Encyclopedia of
Condensed Matter Physics

Second Edition

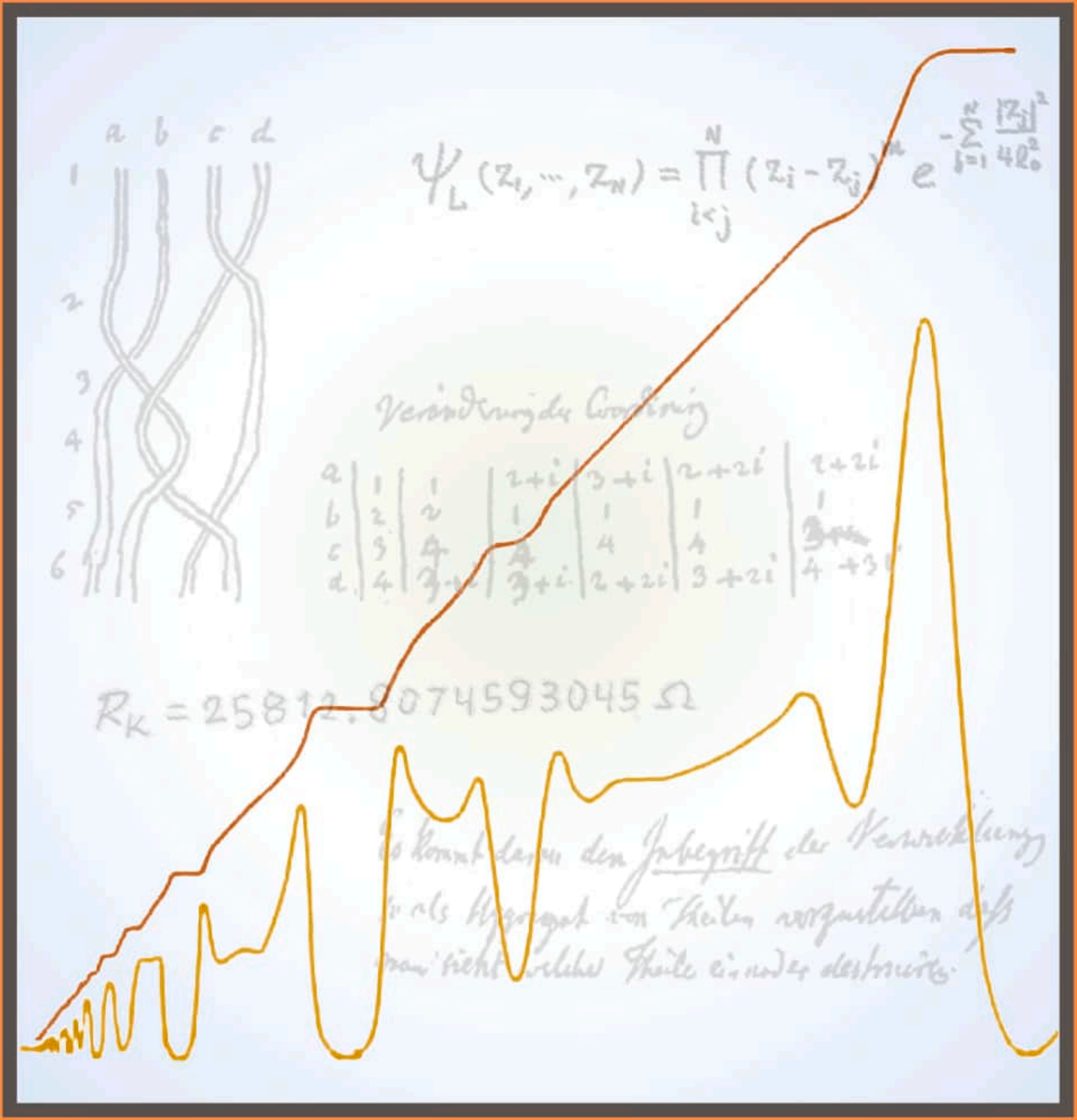
a b c d
1
2
3
4
5
6
$R_K = 25812.807459304 5\ \Omega$

Volume

1

Tapash Chakraborty

Editor-in-Chief

About the pagination of this eBook

This eBook contains a multi-volume set.

To navigate this eBook by page number, you will need to use the volume number and the page number, separated by a hyphen.

For example, to go to page 5 of volume 1, type “1-5” in the Go box at the bottom of the screen and click "Go."

To go to page 5 of volume 2, type “2-5”… and so forth.

ENCYCLOPEDIA OF CONDENSED MATTER PHYSICS

SECOND EDITION

This page intentionally left blank

ENCYCLOPEDIA OF CONDENSED MATTER PHYSICS

SECOND EDITION

EDITOR-IN-CHIEF

Tapash Chakraborty[*]
Professor, Tier-I Canada Research Chair, University of Manitoba, Winnipeg, MB, Canada

VOLUME 1

ELSEVIER

---

[*] Retired.

Elsevier
Radarweg 29, PO Box 211, 1000 AE Amsterdam, Netherlands
The Boulevard, Langford Lane, Kidlington, Oxford OX5 1GB, United Kingdom
50 Hampshire Street, 5th Floor, Cambridge MA 02139, United States

Copyright © 2024 Elsevier Ltd. All rights reserved

No part of this publication may be reproduced or transmitted in any form or by any means, electronic or mechanical, including photocopying, recording, or any information storage and retrieval system, without permission in writing from the publisher. Details on how to seek permission, further information about the Publisher's permissions policies and our arrangements with organizations such as the Copyright Clearance Center and the Copyright Licensing Agency, can be found at our website: www.elsevier.com/permissions.

This book and the individual contributions contained in it are protected under copyright by the Publisher (other than as may be noted herein).

Notices
Knowledge and best practice in this field are constantly changing. As new research and experience broaden our understanding, changes in research methods, professional practices, or medical treatment may become necessary.

Practitioners and researchers may always rely on their own experience and knowledge in evaluating and using any information, methods, compounds, or experiments described herein. In using such information or methods they should be mindful of their own safety and the safety of others, including parties for whom they have a professional responsibility.

To the fullest extent of the law, neither the Publisher nor the authors, contributors, or editors, assume any liability for any injury and/or damage to persons or property as a matter of products liability, negligence or otherwise, or from any use or operation of any methods, products, instructions, or ideas contained in the material herein.

Library of Congress Cataloging-in-Publication Data
A catalog record for this book is available from the Library of Congress

British Library Cataloguing-in-Publication Data
A catalogue record for this book is available from the British Library

ISBN 978-0-32-390800-9

For information on all publications visit our website at http://store.elsevier.com

ELSEVIER Book Aid International
Working together to grow libraries in developing countries
www.elsevier.com • www.bookaid.org

Publisher: Oliver Walter
Acquisitions Editor: Oliver Walter
Content Project Manager: Naman Negi
Associate Content Project Manager: Nandhini Mahendran
Designer: Mark Rogers

EDITOR-IN-CHIEF BIOGRAPHY

Tapash Chakraborty is a retired professor of physics from the University of Manitoba, Canada, where he was also the Canada Research Chair in Nanoscale Physics (2003–17). His research focus has been on many-body theories of various quantum materials, such as nuclear matter, helium liquids, and electron-hole liquids, that he studied under the tutelage of late Professor Manfred Ristig, at the University of Köln (1979–81). Just a year after the discovery of the fractional quantum Hall effect, he (working with his coworkers) demonstrated that electron–electron interactions could actually lead to quantum Hall states with nontrivial spin configurations, and that the low-lying excitations could be described as "spin-reversed quasiparticles." This prediction motivated much experimental work from laboratories around the world, as a result of which the concept of spin-reversed quasi-particles was established.

Similarly, his work on the quantum Hall states in double layer systems has received much attention from the community. Furthermore, Dr. Chakraborty (working with Dr. P. Maksym and others) made pioneering contributions to the many-electron theory of quantum dots. Dr. Chakraborty has also contributed to the theory of electronic properties of various nanoscale systems, such as spin-orbit coupled quantum dots, quantum rings, and single- and double-layer graphene (primarily with Dr. V. Apalkov). He has authored many books and reviews: the book with Dr. Pietiläinen on the quantum Hall effect and the single-authored book on quantum dots have become standard references in their respective fields.

This page intentionally left blank

EDITORIAL ADVISORY BOARD

Ana M. Sanchez
Department of Physics, University of Warwick, Coventry, United Kingdom

Hideo Aoki
Department of Physics, University of Tokyo, Tokyo, Japan

Robert H. Blick
Center for Hybrid Nanostructures, University of Hamburg & DESY, Hamburg, Germany

Roberto Raimondi
Mathematics and Physics Department, Roma Tre University, Rome, Italy

Rudolf A. Roemer
Department of Physics, University of Warwick, Coventry, United Kingdom

Vladimir Mihajlovic Fomin
Leibniz Institute for Solid State and Materials Research (IFW), Dresden, Germany

This page intentionally left blank

INTRODUCTION

> Electrons in orbits contained by the quantum,
> And atoms conjoined by the dipolar force,
> Gravity balanced by pressure
> And flap of a wing.
> Here, I remember the angles and curves,
> Calculus, I learned it all –
> Each bird bit and moon fracture
> Fixed by the symmetries,
> Airborne and airless, aloft.
>
> – Alan Lightman: *Song of Two Worlds*

Condensed matter physics (CMP) is the largest discipline in physics, involving a wide variety of interesting concepts and challenges. To quote Leggett (1992), CMP embraces topics "as diverse as traditional solid-state physics, neutron stars and the physics of biological matter." He further added that, by a liberal definition "just about all of physics outside atomic, nuclear and particle physics and cosmology" fall in this vast enterprise[1]. One of the primary goals of CMP is to explore the fundamental properties of matter—solids, liquids or gasses—comprising a large number of *interacting* constituent particles (Laughlin and Pines, 2000). The quantum-mechanical nature of these many-body systems makes condensed-matter highly nontrivial, sometimes counterintuitive and even astonishing. Superconductivity and the fractional quantum Hall effect (FQHE) naturally fall within that category. In fact, for the past four decades, the quantum Hall effects (QHEs) have been the epitome of elegant CMP (von Klitzing et al., 2020). Our fundamental system of units has been redefined following the discovery of the QHE when the "von Klitzing constant" $R_K = 25,\ 812.8074593045\ \Omega$ came into being (von Klitzing, 2019; Nawrocki, 2019). Observation of the QHE in graphene[2] was crucial in determining the Dirac nature of charge carriers there (see for example, Jiang et al., 2007).

Another effect that outwardly resembles the QHE but is conceptually quite different is the FQHE, which is a quintessential manifestation of electron correlations governed by the Coulomb interaction (Störmer, 1992; Eisenstein and Stormer, 1990). To explain this fascinating effect, Laughlin (1983) introduced his eponymous wave function that not only provided the foundation for understanding the effect but also triggered a new wave of ideas with impact far beyond the realm of CMP[3]. Who would have imagined that a large collection of interacting electrons confined on a plane in a perpendicular magnetic field would result in elementary excitations (quasiholes and quasiparticles) (Chakraborty and Pietiläinen, 1988, 1995; Halperin, 1983; Clark and Maksym, 1989) carrying fractional electron charge and obeying the exotic exchange statistics of anyons (Halperin, 1984; Arovas et al., 1984)? These quasiparticles and quasiholes of the Laughlin state still remain an enigma (Laughlin, 1984; Chakraborty, 1985; Morf and Halperin, 1986). Fractional statistics is a truly path-breaking concept in CMP that was introduced by Leinaas and Myrheim (1977), and has been recently confirmed experimentally (Bartolomei et al., 2020; Nakamura et al., 2020).

Much of the history of CMP can be viewed as a series of paradigm shifts[4]. The field evolved rapidly through frequent ground-breaking discoveries that challenged existing paradigms and opened up new applications, and this evolution is expected to continue (Leggett, 2018; Cohen, 2008). For example, our current understanding of

the FQHE required deep mathematical analysis and a wide range of experimental exploration, which revealed a treasure trove of unique phenomena that are yet to be fully understood or explained. Other studies of electron correlations in low spatial dimensions have ushered in many groundbreaking notions, such as Pfaffian states, Majorana fermions in condensed matter, Chern insulators, and topological quantum materials that promise a fault tolerant means to perform quantum computation. The presence of incompressible FQHE states in monolayer graphene (Apalkov and Chakraborty, 2006), bilayer graphene (Apalkov and Chakraborty, 2010, 2011), and double-layer graphene (Liu et al., 2019) has demonstrated the robustness of the effect, and provides invaluable insight into the nature of this effect.

---

[1] Interestingly, some similarities do exist between the mathematical frameworks that describe low-temperature CMP and early-universe cosmology. See Kibble and Srivastava (2013).

[2] An isolated single layer of graphite consisting of carbon atoms bonded together in a hexagonal structure. See, e.g., Abergel et al. (2010).

[3] For example, an important aspect of Laughlin's theory is its seamless concinnity of classical plasma physics and the planar electron gas that has inspired others to use a similar approach to quark-gluon plasma (Lu, 2022).

[4] A detailed exposition of the meaning and examples of "paradigm shifts" (Kuhn-type) can be found in Leggett (2018).

The dynamics of an electron in a periodic potential subjected to a perpendicular magnetic field has been an intriguing problem for more than half a century (Obermair and Wannier, 1976; Osadchy and Avron, 2001)[5]. Within the nearest neighbor tight-binding description of the periodic potential the electron energy spectrum is described by the Harper equation (Harper, 1955). Numerical solution of this equation (Hofstadter, 1976) has revealed that the applied field splits the Bloch bands into subbands and gaps. As the field is varied, the splitting of band continues indefinitely, leading to bands within bands within bands. When plotted as a function of the magnetic flux per lattice cell, the energy spectrum depicts a *fractal* pattern (a self-similar pattern that repeats at every scale) and is known in the literature as Hofstadter's butterfly because of the resemblance of the pattern to butterflies[6]. Observation of the butterfly spectra in real systems is an arduous task. For example, in ordinary crystalline lattices, the required magnetic field to see the butterflies exceeds 1000 Tesla, which is far beyond the reach of present-day technology. Graphene seems to be the ideal system in the quest of those fractal butterflies (Weiss, 2013). It is interesting to note that a mathematical solution of the Harper equation, in contrast to the numerical solution mentioned above, remained a challenging problem (the so-called Ten Martini Problem) for mathematicians until it was solved (Avila and Jitomirskaya, 2006) in 2006.

Magnetism has been known to mankind since ancient times, and it remains a major topic in CMP. The road to understanding magnetism has been long and tortuous. At various times in history, magnets were claimed to have the healing power to cure a myriad of ailments that included epilepsy, arthritis, gout, and baldness. Magnets were the prime ingredients for the "elixir of life" by Paracelsus (1493–1541). Then there was the healing process of "animal magnetism" proposed by Franz Anton Mesmer (1734–1815) (mesmerism)[7], which was famously mocked in Mozart's *Così fan tutte* (Steptoe, 1986). Our current understanding of magnetism is deeply rooted in quantum mechanics as Van Vleck explained (Van Vleck, 1978): "Quantum mechanics is the key to understand magnetism. When one enters the first room with this key there are unexpected rooms beyond, but it is always the master key that unlocks each door." For centuries, the magnetism of certain rocks and metallic iron was only used for the practical purposes of direction finding, particularly navigation with a compass. Motors, generators, and electrical distribution networks appeared only in the 19th century after the discovery of the deep connection between electricity and magnetism. Magnetic order is a collective phenomenon akin to superconductivity and superfluidity that involves a very large number of particles. The rich variety of magnetically ordered states in solids, not only ferromagnetism but also antiferromagnetism, ferrimagnetism, and a range of noncollinear structures, was confirmed only in the middle of the 20th century, with the availability of neutron beams in research reactors. A range of new magnetic materials are taking their place as active layers in thin film sensors and memory devices (Baltz et al., 2018). Besides information storage (Blundell, 2001), important technical applications include magnetic resonance imaging (MRI) and the use of magnetic nanoparticles in medicine.

Many outstanding discoveries in magnetism and magnetic materials have resulted in rapid advances in information storage technology. Over the last two decades spintronics has emerged as an important field of research both from the point of view of fundamental science and advanced technological applications (Yamaguchi et al., 2021; Pinarbasi and Kent, 2022). The giant magnetoresistance (GMR) effect, the spin Hall effect, and the spin galvanic effects are typical examples of developments in the field. Spintronics aims at understanding how the spin degree of freedom of the electrical carriers can be controlled in order to obtain devices with new functionalities and better performance. This endeavor often combines concepts from different aspects of condensed matter systems, giving the topic a fascinating interdisciplinary flavor. Spintronic phenomena are now being studied in an impressive range of different materials ranging from metals to half-metals to semiconductors, graphene and other two-dimensional systems such as transition metal dichalcogenides.

---

[5] For a recent review on butterflies in graphene, see for example Chakraborty and Apalkov (2015).

[6] However, as one of the authors of this Encyclopedia has (somewhat humorously) pointed out, this butterfly has Lebesgue measure zero, that is, it cannot fly!.

[7] A wonderful account of the use of magnetism in medicine since ancient times can be found in Mourino (1991).

The GMR effect and the related tunnel magnetoresistance effect (TMR) found their first commercial use in magnetic field sensors for hard-disk read-heads, before broadening their field of application to include magnetic sensors for the automobile industry, solid-state compasses, biosensors, and nonvolatile magnetic memory (Hartmann, 2000). The ability to manipulate the magnetic state of ferromagnetic structures led to initial developments in spintronics, where the spin direction was controlled by externally applied magnetic fields. However, the push for downscaling and faster timescales has prompted research advances in the past decade where the manipulation of magnetic configurations is achieved by local electric currents (the spin torque effect) (Brataas et al., 2012; Locatelli et al., 2014). In recent years, various novel concepts, such as chiral spintronics, skyrmionic spin textures, and magnetic domain walls in spintronics, have been actively pursued. The rate of progress in spintronics is truly astounding (Editorial, 2022).

In the past century, superconductivity has raised many theoretical challenges and triggered numerous technical developments. Discovered in mercury in 1911, this unique phenomenon occurs when the electrical resistance of many metals and alloys drops to zero when cooled below about 4 K, the temperature of liquid helium. More significantly, the material expels magnetic flux and becomes perfectly diamagnetic. Superconductivity has been adopted or evaluated for a wide range of technical applications (Rogalla and Kes, 2012). These include electric power generation, electric power transmission, high-speed maglev transportation, and ultra-strong magnetic field generation in high-resolution MRI and other nuclear magnetic resonance (NMR) systems. Interestingly, it took almost 50 years after the original discovery for the phenomena to be explained by the BCS theory (Tinkham, 2004) of reciprocal-space electron pairing, via the electron–phonon interaction. This electron–phonon mediated superconductivity became known as "conventional superconductivity" after the discovery of "high-temperature superconductivity" (Müller and Bednorz, 1987) at liquid nitrogen temperatures in tetragonal copper oxides in 1986. This threw open a new challenge to explain the properties of strongly correlated *anisotropic* electronic systems. Further new classes of superconductors that remain to be properly understood include the iron-based pnictides discovered in 2008 (Hosono et al., 2018). Recently, a two-dimensional superlattice made from a twisted bilayer of "magic angle" graphene was found to exhibit unconventional superconductivity (Cao et al., 2018), driven by electron–electron interactions.

The phenomenon of spontaneous symmetry breaking (SSB) is ubiquitous in physics, and plays a fundamental role in CMP, particle physics, and even in cosmology. A classic illustration of SSB being Heisenberg's 1928 paper on ferromagnetism (Heisenberg, 1928). It is responsible for various collective modes, such as the famous Nambu-Goldstone (NG) and Higgs modes. Named by Baker and Glashow (Baker and Glashow, 1962), SSB corresponds to the case where the ground or lowest-energy state does not have the symmetry of the underlying dynamics. Instead, multiple degenerate ground states are available and the symmetry breaking is *spontaneous* because it is not clear, a priori, which one of those ground states will be chosen. In this well-trodden territory a simple analogy of this abstruse concept given by A. Salam is illuminating (CERN, 1977): "Imagine a banquet where guests sit at round tables. A bird's eye view of the scene presents total symmetry, with serviettes alternating with people around each table. A person could equally well take a serviette from his right or from his left. The symmetry is spontaneously broken when one guest decides to pick up from his left and everyone else follows suit." Over the years, development of the concept of SSB has taken a circuitous route (Gaudenzi, 2022): "from the land of particle physics to the physics of many bodies (solids and nuclei), from there to the province of superconductivity, and from the latter back to particle physics ... ." SSB's significance extends beyond the physics of the Higgs boson to the study of low-energy phenomena such as superconductivity, superfluidity, magnetism, and others. Historically, the particle physics community has been guided by this exploration in their quest to understand and discover particles like the Higgs boson. More to the point, when a continuous symmetry is spontaneously broken, a gapless mode, the NG mode, appears which governs the low-energy behavior of the system. As an example, in a solid, the acoustic phonon is the NG mode associated with translational symmetry breaking and determines the behavior of the specific heat at low temperature (the Debye T^3 law). Recently, signatures of Higgs and Goldstone modes have been proposed to exist in a perovskite oxide (Marthinsen et al., 2018), in other crystalline structures (Vallone, 2019), and also in various other quantum systems (Léonard et al., 2017). On a lighter note, it is the symmetry breaking that is claimed to have prevented the fabled donkey (Weintraub, 2012) in the parable by Jean Buridan (1300–50) from dying of starvation (Fubini, 1974).

Common to the theoretical descriptions of these phenomena across CMP and high-energy physics is Quantum field theory (QFT). QFT was originally developed to describe the fundamental processes in high-energy physics, but has now become a valuable tool to address problems across physics, in particular, in CMP (Fradkin, 2013; see also, Mustafa, 2023), statistical physics, modern quantum chemistry, and even in

pure mathematics (Folland, 2008). Advances in our understanding of strongly correlated electron systems in CMP such as high-temperature superconductivity and the FQHE have been aided by the QFT. It has facilitated the treatment of spontaneous symmetry broken states, such as superfluids. Interestingly, many of the conceptual developments in CMP have, in return, had a reciprocal impact in QFT. A spectacular example being Nambu's work in dynamical symmetry breaking (Weinberg, 1986; Nambu, 2009) in particle physics, based on the BCS theory of superconductivity.

A glass is a noncrystalline solid obtained by quenching a liquid. It has a liquid-like structure, but a transition from liquid to solid behavior occurs on cooling. It may have one of a continuum of possible ground states that exhibit frozen-in liquid-like disorder. The term "spin glass" was coined by B.R. Coles (Mydosh, 1993) in 1970 for a diluted magnetic material with frozen-in paramagnetic-like spin disorder where the magnetic moments interact with randomly varying positive or negative exchange interactions leading to a multitude of possible ground states with different, random orientations of the spins. As in a normal glass, the energy barriers between the continuum of metastable states prevent it from ever reaching equilibrium. This phase of condensed matter has been an important and productive area of research. Spin-glass models are conceptually simple, but embody sophisticated physics. These models have become a paradigm for the solution of complex optimization problems (Mézard, 2022): much like the undulating flight patterns of starlings around the skies over Rome (Parisi, 2023). After cooling from the paramagnetic phase, the spin glass remains out of equilibrium, and it slowly evolves. This aging phenomenon corresponds to the growth of a "spin-glass order" parameter, whose correlation length can be measured (Joh et al., 1999). A cooling temperature step during aging causes a partial "rejuvenation," while the "memory" of previous aging is stored and can be retrieved (Refregier et al., 1987; Bouchaud et al., 2001). Many glassy materials present aging, and rejuvenation and memory effects can be found in other cases, but they are usually less pronounced. Numerical simulations of these phenomena are under active investigation using custom-built computers (Baity-Jesi et al., 2023; Vincent, 2023). A general understanding of glassy systems, to which spin glasses bring some special insight, is being pursued. It was realized decades ago that the physics of spin glasses has deep connections with the behavior of complex biological systems. In fact, spin-glass type states in neural network models offer interesting insights into states of high and low brain activity, as observed in mammals (Recio and Torres, 2016). These analogies are potentially useful for applications in fields such as robotics and artificial intelligence (AI) (Andriuschenko et al., 2022).

One of the most spectacular phenomena in CMP, discovered in the last century, was Bose-Einstein condensation (BEC). This macroscopic quantum phenomenon had its genesis in the work of Satyendra Nath Bose (Bose, 1924; Blanpied, 1972; Tomczyk, 2022) (whose name is forever associated with bosons), and has fascinated physicists for decades, ever since the first observation of this exotic state of matter in an ultracold gas of rubidium atoms (Georgescu, 2020). Among the advances made in this field, we highlight only a few: simulation of correlated electron states, such as the FQHE state and a bosonic analog of the Laughlin state, and the famous BEC-BCS crossover from a BEC to a BCS superfluid of weakly bound Cooper pairs, as the interparticle interaction strength is varied. Noteworthy is the recent measurement of the dynamic structure factor in an ultracold Fermi gas of lithium-6 atoms in the "unitary" limit, where a linear phonon mode for low momentum transfer can be clearly discerned (Biss et al., 2022). Perhaps such a method might one day shed light on the Laughlin quasiparticle gap and the collective modes that are still largely unresolved (Chakraborty and Pietiläinen, 1988, 1995; Halperin, 1983; Clark and Maksym, 1989).

Liquid helium, ^{4}He, and the less common isotope ^{3}He are unique quantum systems (Volovik, 2009). They remain liquid even at absolute zero temperature, a direct manifestation of Heisenberg's uncertainty principle and zero-point energy. The light mass of helium atoms and their weak interatomic attraction leads to a substantial zero-point kinetic energy and the system remains in the liquid state at ambient pressure. Solidification occurs when a pressure of about 25 MPa is applied. The different quantum statistics of the two helium isotopes (^{4}He is a boson while ^{3}He is a fermion) are responsible for the different physical characteristics of the two systems. Microscopic approaches to understand the ground state and low-energy excitations of the liquid state have occupied researchers for many decades (see for example, Ristig and Clark, 1976; Lam et al., 1977). These highly correlated quantum fluids have been established as systems where the efficacies of different many-body theories can be tested (Kallio and Smith, 1977; Lantto et al., 1977). These systems have been described as Ariadne's thread in this Encyclopedia, where the strongly interacting constituent particles are treated by a variety of ingenious theoretical and experimental approaches. Interestingly, liquid helium has been proposed to be a medium to design multiexcitation detectors to probe *dark matter* (Schutz and Zurek, 2016) in the keV mass limit. Although this looks far afield from CMP, the interface between CMP and high-energy particle physics could inspire new horizons in CMP, as discussed earlier.

CMP also has an enormous impact on our daily lives with unceasing technological innovation stemming directly from the advances in CMP research. It is also closely associated with the progress of our understanding of materials science and mechanical, chemical, and electrical engineering that deals with properties of novel materials and devices. As some authors have very aptly pointed out (Chaikin and Lubensky, 1995): The use and understanding of matter in its condensed (liquid or solid) state have gone hand in hand with the advances of civilization and technology since the first use of primitive tools. So important has the control of condensed matter been to man that prehistoric ages—the Stone Age, the Bronze Age, the Iron Age—are named after the material dominating the technology of the time. In fact, modern civilization is entirely dependent on our deep understanding and practical use of materials, old and new: Steel, glass, and concrete have shaped our modern living with comfort, health, longevity, and material wealth. All around us, from a tiny paper clip to giant skyscrapers, from jet planes to modern medicines, and the ubiquitous plastics that are integrated into nearly all aspects of human life, are testaments to our control over the myriad behavior of materials (Miodownik, 2014). Today, a large number of materials are designed by using principles of quantum mechanics (Freeman, 2002).

The Silicon chip that launched the information age is a great example of the effect of CMP on our daily lives. The scaling of transistors down to the nanometer range has enabled them to be embedded in greater numbers in the all-pervasive electronic devices that have transformed every facet of life all around the world. The transition from room-size to pocket-size computers with ever increasing computational power and memory, that occurred in only a few decades, epitomizes the unrelenting progress made in this direction. Advances in nanoscale research have opened the door to exploration of the natural world at the ultra-small scale (Chakraborty, 2022), with the potential to shape our future world.

Quantum dots (QDs), the quasi-zero-dimensional electron systems, are one of the most extensively studied nanostructures in the past three decades. They represent the ultimate reduction in dimensionality of a semiconductor device. Here the electrons are confined (either electrostatically or structurally) in all three directions and occupy spectrally sharp energy levels similar to those found in atoms (Chakraborty, 1999), hence the popular moniker *artificial atoms* (Maksym and Chakraborty, 1990). QDs and other similar nanostructures (Chakraborty, 2003) offer a rich variety of fundamental phenomena that result from manipulation of single electrons (single electronics) or single spins at the nanoscale. The study of interacting electrons in a QD requires large-scale numerical computations involving matrices of dimensions in the millions (“monster matrices”) (Chakraborty and Pietiläinen, 2005; Pietiläinen and Chakraborty, 2006). QDs are also thought to have vast potential for future technological applications. One prominent example being quantum cryptography where the QDs are used in single photon emitters (Nowak et al., 2014), and in single photon detectors (Shields et al., 2000). Quantum cryptography, in turn, forms the basis of the *quantum Internet* (Liao et al., 2018). Other applications include lasers, and spintronics in quantum computing, entertainment industry (Bourzac, 2013), and even in biology (Bruchez and Holz, 2007).

Research in recent years has increasingly revealed that quantum phenomena are also ubiquitous in the natural world (Ball, 2011). They govern how birds are able to navigate around the globe using Earth’s magnetic field or how plants use photosynthesis to harvest sunlight for conversion to chemical energy. All depend on subtle quantum effects that are now coming to light, thereby ushering the topic of quantum biology into CMP. Deoxyribonucleic acid (DNA), the molecule responsible for storage of genetic information in the cells of all living organism, is entrusted with the task of preserving, copying, and transmitting information that are necessary for living beings to grow and function. It is often referred to as the body’s hereditary material as DNA is replicated and transmitted from parents to their offspring. This “molecule of life” was discovered in 1869 by Friedrich Miescher in Tübingen, Germany, who called it “nuclein,” as it was isolated from the nucleus of white blood cells (Dahm, 2005; Thess et al., 2021). It took more than eighty years from that momentous event, to discover that DNA has a right-handed double-helix structure with appropriate base pairing (Watson and Crick, 1953; Klug, 2004). That discovery was so important that it has been compared with the discovery of the atomic nucleus in physics (Frank-Khamenetskii, 1997). Understanding the structure of the atom heralded quantum physics, while understanding of the structure of DNA brought forth the field of molecular biology.

DNA has several remarkable properties that make this molecule a prime candidate for nano-electronic materials (Chakraborty, 2007). These include molecular recognition and the ability to self-assemble via the complementarity of the base sequences on the two strands, which means that DNA can be integrated error-free in current semiconductor technology. DNA can also detect information about its own integrity that can trigger its eventual repair mechanism. All these properties are perfectly suitable for developing nanoscale electronics involving DNA

(Taniguchi and Kawai, 2006). Despite the promise of harnessing biology to realize integrated molecular electronics remains fascinating, much work remains to be done to make it a reality (Braun and Keren, 2004).

Protein molecules play a vital role in all living organisms. They are described as Nature's robots (Tanford and Reynolds, 2001) because for every imaginable task required in a living organism, and for every step of that task, there is a protein designed to carry it out. These proteins are even programmed to know when to turn on or off. Just as the twenty-six letters in the alphabet can spell out hundreds of thousands of words, there are twenty different naturally occurring amino acids that can be combined into many more different proteins than there are atoms in the known universe! Protein's biological function is determined by its unique and native three-dimensional structures that are characteristic of individual proteins (Gomes and Faísca, 2019; Echenique, 2007). The question of how proteins fold to their unique, compact, and highly organized functional states has remained an enduring challenge ("The protein-folding problem") (Chan and Dill, 1993; Dill and MacCallum, 2012; Wolynes and Eaton, 1999). Recently, there has been a tremendous development in this area of research. In November 2020, an AI program called AlphaFold, designed to tackle the problem of protein folding, predicted the three-dimensional structures of almost every protein known to science—about 200 millions in all (Jumper et al., 2021). AlphaFold uses a machine learning methodology to bring together information from preexisting knowledge of protein structures, and other geometric and physical constraints to predict protein structures. While this has been heralded a watershed moment in structural biology (Perrakis and Sixma, 2021), there are many key questions that AlphaFold cannot address yet. These include aspects of protein behavior that cannot be understood from a static structure, such as how proteins respond to their environment or how intrinsically disordered proteins actually are organized. Some authors (Nasser et al., 2021) have likened it to solving a crime story: while AlphaFold presents a snapshot in time, the question about how we get there remains unanswered. Biological systems have developed elaborate mechanisms to ensure that proteins fold correctly, or otherwise, they are detected and degraded before any serious harm can result to the host organism. However, protein misfolding does happen and that misfolding in the cell is linked to an array of diseases, including cancers, cardiovascular disease, type II diabetes, and numerous neurodegenerative diseases, such as Alzheimer's, Parkinson's, and Huntington's disease. NMR spectroscopy has been an important technique to study protein folding where valuable insights are gained into many aspects of the folding process (Jane Dyson and Wright, 1996).

In this Encyclopedia, we strive to present a taste of all the developments in CMP described above (and much more), written by experts in the field. We are keenly aware that many important and interesting topics are not covered here. However, that is not for want of trying. As some authors had rightly pointed out (Hoddeson, 1992): The field is huge and varied and lacks the unifying features beloved of historians, neither a single hypothesis or set of basic equations underpin the field, as in quantum mechanics or relativity theory, nor a single spectacular and fundamental discovery such as uranium fission for nuclear technology or the structure of DNA for molecular biology. CMP owes what unity it has simply to a common concern with solid and liquid materials. This encompasses such a large range of theories and methods that the field resembles a confederation of interest groups rather than a single entity. Clearly, the task of collecting everything in one place is a monumental endeavor, but we do hope that our compilation of a large number of chapters in this five-volume work, covering a broad range of in-depth descriptions of varied phenomena in CMP will be a treasured source of facts and ideas for the community.

It is undeniably true that there would have been no Encyclopedia without the extraordinary contributions of the large number of authors whose valuable time and efforts brought this project to fruition. My sincere thanks to all of them. I also wish to extend my deep appreciation to the staff at Elsevier for their skillful handling of this huge project. The cover image was created by Hong-Yi Chen from National Taiwan Normal University. The image below was created by Elisabetta Collini, one of the authors. My deepest appreciation to them for taking the time to do this work. Finally, my sincere thanks to the Section editors, Vladimir Fomin, Ana Sanchez, Roberto Raimondi, Hideo Aoki, Rudolf Römer, and Robert Blick for the effort they all expended, that has contributed to the success of this venture. Special thanks go to Vladimir Fomin and Ana Sanchez for securing a large share of the chapters and for their enduring help in providing valuable advice and support to bring the project to fruition. Thanks are also due to many of my friends and colleagues, in particular, Michael Coey, Jürg Fröhlich, Sinéad Griffin, Peter Maksym, Eric Vincent, and Jakob Yngvason for their careful and critical reading of the introduction.

Tapash Chakraborty
St. Catharines
Ontario, Canada

References

Abergel DSL, Apalkov V, Berashevich J, Ziegler K, and Chakraborty T (2010) Properties of graphene: A theoretical perspective. *Advances in Physics* 59: 261. https://doi.org/10.1080/00018732.2010.487978.

Andriuschenko P, Kapitan D, and Kapitan V (2022) A new look at the spin glass problem from a deep learning perspective. *Entropy* 24: 697. https://doi.org/10.3390/e24050697.

Apalkov VM and Chakraborty T (2006) Fractional quantum Hall states of Dirac electrons in graphene. *Physical Review Letters* 97: 126801. https://doi.org/10.1103/PhysRevLett.97.126801.

Apalkov VM and Chakraborty T (2010) Controllable driven phase transitions in fractional quantum Hall states in bilayer graphene. *Physical Review Letters* 105: 036801. https://doi.org/10.1103/PhysRevLett.105.036801.

Apalkov VM and Chakraborty T (2011) Stable pfaffian state in bilayer graphene. *Physical Review Letters* 107: 186803. https://doi.org/10.1103/PhysRevLett.107.186803.

Arovas D, Schrieffer JR, and Wilczek F (1984) Fractional statistics and the quantum Hall effect. *Physical Review Letters* 53: 722. https://doi.org/10.1103/PhysRevLett.53.722.

Avila A and Jitomirskaya S (2006) Solving the ten martini problem. *Lecture Notes in Physics* 690: 5. https://doi.org/10.1007/3-540-34273-7_2.

Baity-Jesi M, et al. (2023) Memory and rejuvenation effects in spin glasses are governed by more than one length scale. *Nature Physics* 19: 978–985. https://doi.org/10.1038/s41567-023-02014-6.

Baker M and Glashow SL (1962) Spontaneous breakdown of elementary particle symmetries. *Physics Review* 128: 2462. https://doi.org/10.1103/PhysRev.128.2462.

Ball P (2011) Physics of life: The dawn of quantum biology. *Nature* 474: 272. https://doi.org/10.1038/474272a.

Baltz V, et al. (2018) Antiferromagnetic spintronics. *Reviews of Modern Physics* 90: 015005. https://doi.org/10.1103/RevModPhys.90.015005.

Bartolomei H, et al. (2020) Fractional statistics in anyon collisions. *Science* 368: 173. https://doi.org/10.1126/science.aaz5601.

Biss H, et al. (2022) Excitation spectrum and superfluid gap of an ultracold Fermi gas. *Physical Review Letters* 128: 100401. https://doi.org/10.1103/PhysRevLett.128.100401.

Blanpied WA (1972) Satyendranath Bose: Co-founder of quantum statistics. *American Journal of Physics* 40: 1212. https://doi.org/10.1119/1.1986805.

Blundell S (2001) *Magnetism in Condensed Matter*. New York: Oxford U.P.

Bose SN (1924) Plancks gesetz und lichtquantenhypothese. *Zeitschrift für Physik* 26: 178. https://doi.org/10.1007/BF01327326.

Bouchaud J-P, Dupuis V, Hammann J, and Vincent E (2001) Separation of time and length scales in spin glasses: Temperature as a microscope. *Physical Review B* 65: 024439. https://doi.org/10.1103/PhysRevB.65.024439.

Bourzac K (2013) Quantum dots go on display. *Nature* 493: 283. https://doi.org/10.1038/493283a.

Brataas A, Kent AD, and Ono H (2012) Current-induced torques in magnetic materials. *Nature Materials* 11: 372. https://doi.org/10.1038/nmat3311.

Braun E and Keren K (2004) From DNA to transistors. *Advances in Physics* 53: 441. https://doi.org/10.1080/00018730412331294688.

Bruchez MP and Holz CZ (2007) *Quantum Dots: Applications in Biology*. New Jersey: Humana Press. https://doi.org/10.1385/1597453692.

Cao Y, et al. (2018) Unconventional superconductivity in magic-angle graphene superlattices. *Nature* 556: 43. https://doi.org/10.1038/nature26160.

CERN. (1977) Gauge theories with the lid, partially, off. *CERN Courier* 17: 271. https://cds.cern.ch/record/1730245/files/vol17-issue9-p271-e.pdf.

Chaikin PM and Lubensky TC (1995) *Principles of Condensed Matter Physics*. Cambridge University Press. https://doi.org/10.1017/CBO9780511813467.

Chakraborty T (1985) Elementary excitations in the fractional quantum Hall effect. *Physical Review B* 31: 4026. https://doi.org/10.1103/PhysRevB.31.4026.

Chakraborty T (1999) *Quantum Dots: A Survey of the Properties of Artificial Atoms*. Amsterdam: North-Holland. https://doi.org/10.1016/B978-0-444-50258-2.X5000-7.

Chakraborty T (2003) Nanoscopic quantum rings: A new perspective. *Advances in Solid State Physics* 43: 79. https://doi.org/10.1007/978-3-540-44838-9_6.

Chakraborty T (ed.) (2007) *Charge Migration in DNA*. Springer. https://doi.org/10.1007/978-3-540-72494-0.

Chakraborty T (2022) *Nanoscale Quantum Materials: Musings on the Ultra-Small World*. CRC Press. https://doi.org/10.1201/9781003090908.

Chakraborty T and Apalkov VM (2015) Fractal butterflies of Dirac fermions in monolayer and bilayer graphene. *IET Circuits, Devices and Systems* 9: 19. https://doi.org/10.1049/iet-cds.2014.0275.

Chakraborty T and Pietiläinen P (1988) *The Fractional Quantum Hall Effect*. Springer Verlag. https://doi.org/10.1007/978-3-642-97101-3.

Chakraborty T and Pietiläinen P (1995) *The Quantum Hall Effects*, 2nd. Springer. https://doi.org/10.1007/978-3-642-79319-6.

Chakraborty T and Pietiläinen P (2005) Optical signatures of spin-orbit interaction effects in a parabolic quantum dot. *Physical Review Letters* 95: 136603. https://doi.org/10.1103/PhysRevLett.95.136603.

Chan HS and Dill KA (1993) The protein folding problem. *Physics Today* 46: 24. https://doi.org/10.1063/1.881371.

Clark R and Maksym P (1989) Fractional quantum Hall effect in a spin. *Physics World* 2: 39. https://doi.org/10.1088/2058-7058/2/9/23.

Cohen ML (2008) Fifty years of condensed matter physics. *Physical Review Letters* 101: 250001. https://doi.org/10.1103/PhysRevLett.101.250001.

Dahm R (2005) Friedrich miescher and the discovery of DNA. *Developmental Biology* 278: 274. https://doi.org/10.1016/j.ydbio.2004.11.028.

Dill KA and MacCallum JL (2012) The protein-folding problem, 50 years on. *Science* 338: 1042. https://doi.org/10.1126/science.1219021.

Echenique P (2007) Introduction to protein folding for physicists. *Contemporary Physics* 48: 81. https://doi.org/10.1080/00107510701520843.

Editorial (2022) New horizons in spintronics. Nature Materials 21: 1. https://doi.org/10.1038/s41563-021-01184-z.

Eisenstein JP and Stormer HL (1990) The fractional quantum Hall effect. *Science* 248: 1510. https://doi.org/10.1126/science.248.4962.1510.

Folland GB (2008) *Quantum Field Theory: A tourist guide for Mathematicians*. American Mathematical Society. https://doi.org/10.1090/surv/149.

Fradkin E (2013) *Field Theories of Condensed Matter Physics*. Cambridge University Press. https://doi.org/10.1017/CBO9781139015509.

Frank-Khamenetskii MD (1997) *Unraveling DNA: The Most Important Molecule of life*. Basic Books.

Freeman AJ (2002) Materials by design and the exciting role of quantum computation/simulation. *Journal of Computational and Applied Mathematics* 149: 27. https://doi.org/10.1016/S0377-0427(02)00519-8.

Fubini S (1974) Present trends in particle physics. In: *Proc. Intl. Conf. on High Energy Physics*. Didcot, England: Rutherford Laboratory. https://cds.cern.ch/record/417271/files/CM-P00060491.pdf.

Gaudenzi R (2022) *Historical Roots of Spontaneous Symmetry Breaking: Steps Towards an Analogy*. Springer. https://doi.org/10.1007/978-3-030-99895-0.

Georgescu I (2020) 25 Years of BEC. *Nature Reviews Physics* 2: 396. https://doi.org/10.1038/s42254-020-0211-7.

Gomes CM and Faísca PFN (2019) *Protein Folding: An Introduction*. Springer. https://doi.org/10.1007/978-3-319-00882-0_1.

Halperin BI (1983) Theory of the quantized Hall conductance. *Helvetica Physica Acta* 56: 75. https://doi.org/10.5169/seals-115362.

Halperin BI (1984) Statistics of quasiparticles and the hierarchy of fractional quantized Hall states. *Physical Review Letters* 52: 1583. https://doi.org/10.1103/PhysRevLett.52.1583.

Harper PG (1955) Single band motion of conduction electrons in a uniform magnetic field. *Proceedings of the Physical Society. Section A* 68: 874. https://doi.org/10.1088/0370-1298/68/10/304.

Hartmann U (2000) *Magnetic Multilayers and Giant Magnetoresistance: Fundamentals and Industrial Applications*. Berlin: Springer Verlag. https://doi.org/10.1007/978-3-662-04121-5.

Heisenberg W (1928) Zur theorie des ferromagnetismus. *Zeitschrift für Physik* 49: 619. https://doi.org/10.1007/BF01328601.

Hoddeson L (1992) *Out of the Crystal Maze: Chapters From the History of Solid-State Physics*. N.Y.: Oxford University Press.

Hofstadter D (1976) Energy levels and wave functions of Bloch electrons in rational and irrational magnetic fields. *Physical Review B* 14: 2239. https://doi.org/10.1103/PhysRevB.14.2239.

Hosono H, et al. (2018) Recent advances in iron-based superconductors toward applications. *Materials Today* 21: 278. https://doi.org/10.1016/j.mattod.2017.09.006.

Jane Dyson H and Wright PE (1996) Insights into protein folding from NMR. *Annual Review of Physical Chemistry* 47: 369. https://doi.org/10.1146/annurev.physchem.47.1.369.

Jiang Z, et al. (2007) Quantum Hall effect in graphene. *Solid State Communications* 143: 14. https://doi.org/10.1016/j.ssc.2007.02.046.

Joh YG, Orbach R, Wood JJ, Hammann J, and Vincent E (1999) Extraction of the spin glass correlation length. *Physical Review Letters* 82: 438. https://doi.org/10.1103/PhysRevLett.82.438.

Jumper J, et al. (2021) Highly accurate protein structure prediction with alphafold. *Nature* 596: 583. https://doi.org/10.1038/s41586-021-03819-2.

Kallio A and Smith RA (1977) How simple can HNC be and still be right? *Physics Letters B* 68: 315. https://doi.org/10.1016/0370-2693(77)90483-X.

Kibble T and Srivastava A (2013) Condensed matter analogues of cosmology. *Journal of Physics. Condensed Matter* 25: 400301. https://doi.org/10.1088/0953-8984/25/40/400301.

Klug A (2004) The discovery of the DNA double helix. *Journal of Molecular Biology* 335: 3. https://doi.org/10.1016/j.jmb.2003.11.015.

Lam PM, Clark JW, and Ristig ML (1977) Density matrix and momentum distribution of helium liquids and nuclear matter. *Physical Review B* 16: 222. https://doi.org/10.1103/PhysRevB.16.222.

Lantto LJ, Jackson AD, and Siemens PJ (1977) HNC variational calculations of boson matter. *Physics Letters B* 68: 311. https://doi.org/10.1016/0370-2693(77)90482-8.

Laughlin RB (1983) Anomalous quantum Hall effect: An incompressible quantum fluid with fractionally charged excitations. *Physical Review Letters* 50: 1395. https://doi.org/10.1103/PhysRevLett.50.1395.

Laughlin RB (1984) Primitive and composite ground states in the fractional quantum Hall effect. *Surface Science* 142: 163. https://doi.org/10.1016/0039-6028(84)90301-7.

Laughlin RB and Pines D (2000) The theory of everything. *Proceedings of the National Academy of Sciences of the United States of America* 97: 28. https://doi.org/10.1073/pnas.97.1.28.

Leggett A (1992) On the nature of research in condensed-state physics. *Foundations of Physics* 22: 221. https://doi.org/10.1007/BF01893613.

Leggett A (2018) Reflections on the past, present and future of condensed matter physics. *Science Bulletin* 63: 1019. https://doi.org/10.1016/j.scib.2018.07.004.

Leinaas JM and Myrheim J (1977) On the theory of identical particles. *Il Nuovo Cimento B* 37: 1. https://doi.org/10.1007/BF02727953.

Léonard J, et al. (2017) Monitoring and manipulating higgs and goldstone modes in a supersolid quantum gas. *Science* 358: 1415. https://doi.org/10.1126/science.aan2608.

Liao S-K, et al. (2018) Satellite-relayed intercontinental quantum network. *Physical Review Letters* 120: 030501. https://doi.org/10.1103/PhysRevLett.120.030501.

Liu X, Hao Z, Watanabe K, Taniguchi T, Halperin BI, and Kim P (2019) Interlayer fractional quantum Hall effect in a coupled graphene double layer. *Nature Physics* 15: 893. https://doi.org/10.1038/s41567-019-0546-0.

Locatelli N, Cros V, and Grollier J (2014) Spin-torque building blocks. *Nature Materials* 13: 11. https://doi.org/10.1038/nmat3823.

Lu W (2022) Quark-gluon plasma and nucleons à la Laughlin. *International Journal of Geometric Methods in Modern Physics* 19: 2250061. https://doi.org/10.1142/S021988782250061X.

Maksym P and Chakraborty T (1990) Quantum dots in a magnetic field: Role of electron-electron interactions. *Physical Review Letters* 65: 108. https://doi.org/10.1103/PhysRevLett.65.108.

Marthinsen A, et al. (2018) Goldstone-like phonon modes in a (111)-strained perovskite. *Physical Review Materials* 2: 014404. https://doi.org/10.1103/PhysRevMaterials.2.014404.

Mézard M (2022) Spin glasses and optimization in complex systems. *Europhysics News* 53: 15. https://doi.org/10.1051/epn/2022105.

Miodownik M (2014) *Stuff Matters: Exploring the Marvelous Materials That Shape Our Man-Made World*. N.Y.: Houghton Mifflin Harcourt.

Morf R and Halperin BI (1986) Monte Carlo evaluation of trial wave functions for the fractional quantized Hall effect: Disk geometry. *Physical Review B* 33: 2221. https://doi.org/10.1103/PhysRevB.33.2221.

Mourino MR (1991) From thales to lauterbur, or from the loadstone to MR imaging: Magnetism and medicine. *Radiology* 180: 593. https://doi.org/10.1148/radiology.180.3.1871268.

Müller KA and Bednorz JG (1987) The discovery of a class of high-temperature superconductors. *Science* 237: 1133. https://doi.org/10.1126/science.237.4819.1133

Mustafa MG (2023) An introduction to thermal field theory and some of its application. *The European Physical Journal Special Topics* 232: 1369–1457. https://doi.org/10.1140/epjs/s11734-023-00868-8.

Mydosh JA (1993) *Spin Glasses: An Experimental Introduction*. CRC Press.

Nakamura J, et al. (2020) Direct observation of anyonic braiding statistics. *Nature Physics* 16: 931. https://doi.org/10.1038/s41567-020-1019-1.

Nambu Y (2009) Nobel lecture: Spontaneous symmetry breaking in particle physics: A case of cross fertilization. *Reviews of Modern Physics* 81: 1015. https://doi.org/10.1103/RevModPhys.81.1015.

Nasser R, Dignon GL, Razban RM, and Dill KA (2021) The protein folding problem: The role of theory. *Journal of Molecular Biology* 433: 167126. https://doi.org/10.1016/j.jmb.2021.167126.

Nawrocki W (2019) *Introduction to Quantum Metrology*, 2nd. Springer. https://doi.org/10.1007/978-3-030-19677-6.

Nowak AL, et al. (2014) Deterministic and electrically tunable bright single-photon source. *Nature Communications* 5: 3240. https://doi.org/10.1038/ncomms4240.

Obermair GM and Wannier GH (1976) Bloch electrons in magnetic fields: Rationality, irrationality, degeneracy. *Physica Status Solidi (B)* 76: 217. https://doi.org/10.1002/pssb.2220760122.

Osadchy D and Avron JE (2001) Hofstadter butterfly as quantum phase diagram. *Journal of Mathematical Physics* 42: 5665. https://doi.org/10.1063/1.1412464.

Parisi G (2023) *In a Flight of Starlings: The Wonders of Complex Systems*. Penguin Press.

Perrakis A and Sixma TK (2021) Ai revolutions in biology. *EMBO Reports* 22: e54046. https://doi.org/10.15252/embr.202154046.

Pietiläinen P and Chakraborty T (2006) Energy levels and magneto-optical transitions in parabolic quantum dots with spin-orbit coupling. *Physical Review B* 73: 155315. https://doi.org/10.1103/PhysRevB.73.155315.

Pinarbasi M and Kent AD (2022) Perspectives on spintronics technology: Giant magnetoresistance to spin transfer torque magnetic random access memory. *APL Materials* 10: 020901. https://doi.org/10.1063/5.0075945.

Recio I and Torres JJ (2016) Emergence of low noise frustrated states in E/I balanced neural networks. *Neural Networks* 84: 91. https://doi.org/10.1016/j.neunet.2016.08.010.

Refregier P, Vincent E, Hammann J, and Ocio M (1987) Ageing phenomena in a spin-glass: Effect of temperature changes below Tg. *Journal of Physics (France)* 48: 1533. https://doi.org/10.1051/jphys:019870048090153300.

Ristig ML and Clark JW (1976) Density matrix of quantum fluids. *Physical Review B* 14: 2875. https://doi.org/10.1103/PhysRevB.14.2875.

Rogalla H and Kes PH (2012) *100 Years of Superconductivity*. Boca Raton: Taylor & Francis Group. https://doi.org/10.1201/b11312.

Schutz K and Zurek KM (2016) Detectability of light dark matter with superfluid helium. *Physical Review Letters* 117: 121302. https://doi.org/10.1103/PhysRevLett.117.121302.

Shields AJ, et al. (2000) Detection of single photons using a field-effect transistor gated by a layer of quantum dots. *Applied Physics Letters* 103: 3673. https://doi.org/10.1063/1.126745.

Steptoe A (1986) Mozart, mesmer and 'cosi fan tutte'. *Musics and Letters* 67: 248. https://doi.org/10.1093/ml/67.3.248.

Störmer HL (1992) Two-dimensional electron correlation in high magnetic fields. *Physica B: Condensed Matter* 177: 401. https://doi.org/10.1016/0921-4526(92)90138-I.

Tanford C and Reynolds J (2001) *Nature's Robots: A History of Proteins*. Oxford University Press.

Taniguchi M and Kawai T (2006) Dna electronics. *Physica E: Low-dimensional Systems and Nanostructures* 33: 1. https://doi.org/10.1016/j.physe.2006.01.005.

Thess A, et al. (2021) Historic nucleic acids isolated by Friedrich Miescher contain RNA beside DNA. *Biological Chemistry* 402: 1179. https://doi.org/10.1515/hsz-2021-0226.

Tinkham M (2004) *Introduction to Superconductivity*. N.Y.: Dover.

Tomczyk H (2022) Did Einstein predict Bose-Einstein condensation? *Studies in History and Philosophy of Science* 93: 30. https://doi.org/10.1016/j.shpsa.2022.02.014.

Vallone M (2019) Higgs and goldstone modes in crystalline solids. *Physica Status Solidi* 257: 1900443. https://doi.org/10.1002/pssb.201900443.

Van Vleck JH (1978) Quantum mechanics—The key to understanding magnetism. *Reviews of Modern Physics* 50: 181. https://doi.org/10.1103/RevModPhys.50.181.

Vincent E (2023) Rejuvenated but remembering. *Nature Physics* 19: 926–927. https://doi.org/10.1038/s41567-023-02097-1.

Volovik GE (2009) *The Universe in a Helium Droplet*. Oxford University Press. https://doi.org/10.1093/acprof:oso/9780199564842.001.0001.

von Klitzing K (2019) Essay: Quantum Hall effect and the new international system of units. *Physical Review Letters* 122: 200001. https://doi.org/10.1103/PhysRevLett.122.200001.

von Klitzing K, Chakraborty T, Kim P, Madhavan V, Dai X, McIver J, Tokura Y, Savary L, Smirnova D, Rey AM, Felser C, Gooth J, and Qi X (2020) 40 years of the quantum Hall effect. *Nature Reviews Physics* 2: 397. https://doi.org/10.1038/s42254-020-0209-1.

Watson JD and Crick FHC (1953) Molecular structure of nucleic acids. *Nature* 171: 737. https://doi.org/10.1038/171737a0.

Weinberg S (1986) Superconductivity for particular theorists. *Progress of Theoretical Physics Supplement* 86: 43. https://doi.org/10.1143/PTPS.86.43.

Weintraub R (2012) What can we learn from Buridan's ass? *Canadian Journal of Philosophy* 42: 281. https://doi.org/10.1353/cjp.2012.0013.

Weiss D (2013) The butterfly emerges. *Nature Physics* 9: 395. https://doi.org/10.1038/nphys2680.

Wolynes PG and Eaton WA (1999) The physics of protein folding. *Physics World* 12: 39. https://doi.org/10.1088/2058-7058/12/9/24.

Yamaguchi A, Hirohata A, and Stadler BJH (2021) *Nanomagnetic Materials: Fabrication, Characterization and Application*. Elsevier. (Chapter 5). https://doi.org/10.1016/C2018-0-05445-6.

This page intentionally left blank

LIST OF CONTRIBUTORS FOR VOLUME 1

Ryosuke Akashi
Department of Physics, University of Tokyo, Bunkyo, Japan

Yoichi Ando
Physics Institute II, University of Cologne, Cologne, Germany

Vadym Apalkov
Department of Physics and Astronomy, Georgia State University, Atlanta, GA, United States

Y Avishai
Department of Physics, Ben-Gurion University of the Negev, Beer-Sheva, Israel; Yukawa Institute for Theoretical Physics, Kyoto, Japan

Ajit C Balram
Institute of Mathematical Sciences, CIT Campus, Chennai, India; Homi Bhabha National Institute, Mumbai, India

YB Band
Department of Physics, Ben-Gurion University of the Negev, Beer-Sheva, Israel; Department of Chemistry, Ben-Gurion University of the Negev, Beer-Sheva, Israel; The Ilse Katz Center for Nano-Science, Ben-Gurion University of the Negev, Beer-Sheva, Israel

Jean Bellissard
School of Mathematics, Georgia Institute of Technology, Atlanta, GA, the United States

Giuliano Benenti
Center for Nonlinear and Complex Systems, Dipartimento di Scienza e Alta Tecnologia, Università degli Studi dell'Insubria, Como, Italy; Istituto Nazionale di Fisica Nucleare, Sezione di Milano, Milano, Italy

Emil J Bergholtz
Department of Physics, Stockholm University, AlbaNova University Center, Stockholm, Sweden

IB Bersuker
The University of Texas at Austin, Austin, TX, United States

Jordi Boronat
Department of Physics, Technical University of Catalonia, Barcelona, Spain

AA Burkov
Department of Physics and Astronomy, University of Waterloo, Waterloo, ON, Canada; Perimeter Institute for Theoretical Physics, Waterloo, ON, Canada

Massimo Capone
International School for Advanced Studies (SISSA) and CNR-IOM, Trieste, Italy

Iacopo Carusotto
Pitaevskii BEC Center, CNR-INO and Dipartimento di Fisica, Università di Trento, Trento, Italy

Giulio Casati
Center for Nonlinear and Complex Systems, Dipartimento di Scienza e Alta Tecnologia, Università degli Studi dell'Insubria, Como, Italy

Tapash Chakraborty
Department of Physics and Astronomy, University of Manitoba, Winnipeg, MB, Canada; Department of Physics, Brock University, St. Catharines, ON, Canada

JT Chalker
Theoretical Physics, University of Oxford, Oxford, United Kingdom

James R Chelikowsky
Center for Computational Materials, Oden Institute of Computational Engineering and Sciences, Departments of Physics and Chemical Engineering, University of Texas at Austin, Austin, TX, United States

AG Chronis
Department of Materials Science, University of Patras, Patras, Greece

ML Cohen
University of California at Berkeley, Berkeley, CA, USA

Dimitrie Culcer
School of Physics, The University of New South Wales, Sydney, NSW, Australia

Ippei Danshita
Department of Physics, Kindai University, Higashi-Osaka, Osaka, Japan

Jeanlex Soares de Sousa
Departamento de Física, Universidade Federal do Ceará, Fortaleza, Brazil

SB Dugdale
H.H. Wills Physics Laboratory, University of Bristol, Bristol, United Kingdom

Giuseppe Falci
Physics and Astronomy Department "Ettore Majorana", University of Catania, Catania, Italy; INFN Catania Section, Catania, Italy; CNR-IMM, Catania (University) Unit, Catania, Italy

Dario Ferraro
Dipartimento di Fisica dell'Università degli Studi di Genova & CNR-SPIN, Genova, Italy

G Fève
Laboratoire de Physique de l'Ecole normale supérieure, ENS, Université PSL, CNRS, Sorbonne Université, Université Paris Cité, Paris, France

Christopher Ford
Cavendish Laboratory, University of Cambridge, Cambridge, United Kingdom

Eduardo Fradkin
Department of Physics and Institute for Condensed Matter Theory, University of Illinois at Urbana-Champaign, Urbana, IL, United States

Jürg Fröhlich
Institute for Theoretical Physics, ETH Zurich, Zurich, Switzerland

T Giamarchi
Department of Quantum Matter Physics, University of Geneva, Geneva, Switzerland

Henri Godfrin
Univ. Grenoble Alpes, CNRS, Grenoble INP, Institut Néel, Grenoble, France

Mark O Goerbig
Laboratoire de Physique des Solides, CNRS - Université Paris-Saclay, Orsay, France

Shoushu Gong
Department of Physics, Beihang University, Beijing, China

Sinéad M Griffin
Materials Sciences Division, Lawrence Berkeley National Laboratory, Berkeley, CA, the United States; Molecular Foundry Division, Lawrence Berkeley National Laboratory, Berkeley, CA, the United States

Pertti J Hakonen
Low Temperature Laboratory, Department of Applied Physics, Aalto University, Otaniemi, Finland; InstituteQ—The Finnish Quantum Institute, Espoo, Finland

Yasuhiro Hatsugai
Department of Physics, University of Tsukuba, Tsukuba, Japan

Philipp Hauke
INO-CNR BEC Center and Department of Physics, University of Trento, Italy and INFN-TIFPA, Trento Institute for Fundamental Physics and Applications, Trento, Italy

O Kieler
Quantum Electronics, PTB Braunschweig, Braunschweig, Germany

Eckhard Krotscheck
Department of Physics, The State University of New York at Buffalo, Buffalo, NY, United States

AJ Leggett
Department of Physics, University of Illinois at Urbana-Champaign, Urbana, IL, United States

Jon Magne Leinaas
Department of Physics, University of Oslo, Oslo, Norway

Daniel Leykam
Centre for Quantum Technologies, National University of Singapore, Singapore, Singapore

Zhao Liu
Zhejiang Institute of Modern Physics, Zhejiang University, Hangzhou, China

Douglas Lundholm
Department of Mathematics, Uppsala University, Uppsala, Sweden

Ken KW Ma
National High Magnetic Field Laboratory, Tallahassee, FL, United States

Ryusuke Matsunaga
The Institute for Solid State Physics, The University of Tokyo, Kashiwa, Japan; JST-PRESTO, Saitama, Japan

Edward McCann
Physics Department, Lancaster University, Lancaster, United Kingdom

MJ Mehl
Department of Mechanical Engineering and Materials Sciences, Duke University, Durham, NC, United States

Zi Yang Meng
Department of Physics and HKU-UCAS Joint Institute of Theoretical and Computational Physics, The University of Hong Kong, Pok Fu Lam, Hong Kong, China

Yoshifumi Morita
Faculty of Engineering, Gunma University, Kiryu, Japan

Satoshi Moriyama
Department of Electrical and Electronic Engineering, School of Engineering, Tokyo Denki University, Tokyo, Japan

Nathan M Myers
Department of Physics, Virginia Tech, Blacksburg, VA, United States

Jan Myrheim
Department of Physics, The Norwegian University of Science and Technology, Trondheim, Norway

Joji Nasu
Department of Physics, Tohoku University, Sendai, Japan

Yusuke Nomura
Department of Applied Physics and Physico-Informatics, Keio University, Yokohama, Japan

Kozo Okazaki
The Institute for Solid State Physics, The University of Tokyo, Kashiwa, Japan

Elisabetta Paladino
Physics and Astronomy Department "Ettore Majorana", University of Catania, Catania, Italy; INFN Catania Section, Catania, Italy; CNR-IMM, Catania (University) Unit, Catania, Italy

Gaopei Pan
Beijing National Laboratory for Condensed Matter Physics and Institute of Physics, Chinese Academy of Sciences, Beijing, China; School of Physical Sciences, University of Chinese Academy of Sciences, Beijing, China

DA Papaconstantopoulos
Department of Computational and Data Sciences, George Mason University, Fairfax, VA, United States

Zlatko Papić
School of Physics and Astronomy, University of Leeds, Leeds, United Kingdom

Michael R Peterson
Department of Physics & Astronomy, California State University Long Beach, Long Beach, CA, United States

Sumathi Rao
International Centre for Theoretical Studies, Tata Institute of Fundamental Research, Bangalore, India

Raffaele Resta
Istituto Officina dei Materiali IOM-CNR, Trieste, Italy; Donostia International Physics Center, Donostia-San Sebastián, Spain

Nicolas Rougerie
Ecole Normale Supérieure de Lyon & CNRS, UMPA (UMR 5669), Lyon, France

Eric C Rowell
Department of Mathematics, Texas A&M University, College Station, TX, United States

Maura Sassetti
Dipartimento di Fisica dell'Università degli Studi di Genova & CNR-SPIN, Genova, Italy

VW Scarola
Department of Physics, Virginia Tech, Blacksburg, VA, United States

DN Sheng
Department of Physics and Astronomy, California State University Northridge, Los Angeles, CA, United States

AL Shluger
Department of Physics and Astronomy, University College London, London, United Kingdom

MM Sigalas
Department of Materials Science, University of Patras, Patras, Greece

Tapio Simula
Optical Sciences Centre, Swinburne University of Technology, Melbourne, VIC, Australia

Daria Smirnova
Nonlinear Physics Centre, Research School of Physics, Australian National University, Canberra, ACT, Australia;

AM Stoneham
Department of Physics and Astronomy, University College London, London, United Kingdom

J Strand
Department of Physics and Astronomy, University College London, London, United Kingdom

Jacques Tempere
Departement Fysica, TQC, Universiteit Antwerpen, Antwerp, Belgium

MP Tosi
Scuola Normale Superiore, Pisa, Italy

Shunji Tsuchiya
Department of Physics, Chuo University, Kasuga, Tokyo, Japan

Naoto Tsuji
Department of Physics, University of Tokyo, Hongo, Tokyo, Japan; RIKEN Center for Emergent Matter Science (CEMS), Wako, Saitama, Japan

Marco Vallone
Department of Electronics and Telecommunications. Politecnico of Turin, Turin, Italy

Pedro Vianez
Cavendish Laboratory, University of Cambridge, Cambridge, United Kingdom

G Vignale
Department of Physics and Astronomy, University of Missouri, Columbia, MO, United States

Klaus von Klitzing
Max Planck Institute for Solid State Research, Stuttgart, Germany

Xue-Feng Wang
School of physical science and technology, Soochow University, Suzhou, China

Jürgen Weis
Max Planck Institute for Solid State Research, Stuttgart, Germany

G Wendin
Department of Microtechnology and Nanoscience—MC2, Chalmers University of Technology, Gothenburg, Sweden

Philipp Werner
Department of Physics, University of Fribourg, Fribourg, Switzerland

Kun Yang
Department of Physics and National High Magnetic Field Laboratory, Florida State University, Tallahassee, FL, United States

Wei Yang
Institute of Physics, Chinese Academy of Sciences, Beijing, China

Jakob Yngvason
Fakultät für Physik, Universität Wien, Vienna, Austria; Erwin Schrödinger Institute for Mathematics and Physics, Vienna, Austria

Guangyu Zhang
Institute of Physics, Chinese Academy of Sciences, Beijing, China

CONTENTS OF VOLUME 1

Quantum Hall effect and modern-day metrology 1
Klaus von Klitzing

The pulse-driven AC Josephson voltage standard of Physikalisch-Technische Bundesanstalt (PTB) 9
O Kieler

Field theoretic aspects of condensed matter physics: An overview 27
Eduardo Fradkin

Majorana fermions in condensed-matter physics 132
AJ Leggett

Majorana fermions in Kitaev spin liquids 139
Joji Nasu

Fundamental and emergent particles in condensed matter and high-energy physics 147
Sinéad M Griffin

Phase transitions, spontaneous symmetry breaking, and Goldstone's theorem 158
Jürg Fröhlich

Higgs and Nambu–Goldstone modes in condensed matter physics 174
Naoto Tsuji, Ippei Danshita, and Shunji Tsuchiya

Higgs and Goldstone modes in cold atom systems 187
Jacques Tempere

Higgs and Goldstone modes in crystalline solids 197
Marco Vallone

Quantum mechanics: Foundations 212
AJ Leggett

Aharonov–Bohm and Aharonov–Casher effects in condensed matter physics: A brief review 218
Y Avishai and YB Band

Quantum computation of complex systems 237
Giuliano Benenti and Giulio Casati

Quantum information processing with superconducting circuits: A perspective 246
G Wendin

Braids, motions and topological quantum computing 268
Eric C Rowell

Fibonacci anyon based topological quantum computer 279
Tapio Simula

Fractional quantum Hall effect in semiconductor systems 285
Zlatko Papić and Ajit C Balram

From the integer to the fractional quantum hall effect in graphene 308
Mark O Goerbig

Fractional quantum Hall effect at the filling factor $v = 5/2$ 324
Ken KW Ma, Michael R Peterson, VW Scarola, and Kun Yang

Interacting Dirac fermions and the rise of Pfaffians in graphene 366
Vadym Apalkov and Tapash Chakraborty

On the stability of Laughlin's fractional quantum hall phase 383
Nicolas Rougerie

Fractional statistics in low-dimensional systems 394
Jon Magne Leinaas and Jan Myrheim

Anyon collisions and fractional statistics 402
G Fève

Fractional statistics, gauge invariance and anomalies in condensed matter physics 417
Jürg Fröhlich

Properties of 2D anyon gas 450
Douglas Lundholm

Abelian and non-abelian anyons 485
Sumathi Rao

Statistical anyons 500
Nathan M Myers

Recent developments in fractional Chern insulators 515
Zhao Liu and Emil J Bergholtz

Quantum Hall states in higher Landau levels 539
Jakob Yngvason

Quantum Hall effect 553
Jürgen Weis

The network model and the integer quantum Hall effect 567
JT Chalker

Photonic quantum Hall effects 575
Daniel Leykam and Daria Smirnova

The Anomalous Hall Effect 587
Dimitrie Culcer

Monolayer and bilayer graphene 602
Edward McCann

Quantum spin Hall effect 623
Shoushu Gong and DN Sheng

Quantum hall and synthetic magnetic-field effects in ultra-cold atomic systems 629
Philipp Hauke and Iacopo Carusotto

Quantum Hall phases of cold Bose gases 640
Nicolas Rougerie and Jakob Yngvason

Valley Currents in Graphene 652
Satoshi Moriyama and Yoshifumi Morita

Bulk-edge correspondence 659
Yasuhiro Hatsugai

Berry phase and geometrical observables 670
Raffaele Resta

Topological properties of Dirac and Weyl semimetals 681
AA Burkov

Topological insulators 690
Yoichi Ando

Bloch electrons in a magnetic field 700
Jean Bellissard

The Ten Martini problem 712
Jean Bellissard

Hofstadter butterfly in graphene 724
Wei Yang and Guangyu Zhang

Tight-binding method in electronic structure 732
DA Papaconstantopoulos, MJ Mehl, AG Chronis, and MM Sigalas

Electronic Structure Calculations: Plane-Wave Methods 756
ML Cohen

Plasmons in monolayer and bilayer graphene 765
Xue-Feng Wang and Tapash Chakraborty

Electron gas (theory) 778
G Vignale and MP Tosi

The Jahn-Teller effects 797
IB Bersuker

Fermi surface measurements 815
SB Dugdale

Pseudopotential methods 833
James R Chelikowsky

Effective masses 849
Jeanlex Soares de Sousa

Electronic structure: Impurity and defect states in insulators 856
AM Stoneham, J Strand, and AL Shluger

Density functional theory 867
Yusuke Nomura and Ryosuke Akashi

The sign problem in quantum Monte Carlo simulations 879
Gaopei Pan and Zi Yang Meng

Quantum transport and electron-electron interactions in one dimension 894
Pedro Vianez and Christopher Ford

Quantum physics in one dimension 905
T Giamarchi

The Hubbard model and the Mott–Hubbard transition 914
Massimo Capone

Electron quantum optics: A testbed for the Luttinger paradigma 924
Dario Ferraro and Maura Sassetti

Theoretical approaches to liquid helium 934
Jordi Boronat

The dynamics of quantum fluids 946
Henri Godfrin and Eckhard Krotscheck

Quantum fluids of light 959
Iacopo Carusotto

Floquet states 967
Naoto Tsuji

Pump-probe spectroscopy for non-equilibrium condensed matter 981
Ryusuke Matsunaga and Kozo Okazaki

Nonequilibirum physics, numerical methods 990
Philipp Werner

1/f noise in quantum nanoscience 1003
Giuseppe Falci, Pertti J Hakonen, and Elisabetta Paladino

Quantum Hall effect and modern-day metrology

Klaus von Klitzing, Max Planck Institute for Solid State Research, Stuttgart, Germany

© 2024 Elsevier Ltd. All rights reserved.

Introduction 1
International system of units (SI units) 2
Universality of quantized Hall resistance 2
Is the quantized Hall resistance identical to h/e^2? 4
Integration of electrical quantum units into the official SI system 5
Conclusion 7
References 7

Abstract

The discovery of the quantum Hall effect in 1980 triggered a revolution in metrology. As a result, a modified system of units based on natural constants with a fixed value for the von Klitzing constant h/e^2, where h is the Planck constant and e is the elementary charge, was established worldwide on May 20, 2019. Combined with the Josephson effect, all electrical units today are based on natural constants. Moreover, the quantum Hall effect enabled the kilogram to be defined as an internationally standardized unit of mass based on a fixed value for the Planck constant via the Kibble balance.

Key points

- The discovery of the quantum Hall effect in 1980 was based on experiments that showed the presence of plateaus in the Hall resistance, insensitive to the amount of localized electron states due to disorder.
- High-precision measurements of the quantized Hall resistance performed at various metrology institutes demonstrated the universality of the quantized value.
- A conventional value for the quantized Hall resistance was introduced for metrological applications between 1990 and 2019 (conventional von Klitzing constant).
- The quantized resistance is not affected by the gravitational potential but may have corrections at the 10^{-20} level due to vacuum polarization.
- The CODATA least-squares fit of fundamental constants failed to detect an inexactness of the quantized Hall resistivity with the fundamental constant h/e^2.
- The revised International System of Units introduced in 2019 with fixed values for the fundamental constants h and e integrates the quantized Hall resistance as a resistance standard into the SI system.
- The electric quantum standard for the resistance (QHE) and voltage (Josephson effect) allows the mass unit kilogram to be defined in terms of the Kibble balance based on a fixed value for the Planck constant h.
- The electrical units farad and henry can be traced back to the von Klitzing constant h/e^2 via the ac quantum Hall effect.
- The parallel and series connection of quantum Hall devices allows resistance standards to be defined with arbitrary values.

Introduction

Modern metrology, the science of measurements, originated from the French Revolution, when the metric system with its prototypes for the meter and kilogram was introduced. The rotation frequency and circumference of the Earth as well as one cubic decimeter of water originally served as references for global units of time, length and mass, respectively. This system was internationally adopted by the Metre Convention in 1875. However, Scottish physicist J.C. Maxwell criticized this development, stating that, "The properties of the earth are not stable enough for a precise definition of the units length, time and mass. The wavelength, frequency and mass of atoms are much more suitable for time independent and stable basic units" (Maxwell, 1870). Maxwell's theoretical objections could not be implemented experimentally with high precision until the 1970s, when both the second and the meter were redefined in terms of atomic properties as follows: The standard ephemeris second based on the Earth's orbit around the Sun was replaced by a fixed value of $\Delta\nu_{Cs}$, which denotes the transition between the two hyperfine ground states of cesium-133, and the meter was redefined by a fixed value for the wavelength of a special spectral line of krypton-86. However, the finite linewidth and asymmetry of this spectral line were subsequently found to limit the accuracy of this definition of the meter. Consequently, the meter was redefined yet again in 1983 by something that is even more reliable than atomic properties: The value of a fundamental constant. This radical new concept of defining a unit of measure by fixing the value of a fundamental constant became the blueprint for today's International System of Units and is the most important application of the quantum Hall effect (QHE) (von Klitzing et al., 1980).

https://doi.org/10.1016/B978-0-323-90800-9.00197-9

International system of units (SI units)

The profound industrial importance of electricity, thermodynamics, optics and chemistry requires globally recognized basic units of measure, in addition to the historically most important units of kilogram, meter and second. The International System of Units (SI system) was introduced in 1960 and consists of the seven base units of second, meter, kilogram, ampere, kelvin, mole, and candela (BIPM, SI Brochure, 2019). This system can accommodate an unlimited number of derived units, all of which can be expressed in terms of these seven base units. The 22 most common coherent derived SI units are generally referred to by their own nomenclature, such as ohm for electrical resistance, which is defined in terms of the base units as $1\ \Omega = 1\ \mathrm{kg\ m^2\ s^{-3}\ A^{-2}}$.

The practical importance of standardized units for global commerce requires that the base units can be reproduced worldwide with high accuracy and that these units remain stable over time. Fundamental constants are best suited to fulfill these requirements. For example, in the late 1800s, Max Planck, who discovered the two fundamental constants known today as the Planck and Boltzmann constants h and k, respectively, also developed units for length, mass, time and temperature based on a combination of fundamental constants. Planck determined that "…with the help of fundamental constants, we have the capability to establish units of length, time, mass, and temperature, which necessarily retain their significance for all cultures, even unearthly and nonhuman ones" (Planck, 1900). Unfortunately, these Planck units with length scales of 10^{-35} m or mass units of the order of 10^{-10} kg could not be obtained with high precision and were therefore not useful for practical applications.

Another 80 years would elapse before the velocity of light was chosen as the fundamental constant in terms of which all base units could be defined in today's International System of Units. With the development of lasers, it became possible to measure the velocity of light with such high precision that this replaced the previous definition of the velocity of light in terms of the meter, which had formerly been defined based on the wavelength of ^{86}Kr. Consequently, the official definition of the meter as the base unit of length was redefined in 1983 "by taking the fixed numerical value of the speed of light in vacuum, c, to be 299,792,458 when expressed in the unit m $\mathrm{s^{-1}}$, where the second is defined in terms of the cesium frequency $\Delta\nu_{\mathrm{Cs}}$" (BIPM, SI Brochure, 2019). This definition is identical to a fixed value for the velocity of light and launched the incorporation of fundamental constants into today's SI system, which was established worldwide as the new International System of Units on May 20, 2019.

This landmark accomplishment would not have been possible without the discovery of new quantum phenomena. The theoretical prediction of the Josephson effect (Josephson, 1962) and the experimental demonstration by Tsai et al. (1983) of a voltage based on fundamental constants with a reproducibility of 2 parts in 10^{16} paved the way for further applications of fundamental constants in metrology. The US National Bureau of Standards was the first national metrology institute to introduce a Josephson voltage standard (Field et al., 1973). However, it was not possible simply to replace a base unit with this new "quantum volt", meaning that the volt had to be defined as a unit of electricity outside the official International System of Units. Different countries used different values for the Josephson constant $K_\mathrm{J} = 2e/h$ in order to replace electrochemical Weston cells with the Josephson effect as their voltage standard. Four different voltage standards with differences of up to 6 ppm were adopted by the US, France, Russia and the rest of the world. Ultimately, however, this changed with the discovery of the QHE and the worldwide introduction of conventional standards for electrical quantum units in 1990 (Quinn, 1989).

Universality of quantized Hall resistance

From the very beginning of the "quantum Hall age", the high precision of the quantized Hall plateaus was the most surprising finding. Experiments performed in 1980 at the High Magnetic Field Laboratory in Grenoble, France, (see Fig. 1) showed for the first time that the Hall resistance under the condition of a fully occupied Landau level agrees with the fundamental value of h/e^2, where h is the Planck constant and e is the elementary charge, and is insensitive to device properties. This quantization on a macroscopic level was unexpected. The article by Jürgen Weis (2022) in this encyclopedia provides an introduction to this quantum effect within a model of independent charge carriers. More general explanations of the QHE are based on gage arguments by Laughlin (1981) and topological numbers (Niu et al., 1985; Hastings and Michalakis, 2015). However, at the time the QHE was discovered, it was assumed that disorder in a device influences the Hall effect and that localized states present in the tails of a Landau level are missing in Hall effect measurements (Aoki and Kamimura, 1977). On the other hand, extensive calculations of the Hall effect in two-dimensional systems by Ando et al. (1975) indicated that impurity bands, separated from a Landau level, do not influence the ideal value of the Hall effect for a fully occupied Landau level. Experimental Hall effect data had been published as early as 1978 (Englert and von Klitzing, 1978; Kawaji, 1978). However, the carrier density for these measurements had always been calibrated on the basis of the gate capacitance and the threshold voltage of the device, but not related to the degeneracy of a Landau level. In addition, the discovery of the QHE in 1980 highlighted that the Hall resistance (calculated directly from the measured Hall voltage and the current through the device) is identical to the resistivity tensor component ρ_{xy} used in theoretical calculations.

The first manuscript to describe the discovery of the QHE was submitted to *Physical Review Letters* and originally entitled "Realization of a resistance standard based on natural constant." It remains today the most important application of the QHE in metrology. Peer reviewer Barry Taylor at the National Bureau of Standards requested that the title be changed to "New method for high-accuracy determination of the fine-structure constant based on quantized Hall resistance" (von Klitzing et al., 1980). This change was justified by the fact that, at the time the QHE was discovered, the uncertainty in demonstrating a resistance in terms of SI ohms via the calculable Thompson and Lampard (1956) capacitor was less than the uncertainty regarding the value of

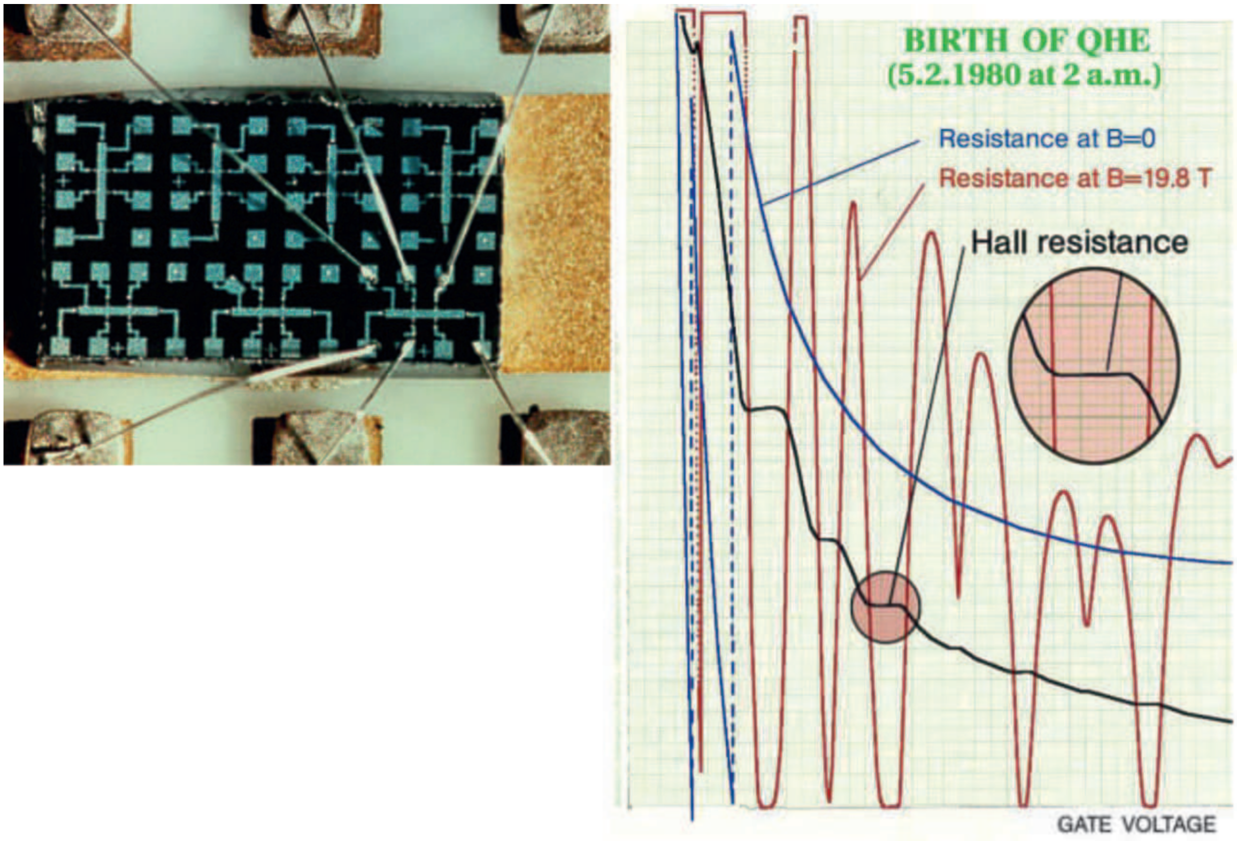

Fig. 1 "Birth" of the quantum Hall effect. Original data (*x-y r*ecorder) of resistance measurements on the silicon field effect transistor shown above.

von Klitzing, K. et al. (1980)	25812.68 (8) Ω
BIPM (France)	25812.809 (2) Ω
PTB (Germany)	25812.802 (3) Ω
NBS (USA)	25812.807 (1) Ω
LCIE (France)	25812.802 (6) Ω
NRC (Canada)	25812.814 (6) Ω
NPL (UK)	25812.809 (1) Ω
ETL (Japan)	25812.806 (7) Ω
IMS (Russia)	25812.807 (8) Ω
VSL (The Netherlands)	25812.802 (5) Ω
NIM (China)	25812.806 (16) Ω
EAM (Switzerland)	25812.809 (4) Ω
conventional von Klitzing constant	25812.807 (0) Ω ≡ $R_{K\text{-}90}$

Fig. 2 Summary of high-precision measurements of fundamental quantized Hall resistance up to 1988, starting with the value of the original publication (von Klitzing et al., 1980). The value for the conventional von Klitzing constant was adopted internationally in 1990 (Quinn, 1989).

the fine-structure constant α. With the introduction of a fixed value for the velocity of light in 1983, however, the inverse fine-structure constant was in fact found to be identical to h/e^2, apart from the exactly known value for the proportionality constant $2\,\varepsilon_0\,c \equiv (2\pi \cdot 29.9792458)^{-1}\,\Omega^{-1}$. (Note that the permittivity constant ε_0 is no longer a fixed number in the current SI). Ironically, the original title of the manuscript "Realization of a resistance standard…" would have proved more appropriate today.

As shown in Fig. 2, many National Metrology Institutes (NMI) have since confirmed the reproducibility of the quantized Hall resistance measured with various devices (Taylor and Witt, 1989). The stability of this quantum resistor was so high that a time-dependent variation of the ohm (represented by a wire resistor) officially established by the U.S. National Bureau of Standards was measured to have a drift of −0.055 ppm/year (Fig. 3). Different NMIs observed similar variations of the national resistance

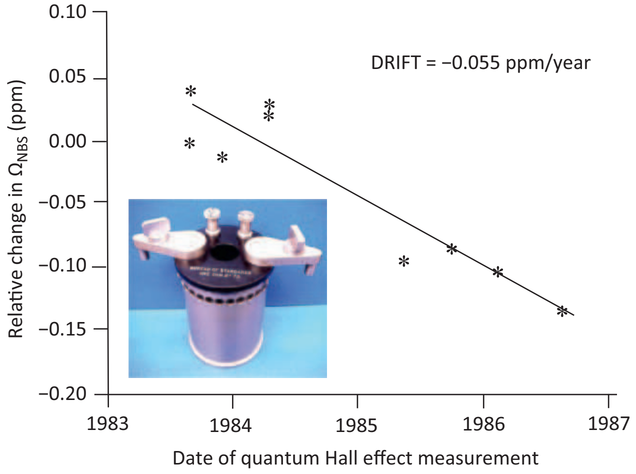

Fig. 3 National Bureau of Standards (NBS) ohm drift based on QHE measurements (https://www.nist.gov/system/files/documents/calibrations/87mscohm.pdf).

standards, originating mainly from strain in the wire. The stability and reproducibility of the quantized Hall resistance was so convincing that, on January 1, 1990, a fixed value for the conventional von Klitzing constant of $R_{K\text{-}90} = 25{,}812.807\ \Omega$ was adopted worldwide for all resistance calibrations based on the QHE (Quinn, 1989). At the same time, a global value for the conventional Josephson constant was fixed, which resulted in very reproducible electrical units outside the official SI units. Delahaye and Jeckelmann (2003) published a guideline that describes the tests and precautions necessary for reliable precision measurements of the quantized Hall resistance with an uncertainty of only a few parts in 10^9, according to the official recommendation of the Consultative Committee for Electricity and Magnetism (CCEM).

Is the quantized Hall resistance identical to h/e^2?

High-precision comparisons obtained using different quantum Hall devices, the results of which included not only the integer QHE but also the fractional quantum Hall effect (FQHE) and the quantum anomalous Hall effect (QAHE), demonstrated the universality of quantized Hall resistance up to an experimental uncertainty of only a few parts in 10^{11} as shown in Fig. 4. However, this does not prove that the quantized resistance is identical to h/e^2 without corrections. Taylor and Cohen (1991) applied a least-squares adjustment of all experimental data to determine the best value for the fine-structure constant (excluding QHE data) to establish that better consistency is achieved if the measured quantized Hall resistance is about 0.06 ppm greater than the corresponding h/e^2 value. However, the 2006 CODATA least-squares adjustment of fundamental constants could not identify a correction for the relation $R_K = h/e^2$ within the uncertainty margin of 2 parts in 10^8. The metrology community accepted the conclusion that there is no experimental evidence for the inaccuracy of $K_J = 2e/h$ nor that of $R_K = h/e^2$ (Mohr et al., 2008).

Another test to verify the correct description of electric quantum units by fundamental constants resulted from the development of electron pumps (Pekola et al., 2013). Such pumps allow the controlled charging and discharging of a quantum dot with one electron leading to a quantum current $I = e{\cdot}f$, where f is the pumping frequency, which can be calibrated from the atomic clock. The combination of an electron pump with a quantum Hall resistor and a Josephson voltmeter (quantum metrology triangle QMT)

Si ⇔ GaAs	**$3.5 \cdot 10^{-10}$**	Hartland et al. (1991)
GaAs ⇔ GaAs	**$3.2 \cdot 10^{-11}$**	Schopfer and Poirier (2007)
Epi C ⇔ GaAs	**$8.7 \cdot 10^{-11}$**	Janssen et al. (2012)
Exfol. C ⇔ GaAs	**$6.3 \cdot 10^{-9}$**	Woszczyna et al. (2012)
$\nu=\frac{1}{3}$ GaAs ⇔ GaAs	**$6.3 \cdot 10^{-8}$**	Ahlers et al. (2017) FQHE
$(Bi,Sb)_2Te_3$ ⇔ GaAs	**$2.5 \cdot 10^{-7}$**	Götz et al. (2018) QAHE
$Cr_x(Bi_{1-y}Sb_y)_{1-x}Te_3$ ⇔ GaAs	**$1.0 \cdot 10^{-8}$**	Okazaki et al. (2022) QAHE

Fig. 4 Universality of quantized Hall resistance. Comparison between different two-dimensional electron systems including fractional quantum Hall effect (FQHE) and quantum anomalous Hall effect (QAHE) (Hartland et al., 1991; Schopfer and Poirier, 2007; Janssen et al., 2012; Woszczyna et al., 2012; Ahlers et al., 2017; Götz et al., 2018; Okazaki et al., 2022).

showed no inconsistency at 1 ppm (Scherer and Camarota, 2012). The accuracy of these experiments is limited by the electron pumps, which produce relatively small currents of approximately 100 pA. Advanced QMT experiments will reduce the uncertainty by about one order of magnitude (Scherer and Schumacher, 2019) and will enhance confidence in our theoretical understanding and the consistency of the quantum electrical effects.

Some theoretical publications have discussed various possible corrections of the relation $R_K = h/e^2$. Even the finite width W of a Hall device in relation to the diameter of the classical cyclotron orbit could contribute to a correction (Shapiro, 1986). However, experiments using devices with different widths ranging from 1 mm to as small as 10 μm showed no width dependence of the quantized Hall resistance within the margin of experimental uncertainty of 1 part in 10^9 (Jeanneret et al., 1995).

Other theoretical publications have discussed the influence of gravity on the QHE. For example, Hehl et al. (2004) found no influence of the gravitational field if it is perpendicular to two-dimensional electron gas (2DEG), but that an additional electric field due to gravity does exist if the gravitational field is parallel to the Hall field. This was analyzed in detail by Hammad et al. (2020). The mere force of the Earth's gravitational field on the electron mass should lead to an electric field of 0.55×10^{-10} V m^{-1}, which is about 13 orders of magnitude less than the Hall field used for high-precision QHE measurements. So far, no experimental data has been published that evaluates the influence of gravity on the quantized Hall resistance. Nevertheless, the gravitational field is not expected to have an effect as long as the gravitational potential does not change within the plane of the two-dimensional electronic system.

Penin (2009) took a quantum electrodynamic (QED) approach to predict a small correction to the von Klitzing constant due to vacuum polarization in strong magnetic fields with the following result:

$$R_K \approx h/e^2 \left[1 - 10^{-20} \cdot (B/10\,\mathrm{T})^2\right].$$

Such a correction of approximately 1 part in 10^{20} under a typical magnetic field of 10 T in QHE experiments is negligible for metrological applications of the QHE, meaning that all measurements of the quantized Hall resistance are consistent with the equation $R_K = h/e^2$.

Integration of electrical quantum units into the official SI system

In 1988, the least-squares adjustment of all measurements of the quantized Hall resistance yielded a value of $R_K = 25{,}812.807\,(5)\,\Omega$ (Taylor and Witt, 1989). The uncertainty margin of some 2 parts in 10^7 was dominated by the uncertainty inherent in expressing ohm in terms of SI units. As the reproducibility of the QHE resistance was significantly greater, a fixed conventional value of $R_{K\text{-}90} \equiv 25{,}812.807\,\Omega$ was introduced in 1990 for metrological applications. This led to international uniformity of all resistance calibrations with uncertainties of less than 10^{-8}. However, such calibrations were outside the official SI system, and more accurate measurements of h/e^2 showed an increasing discrepancy between the von Klitzing constant $R_K = h/e^2$ and the conventional value of $R_{K\text{-}90}$ as shown in Fig. 5. Similar discrepancies appeared between the Josephson constant $K_J = 2e/h$ and the conventional value of $K_{J\text{-}90} \equiv 483{,}597.9 \times 10^9$ Hz V^{-1}. To prevent quantum units from diverging ever further from SI units, the idea was proposed to integrate the von Klitzing constant and the Josephson constant into the International System of Units. However, this would mean abandoning the definitions of two established base units. The breakthrough solution came from Steiner et al. (2005), who presented high-precision measurements with a watt balance (known since 2017 as the Kibble balance). This created the capability to trace the mass unit of the kilogram back to the Planck constant h with sufficient accuracy. In that experiment, the mechanical force of a mass is compensated by the electrical force of a current in a magnetic field, calibrated in accordance with electrical quantum standards. Hence, electrical quantum units gave way to a new definition of the kilogram based on the fundamental constant h.

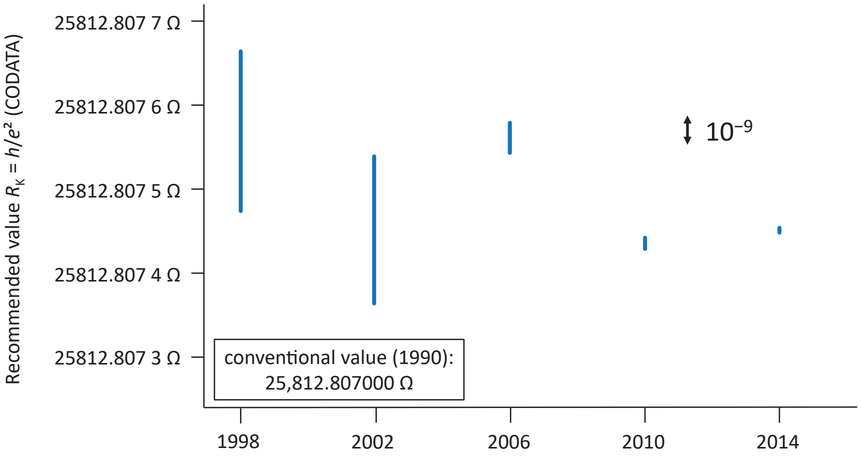

Fig. 5 Recommended CODATA values for the von Klitzing constant $R_K = h/e^2$.

Evidence that the kilogram artifact at the BIPM was not stable in time (Girard, 1994) supported the idea of replacing the kilogram and introducing a new system of units (Mills et al., 2005; Schlamminger and Haddad, 2019). Establishing this revised system was the focus of a historic discussion at the Royal Society in London in 2005 (Quinn and Burnett, 2005). With fixed values for e and h, not only could the base units of ampere and kilogram be related to fundamental constants, but the Josephson and von Klitzing constants could also be integrated into the revised International System of Units. The contribution of C. Borde (2005) at that discussion made it clear that electric metrology is in the midst of a paradigm shift that will play a key role for the entire field of metrology.

A revised international system of units was proposed by Mills et al. (2006), but 12 years would elapse before participants at the 26th General Conference on Weights and Measures voted unanimously to implement a new International System of Units as of May 20, 2019. The fixed values of the constants of nature, which form the basis of today's modified International System of Units, are summarized in Fig. 6. Practical realizations of the SI units have since been published (BIPM, SI Brochure, 2019), which, for example, are defined for the electrical unit ohm as follows:

> The ohm is the electric resistance between two points of a conductor when a constant potential difference of 1 volt, applied to these points, produces in the conductor a current of 1 ampere, the conductor not being the seat of any electromotive force. The ohm can be defined by using the QHE in a manner consistent with the CCEM Guidelines (Delahaye and Jeckelmann, 2003) and using the value of the von Klitzing constant RK = 25,812.8074593045 Ω.

With this recommendation, issued some 40 years after the discovery of the QHE, the vision of the original manuscript describing the application of this quantum effect, which, ironically enough, was rejected, has come to fruition.

With the discovery of graphene as an ideal two-dimensional electron system, it has become simpler to apply the QHE as a resistance standard. In particular, graphene on SiC (epigraphene) exhibits many advantageous features compared to those of GaAs heterostructures, a well-established material. Ribeiro-Palau et al. (2015) demonstrated that the Hall resistance can be accurately quantized to within 1×10^{-9} over a 10-T-wide range of magnetic field starting as low as 3.5 T. Moreover, the same precision can be achieved at temperatures as high as 10 K and device currents up to 500 μA. Further research is needed to optimize epitaxial graphene for quantum Hall applications (Meng et al., 2022).

A special feature of the QHE is that not only the four-terminal Hall resistance but also the two-terminal resistance between any two contacts at the boundary of a QHE device has the quantized resistance. Errors due to finite contact resistance can be reduced to a negligible value by the multiple-series connection scheme (Delahaye, 1993). This created the possibility to establish quantum Hall array standards (QHARS) by combining QHE devices in parallel and in series with quantized resistances at arbitrary levels (Poirier et al., 2004). A scheme for decade-value standards in the range from 100 Ω to 1 MΩ has been presented by Oe et al. (2013). Comparisons of two epigraphene QHARS with 138 devices in parallel (array resistance $R \approx 109\ \Omega$) showed a relative deviation of only 3 parts in 10^{11} and, compared to a single quantum Hall device, was in agreement with the target value of $R_K/276$ within the uncertainty of 2 parts in 10^{10} (He et al., 2022). To eliminate lead resistances, the contacts and interconnects were made of NbN superconducting films, which can support currents on the order of 10 mA at 5 T and 2 K.

Extending the application of the quantized Hall resistance as the primary resistance standard results from the ac QHE in the frequency range from 50 Hz to 20 kHz. This allows direct measurements of impedances (Schurr et al., 2007; Ahlers et al., 2009) with uncertainties of less than 10^{-8}. Calibration of capacitances (Schurr et al., 2009; Schurr and Lee, 2022) in the range from 10 nF to 10 pF and inductances (Overney and Jeanneret, 2010) in the range from 1 μH to 10H were traced back to the von Klitzing constant.

By integrating the conventional electrical quantum units used since 1990 into the International System of Units, the electrical units ohm, farad and henry changed discontinuously on May 20, 2019, by a fractional amount of 17.793×10^{-9}. The corresponding jump for the Josephson volt was nearly four times greater. Such discontinuities for units of measure will never happen again as long as fundamental constants remain constant. Having said that, discussions of possible changes in fundamental constants with time are very important and will focus on the fine-structure constant, which depends on the most important fundamental constants h, e, and c. This has the advantage of being a dimensionless constant independent of units. The most accurate measurements of this constant show that the change is less than 1 part in 10^{17} per year (Safronova, 2019). Possible variations of the fundamental constants at this level are insignificant in metrology for the foreseeable future.

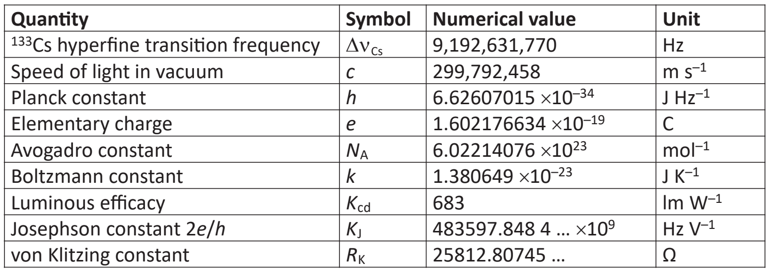

Quantity	Symbol	Numerical value	Unit
^{133}Cs hyperfine transition frequency	$\Delta\nu_{Cs}$	9,192,631,770	Hz
Speed of light in vacuum	c	299,792,458	m s^{-1}
Planck constant	h	$6.62607015 \times 10^{-34}$	J Hz^{-1}
Elementary charge	e	$1.602176634 \times 10^{-19}$	C
Avogadro constant	N_A	$6.02214076 \times 10^{23}$	mol^{-1}
Boltzmann constant	k	1.380649×10^{-23}	J K^{-1}
Luminous efficacy	K_{cd}	683	lm W^{-1}
Josephson constant 2e/h	K_J	483597.848 4 … $\times 10^{9}$	Hz V^{-1}
von Klitzing constant	R_K	25812.80745 …	Ω

Fig. 6 Defining constants of the International System of Units (SI).

Conclusion

The QHE plays a central role in metrology and was crucial for updating the International System of Units based on constants of nature. Even if a complete theory of the QHE for real devices with finite dimensions, electrical contacts, uncontrolled disorder and in the presence of relatively high bias currents has not yet been developed, experiments have demonstrated the reliability of this quantum effect for practical applications. The universality of the quantized Hall resistance has been demonstrated to at least 10 digits, and all high-precision experiments agree with the theoretically predicted value of $R_K = h/e^2$ for the quantum Hall plateaus within the experimental uncertainty of 2 parts in 10^8. The quantized Hall resistance has been officially adopted as a primary realization of the resistance unit ohm. Arrays of quantum Hall devices are used for quantized resistances with arbitrary values in the range from 100 Ω to 10 MΩ. Primary realizations of the electrical units farad and henry are possible with the QHE under ac conditions. The development of an electronic kilogram, where the QHE together with the Josephson effect allowed the mass unit to be defined based on a fixed value for the Planck constant *h*, accelerated the adoption of today's International System of Units. Fig. 7 shows the official logo of this new system that illustrates the relationship to historically introduced base units.

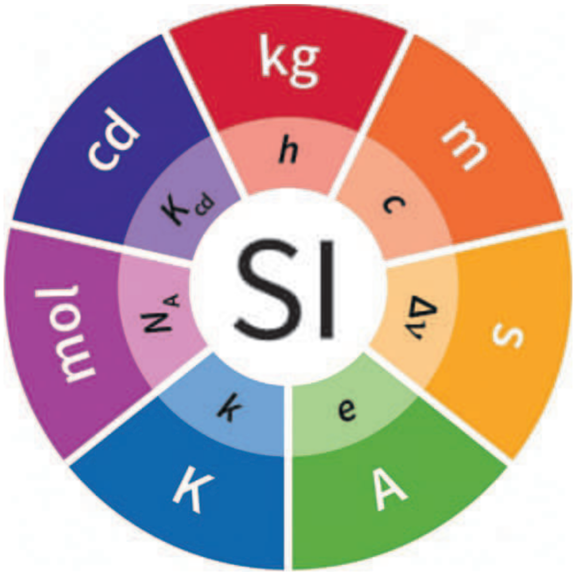

Fig. 7 Official logo for the base units of the International System of Units. The inner ring contains the constants of nature with fixed values connected to the base units introduced historically (outer ring). © BIPM.

References

Ahlers FJ, Jeanneret B, Overney F, Schurr J, and Wood BM (2009) Compendium for precise ac measurements of the quantum Hall resistance. *Metrologia* 46: R1–R11.
Ahlers FJ, Götz M, and Pierz K (2017) Direct comparison of fractional and integer quantized Hall resistance. *Metrologia* 54: 516.
Ando T, Matsumoto Y, and Uemura Y (1975) Theory of Hall effect in a two-dimensional electron system. *Journal of the Physical Society of Japan* 39: 279–288.
Aoki H and Kamimura H (1977) Anderson localization in a two dimensional electron system under strong magnetic fields. *Solid State Communications* 21: 45–47.
BIPM (2019) *The International System of Units (SI)*, 9th edn, updated in 2022. https://www.bipm.org/en/publications/si-brochure.
Borde C (2005) Base units of the SI, fundamental constants and modern quantum physics. *Philosophical Transactions of the Royal Society A* 363: 2177–2201.
Delahaye F (1993) Series and parallel connection of multiterminal quantum Hall-effect devices. *Journal of Applied Physics* 73: 7914.
Delahaye F and Jeckelmann B (2003) Revised technical guidelines for reliable dc measurements of the quantized Hall resistance. *Metrologia* 40: 217–233.
Englert T and von Klitzing K (1978) Analysis of ρ_{xx} minima in surface quantum oscillations on (100) n-type silicon inversion layers. *Surface Science* 73: 70–80.
Field BF, Finnegan TF, and Toots J (1973) Volt maintenance at NBS via 2*e*/*h*: A new definition of the NBS volt. *Metrologia* 9(4): 155.
Girard G (1994) The third periodic verification of national prototypes of the kilogram (1988-1992). *Metrologia* 31: 317–336.
Götz M, Fijalkowski KM, Pesel E, Hartl M, Schreyeck S, Winnerlein M, Grauer S, Scherer H, Brunner K, Gould C, Ahlers FJ, and Molenkamp LW (2018) Precision measurement of the quantized anomalous Hall resistance at zero magnetic field. *Applied Physics Letters* 112: 072102.
Hammad F, Landry A, and Mathieu K (2020) A fresh look at the influence of gravity on the quantum Hall effect. *European Physical Journal - Plus* 135: 449.
Hartland A, Jones K, Williams JM, Gallagher BL, and Galloway T (1991) Direct comparison of the quantized Hall resistance in gallium arsenide and silicon. *Physical Review Letters* 66: 969.
Hastings MB and Michalakis S (2015) Quantization of hall conductance for interacting electrons on a torus. *Communications in Mathematical Physics* 334(1): 433–471.
He H, Cedergren K, Shetty N, Lara-Avila S, Kubatkin S, Bergsten T, and Eklund G (2022) Accurate graphene quantum Hall arrays for the new International System of Units. *Nature Communications* 13: 6933.
Hehl FW, Obukhov YN, and Rosenow B (2004) Is the quantum Hall effect influenced by the gravitational field? *Physical Review Letters* 93: 096804.

Janssen TJBM, Williams JM, Fletcher NE, Goebel R, Tzalenchuk A, Yakimova R, Lara-Avila S, Kubatkin S, and Falko VI (2012) Precision comparison of the quantum Hall effect in graphene and gallium arsenide. *Metrologia* 49: 294.

Jeanneret B, Jeckelmann B, Buhlmann H-J, Houdre R, and Ilegems M (1995) Influence of the device-width on the accuracy of quantization in the integer quantum Hall effect. *IEEE Transactions on Instrumentation and Measurement* 44(2): 254–257.

Josephson B (1962) Possible new effects in superconductive tunneling. *Physics Letters* 1: 251.

Kawaji S (1978) Quantum galvanomagnetic experiments in silicon inversion layers under strong magnetic fields. *Surface Science* 73: 46–69.

Laughlin RB (1981) Quantized Hall conductivity in two dimensions. *Physical Review B* 23: 5632.

Maxwell JC (1870) Address to the mathematical and physical sections of the British Association, Liverpool, reproduced in: Niven WD (Ed.), *The Scientific Papers of James Clerk Maxwell*, Vol. 22. Cambridge University Press, Cambridge, 1890, p. 225.

Meng L, Panna A, Mhatre S, Rigosi A, Payagala S, Saha D, Tran N, Yeh C, Elmquist R, Hight Walker A, Jarrett D, Newell D, and Yang Y (2022) Quantitative characterization of epitaxial graphene for the application of quantum Hall resistance standard. In: *IEEE Proceedings for the Conference on Precision Electromagnetic Measurements 2022, Wellington, NZ.*

Mills IM, Mohr PJ, Quinn TJ, Taylor BN, and Williams ER (2005) Redefinition of the kilogram: A decision whose time has come. *Metrologia* 42: 71–80.

Mills IM, Mohr PJ, Quinn TJ, Taylor BN, and Williams ER (2006) Redefinition of the kilogram, ampere, kelvin and mole: a proposed approach to implementing CIPM recommendation 1. *Metrologia* 43: 227–246.

Mohr P, Taylor BN, and Newel DB (2008) CODATA recommended values of the fundamental physical constants: 2006. *Journal of Physical and Chemical Reference Data* 37: 1258.

Niu Q, Thouless DJ, and Wu Y (1985) Quantized Hall conductance as a topological invariant. *Physical Review B* 31: 3372.

Oe T, Matsuhiro K, Itatani T, Gorwadkar S, Kiryu S, and Kaneko N-H (2013) New design of quantized Hall resistance array device. *IEEE Transactions on Instrumentation and Measurement* 62(6): 1755.

Okazaki Y, Kawamura M, Nakamura S, Takada S, Mogi M, Takahashi KS, Tsukasaki A, Kawasaki M, Tokura Y, and Kaneko N-H (2022) Quantum anomalous Hall effect with a permanent magnet defines a quantum resistance standard. *Nature Physics* 18: 25–29.

Overney F and Jeanneret B (2010) Realization of an inductance scale traceable to the quantum Hall effect using an automated synchronous sampling system. *Metrologia* 47: 690–698.

Pekola JP, Saira OP, Maisi VF, Kemppinen A, Möttönen M, Pashkin YA, and Averin DV (2013) Single-electron current sources: Toward a refined definition of the ampere. *Reviews of Modern Physics* 85(4): 1421.

Penin AA (2009) Quantum Hall effect in quantum electrodynamics. *Physical Review B* 79: 113303. Erratum: Phys. Rev. B 81: 089902.

Planck M (1900) Über irreversible Strahlungsvorgänge. *Annalen der Physik* 306(1): 69–122.

Poirier W, Bounouh A, Piquemal F, and André JP (2004) A new generation of QHARS: discussion about the technical criteria for quantization. *Metrologia* 41: 285–294.

Quinn TJ (1989) News from the BIPM. *Metrologia* 26: 69.

Quinn T and Burnett K (2005) The fundamental constants of physics, precision measurements and the base units of the SI. *Philosophical Transactions of the Royal Society A* 363: 2101–2104.

Ribeiro-Palau R, Lafont F, Brun-Picard J, Kazazis D, Michon A, Cheynis F, Couturaud O, Consejo C, Jouault B, Poirier F, and Schopfer F (2015) Quantum Hall resistance standard in graphene devices under relaxed experimental conditions. *Nature Nanotechnology* 10: 965–971.

Safronova MS (2019) The search for variation of fundamental constants with clocks. *Annals of Physics (Berlin)* 531: 1800364.

Scherer H and Camarota B (2012) Quantum metrology triangle experiments: A status review. *Measurement Science and Technology* 23: 124010.

Scherer H and Schumacher HW (2019) Single-electron pumps and quantum current metrology in the revised SI. *Annals of Physics* 531: 1800371.

Schlamminger S and Haddad D (2019) The new International System of Units. The Kibble balance and the kilogram. *Comptes Rendus Physique* 20: 55–63.

Schopfer F and Poirier W (2007) Testing universality of the quantum Hall effect by means of the Wheatstonebridge. *Journal of Applied Physics* 102: 054903.

Schurr J and Lee J (2022) Realization of the farad from the AC quantum Hall resistance at PTB—14 years of experience. *IEEE Transactions on Instrumentation and Measurement* 71: 1502008.

Schurr J, Ahlers FJ, Hein G, and Pierz K (2007) The ac quantum Hall effect as a primary standard of impedance. *Metrologia* 44: 15–23.

Schurr J, Bürkel V, and Kibble BP (2009) Realizing the farad from two ac quantum Hall resistances. *Metrologia* 46: 619–628.

Shapiro B (1986) Finite-size corrections in the quantum Hall effect. *Journal of Physics C: Solid State Physics* 19: 4709.

Steiner RL, Williams ER, Newell DB, and Liu R (2005) Towards an electronic kilogram: An improved measurement of the Planck constant and electron mass. *Metrologia* 42: 431–441.

Taylor BN and Cohen ER (1991) How accurate are the Josephson and quantum Hall effects and QED? *Physics Letters A* 153: 308–312.

Taylor BN and Witt TJ (1989) New international electrical reference standards based on the Josephson and quantum Hall effects. *Metrologia* 26: 47–62.

Thompson AM and Lampard DG (1956) A new theorem in electrostatics with applications to calculable standards of capacitance. *Nature* 177: 888–890.

Tsai JS, Jain AK, and Lukens JE (1983) High-precision test of the universality of the Josephson voltage-frequency relation. *Physical Review Letters* 51: 316.

von Klitzing K, Dorda G, and Pepper M (1980) New method for high-accuracy determination of the fine-structure constant based on quantized Hall resistance. *Physical Review Letters* 45: 494–497.

Weis J (2022) *Quantum Hall Effect.* this encyclopedia.

Woszczyna M, Friedemann M, Götz M, Pesel E, Pierz K, Weimann T, and Ahlers FJ (2012) Precision quantization of Hall resistance in transferred graphene. *Applied Physics Letters* 100: 164106.

The pulse-driven AC Josephson voltage standard of Physikalisch-Technische Bundesanstalt (PTB)

O Kieler, Quantum Electronics, PTB Braunschweig, Braunschweig, Germany

© 2024 Elsevier Ltd. All rights reserved.

Disclaimer: The commercial instruments and software packages mentioned in this paper merely serve the purpose of adequately specifying the experimental procedure and do not amount to any recommendation or endorsement by PTB whatsoever.

Introduction 9
Fundamental elements of the JAWS 10
JAWS technology 13
JAWS Setup 15
Optical pulse drive and on-chip power divider 16
Applications 21
Conclusion 25
Acknowledgments 25
References 25

Abstract

We present the basic principle of the pulse-driven AC Josephson Voltage Standard, also called "Josephson arbitrary waveform synthesizer" (JAWS). The JAWS is suitable for generating quantized high-precision and arbitrary waveforms in the time and frequency domain with extremely high spectral purity. A brief overview of the fabrication technology for highly integrated JAWS circuits with more than 50,000 junctions per chip will be described. This includes the stacked junction technology with up to 5-stacked junctions. New approaches designed to further increase the output voltage and to simplify the experimental setup are the on-chip power dividers and the optical pulse drive for the JAWS. Some applications of the JAWS that have significant benefits for quantum AC voltage metrology will be presented. Within international research projects, PTB's JAWS chips have been distributed to NMIs in the Netherlands, the United Kingdom, Norway, Italy, Finland, Turkey, Russia, China and Argentina. The technology transfer from PTB to the Supracon company for commercialization purposes has also been initiated to make JAWS available to other NMIs, to calibration laboratories and to industry in the near future.

Key points

- Basic principle of the pulse-driven AC Josephson Voltage Standard (JAWS)
- Design of integrated circuits for JAWS
- Key parameter of JAWS: calculable and arbitrary waveforms, quantum precision
- Circuit fabrication: Nb based thin film and stacked junction technology, fabrication yield
- Experimental setup
- Optical pulse-drive and on-chip power divider
- Applications in Voltage Metrology
- Conclusion

Introduction

This chapter provides an overview of the fundamental principles, practical realization, features and chip design of the AC Josephson voltage standard. To define the electrical units via electrical quantum metrology; the Ohm (quantum Hall effect), the Volt (Josephson effect) and the Ampere (single-electron transport) is one of main tasks of Physikalisch-Technische Bundesanstalt (PTB). The PTB (PTB, 2022) is the national metrology institute of the Federal Republic of Germany. The first such institute in the world, PTB was founded in Berlin as the "Physikalisch-Technische Reichsanstalt "(PTR) in 1887 by Hermann von Helmholtz (its first president) and Werner von Siemens to serve as an interface between science, industry and legal metrology. After World War II, the institute was re-built in Berlin and gained a new, second site in Braunschweig, which was housed in a former research facility. In accordance with the new form of government in Germany established after World War II, the former "Reichsanstalt" was designated "Bundesanstalt" in 1950. PTB is the sole (and thus the highest) authority on the correct and reliable measurements of physical units and forms part of the Federal Ministry for Economic Affairs and Climate Action in Germany. PTB has around 1900 employees and an annual budget of some 200 million euros. Over the years, its advisory board members have included 10 Nobel Prize winners – among them Albert Einstein, Max Planck, Gustav Hertz, Max von Laue and Klaus von Klitzing.

https://doi.org/10.1016/B978-0-323-90800-9.00001-9

The so called "Weston cell," which was previously the electrical voltage standard beginning in 1911, achieved an DC output voltage of about 1 V and precision of about 10^{-6}. This standard was replaced in the 1980s with DC Josephson voltage standards of 1 V/10 V, whose precision was better than 10^{-9}. An AC quantum voltmeter (AC-QVM) based on programmable Josephson voltage standard (PJVS) chips (up to 10 V) was also developed at PTB. Via technology transfer between PTB and the Supracon company (Supracon, 2022), this voltage standard was made commercially available to national metrology institutes (NMIs) and industry worldwide. The AC-QVM only allows waveforms approximated stepwise (i.e., it is only nominally an AC voltage standard). To overcome this issue, a pulse-driven Josephson voltage standard was proposed by NIST (Benz and Hamilton, 1996) and developed at NIST and PTB. This AC Josephson voltage standard is often referred to as the Josephson arbitrary waveform synthesizer (JAWS).

In the following section, we will introduce the fabrication of JAWS circuits in PTB's Clean Room Center via a sophisticated thin-film technology based on Josephson junction properties and stacked-junction technology. The experimental setup used and the most recent developments concerning further improvements to the JAWS will also be discussed, including on-chip power dividers and optical pulse drives. Finally, examples will be given of JAWS applications in electrical quantum metrology where these applications were developed and tested at PTB in close cooperation with our research partners from several NMIs, as well as their impact within the international community.

Fundamental elements of the JAWS

The basic principle of JAWS is as follows: a current pulse with a time-dependent pulse-repetition frequency $f_p(t)$ transfers N flux quanta Φ_0 through M Josephson junctions (Benz and Hamilton, 1996). The signal voltage $V(t)$ in pulse-mode operation can be calculated via the Josephson equation, i.e.,

$$V(t) = N \cdot M \cdot \Phi_0 \cdot f_p(t) \tag{1}$$

According to this equation, a time-dependent voltage, which is quantized at all times, is generated at the junction series array output leads, because only flux quanta $\Phi_0 = h/2e$ (h is Planck's constant and e the elementary charge) are transferred and N and M are integer numbers. The frequency $f_p(t)$ is very well defined by precise knowledge of the time t. The JAWS delivers quantized arbitrary waveforms, when properly biased.

The signal output voltage (RMS) can be obtained from a slight modification of Eq. (1):

$$V_{\text{signal}}\ (\text{RMS}) = A_{\Sigma\Delta} \cdot N \cdot M \cdot \Phi_0 \cdot f_{\text{clock}}, \tag{2}$$

where $A_{\Sigma\Delta}$ is the sigma-delta ($\Sigma\Delta$) code amplitude (details on which are provided below), i.e., a pre-factor in the range $0 < A_{\Sigma\Delta} < 1$ (Schreier and Temes, 2005).

The signal frequency f_{signal} can easily be calculated from

$$f_{\text{signal}} = T_{\Sigma\Delta} \cdot f_{\text{clock}} / L_{\Sigma\Delta}, \tag{3}$$

where $T_{\Sigma\Delta}$ is the number of signal periods in the sigma-delta coded waveform, $L_{\Sigma\Delta}$ is the length of the sigma-delta code, and f_{clock} is the clock frequency of the pulse pattern generator (PPG), which delivers high-frequency pulses to the Josephson array.

For JAWS applications, SNS-type Josephson junctions are used (S = superconductor, N = normal conductor). SNS junctions provide a non-hysteric current-voltage characteristic under microwave irradiation. In pulse-mode operation, Shapiro steps are selected by adjusting the pulse amplitude (see Fig. 1). Large Shapiro steps are generated for all pulse repetition frequencies below the characteristic frequency f_c of the SNS junctions: $f_p \leq f_c$ (Benz and Hamilton, 1996). The maximum pulse-repetition frequencies most frequently used for the JAWS are the 15 GHz return-to-zero pulse, which is typically limited by the maximum clock frequency of commercially available PPGs. This corresponds to a maximum data rate of 30 Gbit/s.

Because a flux-quanta provides only a very small voltage ($\Phi_0 \approx 2\ \mu\text{V/GHz}$), many Josephson junctions must be implemented in a series array in order to achieve practicable large output voltages (e.g. 5000 junctions to achieve 100 mV RMS output voltage at

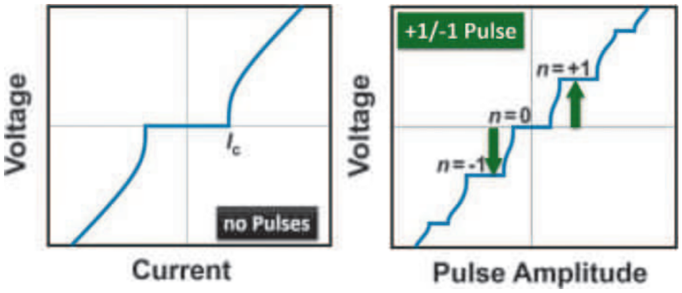

Fig. 1 Current-voltage characteristics of SNS junctions without and with pulse irradiation.

15 GHz clock frequency). Since the pulse repetition frequency is not constant in time ($f_p(t) \neq \text{const.}$), the availability of a broadband circuit design is an important precondition for operating the JAWS properly.

Fig. 2 shows a typical JAWS circuit layout. Two independent JAWS arrays are integrated on a 10 mm × 10 mm silicon chip. The enlarged picture on the right illustrates that the Josephson junctions are embedded in the center line of a coplanar waveguide (CPW). The CPW is matched to a 50 Ω impedance that corresponds to the impedance of the complete JAWS setup (details on which are provided below). A 50 Ω termination (load) is realized at the end of the array to prevent pulse reflections. A CPW taper at the HF pulse input side of the chip is implemented to enable a proper Al wire bond of the chip to a printed circuit board (PCB) carrier. At the current input and voltage output leads, LCR filters (Watanabe et al., 2006) are integrated to prevent the propagation of the input pulses along these lines, as this would lead to distortions in the frequency spectrum of the synthesized waveforms.

The practical realization of the JAWS, i.e., the way in which an arbitrary waveform is quantized with the JAWS chip, is sketched in Fig. 3. Here, we use a sine waveform for the sake of simplicity. Such a waveform is advantageous because, in an ideal case, there will only be one fundamental tone (the signal frequency) in the frequency spectrum, and no higher harmonics will appear. By means of a higher-order sigma-delta modulation (Kieler et al., 2009) ($\Sigma\Delta$ modulation), this analog waveform is digitized into a bit pattern

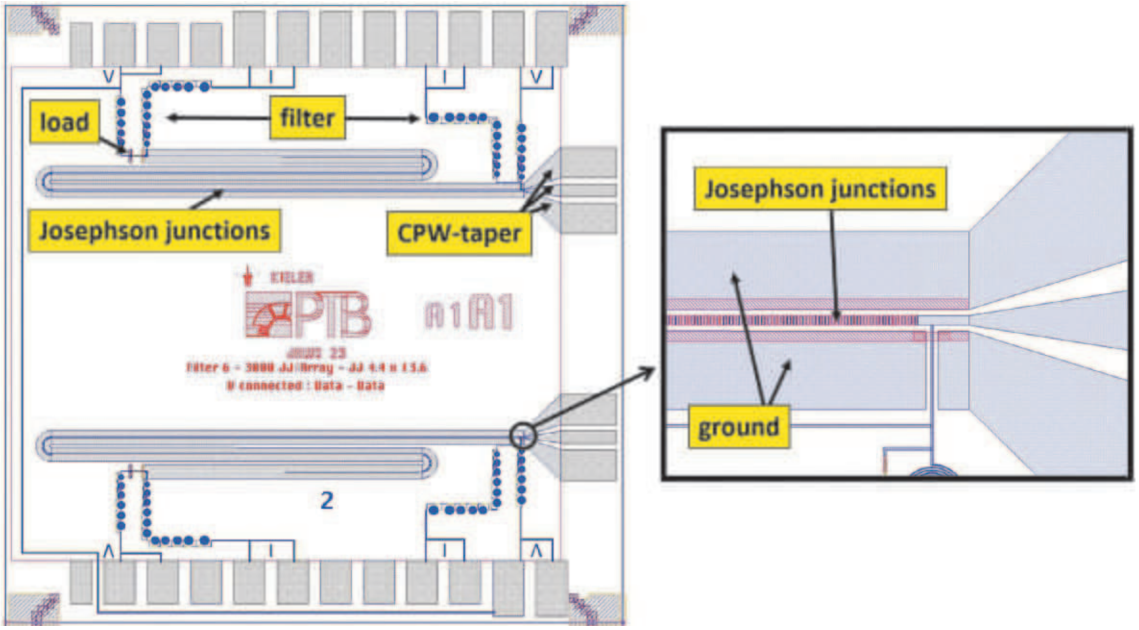
V
I
I
V
load
filter
Josephson junctions
CPW-taper
KIELER
PTB
A1 A1
2
Λ
I
I
Λ
Josephson junctions
ground

Fig. 2 Example of JAWS chip circuit layout.

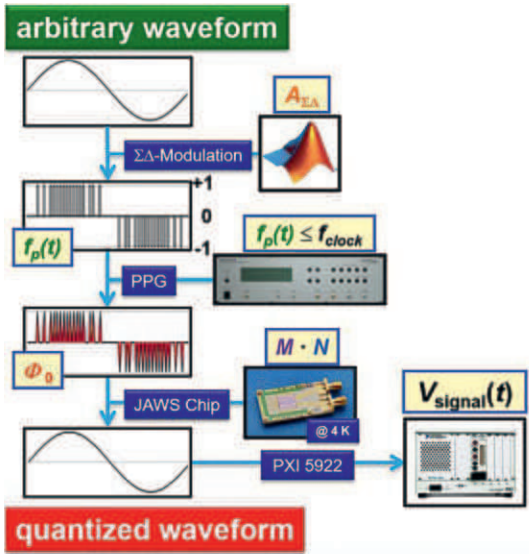
arbitrary waveform
$A_{\Sigma\Delta}$
ΣΔ-Modulation
+1
0
-1
$f_p(t)$
$f_p(t) \leq f_{clock}$
PPG
Φ_0
M · N
JAWS Chip
@4 K
$V_{signal}(t)$
PXI 5922
quantized waveform

Fig. 3 Sketch of the practical realization of quantized waveforms with JAWS.

($\Sigma\Delta$ code) which has the restricted values +1, 0 and −1. The aim of a high-quality Sigma Delta modulation is to ensure that the fast Fourier transform (FFT) of this Sigma Delta code is highly pure on the spectral side, that it has a very low noise floor and a quantization noise shifted to very high frequencies (>1 MHz) far beyond the desired signal frequency. At PTB, a second-order modulator with integrated feedback is typically used, i.e., a CIFB modulator topology (CIFB: cascade of integrators with integrated feedback) (Schreier and Temes, 2005). A stable $\Sigma\Delta$ modulation is realized if $A_{\Sigma\Delta} < 1$. This bit pattern is stored in the memory of the fast PPG. Typical $\Sigma\Delta$ code lengths range from around 2 Mbit to 512 Mbit depending on the desired signal frequency and other properties of the waveform. The ternary pulses (+1, 0, −1) of the PPG are transferred via suitable HF cables to the JAWS chip operating at 4 K. In the Josephson junction array, each input pulse generates a flux pulse. At the array output leads, the quantized waveform can be detected and fed out to a room temperature (300K) environment to be used for applications or further spectral analysis.

Ultimately, the JAWS can be considered a quantum standard characterized by these key features:

- high-precision quantized AC voltage source,
- synthesis of arbitrary waveforms (frequency or time domain),
- excellent spectral purity (signal-to-noise ratio SNR > 130 dBc),
- no drift,
- low noise,
- wide frequency bandwidth (a few Hz, including 0 Hz, up to the MHz range).

These considerable advantages over semiconductor-based waveform synthesis make the JAWS highly suitable for metrological applications. JAWS signals can be synthesized in a very wide frequency range from a few Hertz up to the Megahertz range and DC voltages are possible too. We will briefly explain the relevance of these features by presenting some waveform examples and data.

Fig. 4 shows the frequency spectra of two sine waveforms to demonstrate the concept of "calculable" waveforms. The first waveforms have a signal frequency of 1111.11 Hz and a signal voltage of 111.11 mV RMS, yielding an "11 × 1" sine. This figure also demonstrates spectral purity: no higher harmonics are above the noise floor and the signal-to-noise ratio is about 123 dBc, which corresponds to the dynamic limit of the spectrum analyzer used. The small distortion peak at about 3.3 kHz is related only to the spectrum analyzer (Benz et al., 2015), whereas the JAWS chip is well quantized, while operating in the quantum-locked state (Burroughs et al., 2005) with sufficient operation margins. The second spectrum shows a similar waveform, i.e., a "1 to 9" sine. Here, the signal frequency is 1234.5 Hz and the signal amplitude is 67.89 mV RMS.

Other frequency spectra (Fig. 5) show the wide frequency range of the JAWS. Using an array of 12,000 junctions, different signal frequencies of spectrally pure sine waveforms from 10 Hz to 1 MHz were synthesized at a signal amplitude of 100 mV RMS.

Finally, two arbitrary waveforms are presented in Fig. 6. On the left, an arbitrary signal in the frequency domain is shown: a multitone waveform (132 tones) with different signal amplitudes that resembles the word "JAWS" (Behr et al., 2012). On the right,

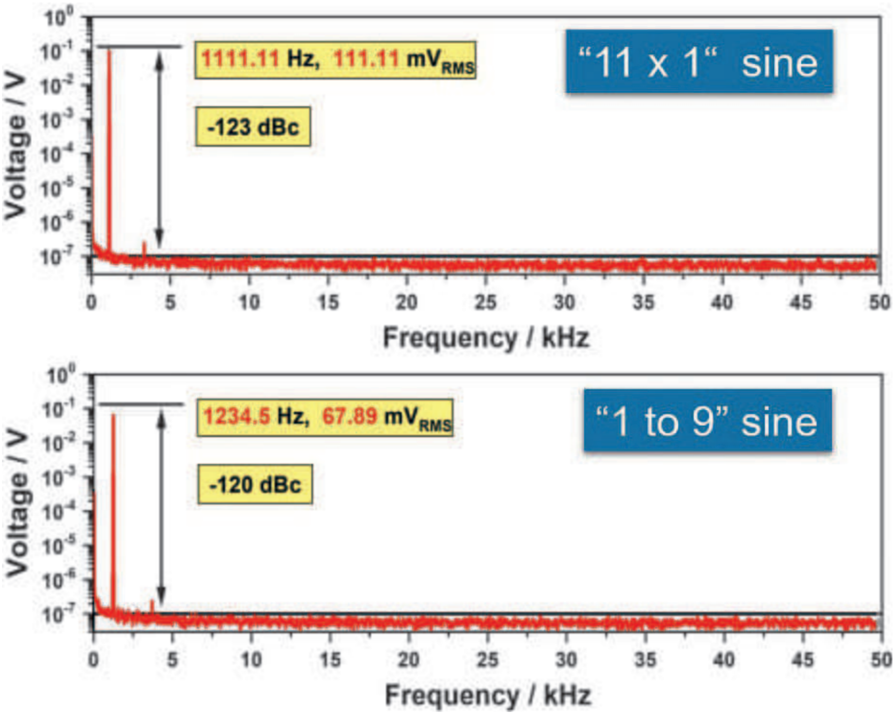

Fig. 4 Frequency spectra of two example sine waveforms.

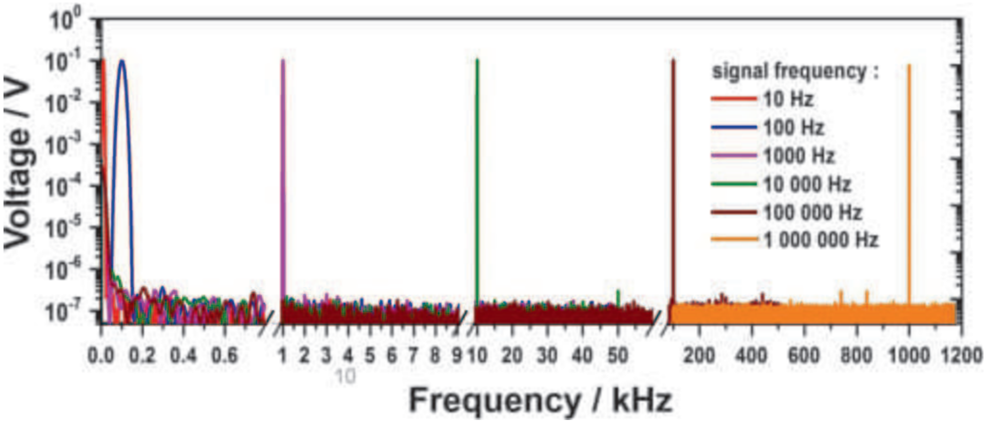

Fig. 5 Frequency spectra of different sine waveforms from 10 Hz to 1 MHz.

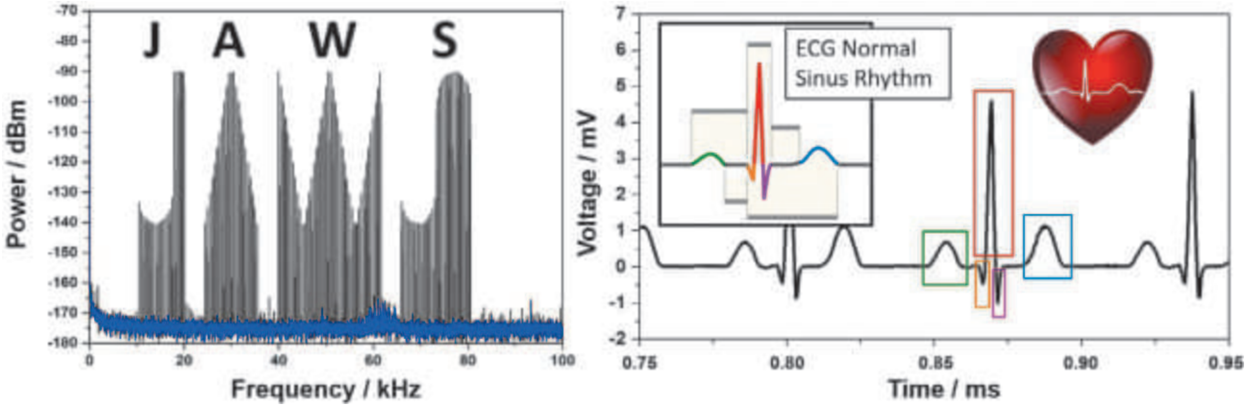

Fig. 6 Left: arbitrary frequency domain waveform, right: arbitrary time domain waveform.

an arbitrary time-domain waveform illustrates an ideal heart-beat signal. Both examples demonstrate that virtually any arbitrary waveform, and even complex waveforms, can be created.

To confirm the quantum precision of the JAWS, we performed a direct comparison between the JAWS and the PTB AC-QVM for voltages at 1 V RMS and 250 Hz. Excellent agreement was achieved: V_{JAWS} - V_{QVM} = (3.5 ± 12) nV (Behr et al., 2015). This comparison was a highlight paper of the journal "Metrologia" in 2015. This direct comparison achieved even better agreement for DC voltages at a 1 V peak: V_{JAWS} - V_{QVM} = (0.3 ± 04) nV (Behr and Kieler, 2020). This quantum precision is a precondition for any application in voltage metrology. In (Kieler et al., 2017), we were able to make 16 arrays operate in parallel with a total number of 162,000 junctions, achieving an output voltage of 2.25 V RMS. This represented an important milestone toward achieving 7 V RMS with the JAWS in order to increase the number of metrological applications possible. Other current JAWS developments include simplifying the experimental setup in order to lower the overall costs of a complete JAWS system, increasing the number of applications to provide greater benefits to NMIs and industry and initiating the technology transfer necessary to make the JAWS commercially available.

JAWS technology

JAWS circuits are fabricated at PTB's Clean Room Center (class ISO 5). This clean room is fully equipped for the high-quality fabrication of superconducting circuits based on Nb as a superconductor. The main fabrication tools used in this process are a cluster sputtering system for highly reproducible deposition conditions and an electron-beam lithography system for high alignment precision and fast prototyping (thus rendering the use of masks unnecessary, in contrast to UV lithography). Previously, SNS Josephson junctions with HfTi as a normal-metal barrier were used at PTB for JAWS applications (Kieler et al., 2007a; Kieler et al., 2007b; Kieler et al., 2009). These junctions were characterized by a high critical current density in the range of >50 kA/cm^2. Consequently, the junction size was limited to the sub-µm range. For large arrays, we observed that these junctions were not suitable because heating effects caused by the high current density degraded the properties of the junctions. This issue prompted the use of SNS Josephson junctions with Nb_xSi_{1-x} as the normal-metal barrier material (Baek et al., 2006; Kieler et al., 2013a). The SNS multilayers are deposited in the cluster sputtering system, which consists of six chambers in total and is fully automatic. The Nb_xSi_{1-x} barrier is deposited in a co-sputter process from two targets (Nb and Si) onto the rotating 3-in. Si wafer. The homogeneous and reproducible deposition conditions are very important to achieve a low parameter spread of the junction's characteristic properties. These junction properties can be adjusted nearly independently over a wide range by choosing the composition x and the thickness of the barrier d as shown in Fig. 7, where the critical current density is plotted against the characteristic voltage. The Josephson junction operation frequency can be tuned from about 1 GHz to 150 GHz (and beyond). An x of about 0.2 and a thickness d of about 30–40 nm are typical parameters in JAWS applications.

Such SNS junctions are advantageous in that they can be deposited and patterned in junction stacks, which increases the integration density of the JAWS circuits. To manufacture 5-stacked junctions, a 12-layer multilayer is first deposited *in-situ* in the cluster system, cf. Fig. 8. On top of a thermally oxidized wafer, a thin etch stop layer made of Al_2O_3 is deposited first to prevent the plasma from etching into the SiO_2. The 5-stacked junctions consist of 6 Nb and 5 Nb_xSi_{1-x} layers. The resulting total layer structure is as follows: $Si/SiO_2/Al_2O_3/Nb/Nb_xSi_{1-x}/Nb/Nb_xSi_{1-x}/Nb/\ Nb_xSi_{1-x}/Nb/\ Nb_xSi_{1-x}/Nb/Nb_xSi_{1-x}/Nb$. A modified "window" process was developed at PTB (Kieler et al., 2021) to fabricate up to 5-stacked Josephson junction series arrays with a high yield. To achieve this, the thicknesses of the Nb and SiO_2 resists were increased. Additionally, the SiO_2 was deposited not only by means of PECVD, but also in a thin ALD layer (before PECVD) to ensure perfect edge coverage for the tall junction stacks. This was necessary to avoid shorts at the uppermost junctions in the stack, which had been problematic without ALD. A soft CMP step was also introduced for the SiO_2 layer to ensure smoothness of the surface before deposition of the Nb-wiring layers. This was done to prevent this superconducting layer from having a weak current capability due to poor edge coverage.

The complete fabrication process consists of six main fabrication steps. First, the Josephson junctions are defined by high-rate RIE-ICP with SF_6 (reactive ion etching with inductive coupled plasma); here, the junction sidewall angle is nearly 90 degrees. This ensures a small parameter spread from one junction floor to the next. Second, the Nb base electrode, which is the lower wiring electrode, is patterned. Third, electrical isolation takes place via atomic layer deposition (ALD) and plasma enhanced chemical vapor deposition (PECVD) SiO_2 and the contact windows on top of each junction stack are opened by via RIE-ICP with CHF_3. Fourth, additional deposition and patterning of the Nb wiring electrode take place via RIE-ICP. Fifth, deposition takes place for AuPd on-chip resistors for impedance matching of the CPW and the on-chip filters by means of a "lift-off" process. Finally, the wire-bond pads are opened by via RIE-ICP to establish contact between the chip and an appropriate PCB carrier. The total process involves 16 layers and about 40 fabrication steps. The clean room cycle time for two wafers is about 3 weeks. More details about this process can be found in (Kieler et al., 2021) for 3-stacked junctions; this process is similar to the modified 5-stacked junction process

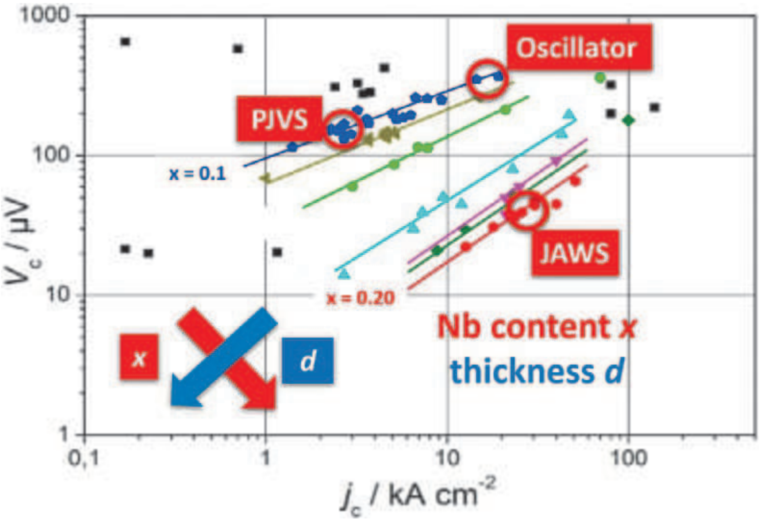

Fig. 7 Critical current density *vs.* characteristic voltage of SNS junctions with a Nb_xSi_{1-x} barrier.

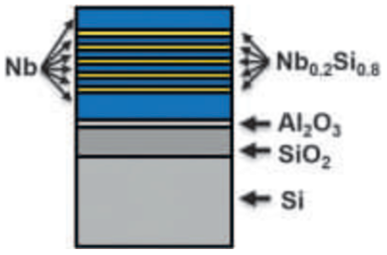

Fig. 8 Multilayer sequence of 5-stacked SNS junctions with Nb_xSi_{1-x} barriers deposited in situ.

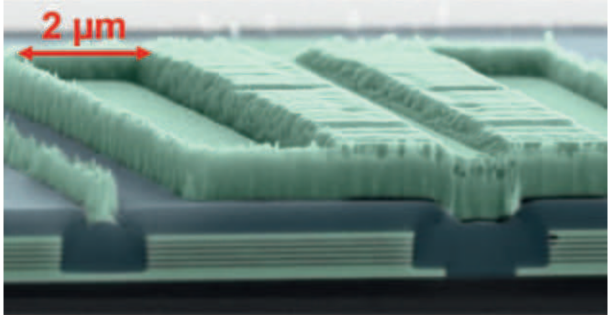

Fig. 9 Cross-section SEM image of a JAWS array with 5-stacked Josephson junctions.

presented in (Kieler et al., 2015). Fig. 9 shows a cross-section SEM image of a JAWS array with 5-stacked Josephson junctions. In this picture, we can clearly recognize the steep junction stacks as required. For the stack on the right, a small under-etch into the stack can be seen. This may be the reason for the slight increase in the parameter spread of the critical current. Compared to the total junction area of 4.4 µm × 13.6 µm, this effect is small enough to ensure a high-quality current-voltage characteristic (IVC). Due to the relatively thick layers combined with long etching times and resist problems, we observed large Nb fence structures (also visible in Fig. 9) that mainly consist of residues of the photo resist and nonvolatile etch products; however, these fence structures did not negatively impact the operation of the JAWS circuits.

Fabricating the highly integrated circuits of JAWS chips, which have many thousands of Josephson junctions, requires a high yield of the functional junctions and a low junction parameter spread. Some information on 3-stacked junctions taken from the wide range of available data will be presented below. The critical current density distribution on a 3-in. wafer shows a deviation of 4.6% from the mean value, which is acceptable for functional JAWS arrays with sufficiently wide operation margins in pulse operation mode. We analyzed the data for 200 arrays that had been fabricated on 20 wafers with a minimum junction count of $N = 5000$ in each array. This corresponded to a total junction count of $N = 1{,}600{,}000$. Only 48 junctions were defective in the sense that the junction were shorted. This is equivalent to a junction yield of 99.997%, which is more than sufficient for our needs. Clearly, the shorted junctions fail to contribute to the IVC as they are "missing" in Shapiro steps. However, the circuit itself is still functional and can be used for JAWS applications, as the signal voltage levels can be adjusted by choosing the $\Sigma\Delta$ code amplitude and the clock frequency. Because these two parameters can be selected with arbitrary precision, there are no limits to the exactness with which the desired signal amplitudes can be adjusted. In contrast to PJVS, the characteristic voltage of a junction does not restrict the voltage resolution of JAWS. Voltage values far below the characteristic voltage can be tuned (see "calibration of nanovoltmeters" in the "Applications" section).

For the 5-stacked junction arrays, the database available is smaller but allows spreads and yields to be estimated. Measuring 28 arrays from two wafers yielded the following data for the spread of the critical current:

1. intra-array: 2.4%
2. intra-wafer: 3.6%
3. inter-wafer: 6.9%

This data is acceptable for our purposes. The intra-wafer uniformity of the critical current density was determined for one of the 5-stacked junction wafers (3-in.): (6.66 ± 0.07) kA/cm^2. Before we implemented ALD into the process, this yield was very poor. By analyzing the data from 58 arrays located on eight wafers, we realized that, on seven wafers, the upper floor of the stack was systematically shorted completely. The reason for this was insufficient edge coverage of the PECVD SiO$_2$ at the top edge of the high pillar, where notches occurred. Only on one wafer were the junctions not shorted. Here, we measured a junction yield of 99.88%. Ever since the implementation of ALD, we have analyzed the data from 28 arrays on two wafers. No stacks were shorted and only 53 out of 440,000 junctions were "missing," corresponding to a junction yield of 99.99%; this result is slightly lower than that of 3-stacked junctions but still very good.

Realizing such 5-stacked junction technology entails significant benefits, as we can synthesize an output voltage of 1 V RMS (2.83 V peak-peak) with four arrays integrated on only two chips instead of eight arrays on four chips (Kieler et al., 2015). The frequency and time domain of a sine waveform generated using 60,000 junctions at 500 Hz is shown in Fig. 10.

JAWS Setup

At PTB, eight JAWS systems are used for different applications. Fig. 11 shows the eight-channel JAWS setup. Using this setup, 1.5 V RMS can be synthesized with 93,000 junctions arranged on 8 arrays (i.e., four chips). These four chips are mounted on four specially designed PCBs made of Rogers3006 (Kieler et al., 2013b). These PCBs are arranged in a cryoprobe, as shown in the upper inset, for operation in a liquid helium dewar at 4 K. An eight-channel PPG (Sympuls) that provides ternary pulses, an eight-channel bias device and a spectrum analyzer (PXI 5922, National Instruments) are the main components of the supply electronics for operation

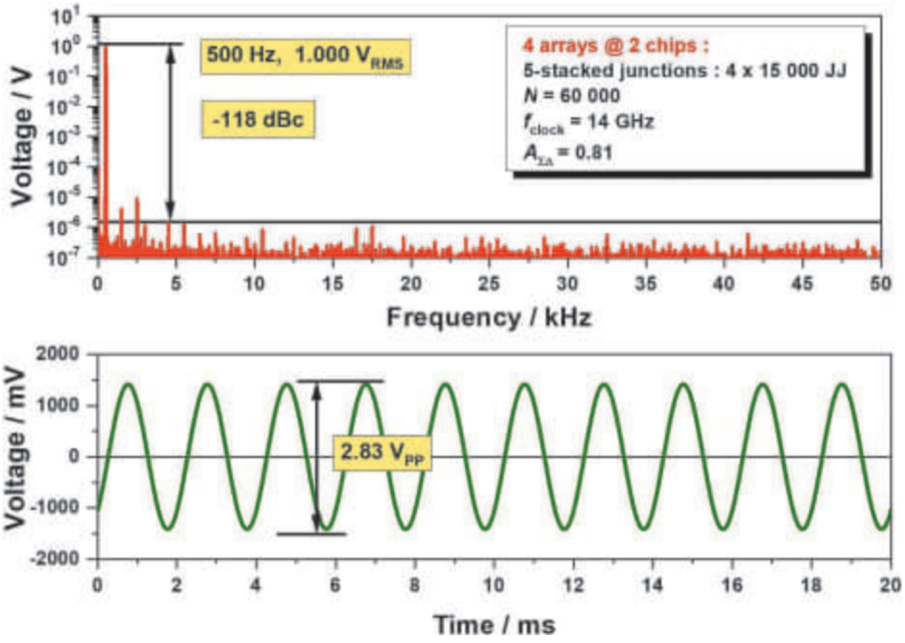

Fig. 10 Frequency and time domain of a sine waveform at 1 V RMS and 500 Hz synthesized with two chips and 60,000 junctions.

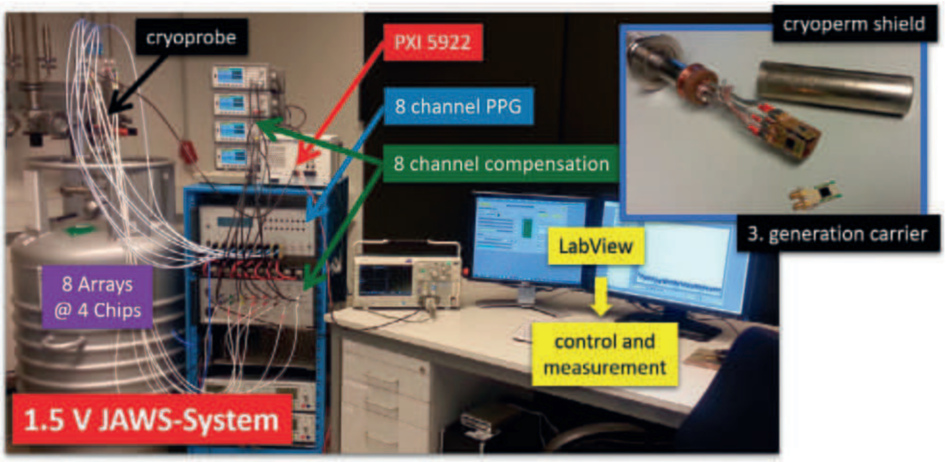

Fig. 11 Photograph of the eight-channel PTB JAWS setup. The inset shows details of the cryoprobe with mounted JAWS chips.

of JAWS circuits. To control the whole system and perform the measurements, customized software (made with Labview) was programmed.

In 2013, we also demonstrated how JAWS circuits can be operated in a pulse-tube cryocooler (Kieler et al., 2013b), cf. Fig. 12 (left). For potential users of JAWS, this is a significant advantage, as it allows the liquid helium infrastructure to be circumvented completely. Modern cryocoolers require only a few hours to cool down, are easy to use and require no or only minimal maintenance work. A second cryocooler is designed for daily use for JAWS applications in the impedance bridge (see Section “Applications”), cf. Fig. 12 (right) (Bauer et al., 2017). A third cryocooler will be installed in the near future to shorten the distance between the JAWS chip at 4 K and 300 K from about 1.2 m to about 0.3 m. This will reduce the uncertainty at high signal frequencies in the range of 100 kHz up to 1 MHz (Brom et al., 2016).

Optical pulse drive and on-chip power divider

Very recently, an optical pulse drive for the JAWS was developed in a collaborative effort between PTB and NPL, JV and the University of South-Eastern Norway (USN) (Kieler et al., 2019; Ireland et al., 2017; Bardalen et al., 2017; Bardalen et al., 2018; Ireland et al., 2019; Karlsen et al., 2019; Bardalen et al., 2020; Karlsen et al., 2020; Herick et al., 2020). Considerable effort was

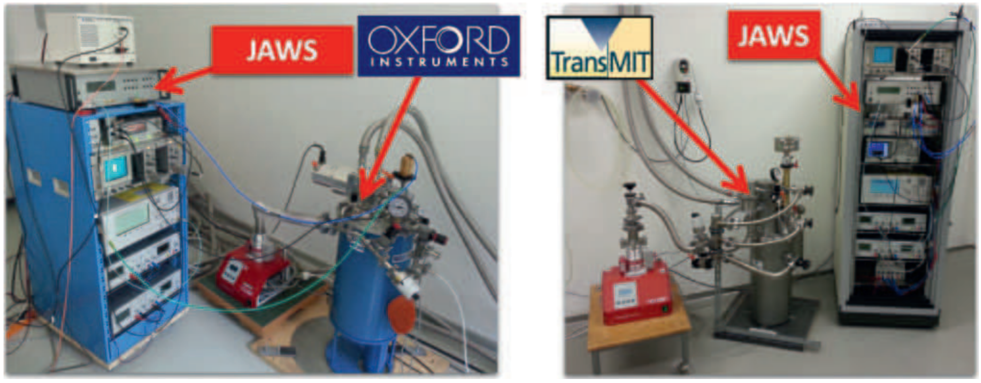
JAWS
OXFORD INSTRUMENTS
TransMIT
JAWS

Fig. 12 Photographs of two JAWS setups operated with pulse-tube cryocoolers from Oxford Instruments (left) and TransMIT (right).

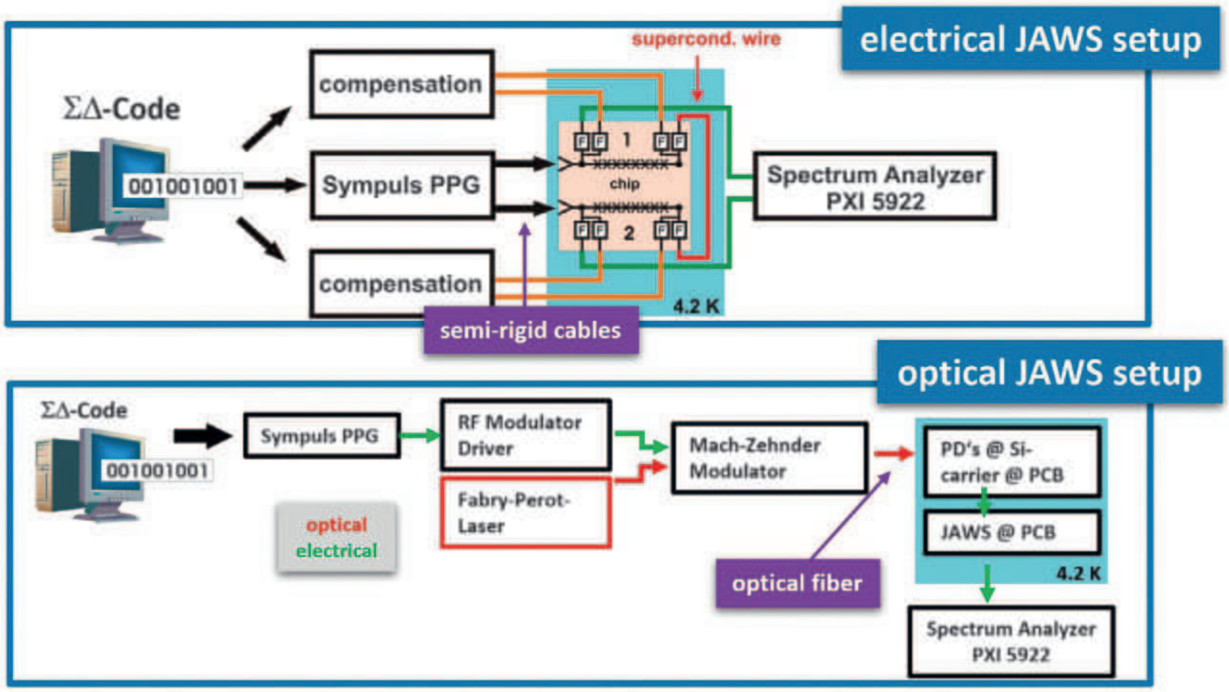
electrical JAWS setup
ΣΔ-Code
001001001
compensation
Sympuls PPG
compensation
supercond. wire
1
chip
2
4.2 K
Spectrum Analyzer PXI 5922
semi-rigid cables
optical JAWS setup
ΣΔ-Code
001001001
Sympuls PPG
RF Modulator Driver
Fabry-Perot-Laser
Mach-Zehnder Modulator
PD's @ Si-carrier @ PCB
JAWS @ PCB
4.2 K
optical
electrical
optical fiber
Spectrum Analyzer PXI 5922

Fig. 13 Schematics of "electrical" *vs.* "optical" JAWS setup.

undertaken by our partner institutions to establish a reliable and robust PD packaging technology with a high yield. The aim of these developments was to create a low-cost solution for the parallel operation of many JAWS arrays by operating fast photodiodes (PD) at 4 K close to the JAWS arrays. Another advantage is that, by using optical fibers (instead of semi-rigid cables), less noise will be introduced – specifically, noise at high signal frequencies in the MHz range. Fig. 13 shows a simplified scheme of the "electrical" JAWS setup *vs.* the "optical" JAWS setup (Kieler et al., 2019). For this application, we used high-performance InGaAs PD from Albis:

- dimensions: 350 μm × 350 μm
- integrated backside lens ➔ suitable for flip-chip bonding
- speed 28 Gbit/s
- wavelength 1310 nm

In a typical JAWS setup at PTB, the electrical pulses are delivered by a PPG and transmitted by an HF coaxial cable about 1.5 m long from the PPG output to the cryoprobe head. The cryoprobe contains a 1.2 m semi-rigid HF coaxial cable to further transfer the pulses to the K-type connectors at the PCB carrier, where the JAWS chip is mounted at 4 K. This electrical pulse transmission is replaced by an optical pulse drive. The pulse pattern is again provided by the PPG and electrically transferred to the RF modulator driver (RF-MD), which serves as an amplifier for the electrical pulses. The amplified pulses are transferred electrically to the Mach-Zehnder Modulator (MZM). The MZM is a LiNbO3-based intensity modulator designed for 1310 nm lasers. We use an

Fabry-Perot steady laser. The optical fiber transfers the pulses to the PD at 4 K. The fiber is attached via a glass tube guide to the PD mounted by a flip-chip process to a customized Si-carrier chip. This carrier chip was designed to provide bias lines and CPW for transfer of the electrical pulses. Those carrier chips were fabricated at PTB using Nb for the DC/HF lines and AuPd for the alignment markers and contact pads (PD and wire bond pads). An additional SiO_2 layer is deposited by PECVD to effectively protect the sensitive on-chip DC block capacitors against electrical damage during handling and operation. A significant advantage for practical use is that the optical fiber, which is connected via the glass tube, is removable. This tube is precisely aligned on-chip to the PD to ensure high efficiency of the illumination. Because the PD has a relatively large lens diameter of 100 μm, it is easy to implement it in the setup to achieve robust and reliable operation. The flip-chip process of the PD is carried out at USN/JV in cooperation with NPL and PTB by using Au stud bumps and thermo-compression. The Si-carrier chip is glued and Al wire-bonded to a PCB. The JAWS-chip PCB and PD-chip PCB are arranged close together (4 cm) and are connected via a K-type edge launcher. Detailed optimizations and investigations of high-speed performance at room temperature and at 4 K were performed (Bardalen et al., 2017; Bardalen et al., 2018); the optical pulse setup is described in (Karlsen et al., 2019). Fig. 14 shows two PDs mounted on a Si-carrier chip made for the unipolar pulse drive of two JAWS arrays (left), a next-generation Si-carrier chip made for a bipolar pulse-drive of one JAWS array, with two PDs and two glass tubes mounted (center), and a glass tube with the removable optical fiber attached (right).

Using a one-channel optical pulse drive, unipolar sine waveforms were synthesized with stable operation margins using a JAWS array of 3000 junctions in a signal frequency range from 60 Hz up to 10 kHz. Clock frequencies up to 15 GHz, which corresponded to the maximum speed of the PPG and the PD, were used to generate output voltages of 6.6 mV RMS resp. 18.6 mV PP with a ΣΔ code amplitude of 0.2 (Kieler et al., 2019). Fig. 15 shows the frequency spectrum and time domain of a sine waveform synthesized at 12 GHz with a ΣΔ code amplitude of 0.2 and a ΣΔ code length of 8 Mbit. This waveform has a signal frequency of 1500 Hz and signal amplitude of 5.26 mV RMS resp. 14.9 mV PP. The signal-to-noise ratio is 90 dBc and the laser-bias operation margins are 1 mA. The time domain clearly shows the DC shift of the waveform generated due to the unipolar pulse-drive with only one PD.

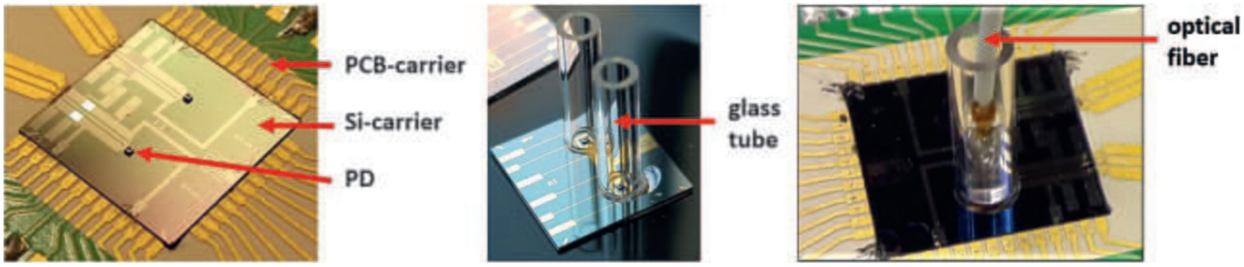

Fig. 14 Photographs of two PDs mounted on a Si-carrier chip (left), a different Si-carrier chip with two PDs and two glass tubes mounted (center), and a glass tube with a removable optical fiber attached (right).

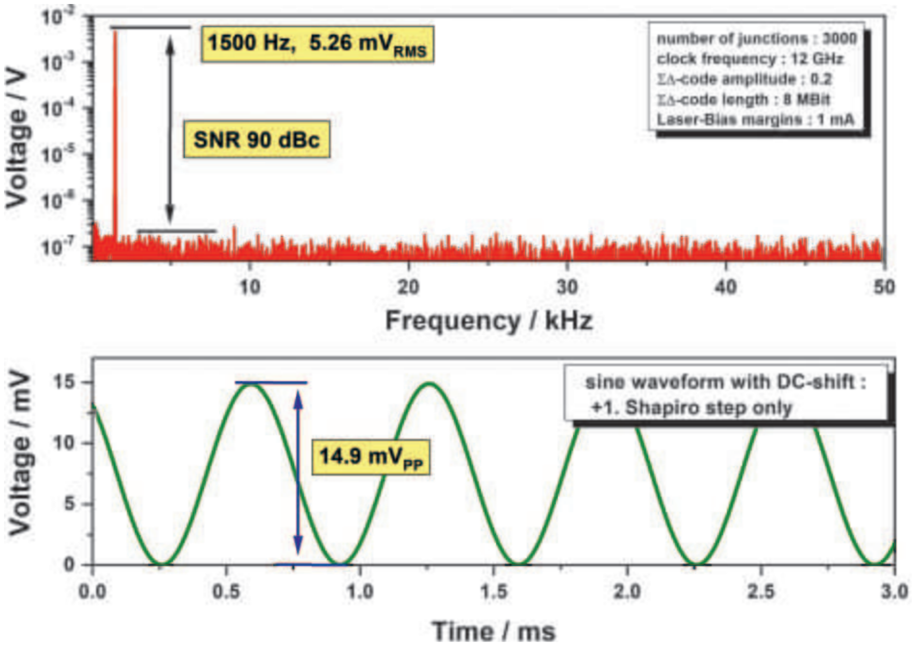

Fig. 15 Frequency spectrum and time domain of a unipolar sine waveform generated with the one-channel optical pulse drive.

Therefore, only one Shapiro step is used, and the output voltage is reduced by 50%. A two-channel optical pulse-drive setup for generating bipolar waveforms is under development at PTB. The first spectrally pure bipolar waveforms were synthesized with a signal amplitude of 12.5 mV RMS resp. 35.4 mV PP at a signal frequency of 10 kHz (Herick et al., 2020).

Another approach to increasing the output voltage of JAWS by parallel operation of several JAWS arrays is to use an on-chip power divider. This approach was successfully implemented by using Wilkinson power dividers for JAWS at NIST (USA) (Flower-Jacobs et al., 2016) and by using CPW-CPS dividers for the programmable voltage standard of AIST (Japan) (Yamamori and Kohjiro, 2016). At PTB, modified versions of both types of dividers were integrated into our JAWS circuits (Tian et al., 2020; Tian et al., 2021; Tian, 2022). Different versions of these dividers were developed to optimize the insertion and return loss and achieve an optimal amplitude balance. Fig. 16 shows an example of the layout (left) and the realized chip (right) of a one-stage three-section Wilkinson divider, wherein two dividers were integrated onto a 10 mm × 15 mm chip. The one-stage divider splits the HF chain into two chains to supply two independent JAWS arrays. Because Wilkinson dividers are known to have a small bandwidth, a three-section divider was integrated. Each section had a different center frequency. Here, the intention was to enlarge the overall bandwidth of this divider and consequently improve the performance of the pulse-mode operation.

The IVC of both arrays of a one-stage Wilkinson divider is shown in Fig. 17. The circuit contains $N = 9000$ per array with 3-stacked junctions, i.e., 18,000 junctions in total. Basic Josephson junction parameters can be derived from this: critical current $I_c = 3.3$ mA, normal resistance $R_n = 3$ mΩ. Thus, the following parameters can be calculated: the critical current density $j_c = 5.5$ kA/cm^2 (junction area $A = 59.84$ μm^2), the characteristic voltage $V_c = 10.3$ μV and the characteristic frequency $f_c = 5.0$ GHz. Both IVCs agree very well and an I_c-spread of about 5% was estimated from these IVCs.

To evaluate the large bandwidth of these dividers, the IVC was measured for different pulse repetition frequencies in the range from 3 GHz to 15 GHz for one array (Fig. 18). For each IVC, the pulse amplitude was adjusted to 0.7 x I_c. For the sake of clarity, the IVCs were derived and plotted using a color-coding scheme: the white area shows the Shapiro steps, while the multicolored areas are the non-quantized parts of the IVC between those steps. First, the +/− first Shapiro steps (SS) are created over the whole frequency

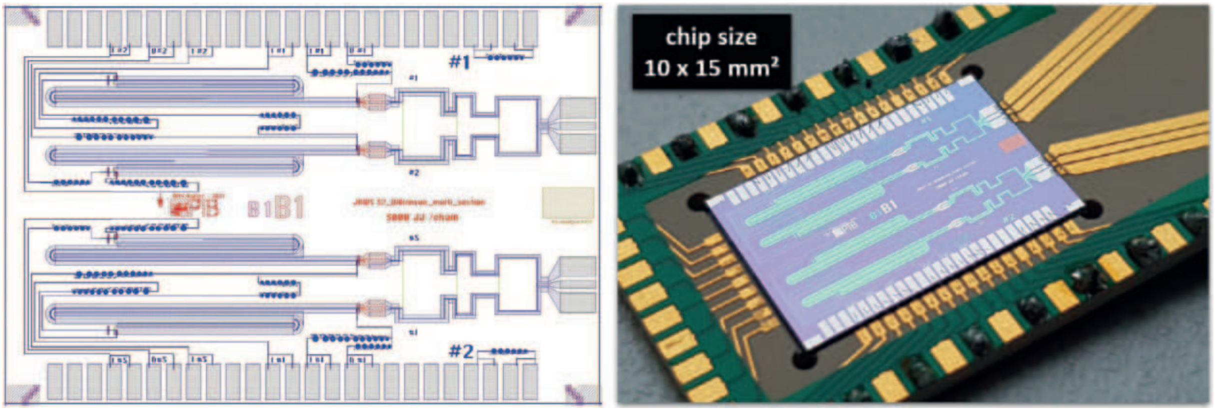

Fig. 16 Layout (left) and photograph (right) of a JAWS chip with two arrays with a one-stage three-section Wilkinson divider.

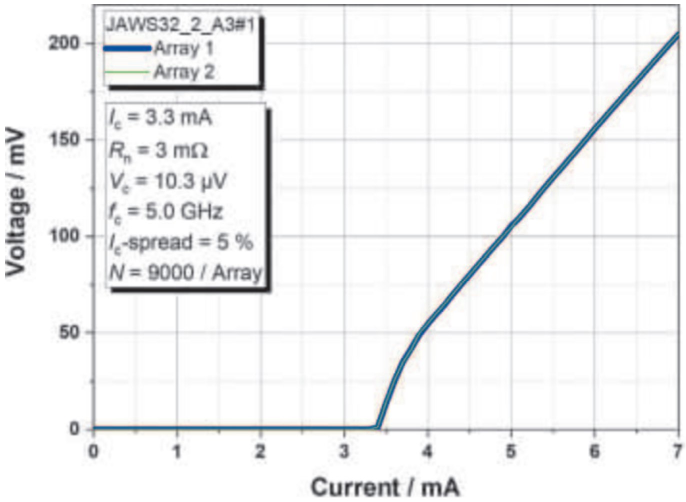

Fig. 17 Current-voltage characteristic of both arrays of a one-stage Wilkinson divider containing 9000 junctions per array.

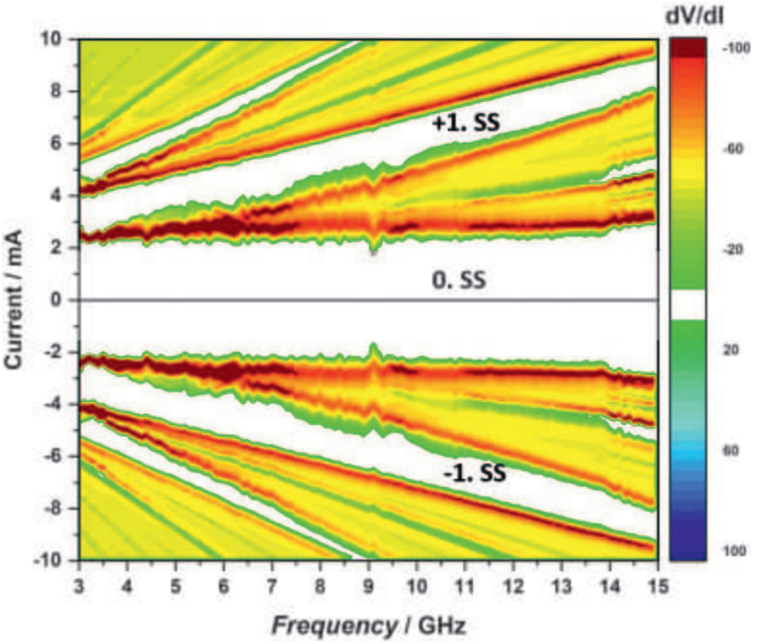

Fig. 18 Derivation of current-voltage characteristic *vs.* pulse repetition frequency for one array of a one-stage Wilkinson divider (9000 junctions).

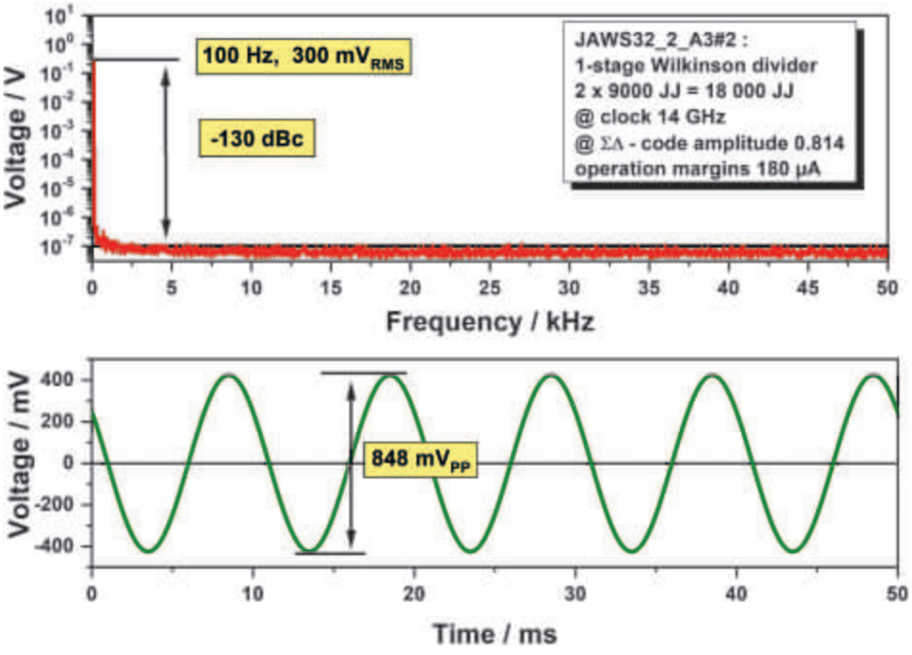

Fig. 19 Frequency spectrum and time domain of a sine waveform generated with the one-section Wilkinson divider.

range with a minimum step width of about 0.8 mA. Second, the Shapiro step generation is (as expected) fairly symmetrical for positive and negative pulses. Both features are the precondition of the synthesis of spectrally pure waveforms in pulse-mode operation.

Below, Fig. 19 illustrates the time and frequency domain of a sine waveform synthesized with both arrays of this Wilkinson divider, which has 18,000 junctions in total. At a clock frequency of $f_{\mathrm{clock}} = 14$ GHz and a ΣΔ code amplitude of $A_{\Sigma\Delta} = 0.814$, it was possible to synthesize a waveform at $f_{\mathrm{signal}} = 100$ Hz and $V_{\mathrm{signal}} = 300$ mV RMS (848 mV PP), providing small but stable operation margins of 180 μA. An excellent signal-to-noise ratio of 130 dBc was achieved.

Applications

The outstanding features of JAWS have already allowed several applications in AC voltage metrology to be demonstrated at PTB. Several international research projects funded in large part by the European Union have helped establish a strong and fruitful collaboration between several national metrology institutes. The following projects were funded from 2001 until 2019: "JAWS" (EU project, 2001), "JoSy" (EU project, 2007), "Q-Wave" (EU project, 2013), "ACQ-Pro" (EU project, 2015), "Dig-AC" (EU project, 2018) and "QuADC" (EU project, 2016). In this way, we were able to extensively explore the limitations of JAWS in the field of voltage metrology, and to set new milestones in the quality of high-precision measurements. The features of the JAWS investigated included the following (the NMI partners of PTB are denoted in parentheses):

1. AC-DC transfer measurements with a trans-conductance amplifier (NMIA [Australia])
2. Characterization of Keysight 3458A (SIQ [Slovenia], CEM [Spain])
3. AC-DC transfer (up to 1 MHz) with Fluke792A in a mini-cryostat (VSL [Netherlands])
4. Characterization of analog-to-digital converters (ADCs) (CMI [Czech Republic)
5. Systematic error analysis (Tübitak [Turkey])
6. Characterization of voltage dividers (SP [Sweden])
7. JAWS based μV-synthesizer
8. JAWS in a cryocooler (INRIM [Italy])
9. Impedance/quadrature bridge (METAS [Switzerland])
10. JAWS Johnson-noise thermometry (JNT) (PTB Berlin)

Some of these activities will be described in the following section.

A novel method for the calibration of fast ADCs using JAWS with a sophisticated constructed waveform was suggested in (Sira et al., 2019). Here, the aim was to determine the gain and time stability of an ADC for different frequencies and amplitudes almost simultaneously, or even in a single measurement if possible. By reordering the sampled data and the numerous steps involved in the data processing, other basic properties of an ADC can also be estimated such as phase, integral nonlinearity (INL), differential nonlinearity (DNL), effective number of bits (ENOB), and signal-to-noise and distortion ratio (SINAD).

The waveform selected is shown in Fig. 20. It consists of 4 sections and 16 subsections, as clearly indicated in the time domain of the signal. The frequency of the sine wave is different for each of the four sections. Each subsection contains four different signal amplitudes, and each amplitude repeats 10 periods of this single-tone sine wave to evaluate the time stability. Frequencies, amplitudes, and periods define the total number of 160 calibration points of this signal. By continuously repeating this waveform, more statistical data can be derived.

We selected a National Instruments PXI 5922 as the device under test (DUT). The PXI 5922 is used in many calibration laboratories because of its flexibility. Its maximum sampling frequency is 15 MSa/s. Because the device has internal ΣΔ modulation

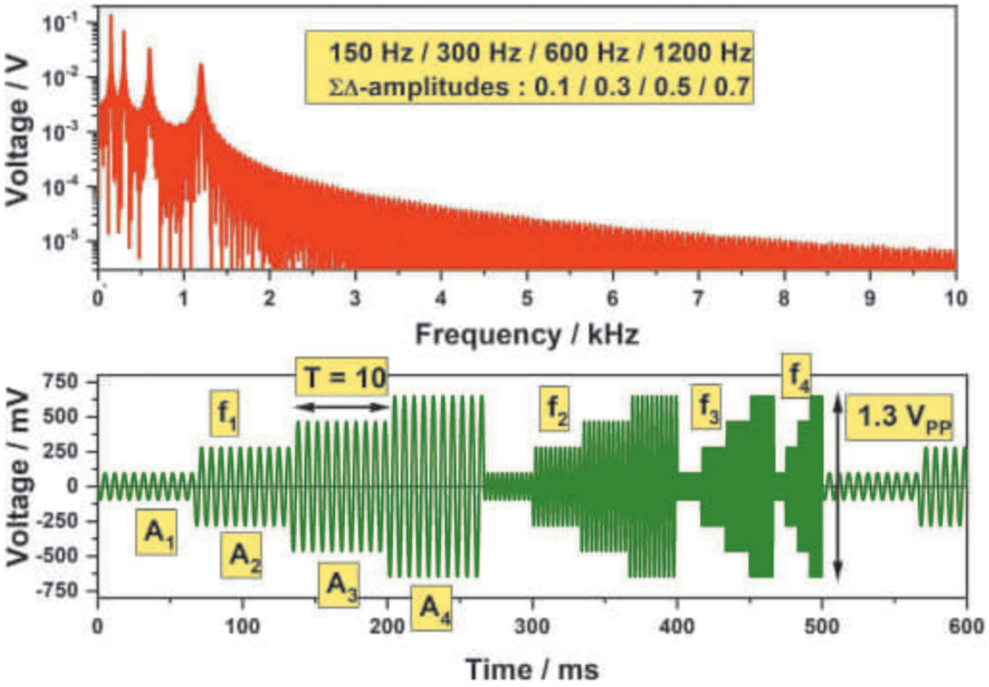

Fig. 20 Frequency spectrum and time domain of a complex multitone sine waveform for calibration of an ADC.

electronics, the resolution increases with decreasing sampling frequency. For sampling frequencies below 500 kSa/s, the resolution is nominally 24 bit. Two full-scale ranges, 2 and 10 V, are available. Because of the small maximum output voltage of the JAWS, only the lower range of the digitizer was used. The waveform was constructed to accommodate some restrictions of the devices used – for example, limited values for the sampling rate of the PXI or the minimum bit resolution of 128 bit for the PPG. These restrictions explain the special values of the PPG clock frequency and code length.

The main waveform properties and settings of the PPG and PXI5922 were the following:

1. Number of junctions $N = 54{,}000$ (six arrays in series)
2. PPG clock frequency $f_{\text{clock}} = 13.762\ 56$ GHz
3. PPG code length $L_{\Sigma\Delta} = 215{,}040{,}000$
4. PPG code amplitude $A_{\Sigma\Delta} = 0.06/\ 0.18/\ 0.30/\ 0.42$
   ($A_{\text{main-}\Sigma\Delta} = 0.6$ x pre-factors $A_{\text{F}} = 0.1/\ 0.3/\ 0.5/0.7$)
5. PPG code repetition rate: 32
6. PXI sampling rate: 480 kSa/s
7. Signal frequencies $f_{\text{signal}} = 150$ /300/600 Hz/1200 Hz
8. Signal amplitudes $V_{\text{signal}} \approx 0.18/\ 0.55/0.92/1.3$ V PP

The main output of the calibration (gain errors) can be obtained at different amplitudes and frequencies. By repeating the waveform, the gain stability can also be measured. The advantage of this method is that all gains are measured in a very short period of time. Thus, the stability is measured at multiple calibration points simultaneously.

Another application is the characterization of a sampling AC voltmeter. The aim of this approach was to evaluate the noise performance of such a device in sampling mode as a function of different device settings, e.g., aperture time.

For this application, a special waveform was again synthesized using the JAWS: a band-limited square waveform (BLSW), which was suggested in (Lapuh et al., 2017) (Fig. 21). This waveform corresponds to a square wave at 52 Hz, where only a certain number of higher harmonics of the frequency spectrum are generated and all other higher harmonics above 20 kHz are cancelled by the signal.

As the DUT, we selected an Keysight 3458A digital multimeter, as it provided high accuracy for sampling low-frequency signals and it is widely used in NMIs and calibration laboratories. Detailed knowledge of the noise performance (among other things) is a precondition for high-accuracy measurements with low uncertainties.

The main waveform properties and settings of the PPG and PXI5922 were the following:

1. Number of junctions $N = 24{,}000$ (two arrays in series)
2. PPG clock frequency $f_{\text{clock}} = 13$ GHz
3. PPG code length $L_{\Sigma\Delta} = 250{,}000{,}000$

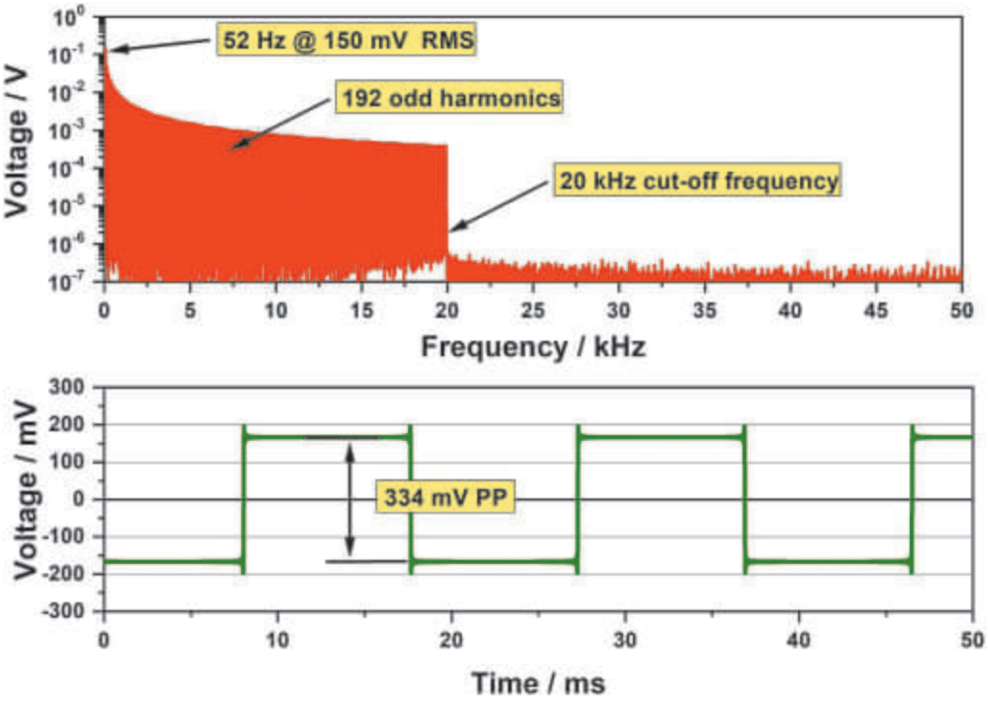

Fig. 21 Frequency spectrum and time domain of a band-limited square waveform for calibration of an AC voltmeter.

4. PPG code amplitude $A_{\Sigma\Delta} = 0.32$
5. PPG code repetition rate: 1
6. JAWS bias current operation margins: 0.5 mA
7. Signal frequencies $f_{\text{signal}} = 52$ Hz
8. Signal amplitude $V_{\text{signal}} = 150$ mV RMS
9. Number of higher harmonics: 192
10. Only odd harmonics are synthesized: 1, 3, 5, . . ., 383

"Simple" sine waveforms at different frequencies and amplitudes are also suitable for this application, as demonstrated in (de Aguilar et al., 2019).

Another application of JAWS is to use it as a precision microvolt synthesizer for the generation of small DC or AC signals (Behr et al., 2017). These signals can be used, for instance, to calibrate nanovoltmeters (DC) or lock-in amplifiers (AC). The JAWS is capable of generating DC/AC signals in the nanovolt range easily if the pulse repetition frequency chosen for the operation of the chip is far below the characteristic voltage of the Josephson junction. In contrast to continuous wave operation, broad Shapiro steps will be generated in this pulse-mode operation regime too (Benz and Hamilton, 1996). We demonstrated this for the first time experimentally for this application.

In order to generate DC voltages by means of the JAWS, two methods can be applied. In the first, more obvious method, simple pulse codes with a constant pulse repetition frequency will be generated. By choosing the pulse code length and the clock frequency, the desired signal voltage can be tuned. The more advanced method invokes higher-order ΣΔ modulation. Here, the pulse repetition frequency in the pulse code is not constant. The advantage of this method is that any desired output voltage can be adjusted easily and precisely by selecting the corresponding ΣΔ code amplitude and (if necessary) the clock frequency.

The typical signal voltage range for the calibration of a nanovoltmeter is about $V = 10$ nV to $V = 100$ μV. For this calibration, we used a JAWS array with $N = 9000$ junctions. For each DC signal voltage, a different ΣΔ code (−1/0/+1) with a constant length of $L_{\Sigma\Delta} = 128$ Mbit was calculated in advance. The clock frequency was also kept constant: $f_{\text{clock}} = 5$ GHz. To synthesize, for example, a DC voltage of 10 nV with these parameters, the resulting ΣΔ code amplitude is very small ($A_{\Sigma\Delta} \approx 1.5 \times 10^{-7}$) and only 1.1×10^{-5}% of the code contains "1"s. To synthesize a "zero" voltage, on the other hand, the ΣΔ code contains only "0"s. When this "zero" code is applied to the JAWS array, no flux quanta are transferred, and the Josephson junctions are kept in the superconducting state below the critical current, giving a "perfect" zero signal output as required for the calibration. The significant advantage of a perfect "zero" voltage being set by choosing the "zero" code automatically by means of a program is that no switches are needed (including those inside an instrument) to set the voltage to zero or to reverse its polarity.

Due to the small voltages, it was not necessary to apply a compensation signal (Benz et al., 2001), i.e., no additional DC bias currents were needed. The Shapiro steps can be centered around the zero bias current simply by tuning the positive or negative pulse amplitude adjusted at the PPG. A positive pulse amplitude is used to select the first positive Shapiro step and the negative pulse amplitude is adjusted for the first negative Shapiro step. Both pulse amplitudes of the PPG were constant for all pulse repetition frequencies in the ΣΔ code (and consequently for all DC voltages) to be generated. Therefore, the entire JAWS setup is comparatively simple. Additionally, this demonstrates that the Shapiro step width is fully independent of the pulse repetition frequency.

To avoid high thermal voltages in the setup, twisted-pair copper wires (in contrast to coaxial wires) were used to connect the array to the DUT (Magnicon NVM1, 10 mV-range), keeping the thermal voltages stable and below 500 nV. Stable and low thermal voltages are important for precise DC voltage measurements.

The minimum pulse repetition frequency applied was only 540 Hz, which is far below the characteristic frequency of $f_c = 7.6$ GHz, which produces a minimum synthesized voltage of only $V_{JJ} = 1.1$ pV per Josephson junction:

1. Minimum pulse repetition frequency: $f_p = 540\ \text{Hz} \approx 0.00000007 \cdot f_c$
2. Minimum voltage per single junction: $V = 1.1\ \text{pV} \approx 0.00000007 \cdot V_c$

The minimum possible voltage has not yet been explored, as it was possible to use the full available PPG memory of 512 MByte, tune down the clock frequency of the PPG, and also reduce the ΣΔ code amplitude. However, from a practical point of view, a minimum voltage of 10 nV is sufficiently small for a typical nanovoltmeter calibration.

The complete measurements were taken fully automatically, and we determined 24 voltage calibration points in 60 min, thus providing a low uncertainty. The results are shown in Fig. 22. The deviation from the linearity is plotted in a measurement range from −4 μV to +4 μV. The error bars indicate Type A uncertainties (k = 1). The measurements agree well with the conventional data achieved by means of a potentiometer method, which shows noticeably higher uncertainties.

By using a similar procedure, the generation of AC voltages is also possible for the calibration of AC devices that are sensitive to small input signals. In (Behr et al., 2017), a lock-in amplifier in the range from 80 Hz to 100 kHz in a signal voltage range from 1 μV to 50 mV was also calibrated. The following features of this device were characterized:

1. Linearity
2. Gain *vs.* frequency
3. Gain *vs.* voltage range
4. AC gain selection
5. Harmonic content influence

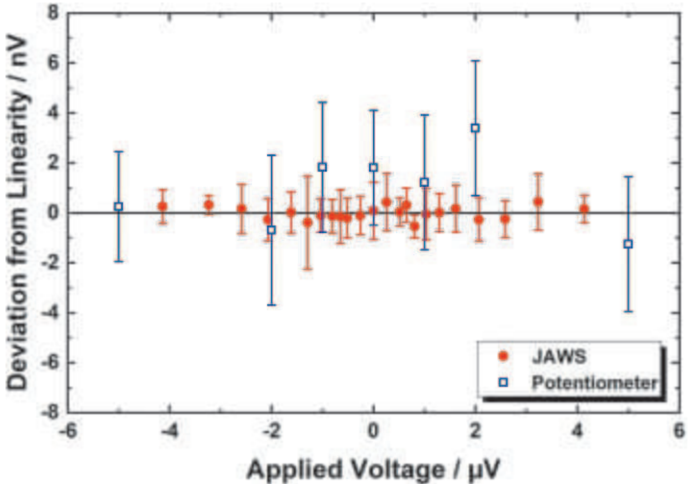

Fig. 22 Deviation from linearity for DC voltages in the µV-range measured for a digital nanovoltmeter with the JAWS and the conventional potentiometer method.

This shows the excellent suitability of the JAWS for this purpose: uncertainties on the nanovolt level can be achieved within short measurement times and the fully automated calibration procedure makes it a useful tool for metrological applications.

Another important application is to integrate two JAWS systems into a quantum-based impedance bridge system for the precise determination of resistor and/or capacitor ratios (Bauer et al., 2017; Bauer et al., 2018; Pimsut et al., 2020; Bauer et al., 2020). In contrast to conventional transformer-based impedance bridges, the JAWS-based setup is very flexible concerning the voltage ratios and phase angles between both voltages. At PTB, a four-terminal-pair impedance bridge was established that can also be directly connected to a graphene quantum Hall resistance (QHR) setup (see schematics in Fig. 23).

The noise level of such a combined setup is extremely low. The QHR device showed a deviation from the quantized value of $\pm 5 \times 10^{-8}$ in a comparison with calibrated 10 nF capacitance standards at 1233.15 Hz. Initial AC measurements with graphene-based quantum Hall resistances show very promising results for measurements with capacitance and resistance standards. Performing a quadrature measurement of the QHR against a capacitance standard allows magnetic field sweeps with lower noise

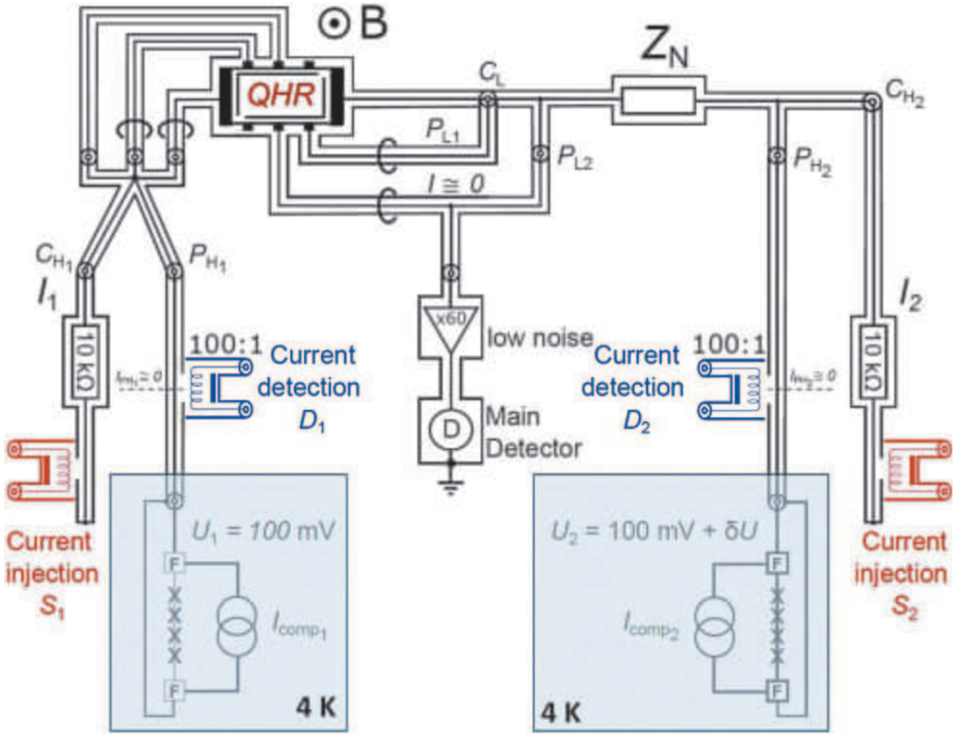
⊙B
QHR
Z_N
C_L
C_{H_2}
P_{L1}
P_{L2}
P_{H_2}
$I \cong 0$
C_{H_1}
P_{H_1}
I_1
I_2
10 kΩ
10 kΩ
$I_{H_1} \cong 0$
$I_{H_2} \cong 0$
100:1
100:1
Current detection D_1
Current detection D_2
x60
low noise
D
Main Detector
Current injection S_1
Current injection S_2
U_1 = 100 mV
U_2 = 100 mV + δU
F
F
F
F
I_{comp_1}
I_{comp_2}
4 K
4 K

Fig. 23 Schematics of the four-terminal-pair impedance bridge of PTB combining two JAWS setups and one QHR setup. Courtesy of Stephan Bauer (PTB).

and therefore reduces the measurement time compared to conventional ratio bridges using room-temperature resistance standards. This can be used to investigate graphene QHR samples and give important feedback on the manufacturing process. Within ratio measurements, the time-dependent drift of a 12.9 k resistance standard was determined in a substitutional measurement and agreed within the fit uncertainty of 0.23 nΩ/Ω with the measurements of a 14-bit cryogenic current comparator. This gives an initial impression of the high reproducibility and flexibility of the whole setup. The excellent features of the four-terminal-pair JAWS-based impedance bridge makes it an ideal tool for future metrological applications.

The PTB JAWS was recently used for the realization of the quantum-based electronic Kelvin. Johnson-noise thermometry (JNT) will enable the development of a primary thermometer up to 1000 K in the future (Kraus et al., 2018; Drung and Krause, 2021; Drung et al., 2022). The JAWS will be implemented in such a system to provide a pseudo-random quantum noise source such as the one suggested by NIST. These activities were prompted by the 2020 re-definition of the basis unit of the Kelvin by setting a fixed value for the Boltzmann constant; this re-definition has enabled the direct definition of the Kelvin in the whole temperature range via primary thermometry. This is important for future objectives in thermodynamical temperature measurements and future development of the international temperature scale. The work on the JAWS-based JNT is still in progress in a collaborative effort between different departments of PTB.

Conclusion

We have presented the basic principle of JAWS and demonstrated the capability of generating quantized high-precision and arbitrary waveforms in the time and frequency domain with extremely high spectral purity. A brief overview of the fabrication technology for highly integrated JAWS circuits with more than 50,000 junctions per chip has been given. We have also introduced stacked junction technology with up to 5-stacked junctions. New approaches designed to further increase the output voltage and to simplify the JAWS setup have been presented, including on-chip power dividers and optical pulse drives for the JAWS. Certain applications of the JAWS that have significant benefits for quantum AC voltage metrology have also been described. These new applications have resulted in numerous publications by PTB scientists in cooperation with our NMI partners over the last several years. For example, from 2018 to 2021, more than 30 papers were published, including conference papers. Within international research projects, PTB's JAWS chips have been distributed to NMIs in the Netherlands, the United Kingdom, Norway, Italy, Finland, Turkey, Russia, China and Argentina. The technology transfer between PTB and the Supracon company for commercialization purposes has also been initiated to make JAWS available to other NMIs, to calibration laboratories and to industry in the near future.

Acknowledgments

R. Behr, L. Palafox, H. Tian, S. Bauer, J. Herick, M. Kraus, Y. Pimsut, J. Kohlmann, T. Weimann, R. Wendisch, R. Gerdau, K. Peiselt, P. Hinze, K. Störr, B. Egeling, J. Felgner, M. Petrich, G. Muchow, S. Gruber, T. Ahbe, A. Zorin, M. Bieler and many international partners from various NMIs.

References

Baek B, Dresselhaus PD, and Benz SP (2006) Co-sputtered amorphous NbxSi1-x barriers for josephson-junction circuits. *IEEE Transactions on Applied Superconductivity* 16(4): 1966–1970.

Bardalen E, et al. (2017) Packaging and demonstration of optical-fiber-coupled photodiode array for operation at 4 K. *IEEE Transactions on Components, Packaging and Manufacturing Technology* 7(9): 1395–1401.

Bardalen E, et al. (2018) Reliability study of fiber-coupled photodiode module for operation at 4 K. *Microelectronics and Reliability* 81: 362–367.

Bardalen E, et al. (2020) Bipolar photodiode module operated at 4 K. In: IEEE 8th Electronics System-Integration Technology Conference *(ESTC), 15–18 Sept. 2020, Tönsberg, Norway*.

Bauer S, et al. (2017) A novel two-terminal-pair pulse-driven Josephson impedance bridge linking a 10 nF capacitance standard to the quantized Hall resistance. *Metrologia* 54(2): 152–160.

Bauer S, et al. (2018) Progress on PTB's Pulse-Driven Josephson Impedance Bridge combined with an AC Quantum Hall Resistance. In: CPEM2018, in Proc. Conference on Precision Electromagnetic Measurements, *Paris, France, 8–13 July 2018*.

Bauer S, et al. (2020) AC quantum hall resistance combined with a four-terminal pair pulse-driven josephson impedance bridge. In: CPEM2020, in Proc. *Conference on Precision Electromagnetic Measurements, Denver, USA, 24–28 Aug. 2020*.

Behr R and Kieler O (2020) unpublished.

Behr R, et al. (2012) Development and metrological applications of Josephson arrays at PTB. *Measurement Science and Technology* 23(12), 124002.

Behr R, et al. (2015) Direct comparison of a 1 V Josephson arbitrary waveform synthesizer and an ac quantum voltmeter. *Metrologia* 52(4): 528–537.

Behr R, Kieler O, and Schumacher B (2017) A precision microvolt-synthesizer based on a pulse-driven josephson voltage standard. *IEEE Transactions on Instrumentation and Measurement* 66(6): 1385. https://doi.org/10.1109/TIM.2016.2619998. (Accessed: 03 March 2022).

Benz SP and Hamilton CA (1996) A pulse-driven programmable Josephson voltage standard. *Applied Physics Letters* 68: 3171–3173.

Benz SP, Burroughs CJ, and Dresselhaus PD (2001) AC coupling technique for Josephson waveform synthesis. *IEEE Transactions on Applied Superconductivity* 11(1): 612–616.

Benz SP, et al. (2015) 1 V Josephson arbitrary waveform synthesizer. *IEEE Transactions on Applied Superconductivity* 25(1).

Brom HVD, et al. (2016) AC-DC calibrations with a pulse-driven AC Josephson voltage standard operated in a small cryostat. In: CPEM2016, in Proc. *Conference on Precision Electromagnetic Measurements, Ottawa, Canada* 1–2. 10–15 July 2016. https://doi.org/10.1109/CPEM.2016.7540605. (Accessed: 03 March 2022).

Burroughs CJ, et al. (2005) Precision measurements of AC Josephson voltage standard operating margins. *IEEE Transactions on Instrumentation and Measurement* 54(2): 624–627.

de Aguilar J, et al. (2019) Characterization of an analog-to-digital converter frequency response by a Josephson arbitrary waveform synthesizer. *Measurement Science and Technology* 30: 035006.

Drung D and Krause C (2021) Dual-mode auto-calibrating resistance thermometer: A novel approach with Johnson noise thermometry. *The Review of Scientific Instruments* 92: 034901. https://doi.org/10.1063/5.0035673. (Accessed: 03 March 2022).

Drung D, Kraus M, and Krause C (2022) Calibration of the dual-mode auto-calibrating resistance thermometer with few-parts-per-million uncertainty. *Measurement Science and Technology* 33. https://doi.org/10.1088/1361-6501/ac2c48. (Accessed: 03 March 2022).

EU-project 'ACQ-Pro' (2015) 14RPT01. Available at: https://www.euramet.org/measurement-research-innovation-issue-14/#c3965. (Accessed: 03 March 2022).

EU-project 'Dig-Ac' (2018) 17RPT03. Available at: https://www.euramet.org/research-innovation/search-research-projects/details/project/a-digital-traceability-chain-for-ac-voltage-and-current/. (Accessed: 03 March 2022).

EU-project 'JAWS' (2001) G6RD-CT-2001-00599. Available at: https://cordis.europa.eu/project/id/G6RD-CT-2001-00599. (Accessed: 03 March 2022).

EU-project 'JoSy' (2007) ERA-NET+ no. 217257. Available at: https://cordis.europa.eu/project/id/217257/de. (Accessed: 03 March 2022).

EU-project 'Q-Wave' (2013) JRP SIB59. Available at: https://www.euramet.org/research-innovation/search-research-projects/details/project/a-quantum-standard-for-sampled-electrical-measurements/. (Accessed: 03 March 2022).

EU-project,QuADC (2016) JRP 15SIB04. Available at: https://www.euramet.org/research-innovation/search-research-projects/details/project/waveform-metrology-based-on-spectrally-pure-josephson-voltages/. (Accessed: 03 March 2022).

Flower-Jacobs NE, et al. (2016) Two-volt Josephson arbitrary waveform synthesizer using Wilkinson dividers. *IEEE Transactions on Applied Superconductivity* 26(6): 1400207. https://doi.org/10.1109/TASC.2016.2532798. (Accessed: 03 March 2022).

Herick J, et al. (2020) Realization of an opto-electronic bias for pulse-driven josephson voltage standards at PTB. In: CPEM2020, in Proc. *Conference on Precision Electromagnetic Measurements, Denver, USA, 24–28 Aug. 2020*.

Ireland J, et al. (2017) Josephson arbitrary waveform system with optoelectronic drive. In: Ext. Abstract, *ISEC-2017*: 16th Int. Supercond. Electron. Conf., *Sorrento, Italy, Jun. 2017* 12–16.

Ireland J, et al. (2019) An optoelectronic pulse drive for quantum voltage synthesizer. *IEEE Transactions on Instrumentation and Measurement* 68(6).

Karlsen B, et al. (2019) Pulsation of InGaAs photodiodes in liquid helium for driving josephson arrays in AC voltage realization. *IEEE Transactions on Applied Superconductivity* 29(7): 1200308. https://doi.org/10.1109/TASC.2019.2901573. (Accessed: 03 March 2022).

Karlsen B, et al. (2020) High-speed pulsation of a cryogenically operable bipolar photodiode module for the Josephson arbitrary waveform synthesizer. In: CPEM2020, in Proc. Conference on Precision Electromagnetic Measurements*, Denver, USA, 24–28 Aug. 2020*.

Kieler O, et al. (2007a) SNS josephson junction series arrays for the Josephson arbitrary waveform synthesizer. *IEEE Transactions on Applied Superconductivity* 17: 187–189.

Kieler O, Kohlmann J, and Müller F (2007b) Improved design of superconductor/normal conductor/superconductor Josephson junction series arrays for an ac Josephson voltage standard. *Superconductor Science and Technology* 20: 318–322.

Kieler O, Iuzzolino R, and Kohlmann J (2009) Sub-μm SNS Josephson junction arrays for the Josephson arbitrary waveform synthesizer. *IEEE Transactions on Applied Superconductivity* 19(3): 230–233.

Kieler O, Behr R, and Kohlmann J (2013a) Development of a pulse-driven AC josephson voltage standard at PTB. In: ISEC 2013, in Proc. 14th International Superconductive Electronics Conference*, Cambridge, USA* 59–61. 7–11 July 2013.

Kieler O, Scheller T, and Kohlmann J (2013b) Cryocooler operation of a pulse-driven AC josephson voltage standard at PTB. *World Journal of Condensed Matter Physics* 3: 193–198.

Kieler O, et al. (2015) Towards a 1 V Josephson arbitrary waveform synthesizer. *IEEE Transactions on Applied Superconductivity* 25(3): 1400305. https://doi.org/10.1109/TASC.2014.2366916. (Accessed: 03 March 2022).

Kieler O, et al. (2017) Arrays of stacked SNS Josephson junctions for pulse-driven Josephson voltage standards. In: EUCAS 2017 - 13th European Conference on Applied Superconductivity*, Geneva, Switzerland, 17–21 September 2017*.

Kieler O, et al. (2019) Optical pulse-drive for the pulse-driven AC Josephson voltage standard. *IEEE Transactions on Applied Superconductivity* 29(5): 1200205.

Kieler O, et al. (2021) Stacked Josephson junction arrays for the pulse-driven AC josephson voltage standard. *IEEE Transactions on Applied Superconductivity* 31(5): 1100705.

Kraus M, et al. (2018) Frequency-dependent verification of the quantum accuracy of a Quantum Voltage Noise Source. In: CPEM2018, in Proc. *Conference on Precision Electromagnetic Measurements, Paris, France, 8–13 July 2018*.

Lapuh R, et al. (2017) Keysight 3458A noise performance in DCV sampling mode. *IEEE Transactions on Instrumentation and Measurement* 66(6): 1089. https://doi.org/10.1109/TIM.2017.2681238. (Accessed: 03 March 2022).

Physikalisch-Technische Bundesanstalt (PTB) (2022) Available at: http://www.ptb.de (Accessed: 03 March 2022).

Pimsut Y, et al. (2020) A four-terminal-pair pulse-driven Josephson impedance bridge for 10 nF:10 nF capacitance ratio measurements. In: CPEM2020, in Proc. *Conference on Precision Electromagnetic Measurements, Denver, USA, 24–28 Aug. 2020*.

Schreier R and Temes T (2005) *Understanding delta-sigma data converters*. Pisctaway, New Jersey: IEEE Press.

Sira M, Kieler O, and Behr R (2019) A novel method for calibration of ADC using JAWS. *IEEE Transactions on Instrumentation and Measurement* 68(6): 2091.

Supracon AG (2022) Jena. Available at: http://www.supracon.de. (Accessed: 03 March 2022).

Tian H (2022) *Development of RF power dividers for high integrated circuits of ACJosephson voltage standards. to be published in PhD thesis*.

Tian H, et al. (2020) Development of RF-power dividers for the Josephson arbitrary waveform synthesizer. *IEEE Transactions on Applied Superconductivity* 30(5): 1100105.

Tian H, et al. (2021) Investigation of broadband wilkinson power dividers for pulse-driven Josephson voltage standards. *IEEE Transactions on Applied Superconductivity* 31(5): 1100305.

Watanabe M, et al. (2006) Resonance-free lowpass filters for the AC Josephson voltage standard. *IEEE Transactions on Applied Superconductivity* 16(1): 49–53.

Yamamori H and Kohjiro S (2016) Fabrication of voltage standard circuits utilizing a serial-parallel power divider. *IEEE Transactions on Applied Superconductivity* 26(8): 1400404.

Field theoretic aspects of condensed matter physics: An overview

Eduardo Fradkin, Department of Physics and Institute for Condensed Matter Theory, University of Illinois at Urbana-Champaign, Urbana, IL, United States

© 2024 Elsevier Ltd. All rights reserved.

Introduction	**29**
Early years: Feynman diagrams and correlation functions	**29**
Critical phenomena	**30**
Classical critical phenomena	30
Landau–Ginzburg theory	30
The renormalization group	31
Scaling	31
The operator product expansion	31
Fixed points	32
Universality	33
RG flows	33
Asymptotic freedom	34
Quantum criticality	**36**
Dynamic scaling	36
The Ising model in a transverse field	36
Quantum antiferromagnets and nonlinear sigma models	38
Spin coherent states	38
Path integral for a spin-*S* degree of freedom	39
Quantum ferromagnet	40
Quantum antiferromagnet	40
Topological excitations	**41**
Topological excitations: Vortices and magnetic monopoles	41
Vortices in two dimensions	42
Magnetic monopoles in compact electrodynamics	45
Nonlinear sigma models and antiferromagnetic quantum spin chains	47
Topology and open integer-spin chains	48
Duality in Ising models	**49**
Duality in the 2D Ising model	49
The 3D duality: $\mathbb{Z}_2$ gauge theory	50
Bosonization	**52**
Dirac fermions in one space dimensions	53
Chiral symmetry and chiral symmetry breaking	55
The chiral anomaly	57
Bosonization, anomalies, and duality	59
Fractional charge	**62**
Solitons in one dimensions	62
Polyacetylene	62
Fractionally charged solitons	63
Fractional statistics	**65**
Basics of fractional statistics	65
What is a topological field theory	66
Chern–Simons gauge theory	66
BF gauge theory	67
Quantization of Abelian Chern–Simons gauge theory	67
Vacuum degeneracy a torus	69
Fractional statistics and braids	70
Topological phases of matter	**72**
Topological insulators	72
Dirac fermions in 2+1 dimensions	72
Dirac fermions and topological insulators	73
Chern invariants	74
The quantum Hall effect on a lattice	76
The anomalous quantum Hall effect	79

https://doi.org/10.1016/B978-0-323-90800-9.00269-9

The parity anomaly 79
Three-dimensional $\mathbb{Z}_2$ topological insulators 83
$\mathbb{Z}_2$ Topological invariants 83
The axial anomaly and the effective action 84
Theta terms, and domain walls: Anomaly and the Callan–Harvey effect 86
Chern–Simons gauge theory and the fractional quantum Hall effect 88
Landau levels and the integer Hall effect 89
The Laughlin wave function 92
Quasiholes have fractional charge 93
The Jain states 93
Quasiholes have fractional statistics 94
Hydrodynamic effective field theory 94
Composite Boson field theory 95
Composite fermion field theory 98
The compressible states 102
Fractional quantum hall wave functions and conformal field theory 103
Edge states and chiral conformal field theory 110
Point contact tunneling and QH chiral edge states 112
Experimental evidence of fractional charge 113
Quantum interferometers and fractional statistics 114
Particle-vortex dualities in 2+1 dimensions 116
Electromagnetic duality 116
Particle-vortex duality in 2+1 dimensions 116
The 3D XY model 116
Scalar QED in 3D 118
The duality mapping 119
Bosonization in 2+1 dimensions 119
Bosonization of the Dirac theory in 2+1 dimensions 120
Bosonization of the fermi surface 124
Conclusion 125
Acknowledgments 125
References 125

Abstract

In this chapter, I discuss the impact of concepts of Quantum Field Theory in modern Condensed matter physics. Although the interplay between these two areas is certainly not new, the impact and mutual cross-fertilization has certainly grown enormously with time, and Quantum Field Theory has become a central conceptual tool in condensed matter physics. In this chapter, I cover how these ideas and tools have influenced our understanding of phase transitions, both classical and quantum, as well as topological phases of matter, and dualities.

Key points

- Quantum Field Theory has a deep and wide impact on our understanding of modern condensed matter physics.
- The conceptual framework of the Renormalization Group and of the UV fixed point is the central concept in the theory and classical and quantum phase transitions.
- The renormalization group is the foundation for universality, scale, and conformal invariance at these fixed points.
- Here, I discuss quantum criticality in the 1D transverse field Ising model and in quantum antiferromagnets.
- Topology is also central to our understanding of condensed matter ranging from the role of vortices and magnetic monopoles to topological terms in effective actions.
- Duality and duality transformations and bosonization and fermionization transformations in condensed matter and gauge theories provide a nonperturbative framework to our understanding of these systems.
- Topology has provided a sharp definition of fractional charge, fractional statistics, braiding, and fusion of quasiparticles.
- Topological phases of matter are physical systems with long-range quantum entanglement characterized by topological invariants.

Introduction

Many (if not most) puzzling problems in condensed matter physics involve systems with a macroscopically large number of degrees of freedom often in regimes of large fluctuations, thermal and/or quantum mechanical. The description of the physics of systems of this type requires the framework provided by Quantum Field Theory. Although quantum field theory has its origins in high-energy physics, notably in the development of Quantum Electrodynamics, it has found a nurturing home in condensed matter physics.

There is a long history of cross-fertilization between both fields. Since the 1950s in many of the most significant developments in Condensed Matter Physics, Quantum Field Theory has played a key role if not in the original development but certainly in the eventual understanding the meaning and the further development of the discoveries. As a result, many of the discoveries and concepts developed in Condensed Matter have had a reciprocal impact in Quantum Field theory. One can already see this interplay in the development of the Bardeen–Cooper–Schrieffer theory of superconductivity (Schrieffer, 1964) and its implications in the theory of dynamical symmetry breaking in particle physics by Nambu (Nambu and Jona-Lasinio, 1961).

The close and vibrant relationship between both fields has continued to these days, and it is even stronger today than before. Many textbooks have been devoted to teaching these ideas and concepts to new generations of condensed matter physicists (and field theorists as well). The earlier texts focused on Green functions which are computed in perturbation theory using Feynman diagrams (Abrikosov et al., 1963; Fetter and Walecka, 1971; Doniach and Sondheimer, 1974), while the more modern ones have a broader scope, use path integrals and attack nonperturbative problems (Feynman and Hibbs, 1965; Feynman, 1972; Faddeev, 1976; Fradkin, 2013, 2021; Altland and Simons, 2010). In two recent books I have discussed many aspects of the interrelation between condensed matter physics and quantum field theory in more depth than I can do in this chapter (Fradkin, 2013, 2021).

Early years: Feynman diagrams and correlation functions

Quantum field theory played a key role in the development of the Theory of the Fermi Liquid (Pines and Nozières, 1966; Baym and Pethick, 1991). The theory of the Fermi liquid was first formulated by Landau using the framework of hydrodynamics and the quantum Boltzmann equation. Landau's ideas were later given a microscopic basis using Green functions and Feynman diagrams (Abrikosov et al., 1963), including the effects of quantum fluctuations at finite temperature and nonequilibrium behavior (Kadanoff and Baym, 1962; Kamenev, 2011). Linear response theory was developed, which allowed the computation of response functions (such as electrical conductivities and magnetic susceptibilities) from the computation of correlation functions for a given microscopic theory (Martin, 1968). In turn, correlation functions can be computed in terms of a set of Feynman diagrams. These concepts and tools borrowed many concepts from field theory including the study of the analytic structure of the generalized susceptibilities and the associated spectral functions (together with the use of dispersion relations). These developments led to the derivation of the fluctuation-dissipation theorem. These ideas were widely applied to metals (Baym and Pethick, 1991) and superconductors (Schrieffer, 1964), as well as to quantum magnets (Mattis, 1965).

The spectrum of an interacting system has low energy excitations characterized by a set of quantum numbers associated with the symmetries of the theory. These low energy excitations are known as *quasiparticles*. In the case of the Landau theory of the Fermi liquid (FL), the quasiparticle is a "dressed" electron: it is a low energy excitation with the same quantum numbers (charge and spin) and an electron but with a renormalized effective mass. There are many such quasiparticles in condensed matter physics. The correlation functions (the propagators) of a physical system have a specific analytic structure. In momentum (and frequency) space, the quasiparticle spectrum is given by the poles of the correlators.

The role of symmetries and, in particular of gauge invariance, in the structure of correlation functions was investigated extensively. A direct consequence of symmetries is the existence of Ward–Takahashi identities, which must be satisfied by all the correlation functions of the theory. Ward–Takahashi identities are exact relations that relate different correlation functions. Such identities contain a host of important results. For example, in a theory with a globally conserved charge, the Hamiltonian (and the action) have a global $U(1)$ symmetry associated with the transformation of the local field operator $\phi(x)$ (which can be fermionic or bosonic) to a new field $\phi'(x) = e^{i\theta}\phi(x)$ (where θ is a constant phase). Theories with a global continuous symmetry have a locally conserved current (and satisfy a continuity equation). The Ward–Takahashi identity requires the correlators of these currents (and densities) to be transverse (i.e., they should have vanishing divergence). In the absence of so-called quantum anomalies (which we will discuss below), global symmetries can be made local and become gauge symmetries.

In many circumstances, a global symmetry can be spontaneously broken. If the global symmetry is continuous, then the Ward–Takahashi identities imply the existence of gapless excitations known as Goldstone bosons. For example in the case of a superfluid, which has a spontaneously broken $U(1)$ symmetry the Goldstone boson is the gapless phase mode. Instead, the Néel phase of a quantum antiferromagnet has two gapless Goldstone bosons, the magnons of the spontaneously broken $SO(3)$ global symmetry of this state of matter. Another example is the Ward–Takahashi identity of quantum electrodynamics (QED), which relates the electron self-energy to the electron–photon vertex function, which also holds in nonrelativistic electron fluids. In addition, these identities implied the existence of sum rules that the spectral functions must satisfy. All of these results became part of the standard toolkit of condensed matter experimentalists in analyzing their data and for theorists to make predictions. Ward–Takahashi identities and sum rules also imply restrictions on the allowed approximations which are often needed to obtain predictions from a microscopic model.

Critical phenomena

Classical critical phenomena

The late 1960s and particularly 1970s brought about an intense back and forth between condensed matter physics and field theory in the context of the problem of classical critical phenomena and phase transitions. This was going to become a profound revolution on the description of macroscopic physical systems with large-scale fluctuations. The problem of continuous ("second order") phase transitions has a long history going back to the work of Landau (Landau, 1937; Landau and Lifshitz, 1959) who introduced the concept of an *order parameter field*. This turned out to be a powerful concept of broad applicability in many physical systems sometimes quite different from each other at the microscopic level.

A simple example is that of a ferromagnet with uniaxial anisotropy in which the spins of the atoms in a crystal are strongly favored to be aligned (or antialigned) along certain directions of the crystal. The simplest microscopic model for this problem is the Ising model, a spin system in which the individual spins are allowed to take only two values, $\sigma = \pm 1$. The partition function of the Ising model (in any dimension) is

$$Z = \sum_{[\sigma]} \exp\left(-\frac{J}{T} \sum_{\langle \boldsymbol{r}, \boldsymbol{r}' \rangle} \sigma(\boldsymbol{r}) \sigma(\boldsymbol{r}') \right) \tag{1}$$

where J is the exchange coupling constant and T is the temperature (measured in energy units); here $[\sigma]$ denotes the sum over the 2^N spin configurations (for a lattice with N sites), and $\langle \boldsymbol{r}, \boldsymbol{r}' \rangle$ are nearest neighbor sites of the lattice. The order parameter of the Ising model is the local magnetization $\langle \sigma(\boldsymbol{r}) \rangle$ which, in the case of a ferromagnet, is uniform. The partition function of the Ising model can be computed trivially in one dimension. The solution of the two-dimensional Ising model by Onsager constituted a tour-de-force in theoretical physics (Onsager, 1944). Its actual meaning remained obscure for some time. The work of Schultz et al. (1964) evinced a deep connection between Onsager's solution and the problem if the spectrum of one-dimensional quantum spin chains (Lieb et al., 1961) [specifically the one-dimensional Ising model in a transverse field (Pfeuty, 1970)]. One important result was that the Ising model was in fact a theory of (free) fermions which, crudely speaking, represented the configurations of domain walls of the magnet. However, even this simple model cannot be solved exactly in general dimension, and approximate mean field theories of various sorts were devised over time to understand its physics.

Landau–Ginzburg theory

Landau's approach assumed that close enough to a phase transition, the important spin configurations are those for which the local magnetization varies slowly on lattice scales. In this picture, the local magnetization, on long enough length scales, becomes an order parameter field that takes values on the real numbers, and can be positive of negative. Thus, the order parameter field is effectively the average of local magnetizations on some scale large compared to the lattice scale, which we will denote by a real field $\phi(x)$. The thermodynamics properties of a system of this type in d dimensions can be described in terms of a free energy

$$F[\phi] = \int d^d x \left[\frac{\kappa}{2} (\nabla \phi(x))^2 + a(T - T_c) \phi^2(x) + u \phi^4(x) + \cdots \right] \tag{2}$$

which is known as the Ginzburg–Landau free energy. Here, κ is the stiffness of the order parameter field; T_c is the (mean-field) critical temperature; and a and u are two (positive) constants. This expression makes sense if the transition is continuous and hence that the order parameter is small near the transition. The energy of the Ising model is invariant under the global symmetry $[\sigma] \mapsto [-\sigma]$. This is the symmetry of the group $\mathbb{Z}_2$. Likewise, the Ginzburg–Landau free energy has the global (discrete) symmetry $[\phi(x)] \mapsto [-\phi(x)]$ and also has a $\mathbb{Z}_2$ global symmetry.

In Landau's approach, which was a mean field theory, the equilibrium state is the global minimum of this free energy. The nature of the equilibrium state depends on whether $T > T_c$ or $T < T_c$: for $T > T_c$ the global minimum is the trivial configuration, $\bar{\phi}(x) = 0$ (this is the paramagnetic state), whereas for $T < T_c$, the equilibrium state is two fold degenerate, $\bar{\phi}(x) = \pm (a(T_c - T)/2)^\beta$, with the two degenerate states being related by the $\mathbb{Z}_2$ symmetry (this is the ferromagnetic state). In the Landau theory, the critical exponent of the magnetization is $\beta = 1/2$ and the critical exponent of the correlation length is $\nu = 1/2$. However, in the case of the 2D Ising model, the order parameter exponent is $\beta = 1/8$ (Yang, 1952) and the correlation length exponent is $\nu = 1$. These (and other) apparent discrepancies led many theorists for much of the 1960s believe that each model was different and that these behaviors reflected microscopic differences. In addition, Landau's theory was regarded as phenomenological and believed to be of questionable validity.

The renormalization group

This situation was to change with the development of the Renormalization Group, due primarily to the work of Kadanoff (Kadanoff, 1966a, b; Efrati et al., 2014) and Wilson (Wilson, 1971a, b; Wilson and Fisher, 1972; Wilson and Kogut, 1974; Wilson, 1975, 1983). The renormalization group was going to have (and still has) a profound effect both in condensed matter physics and in Quantum Field Theory (and beyond).

Scaling

Several phenomenological theories were proposed in the 1960s to describe the singular behavior of physical observables near a continuous phase transition (Patashinskii and Pokrovskii, 1966; Fisher, 1967, 1974). These early works argued that in order to explain the singular behavior of the observables, the free energy density had to have a singular part which should be a homogeneous function of the temperature, magnetic field, etc. A function $f(x)$ is homogeneous if it satisfies the property that it transforms irreducibly under dilations, that is, $f(\lambda x) = \lambda^k f(x)$, there λ is a real positive number (a scale) and k is called the degree. These heuristic ideas then implied that the critical exponents should obey several identities. In 1966, Kadanoff wrote an insightful paper in which he showed that the homogeneity hypothesis implied that in that regime these systems should obey scaling. He showed that this can be justified by performing a sequence of block-spin transformations in which the configurations that vary rapidly at the lattice scale a become averaged at the scale of a larger sized block of length scale $ba > a$, which resulted in a renormalization of the coupling constants from $\{K\}$ at scale a to $\{K'\}$ at the new scale ba (Kadanoff, 1966a; Efrati et al., 2014). In other words, the block spin transformation amounts to a scale transformation and a renormalization of the couplings (and operators). From this condensed matter/statistical physics perspective, the important physics is in the long-distance ("infrared") behavior.

A significant consequence of these ideas was that close enough to a critical point, if the distance $|x - y|$ between two local observables $O(x)$ and $O(y)$ is large compared to the lattice spacing a but small compared to the correlation length ξ, their correlation function takes the form of a power law

$$\langle O(x)O(y)\rangle \sim \frac{\text{const.}}{|x-y|^{2\Delta_O}} \tag{3}$$

where Δ_O is a positive real number known as the scaling dimension of the operator O (Patashinskii and Pokrovskii, 1966; Kadanoff, 1966a; Kadanoff et al., 1967). These conjectures were known to be satisfied in the nontrivial case of the 2D Ising model (Kadanoff, 1966b), as well as in the Landau–Ginzburg theory once the effects of Gaussian fluctuations were included (Kadanoff et al., 1967). For example, in the 2D Ising model, the scaling dimension of the local magnetization σ is $\Delta_\sigma = 1/8$ and of the energy density ε is $\Delta_\varepsilon = 1$, which were sufficient to explain all the singular behaviors known at that time.

The concept of renormalization actually originated earlier in quantum field theory as part of the development of QED. In QED, the notion of renormalization was used to "hide" the short distance ("ultraviolet") divergencies of the Feynman diagrams needed to compute physical processes involving electrons (and positrons) and photons, that is, their strong, divergent, dependence of an artificially introduced short-distance cutoff or regulator. In particular, the sum of the leading diagrams that enter in the electron–photon vertex amounted to a redefinition (renormalization) of the coupling constant. It was observed by Murray Gell-Mann and Francis Low that this renormalization was equivalent to the solution of a first-order differential equation that governed the infinitesimal change of the coupling, the fine structure constant $\alpha = e^2/4\pi$, under an infinitesimal change of the UV cutoff Λ (Gell-Mann and Low, 1954)

$$\Lambda \frac{d\alpha}{d\Lambda} \equiv \beta(\alpha) = \frac{2}{3\pi}\alpha^2 + O(\alpha^3) \tag{4}$$

where $\beta(\alpha)$ is the Gell-Mann–Low beta function. Except for the work by Bogoliubov and Shirkov (1959), this reinterpretation by Gell-Mann and Low was not actively pursued, partly because it predicted that the renormalized coupling became very large at short distances, $\alpha \to \infty$, and, conversely, it vanished in the deep long-distance regime, $\alpha \to 0$ (if the electron bare mass is zero). In other words, QED is strongly coupled in the UV and trivial in the IR. The same behavior was found in the case of the theory of a scalar field $\phi(x)$ with an ϕ^4 interaction, which is relevant in the theory of phase transitions. In addition to these puzzles, the1960s saw the experimental development of the physics of hadrons which involve strong interactions. For these reasons, for much of that decade most high-energy theorists had largely abandoned the use of quantum field theory, and explored other, phenomenologically motivated, approaches (which led to an early version of string theory.) At any rate the notion that the physics may depend on the scale was present as was the notion that in some regimes field theories may exhibit scale invariance at least in an approximate form.

The operator product expansion

The next stage of the development of these ideas was the concept of the operator product expansion (OPE). If we denote by $\{O_j(x)\}$ the set of all possible local operators in a theory (a field theory or a statistical mechanical system near criticality), then the product of two observables on this list closer to each other than to any other observable (and to the correlation length ξ) obeys the expansion

$$\lim_{x\to y} O_j(x)O_k(y) = \lim_{x\to y} \sum_l \frac{C_{jkl}}{|x-y|^{\Delta_j+\Delta_k-\Delta_l}} O_l\left(\frac{x+y}{2}\right) \tag{5}$$

where this equation should be understood as a weak identity, valid inside an expectation value. Remarkably, this concept was derived independently and simultaneously by Kadanoff (1969) (who was working in critical phenomena), by Wilson (1969) (who was interested in the short distance singularities arising in Feynman diagrams), and by Polyakov (1970, 1974) (also working in critical phenomena). In Eq. (5), $\{\Delta_j\}$ are the scaling dimensions of the operators $\{O_j\}$. The coefficients C_{jkl} are (like the dimensions) universal numbers. In a follow-up paper, Polyakov showed that if the theory has conformal invariance, that is, scale invariance augmented by conformal transformations which preserve angles, then, provided the operators O_j are suitably normalized, the coefficients C_{jkl} of the OPE are determined by a three-point correlator

$$\langle O_j(x)O_k(y)O_l(z)\rangle = \frac{C_{jkl}}{|x-y|^{\Delta_{jk}}|y-z|^{\Delta_{kl}}|z-x|^{\Delta_{lj}}} \tag{6}$$

where $\Delta_{jk} = \Delta_j + \Delta_k - \Delta_l$. These results constitute the beginnings of conformal field theory (CFT). In a nontrivial check, Kadanoff and Ceva showed that the OPE holds for the local observables of the 2D Ising model (Kadanoff and Ceva, 1971).

Fixed points

The next and crucial step in the development of the Renormalization Group was made by Wilson. Wilson was a high-energy theorist who wanted to know how to properly define a quantum field theory and the physical meaning of renormalization.

In a Lorentz invariant quantum field theory, one is interested in the computation of the expectation value of time-ordered operators. In the case of a self-interacting scalar field $\phi(x)$ in D-dimensional Euclidean space-time, obtained by analytic continuation from Minkowski spacetime to imaginary time, the observables are computed from the functional (or path) integral by functional differentiation of the partition function

$$Z = \int \mathcal{D}\phi \exp\left(-S(\phi, \partial_\mu \phi) + \int d^D x\, J(x)\phi(x)\right) \tag{7}$$

with respect to the local sources $J(x)$. For a scalar field, the Euclidean action is

$$S = \int d^D x \left[\frac{1}{2}(\partial_\mu \phi(x))^2 + \frac{m^2}{2}\phi^2(x) + \frac{\lambda}{4!}\phi^4(x)\right] \tag{8}$$

which has the same form as the free energy of the Landau–Ginzburg theory of phase transitions shown in Eq. (2). It is apparent that the Landau–Ginzburg theory is the classical limit of the theory of the scalar field whose partition function is a sum over all histories of the field. It is easy to see that an expansion of the partition function (or of a correlator) in powers of the coupling constant λ can be cast in the form of a sum of Feynman diagrams. To lowest order in λ a typical Feynman diagram involves a one-loop integral in momentum space of the form

$$I(p) = \int \frac{d^D q}{(2\pi)^D} \frac{1}{(q^2 + m^2)((q-p)^2 + m^2)} \tag{9}$$

As noted by Wilson in his Nobel Lecture (Wilson, 1983), this integral has large contributions from the IR region of small momenta $q \sim 0$, but for any dimension $D \geq 4$ has a much larger contribution form large the UV region of large momenta, which requires the introduction of a UV cutoff Λ in momentum space (or a lattice spacing a in real space by defining the theory on a hypercubic lattice). In quantum field theory, one then has to require that somehow one takes the limit $a \to 0$ (or $\Lambda \to \infty$). To take this limit in the field theory is very much analogous to the definition of a conventional integral in terms of a limit of a Riemann sum. The difference is that this is a *functional* integral. While for a function of bounded variation in a finite interval (a, b), the limit of a partition of the interval into N steps each of length Δx such that $N\Delta x = b - a$ exists and defines the integral of the function

$$\lim_{\Delta x \to 0} \lim_{N\to\infty} \sum_{j=1}^{N} f(x_j)\Delta x_j = \int_a^b dx\, f(x), \tag{10}$$

the analogous statement does not obviously exists in general for a *functional integral*, that is, an integral over a space of functions, which is what is required. In fact, although thousands of integrals of a function are known to exist, there are extremely few examples for a functional integral. Moreover, in order to take the *continuum limit*, the lattice spacing must approach zero, $a \to 0$. This means that physical scales, such as the correlation length ξ, must diverge in lattice units so that they can be fixed in physical units. But to do that, one has to be asymptotically close to a continuous phase transition! Hence, the problem of defining a quantum field theory is *equivalent* to the problem of critical phenomena at a continuous phase transition!

Wilson gave a systematic formulation to the Renormalization Group by generalizing the earlier ideas introduced by Kadanoff and the earlier work by Gell-Mann and Low. Wilson's key contribution was the introduction of the concept of a *fixed point* of the Renormalization Group transformation (Wilson, 1971a, b; Wilson and Fisher, 1972; Wilson and Kogut, 1974). As we saw, the block-spin transformation is a procedure for coarse graining the degrees of freedom of a physical system resulting in a renormalization of the coupling constants. Upon the repeated action of the RG transformation, its effect can be pictured as a *flow* in the space of coupling constants. However, in addition to integrating short distance degrees of freedom, one needs to restore the units of length, which have changed under that process. This requires a rescaling of lengths. Once this is done, Wilson showed that the resulting RG flows necessarily have *fixed points*, special values of the couplings which are invariant (fixed) under the action of the RG transformation. He then deduced that at a fixed point, the theory has no scales, aside from the linear size L of the system and the microscopic UV cutoff (the lattice spacing a in a spin system).

This analysis means that for length scales long compared to $a \to 0$ but short compared to $L \to \infty$ the theory acquired a new, emergent, symmetry: scale invariance. Therefore, at a fixed point, the correlators of all local observables must be homogeneous functions (hence, must scale).

Universality

A crucial consequence of the concept if the fixed point is that phase transitions can be classified into *universality classes*. Universality means that a large class of physical systems with different microscopic properties have fixed points with the same properties, that is, the same scaling dimensions, OPEs, and correlation functions at long distances independent on how they are defined microscopically. Although the renormalization group transformation is a transformation scheme that we define and, because of that the location in coupling constant space of the fixed point itself does depends on the scheme we choose, its universal properties are the same. Thus, universality classes depend only on features such as the space (and spacetime) dimension and the global symmetries of the system. But the systems themselves may be quite different. This we speak if the Ising universality class in 2D, on the superfluid (or XY) transition class in 3D, etc. This concept, which originated in the theory of phase transition, has been adopted and generalized in the development of CFT.

RG flows

Combined with the condition that the correlators decay at long separations, homogeneity implies that the correlators must have the form of Eq. (3). In addition, this equation also implies that at a fixed point the operators (the local observables) have certain scaling dimensions. Let us consider a theory close to a fixed point whose action we will denote by S^*. Let $\{O_j(x)\}$ be a complete set of local observables whose scaling dimensions are $\{\Delta_j\}$. The total action of the theory close to the fixed point then can be expanded as a linear combination of the operators with dimensionless coupling constants $\{g_j\}$

$$S = S^* + \int d^D x \sum_j g_j a^{\Delta_j - D} O_j(x) \tag{11}$$

Under a change of length scale $x \to x' = bx$, with $b > 1$, the operators (which must transform homogeneously) change as $O_j(bx) = b^{-\Delta_j} O_j(x)$. Since the phase space changes as $d^D x' = b^D d^D x$, we can keep the form of the action provided the coupling constants also change to compensate for these changes as $g_j' = b^{D-\Delta_j} g_j$. Let $b = |x'|/|x| = 1 + da/a$, where da is an infinitesimal change of the UV cutoff a. Then, if we integrate out the degrees of freedom in the range $a < |x| < a + da$, the rate of change of the coupling constants $\{g_j\}$ under this rescaling is

$$a \frac{dg_j}{da} \equiv \beta(g_j) = (D - \Delta_j) g_j + \cdots \tag{12}$$

which we recognize as a Gell-Mann–Low beta function for each coupling constant.

This result says that if the scaling dimension $\Delta_j < D$, then the renormalized coupling will *increase* as we increase the length scale, $g_j' > g_j$, and along this direction in coupling constant space, the RG flows *away* from the fixed point. Conversely, if $\Delta_j > D$ the renormalized coupling flows to smaller values, $g_j' < g_j$ and the RG flows *into* the fixed point. We then say that an operator is *relevant* if its scaling dimension satisfies $\Delta_j < D$, and that it is *irrelevant* if $\Delta_j > D$. If $\Delta_j = D$, then we say that operator is *marginal*.

To go beyond this simple dimensional analysis, one has to include the effects of fluctuations. To lowest orders in the couplings one finds (Cardy, 1996)

$$a \frac{dg_j}{da} = (D - \Delta_j) g_j + \sum_{k,l} C_{jkl}\, g_k g_l + \cdots \tag{13}$$

where $\{C_{jkl}\}$ are the coefficients of the OPE shown in Eq. (6). This expression is the general form of a perturbative renormalization group, and it is valid close enough to a fixed point.

Wilson and Fisher (1972) used a similar approach to analyze how fluctuations alter the results of the Landau–Ginzburg theory. They considered the partition function of Eq. (7) with the action of Eq. (8). Instead of working in real space, they considered the problem in momentum space and partitioned the field configurations into slow and fast modes

$$\phi(x) = \phi_<(x) + \phi_>(x) \tag{14}$$

where $\phi_>(x)$ are configurations whose Fourier components have momenta in the range $b\Lambda < |p| < \Lambda$, where Λ is a UV momentum cutoff and $b < 1$. Hence, if we choose $b \to 1$, the fast modes $\phi_>(x)$ have components in a thin momentum shell near the UV cutoff Λ. Conversely, the slow modes $\phi_<(x)$ have momenta in the range $0 \le |p| < b\Lambda$. One can then use Feynman diagrams to integrate out the fast modes and derive an effective low-energy action with renormalized couplings. In the case of a free field theory (with $\lambda = 0$), the scaling dimension of the ϕ^4 operator is $\Delta_4 = 2(D - 2)$ whereas the ϕ^2 operator has dimension $\Delta_2 = D - 2$. Upon defining a dimensionless mass and coupling constant by $m^2 = t\Lambda^2$ and $\lambda = g\Lambda^{4-D}$, the beta functions are found to be (Fradkin, 2021)

$$\beta(t) = -\Lambda \frac{dt}{d\Lambda} = 2t + \frac{g}{2} - \frac{gt}{2} + \cdots \tag{15}$$

$$\beta(g) = -\Lambda \frac{dg}{d\Lambda} = (4 - D)g - \frac{3}{2}g^2 + \cdots \tag{16}$$

(where we absorbed an uninteresting factor in the definition of the coupling constant).

The RG flows of Eq. (16) show that the free-field (Gaussian) fixed point at $g = 0$ is stable for $D > 4$ and the asymptotic IR behavior is the same as predicted by the Landau–Ginzburg theory. However, for $D < 4$, the free-field fixed point becomes unstable and a new fixed point arises at $g^* = \frac{2}{3}\epsilon + O(\epsilon^2)$, where we have set $\epsilon = 4 - D$. This is the Wilson–Fisher fixed point. At this fixed point, the correlation length diverges with an exponent $\nu = \frac{1}{2} + \frac{\epsilon}{12} + O(\epsilon^2)$, which deviates from the predictions of the Landau–Ginzburg theory. The small parameter of this expansion is ϵ, and this is known as the ϵ expansion.

The Wilson–Fisher (WF) fixed point is an example of a nontrivial fixed point at which the correlation length is divergent. It has only one relevant operator, the mass term, which in the IR flows into the symmetric phase for $t > 0$ and flows to the broken symmetry for $t < 0$. Conversely, in the UV, it flows into the WF fixed point. For these reasons, condensed matter physicists say that this is an IR unstable (or critical) fixed point while high-energy physicists say that it is the UV fixed point. At this fixed point, a nontrivial field theory can be defined with nontrivial interactions. UV fixed points also define examples of what in high-energy physics are called renormalizable field theories and can be used to define a continuum field theory.

The $D = 4$-dimensional theory is special in that the ϕ^4 operator is marginal. As can be seen in Eq. (16), at $D = 4$ the beta function for the dimensionless coupling constant g does not have a linear term and is quadratic in g. In this case the operator is marginally irrelevant, and its beta function has the same behavior as the beta function of Gell-Mann and Low for QED. Such theories are said to have a "triviality problem" since, up to logarithmic corrections to scaling, there are no interactions in the IR and, conversely, become large in the UV.

There are also fixed points at which the correlation length $\xi \to 0$. These fixed points are IR stable (and in a sense trivial). These stable fixed points are sinks of the IR RG flows. Such fixed points define stable phases of matter, for example the broken symmetry state, and the symmetric (or unbroken state). However in the UV, they are unstable and in high-energy physics such fixed points correspond to nonrenormalizable field theories.

More sophisticated methods are needed to go beyond the lowest order beta functions of Eq. (13), and the computation of critical exponents beyond the leading nontrivial order. Possibly, the record high-precision calculations have been done for ϕ^4 theory for which the beta function is known to be $O(\epsilon^5)$. This has been achieved using the method of dimensional regularization ('t Hooft and Veltman, 1972; Bollini and Giambiagi, 1972; Amit, 1980) (with minimal subtraction). Special resummation methods (Borel-Padé) have been used to do these calculations in $D = 3$ dimensions (Zinn-Justin, 2002). Remarkably, these results are so precise that in the case of the superfluid transition, which is well described by a ϕ^4 theory with a complex field, the results could only be tested in the microgravity environment of the International Space Station!

Asymptotic freedom

There are several physical systems of great interest whose beta function has the form

$$\beta(g) = Ag^2 + \cdots \tag{17}$$

The coupling constant has a different interpretation in each theory and the constant $A > 0$, opposite to the sign of the beta function found in QED and ϕ^4 theory in $D = 4$ dimensions. This beta function means that while the associated operator is marginal, with this sign, it is actually marginally relevant. This also means that the fixed point is unstable in the IR but the departure from the fixed point is logarithmically small. Conversely, in the UV, the RG flows into the fixed point and the effective constant is weak at short distances. This is the origin of the term asymptotic freedom (Gross and Wilczek, 1973). The paradigmatic examples of theories with a beta function of this form are the Kondo problem, the 2D nonlinear sigma model, and the $D = 4$ dimensional Yang–Mills non-Abelian gauge theory.

The Kondo problem is the theory of a localized spin-1/2 degree of freedom in a metal. The electrons of the metal couple to this quantum impurity through an exchange interaction of the impurity and the magnetic moment density of the mobile electrons in the metal with coupling constant J. This problem is actually one-dimensional since only the s wave channel of the mobile (conduction band) electrons actually couple to the localized impurity. In 1970, Philip Anderson developed a theory of the Kondo problem in terms of the renormalization of the Kondo coupling constant g as a function of the energy scale (Anderson, 1970). Anderson used perturbation theory in J to progressively integrate the modes of the conduction electrons close to an effective bandwidth E_c and found that the beta function has the form of Eq. (17)

$$E_c \frac{dJ}{dE_c} = -\rho J^2 + \cdots \tag{18}$$

where ρ is the density of states at the Fermi energy of the conduction electrons. This work implied that the free-impurity fixed point is IR unstable and that the effective coupling constant J increases as the energy cutoff E_c is lowered. He argued that at some energy scale, the Kondo scale, perturbation theory breaks down and that there is a crossover to a strong coupling regime, which is not accessible in perturbation theory.

Shortly thereafter, in 1973, Wilson developed a numerical renormalization group approach, which showed that the Kondo problem is indeed a crossover from the free impurity fixed point to the "renormalized" FL (Wilson, 1975). In addition, Wilson used the numerical renormalization group to examine the approach to the strong coupling fixed point and showed that it is characterized by a Wilson ratio, a universal number obtained from the low temperature specific heat and the impurity magnetic susceptibility (in suitable units). Wilson's numerical RG predicted a number close to 2π for this ratio. In 1980, N. Andrei and P. Wiegmann showed (independently) that the Kondo problem is an example of an integrable field theory that can be solved by the Bethe ansatz (Andrei, 1980; Wiegmann, 1980). Their exact result was consistent with Wilson's RG, including the numerical value of the Wilson ratio.

In 1972, Gerard 't Hooft and Martinus Veltman showed that Yang–Mills gauge theory is renormalizable ('t Hooft and Veltman, 1972). This groundbreaking result opened the door to use quantum field theory to develop the theory of strong interactions in particle physics known as Quantum Chromodynamics (QCD). In 1973, Gross and Wilczek (1973) and, independently, Politzer (1973) computed the renormalization group beta function of Yang–Mills theory with gauge group G and found it to be of the same form as Eq. (17),

$$\Lambda\frac{dg}{d\Lambda}=-\frac{g^3}{16\pi^2}\frac{11}{3}C_2(G)+\cdots \tag{19}$$

where g is the Yang–Mills coupling constant and Λ is a UV momentum scale. Here, $C_2(G)$ is the quadratic Casimir for a gauge group G. For $SU(3)$, the case of physical interest, $C_2(SU(3))=3$. This result implies that under the RG at large momenta (short distances), the Yang–Mills coupling constant flows to zero (up to logarithmic corrections). This result holds in the presence of quarks, provided the number of quark flavors is less than a critical value. Hence at short distances, the effective coupling is weak. Gross and Wilczek called this phenomenon asymptotic freedom. This behavior was consistent with the observation of weakly coupled quarks in deep inelastic scattering experiments. However, the flip side of asymptotic freedom is that at low energies (long distances), the coupling constant grows without limit, which implies that at low energies perturbation theory is not applicable. This strong infrared behavior suggested that in QCD quarks are permanently confined in color neutral bound states (hadrons). However, unlike the Kondo problem we just discussed, QCD is not an integrable theory (so far as we know) and to show that it confines has required the development of lattice gauge theory (Wilson, 1974; Kogut and Susskind, 1975). To this date, the best evidence for quark confinement has been obtained using large-scale Monte Carlo simulations in lattice gauge theory (Creutz et al., 1983).

We close this section with a discussion of an important case: the nonlinear sigma models. The $O(N)$ nonlinear sigma model is the continuum limit of the classical Heisenberg model for a spin with N components. Historically, the nonlinear sigma model is the effective field theory for pions in particle physics. We will discuss its role in the theory of quantum antiferromagnets in Section "Quantum antiferromagnets and nonlinear sigma models" and especially in the case of quantum antiferromagnetic spin chains in the Section "Nonlinear sigma models and antiferromagnetic quantum spin chains."

The simplest nonlinear sigma model is a theory of an N-component scalar field $\boldsymbol{n}(x)$ which satisfies the unit length local constraint, $\boldsymbol{n}^2(x)=1$. The Euclidean Lagrangian is

$$\mathcal{L}=\frac{1}{2g}(\partial_\mu\boldsymbol{n}(x))^2 \tag{20}$$

where g is the coupling constant (the temperature in the classical Heisenberg model). At the classical level, that is, in the broken symmetry phase, where $\langle\boldsymbol{n}\rangle\neq 0$, this model describes the $N-1$ massless modes (Goldstone bosons) of the spontaneously broken $O(N)$ symmetry. Dimensional analysis shows that the coupling constant has units of ℓ^{D-2}. Hence, we expect to find marginal behavior at $D=2$. In 1975, Alexander Polyakov used a momentum shell renormalization group in $D=2$ dimensions and showed that the beta function of this model is (here a is the short-distance cutoff) (Polyakov, 1975b)

$$\beta(g)=a\frac{dg}{da}=\frac{N-2}{2\pi}g^2+O(g^3) \tag{21}$$

Hence, in $D=2$ dimensions also this theory is asymptotically free. As in the other examples we just discussed, asymptotic freedom here also implies that the coupling constant g grows to large values in the low-energy (long-distance) regime. In close analogy with Yang–Mills theory in $D=4$ dimensions, Polyakov conjectured that the $O(N)$ nonlinear sigma model also undergoes dynamical dimensional transmutation (Gross and Wilczek, 1973), that the global $O(N)$ symmetry is restored and that for all values of the coupling constant g the theory is in a massive with a finite correlation length $\xi\sim\exp((N-2)/2\pi g)$. Extensive numerical simulations, used to construct a renormalization group using Monte Carlo simulations (Shenker and Tobochnik, 1980), showed that there is indeed a smooth crossover from the weak coupling (low temperature) regime to the high temperature regime where the correlation length is finite. The nonlinear sigma model is a renormalizable field theory in $D=2$ dimensions (Brézin and Zinn-Justin, 1976). For $D>2$ dimensions, it can be studied using the $2+\epsilon$ expansion (Brézin and Zinn-Justin, 1976; Zinn-Justin, 2002), which predicts the existence of a nontrivial UV fixed point and a phase transition from a Goldstone phase to a symmetric phase.

It turns out that there is a significant number of asymptotically free nonlinear sigma models in $D=2$ dimensions, many of physical interest (Friedan, 1985), in particular nonlinear sigma models whose target manifold is a coset space, a quotient of a group G and a subgroup H. The $O(N)$ nonlinear sigma model is an example since the broken symmetry space leaves the $O(N-1)$ subgroup unbroken (the manifold of the Goldstone bosons). In that case, the quotient is $O(N)/O(N-1)$, which is isomorphic to the $N-1$ dimensional sphere S_{N-1}. In later sections, we will discuss other examples in which more general nonlinear sigma models play an important role.

Models on coset spaces arise in the theory of Anderson localization in $D = 2$ dimensions. Anderson localization is the problem of a fermion (an electron) in a disordered system in which the electron experiences a random electrostatic potential. In the limit of strong disorder Philip Anderson showed that all one-particle states are exponentially localized and the diffusion constant (and the conductivity) vanishes (Anderson, 1958). There was still the question of when it is possible for the electron to have a finite diffusion constant (and conductivity). In $D = 2$ dimensions, the conductivity is a dimensionless number which suggests that this may be the critical dimension for diffusion. Abrahams, Anderson, Licciardello, and Ramakrishnan used a weak disorder calculation to construct a scaling theory that implied that in $D = 2$ dimensions, the RG flow of the conductivity at long distances (large samples) flows to zero and all states are localized (Abrahams et al., 1979). Shortly thereafter, Wegner gave strong arguments that showed that the existence of diffusion implied that there are low-energy "diffussion" modes which behaved as Goldstone modes of a nonlinear sigma model on the quotient manifold $O(N_+ + N_-)/O(N_+) \times O(N_-)$ in the "replica limit" $N_\pm \to 0$ (Wegner, 1979). A field theory approach to this nonlinear sigma model was developed by McKane and Stone (1981) and by Hikami (1981).

Quantum criticality

Quantum criticality is the theory of a phase transition of a system (e.g., a magnetic system) at zero temperature that occurs as a coupling constant (or parameter) is varied continuously. Although not necessarily under that name, this question has existed as a conceptual problem for a long time. In particular, already in 1973, Wilson considered the problem of the behavior of quantum filed theories below four spacetime dimensions and their phase transitions (Wilson, 1973).

The modern interest in condensed matter physics stems from discoveries made since the late 1980s. Since that time the behavior of condensed matter systems at a *quantum* critical point has emerged as a major focus in the field. There were several motivations for this problem. One was (and still is) to understand the behavior of quantum antiferromagnets in the presence of frustrating interactions. Frustrating interactions are interactions that favor incompatible types of antiferromagnetic orders. The result is the presence of intermediate nonmagnetic "valence bond" phases that favor the formation of spin singlets between nearby spins. These phases typically either break the point group symmetry of the lattice or are spin liquids (which will be discussed below). Another motivation is that doped quantum antiferromagnets typically harbor superconducting phases (among others) whose high-temperature behavior is a "strange" metal that violates the basic assumptions (and behaviors) of FLs. The most studied version of this problem is the case of the copper oxide high temperature superconductors. It was conjectured that there is a quantum critical point inside the superconducting phase at which the antiferromagnetic order (or other orders) disappears and which may be the reason for the strange metal behavior above the superconducting critical temperature. Many of these questions are discussed in depth by Sondhi et al. (1997) and in the textbook by Sachdev (2011).

Dynamic scaling

We will consider a general quantum phase transition and assume that it is scale invariance. However, except for the case of relativistic quantum field theories, in condensed matter systems, space and time do not need to scale in the same way. Let us assume that the system of interest has just one coupling constant g and that the system of interest has a quantum phase transition (at zero temperature) at some critical value g_c between two phases, for instance one with a spontaneously broken symmetry and a symmetric phase. If the quantum phase transition is continuous, then the correlation length ξ will diverge at g_c and so will the correlation time ξ_t. However, these two scales are in general different and do not necessarily diverge at the same rate. So, in general, if some physical quantity is measured at the quantum critical point at some momentum $\boldsymbol{p}$ and frequency ω, the length scale of the measurement is $2\pi/|\boldsymbol{p}|$ and at a frequency is $\omega \sim |\boldsymbol{p}|^z$, where z is the dynamic critical exponent. Let us say that we measure the observable O at momentum $\boldsymbol{p}$ and frequency ω at g_c. Scale invariance in both space and time means that at g_c, the observable $O(\boldsymbol{p}, \omega)$ at momentum $\boldsymbol{p}$ and frequency ω must scale as

$$O(\boldsymbol{p}, \omega) = |\boldsymbol{p}|^{-\Delta_O} \tilde{O}(|\boldsymbol{p}|^z/\omega) \tag{22}$$

where Δ_O is the scaling dimension of the observable O.

The situation changes at finite temperature T. A quantum field theory at temperature T is described by a path integral on a manifold, which, along the imaginary time direction τ, is finite of length $2\pi/T$ and periodic for a theory bosonic fields and antiperiodic for fermionic fields (Fradkin, 2021). Since the imaginary time direction is finite, the behavior for correlation times $\xi_\tau < 2\pi/T$ and $\xi_\tau > 2\pi/T$ must be different. Indeed, in the first regime, the behavior is essentially the same as at $T = 0$ while in the second, it should be given by the classical theory in the same space dimension. At the quantum critical point g_c, there is only one time scale $\xi_\tau \sim 2\pi/T$ and only one length scale $\xi \sim (2\pi/T)^{1/z}$.

The Ising model in a transverse field

The prototype of the quantum phase transition is the Ising model in a transverse field. This model describes a system of spin-1/2 degrees of freedom with ferromagnetic interactions with uniaxial anisotropy in the presence of a transverse uniform magnetic field. The Hamiltonian is

$$H = -J\sum_{\langle \boldsymbol{r}, \boldsymbol{r}'\rangle}\sigma_3(\boldsymbol{r})\sigma_3(\boldsymbol{r}') - h\sum_{\boldsymbol{r}}\sigma_1(\boldsymbol{r}) \tag{23}$$

where J and h are the exchange coupling constant and the strength of the transverse field, respectively. Here, σ_1 and σ_3 are the two Pauli matrices defined on the sites $\{\boldsymbol{r}\}$ of a lattice with ferromagnetic interactions between spins on nearest neighboring sites. The Hilbert space is the tensor product of the states of the spins at each site of the lattice. At each site, there are two natural bases of states: the eigenstates of σ_3, which we denote by $|\uparrow\rangle$ and $|\downarrow\rangle$ (whose eigenvalues are ± 1), and the eigenstates of σ_1, which we denote by $|\pm\rangle$ (whose eigenvalues are also ± 1).

It is well known that the Ising model in a transverse field on a hypercubic lattice in D dimensions is equivalent to a classical Ising model in $D + 1$ dimensions (Fradkin and Susskind, 1978; Kogut, 1979). These two models are related through the transfer matrix. Indeed, a classical Ising model can be regarded as a path integral representation of the quantum model in one dimension less. For simplicity we will see how this works for the 2D classical ferromagnetic Ising model of Eq. (1), but the construction is general. We will regard the configuration of spins on a row of the 2D lattice as a state of a quantum system, and the set of states on all rows as the evolution of the state along the perpendicular direction that we will regard as a discretized imaginary time. The contribution from two adjacent rows to the partition function defines the matrix element of a matrix between two arbitrary configurations. In Statistical Physics, this matrix is known as the transfer matrix $\hat{T}$ and the full partition function (with periodic boundary conditions) is

$$Z = \mathrm{tr}\hat{T}^{N_\tau} \tag{24}$$

where N_τ is the number of rows. For the case of the ferromagnetic Ising model (actually, for any unfrustrated model), the transfer matrix can always be constructed to be Hermitian. This property holds in fact for any theory that satisfies a property known as reflection positivity which requires that all (suitably defined) correlation functions be positive. For theories of this type, and the Ising model is an example, the matrix elements of the transfer matrix can be identified with the matrix element of the evolution operator of a quantum theory for a small imaginary time step (Fradkin and Susskind, 1978). Also, the positivity of the correlators is equivalent to the condition of positivity of the norm of states in the quantum theory.

For the classical models that satisfy these properties, all directions of the lattice are equivalent. Moreover, asymptotically close to the critical point, the behavior of all the correlators becomes isotropic, that is, invariant under the symmetries of Euclidean space. This means that the arbitrary choice of the direction for the transfer matrix is irrelevant. Consequently, in the quantum model, its equal-time correlators behave the same way as its correlation functions in imaginary time. In other words, space and time behave in the same way and the quantum theory is relativistically invariant. This implies at the quantum critical point the energy $\varepsilon(\boldsymbol{p})$ of its massless excitations should behave as $\varepsilon(\boldsymbol{p}) = v\,|\boldsymbol{p}|$. In a relativistic theory the dynamical critical exponent must be $z = 1$ and the coefficient v is the speed of the excitations (the "speed of light"). We should note that this is not necessarily always the case. There are in fact classical systems, for example, liquid crystals (Chaikin and Lubensky, 1995), which are spatially anisotropic and map onto quantum mechanical theories in one less dimension for which the dynamical critical exponent $z \neq 1$. One such example are the Lifshitz transitions of nematic liquid crystals in three dimensions and the associated quantum Lifshitz model in $D = 2$ dimensions, for which the dynamical exponent is $z = 2$ (Ardonne et al., 2004).

Just as in the classical counterpart in $D + 1$ dimensions, the quantum model in $D \geq 1$ has two phases: a broken symmetry ferromagnetic phase for $J \gg h$ and a symmetric paramagnetic phase for $h \gg J$. In the symmetric phase, the ground state is unique (asymptotically is the eigenstate of σ_1 with eigenvalue $+ 1$) while in the broken symmetry phase, the ground state is doubly degenerate (and asymptotically is an eigenstate of σ_3) and there is a nonvanishing expectation value of the local order parameter $\langle\sigma_3(\boldsymbol{r})\rangle \neq 0$. In the symmetric phase, the correlation function of the local order parameter decays exponentially with distance with a correlation length ξ, as does the connected correlation function in the broken symmetry phase. The model has a continuous quantum phase transition at a critical value of the ratio h/J. For general space dimensions $D > 1$, this model is not exactly solvable and much of what we know about it is due to large-scale numerical simulations.

This problem was solved exactly in one-dimension (Pfeuty, 1970) using the Jordan–Wigner transformation that maps a one-dimensional quantum spin system to a theory of free fermions (Lieb et al., 1961). The fermion operators at site j are

$$\chi_1(j) = K(j-1)\sigma_3(j), \qquad \chi_2(j) = i\hat{K}(j)\sigma_3(j) \tag{25}$$

where $K(j)$ is the kink creation operator (i.e., the operator that creates a domain wall between sites j and $j + 1$ (Fradkin and Susskind, 1978), and is given by

$$K(j) = \prod_{n\leq j}\sigma_1(n) \tag{26}$$

The operators $\chi_1(j)$ and $\chi_2(j)$ are Hermitian, $\chi_j^\dagger(n) = \chi_j(n)$ and obey the *anticommutation* algebra

$$\{\chi_j(n), \chi_{j'}(n')\} = 2\delta_{jj'}\delta_{nn'}. \tag{27}$$

Hence, they are fermionic operators and are Hermitian, anticommute with each other and square to the identity. Operators of this type are called *Majorana fermions*.

Alternatively, we can use the more conventional (Dirac) fermion operators $c(n)$ and its adjoint $c^\dagger(n)$ which are related to the Majorana fermions as

$$c(n) = \chi_1(n) + i\chi_2(n), \qquad c^\dagger(n) = \chi_1(n) - i\chi_2(n) \tag{28}$$

which obey the standard anticommutation algebra

$$\{c(n), c(n')\} = \{c^\dagger(n), c^\dagger(n')\} = 0, \qquad \{c(n), c^\dagger(n')\} = \delta - nn'. \tag{29}$$

In this sense, a Majorana fermion is half of a Dirac fermion.

In terms of the Majorana operators, the Hamiltonian of Eq. (23) becomes

$$H = i\sum_j \chi_1(j)\chi_2(j) + ig\sum_j \chi_2(j)\chi_1(j+1) \tag{30}$$

where we have rescaled the Hamiltonian by a factor of h and the coupling constant is $g = J/h$. Here, we have not specified the boundary conditions (which depend on the fermion parity). Qualitatively, the Majorana fermions can be identified with the domain walls of the classical models. In the Ising model, the number of domain walls on each row is not conserved but their parity is. Likewise, the number of Majorana fermions N_F is not conserved either but the fermion parity $(-1)^{N_F}$ is conserved.

It is an elementary exercise to show that the spectrum of this theory has a gap $G(g)$ that vanishes at $g_c = 1$ as $G(g) \sim |g - g_c|^\nu$, with an exponent $\nu = 1$. Since the Hamiltonian of Eq. (30) is quadratic in the Majorana operators, these operators obey linear equations of motion. In the scaling regime, we take the limit of the lattice spacing $a \to 0$ and the coupling constant $g \to g_c = 1$ while keeping the quantity $m = (g - g_c)/a$ fixed. In this regime, the two-component Hermitian spinor field $\chi = (\chi_1, \chi_1)$, and $\chi^\dagger = \chi$, satisfies a Dirac equation

$$(i\partial\!\!\!/ - m)\chi = 0 \tag{31}$$

where we set the speed $v = 1$, and defined the 2×2 Dirac gamma-matrices $\gamma_0 = \sigma_2$, $\gamma_1 = i\sigma_3$, and $\gamma_5 = \sigma_1$. Upon defining $\bar{\chi} = \chi^T\gamma_0$, we find that the Lagrangian of this field theory is

$$\mathcal{L} = \bar{\chi} i\partial\!\!\!/ \chi - \frac{1}{2} m\, \bar{\chi}\chi \tag{32}$$

which indeed becomes massless at the quantum phase transition of the Ising spin chain. For these considerations, we say that the phase transition of the Ising model (2D classical or 1D quantum) is in the universality class of massless Majorana fermions where $m \to 0$. In Eq. (32), we have used the standard Feynman slash notation, $a\!\!\!/ = \gamma_\mu a^\mu$, where a^μ is a vector.

Quantum antiferromagnets and nonlinear sigma models

As we noted above, the discovery of high temperature superconductors in the copper oxide compounds prompted the study of the behavior of these strongly correlated materials at low temperatures and of possible quantum phase transitions which they may host. The prototypical cuprate material La_2CuO_4 is a quasi two-dimensional Mott insulator that exhibits long-range antiferromagnetic order below a critical temperature T_c. A simple microscopic model is a spin-S quantum Heisenberg antiferromagnet on the 2D square lattice of the Cu atoms, whose Hamiltonian is

$$H = \frac{1}{2}\sum_{\boldsymbol{r},\boldsymbol{r}'} J(|\boldsymbol{r} - \boldsymbol{r}'|)\, \boldsymbol{S}(\boldsymbol{r}) \cdot \boldsymbol{S}(\boldsymbol{r}') \tag{33}$$

where $\boldsymbol{S}$ are the spin-S angular momentum operators. We will consider the case where the exchange interaction for nearest neighbors J is dominant and a weaker $J' \ll J$ for next nearest neighbors. In this section we do not consider the regime $J' \simeq J$ in which the interactions compete for incompatible ground states due to frustration effects.

Spin coherent states

The simplest way to see the physics of this antiferromagnet is to construct a path-integral representation for a spin-S system using spin coherent states (Perelomov, 1986; Fradkin and Stone, 1988; Wiegmann, 1989). For details, see Fradkin (2013) which we follow here. A coherent state of the ($2S + 1$-dimensional) spin-S representation of $SU(2)$ is the state $|\boldsymbol{n}\rangle$, labeled by the spin polarization unit vector $\boldsymbol{n}$

$$|\boldsymbol{n}\rangle = e^{i\theta(\boldsymbol{n}_0 \times \boldsymbol{n}) \cdot \boldsymbol{S}}\, |S, S\rangle \tag{34}$$

where $\boldsymbol{n}^2 = 1$. The states of the spin-S representation are spanned by the eigenstates of S_3 and $\boldsymbol{S}^2$,

$$S_3\, |S, M\rangle = M|S, M\rangle, \qquad \boldsymbol{S}^2|S, M\rangle = S(S+1)|S, M\rangle \tag{35}$$

and $|S, S\rangle$ is the highest weight state with eigenvalues S and $S(S + 1)$. In Eq. (34), $\boldsymbol{n}_0$ is a unit vector along the axis of quantization (the direction $\boldsymbol{e}_3$), and θ is the colatitude, such that $\boldsymbol{n} \cdot \boldsymbol{n}_0 = \cos\theta$. Two spin coherent states, $|\boldsymbol{n}_1\rangle$ and $|\boldsymbol{n}_2\rangle$, are not orthonormal,

$$\langle \boldsymbol{n}_1 | \boldsymbol{n}_2 \rangle = e^{i\Phi(\boldsymbol{n}_1,\boldsymbol{n}_2,\boldsymbol{n}_0)\ S} \left(\frac{1 + \boldsymbol{n}_1 \cdot \boldsymbol{n}_2)}{2} \right)^S \tag{36}$$

where $\Phi(\boldsymbol{n}_1, \boldsymbol{n}_2, \boldsymbol{n}_0)$ is the area of the spherical triangle of the unit sphere spanned by the unit vectors $\boldsymbol{n}_1$, $\boldsymbol{n}_2$, and $\boldsymbol{n}_0$. However, there is an ambiguity in the definition of the area of the spherical triangle since the sphere is a 2-manifold without boundaries: if the "inside" triangle has spherical area Φ, the complement ("outside") triangle has area $4\pi - \Phi$. Thus, the ambiguity of the phase prefactor of Eq. (36) is

$$e^{i4\pi S} = 1 \tag{37}$$

since S is an integer or a half-integer. So, the quantization of the representations of $SU(2)$ makes the ambiguity unobservable. In addition, the spin coherent states $|\boldsymbol{n}\rangle$ satisfy the resolution of the identity

$$I = \int |\boldsymbol{n}\rangle\langle \boldsymbol{n}| \left(\frac{2S+1}{4\pi}\right) \delta(\boldsymbol{n}^2 - 1)\, d^3 n \tag{38}$$

and

$$\langle \boldsymbol{n} | \boldsymbol{S} | \boldsymbol{n} \rangle = S\boldsymbol{n} \tag{39}$$

Path integral for a spin-S degree of freedom

As an example, consider problem of a spin-S degree of freedom coupled to an external magnetic field $\boldsymbol{B}(t)$ that varies slowly in time. The (time-dependent) Hamiltonian is given by the Zeeman coupling

$$H(t) = \boldsymbol{B}(t) \cdot \boldsymbol{S} \tag{40}$$

As usual, the path integral is obtained by inserting the (over-complete) set of coherent states at a large number of intermediate times. The resulting path integral is a sum of the histories of the spin polarization vector $\boldsymbol{n}(t)$

$$Z = \text{tr}\ \exp\left(i \int_0^T dt\ H(t) \right) = \int \mathcal{D}\boldsymbol{n}\ \exp(i\mathcal{S}[\boldsymbol{n}]) \prod_t \delta(\boldsymbol{n}^2(t) - 1) \tag{41}$$

where the action is

$$\mathcal{S} = S\, \mathcal{S}_{WZ}[\boldsymbol{n}] - S \int_0^T dt\ \boldsymbol{B}(t) \cdot \boldsymbol{n}(t) \tag{42}$$

where $\mathcal{S}_{WZ}[\boldsymbol{n}]$ is the Wess–Zumino action

$$\mathcal{S}_{WZ}[\boldsymbol{n}] = \int_0^T dt\ \boldsymbol{A}[\boldsymbol{n}] \cdot \partial_t \boldsymbol{n} \tag{43}$$

$$= \int_0^1 d\tau \int_0^T dt\ \boldsymbol{n}(t,\tau) \cdot \partial_t \boldsymbol{n}(t,\tau) \times \partial_\tau \boldsymbol{n}(t,\tau) \tag{44}$$

where $\boldsymbol{A}[\boldsymbol{n}]$ is the vector potential of a Dirac magnetic monopole (of unit magnetic charge) at the center of the unit sphere. The vector potential $\boldsymbol{A}[\boldsymbol{n}]$ has a singularity associated with the Dirac string of the monopole. We can write an equivalent expression that is singularity-free using Stokes Theorem. We did this in the second line of Eq. (44) which required to extend the circulation of $\boldsymbol{A}$ on the closed path described by $\boldsymbol{n}(t)$ to the flux of the vector potential through the submanifold Σ of the unit sphere S_2 whose boundary is the history $\boldsymbol{n}(t)$, that is, the area of Σ. The smooth (and arbitrary) extension of configuration $\boldsymbol{n}(t)$ to the interior of Σ is done by defining $\boldsymbol{n}(t, \tau)$ such that $\boldsymbol{n}(t, 1) = \boldsymbol{n}_0$, $\boldsymbol{n}(t, 0) = \boldsymbol{n}(t)$, and $\boldsymbol{n}(0, \tau) = \boldsymbol{n}(T, \tau)$. Since $\mathcal{S}_{WZ}$ is the area of the submanifold Σ of the unit sphere S_2, just as in Eq. (37), here too there is an ambiguity of 4π in the definition of the area. Here too, this ambiguity is invisible since the spin S is an integer or a half-integer.

The path integral of Eq. (41) was derived first by Berry (1984) (and extended by Simon (1983)). The first term (which we called Wess–Zumino by analogy with its field theoretic versions) is called the *Berry Phase*. The role of this term, which is first order in time derivatives, is to govern the quantum dynamics of the spin which, in the presence of a uniform magnetic field, executes a precessional motion of the (Bloch) sphere. It is also apparent from this expression that in the large-S limit, the path integral can be evaluated by means of a semiclassical approximation.

The coherent-state construction shows that this problem is equivalent to the path integral of a formally massless nonrelativistic particle of unit electric charge on the surface of the unit sphere with a magnetic monopole of magnetic charge S in its interior! This is not surprising since the Hilbert space of a nonrelativistic particle moving on the surface of a sphere with and radial magnetic field (the field of a magnetic monopole) has a Landau level-type spectrum with a degeneracy given by the flux. The condition of a massless particle means that only the lowest Landau level survives and all other levels have an infinite energy gap.

The coherent state approach has been used to derive a path integral formulation for ferromagnets and antiferromagnets. A detailed derivation can be found in Fradkin (2013).

Quantum ferromagnet

We will consider first the simpler case of a quantum ferromagnet and in Eq. (33) we will set $J = -|J| < 0$ for nearest neighbors and zero otherwise. The action for the path integral for the spin-S quantum Heisenberg ferromagnet on a hypercubic lattice is

$$\mathcal{S} = S\sum_{\boldsymbol{r}} \mathcal{S}_{WZ}[\boldsymbol{n}(\boldsymbol{r},t)] - \frac{|J|S^2}{2}\sum_{\langle \boldsymbol{r},\boldsymbol{r}'\rangle}\int_0^T dt\ (\boldsymbol{n}(\boldsymbol{r},t) - \boldsymbol{n}(\boldsymbol{r}',t))^2 \tag{45}$$

where we have subtracted the classical ground state energy. The order parameter for this theory is the expectation value of the local magnetization, $\boldsymbol{n} = \langle \boldsymbol{n}(\boldsymbol{r})\rangle$, which is constant in space but points in an arbitrary direction in spin space.

In the low-energy regime, the important configurations are slowly varying in space and we can simply approximate the action of Eq. (45) by its continuum version in d space dimensions

$$\mathcal{S} = \frac{S}{a_0^d}\int d^d x\ \ \mathcal{S}_{WZ}[\boldsymbol{n}(\boldsymbol{x},t)] - \frac{|J|S^2}{2a_0^d}\int d^d x\int_0^T dt(\nabla\boldsymbol{n}(\boldsymbol{x},t))^2 \tag{46}$$

where a_0 is the lattice spacing. As before, the path integral is done for a field, which satisfies everywhere in space-time the constraint $\boldsymbol{n}^2(\boldsymbol{x}, t) = 1$. This action can be regarded as nonrelativistic nonlinear sigma model.

It is straightforward to show that the classical equations of motion for this theory are the Landau–Lifshitz equations

$$\partial_t \boldsymbol{n} = |J|Sa_0^2\ \boldsymbol{n}\times\nabla^2\boldsymbol{n} \tag{47}$$

subject to the constraint $\boldsymbol{n}^2 = 1$. Due to the constraint, the Landau–Lifshitz equation is nonlinear. We will decompose the field into a longitudinal and two transverse components, σ and $\boldsymbol{\pi}$, respectively

$$\boldsymbol{n} = \begin{pmatrix}\sigma\\ \boldsymbol{\pi}\end{pmatrix} \tag{48}$$

subject to the constraint $\sigma^2 + \boldsymbol{\pi}^2 = 1$. The linearized Landau–Lifshitz equations become (to linear order in $\boldsymbol{\pi}$)

$$\partial_t\pi_1 \simeq -|J|Sa_0^2\nabla^2\pi_2, \qquad \partial_t\pi_2 \simeq +|J|Sa_0^2\nabla^2\pi_1 \tag{49}$$

The solution to these equations are ferromagnetic spin waves (magnons or Bloch waves) which satisfy the dispersion relation

$$\omega(\boldsymbol{p}) \simeq |J|Sa_0^2\boldsymbol{p}^2 + O(\boldsymbol{p}^4) \tag{50}$$

which shows that the dynamic exponent for a ferromagnet is $z = 2$. Notice that in this case the two transverse components are not independent (they are effectively a dynamical pair). These are the Goldstone bosons of a ferromagnet.

Quantum antiferromagnet

Formally, the quantum antiferromagnet has a coherent state path integral whose action is

$$\mathcal{S} = S\sum_{\boldsymbol{r}} \mathcal{S}_{WZ}[\boldsymbol{n}(\boldsymbol{r},t)] - \frac{JS^2}{2}\sum_{\langle \boldsymbol{r},\boldsymbol{r}'\rangle}\int_0^T dt\ \boldsymbol{n}(\boldsymbol{r},t)\cdot\boldsymbol{n}(\boldsymbol{r}',t) \tag{51}$$

with $J > 0$. For a bipartite lattice, for example, the 1D chain, and the square and cubic lattices, the classical ground state is an antiferromagnet with a Néel order parameter, the staggered magnetization. Let $\boldsymbol{m}(\boldsymbol{r})$ be the expectation value of the local magnetization. A bipartite lattice is the union of two interpenetrating sublattices, and the local magnetization is staggered, that is, it takes values with opposite signs (with equal values) on the two sublattices. Thus, we make the change of variables, $\boldsymbol{n}(\boldsymbol{r}, t) \to (-1)^{\boldsymbol{r}}\boldsymbol{n}(\boldsymbol{r}, t)$ in Eq. (51) and find

$$\mathcal{S} = S\sum_{\boldsymbol{r}}(-1)^{\boldsymbol{r}}\mathcal{S}_{WZ}[\boldsymbol{n}(\boldsymbol{r},t)] - \frac{JS^2}{2}\sum_{\langle \boldsymbol{r},\boldsymbol{r}'\rangle}\int_0^T dt\ (\boldsymbol{n}(\boldsymbol{r},t) - \boldsymbol{n}(\boldsymbol{r}',t))^2 \tag{52}$$

We want to obtain the low energy effective action for the field $\boldsymbol{n}(\boldsymbol{r}, t)$. To this end, we decompose this field into a slowly varying part, that we will call $\boldsymbol{m}(\boldsymbol{r}, t)$, and a small rapidly varying part $\boldsymbol{l}(\boldsymbol{r}, t)$ (which represents ferromagnetic fluctuations)

$$\boldsymbol{n}(\boldsymbol{r},t) = \boldsymbol{m}(\boldsymbol{r},t) + (-1)^{\boldsymbol{r}}a_0\boldsymbol{l}(\boldsymbol{r},t) \tag{53}$$

Since $\boldsymbol{n}^2(\boldsymbol{r}, t) = 1$, we will demand that the slowly varying part also obeys the constraint, $\boldsymbol{m}^2(\boldsymbol{r}, t) = 1$, and require that the two components be orthogonal to each other, $\boldsymbol{m}\cdot\boldsymbol{l} = 0$.

Due to the behavior of the staggered Wess–Zumino terms of Eq. (52), the resulting continuum field theory turns out to have subtle but important differences between one dimension and higher dimensions. Here we will state the results for two and higher dimensions. We will discuss in detail the one-dimensional below when we discuss the role of topology.

It turns out that if the dimension $d > 1$, the contribution of the staggered Wess–Zumino terms for *smooth* field configurations is (Fradkin and Stone, 1988; Dombre and Read, 1988; Haldane, 1988b)

$$\lim_{a_0\to 0} S\sum_{r}(-1)^r \mathcal{S}_{WZ}[\boldsymbol{n}(\boldsymbol{r},t)] = S\int d^3x\, \boldsymbol{l}(\boldsymbol{x},t)\cdot \boldsymbol{m}(\boldsymbol{x},t)\times\partial_t \boldsymbol{m}(\boldsymbol{x},t) \tag{54}$$

The continuum limit of the second term of Eq. (52) in the case of a two-dimensional system is

$$\lim_{a_0\to 0}\frac{JS^2}{2}\sum_{\langle r,r'\rangle}\int_0^T dt\,\left(\boldsymbol{n}(\boldsymbol{r},t)-\boldsymbol{n}(\boldsymbol{r}',t)\right)^2 = a_0\frac{JS^2}{2}\int d^3x\,\left((\nabla \boldsymbol{m}(\boldsymbol{x},t))^2+4\boldsymbol{l}^2(\boldsymbol{x},t)\right). \tag{55}$$

The massive field $\boldsymbol{l}[\boldsymbol{x}, t]$ represents ferromagnetic fluctuations. Since this is a massive field, it can be integrated out leading to an effective field theory for the *antiferromagnetic* fluctuations $\boldsymbol{m}(\boldsymbol{x}, t)$ whose Lagrangian is that of a nonlinear sigma model

$$\mathcal{L}=\frac{1}{2g}\left(\frac{1}{v_s}(\partial_t \boldsymbol{m}(\boldsymbol{x},t)) - v_s(\nabla\boldsymbol{m}(\boldsymbol{x},t))^2\right) \tag{56}$$

where the coupling constant is $g = 2/S$ and the spin-wave velocity is $v_s = 4a_0JS$. If we allow for a weak next-nearest-neighbor interaction $J' > 0$, the coupling constant g and the spin wave velocity v_s become renormalized to $g' \simeq g/\sqrt{1-2J'/J}$ and $v_s' \simeq v_s\sqrt{1-2J'/J}$.

We conclude that the quantum fluctuations about a Néel state are well described by a nonlinear sigma model. Provided the frustration effects of the next-nearest-neighbor interactions are weak enough, the long-range antiferromagnetic Néel order should extend up to a critical value of the coupling constant g_c where the RG beta function has a nontrivial zero, which signals a quantum phase transition to a strong coupling phase without long-range antiferromagnetic order.

Motivated by the discovery of high temperature superconductivity in the strongly correlated quantum antiferromagnet La_2CuO_4 (at finite hole doping) in 1988, Chakravarty et al. (1988) utilized a quantum nonlinear sigma model to analyze this system and its quantum phase transition. La_2CuO_4 is a quasi-two-dimensional material and so it exhibits strong quantum and thermal fluctuations. The upshot of this analysis is that while at $T = 0$ the nonlinear sigma model has a quantum phase transition, at $T > 0$, the long-range order is absent in a strictly 2D system but present in the actual material due to the weak-three-dimensional interaction. So, in the strict 2D case, there is no phase transition but two different *crossover* regimes: a renormalized classical regime (without long-range order), a quantum disordered regime and a quantum critical regime. La_2CuO_4 has long-range Néel (antiferromagnetic) order at $T = 0$ and is in the renormalized classical regime (with long-range order due to the weak 3D interaction).

The nonlinear sigma model does not describe the nature of the ground state for $g > g_c$ beyond saying that there is no long-range order. The problem is that, unlike the Ising model in a transverse field, the microscopic tuning parameter is the next nearest neighbor antiferromagnetic coupling J', and to reach the regime $g \simeq g_c$, one has to make $J' \simeq J$. This is the regime in which frustration effects become strong. In this regime, the assumption that the important configurations are smooth and close to the classical Néel state is incorrect. The nature of the ground state turns out to depend on the value of S.

Topological excitations

Topology has come to play a crucial role both in condensed matter physics and in Quantum Field Theory. Topological concepts have been used to classify topological excitations such as vortices and dislocations and to provide a mechanism for phase transitions, quantum number fractionalization, tunneling processes in field theories, and nonperturbative construction of vacuum states. Here, we will discuss a few representative cases of what has become a very vast subject.

Topological excitations: Vortices and magnetic monopoles

In condensed matter physics, topological excitations play a central role in the description of topological defects and on their role in phase transitions. Here, topology integers in the classification of the configuration space into equivalence classes characterized by topological invariants (Mermin, 1979). The most studied example is vortices. Vortices play a key role in the mixed phase of type II superconductors in a uniform magnetic field (Abrikosov, 1957). Vortices also play a key role in the Statistical Mechanics of 2D superfluids and the 2D classical XY model (Kosterlitz and Thouless, 1973; Kosterlitz, 1974; Berezinskii, 1971, 1972; José et al., 1977). Dislocations and disclinations play an analogous role in the theory of classical melting (Kosterlitz and Thouless, 1973; Halperin and Nelson, 1978; Young, 1979), and 2D and 3D classical liquid crystals (Toner and Nelson, 1981; Nelson and Toner, 1981; Chaikin and Lubensky, 1995).

A similar problem occurs in Quantum Field Theory. Theories with global symmetries, such as the two-dimensional $O(3)$ nonlinear sigma model discussed above, when formulated in Euclidean space-time have *instantons*. Typically, instantons are finite Euclidean action configurations, which are also classified into equivalence classes (associated with homotopy groups) labeled by topological invariants (Coleman, 1985; Rajaraman, 1985). Instantons play a central role in understanding the nonperturbative structure of gauge theories. Gauge theories with a compact gauge group coupled to matter fields have nontrivial vortex (Nielsen and Olesen, 1973) and monopole ('t Hooft, 1976b; Polyakov, 1977, 1987) configurations, as do non-Abelian Yang–Mills gauge theories (Callan et al., 1976). Instantons have also played a central role in condensed matter physics as well, notably in Haldane's work on 1D quantum antiferromagnets (discussed below), and in the problem of macroscopic quantum tunneling and coherence (Caldeira and Leggett, 1983; Leggett et al., 1987).

Vortices in two dimensions

In this section, I will focus on the problem of the superfluid transition in 2D and the closely related problem of the phase transition of a magnet with an easy-plane anisotropy, the classical XY model. A superfluid is described by an order parameter that is a one-component complex field $\phi(\boldsymbol{x})$. If electromagnetic fluctuations are ignored, this description also applies to a superconductor. The complex field can be written in terms of an amplitude $|\phi(\boldsymbol{x})|$, whose square represents the local superfluid density, and a phase $\theta(\boldsymbol{x}) = \arg(\phi(\boldsymbol{x}))$. Deep in the superfluid phase, the amplitude is essentially constant, that we will set to be a real positive number ϕ_0, while the phase field $\theta(\boldsymbol{x})$ is periodic with period 2π and can fluctuate. Similarly, an easy-plane ferromagnet is described by a two-component real order parameter field $\boldsymbol{M}(\boldsymbol{x}) = (M_1(\boldsymbol{x}), M_2(\boldsymbol{x})) = |\boldsymbol{M}(\boldsymbol{x})|(\cos\theta(\boldsymbol{x}), \sin\theta(\boldsymbol{x}))$. Deep in the ferromagnetic phase, the amplitude $|\boldsymbol{M}|$ is essentially constant but the phase field $\theta(\boldsymbol{x})$ can fluctuate.

We will assume that we are in a regime where the local superfluid density $|\phi_0|^2$ is well formed (or, equivalently that $|\boldsymbol{M}|$ is locally well formed) but that the phase field is fluctuating. In this regime, the problem at hand is an $O(2) \simeq U(1)$ nonlinear sigma model, and its partition function takes the form

$$Z = \int \mathcal{D}\theta \exp\left(-\int d^2x \, \frac{1}{2g}\left(\partial_\mu \theta(\boldsymbol{x})\right)^2\right) \tag{57}$$

where we defined the coupling constant $g = T/J|\phi_0|^2$, where T is the temperature, J is an interaction strength, and $|\phi_0|^2$ is the magnitude (squared) of the amplitude of the order parameter, which we will take to be constant; $\kappa = J|\phi_0|^2$ is the phase stiffness.

Except for the requirement that the phase field be *locally* periodic, $\theta \simeq \theta + 2\pi$, superficially this seems to be a trivial free (Gaussian) field theory. We will see that the periodicity (or, *compactification*) condition makes this theory nontrivial. Indeed, configurations of the phase field that are weak enough and do not see the periodicity condition, can for all practical purposes, be regarded as being noncompact and ranging from $-\infty$ to $+\infty$. However there are many configurations for which the periodicity condition is essential. Such configurations are called *vortices*.

Even in the absence of vortices, the periodic (compact) nature of the phase field is essential to the physics of this problem. In fact the only allowed observables must be invariant under local periodic shifts of the phase field. This implies that the phase field θ itself is not a physical observable but that exponentials of the phase of the form $\exp(in\theta(\boldsymbol{x}))$ are physical. This operator is just the order parameter field of the *XY* model. In CFT, operators of this type are called vertex operators (Di Francesco et al., 1997; Ginsparg, 1989). We will see below that this theory has a dual field ϑ, associated with vortices, and that there are vertex operators of the dual field. In String Theory, the model of a compactified scalar is known as the compactified boson and represents the coordinate of a string on a compactified space, in this case a circle S_1 (Polchinski, 1998).

To picture a vortex, consider a large closed curve C on the 2D plane. Hence, topologically a closed curve is isomorphic to a circle, $C \simeq S_1$. The phase field $\theta(\boldsymbol{x})$ is equivalent to a unit circle S_1. Therefore the configuration space are maps of S_1 (the large circle) onto S_1 (the unit circle of the order parameter space). The configurations can be classified by the number of times the phase winds on the large circle C. The winding number is an integer called the topological charge of the configuration, the vorticity. Thus, a vortex is a configuration of the phase field $\theta(\boldsymbol{x})$ that winds by $2\pi m$ (where m is an integer):

$$\frac{(\Delta\theta)_C}{2\pi} = \frac{1}{2\pi}\oint_C d\boldsymbol{x}\cdot\nabla\theta(\boldsymbol{x}) \equiv i\oint_0^{2\pi}\frac{d\varphi}{2\pi}\, e^{i\theta(\varphi)}\partial_\varphi e^{-i\theta(\varphi)} = m \tag{58}$$

where $\varphi \in (0, 2\pi]$ is the azimuthal angle for a vector at the center of the large circle C. Here n is the vorticity or *winding number* of the configuration; $m > 0$ is a vortex and $m < 0$ is an antivortex. The vorticity is a *topological invariant* of the field the configuration $\theta(\boldsymbol{x})$ which does not change under smooth changes.

The winding number of a vortex is a topological invariant that classifies the configurations of the phase field as continuous maps of a large circle S_1 onto the unit circle S_1 defined by the phase field. In topology such continuous maps are called homotopies. The winding number classifies these maps into a discrete set of equivalence classes, which form a *homotopy group* under the composition of two configurations. In this case, the homotopy group is called $\Pi_1(S_1)$. Since the equivalence classes are classified by a topological invariant that takes integer values, the homotopy group $\Pi_1(S_1)$ is isomorphic to the group of integers, $\mathbb{Z}$ (Mermin, 1979).

The field $j_\mu(\boldsymbol{x}) = \partial_\mu\theta(\boldsymbol{x})$ is the superfluid current, and the *vorticity* $\omega(\boldsymbol{x})$ is the curl of the current, that is,

$$\omega(\boldsymbol{x}) = \epsilon_{\mu\nu}\partial_\mu j_\nu(\boldsymbol{x}) = \epsilon_{\mu\nu}\partial_\mu\partial_\nu\theta(\boldsymbol{x}) \tag{59}$$

which vanishes unless $\theta(\boldsymbol{x})$ has a branch-cut singularity across which the phase field jumps by $2\pi n$. Let $\omega(\boldsymbol{x})$ be the vorticity field with singularities at the locations $\{\boldsymbol{x}_j\}$ of vortices with topological charge m_j

$$\omega(\boldsymbol{x}) = 2\pi\sum_j m_j \delta^2(\boldsymbol{x} - \boldsymbol{x}_j) \tag{60}$$

which is satisfied by the phase field configuration

$$\theta(\boldsymbol{x}) = \sum_j 2\pi m_j \mathrm{Im}\ \ln(z - z_j) \tag{61}$$

where we have used the complex coordinates $z = x_1 + ix_2$. Away from the singularities $\{\boldsymbol{x}_j\}$, this configuration obeys the Laplace equation. Hence, it has a Cauchy–Riemann dual field $\vartheta(\boldsymbol{x})$, which satisfies the Cauchy–Riemann equation

$$\partial_\mu \vartheta = \varepsilon_{\mu\nu}\partial_\nu \theta \tag{62}$$

which satisfies the Poisson equation

$$-\nabla^2 \vartheta(\boldsymbol{x}) = \omega(\boldsymbol{x}) \tag{63}$$

whose solution is

$$\vartheta(\boldsymbol{x}) = \int d^2y\ G(|\boldsymbol{x} - \boldsymbol{y}|)\ \omega(\boldsymbol{y}) \tag{64}$$

where $G(|\boldsymbol{x} - \boldsymbol{y}|)$ is the Green function of the 2D Laplacian

$$-\nabla^2 G(|\boldsymbol{x} - \boldsymbol{y}|) = \delta^2(\boldsymbol{x} - \boldsymbol{y}). \tag{65}$$

In 2D, this Green function is

$$G(|\boldsymbol{x} - \boldsymbol{y}|) = \frac{1}{2\pi} \ln\left(\frac{a}{|\boldsymbol{x} - \boldsymbol{y}|}\right) \tag{66}$$

where a is a short distance cutoff (a lattice spacing). In what follows we will assume that the Green function of Eq. (66) has been cutoff so that $G(|\boldsymbol{x} - \boldsymbol{y}|) = 0$ for $|\boldsymbol{x} - \boldsymbol{y}| \leq a$.

The energy of a configuration of vortices $\{n_j\}$ with vanishing total vorticity, $\sum_j m_j = 0$, is

$$\begin{aligned} E[\theta] &= \frac{J\phi_0^2}{2}\int d^2x\ (\partial_\mu\theta)^2 \\ &= \frac{J\phi_0^2}{2}\int d^2x \int d^2y\ \omega(\boldsymbol{x})\ G(|\boldsymbol{x} - \boldsymbol{y}|)\ \omega(\boldsymbol{y}) = 2\pi J\phi_0^2 \sum_{j>k} m_j m_k \ln\left(\frac{a}{|\boldsymbol{x}_j - \boldsymbol{x}_k|}\right) \end{aligned} \tag{67}$$

where we used that configurations with nonvanishing vorticity do not contribute to the partition function since they have infinite energy in the thermodynamic limit. We conclude that, up to an unimportant prefactor, the partition function of Eq. (57) is the same as the partition function a gas of charges $\{m_j\}$ (the vortices) with total vanishing vorticity, $\sum_j m_j = 0$,

$$Z_{2DCG} = \sum_{[\{m_j\}]} \exp\left(-2\pi \frac{J\phi_0^2}{T} \sum_{j<k} m_j m_k \ln\left(\frac{|\boldsymbol{x}_j - \boldsymbol{x}_k|}{a}\right)\right) \tag{68}$$

which is known as the two-dimensional (neutral) Coulomb gas (Kosterlitz and Thouless, 1973).

Kosterlitz and Thouless argued that the neutral two-dimensional Coulomb gas has a phase transition a critical temperature T_{KT} between a low temperature dielectric phase in which vortices and antivortices are bound into neutral pairs and a high temperature phase in which pairs unbind, the vortex charges are screened and the vortex gas is in a plasma phase. A simple estimate of the critical temperature is found by computing the free energy of a single vortex $F_{\text{vortex}} = E_{\text{vortex}} - TS_{\text{vortex}}$, where E_{vortex} is a single vortex and S_{vortex} is the vortex entropy. In 2D, the energy of a single vortex of unit topological charge, $n = 1$, is $\pi J\phi_0^2 \ln(L/a)$, where L is the linear size of the system, and the vortex entropy is $S_{\text{vortex}} = \ln(L/a)^2$, where $(L/a)^2$ is the number of places where a vortex can be located, that is, the area of the system in units of the spacing a. Vortices unbind (proliferate) when the entropy beats the energy. Hence, the critical point occurs at a temperature T_{KT} where the vortex free energy vanishes, $F_{\text{vortex}}[T_{KT}] = 0$. This yields the estimate

$$T_{KT} = \frac{\pi}{2} J\phi_0^2 \tag{69}$$

which is the Kosterlitz–Thouless critical temperature.

There is an alternative, equivalent way to see this physics. Let us consider the theory if Eq. (57) in the background of a $U(1)$ gauge field $A_\mu(x)$

$$Z[A] = \int \mathcal{D}\theta\ \exp\left(-\frac{1}{2g}\int d^2x\left(\partial_\mu\theta - A_\mu\right)^2\right) \tag{70}$$

where the curl of the background gauge field A_μ is chosen to be equal to the local vorticity of Eq. (59),

$$\epsilon_{\mu\nu}\partial_\mu A_\nu(x) = \omega(x) \tag{71}$$

In other words, the gauge A_μ field forces the phase field to have vortices at the locations $\{x_j\}$.

Next we will use a Hubbard–Stratonovich transformation (a Gaussian identity) to write Eq. (70) in the equivalent form

$$Z[A]=\int \mathcal{D}\theta \int \mathcal{D}a_\mu \; \exp\Big(-\frac{g}{2}\int d^2x\, a_\mu^2+i\int d^2x\, a_\mu(x)\big(\partial_\mu\theta(x)-A_\mu(x)\big)\Big) \tag{72}$$

where we neglected an unimportant prefactor. In Eq. (72), the phase field can be integrated out (after an integration by parts) to yield the constraint $\partial_\mu a_\mu=0$. This constraint is solved by introducing the dual field $\vartheta(x)$ such that

$$a_\mu(x)=\epsilon_{\mu\nu}\partial_\nu\vartheta(x) \tag{73}$$

Hence, the partition function $Z[A]$ becomes

$$Z[A]=\int \mathcal{D}\vartheta \; \exp\Big(-\frac{g}{2}\int d^2x\,(\partial_\mu\vartheta)^2+i\int d^2x\,\vartheta(x)\,\omega(x)\Big) \tag{74}$$

where we have assumed that the total vorticity is zero, $\int d^2x\,\omega(x)=2\pi\sum_j m_j=0$. This identity show, that the quantization of the vortex topological charge requires that the dual field ϑ should also be periodic (compact) with period 1.

It is elementary to see that after performing the gaussian integral over the field ϑ in Eq. (74) and summing over all vortex configurations (with total vanishing vorticity), we reproduce the partition function of the 2D neutral Coulomb gas (Kadanoff, 1978; Nienhuis, 1987). Thus, the theory of Eq. (70) defined in terms of the phase field θ and the theory of Eq. (74) are equivalent. This is an example of a *duality transformation* which amounts to the exchange of the fields

$$\theta\leftrightarrow\vartheta, \qquad \text{and} \qquad g\leftrightarrow 1/g \tag{75}$$

A more careful analysis done on the lattice shows that the dual field ϑ is defined on the dual of the square lattice (which is also a square lattice) (José et al., 1977; Kadanoff, 1978). In addition, by differentiating both the partition function of the phase field of Eq. (70) and the partition function of the dual field ϑ of Eq. (74) with respect to the background field A_μ, we obtain the duality identification of the currents

$$\frac{1}{g}\partial_\mu\theta \longleftrightarrow g\epsilon_{\mu\nu}\partial_\nu\vartheta \tag{76}$$

as an operator identity. This identity is the same form as the duality of forms in geometry. In this case, the dual of the current $\partial_\mu\theta$, which is a 1-form field, is another 1-form field, $\partial_\mu\vartheta$. In both cases, the field θ and its dual ϑ are associated with global symmetries. Later, we will encounter similar duality identifications but their content will be different in different dimensions. Moreover, running these identities backwards, it is easy to see that the insertion of the order parameter operator $\exp(ip\theta(x))$ (with p an integer), which acts as a *source* on the phase field θ, in the partition function is equivalent to minimally couple the dual field ϑ to a singular gauge field $B_\mu(x)$ whose curl is p at the location x. In other words, *charges are dual to vortices*.

We will now use the identity we derived in Eq. (74) to compute the full partition function, which is a sum over all vortex configurations. Now we will assume that the vortices have a large core energy (i.e., the energy associated with the short distance behavior of the Green function of Eq. (66)). For a vortex with unit topological charge, we will call this energy u, and for a vortex with charge m the core energy will be um^2. The effects of the core energy can be accounted for in terms of a vortex fugacity $z=\exp(-un^2/T)$. The total partition function now is

$$Z=\sum_{\{m_j\}}\int \mathcal{D}\vartheta \; \exp\Big(-\frac{g}{2}\int d^2x\,(\partial_\mu\vartheta)^2+i\sum_j 2\pi m_j\vartheta(x_j)-\frac{u}{T}\sum_j m_j^2\Big) \tag{77}$$

where, once again, we assumed global charge neutrality.

In the limit in which $z=\exp(-u/T)\ll 1$, only the vortices with the lowest topological charges $m=\pm 1$ contribute and, furthermore, they are dilute. In this limit we can perform over the configurations with the lowest topological charge and derive the effective field theory of the dual field ϑ:

$$Z_{\text{SG}}=\int \mathcal{D}\vartheta\,\exp\Big(-\int d^2x\Big(\frac{g}{2}(\partial_\mu\vartheta)^2-v\cos(2\pi\vartheta)\Big)\Big) \tag{78}$$

which is known as the sine-Gordon field theory. The coupling constant of the sine-Gordon theory is $v=2\exp(-u/T)/a^2$, where a is the core size (the lattice spacing). Hence, the cosine operator of the sine-Gordon theory represents the effects of the vortices.

We can now analyze the role of vortices by looking at the renormalization group of the sine-Gordon theory. The first question is what is the scaling dimension of the cosine operator. This can be computed by looking at the vortex operator correlator in the theory with $v=0$:

$$\langle \exp(i2\pi\vartheta(x))\exp(-i2\pi\vartheta(y))\rangle=\frac{\text{const.}}{|x-y|^{2\pi/g}} \tag{79}$$

which implies that the vortex scaling dimension is

$$\Delta_{\text{vortex}}=\frac{\pi}{g} \tag{80}$$

Eq. (12) implies that in $D = 2$ dimensions the operator is irrelevant if $\Delta > 2$, relevant for $\Delta < 2$ and marginal for $\Delta = 2$. Hence, vortices are marginal if $\Delta_{\text{vortex}} = 2$, which happens if $g = \pi/2$. This is the same as to say that the system is at the Kosterlitz–Thouless critical temperature $T = T_{KT}$. Hence, vortices are irrelevant if $T < T_{KT}$ and relevant for $T > T_{KT}$.

This RG analysis tells us that $T > T_{KT}$, when vortices proliferate, the coupling constant v flows to strong coupling to a regime where ϑ is pinned to an integer value and the theory is in a massive phase. In this phase the connected vortex correlator decays exponentially with distance, which is the same as to say that the vortex charge is screened. This is why in this phase the vortices proliferate. It can be shown that in this phase the correlator of the spins of the *XY* model, that is, the correlator of the vertex operator $\exp(i\theta(x))$, decays exponentially with distance and the system is in its disordered phase.

There is still the question of the nature of the phase with $T < T_{KT}$. The Mermin–Wagner Theorem (Mermin and Wagner, 1966) [and its generalizations by Hohenberg (1967) and Coleman (1973)] states that classical statistical mechanical systems with a global continuous symmetry group cannot undergo spontaneous symmetry breaking in space dimensions $D \leq 2$ (and quantum systems with space-time dimensions $D \leq 2$). Does this theory violate this the Mermin–Wagner Theorem? The answer is no. It is easy to see that in the phase in which the vortices are irrelevant, that is, for $T < T_{KT}$, the correlator of the order parameter operator is always a power law of the distance $|x - y|$,

$$\langle \exp(i\theta(x)) \exp(-i\theta(y)) \rangle = \frac{\text{const.}}{|x-y|^{g/2\pi}} \tag{81}$$

with an exponent that depends on temperature and satisfies

$$\frac{g}{2\pi} = \frac{T}{2\pi J \phi_0^2} \leq \frac{1}{4}. \tag{82}$$

In other words, the entire low temperature phase is not an ordered phase of matter since the correlator is not constant at long-distance. On the other hand, the correlators of the order parameter $\exp(i\theta)$ and of the vortices $\exp(i\vartheta)$ have a power-law behavior for $T < T_{KT}$, we conclude that in this temperature range, the system is scale invariant and that it has a line of critical points.

In summary, we succeeded in expressing the partition function as a sum over configurations of the topological excitations, the vortices. We succeeded in doing that because vortices are labeled by their coordinates on the plane. In addition, we found a nontrivial phase transition since the entropy and the energy both scale logarithmically with the linear size of the system or, equivalently, that vortices became marginally relevant at a critical temperature. This is the mechanism behind the Kosterlitz–Thouless transition.

One may ask if this construction is generic and the answer is no. As an example, consider the Abelian Higgs model in $D = 2$. This model has a complex scalar field minimally coupled to a Maxwell gauge field and, hence, its gauge group is $U(1)$. In the classical spontaneously broken phase, the gauge field becomes massive. In this phase the long-range coherence of the phase field of the vortices of the scalar field is screened at the scale of the penetration depth. As a result, the Euclidean action of the vortices is now finite. Furthermore, on longer scales the interaction energy between vortices becomes short ranged. Hence, instead of a 2D Coulomb gas, now one has a gas of particles (vortices and antivortices) with short-range interactions. In this case the entropy always dominates and the vortices proliferate (Schaposnik, 1978). This behavior is quite analogous to the restoration of symmetry by proliferation of domain walls in one-dimensional classical spin chains (Landau and Lifshitz, 1959) and to the analogous problem of tunneling in the path integral formulation of quantum mechanical double-well potentials (Coleman, 1985). As a caveat, we should note that, in spite of the obvious similarities, the 2D Abelian Higgs model does not describe correctly a 2D superconductor (i.e., a superconducting film) since the electromagnetic field is not confined to the film, and this renders the electromagnetic action nonlocal.

Magnetic monopoles in compact electrodynamics

Instantons are of great interest in Quantum Field Theory since they provide for a mechanism to understand the nonperturbative structure of these theories. For this reason, they have been used to understand the mechanisms of quark confinement and the role of quantum anomalies in non-Abelian gauge theories (Callan et al., 1976; Polyakov, 1977, 1987; 't Hooft, 1976a, b). Instantons in non-Abelian gauge theories are magnetic monopoles and the condensation of monopoles has long been argued to be the mechanism behind quark confinement.

The simplest non-Abelian gauge theory that has magnetic monopoles is the Georgi–Glashow (Georgi and Glashow, 1974). This model has a three-component real field $\boldsymbol{\phi}$ and an $SU(2)$ Yang–Mills gauge field $\boldsymbol{A}_\mu$. In its Higgs phase, the scalar field $\boldsymbol{\phi}$ acquires an expectation value which breaks the gauge symmetry group $SU(2)$ down to its diagonal $U(1)$ subgroup. Since $U(1) \subset SU(2)$, this Abelian gauge group is compact, meaning that its magnetic fluxes are quantized. Polyakov (1975a) and 't Hooft (1976a) showed that in 2+1, Euclidean dimensions have nonsingular instanton solutions which at long distances resemble the magnetic monopole originally proposed by Dirac (1931)

$$B_i(\boldsymbol{x}) = \frac{q}{2}\frac{x_i}{|\boldsymbol{x}|^2} - 2\pi q \delta_{i,3} \delta(x_1) \delta(x_2) \theta(-x_3) \tag{83}$$

The first term in Eq. (83) is the magnetic radial field of a monopole of magnetic charge q. The second term represents an infinitely long infinitesimally thin solenoid ending at the location of the monopole, $\boldsymbol{x} = \boldsymbol{0}$, that supplies the quantized magnetic flux $2\pi q$. This singular term is known as the Dirac string. The string itself (and its orientation) is physically unobservable to any electrically charged particle that obeys the Dirac quantization condition, $qe = 2\pi$ (in units where $\hbar = c = 1$).

In the language of a lattice gauge theory (Wilson, 1975), a theory with a compact (i.e., periodic) $U(1)$ gauge fields on a $D = 3$ cubic lattice, describing a compact gauge field in 2 + 1 dimensions. This theory should have instantons that resemble magnetic monopoles much in the same way as a theory with a compact global $U(1)$ symmetry has vortices. The simplest example is Polyakov's compact electrodynamics (Polyakov, 1977) whose partition function is

$$Z = \prod_{x,\mu}\int_0^{2\pi}\frac{dA_\mu(x)}{2\pi}\ \exp\left(\frac{1}{4e^2}\sum_{x,\,\mu,\,\nu}\cos(F_{\mu\nu}(x))\right) \tag{84}$$

where $F_{\mu\nu}(x) = \Delta_\mu A_\nu(x) - \Delta_\nu A_\mu(x) \equiv \sum_\mu A_\mu$ is the magnetic flux through the elementary plaquette labeled by a site x and a pair of directions, μ and ν, with $\mu = 1, 2, 3$. This theory is invariant under local gauge transformations $A_\mu(x) \to A_\mu(x) + \Delta_\mu\Phi(x)$ and it is also invariant under local periodic shifts of the gauge fields $A_\mu(x) \to A_\mu(x) + 2\pi\ell_\mu(x)$, where $\ell_\mu(x) \in \mathbb{Z}$. The plaquette flux operator satisfies the lattice version of the Bianchi identity that the product of exponentials of the flux on the faces of every elementary cube of the lattice is

$$\prod_{\text{cube faces}} e^{iF_{\mu\nu}(x)} = 1 \tag{85}$$

which says that the theory can have magnetic monopoles of integer magnetic charge.

We will analyze this theory following an approach analogous to what we used for vortices in Section "Vortices in two dimensions." To this end, we will consider the partition function

$$Z[B_{\mu\nu}] = \int \mathcal{D}A_\mu\ \exp\left(-\frac{1}{4e^2}\int d^3x\ \left(F_{\mu\nu}(x) - B_{\mu\nu}(x)\right)^2\right) \tag{86}$$

where $F_{\mu\nu}(x) = \partial_\mu A_\nu - \partial_\nu A_\mu$ is the field strength of the Abelian $U(1)$ Maxwell gauge field A_μ. Here $B_{\mu\nu}(x)$ is an (antisymmetric) two-form background gauge field. The coupling constant of this theory is e^2. Since A_μ is a connection, it has units of length^{-1}, and $F_{\mu\nu}^2$ is a dimension 4 field. Then, in $D = 3$ dimensions, e^2 has units of length^{-1}.

The theory is invariant under two local transformations, namely the usual invariance under gauge transformations

$$A_\mu(x) \to A_\mu(x) + \partial_\mu\Phi(x), \qquad B_{\mu\nu}(x) \to B_{\mu\nu}(x) \tag{87}$$

where $\Phi(x)$ is an arbitrary smooth function of x. The presence of the background two-form field $B_{\mu\nu}$ now requires invariance under one-form gauge transformations

$$A_\mu(x) \to A_\mu(x) + a_\mu(x), \qquad B_{\mu\nu}(x) \to B_{\mu\nu}(x) + \partial_\mu a_\nu - \partial_\nu a_\mu \tag{88}$$

The two-form gauge field $B_{\mu\nu}$ essentially represents the magnetic monopoles. Let $\{m_j\}$ be a configuration of monopoles of charges m_j with coordinates $\{x_j\}$, with total vanishing monopole charge, $\sum_j m_j = 0$. Let $\mathcal{M}(x)$ be the magnetic monopole density at x,

$$\mathcal{M}(x) = 2\pi\sum_j m_j\ \delta^3(x - x_j) \tag{89}$$

which can be expressed as the curl of the two-form gauge field $B_{\mu\nu}$,

$$\mathcal{M}(x) = \frac{1}{2}\epsilon_{\mu\nu\lambda}\partial_\mu B_{\nu\lambda}(x) \tag{90}$$

We will proceed next much in the same way as in Eq. (72) and rewrite the partition function of Eq. (86) in terms of a two-form Hubbard–Stratonovich field $b_{\mu\nu}(x)$ such that

$$\begin{aligned} Z[B] &= \int \mathcal{D}A_\mu \int \mathcal{D}b_{\mu\nu}\exp\left(-\frac{e^2}{4}\int d^3x\ b_{\mu\nu}^2(x) + i\int d^3x\ \frac{1}{2}b_{\mu\nu}(x)\left[F_{\mu\nu}(x) - B_{\mu\nu}(x)\right]\right)\\ &= \int \mathcal{D}A_\mu \int \mathcal{D}b_{\mu\nu}\exp\left(-\frac{e^2}{4}\int d^3x\ b_{\mu\nu}^2(x) + i\int d^3x\left[A_\mu(x)\partial_\nu b_{\mu\nu}(x) - \frac{1}{2}b_{\mu\nu}(x)B_{\mu\nu}(x)\right]\right) \end{aligned} \tag{91}$$

Thus, the gauge field A_μ plays the role of a Lagrange multiplier field the enforces the constraint

$$\partial_\nu b_{\mu\nu}(x) = 0 \tag{92}$$

which is solved in terms of a compact scalar field $\vartheta(x)$

$$b_{\mu\nu}(x) = \epsilon_{\mu\nu\lambda}\partial_\lambda\vartheta(x) \tag{93}$$

Using this identity and the definition of the monopole density $\mathcal{M}(x)$ we find that the partition function $Z[B_{\mu\nu}]$ of Eq. (86) becomes

$$\begin{aligned} Z[B] &= \int \mathcal{D}\vartheta\ \exp\left[-\int d^3x\left(\frac{e^2}{2}(\partial_\mu\vartheta(x))^2 + i\mathcal{M}(x)\vartheta(x)\right)\right]\\ &= \int \mathcal{D}\vartheta\ \exp\left[-\frac{e^2}{2}\int d^3x(\partial_\mu\vartheta(x))^2 + 2\pi i\sum_j m_j\vartheta(x_j)\right] \end{aligned} \tag{94}$$

which requires that the field ϑ obeys the compactification condition $\vartheta \to \vartheta + n$, where n is an arbitrary integer. Eq. (94) says that the magnetic monopole instantons of the compact $U(1)$ gauge theory are dual to charges of the dual phase field ϑ, which has a compact $U(1)$ global symmetry.

The full partition function is obtained by summing over all monopole configurations satisfying the total neutrality condition, $\sum_j m_j = 0$. As in section "Vortices in two dimensions," we will weigh the configurations with a coupling u and find

$$Z = \sum_{\{m_j\}} Z\{m_j\} \int \mathcal{D}\vartheta \, \exp\left(-\frac{e^2}{2} \int d^3x \, (\partial_\mu \vartheta)^2 + \sum_j 2\pi i m_j \vartheta(x_j) - u \sum_j m_j^2 \right) \tag{95}$$

which is the same theory we found in Eq. (77) except that now we are in 3D. Moreover, summing only over dilute configurations of monopoles and antimonopoles we find, once again the sine-Gordon theory but now in $D = 3$ dimensions:

$$Z = \int \mathcal{D}\vartheta \exp\left(- \int d^3x \left(\frac{e^2}{2} (\partial_\mu \vartheta)^2 - v \cos(2\pi\vartheta) \right) \right) \tag{96}$$

with $v = 2\exp(-u)/a^3$.

In spite of the similarities between Eq. (96) and the sine-Gordon theory in 2D, Eq. (78), the physics is very different. It is straightforward to see that, in the limit $v = 0$, the monopole operator correlator is

$$\langle \exp(2\pi i \vartheta(x)) \exp(-2\pi i \vartheta(y)) = \exp\left(\frac{4\pi^2}{e^2} [G(|x-y|) - G(0)] \right) \simeq \exp\left(\frac{\pi}{2e^2} \left[\frac{1}{R} - \frac{1}{a} \right] \right) \tag{97}$$

where a is the short-distance cutoff. Unlike the behavior of the correlator of the vortex operators in 2D found in Eq. (79), Eq. (97) does not show a power-law behavior. The reason is that at $v = 0$ the compactified field ϑ should be regarded as the Goldstone boson of a spontaneously broken $U(1)$ symmetry. However, the cosine operator is now always relevant and the field ϑ is pinned and its fluctuations are actually massive.

Looking back at the partition function of Eq. (95), we could integrate out the field ϑ and obtain an expression with the same form as the Coulomb gas of Eq. (68) except that now this is the three-dimensional neutral Coulomb gas (Polyakov, 1977)

$$Z_{3DCG} = \sum_{[\{m_j\}]} \exp\left(-\frac{\pi}{2e^2} \sum_{j<k} m_j m_k \left[\frac{1}{|\boldsymbol{x}_j - \boldsymbol{x}_k|} - \frac{1}{a} \right] \right) \tag{98}$$

Now the energy of an isolated monopole is finite (in the infrared) while the entropy is still logarithmically divergent. The conclusion is that the monopoles proliferate and the 3D neutral Coulomb gas is always in a plasma phase withe screened interactions. These results also imply that the expectation value of the Wilson loop operator in the $U(1)$ gauge theory decays exponentially with the *area* of the loop. The conclusion is that in 2+1 dimensions compact electrodynamics is in a confining phase for all values of the coupling constant e^2 (Polyakov, 1977, 1987).

Nonlinear sigma models and antiferromagnetic quantum spin chains

We will now discuss the one-dimensional case in which topology plays a crucial role. In one space dimension, the sites of the chain are labeled by an integer $j = 1, \ldots, N$ (with N even). After some simple manipulations, the continuum limit of the staggered Wess–Zumino term of Eq. (52) is

$$\begin{aligned} \lim_{a_0 \to 0} S \sum_{j=1}^{N} (-1)^j \mathcal{S}_{WZ}[\boldsymbol{n}(j,t)] = {} & \frac{S}{2} \int d^2x \, \boldsymbol{m}(x,t) \cdot \partial_t \boldsymbol{m}(x,t) \times \partial_x \boldsymbol{m}(x,t) \\ & + S \int d^2x \, \boldsymbol{l}(x,t) \cdot \boldsymbol{m}(x,t) \times \partial_t \boldsymbol{m}(x,t) \end{aligned} \tag{99}$$

The continuum limit of the second term of Eq. (52) is essentially the same as in Eq. (55).

By putting together the results of Eqs. (99) and (55), we find that in the case of a 1D chain, the continuum field theory has the Lagrangian density

$$\mathcal{L}[\boldsymbol{m}, \boldsymbol{l}] = -2a_0 J S^2 \boldsymbol{l}^2 + S \boldsymbol{l} \cdot \boldsymbol{m} \times \partial_t \boldsymbol{m} - \frac{a_0 J S^2}{2} (\partial_x \boldsymbol{m})^2 + \frac{S}{2} \boldsymbol{m} \cdot \partial_t \boldsymbol{m} \times \partial_x \boldsymbol{m}. \tag{100}$$

Finally, we integrate out the ferromagnetic fluctuations represented by the massive field $\boldsymbol{l}(x, t)$ to find that the effective low-energy Lagrangian has the form

$$\mathcal{L} = \frac{1}{2g} \left(\frac{1}{v_s} (\partial_t \boldsymbol{m})^2 - v_s (\partial_x \boldsymbol{m})^2 \right) + \frac{\theta}{4\pi} \boldsymbol{m} \cdot \partial_x \boldsymbol{m} \times \partial_t \boldsymbol{m} \tag{101}$$

which is a nonlinear sigma model with $N = 3$ components (and hence has a global $O(3)$ symmetry) with a *topological term* whose coupling constant is θ. This result was first derived by Haldane (1985).

In Eq. (101), the effective coupling constant g, the spin-wave velocity v_s, and the θ-angle are given by $g = \frac{2}{S}$, $v_s = 2a_0JS$, and $\theta = 2\pi$. As in the 2D case, since $g = 2/S$, large S implies that the nonlinear sigma model is in the weak coupling regime. Provided that $v_s > 0$, one can always rescale the time and space coordinates without affecting the form of the Lagrangian, including the coupling constant or, as we will see, the value of the θ angle. In what follows we will assume that we have done the rescaling in such a way that we set $v_s = 1$ and, that time and space scale as lengths. Thus we will use a relativistic notation and, after an analytic continuation to imaginary time, we label the time coordinate by x_2 and the space direction by x_1. The partition function now takes the form

$$Z = \int \mathcal{D}\boldsymbol{m} \exp\left(-\frac{1}{2g} \int_{\Omega} d^2x \, \left(\partial_\mu \boldsymbol{n}\right)^2 + i\theta \, Q[\boldsymbol{m}] \right) \tag{102}$$

where Ω is the spacetime manifold. In this notation, the first term of the exponent is called the Euclidean action of the nonlinear sigma model. In Eq. (102), we denoted by $Q[\boldsymbol{m}]$ the quantity

$$Q[\boldsymbol{m}] = \frac{1}{8\pi} \int_{\Omega} d^2x \, \epsilon_{\mu\nu} \boldsymbol{m} \cdot \partial_\mu \boldsymbol{m} \times \partial_\nu \boldsymbol{m} \tag{103}$$

Here we will consider the case in which the spacetime manifold Ω is closed. In particular we will assume that it is a two-sphere S_2. The quantity $Q[\boldsymbol{m}]$ is the integral of a total derivative which counts the number of times the field configuration $\boldsymbol{m}(x_1, x_2)$ wraps around the sphere S_2. In other words, it yields a nonvanishing result only for "large" configurations which wind (or wrap) around the sphere S_2. Since $Q[\boldsymbol{n}]$ is an integer, it has the same for all *smooth* field configuration $\boldsymbol{m}$ that can be smoothly deformed into each other and are homotopically equivalent. If we demand that the field configurations $\boldsymbol{m}$ have finite Euclidean action, which requires that at infinity the configurations take the same (but arbitrary) value of $\boldsymbol{m}$, we have effectively compactified the $x_1 - x_2$ plane into a two sphere S_2. On the other hand the field $\boldsymbol{m}$ is restricted by the constraint $\boldsymbol{m}^2 = 1$ to take values on a two-sphere S_2. Therefore, the field configurations $\boldsymbol{m}(x_1, x_2)$ are smooth maps of the S_2 of the coordinate space to the S_2 of the target space of the field $\boldsymbol{m}$. Hence, the integer $Q[\boldsymbol{m}]$ classifies the smooth field configurations into a set of *equivalence classes* each labeled by the integer Q. Under composition homotopies form groups, and the equivalence classes themselves also form a group which, in this case, is isomorphic to the group of integers, $\mathbb{Z}$. In topology, these statements are summarized by the notation $\Pi_2(S_2) \simeq \mathbb{Z}$. The configurations with nonzero values of Q are called *instantons* which, in the quantum problem, represent tunneling processes of the nonlinear sigma model.

Another consequence of Q being an integer is that the contribution of its term to the weight of the path integral of Eq. (103) is a periodic function of θ angle. On the other hand, since the only allowed values of the θ are $\theta = 0 \pmod{2\pi}$ for S integer, or $\theta = \pi \pmod{2\pi}$ for S a half-integer, the contribution of the topological invariant Q to the weight of the path integral is

$$\exp(i\theta \, Q[\boldsymbol{m}]) = (-1)^{2SQ}. \tag{104}$$

Therefore, for spin chains with S integer, the weight is 1 and the topological invariant does not contribute to the path integral. But, if S is a half-integer, the weight is $(-1)^{Q[\boldsymbol{m}]}$, and it does contribute. Moreover, its contribution is the same for all half-integer values of S.

These results have important consequences for the physics of spin chains which led Haldane to some startling conclusions (Haldane, 1985). In the weak coupling regime, $g \ll 1$ (equivalently, for large S), we can use the perturbative renormalization group and derive the beta function for all these $O(3)$ nonlinear sigma models (with or without topological terms) and find that their beta functions are the same as in Eq. (21) with $N = 3$. Hence, for all S, the effective coupling flows to large values. We can make this inference since the topological term yields no contribution for all configurations which are related by smooth deformations. Thus, we infer that all spin chains with S integer are in a massive phase with an exponentially small energy gap $\sim \exp(-2\pi S)$. This result is nowadays known as the Haldane gap.

On the other hand, these results also imply that all spin chain with half-integer spin S are also the same and, in particular, the same as spin-1/2 chains. However, the Hamiltonian of the quantum spin chain with spin-1/2 degrees of freedom is an example of an integrable system and its spectrum is known to be gapless from its Bethe Ansatz solution (Bethe, 1931; Yang and Yang, 1969). However, the spin-1/2 chain is not only gapless but its low energy states are gapless solitons with a relativistic spectrum. The low energy description of a theory of this type must be described by a conformal field theory. Haldane concluded that the RG flow for spin-1/2 chains must have an IR stable fixed point at some finite (and large) value of the coupling constant. This conjecture was confirmed by Affleck and Haldane (1987) who showed that the spin-1/2 Heisenberg chains are in the universality class of the $SU(2)_1$ Wess–Zumino–Witten model (Witten, 1984) whose CFT was solved by Knizhnik and Zamolodchikov (1984).

Topology and open integer-spin chains

In the preceding section, we showed that integer spin chains have a Haldane gap. We did that by showing that in that case the topological term is absent. However, the derivation is correct provided the spacetime manifold is closed, for example, a sphere and a torus. What happens if the system has a boundary? Let us denote the boundary of Ω by $\Gamma = \partial\Omega$. For example we will take Γ to be along the imaginary time direction and hence that it is a circle of circumference $1/T$, where T is the temperature. The topological term has the same form as the Berry phase term of the path integral for spin, the "Wess–Zumino" term of Eq. (44), but its prefactor is 1/2 as big. Thus, for a system with an open boundary the topological term yields a net contribution equal to a Berry phase with a net prefactor of $S/2$.

In other words, the boundary of the integer spin chain behaves as a localized degree of freedom whose spin is 1/2 (mod an integer). Form the periodicity requirement, we also see that if the spin chain is made of *odd-integer* degrees of freedom, there should be a spin 1/2 degree of freedom localized at the open boundary!. Conversely, if the chain is made of *even-integer* spins, there is no boundary degree of freedom! This line of argument implies that an antiferromagnetic chain with odd-integer spins must have a spin-1/2 degree of freedom at the boundary whereas a chain of even-integer spins should not. Notice that the "bulk" behavior is the same for both odd and even integer spin chains. The difference is whether or not they have a nontrivial "zero-mode" state at the boundary. In particular, the existence of this state is robust, that is, it cannot be removed by making smooth changes to the quantum Hamiltonian or, what is the same, the boundary state is *topologically protected*.

A simple system that displays a protected spin-1/2 zero mode at the boundary is a generalized $S = 1$ spin chain with Hamiltonian

$$H = \alpha \sum_{j=1}^{N} \boldsymbol{S}(j) \cdot \boldsymbol{S}(j+1) + \beta \sum_{j=1}^{N} (\boldsymbol{S}(j) \cdot \boldsymbol{S}(j+1))^2 \tag{105}$$

where $\boldsymbol{S}(j) = (S_x(j), S_y(j), S_z(j)$ are the spin 1 matrices at each lattice site j. This problem was examined in great detail by Affleck et al. (1988) who showed that at the special value of the parameters $\alpha = 1/2$ and $\beta = 1/6$ this Hamiltonian takes the form of a sum of projection operators

$$H = \sum_j P_2(\boldsymbol{S}(j) + \boldsymbol{S}(j+1)) \tag{106}$$

where P_2 is an operator that projects out the spin 2 states. These authors constructed the exact ground state, known as the AKLT state, of this Hamiltonian by writing each spin 1 degree of freedom of two spin-1/2 degrees of freedom at each site. They showed that the ground state is a projected product state in which the "constituent" spin-1/2 degrees of freedom (each labeled by + and −, respectively) on nearby sites j and $j + 1$ are in a valence bond singlet state of the form $\frac{1}{\sqrt{2}}(|\uparrow_{j,+}, \downarrow_{j+1,-}\rangle - \downarrow_{j,+}, \uparrow_{j+1,-}\rangle$ (and symmetrizing at each site to project onto a spin 1 state). This state of the spin-1 chain is translation invariant and gapped and hence agrees with Haldane's result. Moreover, it has a spin-1/2 degree of freedom at each open boundary (Hagiwara et al., 1990).

The arguments discussed above show that the AKLT state is a gapped topological state. The gapless spin-1/2 boundary states are an example of *spin fractionalization*. The spin-1/2 boundary degrees of freedom are an example of an *edge state* which are present in many, thought not all, topological phases of matter. One may ask what symmetry protects the gaplessness of these edge degrees of freedom. The only perturbation that would give a finite energy gap to the spin-1/2 edge states is an external magnetic field. However, this perturbation would break the global $SU(2)$ symmetry of the Hamiltonian as well as time-reversal invariance.

Duality in Ising models

Duality plays a significant role of our understanding of statistical physics and of quantum field theory. Many seemingly unrelated correspondences between different theories have come to be called *dualities*.

Duality in the 2D Ising model

One of the earliest versions of duality transformations was used to relate the high-temperature expansion of the 2D classical Ising model and its low-temperature expansion (Kramers and Wannier, 1941). In all dimensions, for concreteness, we will think of a hypercubic lattice, the high temperature expansion is a representation of the partition function as a sum of contributions of closed loops on the lattice. At temperature T, a configuration of loops γ contributes with a weight which in the Ising model has the form $C(\gamma)\ \tanh^{L(\gamma)}(\beta)$, where $\beta = 1/T$ and $L(\gamma)$ is the length of the loop γ, that is, the number of links on the loop, and $C(\gamma)$ is an entropic factor that counts the number of allowed loops with fixed perimeter $L(\gamma)$. However not all loop configurations are allowed as in the Ising model they satisfy constraints such as being nonoverlapping, etc.

In Section "The Ising model in a transverse field," we noted that the partition function of the classical Ising model (in any dimension) can be interpreted as the path integral of a quantum spin model in one dimension less on a lattice with a discretized imaginary time. In this picture, the loops γ can be regarded as processes in which pairs of particles are created at some initial (imaginary) time, evolve and eventually are annihilated at a later (imaginary) time. In other words, the high-temperature phase is a theory of a massive scalar field. The restrictions on the allowed loop configurations represent interactions among these particles. In the temperature range in which the expansion in loops is convergent, the particles are massive as the loops are small. As the radius of convergence of the expansion is approached, longer and increasingly fractal-like loops begin to dominate the partition function, and concomitantly the mass of the particles decreases. This process is the signal of the approach to a continuous phase transition where the particles become massless. In fact, right at the critical point the particle interpretation is lost as the associated fields acquire anomalous dimensions.

Returning to the 2D classical Ising model, Kramers and Wannier also considered the low temperature expansion. This is an expansion around one of the broken symmetry state, for example, the state with all spins up. In this low temperature, regime the partition function is a sum of configurations of flipped spins. A typical configuration is a set of clusters of flipped spins.

In the absence of a uniform field, a configuration of flipped spins has a energy cost only on links of the lattice with oppositely aligned spins ("broken bonds"). Thus a cluster of flipped spins costs an energy equal to 2 (I assumed that I set $J = 1$) for each broken bond at the *boundary* of the cluster. This boundary is *domain wall*, which is a closed loop on the *dual lattice*. In 2D, the dual of the square lattice is the square lattice of the dual sites (the centers of the elementary plaquettes of the 2D lattice). In 2D, the links of the direct lattice pierce the links of the dual lattice. We can see that this analogous to the geometric duality of forms: sites ("0-forms") are dual to plaquettes ("2-forms") and links ("1-forms") are dual to links (also "1-forms").

Thus, in 2D the low temperature expansion is an expansion in the loops γ^* of the dual lattice that represent the domain walls. We can also regard the domain walls (the dual loops) as the histories the pairs of particles on the dual lattice. However, the weight of each dual loop is $\exp(-2\beta)$ per link of γ^*. Except for that, the counting and restrictions on the dual loops γ^* are the same as those of γ. This means that there is a one-to-one correspondence between the two expansions with the replacement $\tanh\beta \leftrightarrow \exp(-2\beta^*)$. This mapping means that the dual of the 2D classical Ising model (with global $\mathbb{Z}_2$ symmetry) at inverse temperature β is a dual Ising model (also with global $\mathbb{Z}_2$ symmetry) on the dual lattice at inverse temperature β^*. This correspondence is in close analogy with what we discussed in Section "Vortices in two dimensions."

In particular if one assumes that there is a transition at $\beta_c = 1/T_c$ then there should also be a transition at $\beta_c^* = -1/2 \ln \tanh \beta_c$. Moreover, if one further assumes [as Kramers and Wannier did (Kramers and Wannier, 1941)] that there is a unique transition (correct in the Ising model but not in other cases), then the critical point must be such that $\exp(-2\beta_c) = \tanh\beta_c$, which yields the value $T_c = 2/\ln(\sqrt{2} + 1)$, which agrees with the Onsager's result (Onsager, 1944).

In Section "The Ising model in a transverse field," we showed that the classical 2D Ising model is equivalent to the one-dimensional Ising model in a transverse field whose Hamiltonian is given in Eq. (23). The 1D Ising model on a transverse field has spin degrees of freedom defined on the sites of a one-dimensional chain labeled by an integer-valued variable n. The 1D Hamiltonian is expressed in terms of local operators, the Pauli matrices $\sigma_3(n)$ and $\sigma_1(n)$. The 1D chain has a dual lattice whose sites are the midpoints of the chain. Thus in 1D, sites ("0-forms") are dual to links ("1-forms") and vice versa.

We will now see that there is a Hamiltonian version of the Kramers–Wannier duality (Fradkin and Susskind, 1978). In Eq. (26), we introduced the kink creation operator which flips are σ_3 operators to the left and including site j. For clarity we will denote the kink creation operator as $\tau_3(\tilde{n})$, where $\tilde{n}$ is the site of the dual lattice between the sites n and $n + 1$ of the original lattice. We will now define an operator $\tau_1(\tilde{n}) = \sigma_3(n)\sigma_3(n + 1)$. The operators $\tau_1(\tilde{n})$ and $\tau_3(\tilde{n})$ satisfy the same algebra of the Pauli operators $\sigma_1(n)$ and $\sigma_3(n)$. Furthermore, we readily find the Hamiltonian of the dual theory to be the same (up to boundary conditions) as the original Hamiltonian of Eq. (23) except that the dual coupling constant is $\lambda^* = 1/\lambda$. So, once again, if we assume that there is a single (quantum) phase transition we require $\lambda_c^* = \lambda_c$, which is only satisfied by $\lambda_c = 1$. In this language, the kink creation operator plays the role of a disorder operator (Fradkin and Susskind, 1978).

The 3D duality: $\mathbb{Z}_2$ gauge theory

We will now discuss the role of duality in the 3D Ising model on a cubic lattice. This case, and its generalizations to higher dimensions, was considered first by Wegner (1971).

In Section "Duality in the 2D Ising model," we discussed the loop representation of the high temperature expansion and showed that it has the form in all dimensions. Hence, in 3D the high temperature expansion is an expansion in closed loops γ with weight of $\tanh\beta$ per unit link of loop. Hence, in 3D as well, the high temperature phase can be regarded as field theory of a massive scalar field. As in the 2D case, the weight of a loop configuration is $\tanh\beta$ for each link of the loop γ.

However, the low temperature expansion has a radically different form and physical interpretation. Much as in 2D, the low temperature expansion is an expansion in clusters of flipped spins. Here too, in the absence of an external field, the only energy cost resides at the boundary of the clusters of overturned spins, the domain walls. But in 3D, the clusters occupy volumes whose boundaries are closed *surfaces* Σ^*. In 3D a link (bond) is dual to a plaquette (expressing the fact that in 3D a 1-form is dual to a 2-form). Hence the closed domain walls of overturned spins are dual to a closed surface Σ^* on the dual lattice. The weight of each configuration of closed surfaces is $\exp(-2\beta)$ for each plaquette of the surface Σ^*.

These facts mean that the dual theory of the 3D Ising model is a theory on the dual lattice with coupling constant β^*, with $\exp(-2\beta*) = \tanh\beta$, such that its expansion for small β^* is a sum over configurations of closed surfaces σ^*, and for large β^* is a sum of configurations of closed loops γ^* on the dual lattice. The dual theory is the naturally defined on (dual) plaquettes, not on links. To this end, let us define a set of Ising-like degrees of freedom $\sigma_\mu(x) = \pm 1$ located on the links (x, μ) of the dual lattice. These degrees of freedom are coupled on each plaquette of the lattice. Since each plaquette has four links, the coupling involves the degrees of freedom on all four links of each plaquette. The partition function of the dual theory is

$$Z = \sum_{\{\sigma_\mu(x)\}} \exp\left(\beta^* \sum_{\text{plaquettes}} \sigma_\mu(x)\sigma_\nu(x + e_\mu)\sigma_\mu(x + e_\mu + e_\nu)\sigma_\nu(x)\right) \tag{107}$$

where the sum in the exponent (the negative of the "action") runs on all the plaquettes of the dual lattice.

The action of the theory of Eq. (107) is invariant under the reversal of all six Ising degrees of freedom on links sharing a given site x. This is a *local symmetry*. Unlike the 3D Ising model, which has a global $\mathbb{Z}_2$ symmetry of flipping all spins simultaneously, this theory has *local* (or *gauge*) $\mathbb{Z}_2$ symmetry. This is the simplest example of a lattice gauge theory in which the degrees of freedom are gauge fields that take values on the $\mathbb{Z}_2$ gauge group (Wegner, 1971; Wilson, 1975; Kogut, 1979).

We saw that in the spin model the high temperature expansion (i.e., the expansion in powers of $\tanh\beta$) is a sum over loop configurations which can be interpreted in terms of processes in which pairs of particles are created, evolve (in imaginary time), and then are destroyed (also in pairs). The analogous interpretation of the expansion of the $\mathbb{Z}_2$ gauge theory in powers of $\tanh\beta^* = \exp(-2\beta)$ as a sum over the configurations of closed surfaces is not in terms of the histories of *particles* but in terms of the histories of closed strings which, as they evolve, sweep the closed surfaces. The physics is, however, more complex as the sum over surfaces runs over all surfaces of arbitrary topology with arbitrary number of handles (or *genus*). Thus, over (imaginary) time a closed strong is created, evolves, splits into two closed strings, etc.

Therefore, the 3D Ising model, which has a $\mathbb{Z}_2$ global symmetry, is dual to a $\mathbb{Z}_2$ gauge theory, which has a $\mathbb{Z}_2$ local symmetry. The duality maps the high temperature (disordered) phase of the Ising model to the strong coupling (small β^*) phase of the gauge theory. In the gauge theory language, this is the *confining* phase. This can be seen by computing the expectation value of the Wilson loop operator on the closed loop Γ, which here reads $\langle \prod_{(x,\mu)\in\Gamma} \sigma_\mu(x)\rangle$. In the small β^* phase, this expectation value decays exponentially with the size of the minimal surface bounded by the loop Γ. This behavior of the area law of the Wilson loop. Under duality, the insertion of this operator is equivalent to an Ising model with a domain wall terminating on the loop Γ, and the area law of the Wilson loop is the consequence of the fact that if the Ising model has long-range order, the free energy cost of the domain wall scales with its area. Moreover, in this phase of the gauge theory, the closed strings are small meaning that the string tension (the energy per unit length of string) is finite. In the Ising model language, the string tension becomes surface tension of the domain wall.

In the preceding section, we discussed a Hamiltonian version of the duality. We will briefly do the same in the case of the 2+1 dimensional Ising model. The Hamiltonian of the Ising model in a transverse field on a square lattice is

$$H_{\text{2D}-\text{TFIM}} = -\sum_{\boldsymbol{r}} \sigma_1(\boldsymbol{r}) - \lambda \sum_{\boldsymbol{r},\, j=1,\,2} \sigma_3(\boldsymbol{r})\sigma_3(\boldsymbol{r}+\boldsymbol{e}_j) \tag{108}$$

where $\boldsymbol{r}$ labels the sites of the square lattice and $\boldsymbol{e}_j$ (with $j = 1, 2$) are the two (orthonormal) primitive unit vectors of the lattice. Here too, at each site we have a two-level system (the spins), σ_1 and σ_3 are Pauli matrices acting on these states at each site and λ is the coupling constant. Just as in the 1D case, this system has two phases: an ordered phase for $\lambda > \lambda_c$ and a disordered phase for $\lambda < \lambda_c$, where λ_c is a critical coupling. This Hamiltonian is invariant under the global $\mathbb{Z}_2$ symmetry generated by the global spin flip operator $Q = \prod_{\boldsymbol{r}} \sigma_1(\boldsymbol{r})$ which commutes with the Hamiltonian, $[Q, H_{\text{2D-TFIM}}] = 0$.

Let us consider now a $\mathbb{Z}_2$ gauge theory on the dual of the square lattice. We will now define a two-dimensional Hilbert space on each link, denoted by $(\tilde{\boldsymbol{r}}, j)$ (with $j = 1, 2$) of the dual lattice with sites labeled by $\tilde{\boldsymbol{r}}$. We will further define at each link $(\tilde{\boldsymbol{r}}, j)$ the Pauli operators $\sigma_j^1(\tilde{\boldsymbol{r}})$ and $\sigma_j^3(\tilde{\boldsymbol{r}})$. The Hamiltonian of the $\mathbb{Z}_2$ gauge theory is

$$H_{\mathbb{Z}_2\text{gauge}} = -\sum_{\tilde{\boldsymbol{r}},\, j} \sigma_j^1(\tilde{\boldsymbol{r}}) - g\sum_{\tilde{\boldsymbol{r}}} \sigma_1^3(\tilde{\boldsymbol{r}})\sigma_2^3(\tilde{\boldsymbol{r}}+\tilde{\boldsymbol{e}}_1)\sigma_1^3(\tilde{\boldsymbol{r}}+\tilde{\boldsymbol{e}}_1+\tilde{\boldsymbol{e}}_2)\sigma_2^3(\tilde{\boldsymbol{r}}) \tag{109}$$

where $\tilde{\boldsymbol{e}}_j = \epsilon_{jk}\boldsymbol{e}_k$ (with $j, k = 1, 2$).

Unlike the Hamiltonian of Eq. (108), the Hamiltonian of Eq. (109) has a local symmetry. Let $\tilde{Q}(\tilde{\boldsymbol{r}})$ be the operator that flips the $\mathbb{Z}_2$ gauge degrees of freedom on the four links that share the site $\tilde{\boldsymbol{r}}$,

$$\tilde{Q}(\tilde{\boldsymbol{r}}) = \prod_{j=1,\,2} \sigma_j^1(\tilde{\boldsymbol{r}})\sigma_j^1(\tilde{\boldsymbol{r}}-\tilde{\boldsymbol{e}}_j) \tag{110}$$

These operators commute with each other, $[\tilde{Q}(\tilde{\boldsymbol{r}}), \tilde{Q}(\tilde{\boldsymbol{r}}')] = 0$, and commute with the Hamiltonian, $[H_{\mathbb{Z}_2\text{gauge}}, \tilde{Q}(\tilde{\boldsymbol{r}})] = 0$. The Hilbert space of gauge-invariant states is eigenstates of $\tilde{Q}(\boldsymbol{r})$ with unit eigenvalue,

$$\tilde{Q}(\boldsymbol{r})|\text{Phys}\rangle = |\text{Phys}\rangle \tag{111}$$

(for all $\boldsymbol{r}$). This constraint is the $\mathbb{Z}_2$ Gauss Law. The Hamiltonian $H_{\mathbb{Z}_2\text{gauge}}$ has two phases: a *confining* phase for $g < g_c$ and a *deconfined* phase for $g > g_c$ (where g_c is a critical coupling).

The duality transformation is defined so that

$$\sigma_1(\boldsymbol{r}) = \prod_{\text{plaquette}(\boldsymbol{r})} \sigma_j^3(\tilde{\boldsymbol{r}}) \tag{112}$$

is the product of the σ_j^3 operators of the gauge theory on a dual plaquette centered at the site $\boldsymbol{r}$, and

$$\sigma_1^1(\tilde{\boldsymbol{r}}) = \sigma_3(\boldsymbol{r})\sigma_3(\boldsymbol{r}+\boldsymbol{e}_2), \qquad \sigma_2^1(\tilde{\boldsymbol{r}}) = \sigma_3(\boldsymbol{r})\sigma_3(\boldsymbol{r}+\boldsymbol{e}_1) \tag{113}$$

These identities imply that the gauge theory constraint of the $\mathbb{Z}_2$ Gauss Law, Eq. (111), is satisfied. This also means that duality is a mapping of the *gauge-invariant* sector of the $\mathbb{Z}_2$ gauge theory to the Hilbert space of the Ising model in a transverse field.

Eqs. (112) and (113) imply that the Hamiltonians $H_{\text{2D-TFIM}}$ and $H_{\mathbb{Z}_2\text{gauge}}$ are equal to each other with the identification of the coupling constants $g = 1/\lambda$. Hence, the *ordered phase* of the Ising model, $\lambda > \lambda_c$, maps onto the *confining phase* of the $\mathbb{Z}_2$ gauge theory and, conversely, the *disordered phase* of the Ising model maps onto the *deconfined phase* of the gauge theory.

Eq. (113) also implies that the operator $\sigma_3(\boldsymbol{r})$ of the Ising model can be identified with the operator

$$\sigma_3(\boldsymbol{r}) = \prod_{\gamma(\boldsymbol{r})} \sigma_j^1(\tilde{\boldsymbol{r}}) \tag{114}$$

where the product is on the links of the dual lattice pierced by the path $\gamma(\boldsymbol{r})$ on the direct lattice ending at the site $\boldsymbol{r}$.

While $\sigma_3(\boldsymbol{r})$ is of course just the order parameter of the Ising model, the dual operator defined by Eq. (114) anticommutes with the plaquette term of the Hamiltonian of Eq. (109) and creates an $\mathbb{Z}_2$ flux excitation at the plaquette. With some abuse of language, this operator can be regarded as creating a $\mathbb{Z}_2$ "magnetic monopole." Since in the confining phase this operator has an expectation value, we can regard this phase as a magnetic condensate.

We will now discuss the role of boundary conditions, which is different in both theories. Let us examine the behavior of the $\mathbb{Z}_2$ gauge theory with periodic boundary conditions. Periodic boundary conditions means that the 2D space is topologically a 2-torus. It is straightforward to show that the ground state in the confining phase is unique and insensitive to boundary conditions. The physics of the deconfined phase is more subtle. We will now see that on a 2-torus it has a fourfold degenerate ground state and that the degeneracy is not due to the spontaneous breaking of a global symmetry.

Let γ_1 and γ_2 be two noncontractible loops on the torus along the directions 1 and 2, respectively. Let us consider the ("electric") Wilson loop operators along γ_1 and γ_2, $W[\gamma_1] = \prod_{(\boldsymbol{r},j)\in\gamma_1} \sigma_j^3(\boldsymbol{r})$ and similarly for γ_2. Similarly let us consider the ("magnetic") 't Hooft operators $\tilde{W}[\tilde{\gamma}_1]$ and $\tilde{W}[\gamma_2]$ defined on the noncontractible closed paths of the dual lattice $\tilde{\gamma}_1$ and $\tilde{\gamma}_2$, such that $\tilde{W}[\tilde{\gamma}_1] = \prod_{\tilde{\gamma}_1} \sigma_2^1(\tilde{\boldsymbol{r}})$ and $\tilde{W}[\tilde{\gamma}_2] = \prod_{\tilde{\gamma}_2} \sigma_1^1(\tilde{\boldsymbol{r}})$. It is easy to see that the Wilson and't Hooft operators satisfy that $W[\gamma_i]^2 = \tilde{W}[\tilde{\gamma}_j]^2 = I$, and that

$$[W[\gamma_i], W[\gamma_j]] = [\tilde{W}[\tilde{\gamma}_i], \tilde{W}[\tilde{\gamma}_j]] = 0, \qquad \{W[\gamma_1], \tilde{W}[\tilde{\gamma}_2]\} = \{W[\gamma_2], \tilde{W}[\tilde{\gamma}_1]\} = 0 \tag{115}$$

Let us consider the special limit of $g \to \infty$. In this limit the Wilson loop operators $W[\gamma_i]$ on the two noncontractible loops of the 2-torus commute with the Hamiltonian $H_{\mathbb{Z}_2\text{gauge}}$ of Eq. (109). Therefore the eigenstates of the Hamiltonian can be chosen to be the eigenstates of these two Wilson loops. Since the Wilson loop operators are Hermitian and obey $W[\gamma_i]^2 = I$, the spectrum of each loop is two-dimensional $|\pm 1\rangle_i$ ($i = 1, 2$) with eigenvalues $\pm$ 1, respectively. At $g \to \infty$, these states are also eigenstates of $H_{\mathbb{Z}_2\text{gauge}}$. Thus, the ground state of $H_{\mathbb{Z}_2\text{gauge}}$ is four dimensional. The 't Hooft loops $\tilde{W}[\tilde{\gamma}_i]$ act as ladder operators in this restricted Hilbert space.

The conclusion is that, on a 2-torus, at least in the limit $g \to \infty$, the ground state of $H_{\mathbb{Z}_2\text{gauge}}$ is degenerate. However, this degeneracy is not due to the spontaneous breaking of a global symmetry. Rather, it reflects the topological character of the theory. To see this, one can extend this analysis to a theory to be on a more general two-dimensional and instead of a 2-torus we can consider a surface with g handles (not to be confused with the coupling constant!), for example, $g = 0$ for a sphere (or disk), $g = 1$ for a 2-torus, $g = 2$ for a pretzel, etc. For each of these two-dimensional surfaces, the different number of noncontractible loops is g, and the Wilson loops defined on them commute with each other (and with $H_{\mathbb{Z}_2\text{gauge}}$). Hence, in the limit $g \to \infty$, $H_{\mathbb{Z}_2\text{gauge}}$ has a ground state degeneracy of 2^g which, clearly, depends only on the topology of the surface. We conclude that, at least as $g \to \infty$, the Hamiltonian $H_{\mathbb{Z}_2\text{gauge}}$ is in a *topological phase*.

However, is the exact degeneracy found in the limit $g \to \infty$ a property of the entire deconfined phase? For a finite system, the expansion in powers of $1/g$ is convergent. On the other hand, in the thermodynamic limit, $L \to \infty$, the expansion has a finite radius of convergence with g_c being an upper bound. Let us consider the ground state at $g = \infty$ with eigenvalue + 1 for the Wilson loop $W[\gamma_1]$. The degenerate state with eigenvalue − 1 is created by the 't Hooft loop $\tilde{W}[\tilde{\gamma}_2]$, that is, $|{-1}\rangle_1 = \tilde{W}[\tilde{\gamma}_2]\, |{+1}\rangle_1$. The 't Hooft operator is a product of σ^1 operators on links along the direction 1 crossed by the path $\tilde{\gamma}_2$ of the dual lattice, which involves (at least) L links. Then, it takes L orders in the expansion in powers of $1/g$ to mix the state $|+1\rangle_1$ with the state $|-1\rangle_1$, and this amplitude is of order $1/g^L$, which is exponentially small. The same argument applies to the mixing between all four states. For a finite but large system of linear size L, the degeneracy is lifted but the energy splitting is exponentially small in the system size. Hence, the topological protection is a feature of the deconfined phase in the thermodynamic limit $L \to \infty$.

We conclude that the deconfined phase of the $\mathbb{Z}_2$, lattice gauge theory is a topological phase. This result extends to the case of a gauge theory with discrete gauge group $\mathbb{Z}$, the cyclic group of k elements. In general spacetime dimension $D > 2$, the $\mathbb{Z}_k$ gauge theory also has confined and deconfined phases and if $k \gtrsim 4$, it also has an intermediate "Coulomb phase" (Elitzur et al., 1979; Ukawa et al., 1980). In Section "BF gauge theory," we will see that the low-energy (IR) regime of the deconfined phase is described by a topological quantum field theory known as the level k BF theory.

Bosonization

The behavior of one-dimensional electronic systems is of great interest in condensed matter physics for many reasons. One is that, even for infinitesimally weak interactions, these one-dimensional metals violate the basic principles of the Landau Theory of the FL (Baym and Pethick, 1991). A central assumption of Femi Liquid theory is that at low energies the excitation energy of the fermion (electron) quasiparticle is always much larger than its width. Hence, at asymptotically low energies, the quasiparticle excitations become increasingly sharp.

A manifestation of this feature is that the quasiparticle propagator (the "Green function") has a pole on the real frequency axis with a finite residue Z. In one-dimensional metals, this assumption always fails since the residue Z vanishes, the Fermi field acquires a nontrivial anomalous dimension, and the pole is replaced by a branch cut. To this date this is the best example of what is called a "non-Fermi liquid." In one-dimensional metals, this non-Fermi liquid is often called a "Luttinger Liquid" (Haldane, 1981). A detailed analysis can be found in Chapter 6 of Fradkin (2013), and in other books.

Bosonization provides for a powerful tool to understand the physics of these nontrivial systems. Bosonization is a duality between a massless Dirac field in 1+1 dimensions and a (also massless) relativistic Bose (scalar) field (Mattis and Lieb, 1965; Luther and Emery, 1974; Mandelstam, 1975; Coleman, 1975). In this context, bosonization is a set of operator identities relating observables between two different (dual) continuum field theories. These identities have a close resemblance to the Jordan–Wigner transformation, which relates operators of a theory of spinless (Dirac) fermions on a one-dimensional lattice to a theory of bosons with hard cores (i.e., spins) on the same lattice (Lieb et al., 1961).

Dirac fermions in one space dimensions

To understand how these operator identities come about and what these fields mean in the Condensed Matter, context we will consider the simple problem of a system of noninteracting spinless fermions $c(n)$ on a one-dimensional chain of length L (with $L \to \infty$) for simplicity with periodic boundary conditions. The Hamiltonian is

$$H_0 = -t \sum_{n=1}^{L} c(n)^\dagger c(n+1) + \text{h.c.} \tag{116}$$

In momentum space, and in the thermodynamic limit $L \to \infty$, the Hamiltonian becomes

$$H_0 = \int_{-\pi}^{\pi} \frac{dp}{2\pi} (\varepsilon_0(p) - \mu)\, c^\dagger(p) c(p) \tag{117}$$

where $-\pi \leq p \leq \pi$, μ is the chemical potential (which fixes the fermion number) and $\varepsilon_0(p)$ is the (free) quasiparticle energy which, in this case, is

$$\varepsilon_0(p) = -2t \cos p. \tag{118}$$

This simple system has a global internal symmetry

$$c'(n) = e^{i\alpha} c(n), \qquad c'(n)^\dagger = e^{-i\alpha} c(c) \tag{119}$$

where α is a constant phase (with period 2π). This global symmetry reflects the conservation of fermion number

$$N_F = \sum_n c^\dagger(n) c(n). \tag{120}$$

The free fermion Hamiltonian of Eq. (116) is also invariant under lattice translations.

The ground state of this system is obtained by occupying all single particle states with energy below the chemical potential, $E \leq \mu \equiv EF$, which defines the Fermi energy E_F. In what follows we will redefine the zero of the energy at the Fermi energy. In the thermodynamic limit, the one-particle states are labeled by momenta defined in the first Brillouin zone $[-\pi, \pi)$. The ground state $|G\rangle$ of this system is obtained by filling up all single-particle states with momentum p in the range $[-p_F, p_F)$, where p_F is the Fermi momentum. Hence, the occupied states have energy $\varepsilon_0(p) \leq E_F$. The ground state is

$$|G\rangle = \prod_{|p| \leq p_F} c^\dagger(p) |0\rangle \tag{121}$$

and is called the *filled Fermi sea*. We will further assume that the fermionic system is dense in the sense that the occupied states are a finite fraction of the available states, that is, we assume that $|E_F|$ is a *finite* fraction of the bandwidth $W = 4t$.

The single-particle excitations have low energy if $|\varepsilon_0(p) - E_F| \ll |E_F|$. This range can only be accessed by quasiparticles with momenta p close to $\pm p_F$. For states with p close to p_F, we can a linearized approximation and write

$$\varepsilon_0(p) \simeq v_F(p - p_F) + \cdots \tag{122}$$

and similarly for the states near $-p_F$. Here $v_F = \left.\frac{\partial \varepsilon_0}{\partial p}\right|_{p_F} = 2t \sin p_F$ is the Fermi velocity. Let q being the momentum measured from p_F (or $-p_F$ in the other case), this approximation is correct in a range of momenta $-\Lambda \leq q \leq \Lambda$, where $\frac{2\pi}{L} \ll \Lambda \ll \pi$. In this regime we can approximate the lattice fields $c(n)$ with two continuum right moving $\psi_R(x)$ and left moving $\psi_L(x)$ Fermi fields such that (with $x = na_0$)

$$c(n) \sim e^{ip_F x} \psi_R(x) + e^{-ip_F x} \psi_L(x) \tag{123}$$

in terms of which the Hamiltonian takes the continuum form

$$\begin{aligned} H_{\text{continuum}} &= \int dx \left(\psi_R^\dagger(x)(-iv_F)\partial_x \psi_R(x) - \psi_L^\dagger(x)(-iv_F)\partial_x \psi_L(x) \right) \\ &= \int \frac{dq}{2\pi} q v_F \left(\psi_R^\dagger(q)\psi_R(q) + \psi_R^\dagger(q)\psi_R(q) \right). \end{aligned} \tag{124}$$

In what follows I will rescale time and space in such a way as to set $v_F = 1$.

Eq. (124) is the Hamiltonian of a massless Dirac field in 1+1 dimensions. It describes the effective low energy behavior of the excitations of the fermionic system defined on a lattice by the Hamiltonian of Eq. (116). Here low energy means asymptotically close to the Fermi energy (which we have set to zero) and momenta close to $\pm p_F$. We will see that this effective relativistic field theory gives a complete description of the universal low energy physics encoded in the microscopic model of Eq. (116) up to some subtle issues associated with what are called quantum anomalies.

Let us denote by $\psi(x)$ the bi-spinor field $\psi(x) = (\psi_R(x), \psi_L(x))$ and the 2×2 Dirac gamma-matrices in terms of the three Pauli matrices are

$$\gamma_0 = \sigma_1, \qquad \gamma_1 = -i\sigma_2, \qquad \gamma_5 = \sigma_3 \tag{125}$$

which obey the Dirac algebra

$$\{\gamma_\mu, \gamma_\nu\} = 2g_{\mu\nu} \tag{126}$$

where $g_{\mu\nu}$ is the metric tensor in 1+1-dimensional Minkowski spacetime

$$g_{\mu\nu} = \begin{pmatrix} 1 & 0 \\ 0 & -1 \end{pmatrix}. \tag{127}$$

Using the standard notation $\bar{\psi}(x) = \psi^\dagger(x)\gamma_0$ (where I left the spinor index $\alpha = 1, 2$ implicit), the Lagrangian density of the free massless Dirac fermion is

$$\mathcal{L} = \bar{\psi} i \not{\partial} \psi \tag{128}$$

where we have used the Feynman slash notation, which denotes the contraction of a vector field, say A_μ with the Dirac gamma matrices with a slash, $A_\mu \gamma^\mu \equiv \not{A}$.

Formally, the Dirac Lagrangian of Eq. (128) (and the Dirac Hamiltonian of Eq. (124)) is invariant under two separate global transformations. It has a global $U(1)$ (gauge) symmetry transformation

$$\psi'(x) = e^{i\theta}\psi(x) \tag{129}$$

(where θ is constant) under which the two components of the bi-spinor ψ transform in the same way

$$\psi'_R(x) = e^{i\theta}\psi_R(x), \qquad \psi'_L(x) = e^{i\theta}\psi_L(x). \tag{130}$$

The massless Dirac theory is also invariant under a global gauge $U(1)$ chiral transformation

$$\psi'(x) = e^{i\theta\gamma_5}\psi(x) \tag{131}$$

which in components reads

$$\psi'_R(x) = e^{i\theta}\psi_R(x), \qquad \psi'_L(x) = e^{-i\theta}\psi_L(x). \tag{132}$$

In general, if a system has a global continuous symmetry, it should have a locally conserved current and a globally conserved charge. This is the content of Noether's Theorem. Since the massless Dirac theory has these two global symmetries, one would expect that it should have two separately conserved currents.

The global $U(1)$ symmetry has an associated current $j_\mu = (j_0, j_1)$ given by

$$j_\mu = \bar{\psi}\gamma_\mu\psi \tag{133}$$

which is invariant under the global $U(1)$ symmetry. In terms of the right and left moving Dirac fields, ψ_R and ψ_L, the components of the current are

$$j_0 = \psi_R^\dagger\psi_R + \psi_L^\dagger\psi_L, \qquad j_1 = \psi_R^\dagger\psi_R - \psi_L^\dagger\psi_L. \tag{134}$$

This current is locally conserved and satisfies the continuity equation

$$\partial_\mu j^\mu = 0. \tag{135}$$

It has an associated conserved global charge, which we will call fermion number

$$Q = \int_{-\infty}^{\infty} dx j_0(x) = \int_{-\infty}^{\infty} dx \left(\psi_R^\dagger\psi_R + \psi_L^\dagger\psi_L\right). \tag{136}$$

This is the continuum version of the conservation of fermion number N_F of the free fermion lattice model discussed above.

Since this current is conserved, it can be coupled to an electromagnetic field through a term in the Lagrangian

$$\mathcal{L}_{\text{int}} = -e j_\mu A^\mu \tag{137}$$

where A^μ is the electromagnetic vector potential, which in 1+1 dimensions has only two components, $A^\mu = (A_0, A_1)$. Here, e is a coupling constant, which is interpreted as the electric charge. This coupling amounts to making the $U(1)$ symmetry a local gauge symmetry under which the fields transform as

$$\psi'(x) = e^{i\theta(x)}\psi(x), \qquad A'_\mu(x) = A_\mu(x) + \frac{1}{e}\partial_\mu\theta(x). \tag{138}$$

Now the conservation of fermion number becomes the conservation of the total electric charge

$$Q_e = -eQ. \tag{139}$$

In a continuum nonrelativistic model, the Fermi field is $\psi(x)$ (ignoring spin), for example, an electron gas in one dimension such as a quantum wire, the analog of decomposition shown in Eq. (123) of the electron field $\psi(x)$ becomes

$$\psi(x) = e^{ip_F x}\psi_R(x) + e^{-ip_F x}\psi_L(x). \tag{140}$$

The electron field $\psi(x)$ transforms as $\psi'(x) = e^{i\alpha}\psi(x)$ under the global $U(1)$ gauge symmetry of Eq. (130). In particular, the local density operator $\rho(x) = \psi^\dagger(x)\psi(x)$ is invariant under this symmetry. Under both decompositions of Eqs. (123) and (140), the local density operator becomes

$$\rho(x) = \psi_R^\dagger(x)\psi_R(x) + \psi_L^\dagger(x)\psi_L(x) + e^{i2p_F x}\psi_R^\dagger(x)\psi_L(x) + e^{-i2p_F x}\psi_L^\dagger(x)\psi_R(x) \tag{141}$$

Clearly the nonrelativistic density operator $\rho(x)$ is invariant under the global $U(1)$ gauge symmetry. The same considerations apply to the lattice version of the density operator (the local occupation number).

Thus, the density operator $\rho(x)$ can be decomposed into a slowly varying part (the first two terms in Eq. (141)) and the last two terms which oscillate with wave vectors $Q = \pm 2p_F$. These observations imply that we can express $\rho(x)$ in the form

$$\rho(x) = \bar{\rho} + j_0(x) + e^{iQx}\psi_Q(x) + e^{-iQx}\psi_{-Q}(x). \tag{142}$$

This decomposition can be interpreted as a Fourier expansion of the density operator in term of newly defined slowly varying fields. In Eq. (142), $Q = 2p_F$ and $\bar{\rho}$ is the average density, where we assumed that the Dirac density operator $j_0(x)$ has vanishing expectation value (i.e., it is normal-ordered). In Eq. (142), we defined the (bosonic) operators

$$\psi_Q(x) = \psi_R^\dagger(x)\psi_L(x), \qquad \psi_{-Q}(x) = \psi_L^\dagger(x)\psi_R(x) \tag{143}$$

which characterize the oscillatory component of the density. The operators $\psi_{\pm Q}(x)$ are the order parameters of a charge density wave state in one dimension and Q is the ordering wavevector.

Repulsive interactions between the electrons can cause scattering process between the right and left moving components to become relevant (in the Renormalization Group sense) leading to the spontaneous breaking of translation invariance. The resulting state is known as a charge-density-wave (CDW). In this state the operators $\psi_{\pm Q}(x)$ (or a linear combination of them) acquire a nonvanishing expectation value, and the expectation value of the density operator $\rho(x)$ has a (static) modulated component, and the Dirac Hamiltonian density becomes

$$\mathcal{H} = \psi_R^\dagger(x)(-i)\partial_x\psi_R(x) - \psi_L^\dagger(x)(-i)\partial_x\psi_L(x) + m\left(\psi_R^\dagger(x)\psi_L(x) + \psi_L^\dagger(x)\psi_R(x)\right) \tag{144}$$

where m is the Dirac mass. The operator in the second term of Eq. (144) mixes the right and left moving components of the Dirac spinor. This Hermitian operator is known as the Dirac mass term. In relativistic notation this operator is written as

$$\bar{\psi}\psi = \psi_R^\dagger(x)\psi_L(x) + \psi_L^\dagger(x)\psi_R(x). \tag{145}$$

When $m \neq 0$, that is, when $\langle\bar{\psi}\psi\rangle \neq 0$, the fermionic spectrum has a mass gap, and the electronic states with momenta $\pm\, p_F$ have an energy gap. Alternatively we could have considered a state with the in which the (Hermitian) operator that has an expectation value is

$$i\bar{\psi}\gamma_5\psi = i\left(\psi_R^\dagger(x)\psi_L(x) - \psi_L^\dagger(x)\psi_R(x)\right) \tag{146}$$

which is known as the γ_5 mass term. In a more general CDW state both mass terms can be present.

Chiral symmetry and chiral symmetry breaking

The CDW states we introduced have different symmetries. To see this let us observe that the operators $\psi_{\pm Q}(x)$ transform nontrivially under a global $U(1)$ chiral transformation

$$\psi'_{\pm Q}(x) = e^{\mp 2i\theta}\psi_{\pm Q}(x). \tag{147}$$

Upon substituting this transformation in the expansion of the density $\rho(x)$ of Eq. (142), we see that a chiral transformation is equivalent to a uniform displacement of the density operator by θ/p_F,

$$\rho(x) \to \rho(x + \theta/p_F). \tag{148}$$

Under a chiral transformation with arbitrary angle θ, the Dirac and γ_5 mass term operators transform as an orthogonal transformation of a two-component vector. In particular for a chiral transformation with $\theta = \pi/4$,

$$\bar{\psi}\psi \mapsto i\bar{\psi}\gamma_5\psi, \qquad i\bar{\psi}\gamma_5\psi \mapsto -\bar{\psi}\psi \tag{149}$$

which is equivalent to a displacement of the density by 1/4 of the period of the CDW. In this sense these two states are equivalent, as is the state with a more general linear combination.

The microscopic lattice model (and the continuum nonrelativistic model) is invariant under the spatial inversion symmetry $x \leftrightarrow -x$. This also implies a symmetry under the exchange of right and left moving components of the Dirac spinor, $\psi_R \leftrightarrow \psi_L$. In the massless Dirac theory this operation is equivalent to the multiplication of the spinor by the Pauli matrix σ_1. In the massless theory, the multiplication by σ_2 (followed by a chiral transformation with $\theta = \pi/2$) has the same effect.

These symmetries have an important effect on the fermionic spectrum. To understand what they do let us consider the one-particle Dirac Hamiltonian with a Dirac mass m (jn momentum space)

$$h = \begin{pmatrix} p & m \\ m & -p \end{pmatrix}. \tag{150}$$

This operator anticommutes with the Pauli matrix σ_2, $\{h, \sigma_2\} = 0$. Let $|E\rangle$ be an eigenstate of the Hamiltonian h with energy eigenvalue $E = \sqrt{p^2 + m^2}$. Let us consider the state $\sigma_2|E\rangle$. It is also an eigenstate of h but with energy $-E$, that is,

$$h\sigma_2|E\rangle = -\sigma_2 h|E\rangle = -E|E\rangle, \qquad \Rightarrow \sigma_2|E\rangle = |-E\rangle. \tag{151}$$

Hence if $|E\rangle$ is an eigenstate of energy E, then $\sigma_2|E\rangle$ is an eigenstate of energy $-\ E$. This means that the spectrum is invariant under charge conjugation symmetry. Notice that under this operation the spinor transforms as

$$\sigma_2 \begin{pmatrix} \psi_R \\ \psi_L \end{pmatrix} = \begin{pmatrix} -i\psi_L \\ i\psi_R \end{pmatrix} = e^{-i\gamma_5\pi/2} \begin{pmatrix} \psi_L \\ \psi_R \end{pmatrix}. \tag{152}$$

In other words, this theory is invariant under charge conjugation C and parity $\mathcal{P}$ which, combined, it implies that it is invariant under time-reversal $\mathcal{T}$.

The same consideration applies in the case of a γ_5 mass term in which case the one-particle Dirac Hamiltonian now is

$$h = \begin{pmatrix} p & -im_5 \\ im_5 & -p \end{pmatrix}. \tag{153}$$

This Hamiltonian now anticommutes with the Pauli matrix σ_1 which also implies that the same charge conjugation symmetry C, $|E\rangle \leftrightarrow |-\ E\rangle$ is present in the spectrum of the case of a γ_5 mass. We can also repeat the argument on parity invariance $\mathcal{P}$, which is now multiplication by σ_1, Thus the theory is invariant under time-reversal $\mathcal{T}$.

However, if the theory has both a Dirac mass m and a γ_5 mass m_5, these symmetries are broken. Indeed, the one-particle Dirac Hamiltonian now is

$$h = \begin{pmatrix} p & m - im_5 \\ m + im_5 & -p \end{pmatrix} = p\sigma_3 + m\sigma_1 + m_5\sigma_2 \tag{154}$$

which no longer has a spectral symmetry. In this case $C\mathcal{P}$ is broken and, hence, so it $\mathcal{T}$ since $C\mathcal{P}\mathcal{T}$ remains unbroken (as it should).

In a lattice system, this is a symmetry transformation only if $\theta = \pi n/p_F$ is a lattice displacement, which restricts the allowed values of the chiral angle to be discrete. Although this is true, interactions play a significant role in the actual behavior. In fact, there are physical situations in which an effective continuous symmetry actually emerges in this he infrared (long-distance) limit. This is what happens when the CDW is incommensurate and, as we will see in the next section, it slides under the action of an electric field.

In the case of a half-filled system (with only nearest-neighbor hopping matrix elements) the Fermi wave vectors are $\pm\,\pi/2$. In this case the allowed discrete chiral transformation has a chiral angle $\pi/2$ under which $\bar{\psi}\psi \ \mapsto\ -\bar{\psi}\psi$ (and similarly for $i\bar{\gamma}_5\psi$) corresponding by a translation by one lattice spacing. The allowed four fermion operator is $(\bar{\psi}\psi)^2$. If the lattice fermions are spinless this operator reduces to

$$(\bar{\psi}\psi)^2 = -2j_R(x)j_L(x) + \lim_{y\to x} \psi_R^\dagger(x)\psi_L^\dagger(x)\psi_L(y)\psi_R(y) + \text{h.c.} \tag{155}$$

where introduced the right and left moving (chiral) components of the current operator

$$j_R(x) = \frac{1}{2}(j_0(x) + j_1(x)) = \psi_R^\dagger(x)\psi_R(x), \qquad j_L(x) = \frac{1}{2}(j_0(x) - j_1(x)) = \psi_L^\dagger(x)\psi_L(x) \tag{156}$$

The first term in Eq. (155) is known as the backscattering interaction and has scaling dimension 2. Hence, it is a marginal operator. The theory with only the first term is known in condensed matter physics as the Luttinger model and in High-Energy Physics as the (massless) Thirring model. The second operator in Eq. (155) formally violates momentum conservation as its total momentum is $4p_F = 2\pi$, which is a reciprocal lattice vector and, as such, it is equivalent to zero (mod 2π). Such an operator is not formally allowed in a (naive) continuum theory. This operator is due to a lattice Umklapp process and breaks the formal continuous chiral symmetry to a discrete $\mathbb{Z}_2$ subgroup. Although the naive scaling dimension of this operator is 2 (and hence it is formally marginal). If the fermions are spinless, the leading operator actually vanishes and the leading nonvanishing operator actually has dimension 4, which is irrelevant. However, as shown above, backscattering processes of the form $j_R(x)\, j_L(x)$ are part of this operator and are exactly marginal.

If the interaction is strong enough, the backscattering interaction can make the Umklapp operator relevant. When this happens, the fermionic system has a quantum phase transition to an insulating state with a period 2 (commensurate) CDW state. On the other hand, for spin 1/2 fermions, the operator $(\bar{\psi}\psi)^2$ is allowed and is marginally relevant. If the interactions are repulsive, the resulting state is an antiferromagnetic Néel state at quantum criticality, while for attractive interactions it is a period 2 CDW. This is what happens in the 1D Hubbard model (see, e.g., Fradkin, 2013 for a detailed analysis).

There are two theories in relativistic systems, which are closely related to this problem. One if the Gross–Neveu model (Gross and Neveu, 1974) which is a theory of N species of massless Dirac spinors with Lagrangian density

$$\mathcal{L}_{\rm GN} = \bar{\psi}_a i\partial\!\!\!/\psi_a + g(\bar{\psi}_a\psi_a)^2 \tag{157}$$

with $a = 1, \ldots, N$ (summation of repeated induces is implies). The spin-1/2 Hubbard model corresponds to the case $N = 2$. This Lagrangian is invariant only under the discrete chiral symmetry $\bar{\psi}_a\psi_a \mapsto -\bar{\psi}_a\psi_a$. This is a discrete, $\mathbb{Z}_2$, symmetry and as such it can be spontaneously broken in 1+1 dimensions. For $N \geq 2$, the resulting state has a (dynamically) broken $\mathbb{Z}_2$ chiral symmetry and that there is a chiral condensate $\langle\bar{\psi}_a\psi_a\rangle \neq 0$ corresponding to a period 2 CDW.

The other theory is known as the chiral Gross–Neveu model whose Lagrangian density is

$$\mathcal{L}_{\rm cGN} = \bar{\psi}_a i\partial\!\!\!/\psi_a + g\left((\bar{\psi}_a\psi_a)^2 - (\bar{\psi}_a\gamma_5\psi_a)^2\right) \tag{158}$$

which has the full continuous chiral symmetry. For $N = 1$, this theory is equivalent to the Luttinger model (and to the Gross–Neveu model if we ignore the Umklapp term). For $N \geq 2$ the chiral symmetry is formally broken. If this were true, this theory would violate the Mermin–Wagner theorem. However a detailed study (most easily done using bosonization methods) shows that instead of long-range order the correlator of both mass terms decay as a power law as a function of distance, consistent with the requirements by this theorem.

We close this section by noting that if the lattice model is not half filled but its density is either incommensurate or has a higher degree of commensurability, say p/q, the chiral symmetry is actually continuous (in the incommensurate case) or effectively continuous since the requisite Umklapp terms are strongly irrelevant. However, if the lattice model is not at half filling charge conjugation symmetry C is broken at the lattice scale (in the UV), where it is equivalent to particle–hole symmetry, but it is recovered in the low-energy, IR, regime (up to irrelevant operators). In this sense, both the continuous chiral symmetry and charge conjugation symmetry can be regarded as emergent IR symmetries

The chiral anomaly

In Section "Chiral symmetry and chiral symmetry breaking" we showed that the theory of massless Dirac fermions, in addition to a global $U(1)$ gauge symmetry, has a second conservation law which we called a global $U(1)$ chiral symmetry, shown in Eq. (131). This symmetry implies that there is a locally associated chiral current j_μ^5, given by

$$j_\mu^5(x) = \bar{\psi}(x)\gamma_\mu\gamma_5\psi(x) \tag{159}$$

which also satisfies a continuity equation

$$\partial^\mu j_\mu^5 = 0 \tag{160}$$

and there is a globally conserved chiral charge Q^5

$$Q^5 = \int_{-\infty}^{\infty} dx\, j_0^5(x) = \int_{-\infty}^{\infty} dx\left(\psi_R^\dagger\psi_R - \psi_L^\dagger\psi_L\right). \tag{161}$$

It is easy to check that the Dirac current j_μ and the chiral current j_μ^5 are related by

$$j_\mu^5 = \epsilon_{\mu\nu} j^\mu \tag{162}$$

where $\varepsilon_{\mu\nu}$ is the second rank Levi-Civita tensor.

The simultaneous conservation of both currents j_μ and j_μ^5 in the massless Dirac theory implies that the right and left moving densities j_R and j_L, defined in Eq. (156), should be separately conserved. In fact, if the Dirac theory has a mass term

$$\mathcal{L} = \bar{\psi} i \partial\!\!\!/ \psi - m \bar{\psi}\psi \tag{163}$$

it is straightforward to show that

$$\partial^\mu j_\mu^5 = 2mi\bar{\psi}\gamma^5\psi \tag{164}$$

which means that in the massive theory, the axial current is not conserved. This is easy to understand since the mass term mixes the right and left moving components of the Dirac spinor and, hence, the right and left moving densities are not conserved.

What happens in the *massless* limit, $m \to 0$, is more subtle. This problem was investigated in the late 1960s in 3+1 dimensions by Adler (1969) and by Bell and Jackiw (1969), who were interested in the anomalous decay of a neutral pion into two photons, $\pi^0 \to 2\gamma$. This process appears at third order of perturbation theory and it involves the computation of a triangle diagram (a fermion loop). In 3+1 dimensions, this process has a UV divergence which needed to be regulated. These authors showed that it is not possible to find a regularization in which both the Dirac (gauge) current $j_\mu = \bar{\psi}\gamma_\mu\psi$ and the axial current $j_\mu^5 = \bar{\psi}\gamma_\mu\gamma^5\psi$ are conserved. In other words, if gauge invariance is preserved then the axial current is not and has an *anomaly* and results in a nonconservation of the axial current, $\partial^\mu j_\mu^5 \neq 0$. On the other hand, at least in the case of the physical gauge-invariant regularization, the obtained expression for the anomaly in the axial current is *universal*, independent of the value of the UV regulator (the cutoff). Sometime later G. 't Hooft showed that in non-Abelian gauge theories instant processes also lead to anomalies and, furthermore, the result was also universal ('t Hooft, 1976a, b). Since the result is universal and, hence, independent of the UV scale, this led to the concept of anomaly matching conditions.

We will examine this problem in 1+1 dimensions (although it plays a key role in the theory of topological insulators in three space dimensions, Qi et al., 2008). As we noted above, the lattice model is gauge-invariant and has only one conserved current. The conserved axial current appeared only in the low-energy regime in which the lattice model is described by a theory of massless Dirac fermions. To understand this problem, we will consider the theory of fermions in 1+1 dimensions coupled to a $U(1)$ gauge field. In the presence of a background (i.e., not quantized) electromagnetic field in the $A_0 = 0$ gauge, the free fermion Hamiltonian of Eq. (116) becomes

$$H[A] = -t\sum_{n=1}^{L} c^\dagger(n) e^{ieA(n,t)/\hbar} c(n) + \text{h.c.} \tag{165}$$

An uniform and constant electric field is E, which is represented by a vector potential $A = -cEt$ (with c being the speed of light). The net effect of this gauge field is to shift of the momentum of the fermion quasiparticles $p \to p + ecEt/\hbar$ or, what is the same, to displace the fermion dispersion relation in momentum by the $ecEt/\hbar$. This means that the Fermi points are also shifted by that amount, $p_F \to p_F + ecEt/\hbar$ and $-p_F \to -p_F + ecEt/\hbar$. This means that the single particle states between p_F and $p_F + ecEt/\hbar$ that were empty for $E = 0$ are now occupied and the states between $-p_F$ and $-p_F + ecEt/\hbar$ that were occupied for $E = 0$ are now empty. This means that number of right-moving fermions is increasing at a rate of $ecE/\hbar$ and that the number of left-moving fermions decreases at the same rate. This results in a net current. Throughout this process the total number of fermions is not changed, gauge invariance is satisfied, but the number of right and left moving fermions is not separately concerned. Notice that this is an effect that involved the entire Femi sea but the net effect is at low energies.

Let us see now how this plays out in the effective Dirac theory. The massless Dirac Lagrangian density in the background of an unquantized electromagnetic field A_μ is

$$\mathcal{L} = \bar{\psi}(i\partial\!\!\!/ - eA\!\!\!/)\psi. \tag{166}$$

Since there is no mass term, the Dirac equation still decouples into two equations, for the right and left moving components of the Dirac spinor. In the $A_0 = 0$, gauge they are

$$i\partial_0\psi_R = (-i\partial_1 - A^1)\psi_R, \qquad i\partial_0\psi_L = (i\partial_1 - A^1)\psi_L. \tag{167}$$

In the temporal gauge, $A_0 = 0$, a uniform electric field $E = \partial_0 A^1$, and A^1 increases linearly with time. As A^1 increases, the Fermi momentum p_F (which is equal to the Fermi energy E_F) also increases at the rate eE. The density of states of a system of length L is $L/(2\pi)$. So, the rate of change of the number of right-moving fermions is

$$\frac{dN_R}{dx_0} = \frac{e}{2\pi}E \tag{168}$$

where we defined $N_R = \int_0^L dx\, j_R$ and similarly for N_L. If the UV regulator of the theory is compatible with gauge invariance, then the total fermion number must be conserved and the total vacuum charge must remain equal to zero,

$$Q = \int_0^L dx\, j_0(x) = N_R + N_L = 0. \tag{169}$$

Thus, if N_R increases, then N_L must decrease by the same amount. Or, equivalently, the electric field E creates an equal number of particles N_R and of antiparticles $\overline{N}_L = -N_L$.

On the other hand, the chiral charge $Q^5 = N_R - N_L$ must increase at the rate

$$\frac{dQ^5}{dx_0} = \frac{dN_R}{dx_0} + \frac{d\bar{N}_L}{dx_0} = \frac{e}{\pi}E. \tag{170}$$

Again, the details of the UV regularization do not matter, only that it is gauge-invariant. We can also interpret Eq. (170) as the rate of particle–antiparticle pair creation by an electric field.

In a relativistic notation, these results are expressed as

$$\partial^\mu j^5_\mu = \frac{e}{2\pi}\epsilon_{\mu\nu}F^{\mu\nu}. \tag{171}$$

Hence, the formally conserved current j^5_μ has an anomaly and is not conserved due to quantum effects. Since it is not conserved, we cannot gauge the chiral symmetry. In the next section, we will see that the anomaly is closely related with bosonization.

Bosonization, anomalies, and duality

We will reexamine the problem at hand from the point of view of the fermionic currents of the Dirac theory j_μ as operators. Since the currents obey the continuity equation, $\partial_\mu j^\mu = 0$ one expects that this would imply that it may be possible to write them as a curl of a scalar field, that is, $j_\mu(x) = \epsilon_{\mu\nu}\partial^\nu\phi(x)$ where $\phi(x)$ should be a scalar field. Since this should be an operator identity, we will need to understand how the currents act on the physical Hilbert space.

The Fermi-Bose mapping in 1D systems is closely related to the chiral anomaly we just discussed. Bosonization of a system of 1+1 dimensional massless Dirac fermions is a set of operator identities understood as matrix elements of the observables in the physical Hilbert space. These identities were first derived by Mattis and Lieb (1965), based on earlier work by Schwinger (1959). These identities were rediscovered (and their scope greatly expanded) by Luther and Emery (1974), by Coleman (1975), by Mandelstam (1975), and by Witten (1978). A non-Abelian version of bosonization was subsequently derived by Witten (1984).

The physical Hilbert space is defined as follows: Let $|\text{FS}\rangle \equiv |0\rangle$ denote the *filled Fermi sea*. In what follows we will assume that the physical system is macroscopically large and that local operators create the physical states by acting *finitely* on the filled Fermi sea. Physical observables, such as the right and left moving densities $j_R(x)$ and $j_L(x)$, need to be *normal-ordered* with respect to the physical vacuum state, the filled Fermi (Dirac) sea $|0\rangle$. The normal ordered densities are $j_R(x) : \equiv j_R(x) - \langle 0|j_R(x)|0\rangle$ and $: j_L(x) : \equiv j_L(x) - \langle 0|j_R(x)|0\rangle$. Since the densities are products of fermion operators, they need to be defined as a limit in which the operators are separated by a short distance η. Crucial to this construction is that the computation of the expectation values be regularized in such a way that the charge (gauge) current $j_\mu(x)$ is locally conserved and satisfies the continuity equation $\partial_\mu j^\mu = 0$ as an operator identity. In what follows, all expectation values will refer to the filled Fermi sea state $|0\rangle$.

The propagators of the right and left moving Fermi fields are given by

$$\langle \psi_R^\dagger(x_0, x_1)\psi_R(0,0)\rangle = \frac{-i}{2\pi(x_0 - x_1 + i\epsilon)}, \qquad \langle \psi_L^\dagger(x_0, x_1)\psi_L(0,0)\rangle = \frac{i}{2\pi(x_0 + x_1 + i\epsilon)} \tag{172}$$

The expectation values of the currents at a space location x_1 are

$$\langle j_R(x_1)\rangle = \lim_{\eta\to 0}\langle \psi_R^\dagger(x_1+\eta)\psi_R(x_1-\eta)\rangle = \frac{i}{4\pi\eta}, \quad \langle j_L(x_1)\rangle = \lim_{\eta\to 0}\langle \psi_L^\dagger(x_1+\eta)\psi_L(x_1-\eta)\rangle = \frac{-i}{4\pi\eta} \tag{173}$$

which are divergent at short distances. It follows that the normal-ordered right and left moving current densities satisfy the equal-time commutation relations

$$[j_R(x_1), j_R(x'_1)] = -\frac{i}{2\pi}\partial_1\delta(x_1 - x'_1), \quad [j_L(x_1), j_L(x'_1)] = +\frac{i}{2\pi}\partial_1\delta(x_1 - x'_1) \tag{174}$$

These identities imply that the normal-ordered space-time components of the current $j_\mu = (j_0, j_1)$ satisfy the equal-time commutation relations

$$[j_0(x_1), j_1(x'_1)] = -\frac{i}{\pi}\partial_1\delta(x_1 - x'_1), \qquad [j_0(x_1), j_0(x'_1)] = [j_i(x_1), j_1(x'_1)] = 0 \tag{175}$$

The nonvanishing right-hand sides of these commutators are known as Schwinger terms. These identities define the $U(1)$ (Kac-Moody) current algebra.

We should note that in a theory of *nonrelativistic* Fermi fields $\psi(\boldsymbol{x}, t)$ in all dimensions, the charge density $\rho(\boldsymbol{x})$ and the current operators $\boldsymbol{j}(\boldsymbol{x}) = \frac{1}{2i}\left(\psi^\dagger(\boldsymbol{x})\nabla\psi(\boldsymbol{x}) - \nabla\psi^\dagger(\boldsymbol{x})\nabla\psi(\boldsymbol{x})\right)$ satisfy a similar expression (also at equal times)

$$[\rho(\boldsymbol{x}), j_k(\boldsymbol{x}')] = -i\frac{e^2}{mc^2}\partial_k(\delta(\boldsymbol{x} - \boldsymbol{x}')\rho(\boldsymbol{x})), \quad [\rho(\boldsymbol{x}), \rho(\boldsymbol{x}')] = 0, \quad [j_k(\boldsymbol{x}), j_l(\boldsymbol{x}')] = 0 \tag{176}$$

In one dimension, and in the regime in which the fermions have a macroscopic density so that $\rho(x) \simeq \langle\rho(x)\rangle$, after a multiplicative rescaling of the operators, the nonrelativistic identities of Eq. (176) are equivalent to the $U(1)$ current algebra of Eq. (175).

The $U(1)$ current algebra of Eq,(175) is reminiscent of the equal-time canonical commutation relations of a scalar field. Indeed, if $\phi(x)$ is a scalar field and $\Pi(x) = \partial_0\phi(x)$ is its canonically conjugate momentum, then they obey the equal-time canonical commutation relations

$$[\phi(x_1), \Pi(x_1')] = i\delta(x_1 - x_1'). \tag{177}$$

We can then identify the charge density j_0 and the current density j_1 with the scalar field operators

$$j_0(x) = \frac{1}{\sqrt{\pi}}\partial_1\phi(x), \qquad j_1(x) = -\frac{1}{\sqrt{\pi}}\Pi(x) = -\frac{1}{\sqrt{\pi}}\partial_0\phi(x) \tag{178}$$

which obey the $U(1)$ current algebra of Eq. (175) as a consequence of the canonical commutation relations, Eq. (177). Furthermore, we can rewrite Eq. (177) in the Lorentz covariant form

$$j_\mu(x) = \frac{1}{\sqrt{\pi}}\epsilon_{\mu\nu}\partial^\nu\phi(x) \tag{179}$$

which is clearly consistent with the local conservation of the current j_μ,

$$\partial_\mu j^\mu(x) = 0. \tag{180}$$

Let us examine now the question of the conservation of the chiral current j_μ^5. In Eq. (162), we showed that the gauge current and the chiral current are related by $j_\mu^5 = \epsilon_{\mu\nu}j^\nu$. Therefore the divergence of the chiral current is

$$\partial^\mu j_\mu^5 = \epsilon_{\mu\nu}\partial^\mu j^\nu = \frac{1}{\sqrt{\pi}}\epsilon_{\mu\nu}\epsilon^{\nu\lambda}\partial^\mu\partial_\lambda\phi = -\frac{1}{\sqrt{\pi}}\partial^2\phi \tag{181}$$

where we used the identification of the gauge current in terms of the scalar field ϕ, Eq. (179). Therefore we conclude that

$$\partial^\mu j_\mu^5 = 0 \Leftrightarrow \partial^2\phi = 0. \tag{182}$$

This equation states that the chiral current as an operator identity is conserved if and only if the field ϕ is a free massless scalar field, whose Lagrangian density is

$$\mathcal{L}_B = \frac{1}{2}(\partial_\mu\phi)^2. \tag{183}$$

In Eq. (166), we considered the free massless Dirac Lagrangian coupled to a background (not quantized) gauge field A_μ through the usual minimal coupling which here is $\mathcal{L}_{\text{int}} = -ej_\mu A^\mu$. using the bosonization identity for the gauge current, Eq. (179) we see that the Lagrangian density of the bosonized theory now becomes

$$\begin{aligned}\mathcal{L}_B[A] &= \frac{1}{2}(\partial_\mu\phi)^2 - \frac{e}{\sqrt{\pi}}\epsilon_{\mu\nu}\partial^\nu\phi(x)\, A^\mu(x)\\ &\equiv \frac{1}{2}(\partial_\mu\phi)^2 + J(x)\phi(x)\end{aligned} \tag{184}$$

where the source $J(x)$ is

$$J(x) = \frac{e}{\sqrt{\pi}}\epsilon_{\mu\nu}\partial^\nu A^\mu(x) = \frac{e}{\sqrt{4\pi}}F^*(x) \tag{185}$$

where $F^*(x) = \epsilon_{\mu\nu}F^{\nu\mu}(x)$ is the (Hodge) dual of the field strength $F_{\mu\nu}$. Hence, F^* is (essentially) the source for the scalar field $\phi(x)$. This implies that the equation of motion of the scalar field must be

$$-\partial^2\phi(x) = J(x) = \frac{e}{\sqrt{\pi}}\epsilon_{\mu\nu}\partial^\nu A^\mu. \tag{186}$$

Retracing our steps, we find that the chiral current j_μ^5 obeys

$$\partial^\mu j_\mu^5 = -\frac{1}{\sqrt{\pi}}\partial^2\phi = \frac{e}{2\pi}\epsilon_{\mu\nu}F^{\mu\nu} \tag{187}$$

which reproduces the chiral anomaly given in Eq. (170).

These results suggest that the theory of a free massless Dirac spinor must be equivalent to the theory of the free massless scalar field. This statement is known as bosonization. However for this identification to be correct, there must be an identification of the Hilbert spaces and of all the operators of each theory. We will not do this detailed analysis here but will highlight the most significant statements.

Let us begin with the fermion number of the Dirac theory. Consider a system of fermions of total length L. Using the bosonization identity of Eq. (179), we find that the fermion number $N_F \equiv Q$ is given by

$$N_F = \int_0^L dx_1\, j_0(x_0, x_1) = \frac{1}{\sqrt{\pi}} \int_0^L dx_1\, \partial_1 \phi(x_0, x_1) = \frac{1}{\sqrt{\pi}} (\phi(x_0, L) - \phi(x_0, 0)). \tag{188}$$

Thus, the vacuum sector of the Dirac theory, with $N_F = 0$, corresponds to the theory of the scalar field with periodic boundary conditions, $\phi(x_1 = 0) = \phi(x_1 = L)$. Furthermore, since the fermion number is quantized, $N_F \in \mathbb{Z}$, changing the fermion number is the same as twisting the boundary conditions of the scalar so that

$$\phi(x_1 + L) = \phi(x_1) + \sqrt{\pi} N_F. \tag{189}$$

In String Theory (Polchinski, 1998) the scalar field is interpreted as the coordinate of a string. Compactifying the space where the string lives to be a circle of radius R means that the string coordinate is defined modulo $2\pi Rn$, where n is an integer. We see that the condition imposed by Eq. (189) is equivalent to say that the scalar field is *compactified* and that the compactification radius is $R = 1/\sqrt{4\pi}$. This identification also imposes the restriction that the allowed operators of the scalar field must obey the identification

$$\phi(x) \sim \phi(x) + 2\pi R n \tag{190}$$

as an equivalency condition.

The simplest bosonic operators that obey the compactification condition are the vertex operators $V_\alpha(x)$,

$$V_\alpha(x) = \exp(i\alpha\phi(x)). \tag{191}$$

The compactification condition then requires that the allowed vertex operators should have $\alpha = n/R = \sqrt{4\pi}\, n$, where n is an integer. Since the propagator of the scalar field in 1+1-dimensional (Euclidean) spacetime is

$$G(x - x') = -\frac{1}{2\pi} \ln\left(\frac{|x - x'|}{a}\right) \tag{192}$$

where a is a short-distance cutoff, we find that the scaling dimension of the vertex operator is $\Delta_\alpha = \alpha^2/(4\pi) = n^2$. We will see shortly that the vertex operator with $\alpha = \sqrt{4\pi}$ is essentially the Dirac mass operator (which has scaling dimension 1).

The free massless scalar field can be decomposed into right and left moving components, ϕ_R and ϕ_L respectively,

$$\phi = \phi_R + \phi_L, \qquad \vartheta = -\phi_R + \phi_L \tag{193}$$

where

$$\vartheta(x_0, x_1) = \int_{-\infty}^{x_1} dx'_1\, \Pi(x_0, x'_1) \tag{194}$$

is the Cauchy–Riemann dual of the field $\phi(x)$ since they satisfy the Cauchy–Riemann equation

$$\partial_\mu \phi = \epsilon_{\mu\nu} \partial^\nu \vartheta. \tag{195}$$

The right and left moving components of the Dirac spinor are found to have the bosonized expression (Mandelstam, 1975)

$$\psi_R(x) = \frac{1}{\sqrt{2\pi a}} : \exp(i\sqrt{4\pi}\phi_R(x)) : , \qquad \psi_L(x) = \frac{1}{\sqrt{2\pi a}} : \exp(-i\sqrt{4\pi}\phi_L(x)) : \tag{196}$$

It is easy to check that the propagators of these operators agree with the expressions given in Eq. (172), and that they have scaling dimension 1/2 and spin 1/2.

How does a chiral transformation act on the scalar field? A chiral transformation by an angle θ, c.f. Eq. (132), acts on the right and moving fermions as $\psi'_R = \exp(i\theta)\psi_R$ and $\psi'_L = \exp(-i\theta)\psi_L$. From Eq. (196), we see that the right and left moving components of the scalar field transform as $\phi'_R = \phi_R + \theta/\sqrt{4\pi}$ and $\phi'_L = \phi_L + \theta/\sqrt{4\pi}$. This means that a chiral transformation by an angle θ of the Dirac fermion is equivalent to a translation (a shift) of the scalar field $\phi' = \phi + 2\theta/\sqrt{4\pi}$.

We can use the operator product expansion discussed in Section "The operator product expansion" to show that the fermion mass terms $\bar\psi\psi$ and $i\bar\psi\gamma^5\psi$ are given by the following identifications

$$\bar\psi\psi = \frac{1}{2\pi a} : \cos(\sqrt{4\pi}\phi) : , \qquad i\bar\psi\gamma^5\psi =: \sin(\sqrt{4\pi}\phi) : \ . \tag{197}$$

These operators have scaling dimension 1 and transform properly under chiral transformations. These identifications imply that a theory of free *massive* Dirac fermions

$$\mathcal{L}_D = \bar\psi i\partial\!\!\!/\, \psi - m\bar\psi\psi \tag{198}$$

is equivalent to the sine-Gordon field theory (Coleman, 1975) whose Lagrangian is

$$\mathcal{L}_{SG} = \frac{1}{2}(\partial_\mu\phi)^2 - g : \cos(\sqrt{4\pi}\phi) : \tag{199}$$

where $g = m/(2\pi a)$.

Given the central role played by the current algebra identities of Eq. (175), one may wonder if a similar approach might apply in higher dimensions. Schwinger terms in current algebra play an important role in relativistic field theories. However in higher dimensions, their structure is more complex and does not lead to identities of the type we have discussed. The reason at the root of this problem is largely kinematical. The Bose (scalar) field ϕ is qualitatively a bound state, a collective mode in the language of condensed matter physics. In 1+1 dimensions, this collective mode exhausts the spectrum at low energies due to the strong kinematical restriction on one spatial dimension.

The equivalency between the theory of free massive Dirac fermions and the sine-Gordon theory is an example of the power of bosonization. On the Dirac side, mapping the theory is free and its spectrum is well understood. But on the sine-Gordon side, the theory is nonlinear. In fact in the sine-Gordon theory, the fermions are essentially solitons, domain walls of the scalar field. For these and many other reasons that we do not have space here bosonization plays a huge role in understanding the nonperturbative behavior of systems both in condensed matter physics and in Quantum Field Theory in 1+1 dimensions. We will see in Section "Bosonization of the Dirac theory in 2+1 dimensions" that to an extent some of these ideas can and have been extended to relativistic systems and classical statistical mechanical systems in 2+1 dimensions.

Fractional charge

Solitons in one dimensions

We begin by returning to the equivalency between the theory of free massive Dirac fermions and sine-Gordon theory, in 1+1 dimensions. In Eq. (188), we showed that the boundary conditions of the compactified scalar field $\phi(x)$ are determined by the fermion number N_F of the dual Dirac theory, and that the vacuum sector of the Dirac theory maps onto the sine-Gordon theory with periodic boundary conditions. We will now examine the sector with one fermion, $N_F = 1$. This sector of the Dirac theory maps onto the sine-Gordon theory with *twisted* boundary conditions,

$$\phi(L) - \phi(0) = \sqrt{\pi}. \tag{200}$$

The Hamiltonian of the sine-Gordon theory is

$$H_{\text{SG}} = \int_{-\infty}^{\infty} dx \left[\frac{1}{2}\Pi^2(x) + \frac{1}{2}(\partial_x\phi(x)) + g\cos\left(\sqrt{4\pi}\phi(x)\right)\right] \tag{201}$$

In the sector with periodic boundary conditions, the classical ground states are static and uniform configurations that minimize the potential energy. Since the potential energy is a periodic functional of $\phi(x)$, the classical minima are at $\phi_n(x) = (n + 1/2)\sqrt{\pi}$, where n is an arbitrary integer. The classical energy of these ground states is extensive and is given by $E_{\text{gnd}} = -gL$ where L is the linear size of the system.

The classical ground state in the twisted sector is a *domain wall* (or *soliton*) that interpolates between the static and uniform ground states $\phi(x) = \pm\sqrt{\pi}/2$. The classical ground state in this sector is the static solution of the Euler-Lagrange equation

$$\frac{d^2\phi}{dx^2} = -2g\sqrt{\pi}\sin\left(2\sqrt{\pi}\phi(x)\right) \tag{202}$$

such that asymptotically satisfies $\lim_{x\to\pm\infty} = \pm\sqrt{\pi}/2$. The solution is the classical soliton configuration

$$\phi(x) = \frac{2}{\sqrt{\pi}}\tan^{-1}\left(\exp(2\sqrt{\pi}g(x - x_0))\right) - \frac{\sqrt{\pi}}{2} \tag{203}$$

The soliton solution represents a *domain wall* between two symmetry-related classical ground states with $\phi = \pm\sqrt{\pi}/2$.

The energy of the soliton (measured from the energy of the ground state in the trivial sector) is finite and is given by

$$E_{\text{soliton}} = 4\sqrt{\frac{g}{\pi}} \tag{204}$$

where x_0 is a zero mode of the soliton solution and represents its coordinate. By coupling the bosonized theory to a weak electromagnetic field A_μ, as given in Eq. (184), it is easy to check that it has electric charge $-e$ and, in this sense represents the electron. Then the identities of Eq. (196) can be used that as a quantum state it is indeed a fermion.

Polyacetylene

In Section "Bosonization, anomalies, and duality," we saw that solitons of a scalar field can be regarded as being equivalent to electrons, fermions with charge $-$ e. We will now see that in a theory of fermions coupled to a domain wall of a scalar field, the soliton carries fractional charge. This problem has been extensively studied in one-dimensional conductors such as polyacetylene, in particular by the work of Su et al. (1979) and by Jackiw and Schrieffer (1981). In quantum field theory, this problem was first discussed by Jackiw and Rebbi (1976) and by Goldstone and Wilczek (1981).

In Section "Dirac fermions in one space dimensions," we showed that the physics of lattice fermions in one dimension at low energies is well described by a theory of massless Dirac fermions. In a one-dimensional conductor, such as polyacetylene, the fermions couple to the lattice vibrations (phonons). Su, Schrieffer, and Heeger (SSH) (Su et al., 1979) proposed a simple model in which the electrons couple to the lattice vibrations through a modulation of the hopping amplitude between two consecutive sites n and $n+1$, instead of being a constant t, becomes $t_{n,n+1} = t - g(u_{n+1} - u_n)$, where u_n is the displacement of the ion (a CH group in polyacetylene) at site n from its classical equilibrium position and g is the electron–phonon coupling constant. In polyacetylene, the number of electrons (which are spin-1/2 fermions) is equal to the number of sites of the lettuce and the electronic band is half-filled. At half filling, this simple band structure is invariant under a particle–hole transformation. If the coupling to the lattice vibrations is included, this symmetry remains respected provided the displacements change sign $u_n \to -u_n$ for all lattice sites. In polyacetylene, the lattice dimerizes (a process known as a Peierls distortion) and the discrete translation symmetry by one lattice spacing is spontaneously broken: the system becomes a period 2 CDW on the bonds of the lattice. The broken symmetry state is still invariant under a particle–hole transformation.

The effective field theory of this system is a theory of two Dirac spinors $\psi_{\alpha,\sigma}(x)$, where $\alpha = 1, 2$ denotes right and left-moving fermions, and $\sigma = \uparrow, \downarrow$ are the two spin polarizations. The Lagrangian density of this system is

$$\mathcal{L} = \bar{\psi}_\sigma i\partial\!\!\!/ \psi_\sigma - g\phi(x)\bar{\psi}_\sigma(x)\psi_\sigma(x) - \frac{1}{2}\phi(x)^2. \tag{205}$$

The real scalar field $\phi(x)$ represents the distortion field of the polyacetylene chain. Here we will assume that the chains have spontaneously distorted and we will regard the scalar field as static and classical. This is a good approximation since the masses of the CH complexes are much bigger than the electron mass. This continuum model is due to Takayama et al. (1980) and further developed by Campbell and Bishop (1981, 1982). Many of the results fund in this (adiabatic) approximation remain qualitatively correct upon taking into account the quantum dynamics of the chain, even in the limit in which the ions are treated as being "light" (provided the spin of the fermions is taken into account) (Hirsch and Fradkin, 1982; Fradkin and Hirsch, 1983).

In the field theory, the discrete symmetry of displacements by one lattice spacing becomes the $\mathbb{Z}_2$ symmetry $\phi \to -\phi$. This is a symmetry of the electron–phonon system once combined with the discrete chiral transformation $\psi \to \gamma_5\psi$ under which $\bar{\psi}\psi \to -\bar{\psi}\psi$. The ground state is twofold degenerate $\pm\,\phi_0$ with

$$\phi_0 = \frac{2\Lambda v_F}{g} \exp\left(-\frac{\pi v_F}{g^2}\right) \tag{206}$$

and the Dirac fermion (the electron) has a exponentially small mass, $m = g\phi_0$.

Fractionally charged solitons

Jackiw and Rebbi showed that the 1+1-dimensional classical ϕ^4 theory has the following soliton solution that interpolates between the two classically ordered states at $\pm\,\phi_0$ (Jackiw and Rebbi, 1976)

$$\phi(x) = \phi_0 \tanh\left(\frac{x - x_0}{\xi}\right) \tag{207}$$

where ξ is the correlation length of ϕ^4 theory, and x_0 is the (arbitrary) location of the soliton. They further showed that, when coupled to a theory of massless relativistic fermions through a Yukawa coupling, as in Eq. (205), this soliton carries fractional charge. The argument goes as follows. The one-particle Dirac Hamiltonian for a Dirac fermion with a position-dependent mass $m(x)$ is

$$H = -i\sigma_1\partial_x + m(x)\sigma_3 = \begin{pmatrix} m(x) & -i\partial_x \\ -i\partial_x & -m(x) \end{pmatrix} \tag{208}$$

where $m(x) = g\phi(x)$, with $\phi(x)$ being the soliton solution of Eq. (207). This Hamiltonian is Hermitian and real. Furthermore, this Hamiltonian anticommutes with the Pauli matrix σ_2. This implies that for every positive-energy state $|E\rangle$ with energy $+E$, there is a negative-energy eigenstate with energy $-E$ given by $\sigma_2|E\rangle$. Hence, the spectrum is particle–hole symmetric (or, what is the same, charge-conjugation invariant). In addition, and consistent with charge-conjugation symmetry, the Hamiltonian of Eq. (208) has state with $E = 0$, a zero mode, with a normalizable spinor wave function

$$\psi_0(x) = \frac{1}{\sqrt{2}}\begin{pmatrix} -i \\ 1 \end{pmatrix} \exp\left(-\mathrm{sgn}(m)\int_0^x dx'\, m(x')\right) \tag{209}$$

which exists for an arbitrary function $m(x)$, which changes sign once at some location (which we took to be $x_0 = 0$). Jackiw and Rebbi further showed that the soliton (antisoliton) carries fractional charge

$$Q = \mp \frac{e}{2}. \tag{210}$$

This result follows from the spectral asymmetry identity of the density of states $\rho_S(E)$ in the presence of the soliton

$$Q = -\frac{e}{2}\int_0^{\infty} (\rho_S(E) - \rho_S(-E)) = -\frac{e}{2}\eta \tag{211}$$

where η is the spectral asymmetry of the Dirac operator in the soliton background, and it is known as the APS η-invariant of Atiyah et al. (1975). Given the one-to-one correspondence that exists between positive and negative energy states in the spectrum, the spectral asymmetry follows from the condition that the zero mode be half-filled, which is required by normal ordering or, what is the same, by charge neutrality. Another way to understand this result is that adding (or removing) a fermion of charge $-e$ results in the creation of a soliton–antisoliton pair, with each topological excitation carrying half of the charge of the electron. In other words, in the dimerized phase, the electron is fractionalized. In this analysis, we ignored the spin of the electron. If we take it into account the spin degree of freedom, the soliton is instead a boson with charge $\mp e$.

There is an alternative, complementary, way to think about the charge of the soliton. Goldstone and Wilczek (1981) considered a theory in which the (massless) Dirac fermion is coupled to two real scalar fields, φ_1 and φ_2, with Lagrangian

$$\mathcal{L} = \bar{\psi} i \partial\!\!\!/ \psi - g\varphi_1 \bar{\psi}\psi - ig\varphi_2 \bar{\psi}\gamma_5 \psi \equiv \bar{\psi} i \partial\!\!\!/ \psi - g|\varphi| \bar{\psi} \exp(i\theta\gamma_5)\psi \tag{212}$$

where $|\varphi|^2 = \varphi_1^2 + \varphi_2^2$ and $\theta = \tan^{-1}(\varphi_2/\varphi_1)$. They considered a soliton in which $g\varphi_1 = m$ is the constant (in space) Dirac mass and φ_2 winds slowly between two values $\pm\varphi_0$ for $x \to \pm\infty$. In this theory, the one-particle Dirac Hamiltonian is

$$H = -i\sigma_1 \partial_x + g\varphi_1 \sigma_3 + g\varphi_2 \sigma_2 \tag{213}$$

which is Hermitian and complex and, hence, it violates CP invariance.

A perturbative calculation of the induced (gauge-invariant) current j_μ, which is given by the triangle diagram of a fermion loop with two gauge field insertions and a coupling of the scalar fields, yields the result (with $a = 1, 2$)

$$\langle j_\mu(x) \rangle = \frac{1}{2\pi}\epsilon_{\mu\nu}\epsilon_{ab}\frac{\varphi_a \partial^\nu \varphi_b}{|\varphi|^2} = \frac{1}{2\pi}\epsilon_{\mu\nu}\partial^\nu \theta \tag{214}$$

which is locally conserved. Notice, however, that the induced axial current j_μ^5 is not conserved, $\partial^\mu \langle j_\mu^5 \rangle = -\frac{1}{2\pi}\partial^2\theta \neq 0$ and, hence, this current is anomalous. We can now compute the total charge accumulated as the soliton is created adiabatically to be given by the Goldstone–Wilczek formula

$$Q = -e\frac{\Delta\theta}{2\pi} \tag{215}$$

where $\Delta\theta = \theta(+\infty) - \theta(-\infty)$. Since $\lim_{x\to\pm\infty}\varphi_2(x) = \pm\varphi_0$, we obtain the result

$$Q = -\frac{e}{\pi}\tan^{-1}\left(\frac{g\varphi_0}{m}\right). \tag{216}$$

In the limit $m = g\varphi \to 0$, where CP (or T) invariance is recovered, we get

$$\lim_{m\to 0} Q = -\frac{e}{2} \tag{217}$$

which is the Jackiw–Rebbi result for the fractional charge of a soliton of Eq. (210).

The results for the fractional charge of the soliton can also be derived using the bosonization identities of Section "Bosonization, anomalies, and duality." Indeed, the bosonized expression for the Lagrangian of Eq. (212) is

$$\mathcal{L} = \frac{1}{2}(\partial_\mu \phi)^2 - \frac{g|\varphi|}{2\pi a}\cos\left(\sqrt{4\pi}\phi - \theta\right). \tag{218}$$

Deep in the phase in which the Bose field ϕ is massive, the nonlinear term in Eq. (218) locks this field to the chiral angle θ, that is,

$$\phi = \frac{1}{\sqrt{4\pi}}\theta. \tag{219}$$

However, the bosonization identities also tell us that the gauge current j_μ is given by the curl of the scalar field ϕ. Therefore, in this state the current j_μ is

$$j_\mu = \frac{1}{\sqrt{\pi}}\epsilon_{\mu\nu}\partial^\nu \phi = \frac{1}{2\pi}\epsilon_{\mu\nu}\partial^\nu \theta \tag{220}$$

which is the same as the Goldstone–Wilczek result of Eq. (214). That these two seemingly different approaches yield the same result is not accidental as they both follow from the axial anomaly.

Fractional statistics

A fundamental axiom of Quantum Mechanics is that identical particles are indistinguishable (Dirac, 1930; Landau and Lifshitz, 1957). In nonrelativistic Quantum Mechanics, this leads to the requirement that the quantum states of a system of identical particles must be eigenstates of the pairwise particle exchange operator. Since two exchanges are equivalent to the identity operation, this implies that the states must be even or odd under pairwise exchanges. This result, in turn, implies that particles can be classified as being either bosons (whose states are invariant under pairwise exchanges) or fermions (whose states change sign under pairwise particle exchanges). A consequence is that bosons obey the Bose-Einstein (and can condense into a single particle state) whereas fermions obey the Fermi–Dirac distribution and must obey the Pauli exclusion principle. It is an implicit assumption of this line of reasoning that all relevant states of a system of identical particles can be efficiently represented by a (suitably symmetrized or antisymmetrized) product state.

This classification is present at an even deeper level in (relativistic) Quantum Field Theory where locality, unitarity, and Lorentz invariance require that the fields be classified as representations of the Lorentz group and obey the Spin-Statistics Theorem (Weinberg, 2005). The Spin-Statistics Theorem is actually an *axiom* of local relativistic Quantum Field theory that requires that fields that transform with an integer spin representation of the Poincaré group (i.e., scalars, gauge fields, gravitational fields) must be bosons while fields that transform with a half-integer spin representation (i.e., Dirac spinors) must be fermions. This spin-statistics connection is intrinsic to the construction of String Theory Polchinski (1998).

Given these considerations, there was a general consensus that fermions and bosons were the only possible types of statistics. Nevertheless several exceptions to this rule were known to exist. One is the construction of the magnetic monopole in 3+1 dimensional gauge theory by Tai-Tsun Wu and Chen-Ning Yang who showed that a scalar coupled to a Dirac magnetic monopole behaves as a Dirac spinor (Wu and Yang, 1976). This was an early example of statistical transmutation by coupling a matter field to a nontrivial configuration of a gauge field. As we will note below, the construction of anyons (particles with fractional statistics) in 2+1 dimensions has a close parentage to the Wu-Yang example. Examples of statistical transmutation were known to exist in 1+1 dimensional theories where a system of hard-core bosons was shown to be equivalent to a theory of free fermions using the Jordan–Wigner transformation (Lieb et al., 1961), which represents a fermion as a composite operator of a hard-core boson and an operator that creates a kink (or soliton). This construction also underlies the fermion-boson mapping in 1+1 dimensional field theories (Mattis and Lieb, 1965; Luther and Emery, 1974; Coleman, 1975; Mandelstam, 1975) that we discussed in Section "Bosonization, anomalies, and duality." Finally, in the late 1970s, it was found that 1+1 dimensional $\mathbb{Z}_N$ spin systems harbor operators known as parafermions, which obey the same algebra shortly afterwards found to be obeyed by anyons in 2+1 dimensions (Fradkin and Kadanoff, 1980).

Basics of fractional statistics

Jon Magne Leinaas and Jan Myrheim wrote an insightful paper in 1977 in which they examined the structure of the configuration space of the histories of a system of N identical particles (Leinaas and Myrheim, 1977). Using the Feynman path-integral approach, they showed that if the worldlines of the identical particles are not allowed to cross, then the configuration space is topologically nontrivial. Through a detailed analysis they showed that the three and higher dimensions under a pairwise particle exchange the states must be either even or odd and hence the particles are either bosons or fermions. Leinaas and Myrheim also showed that in one and two space dimensions, the wave functions can change by a *phase*, nowadays known as the statistical angle. In retrospect this result could have been anticipated (but was not) in an earlier paper by Laidlaw and DeWitt (1971), who did a similar analysis of the configuration space of identical particles in the Feynman path integral.

Frank Wilczek generalized the Aharonov–Bohm effect (Aharonov and Bohm, 1959) to describe the quantum mechanics of composite objects made of electric charge and magnetic flux in two space dimensions (Wilczek, 1982a). Wilczek showed that composite objects made of a nonrelativistic particle of charge q bound to a magnetic flux of (magnetic) charge Φ behaves as an object with fractional angular momentum $q\Phi/2\pi$. Here Φ is measured in units of the flux quantum 2π (in units in which $\hbar = c = e = 1$). Furthermore, in a subsequent paper, Wilczek (1982b) showed that, upon an adiabatic process in which the two composites exchange positions without their worldlines coinciding, the wave function of two identical flux-charge composites changes by a phase factor $\exp(\pm iq\Phi)$. For instance if $\Phi = \pi$ (i.e., a half-flux quantum), the acquired phase is equal to $\exp(i\pi) = -1$. Thus if the particle was a boson, the composite becomes a fermion and vice versa. Wilczek coined the term *anyon* to describe the behavior of an arbitrary charge-flux composite. Furthermore, this construction also implies that not only *fractional statistics* but also *fractional spin*, consistent with a generalization of the Spin-Statistics Theorem. In other terms, "flux-attachment" implies fractional statistics (and fractional spin). Clearly Wilczek's construction gave an explicit physical grounding to the general arguments of the 1977 paper by Leinaas and Myrheim. It is worth to note the close analogy between this construction in 2+1 dimensions and the Wu-Yang construction in 3+1 dimensions [whose consistency with the Spin-Statistics Theorem had been shown earlier on by Goldhaber (1976)].

In this description, the statistics of the composites (the anyons) enters in the form of complex weights (phases) given in terms of the *linking numbers* of the worldlines. Hence, the concept of fractional statistics is intimately related to the theory of knots and of the representations of the braid group. These concepts were originally introduced in physics to describe statistical transmutation in the theory of solitons (Finkelstein and Rubinstein, 1968) in the context of the Skyrme model (Skyrme, 1962). Wu (1984) developed an explicit connection between the work of Leinaas and Myrheim and Wilczek's work on anyons in terms of operations acting on the worldlines of the anyons and described by the Braid Group. Wu's work and the somewhat early paper by Wilczek and Zee on the statistics of solitons (Wilczek and Zee, 1983) marked the definite entry of the theory of knots (and of the braid group) in physics in general and in condensed matter physics in particular. The classification of anyons in terms of representations of the braid group labeled by the fractional statistics (determined by linking numbers) as well as of fractional (or topological) spin (determined by the writhing number of the worldlines) leads to a rich set of physical consequences. As it will turn out, Wilczek's anyons are described one-dimensional representations of the braid group. As we will see below, additional and intriguing (non-Abelian) representations will also play a role.

What is a topological field theory

We will now consider a special class of gauge theories known as topological field theories. These theories often (but not always) arise as the low energy limit of more complex gauge theories. In general, one expects that at low energies the phase of a gauge theory be either confining or deconfined. While confining phases have (from really good reasons!) attracted much attention, deconfined phases are often regarded as trivial, in the sense that the general expectation is that their vacuum states be unique and the spectrum of low lying states is either massive or massless.

Let us consider a gauge theory whose action on a manifold $\mathcal{M}$ with metric tensor $g_{\mu\nu}(x)$ is

$$S = \int_{\mathcal{M}} d^D x \, \sqrt{g} \, \mathcal{L}(g, A_\mu). \tag{221}$$

At the classical level, the energy–momentum tensor $T^{\mu\nu}(x)$ is the linear response of the action to an infinitesimal change of the local metric,

$$T^{\mu\nu}(x) \equiv \frac{\delta S}{\delta g_{\mu\nu}(x)}. \tag{222}$$

That a theory is topological means that depends only on the topology of the space in which is defined and, consequently, it is independent of the local properties that depend on the metric, for example, distances, angles. Therefore, at least at the classical level, the energy–momentum tensor of a topological field theory must vanish identically,

$$T^{\mu\nu} = 0. \tag{223}$$

In particular, if the theory is topological, the *energy* (or Hamiltonian) is also zero. Furthermore, if the theory is independent of the metric, it is invariant under *arbitrary* coordinate transformations. Thus, if the theory is a gauge theory, the expectation values of Wilson loops will be independent of the size and shape of the loops. Whether or not a theory of this type can be consistently defined at the quantum level is a subtle problem which we will briefly touch on below.

It turns out that, due to the nonlocal nature of the observables of a gauge theory, the low-energy regime of a theory in its deconfined phase can have nontrivial global properties. In what follows, we will say that a gauge theory is topological if all local excitations are massive (and in fact we will send their mass gaps to infinity). The remaining Hilbert space of states is determined by global properties of the theory, including the topology of the manifold of their space-time. In several cases, the effective action of a topological field theory does not depend on the metric of the space-time, at least at the classical level. In all cases, the observables are nonlocal objects, Wilson loops and their generalization.

Chern–Simons gauge theory

Gauge theories play a key role in physics. In 2+1 dimensions, it is possible to define a special gauge theory which is odd under time-reversal invariance and parity: Chern–Simons gauge theory. Originally introduced in Quantum Field Theory in 1982 by Deser et al. (1982a,b), Chern–Simons gauge theory can be defined for any compact Lie group, as well as an extension of Einstein's gravity in 2+1 dimensions. In 1989, Witten (1989) showed that Chern–Simons gauge theory computes the expectation values of configurations of Wilson loops, regarded as the worldlines of heavy particles, in terms of a set of topological invariants known as the Jones polynomial that classify knots in three dimensions.

We will consider the simplest case, the $U(1)$ Chern–Simons gauge theory. The Chern–Simons action for a $U(1)$ gauge field A_μ in 2+1 dimension is

$$S[A] = \frac{k}{4\pi} \int_{\Omega} d^3x \, \epsilon_{\mu\nu\lambda} A^\mu \partial^\nu A^\lambda + \int_{\Omega} d^3x \, J_\mu A^\mu \tag{224}$$

where J_μ is a set of conserved currents (representing the worldlines of a set of heavy particles). On a closed 3-manifold Ω (e.g., a sphere, a torus) the Chern–Simons action is gauge invariant provided the parameter k (known as the level) is an integer. If the manifold Ω has a boundary, the action is not gauge invariant at the boundary. Gauge invariance is restored by additional boundary degrees of freedom. This structure is general, and not just a feature of the $U(1)$ theory.

Since the Chern–Simons action is first order in derivatives, it is not invariant under time reversal and under parity (which in 2+1 dimensions is a reflection). These symmetries make this theory relevant to the description of the fractional quantum Hall effect. In the absence of external sources, $J_\mu = 0$, at the classical level the Chern–Simons action is invariant under arbitrary changes of coordinates. This means that the theory is, at least classically, a topological field theory.

For a general non-Abelian gauge group G, the Chern–Simons action becomes

$$S = \frac{k}{4\pi}\int_{\mathcal{M}} d^3x \ \mathrm{tr}\left(AdA + \frac{2}{3}A \wedge A \wedge A\right). \tag{225}$$

Here, the cubic term is shorthand for

$$\mathrm{tr}(A \wedge A \wedge A) \equiv \mathrm{tr}\left(\epsilon_{\mu\nu\lambda}A^\mu A^\nu A^\lambda\right) \tag{226}$$

for a gauge field A^μ that takes values on the algebra of the gauge group G.

BF gauge theory

A closely related (abelian) gauge theory is the so-called *BF* theory (Horowitz, 1989) which, in a general spacetime dimension D (even or odd), is a theory of a vector field A^μ (a one-form) and an antisymmetric tensor field B with $D - 2$ Lorentz indices (a $D2$ form), known as a Kalb–Ramond field. In 2+1 dimensions, the action of the BF theory is

$$S = \frac{k}{2\pi}\int_{\mathcal{M}} d^3x \ \epsilon_{\mu\nu\lambda}B^\lambda \partial^\mu A^\nu \tag{227}$$

where, once again, k is an integer.

The BF gauge theory has the same content as the topological sector of a discrete $\mathbb{Z}_k$ gauge theory. To see this, we will consider the theory of compact electrodynamics which is a $U(1)$ gauge theory minimally coupled to charged scalar field ϕ. The will assume that the gauge theory is defined for a compact $U(1)$ gauge group (meaning that the gauge flux is quantized) and that the complex scalar field has charge integer $k \in \mathbb{Z}$. As usual minimal coupling is implemented by introducing the covariant derivative $D_\mu - \partial_\mu + ikA_\mu$, where A_μ is the $U(1)$ gauge field. Deep in the phase in which the global $U(1)$ symmetry is spontaneously broken, usually called the Higgs regime, the amplitude of the scalar field is frozen at its (real) vacuum expectation value ϕ_0 but its phase ω, representing the Goldstone mode, is unconstrained. In this limit, the Lagrangian of this theory becomes

$$\mathcal{L} = |\phi_0|^2\left(\partial_\mu\omega - kA_\mu\right)^2 - \frac{1}{4e^2}F_{\mu\nu}^2 \tag{228}$$

where e is the coupling constant of the gauge field (the electric charge) and $F_{\mu\nu}$ is the field strength of the gauge field A_μ. In general spacetime dimension D the charge e has units of length$^{(D-4)/2}$. In this limit the gauge field becomes massive (this is the Higgs mechanism). This theory has fluxes quantized in units of $2\pi/k$ and has only k distinct fluxes. This is the $\mathbb{Z}_k$ gauge theory.

Here we will consider this theory in 2+1 dimensions. We will use a Gaussian (Hubbard–Stratonovich) decoupling of the first term of Eq. (228) in terms of a gauge field C_μ to write the Lagrangian in the equivalent form

$$\mathcal{L} = -\frac{1}{4|\phi_0|^2}C_\mu^2 + C^\mu(\partial_\mu\omega - kA_\mu) - \frac{1}{4e^2}F_{\mu\nu}^2. \tag{229}$$

Up to an integration by parts, we see that the phase field ω plays the role of a Lagrange multiplier field, which forces the vector field B_μ to obey the constraint $\partial_\mu C^\mu = 0$. This constraint is solved by writing C_μ as

$$C_\mu = \frac{1}{2\pi}\epsilon_{\mu\nu\lambda}\partial^\nu B^\lambda \tag{230}$$

of a 1-form gauge field B_μ. Upon solving the constraint, the Lagrangian of Eq. (229) becomes

$$\mathcal{L} = \frac{k}{2\pi}\epsilon_{\mu\nu\lambda}A^\mu\partial^\nu B^\lambda - \frac{1}{4e^2}F_{\mu\nu}(A)^2 - \frac{1}{32\pi^2|\phi_0|^2}F_{\mu\nu}(B)^2. \tag{231}$$

For spacetime dimensions $D < 4$ the IR the Maxwell terms for the fields A^μ and B_μ are irrelevant in the IR and, in this limit, this theory reduces to the BF theory at level k of Eq. (227). Therefore, $\mathbb{Z}_k$ gauge theory is equivalent to the BF theory at level k. In fact, this result is essentially valid in all dimensions with the main difference being that the field B_μ is, in general, a rank $D - 2$ Kalb–Ramond antisymmetric field.

Quantization of Abelian Chern–Simons gauge theory

By expanding the action of Eq. (224), the Lagrangian density becomes

$$\mathcal{L} = \frac{k}{4\pi}\epsilon_{ij}A_i\partial_0 A_j + A_0\left(\frac{k}{2\pi}B - J_0\right) - J_iA_i \tag{232}$$

where $B = \epsilon_{ij}\partial_i A_j$ is the local flux, J_0 is a local classical density, and J_i is a local classical current. Then, the first term of Eq. (232) implies that the spatial components of the gauge field obey equal-time canonical commutation relations

$$[A_1(x), A_2(x')] = i\frac{2\pi}{k}\delta(x - x'). \tag{233}$$

The second term of the Lagrangian enforces the Gauss Law which for this theory simply implies that the states in the physical Hilbert space obey the constraint

$$B(x) = \frac{2\pi}{k}J_0(x). \tag{234}$$

Thus the Gauss's Law requires that a charge density necessarily has a magnetic flux attached to it. In other terms, the physical states are charge-flux composites as postulated in Wilczek's theory (Wilczek, 1982b). This is the theoretical basis to the concept of flux attachment which, as we will see in Section "Chern–Simons gauge theory and the fractional quantum Hall effect," is widely used in the theory of the fractional quantum Hall effect.

The third term in Eq. (232) simply states that the Hamiltonian density is just

$$\mathcal{H} = J_i A_i \tag{235}$$

Hence, in the absence of sources, the Hamiltonian vanishes, $\mathcal{H} = 0$.

The Chern–Simons action is locally gauge-invariant, up to boundary terms. To see this, let us perform a gauge transformation, $A_\mu \to A_\mu + \partial_\mu \Phi$, where $\Phi(x)$ is a smooth, twice differentiable function. Then,

$$\begin{aligned} S[A^\mu + \partial^\mu\Phi] &= \int_{\mathcal{M}} (A^\mu + \partial^\mu\Phi)\epsilon_{\mu\nu\lambda}\partial^\nu(A^\lambda + \partial^\lambda\Phi) \\ &= \int_{\mathcal{M}} d^3x\, \epsilon_{\mu\nu\lambda}A^\mu\partial^\nu A^\lambda + \int_{\mathcal{M}} d^3x\, \epsilon_{\mu\nu\lambda}\partial^\mu\Phi\partial^\nu A^\lambda \end{aligned} \tag{236}$$

Therefore, the change is

$$S[A^\mu + \partial^\mu\Phi] - S[A^\mu] = \int_{\mathcal{M}} d^3x\, \partial^\mu\Phi F^*_\mu = \int_{\mathcal{M}} d^3x\, \partial^\mu(\Phi F^*_\mu) - \int_{\mathcal{M}} d^3x\, \Phi\partial^\mu F^*_\mu \tag{237}$$

where $F^*_\mu = \epsilon^{\mu\nu\lambda}\partial_\nu A_\lambda$ is the dual field strength. However, in the absence of magnetic monopoles, this field satisfies the Bianchi identity, $\partial^\mu F^*\mu = \partial^\mu(\epsilon_{\mu\nu\lambda}\partial^\nu A^\lambda) = 0$. Therefore, using the Gauss Theorem, we find that the change of the action is a total derivative and integrates to the boundary

$$\delta S = \int_{\mathcal{M}} d^3x\, \partial^\mu(\Phi F^*_\mu) = \int_{\Sigma} dS^\mu \Phi F^*_\mu \tag{238}$$

where $\Sigma = \partial\mathcal{M}$ is the boundary of $\mathcal{M}$. In particular, if Φ is a nonzero constant function on $\mathcal{M}$, then the change of the action under such a gauge transformation is

$$\delta S = \Phi \times \text{flux}(\Sigma). \tag{239}$$

Hence, the action is not invariant if the manifold has a boundary, and the theory must be supplied with additional degrees of freedom at the boundary.

Indeed, the flat connections, that is, the solution of the equations of motion, $F_{\mu\nu} = 0$, are pure gauge transformations, $A_\mu = \partial_\mu\phi$, and have an action that integrates to the boundary. Let $\mathcal{M} = D \times \mathbb{R}$ where D is a disk in space and $\mathbb{R}$ is time. The boundary manifold is $\Sigma = S^1 \times \mathbb{R}$, where S^1 is a circle. Thus, in this case, the boundary manifold Σ is isomorphic to a cylinder. The action of the flat configurations reduces to

$$S = \int_{S^1\times\mathbb{R}} d^2x \frac{k}{4\pi}\partial_0\phi\partial_1\phi \tag{240}$$

This implies that the dynamics on the boundary is that of a scalar field on a circle S^1, and obeys periodic boundary conditions.

Although classically the theory does not depend on the metric, it is invariant under arbitrary transformations of the coordinates. However, any gauge fixing condition will automatically break this large symmetry. For instance, we can specify a gauge condition at the boundary in the form of a boundary term of the form $\mathcal{L}_{\text{gauge fixing}} = A_1^2$. In this case, the boundary action of the field φ becomes

$$S[\varphi] = \int_{S^1\times\mathbb{R}} d^2x\, \frac{k}{4\pi}\, \left[\partial_0\phi\partial_1\phi - (\partial_1\phi^2)\right]. \tag{241}$$

The solutions of the equations of motion of this compactified scalar field have the form $\phi(x_1 \mp x_0)$, and are right (left) moving chiral fields depending of the sign of k. This boundary theory is not topological but is conformally invariant.

A similar result is found in non-Abelian Chern–Simons gauge theory. In the case of the $SU(N)_k$ Chern–Simons theory on a manifold $D \times \mathbb{R}$, where D is a disk whose boundary is Γ, and $\mathbb{R}$ is time, the action is

$$S_{\mathrm{CS}}[A] = \int_{D\times\mathbb{R}} d^3x \left[\frac{k}{8\pi}\mathrm{tr}\left(\epsilon_{\mu\nu\lambda}A^\mu\partial^\nu A^\lambda + \frac{2}{3}\epsilon^{\mu\nu\lambda}A_\mu A_\nu A_\lambda\right)\right]. \tag{242}$$

This theory integrates to the boundary, $\Gamma \times \mathbb{R}$ where it becomes the chiral (right-moving) $SU(N)_k$ Wess–Zumino–Witten model (at level k) at its IR fixed point, $\lambda_c^2 = 4\pi/k$

$$S_{WZW}[g] = \frac{1}{4\lambda_c^2}\int_{\Gamma\times\mathbb{R}} d^2x\, \mathrm{tr}\left(\partial_\mu g\partial^\mu g^{-1}\right) + \frac{k}{12\pi}\int_B \epsilon^{\mu\nu\lambda}\mathrm{tr}\left(g^{-1}\partial_\mu g\, g^{-1}\partial_\nu g\, g^{-1}\partial_\lambda g\right). \tag{243}$$

Here, $g \in SU(N)$ parametrizes the flat configurations of the Chern–Simons gauge theory. The boundary theory is a nontrivial CFT, the chiral Wess–Zumino–Witten CFT (Witten, 1989).

Vacuum degeneracy a torus

We will now construct the quantum version of the $U(1)$ Chern–Simons gauge theory on a manifold $\mathcal{M} = T^2 \times \mathbb{R}$, where T^2 is a spatial torus, of linear size L_1 and L_2. Since this manifold does not have boundaries, the flat connections, $\epsilon_{ij}\partial_i A_j = 0$, do not reduce to local gauge transformations of the form $A_i = \partial_i\Phi$. Indeed, the holonomies of the torus T^2, that is, the Wilson loops on the two noncontractible cycles of the torus Γ_1 and Γ_2, are gauge-invariant observables:

$$\int_0^{L_1} dx_1 A_1 \equiv \bar{a}_1, \qquad \int_0^{L_2} dx_1 A_2 \equiv \bar{a}_2 \tag{244}$$

where $\bar{a}_1$ and $\bar{a}_2$ are time-dependent. Thus, the flat connections now are

$$A_1 = \partial_1\Phi + \frac{\bar{a}_1}{L_1}, \qquad A_2 = \partial_2\Phi + \frac{\bar{a}_2}{L_2} \tag{245}$$

whose action is

$$S = \frac{k}{4\pi}\int dx_0 \epsilon_{ij}\bar{a}_i\partial_0\bar{a}_j \tag{246}$$

Therefore, the global degrees of freedom $\bar{a}_1$ and $\bar{a}_2$ at the quantum level become operators that satisfy the commutation relations

$$[\bar{a}_1, \bar{a}_2] = i\frac{2\pi}{k}. \tag{247}$$

We find that the flat connections are described by the quantum mechanics of $\bar{a}_1$ and $\bar{a}_2$. A representation of this algebra is

$$\bar{a}_2 \equiv -i\frac{2\pi}{k}\frac{\partial}{\partial\bar{a}_1}. \tag{248}$$

Furthermore, the Wilson loops on the two cycles become

$$W[\Gamma_1] = \exp\left(i\int_0^{L_1} A_1\right) \equiv e^{i\bar{a}_1}, \quad W[\Gamma_2] = \exp\left(i\int_0^{L_2} A_2\right) \equiv e^{i\bar{a}_2} \tag{249}$$

and satisfy the algebra

$$W[\Gamma_1]W[\Gamma_2] = \exp(-i2\pi/k)W[\Gamma_2]W[\Gamma_1]. \tag{250}$$

Under large gauge transformations

$$\bar{a}_1 \to \bar{a}_1 + 2\pi, \qquad \bar{a}_2 \to \bar{a}_2 + 2\pi. \tag{251}$$

Therefore, invariance under large gauge transformations on the torus implies that $\bar{a}_1$ and $\bar{a}_2$ define a two-torus target space.

Let us define the unitary operators

$$U_1 = \exp(ik\bar{a}_2), \quad U_2 = \exp(-ik\bar{a}_1) \tag{252}$$

which satisfy the algebra

$$U_1U_2 = \exp(i2\pi k)U_2U_1. \tag{253}$$

The unitary transformations U_1 and U_2 act as shift operators on $\bar{a}_1$ and $\bar{a}_2$ by 2π, and hence generate the large gauge transformations. Moreover, the unitary operators U_1 and U_2 leave the Wilson loop operators on noncontractible cycles invariant,

$$U_1^{-1}W[\Gamma_1]U_1 = W[\Gamma_1], \quad U_2^{-1}W[\Gamma_2]U_2 = W[\Gamma_2]. \tag{254}$$

Let $|0\rangle$ be the eigenstate of $W[\Gamma_1]$ with eigenvalue 1, that is, $W[\Gamma_1]||0\rangle = |0\rangle$. The state $W[\Gamma_2]|0\rangle$ is also an eigenstate of $W[\Gamma_1]$ with eigenvalue $\exp(-i2\pi/k)$, since

$$W[\Gamma_1]W[\Gamma_2]|0\rangle = e^{i2\pi/k}W[\Gamma_2]W[\Gamma_1]|0\rangle = e^{-i2\pi/k}W[\gamma_2|0]\rangle. \tag{255}$$

More generally, since

$$W[\Gamma_1]W^p[\Gamma_2] \parallel 0\rangle = e^{-i2\pi p/k}W^p[\Gamma_2]|0\rangle \tag{256}$$

we find that, provided $k \in \mathbb{Z}$, there are k linearly independent vacuum states $|p\rangle = W^p[\Gamma_2]|0\rangle$, for the $U(1)$ Chern–Simons gauge theory at level k. It is denoted as the $U(1)_k$ Chern–Simons theory. Therefore the finite-dimensional topological space on a two-torus is k-dimensional. It is trivial to show that, on a surface of genus g, the degeneracy is k^g.

We see that in the Abelian $U(1)_k$ Chern–Simons theory, the Wilson loops must carry k possible values of the unit charge. This property generalizes to the non-Abelian theories, which are technically more subtle. We will only state some important results. For example, if the gauge group is $SU(2)$, we expect that the Wilson loops will carry the representation labels of the group $SU(2)$, that is, they will be labeled by (j, m), where $j = 0, \frac{1}{2}, 1, \ldots$ and the $2j + 1$ values of m satisfy $|m| \leq j$. However, it turns that out $SU(2)_k$ Chern–Simons theory has fewer states, and that the values of j are restricted to the range $j = 0, \frac{1}{2}, \ldots, \frac{k}{2}$.

Fractional statistics and braids

Another aspect of the topological nature of Chern–Simons theory is the behavior of expectation values of products of Wilson loop operators. Let us compute the expectation value of a product of two Wilson loop operators on two positively oriented closed contours γ_1 and γ_2. We will do this computation in the Abelian Chern–Simons theory $U(1)_k$ in 2+1-dimensional Euclidean space. Note that the Euclidean Chern–Simons action is pure imaginary since the action is first order in derivatives. The expectation value to be computed is

$$W[\gamma_1 \cup \gamma_2] = \left\langle \exp\left(i \oint_{\gamma_1 \cup \gamma_2} dx_\mu A_\mu \right) \right\rangle_{\text{CS}}. \tag{257}$$

The result changes depending on whether the loops γ_1 and γ_2 are linked or unlinked. In this section, we will compute the contribution to this expression for a pair of contours γ_1 and γ_2. Here we will not include the contribution to this expectation value for each contours. We will return to this problem in Section "Bosonization of the Dirac theory in 2+1 dimensions" where we discuss the problem of fractional spin.

The expectation value of a Wilson loop on the union of two contours, as in the present case, γ can be written as

$$\left\langle \exp\left(i \oint_\gamma dx_\mu A_\mu \right) \right\rangle_{\text{CS}} = \left\langle \exp\left(i \int d^3x J_\mu A_\mu \right) \right\rangle_{\text{CS}} \tag{258}$$

where the current J_μ is

$$J_\mu(x) = \delta(x_\mu - z_\mu(t)) \frac{dz_\mu}{dt} \tag{259}$$

Here, $z_\mu(t)$ is a parametrization of the contour γ. Therefore, the expectation value of the Wilson loop is (Witten, 1989)

$$\left\langle \exp\left(i \oint_\gamma dx_\mu A_\mu \right) \right\rangle_{\text{CS}} \equiv \exp(iI[\gamma]_{\text{CS}}) = \exp\left(-\frac{i}{2} \int d^3x \int d^3y \, J_\mu(x) G_{\mu\nu}(x-y) J_\nu(y) \right) \tag{260}$$

where $G_{\mu\nu}(x - y) = \langle A_\mu(x) A_\nu(y) \rangle_{\text{CS}}$ is the propagator of the Chern–Simons gauge field. Since the loops are closed, the current J_μ is conserved, that is, $\partial_\mu J_\mu = 0$, and the effective action $I[\gamma]_{\text{CS}}$ of the loop γ is gauge-invariant.

The Euclidean propagator of Chern–Simons gauge theory (in the Feynman gauge) is

$$G_{\mu\nu}(x-y) = \frac{2\pi}{k} G_0(x-y) \epsilon_{\mu\nu\lambda} \partial_\lambda \delta(x-y) \tag{261}$$

where $G_0(x - y)$ is the propagator of the massless Euclidean scalar field, which satisfies

$$-\partial^2 G_0(x-y) = \delta^3(x-y). \tag{262}$$

Using these results, we find the following expression for the effective action

$$\begin{aligned} I[\gamma]_{\text{CS}} &= \frac{\pi}{k} \int d^3x \int d^3y \, J_\mu(x) J_\nu(y) G_0(x-y) \epsilon_{\mu\nu\lambda} \partial_\lambda \delta(x-y) \\ &= \frac{\pi}{k} \oint_\gamma dx_\mu \oint_\gamma dy_\nu \epsilon_{\mu\nu\lambda} \partial_\lambda G_0(x-y). \end{aligned} \tag{263}$$

Since the current J_μ is conserved, it can be written as the curl of a vector field, B_μ, as

$$J_\mu = \epsilon_{\mu\nu\lambda} \partial_\nu B_\lambda. \tag{264}$$

In the Lorentz gauge, $\partial_\mu B_\mu = 0$, we can write

$$B_\mu = \epsilon_{\mu\nu\lambda}\partial_\nu \phi_\lambda. \tag{265}$$

Hence,

$$J_\mu = -\partial^2 \phi_\mu \tag{266}$$

where

$$\phi_\mu(x) = \int d^3y \; G_0(x-y) J_\mu(y) \tag{267}$$

Upon substituting this result into the expression for B_μ, we find

$$B_\mu = \int d^3y \epsilon_{\mu\nu\lambda}\partial_\nu G_0(x-y) J_\lambda(y) = \oint_\gamma \epsilon_{\mu\nu\lambda}\partial_\nu G_0(x-y) dy_\lambda. \tag{268}$$

Therefore, the effective action $I[\gamma]_{\text{CS}}$ becomes

$$I[\gamma]_{\text{CS}} = \frac{\pi}{k}\oint_\gamma dx_\mu \oint_\gamma dy_\nu \epsilon_{\mu\nu\lambda}\partial_\lambda G_0(x-y) = \frac{\pi}{k}\oint_\gamma dx_\mu B_\mu(x). \tag{269}$$

Let Σ be an oriented open surface of the Euclidean three-dimensional space whose boundary is the oriented loop (or union of loops) γ, that is, $\partial\Sigma = \gamma$. Then, using Stokes Theorem we write in the last line of Eq. (269) as

$$I[\gamma]_{\text{CS}} = \frac{\pi}{k}\int_\Sigma dS_\mu \epsilon_{\mu\nu\lambda}\partial_\nu B_\lambda = \frac{\pi}{k}\int_\Sigma dS_\mu J_\mu. \tag{270}$$

The integral in the last line of this equation is the flux of the current J_μ through the surface Σ. Therefore, this integral counts the number of times n_γ the Wilson loop on γ pierces the surface Σ (whose boundary is γ), and therefore it is an integer, $n_\gamma \in \mathbb{Z}$. We will call this integer the *linking number* (or Gauss invariant) of the configuration of loops. In other words, the expectation value of the Wilson loop operator is

$$W[\gamma]_{\text{CS}} = e^{i\pi n_\gamma/k}. \tag{271}$$

The linking number is a *topological invariant* since, being an integer, its value cannot be changed by smooth deformations of the loops, provided they are not allowed to cross.

We will now see that this property of Wilson loops in Chern–Simons gauge theory leads to the concept of fractional statistics. Let us consider a scalar matter field that is massive and charged under the Chern–Simons gauge field. The excitations of this matter field are particles that couple minimally to the gauge field. Here we will be interested in the case in which these particles are very heavy. In that limit, we can focus on states that have a few of this particles which will be in their nonrelativistic regime.

Consider, for example, a state with two particles which in the remote past, at time $t = -T \to -\infty$, are located at two points A and B. This initial state will evolve to a final state at time $t = T \to \infty$, in which the particles go back either to their initial locations (the direct process) or to another one in which they exchange places, $A \leftrightarrow B$. At intermediate times, the particles follow smooth worldlines. These are two processes, direct and exchange. There we see that the direct process is equivalent to a history with two unlinked loops (the worldlines of the particles), whereas in the exchange process, the two loops form a link. It follows from the preceding discussion that the two amplitudes differ by the result of the computation of the Wilson loop expectation value for the loops γ_1 and γ_2. Let us call the first amplitude W_{direct} and the second W_{exchange}. The result is

$$W_{\text{exchange}} = W_{\text{direct}} e^{\pm i\pi/k} \tag{272}$$

where the sign depends on how the two worldlines wind around each other.

An equivalent interpretation of this result is that if $\Psi[A, B]$ is the wave function with the two particles at locations A and B, the wavefunction where their locations are exchanged is

$$\Psi[B, A] = e^{\pm i\pi/k}\Psi[A, B] \tag{273}$$

where the sign depends on whether the exchange is done counterclockwise or clockwise. Clearly, for $k = 1$, the wave function is antisymmetric and the particles are fermions, while for $k \to \infty$, they are bosons. At other values of k, the particles obey *fractional statistics* and are called *anyons* (Wilczek, 1982a; Leinaas and Myrheim, 1977). The phase factor $\phi = \pm\pi/k$ is called the statistical phase.

Notice that while for fermions and bosons the statistical phase $\varphi = 0, \pi$ is uniquely defined (mod 2π), for other values of k, the statistical angle is specified up to a sign that specifies how the worldlines wind around each other. Indeed, mathematically the exchange process is known as a *braid*. Processes in which the worldlines wind clock and counterclockwise are braids that are inverse of each other. Braids can also be stack sequentially yielding multiples of the phase φ. In addition to stacking braids, Wilson loops can be fused: seen from some distance, a pair of particles will behave as a new particle with a well-defined behavior under braiding. This process of fusion is closely related to the concept of fusion of primary fields in CFT.

Furthermore, up to regularization subtleties (Grundberg et al., 1990), the self-linking terms (those with $a = b$) yield a topological spin $1/2k$, consistent with the spin-statistics connection (Polyakov, 1988). For $k = 1$, this means that the flux-charge composites have spin $1/2$.

What we have just described is a mathematical structure called the *Braid* group. The example that we worked out using Abelian Chern–Simons theory yields one-dimensional representations of the Braid group with the phase φ being the label of the representations. For $U(1)_k$, there are k types of particles (anyons). That these representations are Abelian means that, in the general case of $U(1)_k$, acting on a one-dimensional representation p (defined mod k) with a one-dimensional representation q (also defined mod k) yields the representation one-dimensional $p + q$ (mod k). We will denote the operation of *fusing* these representations (particles!) as $[q]_{\text{mod } k} \times [p]_{\text{mod } k} = [q+p]_{\text{mod } k}$. These representations are in one-to-one correspondence with the inequivalent charges of the Wilson loops, and with the vacuum degeneracy of the $U(1)_k$ Chern–Simons theory on a torus.

A richer structure arises in the case of the non-Abelian Chern–Simons theory at level k (Witten, 1989), such as $SU(2)_k$. For example, for $SU(2)_1$, the theory has only two representations, both are one-dimensional, and have statistical angles $\varphi = 0, \pi/2$.

However, for $SU(2)_k$, the content is more complex. In the case of $SU(2)_2$, the theory has (a) a trivial representation [0] (the identity, $(j, m) = (0, 0)$), (b) a (spinor) representation [1/2] ($(j, m) = (1/2, \pm 1/2)$), and (c) a the representation [1] ($(j, m) = (1, m)$, with $m = 0, \pm 1$). These states will fuse obeying the following rules: $[0] \times [0] = [0]$, $[0] \times [1/2] = [1/2]$, $[0] \times [1] = [1]$, $[1/2] \times [1/2] = [0] + [1]$, $[1/2] \times [1] = [1/2]$, and $[1] \times [1] = [0]$ (note the truncation of the fusion process!).

Of particular interest is the case $[1/2] \times [1/2] = [0] + [1]$. In this case, we have two fusion channels, labeled by [0] and [1]. The braiding operations now will act on a two-dimensional Hilbert space and are represented by 2×2 matrices. This is an example of a non-Abelian representation of the braid group. These rather abstract concepts have found a physical manifestation in the physics of the fractional quantum Hall fluids, whose excitations are vortices that carry fractional charge and anyon (braid) fractional statistics.

Why this is interesting can be seen by considering a Chern–Simons gauge theory with four quasi-static Wilson loops. For instance in the case of the $SU(2)_2$ Chern–Simons theory the Wilson loops carry the spinor representation, [1/2]. If we call the four particles A, B, C, and D, we would expect that their quantum state would be completely determined by the coordinates of the particles. This, however, is not the case since, if we fuse A with B, the result is either a state [0] or a state [1]. Thus, if the particles were prepared originally in some state, braiding (and fusion) will lead to a linear superposition of the two states. This braiding process defines a unitary matrix, a representation of the Braid Group. The same is true with the other particles. However, it turns out that for four particles, there are only two linearly independent states. This twofold degenerate Hilbert space of topological origin is called a topological qubit.

Moreover, if we consider a system with N (even) number of such particles, the dimension of the topologically protected Hilbert space is $2^{\frac{N}{2}-1}$. Hence, for large N, the entropy per particle grows as $\frac{1}{2}\ln 2 = \ln\sqrt{2}$. Therefore the qubit is not an "internal" degree of freedom of the particles but a collective state of topological origin. Interestingly, there are physical systems, known as non-Abelian fractional quantum Hall fluids that embody this physics and are accessible to experiments! For these reasons, the non-Abelian case has been proposed as a realization of a topological qubit (Kitaev, 2003; Das Sarma et al., 2008).

Topological phases of matter

Topological insulators

We will now give a brief discussion of the physics of Topological Insulators from a field-theoretic perspective. Topological insulators are systems whose electronic states (band structures) have special topological properties that manifest in the existence of symmetry-protected edge states. For this reason these systems are known as symmetry-protected topological states (or SPTs). The simplest example is found in one space dimension where it is related to the fascinating problem of fractionally charged solitons and electron fractionalization. In several ways many of the concepts involved in these 1+1-dimensional systems can and have been extended to higher dimensions.

Dirac fermions in 2+1 dimensions

We will now see that, in spite of the formal similarities with the 1+1 dimensional case, this theory has different symmetries, particularly concerning parity and time-reversal invariance. In addition, in 2+1 dimensions, it is not possible to define a γ^5 Dirac matrix, which implies that there is no chiral symmetry and no chiral anomaly. We will consider first a theory of a Dirac field which in 2+1 dimensions is a bi-spinor (as is in 1+1 dimensions). The Lagrangian of the Dirac theory coupled to a background gauge field A_μ is

$$\mathcal{L} = \bar{\psi} i\gamma^\mu \partial_\mu \psi - m\bar{\psi}\psi - eA_\mu \bar{\psi}\gamma_\mu \psi \equiv \bar{\psi} i\gamma^\mu D_\mu(A)\psi - m\bar{\psi}\psi \tag{274}$$

where $\bar{\psi} = \psi^\dagger \gamma_0$, $\bar{\psi}\gamma_\mu\psi \equiv j_\mu$ is the gauge-invariant (and conserved) Dirac current, and $D_\mu(A) = \partial_\mu + ieA_\mu$ is the covariant derivative.

In Eq. (274), γ_μ are the three 2×2 Dirac matrices which obey the algebra, $\{\gamma_\mu, \gamma_\nu\} = 2g_{\mu\nu}$, where $g_{\mu\nu} = \text{diag}(1, -1, -1)$ is the metric of 2+1 dimensional Minkowski spacetime. The Dirac matrices γ_μ can be written in terms of the three 2×2 Pauli matrices. For instance we can choose $\gamma_0 = \sigma_3$, $\gamma_1 = i\sigma_2$ and $\gamma_2 = -i\sigma_1$, which satisfy the Dirac algebra. Since the three gamma matrices involve all tree Pauli matrices, it is not possible to define a γ_5 matrix, which would anticommute with the gamma matrices. In this sense, it is not possible to define a chirality for bi-spinors in 2+1 dimensions

We could have also chosen a different set of gamma matrices. For instance, we could have chosen $\gamma_0 = \sigma_3$, $\gamma_1 = i\sigma_2$, and $\gamma_2 = +i\sigma_1$, which also satisfy the Dirac algebra. These two choices are equivalent to the 2D parity transformation $x_1 \to x_1$ and $x_2 \to -x_2$. In other words, we can choose the three gamma matrices to be defined in terms of a right-handed or a left-handed frame (or triad). Thus, the choice of handedness of the frame used to define the gamma matrices can be regarded as a chirality.

The parity transformation is also equivalent to a unitary transformation (a change of basis) $U = \gamma_1 = i\sigma_1$ which flips the sign of both γ_2 and γ_0. Thus, a parity transformation is equivalent to a change of the sign of γ_0 or, what is the same, as changing the *sign* of the Dirac mass $m \to -m$. Since the Dirac theory is charge conjugation invariant, the parity transformation is equivalent to time reversal. It is easy to see that in 2+1 dimensions, the massive Dirac theory is not invariant under time reversal since the single particle Dirac Hamiltonian $H(\boldsymbol{p})$ for momentum $\boldsymbol{p}$ involves all three Pauli matrices,

$$H(\boldsymbol{p}) = \boldsymbol{\alpha} \cdot \boldsymbol{p} + \beta m \tag{275}$$

where, as usual, $\boldsymbol{\alpha} = \gamma_0 \boldsymbol{\gamma}$ and $\beta = \gamma_0$. In fact, time reversal is equivalent to the change of the sign of the Dirac mass. These considerations also apply to the massless Dirac theory coupled to a background gauge field.

Dirac fermions and topological insulators

In addition systems in one space dimension, discussed in Section "Dirac fermions in one space dimensions," in which Dirac fermions naturally describe the low energy electronic degrees of freedom, Dirac fermions also play a role in many other systems in condensed matter physics. Such systems range from the nodal Bogoliubov fermionic excitations of d-wave superconductors in 2D and p-wave superfluids in 3D, to Chern and $\mathbb{Z}_2$ topological insulators in 2D and $\mathbb{Z}_2$ topological insulators and Weyl semimetals in 3D. They also play a role in spin liquid phases of frustrated spin-1/2 quantum antiferromagnets, such as Dirac and chiral spin liquids. Dirac fermions also play a significant role in our understanding of the compressible limit of 2D electron gases (2DEG) in large magnetic fields (see Section "Chern–Simons gauge theory and the fractional quantum Hall effect"). We will not cover here all of these examples. Instead we will focus on the 2D Chern topological insulators (which exhibit the anomalous quantum Hell effect) and on the 3D $\mathbb{Z}_2$ topological insulators.

In condensed matter physics the important low energy electronic degrees of freedom belong to the electronic states close to the Fermi energy. In such systems, the lattice periodic potential determines the properties of their band structures. The only significant exception to this general rule is the case of the 2DEGs in GaAs-AlAs heterostructures (the most commonly used platform for the study of quantum hall effects) whose electronic densities are low enough so that the lattice periodic potential can for practical purposes almost always be ignored.

In general, Dirac (and Weyl) fermions arise when the conduction and valence bands cross at isolated points of the Brillouin zone. In such situations, the near the crossing points the low energy electronic states locally (in momentum space) look like cones and, ignoring possible anisotropies, look like the states of a Dirac-Weyl theory. For these reasons, Dirac fermions play a central role in the theory of graphene type materials (Castro Neto et al., 2009) and, more significantly, in the theory of topological insulators (Qi and Zhang, 2011).

Dirac fermions play a central role in Quantum Electrodynamics and in the Standard Model of Particle Physics. The problem of quark confinement requires an understanding of these theories in a regime inaccessible to Feynman-diagrammatic perturbation theory and an intrinsically nonperturbative formulation, known as Lattice Gauge Theory (Wilson, 1974; Kogut and Susskind, 1975; Susskind, 1977), needed to be developed. For this reason, in the 1970s, fermionic Hamiltonians with crossings at points became of great interest in High Energy Physics as a way to describing the short-distance dynamics of quarks in lattice gauge theory.

This program runs into difficulties when extended to the theory of Weak Interactions, which have an odd number of species of chiral (Weyl) Dirac fermions. All local discretizations of the Dirac equation yield an even number of species. This fact came to be known as the fermion doubling problem. These results are special cases of a general theorem, due to Nielsen and Ninomiya (1981a, b, 1983) [and extended by Friedan (1982)], which proves that for systems whose kinetic energy is *local* in space (as it must be) there must always be an *even* number of crossings. Therefore, it is impossible to write a local theory with an odd number of chiral fermionic species.

In the context of condensed matter physics, the simplest example of Dirac fermions is found in the electronic structure of graphene (a single layer of graphite) discussed by Castro Neto et al. (2009). Graphene is an allotrope of crystalline carbon in which the carbon atoms are arranged in a 2D hexagonal lattice, which is a lattice with two inequivalent sites in its unit cell, labeled by A and B. Let $\boldsymbol{r}_A$ and $\boldsymbol{r}_B$ be the sites of the two sublattices. Each site $\boldsymbol{r}_A$ has three nearest neighbors on the B sublattice located at $\boldsymbol{r}_B^i = \boldsymbol{r}_A + \boldsymbol{d}_i$, where $i = 1, 2, 3$ and

$$\boldsymbol{d}_1 = \left(\frac{1}{2\sqrt{3}}, \frac{1}{2}\right), \qquad \boldsymbol{d}_2 = \left(\frac{1}{2\sqrt{3}}, -\frac{1}{2}\right), \qquad \boldsymbol{d}_3 = \left(-\frac{1}{\sqrt{3}}, 0\right) \tag{276}$$

(in units in which the lattice spacing is $a = 1$). The nearest neighbor A sites are related by the vectors

$$\boldsymbol{a}_1 = \left(\frac{\sqrt{3}}{2}, -\frac{1}{2}\right), \qquad \boldsymbol{a}_2 = (0, 1), \qquad \boldsymbol{a}_3 = \left(-\frac{\sqrt{3}}{2}, -\frac{1}{2}\right) \tag{277}$$

where $\boldsymbol{a}_1$ and $\boldsymbol{a}_2$ are the primitive lattice vector of the hexagonal lattice. The nearest neighbor sites of the B sublattice are also related by these same three vectors.

The low energy electronic degrees of freedom of graphene can be described by a single fermionic state (ignoring spin) at each carbon atom. Let $c^\dagger(\boldsymbol{r}_A)$ and $c^\dagger(\boldsymbol{r}_B)$ be the fermion operators that create an electron at the site $\boldsymbol{r}_A$ and at the site nearest neighbor sites $\boldsymbol{r}_B$, respectively. The Hamiltonian is

$$H = t_1 \sum_{\boldsymbol{r}_A, i=1,2,3} c^\dagger(\boldsymbol{r}_A) c(\boldsymbol{r}_A + \boldsymbol{d}_i) + \text{h.c.} \tag{278}$$

where t_1 is the hopping matrix element between nearest neighbor A and B sites.

In Fourier space

$$c(\boldsymbol{r}_A) = \int_{\text{BZ}} \frac{d^2k}{(2\pi)^2} \psi_A(\boldsymbol{k}) \exp(i\boldsymbol{k}\cdot\boldsymbol{r}_A), \quad c(\boldsymbol{r}_B) = \int_{\text{BZ}} \frac{d^2k}{(2\pi)^2} \psi_B(\boldsymbol{k}) \exp(i\boldsymbol{k}\cdot\boldsymbol{r}_B) \tag{279}$$

where BZ is the first Brillouin zone of the hexagonal lattice, a hexagonal region of reciprocal space with vertices at $\pm 2\pi/\sqrt{3}(1, 1/\sqrt{3})$ (which are denoted by K and K', respectively) and their two images under $2\pi/3$ rotations. In momentum space the Hamiltonian is (Semenoff, 1984)

$$H = t_1 \int_{\text{BZ}} \frac{d^2k}{(2\pi)^2} \left(\psi_A(\boldsymbol{k}) \;\; \psi_B(\boldsymbol{k})\right) \begin{pmatrix} 0 & \sum_{j=1,2,3} \exp(i\boldsymbol{k}\cdot\boldsymbol{d}_j) \\ \sum_{j=1,2,3} \exp(-i\boldsymbol{k}\cdot\boldsymbol{d}_j) & 0 \end{pmatrix} \begin{pmatrix} \psi_A(\boldsymbol{k}) \\ \psi_B(\boldsymbol{k}) \end{pmatrix} \tag{280}$$

The one-particle states of this Hamiltonian have eigenvalues $E(\boldsymbol{k}) = \pm\left|\sum_{j=1,2,3} \exp(i\boldsymbol{k}\cdot\boldsymbol{d}_j)\right|$. Clearly $E(\boldsymbol{k})$ vanishes at the K and K' points, the corners of the Brillouin zone. Hence, there is a crossing of the two bands at the K and K' points near which the energy eigenvalues are a two cones at K and K', respectively. Thus, the low energy states of graphene consist of two massless (gapless) Dirac bi-spinors, with opposite chirality/parity.

Other examples with similar fermion content are a theory of fermions on a 2D square lattice with a π magnetic flux (1/2 of the flux quantum) per plaquette which arises, for instance, in the theory of the integer quantum Hall effect on lattices by Thouless et al. (1982) (albeit for more general flux per plaquette), and in the theory of flux phases of 2D spin liquids of Affleck and Marston (1988). It also arises in the theory of the chiral spin liquid of Wen et al. (1989). We will discuss these theories in Section "Topological phases of matter."

Chern invariants

The single-particle quantum states of free fermions (electrons) in the periodic potential of a crystal are Bloch wave functions labeled by the lattice momentum $\boldsymbol{k}$ and band indices m. The Bloch states are periodic functions of the lattice momenta whose periods are the Brillouin zones. Topologically each Brillouin zone is a torus: in 1D is a 1-torus, in 2D a 2-torus, etc. The symmetries (and shapes) of the Brillouin zone are dictated by the symmetries of the host crystal.

In this section we will consider the quantum states of systems of fermions on a 2D lattice with M bands with eigenvalues $\{E_m(\boldsymbol{k})\}$ with $m = 1, \ldots, M$. The eigenstates are Bloch states $\{|u_m(\boldsymbol{k})\rangle\}$ such that the wave functions are $\psi_m(\boldsymbol{x}) = u_m(\boldsymbol{k})\exp(i\boldsymbol{k}\cdot\boldsymbol{x})$, where $\boldsymbol{k}$ is a (quasi) momentum in the first Brillouin zone (Bloch, 1929). We will assume that the band spectrum is such that all the bands are separated from each other by a finite gap for all momenta in the first Brillouin zone. Hence, the eigenvalues obey the inequality $|E_m(\boldsymbol{k}) - E_n(\boldsymbol{k})| > 0$. We will assume that the system of interest has $N < M$ filled bands and, consequently, that there is a gap separating the top-most occupied band N (the "valence band") and the lowest unoccupied band $N+1$ (the "conduction band") that does not close everywhere in the first Brillouin zone.

Let us consider specifically a 2D system and a Bloch state $|u_m(\boldsymbol{k})\rangle$ at a momentum $\boldsymbol{k}$, and let $\partial_k|u_m(\boldsymbol{k})\rangle$ be an infinitesimally close Bloch state with momentum $\boldsymbol{k}' = \boldsymbol{k} + d\boldsymbol{k}$. The inner product of these two infinitesimally close Bloch states is the vector field (defined on the first Brillouin zone for each band m)

$$\mathcal{A}_j^{(m)}(\boldsymbol{k}) = i\langle u_m(\boldsymbol{k})|\partial_j|u_m(\boldsymbol{k})\rangle \tag{281}$$

where $j = 1, 2$ are the orthogonal directions in momentum space, and we have used the notation $\partial_i = \partial/\partial k_i$. This vector field is known as the *Berry Connection* of the electronic states in the mth band.

The theory of the quantum states of noninteracting electrons in periodic potentials as developed by Bloch (1929) is the foundation of much of what we know about the physics of many semiconductors and simple metals. This theory is the core subject of many textbooks (Kittel, 1996; Ashcroft and Mermin, 1976). This theory is based on the classification of the electronic states as representations of the group of lattice translations and point (and spatial) group symmetry transformations. A key unstated assumption in much of this body of work is that the Bloch states are globally well-defined functions on the Brillouin zone of a given crystal. It is rather remarkable that this assumption was not stated explicitly since the original work by Bloch in 1929 until the work by Thouless, Kohmoto, Nightingale and den Nijs on the quantum states of electrons on 2D lattices in the presence of an uniform magnetic field (Thouless et al., 1982). The realization that there is a topological obstruction to define the electronic states globally in the Brillouin zone is the key to the development of the theory of topological insulators and, more generally, of the modern theory of band structures (Bradlyn et al., 2017; Cano and Bradlyn, 2021).

In quantum mechanics, states are defined up to a *phase*. This means that Bloch states that differ by a phase describe the same quantum state. In other words, each quantum state $|u_m(\boldsymbol{k})\rangle$ is a member of a *ray* (or *fiber*) of states each labeled by a phase

$$|(u_m)(\boldsymbol{k})\rangle \mapsto \exp(if_m(\boldsymbol{k}))\,|u_m(\boldsymbol{k})\rangle. \tag{282}$$

Changing the states by phase factors defines a $U(1)^M$ unitary transformation of physically equivalent states. Since we have a fiber at each point $\boldsymbol{k}$, this amount at defining a *fiber bundle*. However, under this transformation, the Berry connection $\mathcal{A}_j^{(m)}(\boldsymbol{k})$ changes by a gradient of the phases

$$\mathcal{A}_j^{(m)}(\boldsymbol{k}) \mapsto \mathcal{A}_j^{(m)}(\boldsymbol{k}) + \partial_j f_m(\boldsymbol{k}) \tag{283}$$

where we assumed that the phases $f_m(\boldsymbol{k})$ are continuous and differentiable functions on the entire first Brillouin zone. Since the physical states cannot change by redefinitions of the phases of the basis states, we are led to the condition that only the data that is invariant under the gauge transformations defined by Eqs. (282) and (283) is physically meaningful, which is encoded in the gauge-invariant pseudo-scalar quantity $\mathcal{F}^{(m)}(\boldsymbol{k})$

$$\mathcal{F}^{(m)}(\boldsymbol{k}) = \epsilon_{ij}\partial_i\mathcal{A}_j^{(m)}(\boldsymbol{k}) \tag{284}$$

which is known as the *Berry curvature*.

In what follows we will be interested in the quantity

$$C_1^{(m)} = \frac{1}{2\pi}\oint_\Gamma dk_j\mathcal{A}_j^{(m)}(\boldsymbol{k}) = \frac{1}{2\pi}\int_{\mathrm{BZ}} d^2k\,\mathcal{F}^{(m)}(\boldsymbol{k}) \tag{285}$$

where Γ is the boundary of the 1st Brillouin zone (which we denote by BZ). We will now show that the quantity $C_1^{(m)}$, which measures the *flux* of the Berry connection $\mathcal{A}_j^{(m)}(\boldsymbol{k})$ through the first Brillouin zone (in units of 2π), is an integer independent of the particular connection $\mathcal{A}_j^{(m)}(\boldsymbol{k})$ that we have chosen. This integer-valued quantity is a topological invariant known as the first Chern number.

However, since the first Brillouin zone is a 2-torus,which is a closed manifold, a Berry connection with a net flux cannot obey periodic boundary conditions. Instead, we must allow for generalized (large) gauge transformations that wrap around the 2-torus of the first Brillouin zone. This problem is similar (and closely related) to the problem of the wave functions of a charged particle moving in the presence of a magnetic monopole (Wu and Yang, 1976). We will consider a 2D system whose first Brillouin zone is spanned by two reciprocal lattice vectors $\boldsymbol{b}_1$ and $\boldsymbol{b}_2$, related by the two primitive lattice vectors $\boldsymbol{a}_1$ and $\boldsymbol{a}_2$ by the relation $\boldsymbol{b}_i\cdot\boldsymbol{a}_j = 2\pi\delta_{ij}$ (with $i, j = 1, 2$). The generalized gauge transformations now are

$$\begin{aligned} |u_m(\boldsymbol{k}+\boldsymbol{b}_1)\rangle &= \exp(if_m^{(1)}(\boldsymbol{k}))\,|u_m(\boldsymbol{k})\rangle, \qquad & |u_m(\boldsymbol{k}+\boldsymbol{b}_2)\rangle &= \exp(if_m^{(2)}(\boldsymbol{k}))\,|u_m(\boldsymbol{k})\rangle \\ \mathcal{A}_j^{(m)}(\boldsymbol{k}+\boldsymbol{b}_1) &= \mathcal{A}_j^{(m)}(\boldsymbol{k}) + \partial_j f_m^{(1)}(\boldsymbol{k}), \qquad & \mathcal{A}_j^{(m)}(\boldsymbol{k}+\boldsymbol{b}_2) &= \mathcal{A}_j^{(m)}(\boldsymbol{k}) + \partial_j f_m^{(2)}(\boldsymbol{k}) \end{aligned} \tag{286}$$

where $f_m^{(1)}(\boldsymbol{k})$ and $f_m^{(2)}(\boldsymbol{k})$ are smooth functions of $\boldsymbol{k}$.

We will now show that the Bloch states cannot be defined globally over the Brillouin zone if the flux of the Berry connection does not vanish. More specifically let us assume that at some point $\boldsymbol{k}_0 \in T$, we know the Bloch state $|u_m(\boldsymbol{k}_0)\rangle$ which satisfies the generalized periodic boundary conditions of Eq. (286). The question is, can we determine the Bloch state at some other also *arbitrary* point $\boldsymbol{k}_0'$? We will know that there is a topological obstruction that does not allow it if the flux of the Berry phase is not zero. The reason is that the *phase* of the Bloch state cannot be defined since, in general, the Bloch state will vanish at some point of the Brillouin zone where the phase is undefined.

We will prove that this is true by following an elegant construction due to Mahito Kohmoto which goes as follows (Kohmoto, 1985): The Brillouin zone is a torus that, we will denote by T, can be regarded as the tensor product of two circles, $T \equiv S_1 \times S_1$. Let us split the torus T into two disjoint subsets (or patches) H_I and H_{II} such that $T = H_I \bigcup H_{II}$. We will assume that in region H_I, the Bloch state vanishes at some point $\boldsymbol{k}_0 \in T_I$ and that the Bloch state does not vanish for all points $\boldsymbol{k} \in H_{II}$. This means that we can choose the Bloch state $|u_m(\boldsymbol{k})\rangle$ to be real for all $\boldsymbol{k} \in H_{II}$. On the other hand, we can always assign some arbitrary phase to the Bloch state at $\boldsymbol{k}_0 \in T_I$. Once we have done that, we can extend the definition of the phase to a neighborhood of $\boldsymbol{k}_0$ wholly included in H_I. If we assume that there is only one zero, then the phase can be defined over all of H_I. The result is that we now have two different definitions of the phase of the Bloch state on H_I and on H_{II}. Let $|u_m(\boldsymbol{k})\rangle_I$ and $|u_m(\boldsymbol{k})\rangle_{II}$ be the two resulting definitions of the Bloch state. Let the closed curve γ be the common boundary of regions H_I and H_{II}, $\gamma = \partial H_I = \partial H_{II}$. However on the common boundary γ, these two definitions of the Bloch state must be a gauge transformation,

$$|u_m(\boldsymbol{k})\rangle_I = \exp(if_m(\boldsymbol{k}))\,|u_m(\boldsymbol{k})\rangle_{II} \tag{287}$$

on all points $\boldsymbol{k} \in \gamma$. The gauge transformation $f_m(\boldsymbol{k})$, known as the transition function, is a smooth periodic function of the points $\boldsymbol{k}$ on the closed curve γ. Likewise, the Berry connection $\mathcal{A}_j^{(m)}(\boldsymbol{k})$ has two definitions on the regions H_I and H_{II}, which differ by a gauge transformation on all the points $\boldsymbol{k}$ of the common boundary γ,

$$\mathcal{A}_j^{(m)}(\boldsymbol{k})\Big|_I - \mathcal{A}_j^{(m)}(\boldsymbol{k})\Big|_{II} = \partial_j f_m(\boldsymbol{k}). \tag{288}$$

The transition function defines a mapping of the closed curve γ, which is topologically equivalent to a circle S_1, to the phase of the Bloch state, which is defined mod 2π and hence is also a circle S_1. Hence the transition functions $f_m(\boldsymbol{k})$ are homotopies that can be classified by the homotopy group $\Pi_1(S_1) \simeq \mathbb{Z}$. We recognize that the classification of the transition functions is the same that we used for the vortices of Section "Vortices in two dimensions." Hence, the change of the transition function on a full revolution of the closed curve γ must be an integer multiple of 2π.

We will now compute the quantity $C_1^{(m)}$, given in Eq. (285), which measures the flux of the Berry connection through the 2-torus T that defines the first Brillouin zone. Using the partition of the torus $T = T_I \bigcup T_{II}$, we can write

$$C_1^{(m)} = \frac{1}{2\pi}\int_T d^2k\, \mathcal{F}^{(m)}(\boldsymbol{k}) = \frac{1}{2\pi}\left(\int_{H_I} d^2k\, \mathcal{F}^{(m)}(\boldsymbol{k}) + \int_{H_{II}} d^2k\, \mathcal{F}^{(m)}(\boldsymbol{k})\right) \tag{289}$$

Using Stokes Theorem on the two regions H_I and H_{II}, we get

$$C_1^{(m)} = \frac{1}{2\pi}\oint_\gamma dk_j\left(\mathcal{A}_j(\boldsymbol{k})\big|_I - \mathcal{A}_j(\boldsymbol{k})\big|_{II}\right). \tag{290}$$

Since the two definitions of the Berry connection differ by a gauge transformation, Eq. (288), we can express $C_1^{(m)}$ in terms of the transition function $f_m(\boldsymbol{k})$ on the curve γ

$$C_1^{(m)} = \frac{1}{2\pi}\oint_\gamma d\boldsymbol{k}\cdot\partial f_m(\boldsymbol{k}) = \frac{1}{2\pi}(\Delta f_m(\boldsymbol{k}))_\gamma = n \tag{291}$$

where we used that the transition functions are classified by the integer-valued quantity $n \in \mathbb{Z}$.

We conclude that the flux of the Berry curvature $C_1^{(m)}$ takes only integer values. It is known of the first Chern number $C_1^{(m)}$, which is a topological invariant since it cannot change by a smooth redefinition of the curve γ. Since $C_1^{(m)} \neq 0$ implies that the Bloch states must vanish at least at some point (or points) $\boldsymbol{k} \in H_I$, then the integer-valued Chern number can only change if a redefinition of the curve γ crosses at least one point $\boldsymbol{k}$ at which the Bloch state vanishes.

The conclusion of this analysis is that whenever the flux of the Berry curvature through the Brillouin zone does not vanish, the Bloch states cannot be defined globally on the Brillouin zone. A direct consequence is that in this case the band is characterized by a topological invariant called the first Chern number. This number is a property of a given band and, in general, it is different for each band. This is a particular case of a more general topological classification of the states of free fermions on a lattice which depends on the dimensionality of the system (Schnyder et al., 2008; Kitaev, 2009; Moore and Balents, 2007).

The quantum Hall effect on a lattice

We will now show that 2D free fermion systems with Chern bands, that is, bands characterized by a nonvanishing Chern number, are insulators that have a quantized Hall conductivity. We will do this for the theory of the integer quantum Hall effect on a 2D lattice of Thouless, Kohmoto, Nightingale and den Nijs (TKNN) (Thouless et al., 1982; Kohmoto, 1985) [see also, Fradkin and Kohmoto (1987)]. Although this problem played a key role in the development of the theory of topological phases of matter, for many years it was viewed as an academic problem since it would require gigantic magnetic fields to be in the regime of interest for typical solids. The situation changed with the development of twisted bilayer graphene and similar systems which have unit cells large enough for this physics to be observable. These new materials have allowed to study this problem experimentally.

TKNN considered a system of free fermions on a planar (actually square) lattice in a uniform magnetic field B with flux $2\pi p/q$ per plaquette (in units in which the flux quantum $\phi_0 = e\hbar/c = 1$) with p and q two co-prime integers. The tight-binding Hamiltonian for this simple problem is

$$H = \sum_{\boldsymbol{r},\, j=1,\,2} t_j\, c^\dagger(\boldsymbol{r})\, e^{iA_j(\boldsymbol{r})}\, c(\boldsymbol{r}+\boldsymbol{e}_j) + \text{h.c.} \tag{292}$$

where $c(\boldsymbol{r})$ and $c^\dagger(\boldsymbol{r})$ are fermion creation and annihilation operators on the lattices sites $\{\boldsymbol{r} = (m, n)\}$, $\boldsymbol{e}_j$ are lattice unit vectors, and t_j, with $j = x, y$, is a hopping matrix element between nearest neighbor sites of the square lattice along the x and y directions. On each link of the lattice, we defined a vector potential $A_j(\boldsymbol{r})$, where the oriented sum of the lattice vector potentials on each plaquette $2\pi\phi$, where $\phi = \frac{p}{q}$, is the flux on each plaquette of the square lattice. In the axial (Landau) gauge $A_1(m, n) = 0$, $A_2(m, n) = 2\pi m\phi$ is a periodic function of m with period q. In this gauge, the Hamiltonian becomes

$$\begin{aligned} H = t&\sum_{m,n}\left(c^\dagger(m+1,n)c(m,n) + c^\dagger(m,n)c(m+1,n)\right) \\ &+ t\sum_{m,n}\left(c^\dagger(m,n+1)\, e^{i2\pi\phi m}\, c(m,n) + c^\dagger(m,n)\, e^{-i2\pi\phi m}\, c(m,n+1)\right) \end{aligned} \tag{293}$$

In this gauge, the problem reduces to a system with a theory with a $q \times 1$ unit cell with q inequivalent sites. In momentum space, the (*magnetic*) Brillouin zone of this system is $-\frac{\pi}{q} \leq k_1 \leq \frac{\pi}{q}$ and $-\pi \leq k_2 \leq \pi$. The Fourier transform of the operators $c^\dagger(\boldsymbol{r})$ and $c(\boldsymbol{r})$ is, respectively, $c^\dagger(\boldsymbol{k})$ and $c(\boldsymbol{k})$, which obey the standard anticommutation relations, $\{c(\boldsymbol{k}), c(\boldsymbol{q})\} = \{c^\dagger(\boldsymbol{k}), c^\dagger(\boldsymbol{q})\} = 0$, and $\{c^\dagger(\boldsymbol{k}), c(\boldsymbol{q})\} = \delta(\boldsymbol{k}-\boldsymbol{q})$. In momentum space, the Hamiltonian becomes

$$H = q\int_{-\pi/q}^{\pi/q}\frac{dk_x}{2\pi}\int_{-\pi}^{\pi}\frac{dk_y}{2\pi}\widetilde{H}(k_x, k_y) \tag{294}$$

where

$$\begin{aligned}\widetilde{H}(k_x,k_y)=\frac{1}{q}\sum_{n=0}^{q-1}\big\{&2t_x\ \cos(k_x+2\pi\phi n)\ c^\dagger(k_x+2\pi\phi n,k_y)\ c(k_x+2\pi\phi n,k_y)\\&+t_y\big[e^{-ik_y}\ c^\dagger(k_x+2\pi(n+1)\phi,k_y)\ c(k_x+2\pi n\phi,k_y)+e^{ik_y}\ c^\dagger(k_x+2\pi(n-1)\phi,k_y)\ c(k_x+2\pi n\phi,k_y)\big]\big\}\end{aligned} \tag{295}$$

The spectrum of this system was first investigated by Hofstadter (1876) consists of q bands which for q an odd integer are separated by finite energy gaps.

For fixed values of k_x and k_y (in the magnetic Brillouin zone), the Hamiltonian $\widetilde{H}(k_x,k_y)$ is the tight-binding model of a one-dimensional chain on the 1D lattice of q sites located at $k_x+2\pi n\phi$ with nearest neighbor hopping. The single-particle (Bloch) states $u_n(\boldsymbol{k})$ of this 1D model obeys the Schrödinger Equation

$$2t_x\ \cos(k_x+2\pi n\phi)u_n(\boldsymbol{k})+t_y\left(e^{-ik_y}\ u_{n-1}(\boldsymbol{k})+e^{ik_y}\ u_{n+1}(\boldsymbol{k})\right)=E_n u_n \tag{296}$$

which is known as Harper's equation. In general, this equation does not admit an analytic solution. However, the nature qualitative features of the spectrum can be obtained by an expansion either on t_x/t_y or on t_y/t_x. TKNN used degenerate perturbation theory to show that the spectrum has q bands and that the r-th band is characterized by two integers s_r and ℓ_r, which are the solution of the Diophantine equation

$$r=q\ s_r+p\ \ell_r \tag{297}$$

with $\ell_0=s_0=0$. It is also obvious that for $r=q\ s_q=1$ and $\ell_q=0$ (for all p).

Furthermore, TKNN showed that there was an, until then unsuspected, relation between the Hall conductivity σ_{xy} of a gapped system of electrons in periodic potentials in a uniform magnetic field and the Berry connection of the filled bands. This relation implies the quantization of the Hall conductivity and its computation in terms of a topological invariant, the Chern number of the occupied bands. They showed that in this context, each band has a nontrivial Berry connection $\mathcal{A}_j^{(r)}=i\langle u_r(\boldsymbol{k})|\partial_j|u_r(\boldsymbol{k}\rangle$ (with $\partial_j=\partial_{k_j}$) of the form of Eq. (281) with a nonvanishing (first) Chern number $C_1^{(r)}$, that is, the flux through the magnetic Brillouin zone.

The conductivity tensor characterizes the electrical properties of a physical system. Linear Response Theory provides a framework for computing the conductivity tensor by perturbing the system with a weak external electromagnetic field A_μ and computing the currents that they induce (Martin, 1967; Fradkin, 2021). The expectation value of the gauge-invariant current operator $J_\mu(x)$ is

$$\langle J_\mu(x)\rangle=-\frac{i}{\hbar}\frac{\delta}{\delta A_\mu(x)}\ln Z[A_\mu] \tag{298}$$

where $Z[A_\mu]$ is the partition function in the presence of a background (i.e., classical) electromagnetic field $A_\mu(x)$. In general spacetime dimension $D=d+1$, the lowest order in the vector potential A_μ, the induced current is given in terms of the polarization tensor $\Pi_{\mu\nu}(x,y)$

$$\ln Z[A_\mu]=\frac{i}{2}\int d^Dx\int d^Dy\ A_\mu(x)\ \Pi^{\mu\nu}(x,y)\ A_\nu(y)+O(A^3). \tag{299}$$

Therefore, the induced current is related to the external field by

$$\langle J_\mu(x)\rangle\equiv J_\mu(x)=\int d^Dy\ \Pi_{\mu\nu}(x,y)\ A^\nu(y). \tag{300}$$

Expressions of this type are known as a *Kubo formula*. The polarization tensor can be regarded as a *generalized susceptibility*.

Although we are using a continuum relativistic notation, these expressions are generally valid, even in lattice systems. Gauge invariance requires that the polarization tensor be conserved

$$\partial_\mu\Pi^{\mu\nu}(x,y)=0. \tag{301}$$

In general, the (retarded) polarization tensor $\Pi^{\mu\nu}(x,y)$ is related to the (retarded) current–current correlation function $\mathcal{D}^R_{\mu\nu}(x,y)$,

$$\mathcal{D}^{\mu\nu}(x,y)=-\frac{i}{\hbar}\Theta(x_0-y_0)\langle[J_\mu(x),J_\nu(y)]\rangle \tag{302}$$

by the identity

$$\Pi^R_{\mu\nu}(x,y)=\mathcal{D}^R_{\mu\nu}(x,y)-i\hbar\left\langle\frac{\delta J_\mu(x)}{\delta A_\nu(y)}\right\rangle. \tag{303}$$

The last term in Eq. (303) is usually called a "contact term." This term vanishes only for a theory of relativistic fermions (in the continuum). In all other cases, lattice or continuum, relativistic or not, the contact term does not vanish and its form depends on the specific theory. In nonrelativistic systems, for example, in a FL, this term is the origin of the *f*-sum rule (Martin, 1967; Nozières and Pines, 1966).

When the external field A_μ represents is a (locally) uniform electric field $\boldsymbol{E}$, the induced current is $J_i = \sigma_{ij} E_j$, where σ_{ij} is the conductivity tensor, which can be obtained from the polarization tensor as the limit

$$\sigma_{ij} = \lim_{\omega \to 0} \frac{1}{i\omega} \lim_{\boldsymbol{q} \to 0} \Pi_{ij}(\omega, \boldsymbol{q}) \tag{304}$$

In a metal, which has a Fermi surface, the order of limits in which ω and $\boldsymbol{q}$ vanish matters and only the order of limits specified above is the correct one to take. In Dirac systems, that we will discuss below, the order does not matter due to relativistic invariance. The other case in which the order does not matter is the Chern insulator that we are interested in. In general, in an isotropic system, the conductivity tensor has a symmetric part and an antisymmetric part. The symmetric part of the conductivity tensor yields the longitudinal conductivity, which has all the effects of dissipation. The antisymmetric part does not vanish in the presence of a magnetic field or, more generally, if time reversal symmetry is broken, and yields the Hall conductivity.

A Chern insulator is an insulator and as such is a state with an energy gap. In such a state, the longitudinal conductivity vanishes since there is no dissipation in a gapped state. But in a Chern insulator time-reversal invariance is broken. In the system that we are discussing is broken by the magnetic field. The Hall conductivity can be calculated from the antisymmetric part of the polarization tensor as the limit

$$\sigma_{xy} = \lim_{\omega \to 0} \frac{i}{\omega} \Pi_{xy}(\omega, 0). \tag{305}$$

In addition, the contact term does not contribute to the Hall conductivity. As a result, the hall conductivity can be computed in terms of the antisymmetric component of the current-correlation function.

Let us now return to the theory of free fermions on a lattice in a (commensurate) magnetic field takes. As we saw, the electronic states are split into q bands with single particle states $|\psi_n(\boldsymbol{k})\rangle$ where $\boldsymbol{k}$ takes values on the first magnetic Brillouin zone. We will compute the Hall conductivity for this system assuming that the Fermi energy E_F lies in the gap between the n-th and the $n-1$-th bands. Let us label by α the occupied bands and by β the unoccupied bands. Hence $E_\alpha(\boldsymbol{k}) < E_F < E_\beta(\boldsymbol{k})$. In this case, the Kubo formula for the Hall conductivity becomes

$$\sigma_{xy} = i\frac{e^2}{\hbar} \sum_{E_\alpha < E_F < E_\beta} \int_{BZ} \frac{d^2k}{(2\pi)^2} \frac{\langle u_\alpha(\boldsymbol{k})|J_y|u_\beta(\boldsymbol{k})\rangle\langle u_\beta(\boldsymbol{k})|J_x|u_\alpha(\boldsymbol{k})\rangle - \langle u_\alpha(\boldsymbol{k})|J_x|u_\beta(\boldsymbol{k})\rangle\langle u_\beta(\boldsymbol{k})|J_y|u_\alpha(\boldsymbol{k})\rangle}{(E_\alpha(\boldsymbol{k}) - E_\beta(\boldsymbol{k}))^2}. \tag{306}$$

In the lattice model, the current operator is simply

$$\boldsymbol{J} = \frac{e}{\hbar} \partial_{\boldsymbol{k}} \widetilde{H}(\boldsymbol{k}) \tag{307}$$

Using this form of the current and the Schrödinger equation of Eq. (296), we can rewrite the Kubo formula for the Hall conductivity, Eq. (306), as a sum over only the occupied states labeled by α. The expression for the Hall conductivity now takes the more compact form

$$\sigma_{xy} = \frac{e^2}{\hbar} \sum_\alpha \int_{BZ} \frac{d^2k}{(2\pi)^2} \epsilon_{jl} \partial_j \langle u_\alpha(\boldsymbol{k})|\partial_k|u_\alpha(\boldsymbol{k})\rangle = \frac{e^2}{h} \sum_\alpha \frac{1}{2\pi} \int_{BZ} \mathcal{F}^{(\alpha)}(\boldsymbol{k}) = \frac{e^2}{h} \sum_\alpha C_1^{(\alpha)}. \tag{308}$$

Therefore, we conclude that each occupied band contributes to the Hall conductivity an amount equal to its first Chern number (multiplied by e^2/h). This is the main result of TKNN (Thouless et al., 1982).

In the specific case of the model that we are discussing here, the Chern number is given explicitly in terms of the solution of the Diophantine equation, Eq. (297)

$$C_1^{(r)} = \frac{1}{2\pi} \oint_\Gamma dk_j \mathcal{A}_j^{(r)}(\boldsymbol{k}) = \ell_r - \ell_{r-1} \tag{309}$$

where the integers ℓ_r and ℓ_{r-1} are the solutions of the Diophantine equation for the bands r and $r-1$ (A detailed derivation can be found in Fradkin (2013), Chapter 12). The TKNN integers ℓ_r are topological invariants of the bands.

We conclude, with TKNN, that for a system with r filled bands, the Hall conductivity $\sigma_{xy}^{(r)}$ is given by the expression

$$\sigma_{xy}^{(r)} = \frac{e^2}{h} \sum_{n=1}^{r} (\ell_r - \ell_{r-1}) = \frac{e^2}{h} \ell_r \tag{310}$$

thus showing that this system exhibits an integer quantum Hall effect and that the Hall conductivity is (up to the ratio of universal constants e^2/h) given by a topological invariant, the first Chern number of the band.

We conclude with two comments. The first is that when *all* the bands are occupied, the Hall conductivity vanishes. This obvious physical constraint is automatically satisfied by the Diophantine equation. The other comment concerns the case of what happens when q is an even integer. In this case it is possible to show that there are band crossings. This is what happens for $q = 2$, which is the π flux lattice. In this case, one has a theory of two species of Dirac bi-spinors. As we will see in Section "The anomalous quantum Hall effect," what happens depends on how the gapless state is reached.

The anomalous quantum Hall effect

We will now discuss a simple and insightful model of a Chern insulator that displays the quantum anomalous Hall effect, that is, a Hall effect in a system with broken time reversal symmetry in the absence of a uniform magnetic field. In order to do that, we will reconsider the graphene model with additional terms in the Hamiltonian of Eq. (280) that will open up energy gaps in its spectrum. There are several ways to do this. One way requires breaking the symmetry between the two sublattices *A* and *B*, by assigning them a site energy of $\pm M$, which breaks the mirror reflection symmetry of the hexagon. This is what happens with graphene on a boron nitrade substrate (Semenoff, 1984) [there are other ways that involve breaking the point group symmetry (Ryu et al., 2009)]. Another way to open a gap is to break time reversal symmetry, which is accomplished by complex hopping amplitudes $t_2 \exp(i\phi)$ between nearest neighbor *A* sites (and between nearest neighbor *B* sites as well). The phase ϕ is oriented from $\boldsymbol{r}_A$ to $\boldsymbol{r}_A + \boldsymbol{a}_i$, where $\boldsymbol{a}_1 = \boldsymbol{d}_2 - \boldsymbol{d}_3$, etc. (and similarly for the *B* sites). Physically, the oriented sum of the phases ϕ on the triangles generated by the hopping terms t_1 and t_2 represents the magnetic fluxes through each triangle such that the total flux on the elementary hexagon is zero. This model was considered by Haldane (1988a). With these changes, the one-particle Hamiltonian becomes 2×2 Hermitian matrix

$$H(\boldsymbol{k}) = h_0(\boldsymbol{k})\ \mathbf{1} + \boldsymbol{h}(\boldsymbol{k}) \cdot \boldsymbol{\sigma} \tag{311}$$

where **I** is the 2×2 identity matrix and $\boldsymbol{\sigma} = (\sigma_1, \sigma_2, \sigma_3)$ is a vector made of the three Pauli matrices. The functions $h_0(\boldsymbol{k})$ and $\boldsymbol{h}(\boldsymbol{k}) = (h_1(\boldsymbol{k}), h_2(\boldsymbol{k}), h_3(\boldsymbol{k}))$ are, respectively, given by

$$\begin{aligned} h_0(\boldsymbol{k}) &= 2t_2 \cos\phi \sum_{i=1,2,3} \cos(\boldsymbol{k}\cdot\boldsymbol{a}_i), \qquad & h_1(\boldsymbol{k}) &= t_1 \sum_{i=1,2,3} \cos(\boldsymbol{k}\cdot\boldsymbol{d}_i), \\ h_2(\boldsymbol{k}) &= t_1 \sum_{i=1,2,3} \sin(\boldsymbol{k}\cdot\boldsymbol{d}_i), \qquad & h_3(\boldsymbol{k}) &= M - 2t_2 \sin\phi \sum_{i=1,2,3} \sin(\boldsymbol{k}\cdot\boldsymbol{a}_i). \end{aligned} \tag{312}$$

Provided $|t_2/t_1| < 1/3$, the spectrum of the Hamiltonian of Eq. (280) has two bands that do not overlap and have a finite energy gap unless they cross at the corners K and K', the Brillouin zone where the gap is smallest. The two bands cross at K and/or K' if $M = \pm 3\sqrt{3} t_2 \sin\phi$ (for K and K', respectively). When either one of these conditions is not met, the spectrum is gapped at either K or K' or, more generally, at both. For values of the parameters for which the band gaps are small, the low energy states of the Hamiltonian of Eq. (280) is that of a theory of two Dirac fields, that we will label as $\psi_1(x)$ and $\psi_2(x)$, whose one-particle Hamiltonians have the form of Eq. (275) but with generally different masses $m_1 \propto M - 3\sqrt{3} t_2 \sin\phi$ and $m_2 \propto M + 3\sqrt{3} t_2 \sin\phi$. So, in general, both fields will have nonvanishing masses, which can have the same sign or opposite sign.

We conclude that the effective low-energy theory consists of two species of massive Dirac bi-spinors, albeit generally with different masses. To examine the electromagnetic response, we will couple the lattice model and the effective low energy theory to a slowly varying background electromagnetic field A_μ. The Lagrangian of the low energy theory is

$$\mathcal{L} = \bar{\psi}_1 (i\partial\!\!\!/ - m_1)\psi_1 + \bar{\psi}_2 (i\partial\!\!\!/ - m_2)\psi_2 - eA_\mu(\bar{\psi}_1\gamma^\mu\psi_1 + \bar{\psi}_1\gamma^\mu\psi_1). \tag{313}$$

In general, the two masses will be different in magnitude and sign. Equivalently the Dirac fermions may have the same or opposite chirality. We will examine the electromagnetic response for both cases in Section "The parity anomaly" where we will see that in the phase in which the masses of both Dirac fermions have the same sign, this model describes a topological insulator that exhibits the anomalous quantum Hall effect, whereas in the phase where the signs are opposite, it is a conventional insulator.

However, by varying the parameters, we can tune to special values of these parameters where one of the two masses vanishes. In Section "The parity anomaly," we will see that these special values of the parameters correspond to quantum phase transitions at which the topological properties of the ground state change. We will see that this is a quantum critical point with special properties. In particular, time-reversal invariance is explicitly broken at this quantum critical point. In this regime, the heavy Dirac fermion plays the role of the heavy regulating field as in the Pauli–Villars regularization of the theory of a single Dirac fermion. In the lattice model, this is a manifestation of the Nielsen–Ninomiya theorem which requires that there should be an even number of Dirac fermions (Nielsen and Ninomiya, 1981a, b; Friedan, 1982). In this context, the heavy fermion is the "doubler."

The parity anomaly

We saw in Section "The chiral anomaly" that Dirac fermions in 1+1 dimensions have a chiral anomaly. That statement mean, that although the theory of free massless Dirac fermions has a global chiral symmetry, the associated current, which we called j^5_μ, is not conserved when the system is coupled to an external gauge field. This effect happened because the right and left moving (Weyl) components of the massless Dirac fermion cannot be separately conserved in the presence of a gauge field.

Analogs of the 1+1-dimensional chiral anomaly exist on 3+1 dimensions (and, more generally, in all even spacetime dimensions). The cancelation of these anomalies is a key condition for the consistency of gauge theories ('t Hooft, 1976b). We will see in Section "Topological phases of matter" that these anomalies play a role on the theory of 3D topological insulators. More generally, anomalies play a central role in the theory of symmetry-protected topological (SPT) phases of matter (Chen et al., 2012; Senthil, 2015; Witten, 2016).

Dirac fermions in 2+1 dimensions do not have an analog of the chiral anomaly for the simple reason that the chiral symmetry does not exist. There is, however, an anomaly involving parity or, equivalently, time-reversal invariance, known as the parity anomaly. The parity anomaly was discovered in the computation of the effective action of the electromagnetic field in a theory of massive Dirac fermions in 2+1 dimensions by Redlich (1984a,b).

Consider theory on a single massive Dirac fermion (a bi-spinor) $\psi(x)$ in 2+1 dimensions coupled to a background $U(1)$ gauge field A_μ. The Lagrangian is

$$\mathcal{L}[\psi, \bar{\psi}, A_\mu] = \bar{\psi} i \not{D} \psi - m\bar{\psi}\psi \tag{314}$$

where the covariant derivative is $D_\mu = \partial_\mu + iA_\mu$. The effective action $S_{\text{eff}}[A_\mu]$ of the gauge field A_μ is formally obtained by computing the path integral

$$Z[A_\mu] = \exp(iS_{\text{eff}}[A_\mu]) = \int \mathcal{D}\psi \mathcal{D}\bar{\psi} \exp(i \int d^3x \, \mathcal{L}[\psi, \bar{\psi}, A_\mu]) = \text{Det}(i\not{D}[A_\mu] - m) \tag{315}$$

where we used that the theory is free to write the partition function as a functional determinant. In 1+1 dimensions, in the case of a massless theory, this determinant can be computed exactly using the heat kernel (or zeta-function) technique (Fujikawa, 1979; Gamboa Saraví et al., 1984). Aside from important technicalities, the reason for why this works is that as a consequence of the chiral anomaly, the effective action computed at one loop order in the fermions is exact in 1+1 dimensions. In higher dimensions, this is no longer true.

We will sketch the computation of the effective action to one loop order, which means quadratic in the gauge field A_μ, which has the form

$$S_{\text{eff}}[A_\mu] = \frac{1}{2}\int d^3x \int d^3y \, A_\mu(x) \, \Pi^{\mu\nu}(x-y) \, A_\nu(y) + \cdots \tag{316}$$

where the ellipsis contains the higher order contributions. The polarization operator $\Pi^{\mu\nu}(x-y)$ in momentum space is (here p_μ is the momentum transfer) by the one-loop result

$$\Pi^{\mu\nu}(p) = \int \frac{d^3q}{(2\pi)^3} \text{tr}[S(q+p/2)\gamma^\mu S(q-p/2)\gamma^\nu]. \tag{317}$$

The symbol tr signifies the trace over the spinor labels and $S(p)$ is the (massive) Feynman propagator

$$S(p) = \frac{1}{\not{p} - m + i\epsilon}. \tag{318}$$

The polarization tensor $\Pi^{\mu\nu}(p)$ has the explicit decomposition into a parity even and a parity odd contributions

$$\Pi^{\mu\nu}(p) = (p^2 g^{\mu\nu} - p^\mu p^\nu) \, \Pi_0(p^2) - i\epsilon^{\mu\nu\lambda} p_\lambda \, \Pi_A(p^2) \tag{319}$$

where $p^2 = p_0^2 - \boldsymbol{p}^2$. The polarization tensor is manifestly transverse, $p_\mu \Pi^{\mu\nu}(p) = 0$ and, hence, the one-loop effective action of Eq. (316) is gauge-invariant (as it should be). The parity even $\Pi_0(p^2)$ and parity odd $\Pi_A(p^2)$ kernels are given by

$$\Pi_0(p^2) = -\frac{|m|}{4\pi p^2} + \frac{1}{8\pi\sqrt{p^2}}\left(\frac{4m^2}{p^2} + 1\right) \sinh^{-1}\left(\frac{\sqrt{p^2}}{\sqrt{4m^2 - p^2}}\right) \tag{320}$$

$$\Pi_A(p^2) = -\frac{m}{2\pi\sqrt{p^2}} \sinh^{-1}\left(\frac{\sqrt{p^2}}{\sqrt{4m^2 - p^2}}\right). \tag{321}$$

These two results are obtained in the limit in which the regulator scales are sent to infinity leaving behind these finite results, which hold provided the Dirac mass m does not vanish.

In the low-energy regime, $|p^2| \ll m^2$, the kernels take the asymptotic values

$$\Pi_0(p^2) \simeq \frac{1}{16\pi|m|} \qquad \Pi_A(p^2) \simeq -\frac{1}{4\pi}\text{sgn}(m). \tag{322}$$

This result is the leading contribution to the parity even term (the first term) up to corrections of the order of p^2/m^2. However, the second term, which is parity odd, is the exact contribution in the limit $p \to 0$ for all nonvanishing values of the Dirac mass. In this regime, the effective Lagrangian of the gauge field A_μ takes the local form of the sum of a Maxwell term and a Chern–Simons term

$$\mathcal{L}_{\text{eff}}[A_\mu] = -\frac{1}{4\pi|m|} F_{\mu\nu}F^{\mu\nu} \pm \frac{1}{2}\frac{1}{4\pi} \epsilon_{\mu\nu\lambda} \, A^\mu \partial^\nu A^\lambda \tag{323}$$

where $F_{\mu\nu} = \partial_\nu A_\nu - \partial_\nu A_\mu$ is the field strength of the gauge field. Clearly, since the Maxwell term has two derivatives while the Chern–Simons term has one derivative, in the long-distance regime the Maxwell term is irrelevant (subdominant). Also, while the prefactor of the Chern–Simons term is a pure number, the prefactor of the Maxwell term is proportional to $\frac{1}{|m|}$ (as required by dimensional analysis).

The second term in the Lagrangian of Eq. (323) is a Chern–Simons term for the background gauge field A_μ (Deser et al., 1982a,b). This term is gauge-invariant (up to boundary terms) but breaks parity and time-reversal invariance. This phenomenon is called the *parity anomaly* (Redlich, 1984a), although Witten (2016) has argued that it is better to call this phenomenon a *time-reversal anomaly*.

The *sign* of the prefactor of the Chern–Simons term depends on the *sign* of the Dirac mass m: positive for $m > 0$ and negative for $m < 0$ or, alternatively for positive and negative chirality of the Dirac (bi-spinor) field which fixes the sign of the breaking of time-reversal invariance.

In addition to the sign, the prefactor of the Chern–Simons term is equal to $\frac{1}{2}$, and it is not an integer. In Section "Vacuum degeneracy a torus," we showed that for a *dynamical* Chern–Simons gauge theory to be defined consistently on a closed surface, this coefficient must be quantized and should take *integer* values. The fact that the coefficient is half-quantized means that the classical global symmetry of a theory of a single Dirac bi-spinor cannot be gauged, which means that the gauge theory cannot be quantized. This is an example of an obstruction to the quantization of a gauge theory due to an anomaly ('t Hooft, 1976b).

We will now use these results to compute the effective low-energy action for the theories of lattice Dirac fermions of Section "Dirac fermions and topological insulators." In those systems, the low energy theory is that of *two* Dirac (bi-spinors) with different masses m_1 and m_2. Since both Dirac fields are coupled (minimally) to the same background gauge field A_μ, the effective Lagrangian is just the sum of the contribution for each Dirac fermion

$$\mathcal{L}_{\text{eff}}[A_\mu] = -\frac{1}{4\pi|m|_{\text{eff}}} F_{\mu\nu}F^{\mu\nu} + \frac{1}{2}\left(\text{sgn}(m_1) + \text{sgn}(m_2)\right)\frac{1}{4\pi}\epsilon_{\mu\nu\lambda}A^\mu\partial^\nu A^\lambda \tag{324}$$

where $|m|_{\text{eff}}$ is

$$\frac{1}{|m|_{\text{eff}}} = \frac{1}{|m_1|} + \frac{1}{|m_2|}. \tag{325}$$

This result implies that, as anticipated in Section "Dirac fermions and topological insulators," this theory has two phases: a parity even phase and a parity-odd phase. In the regime in which the signs of the two mass terms are equal and opposite, $\text{sgn}(m_1) = -\text{sgn}(m_2)$, the coefficient of the Chern–Simons term cancels and the low-energy effective Lagrangian is a Maxwell term (generally with an effective speed of light much smaller than that in vacuum): this phase is a conventional insulator.

Conversely, in the phase in which the two masses have the same sign, $\text{sgn}(m_1) = \text{sgn}(m_2)$, the coefficient of the Chern–Simons terms does not cancel, and it is given by $\pm\frac{1}{4\pi}$, where the sign is the sign of both mass terms. This phase is also an insulator but one in which time-reversal invariance is broken. Moreover, in this phase, the induced current j_μ by the background field A_μ in the long-distance limit is controlled by the Chern–Simons term, and it is given by

$$j_\mu = \frac{\delta\mathcal{L}_{\text{eff}}}{\delta A_\mu(x)} = \pm\frac{e^2}{2\pi\hbar}\epsilon_{\mu\nu\lambda}\partial^\nu A^\lambda. \tag{326}$$

From this result, we see that in the parity-broken anomalous quantum Hall phase, the system has a correctly quantized and nonvanishing Hall conductivity

$$\sigma_{xy} = \pm\frac{e^2}{h}. \tag{327}$$

Therefore, the phase with $\text{sgn}(m_1) = \text{sgn}(m_2)$ displays the *quantum anomalous Hall* effect with a Hall conductivity whose sign equals the signs of both masses. Notice that this is true regardless the magnitudes of the masses m_1 and m_2, and that only their signs matter. In Section "Topological insulators," we will identify this phase with a topological phase of matter known as the *Chern Insulator*.

We showed that the Hall conductivity of the anomalous quantum Hall phase is, as expected, equal to e^2/h using the effective low energy Dirac theory. One may wonder if this approximation may be missing some contributions to the Hall conductivity. Fortunately there is an alternative, quite elegant way of computing the Hall conductivity as a property of the entire occupied band. This approach, originally introduced by Volovik (1987) in the context of superfluid ^{3}He-A, and adapted to the theory of the quantum anomalous Hall effect by Yakovenko (1990), by Maarten Golterman, Karl Jansen, and David Kaplan for a theory of Wilson fermions in odd dimensional hypercubic lattices (Golterman et al., 1993), and by Qi et al. (2006), involves the derivation of a topological invariant for a two-band model.

As we saw above, the Hall conductivity is obtained from the xy component of the polarization operator as the limit

$$\sigma_{xy} = \lim_{\omega\to 0}\frac{i}{\omega}\lim_{q\to 0}\Pi_{xy}(\omega, \boldsymbol{q}). \tag{328}$$

For a free fermion system, $\Pi_{xy}(\omega, 0)$ is given by the current correlator

$$\Pi_{xy}(\omega, 0) = \int_{\text{BZ}}\frac{d^2k}{(2\pi)^2}\int_{-\infty}^{\infty}\frac{d\Omega}{2\pi}\,\text{tr}\left[J_x(\boldsymbol{k})G(\boldsymbol{k}, \omega + \Omega)J_y(\boldsymbol{k})G(\boldsymbol{k}, \Omega)\right] \tag{329}$$

where $G(\boldsymbol{k}, \Omega)$ is the propagator for a two-band free fermion system. A generic two-band free fermion system has a one-particle Hamiltonian of the form given in Eq. (311). The (one-body) current operator for such a system is obtained as

$$J_l(\boldsymbol{k}) = \frac{\partial h_0(\boldsymbol{k})}{\partial k_l}\,\mathbf{1} + \frac{\partial h_a(\boldsymbol{k})}{\partial k_l}\,\sigma_a. \tag{330}$$

The propagator $G(\boldsymbol{k}, \omega)$ is the 2×2 matrix (in band indices)

$$G(\boldsymbol{k}, \omega) = \frac{1}{\omega \mathbf{1} - \boldsymbol{h}(\boldsymbol{k}) \cdot \boldsymbol{\sigma} + i\epsilon} = \frac{P_+(\boldsymbol{k})}{\omega - E_+(\boldsymbol{k}) + i\epsilon} + \frac{P_-(\boldsymbol{k})}{\omega - E_-(\boldsymbol{k}) + i\epsilon} \tag{331}$$

where $P_\pm(\boldsymbol{k})$ are the operators that project onto the (empty) conduction band and the (filled) valence band whose energies are, respectively $E_\pm(\boldsymbol{k})$,

$$P_\pm(\boldsymbol{k}) = \frac{1}{2}\left(\mathbf{1} \pm \hat{\boldsymbol{h}}(\boldsymbol{k}) \cdot \boldsymbol{\sigma}\right) \tag{332}$$

where $\hat{\boldsymbol{h}}(\boldsymbol{k})$ is the unit vector defined for every momentum $\boldsymbol{k}$ of the first Brillouin zone

$$\hat{\boldsymbol{h}}(\boldsymbol{k}) = \frac{\boldsymbol{h}(\boldsymbol{k})}{||\boldsymbol{h}(\boldsymbol{k})||}. \tag{333}$$

Upon performing the frequency integration and the band traces in the expression for $\Pi_{xy}(\omega, 0)$ of Eq. (329), we find that the Hall conductivity takes the form

$$\sigma_{xy} = \frac{e^2}{2\hbar} \int_{\text{BZ}} \frac{d^2k}{(2\pi)^2}\, \epsilon_{abc} \frac{\partial \hat{h}_a(\boldsymbol{k})}{\partial k_x} \frac{\partial \hat{h}_b(\boldsymbol{k})}{\partial k_y} \hat{h}_c(\boldsymbol{k}) (n_+(\boldsymbol{k})) - n_-(\boldsymbol{k})) \tag{334}$$

where $n_\pm(\boldsymbol{k})$ are the Fermi functions (at zero temperature) for the two bands. Since

$$E_+(\boldsymbol{k}) - E_-(\boldsymbol{k}) = 2||\boldsymbol{h}(\boldsymbol{k})|| = 2\sqrt{\boldsymbol{h}^2(\boldsymbol{k})} > 0 \tag{335}$$

there is a nonvanishing gap on the entire Brillouin zone between the occupied valence band, with $n_-(\boldsymbol{k}) = 1$, and the unoccupied conduction band, with $n_+(\boldsymbol{k}) = 0$. For the insulating state, the Fermi energy lies inside this gap and the expression for the Hall conductivity reduces to the following

$$\sigma_{xy} = -\frac{e^2}{2\hbar} \int_{\text{BZ}} \frac{d^2k}{(2\pi)^2}\, \epsilon_{abc} \frac{\partial \hat{h}_a(\boldsymbol{k})}{\partial k_x} \frac{\partial \hat{h}_b(\boldsymbol{k})}{\partial k_y} \hat{h}_c(\boldsymbol{k}). \tag{336}$$

In our discussion of quantum antiferromagnets in one space dimensions in Section "Nonlinear sigma models and antiferromagnetic quantum spin chains," we found that their effective low-energy action contained a crucial topological term proportional to the integer-valued topological invariant Q (the winding number) of Eq. (103) which classifies the smooths maps (homotopies) of the 2D surface (say a sphere S^2) onto the target space of a three-component unit vector field which also a sphere S^2. These equivalence classes are represented by the notation $\Pi_2(S^2) \simeq \mathbb{Z}$. In the case at hand, the unit vector $\hat{\boldsymbol{h}}(\boldsymbol{k})$ are points on a 2-sphere. Hence, $\hat{\boldsymbol{h}}(\boldsymbol{k})$ is a map of the first Brillouin zone (which is a 2-torus) to the sphere S^2. Such maps are also classified by the same integer-valued topological invariant defined in Eq. (103). These results imply that the Hall conductivity of the two-band system is

$$\sigma_{xy} = \frac{e^2}{2\pi\hbar} Q[\hat{\boldsymbol{h}}]. \tag{337}$$

In other words, we have shown that the Hall conductivity is given in terms of a topological invariant of the occupied band (in units of e^2/h), the winding number Q. In the two-band model the topological invariant Q plays the same role as the Chern number does in the work of TKNN (Thouless et al., 1982; Kohmoto, 1985). When $Q \neq 0$, the two-band system exhibits the quantized anomalous quantum Hall effect. This is a property of the entire band of occupied states, and not just a consequence of the low energy approximation. This result implies that the low energy approximation captures all of the topology of the band. It also implies that in these lattice models, the Berry curvature is highly concentrated near the points in momentum space where the two bands are close in energy.

We will now consider the problem of the quantum phase transition between the trivial and the Chern insulator. To address this problem, we will tune the parameters of the lattice model discussed in Section "Dirac fermions and topological insulators," the phase ϕ and the ratio of hopping amplitudes t_2/t_1, to the point at which the mass of one of the two species of Dirac fermions, say the fermion ψ_1, is zero, $m_1 = 0$, while keeping the fermion ψ_2 massive, $m_2 \neq 0$. In the low-energy regime we have a massless fermion and a massive fermion. This point in parameter space is a quantum phase transition between a trivial insulator and a Chern insulator. In the low-energy regime, the fermion ψ_1 is massless. A massless fermion is a scale-invariant system in the sense that the correlators of all its observables exhibit power law behavior (free field in this case).

We will now discuss briefly the electromagnetic response of this system at the quantum phase transition where one fermion becomes massless. In particular, it is natural to ask if the coefficient of the parity-odd (Chern–Simons) term nonvanishing *at the quantum phase transition*. To answer this question, we will look at the behavior of the parity-even kernel $\Pi_0(p^2)$ and the parity-odd kernel $\Pi_A(p^2)$ in the massless limit for the light fermion, $m_1 \to 0$. We find that the *total* contribution of both the light fermion and the heavy fermion to the polarization kernels is (assuming $m_2/m_1 \to \infty$)

$$\lim_{m_1 \to 0} \Pi_0(p^2) = \frac{i}{16\sqrt{p^2}}, \qquad \lim_{|m_2| \to \infty} \Pi_A(p^2) = -\frac{1}{4\pi} \text{sgn}(m_2). \tag{338}$$

The important conclusion is that at this quantum critical point, the parity-even kernel $\Pi_0(p^2)$ is *nonlocal* and that the heavy regulator fermion (the "doubler") yields the leading finite nonvanishing and local contribution to the parity-odd kernel $\Pi_A(p^2)$.

We can now use these results to compute the conductivity *tensor* σ_{ij} at the quantum critical point where $m_1 \to 0$. Since the system is spatially isotropic, the conductivity tensor has the form

$$\sigma_{ij} = \begin{pmatrix} \sigma_{xx} & \sigma_{xy} \\ -\sigma_{xy} & \sigma_{xx} \end{pmatrix} \tag{339}$$

where we used that $\sigma_{yy} = \sigma_{xx}$ since the system is isotropic. The *longitudinal* conductivity σ_{xx} and the Hall conductivity σ_{xy} are

$$\sigma_{xx} = \frac{\pi}{8}\frac{e^2}{h}, \qquad \sigma_{xy} = \pm\frac{1}{2}\frac{e^2}{h}. \tag{340}$$

In other words, *at* the quantum critical point the system has a finite (and universal) longitudinal conductivity. This result may seem surprising as there is no disorder in this model. A finite universal longitudinal conductivity is a standard occurrence in 2D systems at a quantum critical point. For example, at the superconductor–insulator transition, the conductivity is (conjectured to be) $\sigma_{xx} = e^2/2h$ (with $\sigma_{xy} = 0$). In addition, it also has finite and universal Hall conductivity. The Hall conductivity at the quantum critical point is due to the heavy fermionic "doubler" and is equal to 1/2 (in units of e^2/h). So, the quantum critical point is not time-reversal invariant since this symmetry is broken at the UV (lattice).

We can examine the massless theory using a more formal approach (Witten, 2016; Seiberg et al., 2016). In a gauge-invariant regularization of the massless theory the partition function of a Dirac fermion coupled to a background (unquantized) $U(1)$ gauge field, the partition function is not time-reversal invariant. It is given by

$$Z[A_\mu] = \int \mathcal{D}\bar{\psi}\mathcal{D}\psi\ \exp\left(i\int d^3x\ \bar{\psi} i\not{D}[A_\mu]\psi\right) = \det(i\not{D}[A_\mu]) = \left|\det(i\not{D}[A_\mu])\right|\ \exp\left(\pm i\frac{\pi}{2}\eta[A_\mu]\right) \tag{341}$$

where the sign depends on how time-reversal invariance is broken by the choice of regularization. The quantity $\eta[A_\mu]$ that appears in the phase factor is the Atiyah-Patodi-Singer η-invariant (Atiyah et al., 1975) which we already encountered in the discussion of the fractionally charged solitons in Section "Fractionally charged solitons." With some caveats (Witten, 2016; Seiberg et al., 2016), the phase factor of the partition function of Eq. (341) is commonly written in the form of a 1/2-quantized Chern–Simons term

$$\frac{\pi}{2}\eta[A_\mu] \equiv \pm\frac{1}{2}\int d^3x\ \frac{1}{4\pi}\epsilon_{\mu\nu\lambda}A^\mu\partial^\nu A^\lambda \tag{342}$$

often denoted as a $U(1)_{1/2}$ Chern–Simons term. This term plays the same role as the contribution of the heavy fermion doubler in the lattice theory.

However, we can also wonder if there is a way to have a time-reversal invariant theory of a *single* massless Dirac fermion, $m \to 0$. This case cannot be realized in a y 2D lattice model but, as will see, it can be realized on the surface states of a 3D time-reversal invariant $\mathbb{Z}_2$ topological insulator, which we will discuss in Section "Topological insulators."

Three-dimensional $\mathbb{Z}_2$ topological insulators

The classification of topological insulators in terms of a Chern number is only possible in even space dimensions in systems with broken time reversal symmetry: in $d = 2$, the Berry connection is Abelian and the topological invariant is the first Chern number while in $d = 4$, the Berry connection in a non-Abelian $SU(2)$ gauge field and the topological invariant is the second Chern number (Qi et al., 2008), etc. We will now discuss the time-reversal invariant topological insulators (Fu and Kane, 2007; Moore and Balents, 2007; Qi et al., 2008) and, in particular, those that are invariant under inversion symmetry. Such states exist in both two and space dimensional insulator with strong spin-orbit coupling.

$\mathbb{Z}_2$ Topological invariants

Let $\{|u_n(\boldsymbol{k})\rangle\}$ be the Bloch states. We will represent time reversal by the antiunitary operator Θ that acts on the single particle (Bloch) states by complex conjugating the state and reversing the spin. For spin-1/2 fermions $\Theta = \exp(i\pi\sigma_2)\mathcal{K}$, where $\mathcal{K}$ is the complex conjugation operator. In this case, $\Theta^2 = -\mathbf{1}$. Let us assume that we have two occupied Bloch bands for each point $\boldsymbol{k}$ of the Brillouin zone. In this case, the states form a rank-2 vector bundle over the torus of the Brillouin zone. In time-reversal invariant systems, the antiunitary time reversal transformation $\mathcal{T}$ induces an involution in the Brillouin zone that identifies the points $\boldsymbol{k}$ and $-\boldsymbol{k}$. Time reversal acts on the one-particle (Bloch) Hamiltonian as $\Theta H(\boldsymbol{k})\Theta^{-1} = H(-\boldsymbol{k})$. The states $|u_n(\pm\boldsymbol{k})\rangle$ are related by time reversal as $|u_n(-\boldsymbol{k})\rangle = \Theta|u_n(\boldsymbol{k})\rangle$, which implies that the bundle is real. The condition $\Theta^2 = -\mathbf{1}$ implies that the bundle is real. In algebraic topology, these bundles are classified by an integer (here the number of occupied bands) and a $\mathbb{Z}_2$ index that will allow us to classify these states.

In a periodic lattice, there exists a set of points $\boldsymbol{Q}_i$ of the Brillouin zone with the property that they differ by their images under the action of time reversal by a reciprocal lattice vector, $-\boldsymbol{Q}_i = \boldsymbol{Q}_i + \boldsymbol{G}$. In $d = 2$, there are four such points and $d = 3$, there are eight points, and are given by $\boldsymbol{Q}_i = \frac{1}{2}\sum_j n_j \boldsymbol{b}_j$, where $n_j = 0, 1$, $j = 1, 2$ in $d = 2$ and $j = 1, 2, 3$ in $d = 3$. Here, $\boldsymbol{b}_j$ are the primitive lattice vectors. Kane and Mele (2005) defined the $2N \times 2N$ antisymmetric matrix $w_{m,n}(\boldsymbol{k}) = \langle u_m(-k)|\Theta|u_n(\boldsymbol{k})\rangle$. They showed that at each time-reversal invariant point $\boldsymbol{Q}_i$, one can define an index δ_i

$$\delta_i = \frac{\sqrt{\det[w(\boldsymbol{Q}_i)]}}{\mathrm{Pf}[w(\boldsymbol{Q}_i)]} = \pm 1 \tag{343}$$

where $\det[w]$ and $\mathrm{Pf}[w]$ are, respectively, the determinant and the Pfaffian of the matrix w, and $\det[w] = \mathrm{Pf}[w]^2$. The sign of the quantities δ_i can be made unambiguous by requiring that the Bloch states be continuous. In addition, the quantities δ_i are gauge-dependent. However the products

$$(-1)^{\nu} = \prod_{i=1}^{4} \delta_i \tag{344}$$

in $d = 2$, and

$$(-1)^{\nu_0} = \prod_{i=1}^{8} \delta_i, \qquad (-1)^{\nu_k} = \prod_{n_k=1,\, n_{j\neq k}=0,1} \delta_i(n_1, n_2, n_3) \tag{345}$$

are gauge and are also topological invariant. The $\mathbb{Z}_2$-valued indices ν and ν_0 are robust to disorder and are called strong topological indices. Furthermore, Fu and Kane showed that if $\xi_n(\boldsymbol{Q}_i) = \pm 1$ are the parity eigenvalues of the occupied parity eigenstates, the quantities δ_i are given by $\delta_i = \prod_{m=1}^{N} \xi_{2m}(\boldsymbol{Q}_i)$. In $d = 3$, the index ν_0 does not rely on the existence of inversion symmetry.

In the case of a two-band model in $d = 2$ and in $d = 3$, the states are four-component spinors reflecting the two bands and the two spin components. In the context of these systems with strong spin-orbit coupling spin is actually the z-component of the atomic total angular momentum $\boldsymbol{J}$ of the electrons with energies close to the Fermi energy. In these systems, the one-particle Hamiltonian $H(\boldsymbol{k})$ is a 4×4 Hermitian matrix, which can be expanded as a linear combination of Dirac matrices. A simple and very useful model of systems of this type is the Wilson fermion model (with continuous time) (Wilson, 1974; Bernevig et al., 2006; Qi et al., 2008) of a square (cubic) lattice with 4 states per site (parity and spin) whose Hamiltonian in three dimensions is

$$H(\boldsymbol{k}) = \sin \boldsymbol{k} \cdot \boldsymbol{\alpha} + M(\boldsymbol{k})\, \beta \tag{346}$$

where $\boldsymbol{\alpha} = \gamma_0 \boldsymbol{\gamma}$ and $\beta = \gamma_0$ are the conventional 4×4 Dirac matrices. The γ matrices satisfy the Clifford algebra $\{\gamma_\mu, \gamma_\nu\} = 2g_{\mu\nu}\mathbf{1}$, where $g_{\mu\nu} = \mathrm{diag}(1, -1, -1, -1)$ is the metric tensor of four-dimensional Minkowski space time. An additional γ matrix of interest is $\gamma_5 = i\gamma_0\gamma_1\gamma_2\gamma_3$.

The (Wilson) mass term $M(\boldsymbol{k})$ in two dimensions is $M(\boldsymbol{k}) = M + \cos k_1 + \cos p_2 - 2$, and in three dimensions is $M(\boldsymbol{k}) = M + \cos k_1 + \cos k_2 + \cos k_3 - 3$. In Eq. (346), we see that, consistent with the requirements of the Nielsen–Ninomiya theorem (Nielsen and Ninomiya, 1981a,b), in addition to a possible low energy Dirac fermion (if M is small), there are three more massive Dirac fermions (in $d = 2$) and seven other Dirac fermions in $d = 3$ so that the total number of Dirac fermions is always even, 8 in this case. With Wilson's mass term, the additional Dirac fermions (the "doublers") are always heavy even if the Dirac fermion near the Γ point $\boldsymbol{Q} = 0$ is light.

In the Dirac basis time reversal is the operation $\Theta = (i\sigma_2 \otimes I)\mathcal{K}$, where $\mathcal{K}$ is complex conjugation and parity is $P = \beta$. The matrices $\boldsymbol{\alpha}$ and β commute with $P\Theta$. At the time-reversal and parity invariant points of the Brillouin zone $\{\boldsymbol{Q}_i\}$, the Hamiltonian only depends on the matrix β, $H(\boldsymbol{Q}_i) = M(\boldsymbol{Q}_i)\beta$. Since the parities of the spinors are the eigenvalues of the matrix β, we conclude that in the two-band models, the quantities δ_i are simply equal to the sign of the mass of the fermions defined at the time-reversal-invariant points $\boldsymbol{Q}_i$ of the BZ (Fu and Kane, 2007; Qi et al., 2008), $\delta_i = \delta(\boldsymbol{Q}_i) = -\mathrm{sgn}\, M(\boldsymbol{Q}_i)$. Using this result, it follows that in two dimensions the system is a $\mathbb{Z}_2$ topological insulator with index $\nu = 1 \pmod 2$ if $0 < M < 4$ while it is trivial for other values of M, that is, $\nu = 0$ mod 2. Similarly, in three dimensions, a $\mathbb{Z}_2$ (strong) topological insulator exists only if $0 < M < 2$ (in the other regimes, this system is in a weak topological insulator state or in a trivial one).

We conclude that both in two and three dimensions, the low energy theory of the $\mathbb{Z}_2$ topological insulators consists of a single Dirac fermion whose mass is small compared to that of the fermion doublers and has the opposite sign. In both cases, there is a quantum phase transition between a trivial insulator and the time-reversal invariant topological insulator at the point where the mass of the light fermion vanishes.

The axial anomaly and the effective action

We will now look at the electromagnetic response of a $\mathbb{Z}_2$ topological insulator in 3+1 dimensions. This problem can be addressed more easily using the continuum field theory description, which is valid in the regime where the mass M is weak. In this regime, one species of Dirac fermions is light (i.e., its mass is small) while the Dirac doublers remain heavy. Much as we did in our discussion of the Chern insulators and the *parity anomaly* in Section "The parity anomaly," we will keep in mind that the fermion doublers play the role of heavy regulators, such as in the Pauli–Villars scheme, in Quantum Field Theory. Here too, we will see that a field-theoretic anomaly, known as the *axial anomaly*, plays a central role in the physics. The analysis is very similar to what we did with the *chiral anomaly* in 1+1 dimensions in Section "The chiral anomaly."

Let us begin with a theory of a single massive Dirac fermion in 3+1 dimensions. The Lagrangian of the free massive Dirac theory is

$$\mathcal{L} = \bar{\psi}(\, i\not{\partial} - m)\psi. \tag{347}$$

The equation of motion of the spinor field operator $\psi(x)$ (I omit the spinor indices here) is the Dirac equation

$$(i\not{\partial} - m)\psi = 0. \tag{348}$$

The Dirac Lagrangian has a global gauge symmetry $\psi \to e^{i\theta}\psi$, which requires that the Dirac current $j_\mu = \bar{\psi}\gamma_\mu\psi$ is locally conserved, $\partial_\mu j^\mu = 0$. The *massless* Dirac theory can be decomposed into a theory of two Weyl bi-spinor fields that obey separate Dirac Lagrangians. Furthermore, the massless theory has the additional global symmetry under the transformation $\psi \to e^{i\theta\gamma_5}\psi$ and the additional formally locally conserved *axial* current $j^5_\mu = i\bar{\psi}\gamma_\mu\gamma^5\psi$. However the conservation law of the axial current is violated in the *massive* Dirac theory

$$\partial^\mu j^5_\mu = -2mi\bar{\psi}\gamma^5\psi \tag{349}$$

since the two Weyl bi-spinors transmute into each other in the presence of a mass term. This is the origin of the phenomenon of neutrino oscillations. In the condensed matter physics, context there is a similar phenomenon in systems of Weyl semimetals which have crossings between the valence and conducting bands at two locations $\pm\boldsymbol{Q}$ of the BZ, with each crossing associated with each Weyl bi-spinor. A charge density wave with ordering wavevector $2\boldsymbol{Q}$ mixes the two Weyl fermions that become gapped, becoming effectively a single massive Dirac fermion (Gooth et al., 2019). This state is often called an "axionic"-charge-density-wave.

We will now show that the axial symmetry has an anomaly and cannot be gauged. Thus, we will consider the problem of a Dirac theory coupled to a background $U(1)$ gauge field A_μ and reexamine the putative conservation of the axial current j^5_μ. This question can be addressed in different ways. Quite early on Adler (1969), and Bell and Jackiw (1969) examined this problem by computing a Dirac fermion triangle diagram for the process of a neutral pion decaying into two photons, $\pi^0 \to 2\gamma$. In particle physics, the pion is the Goldstone boson of the spontaneously broken chiral symmetry. The analog of this problem in condensed matter physics is the phase mode of an incommensurate charge density wave. The relativistic Lagrangian for this problem is a theory of Dirac fermions coupled to a complex scalar field $\phi = \phi_1 + i\phi_2$ through two Yukawa couplings

$$\mathcal{L} = \bar{\psi}i\not{D}\psi + g\phi_1\bar{\psi}\psi + ig\phi_2\bar{\psi}\gamma^5\psi - V(\phi_1, \phi_2) = \bar{\psi}i\not{D}\psi + g|\phi|\bar{\psi}e^{i\gamma_5\theta}\psi - V(|\phi|^2) \tag{350}$$

where $|\phi|^2 = \phi_1^2 + \phi_2^2$, $\tan\theta = \phi_2/\phi_1$, and $D_\mu = \partial_\mu + ieA_\mu$ is the covariant derivative. Here we are regarding the gauge field A_μ as a background probe field.

The triangle Feynman diagram computes the polarization tensor for the electromagnetic field A_μ with an insertion of the coupling to the complex scalar field in an otherwise massless theory. Assuming a gauge-invariant regularization of the diagram, this computation finds that the axial current j^5_μ is anomalous and is not conserved even in the massless theory (Adler, 1969; Bell and Jackiw, 1969)

$$\partial^\mu j^5_\mu = -\frac{e^2}{16\pi^2}F^{\mu\nu}F^*_{\mu\nu} \tag{351}$$

where $F^*_{\mu\nu} = \frac{1}{2}\epsilon_{\mu\nu\lambda\rho}F^{\lambda\rho}$ is the dual of the electromagnetic field tensor. This is the *axial anomaly*.

To see how the axial anomaly arises, we will follow the physically transparent approach of Nielsen and Ninomiya (1983), which we also employed in Section "The chiral anomaly" in 1+1 dimensions. We will consider a theory of free massless dirac fermions coupled to a background electromagnetic field. Since the theory is massless, the Dirac equation decouples into an equation to the right-handed Weyl fermion ψ_R (with positive chirality $\gamma_5\psi_R = +\psi_R$) and a left-handed Weyl fermion ψ_L (with negative chirality, $\gamma_5\psi_L = -\psi_L$). In the gauge $A_0 = 0$, the Dirac equations become

$$[i\partial_0 - (-i\partial - e\boldsymbol{A})\cdot\boldsymbol{\sigma}]\psi_R = 0, \qquad [i\partial_0 - (i\partial - e\boldsymbol{A})\cdot\boldsymbol{\sigma}]\psi_L = 0 \tag{352}$$

Let us now consider looking at the solutions of the Weyl equation for right-handed fermions ψ_R, Eq. (352). The left-handed fermions ψ_L are analyzed similarly. Wd will consider a gauge field $A_1 = 0$ and $A_2 = Bx_1$ representing a uniform static magnetic field of strength B pointing along the x_3 direction. In this gauge, the eigenstates are plane waves along the directions x_2 and x_3 and harmonic oscillator states along the direction x_1. The eigenvalue spectrum consists of Landau levels with energies

$$E(n, p_3, \sigma_3) = \pm\left[2eB\left(n + \frac{1}{2}\right) + p_3^2 + eB\sigma_3\right]^{1/2} \tag{353}$$

for $n = 0, 1, 2, \ldots$, except for the *zero mode* with $n = 0$ and $\sigma_3 = -1$, for which

$$E(n = 0, p_3, \sigma_3 = -1) = \pm p_3 \tag{354}$$

where the + sign holds for ψ_R and the − sign for ψ_L. Just as in the case of nonrelativistic fermions, the relativistic Landau levels are degenerate. We will consider a system of Dirac fermions at charge neutrality and, hence, $E_F = 0$. The positive and negative energy states are charge conjugate of each other and the negative energy states are filled. For right-handed fermions, the zero mode states with $p_3 < 0$ are filled while for right-handed states the zero modes with $p_3 > 0$ are filled. The density of states of the zero modes is $LeB/(4\pi^2)$ (where L is the linear size of the system).

Let us consider now turning on an external electric field E *parallel* to the magnetic field B. Just as we saw in 1+1 dimensions in Section "The chiral anomaly," the electric field leads to pair creation by shifting the Fermi momentum to p_F for the zero modes. There is no particle creation for the states with $n \neq 0$ and they do not contribute to the anomaly. The rate of creation of right-handed fermions, N_R is

$$\frac{dN_R}{dx_0} = \frac{1}{L}\frac{LeB}{4\pi^2}\frac{p_F}{dx_0} = \frac{e^2}{4\pi^2}EB. \tag{355}$$

The annihilation rate of left-handed particles is

$$\frac{dN_L}{dx_0} = -\frac{1}{L}\frac{LeB}{4\pi^2}\frac{p_F}{dx_0} = -\frac{e^2}{4\pi^2}EB \tag{356}$$

and the creation rate of left-handed antiparticles is

$$\frac{d\bar{N}_L}{dx_0} = \frac{1}{L}\frac{LeB}{4\pi^2}\frac{p_F}{dx_0} = \frac{e^2}{4\pi^2}EB. \tag{357}$$

The axial anomaly is the total rate of creation of right-handed particles and of left-handed antiparticles:

$$\frac{dQ_5}{dx_0} = \frac{dN_R}{dx_0} + \frac{d\bar{N}_L}{dx_0} = \frac{e^2}{2\pi^2}EB \tag{358}$$

which agrees with the expression of Eq. (351).

We now turn to the $\mathbb{Z}_2$ topological insulator. As we saw, this is a system with two species of (4 component) Dirac spinors. In the topological phase, the sign of the Dirac mass term one of the Dirac fermions (the one near the Γ point in the lattice model) is opposite (negative) to the sign of the mass term of the of the other Dirac fermion (the fermion doubler). Explicit calculations (Qi et al., 2008; Essin et al., 2009; Hosur et al., 2010) on the lattice model obtain the result that the effective low-energy action for the electromagnetic gauge field A_μ in the topological phase is

$$S_{\text{eff}}[A_\mu] = \int d^4x \left[-\frac{1}{4e^2} F_{\mu\nu}F^{\mu\nu} + \frac{\theta}{32\pi^2} e^2 \epsilon_{\mu\nu\lambda\rho} F^{\mu\nu} F^{\lambda\rho} \right] + \cdots \tag{359}$$

In a time-reversal invariant system, the allowed values of the θ angle of Eq. (359) are restricted to be $\theta = n\pi$, with $n \in \mathbb{Z}$. The case $\theta = 0 \pmod{2\pi}$ represents a trivial insulator, whereas $\theta = \pi \pmod{2\pi}$ holds for a $\mathbb{Z}_2$ time-reversal invariant topological insulator.

The second term in the effective action of the electromagnetic gauge field of Eq. (359), known as the θ term, has been extensively discussed in the high-energy physics literature (Fujikawa, 1979; Wilczek, 1987; Peskin and Schroeder, 1995). The derivation of this term is subtle. As it stands, unless θ is varying in space-time (in which case this is known a the axion field), this term is a total derivative. In non-Abelian Yang–Mills gauge theories, this term is proportional to a topological invariant known as the Pontryagin index which counts the instanton number of the gauge field configurations (Callan et al., 1976; Coleman, 1985). In the context of the Lagrangian of Eq. (350), this term is induced by the coupling of the Dirac fermion to the Yukawa coupling of the complex scalar field ϕ to the Dirac and γ_5 mass terms. In this case, the lowest order contribution is given by the triangle diagram. The fact that this term is exact at lowest order reflects the fact that the axial anomaly is in fact a nonperturbative effect, which is the same in both the weak coupling and the strong coupling regimes ('t Hooft, 1976b).

In the phase where the potential $V(|\phi|^2)$ in the Lagrangian of Eq. (171) has a minimum at $|\phi_0| \exp(i\theta)$, the chiral symmetry is spontaneously broken and the phase field $\theta(x)$ is the Goldstone boson of the spontaneously broken chiral symmetry. In this phase, the Dirac fermions become massive through the Yukawa couplings to the complex scalar field, and the phase of the field ϕ enters in the effective action as an axion field which couples to the gauge field A_μ through the θ term of the effective action. We should note that in a recently studied axionic CDW state of a Weyl semimetal (Gooth et al., 2019), the phase of the CDW plays the role of the axion field.

Theta terms, and domain walls: Anomaly and the Callan–Harvey effect

We will now discuss some remarkable behaviors of three-dimensional $\mathbb{Z}_2$ topological insulators. We will begin with the electromagnetic response encoded in the effective action of Eq. (359). We will assume that the θ angle is effectively a slowly varying Goldstone mode of the spontaneously broken $U(1)$ chiral symmetry (i.e., the axion field) present in the Lagrangian of Eq. (350). If the field θ is constant, the θ term will be a total derivative and it will not contribute to the local equations of motion. We will see below that this term plays a key role in the physics of a domain wall, which we will regard as the interface of a $\mathbb{Z}_2$ topological insulator and a trivial insulator. In the general case in which θ varies slowly (as Goldstone modes do), its presence leads to interesting modification of Maxwell's equations, known as axion electrodynamics (Wilczek, 1987):

$$\begin{aligned} \nabla \cdot \boldsymbol{E} &= \tilde{\rho} - e^2 \nabla\theta \cdot \boldsymbol{B}, & \nabla \times \boldsymbol{E} &= -\partial_t \boldsymbol{B} \\ \nabla \times \boldsymbol{B} &= \partial_t \boldsymbol{E} + \tilde{\boldsymbol{j}} + e^2(\partial_t\theta + \nabla\theta \times \boldsymbol{E}), & \nabla \cdot \boldsymbol{B} &= 0 \end{aligned} \tag{360}$$

where $\tilde{\boldsymbol{\rho}}$ and $\tilde{\boldsymbol{j}}$ are external probe electric charge and current densities. The equations of axion electrodynamics have many remarkable properties. Here we will focus on effects: the topological magnetoelectric effect (Qi et al., 2008) and the Witten effect (Witten, 1979).

Let us consider a $\mathbb{Z}_2$ topological insulator with a flat open boundary (the $x_1 - x_2$ plane) perpendicular to the direction x_3. We will assume that the topological insulator lies at $x_3 < 0$. This means that for $x_3 < 0$, and far from the surface, $\theta(x_3) \to \pi$, while in the trivial vacuum, and also far from the surface, $\theta(x_3) \to 0$. We will assume that the change of θ from 0 to π occurs on a short distance ξ. We will call this configuration an axion domain wall. In the region where $\theta(x_3)$ is changing, $|x_3| \lesssim \xi$, an applied uniform magnetic field $\boldsymbol{B}$ induces a uniform electric field $\boldsymbol{E}$ parallel to $\boldsymbol{B}$ whose magnitude is proportional to the change in θ. This is the topological magnetoelectric effect (Qi et al., 2008).

A similar striking effect is obtained by considering the case of a magnetic monopole of magnetic charge $2\pi/e$ (as required by Dirac quantization) inside a sphere of the trivial region of radius R, with $\theta = 0$, surrounded by a region with $\theta \neq 0$. The two regions are separated by a thin (axion) wall in which θ changes for 0 to π in a narrow shell of thickness $\xi \ll R$. The equations of axion electrodynamics imply that the magnetic monopole induces an electric charge Q_e on the surface of the sphere

$$Q_e = e\frac{\Delta\theta}{2\pi}. \tag{361}$$

Thus, a magnetic monopole acquires an electric charge and becomes a *dyon*. This is the Witten effect (Witten, 1979). In the particular case of a $\mathbb{Z}_2$ topological insulator, time-reversal invariance requires that $\Delta\theta = \pi$, which implies that a monopole with unit magnetic charge has an electric charge $e/2$. A similar argument implies that an external magnetic field perpendicular to the open surface of the $\mathbb{Z}_2$ topological insulator (which is essentially an axion domain wall) induces an *electric charge polarization* on the surface proportional to the total magnetic flux, which is another manifestation of the topological magnetoelectric effect.

The reader should readily recognize that the result of Eq. (361) for the electric charge induced by the magnetic monopole is the same as the Goldstone–Wilczek equation for the fractional charge for a one-dimensional soliton of Eq. (215). We will now see that this is not just an analogy. We will follow here the general approach of Callan and Harvey (1985) who extended the earlier work of Goldstone and Wilczek (1981). Let us consider the bulk of a $\mathbb{Z}_2$ topological insulator and assume that $\theta(x)$ is slowly varying. We can use the triangle diagram calculation to find that an electromagnetic gauge field A_μ induces a current $\langle J_\mu(x)$ given by

$$\langle J_\mu(x)\rangle = -i\frac{e}{16\pi^2}\epsilon_{\mu\nu\lambda\rho}\frac{\phi^*(x)\partial^\nu\phi(x) - \phi(x)\partial^\nu\phi^*(x)}{|\phi(x)|^2}F^{\lambda\rho}(x) = \frac{e}{8\pi^2}\epsilon_{\mu\nu\lambda\rho}\partial^\nu\theta(x)F^{\lambda\rho}(x) \tag{362}$$

This result implies that, in the case of a domain wall in the $x_1 - x_2$ plane, a magnetic field perpendicular to the wall induces a current toward the wall and, hence, a charge accumulation on the wall. Where does this charge come from? To understand this problem, we will consider a $\mathbb{Z}_2$ topological insulator occupying a slab of macroscopic size L between a wall at $x_3 = 0$ and a far way "anti-wall" at $x_3 = L$. In this configuration, a magnetic field normal to the wall(s) induces a transfer of charge from one wall to the other. Similarly, an electric field *parallel* to the wall induces a current also parallel to the wall and *perpendicular* to the electric field, that is, a Hall current.

In 1+1 dimensions, we saw that soliton configurations acquire a fractional charge associated to states bound to the soliton (which are zero modes when $\Delta\theta = \pi$). We will see that the surfaces of the 3D $\mathbb{Z}_2$ topological insulators also have zero modes which are Weyl fermions propagating on the wall. To see how this works, we will consider a 3+1 dimensional Dirac fermion with a Dirac mass that changes sign at $x_3 = 0$. The Lagrangian now ill be

$$\mathcal{L} = \bar{\psi}i\partial\!\!\!/\psi + g\phi(x)\bar{\psi}\psi \tag{363}$$

where $\phi(x)$ is now a *real* scalar field that has the asymptotic behaviors $\phi(x_3) = \phi_0 f(x_3)$ such that $\lim_{x_3\to\pm\infty} f(x_3) = \pm 1$. We will assume that $f(x_3)$ is a monotonous function of x_3, but its actual dependence on x_3 is immaterial aside from the requirement that it should change sign at some point which we will take to be $x_3 = 0$. This is a special case of Eq. (350) with $\phi_1 = \phi$ and $\phi_2 = 0$. We will now recognize that this is just a Dirac fermion with a position-dependent Dirac mass $m(x_3) = g\phi(x_3)$. The one-particle Dirac Hamiltonian for this system is

$$H = -i\boldsymbol{\alpha}\cdot\nabla + m(x_3)\beta \tag{364}$$

where $\boldsymbol{\alpha}$ and β are the four 4×4 Dirac matrices. By symmetry, this Hamiltonian can be split into two Hamiltonians, $H = H_{\text{wall}} + H_\perp$,

$$H_{\text{wall}} = -i\alpha_1\partial_1 - i\alpha_2\partial_2, \qquad H_\perp = -i\alpha_3\partial_3 + m(x_3)\beta. \tag{365}$$

Let the spinor $\psi_\pm$ be an eigenstate of the anti-Hermitian Dirac matrix $\gamma_3 = \beta\alpha_3$ with eigenvalues $\pm\, i$, respectively

$$\gamma_3\psi_\pm = \pm i\psi_\pm. \tag{366}$$

We seek a spinor solution $\psi_\pm$ of the Dirac equation (Eq. 364) such that $H_\perp\psi_\pm = 0$

$$\pm\,\partial_3\psi_\pm + m(x_3)\psi_\pm = 0 \tag{367}$$

which is also a solution of

$$(i\gamma_0 - i\gamma_1\partial_1 - i\gamma_2\partial_2)\psi_\pm = 0. \tag{368}$$

In other words, it is a solution of the massless Dirac equation in 2+1 dimensions. The requirement that $\psi_\pm$ is an eigenstate of γ_3 reduces the number of spinor components from four to two. The full solution has the form

$$\psi_\pm = \eta_\pm(x_0, x_1, x_2) F_\pm(x_3), \qquad \pm\,\partial_3 F_\pm(x_3) = -m(x_3) F_\pm(x_3). \tag{369}$$

For a domain wall with $\lim_{x_3 \to \infty} m(x_3) = +m$, the normalizable solution of $F_+(x_3)$ is

$$F_+(x_3) = F(0)\ \exp\left(-\int_0^\infty dx_3'\ m(x_3')\right) \tag{370}$$

where $F(0)$ is a constant. For the antidomain wall, for which $\lim_{x_3 \to \infty} m(x_3) = -m$, the normalizable solution is $F_-(x_3)$.

We conclude that there is a 2+1-dimensional massless Dirac theory that describes the quantum states bound to the wall, which propagate along the wall. These states are the generalization of the fractionally charged midgap states of solitons in one dimension discussed in Section "Fractionally charged solitons." The energy of these states is $E(\boldsymbol{p}) = \pm|\boldsymbol{p}|$, where $\boldsymbol{p} = (p_1, p_2)$ (where I set the Fermi velocity to unity). Experimental evidence for 2+1 dimensional massless Dirac fermions on the surface of the 3D $\mathbb{Z}_2$ topological insulator Bi_2Te_3 has been found in spin-polarized angle-resolved photoemission studies of the surface states, which showed that they have a linear energy–momentum relation (expected of massless Dirac fermions) as well as the spin-momentum locking characteristic of these spinor states (Hsieh et al., 2009).

Having succeeded in showing that the surface of the $\mathbb{Z}_2$ time-reversal invariant 3D topological insulator has a two-component massless Dirac spinor, we now want to determine its electromagnetic response. In fact we have already discussed this problem in our discussion of the parity anomaly in Section "The parity anomaly" where we showed that the effective action for the electromagnetic field A_μ of Eq. (342) of a single massless Dirac bi-spinor is a Chern–Simons term with a prefactor, which is 1/2 of the allowed value. In that purely 2+1-dimensional context we saw that time-reversal invariance is actually broken. However, the 3D problem is time-reversal invariant so there must be a contribution that cancels this time-reversal anomaly. The answer is that the requisite cancellation is supplied by the bulk.

To see how this can happen, we return to the bulk effective action of the 3D topological insulator of Eq. (359) where we observed that the θ term is a total derivative. Suppose that the system has a boundary at $x_3 = 0$ and that the topological insulator exists for $x_3 > 0$ (where the fermion mass is negative, $m < 0$) and trivial for $x_3 < 0$ (where $m > 0$). Only the region with $m < 0$ contributes to the θ term. The region of four-dimensional space time occupied by the topological insulator is $\mathcal{M}$ and in this region the θ term becomes

$$S_\theta[A] = \frac{\theta}{32\pi^2}\int_{\mathcal{M}} d^4x\ \epsilon_{\mu\nu\lambda\rho} F^{\mu\nu} F^{\rho\lambda} = \frac{\theta}{8\pi^2}\int_{\mathcal{M}} d^4x\ \epsilon_{\mu\nu\lambda\rho}\partial^\mu A^\nu \partial^\lambda A^\lambda = \frac{\theta}{8\pi^2}\int_{\partial\mathcal{M}} d^3x\ \epsilon_{\mu\nu\lambda} A^\mu \partial^\nu A^\lambda \tag{371}$$

where $\partial\mathcal{M} \equiv \Sigma \times \mathbb{R}$ is the boundary of the region $\mathcal{M}$, Σ is the surface of the 3D topological insulator, and $\mathbb{R}$ is time.

Thus we see that the θ term of the effective action $S_\theta[A]$ integrates to the boundary where it has the form of a 2+1-dimensional Chern–Simons term. Since for a time-reversal-invariant 3D topological insulator $\theta = \pi$, we see that in this case the boundary Chern–Simons term becomes

$$S_{\theta=\pi}[A] = \frac{1}{8\pi}\int_{\partial\mathcal{M}} d^3x\ \epsilon_{\mu\nu\lambda} A^\mu \partial^\nu A^\lambda \tag{372}$$

with a coefficient which is 1/2 of the allowed value. This bulk contribution cancels the parity anomaly of the boundary state, rendering the full system time-reversal invariant. In other words, in this system, time-reversal symmetry is realized by cancellation of the anomaly between the bulk of the topological insulator and the boundary or, equivalently, by an *inflow* of the parity anomaly between the boundary and the bulk of the system. Another way to phrase this result is the statement that a single Dirac fermion cannot exist on its own in 2+1 dimensions but it can as the boundary state of a 3+1-dimensional system whose anomaly cancels the anomaly of the boundary.

Chern–Simons gauge theory and the fractional quantum Hall effect

We will now turn to the problem of the quantum Hall effects. This is a problem that revealed the existence of profound and far-reaching connections between condensed matter physics, quantum field theory, CFT, and topology. In particular, the *fractional* quantum hall effect is the best studied and best understood topological phase of matter. As such, it has become the conceptual springboard for its manifold generalizations.

The integer (IQHE) and fractional (FQHE) quantum Hall effects are fascinating phenomena observed in fluids of electrons in two dimensions in strong perpendicular magnetic fields. The integer quantum Hall effect was discovered by von Klitzing et al. (1980) in transport measurements of the longitudinal and Hall resistivity of the surface states of metal oxide field-effect transistors (MOSFET) in magnetic field of up to 15 Tesla. The effect that von Klitzing discovered (for which he was awarded the 1985 Nobel Prize in Physics) was that in the high-field regime the measured Hall conductivity showed a series of sharply defined plateaus at which took the values $\sigma_{xy} = ne^2/h$, where n is an integer, and the longitudinal conductivity appeared to vanish $\sigma_{xx} \to 0$ as the temperature was lowered down to $T \simeq 1.5$ K. Remarkably the measured value of the Hall conductivity was obtained with a precision of $\sim 10^{-9}$. To this date, the measurement of the Hall conductivity in the IQHE yields the most precise definition of the fine structure constant.

Subsequent transport experiments in ultra-high-purity GaAs-AlAs heterostructures by Dan Tsui, Horst Störmer, and Art Gossard found that, in addition to the IQHE, two-dimensional electron fluids in high magnetic fields exhibit the *fractional* quantum Hall effect meaning that there are equally sharply defined plateaus of the Hall conductivity at the values $\sigma_{xy} = \frac{p}{q}\frac{e^2}{h}$, where p and q are co-prime integers (Tsui et al., 1982). Much as in the IQHE case, in the FQHE, the longitudinal conductivity vanishes at low temperatures. It is important to note that both in the IQHE and in the FQHE, the observed temperature dependence in the highest purity samples of the longitudinal conductivity is activated, $\sigma_{xx} \sim \exp(-W/T)$. The observed value of the energy scale W is the experimental estimate of an energy gap in the electron fluid in the quantum Hall states.

In addition to MOSFETS and GaAs-AlAs, heterostructures, both the IQHE and the FQHE, have been seen in several other experimental platforms, particularly in graphene and other 2D materials (Du et al., 2009; Zibrov et al., 2017). The explanation of these effects and of a panoply of startling consequences that were uncovered in the course of understanding this phenomenon is the focus of this section.

Landau levels and the integer Hall effect

At some level, the integer quantum Hall effect can be explained by the Landau quantization of the energy levels of a free charged moving in two dimensions in a perpendicular magnetic field (Landau, 1930). The Hamiltonian for a nonrelativistic particle of charge $-e$ and mass M in a perpendicular magnetic field B is

$$H = \frac{1}{2M}\left(-i\hbar\nabla + i\frac{e}{c}\boldsymbol{A}(\boldsymbol{x})\right)^2 \tag{373}$$

for a uniform perpendicular magnetic field $\boldsymbol{B} = B\,\widehat{\boldsymbol{e}_z} = \nabla \times \boldsymbol{A}(\boldsymbol{x})$.

In the circular gauge, the vector potential is $A_i = -\frac{1}{2}B\epsilon_{ij}x_j$. We will assume that the 2D plane has linear size L. The total magnetic flux is $\Phi = BL^2$ and we will assume that there is an integer number N_ϕ of magnetic flux quanta piercing the plane, $\phi = N_\phi\phi_0$, where $\phi_0 = hc/e$ is the flux quantum. In units such that $\hbar = e = c = 1$, the flux quantum is $\phi_0 = 2\pi$ and $\Phi = 2\pi N_\phi$.

In the presence of a magnetic field, the components of the canonical momentum operator $\boldsymbol{p} = -i\hbar\nabla - \frac{e}{c}\boldsymbol{A}$ do not commute with each other

$$[p_i, p_j] - i\frac{e\hbar}{c}B\epsilon_{ij}. \tag{374}$$

This means that translations in two directions do not commute with each other. However, the components of the operator $\boldsymbol{k} = \boldsymbol{p}$ $(-B)$ commute with $\boldsymbol{p}$ (and hence with the one-particle Hamiltonian) but do not commute with each other: the commutator is the same as in Eq. (374). Since $[\boldsymbol{k}, H] = 0$, they act as symmetry generators of the group of *magnetic translations*. For arbitrary displacements $\boldsymbol{a}$ and $\boldsymbol{b}$, the translation operators $t(\boldsymbol{a}) = \exp(i\boldsymbol{a}\cdot\boldsymbol{k}/\hbar)$ (and similarly with $\boldsymbol{b}$) satisfy

$$t(\boldsymbol{a})t(\boldsymbol{b}) = \exp(i\boldsymbol{a}\times\boldsymbol{b}\ \cdot\boldsymbol{e}_z/\ell_0^2)t(\boldsymbol{b})t(\boldsymbol{a}). \tag{375}$$

Magnetic translations only commute with each other is the area subtended by $\boldsymbol{a}$ and $\boldsymbol{b}$ contains an integer number of magnetic flux quanta.

Given the rotational symmetry of the circular gauge, it is natural to work in complex coordinates $z = x_1 + ix_2$. We will also use the notation $\partial_z = (\partial_1 - i\partial_2)/2$ and $\partial_{\bar{z}} = (\partial_1 + i\partial_2)/2$. In this gauge, up to a normalization, the eigenstate wave functions have the form

$$\psi(z,\bar{z}) = f(z,\bar{z})\ \exp\left(-\frac{|z|^2}{4\ell_0^2}\right) \tag{376}$$

where $\ell_0 = \sqrt{\frac{\hbar c}{e|B|}}$ is the magnetic length. In this gauge (and in complex coordinates), the angular momentum operator $L_z = -i\hbar(x_1\partial_2 - x_2\partial_1) = \hbar(z\partial_z - \bar{z}\partial_{\bar{z}})$.

Any analytic function $f(z)$ is an eigenstate with energy $E_0 = \frac{1}{2}\hbar\omega_c$. A complete basis of analytic functions are the monomials $f_n(z) = z^n$ and have energy E_0 and angular momentum $L_z = n\hbar$. This is the lowest Landau level whose wave functions are $\psi_n(z) = z^n\exp(-|z|^2/4\ell_0^2)$. On the other hand, an antianalytic function $f_N = \bar{z}^N$ is an eigenstate of energy $E_N = \hbar\omega_c\left(N + \frac{1}{2}\right)$, where $\omega_c = \frac{e|B|}{Mc}$ is the cyclotron frequency, and angular momentum $L_z = -N\hbar$. States with angular momentum $n\hbar$ have the same energy, and the degeneracy is equal to the number of flux quanta N_ϕ. For the most part, we will be interested in the states in the lowest Landau level.

In the absence of disorder, the Landau levels have an extensive degeneracy equal to the number of flux quantum N_ϕ. If we consider a system of N electrons in a Landau level the natural measure of density is not the areal density $\rho = \frac{N_e}{L^2}$ but the fraction $\nu = \frac{N_e}{N_\phi}$ the states in the Landau level which are occupied by electrons. The many-body state in which all N_ϕ states of the lowest Landau level has filling fraction $\nu = 1$. The wave function for this state is the Slater determinant of the Landau states in the $m = 0$ level. After some simple algebra, the wave function of this state is found to be

$$\Psi_{\nu=1}(z_1,\ \ldots, z_{N_e}) = \prod_{i<j}(z_i - z_j)\ \exp\left(-\sum_{i=1}^{N_e}\frac{|z_i|^2}{4\ell_0^2}\right). \tag{377}$$

This is the ground state of the noninteracting system and it is nondegenerate. It is easy to see that this state has a finite energy gap. Indeed, in the Hilbert space with a fixed number of electrons, the lowest energy excitation is a particle–hole pair in which the particle is in an unoccupied state of the first excited Landau level, with $m = 1$ and energy $E_1 = \frac{3}{2}\hbar\omega_c$ and a hole a single-particle state in the lowest Landau level, with energy $E_0 = \hbar\omega_c$. The excitation energy of the electron–hole pair is just $\hbar\omega_c$, which is finite. However, in the free particle system, this excited state has a huge degeneracy as the particle and the hole can be in any single particle state of the Landau level.

At a very naive level, one can estimate the Hall conductivity for a translationally invariant system filling up n Landau level by the following simple argument. If n Landau levels are filled, the number of electrons $N = nN_\phi$ and the total charge are then $Q = eN = e\, n\, N_\phi = e\, n\, BL^2/\phi_0 = ne^2BL^2/hc$. If a weak and uniform in-plane electric field $\boldsymbol{E}$ is applied in the presence of a perpendicular magnetic field $\boldsymbol{B} = B\, \boldsymbol{e}_z$, then the entire system (its center of mass) moves at the drift velocity $\boldsymbol{v}$ such that $\boldsymbol{v} \times \boldsymbol{B} = -\boldsymbol{E}c$. Thus, there is a Hall current $\boldsymbol{J} = Q\boldsymbol{v}$. The current density is $\boldsymbol{j} = \boldsymbol{J}/L^2 = Q\boldsymbol{v}/L^2$. Hence, $j_i = \frac{Qc}{BL^2}\, \epsilon_{ij}\, E_j$, which implies that the Hall conductivity is $\sigma_{xy} = Qc/BL^2 = ne^2/h$.

While the above argument is formally correct and yields the correct value of the Hall conductivity in this highly idealized setting, at a very basic level, it is faulty. To begin with, it assumes exact translational invariance and, hence, Galilean symmetry, which are not obeyed in any realistic system. The second objection is that, even in this idealized system, as the number of electrons is varied, the chemical potential (and hence the Fermi energy) jumps discontinuously from one Landau level to the next, resulting in a linearly increasing Hall conductivity (as predicted classically) without any of the observed plateaus. Furthermore, this argument does not explain which the Hall conductivity is so precisely quantized whereas, a priori, one would expect that being a transport coefficient, the Hall conductivity would depend on lots of complicated material details. But, it turns out that it does not!

Let us first discuss the observed *universality* of the Hall conductivity, namely its robustness and independence of microscopic details. In a remarkable paper, Niu et al. (1985) showed that, provided the ground state is separated by a finite energy gap from the excited states, the Hall conductivity is actually a topological invariant. The argument has a similarity with what we discussed in the case of the Hall effect on a 2D lattice (in Section "The quantum Hall effect on a lattice") but in this more general system, one considers the full many-body wave function rather than the one-particle states. To show that this is true, they considered a system of N electrons with periodic boundary conditions, that is, on a two-dimensional torus, $T^2 = S_1 \times S_1$, with N_ϕ flux quanta going through the torus. The torus is a rectangle of dimensions L_1 and L_2 with opposite ends identified. This is necessary to allow for a Hall current to be globally allowed. The electromagnetic gauge field for a system on a torus with uniform nonvanishing flux cannot obey periodic boundary conditions but rather across the torus, the gauge fields must differ by (large) gauge transformations

$$A_1(x_1, x_2 + L_2) = A_1(x_1, x_2) + \partial_1\beta_2(x_1, x_2), \qquad A_2(x_1 + L_1, x_2) = A_2(x_1, x_2) + \partial_2\beta_1(x_1, x_2) \tag{378}$$

while the wave functions themselves obey twisted boundary conditions

$$\begin{aligned} \Psi([\boldsymbol{x}^{(j)} + L_1\boldsymbol{e}_1]) &= \exp\left(-i\frac{e}{\hbar c}\sum_{j=1}^{N_e}\beta_1([\boldsymbol{x}^{(j)}]) + i\theta_1 \right) \times \Psi([\boldsymbol{x}^{(j)}]) \\ \Psi([\boldsymbol{x}^{(j)} + L_2\boldsymbol{e}_2]) &= \exp\left(-i\frac{e}{\hbar c}\sum_{j=1}^{N_e}\beta_2([\boldsymbol{x}^{(j)}]) + i\theta_2 \right) \times \Psi([\boldsymbol{x}^{(j)}]) \end{aligned} \tag{379}$$

where $\boldsymbol{e}_j$ (with $j = 1, 2,$) are two unit vectors on the torus, and θ_1 and θ_2 are two angles that *twist* the boundary conditions of the wave functions.

In order to have a current on the torus, they assumed that, in addition to the uniform flux going through the torus, there a weak uniform electric field $\boldsymbol{E}$ on the torus represented by the constant in space vector potential $\delta\boldsymbol{A} = \boldsymbol{E}\, t = \nabla[U(\boldsymbol{x})t]$ whose circulation on the two noncontractible circles Γ_1 and Γ_2, which wrap around the directions x_1 and x_2 of the torus T^2, are

$$I_j = \oint_{\Gamma_j} \delta\boldsymbol{A}\cdot d\boldsymbol{x} = t\oint_{\Gamma_j} \boldsymbol{E}\cdot d\boldsymbol{x} = itE_jL_j. \tag{380}$$

Line integrals of a gauge field on noncontractible loops in space (or space-time) are called *holonomies*. By inspection, we see that the angles θ_1 and θ_2 are given by

$$\theta_j = \frac{e}{\hbar c} I_j \tag{381}$$

Alternatively, the angles $\boldsymbol{\theta} = (\theta_1, \theta_2)$ can be interpreted as magnetic fluxes (in units of the flux quantum ϕ_0) through the two noncontractible circles of the torus T^2.

The angles $\boldsymbol{\theta}$ are defined as mod 2π since they are phase factors that twist the phase of the wave functions, and define a 2-torus of boundary conditions. By comparing with what we did in Section "The quantum Hall effect on a lattice" in the case of the single-particle wave functions in the lattice model, we see that the *many-body wave function* $\Psi_{\boldsymbol{\theta}}$ and the twist angles $\boldsymbol{\theta}$ are the same as the relation between the phase of the Hofstadter wave functions and the momentum $\boldsymbol{k}$ of the magnetic BZ (which is also a 2-torus). Indeed, as it is always the case, while the phase of (in this case) the many-body wave function $\Psi_{\boldsymbol{\theta}}$ is arbitrary, the changes of this phase as the twist angle $\boldsymbol{\theta}$ is changed are not. To quantify this dependence, for a given many-body state $\Psi_{\boldsymbol{\theta}}^{(\alpha)}$, where α labels the state, we define a Berry connection $\mathcal{A}^{(\alpha)}(\boldsymbol{\theta})$ on the torus of boundary conditions $\boldsymbol{\theta}$

$$\mathcal{A}^{(\alpha)}(\boldsymbol{\theta}) = i\left\langle \Psi_{\boldsymbol{\theta}}^{(\alpha)} \middle| \partial_{\boldsymbol{\theta}} \middle| \Psi_{\boldsymbol{\theta}}^{(\alpha)} \right\rangle. \tag{382}$$

Under a redefinition of the phase of the state

$$\Psi_{\boldsymbol{\theta}}^{(\alpha)} \to \exp(if(\boldsymbol{\theta}))\, \Psi_{\boldsymbol{\theta}}^{(\alpha)} \tag{383}$$

the Berry connection $\mathcal{A}^{(\alpha)}(\boldsymbol{\theta})$ changes by a gauge transformation

$$\mathcal{A}^{(\alpha)}(\theta) \to \mathcal{A}^{(\alpha)}(\theta) - \partial_{\boldsymbol{\theta}} f(\boldsymbol{\theta}). \tag{384}$$

Niu et al. (1985) showed that the expression of the Kubo formula for the Hall conductivity of the state $\Psi_{\boldsymbol{\theta}}^{(\alpha)}$, averaged over the boundary conditions $\boldsymbol{\theta}$, is given in terms of the flux of the Berry connection $\mathcal{A}^{(\alpha)}(\boldsymbol{\theta})$ through the 2-torus of boundary conditions, by the gauge-invariant quantity

$$\langle (\sigma_{xy})_\alpha \rangle_{\boldsymbol{\theta}} = \frac{e^2}{\hbar} \int_0^{2\pi} \frac{d\theta_1}{2\pi} \int_0^{2\pi} \frac{d\theta_2}{2\pi} \left(\partial_1 \mathcal{A}_2^{(\alpha)} - \partial_2 \mathcal{A}_1^{(\alpha)} \right) = \frac{e^2}{h} \frac{1}{2\pi} \oint_\gamma \mathcal{A}^{(\alpha)}(\boldsymbol{\theta}) \cdot d\boldsymbol{\theta} \tag{385}$$

where γ is the square contour with corners at $(0, 0)$, $(2\pi, 0)$, $(0, 2\pi)$, and $(2\pi, 2\pi)$, which defines the 2-torus of boundary conditions $\boldsymbol{\theta}$. This result is known as the Niu–Thouless–Wu formula.

Eq. (385) implies that for the Hall conductivity to be nonvanishing, the Berry connection $\mathcal{A}^{(\alpha)}(\boldsymbol{\theta})$ must have a nonvanishing flux through the torus of boundary conditions. For this to be true, just as we did in Section "Chern invariants," we must consider large gauge transformations of the form

$$\begin{aligned} \mathcal{A}_1(\boldsymbol{\theta} + 2\pi \boldsymbol{e}_2) &= \mathcal{A}_1(\boldsymbol{\theta}) + \partial_1 f_2(\boldsymbol{\theta}) \\ \mathcal{A}_2(\boldsymbol{\theta} + 2\pi \boldsymbol{e}_1) &= \mathcal{A}_2(\boldsymbol{\theta}) + \partial_2 f_1(\boldsymbol{\theta}) \\ \Psi^{(\alpha)}(\{\boldsymbol{x}^{(j)}\}; \boldsymbol{\theta} + 2\pi\, \boldsymbol{e}_1) &= \exp(i f_1(\boldsymbol{\theta}))\, \Psi^{(\alpha)}(\{\boldsymbol{x}^{(j)}\}; \boldsymbol{\theta}) \\ \Psi^{(\alpha)}(\{\boldsymbol{x}^{(j)}\}; \boldsymbol{\theta} + 2\pi\, \boldsymbol{e}_2) &= \exp(i f_2(\boldsymbol{\theta}))\, \Psi^{(\alpha)}(\{\boldsymbol{x}^{(j)}\}; \boldsymbol{\theta}) \end{aligned} \tag{386}$$

where $\boldsymbol{e}_1$ and $\boldsymbol{e}_2$ are two orthogonal unit vectors on the torus of boundary conditions. We can now repeat the analysis we did in Section "Chern invariants" which, in this context, implies that the wave function $\Psi_{\boldsymbol{\theta}}^{(\alpha)}$ cannot be globally well defined on the torus of boundary conditions, where it must have zeros, and where it should be defined in patches. The end result is that the wave functions labeled by α are classified by a *topological invariant*, the first-valued Chern number $C_1^{(\alpha)}$, which is given here by

$$C_1^{(\alpha)} = \frac{1}{2\pi} \oint_\gamma \mathcal{A}^{(\alpha)}(\boldsymbol{\theta}) \cdot d\boldsymbol{\theta} \tag{387}$$

and, hence, that the Hall conductivity in the state α (averaged over the twisted boundary conditions) exhibits the integer quantum Hall effect,

$$\langle (\sigma_{xy})^{(\alpha)} \rangle_{\boldsymbol{\theta}} = C_1 \frac{e^2}{h}. \tag{388}$$

Expressing the Hall conductivity in terms of the first Chern number, which is a topological invariant, proves that the value of the conductivity cannot be changed by local physics effects, such as disorder. The topological nature of the Hall conductivity is the reason for the robustness and high precision of the measured value of the Hall conductivity. In subsequent work Niu and Thouless showed that, provided the state has a finite energy gap to all excitations, in the thermodynamic limit the Hall conductivity averaged over boundary conditions and for a given boundary condition are equal.

The result of Eq. (388) seemingly implies that there can only be an *integer* quantum Hall effect which, as we see shortly, is not the case: there is a fractional quantum Hall effect in which the Hall conductivity is a *fraction*, $\sigma_{xy} = \frac{p}{q} \frac{e^2}{h}$, where p and q are co-prime integers. This value of the Hall conductivity is also found experimentally to be obeyed with the same precision as in the integer quantum Hall effect. In other words, the Hall conductivity in the fractional case must also have a topological character. To understand why this can be the case, we need an implicit assumption that we made in our derivation. In fact, in deriving the result of Eq. (388), we assumed (implicitly) that for each value of $\boldsymbol{\theta}$ there is only one many body state $\Psi_{\boldsymbol{\theta}}^{(\alpha)}$ (up to gauge transformations). As we will see below, in the *fractional* quantum Hall effect on a torus (and, in fact on any closed surface except the sphere), the ground state is degenerate in the thermodynamic limit. We will also see that traversing the torus of boundary conditions once maps one degenerate state to another one. In general, we will find that on the 2-torus in the thermodynamic limit, there are $m \in \mathbb{Z}$ exactly degenerate states. In this case, one returns to the original state after sweeping m times the torus of boundary conditions. We will also see below that the degenerate states are labeled by quantum numbers related to the *anyons* that they support.

While the topological argument proves the robustness (and universality) of the value of the Hall conductivity, it does not provide an insight for why there are plateaus in its magnetic field dependence. If for some value of the filling fraction $\nu = N/N_\phi$, the electron fluid is exactly at a ground state $\Psi^{(\alpha)}$ upon changing either the number of particles N or the magnetic field B (but not both), the fluid will now be at the state $\Psi^{(\alpha)}$ plus or minus some number of electrons. The existence of the plateau in σ_{xy} can be understood if the extra electrons (or holes) do not contribute to the Hall conductivity. This happens in the presence of disorder as these extra particles will be localized by the disorder and localized states, whose wave functions decay exponentially are insensitive to boundary conditions and, hence, these states do not contribute to the conductivity. This argument was first put forth by Laughlin (1981) who built on the result that in a disordered system in two dimensions, all states are localized (Abrahams et al., 1979) but made the key assumption that the state at the center of the Landau level (broadened by disorder) is extended and contributes to the conductivity if this state is filled. This picture implies that this is actually a quantum phase transition from an insulator (dubbed a Hall insulator) to a state with a quantized Hall conductivity.

This intuitive and appealing proposal has been the focus of research for many years and it is largely an unsolved problem. There is in fact a proposed field theory for this quantum phase transition based on a nonlinear sigma model (in replica space) with a topological θ term (Levine et al., 1983; Pruisken, 1984), analogous to the theory we discussed in Section "Nonlinear sigma models and antiferromagnetic quantum spin chains" for quantum antiferromagnets in 1+1 dimensions. In this proposal, the (Boltzmann) longitudinal conductivity σ_{xx} plays the role of the inverse of the coupling constant of the nonlinear sigma model while σ_{xy} plays the role of the coefficient of the θ term. Although the RG flows suggested by this approach qualitatively agree with currently existing experimental data, actual derivation is still wanting.

However, aside from the fact that it is still an unsolved problem, there is the problem that this explanation ignores the fact that in a Landau level interactions are dominant and are the key to the understanding of the fractional case even in the same samples! A symptom of this problem is that, at least in the cleaner samples, as we noted above, the longitudinal conductivity vanishes exponentially with temperature. This dependence means that there is a clean energy gap (and not just a mobility gap), which suggests that the state with additional excitations may have some sort of at least local order, which would provide for a local energy gap. An actual theory based on this picture has yet to be developed.

The Laughlin wave function

We will turn now to the *fractional* quantum Hall effect (FQHE). The FQHE is observed in fractionally filled Landau levels. These states have fractional filling fractions, namely that $\nu = \frac{N_e}{N_\phi}$ is a fraction. Most of the observed states are in the lowest Landau level, with $N = 0$, but a few states with very intriguing properties are seen in the first excited Landau Level with $N = 1$.

Let us consider for now the states in the lowest Landau level, $N = 0$. We will assume that there is no disorder and, for now, we will ignore the effects of boundaries of the sample. Physically, the important interaction here is the Coulomb interaction although, in some samples with screening layers, short-range interactions may be important as well. Since there is a large magnetic field, the Zeeman interaction is typically a large energy scale and the electros are expected to be fully polarized. However, there are situations under which the gyromagnetic factor can be made small (and even zero) and spin unpolarized states have to be considered. In some platforms, such as graphene, additional quantum numbers are present, such as "flavor" associated with the different Dirac states. In our discussion we will not cover these richer possibilities.

Under these circumstances, we have a problem in which all N_ϕ available one-particle states are exactly degenerate (the Landau level is "flat") but only a fraction of them are filled. In this limit, this system as strongly interaction as it gets. Not surprisingly, in a system of this type, time-honored standard approximations fail, such as Hartree–Fock. Given the macroscopic degeneracy and the nature of the states in a magnetic field, a system of this type may harbor many different types of actual ground states depending of the types of interactions that are considered.

Tsui et al. (1982) did transport experiments in the two-dimensional electron gas (2DEG) in high-purity GaAs-AlAs heterostructures and reported the discovery of a state with a highly precise value of the Hall conductivity of $\sigma_{xy} = \frac{1}{3}\frac{e^2}{h}$. Such a state cannot be understood in any obvious way in terms of the integer quantum Hall effect. The observation of a clean gap in the low temperature longitudinal resistivity $\sigma_{xx} \to 0$ as $T \to 0$ implied that the 2DEG is incompressible and quite likely uniform.

The first breakthrough was Laughlin's unique insight, which led to his explanation of the experiments in terms of a novel quantum liquid of fully spin-polarized electrons at filling fractions $\nu = \frac{1}{m}$ (with m and odd integer) whose wave function he proposed to be

$$\Psi_m(z_1, \ldots, z_N) = \prod_{i<j}(z_i - z_j)^m \times \exp\left(-\sum_{i=1}^{N_e} \frac{|z_i|^2}{4\ell_0^2} \right) \tag{389}$$

where $N = N_e$ is the number of electrons, $\{z_i\}$ are their (complex) coordinates, and m is an odd integer (which makes the wave function antisymmetric, as required by Fermi statistics).

Laughlin extracted the physics encoded in this wave function by considering the probability $|\Psi_m(z_1, \ldots, z_N)|^2$ of finding the N electrons in the locations $\{z_i\}$ (with $i = 1, \ldots, N$). The norm of the Laughlin wave function is

$$\left|\left|\Psi_m\right|\right|^2 = \int d^2z_1 \ldots d^2z_N \left|\Psi_m(z_1, \ldots, z_N)\right|^2. \tag{390}$$

The Laughlin wave function $\Psi_m(z_1, \ldots, z_N)$ is an eigenstate of angular momentum with eigenvalue $L_m = \frac{1}{2}mN(N-1)$. This remarkable wave function has a large overlap ($\sim$ 98%) with the exact wave function with $V(R) = \frac{e^2}{\varepsilon R}$ (Coulomb) interactions in systems of up to eight particles (ε is the dielectric constant).

The norm of the state can then be interpreted as the classical partition function of a system of a system of N particles at the locations $\{z_i\}$ at inverse temperature $\beta = m$ with the effective interaction

$$U(z_1, \ldots, z_N) = -2 \sum_{1 \le i < j \le N} \ln|z_1 - z_j| + \frac{1}{2m\ell_0^2} \sum_{j=1}^{N} |z_j|^2. \tag{391}$$

This classical partition function is a one-component plasma, of a gas of particles with unit (negative) charge interacting with each other with the repulsive 2D classical (logarithmic!) Coulomb interaction, $V_{\rm CG} = -\ln|z_i - z_j|$ (not $1/R$!). The last term represents the contribution of a neutralizing background positive charge (which here it originates in the Gaussian factor of the wave function).

In other words, this is a one-component plasma. We can check that this is correct since $\nabla^2\left(\frac{|z|^2}{2m\ell_0^2}\right) = \frac{2}{m\ell_0^2}$, which corresponds to a uniform (areal) charge density $\rho_0 = \frac{1}{2\pi m\ell_0^2}$. Classical Monte Carlo simulations of this probability distribution showed that this wave function describes an incompressible fluid state if $m \lesssim 7$ while for larger values, it represents a crystalline state. This approach is known as the plasma analogy.

Quasiholes have fractional charge

Laughlin considered a vortex-like excitation in the fluid created by the adiabatic insertion of an infinitesimally thin solenoid at some coordinate z_0 carrying a magnetic flux Φ, a *fluxoid*. In the presence of this solenoid, the single particle state $z^n \exp(|z|^2/4\ell_0^2)$ acquires a branch cut and becomes the state $z^{n+\alpha} \exp(|z|^2/4\ell_0^2)$ where $\alpha = \Phi/\phi_0$, with $\phi_0 = hc/e$ being the flux quantum. This analytic structure is the Aharonov–Bohm effect (Aharonov and Bohm, 1959).

However, if the solenoid carries just one flux quantum $\alpha = 1$ and the net effect is that the state becomes $z^{n+1} \exp(-|z|^2/4\ell_0^2)$ which has one more unit of angular momentum. For these reasons, in the presence of a solenoid with one flux quantum inserted at z_0, the Laughlin wave function for the 2DEG in a large magnetic field now becomes

$$\Psi_m^{qh}(z_0; z_1, \ldots, z_N) = \prod_{i=1}^{N} (z_i - z_0) \times \Psi_m(z_1, \ldots, z_N). \tag{392}$$

A calculation using the plasma analogy reveals that the net effect of the solenoid is to expel a charge equal to $-e/m$ from the vicinity of the location of the solenoid or, equivalently, to create a *fractionally charged quasihole* at z_0 with charge $Q_{\text{qh}} = +e/m$. The charge distribution is uniform at long distances but is depleted (hence a quasihole) on a length scale ξ. One can check that this state costs a finite energy ε_0, which depends on the particular interaction.

On the other hand, if we consider a system in which the solenoid is inserted adiabatically so that after a long time t there is a quasihole at z_0, an amount of charge equal to $-e/m$ will flow radially outwards to the outer edge of the 2DEG. The adiabatic insertion of the solenoid generates a azimuthal electric field (an e.m.f.) and a radial Hall current, and a Hall conductivity $\sigma_{xy} = \frac{1}{m}\frac{e^2}{h}$. Hence, the Laughlin wave function exhibits the fractional quantum Hall effect and its excitations are vortices with fractional charge e/m.

It is important to note the nonlocal nature of the Laughlin quasihole. The nonlocality is inherited from the fluxoid (the solenoid) inserted at z_0: even though the magnetic field of the fluxoid vanishes away from it, $B(\boldsymbol{x}) = \Phi\, \delta^2(\boldsymbol{x} - \boldsymbol{x}_0)$, its vector potential $\boldsymbol{A}(\boldsymbol{x})$ does not since its circulation on any noncontractible loop γ that contains the location of the fluxoid inside must be equal to the flux Φ carried by the fluxoid. Although in principle one can choose a singular gauge in which $\boldsymbol{A}(\boldsymbol{x})$ vanishes locally, this cannot be true everywhere as it must leave behind a Dirac-like string on a curve Γ ranging form the location z_0 of the fluxoid to the boundary of the system with $\boldsymbol{A}$ taking a singular value on Γ. This feature has the same form as the 2D vortex that we discussed in Section "Vortices in two dimensions." Kievelson and Ro·ek (1985) showed that the existence of this Dirac string causes the *phase* of a quantum state that carries charge e^* to have a branch cut on the curve Γ and to change by $\exp(i2\pi(e^*/e)\Phi/\phi_0)$, as required by the Aharonov–Bohm effect (Aharonov and Bohm, 1959). This effect is unobservable for integer-charged states, that is, electrons.

The Jain states

The construction of the Laughlin quasihole motivated Jain (1989a,b) to rewrite the Laughlin wave function in the form

$$\Psi_m(z_1, \ldots, z_N) = \prod_{i<j} (z_i - z_j)^{m-1} \times \Psi_{\nu=1}(z_1, \ldots, z_N). \tag{393}$$

Here the prefactor represents particles each attached with an even number, $m-1$, of flux quanta. The second factor, $\Psi_{\nu=1}(z_1, \ldots, z_N)$, is the wave function of fermions filling up a lowest Landau level, that is, the Vandermonde determinant of Eq. (377). In this form, the inverse of the filling factor, $1/\nu$, which is the number of flux quanta per particle, is written as $\frac{1}{\nu} = (m-1) + 1 = m$. The interpretation now is that the $(m-1)\phi_0$ magnetic flux carried by each particle, which partially screens the uniform field down to an effective field $B_{\text{eff}} = B - (m-1)\phi_0$ corresponding to one effective flux quantum per particle, that is, a filled lowest Landau level of the effective field B_{eff}. In other words, the wave function for the $\nu = 1/m$ FQH state is reinterpreted as the $\nu_{\text{eff}} = 1$ *integer* QH state of *N composite fermions*, each being an electron carrying attached an even integer $m-1$ flux quanta.

This procedure is known as flux attachment. Physically it means that the strong interactions between the electrons for other electrons to be further away which, in virtue of being in a strong magnetic field, is equivalent to an increase of their relative angular momentum, as if there was a local change in the magnetic field. There is no reason to believe that the composite fermions are weakly coupled, even though this is frequently stated in the literature without any real supporting evidence.

Jain then generalized this reinterpretation of the Laughlin state to a whole sequence of FQH states obtained by filling p levels of these partially screened magnetic fluxes

$$\Psi_{m,p}(z_1, \ldots, z_N) = P_{LLL} \prod_{i<j} (z_i - z_j)^{m-1} \Psi_{\nu=p}(z_1, \ldots, z_N) \tag{394}$$

where $\Psi_{\nu=p}(z_1, \ldots, z_N)$ is the wave function of p-filled Landau levels (of composite fermions), and P_{LL} is an operator that projects onto the lowest Landau level. By counting fluxes, we see that the filling fractions for the Jain states satisfy

$$\frac{1}{\nu(m,p)} = m - 1 \pm \frac{1}{p} \tag{395}$$

where we allowed for the possibility that the external fluxes may be over-screened by the composite fermions. Alternatively we can write

$$\nu(m,p) = \frac{p}{p(m-1) + \pm 1}. \tag{396}$$

The Jain states with $p = 1$ are the Laughlin states and each is called the primary state of a Jain sequence. Almost all the observed FQH states belong to one of these sequences (and its generalizations). In particular, the most prominent states (i.e., those with larger plateaus) belong to the sequence $\frac{1}{3}, \frac{2}{5}, \frac{3}{7}, \frac{4}{9}, \frac{5}{11}, \ldots$ and to the reversed sequence $1, \frac{2}{3}, \frac{3}{5}, \frac{4}{7}, \ldots$. For $p \to \infty$, the Jain sequences converge to the values of the filling fraction $\lim_{p\to\infty} \nu(m,p) = \frac{1}{m-1}$. In this limit, the $m - 1$ fluxes attached to each particle exactly cancels the external flux leading us to a (possibly) FL of composite fermions (Halperin et al., 1993).

Quasiholes have fractional statistics

The nonlocality and topological nature of the Laughlin quasihole imply that this state must be regarded as a soliton (or vortex) of the charged quantum fluid. The vortex-like state with wave function $\Psi_m^{qh}(z_0; z_1, \ldots, z_N)$ is called the Laughlin quasihole. This state represents a composite object of a flux quantum and a fractional charge. This structure of this quantum state is strongly reminiscent of the flux-charge composite objects considered by Frank Wilczek who showed that such objects should be *anyons*, states that exhibit *fractional statistics* (Wilczek, 1982a). Although at a conceptual level anyons were proposed (almost) prior to the discovery of the FQHE, it is in this setting that fractional statistics entered actual physics. The actual experimental observation took work by many people, and was only confirmed in 2020 (Nakamura et al., 2020).

Fractional statistics dictates the analytic form of the wave functions of two or more quasiholes (Halperin, 1984). Let us consider a Laughlin-type wave function for two quasiholes located at (complex) coordinates u and w. Naively we expect the wave function for two quasiholes in the $\nu = 1/m$ Laughlin state to have the form

$$\Psi(u, w; z_1, \ldots, z_N) = N(u, w) \prod_{j=1}^{N} (z_j - u)(z_j - w)\, \Psi_m(z_1, \ldots, z_N) \tag{397}$$

The prefactor $N(u, w)$ must be chosen to account for the fact that there is an additional change of angular momentum due to the additional fluxoid at w. We also expect that as the quasihole with charge e/m is adiabatically carried around the other quasihole (also with charge e/m), there will be an accrued phase in the wave function due to the Aharonov–Bohm effect of the charge of one quasihole circling around the flux of the other (or, equivalently, crossing the branch cut) (Kievelson and Ro·ek, 1985). The requirement of translation invariance and analyticity is met by the choice (Halperin, 1984) (ignoring a multiplicative normalization constant)

$$N(u, w) = (u - w)^{1/m} \exp\left(-\frac{1}{4\ell_0^2 m} \left(|u|^2 + |w|^2\right) \right) \tag{398}$$

which has a branch cut stretching from u to w. A calculation using the plasma analogy represents this state as a set of N charge -1 particles interacting with two additional particles of charge $-1/m$ at u and w (and a neutralizing background). The branch cut implies that dragging a quasihole around the other during a π rotation followed by a translation (i.e., an exchange) induces a monodromy in the wave with a jump in its phase of $\exp(\pm i\pi/m)$ (with the sign determined by the orientation of the monodromy) in such a way that the wave function changes by a phase factor

$$\Psi(u, w; z_1, \ldots, z_N) \mapsto e^{\pm i\frac{\pi}{m}}\, \Psi(u, w; z_1, \ldots, z_N). \tag{399}$$

In other words, the quasihole is an *anyon* with fractional statistics π/m. Arovas et al. (1984) further refined this argument by showing that under such a slow adiabatic change the wave function of two quasiholes acquires a Berry phase, which accounts for the fractional statistics. An explicit path-integral derivation of this effect, which uses the fact that the quasihole states are coherent states can be found in Fradkin (2013), Chapter 13.

Hydrodynamic effective field theory

We will now turn to the approaches to the FQHE using the methods of quantum field theory. As we will see, the concept of flux attachment plays a key role. In Section "Quantization of Abelian Chern–Simons gauge theory," we showed that Chern–Simons gauge theory is in fact a theory of flux attachment. Thus we expect that Chern–Simons gauge theory should play a key role as well.

It is useful to ask first why should Chern–Simons gauge theory play a central role at least in the description of the low energy physics. There is a simple, yet powerful, phenomenological argument due to Jörg Fröhlich and Anthony Zee that shows why this should be the case (Fröhlich and Zee, 1991). This in essence a hydrodynamic argument. The fractional quantum Hall effect occurs in a 2DEG in the presence of a large magnetic field which breaks explicitly time-reversal invariance. In the regime of the FQHE, the 2DEG is a uniform charged incompressible fluid in which charge is conserved. This means that the charge 3-current $j_\mu = (j_0, \boldsymbol{j})$ (where j_0 is the charge density and $\boldsymbol{j}$ is the charge current density) must be locally conserved,

$$\partial_\mu j^\mu = 0 \tag{400}$$

which is the continuity equation. The solution of this equation is that the conserved current can be written in terms of a *dual* (in the Hodge sense) vector field $\mathcal{B}_\mu$such that

$$j_\mu = \frac{1}{2\pi}\epsilon_{\mu\nu\lambda}\partial^\nu\mathcal{B}^\lambda. \tag{401}$$

The factor of $\frac{1}{2\pi}$ is introduced for later convenience. The current field j_μ is not changed by a smooth redefinition of the vector field $\mathcal{B}_\mu \to \mathcal{B}_\mu + \partial_\mu\Phi$, where $\Phi(x)$ is a nonsingular field. This means that the vector field $\mathcal{B}_\mu$ is a gauge field.

The effective action of this theory is a functional of the current distribution ${}_\mu$ and, hence, of the gauge field $\mathcal{B}_\mu$. It should be gauge-invariant, and odd under parity and time reversal. Since the fluid is incompressible and uniform, at long distances and low energies the action must be a local functional of the gauge field which should be at least Galilean invariant. In addition, the coupling of the fluid to an external electromagnetic probe field A_μ must be of the usual form $- ej^\mu A_\mu$. To lowest orders in derivatives, there the unique local and gauge-invariant Lagrangian density which is odd under time reversal (and parity) is the Chern–Simons theory

$$\mathcal{L}_{\text{eff}}[\mathcal{B}_\mu] = \frac{m}{4\pi}\epsilon_{\mu\nu\lambda}\mathcal{B}^\mu\partial^\nu\mathcal{B}^\lambda - \frac{1}{4g^2}\mathcal{F}^2_{\mu\nu} - \frac{e}{2\pi}A^\mu\epsilon_{\mu\nu\lambda}\partial^\nu\mathcal{B}^\lambda + \cdots \tag{402}$$

The first term is the Chern–Simons term of the Lagrangian. The coefficient m is a dimensionless integer which, as we saw in Section "Chern–Simons gauge theory" is required for the theory to be invariant on a closed manifold. The second is a Maxwell term. Here $\mathcal{F}_{\mu\nu} = \partial_\mu\mathcal{B}_\nu - \partial_\nu\mathcal{A}_\mu$ is the field strength tensor of the gauge field $\mathcal{B}_\mu$. By power counting, we see that the coupling constant g^2 has units of length^{-1} and, hence this term is irrelevant at long distances and will be neglected. The third term is the coupling of the current j_μ to the electromagnetic field A_μ. Upon an integration by parts this term can be written as $\mathcal{B}_\mu\mathcal{J}^\mu$ where

$$\mathcal{J}_\mu = -\frac{e}{2\pi}\epsilon_{\mu\nu\lambda}\partial^\nu A^\lambda \tag{403}$$

is a current minimally coupled to $\mathcal{B}_\mu$.

The equation of motion of the (dynamical) gauge field $\mathcal{B}_\mu$ is

$$\frac{\delta\mathcal{L}}{\delta\mathcal{B}} = 0 \tag{404}$$

which yields the relation

$$\frac{m}{2\pi}\epsilon_{\mu\nu\lambda}\mathcal{B}^\mu\partial^\nu\mathcal{B}^\lambda = \mathcal{J}_\mu \tag{405}$$

From the definition of the current $\mathcal{J}_\mu$, Eq. (403), we see that the solution of the equation of motion of Eq. (405), up to a gauge transformation, is

$$m\mathcal{B}_\mu = -eA_\mu. \tag{406}$$

By plugging this relation back into the Lagrangian for the gauge field $\mathcal{B}_\mu$, Eq (402) (which si equivalent to integrate out the gauge field $\mathcal{B}_\mu$) we find that the effective Lagrangian of the electromagnetic field A_μ is just a Chern–Simons term

$$\mathcal{L}_{\text{eff}}[A_\mu] = \frac{e^2}{4\pi m}\epsilon_{\mu\nu\lambda}A^\mu\partial^\nu A^\lambda + \cdots \tag{407}$$

This result allows us to read-off the Hall conductivity of the fluid

$$\sigma_{xy} = \frac{1}{m}\frac{e^2}{2\pi\hbar} \tag{408}$$

where we restored units such that $\hbar$ is not unity. In other words, this fluid exhibits the fractional quantum Hall effect for a fluid at filling fraction $\nu = 1/m$.

We should note that this heuristic argument applies equally to systems of fermions, for which m is odd, as well as to systems of bosons, for which m is even.

Composite Boson field theory

We will now discuss two field-theoretic approaches to the FQHE. These approaches use the concept of flux attachment as a mapping of fermions to bosons and as a mapping of fermions to fermions. These approaches are a form of duality transformation that engineers a form of statistical transmutation. We will first show that Chern–Simons theory can be used to effect such a mapping. That this is possible should not be surprising since, as we saw in Section "Fractional statistics and braids," Chen-Simons theory is a theory of fractional statistics and, hence, of anyons.

We should make some important comments on both approaches before we get into a detailed description. While the mapping of fermions to composite bosons and fermions to composite bosons is correct, their approximate mean field descriptions violate symmetries of the 2DEG in a magnetic field. At the root level is the fact that the flux attachment is local in space time and approximate descriptions of these theories bring about a large amount of Landau level mixing, even in the large field limit.

For instance, at the mean field theory level, the composite boson approach is equivalent to a Bose-Einstein condensate which is invariant under translations and under time reversal. In this picture the breaking of time reversal is present in the coupling to a Chern–Simons gauge field. Likewise, the mean field theory of the composite fermion theory is a problem of composite fermions in a partially screened. While a partially screened magnetic field still breaks time reversal, it does not behave properly under magnetic translations. As we will see, these problems will be solved, at least in the low-energy regime, by quantum fluctuations which restore the symmetries. In both cases, in the fractional states, one recovers an effective topological field theory, which captures the universal physics of these states. Needless to say it, both approaches do poorly in the computation of nonuniversal dimensionful quantities such as energy gaps. These difficulties become very severe in the compressible states whose low energy behavior is not topological.

Unlike the wave function approaches, which project these states into a specific Landau level (usually the lowest), the field theoretic approach does not effect such projection. Several papers have been written attempting to do a field theory projected into a Landau level. These approaches transformed the problem into quantum field theory on a noncommutative plane, which is inherent in the nature of the states in a magnetic field. Although some significant progress has been made in this direction, these theories remain poorly understood (Pasquier and Haldane, 1998; Read, 1998; Susskind, 2001; Polychronakos, 2001; Fradkin et al., 2002; Dong and Senthil, 2020; Goldman and Senthil, 2022).

In this section, we will focus on the composite boson theory. Let us consider a theory in 2+1 dimensions with two dynamical Abelian gauge fields $\mathscr{A}_\mu$ and $\mathscr{B}_\mu$, whose Lagrangian is a sum of a Chern–Simons term at level k and a BF term:

$$\mathcal{L} = \frac{k}{4\pi}\epsilon_{\mu\nu\lambda}\mathscr{A}^\mu\partial^\nu\mathscr{A}^\lambda + \frac{1}{2\pi}\epsilon_{\mu\nu\lambda}\mathscr{A}^\mu\partial^\nu\mathscr{B}^\lambda \tag{409}$$

The equation of motion for the field $\mathscr{A}_\mu$ is

$$\frac{k}{2\pi}\epsilon_{\mu\nu\lambda}\partial^\nu\mathscr{A}^\lambda + \frac{1}{2\pi}\epsilon_{\mu\nu\lambda}\partial^\nu\mathscr{B}^\lambda = 0 \tag{410}$$

whose solution (up to a gauge transformation) is $k\mathscr{A}_\mu = -\mathscr{B}_\mu$. Plugging this relation into the Lagrangian of Eq. (409) we find that the effective Lagrangian for the field $\mathscr{B}_\mu$ is

$$\mathcal{L}[\mathscr{B}_\mu] = -\frac{1}{4\pi k}\epsilon_{\mu\nu\lambda}\mathscr{B}^\mu\partial^\nu\mathscr{B}^\lambda \tag{411}$$

which states that exchanging $\mathscr{A}_\mu \leftrightarrow \mathscr{B}_\mu$ is equivalent to the "duality" $k \leftrightarrow -1/k$.

In Section "Fractional statistics and braids," we showed that particles coupled to a Chern Simons gauge field at level k have fractional statistics $\exp(\pm i\pi/k)$. Hence, we see that particles coupled to the field $\mathscr{B}_\mu$ have fractional statistics $\exp(\pm i\pi k)$. In other words, for k odd, this coupling amounts to exchanging a theory of fermions to a theory of bosons coupled to the gauge field $\mathscr{B}_\mu$. This is a form of bosonization. Alternatively, for k, even it maps a theory of fermions to another theory of fermions coupled to a gauge field $\mathscr{B}_\mu$. These observations have led to distinct, but ultimately equivalent description of the quantum Hall effect.

We will begin the approach of mapping fermions to bosons and use it in the problem of the FQHE. This is the Landau–Ginzburg theory (or *composite boson theory*) of Zhang et al. (1989) (ZHK). In this approach, the problem of fermions coupled to a magnetic field interacting with each other through a two-body potential (that we will assume is ultra with coupling constant λ, for simplicity) becomes the same problem but for a theory of bosons which are also coupled to a Chern–Simons gauge field, which we will denote by $\mathscr{A}_\mu$. The Lagrangian density for this equivalent system of *composite bosons* is

$$\mathcal{L}_{\rm CB} = \phi^*(x)[iD_0 + \mu]\phi(x) + \frac{1}{2M}|\boldsymbol{D}\phi(x)|^2 - \lambda(|\phi(z)|^4 + \frac{1}{4\pi m}\epsilon_{\mu\nu\lambda}\mathscr{A}^\mu\partial^\nu\mathscr{A}^\lambda) \tag{412}$$

where $x = (x_0, \boldsymbol{x})$ are the space-time coordinates, μ is the chemical potential, M is the mass of the fermions, and m is an arbitrary odd integer. The covariant derivative

$$D_\mu = \partial_\mu + i\frac{e}{\hbar c}A_\mu + i\mathscr{A}_\mu \tag{413}$$

which effects the minimal coupling of the complex scalar field $\phi(x)$ to the background electromagnetic field A_μ and to the Chern–Simons gauge field $\mathscr{A}_\mu$, known in this context os known as the statistical gauge field.

ZHK showed that the FQH state can be thought as being closely related to a phase in which the complex scalar field condenses, much as in the case of a superfluid even though the FQH *is not* a superfluid. To see how this works, we will write

$$\phi(x) = \sqrt{\rho(x)}\ \exp(i\omega(x)). \tag{414}$$

The classical equations of motion of the theory of composite bosons, Eq. (412), are

$$\frac{\delta\mathcal{L}_{\rm CB}}{\delta\phi^*(x)} = 0 \quad\Rightarrow\quad (iD_0 + \mu)\phi(x) - \frac{1}{2M}\boldsymbol{D}^2\phi(x) - 2\lambda|\phi(x)|^2\phi(x) = 0 \tag{415}$$

$$\frac{\mathcal{L}_{\rm CB}}{\delta\mathscr{A}_0(x)} = 0 \quad\Rightarrow\quad \frac{1}{2\pi m}\epsilon_{ij}\partial_i\mathscr{A}_j + |\phi(x)|^2 = 0 \tag{416}$$

$$\frac{\mathcal{L}_{\rm CB}}{\delta\mathscr{A}_i(x)} = 0 \quad\Rightarrow\quad \frac{1}{2\pi m}\epsilon_{i\alpha\beta}\partial^\alpha\mathscr{A}^\beta + \frac{i}{2M}[\phi^*(x)D_i\phi(x) - (D_i\phi(x))^*\phi(x)] = 0 \tag{417}$$

$$\frac{\mathcal{L}_{\rm CB}}{\delta\mu} = \rho_0L^2T \quad\Rightarrow\quad \int d^3x\ |\phi(x)|^2 = \rho_0L^2T \tag{418}$$

where ρ_0 is the areal density of electrons.

A uniform solution of Eqs. (415)–(418) with constant amplitude of the composite bosons, that is, a uniform and static condensate $\bar{\phi}$, with uniform statistical gauge field strength $\bar{\mathscr{B}}$, requires that the there should be no current in the ground state and that each term of Eq. (417) should be zero. This condition implies that the external field is canceled by the average statistical field, $\frac{eB}{\hbar c} + \bar{\mathscr{B}} = 0$. This condition together with Eqs. (416) and (418) implies that

$$\rho_0 = \frac{1}{m}\frac{eB}{\hbar c} = \frac{1/m}{2\pi\ell_0^2} \tag{419}$$

and we conclude that the filling fraction is $\nu = \frac{1}{m}$, which are the Laughlin states. In addition we get that the chemical potential is $\mu = 2\lambda\rho_0$ and that $|\bar{\phi}|^2 = \rho_0$, with ρ_0 given in Eq. (419).

However, these mean field results seeming imply that this system is a Bose-Einstein condensate. To understand why this is incorrect, and to determine what it actually is, we need to go beyond the mean field theory that we just described and evaluate the effects of quantum fluctuations and write

$$\phi(x) = (\rho_0 + \delta\rho(x))^{1/2}\ \exp(i\omega(x)), \qquad \frac{eA_\mu}{\hbar c} + \mathscr{A}_\mu = \delta\mathscr{A}_\mu. \tag{420}$$

The partition function of this theory is a path integral over the fluctuating density fields $\delta\rho$, the Goldstone field ω, and the fluctuation of the Chern–Simons gauge field $\delta\mathscr{A}_\mu$. Upon integrating out the massive density fluctuations to lowest (quadratic) order, we find that the effective Lagrangian for ω and $\delta\mathscr{A}_\mu$ is

$$\mathcal{L}_{\text{eff}}[\omega, \delta\mathscr{A}_\mu] = \frac{\kappa}{2}(\partial_0\omega - \delta\mathscr{A}_0)^2 - \frac{\rho_s}{2}(\partial_i\omega - \delta\mathscr{A}_i)^2 + \frac{1}{4\pi m}\epsilon_{\mu\nu\lambda}\delta\mathscr{A}^\mu\partial^\nu\delta\mathscr{A}^\lambda + \cdots \tag{421}$$

The first two terms of Eq. (421) is the effective Lagrangian of the Goldstone mode ω in the Bogoliubov theory of superfluidity a compressibility κ and a superfluid stiffness ρ_s given by

$$\kappa = \frac{1}{2\lambda}, \qquad \rho_s = \frac{\rho_0}{M} = \frac{\nu}{2\pi}\hbar\omega_c. \tag{422}$$

However, as we see, this is not a superfluid since the phase field is "eaten" by the Chern–Simons gauge field $\delta\mathscr{A}_\mu$, which now acquires a mass term. In this sort of Higgs mechanism, the fluctuating gauge field has a massive longitudinal mode and a massive transverse mode. Thus, this state doe not have any massless modes.

To see that this theory describes the fractional quantum Hall effect, we need to compute the linear response to a weak electromagnetic perturbation $\delta A_\mu(x)$. This can be accomplished by considering the new Lagrangian

$$\mathcal{L}_{\text{eff}}[\omega, \delta\mathscr{A}_\mu, \delta A_\mu] = \frac{\kappa}{2}\left(\partial_0\omega - \delta\mathscr{A}_0 - \frac{e}{\hbar c}\delta A_0\right)^2 - \frac{\rho_s}{2}\left(\partial_i\omega - \delta\mathscr{A}_i - \frac{e}{\hbar c}\delta A_i\right)^2 + \frac{1}{4\pi m}\epsilon_{\mu\nu\lambda}\delta\mathscr{A}^\mu\partial^\nu\delta\mathscr{A}^\lambda + \cdots \tag{423}$$

and integrate the phase field ω (which can be set to zero in the London/unitary gauge) and the fluctuation of the statistical field $\delta\mathscr{A}_\mu$ to find that effective electromagnetic action is

$$S_{\text{eff}}[\delta A_\mu] = \frac{1}{4\pi m}\frac{e^2}{\hbar}\int d^3x\ \epsilon_{\mu\nu\lambda}\delta A^\mu\partial^\nu\delta A^\lambda + \cdots \tag{424}$$

from which we conclude that the Hall conductivity predicted by the composite boson theory is

$$\sigma_{xy} = \frac{1}{m}\frac{e^2}{h} \tag{425}$$

as it should be for a FQHE at filling fraction $\nu = 1/m$.

We conclude by looking at vortex states in the composite boson theory. A vortex state is a time-independent solution of the equations of motion Eqs. (415)–(418) with the asymptotic behavior (in the temporal gauge $\delta\mathscr{A}_0 = 0$)

$$\lim_{|\boldsymbol{x}|\to\infty}\phi(\boldsymbol{x}) = \sqrt{\rho_0}\ e^{i\varphi(\boldsymbol{x})} \tag{426}$$

$$\lim_{|\boldsymbol{x}|\to\infty}\delta\mathscr{A}_i(\boldsymbol{x}) = \pm\partial_i\varphi(\boldsymbol{x}) = \pm\epsilon_{ij}\frac{x_j}{|\boldsymbol{x}|^2} \tag{427}$$

where $\varphi(\boldsymbol{x})$ is the azimuthal angle on the plane

$$\varphi(\boldsymbol{x}) = \tan^{-1}\left(\frac{x_2}{x_1}\right). \tag{428}$$

The energy of a neutral vortex (i.e., not coupled to a gauge field) is logarithmically divergent, $E_{\text{vortex}} \simeq \frac{\rho_s}{2}\ln(R/a_0)$ where R is the linear size of the system and a_0 is a short-distance cutoff (see Section "Vortices in two dimensions"). However, the situation here is different since the complex scalar field $\phi(x)$ is coupled to a dynamical Chern–Simons gauge field $\mathscr{A}_\mu$. Except for the Chern–Simons nature of this gauge field, the problem we are dealing with is similar to that of a superconductor coupled to a dynamical gauge field or to the Abelian-Higgs model in quantum field theory. In the case of interest, here we have finite energy vortex solutions that satisfy the asymptotic condition

$$\lim_{|\boldsymbol{x}|\to\infty}\left|\left(i\partial_j - \delta\mathscr{A}_j\right)\phi(\boldsymbol{x})\right|^2 = 0 \tag{429}$$

which is obeyed by configurations that obey Eq. (427). Thus, at long distances, the circulation of the Chern–Simons gauge field on a large closed contour Γ that contains the vortex satisfies

$$\oint_\Gamma \delta\mathscr{A}_j dx_j = \pm 2\pi. \tag{430}$$

This vortex carries charge. To see this we compute the local charge density $j_0(\boldsymbol{x})$

$$j_0(\boldsymbol{x}) = -\frac{\delta S_{\text{eff}}}{\delta A_0(x)} = -e\frac{\delta S_{\text{eff}}}{\delta\delta\mathscr{A}_0(x)} = +e\frac{\delta S_{\text{CS}}}{\delta\delta\mathscr{A}_0(x)} = \frac{e}{2\pi m}\epsilon_{ij}\partial_i\delta\mathscr{A}_j(x) \tag{431}$$

and compute the total charge of the vortex on a larger region Σ whose boundary is Γ and obtain

$$Q = e\int d^2x j_0(\boldsymbol{x}) = \frac{e}{2\pi m}\int_\Sigma d^2x\,\epsilon_{ij}\partial_i\delta\mathscr{A}_j(\boldsymbol{x}) = \frac{e}{m}\frac{1}{2\pi}\oint_\Gamma dx_j\delta\mathscr{A}_j(x) = \pm\frac{e}{m}. \tag{432}$$

Therefore, the vortex of the composite boson theory has the same charge as the Laughlin quasihole.

To determine the statistics of the vortex, we go back to the effective Lagrangian written in the form of Eq. (409), (from now on we set $\delta\mathscr{A}^\mu \equiv \mathscr{A}^\mu$)

$$\mathcal{L}_{\text{eff}} = \frac{\kappa}{2}(\partial_0\omega - \mathscr{A}_0)^2 - \frac{\rho_s}{2}(\partial_j\omega - \mathscr{A}_j)^2 + \frac{1}{2\pi}\epsilon_{\mu\nu\lambda}\mathscr{A}^\mu\partial^\nu\mathscr{B}^\lambda - \frac{e}{2\pi}\epsilon_{\mu\nu\lambda}A^\mu\partial^\nu\mathscr{B}^\lambda - \frac{m}{4\pi}\epsilon_{\mu\nu\lambda}\mathscr{B}^\mu\partial^\nu\mathscr{B}^\lambda \tag{433}$$

where A_μ is the external electromagnetic probe field, and where we used units with $\hbar = c = 1$. The first two terms make the statistical gauge field $\mathscr{A}_\mu$ massive. In the low energy limit, the statistical gauge field is frozen to the vortex configurations of the complex scalar field ϕ or, equivalently, to the vortex singularities of its phase field ω. The vorticity current Ω_μ is

$$\Omega_\mu = \epsilon_{\mu\nu\lambda}\partial^\nu\mathscr{A}^\lambda. \tag{434}$$

The effective Lagrangian for the field $\mathscr{B}_\mu$ is

$$\mathcal{L}_{\text{eff}}[\mathscr{B}_\mu] = -\frac{m}{4\pi}\epsilon_{\mu\nu\lambda}\mathscr{B}^\mu\partial^\nu\mathscr{B}^\lambda - \frac{e}{2\pi}A^\mu\epsilon_{\mu\nu\lambda}\partial^\nu\mathscr{B}^\lambda + \Omega_\mu\mathscr{B}^\mu \tag{435}$$

which, except for the coupling to the electromagnetic field, has the same form as in Eq. (224), and of the effective action introduced in Section "Hydrodynamic effective field theory" on phenomenological grounds.

The effective topological field theory of Eq. (435) encodes al the *universal* data of fractional quantum Hall fluids. Being topological, this effective field theory has no energy scales and describes the physics at energies low compared to any excitation energy gap. In addition to yielding the correct Hall conductivity $\sigma_{xy} = \nu e^2/h$ (with $\nu = 1/m$) and the fractional vortex charge $Q = e/m$, this theory will allow us to draw important additional results about the low energy physics.

By using the results of Section "Fractional statistics and braids," we conclude that the vortices of the composite boson are anyons with fractional statistics $\exp(\pm i\pi/m)$, consistent with the conclusions of Section "Quasiholes have fractional statistics." In addition, on a 2-torus the ground state of this system is m-fold degenerate. This feature, characteristic of systems with *topological order*, is that the ground state degeneracy depends on the topology of the surface on which the 2DEG resides. The ground state on a torus degeneracy was shown by Haldane and Rezayi (1985) by an explicit construction of a model wave function for the Laughlin states on a torus. On a surface with g handles (i.e., genus g), the degeneracy is m^g. Wen and Niu (1990) showed that these results hold for any FQH state which are, quite generally, topological quantum fluids.

Finally, we may ask how many *distinct* types of vortices does this theory have. The fundamental (Laughlin) vortex has charge e/m and statistics π/m. In principle we could have a vortex with any integer topological charge (winding number) $n \in \mathbb{Z}$. Such a vortex has charge ne/m and statistics $\pi n^2/m$. However, a vortex with topological charge $n = m$ has charge e and statistics $m\pi$. This vortex is indistinguishable from a hole (a missing electron) since it has the same charge and statistics. We conclude that a Laughlin state has m distinct vortices with $n = 1, 2, \ldots, m - 1$. We notice that this number is the as the number of degenerate states on a torus. In Section "Fractional quantum hall wave functions and conformal field theory," we will see that this fact is closely related to the number of primary fields of a CFT associated with the FQH states.

Composite fermion field theory

At the beginning of Section "Composite Boson field theory," we noted that flux attachment can be used to define equivalent theories: (a) by attaching an *odd* number, m, fluxes to each electron thereby becoming a composite boson, and (b) by attaching an *even* number, $m - 1$, fluxes by which the electrons turn into *composite fermions*, as in Jain's construction (Jain, 1989b). In this section we discuss the most salient features of the field theory approach to composite fermions, introduced by López and Fradkin (1991, 1993) as a theory of all the Jain states. This approach was extended in 1993 by Halperin et al. (1993) to the case of the compressible states.

By following the same approach that we used in Section "Composite Boson field theory," but adapted to the case in which we map to a theory of a composite Fermi field $\psi(x)$, we find their dynamics is described by the effective action (López and Fradkin, 1991)

$$\begin{aligned}\mathcal{S}_{\rm CF} = &\int d^3x \left\{\psi^*(x)[iD_0 + \mu]\psi(x) + \frac{1}{2M}|\boldsymbol{D}\psi(x)|^2\right\} + \frac{1}{4\pi n}\int d^3x \epsilon_{\mu\nu\lambda}\mathscr{A}^\mu\partial^\nu\mathscr{A}^\lambda \\ &-\frac{1}{2}\int d^3x \int d^3x' \, (|\psi(x)|^2 - \rho_0)V(x-x')(|\psi(x')|^2 - \rho_0)\end{aligned} \tag{436}$$

where $n = m - 1$ is an even integer. Here $V(x - x') = \delta(x_0 - x_0')V(|\boldsymbol{x} - \boldsymbol{x}'|)$ is the instantaneous electron–electron repulsive interaction, and ρ_0 is the average areal neutralizing charge density. As before, the covariant derivative is $D_\mu = \partial_\mu + ieA_\mu + \mathscr{A}_\mu$, where A_μ is the electromagnetic field (including the uniform magnetic field B), and $\mathscr{A}_\mu$ is the statistical gauge field. We are using units such that $\hbar = c = 1$.

We can simplify somewhat the form of the actions for the composite fermions by using the fact that the Gauss law of Chern–Simons gauge theory states that the particle density and the gauge flux are rigidly tied together, $|\psi(x)|^2 = \frac{1}{2\pi n}\mathscr{B} \equiv \epsilon_{ij}\partial_i\mathscr{A}_j$ (this is the flux attachment) as a operator identity. Thus, we can write the action as

$$\begin{aligned}\mathcal{S}_{\rm CF} = &\int d^3x \left\{\psi^*(x)[iD_0 + \mu]\psi(x) + \frac{1}{2M}|\boldsymbol{D}\psi(x)|^2\right\} + \frac{1}{4\pi n}\int d^3x \, \epsilon_{\mu\nu\lambda}\mathscr{A}^\mu\partial^\nu\mathscr{A}^\lambda \\ &-\frac{1}{2}\int d^3x \int d^3x' \left(\frac{\mathscr{B}(x)}{2\pi n} - \rho_0\right)V(x-x')\left(\frac{\mathscr{B}(x')}{2\pi n} - \rho_0\right).\end{aligned} \tag{437}$$

Since this action is a quadratic form in the Fermi (Grassmann) fields ψ, we can integrate them out to obtain the following effective action for the statistical gauge field $\mathscr{A}_\mu$

$$S_{\rm eff}[\mathscr{A}_\mu] = -i{\rm tr}\left(iD_0 + \mu + \frac{\boldsymbol{D}^2}{2M}\right) + \frac{1}{4\pi n}\int d^3x \, \epsilon_{\mu\nu\lambda} \, (\mathscr{A}^\mu - eA^\mu)\partial^\nu \, (\mathscr{A}^\lambda - eA^\lambda) + S_{\rm int}[\mathscr{A}_\mu - eA_\mu] \tag{438}$$

where A_μ is a probe external electromagnetic field (with vanishing average) and does not include the uniform magnetic field. The interaction term is

$$S_{\rm int}[\mathscr{A}_\mu - eA_\mu] = -\frac{1}{2}\int d^3x \int d^3x' \left(\frac{(\mathscr{B}(x) - eB(x))}{2\pi n} - \rho_0\right) V(x-x') \left(\frac{(\mathscr{B}(x') - eB(x'))}{2\pi n} - \rho_0\right). \tag{439}$$

Here too $B(x)$ is an external probe with vanishing average.

We will investigate the properties of the path integral for the statistical gauge field

$$Z[A_\mu] = \int \mathcal{D}\mathscr{A}_\mu \, \exp(iS_{\rm eff}[\mathscr{A}_\mu, A_\mu]) \tag{440}$$

using a saddle point expansion. The saddle-point condition of the effective action of Eq. (438)

$$\frac{\delta S_{\rm eff}}{\delta \mathscr{A}_\mu(x)} = 0 \tag{441}$$

leads to the equation of motion for the field $\mathscr{A}_\mu$

$$\langle j_\mu^F(x)\rangle + \frac{1}{4\pi n}\epsilon_{\mu\nu\lambda}\left[\mathcal{F}^{\nu\lambda}(x) - eF^{\nu\lambda}\right] = 0 \tag{442}$$

where $\langle j_\mu^F\rangle$ is the expectation value of the fermionic current. In addition we need to impose the condition for the particle density to be uniform and equal to the neutralizing background charge $\langle j_0^F(x)\rangle = \rho_0$.

We will assume that the electromagnetic field A_μ describes just a static uniform magnetic field of strength B. Under these conditions, the ground state should also be static and uniform. This means that the field strength of the statistical gauge field should be constant and uniform value $\langle\mathscr{B}\rangle$, and that the current $\langle \boldsymbol{j}^F\rangle$ should vanish in the ground state. On the other hand, the Gauss Law of the Chern–Simons gauge field implies that $\langle\mathscr{B}\rangle = -2\pi n \, \rho_0$ while the zero current condition requires the (statistical) electric field vanishes, $\langle\mathcal{E}\rangle = 0$. Since the composite fermion couples in the same way to the electromagnetic field A_μ and to the statistical field $\mathscr{A}_\mu$ we conclude that they experience an effective magnetic field

$$B_{\rm eff} = B + \frac{1}{e}\langle\mathscr{B}\rangle = B - 2\pi n \, \frac{\rho_0}{e}. \tag{443}$$

If the total number of electrons is N, then $\rho_0/e = N/L^2$, where L is the linear size of the system. Let us denote by $N_\phi^{\rm eff}$ the total number of flux quanta of the effective magnetic field (in units of $\hbar = c = 1$ in which the flux quantum is $\phi_0 = 2\pi$), and $2\pi N_\phi = BL^2$ is the total flux. Then, the total effective flux is

$$2\pi N_\phi^{\rm eff} = 2\pi N_\phi - 2\pi n \, N. \tag{444}$$

Let $\nu = N/N_\phi$ be the filling fraction and $\nu^{\text{eff}} = N/N_\phi^{\text{eff}}$ be the effective filling fraction. Eq. (444) implies that these filling fractions are related by

$$\frac{1}{\nu^{\text{eff}}} = \frac{1}{\nu} - n. \tag{445}$$

Recall that n is an *even* integer. However, the system will be incompressible only if $\nu^{\text{eff}} = p \in \mathbb{Z}$. In other words, the composite fermions fill an integer number p of the partially screened Landau levels, which is Jain's condition. For this condition to be satisfied, the filling fraction $\nu(p, n)$ is

$$\nu_\pm(n, p) = \frac{p}{np \pm 1} \tag{446}$$

which are the Jain fractions. In the special case $p = 1$, the Jain fractions are the Laughlin fractions, with $n = m - 1$. Similarly we find that B_{eff} is

$$B_{\text{eff}} = \pm \frac{B}{np \pm 1}. \tag{447}$$

So we see that the external field B is partially screened to the smaller value B_{eff} which can be parallel (screened) to B or antiparallel (overscreened) to B. For the same reason, at this mean field level, the cyclotron frequency ω_c is reduced by the same amount to $\omega_c^{\text{eff}} = \omega_c/(np \pm 1)$.

We will discuss now the effects of quantum fluctuations for the action of Eq. (438) about the saddle-point solutions. We will work to the lowest order (quadratic) in the fluctuations, which can be regarded as a semiclassical (or "RPA") treatment of this theory. The quadratic effective action for the fluctuations of statistical gauge field, which we will still denote by $\mathscr{A}_\mu$ is

$$\begin{aligned} S_{\text{eff}}^{(2)}[\mathscr{A}_\mu] = & \frac{1}{2}\int d^3x \int d^3y \; \mathscr{A}^\mu(x)\Pi_{\mu\nu}^{CF}(x, y) \; \mathscr{A}^\nu(y) \\ & + \frac{1}{4\pi n}\int d^3x \; \epsilon_{\mu\nu\lambda}(\mathscr{A}_\mu(x) - eA_\mu(x))\partial^\nu(\mathscr{A}_\nu(x) - eA_\nu(x)) + S_{\text{int}}(\mathscr{A}_\mu - eA_\mu). \end{aligned} \tag{448}$$

Here, $\Pi_F^{\mu\nu}(x, y)$ is the polarization tensor of the composite fermions for p-filled effective Landau levels. The interaction term of the action is given in Eq. (439).

As required by gauge invariance, the composite fermion polarization tensor is transverse, $\partial^\mu \Pi_{\mu\nu}^{CF} = 0$, which fixes the tensorial structure. In momentum and frequency space, the composite fermion polarization tensor $\Pi_{\mu\nu}^{CF}(\boldsymbol{q}, \omega)$ depends on three kernels $\Pi_0^{CF}(\boldsymbol{q}, \omega)$, $\Pi_1^{CF}(\boldsymbol{q}, \omega)$, and $\Pi_2^{CF}(\boldsymbol{q}, \omega)$, where Π_0^{CF} and Π_2^{CF} contain the parity-even response of the composite fermions and Π_1^{CF} is their parity-odd response. Each kernel is given as a series terms representing particle–hole processes with simple poles at the excitations energies $\omega_{rs} = (r - s)\omega_c^{\text{eff}}$, with $r > p$ (particles) and $s \leq p$ (holes). Each term has a residue, which is an integer power of $\boldsymbol{q}^2$ times a Laguerre polynomial in $\boldsymbol{q}^2$. Details of these kernels can be found in López and Fradkin (1991) and in Chapter 13 of Fradkin (2013). However, what will be important here is that, in the gapped states these kernels have a low energy and low momentum limit which is local. This will enable us to find a local topological effective action only for the gapped states.

After integrating out the statistical gauge field $\mathscr{A}_\mu$, we find the effective action for the external electromagnetic probe field A_μ, which has the standard form

$$S_{\text{eff}}[A_\mu] = \frac{1}{2}\int d^3x \int d^3y \; A_\mu(x) \; \Pi^{\mu\nu}(x - y) \; A_\nu(y) \tag{449}$$

which encodes the full electromagnetic response of the system, not just of the composite fermions. Once again, gauge invariance requires that the full polarization tensor be transverse, $\partial^\mu \Pi_{\mu\nu} = 0$.

In Section "The quantum Hall effect on a lattice," we showed that there is a relation between the polarization tensor $\Pi_{\mu\nu}$ and the current-current correlation function $\mathcal{D}_{\mu\nu}$. There we mentioned that these correlators are required (by gauge invariance) to satisfy a Ward–Takahashi identity known as the f-sum rule:

$$\int_{-\infty}^{\infty} \frac{d\omega}{2\pi} \; i\omega \; \mathcal{D}_{00}^R(\omega, \boldsymbol{q}) = \frac{\rho_0}{M}\boldsymbol{q}^2 \tag{450}$$

where the (retarded) density–density correlation function is related to the (retarded) polarization tensor, $\mathcal{D}_{00}^R(\omega, \boldsymbol{q}) = \Pi_{00}^R(\omega, \boldsymbol{q})$. In the limit of low momentum $\boldsymbol{q}$, at fixed frequency ω, the expression for $\Pi_{00}^R(\omega, \boldsymbol{q})$ is

$$\Pi_{00}^R(\omega, \boldsymbol{q}) \simeq \boldsymbol{q}^2 \Pi_0^R(\omega, \boldsymbol{q}) = -\frac{\rho_0}{M} \frac{\boldsymbol{q}^2}{(\omega + i\epsilon)^2 - \omega_c^2} \tag{451}$$

where $\omega_c = eB/(Mc)$ is the cyclotron frequency of the *electrons*. This expression saturates the sum rule. This means that whichever corrections Eq. (451) may have must vanish in the low $\boldsymbol{q}$ limit. In other words, in this limit, the approximation that we made is actually exact. This is well-known result in the theory of the FL (Nozières and Pines, 1966).

In addition, the result of Eq. (451) implies that there is a particle–hole (density) collective mode which at low momentum has energy $\hbar\omega_c$, without corrections. This result is known as Kohn's theorem (Kohn, 1961), which states that in a Galilean invariant system, the 2DEG must have an exact eigenstate at the cyclotron frequency. More intuitively, the center of mass of the 2DEG executes a cyclotron motion regardless of whether the particles are free, interacting or not, fermions, bosons, or anyons. This is a general result. Notice that the composite fermions do not satisfy Kohn's theorem as the cyclotron mode would be at the effective cyclotron frequency ω_c^{eff}, and that the leading quantum fluctuations have restored the magnetic symmetry.

In the limit of low energy $\omega \to 0$ and low momentum $\boldsymbol{q} \to 0$ of the kernels Π_0^{CF}, Π_1^{CF} and Π_2^{CF} become

$$\Pi_0^{CF}(0,0) = \frac{p}{2\pi}\frac{M}{B_{\text{eff}}} \equiv \varepsilon^{CF}, \qquad \Pi_1^{CF}(0,0) = \pm\frac{p}{2\pi} \equiv \sigma_{xy}^{CF}, \qquad \Pi_2^{CF}(0,0) = -\frac{1}{2\pi}\frac{p^2}{M} \equiv -\chi^{CF} \tag{452}$$

where ε^{CF} is the "dielectric constant" of the composite fermions, χ^{CF} is their effective "permeability," and σ_{xy}^{CF} is the (integer) composite fermion Hall conductivity. We then find that low-energy effective action of the statistical gauge field $\mathscr{A}_\mu$ is

$$\begin{aligned}
S_{\text{eff}}[\mathscr{A}_\mu] = {} & \frac{1}{2}\left(\sigma_{xy}^{CF} + \frac{1}{2\pi n}\right) \int d^3x\, \epsilon_{\mu\nu\lambda} \mathscr{A}^\mu(x)\, \partial^\nu\, \mathscr{A}^\lambda(x) \\
& - \frac{e}{2\pi n} \int d^3x\, \epsilon_{\mu\nu\lambda} \mathscr{A}^\mu(x)\, \partial^\nu\, A^\lambda(x) + \frac{e^2}{4\pi n} \int d^3x\, \epsilon_{\mu\nu\lambda} A^\mu(x)\, \partial^\nu\, A^\lambda(x) \\
& + \int d^3x \frac{1}{2}\left(\varepsilon^{CF}\, \mathscr{E}_i^{\,2}(x) - \chi^{CF}\, \mathscr{B}^2(x)\right) \\
& - \frac{1}{8\pi^2 n^2} \int d^3x \int d^3y (\mathscr{B}(x) - eB(x))\, V(x-y)\, (\mathscr{B}(y) - eB(y)).
\end{aligned} \tag{453}$$

Notice that, except possibly for the last term, the effective action is a local. This is possible because the mean field theory state is gapped.

In what follows we will focus only on the leading terms of the effective action and neglect the subleading terms, the least two terms of the effective action which have the form of a Maxwell term and an additional (possibly nonlocal) term. The remaining leading terms have a Chern–Simons form and a BF form whose effective Lagrangian is

$$\mathcal{L}_{\text{eff}}[\mathscr{A}_\mu] = \frac{1}{4\pi}\left(\pm p + \frac{1}{n}\right) \epsilon_{\mu\nu\lambda} \mathscr{A}^\mu(x)\, \partial^\nu\, \mathscr{A}^\lambda(x) - \frac{e}{2\pi n}\, \epsilon_{\mu\nu\lambda} \mathscr{A}^\mu(x)\, \partial^\nu\, A^\lambda(x) + \frac{e^2}{4\pi n}\, \epsilon_{\mu\nu\lambda} A^\mu(x)\, \partial^\nu\, A^\lambda(x). \tag{454}$$

If integrating the statistical gauge field $\mathscr{A}_\mu$ we find the electromagnetic field A_μ has the effective Lagrangian

$$\mathcal{L}_{\text{eff}}[A_\mu] = \frac{\sigma_{xy}}{2}\, \epsilon_{\mu\nu\lambda} A_\mu(x)\, \partial^\nu\, A_\nu(x) \tag{455}$$

from where we find that the Hall conductivity σ_{xy} *of the 2DEG* is

$$\sigma_{xy} = \frac{e^2}{2\pi\hbar}\frac{p}{pn \pm 1} \tag{456}$$

which is the Hall conductivity of the Jain states (in standard units). Here, as before, n is an even integer.

We will now return to the effective Lagrangian of Eq. (454). As it stands, since the Chern–Simons term has fractional level, it is not invariant under large gauge transformations and, as such, cannot be defined on a closed manifold. To remedy this problem, we can now write this Lagrangian in terms of a theory with two dynamical gauge fields $\mathscr{A}_\mu$ and $\mathscr{B}_\mu$ as follows:

$$\begin{aligned}
\mathcal{L}_{\text{eff}}[\mathscr{A}_\mu, \mathscr{B}_\mu] = {} & \frac{p}{4\pi} \epsilon_{\mu\nu\lambda} \mathscr{A}^\mu(x)\, \partial^\nu\, \mathscr{A}^\lambda(x) - \frac{n}{4\pi} \epsilon_{\mu\nu\lambda} \mathscr{B}^\mu(x)\, \partial^\nu\, \mathscr{B}^\lambda(x) \\
& + \frac{1}{2\pi} \epsilon_{\mu\nu\lambda} \mathscr{A}^\mu(x)\, \partial^\nu\, \mathscr{B}^\lambda(x) - \frac{e}{2\pi} \epsilon_{\mu\nu\lambda} \mathscr{B}^\mu(x)\, \partial^\nu A^\lambda
\end{aligned} \tag{457}$$

This is a topological quantum field theory for all the Jain states (López and Fradkin, 1999). This theory can be defined on any manifold no matter its topology. It is easy to see that upon integrating out the field $\mathscr{B}_\mu$, we recover the effective field theory for $\mathscr{A}_\mu$ of Eq. (454). Also, in the special case of the Laughlin states, for which $p = 1$, we can integrate out the field $\mathscr{A}_\mu$, and arrive to the effective topological field theory for the field $\mathscr{B}_\mu$ of Eq. (435) that we derived in the composite boson theory in Section "Composite Boson field theory."

Let us rewrite the Lagrangian of Eq. (457) in a more compact yet general form. To this end, we define a multicomponent gauge field $\mathscr{A}_\mu^I$ with $I = 1, \ldots, L$, an L-component *charge* vector $\boldsymbol{t}$, and an $L \times L$ second rank symmetric matrix K_{IJ}. Wen and Zee have given a general classification of a large class of fractional quantum Hall states, said to be *abelian*, whose topological field theory is defined by the Lagrangian (Wen and Zee, 1992; Wen, 1995)

$$\mathcal{L} = \frac{1}{4\pi} K_{IJ} \epsilon^{\mu\nu\lambda} \mathscr{A}_\mu^I(x)\, \partial^\nu\, \mathscr{A}_\lambda^J(x) - \frac{e}{2\pi} t_I \epsilon^{\mu\nu\lambda} A_\mu(x)\, \partial^\nu\, \mathscr{A}_I^\lambda(x). \tag{458}$$

In the case of the theory of Eq. (457) which has two components, $L = 2$, with $\mathscr{A}_\mu^1 = \mathscr{A}_\mu$ and $\mathscr{A}_\mu^2 = \mathscr{B}_\mu$. The two-component vector is $\boldsymbol{t} = (0, 1)$ and the matrix 2×2 matrix is

$$K = \begin{pmatrix} -p & 1 \\ 1 & n \end{pmatrix}. \tag{459}$$

Wen and Zee showed that, quite generally, a theory of the K-matrix form has a vacuum degeneracy on a torus of $|\det K|$ and, on a surface of genus g, the degeneracy is $|\det K|^g$. They also showed that the Hall conductivity is $\sigma_{xy} = \nu\, e^2/h$ where the filling fraction is

$$\nu = \sum_{I,J=1}^{L} t_I\, K_{IJ}^{-1}\, t_J. \tag{460}$$

The properties of the quasiparticles can be determined by computing the appropriate correlator. In the composite fermion theory, whose Lagrangian is given in Eq. (437), the *gauge-invariant* composite fermion propagator is

$$G_{CF}(x-y;\gamma(x,y)) = \left\langle \psi^\dagger(x) \exp(i \int_{\gamma(x,y)} dz_\mu (eA^\mu(z) + \mathscr{A}^\mu))\psi(y) \right\rangle \tag{461}$$

which, as in any gauge theory, it is gauge-invariant but path-dependent. Here γ is an oriented open path with endpoints that the space-time locations x and y. The composite fermion propagator has information about many of the properties of the quasiparticles, including their electric charge. To find what is the statistics of the quasiparticles, we need to compute a two-particle correlator (a four-point function), which is defined in terms of two open oriented paths, say $\gamma_1(x, y)$ and $\gamma_2(u, w)$, with endpoints at the locations of the two particles, respectively.

The computation of these correlators is done using a feynman sum over trajectories with different weights, which depend on the gauge field configurations. To do these calculations is, in general, a complicated problem. However, in a gapped state, the quasiparticles are massive and in the low-energy regime, these expressions are dominated by a classical trajectory on an oriented path $\tilde{\gamma}(x,y)$ with the same endpoints x and y. The end result reduces to the computation of the expectation value of a Wilson loop operator

$$W[\Gamma] = \left\langle \exp(i \oint_\Gamma dz_\mu (eA_\mu(z) + \mathscr{A}^\mu(z))) \right\rangle_{\mathscr{A}^\mu} \tag{462}$$

on the *closed* oriented path $\Gamma = \gamma \bigcup \tilde{\gamma}^-$ (where $\tilde{\gamma}^-(y,x)$ has the opposite orientation as $\tilde{\gamma}(x,y)$ and runs from y to x). The explicit dependence on the external electromagnetic field yields the value of the charge of the quasiparticle through the Aharanov-Bohm effect. Likewise, the two-particle correlator is reduced, in the asymptotic low-energy regime, to the computation of an expectation value of two Wilson loops in the effective Chern–Simons theory, as was done in Section "Fractional statistics and braids," which yields the fractional statistics of the quasiparticles. The interested reader can find details in Chapter 13 of Fradkin (2013).

A system described by a theory of the form of Eq. (458) has different types of quasiparticles. In general we can assign an integer-valued quantum number $\ell_I \in \mathbb{Z}$ as the charge of the quasiparticle with respect to the gauge field $\mathscr{A}_I^\mu$. The general coupling of a quasiparticle current has the form $\mathcal{L}_{qp} = j_\mu \ell_I \mathscr{A}_I^\mu$. Then, the charge $Q[\boldsymbol{\ell}]$ and the statistics $\delta[\boldsymbol{\ell}]$ of a general quasiparticle defined by the integer-valued L-component vector $\boldsymbol{\ell}$ are

$$Q[\ell] = -e t_I K_{IJ}^{-1} \ell_J, \qquad \frac{\delta[\ell]}{\pi} = \ell_I K_{IJ}^{-1} \ell_J + 1 \tag{463}$$

where +1 is required to refer the statistics to fermions (not bosons) (López and Fradkin, 1999). These results are general and hold for any Abelian FQH state (Wen and Zee, 1992).

In the case of the Jain states, the charge vector is $\boldsymbol{t} = (0, 1)$ and the quasiparticle is labeled by the vector $\boldsymbol{\ell} = (1, 0)$, which yield the results for the charge Q and the statistics δ

$$Q = \frac{-e}{np+1}, \qquad \delta = \pi\left(\frac{-n}{np+1} + 1\right) \tag{464}$$

which are the quantum numbers of the quasiparticles of the Jain states. For the Laughlin state at $\nu = 1/3$, we obtain $Q = -e/3$ and $\delta = \pi/3$ (as we should), which for the first Jain state at $\nu = 2/5$, the charge Q, and the statistics δ are $Q = -e/5$ and $\delta = 3\pi/5$. With some caveats, the predictions for the quasiparticle charge in the FQH states with $\nu = 1/3$ and $\nu = 2/5$ have been confirmed in noise measurements at a quantum point contact by de Picciotto et al. (1997) and by Saminadayar et al. (1997). Fractional statistics has been measured experimentally in both FQH states at $\nu = 1/3$ and $\nu = 2/5$ in (Fabry-Perot) interferometers by Nakamura et al. (2020).

The compressible states

At large values $p \to \infty$, the Jain sequences converge to the even-denominator fractions $\nu_\infty(n) = 1/n$. In this limit, $B_{\text{eff}} \to 0$ and $\omega_c^{\text{eff}} \to 0$. In other words, at the filling fractions $\nu_\infty(n)$, the average effective field experienced by the composite fermions is zero. This mean field theory then would predict that this state is essentially a FL of composite fermions which is a compressible state. In addition, one can compute the effective charge of the composite fermion and find that it is $e/(np \pm 1)$, which also vanishes in the compressible limit. It is straightforward to see that the Fermi sea of the composite fermions is a disk with Fermi momentum

$p_F = (2\nu_\infty(n))^{1/2}\hbar/\ell_0$ and that the Fermi energy is $E_F = \nu_\infty(n)\hbar/(M\ell_0^2)$. Halperin et al. (1993) did an in-depth analysis of the consequences of this compressible state, which are largely in agreement with experiment.

In our discussion of the incompressible FQ states, both in the composite boson and in the composite fermion approaches in Sections "Composite Boson field theory" and "Composite fermion field theory," we saw that the mean field approximation violated symmetries that were restored by quantum fluctuations. This fact allowed us the derive effective filed theories which are asymptotically exact in the low energy IR regime. What allowed us to obtain these exact results is the existence of a gap. However, the compressible states are gapless and in some sense should be regarded theories of a quantum critical system.

In fact, if we reexamine the field theory of composite fermions of Section "Composite fermion field theory," we see that, in the compressible limit $p \to \infty$, the action of Eq. (437) describes a system of fermions at finite density coupled to the *fluctuations* $\mathscr{A}_\mu$ of the statistical gauge field with a Chern–Simons term, but without an external uniform field (which has been canceled by the flux of the average statistical gauge field). This theory has two salient features. one is that the only trace left of the explicitly broken time-reversal symmetry is in the presence of the Chern–Simons term. This means that while the mean field theory looks like a FL, the consequences of the broken time-reversal invariance only enters in the quantum fluctuations. In addition, in this regime, this theory also breaks the particle–hole symmetry of a half-filled Landau level (in the high magnetic field regime).

However, these contributions, already at one-loop order, typically contain IR divergencies. These IR divergencies are due to singular forward scattering processes of the composite fermions by the gauge fields. They are most severe in the computation of the fermion self energy and depend on the form of the electron–electron interactions. For instance if the interaction potential $V(R)$ is short range, the one-loop contribution to the fermion self-energy has an imaginary part with the behavior $\Sigma''(\omega) \sim \omega^{2/3}$, which is *much larger* than the real part $\Sigma'(\omega)$ as $\omega \to 0$ and the Fermi energy E_F is approached (Halperin et al., 1993). This behavior, which is found in many metallic systems at quantum criticality (Hertz, 1976; Millis, 1993; Sachdev, 2011), implies that the width of the quasiparticle is asymptotically much larger than the energy as the Femi surface is approached. This one-loop result means that perturbation theory fails in the IR and that actual behavior may be nonperturbative. This problem is present even in the case of unscreened $\frac{e^2}{R}$ (Coulomb) interactions where the singular behavior is milder with $\Sigma''(\omega) \sim \omega \ln \omega$ [known as Marginal Fermi Liquid scaling (Varma et al., 1989)].

At any rate, these IR singular behaviors imply that the quasiparticle picture is inadequate and the that in these regimes there may be no quasiparticles. These systems are generally known as "Strange Metals." Many strongly interacting physical systems of interest, ranging form high T_c superconductors to (largely conjectured) spin liquids with spinon Fermi surfaces to even quark-gluon plasmas, share these types of singular IR behaviors (Varma et al., 1989; Polchinski, 1994). In spite of a large body of theoretical work, it has remained largely unsolved problem. Perturbative renormalization group methods used to justify the Landau theory of the Fermi liquid (Shankar, 1994; Polchinski, 1993) generally fail in these regimes, although in some cases long-range interactions have allowed some degree of control (Nayak and Wilczek, 1994b, a). Remarkably, the AdS/CFT Gauge/Gravity Duality (Maldacena, 1998) has brought new insights into strange metal behaviors (Faulkner et al., 2010). We will see below that relativistic dualities have given addition insights into the physics of compressible states.

Fractional quantum hall wave functions and conformal field theory

The Laughlin wave function and its generalizations share the remarkable feature of being essentially universal. Aside form the dependence on the magnetic length ℓ_0 in the Gaussian factors, which ensure that the function is integrable at long distances (a feature inherited from the single-particle states in the Landau level), the FQH "ideal" wave functions do not have any length scales. In addition, in almost all cases, the ideal wave functions are the exact ground state wave functions of some suitable ultra-local Hamiltonian projected onto the lowest Landau level. Another feature, closely related to their universality and analyticity, is that these wave functions look similar to correlation functions in two-dimensional critical (chiral) critical systems. We will now see that these features are not accidental and point to a deep relation between quantum Hall states and CFT.

Although the relation between the simpler case of the Laughlin state was known to several people, such as Fubini (1991), this deep connection with *rational* CFT was articulated in considerable generality in a somewhat earlier paper by Moore and Read (1991). This approach showed its full power in the formulation of the non-Abelian quantum Hall states.

Let us begin with the simpler case of the Laughlin states with $\nu = 1/m$, where m is odd for fermions and even for bosons. We will consider a $U(1)$ *Euclidean* CFT of a compact boson (a scalar field) $\phi(x)$ closely related to our discussion of bosonization in 1+1 dimensions in Section "Bosonization, anomalies, and duality." This theory has been extensively studied in the CFT literature (Ginsparg, 1989; Di Francesco et al., 1997; Polchinski, 1998). The Euclidean action for this theory is

$$S = \frac{1}{8\pi}\int d^2x \, \left(\partial_\mu \phi\right)^2. \tag{465}$$

This theory is compactified by the condition that the only allowed observables are invariant under the discrete symmetry

$$\phi(x) \mapsto \phi(x) + 2\pi R n \tag{466}$$

where R is the compactification radius and n is an arbitrary integer. The observables that satisfy this condition are vertex operators of the form

$$V_p(x) = \exp\left(i \frac{p}{R} \phi(x)\right) \tag{467}$$

where p is an integer.

The correlators of this theory are products of holomorphic (right-moving in Minkowski spacetime) and antiholomorphic (left-moving in Minkowski spacetime) factors. In the context of the FQH states, we will be interested in a it chiral theory, whose correlators are holomorphic (analytic) functions in complex coordinates $z = x_1 + ix_2$. Formally, the field $\phi(z, \bar{z})$ is decomposed into a sum of a holomorphic field $\phi(z)$ and antiholomorphic field $\phi(\bar{z})$ so that the propagator is

$$\langle \phi(z, \bar{z})\ \phi(w, \bar{w}) \rangle = -\ln(z - w) - \ln(\bar{z} - \bar{w}). \tag{468}$$

In what follows we will focus on the chiral(holomorphic) field $\phi(z)$ whose propagator is

$$\langle \phi(z)\phi(w) = -\ln(z - w). \tag{469}$$

The correlator of the chiral current operator

$$j(z) = \frac{i}{R} \partial_z \phi(z) \tag{470}$$

is given by

$$\langle i\partial_z \phi(z)\ i\partial_w \phi(w) \rangle \sim \frac{1}{(z - w)^2} \tag{471}$$

which tells us that this operator has (chiral) scaling dimension $\Delta = 1$. Similarly the correlator of two *chiral* vertex operators

$$V_p(z) = \exp\left(i \frac{p}{R} \phi(z)\right) \tag{472}$$

is

$$\langle V_p(z)\ V_{-p}(w) \rangle = \frac{1}{(z - w)^{p^2/R^2}} \tag{473}$$

whose (chiral) scaling dimension is $\Delta_p = p^2/(2R^2)$. These expressions are very similar to the operators that we used in Section "Vortices in two dimensions" to describe vortices in 2D superfluids (and planar magnets). The main difference is that here the fields and their correlators are holomorphic where is Section "Vortices in two dimensions" the correlators are the product of a holomorphic and antiholormophic factors.

For general p and R, the correlator of Eq. (473) has a branch cut from z to w. This means that the *monodromies* of the operators, that is, dragging an operator around the other, induce a change in the *phase* of the correlator equal to $2\pi p^2/R^2$. This behavior is reminiscent of the analytic structure of the quasiparticle wave function in the FQH states and of the *braiding* operation between anyons.

Moore and Read (1991) showed that the following correlator in a $U(1)$ compactified boson CFT (with compactification radius $R = \sqrt{m}$) is equal to the Laughlin wave function at filling fraction $\nu = 1/m$,

$$\Psi_m(z_1, \ldots .z_N) = \left\langle \left(\prod_{i=1}^{N} \exp\left(i\sqrt{m}\phi(z_i)\right) \right) \exp\left(-i \int d^2z' \sqrt{m}\ \rho_0\ \phi(z')\right) \right\rangle \tag{474}$$

$$= \prod_{i<j} (z_i - z_j)^m \exp\left(-\frac{1}{4} \sum_{i=1}^{N} |z_i|^2 \right) \tag{475}$$

where we have used units in which the magnetic length is $\ell_0 = 1$.

In Section "Vortices in two dimensions," we saw that correlators of vertex operators are nonvanishing only if their total charge (vorticity) is zero. The reason for this condition is that the (Euclidean) action is invariant under arbitrary uniform shifts of the field ϕ. Now, in the correlator on the right-hand side of Eq. (475), we have a product of N vertex operators, each with the same charge $\sqrt{m}$. Then, under an arbitrary shift by α of the field $\phi(z)$, the product of vertex operators changes by a phase equal to $N\sqrt{m}\alpha$. On the other hand the other operator in the correlator, which describes a continuum background charge, changes by a phase $-\sqrt{m}\rho_0 L^2\alpha$, where L^2 is the area. Since ρ_0 is the areal particle density, N/L^2, the two changes of the phase cancel each other exactly. Thus, the operator in the expectation value of Eq. (475) is charge neutral and has a nonvanishing expectation value.

The other important feature of the correlator of Eq. (475) is the choice of compactification radius, $R = \sqrt{m}$, and of the vertex operator $V_p(z)$ with $p = m$:

$$V_m(z) = \exp(i\sqrt{m}\phi(z)) \tag{476}$$

whose correlation function is

$$\langle V_m(z)\, V_{-m}(w)\rangle = \frac{1}{(z-w)^m}. \tag{477}$$

Which is invariant under a 2π rotation (since $m \in \mathbb{Z}$). However under a rotation by π (i.e., an *exchange*), it changes by $(-1)^m$. Hence, for m odd it changes sign, and the vertex operator V_m behaves as a *fermion*, while for m even the vertex operator behaves as a *boson*. We will call the vertex operator $V_m \equiv V_e$ the electron operator.

In other words, the correlator of Eq. (475) is the expectation value of N vertex operators, each describing an *electron* (for m odd) and a neutralizing background charge. Then, an elementary calculation yields the expression of the Laughlin wave function.

In this formulation the ground state wave function for the integer QH state at $\nu = 1$, which has the for of a Vandermonde determinant shown in Eq. (377), is interpreted as the correlator of N electron operators in the $U(1)$ CFT with compactification radius $R = 1$. In this simple case, the electron operator is the vertex operator $V_1(z) = \exp(i\phi(z))$, and there are no other operators (aside from the current $j(z) = i\partial_z\phi$). The propagator of this vertex operator is

$$\langle V_1(z) V_{-1}(w)\rangle = \frac{1}{z-w} \tag{478}$$

which indeed represents a fermion with electric charge e.

We will now see that the vertex operator of Eq. (472) with $p = 1$ (and $R = \sqrt{m}$)

$$V_1(z) = \exp\left(\frac{i}{\sqrt{m}}\phi(z)\right) \tag{479}$$

represents the Laughlin quasihole. The correlator of this vertex operator is

$$\langle V_1(z)\, V_{-1}(w)\rangle = \frac{1}{(z-w)^{1/m}} \tag{480}$$

which has a branch cut stretching from z to w and, as a result, under a rotation by $\pm\,\pi$, its phase changes by $\pm\,\pi/m$, just as the Laughlin anyons do. To see that this operator indeed is related to the Laughlin quasihole, we will compute the effect of inserting the vertex operator $V_1(z)$ in the correlator of Eq. (475) and find

$$\begin{aligned}
&\left\langle \exp\left(\frac{i}{\sqrt{m}}\phi(w)\right)\left(\prod_{i=1}^{N}\exp(i\sqrt{m}\phi(z_i))\right)\ \exp\left(-i\int d^2z'\sqrt{m}\,\rho_0\ \phi(z')\right)\right\rangle\\
&= \prod_{i=1}^{N}(z_i - w)\prod_{i<j}(z_i - z_j)^m\ \exp\left(-\frac{1}{4}\sum_{i=1}^{N}|z_i|^2 - \frac{1}{4m}|w|^2\right)\\
&= \Psi_m(w; z_1, \ldots, z_N)
\end{aligned} \tag{481}$$

which is, indeed, the wave function for the Laughlin quasihole of Eq. (392). The insertion of an additional vertex operator $V_1(u)$ at u inside the expectation value of Eq. (481) yields the two-quasihole wave function of Eq. (397), proposed by Halperin (1984) and discussed in Section "Quasiholes have fractional statistics," with the same branch cut shown in Eq. (398) and, therefore carry fractional statistics π/m.

The operator product expansion discussed in Section "The operator product expansion" of the vertex operators of this CFT yields new insight on the quasiholes. Indeed the OPE of two vertex operators of charges p and q is

$$\lim_{w\to u} V_p(w)V_q(u) = \lim_{w\to u}\frac{1}{(w-u)^{\Delta_p+\Delta_q-\Delta_{[p+q]_m}}}V_{[p+q]_m}(u) \tag{482}$$

where $[p]_m$ is the integer p modulo a multiple of m, that is, if $p = mr + s$ (with r a nonnegative integer and $0 \leq s < m$, then $[p]_m = s$. Eq. (482) is understood in the sense that the contribution of all additional operators to the right-hand side vanish as $w \to u$. In other words, the vertex operators are primary fields of this CFT and there are only m primary fields. The physical process described by the OPE is called *fusion*.

A CFT with a finite number of primaries is called a rational CFT (Ginsparg, 1989; Di Francesco et al., 1997). This result is, of course, the same statement that we made is Section "Composite Boson field theory" that the FQH state has m distinct anyons (vortices). This result also means that a vertex operator of charge m, that is, an electron, is indistinguishable from the *identity operator*, V_0. In this sense, the allowed primaries are fields that are *local* with respect to the electron operator V_m. From the point of view of the FQH state, an operator that creates or destroys an electron (at fixed filling fraction) has no effect, as the FQH state is a fluid made of electrons. This also means that all physical operators must braid trivially with the electron operator. In a CFT, an operator of this type is said to generate and extend symmetry algebra (Moore and Seiberg, 1989b, a).

Furthermore, the OPE of the chiral current $j(z)$ with the vertex operator $V_1(z)$ is

$$\lim_{w\to u} j(w)V_1(u) = \frac{1/m}{z-w}V_1(u) \tag{483}$$

which implies that the vertex operator represents a state with charge $1/m$ (in units of the electric charge e).

The CFT approach to construct FQH states has become a very powerful tool. We will see in Section "Edge states and chiral conformal field theory" that FQH states on an open geometry (e.g., a disk) have edge states, which can be understood as chiral CFTs. In addition to providing a deeper understanding of more general Abelian (multicomponent) FQH states with a K-matrix structure, new classes of FQH states with non-Abelian (multidimensional) representations of the Braid Group has been proposed. The anyons of these states are of particular interest since they have been proposed originally by Kitaev in 1997 (Kitaev, 2003) that anyons can be used as physical qubits for topologically protected quantum computation (Kitaev, 2003; Freedman et al., 2002b, a; Preskill, 2004; Das Sarma et al., 2008).

So far, we discussed the case of Abelian anyons. Abelian anyons have the property that the fusion of two anyons is another anyon. Similarly, a braiding operation between two anyons is equivalent (up to a phase factor) to another anyon. Mathematically this means that Abelian anyons are one-dimensional representations of the Braid group. The fractional statistics of an anyon is then a label of the representation of the Braid group. As we saw, the same holds under fusion.

However, the Braid group generally admits multidimensional representations. In this more general case, the fusion (or braiding) of two anyons is represented by a linear combination (superposition) of anyon states. Linear combinations of anyon states are represented by unitary matrices of rank greater than 1. Since matrices generally do not commute braiding and/or fusion processes correspond to a multiplication of these matrices. Such unitary processes are then regarded as quantum gates. This concept is the physical basis of topological quantum computation. It is currently the cutting edge of research in the field.

We will now discuss the simplest non-Abelian FQH states, the Moore-Read (MR) states (Moore and Read, 1991). The Moore-Read wavefunctions are

$$\Psi_{MR}(z_1,\ldots,z_N)=\mathrm{Pf}\left(\frac{1}{z_i-z_j}\right)\prod_{i<j}(z_i-z_j)^n\ \exp(-\frac{1}{4\ell_0^2}\sum_{i=1}^{N}|z_i|^2) \tag{484}$$

which describes an FQH of electrons at filling fraction $\nu = 1/n$, with n an *even* integer. Here, $\mathrm{Pf}\big(1/(z_i - z_j)$ is the Pfaffian of the matrix $1/(z_i - z_j)$.

This state was motivated by the discovery of an unexpected FQH state in the $N = 1$ Landau level with an *even denominator* filling fraction $\nu = 5/2$ by Willett and coworkers in 1987 (Willett et al., 1987; Eisenstein et al., 1988; Pan et al., 2008). Until then, (and since then) this is the only FQH state with an even denominator filling fraction. The Pfaffian factor has a simple pole when two coordinates approach each other. However, provided $n \geq 1$, the "Laughlin factor" in the MR wavefunction cancels the singularity. We will shortly discuss the CFT construction of the Moore-Read state. The poles in the MR wavefunction suggest that in this state the electrons can get closer to each other than in a Laughlin state. This observation suggests that there may be some form of attraction (or suppression of repulsion) between the electrons in the MR state and motivated the notion that the observed even-denominator plateau may be physically related to some sort of pairing interaction. Shortly after the Moore-Read proposal was made, a paired wave function at $\nu = 1/2$ with a Pfaffian factor was also proposed by Greiter et al. (1991, 1992) and Wen (1991) who suggested that it reflects electrons pairing in the $\ell = 1$ angular momentum channel in time-reversal breaking condensate with symmetry $p_x + ip_y$.

Although following the logic behind the Kohn-Luttinger mechanism for paring in angular momentum state $\ell geq1$ with repulsive interactions (Kohn and Luttinger, 1965; Chubukov, 1993; Raghu and Kivelson, 2011), it may be possible to get a paired state even in the lowest Landau level (although there is no evidence for it, so far), the $N = 1$ Landau level may be more hospitable to such a state. Indeed, in the $N = 1$ Landau level the single-particle states i have angular momentum greater or equal than 1, and their probability distributions are suppressed both at short and long distances; these states look like smoke-rings. The matrix elements of the Coulomb potential in the $N = 1$ Landau level are parametrically suppressed at short distances (compared with the states in the lowest, $N = 0$, Landau level). In this scenario, the $\nu = 5/2$ plateau is interpreted as a $\nu = 1/2$ fully polarized state of the $N = 1$ Landau level, with an $N = 0$ Landau level filled with electrons with both spin polarizations in a state with $\nu = 2$. There is numerical evidence that an instability in a p-wave paired state such as the MR state is favored if the short-distance repulsion between the *composite fermions* is softened (Park et al., 1998).

In fact, in 1983, Halperin (1983) considered generalizations of the Laughlin state in which due to very strong attractive interactions, electrons would form clusters which then condense into a Laughlin-type state. The simplest example was Laughlin state of bosons (paired electrons) a paired state at $\nu = 1/2$ whose Laughlin quasihole carries charge $e/4$. Extensive numerical calculations are more compatible with the MR state than with the Halperin state of pairs (Morf, 1998). We will see shortly that the Halperin state is an Abelian relative of the MR state.

Moore and Read derived the wave function of Eq. (484) by considering a CFT with two sectors: a chiral boson CFT with compactification radius $R = \sqrt{n}$, and a chiral Majorana fermion CFT, i.e. the chiral part of the 2D Ising CFT, discussed in Section "The Ising model in a transverse field." The chiral Ising CFT has central charge $c = 1/2$ and several primary fields: the identity I, the twist field σ, and the (chiral) Majorana fermion χ with (chiral) scaling dimensions 0, 1/16, and 1/2, respectively. The propagator of the Majorana fermion, which is a free field, is

$$\langle\chi(z)\ \chi(w)\rangle=\frac{1}{z-w}. \tag{485}$$

The primary field σ, the "twist field," is nonlocal with respect to the Majorana fermion χ, and changes its boundary conditions from periodic to antiperiodic.

The fusion rules of the chiral Ising CFT are

$$\chi\star\chi=I,\qquad\sigma\star\sigma=I+\chi,\qquad\sigma\star\chi=\chi. \tag{486}$$

What will be important below is that the σ field has two fusion channels. As in the analysis of the Laughlin states, the compactified boson n primaries (anyons), the vertex operators $V_p(x) = \exp(ip\phi(x)/n)$, with $n = 0, 1, \dots n$ and there are n types of anyons, and a (charge) current $J = \frac{i}{\sqrt{n}}\partial_z\phi(z)$.

The first task is to identify the electron operator, which has to be a fermion and has to carry electric charge. This means that it is a composite of an operator (with Fermi statistics) the (neutral) chiral ising CFT and a vertex operator whose charge is an integer multiple of e. The desired electron operator is $\psi_e(z) = \chi(z)\ \exp(i\sqrt{n}\phi(z))$ whose correlator is $\langle\chi(z)V_n(z)\chi(w)V_{-n}(z)\rangle = 1/(z-w)^{1+n}$, which is a fermion with charge e.

The n-point function of the chiral Majorana fermions is

$$\langle\chi(z_1)\dots\chi(z_N)\rangle = \mathrm{Pf}\left(\frac{1}{z_i - z_j}\right) \tag{487}$$

which follows from applying Wick's theorem. Then we see that the MR wave function is the expectation value

$$\Psi_{MR}(z_1, \dots, z_N) = \langle\chi(z_1)\dots\chi(z_N)\rangle \times \left\langle \left(\prod_{i=1}^{N}\exp\big(i\sqrt{n}\phi(z_i)\big)\right)\ \exp\left(-i\int d^2z'\sqrt{n}\,\rho_0\ \phi(z')\right)\right\rangle \tag{488}$$

Next we need to identify the primary fields of the tensor product of the chiral Ising CFT, $\mathbb{Z}_2$, and the chiral $U(1)$ CFT with compactification radius $R = \sqrt{n}$. The allowed primary field must be *local* with respect to the electron operator, ψ_e. This leaves us with four primary fields: (a) the identity I, (b) the non-Abelian vortex $\sigma(z) \times \exp\left(\frac{i}{2\sqrt{n}}\phi(z)\right)$ with charge $e/(2n)$ and non-Abelian statistics, (c) the charge-neutral Majorana fermion χ, and (d) the Abelian vortex (the Laughlin quasihole) $\exp\left(\frac{i}{\sqrt{n}}\phi(z)\right)$, with charge e/n and Abelian statics $\delta = \pi/n$.

The new feature here is the non-Abelian fractional statistics of the non-Abelian vortex sometimes called a "half-vortex." Its non-Abelian character is a consequence of the fact that the fusion of two twist fields has two channels, see Eq. (486). This implies that the wave function of four non-Abelian vortices can be expressed as a linear combination of two so-called conformal blocks. In other words, this wave function belongs to a degenerate two-dimensional Hilbert space, each component labeled by a conformal block (Di Francesco et al., 1997). A braiding operation between two non-Abelian vortices is a monodromy of the wave function that induces a unitary transformation U in this Hilbert space

$$U = \frac{1}{\sqrt{2}}\exp\left[i\pi\left(\frac{1}{8} + \frac{1}{4n}\right)\right] \times \begin{pmatrix} 1, & 1 \\ -1 & 1 \end{pmatrix} \tag{489}$$

Therefore, the degenerate Hilbert space of four quasiholes provides a two-dimensional representation of the Braid Group. This observation is the basis for regarding a state of four non-Abelian quasiholes as a qubit. Furthermore, Nayak and Wilczek showed that a state of $2p$ quasiholes spans a 2^{p-1}-dimensional degenerate Hilbert space (Nayak and Wilczek, 1996). This means that, for large p, the degeneracy *per quasihole* is $\sqrt{2}$. In other words, this degeneracy is not due to a local degree of freedom attached to each quasihole but that it is shared in a nonlocal fashion!

In what sense are the Moore-Read states paired? In an insightful paper Read and Green (2000) used a BCS theory approach to investigate the pairing properties of a condensate of composite fermions in the $p_x + ip_y$ channel. The mean-field BCS Hamiltonian is

$$H_F = \int d^2k\left[(\varepsilon(\boldsymbol{k}) - \mu)\psi^\dagger(\boldsymbol{k})\psi(\boldsymbol{k}) + \frac{1}{2}\left(\Delta^*(\boldsymbol{k})\psi(-\boldsymbol{k})\psi(\boldsymbol{k}) + \Delta(\boldsymbol{k})\psi^\dagger(\boldsymbol{k})\psi^\dagger(-\boldsymbol{k})\right)\right] \tag{490}$$

where $\psi(\boldsymbol{k})$ is the composite fermions field, $\varepsilon(\boldsymbol{k}) = \frac{\boldsymbol{k}^2}{2M}$, and $\Delta(\boldsymbol{k})$ is the gap function. For a $p_x + ip_y$ condensate, the gap function transforms under rotations as an $\ell = -1$ angular momentum eigenstate, and for $\boldsymbol{k} \to 0$, it behaves as $\Delta(\boldsymbol{k}) = (k_x - ik_y)\Delta$, where Δ is a constant pairing amplitude.

The BCS ground state has the form

$$|G\rangle = \prod_{\boldsymbol{k}}\left(u(\boldsymbol{k}) + v(\boldsymbol{k})\psi^\dagger(\boldsymbol{k})\psi^\dagger(-\boldsymbol{k})\right)|0\rangle \tag{491}$$

where $|u(\boldsymbol{k})|^2 = |v(\boldsymbol{k})|^2 = 1$. The amplitudes $u(\boldsymbol{k})$ and $v(\boldsymbol{k})|$ satisfy the Bogoliubov–de Gennes equation (BdG)

$$\begin{pmatrix} \xi(\boldsymbol{k}) & -\Delta^*(\boldsymbol{k}) \\ -\Delta(\boldsymbol{k}) & -\xi^*(\boldsymbol{k}) \end{pmatrix}\begin{pmatrix} u(\boldsymbol{k}) \\ v(\boldsymbol{k}) \end{pmatrix} \equiv E(\boldsymbol{k})\hat{\boldsymbol{n}}(\boldsymbol{k})\cdot\boldsymbol{\sigma}\begin{pmatrix} u(\boldsymbol{k}) \\ v(\boldsymbol{k}) \end{pmatrix} = E(\boldsymbol{k})\begin{pmatrix} u(\boldsymbol{k}) \\ v(\boldsymbol{k}) \end{pmatrix} \tag{492}$$

where $\xi(\boldsymbol{k}) = \varepsilon(\boldsymbol{k}) - \mu$, $\boldsymbol{\sigma} = (\sigma_x, \sigma_y, \sigma_z)$ are the Pauli matrices, and $\hat{\boldsymbol{n}}(\boldsymbol{k}) = (-\mathrm{Re}\Delta(\boldsymbol{k}), \mathrm{Im}\Delta(\boldsymbol{k}), \xi(\boldsymbol{k}))$ is a unit vector defined for every $\boldsymbol{k}$. The eigenvalues $E(\boldsymbol{k})$ and the eigenvectors $(u(\boldsymbol{k}), v(\boldsymbol{k})$ are

$$E(\boldsymbol{k}) = \sqrt{\xi^2(\boldsymbol{k}) + |\Delta(\boldsymbol{k})|^2}, \qquad \frac{v(\boldsymbol{k})}{u(\boldsymbol{k})} = -\frac{E(\boldsymbol{k}) - \xi(\boldsymbol{k})}{\Delta^*(\boldsymbol{k})}. \tag{493}$$

The spinor amplitudes are $|u(\boldsymbol{k})|^2 = \frac{1}{2}\left(1 + \frac{\xi(\boldsymbol{k})}{E(\boldsymbol{k})}\right)$ and $v(\boldsymbol{k}) = \frac{1}{2}\left(1 - \frac{\xi(\boldsymbol{k})}{E(\boldsymbol{k})}\right)$.

In the low momentum limit and in real space, the BdG equations become

$$\begin{aligned} i\partial_t u &= -\mu u + \Delta^* i(\partial_x + i\partial_y)v \\ i\partial_t v &= \mu v + \Delta i(\partial_x - i\partial_y)u \end{aligned} \tag{494}$$

which is just the Dirac equation in 2+1 dimensions, with μ playing the role of the mass, and with the restriction that the spinor (u, v) obeys the Majorana condition

$$(u, v)\begin{pmatrix} 0 & 1 \\ 1 & 0 \end{pmatrix} = \begin{pmatrix} u \\ v \end{pmatrix}. \tag{495}$$

The Majorana condition is obeyed in all superconductors and reflects the fact that in these condensates only the fermion parity $(-1)^{N_F}$ (with N_F being the number of fermions) is conserved while the fermion number N_F is not.

This is a good BCS state in that it is fully gapped and is chiral. Assuming that the pair fields in the p_x and p_y channels are equal, they showed that the BCS ground state $|G\rangle$ has the form

$$|G\rangle \sim \exp\left(\frac{1}{2}\sum_{\boldsymbol{k}} g(\boldsymbol{k})\psi^\dagger(\boldsymbol{k})\psi^\dagger(-\boldsymbol{k})\right)|0\rangle. \tag{496}$$

Projected onto a state with N fermions with real space coordinates $\boldsymbol{x}_i$, the wave function is a Pfaffian

$$\Psi(\boldsymbol{x}_1, \ldots, \boldsymbol{x}_N) = \langle \boldsymbol{x}_1, \ldots, \boldsymbol{x}_N | G\rangle = \mathrm{Pf}(g(\boldsymbol{x}_i - \boldsymbol{x}_j)). \tag{497}$$

The long-distance behavior of this wave function depends on whether the chemical potential $\mu > 0$ (this is the weak-pairing or BCS regime) or $\mu < 0$ (which is the strong pairing BEC-like regime). While in the case of an s-wave superconductor these two regimes are smoothly connected by a crossover, in the $p_x + ip_y$ case, they are separated by a quantum phase transition at $\mu = 0$. In the weak pairing regime, the function $g(\boldsymbol{k})$ has the asymptotic long-distance form, as $\boldsymbol{k} \to 0$,

$$g(\boldsymbol{k}) \simeq -\frac{2\mu}{(k_x + ik_y)\Delta^*} \tag{498}$$

where the pair field behaves as $\Delta(\boldsymbol{k}) \simeq (k_x - ik_y)\Delta$. In real space (in complex coordinates), the function $g(z)$ becomes

$$g(z) = \left(\frac{i\mu}{\pi\Delta^*}\right)\frac{1}{z} \tag{499}$$

which is the form used in the Pfaffian wave function. On the other hand, in the strong pairing regime, $\mu < 0$, $g(\boldsymbol{k})$ has the asymptotic behavior

$$g(\boldsymbol{k}) \simeq -A\frac{(k_x - ik_y)}{a_0^{-2} + \boldsymbol{k}^2} \tag{500}$$

where A and a_0 are functions of Δ and μ,

$$A = \frac{2|\mu|M\Delta}{2|\mu| + m|\Delta|^2}, \qquad a_0 = \frac{1}{2|\mu|}\sqrt{\frac{2|\mu|}{M} + |\Delta|^2}. \tag{501}$$

In real space, at distances $|\boldsymbol{x}| \gg a_0$, the Fourier transform of $g(\boldsymbol{k})$ decays exponentially, and as $a_0 \to \infty$, $\mu \to 0$, and the Fourier transform $g(z)$ has the power-law behavior

$$g(z) \simeq \left(\frac{i|\Delta|}{2\pi\Delta^*}\right)\frac{1}{z|z|} \tag{502}$$

This means that $\mu = 0$ is a quantum critical point that separates the weak pairing phase from the strong pairing phase, which have distinct properties.

Read and Green then used a topological argument, originally formulated by Volovik (1988) in the context of superfluid ^{3}He films. To see this, we notice that the three-component unit vector $\hat{\boldsymbol{n}}(\boldsymbol{k})$ takes values on the surface of a sphere S_2. In addition, since $v(\boldsymbol{k}) \to 0$ for $\boldsymbol{k} \to \infty$(and, hence $u(\boldsymbol{k}) \to 1$), we can wrap the momentum space $\boldsymbol{k}$ onto a sphere S_2. Thus $\hat{\boldsymbol{n}}(\boldsymbol{k})$ are smooth functions of $S_2 \mapsto S_2$. such maps are classified into the homotopy classes of $\pi_2(S_2) \simeq \mathbb{Z}$ given in terms of the integer-valued topological invariant

$$Q = \frac{1}{4\pi}\int d^2k\, \hat{\boldsymbol{n}}(\boldsymbol{k}) \cdot \partial_{k_x}\hat{\boldsymbol{n}}(\boldsymbol{k}) \times \partial_{k_y}\hat{\boldsymbol{n}}(\boldsymbol{k}). \tag{503}$$

In the strong pairing phase $\mu < 0$, and $\xi(\boldsymbol{k}) > 0$ and $\hat{\boldsymbol{n}}(\boldsymbol{k})$ takes values only on the northern hemisphere of the target space S_2. Such maps can be deformed continuously to the North Pole and, hence, are topologically trivial, $Q = 0$. On the other hand, in the weak pairing phase, $\mu > 0$, $\xi(\boldsymbol{k})$ takes both positive and negative values. In this phase, $\hat{\boldsymbol{n}}(\boldsymbol{k})$ is topologically nontrivial and the topological invariant Q takes nontrivial values $\pm$ 1.

The upshot of this analysis is that, in the weak pairing phase, the paired FQH state is, at this mean field level, a two-dimensional *topological superconductor*. Read and Green (2000) further showed that this pairing state has vortices with an interesting fermionic spectrum. A vortex is a state win which at long distances the (complex) amplitude of the $p_x + ip_y$ condensate behaves as $\Delta \exp(i\varphi)$, where φ is the azimuthal angle, which winds by 2π on a circumference of large radius R. The BdG equation, Eq. (494), has zero mode solutions. In polar coordinates (r, φ) the BdG equation the zero modes satisfy

$$\begin{aligned} \Delta i e^{i\varphi}\left(\partial_r + \frac{i}{r}\partial_\varphi\right)v &= \mu u \\ \Delta i e^{-i\varphi}\left(\partial_r - \frac{i}{r}\partial_\varphi\right)u &= -\mu v \end{aligned} \tag{504}$$

The normalizable zero mode spinor solution is

$$\begin{pmatrix} u(r,\varphi) \\ v(r,\varphi) \end{pmatrix} = \frac{f(r)}{\sqrt{r}} \begin{pmatrix} \frac{1}{\sqrt{i}} e^{i\varphi/2} \\ \frac{1}{\sqrt{-i}} e^{-i\varphi/2} \end{pmatrix} \tag{505}$$

where $f(r)$ is given by

$$f(r) \sim \exp\left(-\int_0^r dr' \frac{\mu(r')}{|\Delta|}\right) \sim \exp(-\mu r/|\Delta|). \tag{506}$$

Under a 2π rotation, this spinor solution is double-valued

$$(u(r,\varphi+2\pi), v(r,\varphi+2\pi)) = -(u(r,\varphi), v(r,\varphi)) \tag{507}$$

which follows from the global phase invariance. I fact, in all paired states, topological or not, under a global transformation of the pair field by a phase θ, the (composite) fermion must transform with a phase of $\theta/2$,

$$\Delta(\boldsymbol{x}) \mapsto e^{i\theta}\Delta(\boldsymbol{x}), \qquad \psi(\boldsymbol{x}) \mapsto e^{i\theta/2}\psi(\boldsymbol{x}), \qquad \psi^\dagger(\boldsymbol{x}) \mapsto e^{-i\theta/2}\psi^\dagger(\boldsymbol{x}). \tag{508}$$

In other words, in a paired state, the fermion is nonlocal to the vortex. Hence, under a 2π phase transformation of the pair field, the fermions must change sign, and the spinor zero mode solution must be double-valued. This means that this state has a branch cut.

The structures of the vortex and the fermion zero mode are closely related to the problem of solitons with fractional charge that we discussed in Section "Fractionally charged solitons." In fact, Jackiw and Rossi (1981) investigated a closely related problem of a theory of Dirac field in 2+1 dimensions coupled to a charged scalar field through a Yukawa coupling with the form of a Majorana mass. They showed that such a theory admits vortex solutions with fermion zero modes. In a subsequent paper, Weinberg (1981) showed that these zero modes are counted by an index theorem which relates the number of zero modes to the vorticity. More recently, Nishida et al. (2010) showed that the relativistic theory of Jackiw and Rossi in the nonrelativistic approximation reduces to the theory of a $p_x + ip_y$ superconductor.

There is, however, a subtle but profound difference between the fermion zero modes of the one-dimensional fractionally charged solitons and the fermion zero modes of a superconductor. In the case of the 1D solitons, the zero modes can be either occupied or empty rendering a soliton charge of $-e/2$ or $+e/2$. However, in the case of the superconductor, the BdG fermions are charge-neutral since their charge has gone into the condensate. Thus, in a superconductor, fermion number is not conserved, and only the fermion parity is conserved. This means that the field operator associated with the vortex zero mode, which we will denote by γ, must be a self-adjoint operator, $\gamma^\dagger = \gamma$.

Ivanov (2001) showed that this behavior is the origin of the non-Abelian fractional statistics in this system. Indeed, if one considers a configuration with $2n$ vortices, each will carry a Majorana zero mode γ_i. Since these are fermion operators, they satisfy the usual anticommutator algebra, $\{\gamma_i, \gamma_j\} = 2\delta_{ij}$. We can (arbitrarily) group the $2n$ Majorana fermion operators into n pairs. For each *pair* we can define a complex Dirac operator $\psi_j = (\gamma_{2j} + i\gamma_{2j+1})/2$ (and its adjoint), which satisfies the usual fermionic algebra, $\{\psi_j, \psi_k^\dagger\} = \delta_{jk}$. Each Dirac fermion can be either in an empty state or in an occupied state. Thus a system of $2n$ vortices supports a degenerate Hilbert space of dimension 2^{n-1}, which agrees with the results of Nayak and Wilczek (1996). However, the assignment of Majorana operators to specific pairs is actually arbitrary, which amounts to a particular definition of the branch cuts. Changing the assignment of the operators into pairs is then equivalent to a rearrangement of the cuts. In 2006, Stone and Chung (2006) showed that these vortices obey the braiding and fusion properties of *Ising* anyons. These properties follow from the branch-cut configurations that affect the monodromies of the vortices. It is important to stress that the vortices with zero modes are the non-abelions. Majorana fermions are fermions and, as such, are abelian.

In addition to the Moore-Read Pfaffian state, the CFT approach has led to the formulation of new nontrivial FQH states. Read and Rezayi (1999) proposed a series of so-called cluster states, which generalize the concept of paired states. They investigated a particular type of cluster states in which the Pfaffian factor of the MR state is replaced by a correlator of *parafermion* primary fields of a $\mathbb{Z}_k$ CFT of Zamolodchikov and Fateev (1985). Parafermions were originally introduced by Fradkin and Kadanoff (1980) (see also Alcaraz and Köberle, 1981) as a generalization of the fermions of the 2D Ising model to the $\mathbb{Z}_k$ clock model. In this model, one can define several types of parafermions each consisting of the fusion of a charge operator and a magnetic (disorder) operator. These operators obey an algebra of the type $AB = \exp(ip2\pi/k)BA$, where the integer p depends on the electric and magnetic charges of the parafermions, which is reminiscent of fractional statistics. In close analogy with the Majorana fermions of the 2D Ising model, $\mathbb{Z}_k$ CFT describes the behavior of these systems their self-dual points.

The $\mathbb{Z}_k$ CFT is actually much richer and has more primary fields than the $\mathbb{Z}_2$ case of the Ising model. As a CFT, the $\mathbb{Z}_k$ theory is the same as the CFT on the coset $SU(2) - k/U(1)$. A coset means that a $U(1)$ sector has been projected out of the spectrum. Here we will focus on a special case of the $\mathbb{Z}_3$ CFT. This CFT has a parafermion primary field, which we will call ψ, and a non-Abelian primary that we will call τ. Read and Rezayi (1999) proposed to replace the Pfaffian factor of the MR state with a correlator of N parafermions of a $\mathbb{Z}_3$ CFT and a Laughlin factor with an exponent of $n + 2/3$. Such states require that the number of electrons N be a multiple of 3. Thus, these states can be viewed as sates in which the electrons cluster in groups of 3. They also considered the more general case of the $\mathbb{Z}_k$ CFT in which case N is a multiple of k. The resulting filling fractions are $\nu = k/(mk + 2)$ (with $m \geq 0$). The Read-Rezayi $k = 3$ parafermion state is a leading candidate for the observed FQH plateau at $\nu = 12/5 = 2 + 2/5$ (Pan et al., 2003; Xia et al., 2004) (the compering state being the 2/5 Jain state). There is strong numerical support for the 12/5 state being a $\mathbb{Z}_3$ parafermion (Rezayi and Read, 2009).

The quasiholes obtained by inserting the primary fields τ in the correlator of parafermions have interesting properties that stem from their basic fusion rule

$$\tau \star \tau = I + \tau \tag{509}$$

Read and Rezayi (1999) showed that the number of conformal blocks for $3n$ quasiholes, that is, the number of degenerate states, in the parafermion theory is the Fibonacci number F_{3n-2}, where $F1 = 1$, $F_2 = 2$, $F_3 = 3$, $F_4 = 5$. In general $F_m = F_{m-1} + F_{m-2}$. For $m \to \infty$, the rate of increase approaches the limit $\lim_{m\to\infty} F_m/F_{m-1} = (1 + \sqrt{5})/2$, which is known as the Golden Mean. In other words, for large m, the dimension of the Hilbert space increases exponentially as $((1 + \sqrt{5})/2)^m$. Aside from these interesting mathematical curiosities, the significance of this fusion rule is that these states, regarded as"qubits," define unitary transformations that cover uniformly the Bloch sphere, which is required for universal quantum computation (Freedman et al., 2002a).

At the level of topological quantum field theory, the Moore-Read and Read-Rezayi states are related to the non-Abelian Chern–Simons gauge theory with gauge group $SU(2)$ at Chern–Simons level k. In the more general case of the gauge group, $SU(N)$ on a manifold $\mathcal{M}$ action is given by

$$S_{\mathrm{CS}}[A_\mu] = \frac{k}{4\pi}\int_{\mathcal{M}} d^3x\, \epsilon_{\mu\nu\lambda}\left(A_a^\mu \partial^\nu A_a^\lambda + \frac{2}{3} f_{abc} A_a^\mu A_b^\nu A_c^\lambda\right) \tag{510}$$

where $k \in \mathbb{Z}$ is the level, the gauge fields $A^\mu = A_a^\mu t_a$ take values in the algebra of $SU(N)$, with $\{t_a\}$ being the $N^2 - 1$ generators, and f_{abc} are the structure constants of $SU(N)$. The expectation values of Wilson loop operators of this theory compute the Jones polynomials that are topological invariants of knot theory (Witten, 1989). The connection with $SU(2)_k$ Chern–Simons gauge theory has been essential in formulating effective low energy quantum field theories for the non-Abelian states (Fradkin et al., 1998, 1999; Barkeshli and Wen, 2010; Goldman et al., 2019, 2020, 2021).

Edge states and chiral conformal field theory

We will now discuss the edge states of the FQH states. As we saw, the FQH states are incompressible in the bulk and all bulk excitations are gapped. The edge of the region occupied by the fluid (in many cases that edge of the physical sample) is where the bulk gap collapses and hence where the system has low energy excitations.

The role of edges and their nature can be seen already in the simple case of the integer Hall effect treated as a system of free fermions in the lowest Landau level. In this state, all single particle states are occupied, and the bulk ground state wave function is a Slater state that takes the form of the Vandermonde determinant of Eq. (377). The potential that keeps the electrons inside the sample increases monotonously near the edge. As we discussed in Section "Landau levels and the integer Hall effect," in this region, the electrons experience an electric field E that pushes them into the sample, and in the presence of the perpendicular magnetic field B, the electrons move *along the edge* at the drift velocity $v = c|E|/|B|$. At some spatial location, corresponding to the locus of a single particle Landau state, the potential crosses the Fermi energy and in that region, potential is essentially a linear function of the coordinate and hence of momentum (or angular momentum depending on the gauge that is being used). In other words, the low energy states are one branch of a one-dimensional chiral excitation, such as in the right-moving states of our discussion of the chiral anomaly in Section "Chiral symmetry and chiral symmetry breaking."

In Section "Quantization of Abelian Chern–Simons gauge theory," we showed that a Chern–Simons gauge theory on a manifold with a boundary projects onto a chiral CFT on that boundary. In that section we showed that an Abelian Chern–Simons theory $U(1)_m$ integrates to the boundary, the 1+1-dimensional Minkowski spacetime $S^1 \times \mathbb{R}$, as a chiral $U(1)_m$ CFT for a compactified boson with compactification radius $R = 1$ whose action is given by

$$S[\varphi] = \int_{S^1\times\mathbb{R}} d^2x\, \frac{1}{4\pi}\, \left[\partial_0\phi\partial_1\phi - v(\partial_1\phi^2)\right] \tag{511}$$

where we rescaled the compactified scalar by a factor of $\sqrt{m}$ to that its compactification radius $R = \sqrt{m}$ as in Section "Fractional quantum hall wave functions and conformal field theory." The only difference between the theory of Eq. (241) and what we did in Section "Fractional quantum hall wave functions and conformal field theory" is that this theory is in a 1+1-dimensional Minkowski spacetime $S_1 \times \mathbb{R}$ while before we were in Euclidean spacetime. In the case of the integer quantum Hall effect $\nu = 1$ (and hence $m = 1$) and the (time-ordered) correlator of the vertex operator, $V_1(x,t) = \exp(i\phi(x,t))$ is

$$\langle T \exp(i\phi(x,t)) \exp(-i\phi(0,0)) \rangle = \frac{1}{x - vt - i\varepsilon} \tag{512}$$

which is, indeed, the propagator of a chiral free fermion.

On the other hand, for the Laughlin states at filling fraction $\nu = 1/m$ (and compactification radius $R = \sqrt{m}$), the propagator of the electron $\psi_e \sim \exp(i\sqrt{m}\phi)$ is

$$\langle T \exp(i\sqrt{m}\phi(x,t)) \exp(-i\sqrt{m}\phi(0,0)) \rangle \sim \frac{1}{(x - vt - i\varepsilon)^m} \tag{513}$$

while the propagator of the quasihole $\exp\left(\frac{i}{\sqrt{m}}\phi\right)$ is

$$\left\langle T \exp\left(\frac{i}{\sqrt{m}}\phi(x,t)\right) \exp\left(-\frac{i}{\sqrt{m}}\phi(0,0)\right) \right\rangle \sim \frac{1}{(x - vt - i\varepsilon)^{1/m}}. \tag{514}$$

Therefore, the CFT of the edge is the same as the CFT of the ideal wavefunction with the only difference that the former is in Minkowski spacetime while the latter is in Euclidean spacetime.

In this sense, there is a one-to-one correspondence between the bulk and the edge. We can also see how that works by considering a fundamental Wilson arc in the bulk along a path $\gamma(x, y)$ where x and y are at the boundary

$$\langle W[\gamma] \rangle = \langle \exp(i \int_{\gamma(x,y)} dx_\mu \mathscr{A}^\mu) \equiv \langle \exp(\frac{i}{\sqrt{m}}\phi(x)) \exp(-\frac{i}{\sqrt{m}}\phi(y)) \rangle \tag{515}$$

where on the right-hand side we have rescaled the field by $\sqrt{m}$, as before. The scaling dimensions of the electron, the quasihole, and the current are $\Delta_e = \frac{m}{2}$, $\Delta_{qh} = \frac{1}{2m}$, and $\Delta_{\text{current}} = 1$. These results will be important shortly.

The same structure applies to the multicomponent Abelian FQH states. The only difference is that in multicomponent FQH states, the edge consists, in general, of a charge field that couples to the electromagnetic field and one or more neutral edge states. An example is the theory of the non-Abelian Pfaffian states at filling fraction $\nu = 1/n$. In this case the edge theory consists of a compactified chiral boson ϕ of radius $R = \sqrt{n}$ and a chiral Majorana (neutral) fermion χ. At a formal level, the Lagrangian for the edge state(s) is a sum of two terms

$$\mathcal{L} = \frac{1}{4\pi}(\partial_x\phi\partial_t\phi - v_c(\partial_x\phi)^2) + \chi i(\partial_t - v_n\partial_x)\chi \tag{516}$$

where v_c and v_n are the velocities of the (charged) compactified chiral scalar ϕ and of the neutral Majorana field χ. Numerically (and experimentally) it is known that the charge mode is (substantially) faster than the neutral mode(s), $v_c > v_n$, and often by significant factors.

A superficial reading of this Lagrangian suggests that these degrees of freedom are decoupled. However this is not correct. Only operators from both sectors, which are local with respect to the electron $\psi_e \sim \chi \exp(i\sqrt{n}\phi)$, are physically allowed. Here an operator is local with respect to the electron means that the operator braids trivially with the electron. This condition restricts the allowed observables. In the case of the fermionic MR state, with $n = 2$, the allowed operators are the non-abelion $\sigma \exp(i\phi/2\sqrt{2})$, where scaling dimension is $\Delta = 1/8$ and electric charge is $Q = 1/4$, the Majorana fermion with scaling dimension $\Delta = 1/2$ and no electric charge $Q = 0$, and the Laughlin quasiparticle with scaling dimension $\Delta = 1/4$ and charge $Q = 1/2$. Its electron operator has scaling dimension $\Delta = 3/2$ and charge $Q = 1$.

CFT has an important defining universal quantity called the central charge, which is closely related to the energy–momentum tensor of the theory (Di Francesco et al., 1997). For pedagogical introductions to CFT, see Affleck (1990) and Cardy (1996) and Chapter 21 of Fradkin (2021). The energy–momentum tensor $T_{\mu\nu}$ is a locally conserved current, $\partial^\mu T_{\mu\nu} = 0$. Its local conservation implies the global conservation of energy and momentum. As such, the energy–momentum tensor is a fundamental observable of any quantum field theory. In a CFT, the energy–momentum tensor is also the generator of local scale and conformal transformations. In the special case of 1+1-dimensional systems, such as the edge states of the FQH fluids, the energy-momentum tensor has special and crucially important properties. In addition to being locally conserved, conformal invariance requires that $T_{\mu\nu}$ must be traceless, $T^\mu_\nu = 0$, since its trace is the generator of dilations. In this case, if the theory is chiral, the energy-momentum tensor has only one (right-moving) component $T = (T_{00} - T_{11})/2$. In complex coordinates of the Euclidean metric, the correlator of the energy momentum tensor $T = T_{zz}$ is (Belavin et al., 1984)

$$\langle T(z) T(w) \rangle = \frac{c/2}{(z - w)^4} \tag{517}$$

where c is a universal quantity known as the central charge of the CFT. In the case of the compactified boson, the central charge is $c = 1$, whereas for a massless Majorana fermion, $c = 1/2$.

The central charge of the CFT enters in many observables of fundamental physical importance. For example, for a 1+1-dimensional system of length L, such as the edge state of an FQH droplet, the ground state energy E_{gnd} for large L has the behavior (Affleck, 1986; Blöte et al., 1986)

$$E_{\text{gnd}} = \varepsilon_0 L - c\frac{\pi v}{6L} + O(1/L^2) \tag{518}$$

where ε_0 is the ground state energy density, which is a nonuniversal quantity, c is the central charge of the CFT, and v is the velocity of the massless modes. The second term in Eq. (518) is known as the Casimir energy. Similarly, the free energy density $f(T)$ of a CFT has the low temperature Stefan–Boltzmann behavior (in one dimension)

$$f(T) = \varepsilon_0 + c\frac{\pi T^2}{6v} + O(T^3) \tag{519}$$

where we set the Boltzmann constant to unity. The low-temperature specific heat $c(T)$ is

$$c(T) = c\frac{\pi T}{3v} + O(T^2). \tag{520}$$

In a chiral CFT, such as the edge states of the FQH fluids, the central charge enters in the low temperature behavior of the (Hall) thermal conductivity κ_{xy}, (Read and Green, 2000)

$$\kappa_{xy} = c\frac{\pi T}{6\hbar}. \tag{521}$$

Much of what is known about FQH states comes form experiments involving their edge states. In a series of exquisite experiments of Granger et al. (2009) measured κ_{xy} in the edge states of a $\nu = 1$ quantum Hall fluid and showed that the heat transport is indeed chiral, that is, the edge state behaves as a heat "diode." This effect was confirmed in the FQH states by Bid et al. (2010) who, in addition, used this effect to detect the neutral modes in several Jain states at filling fractions 2/3 and 2/5 and in the non-Abelian state at $\nu = 5/2$. These experiments are a key confirmation that the edge states of fractional quantum Hall states are indeed chiral Luttinger liquids (CLL).

Point contact tunneling and QH chiral edge states

The simplest experimental probes are quantum point contacts and typically are of two types: inter-edge tunneling inside an FQH liquid or tunneling of electrons into the edge state of a FQH liquid. Since the bulk is gapped, only the edge states participate in these tunneling processes. In the general case we will have two edges and a tunnel process at a point contact. Here the two edges can be either the two edges of the same FQH state, in which case the process happens inside the FQH liquid and involves tunneling of quasiparticles, or the edges of different liquids, in which case this process is external and involves tunneling of electrons. Problems of these types were first investigated by Kane and Fisher (1992), which led to a considerable amount of work on these problems.

Let us consider first the case of tunneling into the edge state of a $\nu = 1/m$ Laughlin state from a FL, which we will take to be a QH fluid in the $\nu = 1$ state. The point contact is at $x = 0$. The total Lagrangian is

$$\mathcal{L} = \mathcal{L}_{\text{edge}} + \mathcal{L}_{\text{FL}} - \Gamma\, e^{i\omega_0 t}\, \psi^\dagger_{e,\text{edge}}(0,t)\, \psi_{e,\text{FL}}(0,t) + \text{h.c.} \tag{522}$$

where $\omega_0 = eV/\hbar$, V is the bias voltage between the two fluids, and Γ is a tunneling matrix element. The local electron spectral density (the density of states) $N(\omega)$ at energy ω is

$$N(\omega) = \text{Im} \lim_{x\to 0^+} \int_{-\infty}^{\infty} dt\; G_e(x,t)\; e^{i\omega t} = \text{const.}\; |\omega|^{m-1} \tag{523}$$

where $G_e(x,t) = \langle T\psi_e^\dagger(x,t)\psi_e(0,0)\rangle$ is the electron correlator in the FQH edge, shown in Eq. (512). This result, combined with Fermi's Golden Rule for a point contact with voltage bias V, predicts a tunneling current from a FL into the chiral Luttinger liquid CLL of the edge state to be (Chamon and Fradkin, 1997)

$$I(V) = 2\pi\frac{e}{\hbar}|\Gamma|^2 \int_{-eV}^{0} dE\; N_{\text{CLL}}(E,T) N_{\text{FL}}(E+eV,T) \propto V^m \tag{524}$$

and a tunneling differential conductance $G(V)$

$$G(V) = \frac{dI}{dV} = 2\pi\frac{e}{\hbar}|\Gamma|^2 N_{\text{FL}}(0) N_{\text{CLL}}(V,T) \propto V^{m-1} \tag{525}$$

which is non-Ohmic and vanishes as $V \to 0$.

Early experiments by Chang et al. (1996) [reviewed by Chang (2004)], on a geometry that (most likely) had many point contacts, confirmed the predicted CLL behavior, although there were discrepancies in the measured exponents. The behavior seen in more recent experiments by Hashisaka et al. (2021) and Cohen et al. (2022) on a point contact in graphene is consistent with the theoretical predictions of Chamon and Fradkin (1997). Interestingly, these newer class of experiments also show evidence of an analog of Andreev reflection predicted to exist near the strong coupling fixed point of the theory of Sandler et al. (1999) as a consequence of electron fractionalization.

Most experiments are done on a geometry call a Hall bar in which the QH fluid occupies a rectangular region with its length L larger than its width W. In this geometry, there are chiral edge states at opposite sides of the Hall bar propagating in opposite directions. One type of point contact consists in creating a constriction in the quantum Hall fluid by applying a gate, a bias potential on a narrow strip across the Hall bar. This gate repels the electrons in the QH fluid, forcing the opposite edges to approach each other in the proximity of the gate. In the absence of the gate, momentum is conserved on each edge, which forbids tunneling across the Hall bar since the edge states have opposite Fermi momentum. However, the gate breaks translation invariance on both edges and tunneling between them is now allowed. In other words, the gate creates a point contact between the opposite propagating edge states leading to a tunneling process between the edges of the QH liquid. Thus, this is internal tunneling as opposed to the process of tunneling between two different liquids that we discussed above.

The tunneling Lagrangian for this system has the same form as in Eq. (522) except that now the two edges are identical. The theory by Kane and Fisher shows that in the factional case, the most relevant process is the tunneling of FQH quasiparticles. The Fermi Golden Rule argument used in Eq. (525) to compute the differential conductance also applies in the present case except that now the two densities of states are the densities of states of the (Laughlin) quasiparticles (instead of electrons). The local quasiparticle density of states is $N_{qp}(\omega) \sim |\omega|^{\frac{2}{m}-1}$. Then, the differential tunneling conductance $G(V)$ in this case is

$$G(v) \sim V^{2(\frac{1}{m}-1)}. \tag{526}$$

This behavior is also non-Ohmic but, unlike the case of electron tunneling of Eq. (522), the differential tunneling conductance now *diverges* as $V \to 0$. This behavior means that the $\Gamma \to 0$ fixed point is *unstable* and that the point contact flow to a *strong coupling fixed point* at $\Gamma \to \infty$. Early experiments by Milliken et al. (1996) showed indications of CLL behavior. The predicted behavior was confirmed in the experiments of Roddaro et al. (2004a, b).

In the RG language, we can define a dimensionless tunneling amplitude g by $\Gamma = a^{\Delta-1}g$, where Δ is the scaling dimension of the tunneling operator and a is a UV cutoff. The "tree-level" beta function is readily found to be

$$\beta(g) = a\frac{\partial g}{\partial a} = (1 - \Delta)\, g + O(g^2) \tag{527}$$

which shows that if the scaling dimension of the operator of the tunneling particle is $\Delta < 1$, then this tunneling process is relevant, while $\Delta > 1$ is irrelevant.

Kane and Fisher argued that there should be a crossover from the IR unstable weak-coupling fixed point governed by quasiparticle tunneling to an IR stable strong coupling fixed point governed by electron tunneling. This crossover is reminiscent of the crossover in quantum impurity problems such as the Kondo problem of a magnetic impurity in a metal (Anderson et al., 1970; Wilson, 1975; Andrei, 1980; Wiegmann, 1980; Read and Newns, 1983). The main difference is that the impurity coupling is marginal and the crossover scale, the Kondo temperature T_K, which is related to the coupling constant g as $T_K \sim \exp(-1/g)$, while in the FQH constriction, the crossover scale is $T_K(g) \sim g^{1/(1-\Delta)}$. Kane and Fisher argued that this crossover can be viewed as a process that interpolated between an FQH fluid with a weak constriction to a regime in which the Hall bar splits into two pieces with weak electron tunneling between them.

It turns out that, after some manipulations, the model of the constriction can be mapped into a one-dimensional compactified boson φ on a semi-infinite line, $x \geq 0$, with a vertex operator acting on the boundary. The action of this system, known as boundary sine-Gordon, is

$$S = \frac{1}{8\pi}\int_{-\infty}^{\infty} dt \int_{0}^{\infty} dx\, (\partial_\mu \varphi)^2 + \Gamma_{qp}\int_{-\infty}^{\infty} dt\ \cos\left(\sqrt{\frac{v}{2}}\varphi(0,t)\right). \tag{528}$$

This theory has two fixed points: (a) the IR unstable fixed point at $\Gamma_{qp} = 0$ where the field Neumann boundary conditions at $x = 0$, $\partial_x \varphi = 0$, and (b) an IR stable fixed point at $\Gamma_{qp} \to \infty$ where the field has Dirichlet boundary conditions, $\varphi = 2\pi\sqrt{2/v}\, n$ (with $n \in \mathbb{Z}$). It turns out that this is an integrable field theory. Fendley et al. (1995b) used the thermodynamic Bethe Ansatz to calculate the differential tunneling conductance for the Laughlin state at $v = 1/3$ as a function of voltage V and temperature T and obtained the full weak to strong crossover RG flow. Detailed predictions of this theory have been verified experimentally by the work of Roddaro et al. (2004a, b). Point-contact experiments were performed in the more challenging $v = 5/2$ FQH state by Miller et al. (2007) and Radu et al. (2008). They found that the MR state is the one that best fits their experimental results.

Experimental evidence of fractional charge

The charge of a quasiparticle can, in principle, be found directly by measuring the noise of a weak current. This process is known as shot noise. In the case of the constriction, the quasiparticle current operator is $I_{qp} = 2ev\Gamma_{qp}\sin\left(\sqrt{v/2}\phi + \omega_0^* t\right)$, where $\omega_0^* = evV/\hbar$. The noise spectrum, $S(\omega)$, of the tunneling current I_{qp} is (Kane and Fisher, 1994)

$$S(\omega) = \int_{-\infty}^{\infty} dt\ \langle\{I_{qp}(t), I_{qp}(0)\}\rangle\ e^{i\omega t}. \tag{529}$$

Using the expression of the quasiparticle correlator of Eq. (514), one readily finds that, to leading order in Γ_{qp}, the noise spectrum is

$$S(\omega) = ev\langle I_{qp}\rangle\left[\left(1 - \frac{\omega}{\omega_0^*}\right)^{2v-1} + \left(1 + \frac{\omega}{\omega_0^*}\right)^{2v-1}\right]. \tag{530}$$

In the limit of zero frequency, the noise spectrum takes the shot noise form

$$\lim_{\omega\to 0} S(\omega) = 2e^{*}\langle I_{qp}\rangle \tag{531}$$

where the expectation value of the tunneling current is

$$\langle I_{qp}\rangle = \frac{2\pi}{\Gamma(2\nu)} e\nu |\Gamma_{qp}|^2\ \omega_0^{*\,2\nu-1}. \tag{532}$$

Chamon et al. (1996) calculated the exact noise spectrum for the case of a $\nu = 1/2$ bosonic FQH state and were able to investigate the crossover as well, and Fendley et al. (1995a) used the Bethe Ansatz to construct a soliton basis to compute the DC shot noise.

These theoretical predictions were tested in tour-de-force experiments by de Picciotto et al. (1997) and by Saminadayar et al. (1997) who were able to measure the fractional charge of $e/3$ in the $\nu = 1/3$ state and, with some caveats, $e/5$ in the $\nu = 2/5$ state. Subsequent experiments by Dolev et al. (2008) went on to measure the charge from noise experiments in the non-Abelian state at $\nu = 5/2$ and obtained results consistent with $e^* = e/4$ as predicted by theory. A separate experiment by Venkatachalam et al. (2011) used a local electrometer device to measure the electric charge in localized quasiparticles in puddles of the 2DEG at filling fractions $\nu = 5/2$ and $\nu = 7/3$. A statistical analysis of the data showed that the quasiparticle charges are consistent with the theoretical predictions of $e^* = e/4$ for $\nu = 5/2$ and $e^* = e/3$ for $\nu = 7/3$.

Quantum interferometers and fractional statistics

We will now consider experiments on Hall bars with two quantum point contacts created by two narrow gates transversal to the bar and separated at some distance d from each other. Quantum devices of this type are Fabry-Pérot quantum interferometers. The way they operate is as follows: A current is injected in the bottom edge. At the first quantum point contact (QPC), part of the current I_1 tunnels to the opposite edge and the other part I_2 goes on and tunnels at the second QPC. The FQH fluid is assumed to occupy uniformly the region between the two QPCs. There is some magnetic flux Φ in that region, which also contains a number of localized vortices (quasiparticles). When both currents rejoin at the top edge, they interfere and the interference has information on the charge of the particles that tunnels through the Aharonov–Bohm effect with the flux Φ. The interference also has information on the fractional statistics of the quasiparticles that tunneled through their braiding with the static vortices. Chamon, Freed, Kivelson, Sondhi, and Wen proposed a setup of this type to measure the fractional statistics of the quasiparticles for the Abelian states (Chamon et al., 1997). They showed that the total current $I_t = I_1 + I_2$ is given by

$$I_t = e^{*}|\Gamma_{\text{eff}}|^2 \frac{2\pi}{\Gamma(2\nu)}\ |\omega_0|^{2\nu-1}\ \text{sign}(\omega_0^{*}) \tag{533}$$

where Γ_{eff} is given by

$$|\Gamma_{\text{eff}}|^2 = |\Gamma_1|^2 + |\Gamma_2|^2 + \left(\Gamma_1\Gamma_2^{*} + \Gamma_1^{*}\Gamma_2\right) F_\nu\left(\frac{\omega_0^{*}d}{v}\right). \tag{534}$$

Here Γ_1 and Γ_2 are the tunneling amplitudes at the two QPCs, $\nu = 1/m$ is the filling fraction, v is the velocity of the edge modes, d is the distance between the two QPCs and

$$F_\nu(x) = \sqrt{\pi}\frac{\Gamma(2\nu)}{\Gamma(\nu)}\frac{J_{\nu-1/2}(x)}{(2x)^{\nu-1/2}} \tag{535}$$

where $\Gamma(z)$ is the Euler Gamma function and $J_{\nu-1/2}(z)$ is the Bessel function of the first kind. In the presence of N_q localized quasiparticles in the area between the two QPCs, the contribution of the phases of the tunneling matrix elements gets shifted to

$$\Gamma_1^{*}\Gamma_2 = \bar{\Gamma}_1^{*}\bar{\Gamma}_2\ \exp\left[-2\pi i\left(\nu\frac{\Phi}{\phi_0} - \nu N_q\right)\right] \tag{536}$$

where ϕ_0 is the flux quantum. In Eq. (536), the first term in the phase shift is the Aharonov–Bohm effect of the tunneling quasiparticles while the second term in the phase shift $2\pi\nu N_q$ is the contribution of the fractional statistics of the tunneling quasiparticle as its worldline braids with the N_q localized quasiparticles. This means that there is an interference contribution to the tunneling current (and also to the transmitted current), which is sensitive to both the charge and the fractional statistics of the quasiparticles. This is this effect that is being measured in experiments.

Early attempts at doing this experiment were made by Camino et al. (2005) but were difficult to interpret partly due to subtle reasons related to the difficulty in controlling the actual area of the region comprised between the two QPCs (Halperin et al., 2011). Recent theoretical work by Halperin et al. (2011) showed that the size of the 2DEG in the region comprised by the interferometer plays an important role in the interpretation of these experiments. Thus, if the 2DEG in the region between the two constrictions is small, the device is in a Coulomb blockade regime. A properly working interferometer requires that the interferometer be large enough (and the 2DEG be uniform enough) not to be in this regime. These authors also provided a tell-tale pattern of the oscillations that reveal the detection of fractional statistics. Technical advances in the fabrication and design of these quantum interferometers led in 2020 to the first successful measurement of the fractional statistics of the quasiholes of the Laughlin state at $\nu = 1/3$ (and also at the Jain state at $\nu = 2/5$) by Nakamura et al. (2020).

The non-Abelian case is more subtle both theoretically and experimentally. The theory of the Abelian interferometer of Chamon et al. (1997) was generalized to the non-Abelian FQH states by Fradkin et al. (1998). The structure of the interferometer is the same as in the Abelian case but the interference effects are different. In addition, in the case of the MR state, aside from the non-Abelian quasiparticle $\sigma \sim \chi \exp(i\phi/2\sqrt{2})$ has charge $e/4$ and non-Abelian fractional statistics, the MR state has two more Abelian anyons, the charge neutral Majorana fermion χ and the charge $e/2$ Laughlin quasiparticle. The number of anyons and their properties are very different in different non-Abelian FQH states.

Ignoring for now the existence of more quasiparticles, let us focus now on the fundamental anyon that is nonabelian. Fradkin et al. (1998) considered a non-Abelian quasihole that is injected to the bottom edge, tunneled at the first QPC, and arrived at the left end of the top edge in state $|\psi\rangle$. If a second such quasiparticle is now injected but now tunnels to the top edge at the second QPC, arriving at the left end of the top edge in the state $e^{i\alpha}B_{N_q}|\psi\rangle$, where α is the Aharonov–Bohm phase determined by the flux Φ piercing the interferometer and B_{N_q} is the braiding operator of the second quasiparticle that is circling around the N_q localized quasiparticles in the interferometer. Then the tunneling conductance measured at the left exit of the top edge has an interference contribution

$$\sigma_{xx} \propto |\Gamma_1|^2 + |\Gamma_2|^2 + \mathrm{Re}\left[\Gamma_1^* \Gamma_2 e^{i\alpha} \langle \psi | B_{N_q} | \psi \rangle\right]. \tag{537}$$

The matrix element $\langle \psi | B_{N_q} | \psi \rangle$ is given in terms of the expectation value of the Wilson loop operators of the tunneling quasiparticles braided with the Wilson loops of the N_q localized quasiparticles in the area of the interferometer. In 1989, Witten (1989) showed that this expectation value, which is computed in the non-Abelian Chern–Simons gauge theory, is equal to a topological invariant of the braid known as the Jones polynomial $V_{N_q}\left(e^{1\pi/4}\right)$. Fradkin et al. (1998) showed that the Verlinde algebra yields a general algorithm for the computation of this matrix element. Therefore, the oscillatory component of the tunneling current (and of the conductance) measures a topological invariant!

However, in the particular case of the MR states, the non-Abelian gauge theory associated with these states is the $SU(2)_2$-Chern–Simons gauge theory. In this case, an explicit calculation Bonderson et al. (2006) and by Stern and Halperin (2006) leads to the result

$$\begin{aligned} \sigma_{xx} &\propto |\Gamma_1|^2 + |\Gamma_2|^2, && \text{for } N_q \text{ odd} \\ \sigma_{xx} &\propto |\Gamma_1|^2 + |\Gamma_2|^2 + 2\,|\Gamma_1||\Gamma_2|(-1)^{N_\psi}\, \cos\left(\alpha + \arg\left(\frac{\Gamma_2}{\Gamma_1}\right) + \frac{\pi}{4} N_q\right), && \text{for } N_q \text{ even} \end{aligned} \tag{538}$$

Here, $N_\psi = 1$ when the N_q quasiparticles fuse into the state ψ and $N_\psi = 0$ otherwise. The interference effect is absent for N_q odd since an odd number of σ quasiparticles cannot fuse into the identity state I. This simple even-odd effect is special for $SU(1)_2$. In the general case and, in particular in the $SU(2)_3$ case which applies to the $k = 3$ Read-Rezayi ("Fibonacci") state, the expressions are more complex.

At any rate, even in the MR state the situation is more complicated for two reasons. One is that the charge $e/2$ Abelian Laughlin quasiparticle is always able to tunnel thus spoiling the even-odd effect. The other complication is that the non-Abelian FQH occurs in the $N = 1$ Landau level and the edge states of the non-Abelian FQH state are surrounded by an Abelian $\nu = 2$ state, which makes accessing the interesting edge states more difficult. Robert Willett has pioneered the fabrication and operation of the interferometer for the non-Abelian state at $\nu = 5/2$ (Willett et al., 2009, 2013, 2023). With some significant caveats, these experiments provide solid evidence of non-Abelian braiding, although more work remains to be done on this system.

A variant of the Fabry-Perot interferometer is the Mach–Zehnder well known from quantum optics. Much like the Fabry-Pérot interferometer, this setup has a source and a drain and two "beam splitters." However, many features of the Fabry-Pérot interferometer which make its operation complex, such as the role of Coulomb interactions and the control of the area of the interferometer, do not play an essential role in the Mach–Zehnder system. In a recent paper, Kundu et al. (2023) report experiments in an electronic Mach–Zehnder interferometer, developed originally by Ji et al. (2003), done in fractional quantum Hall states at $\nu = 1/3$ and $\nu = 2/5$, and found values of the fractional statistics consistent with theoretical predictions.

Quantum Mechanics predicts that in collision experiments of identical particles bosons tend to have enhanced correlations localized in space, effect known as "bunching" while fermions exclude each other, due to the exclusion principle, an effect known as "anti-bunching." The bunching effect of photons was first confirmed by the celebrated experiments of Hanbury Brown and Twiss (1956). In 2003, Vishveshwara proposed a collider-type setup for anyons in a quantum Hall bar with a "beam" of anyons created by two sources colliding at a "beam splitter," and detected at two sinks (Vishveshwara, 2003). In that setup, fractional statistics is manifest in the cross correlations of the currents detected at the two sinks. Such correlations are present in the noise (quantum fluctuations) of the detected currents. There were several subsequent proposals for detecting the role of fractional statistics in current noise, for example in quantum point contacts at a tri-junction (Kim et al., 2005). Further theoretical work on the collider setup by Vishveshwara and Cooper (2010) and by Rosenow et al. (2016) refined and clarified the role of fractional statistics in anyon collider setups. An experiment by Bartolomei et al. (2020) confirmed the theoretical prediction that, compared to fermions, anyons of a fractional quantum Hall state with filling fraction $\nu = 1/3$ have a bunching tendency (compared to fermions) at a beam splitter consistent with the predicted fractional statistics $\pi/3$.

Particle-vortex dualities in 2+1 dimensions

Electromagnetic duality

The oldest form of duality in Physics is, perhaps, Dirac's observation that in the absence of electric charges and currents, Maxwell's equations are invariant under the exchange of electric and magnetic fields, $\boldsymbol{E} \to \boldsymbol{B}$ and $\boldsymbol{B} \to -\boldsymbol{E}$ (Dirac, 1931). This observation led him to conjecture the existence of magnetic monopoles. In a relativistic invariant formulation, Maxwell's equations in free space can be expressed in terms of the electromagnetic field tensor $F_{\mu\nu}$ and the dual field tensor $F^*_{\mu\nu}$

$$\partial^\mu F_{\mu\nu} = 0, \qquad \partial^\mu F^*_{\mu\nu} = 0 \tag{539}$$

where $F^*_{\mu\nu} = \frac{1}{2}\epsilon_{\mu\nu\lambda\rho}F^{\lambda\rho}$, and where $\epsilon_{\mu\nu\lambda\rho}$ is the fourth-rank antisymmetric Levi-Civita tensor. The first Maxwell equation in Eq. (539) is just the wave equation in free Minkowski spacetime. The second equation in Eq. (539) is known as the Bianchi identity. The Bianchi identity is a *constraint* that implies that there are no magnetic monopoles and that the second rank antisymmetric field strength tensor can be expressed in terms of the vector potential A_μ as $F_{\mu\nu} = \partial_\mu A_\nu - \partial_\nu A_\mu$.

This is an example of what in differential geometry is called *Hodge duality*, which relates a vector or more generally a tensor field to its Hodge dual. In general in D dimensions, the Hodge dual of a (fully antisymmetric) tensor of rank p is an antisymmetric tensor of rank $D - p$. When contracted with the oriented infinitesimal element of a p-dimensional hypersurface, $dx_1 \wedge dx_2 \wedge \ldots \wedge dx_p$, an antisymmetric tensor of rank p, $F_{\mu_1\mu_2\ldots\mu_p}$, defines a p-differential form, called a p-form. Differential forms embody the physically intuitive notions of circulation of a vector field, flux of a second rank tensor, etc. We will see below that duality transformations are closely related to these geometric notions of duality.

Particle-vortex duality in 2+1 dimensions

In this section, we will extend the particle-vortex duality discussed in 2D in Section "Vortices in two dimensions" (see Eq. 75) to 3D. In the field theory interpretation, 2D is a 1+1-dimensional Minkowski spacetime and the XY model is a representation of a complex scalar field of unit modulus. In the duality, the particles are the particle-like excitations of the complex scalar field. The high temperature phase of the XY model is viewed as a partition function of a set of oriented loops that carry charge. the loops are the worldlines of the particles of the XY model.

The 3D XY model

This picture can be seen as follows: Consider an XY model on a D-dimensional hypercubic lattice whose sites are labeled by $\{\boldsymbol{r}\}$. At each site, there is a periodic variable $\theta(\boldsymbol{r}) \in [0, 2\pi)$. The partition function is

$$Z_{\text{XY}} = \prod_{\boldsymbol{r}} \int_0^{2\pi} \frac{d\theta(\boldsymbol{r})}{2\pi} \exp\left(\frac{1}{T}\sum_{\boldsymbol{r}}\sum_{j=1,\ldots,D}(\cos\Delta_j\theta(\boldsymbol{r}))\right) \tag{540}$$

where $\Delta_j\theta(\boldsymbol{r}) = \theta(\boldsymbol{r} + \boldsymbol{e}_j) - \theta(\boldsymbol{r})$, with $j = 1, \ldots, D$, is the lattice difference, and T is the temperature (in the classical statistical mechanical picture). Since the interaction on each link is a periodic function of the phase difference $\Delta_j\theta(\boldsymbol{r})$, we can expand the Gibbs weight (for each link!) in a Fourier series or, what is the same, in the integer-valued representations of the group $U(1)$ (which is the global symmetry of the XY model) to obtain

$$Z_{\text{XY}} = \prod_{\boldsymbol{r}} \int_0^{2\pi} \frac{d\theta(\boldsymbol{r})}{2\pi} \sum_{\ell_j(\boldsymbol{r})=-\infty}^{\infty} \exp\left(-\sum_{\boldsymbol{r},j}\frac{T}{2}\ell_j^2(\boldsymbol{r}) + i\sum_{\boldsymbol{r}}\theta(\boldsymbol{r})\Delta_j\ell_j(\boldsymbol{r})\right) \tag{541}$$

where we used a Gaussian approximation for the modified Bessel function $I_n(z)$, and $\Delta_j\ell_j(\boldsymbol{r}) = \sum_{j=1}^{D}(\ell_j(\boldsymbol{r}) - \ell_j(\boldsymbol{r} - \boldsymbol{e}_j))$ (where $\boldsymbol{e}_j$ is the lattice unit vector along the direction j) denotes the lattice divergence. Integrating out the phase variables $\theta(\boldsymbol{r})$, we obtain

$$Z_{\text{XY}} = \prod_{\boldsymbol{r}} \sum_{\ell_j(\boldsymbol{r})=-\infty}^{\infty} \prod_{\boldsymbol{r}} \delta(\Delta_j\ell_j(\boldsymbol{r})) \exp\left(-\sum_{\boldsymbol{r}}\sum_{j=1}^{D}\frac{T}{2}\ell_j^2(\boldsymbol{r})\right). \tag{542}$$

Therefore, the partition function is given by a sum over loops of conserved currents $\ell_j(\boldsymbol{r})$ defined on the links of the lattice, with a weight on each link $\propto \exp(-\ell_j^2/2\beta)$. These loops are the (lattice) worldlines of the particles of the complex scalar field. In the phase where this representation is convergent, the complex scalar field is massive, the XY model is gapped, and these particles have short-range interactions. This picture is true in all dimensions, 3D included.

On the other hand, in 2D, the vortices are point-like events in Euclidean spacetime, which interact with each other through long-range, logarithmic, interactions. In the field theory language, in 2D the point-like vortices are *instantons*, which govern the low temperature phase of the XY model. In spacetime dimensions $D > 2$, the vortices become extended objects: vortex loops (or strings) in 3D, closed vortex surfaces in 4D, etc. In 3D, the vortex loops are magnetic flux tubes, which interact with each other through a Biot-Savart-type interaction, namely bits of vortices interact with each other with a 3D Coulomb interaction much in the same way as with loops of current in magnetostatics,

$$Z_{3\text{D XY}} = \sum_{\{m_j(\tilde{\boldsymbol{r}})\}} \prod_{\tilde{\boldsymbol{r}}} \delta(\Delta_j m_j(\tilde{\boldsymbol{r}})) \exp\left(-\frac{2\pi^2}{T} \sum_{\tilde{\boldsymbol{r}}, \tilde{\boldsymbol{r}}'} \sum_{j=1}^{3} m_j(\tilde{\boldsymbol{r}}) G_0(\tilde{\boldsymbol{r}} - \tilde{\boldsymbol{r}}') m_j(\tilde{\boldsymbol{r}}') - \alpha \sum_{\tilde{\boldsymbol{r}}, j} m_j^2(\tilde{\boldsymbol{r}}) \right) \tag{543}$$

where $\{\tilde{\boldsymbol{r}}\}$ labels the sites of the dual (cubic) lattice, the variables $m_j(\tilde{\boldsymbol{r}})$ take values on the integers, α is a (short-distance) vortex core energy, and $G_0(\tilde{\boldsymbol{r}} - \tilde{\boldsymbol{r}}')$ is the 3D lattice propagator (Green function), which, at long distances, has the standard form

$$G_0(\boldsymbol{x} - \boldsymbol{x}') = \frac{1}{4\pi|\boldsymbol{x} - \boldsymbol{x}'|} \tag{544}$$

In Eq. (543), the vortex loops are represented by the integer-valued conserved currents $m_j(\tilde{\boldsymbol{r}})$, which are naturally interpreted as the world lines of magnetic charges.

We could have also reached the same result by following the line of reasoning that we used in Section "Vortices in two dimensions." Indeed, let $\theta(x)$ be the phase field of a complex scalar field $\phi(x)$ deep in its broken symmetry state where the amplitude of the field $\phi(x)$ can be taken to be approximately fixed. The partition function in this phase reduces to

$$Z[a_\mu] = \int \mathcal{D}\theta \, \exp\left(-\frac{1}{2g} \int d^3x \left(\partial_\mu \theta - a_\mu\right)^2 \right) \tag{545}$$

where g is a coupling constant, which in the XY model is proportional to the temperature. Here, much as in Eq. (70), the gauge field a_μ represents the vortices. Indeed, in 3D, the vorticity is represented by a locally conserved vector field ω_μ

$$\omega_\mu = \epsilon_{\mu\nu\lambda} \partial_\nu a_\lambda = 2\pi \sum_k m_\mu^k \delta(x - x_k) \tag{546}$$

where m_μ^k are the integer-valued vortex (magnetic) currents we used above. As before, the periodic nature of the phase field $\theta(x)$ implies that the vortex currents must be quantized and be integer-valued.

Here too, we can perform a Hubbard–Stratonovich transformation in terms of a vector field b_μ to find a dual theory, which now is

$$Z(a_\mu) = \int \mathcal{D}b_\mu \mathcal{D}\theta \exp\left(-\frac{g}{2} \int d^3x \, b_\mu^2 - i \int d^3x \, b_\mu(\partial_\mu \theta - a_\mu) \right). \tag{547}$$

Upon integrating out the phase field θ, which acts as a Lagrange multiplier which imposes the constraint $\partial_\mu b_\mu = 0$. This constraint implies that we can write the field b_μ in terms of a dual gauge field ϑ_μ

$$b_\mu = \epsilon_{\mu\nu\lambda} \partial_\nu \vartheta_\lambda. \tag{548}$$

Therefore, we can rewrite the partition function as

$$Z(a_\mu) = \int \mathcal{D}\vartheta \, \exp\left(-\frac{g}{4} \int d^3x \, f_{\mu\nu}^2 + i \int d^3x \, \omega_\mu \vartheta_\mu \right) \tag{549}$$

where $f_{\mu\nu} = \partial_\mu \vartheta_\nu - \partial_\nu \vartheta_\nu$ is the field strength of the dual gauge field ϑ_μ. Notice that the vortex current ω_μ is minimally coupled to the dual gauge field ϑ_μ. If we now integrate out the gauge field ϑ_μ, we obtain an expression for the weight in the path integral for a configuration of vortices m_μ^k, which is identical to the result of Eq. (543).

What we have shown above is that in 3D, the Goldstone phase of a complex scalar field with coupling constant g is the dual of a Maxwell gauge theory with coupling constant $1/g$. Moreover, the periodicity of the phase field implies that the dual gauge field ϑ_μ is compact in the sense that its fluxes must obey flux quantization. It is straightforward to show that a charge operator $V_n = \exp(in\theta)$ with electric charge n in the scalar field theory is represented in the dual gauge theory by a magnetic monopole of magnetic charge n.

In summary, we showed that the 3D XY model (equivalent to the theory of the complex scalar field) can be written in terms of two different models of loop configurations. We saw that the XY model is a theory of particle (electric) loops in the high-temperature phase and of vortex (magnetic) loops in the low-temperature phase. However the particle loops have short-range interactions while the vortex loops have long-range interactions. Thus, the 3D XY model not self-dual. In spite of having a representation in terms of vortex loops, the 3D XY model is in reality has a very different behavior than the 2D system. The Kosterlitz–Thouless theory describes the phase transition in terms of a vortex–antivortex unbinding transition upon which the vortices proliferate. In addition, in 2D, the Goldstone phase is actually a line of fixed points; there is never true long-range order but, instead, power-law correlations of the physical observables. In the Kosterlitz–Thouless theory the disordered phase arises the strong fluctuations of the phase field due to the proliferation of vortices while, at the local level, the order parameter still has a finite magnitude. A consequence of this behavior is that the superfluid density has a universal jump at the Kosterlitz–Thouless transition (Nelson and Kosterlitz, 1977).

In contrast in the 3D XY model, the Goldstone phase is a true phase with long-range order. The theory has a continuous phase transition (the thermodynamic superfluid transition) at which the superfluid density vanishes continuously. This means that the phase transition of the 3D XY is better described by the Wilson–Fisher fixed point of a complex scalar field (Wilson and Fisher, 1972; Amit, 1980), rather than by a vortex proliferation picture of the Kosterlitz–Thouless theory (Kosterlitz and Thouless, 1973;

Kosterlitz, 1974). In particular, since this theory does not have magnetic monopoles, the vortex loops cannot proliferate as they do in 2D. Instead, as the phase transition is approached, the vortex loops not only grow large in size but also become fractal-like objects whose effective core size diverges as the transition is approached. In fact, qualitative vortex proliferation arguments readily lead to the incorrect conclusion that the transition should be (strongly) first order (Thomas and Stone, 1978).

In spite of these differences, particle-vortex duality still plays an important role in 3D by relating the 3D XY model to another theory, which is its dual under electromagnetic duality. Here electromagnetic duality is understood as the exchange of the electric worldlines (electric loops) and the magnetic loops (vortex loops) while exchanging strong and weak coupling, $T \leftrightarrow 1/T$, in this case between different theories. This duality was investigated by Peskin (1978), by Thomas and Stone (1978), and by Dasgupta and Halperin (1981).

Scalar QED in 3D

These authors considered a theory of a superconductor represented by a complex scalar field $\varphi(x)$, coupled to a fluctuating electromagnetic (Maxwell) field, also known as the Abelian Higgs model, or scalar electrodynamics (scalar QED) a_μ, with $\mu = 1, 2, 3$. The partition function of this theory is

$$Z_{\text{SC}} = \int \mathcal{D}\varphi \mathcal{D}\varphi^* \mathcal{D}a_\mu \exp\left(- \int d^3x \, \mathcal{L}[\varphi, \varphi^*, a_\mu]\right) \tag{550}$$

where

$$\mathcal{L} = |D_\mu(a)\varphi|^2 + m^2|\varphi|^2 + u|\varphi|^4 + \frac{1}{4e^2} f_{\mu\nu}^2 \tag{551}$$

where the covariant derivative is $D_\mu(a) = \partial_\mu + iqa_\mu$, with the integer q being the charge of the scalar field (in units of the coupling constant e), and $f_{\mu\nu} = \partial_\mu a_\nu - \partial_\nu a_\mu$ is the field strength. This theory is known as (Euclidean) scalar electrodynamics (or the Abelian Higgs model).

The scalar electrodynamics was extensively studied using the perturbative renormalization group within the epsilon expansion (near 4 dimensions), which leads to the conclusion that it has a weakly (fluctuation-induced) first-order phase transition (Coleman, 1973; Halperin et al., 1974). Scalar QED of an N-component scalar field coupled to a Maxwell gauge field has a continuous phase transition with a nontrivial fixed point for $N \geq N_c \simeq 183$ (!) (Moshe and Zinn-Justin, 2003). Since these results rely on perturbation theory (or in the large-N limit), it was long suspected that the physics may be different in $D = 3$. We will see that particle-vortex duality provides the answer to this question (Dasgupta and Halperin, 1981).

We begin by writing the lattice version of Eq. (550), which is obtained by coupling the XY model of Eq. (540) to a dynamical (Euclidean) Maxwell field

$$Z_{\text{SC}} = \prod_{\mathbf{r}} \int_0^{2\pi} \frac{d\theta(\mathbf{r})}{2\pi} \int_{-\infty}^{\infty} \frac{da_\mu(\mathbf{r})}{2\pi} \, \exp\left(-S(\theta, a_\mu)\right) \tag{552}$$

where the action $S(\theta, a_\mu)$ is

$$S(\theta, a_\mu) = -\frac{1}{T}\sum_{\mathbf{r},\mu} \cos\left(\Delta_\mu \theta(\mathbf{r}) - qa_\mu(\mathbf{r})\right) + \frac{1}{4e^2}\sum_{\mathbf{r},\mu,\nu}\left(\Delta_\mu a_\nu(\mathbf{r}) - \Delta_\nu a_\mu(\mathbf{r})\right)^2. \tag{553}$$

In this action we assumed that the Abelian gauge fields do not have monopole configurations.

The partition function of Eq. (550) admits a representation as a sum over loops. We can then use the same line of reasoning that led to Eq. (542) and write the partition function as a sum over loops of the worldlines of the particles (charges) of the complex scalar field

$$\frac{Z_{\text{SC}}}{Z_0^{\text{gauge}}} = \prod_{\mathbf{r}} \sum_{\ell_\mu(\mathbf{r})=-\infty}^{\infty} \delta(\Delta_\mu \ell_\mu(\mathbf{r})) \exp\left(-\sum_{\mathbf{r},\mu} \frac{T}{2}\ell_\mu^2(\mathbf{r})\right) \left\langle \exp\left(iq \sum_{\mathbf{r},\mu} \ell_\mu(\mathbf{r}) a_\mu(\mathbf{r})\right)\right\rangle_a \tag{554}$$

where $\langle O[a]\rangle_a$ is the expectation value of the operator $O[a]$ over the gauge fields a_μ, and Z_0^{gauge} is the partition function of the free gauge fields. After computing this free-field expectation value, we obtain the result

$$\frac{Z_{\text{SC}}}{Z_0^{\text{gauge}}} = \sum_{\{\ell_\mu(\mathbf{r})\}=-\infty}^{\infty} \delta(\Delta_\mu \ell_\mu(\mathbf{r})) \exp\left(-\sum_{\mathbf{r},\mu} \frac{T}{2}\ell_\mu^2(\mathbf{r}) - \frac{q^2e^2}{2}\sum_{\mathbf{r},\mu}\sum_{\mathbf{r}',\nu} \ell_\mu(\mathbf{r}) \, G_{\mu\nu}(\mathbf{r} - \mathbf{r}') \, \ell_\nu(\mathbf{r}')\right) \tag{555}$$

where

$$G_{\mu\nu}(\mathbf{r} - \mathbf{r}') = \langle a_\mu(\mathbf{r}) a_\nu(\mathbf{r}')\rangle \tag{556}$$

is the Euclidean propagator of the free gauge fields. Since the configurations of the worldlines, the currents represented by $\ell_\mu(\mathbf{r})$ are conserved and satisfy the local constraint $\Delta_\mu \ell_\mu = 0$, the second term in the exponent of Eq. (555) is gauge invariant. Hence, we can use the propagator in the Feynman gauge

$$G_{\mu\nu}(\boldsymbol{r}-\boldsymbol{r}') = \delta_{\mu\nu} G_0(\boldsymbol{r}-\boldsymbol{r}') \tag{557}$$

where $G_0(\boldsymbol{r}-\boldsymbol{r}')$ is the 3D lattice propagator that has the same Coulomb form at long distances already given in Eq. (544).

Therefore we can write the partition function of the scalar QED model (the superconductor) as a sum over worldline loop configurations of the particles of the scalar field in the equivalent form

$$\frac{Z_{\text{SC}}}{Z_0^{\text{gauge}}} = \sum_{\{\ell_\mu(\boldsymbol{r})\}=-\infty}^{\infty} \delta(\Delta_\mu \ell_\mu(\boldsymbol{r})) \exp\left(-\sum_{\boldsymbol{r},\mu} \frac{T}{2}\ell_\mu^2(\boldsymbol{r}) - \frac{q^2 e^2}{2} \sum_{\boldsymbol{r},\boldsymbol{r}',\mu} \ell_\mu(\boldsymbol{r})\, G_0(\boldsymbol{r}-\boldsymbol{r}')\, \ell_\mu(\boldsymbol{r}') \right) \tag{558}$$

which is the same as the partition function of the 3D XY model in the broken symmetry state, given in Eq. (543), with the identification of the particle loops of the Abelian Higgs model with the vortices of the 3D XY model and a relation between the coupling constants. Hence we obtain the duality between the broken symmetry phase of the 3DXY model ("low T") and the symmetric phase of the Abelian Higgs model ("high T")

$$\ell_\mu \leftrightarrow m_\mu, \qquad q^2 e^2 \leftrightarrow \frac{2\pi^2}{T}, \qquad \frac{T}{2} \leftrightarrow \alpha \tag{559}$$

where the quantities on the left-hand side of the identifications refer to the 3D Abelian Higgs model and the quantities on the right-hand side to the 3D XY model.

We can now repeat the same analysis but in the broken symmetry of the Abelian Higgs model. In this phase the gauge field a_μ becomes massive by the Higgs mechanism (or, what is the same, by the Meissner effect of the superconductor), and in this phase, the vortex loops m_μ of the complex scalar field have short-range interactions. This phase then is mapped onto the unbroken phase of the 3DXY model with the screened vortex loops of the Abelian Higgs model identified with the particle loops of the 3D XY model, and with the same identifications between the coupling constants of the two theories given in Eq. (559). The identification between the two partition functions implies that the phase transitions must be the same. In other words, the duality implies that the 3D Abelian Higgs model has a continuous phase transition with the same fixed point as that of the complex scalar field in 3D. The only difference is that the phases are reversed and, for this reason, this is sometimes called an "inverted" 3D XY transition (Dasgupta and Halperin, 1981).

The duality mapping

We can summarize these results with the following identification of two Lagrangians (in real time, Minkowski signature) (Seiberg et al., 2016)

$$|\partial_\mu(B)\phi|^2 - m^2|\phi|^2 - u|\phi|^4 \leftrightarrow |\partial_\mu(a)\varphi|^2 + m^2|\varphi|^2 - u|\varphi|^4 - \frac{1}{4e^2} f_{\mu\nu}^2 + \frac{1}{2\pi}\epsilon_{\mu\nu\lambda} a^\mu \partial^\nu B^\lambda. \tag{560}$$

The left-hand side of this equivalence is the Lagrangian of the 3D complex scalar field ϕ and B_μ is a background electromagnetic gauge field. The right-hand side is the Lagrangian of the Abelian Higgs model with a scalar field φ and a $U(1)$ gauge field a_μ. Notice that the mass terms of the two sides are inverted reflecting the reverse order of their two phases. This identification also shows that the current of the scalar field $j_\mu = -\frac{i}{2}(\phi^* \partial_\mu \phi - \phi \partial_\mu \phi^*)$ is identified as

$$j_\mu \leftrightarrow \frac{1}{2\pi}\epsilon_{\mu\nu\lambda}\partial_\nu a_\lambda. \tag{561}$$

The field operator of the complex scalar field creates worldlines (as opposed to loops) of charged particles. In the dual Abelian Higgs theory, this operator is identified with an operator that creates a magnetic monopole of the $U(1)$ gauge field a_μ with unit magnetic charge. It is easy to see that in the broken symmetry phase of the Abelian Higgs model, a monopole–antimonopole pair creation operator decays exponentially with distance due to the flux expulsion effect (the Meissner effect of a superconductor). This means that the monopoles are confined with a linear potential. This is the same behavior of the complex scalar field ϕ in its symmetric phase where the propagator of the complex scalar field decays exponentially with distance. Conversely, in the broken symmetry phase of the complex scalar field theory, the field operator ϕ condenses and its propagator approaches the value $|\langle\phi\rangle|^2$ at long distances. This is the same behavior one readily finds for the monopole operator of the Abelian Higgs model in the symmetric phase.

Bosonization in 2+1 dimensions

The particle-vortex duality that we discussed in Section "Particle-vortex duality in 2+1 dimensions" essentially has been understood since the 1980s. In Section "Bosonization, anomalies, and duality," we discussed in detail the problem of bosonization in 1+1 dimensions, whic, is a mapping between a massless Dirac fermion and a massless compactified scalar field. As we noted, this mapping is a powerful theoretical tool to investigate nonperturbatively the structure of many theories in 1+1 dimensions of great physical interest. This success has motivated a sustained effort to extend these concepts to higher dimensions where the problem in many ways is more subtle.

Fermi systems in dimensions higher differ from the 1+1-dimensional case in two significant ways. Due to the kinematic restriction of one space dimension, a massless relativistic fermion and a theory of fermions (relativistic or not) at finite density are mostly equivalent to each other. The reason is quite simple. Consider a free massless Dirac theory in 1+1 dimensions. As we saw, it is equivalent to a theory of two chiral fermions, the right- and left-moving components of the spinor. If we add a chemical potential μ, the right- and left-moving states will be filled up to μ, which is the Fermi energy. While in space dimensions $d > 1$ a finite chemical potential leads to a finite fermi surface, in $d = 1$ space dimensions the Fermi "surface" is just two points, for the right and left moving fermion modes respectively. The Dirac Hamiltonian at finite chemical potential is

$$\mathcal{H} = \psi^{\dagger}(-i)\alpha\partial_x\psi - \mu\psi^{\dagger}\psi. \tag{562}$$

Under a chiral transformation with angle $\theta(x)$, the field operators change as $\psi_R \rightarrow e^{i\theta}\psi_R$ and $\psi_L \rightarrow e^{-i\theta}\psi_L$ and the Hamiltonian becomes

$$\mathcal{H} = \psi^{\dagger}(-i)\alpha\partial_x\psi - (\mu - \partial_x\theta)\, \psi^{\dagger}\psi. \tag{563}$$

Clearly if we choose $\partial_x\theta = \mu$ (or, what is the same, $\theta = \mu x$), the explicit dependence on the chemical potential will be cancelled and the transformed Dirac Hamiltonian will be the same as the Hamiltonian at zero chemical potential. However under this transformation the mass operators transform as $\bar{\psi}\psi \rightarrow \cos(2\mu x)\, \bar{\psi}\psi$ and $i\bar{\psi}\gamma_5\psi \rightarrow \sin(2\mu x)\, i\bar{\psi}\gamma_5$. In the nonrelativistic context, this change amounts to a modulation of the charge density with wave vector $Q = 2p_F(\mu)$.

In contrast, in space dimensions $d > 1$, the massless Dirac system and a system of fermions at finite density (relativistic or not) are no longer equivalent to each other as the latter system has a Fermi surface (of codimension $d - 1$) while the former system has not. This difference has profound effects on their dynamics: the system of fermions at finite density is, at least in the weak coupling regime, is expected to be a FL (except for an instability to a superconducting state even for infinitesimal attractive interactions) while the massless Dirac theory is stable as all local interactions are irrelevant.

Bosonization of the Dirac theory in 2+1 dimensions

We will now turn to the problem of Bose-Fermi mappings in relativistic systems in 2+1 dimensions. This problem is of great interest in both condensed matter physics and in High Energy Physics.

Bosonization in 2+1 dimensions is a more subtle problem than in 1+1 dimensions that we discussed in Section "Bosonization, anomalies, and duality." There we saw, in 1+1 dimensions, bosonization consists of a set of operator identities relating two free field theories, a theory of massless Dirac fermions and a compactified massless free scalar field $\phi(x)$. The success of that program is largely based on the fact that both theories are massless (and hence are scale and conformally invariant), on the chiral anomaly, and on the relation between the gauge current of the Dirac theory with the topological current of the compactified boson.

The physics in 2+1 dimensions (and in general) is very different. For instance, instead of the chiral anomaly in 2+1 dimensions theories of relativistic fermions have a parity anomaly, discussed in Section "The parity anomaly." We will also see that although in 2+1 dimensions there are theories of free massless Dirac fermions and free massless compactified bosons, they are no longer dual to each other. For these and other reasons, it has been difficult to extend the bosonization program to 2+1 dimensions.

One of the first bosonization constructions for a theory of massive (relativistic) Dirac fields was put forth by Polyakov (1988) and Grundberg et al. (1990). For reasons that were no longer relevant, Polyakov considered a theory of CP^1 complex scalar fields (in its unbroken phase) coupled to a $U(1)_1$ Chern–Simons gauge theory. Nevertheless, his main argument, with some corrections associated with the parity anomaly, still holds correct.

Here we will follow the work of Goldman and Fradkin (2018b) and consider instead a theory of a single massive complex field coupled to a $U(1)_1$ Chern–Simons gauge theory whose Lagrangian density is

$$\mathcal{L} = |D_{\mu}(\mathscr{A}_{\mu})\phi|^2 - m^2|\phi|^2 - \lambda|\phi|^4 + \frac{1}{4\pi}\epsilon_{\mu\nu\lambda}\mathscr{A}^{\mu}\partial^{\nu}\mathscr{A}^{\lambda}. \tag{564}$$

In essence, this theory is a relativistic version of what we did in Section "Composite Boson field theory" where we mapped nonrelativistic fermions to (also nonrelativistic) bosons whereas here the theory is relativistic and we are mapping bosons to fermions. In his work, Polyakov actually considered the problem of the propagator of a free massive scalar field coupled to the Chern–Simons gauge field. In this limit, the propagator $G(x, x')$ is the transition amplitude from x to x' (in Minkowski spacetime). In the case in which $\phi(x)$ is a free massive field, this propagator can be expressed in the for of a Feynman path integral as a sum over all open-oriented paths $\{P_{x,x'}\}$ with endpoints at x and x' which in Euclidean spacetime is

$$G_{\gamma(x,x')} = \sum_{\{P_{x,x'}\}} \exp(-mL(P_{x,x'})) \left\langle \exp\left(i\int_{P_{x,x'}} dz_{\mu}\mathscr{A}^{\mu}(z) \right) \right\rangle_{U(1)_1} \tag{565}$$

where the expectation value is over the Chern–Simons gauge fields $\mathscr{A}_{\mu}$ of Eq. (564).

Let us consider now the partition function of the bosons, which is a sum over all closed paths $\{P\}$, which we will assume to be nonintersecting (which requires a short distance repulsion)

$$Z = \sum_{\{P\}} \exp(-mL(P)) \left\langle \exp(i\oint_P dz_{\mu}\mathscr{A}^{\mu}(z)) \right\rangle_{U(1)_1} \tag{566}$$

The expectation value is given by

$$\left\langle \exp\left(i\int_P dz_\mu \mathscr{A}^\mu(z)\right)\right\rangle_{U(1)_1} = \exp\left(-\frac{1}{2}\oint_P\oint_P dx_\mu dy_\nu \langle \mathscr{A}_\mu(x)\mathscr{A}_\nu(y)\rangle\right) \equiv \exp(i\pi W(P)) \tag{567}$$

where $W(P)$ is the *writhe* of the closed path P. The computation of the writhe requires a regularization. One possible regularization is to thicken the path which is equivalent to including a Maxwell term for the gauge field in the Lagrangian. In general, the writhe of the path P is

$$W(P) = SL(P) - T(P) \tag{568}$$

where $SL(P)$ is an integer-valued topological invariant called the self-linking number and $T(P)$ is the twist (or torsion) of the path. The twist $T(P)$ is a Berry phase, which depends on the coordinates of the space in which the path P is embedded, and it is not a topological invariant.

We will now compute the Berry phase $T(P)$. Let $\hat{\boldsymbol{e}}(s)$ be a unit vector tangent to the path P and where we parametrized the closed path P by a coordinate $s \in [0, L]$. The closed path P is the boundary of a surface Σ we can take to be a disk. We will write the Berry phase by extending $\hat{\boldsymbol{e}}(s)$ smoothly to the interior of Σ as $\hat{\boldsymbol{e}}(s, u)$, where $0 \leq u \leq 1$ and $\hat{\boldsymbol{e}}(s, u = 1) = \hat{\boldsymbol{e}}(s)$ and $\hat{\boldsymbol{e}}(s, u = 0) = \hat{\boldsymbol{e}}_0 \equiv$ constant. With this definition, the Berry phase is

$$T(P) \equiv W(\hat{\boldsymbol{e}}) = \frac{1}{2\pi}\int_0^L ds \int_0^1 du\, \hat{\boldsymbol{e}} \cdot \partial_s \hat{\boldsymbol{e}} \times \partial_u \hat{\boldsymbol{e}} \tag{569}$$

which is defined modulo an integer.

In this formulation, in the bosonic theory, the amplitude for a path of length L with tangent vector $\hat{e}(s)$ with endpoints at x and x' is

$$G(x - x') = \int_0^\infty dL \int \mathcal{D}\, \hat{e}(s)\, \delta\left(1 - |\hat{e}|^2\right) \delta\left(x - x' - \int_0^L ds\, \hat{e}(s)\right) \exp(-|m|L \pm i\pi W(\hat{\boldsymbol{e}})). \tag{570}$$

In momentum space, we find

$$G(p) = \int_0^\infty dL \int \mathcal{D}\hat{e}\, \delta(1 - |\hat{e}|^2)\, \exp(-|m|L \pm i\pi\, W(\hat{e}))\, \exp(ip^\mu \int_0^L ds\, \hat{e}_\mu(s)). \tag{571}$$

By inspection of Eq. (569), we see that this is the same expression that we looked in the theory of the path integral for spin in Section "Path integral for a spin-S degree of freedom." for spin $S = 1/2$ particle in a magnetic field $b_\mu = \pm 2p_\mu$.

The equation of motion for $\hat{e}$ is

$$\partial_s \hat{e}_\mu = \pm 2\epsilon_{\mu\nu\lambda}\hat{e}^\lambda = i[H, \hat{e}_\mu] \tag{572}$$

where $H = \mp p_\mu \hat{e}^\mu$ is the Hamiltonian. Upon quantization, $\hat{e}_\mu$ satisfies the commutation relations

$$[\hat{e}_\mu, \hat{e}_\nu] = 2i\epsilon_{\mu\nu\lambda}\hat{e}^\lambda. \tag{573}$$

This means that we should make the identification $\hat{e}_\mu \to \sigma_\mu$ where σ_μ are the three 2 × 2 Pauli matrices. Up to rescaling of the mass $m \to M$, upon performing the path integral of Eq. (571), we find that $G(P)$ is the (Euclidean) Dirac propagator (Polyakov, 1988)

$$G(p) = \frac{1}{ip_\mu \sigma^\mu - M}. \tag{574}$$

Using these results, the partition function of Eq. (566) becomes

$$Z_{\text{fermion}} = \det[i\partial\!\!\!/ - M] = \int \mathcal{D}J\, \delta(\partial_\mu J^\mu)\, \exp(\, -|m|L[J] - i\,\text{sgn}(M)\pi\Phi[J]) \tag{575}$$

where $\Phi[J] = W[J]$, defined in Eq. (568).

We will return to this construction shortly below when we include the effects of the parity anomaly.

Early attempts at deriving a mapping for a theory of Dirac fermions in 2+1 dimensions were based on their behavior in the presence of gauge fields and the associated parity anomaly, discussed in Section "The parity anomaly." These early theories are essentially a hydrodynamic description of the Dirac theory deep in the massive phase. With minor differences, the same results were derived independently (and simultaneously) by two groups, Fidel Fradkin and Schaposnik (1994) and Burgess and Quevedo (1994). This approach was reexamined more recently by Chan, Hughes, Ryu, and myself in 2016 in a derivation of a hydrodynamic effective field theory for topological insulators in different dimensions (Chan et al., 2013, 2016). These derivations are similar in spirit to what we discussed in Section "Hydrodynamic effective field theory" for the fractional quantum Hall effect. We will follow the approach of Chan et al. (2013) for the special case of a Chern insulator 2+1 dimensions.

The Dirac theory, in any dimension, is globally gauge invariant. By Noether's theorem, this means that it has a locally conserved current, $j_\mu = \bar{\psi}\gamma_\mu\psi$ which thus satisfies $\partial_\mu j^\mu = 0$. Here too, this means that we can write $j_\mu = \epsilon_{\mu\nu\lambda}\partial^\nu b^\lambda$, where b_μ is a gauge field.

We expect that the effective action of the gauge field b_μ should be local, gauge invariant and, in this case, relativistic invariant. In 2+1 dimensions, the effective action should break time-reversal invariance and hence it should have a Chern–Simons term.

We will consider the free massive Dirac theory coupled to a background probe gauge field A_μ. The Lagrangian is $\mathcal{L} = \bar{\psi}(i\not{D}) - M)\psi$, where $D_\mu = \partial_\mu + iA_\mu$. As we saw in Section "The parity anomaly," gauge invariance and locality require that we have an even number of Dirac fermions. Here we will assume that one of the Dirac fermions is massive and acts as a regulator. The partition function

$$Z[A_\mu] = \int \mathcal{D}\bar{\psi}\mathcal{D}\psi \ \exp(iS_F[\bar{\psi}, \psi, A_\mu]). \tag{576}$$

By definition the expectation value of a product of current operators j_μ can be obtained by functional differentiation of the partition function with respect to A_μ.

The partition function is gauge invariant, that is,

$$Z[A_\mu = Z[A_\mu + a_\mu] \tag{577}$$

where the vector field a_μ is a pure gauge, $a_\mu = \partial_\mu \phi$ and $f_{\mu nu} = \partial_\mu a - \nu - \partial_\mu a_\mu = 0$. Hence, a_μ is said to be flat. Therefore, up to a normalization

$$\begin{aligned} Z[A_\mu] &= \int \mathcal{D}[a_\mu]_{\text{pure}} \, Z[A_\mu + a_\mu] \\ &= \int \mathcal{D}a_\mu \ \delta(f_{\mu\nu} = 0) \ Z[A_\mu + a_\mu] \\ &= \int \mathcal{D}a_\mu \mathcal{D}b_\mu \ Z[A_\mu + a_\mu] \ \exp\left(-\frac{i}{2} \int d^3x \ \epsilon^{\mu\nu\lambda} \ b_\mu \, f_{\nu\lambda} \right) \end{aligned} \tag{578}$$

where in the last equality we introduced a representation of the delta function and the vector field b_μ plays the role of a Lagrange multiplier field. Using the invariance of the integration measure under $a_\mu \to a_\mu - A_\mu$, we find

$$Z[A_\mu] = \int \mathcal{D}a_\mu \mathcal{D}b_\mu Z[a_\mu] \ \ \exp\left(-\frac{i}{2} \int d^3x \ \epsilon^{\mu\nu\lambda} \ b_\mu \ (f_{\nu\lambda} - F^{\nu\lambda}) \right) \tag{579}$$

where $F_{\mu\nu}$ is the field strength of the external field A_μ. From these identities and by differentiation of Eq. (579), it follows that a general expectation value of products of currents is

$$\langle j_\mu(x) \, j_\nu(y) \ldots \rangle = \frac{\delta}{\delta A_\mu(x)} \frac{\delta}{\delta A_\nu(y)} \ldots Z[A_\mu] = \langle \epsilon_{\mu\alpha\beta} \partial^\alpha b^\beta \ \epsilon_{\nu\gamma\delta} \partial^\gamma b^\delta \ldots \rangle \tag{580}$$

which means that, at the operator level, we can identify (Fradkin and Schaposnik, 1994)

$$j_\mu(x) \leftrightarrow \epsilon_{\mu\nu\lambda} \partial^\nu b^\lambda. \tag{581}$$

This result is actually general. The only difference is the nature of the field b is different dimensions: in 1+1 is a pseudo-scalar, in 2+1 is a vector (gauge) field, in 3+1 is an antisymmetric (Kalb–Ramond) tensor field, etc.

Returning to the partition function of Eq. (579) we find, using the result of Eq. (324) applied the partition function $Z[a_\mu]$, that $Z[A_\mu]$ is given by

$$Z[A_m u] = \int \mathcal{D}a_\mu \mathcal{D}b_\mu \exp\left(i \int d^3x \ \mathcal{L}_{\text{eff}}[a_\mu, b_\mu, A_\mu] \right) \tag{582}$$

where the effective Lagrangian is

$$\mathcal{L}_{\text{eff}} = -\epsilon^{\mu\nu\lambda} \ b_\mu \ \partial_\nu a_\lambda + \frac{s}{4\pi} \epsilon^{\mu\nu\lambda} a_\mu \partial_\nu a_\lambda - \frac{1}{4g_{\text{eff}}} f_{\mu\nu} f^{\mu\nu} + A_\mu \epsilon^{\mu\nu\lambda} \partial_\nu b_\lambda + \cdots \tag{583}$$

where $f_{\mu\nu} = \partial_\mu a_\nu - \partial_\nu a_\mu$. Here, $s = 1$ in the Chern insulator, $s = 0$ in the trivial insulator and $s = 1/2$ at the quantum critical point, and g_{eff} an effective coupling constant (with dimensions of length^{-1}). Here we included the effects of the parity anomaly. We recognize that the first term of the effective Lagrangian of Eq. (583) is a BF term.

In Chan et al. (2013), a similar result is also derived for a 3+1-dimensional topological insulator. The main differences are that there is no parity anomaly but an axial anomaly and that the Lagrange multiplier field is a Kalb–Ramond field,

$$\mathcal{L}_{\text{eff}}[a_\mu, b_{\mu\nu}, A_\mu] = \epsilon^{\mu\nu\lambda\rho} \ b_{\mu\nu} \ \partial_\lambda a_\rho + \frac{\theta}{8\pi^2} \epsilon^{\mu\nu\lambda\rho} \partial_\mu a_\nu \partial_\lambda a_\rho - \frac{1}{4g^2} f_{\mu\nu} f^{\mu\nu} + A_\mu \epsilon^{\mu\nu\lambda\rho} \partial_\nu b_{\lambda\rho} + \cdots \tag{584}$$

where $\theta = \pi$ in the topological insulator and $\theta = 0$ in the trivial insulator.

Although these results are correct, they do not give a full bosonization mapping. In particular, these results do not identify a fixed point for the dual bosonic theory and, along with it, a full mapping of the observables. Progress on this problem has only been achieved in the past few years both in the high energy literature (Giombi et al., 2012; Jain et al., 2013; Aharony et al., 2012b, a; Aharony, 2016; Witten, 2016; Seiberg and Witten, 2016; Karch and Tong, 2016), and in the condensed matter physics literature (Son, 2015; Metlitski and Vishwanath, 2016; Wang and Senthil, 2015; Chen et al., 2018; Mross et al., 2016). Much of that new insight was presented in a 2016 insightful paper by Seiberg et al. (2016). Many of the dualities are actually conjectures supported by strong consistency checks. A derivation of the basic bosonization duality based on loop models was constructed by Goldman and Fradkin (2018b).

The basic conjectured bosonization duality is a mapping of a free Dirac fermion to a gauge complex scalar field with a Chern–Simons term (Aharony, 2016; Seiberg et al., 2016). We can think of the Dirac theory as either being defined entirely in 2+1 dimensions or as being defined at the boundary of a nontrivial 3+1 dimensional topological insulator. In the first scenario we need to take into account the contribution of the fermionic doublers (this is what happens in the case of a lattice theory) or as the Pauli–Villars heavy fermionic regulators. In both cases, the additional heavy degrees of freedom cancel the anomaly of the 2+1-dimensional Dirac fermion, see Section "The parity anomaly." In the second scenario, there is only one Dirac fermion at the boundary and the bulk θ term cancels the anomaly of the boundary theory, see Section "Theta terms, and domain walls: Anomaly and the Callan–Harvey effect." With these provisos, the Lagrangian $\mathcal{L}_A$ of the free massive (or massless) Dirac fermion in 2+1 dimensions coupled to the electromagnetic gauge field A_μ is

$$\mathcal{L}_A = \bar{\psi}(i\not{D}(A_\mu) - M)\psi - \frac{1}{8\pi}\epsilon_{\mu\nu\lambda}A^\mu\partial^\nu A^\lambda \tag{585}$$

where M is the Dirac mass. We will call this Theory A. Here $\not{D}_\mu(A) = \gamma^\mu(\partial_\mu - iA_\mu)$ and A_μ is a background (nondynamical) gauge field. The last term in Eq. (585) is the Chern–Simons term with the 1/2-quantized coefficient, the usual short-hand for the η-invariant term of Eq. (342) needed to cancel the parity anomaly.

From the effective field theories we discussed above we know that the fermionic current maps to the curl of a gauge field, see Eq (581). Then, the conjectured bosonic dual is given by the Lagrangian of Eq (564) with an extra term for the (dual) coupling to the electromagnetic gauge filed. We will call this Theory B whose Lagrangian $\mathcal{L}_B$ is

$$\mathcal{L}_B = |D_\mu(\mathscr{A}_\mu)\phi|^2 - m^2|\phi|^2 - \lambda|\phi|^4 + \frac{1}{4\pi}\epsilon_{\mu\nu\lambda}\mathscr{A}^\mu\partial^\nu\mathscr{A}^\lambda + \frac{1}{2\pi}\epsilon_{\mu\nu\lambda}A^\mu\partial^\nu\mathscr{A}^\lambda. \tag{586}$$

To check the consistence we first observe that both theories are anomaly free. By functional differentiation of the two partition functions, we check that we get the correct mapping for the fermionic current, $j_\mu \leftrightarrow \epsilon_{\mu\nu\lambda}\partial^\nu\mathscr{A}^\lambda$. This mapping implies that the charge density of Theory A maps onto the gauge field flux of Theory B, which is electromagnetic duality. We see that this bosonization is a relativistic version of flux attachment.

Let us now identify the mapping of the phases of both theories. If the Dirac mass $M < 0$, Theory A describes an anomalous quantum Hall insulator. Integrating out the massive fermions, we find that the effective action for the electromagnetic gauge field A_μ is a $U(1)_1$ Chern–Simons theory. This means that in this phase $\sigma_{xy} = -1/(2\pi)$ (in units in which $e = \hbar = c = 1$). Looking now at Theory B, we see that if $m^2 > 0$, the scalar field is in the unbroken phase, and it is massive. In this phase we set $\phi = 0$ and find that the low energy resulting theory if just a $U(1)_1$ Chern–Simons gauge theory coupled to the curl of the electromagnetic field. Upon integrating out the $\mathscr{A}_\mu$ gauge field, we find that the effective action of A_μ is also a $U(1)_1$ Chern–Simons term, which implies that $\sigma_{xy} = -1/(2\pi)$.

Conversely, for $M > 0$, the effective electromagnetic action of the fermionic theory is a Maxwell term (the Chern–Simons term canceled). This phase is a trivial insulator. Looking now at Theory B, we see that for $m^2 < 0$, this theory is in its Higgs phase where $\langle\phi\rangle \neq 0$ and the gauge field $\mathscr{A}_\mu$ now has a mass term, $\propto \mathscr{A}_\mu^2$. In the low energy limit $\mathscr{A}_\mu \to 0$, and the Hall conductivity vanishes, consistent to what is expected from Theory A.

On the other hand, for $M = 0$, Theory A is at a quantum critical point with a very simple CFT structure but a nonvanishing Hall conductivity $\sigma_{xy} = 1/(4\pi)$. It is natural to map this CFT to a Wilson–Fisher (WF) fixed point of Theory B. At the WF, one sets the (renormalized!) mass $m_R^2 = 0$ (not the *bare* mass). In the absence of the Chern–Simons gauge field, this WF fixed point in well-understood forms high-quality (five loop!) epsilon expansion calculations (enhanced with Borel resummation) (Zinn-Justin, 2002), and by more recent numerical Conformal Bootstrap methods (Simmons-Duffin, 2017). However, not much is known of the *gauged* version of the CFT of Theory B since it cannot be accessed by either methods. If the mapping to Theory A is correct, it should have a Hall conductivity of $\sigma_{xy} = 1/(4\pi)$. This conjectured value hast not yet been confirmed.

Consider now a monopole operator of the gauge field $\mathscr{A}_\mu$ of Theory B. We will denote this operator $\mathcal{M}_{\mathscr{A}}$. The Chern–Simons term is not gauge invariant in a monopole background. To put it differently, it has charge 1 under the Chern–Simons gauge field $\mathscr{A}_\mu$. It also has charge 1 under the electromagnetic field A_μ. Likewise the scalar field ϕ has charge 1 under the Chern–Simons gauge field $\mathscr{A}_\mu$. The operator $\phi^\dagger\mathcal{M}_{\mathscr{A}}$ is gauge-invariant under the Chern–Simons gauge field $\mathscr{A}_\mu$ (i.e., it has charge 0). This composite operator has electromagnetic charge 1 (which it inherited from the monopole). Moreover, it has spin-1/2 required by the Wu-Yang construction (Wu and Yang, 1976). In other words, the operator $\phi^\dagger\mathcal{M}_{\mathscr{A}}$ has the *same* quantum numbers as the Dirac fermion and are identified by this conjecture. Notice, however, that the free massless Dirac field has scaling dimension $\Delta_\psi = 1$ in 2+1 dimensions. The conjecture implies the composite operator $\phi^\dagger\mathcal{M}_{\mathscr{A}}$ should also have scaling dimensions 1 at the (gauged) WF fixed point of Theory B. Many of these conjectures have been verified in non-Abelian versions of Theory A and Theory B: a theory of free massless Dirac fermions coupled to a Chern–Simons gauge theory with gauge group $SU(N)_k$ and a theory of complex scalars coupled to a non-Abelian Chern–Simons gauge theory with gauge group $SU(k)_N$, both in the limits $N \to \infty$ and $k \to \infty$ with N/k fixed (Giombi et al., 2012; Jain et al., 2013; Aharony et al., 2012b, a; Aharony, 2016).

The particle-vortex duality discussed in Section "Particle-vortex duality in 2+1 dimensions" combined with the fermion-vortex duality we sketched here provide a web of dualities. These identifications constitute a powerful nonperturbative tool, which has led to many significant developments. For instance, Goldman and Fradkin (2018a) used the web of dualities to explain the experimentally observed self-duality at fractional quantum Hall plateau transitions, which was a long standing puzzle. It has also provided a powerful new tool to derive effective field theories of non-Abelian fractional quantum Hall states (Goldman et al., 2019) and even to propose novel states with a single (Fibonacci) anyon (Goldman et al., 2021).

Bosonization of the fermi surface

A form of bosonization has been developed for the case of systems of fermions with a Fermi surface. Dense Fermi systems at sufficiently weak coupling are well described by the Landau theory of the Fermi liquid (Baym and Pethick, 1991; Abrikosov et al., 1963; Nozières and Pines, 1966; Polchinski, 1993; Shankar, 1994). In this regime, the system of fermions has a collective mode, a bound state of particles and holes, which at long wavelengths is well described by the random phase approximation (RPA) (Bohm and Pines, 1953). However, in space dimensions $d > 1$, there is no kinematical restriction and quasi-particles and quasi-holes may move in their separate ways. The result is that, in addition to the collective modes, there is a low-energy spectrum of renormalized but essentially free quasi-particles. Because of the existence of this quasi-particle spectrum, the collective modes generally (but not always) decay into particle–hole pairs, resulting in a finite lifetime of the collective modes.

Superficially, the particle–hole collective modes are similar to the scalar field of the bosonized theory in $d = 1$. To an extent it has been possible to "bosonize the Fermi surface" and to treat it as a quantum mechanical object (Haldane, 1994; Houghton and Marston, 1993; Castro Neto and Fradkin, 1994b, a; Houghton et al., 2000; Delacrétaz et al., 2022). In this approach, one essentially regards each direction normal to the Fermi surface as a one-dimensional chiral fermion, including the current algebra structure, subject to global constraints that cancels the anomalies. This point of view ensures that the total fermion number in the Fermi sea is conserved. Here I will only present a short summary of the main ideas.

As in the one-dimensional case, one defines a filled Fermi sea state $|\mathrm{FS}\rangle$. This is a state of noninteracting fermions filling up all one-particle states up to the Fermi energy E_F. For concreteness, we consider a system in two space dimensions. In this case, neglecting lattice effects, the Fermi surface is a circumference of radius p_F, the Fermi momentum. At fixed fermion number, the excitations are particle–hole pairs. The operator $n_{\boldsymbol{k}}(\boldsymbol{q}) = c^\dagger(\boldsymbol{k} + \frac{\boldsymbol{q}}{2})\, c(\boldsymbol{k} - \frac{\boldsymbol{q}}{2})$ creates a particle–hole pair with relative momentum $\boldsymbol{q}$ with total momentum $\boldsymbol{k}$. In the low-energy regime, $\boldsymbol{k}$ is a point on the Fermi surface (with $|\boldsymbol{k}| = p_F$) and $\boldsymbol{q}$ is small momentum compared with p_F. In what follows we will label the point $\boldsymbol{k}$ on the Fermi surface by the angle θ of the arc spanned by $\boldsymbol{k}$ and an arbitrary origin on the Fermi surface.

We will normal-order the particle–hole creation operator with respect to the filled Fermi sea and define $\delta(\boldsymbol{q}, \theta) =: n_{\boldsymbol{k}}(\boldsymbol{q}) := n_{\boldsymbol{k}}(\boldsymbol{q}) - \langle \mathrm{FS}|n_{\boldsymbol{k}}(\boldsymbol{q})|\mathrm{FS}\rangle$. Haldane (1994), Houghton and Marston (1993), Houghton et al. (2000), and Castro Neto and Fradkin (1994a, b) showed that in real space these normal ordered density operators obey the equal-time commutation relations

$$[\delta n(\boldsymbol{x}, \theta), \delta n(\boldsymbol{x}', \theta')] = -\frac{1}{2\pi}\boldsymbol{k}_F(\theta) \cdot \nabla \delta^2(\boldsymbol{x} - \boldsymbol{x}')\delta(\theta - \theta') \tag{587}$$

where $\boldsymbol{k}_F(\theta)$ is a unit vector normal to the Fermi surface at angle θ. This is the algebra of the quantum fluctuations of the Fermi surface. We can further define at each point θ on the Fermi surface a Bose field $\varphi(\boldsymbol{x}, \theta)$ such that

$$\delta n(\boldsymbol{x}, \theta) = N(0)\boldsymbol{v}_F(\theta) \cdot \nabla \varphi(\boldsymbol{x}, \theta) \tag{588}$$

where $N(0)$ is the density of one-particle states at the Fermi surface and $\boldsymbol{v}_F(\theta)$ is the Fermi velocity at the location θ. The scalar field $\varphi(\boldsymbol{x}, \theta)$ is a chiral boson at θ which parametrizes the quantum fluctuations of the Fermi surface. The quantum dynamics of the chiral bosons $\varphi(\boldsymbol{x}, \theta)$ is governed by the action

$$\begin{aligned} S = & \frac{1}{2}N(0)\int_0^{2\pi}\frac{d\theta}{2\pi}\int d^2x\, dt\, \left(-\partial_t\varphi(x, \theta)\, \boldsymbol{v}_F(\theta) \cdot \nabla\varphi(x, \theta) - (\boldsymbol{v}_F(\theta) \cdot \nabla\varphi(x, \theta))^2 \right) \\ & + \frac{1}{2}N(0)\int_0^{2\pi}\frac{d\theta}{2\pi}\int_0^{2\pi}\frac{d\theta'}{2\pi}\int d^2x\, d^2x'\, dt\, F(\boldsymbol{x} - \boldsymbol{x}'; \theta - \theta')\, \boldsymbol{v}_F(\theta) \cdot \nabla\varphi(x, \theta)\, \boldsymbol{v}_F(\theta') \cdot \nabla\varphi(x, \theta') \end{aligned} \tag{589}$$

where $x = (\boldsymbol{x}, t)$, and $F(\boldsymbol{x} - \boldsymbol{x}';\theta - \theta')$ are the FL parameters that parametrize the effective forward scattering interactions among the fermion quasiparticles on the Fermi surface (Baym and Pethick, 1991). The equation of motion predicted by this (quadratic) action is equivalent to the linearized quantum Boltzmann equation familiar from the Landau theory of the Fermi liquid. A nonlinear extension has been introduced recently by Delacrétaz et al. (2022). Recent work on the role of quantum anomalies in dense Fermi systems has yielded new insights on these problems (Shi et al., 2022).

In the regime, where the Landau theory of the Fermi liquid is expected to work (Baym and Pethick, 1991), bosonization of the Fermi surface approach has reproduced the previously known results. There remain many open problems in this approach (and others) in the vicinity of quantum phase transitions. In spite of intense research using many different approaches, quantum phase transitions in metallic systems are not yet fully understood beyond perturbation theory (Hertz, 1976; Millis, 1993). Nonperturbative ideas such as deconfined quantum criticality have been proposed (Senthil et al., 2004) and significant work has been done using large-N methods (Fitzpatrick et al., 2013; Metlitski et al., 2015). A particularly important metallic quantum phase transition (and perhaps the simplest) occurs near the Pomeranchuk instability of the FL. A quantum phase transition to an electron nematic state (Oganesyan et al., 2001) has been predicted and studied within the Hertz-Millis approach. It has also been studied using higher dimensional bosonization (Oganesyan et al., 2001; Lawler et al., 2006; Lawler and Fradkin, 2007). Quantum Monte Carlo simulations by Lederer et al. (2015) have shown that the vicinity of a nematic quantum critical point can trigger a superconducting state. Nematic Fermi fluids have been found in many physical systems of interest ranging from high temperature superconductors (such as cuprates and iron superconductors), to electron gases in large magnetic fields (Kivelson et al., 1998; Fradkin et al., 2010, 2015; Fernandes et al., 2019).

Conclusion

In this chapter, I presented the deep and broad role that Quantum Field Theory has in modern condensed matter physics. In spite of the length of this chapter, I have not done justice to its role in many important areas that I did not cover. In particular, I have not touched on the theory of quantum spin liquids, fractions, and particularly topological phases in three space dimensions, among others. An area in which the ideas and concepts of QFT have a huge impact, both conceptually and as a tool, is in the problem of quantum entanglement in Condensed Matter. The concept of quantum entanglement as applied to condensed matter systems, both in equilibrium and out of equilibrium, is a major area of current research and has become a crucial tool for characterizing systems at quantum criticality as well as topological phases of matter.

Acknowledgments

This work was supported in part by the US National Science Foundation through grant numbers DMR 1725401 and DMR 225920 at the University of Illinois.

References

Abrahams E, Anderson PW, Licciardello DC, and Ramakrishnan TV (1979) Scaling theory of localization: Absence of quantum diffusion in two dimensions. *Physical Review Letters* 42: 673.

Abrikosov AA (1957) On the magnetic properties of superconductors of the second group. *Soviet Physics JETP* 5: 1174 [(1957) Zh. Ekzp. i Teor. Fiz. 32: 1442].

Abrikosov AA, Gorkov LP, and Dzyaloshinski IE (1963) *Methods of Quantum Field Theory in Statistical Physics*. Englewood Cliffs, New Jersey: Prentice-Hall, Inc.

Adler SE (1969) The axial-vector vertex in spinor electrodynamics. *Physical Review* 177: 2426.

Affleck I (1986) Universal term in the free energy at a critical point and the conformal anomaly. *Physical Review Letters* 56: 746.

Affleck I (1990) Field theory methods and quantum critical phenomena. In: *Strings, Fields and Critical Phenomena*, p. 563. Amsterdam, The Netherlands: North-Holland.

Affleck I and Haldane FDM (1987) Critical theory of quantum spin chains. *Physical Review B* 36: 5291.

Affleck I and Marston JB (1988) Large-N limit of the Heisenberg-Hubbard model: Implications for high-T_c superconductors. *Physical Review B* 37: 3774.

Affleck I, Kennedy T, Lieb EH, and Tasaki H (1988) Valence bond ground states in isotropic quantum antiferromagnets. *Communications in Mathematical Physics* 115: 477.

Aharonov Y and Bohm D (1959) Significance of electromagnetic potentials in the quantum theory. *Physics Review* 115: 485–491.

Aharony O (2016) Baryons, monopoles and dualities in chern-simons-matter theories. *Journal of High Energy Physics* 2: 93.

Aharony O, Gur-Ari G, and Yacoby R (2012a) Correlation functions of large N Chern-Simons-matter theories and bosonization in three dimensions. *Journal of High Energy Physics* 2012: 28.

Aharony O, Gur-Ari G, and Yacoby R (2012b) $d = 3$ Bosonic vector models coupled to Chern-Simons gauge theories. *Journal of High Energy Physics* 3: 37.

Alcaraz FC and Köberle R (1981) Hidden parafermions in $Z(N)$ theories. *Physical Review D* 24: 1652.

Altland A and Simons BD (2010) *Condensed Matter Field Theory*. Cambridge U.K: Cambridge University Press.

Amit DJ (1980) *Field Theory, the Renormalization Group and Critical Phenomena*. New York, NY: McGraw Hill.

Anderson PW (1958) Absence of diffusion in certain random lattices. *Physics Review* 109: 1492.

Anderson PW (1970) A poor man's derivation of the scaling laws of the Kondo problem. *Journal of Physics C: Solid State Physics* 3: 2436.

Anderson PW, Yuval G, and Hammann DR (1970) Exact results in the kondo problem. II. Scaling theory, qualitatively correct solution, and some new results on one-dimensional classical statistical models. *Physical Review B* 1: 4464.

Andrei N (1980) Diagonalization of the Kondo Hamiltonian. *Physical Review Letters* 45: 379.

Ardonne E, Fendley P, and Fradkin E (2004) Topological order and conformal quantum critical points. *Annals of Physics* 310: 493.

Arovas D, Schrieffer JR, and Wilczek F (1984) Fractional statistics and the quantum Hall effect. *Physical Review Letters* 53: 722.

Ashcroft N and Mermin DN (1976) *Solid State Physics*. New York, New York: Holt, Reinhart and Winston.

Atiyah MF, Patodi VK, and Singer IM (1975) Spectral asymmetry and Riemannian geometry. I. *Mathematical Proceedings of the Cambridge Philosophical Society* 77: 43.

Barkeshli M and Wen XG (2010) Effective field theory and projective construction for $\mathbb{Z}_k$ parafermion fractional quantum Hall states. *Physical Review B* 81: 155302.

Bartolomei H, Kumar M, Bisognin R, Marguerite A, Berroir JM, Bocquillon E, Plaçais B, Cavanna A, Dong Q, Gennser U, Jin Y, and Fève G (2020) Fractional statistics in anyon collisions. *Science* 368: 173–177.

Baym G and Pethick CJ (1991) *Landau Fermi Liquid Theory*. New York, NY: John Wiley & Sons.

Belavin AA, Polyakov AM, and Zamolodchikov AB (1984) Infinite conformal symmetry in two-dimensional quantum field theory. *Nuclear Physics B* 241: 333.

Bell JS and Jackiw R (1969) The PCAC puzzle: $\pi^0\gamma$ in the σ-model. *Nuovo Cimento A* 60: 47.

Berezinskii VL (1971) Destruction of long-range order in one-dimensional and two-dimensional systems having a continuous symmetry group I. Classical systems. *Soviet Physics JETP* 32: 493.

Berezinskii VL (1972) Destruction of long-range order in one-dimensional and two-dimensional systems having a continuous symmetry group II. Quantum systems. *Soviet Physics JETP* 34: 610.

Bernevig BA, Hughes TL, and Zhang SC (2006) Quantum spin Hall effect and topological phase transition in HgTe quantum wells. *Science* 314: 1757.

Berry MV (1984) Quantal phase factors accompanying adiabatic changes. *Proceedings of the Royal Society of London A* 392: 45.

Bethe H (1931) *Theory of metals. I. Eigenvalues and eigenfunctions of the linear atomic chain* 71: 205.

Bid A, Ofek N, Inoue H, Heiblum M, Kane CL, Umansky V, and Mahalu D (2010) Observation of neutral modes in the fractional quantum Hall regime. *Nature* 466: 585–590.

Bloch F (1929) über der quantenmechanik der elektronen in kristallgittern. *Zeitschrift für physik* 52: 555–600.

Blöte H, Cardy JL, and Nightingale MP (1986) Conformal invariance, the central charge, and universal finite-size amplitudes at criticality. *Physical Review Letters* 56: 742.

Bogoliubov NN and Shirkov DV (1959) *Introduction to the Theory of Quantized Fields*. New York, New York: Interscience.

Bohm D and Pines D (1953) A collective description of electron interactions: III. Coulomb interactions in a degenerate electron gas. *Physical Review* 92: 609–625.

Bollini CG and Giambiagi JJ (1972) Dimensional renormalization: The number of dimensions as a regularizing parameter. *Il Nuovo Cimento B* 12: 20.

Bonderson P, Shtengel K, and Slingerland JK (2006) Probing non-abelian statistics with quasiparticle interferometry. *Physical Review Letters* 97: 016401.

Bradlyn B, Elcoro L, Cano J, Vergniory MG, Wang Z, Felser C, Aroyo MI, and Bernevig BA (2017) Topological quantum chemistry. *Nature* 547: 298–305.

Brézin E and Zinn-Justin J (1976) Renormalization of the nonlinear σ model in $2 + \varepsilon$ dimensions: Application to the Heisenberg ferromagnets. *Physical Review Letters* 36: 691.

Burgess CP and Quevedo F (1994) Bosonization as duality. *Nuclear Physics B* 421: 373.

Caldeira AO and Leggett AJ (1983) Quantum tunneling in a dissipative system. *Annals of Physics* 149: 374–456.

Callan CG and Harvey JA (1985) Anomalies and fermion zero modes on strings and domain walls. *Nuclear Physics B* 250: 427.

Callan CG, Dashen RF, and Gross DJ (1976) The structure of the gauge theory vacuum. *Physics Letters B* 63: 334.

Camino FE, Zhou W, and Goldman VJ (2005) Realization of a Laughlin quasiparticle interferometer: Observation of fractional statistics. *Physical Review B* 72: 075342.

Campbell DK and Bishop AR (1981) Solitons in polyacetylene and relativistic-field-theory models. *Physical Review B* 24: 4859–4862.

Campbell D and Bishop A (1982) Soliton excitations in polyacetylene and relativistic field theory models. *Nuclear Physics B* 200: 297–328.

Cano J and Bradlyn B (2021) Band representations and topological quantum chemistry. *Annual Review of Condensed Matter Physics* 12: 225–246.

Cardy J (1996) Scaling and Renormalization in Statistical Physics. *Cambridge Lecture Notes in Physics*. Cambridge, U.K.: Cambridge University Press.

Castro Neto AH and Fradkin E (1994a) Bosonization of fermi liquids. *Physical Review B* 49: 10877.

Castro Neto AH and Fradkin E (1994b) Bosonization of the low energy excitations of fermi liquids. *Physical Review Letters* 72: 1393.

Castro Neto AH, Guinea F, Peres NMR, Novoselov KS, and Geim AK (2009) The electronic properties of graphene. *Reviews of Modern Physics* 81: 109–162.

Chaikin PM and Lubensky TC (1995) *Principles of Condensed Matter Physics*. Cambridge, U.K.: Cambridge University Press.

Chakravarty S, Halperin BI, and Nelson DR (1988) Low-temperature behavior of two-dimensional quantum antiferromagnets. *Physical Review Letters* 60: 1057.

Chamon C and Fradkin E (1997) Distinct universal conductances in tunneling to quantum Hall states: The role of contacts. *Physical Review B* 56: 2012.

Chamon C, Freed DE, and Wen XG (1996) Nonequilibrium quantum noise in chiral Luttinger liquids. *Physical Review B* 53: 4033.

Chamon C, Freed DE, Kivelson SA, Sondhi SL, and Wen XG (1997) Two point-contact interferometer for quantum Hall systems. *Physical Review B* 55: 2331.

Chan A, Hughes TL, Ryu S, and Fradkin E (2013) Effective field theories for topological insulators by functional bosonization. *Physical Review B* 87: 085132.

Chan APO, Kvorning T, Ryu S, and Fradkin E (2016) Effective hydrodynamic field theory and condensation picture of topological insulators. *Physical Review B* 93: 155122.

Chang AM (2004) chiral Luttinger liquids at the fractional quantum Hall edge. *Reviews of Modern Physics* 75: 1449.

Chang AM, Pfeiffer LN, and West KW (1996) Observation of chiral Luttinger behavior in electron tunneling into fractional quantum Hall edges. *Physical Review Letters* 77: 2538.

Chen X, Gu ZC, Liu ZX, and Wen XG (2012) Symmetry-protected topological orders in interacting bosonic systems. *Science* 338: 1604–1606.

Chen JY, Son JH, Wang C, and Raghu S (2018) Exact boson-fermion duality on a 3D Euclidean lattice. *Physical Review Letters* 120.

Chubukov AV (1993) Kohn-Luttinger effect and the instability of a two-dimensional repulsive fermi liquid at $T = 0$. *Physical Review B* 48: 1097.

Cohen LA, Samuelson NL, Wang T, Taniguchi T, Watanabe K, Zaletel MP, and Young AF (2022) Universal chiral Luttinger liquid behavior in a graphene fractional quantum Hall point contact. *arXiv:2212.01374* (unpublished).

Coleman S (1973) There are no goldstone bosons in two dimensions. *Communications in Mathematical Physics* 31: 259–264.

Coleman S (1975) Quantum sine-Gordon equation as the massive Thirring model. *Physical Review D* 11: 2088.

Coleman S (1985) *Aspects of Symmetry*. Cambridge U.K: Cambridge University Press.

Creutz M, Jacobs L, and Rebbi C (1983) Monte Carlo computations in lattice gauge theories. *Physics Reports* 95: 201–282.

Das Sarma S, Freedman M, Nayak C, Simon SH, and Stern A (2008) Non-abelian anyons and topological quantum computation. *Reviews of Modern Physics* 80: 1083.

Dasgupta C and Halperin BI (1981) Phase transition in a lattice model of superconductivity. *Physical Review Letters* 47: 1556–1560.

de Picciotto R, Reznikov M, Heiblum M, Umansky V, Bunin G, and Mahalu D (1997) Direct observation of a fractional charge. *Nature* 389: 162.

Delacrétaz LV, Du YH, Mehta U, and Son DT (2022) Nonlinear bosonization of fermi surfaces: The method of coadjoint orbits. *Physical Review Research* 4: 033131.

Deser S, Jackiw R, and Templeton S (1982a) Three-dimensional massive gauge theories. *Physical Review Letters* 48: 975.

Deser S, Jackiw R, and Templeton S (1982b) Topologically massive gauge theories. *Annals of Physics* 140: 372–411.

Di Francesco P, Mathieu P, and Sénéchal D (1997) *Conformal Field Theory*. Berlin: Springer-Verlag.

Dirac P (1930) *The Principles of Quantum Mechanics*. Oxford, U.K.: Oxford University Press.

Dirac P (1931) Quantised singularities in the electromagnetic field. *Proceedings of the Royal Society of London* 133: 60.

Dolev M, Heiblum M, Umansky V, Stern A, and Mahalu D (2008) Observation of a quarter of an electron charge at the $\nu = 5/2$ quantum Hall state. *Nature* 452: 829.

Dombre D and Read N (1988) Absence of the hopf invariant in the long-wavelength action of two-dimensional antiferromagnets. *Physical Review B* 38: 7181.

Dong Z and Senthil T (2020) Noncommutative field theory and composite fermi liquids in some quantum Hall systems. *Physical Review B* 102: 205126.

Doniach S and Sondheimer EH (1974) Green's Functions for Solid State Physicists. *Frontiers in Physics*. New York, New York: W. A. Benjamin Inc.

Du X, Skachko I, Duerr F, Lucian A, and Andrei EY (2009) Fractional quantum Hall effect and insulating phase of Dirac electrons in graphene. *Nature* 462: 192–195.

Efrati E, Wang Z, Kolan A, and Kadanoff LP (2014) Real-space renormalization in statistical mechanics. *Reviews of Modern Physics* 86: 647–667.

Eisenstein JP, Willett R, Störmer HL, Tsui DC, Gossard AC, and English JH (1988) Collapse of the even-denominator fractional quantum Hall effect in tilted fields. *Physical Review Letters* 61: 997.

Elitzur S, Pearson RB, and Shigemitsu J (1979) Phase structure of discrete Abelian spin and gauge systems. *Physical Review D* 19: 3698.

Essin AM, Moore JE, and Vanderbilt D (2009) Magnetic polarizability and axion electrodynamics in crystalline insulators. *Physical Review Letters* 102: 146805.

Faddeev LD (1976) Introduction to functional methods. In: *Methods of Field Theory*, pp. 1–40. Amsterdam: North Holland.

Faulkner T, Iqbal N, Liu H, McGreevy J, and Vegh D (2010) Strange metal transport realized by gauge/gravity duality. *Science* 329: 1043–1047.

Fendley P, Ludwig A, and Saleur H (1995a) Exact nonequilibrium dc shot noise in Luttinger liquids and fractional quantum Hall devices. *Physical Review Letters* 75: 2196.

Fendley P, Ludwig AWW, and Saleur H (1995b) Exact conductance through point contacts in the $\nu = 1/3$ fractional quantum Hall effect. *Physical Review Letters* 74: 3005.

Fernandes RM, Orth PP, and Schmalian J (2019) Intertwined vestigial order in quantum materials: Nematicity and beyond. *Annual Review of Condensed Matter Physics* 10: 133–154.

Fetter AL and Walecka JD (1971) *Quantum Theory of Many-Particle Systems*. New York, New York: McGraw-Hill.

Feynman RP (1972) Statistical Mechanics, A Set of Lectures. *Frontiers in Physics*. Reading, Massachusetts: W. A. Benjamin Inc.

Feynman RP and Hibbs AR (1965) *Quantum Mechanics and Path Integrals*. New York, New York: McGraw-Hill.

Finkelstein D and Rubinstein J (1968) Connection between spin, statistics, and kinks. *Journal of Mathematical Physics* 9: 1762–1779.

Fisher ME (1967) The theory of equilibrium critical phenomena. *Reports on Progress in Physics* 30: 615.

Fisher ME (1974) The renormalization group in the theory of critical behavior. *Reviews of Modern Physics* 46: 597–615.

Fitzpatrick AL, Kachru S, Kaplan J, and Raghu S (2013) Non-fermi-liquid fixed point in a Wilsonian theory of quantum critical metals. *Physical Review B* 88: 125116.

Fradkin E (2013) *Field Theories of Condensed Matter Physics*, second ed. Cambridge, U.K: Cambridge University Press (expanded 2nd edition of the originally published book in 1991).

Fradkin E (2021) *Quantum Field Theory: An Integrated Approach*. Princeton, N. J.: Princeton University Press.

Fradkin E and Hirsch JE (1983) Phase diagram of one-dimensional electron-phonon systems. I. The Su-Schrieffer-Heeger model. *Physical Review B* 27: 1680.

Fradkin E and Kadanoff LP (1980) Disorder variables and para-fermions in two-dimensional statistical mechanics. *Nuclear Physics B* 170: 1.

Fradkin E and Kohmoto M (1987) Quantized Hall effect and geometric localization of electrons on lattices. *Physical Review B* 35: 6017–6023.

Fradkin E and Schaposnik FA (1994) The fermion-boson mapping in three dimensional quantum field theory. *Physics Letters B* 338: 253.

Fradkin E and Stone M (1988) Topological terms in one- and two-dimensional quantum Heisenberg antiferromagnets. *Physical Review B* 38: 7215(R).

Fradkin E and Susskind L (1978) Order and disorder in gauge systems and magnets. *Physical Review D* 17: 2637.

Fradkin E, Nayak C, Tsvelik A, and Wilczek F (1998) A Chern-Simons effective field theory for the pfaffian quantum Hall state. *Nuclear Physics B* 516: 704.

Fradkin E, Nayak C, and Schoutens K (1999) Landau-Ginzburg theories for non-abelian quantum Hall states. *Nuclear Physics B* 546: 711.

Fradkin E, Jejjala V, and Leigh RG (2002) Non-commutative Chern-Simons for the quantum Hall system and duality. *Nuclear Physics B* 642: 483–500.

Fradkin E, Kivelson SA, Lawler MJ, Andrew P, and Mackenzie JPE (2010) Nematic fermi fluids in condensed matter physics. *Annual Review of Condensed Matter Physics* 1: 153–178.

Fradkin E, Kivelson SA, and Tranquada JM (2015) Colloquium: Theory of intertwined orders in high temperature superconductors. *Reviews of Modern Physics* 87: 457–482.

Freedman MH, Kitaev A, Larsen MJ, and Wang Z (2002a) Topological quantum computation. *Communications in Mathematical Physics* 227: 605.

Freedman MH, Kitaev A, and Wang Z (2002b) Simulation of topological field theories by quantum computers. *Communications in Mathematical Physics* 227: 587.

Friedan D (1982) A proof of the Nielsen-Ninomiya theorem. *Communications in Mathematical Physics* 85: 481–490.

Friedan DH (1985) Nonlinear models in $2+\varepsilon$ dimensions. *Annals of Physics* 163: 318.

Fröhlich J and Zee A (1991) Large-scale physics of the quantum Hall fluid. *Nuclear Physics B* 364: 517.

Fu L and Kane CL (2007) Topological insulators with inversion symmetry. *Physical Review B* 76.

Fubini S (1991) Vertex operators and the quantum Hall effect. *Modern Physics Letters A* 6: 347–358.

Fujikawa K (1979) Path-integral measure for gauge-invariant fermion theories. *Physical Review Letters* 42: 1195.

Gamboa Saraví RE, Muschietti MA, Schaposnik FA, and Solomin JE (1984) Chiral symmetry and functional integral. *Annals of Physics* 157: 360.

Gell-Mann M and Low FE (1954) Quantum electrodynamics at small distances. *Physical Review* 95: 1300.

Georgi H and Glashow S (1974) Unity of all elementary-particle forces. *Physical Review Letters* 32: 438.

Ginsparg P (1989) Applied conformal field theory. In: Brézin E and Zinn-Justin J (eds.) *Champs, Cordes et Phénoménes Critiques/Fields, Strings and Critical Phenomena*, pp. 1–168. Amsterdam, The Netherlands: Elsevier Science Publishers B.V.

Giombi S, Minwalla S, Prakash S, Trivedi SP, Wadia SR, and Yin X (2012) Chern-Simons theory with vector fermion matter. *European Physical Journal C: Particles and Fields* 72: 1–65.

Goldhaber AS (1976) Connection of spin and statistics for charge-monopole composites. *Physical Review Letters* 36: 1122–1125.

Goldman H and Fradkin E (2018a) Dirac composite fermions and emergent reflection symmetry about even-denominator filling fractions. *Physical Review B* 98: 165137.

Goldman H and Fradkin E (2018b) Loop models, modular invariance, and three dimensional bosonization. *Physical Review B* 97: 195112.

Goldman H and Senthil T (2022) Lowest Landau level theory of the bosonic Jain states. *Physical Review B* 105.

Goldman H, Sohal R, and Fradkin E (2019) Landau-Gizburg theories of non-Abelian quantum Hall states from non-abelian bosonization. *Physical Review B* 100: 115111.

Goldman H, Sohal R, and Fradkin E (2020) Non-abelian fermionization and the landscape of quantum Hall phases. *Physical Review B* 102: 195151.

Goldman H, Sohal R, and Fradkin E (2021) Composite particle construction of the fibonacci fractional quantum Hall state. *Physical Review B* 103: 235118.

Goldstone J and Wilczek F (1981) Fractional quantum numbers on solitons. *Physical Review Letters* 47: 986.

Golterman MF, Jansen K, and Kaplan DB (1993) Chern-Simons currents and chiral fermions on the lattice. *Physics Letters B* 301: 219.

Gooth J, Bradlyn B, Honnali S, Schindler C, Kumar N, Noky J, Qi Y, Shekhar C, Sun Y, Wang Z, Bernevig BA, and Felser C (2019) Axionic charge-density wave in the Weyl semimetal $(TaSe_4)_2I$. *Nature* 575: 315–319.

Granger G, Eisenstein JP, and Reno JL (2009) Observation of chiral heat transport in the quantum Hall regime. *Physical Review Letters* 102: 086803.

Greiter M, Wen XG, and Wilczek F (1991) Paired Hall state at half filling. *Physical Review Letters* 66: 3205.

Greiter M, Wen XG, and Wilczek F (1992) Paired Hall states. *Nuclear Physics B* 374: 567–614.

Gross DJ and Neveu A (1974) Dynamical symmetry breaking in asymptotically free field theories. *Physical Review D* 10: 3235.

Gross DJ and Wilczek F (1973) Ultraviolet behavior of non-Abelian gauge theories. *Physical Review Letters* 30: 1343–1346.

Grundberg J, Hansson TH, and Karlhede A (1990) On Polyakov's spin factors. *Nuclear Physics B* 347: 420–440.

Hagiwara M, Katsumata K, Affleck I, Halperin BI, and Renard JP (1990) Observation of $S=1/2$ degrees of freedom in an $S=1$ linear-chain Heisenberg antiferromagnet. *Physical Review Letters* 65: 3181.

Haldane F (1981) Luttinger liquid theory of one-dimensional quantum fluids. I. Properties of the Luttinger model and their extension to the general 1D interacting spinless fermi gas. *Journal of Physics C: Solid State Physics* 14: 2585.

Haldane FDM (1985) 'θ' Physics' and quantum spin chains. *Journal of Applied Physics* 57: 3359.

Haldane FDM (1988a) Model for a quantum Hall effect without Landau levels: Condensed-matter realization of the "parity anomaly". *Physical Review Letters* 61: 2015–2018.

Haldane FDM (1988b) $O(3)$ non-linear σ model and the topological distinction between integer and half-integer-spin antiferromagnets in two dimensions. *Physical Review Letters* 61: 1029.

Haldane FDM (1994) Luttinger's theorem and bosonization of the fermi surface. In: Broglia RA and Schrieffer JR (eds.) *Proceedings of the International School of Physics "Enrico Fermi", Course CXXI "Perspectives in Many-Particle Physics", International School of Physics "Enrico Fermi"*, pp. 5–29. Amsterdam, The Netherlands: North-Holland. ArXiv:cond-mat/0505529.

Haldane F and Rezayi EH (1985) Periodic Laughlin-Jastrow wave functions for the fractional quantized Hall effect. *Physical Review B* 31: 2529.

Halperin BI (1983) Theory of the quantized Hall conductance. *Helvetica Physica Acta* 56: 75–102.

Halperin BI (1984) Statistics of quasiparticles and the hierarchy of fractional quantized Hall states. *Physical Review Letters* 52: 1583.

Halperin BI and Nelson DR (1978) Theory of two-dimensional melting. *Physical Review Letters* 41: 121.

Halperin BI, Lubensky TC, and Ma S-K (1974) First-order phase transitions in superconductors and smectic-A liquid crystals. *Physical Review Letters* 32: 292.

Halperin BI, Lee PA, and Read N (1993) Theory of the half-filled Landau level. *Physical Review B* 47: 7312.

Halperin BI, Stern A, Neder I, and Rosenow B (2011) Theory of the Fabry-Pérot quantum Hall interferometer. *Physical Review B* 83: 155440.

Hanbury Brown R and Twiss RQ (1956) Correlation between photons in two coherent beams of light. *Nature* 177: 27–29.

Hashisaka M, Jonckheere T, Akiho T, Sasaki S, Rech J, Martin T, and Muraki K (2021) Andreev reflection of fractional quantum Hall quasiparticles. *Nature Communications* 12: 2794.

Hertz JA (1976) Quantum critical phenomena. *Physical Review B* 14: 1165–1184.

Hikami S (1981) Anderson localization in a non-lienar σ-model representation. *Physical Review B* 24: 2671–2679.

Hirsch JE and Fradkin E (1982) Effect of quantum fluctuations on the Peierls instability: A Monte Carlo study. *Physical Review Letters* 49: 402–405.

Hofstadter DR (1876) Energy levels and wave functions of Bloch electrons in rational and irrational magnetic fields. *Physical Review B* 14: 2239.

Hohenberg PC (1967) Existence of long-range order in one and two dimensions. *Physics Review* 158: 383–386.

Horowitz GT (1989) Exactly soluble diffeomorphism invariant theories. *Communications in Mathematical Physics* 125: 417.

Hosur P, Ryu S, and Vishwanath A (2010) Chiral topological insulators, superconductors, and other competing orders in three dimensions. *Physical Review B* 81: 045120.

Houghton A and Marston JB (1993) Bosonization and fermion liquids in dimensions greater than one. *Physical Review B* 48: 7790–7808.

Houghton A, Kwon HJ, and Marston JB (2000) Multidimensional bosonization. *Advances in Physics* 49: 141–228.

Hsieh D, Xia Y, Qian D, Wray L, Dil JH, Meier F, Osterwalder J, Patthey L, Checkelsky JG, Ong NP, Fedorov AV, Lin H, Bansil A, Grauer D, Hor YS, Cava RJ, and Hasan MZ (2009) A tunable topological insulator in the spin helical Dirac transport regime. *Nature* 460: 1101–1105.

Ivanov DA (2001) Non-abelian statistics of half-quantum vortices in p-wave superconductors. *Physical Review Letters* 86: 268.

Jackiw R and Rebbi C (1976) Solitons with fermion number 1/2. *Physical Review D* 13: 3398.

Jackiw R and Rossi P (1981) Zero modes of the vortex-fermion system. *Nuclear Physics B* 190: 681.

Jackiw R and Schrieffer JR (1981) Solitons with fermion number 1/2 in condensed matter and relativistic field theories. *Nuclear Physics B* 190: 253.

Jain JK (1989a) Composite-fermion approach for the fractional quantum Hall effect. *Physical Review Letters* 63: 199.

Jain JK (1989b) Incompressible quantum Hall states. *Physical Review B* 40: 8079.

Jain S, Minwalla S, and Yokoyama S (2013) Chern Simons duality with a fundamental boson and fermion. *Journal of High Energy Physics* 2013: 37.

Ji Y, Chung Y, Sprinzak D, Heiblum M, Mahalu D, and Shtrikman H (2003) An electronic Mach-Zehnder interferometer. *Nature* 422: 415–418.

José JV, Kadanoff LP, Kirkpatrick S, and Nelson DR (1977) Renormalization, vortices, and symmetry-breaking perturbations in the two-dimensional planar model. *Physical Review B* 16: 1217.

Kadanoff LP (1966a) Scaling laws for Ising models near T_c. *Physics* 2: 263.

Kadanoff LP (1966b) Spin-spin correlations in the two-dimensional ising model. *Il Nuovo Cimento B* 44: 276.

Kadanoff LP (1969) Operator algebra and the determination of critical indices. *Physical Review Letters* 23: 1430.

Kadanoff LP (1978) Lattice Coulomb gas representations of two-dimensional problems. *Journal of Physics A: Mathematical and Theoretical* 11: 1399.

Kadanoff LP and Baym G (1962) Quantum Statistical Mechanics: Green's Function Methods in Equilibrium and Non-Equilibrium Problems. *Frontiers in Physics.* New York, New York: W. A. Benjamin Inc.

Kadanoff LP and Ceva H (1971) Determination of an operator algebra for the two-dimensional ising model. *Physical Review B* 3: 3918.

Kadanoff LP, Götze W, Hamblen D, Hecht R, Lewis EAS, Palciauskas VV, Rayl M, Swift J, Aspnes D, and Kane J (1967) Static phenomena near critical points: Theory and experiment. *Reviews of Modern Physics* 39: 395–431.

Kamenev A (2011) *Field theory of Non-Equilibrium Systems.* Cambridge, U.K.: Cambridge University Press.

Kane CL and Fisher M (1992) Transmission through barriers and resonant tunneling in an interacting one-dimensional electron gas. *Physical Review B* 46: 15233.

Kane CL and Fisher M (1994) Nonequilibrium noise and fractional charge in the quantum Hall effect. *Physical Review Letters* 72: 724.

Kane CL and Mele EJ (2005) Z_2 topological order and the quantum spin Hall effect. *Physical Review Letters* 95: 146802.

Karch A and Tong D (2016) Particle-vortex duality from 3D bosonization. *Physical Review X* 6: 031043.

Kievelson S and Ro·ek M (1985) Consequences of gauge invariance for fractionally charged quasi-particles. *Physics Letters B* 156: 85.

Kim EA, Lawler M, Vishveshwara S, and Fradkin E (2005) Signatures of fractional statistics in noise experiments in quantum Hall fluids. *Physical Review Letters* 95: 176402.

Kitaev AY (2003) Fault-tolerant quantum computation by anyons. *Annals of Physics* 303: 2 (arXiv:quant-ph/9707021).

Kitaev A (2009) Periodic table for topological insulators and superconductors. In: Feigelman M (ed.) *Advances in Theoretical Physics: Landau Memorial Conference. AIP Conference Proceedings*, p. 22. College Park, Maryland: American Institute of Physics.

Kittel C (1996) *Introduction to Solid State Physics.* New York, New York: John Wiley & Sons.

Kivelson SA, Fradkin E, and Emery VJ (1998) Electronic liquid-crystal phases of a doped mott insulator. *Nature* 393: 550–553.

Knizhnik VG and Zamolodchikov AB (1984) Current algebra and Wess-Zumino model in two dimensions. *Nuclear Physics B* 247: 83.

Kogut JB (1979) An introduction to lattice gauge theory and spin systems. *Reviews of Modern Physics* 51: 659.

Kogut J and Susskind L (1975) Hamiltonian formulation of Wilson's lattice gauge theories. *Physical Review D* 11: 395.

Kohmoto M (1985) Topological invariant and the quantization of the Hall conductance. *Annals of Physics* 160: 343.

Kohn W (1961) Cyclotron resonance and de Haas-van Alphen oscillations of an interacting electron gas. *Physical Review* 123: 1242.

Kohn W and Luttinger JM (1965) New mechanism for superconductivity. *Physical Review Letters* 15: 524.

Kosterlitz JM (1974) The critical properties of the two-dimensional *XY* model. *Journal of Physics C: Solid State Physics* 7: 1046.

Kosterlitz JM and Thouless DJ (1973) Order, metastability and phase transitions in two-dimensional systems. *Journal of Physics C: Solid State Physics* 6: 1181.

Kramers HA and Wannier GH (1941) Statistics of the two-dimensional ferromagnet part I. *Physical Review* 60: 252.

Kundu HK, Biswas S, Ofek N, Umansky V, and Heiblum M (2023) Anyonic interference and braiding phase in a Mach-Zehnder interferometer. *Nature Physics* 19: 515–521. https://doi.org/10.1038/s41567-022-01899-z (published online).

Laidlaw MGG and DeWitt CM (1971) Feynman functional integrals for systems of indistinguishable particles. *Physical Review D* 3: 1375–1378.

Landau L (1930) Diamagnetismus der metalle. *Zeitschrift für Physik* 64: 629–637.

Landau LD (1937) On the theory of phase transitions. *Zhurnal Eksperimental'noi i Teoreticheskoi Fiziki* 7: 19.

Landau LD and Lifshitz EM (1957) Quantum Mechanics: Non-Relativistic Theory. *Course of Theoretical Physics.* , first ed, vol. 3. Oxford, U.K.: Pergamon Press.

Landau LD and Lifshitz EM (1959) Statistical Physics. *Course of Theoretical Physics.* vol. 5. Oxford, U.K.: Pergamon Press.

Laughlin RB (1981) Quantized Hall conductivity in two dimensions. *Physical Review B* 23: 5632–5633.

Lawler MJ and Fradkin E (2007) Local quantum criticality at the nematic quantum phase transition. *Physical Review B* 75: 0333304.

Lawler MJ, Barci DG, Fernández V, Fradkin E, and Oxman L (2006) Non-perturbative behavior of the quantum phase transition to a nematic fermi liquid. *Physical Review B* 73: 085101.

Lederer S, Schattner Y, Berg E, and Kivelson SA (2015) Enhancement of superconductivity near a nematic quantum critical point. *Physical Review Letters* 114: 097001.

Leggett AJ, Chakravarty S, Dorsey AT, Fisher M, Garg A, and Zwerger W (1987) Dynamics of the dissipative two-state system. *Reviews of Modern Physics* 59: 1–85.

Leinaas JM and Myrheim J (1977) On the theory of identical particles. *Il Nuovo Cimento B (1971–1996)* 37: 1–23.

Levine H, Libby SB, and Pruisken A (1983) Electron delocalization by a magnetic field in two dimensions. *Physical Review Letters* 51: 1915.

Lieb E, Schultz T, and Mattis DC (1961) Two soluble models of an antiferromagnetic chain. *Annals of Physics (N. Y.)* 16: 407.

López A and Fradkin E (1991) Fractional quantum Hall effect and Chern-Simons gauge theories. *Physical Review B* 44: 5246.

López A and Fradkin E (1993) Response functions and spectrum of collective excitations of fractional quantum Hall effect systems. *Physical Review B* 47: 7080.

López A and Fradkin E (1999) Universal structure of the edge states of the fractional quantum Hall states. *Physical Review B* 59: 15323.

Luther A and Emery VJ (1974) Backward scattering in the one-dimensional electron gas. *Physical Review Letters* 33: 589.

Maldacena JM (1998) Large *N* limit of superconformal field theories and supergravity. *Advances in Theoretical and Mathematical Physics* 2: 231.

Mandelstam S (1975) Soliton operators for the quantized sine-Gordon equation. *Physical Review D* 11: 3026.

Martin PC (1967) *Measurements and Correlation Functions.* Philadelphia, Pennsylvania: Gordon & Breach.

Martin PC (1968) *Measurements and Correlation Functions.* New York/London/Paris: Gordon and Breach Science Publishers Ltd.

Mattis DC (1965) *The Theory of Magnetism.* New York, New York: Harper & Row.

Mattis DC and Lieb EH (1965) Exact solution of a many-fermion system and its associated boson field. *Journal of Mathematical Physics* 6: 304.

McKane AJ and Stone M (1981) Localization as an alternative to Goldstone's theorem. *Annals of Physics* 131: 36–55.

Mermin ND (1979) The topological theory of defects in ordered media. *Reviews of Modern Physics* 51: 591.

Mermin ND and Wagner H (1966) Absence of ferromagnetism or antiferromagnetism in one- or two-dimensional isotropic Heisenberg models. *Physical Review Letters* 17: 1133–1136.

Metlitski MA and Vishwanath A (2016) Particle-vortex duality of two-dimensional Dirac fermion from electric-magnetic duality of three-dimensional topological insulators. *Physical Review B* 93: 245151.

Metlitski MA, Mross DF, Sachdev S, and Senthil T (2015) Cooper pairing in non-fermi liquids. *Physical Review B* 91: 115111.

Miller JB, Radu IP, Zumbühl DZ, Levenson-Falk E, Kastner MA, Marcus CM, Pfeiffer LN, and West KW (2007) Fractional quantum Hall effect in a quantum point contact at filling fraction 5/2. *Nature Physics* 3: 561.

Milliken FP, Umbach CP, and Webb RA (1996) Indications of a Luttinger liquid in the fractional quantum Hall regime. *Solid State Communications* 97: 309–313.

Millis AJ (1993) Effect of a nonzero temperature on quantum critical points in itinerant fermion systems. *Physical Review B* 48: 7183–7196.

Moore JE and Balents L (2007) Topological invariants of time-reversal-invariant band structures. *Physical Review B* 75: 121306.

Moore G and Read N (1991) Non-Abelians in the fractional quantum Hall effect. *Nuclear Physics B* 360: 362.

Moore G and Seiberg N (1989a) Classical and quantum conformal field theory. *Communications in Mathematical Physics* 123: 177.

Moore G and Seiberg N (1989b) Taming the conformal zoo. *Physics Letters B* 220: 422.

Morf RH (1998) Transition from quantum Hall to compressible states in the second Landau level: New light on the $\nu = 5/2$ enigma. *Physical Review Letters* 80: 1505.

Moshe M and Zinn-Justin J (2003) Quantum field theory in the large *N* limit: A review. *Physics Reports* 385: 69–228.

Mross DF, Alicea J, and Motrunich OI (2016) Explicit derivation of duality between a free Dirac cone and quantum electrodynamics in $(2+1)$ dimensions. *Physical Review Letters* 117: 016802.

Nakamura J, Liang S, Gardner GC, and Manfra MJ (2020) Direct observation of anyonic braiding statistics. *Nature Physics* 16: 931–936.

Nambu Y and Jona-Lasinio G (1961) Dynamical model of elementary particles based on an analogy with superconductivity. I. *Physical Review* 122: 345.

Nayak C and Wilczek F (1994a) Non-fermi liquid fixed point in $2+1$ dimensions. *Nuclear Physics B* 417: 359–373.

Nayak C and Wilczek F (1994b) Renormalization group approach to low temperature properties of a non-fermi liquid metal. *Nuclear Physics B* 430: 534–562.

Nayak C and Wilczek F (1996) $2n$-Quasihole states realize 2^{n-1}-dimensional spinor braiding statistics in paired quantum Hall states. *Nuclear Physics B* 479: 529–553.

Nelson DR and Kosterlitz JM (1977) Universal jump in the superfluid density of two-dimensional superfluids. *Physical Review Letters* 39: 1201–1205.

Nelson DR and Toner J (1981) Bond-orientational order, dislocation loops, and melting of solids and smectic-*A* liquid crystals. *Physical Review B* 24: 363.

Nielsen HB and Ninomiya M (1981a) Absence of neutrinos on a lattice (I). Proof by homotopy theory. *Nuclear Physics B* 185: 20–40.

Nielsen HB and Ninomiya M (1981b) Absence of neutrinos on a lattice (II). Intuitive topological proof. *Nuclear Physics B* 193: 173–194.

Nielsen HB and Ninomiya M (1983) The Adler-Bell-Jackiw anomaly and Weyl fermions in a crystal. *Physics Letters B* 130: 389.

Nielsen HB and Olesen P (1973) Vortex-line models for dual strings. *Nuclear Physics B* 61: 45.

Nienhuis B (1987) Two-dimensional critical phenomena and the Coulomb gas. In: Domb C, Green M, and Lebowitz JL (eds.) *Phase Transitions and Critical Phenomena*, p. 1. London, U.K.: Academic Press.

Nishida Y, Santos L, and Chamon C (2010) Topological superconductors as nonrelativistic limits of Jackiw-Rossi and Jackiw-Rebbi models. *Physical Review B* 82: 144513.

Niu Q, Thouless DJ, and Wu YS (1985) Quantized Hall conductance as a topological invariant. *Physical Review B* 31: 3372.

Nozières P and Pines D (1966) *The Theory of Quantum Liquids: Normal Fermi Liquids*. New York, New York: W. A. Benjamin Inc.

Oganesyan V, Kivelson SA, and Fradkin E (2001) Quantum theory of the nematic fermi liquid. *Physical Review B* 64: 195109.

Onsager L (1944) Crystal statistics. I. A two-dimensional model with an order-disorder transition. *Physical Review* 65: 117.

Pan W, Störmer HL, Tsui DC, Pfeiffer LN, Baldwin KW, and West KW (2003) Fractional quantum Hall effect of composite fermions. *Physical Review B* 90.

Pan W, Xia JS, Störmer HL, Tsui DC, Vicente C, Adams ED, Sullivan NS, Pfeiffer LN, Baldwin KW, and West KW (2008) Experimental studies of the fractional quantum Hall effect in the first excited Landau level. *Physical Review B* 77: 075307.

Park K, Melik-Alaverdian V, Bonesteel NE, and Jain JK (1998) Possibility of *p*-wave pairing of composite fermions at $\nu = 1/2$. *Physical Review B* 58: R10167.

Pasquier V and Haldane F (1998) A dipole interpretation of the $\nu = 1/2$ state. *Nuclear Physics B* 516: 719.

Patashinskii AZ and Pokrovskii VL (1966) Behavior of ordered systems near the transition point. *Soviet Physics JETP* 23: 292 [(1966) Zh. Ekzp. i Teor. Fiz. 50: 439].

Perelomov A (1986) *Generalized Coherent States and Their Applications*. Berlin: Springer-Verlag.

Peskin ME (1978) Mandelstam-'t Hooft duality in abelian lattice models. *Annals of Physics* 113: 122–152.

Peskin ME and Schroeder DV (1995) An Introduction to Quantum Field Theory. *The Advanced Book Program.* Reading, Massachusetts: Perseus Books Publishing L.L.C.

Pfeuty P (1970) The one-dimensional ising model with a transverse field. *Annals of Physics* 57: 79.

Pines D and Nozières P (1966) *The Theory of Quantum Liquids*, vol. I. New York, New York: W. A. Benjamin Inc.

Polchinski J (1993) Effective field theory and the fermi surface. In: Harvey JA and Polchinski J (eds.) *Theoretical Advanced Study Institute (TASI 92): From Black Holes and Strings to Particles*, pp. 235–276. Singapore: World-Scientific Publishing Co. (Proceedings of TASI 1992, Boulder (Colorado, USA), June 1–26 (1992)).

Polchinski J (1994) Low-energy dynamics of the spinon-gauge system. *Nuclear Physics B* 422: 617–633.

Polchinski J (1998) *String Theory*. Cambridge U.K: Cambridge University Press.

Politzer HD (1973) Reliable perturbative results for strong interactions? *Physical Review Letters* 30: 1346.

Polyakov AM (1970) Conformal symmetry of critical fluctuations. *JETP Letters* 12: 381.

Polyakov AM (1974) Non-Hamiltonian approach to quantum field theory. *Soviet Physics JETP* 39: 10.

Polyakov A (1975a) Compact gauge fields and the infrared catastrophe. *Physics Letters B* 59: 82–84.

Polyakov AM (1975b) Interaction of goldstone particles in two dimensions. Applications to ferromagnets and massive yang-mills fields. *Physics Letters B* 59: 79.

Polyakov AM (1977) Quark confinement and topology of gauge theories. *Nuclear Physics B* 120: 429.

Polyakov AM (1987) *Gauge Fields and Strings*. London: Harwood Academic Publishers.

Polyakov AM (1988) Fermi-bose transmutations induced by gauge fields. *Modern Physics Letters A* 3: 325.

Polychronakos AP (2001) quantum Hall states as matrix Chern-Simons theory. *Journal of High Energy Physics* 2001: 011.

Preskill J (2004) Topological Quantum Computation. *Lecture Notes for Physics 219: Quantum Computation.* Caltech. http://www.theory.caltech.edu//tilde/preskill/ph219/topological.pdf. (Chapter 9; unpublished).

Pruisken A (1984) On localization in the theory of the quantized Hall effect: A two-dimensional realization of the θ-vacuum. *Nuclear Physics B* 235: 277.

Qi XL and Zhang SC (2011) Topological insulators and superconductors. *Reviews of Modern Physics* 83: 1057.

Qi XL, Wu YS, and Zhang SC (2006) Topological quantization of the spin Hall effect in two-dimensional paramagnetic semiconductors. *Physical Review B* 74: 085308.

Qi XL, Hughes TL, and Zhang SC (2008) Topological field theory of time-reversal invariant insulators. *Physical Review B* 78: 195424.

Radu I, Miller JB, Marcus CM, Kastner MA, Pfeiffer LN, Baldwin KW, and West KW (2008) Quasi-particle properties from tunneling in the $\nu = 5/2$ fractional quantum Hall state. *Science* 320: 899.

Raghu S and Kivelson SA (2011) Superconductivity from repulsive interactions in the two-dimensional electron gas. *Physical Review B* 83: 094518.

Rajaraman R (1985) *Solitons and Instantons*. Amsterdam, The Netherlands: North-Holland.

Read N (1998) Lowest-Landau-level theory of the quantum Hall effect: The fermi-liquid-like state of bosons at filling factor one. *Physical Review B* 58: 16262.

Read N and Green D (2000) Paired states of fermions in two dimensions with breaking of parity and time-reversal symmetries and the fractional quantum Hall effect. *Physical Review B* 61: 10267.

Read N and Newns DM (1983) On the solution of the Coqblin-Schreiffer Hamiltonian by the large-*N* expansion technique. *Journal of Physics C: Solid State Physics* 16: 3273.

Read N and Rezayi E (1999) Beyond paired quantum Hall states: Parafermions and incompressible states in the first excited Landau level. *Physical Review B* 59: 8084.

Redlich AN (1984a) Gauge noninvariance and parity nonconservation of three-dimensional fermions. *Physical Review Letters* 52: 18.

Redlich AN (1984b) Parity violation and gauge noninvariance of the effective gauge field action in three dimensions. *Physical Review D* 29: 2366.

Rezayi EH and Read N (2009) Non-Abelian quantized Hall states of electrons at filling factors 12/5 and 13/5 in the first excited Landau level. *Physical Review B* 79: 075306.

Roddaro S, Pellegrini V, and Beltram F (2004a) Quasi-particle tunneling at a constriction in a fractional quantum Hall state. *Solid State Communications* 131: 565.

Roddaro S, Pellegrini V, Beltram F, Biasiol G, and Sorba L (2004b) Interedge strong-to-weak scattering evolution at a constriction in the fractional quantum Hall regime. *Physical Review Letters* 93: 046801.

Rosenow B, Levkivskyi IP, and Halperin BI (2016) Current correlations from a mesoscopic anyon collider. *Physical Review Letters* 116: 156802.

Ryu S, Mudry C, Hou CY, and Chamon C (2009) Masses in graphene-like two-dimensional electronic systems: Topological defects in order parameters and their fractional exchange statistics. *Physical Review B* 80: 205319.

Sachdev S (2011) *Quantum Phase Transitions*. Cambridge, UK: Cambridge University Press.

Saminadayar L, Glattli DC, Jin Y, and Etienne B (1997) Observation of the *e*/3 fractionally charged Laughlin quasiparticle. *Physical Review Letters* 79: 2526.

Sandler NP, Chamon C, and Fradkin E (1999) Noise measurements and fractional charge in fractional quantum Hall liquids. *Physical Review B* 59: 12521.

Schaposnik FA (1978) Pseudoparticles and confinement in the two-dimensional Abelian Higgs model. *Physical Review D* 18: 1183.

Schnyder AP, Ryu S, Furusaki A, and Ludwig AWW (2008) Classification of topological insulators and superconductors in three spatial dimensions. *Physical Review B* 78: 195125.

Schrieffer JR (1964) Theory of Superconductivity. *Frontiers in Physics*. New York, New York: Addison-Wesley.

Schultz TD, Mattis DC, and Lieb EH (1964) Two-dimensional ising model as a soluble problem of many fermions. *Reviews of Modern Physics* 36: 856.

Schwinger J (1959) Field theory commutators. *Physical Review Letters* 3: 296.

Seiberg N and Witten E (2016) Gapped boundary phases of topological insulators via weak coupling. *Progress of Theoretical and Experimental Physics* 2016: ptw083.

Seiberg N, Senthil T, Wang C, and Witten E (2016) A duality web in 2+1 dimensions and condensed matter physics. *Annals of Physics* 374: 395–433.

Semenoff GW (1984) Condensed-matter simulation of a three-dimensional anomaly. *Physical Review Letters* 53: 2449.

Senthil T (2015) Symmetry-protected topological phases of quantum matter. *Annual Review of Condensed Matter Physics* 6: 299–324.

Senthil T, Vishwanath A, Balents L, Sachdev S, and Fisher MPA (2004) Deconfined quantum critical points. *Science* 303: 1490.

Shankar R (1994) Renormalization-group approach to interacting fermions. *Reviews of Modern Physics* 66: 129–192.

Shenker SH and Tobochnik J (1980) Monte Carlo renormalization group analysis of the classical Heisenberg model in two dimensions. *Physical Review B* 22: 4462.

Shi ZD, Goldman H, Else DV, and Senthil T (2022) Gifts from anomalies: Exact results for Landau phase transitions in metals. *SciPost Physics* 13: 102.

Simmons-Duffin D (2017) The conformal bootstrap. In: Polchinski J, Vieira P, and DeWolfe O (eds.) *TASI 2015: Proceedings of the 2015 Theoretical Advanced Study Institute in Elementary Particle Physics*, pp. 1–74. Singapore: World Scientific.

Simon B (1983) Holonomy, the quantum adiabatic theorem, and Berry's phase. *Physical Review Letters* 51: 2167.

Skyrme T (1962) A unified theory of mesons and baryons. *Nuclear Physics* 31: 556–569.

Son DT (2015) Is the composite fermion a Dirac particle? *Physical Review X* 5: 031027.

Sondhi SL, Girvin SM, Carini JP, and Shahar D (1997) Continuous quantum phase transitions. *Reviews of Modern Physics* 69: 315.

Stern A and Halperin BI (2006) Proposed experiments to probe the non-Abelian $\nu = 5/2$ quantum Hall state. *Physical Review Letters* 96: 016802.

Stone M and Chung SB (2006) Fusion rules and vortices in $p_x + ip_y$ superconductors. *Physical Review B* 73: 014505.

Su WP, Schrieffer JR, and Heeger AJ (1979) Solitons in polyacetylene. *Physical Review Letters* 42: 1698.

Susskind L (1977) Lattice fermions. *Physical Review D* 16: 3031.

Susskind L (2001) The Quantum Hall Fluid and Non-Commutative Chern Simons Theory. https://arxiv.org/abs/hep-th/0101029v3.

't Hooft G (1976) Computation of the quantum effects due to a four-dimensional pseudoparticle. *Physical Review D* 14: 3432–3450.

't Hooft G (1976) Symmetry breaking through Bell-Jackiw anomalies. *Physical Review Letters* 37: 8.

't Hooft G and Veltman M (1972) Regularization and renormalization of gauge fields. *Nuclear Physics B* 44: 189.

Takayama H, Lin-Liu YR, and Maki K (1980) Continuum model for solitons in polyacetylene. *Physical Review B* 21: 2388–2393.

Thomas PR and Stone M (1978) Nature of the phase transition in a non-linear $O(2)_3$ model. *Nuclear Physics B* 144: 513–524.

Thouless DJ, Kohmoto M, Nightingale MP, and den Nijs M (1982) Quantized Hall conductance in a two-dimensional periodic potential. *Physical Review Letters* 49: 405.

Toner J and Nelson DR (1981) Smectic, cholesteric, and Rayleigh-Benard order in two dimensions. *Physical Review B* 23: 316.

Tsui DC, Stormer HL, and Gossard AC (1982) Two-dimensional magnetotransport in the extreme quantum limit. *Physical Review Letters* 48: 1559.

Ukawa A, Windey P, and Guth AH (1980) Dual variables for lattice gauge theories and the phase structure of $Z(N)$ systems. *Physical Review D* 21: 1013.

Varma CM, Littlewood PB, Schmitt-Rink S, Abrahams E, and Ruckenstein AE (1989) Phenomenology of the normal state of Cu-O high-temperature superconductors. *Physical Review Letters* 63: 1996–1999.

Venkatachalam V, Yacoby A, Pfeiffer L, and West K (2011) Local charge of the $\nu = 5/2$ fractional quantum Hall state. *Nature* 469: 185–188.

Vishveshwara S (2003) Revisiting the hanbury Brown-Twiss setup for fractional statistics. *Physical Review Letters* 91: 196803.

Vishveshwara S and Cooper NR (2010) Correlations and beam splitters for quantum Hall anyons. *Physical Review B* 81: 201306.

Volovik GE (1987) Zeros in the fermion spectrum in superfluid systems as diabolical points. *Journal of Experimental and Theoretical Physics Letters* 46: 98.

Volovik GE (1988) An analog of the quantum Hall effect in a superfluid ^{3}He film. *Soviet Physics JETP* 67: 1804.

von Klitzing K, Dorda G, and Pepper M (1980) New method for high-accuracy determination of the fine-structure constant based on quantized Hall resistance. *Physical Review Letters* 45: 494.

Wang C and Senthil T (2015) Dual Dirac liquid on the surface of the electron topological insulator. *Physical Review X* 5: 041031.

Wegner FJ (1971) Duality in generalized ising models and phase transitions without local order parameters. *Journal of Mathematical Physics* 12: 2259.

Wegner FJ (1979) The mobility edge problem: Continuous symmetry and a conjecture. *Zeitschrift für Physik B Condensed Matter* 35: 207.

Weinberg EJ (1981) Index calculations for the fermion-vortex system. *Physical Review D* 24: 2669.

Weinberg S (2005) *The Quantum Theory Of Fields*, first ed, vols. I-III. Cambridge, U.K.: Cambridge University Press.

Wen XG (1991) Non-abelian statistics in the fractional quantum Hall states. *Physical Review Letters* 66: 802.

Wen XG (1995) Topological orders and edge excitations in fractional quantum Hall states. *Advances in Physics* 44: 405.

Wen XG and Niu Q (1990) Ground-state degeneracy of the fractional quantum Hall states in the presence of a random potential and on high-genus Riemann surfaces. *Physical Review B* 41: 9377.

Wen XG and Zee A (1992) Classification of Abelian quantum Hall states and matrix formulation of topological fluids. *Physical Review B* 46: 2290.

Wen XG, Wilczek F, and Zee A (1989) Chiral spin states and superconductivity. *Physical Review B* 39: 11413–11423.

Wiegmann PB (1980) Exact solution of the Kondo problem. *JETP Letters* 31: 392.

Wiegmann PB (1989) Multivalued functionals and geometrical approach for quantization of relativistic particles and strings. *Nuclear Physics B* 323: 311.

Wilczek F (1982a) Magnetic flux, angular momentum, and statistics. *Physical Review Letters* 48: 1144.

Wilczek F (1982b) Quantum mechanics of fractional-spin particles. *Physical Review Letters* 49: 957–959.

Wilczek F (1987) Two applications of axion electrodynamics. *Physical Review Letters* 58: 1799–1802.

Wilczek F and Zee A (1983) Linking numbers, spin, and statistics of solitons. *Physical Review Letters* 51: 2250.

Willett R, Eisenstein JP, Störmer HL, Tsui DC, Gossard AC, and English JH (1987) Observation of an even-denominator quantum number in the fractional quantum Hall effect. *Physical Review Letters* 59: 1776.

Willett RL, Pfeiffer LN, and West KW (2009) Measurement of filling factor 5/2 quasiparticle interference with observation of charge e/4 and e/2 period oscillations. *Proceedings of the National Academy of Sciences* 106: 8853–8858.

Willett RL, Nayak C, Shtengel K, Pfeiffer LN, and West KW (2013) Magnetic-field-tuned Aharonov-Bohm oscillations and evidence for non-Abelian anyons at $\nu = 5/2$. *Physical Review Letters* 111: 186401.

Willett RL, Shtengel K, Nayak C, Pfeiffer LN, Chung YJ, Peabody ML, Baldwin KW, and West KW (2023) Interference measurements of non-Abelian e/4 & abelian e/2 quasiparticle braiding. *Physical Review X* 13: 011028.

Wilson KG (1969) Non-Lagrangian models of current algebra. *Physics Review* 179: 1499.

Wilson KG (1971a) Renormalization group and critical phenomena. I. Renormalization group and the Kadanoff scaling picture. *Physical Review B* 4: 3174–3183.

Wilson KG (1971b) Renormalization group and critical phenomena. II. Phase-space cell analysis of critical behavior. *Physical Review B* 4: 3184–3205.

Wilson KG (1973) Quantum field theory models in less than 4 dimensions. *Physical Review D* 7: 2911.

Wilson KG (1974) Confinement of quarks. *Physical Review D* 10: 2445.

Wilson KG (1975) The renormalization group: Critical phenomena and the kondo problem. *Reviews of Modern Physics* 47: 773.

Wilson KG (1983) The renormalization group and critical phenomena. *Reviews of Modern Physics* 55: 583.

Wilson KG and Fisher ME (1972) Critical exponents in 3.99 dimensions. *Physical Review Letters* 28: 240.

Wilson KG and Kogut JB (1974) The renormalization group and the ε expansion. *Physics Reports C* 12: 75.

Witten E (1978) Some properties of the $(\bar{\psi}\psi)^2$ model in two dimensions. *Nuclear Physics B* 142: 285.

Witten E (1979) Dyons of charge $e\theta/2\pi$. *Physics Letters B* 86: 283.

Witten E (1984) Non-abelian bosonization in two dimensions. *Communications in Mathematical Physics* 92: 455.

Witten E (1989) Quantum field theory and the Jones polynomial. *Communications in Mathematical Physics* 121: 351.

Witten E (2016) Fermion path integrals and topological phases. *Reviews of Modern Physics* 88: 035001.

Wu YS (1984) General theory for quantum statistics in two dimensions. *Physical Review Letters* 52: 2103–2106.

Wu TT and Yang CN (1976) Dirac monopole without strings: Monopole harmonics. *Nuclear Physics B* 107: 365.

Xia JS, Pan W, Vicente CL, Adams ED, Sullivan NS, Stormer HL, Tsui DC, Pfeiffer LN, Baldwin KW, and West KW (2004) Electron correlation in the second Landau level: A competition between many nearly degenerate quantum phases. *Physical Review Letters* 93: 176809.

Yakovenko VM (1990) Chern-Simons terms and *n* field in Haldane's model for the quantum Hall effect without Landau levels. *Physical Review Letters* 65: 251.

Yang CN (1952) The spontaneous magnetization of a two-dimensional ising model. *Physical Review* 85: 808.

Yang CN and Yang CP (1969) Thermodynamics of a one-dimensional system of bosons with repulsive delta-function interaction. *Journal of Mathematical Physics* 10: 1115.

Young AP (1979) Melting and the vector coulomb gas in two dimensions. *Physical Review B* 19: 1855.

Zamolodchikov AB and Fateev VA (1985) Nonlocal(parafermion) currents in two-dimensional conformal quantum field theory and self-dual critical points in $\mathbb{Z}_N$-symmetric statistical systems. *Soviet Physics JETP* 62: 215.

Zhang SC, Hansson TH, and Kivelson S (1989) Effective-field-theory model for the fractional quantum Hall effect. *Physical Review Letters* 62: 82.

Zibrov AA, Kometter C, Zhou H, Spanton EM, Taniguchi T, Watanabe K, Zaletel MP, and Young AF (2017) Tunable interacting composite fermion phases in a half-filled bilayer-graphene Landau level. *Nature* 549: 360–364.

Zinn-Justin J (2002) Quantum Field Theory and Critical Phenomena. *International Series of Monographs in Physics*. Oxford, U.K.: Oxford University Press.

Majorana fermions in condensed-matter physics[☆]

AJ Leggett, Department of Physics, University of Illinois at Urbana-Champaign, Urbana, IL, United States

© 2024 Elsevier Ltd. All rights reserved.

Introduction 132
Acknowledgments 138
References 138

Abstract

This chapter reviews the standard theoretical wisdom, based on the Bogoliubov-de Gennes mean-field equations, concerning Majorana fermions in so-called topological superconductors and (Fermi) superfluids, and attempts to provide some intuition concerning their nature. The experimental situation is briefly discussed. At the end some doubts about the standard wisdom are expressed.

Abbreviations

ACR	Anticommutation relation
BdG	Bogoliubov-de Gennes
HQV	Half-quantum vortices
SRO	Single-layer strontium ruthenate
TQC	Topological quantum computing

Introduction

The concept of a Majorana fermion (hereafter MF) was originally introduced (Majorana, 1937) in a particle-physics context, by Ettore Majorana in 1937; it is a fermionic quasiparticle which is its own antiparticle. More formally, the field operator $\hat{\psi}(\mathbf{r})$ which creates a MF has the property

$$\hat{\psi}(\mathbf{r}) = \hat{\psi}^{\dagger}(\mathbf{r}), \tag{1}$$

from which follows (with appropriate normalization conventions) the anticommutation relation (ACR)

$$\left\{\hat{\psi}(\mathbf{r}),\ \ \hat{\psi}(\mathbf{r}')\right\} = \delta(\mathbf{r} - \mathbf{r}') \tag{2}$$

(instead of the standard fermionic ACR which would have zero on the right-hand side).

How can such a particle arise in condensed matter physics? The standard example is the case of a so-called "topological superconductor" (TS), as described by the standard "mean-field" theory which is a generalization of that developed for a simple Bardeen-Cooper-Schrieffer (BCS) superconductor; for the latter, see e.g., Chapter 5 of Ref. (de Gennes, 1966). Consider a general nonrelativistic Hamiltonian of the form $\widehat{\mathcal{H}}_0 + \hat{V}$, where

$$\begin{aligned}\widehat{\mathcal{H}}_0 \equiv \frac{\hbar^2}{2m}\int d\mathbf{r}\Bigg\{&\sum_{\alpha}\nabla\hat{\psi}^{\dagger}_{\alpha}(\mathbf{r})\cdot\nabla\hat{\psi}_{\alpha}(\mathbf{r})\\ &+\sum_{\alpha\beta}U_{\alpha\beta}(\mathbf{r})\hat{\psi}^{\dagger}_{\alpha}(\mathbf{r})\hat{\psi}_{\beta}(\mathbf{r})\Bigg\}\end{aligned} \tag{3}$$

$$\begin{aligned}\hat{V} \equiv \frac{1}{2}\sum_{\alpha\beta\gamma\delta}\iint d\mathbf{r}d\mathbf{r}'\, V_{\alpha\beta\gamma\delta}(\mathbf{r},\mathbf{r}')\cdot\\ \cdot\hat{\psi}^{\dagger}_{\alpha}(\mathbf{r})\hat{\psi}^{\dagger}_{\beta}(\mathbf{r}')\hat{\psi}^{\dagger}_{\gamma}(\mathbf{r}')\hat{\psi}^{\dagger}_{\delta}(\mathbf{r}).\end{aligned} \tag{4}$$

Here the suffix $\alpha = \pm 1$ is the spin index, and the quantity $\hat{\psi}_{\alpha}(\mathbf{r})$ and its Hermitian conjugate $\hat{\psi}^{\dagger}_{\alpha}(\mathbf{r})$ are field operators satisfying the standard fermionic ACRs

$$\begin{aligned}\left\{\hat{\psi}_{\alpha}(\mathbf{r}),\ \ \hat{\psi}^{\dagger}_{\beta}(\mathbf{r}')\right\} &= \delta_{\alpha\beta}\delta(\mathbf{r} - \mathbf{r}'),\\ \left\{\hat{\psi}_{\alpha}(\mathbf{r}),\ \ \hat{\psi}_{\beta}(\mathbf{r}')\right\} &= 0.\end{aligned} \tag{5}$$

[☆] *Change History*: July 2022. AJ Leggett updated the chapter.

https://doi.org/10.1016/B978-0-323-90800-9.00050-0

For the moment, we place no particular constraints on the form of the single-particle potential $U_{\alpha\beta}(\boldsymbol{r})$ or that of the two-particle interaction $V_{\alpha\beta\gamma\delta}(\boldsymbol{r}, \boldsymbol{r}')$. Note that the Hamiltonian (3) is automatically invariant under the global $U(1)$ transformation

$$\hat{\psi}_\alpha(\boldsymbol{r}) \to \mathbf{e}^{\mathrm{i}\phi}\hat{\psi}_\alpha(\boldsymbol{r}), \quad \hat{\psi}^\dagger_\alpha(\boldsymbol{r}) \to \mathbf{e}^{-\mathrm{i}\phi}\hat{\psi}^\dagger_\alpha(\boldsymbol{r}), \tag{6}$$

where φ is a real position-independent constant. (We could of course introduce a vector potential $\mathbf{A}(\mathbf{r})$ and more general gage transformations, but for simplicity of presentation I do not do so here).

The essence of the mean-field (mf) theory of superconductivity (de Gennes, 1966) consists in introducing the notion of spontaneous breaking of the U(1) symmetry (hereafter abbreviated SBU(1)S) or equivalently the idea that we are free to describe the system by quantum-mechanical states which are not eigenstates of the total particle number operator

$$\hat{N} \equiv \sum_\alpha \int d\boldsymbol{r}\ \hat{\psi}^\dagger_\alpha(\boldsymbol{r})\hat{\psi}_\alpha(\boldsymbol{r}). \tag{7}$$

Indeed, in mf theory, the ground state of a superconducting system containing an even number of fermions is (explicitly or implicitly) taken in the form

$$\Psi_{(\mathrm{even})} = \sum_{N=\mathrm{even}} C_N \Psi_N, \tag{8}$$

where the quantities C_N are complex coefficients. As a result of the ansatz (8), the "anomalous averages", that is, expectation values of the form

$$F_{\alpha\beta}(\boldsymbol{r},\ \ \boldsymbol{r}') \equiv \left\langle \psi_\alpha(\boldsymbol{r})\ \ \hat{\psi}_\beta(\boldsymbol{r}')\right\rangle \tag{9}$$

can legitimately be taken to be nonzero in the ground state (and more generally in the superconducting phase). The quantity $F_{\alpha\beta}(\boldsymbol{r}, \boldsymbol{r}')$ may be intuitively regarded (apart from its normalization) as the wave function of the Cooper pairs which form in the superconductor (on this see e.g., Ref. (Leggett, 2006), Chapter 5).

The mf method then proceeds by decoupling the expression for the potential energy operator $\hat{V}$, Eq. (4), by a "generalized Hartree-Fock" approximation, in which not only operators of the form $\hat{\psi}^\dagger_\alpha(\boldsymbol{r})\ \hat{\psi}_\beta(\boldsymbol{r}')$ but also those of the form $\hat{\psi}_\alpha(\boldsymbol{r})\ \hat{\psi}_\beta(\boldsymbol{r}')$ are (partially) replaced by their averages. The resulting form of $\hat{V}$ contains not only the standard Hartree and Fock terms, which for simplicity of presentation I will omit, but also the "pairing" ("mf") term

$$\hat{V}_{\mathrm{mf}} = \sum_{\alpha\beta} \iint d\boldsymbol{r}\ d\boldsymbol{r}' \left\{\Delta_{\alpha\beta}(\boldsymbol{r},\ \ \boldsymbol{r}')\hat{\psi}^\dagger_\alpha(\boldsymbol{r})\hat{\psi}^\dagger_\beta(\boldsymbol{r}') + \mathrm{h.c.}\right\}, \tag{10}$$

where the $\hat{\psi}^\dagger_{\alpha,\beta}$ are still operators, but the quantity

$$\Delta_{\alpha\beta}(\boldsymbol{r},\ \ \boldsymbol{r}') \equiv \sum_{\gamma\delta} V_{\alpha\beta\gamma\delta}(\boldsymbol{r},\ \ \boldsymbol{r}')\left\langle \hat{\psi}_\gamma(\boldsymbol{r}')\ \ \hat{\psi}_\delta(\boldsymbol{r})\right\rangle \tag{11}$$

is a c-number; Δ is often regarded as a sort of effective mf. While the general expression (10) looks dauntingly complicated, readers may be familiar with the simpler form it takes in the case of a contact interaction $V_0\delta(\boldsymbol{r})$ and s-wave pairing:

$$\begin{gathered}\hat{V}_{\mathrm{mf}} = \int d\boldsymbol{r}\left\{\Delta(\boldsymbol{r})\ \ \hat{\psi}^\dagger_\uparrow(\boldsymbol{r})\ \ V(\boldsymbol{r})\ \ \hat{\psi}^\dagger_\downarrow(\boldsymbol{r}) + \mathrm{h.c.}\right\}, \\ \Delta(\boldsymbol{r}) \equiv V_0\left\langle \hat{\psi}_\downarrow(\boldsymbol{r})\ \ \hat{\psi}_\uparrow(\boldsymbol{r})\right\rangle \end{gathered} \tag{12}$$

Before we proceed further, it is necessary to state one caveat: were we to minimize the sum of $\widehat{\mathcal{H}}_0$ and $\hat{V}_{\mathrm{mf}}$ as it stands, then since there is now no explicit restriction on the total particle number N the expectation value of the latter would likely turn out to be zero or at most very small (certainly this will be so if the potential is too weak to form a two-particle bound state in free space). Thus, we need to add to the single-particle energy $\widehat{\mathcal{H}}_0$ a term $-\mu\hat{N}$. With this correction, and continuing to omit the Hartree and Fock terms (which do not affect subsequent arguments qualitatively) the mf [Bogoliubov-de Gennes (BdG)] Hamiltonian is schematically of the form

$$\begin{gathered}\widehat{\mathcal{H}}_{\mathrm{mf}} = \sum_{\alpha\beta}\left\{\int d\boldsymbol{r}\ \ K_{\alpha\beta}(\boldsymbol{r})\ \ \hat{\psi}^\dagger_\alpha(\boldsymbol{r})\ \ \hat{\psi}_\beta(\boldsymbol{r})\right. \\ \left. + \frac{1}{2}\iint d\boldsymbol{r}\ \ d\boldsymbol{r}'\ \ \Delta_{\alpha\beta}(\boldsymbol{r},\ \ \boldsymbol{r}')\ \ \hat{\psi}^\dagger_\alpha(\boldsymbol{r})\ \ \psi^\dagger_\beta(\boldsymbol{r}') + \mathrm{h.c.}\right\}\end{gathered} \tag{13}$$

where the notation $K_{\alpha\beta}(\boldsymbol{r})$ is introduced in the first term as a shorthand for the quantity

$$\delta_{\alpha,\beta}\left(\frac{\hbar^2}{2m}\nabla\hat{\psi}^\dagger_\alpha(\boldsymbol{r})\cdot\nabla\hat{\psi}_\beta(\boldsymbol{r}') - \mu\hat{\psi}^\dagger_\alpha(\boldsymbol{r})\hat{\psi}_\beta(\boldsymbol{r})\right). \tag{14}$$

The operator $\widehat{\mathscr{H}}_{\text{mf}}$ does not conserve particle number, but does conserve the parity of the latter (i.e., it does not mix states with even and odd parity); note that the occurrence of terms proportional to (the operator) $\hat{\psi}^{\dagger}\hat{\psi}^{\dagger}$ leads rather naturally to eigenstates of the form (8).

In principle, we may try to use the mf Hamiltonian (13) for either of two purposes: (1) we could try to determine the form of the even-parity ground state [i.e., of the state vectors $\hat{\psi}_N$ and coefficients C_N in Eq. (8)]. This is possible, but actually quite complicated (see e.g., Appendix A of Ref. (Stone and Chung, 2006)), and in fact we need to proceed via the solution of task (2), namely to determine the *relation* between the even-parity ground state and the simplest ("single-fermion") odd-parity states. It is the latter problem which is central to the question of MF, so I shall from now on specialize to that.

The "textbook" prescription for creating, from the even-parity ground state ψ_{even}, the simplest odd-parity states goes as follows [for simplicity of notation I omit in the following the spin indices: in reality the quantities $\hat{\psi}(\mathbf{r})$, etc., are spinors in *real* spin space (not "Nambu space," see below): and the *u*s and vs are matrices.] We construct an operator of the form

$$\gamma_i^{\dagger} = \int d\mathbf{r}\left\{u_i(\mathbf{r})\ \hat{\psi}^{\dagger}(\mathbf{r}) + v_i(\mathbf{r})\ \hat{\psi}(\mathbf{r})\right\} \tag{15}$$

and determine the coefficients $u_i(\mathbf{r})$, $v_i(\mathbf{r})$ by requiring $\gamma_i^{\dagger}$ to satisfy the eigenvalue equation (with E_i the value of $\widehat{\mathscr{H}}_{\text{mf}}$ relative to the even-parity ground state).

$$\left[\widehat{\mathscr{H}}_{\text{mf}},\ \gamma_i^{\dagger}\right] = E_i\gamma_i^{\dagger}, \tag{16}$$

so that (with appropriate normalization of u_i and v_i, see below)

$$\mathscr{H}_{\text{mf}} = \sum_i E_i\gamma_i^{\dagger}\gamma_i + \text{const.} \tag{17}$$

The states $\gamma_i^{\dagger}|\psi_{\text{even}}\rangle$ are then the simplest ("single-fermion") odd-parity energy eigenstates of the system, and are said to contain a single "Bogoliubov quasiparticle."

When written out explicitly in terms of the amplitudes $u(\mathbf{r})$, $v(\mathbf{r})$ Eq. (15) becomes a set of linear equations which can be written *schematically* in the form

$$\begin{pmatrix} \hat{K} & \hat{\Delta} \\ \hat{\Delta} & -K** \end{pmatrix}\begin{pmatrix} u \\ v \end{pmatrix} = E\begin{pmatrix} u \\ v \end{pmatrix} \tag{18}$$

where the matrix elements $\hat{K}$ and $\hat{\Delta}$ are themselves matrices in the (real) spin space, and may also be integral operators in (real) coordinate space, cf. Eq. (13). $\hat{\Delta}$ must be calculated self-consistently according to Eq. (11). In the best-known case of simple BCS pairing, the equations take the possibly more familiar form

$$\begin{aligned} \left(\widehat{\mathscr{H}}_0 - \mu\right) u(\mathbf{r}) + \Delta(\mathbf{r})\ u(\mathbf{r}) &= E\ u(\mathbf{r}), \\ \Delta^*(\mathbf{r})\ u(\mathbf{r}) - \left(\widehat{\mathscr{H}}_0 - \mu\right) v(\mathbf{r}) &= E\ v(\mathbf{r}), \end{aligned} \tag{19}$$

where $u(\mathbf{r})$, $v(\mathbf{r})$ and $\Delta(\mathbf{r})$ are all simple complex scalars. Equations (18) are called the BdG equations, and have been very widely used over the last 50 years in the theoretical literature on superconductivity, including cases more complicated than simple *s*-wave pairing. It is convenient to normalize the *u*s and vs so that

$$\int d\mathbf{r}\left(|u|^2(\mathbf{r}) + |v|^2(\mathbf{r})\right) = 1, \tag{20}$$

whereupon the γ_is satisfy the standard fermionic ACRs,

$$\left\{\gamma_i,\ \gamma_j^{\dagger}\right\} = \delta_{ij}, \quad \left\{\gamma_i,\ \gamma_j\right\} = 0 \tag{21}$$

thereby justifying Eq. (17).

All the above is standard textbook stuff, but it is important to note a crucial point: in this mf treatment, the fermionic quasiparticles are quantum superpositions of a state corresponding to an extra real fermion [with probability amplitude $u(\mathbf{r})$] and one with an extra (real) hole [with amplitude $v(\mathbf{r})$]; this is usually justified by appealing to SBU(1)S. It is conventional to represent this situation by a spinor in the 2D "Nambu space" corresponding to the particle and the hole degrees of freedom:

$$\gamma_j^{\dagger} \to \begin{pmatrix} u_j(\mathbf{r}) \\ v_j(\mathbf{r}) \end{pmatrix} \tag{22}$$

and to regard it (to my mind misleadingly, cf. below) as analogous to the mixing of different bands in an insulator by spin orbit coupling; then by analogy with the standard use of the term "topological insulator" for the latter case when the mixing is topologically nontrivial, in the corresponding case for a superconductor one talks about a "topological superconductor". In the recent literature, it has become common to refer to both of these cases, in the absence of more sophisticated terms than (14) in the

Hamiltonian, as "noninteracting-electron" problems, although the occurrence of the self-consistency condition (11) makes this phrasing rather misleading.

Before proceeding, we need to note a couple of easily verified properties of the γ_is:

(1) $\gamma_i|\hat{\psi}_{\text{even}}\rangle = 0, \ \forall_i$ s.t. $E_i \neq 0$.
(2) If there exists a formal solution to the BdG equations with some positive energy E_i, then by interchanging $u(\mathbf{r})$ and $v(\mathbf{r})$ (and appropriate attention to signs and spin suffixes) we can always construct a solution with negative energy $-E_i$. These "negative-energy" solutions are often regarded (in my opinion misleadingly, cf. below) as analogous to the "positron" solutions in quantum field theory.

Let us now raise (for the moment for no obviously good reason!) the question: do there exist "Majorana-like" solutions to the BdG equations, that is, solutions such that

$$\gamma_i^\dagger = \gamma_i. \tag{23}$$

It is clear from the definition (15) that this requires $u_i^*(\mathbf{r}) = v_i(\mathbf{r})$, (with appropriate spin-dependences, see below) and it furthermore follows from(16) that the corresponding energy eigenvalue E_i is exactly zero. However, these two conditions are not sufficient for an "interesting" Majorana; they would, for example, be satisfied by an ordinary Bogoliubov quasiparticle created in a "polar" p-wave superfluid (which has no particularly interesting topological properties) exactly at a node of the gap $\Delta(\mathbf{k})$, but one would not normally call such a quasiparticle a "Majorana". What is missing in the above definition is that the solutions of the BdG equations are spatially *localized*, i.e., that both $u(\mathbf{r})$ and $v(\mathbf{r})$ tend to zero exponentially outside a small spatial region,[1] typically a volume $\sim \xi^d$ where ξ is the Cooper pair radius and d the spatial dimension. It turns out that in addition to the requirement that the pair spin structure is a triplet [necessary to guarantee the self-conjugacy condition (23)], such localized solutions only occur if the pair wave function (order parameter) has a sufficiently interesting structure, typically involving spontaneous breaking of time-reversal invariance (TRI).

At this point, rather than trying to review the general picture, let me specialize to what seems to be the most promising state for the real-life realization of MFs, namely the so-called "p + ip" state. This state is characterized by the fact that either there is only a single spin state involved, or the amplitudes for ↑↑ and ↓↓ pairs may be treated as independent, and that as the name implies, in homogeneous conditions the order parameter $\Delta(\hat{p})$ written as a function of the direction of relative momentum $\mathbf{p}$ on the Fermi surface has the form

$$\Delta(\hat{p}) \propto \hat{p}_x + i\hat{p}_y \tag{24}$$

thereby violating (*inter alia*) the time-reversal invariance of the mf Hamiltonian [or of the original one of Eqs. (3), which for now we assume does not include TRI-violating terms]. The "p + ip" state is believed to describe the A phase of superfluid ^{3}He and, (possibly, though this is controversial), the superconducting state of the metal Sr_2RuO_4; in the future it may be possible to realize a (p + ip) state of an ultracold Fermi gas which has only a single spin population paired.

In the case of ^{3}He-A and Sr_2RuO_4, which contain both types $|\uparrow\uparrow\rangle$ and $|\downarrow\downarrow\rangle$ of Cooper pairs, it is believed (and in the latter case consistent with experiment (Jang et al., 2011)) that the system may sustain so-called "half-quantum vortices" (HQVs), that is, configurations in which (say) the ↑↑ pair wave function exhibits a simple vortex similar to those realized in the Bose system ^{4}He, while that of the ↓↓ pairs remains perfectly uniform. If this is so, then it appears that Majorana-type solutions not only can but must exist in the vicinity of these vortices (and possibly on the boundary of the system, if the number of vortices is odd). The general proof of this statement follows from the celebrated Atiyah-Patodi-Singer theorem in algebraic topology, but for any specified form of the order parameter near the vortex the existence of these solutions can be established by directly solving the BdG equations (18) (see Refs. (Kopnin and Salomaa, 1991; Volovik, 1999)).

The most exciting consequence of the existence of these MFs in a condensed-matter context is the prospect of possibly being able to use them for topological quantum computing (TQC), that is, a form of quantum computing in which the ubiquitous decoherence is frustrated by burying the relevant quantum information in strongly entangled many-body degrees of freedom in a way which is topologically protected. Why might MFs be a good prospect for TQC? There are essentially two major reasons (within the standard mf treatment, cf. below):

(1) Because a MF is an exactly equal superposition of particle and hole, it is undetectable by any local probe.
(2) MFs should behave under braiding as "Ising anyons": if two HQVs each carrying a MF, are interchanged, the phase of the many-body wave function is changed (relative to the zero-MF state) by $\pi/2$: note this is different from the standard result of π which one would obtain for ordinary fermions.

This then leads to the following scheme to create a TQC (for details see Ref. (Stone and Chung, 2006)):

(1) Create a set of HQVs, with and without MFs on them.
(2) Braid the vortices adiabatically.
(3) Recombine them and "measure" the result.

---

[1] Or in some cases away from the boundary.

Then provided that during the braiding processes, the HQVs are kept at mutual distance $\gg \xi$, all decoherence should be proportional to $\exp(-L/\xi)$ and thus at least a class[2] (Nayak et al., 2008) of quantum computing operations will be topologically protected.

The above is an extremely "potted" version of the standard wisdom concerning MF in condensed matter physics. Now for a few comments:

What exactly *is* a MF?

Recall: its creation operator $\gamma_i^\dagger$ satisfies (since $E_i = 0$ exactly) the equation

$$\left[\widehat{\mathcal{H}},\ \gamma_i^\dagger\right]\ \hat{\psi}_{\text{even}}\big|\big\rangle = 0. \tag{25}$$

But this equation actually has two possible interpretations: the more obvious one is that $\gamma_i^\dagger$ creates an odd-number-parity state (a Bogoliubov quasiparticle)with energy exactly equal to that of the even-parity one. However, an equally viable interpretation is that $\gamma_i^\dagger$ simply annihilates the ground state ("pure annihilator")! Now it is in fact easy to show (cf. Ref. (Leggett, 2010)) that neither of these possibilities can satisfy the self-conjugacy condition $\gamma_i^\dagger = \gamma_i$. To satisfy it, we must superpose the two possibilities: that is, formally, *a MF is simply a quantum superposition of a "real" Bogoliubov quasiparticle with zero energy and a pure annihilator.*

Consider now a situation in which we have just two HQVs, labeled 1 and 2, arbitrarily far apart. There exists on each vortex a Majorana solution, $\gamma_1^\dagger$ and $\gamma_2^\dagger$, respectively. As we have just seen, neither of these individually corresponds to creation of an extra zero-energy Bogoliubov quasiparticle. However, the combination

$$\alpha^+ \equiv \gamma_1^\dagger + i\gamma_2^\dagger \tag{26}$$

does so and satisfies the standard ACRs (5)! Thus, the two individual Majoranas, when suitably combined, indeed represent such a quasiparticle. The curious point is that this single extra fermion is spatially "split": it has support from two very different regions of space. In this light, the "braiding" of two HQVs each carrying an MF may be regarded as the rotation through π of this zero-energy fermion (note that the predicted phase change of $\pi/2$ is exactly the mean of what we would expect, for the "standard" double-well case, for the symmetric and antisymmetric combinations of the states localized on 1 and 2, respectively).

An intuitive appreciation of the nature of MFs may be obtained by considering the "Kitaev quantum wire" (Kitaev, 2001), a set of equally spaced sites described by the BdG-type Hamiltonian

$$\widehat{\mathcal{H}} = \sum_i t_i\left(a_i^\dagger a_{i+1} + \text{h.c.}\right) + \sum_i \Delta_i\left(a_i^\dagger a_{i+1}^\dagger + \text{h.c.}\right) \tag{27}$$

with the special choice $t_i = \Delta_i \equiv X_i$ (but the X_i are not necessarily identical). Let us start with a ring geometry [Fig. 1 (a)]. Then the Bogoliubov quasiparticles are created by the operators

$$\alpha_i^+ \equiv \left(a_i^\dagger - a_i\right) + \left(a_{i-1}^\dagger + a_{i-1}\right) \tag{28}$$

and have excitation energies X_i: note that they are localized on the links rather than the sites.

Now, imagine that we gradually turn down to zero the "strength" X_i of some link i, say 0, [see Fig. 1B]. There is still a fermionic (Bogoliubov) excitation associated with this link, but the energy of the corresponding odd-parity many-body state is degenerate with that of the even-parity ground state. Finally, we break the i-th link, and reconfigure the set of sites into Kitaev's original open

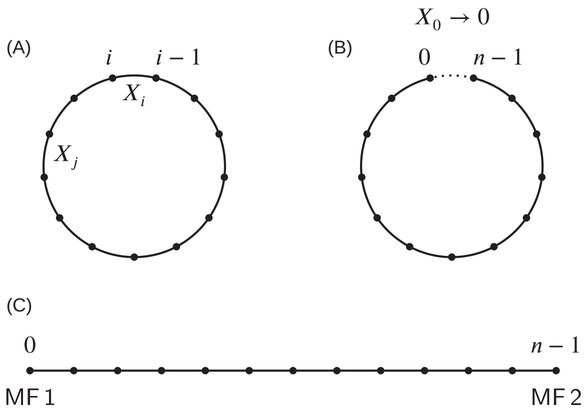

Fig. 1 Origin of two Majorana fermions in the Kitaev quantum wire.

---

[2] As in other putative realizations of an Ising quantum computer, there is no complete topological protection: for that one needs to go to e.g., a "Fibonacci" QC, see e.g., Ref. (Nayak et al., 2008), Sec. IV·B

"wire" [Fig. 1C]; since the energy associated with this link is zero, the structure of the fermionic states cannot change and we must still have the zero-energy state. But where is it localized? In view of the symmetry of the situation, it must be localized equally on the two open ends of the wire! It should be mentioned that while this argument seems rather straightforward, the actual wave functions of both the even- and odd-parity ground states individually are highly entangled and the derivation of the correct forms is not entirely trivial.

I now turn briefly to the question of the experimental evidence for Majorana fermions. It should be stated at the outset that, at least as regards MF's in topological superfluids/superconductors or related systems, the situation at the time of this writing is confused and controversial in the extreme. Whether by the time this chapter is published it will have become any clearer is anyone's guess.

Let me first briefly review the physical systems which are of interest in this context. The one originally favored was a bulk topological superfluid, usually with an order parameter of the $p + ip$ type; this class includes bulk liquid ^{3}He-A and possibly some metallic superconductors, the originally favored candidate being Sr_2RuO_4 (single-layer strontium ruthenate, SRO). In such a system a necessary precondition for the appearance of MF's would be the existence of half-quantum vortices (HQV's). Unfortunately, to the present author's knowledge there is to date no experimental evidence for HQV's in the bulk A phase[3] of ^{3}He, even in circumstances where theory would apparently predict them; the reason for this is not currently understood. In SRO the experimental picture seems internally inconsistent: magnetotorque experiments are naturally interpreted in terms of the appearance of (single) HQV's, while recent Knight-shift experiments have given results which are widely interpreted as inconsistent with the spin triplet order parameter which is a necessary precondition for the latter. (For a discussion of this and other current puzzles related to SRO, see the mini-review (Leggett and Liu, 2021)). Other superconductors (e.g., UTe_2) have been identified as possibly having a $(p + ip)$ order parameter, but at the time of writing there is no direct evidence for HQV's in them.

Actually, HQV's as such are not essential to the existence of MF's: all that is necessary is that the topological phase (e.g., the $p + ip$ phase) has one or more "edges" where it abuts on a region where the order parameter goes to zero. In the case of HQV's, this region is the vortex core; however, the physical boundary of the sample can play a similar role. This realization has led to a proposal (Sau et al., 2010) which has attracted much interest in the experimental community, namely that a suitable system might be a semiconducting wire with strong spin-orbit interaction in proximity to a simple BCS superconductor. In this case the combination of the proximity effect and the spin-orbit interaction can generate in part of the wire a $p + ip$-like (topological) superconducting state; while the rest of the wire remains normal; the two Majoranas are then predicted to reside at the edges of the topological region. In part because of the rich variety of parameters which can be tuned so as to affect the predicted properties of the MF's, this idea has generated over the last decade a large number of experiments which use this setup to attempt to detect the latter; in most of these the raw date has been the current-voltage (I-V) characteristics of the wire as a function of spin-orbit interaction, *s*-wave gap, magnitude and direction of the magnetic field etc., and in many of the papers in question evidence for the existence of MF's has been claimed. Unfortunately, the logic underlying these claims has mostly been of the "what else could it be?" variety, and there have been plenty of theoretical papers proposing other things it could be. In addition, in many cases the selection procedures used in the reporting of the data have been questioned (for a hard-hitting critique by an active worker in the field, see Ref. (Frolov, 2021)). So at this point the jury seems to be still out on these claims.

If one does not find spectroscopic (I-V) experiments particularly conclusive, an alternative is to look for evidence of behavior which is predicted to be qualitatively different for MFs and for ordinary quasiparticles. One possibility which has been suggested concerns Josephson circuits whose geometry and topology permits MFs, for example, some generated using *p*-wave-like superconductivity: the current-phase relation $I(\varphi)$ of such circuits is predicted to have not just the straightforward "2π-periodicity" in the Cooper-pair phase drop φ, but an extra $4\pi-$periodic component. Unfortunately, when translated into the language of flux Φ, this simply corresponds to the generic h/e periodicity required by the Byers-Yang theorem, so it is not clear that its observation would be particularly definitive.

At first sight, a unique signature of the presence of a pair of MFs might seem to be the phenomenon of "teleportation": since the corresponding single zero-energy Bogoliubov quasiparticle is delocalized between two spatially very distant sites, one might imagine that a "cause" at HQV 1, say the addition of an extra electron, might have "effects" at HQV 2 within a very short time compared to the time $\Delta t \sim L/v_F$ for ordinary physical impulses to travel the distance L between the HQVs ($v_F =$ Fermi velocity). Unfortunately, there seem to be a number of reasons to doubt these conclusions, and the relevant theoretical community appears at the time of writing to be split/confused about it. In sum, while there is some circumstantial evidence for MFs in condensed matter physics, their existence cannot be said to have been established beyond reasonable doubt. Probably, the community will be totally convinced of their existence only if and when their predicted behavior under braiding is definitively established; at the time of writing several experimental groups are working toward this goal.

All the discussion up to this point has been within the framework of the standard mean-field approach to superconductivity (or fermion superfluidity). Actually, the present author has some doubts as to whether this approach is adequate for the MF problem, and it may be appropriate to conclude this chapter by explaining briefly why.

The problem lies in the very notion of spontaneously broken U(1) symmetry (SBU(1)S). To recap, if we proceed as above using this idea, we relax particle number conservation and thus write the even-parity ground state in the form

---

[3] A 2016 paper (Autti et al., 2016) claims evidence for HQV's in a different phase (the so called polar phase, believed to be unstable in bulk) in the pores of a certain kind of aerogel; while this phase as such is believed not to sustain MF's, a modification of it might do so.

$$\psi_{\text{even}} \sim \sum_{N=\text{even}} C_N \psi_N \tag{29}$$

this then allows us to seek the simplest odd-parity states in the form

$$\gamma_i^\dagger = \int d\boldsymbol{r}\ \left[u_i(\boldsymbol{r})\ \hat{\psi}^\dagger(\boldsymbol{r}) + v_i(\boldsymbol{r})\ \hat{\psi}(\boldsymbol{r})\right]. \tag{30}$$

But in real life, SBU(1)S is a myth! Indeed, if we consider a system contained in a well-defined volume, then either the boundaries of that volume are real physical walls, in which case a rigorous superselection rule forbids any nontrivial form of Eq. (29), or they are not, in which case, while the reduced density matrix of the system in the number representation may have different nonzero elements along the diagonal, ($\rho_{NN} \neq 0$ for several N), its *off-diagonal* elements $\rho_{NN'}(N \neq N')$ are rigorously zero and hence $\hat{\rho}$ cannot correspond to the ansatz (29). This state of affairs does not matter too much while we are considering only the even-parity states, since we can use the "Anderson trick" to write

$$\hat{\psi}_N \sim \int d\varphi\ \hat{\psi}_{\text{even}}(\varphi)\ e^{-iN\varphi} \tag{31}$$

[where φ is the overall phase of the pair wave function as defined under the assumption of SBU(1)S]. Similarly, it does not matter to the extent that we consider only the odd-parity situation (where a similar trick is possible). But if we want to discuss the *relation* between the even- and odd-parity states (which is the crux of what we have been doing above) it may be fatal! An example of a situation where the use of (30) leads to contradictions is the theory of NMR of a surface MF in ^{3}He—B (Taylor et al., 2015).

The problem may be fixed by properly taking into account the effect of the condensate, in particular by replacing formula (15) for $\gamma_i^\dagger$ by

$$\gamma_i^\dagger = \int d\boldsymbol{r}\ \left[u(\boldsymbol{r})\ \hat{\psi}^\dagger(\boldsymbol{r}) + v(\boldsymbol{r})\ \hat{\psi}(\boldsymbol{r})\ \mathrm{C}^\dagger\right], \tag{32}$$

where the operator $\mathrm{C}^\dagger$ creates an extra Cooper pair so as to conserve total particle number. This makes essentially no difference in simple situations such as that of a BCS *s*-wave condensate at rest, in which the Cooper pairs have no "interesting" properties, but the moment they have a nontrivial degree of freedom (spin, center-of-mass momentum, angular momentum, etc.) it may change the picture qualitatively. But the very existence of MFs rests on the fact that the pairs indeed have "interesting" properties!

In this situation, we really need to go back to first principles and examine how the replacement of (15) by (32) (and also the question of whether $\mathrm{C}^\dagger$ is simply the same quantity as appears in the even-parity ground state wave function) affects the "established" arguments about MFs and TQC. A preliminary conclusion is that it probably does not affect the existence of MFs (though they are no longer strictly their own antiparticles), but it may well destroy much of the current orthodoxy concerning their local undetectability, behavior under braiding, etc. This is work waiting to be done.

Acknowledgments

I am very grateful to Prof. Tapash Chakraborty and Prof. Martin Greiter for assistance in the preparation of the manuscript.

References

Autti S, Dmitriev VV, Mäkinen JT, Soldatov AA, Volovik GE, Yudin AN, Zavjalov VV, and Eltsov VB (2016) *Observation of half-quantum vortices in topological superfluid* ^{3}He. *Physical Review Letters* 117: 255301. https://doi.org/10.1103/PhysRevLett.117.255301.

de Gennes P (1966) *Superconductivity of Metals and Alloys*. New York: W.A. Benjamin.

Frolov S (2021) Quantum computings reproducibility crisis: Majorana fermions. *Nature* 592: 350. 202s2112 https://doi.org/10.1038/d41586-021-00954-8.

Jang J, Ferguson DG, Vakaryuk V, Budakian R, Chung SB, Goldbart PM, and Maeno Y (2011) *Observation of half-height magnetization steps in* Sr_2RuO_4. *Science* 331: 186. https://doi.org/10.1126/science.1193839.

Kitaev AY (2001) Unpaired majorana fermions in quantum wires. *Physics-Uspekhi* 44: 131. https://doi.org/10.1070/1063-7869/44/10S/S29.

Kopnin N and Salomaa M (1991) *Mutual friction in superfluid* ^{3}*he: Effects of bound states in the vortex core. Physical Review B* 44: 9667. https://doi.org/10.1103/PhysRevB.44.9667.

Leggett A (2006) *Quantum Liquids: Bose Condensation and Cooper Pairing in Condensed-Matter Systems*. Oxford: Oxford University Press.

Leggett A (2010) Majorana fermions in fermi superfluid: A pedagogical note. In: Johnson P (ed.) *Doing Physics: A Festscrift for Thomas Erber*, pp. 173–184. IIT Press.

Leggett A and Liu Y (2021) *Symmetry properties of superconducting order parameter in* Sr_2RuO_4. *Journal of Superconductivity and Novel Magnetism* 34: 1647. https://doi.org/10.1007/s10948-020-05717-6.

Majorana E (1937) Teoria simmetrica della elettrone e del positrone. *Il Nuovo Cimento* 14: 171. https://doi.org/10.1007/BF02961314.

Nayak C, Simon SH, Stern A, Freedman M, and Das Sarma S (2008) Non-Abelian anyons and topological quantum computation. *Reviews of Modern Physics* 80: 1083. https://doi.org/10.1103/RevModPhys.80.1083.

Sau JD, Lutchyn RM, Tewari S, and Das Sarma S (2010) Generic new platform for topological quantum computation using semiconductor heterostructures. *Physical Review Letters* 104: 040502. https://doi.org/10.1103/PhysRevLett.104.040502.

Stone M and Chung S-B (2006) *Fusion rules and vortices in* $p_x + ip_y$ *superconductors. Physical Review B* 73: 014505. https://doi.org/10.1103/PhysRevB.73.014505.

Taylor E, Berlinsky AJ, and Kallin C (2015) *Locally gauge-invariant spin response of* ^{3}He $-$ *B films with Majorana surface states. Physical Review B* 91: 134505. https://doi.org/10.1103/PhysRevB.91.134505.

Volovik G (1999) Fermion zero modes on vortices in chiral superconductors. *JETP Letters* 70: 609. https://doi.org/10.1134/1.568223.

Majorana fermions in Kitaev spin liquids

Joji Nasu, Department of Physics, Tohoku University, Sendai, Japan

© 2024 Elsevier Ltd. All rights reserved.

Introduction 139
Majorana fermions in Kitaev model 140
Fingerprint of Majorana fermions 143
Experimental realizations 144
Conclusion 145
References 145

Abstract

This chapter reviews Majorana fermions emergent in insulating magnets, particularly the Kitaev quantum spin liquid. The Kitaev model, an $S = 1/2$ quantum spin model on a honeycomb lattice, can be solved by introducing four Majorana fermions. Three of them consist of local gage fields defined on the bonds of the honeycomb lattice, and they are local conserved quantities. One of the four Majorana fermions moves freely on the lattice under fixed gage fields. Thus, the elementary excitations are governed by the two quasiparticles, itinerant Majorana fermions and local gage fields, which are interpreted as fractionalization of quantum spin. The signatures of the Majorana fermions can be observed in thermodynamic and dynamical properties, such as the specific heat, dynamical spin structure factor, and Raman spectrum. Moreover, the Majorana fermion system becomes topologically nontrivial by applying magnetic fields, and an excited gage field traps an isolated Majorana fermion (Majorana zero mode). This causes a half quantization of thermal Hall coefficient, which should be one of the most demonstrable signatures of the existence of Majorana fermions. Transition metal compounds with strong spin–orbit coupling are proposed as candidate materials whose magnetic properties are dominantly governed by the Kitaev model. Different experimental probes have observed manifestations of Majorana fermions in these materials. However, further investigations are needed in the candidate materials to establish the presence of the Majorana fermions, particularly Majorana zero modes, which can be applied to topological quantum computing.

Key points

- The ground state of the Kitaev model is a quantum spin liquid with short-range spin correlations.
- Elementary excitations from the Kitaev quantum spin liquid are two quasiparticles: itinerant Majorana fermions and local gauge fields.
- The itinerant Majorana fermions and local gauge fields are emergent quasiparticles due to spin fractionalization.
- An applied magnetic field induces the band structure of the emergent Majorana fermions to be topologically nontrivial and the excitation of local gauge fields to be accompanied by a Majorana zero mode.
- The Kitaev model is believed to be realized in transition metal compounds with strong spin–orbit coupling.
- Recent experiments for the Kitaev candidate materials have observed signatures of the existence of Majorana fermions.

Introduction

In strongly correlated electron systems, quasiparticles with distinct natures appear as elementary excitations due to electron correlations despite electrons being merely Fermi-Dirac particles. In particular, insulating magnets possess quasiparticles originating from magnetic excitations. For example, collective excitations from a magnetic order are known as magnons, which are bosonic excitations. On the other hand, it has been suggested that fermionic excitations are present as elementary excitations in quantum spin liquids (QSLs), where any magnetic orders do not appear even at zero temperature. Such quasiparticles are called spinons, and the signatures, such as a T-linear specific heat and continuum in excitation spectra, have been observed in candidate materials of the QSL, although they are insulating (Yamashita et al., 2008, 2010; Han et al., 2012; Isono et al., 2014).

In QSLs, other quasiparticles with striking features can emerge due to strong quantum fluctuations. For example, a Majorana fermion can be realized as a quasiparticle. A Majorana fermion was introduced by E. Majorana in 1937 as a real-valued solution of the Dirac equation (Majorana, 1937). The characteristic, unlike conventional fermions, is that it is identical to its own antiparticle,

https://doi.org/10.1016/B978-0-323-90800-9.00178-5

and thereby, the Majorana particle is a charge-neutral fermion. In the field of particle physics, neutrinos are the candidates for Majorana fermions. On the other hand, condensed matter physics also provides a playground for Majorana fermions as elementary excitations.

Here, we briefly show the fundamental properties of Majorana fermions. We introduce two Majorana fermion operators, γ_1 and γ_2. Owing to the Majorana nature, creation and annihilation operators are identical: $\gamma_i = \gamma_i^\dagger$ $(i = 1, 2)$. Moreover, as they are fermion operators, these satisfy the following relations: $\{\gamma_i, \gamma_j\} = 2\delta_{ij}$. Using the two Majorana fermions, a fermion operator f is introduced as

$$\begin{aligned} f &= \frac{1}{2}(\gamma_1 + i\gamma_2) \\ f^\dagger &= \frac{1}{2}(\gamma_1 - i\gamma_2). \end{aligned} \tag{1}$$

The relations indicate that the degree of freedom of a Majorana fermion is half that of a conventional fermion.

In condensed matter physics, one of the most familiar systems with Majorana quasiparticles is the Kitaev model. This model was introduced by A. Kitaev in 2006 for realizing the toric code with topological order and a system with non-Abelian anyons, which is applicable to topological quantum computing (Kitaev, 2006). This model is a simple quantum spin model, but the ground state is a QSL due to strong quantum fluctuations, and its elementary excitations are described as Majorana fermions (Nussinov and van den Brink, 2015; Hickey and Trebst, 2022; Hermanns et al., 2018; Knolle and Moessner, 2019; Takagi et al., 2019; Motome and Nasu, 2020). In the following section, we review the fundamental properties of the Kitaev model.

Majorana fermions in Kitaev model

The Kitaev model is a quantum spin model, which describes interactions between neighboring $S = 1/2$ spins located on sites of a honeycomb lattice (Kitaev, 2006). On this lattice, there are three types of bonds connecting sites i and j, which we term x bond $\langle ij\rangle_x$, y bond $\langle ij\rangle_y$, and z bond $\langle ij\rangle_z$ [see Fig. 1A]. Using these representations, the Hamiltonian is given by

$$\mathcal{H}_{\mathrm{K}} = -J_x \sum_{\langle ij\rangle_x} S_i^x S_j^x - J_y \sum_{\langle ij\rangle_y} S_i^y S_j^y - J_z \sum_{\langle ij\rangle_z} S_i^z S_j^z, \tag{2}$$

where $\mathbf{S}_i$ is an $S = 1/2$ spin on site i and J_μ $(\mu = x, y, z)$ is a coupling constant on the μ bonds, as shown in Fig. 1A. We assume that all exchange constants are positive for simplicity. As shown in Eq. (2), the Kitaev model comprises bond-dependent Ising-type interactions. This leads to a kind of frustration even in the ferromagnetic couplings with $J_\mu > 0$, where all bond energies cannot be minimized simultaneously. The situation expects an exotic quantum ground state. Indeed, the ground state of the Kitaev model is exactly shown to be a QSL.

In the Kitaev model, there is a local conserved quantity on each hexagon in the honeycomb lattice, which is given by

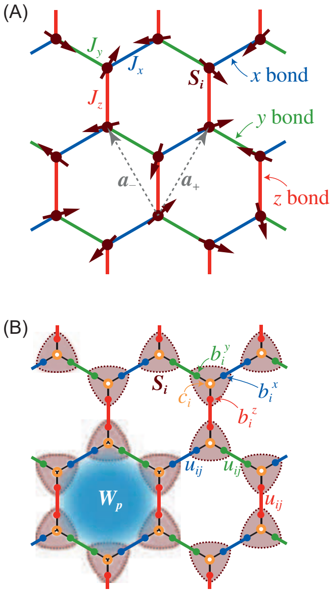

Fig. 1 (A) Bond-dependent interactions of the Kitaev model defined on a honeycomb lattice. The x, y, and z bonds with exchange constants J_x, J_y, and J_z are shown by *blue*, *green*, and *red*, respectively. $\boldsymbol{a}_+$ and $\boldsymbol{a}_-$ are the primitive transformation vectors of the honeycomb lattice. (B) Schematic picture of Majorana fermion representation of an $S = 1/2$ quantum spin in the Kitaev model. The quantity u_{ij} is defined on each bond, and the flux W_p is on each hexagon plaquette (Kitaev, 2006).

$$W_p = 2^6 \prod_{i \in p} S_i^{\mu_i}, \tag{3}$$

where W_p is given by the product of six spins on hexagon plaquette p, and μ_i is the spin component corresponding to the bond not belonging to the hexagon. This quantity is called "flux" or "vison" and satisfies the following relations: $W_p^2 = 1$ and $[W_p, W_{p'}] = 0$ with $p \neq p'$ in addition to $[\mathcal{H}_{\mathrm{K}}, W_p] = 0$. These relations indicate that the eigenstates of the Kitaev model are characterized by the set of the eigenvalues of W_p taking ± 1 for all hexagon plaquettes. The presence of the local conserved quantities straightforwardly results in the absence of long-range spin correlations (Baskaran et al., 2007). Hence, the Kitaev model exhibits a QSL ground state.

While all eigenstates of the Kitaev model are assigned by flux configurations $\{W_p = \pm 1\}$, the dynamics in each fixed flux sector can be described by using Majorana fermions. Let us introduce four Majorana fermions $\{c_i, b_i^x, b_i^y, b_i^z\}$ at each site [see Fig. 1B] and represent the spin operator as

$$S_i^\mu = \frac{i}{2} b_i^\mu c_i. \tag{4}$$

Here, the commutation relations of the spin operators are reproduced by those of Majorana fermions. Note that spin operators also satisfy the following equation:

$$i = 2^3 S_i^x S_i^y S_i^z = i b_i^x b_i^y b_i^z c_i \equiv iD, \tag{5}$$

which indicates that original spin space enforces $D = +1$ for all site. On the other hand, $D = b_i^x b_i^y b_i^z c_i$ takes ± 1 in the Majorana representation, suggesting that the present Majorana representation extends the model space to that with $D = \pm 1$. This implies that the projection onto the model space with $D = +1$ is essential to obtain correct results.

Using Eq. (4), the Hamiltonian given in Eq. (2) is rewritten as

$$\mathcal{H}_{\mathrm{K}} = \frac{i}{4} \sum_{\langle ij \rangle_\mu} J_\mu u_{ij} c_i c_j, \tag{6}$$

where u_{ij} are given by $u_{ij} = i b_i^\mu b_j^\mu$ on μ bonds. Each u_{ij} commutes with the Hamiltonian and satisfies $u_{ij}^2 = 1$, and therefore, it is a Z_2 conserved quantity on each bond. This indicates that the dynamics of the Majorana fermion c_i is separated from that of b_i^μ although the spin operator, which is an observable, is written as the product of these two Majorana fermions. This is interpreted as the fractionalization of spin into two Majorana fermions. Note that u_{ij} is related to the flux operator given in Eq. (3) as follows:

$$W_p = \prod_{\langle ij \rangle \in p} u_{ij}, \tag{7}$$

where the product is taken for the six bonds of the hexagon p. The flux operator W_p is written by the spin operators, and hence it is an observable. On the other hand, u_{ij} is not directly given by the spin operators and is not observable. Moreover, the number of W_p is $N/2$, but that of u_{ij} is $3N/2$, where N is the number of sites, indicating the presence of the redundancy in u_{ij}. Thus, u_{ij} is regarded as a Z_2 gauge field.

Since u_{ij} is a Z_2 local conserved quantity, this can be treated as a classical number taking ± 1 in Eq. (6). From Lieb's theorem, one can prove that the flux configuration with all $W_p = +1$ gives the lowest energy manifold. This configuration is reproduced by all $u_{ij} = +1$. In this subspace, the Hamiltonian is written as

$$\mathcal{H}_{\mathrm{K}} = \frac{i}{4} \sum_{\langle ij \rangle_\mu} J_\mu c_i c_j, \tag{8}$$

which is regarded as a free Majorana fermion system. By introducing the Fourier transformation of c_i, the Hamiltonian is diagonalized as

$$\mathcal{H}_{\mathrm{K}} = \sum_{\boldsymbol{k}} \varepsilon_{\boldsymbol{k}} \left(d_{\boldsymbol{k}}^\dagger d_{\boldsymbol{k}} - \frac{1}{2} \right), \tag{9}$$

where $\varepsilon_{\boldsymbol{k}} = |J_x e^{i\boldsymbol{k}\cdot\boldsymbol{a}_+} + J_y e^{i\boldsymbol{k}\cdot\boldsymbol{a}_-} + J_z|/2$ with $\boldsymbol{a}_\pm = (\pm 1/2, \sqrt{3}/2)$ being the primitive transformation vectors shown in Fig. 1A. By changing the exchange constants, the band structure $\varepsilon_{\boldsymbol{k}}$ exhibits both gapless and gapped. In the isotropic case with $J_x = J_y = J_z$, there are point nodes at the K and K′ points, as shown in Fig. 2. In general, in the case of $J_x \leq J_y + J_z$ and its cyclic permutations, the dispersion is gapless, and the excitation gap opens elsewhere. The phase diagram is presented in Fig. 3. As shown in this figure, the Kitaev model shows the gapless and gapped QSLs, determined by the spectrum of the Majorana fermion excitations. On the other hand, the excitation energy of fluxes is nonzero regardless of the values of the exchange constants. This leads to the fact that spin excitations should be gapped because the γ component of the spin operators is given by the product of c_i and b_i^γ, the latter of which changes the flux configuration. The dynamical spin structure factor is calculated exactly in the Kitaev model (Knolle et al., 2014b), and it exhibits the spin gap, whose energy reflects the flux gap Δ_f. The details are given later. The presence of the spin gap is consistent with short-range spin correlations even in the gapless phase, where the excitation spectrum of the Majorana fermion c_i is gapless.

In the Kitaev model without magnetic fields, the dynamics of Majorana fermions c is separated from that of b^γ. This feature is the origin of the exact solvability. Since the spin operators hybridize these dynamics, the introduction of the magnetic fields renders the

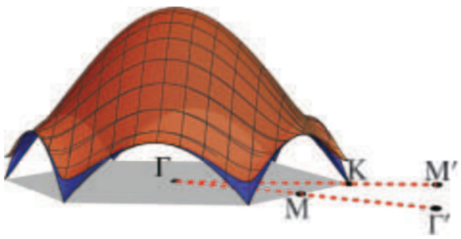

Fig. 2 Dispersion relation $\varepsilon_{\boldsymbol{k}}$ in Eq. (9) without magnetic fields and $\tilde{\varepsilon}_{\boldsymbol{k}}$ in Eq. (12) with the effective magnetic field, which are shown by *blue* and *brown*, respectively. The *red dashed line* represents the horizontal axis of Fig. 4A.

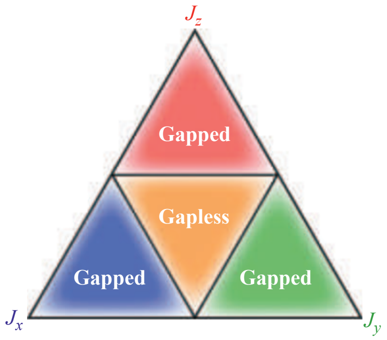

Fig. 3 Phase diagram of the Kitaev model without magnetic fields on the plane of $J_x + J_y + J_z = 1$ (Kitaev, 2006).

system unsolvable. To avoid this difficulty, one considers the effect of the magnetic field as a perturbation in the ground-state flux sector with all $W_p = +1$. The third-order perturbation for the Zeeman term $\mathcal{H}_h = -\sum_i \boldsymbol{h} \cdot \boldsymbol{S}_i$ leads to the effective magnetic field, which is given by

$$\mathcal{H}_h^{\mathrm{eff}} = -\kappa \sum_{[ijk]_{\mu\mu'}} S_i^{\mu} S_j^{\mu''} S_k^{\mu'}, \tag{10}$$

where κ is the effective magnetic field proportional to $h^x h^y h^z/\Delta_f^2$, and $[ijk]_{\mu\mu'}$ stands for neighboring three sites on the two bonds $\langle ij\rangle_\mu$ and $\langle jk\rangle_{\mu'}$ with μ'' neither μ nor μ'. This effective Zeeman term is rewritten by the Majorana representation of the spin operators given in Eq. (4) as

$$\mathcal{H}_h^{\mathrm{eff}} = \frac{i\kappa}{8} \sum_{[ik]} c_i c_k, \tag{11}$$

in the case with all $W_p = +1$, where $[ik]$ represents the next nearest neighbor pair for sites i and k. The total Hamiltonian $\mathcal{H}_{\mathrm{K}} + \mathcal{H}_h^{\mathrm{eff}}$ describes the Majorana fermions with nearest neighbor hopping J_μ and next nearest neighbor hopping κ on the honeycomb lattice, which is regarded as a Majorana version of the Haldane model showing the quantum Hall effect (Haldane, 1988). One can expect the topologically nontrivial band structure originating from the Majorana fermions in the presence of the effective magnetic field. Indeed, the band structure is modified by introducing the magnetic field as

$$\tilde{\varepsilon}_{\boldsymbol{k}} = \sqrt{\varepsilon_{\boldsymbol{k}}^2 + \Delta_{\boldsymbol{k}}^2}, \tag{12}$$

where $\Delta_{\boldsymbol{k}} = \kappa[\sin(-\boldsymbol{k}\cdot\boldsymbol{a}_+) + \sin(\boldsymbol{k}\cdot\boldsymbol{a}_-) + \sin(\boldsymbol{k}\cdot(\boldsymbol{a}_+ - \boldsymbol{a}_-))]$. In the case of $\kappa = 0$, there are two point nodes for the isotropic case with $J_x = J_y = J_z$ as mentioned before. The effective magnetic field opens the gap at these points, given by $3\sqrt{3}\kappa/4$. As a result, the Chern number of the fermionic band is quantized to ± 1, and a chiral edge mode appears in the gap around the zero energy when open boundary conditions are imposed.

Note that a flux excitation traps a Majorana fermion with $W_p = -1$ at a hexagon plaquette p, which appears as a counterpart of the chiral edge mode. When the trapped Majorana fermion is localized and isolated, the energy should be zero. This implies that a flux excitation accompanies a Majorana zero mode in the presence of the effective magnetic field. Since the quantum states of Majorana zero modes can change in exchanging them, the composite quasiparticle consisting of a Majorana zero mode and an excited flux is regarded as a non-Abelian anyon. The exchange procedure called "braiding" should be achieved by manipulating the positions of excited fluxes and is known to be applicable to topological quantum computing.

Fingerprint of Majorana fermions

In this section, we show how the signature of Majorana fermions appears in the Kitaev QSL. In particular, we focus on the isotropic case with $J_x = J_y = J_z \equiv J$ hereafter. The Kitaev model hosts two elementary excitations: the itinerant Majorana fermion c_i and localized flux excitation W_p originating from the Majorana fermion b_i^μ. In the present case, the band structure of the itinerant Majorana fermions is gapless, whereas the localized flux excitations are gapped. As shown in Eq. (4), the spin operator is represented as the product of the two Majorana fermions, which indicates that spin excitations involve the dynamics of both of them. Thus, fingerprints of the Majorana fermions should appear in the spectrum of the dynamical spin structure factor, which is defined as

$$\mathcal{S}(\boldsymbol{q},\omega)=\frac{1}{N}\sum_{ij}\int_{-\infty}^{\infty}\frac{dt}{2\pi}\sum_{\mu\mu'}\langle S_i^\mu(t)S_j^\mu\rangle e^{i\omega t-i\boldsymbol{q}\cdot(\boldsymbol{r}_i-\boldsymbol{r}_j)},\tag{13}$$

where $\mathcal{O}(t)=e^{i\mathcal{H}_{\rm K}t}\mathcal{O}e^{-i\mathcal{H}_{\rm K}t}$ is the Heisenberg representation of an operator $\mathcal{O}$. This quantity corresponds to the spectrum of inelastic neutron scattering in experiments, and theoretically, it can be exactly evaluated using the Majorana representation in the Kitaev model (Knolle et al., 2014b, 2015). Fig. 4A shows the contour map of $\mathcal{S}^{\mu\mu}(\boldsymbol{q},\omega)$ on the plane of $\boldsymbol{q}$ and ω. There is a strong peak at $\omega \simeq 0.1J$ and a broad continuum around $\omega \sim J$. These two types of structure does not strongly depend on $\boldsymbol{q}$ because the long-range spin correlations beyond nearest neighbor sites are absent in the Kitaev model. The energy of the low-energy coherent peak is close to the flux gap, and the incoherent structure has a spectral weight up to $\omega \sim 1.5J$ corresponding to the bandwidth of the itinerant Majorana fermions c_i. Therefore, two Majorana fermions b_i^μ and c_i manifest themselves as distinctly different types of structure in $\mathcal{S}^{\mu\mu}(\boldsymbol{q},\omega)$.

In the dynamical spin correlations, the signatures of the two Majorana fermions are observed simultaneously, but separated observations for them are desired to clarify the presence of the fractionalization into Majorana fermions in the Kitaev QSL. One of the measurements capable of observing the quasiparticles separately is the Raman scattering. This is an optical measurement to obtain information on low-energy excitations by irradiating light and observing scattered light with a different frequency. The Raman spectrum $I_R(\omega)$ is given by a function of the frequency difference of the incoming and outgoing phonons, which is called the Raman shift ω. To calculate the Raman spectrum, Loudon and Fleury developed a theory for insulating magnets (Fleury and Loudon, 1968). In the Loudon–Fleury approach, the Raman operator is given by $\mathcal{R}=\sum_{\langle ij\rangle_\mu}(\boldsymbol{\varepsilon}_{\rm in}\cdot\boldsymbol{d}^\mu)(\boldsymbol{\varepsilon}_{\rm out}\cdot\boldsymbol{d}^\mu)J^\mu S_i^\mu S_j^\mu$, where $\varepsilon_{\rm in}$ and $\varepsilon_{\rm out}$ are the polarization vectors of the incoming and outgoing photons, and $\boldsymbol{d}^\mu$ are the vectors connecting the nearest neighbor sites (Knolle et al., 2014a; Perreault et al., 2015). Using the Raman operator, the Raman intensity $I_R(\omega)$ is given by

$$I_R(\omega)=\frac{1}{N}\int_{-\infty}^{\infty}\langle\mathcal{R}(t)\mathcal{R}\rangle e^{i\omega t}dt.\tag{14}$$

Note that this is independent of the polarization directions of the incoming and outgoing phonons in the isotropic case. Importantly, because the Raman operator commutes with all fluxes W_p, the itinerant Majorana fermions c_i are only excited in the Raman process. This characteristic is in stark contrast to the dynamical spin structure factor in Eq. (13); the spin operator does not commute with W_p. Thus, the itinerant Majorana fermions c_i are only excited in the Raman process, which is one of the striking features of the Raman scattering.

In the Kitaev model, the Raman spectrum in the Kitaev model is also calculated exactly based on the Loudon–Fleury approach. Fig. 4B shows the Raman intensity as a function of the Raman shift ω (Knolle et al., 2014a; Perreault et al., 2015). There is a broad continuum between 0 and $3J$, which is twice of the bandwidth of the itinerant Majorana fermions. This is understood from the fact that a phonon creates two Majorana fermions in the Raman process, and hence the spectral structure of the Raman scattering directly reflects the presence of the Majorana fermions and is unrelated to the flux excitations.

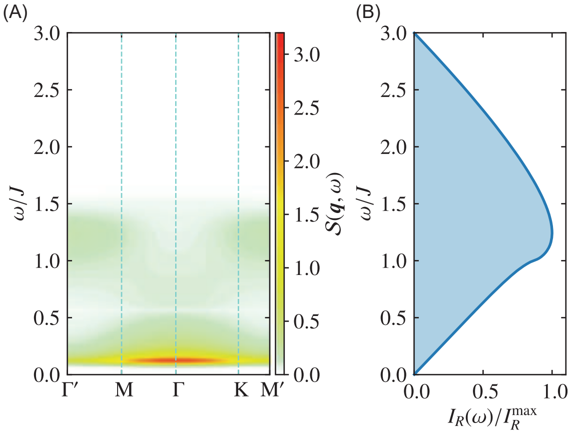

Fig. 4 (A) Dynamical spin structure factor $\mathcal{S}(\boldsymbol{q},\omega)$ on the plane of $\boldsymbol{q}$ and ω (Knolle et al., 2014b), and (B) intensity of the Raman spectrum $I_R(\omega)$ normalized by its maximum (Knolle et al., 2014a).

The topological properties of the Majorana fermions can be observed as a heat transport because the charge neutrality intrinsic in the Majorana fermion hinders observations by electric responses, but its flow can carry heat. Here, we focus on the thermal Hall effect, where a temperature gradient generates a heat current perpendicular to it. As discussed in the previous section, we show that the Majorana fermion system becomes topologically nontrivial in the presence of the effective magnetic field $\mathcal{H}_h^{\mathrm{eff}}$. Here, we introduce the thermal Hall conductivity κ^{xy} defined by $\langle J_Q^x \rangle_{\nabla T} = \kappa^{xy}(-\nabla T)_y$, where ∇T is an applied temperature gradient along the y direction and $\langle J_Q^x \rangle_{\nabla T}$ is the expectation value of the x component of the heat current in the presence of the temperature gradient. In Majorana fermion systems with topologically nontrivial band structure with Chern number $C = +1$, the low-temperature thermal Hall conductivity is quantized as

$$\frac{\kappa^{xy}}{T} = \frac{\pi}{12}\frac{k_B^2}{\hbar}, \tag{15}$$

where k_B and $\hbar$ are the Boltzmann and reduced Planck constants, respectively (Nomura et al., 2012; Sumiyoshi and Fujimoto, 2013). In contrast, thermal Hall conductivity divided by T is quantized by $\frac{\pi}{6}\frac{k_B^2}{\hbar}$ at $T \to 0$ in conventional fermion systems, which is twice in the Majorana fermion system. The quantized thermal Hall conductivity Eq. (15) is the consequence of the nature inherent in a Majorana fermion, which carries a half degree of freedom of a conventional fermion. Therefore, the half-quantization of the thermal Hall conductivity can provide compelling evidence of realizing Majorana fermions.

The fractionalization of spin into itinerant Majorana fermions and flux excitations manifests itself in the temperature dependence. As mentioned, these two elementary excitations in Kitaev QSL have completely different energy scales. As a result, the entropy releases are expected to occur at different temperatures. The specific heat exhibits a double-peak structure in the specific heat, and half of the entropy is released at each peak (Nasu et al., 2014, 2015). The detailed analysis clarifies that the low-temperature entropy release originates from the flux excitations, and the high-temperature one corresponds to the itinerant Majorana fermions. The half-entropy release should also be convincing evidence of the fractionalization of spin into Majorana fermions in the temperature evolution of the Kitaev QSL.

Experimental realizations

The Kitaev model is believed to be realized in strongly correlated electron systems with the strong relativistic spin–orbit coupling (Jackeli and Khaliullin, 2009). We focus on transition metal ions with the t_{2g}^5 configuration in $4d$ or $5d$ orbitals, for example, Ir^{4+} and Ru^{3+} ions. Since the t_{2g} orbitals possess effective angular momentum with $l_{\mathrm{eff}} = 1$, the t_{2g} orbital degeneracy is lifted into $j_{\mathrm{eff}} = 1/2$ and $j_{\mathrm{eff}} = 3/2$ states due to the strong spin–orbit coupling. There is a hole in the doubly degenerate $j_{\mathrm{eff}} = 1/2$ states for the t_{2g}^5 configuration, and the degree of freedom of which state a hole occupies is described by introducing a pseudo-spin $\boldsymbol{S}$. The effective interaction between pseudo-spins in neighboring transition metal ions is derived from a multiorbital Hubbard model by considering the second perturbation with respect to the hopping of t_{2g} electrons in the strong correlation limit. Suppose that each transition ion is surrounded by six ligand ions forming an octahedron with cubic symmetry, and neighboring octahedra share their edges. Moreover, one only considers the virtual hopping between t_{2g} electrons in neighboring sites via ligand ions located between the transition metal ions in the perturbation procedure. In these conditions, the interaction between the pseudo-spins is Ising-type, and the interacting component of the pseudo-spin depends on the bonding direction. When transition ions form a honeycomb lattice, the interactions between the pseudo-spins are given by the Kitaev model. As the candidate materials, iridium oxides $A_2\mathrm{IrO}_3$ (A = Li, Na) (Singh and Gegenwart, 2010; Singh et al., 2012; Comin et al., 2012; Choi et al., 2012) and α-RuCl_3 (Sears et al., 2015; Kubota et al., 2015; Sandilands et al., 2015; Majumder et al., 2015) were proposed, and thermodynamic and magnetic properties of them have been intensively investigated.

In these materials, magnetic orders appear at low temperatures while the ground state of the Kitaev model is a QSL. This is due to additional interactions, such as Heisenberg and off-diagonal symmetric interactions (Chaloupka et al., 2010, 2013; Rau et al., 2014; Winter et al., 2016). Nevertheless, the Kitaev interaction is believed to be predominant over these additional terms, and the signature of the Kitaev physics appears above the temperature of the magnetic ordering. For example, it has been reported that the specific heat exhibits a peak in addition to the low-temperature anomaly originating from the magnetic ordering in the iridium oxide $\mathrm{Na_2IrO_3}$ (Mehlawat et al., 2017) and ruthenium compound α-RuCl_3 (Do et al., 2017; Widmann et al., 2019). By integrating the specific heat around the high-temperature peak, the entropy release is estimated at about $0.5k_B \ln 2$, which is considered to be a manifestation of the spin fractionalization into Majorana fermions.

Signatures of Majorana fermions are also observed in excitation spectra as discussed in Section "Fingerprint of Majorana fermions". Inelastic neutron scattering measurements have clarified that there is the continuum of magnetic excitations whose energy scale corresponds to the exchange energy in α-RuCl_3, and this broad structure survives even above the critical temperature of the magnetic order (Banerjee et al., 2016, 2017). Since the dominant exchange energy originates from the Kitaev interaction, which is much larger than the energy scale of the critical temperature, the broad continuum is considered to correspond to the structure at $\omega \sim J$ of $\mathcal{S}(\boldsymbol{q}, \omega)$ in the Kitaev model [see Fig. 4A]. The results suggest that the neutron scattering observes excitations of the Majorana fermions. It has also been pointed out that the broad continuum in the candidate compounds should be explained by the magnon damping (Winter et al., 2017).

In addition to the neutron scattering, the Raman scattering measurement has also been performed in α-RuCl_3 (Sandilands et al., 2015). Similar to the inelastic neutron scattering, the broad continuum has been observed in the Raman spectrum, which corresponds to that of the Kitaev model shown in Fig. 4B. More interestingly, the temperature dependence of the spectral weight observed in α-$RuCl_3$ is well fitted using the Fermi distribution function (Nasu et al., 2016). The result implies that the experimentally observed broad continuum is attributed to fermionic excitations.

As mentioned in Section "Fingerprint of Majorana fermions", the thermal Hall effect is crucial to clarify the presence of Majorana fermions in Kitaev candidate materials. When a topological chiral edge mode comes from a Majorana fermion, the thermal Hall coefficient is quantized. The value given in Eq. (15) is half of the case of a conventional fermion, which is a consequence of the presence of Majorana fermions. The half-quantization of the thermal Hall coefficient was reported in the Kitaev candidate material α-$RuCl_3$ (Kasahara et al., 2018). Furthermore, it was reported that the half quantization is also observed even when the magnetic field is applied on the plane of the temperature gradient and resultant heat current (Yokoi et al., 2021). Note that some research groups claimed that these results were reproduced (Yamashita et al., 2020; Bruin et al., 2022), but other groups reproduced a nonzero thermal Hall coefficient while they claimed the absence of its quantization. Instead, they provided another origin such as magnons or phonons (Hentrich et al., 2019; Czajka et al., 2021; Lefrançois et al., 2022; Czajka et al., 2022). Thus, further investigations are need to clarify the presence of the half quantization, which is compelling evidence of the presence of Majorana fermions in real materials.

Conclusion

In summary, we have reviewed the properties of Majorana fermions emergent in the Kitaev QSL and how to observe them in real compounds. The Kitaev model possesses two elementary excitations, itinerant Majorana fermions, and flux excitations. The itinerant Majorana fermions are accessible from several experimental probes, and the presence is becoming established. The next step is the local manipulation of a Majorana fermion (Majorana zero mode), which is essential to topological quantum computing. We hope that in the future, Majorana fermions in condensed matter physics, including QSLs, will be applied in various fields, taking advantage of their unique features.

References

Banerjee A, Bridges C, Yan JQ, Aczel A, Li L, Stone M, Granroth G, Lumsden M, Yiu Y, Knolle J, et al. (2016) Proximate kitaev quantum spin liquid behaviour in a honeycomb magnet. *Nature Materials* 15: 733–740. https://doi.org/10.1038/nmat4604.

Banerjee A, Yan J, Knolle J, Bridges CA, Stone MB, Lumsden MD, Mandrus DG, Tennant DA, Moessner R, and Nagler SE (2017) Neutron scattering in the proximate quantum spin liquid α-$RuCl_3$. *Science* 356: 1055–1059. https://doi.org/10.1126/science.aah6015.

Baskaran G, Mandal S, and Shankar R (2007) Exact results for spin dynamics and fractionalization in the kitaev model. *Physical Review Letters* 98: 247201. https://doi.org/10.1103/PhysRevLett.98.247201.

Bruin J, Claus R, Matsumoto Y, Kurita N, Tanaka H, and Takagi H (2022) Robustness of the thermal hall effect close to half-quantization in α-rucl3. *Nature Physics* 18: 401–405. https://doi.org/10.1038/s41567-021-01501-y.

Chaloupka J, Jackeli G, and Khaliullin G (2010) Kitaev-heisenberg model on a honeycomb lattice: Possible exotic phases in iridium oxides A_2iro_3. *Physical Review Letters* 105: 027204. https://doi.org/10.1103/PhysRevLett.105.027204.

Chaloupka J, Jackeli G, and Khaliullin G (2013) Zigzag magnetic order in the iridium oxide na_2iro_3. *Physical Review Letters* 110: 097204. https://doi.org/10.1103/PhysRevLett.110.097204.

Choi SK, Coldea R, Kolmogorov AN, Lancaster T, Mazin II, Blundell SJ, Radaelli PG, Singh Y, Gegenwart P, Choi KR, Cheong SW, Baker PJ, Stock C, and Taylor J (2012) Spin waves and revised crystal structure of honeycomb iridate na_2iro_3. *Physical Review Letters* 108: 127204. https://doi.org/10.1103/PhysRevLett.108.127204.

Comin R, Levy G, Ludbrook B, Zhu ZH, Veenstra CN, Rosen JA, Singh Y, Gegenwart P, Stricker D, Hancock JN, van der Marel D, Elfimov IS, and Damascelli A (2012) Na_2IrO_3 as a novel relativistic mott insulator with a 340-mev gap. *Physical Review Letters* 109: 266406. https://doi.org/10.1103/PhysRevLett.109.266406.

Czajka P, Gao T, Hirschberger M, Lampen-Kelley P, Banerjee A, Yan J, Mandrus DG, Nagler SE, and Ong N (2021) Oscillations of the thermal conductivity in the spin-liquid state of α-rucl3. *Nature Physics* 17: 915–919. https://doi.org/10.1038/s41567-021-01243-x.

Czajka P, Gao T, Hirschberger M, Lampen-Kelley P, Banerjee A, Quirk N, Mandrus D, Nagler S, and Ong NP (2022) Planar thermal hall effect of topological bosons in the kitaev magnet α-rucl3. *Nature Materials*. https://doi.org/10.1038/s41563-022-01397-w.

Do SH, Park SY, Yoshitake J, Nasu J, Motome Y, Kwon YS, Adroja D, Voneshen D, Kim K, and Jang TH (2017) Majorana fermions in the kitaev quantum spin system α-rucl 3. *Nature Physics* 13: 1079–1084. https://doi.org/10.1038/nphys4264.

Fleury PA and Loudon R (1968) Scattering of light by one- and two-magnon excitations. *Physics Review* 166: 514–530. https://doi.org/10.1103/PhysRev.166.514.

Haldane FDM (1988) Model for a quantum hall effect without landau levels: Condensed-matter realization of the "parity anomaly". *Physical Review Letters* 61: 2015–2018. https://doi.org/10.1103/PhysRevLett.61.2015.

Han TH, Helton JS, Chu S, Nocera DG, Rodriguez-Rivera JA, Broholm C, and Lee YS (2012) Fractionalized excitations in the spin-liquid state of a kagome-lattice antiferromagnet. *Nature* 492: 406–410.

Hentrich R, Roslova M, Isaeva A, Doert T, Brenig W, Büchner B, and Hess C (2019) Large thermal hall effect in α-$RuCl_3$: Evidence for heat transport by kitaev-heisenberg paramagnons. *Physical Review B* 99: 085136. https://doi.org/10.1103/PhysRevB.99.085136.

Hermanns M, Kimchi I, and Knolle J (2018) Physics of the kitaev model: Fractionalization, dynamic correlations, and material connections. *Annual Review of Condensed Matter Physics* 9: 17–33. https://doi.org/10.1146/annurev-conmatphys-033117-053934.

Hickey C and Trebst S (2022) Kitaev materials. *Physics Reports* 950: 1–37. https://doi.org/10.1016/j.physrep.2021.11.003.

Isono T, Kamo H, Ueda A, Takahashi K, Kimata M, Tajima H, Tsuchiya S, Terashima T, Uji S, and Mori H (2014) Gapless quantum spin liquid in an organic spin-1/2 triangular-lattice $\kappa-h_3(\text{cat-edt-ttf})_2$. *Physical Review Letters* 112: 177201. https://doi.org/10.1103/PhysRevLett.112.177201.

Jackeli G and Khaliullin G (2009) Mott insulators in the strong spin-orbit coupling limit: From heisenberg to a quantum compass and kitaev models. *Physical Review Letters* 102: 017205. https://doi.org/10.1103/PhysRevLett.102.017205.

Kasahara Y, Ohnishi T, Mizukami Y, Tanaka O, Ma S, Sugii K, Kurita N, Tanaka H, Nasu J, Motome Y, Shibauchi T, and Matsuda Y (2018) Majorana quantization and half-integer thermal quantum hall effect in a kitaev spin liquid. *Nature* 559: 227. https://doi.org/10.1038/s41586-018-0274-0.

Kitaev A (2006) Anyons in an exactly solved model and beyond. *Annals of Physics (New York)* 321: 2–111. https://doi.org/10.1016/j.aop.2005.10.005.

Knolle J and Moessner R (2019) A field guide to spin liquids. *Annual Review of Condensed Matter Physics* 10: 451–472. https://doi.org/10.1146/annurev-conmatphys-031218-013401.

Knolle J, Chern GW, Kovrizhin DL, Moessner R, and Perkins NB (2014a) Raman scattering signatures of kitaev spin liquids in A_2iro$_3$ iridates with $a =$ Na or li. *Physical Review Letters* 113: 187201. https://doi.org/10.1103/PhysRevLett.113.187201.

Knolle J, Kovrizhin DL, Chalker JT, and Moessner R (2014b) Dynamics of a two-dimensional quantum spin liquid: Signatures of emergent majorana fermions and fluxes. *Physical Review Letters* 112: 207203. https://doi.org/10.1103/PhysRevLett.112.207203.

Knolle J, Kovrizhin DL, Chalker JT, and Moessner R (2015) Dynamics of fractionalization in quantum spin liquids. *Physical Review B* 92: 115127. https://doi.org/10.1103/PhysRevB.92.115127.

Kubota Y, Tanaka H, Ono T, Narumi Y, and Kindo K (2015) Successive magnetic phase transitions in α −rucl$_3$: Xy-like frustrated magnet on the honeycomb lattice. *Physical Review B* 91. https://doi.org/10.1103/PhysRevB.91.094422.

Lefrançois E, Grissonnanche G, Baglo J, Lampen-Kelley P, Yan JQ, Balz C, Mandrus D, Nagler SE, Kim S, Kim YJ, Doiron-Leyraud N, and Taillefer L (2022) Evidence of a phonon hall effect in the kitaev spin liquid candidate α-RuCl$_3$. *Physical Review X* 12: 021025. https://doi.org/10.1103/PhysRevX.12.021025.

Majorana E (1937) Teoria simmetrica dell'elettrone e del positrone. *Il Nuovo Cimento (1924-1942)* 14: 171–184. https://doi.org/10.1007/BF02961314.

Majumder M, Schmidt M, Rosner H, Tsirlin AA, Yasuoka H, and Baenitz M (2015) Anisotropic ru^{3+}4d^5 magnetism in the α−rucl$_3$ honeycomb system: Susceptibility, specific heat, and zero-field nmr. *Physical Review B* 91: 180401. https://doi.org/10.1103/PhysRevB.91.180401.

Mehlawat K, Thamizhavel A, and Singh Y (2017) Heat capacity evidence for proximity to the kitaev quantum spin liquid in A_2iro$_3$ ($a =$ Na, li). *Physical Review B* 95: 144406. https://doi.org/10.1103/PhysRevB.95.144406.

Motome Y and Nasu J (2020) Hunting majorana fermions in kitaev magnets. *Journal of the Physical Society of Japan* 89: 012002. https://doi.org/10.7566/JPSJ.89.012002.

Nasu J, Udagawa M, and Motome Y (2014) Vaporization of kitaev spin liquids. *Physical Review Letters* 113: 197205. https://doi.org/10.1103/PhysRevLett.113.197205.

Nasu J, Udagawa M, and Motome Y (2015) Thermal fractionalization of quantum spins in a kitaev model: Temperature-linear specific heat and coherent transport of majorana fermions. *Physical Review B* 92: 115122. https://doi.org/10.1103/PhysRevB.92.115122.

Nasu J, Knolle J, Kovrizhin DL, Motome Y, and Moessner R (2016) Fermionic response from fractionalization in an insulating two-dimensional magnet. *Nature Physics* 12: 912–915. https://doi.org/10.1038/nphys3809.

Nomura K, Ryu S, Furusaki A, and Nagaosa N (2012) Cross-correlated responses of topological superconductors and superfluids. *Physical Review Letters* 108: 026802. https://doi.org/10.1103/PhysRevLett.108.026802.

Nussinov Z and van den Brink J (2015) Compass models: Theory and physical motivations. *Reviews of Modern Physics* 87: 1–59. https://doi.org/10.1103/RevModPhys.87.1.

Perreault B, Knolle J, Perkins NB, and Burnell FJ (2015) Theory of raman response in three-dimensional kitaev spin liquids: Application to β- and γ −li$_2$iro$_3$ compounds. *Physical Review B* 92: 094439. https://doi.org/10.1103/PhysRevB.92.094439.

Rau JG, Lee EKH, and Kee HY (2014) Generic spin model for the honeycomb iridates beyond the kitaev limit. *Physical Review Letters* 112: 077204. https://doi.org/10.1103/PhysRevLett.112.077204.

Sandilands LJ, Tian Y, Plumb KW, Kim YJ, and Burch KS (2015) Scattering continuum and possible fractionalized excitations in α-rucl$_3$. *Physical Review Letters* 114: 147201. https://doi.org/10.1103/PhysRevLett.114.147201.

Sears JA, Songvilay M, Plumb KW, Clancy JP, Qiu Y, Zhao Y, Parshall D, and Kim YJ (2015) Magnetic order in α −rucl$_3$: A honeycomb-lattice quantum magnet with strong spin-orbit coupling. *Physical Review B* 91: 144420. https://doi.org/10.1103/PhysRevB.91.144420.

Singh Y and Gegenwart P (2010) Antiferromagnetic mott insulating state in single crystals of the honeycomb lattice material na$_2$iro$_3$. *Physical Review B* 82: 064412. https://doi.org/10.1103/PhysRevB.82.064412.

Singh Y, Manni S, Reuther J, Berlijn T, Thomale R, Ku W, Trebst S, and Gegenwart P (2012) Relevance of the heisenberg-kitaev model for the honeycomb lattice iridates A_2iro$_3$. *Physical Review Letters* 108: 127203. https://doi.org/10.1103/PhysRevLett.108.127203.

Sumiyoshi H and Fujimoto S (2013) Quantum thermal hall effect in a time-reversal-symmetry-broken topological superconductor in two dimensions: Approach from bulk calculations. *Journal of the Physical Society of Japan* 82: 023602. https://doi.org/10.7566/JPSJ.82.023602.

Takagi H, Takayama T, Jackeli G, Khaliullin G, and Nagler SE (2019) Concept and realization of kitaev quantum spin liquids. *Nature Reviews Physics*: 1. https://doi.org/10.1038/s42254-019-0038-2.

Widmann S, Tsurkan V, Prishchenko DA, Mazurenko VG, Tsirlin AA, and Loidl A (2019) Thermodynamic evidence of fractionalized excitations in α - RuCl$_3$. *Physical Review B* 99: 094415. https://doi.org/10.1103/PhysRevB.99.094415.

Winter SM, Li Y, Jeschke HO, and R., V. (2016) Challenges in design of kitaev materials: Magnetic interactions from competing energy scales. *Physical Review B* 93: 214431. https://doi.org/10.1103/PhysRevB.93.214431.

Winter SM, Riedl K, Maksimov PA, Chernyshev AL, Honecker A, and Valentí R (2017) Breakdown of magnons in a strongly spin-orbital coupled magnet. *Nature communications* 8: 1152. https://doi.org/10.1038/s41467-017-01177-0.

Yamashita S, Nakazawa Y, Oguni M, Oshima Y, Nojiri H, Shimizu Y, Miyagawa K, and Kanoda K (2008) Thermodynamic properties of a spin-1/2 spin-liquid state in a κ-type organic salt. *Nature Physics* 4: 459–462.

Yamashita M, Nakata N, Senshu Y, Nagata M, Yamamoto HM, Kato R, Shibauchi T, and Matsuda Y (2010) Highly mobile gapless excitations in a two-dimensional candidate quantum spin liquid. *Science* 328: 1246–1248. https://doi.org/10.1126/science.1188200.

Yamashita M, Gouchi J, Uwatoko Y, Kurita N, and Tanaka H (2020) Sample dependence of half-integer quantized thermal hall effect in the kitaev spin-liquid candidate α-RuCl$_3$. *Physical Review B* 102: 220404. https://doi.org/10.1103/PhysRevB.102.220404.

Yokoi T, Ma S, Kasahara Y, Kasahara S, Shibauchi T, Kurita N, Tanaka H, Nasu J, Motome Y, and Hickey C (2021) Half-integer quantized anomalous thermal hall effect in the kitaev material candidate α-rucl3. *Science* 373: 568–572. https://doi.org/10.1126/science.aay5551.

Fundamental and emergent particles in condensed matter and high-energy physics

Sinéad M Griffin, Materials Sciences Division, Lawrence Berkeley National Laboratory, Berkeley, CA, the United States; Molecular Foundry Division, Lawrence Berkeley National Laboratory, Berkeley, CA, the United States

© 2024 Elsevier Ltd. All rights reserved.

Introduction 147
Spontaneous symmetry breaking 148
Goldstone and Higgs modes 149
Nambu–Goldstone modes 149
Example: Goldstone modes in U(1) scalar field theory 149
Example: Goldstone modes in the Heisenberg model 151
Higgs modes 152
Higgs mechanism 154
Example: Higgs mechanism 154
Topological phases and emergent quasiparticles 155
Dark matter detection 155
Conclusion 156
Acknowledgments 156
References 156

Abstract

This chapter explores the origins and descriptions of collective modes, traversing the vast spectrum of physics from the subatomic particles in the Standard Model to quasiparticle phenomena in condensed matter. Spontaneous symmetry breaking (SSB) plays a crucial role, as Goldstone modes and Higgs bosons emerge, shaping our understanding of matter's properties across various energy scales. We discuss their origins and provide explicit examples in field theories and in solid-state physics. This interdisciplinary exploration enhances our comprehension of the underlying laws of nature, bridging the realms of condensed matter and high-energy physics.

Key points

- Explore the origins and descriptions of collective modes in physics, spanning field theories to quasiparticle phenomena in condensed matter.
- Discuss the role of spontaneous symmetry breaking (SSB) in the emergence of Goldstone modes and Higgs bosons, shaping our understanding of matter's properties across energy scales.
- Provide explicit examples of SSB in field theories and solid-state physics.
- Enhance comprehension of the underlying laws of nature by bridging condensed matter and high-energy physics.
- Investigate the crucial role of collective excitations, such as Goldstone and Higgs modes, in understanding matter at low and high energy scales.
- Highlight the potential of quasiparticle excitations in both condensed matter and high-energy physics to uncover new physics beyond the Standard Model such as for scattering targets for low-mass dark matter, expanding the parameter space for dark matter searches.

Introduction

The use of a particle description of our physical universe is common across all lengthscales in physics ranging from quarks at the subatomic scale to astronomical objects such as stars (Grossman, 2014). There are intriguing analogies between the formulation of quantum field theory (QFT) for elementary particles and many-body theory for condensed matter systems. For instance, QFT associates elementary particles such as photons (particles of light) and gravitons (particles mediating gravitational forces) with quanta of radiation fields and gravitational fields, respectively. These particles are intricately linked to the fundamental forces of nature, and in the case of gravitons have not yet been directly observed (Carney, 2022). On the other hand, condensed matter systems exhibit collective behaviors and waves that can be effectively described using many-body theory. Here, entities like phonons

https://doi.org/10.1016/B978-0-323-90800-9.00258-4

(quanta of lattice vibrations) and plasmons (quanta of collective electronic oscillations) emerge through the quantization of these collective waves. Unlike elementary particles, these quasiparticles arise as collective excitations within the solid-state structure, influenced by interatomic interactions and the underlying lattice structure.

The concept of spontaneous symmetry breaking (SSB) plays a significant role in the description and understanding of quasiparticle excitations in this wide range of physical systems, from the microscopic to the galactic (Guralnik et al., 1968). Goldstone modes are perhaps the most well-known example of collective excitations that arise from SSB as they play a fundamental role in determining the properties of materials at low temperatures. On the other hand, in high-energy physics, SSB is deeply connected to the Higgs mechanism, which gives rise to the Higgs boson and is responsible for the spontaneous breaking of the electroweak symmetry in the Standard Model. The Higgs mechanism also has substantial implications in condensed matter physics, where Higgs modes are now the emergent quasiparticle excitations.

At low energies, the study of quasiparticle excitations, such as Goldstone and Higgs modes, is crucial for our understanding of matter. These collective excitations can also provide new insights into the behavior of matter at high-energy scales, such as those found in collider experiments. Exploring quasiparticle excitations in both condensed matter and high-energy physics allows us to better understand and connect the fundamental laws of nature across lengthscales. Condensed matter systems can provide a unique opportunity to study quasiparticle excitations in more easily accessible table-top experiments while high-energy physics can provide new insights into the nature of matter and the universe at extreme scales. For instance, an emerging area in high-energy physics is the use of quasiparticle excitations in condensed matter systems as scattering targets for low-mass dark matter (DM). This bridging of high- and low-energy physics has the potential to expand the parameter space for DM searches and uncover new physics beyond the Standard Model.

Spontaneous symmetry breaking

SSB occurs when the underlying laws of a physical system exhibit a symmetry, but the system itself behaves in a way that apparently breaks that symmetry. While this may sound paradoxical, it is in fact a common occurrence in nature and plays a crucial role in many areas of physics, from particle physics to condensed matter physics.

The concept of symmetry breaking has roots far deeper than its modern usage in contemporary physics, tracing back to Aristotle's work, "On the Heavens 295b," circa 350 BC. Aristotle satirically posits that an individual, situated equidistantly between food and drink, would rather perish than disrupt the symmetry and choose between the two options (Rescher, 2013). This ancient paradox was later recast by philosophers as a commentary on moral determinism, replacing the famished and parched human with a donkey (as illustrated in Fig. 1). At the top of the "wine bottle" potential, there is full rotational symmetry—the landscape appears identical from the donkey's perspective even as he rotates about his position. However, a minor perturbation—perhaps prompted by the donkey's own need for sustenance—can cause the donkey to topple down the potential, landing at a select point in the circle making up the trough at the bottom of the potential. Now the situation has dramatically changed: as the donkey rotates, each direction presents a distinct view. The ground-state solution no longer exhibits rotational symmetry even though the potential hasn't

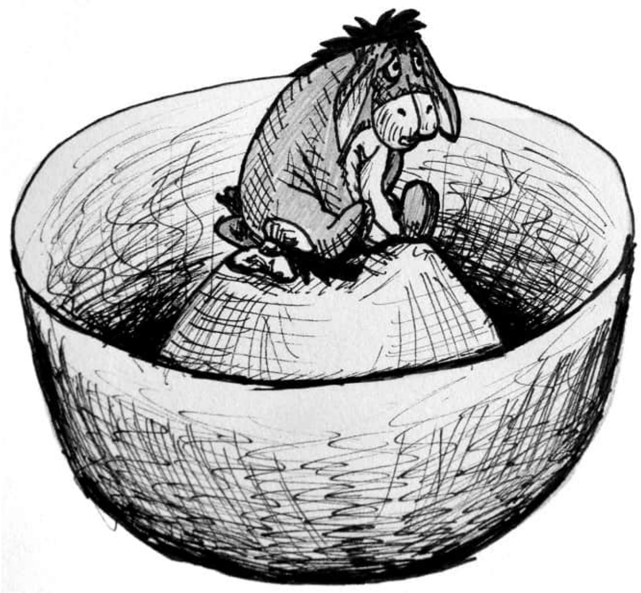

Fig. 1 Buridan's donkey sitting on top of the "wine bottle" potential. In the high-symmetry state on top of the potential, the system has full rotational symmetry. Falling down the hill results in a choice of ground state which at the same time breaks rotational symmetry.

changed. Luckily, the donkey can traverse the flat trough in a complete circle without expending energy. Upon descending the potential, the system's symmetry remains unchanged; however, the particular choice of ground-state solution breaks this symmetry. Nature's predilection for lower energy solutions resolves the indecisive philosopher's quandaries.

SSB occurs when the ground state of a system appears not to share the same symmetries as the theory that describes it. In these cases, a continuous transformation, such as rotation or translation, that leaves the equations of motion unchanged does not leave the ground state unchanged. We see SSB across all fields of physics, and most frequently discussed in condensed matter physics and high-energy physics. A common example of SSB is the paramagnetic to ferromagnetic phase transition in a magnetic material (see Fig. 2). Above the Curie temperature, T_C, the spins on each site are randomly oriented. The system has rotational symmetry with a net magnetization of zero. As the system is cooled below T_C, it undergoes a phase transition where the spins now spontaneously order and point in a particular direction. This choice of ground state breaks the rotational symmetry and results in a net magnetization in the direction of the broken symmetry. Table 1 gives several further examples of SSB at disparate lengthscales and the corresponding broken symmetries for each case.

Goldstone and Higgs modes

Nambu–Goldstone modes

Upon symmetry breaking, we noted that the donkey now has the freedom to wander around the base of the potential—this new excitation is a direct result of the SSB. Such an excitation is referred to as a Goldstone mode, also known as a Nambu–Goldstone boson or a Goldstone boson (Nambu, 1960; Goldstone, 1961). It is a collective excitation in a theory that appears when a continuous symmetry is spontaneously broken. Goldstone modes are massless or nearly massless fluctuations that are associated with this broken symmetry. Due to their low energy cost, they can propagate throughout the system, giving rise to long-range correlations and other emergent phenomena. In condensed matter, Goldstone modes are used to describe an array of collective excitations in systems such as crystals, magnets, and superfluids.

Example: Goldstone modes in U(1) scalar field theory

To illustrate the appearance of Goldstone modes with SSB, we consider the case of a complex scalar field, $\phi(x)$ which is charged under $U(1)$ global symmetry:

$$\phi(x) \to e^{i\theta}\phi(x) \tag{1}$$

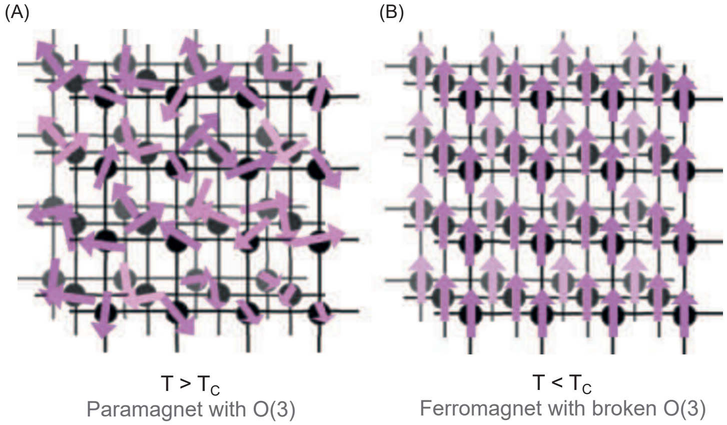

Fig. 2 Paramagnetic to ferromagnetic phase transition. Above the Curie temperature (T_C), the spins are randomly oriented and have full rotational symmetry (A). Below T_C, spontaneous symmetry breaking occurs that breaks the rotational symmetry resulting in a macroscopic magnetization (B).

Table 1 Examples of spontaneous symmetry breaking (SSB) in physics including those in solid-state systems and in the standard model.

Phenomenon	*Symmetry broken*	*Observable/manifestation*
Ferromagnetism	$SO(3)$	Spontaneous magnetization
Superconductivity	$U(1)$	Zero resistance, Meissner effect
Higgs mechanism	$SU(2) \times U(1)$	Mass of W and Z Bosons
Chiral symmetry breaking in QCD	$SU(3)_L \times SU(3)_R$	Appearance of pions, larger nucleon masses

where θ is the phase associated with the $U(1)$ symmetry (Peskin and Schroeder, 2018). The Lagrangian is then the sum of the familiar kinetic term, and a yet undefined potential, V:

$$\mathcal{L} = \frac{1}{2}\partial_\mu \phi^* \partial^\mu \phi - V(\phi) \tag{2}$$

To write down the potential, we consider the restrictions on its form from both the symmetry of the theory and our desire for a renormalizable theory. First, we cannot have odd powers of ϕ as this would result in an unstable theory (solutions would "roll down" the potential). Additionally, the $U(1)$ global symmetry requirement restricts us to even powers of ϕ. Second, a theory with $\mathcal{O}(\phi^6)$ terms is not renormalizable, limiting us to a square and a quartic term for a simple form. This leads us to the famous "wine bottle" potential:

$$V(\phi) = \frac{\mu}{2}|\phi|^2 + \frac{\lambda}{4}|\phi|^4 \tag{3}$$

where μ and λ are coupling constants. Since the potential must be bounded from below, we require that $\lambda > 0$. However we have no such restrictions on the sign of μ, so we consider the two cases of $\mu > 0$ and $\mu < 0$, with the corresponding potentials illustrated in Fig. 3. For $\mu > 0$, the ground state is unique and the vacuum expectation value (VEV) $\langle \phi_0 \rangle = 0$. In this case both the theory and the unique solution to the theory have $U(1)$ symmetry.

However, an interesting case emerges for $\mu < 0$, as shown in Fig. 3B. Now the scalar potential has a collection of local minima rather than a single unique vacuum. The theory still retains its $U(1)$ symmetry; however, the ground-state solutions to the theory do not. Instead, the vacuum manifold is invariant under $U(1)$ symmetry such that we can transform between these different degenerate vacuum states (the donkey can walk around the base of the potential). This continuum of vacua has amplitude $|\phi_0| = \sqrt{\frac{|\mu|}{\lambda}}$ and can be described as a collection of points on a circle, S^1. Since the minimum of the potential is not at $|\phi_0| = 0$, symmetry breaking must occur. The process of choosing a particular solution out of these degenerate vacua is *spontaneous*. The order parameter space is the quotient space of $U(1)/1 \simeq U(1)$ which classifies all possible broken-symmetry states.

We next explore what new excitations (if any) are present in the broken-symmetry solution of the vacuum. We do this by picking a vacuum state and examining fluctuations away from the minimum at $|\phi_0| = \sqrt{\frac{|\mu|}{\lambda}}$. Since our collection of vacuum states are invariant under $U(1)$ symmetry, we parametrize the fluctuations around the minimum of our scalar field ϕ in terms of radial and angular contributions:

$$\phi = \frac{1}{\sqrt{2}}\left(h + \sqrt{\frac{-\mu}{\lambda}}\right)e^{i\theta} \tag{4}$$

Here, h and θ are real scalar fields representing the radial and angular fluctuations around the minimum, respectively. Substituting this parameterization into the Lagrangian density, we get:

$$\mathcal{L} = \frac{1}{2}\left(\partial_\mu h \partial^\mu h + \frac{-\mu}{\lambda}\partial_\mu \theta \partial^\mu \theta\right) - \frac{\lambda}{4}h^4 - \frac{1}{2}\mu h^2 + O(h) \tag{5}$$

First focusing on the angular mode, θ, we find that it is massless, corresponding to the Goldstone mode. This Goldstone mode arises as a consequence of the spontaneous breaking of the $U(1)$ global symmetry and represents the continuous shift in the phase of the complex scalar field ϕ around the minimum of the potential (see Fig. 4). We also see that the radial mode h is massive, with mass $m_h = \sqrt{2|\mu|}$. This will be discussed later and identified as a Higgs mode. In summary, in a $U(1)$ global scalar field theory with a potential of the form given in Eq. (3) where $\mu < 0$, the Goldstone mode arises as a massless excitation corresponding to the phase fluctuation of the complex scalar field. The radial mode corresponds to the massive amplitude fluctuation (Higgs-like particle). The existence of the Goldstone mode is a direct consequence of the spontaneous breaking of the continuous global symmetry.

Although demonstrated here for the straightforward case of SSB in a global $U(1)$ scalar theory, Goldstone's predictions have broad applicability across a wide range of physical systems that undergo SSB of a continuous symmetry. It is summarized by Goldstone's Theorem, which states that when a continuous symmetry is spontaneously broken, a corresponding gapless excitation must emerge in the system's low-energy spectrum (Goldstone, 1961). The excitation is the Goldstone mode and is characterized by

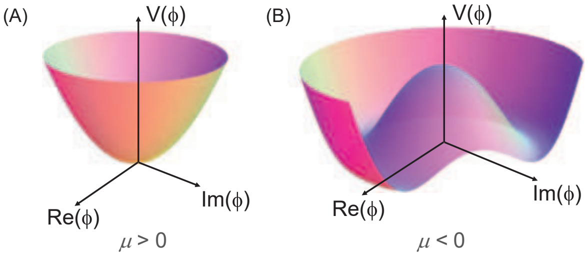

Fig. 3 "Wine bottle" potentials for the form ϕ^4 for (A) $\mu > 0$ and (B) $\mu < 0$. Only (B) exhibits spontaneous symmetry breaking.

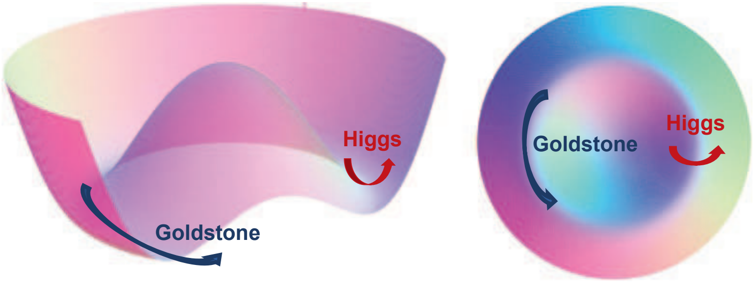

Fig. 4 Goldstone (phase) and Higgs (amplitude) modes depicted for a $U(1)$ global theory. The Goldstone modes correspond to fluctuations in angle; Higgs modes correspond to amplitude fluctuations.

its long wavelength and low energy and arises due to the broken symmetry in the system. Furthermore, the theorem predicts that the number of Goldstone modes appearing from the SSB is equal to the number of broken symmetry generators. For the complex scalar field under $U(1)$ global symmetry considered earlier, one broken symmetry (rotational symmetry) resulted in the appearance of one Goldstone mode. Viewed another way, when SSB occurs the symmetry is not completely "broken," but rather manifests as gapless excitations of the ground state. This allows us to redefine the excitations in the ground state manifold as emergent modes and to use a particular description for their behavior. In more complex systems with multiple broken continuous symmetries, multiple Goldstone modes may emerge, each representing a distinct facet of the broken symmetry with examples given in Table 1.

The emergence of three branches of gapless acoustic phonon modes in a crystalline material is a example of the Goldstone theorem in condensed matter. Crystals are characterized by the spontaneous breaking of translation symmetry—in a three-dimensional crystal there are three generators of translation. The theorem then predicts that these three broken translational symmetries result in the appearance of three gapless modes, corresponding to the three gapless acoustic phonon modes. In general, we expect d branches of gapless (acoustic phonon) modes in a d-dimensional crystal (Nielsen and Chadha, 1976).

One of the most important manifestations of Goldstone modes appears in the theory of the strong nuclear force, as described by quantum chromodynamics (QCD) (Nambu and Jona-Lasinio, 1961; Ryan, 2023). The QCD Lagrangian captures the interaction between quarks and gluons in the Standard Model and exhibits several symmetries, including $SU(3)$ gauge symmetry, chiral, flavor, and isospin symmetry of quarks and baryon number. Of these symmetries, chiral symmetry plays a key role in the appearance of Goldstone modes in QCD. Here, chiral symmetry describes the invariance of the QCD Lagrangian under the separate transformations of left-handed and right-handed components of the quark fields. When chiral symmetry is exact, left- and right-handed components of quarks are indistinguishable. However, the nonzero masses of the quarks only allow for approximate conservation of chiral symmetry. At lower energies, where quarks become strongly coupled, chiral symmetry is spontaneously broken, resulting in the creation of Goldstone bosons called pions. The pion is the lightest meson and plays a crucial role in the behavior of hadrons, the composite particles made up of quarks and gluons. Pions are the Goldstone modes associated with the breaking of chiral symmetry in QCD, and their properties are central in understanding the dynamics of the strong force.

Example: Goldstone modes in the Heisenberg model

We now consider a specific case of SSB and Goldstone modes in condensed matter with the emergence of Goldstone modes in the Heisenberg model. This elegant yet highly informative model describes a cubic lattice of spin-$\frac{1}{2}$ sites interacting via an isotropic exchange interaction:

$$H = -J\sum_{\langle i,j\rangle}\mathbf{S}_i\cdot\mathbf{S}_j \tag{6}$$

where J is the exchange interaction strength and $\mathbf{S}_i = \hbar\sigma_i$ is the spin operator on site i, and σ_i are the Paul matrices. The sites are labeled by i, j, and the sum is taken over all nearest-neighbor pairs. This H is characterized by the orientation of the spins, which can be rotated together without affecting our theory. This gives a net zero expectation value for spin in the absence of symmetry breaking. However, the dot product between nearest-neighbor spins in H, the sign of the exchange interaction, J, dictates the preferred relative orientation of spins in the system. For $J > 0$, the energy is minimized when the spins are parallel, leading to a ferromagnetic ground state. Conversely, when $J < 0$, antialignment of spins is favored, resulting in an antiferromagnetic ground state. These magnetic ground states spontaneously break the rotational symmetry in our theory, and give rise to a gapless Goldstone mode.

To illustrate this concept, let us consider the 1D Heisenberg model with $J > 0$ and explore its low-energy citations (The general case can be derived of an n-dimensional spin model by performing a Holstein–Primakoff transformation to express H in terms of bosonic creation and annihilation operators.). We rewrite the Hamiltonian in terms of the spin operators $S_i^{\pm}$:

$$
\begin{aligned}
H &= -J\sum_{\langle i,j\rangle}\mathbf{S}_i\cdot\mathbf{S}_j \\
&= -J\sum_{\langle i,j\rangle}S_i^zS_j^z - \frac{1}{2}\left(S_i^+S_j^- + S_i^-S_j^+\right)
\end{aligned}
\tag{7}
$$

The S_i^+ and S_i^- correspond to the spin raising and lowering operators at site i. Since $J > 0$, the ground state, ϕ_G, corresponds to all spins being aligned:

$$
\begin{aligned}
H|\phi_G\rangle &= -J\sum_{\langle i,\,j\rangle}S_i^zS_j^z|\phi_G\rangle - \frac{J}{2}\left(S_i^+S_j^- + S_i^-S_j^+\right)|\phi_G\rangle \\
&= -JNs^2|\phi_G\rangle \\
&= E_G|\phi_G\rangle
\end{aligned}
\tag{8}
$$

To examine low-energy excitations, we rewrite H as linear combinations of states $|i\rangle$ with a single spin flip at site i giving

$$
H = \sum_{ij}|i\rangle\langle i|H|j\rangle\langle j|
\tag{9}
$$

When one spin is flipped, it results in a reversal of two J couplings, at an energy cost of $2JS^2$. Since the interactions are restricted to nearest-neighbor only, all off-diagonal matrix elements vanish except for the nearest-neighbor terms, which lead to the diagonal matrix elements and the nonvanishing off-diagonal terms in Eq. (9). The energy spectrum of these low-energy excitations is then

$$
H = (E_G + 2JS^2)\sum_i|i\rangle\langle i| - JS^2\sum_i(|i+1\rangle\langle i| + |i\rangle\langle i+1|)
\tag{10}
$$

Taking the Fourier transform of this and diagonalizing the corresponding $H(q)$ we get:

$$
E_q = E_G + 2JS^2[1 - \cos(qa)]
\tag{11}
$$

The excited state energies in the long wavelength limit ($q \to 0$) are $\sim Ja^2q^2$, where a is the lattice spacing and q is the wavenumber, These low-energy excitations are the Goldstone modes associated with the SSB magnetic phase transition, known as magnons. These collective excitations are the magnetic analog of phonons and are generally linear in q for magnetic materials. An exception to this is the ferromagnetic case considered here, which is quadratic in q.

Higgs modes

An alternative description of Goldstone modes is as fluctuations in the phase of the order parameter. For instance, in a conventional superconductor, the continuous $U(1)$ symmetry is spontaneously broken leading to our "wine-bottle" potential with a degenerate circle of minima described by the order parameter $\phi = Ae^{i\theta}$. Fluctuations from the ground state can be classified as transverse Goldstone (phase) modes and longitudinal (amplitude) Higgs modes. Here, the order parameter corresponds to the wave function of Cooper pairs with fluctuations in the phase representing their orientation. In our scalar field theory above, Goldstone modes are the gapless excitations around the bottom of the potential, tracing out a circle. Higgs modes, on the other hand, are characterized by fluctuations of the order parameter around its VEV and are gapped.

We return to the Lagrangian for a $U(1)$-symmetric complex scalar field Eq. (2) with the potential expressed as:

$$
V(\phi) = \frac{\mu}{2}|\phi|^2 + \frac{\lambda}{4}|\phi|^4
\tag{12}
$$

By examining fluctuations around the ground-state vacua, we found a radial mode h with mass $m_h = \sqrt{2|\mu|}$, which we identified as a "Higgs"-type excitation. This mode is associated with the amplitude of the scalar field, which means that its excitations correspond to changes in the field's magnitude. As a result, the Higgs mode plays a fundamental role in defining the energy landscape of the scalar field, as well as the characteristics of the phase where symmetry is spontaneously broken. We see that the Higgs field has acquired a mass *due* to the symmetry breaking, and this is the Higgs mode. Its mass is determined by the Higgs field VEV μ and the coupling strength λ in a $U(1)$ symmetric complex scalar theory.

The Higgs mode was originally theoretically proposed for relativistic theories where the equations of motion have Lorentz symmetry (Higgs, 1964, 1966; Englert and Brout, 1964; Guralnik et al., 1964). In these relativistic theories, the Higgs modes can be well defined and decoupled from Goldstone modes near particle-hole symmetry. Since the presence of Lorentz symmetry imposes constraints on the dispersion relation of the excitations, we then expect the Higgs modes to have a flat dispersion near particle-hole symmetry while Goldstone modes generally have a linear dispersion (Fig. 5). The Higgs' flat dispersion has important consequences: it implies that the Higgs mode extends over a vast spatial region and possesses minimal energy. Because of this, it can avoid rapid decay into particle-hole pairs. Therefore, particle theories with both Lorentz symmetry and particle-hole symmetry can have observable Higgs modes that are also effectively decoupled from the Goldstone modes.

The observation of Higgs modes is extremely challenging in condensed matter systems for two key reasons (Pekker and Varma, 2015; Podolsky et al., 2011). First, particle-hole symmetry is required to fully decouple the Goldstone and Higgs modes to avoid their rapid decay into other excitations. In such systems, the Fermi level is located at the center of the energy gap, and the electron

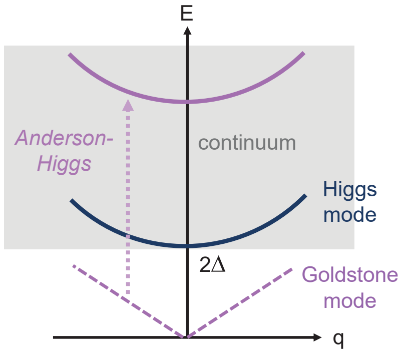

Fig. 5 A schematic excitation spectrum of an *s*-wave superconductor. Due to the Anderson–Higgs mechanism, the Nambu–Goldstone mode acquires an energy gap in the order of the plasma frequency ω_p while the Higgs mode remains in low energy with an energy gap 2Δ, above which the quasiparticle excitation continuum overlaps.

and hole states are degenerate in energy. Careful tuning of the chemical potential in systems ranging from trapped atoms and uniaxial antiferromagnets to superconductors can achieve approximate particle-hole symmetry allowing for the detection of Higgs modes in principle. In particular the search for Higgs modes in superconductors is appealing since they are particle-hole symmetric at low energies surrounding the superconducting gap.

The second, perhaps more fundamental, challenge for the detection of Higgs modes in solid-state systems relates to its scalar nature. In condensed matter systems, the Higgs mode is a scalar, lacking charge, spin, or any other distinguishable quantum number, making it "dark" to conventional experimental probes that linearly couple to quantum numbers. Therefore observation of the Higgs mode in condensed matter systems relies on indirect probes requiring nonlinear couplings to conventional states in quantum matter or on rapid nonequilibrium probes of the system (Shimano and Tsuji, 2020).

In the quest to observe the elusive Higgs mode, a promising proposal involves examining spectral weight redistribution between the Higgs mode and optical phonons in superconductors. This can be observed in low-temperature Raman spectroscopy in close proximity to the superconducting transition temperature (T_C). When Raman active modes couple with Higgs mode, a shift in spectral weight occurs which can be identified as a pole in the self-energy of the Raman-active phonon. This results in two resonances with an aggregate weight equal to the single resonance above the superconducting transition temperature.

The conservation of total spectral weight emerges naturally when the Higgs mode is linearly coupled to Raman active optical phonons. However, this coupling seems to violate particle number conservation while conserving charge conservation. In principle, this can be allowed if lattice vibrations only couple with electronic charge density. In this scenario, the Higgs mode can be observed through a process in which the lattice vibration "shakes" the condensate and generates a particle-number nonconserving condensate (Littlewood and Varma, 1982).

Recent experimental advancements in Raman scattering on metals have successfully detected spectral weight transfer which can be attributed to the Higgs mode (Méasson et al., 2014). When Higgs-phonon coupling is present, the combined spectral weight of the two resonances below the superconducting transition temperature is predicted to equal the weight of a single resonance above it. Investigations using Raman spectroscopy on $NbSe_2$ in both normal and superconducting states have revealed optical phonons at 2 K and above the superconducting transition ($T_C = 7.2$ K). Furthermore, an additional peak emerges at roughly twice the superconducting gap or 2Δ. This conservation of spectral weight in each channel provides compelling evidence for the vertex responsible for coupling the Higgs mode; however, other possible causes of these resonances have also been proposed (Balseiro and Falicov, 1980).

A direct coupling of the Higgs mode to experimental probes can in principle be achieved using the Josephson effect. By coupling two superconductors with the same symmetries but different amplitudes, one can drive both Goldstone and Higgs mode by applying a time-dependent voltage. This was used in experiments near T_C by Carlson and Goldman and Kadin and Goldman, who identified a new set of phase modes, known as the Carlson–Goldman modes (Carlson and Goldman, 1975; Kadin and Goldman, 1982). However, despite these observations, the corresponding amplitude modes (Higgs modes) have yet to be observed using this technique.

Ongoing research in the field of superconductivity has revealed that more complex scenarios with multiple Higgs modes are possible, potentially shedding light on open questions about the nature of superconductivity. Superfluid 3He, which possesses a multicomponent order parameter, displays various collective oscillation modes between the different components of the order parameter (Vollhardt and Wolfle, 2013). In the case of cuprate superconductors, a mysterious mode has been observed directly in Raman scattering at an energy of approximately 1.5Δ, where Δ is the maximum gap. This mode has been identified as the amplitude mode of the superconductor, which is suggested to draw spectral weight from the continuum in a similar coupling mechanism to the Higgs-phonon scenario described above (Katsumi et al., 2018). It has also been suggested that non-*s*-wave order parameters can give rise to multiple symmetry-dependent Higgs modes, leading to a complex superconducting state with several competing mechanisms. These findings highlight the importance of understanding the appearance and control of Higgs modes in quantum materials with complex order parameters spaces such as high-T_C superconductors (Schwarz et al., 2020).

Higgs mechanism

The SSB cases we have explored in detail to now have focused on the spontaneous breaking of a global symmetry which we show via Goldstone's Theorem results in the creation of a massless Goldstone boson. However, when a local (gauge) symmetry instead is broken, the Goldstone bosons are "eaten" by the gauge bosons, giving them mass and leaving no massless Goldstone bosons in the resulting theory. This process is commonly known as the Higgs mechanism (Several papers published in close succession proposed a mechanism whereby massless Goldstone bosons interact with massless gauge bosons to produce a massive vector mode. This motivates the more complete title—the Anderson-Brout-Englert-Guralnik-Hagen-Kibble-Higgs phenomenon.), and it plays a pivotal role in the electroweak symmetry breaking that gives mass to the W and Z bosons, which are responsible for mediating the weak nuclear force.

Example: Higgs mechanism

We first derive the Higgs mechanism for an explicit theory to demonstrate how it imbues mass on otherwise massless particles. Following this, we will discuss the important of the Higgs mechanism for understanding particles in condensed matter and in high-energy physics. We begin with our previous $U(1)$ complex scalar theory, but now couple it to electromagnetism. This results in an abelian $U(1)$ gauge theory:

$$\mathcal{L} = (D_\mu \phi)^\dagger (D^\mu \phi) - V(\phi) - \frac{1}{4} F_{\mu\nu} F^{\mu\nu} \tag{13}$$

Where $D_\mu = \partial_\mu + ieA_\mu$ is the covariant derivative, e is the gauge coupling constant, $V(\phi)$ is a Higgs potential, and $F_{\mu\nu} = \partial_\mu A_\nu - \partial_\nu A_\mu$ is the field strength tensor for the $U(1)$ gauge field. We choose a Higgs potential with SSB, such as the "wine bottle" potential in Eq. (12). Since the minimum of the potential is not at $\phi_0 = 0$, SSB occurs. Again we can parameterize the complex scalar field ϕ in terms of the radial and angular fluctuations around the minimum, respectively. Substituting this parameterization into the Lagrangian density, we get:

$$\mathcal{L} = \frac{1}{2} (\partial_\mu h)^2 + \frac{1}{2} \left(h + \sqrt{\frac{-\mu}{\lambda}} \right)^2 (\partial_\mu \theta - eA_\mu)^2 - V(h) - \frac{1}{4} F_{\mu\nu} F^{\mu\nu} \tag{14}$$

In this expression, the gauge field A_μ acquires a mass term proportional to $\left(h + \sqrt{\frac{-\mu}{\lambda}}\right)^2$. The mass of the gauge boson is given by:

$$m_A = e\sqrt{\frac{-\mu}{\lambda}} \tag{15}$$

The radial mode h is massive, while the angular mode θ is "eaten" by the gauge field through the Higgs mechanism, providing the gauge boson with mass. In this case, the massless Goldstone mode associated with the phase fluctuation does not manifest as a separate physical excitation. The scalar field's angular mode, θ, becomes part of the longitudinal degree of freedom of the now massive gauge boson, and the Goldstone mode disappears as an independent excitation.

The Higgs mechanism and the concept of SSB are essential components of our current understanding of fundamental particles and their interactions. It predicts how a massive boson can be created when massless Goldstone modes combine with gauge bosons upon SSB, and is generally applicable in both nonrelativistic and relativistic theories. These descriptions and mechanisms are broadly applied across the landscape of physics ranging from condensed matter and particle physics to cosmology, where they help explain the emergence of various ordered states and phase transitions.

In particle physics, the Abelian Higgs mechanism described above can be extended to non-Abelian gauge theories, such as the $SU(2) \times U(1)$ electroweak gauge theory, which is a cornerstone of the Standard Model of particle physics. In the electroweak theory, the Higgs mechanism is responsible for giving mass to the W and Z bosons, which mediate the weak nuclear force, as well as providing masses to the quarks and charged leptons through Yukawa interactions with the Higgs field. In the context of Standard Model, SSB of the electroweak gauge theory creates a massive scalar particle—the Higgs boson—which give mass to other Standard Model particles. The discovery of the Higgs boson with a mass of $\sim$125 GeV at CERN in 2012 validated the Higgs mechanism and existence of the Higgs field.

The Higgs mechanism plays a key role in the theoretical understanding of superconductors, and was in fact originally proposed in the context of superconductors by Anderson (and is often dubbed the Anderson–Higgs mechanism because of this) (Anderson, 1963). Superconductors undergo a phase transition from the normal conducting state to the superconducting state below a critical temperature, which is characterized by the onset of a Cooper pair condensate. This phase transition is described as the spontaneous breaking of the $U(1)$ gauge symmetry associated with electromagnetism. The interplay between the SSB and the breaking of a gauge symmetry result in the massless gauge boson (the photon in this case) acquiring mass. Therefore the effective mass of photons within the superconductor increases because of their interaction with the Cooper pair condensate. The appearance of this massive gauge boson leads to the Meissner effect, where magnetic fields are expelled from the bulk of a superconductor.

Topological phases and emergent quasiparticles

While SSB plays a key role in the appearance of Goldstone and Higgs modes, it can also lead to other particle-like phenomena. A particular interesting class of SSB-induced phenomena is the emergence of topological defects (TDs) that are determined by the system's topology. TDs emerge in regions where a continuous symmetry is broken, giving rise to nontrivial configurations that cannot be locally rearranged (Griffin and Spaldin, 2017). The stability of TDs against local deformations stems from the global characteristics of the order parameter, which are inherently embedded in its topology. TDs occur when the SSB of a continuous symmetry in a system also corresponds to a change in the homotopy group during a phase transition (Kibble, 1976). While Goldstone modes represent massless fluctuations around a vacuum that are caused by SSB, TDs originate from distinct choices of local configurations within the order parameter field. This leads to the formation of various phenomena, including vortices in superfluids, dislocations in crystalline solids, and topological solitons such as domain walls and skyrmions in magnetic materials.

Originally proposed in the context of nuclear physics, skyrmions are TDs that emerge in ferroic systems. They are solitonic solutions to the relevant effective theory that have a twist or kink the order parameter field that cannot be removed. As emergent quasiparticles, skyrmions display particle-like attributes, such as individual mobility, mutual interactions, and the ability to act collectively. TDs can also act to induce and localize physics that does not appear in a bulk system. For instance, the appearance of Majorana fermions in topological superconductors is predicted to occur at one-dimensional TDs or vortices. Majoranas are quasiparticles that act as their own antiparticles and are the key building block for topological quantum computing. Finally, the effective description of TDs can be mapped onto other models of emergent quasiparticles such as the magnetic behavior in "spin ice" and the emergent magnetic monopoles that appear (Bramwell et al., 2009).

The interplay between TDs and emergent quasiparticles opens up a rich and complex phase space where new, exotic quasiparticles can appear. Studying these connections can provide valuable insights into the emergent behavior of many-body systems and unveil new possibilities for the manipulation and control of their properties. Understanding these interactions also allows us to manipulate and control the properties of these systems more effectively. For instance, through various physical and chemical methods like applying fields or doping, we can refine the systems for optimal performance.

Dark matter detection

Standard Model matter described above constitute only 25% of the matter mass in the universe; the rest is dubbed "dark" as it does not couple to electromagnetism. There is an increasing litany of indirect evidence for DM ranging from Vera Rubin's observations of the rotational curves of galaxies to gravitational lensing and structure in the cosmic microwave background. These all suggest that there is significantly more matter in the universe that cannot be accounted for by Standard Model matter. However, despite the wealth of indirect evidence for DM, so far it has evaded direct detection making it one of the biggest open questions in modern physics.

Current evidence for DM suggests that it makes up the majority of matter in the universe, inferred from the "missing" matter that is needed to account for existing observations. However, this evidence does not give us information on the mass of individual DM particles/waves. Because of this, the search for DM must extend across a vast range of magnitudes, from massive galactic objects like black holes to subatomic particles and wave-like phenomena. Among the most promising DM candidates are weakly interacting massive particles (WIMPs), with masses ranging from 10 GeV/c^2 to 10 TeV/c^2 down to lighter "wave-like" modes of DM, such as the axion, are theorized to have masses in the range of 10^{-22}–10^{-6} eV/c^2.

Direct detection experiments commonly seek to detect DM through their interaction with our known matter that is described by Standard model. For instance, particle-like DM, since it has mass, has well-defined momentum and kinetic energy and so can scatter from DM particles, given the right kinematic constraints. This principle is used in the current searches for WIMPs which look for DM-induced recoil of nuclei in large volumes of target materials. Yet, despite significant effort, these searches have yet to uncover definitive evidence of DM, and so new strategies are needed to expand the parameter space in the search for DM. One promising approach involves the use of more sensitive detection schemes capable of detecting lower-mass DM than many of the existing searches. However, this requires a rethinking of the experimental and sensing setup to make it sensitive to DM masses lower than the WIMP scale (Essig, 2020). One potential avenue is to explore collective excitations in quantum materials such as phonons, electrons, and magnons as scattering targets for such low-mass DM (see Fig. 6).

Condensed matter physics provides valuable insights and techniques for the detection of DM. For example, cryogenic detectors for studying condensed matter systems, such as superconductors, has led to the development of similar detectors for DM searches. These detectors rely on the detection of tiny amounts of energy released when DM particles scatter off of the detector material, which can be measured using sensitive electronics. In addition, condensed matter physics has also contributed to the development of new materials and technologies that can enhance the sensitivity of DM detectors. For example, the use of superconducting materials can allow for the detection of smaller energy signals from DM interactions while the use of quantum-enhanced sensing can potentially improve signal-to-noise ratios, which are key for these highly sensitive searches.

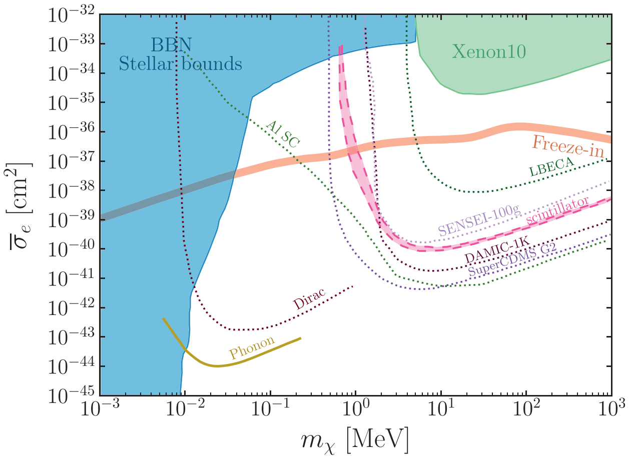

Fig. 6 Projected reach for dark photon-mediated dark matter (DM) scattering via Dirac electron and single phonon excitations with 1 kg-year exposure and no background. For the Dirac electron case, the sensitivity is shown for $ZrTe_5$ (Hochberg et al., 2018) while for the single phonon case, the sensitivity is shown for H_2O with a 20 meV detector threshold (Taufertshöfer et al., 2023). Existing constraints and other proposed experiments are included for comparison.

Conclusion

SSB and its role in describing matter in the form of quasiparticle excitations pervades all areas of physics ranging from the micro- to macroscopic. The common description of collective excitations across high-energy physics and condensed matter has served as an important bridge in connecting the communities. This unity has paved the way for groundbreaking discoveries, such as superconductivity and the discovery of the Higgs boson. As more complex manifestations and interactions of these collective excitations emerge, the need for comprehensive theoretical descriptions and novel measurement probes will maintain the search and understanding for new quasiparticles as an exciting and vibrant area of research.

Acknowledgments

This work was supported by the U.S. Department of Energy under contract DEAC02-05CH11231 and Quantum Information Science Enabled Discovery (QuantISED) for High Energy Physics grant KA2401032. The work performed at the Molecular Foundry was supported by the Office of Science, Office of Basic Energy Sciences, of the U.S. Department of Energy under the same contract. Thanks to Omar Ashour for plotting Fig. 6 and to Ali Mozaffari and Daniel Carney for their insights and sometimes useful discussions.

References

Anderson PW (1963) Plasmons, gauge invariance, and mass. *Physical Review* 130(1): 439.
Balseiro CA and Falicov LM (1980) Phonon Raman scattering in superconductors. *Physical Review Letters* 45: 662–665. https://doi.org/10.1103/PhysRevLett.45.662.
Bramwell ST, Giblin SR, Calder S, Aldus R, Prabhakaran D, and Fennell T (2009) Measurement of the charge and current of magnetic monopoles in spin ice. *Nature* 461(7266): 956–959.
Carlson RV and Goldman AM (1975) Propagating order-parameter collective modes in superconducting films. *Physical Review Letters* 34: 11–15. https://doi.org/10.1103/PhysRevLett.34.11.
Carney D (2022) Newton, entanglement, and the graviton. *Physical Review D* 105: 024029. https://doi.org/10.1103/PhysRevD.105.024029.
Englert F and Brout R (1964) Broken symmetry and the mass of gauge vector mesons. *Physical Review Letters* 13: 321–323. https://doi.org/10.1103/PhysRevLett.13.321.
Essig R (2020) The low-mass dark matter frontier. *Physics* 13: 172.
Goldstone J (1961) Field theories with superconductor solutions. *Il Nuovo Cimento (1955–1965)* 19: 154–164.
Griffin SM and Spaldin NA (2017) On the relationship between topological and geometric defects. *Journal of Physics: Condensed Matter* 29(34): 343001.
Grossman MI (2014) John Dalton and the London atomists: William and Bryan Higgins, William Austin, and new Daltonian doubts about the origin of the atomic theory. *Notes and Records: the Royal Society Journal of the History of Science* 68(4): 339–356.
Guralnik GS, Hagen CR, and Kibble TWB (1964) Global conservation laws and massless particles. *Physical Review Letters* 13: 585–587. https://doi.org/10.1103/PhysRevLett.13.585.
Guralnik GS, Hagen CR, and Kibble TWB (1968) Broken symmetries and the goldstone theorem. *Advances in Particle Physics* 2: 567–708.
Higgs PW (1964) Broken symmetries and the masses of gauge bosons. *Physical Review Letters* 13(16): 508.
Higgs PW (1966) Spontaneous symmetry breakdown without massless Bosons. *Physical Review* 145: 1156–1163. https://doi.org/10.1103/PhysRev.145.1156.
Hochberg Y, Kahn Y, Lisanti M, Zurek KM, Grushin AG, Ilan R, Griffin SM, Liu Z-F, Weber SF, and Neaton JB (2018) Detection of sub-Mev dark matter with three-dimensional Dirac materials. *Physical Review D* 97(1): 015004.
Kadin AM and Goldman AM (1982) Pair-field susceptibility and superconducting tunneling: A macroscopic approach. *Physical Review B* 25: 6701–6710. https://doi.org/10.1103/PhysRevB.25.6701.

Katsumi K, Tsuji N, Hamada YI, Matsunaga R, Schneeloch J, Zhong RD, Gu GD, Aoki H, Gallais Y, and Shimano R (2018) Higgs mode in the *d*-wave superconductor $Bi_2Sr_2CaCu_2O_{8+x}$ driven by an intense terahertz pulse. *Physical Review Letters* 120: 117001. https://doi.org/10.1103/PhysRevLett.120.117001.

Kibble TWB (1976) Topology of cosmic domains and strings. *Journal of Physics A: Mathematical and General* 9(8): 1387.

Littlewood PB and Varma CM (1982) Amplitude collective modes in superconductors and their coupling to charge-density waves. *Physical Review B* 26: 4883–4893. https://doi.org/10.1103/PhysRevB.26.4883.

Méasson M-A, Gallais Y, Cazayous M, Clair B, Rodière P, Cario L, and Sacuto A (2014) Amplitude Higgs mode in the 2H-$NbSe_2$ superconductor. *Physical Review B* 89: 060503. https://doi.org/10.1103/PhysRevB.89.060503.

Nambu Y (1960) Quasi-particles and gauge invariance in the theory of superconductivity. *Physical Review* 117(3): 648.

Nambu Y and Jona-Lasinio G (1961) Dynamical model of elementary particles based on an analogy with superconductivity. II. *Physical Review* 124(1): 246.

Nielsen HB and Chadha S (1976) On how to count goldstone bosons. *Nuclear Physics B* 105(3): 445–453.

Pekker D and Varma CM (2015) Amplitude/Higgs modes in condensed matter physics. *Annual Review of Condensed Matter Physics* 6(1): 269–297.

Peskin ME and Schroeder DV (2018) *An Introduction to Quantum Field Theory*. CRC Press.

Podolsky D, Auerbach A, and Arovas DP (2011) Visibility of the amplitude (Higgs) mode in condensed matter. *Physical Review B* 84: 174522. https://doi.org/10.1103/PhysRevB.84.174522.

Rescher N (2013) *Cosmos and Logos: Studies in Greek Philosophy*, vol. 1. Walter de Gruyter.

Ryan SM (2023) *INT lectures on hadron spectroscopy*. https://www.maths.tcd.ie/ryan/INT2012/. (accessed 20.04.23).

Schwarz L, Fauseweh B, Tsuji N, Cheng N, Bittner N, Krull H, Berciu M, Uhrig GS, Schnyder AP, Kaiser S, et al. (2020) Classification and characterization of nonequilibrium Higgs modes in unconventional superconductors. *Nature Communications* 11(1): 287.

Shimano R and Tsuji N (2020) Higgs mode in superconductors. *Annual Review of Condensed Matter Physics* 11: 103–124.

Taufertshöfer N, Garcia-Sciveres M, and Griffin SM (2023) Broad-range directional detection of light dark matter in cryogenic ice. *arXiv:2301.04778*.

Vollhardt D and Wolfle P (2013) *The Superfluid Phases of Helium 3*. Courier Corporation.

Phase transitions, spontaneous symmetry breaking, and Goldstone's theorem

Jürg Fröhlich, Institute for Theoretical Physics, ETH Zurich, Zurich, Switzerland

© 2024 Elsevier Ltd. All rights reserved.

Introduction to spontaneous symmetry breaking and the Higgs mechanism 158
The phase transition in the $\lambda|\phi|_3^4$-Euclidean field theory in three dimensions 160
Proof of the Goldstone theorem for Euclidean field theories 164
  The example of $\lambda|\phi|^4$-theory 166
Phase transitions and symmetry breaking in classical and quantum lattice systems 167
Conclusion 171
Acknowledgments 171
References 171

Abstract

Some important rigorous results on phase transitions accompanied by the spontaneous breaking of symmetries in statistical mechanics and relativistic quantum field theory are reviewed. Basic ideas, mainly inspired by quantum field theory, underlying the proofs of some of these results are sketched. The Goldstone theorem is proven, and the Mermin–Wagner–Hohenberg theorem concerning the absence of continuous symmetry breaking in one and two dimensions is recalled. Comments concerning rigorous results on the Kosterlitz–Thouless transition in the two-dimensional classical XY model are made.

Key points

- A heuristic introduction to the subject of spontaneous symmetry breaking, Goldstone's theorem and the Anderson–Higgs mechanism in the context of quantum field theory is given. The Wick rotation from real to imaginary time and the equivalence of real-time relativistic quantum field theory (RQFT) and imaginary-time Euclidean field theory (EFT) are recalled.
- The $\lambda|\phi|^4$-Euclidean field theory of a real or complex scalar field ϕ in three dimensions is introduced. Its relevance for understanding various systems of statistical mechanics and condensed matter physics, for example, Bose gases, is commented upon. It is shown that the broken-symmetry phase of the theory of a complex field exhibits massless modes, in accordance with the Goldstone theorem.
- A general proof of the Goldstone theorem in the formalism of EFT is presented. The example of $\lambda|\phi|^4$-theory of a complex scalar field in three dimensions is considered in more detail. Bounds on critical exponents for the susceptibility of the theory and its correlation length, as phase transition points in zero magnetic field are approached, are reviewed.
- A summary of results on phase transitions accompanied by spontaneous symmetry breaking for classical and quantum (lattice) spin systems is presented. The role of "Reflection Positivity" and "Infrared Bounds" in the analysis of phase transitions is emphasized. For the classical XY model, the usefulness of a representation as a vortex gas for the analysis of the massless low-temperature phase and for the analysis of the Kosterlitz–Thouless transition is indicated.

Introduction to spontaneous symmetry breaking and the Higgs mechanism

This contribution is **not** an exhaustive review of the subject of spontaneous breaking of (continuous) symmetries or its absence, the Goldstone theorem, the Mermin–Wagner–Hohenberg theorem, the Anderson–Higgs mechanism, etc. My modest goal is to provoke the readers' interest in this subject, to draw attention to the fruitful intertwining between statistical mechanics and particle physics, in particular quantum field theory, and to draw some attention to the more mathematical literature on these matters. I will not state the relevant results in all detail, let alone describe proofs. For further information, the readers are invited to consult the papers quoted in the text.

Phase transitions in systems of condensed matter have been studied ever since the 19th century, using the formalism of thermodynamics, by *Clausius, Clapeyron, Maxwell, Gibbs* and others. Their findings are well known and are taught in every introductory course on the theory of heat. Toward the end of the 19th and at the beginning of the 20th century, statistical mechanics was created by Maxwell, *Boltzmann*, Gibbs, and *Einstein.* The first example of a phase transition accompanied by the breaking of a continuous symmetry, treated by using the methods of equilibrium statistical mechanics, was *Bose–Einstein*

https://doi.org/10.1016/B978-0-323-90800-9.00275-4

condensation exhibited by ideal Bose gases when the temperature is lowered at some fixed positive density. Further examples relevant for the description of liquid–gas transitions and anisotropic magnetism, mostly with discrete symmetries, were studied subsequently. A famous model in this context is the Ising model. The phenomena of superconductivity and ferromagnetism inspired many further efforts to understand phase transitions, spontaneous symmetry breaking, and critical phenomena near continuous transitions. It is not the purpose of this contribution to provide a detailed overview on this field. General surveys of equilibrium statistical mechanics, including the theory of phase transitions, can be found in the monographs (Ruelle, 1969; Bratteli and Robinson, 1979, 1981; Simon, 1993), which are written in the style of mathematical physics. Rich sources of results on continuous phase transitions, symmetry breaking and critical phenomena are Domb and Green (1972–1976), Domb and Lebowitz (1983–2001), and Itzykson and Drouffe (1989). Phase transitions accompanied by spontaneous symmetry breaking and the Anderson–Higgs mechanism later came to play a fundamental role in particle physics; see Weinberg (1995–2000) and references given there. As already mentioned, a very attractive feature of this subject is that it is a great example of productive interactions between statistical and condensed matter physics, on one hand, and particle physics and quantum field theory, on the other hand.

I begin my tale by briefly recalling the heuristics of spontaneous symmetry breaking and the Anderson–Higgs mechanism in relativistic quantum field theory (RQFT). The simplest theory is one of a complex scalar field ϕ, which I write in polar coordinates

$$\phi(x) = e^{i\theta(x)}\,\rho(x), \qquad x \in \mathbb{M}^4, \tag{1}$$

where $\theta(x) \in [0, 2\pi)$ is the azimuthal angular variable and $\rho(x) \equiv |\phi(x)| \in [0, \infty)$ is the radial variable, for every space-time point x in Minkowski space $\mathbb{M}^4$. The symmetry group of the theory is $U(1)$. In order to distinguish spontaneous symmetry breaking from the Anderson–Higgs mechanism, I couple ϕ to a $U(1)$-gauge field/connection, A_μ, with $\mu = 0, 1, 2, 3$. In studies of superconductivity this gauge field is the electromagnetic four-vector potential. A typical action functional for the fields ϕ and A_μ has the form

$$S(\phi, A_\mu) = \frac{1}{2}\int d^4x\left\{[\partial_\mu + ieA_\mu(x)]\bar{\phi}(x)\cdot[\partial^\mu - ieA^\mu(x)]\phi(x) - U(|\phi(x)|)\right\}, \tag{2}$$

where e is the gauge charge (i.e., twice the elementary electric charge, in the case of superconductivity) and $U(|\phi|)$ is the self-interaction potential for the scalar field, which is assumed to be invariant under the transformation $\phi \mapsto e^{i\theta_0}\,\phi$, where $e^{i\theta_0}$ belongs to the symmetry group $U(1)$. If ϕ is written in polar coordinates, $S(\phi, A_\mu)$ takes the form

$$S(\phi, A_\mu) = \frac{1}{2}\int d^4x\left\{\rho(x)^2[\partial_\mu\theta(x) - eA_\mu(x)]\cdot[\partial^\mu\theta(x) - eA^\mu(x)] + \partial_\mu\rho(x)\cdot\partial^\mu\rho(x) - U(\rho(x))\right\}. \tag{3}$$

I assume that the self-interaction potential $U(\rho)$ is nonnegative and has the shape of a Mexican hat, with a sharp minimum at $\rho = R > 0$ (so that $\rho(x)^2 \approx R^2$).

One distinguishes the following two situations.

1. *Continuous symmetry breaking with Goldstone bosons:* We set $e = 0$, so that the gauge field is absent, and write $S(\phi)$ instead of $S(\phi, A_\mu)$. Then

$$\begin{aligned} S(\phi) &\simeq S_1(\theta) + S_2(\rho), \quad \text{where} \\ S_1(\theta) &= (R^2/2)\int d^4x\;\partial_\mu\theta\cdot\partial^\mu\theta, \end{aligned} \tag{4}$$

$$S_2(\rho) = \frac{1}{2}\int d^4x\;\left\{\partial_\mu\rho\cdot\partial^\mu\rho - U(\rho)\right\}, \tag{5}$$

and the vacuum expectation value of ϕ in a pure vacuum state, $|\varnothing\rangle_{\theta_0} \equiv |\varnothing\rangle$, can be expected to be given by

$$\langle\varnothing|\phi|\varnothing\rangle \approx e^{i\theta_0}R \neq 0, \qquad \text{for some}\;\; \theta_0 \in [0, 2\pi).$$

The fact that $\langle\varnothing|\phi|\varnothing\rangle \neq 0$ and the appearance of the angular parameter θ_0 are a signal of spontaneous symmetry breaking. Expression (4) shows that the modes described by the angular field θ are massless—these are the modes describing the Goldstone bosons that accompany spontaneous symmetry breaking—while the fluctuations of the radial modes described by the field ρ around the minimum of U at $\rho = R$ may seem to be massive, assuming that the curvature of $U(\rho)$ at $\rho = R$ is positive. Actually, these modes are unstable and decay into pairs of Goldstone bosons. This can be understood by expanding the self-interaction potential $U(|\phi|)$ around one of its minima and then noticing that the fluctuations of the radial field ρ couple to pairs of Goldstone bosons. There is a rigorous result confirming this claim (see Dunlop and Newman, 1975).

Note that, for a theory in *two* space-time dimensions, the form of the action functional (4) suggests that the fluctuations of the angular field θ diverge in the infrared, which implies that there is no spontaneous symmetry breaking. This is the content of the Mermin–Wagner–Hohenberg (-Coleman) theorem. Continuous symmetries can only be broken in space-times of dimension ≥ 3.

2. *Anderson–Higgs mechanism:* The gauge charge e does *not* vanish, and A_μ is a dynamical gauge field, with a gauge-field action given by

$$S_0(A_\mu) = \frac{1}{4}\int d^4x\, F_{\mu\nu}\cdot F^{\mu\nu}.$$

   We may then set

$$\hat{A}_\mu := A_\mu - e^{-1}\partial_\mu\theta.$$

   Obviously, the vector potential $\hat{A}_\mu$ is gauge-equivalent to A_μ. We observe that the angular field θ can be eliminated from the theory by a gauge transformation, and the action $S(\phi, A_\mu)$ becomes

$$S(\rho, A_\mu) \simeq \frac{1}{4}\int d^4x\left\{\hat{F}_{\mu\nu}\cdot\hat{F}^{\mu\nu} + 2e^2R^2\hat{A}_\mu\,\hat{A}^\mu\right\} + S_2(\rho),$$

   where we have used that $\hat{F}_{\mu\nu} = F_{\mu\nu}$ (by gauge invariance).

   We observe that the gauge field $\hat{A}$ is **massive**, with a mass proportional to eR, and the radial modes described by ρ remain present and are massive; these modes are the ones that describe the Higgs bosons. Actually, Higgs bosons are usually unstable particles—resonances—that decay into lighter particles, which the field ρ couples to.

Spontaneous symmetry breaking has first been studied, quite a long time ago, for example in the theory of ferromagnetism (Weiss, 1907; Renker, 1913; Heisenberg, 1928) and, in particle physics, in the celebrated work of Nambu and Jona-Lasinio (1961a, b). The fact that the spontaneous breaking of a continuous symmetry is accompanied by the emergence of massless scalar or pseudo-scalar bosons is the content of the Goldstone theorem (Goldstone, 1961; Goldstone et al., 1962).

The arguments leading up to the Higgs mechanism described in item 2 go back, originally, to work by Stückelberg (1938a, b, c) and Anderson (1962). In particle physics, the Higgs mechanism was then studied by Englert and Brout (1964), Higgs (1964), and Guralnik et al. (1964). The Higgs mechanism also works for *non-Abelian gauge fields*, which is relevant for the Standard Model of Particle Physics. The renormalizability of non-Abelian gauge fields coupled to Higgs scalars has first been analyzed in 'tHooft and Veltman (1972), and in Lee and Zinn-Justin (1972a, b, c).

If the scalar field ϕ is coupled to a dynamical gauge field A_μ, then it does not make sense to speak of spontaneous symmetry breaking. The vacuum expectation value of ϕ vanishes unless a special gauge is chosen, in which case it can be given an arbitrary value that is irrelevant for the physical properties of the theory. A manifestly gauge-invariant formulation of the Higgs mechanism (not involving any artificial assumptions concerning the vacuum expectation value of the Higgs scalar ϕ) has been given in Fröhlich et al. (1981).

The following survey is limited to the mathematical theory of spontaneous symmetry breaking, the Goldstone theorem and the Mermin–Wagner–Hohenberg theorem in the context of statistical mechanics and condensed matter physics. I do not pursue the study of the Higgs mechanism; but see, for example, Weinberg (1995–2000).

If a Wick rotation to imaginary time is performed on an RQFT, one obtains what is called a *Euclidean field theory* (EFT). It has been shown by Osterwalder and Schrader (1975) (see also Glaser, 1974) that from the Euclidean Green functions, also called Schwinger functions, of an EFT satisfying *Reflection Positivity* (which is a manifestation of unitarity at imaginary time) one can reconstruct the vacuum expectation values of products of the relativistic (real-time) fields of a corresponding RQFT. EFT's of scalar fields can be viewed as systems of statistical mechanics in a state of thermal equilibrium, as first understood by *Schwinger*, *Symanzik*, and *Nelson*; see Simon (1974), Glimm and Jaffe (1981), and references given there. For classical and quantum lattice systems, Reflection Positivity expresses the self-adjointness of the transfer matrix of the system in question and gives rise to a variety of crucial bounds on numerous physical quantities. It plays a central role in many studies of phase transitions and symmetry breaking in EFT and in important models of classical and quantum lattice systems, as indicated below.

After a sketch of how the phase transition accompanied by continuous symmetry breaking is treated in a concrete example of EFT, namely $\lambda|\phi|^4$-theory in three dimensions (see Section "The phase transition in the $\lambda|\phi|^4_3$-Euclidean field theory in three dimensions"), I will present a proof of the Goldstone theorem in the formalism of EFT (Section "Proof of the Goldstone theorem for Euclidean field theories") and outline consequences for $\lambda|\phi|^4$-theory in three dimensions (Section "The example of $\lambda|\phi|^4$-theory"). In Section "Phase transitions and symmetry breaking in classical and quantum lattice systems," I focus attention on systems of classical and quantum statistical mechanics in states of thermal equilibrium, and I will summarize some important results for lattice theories; see also Fröhlich (1978, 2011) for more detailed surveys.

The phase transition in the $\lambda|\phi|^4_3$-Euclidean field theory in three dimensions

The analysis of the phase transition in $\lambda|\phi|^4$-theory in three dimensions presented in this section follows the original work reported in Fröhlich et al. (1976).

Henceforth I will always assume that the Wick rotation to purely imaginary time has been made (see Jost, 1965; Osterwalder and Schrader, 1975), and I will thus only consider Euclidean field theories. Such theories are equivalent to classical Hamiltonian systems in a state of thermal equilibrium. In this interpretation, the Euclidean action functional becomes the Hamilton functional of the classical system. I will focus my attention on $\lambda|\phi|^4$-theory at imaginary time.

The Euclidean action functional of $\lambda|\phi|^4$-theory is given by

$$\begin{aligned} S_\Lambda(\phi) &:= \int_\Lambda d^3x \Big\{ \frac{1}{2} |\nabla \phi(x)|^2 + U(|\phi(x)|) + c.t. \Big\}, \quad \text{with} \\ U(|\phi|) &= \frac{\lambda}{4!} \left[|\phi|^2 - R^2 \right]^2 - h\varphi^1, \end{aligned} \tag{6}$$

where $\phi = (\varphi^1, \ldots, \varphi^N)$ is a scalar field with $N = 1, 2, \ldots$ real-valued components (equivalent to a complex scalar field, for $N = 2$), Λ is a cube in $\mathbb{R}^3$ with sides of length L and with periodic boundary conditions imposed at the boundary $\partial\Lambda$, "*c.t.*" stands for a logarithmically divergent mass counterterm, $\delta m^2(\lambda)\ |\phi|^2$ (with $\delta m^2(\lambda) \propto \lambda^2$), and a divergent (c-number) vacuum-energy counterterm, $\lambda > 0$ is a coupling constant (not renormalized in the three-dimensional theory), R^2 is a real parameter tuning the location of the minima of U in field space and thereby driving a phase transition accompanied by spontaneous symmetry breaking, and $h \geq 0$ plays the role of a small symmetry breaking "magnetic field" in the 1-direction in field space.

We note that, for $h = 0$, the $\lambda|\phi|^4$-theory with action functional as given in (6) has a global $O(N)$ symmetry (with $O(1) = \mathbb{Z}_2$). The theory is of obvious physical interest. For $N = 1$, it is expected to have the same critical properties as the three-dimensional Ising model, thus describing critical phenomena encountered in liquid-gas transitions. Next, we consider the theory of a complex scalar field equivalent to the theory of a field with $N = 2$ real scalar components.

- This theory turns out to describe the "mean-field limit" of translation-invariant Bose gases with repulsive two-body interactions of very short range (approaching δ-function interactions); see, for example, Fröhlich et al. (2020, 2023). The fact that $\lambda|\phi|^4$-theory undergoes a phase transition accompanied by spontaneous symmetry breaking, the proof of which is sketched below, is an indication that Bose gases with weak repulsive two-body interactions of short range exhibit Bose–Einstein condensation, as the temperature is lowered at some fixed positive density—a conjecture/claim whose mathematical proof has remained elusive, so far.
- The critical phenomena observed near the point in parameter space where $\lambda|\phi|^4$-theory with $N = 2$ real scalar fields undergoes a continuous phase transition are expected to be identical to those observed for the classical XY-model (rotator) and to be relevant for understanding critical phenomena exhibited by superfluid Helium, to mention an example. Moreover, for $N = 3$, the theory is expected to describe critical phenomena observed in three-dimensional ferromagnets near their critical point. See Domb and Green (1972–1976), Domb and Lebowitz (1983–2001), and references given there.

In $d = 3$ dimensions, $\lambda|\phi|^4$-theory with an action functional given by (6) is a superrenormalizable theory that can be constructed nonperturbatively by using functional integration. There are no field strength and coupling constant renormalizations. It makes perfect mathematical sense! The control of ultraviolet divergences of the theory was first accomplished in Glimm and Jaffe (1973), the infinite-volume limit, $L \to \infty$, was shown to exist in Feldman and Osterwalder (1975, 1977) and Park (1977); see also Glimm and Jaffe (1981) and Brydges et al. (1983).

In the following, we consider the theory in the infinite-volume ("thermodynamic") limit $L \to \infty$, unless stated otherwise. If $\lambda = 0$ (and $L = \infty$) the theory is determined by the free-field *Gaussian measure* of mean 0 and covariance $\delta^{ij}(-\Delta)^{-1}$ defined on a space of $\mathbb{R}^N$-valued tempered distributions, $\mathcal{S}'(\mathbb{R}^3)^{\times N}$; ($\Delta$ is the three-dimensional Laplacian). The Euclidean one-point and two-point Green functions, that is, the first and second moments of the free-field Gaussian measure, are given by

$$\left\langle \varphi^j(x) \right\rangle_0 \equiv 0, \quad \text{and} \quad \left\langle \varphi^i(x)\ \varphi^j(y) \right\rangle_0 = \frac{\delta^{ij}}{4\pi|x - y|}. \tag{7}$$

The two-point function, $\langle \varphi^i(x)\ \varphi^i(y) \rangle_0$, is given by the Green function of the Laplacian Δ, for all $i = 1, \ldots N$. In the following, $:(\cdot):$ indicates standard Wick ordering with respect to the massless free field introduced in (7); for example,

$$:\varphi^i(x)\ \varphi^j(y) := \varphi^i(x)\ \varphi^j(y) - \frac{\delta^{ij}}{4\pi|x - y|}.$$

We rewrite the contribution of the self-interaction potential $U(|\phi|)$ to the action functional S_Λ as follows:

$$\begin{aligned} U_\Lambda(R^2, h; |\phi|) &:= \int_\Lambda d^3x \left[: U(|\phi(x)|) : - \frac{\lambda R^4}{4!} \right] \\ &= \int_\Lambda d^3x \Big\{ \lambda : |\phi(x)|^4 : - \frac{\lambda R^2}{12} : |\phi(x)|^2 : - h\varphi^1(x) \Big\} \\ &= U_\Lambda(0, h; |\phi|) - \frac{\lambda R^2}{12} \int_\Lambda d^3x : |\phi(x)|^2 : . \end{aligned} \tag{8}$$

We then define the "partition function" of the theory by

$$Z_\Lambda(R^2, h) := Z_\Lambda(0,0)^{-1} \int \mathcal{D}\phi \ \exp\left[-\frac{1}{2} \int_\Lambda d^3x\ |\nabla\phi(x)|^2 + \frac{\lambda R^2}{6} : |\phi(x)|^2 : + c.t. \right] e^{-U_\Lambda(0,h;\ |\phi|)}, \tag{9}$$

and the "free energy" as

$$F(R^2, h) := \lim_{L\to\infty} L^{-3} \ell n Z_\Lambda (R^2, h). \tag{10}$$

The functional integral in (9) can be given a precise mathematical meaning (see Glimm and Jaffe (1981) and references given there). Expectation values with respect to the normalized functional measure appearing under the integral of the right side of (9) are denoted by $\langle(\cdot)\rangle_{R,h}$. The following properties of the function $F(R^2, h)$ are known.

I. $F(R^2, h)$ is a convex function of R^2, with

$$\frac{\lambda}{12}\left\langle : |\phi(0)|^2 : \right\rangle_{R,h} = \frac{\partial F(R^2, h)}{\partial R^2} \nearrow \infty, \quad \text{as} \quad R^2 \to +\infty. \tag{11}$$

II. For fields ϕ with $N = 1, 2, 3$ components, the function $F(R^2, h)$ is analytic in h away from the imaginary axis. This is a consequence of a generalized Lee–Yang theorem; see Lee and Yang (1952), Simon and Griffiths (1973), and Dunlop and Newman (1975).

These statements and the following analysis of the phase transition in $\lambda|\phi|^4$-theory in three dimensions are discussed in detail in Fröhlich et al. (1976).

From (11) it follows that, given a finite constant $M^2 > 0$, there exists a constant $R_M^2 < \infty$ such that

$$\left\langle : |\phi(0)|^2 : \right\rangle_{R,h} \geq M^2 > 0, \quad \text{for} \quad R^2 \geq R_M^2 \quad \text{and all} \quad h \geq 0. \tag{12}$$

Next we note that

$$\begin{aligned} \left\langle : |\phi(0)|^2 : \right\rangle_{R,h} &= \lim\nolimits_{y\to 0}\left\{ \langle \phi(y)\cdot\phi(0)\rangle_{R,h} - \frac{N}{4\pi|y|}\right\} \\ &= \lim\nolimits_{y\to 0}\left\{ \langle \phi(y)\cdot\phi(0)\rangle_{R,h}^c + \langle \varphi^1(0)\rangle_{R,h}^2 - \frac{N}{4\pi|y|}\right\}. \end{aligned} \tag{13}$$

Here $\langle(\cdot)\rangle_{R,h}^c$ stands for "connected (truncated) expectation values." Since the "magnetic field" h only couples to φ^1, we have that $\langle\varphi^i(0)\rangle_{R,h} = 0$, for $i = 2, \ldots, N$, by symmetry, but that

$$\left\langle \varphi^1(0)\right\rangle_{R,h} \geq 0, \quad \text{for} \quad h \geq 0. \tag{14}$$

In fact, $\langle\varphi^1(0)\rangle_{R,h}$ is an increasing function of h on the positive half-axis, as follows from the fact that the connected two-point function defines a positive quadratic form.

Next, we remind the readers of the so-called Källen–Lehmann representation of connected two-point functions (see, e.g., Jost (1965) and references given there), which says that

$$\begin{aligned} \left\langle \varphi^i(y)\cdot\varphi^i(0)\right\rangle_{R,h}^c &= \int_0^\infty d\mu^{(i)}(a^2)\left[-\Delta + a^2\right]^{-1}(y) \\ &\overset{d=3}{=} \int_0^\infty d\mu^{(i)}(a^2)\frac{e^{-a|y|}}{4\pi|y|}, \quad \text{for} \quad i = 1, \ldots, N, \end{aligned} \tag{15}$$

where $d\mu^{(i)} = d\mu^{(j)}$, for $i, j = 2, \ldots, N$. In $d = 3$ dimensions, $\lambda|\phi|^4$-theory is a canonical field theory (there is no field strength renormalization!). The real-time quantum fields satisfy equal-time canonical commutation relations; that is,

$$\left[\varphi^j(\vec{x}, t), \pi^k(\vec{y}, t)\right] = i\delta^{jk}\delta(\vec{x} - \vec{y}), \quad \text{where} \quad \pi^k = \dot{\varphi}^k,$$

and these commutation relations imply that

$$\int_0^\infty d\mu^{(i)}(a^2) = 1, \quad \forall \ i = 1, \ldots, N.$$

It then follows that

$$\langle \phi(y)\cdot\phi(0)\rangle_{R,h}^c - \frac{N}{4\pi|y|} \leq 0, \quad \forall \ y,$$

and, using (12) and (13), we conclude that

$$M^2 \leq \left\langle : |\phi(0)|^2 : \right\rangle_{R,h} \leq \left\langle \varphi^1(0)\right\rangle_{R,h}^2, \tag{16}$$

for $R^2 \geq R_M^2$, uniformly in $h \geq 0$. Thus, for R^2 large enough, the theory predicts "spontaneous magnetization," in the sense that

$$\lim_{h \searrow 0} \left\langle \varphi^1(o)\right\rangle_{R,h} =: M(R) > 0. \tag{17}$$

Spontaneous magnetization implies that the $O(N)$-symmetry of the action functional of the theory at $h = 0$—see (6)—is spontaneously broken. For one-component fields ($N = 1$), the existence of a phase transition accompanied by spontaneous breaking of the $\phi \to -\phi$—symmetry can also be proven in two dimensions; but the proof is more involved; (it is based on the so-called Peierls argument—see Glimm et al. (1975) and references given there). For $N \geq 2$, spontaneous magnetization, as stated in (17), implies that the Fourier transform of the two-point function satisfies a lower bound

$$\left\langle \hat{\varphi}^i(k)\ \hat{\varphi}^i(-k)\right\rangle_{R,h=0} \geq \frac{\mathfrak{R}}{|k|^2}, \quad \forall\ i = 2, \ldots, N, \tag{18}$$

for some positive constant $\mathfrak{R} = \mathcal{O}(M(R)^2)$, for small $M(R)$, which shows that, in two dimensions and for $N \geq 2$, $M(R)$ must vanish at $h = 0$, for arbitrary values of R^2, and there is no spontaneous breaking of the $O(N)$-symmetry, because $|k|^{-2}$ is not integrable at the origin ($k = 0$) in momentum space. The lower bound in (18) can be derived from the analysis in Mermin and Wagner (1966) and Mermin (1967) and can also be extracted from the material in Section "Proof of the Goldstone theorem for Euclidean field theories." For a more detailed analysis and further references see Wreszinski (1976), and vol. 2 of Simon (1993).

Next, I draw attention to the fact that, for $N \leq 3$, if the real part, Reh, of the magnetic field h does not vanish then the Green functions of the theory, such as $\langle \phi(x) \cdot \phi(0)\rangle_{R,h}$, are analytic functions of h, and the connected Green functions decay exponentially in the separation of the field insertion points; in particular $\langle \phi(x) \cdot \phi(0)\rangle^c_{R,h}$ decays exponentially in $|x|$ if Re$h \neq 0$. This implies that, for real $h \neq 0$, the physical mass of all modes described by the theory is strictly positive. For proofs see, for example, Fröhlich and Rodriguez (2012, 2017) and references given there. But, for theories with fields of $N \geq 2$ components at $h = 0$, the Green functions have slow power-law decay if the spontaneous magnetization, $M(R)$, does not vanish. In particular, the susceptibility

$$\chi(R, h) := \int_{\mathbb{R}^3} d^3x \left\langle \varphi^i(x)\ \varphi^i(0)\right\rangle_{R,h}, \quad \text{for} \quad i \geq 2, \tag{19}$$

has the property that if the spontaneous magnetization $M(R) = \lim_{h \searrow 0} \langle \varphi^1(0)\rangle_{R,h}$ is strictly positive then

$$\chi(R, h) \simeq \frac{M(R)}{h}, \quad \text{as} \quad h \searrow 0. \tag{20}$$

Hence, if R^2 is chosen such that there is spontaneous magnetization, in the sense that $M(R) > 0$, then, at $h = 0\,+$, the two-point Green functions $\langle \varphi^i(x)\ \varphi^i(0)\rangle_{R,0+}$, $i \geq 2$, have nonintegrable decay in x, which shows that there must be massless modes in the theory. It may be appropriate to sketch the proof of (20). We consider a change of variables in the (φ^1, φ^2)-plane of field space, namely

$$\begin{aligned} \varphi^1_\theta &:= \quad \cos\theta\ \varphi^1 + \sin\theta\ \varphi^2, \\ \varphi^2_\theta &:= -\sin\theta\ \varphi^1 + \cos\theta\ \varphi^2. \end{aligned} \tag{21}$$

where θ is an x-independent angle. In the following, I drop reference to the parameter R (which will be kept fixed) from my notations and rewrite the action functional, $S(\phi)$, of the theory introduced in (6) as

$$S(\phi) = \tilde{S}(\phi) - h \int d^3x\ \varphi^1(x),$$

where the functional $\tilde{S}(\phi)$ is manifestly $O(N)$-invariant. Then we have that

$$\begin{aligned} 0 &= \langle \varphi^2(0)\rangle_h \\ &= \frac{1}{Z(h)} \int \mathcal{D}\phi\ e^{-\tilde{S}(\phi)+h\int d^3x\ \varphi^1(x)} \varphi^2(0) \\ &= \frac{1}{Z(h)} \int \mathcal{D}\phi_\theta\ e^{-\tilde{S}(\phi)+h\int d^3x\ \varphi^1_\theta(x)}\ \varphi^2_\theta(0) \end{aligned} \tag{22}$$

identically in θ, where we have used that $\tilde{S}(\phi_\theta) = \tilde{S}(\phi)$, by $O(N)$-symmetry. We note that

$$\mathcal{D}\phi_\theta = \mathcal{D}\phi,$$

because the Jacobian of the change of variables in (21) is unity. By taking the derivative in the variable θ and subsequently setting $\theta = 0$ the identity in (22) is seen to imply that

$$\begin{aligned} 0 &= \tfrac{d}{d\theta} \langle \varphi^2(0)\rangle_h \big|_{\theta=0} \\ &= \frac{1}{Z(h)} \int \mathcal{D}\phi\ e^{-\tilde{S}(\phi)+h\int d^3x\ \varphi^1(x)} \left[h \int d^3x\ \varphi^2(x)\right]\ \varphi^2(0) \\ &\quad - \frac{1}{Z(h)} \int \mathcal{D}\phi\ e^{-\tilde{S}(\phi)+h\int d^3x\ \varphi^1(x)}\ \varphi^1(0) \\ &= h\ \chi(h) - \langle \varphi^1(0)\rangle_h. \end{aligned} \tag{23}$$

After re-introducing the parameter R in our notations we see that (23) and (17) imply that

$$\chi(R,h) = h^{-1}\langle \varphi^1(0)\rangle_{R,h} \geq \frac{M(R)}{h},$$

which yields (20). The arguments presented here have been worked out in Spencer and Fröhlich (2013–2014).

Proof of the Goldstone theorem for Euclidean field theories

The following analysis is inspired by a paper on the Goldstone theorem; see Symanzik (1967).

In comparison with the previous section, we consider a somewhat more general set-up and consider an RQFT of a scalar field ϕ in $d \geq 3$ dimensions with a continuous internal symmetry described by a compact Lie group G whose Lie algebra is denoted by $\mathfrak{g}$. A symmetry transformation generated by an element $X \in \mathfrak{g}$ corresponds to a conserved Noether current $j^{\mu}_{X}(x), x = (\vec{x}, t) \in \mathbb{M}^d$, of the theory; (see, e.g., Buchholz et al. (1986) for a somewhat abstract treatment of Noether's theorem in RQFT). In the example of $\lambda|\phi|^4$-theory with an action functional as in (6), setting $h = 0$, the symmetry group is $G = O(N)$, and, for $X \equiv X_{ij} := E_{ij} - E_{ji}$, where E_{ij} is a matrix unit with a 1 in the position ij, for $i, j = 1, \ldots, N$, the corresponding conserved Noether current is given by

$$j^{\mu}_{X_{ij}}(x) = i(\partial^{\mu}\varphi^{i}(x))\varphi^{j}(x) - i(\partial^{\mu}\varphi^{j}(x))\varphi^{i}(x), x \in \mathbb{M}^d. \tag{24}$$

Returning to the general framework, the field ϕ of the theory is assumed to transform under a representation π of the symmetry group G, which we assume not to contain the trivial representation of G as a subrepresentation. A generator $X \in \mathfrak{g}$ therefore acts on field space in the representation $d\pi$ of $\mathfrak{g}$, that is,

$$d\pi(X): \ \phi(x) \mapsto d\pi(X)\phi(x) \equiv \phi^{X}(x).$$

Since the currents j^{μ}_{X} are conserved, that is, satisfy the continuity equation,

$$\partial_{\mu} j^{\mu}_{X}(x) = 0, \tag{25}$$

the charges

$$Q_X := \int\limits_{t=\text{const.}} d^{d-1}x \ \ j^{0}_{X}(\vec{x}, t) \tag{26}$$

are conserved, and we have that

$$[Q_X, \phi(x)] = \phi^{X}(x). \tag{27}$$

We now assume that the theory has a vacuum state, denoted by $|\varnothing\rangle =: \Omega_{\phi_c}$, which is **not** invariant under the action of G on the state space of the theory, i.e, breaks the symmetry G spontaneously, with

$$\langle \Omega_{\phi_c}|\phi(x)|\Omega_{\phi_c}\rangle = \phi_c \neq 0. \tag{28}$$

Let H_{ϕ_c} denote the subgroup of G that leaves ϕ_c invariant, and let $\mathfrak{h}_{\phi_c}$ denote its Lie algebra. Then

$$\phi^{X}_{c} \equiv d\pi(X)\phi_c = 0, \qquad \forall X \in \mathfrak{h}_{\phi_c}.$$

Since π does not contain the trivial representation of G as a subrepresentation, $\mathfrak{h}_{\phi_c}$ is a subspace of $\mathfrak{g}$ of dimension smaller than the dimension of $\mathfrak{g}$. For a generator $Y \in \mathfrak{g}$ that belongs to the complement, $\mathfrak{h}^{\perp}_{\phi_c}$, of $\mathfrak{h}_{\phi_c}$, we then have that

$$\phi^{Y}_{c} := \langle \Omega_{\phi_c}|\phi^{Y}(x)|\Omega_{\phi_c}\rangle \neq 0. \tag{29}$$

Combining (27) with (29), we find that

$$\langle \Omega_{\phi_c}|[Q_Y, \phi(0)]|\Omega_{\phi_c}\rangle = \langle \Omega_{\phi_c}|\phi^{Y}(0)|\Omega_{\phi_c}\rangle = d\pi(Y)\phi_c \equiv \phi^{Y}_{c}, \tag{30}$$

for an arbitrary $Y \in \mathfrak{h}^{\perp}_{\phi_c}$. On the left side of (30) we re-write Q_Y using (26) and then use a standard formula involving the Hamiltonian $H \geq 0$ of the associated RQFT. This yields

$$\begin{aligned}
\phi^{Y}_{c} &= \langle \Omega_{\phi_c}|[Q_Y, \phi(0)]|\Omega_{\phi_c}\rangle \\
&= \int\limits_{t=0} d^{d-1}x \left\langle \Omega_{\phi_c}\middle|\left[j^{0}_{Y}(\vec{x}, 0), \phi(0)\right]\middle|\Omega_{\phi_c}\right\rangle \\
&= \lim_{\varepsilon \searrow 0} \int d^{d-1}x \left\langle \Omega_{\phi_c}\middle| j^{0}_{Y}(\vec{x}, 0)e^{-\varepsilon H}\phi(0) - \phi(0)e^{-\varepsilon H} j^{0}_{Y}(\vec{x}, 0)\middle|\Omega_{\phi_c}\right\rangle \\
&= \lim_{\varepsilon \searrow 0} \int d^{d-1}x \left\langle \left[j^{0}_{Y}(\vec{x}, \varepsilon) - j^{0}_{Y}(\vec{x}, -\varepsilon)\right] \phi(0)\right\rangle,
\end{aligned} \tag{31}$$

where the integrand on the very right side of these equations is a Euclidean Green or Schwinger function of the 0 component of the current j_Y^μ and the field ϕ (which, in the example of $\lambda|\phi|^4$-theory in two or three dimensions, can be expressed by a functional integral). We define distributions $W_Y^\mu(x),\ x = (\vec{x}, t) \in \mathbb{E}^d$, by

$$\begin{aligned} W_Y^\mu(x) &:= \left\langle j_Y^\mu(\vec{x}, t)\ \phi(0) \right\rangle \\ &= \begin{cases} \left\langle \Omega_{\phi_c} \middle| j_Y^\mu(\vec{x}, 0)\ e^{-tH}\ \phi(0) \middle| \Omega_{\phi_c} \right\rangle, & \text{for} \quad t > 0, \\ \left\langle \Omega_{\phi_c} \middle| \phi(0)\ e^{tH}\ j_Y^\mu(\vec{x}, 0) \middle| \Omega_{\phi_c} \right\rangle, & \text{for} \quad t < 0, \end{cases} \end{aligned} \tag{32}$$

where we have used that $e^{\pm tH}|\Omega_{\phi_c}\rangle = |\Omega_{\phi_c}\rangle$, for arbitrary t. Combining (30) through (32), we find that

$$\phi_c^Y = \lim_{\varepsilon \searrow 0} \int_{S_\varepsilon} d\sigma_\mu(x)\ W_Y^\mu(x) \neq 0, \tag{33}$$

where S_ε is the union of two oriented planes given by

$$S_\varepsilon := \bigcup_{t = \pm\varepsilon} \left\{ x \in \mathbb{R}^d \mid x = (\vec{x}, t), t = \text{const.} \right\},$$

and $d\sigma_\mu(\cdot)$ is the oriented surface measure on S_ε. Next, we use that j_Y^μ is a conserved current, that is, that it satisfies the continuity equation (25) (with X replaced by Y), which implies that

$$\partial_\mu W_Y^\mu(x) = 0, \quad \text{for} \quad x \overset{!}{\neq} 0. \tag{34}$$

This identity will permit us to apply Gauss' theorem in a useful way. We define two "half-balls," $B_{r,\varepsilon}^+$ and $B_{r,\varepsilon}^-$, in $\mathbb{R}^d$ with oriented boundaries by

$$\begin{aligned} B_{r,\varepsilon}^+ &:= \left\{ x = (\vec{x}, t) \,\middle|\, |x| \le r, t \ge \varepsilon > 0 \right\}, \quad \text{with} \quad |x| := \sqrt{x^2}, \\ B_{r,\varepsilon}^- &:= \left\{ x = (\vec{x}, t) \,\middle|\, |x| \le r, t \le -\varepsilon < 0 \right\}. \end{aligned} \tag{35}$$

Since $0 \notin B_{r,\varepsilon}^+ \cup B_{r,\varepsilon}^-$, we can apply Gauss' theorem to $W_Y^\mu|_{B_{r,\varepsilon}^+ \cup B_{r,\varepsilon}^-}$, which then yields

$$\begin{aligned} 0 \neq \phi_c^Y &= \lim_{\varepsilon \searrow 0} \left\{ \int_{S_\varepsilon} d\sigma_\mu(x)\ W_Y^\mu(x) + \sum_{\kappa = \pm} \underbrace{\int_{\partial B_{r,\varepsilon}^\kappa} d\sigma_\mu(x)\ W_Y^\mu(x)}_{=0,\ \text{by (34) and Gauss' theorem}} \right\} \\ &= \int_{\partial B_r} d\sigma_\mu(x)\ W_Y^\mu(x), \end{aligned} \tag{36}$$

for an arbitrary $r > 0$, where B_r is a ball in $\mathbb{R}^d$ of radius r centered at the origin, $x = 0$; (the reader is invited to make a drawing to verify this). The second (last) equality in (36) follows by using Gauss' theorem again. Euclidean covariance of W_Y^μ implies that

$$W_Y^\mu(x) = \phi_c^Y \cdot x^\mu f(|x|),$$

for some rotation-invariant function f. It then follows from (36) that

$$W_Y^\mu(x) = \frac{\phi_c^Y}{s_{d-1}} \cdot \frac{x^\mu}{|x|^d}, \tag{37}$$

where s_{d-1} is the area of the $(d\text{-}1)$-dimensional unit sphere in d dimensions. The definition of W_Y^μ in (32) and Eq. (37) show that the field ϕ and the charge density j_Y^0 couple the vacuum state, Ω_{ϕ_c}, of the theory to a massless scalar one-particle state, which describes a Goldstone boson. Apparently, there are at least as many distinct Goldstone bosons in this theory as there are linearly independent generators in the complement, $\mathfrak{h}_{\phi_c}^\perp$, of $\mathfrak{h}_{\phi_c} \subset \mathfrak{g}$. Furthermore, if $\phi_c \neq 0$ then the connected two-point function of the field ϕ has the form

$$\langle \phi(x) \cdot \phi(0) \rangle^c = \int_0^\infty d\mu(a^2) \left[-\Delta + a^2 \right]^{-1}(x), \tag{38}$$

with

$$d\mu(a^2) = \mathfrak{R} \cdot \delta(a^2)\ da^2 + \text{regular at } a^2 = 0, \tag{39}$$

where $\mathfrak{R}$ is the residue of a one-particle pole of zero mass.

Well, we have apparently just recovered a (somewhat novel) proof of the Goldstone theorem in the imaginary-time (Euclidean) formalism of quantum field theory; (see Symanzik (1967) for the original arguments).

In two dimensions, the residue $\mathfrak{R}$ must vanish if the two-point function of the field ϕ is well defined. We thus conclude that ϕ_c must vanish, that is, continuous symmetries cannot be broken in two dimensions. This is the content of the Mermin–Wagner–Hohenberg–Coleman theorem; see Hohenberg (1967), Mermin and Wagner (1966), Mermin (1967), and Coleman (1973).

Interesting general results on spontaneous symmetry breaking, Goldstone bosons, and effective Lagrangians (also for nonrelativistic systems of condensed matter) can be found in Leutwyler (1994, 1997).

The example of $\lambda|\phi|^4$-theory

We conclude this section with some remarks on the $\lambda|\phi|^4$-theories with fields ϕ of $N = 1$, 2 or 3 real components. For $N = 1$, the symmetry group is discrete, namely $\mathbb{Z}_2$. The breaking of discrete groups does not give rise to Goldstone bosons and is possible not only in three but also in two dimensions, as shown in Glimm et al. (1975), where a Peierls-type argument is used to prove the existence of a phase transition accompanied by the breaking of the $\mathbb{Z}_2$-symmetry. For $N = 2$, the symmetry group is $U(1)$, and symmetry breaking is only possible in dimension $d \geq 3$. However, one expects that, in two dimensions, the theory exhibits a Berezinskii–Kosterlitz–Thouless transition (Kosterlitz and Thouless, 1973) from a massive to a massless phase, but without spontaneous symmetry breaking. The existence of this transition has been proven rigorously for the classical XY-model on the square lattice and the related Villain model, as well as for some other lattice models, such as the two-component Coulomb gas, in Fröhlich and Spencer (1981); see also Falco (2012). But it remains conjectural for the continuum $\lambda|\phi|^4$- theory of a complex scalar field. For $N \geq 3$, many people expect that, in two dimensions, the theory is always massive, that is, the lowest mass in the theory is strictly positive; see, for example, Polyakov (1975).

We now turn to the $\lambda|\phi|^4$-theories with $N \geq 2$ components in three dimensions. For these theories, we have established the existence of a phase transition to a phase with a nonvanishing vacuum expectation value of the field ϕ in a vanishing magnetic field $h = 0+$ signaling spontaneous symmetry breaking. The analysis presented above shows that if the $O(N)$-symmetry is broken, then there are $N - 1$ distinct Goldstone bosons.

The Lee–Yang theorem implies that, for $N \leq 3$, the connected Green functions of the theory are analytic in h and have exponential decay in the separation of their arguments, provided $\mathrm{Re}h \neq 0$. As a corollary, it follows that, for real $h \neq 0$, the theory has a strictly positive mass gap $m(h)$, that is, the masses of all excitations in the theory are bounded below by $m(h) > 0$.

The results in Section "The phase transition in the $\lambda|\phi|^4_3$-Euclidean field theory in three dimensions" yield information on some of the critical exponents of the theories with $N = 2$, 3. We return to Eq. (20), which says that the susceptibility $\chi(h)$ of the theory diverges like $\frac{1}{h}$, as $h \to 0$, provided the "spontaneous magnetization" $M(R)$ (see (17)) does not vanish. A related bound on the mass gap $m(h)$ is plausible, but remains conjectural. I briefly sketch it here. We have seen in (38) and (39) that if there is spontaneous symmetry breaking, then the connected two-point Green function has a one-particle pole at zero mass, which, for the example of $\lambda|\phi|^4$-theory, with $N \geq 2$ and at $h = 0+$, implies that

$$\left\langle \varphi^i(x)\cdot\varphi^i(0)\right\rangle_{h=0+} = \mathfrak{R}\,[-\Delta]^{-1}(x) + \int_0^\infty d\mu_{reg}(a^2)[-\Delta + a^2]^{-1}(x), \qquad \text{for} \quad i \geq 2, \tag{40}$$

where the residue $\mathfrak{R}$ of the one-particle pole at zero mass is strictly positive in the symmetry-broken phase, and the measure $d\mu_{reg}(a^2)$ is regular at $a^2 = 0$. (It is assumed here that the parameter R^2 is large enough such that there is spontaneous symmetry breaking; but we do not display the R-dependence explicitly.) If $h > 0$, this representation takes the form

$$\left\langle \varphi^i(x)\cdot\varphi^i(0)\right\rangle_h = \mathfrak{R}(h)\,\left[-\Delta + m^2(h)\right]^{-1}(x) + \int_{m^2(h)}^\infty d\tilde{\mu}(a^2)\left[-\Delta + a^2\right]^{-1}(x), \quad i \geq 2, \tag{41}$$

where the physical mass, that is, the inverse correlation length, $m(h)$, is strictly positive, as follows from the Lee–Yang theorem, and $d\tilde{\mu}(a^2)$ is regular at $a^2 = m^2(h)$. It is plausible to expect that $\mathfrak{R}(h) \approx \mathfrak{R}$ is strictly positive, for $h > 0$ small enough, that is,

$$\mathfrak{R}(h) \geq \mathfrak{R}_* > 0, \qquad \text{for} \quad h > 0 \quad \text{small enough}. \tag{42}$$

Using convergent expansions, this expectation is known to be true if h is real and $|h|$ is large enough. However, the strict positivity of $\mathfrak{R}(h)$ for small, but positive values of h is a conjecture that has not been proven so far. Assuming that it holds true, we conclude from (41) and (42) that, for $i \geq 2$,

$$\chi(h) = \int d^3x\left\langle \varphi^i(x)\cdot\varphi^i(0)\right\rangle_h \geq \frac{\mathfrak{R}_*}{m^2(h)}, \qquad \text{with} \quad \mathfrak{R}_* > 0. \tag{43}$$

Combining this lower bound with expression (20) for the susceptibility $\chi(h)$, we find that the mass gap $m(h)$ of the theory satisfies the lower bound (predicted by heuristic arguments)

$$m(h) \geq \text{const.}\sqrt{h}, \qquad \text{as} \quad h \searrow 0. \tag{44}$$

We remark that it follows from the Lee–Yang theorem that $m(h)$ is bounded below by const. h, for small values of $h > 0$. One can rigorously prove a related upper bound on $m(h)$ as follows: From the Källen–Lehmann representation,

$$\left\langle \varphi^i(y)\cdot\varphi^i(0)\right\rangle^c_{\rho,h} = \int_{m^2(h)}^{\infty} d\mu^{(i)}(a^2)\left[-\Delta + a^2\right]^{-1}(y), \qquad i \geq 2,$$

see (15), the fact that $\int d\mu^{(i)}(a^2) = 1$, and (20) we derive that

$$\frac{M(R)}{h} \leq \chi(h) \leq \frac{1}{m(h)^2}$$

hence if there is spontaneous magnetization ($M(R) > 0$) then, for positive h,

$$m(h) \leq \text{const.}\sqrt{h}, \qquad \text{as} \quad h \searrow 0. \tag{45}$$

It is evident that whatever is written here for $h > 0$ also holds for $h < 0$ (by replacing φ^1 by $-\varphi^1$).

Eqs. (20), (44), and (45) are results on critical exponents describing the behavior of the susceptibility and of the mass gap, as $h \searrow 0$, assuming that the spontaneous magnetization is strictly positive. It would be of considerable interest to understand the behavior of the spontaneous magnetization, $M(R)$, defined in (17), as the parameter R^2 approaches the phase-transition point, that is, $R^2 \searrow R_c^2$, with $M(R) = 0$, for $R^2 < R_c^2$. One expects that $M(R) \searrow 0$ continuously, as $R^2 \searrow R_c^2$. But this has only been proven rigorously for the three-dimensional Ising model (corresponding to $N = 1$), with $M(R) \geq \mathcal{O}([R^2 - R_c^2]^{1/2})$; see Aizenman et al. (2015).

One may ask how, in zero magnetic field, $h = 0$, the susceptibility, $\chi(R, h = 0)$, and the mass gap, $m(R, h = 0)$, behave when $R^2 \nearrow R_c^2$. A correlation inequality for the connected four-point (Ursell) function due to Lebowitz (1974) implies that, for one-component real fields ($N = 1$), $\chi(R, 0)$ diverges at least as rapidly as $(R_c^2 - R^2)^{-1}$, and the mass gap $m(R,0)$ tends to 0 continuously, as $R^2 \nearrow R_c^2$; see Glimm and Jaffe (1974) and McBryan and Rosen (1976). These results are also known to hold for complex scalar fields ($N = 2$), but not for $N \geq 3$.

The reader may wonder why the $\lambda|\phi|^4$-theory in four (or more) dimensions has not been considered so far. The reason is that if all ultraviolet cutoffs are removed this theory is expected to be equivalent to a (generalized) free field. Assuming that one regularizes the theory by putting it on a hypercubic lattice, this result has been proven for the theories in dimension $d > 4$, with fields of $N = 1$ or 2 components, in Aizenman (1982) and Fröhlich (1982). In four dimensions, this result is only known for the scaling limit of the Ising model and for $\lambda\phi_4^4$-theory of a one-component real scalar field, the very beautiful, subtle proof appearing in Aizenman and Duminil-Copin (2021). Partial results for $\lambda|\phi|_4^4$-theory of a complex scalar field in four dimensions have been reported in Fröhlich (1982); but these results remain incomplete. For $N \geq 3$, there are no rigorous results known, yet (except at weak coupling).

These remarks motivate us to consider classical and quantum lattice systems, which do not have an ultraviolet (short-distance) problem. I will provide a guide to the literature in the next section, but won't discuss any details.

Phase transitions and symmetry breaking in classical and quantum lattice systems

For applications in statistical mechanics and condensed matter physics, classical and quantum lattice systems are usually more relevant than continuum field theories, although the latter tend to describe critical phenomena of lattice systems near continuous phase transitions.

We limit our review to sketching some results for classical or quantum spin systems on a lattice $\mathbb{Z}^d$, with $d = 2, 3, 4$. The Hamiltonian of such systems is given by

$$H \equiv H(\{\vec{S}\}) := -\sum_{x,\,y\in\mathbb{Z}^d}\left\{J_\perp(x-y)\left[S_x^1\cdot S_y^1 + S_x^2\cdot S_y^2\right] + J_\parallel(x-y)S_x^3\cdot S_y^3\right\} - h\sum_{x\in\mathbb{Z}^d} S_x^3, \tag{46}$$

where $J_\perp(x-y)$ and $J_\parallel(x-y)$ are exchange couplings (see Heisenberg, 1928), h is proportional to the strength of an external magnetic field in the 3-direction, and $\vec{S}_x = (S_x^1, S_x^2, S_x^3)$ is either a classical spin in $\mathbb{R}^3$ or a quantum spin with spin quantum number $s = \frac{1}{2}, 1, \ldots$

(i) If $J_\parallel(x-y) \gg |J_\perp(x-y)|$, $\forall\, x, y$, this Hamiltonian describes uniaxial magnetism. For classical spins or quantum spins with $s = \frac{1}{2}$, the model behaves like an Ising model with $J_\perp \equiv 0$. Phase transitions only occur when $h = 0$, in which case the model has a $\mathbb{Z}_2$-symmetry. Rigorous results for quantum spins can be found in Ginibre (1969) and Kennedy (1985) and references given there.

(ii) If $J_\perp(x-y) \gg |J_\parallel(x-y)|$, $\forall\, x, y$, the model describes a classical or quantum XY (rotator) model, which has a continuous symmetry $U(1)$.

(iii) If $J_\perp \equiv J_\parallel =: J$ the model describes an isotropic magnet and, for $h = 0$, has a continuous symmetry given by $SO(3)$ or $\widetilde{SO}(3) = SU(2)$.

Let us first consider the classical models. They have been studied in Fröhlich et al. (1976) and, using totally different methods, in Garban and Spencer (2022); and references given there. We briefly review the results and methods used in Fröhlich et al. (1976), which are inspired by properties of RQFT's and EFT's, in particular by the Källen–Lehmann representation (15).

For classical spin systems, the number of components of the spin $\vec{S}$ is irrelevant; we may replace (S^1, S^2) by $(S^1, \ldots, S^{N-1})$ and S^3 by S^N, $N = 1, 2, 3, \ldots$ We begin by explaining what it means for exchange couplings J to be "reflection positive." Let Π be a hyperplane in $\mathbb{R}^d$ of codimension 1 that lies in between two lattice planes of $\mathbb{Z}^d$ (viewed as a subset of $\mathbb{R}^d$), and let θ denote reflection at Π. Then the two sites $x \in \mathbb{Z}^d$ and $\theta x \in \mathbb{Z}^d$ lie symmetrically on two different sides of the hyperplane Π. We define $\mathbb{Z}^d_+$ and $\mathbb{Z}^d_-$ to be the two half-lattices on the two different sides of the hyperplane Π. Let $J(x-y), x, y \in \mathbb{Z}^d,$ be exchange couplings.

Definition: J is said to be "reflection positive" iff

$$\sum_{x,\, y \in \mathbb{Z}^d_+} J(x-\theta y) z_x \bar{z}_y \geq 0, \tag{47}$$

for an arbitrary complex-valued function z on the half-lattice $\mathbb{Z}^d_+$.

The equilibrium state of a classical spin system with a Hamiltonian given by (46) at inverse temperature β is given by the formal probability measure

$$dP(\{\vec{S}\}) := \frac{1}{Z_\beta} e^{-\beta H(\{\vec{S}\})} \prod_{x \in \mathbb{Z}^d} d\rho(\vec{S}_x). \tag{48}$$

where $d\rho(\vec{S})$ is a finite measure on $\mathbb{R}^N$, for example

$$d\rho(\vec{S}) = \begin{cases} \exp\left(-\frac{\lambda}{4!} \left[\left| \vec{S} \right|^2 - R^2 \right]^2 \right) d\vec{S}, & \text{or} \\ \delta(|\vec{S}|^2 - R^2)\, d\vec{S}, \end{cases} \tag{49}$$

with $d\vec{S}$ the Lebesgue measure on $\mathbb{R}^N$, $N = 1, 2, 3, \ldots$, and Z_β is the partition function, which is chosen such that $\int dP(\{\vec{S}\}) = 1$. Since we have not normalized the exchange couplings, we may henceforth set $\beta = 1$ and omit it. Expectations of products of components of spins with respect to the measure $dP(\{\vec{S}\})$ are denoted by $\langle (\cdot) \rangle_{J_\perp, J_\parallel, h} \equiv \langle (\cdot) \rangle$.

It turns out that, for classical spin systems with a Hamiltonian given by (46) and reflection-positive exchange couplings $J_\perp$ and $J_\parallel$ satisfying (47), there is an analog of the Källen–Lehmann representation in the form of upper bounds, so-called **Infrared Bounds**, on the Fourier transforms of connected spin–spin correlation functions: for $k \neq 0$,

$$\begin{aligned} 0 < \left\langle \hat{S}^i(k)\, \hat{S}^i(-k) \right\rangle &\leq \frac{1}{\hat{J}_\perp(0) - \hat{J}_\perp(k)}, \quad \text{for} \quad i = 1, \ldots, N-1, \\ 0 < \left\langle \hat{S}^N(k)\, \hat{S}^N(-k) \right\rangle &\leq \frac{1}{\hat{J}_\parallel(0) - \hat{J}_\parallel(k)}, \end{aligned} \tag{50}$$

where $\widehat{(\cdot)}$ denotes Fourier transformation, that is $\hat{S}^i(k)$ is the Fourier transform of S^i_x, for $i = 1, \ldots, N$, and $k \in B$, where B is the Brillouin zone (i.e., a d-dimensional torus, for the lattice $\mathbb{Z}^d$). At the origin, $k = 0$, in quasi-momentum space, these two-point functions may include δ-function contributions, $M_i^2\, \delta_0(k)\, d^dk$, where the constants M_i^2 manifest long-range order (LRO), for $i = 1, 2, \ldots, N$. In an extremal equilibrium state, the absolute value of the spontaneous magnetization is then given (in average) by $\mathcal{M} = \sqrt{\sum_{i=1}^N M_i^2}$. The bounds in (50) have been established rigorously in Fröhlich et al. (1976) and Fröhlich et al. (1978).

We now show that, in $d \geq 3$ dimensions and for exchange couplings $J_\perp$ and $J_\parallel$ of short range, the quantity $\mathcal{M}$ must be strictly positive, provided the parameter R is large enough. First we note that, for $d\rho$ as in (49),

$$\sum_{i=1}^N \int_B d^dk \left\langle \hat{S}^i(k)\, \hat{S}^i(-k) \right\rangle = \left\langle \vec{S}_0 \cdot \vec{S}_0 \right\rangle = c \cdot R^2, \tag{51}$$

for some strictly positive constant c. (This is obvious for the choice $d\rho(\vec{S}) = \delta(|\vec{S}|^2 - R^2)\, d\vec{S}$, in which case $c = 1$.) But, by (50), the left side is bounded from above by

$$\left\langle \vec{S}_0 \cdot \vec{S}_0 \right\rangle \leq \int_B d^dk \left[\frac{N-1}{\hat{J}_\perp(0) - \hat{J}_\perp(k)} + \frac{1}{\hat{J}_\parallel(0) - \hat{J}_\parallel(k)} \right] + \mathcal{M}^2. \tag{52}$$

If the exchange couplings $J_\perp$ and $J_\parallel$ are of short range, then

$$\left[\hat{J}_\alpha(0) - \hat{J}_\alpha(k) \right]^{-1} \leq J_\alpha^{-1} |k|^{-2}, \tag{53}$$

for some positive constants J_α, with $\alpha = \perp$ or $\parallel$. Taking $J := \min(J_\perp, J_\parallel)$ we find that

$$c \cdot R^2 = \left\langle \vec{S}_0 \cdot \vec{S}_0 \right\rangle \leq \frac{N}{J} I_d + \mathcal{M}^2. \tag{54}$$

where $I_d = \int_B \frac{d^dk}{k^2}$. Obviously, I_d diverges in $d = 1$ and 2 dimensions, in which case (54) is useless. But I_d is finite for $d \geq 3$, and it then follows that

$$\mathcal{M}^2 \geq c \cdot R^2 - \frac{N}{J} I_d > 0, \quad \text{for} \quad R^2 \text{ big enough},$$

that is, there is spontaneous magnetization and symmetry breaking if R^2 or J are big enough.

For the Ising model ($N = 1$) and the classical XY model ($N = 2$), these results on the existence of phase transitions accompanied by symmetry breaking can be extended to a large class of not necessarily translation-invariant and not necessarily reflection-positive exchange couplings by using what one calls "correlation inequalities." The relevant inequalities can be found in Messager et al. (1978).

One expects that if $J_\parallel > J_\perp$, then the spontaneous magnetization is parallel to the N-axis (with $N = 3$ for the Hamiltonian in (46)). In this case, the discrete symmetry $S^N \to -S^N$ is broken; for results in this direction, see Kennedy (1985) and references given there. But if $J_\perp > J_\parallel$, then the spontaneous magnetization is expected to lie in the plane $\{\vec{S} \mid S^N = 0\}$, and the continuous symmetry $O(N-1)$ of the Hamiltonian is broken, which, for $N \geq 3$, is accompanied by the emergence of $N-2$ Goldstone bosons. If $J_\parallel = J_\perp \equiv J$, then the model exhibits an $O(N)$-symmetry, and the spontaneous magnetization can have an arbitrary direction in $\mathbb{R}^N$, which can be chosen by introducing a small symmetry breaking term, $-\vec{h} \cdot \sum_x \vec{S}_x$, in the Hamiltonian and letting $|\vec{h}|$ tend to 0 eventually. All these predictions can be shown to hold rigorously for $N = 1, 2, 3$, under suitable assumptions on the parameters.

It may be appropriate to sketch a heuristic idea that originally inspired a stronger (exponential) version of the Infrared Bounds in (50), and which could then be extended to quantum lattice systems. We consider a canonical quantum field theory of a real scalar field φ on d space-time dimensions with a Hamiltonian, denoted by H, whose energy spectrum is bounded from below by 0. Such a theory (if it existed) would have the following properties:

$$\begin{gathered}\dot{\varphi}(\vec{x}, t) = i\Big[H, \varphi(\vec{x}, t)\Big] =: \pi(\vec{x}, t), \quad \text{with} \\ \Big[\varphi(\vec{x}, t), \pi(\vec{y}, t)\Big] = i\,\delta(\vec{x} - \vec{y}),\end{gathered} \tag{55}$$

where t denotes time and $\vec{x}$ is a point in space. Let f and g be real-valued test functions on $\mathbb{R}^{d-1}$, and let

$$\varphi(f, t) := \int_{\mathbb{R}^{d-1}} d\vec{x}\;\; \varphi(\vec{x}, t)\, f(\vec{x}), \tag{56}$$

$$\pi(g, t) := \int_{\mathbb{R}^{d-1}} d\vec{x}\;\; \pi(\vec{x}, t)\, g(\vec{x}), \quad \text{with} \tag{57}$$

$$[\varphi(f, t), \pi(g, t)] = i \int_{\mathbb{R}^{d-1}} d\vec{x}\;\; f(\vec{x})\, g(\vec{x}) \equiv i\,\langle f, g\rangle. \tag{58}$$

Since φ is a real field, we may expect that, at all times t, $\varphi(f, t)$ is a self-adjoint operator on the Hilbert space, $\mathcal{H}$, of the theory. From our assumption that $H \geq 0$ it follows that $U\,H\,U^* \geq 0$, for an arbitrary unitary operator U on $\mathcal{H}$, and we then find that

$$0 \leq e^{i\varphi(f,t)}\; H\; e^{-i\varphi(f,t)} = H - \pi(f, t) + \frac{1}{2}\, \| f \|_2^2 \cdot \mathbf{1}, \tag{59}$$

where $\| f \|_2^2 := \langle f, f\rangle$. Using a Feynman–Kac formula, one can translate this bound to one that holds for a corresponding EFT at imaginary time. We denote the Euclidean field corresponding to the quantum field φ by ϕ, as before, and expectations with respect to the functional measure describing the EFT corresponding to the QFT are denoted by $\langle(\cdot)\rangle$. For a real-valued test function h on $\mathbb{R}^d$, we define $\phi(h) := \int d^d x\;\; \phi(x)\, h(x)$. Then (59) implies that

$$\left\langle e^{\frac{\partial \phi}{\partial t}(h)} \right\rangle \leq e^{\frac{1}{2}\|h\|_2^2}.$$

By Euclidean invariance, it then follows that

$$\langle \exp[\underline{\nabla}\phi(\underline{h})] \rangle \leq e^{\frac{1}{2}\|\underline{h}\|_2^2}, \tag{60}$$

where $\underline{h} = (h_1, \ldots, h_d)$ is a d-tuple of test functions. This bound readily implies that, in momentum space and for $k \neq 0$,

$$\left\langle \hat{\phi}(k)\;\hat{\phi}(-k) \right\rangle \leq \frac{1}{|k|^2},$$

which is an Infrared Bound similar to (50) in the special case where $N = 1$ and where $J_\parallel$ is a nearest-neighbor coupling of strength 1. Obviously, one can extend these arguments to canonical theories of N-component real fields, $\vec{\varphi} = (\varphi^1, \ldots, \varphi^N)$, $N \geq 2$. (Of course, the bound on $\langle \hat{\phi}(k)\;\hat{\phi}(-k)\rangle$ also follows from the Källen–Lehmann representation (15).)

For classical lattice spin systems with nearest-neighbor exchange couplings, bounds of the form of (60) have first been proven in Fröhlich et al. (1976). They were subsequently extended, mutatis mutandis, to classical models with general reflection-positive exchange coupling, including long-range couplings, in Fröhlich et al. (1978) and to quantum spin systems in Dyson et al. (1978).

A much more ambitious, more robust analysis of classical lattice spin systems with phase transitions accompanied by the spontaneous breaking of continuous $O(N)$-symmetries has been undertaken in Balaban (1998) and Balaban and O'Carroll (1999), using mathematically controlled renormalization group methods. (See also Bauerschmidt et al. (2021) for a somewhat related, but simpler analysis of a different model.)

A new, quite surprising and original approach to proving the existence of phase transitions accompanied by spontaneous symmetry breaking has been proposed in Garban and Spencer (2022). The advantage of their method is that it also applies to classical models that are neither translation-invariant nor do they satisfy Reflection Positivity. The price to pay is that the models describe disordered systems and have random exchange couplings. (For the Ising- and the classical XY model, one can, however, use the correlation inequalities in Messager et al. (1978) to extend their results to the usual choice of exchange couplings; see Garban and Spencer, 2022.)

It turns out that Infrared Bounds analogous to those in (50)—but for so-called Duhamel two-point correlations—can also be proven for quantum lattice spin systems satisfying Reflection Positivity, as discovered in Dyson et al. (1978). It turns out that, among the quantum Heisenberg models, only the antiferromagnets satisfy Reflection Positivity, but not the ferromagnets. For antiferromagnets, the Infrared Bounds can be used to establish phase transitions accompanied by spontaneous symmetry breaking and the emergence of Goldstone modes (magnons); see Dyson et al. (1978). More general results on phase transitions and spontaneous symmetry breaking for a large family of quantum lattice systems satisfying Reflection Positivity have been established in Fröhlich et al. (1978) and Albert et al. (2006); see also Fröhlich (1978, 2011) for reviews. I cannot go into any details about these results. For the isotropic quantum Heisenberg ferromagnet on the complete graph, the existence of a phase transition accompanied by the spontaneous breaking of the $SU(2)$-symmetry has been proven in Björnberg et al. (2020), using exact calculations that do not rely on Reflection Positivity; but rigorous results concerning phase transitions in isotropic quantum Heisenberg ferromagnets with continuous internal symmetries on finite-dimensional lattices are not known so far.

I conclude this review with a few comments on the Ising model and the classical XY model. By Kramers–Wannier duality, these models are equivalent to gases of "topological defects." For the Ising model, these defects are domain walls (also called Peierls contours) separating domains with opposite spin orientation. For the XY model the defects are (codimension-2) vortices. It turns out that, in dimension $d \geq 2$ and at low temperatures, these defect gases are dilute. This feature enables one to analyze them by using mathematically controlled versions of energy-entropy arguments underpinned by "multiscale analysis." For the Ising model, this strategy is implemented in what is commonly called a "Peierls argument," in honor of its inventor. For the XY model, the analysis is considerably more subtle, due to the presence of massless Goldstone modes at low temperatures. In particular, the analysis of the low-temperature phase of the two-dimensional classical XY model, viewed as a dilute gas of point vortices with long-range (Coulomb) interactions, is really rather involved. An interesting, fairly precise upper bound on spin–spin correlations in the two-dimensional XY model at low temperatures has been proven in McBryan and Spencer (1977). Techniques (involving complex translations in the space of spin configurations) developed in this paper have provided some of the tools used in Fröhlich and Spencer (1981), where, using rather heavy multiscale analysis, the existence of the Kosterlitz–Thouless transition for the two-dimensional classical XY model and other related models has been established rigorously; see also Falco (2012). New, simpler proofs have recently appeared in Lammers (2022, 2023) (and references given there).

One of the key results established in McBryan and Spencer (1977) and Fröhlich and Spencer (1981) is the following bound on the spin–spin correlation. For ferromagnetic exchange couplings $J > J_c$, where J_c is the coupling at which the Kosterlitz–Thouless transition occurs,

$$\begin{gathered}\left\langle \vec{S}_0 \cdot \vec{S}_x \right\rangle_{J,h=0} \simeq \mathcal{O}\left([|x|+1]^{-\{1/2\pi\varepsilon(J)\}}\right), \quad \text{with} \\ 0 < \varepsilon(J) \to J, \quad \text{as} \quad J \to \infty. \end{gathered} \tag{61}$$

Here, $\vec{S}_x = (\cos\theta_x, \sin\theta_x)$, $\theta_x \in [0, 2\pi)$, is the planar spin variable of the classical XY model at site $x \in \mathbb{Z}^2$, and the external magnetic field h vanishes, $h = 0$. The Lee–Yang theorem, which holds for the classical XY model, implies that the susceptibility

$$\chi(J,h) = \sum_{x \in \mathbb{Z}^2} \left\langle \vec{S}_0 \cdot \vec{S}_x \right\rangle_{J,h}$$

is finite if $h > 0$. By (61), $\chi(J,h)$ diverges, as $h \searrow 0$, provided J is large enough. The magnetization, $M(J,h)$, is nonzero, for $h > 0$, but approaches 0, as $h \searrow 0$, by the Mermin–Wagner–Hohenberg theorem (Hohenberg, 1967; Mermin and Wagner, 1966; Mermin, 1967). Using that

$$\chi(J,h) = \frac{M(J,h)}{h},$$

see (20), we conclude that, for J large enough,

$$\begin{gathered} M(J,h) \to 0, \qquad \text{but} \quad \frac{M(J,h)}{h} \quad \text{diverges, as} \quad h \searrow 0, \quad \text{and} \\ \chi(J,h) = \mathfrak{o}(h^{-1}), \quad \text{as} \quad h \searrow 0, \end{gathered} \tag{62}$$

while, for $J < J_c$, where the spin–spin correlation decays exponentially, as $|x| \to \infty$, and the susceptibility remains finite, as $h \searrow 0$, we have that $M(J, h) \propto h$, as $h \searrow 0$.

For the three-dimensional classical XY model, the analysis is simpler, because, in $d = 3$, the vortices are one-dimensional objects and form loops. At high temperatures, these vortex loops condense; but, at low temperatures, they form a dilute gas. They have long-range interactions mediated by massless Goldstone modes. Somewhat surprisingly, these long-range interactions do not cause any major complications in the mathematical analysis of the low-temperature phase of the model. In fact, the vortex-loop representation has been used to rigorously prove that, at low enough temperatures, the three-dimensional classical XY model has spontaneous magnetization and that its connected spin–spin correlations decay very slowly, namely like r^{-1}, where r is the distance between the spin insertion points. It is easy to show that, at high temperatures, the spin–spin correlations decay exponentially fast. These findings establish again the existence of a phase transition accompanied by the spontaneous breaking of a $U(1)$-symmetry and the emergence of Goldstone bosons; see Fröhlich and Spencer (1983). Translation invariance of the Hamiltonian is not essential in this method.

Ideas somewhat related to those in Fröhlich and Spencer (1983) have earlier been used in Guth (1980) in an analysis of the deconfining transition in the four-dimensional $U(1)$-lattice gauge theory; see also Fröhlich and Spencer (1982).

Conclusion

I hope this short review convinces the reader that many nontrivial facts about phase transitions accompanied by spontaneous symmetry breaking and about Goldstone bosons of considerable interest in condensed matter and particle physics are now known in the form of mathematically precise results. Work on this subject has given rise to many important insights into properties of physical systems and to the development of numerous interesting techniques of analysis that can also be used in other contexts. Ideas from statistical and condensed matter physics have been fruitfully imported into particle physics and quantum field theory, and conversely. Without this cross-fertilization, many significant results would presumably not have been found, yet.

I expect that I have quoted sufficiently much of the relevant literature to enable the reader to access without effort the nitty-gritty of the topics discussed in this review. (I offer my apologies to all colleagues whose work I should have quoted, but did not.)

Despite all the progress that has been made during more than half a century, many important questions remain open, at least if one insists on adhering to the standards of mathematical physics. Among the most important such questions are the following ones.

1. Find a continuum model with a translation-invariant Hamiltonian for which one can prove that the ground-state and the extremal low-temperature equilibrium states break translation invariance spontaneously and exhibit crystalline ordering.
2. Show that translation-invariant interacting Bose gases with physically realistic repulsive two-body interactions can exhibit Bose–Einstein condensation as the temperature is lowered at a fixed, positive density.
3. Show that the isotropic quantum Heisenberg ferromagnet in $d \geq 3$ dimensions undergoes a phase transition accompanied by the spontaneous breaking of its $SU(2)$-symmetry.
4. Show that the quantum-mechanical XY model and the $\lambda|\phi|^4$-theory of a complex scalar field in two dimensions undergo a Kosterlitz–Thouless transition.
5. Prove rigorously that the classical Heisenberg model and the classical N-vector models, with $N > 3$, in two dimensions have a strictly finite correlation length at all positive temperatures.
6. Extend the results in Aizenman et al. (2015) and Aizenman and Duminil-Copin (2021) concerning the magnetization in the three-dimensional Ising model, and the Gaussian nature of the scaling limit of the four-dimensional Ising- and $\lambda\phi^4$-model ($N = 1$), respectively, to two-component models, in particular to the classical XY model.

Acknowledgments

This review could not have been written without my collaborations, mostly many years ago, with E. H. Lieb, B. Simon, and T. Spencer. They have taught me very many important things about statistical mechanics and quantum field theory. My collaboration and my countless discussions, also in more recent times, with T. Spencer count among the highlights in my scientific life, and I am deeply grateful to him for his generosity and his friendship. I have profited from interactions and collaboration with numerous other colleagues, postdocs and PhD students, too many to list them all.
I thank T. Chakraborty for encouraging me to write this review and for his patience.

AIPP-Data availability statement

Data sharing is not applicable to this article as no new data were created or analyzed in this study.

References

Aizenman M (1982) Geometric analysis of φ^4 fields and Ising models. I, II. *Communications in Mathematical Physics* 86(1): 1–48.
Aizenman M and Duminil-Copin H (2021) Marginal triviality of the scaling limits of critical 4D Ising and ϕ_4^4 models. *Annals of Mathematics* 194(1): 163–235.
Aizenman M, Duminil-Copin H, and Sidoravicius V (2015) Random currents and continuity of Ising model's spontaneous magnetization. *Communications in Mathematical Physics* 334(2): 719–742.
Albert C, Ferrari L, Fröhlich J, and Schlein B (2006) Magnetism and the Weiss exchange field—A theoretical analysis motivated by recent experiments. *Journal of Statistical Physics* 125(1): 77–124.

Anderson PW (1962) Plasmons, gauge invariance, and mass. *Physical Review* 130(1): 439–442.

Balaban T (1998) The large field renormalization operation for classical N-vector models. *Communications in Mathematical Physics* 198(3): 493–534.

Balaban T and O'Carroll M (1999) Low temperature properties for correlation functions in classical n-vector spin models. *Communications in Mathematical Physics* 199(3): 493–520.

Bauerschmidt R, Crawford N, and Helmuth T (2021) Percolation transition for random forests in $d \geq 3$. *arXiv:2107.01878v2 [math.PR]*.

Björnberg JE, Fröhlich J, and Ueltschi D (2020) Quantum spins and random loops on the complete graph. *Communications in Mathematical Physics* 375: 1629–1663.

Bratteli O and Robinson DW (1979) In: Balian R, et al. (eds.) *Operator Algebras and Quantum Statistical Mechanics. Texts and Monographs in Physics*, vol. 1. New York, Berlin, Heidelberg: Springer-Verlag.

Bratteli O and Robinson DW (1981) *Operator Algebras and Quantum Statistical Mechanics. Texts and Monographs in Physics*, vol. 2. New York, Berlin, Heidelberg: Springer-Verlag.

Brydges D, Fröhlich J, and Sokal A (1983) A new proof of the existence and non-triviality of the continuum ϕ_2^4 and ϕ_3^4 quantum field theories. *Communications in Mathematical Physics* 91: 141–186.

Buchholz D, Doplicher S, and Longo R (1986) On Noether's theorem in quantum field theory. *Annals of Physics* 170: 1–17.

Coleman S (1973) There are no Goldstone Bosons in two dimensions. *Communications in Mathematical Physics* 31: 259–264.

Domb C and Green MS (1972–1976) *Phase Transition and Critical Phenomena*, vols. 1–6. San Diego, New York: Harcourt, Brace & World.

Domb C and Lebowitz JL (1983–2001) *Phase Transition and Critical Phenomena*, vols. 7–20. San Diego, New York: Harcourt, Brace & World.

Dunlop F and Newman C (1975) Multicomponent field theories and classical rotators. *Communications in Mathematical Physics* 44: 223–235.

Dyson F, Lieb EH, and Simon B (1978) Phase transitions in quantum spin systems with isotropic and nonisotropic interactions. *Journal of Statistical Physics* 18: 335–383.

Englert F and Brout R (1964) Broken symmetry and the mass of gauge vector mesons. *Physical Review Letters* 13(9): 321–323.

Falco P-L (2012) Kosterlitz-Thouless transition line for the two dimensional Coulomb Gas. *Communications in Mathematical Physics* 312: 559–609.

Feldman J and Osterwalder K (1975) The Wightman axioms and the mass gap for weakly coupled ϕ_3^4 quantum field theories. In: Araki H (ed.) *Mathematical Problems in Theoretical Physics*. Berlin, Heidelberg, New York: Springer-Verlag.

Feldman J and Osterwalder K (1977) The Wightman axioms and the mass gap for weakly coupled ϕ_3^4 quantum field theories. *Annals of Physics (NY)* 97: 80–135.

Fröhlich J (1978) The pure phases (harmonic functions) of generalized processes—Or: Mathematical physics of phase transitions and symmetry breaking. *Bulletin of the AMS* 84(2): 165–193.

Fröhlich J (1982) On the triviality of $\lambda\varphi_d^4$ theories and the approach to the critical point in $d > 4$ dimensions. *Nuclear Physics B* 200(2): 281–296.

Fröhlich J (2011) *Phase Transitions and Continuous Symmetry Breaking*. Vienna: Erwin-Schrödinger Institute (available from the author on request).

Fröhlich J and Rodriguez P-F (2012) Some applications of the Lee-Yang theorem. *Journal of Mathematical Physics* 53. 095218-1–095218-15.

Fröhlich J and Rodriguez P-F (2017) On cluster properties of classical ferromagnets in an external magnetic field. *Journal of Statistical Physics* 166: 828–840.

Fröhlich J and Spencer T (1981) The Kosterlitz-Thouless transition in two-dimensional abelian spin systems and the Coulomb gas. *Communications in Mathematical Physics* 81: 527–602.

Fröhlich J and Spencer T (1982) Massless phases and symmetry restoration in Abelian Gauge theories and spin system. *Communications in Mathematical Physics* 83: 411–454.

Fröhlich J and Spencer T (1983) The Berezinskii-Kosterlitz-Thouless transition. In: Fröhlich J (ed.) *Scaling and Self- Similarity in Physics. Progress in Physics*, vol. 7, pp. 29–138. Basel, Boston: Birkhäuser Verlag.

Fröhlich J, Simon B, and Spencer T (1976) Infrared bounds, phase transitions and continuous symmetry breaking. *Communications in Mathematical Physics* 50: 79–95.

Fröhlich J, Israel R, Lieb EH, and Simon B (1978) Phase transitions and reflection positivity. I. General theory and long range lattice models. *Communications in Mathematical Physics* 62: 1–34.

Fröhlich J, Morchio G, and Strocchi F (1981) Higgs phenomenon without symmetry breaking order parameter. *Nuclear Physics B* 190(3): 553–582.

Fröhlich J, Knowles A, Schlein B, and Sohinger V (2020) A path-integral analysis of interacting Bose gases and loop gases. *Journal of Statistical Physics* 180: 810–831.

Fröhlich J, Knowles A, Schlein B, and Sohinger V (2023) The Euclidean ϕ_2^4 theory as a limit of an interacting Bose gas. *arXiv:2201.07632v2 [math-ph]*.

Garban C and Spencer T (2022) Continuous symmetry breaking along the Nishimori line. *J. Math. Phys.* 63(9): 093302.

Ginibre J (1969) Existence of phase transitions for quantum lattice systems. *Communications in Mathematical Physics* 14: 205–234.

Glaser V (1974) On the equivalence of the Euclidean and Wightman formulation of field theory. *Communications in Mathematical Physics* 37(4): 257–272.

Glimm J and Jaffe A (1973) Positivity of the ϕ_3^4 Hamiltonian. *Fortschritte der Physik* 21: 327–376.

Glimm J and Jaffe A (1974) φ_2^4 quantum field model in the single-phase region: Differentiability of the mass and bounds on critical exponents. *Physical Review D* 10: 536–539.

Glimm J and Jaffe A (1981) *Quantum Physics—A Functional Integral Point of View*. New York, Berlin, Heidelberg: Springer-Verlag.

Glimm J, Jaffe A, and Spencer TC (1975) Phase transition for ϕ_2^4 quantum fields. *Communications in Mathematical Physics* 45: 203–216.

Goldstone J (1961) Field Theories with "Superconductor" Solutions. *Il Nuov Cimento* XIX: 154–164.

Goldstone J, Salam A, and Weinberg S (1962) Broken symmetries. *Physical Review* 127: 965–970.

Guralnik GS, Hagen CR, and Kibble TWB (1964) Global conservation laws and massless particles. *Physical Review Letters* 13(20): 585–587.

Guth A (1980) Existence proof of a nonconfining phase in four-dimensional $U(1)$ lattice gauge theory. *Physical Review D* 21: 2291–2307.

Heisenberg W (1928) Zur Theorie des Ferromagnetismus. *Zeitschrift für Physik* 49: 619–636.

Higgs PW (1964) Broken symmetries and the masses of gauge bosons. *Physical Review Letters* 13(16): 508–509.

Hohenberg P (1967) Existence of long-range order in one and two dimensions. *Physical Review* 158: 383–386.

Itzykson C and Drouffe J-M (1989) Statistical Field Theory. *Cambridge Monographs on Mathematical Physics.* , vol. I & II. Cambridge, New York: Cambridge University Press.

Jost R (1965) *The General Theory of Quantized Fields*. Providence RI: AMS publ.

Kennedy T (1985) Long range order in the anisotropic quantum ferromagnetic Heisenberg model. *Communications in Mathematical Physics* 100: 447–462.

Kosterlitz M and Thouless DJ (1973) Ordering, metastability and phase transitions in two-dimensional systems. *Journal of Physics C* 6: 1181–1203.

Lammers P (2022) Height function delocalisation on cubic planar graphs. *Probability Theory and Related Fields* 182(1): 531–550.

Lammers P (2023) Bijecting the BKT transition. *arXiv:2301.06905v1 [math.PR]*.

Lebowitz JL (1974) GHS and other inequalities. *Communications in Mathematical Physics* 35: 87–92.

Lee TD and Yang CN (1952) Statistical theory of equations of state and phase transitions II. Lattice gas and Ising model. *Physical Review* 87: 410–419.

Lee BW and Zinn-Justin J (1972a) Spontaneously broken gauge symmetries. I. Preliminaries. *Physical Review D* 5: 3121–3137.

Lee BW and Zinn-Justin J (1972b) Spontaneously broken gauge symmetries. II. Perturbation theory and renormalization. *Physical Review D* 5: 3137–3155.

Lee BW and Zinn-Justin J (1972c) Spontaneously broken gauge symmetries. III. Equivalence. *Physical Review D* 5: 3155–3160.

Leutwyler H (1994) Non-relativistic effective lagrangians. *Physical Review D* 49(6): 3033–3043.

Leutwyler H (1997) Phonons as Goldstone bosons. *Helvetica Physica Acta* 70: 275–286.

McBryan O and Rosen J (1976) Existence of the critical point in ϕ^4 field theory. *Communications in Mathematical Physics* 51: 91–105.

McBryan OA and Spencer TC (1977) On the decay of correlations in SO(n)-symmetric ferromagnets. *Communications in Mathematical Physics* 53: 299–302.

Mermin ND (1967) Absence of ordering in certain classical systems. *Journal of Mathematical Physics* 6: 1061–1064.

Mermin ND and Wagner H (1966) Absence of ferromagnetism or antiferromagnetism in one- or two-dimensional isotropic Heisenberg models. *Physical Review Letters* 17: 1133–1136.

Messager A, Miracle-Sole S, and Pfister C (1978) Correlation inequalities and uniqueness of the equilibrium state for the plane rotator ferromagnetic model. *Communications in Mathematical Physics* 58(1): 19–29.

Nambu Y and Jona-Lasinio G (1961a) Dynamical model of elementary particles based on an analogy with superconductivity. I. *Physical Review* 122: 345–358.

Nambu Y and Jona-Lasinio G (1961b) Dynamical model of elementary particles based on an analogy with superconductivity. II. *Physical Review* 124: 246–254.

Osterwalder K and Schrader R (1975) Axioms for Euclidean Green's functions II. *Communications in Mathematical Physics* 42(3): 281–305 (this paper is a sequel to a previous paper by the same authors from the year 1973 that contained a gap in the arguments).

Park YM (1977) Convergence of lattice approximation and infinite volume limit in the $(\lambda\phi^4 - \phi^2 - \phi)_3$ field theory. *Journal of Mathematical Physics* 18: 354–366.

Polyakov AM (1975) Interaction of Goldstone particles in two dimensions. Applications to ferromagnets and massive Yang-Mills fields. *Physics Letters* 59B: 79–81.

Renker, H., 1913. Magnetische Untersuchungen an Legierungen der Eisengruppe oberhalb des Curie-Punktes. 10.3929/ethz-a-000092025. (Promotionsarbeit ETH Zurich (Referent: Herr Prof. Dr. P. Weiss, Korreferent: Herr Prof. Dr. A. Einstein)-and references given there).

Ruelle D (1969) *Statistical Mechanics: Rigorous Results*. Reading MA: W. A. Benjamin, Inc.

Simon B (1974) The $P(\phi)_2$ Euclidean (Quantum) Field Theory. *Princeton Series in Physics*. Princeton NJ: Princeton University Press.

Simon B (1993) *The Statistical Mechanics of Lattice Gases*, vol. 1. Princeton NJ: Princeton University Press (vol. 2 in preparation).

Simon B and Griffiths R (1973) The ϕ_2^4-field theory as a classical Ising model. *Communications in Mathematical Physics* 33: 145–164.

Spencer T and Fröhlich J (2013–2014) *Discussions and Unpublished Notes on the Classical XY Model*. Princeton: IAS.

Stückelberg ECG (1938a) Die Wechselwirkungs Kräfte in der Elektrodynamik und in der Feldtheorie der Kernkräfte (I). *Helvetica Physica Acta* 11: 225–244.

Stückelberg ECG (1938b) Die Wechselwirkungs Kräfte in der Elektrodynamik und in der Feldtheorie der Kernkräfte (II). *Helvetica Physica Acta* 11: 299–312.

Stückelberg ECG (1938c) Die Wechselwirkungs Kräfte in der Elektrodynamik und in der Feldtheorie der Kernkräfte (III). *Helvetica Physica Acta* 11: 312–328.

Symanzik K (1967) Euclidean proof of the Goldstone theorem. *Communications in Mathematical Physics* 6: 228–232.

'tHooft G and Veltman M (1972) Regularization and renormalization of gauge fields. *Nuclear Physics B* 44(1): 189–219.

Weinberg S (1995–2000) *The Quantum Theory of Fields*. Volumes I–III. Cambridge and New York: Cambridge University Press.

Weiss P (1907) L'hypothèse du champ moléculaire et la propriété ferromagnétique. *Journal de Physique* 6: 661–690.

Wreszinski W (1976) Goldstone's theorem for quantum spin systems of finite range. *Journal of Mathematical Physics* 17: 109–111.

Higgs and Nambu–Goldstone modes in condensed matter physics

Naoto Tsuji[a,b], **Ippei Danshita**[c], **and Shunji Tsuchiya**[d], [a]Department of Physics, University of Tokyo, Hongo, Tokyo, Japan; [b]RIKEN Center for Emergent Matter Science (CEMS), Wako, Saitama, Japan; [c]Department of Physics, Kindai University, Higashi-Osaka, Osaka, Japan; [d]Department of Physics, Chuo University, Kasuga, Tokyo, Japan

© 2024 Elsevier Ltd. All rights reserved.

Introduction 174
Higgs mode in superconductors 176
Higgs modes in atomic Fermi gases 179
Higgs and Nambu–Goldstone modes in other systems 181
Conclusion 183
References 184

Abstract

Collective dynamics of many particle systems is tightly linked to their underlying symmetry and phase transitions. Higgs and Nambu–Goldstone (NG) modes are, respectively, collective amplitude and phase modes of the order parameter that are widely observed in various physical systems at different energy scales, ranging from magnets, superfluids, and superconductors to our universe. The Higgs mode is a massive excitation, which is a condensed-matter analog of Higgs particle in high-energy physics, while the NG mode is a massless excitation that appears when a continuous symmetry is spontaneously broken. They provide important information on the fundamental aspects of many particle systems, such as symmetry, phases, dynamics, and response to external fields. In this article, we review the physics of Higgs and NG modes in condensed matter physics. Especially, we focus on the development on the study of collective modes in superconductors and cold-atom systems.

Key points

- Introduces collective modes of an order parameter in condensed matter physics, including Higgs and Nambu–Goldstone modes.
- Describes basic theories for Higgs and Nambu–Goldstone modes in superconductors and cold-atom systems (including fermionic and bosonic superfluids).
- Reviews experimental observations of Higgs and Nambu–Goldstone modes in condensed matter systems.

Introduction

A phenomenon of phase transition is widely observed in various physical systems at different energy scales, ranging from condensed-matter to high-energy physics. For example, when temperature decreases, a paramagnet turns into a ferromagnet, and a metal turns into a superconductor. Those phenomena can be universally understood with the concept of spontaneous symmetry breaking: Physical laws are invariant under a certain symmetry transformation while a physically realized state at low energy does not necessarily exhibit the same symmetry. In the case of magnets having spin rotation symmetry, individual spins are randomly oriented at high temperature, whereas at low temperature, they are aligned to one particular direction, which is spontaneously chosen. In the case of superconductors, a complex phase of a macroscopic wavefunction of electrons is aligned spontaneously.

In the conventional Landau paradigm, phase transition is characterized by an order parameter, which grows in ordered phases, such as magnetization or condensate (superfluid) density. When a continuous symmetry is spontaneously broken, there typically appear two types of collective motions of the order parameter: One is a phase fluctuation of the order parameter and the other is an amplitude fluctuation of the order parameter (Fig. 1). The former is often referred to as Nambu–Goldstone (NG) mode while the latter is called Higgs mode, which recently attracts interests in condensed matter physics. As the name suggests, the Higgs mode is a condensed-matter analog of a Higgs particle in high-energy physics, which emerges as a result of quantization of the amplitude fluctuation of a complex scalar field. The Higgs particle plays an important role in generating a mass of gauge fields due to the Higgs mechanism, making a force mediated by gauge bosons short-ranged.

Historically, on the other hand, the physics of Higgs particle and Higgs mechanism arose from the study of superconductivity. The macroscopic phenomenological theory of superconductivity had been developed by Ginzburg and Landau (1950), which can be viewed as a nonrelativistic version of the complex scalar field theory adopted by Higgs and others in the study of the Higgs mechanism. The microscopic theory of superconductivity had been presented by Bardeen et al. (1957), known as the BCS theory,

https://doi.org/10.1016/B978-0-323-90800-9.00256-0

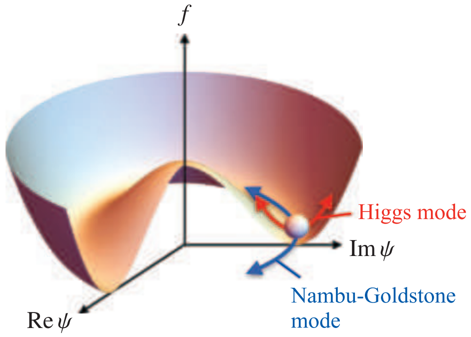

Fig. 1 Free-energy surface in the plane of a complex order parameter ψ. The *red* (*blue*) *arrows* represent Higgs (Nambu–Goldstone) mode, corresponding to amplitude (phase) fluctuation of the order parameter.

which had a broad impact on various branches of physics. In 1958, just one year after the BCS theory, Anderson and Bogoliubov had already discussed collective modes in superconductors (Bogoliubov et al., 1958; Anderson, 1958a, b). Especially, Anderson mentioned the existence of what is known as the Higgs mode in superconductors, whose energy was found to be twice as large as the superconducting gap. Physically, the Higgs mode in superconductors corresponds to a collective oscillation of the superfluid density (density of condensed Cooper pairs), which should be distinguished from an individual excitation of Cooper-pair breaking.

Stimulated by the development of the BCS theory, Nambu had introduced the concept of spontaneous symmetry breaking in particle physics. Based on an analogy with the BCS theory (Nambu, 1960), a possibility of spontaneous symmetry breaking is postulated for a vacuum ground state in a relativistic field theory (Nambu and Jona-Lasinio, 1961; Goldstone, 1961). It was found that a massless boson appears as a phase fluctuation of the order parameter in a symmetry broken phase, in much the same way as a spin wave appears as a collective excitation in magnets. In parallel, Goldstone and others proved a theorem (Goldstone et al., 1962) that massless particles must appear when a continuous symmetry is spontaneously broken in a relativistic field theory, and the number of those correspond to the number of degrees of broken symmetries. Later, the theorem has been extended to nonrelativistic cases (Watanabe and Murayama, 2012; Hidaka, 2013), where the counting rule of the NG modes has been established.

In the application of symmetry breaking in particle physics, one has to avoid Goldstone's theorem since no such massless particle had been observed in our universe. In 1964, Englert, Brout, Higgs, and others had noticed that there is a way to go around Goldstone's theorem when the system is coupled to gauge fields (Englert and Brout, 1964; Higgs, 1964; Guralnik et al., 1964): The phase mode is absorbed into the longitudinal component of gauge fields, which results in generating a mass of gauge bosons (Higgs mechanism). What remains after this is the amplitude mode of the scalar field, which corresponds to a massive scalar particle (Higgs boson). In 2012, the Higgs particle has been finally discovered in the LHC experiment at CERN (ATLAS Collaboration, 2012; CMS Collaboration, 2012), after almost 50 years since the theoretical prediction.

It should be emphasized that the Higgs mechanism had been discussed earlier by Anderson in the context of superconductivity in condensed matter physics (Anderson, 1958a, b, 1963): In superconductors, an interior magnetic field is completely excluded due to the Meissner—Ochsenfeld effect. This phenomenon can be understood by the fact that electromagnetic fields acquire a mass and cannot propagate freely inside superconductors (Anderson–Higgs mechanism). Anderson's argument was based on a nonrelativistic theoretical formalism, but essentially the same thing happens in relativistic field theories.

While the physics of Higgs phenomena has originated from the study of superconductivity, the Higgs mode in superconductors (Pekker and Varma, 2015; Shimano and Tsuji, 2020), which manifests the existence of an effective scalar potential with a Mexican-hat shape (Fig. 1) that causes the Higgs mechanism, has not been observed for a long time. An exception at an early stage was the Raman scattering experiment reported in 1980 for 2H-NbSe$_2$ (Sooryakumar and Klein, 1980), which is rather a special material in the sense that superconductivity coexists with a charge-density-wave (CDW) order. Only in this particular regime, a resonance peak corresponding to the amplitude mode has been observed in Raman spectra.

In 2013, a coherent long-lived oscillation induced by a mono-cycle terahertz laser pulse was observed for a pure superconductor NbN ("pure" means the one without coexistence of any other long-range orders) (Matsunaga et al., 2013). The oscillation frequency agrees with the superconducting gap energy, implying that the Higgs mode is excited in the terahertz laser experiment. In the subsequent experiment, a multicycle terahertz pulse has been applied to NbN, showing a coherent oscillation with the frequency twice as large as the pump laser frequency (Matsunaga et al., 2014). This is consistent with the fact that the Higgs mode can be generated by a two-photon absorption process through the nonlinear light-Higgs coupling (Tsuji and Aoki, 2015). At the same time, the resonant enhancement of third harmonic generation has been observed in NbN when the superconducting gap coincides with twice the pump frequency (Fig. 2) (Matsunaga et al., 2014). Later, it turns out that impurities play an essential role in the resonant enhancement of third harmonic generation mediated by the Higgs mode (Jujo, 2018; Murotani and Shimano, 2019; Silaev, 2019; Tsuji and Nomura, 2020; Seibold et al., 2021).

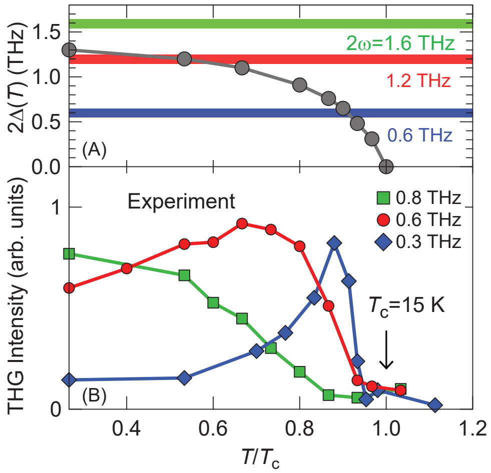

Fig. 2 Temperature dependence of (A) the superconducting gap compared with twice the pump frequencies and (B) the intensity of third harmonic generation in NbN superconductors. Adapted from Matsunaga R, Tsuji N, Fujita H, Sugioka A, Makise K, Uzawa Y, Terai H, Wang Z, Aoki H, and Shimano R (2014) Light-induced collective pseudospin precession resonating with Higgs mode in a superconductor. Science 345(6201): 1145–1149. ISSN 0036-8075

Table 1 Examples of phase and amplitude modes in various physical systems.

System	*Nambu–Goldstone (phase) mode*	*Higgs (amplitude) mode*	*Broken symmetry*
Magnet	Magnon	Amplitude mode	Spin rotation
(Incommensurate) Charge density wave	Phason	Amplitudon	Space translation
Superfluid ^{4}He	Phase mode	–	Phase rotation
Weakly interacting superfluid Bose gas	Phase mode	–	Phase rotation
Strongly interacting superfluid Bose gas in an optical lattice at commensurate filling	Phase mode	Amplitude mode	Phase rotation
Superfluid Fermi gas	Phase mode	Amplitude mode	Phase rotation
Superfluid ^{3}He (B phase)	Phase mode	Squashing mode	SO(3)×SO(3)×U(1)
Superconductor	–	Amplitude mode	Phase rotation
Atomic nuclei	Pion	σ Particle	Chiral symmetry
Standard model in high-energy physics	–	Higgs particle	SU(2)×U(1)

In the case of superconductors and the standard model in high-energy physics, the system is coupled to gauge fields, and the phase mode disappears due to the Anderson–Higgs mechanism.

If one is not limited to charged systems in which the order parameter is coupled with gauge fields, the phase and amplitude modes of order parameters have been widely observed in symmetry broken phases (see Table 1). For example, magnons, or spin waves, correspond to phase modes in magnetically ordered systems. Liquid helium and cold atomic gases are other examples of physical systems in which collective modes of bosonic and fermionic superfluids are well studied. These collective modes provide important information on the underlying system, such as symmetries, phases, dynamics, and response to external fields.

Throughout the article, we put $\hbar = 1$.

Higgs mode in superconductors

The emergence of collective modes in symmetry broken phases can be understood with a simple macroscopic phenomenological model. For example, the low-energy effective theory of superconductors corresponds to the Ginzburg–Landau (GL) theory, whose Lagrangian density is given, as a functional of a complex scalar field $\psi(\boldsymbol{r})$ (a "macroscopic wavefunction" of electrons), by

$$\mathcal{L} = -\left[a|\psi(\boldsymbol{r})|^2 + \frac{b}{2}|\psi(\boldsymbol{r})|^4 + \frac{1}{2m^*}|(-i\nabla - e^*\boldsymbol{A})\psi(\boldsymbol{r})|^2\right] + c_1\psi(\boldsymbol{r})^\dagger(i\partial_t - e^*\phi)\psi(\boldsymbol{r}) + c_2|(i\partial_t - e^*\phi)\psi(\boldsymbol{r})|^2. \tag{1}$$

Here a, b, c_1, and c_2 are constants; m^* and e^* are effective mass and charge of condensates, and ϕ and $\boldsymbol{A}$ are scalar and vector potentials for external electromagnetic fields, respectively. The time derivative terms are included phenomenologically. The amplitude of the scalar field $\psi(\boldsymbol{r})$ serves as an order parameter, and its squared absolute value has a meaning of the superfluid density ($|\psi(\boldsymbol{r})|^2 = n_s$). The Lagrangian is invariant under the global phase rotation, $\psi \to e^{i\theta}\psi$. The coefficient a is assumed to behave as $a = a_0(T - T_c)$ ($a_0 > 0$) near the critical point, where T is a temperature of the system, and T_c is a critical temperature at which superconductivity emerges. At high temperature, the effective potential (the first two terms in the square bracket in Eq. (1)) has a parabolic cylindrical shape with a single minimum at the origin ($\psi = 0$). As the temperature goes down below T_c, the potential turns into a Mexican-hat shape (Fig. 1), where degenerate minima appear along the circle at the bottom of the potential ($|\psi| = \psi_0 > 0$). One of the minima is realized as the ground state, which spontaneously breaks the phase rotation symmetry. Without loss of generality, one can assume that the order parameter takes a real positive value in the ground state.

One can consider fluctuations of the order parameter around the ground state by expanding as

$$\psi(\boldsymbol{r}) = (\psi_0 + H(\boldsymbol{r}))e^{i\theta(\boldsymbol{r})}, \tag{2}$$

where $H(\boldsymbol{r})$ and $\theta(\boldsymbol{r})$ represent amplitude and phase fluctuations, respectively. The Lagrangian is then expanded in the following way:

$$\begin{aligned} \mathcal{L} = {} & 2aH^2 - \frac{1}{2m^*}(\nabla H)^2 - \frac{e^{*2}}{2m^*}\left(\boldsymbol{A} - \frac{1}{e^*}\nabla\theta\right)^2 \\ & \times (\psi_0 + H)^2 - c_1 e^*\left(\phi + \frac{1}{e^*}\partial_t\theta\right)(\psi_0 + H)^2 \\ & + c_2(\partial_t H)^2 + c_2 e^{*2}\left(\phi + \frac{1}{e^*}\partial_t\theta\right)^2(\psi_0 + H)^2 \\ & + \cdots . \end{aligned} \tag{3}$$

The first term indicates that the Higgs mode represented by H has a finite mass, reflecting the fact that the effective potential has a finite curvature along the amplitude direction. The second term in Eq. (3) corresponds to the kinetic term of the Higgs mode. The phase field θ appears without a mass term ($\propto \theta^2$). Hence, θ would be thought of as a massless NG mode. However, θ always appears in the combination of $\boldsymbol{A} - \frac{1}{e^*}\nabla\theta$ or $\phi + \frac{1}{e^*}\partial_t\theta$, due to which one can remove θ by performing a gauge transformation, $\boldsymbol{A} \to \boldsymbol{A}' = \boldsymbol{A} - \frac{1}{e^*}\nabla\theta$ and $\phi \to \phi' = \phi + \frac{1}{e^*}\partial_t\theta$ (unitary gauge). By rewriting $\boldsymbol{A}'$ and ϕ' as $\boldsymbol{A}$ and ϕ, one obtains an expression in terms of H,

$$\begin{aligned} \mathcal{L} = {} & 2aH^2 - \frac{1}{2m^*}(\nabla H)^2 - \frac{e^{*2}}{2m^*}\boldsymbol{A}^2(\psi_0 + H)^2 \\ & - c_1 e^*\phi(\psi_0 + H)^2 + c_2(\partial_t H)^2 + c_2 e^{*2}\phi^2(\psi_0 + H)^2 \\ & + \cdots . \end{aligned} \tag{4}$$

The phase mode θ disappears from the expression, and a mass term of the gauge field ($\propto\boldsymbol{A}^2$) appears in the third term. This is nothing but the Anderson–Higgs mechanism. One can count the number of degrees of freedom before and after the Anderson–Higgs mechanism:

$$\begin{aligned} & 2\ (\text{transverse components of } \boldsymbol{A}) + 2\ (\text{real and imaginary parts of } \psi) \\ & \to 3\ (\text{transverse and longitudinal components of } \boldsymbol{A}) + 1\ (\text{Higgs mode}) \end{aligned}$$

The electromagnetic field, that mediates the long-range Coulomb interaction, screens phase fluctuations of the superconducting order parameter, pushing them up to high energy (in the scale of plasma frequency). As a result of the Anderson–Higgs mechanism, the electromagnetic field itself becomes short-ranged and decays exponentially within the London penetration depth (Meissner–Ochsenfeld effect). The remaining low-energy excitation mode is the Higgs mode. In the vicinity of T_c, however, the phase mode may have a possibility to revive without damping [known as the Carlson–Goldman mode (Carlson and Goldman, 1975)] due to the presence of a large number of normal electrons which screen the long-range Coulomb interaction.

If the system is electrically neutral (i.e., $e^* = 0$), the order parameter is not coupled to gauge fields, and the Anderson–Higgs mechanism does not take place. In this case, the NG mode survives as a massless excitation, which dominates the low-energy behavior. In particular, the Higgs mode can hybridize with the NG mode if $c_1 \neq 0$, which causes a mixing between amplitude and phase modes. In order to decouple the amplitude and phase modes, one often requires an effective particle-hole symmetry, which suppresses the c_1 term and makes the Lagrangian relativistic with an emergent Lorentz symmetry.

In superconductors, there is an approximate particle-hole symmetry at low energy so that one can practically neglect the c_1 term. From Eq. (4), one can see that there is no linear coupling between H and $\boldsymbol{A}$ (or ϕ). This means that the Higgs mode cannot be excited within the linear response regime, which is well expected from the fact that the Higgs mode is a scalar excitation having no electric charge or magnetic moment. On the other hand, if one goes beyond the linear response, the Higgs mode can be excited by electromagnetic fields through the nonlinear coupling (e.g., $\propto\boldsymbol{A}^2H$) (Tsuji and Aoki, 2015), which has been used to observe the Higgs mode in terahertz laser experiments.

The GL theory does not predict the precise value of the mass of the Higgs mode. It only tells that the mass is proportional to $(-a)^{\frac{1}{2}} \propto (T_c - T)^{\frac{1}{2}}$. From a microscopic theory, the mass is found to coincide with the superconducting gap energy 2Δ. That is, the minimum energy that is required to excite the Higgs mode is the same as the energy to break a single Cooper pair. This causes a problem of using the GL theory in the energy scale of the Higgs mode. In the GL theory, the order parameter is supposed to vary sufficiently slowly in space and time, whereas the order parameter oscillates with the frequency of 2Δ when the Higgs mode is excited. This already reaches the energy scale of pair breaking, and thus one cannot neglect the effect of quasiparticle excitations, invalidating the basic assumption of the GL description.

The aforementioned issue motivates one to move to a microscopic description of superconductivity, that is, the BCS theory. In the BCS theory, one adopts the Hamiltonian that includes the kinetic energy of electrons and the pairing interaction (usually mediated by phonons),

$$H_{\mathrm{BCS}} = \sum_{\boldsymbol{k},\sigma} \varepsilon_{\boldsymbol{k}} c^{\dagger}_{\boldsymbol{k}\sigma} c_{\boldsymbol{k}\sigma} - \frac{V}{N} \sum_{\boldsymbol{k},\boldsymbol{k}'} c^{\dagger}_{\boldsymbol{k}\uparrow} c^{\dagger}_{-\boldsymbol{k}\downarrow} c_{-\boldsymbol{k}'\downarrow} c_{\boldsymbol{k}'\uparrow}, \tag{5}$$

where $c_{\boldsymbol{k}\sigma}$ is the annihilation operator of electrons with momentum $\boldsymbol{k}$ and spin σ, $\varepsilon_{\boldsymbol{k}}$ is the energy dispersion, $V\ (> 0)$ is the pairing interaction strength, and N is the number of $\boldsymbol{k}$ points.

In the mean-field approximation, the Hamiltonian (5) is replaced by $H_{\mathrm{MF}} = \sum_{\boldsymbol{k}} \Psi^{\dagger}_{\boldsymbol{k}} h(\boldsymbol{k}) \Psi_{\boldsymbol{k}}$, where $\Psi_{\boldsymbol{k}} = (c_{\boldsymbol{k}\uparrow} c^{\dagger}_{-\boldsymbol{k}\downarrow})^T$ is the Nambu spinor and

$$h(\boldsymbol{k}) = \begin{pmatrix} \varepsilon_{\boldsymbol{k}} & -\Delta^* \\ -\Delta & -\varepsilon_{\boldsymbol{k}} \end{pmatrix} \tag{6}$$

is the Bogoliubov–de-Gennes Hamiltonian. The off-diagonal element Δ is defined by

$$\Delta = \frac{V}{N} \sum_{\boldsymbol{k}} \langle c^{\dagger}_{\boldsymbol{k}\uparrow} c^{\dagger}_{-\boldsymbol{k}\downarrow} \rangle. \tag{7}$$

We assume that Δ takes a real positive value. The eigenvalues of $h(\boldsymbol{k})$ are found to be $\pm E_{\boldsymbol{k}} := \pm\sqrt{\varepsilon^2_{\boldsymbol{k}} + \Delta^2}$, and thus the single-particle spectrum shows an energy gap of 2Δ. At zero temperature, Δ satisfies the gap equation,

$$\Delta = \frac{V}{N} \sum_{\boldsymbol{k}} \frac{\Delta}{2E_{\boldsymbol{k}}}. \tag{8}$$

The dynamics of superconductors is determined by the time-dependent Bogoliubov–de-Gennes equation,

$$i \frac{\partial}{\partial t} \Psi_{\boldsymbol{k}} = h(\boldsymbol{k}) \Psi_{\boldsymbol{k}}. \tag{9}$$

To analyze the equation, it is convenient to introduce Anderson's pseudospins,

$$\sigma^{\alpha}_{\boldsymbol{k}} = \frac{1}{2} \langle \Psi^{\dagger}_{\boldsymbol{k}} \tau^{\alpha} \Psi_{\boldsymbol{k}} \rangle \quad (\alpha = x, y, z). \tag{10}$$

Here τ^{α} denotes the Pauli matrices. Physically, the x and y components of the pseudospins correspond, respectively, to the real and imaginary parts of Cooper pairs' amplitude $\langle c^{\dagger}_{\boldsymbol{k}\uparrow} c^{\dagger}_{-\boldsymbol{k}\downarrow} \rangle$, and the z component represents the momentum-dependent occupation of electrons. From Eq. (9), one finds that the time evolution of the pseudospins is given by

$$\frac{\partial}{\partial t} \boldsymbol{\sigma}_{\boldsymbol{k}} = 2\boldsymbol{b}_{\boldsymbol{k}} \times \boldsymbol{\sigma}_{\boldsymbol{k}}, \tag{11}$$

which resembles the Bloch equation that describes precession motion of spins in a magnetic field. Here $\boldsymbol{b}_{\boldsymbol{k}} = (-\mathrm{Re}\,\Delta, -\mathrm{Im}\,\Delta, \varepsilon_{\boldsymbol{k}})$ plays a role of a magnetic field for pseudospins.

In general, the equation of motion (11) becomes a nonlinear equation since it is supplemented by the self-consistency condition (8). However, one can linearize the equation if the deviation from the initial ground state is sufficiently small. By writing $\boldsymbol{\sigma}_{\boldsymbol{k}}(t) = \boldsymbol{\sigma}_{\boldsymbol{k}}(0) + \delta\boldsymbol{\sigma}_{\boldsymbol{k}}(t)$ and $\Delta(t) = \Delta + \delta\Delta(t)$, the linearized equation is expressed as

$$\frac{\partial}{\partial t} \delta\sigma^x_{\boldsymbol{k}} = -2\varepsilon_{\boldsymbol{k}} \delta\sigma^y_{\boldsymbol{k}}, \tag{12}$$

$$\frac{\partial}{\partial t} \delta\sigma^y_{\boldsymbol{k}} = 2\varepsilon_{\boldsymbol{k}} \delta\sigma^x_{\boldsymbol{k}} + 2\Delta\delta\sigma^z_{\boldsymbol{k}} - \frac{\varepsilon_{\boldsymbol{k}}}{E_{\boldsymbol{k}}} \delta\Delta, \tag{13}$$

$$\frac{\partial}{\partial t} \delta\sigma^z_{\boldsymbol{k}} = -2\Delta\delta\sigma^y_{\boldsymbol{k}}. \tag{14}$$

By using the relation $\Delta\delta\sigma^x_{\boldsymbol{k}} = \varepsilon_{\boldsymbol{k}} \delta\sigma^z_{\boldsymbol{k}}$, one can further simplify the equation into

$$\frac{\partial^2}{\partial t^2} \delta\sigma^x_{\boldsymbol{k}} = -\,4E^2_{\boldsymbol{k}} \delta\sigma^x_{\boldsymbol{k}} + \frac{2\varepsilon^2_{\boldsymbol{k}}}{E_{\boldsymbol{k}}} \delta\Delta. \tag{15}$$

After Fourier transformation, one obtains

$$\delta\sigma^x_{\boldsymbol{k}}(\omega) = \frac{2\varepsilon^2_{\boldsymbol{k}}}{E_{\boldsymbol{k}}(4E^2_{\boldsymbol{k}} - \omega^2)} \delta\Delta(\omega) \tag{16}$$

Combining with the linearized gap equation, $\delta\Delta(\omega) = \frac{V}{N}\sum_{\boldsymbol{k}}\delta\sigma^x_{\boldsymbol{k}}(\omega)$, one finds that a nontrivial solution exists if the following condition is satisfied:

$$\frac{V}{N}\sum_{\boldsymbol{k}}\frac{2\varepsilon^2_{\boldsymbol{k}}}{E_{\boldsymbol{k}}(4E^2_{\boldsymbol{k}} - \omega^2)} = 1. \tag{17}$$

This is precisely the condition that has been derived by Anderson (1958b). One can quickly verify that $\omega = 2\Delta$ is a solution of Eq. (17) since it is reduced to the gap equation (8) at this frequency. The solution $\Delta(t)$ consists of a collective amplitude oscillation of the order parameter, and hence is identified to the Higgs mode that has been expected to exist in the GL theory.

Subsequently, the equation of motion for a quench problem has been studied by Volkov and Kogan (1974), who showed that the amplitude oscillation of the gap function does not persist but decays in a power law as

$$\Delta(t) \sim \Delta + \frac{c}{\sqrt{2\Delta t}}\cos(2\Delta t + \varphi) \tag{18}$$

with certain constants c and φ. This slight instability (power-law decay) of the Higgs mode is related to the fact that the energy of the Higgs mode lies right at the bottom edge of the quasiparticle excitation continuum. The decay into quasiparticles occurs without collisions, similar to the case of Landau damping for plasma waves. The energy dispersion of the Higgs mode at finite momentum, $\omega_H(\boldsymbol{q})$, has the following form (Littlewood and Varma, 1982),

$$\omega_H(\boldsymbol{q}) = \sqrt{(2\Delta)^2 + \frac{1}{3}v_F^2q^2} - i\frac{\pi^2}{24}v_Fq, \tag{19}$$

where v_F is the Fermi velocity and $q = |\boldsymbol{q}|$. The presence of the imaginary part indicates that the Higgs mode has a finite lifetime at finite $\boldsymbol{q}$ due to the decay into quasiparticles. Especially, the mode becomes overdamped when $v_Fq/\Delta \gtrsim 1$.

In multiband superconductors, the system may possess multiple order parameters (multigap superconductors) such as MgB_2. In this case, there can arise a collective oscillation of the relative phase between two order parameters, known as the Leggett mode (Leggett, 1966). Since the relative phase oscillation does not induce the net current and hence does not couple to gauge fields linearly, the Leggett mode can evade the Anderson–Higgs mechanism, remaining to survive at low energy.

If there is a hidden competing order that stays close to the primary order, the so-called Bardasis–Schrieffer mode can emerge as a collective oscillation of the amplitude of the secondary order parameter (Bardasis and Schrieffer, 1961). For example, some of iron-based superconductors are expected to have a close competition between the $s_\pm$ pairing ground state with the d-wave pairing instability. The Bardasis–Schrieffer mode can be used to probe such hidden instabilities that are difficult to detect by other means.

In strongly correlated systems, one may need to go beyond the BCS theory and take into account quantum correction effects to treat Higgs modes, which can be defined by the peak of the superconducting amplitude-amplitude correlation function. It is expected that the lifetime (i.e., inverse of the peak width) of the Higgs mode would become shorter and shorter as one goes into strongly correlated regimes due to the decay to quasiparticles, and the amplitude oscillation of the order parameter would become overdamped at some point. Such kind of behavior has been observed in the ordered phase of the Hubbard model with an interaction quench (Werner et al., 2012; Tsuji et al., 2013).

Higgs modes in atomic Fermi gases

The Higgs mode appears not only in superconductors but also in neutral fermionic superfluids. The only traditional condensed-matter system that falls into the latter category had been the system of superfluid ^{3}He. In the last few decades, a new system arose in the field of atomic physics: Superfluidity in a dilute gas of fermionic atoms has been realized in 2004 (Regal et al., 2004; Zwierlein et al., 2004). Since then, this system has been offering a unique opportunity for studying Higgs modes in fermionic superfluids.

Atomic gases have several advantages over solid-state systems. One of them is high controllability of system parameters. Using experimental techniques developed in atomic, molecular, and optical physics, various parameters can be tuned with unprecedented precision. In atomic Fermi gases, the interaction strength between fermions can be tuned by external fields via the Feshbach resonance. Employing this technique, one can observe a smooth crossover between the BCS-type state with large overlapping Cooper pairs and Bose–Einstein condensation (BEC) of tightly bound molecules of two fermions, known as the "BEC-BCS crossover," which has been realized also in 2004 (Regal et al., 2004; Zwierlein et al., 2004). This phenomenon had never been directly observed in condensed-matter systems, though it was theoretically speculated by Leggett (1980) and Eagles (1969). This experimental progress allows one to study the evolution of the Higgs mode in the BEC-BCS crossover.

The interaction strength in this system is often described by the dimensionless parameter $1/(k_Fa)$, where k_F and a are the Fermi wave number and the s-wave scattering length, respectively. The s-wave scattering length can be tuned by an external magnetic field due to the Feshbach resonance. The weak-coupling BCS regime and strong-coupling BEC regime correspond to $1/(k_Fa) < 0$ and $1/(k_Fa) > 0$, respectively. The crossover between the BCS and BEC physics occurs at the unitary limit $1/(k_Fa) = 0$, at which a diverges.

The Higgs mode in a superfluid Fermi gas of ^{6}Li atoms has been observed in 2018 (Behrle et al., 2018). A novel scheme to induce the Higgs mode has been developed in the experiment: One of the two hyperfine states involved in pairing is coupled with an initially unoccupied third state by a radiofrequency field. In this manner, a periodic modulation of the amplitude of the gap

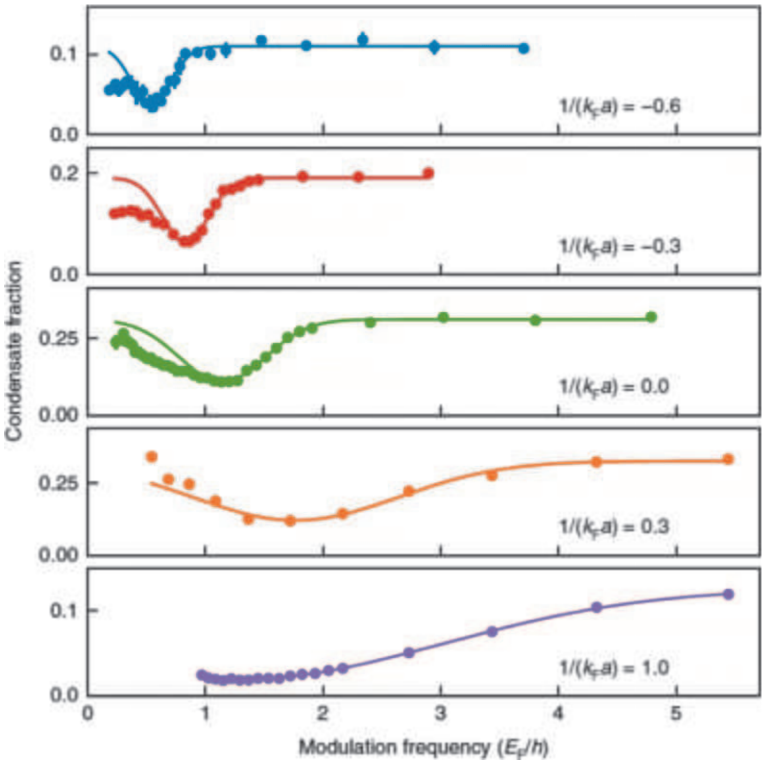

Fig. 3 Measured excitation spectra of the Higgs mode in a superfluid Fermi gas for different interaction strength $1/(k_Fa)$. Adapted from Behrle A, Harrison T, Kombe J, Gao K, Link M, Bernier J-S, Kollath C, and Köhl M (2018) Higgs mode in a strongly interacting fermionic superfluid. Nature Physics 14(8): 781–785. ISSN 1745-2481

function was induced. The Higgs mode was searched by rapidly sweeping the magnetic field onto the molecular side of the Feshbach resonance and measuring the energy absorption spectrum. The excitation spectra in Fig. 3 show the clear resonance at 2Δ in the BCS side ($1/(k_Fa) < 0$) while the peak broadens significantly signaling the instability of the Higgs mode in the BEC side ($1/(k_Fa) > 0$).

The time-dependent Bogoliubov–de-Gennes (tdBdG) formalism has been extensively used to study the dynamical properties of superfluid Fermi gases. In this formalism, the gap function $\Delta(\mathbf{r}, t)$ obeys the tdBdG equation

$$i\frac{\partial}{\partial t}\begin{pmatrix} u_\nu(\mathbf{r},t) \\ v_\nu(\mathbf{r},t) \end{pmatrix} = \begin{pmatrix} \hat{h} & \Delta \\ \Delta^* & -\hat{h} \end{pmatrix}\begin{pmatrix} u_\nu(\mathbf{r},t) \\ v_\nu(\mathbf{r},t) \end{pmatrix}, \tag{20}$$

where $\hat{h} = -\nabla^2/2m + U(\mathbf{r}) - \mu$, m is the atomic mass, μ is the chemical potential, $U(\mathbf{r})$ is the trapping potential, ν is the index for the eigenstates, and u_ν and v_ν are the time-dependent quasi-particle amplitudes, respectively. The tdBdG equation needs to be solved self-consistently with the gap equation,

$$\Delta(\mathbf{r}, t) = \frac{V}{N}\sum_\nu u_\nu(\mathbf{r}, t)v_\nu^*(\mathbf{r}, t), \tag{21}$$

and the equation for the total number of atoms $\mathcal{N}$,

$$\mathcal{N} = 2\int d\mathbf{r}\sum_\nu |u_\nu(\mathbf{r}, t)|^2. \tag{22}$$

In a uniform system ($U(\mathbf{r}) = 0$), substituting the static solution of Eq. (20) $u_k^2 = (1 + \varepsilon_k/E_k)/2$ and $v_k^2 = (1 - \varepsilon_k/E_k)/2$ ($\varepsilon_k = k^2/2m - \mu$ and $E_k = \sqrt{\varepsilon_k^2 + \Delta^2}$) into Eqs. (22) and (22), the former reduces to the gap equation (8), while the latter reduces to

$$\mathcal{N} = \sum_k\left(1 - \frac{\varepsilon_k}{E_k}\right). \tag{23}$$

The self-consistent solution of (Δ, μ) for the gap equation (8) and the number equation (23) smoothly connects the weak-coupling BCS limit with $((8\varepsilon_F/e^2)e^{-\pi/2k_F|a|}, \varepsilon_F)$ and the strong-coupling BEC limit with $(\sqrt{16/3\pi}|\mu|^{1/4}\varepsilon_F^{3/4}, -1/2ma^2)$, where e is Napier's constant and ε_F is the Fermi energy. Note that μ coincides with the binding energy of molecules in the BEC limit. The above tdBdG formalism thus correctly captures the dynamical properties of a superfluid Fermi gas including the Higgs mode throughout the entire BEC-BCS crossover.

One can study small amplitude oscillations of the gap function (Higgs mode) induced by a quench of the interaction strength in the tdBdG formalism. The gap function evolves in time according to Eq. (18) in the BCS regime, where the amplitude oscillates with the frequency $\omega_H = 2\Delta$ and the oscillation decays in a power law ($\sim t^{\gamma}$) with the exponent $\gamma = -1/2$ (Volkov and Kogan, 1974). In the BEC regime, on the other hand, the frequency $\omega_H = 2\sqrt{\Delta^2 + \mu^2}$ and the exponent of the power-law decay $\gamma = -3/2$ for the amplitude oscillation have been predicted (Gurarie, 2009). The former coincides with twice of the energy threshold for the creation of fermionic excitations by pair-breaking. The evolution of the frequency ω_H and the power γ through the BEC-BCS crossover is of particular interest and worth investigating in future experiments (Tokimoto et al., 2019).

The NG mode has also been investigated in atomic fermi superfluids. It manifest itself as the Anderson–Bogoliubov (AB) phonon (phase) mode as shown in Table 1. Anderson predicted the sound velocity $c = v_F/\sqrt{3}$ for the AB phonon mode in the BCS limit by the generalized random-phase approximation (Anderson, 1958b). The evolution of the excitation spectra throughout the BEC-BCS crossover has been studied using two-photon Bragg spectroscopy, which allows characterization of the dispersion relation of the AB phonon mode (Hoinka et al., 2017).

Higgs and Nambu–Goldstone modes in other systems

The NG and Higgs modes exist ubiquitously in quantum many-body systems that possess both a spontaneously broken continuous symmetry and an approximate particle-hole symmetry. In the previous sections, we have taken superconductors and superfluid states of ultracold two-component Fermi gases as specific examples that possess either or both of the NG and Higgs modes. In this section, we explain several other significant examples of the NG and Higgs modes in the contexts of condensed matter and ultracold-atom physics in order to illustrate broad applicability of the concepts.

We first consider a superfluid state of ultracold spinless Bose gases in optical lattices. An optical lattice means a periodic potential for atoms that is created by two counter-propagating laser beams. When the optical lattice potential is sufficiently deep, the system is well described by the Bose–Hubbard model,

$$\hat{H}_{\mathrm{BH}} = -J\sum_{\langle j,l\rangle}\left(\hat{b}_j^{\dagger}\hat{b}_l + \mathrm{h.c.}\right) + \frac{U}{2}\sum_j \hat{b}_j^{\dagger}\hat{b}_j^{\dagger}\hat{b}_j\hat{b}_j + \sum_j(\varepsilon_j - \mu)\hat{b}_j^{\dagger}\hat{b}_j, \tag{24}$$

where $\hat{b}_j$, U, J, and μ denote, respectively, the annihilation operator of bosons at site j, the onsite interaction, the hopping, and the chemical potential. The external field potential ε_j is present for trapped atoms in standard experiments. In Fig. 4, we show a ground-state phase diagram of the homogeneous Bose-Hubbard model in the (ZJ/U, μ/U) plane, where Z is the coordination number. When the filling factor, which is the number of particles per lattice site, is integer and ZJ/U is small, the ground state is a Mott insulating (MI) state. Otherwise, it is a superfluid state. There is a continuous quantum phase transition from the MI to the

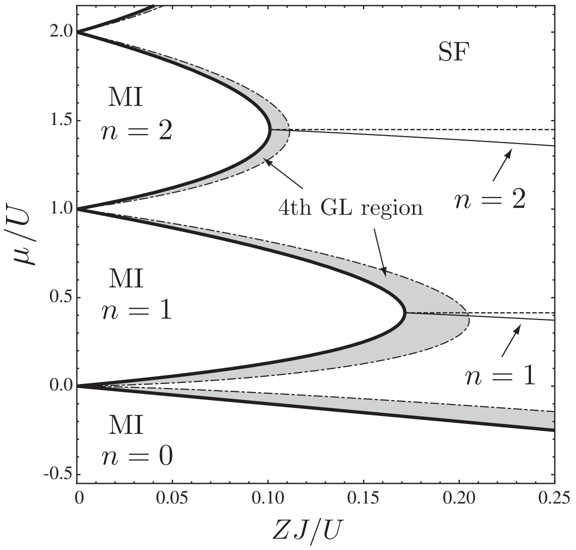

Fig. 4 Ground-state phase diagram of the homogeneous Bose–Hubbard model obtained by using a mean-field theory. The *gray shaded areas* near the Mott insulator (MI) regions roughly mark the regions where the superfluid (SF) order parameter is small enough for the fourth-order GL approximation (i.e., the effective action can be written by the expansion up to fourth order in the order parameter) to be valid. On the *dashed lines* in the SF region, the effective particle-hole symmetry is present. *n* denotes the filling factor. Adapted from Nakayama T, Danshita I, Nikuni T, and Tsuchiya S (2015) Fano resonance through Higgs bound states in tunneling of Nambu-Goldstone modes. Physical Review A 92(4): 043610

superfluid state, where the U(1) symmetry is spontaneously broken. In the superfluid region near the quantum phase transitions, which is the *gray-shaded area* in Fig. 4, low-energy properties of the system can be effectively described by the GL theory (Sachdev, 2011). At the tip of the lobe of the Mott insulating region, where the quantum phase transition to a superfluid with commensurate filling occurs, there emerges particle-hole symmetry. In the nearby superfluid state at the commensurate filling, the emergent particle-hole symmetry survives approximately so that the effective theory coincides with the Lagrangian of Eq. (1) with $e^* = 0$. Consequently, the Higgs mode is present as an approximately independent collective mode. Note that there is no Higgs mode in a bosonic superfluid state without particle-hole symmetry as in the cases of superfluid ^{4}He and Bose–Einstein condensates of weakly-interacting atomic Bose gases. When ZJ/U decreases toward the critical value $(ZJ/U)_c$, the energy gap of the Higgs mode Δ_g approaches zero as $\Delta_g \propto |zJ/U - (zJ/U)_c|^{\nu}$, where ν is the critical exponents for the correlation length of the $(D + 1)$-dimensional classical XY model and D denotes the spatial dimension of the system.

In 2012, Endres et al. have investigated dynamics of two-dimensional gas of ^{87}Rb atoms (bosons) in optical lattices in response to the temporal modulation of the lattice depth in order to measure the gap of the Higgs mode (Endres et al., 2012). Fig. 5B shows the temperature of the system after the application of the lattice modulation as a function of the modulation frequency for the superfluid state at $J/J_c = 1.2$, where J_c is the transition value of the hopping for a given U at unit filling. Above an onset frequency ν_0, the response exhibits a broad spectrum. Quantitative comparisons with theoretical analyses have revealed that the onset frequency (Fig. 5A) coincides with the gap of the Higgs mode at zero momentum. It is worth noticing that the Higgs mode has not been observed as a resonance peak in the response. This smearing of the resonance can be attributed to combined effects of the spatial inhomogeneity due to the trapping potential and the finite temperatures (Pollet and Prokof'ev, 2012).

We next consider antiferromagnetic materials consisting of dimers of $S = 1/2$ spins, such as $\mathrm{TlCuCl_3}$ (Rüegg et al., 2008) and $\mathrm{KCuCl_3}$ (Kuroe et al., 2012), which can be effectively described by the following Hamiltonian,

$$\hat{H}_{\mathrm{AFD}} = \sum_{j}\left(J\hat{\mathbf{S}}_{j,R}\cdot\hat{\mathbf{S}}_{j,L} - J_{xx}\hat{S}^{x}_{j,R}\cdot\hat{S}^{x}_{j,L}\right) + \sum_{j,\,l;\,m,\,m'} J_{j,l;\,m,m'}\hat{\mathbf{S}}_{l,m}\cdot\hat{\mathbf{S}}_{j,m'}. \tag{25}$$

Here, $\hat{\mathbf{S}}_{j,m} = (\hat{S}^{x}_{j,m}, \hat{S}^{y}_{j,m}, \hat{S}^{z}_{j,m})$ denotes the $S = 1/2$ spin operator at spin $m(= L, R)$ of dimer j. $J(> 0)$, $J_{xx}(> 0)$ and $J_{j,l;m,m'}$ are the intradimer isotropic interaction, the intradimer anisotropic interaction, and the interdimer isotropic interaction, respectively. In Fig. 6, the spatial configuration of the interdimer interactions is illustrated (Matsumoto et al., 2004). To be concrete, we hereafter focus on the case of $\mathrm{TlCuCl_3}$, in which the Higgs mode has been observed via neutron scattering experiments. In this case, the most dominant interdimer interaction is J_2 that is antiferromagnetic. Although J_{xx} is about 1% of J, it is important for discussing the NG and Higgs modes in the sense that it reduces the spin rotation symmetry from SU(2) to U(1).

At atmospheric pressure, J is dominant over J_2 so that the low-temperature magnetic state is a dimerized state in that two spins on each dimer form a spin singlet and there is no magnetic order. When the hydrostatic pressure p is increased, J_2/J increases and a continuous quantum phase transition to an antiferromagnetic ordered state occurs at $p = p_c \simeq 1.08$ kbar. Associated with the

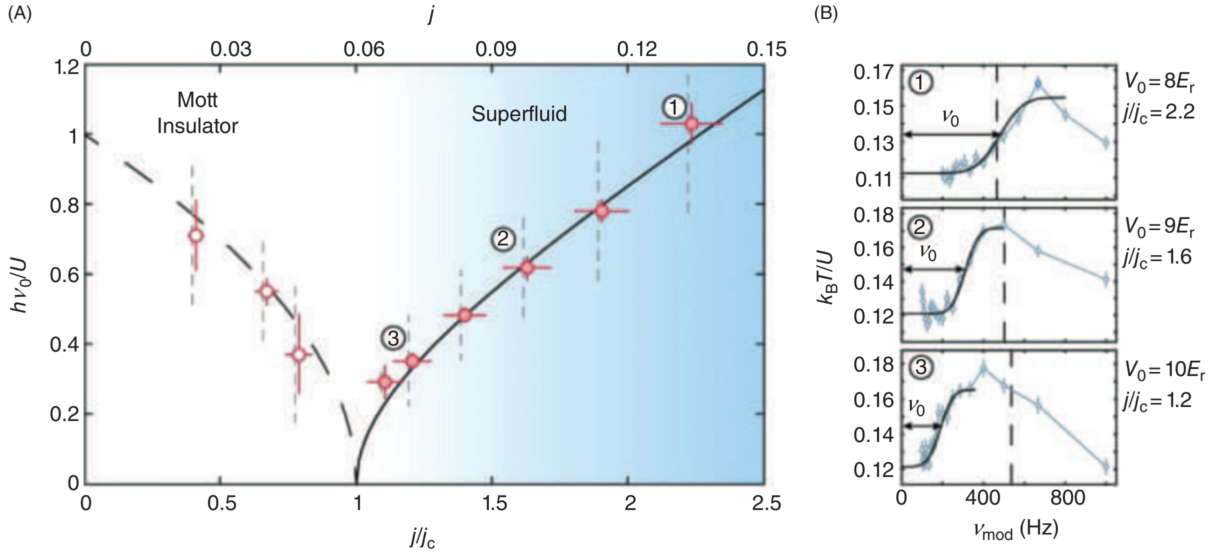

Fig. 5 Experimental observation of the Higgs gap in the system of ultracold Bose gases in optical lattices. (A) Excitation gap versus the hopping parameter j, which is denoted by J in the main text, in unit of its critical value j_c. *Solid line* and *dashed line*, respectively, stand for the Higgs and Mott gaps calculated by the Gutzwiller mean-field theory for a homogeneous system with unit filling. (B) Temperature response to temporal modulation of the lattice depth for three values of j/j_c. Adapted from Endres M, Fukuhara T, Pekker D, Cheneau M, SchaußP, Gross C, Demler E, Kuhr S, and Bloch I (2012) The 'Higgs' amplitude mode at the two-dimensional superfluid/Mott insulator transition. Nature 487(7408): 454–458. ISSN 1476-4687

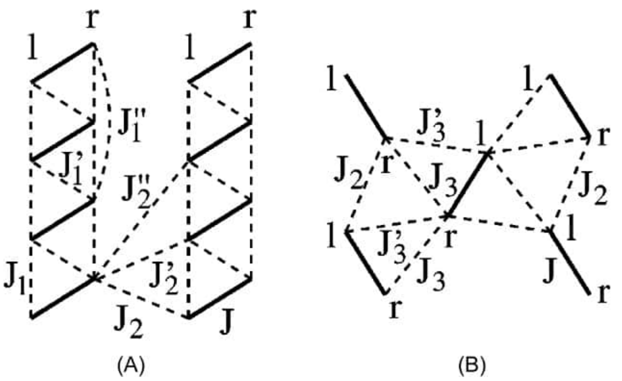

Fig. 6 Schematic diagram of the interdimer interaction between each pair of spins of $XCuCl_3$ in (A) *a–c* plane and (B) *b–c* plane, where X is for example Tl or K. One spin with $S = 1/2$ lives at each vertex. Adapted from Matsumoto M, Normand B, Rice TM, and Sigrist M (2004) Field- and pressure-induced magnetic quantum phase transitions in $TlCuCl_3$. Physical Review B 69(5): 054423

transition, the spin-rotation symmetry is spontaneously broken. The quantum phase transition can be qualitatively captured by a mean-field approximation in which the many-body wave function is assumed to be a product state,

$$|\Psi_{\mathrm{MF}}\rangle = \bigotimes_j |\phi\rangle_j \tag{26}$$

where

$$|\phi\rangle_j = a_{j,0}|s\rangle_j + a_{j,1}|t_1\rangle_j + a_{j,2}|t_2\rangle_j + a_{j,3}|t_3\rangle_j. \tag{27}$$

The local state at dimer j is spanned by the spin-singlet and triplet states, namely, $|s\rangle = 2^{-\frac{1}{2}}(|\uparrow,\downarrow\rangle - |\downarrow,\uparrow\rangle)$, $|t_1\rangle = 2^{-\frac{1}{2}}(|\uparrow,\downarrow\rangle + |\downarrow,\uparrow\rangle)$, $|t_2\rangle = 2^{-\frac{1}{2}}(|\uparrow,\uparrow\rangle + |\downarrow,\downarrow\rangle)$, and $|t_3\rangle = 2^{-\frac{1}{2}}(|\uparrow,\uparrow\rangle - |\downarrow,\downarrow\rangle)$. The coefficients satisfy the normalization condition $\sum_{\alpha=0}^{3}|a_{j,\alpha}|^2 = 1$. In the limit of $J_{j,l;m,m'} \to 0$, the four states are the eigenstates of each local Hamiltonian, where $|s\rangle$ is the ground state, $|t_1\rangle$ and $|t_2\rangle$ are the degenerate first excited states, and $|t_3\rangle$ is the highest energy state. When J_2/J is finite but smaller than the critical value, the ground state remains to be $|\phi\rangle = |s\rangle$ for all the dimers and there is the energy gap to create triplet states. The energy cost for creating $|t_1\rangle$ is equivalent to that for creating $|t_2\rangle$ so that this symmetry can be regarded as a particle-hole symmetry. At the critical value of J_2/J, the energy gap closes. When J_2/J increases further, the coefficients $a_{j,\alpha}$ for $\alpha = 1, 2, 3$ become finite and the antiferromagnetic order emerges. The low-energy properties in the ordered phase can be effectively described by the GL theory of Eq. (1), thanks to the spontaneous breaking of the U(1) symmetry and the presence of the particle-hole symmetry. Hence, there are the NG and Higgs modes in the ordered phase. In addition, there is another gaped mode that dominantly includes the $|t_3\rangle$ excitation.

In 2008, Rüegg et al. have observed the excitation modes explained above by means of inelastic neutron scattering (Rüegg et al., 2008). Fig. 7 shows the energy gaps of the excitation modes at specific momenta, which are detected as resonance peaks in the spectra of inelastic neutron scattering. In the dimerized phase at low pressure, there are three gapped modes corresponding to the creation of a triplet excitation. The gap of the two modes (*blue symbols*) closes at the quantum critical point whereas that of the other mode (*black symbols*) remains gappped. In the antiferromagnetic ordered phase at high pressure, the former two modes transform into the Higgs and NG modes, which correspond to longitudinal and transverse fluctuations of the magnetic order parameter.

In the last place, we briefly mention another important example, namely, materials with incommensurate CDW (ICDW) order (Grüner, 1988). Specifically, in solid-state materials with quasi-1D lattice structure, such as $2H$-$NbSe_2$ (Tsang et al., 1976) and $K_{0.3}MoO_3$ (Yusupov et al., 2010), electron–phonon interactions induce the condensation of particle-hole pairs with momenta $2k_F$ and $-2k_F$, leading to the formation of ICDW states at low temperatures. In the ICDW state, the electron density is given by

$$\rho(x) \simeq \rho_0 + \rho_1 \cos(2k_F x + \varphi), \tag{28}$$

where k_F, ρ_0, ρ_1, and φ denote, respectively, the Fermi momentum, the average electron density, the amplitude, and the phase of ICDW. The oscillation of the amplitude ρ_1, which is often called amplitudon, corresponds to the Higgs mode whereas that of the phase φ (phason) does to the NG mode. The Higgs mode has been observed in several ICDW materials via Raman spectroscopy.

Conclusion

We have reviewed various order-parameter dynamics that appear in condensed matter systems. Especially, we have focused on Higgs and Nambu–Goldstone (NG) modes, corresponding to amplitude and phase oscillations of order parameters. They provide important information on the fundamental properties of underlying quantum many-body systems, including symmetries, phase transitions, dynamics, and response to external perturbations. Target systems range from superconductors to cold-atom systems (bosonic and fermionic superfluids), quantum magnets, charge density waves, and so on. Here one can see the universality of

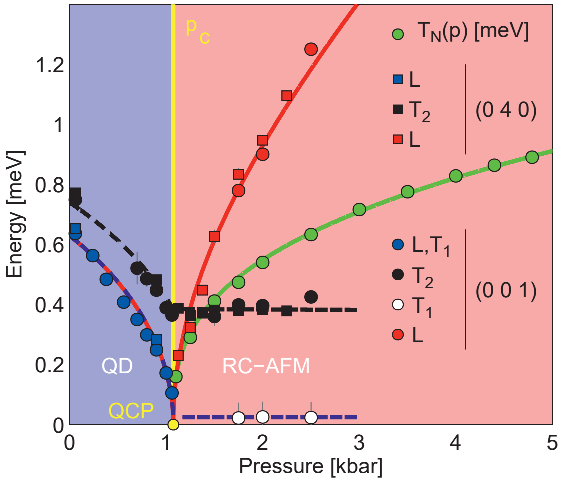

Fig. 7 Energy gaps of the magnetic excitations in $TlCuCl_3$ versus pressure, which has been detected via inelastic neutron scattering. The *red symbols* correspond to the gap of the Higgs mode in the ordered phase, namely, the renormalized classical antiferromagnetic (RC-AFM) phase. QD and QCP stand for the quantum disordered phase and quantum critical point, respectively. p_c, L, and T denote the critical pressure, longitudinal magnetic excitation, and transverse magnetic excitation, respectively. (0 4 0) or (0 0 1) means the value of the momentum transfer in the neutron scattering. Adapted from Rüegg C, Normand B, Matsumoto M, Furrer A, McMorrow DF, Krämer KW, Güdel HU, Gvasaliya SN, Mutka H, and Boehm M (2008) Quantum magnets under pressure: Controlling elementary excitations in $TlCuCl_3$. Physical Review Letters 100(20): 205701

order-parameter dynamics, which may not depend so much on details of the system, partly because they are effectively described by a "common language" based on quantum field theories at low energies.

There are many open issues that remain to be addressed. In the case of superconductors, it is experimentally important to understand various aspects of Higgs modes in superconductors, especially for those beyond NbN and the coexisting phase of CDW and superconductivity in $NbSe_2$. The difficulty lies in the fact that there are always competitions between the Higgs mode and quasiparticle excitations (Cea et al., 2016), both of which have similar characters with respect to symmetries and excitation energies. To distinguish them, one has to carefully compare experimental results with theoretical calculations, which may depend on details of materials, impurities, electron–phonon couplings, and so on (Tsuji and Nomura, 2020). This reflects the situation that one has not fully understood the universal (i.e., material-independent) condition that the Higgs mode becomes visible in experiments. To see enriched order-parameter dynamics, it will be fascinating to extend the observation of Higgs modes in various multiband superconductors such as MgB_2 (Kovalev et al., 2021) and unconventional superconductors (Schwarz et al., 2020) such as cuprates (Barlas and Varma, 2013; Katsumi et al., 2018; Chu et al., 2020) and iron-based superconductors (Vaswani et al., 2021; Grasset et al., 2022). A potential application of the Higgs mode includes detection of light-induced orders (Isoyama et al., 2021; Katsumi et al., 2022) and hidden fluctuations (Katsumi et al., 2020).

In the case of cold-atom systems, further investigations, both experimentally and theoretically, are needed to better understand the evolution of the Higgs modes across the BCS-BEC crossover in a superfluid fermi gas and the SF-MI phase transition in a bosonic superfluid in an optical lattice. In the lattice-boson systems, in particular, it is a long-standing problem whether or not the Higgs mode can be detected as a resonance peak in the response to temporal modulation of an external potential. Since recent experiments on optical-lattice systems have realized almost homogeneous samples of ultracold gases (e.g., Mazurenko et al., 2017), it will be interesting to experimentally address such a problem. Last but not least, taking advantage of the high degree of ability to control the system, it may be worthwhile to investigate previously unexplored aspects of Higgs modes, such as tunneling properties (Nakayama et al., 2015; Nakayama and Tsuchiya, 2019), which are typically difficult to study in solid-state systems.

References

Anderson PW (1958a) Coherent excited states in the theory of superconductivity: Gauge invariance and the Meissner effect. *Physical Review* 110(4): 827–835.
Anderson PW (1958b) Random-phase approximation in the theory of superconductivity. *Physical Review* 112(6): 1900–1916.
Anderson PW (1963) Plasmons, gauge invariance, and mass. *Physical Review* 130(1): 439–442.
ATLAS Collaboration. (2012) Observation of a new particle in the search for the Standard Model Higgs Boson with the ATLAS detector at the LHC. *Physics Letters B* 716(1): 1–29. ISSN: 0370-2693.
Bardasis A and Schrieffer JR (1961) Excitons and plasmons in superconductors. *Physical Review* 121(4): 1050–1062.
Bardeen J, Cooper LN, and Schrieffer JR (1957) Theory of superconductivity. *Physical Review* 108(5): 1175–1204.
Barlas Y and Varma CM (2013) Amplitude or Higgs modes in *d*-wave superconductors. *Physical Review B* 87(5): 054503.
Behrle A, Harrison T, Kombe J, Gao K, Link M, Bernier J-S, Kollath C, and Köhl M (2018) Higgs mode in a strongly interacting fermionic superfluid. *Nature Physics* 14(8): 781–785. ISSN: 1745-2481.
Bogoliubov NN, Tolmachev VV, and Shirkov DV (1958) *A New Method in the Theory of Superconductivity.* Moscow: Academy of Sciences of USSR.
Carlson RV and Goldman AM (1975) Propagating order-parameter collective modes in superconducting films. *Physical Review Letters* 34(1): 11–15.

Cea T, Castellani C, and Benfatto L (2016) Nonlinear optical effects and third-harmonic generation in superconductors: Cooper pairs versus Higgs mode contribution. *Physical Review B* 93(18): 180507.

Chu H, Kim M-J, Katsumi K, Kovalev S, Dawson RD, Schwarz L, Yoshikawa N, Kim G, Putzky D, Li ZZ, Raffy H, Germanskiy S, Deinert J-C, Awari N, Ilyakov I, Green B, Chen M, Bawatna M, Cristiani G, Logvenov G, Gallais Y, Boris AV, Keimer B, Schnyder AP, Manske D, Gensch M, Wang Z, Shimano R, and Kaiser S (2020) Phase-resolved Higgs response in superconducting cuprates. *Nature Communications* 11(1): 1793.

CMS Collaboration. (2012) Observation of a new boson at a mass of 125 GeV with the CMS experiment at the LHC. *Physics Letters B* 716(1): 30–61. ISSN: 0370-2693.

Eagles DM (1969) *Physical Review* 186(2): 456–463.

Endres M, Fukuhara T, Pekker D, Cheneau M, Schauß P, Gross C, Demler E, Kuhr S, and Bloch I (2012) The 'Higgs' amplitude mode at the two-dimensional superfluid/Mott insulator transition. *Nature* 487(7408): 454–458. ISSN: 1476-4687.

Englert F and Brout R (1964) Broken symmetry and the mass of gauge vector mesons. *Physical Review Letters* 13(9): 321–323.

Ginzburg VL and Landau LD (1950) On the theory of superconductivity. *Zhurnal Eksperimental'noi i Teoreticheskoi Fiziki* 20: 1064.

Goldstone J (1961) Field theories with superconductor solutions. *Il Nuovo Cimento* 19(1): 154–164.

Goldstone J, Salam A, and Weinberg S (1962) Broken symmetries. *Physical Review* 127(3): 965–970.

Grasset R, Katsumi K, Massat P, Wen H-H, Chen X-H, Gallais Y, and Shimano R (2022) Terahertz pulse-driven collective mode in the nematic superconducting state of Ba$_{1-x}$K$_x$Fe$_2$As$_2$. *npj Quantum Materials* 7(1): 4.

Grüner G (1988) The dynamics of charge-density waves. *Reviews of Modern Physics* 60(4): 1129–1181.

Guralnik GS, Hagen CR, and Kibble TWB (1964) Global conservation laws and massless particles. *Physical Review Letters* 13(20): 585–587.

Gurarie V (2009) Nonequilibrium dynamics of weakly and strongly paired superconductors. *Physical Review Letters* 103(7): 075301.

Hidaka Y (2013) Counting rule for Nambu-Goldstone modes in nonrelativistic systems. *Physical Review Letters* 110(9): 091601.

Higgs PW (1964) Broken symmetries and the masses of gauge Bosons. *Physical Review Letters* 13(16): 508–509.

Hoinka S, Dyke P, Lingham MG, Kinnunen JJ, Bruun GM, and Vale CJ (2017) Goldstone mode and pair-breaking excitations in atomic Fermi superfluids. *Nature Physics* 13(10): 943–946. ISSN: 1745-2481.

Isoyama K, Yoshikawa N, Katsumi K, Wong J, Shikama N, Sakishita Y, Nabeshima F, Maeda A, and Shimano R (2021) Light-induced enhancement of superconductivity in iron-based superconductor FeSe$_{0.5}$Te$_{0.5}$. *Communications on Physics* 4(1): 160.

Jujo T (2018) Quasiclassical theory on third-harmonic generation in conventional superconductors with paramagnetic impurities. *Journal of the Physical Society of Japan* 87(2): 024704.

Katsumi K, Tsuji N, Hamada YI, Matsunaga R, Schneeloch J, Zhong RD, Gu GD, Aoki H, Gallais Y, and Shimano R (2018) Higgs mode in the *d*-wave superconductor Bi$_2$Sr$_2$CaCu$_2$O$_{8+x}$ driven by an intense terahertz pulse. *Physical Review Letters* 120(11): 117001.

Katsumi K, Li ZZ, Raffy H, Gallais Y, and Shimano R (2020) Superconducting fluctuations probed by the Higgs mode in Bi$_2$Sr$_2$CaCu$_2$O$_{8+x}$ thin films. *Physical Review B* 102(5): 054510.

Katsumi K, Nishida M, Kaiser S, Miyasaka S, Tajima S, and Shimano R (2022) Absence of the superconducting collective excitations in the photoexcited nonequilibrium state of underdoped YBa$_2$Cu$_3$O$_y$. *arXiv:2209.01633*.

Kovalev S, Dong T, Shi L-Y, Reinhoffer C, Xu T-Q, Wang H-Z, Wang Y, Gan Z-Z, Germanskiy S, Deinert J-C, Ilyakov I, van Loosdrecht PHM, Wu D, Wang N-L, Demsar J, and Wang Z (2021) Band-selective third-harmonic generation in superconducting MgB$_2$: Possible evidence for the Higgs amplitude mode in the dirty limit. *Physical Review B* 104(14): L140505.

Kuroe H, Takami N, Niwa N, Sekine T, Matsumoto M, Yamada F, Tanaka H, and Takemura K (2012) Longitudinal magnetic excitation in KCuCl$_3$ studied by Raman scattering under hydrostatic pressures. *Journal of Physics Conference Series* 400(3): 032042.

Leggett AJ (1966) Number-phase fluctuations in two-band superconductors. *Progress in Theoretical Physics* 36(5): 901–930. ISSN: 0033-068X.

Leggett AJ (1980) Diatomic molecules and cooper pairs. In: Pękalski A and Przystawa JA (eds.) *Modern Trends in the Theory of Condensed Matter*, vol. 115. Berlin, Heidelberg: Springer.

Littlewood PB and Varma CM (1982) Amplitude collective modes in superconductors and their coupling to charge-density waves. *Physical Review B* 26(9): 4883–4893.

Matsumoto M, Normand B, Rice TM, and Sigrist M (2004) Field- and pressure-induced magnetic quantum phase transitions in TlCuCl$_3$. *Physical Review B* 69(5): 054423.

Matsunaga R, Hamada YI, Makise K, Uzawa Y, Terai H, Wang Z, and Shimano R (2013) Higgs amplitude mode in the BCS superconductors Nb$_{1-x}$Ti$_x$N induced by terahertz pulse excitation. *Physical Review Letters* 111(5): 057002.

Matsunaga R, Tsuji N, Fujita H, Sugioka A, Makise K, Uzawa Y, Terai H, Wang Z, Aoki H, and Shimano R (2014) Light-induced collective pseudospin precession resonating with Higgs mode in a superconductor. *Science* 345(6201): 1145–1149. ISSN: 0036-8075.

Mazurenko A, Chiu CS, Ji G, Parsons MF, Kanász-Nagy M, Schmidt R, Grusdt F, Demler E, Greif D, and Greiner M (2017) A cold-atom Fermi-Hubbard antiferromagnet. *Nature* 545 (7655): 462–466. ISSN: 1476-4687.

Murotani Y and Shimano R (2019) Nonlinear optical response of collective modes in multiband superconductors assisted by nonmagnetic impurities. *Physical Review B* 99(22): 224510.

Nakayama T and Tsuchiya S (2019) Perfect transmission of Higgs modes via antibound states. *Physical Review A* 100(6): 063612.

Nakayama T, Danshita I, Nikuni T, and Tsuchiya S (2015) Fano resonance through Higgs bound states in tunneling of Nambu-Goldstone modes. *Physical Review A* 92(4): 043610.

Nambu Y (1960) Quasi-particles and gauge invariance in the theory of superconductivity. *Physical Review* 117(3): 648–663.

Nambu Y and Jona-Lasinio G (1961) Dynamical model of elementary particles based on an analogy with superconductivity. I. *Physical Review* 122(1): 345–358.

Pekker D and Varma CM (2015) Amplitude/Higgs modes in condensed matter physics. *Annual Review of Condensed Matter Physics* 6(1): 269–297.

Pollet L and Prokof'ev N (2012) Higgs mode in a two-dimensional superfluid. *Physical Review Letters* 109(1): 010401.

Regal C, Greiner M, and Jin DS (2004) Observation of resonance condensation of Fermionic atom pairs. *Physical Review Letters* 92(4): 040403.

Rüegg C, Normand B, Matsumoto M, Furrer A, McMorrow DF, Krämer KW, Güdel HU, Gvasaliya SN, Mutka H, and Boehm M (2008) Quantum magnets under pressure: Controlling elementary excitations in TlCuCl$_3$. *Physical Review Letters* 100(20): 205701.

Sachdev S (2011) *Quantum Phase Transitions*, 2nd edn. Cambridge University Press.

Schwarz L, Fauseweh B, Tsuji N, Cheng N, Bittner N, Krull H, Berciu M, Uhrig GS, Schnyder AP, Kaiser S, and Manske D (2020) Classification and characterization of nonequilibrium Higgs modes in unconventional superconductors. *Nature Communications* 11(1): 287.

Seibold G, Udina M, Castellani C, and Benfatto L (2021) Third harmonic generation from collective modes in disordered superconductors. *Physical Review B* 103(1): 014512.

Shimano R and Tsuji N (2020) Higgs mode in superconductors. *Annual Review of Condensed Matter Physics* 11(1): 103–124.

Silaev M (2019) Nonlinear electromagnetic response and Higgs-mode excitation in BCS superconductors with impurities. *Physical Review B* 99(22): 224511.

Sooryakumar R and Klein MV (1980) Raman scattering by superconducting-gap excitations and their coupling to charge-density waves. *Physical Review Letters* 45(8): 660–662.

Tokimoto J, Tsuchiya S, and Nikuni T (2019) Excitation of Higgs mode in superfluid fermi gas in BCS-BEC crossover. *Journal of the Physical Society of Japan* 88(2): 023601.

Tsang JC, Smith JE, and Shafer MW (1976) Raman spectroscopy of soft modes at the charge-density-wave phase transition in 2H–NbSe$_2$. *Physical Review Letters* 37(21): 1407–1410.

Tsuji N and Aoki H (2015) Theory of Anderson pseudospin resonance with Higgs mode in superconductors. *Physical Review B* 92(6): 064508.

Tsuji N and Nomura Y (2020) Higgs-mode resonance in third harmonic generation in NbN superconductors: Multiband electron-phonon coupling, impurity scattering, and polarization-angle dependence. *Physical Review Res.* 2(4): 043029.

Tsuji N, Eckstein M, and Werner P (2013) Nonthermal antiferromagnetic order and nonequilibrium criticality in the Hubbard model. *Physical Review Letters* 110(13): 136404.

Vaswani C, Kang JH, Mootz M, Luo L, Yang X, Sundahl C, Cheng D, Huang C, Kim RHJ, Liu Z, Collantes YG, Hellstrom EE, Perakis IE, Eom CB, and Wang J (2021) Light quantum control of persisting Higgs modes in iron-based superconductors. *Nature Communications* 12(1): 258.

Volkov AF and Kogan SM (1974) Collisionless relaxation of the energy gap in superconductors. *Soviet Physics–JETP* 38: 1018.

Watanabe H and Murayama H (2012) Unified description of Nambu-Goldstone Bosons without Lorentz invariance. *Physical Review Letters* 108(25): 251602.

Werner P, Tsuji N, and Eckstein M (2012) Nonthermal symmetry-broken states in the strongly interacting Hubbard model. *Physical Review B* 86(20): 205101.

Yusupov R, Mertelj T, Kabanov VV, Brazovskii S, Kusar P, Chu J-H, Fisher IR, and Mihailovic D (2010) Coherent dynamics of macroscopic electronic order through a symmetry breaking transition. *Nature Physics* 6(9): 681–684. ISSN: 1745-2481.

Zwierlein MW, Stan CA, Schunck CH, Raupach SMF, Kerman AJ, and Ketterle W (2004) Condensation of pairs of Fermionic atoms near a Feshbach resonance. *Physical Review Letters* 92(12): 120403.

Higgs and Goldstone modes in cold atom systems

Jacques Tempere, Departement Fysica, TQC, Universiteit Antwerpen, Antwerp, Belgium

© 2024 Elsevier Ltd. All rights reserved.

Introduction 187
Collective modes in Bose condensates 188
Order parameter for the superfluid Fermi gas 189
Gaussian fluctuations of the pair field 190
Anderson–Bogoliubov mode in superfluid Fermi gases 192
Amplitude mode in superfluid Fermi gases 194
Conclusion 195
References 195

Abstract

Many superfluid and superconducting systems can be well characterized by a complex order parameter that obtains a nonzero expectation value after spontaneous U(1) symmetry breaking. The complex order parameter can exhibit oscillations in phase or in amplitude, corresponding to Goldstone and Higgs excitations, respectively. These modes are also expected to be present in superfluid atomic Bose and Fermi gases. The excellent level of experimental control over interaction strength, atom numbers, and trapping geometry motivated theoretical and experimental efforts to study the Goldstone and Higgs modes in these cold atom systems. In atomic Fermi superfluids in particular, there exists a tunable coupling between these modes, as well as a coupling to a nearby continuum of single-particle excitations, and this leads to a much richer physics than can be initially expected from simple field-theoretical models. In this contribution, the recent theoretical and experimental developments for the collective modes in superfluid atomic systems are reviewed and placed in the context of earlier research both in particle physics and solid-state physics. The focus is on superfluid Fermi gases, as they include the case of the Bose gas in the limit of strong pairing. For this system, the state-of-the-art theoretical understanding of these modes is provided and compared to recent experimental observations of the collective modes.

Key points

- Description of the Anderson–Bogoliubov mode in superfluid quantum gases
- Description of the Higgs mode in superfluid quantum gases
- Review of experiment and theory for elementary excitations in superfluid atomic gases

Introduction

Collective modes of many-body quantum systems are crucial ingredients in the description of the low-temperature dynamics and thermodynamics of these systems. They allow to construct simplified models for many phenomena, based on fewer and more weakly interacting constituents than those of the original many-body system. Very often, these modes also reveal emergent properties not easily understood from the viewpoint of the original building blocks of the system.

Here, we focus on collective modes arising from spontaneously breaking a continuous symmetry. The paradigmatic example that we will explore in more detail is the case of a complex scalar order parameter[1], for which the U(1) symmetry can be spontaneously broken. This is up to now also the most relevant case in cold atom systems, both for Bose gases where the order parameter represents the macroscopic wave function of the condensate, and for superfluid Fermi gases where the order parameter corresponds to the wave function characterizing the pair condensate. In both cases, we will denote the order parameter by $\Psi(\mathbf{r}, t)$.

When the U(1) symmetry is spontaneously broken, collective modes of the order parameter appear (for an excellent review, see Pekker and Varma (2015)). One mode is associated to the modulation of the phase of the order parameter. Since any choice of phase is equivalent by the U(1) symmetry, any modulation in the phase in the symmetry-broken phase should have an energy tending to zero as its wavelength tends to infinity. This gapless mode was described by Nambu (1960), and later refined by

---

[1] Superfluid Helium-3 is an example of a system with a more complicated order parameter, and hence more collective modes.

https://doi.org/10.1016/B978-0-323-90800-9.00212-2

Goldstone (1961), in the context of particle physics. From this, it got its name the "Goldstone mode." In the context of condensed matter physics, more precisely superconductivity, this mode had already been identified earlier by Bogoliubov et al. (1958) and Anderson (1958a), who also realized that for a charged system, the Goldstone mode acquires a gap (Anderson, 1958b). However, in the context of quantum gases, the mode is gapless, since the system consists of neutral atoms. Within the quantum gas community, this mode is most commonly referred to as the "Anderson–Bogoliubov mode."

The complex order parameter is characterized by phase and amplitude, so besides the gapless Goldstone mode, there is also a mode associated with oscillations of the modulus of the order parameter, commonly called the "Higgs" mode. In particle physics, this mode plays an important role, as pointed out by Higgs (1964) and Englert and Brout (1964), who based themselves on an observation by Anderson (1963) on plasma oscillations. In the context of the standard model, the order parameter is associated to the condensate a new quantum field invoked to generate the masses of the gauge bosons. At first, condensed matter physics did not take much note of the standard model Higgs mode. It was not until the detection of the amplitude mode in superconductors by Sooryakumar and Klein (1980) and the subsequent theoretical description (Littlewood and Varma, 1981, 1982) for the case of superconductors that the concept of a Higgs mode came fully to the attention of the condensed matter community. Most recently, the advent of ultracold quantum gases with their exquisite experimental controllability and tunability has spurred a renewed interest in the Higgs/amplitude and Goldstone/Anderson–Bogoliubov modes in superfluid systems.

Before we discuss the realizations of these modes in atomic gases in the next sections, there are a few important remarks to be made about the difference with their particle physics counterparts. A well-known graphical depiction of the Higgs field is that of the Mexican hat potential. The Goldstone mode follows the valley, whereas the Higgs mode is a radial oscillation up and down the hat's rim. An objection to this graph, from the point of view of Fermi superfluids and superconductors, is that it seems to suppose that the (free) energy as a function of the order parameter can be expanded in series around its value in the normal (nonsuperfluid) state, which is not the case, in contrast to the standard model Higgs field where the Mexican hat potential is assumed from the start. Another difference, as noted in Pekker and Varma (2015), is that the original Higgs theory is a locally gauge invariant theory, which need not be the case for realizations in atomic gases. Moreover, in contrast to the field theoretical counterpart, the Higgs mode in Fermi superfluids lies inside the continuum of pair-breaking excitations and is strongly influenced by it. A final point to keep in mind, and that will be discussed in more detail below, is that the phase and amplitude modes are in general coupled in superfluid gases, so the eigenmodes have a mixed nature and may even become degenerate—even in the presence of a Mexican hat potential. To decouple these modes, one needs exact particle–hole symmetry, which is not present in general. It can be realized only in special cases: in the Bardeen–Cooper–Schrieffer (BCS) limit of a fermionic superfluid, or by fine-tuning a system in an optical lattice.

Collective modes in Bose condensates

Bose–Einstein condensates (BEC) in cold atomic gases are characterized by a complex scalar order parameter $\Psi(\mathbf{r}, t)$ that obeys the Gross–Pitaevskii equation (see Pitaevskii and Stringari, 2003),

$$i\hbar\frac{\partial\Psi}{\partial t} = -\frac{\hbar^2}{2m}\nabla^2\Psi + V\Psi + g|\Psi|^2\Psi, \tag{1}$$

where m is the mass of the atoms, V is an external potential, and g denotes the strength of the contact potential, related to the s-wave scattering length between the atoms. This equation describes condensates well for temperatures sufficiently below the critical temperature so that effects of thermal excitations are negligible. The description in terms of the order parameter neglects quantum fluctuations of the Bose field, which is justified when the bosons macroscopically occupy a single mode. The order parameter is interpreted straightforwardly: its modulus squared $|\Psi|^2$ represents the density n of Bose condensed atoms, and its phase θ is related to the velocity field through $\mathbf{v} = (\hbar/m)\nabla\theta$.

This equation does not allow for uncoupled phase and amplitude modes; the only collective mode (in the uniform system, $V = 0$) is the Bogoliubov mode with dispersion

$$\omega = ck\sqrt{1 + \frac{1}{2}(k\xi)^2}, \tag{2}$$

where $c = \sqrt{gn/m}$ is the sound velocity, and $\xi = \sqrt{\hbar^2/(2mgn)}$ is the healing length of the condensate (Pitaevskii and Stringari, 2003). This can be considered as the Goldstone mode of the condensate, and no separate Higgs mode exists. In the long wavelength limit ($k \to 0$), the mode turns to a sound mode. As the wave number of the mode grows to become comparable to the healing length $k\xi \gtrsim 1$, the mode no longer represents a collective oscillation. Rather it becomes a single-particle excitation, taking an atom out of the condensate and into the normal-state cloud.

The Bogoliubov sound mode was observed experimentally, shortly after the first realization of BEC in cold trapped gases, by modulating the trapping potential to excite these modes (Jin et al., 1996; Andrews et al., 1997). A more refined technique to probe this excitation is through Bragg spectroscopy, where a fixed amount of energy at a fixed wavelength can be imparted on the condensate via two crossed laser beams, as the condensate absorbs a photon from one beam and emits it in the other. This technique reveals the structure factor, in which the Bogoliubov modes were characterized (Stamper-Kurn et al., 1999).

As mentioned above, the amplitude mode is not independently present in uniform BECs (nor in the case of a trapping potential that varies slowly with respect to the healing length). However, condensates can be placed in optical lattices, realizing the Bose–Hubbard model, and allowing both the nearest-neighbor hopping amplitude J and the on-site interaction U to be tuned experimentally. Huber et al. (2007) have shown that along certain curves in the J–U phase diagram, particle–hole symmetry is restored. In the superfluid phase, this leads to the existence of gapped amplitude modes. These were subsequently discovered experimentally, again using Bragg scattering, by Bissbort et al. (2011). Following theoretical work (Podolsky et al., 2011; Pollet and Prokofiev, 2012), that showed that the amplitude mode is also present in a two-dimensional optical lattice, the amplitude mode was excited and observed in two-dimensional systems by modulating the lattice depth (Endres et al., 2012), or by Bragg spectroscopy using two crossed optical cavities (Léonard et al., 2017).

So, in summary, for cold atomic Bose gases, the Bogoliubov (Goldstone) mode is easily accessible by disturbing and probing the condensate density, but the amplitude (Higgs) mode has to be engineered into the system, by using optical lattices. The study of the Higgs mode and its visibility in quantum simulations of the Bose–Hubbard model has been the subject of a large amount of theoretical work that would require a much longer review paper than this encyclopedia entry. Instead, and for the remainder of this paper, we turn to superfluid Fermi gases. Superfluid Fermi gases are the neutral counterpart of superconductors, and they are most relevant to link the cold atomic systems to solid-state physics in general and superconductors in particular. Moreover, as will be discussed below, the interaction strength between the fermionic atoms can be tuned, and the case of a condensate of point bosons is retrieved in the limit of tightly bound pairs.

Order parameter for the superfluid Fermi gas

In atomic Fermi gases, superfluidity requires the presence of pairing between the atoms. The pairing partners are typically different hyperfine states of a given fermionic isotope; for the sake of simplicity we will refer to the two pairing states as "spin-up" and "spin-down." At low temperatures (such that the de Broglie wavelength is much larger than the range of the interatomic potential) scattering between atoms is dominated by the s-wave channel, and fully characterized by the s-wave scattering length a_s. For fermionic atoms, the requirement of antisymmetry precludes s-wave interactions between same spin atoms.

Pairing between ultracold, neutral atoms was first investigated theoretically in the framework of BCS theory by Houbiers and Stoof (1999). In the conventional BCS model, the parameter that controls the strength of the pairing is the inverse product of the BCS interaction strength with the density of states at the Fermi level. In (three-dimensional) cold Fermi gases, this parameter is replaced by $1/(k_F a_s)$, with k_F, the Fermi wave number. Remarkably, the s-wave scattering length a_s can be tuned experimentally using Feshbach resonances. These are scattering resonances between a bound state in a closed scattering channel, and the scattering state of colliding atoms in the open channel. Here, these channels are characterized by different hyperfine states so that the resonance can be tuned via an external magnetic field through the Zeeman effect. This allows to enhance the strength of the attractive interaction (and raise the critical temperature), by making a_s more strongly negative. As the bound state of the closed channel dips below the scattering energy (and a_s becomes positive), the bound molecular state mixes with the scattering state, and allows for a BEC of strongly bound molecules. Experimentally, the BEC–BCS crossover region $(1 \gtrsim 1/(k_F a_s) \gtrsim -1)$ is entirely accessible, including the unitary limit $(1/(k_F a_s) = 0)$. This results in a much richer physics than for the limiting case of a BEC discussed in the previous section.

The order parameter $\Psi(\mathbf{r}, t)$ now represents the pair condensate. To see what that means, we turn to the path integral formalism, and start from the imaginary time action functional S for the Fermi gas described by Grassmann variables ψ_σ for fermions with spin σ:

$$S = \int_0^\beta \mathrm{d}\tau \int \mathrm{d}\mathbf{r} \left[\sum_\sigma \overline{\psi}_\sigma \left(\partial_\tau - \frac{1}{2m} \nabla_\mathbf{r}^2 - \mu_\sigma \right) \psi_\sigma + g \overline{\psi}_\uparrow \overline{\psi}_\downarrow \psi_\downarrow \psi_\uparrow \right], \tag{3}$$

where we have set $\hbar = k_B = 1$, and $\beta = 1/k_B T$ represents the inverse temperature. The chemical potentials for each spin species μ_σ can in principle be set independently. The interaction strength g is related to the scattering length a_s via the renormalization relation

$$\frac{1}{g} = \frac{m}{4\pi a_s} - \int_{k<k_c} \frac{\mathrm{d}^3 k}{(2\pi)^3} \frac{m}{k^2}. \tag{4}$$

The complex order parameter for the pair superfluid can then be interpreted as arising from a Hubbard–Stratonovich auxiliary field introduced to decouple the interaction term and integrate out the fermionic degrees of freedom. The Hubbard–Stratonovic identity allows to transform the fermionic action into an equivalent effective bosonic action for the fermionic pairs such that the functional integral over this field yields the same partition sum

$$\mathcal{Z} = \int \mathcal{D}\psi \exp\{-S[\psi]\} = \int \mathcal{D}\Delta \exp\{-S_{\text{eff}}[\Delta]\}, \tag{5}$$

with

$$S_{\text{eff}} = \int_0^\beta \mathrm{d}\tau \int \mathrm{d}\mathbf{r} \frac{|\Delta_{\mathbf{r},\tau}|^2}{g} - \mathrm{Tr}[\log(\mathbb{G}^{-1})], \tag{6}$$

where

$$\mathbb{G}^{-1} = \begin{pmatrix} -\partial_\tau + \frac{1}{2m}\nabla_\mathbf{r}^2 + \mu_\uparrow & \Delta_{\mathbf{r},\tau} \\ \Delta_{\mathbf{r},\tau}^* & -\partial_\tau - \frac{1}{2m}\nabla_\mathbf{r}^2 - \mu_\downarrow \end{pmatrix}. \tag{7}$$

The path integral over the pair field $\Delta_{\mathbf{r},\tau}$ cannot be taken analytically, but if one assumes a condensate of pairs is present, then the Bogoliubov shift can be introduced, writing the pair field as

$$\Delta_{\mathbf{r},\tau} = \Delta + \delta_{\mathbf{r},\tau}. \tag{8}$$

Here Δ is the (saddle-point) order parameter of the uniform system, assumed independent of position and imaginary time, and chosen real. It represents a shift of the pair field such that the quantum (and thermal) fluctuations $\delta_{\mathbf{r},\tau}$ can be treated as small. In that case, the Gaussian approximation can be made in which the effective action is expanded up to second order in the fluctuations. Thus, the effective action for the pair field is written as

$$S_{\text{eff}} \approx S_{\text{sp}} + S_{\text{fluct}}, \tag{9}$$

where S_{fluct} is the fluctuation action described in the next section. This fluctuation action contains the information on the Anderson and Higgs modes, and is the main subject of this paper. For completeness, we mention that the saddle point action S_{sp} is given by

$$S_{\text{sp}} = -\frac{\beta V}{g}|\Delta|^2 - \frac{V}{(2\pi)^3} \int \mathrm{d}\mathbf{k} \{\log[2\cosh(\beta E_k) + 2\cosh(\beta\zeta)] - \beta\xi_k\}, \tag{10}$$

with $\xi_\mathbf{k} = k^2/(2m) - \mu$ where $\mu = (\mu_\downarrow + \mu_\uparrow)/2$, $\zeta = (\mu_\uparrow - \mu_\downarrow)/2$, and V is the volume. The Bogoliubov energy related to breaking up a pair is given by

$$E_\mathbf{k} = \sqrt{\xi_\mathbf{k}^2 + |\Delta|^2}. \tag{11}$$

Note that the precise value of the saddle point is obtained from the gap equation $\partial S_{\text{sp}}/\partial\Delta = 0$, which corresponds to minimizing the action for the pair field. This equation should be solved in conjunction with the number equation, fixing the density $n = -\partial\Omega/\partial\mu$ where Ω is the thermodynamic potential. However, the question of the value of the saddle point and the equation of state is separate from the study of the fluctuations. As we discuss below, the fluctuation propagator depends only on the ratio μ/Δ (and the temperature). This means that one can use an equation of state of one's own choice to relate this quantity to the density and the interaction strength: the mean-field equation of state, the experimentally determined one, or the one from Monte Carlo simulations. This is an often overlooked but important aspect of the study of small-amplitude fluctuations in fermi superfluids.

Gaussian fluctuations of the pair field

Having introduced the order parameter Δ in the previous section, we now turn to the question of small amplitude variations of this field. Since we are interested in phase (Anderson–Bogoliubov) and amplitude (Higgs) modes, it is convenient to write the fluctuations also in amplitude and phase representation:

$$\Delta_{\mathbf{r},\tau} = (\Delta + a_{\mathbf{r},\tau})\exp\{i\theta_{\mathbf{r},\tau}\}. \tag{12}$$

The fluctuation action is best expressed not in real space but in reciprocal space coordinates, namely, the center-of-mass wavenumber $\mathbf{q}$ of the pair and the bosonic Matsubara frequencies $\omega_n = 2\pi n/\beta$. In terms of the reciprocal space fluctuation fields $a_{\mathbf{q},n}$ and $\theta_{\mathbf{q},n}$, the fluctuation action in Nambu notation is given by

$$S_{\text{fluct}} = \frac{1}{\beta V}\sum_{\mathbf{q},n}\begin{pmatrix}\theta_{\mathbf{q},n} & \Delta a_{\mathbf{q},n}\end{pmatrix}\cdot\begin{pmatrix}M_{++} & -iM_{+-}\\ iM_{-+} & M_{--}\end{pmatrix}\cdot\begin{pmatrix}\theta_{\mathbf{q},n}\Delta\\ a_{\mathbf{q},n}\end{pmatrix}. \tag{13}$$

The "fluctuation" matrix in (13) will be denoted by $\mathbb{M}(\mathbf{q}, i\omega_n)$. The inverse fluctuation matrix $\mathbb{M}^{-1}(\mathbf{q}, i\omega_n)$ is interpreted as the propagator for the (coupled) amplitude and phase modes, and as such it takes center stage in our study of these modes. The dispersion and the lifetime of the coupled phase (Anderson–Bogoliubov) and amplitude (Higgs) modes are found via the real and imaginary poles of the propagator $\mathbb{M}^{-1}(\mathbf{q}, i\omega_n)$, analytically continued to the complex plane ($i\omega_n \to z$), or equivalently, via the roots of $\det(\mathbb{M})$. Its matrix elements are given by

$$\begin{aligned}M_{\pm\pm}(\mathbf{q},z) = {} & \sum_{\mathbf{k}}\frac{X(E_+)+X(E_-)}{8E_+E_-}\left(E_+E_- + \xi_+\xi_- \pm \Delta^2\right)\left(\frac{1}{z-(E_++E_-)} - \frac{1}{z+(E_++E_-)}\right)\\ & + \sum_{\mathbf{k}}\frac{X(E_+)-X(E_-)}{8E_+E_-}\left(E_+E_- - \xi_-\xi_+ \pm \Delta^2\right)\left(\frac{1}{z-(E_+-E_-)} - \frac{1}{z+(E_+-E_-)}\right) + \sum_{\mathbf{k}}\frac{X(E_{\mathbf{k}})}{2E_{\mathbf{k}}},\end{aligned} \tag{14}$$

and

$$\begin{aligned}M_{+-}(\mathbf{q},z) = {} & \sum_{\mathbf{k}}\frac{X(E_+)+X(E_-)}{8E_+E_-}\left(E_-\xi_+ + E_+\xi_-\right)\left(\frac{1}{z-(E_++E_-)} + \frac{1}{z+(E_++E_-)}\right)\\ & + \sum_{\mathbf{k}}\frac{X(E_+)-X(E_-)}{8E_+E_-}\left(E_-\xi_+ - E_+\xi_-\right)\left(\frac{1}{z-(E_+-E_-)} + \frac{1}{z+(E_+-E_-)}\right),\end{aligned} \tag{15}$$

where we used shorthand notations $E_\pm = E_{\mathbf{k}\pm\mathbf{q}/2}$ and $\xi_\pm = \xi_{\mathbf{k}\pm\mathbf{q}/2}$ and introduced the function

$$X(E) = \frac{\sinh(\beta E)}{\cosh(\beta E) + \cosh(\beta\zeta)}. \tag{16}$$

These matrix elements, discussed here in the context of the path-integral description, can equally be found in the Gaussian random-phase approximation. In the form given above, the matrix elements have units of inverse energy, and when multiplied by $1/\beta$ in expression (13), the result becomes dimensionless, and will depend only on the ratio μ/Δ and on the reduced temperature $\beta\Delta$. This means that the result is expressed in a form independent of the chosen equation of state that is used to relate the system parameters a_s and k_F to μ/Δ and $\beta\Delta$.

Care must be taken with the analytic continuation for values of z in the lower half complex plane $\text{Im}(z) < 0$. Both formalisms yield the propagator as a thermal Green's function, defined for the bosonic Matsubara frequencies $i\omega_n$. Experiments measure response functions, given in Kubo's formalism by the retarded Green's functions obtained by replacing $i\omega_n \to \omega + i\varepsilon$ with ε an infinitesimal. When we search for quasiparticles (Anderson–Bogoliubov phonons or Higgs particles) in the superfluid, we need to look for poles in the lower half complex plane. However, the real axis itself is a branch cut since the integrations over the wave numbers $\mathbf{k}$ yield integrals of the form

$$F(z) = \int_{-\infty}^{+\infty}\frac{f(v)}{z-v}\,\mathrm{d}v. \tag{17}$$

At temperature zero, this cut starts from $\min_{\mathbf{k}}(E_+ + E_-) = 2\Delta$, and at nonzero temperature, the entire real line is a branch cut. To cross this branch cut, one must follow Nozières' prescription

$$\text{Im}(z) < 0 \to F(z) = \int_{-\infty}^{+\infty}\frac{f(v)}{z-v}\,\mathrm{d}v + 2\pi i f(z). \tag{18}$$

This brings another difficulty: the function in the numerator $f(v)$ must itself be analytically continued into the lower half plane. For the integrals in (14) and (15), the functions in the numerator are piecewise analytic as they contain kinks at energies where new channels for decay open up. Hence one must choose the window through which the analytic continuation is performed. The natural choice for this is to choose the window in which $v = \Re(z)$ is contained. The switching of windows as $\Re(z)$ is varied leads to kinks or discontinuities in the dispersion and lifetimes of the Anderson and Higgs modes, which can be interpreted as physically resulting from additional decay modes becoming available.

Before looking in more detail at the collective modes calculated from this theory, it is useful to start with a schematic overview of the commonly agreed qualitative results (at low temperature), as shown in Fig. 1. The collective mode spectrum is influenced by the presence of a continuum of single-particle (pair-breaking) excitations, shown as a shaded region. This influence becomes negligible

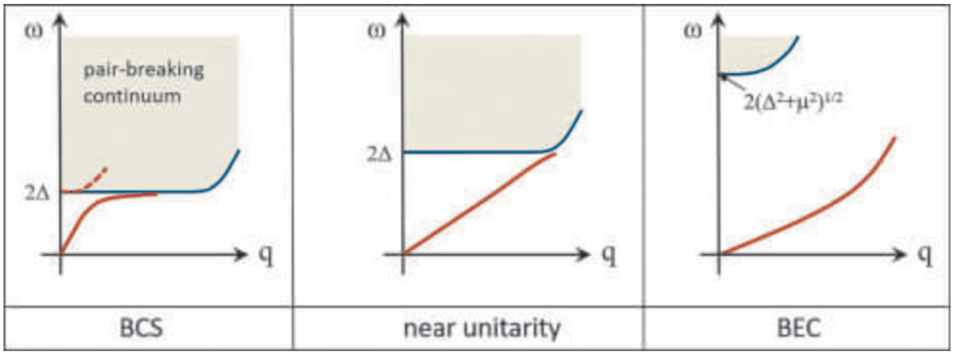

Fig. 1 Schematic overview of the collective modes in the BEC–BCS crossover of a fermionic superfluid at low temperature. The pair-breaking continuum is shown as a *shaded region*. The Anderson–Bogoliubov mode (*full red curve*) starts as a sound mode at low momentum. The Higgs mode is only present in the BCS regime and is indicated by a *dashed red curve*.

in the BEC limit, as the pair breaking continuum shifts to higher and thermally inaccessible energies. In the BEC limit, the Anderson–Bogoliubov mode (shown as a full red curve) corresponds to the Bogoliubov spectrum of Eq. (2) for a gas of point bosons (the tightly bound pairs). The spectrum starts linear, and curves up at higher momenta. There is no Higgs (amplitude) mode present in the BEC case, as discussed in section "Collective modes in Bose condensates." However, as one shifts to the BCS side of the crossover, the pair breaking continuum comes down in energy as the sound velocity increases. The Anderson–Bogoliubov mode is repelled by the continuum and the curvature turns from positive to negative. In addition, the amplitude mode (dashed red curve) appears close to the pair breaking gap 2Δ, and disperses upward while also acquiring a larger damping, washing out this mode at larger momenta. In the next sections, we will go into detail about the Anderson–Bogoliubov mode and the amplitude mode, and sketch how the above picture originated from the various theoretical and experimental investigations.

Anderson–Bogoliubov mode in superfluid Fermi gases

The poles of the propagator are found by solving $\det[\mathbb{M}(\mathbf{q},z)] = 0$ with respect to z for any given wave number $\mathbf{q}$. These poles reveal the collective modes of the Fermi superfluid, as already noted by Sa de Melo et al. (1993). However, it was only recently that this equation was solved in its entire complexity. Initial studies focused on simplifications (ignoring the coupling between amplitude and phase modes, ignoring damping) and limiting cases (long wavelength and temperature zero). Below, we take the reader more or less chronologically through the various steps taken in the study of the Anderson–Bogoliubov mode in the Fermi superfluid gas.

The Anderson–Bogoliubov mode at long wavelength $q \to 0$ has a sound-like dispersion $\omega = cq$, and initially the sound velocity was obtained at zero temperature (Sa de Melo et al., 1993; Marini et al., 1998; Huang and Wan, 2007; Diener et al., 2008) by expanding the matrix elements of $\mathbb{M}(q, \omega)$ for small q and small ω. However, this expansion turns out to be problematic as the point $(q, \omega) = (0, 0)$ is a branch point for the matrix (at any temperature) such that the limiting value depends on the path followed in the q, ω plane. Therefore, there is no Taylor expansion valid everywhere in the vicinity of the $(q, \omega) = (0, 0)$ point.

Other initial investigations, such as Ohashi and Griffin (2003) focused on solving $M_{++} = 0$ and thus neglecting the coupling between the phase and amplitude modes. In the BCS limit, $\mu/\Delta \to \infty$ as the gap approaches zero exponentially. In that case, M_{+-} approaches zero, and the phase and amplitude sectors decouple so that the phase mode is indeed solved by $M_{++} = 0$. However, for a general coupling strength in the BEC–BCS crossover, this is no longer the case, and the mixing of phase and amplitude modes must be taken into account.

The full dispersion at temperature zero was obtained by Combescot et al. (2006), which matches results obtained by the random phase approximation (Kurkjian et al., 2016). These results are in the collisionless regime, but they agree reasonably well with the results obtained in the hydrodynamic regime (Heiselberg, 2006; He et al., 2007) via the relation $c = (n/m)\partial\mu/\partial n$, which however requires a choice of equation of state, for which Astrakharchik et al. (2005) used the Monte Carlo equation of state.

The Anderson–Bogoliubov mode has a finite lifetime, even at zero temperature. Sophisticated low-energy effective theories were developed to go beyond hydrodynamics and capture the first dispersive correction to the spectrum (Salasnich and Toigo, 2008; Mañes and Valle, 2009; Rupak and Schäfer, 2009). The finite lifetime of the phonons at $T = 0$ was obtained by considering Beliaev processes (Kurkjian et al., 2017). In these results the lifetime is calculated in a perturbative way, by including the decay processes diagrammatically, for example. However, a nonperturbative result can be found by locating the zeroes of $\det[\mathbb{M}(\mathbf{q}, z)]$ numerically in the lower complex z plane, using the analytic continuation (18), as shown by Klimin et al. (2019a,b). This work also addressed the temperature dependence of the mode's dispersion and damping.

In contrast with the low-temperature regime, the behavior of the collective branches near T_c long remained a controversial problem. Whereas Andrianov and Popov (1976) find a purely imaginary dispersion, Ohashi and Takada (1997) find a real dispersion. Both studies were performed in the BCS limit $\mu/\Delta \to \infty$, whereas a more recent study is limited to the strong-coupling regime (Kosztin et al., 2000). The controversy was solved in Klimin et al. (2019b), where it is shown that in the vicinity of the transition temperature T_c a second sound-like mode appears, corresponding to a second solution of $\det[\mathbb{M}(\mathbf{q}, cq)] = 0$. The second mode is not present in the BEC regime. The two-mode nature is also visible in the order-parameter phase response function which displays two distinct resonance peaks, at temperatures relatively close to T_c, and in the BCS regime. The second mode, obtained in the random phase approximation as well as in the Gaussian pair fluctuation approach outlined in the previous sections, has a counterpart in superconductors, where it is known as the Carlson–Goldman mode, observed experimentally by Carlson and Goldman (1973, 1976). There, the Anderson–Bogoliubov mode is no longer sound-like due to the charged nature of the pairs, but the second mode, existing only close to T_c, remains sound-like.

Let us now turn to experiments in ultracold Fermi gases. As discussed in the section "Order parameter for the superuid Fermi gas," Feshbach resonances allowed to boost the critical temperature for pair formation and superfluidity to within experimental reach. The sound velocity in these systems was first observed by creating a density perturbation and observing its displacement grow linearly with time (Joseph et al., 2007; Sidorenkov et al., 2013; Weimer et al., 2015). In the BEC regime the sound velocity determines the Landau critical velocity for superfluid flow (whereas in the BCS regime, the pair-breaking excitations do), and this provides an indirect way to determine the velocity of the sound mode on the BEC side of unitarity (Miller et al., 2007).

The complete excitation spectrum (i.e., beyond the long-wavelength limit given by the sound velocity) was measured in a seminal experiment by (Hoinka et al., 2017), using Bragg spectroscopy. When the imparted momentum and energy are resonant to an elementary excitation (such as an Anderson–Bogoliubov excitation), a peak in the number of Bragg scattered atom number is detected. Strongly speaking, the Bragg probe couples to the atom density rather than to the pair phase, but the two are coupled such that the Anderson–Bogoliubov mode can be both excited and probed by this technique.

A comparison between the experimentally measured Anderson–Bogoliubov response and the Gaussian pair fluctuation theory (Klimin et al., 2019b) is shown in Fig. 2. Theory and experiment are seen to be in fair agreement. Nevertheless, many questions remain, such as how to improve qualitative results of the curvature of the Anderson–Bogoliubov mode as a function of the interaction strength. The precise value of the interaction strength where the curvature switches from positive to negative is very

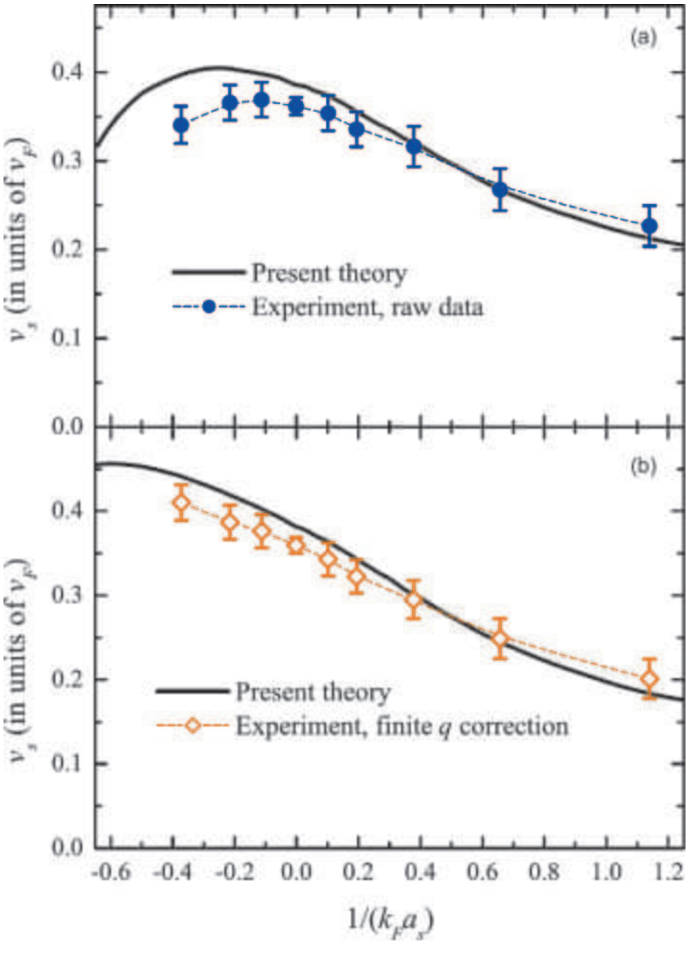

Fig. 2 Comparison between theory and experiment for the Anderson–Bogoliubov mode. The symbols correspond to Bragg spectroscopy measurements (Hoinka et al., 2017), the *full line* is the result from Gaussian pair fluctuation theory (Klimin et al., 2019b). The measurements were performed at finite wave number $k \approx k_F/2$ (panel A), from which the long-wavelength $k \longrightarrow 0$ data was extrapolated (panel B). Reproduced with permission from Klimin SN, Kurkjian H, Tempere J (2019a.) Anderson-Bogoliubov collective excitations in superfluid Fermi gases at nonzero temperatures. Journal of Low Temperature Physics 196: 102–110.

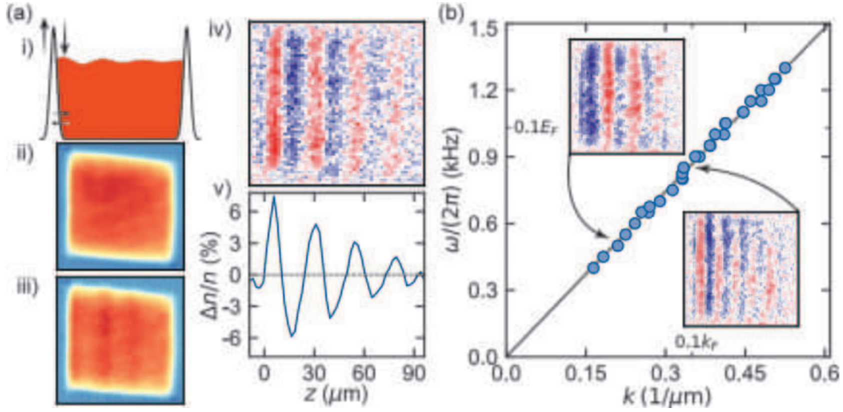

Fig. 3 (A) In the experiment of Patel et al. (2020), a density wave is excited by shaking one of the walls of a box trap containing a Fermi superfluid near unitarity. The damping of the wave away from the wall is visible. (B) The measured resonant frequency (*dots*) corresponds to that of the Anderson–Bogoliubov mode (*full line*) since near unitarity there is a good coupling between the phase mode of the order parameter and the density oscillation. Reproduced with permission from Patel PB, Yan Z, Mukherjee B, Fletcher RJ, Struck J, Zwierlein MW (2020). Universal sound diffusion in a strongly interacting Fermi gas. Science 370: 1222–1226.

sensitive to the microscopic theory for the pairing and can be seen as test for it. Experimentally, the Carlson–Goldman mode near the critical temperature, and, in general, the temperature dependence remain to be measured.

The damping of the Anderson–Bogoliubov mode has only recently been observed directly, although it possibly could be extracted from the width of the Bragg excitation peaks in Hoinka et al. (2017). A recent experiment by Patel et al. (2020) takes a more direct approach; its results are shown in Fig. 3. In this experiment, the Fermi superfluid is enclosed in a box trap in which one of the walls of the box is shaken to excite the sound mode. The damping of the amplitude of the mode away from the wall can then be related to the sound attenuation in the Fermi superfluid (Braby et al., 2010). A difficulty that remains is that the shaking excites a density wave, which is strictly speaking different from the phase mode—however, both are coupled in such a way that at the resonant frequency, the phase mode is visible in the density response.

Amplitude mode in superfluid Fermi gases

The first theoretical efforts to describe the amplitude mode were performed in the context of superconductors. There, the Coulomb interactions between the charged pairs create a gap for the phase mode, lifting it to a plasmonic start. However, the amplitude mode is expected to remain present near 2Δ. Initial studies (Schmid, 1968; Kulik et al., 1981; Littlewood and Varma, 1981, 1982) assumed particle–hole symmetry, which is only valid in the BCS limit, as well as the long-wavelength limit $q \to 0$. This corresponds to solving $M_{--}(\mathbf{q} \to 0, z) = 0$, rather than $\det[\mathbb{M}(\mathbf{q}, z)] = 0$. As mentioned in the introduction, this approximation is not valid for superfluid Fermi gases.

Liu et al. (2016) studied the amplitude mode through the Ginzburg–Landau equation for the superfluid Fermi gas. This can be obtained by a gradient expansion of the action, valid for slow frequencies and long wavelength. However, it is not clear whether this approach is valid at frequencies comparable to $2\Delta/\hbar$. The result of $\det[\mathbb{M}(\mathbf{q}, z)] = 0$ at arbitrary wave number was first studied in Kurkjian et al. (2019), obtaining the full dispersion relation of the amplitude mode, accounting for amplitude–phase coupling. This includes a calculation of the damping rate, which is shown to have a quadratic start at low wave number rather than the previously assumed linear one (Littlewood and Varma, 1982). The amplitude mode is shown to appear in the BCS regime at $\mu/\Delta \simeq 0.8267$. At zero temperature, analytical results for the dispersion were obtained in Kurkjian and Castin (2020). Analysis of the fluctuation matrix at nonzero temperature reveals that when approaching the critical temperature from below, the Anderson–Bogoliubov mode persists only in a relatively low energy-momentum region, and is gradually replaced by a quadratically dispersed pairing resonance (Klimin et al., 2021). This also leads to a decrease in the Landau critical velocity, which tends to zero as the temperature tends to the critical temperature. The general conclusion for the amplitude mode is that it persists well into the crossover regime of strongly correlated fermionic superfluids, and is not overdamped so that it should be experimentally detectable. Fig. 4 (reproduced from Kurkjian et al., 2019) shows the response function of the superfluid in the pair-breaking continuum, and in the BCS regime at $\mu/\Delta = 10$. The Higgs mode is clearly visible at low momentum, and the long-wavelength analytic results for the dispersion match the peak of response function well, even as it becomes more strongly damped.

However, in contrast to the Anderson–Bogoliubov mode, the amplitude mode is much harder to detect in practice. The presence of the broken-pair continuum dampens the mode, and it is not a priori clear how to disentangle the signal of the amplitude mode from the response of the pair-breaking excitations (Cea et al., 2016). The amplitude mode is also much harder to excite: many "pump" protocols (such as Bragg scattering) use fields the couple to the density rather than to the amplitude of the order parameter. Whereas the phase sector couples well to the density, a question remained as to how strongly the amplitude of the order parameter couples to it. Following a suggestion made by Volkov and Kogan (1974) for superconductors, Scott et al. (2012) therefore propose to modulate the scattering length via a Feshbach resonance as a way to excite the (long-wavelength) amplitude mode directly. This

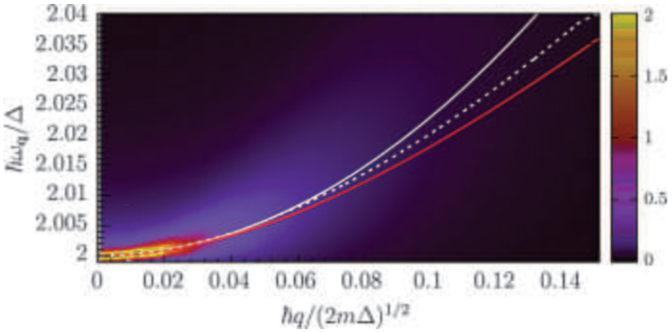

Fig. 4 The pair-field response function of the Fermi superfluid is shown in the pair-breaking continuum region ($\omega > 2\Delta$). Despite the presence of strong damping at larger wave numbers, the amplitude mode is clearly visible at lower momenta. The analytic dispersion (*full red line*) matches with the maximum of the broadening peak (*dashed line*) in the numerically computed response. The *white dashed line* is the quadratic long-wavelength limit. Reproduced with permission from Kurkjian H, Klimin SN, Tempere J, Castin Y (2019). Pair-breaking collective branch in BCS superconductors and superfluid Fermi gases. Physical Review Letters 122: 093403.

proposal was investigated theoretically in the framework of the Bogoliubov–de Gennes approach (but still in the long-wavelength limit) by Tokimoto et al. (2017). Kurkjian et al. (2020) studied the linear response functions where both the pump and the probe can couple to amplitude, phase, or density and showed that an experiment where the pump couples to the amplitude of the order parameter (such as the "wiggling" of the scattering length) will provide a measurable signal of the amplitude mode in the density channel. Crucially, Kurkjian et al. (2020) also showed that the amplitude mode is detectable not only in the amplitude–amplitude and amplitude–density response functions but also in the density–density responses.

Behrle et al. (2018) developed a scheme for exciting the amplitude mode that does not rely on modulating the scattering length. Rather, they induce a radio-frequent coupling between one of the pairing states, denoted by $|2\rangle$ and an unoccupied hyperfine spin state, $|3\rangle$. This modulates the pairing between the two states $|1\rangle$ and $|2\rangle$ that form the superfluid. After the excitation, the condensate fraction is measured by a quick sweep to the BEC regime, projecting onto tightly bound pairs. Thus, the detection is also more closely linked to the amplitude channel than to the density channel. Behrle et al. (2018) detect a resonance at the modulation frequency 2Δ that is attributed to the amplitude mode, and that broadens when the system is tuned to the BEC side. To this date, this remains the only observation of the amplitude mode in superfluid Fermi gases, although a full theoretical analysis of the particular experimental procedure is still lacking. Other researchers follow more closely the proposal of modulating the interaction strength. In particular, Dyke et al. (2021) mapped the response of the order parameter to a quench in the interaction strength. This reveals the formation of the pairs, but the long-wavelength response is much slower. Supposedly, extending this experiment from a quench to a periodical modulation will allow to reveal the amplitude mode. However, at the time of writing, this measurement remains to be performed.

Conclusion

It is clear that the advent of superfluid Bose and Fermi gases offer a new and versatile approach to studying the phase and amplitude mode that follow from breaking U(1) symmetry. These modes were originally defined and studied in the context of particle physics and superconductors, but the atomic gases offer a much cleaner system, where interaction strength, dimensionality, and composition can be finely tuned experimentally. This has allowed to extend earlier studies to now encompass damping, nonzero wave number, and temperature effects of these modes. At the same time, differences have been revealed with superconducting systems, due to the charge neutrality of the superfluid gases. Despite these advances, challenges remain to excite and probe these modes experimentally, for which the coupling between the modes and the coupling with the suitable experimental probes should be better understood, perhaps even beyond the linear regime.

References

Anderson PW (1958a) Coherent excited states in the theory of superconductivity: Gauge invariance and the Meissner effect. *Physical Review* 110: 827–835.
Anderson PW (1958b) Random-phase approximation in the theory of superconductivity. *Physical Review* 112: 1900–1916.
Anderson PW (1963) Plasmons, gauge invariance, and mass. *Physical Review* 130: 439.
Andrews MR, Kurn DM, Miesner HJ, Durfee DS, Townsend CG, Inouye S, and Ketterle W (1997) Propagation of sound in a Bose-Einstein condensate. *Physical Review Letters* 79: 553–556.
Andrianov VA and Popov VN (1976) Hydrodynamic action and Bose spectrum of superfluid Fermi systems. *Teoreticheskaya i Matematicheskaya Fizika* 28: 341.
Astrakharchik GE, Combescot R, Leyronas X, and Stringari S (2005) Equation of state and collective frequencies of a trapped Fermi gas along the BEC-unitarity crossover. *Physical Review Letters* 95: 030404.
Behrle A, Harrison T, Kombe J, Gao K, Link M, Bernier J-S, Kollath C, and Köhl K (2018) Higgs mode in a strongly interacting fermionic superfluid. *Nature Physics* 14: 781–785.
Bissbort U, Götze S, Li Y-Q, Heinze J, Krauser JS, Weinberg M, Becker C, Sengstock K, and Hofstetter W (2011) Detecting the amplitude mode of strongly interacting lattice bosons by Bragg scattering. *Physical Review Letters* 106: 205303.

Bogoliubov NN, Tolmachov VV, and Sirkov DV (1958) A new method in the theory of superconductivity. *Fortschritte der Physik* 6: 605–682.

Braby M, Chao J, and Schafer T (2010) Thermal conductivity and sound attenuation in dilute atomic Fermi gases. *Physical Review A* 82: 033619.

Carlson RV and Goldman AM (1973) Superconducting order-parameter fluctuations below Tc crossover scenario. *Physical Review Letters* 31: 880.

Carlson RV and Goldman AM (1976) Dynamics of the order parameter of superconducting aluminum films. *Journal of Low Temperature Physics* 25: 67.

Cea T, Castellani C, and Benfatto L (2016) Nonlinear optical effects and third-harmonic generation in superconductors: Cooper pairs versus Higgs mode contribution. *Physical Review B* 93: 180507.

Combescot R, Kagan MY, and Stringari S (2006) Collective mode of homogeneous superfluid Fermi gases in the BEC-BCS crossover. *Physical Review A* 74: 042717.

Diener RB, Sensarma R, and Randeria M (2008) Quantum fluctuations in the superfluid state of the BCS-BEC crossover. *Physical Review A* 77: 023626.

Dyke P, Hogan A, Herrera I, Kuhn CCN, and Vale CJ (2021) Dynamics of a Fermi gas quenched to unitarity. *Physical Review Letters* 124: 100405.

Endres M, Fukuhara T, Pekker D, Cheneau M, Schauss P, Gross C, Demler E, Kuhr S, and Bloch I (2012) The ‘Higgs’ amplitude mode at the two-dimensional superfluid/Mott insulator transition. *Nature* 487: 454–458.

Englert F and Brout R (1964) Broken symmetry and the mass of gauge vector mesons. *Physical Review Letters* 13: 321.

Goldstone J (1961) Field theories with superconductor solutions. *Nuovo Cimento* 19: 154–164.

He Y, Chen Q, Chien C-C, and Levin K (2007) First- and second-sound-like modes at finite temperature in trapped Fermi gases from BCS to BEC. *Physical Review A* 76: 051602.

Heiselberg H (2006) Sound modes at the BCS-BEC crossover. *Physical Review A* 73: 013607.

Higgs PW (1964) Broken symmetries and the masses of gauge bosons. *Physical Review Letters* 13: 508.

Hoinka S, Dyke P, Lingham MG, Kinnunen JJ, Bruun GM, and Vale CJ (2017) Goldstone mode and pair-breaking excitations in atomic Fermi superfluids. *Nature Physics* 13: 943–946.

Houbiers M and Stoof HTC (1999) Cooper-pair formation in trapped atomic Fermi gases. *Physical Review A* 59: 1556.

Huang B and Wan S (2007) Collective modes in a uniform Fermi gas with Feshbach resonances. *Physical Review A* 75: 053608.

Huber SD, Altman E, Büchler HP, and Blatter G (2007) Dynamical properties of ultracold bosons in an optical lattice. *Physical Review Letters* 358: 1415–1418.

Jin DS, Ensher JR, Matthews MR, Wieman CE, and Cornell EA (1996) Collective excitations of a Bose-Einstein condensate in a dilute gas. *Physical Review Letters* 77: 420–423.

Joseph J, Clancy B, Luo L, Kinast J, Turlapov A, and Thomas JE (2007) Measurement of sound velocity in a Fermi gas near a Feshbach resonance. *Physical Review Letters* 98: 170401.

Klimin SN, Kurkjian H, and Tempere J (2019a) Anderson-Bogoliubov collective excitations in superfluid Fermi gases at nonzero temperatures. *Journal of Low Temperature Physics* 196: 102–110.

Klimin SN, Kurkjian H, and Tempere J (2019b) Phononic collective excitations in superfluid Fermi gases at nonzero temperatures. *Physical Review A* 100: 063634.

Klimin SN, Tempere J, and Kurkjian H (2021) Collective excitations of superfluid Fermi gases near the transition temperature. *Physical Review A* 103: 043336.

Kosztin I, Chen Q, Kao Y-J, and Levin K (2000) Pair excitations, collective modes, and gauge invariance in the BCS-Bose-Einstein crossover scenario. *Physical Review B* 61: 11662.

Kulik IO, Entin-Wohlman O, and Orbach R (1981) Pair susceptibility and mode propagation in superconductors: A microscopic approach. *Journal of Low Temperature Physics* 43: 591–620.

Kurkjian H and Castin Y (2020) Collective excitation branch in the continuum of pair-condensed Fermi gases : Analytical study et scaling laws. *Comptes Rendus : Physique* 21: 253–310.

Kurkjian H, Castin Y, and Sinatra A (2016) Concavity of the collective excitation branch of a Fermi gas in the BEC-BCS crossover. *Physical Review A* 93: 013623.

Kurkjian H, Castin Y, and Sinatra A (2017) Three-phonon and four-phonon interaction processes in a pair-condensed Fermi gas. *Annals of Physics A* 529: 1600352.

Kurkjian H, Klimin SN, Tempere J, and Castin Y (2019) Pair-breaking collective branch in BCS superconductors and superfluid Fermi gases. *Physical Review Letters* 122: 093403.

Kurkjian H, Tempere J, and Klimin SN (2020) Linear response of a superfluid Fermi gas inside its pair-breaking continuum. *Scientific Reports* 10: 11591.

Léonard J, Morales A, Zupancic P, Donner T, and Esslinger T (2017) Monitoring and manipulating Higgs and Goldstone modes in a supersolid quantum gas. *Science* 358: 1415–1418.

Littlewood PB and Varma CM (1981) Gauge-invariant theory of the dynamical interaction of charge density waves and superconductivity. *Physical Review Letters* 47: 811.

Littlewood PB and Varma CM (1982) Amplitude collective modes in superconductors and their coupling to charge-density waves. *Physical Review B* 26: 4883.

Liu B, Zhai H, and Zhang S (2016) Evolution of the Higgs mode in a fermion superfluid with tunable interactions. *Physical Review A* 93: 033641.

Mañes JL and Valle MA (2009) Effective theory for the Goldstone field in the BCS-BEC crossover at T = 0. *Annals of Physics A* 324: 1136.

Marini M, Pistolesi F, and Strinati GC (1998) Evolution from BCS superconductivity to Bose condensation: Analytic results for the crossover in three dimensions. *European Physical Journal B* 1: 151–159.

Miller DE, Chin JK, Stan CA, Liu Y, Setiawan W, Sanner C, and Ketterle W (2007) Critical velocity for superfluid flow across the BEC-BCS crossover. *Physical Review Letters* 99: 070402.

Nambu Y (1960) Quasiparticles and gauge invariance in the theory of superconductivity. *Physical Review* 117: 648–663.

Ohashi Y and Griffin A (2003) Superfluidity and collective modes in a uniform gas of Fermi atoms with a Feshbach resonance. *Physical Review A* 67: 063612.

Ohashi Y and Takada S (1997) Goldstone mode in charged superconductivity: Theoretical studies of the Carlson-Goldman mode and effects of the Landau damping in the superconducting state. *Journal of the Physical Society of Japan* 66: 2437.

Patel PB, Yan Z, Mukherjee B, Fletcher RJ, Struck J, and Zwierlein MW (2020) Universal sound diffusion in a strongly interacting Fermi gas. *Science* 370: 1222–1226.

Pekker D and Varma CM (2015) Amplitude / Higgs modes in condensed matter physics. *Annual Reviews of Condensed Matter Physics* 6: 269–297.

Pitaevskii LP and Stringari S (2003) *Bose-Einstein condensation*. Oxford: Clarendon Press.

Podolsky D, Auerbach A, and Arovas DP (2011) Visibility of the amplitude (Higgs) mode in condensed matter. *Physical Review B* 84: 174522.

Pollet L and Prokofiev NV (2012) The Higgs mode in a two-dimensional superfluid. *Physical Review Letters* 109: 010401.

Rupak G and Schäfer T (2009) Density functional theory for non-relativistic fermions in the unitarity limit. *Nuclear Physics A* 816: 52.

Sa de Melo CAR, Randeria M, and Engelbrecht JR (1993) Crossover from BCS to Bose superconductivity: Transition temperature and time-dependent Ginzburg-Landau theory. *Physical Review Letters* 71: 3202–3205.

Salasnich L and Toigo F (2008) Extended Thomas-Fermi density functional for the unitary Fermi gas. *Physical Review A* 78: 053626.

Schmid A (1968) The approach to equilibrium in a pure superconductor. The relaxation of the Cooper pair density. *Physik der kondensierten Materie* 8: 129–140.

Scott RG, Dalfovo F, Pitaevskii LP, and Stringari S (2012) Rapid ramps across the BEC-BCS crossover: A route to measuring the superfluid gap. *Physical Review A* 86: 053604.

Sidorenkov LA, Tey MK, Grimm R, Hou Y-H, Pitaevskii LP, and Stringari S (2013) Second sound and the superfluid fraction in a resonantly interacting Fermi gas. *Nature* 498: 78–81.

Sooryakumar R and Klein MV (1980) Raman scattering by superconducting-gap excitations and their coupling to charge-density waves. *Physical Review Letters* 45: 660.

Stamper-Kurn DM, Chikkatur AP, Görlitz A, Inouye S, Gupta S, Pritchard DE, and Ketterle W (1999) Excitation of phonons in a Bose-Einstein condensate by light scattering. *Physical Review Letters* 83: 2876–2879.

Tokimoto J, Tsuchiya S, and Nikuni T (2017) Higgs mode in a trapped superfluid Fermi gas. *Journal of Low Temperature Physics* 187: 765–770.

Volkov AF and Kogan SM (1974) Collisionless relaxation of the energy gap in superconductors. *Soviet Physics: JETP* 38: 1018.

Weimer W, Morgener K, Singh VP, Siegl J, Hueck K, Luick N, Mathey L, and Moritz H (2015) Critical velocity in the BEC-BCS crossover. *Physical Review Letters* 114: 095301.

Higgs and Goldstone modes in crystalline solids

Marco Vallone, Department of Electronics and Telecommunications. Politecnico of Turin, Turin, Italy

© 2024 Elsevier Ltd. All rights reserved.

Introduction 197
Overview and outline of the chapter 198
Notation 198
Symmetry and invariance 199
Symmetry of states 199
Symmetry of the physical laws 199
Gauging translations in crystal lattice: Acoustic phonons as gauge bosons 200
Emerging of Goldstone modes 200
Pseudo-relativistic metric 201
Gauging spatial translations 201
Peculiarities of spatial translations 202
Yang–Mills theory of acoustic phonons in crystal 202
Optical phonons remain still undescribed 204
Spontaneous symmetry breaking and order parameter 205
Ginzburg–Landau approach and SSB 206
SSB in crystalline solids 206
Experimental evidences of SSB in structural phase transitions in metals 209
Conclusion 210
References 210

Abstract

Optical and acoustic phonons play a central role in solid-state physics. Acoustic phonons can be thought of either as Goldstone bosons, which arise from the breaking of the translational invariance, or as gauge bosons within a non-Abelian gauge theory framework. Nevertheless, optical phonons are left out. Spontaneous symmetry breaking provides a unified framework in which optical and acoustic phonons appear together. After a general overview of this subject, the concept was applied specifically to crystalline phase transitions. Goldstone and Higgs modes arise naturally as a result of spontaneous breaking of a global, continuous crystal symmetry and can be identified with acoustic and optical phonons, respectively.

Key points

- The emergence of Goldstone modes in crystals, ensuing from the spontaneous breakdown of the translational invariance due to the lattice.
- Solid crystal lattice, phonons, and sonic metric: similarities with the general relativity formalism.
- By requiring Lagrangian gauge invariance, the acoustic phonons appear as gauge bosons. They are self-interacting due to the noncommutative Lie algebra of group generators.
- Introduction to the Spontaneous Symmetry Breaking: the emergence of order parameters and Higgs modes.
- Optical and acoustic phonons in crystals are Higgs and Goldstone lattice excitations caused by the spontaneous breaking of a global, continuous symmetry.
- Phase transitions in metals and experimental evidences of spontaneous symmetry breaking.

Introduction

When a continuous symmetry breaks, a massless bosonic particle appears for each broken generator. This is the short version of the Nambu–Goldstone theorem (Nambu, 1960; Goldstone, 1961), which forms the basis of the Standard Model of fundamental interactions. However, the Goldstone theorem is very general and is valid also in the nonrelativistic condensed matter, where the massless bosons correspond to collective excitations with wavevector $\boldsymbol{k}$ and gapless frequency dispersion relation ω_k, that is, $\omega_{k\to 0} \to 0$, where $k = |\boldsymbol{k}|$. Some examples: Spin waves in the Heisenberg model are bosons that appear when the ground state of the

https://doi.org/10.1016/B978-0-323-90800-9.00227-4

Heisenberg–Hamiltonian is magnetically ordered (Kendziora et al., 2005); collective density excitations in superconductors arise from spontaneous breaking of the electronic phase rotation symmetry $U(1)$ (Pracht, 2017; Pracht et al., 2017). A more known example is given by acoustic phonons (Ashcroft and Mermin, 1976), collective excitations in crystalline solids associated with lattice vibrational modes. They correspond to Goldstone modes arising from the breaking of a continuous spatial symmetry, the translational invariance, which is broken by the presence of the crystal lattice (Leutwyler, 1994, 1997). All of these collective excitations are said to arise from one of the so-called emergence principles, in this case the Goldstone theorem, since they arise from the beginning.

The nature of acoustic phonons can be reinterpreted in the context of a non-Abelian gauge theory in which translations play the role of the gauge group. Following a formalism very similar to the Yang–Mills theory of the affine group, the local gauge invariance imposed on the Lagrangian leads to gauge fields identified with acoustic phonon modes (Vallone, 2019).

An important topic in physics is spontaneous symmetry breaking (SSB): it is widely known in the Standard Model of particle physics, where the mass-generating mechanism described by Higgs (1964) removed the obstacles encountered in the attempt to construct a unified gauge invariant theory of the electromagnetic and weak interactions (Mandl and Shaw, 2010). In condensed matter physics a similar concept was formulated by Ginzburg and Landau (Ginzburg and Landau, 1950; Landau, 1965), an approach that inspired Anderson (1963) to describe the plasmon phenomenon in a way that was recognized by Higgs himself as cornerstone for his own work. The existence of such oscillating modes seems to be ubiquitous. The Higgs mechanism has been recognized in topological insulators, Weyl semimetals, and in cuprates (Hasan and Kane, 2010; Ando, 2013; Wan et al., 2011; Burkov and Balents, 2011; Singh et al., 2012; Raines et al., 2015); in the quantum phase transition between superfluid and insulating phases (Littlewood and Varma, 1981; Endres et al., 2012); in the transition from a sea of spin-singlet pairs to a long-range antiferromagnet (Rüegg et al., 2008); in superconductors (Pracht, 2017; Pracht et al., 2017), etc. Recently, the presence of structural Goldstone and Higgs modes was suggested by first-principles calculations (Marthinsen et al., 2018) on a perovskite oxide, $SrMnO_3$, and demonstrated in a supersolid quantum gas (Léonard et al., 2017).

It has been shown that even the well-known optical and acoustic phonons in crystalline solids (metals, semiconductors, etc.) can be identified, respectively, with Higgs and Goldstone excitations of the crystal lattice which arise from the spontaneous breaking of a global, continuous symmetry in structural phase transitions that occur in widely available, natural crystalline solids (Vallone, 2019; Meier et al., 2019; Juraschek et al., 2020; Vallone, 2020). This important fact complements similar occurrences in quantum phase transitions and shows how widespread such concepts are in seemingly unrelated branches of physics.

Overview and outline of the chapter

In order to depict what will be covered in the sections that follow, it is important to note that the current chapter includes a number of concepts and themes that are strictly related to one another.

Section “Symmetry and invariance” provides an overview of the concepts of symmetry of states, symmetry of Hamiltonian (or action), and invariance, which are required to address what follows, particularly the concept of spontaneous symmetry breaking.

In Section “Gauging translations in crystal lattice: Acoustic phonons as gauge bosons,” after a description of the acoustic phonons as Goldstone bosons arising from the breaking of the translational invariance, we introduce a different concept: the gauging of spatial translations on the lattice. This reinterprets the acoustic phonons in the framework of a non-Abelian gauge theory, in which translations play the role of the gauge group. From this point of view, the nonlinearity of phonon–phonon interactions arises naturally from the noncommutative Lie algebra of the group generators involved. However, this approach does not describe another, even more important oscillatory mode of the crystal lattice: optical phonons.

In Section “Spontaneous symmetry breaking and order parameter” we first discuss the general concept of SSB. Then we show how acoustic and optical phonons in crystals can be described as Goldstone and Higgs modes emerging from an SSB caused by a transition from a symmetric crystalline phase to a less symmetric phase. Considering the great importance of optical phonons for electronic transport in semiconductors (Brum and Bastard, 1986; Vallone et al., 2015, 2017), this topic is particularly important. We also emphasize that nonlinear multiphonon coupling, phonon decay, and the acousto-optical coupling are all described by this unifying approach, and they are the result of the Lagrangian nonlinearities (Vallone, 2020; Xie, 2022).

Notation

In the present work A^{α} and B_{β} are contravariant and covariant four-vectors, ∂_{μ} is the partial derivative $\partial/\partial x^{\mu}$, where Greek indices $\alpha, \beta, \mu, \ldots = 0, \ldots 3$ mark space–time coordinates on a four-dimensional differentiable manifold with metric $g_{\mu\nu}$ and connection $\Gamma^{\alpha}_{\mu\nu}$. Latin indices $(i, j, k, \ldots = 1, 2, 3)$ indicate spatial components, while Greek indices with a ‘hat’ $\hat{\mu}, \hat{\nu}, \ldots = 0, \ldots 3$ are used for indices of local four-dimensional frames (vierbeins or tetrad indices) on a flat Lorentzian space–time with Minkowski metric $\eta_{\hat{\mu}\hat{\nu}} = \mathrm{diag}(+1, -1, -1, -1)$. Einstein summation over the repeated index is always understood, the nonitalicized ‘i’ is the imaginary unit, square brackets $[A, B]$ represent the commutator $AB - BA$, the operator $\hat{U}^{\dagger}$ is the Hermitian conjugate of $\hat{U}$, and ψ^{*} is the complex conjugate of ψ.

Symmetry and invariance

Until the 20th century, the principles of symmetry played little role in theoretical physics. This changed dramatically with A. Einstein, whose breakthrough in 1905 was to put symmetry first and to regard the principle of symmetry as the primary feature of nature that restricts dynamical laws to an admissible path. From this new perspective, the transformation properties of the electromagnetic field do not derive from Maxwell's equations, but rather are a consequence of relativistic invariance, from which the form of Maxwell's equations follows.

With the development of quantum mechanics in the 1920s, symmetry principles were elevated to an even more fundamental role, which is now the predominant concept in the study of the properties of matter and the universe at the deepest level and serves as the guiding principle in the search for the grand unification laws.

To get to our topic and discuss what a spontaneous symmetry breaking is, we must first briefly recall what a symmetry is. To this end, we must distinguish the symmetry of physical states, objects, and solutions of equations of motion from the symmetry of the laws that govern them, which is a different concept.

Symmetry of states

When an object appears identical from different angles, we say that it is symmetrical. For example, if it is rotated through any angle, it may appear identical. A sphere is a classic case, and we say that it has continuous rotational symmetry: its shape is invariant by rotations. A book, a cat, a man, etc. have no rotational symmetry. A cylinder has cylindrical symmetry, that is, it looks the same—it is invariant—when rotated about its longitudinal axis (but this is not true for rotation about any other axis). These are continuous symmetries, but there are also discrete symmetries. One example is spatial parity, which is defined by a change in the sign of all spatial coordinates. A reflection symmetry is the flipping of one spatial coordinate (e.g., x, y, z, $\rightarrow -x$, y, z): we have roughly reflection symmetry since our shape is approximately invariant when mirrored. However, in this paper, we will only consider continuous symmetries.

Although the concept of symmetry and the related conservation laws can be presented in a classical context, they can be discussed in quantum mechanics in a much simpler yet general form. A state $|\psi\rangle$ is said to be symmetric under a transformation U (e.g., represented as a matrix) if the transformed state is the same initial state except for a phase factor, that is, $U|\psi\rangle = e^{i\phi}|\psi\rangle$, where ϕ is a real parameter. Since a phase factor does not correspond to any observable, the new state has the same properties as the initial state, including the same norm. The last point implies that the associated operator $\hat{U}$ is unitary.

The unitary transformations form a group, and $\hat{U}$ can be given the exponential form $\hat{U} = e^{i\phi^i \hat{P}_i}$, where ϕ^i are real parameters and $\hat{P}_i$ are called the generators of the group ($i = 1, 2, 3$, in the ordinary space). Continuous spatial translations in the ordinary space have three generators (the momentum operator components) that fulfill the Lie algebra $[\hat{P}_j, \hat{P}_k] = \mathrm{i} f^i_{jk} \hat{P}_i$, where f^i_{jk} are called structure constants of the algebra (Ziman, 1969; Peskin and Schroeder, 1995; Lipkin, 2002).

An important note: The transformed state is not the same as the initial state, but it seems that the difference is not observable. However, this is not the case: if $\hat{U}$ is applied to another state $|\chi\rangle$ and the transformed state cannot be expressed by $e^{i\phi}|\chi\rangle$, we say that $|\chi\rangle$ is not symmetric with respect to the group of transformations represented by $\hat{U}$. From the comparison we conclude that $|\psi\rangle$ is symmetric and $|\chi\rangle$ is not, while without the comparison we could conclude that $\hat{U}$ is the identity operator, which is not true.

Symmetry of the physical laws

The second point we need to discuss is the symmetry of the physical laws governing quantum states: in particular, the symmetry of the equations of motion (e.g., the Euler–Lagrange or Schrödinger equations), which derive their symmetry properties from the symmetry of Hamiltonians, Lagrangians, or action.

A system is called symmetric if it is described by a Hamiltonian operator $\hat{H}$ (or by a Lagrangian operator $\hat{\mathcal{L}}$), which is invariant under a unitary transformation $\hat{U}$ which commutes with the Hamiltonian operator, $[\hat{U}, \hat{H}] = 0$, or equivalently $\hat{U}^\dagger \hat{H} \hat{U} = \hat{H}$. The reason is the following: It is easy to prove that the energy E_n associated to an eigenstate $|\psi_n\rangle$ of $\hat{H}$ does not change if we transform the state to $\hat{U}|\psi_n\rangle$ provided $[\hat{U}, \hat{H}] = 0$, even if $|\psi_n\rangle$ itself is not symmetric under the transformation $\hat{U}$:

$$\hat{H}\left(\hat{U}|\psi_n\rangle\right) = \hat{U}\left(\hat{H}|\psi_n\rangle\right) = E_n\left(\hat{U}|\psi_n\rangle\right). \tag{1}$$

In Eq. (1), we have only exploited the commutation rule $[\hat{U}, \hat{H}] = 0$, but no symmetry constraints have been set for the state $|\psi_n\rangle$. More formally, $\hat{H}$ and $\hat{U}^\dagger \hat{H} \hat{U}$ represent the same dynamics: if $\hat{U}$ commutes with the Hamiltonian, the eigenstates of $\hat{H}$ are also eigenstates of the transformed Hamiltonian $\hat{U}^\dagger \hat{H} \hat{U}$ with the same eigenvalues. We say that the transformation represented by $\hat{U}$ is a symmetry of the Hamiltonian.

All this is closely related to conservation laws. The relationship between symmetries and conserved quantities can be understood by noting that the Hamiltonian operator defines the time evolution unitary operator $\hat{T} = e^{i\hat{H}t}$, for which $[\hat{T}, \hat{H}] = 0$ holds. $\hat{T}$ can also be written in the exponential form $\hat{T} = e^{i\hat{Q}}$, and since $[\hat{Q}, \hat{T}] = 0$ also holds, the expectation value of $\hat{Q}$ in any state $|\psi\rangle$ is conserved in time (Heisenberg equation): its eigenvalue is a conserved quantity, a constant of motion.

All this has an important consequence: the existence of a symmetry transformation implies a conservation law. For example, symmetry with respect to translations implies conservation of momentum, and symmetry with respect to rotations implies conservation of angular momentum. Moreover, for continuous symmetry transformations parameterized by a continuous variable, there is an even stronger result, the Noether theorem: a continuous symmetry always implies a current $j^\nu(\boldsymbol{r}, t)$ for which a local conservation law holds: $\partial_\nu j^\nu(\boldsymbol{r}, t) = 0$. There are many more details behind this, but they are far beyond the scope of the present work. The interested reader can find much further food for thought in Gross (1996), and Beekman et al. (2019), beside a demonstration of the Noether theorem in Peskin and Schroeder (1995).

What is still important here is the fact that the local form of the Noether theorem $\partial_\nu j^\nu(\boldsymbol{r}, t) = 0$ only depends on the symmetry of the action with respect to $\hat{U}$ and is also valid for a stable state which does not have the same symmetry. In the latter case we say that the symmetry of the action is spontaneously broken, a concept that will be presented in detail in Section "Spontaneous symmetry breaking and order parameter."

Gauging translations in crystal lattice: Acoustic phonons as gauge bosons

The dynamics of nonrelativistic Pauli electrons in crystal lattice (e.g., in a semiconductor, in a metal) with effective mass m_e, wavefunction $\psi_{\boldsymbol{k}}(t, \boldsymbol{r})$, and wavevector $\boldsymbol{k}$ can be described by the Lagrangian density

$$\mathcal{L} = \mathrm{i}\psi^*_{\boldsymbol{k}}\partial_t\psi_{\boldsymbol{k}} - \frac{1}{2m_e}\nabla\psi^*_{\boldsymbol{k}} \cdot \nabla\psi_{\boldsymbol{k}}, \tag{2}$$

which is symmetric (i.e., invariant) under global, continuous transformations described by the Galilei group G (Sternberg, 1994; Gilmore, 2008). If H is the group of time translations, the generators of the quotient group G/H are the momentum $\boldsymbol{p}$ (spatial translations), the angular momentum $\boldsymbol{J}$ (rotations), and the boosts $\boldsymbol{K}$. The spatial translations form the subgroup $T(3)$ in the ordinary space, and the elements of its infinitesimal form are the operators $U_T = 1 - \mathrm{i}\boldsymbol{k} \cdot \delta\boldsymbol{R}$, where $\delta\boldsymbol{R}$ is an infinitesimal displacement of the crystal ions in space around a Bravais lattice translation vector $\boldsymbol{R}$ (Ashcroft and Mermin, 1976). U_T may be written as $U_T = 1 - \varepsilon^j p_j$, where ε_j are real parameters, and the momentum components $p_j = -\mathrm{i}\hbar\partial_j$ are the three generators of $T(3)$, which obey the Lie algebra $[p_i, p_j] = 0$. Similar considerations could be made for the other two subgroups.

Emerging of Goldstone modes

The underlying crystal lattice can be described (Peskin and Schroeder, 1995) as a periodic potential $V(\phi)$ to be inserted into a Lagrangian given by $\mathcal{L} =$ kinetic term $-V(\phi)$. The fields ϕ^j transform under the action of U_T as $\phi^j \rightarrow \phi^j + \alpha(\phi)p^j$, where $\alpha(\phi)$ is an infinitesimal parameter. As a consequence, the lattice breaks both translational and rotational invariances, making the system ground state not symmetric. On the other hand, the Lagrangian symmetry may remain exact, provided

$$V(\phi^j) = V(\phi^j + \alpha(\phi)p^j). \tag{3}$$

Taylor expanding the Eq. (3), the same condition can be written as

$$\alpha(\phi)\frac{\partial V(\phi)}{\partial \phi^j} = 0, \tag{4}$$

and differentiating the Eq. (4) with respect to ϕ^k around a potential minimum ϕ_0 (corresponding to one of the ions equilibrium positions), we obtain

$$\left(\frac{\partial\alpha(\phi)}{\partial\phi^k}\frac{\partial V}{\partial\phi^j}\right)_{\phi_0} + \alpha(\phi_0)\left(\frac{\partial^2 V}{\partial\phi^k\partial\phi^j}\right)_{\phi_0} = 0. \tag{5}$$

The first term vanishes because ϕ_0 is a minimum of V. Regarding the second term, since the increment $\alpha(\phi_0)$ is nonzero, it must be

$$\left(\frac{\partial^2 V}{\partial\phi^k\partial\phi^j}\right)_{\phi_0} = 0, \tag{6}$$

which specifies the null eigenvector of the mass matrix $\partial^2 V/\partial\phi^k\partial\phi^j$ (and hence the corresponding zero-mass eigenvalue). This states the emergence of a massless field, the Goldstone mode, which can be shown to obey the Bose–Einstein statistics (Leutwyler, 1997).

In summary, the crystal lattice makes a massless field ϕ^j to arise, the Goldstone excitation associated with p^j. In the end, we expect three Goldstone bosons, one for each broken translation generator, and the ground-state symmetry is said to be spontaneously broken.[1]

---

[1] It is possible to see that apart from $\boldsymbol{p}$, also $\boldsymbol{J}$ and $\boldsymbol{K}$ are broken generators (i.e., the system ground state is not symmetric under the corresponding transformations they generate), but it has been shown that they do not give rise to Goldstone bosons (Brauner, 2010; Brauner and Watanabe, 2014).

Pseudo-relativistic metric

A pseudo-relativistic notation can be introduced to describe Goldstone modes as sound-like four-momenta states p_μ in a locally flat manifold $\mathcal{M}$. The tangent space to any point of $\mathcal{M}$ is a four-dimensional manifold $T_\mathcal{M}$ with the same local pseudo-Minkowskian metric expression $\eta_{\hat{\mu},\hat{\nu}}$ as in special relativity and is referred to as the acoustic or sonic metric (Unruh, 1981; Barceló et al., 2011; Dartora and Cabrera, 2014). The space–time coordinates on $\mathcal{M}$ are expressed as $x^\mu = (c_s t, \mathbf{r})$, and the world *pseudo* means that the relevant velocity is the speed of sound c_s in the medium under consideration, which of course is not a limiting velocity.

Following this convenient formalism, instead of $T(3)$ we can consider the group of translations $T(4)$ with elements

$$U_T = 1 - \varepsilon^\mu p_\mu \tag{7}$$

on the space–time $\mathcal{M}$, where the parameters ε^μ are point dependent. The four $T(4)$ generators are $p_\mu = -i\hbar\partial_\mu$, and the crystal lattice breaks the three spatial components $p_{1\ldots3}$, but not p_0. Since $p_\mu p^\mu = 0$ (they are sound-like four-momenta in $\mathcal{M}$), a wave-like solution for them yields, as expected, the gapless dispersion relation $\omega_k = c_s k$. This relation is valid for small k and describes the Goldstone bosons as quasiparticles that are excitations of the field of lattice displacements, which are referred to as acoustic phonons.

Gauging spatial translations

The occurrence of Goldstone bosons is strongly connected to gauge theories of interactions. Weyl (1929) elevated the freedom to modify a local parameter without changing the physics of a system as a general principle known as local gauge invariance. It turns out that if a Lagrangian density $\mathcal{L}(\psi_\mathbf{k})$ must be invariant under the action of an element U_G of a Lie group G of local transformations $\psi_\mathbf{k} \rightarrow U_G\psi_\mathbf{k}$, one or more compensating fields emerge to mediate an interaction. As an example, in the description of the electromagnetism the compensating—or gauge—field is the vector potential A_μ mediating the electromagnetic interaction, and the involved gauge group is the Lie group $U(1)$ whose elements induce phase rotations on $\psi_\mathbf{k}$ (Mandl and Shaw, 2010).

Similar to electromagnetism or, more generally, Yang–Mills theories, it is tempting to represent acoustic phonons as gauge fields using the local (coordinate-dependent) version of U_T, that is, $U_T = 1 - \varepsilon^j(\mathbf{r})p_j$ (Jackiw, 1980; 't Hooft, 2005). The Lagrangian $\mathcal{L}$ in Eq. (2) is not invariant when U_T acts on $\psi_\mathbf{k}$, despite the fact that U_T is unitary, because of the presence of spatial derivatives in the generators' expressions. The naive method of elevating $T(4)$ to the status of a gauge group in order to make $\mathcal{L}$ invariant under local spatial translations, however, is not straightforward. Given the significance of this matter, it is important to first explain why gauging a spatial translation differs significantly from gauging, for instance, the phase transformation of a wavefunction.

In electromagnetism, it is stated that an internal symmetry is gauged since the transformation only affects a phase rather than space–time coordinates. All of this has a clear geometric meaning: Referring to Fig. 1A, a fiber bundle is a space with topological structure $(\pi : \mathcal{E} \rightarrow \mathcal{M}, L, G)$, where $\mathcal{E}$ is known as total space, and for each point $P \in \mathcal{M}$, a fiber $L(P)$ is connected to P such that a neighborhood V_P of P is mapped into $\mathcal{E}$ according to $\pi^{-1}(V_P)$, and that $\pi^{-1}(V_P)$ is homeomorphic to the Cartesian product $V_P \times L$. We can also say that the total space can be written locally as a product $\mathcal{E} = \mathcal{M} \times L$. The fiber bundle is defined alongside a group G, which acts as a transformation group on the fiber and represents the various ways in which the fiber can be considered equivalent. The covariant derivative D_μ is a connection that allows a vector in $\mathcal{E}$ to be parallel-transported (Daniel and Viallet, 1980; Fré, 2013). The n-dimensional manifold $\mathcal{M}$ can also be thought of as a n-surface, with an internal space L associated with each point $P \in \mathcal{M}$ with a given topological structure. In electromagnetism, $\mathcal{M}$ is the ordinary four-dimensional space–time of special relativity, and a phase transformation on $\psi_\mathbf{k}$ is a vertical automorphism of the bundle and a diffeomorphism of L such that the fiber over each point

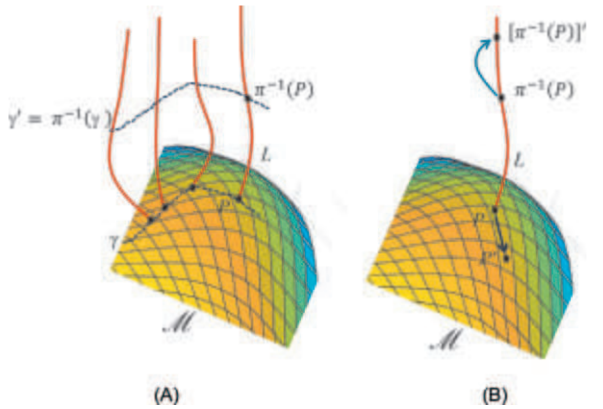

Fig. 1 (A) Scheme of a fiber bundle, a map $(\pi : E \rightarrow M, L, G)$, with the base space M and the fiber L, on which the associated group G acts. A trajectory γ in M is mapped to γ' in the total space E. (B) The usual picture of a gauge theory for an internal symmetry: a gauge transformation in E moves the point $\pi^{-1}(P)$ to $[\pi^{-1}(P)]'$, preserving the point P on M. Translations are defined on the base manifold M itself, where the gauge transformation changes the point P to P', which prevents a straightforward definition of a fiber bundle.

in $\mathcal{M}$ remains unchanged (Fig. 1B). Since only the phase changes, the point in the total space $\mathcal{E}$ in fact moves only vertically along the fiber $L(P)$. This is the gauge freedom carried by the fiber bundle within its fibers.

By contrast, when attempting to gauge a space–time transformation group such as $T(4)$, it is clear that translations in $\mathcal{M}$ induced by $T(4)$ are horizontal diffeomorphisms of $\mathcal{M}$ (Fig. 1B, the straight arrow) since a translation by definition changes the point P in the base space, involving spatial coordinates. As a result, an invariance under the action of $T(4)$ is referred to as an external symmetry. In this context, identifying a fiber as an internal space L for which $\mathcal{E} = \mathcal{M} \times L$ locally holds is difficult, preventing a straightforward definition of a fiber bundle as $(\pi : \mathcal{E} \to \mathcal{M}, L, T(4))$.

Peculiarities of spatial translations

Gauging $T(4)$ on the pseudo-Lorentzian locally flat manifold endowed with the sonic metric and potentially suitable to describe the dynamics, propagation, and interactions of acoustic phonons appears to be mathematically similar to gauging $T(4)$ on the ordinary Lorentzian manifold of general relativity, which, however, was a difficult goal to achieve.

The groundbreaking works (Utiyama, 1956; Kibble, 1961; Sciama, 1964) followed the Yang–Mills formalism and defined the covariant derivative as $D_{\hat{\nu}} = \partial_{\hat{\nu}} + W_{\hat{\nu}}$. Here $W_{\hat{\nu}}$ is a gauge field that, when written in terms of its components $R^{\mu}_{\hat{\nu}}$, reads

$$W_{\hat{\nu}} = R^{\mu}_{\hat{\nu}} p_{\mu}. \tag{8}$$

Employing Eq. (8), $D_{\hat{\nu}}$ was written as

$$D_{\hat{\nu}} = h^{\mu}_{\hat{\nu}} \partial_{\mu} \tag{9}$$

where

$$h^{\mu}_{\hat{\nu}} = \delta^{\mu}_{\hat{\nu}} - \mathrm{i}\hbar R^{\mu}_{\hat{\nu}}. \tag{10}$$

If the covariant index $\hat{\nu}$ is a local Lorentz index, the field $h^{\mu}_{\hat{\nu}}$ defines a set of four orthonormal vectors $h^{\mu}_{\hat{\nu}}\partial_{\mu}$, the tetrad or vierbein. After a partial success of this still unsatisfactory formulation, Cho (1976) developed a gauge theory of translations with a Yang–Mills-type Lagrangian in which the gauge potentials were correctly interpreted as connections (in particular, they are the nontrivial part of the vierbein fields $h^{\mu}_{\hat{\nu}}$). D. Grensing and G. Grensing reached similar conclusions (Grensing and Grensing, 1983), obtaining the gauging of the Poincaré group in a form that allowed the general relativity to be expressed as a gauge theory of $T(4)$. More recently, the Yang–Mills theory of the affine group was developed (Tresguerres and Mielke, 2000; Martín-Martín and Tiemblo, 2010), where tetrads have been identified with nonlinear connections, for which the given $h^{\mu}_{\hat{\nu}}\partial_{\mu}$ expression is a simplified yet correct version of the general formulation.

These concepts were developed to describe gravity, which is now correctly formulated as a Yang–Mills theory. Nonetheless, the same formulation holds and can be used to develop a Yang–Mills theory of elasticity in solid crystals by considering the crystal lattice manifold $\mathcal{M}$, its metric $g_{\mu\nu}$, and its pseudo-Minkowski tangent space $T_{\mathcal{M}}$ equipped with the sonic metric $\eta_{\hat{\mu}\hat{\nu}}$ instead of the ordinary space–time. In this case, the field components $R^{\mu}_{\hat{\nu}}$ correspond to the tensor components of the crystal elasticity field, whereas in gravity theory they correspond to the Ricci tensor (Weinberg, 1972). This allows to formulate the physics of lattice vibrations in crystals (acoustic phonons) in a way that results somehow similar to the physics of gravitational waves in the ordinary space–time, as described in part by Dartora and Cabrera (2014), developed in more detail by the author of the present work (Vallone, 2019), and shortly discussed in Section "Yang–Mills theory of acoustic phonons in crystal."

Yang–Mills theory of acoustic phonons in crystal

The infinitesimal displacement of the crystal lattice induces a local translation $\psi_{\boldsymbol{k}}(x^{\mu}) \to \psi'_{\boldsymbol{k}}(x^{\mu}) = U_T(x^{\mu})\psi_{\boldsymbol{k}}(x^{\mu})$ on the electronic wavefunction. Let us define a gauge-covariant derivative $D_{\hat{\nu}} = h^{\mu}_{\hat{\nu}}\partial_{\mu}$, with $T(4)$ as gauge group. Following the standard gauge prescriptions, all ordinary derivatives in the Lagrangian must be replaced by $D_{\hat{\nu}}$, and the field $W_{\hat{\nu}}$ must transform in turn according to $W_{\hat{\nu}} \to W'_{\hat{\nu}} = U_T W_{\hat{\nu}} U_T^{\dagger} - (\partial_{\hat{\nu}} U_T) U_T^{\dagger}$, which implies

$$(D_{\hat{\nu}}\psi_{\boldsymbol{k}})' = U_T(D_{\hat{\nu}}\psi_{\boldsymbol{k}}), \tag{11}$$

a position that makes the Lagrangian gauge invariant under the local action of $T(4)$.

The translational symmetry is manifested by the appearance of conserved currents j_{μ}, according to the Noether theorem. In the present case, the relevant gauge charges are the three generators $p_k = \int d^3x\, j_k(x) = \int d^3x\, T_{0k}(x)$ of the spatial translations, whose corresponding currents are the components of the symmetric energy–momentum tensor T_{0k}. Moreover, the total energy operator (Hamiltonian) $H = \int d^3x\, c_s^2\, T_{00}(x)$ is written in terms of p_0, the unbroken generator of the translations in the time coordinate.

An essential difference from electromagnetism is the fact that the elements of $T(4)$ do not commute, even if the group generators commute on a flat space–time, $[p_{\hat{\mu}}, p_{\hat{\nu}}] = 0$. Indeed, if $U_T(x)$ and $U_T(y)$ are two elements of $T(4)$, then it holds

$$[U_T(x), U_T(y)] = -\hbar^2 \left[\varepsilon^{\mu}(x)\partial_{\mu}\varepsilon^{\nu}(y) - \varepsilon^{\mu}(y)\partial_{\mu}\varepsilon^{\nu}(x)\right]\partial_{\nu}. \tag{12}$$

The intrinsic difference between the structure of the global and the local version of $T(4)$ can be expressed more formally by writing the algebra of currents

$$[j_\mu(x), j_\nu(y)] = -i\hbar\Big(\partial_\mu j_\nu(y) - \partial_\nu j_\mu(x)\Big)\delta^3(x-y), \tag{13}$$

where the commutator is in general nonzero for $x \neq y$, which makes the local form of the gauge group non-Abelian. Finally, the algebra of generators can be written as in Gegenberg et al. (2016)

$$[p_\mu, p_\nu] = igf^{\gamma}_{\mu\nu}p_\gamma \tag{14}$$

where $f^{\gamma}_{\mu\nu}$ are the structure constants and g is the coupling constant of the theory, with $f^{\gamma}_{\mu\mu} = 0$ and $f^{\gamma}_{\mu\nu} = -f^{\gamma}_{\nu\mu} = 1$ for $\mu \neq \nu$. In a flat space–time like $T_{\mathcal{M}}$, it is $[p_{\hat{\mu}}, p_{\hat{\nu}}] = 0$, but this is not true for $\mathcal{M}$. This is a central point of the theory, and the non-Abelianity of the local symmetry expressed by the algebra of Eq. (14) is responsible for the phonon–phonon interactions. On this basis it follows also

$$[W_{\hat{\mu}}, W_{\hat{\nu}}] = igf^{\alpha}_{\beta\gamma}R^{\beta}_{\hat{\mu}}R^{\gamma}_{\hat{\nu}}p_\alpha. \tag{15}$$

Making use of Eq. (9), the commutator $[D_{\hat{\mu}}, D_{\hat{\nu}}]$ can be written in the alternative forms

$$[D_{\hat{\mu}}, D_{\hat{\nu}}] = G^{\alpha}_{\hat{\mu}\hat{\nu}}p_\alpha = G_{\hat{\mu}\hat{\nu}} \tag{16}$$

where the field strength tensor $G_{\hat{\mu}\hat{\nu}}$ and its components $G^{\alpha}_{\hat{\mu}\hat{\nu}}$ are given by

$$\begin{aligned} G_{\hat{\mu}\hat{\nu}} &= \partial_{\hat{\mu}}W_{\hat{\nu}} - \partial_{\hat{\nu}}W_{\hat{\mu}} + [W_{\hat{\mu}}, W_{\hat{\nu}}] \\ G^{\alpha}_{\hat{\mu}\hat{\nu}} &= \partial_{\hat{\mu}}R^{\alpha}_{\hat{\nu}} - \partial_{\hat{\nu}}R^{\alpha}_{\hat{\mu}} + igf^{\alpha}_{\beta\gamma}R^{\beta}_{\hat{\mu}}R^{\gamma}_{\hat{\nu}}. \end{aligned} \tag{17}$$

It is worth noting that Eq. (17) resembles expressions typical of classical Yang–Mills theories, although it should be remembered that the symmetry group governs an external symmetry and the gauge field $W_{\hat{\mu}}$ contains spatial partial derivatives since the infinitesimal group generators act as differential operators.

The Lagrangian density for the free gauge field is

$$\mathcal{L}_R = \frac{1}{4}G^{\alpha}_{\hat{\mu}\hat{\nu}}G^{\hat{\mu}\hat{\nu}}_{\alpha}, \tag{18}$$

that explicitly reads

$$\mathcal{L}_R = \frac{1}{2}\left(\partial_{\hat{\mu}}R^{\alpha}_{\hat{\nu}}\partial^{\hat{\mu}}R^{\hat{\nu}}_{\alpha} - \partial_{\hat{\mu}}R^{\alpha}_{\hat{\nu}}\partial^{\hat{\nu}}R^{\hat{\mu}}_{\alpha}\right) + igf^{\gamma\delta}_{\alpha}\ \ R^{\hat{\mu}}_{\gamma}R^{\hat{\nu}}_{\delta}\ \left(\partial_{\hat{\mu}}R^{\alpha}_{\hat{\nu}}\right) - \frac{g^2}{4}f^{\sigma}_{\beta\gamma}f^{\delta\varepsilon}_{\sigma}R^{\beta}_{\hat{\mu}}R^{\gamma}_{\hat{\nu}}R^{\hat{\mu}}_{\delta}R^{\hat{\nu}}_{\varepsilon} \tag{19}$$

and describes the dynamics of a field with cubic and quartic (self-interacting) terms. Writing the Euler–Lagrange equation

$$\partial^{\hat{\mu}}\frac{\partial\mathcal{L}_R}{\partial\left(\partial^{\hat{\mu}}R^{\hat{\nu}}_{\alpha}\right)} = \frac{\partial\mathcal{L}_R}{\partial R^{\hat{\nu}}_{\alpha}} \tag{20}$$

and imposing the Lorenz gauge (that allows for great simplification of all the expressions), the equation of motion for the free fields $R^{\alpha}_{\hat{\nu}}$ results (defining $\lambda = g^2$ and $\Box = \partial_{\hat{\mu}}\partial^{\hat{\mu}}$) in

$$\Box R^{\alpha}_{\hat{\nu}} + \lambda\, f^{\sigma}_{\beta\gamma}f^{\delta\alpha}_{\sigma}R^{\beta}_{\hat{\mu}}R^{\gamma}_{\hat{\nu}}R^{\hat{\mu}}_{\delta} = 0. \tag{21}$$

This equation does not contain any mass term (it would be a linear term in $R^{\alpha}_{\hat{\nu}}$), but a cubic self-interacting term is present, coming from the quartic term in the Lagrangian.

All components are strongly coupled and difficult to handle. To understand the underlying physics, it is particularly interesting to consider in more detail the case of a simple one-dimensional atomic chain along x. Here we assume—without loss of generality—that the perturbation is along the longitudinal direction (longitudinal acoustic phonon), that is, $R^0_0 = 0$. From the group commutation rules in Eq. (14), the equations of motion for the nonzero field components $\hat{R} = R^1_0$ (the longitudinal acoustic phonon field) and $\hat{S} = R^1_1$ (the spatial strain field) decouple, yielding

$$\left(\partial_t^2 - c_s^2\partial_x^2\right)\hat{R} + \lambda c_s^2|\hat{R}|^2\hat{R} = 0 \tag{22}$$

$$\left(\partial_t^2 - c_s^2\partial_x^2\right)\hat{S} = 0. \tag{23}$$

$\hat{S}(x,t)$ describes the fluctuations of the crystalline strain field (coupled to phonons in higher dimensional domains, and which can be scattered by them). Concerning the equation for the acoustic phonon field $\hat{R}(x,t)$, the parameter λ leads to a nonlinear oscillatory solution for $\hat{R}$ with a dispersion relation given by (Frasca, 2011, 2017)

$$\omega_k^2 = \sqrt{\frac{\lambda c_s^2}{2}\rho_R^2 + c_s^2 k^2} \tag{24}$$

where ρ_R is an integration constant that depends on cell properties. Eq. (22) can be promptly derived by the Euler–Lagrange equation from a Lagrangian that is a simplified form of Eq. (19),

$$\mathcal{L}_R = \frac{1}{2}\left(\eta^{\hat{\mu}\hat{\nu}}\partial_{\hat{\mu}}\hat{R}\ \partial_{\hat{\nu}}\hat{R} - \frac{1}{2}\lambda\hat{R}^4\right), \tag{25}$$

the well-known Lagrangian with ϕ^4-potential describing a massless self-interacting scalar field (Mandl and Shaw, 2010).

To summarize, apart from their description as Goldstone bosons, acoustic phonons can also be viewed as gauge bosons mediating lattice interactions, described in terms of a non-Abelian gauge theory. The local gauge invariance imposed on the Lagrangian in Eq. (2) gives rise to three gauge fields identified with acoustic phonon modes, one longitudinal and two transverse. Their Lagrangian is Eq. (19), for which a simplified one-dimensional form is Eq. (25), which describes phonon–phonon interactions by the nonlinear (quartic) term proportional to λ, a feature that arises from the commutator $[W_{\hat{\mu}}, W_{\hat{\nu}}]$ in the field strength tensor, which is not zero.

It is worthwhile to consider that Eq. (24) reduces to the well-known Debye form (Ashcroft and Mermin, 1976) $\omega_k = c_s|k|$, provided the nonlinear term in the Lagrangian can be neglected. However, a relevant and rather unexpected result is that ω_k is gapped in its general form due to self-interactions when the latter are relevant (i.e., $\omega_k \neq 0$ in the limit $k \to 0$), even though the gauge field remains massless (see a more extended discussion in Vallone (2019)).

As a side feature already noticed by Dartora and Cabrera (2014), the commutator $[D_{\hat{\mu}}, D_{\hat{\nu}}]$ satisfies a cyclic identity that can be written as

$$D_{\hat{\sigma}}G_{\hat{\mu}\hat{\nu}} + D_{\hat{\nu}}G_{\hat{\sigma}\hat{\mu}} + D_{\hat{\mu}}G_{\hat{\nu}\hat{\sigma}} = 0, \tag{26}$$

an equation known as the Bianchi identity for the field strength tensor. The tensor $R_{\hat{\mu}}^{\nu}$ plays the same role as the Ricci tensor in general relativity and obeys the same dynamical equations implied by Eq. (26). It describes the local perturbation of the sonic metric $\eta_{\hat{\mu}\hat{\nu}}$ of the solid crystal caused by the propagation of an acoustic phonon, in strict analogy to the space–time Lorentz metric perturbation induced by the propagation of a gravitational wave as described in general relativity.

Optical phonons remain still undescribed

In the previous considerations, optical phonons were never considered. Nevertheless, they play a central role in semiconductor physics, as they can support Auger recombinations, describe the carriers relaxation, and are crucial for understanding quantum transport and carriers capture in quantum-confined heterostructures (Vallone, 2010, 2013). However, they do not arise from the breaking of translational symmetry or as gauge modes described so far.

We recall that for several binary compounds of interest in electronics, such as GaAs, InP, and GaN, the crystal can be viewed as composed of two interacting sublattices, one for each atomic species. Textbook toy models describe the relevant physics considering a one-dimensional Bravais lattice with two ions per unit cell. Considering it as a set of elementary classical oscillators, one can show that two different modes of oscillation exist (Ashcroft and Mermin, 1976):

(a) the two atoms in the cell oscillate at frequency ω_k around their equilibrium position with the same direction and phase, Fig. 2A, leaving their relative displacement σ_d unchanged. The perturbation is the acoustic mode, an elastic wave propagating in the lattice with the speed of sound c_s, and the corresponding collective excitation is the acoustic phonon. Its dispersion relation has an expression that can be approximated in the long-wavelength limit as $\omega_k = c_s|k|$, indicating that the acoustic mode can be excited with arbitrarily small energy (there is no gap in ω_k);

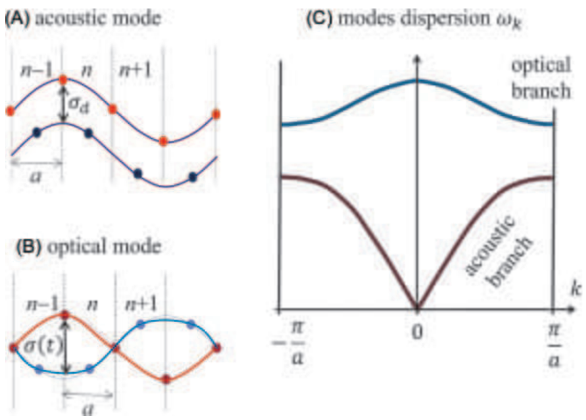

Fig. 2 Acoustic (A) and optical (B) oscillation modes of a two-atom elementary cell. In (C), the modes dispersion ω_k.

(b) conversely, the two atoms in the cell oscillate with respect to each other, Fig. 2B, and their relative displacement $\sigma(t)$ oscillates about an equilibrium position along a well-defined direction with respect to a reference frame, defining an oscillating dipole moment of the cell when the solid is ionic. This is the optical mode, and the associated collective excitation is the optical phonon, whose role in semiconductor transport theory and electron dynamics is of great importance. It has been shown that $\omega_{k\to 0} \to \omega_0 \neq 0$: in other words, the optical phonon dispersion ω_k is gapped, and the excitation of the optical mode costs a fixed energy $\hbar\omega_0$, which is nonzero even for $k \to 0$, see Fig. 2C.

Section "Spontaneous symmetry breaking and order parameter" shows that the concept of SSB allows a unified description of the two phonon modes. To follow this path, in the next section we will first describe what is meant by spontaneous symmetry breaking in general. We will then discuss how this concept can be applied to acoustic and optical phonons in solid-state physics.

Spontaneous symmetry breaking and order parameter

A system consisting of a sphere that is free to move on the underside of a paraboloid can remain in a stable equilibrium state, as in Fig. 3A. A small displacement would cause the sphere to return to the bottom of the paraboloid, that is, to its equilibrium state, regardless of the displacement direction.

In quantum field theory, we can consider an electron instead of a sphere, and the paraboloid can represent a potential energy profile whose vertex lies at the origin of a reference frame. In its simplest formulation, the dynamics of the system can be described by a complex scalar field ϕ and a potential energy profile $V(\phi) = \phi^* \phi$, whose only minimum is in $\phi = 0$. The ground state $|\psi_0\rangle$ of the system is a stable vacuum state.

We can now introduce an operator $\hat{\phi}$ corresponding in coordinates to the field ϕ (in elementary quantum mechanics it corresponds to the position operator). In this very simple example this operator is not very useful, but we can easily notice that its expectation value on the vacuum state is $\langle\psi_0|\hat{\phi}|\psi_0\rangle =< \hat{\phi} >= 0$. This operator is called order parameter, and its zero expectation value expresses the concept that the system is in a symmetric (i.e., not ordered) state. The Lagrangian density for the scalar field ϕ moving in the potential $V(\phi)$ is $\mathcal{L} = \partial_\mu\partial^\mu\phi - V(\phi)$ and it is $U(1)$ invariant, that is, it is invariant for $\phi \to e^{i\theta}\phi$, and the same invariance holds for the state $|\psi_0\rangle$.

As shown in Fig. 3B, the situation is quite different if we assume that the paraboloid suddenly becomes a Mexican hat because of some phase transition: its vertex $\phi = 0$ no longer represents an equilibrium position for the sphere in classical terms, and even a slight perturbation leads to the sphere falling into the brim of the hat. The sphere can move along the brim without spending energy,

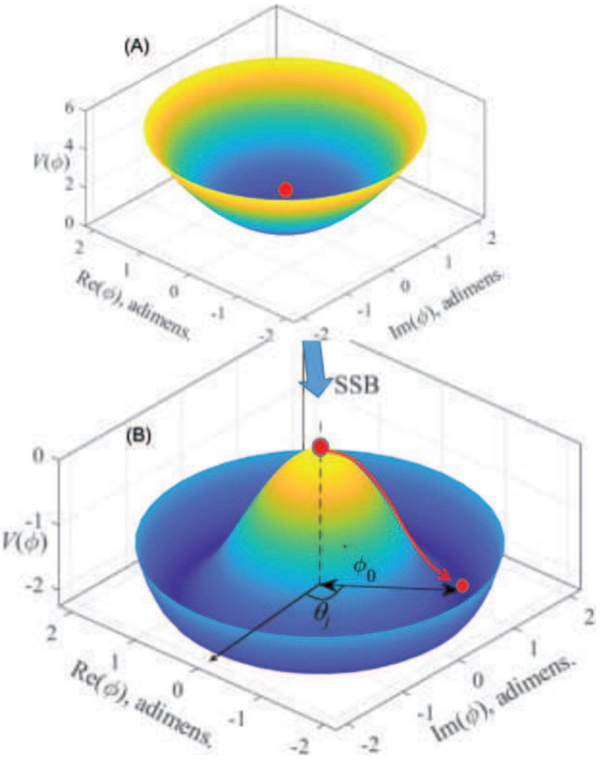

Fig. 3 (A) The sphere in the paraboloid origin is in a stable equilibrium ground state. (B) For a Mexican hat-shaped potential $V(\phi)$, the origin is no more a stable state. Conversely, stable ground states are the infinitely degenerate states $|\psi_j\rangle$ into the brim. However, a nonzero order parameter arises.

whereas a small perturbation that makes the sphere climb the hat crown costs a certain amount of energy. As a result, the sphere tends to return to the brim.

Coming back to the quantum world, the Mexican hat potential can be written as $V(\phi) = -a(\phi^* \phi) + b(\phi^* \phi)^2$ with a and b positively defined real parameters. A possible vacuum state corresponds to $< \hat{\phi} > = 0$, which has $U(1)$ symmetry as well as the Lagrangian, but it is not the ground state of the system. Therefore, the system will spontaneously decay into a specific stable ground state $|\psi_j\rangle$.

In this different situation, the expectation value of $\hat{\phi}$ on the new vacuum state is $< \hat{\phi} > = \sqrt{a/2b}\, e^{i\theta_j}$ for a given real θ_j between 0 and 2π. Since $\mathcal{L}$ is symmetric with respect to a rotation $\hat{U}$, but $|\psi_j\rangle$ is not, the $U(1)$ symmetry has been broken, and a SSB has occurred, because of the choice of a particular θ_j. Moreover, a small translation around the hat brim consists of a transition between two stable degenerate ground states, and it does not cost energy. In contrast, a small shift in the orthogonal direction costs energy, and this has profound consequences.

It is important to emphasize that we found for $< \hat{\phi} >$ a value of zero in the symmetric state, and a nonzero value for each broken-symmetry states. This is what characterizes the order parameter operator, whose eigenvalues in the broken $U(1)$ symmetry phase are the couples $< \hat{\phi} > = (\phi_0, \theta_j)$, where $\phi_0 = \sqrt{a/2b}$ is the radius of the hat brim and θ_j is an angle measured with respect an arbitrary reference direction.

Ginzburg–Landau approach and SSB

As indicated in Introduction, the concept of SSB was first formulated in the context of condensed matter physics by Ginzburg and Landau in a paper on superconductivity (Landau, 1965). In a completely different context, Higgs (1964) started by writing a gauge-invariant Lagrangian density containing a potential showing a spontaneous breakdown of the $U(1)$ (rotational) symmetry. We should follow in the footsteps of Ginzburg and Landau.

When they studied superconductivity, they considered a complex scalar field with continuous $U(1)$ invariance in the symmetric normal (i.e., not superconducting) phase. A phase transition from the normal to superconducting state breaks the phase rotation symmetry. The ordering transition can be described by the Landau free energy functional for the complex order parameter ϕ as

$$F(\phi) = -\frac{\mu_0^2}{2}(\phi\phi^*) + \frac{\lambda}{4}(\phi\phi^*)^2 + O(|\phi|^6), \tag{27}$$

where μ_0^2 and λ are real and positively defined parameters. The microscopic origin of $U(1)$ symmetry breaking appeared only some years later, thanks to the work of Bardeen, Cooper, and Schrieffer (BCS theory) (Bardeen et al., 1957a, b): phonons mediate an attractive interaction between electrons, and the simplest scalar state that can be constructed from an electron pair with total spin zero is $|\psi\rangle = c^\dagger_{\mathbf{k}\uparrow} c^\dagger_{-\mathbf{k}\downarrow}|0\rangle$, where $c^\dagger_{\mathbf{k}\uparrow}$ creates from the vacuum an electron state with wavevector $\mathbf{k}$ and the arrow represents the electron spin state. The interaction term in the Hamiltonian $H_{\text{BCS}} \propto c^\dagger_{\mathbf{k}\uparrow} c^\dagger_{-\mathbf{k}\downarrow} c_{\mathbf{k}\uparrow} c_{-\mathbf{k}\downarrow}$ is locally gauge invariant with $U(1)$ as gauge group with parameter θ transforming $|\psi\rangle$ into $e^{i\theta(x)}|\psi\rangle$. However, in the mean field approximation, the interaction term becomes $\hat{H}_{\text{BCS}} \propto \Delta_{\mathbf{k}} c^\dagger_{\mathbf{k}\uparrow} c^\dagger_{-\mathbf{k}\downarrow} + \Delta^*_{\mathbf{k}} c_{\mathbf{k}\uparrow} c_{-\mathbf{k}\downarrow}$, and the continuous $U(1)$ symmetry is broken since only the special values $\theta = 0$ and $\theta = \pi$ make $\hat{H}_{\text{BCS}}$ gauge invariant. Here $\Delta_{\mathbf{k}}$ is the energy gap of the Cooper pair (Bardeen et al., 1957a, b), the superconducting phase is the ordered phase, and, in particular, Gor'kov and Melik-Barkhudarov (1964) showed that a rigorous microscopic evaluation of $\hat{H}_{\text{BCS}}$ provides the expression for the Ginzburg–Landau free energy in Eq. (27), with $\Delta_{\mathbf{k}}$ as the order parameter.

Eq. (27) also describes other quantum phase transitions, for example, in materials changing from a paramagnetic (disordered) to a ferromagnetic (ordered) phase when the system temperature T falls below the Curie temperature. In this case, the field ϕ—the order parameter—is the magnetization, and in the ordered phase, the system chooses a particular spatial direction along which the atomic spins self-align: The system is no longer $U(1)$-invariant. In these materials, the Higgs and Goldstone modes correspond respectively to the modulation of the amplitude and phase of the magnetization, the order parameter that emerges when the continuous rotational symmetry is broken.

SSB in crystalline solids

The expansion of the total energy of crystal atoms with mass μ_n around their equilibrium positions, displaced by $\vec{a}_n$ at temperature T, can be written as

$$E = \frac{1}{2}\sum_{n\hat{i}} \mu_n \left(\partial_t a_n^{\hat{i}}\right)^2 + \sum_{nm} \sum_{\hat{i}\hat{j}} Q_{nm;\,\hat{i}\hat{j}} a_n^{\hat{i}} a_m^{\hat{j}} + \sum_{nmqr} \sum_{\hat{i}\hat{j}\hat{k}\hat{l}} R_{nmqr;\,\hat{i}\hat{j}\hat{k}\hat{l}} a_n^{\hat{i}} a_m^{\hat{j}} a_q^{\hat{k}} a_r^{\hat{l}} + \cdots, \tag{28}$$

where the sum runs over the N atoms index $n \in \{1^{\hat{i}}, 1^{\hat{j}}, 1^{\hat{k}}, \ldots N^{\hat{i}}, N^{\hat{j}}, N^{\hat{k}}\}$, and $a_n^{\hat{i}}$ are the spatial components of $\vec{a}_n$. The first term is the kinetic energy of the atoms and the second term is the potential harmonic term, followed by the fourth-order anharmonic term. In the harmonic approximation, the $Q_{nm;\,\hat{i}\hat{j}}$ matrix represents the energy cost associated with moving atoms from their equilibrium position. In a field-theoretic approach, the displacements are defined by a complex vector field $\vec{\phi}$, and the free energy can be conveniently written in terms of the spatial components of $\vec{\phi}$ as

$$F(\phi) = \frac{1}{2!}\mathcal{Q}_{\hat{i}\hat{j}}\phi^{\hat{i}}\phi^{\hat{j}} + \frac{1}{4!}\mathcal{R}_{\hat{i}\hat{j}\hat{k}\hat{l}}\phi^{\hat{i}}\phi^{\hat{j}}\phi^{\hat{k}}\phi^{\hat{l}} + O(|\phi|^6), \tag{29}$$

where

$$\mathcal{Q}_{\hat{i}\hat{j}} = \frac{\partial^2 F(\phi)}{\partial\phi^{\hat{i}}\partial\phi^{\hat{j}}}, \quad \mathcal{R}_{\hat{i}\hat{j}\hat{k}\hat{l}} = \frac{\partial^4 F(\phi)}{\partial\phi^{\hat{i}}\partial\phi^{\hat{j}}\partial\phi^{\hat{k}}\partial\phi^{\hat{l}}} \tag{30}$$

are evaluated at equilibrium. More generally, and considering a three-dimensional crystal, we can rewrite the Eq. (29) in a more compact way as

$$F(\phi) = \frac{1}{2}\mathcal{A}\phi^*\phi + \frac{1}{4}\mathcal{B}\left(\phi^*\phi\right)^2 + O(|\phi|^6), \tag{31}$$

where $\mathcal{A}$ and $\mathcal{B}$ are real coefficients and the complex field ϕ is an atomic displacement matrix whose rank and symmetry properties depend on the unitary cell under consideration (Vaks and Khromov, 2008). It should be noted that odd powers of ϕ are usually excluded in the free energy expansion. This is because the free energy cannot contain a phase, in order to be an observable. This choice does not prevent important interactions from occurring (such as the coupling of three phonons and the decay of phonons), and this important point will be clarified at the end of this section.

In our discussion we consider the transition from a parent (*bcc*, symmetric) and a product (*hcp*, with broken symmetry) crystalline phase. It is worth mentioning that in the framework of Ginzburg and Landau theory, the difference of their free energy $F(\phi)$ was calculated in Sanati et al. (2001) as

$$\tilde{F}(\phi) = \frac{A_0(T - T_0)}{2}\phi^2 + B\phi^4 + C\phi^6, \tag{32}$$

where ϕ is a scalar order parameter (the same arguments would of course apply to the structural transition between *fcc* and *hcp* phases). $\tilde{F}(\phi)$ was derived from a one-dimensional (or scalar) model and has the same functional form as the Eq. (31), except that the expansion in powers of ϕ also retains the sixth-order term. Here T_0 is a characteristic temperature, and A_0 and C are real and positively defined parameters, while B is negative. Moreover, it can be observed that for $T < T_0$, also the coefficient of ϕ^2 is negative.

The Ginzburg and Landau theory, and even the Higgs mechanism, have no intrinsic constraints on the number of expansion terms of $F(\phi)$ in powers of ϕ since both theories are phenomenological and provide a way to describe global symmetry breaking, that is, a second-order transition, at least in their original formulations. Nevertheless, the same theory can be applied to first-order structural phase transitions (Krumhansl, 1992), for which an expansion to the sixth-order is customary, when an accurate free energy fit and a description of the behavior around T_0 are required. However, this is not the focus of the present discussion: the main requirement for the present phenomenological approach is to correctly describe the SSB, that is, the properties of the structural phase for $T \ll T_0$ and for $T \gg T_0$. Nevertheless, an extensive discussion about this point can be found in Vallone (2020), where it is shown that the functional $F(\phi)$ given by the Eq. (27) correctly describes the SSB occurring during a crystalline phase transition, provided we identify the coefficients according to

$$-\mu_0^2 = A_0(T - T_0), \quad \frac{\lambda}{4} = B, \tag{33}$$

with $T < T_0$, $A_0 > 0$, $B > 0$, hence $\lambda > 0$.

Exploiting the similarities between the sonic metric and the Lorentzian metric of ordinary spacetime, the dynamics of ϕ can be described by the Lagrangian density

$$\mathcal{L}_\phi = \frac{1}{2}\partial_\mu\phi^*\,\partial^\mu\phi - V(\phi) \tag{34}$$

$$V(\phi) = -\frac{\mu_0^2}{2}\phi^*\phi + \frac{\lambda}{4}\left(\phi^*\phi\right)^2 + V_c(\phi), \tag{35}$$

where the potential energy $V(\phi)$ has been identified with the crystal free energy in the *hcp* phase supplied by $F(\phi)$. We have included in the potential an additional term $V_c(\phi)$ which depends on the particular crystal we are considering. For example, in a cubic crystal it is (Plischke and Bergersen, 2006) $V_c(\phi) = \lambda_1[\mathrm{Re}(\phi)\mathrm{Im}(\phi)]^2 = \lambda_1/4\left(\phi^*\phi\right)^2\sin^2(n\arctan(\phi))$, where $n = 2$ and λ_1 is a constant. $V_c(\phi)$ provides four pairs of minima and maxima in the potential brim, corresponding to ion positions. In hexagonal crystals $n = 3$, there are six pairs of local minima and maxima, but this is only a minor detail. What matters is the Mexican hat shape of $V(\phi)$, which is typical of the Higgs SSB theory, slightly modified by the $V_c(\phi)$ term (Fig. 4A).

In the neighborhood of $\phi = 0$, the Lagrangian $\mathcal{L}_\phi$ is still $U(1)$ invariant, but its symmetric vacuum state is unstable. When $\lambda_1 = 0$, all ϕ values on the circle of radius $\phi_0 = \sqrt{\mu_0^2/\lambda}$ are minima, and the brim is flat. The order parameter takes nonzero values here, and the only stable vacuum states are those characterized by an order parameter expectation value $\langle\hat{\phi}\rangle = \phi_0 e^{i\theta}$. Among them, the system chooses the ordered state for which θ has a given value θ_j, and this fixes the true vacuum state of the system. Therefore, the vacuum is not $U(1)$-invariant since the rotational symmetry described by the Lie group $U(1)$ is broken: the value θ_j fixes the expectation value of the order parameter ϕ.

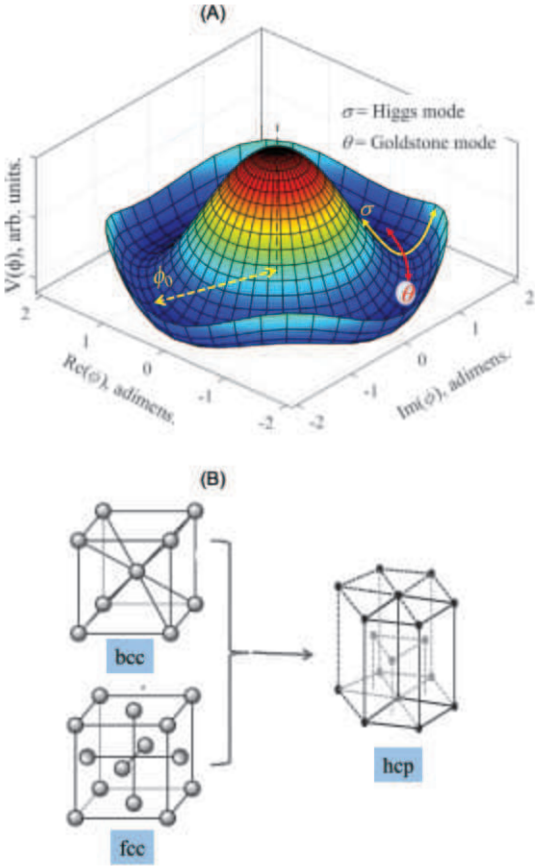

Fig. 4 (A) The Higgs potential $V(\phi)$, leading to the excitation of the amplitude (or Higgs) and phase (or Goldstone) modes, σ and θ, for the *hcp* phase. (B) Illustrative scheme of *bcc*, *fcc*, and *hcp* crystal structures (the *dots* represent the ions).

The Higgs SSB formalism, as well as the identification of $U(1)$ as the symmetry group for the Lagrangian, indicates that there is also a more fundamental reason for the selection of the quartic expression $F(\phi)$ of Eq. (27) as an appropriate potential, instead of a more complicated sixth-order expression. It is possible to demonstrate a theorem (Michel and Radicati, 1971; Brauner, 2010), according to which, if G is a compact Lie group (in the present case, $U(1)$) that acts smoothly on the real manifold $\mathcal{M}$ with $\phi \in \mathcal{M}$, the orbit $G(\phi)$ is critical, that is, every smooth real $\mathcal{G}$-invariant function on $\mathcal{M}$ is stationary on $\mathcal{G}(\phi)$ if and only if $\mathcal{G}(\phi)$ is isolated in its stratum (a *stratum* consists of all points of the same symmetry class). Very shortly and informally, we remind that an orbit $\mathcal{G}(\phi)$ is the ensemble of all points of $\mathcal{M}$ which can be reached from ϕ via a (eventually broken) symmetry transformation, that is, $\mathcal{G}(\phi) = \{g\phi | g \in G\}$. Two points on the same orbit have isotropy groups H_ϕ that are isomorphic (the isotropy group H_ϕ is formed by the set of all group elements that leave ϕ invariant, i.e., $H_\phi = \{g\phi = \phi | g \in G\}$: it is formed by those transformations that are left unbroken when the order parameter takes the value ϕ). Any potential V on the manifold $\mathcal{M}$ that is invariant under the group action, that is $V(\phi) = V(g\phi)$ for all $\phi \in \mathcal{M}$ and $g \in G$, can therefore be viewed as functions on the orbits: thus, the minimization of a given potential $V(\phi)$ can be reformulated as a minimization of a function on the space of orbits, where a transformation $\phi \to g\phi$ along one orbit does not require energy: this is the origin of the Goldstone boson. Changing orbit requires an energy cost, which will give rise to the Higgs boson, for which a mass term is expected. An interesting fact for our discussion is that (Brauner, 2010) *the theorem makes no particular assumption about the form of the invariant function, so it may be a Higgs-type quartic potential as well as the full quantum effective potential whose power expansion may contain terms of arbitrarily high orders in* ϕ.

With reference to Fig. 4A, we can expand $\mathcal{L}_\phi$ around the vacuum (ϕ_0, θ_j) in terms of small oscillations σ and θ, obtaining the Lagrangian density

$$\mathcal{L}_{\sigma\theta} = \frac{1}{2}\left(\partial_\mu\theta\ \partial^\mu\theta - \frac{\lambda\theta^4}{2}\right) + \frac{1}{2}\left(\partial_\mu\sigma\ \partial^\mu\sigma - 2\mu_0^2\sigma^2 - 2\mu_0\sqrt{\lambda}\sigma^3 - \frac{\lambda\sigma^4}{2}\right) - \mu_0\sqrt{\lambda}\sigma\theta^2 - \frac{\lambda}{2}\theta^2\sigma^2 + \frac{\lambda}{4}\left(\sigma^2 + \theta^2\right)\theta^2, \tag{36}$$

that can be simplified neglecting nonlinear terms higher than second order:

$$\mathcal{L}_{\sigma\theta} = \frac{1}{2}\partial_\mu\theta\ \partial^\mu\theta + \frac{1}{2}\partial_\mu\sigma\ \partial^\mu\sigma - \mu_0^2\sigma^2. \tag{37}$$

Eq. (37) provides two oscillatory solutions for the fields θ and σ when plugged into the Euler–Lagrange equations. The solution of θ is a Nambu–Goldstone mode with frequency dispersion relation $\omega_\theta^2 = c_s^2k^2$, and it is a phase oscillation mode along the Mexican hat brim. Because there is no mass term, the dispersion relation is gapless. The solution for σ describes amplitude oscillations and is a Higgs mode, whose frequency dispersion relation is $\omega_\sigma^2 = 2\mu_0^2 + c_s^2 k^2$. It is gapped because the Lagrangian contains the mass term $\mu_0\sqrt{2}$.

The field θ is a pure gauge field associated with the acoustic phonon in the lattice, which breaks continuous translational invariance because of the lattice itself. Since the ground state of θ may be changed by simply executing a gauge transformation along the valley of the Mexican hat, it is a massless Goldstone mode. Moreover, the Higgs mode can be identified with the optical phonon, whose frequency in the long-wavelength limit is given by the mass-like term, $\omega_0 = \mu_0\sqrt{2}$.

Eq. (36) also describes multiphonon scattering terms and phonon decay (the terms proportional to $\theta^2\sigma^2$, σ^3, σ^4, θ^4, and $\sigma\theta^2$). All these effects can be significant in systems where phonons are strongly coupled to the strain field. As an example, retaining the term in $\sigma\theta^2$ (i.e., the nonlinear term at the lowest order in σ), the Lagrangian describes the acousto-optical phonon coupling, and the resulting frequency dispersion relation is shown in Fig. 5, characterized by the opening of minigaps in the acoustic branch ω_θ (Duggen and Willatzen, 2017; Xie, 2022). The result was obtained by solving numerically the wave equations arising from Eq. (36) at the lowest order in λ and approximating ω_σ with ω_0 (see Vallone, 2019, for details).

Experimental evidences of SSB in structural phase transitions in metals

Observations of the experimental phonon dispersion of Co at room temperature and at 833 K (Wakabayashi et al., 1982; Strauss et al., 1996) confirm the existence of optical phonon branches only at the lowest temperatures.

In contrast to high energy physics, it is quite easy to restore hidden symmetry; all that is required is to raise the temperature above the value of T_0 of the crystal under consideration (in our example, Zr, Ti, and Co). In the symmetric phase, a structural phase transition *hcp* → (*bcc, fcc*) occurs, and the coefficient of the quadratic term in Eq. (27) becomes positive. The system has recovered the $U(1)$ invariance that was lost in the *hcp*, and the expectation value of $\hat{\phi}$ in the stable vacuum state is now $\langle\hat{\phi}\rangle = 0$. The only broken continuous symmetry is translational invariance, which still allows for the emergence of the acoustic phonon, the Nambu–Goldstone mode. However, there is no Higgs mode in Co at $T = 833$ K (Strauss et al., 1996), where the structural phase changes to *bcc* and only the acoustic phonon branch remains. Similar considerations and experimental results can be found in literature for Zr and Ti (*fcc* → *hcp*) (Stassis et al., 1979; Wakabayashi et al., 1982; Strauss et al., 1996; Schnell et al., 2006; Purja and Mishin, 2012; Grimvall et al., 2012). Even though it is a much simpler formulation, the hidden symmetry restoration represented by the *hcp* → (*bcc, fcc*) phase transition when temperature increases above T_0 is conceptually similar to what occurs in the Standard Model for the electroweak interaction above the electroweak symmetry breaking energy (≈159 GeV (D'Onofrio and Rummukainen, 2014)).

The number of oscillating modes for θ and σ depends on the crystal unitary cell, and on the dimension of the matrix associated with the operatorial form of the order parameter $\hat{\phi}$. In the considered examples, the crystal broken phase is *hcp*, and it is possible to write the displacement matrices Q evaluated at symmetry points of the Brillouin zone. They can be employed to build the dynamical matrix as blocks of submatrices, substantially the Q themselves. The dynamical matrix has six eigenvalues, and so it is for $\hat{\phi}$ at the same symmetry points. In the ground state of the broken phase, there will be three eigenvalues belonging to θ and three belonging to σ. Hence, there will be three fields θ (acoustic branches) and three fields σ (optical branches). For each branch, two fields represent oscillations in the *hcp* basal plane (transversal modes), and one field represents an oscillation orthogonal to the plane (longitudinal mode).

As an aside, even if one has conceptually identified free energy with the Higgs potential, it is generally not possible to assign a particular type of phonon to the Higgs and Goldstone modes (Meier et al., 2019). Since $Q_{n,m}$ is the matrix of the force constant, its

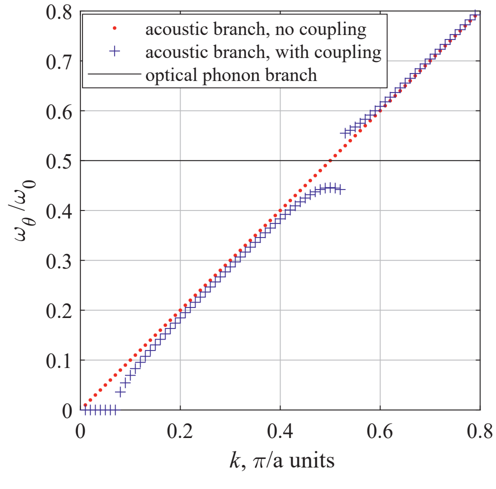

Fig. 5 The nonlinear coupling between Goldstone and Higgs modes, which gives origin to acousto-optic coupling.

value depends on the atomic masses in the unit cell, and the phonons are eigenvectors of $Q_{n,m}/\sqrt{\mu_n\mu_m}$, which, according to our description, correspond to the Goldstone and Higgs modes only when the crystal contains atoms with only one mass μ_n, as in the examples considered in this work (crystals of Co, Zr, Ti). In summary, the phase (or Goldstone) and amplitude (or Higgs) oscillations always start from an SSB, but only in some special cases it is possible to associate them with a unique character of the acoustic and optical phonon (Meier et al., 2019; Juraschek et al., 2020).

Conclusion

A recently introduced viewpoint enabled the description of Goldstone and Higgs modes in clearly identifiable structural phase transitions occurring in widely available natural crystalline solids.

Within the Ginzburg–Landau theory formalism, we identified the potential energy term with the crystal free energy difference $F(\phi)$ between a parent, symmetric phase and a product phase with broken symmetry by expanding the total energy of crystal atoms around their equilibrium positions.

Goldstone (phase) and Higgs (amplitude) modes emerge when the initial system symmetry is broken during the phase transition to the *hcp* phase. These modes can be identified with the acoustic and optical phonons in the special case of crystals made of only one atomic species.

This perspective offers an example of what in the Standard Model of particle physics is difficult to achieve, that is, the symmetry restoration. A phase transition to a more symmetric *bcc* or *fcc* phase restores the $U(1)$ symmetry, stabilizes the symmetric vacuum state with $\phi_0 = 0$, and reveals a greater crystal symmetry that was hidden in the *hcp* broken phase.

In the event that an SSB is not observed, the acoustic phonons still exist. It is possible to view them as either Goldstone bosons resulting from the breakdown of translational invariance or gauge bosons that mediate lattice interactions within a non-Abelian gauge theory, a subject to be explored in greater detail in future publications.

References

Anderson PW (1963) Plasmons, gauge invariance, and mass. *Physics Review* 130(1): 439–442. https://doi.org/10.1103/PhysRev.130.439.

Ando Y (2013) Topological insulator materials. *Journal of the Physical Society of Japan* 82(10): 102001. https://doi.org/10.7566/JPSJ.82.102001.

Ashcroft NW and Mermin ND (1976) *Solid State Physics*. Philadelphia: Saunders.

Barceló C, Liberati S, and Visser M (2011) Analogue gravity. *Living Reviews in Relativity* 14(1): 3–159. https://doi.org/10.12942/lrr-2011-3.

Bardeen J, Cooper LN, and Schrieffer JR (1957a) Microscopic theory of superconductivity. *Physics Review* 106(1): 162–164. https://doi.org/10.1103/PhysRev.106.162.

Bardeen J, Cooper LN, and Schrieffer JR (1957b) Theory of superconductivity. *Physics Review* 108(5): 1175–1204. https://doi.org/10.1103/PhysRev.108.1175.

Beekman AJ, Rademaker L, and van Wezel J (2019) An introduction to spontaneous symmetry breaking. *SciPost Physics Lecture Notes*: 11. https://doi.org/10.21468/SciPostPhysLectNotes.11.

Brauner T (2010) Spontaneous symmetry breaking and Nambu-Goldstone bosons in quantum many-body systems. *Symmetry* 2(2): 609–657. https://doi.org/10.3390/sym2020609.

Brauner T and Watanabe H (2014) Spontaneous breaking of spacetime symmetries and the inverse Higgs effect. *Physical Review D* 89(8): 085004. https://doi.org/10.1103/PhysRevD.89.085004.

Brum JA and Bastard G (1986) Resonant carrier capture by semiconductor quantum wells. *Physical Review B* 33(2): 1420–1423.

Burkov AA and Balents L (2011) Weyl semimetal in a topological insulator multilayer. *Physical Review Letters* 107(12): 127205. https://doi.org/10.1103/PhysRevLett.107.127205.

Cho YM (1976) Einstein Lagrangian as the translational Yang-Mills Lagrangian. *Physical Review D* 14(10): 2521–2525. https://doi.org/10.1103/PhysRevD.14.2521.

Daniel M and Viallet CM (1980) The geometrical setting of gauge theories of the Yang-Mills type. *Reviews of Modern Physics* 52(1): 175–197. https://doi.org/10.1103/RevModPhys.52.175.

Dartora C and Cabrera G (2014) The electron-phonon interaction from fundamental local gauge symmetries in solids. *Journal of Physics A* 47(3): 035004. https://doi.org/10.1088/1751-8113/47/3/035004.

D'Onofrio M and Rummukainen K (2014) Standard model cross-over on the lattice. *Physical Review D* 93(2): 025003. https://doi.org/10.1103/PhysRevD.93.025003.

Duggen L and Willatzen M (2017) Acousto-optical phonon excitation in cubic piezoelectric slabs and crystal growth orientation effects. *Physical Review B* 95(3): 035310. https://doi.org/10.1103/PhysRevB.95.035310.

Endres M, Fukuhara T, Pekker D, Cheneau M, Schauß P, Gross C, Demler E, Kuhr S, and Bloch I (2012) The Higgs amplitude mode at the two-dimensional superfluid/Mott insulator transition. *Nature* 487: 454–458. https://doi.org/10.1126/science.aan2608.

Frasca M (2011) Exact solutions of classical scalar field equations. *Journal of Nonlinear Mathematical Physics* 18(2): 291–297. https://doi.org/10.1142/S14029251110014416.

Frasca M (2017) Quantum Yang-Mills field theory. *The European Physical Journal Plus* 132(1): 38. https://doi.org/10.1140/epjp/i2017-11321-4.

Fré P (2013) Basic concepts about manifolds and fibre bundles. *Gravity, a Geometrical Course*, pp. 25–84. Dordrecht, Germany: Springer.

Gegenberg J, Rahmati S, and Seahra SS (2016) Infrared modification of gravity from conformal symmetry. *Physical Review D* 93(6): 064025. https://doi.org/10.1103/PhysRevD.93.064025.

Gilmore R (2008) *Lie Groups, Physics, and Geometry: An Introduction for Physicists, Engineers and Chemists*. New York, UK: Cambridge University Press, ISBN:9781139469074.

Ginzburg VL and Landau LD (1950) On the theory of superconductivity. *Zhurnal Eksperimental'noi i Teoreticheskoi Fiziki* 20: 1064–1082.

Goldstone J (1961) Field theories with superconductor solutions. *Il Nuovo Cimento* 19(1): 154–164. https://doi.org/10.1007/BF02812722.

Gor'kov LP and Melik-Barkhudarov TK (1964) Microscopic derivation of the Ginzburg-Landau equations for an anisotropic superconductor. *Journal of Experimental and Theoretical Physics* 18(4): 1031–1034.

Grensing D and Grensing G (1983) General relativity as a gauge theory of the Poincaré group, the symmetric momentum tensor of both matter and gravity, and gauge-fixing conditions. *Physical Review D* 28(2): 286–296. https://doi.org/10.1103/PhysRevD.28.286.

Grimvall G, Magyari-Köpe B, Ozoliņš V, and Persson KA (2012) Lattice instabilities in metallic elements. *Reviews of Modern Physics* 84(2): 945–986. https://doi.org/10.1103/RevModPhys.84.945.

Gross DJ (1996) The role of symmetry in fundamental physics. *Proceedings. National Academy of Sciences. United States of America* 93: 14256–14259. https://doi.org/10.1073/pnas.93.25.14256.

Hasan MZ and Kane CL (2010) Colloquium: Topological insulators. *Reviews of Modern Physics* 82(4): 3045–3067. https://doi.org/10.1103/RevModPhys.82.3045.

Higgs PW (1964) Amplitude collective modes in superconductors and their coupling to charge-density waves. *Physical Review Letters* 13(16): 508–509. https://doi.org/10.1103/PhysRevLett.13.508.

Jackiw R (1980) Introduction to the Yang-Mills quantum theory. *Reviews of Modern Physics* 52(4): 661–673. https://doi.org/10.1103/RevModPhys.52.661.

Juraschek DM, Meier QN, and Narang P (2020) Parametric excitation of an optically silent Goldstone-like phonon mode. *Physical Review Letters* 124(11): 117401. https://doi.org/10.1103/PhysRevLett.124.117401.

Kendziora CA, Sergienko IA, Jin R, He J, Keppens V, Sales BC, and Mandrus D (2005) Goldstone-mode phonon dynamics in the pyrochlore $Cd_2Re_2O_7$. *Physical Review Letters* 95(12): 125503. https://doi.org/10.1103/PhysRevLett.95.125503.

Kibble TWB (1961) Lorentz invariance and the gravitational field. *Journal of Mathematical Physics* 2(2): 212–221. https://doi.org/10.1063/1.1703702.

Krumhansl JA (1992) Landau models for structural phase transitions: Are soft modes needed? *Solid State Communications* 84(1): 251–254. https://doi.org/10.1016/0038-1098(92)90334-6.

Landau LD (1965) On the theory of superconductivity. *Collected Papers of L. D. Landau*, pp. 546–568. Oxford, UK: Pergamon.

Léonard J, Morales A, Zupancic P, Donner T, and Esslinger T (2017) Monitoring and manipulating Higgs and Goldstone modes in a supersolid quantum gas. *Science* 358(6369): 1415–1418. https://doi.org/10.1126/science.aan2608.

Leutwyler H (1994) Nonrelativistic effective Lagrangians. *Physical Review D* 49(6): 3033–3043. https://doi.org/10.1103/PhysRevD.49.3033.

Leutwyler H (1997) Phonons as Goldstone bosons. *Helvetica Physica Acta* 70(1-2): 275–286. https://doi.org/10.5169/seals-117020.

Lipkin HJ (2002) *Lie Groups for Pedestrians*. New York, USA: Dover Publications, ISBN:0486421856.

Littlewood PB and Varma CM (1981) Gauge-invariant theory of the dynamical interaction of charge density waves and superconductivity. *Physical Review Letters* 47(11): 811–814. https://doi.org/10.1103/PhysRevLett.47.811.

Mandl F and Shaw B (2010) *Quantum Field Theory*, 2nd ed. UK: Wiley, ISBN:978-0-471-49683-0.

Marthinsen A, Griffin SM, Moreau M, Grande T, Tybell T, and Selbach SM (2018) Goldstone-like phonon modes in a (111)-strained perovskite. *Physical Review Materials* 2(1): 014404. https://doi.org/10.1103/PhysRevMaterials.2.014404.

Martín-Martín J and Tiemblo A (2010) Gravity as a gauge theory of translations. *International Journal of Geometric Methods in Modern Physics* 7(2): 323–335. https://doi.org/10.1142/S0219887810003999.

Meier QN, Stucky A, Teyssier J, Griffin SM, van der Marel D, and Spaldin NA (2019) Manifestation of structural Higgs and Goldstone modes in the hexagonal manganites. *arXiv*. arXiv:1912.04942v2.

Michel L and Radicati LA (1971) Properties of the breaking of hadronic internal symmetry. *Annals of Physics* 66(2): 758–783. https://doi.org/10.1016/0003-4916(71)90079-0.

Nambu Y (1960) Axial vector current conservation in weak interactions. *Physical Review Letters* 4(7): 380–382. https://doi.org/10.1103/PhysRevLett.4.380.

Peskin ME and Schroeder DV (1995) *An Introduction to Quantum Field Theory*. Reading, MA: Westview Press, Perseus Books Group, ISBN:0-201-50397-2.

Plischke M and Bergersen B (2006) *Equilibrium Statistical Physics*. Singapore: World Scientific, ISBN:9812560483.

Pracht US (2017) *Electrodynamics of quantum-critical conductors and superconductors*. Springer, ISBN:9783319728025.

Pracht US, Cea T, Bachar N, Deutscher G, Farber E, Dressel M, Scheffler M, Castellani C, Garcia-Garcia AM, and Benfatto L (2017) Optical signatures of the superconducting Goldstone mode in granular aluminum: Experiments and theory. *Physical Review B* 96(9): 094514. https://doi.org/10.1103/PhysRevB.96.094514.

Purja GP and Mishin Y (2012) Embedded-atom potential for hcp and fcc cobalt. *Physical Review B* 86(13): 134116. https://doi.org/10.1103/PhysRevB.86.134116.

Raines ZM, Stanev VG, and Galitski VM (2015) Hybridization of Higgs modes in a bond-density-wave state in cuprates. *Physical Review B* 92(18): 184511. https://doi.org/10.1103/PhysRevB.92.184511.

Rüegg C, Normand B, Matsumoto M, Furrer A, McMorrow DF, Krämer KW, Güdel HU, Gvasaliya SN, Mutka H, and Boehm M (2008) Quantum magnets under pressure: Controlling elementary excitations in $TlCuCl_3$. *Physical Review Letters* 100(20): 205701. https://doi.org/10.1103/PhysRevLett.100.205701.

Sanati M, Saxena A, Lookman T, and Albers RC (2001) Landau free energy for a bcc-hcp reconstructive phase transformation. *Physical Review B* 63(22): 224114. https://doi.org/10.1103/PhysRevB.63.224114.

Schnell I, Jones MD, Rudin SP, and Albers RC (2006) Tight-binding calculations of the elastic constants and phonons of hcp Zr: Complications due to anisotropic stress and long-range forces. *Physical Review B* 74(5): 054104. https://doi.org/10.1103/PhysRevB.74.054104.

Sciama DW (1964) The physical structure of general relativity. *Reviews of Modern Physics* 36(1): 463–469. https://doi.org/10.1103/RevModPhys.36.463.

Singh B, Sharma A, Lin H, Hasan MZ, Prasad R, and Bansil A (2012) Topological electronic structure and Weyl semimetal in the $TlBiSe_2$ class of semiconductors. *Physical Review B* 86(11): 115208. https://doi.org/10.1103/PhysRevB.86.115208.

Stassis C, Arch D, Harmon BN, and Wakabayashi N (1979) Lattice dynamics of hcp Ti. *Physical Review B* 19(1): 181–188. https://doi.org/10.1103/PhysRevB.19.181.

Sternberg S (1994) *Group Theory and Physics*. Cambridge, UK: Cambridge University Press, ISBN:0521558859.

Strauss B, Frey F, Petry W, Trampenau J, Nicolaus K, Shapiro SM, and Bossy J (1996) Martensitic phase transformation and lattice dynamics of fcc cobalt. *Physical Review B* 54(9): 6035–6038. https://doi.org/10.1103/PhysRevB.54.6035.

't Hooft G (2005) *50 Years of Yang-Mills Theory*. World Scientific Publishing Company, ISBN:9789814482196.

Tresguerres R and Mielke EW (2000) Gravitational Goldstone fields from affine gauge theory. *Physical Review D* 62(4): 044004. https://doi.org/10.1103/PhysRevD.62.044004.

Unruh WG (1981) Experimental black-hole evaporation. *Physical Review Letters* 46(21): 1351–1353. https://doi.org/10.1103/PhysRevLett.46.1351.

Utiyama R (1956) Invariant theoretical interpretation of interaction. *Physics Review* 101(5): 1597–1607. https://doi.org/10.1103/PhysRev.101.1597.

Vaks VG and Khromov KY (2008) Construction of a dynamical matrix for an HCP crystal using phonon data at the symmetry points of the Brillouin zone and elastic constants. *Journal of Experimental and Theoretical Physics* 106(3): 495–516. https://doi.org/10.1134/S1063776108030102.

Vallone M (2010) Many-body formulation of carriers capture time in quantum dots applicable in device simulation codes. *Journal of Applied Physics* 107(5): 053718. https://doi.org/10.1063/1.3309838.

Vallone M (2013, Aug) Quantum well electron scattering rates through longitudinal optic-phonon dynamical screened interaction: An analytic approach. *Journal of Applied Physics* 114(5): 053704. https://doi.org/10.1063/1.4817242.

Vallone M (2019) Higgs and Goldstone modes in crystalline solids. *Physica Status Solidi B* 257(3): 1900443. https://doi.org/10.1002/pssb.201900443.

Vallone M (2020) Structural phase transitions in crystals: Phonons as Higgs and Goldstone excitations. *Physica Status Solidi RRL: Rapid Research Letters* 14(9): 2000265. https://doi.org/10.1002/pssr.202000265.

Vallone M, Bertazzi F, Goano M, and Ghione G (2015) Model for carrier capture time through phonon emission in InGaN/GaN quantum wells. *Physica Status Solidi B* 252(5): 971–976. https://doi.org/10.1002/pssb.201451580.

Vallone M, Bertazzi F, Goano M, and Ghione G (2017) Carrier capture in InGaN/GaN quantum wells: Role of electron-electron scattering. *Journal of Applied Physics* 121(12): 123107. https://doi.org/10.1063/1.4979010.

Wakabayashi N, Scherm RH, and Smith HG (1982) Lattice dynamic of Ti, Co, Tc, and other hcp transition metals. *Physical Review B* 25(8): 5122–5132. https://doi.org/10.1103/PhysRevB.25.5122.

Wan X, Turner AM, Vishwanath A, and Savrasov SY (2011) Topological semimetal and fermi-arc surface states in the electronic structure of pyrochlore iridates. *Physical Review B* 83(20): 205101. https://doi.org/10.1103/PhysRevB.83.205101.

Weinberg S (1972) *Gravitation and Cosmology: Principles and Applications of the General Theory of Relativity*. New York: Wiley, ISBN:0-471-92567-5.

Weyl H (1929) Electron und gravitation. *Zeitschrift für Physik* 56(5-6): 330–352. https://doi.org/10.1007/BF01339504.

Xie H (2022) The role of off-centering behavior and acoustic-optical phonon coupling in heat transport. *Materials Lab*: 220051. https://doi.org/10.54227/mlab.20220051.

Ziman JM (1969) *Elements of Advanced Quantum Theory*. London, UK: Cambridge University Press, ISBN:0521099498.

Quantum mechanics: Foundations[☆]

AJ Leggett, Department of Physics, University of Illinois at Urbana-Champaign, Urbana, IL, United States

© 2024 Elsevier Ltd. All rights reserved.

This is an update of A.J. Leggett, Quantum Mechanics: Foundations, Editor(s): Franco Bassani, Gerald L. Liedl, Peter Wyder, Encyclopedia of Condensed Matter Physics, Elsevier, 2005, Pages 51–56, ISBN 9780123694010, https://doi.org/10.1016/B0-12-369401-9/00616-1.

Introduction 212
Quantum statistics 212
Aharonov–Bohm effect 214
Limits on the validity of quantum mechanics 215
Further reading 217

Abstract

This chapter discusses three different points at which condensed matter physics makes contact with foundational issues of quantum mechanics: (i) The effects of Fermi and Bose "statistics" in macroscopic systems. (ii) The Aharonov-Bohm effect. (iii) Does quantum-mechanics retain its validity at the everyday level?

Introduction

When one thinks about fundamental tests of the principles of quantum mechanics, the area of condensed matter physics is not the first that springs to mind. At least at first sight, such tests would seem to require the use of physical systems which are very well characterized, well isolated from their environments, and (for certain kinds of tests) propagate at or close to the speed of light. None of these conditions is at all well satisfied by a typical condensed matter system. Nevertheless, there are certain kinds of fundamental tests for which such systems are indispensable and others for which they permit substantial extensions of the results obtained on more "microscopic" systems, and this is the subject of this article. Apart from "quantum statistics," the issues discussed are: one aspect of nonlocality in quantum mechanics, and the universal validity of the quantum description.

Quantum statistics

It is a well-known consequence of the basic principles of the quantum field theory that "elementary" particles can be partitioned into two and only two classes, based on their possessing integral or half-odd-integral spin in units of $\hbar$; these are called bosons and fermions respectively (cf. below for the names). A very fundamental consequence of the indistinguishability in principle of elementary particles, coupled with considerations peculiar to the relativistic quantum field theory, is the spin-statistics theorem: the wave function of any quantum-mechanical system containing more than one particle must be unchanged under the exchange of any two identical bosons, and must change sign under the exchange of any two identical fermions. (A conventional, if somewhat imprecise, phrasing of this principle is that particles of integral (half-odd-integral) spin obey Bose (Fermi) "statistics.") The spin-statistics theorem has been well confirmed at the level of particle physics, for example, in the selection rules on decay processes, and in the case of fermions one of its consequences, the Pauli exclusion principle which forbids more than one fermion from occupying any single-particle state, has well-known effects for the structure of both atoms and nuclei. The spin-statistics theorem applies not only to "elementary" particles but also to complexes built up from the latter, provided that (1) the "internal" structure of the composites is identical, and (2) they remain undissociated in the regime of interest. This follows because if S is the total spin of the complex, the parity of $2S$ is just that of the total number of fermions contained in it, and this is also the parity of the wave function under the simultaneous exchange of all the fermions between two such complexes. Thus, for example, the ^{4}He atom (2 electrons, 2 protons, 2 neutrons, $S = 0$) behaves as a boson, while the ^{3}He atom (2 electrons, 2 protons, 1 neutron, $S = 1/2$) behaves as a fermion. The same conclusion obviously applies to the even and odd isotopic species of any chemical element. Does this difference in "statistics" have any effect in the macroscopic limit?

Actually, it is an experimental fact that the properties of most substances do not depend qualitatively on their isotopic composition. The reason is that for the effects of the statistics to be appreciable, two conditions must hold simultaneously. The first is that the behavior predicted by a quantum-mechanical calculation should differ appreciably from that obtained in the classical approximation (if this is not true, then the whole concept of a wave function becomes unnecessary, so its symmetry clearly cannot affect any physical property); this requires that the thermal de Broglie wavelength of the particles in question should be greater than, or at least comparable to, the average interparticle spacing. The second condition is that the particles in question can

---

[☆] *Change History*: Change History: August 2022. AJ Leggett updated section "Limits on the validity of quantum mechanics."

exchange places fairly readily; if this is not so, it is easy to show that the symmetry of the wave function under interchange can have no substantial consequences. Now for almost all elements and compounds, at temperatures low enough for the first condition to be satisfied the system is already solid, so that the second condition is violated (in a solid the atoms change places, if at all, only very rarely). In fact, by the traditional definition the only "condensed matter" systems where the two conditions are simultaneously satisfied are the above two stable isotopes of helium, both of which are unique in remaining liquid under their own vapor pressure down to the lowest temperatures investigated.

The effect of the "statistics" on the behavior of liquid helium is indeed spectacular. The two isotopes, ^{4}He and ^{3}He, are essentially identical in their electronic structure and interatomic interactions, and the difference in nuclear mass does not seem to have any major qualitative effect; indeed, in the solid phase the properties of the two species are very similar (with the exception, of course, of those associated explicitly with the nuclear spin degree of freedom, which is peculiar to ^{3}He). Despite this, the properties in the liquid phase are completely different: in the case of liquid ^{4}He, the liquid enters, below the so-called λ-temperature of $\sim$2.17 K, a "superfluid" phase which displays a variety of exotic properties (persistent currents, nonclassical rotational inertia, film creep, fountain effect, etc.). By contrast, liquid ^{3}He behaves, right down to temperatures below 3 mK, in a way qualitatively similar to that of any other liquid, and in particular, shows none of the above exotic effects. (Below 2.6 mK, liquid ^{3}He does indeed become superfluid, but as shall be seen below, the character of the superfluid phase(s) is/are rather different from that occurring in ^{4}He.)

The origin of this spectacular difference in the behavior of the two isotopes (or at least of much of it) may be understood, at least qualitatively, by asking how they would behave in the complete absence of interactions between the atoms. If N identical noninteracting atoms (of either species) are considered to be moving in a volume V, the relevant single-particle energy eigenstates are plane waves of the form

$$\psi_k(r) = V^{-1/2} \exp(\mathrm{i}k \cdot r) \tag{1}$$

If the system is considered to be in thermal equilibrium at temperature T and the standard principles of statistical mechanics are applied subject to the constraints imposed on the many-particle wave function by the spin-statistics theorem, one finds that the distribution $n_k(T)$ of atoms between the single-particle plane-wave states (1) is given by the formula

$$n_k(T) = (\exp((\varepsilon_k - \mu)/k_B T) \pm 1)^{-1}, \varepsilon_k \equiv \hbar^2 k^2/2m \tag{2}$$

where the plus sign applies for fermions and the minus sign for bosons. In these formulas, the quantity $\mu(T)$ is the chemical potential, and its value is fixed, for either sign, by the self-consistency condition

$$\sum_k n_k(T : \mu(T)) = N \tag{3}$$

The consequences of the sign difference are profound: for fermions, in the limit $T \to 0$, the N lowest-energy single-particle states are each occupied by a single atom, in accordance with the Pauli exclusion principle; one can say that they fill up a "Fermi sea" or "Fermi sphere" in momentum space, with a radius k_F given (for spin 1/2) by the formula $k_F = (3\pi^2 n)^{1/3}$, where $n \equiv N/V$. At nonzero but low temperatures, particles can be excited to states which lie $\lesssim k_B T$ in energy above the top of the Fermi sea, leaving "holes" in a similar range in the sea. Although such a "free Fermi gas" model is of course not a realistic picture of real liquid ^{3}He, it turns out that the modifications necessary to take account of the interatomic interactions do not change the situation qualitatively (this is the essential content of Landau's "Fermi-liquid" theory), and that the behavior of the resulting system is overall not very different from that of a classical liquid; in particular, it is predicted to show none of the exotic effects seen in liquid ^{4}He.

In the case of a system of noninteracting bosons, which is described by Eq. (2) with the minus sign, the behavior is again not qualitatively very different from that of a normal liquid so long as the chemical potential μ has a finite negative value (which is the case at sufficiently high temperatures). As the temperature falls, however, the value of $\mu(T)$ increases, and for a system moving in free space there exists a nonzero temperature T_c (whose value depends on the density n) below which such a nonzero negative value of μ is incompatible with the self-consistency relation (3). For $T < T_c$, the chemical potential tends to zero, and a finite fraction of all the atoms (i.e., a macroscopically large number N_0) occupies the lowest-energy single-particle state, namely that with $\boldsymbol{k} = 0$. This is the phenomenon known as Bose–Einstein condensation (BEC). For a gas of atoms with the mass and density of ^{4}He, the onset temperature T_c of BEC is $\sim$3.3 K, not far from the temperature (2.17 K) of the onset of superfluidity in liquid ^{4}He. It is the almost universal belief that below this latter temperature, BEC indeed occurs in liquid ^{4}He, and that this is the origin of the complex of exotic properties observed in that system.

To illustrate how BEC can give rise to this kind of exotic behavior, let us focus, for definiteness, on the property of "nonclassical rotational inertia." Consider a free gas of N identical atoms (of any species) in a toroidal (annular) container of radius R and thickness $d \ll R$, which rotates at an angular velocity $\omega < \omega_c/2$, where $\omega_c \equiv \hbar/mR^2$. What is the angular momentum of the system in thermal equilibrium? Classical intuition suggests that the system would like to rotate so that its mean velocity exactly matches that of the container, and that its angular momentum will then be simply $NmR^2\omega$. It is easy to show that a system which is well described by classical (Newtonian) mechanics will indeed behave in just this way. For a quantum-mechanical system, it turns out that the effect of the rotation is to change the "effective" energy of a single-particle state with angular momentum l from its original energy $l^2\hbar^2/2mR^2$ to $l^2\hbar^2/2mR^2$—$\hbar\omega l$. For a system of any species which is not Bose-condensed, the distribution given by formula (2) is a smooth function of energy, and provided only that the thermal energy $k_B T$ is $\gg \hbar^2/mR^2$ (a condition very well satisfied in any currently realistic experiment), the classical result for the total angular momentum is obtained. However, for a boson system below T_c, a macroscopic fraction of all the atoms must occupy the single lowest-(effective)-energy single-particle state; for $\omega < (1/2)\omega_c$, this is a state with $l = 0$, so a fraction of the atoms stays at rest in the laboratory frame and the observed angular momentum is less than the classical value. Again, this simple model is not a realistic description of liquid ^{4}He (and in fact, cannot account for all the exotic behavior of the latter), but a model which takes adequate account of the interatomic interactions while still assuming the existence of BEC has been very successful in explaining all the main phenomena of superfluidity in that system.

Finally, it is generally believed that below 2.6 mK the fermions in liquid ^{3}He form "Cooper pairs"—a sort of giant "diatomic molecules." (A similar phenomenon occurs for the electrons in metals below the transition temperature for superconductivity, but the Cooper pairs in ^{3}He have a more sophisticated structure). Since such pairs of fermions have integral spin, they are in effect bosons and can (and do) undergo Bose condensation. One, therefore, expects the system to show exotic properties such as those displayed by ^{4}He below the λ-temperature, and indeed such are found.

Thus, the two isotopes of liquid helium manifest, in a dramatic way, the consequences of a fundamental principle, the indistinguishability, in principle, of elementary particles.

Aharonov–Bohm effect

In the classical electromagnetic theory, all electromagnetic effects on charged particles can be obtained from a knowledge of the electric and magnetic fields "seen" by the particle, that is, the fields at the position of the latter; the electromagnetic vector potential $A(r, t)$ is introduced purely as an auxiliary function to simplify some of the calculations. However, in quantum mechanics the situation is different. Consider an experimental arrangement in which a solenoid, regarded here as of infinite length, carries a finite steady current (see Fig. 1). The magnetic field produced by the current is entirely confined to the interior of the solenoid; outside it is zero. Now consider a beam of electrons which is split so as to pass on either side of the solenoid, and detected on a screen behind it (Fig. 1). According to a quantum-mechanical calculation, the position of the interference fringes observed on the screen should depend on the current in the solenoid, being periodic in the flux through the latter with period h/e. This is despite the fact that there are no electric or magnetic fields at any point on the trajectories of the electrons! This strange behavior, usually known as the Aharonov–Bohm effect, can be interpreted as showing either that the electrons can "feel" fields even at points they never travel to, or that the vector potential has a "physical reality" not envisaged in the classical electromagnetic theory.

While the most loophole-free tests of the Aharonov–Bohm effect have been done with electron beams in free space, the use of condensed-matter systems permits one to display the effects of this "nonlocality" on a macroscopic scale. This is possible in a superconductor, since, to produce the superconducting state, the electrons must form Cooper pairs (as in the superfluid phase of liquid ^{3}He, see above), and these pairs then effectively form bosons and undergo a sort of BEC (again just as in ^{3}He). Suppose now one forms the completely superconducting device shown in Fig. 2; in the present context it is enough to know that each junction by itself can carry, without dissipation, a certain maximum ("critical") current I_c, which is assumed for simplicity to be the same for the two junctions. Thus, if one of the arms were blocked the critical current of the device would simply be I_c, while if both are open and there is no current in the solenoid S, the currents in the two arms just add and the critical current of the device is $2I_c$. If however, one imposes a current through the solenoid and thus generates a total flux ϕ through the device, it turns out that the critical current of the latter should be modulated by a factor $|\cos(\pi\phi/\phi_0)|$; thus it is periodic in the (superconducting) "flux quantum" $\phi_0 \equiv h/2e$. (The reason the period is $h/2e$ rather than h/e as in the electron beam case is that the Cooper pairs have charge $2e$, not e.) As in the electron-beam case, this is despite the fact that the electrons which carry this current never experience any electric or magnetic fields. This prediction is well verified experimentally, showing that the Aharonov–Bohm effect has not merely atomic-level but also macroscopic manifestations.

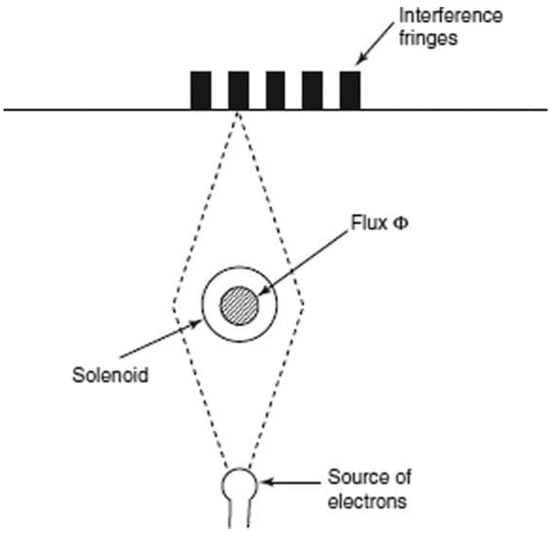

Fig. 1 The Aharonov–Bohm effect. The magnetic field of the solenoid is confined to its interior, so there are no fields at any point on the paths taken by the electrons.

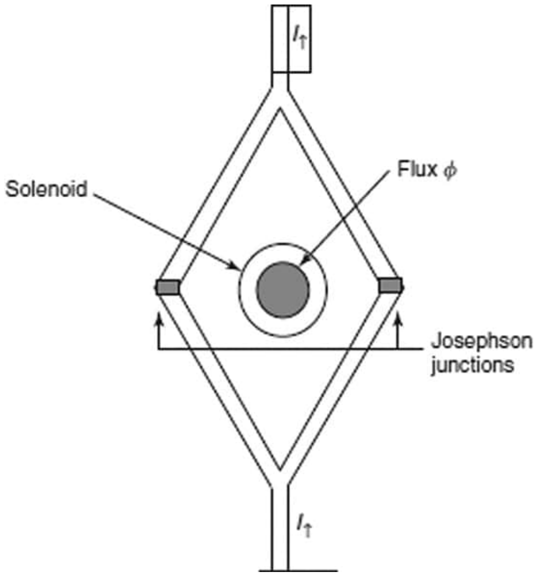

Fig. 2 The Aharonov–Bohm effect in a superconducting circuit. The solenoid produces no field anywhere in the metal.

Limits on the validity of quantum mechanics

The quantum measurement paradox (or, as it is sometimes known after its most famous instantiation, the "Schrödinger's Cat" paradox) may be stated succinctly as follows: at the microscopic level, if one considers a standard example such as the Young's slits experiment with attenuated beams of single electrons, the fact that the probability amplitude (wave function) which in quantum mechanics describes the ensemble in question, has a finite value at each of the two slits of the intermediate screen cannot, at least without extreme contortions, be interpreted as implying that each individual electron of the ensemble passed through a definite slit (so that the only significance of the amplitude is that its square is a measure of the probability of a given electron passing through the slit in question). The evidence for the above statement is the phenomenon of interference at the final screen. Now, if one believes (as most physicists do) that quantum mechanics is, in principle, the complete truth about the physical universe, it can be applied not just to single electrons and atoms, but to arbitrarily complex objects composed of them, and in this process the formalism itself is in no way modified. This means that it is perfectly possible to devise thought-experiments (such as Schrödinger's original example involving the cat) such that the unambiguous description given by quantum mechanics of the final state of the universe (or more precisely the relevant "ensemble of universes") is a linear superposition of amplitudes corresponding to macroscopically distinct outcomes (e.g., living or dead cat). Thus, unless the interpretation of the quantum formalism is changed significantly between the microscopic and macroscopic levels, one is forced to conclude that it is not true that, for example, each individual cat was either alive or dead before inspection. Yet it is (or at least appears to be!) a fact of our direct experience that inspection reveals each cat to be in one state or the other!

In the literature it is often claimed that the apparent paradox can be resolved by appealing to the phenomenon known as "decoherence": when an object is sufficiently macroscopic, and/or interacts with a sufficiently complex environment, then one effect of this interaction is, in effect, to "scramble" the relative phases of the amplitudes representing the two macroscopically distinct states, so that the reduced density matrix of the system becomes equivalent to that of a classical "mixture" of the two states (which *inter alia* gives no possibility of interference), and can thus (it is claimed) be interpreted as simply saying that one or other of the two states is definitely realized for each cat, but one does not know which, and thus have to give a probabilistic description. While the occurrence and ubiquity of the decoherence phenomenon at the macroscopic level is not in serious dispute, the validity of the last, crucial step in the argument (which is equivalent to a major change in the interpretation of the quantum formalism between the micro- and macro-levels) is controversial in the extreme, so that it is by no means universally agreed in the physics community that the measurement paradox is "solved."

The premise underlying the above discussion is that since the pristine quantum formalism describes, apparently perfectly, the behavior of individual atoms and molecules, it must likewise describe perfectly, at least in principle, the behavior of arbitrarily complex objects composed of them. Given the situation just described concerning the measurement paradox, it would appear to make sense to ask if one is sure that this premise is actually true, or could it perhaps be that by the time one gets from the level of atoms to that of cats, some new physics comes into play which, *inter alia*, has the effect of reducing any superposition of macroscopically distinct states, not to a mixture as the "decoherence" argument would have it, but to a definite one of its branches for any given system of the ensemble? The class of theories which have these properties are termed "macrorealistic"; a number of such theories have appeared in literature, the most fully developed probably being that associated with the names of Ghirardi, Rimini, Weber, and Pearle. The question is whether one could actually devise an experimental test of the class of macrorealistic theories against quantum mechanics.

It is fairly obvious that to the extent that a superposition of macroscopically distinct states is *ipso facto* automatically subject to a degree of decoherence sufficient to reduce the density matrix to that of a classical mixture, it will be impossible to implement such a test, because the experimental predictions of the "mixture" description are, by definition, equivalent to those of a theory in which a definite outcome is realized for each system, that is, a macrorealistic theory. The experimental challenge is thus to find a system where the superposition is both of "macroscopically distinct" states and at the same time sufficiently resistant to decoherence. Of course, the possibility of doing so rests on the definition of "macroscopically distinct," and this point has had considerable discussion in literature; for present purposes, it is adequate to define two states as having this property relative to one another if there is at least one extensive physical quantity whose expectation value in the two states is different by some large number (say 10^4–10^9, see below) in the "natural" (atomic) units. Below, for convenience, this number is denoted by the symbol Λ.

Suppose, for the sake of argument, that one has found such a system; then one can try to engineer a situation where, if quantum mechanics is indeed the whole story, at some stage the correct description of the relevant ensemble is indeed a linear superposition of two (or more) macroscopically distinct states. At that point one can, in principle, (1) test whether the predictions of quantum mechanics in fact correspond to experiment, and (2) test whether predictions made on the basis of a macrorealistic theory correspond to experiment. While it can be shown that there exist experimental situations in which a positive answer to (1) automatically implies a negative answer to (2) (i.e., confirmation of the quantum-mechanical predictions automatically refutes the whole class of macrorealistic theories), such experiments have been realized only quite recently, and the experiments to be described in the next paragraph have been of type (1) only. In such tests, the interpretation of the raw data is always done in explicitly quantum-mechanical terms, and the question being asked is whether the experimentally realized state is, as predicted by theory, a superposition or rather a mixture of macroscopically distinct states.

Condensed matter experiments which were consciously designed to test the validity of quantum mechanics at the macroscopic level were started as early as 1980. The first generation of these experiments looked for, and saw, the essentially quantum-mechanical phenomenon of tunneling out of a metastable well (often referred to, in this context, as "macroscopic quantum tunneling" or MQT). A second generation of experiments has looked more directly for the effects of superposition, by testing for NH_3-type oscillations or a related phenomenon. The system of choice is usually a bulk superconducting ring interrupted by a single Josephson junction ("flux qubit"), or some variant thereof, and the two states in question are states in which the current circulates clockwise or counterclockwise respectively; depending on the details of the geometry, the value of Λ can range from 10^4 to 10^9. If such a system is subjected to an external flux f_{ext}, the energy eigenstates are (in the absence of decoherence) linear superpositions of the above two states; for the special case $\phi_{ext} = \phi_0/2 = h/4e$, the ground state has even parity and the excited state odd parity, and the level splitting is twice the matrix element t for tunneling between the clockwise- and anticlockwise-circulating states. More generally, as a function of flux the level splitting has the form

$$\Delta E = 2\sqrt{t^2 + \text{const.}(\phi - \phi_0/2)^2} \tag{4}$$

as shown by the solid lines in Fig. 3. By contrast, if the true density matrix of the system is a mixture then the splitting should be linear in the flux, as indicated by the broken lines. In the experiments (which used a spectroscopic technique to measure the splitting), it was unambiguously the solid line which was found.

In one set of experiments, the value of Λ was $\sim 10^9$, which is probably a record at the time of writing. Note however that these experiments, while verifying that the behavior at this level is consistent with the predictions of quantum mechanics, have not explicitly excluded theories of the macrorealistic class.

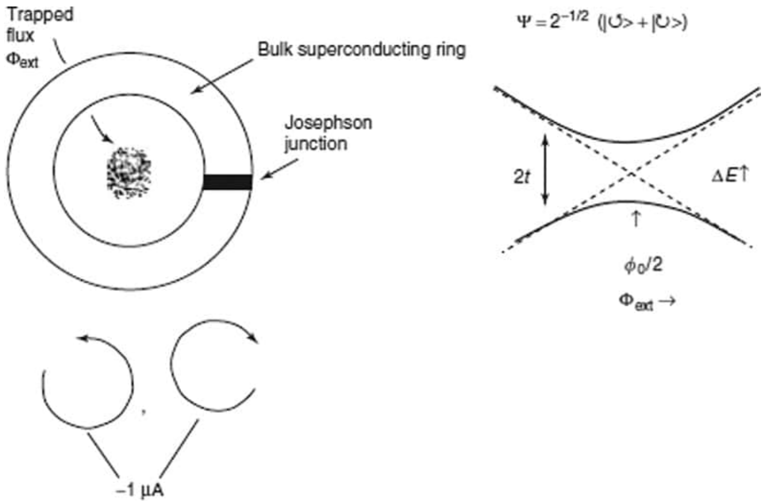
Trapped flux Φ_{ext}
Bulk superconducting ring
Josephson junction
−1 μA
$\Psi = 2^{-1/2}$ (|↺> + |↻>)
2t
ΔE↑
↑
$\phi_0/2$
Φ_{ext} →

Fig. 3 The predicted dependence of the energies of the two lowest states of an RF SQUID ring on the externally applied flux, under the assumption of a coherent superposition (solid lines) or a mixture (broken lines).

In 2016 the NTT group in Japan Knee (2016) reported the first definitive experiment of type (2). This was essentially a simple "Young's slits" experiment in which the "slits" were two states of a flux qubit which were,at least arguably, macroscopically distinct (see supplementary note 3 of Knee et al.), and in which the raw data was the dependence of the post-slit behavior on whether or not an observation was made on which "slit" was traversed. The results are in agreement,within the error bars, with the predictions of quantum mechanics,and violate those of any macrorealistic theory by more than 80 standard deviations. Thus it seems that the idea of macrorealism is untenable at least at the level of flux qubits. Whether it may become viable at a level closer to that of direct human experience is a matter for further experiments in the future.

Further reading

Knee GC (2016) *Nature Communications* 13253.

Leggett AJ (1989) In: Davies P (ed.) *The New Physics*, pp. 268–288. Cambridge: Cambridge University Press.

Leggett AJ (2002R) *Journal of Physics: Condensed Matter* 14: 415–451.

Wilks J (1970) *An Introduction to Liquid Helium*. Oxford: Clarendon Press.

Aharonov–Bohm and Aharonov–Casher effects in condensed matter physics: A brief review

Y Avishai[a,b] **and YB Band**[a,c,d], [a]Department of Physics, Ben-Gurion University of the Negev, Beer-Sheva, Israel; [b]Yukawa Institute for Theoretical Physics, Kyoto, Japan; [c]Department of Chemistry, Ben-Gurion University of the Negev, Beer-Sheva, Israel; [d]The Ilse Katz Center for Nano-Science, Ben-Gurion University of the Negev, Beer-Sheva, Israel

© 2024 Elsevier Ltd. All rights reserved.

Introduction **218**
Aharonov–Bohm effect **219**
Periodicity in the Aharonov–Bohm phase 220
Gauge invariance 220
Examples in condensed matter physics 220
Interference 220
Electrons on a ring 220
Spectrum 220
Persistent current 221
Aharonov–Bohm interferometer 222
Aharonov–Casher effect **224**
Aharonov–Casher effect and non-Abelian gauge transformations 225
Examples in condensed matter physics 226
Aharonov–Casher interferometer in a perpendicular electric field 227
Conductance and polarization in transmission through a square interferometer 228
Analogy of Aharonov–Bohm effect in cold atoms physics **229**
Magnetic monopoles **230**
Dirac quantization and phase factors 230
Tight-binding spectra on spherical graphs: Avoiding the Dirac string 231
Relation to Aharonov–Casher effect 231
Conclusion **233**
Acknowledgments **234**
References **234**

Abstract

We briefly review the theoretical formulations and applications of the Aharonov–Bohm effect and the Aharonov–Casher effect in condensed physics with emphasis on mesoscopic physics. Topics relating to the Aharonov–Bohm effect include locality, periodicity, nonintegrable phase factors, Abelian gauge theory, interference, the spectrum and persistent current of electrons on a ring pierced by a magnetic field, Onsager reciprocity relations, and Aharonov–Bohm interferometer. Topics relating to the Aharonov–Casher effect include a magnetic dipole in an electric field, locality, periodicity, non-Abelian gauge invariance, SU(2) nonintegrable phase factors, spin–orbit coupling, Pauli equation, Rashba Hamiltonian, Aharonov–Casher interferometer, conductance and polarization in two-channel systems due to the Aharonov–Casher effect. We also touch upon Aharonov–Bohm effect in cold atom physics and the topic of magnetic monopoles.

Introduction

The Aharonov–Bohm effect (Aharonov and Bohm, 1959) and Aharonov–Casher effect (Aharonov and Casher, 1984) are purely quantum mechanical in nature. They highlight the crucial role of the phase of the wave function and its experimental significance (Berry, 1984; Loss et al., 1990; Stern et al., 1990; Stern, 1992; Aronov and Lyanda-Geller, 1993; Qian and Su, 1994). The Aharonov–Bohm effect shows that a charged particle is affected by a magnetic field even if the particle is confined to a region in which the magnetic field **B** is absent. Thus, the magnetic field acts nonlocally on charged particles, and the fundamental pertinent field affecting charged particle is the vector potential **A**, and the relevant theory is characterized by Abelian gauge invariance.

The Aharonov–Casher effect applies to particles with an intrinsic magnetic moment (they need not necessarily be charged), whose (spinor) wave function acquires a matrix-valued phase factor. Consequently, the relevant theory is characterized by non-Abelian gauge invariance (Yang and Mills, 1954).

Several examples relevant to condensed matter physics are discussed, mainly for mesoscopic systems (Stone, 1985; Lee and Stone, 1985; Imry, 1997; Akkermans and Montambaux, 2007), supported by short derivations of the basic equations that model the observed phenomena.

https://doi.org/10.1016/B978-0-323-90800-9.00183-9

Aharonov–Bohm effect

The Aharonov–Bohm effect (Aharonov and Bohm, 1959, 1961; Aharonov and Anandan, 1987) is a spectacular manifestation of the difference between classical and quantum theories of charged particles interacting with electromagnetic forces; it stresses the crucial role of the phase of the charged particle's wave function. It predicts that the behavior of a charged particle is affected by the electromagnetic field even when the particle is always in a region where the field vanishes. Shortly after being predicted, it was first confirmed experimentally (Chambers, 1960). An experimental verification in a toroidal magnetic field was reported in Osakabe (1986) and its verification in carbon nano tubes was reported in Bachtold et al. (1999). It was also confirmed in tunneling experiments (Noguchi et al., 2014) and tomography (Valagiannopoulos et al., 2018).

In classical electrodynamics, the electric and magnetic fields **E** and **B** fully describe the electromagnetic field and the phenomena involving the interaction of matter and photons. The vector potential **A** is introduced as an auxiliary field in order to solve Maxwell's equations (see however Vaidman, 2011). In quantum mechanics, the Aharonov–Bohm effect shows that this is not the case. For charged particles, knowing **B** (assume $\mathbf{E} = 0$ for simplicity) does not completely determine all the electromagnetic effects on the particle. Experimental and theoretical consequences of the Aharonov–Bohm effect were elaborated in numerous papers and books, see for example Olariu and Popescu (1985), Peshkin and Tonomura (1989), and Tonomura (2006).

In order to describe the effect in simple terms, let us consider, as in Fig. 1 (Shech, 2022), a two-slit interference pattern of electrons moving in the x-y plane. The plane is pierced by a circular tube of radius R centered at the origin, namely $\sqrt{x^2 + y^2} < R$, in which there is a uniform perpendicular magnetic field, $\mathbf{B} = B_z\Theta(R - r)$ (see the small circle with B in Fig. 1). Outside the tube $\mathbf{B} = 0$ yet $\mathbf{A} \neq 0$ (but nevertheless, the magnetic field $\nabla \times \mathbf{A} = 0$), see Tonomura (2006) and Batelaan and Tonomura (2009). The electron wave function is $\psi(\mathbf{r})$ and the density pattern on the screen on the right is proportional to $|\psi(\mathbf{r})|^2$. The line integral $\oint \mathbf{A} \cdot d\mathbf{r} = \pi R^2 B \neq 0$ along *any closed curve encircling the tube* equals the magnetic flux through the tube. Because of the Aharonov–Bohm effect, experiments performed on electrons that are located outside the flux tube (where $\mathbf{B} = 0$), for example, measuring the density on the screen), yield results that depends solely on the (dimensionless) quantity

$$\Phi_{AB} \equiv \frac{e}{\hbar c} \oint \mathbf{A} \cdot d\mathbf{r} \neq 0. \tag{1}$$

This quantity is called the Aharonov–Bohm phase. In a sense, the magnetic field acts where it is not present (see however Avishai et al. 1972; Roy 1980; Vaidman 2008; Popescu 2010, Vaidman 2012, Pearle and Rizzi 2017; Heras 2022). In other words, knowledge of the scalar potential V and the vector potential **A** contain more information than the information about the fields **E** and **B**. The Aharonov–Bohm effect can also test the role of the gravitational potential versus that of the gravitational field (Dowker, 1967; Hohensee et al., 2012; Overstreet et al., 2022).

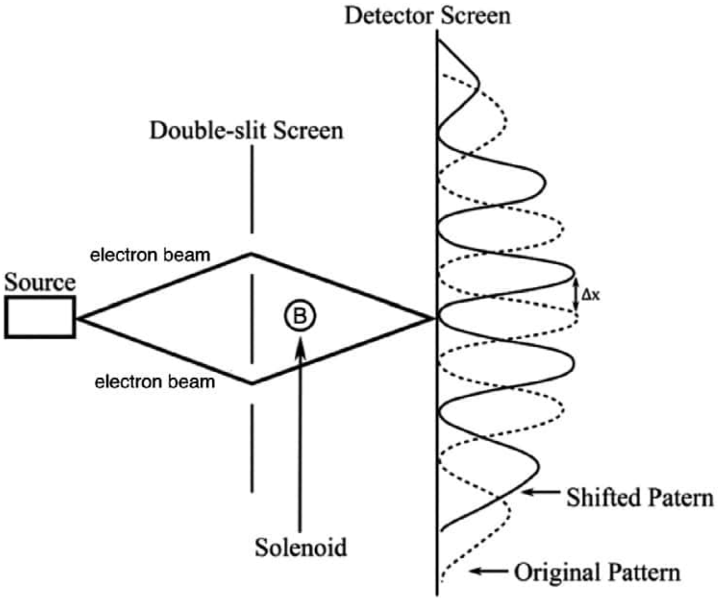

Fig. 1 Aharonov–Bohm interference experiment (schematic): A coherent electron beam emanating for the source propagates in a region where there is no magnetic field but is affected by a flux tube of radius R (with the electron beam not able to enter the tube) within which the magnetic field **B** (along the axis of the tube) is finite and uniform; hence, the magnetic flux is $\Phi_{AB} = \pi R^2 B$. The interference pattern on the screen is a periodic function of Φ_{AB} with period $\frac{hc}{e}$. The original pattern (*bold line*) is obtained for $\Phi_{AB} = n\Phi_0$ and the shifted pattern (*dashed line*) is obtained for $\Phi_{AB} \neq n\Phi_0$ ($n =$ integer). Modified from Shech E (2022) Scientific understanding in the Aharonov-Bohm effect. Theoria 88: 943, Fig. 2

Periodicity in the Aharonov–Bohm phase

As predicted by Aharonov and Bohm and substantiated shortly after their publication (Byers and Yang, 1961), such experimental results are periodic functions of Φ_{AB} with period

$$\Phi_0 \equiv \frac{hc}{e} = 4.1414 \times 10^{-7}\ \text{Gauss} - \text{cm}^2, \tag{2}$$

which serves as a quantum unit of flux. Consequently, Wu and Yang (1975) introduced the concept of *phase factor*,

$$\Lambda_{AB} \equiv e^{i\Phi_{AB}}, \tag{3}$$

and stressed that, although Φ_{AB} contains more information than Λ_{AB}, this extra information is not measurable. In other words, the result of experiments depend solely on the phase factor Λ_{AB}. If there are two cases a and b such that $\Phi^a_{AB} - \Phi^b_{AB} = n\frac{hc}{e}$ ($n =$ integer), no experiment performed on an electron *outside the tube* can distinguish between the two cases.

Gauge invariance

The proof of the statement above (Wu and Yang, 1975) proceeds by applying a (unitary) *gauge transformation* between the corresponding electron wave functions, $\psi_b(\mathbf{r}) = e^{i\alpha(\mathbf{r})}\psi_a(\mathbf{r}) \equiv S(\mathbf{r})\psi_a(\mathbf{r})$, implying $\mathbf{A}_b(\mathbf{r}) - \mathbf{A}_a(\mathbf{r}) = \frac{\hbar c}{e}\nabla\alpha(\mathbf{r})$. Since the curl of the left-hand side vanishes, the solution for $\alpha(\mathbf{r})$ is $\alpha(\mathbf{r}) = \frac{e}{\hbar c}\int_{\mathbf{r}_0}^{\mathbf{r}}[\mathbf{A}_b(\mathbf{r}) - \mathbf{A}_a(\mathbf{r})]\cdot d\mathbf{r}$, where $\mathbf{r}$ and $\mathbf{r}_0$ are two points along the chosen curve outside the tube. Therefore,

$$\frac{e}{\hbar c}\oint[\mathbf{A}_b(\mathbf{r}) - \mathbf{A}_a(\mathbf{r})]\cdot d\mathbf{r} = \Phi^b_{AB} - \Phi^a_{AB} = 2n\pi, \tag{4}$$

hence, $[\Lambda_{AB}]_a = [\Lambda_{AB}]_b$. In the language of Wu and Yang (1975), *the two cases are gauge transformable into each other and no physically observable effects can differentiate between them*.

The concept of gauge transformation is generalized to the case where the line integral is performed for any curve between $\mathbf{r}_0$ and $\mathbf{r}$ by introducing a *nonintegrable (path dependent) phase factor*,

$$\Lambda_{pq} \equiv e^{\frac{ie}{\hbar c}\int_{\mathbf{r}_p}^{\mathbf{r}_q}\mathbf{A}(\mathbf{r})\cdot d\mathbf{r}}, \tag{5}$$

such that an arbitrary gauge transformation $e^{\frac{ie}{\hbar c}f(\mathbf{r}_p)}\Lambda_{pq}e^{\frac{-ie}{\hbar c}f(\mathbf{r}_q)}$ does not affect the result of measurements. Here $f(\bullet)$ is any continuous function taking $\mathbf{r}_p$ outside the tube to $\mathbf{r}_q$ outside the tube, and the factor $e^{\frac{ie}{\hbar c}f(\mathbf{r})}$ is a transformation of the wave function $\psi(\mathbf{r})$. Wu and Yang then conclude that *electromagnetism is the gauge-invariant manifestation of nonintegrable phase factors*.

Examples in condensed matter physics

In the Aharonov–Bohm effect, phase coherence is a crucial factor. Hence, pertinent experiments must be carried out at low temperature and with systems of small size (up to a few microns). The underlying physics of systems whose size is larger than the atomic size but much smaller than macroscopic size is termed *mesoscopic physics* (Lee and Stone, 1985; Stone, 1985; Imry, 1997; Akkermans and Montambaux, 2007). In the examples discussed below, the spin of the electron does not play a role. The Aharonov–Bohm effect for particles with spin is discussed in Hagen (1990), Nitta et al. (1997), Morpurgo et al. (1998), Nitta et al. (1999), Yau et al. (2002), and Grbic et al. (2007).

Interference

Fig. 1 is a schematic description of an Aharonov–Bohm interference wherein a beam of electrons propagates toward a screen. The electrons avoid the tube through which a magnetic field generates a magnetic flux Φ_{AB}. Outside the tube the magnetic field vanishes but the vector potential **A** is finite. The electrons do not feel the magnetic field, but on going outside the tube from a point q to a point p the wave function of the electron gains a phase as given in Eq. (5). This leads to an interference pattern whose intensity is shown on the screen. The intensity pattern is periodic in Φ_{AB} with period $\Phi_0 = \frac{hc}{e}$.

Electrons on a ring

Impressive progress in experimental techniques has enabled fabrication of micron-sized conducting rings (Webb et al., 1985; Imry and Webb, 1986). Specifically, consider uniformly distributed electrons propagating in a small metallic ring of radius R and length $L = 2\pi R$. The ring is placed on a plane and pierced by a perpendicular magnetic field $\mathbf{B}$ such that the magnetic flux is $\Phi_{AB} = \pi R^2 B$, and the corresponding vector potential $\mathbf{A} = \frac{\Phi_{AB}}{L}\hat{\boldsymbol{\theta}}$ is along the ring (the magnetic field acting on the circumference of the ring vanishes). Here the electrons are treated as noninteracting spin less fermions of charge $-e$ and mass m (see however, Hagen (1990)). Due to the Aharonov–Bohm effect, this simple system exhibits beautiful phenomena both in equilibrium and, if coupled to leads with a small potential difference, out of equilibrium (see the Section Aharonov–Bohm interferometer below).

Spectrum

Let $0 \leq x \leq L$ denote an electron coordinate along the ring. The time-independent Schrödinger equation for electrons (charge $-e$ and mass m_e) moving on the ring is,

$$H\psi = \frac{1}{2m_e}\left(p + \frac{e}{c}\frac{\Phi_{AB}}{L}\right)^2 \psi = \varepsilon\psi, \tag{6}$$

where $p = -i\hbar\frac{d}{dx}$ is the momentum operator and c is the speed of light. Note that $[p, H] = 0$ since Φ_{AB} is independent of x. The periodic solutions are plane waves, $\psi(x) = L^{-1/2}\ e^{ikx}$. Since the wave function must be single valued, the wave numbers are quantized, $k = k_n = 2n\pi/L = n/R$, with $n = 0, \pm 1, \pm 2\ldots$ Substituting this wave function into Eq. (6), one obtains the energy eigenvalues E_n,

$$\begin{aligned}\varepsilon_n(\Phi_{AB}) &= \frac{1}{2m_e}\left(\hbar k_n + \frac{e\Phi_{AB}}{cL}\right)^2 \\ &= \frac{\hbar^2}{2m_eR^2}\left(n + \frac{\Phi_{AB}}{\Phi_0}\right)^2,\end{aligned} \tag{7}$$

Note that $\varepsilon_n(\Phi_{AB})$ is not periodic in Φ_{AB} and also, $\varepsilon_n(\Phi_{AB}) \neq \varepsilon_n(-\Phi_{AB})$ (which is physically wrong). Using the degeneracy $\varepsilon_{n+1}(\Phi_{AB}) = \varepsilon_n(\Phi_{AB} + \Phi_0)$ we can reorder the quantum numbers $\{n \in \mathbb{Z}\}$ and the energies $\{\varepsilon_n(\Phi_{AB})\}$ such that (see Fig. 2),

$$0 \leq E_n(\Phi_{AB}) \leq E_{n+1}(\Phi_{AB}), \tag{8}$$

$$E_n(\Phi_{AB}) = E_n(\Phi_{AB} \pm m\Phi_0) = E_n(-\Phi_{AB}), \tag{9}$$

where $n, m = 0, 1, 2\ldots$

At zero temperature, the ground-state energy is given by the sum of single-particle energies of levels below the Fermi energy E_F,

$$E_{\text{gs}}(\Phi_{AB}) = 2\sum_{E_n(\Phi_{AB})<E_F} E_n(\Phi_{AB}). \tag{10}$$

where the factor 2 is due to spin degeneracy. At higher temperature, the levels are occupied according to the Fermi-Dirac distribution function.

Persistent current

One of the important consequences of the Aharonov–Bohm effect in the ring geometry is that there can exist a nonzero steady-state current in the ring. This was first suggested in Büttiker et al. (1983), and was observed experimentally several years later (Schwarzschild, 1986; Levy et al., 1990). The existence of the current is related to the fact that in a magnetic field, time-reversal symmetry is violated and the Hamiltonian is complex (albeit Hermitian). This current is not the usual conduction current where electrons in a metal at the Fermi energy exchange energy with an external electric field. Rather, it is an equilibrium property of the system, and there is no dissipation associated with this current. For the moment, confining our discussion to zero temperature, all the electrons in the levels below the Fermi energy E_F contribute to the current. The current operator can be written as

$$\hat{I} = -c\frac{\partial H}{\partial \Phi_{AB}} = \frac{-e}{L}\left[\frac{1}{m}(p + \frac{e\Phi_{AB}}{cL})\right] = \frac{-e}{L}\hat{v}, \tag{11}$$

where $\hat{v}$ is the velocity operator. The contribution of level n below the Fermi energy to the current is obtained by taking the expectation value of $\hat{I}$ with the wave function ψ_n. Using the Feynman-Hellman theorem, we can equate the expectation $\langle\psi_n|\frac{\partial H}{\partial \Phi_{AB}}|\psi_n\rangle$ to $\frac{\partial E_n(\Phi_{AB})}{\partial \Phi_{AB}}$. The total current at zero temperature is then given by

$$I(\Phi_{AB}) = -c\sum_{E_n(\Phi_{AB})<E_F}\frac{\partial E_n(\Phi_{AB})}{\partial \Phi_{AB}} = -c\frac{dE_{\text{gs}}}{d\Phi_{AB}}. \tag{12}$$

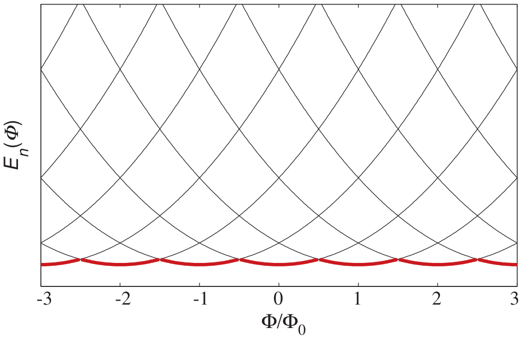

Fig. 2 Energy eigenvalues $E_n(\Phi_{AB})$ versus magnetic flux Φ_{AB}/Φ_0. Level crossings occur at $\Phi_{AB} = m\Phi_0$ and $\Phi_{AB} = (m + 1/2)\Phi_0$ in a clean system (m=integer). However, any amount of disorder or imperfection leads to avoided crossings and a pattern of energy bands with small gaps between them. For any fixed value of the flux, the levels should be ordered from low energy to higher energy. The ground-state energy of a single electron is shown as the thick red line. With this ordering, the spectrum is a periodic function of the flux with period Φ_0. Taken from Band Y and Avishai Y (2012) Quantum Mechanics with Application to Nanotechnology and Information Science, Elsevier.

As a result of the properties of the spectrum listed above, it is clear that the current is a periodic function of Φ_{AB} with period Φ_0 and is an antisymmetric function of the flux

$$I(\Phi_{AB}) = -I(-\Phi_{AB}), \quad I(\Phi_{AB} + m\Phi_0) = I(\Phi_{AB}). \tag{13}$$

The above analysis is pertinent to a one-dimensional metallic ring geometry. It is worthwhile mentioning other geometries. Persistent current is analyzed for a Corbino disk geometry (Avishai et al., 1993; Avishai and Kohmoto, 1993; Yerin et al., 2021), and for a closed flux line of arbitrary shape and size (Heras, 2022). The Aharonov–Bohm effect for an electron on a spherical shell was discussed by Wu and Yang (1975).

What happens if the ring is not "clean," for example, if a disordered potential is present in the ring? (Altshuler et al., 1981; Imry, 1997). In this case, the electrons can be scattered elastically from numerous fixed scattering centers. Such scattering centers are related to imperfections and impurities. Experimentally, they are often unavoidable. In many cases, the positions and potential strengths of these impurities are generically random; this kind of potential is called *quenched disorder*. The main consequences of the presence of quenched disorder in the ring are as follows:

1. Level crossings shown in Fig. 2 are avoided and the dependence of energy levels on the flux is smooth.
2. The periodicity and symmetry relations of the energy and current remain unchanged. The Fourier expansion of the current is

$$I = \sum_{k=1}^{\infty} I_k \sin(2\pi k \Phi_{AB}/\Phi_0). \tag{14}$$

   In some experiments, the current is found to have an effective period of $\Phi_0/2$ because, in the presence of weak disorder, the dominant Fourier components have even k (Imry, 1997).
3. In the presence of quenched disorder, the wave functions in one dimension decay exponentially at long distance with some characteristic length scale ξ which depends on energy and strength of disorder, and referred to as the *localization length*. This phenomena is termed as *Anderson localization* (Anderson 1958). Thus, if the ring size is such that $L > \xi$, we expect the current to decay exponentially with L.
4. For $L < \xi$, the current persists and is measurable.
5. The order of magnitude of persistent current in the presence of quenched disorder depends on the experimental situation. There are experiments on a single ring and then one speaks of a *sample-specific* persistent current. In this case the order of magnitude is E_c/Φ_0, where according to the Thouless relation, $E_c = \hbar D/\ell^2$ (Edwards and Thouless 1972; Altland et al. 1996), where D is the diffusion constant and ℓ is a typical random walk step.

   On the other hand, experiments involving hundreds of rings are referred to as *impurity-ensemble* experiments. The contribution of many currents tends to cancel out since it has, for example, a random slope at the origin ($\Phi_{AB} = 0$). Thus, ensemble averaging is expected to reduce the magnitude of the persistent currents. Calculations pertaining to weak disorder performed at finite temperature within the grand canonical ensemble (Entin-Wohlman and Gefen, 1989) conclude that after sample averaging, the persistent current virtually vanishes. "Grand canonical" means in this connection that the rings are taken to be connected to a particle bath at temperature T, having a chemical potential μ, and the electron number N may change with Φ_{AB} in each ring.

An important aspect of the behavior of such systems is how the interaction between electrons affects the persistent current. Numerical calculations (Berkovits and Avishai, 1995, 1996) reveal significant interaction-induced enhancement of persistent currents in 2D disordered cylinders. In the paper by Entin-Wohlman et al. (2003), it is shown that persistent currents in interacting Aharonov–Bohm interferometers are enhanced by acoustic radiation. See also Zvyagin (2020).

Aharonov–Bohm interferometer

Electron-based interferometry is a powerful method for probing coherent quantum phenomena in condensed matter physics. An example of the relevance of the Aharonov–Bohm effect in a nonequilibrium situation is an electron interferometer, which is experimentally easier to control than an isolated ring. The measured quantities are conductance and current, which are easier to measure than the persistent current. The underlying tool used to calculate these observables is quantum scattering theory. The Aharonov–Bohm interferometer highlights some fundamental concepts in quantum mechanics such as interference, coherence (Imry, 1995), gauge invariance, current conservation, and Onsager reciprocity relations (Onsager, 1931).

In its simplest version, an Aharonov–Bohm interferometer (see Fig. 3) consists of two one-dimensional ideal conductors L and R (for left and right) connected by three port contacts S_L and S_R, sometimes referred to as *splitters*, to an ideal ring-shaped conductor of radius ρ threaded by a central magnetic flux. The conductors are connected on their other side to electron reservoirs at potentials $V_L \gtrsim V_R$ so there is a small potential difference between the left and right reservoirs, and a small current from left to right. There is a single incoming channel and a single outgoing channel, and therefore, according to the Landauer formula (Landauer, 1957; Büttiker et al., 1985), the conductance of the interferometer (in units of the quantum conductance $G_0 \equiv e^2/h$) is equal to the transmission coefficient. The magnetic field vanishes everywhere except at the small aperture marked as black circle. The electrons stay on the wires of the interferometer and do not reach the region where the magnetic field is present. Nevertheless, the transmission (and hence the conductance) depends on the magnetic flux. This is a purely quantum mechanical effect with no classical analog.

To describe the underlying physics, it is useful to introduce dimensionless variables using the radius ρ of the ring as the unit of length. The dimensionless coordinate is x (in units of ρ), the wave number is k (in units of $1/\rho$), the dimensionless energy is

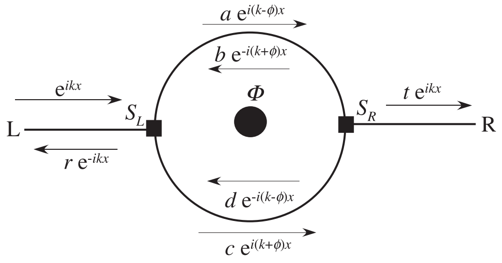

Fig. 3 Schematic illustration of scattering through an Aharonov–Bohm interferometer. Modified from Imry Y (1997) Introduction to Mesoscopic Physics. Oxford University Press. page 110 Fig. 5.4

$\varepsilon = \frac{2mE\rho^2}{\hbar^2} = k^2$ (where E is the energy in physical units), and the dimensionless magnetic flux is $\phi = \Phi_{AB}/\Phi_0$, where $\Phi_0 \equiv \frac{hc}{e}$. The incoming plane wave with (dimensionless) energy $\varepsilon = k^2$ propagates toward the interferometer from the left and is partially reflected at S_L leftward with reflection amplitude r and partially transmitted into the two arms of the ring. After traveling through the two arms of the ring, it is partially transmitted at S_R with transmission amplitude t at partially reflected back to the arms of the ring. The goal is to calculate the transmission and hence, according to the Landauer formula (Landauer, 1957), the conductance $G(k, \Phi_{AB}) = 2\frac{e^2}{h}|t|^2$. The external flux is a convenient control parameter, and the dependence of $G(k, \Phi_{AB})$ on energy and magnetic flux reflects the roles of quantum interference (at the splitters) and gauge invariance (the periodicity of $G(k, \Phi_{AB})$). Note that the system cannot be regarded as purely one dimensional since part of it (the ring with the flux) is not simply connected. The calculation requires finding the two linearly independent solutions on every 1D arm of the ring and matching the solutions at the two splitters. The motion of the electron on the ring is governed by the Schrödinger equation in the presence of magnetic flux. The variable x in Fig. 3 assumes values $-\infty < x \leq 0$ on L, $0 \leq x < \infty$ on R and $0 \leq x \leq \pi$ on either arm of the ring where $x = 0$ at S_L. Gauge invariance requires that all measurable quantities are periodic functions of ϕ with period 1, and Onsager reciprocity relations require that the conductance is symmetric with respect to ϕ (see Eq. (19). Thus, we have

$$-\frac{d^2}{dx^2}\psi(x) = k^2\psi(x), \quad (x < S_L, \quad x > S_R), \tag{15a}$$

$$\left(-i\frac{d}{dx} + \phi\right)^2 \psi(x) = k^2\psi(x), \quad (S_L \leq x \leq S_R). \tag{15b}$$

The solutions corresponding to an incoming wave from the left (see Fig. 3) are

$$\psi(x) = e^{ikx} + r\ e^{-ikx} \quad (x < S_L), \tag{16a}$$

$$\psi(x) = t\ e^{-ikx} \quad (x > S_R), \tag{16b}$$

$$\psi(x) = a\ e^{i(k-\phi)x} + b\ e^{-i(k+\phi)x}(S_L \leq x \leq S_R, \text{ upper arm}), \tag{16c}$$

$$\psi(x) = c\ e^{i(k+\phi)x} + d\ e^{-i(k-\phi)x}(S_L \leq x \leq S_R, \text{ lower arm}). \tag{16d}$$

The junctions at points S_L and S_R are referred to as splitters. The precise relations between the incoming and outgoing amplitudes at each splitter depend on the detailed structure of the device. The only restriction is that current should be conserved at each splitter. To satisfy this restriction, we characterize the splitters S_L and S_R by two unitary 3×3 S matrices $\mathcal{S}_L$ and $\mathcal{S}_R$ relating the three amplitudes of the incoming waves in the junction to the three amplitudes of the outgoing waves at this junction. The form of these S matrices is dictated by the requirements of wave function continuity and current conservation but otherwise they are dependent on the structure of the contacts and the experimental setup. Continuity and current conservation at the two junctions yields

$$\mathcal{S}_L \begin{pmatrix} 1 \\ b \\ d \end{pmatrix} = \begin{pmatrix} r \\ a \\ c \end{pmatrix}, \quad \mathcal{S}_R \begin{pmatrix} 0 \\ ae^{i(k-\phi)\pi} \\ ce^{i(k+\phi)\pi} \end{pmatrix} = \begin{pmatrix} t \\ be^{-i(k+\phi)\pi} \\ de^{-i(k-\phi)\pi} \end{pmatrix}. \tag{17}$$

These are six linear inhomogeneous equations for the six unknowns a, b, c, d, r, and t, which can be solved once the unitary matrices $\mathcal{S}_L$ and $\mathcal{S}_R$ are given. The solution must satisfy continuity of the wave function at the junction and obey the current conservation constraint (Kirchhoff's law). These constraints determine the form of the unitary matrices in the splitters (Shapiro, 1983),

$$\mathcal{S}_L = \mathcal{S}_R = \begin{pmatrix} 0 & -\frac{1}{\sqrt{2}} & -\frac{1}{\sqrt{2}} \\ -\frac{1}{\sqrt{2}} & \frac{1}{2} & -\frac{1}{2} \\ -\frac{1}{\sqrt{2}} & -\frac{1}{2} & \frac{1}{2} \end{pmatrix}. \tag{18}$$

Current conservation implies that $|t|^2 + |r|^2 = 1$. Another test is that the conductance through the interferometer $G(\phi) = 2\frac{e^2}{h}|t(\phi)|^2$ (the factor 2 is due to spin degeneracy) should be a symmetric and periodic function of ϕ with period 1

$$G(\phi) = G(-\phi), \quad G(\phi) = G(\phi + 1). \tag{19}$$

The first equality is a special case of a more general set of constraints resulting from the combination of time-reversal invariance and magnetic field reversal, known as *Onsager relations* (Onsager, 1931). The second relation, the periodicity of $G(\phi)$, is a consequence of gauge invariance, as demonstrated in the *Byers-Yang theorem* (Byers and Yang, 1961; Bloch, 1970). As already discussed above, it states that every physical quantity that is measured in a system which is not simply connected and threaded by a magnetic flux Φ_{AB} is a periodic function of Φ_{AB} with period given by the flux quantum $\Phi_0 = hc/e$.

This system is a beautiful manifestation of the Aharonov–Bohm effect, and, in addition, reveals numerous fundamental concepts in quantum mechanics (Gefen et al., 1984; van Oudenaarden et al., 1998; Cheung et al., 1989; Entin-Wohlman and Gefen, 1989; Aharony et al., 2002, 2003; Entin-Wohlman et al., 2004; Aharony et al., 2005, 2006, 2014, 2019). The example analyzed above involves only two-port systems. The scattering theory and Aharonov–Bohm effect in multi-port systems have been developed in Büttiker (1985), Büttiker (1986), Imry (1986), Avishai and Band (1987), Büttiker (1988), Büttiker (2901), Büttiker (1992), and Cernicchiaro et al. (1997).

The Aharonov–Bohm effect was predicted to be a possible tool for identifying the set of sites visited by a wave packet such that for particular values of the magnetic flux, the wave packet is bound, and this effect is referred to as Aharonov–Bohm caging (Vidal et al., 1998, see also Vaidman, 2000). This effect was recently observed in cold atom systems (Li et al., 2022). Peculiar aspects of the Aharonov–Bohm effect in graphene are reported by Recher et al. (2007) and Rycerz and Beenakker (2007), and in molecular physics by Sjoqvist (2014). Recently, two experiments were performed manifesting the Aharonov–Bohm effect in the study of anyons (Ronen et al., 2021) (using a Fabry–Pérot quantum Hall interferometer), and (Hemanta et al., 2023) using a Mach–Zehnder interferometer. Both experiments exposed the unconventional exchange statistics of these exotic quasiparticles which occur only in two-dimensional systems, and play a crucial role in the fractional quantum Hall effect. The latter experiment also studies the braiding phases of anyons.

Aharonov–Casher effect

The Aharonov–Casher effect (Aharonov and Casher, 1984; Aharonov et al., 1988; Bergsten et al., 2006; Rohrlich, 2009) is an astounding quantum phenomena which is related to the Aharonov–Bohm effect. The relation is sketched in Fig. 4. The Aharonov–Casher effect occurs when a particle with nonzero magnetic moment $\boldsymbol{\mu} = g\mu_B\mathbf{S}/\hbar$ moves in a doubly connected region and is affected by an *electric field* that leads to spin–orbit interaction. The particle need not be charged. It can be an electron (Köenig et al., 2006), a neutron (Cimmino et al., 1989), a magnetic vortex (Elion et al., 1993), or a neutral atom with nonzero spin. An essential point is that no force acts on the particle. In condensed matter physics, the effect is mainly relevant for electrons (Mathur and Stone 1992; Bogachek and Landman 1994; Frustaglia and Richter 2004; Saarikoski et al. 2015; Frustaglia and Nitta 2020; Shekhter et al., 2022).

First we consider a simple case wherein an electron moves on a ring threaded through its center by a charged line of charge density λ which is perpendicular to the plane of the ring. The setup is shown in Fig. 4B, where a comparison of the ring geometries of the Aharonov–Bohm (see Fig. 4A) and Aharonov–Casher effects is illustrated.

A heuristic explanation of the role of spin–orbit in the Aharonov–Casher effect (Aharonov and Casher 1984) for charged particles, for example, electrons, goes as follows: A particle (say, an electron of mass m_e), subject to an electric field $\mathbf{E}$ feels, in its rest frame, an effective magnetic field $\mathbf{H}_{\text{eff}} = (\mathbf{v}/c) \times \mathbf{E} = \frac{1}{m_e c}\mathbf{p} \times \mathbf{E}$, where $\mathbf{v}$ is the particle's velocity and $\mathbf{p}$ is its momentum. This results in an effective Zeeman Hamiltonian, $H_Z \equiv -\boldsymbol{\mu} \cdot \mathbf{H}_{\text{eff}} = g(\mu_B/m_e c)(\mathbf{S}/\hbar) \cdot \mathbf{p} \times \mathbf{E}$, where $g \approx 2$ reflects the anomalous magnetic moment of the electron. For an electron subject to an electric field $\mathbf{E}$, the spin–orbit term of the Hamiltonian is written (in proper Hermitian form) as

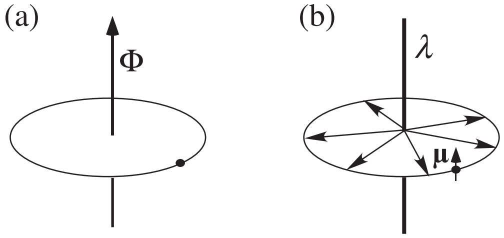

Fig. 4 A schematic illustration of the Aharonov–Bohm and Aharonov–Casher effects. (A) Aharonov–Bohm Effect: An electron moving on a metallic ring threaded by a magnetic flux Φ_{AB}. When the electron encircles the ring, its wave function gains a phase $e^{2\pi i\phi}$, where $\phi = \Phi_{AB}/\Phi_0$. The spin of the electron does not play a role. (B) Aharonov–Casher Effect: An electron with magnetic moment $\boldsymbol{\mu}$ moving on a metallic ring threaded by a charged wire of longitudinal charge density λ. This results in a radial electric field $\mathbf{E} = \frac{\lambda}{L}\hat{\mathbf{r}}$ (black arrows), where R is the radius of the ring. When the electron encircles the ring, its wave function (a two component spinor) is multiplied by a unitary matrix $e^{2\pi i\gamma\sigma_z}$ where $\gamma = \frac{g\mu_B\lambda}{2hc}$. The charge of the electron does not play a role here. Taken from Band Y and Avishai Y (2012) Quantum Mechanics with Application to Nanotechnology and Information Science, Elsevier.

$$H_{\mathrm{so}} = \eta(\mathbf{p}\cdot\boldsymbol{\sigma}\times\mathbf{E} + \boldsymbol{\sigma}\times\mathbf{E}\cdot\mathbf{p}), \tag{20}$$

where $\eta = \frac{g\mu_B}{4m_e c}$. For electrons, the Hamiltonian H_{so} appears in the Pauli Hamiltonian (Pauli, 1927), which arises in the context of working out the nonrelativistic limit of the Dirac equation by expanding it in the Foldy–Wouthuysen scheme (Foldy and Wouthuysen, 1950). It is responsible for a myriad of phenomena. In condensed matter physics, this Hamiltonian is related to the Rashba Hamiltonian (Rashba, 2006; Engel et al., 2006). In contrast with the Hamiltonian H defined in Eq. (6), the Hamiltonian H_{so} is invariant under time reversal that reverses the signs of both $\mathbf{p}$ and $\boldsymbol{\sigma}$.

A simple example of the Aharonov–Casher effect is illustrated by considering the ring geometry shown in Fig. 4B. An electron moving on a ring of radius R experiences a static electric field $\mathbf{E} = \frac{\lambda}{L}\hat{\mathbf{r}}$ produced by a uniformly charged wire with constant charge per unit length λ, stretched along the z-axis passing through the ring's center (here, $L = 2\pi R$). It is instructive to write the Hamiltonian in a form similar to that of Eq. (6),

$$\mathcal{H} = \frac{\mathbf{p}^2}{2m_e} + H_{\mathrm{so}} = \frac{1}{2m_e}\left(\mathbf{p} + \frac{g\mu_B}{2c}\boldsymbol{\sigma}\times\mathbf{E}\right)^2 - \frac{(g\mu_B\mathbf{E})^2}{8m_e c^2}. \tag{21}$$

The term $(\mathbf{p} + \frac{g\mu_B}{2c}\boldsymbol{\sigma}\times\mathbf{E})$ is the *covariant SU(2) momentum* (a 2×2 matrix in spin space), in which the factor $\frac{g\mu_B}{2}\boldsymbol{\sigma}\times\mathbf{E}$ is proportional to an *SU(2) vector potential*. In the ring geometry of Fig. 4B, the magnitude of the electric field is constant but its direction is angle dependent—it points radially outward, $\mathbf{E} = (\lambda/L)\hat{\mathbf{r}}$. The last term on the RHS of (21) is a constant, $\bar{\varepsilon} = \frac{(g\mu_B\mathbf{E})^2}{8m_e c^2}$. The Schrödinger equation for an electron on the ring involves only the angular direction $\hat{\theta}$ along the ring, $\boldsymbol{\sigma}\times\mathbf{E}$ is proportional to σ_z, so

$$\frac{1}{2m_e}\left(p_\theta + \frac{e}{c}\frac{\Phi_{AC}}{L}\sigma_z\right)^2\psi = \varepsilon(\Phi_{AC})\psi, \quad \Phi_{AC} \equiv \frac{g\mu_B\lambda}{2e}. \tag{22}$$

where p_θ is the tangential momentum and the Aharonov–Casher phase $\Phi_{AC} \equiv \frac{g\mu_B\lambda}{2e}$ has units of magnetic flux. Thus, in this simple example, the operator

$$A_\theta \equiv \frac{g\mu_B\lambda}{2eL}\sigma_z = \frac{\Phi_{AC}}{L}\sigma_z \tag{23}$$

can be viewed as a tangential component of a 2 × 2 matrix SU(2) vector potential. The similarity of (6) and (22) is evident. In Eq. (6), Φ_{AB}/L is the vector potential on the ring responsible for the Aharonov–Bohm effect, whereas in Eq. (22), $\Phi_{AC}\sigma_z/L$ can be interpreted as a 2 × 2 matrix vector potential on the ring responsible for the Aharonov–Casher effect. This analogy is not perfect because in the latter case, the energy eigenvalue contains a constant $\bar{\varepsilon} = \left[\frac{e}{c}\frac{\Phi_{AC}}{L}\right]^2$; hence strictly speaking, $\varepsilon(\Phi_{AC})$ is not periodic in Φ_{AC}. However, the ratio between $\bar{\varepsilon}$ and the kinetic energy at the Fermi momentum p_F can be shown to be extremely small; it is legal to assume that $\bar{\varepsilon}$ can safely be neglected. Then, Φ_{AB}/L and $\Phi_{AC}\sigma_z/L$ appear on the same footing as $U(1)$ and $SU(2)$ vector potentials, respectively.

The energy spectrum can be understood in analogy with the discussion of the spectrum of the Aharonov–Bohm system of electrons on a ring. The wave functions for spin-up electrons ($|+\rangle \equiv |\uparrow\rangle$) and spin-down electrons ($|-\rangle \equiv |\downarrow\rangle$) are $\psi_n^{(\pm)}(x) = L^{-1}e^{ik_n x}|\pm\rangle$, where $k_n = \frac{2\pi n}{L}$ with $n = 0, \pm 1, \pm 2, \ldots$, and the energy eigenvalues are

$$E_n^{(\pm)} = \frac{\hbar^2}{2m_e R^2}(n \pm \gamma)^2 - \bar{E} = \frac{\hbar^2}{2m_e R^2}(n^2 \pm 2n\gamma)\ , \tag{24}$$

where $\gamma = \Phi_{AC}/\Phi_0 = \frac{g\mu_B\lambda}{2hc} = \frac{ge\lambda}{2\pi m_e c^2}$, and $\bar{E} = \frac{(g\mu_B\mathbf{E})^2}{8m_e c^2} = \frac{\hbar^2\gamma^2}{2m_e R^2}$.

Aharonov–Casher effect and non-Abelian gauge transformations

The example discussed above and illustrated in Fig. 4B is a simple particular case wherein the vector potential $\frac{g\mu_B\lambda}{2eL}\sigma_z$ involves a *single Pauli matrix* and a line integral between two points, for example, $\int_{x_q}^{x_p} e^{-i\frac{e}{\hbar c}\frac{\Phi_{AC}}{L}\sigma_z}dx$, makes sense. Generically, (as shown below) $SU(2)$ vector potentials depend on space point $\mathbf{r}$. The components of the $SU(2)$ vector potential along a line involve combinations of Pauli matrices such as $a_x(\mathbf{r})\sigma_x + a_y(\mathbf{r})\sigma_y + a_z(\mathbf{r})\sigma_z$, where the coefficients are real numbers. Thus, in the language of non integrable phase factors, the phase factor Λ_{pq}, Eq. (5), is an element of the $U(1)$ gauge Abelian group represented here by complex numbers on the unit circle. On the other hand, in the Aharonov–Casher effect, we encounter the case where nonintegrable phase factors require integration along a given curve connecting points p and q that should be path ordered, that is, the $SU(2)$ nonintegrable phase factor is

$$\eta_{pq} = \left[\int_{\mathbf{r}_q}^{\mathbf{r}_p} e^{-i\frac{e}{\hbar c}\mathbf{A}\cdot d\mathbf{r}}\right]_{\text{path ordered}}, \tag{25}$$

Gauge theories play a central role in many fields of modern physics. Non-Abelian gauge theories were introduced into physics in a seminal paper (Yang and Mills, 1954).

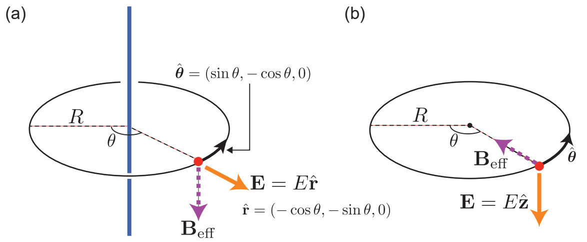
(a)
(b)
$\hat{\boldsymbol{\theta}} = (\sin\theta, -\cos\theta, 0)$
R
θ
$\mathbf{E} = E\hat{\mathbf{r}}$
$\hat{\mathbf{r}} = (-\cos\theta, -\sin\theta, 0)$
$\mathbf{B}_{\text{eff}}$
R
θ
$\mathbf{B}_{\text{eff}}$
$\hat{\boldsymbol{\theta}}$
$\mathbf{E} = E\hat{\mathbf{z}}$

Fig. 5 Two cases where an electron on a ring is subject to an electric field that is responsible for spin–orbit coupling. (A) As in Fig. 4B, the electron is subject to a *radial electric field* $\mathbf{E} = E\hat{\mathbf{r}}$ generated by an infinite uniformly charged wire stretched along the ring axis. In its rest frame, the electron feels a constant effective magnetic field along $\hat{\mathbf{z}}$. In (B), the electric field (generated, e.g, by a gate voltage) is perpendicular to the ring $\mathbf{E} = E\hat{\mathbf{z}}$. Note that in (A) the effective magnetic field is constant and the phase factor is calculated by an ordinary integral. However, in (B) the electric field generates a *position-dependent effective magnetic field*, and the phase factor is calculated by a path-ordered integral as in Eq. (25). The pertinent coupling is referred to as *Rashba spin–orbit coupling*. Taken from Avishai Y, Totsuka K, and Nagaosa N (2019) AharonovCasher Phase Factor in Mesoscopic Systems. Journal of the Physical Society of Japan 88(8): 084705.

Examples in condensed matter physics

Let us consider an electron moving on a metallic ring of radius R lying on the plane $z = 0$ centered at the origin of the x-y plane (Meijer et al., 2002). Its position is specified by the polar vector $\mathbf{r} = (R, \theta)$ (see Fig. 5B).

The electron is subject to an electric field $\mathbf{E} = E\hat{\mathbf{z}} \perp \hat{\boldsymbol{\theta}}$. Introducing R as the length unit enables us to rewrite the corresponding Schrödinger equation for the electron on the ring in terms of dimensionless quantities. The mechanical momentum is $p_\theta = -i\frac{d}{d\theta}$. Within the SU(2) formulation of the Pauli equation (Pauli, 1927; Anandan, 1989; Fröhlic and Studer, 1993), the SU(2) vector potential in the ring geometry takes the form

$$A(\theta) = \beta(\theta)\hat{\mathbf{E}}(\theta) \times \boldsymbol{\sigma}, \tag{26}$$

where the real parameter $\beta(\theta)$ specifies the strength of the local spin–orbit coupling (Meir et al., 1989, 1990; Entin-Wohlman et al., 1992) (compare with Eq. (23) applicable for case Fig. 5B). For simplicity it is assumed that β is independent of θ. For example, if the Rashba Hamiltonian [relevant for the present discussion based on figure 5 (b)] is written as $H_{\text{R}} = -\alpha_{\text{R}}(\boldsymbol{\sigma} \times \mathbf{p}) \cdot \hat{\mathbf{E}}$ (where $\alpha_{\text{R}} = -\frac{1}{2mc} g\mu_{\text{B}}|\mathbf{E}|$ is the Rashba SOC strength parameter), then $\beta = 2mR\alpha_{\text{R}}/\hbar^2$.

In the present ring geometry, $\mathbf{k}$ is parallel to the tangential unit vector $\hat{\boldsymbol{\theta}}$ and we are concerned only with the tangential component of $A(\theta)$, that is an element of the su(2)-algebra,

$$\mathcal{A}(\theta) = A(\theta) \cdot \hat{\boldsymbol{\theta}} = \beta[\hat{\boldsymbol{\theta}} \times \hat{\mathbf{E}}] \cdot \boldsymbol{\sigma} \equiv \beta\ \hat{\mathbf{n}} \cdot \boldsymbol{\sigma}\ [\in \text{su}(2)]. \tag{27}$$

Classically, $\hat{\boldsymbol{\theta}} \parallel \mathbf{v}$ (where $\mathbf{v}$ is the electron velocity) so that $\hat{\mathbf{n}}$ points along $\mathbf{E} \times \mathbf{v}$ that is the direction of the effective magnetic field $\mathbf{B}_{\text{eff}}$ felt by the electron in its rest frame. Quantum mechanically, $\hat{\mathbf{n}}$ encodes the nature of the spin–orbit coupling. In our example for electrons on a ring subject to a perpendicular electric field, $\hat{\mathbf{n}} = \hat{\boldsymbol{\theta}} \times \hat{\mathbf{E}}$. In two-dimensional semiconductors, it is possible to have also an intrinsic spin–orbit coupling (Engel et al., 2006). In one simplified form (Dresselhaus, 1955), derived from the Kane model of $\mathbf{k} \cdot \mathbf{p}$ perturbation theory (Kane, 1957), $\hat{\mathbf{n}}$ is defined through $\hat{\mathbf{n}} \cdot \boldsymbol{\sigma} = \cos\theta\ \sigma_x - \sin\theta\ \sigma_y$ (Engel et al. 2006, Eq. (8)). With the unit vector $\hat{\mathbf{n}}$, the SU(2)-invariant Schrödinger equation (in dimensionless units) for the spinor $\psi(\theta) = \binom{\psi_\uparrow(\theta)}{\psi_\downarrow(\theta)}$ is written as:

$$\left[-i\frac{d}{d\theta} + \beta\ \hat{\mathbf{n}}(\theta) \cdot \boldsymbol{\sigma}\right]^2 \psi(\theta) = \varepsilon\psi(\theta)\ , \tag{28}$$

where $\varepsilon = \frac{2mR^2}{\hbar^2}\mathcal{E} \equiv k^2$, with $\mathcal{E}$ being the electron energy in physical units.

Now we are in a position to express the nonintegrable phase factor. If the SU(2) vector potential is changed from θ to $\theta + d\theta$ along an infinitesimal directed arc $d\ell = R\hat{\boldsymbol{\theta}}d\theta$, it gains an SU(2) *matrix-valued* phase factor according to

$$\mathbf{A}(\theta + d\theta) = e^{i\beta\ \hat{\mathbf{n}}(\theta) \cdot \boldsymbol{\sigma} d\theta}\mathbf{A}(\theta). \tag{29}$$

If the spin–orbit coupling strength β and/or the unit vector $\hat{\mathbf{n}}$ depend on the position θ, two phase factors do not commute. Thus, the SU(2) non integrable phase factor accumulated from $\theta = 0$ up to a finite angle θ is given by the following path-ordered integral, or equivalently, an ordered product of infinitesimal phase factors (Wu and Yang 1975, Anandan 1989). The *non-Abelian* gauge transformation $\psi(\theta) \to \xi(\theta)$ that eliminates the vector potential is

$$\begin{aligned}\psi(\theta) &= \mathcal{P}\exp\left\{\int_0^\theta i\beta\ \hat{\mathbf{n}}(\theta')\cdot\boldsymbol{\sigma}d\theta'\right\}\xi(\theta)\\ &= \lim_{N\to\infty}\left\{\prod_{\substack{j=1\\ \longleftarrow}}^{N} \mathrm{e}^{i\beta\ \hat{\mathbf{n}}(j\Delta\theta)\cdot\boldsymbol{\sigma}\Delta\theta}\right\}\xi(\theta)\equiv\Lambda_{\mathrm{AC}}[\theta;\beta]\xi(\theta),\end{aligned} \tag{30}$$

where $\mathcal{P}$ is path ordering, $\Delta\theta = \theta/N$, and the arrow ← means that matrices are multiplied from the right to the left. The 2 × 2 matrix function $\Lambda_{\mathrm{AC}}[\theta;\beta]$ satisfies a first-order differential equation that can be solved analytically (Avishai et al., 2019). The function $\xi(\theta)$ then satisfies Eq. (28) in the absence of the vector potential. The procedure of multiplying phase factors as in Eq. (30) and defining λ_{AC} by Eq. (31) can be extended straightforwardly to any continuous closed curve.

Since the gauge transformation $\Lambda_{\mathrm{AC}}[\theta;\beta]$ is an SU(2) matrix, it can be written as $\Lambda_{\mathrm{AC}}[\theta;\beta] = \mathrm{e}^{i\lambda(\theta,\beta)\hat{\mathbf{b}}[\theta,\beta]\cdot\boldsymbol{\sigma}}$, where $\lambda(\theta,\beta)$ and the two dimensional unit vector $\hat{\mathbf{b}}[\theta,\beta]$ should be calculated within a given spin–orbit coupling scheme (see for example, the analysis of the scattering in the square geometry below). The Aharonov–Casher phase λ_{AC} is here defined as a single number in terms of the SU(2) phase acquired along the entire circle:

$$F_{\mathrm{AC}}[2\pi;\beta] = \mathcal{P}\exp\left\{\oint i\beta\ \hat{\mathbf{n}}(\theta')\cdot\boldsymbol{\sigma}d\theta'\right\} \equiv e^{i\lambda_{\mathrm{AC}}\hat{\mathbf{b}}\cdot\boldsymbol{\sigma}} = \underbrace{\cos\lambda_{\mathrm{AC}}\ \mathbf{1}_{2\times2}}_{\text{nonvanishing trace}} + \underbrace{i\sin\lambda_{\mathrm{AC}}\ \hat{\mathbf{b}}\cdot\boldsymbol{\sigma}}_{\text{traceless}}. \tag{31}$$

Consequently, three real parameters, that is, the angle λ_{AC} and the two-component unit vector $\hat{\mathbf{b}}$ determine the Aharonov–Casher phase factor unambiguously. The wave function $\psi(\theta) = \Lambda_{\mathrm{AC}}[\theta;\beta]\xi(\theta)$ should be periodic, that is, $\psi(2\pi) = \psi(0)$, and this equality determines the energy eigenvalues.

In analogy with persistent charge current discussed in relation to the Aharonov–Bohm effect we encounter here the possible occurrence of *spin current* (Sun and Xie 2005; Niu 2006). It is formally defined as $J_S(\theta) = \frac{1}{2}\psi^\dagger(\theta)\{\mathbf{v},\boldsymbol{\sigma}\}\psi(\theta)$, where $\mathbf{v} = \left[-i\frac{d}{d\theta} + \beta\ \hat{\mathbf{n}}(\theta)\cdot\boldsymbol{\sigma}\right]$ is the velocity operator. Unlike charge current, spin current is time reversal invariant and (generically) space dependent.

Aharonov–Casher interferometer in a perpendicular electric field

Having studied the physics of an Aharonov–Bohm interferometer, it is expected, following an experiment by Borunda et al. (2008), that there is an analogous system for the Aharonov–Casher effect. The setup of a simple example of Aharonov–Casher interferometer is illustrated in Fig. 6. To write down the Schrödinger equation, we use, as before, dimensionless quantities. The electron wave function at point $\mathbf{r}$ (any point on the ring or on either wire) for a boundary condition that an initial incoming electron has spin projection σ is expressed as a spinor: $\Psi_\sigma(\mathbf{r}) = \binom{\psi_{\uparrow\sigma}(\mathbf{r})}{\psi_{\downarrow\sigma}(\mathbf{r})}$. The two spinors for the spin projections $\sigma =\uparrow,\downarrow$ of the incoming electron can be arranged into a 2 × 2 wave function matrix

$$\boldsymbol{\Psi}(\mathbf{r}) = \begin{pmatrix}\psi_{\uparrow\uparrow}(\mathbf{r}) & \psi_{\uparrow\downarrow}(\mathbf{r})\\ \psi_{\downarrow\uparrow}(\mathbf{r}) & \psi_{\downarrow\downarrow}(\mathbf{r})\end{pmatrix},$$

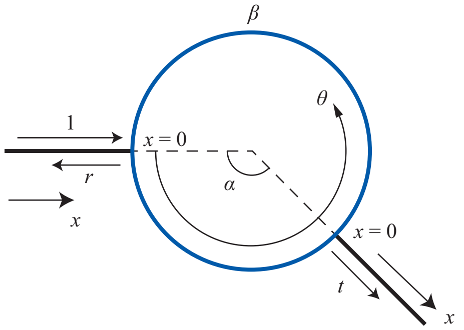

Fig. 6 Aharonov–Casher Interferometer: Similar to Fig. 3, two wires at different potentials $V_L \gtrapprox V_R$ are connected to a metallic ring. Electrons approaching the ring from the left at polar angle $\theta = 0$ are partially reflected back to the left wire and partially transmitted to the right wire at polar angle $\theta = \alpha$ (reflection matrix *r* and transmission matrix *t*). The ring is subject to a perpendicular electric field so that the Rashba spin–orbit mechanism generates an effective magnetic field along the radial direction $\hat{\mathbf{n}}(\theta) = (\cos\theta, \sin\theta, 0)$ (Fig. 5B). The electric field is *homogeneous and acts only on the circular area confined by the ring.* The local phase factor for **any** polar angle θ is $e^{i\beta\ \hat{\mathbf{n}}(\theta)\cdot\boldsymbol{\sigma}}$. Taken from Avishai et al. (2019), where an analysis of Aharonov–Casher interferometer subject to some version of Dresselhaus spin–orbit coupling is also analyzed. Taken from Avishai Y, Totsuka K, and Nagaosa N (2019) Aharonov–Casher Phase Factor in Mesoscopic Systems. Journal of the Physical Society of Japan 88(8): 084705.

so we have

$$\begin{cases} -\dfrac{d^2}{dx^2}\mathbf{\Psi}(x) = k^2\mathbf{\Psi}(x), \quad \text{(when the electron is on left or right wire)} \\ \left[-i\frac{d}{d\theta} - \beta\hat{\mathbf{n}}(\theta)\cdot\boldsymbol{\sigma}\right]^2\mathbf{\Psi}(\theta) = k^2\mathbf{\Psi}(\theta) \quad \text{(when the electron is on the ring).} \end{cases} \tag{32}$$

We consider an electron with spin projection $\sigma = \uparrow, \downarrow$ approaching the ring from the left wire at energy $\varepsilon = k^2$. It is partly transmitted into the right wire with spin projection $\mu = \uparrow, \downarrow$ and partly reflected back into the left wire with $\mu = \uparrow, \downarrow$. The corresponding matrix elements of the 2×2 transmission and reflection matrices are $t_{\mu\sigma}$, $r_{\mu\sigma}$, explicitly

$$t = \begin{pmatrix} t_{\uparrow\uparrow} & t_{\uparrow\downarrow} \\ t_{\downarrow\uparrow} & t_{\downarrow\downarrow} \end{pmatrix} \quad r = \begin{pmatrix} r_{\uparrow\uparrow} & r_{\uparrow\downarrow} \\ r_{\downarrow\uparrow} & r_{\downarrow\downarrow} \end{pmatrix}.$$

The technique for calculating t and r is similar to that used in the Aharonov–Bohm interferometer, but is slightly more complicated. The conductance through the interferometer is given by the Landauer formula (Landauer, 1957), $g = \frac{e^2}{h}\text{Tr}[t^\dagger t]$.

Fig. 7 plots the cosine of the Aharonov–Casher phase λ_{AC} and the conductance g (in units of $\frac{e^2}{h}$) as a function of the spin–orbit strength β for two values of the right splitter angle α.

Conductance and polarization in transmission through a square interferometer

It was shown in the discussion of Eq. (31) that the SU(2) phase factor $e^{i\lambda_{\text{AC}}\hat{\mathbf{b}}\cdot\boldsymbol{\sigma}}$ can be written as a sum of two 2×2 matrices, one has nonvanishing trace and one is traceless. Both depend on the Aharonov–Casher phase λ_{AC}, but the role of the traceless term (in particular the unit vector $\hat{\mathbf{b}}$) was not explained. Using a relatively simple tight-binding model that can be solved analytically, it will be shown that this term is responsible for electron polarization. Note that spin–orbit coupling obeys time reversal invariance but the specification of scattering boundary condition destroys it so that polarization is feasible (Meijer et al., 2005; Entin-Wohlman et al., 2010; Nagasawa et al., 2012, 2013; Avishai and Band, 2017).

It can be shown (Avishai et al., 2019) that in two-port systems like the Aharonov–Casher interferometer discussed above, there is no polarization in the outgoing lead (assuming that the incoming beam is not polarized). Here we show that in a multiport system, it is possible to get a polarized outgoing beam due to Rashba spin–orbit coupling. Consider, as in Fig. 8, a tight-binding model of noninteracting electrons moving along two wires and scattered from a region that carries an SU(2) flux where the phase factors in the product do not commute and depend on the spin–orbit strength. The system is laid on the $x-z$ plane and consists of two chains (metallic wires) numbered $\alpha = 1, 2$ with each chain consisting of sites $-\infty < n < \infty$, which are then connected to each other by the two rungs of the square at $n = 0$ and $n = 1$ (see Fig. 8). A uniform electric field acts along $\hat{\mathbf{y}}$ upon the square, thereby lead to a Rashba spin–orbit coupling along the links of the square. This tight-binding model is treated within the formalism of second quantization.

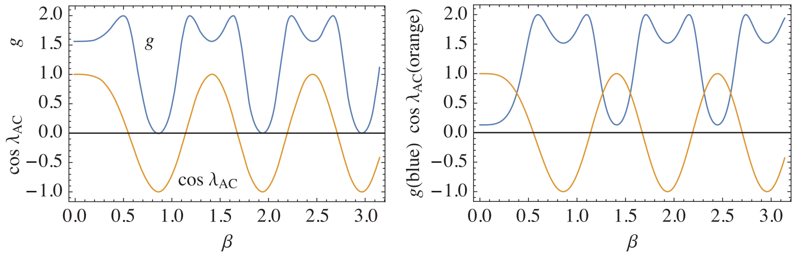

(a) (b)

Fig. 7 Plots of dimensionless conductance g (*blue curve*) and cosine of the Aharonov–Casher phase $\cos\lambda_{\text{AC}}$ (*orange curve*) as function of spin–orbit strength β for the ring interferometer schematically depicted in Fig. 6. The wave number is set to $kR = 1.25$, and (A) $\alpha = \pi$, and (B) $\alpha = 1.7$. As a property of the closed loop, λ_{AC} is independent of α. The conductance, that also encodes the geometric properties of the interferometer, naturally depends on α, but in both cases it is periodic in the Aharonov–Casher phase λ_{AC}. Taken from Avishai Y, Totsuka K, and Nagaosa N (2019) Aharonov–Casher Phase Factor in Mesoscopic Systems. Journal of the Physical Society of Japan 88(8): 084705.

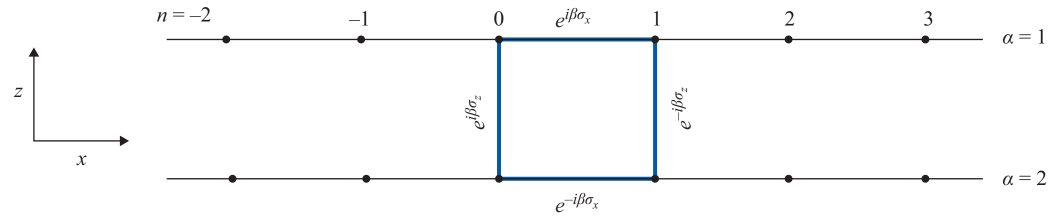

Fig. 8 Two-channel tight-binding model for electron scattering from a square region in the *x-z* plane (shown by *bold blue lines*) subject to a uniform electric field $E\hat{\mathbf{y}}$ acting only on the square. The corresponding SU(2) hopping matrix elements are given by $e^{\pm i\beta\sigma_x}$ along the horizontal links and $e^{\mp i\beta\sigma_z}$ along the vertical links. Taken from Avishai Y, Totsuka K, and Nagaosa N (2019) AharonovCasher Phase Factor in Mesoscopic Systems. Journal of the Physical Society of Japan 88 (8): 084705.

The creation and annihilation operators for the spin projection $\sigma = \uparrow, \downarrow$ are indexed as $c^{\dagger}_{\alpha,n,\sigma}$ and $c_{\alpha,n,\sigma}$, respectively, and the spin–orbit interaction is active only on the four links forming the square (shown by the bold lines in Fig. 8). The Hamiltonian is written as $H = H_0 + H_1$ with

$$\begin{aligned} H_0 = & -t \sum_{\alpha=1,2} \sum_{n \le 0} \mathbf{c}^{\dagger}_{\alpha,-(n+1)} \mathbf{c}_{\alpha,-n} \\ & -t \sum_{\alpha=1,2} \sum_{n \ge 1} \mathbf{c}^{\dagger}_{\alpha,(n+1)} \mathbf{c}_{\alpha,n} + \text{h.c.}, \\ H_1 = & \sum_{n=0,1} \mathbf{c}^{\dagger}_{1,n} e^{-i\beta\sigma_x} \mathbf{c}_{2,n} + \sum_{\alpha=1,2} \mathbf{c}^{\dagger}_{\alpha,0} e^{i\beta\sigma_z} \mathbf{c}_{\alpha,1} + \text{h.c.}, \end{aligned} \tag{33}$$

where $\mathbf{c}^{\dagger}_{\alpha,n} \equiv (c^{\dagger}_{\alpha,n,\uparrow}, c^{\dagger}_{\alpha,n,\downarrow})$.

The solution of the scattering problem yields the 4 × 4 (2 for spin and 2 for channel) transmission and reflection matrices t and r whose matrix elements $t_{\alpha'\sigma';\alpha\sigma}$ and $r_{\alpha'\sigma';\alpha\sigma}$ give the transmission and reflection amplitudes for scattering of a spin-σ electron impinging from channel α to one in the channel α' with spin projection σ'. They depend on the SOC strength, and the wave number k that determines the energy $\varepsilon = -2t \cos k$. On the other hand, the Aharonov–Casher phase λ_{AC} is a property of the closed loop irrespective of the scattering energy. In the present case, it is given by calculating the product of the four matrices shown in Fig. 8, and using Eq. (31), giving

$$\cos \lambda_{\text{AC}}(\beta) = 1 - 2 \sin^4 \beta. \tag{34}$$

Before presenting results related to the scattering problem, it is worthwhile to check the eigenvalue problem of a system of an electron hopping on an isolated square (without wires; the square shown by bold lines in Fig. 8) as a closed system, especially whether they depend only on the Aharonov–Casher phase. The tight-binding Hamiltonian assumes the following form

$$H_{\square} = \begin{pmatrix} 0 & e^{i\beta\sigma_z} & e^{-i\beta\sigma_x} & 0 \\ e^{-i\beta\sigma_z} & 0 & 0 & e^{-i\beta\sigma_x} \\ e^{i\beta\sigma_x} & 0 & 0 & e^{i\beta\sigma_z} \\ 0 & e^{i\beta\sigma_x} & e^{-i\beta\sigma_z} & 0 \end{pmatrix}, \tag{35}$$

where each entry is a 2 × 2 matrix acting on the spin space at each site of the square. Simple calculations show that there are four different eigenvalues each of which is twofold (Kramers') degenerate:

$$E_{\square} = \pm 2 \cos \frac{\lambda_{\text{AC}}(\beta)}{4}, \quad \pm 2 \sin \frac{\lambda_{\text{AC}}(\beta)}{4}. \tag{36}$$

In any case, the eigenvalues depend on β only through $\lambda_{\text{AC}}(\beta)$ as defined in Eq. (34).

The solution of the scattering problem yields the 4 × 4 (2 for spin and 2 for channel) transmission and reflection matrices t and r whose matrix elements $t_{\alpha'\sigma';\alpha\sigma}$ and $r_{\alpha'\sigma';\alpha\sigma}$ give the transmission and reflection amplitudes for scattering of a spin-σ electron impinging from channel α to one in the channel α' with spin projection σ'. They depend on the spin–orbit coupling strength β and the wave number k that determines the energy $\varepsilon = -2t \cos k$. Going back to the scattering problem, we will now inspect the relation between the ACP and a couple of experimental observables. Specifically, we are interested in the conductance g and the transmitted polarization vector $\mathbf{P}$, defined as

$$g(k;\beta) = \text{Tr}[t^{\dagger} t], \quad \mathbf{P} = \frac{\text{Tr}[t^{\dagger} \boldsymbol{\Sigma} t]}{g}, \quad \boldsymbol{\Sigma} = \mathbf{1}_{2\times 2} \otimes \boldsymbol{\sigma}. \tag{37}$$

The following expressions for the conductance g and the transmitted polarization P_y are as follows:

$$\begin{aligned} g &= \frac{16(-5 + 4\cos 2k(1 - \cos \lambda_{\text{AC}}) \sin^2 k}{-17 + 8\cos 2k + 8(\cos 4k - 4\cos 2k)(1 - \cos \lambda_{\text{AC}}) - 16(1 - \cos \lambda_{\text{AC}})^2}, \\ P_y &= \frac{2 \sin 2k(1 - \cos \lambda_{\text{AC}})}{5 - 2\cos 2k(1 - \cos \lambda_{\text{AC}})}, \quad P_x = P_z = 0. \end{aligned} \tag{38}$$

When the spin–orbit coupling strength $\beta \to 0$ then $\lambda_{\text{AC}} \to 0$. The conductance remains finite but the polarization vanishes (as it must). But when $\lambda_{\text{AC}} \to 0$, the traceless part of the Aharonov–Casher phase factor in Eq. (31) tends to zero as well. Hence, this part of the phase factor is related (albeit in a complex way) to an experimental quantity.

Analogy of Aharonov–Bohm effect in cold atoms physics

In the Aharonov–Bohm effect, electrons (charged particles) encircle a magnetic flux in configuration space. There is a beautiful analog pertaining to *neutral atoms*. When cold atoms are subject to a periodic optical potential the corresponding dynamics is similar to that of Bloch electrons in crystals, and the wave functions are Bloch functions at crystal momentum $\mathbf{k}$ and energy $\varepsilon_n(\mathbf{k})$. Since the atoms are neutral, and one cannot speak of Aharonov–Bohm phase. However, moving an atom along a closed curve in $\mathbf{k}$ space endows its wave function with a phase denoted as *Berry phase* (Berry 1984; Xiao et al., 2010).

Thus, in cold atom systems, instead of the Aharonov–Bohm phase, the object of study is the Berry phase, that contains information on the pertinent energy band. In addition, the Berry phase is related to the topological invariant known as the Chern number (Thouless et al., 1982). For a graphene-like optical potential forming a hexagonal lattice, the Berry phase is obtained by moving an atom that encircles a Berry flux along a closed loop C around a Dirac point *in momentum space* (see Fig. 1 in Duca et al., 2015). For a Bloch function $\psi^n_{\mathbf{k}}(\mathbf{r}) = e^{i\mathbf{k}\cdot\mathbf{r}}u^n_{\mathbf{k}}(\mathbf{r})$ corresponding to an energy band n and lattice momentum $\mathbf{k}$, the analog of the vector potential $\mathbf{A}$ is the *Berry connection* $\mathbf{A}_n(\mathbf{k}) = i\langle u^n_{\mathbf{k}}|\nabla_{\mathbf{k}}|u^n_{\mathbf{k}}\rangle$, and the analog of the magnetic field is the *Berry curvature* $\Omega_n(\mathbf{k}) = \nabla_{\mathbf{k}} \times \mathbf{A}_n(\mathbf{k})$. The Berry phase is then defined as

$$\varphi_n = \oint_C \mathbf{A}_n(\mathbf{k})d\mathbf{k} = \int_S \Omega_n(\mathbf{k})d^2k, \tag{39}$$

where S is the area encircled by the curve C in momentum space. The Berry phase includes information on the geometry of the corresponding Bloch band. It is gauge invariant and hence it can be measured. For a graphene hexagonal lattice, the authors of Duca et al. (2015) built an interferometer that enabled the detection of the Berry flux at each Dirac point. Thereby, they could determine the Berry curvature with high momentum resolution.

As it turns out, understanding the physics of multiple bands with degeneracies in topological insulators, requires other concepts beyond the Berry phases. As shown in Li et al. (2016), such systems can be described using the technique of Wilson lines (Yu et al., 2011; Alexandradinata et al., 2014).

Chern numbers are topological invariants that classify bands in topological materials (Hasan and Kane, 2010; Asbóth et al., 2016 ; Qi and Zhang, 2011; Goldman et al., 2014; Cooper et al., 2019). They can be calculated using the Berry curvature of the band (Fukui et al., 2005). The Chern numbers determine properties of the edge state of materials. This generalization of Aharonov phase has become a very important part of condensed mater physics.

Magnetic monopoles

A magnetic monopole is an elementary particle with a magnetic charge. The existence of a magnetic monopole would violate Gauss's law for magnetism $\nabla \cdot B = 0$ and help to explain the law of charge quantization as formulated by Dirac (1931). So far, magnetic monopoles have not been observed (Milton, 2006). The theoretical investigation of Dirac monopoles is extremely rich but will not be considered here.

In condensed matter physics (specifically in strongly interacting systems), there are objects that behave as monopole (although they do not exist as elementary particles) are encountered. An example is that of quasi-particles with fractional charge (suggested by Laughlin) in the fractional quantum Hall effect (Willet et al., 2013; Nakamura et al., 2019). In spin ice materials, electron correlations lead to phenomena that are similar to those of magnetic monopoles (e.g., see Castelnovo et al., 2008; Diamentiny et al., 2021, and references therein) but, again, they should not be confused with elementary particles having magnetic charge. An experimental imitation of a magnetic monopole at the tip of a long nanoscopically thin magnetic needle was reported in Béché et al. (2014).

Dirac quantization and phase factors

If a monopole does exist, it is interesting to consider the spectrum of an electron of charge $-e$ in the central field of a monopole of magnetic charge g such that the magnetic field is $\mathbf{B} = g\frac{\widehat{\mathbf{r}}}{r^2}$, and as shown in Wu and Yang (1975), in this case there does not exist a singularity-free vector potential $\mathbf{A}(\mathbf{r})$ in 3D space. To show this, assume the monopole to be fixed at the origin and denote the electron position in spherical coordinates r, θ, φ. Denote by $\Phi(r,\theta)$ the magnetic flux through a cup bounded by the circular loop r, θ, $0 \le \varphi \le 2\pi$. From Maxwell equations we have,

$$\Phi(r,\theta) = \oint A_\varphi(r,\theta)d\varphi. \tag{40}$$

Evidently, $\Phi(r,\theta) = 2\pi g(1 - \cos\theta)$. For $\theta = 0$ (the north pole) we indeed get $\Phi(r,0) = 0$, which is reasonable, but for $\theta = \pi$ (the south pole) we get $\Phi(r,\pi) = 4\pi g$ which is not reasonable because the length of the loop is zero. Thus A_φ is singular at $\theta = \pi$ and the concept of phase factors introduced in the "Gauge invariance" section should be reexamined. This singularity is sometimes termed as *the Dirac string*.

The solution to this contradiction (Wu and Yang, 1975) is to divide the spherical shell for fixed r and φ into three regions, $0 \le \theta \le \frac{\pi}{2} - \delta$, $\frac{\pi}{2} - \delta \le \theta \le \frac{\pi}{2} + \delta$ and $\frac{\pi}{2} + \delta \le \theta \le \pi$ where $0 < \delta < \frac{\pi}{2}$. In the first and third regions, the corresponding vector potentials are,

$$\begin{aligned} A_\varphi(r,\theta) &= \frac{g}{r\sin\theta}(1 - \cos\theta) \qquad 0 \le \theta \le \frac{\pi}{2} - \delta, \\ A_\varphi(r,\theta) &= \frac{-g}{r\sin\theta}(1 + \cos\theta) \qquad \frac{\pi}{2} + \delta \le \theta \le \pi, \end{aligned} \tag{41}$$

so that there is no singularity, not at $\theta = 0$ nor at $\theta = \pi$. In the overlap region the two vector potentials are related by a gauge transformation

$$S(\varphi) = e^{\frac{2ige}{\hbar c}\varphi}. \tag{42}$$

Since $S(\varphi)$ must be uniquely defined we must have the Dirac quantization rule,

$$\frac{2ge}{\hbar c} = n = \text{integer}. \tag{43}$$

Wu and Yang then show that if Dirac quantization holds, the concept of phase factors is valid for the description of electromagnetism also if monopoles do exist. In a subsequent paper (Wu and Yang, 1976) the authors introduced the concept of *Dirac monopole without strings*.

Tight-binding spectra on spherical graphs: Avoiding the Dirac string

We now analyze a tight-binding model for an electron in the field of a magnetic monopole, in which the Dirac string is avoided (Avishai and Luck, 2008a). It is based on the use of the *group* $U(1)$ (whose elements are the phase factors) and not on its *algebra* (whose elements are the path integrals of the vector potentials). The simplest example of this model is that of an electron hopping on the vertices of a tetrahedron at whose center there is a magnetic monopole of magnetic charge $g = \frac{n\hbar c}{2e}$. The tetrahedron has $V = 4$ vertices, $F = 4$ faces, and $L = 6$ links. According to Euler theorem $L = F + V - 2$. Denote by $a_i^\dagger$ and a_i the creation and annihilation operators of the electron on vertex i, and by U_{ij} the phase factor between two adjacent vertices i, j by U_{ij} (these are elements of the gauge group U(1) living on these links). The tight-binding Hamiltonian of the system is

$$\widehat{\mathcal{H}} = \sum_{<ij>} a_i^\dagger U_{ij} a_j + h.c, \tag{44}$$

where the sum runs over the $L = 4$ oriented links $\langle\, ij \,\rangle$ of a tetrahedron. The Hamiltonian $\widehat{\mathcal{H}}$ is complex, i.e., it is not invariant under time reversal. One has

$$U_{ij} = U_{ji}^{-1} = U_{ji}^{*}. \tag{45}$$

The product of the phase factors around *each face* is related to the outgoing magnetic flux φ through this face as

$$U_{ij} U_{jk} U_{ki} = e^{(2\pi i\varphi/\Phi_0)}, \tag{46}$$

where $\Phi_0 = \frac{hc}{e}$ is the quantum flux unit. By Gauss's theorem the total outgoing magnetic flux is $\Phi = 4\pi g$ so that $\varphi = \pi g$. The Hamiltonian $\widehat{\mathcal{H}}$ is thus represented by a $V \times V = 4 \times 4$ complex Hermitian matrix $\mathcal{H}$ such that $\mathcal{H}_{ij} = U_{ij}$. It is easy to check that $\mathrm{tr}\mathcal{H} = 0$ and $\mathrm{tr}\mathcal{H}^2 = 2L = 12$. The main step in the explicit construction of the Hamiltonian matrix consists in finding a configuration of the gauge field, i.e., a set of phase factors U_{ij}, so that Eq. (46) is satisfied. This procedure is carried out in Avishai and Luck (2008a) and results in the spectrum shown in Table 1.

Calculations are reported for the five platonic solids tetrahedron, cube, octahedron, dodecahedron, icosahedron (for which the spectrum is periodic in the number of faces F, namely $E(n + F) = E(n)$, $n = 0, 1, \ldots F - 1$), and the fullerene (for which the spectrum is *not periodic in n* because the ratio between the areas of a hexagon and a pentagon is not a rational number.

Relation to Aharonov–Casher effect

In Avishai and Luck (2008b), the authors investigate a tight-binding model for an electron confined to move on a two-dimensional surface with spherical topology and subject to a spin-orbit interaction. The latter is assumed to be generated by the radial electric field produced by a static point charge sitting at the center of the sphere. The tight-binding Hamiltonian considered is a discretization of the familiar form of the spin-orbit Hamiltonian $\boldsymbol{L} \cdot \boldsymbol{S}$. It involves SU(2) hopping matrices (phase factors) of the form $\exp(i\mu\mathbf{n} \cdot \boldsymbol{\sigma})$ living on the oriented links of the graph and $\mathbf{n}$ is a unit vector along the link. For a given structure, the dimensionless coupling constant μ is the only parameter of the model (see below the expression for μ).

Table 1 Energy levels *E* of the tetrahedron and their multiplicities *m*, for each value of the magnetic charge *n* over one period.

n	*E*	*m*
0	3	1
	−1	3
1,3	$\sqrt{3}$	2
	$-\sqrt{3}$	2
2	1	3
	−3	1

For definiteness let us consider an electron hoping on the vertices A, B, C, D of a tetrahedron (a spherical graph of sphere radius R), at whose center O there is a charge $q = Ze$. Denote by Θ the angle of the triangle $A\widehat{O}B$. The tight-binding model is defined by means of the Hamiltonian

$$\widehat{\mathcal{H}} = \sum_{(\mathrm{AB})} \left(\boldsymbol{a}_{\mathrm{A}}^{\dagger} U_{\mathrm{AB}} \boldsymbol{a}_{\mathrm{B}} + \mathrm{h.c.} \right), \tag{47}$$

where the sum runs over the six oriented links (AB) of the tetrahedron, whereas

$$\boldsymbol{a}_{\mathrm{A}}^{\dagger} = \left(a_{\mathrm{A}\uparrow}^{\dagger}, a_{\mathrm{A}\downarrow}^{\dagger} \right), \mathbf{a} = \begin{pmatrix} a_{A\uparrow} \\ a_{A\downarrow} \end{pmatrix} \tag{48}$$

are respectively the electron creation and annihilation operators at site A, and the matrices U_{AB} are elements of the non-Abelian gauge group SU(2), i.e., 2×2 unitary matrices with unit determinant, describing the spin-orbit coupling on an electron hopping from site A to a neighboring site B. In analogy with the Abelian case the phase factor U_{AB} is expressed as a *path-ordered integral*:

$$U_{\mathrm{AB}} = \mathrm{P}\ \exp\left\{ -ig \int_{\gamma(\mathrm{A,B})} (\mathbf{E} \times \boldsymbol{\sigma}) \cdot d\mathbf{r} \right\}, \tag{49}$$

where

$$g = \frac{e}{4mc^2}, \quad \mathbf{E} = q\frac{\mathbf{r}}{r^3}. \tag{50}$$

and $\gamma(A, B)$ is a curve joining A and B. If the path $\gamma(\mathrm{A, B})$. is planar, i.e., entirely contained in the OAB plane, In this case, at every point of the path the infinitesimal vector $\boldsymbol{r} \times d\mathbf{r}$ is perpendicular to the latter plane, i.e., aligned with the vector $\boldsymbol{n}_{\mathrm{AB}} = \widehat{\mathbf{A}} \times \widehat{\mathbf{B}}$. As a consequence, the path-ordering prescription is not needed, and Eq. (49) can be recast as an *ordinary integral*

$$\begin{aligned} U_{\mathrm{AB}} &= \exp\left\{ igq \left(\int_{\gamma(\mathrm{A,B})} \frac{\mathbf{r} \times d\mathbf{r}}{r^3} \right) \cdot \boldsymbol{\sigma} \right\}, \\ &= \exp(i\mu(\Theta)\, \boldsymbol{n}_{\mathrm{AB}} \cdot \boldsymbol{\sigma}) = \cos\mu + \mathrm{i}\sin\mu\, \boldsymbol{n}_{\mathrm{AB}} \cdot \boldsymbol{\sigma}. \end{aligned} \tag{51}$$

The functional form of $\mu(\Theta)$ depends on the form of the planar curve $\gamma(A, B)$. Intuitively, we can choose either a link or an arc of a great circle joining A and B. Consequently, we are left with the following expression for the parameter μ, for both choices of the path $\gamma(\mathrm{A, B})$:

$$\mu(\Theta) = \varepsilon \times \begin{cases} 2\tan(\Theta/2) & (\text{path along link}), \\ \Theta & (\text{great-circle path}) \end{cases} \tag{52}$$

with

$$\varepsilon = \frac{gq}{R} = \frac{qe}{4mc^2 R}, q = Ze. \tag{53}$$

An analysis of the energy spectrum is carried out for the five Platonic solids (tetrahedron, cube, octahedron, dodecahedron, and icosahedron) and the C_{60} Fullerene. Except for the latter, the μ-dependence of all the energy levels is obtained analytically in closed form (Table 2).

Special values of μ. The following two values of the parameter μ:

$$\mu_0 = \Theta/2, \quad \mu_1 = \Theta/2 + \pi, \tag{54}$$

are special in several respects. First, the $\mu \leftrightarrow \Theta - \mu$ symmetry and the semi-periodicity imply that μ_0 and μ_1 are symmetry axes of the energy spectrum, if displayed as a function of μ. Second, the Kramers degeneracy and the $\mu \leftrightarrow \Theta - \mu$ symmetry imply that all energy levels are at least fourfold degenerate, i.e., that all the multiplicities are integer multiples of 4. Third, there is a striking

Table 2 Energy levels $E_a(\mu)$ of the tetrahedron and their multiplicities m_a. Horizontal lines separate groups of levels related to each other by the $\mu \leftrightarrow \Theta - \mu$ symmetry.

a	E_a	m_a
1	$3\cos\mu$	2
2	$-cos\mu + 2\sqrt{2}\sin\mu$	2
3	$\sqrt{3}$	2
	$-\sqrt{3}$	2
3	$-cos\mu - 2\sqrt{2}\sin\mu$	4

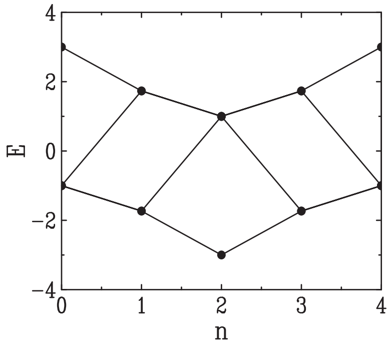

Fig. 9 Energy levels E of the tetrahedron as a function of the magnetic charge n over one period. Line segments show how individual levels 'jump' as n is increased by one unit.

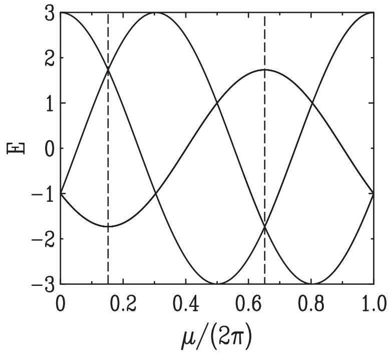

Fig. 10 Plot of the energy spectrum of the tetrahedron against $\mu/(2\pi)$ over one period. *Vertical dashed lines*: symmetry axes at the special values of μ given in Eq. (54). The energies at the intersection point of the first vertical dashed line are identical with the two energies corresponding to the energies of an electron in the field of $n = 1$ quantized magnetic dipole, shown in Fig. 9.

correspondence between the present problem at the special value μ_0 and the tight-binding problem in the presence of a magnetic monopole investigated in "Tight-binding spectra on spherical graphs: Avoiding the Dirac string" subsection. For the symmetric point $\mu = \Theta/2$, the problem can be exactly mapped onto a tight-binding model in the presence of the magnetic field generated by a Dirac monopole, studied in "Tight-binding spectra on spherical graphs: Avoiding the Dirac string" subsection. Thus, in Fig. 10, the energies at the intersection point of the first vertical dashed line are identical with the two energies corresponding to the energies of an electron in the field of $n = 1$ quantized magnetic dipole, shown in Fig. 9. This result, proved analytically in Avishai and Luck (2008b), is a beautiful manifestation of the relation between Aharonov–Bohm and Aharonov–Casher effects.

Conclusion

Aharonov–Bohm and Aharonov–Casher effects substantiate the fundamental role of quantum mechanics as a solid theory of Nature (Richter, 2012). In addition, they expose its beauty and peculiarities, and, at the same time, point out the possible occurrence of its puzzles. The Aharonov–Bohm effect constitutes a simple manifestation of Abelian gauge theory, while the Aharonov–Casher effect constitutes a simple manifestation of non-Abelian gauge theory. These two effects are published several decades ago, and remain among the building blocks of quantum mechanics ever since. The question of duality between the Aharonov–Casher and Aharonov–Bohm effects is raised by Hegen (1990), Bogachek and Landman (1994), Borunda et al. (2008), Rohrlich (2010), and Vaidman (2012). A theoretical analysis relating the two effects is suggested in Avishai and Luck (2009). Paradoxes of the Aharonov–Bohm and the Aharonov–Casher effects are discussed by Vaidman (2013).

Both effects stress the essential role of phase of the wave functions (Berry, 1984). The Aharonov and Bohm effect involves the motions of charged particles (e.g., electrons) around but away from a region in which the magnetic field is finite. In the Aharonov and Casher effect (Aharonov and Casher, 1984), an electrical field is considered and its effect on particles with nonzero magnetic moment such as electrons (but also neutrons as they need not be charged) is analyzed. Both of these effects have direct relevance to condensed matter systems. Here we described these two effects and reviewed their relevance in condensed matter (mainly in mesoscopic systems).

In this short review, some aspects of the relevance of these effects to condensed matter physics are illuminated. In particular, we focus on the physics of mesoscopic systems, for which numerous experiments confirm the two effects. For the Aharonov–Bohm effect, examples of interference around a tube carrying magnetic flux, electrons on the ring (spectrum and persistent current) and an interferometer are analyzed. For the Aharonov–Casher effect, examples of an interferometer, and an analysis of transmission and polarization in a two channel system are presented.

It is the authors' hope that the broad list of references will enable the readers to become acquainted with additional aspects of these effects in condensed matter physics.

Acknowledgments

The authors thank Tapash Chakraborty for suggesting this project, and Lev Vaidman for valuable comments.

References

Aharonov Y and Anandan J (1987) Phase change during a cyclic quantum evolution. *Physical Review Letters* 58: 1593.
Aharonov Y and Bohm D (1959) Significance of electromagnetic potentials in quantum theory. *Physics Review* 115(3): 485–491.
Aharonov Y and Bohm D (1961) Further considerations on electromagnetic potentials in the quantum theory. *Physical Review* 123(4): 1511–1524.
Aharonov Y and Casher A (1984) Topological quantum effects for neutral particles. *Physical Review Letters* 53(4): 319–321.
Aharonov Y, Pearle P, and Vaidman L (1988) Comment on proposed Aharonov-Casher effect: Another example of an Aharonov-Bohm effect arising from a classical lag. *Physics Review A* 37: 4052–4055.
Aharony A, Entin-Wohlman O, Halperin BI, and Imry Y (2002) Phase measurement in the mesoscopic Aharonov-Bohm interferometer. *Physical Review B* 66: 115311.
Aharony A, Entin-Wohlman O, and Imry Y (2003) Measuring the transmission of a quantum dot using Aharonov-Bohm interferometers. *Journal of the Physical Society of Japan* 72(Supp. A): 112 (cond-mat/0208068).
Aharony A, Entin-Wohlman O, and Imry Y (2005) Phase measurements in open and closed Aharonov-Bohm interferometers. *Physica E: Low-Dimensional Systems and Nanostructures* 28: 283 (cond-mat/0412027).
Aharony A, Entin-Wohlman O, Otsuka T, Katsumoto S, Aikawa H, and Kobayashi K (2006) Breakdown of phase rigidity and variations of the Fano effect in closed Aharonov-Bohm interferometers. *Physical Review B*: 73.
Aharony A, Takada S, Entin-Wohlman O, Yamamoto M, and Tarucha S (2014) Aharonov-Bohm interferometry with a tunnel-coupled wire. *New Journal of Physics* 16.
Aharony A, Entin-Wohlman O, Tzarfati L, Hevroni H, Karpovski R, Shelukhina M, Umansky V, and Palevski A (2019) Possible observation of Berry phase in Aharonov-Bohm rings of InGaAs. *Solid State Electronics* 155: 117.
Akkermans E and Montambaux G (2007) *Mesoscopic Physics of Electrons and Photons*. Cambridge University Press.
Alexandradinata A, Dai X, and Bernevig BA (2014) Wilson-loop characterization of inversion-symmetric topological insulators. *Physical Review B* 89: 155114.
Altland A, Gefen Y, and Montambaux G (1996) What is the Thouless energy for ballistic systems? *Physical Review Letters* 76: 1130.
Altshuler BL, Aronov AG, and Spivak BZ (1981) The Aharonov-Bohm effect in disordered conductors. *JETP Letters* 33: 94.
Anandan J (1989) Electromagnetic effects in the quantum interference of dipoles. *Physics Letters A* 138: 347.
Anderson PW (1958) Absence of diffusion in certain random lattices. *Physical Review* 109: 1492.
Aronov AG and Lyanda-Geller Y (1993) Spin-orbit Berry phase in conducting rings. *Physical Review Letters* 70: 343.
Asbóth JK, Oroszlány L, and Pályi A (2016) *A Short Course on Topological Insulators*. Springer International Publishing.
Avishai Y and Band Y (1987) Quantum scattering determination of magneto-conductance for 2D systems. *Physical Review Letters* 58: 2251.
Avishai Y and Band Y (2017) Simple spin-orbit based devices for electron spin polarization. *Physical Review B* 95: 104429.
Avishai Y and Kohmoto M (1993) Quantized persistent currents in quantum dot at strong magnetic field. *Physical Review Letters* 71: 279.
Avishai Y and Luck JM (2008a) Tight-binding electronic spectra on graphs with spherical topology. I. The effect of a magnetic charge. *Journal of Statistical Mechanics*. P06007, arXiv:0801.1460.
Avishai Y and Luck JM (2008b) Tight-binding electronic spectra on graphs with spherical topology. II. The effect of spin orbit interaction. *Journal of Statistical Mechanics*. P06008, arXiv:0802.0795.
Avishai Y and Luck JM (2009) Magnetization of two coupled rings. *Journal of Physics A: Mathematical and Theoretical* 42: 175301.
Avishai Y, Ekstein H, and Moyal JE (1972) Is the Maxwell field local? *Journal of Mathematical Physics* 13: 1139.
Avishai Y, Hatsugai Y, and Kohmoto M (1993) Persistent currents and edge states in a magnetic field. *Physical Review B* 47: 9501.
Avishai Y, Totsuka K, and Nagaosa N (2019) Aharonov-Casher phase factor in mesoscopic systems. *Journal of the Physical Society of Japan* 88(8): 084705.
Bachtold A, Strunk C, Salvetat J-P, Bonard J-M, Forró L, Nussbaumer T, and Schönenberger C (1999) Aharonov-Bohm oscillations in carbon nanotubes. *Nature* 397(6721): 673.
Band Y and Avishai Y (2012) *Quantum Mechanics with Application to Nanotechnology and Information Science*. Elsevier.
Batelaan H and Tonomura A (2009) The Aharonov-Bohm effects: Variations on a subtle theme. *Physics Today* 62(9): 38–43.
Béché A, Van Boxem R, Van Tendeloo G, and Verbeeck J (2014) Magnetic monopole field exposed by electrons. *Nature Physics* 10: 26.
Bergsten T, Kobayashi T, Sekine Y, and Nitta J (2006) Experimental demonstration of the time reversal Aharonov-Casher effect. *Physical Review Letters* 97: 196803.
Berkovits R and Avishai Y (1995) Significant interaction-induced enhancement of persistent currents in 2D disordered cylinders. *Europhysics Letters* 29: 475.
Berkovits R and Avishai Y (1996) Interacting electrons in disordered potentials: Conductance versus persistent currents. *Physical Review Letters* 76: 261.
Berry MV (1984) Quantal phase factors accompanying adiabatic changes. *Proceedings of the Royal Society of London, Series A* 392: 45.
Bloch F (1970) Josephson effect in a superconducting ring. *Physics Review B* 2: 109.
Bogachek EN and Landman U (1994) Aharonov-Bohm and Aharonov-Casher tunneling effects and edge states in double-barrier structures. *Physical Review B* 50(4): 2678–2680.
Borunda MF, Liu X, Kovalev AA, Xiong-Jun L, Jungwirth T, and Sinova J (2008) Aharonov-Casher and spin Hall effects in two-dimensional mesoscopic ring structures with strong spin-orbit interaction. *Physical Review B* 78(24): 245315.
Büttiker M (1985) Small normal-metal loop coupled to an electron reservoir. *Physical Review B* 32: 1846.
Büttiker M (1986) Four-terminal phase-coherent conductance. *Physical Review Letters* 57: 1761.
Büttiker M (1988) Symmetry of electrical conduction. *IBM Journal of Research and Development* 32: 317.
Büttiker M (1992) Flux-sensitive correlations of mutually incoherent quantum channels. *Physical Review Letters* 68: 843.
Büttiker, M., 2901. Scattering theory of thermal and excess noise in open conductors. Physical Review Letters 65.
Büttiker M, Imry Y, and Landauer R (1983) Josephson behavior in small normal one-dimensional rings. *Physics Letters* 96: 365.
Büttiker M, Imry Y, Landauer R, and Pinhas S (1985) Generalized many-channel conductance formula with application to small rings. *Physical Review B* 31: 6207.
Byers N and Yang CN (1961) Theoretical considerations concerning quantized magnetic flux in superconducting cylinders. *Physical Review Letters* 7: 46.
Castelnovo C, Moessner R, and Sondhi SL (2008) Magnetic monopoles in spin ice. *Nature* 451: 42.
Cernicchiaro G, Martin T, Hasselbach K, Mailly D, and Benoit A (1997) Channel interference in a quasi-ballistic Aharonov-Bohm experiment. *Physical Review Letters* 79: 273.

Chambers RG (1960) Shift of an electron interference pattern by enclosed magnetic flux. *Physical Review Letters* 5(1): 3–5.

Cheung HF, Riedel EK, and Gefen Y (1989) Persistent currents in mesoscopic rings and cylinders. *Physical Review Letters* 62(5): 587.

Cimmino A, Opat GI, Klein AG, Kaiser H, Werner SA, Arif M, and Clothier R (1989) Observation of the topological Aharonov-Casher phase shift by neutron interferometry. *Physical Review Letters* 63(4): 380–383.

Cooper NR, Dalibard J, and Spielman IB (2019) Topological bands for ultracold atoms. *Reviews of Modern Physics* 91: 015005.

Diamentiny MC, Trugenberger CA, and Vinokur VM (2021) Quantum magnetic monopole condensate. In: *Communications Physics*, 4. article 25.

Dirac PAM (1931) Quantised singularities in the electromagnetic field. *Proceedings of the Royal Society A* 133: 60–72.

Dowker JS (1967) A gravitational Aharonov-Bohm effect. *Nuovo Cimento B (1965-1970)* 52: 129–135.

Dresselhaus G (1955) Spin-orbit coupling effects in zinc blende structures. *Physics Review* 100(2): 580.

Duca L, Reitter T, Bloch M, Schleier-Smith M, and Schneider U (2015) An Aharonov-Bohm interferometer for determining Bloch band topology. *Science* 347: 288.

Edwards JT and Thouless DJ (1972) Numerical studies of localization in disordered systems. *Journal of Physics C: Solid State Physics* 5: 807.

Elion WJ, Wachters JJ, Sohn LL, and Mooij JD (1993) Observation of the Aharonov-Casher effect for vortices in Josephson-junction arrays. *Physical Review Letters* 71(14): 2311–2314.

Engel HA, Rashba EI, and Halperin BI (2006) Theory of spin hall effects in semiconductors. In: *Handbook of Magnetism and Advanced Magnetic Materials*. John Wiley and Sons, Ltd (cond-mat/0603306).

Entin-Wohlman O and Gefen Y (1989) Persistent currents in two-dimensional metallic cylinders: A linear response analysis. *Europhysics Letters* 8(5): 477.

Entin-Wohlman O, Gefen Y, Meir Y, and Oreg Y (1992) Effects of spin-orbit scattering in mesoscopic rings: Canonical-versus grand-canonical-ensemble averaging. *Physical Review B* 45(20): 11890.

Entin-Wohlman O, Imry Y, and Aharony A (2003) Persistent currents in interacting Aharonov-Bohm interferometers, and their enhancement by acoustic radiation. *Physical Review Letters* 91 (cond-mat/0302146).

Entin-Wohlman O, Imry Y, and Aharony A (2004) *Effects of external radiation on biased Aharonov-Bohm rings*.

Entin-Wohlman O, Aharony A, Tokura Y, and Avishai Y (2010) Spin-polarized electric currents in quantum transport through tubular two-dimensional electron gases. *Physical Review B* 81. 075439–075445.

Foldy LL and Wouthuysen SA (1950) On the Dirac theory of spin 1/2 particles and its non-relativistic limit. *Physics Review* 78(1): 29–36.

Fröhlic J and Studer UM (1993) Gauge invariance and current algebra in non-relativistic many-body theory. *Journal of Mathematical Physics* 65: 733.

Frustaglia D and Nitta J (2020) Geometric spin phases in Aharonov-Casher interference. *Solid State Communications* 311: 113864.

Frustaglia D and Richter K (2004) Spin interference effects in ring conductors subject to rashba coupling. *Physical Review B* 69: 235310.

Fukui T, Hatsugai Y, and Suzuki H (2005) Chern numbers in discretized Brillouin zone: Efficient method of computing (spin) Hall conductances. *Journal of the Physical Society of Japan* 74: 1674.

Gefen Y, Imry Y, and Azbel MY (1984) Quantum oscillations and the Aharonov-Bohm effect for parallel resistors. *Physical Review Letters* 52(2): 129.

Goldman N, Juzeliūnas G, Öhberg P, and Spielman IB (2014) Light-induced gauge fields for ultracold atoms. *Reports on Progress in Physics* 77: 126401.

Grbic B, Leturcq R, Ihn T, Ensslin K, Reuter D, and Wieck AD (2007) Aharonov-Bohm oscillations in the presence of strong spin-orbit interactions. *Physical Review Letters* 99: 176803.

Hagen CR (1990) Aharonov-Bohm scattering of particles with spin. *Physical Review Letters* 64(5): 503.

Hasan MZ and Kane CL (2010) Colloquium: Topological insulators. *Reviews of Modern Physics* 82: 3045.

Hegen CR (1990) Exact equivalence of spin-1/2 Aharonov-Bohm and Aharonov-Casher effects. *Physical Review Letters* 64: 2347.

Hemanta KK, Biswas S, Ofek N, Umansky V, and Heiblum M (2023) Anyonic interference and braiding phase in a Mach-Zehnder interferometer. *Nature Physics* 19: 515–521. https://doi.org/10.1038/s41567-022-01899-z.

Heras R (2022) The Aharonov-Bohm effect in a closed flux line. *The European Physical Journal Plus* 137: 641.

Hohensee MA, Estey B, Hamilton P, Zeilinger A, and Muller H (2012) Force-ffee gravitational redshift: Proposed gravitational Aharonov-Bohm experiment. *Physical Review Letters* 108 (23): 230404.

Imry Y (1986) Active transmission channels and universal conductance fluctuations. *Europhysics Lett* 1: 249.

Imry Y (1995) Coherent propagation of two interacting particles in a random potential. *Europhysics Letters* 30: 405.

Imry Y (1997) *Introduction to Mesoscopic Physics*, p. 110. Oxford University Press (Fig. 5.4).

Imry Y and Webb RA (1986) Quantum interference and the Aharonov-Bohm effect. *Scientific American* 260(4): 56–62.

Kane EO (1957) Band structure of indium antimonide. *Journal of Physics and Chemistry of Solids* 1: 249.

Köenig M, Tschetschetkin A, Hankiewicz EM, Sinova J, Hock V, Daumer V, et al. (2006) Direct observation of the Aharonov-Casher phase. *Physical Review Letters* 96.

Landauer R (1957) Spatial variation of currents and fields due to localized scatterers in metallic conduction. *IBM Journal of Research and Development* 1: 223.

Lee PA and Stone AD (1985) Universal conductance fluctuations in metals. *Physical Review Letters* 55: 1622.

Levy LP, Dolan G, Dunsmuir J, and Bouchiat H (1990) Magnetization of mesoscopic copper rings: Evidence for persistent currents. *Physical Review Letters* 64: 2074.

Li T, Duca L, Reitter M, Grusdt F, Demler E, Endres M, Schleier-Smith M, Bloch I, and Schneider U (2016) Bloch state tomography using Wilson lines. *Science* 352: 1094–1097.

Li H, Dong Z, Longhi S, Liang Q, Xie D, and Yan B (2022) Aharonov-Bohm caging and inverse Anderson transition in ultra-cold atoms. *Physical Review Letters* 129: 220403.

Loss D, Goldbart P, and Balatsky AV (1990) Berry's phase and persistent charge and spin currents in textured mesoscopic rings. *Physical Review Letters* 65: 1655.

Mathur H and Stone AD (1992) Quantum transport and the electronic Aharonov-Casher effect. *Physical Review Letters* 68: 2964.

Meijer FE, Morpurgo AF, and Klapwijk TM (2002) One dimensional ring in the presence of rashba spin-orbit interaction: Derivation of the correct hamiltonian. *Physical Review B* 66.

Meijer FE, Morpurgo AF, Klapwijk TM, and Nitta J (2005) Universal spin-induced time reversal symmetry breaking in two-dimensional electron gases with rashba spin- orbit interaction. *Physical Review Letters* 95: 186805.

Meir Y, Gefen Y, and Entin-Wohlman O (1989) Universal effects of spin-orbit scattering in mesoscopic systems. *Physical Review Letters* 63(7): 798.

Meir Y, Entin-Wohlman O, and Gefen Y (1990) Magnetic-field and spin-orbit interaction in restricted geometries: Solvable models. *Physical Review B* 42(13): 8351.

Milton KA (2006) Theoretical and experimental status of magnetic monopoles. *Reports on Progress in Physics* 69: 1637–1712.

Morpurgo AF, Heida JP, Klapwijk TM, van Wees BJ, and Borghs G (1998) Ensemble- average spectrum of Aharonov-Bohm conductance oscillations: Evidence for spin- orbit-induced Berry's phase. *Physical Review Letters* 80: 1050.

Nagasawa F, Takagi J, Kunihashi Y, Kohda M, and Nitta J (2012) Experimental demonstration of spin geometric phase: Radius dependence of time- reversal Aharonov-Casher oscillations. *Physical Review Letters* 108.

Nagasawa F, Frustaglia D, Saarikoski H, Richter K, and Nitta J (2013) Control of the spin geometric phase in semiconductor quantum rings. *Nature Communications* 4: 2526.

Nakamura J, Fallahi S, Sahasrabudhe H, Rahman R, Liang S, Gardner GC, and Manfra MJ (2019) Aharonov-Bohm interference of fractional quantum Hall edge modes. *Nature Physics* 15: 563.

Nitta J, Akazaki T, Takayanagi H, and Enoki T (1997) Gate control of spin-orbit interaction in an inverted InGaAs/InAlAs heterostructure. *Physical Review Letters* 78: 1335.

Nitta J, Meijer FE, and Takayanagi H (1999) Spin-interference device. *Applied Physics Letters* 75: 695–697.

Niu Q (2006) On a proper definition of spin current. *Physical Review Letters* 96.

Noguchi A, Shikano Y, Toyoda K, and Urabe S (2014) Aharonov-Bohm effect in the tunneling of a quantum rotor in a linear Paul trap. *Nature Communications* 5: 3868.

Olariu S and Popescu S (1985) The quantum effects of electromagnetic fluxes. *Reviews of Modern Physics* 57(2): 339.

Onsager L (1931) Reciprocal relations in irreversible processes. *Physics Review* 37(4): 405–426.

Osakabe N (1986) Experimental confirmation of Aharonov-Bohm effect using a toroidal magnetic field confined by a superconductor. *Physical Review A* 34(2): 815–822.

Overstreet C, Asenbaum P, Curti J, Kim M, and Kasevich MA (2022) Observation of a gravitational Aharonov-Bohm effect. *Science* 375(6577): 226–229.

Pauli W (1927) Zur quantenmechanik des magnetischen elektrons. *Zeitschrift für Physik* 43: 601–623.

Pearle P and Rizzi A (2017) Quantum-mechanical inclusion of the source in the Aharonov-Bohm effect. *Physical Review A* 95(5): 052123. ArXiv:1507.00068.

Peshkin M and Tonomura A (1989) *The Aharonov-Bohm effect*. Berlin Heidelberg New York London Paris Tokyo Hong Kong: Springer-Verlag.

Popescu S (2010) Dynamical quantum non-locality. *Nature Physics* 6(3): 151–153.

Qi X-L and Zhang S-C (2011) Topological insulators and superconductors. *Reviews of Modern Physics* 83: 1057.

Qian TZ and Su Z-B (1994) Spin-orbit interaction and Aharonov-Anandan phase in mesoscopic rings. *Physical Review Letters* 72: 2311.

Rashba EI (2006) Spin-orbit coupling and spin transport. *Physica E: Low-Dimensional Systems and Nanostructures* 34: 31.

Recher P, Trauzettel B, Rycerz A, Blanter YM, Beenakker CWJ, and Morpurgo AF (2007) Aharonov-Bohm effect and broken valley degeneracy in graphene rings. *Physical Review B* 76: 235404.

Richter K (2012) Viewpoint: The ABC of Aharonov effects. *Physics* 5: 22.

Rohrlich D (2009) Aharonov-Casher effect. In: Greenberger D, Hentschel K, and Weinert F (eds.) *Compendium of Quantum Physics*. Berlin, Heidelberg: Springer.

Rohrlich D (2010) Duality in the Aharonov-Casher and Aharonov-Bohm effects. *Journal of Physics A Mathematical and Theoretical* 43(35): 354028.

Ronen Y, Werkmeister T, Najafabadi DH, Pierce AT, Anderson LE, Jae Y, Si S, Lee U, Lee YH, Johnson B, Watanabe K, Takashi T, Yacoby A, and Kim P (2021) Aharonov-Bohm effect in graphene-based Fabry-Pérot quantum hall interferometers. *Nature Nanotechnology* 16: 563.

Roy SM (1980) Condition for nonexistence of Aharonov-Bohm effect. *Physical Review Letters* 44(3): 11–14.

Rycerz A and Beenakker CWJ (2007) Aharonov-Bohm effect for a valley-polarized current in graphene. arXiv:0709.3397.

Saarikoski H, Vázquez-Lozano JE, Baltanás JP, Nagasawa F, Nitta J, and Frustaglia D (2015) Topological transitions in spin interferometers. *Physical Review B* 91(R): 241406.

Schwarzschild B (1986) Currents in normal-metal rings exhibit Aharonov-Bohm effect. *Physics Today* 39(1): 17–20.

Shapiro B (1983) Quantum conduction on a cayley tree. *Physical Review Letters* 50: 747.

Shech E (2022) Scientific understanding in the Aharonov-Bohm effect. *Theoria* 88: 943.

Shekhter RI, Entin-Wohlman O, Jonson M, and Aharony A (2022) Magnetoconductance anisotropies and Aharonov-Casher phases. *Physical Review Letters* 129.

Sjoqvist E (2014) Locality and topology in the molecular Aharonov-Bohm effect. *Physical Review Letters* 89(21): 210401.

Stern A (1992) Berry's phase, motive forces, and mesoscopic conductivity. *Physical Review Letters* 68: 1022.

Stern A, Aharonov Y, and Imry Y (1990) Phase uncertainty and loss of interference: A general picture. *Physical Review A* 41: 3436.

Stone AD (1985) Magnetoresistance fluctuations in mesoscopic wires and rings. *Physical Review Letters* 54: 2692.

Sun QF and Xie XC (2005) Definition of the spin current: The angular spin current and its physical consequences. *Physical Review B* 72: 245305.

Thouless DJ, Kohmoto M, Nightingale MP, and den Nijs M (1982) Quantized Hall conductance in a two-dimensional periodic potential. *Physical Review Letters* 49: 405–408.

Tonomura A (2006) The Aharonov-Bohm effect and its application to electron phase microscopy. *Proceedings of the Japan Academy. Series B*: 82.

Vaidman L (2000) Torque and force on a magnetic dipole. *American Journal of Physics* 58: 978–983.

Vaidman L (2008) Many-worlds interpretation of quantum mechanics. *Stanford Encyclopedia of Philosophy*. https://plato.stanford.edu/entries/qm-manyworlds.

Vaidman L (2011) On the role of potentials in the Aharonov-Bohm effect. *Physics Review* A86.

Vaidman L (2012) Role of potentials in the Aharonov-Bohm effect. *Physical Review A* 86. 040101(R).

Vaidman L (2013) *Paradoxes of the Aharonov-Bohm and the Aharonov-Casher effects*. Arxiv1301/6153, published in Yakir Aharonov 80th birthday Festschrift.

Valagiannopoulos C, Marengo EA, Dimakis AG, and Alù A (2018) Aharonov-Bohm-inspired tomographic imaging via compressive sensing. *IET Microwaves, Antennas Propagation* 12: 1890.

van Oudenaarden A, Devoret MH, Nazarov YV, and Mooij JE (1998) Magneto-electric Aharonov-Bohm effect in metal rings. *Nature* 391(6669): 768.

Vidal J, Mosseri R, and Doucot B (1998) Aharonov-Bohm cages in two-dimensional structures. *Physical Review Letters* 81: 5888.

Webb RA, Washburn S, Umbach CP, and Laibowitz RB (1985) Observation of *h*/*e* Aharonov-Bohm oscillations in normal-metal rings. *Physical Review Letters* 54(25): 2696–2699.

Willett RL, Nayak C, Shtengel K, Pfeiffer LN, and West KW (2013) Magnetic-field-tuned Aharonov-Bohm oscillations and evidence for non-Abelian anyons at $\nu = 5/2$. *Physical Review Letters* 111: 186401.

Wu TT and Yang CN (1975) Concept of non-integrable phase factors and global formulation of gauge fields. *Physics Review D* 12: 3845–3857.

Wu TT and Yang CN (1976) Dirac monopole without strings: Monopole harmonics. *Nuclear Physics B* 107: 365–380.

Xiao D, Chang M-C, and Niu Q (2010) Berry phase effects on electronic properties. *Reviews of Modern Physics* 82: 1959–2007.

Yang CN and Mills RL (1954) Conservation of isotopic spin and isotopic gauge invariance. *Physics Review* 96: 191.

Yau J-B, De Poortere EP, and Shayegan M (2002) AharonovBohm oscillations with spin: Evidence for Berry's phase. *Physical Review Letters* 88: 146801.

Yerin Y, Gusynin VP, Sharapov SG, and Varlamov AA (2021) Genesis and fading away of persistent currents in a Corbino disk geometry. *Physical Review B* 104.

Yu R, Qi XL, Bernevig A, Fang Z, and Dai X (2011) Equivalent expression of Z_2 topological invariant for band insulators using the non-Abelian Berry connection. *Physical Review B* 84: 075119.

Zvyagin AA (2020) Persistent currents in the two-chain correlated electron model. *Low Temperature Physics* 46: 507.

Quantum computation of complex systems☆

Giuliano Benenti[a,b] **and Giulio Casati**[a], [a]Center for Nonlinear and Complex Systems, Dipartimento di Scienza e Alta Tecnologia, Università degli Studi dell'Insubria, Como, Italy; [b]Istituto Nazionale di Fisica Nucleare, Sezione di Milano, Milano, Italy

© 2024 Elsevier Ltd. All rights reserved.

This is an update of G. Casati, G. Benenti, Quantum Computation and Chaos, Editor(s): Franco Bassani, Gerald L. Liedl, Peter Wyder, Encyclopedia of Condensed Matter Physics, Elsevier, 2005, Pages 9–17, ISBN 9780123694010, https://doi.org/10.1016/B0-12-369401-9/01146-3.

Introduction 237
Quantum logic 238
Quantum algorithms 239
Quantum simulation of physical systems 240
Simulating complex dynamics on actual quantum hardware 243
Conclusion 244
Acknowledgments 244
References 245

Abstract

Miniaturization provides us with an intuitive way of understanding why, in the near future, quantum mechanics will become important for computation. The electronics industry for computers grows hand-in-hand with the decrease in size of integrated circuits. This miniaturization is necessary to increase computational power, that is, the number of floating-point operations per second (flops) a computer can perform. In the 1950s, electronic computers based on vacuum-tube technology were capable of performing approximately 10^3 floating-point operations per second, while nowadays (2022) there exist supercomputers whose power is greater than 100 petaflops (a 1 petaflops computer is capable of performing 10^{15} floating-point operations per second). This enormous growth of computational power has been made possible owing to progress in miniaturization, which may be quantified empirically in Moore's law. This law is the result of a remarkable observation made by Gordon Moore in 1965: the number of transistors on a single integrated-circuit chip doubles approximately every 18–24 months. This exponential growth has not yet saturated and Moore's law is still valid. At the present time the limit is close to 10^{10} transistors per chip and the typical size of circuit components is of the order of 5–10 nm. Extrapolating Moore's law, it is estimated that within a few years, one would reach the atomic size for storing a single bit of information. At that point, quantum effects will become unavoidably dominant.

Key points

- Quantum logic: superposition and entanglement
- Quantum algorithms for complex dynamical systems
- Quantum simulations on actual quantum hardware

Introduction

Miniaturization provides us with an intuitive way of understanding why, in the near future, quantum mechanics will become important for computation. The electronics industry for computers grows hand-in-hand with the decrease in size of integrated circuits. This miniaturization is necessary to increase computational power, that is, the number of floating-point operations per second (flops) a computer can perform. In the 1950s, electronic computers based on vacuum-tube technology were capable of performing approximately 10^3 floating-point operations per second, while nowadays (2022) there exist supercomputers whose power is greater than 100 petaflops (a 1 petaflops computer is capable of performing 10^{15} floating-point operations per second). This enormous growth of computational power has been made possible owing to progress in miniaturization, which may be quantified empirically in Moore's law. This law is the result of a remarkable observation made by Gordon Moore in 1965: the number of transistors on a single integrated-circuit chip doubles approximately every 18–24 months. This exponential growth has not yet saturated and Moore's law is still valid. At the present time the limit is close to 10^{10} transistors per chip and the typical size of circuit components is of the order of 5–10 nm. Extrapolating Moore's law, it is estimated that within a few years, one would reach the atomic size for storing a single bit of information. At that point, quantum effects will become unavoidably dominant.

☆Change History: September 2022. G Benenti, G Casati updated the chapter. Section "Simulating complex dynamics on actual quantum hardware" is newly added. Updated outlook.

Quantum physics sets fundamental limitations on the size of the circuit components. The first question under debate is whether it would be more convenient to push the silicon-based transistor to its physical limits or instead to develop alternative devices, such as quantum dots, single-electron transistors or molecular switches. A common feature of all these devices is that they are at the nanometer length scale, and therefore quantum effects play a crucial role.

So far, the quantum switches that could substitute silicon-based transistors and possibly be connected together to execute classical algorithms based on Boolean logic were discussed. In this perspective, quantum effects are simply unavoidable corrections that must be taken into account owing to the nanometer size of the switches. A quantum computer represents a radically different challenge: the aim is to build a machine based on quantum logic, that is, it processes the information and performs logic operations in agreement with the laws of quantum mechanics (Benenti et al., 2019).

Quantum logic

The elementary unit of quantum information is called a qubit (the quantum counterpart of the classical bit) and a quantum computer may be viewed as a many-qubit system. Physically, a qubit is a two-level system, like the two spin states of a spin-1/2 particle, the vertical and horizontal polarization states of a single photon or two levels of an atom.

A classical bit is a system that can exist in two distinct states, which are used to represent 0 and 1, that is, a single binary digit. The only possible operations (gates) in such a system are the identity (0 → 0, 1 → 1) and NOT (0 → 1, 1 → 0). In contrast, a quantum bit (qubit) is a two-level quantum system, described by a two-dimensional complex Hilbert space. In this space, one may choose a pair of normalized and mutually orthogonal quantum states, called $|0\rangle$ and $|1\rangle$ (say, the eigenstates of the Pauli operator σ_z), to represent the values 0 and 1 of a classical bit. These two states form a computational basis. From the superposition principle, any state of the qubit may be written as

$$|\Psi\rangle = \alpha|0\rangle + \beta|1\rangle, \tag{1}$$

where the amplitudes α and β are complex numbers, constrained by the normalization condition $|\alpha|^2 + |\beta|^2 = 1$.

A quantum computer can be seen as a collection of n qubits and therefore its wave function resides in a 2^n- dimensional complex Hilbert space. While the state of an n-bit classical computer is described in binary notation by an integer $k \,\varepsilon\, [0,2^n - 1]$,

$$k = k_{n-1}2^{n-1} + \cdots + k_1 2 + k_0, \tag{2}$$

with $k_0, k_1, \ldots k_{n-1} \,\varepsilon\, [0,1]$ binary digits, the state of an n-qubit quantum computer is

$$\begin{aligned} |\Psi\rangle &= \sum_{k=0}^{2^n-1} c_k|k\rangle \\ &= \sum_{k_{n-1},\ldots k_1,k_0=0}^{1} c_{k_{n-1},\ldots,k_1,k_0}|k_{n-1}\ldots k_1 k_0\rangle, \end{aligned} \tag{3}$$

where $|k_{n-1}\ldots k_1 k_0\rangle \equiv |k_{n-1}\rangle \otimes \cdots \otimes |k_1\rangle \otimes |k_0\rangle$. Notice that the complex numbers c_k are constrained by the normalization condition $\sum_{k=0}^{2^n-1}|c_k|^2 = 1$.

The superposition principle is clearly visible in Eq. (3): while n classical bits can store only a single integer k, the n-qubit quantum register can be prepared in the corresponding state $|k\rangle$ of the computational basis, but also in a superposition. The number of states of the computational basis in this superposition can be as large as 2^n, which grows exponentially with the number of qubits. The superposition principle opens up new possibilities for computation. When one performs a computation on a classical computer, different inputs require separate runs. In contrast, a quantum computer can perform a computation for exponentially many inputs on a single run. This huge parallelism is the basis of the power of quantum computation.

The superposition principle is not a uniquely quantum feature. Indeed, classical waves satisfying the superposition principle do exist. For instance, consider the wave equation for a vibrating string with fixed endpoints. Its solutions $|\varphi_k\rangle$ satisfy the superposition principle and one can write the most general state $|\varphi\rangle$ of a vibrating string as a linear superposition of these solutions, analogously to Eq. (3): $|\varphi\rangle = \sum_{k=0}^{2^n-1} c_k|\varphi_k\rangle$. It is therefore also important to point out the importance of entanglement for the power of quantum computation, as compared to any classical computation. Entanglement is the most spectacular and counter-intuitive manifestation of quantum mechanics, observed in composite quantum systems: it signifies the existence of non-local correlations between measurements performed on well-separated particles. After two classical systems have interacted, they are in well-defined individual states. In contrast, after two quantum particles have interacted, in general, they can no longer be described independently of each other. There will be purely quantum correlations between two such particles, independently of their spatial separation. Examples of two-qubit entangled state are the four states of the so-called Bell basis, $|\phi^{\pm}\rangle = \frac{1}{2}(|00\rangle \pm |11\rangle)$ and $|\varphi^{\pm}\rangle = \frac{1}{2}(|01\rangle \pm |10\rangle)$. The measure of the polarization state of one qubit will instantaneously affect the state of the other qubit, whatever their distance is. There is no entanglement in classical physics. Therefore, in order to represent the superposition of $N = 2^n$ levels by means of classical waves, these levels must belong to the same system. Indeed, classical states of separate systems can never be superposed. Thus, any computation based on classical waves requires a number N of levels that grows exponentially with n. If Δ is the typical energy separation between two consecutive levels, the amount of energy required for this computation is given by $\Delta 2^n$. Hence, the amount of physical resources needed for the computation grows exponentially with n. In contrast, due to entanglement, in quantum physics a general superposition of 2^n levels may be represented by means of n qubits. Thus, the amount of physical resources (energy) grows only linearly with n.

To implement a quantum computation, one must be able to control the evolution in time of the many-qubit state describing the quantum computer. As far as the coupling to the environment may be neglected, this evolution is unitary and governed by the

Schrödinger equation. It is well known that a small set of elementary logic gates allows the implementation of any complex computation on a classical computer. This is very important: it means that, when one changes the problem, one does not need to modify one's computer hardware. Fortunately, the same property remains valid for a quantum computer. It turns out that, in the quantum circuit model, any whatever complex unitary transformation acting on a many-qubit system can be decomposed into quantum gates acting on a single qubit and a suitable quantum gate acting on two qubits. Any unitary operation on a single qubit can be constructed using only Hadamard and phase-shift gates. The Hadamard gate is defined as follows: it turns $|0\rangle$ into $(|0\rangle + |1\rangle)/\sqrt{2}$ and $|1\rangle$ into $(|0\rangle - |1\rangle)/\sqrt{2}$. The phase-shift gate (of phase δ) turns $|0\rangle$ into $|0\rangle$ and $|1\rangle$ into $e^{i\delta}|1\rangle$.. One can decompose a generic unitary transformation acting on a many-qubit state into a sequence of Hadamard, phase-shift and CNOT gates, where CNOT is a two-qubit gate, defined as follows: it turns $|00\rangle$ into $|00\rangle$, $|01\rangle$ into $|01\rangle$, $|10\rangle$ into $|11\rangle$, and $|11\rangle$ into $|10\rangle$ As in the classical XOR gate, the CNOT gate flips the state of the second (target) qubit if the first (control) qubit is in the state $|1\rangle$ and does nothing if the first qubit is in the state $|0\rangle$. Of course, the CNOT gate, in contrast to the classical XOR gate, can also be applied to any superposition of the computational basis states.

The decomposition of a generic unitary transformation of a n-qubit system into elementary quantum gates is in general inefficient, that is, it requires a number of gates exponentially large in n (more precisely, $O(n^2 4^n)$ quantum gates). However, there are special unitary transformations that can be computed efficiently in the quantum circuit model, namely by means of a number of elementary gates polynomial in n. A very important example is given by the quantum Fourier transform, mapping a generic n-qubit state $\sum_{k=0}^{2^n-1} a_k|k\rangle$ into $\sum_{l=0}^{2^n-1} b_l|l\rangle$, where the vector $\{b_0, \cdots, b_{N-1}\}$ is the discrete Fourier transform of the vector $\{a_0, \cdots a_{N-1}\}$, that is, $b_l = \sum_{k=0}{}^{N-1} e^{2\pi ikl/2^n} a_k$. It can be shown that this transformation can be efficiently implemented in $O(n^2)$ elementary quantum gates, whereas the best known classical algorithm to simulate the Fourier transform, the fast Fourier transform, requires $O(n2^n)$ elementary operations. The quantum Fourier transform is an essential subroutine in many quantum algorithms.

Quantum algorithms

As shown above, the power of quantum computation is due to the inherent quantum parallelism associated with the superposition principle. In simple terms, a quantum computer can process a large number of classical inputs in a single run. For instance, starting from the input state $\sum_{k=0}^{2^n-1} c_k|k\rangle \otimes |0 \cdots 0\rangle$, one may obtain the output state.

$$\sum_{k=0}^{2^n-1} c_k|k\rangle \otimes |f(k)\rangle. \tag{4}$$

Therefore, the function $f(k)$ is computed for all k in a single run (note that one needs two quantum registers to compute by means of a reversible unitary transformation $f(k)$; the second register requires enough qubits to load the output $f(k)$ for all input values $k = 0, 1, \ldots, 2^n$, with n number of qubits in the first register). However, it is not an easy task to extract useful information from the output state. The problem is that this information is, in a sense, hidden. Any quantum computation ends up with a projective measurement in the computational basis: the qubit polarization is measured along the z-axis for all the qubits. The output of the measurement process is inherently probabilistic and the probabilities of the different possible outputs are set by the basic postulates of quantum mechanics. Given the state (4), one obtains $|\bar{k}\rangle|f(\bar{k})\rangle$ with probability $|c_{\bar{k}}|^2$, hence, the evaluation of the function $f(k)$ for a single $k = \bar{k}$, exactly as with a classical computer. However, there exist quantum algorithms that exploit quantum interference to efficiently extract useful information.

In 1994, Peter Shor proposed a quantum algorithm that efficiently solves the prime-factorization problem: given a composite odd positive integer N, find its prime factors. This is a central problem in computer science and it is conjectured, though not proven, that for a classical computer it is computationally difficult to find the prime factors. Indeed, the best classical algorithm, the number field sieve, requires exp. $(O(n^{1/3}(\log n)^{2/3}))$ operations. Shor's algorithm instead efficiently solves the integer factorization problem in $O((n^2 \log n \log\log n))$ elementary quantum gates, where $n = \log N$ is the number of bits necessary to code the input N. Therefore it provides an exponential improvement in speed with respect to any known classical algorithm. The integer factoring problem can be reduced to the problem of finding the period of the function $f(k) = \mathrm{a}^k \bmod N$, where N is the number to be factorized and $\mathrm{a} < N$ is chosen randomly. The modular exponentiation can be computed efficiently on a quantum computer and, starting from the state $\frac{1}{\sqrt{N}}\sum_{k=0}^{2^n-1}|k\rangle|0\ldots0\rangle$ (the equal superposition of all basis states in the first register can be obtained by applying one Hadamard gate for each qubit), one arrives at $\frac{1}{\sqrt{N}}\sum_{k=0}^{2^n-1}|k\rangle|f(k)\rangle$. Notice that there are two quantum registers, the first one stores k, the second $f(k)$. By measuring the second register, one obtains the outcome $f(\bar{k})$. Thus, the quantum computer wave function collapses onto $\frac{1}{\sqrt{m}}\sum_{j=0}^{m-1}|\bar{k} + jr\rangle|f(\bar{k})\rangle$, where m is the number of k values such that $f(k) = f(\bar{k})$, and r is the period of $f(k)$, that is $f(k) = f(k + r)$. To determine the period r, one has to perform the quantum Fourier transform of the first register. The resulting wave function is peaked around integer multiples of N/r. From the measurement of this state, one can extract the period r. It is worth mentioning that there are cryptographic systems, such as RSA, that are used extensively today and that are based on the conjecture that no efficient algorithms exist for solving the prime factorization problem. Hence Shor's algorithm, if implemented on a large scale quantum computer, would break the RSA cryptosystem.

Other quantum algorithms have been developed. In particular, Grover has shown that quantum computers can also be useful for solving the problem of searching for a marked item in an unstructured database of $N = 2^n$ items. The best one can do with a classical computer is to go through the database, until one finds the solution. This requires $O(N)$ operations. In contrast, the same problem can be solved by a quantum computer in $O(\sqrt{N})$ operations. In this case, the gain with respect to classical computation is quadratic.

Quantum simulation of physical systems

The simulation of quantum many-body problems on a classical computer is a difficult task as the size of the Hilbert space grows exponentially with the number of particles. For instance, if one wishes to simulate a chain of n spin-1/2 particles, the size of the Hilbert space is 2^n. Namely, the state of this system is determined by 2^n complex numbers. As observed by Feynman in the 1980s, the growth in memory requirement is only linear on a quantum computer, which is itself a many-body quantum system. For example, to simulate n spin-1/2 particles one only needs n qubits. Therefore, a quantum computer operating with only a few tens of qubits can outperform a classical computer. Of course, this is only true if one can find an efficient quantum algorithm and if one can efficiently extract useful information from the quantum computer. Quite interestingly, a quantum computer can outperform a classical computer not only for the investigation of the properties of many-body quantum systems, but also for the study of the quantum and classical dynamics of complex single-particle systems.

For a concrete example, consider the quantum-mechanical motion of a particle in one dimension (the extension to higher dimensions is straightforward). It is governed by the Schrödinger equation

$$i\hbar \frac{d}{dt}\Psi(x,t) = H\Psi(x,t), \tag{5}$$

where the Hamiltonian H is given by

$$H = H_0 + V(x,t) = -\frac{\hbar^2}{2m}\frac{d^2}{dx^2} + V(x,t). \tag{6}$$

The Hamiltonian $H_0 = -(\hbar^2/2m)d^2/dx^2$ governs the free motion of the particle, while $V(x, t)$ is a (possibly time-dependent) one-dimensional potential. To solve Eq. (5) on a quantum computer with finite resources (a finite number of qubits and a finite sequence of quantum gates), one must first of all discretize the continuous variables x and t. If the motion essentially takes place inside a finite region, say $-d \le x \le d$, decompose this region into 2^n intervals of length $\Delta = 2d/2^n$ and represent these intervals by means of the Hilbert space of an n-qubit quantum register (this means that the discretization step drops exponentially with the number of qubits). Hence, the wave function $|\Psi(t)\rangle$ is approximated as follows:

$$\left|\tilde{\Psi}(t)\right\rangle = \frac{1}{N}\sum_{i=0}^{2^n-1}\Psi(x_i,t)|i\rangle, \tag{7}$$

where $x_i \equiv -d + \left(i + \frac{1}{2}\right)\Delta$, $|i\rangle = |i_{n-1}\rangle \otimes \cdots \otimes |i_0\rangle$ is a state of the computational basis of the n-qubit quantum register a d $N \equiv \sqrt{\sum_{i=0}^{2^n-1}|\Psi(x_i,t)|^2}$ is a factor that ensures correct normalization of the wave function. It is intuitive that $\left|\tilde{\Psi}\right\rangle$ provides a good approximation to $|\Psi\rangle$ when the discretization step Δ is much smaller than the shortest length scale relevant for the motion of the system. The Schrödinger Eq. (5) may be integrated by propagating the initial wave function $\Psi(x, 0)$ for each time-step ε as follows:

$$\Psi(xt + \varepsilon) = \mathscr{T}e^{-\frac{i}{\hbar}[H_0 + V(xt)]\in}\Psi(xt), \tag{8}$$

where $\mathscr{T}$ is the time-ordering operator. If the time-step ε is small enough, it is possible to write the Trotter decomposition

$$e^{-\frac{i}{\hbar}[H_0 + V(x,t)]\in} \approx e^{-\frac{i}{\hbar}H_0\in}e^{-\frac{i}{\hbar}V(x,t)\in}, \tag{9}$$

which is exact up to terms of order ε^2. The operator on the right-hand side of Eq. (9) is still unitary, simpler than that on the left-hand side, and, in many interesting physical problems, can be efficiently implemented on a quantum computer. Advantage is taken of the fact that the Fourier transform can be efficiently preformed by a quantum computer. One can then write the first operator in the right-hand side of (9) as

$$e^{-\frac{i}{\hbar}H_0\in} = F^{-1}e^{+\frac{i}{\hbar}\left(\frac{\hbar^2k^2}{2m}\right)\in}F, \tag{10}$$

where k is the variable conjugated to x and F the discrete Fourier transform. This represents a transformation from the x-representation to the k-representation, in which this operator is diagonal. Then, using the inverse Fourier transform F^{-1}, one returns to the x-representation, in which the operator $\exp(-iV(x, t)\varepsilon/\hbar)$ is diagonal. The wave function $\Psi(x, t)$ at time $t = l\varepsilon$ is obtained from the initial wave function $\Psi(x, 0)$ by applying l times the unitary operator.

$$F^{-1}e^{+\frac{i}{\hbar}\left(\frac{\hbar^2k^2}{2m}\right)\in}Fe^{-\frac{i}{\hbar}V(x,t)\in}. \tag{11}$$

Therefore, simulation of the Schrödinger equation is now reduced to the implementation of the Fourier transform plus diagonal operators of the form where c is some real constant. Note that an operator of the form

$$|x\rangle \to e^{icf(x)}|x\rangle, \tag{12}$$

where c is some real constant. Note that an operator of the form (12) appears both in the computation of $\exp(-iV(x, t)\varepsilon/\hbar)$ and of $\exp(-iH_0\varepsilon/\hbar)$, when this latter operator is written in the k-representation. The quantum computation of (12) is possible, using an ancillary quantum register $|y\rangle_a$, by means of the following steps:

$$|0\rangle_a \otimes |x\rangle \to |f(x)\rangle_a \otimes |x\rangle \to e^{icf(x)}|f(x)\rangle_a \otimes |x\rangle \to e^{icf(x)}|0\rangle_a \otimes |x\rangle = |0\rangle_a \otimes e^{icf(x)}|x\rangle. \tag{13}$$

The first step is a standard function evaluation and may be implemented by means of $O(n2^n)$ elementary quantum gates. Of course, more efficient implementations (polynomial in n) are possible when the function $f(x)$ has some structure, as it is the case for the potentials $V(x, t)$ usually considered in quantum-mechanical problems. The second step in (13) is the transformation $|\gamma\rangle_a \to e^{ic\gamma}|\gamma\rangle_a$ and can be performed in m single-qubit phase-shift gates, m being the number of qubits in the ancillary register. Indeed, one may write the binary decomposition of an integer $\gamma \,\varepsilon\, [0, 2-1]$ as $\gamma = \sum_{j=0}^{m-1} \gamma_j 2^j$, with $\gamma_j \in \{0, 1\}$. Therefore,

$$\exp(i\gamma) = \exp\left(\sum_{j=0}^{m-1} ic\gamma_j 2^j\right) = \prod_{j=0}^{m-1} \exp\left(ic\gamma_j 2^j\right), \tag{14}$$

which is the product of m single-qubit gates, each acting non-trivially (differently from identity) only on a single qubit. The j-th gate operates the transformation $|\gamma_j\rangle_a \to \exp(ic\gamma_j 2^j)|\gamma_j\rangle_a$, with $|\gamma_j\rangle_a \in \{|0\rangle, |1\rangle\}$ vectors of the computational basis for the j-th ancillary qubit. The third step in (13) is just the reverse of the first and may be implemented by the same array of gates as the first but applied in the reverse order. After this step the ancillary qubits are returned to their standard configuration $|0\rangle_a$ and it is therefore possible to use the same ancillary qubits for every time-step. Note that the number of ancillary qubits m determines the resolution in the computation of the diagonal operator (12). Indeed, the function $f(x)$ appearing in (12) is discretized and can take 2^m different values.

An example of an interesting dynamical model that can be simulated efficiently (and without ancillary qubits) on a quantum computer is the so-called quantum sawtooth map. This map represents the dynamics of a periodically driven system and is derived from the Hamiltonian

$$H(\theta, I; \tau) = \frac{I^2}{2} + V(\theta) \sum_{j=-\infty}^{+\infty} \delta(\tau - jT), \tag{15}$$

where (I, θ) are conjugate action-angle variables $(0 \le \theta < 2\pi)$, with the usual quantization rules, $\theta \to \theta$ and $\mathrm{I} \to \mathrm{I} = -i\partial/\partial\theta$ (set $\hbar = 1$) and $\mathrm{V}(\theta) = -k(\theta - \pi)^2/2$. This Hamiltonian is the sum of two terms, $\mathrm{H}(\theta, I; \tau) = \mathrm{H}_0(I) + U(\theta; \tau)$, where $\mathrm{H}_0(I) = I^2/2$ is just the kinetic energy of a free rotator (a particle moving on a circle parametrized by the coordinate θ), while $U(\theta; \tau) = V(\theta)\sum_j \delta(\tau - jT)$ represents a force acting on the particle that is switched on and off instantaneously at time intervals T. Therefore, its is said that the dynamics described by Hamiltonian (15) is kicked. The (quantum) evolution from time tT^- (prior to the t-th kick) to time $(t+1)T^-$ (prior to the $(t+1)$-th kick) is described by a unitary operator U acting on the wave function Ψ:

$$\Psi_t + 1 = U\Psi_t = U_T U_k \Psi_t;$$

$$U_T = e^{-iTI^2/2}, U_k = e^{ik(\theta-\pi)^2/2}. \tag{16}$$

This map is called the quantum sawtooth map, since the force $F(\theta) = -dV(\theta)/d\theta = k(\theta - \pi)$ has a sawtooth shape, with a discontinuity at $\theta = 0$.

In the following, an exponentially efficient quantum algorithm for simulation of the map (16) is described. It is based on the forward/backward quantum Fourier transform between action and angle bases. Such an approach is convenient since the operator U is the product of the two operators U_k and U_T, which are diagonal in the θ and I representations, respectively. This quantum algorithm requires the following steps for one map iteration:

1. Apply U_k to the wave function $\Psi(\theta)$. In order to decompose the operator U_k into one- and two-qubit gates, we first of all write θ in binary notation:

$$\theta = 2\pi \sum_{j=1}^{n} \alpha_j 2^{-j}, \tag{17}$$

with $\alpha_i \,\varepsilon\, \{0,1\}$. Here n is the number of qubits, so that the total number of levels in the quantum sawtooth map is $N = 2^n$. One can insert (17) into the unitary operator U_k, obtaining the decomposition

$$e^{\imath k(\theta-\pi)^2/2} = \prod_{i,j=1}^{n} e^{\imath 2\pi^2} k\left(\alpha_i 2^{-i} - \frac{1}{2n}\right)\left(\alpha_j 2^{-j} - \frac{1}{2n}\right), \tag{18}$$

which is the product of n^2 two-qubit gates, each acting non-trivially only on the 4-dimensional subspace spanned by the qubits i and j.

2. The change from the θ to the I representation is obtained by means of the quantum Fourier transform, which requires and $\frac{1}{2}n(n+1)$elementary quantum gates.
3. In the I representation, the operator U_T has essentially the same form as the operator U_k in the θ representation, and therefore it can be decomposed into n^2 two-qubit gates, similarly to Eq. (18).
4. Return to the initial θ representation by application of the inverse quantum Fourier transform.

Thus, overall, this quantum algorithm requires $3n^2 + n$ gates per map iteration. This number is to be compared with the $O(n2^n)$ operations required by a classical computer to simulate one map iteration by means of a fast Fourier transform. Thus, the quantum simulation of the quantum sawtooth map dynamics is exponentially faster than any known classical algorithm. Note that the resources required to the quantum computer to simulate the evolution of the sawtooth map are only logarithmic in the Hilbert space dimension N.

As an example of the efficiency of this quantum algorithm, Fig. 1 shows the Husimi functions, taken after 1000 map iterations. It is noted that $n = 9$ qubits are sufficient to observe the appearance of integrable islands, while at $n = 16$ these islands exhibit a complex hierarchical structure in the phase space.

However, there is an additional aspect to be taken into account. Any quantum algorithm has to address the problem of efficiently extracting useful information from the quantum computer wave function. Indeed, the result of the simulation of a quantum system is the wave function of this system, encoded in the n qubits of the quantum computer. The problem is that, in order to measure all $N = 2^n$ wave function coefficients by means of standard polarization measurements of the n qubits, one has to repeat the quantum simulation a number of times exponential in the number of qubits. This procedure would spoil any quantum algorithm, even in the case, like the present one, in which such algorithm could compute the wave function with an exponential gain with respect to any classical computation. Nevertheless, there are some important physical questions that can be answered in an efficient way.

The quantum computation can provide an exponential gain (with respect to any known classical computation) in problems that require the simulation of dynamics up to a time t which is independent of the number of qubits. In this case, provided that one can extract the relevant information in a number of measurements polynomial in the number of qubits, one should compare, in the example of the quantum sawtooth map, $O(t(\log N)^2)$ elementary gates (quantum computation) with $O(tN \log N)$ elementary gates (classical computation). This is, for instance, the case of dynamical correlation functions of the form

$$C_t \equiv \langle \Psi_0 | A_t^\dagger B_0 | \Psi_0 \rangle = \langle \Psi_0 | \left(U^\dagger\right)^t A_0^\dagger U^t B_0 | \Psi_0 \rangle, \tag{19}$$

where U is the time-evolution operator (16) for the quantum sawtooth map. Similarly, one can efficiently compute the fidelity of quantum motion, which is a quantity of central interest in the study of the stability of quantum motion under perturbations. The fidelity $f(t)$ (also called the Loschmidt echo), measures the accuracy with which a quantum state can be recovered by inverting, at time t, the dynamics with a perturbed Hamiltonian. It is defined as

$$f(t) = \langle \Psi | \left(U_\in^\dagger\right)^t U^t | \Psi \rangle = \langle \Psi | e^{iH_\in t} e^{-iHt} | \Psi \rangle. \tag{20}$$

Here the wave vector $|\Psi\rangle$ evolves forward in time with Hamiltonian H up to time t and then evolves backward in time with a perturbed Hamiltonian H_ε. If the evolution operators U and U_ε can be simulated efficiently on a quantum computer, as is the case in many physically interesting situations, then the fidelity of quantum motion can be evaluated with exponential speed up with respect to known classical computations. As shown in Fig. 2, it is possible to measure the fidelity by means of a Ramsey-type quantum interferometer method. A single ancillary qubit is needed, initially prepared in the state $|0\rangle$, while the input state for the other n qubits is a given initial state $|\Psi_0\rangle$ for the quantum sawtooth map. Two Hadamard gates are applied to the ancillary qubit, and in between these operations a controlled-W operation is applied (W is a unitary operator), namely W is applied to the other n qubits only if the ancillary qubit is in its $|1\rangle$ state. As a result, one obtains the following final overall state for the $n + 1$ qubits:

$$\frac{1}{2}\left[(|0\rangle + |1\rangle)|\Psi_0\rangle + (|0\rangle - |1\rangle)W|\Psi_0\rangle\right]. \tag{21}$$

If $W = (U_\in^\dagger)^t U^t$, then one can derive the fidelity from polarization measurements of the ancillary qubit. One obtains

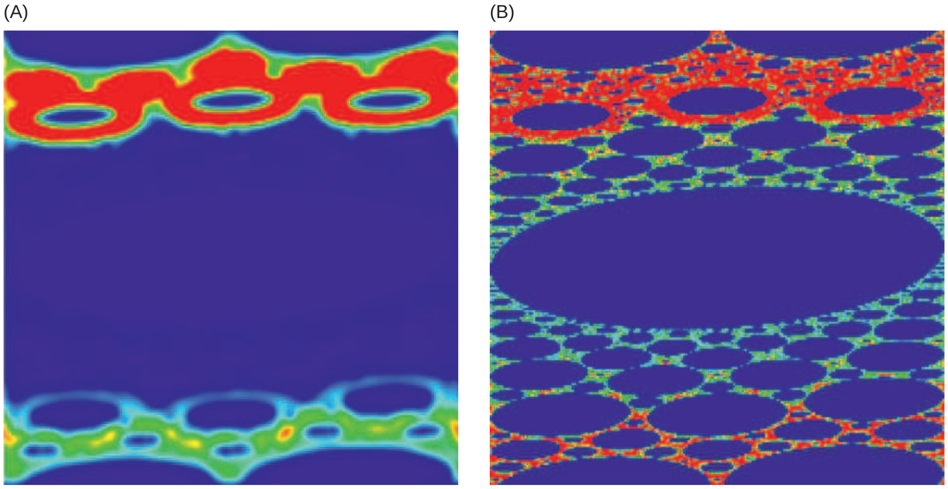

Fig. 1 Husimi function for the sawtooth map for $n = 9$ (left) and $n = 16$ (right) qubits, in action angle variables (I, θ), with $-N/2 \leq I < N/2$ (vertical axis, $N = 2^n$) and $0 \leq \theta < 2\pi$ (horizontal axis), averaged in the interval $950 \leq t \leq 1000$, for $T = 2\pi/N$ and $kT = -0.1$. An action eigenstate, $|\psi_0\rangle = |m_0\rangle$, with $m_0 = [0.38\ N]$ is considered as initial state at time $t = 0$. The color is proportional to the density: blue for zero and red for maximal density. Casati G and Benenti G (2005) Quantum computation and chaos, in: Bassani G, Liedl G and Wyder P (eds.) *Enciclopedia of Condensed Matter Physics*, Oxford, United Kingdom: Elsevier Science, Benenti G and Casati G (2016) Quantum computation of complex systems, in: Hashmi S (eds.) *Reference Module in Materials Science and Materials Engineering*, United Kingdom: Elsevier Science.

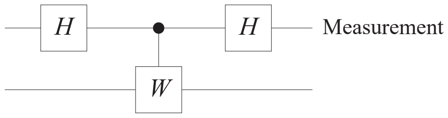

Fig. 2 Schematic drawing of a quantum circuit implementing a Ramsey-type quantum interferometer. The top line denotes a single ancillary qubit, the bottom line a set of *n* qubits, *H* the Hadamard gate and *W* a unitary transformation. Benenti G and Casati G (2016) Quantum computation of complex systems, in: Hashmi, S (ed.) *Reference Module in Materials Science and Materials Engineering*, United Kingdom: Elsevier Science.

$$f(t) = \langle \sigma_z \rangle^2 + \langle \sigma_y \rangle^2, \tag{22}$$

where $\langle \sigma_z \rangle$ and $\langle \sigma_y \rangle$ are the expectation values of the Pauli operators σ_z and σ_y. Provided that the quantum algorithm implementing U is efficient, as it is the case for the quantum sawtooth map, the fidelity can then be computed efficiently.

Simulating complex dynamics on actual quantum hardware

Present-day quantum computers, whether they are based on superconducting qubits or on trapped ions, suffer from significant decoherence and the effects of various noise sources. Therefore, achieving the quantum advantage in practically relevant problems such as chemical reactions, new materials design, or biological processes, is an imposing task. Note that quantum advantage is achieved when a quantum computer can solve a problem that no classical computer can solve in a feasible amount of time. The progress of currently available quantum processors can nevertheless be benchmarked by simulating complex dynamics.

An illustrative example is again provided by the quantum sawtooth map. The classical limit of such map is chaotic when $kT < -4$ or $kT > 0$. Although the sawtooth map is a deterministic system, in the chaotic regime the motion along the action direction is in practice indistinguishable from a random walk, with diffusion in the action variable. If one considers a classical ensemble of trajectories with fixed initial action m_0 and random initial angle θ, the second moment of the action distribution grows linearly with the number t of map iterations, $\langle (\Delta I)^2 \rangle \approx D(k)t$, with a diffusion coefficient D dependent on k. The quantum sawtooth map, in agreement with the correspondence principle, initially exhibits diffusive behavior, with the classical diffusion coefficient D. However, after a break time t^*, quantum interference leads to suppression of diffusion. For $t > t^*$, the quantum distribution reaches a steady state which decays exponentially over the action eigenbasis:

$$W_m \equiv |\langle m|\Psi\rangle|^2 \approx \frac{1}{\ell} \exp\left[-\frac{2|m - m_0|}{\ell}\right], \tag{23}$$

where the index m singles out the action eigenstates ($I|m\rangle = m|m\rangle$), the system is initially prepared in the eigenstate $|m_0\rangle$, and ℓ is known as the localization length of the system. Therefore, for $t > t^*$ only

$$\sqrt{\langle (\Delta I)^2 \rangle} \approx \sqrt{Dt^*} \approx \ell \tag{24}$$

levels are populated. This phenomenon, known as dynamical localization, is due to quantum interference effects, suppressing the underlying classical diffusion process after a time $t^* \approx \ell \approx D$.

Fig. 3 shows the results of a dynamical localization experiment with $n = 3$ qubits on a real and freely available IBM quantum processor, with superconducting qubits, remotely accessed through cloud quantum programming (Pizzamiglio et al., 2021). The initial condition is peaked in action, $\Psi_0(m) = \langle m \mid \Psi_0 \rangle = \delta_{m,m_0}$, with $m_0 = 0$. The quantum algorithm for the sawtooth map allows

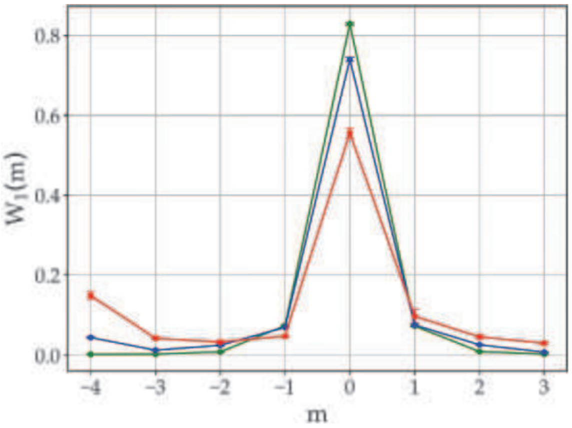

Fig. 3 Dynamical localization in the quantum sawtooth map with $n = 3$ qubits, $kT = 1{:}5$, $k \approx 0.273$. Data from the IBM quantum processors *lima* (red) are obtained after averaging over 10 repetitions of 8192 experimental runs, and compared with the Qiskit simulator (blue) and the noiseless simulation (green). Pizzamiglio A, Chang SY, Bondani M, Montangero S, Gerace D and Benenti G (2021) Dynamical localization simulated on actual quantum hardware, *Entropy* 23: 654.

one to compute the wave vector $\Psi_t(m)$ as a function of the number of map steps, and then the probability distribution $W_t(m) = |\Psi_t(m)|^2$. In the figure $k \approx 0{:}273 < 1$, so that the distribution is already localized after a single map step. On the other hand, here $kT = 1{:}5$, corresponding to diffusive, chaotic behavior for the underlying classical dynamics. In Fig. 3 the ideal, noiseless distribution after $t = 1$ map step is compared with the results of the real quantum hardware and with a simulator (Qiskit, provided by IBM), which takes into account a few relevant noise sources, modeling in particular dephasing, relaxation, and readout errors. The results show that the quantum hardware exhibits a localization peak, which emerges from quantum interference. Note that the quantum algorithm performs forward-backward Fourier transform, thus exploring the entire Hilbert space of the quantum register in a complex multiple-path interferometer that leads to wave-function localization. As such, dynamical localization is a very fragile quantum phenomenon, extremely sensitive to noise. The height of the peak, is significantly smaller than the noiseless value and the prediction of the Qiskit simulator. These results show that the Qiskit simulator underestimate some of the relevant noise channels, such as fluctuations of the qubit quality parameters between calibrations of the quantum computer, memory effects, and cross-talks between qubits.

The presence of these noise channels also shows the imposing difficulties in scaling quantum algorithms to a large number of qubits and of quantum gates. On the other hand, striking progress has been reported in recent years, quantified for instance by the quantum volume V_Q, a single number meant to encapsulate the quantum computer performance, including number of available qubits and number of quantum gates that can be reliably implemented, before errors dominate (Cross et al., 2019). The quantum volume is defined as

$$\log_2 V_Q = \arg\max_{\kappa \le n}\{\min[\kappa,\ d(\kappa)]\}, \tag{25}$$

where n is the number of qubits in the quantum computer, and $d(\kappa) = 1/(\kappa\varepsilon_{\text{eff}}(\kappa))$, known as circuit depth, is determined by an effective error rate $\varepsilon_{\text{eff}}(\kappa)$ for a subset of $\kappa \le n$ qubits, on which sequences of random two-qubit unitaries are implemented. From January 2020 to December 2021, the reported values of V_Q have increased from $V_Q = 32$ to $V_Q = 2048$ (for a comparison, data from Fig. 3 have been obtained with a machine with quantum volume $V_Q = 8$).

Conclusion

A few significant examples have been discussed showing the capabilities of a quantum computer in the simulation of complex physical systems. A quantum computer with a few tens of qubits and a long enough decoherence time to allow the implementation of a large number of quantum gates, would outperform a classical computer in this kind of problems.

Any practical implementation of a quantum computer has to face errors, due to the inevitable coupling of the computer to the surrounding environment or to imperfections in the quantum computer hardware. The first kind of error is known as decoherence and is a threat to the actual implementation of any quantum computation. More generally, decoherence theory has a fundamental interest beyond quantum information science, since it provides explanations for the emergence of classicality in a world governed by the laws of quantum mechanics (Zurek, 2003). The core of the problem is the superposition principle, according to which any superposition of quantum states is an acceptable quantum state. This entails consequences that are absurd according to classical intuition, like the superposition of "cat alive" and "cat dead" that is considered in the Schrödinger's cat paradox. The interaction with the environment can destroy the coherence between the states appearing in a superposition (for instance, the "cat alive" and "cat dead" states). Therefore, decoherence invalidates the quantum superposition principle, which is at the heart of the power of quantum algorithms. The presence of device imperfections, although not leading to any decoherence, also hinders the implementation of any quantum computational task, introducing errors. Therefore, decoherence and imperfection effects appear to be the ultimate obstacle to the realization of a large-scale quantum computer.

Note that a quantum computer is not necessarily required for implementing quantum simulation. Simpler quantum devices, called (analog) quantum simulators can mimic the evolution of other quantum systems in an analog manner. Such simulators are problem-specific quantum machines, namely controllable quantum systems used to simulate other quantum systems (Georgescu et al., 2014).

At present (2022) it is not clear if and when a useful quantum computer, capable of outperforming existing classical computers in important computational tasks, will be built. In order to perform coherent controlled evolution of a many-qubit system, one needs to take into account the problem of decoherence, and therefore large-scale quantum computers appear unrealistic with present technology. On the other hand, progress in the field has been huge in recent years. Moreover, we should bear in mind that technological breakthroughs (such as the transistor was for the classical computer) are always possible and that no fundamental objections have been found against the possibility of building a quantum computer.

Acknowledgments

We acknowledge use of the IBM Quantum Experience for Fig. 3 of this work. The views expressed are those of the authors and do not reflect the official policy or position of IBM company or the IBM-Q team.

References

Benenti G, Casati G, Rossini D, and Strini G (2019) *Principles of Quantum Computation and Information (A comprehensive textbook)*. Singapore: World Scientific.
Cross AW, Bishop LS, Sheldon S, Nation PD, and Gambetta JM (2019) Validating quantum computers using randomized model circuits. *Physical Review A* 100: 032328.
Georgescu IM, Ashhab A, and Nori F (2014) Quantum simulation. *Reviews of Modern Physics* 86: 153.
Pizzamiglio A, Chang SY, Bondani M, Montangero S, Gerace D, and Benenti G (2021) Dynamical localization simulated on actual quantum hardware. *Entropy* 23: 654.
Zurek WH (2003) Decoherence, einselection, and the quantum origins of the classical. *Reviews of Modern Physics* 75: 715.

Quantum information processing with superconducting circuits: A perspective

G Wendin, Department of Microtechnology and Nanoscience—MC2, Chalmers University of Technology, Gothenburg, Sweden

© 2024 Elsevier Ltd. All rights reserved.

Introduction **247**
Overview **248**
Quantum processor systems: Hardware and software 248
Quantum algorithms 248
Quantum supremacy 249
Performance metrics 250
Cross entropy benchmarking—XEB 250
Quantum volume—QV 250
Relevance of metrics for usefulness 251
Applications **251**
Quantum approximate optimization algorithm—QAOA 251
QAOA basics 251
QAOA applied to air transportation—Tail assignment 252
Variational quantum eigensolver—VQE 253
VQE basics 253
VQE applied to chemistry 253
Simulating physical systems on engineered quantum platforms 255
Quantum transport and localization 255
Quantum information scrambling 255
Many-body Hilbert space scarring 256
Key issues **256**
Noise and loss of information—A common experience 256
Fighting imperfections and noise in quantum processors 257
Quantum error suppression 257
Quantum error mitigation 257
Quantum error correction 258
Scaling up for practical quantum advantage 258
QPU-centric approach 258
HPC-centric approach 258
Useful NISQ digital quantum advantage—Mission impossible? 259
Future directions **260**
Improved and alternative superconducting qubits 260
Hybrid distributed computing 261
Continuous variables—Computing with resonators 261
Biochemistry and life science—Drivers of quantum computing? 262
Conclusion **262**
Acknowledgments **263**
References **263**

Abstract

The last 5 years have seen a dramatic evolution of platforms for quantum computing, taking the field from physics experiments to quantum hardware and software engineering. Nevertheless, despite this progress of quantum processors, the field is still in the noisy intermediate-scale quantum (NISQ) regime, seriously limiting the performance of software applications. Key issues involve how to achieve quantum advantage in useful applications for quantum optimization and materials science. In this article we will describe recent work to establish relevant benchmarks for quantum supremacy and quantum advantage, present recent work on applications of variational quantum algorithms for optimization and electronic structure determination, discuss how to achieve practical quantum advantage, and finally outline current work and ideas about how to scale up to competitive quantum systems.

https://doi.org/10.1016/B978-0-323-90800-9.00226-2

Key points

- Progress of gate-based superconducting quantum processors
- Status of quantum supremacy and quantum advantage
- Quantum approximate optimization algorithm (QAOA) applied to flight logistics
- Variational quantum eigensolver (VQE) applied to molecular ground state energies
- Methods for quantum error mitigation in noisy quantum processors
- Prospects of useful quantum advantage in current efforts to scale up superconducting quantum processors
- Improved and alternative superconducting qubits and architectures
- Superconducting platforms for quantum simulation of fundamental and applied physics problems

Introduction

Since around 1980, quantum computing (QC) and quantum simulation (QS) have gone from fantasy to possibility, from concept to application, from basic science to engineering (Wendin, 2017; Gu et al., 2019; Krantz et al., 2019; Kjaergaard et al., 2020; Blais et al., 2020, 2021; Bruzewicz et al., 2019; Brown et al., 2021; Daley et al., 2022). In 2011, at a workshop at Benasque in the Spanish Pyrenees, at a memorable session we discussed in particular the future of QC. Myself, I predicted 20–30 years for useful applications, while Rainer Blatt emphasized that if we did not have any decisive results in 5 years, QC would soon be dead. It seems we were both right: QC did take off around 2016 at engineering levels, while really useful competitive applications showing practical quantum advantage may still be 10–20 years ahead. The intense discussions in the European quantum community then led to the 2016 Quantum Manifesto, and to the EU Quantum Flagship setting sail in 2018.

From 2019, the field has seen a huge development of platforms for QC and simulation with superconducting devices and systems (Arute et al., 2019; Wu et al., 2021; Zhu et al., 2022; Córcoles et al., 2020; Gambetta, 2022a), including experiments indicating quantum supremacy (Arute et al., 2019; Wu et al., 2021; Zhu et al., 2022), a concept introduced by Preskill (2012). However, we are living in the era of noisy intermediate-scale quantum (NISQ) devices (Preskill, 2018), and it is currently impossible to build superconducting quantum processing units (QPUs) where one can entangle more than 10–15 qubits with high probability during the coherence time. Which means there is no time for useful computation with deep quantum circuits, only time to characterize the device and demonstrate physical entanglement—impressive but not necessarily useful. Nevertheless, IBM is now scaling superconducting QPUs to more than 1000 qubits in 2023 and over 4000 qubits in 2025 (Gambetta, 2022a; Bravyi et al., 2022), aiming for seamless integration of high-performance computers (HPCs) and QPU accelerators. Google (Lucero, 2021) seems to focus on modest-size quantum error-corrected QPUs for large-scale quantum computational breakthroughs already by 2029, while at the same time there seems to be some consensus (Sanders et al., 2020; Babbush et al., 2021; Beverland et al., 2022) that practical quantum advantage may take much longer to achieve.

To create useful applications showing quantum advantage, it is necessary to scale up QPUs and related classical-quantum hybrid (HPC+QC) infrastructure. This explains a number of current trends: (i) stay at "small" scales ($\leq$100 qubits) and try to solve coherence problems and create useful applications before scaling up; (ii) go for large scales ($\geq$1000 qubits) and try to implement quantum error correction (QEC) for quantum advantage or superiority while scaling up; (iii) scale up and solve large-scale hardware (HW) and software (SW) integration at systems levels, waiting for practical quantum advantage for use cases to emerge.

The question of the feasibility of powerful quantum computers beating classical super-HPC hinges on that it will be ultimately possible to perform QEC. When John Martinis' group announced that their superconducting quantum circuits were at the surface code threshold for fault tolerance (Barends et al., 2014), then the field opened up and went from quantum physics toward QC, scaling up HW and SW (Barends et al., 2015, 2016; Song et al., 2017; Kandala et al., 2017, 2019; Arute et al., 2019; Gong et al., 2019, 2021, 2022), and implementing significant quantum algorithms and quantum physics experiments (Barends et al., 2015, 2016; Kandala et al., 2017, 2019; Arute et al., 2020b, a; Neill et al., 2021; Gong et al., 2019, 2021, 2022; Zhang et al., 2022b; Mi et al., 2022b; Stanisic et al., 2022), including demonstrations of significant steps toward QEC (Andersen et al., 2020; Chen et al., 2021b; Marques et al., 2022; Krinner et al., 2022; Acharya et al., 2023).

Much of the current discussion concerns how to get from proofs of concept to useful applications. Consider the way QC is being promoted by Google (Lucero, 2021): "Within the decade, Google aims to build a useful, error-corrected quantum computer. This will accelerate solutions for some of the world's most pressing problems, like sustainable energy and reduced emissions to feed the world's growing population, and unlocking new scientific discoveries, like more helpful AI."

This tells us that the world's most pressing problems, like benchmarking climate models, are already subject to large-scale calculations, pushing super-HPCs to their limits set by NP-hard problems. The intended role of QPUs is to provide quantum superiority and to go far beyond those classsical limits. However, in the short term, at least during this decade, this can only be achieved by experimental quantum co-processors running specific subroutines addressing classically hard problems, omnipresent in industrial use cases (QUTAC, 2021; Kim et al., 2022). In the short term, industry will effectively be co-developing quantum algorithms as subroutines, and benchmark them against competing classical algorithms. If this leads to quantum advantage already in the short term, that will be a great bonus. The important thing to understand is that lack of quantum advantage for now does not jeopardize powerful computing—exascale super-HPC platforms will continue addressing the world's most pressing problems, and eventually QPU accelerators may provide quantum leaps.

This perspective article can be looked upon as a self-contained second part of a research and review paper (Wendin, 2017) that stopped short at the beginning of the current engineering era of scaling up devices and building QC ecosystems. The purpose is to focus on addressing the quite dramatic development since then, trying to "predict the future" based on current visions, roadmaps, efforts, and investments that aim for the next 10 years (Alexeev et al., 2021; Altman et al., 2022; Ang et al., 2022), outlining a sustainable quantum evolution that hopefully survives the quantum hype (Ezratty, 2022; Das Sarma, 2022). To be able to do so in this brief article, we will frequently refer to Wendin (2017) and to recent reviews for basic background, technology, and methods. This review will focus on superconducting technology and systems based on circuit quantum electrodynamics (cQED) (Gu et al., 2019; Blais et al., 2021), but will also provide glimpses of the broader development.

Overview

Quantum processor systems: Hardware and software

With NISQ devices with limited coherence time, the necessary circuits are much too deep to achieve reasonable accuracy. It is therefore necessary to break up the quantum circuits in short, low-depth pieces with a small number of gates that can be run on QPUs during the coherence time. These often make use of variational quantum algorithms (VQAs) where one calculates the expectation value of a cost function, for example, a Hamiltonian, using a parameterized trial function. A classical HPC controls and executes the classical optimization loop: computes averages, searches for improved energies, computes new parameters, and updates the quantum circuit.

Fig. 1 illustrates the basics of QC from a user perspective. The program code is typically prepared on a small classical computer and then submitted to the application programming interface (API) of an HPC frontend. The HPC interprets the quantum part and prepares the code defining the quantum circuit. This is finally loaded into the stack of the QPU. In the case of an ideal QPU, the code is executed on the QPU until solution is achieved, and the results finally read out and sent back to the HPC for postprocessing. In the NISQ world of QPUs, the quantum execution has to be limited to low-depth (shallow) quantum circuits that can be executed within the coherence time. This necessitates repeated quantum-classical processing loops for optimization of variational problems.

Here the classical computer is a bottleneck. The HPC calculation takes much longer time than the QPU execution time, even if the HPC responds without delay (no latency) and the QPU backend is available immediately on request. This is hybrid HPC+QC computation, and is algorithm dependent.

Quantum advantage in the NISQ era depends critically on efficient representation and coding of problems. There is a distinct difference between binary decision and optimization problems that can be mapped directly on qubits, and electron structure problems that need additional extensive transformations from fermionic operators to qubits.

Quantum algorithms

An ideal digital quantum computer executes perfect gates on ideal qubits with infinite coherence time. It evolves the time-evolution operator e^{-iHt} corresponding to a given Hamiltonian describing the problem (see e.g., Wendin, 2017). e^{-iHt} is then broken down

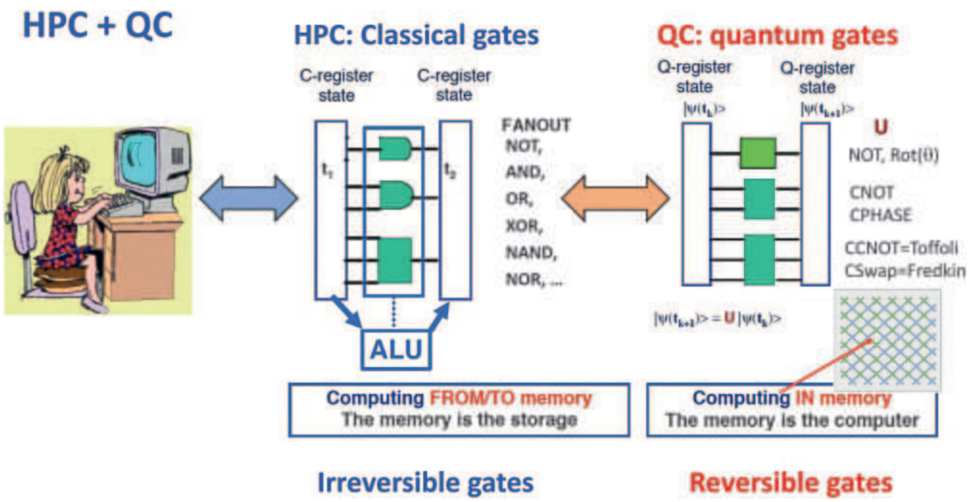

Fig. 1 HPC + QC. The user prepares a program and submits it to the classical frontend. The HPC prepares the quantum circuit and sends it to the QC. The HPC/QC registers have N bits/qubits, that is, $n = 2^N$ possible configurations/states. The HPC register can only be in one of 2^N states: $|00\ldots00\rangle, |00\ldots01\rangle, |00\ldots10\rangle, \ldots |11\ldots11\rangle$ at each instance of time *t*, while the QC register can be in a *superposition of all states*: $f_1(t)|00\ldots00\rangle + f_2(t)|00\ldots01\rangle + f_3(t)|00\ldots10\rangle, \ldots + f_{n-1}(t)|11\ldots10\rangle + f_n(t)|11\ldots11\rangle$. This describes *time-dependent quantum superposition and entanglement* and can, at best, lead to exponential quantum advantage (EQA).

into a product of factors for the different terms of the Hamiltonian. These factors are finally represented in terms of products of quantum gates constituting a quantum circuit. In this case, the role of a classical computer is exclusively pre- and post-processing: preprocessing to construct the quantum circuit and postprocessing to read out and treat the results. Both of these are in principle NP-hard. To get desired results, the QC must be able to run for sufficiently long times to execute deep quantum circuits, which requires perfect qubits and gates. With NISQ devices, it is not possible to run phase-estimation algorithms (PEAs) to compute the energies of molecules—the needed quantum circuits are far too long with respect to the coherence time. This has led to alternative approaches, calculating the expectation value of the problem Hamiltonian with respect to parametrized trial functions and then optimizing the parameters for lowest energy.

VQAs are generally based on constructing parametrized trial functions to compute and minimize the expectation value of a cost function. In the quantum case, the specific quantum computation involves computing the expectation value of a Hamiltonian cost function, while the classical computer prepares the trial function, computes the energy, updates the trial function parameters and minimizes the energy in an optimization loop. Extensive discussions and reviews of quantum methods and algorithms are presented by Wang et al. (2019), Cerezo et al. (2021), Franca and Garcia-Patron (2021), Tilly et al. (2022), Bharti et al. (2022), Abhijith et al. (2022), and Kowalsky et al. (2022).

Quantum supremacy

John Preskill was the first one to explicitly introduce the concept of quantum supremacy in a 2012 paper discussing QC and the entanglement frontier (Preskill, 2012). In 2016, Boixo et al. then described how to characterize quantum supremacy in near-term devices (Boixo et al., 2018) preparing for the 2019 Google experiment to demonstrate quantum supremacy (Arute et al., 2019). The idea was to measure the output of a pseudo-random quantum circuit (Fig. 2) to produce a distribution of samples, and to compute the cross-entropy describing the "overlap" between the quantum and classical distributions (see Hangleiter and Eisert (2022) for a review of quantum random sampling).

Aaronson and Chen (2017) put this on complexity-theoretic foundations. They noted that for the sampling tasks, not only simulation but also verification might need classical exponential time. This made it advantageous to directly consider the probability of observed bitstrings, rather than the distribution of sampled bitstrings. To this end, Aaronson and Chen (2017) showed that there is a natural average-case hardness assumption (Heavy Output Generation, HOG), which has nothing to do with sampling, yet implies that no polynomial-time classical algorithm can pass a statistical test passed by the outputs of the quantum sampling procedure. The quantum volume benchmark of IBM (see Section "Quantum volume—QV") is based on HOG.

As mentioned, Google based their quantum supremacy demonstration (Arute et al., 2019) on sampling quantum and classical distributions, calculating the cross-entropy as described by Boixo et al. (2018). Cross-entropy benchmarking (XEB) has the advantage that it provides deeper insight than HOG, including measures of fidelity, and allows tracing of the development from small processors to devices that can only be simulated approximately.

The Google paper (Arute et al., 2019) stated that an HPC would take 10,000 years. That statement immediately met with a rebuttal on the IBM Research blog by Pednault et al. (2019), explaining that an ideal simulation of the same task in a conservative, worst-case estimate could be performed on a classical system in 2.5 days and with far greater fidelity. Therefore the quantum supremacy threshold had not been met by Google using 53 qubits.

This was of course valid criticism, but effectively just delaying the inevitable. An experiment that more decisively passed the quantum supremacy threshold was soon announced by Chinese researchers (Wu et al., 2021; Zhu et al., 2022) using the Zuchongzhi processor, closely following Google's recipes, to demonstrate distinct quantum computational advantage. In the most recent experiment (Zhu et al., 2022) using 60-qubit 24-cycle random circuit sampling (RCS), the state-of-the-art HPC classical

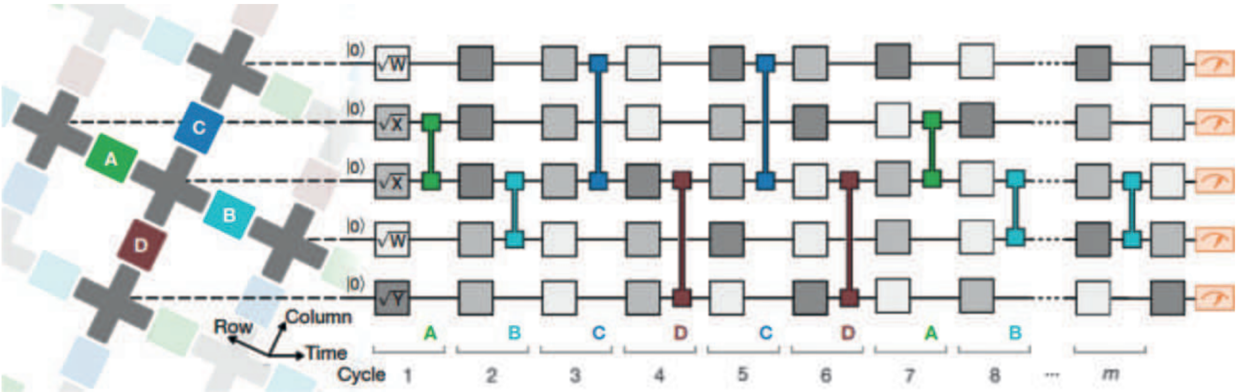

Fig. 2 Control operations for generating the pseudo-random quantum circuits for Google's quantum supremacy benchmarking protocol. Adapted from Arute F, et al. (2019) Quantum supremacy using a programmable superconducting processor. Nature 574: 505–510.

simulation would have taken tens of thousands of years, while Zuchongzhi 2.1 only took about 4.2 h, thereby significantly enhancing the quantum computational advantage.

As emphasized by Pednault et al. (2019), quantum supremacy is a threshold that does not automatically certify the quantum processor to be useful for running useful algorithms. However, it does benchmark the quality of the processor. The original Google experiment used a 53-qubit quantum processor that implements a large two-qubit gate quantum circuit of depth 20, with 430 two-qubit and 1,113 single-qubit gates, and with predicted total fidelity of $F_{XEB} = 0.2\% > 0$. The condition for quantum supremacy, $F_{XEB} > 0$, is based on statistics of creating an ensemble of a million runs of quantum circuits. The problem is that to solve, for example, a quantum chemistry problem based on 53 qubits, the depth of the quantum circuit would have to be in the range of a million. To solve useful problems challenging HPCs one must be able to run perfect quantum circuits with depth much larger than the circuit width, involving a very large number of 2-qubit gates. The name of the game is how to achieve practical quantum advantage.

Performance metrics

Cross entropy benchmarking—XEB

The task is to sample the 2^N bitstring output of a pseudo-random quantum circuit (Fig. 2). XEB compares the probability for observing a bitstring experimentally with the corresponding ideal probability computed via simulation on a classical computer.

For a given circuit, one collects the measured bitstring sample $\{x_i\}$ and computes the linear XEB fidelity (Arute et al., 2019)

$$F_{XEB} = 2^N \langle P(x_i) \rangle_i - 1 \tag{1}$$

where N is the number of qubits, $P(x_i)$ is the probability of the *experimental* bitstring $\{x_i\}$ computed for the *ideal quantum circuit*, and the average is over the observed bitstrings. F_{XEB} is correlated with how often one samples high-probability bitstrings. If the distribution is uniform, then $\langle P(x_i) \rangle_i = 1/2^N$ and $F_{XEB} = 0$. Values of F_{XEB} between 0 and 1 correspond to the probability that no error has occurred while running the circuit. In the Google case (Arute et al., 2019), the computed values are very small, $F_{XEB} \sim 10^{-3}$. This may represent proof of principle, but hardly provides any useful result. One needs to have $F_{XEB} \sim 1$ to be able to run algorithms, useful or not.

To demonstrate quantum supremacy, one must achieve a high enough F_{XEB} for a circuit with sufficient width and depth such that the classical computing cost of $P(x_i)$ for the full circuit is intractable. $P(x_i)$ must be calculated classically by simulating the ideal quantum circuit, which is formally intractable in the region of quantum supremacy. Since 2016, or even before, it has been understood that RCS, the task to sample the 2^N bitstring output of a pseudo-random quantum circuit, will not scale to arbitrarily many qubits without error correction (Aaronson and Chen, 2017). Bouland et al. (2019) provided strong complexity theoretic evidence of classical hardness of RCS, placing it on par with the best theoretical proposals for supremacy. However, very recently Aharonov et al. (2022) (see also Brubaker, 2023) produced a polynomial time classical algorithm for sampling from the output distribution of a noisy random quantum circuit. This gives strong evidence that, in the presence of a constant rate of noise per gate, RCS cannot be the basis of a *scalable* experimental violation of the extended Church-Turing thesis. Noise kills entanglement and makes RCS classically tractable (provided the HPC has enough memory to do the calculation).

However, the algorithm does not directly address finite-size RCS-based quantum supremacy experiments (Aharonov et al., 2022), so the result is not directly applicable to current attempts to invalidate the quantum supremacy results (Arute et al., 2019; Wu et al., 2021; Zhu et al., 2022) using classical HPC. Pan et al. (2022) solved the Google sampling problem classically in about 15 h on a computational cluster with 512 GPUs with state fidelity 0.0037 (Google 0.00224), and claimed that it would only take few dozen seconds on an exascale machine, much faster than Google.

Clearly it provides some satisfaction to demonstrate in practice that an HPC can beat the noisy 53q Sycamore QPU. However, a more challenging target for the HPC may now be to beat the 66q Zuchongzhi 2.1 with its 60-qubit 24-cycle RCS (Zhu et al., 2022).

Quantum volume—QV

The fundamental challenges in the NISQ era can be illustrated using the concept of quantum volume (QV) introduced by IBM (Cross et al., 2019). QV is linked to system error rates, and quantifies the largest random circuit of equal width and depth that a specific computer can successfully implement given decoherence, gate fidelities, connectivity, and more (Cross et al., 2019; Pelofske et al., 2022).

QV is a benchmarking protocol based on the execution of a pseudo-random quantum circuit with a fixed but generic form producing a bitstring $\{x\}$ (Fig. 3). QV quantifies the largest random circuit U of equal width N (number of qubits) and depth d (number of layers) that the computer successfully implements $U = U(d), \ldots, U(2)U(1)$ and produces the ideal output distribution $p_U(x) = |\langle x|U|0\rangle|^2$ where $\{x\}$ is an observable bit string.

Benchmarking the QV, one runs circuits with an increasing number of cycles $d = 1, \ldots, d_{max}$ with $d = N$, and measures the success rate for increasing the depth d until one reaches a prescribed success threshold. To define when a model circuit U has been successfully implemented in practice, Cross et al. (2019) use the HOG problem formulated by Aaronson and Chen (2017): "Given as input a random quantum circuit C (drawn from some suitable ensemble), generate output strings $x_1, \ldots, x_k$, at least a 2/3 fraction of which have greater than the median probability in C's output distribution." This means that the set of output probabilities $p_U(x)$ are sorted in ascending order of probability, and the heavy (high probability) output generation problem is to produce a set of output strings $\{x\}$ such that more than two-thirds are heavy, that is, greater than the median probability.

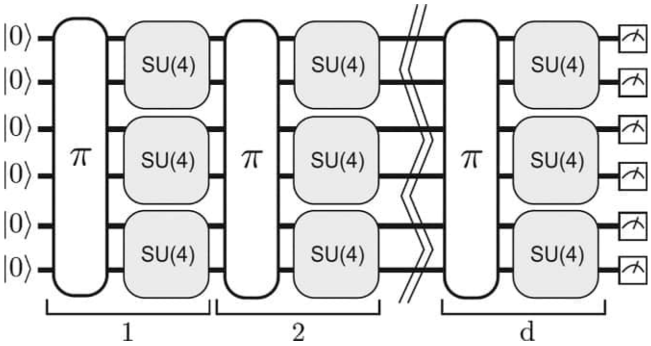

Fig. 3 IBM QV pseudo-random quantum circuit (Cross et al., 2019) consisting of d layers (depth) of random permutations π of the N qubit labels, followed by random SU(4) two-qubit gates. When the circuit width N is odd, one of the qubits is idle in each layer. From Cross AW, Bishop LS, Sheldon, S, Nation, PD, Gambetta, JM, (2019) Validating quantum computers using randomized model circuits. Physical Review A 100: 032328.

Aaronson and Chen (2017) state: "HOG is easy to solve on a quantum computer, with overwhelming success probability, by the obvious strategy of just running C over and over and collecting k of its outputs," and demonstrate that HOG is exponentially hard for a classical computer. The important thing is that the approach makes no reference to sampling or relation problems. Thus, one can shift focus from sampling algorithms to algorithms that simply estimate amplitudes.

Pelofske et al. (2022) recently published a guide to the QV: "Quantum Volume in Practice: What Users Can Expect from NISQ Devices." QV provides a standard benchmark to quantify the capability of NISQ devices. Interestingly, the QV values achieved in the tests (Pelofske et al., 2022) typically lag behind officially reported results and also depend significantly on the classical compilation effort. This is important to have in mind when popular articles announce QC breakthroughs in terms of higher QV values.

Relevance of metrics for usefulness

The definition of QV: $d = N$ stops short of benchmarking what is needed for useful applications. Useful algorithms often require the quantum circuit depth d to be much larger than the width N (number of qubits): $d \gg N$. This is typically the case when describing the ground-state energy of a molecule with reasonable accuracy. For example, a small molecule like HCN can be described (STO-6G basis) using Qiskit with $N = 15$ and $d \approx 33000 = 2200$ N ($N = 14$ and $d \approx 3000 \approx 200$N within an optimized scheme of Tranter et al., 2022). Similarly, HCN (6–31 G basis) can be described using Qiskit with $N = 69$ and $d = 6 \times 10^6 \sim 87000$ N (Lolur et al., 2021). These huge circuit depths can most likely be reduced with improved compilation methods (like in Tranter et al. (2022)), but nevertheless indicate the nature of the problem to perform useful calculations.

For comparison, instead of using random circuits and XEB or QV/HOG as targets, one can generate specific quantum states showing genuine multipartite entanglement (GME) with sufficient fidelity. Mooney et al. (2021) investigated multiple quantum coherences of Greenberger-Horne-Zeilinger (GHZ) states on 11–27 qubits prepared on the IBM Quantum Montreal (ibmq_montreal) device (27 qubits), applying quantum readout error mitigation and parity verification error detection to the states. In this way, a fidelity of $0.546 \pm 0.017 > 0.5$ was recorded for a 27-qubit GHZ state, demonstrating rare instances of GME across the full device.

Although this experiment may feel more interesting and useful than testing with random circuits, it nevertheless demonstrates that there is a very low probability for creating a 27-qubit GHZ state. For it to be useful, the GHZ state must be created with 100% probability to serve as starting point for useful information processing.

Applications

Quantum approximate optimization algorithm—QAOA

The quantum approximate optimization algorithm (QAOA) was proposed as a heuristic variational method for solving NP-hard combinatorial optimization problems on near-term quantum computers (Farhi et al., 2014; Farhi and Harrow, 2016), and constitutes one of the most widespread and active current methods for using NISQ computers (Farhi et al., 2022; Zhou et al., 2020; Morales et al., 2020; Zhang et al., 2022a; Harrigan et al., 2021; Herrman et al., 2021; Borle et al., 2021; Dupont et al., 2022; Chen et al., 2022b; Sreedhar et al., 2022; Willsch et al., 2020; Bengtsson et al., 2020; Fitzek et al., 2021; Lacroix et al., 2020; Weggemans et al., 2022; Verdon et al., 2019; Moussa et al., 2022; Patel et al., 2022; Bravyi et al., 2020, 2022; Egger et al., 2021; Guerreschi and Matsuura, 2019; Wurtz and Love, 2022; Chandarana et al., 2022; Hegade et al., 2022).

QAOA basics

The QPU prepares a variational quantum state $|\psi(\gamma,\beta)\rangle$ with N qubits starting from an initial uniform superposition of all possible computational basis states $|+\rangle^{\otimes N}$ generated by Hadamard gates from $|0\rangle^{\otimes N}$ (Fig. 4). The second step of QAOA is then to apply an alternating sequence $U = U(p), \ldots, U(2)U(1)|+\rangle^{\otimes N}$ of two parametrized noncommuting quantum gates $U(i) = U(i,\beta_i)U(i,\gamma_i) = e^{-i\beta_i\hat{B}}e^{-i\gamma_i\hat{C}}$, followed by measurement generating an n-qubit bitstring. Many repetitions (shots) of the

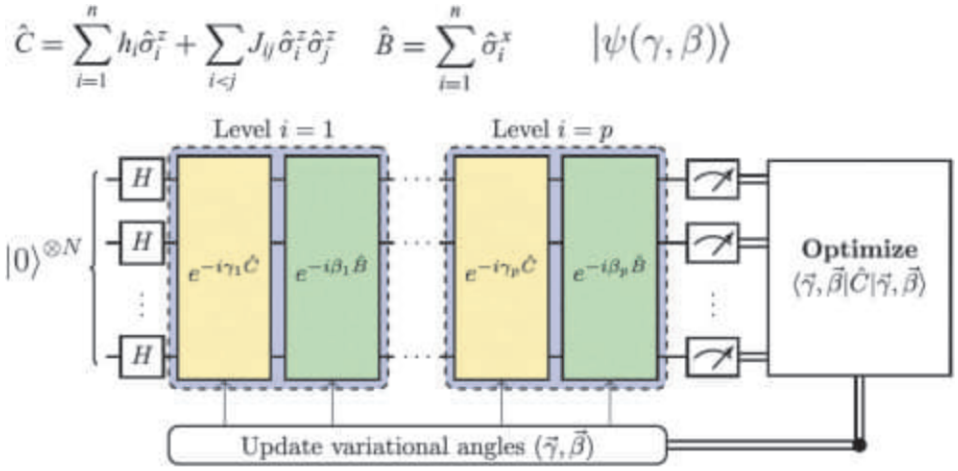
$\hat{C} = \sum_{i=1}^{n} h_i \hat{\sigma}_i^z + \sum_{i<j} J_{ij} \hat{\sigma}_i^z \hat{\sigma}_j^z$
$\hat{B} = \sum_{i=1}^{n} \hat{\sigma}_i^x$
$|\psi(\gamma, \beta)\rangle$
Level $i = 1$
Level $i = p$
$|0\rangle^{\otimes N}$
H
H
H
$e^{-i\gamma_1 \hat{C}}$
$e^{-i\beta_1 \hat{B}}$
$e^{-i\gamma_p \hat{C}}$
$e^{-i\beta_p \hat{B}}$
Optimize
$\langle \vec{\gamma}, \vec{\beta} | \hat{C} | \vec{\gamma}, \vec{\beta} \rangle$
Update variational angles $(\vec{\gamma}, \vec{\beta})$

Fig. 4 Quantum circuit for the quantum approximate optimization algorithm (QAOA). The QAOA for a problem specified by the Ising Hamiltonian $\hat{C}$. An alternating sequence of the Ising Hamiltonian $\hat{C}$ and the transverse mixing Hamiltonian $\hat{B}$ is applied to an equal superposition of N qubits, producing a trial state function $|\psi(\gamma, \beta)\rangle = \prod_{l=1}^{p} e^{-i\beta_l \hat{B}} e^{-i\gamma_l \hat{C}} | + \rangle^n$. Measurement of the qubit state produces a specific N-qubit bitstring, and many repetitions (shots) of the identical quantum circuit (loop not shown) creates a distribution used for estimating the cost function $\langle \psi(\gamma, \beta) | C | \psi(\gamma, \beta) \rangle$. A classical optimization loop then minimizes the cost function by updating the variational parameters γ, β. The level p represents the depth of the circuit, determining the number of variational parameters and gates used in the trial function $|\psi(\gamma, \beta)\rangle$. A large circuit width N requires a (very) large depth p for accuracy. Adapted from Bengtsson A, et al. (2020) Quantum approximate optimization of the exact cover problem on a superconducting quantum processor. Physical Review Applied 14: 034010.

same circuit generate a distribution of bitstrings used to evaluate the cost function $\langle \psi(\gamma, \beta) | C | \psi(\gamma, \beta) \rangle$. The variational parameters are then updated in a closed loop using a classical optimizer to minimize the cost function.

QAOA applied to air transportation—Tail assignment

Industrial optimization has a long history (Ong and Teo, 2021), one of the most famous applications being Toyota's Just-In-Time production system first implemented in 1973 (Monden, 2012). There is an extensive recent literature on optimization for industrial engineering and logistics (see e.g., de Sousa Junior et al., 2019; Csalódi et al., 2021; Ong and Teo, 2021; Monden, 2012), since around 2015 often referred to as Industry 4.0 (Csalódi et al., 2021; Rai et al., 2021).

In the following we will discuss one specific example addressing airline scheduling (Wedelin, 1995): the performance of the QAOA algorithm for optimizing small but realistic instances of logistic scheduling relevant to airlines. The problem addressed is called tail assignment (TAS) (Grönkvist, 2005; Vikstål et al., 2020; Svensson et al., 2021), assigning individual aircraft (identified by the number on its tail fin) to particular routes, deciding which individual aircraft (tail) should operate each flight.

A full approach to TAS is discussed in detail by Svensson et al. (2021), separating TAS into a generation problem and a selection problem. In this way, the complex rules only affect the generation problem, whereas the selection problem is often a pure Set Cover or Set Partitioning problem.

The TAS generation problem is responsible for generating the complex aircraft routes. A flight is a connection between two airports. A set of flights operated in sequence by the same aircraft (tail) is called a route (Vikstål et al., 2020). To formulate the TAS problem, let F denote the set of flights f, T the set of tails t, and R the set of all legal routes r. In order for a route to be considered legal to operate, it needs to satisfy a number of constraints.

In a full problem description one would include various costs, like the cost of flying a route and the cost of leaving a flight unassigned. In the decision version of TAS, the goal is to find any solution satisfying all the constraints, disregarding the costs. Essential aspects of the full TAS selection problem can then be reduced to an Exact Cover decision problem with the constraint

$$\sum_{r \in R} a_{fr} x_r = 1; \quad x_r \in \{0, 1\} \tag{2}$$

The constraint matrix $\{a_{fr}\}$ defines the relationship between F and R and tells whether a flight f is included in route r: $a_{fr} = 1$ if flight f is covered by route r and 0 otherwise. Given the *generated constraint matrix* $\{a_{fr}\}$, the solutions for the decision variable x_r will follow from the solution of the Exact Cover decision problem: $x_r = 1$ if route r should be used in the solution, and is 0 otherwise.

The constraint can be turned into a cost function

$$C = \sum_{f \in F} \left(\sum_{r \in R} a_{fr} x_r - 1 \right)^2 \tag{3}$$

that can be converted to the classical QUBO model—quadratic unrestricted binary optimization, which then maps over onto the quantum Ising model (Glover et al., 2022a, b; Ajagekar et al., 2022). In the final cost function, the Ising Hamiltonian, the constants (external field and spin interactions) are then determined by the constraint matrix $\{a_{fr}\}$ (Eq. 2).

Vikstål et al. (2020) reduced real-world instances obtained from real flight scheduling to instances with 8, 15, and 25 decision variables, which could be solved using QAOA on a quantum computer laptop simulator with 8, 15, and 25 qubits (routes), respectively. For these small instances, the problem was reduced to an exact cover problem with one solution in each instance. Elementary instances have been studied experimentally by Bengtsson et al. (2020) and Lacroix et al. (2020).

The same TAS problem was studied by Willsch et al. (2022) mapped onto a 40-qubit problem and 472 flights. For each of the 40 routes, the constraint matrix defines all flights that are covered by this route. As explained, the exact cover problem is to find a selection of routes (i.e., a subset of rows of the constraint matrix) such that all 472 flights are covered exactly once. The exact cover problem was programmed on D-Wave Advantage and 2000Q. The problem instance has the unique ground state $|0000000001010010011001000001000000000110\rangle$, where each qubit represents a flight route. The ground state contains nine 1′s meaning that for this particular instance, the solution consists of nine routes. Each route is assigned to an aircraft. All other states represent invalid solutions, in the sense that not all 472 flights are covered exactly once. However, the fact that the D-Wave quantum annealers (simulators) were able to solve this problem does not imply quantum advantage (Kowalsky et al., 2022).

Variational quantum eigensolver—VQE

VQE basics

The VQE implements the Rayleigh-Ritz variational principle (Fig. 5) (Wendin, 2017; Lee et al., 2019):

$$E(\theta) = \langle \psi(\theta) | \hat{H} | \psi(\theta) \rangle \geq E_0 \tag{4}$$

The VQE is a classical-quantum hybrid algorithm where the trial function $|\psi(\theta)\rangle$ is created in the qubit register by gate operations. Calculating the expectation value on a QPU, the energy is estimated via repeated generation and readout of the quantum state, generating a distribution used to evaluate the Pauli operator products of $\hat{H}$. In quantum simulation on an HPC, the state vector is available classically, and the expectation value of H can be evaluated directly. The VQE scales badly for large molecules due to repeated measurements or tomography to form the expectation value of the Hamiltonian, $\langle \hat{H} \rangle$. Nevertheless, the VQE is the common approach for small molecules with present NISQ QPUs (Cao et al., 2019; McArdle et al., 2020; McClean et al., 2021; Fedorov et al., 2022). The PEA scales better, but involves much deeper circuits, puts much higher demands on the coherence time of the q-register, and needs advanced QEC.

VQE applied to chemistry

For an overview of applications to chemistry, see reviews (McArdle et al., 2020; McClean et al., 2021; Fedorov et al., 2022) and specific applications (Lee et al., 2019; Kim et al., 2022; Sokolov et al., 2020; Elfving et al., 2021; Sapova and Fedorov, 2022; Lolur et al., 2021; Tranter et al., 2022; Lolur et al., 2023; Sugisaki et al., 2019, 2022; Chen et al., 2021a; Zhang et al., 2022c; de Gracia-Treviño et al., 2023; Grimsley et al., 2019; Tang et al., 2021; Tkachenko et al., 2021; Lan and Liang, 2022).

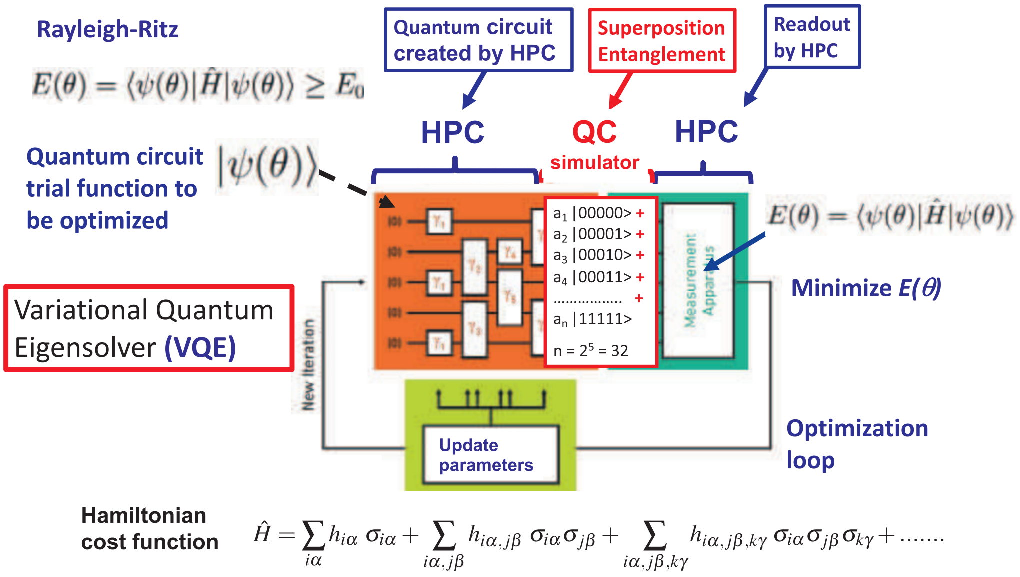
Rayleigh-Ritz
$E(\theta) = \langle \psi(\theta) | \hat{H} | \psi(\theta) \rangle \geq E_0$
Quantum circuit created by HPC
Superposition Entanglement
Readout by HPC
HPC
QC
simulator
HPC
Quantum circuit trial function to be optimized
$|\psi(\theta)\rangle$
Variational Quantum Eigensolver (VQE)
$a_1\,|00000\rangle$ +
$a_2\,|00001\rangle$ +
$a_3\,|00010\rangle$ +
$a_4\,|00011\rangle$ +
.... +
$a_n\,|11111\rangle$
$n = 2^5 = 32$
Measurement Apparatus
$E(\theta) = \langle \psi(\theta) | \hat{H} | \psi(\theta) \rangle$
Minimize $E(\theta)$
New iteration
Update parameters
Optimization loop
Hamiltonian cost function
$\hat{H} = \sum_{i\alpha} h_{i\alpha}\,\sigma_{i\alpha} + \sum_{i\alpha,j\beta} h_{i\alpha,j\beta}\,\sigma_{i\alpha}\sigma_{j\beta} + \sum_{i\alpha,j\beta,k\gamma} h_{i\alpha,j\beta,k\gamma}\,\sigma_{i\alpha}\sigma_{j\beta}\sigma_{k\gamma} + \ldots\ldots$

Fig. 5 The Variational Quantum Eigensolver (VQE) implements the Rayleigh-Ritz variational principle: $E(\theta) = \langle \psi(\theta) | \hat{H} | \psi(\theta) \rangle \geq E_0$. The trial function $|\psi(\theta)\rangle$ is created as a quantum circuit by the HPC and sent to the backend QPU (or simulator). The gates are then executed in the QPU by pulses generated by the classical electronics and software control system in the stack. The quantum register is finally measured, producing a bitstring used to evaluate the Hamiltonian cost function $\hat{H}$. This is repeated many times to evaluate the energy $\langle \psi(\theta) | \hat{H}_i | \psi(\theta) \rangle$ with sufficient accuracy. The optimization loop then updates the parameters $\{\theta_i\}$ to minimize the energy.

In VQE calculations for quantum chemistry (Wendin, 2017; Lee et al., 2019), one typically starts from an ansatz of the quantum state $|\psi(\theta)\rangle = U(\theta)|\psi_{ref}\rangle$ with variational parameters θ, where $U(\theta)$ is a unitary operator describing the quantum circuit, and $|\psi_{ref}\rangle$ is the initial state. $U(\theta)$ could be a heuristic "hardware efficient" quantum circuit (Kandala et al., 2017) or a more elaborate unitary coupled cluster (UCC) expansion, with a Hartree-Fock (Wendin, 2017; Lee et al., 2019; Sokolov et al., 2020) or multiconfiguration (Sugisaki et al., 2019, 2022) initial reference state.

The UCC ansatz of the quantum state $|\psi(\theta)\rangle$:

$$|\psi(\theta)\rangle = \hat{U}(\theta)|\psi_{ref}\rangle = e^{T(\theta) - T(\theta)^{\dagger}}|\psi_{ref}\rangle \tag{5}$$

can be expanded:

$$T(\theta) = T_1 + T_2 + T_3 + \ldots + T_N \tag{6}$$

producing $1, 2, 3, \ldots, N$ electron-hole excitations from the N-electron reference state. The first two terms

$$T_1 = \sum_{pq} t(\theta)_{pq}\, c_p^{\dagger} c_q; \quad T_2 = \sum_{pqrs} t(\theta)_{pqrs}\, c_p^{\dagger} c_q^{\dagger} c_r c_s \tag{7}$$

with fermionic creation ($c_i^{\dagger}$) and annihilation (c_i) operators generate single (S) and double (D) excitations and produce the parametrized UCCSD trial-state approximation. In particular $t(\theta)_{pq} = \theta_i$ and $t(\theta)_{pqrs} = \theta_j$ for all combinations of the indices $pqrs$.

The trial-state fermionic operator $U(\theta)$ must now be mapped onto qubit spin operators. Common transformations (codings) are Jordan-Wigner (JW), Bravyi–Kitaev (BK) and Parity, all designed to impose the anticommutation rules. In the case of the UCC ansatz, the exponential is expanded into exponentials of large numbers of products of Pauli spin operators acting on qubits. The initial trial state is then constructed through entangled quantum circuits: combinations of parametrized 1q-rotation gates and entangling 2q gates. The size of the quantum circuit can finally be reduced by qubit reduction schemes. All this results in a state vector for the trial state.

The fermionic operators $c_i^{\dagger}$ and c_i in the molecular Hamiltonian

$$\hat{H} = \sum_{pq} h_{pq} c_p^{\dagger} c_q + \frac{1}{2} \sum_{pqrs} h_{pqrs} c_p^{\dagger} c_q^{\dagger} c_r c_s \tag{8}$$

must also be expanded in products of Pauli spin operators using codings like JW, BK, or Parity, resulting in the generic interaction form:

$$\hat{H} = \sum_{i\alpha} h_{i\alpha}\, \sigma_{i\alpha} + \sum_{i\alpha,\, j\beta} h_{i\alpha,j\beta}\, \sigma_{i\alpha}\sigma_{j\beta} + \sum_{i\alpha,\, j\beta,\, k\gamma} h_{i\alpha,j\beta,k\gamma}\, \sigma_{i\alpha}\sigma_{j\beta}\sigma_{k\gamma} + \ldots\ldots \tag{9}$$

where $\sigma_{i\alpha}$ corresponds to the Pauli matrix σ_α for $\alpha \in \{0, x, y, z\}$, acting on the i-th qubit. The expectation value $\langle\hat{H}\rangle$ can then be calculated in two ways: (1) State vector approach: direct calculation of by matrix operations; (2) Measurement approach: generating an ensemble of identical trial states and evaluating the Pauli operators of the Hamiltonian terms $\hat{H}_i$.

The original UCC exponential (Eq. 5) is then expanded into exponentials of large numbers of products of Pauli spin operators acting on qubits: $e^{-i\theta\sigma_{1z}\sigma_{2z}}$; $e^{-i\theta\sigma_{1z}\sigma_{2z}\sigma_{3z}}$, etc. The parametrized initial entangled quantum circuit $U(\theta)$ for the UCCSD trial state is then finally constructed through combinations of parametrized one-qubit rotation gates and entangling two-qubit CNOT gates, resulting in a state vector $|\psi(\theta)\rangle = U(\theta)|\psi_{HF}\rangle$ for the trial state.

Lolur et al. (2021) have benchmarked the VQE as implemented in the Qiskit software package on laptops and HPCs, applying it to computing the ground state energy of water, H_2O, hydrogen cyanide, HCN, and a number of related molecules.[a] The energies have been determined using the noise-free Qiskit statevector backend to directly calculate $\langle\psi(\theta)|\hat{H}|\psi(\theta)\rangle$ through matrix multiplication rather than repeated measurement. Clearly, substantial classical computational resources are needed to compute these systems on classical HPC quantum simulators. It is evident that for problems with QChem-inspired ansätze, even small numbers of qubits lead to large numbers of gates. And this is then amplified by the variational procedure with many parameters and iterations. The large number of gates will severely limit the types of molecules that can be used for benchmarking real quantum HW. And it will also limit what can be simulated on HPC quantum simulators. QChem problems will provide serious challenges and benchmarks for testing HPC and quantum HW NISQ implementations.

To utilize VQE and achieve near chemical accuracy will be extremely challenging for NISQ processors. It is problematic or impossible to achieve chemical accuracy with conventional HPC VQE simulators already for small molecules such as HCN. But, there is no way around it: one must benchmark and challenge existing quantum HW and SW with available resources. The water molecule is a kind of "gold standard" even for forefront HPC applications, and H_2O is an excellent candidate for testing the VQE on quantum HW. Nevertheless, at the present stage of the NISQ era, one has to start with "easy" applications and simple approximations just to benchmark the quantum HW.

---

[a] Wendin G., 'The Main Results of Lolur et al. (2021) are Produced with an iMac i9, 8-Cores Workstation with 128 GB RAM (max 32 Qubits). The Practical Limit for the iMac to Achieve an Accurate Ground-State Energy Minimum is so far Connected with H2O (6-31G): 20 Qubits and 73 000 Gates, Taking 66.5 Hours to Converge to 10–6 Ha Precision of the Ground-State Energy for the Equilibrium Geometry. In the Case of N=C=C=N (STO-6G: 29 Qubits, 2815 Variational Parameters, 515611 Gates) it Took 132 CPU-Hours (5.5 days) to Produce the First Energy Value. This Must then be Multiplied by 2815 to Evaluate one Gradient Vector for the First Energy Estimate by the Optimizer. And then this will need to be Iterated at Least 10 Times to Converge to an Accurate Ground State Energy Value. The Time-to-Solution (TTS) is then about 3.7 · 106 CPU-Hours. For Comparison, SUMMIT at ORNL, USA, with in total 202752 Cores, Would Finish the N=C=C=N Instance in 147 Hours = 6 days. In the QChem Case, the Challenge Lies in the Number of Variational Parameters and the number of Gates Needed, not in the number of Qubits. Smart Compilation can Greatly Reduce the number of Gates Tranter et al. (2022), but does not really change the poor scaling.

The concept of "hardware-efficient" trial functions (Kandala et al., 2017) is an attempt to short-circuit standard UCCSD approaches and still introduce essential electron correlation. The recently developed adaptive VQE (Grimsley et al., 2019; Tang et al., 2021) and related further developments (Tkachenko et al., 2021; Lan and Liang, 2022) provide a more systematic approach to including electron correlation processes in order of monotonically decreasing weight. Nevertheless, the electron-correlation problem is computationally hard (NP-hard), so there is no easy way around it. State-of-the-art HPC computation of accurate molecular energies based on the Schrödinger equation defines the resources needed, and they are indeed huge (Calvin et al., 2021; Jones et al., 2022).

HPC quantum simulators cannot be more efficient than systematic HPC brute-force full CI calculations. Quantum advantage will be possible by definition as soon as a quantum register exceeds the available RAM memory of an HPC. But to profit from that potential quantum advantage, the QPU must be able to run the q-algorithm to solution, and that will involve a very large number of gate operations even for the VQE. So, this is the ultimate challenge of the NISQ era.

Simulating physical systems on engineered quantum platforms

Feynman's original idea was to simulate quantum systems with engineered quantum systems. Using analog quantum circuits one tunes the interactions in a controllable quantum substrate to describe the Hamiltonian of the system to be simulated, and then anneals the systems toward their ground states by lowering the temperature.

A comprehensive review (Daley et al., 2022) describes how quantum simulation can be performed already today through special-purpose analog HW quantum simulators, arguing that a first practical quantum advantage already exists in the case of specialized applications of analog devices. A particular example is simulation of 2D antiferromagnets with hundreds of Rydberg atoms trapped in an array by optical tweezers (Scholl et al., 2021), and the development of digital-analog QS for superconducting circuits (Lamata et al., 2018; Yu et al., 2022).

The recent development of large-scale superconducting arrays makes it possible to design qubit circuits that simulate a specific physical device, and perform experiments on it (Arute et al., 2020b; Neill et al., 2021; Gong et al., 2021; Mi et al., 2022b; Zhang et al., 2022b; Karamlou et al., 2022; Landsman et al., 2019; Touil and Deffner, 2020; Mi et al., 2021; Braumüller et al., 2022; Frey and Rachel, 2022; Mi et al., 2022a). In this way, Arute et al. (2020b) simulated separation of the dynamics of charge and spin in the Fermi-Hubbard model, Neill et al. (2021) simulated the electronic properties of a quantum ring created in the Sycamore substrate, and Mi et al. (2022b) investigated discrete time crystals in an open-ended, linear chain of 20 superconducting transmon qubits that were isolated from the two-dimensional Sycamore grid. Kim et al. (2023) studied the evolution of quench dynamics of a 2D transverse-field Ising model with up to 26 spins on a 27q IBM Falcon processor, and similar experiments with the 127q Eagle processor are in the pipeline. In this case the results may be classically intractable.

We will now discuss a few recent experiments addressing transport, information scrambling, and scarring in quantum circuits.

Quantum transport and localization

Tight-binding lattice Hamiltonians are canonical models for particle transport and localization phenomena in condensed-matter systems. To study the propagation of entanglement and observe Anderson and Wannier–Stark localization, Karamlou et al. (2022) experimentally investigated quantum transport in one- and two-dimensional tight-binding lattices, emulated by a fully controllable 3 x 3 array of superconducting qubits in the presence of site-tunable disorder strengths and gradients.

The dynamics are hard to observe in natural solid-state materials, but they can be directly emulated and experimentally studied using engineered quantum systems. The close agreement between the experimental results, simulations, and theoretical predictions (Karamlou et al., 2022) results from high-fidelity, simultaneous qubit control and readout, accurate calibration, and taking into account the relevant decoherence mechanisms in the system.

Karamlou et al. (2022) emphasize that although the experiments are performed on a small lattice that can still be simulated on a classical computer, they demonstrate a platform for exploring larger, interacting systems where numerical simulations become intractable.

Quantum information scrambling

Quantum scrambling is the dispersal of local information into many-body quantum entanglements and correlations distributed throughout an entire system, leading to the loss of local recoverability of quantum information (Landsman et al., 2019; Touil and Deffner, 2020; Mi et al., 2021; Braumüller et al., 2022).

Following Mi et al. (2021), the approach is based on measuring the out-of-time-order correlator (OTOC) $C = \langle |\hat{O}^*(t)\hat{M}^*\hat{O}(t)\hat{M}| \rangle$ between a unitary local perturbation operator $\hat{O}(t)$ and unitary operator $\hat{M}$ which is a Pauli operator on a different qubit. Scrambling means a local perturbation is rapidly amplified over time. During the time evolution, $\hat{O}(t)$ becomes increasing nonlocal, which leads to decay of correlation function due to the spreading of the excitation all over the system.

The perturbation operator can be modeled as $\hat{O}(t) = \sum_i w_i \hat{B}_i$, where $\hat{B}_i = b_1(i) \otimes b_2(i) \otimes b_3(i) \ldots$ is a string of single-qubit basis operators acting on different qubits, and w_i are the weights of the operator strings. Scrambling involves two different mechanisms: (i) Operator spreading, and (ii) generation of operator entanglement. Operator spreading (i) means that the strings of single-qubit basis operators $\hat{B}_i$ get expanded, spreading over more qubits, while (ii) generation of operator entanglement is reflected in the growth in time of the minimum number of terms needed to expand $\hat{O}(t) = \sum_i w_i \hat{B}_i$ with a broad distribution of coefficients w_i.

By measuring the OTOC, Mi et al. (2021) experimentally investigated the dynamics of quantum scrambling on a 53-qubit Sycamore quantum processor. Engineering quantum circuits that distinguished between operator spreading and operator entanglement, they showed that operator spreading is captured by an efficient classical model, while operator entanglement in idealized circuits requires exponentially scaled computational resources to simulate. However, the quantum-supremacy discussion of the influence of noise, making possible classical simulation of large noisy QPUs, suggests that the noise level needs to be reduced substantially before exponentially scaled computational resources are needed.

Recently Braumüller et al. (2022) also probed quantum information propagation with out-of-time-ordered correlators (OTOCs). They implemented a 3 × 3 two-dimensional hard-core Bose–Hubbard lattice with a superconducting circuit, studied its time reversibility, and measured out-of-time-ordered correlators. The method relies on the application of forward and backward time evolution steps implemented by interleaving blocks of unitary time evolution and single-qubit gates. Extracting OTOCs made it possible to study quantum information propagation in lattices with various numbers of particles, enabling observation of a signature of many-body localization in the 2D hard-core Bose–Hubbard model.

Braumüller et al. (2022) propose that applying the technique to larger lattices may improve our understanding of quantum thermodynamics and black-hole dynamics, as well as of using many-body systems for quantum memories. In addition, experimentally accessing OTOCs in large quantum circuits may provide a powerful benchmarking tool to study future quantum processors. But again, here noise will likely become an issue.

Many-body Hilbert space scarring

Moudgalya et al. (2022) and Chandran et al. (2023) recently presented reviews of work on quantum many-body scars and Hilbert space fragmentation, describing dynamical process that is weakly nonergodic, not completely filling the entire phase space.

Zhang et al. (2022b) and Chen et al. (2022a) studied many-body Hilbert space scarring (QMBS) on superconducting processors. QMBS is a weak form of ergodicity breaking in strongly interacting quantum systems, meaning that the system does not visit all parts of phase space. This presents opportunities for mitigating thermalization-induced decoherence due to scrambling in quantum information processing applications.

Utilizing a programmable superconducting processor with 30 qubits and tunable couplings, Zhang et al. (2022b) created Hilbert space scarring in a nonconstrained model in different geometries, including a linear chain and quasi-one-dimensional comb geometry, by approximately decoupling from the qubit substrate. By reconstructing the full quantum state through quantum state tomography on four-qubit subsystems, they present strong evidence for QMBS states by measuring qubit population dynamics, quantum fidelity, and entanglement entropy after a quench from initial unentangled states. The QMBS is found to be robust to various imperfections such as random cross-couplings between qubits, and it persists beyond 1D systems. The experimental findings also broaden the realm of scarring mechanisms and identify correlations in QMBS states for quantum technology applications. Comparing with other qubit platforms, Zhang et al. (2022b) state that the superconducting platform can process the same quantum information in a shorter time, implying advantages of QMBS in a superconducting platform for more practical quantum-sensing and metrology applications.

Also, Chen et al. (2022a) recently used pulse-level control and a variety of quantum error-mitigation (QEM) techniques to simulate the dynamics of a spin chain with QMBS on IBM QPUs for chains of up to 19 qubits. They conclude that the results demonstrate the power of error-mitigation techniques and pulse-level control to probe many-body coherence and correlation effects on present-day quantum hardware.

Key issues

Noise and loss of information—A common experience

A common classical experience might illuminate what QC is facing in the present NISQ era. Onboard an airplane, listening to music using the cheap versions of headphones offered by airlines in economy class can be a less-than-satisfactory experience. To start with, the headphone sound emitters have narrow bandwidth and large distortion, certainly not improving the limited quality of the source itself. Then the high-frequency background noise in the cabin from the air conditioning and engines may swamp the music signal. And finally, the sensitivity and frequency response of passenger's ears, and the processing in the brain (CPS, 2023; CAPD, 2023; Souffi, 2023), may be less than perfect, making it difficult to discriminate against the noise. For the traveler, high-quality headphones with noise suppression therefore make a big difference. Then the external noise from the environment is processed in real time: recorded, inverted, and subtracted.

This is a useful analogy in the case of a single qubit in a noisy environment. However, in order to describe the influence of noise on a multiqubit processor, one might better illustrate the situation in terms of the "Cocktail Party Syndrome" (CPS, 2023), referring to the difficulty to entertain a meaningful conversation within a group of people in a very noisy environment. Here, also simultaneous "two-body interactions" between members of the group add "correlated" noise to the "random" noise from the background.

In our classical example, one can informally define error suppression, error mitigation, and error correction: Error suppression means creating high-quality hardware: the signal input is perfect; the classical bits are perfect; the sound generators in the headphones are perfect. Error mitigation means eliminating background cocktail party (channel) noise, for example, via noise inverting devices, as well as eliminating noise generated within the group (e.g., noise within the brain from alcohol consumption and tinnitus). Error mitigation would also include recording of the session and providing a clean edited transcript afterwards (postprocessing). Error correction means coding the information such that any errors can be traced and corrected, in real time or at the end.

When it comes to real quantum computers, similar concepts and actions apply: one talks about quantum error suppression (QES), quantum error mitigation (QEM), and quantum error correction (QEC).

Fighting imperfections and noise in quantum processors

Key issues concern the impact of imperfections and noise on computational capacity. NISQ devices are noisy, which creates decoherence and computational errors due to qubit relaxation and dephasing. One talks about three main types of noise: incoherent, coherent, and correlated. JJ qubits are embedded in a sea of fluctuating defects creating stochastic charge fluctuations—incoherent noise—capable of driving unwanted qubit transitions causing relaxation. Moreover, qubit control via microwave waveguides and magnetic flux lines is subject to stochastic fluctuations influencing the precision of quantum operations. These fluctuating fields may lead to incoherent dephasing of individual qubits, as well as to systematic miscalibrations, drift, and crosstalk—coherent noise—that in principle can be reversed (Krantz et al., 2019; Hashim et al., 2021; Ahsan et al., 2022). Finally, recent work shows that impact of cosmic rays can generate quasiparticles that create correlated charge noise and qubit relaxations on a length scale of hundreds of micrometers (Vepsäläinen et al., 2020; Wilen et al., 2021).

Quantum error suppression

QES refers to various efforts to maximize the QV by improving the fabrication and operation of the quantum hardware (HW). (This excludes active feedback, treated as QEC).

On the fabrication side, the main issues concern minimizing decoherence (Krantz et al., 2019; Burnett et al., 2019; Vepsäläinen et al., 2020; Wilen et al., 2021; Spring et al., 2022; Müller et al., 2019; Bilmes et al., 2020; Carroll et al., 2022) and cross talk (Zhao et al., 2022; Spring et al., 2022). For a given QPU circuit, the issue is to maximize gate fidelities and speed via optimal control (e.g., pulse shaping) based on advanced characterization of the device (Wittler et al., 2021).

Quantum error mitigation

QEM aims to produce accurate expectation values of observables. It refers to various software methods to alleviate the effects of noise on computational results during execution of an algorithm on a QPU (Temme et al., 2017; Li and Benjamin, 2017; Kandala et al., 2017; Endo et al., 2018; Song et al., 2019; van den Berg et al., 2022; Takagi et al., 2022; Lolur et al., 2023).

QEM effectively involves creating a noisy distribution of results, and then extracting the desired quantum information via postprocessing. Currently, the main principles are zero-noise extrapolation (ZNE) (Temme et al., 2017; Li and Benjamin, 2017; Kandala et al., 2017; Endo et al., 2018) and probabilistic error cancellation (PEC) (Temme et al., 2017; Li and Benjamin, 2017; Endo et al., 2018; Song et al., 2019; van den Berg et al., 2022; Takagi et al., 2022). The first scheme (ZNE) does not make any assumption about the noise model other than it being weak and constant in time (Temme et al., 2017). The second scheme (PEC) can tolerate stronger noise; however, it requires detailed knowledge of the noise model (Temme et al., 2017).

ZNE works by physically increasing the impact of noise, determining a curve describing how the expectation value of some observable varies with noise. Variation of the noise strength can be done or simulated by varying the 1q- and 2q-gate times. Given enough points to determine the variation, the curve is then extrapolated back to zero noise, providing a best estimate of the expectation value. This has been implemented successfully in a number of experimental and theoretical investigation (Kandala et al., 2019; Giurgica-Tiron et al., 2020; Schultz et al., 2022; Pascuzzi et al., 2022, Kim et al., 2023).

The ZNE requires sufficient control of the time evolution to implement the rescaled dynamics and hinges on the assumption of a large time-scale separation between the dominant noise and the controlled dynamics (Temme et al., 2017).

PEC works by measuring the noise spectrum and applying an inverted quasiprobability distribution to the result of the computation via postprocessing (Temme et al., 2017; Li and Benjamin, 2017; Endo et al., 2018; Song et al., 2019; van den Berg et al., 2022; Takagi et al., 2022). PEC requires a full characterization of the noisy computational operations. To obtain this to sufficient precision is challenging in practice (Temme et al., 2017). Nevertheless, Song et al. (2019) experimentally demonstrated that PEC based on a combination of gate set tomography (GST) and quasiprobability decomposition can substantially reduce the error in quantum computation on a noisy quantum device. Moreover, van den Berg et al. (2022) have presented a practical protocol for learning and inverting a sparse noise model that is able to capture correlated noise and scales to large quantum devices, demonstrating PEC on a superconducting quantum processor with crosstalk errors.

In contrast, Leyton-Ortega et al. (2023) present a method to improve the convergence of variational algorithms by replacing the hardware implementation of certain Hermitian gates with their inverses, resulting in noise cancellation and a more resilient quantum circuit. This is demonstrated on superconducting quantum processors running the VQE algorithm to find the H_2 ground-state energy.

Another QEM method has been developed by Lolur et al. (2023) for quantum chemical computations on NISQ devices—Reference-State Error Mitigation (REM). The method relies on determining the exact error in energy due to hardware and environmental noise for a reference wavefunction that can be feasibly evaluated on a classical computer. REM is shown to drastically improve the computational accuracy at which total energies of molecules can be computed using current quantum hardware.

Quantum error correction

QEC refers to methods to code quantum information into logical qubits that can be measured, errors detected and identified, and logical qubits restored (Fowler et al., 2012; Kelly et al., 2015; Terhal, 2015; Wendin, 2017; Roffe, 2015; Bravyi et al., 2022; Ryan-Anderson et al., 2021, 2022; Postler et al., 2022; Andersen et al., 2020; Marques et al., 2022; Chen et al., 2021b; Krinner et al., 2022; Acharya et al., 2023; Piveteau et al., 2021; Ouyang, 2021; Suzuki et al., 2022). The initial application of the surface code to superconducting devices (Kelly et al., 2015) was followed up by several groups (Andersen et al., 2020; Marques et al., 2022; Chen et al., 2021b), and has recently resulted in demonstrations of repeated cycles of QEC. Krinner et al. (2022) implemented a 17-qubit distance-3 surface code, while Acharya et al. (2023) implemented a 49-qubit distance-5 code.

Acharya et al. (2023) draw particular attention to the question whether scaling up the error-correcting code size will reduce logical error rates in a real device. They answer it by reporting on a 72-qubit superconducting device supporting a 49-qubit distance-5 ($d = 5$) surface code that narrowly outperforms its average subset 17-qubit distance-3 ($d = 3$) surface code, demonstrating a critical step toward scalable QEC.

Even though John Martinis' group at USCB in 2014 announced that superconducting quantum circuits were at the surface code threshold for fault tolerance (Barends et al., 2014), this did not mean that the route to QEC was a straight one—it is all about scaling. When the physical error rate is high, the logical error probability increases with increasing system size while sufficiently low physical error rates will eventually lead to the desired exponential suppression of logical errors.

Acharya et al. (2023) show that their experiment lies in a crossover regime where increasing system size initially suppresses the logical error rate before, due to finite-size effects, later increasing it. They estimate that component performance must improve significantly to achieve practical scaling. In any case, the work demonstrates the first step in the process of suppressing logical errors by scaling up a quantum error-correcting code.

Scaling up for practical quantum advantage

The concept of quantum advantage (QA) has emerged as a reaction to the more dramatic notion of quantum superiority (QS) (Preskill, 2012). In principle, QS is what we need—exponential advantage of over classical computers. However, this is only possible with functional QEC. QA emphasizes enhanced performance relative to specific classical algorithms for real-world use cases, typically addressing variational problems like QAOA and VQE.

Currently there seems to be two opposite uses of practical QA: (i) effectively describing QS in huge QEC machines and (ii) mainly providing some useful speedup relative to classical algorithms. In the present NISQ era, there are essentially two ways to look at the scaling up of QPUs, what we will refer to as *QPU-centric* and *HPC-centric*.

QPU-centric approach

Here QPUs are scaled up in tune with HW progress to push the limits in experiments testing quantum supremacy (Arute et al., 2019; Wu et al., 2021; Zhu et al., 2022), QEC (Andersen et al., 2020; Chen et al., 2021b; Marques et al., 2022; Krinner et al., 2022; Acharya et al., 2023), and physics (Barends et al., 2015, 2016; Kandala et al., 2017, 2019; Gong et al., 2019; Arute et al., 2020b, a; Neill et al., 2021; Gong et al., 2021, 2022; Zhang et al., 2022b; Mi et al., 2022b; Stanisic et al., 2022). The main role of the classical computer is to serve a single "free-standing" QPU with pre- and post-processing resources for running quantum circuits. The maximum number of qubits in the QPU so far is 72 (Acharya et al., 2023). Further scaling up the number of qubits will make it possible to systematically build larger logical qubits and larger code distances. In a blog post in May 2021, Erik Lucero at Google (Lucero, 2021) began with a bold statement: "Within the decade, Google aims to build a useful, error-corrected quantum computer." The key issue in 2029 will most likely be "useful to whom?" Researchers or industry?

HPC-centric approach

Here the HPC supercomputer seamlessly integrates collections of parallel CPUs, GPUs, and QPUs. The quantum big picture is to boost classical performance by including QPU subroutines approximately solving specific NP-hard problems that form classical bottlenecks. In this sense, the IBM roadmap and philosophy look *HPC-centric*, even though it is described by IBM rather as quantum-centric supercomputing (Gambetta, 2022a; Bravyi et al., 2022). The maximum number of qubits is currently 433, in the Osprey QPU (IBM, 2022). Osprey will be operated as a system of small parallel QPUs to achieve a computational advantage in the near term by combining multiple QPUs through circuit knitting techniques (Bravyi et al., 2022; Piveteau and Sutter, 2022), improving the quality of solutions through error suppression and mitigation, and focusing on heuristic versions of quantum algorithms with asymptotic speedups. Much of this is controlled by fast electronics and software that must effectively be incorporated as a dedicated HPC in the QPU stack. In this sense, the IBM approach is indeed QPU-centric, and the HPC mainframe becomes more of a server. The work distribution between the HPC and the QC/QPU is basically floating, and the terminology rather reflects HPC/QC attitudes: who serves who?

The IBM Q Experience has created an ecosystem based on Qiskit, providing a versatile programming and testbed environment (García-Pérez et al., 2020; Bravyi et al., 2022), beginning to emerge as an industry standard. However, superpolynomial speedup does not belong to the NISQ era, and practical quantum advantage is elusive. Realistically, industrial users will not profit from quantum accelerators in the near term, so how can this large quantum effort be justified? The answer seems to be that IBM is going for useful quantum advantage via quantum parallel processing provided by QPU accelerators integrated in an efficient runtime HPC environment. Again the question is: useful to whom? Researchers or industry? And is useful quantum advantage possible without QEC?

The quantum volume (QV) effectively represents the size of a qubit register for which one can entangle all of its qubits in a single shot. Currently, for IBM the best published value is $QV = 2^9 = 512$, corresponding to a 9-qubit quantum circuit 9 levels deep. This means that there is no point running algorithms requiring more than that. Instead, one can configure the operating system to run a number of 9-qubit mini-QPUs in parallel to speed up the rate for creating measured distributions, thus reducing the time to solution for computing expectation values of physical variables, like energy.

Scale, quality, and speed are three key attributes to measure the performance of near-term quantum computers (Gambetta, 2022a; Bravyi et al., 2022). In the NISQ era, the QPU will spend very little time computing compared with the time spent by the CPU on pre- and post-processing before and after every call to the QPU. Calls that will be very frequent when solving variational problems. Circuit Layer Operations per Second (CLOPS) (Wack et al., 2021) is a measure correlated with how many QV circuits (mini-QPUs) a QPU can execute per unit of time, therefore shortening the time to solution.

At the IBM Summit 2022, Gambetta (2022b) pledged that in 2024, IBM will offer a system that will generate reliable outcomes running 100 qubits with gate depth of 100: "So creating this 100 × 100 device will really allow us to set up a path to understand how can we get quantum advantage in these systems and lay a future going forward." It must be noted, however, that this does not mean executing a 100q quantum circuit with depth 100 coherently "in a single shot," achieving $QV = 2^{100}$—that would be a quantum-earth shaking demonstration of quantum supremacy.

Microsoft has developed a framework for quantum resource estimation (Beverland et al., 2022) to estimate resources required across the stack layers for large-scale quantum applications, finding (as expected) that hundreds of thousands to many millions of physical qubits are needed to achieve practical quantum advantage. Beverland et al. (2022) maintain that the best solution is a monolithic QPU with, say, 10 million controllable, fast, and small qubits. The stack control system must be able to run millions of parallel high-fidelity gates at high speed, as well as reading out millions of qubits in parallel.

Not surprisingly, no qubit technology currently implemented satisfies all of these requirements. However, Microsoft suggests that the recent proposals of electro-acoustic qubits (Chamberland et al., 2022) and the topological qubit approach based on Majorana Zero Modes (MZMs) (Karzig et al., 2017) might do it in future. Practical quantum advantage is on the horizon but needs to be accelerated through a variety of breakthrough techniques. The Microsoft view is that these research directions can be best studied in the context of resource estimation to unlock quantum at scale.

Useful NISQ digital quantum advantage—Mission impossible?

The short answer is: yes, unfortunately probably mission impossible in the NISQ era. There are two fundamental questions: (1) Does the physical problem itself provide a quantum advantage? and (2), does a quantum algorithm have any advantage over a corresponding classical algorithm?

Both questions were the original drivers of QC: the exponential advantage of Shor's algorithm for factorization into prime numbers. However, the need for QEC put that problem far in the future. Instead, Matthias Troyer and coworkers (Reiher et al., 2017) promoted quantum chemistry for catalysts as the most useful killer application motivating the quest for scaling up QC. The paper argues that "quantum computers will be able to tackle important problems in chemistry without requiring exorbitant resources," but at the same time concludes that "The required space and time resources for simulating FeMoco are comparable to that of Shor's factoring algorithm." Berry et al. (2019) improved on those results, obtaining circuits requiring less surface code resources, despite using a larger and more accurate active space. Nevertheless, also this needs extensive QEC and is far beyond NISQ computers. Liu et al. (2022) further elaborate on the potential benefits of QC in the molecular sciences, that is, in molecular physics, chemistry, biochemistry, and materials science, emphasizing the competition with classical methods that will ultimately decide on the usefulness of quantum computation for molecular science. Lee et al. (2022) have examined the case for the exponential quantum advantage (EQA) hypothesis for the central task of ground-state determination in quantum chemistry. Key for EQA is for the quantum state preparation to be exponentially easy compared to classical heuristics, which is far from clear and perhaps not even likely (Wang et al., 2021; Bittel and Kliesch, 2021). Identifying relevant quantum chemical systems with strong evidence of EQA remains an open question (Lee et al., 2022).

The second question: "does a quantum algorithm have any advantage over a corresponding classical algorithm?" is currently a hot topic. Understanding whether, for example, quantum machine learning (QML) algorithms present a genuine computational advantage over classical approaches is extremely challenging. It seems that quantum-inspired classical algorithms "dequantizing" quantum algorithms (Tang, 2021, 2022; Cotler et al., 2021; Gharibian and Gall, 2022) can compete in polynomial time as long as one is not demanding exponentially accurate results.

Tang and coworkers (Tang, 2022) developed a dequantization framework for analyzing QML algorithms to produce formal evidence against EQA. These are fully classical algorithms that, on classical data, perform only polynomially slower than their quantum counterparts. The existence of a dequantized algorithm means that its quantum counterpart cannot give exponential speedups on classical data, suggesting that the quantum exponential speedups are simply an artifact of state preparation assumptions. QML has the best chance of achieving large speedups whenever classical computation cannot get access to this data (which occurs when input states come from quantum circuits and other physical quantum systems). This does not yet rule out the possibility of large polynomial speedups on classical data, which could still lead to significant performance improvements in practice with sufficiently good quantum computers (Tang, 2022).

Lloyd et al. (2016), however, proposed an algorithm for topological data analysis (TDA) that could not to be directly dequantized using the same techniques, raising the question whether a greater speedup was possible with TDA algorithms. This question has now been analyzed in depth by Berry et al. (2022), proposing a dequantization of the quantum TDA algorithm which shows that having exponentially large dimension and Betti number is necessary for superpolynomial advantage. The speedup is quartic, which will not be killed by QEC overhead (Babbush et al., 2021). Based on that, Berry et al. (2022) estimate that tens of billions of Toffoli gates will be sufficient to estimate a Betti number that should be classically intractable. This number of Toffoli gates is considered to be reasonable for early generations of fully fault-tolerant quantum computers (Berry et al., 2022), falling somewhere in between quantum chemistry applications and Shor's algorithm in terms of the resources required for quantum advantage.

Recently Akhalwaya et al. (2022) presented an NISQ-TDA QML algorithm needing only a short circuit depth with provable asymptotic speedup for certain classes of problems. How this goes together with Berry et al. (2022) remains to be understood in greater depth, as nicely explained by Quanta Magazine (Parshall, 2022), pointing out that the number of high-dimensional holes needs to be unthinkably large for quantum advantage.

Reconnecting here to quantum chemistry, Gharibian and Gall (2022) have shown how to design classical algorithms that estimate, with constant precision, the singular values of a sparse matrix, implying that the ground state energy in quantum chemistry can be solved efficiently with constant precision on a classical computer. However, Gharibian and Gall (2022) also prove that with inverse-polynomial precision, the same problem becomes BQP-complete, suggesting that the superiority of quantum algorithms for chemistry stems from the improved precision achievable in the quantum setting.

Finally, Huang et al. (2022) investigate quantum advantage in learning from experiments that processes quantum data with a quantum computer. That could have substantial advantages over conventional experiments in which quantum states are measured and outcomes are processed with a classical computer. Huang et al. (2022) prove that quantum machines can learn from exponentially fewer experiments than the number required by conventional experiments. They do that by assuming having access to data obtained from quantum-enhanced experiments like quantum sensing systems and stored in quantum memory (QRAM), allowing the QPU to process quantum input data. Exponential advantage is shown for predicting properties of physical systems, performing quantum principal component analysis, and learning about physical dynamics. Huang et al. (2022): "Although for now we lack suitably advanced sensors and transducers, we have conducted proof-of-concept experiments in which quantum data were directly planted in our quantum processor."

In the absence of perfect physical qubits, or QEC, quantum memory is a great challenge. Quantum memory may be far away for QC as needed by, for example, Huang et al. (2022), but it is essential for the development of quantum repeaters for quantum communication networks. O'Sullivan et al. (2022) investigate random-access quantum memory using chirped-pulse phase encoding. The protocol is implemented using donor spins in silicon coupled to a superconducting cavity, offering the potential for microwave random access quantum memories with lifetimes exceeding seconds.

Future directions

Improved and alternative superconducting qubits

A recent comprehensive review by Calzona and Carrega (2023) describes and analyzes the basic concepts and ideas behind the implementation of novel superconducting circuits with intrinsic protection against decoherence at the hardware level. The review explains the basics and performance of state-of-the-art transmons and other single-mode superconducting quantum circuits, and goes on to describe multimode superconducting qubits, toward the realization of fully protected qubits engineered in systems with more than one degree of freedom and/or characterized by the presence of specific symmetries.

Regarding state-of-the-art tantalum-based transmons Place et al. (2021), Wang et al. (2022b) and Tennant et al. (2022) performed low-frequency charge-noise spectroscopy on Ta-based transmons and found distinctly different behavior compared with Al- and Nb-based transmons. They conclude that the temperature-dependent behavior of the neighboring charge-configuration transitions is caused by jumps between local charge configurations in the immediate vicinity of the transmon. This is in contrast to Al- and Nb-based transmons which are dominated by a TLS distribution giving rise to 1/f noise, apparently ruling out a TLS collection as the basis of the quasistable charge offsets in Ta-based transmons.

Very different types of superconducting devices are semiconductor–superconductor hybrid structures containing Andreev bound states (ABS) (Wendin and Shumeiko, 2022) and topological MZMs (Das Sarma et al., 2015; Pikulin et al., 2021; Aghaee et al., 2022). Recently Pikulin et al. (2021) developed an experimental protocol (Topological Gap Protocol, TGP) to determine the presence and extent of a topological phase with MZMs in a hybrid semiconductor–superconductor three-terminal device with two normal leads and one superconducting lead. Now Aghaee et al. (2022) have presented measurements and simulations of InAs-Al hybrid three-terminal devices that are consistent with the observation of topological superconductivity and MZM, passing the TGP. Passing the protocol indicates a high probability of detection of a topological phase hosting MZMs as determined by large-scale disorder simulations and is a prerequisite for experiments involving fusion and braiding of MZMs.

Hybrid distributed computing

In Section "HPC-centric approach" we talked about distributed quantum processing, running many QPU modules in parallel. It is a matter of debate whether future large-scale algorithms can be run on monolithic or modular QPUs fitting inside a single fridge, or whether the algorithms have to be distributed over several fridges and locations. Eventually one will be able to work with clusters of quantum computers connected via local or global quantum networks, but for now this represents a great challenge waiting for great breakthroughs and a quantum infrastructure.

On a smaller scale, recent work has connected superconducting qubit circuits between two separate chips linked by a microwave cable: Wallraff's group (Magnard et al., 2020) produced multiqubit entanglement between single transmons in separate fridges while Cleland's group (Zhong et al., 2021; Yan et al., 2022) demonstrated entanglement, purification, and protection between two separately enclosed three-transmon nodes inside the same fridge. The microwave connections are photonic, but limited to local clusters. The needed interfaces for long-distance optical connections are emerging (Chu and Gröblacher, 2020), but will probably remain research endeavors for quite some time (Arnold et al., 2020; Wang et al., 2022a; Kumar et al., 2022; Tsuchimoto et al., 2022).

On a larger scale, Ang et al. (2022) have developed architectures for superconducting modular, distributed, or multinode quantum computers (MNQCs), employing a "co-design"-inspired approach to quantify overall MNQC performance in terms of hardware models of internode links, entanglement distillation, and local architecture. In the particular case of superconducting MNQCs with microwave-to-optical interconnects, Ang et al. (2022) describe how compilers and software should optimize the balance between local gates and internode gates, discuss when noisy quantum internode links have an advantage over purely classical links, and introduce a research roadmap for the realization of early MNQCs. This roadmap illustrates potential improvements to the hardware and software of MNQCs and outlines criteria for evaluating the improvement landscape, from progress in entanglement generation to the use of quantum memory in entanglement distillation and dedicated algorithms such as distributed quantum phase estimation.

As a concrete example, DiAdamo et al. (2021) consider an approach for distributing the VQE algorithm over distributed quantum computers with arbitrary number of qubits in a systematic approach to generate distributed quantum circuits for QC. This includes a proposal for software-based system for controlling quantum systems at the various classical and quantum hardware levels. DiAdamo et al. (2021) emphasize that much effort has gone into distributed computing in the classical computing domain. And since the overlap between the fields is high, one can use this knowledge to design robust and secure distributed quantum computers, and as quantum technologies improve, this may become a reality.

Continuous variables—Computing with resonators

In this field, the resonator modes are the logical qubits, and the transmon qubits provide ancillas for loading and readout. The Yale group is leading the development, and has recently demonstrated some decisive breakthroughs (Sivak et al., 2022b). The name of the game is to construct logical qubits from linear combinations of (already long-lived) resonator states representing the Gottesman-Kitaev-Preskill (GKP) bosonic code, encoding a logical qubit into grid states of an oscillator. Sivak et al. (2022b) demonstrate a fully stabilized and error-corrected logical qubit whose quantum coherence is significantly longer than that of all the imperfect quantum components involved in the QEC process, beating the best of them with a coherence gain of $G \approx 2.3$. This was achieved by combining innovations in several domains including the fabrication of superconducting quantum circuits and model-free reinforcement learning (Sivak et al., 2022a).

To correct for single-photon loss, Kudra et al. (2022) have implemented two photon transitions that excite the cavity and the qubit at the same time. The additional degree of freedom of the qubit makes it possible to implement a coherent, unidirectional mapping between spaces of opposite photon parity. The successful experimental implementation, when supplemented with qubit reset, is suitable for autonomous QEC in bosonic systems, opening up the possibility to realize a range of nonunitary transformations on a bosonic mode.

For full-scale QEC, various groups have recently investigated the concatenation of CV and DV codes, such as concatenating the single-mode GKP code with the surface code. Instead, Guillaud and Mirrahimi (2019) present a 1D repetition code based on a cat code as the base qubit for which the noise structure is modified in such a way that QEC becomes of similar complexity as classical error correction and can be performed using a simple repetition code. According to Guillaud and Mirrahimi (2019), the specific noise structure can be preserved for a set of fundamental operations which at the level of the repetition code lead to a universal set of protected logical gates.

Regarding scaling up CV resonator technology, Axline et al. (2018) have experimentally realized on-demand, high-fidelity state transfer and entanglement between two isolated superconducting cavity quantum memories. By transferring states in a multiphoton encoding, they show that the use of cavity memories and state-independent transfer creates the striking opportunity to deterministically mitigate transmission loss with QEC. The results establish a basis for deterministic quantum communication across networks, and will enable modular scaling of CV superconducting quantum circuits.

The size of superconducting 3D microwave resonators makes it challenging to scale up large 3D multiqubit CV systems. An alternative may be provided by nanomechanical phononic nanostructures (Chu and Gröblacher, 2020). Chu et al. (2017) experimentally demonstrated strong coupling between a superconducting transmon qubit and the long-lived longitudinal phonon modes of a high-overtone bulk acoustic wave disk resonator (HBAR) formed in thin-film aluminum nitride (AlN). Recently, von

Lüpke et al. (2022) demonstrated HBAR parity measurement in the strong dispersive regime of circuit quantum acoustodynamics, providing basic building blocks for constructing acoustic quantum memories and processors. Moreover, Schrinski et al. (2022) measured long-lived HBAR Wigner states, monitoring the gradual decay of negativities over tens of microseconds. Wollack et al. (2022) use a superconducting transmon qubit to control and read out the quantum state of a pair of nanomechanical resonators made from thin-film lithium niobate (LN). The device is capable of fast swap operations, used to deterministically manipulate the nonclassical and entangled mechanical quantum states. This creates potential for feedback-based operation of quantum acoustic processors. Finally, Chamberland et al. (2022) have presented a comprehensive architectural analysis for a proposed fault-tolerant quantum computer based on cat codes concatenated with outer quantum error-correcting codes applied to a system of acoustic resonators coupled to superconducting circuits with a two-dimensional layout.

Biochemistry and life science—Drivers of quantum computing?

Biochemistry and life science are, as always, at the focus of high-performance computing, driving the development of exascale and postexascale supercomputers, experiencing the limitations and bottlenecks. These are topics and areas that would profit immensely from quantum advantage. As already mentioned, Reiher et al. (2017) practically created the vision of quantum chemistry as the killer application for quantum computers, needed to design new catalysts for efficient biochemistry, beyond the reach of classical computers. Since then, if not before, quantum chemistry and materials science present a kind of mission for QC to benchmark methods, algorithms, and computers (Santagati et al., 2023; Rubin et al., 2023; Babbush et al., 2023; O'Brien et al., 2022; Liu et al., 2022; Lee et al., 2022; Goings et al., 2022; Cheng et al., 2020).

In computational science there is the well-established method of multiscale modeling (Fish et al., 2021) that gave the Nobel Prize in Chemistry in 2014 to Arieh Warshel for modeling biological functions, from enzymes to molecular machines (Warshel, 2014). Multiscale modeling describes methods that simulate continuum-scale behavior using information derived from computational models of finer scales in the system, down to molecular quantum levels, bridging across multiple length and time scales. It is then natural to consider using a quantum computer to address the case of a quantum system embedded in a multiscale environment. Cheng et al. (2020) review these methods and propose the embedding approach as a method for describing complex biochemical systems, with the parts treated at different levels of theory and computed with hybrid classical and quantum algorithms.

Considering healthcare, life science, and artificial intelligence in a broad sense, from the huge databases of cell biology and human diseases, one can design network models describing the networks of Life. In particular Barabasi, Loscalzo, and collaborators (Barabasi et al., 2011; Lee and Loscalzo, 2019) developed the science of network medicine, and machine learning is essential for creating models for therapies that can design and control the action of drugs (de Siqueira Santos et al., 2022; Infante et al., 2021).

Maniscalco et al. (2022) recently published a forward-looking white paper: "Quantum network medicine: rethinking medicine with network science and quantum algorithms," and posit that QC may be a key ingredient in enabling the full potential of network medicine, laying the foundations of a new era of disease mechanism, prevention, and treatment. This challenging vision reflects the mission of the entire field of QC—to achieve the elusive Quantum Advantage. The difficulty is amply illustrated by Goings et al. (2022) who discussed the ways to "explore the quantum computation and classical computation resources required to assess the electronic structure of cytochrome P450 enzymes (CYPs) and thus define a classical-quantum advantage boundary." One conclusion (Goings et al., 2022) is that a large classically intractable CYP model simulation may need 5 million qubits and nearly 10 billion Toffoli gates, and may take 100 QPU hours. Another, less surprising, conclusion is that deep classical chemical insight is essential for guiding quantum algorithms and defining the computational frontier for chemistry.

Conclusion

Quantum computers and QC have evolved in ways that seemed almost impossible a few decades ago. When David DiVincenzo published his famous seven points stating the conditions for creating functional quantum computers (DiVincenzo, 2000), the first superconducting solid-state qubit had just been born (Nakamura et al., 1999). And 10 years later, demonstrating elementary operations on two-three superconducting transmon qubits still represented the state of the art in that field. Scaling to larger systems was not meaningful until the quality of qubits and the technology of electronic and optical control systems for driving and reading out qubits had improved. However, during the following 10 years, the telecommunication development has provided many of the tools needed, and some areas of the field have gone from academic science to engineering.

Strictly speaking, the current technology for quantum computers is nevertheless not yet scalable. Classical digital computers became scalable when high-quality integrated transistor circuits were combined with error correction in the 1960s—then the road was open toward scaling, as manifested by Moore's Law (Moore, 1965). Morover, the subsequent invention of microprocessors in the 1970s opened up the landscape for classical computers. Nevertheless it took 60 years to get to where we are now, in continuous mutual adaptation of problem solving and technology development. This has led to exascale supercomputers with currently ten million cores that still uphold Moore's Law when it comes to computing power. However, as Landauer (May, 1991) pointed out, information is physical, which explains the current explosion of electrical power consumption for computing.

That long timescale is very different from today's visions of what QC will be able to do already in a not-so-distant future, and certainly different from the mission of several academic and industry projects to deliver useful quantum advantage by the end of this decade. Fortunately there are very few problems of importance to mankind that rely on the imminent arrival of quantum computers with quantum advantage. This is not to say that we do not need still more powerful computers—the problem is that the complex problems we may urgently want to solve, like the evolution of global climate dynamics, are NP-hard and can only be solved approximately, even by quantum computers. This means that predictions over time are necessarily uncertain. Adding to this the necessarily incomplete knowledge of models and background information, computation of our future unavoidably has huge error bars— uncertain predictions of the effects of global warming around the year 2100 are just one aspect of that.

The advantage of digital quantum computers beyond classical computing and algorithms must be established by benchmarking performance in practical applications. A common view in the HPC community is to regard QPUs as a kind of GPUs, closely integrated with the HPC and expected to accelerate the CPUs when handling hard problems that present classical bottlenecks. The development of HPC+QC integration is happening right now, and during the next 5 years, it will be taken to high levels—IBM is one prominent example. For sure this will challenge and boost the development of competitive classical algorithms and dedicated hardware—but useful quantum advantage for digital quantum computers may remain problematic in the NISQ era. It is therefore desirable to dampen some of the hype and promote realistic views of the near-future power of quantum computers. Industry currently involved in testing QC is certainly aware of what to expect, but that is not obvious when it comes to journalists and the public.

In the near term, the most important use of quantum processors may actually be to follow Feynman's original idea and create quantum hardware platforms for emulating physical systems with properties that are hard to describe by classical computers.

An important use of HPC is to make virtual rather than real-life experiments. One example is to describe the liquid environment of molecules via molecular dynamics simulations (Warshel, 2014). Another example is simulation of the behavior of aircraft in wind tunnels through extensive hydrodynamics calculations without need for real wind tunnels. In the same spirit, quantum processors already provide platforms for performing computer experiments, simulating fundamental quantum physics problems that are hard or impossible, in practice, for classical computers to describe. There are already impressive results for ion traps (Kokail et al., 2019, 2021), arrays of atoms (Scholl et al., 2021; Daley et al., 2022), and superconducting transmon processors (Arute et al., 2020b; Neill et al., 2021; Gong et al., 2021; Mi et al., 2022b; Zhang et al., 2022b; Karamlou et al., 2022; Landsman et al., 2019; Touil and Deffner, 2020; Mi et al., 2021; Braumüller et al., 2022; Mi et al., 2022a; Frey and Rachel, 2022; Kim et al., 2023). The near-term mission for superconducting processors might therefore be to emulate basic and applied physics experiments by mapping them on large superconducting controllable multiqubit networks that are impossible for classical digital supercomputers to simulate.

The next assessment of the future of quantum information processing is planned for 2028 (Wendin, 2028) and then we can perhaps compare notes.

Acknowledgments

This work was supported from the Knut and Alice Wallenberg Foundation through the Wallenberg Center for Quantum Technology (WACQT).

References

Aaronson S and Chen L (2017) Complexity-theoretic foundations of quantum supremacy experiments. *32nd Computational Complexity Conference CCC'17; arXiv: 1612.05903*, pp. 1–67.

Abhijith J, et al. (2022) Quantum algorithm implementations for beginners. *ACM Transactions on Quantum Computings* 3(4): 1–92.

Acharya R, et al. (2023) Suppressing quantum errors by scaling a surface code logical qubit. *Nature* 614(7949): 676–681.

Aghaee M, et al. (2022) InAs-Al hybrid devices passing the topological gap protocol. *arXiv:2207.02472v3*.

Aharonov D, Gao X, Landau Z, Liu Y, and Vazirani U (2022) A polynomial-time classical algorithm for noisy random circuit sampling. *arXiv:2211.03999v1*.

Ahsan M, Abbas S, Naqvi Z, and Anwer H (2022) Quantum circuit engineering for correcting coherent noise. *Physical Review A* 15: 022428.

Ajagekar A, Hamoud KA, and You F (2022) Hybrid classical-quantum optimization techniques for solving mixed-integer programming problems in production scheduling. *IEEE Transactions on Quantum Engineering* 3: 3102216.

Akhalwaya IY, et al. (2022) Towards quantum advantage on noisy quantum computers. *arXiv:2209.09371v2*.

Alexeev Y, et al. (2021) Quantum computer systems for scientific discovery. *PRX Quantum* 2: 017001.

Altman E, et al. (2022) Quantum simulators: Architectures and opportunities. *PRX Quantum* 2: 017003.

Andersen CK, Remm A, Lazar S, Krinner S, Lacroix N, Norris GJ, Gabureac M, Eichler C, and Wallraff A (2020) Repeated quantum error detection in a surface code. *Nature Physics* 16(8): 875.

Ang J, et al. (2022) Architectures for multinode superconducting quantum computers. *arXiv:2212.06167v1*.

Arnold G, Wulf M, Barzanjeh S, Redchenko ES, Rueda A, Hease WJ, Hassani F, and Fink JM (2020) Converting microwave and telecom photons with a silicon photonic nanomechanical interface. *Nature Communications* 11: 4460.

Arute F, et al. (2019) Quantum supremacy using a programmable superconducting processor. *Nature* 574: 505–510.

Arute F, et al. (2020a) Hartree-Fock on a superconducting qubit quantum computer. *Science* 369: 1084–1089.

Arute F, et al. (2020b) Observation of separated dynamics of charge and spin in the Fermi-Hubbard model. *arXiv:2010.07965v1*.

Axline CJ, Burkhart LD, Pfaff W, Zhang M, Chou K, Campagne-Ibarcq P, Reinhold P, Frunzio L, Girvin SM, Jiang L, Devoret MH, and Schoelkopf RJ (2018) On-demand quantum state transfer and entanglement between remote microwave cavity memories. *Nature Physics* 14: 705–710.

Babbush R, McClean JR, Newman M, Gidney C, Boixo S, and Neven H (2021) Focus beyond quadratic speedups for error-corrected quantum advantage. *PRX Quantum* 2: 010103.

Babbush R, Huggins WJ, Berry DW, Ung SF, Zhao A, Reichman DR, Neven H, Baczewski AD, and Lee J (2023) Quantum simulation of exact electron dynamics can be more efficient than classical mean-field methods. *arXiv:2301.01203v1*.

Barabasi AL, Gulbahce N, and Loscalzo J (2011) Network medicine: A network-based approach to human disease. *Nature Reviews. Genetics* 12: 56e68.

Barends R, et al. (2014) Superconducting quantum circuits at the surface code threshold for fault tolerance. *Nature* 508: 500–503.

Barends R, et al. (2015) Digital quantum simulation of fermionic models with a superconducting circuit. *Nature Communications* 6: 7654.

Barends R, et al. (2016) Digitized adiabatic quantum computing with a superconducting circuit. *Nature* 534(7606): 222–226.

Bengtsson A, et al. (2020) Quantum approximate optimization of the exact-cover problem on a superconducting quantum processor. *Physical Review Applied* 14: 034010.

Berry DW, Gidney C, Motta M, McClean JR, and Babbush R (2019) Qubitization of arbitrary basis quantum chemistry by low rank factorization. *Quantum* 3: 208.

Berry DW, et al. (2022) Quantifying quantum advantage in topological data analysis. *arXiv:2209.13581v1*.

Beverland ME, et al. (2022) Assessing requirements to scale to practical quantum advantages. *arXiv:2211.07629v1*.

Bharti K, et al. (2022) Noisy intermediate-scale quantum algorithms. *Reviews of Modern Physics* 94: 015004.

Bilmes A, Megrant A, Klimov P, Weiss G, Martinis JM, Ustinov AV, and Lisenfeld J (2020) Resolving the positions of defects in superconducting quantum bit. *Science Reports* 10: 3090.

Bittel L and Kliesch M (2021) Training variational quantum algorithms is NP-hard. *Physical Review Letters* 127: 120502.

Blais A, Girvin SM, and Oliver WD (2020) Quantum information processing and quantum optics with circuit quantum electrodynamics. *Nature Physics* 16: 247.

Blais A, Grimsmo AL, Girvin SM, and Wallraff A (2021) Circuit quantum electrodynamics. *Reviews of Modern Physics* 93: 025005.

Boixo S, Isakov SV, Smelyanskiy VN, Babbush R, Ding N, Jiang Z, Bremner MJ, Martinis JM, and Neven H (2018) Characterizing quantum supremacy in near-term devices. *Nature Physics* 14: 595–600.

Borle A, Elfving VE, and Lomonaco SJ (2021) Quantum approximate optimization for hard problems in linear algebra. *SciPost Physics Core* 4: 031.

Bouland A, Fefferman B, Nirkhe C, and Vazirani U (2019) On the complexity and verification of quantum random circuit sampling. *Nature Physics* 15: 159–163.

Braumüller J, et al. (2022) Probing quantum information propagation with out-of-time-ordered correlators. *Nature Physics* 18: 172–178.

Bravyi S, Kliesch A, Koenig R, and Tan E (2020) Obstacles to variational quantum optimization from symmetry protection. *Physical Review Letters* 125: 260505.

Bravyi S, Dial O, Gambetta JM, Gil D, and Nazario Z (2022) The future of quantum computing with superconducting qubits. *Journal of Applied Physics* 132(16): 160902.

Brown KR, Chiaverini J, Sage JM, and Häffner H (2021) Materials challenges for trapped-ion quantum computers. *Nature Reviews Materials* 6: 893–905.

Brubaker B (2023) New algorithm closes quantum supremacy window. *Quanta Magazine January 9, 2023*.

Bruzewicz CD, Chiaverini J, McConnell R, and Sage JM (2019) Trapped-ion quantum computing: Progress and challenges. *Applied Physics Reviews* 6: 021314.

Burnett JJ, Bengtsson A, Scigliuzzo M, Niepce D, Kudra M, Delsing P, and Bylander J (2019) Decoherence benchmarking of superconducting qubits. *npj Quantum Information* 5: 54.

Calvin JA, Peng C, Rishi V, Kumar A, and Valeev EF (2021) Many-body quantum chemistry on massively parallel computers. *Chemical Reviews* 121: 1203–1231.

Calzona A and Carrega M (2023) Muti-mode architectures for noise-resilient superconducting qubits. *Superconductor Science and Technology* 36: 023001.

Cao Y, et al. (2019) Quantum chemistry in the age of quantum computing. *Chemical Reviews* 119: 10856.

CAPD. (2023) *Central Auditory Processing Disorder (CAPD) is a Deficiency in the Central Auditory Nervous System (CANS).* https://www.asha.org/practice-portal/clinical-topics/central-auditory-processing-disorder/; https://www.additudemag.com/central-auditory-processing-disorder/.

Carroll M, Rosenblatt S, Jurcevic P, Lauer I, and Kandala A (2022) Dynamics of superconducting qubit relaxation times. *npj Quantum Information* 8: 132.

Cerezo M, et al. (2021) Variational quantum algorithms. *Nature Reviews Physics* 3: 625–644.

Chamberland C, et al. (2022) Building a fault-tolerant quantum computer using concatenated cat codes. *PRX Quantum* 3: 010329.

Chandarana P, Hegade NN, Paul K, Albarrán-Arriagada F, Solano E, del Campo A, and Chen X (2022) Digitized-counterdiabatic quantum approximate optimization algorithm. *Physical Review Research* 4: 013141.

Chandran A, Iadecola T, Khemani V, and Moessner R (2023) Quantum many-body scars: A quasiparticle perspective. *Annual Review of Condensed Matter Physics* 14: 443–469.

Chen H, Nusspickel M, Tilly J, and Booth GH (2021a) Variational quantum eigensolver for dynamic correlation functions. *Physical Review A* 104: 032405.

Chen Z, et al. (2021b) Exponential suppression of bit or phase errors with cyclic error correction. *Nature* 595(7867): 383–387.

Chen I-C, et al. (2022a) Error-mitigated simulation of quantum many-body scars on quantum computers with pulse-level control. *Physical Review Research* 4: 043027.

Chen Y, Zhu L, Liu C, Mayhall NJ, Barnes E, and Economou SE (2022b) How much entanglement do quantum optimization algorithms require?. *Quantum 2.0 Conference 2022; arXiv:2205.12283*.

Cheng H-P, Deumens E, Freericks JK, Li C, and Sanders BA (2020) Application of quantum computing to biochemical systems: A look to the future. *Frontiers in Chemistry* 8: 587143.

Chu Y and Gröblacher S (2020) A perspective on hybrid quantum opto- and electromechanical systems. *Applied Physics Letters* 117: 150503.

Chu Y, Kharel P, Renninger WH, Burkhart LD, Frunzio L, Rakich PT, and Schoelkopf RJ (2017) Quantum acoustics with superconducting qubit. *Science* 358(6360): 199–202.

Córcoles AD, Kandala A, Javadi-Abhari A, McClure DT, Cross AW, Temme K, Nation PD, Steffen M, and Gambetta JM (2020) Challenges and opportunities of near-term quantum computing systems. *Proceedings of the IEEE* 108(8): 1338.

Cotler J, Huang H-Y, and McClean JR (2021) Revisiting dequantization and quantum advantage in learning tasks. *arXiv:2112.00811v2*.

CPS. (2023) *The "Cocktail Party Syndrome" is the name given to the inability to differentiate sound from background noise.* https://en.wikipedia.org/wiki/Cocktail_party_effect.

Cross AW, Bishop LS, Sheldon S, Nation PD, and Gambetta JM (2019) Validating quantum computers using randomized model circuits. *Physical Review A* 100: 032328.

Csalódi R, Süle Z, Jaskó S, Holczinger T, and Abonyi J (2021) Industry 4.0-driven development of optimization algorithms: A systematic overview. *Complexity* 2021: 1–22.

Daley AJ, Bloch I, Kokail C, Flannigan S, Pearson N, Troyer M, and Zoller P (2022) Practical quantum advantage in quantum simulation. *Nature* 607: 667–676.

Das Sarma S, Freedman MH, and Nayak C (2015) Majorana zero modes and topological quantum computation. *npj Quantum Information* 1: 15001.

Das Sarma S (2022) Quantum computing has a hype problem. *MIT Technology Review (March 28, 2022)*.

de Gracia-Treviño JA, Delcey MG, and Wendin G (2023) Complete active space methods for NISQ devices: The importance of canonical orbital optimization for accuracy and noise resilience. *ChemRxiv*.

de Siqueira Santos S, Torres M, Galeano D, del Mar Sánchez M, Cernuzzi L, and Paccanaro A (2022) Machine learning and network medicine approaches for drug repositioning for COVID-19. *Patterns (New York)* 3(1): 100396.

de Sousa Junior WT, Montevechi JAB, de Carvalho Miranda R, and Campos AT (2019) Discrete simulation-based optimization methods for industrial engineering problems: A systematic literature review. *Computers & Industrial Engineering* 128: 526–540.

DiAdamo S, Ghibaudi M, and Cruise J (2021) Distributed quantum computing and network control for accelerated VQE. *IEEE Transactions on Quantum Engineering* 2: 3100921.

DiVincenzo D (2000) The physical implementation of quantum computation. *Fortschritte der Physik* 9–11: 771–783.

Dupont M, Didier N, Hodson MJ, Moore JE, and Reagor MJ (2022) An entanglement perspective on the quantum approximate optimization algorithm. *Physical Review A* 106: 022423.

Egger DJ, Marecek J, and Woerner S (2021) Warm-starting quantum optimization. *Quantum* 5: 479.

Elfving VE, Millaruelo M, Gámez JA, and Gogolin C (2021) Simulating quantum chemistry in the seniority-zero space on qubit-based quantum computers. *Physical Review A* 103: 032605.

Endo S, Benjamin SC, and Li Y (2018) Practical quantum error mitigation for near-future applications. *Physical Review X* 8: 031027.

Ezratty O (2022) Mitigating the quantum hype. *arXiv:2202.01925*.

Farhi E and Harrow AW (2016) Quantum supremacy through the quantum approximate optimization algorithm. *arXiv:1602.07674v1*.

Farhi E, Goldstone J, and Gutmann S (2014) A quantum approximate optimization algorithm. *arXiv:1411.4028*.

Farhi E, Goldstone J, Gutmann S, and Zhou L (2022) The quantum approximate optimization algorithm and the Sherrington-Kirkpatrick model at infinite size. *Quantum* 6: 759.

Fedorov DA, Peng B, Govind N, and Alexeev Y (2022) VQE method: A short survey and recent developments. *Materials Theory* 6: 2.

Fish J, Wagner GJ, and Keten S (2021) Mesoscopic and multiscale modelling in materials. *Nature Materials* 20: 774.

Fitzek D, Ghandriz T, Laine L, Granath M, and Kockum AF (2021) Applying quantum approximate optimization to the heterogeneous vehicle routing problem. *arXiv:2110.06799*.

Fowler AG, Mariantoni M, Martinis JM, and Cleland AN (2012) Surface codes: Towards practical large-scale quantum computation. *Physical Review A* 86: 032324.

Franca DS and Garcia-Patron R (2021) Limitations of optimization algorithms on noisy quantum devices. *Nature Physics* 17: 1221.

Frey P and Rachel S (2022) Realization of a discrete time crystal on 57 qubits of a quantum computer. *Science Advances* 8: eabm7652.

Gambetta J (2022a) *Expanding the IBM Quantum Roadmap to Anticipate the Future of Quantum-Centric Supercomputing (10 May 2022).* https://research.ibm.com/blog/ibm-quantum-roadmap-2025.

Gambetta J (2022b) *IBM Quantum Summit 2022, IBM Quantum State of the Union 2022.* https://www.ibm.com/quantum/summi.

García-Pérez G, Rossi MAC, and Maniscalco S (2020) IBM Q Experience as a versatile experimental testbed for simulating open quantum systems. *npj Quantum Information* 6: 1.

Gharibian S and Gall FL (2022) Dequantizing the quantum singular value transformation: Hardness and applications to quantum chemistry and the quantum PCP conjecture. *STOC 2022: Proceedings of the 54th Annual ACM SIGACT Symposium on Theory of ComputingJune (STOC 2022)*, pp. 19–32.

Giurgica-Tiron T, Hindy Y, LaRose R, Mari A, and Zeng WJ (2020) Digital zero noise extrapolation for quantum error mitigation. *2020 IEEE International Conference on Quantum Computing and Engineering (QCE)*.

Glover F, Kochenberger G, and Du Y (2022a) Quantum bridge analytics I: A tutorial on formulating and using QUBO models. *Annuals of Operations Research* 17: 335–337.

Glover F, Kochenberger G, Ma M, and Du Y (2022b) Quantum bridge analytics II: QUBO-Plus, network optimization and combinatorial chaining for asset exchange. *Annals of Operations Research* 314: 185.

Goings JJ, White A, Lee J, Tautermann CS, Degroote M, Gidney C, Shiozaki T, Babbush R, and Rubin NC (2022) Reliably assessing the electronic structure of cytochrome P450 on today's classical computers and tomorrow's quantum computers. *PNAS* 119. e2203533119.

Gong M, et al. (2019) Genuine 12-qubit entanglement on a superconducting quantum processor. *Physical Review Letters* 122: 110501.

Gong M, et al. (2021) Quantum walks on a programmable two-dimensional 62-qubit superconducting processor. *Science* 372: 948–952.

Gong M, et al. (2022) Quantum neuronal sensing of quantum many-body states on a 61-qubit programmable superconducting processors. *arXiv:2201.05957v1*.

Grimsley HR, Economou SE, Barnes E, and Mayhall NJ (2019) An adaptive variational algorithm for exact molecular simulations on a quantum computer. *Nature Communications* 10: 3007.

Grönkvist, M., 2005. The Tail Assignment Problem. (Ph.D. thesis), Chalmers University of Technology.

Gu X, Kockum AF, Miranowicz A, Liu Y-X, and Nori F (2019) Microwave photonics with superconducting quantum circuits. *Physics Reports* 718–719: 1.

Guerreschi GG and Matsuura AY (2019) QAOA for Max-Cut requires hundreds of qubits for quantum speed-up. *Scientific Reports* 9: 6903.

Guillaud J and Mirrahimi M (2019) Repetition cat qubits for fault-tolerant quantum computation. *Physical Review X* 9: 041053.

Hangleiter D and Eisert J (2022) Computational advantage of quantum random sampling. *aXiv:2206.04079v3*.

Harrigan MP, et al. (2021) Quantum approximate optimization of non-planar graph problems on a planar superconducting processor. *Nature Physics* 17: 332–336.

Hashim A, et al. (2021) Randomized compiling for scalable quantum computing on a noisy superconducting quantum processor. *Physical Review X* 11: 041039.

Hegade NN, Chen X, and Solano E (2022) Digitized counterdiabatic quantum optimization. *Physical Review Research* 4: L042030.

Herrman R, Ostrowski J, Humble TS, and Siopsis G (2021) Lower bounds on circuit depth of the quantum approximate optimization algorithm. *Quantum Information Processing* 20: 59.

Huang H-Y, Broughton M, Cotler J, Chen S, Li J, Mohseni M, Neven H, Babbush R, Kueng R, Preskill J, and McClean JR (2022) Quantum advantage in learning from experiments. *Science* 376: 1182.

IBM. (2022) *Osprey.* https://newsroom.ibm.com/2022-11-09-IBM-Unveils-400-Qubit-Plus-Quantum-Processor-and-Next-Generation-IBM-Quantum-System-Two.

Infante T, et al. (2021) Machine learning and network medicine: A novel approach for precision medicine and personalized therapy in cardiomyopathies. *Journal of Cardiovascular Medicine* 22(6): 429.

Jones GM, Pathirage PDVS, and Vogiatzis KD (2022) Data-driven acceleration of coupled-cluster theory and perturbation theory methods. In: Pavlo Dral (ed.) *Quantum Chemistry in the Age of Machine Learning*, pp. 509–529. Elsevier.

Kandala A, Mezzacapo A, Temme K, Takita M, Brink M, Chow JM, and Gambetta JM (2017) Hardware-efficient quantum optimizer for small molecules and quantum magnets. *Nature* 549(7671): 242–246.

Kandala A, Temme K, Córcoles AD, Mezzacapo A, Chow JM, and Gambetta JM (2019) Error mitigation extends the computational reach of a noisy quantum processor. *Nature* 567 (7749): 491.

Karamlou AH, et al. (2022) Quantum transport and localization in 1d and 2d tight-binding lattices. *npj Quantum Information* 8: 35.

Karzig T, et al. (2017) Scalable designs for quasiparticle-poisoning-protected topological quantum computation with majorana zero modes. *Physical Review B* 95: 235305.

Kelly J, et al. (2015) State preservation by repetitive error detection in a superconducting quantum circuit. *Nature* 519: 66–69.

Kim IH, Liu Y-H, Pallister S, Pol W, and Roberts S (2022) Fault-tolerant resource estimate for quantum chemical simulations: Case study on Li-ion battery electrolyte molecules. *Physical Review Research* 4: 023019.

Kim Y, et al. (2023) Scalable error mitigation for noisy quantum circuits produces competitive expectation values. *Nature Physics*. https://doi.org/10.1038/s41567-022-01914-3.

Kjaergaard M, Yan F, Orlando TP, Gustavsson S, and Oliver WD (2020) Superconducting qubits: Current state of play. *Annual Review of Condensed Matter Physics* 11: 369.

Kokail C, et al. (2019) Self-verifying variational quantum simulation of lattice models. *Nature* 569: 355–360.

Kokail C, van Bijnen R, Elben A, Vermisch B, and Zoller P (2021) Entanglement Hamiltonian tomography in quantum simulation. *Nature Physics* 17: 936–942.

Kowalsky M, Albash T, Hen I, and Lidar DA (2022) 3-regular three-XORSAT planted solutions benchmark of classical and quantum heuristic optimizers. *Quantum Science and Technology* 7: 025008.

Krantz P, Kjaergaard M, Yan F, Orlando TP, Gustavsson S, and Oliver WD (2019) A quantum engineer's guide to superconducting qubits. *Applied Physics Reviews* 6: 021318.

Krinner S, et al. (2022) Realizing repeated quantum error correction in a distance-three surface code. *Nature* 605: 669.

Kudra M, Abad T, Kervinen M, Eriksson AM, Quijandrá F, Delsing P, and Gasparinetti S (2022) Experimental realization of deterministic and selective photon addition in a bosonic mode assisted by an ancillary qubit. *arXiv:2212.12079v1*.

Kumar A, Suleymanzade A, Stone M, Taneja L, Anferov A, Schuster DI, and Simon J (2022) Quantum-limited millimeter wave to optical transduction. *arXiv:2207.10121v1*.

Lacroix N, et al. (2020) Improving the performance of deep quantum optimization algorithms with continuous gate sets. *PRX Quantum* 1: 020304.

Lamata L, Parra-Rodriguez A, Sanz M, and Solano E (2018) Digital-analog quantum simulations with superconducting circuits. *Advances in Physics: X* 3: 1457981.

Lan Z and Liang WZ (2022) Amplitude reordering accelerates the adaptive variational quantum eigensolver algorithms. *Journal of Chemical Theory and Computation* 18: 5267.

Landauer R (1991) Information is physical. *Physics Today, May 1991*.

Landsman KA, Figgatt C, Schuster T, Linke NM, Yoshida B, Yao NY, and Monroe C (2019) Verified quantum information scrambling. *Nature* 567: 61–65.

Lee LY-H and Loscalzo J (2019) Network medicine in pathobiology. *The American Journal of Pathology* 189: 1311.

Lee J, Huggins WJ, Head-Gordon M, and Whaley KB (2019) Generalized unitary coupled cluster wave functions for quantum computation. *Journal of Chemical Theory and Computation* 15: 311.

Lee S, et al. (2022) Is there evidence for exponential quantum advantage in quantum chemistry? *arXiv:2208.02199v3*.

Leyton-Ortega V, Majumder S, and Pooser RC (2023) Quantum error mitigation by hidden inverses protocol in superconducting quantum devices. *Quantum Science and Technology* 8: 014008.

Li Y and Benjamin SC (2017) Efficient variational quantum simulator incorporating active error minimization. *Physical Review X* 7: 021050.

Liu H, Low GH, Steiger DS, Häner T, Reiher M, and Troyer M (2022) Prospects of quantum computing for molecular sciences. *Materials Theory* 6: 11.

Lloyd S, Garnerone S, and Zanardi P (2016) Quantum algorithms for topological and geometric analysis of data. *Nature Communications* 6: 10138.

Lolur P, Rahm M, Skogh M, García-Álvarez L, and Wendin G (2021) Benchmarking the variational quantum eigensolver through simulation of the ground state energy of prebiotic molecules on high-performance computers. *AIP Conference Proceedings* 2362: 030005.

Lolur P, Skogh M, Dobrautz W, Warren C, Biznárová J, Osman A, Tancredi G, Wendin G, Bylander J, and Rahm M (2023) Reference-state error mitigation: A strategy for high accuracy quantum computation of chemistry. *Journal of Chemical Theory and Computation* 19: 783–789.

Lucero E (2021) *Google: Unveiling our new Quantum AI campus, May 18, 2021*. https://qt.eu/app/uploads/2018/04/93056_Quantum-Manifesto_WEB.pdf.

Magnard P, et al. (2020) Microwave quantum link between superconducting circuits housed in spatially separated cryogenic systems. *Physical Review Letters* 125: 260502.

Maniscalco S, et al. (2022) Quantum network medicine: Rethinking medicine with network science and quantum algorithms. *arXiv:2206.12405v1*.

Marques JF, et al. (2022) Logical-qubit operations in an error-detecting surface code. *Nature Physics* 18(1): 80–86.

McArdle S, Endo S, Aspuru-Guzik A, Benjamin SC, and Yuan X (2020) Quantum computational chemistry. *Reviews of Modern Physics* 92: 015003.

McClean JR, et al. (2021) What the foundations of quantum computer science teach us about chemistry. *The Journal of Chemical Physics* 155: 150901.

Mi X, et al. (2021) Information scrambling in quantum circuits. *Science* 374: 1479–1483.

Mi X, et al. (2022a) Noise-resilient edge modes on a chain of superconducting qubits. *Science* 378(6621): 785–790.

Mi X, et al. (2022b) Time-crystalline eigenstate order on a quantum processor. *Nature* 601(7894): 531–536.

Monden Y (2012) *TOYOTA Production System an Integrated Approach to Just-In-Time*. CRC Press, Taylor & Francis Group.

Mooney GJ, White GAL, Hill CD, and Hollenberg LCL (2021) Generation and verification of 27-qubit Greenberger-Horne-Zeilinger states in a superconducting quantum computer. *Journal of Physics Communications* 5: 095004.

Moore GE (1965) Cramming more components onto integrated circuits. *Electronics*. April 19, 1965.

Morales MES, Biamonte JD, and Zimborás Z (2020) On the universality of the quantum approximate optimization algorithm. *Quantum Information Processing* 19: 291.

Moudgalya S, Bernevig BA, and Regnault N (2022) Quantum many-body scars and Hilbert space fragmentation: A review of exact results. *Reports on Progress in Physics* 85: 086501.

Moussa C, Wang H, Bäck T, and Dunjko V (2022) Unsupervised strategies for identifying optimal parameters in quantum approximate optimization algorithm. *EPJ Quantum Technology* 9: 11.

Müller C, Cole JH, and Lisenfeld J (2019) Towards understanding two-level-systems in amorphous solids: Insights from quantum circuits. *Reports on Progress in Physics* 82: 124501.

Nakamura Y, Pashkin YA, and Tsai J-S (1999) Coherent control of macroscopic quantum states in a single-Cooper-pair box. *Nature* 398: 786–788.

Neill C, et al. (2021) Accurately computing the electronic properties of a quantum ring. *Nature* 594(7864): 508–551.

O'Brien TE, et al. (2022) Efficient quantum computation of molecular forces and other energy gradients. *Physical Review Research* 4: 043210.

Ong JH and Teo J (2021) Systematic review and open challenges in hyper-heuristics usage on expensive optimization problems with limited number of evaluations. *2021 IEEE Symposium on Industrial Electronics & Applications (ISIEA)*.

O'Sullivan J, et al. (2022) Random-access quantum memory using chirped pulse phase encoding. *Physical Review X* 12: 041014.

Ouyang Y (2021) Avoiding coherent errors with rotated concatenated stabilizer codes. *npj Quantum Information* 7: 87.

Pan F, Chen K, and Zhang P (2022) Solving the sampling problem of the Sycamore quantum circuits. *Physical Review Letters* 129: 090502.

Parshall A (2022) After a quantum clobbering, one approach survives unscathed. *Quanta Magazine Dec 7, 2022*.

Pascuzzi VR, He A, Bauer CW, de Jong WA, and Nachman B (2022) Computationally efficient zero-noise extrapolation for quantum-gate-error mitigation. *Physical Review A* 105: 042406.

Patel YJ, Jerb S, Bäck T, and Dunjko V (2022) Reinforcement learning assisted recursive QAOA. *arXiv:2207.06294v1*.

Pednault E, Gunnels J, Maslov D, and Gambetta J (2019) *On "Quantum Supremacy"*. https://qt.eu/app/uploads/2018/04/93056_Quantum-Manifesto_WEB.pdf.

Pelofske E, Bärtschi A, and Eidenbenz S (2022) Quantum Volume in practice: What users can expect from NISQ devices. *arXiv:2203.03816v4*.

Pikulin DI, et al. (2021) Protocol to identify a topological superconducting phase in a three-terminal device. *arXiv:2103.12217v1*.

Piveteau C and Sutter D (2022) Circuit knitting with classical communication. *arXiv:2205.00016*.

Piveteau C, Sutter D, Bravyi S, Gambetta JM, and Temme K (2021) Error mitigation for universal gates on encoded qubits. *Physical Review Letters* 127: 200505.

Place APM, et al. (2021) New material platform for superconducting transmon qubits with coherence times exceeding 0.3 milliseconds. *Nature Communications* 12: 1779.

Postler L, et al. (2022) Demonstration of fault-tolerant universal quantum gate operations. *Nature* 605(7911): 675–680.

Preskill J (2012) Quantum computing and the entanglement frontier. *arXiv:1203.5813*.

Preskill J (2018) Quantum computing in the NISQ era and beyond. *Quantum* 2: 79.

QUTAC. (2021) QUTAC, industry quantum computing applications. *EPJ Quantum Technology* 8: 25.

Rai R, Tiwari MK, Ivanov D, and Dolgui A (2021) Machine learning in manufacturing and industry 4.0 applications. *International Journal of Production Research* 59: 4773.

Reiher M, Wiebe N, Svore KM, Wecker D, and Troyer M (2017) Elucidating reaction mechanisms on quantum computers. *PNAS* 114: 7555.

Roffe J (2015) Quantum error correction: An introductory guide. *Contemporary Physics* 60(3): 226.

Rubin NC, et al. (2023) Fault-tolerant quantum simulation of materials using Bloch orbitals. *arXiv:2302.05531v1*.

Ryan-Anderson C, et al. (2021) Realization of real-time fault-tolerant quantum error correction. *Physical Review X* 11: 041058.

Ryan-Anderson C, et al. (2022) Implementing fault-tolerant entangling gates on the five-qubit code and the color code. *arXiv: 2208.01863v1*.

Sanders YR, Berry DW, Costa PCS, Tessler LW, Wiebe N, Gidney C, Neven H, and Babbush R (2020) Compilation of fault-tolerant quantum heuristics for combinatorial optimization. *PRX Quantum* 1: 020312.

Santagati R, et al. (2023) Drug design on quantum computers. *arXiv:2301.04114v1*.

Sapova MD and Fedorov AK (2022) Variational quantum eigensolver techniques for simulating carbon monoxide oxidation. *Communications Physics* 5: 19.

Scholl P, et al. (2021) Quantum simulation of 2D antiferromagnets with hundreds of Rydberg atoms. *Nature* 595: 233–238.

Schrinski B, et al. (2022) Macroscopic quantum test with bulk acoustic wave resonators. *arXiv:2209.06635v1*.

Schultz K, et al. (2022) Impact of time-correlated noise on zero-noise extrapolation. *Physical Review A* 106: 052406.

Sivak VV, et al. (2022a) Model-free quantum control with reinforcement learning. *Physical Review X* 12: 011059.

Sivak VV, et al. (2022b) Real-time quantum error correction beyond break-even. *arXiv:2211.09116v1*.

Sokolov IO, Barkoutsos PK, Ollitrault PJ, Greenberg D, Rice J, Pistoia M, and Tavernelli I (2020) Quantum orbital-optimized unitary coupled cluster methods in the strongly correlated regime: Can quantum algorithms outperform their classical equivalents? *The Journal of Chemical Physics* 152: 124107.

Song C, et al. (2017) 10-qubit entanglement and parallel logic operations with a superconducting circuit. *Physical Review Letters* 119: 180511.

Song C, Cui J, Wang H, Hao J, Feng H, and Li Y (2019) Quantum computation with universal error mitigation on a superconducting quantum processor. *Science Advances* 5: eaaw5686.

Souffi S (2023) Reduction in sound discrimination in noise is related to envelope similarity and not to a decrease in envelope tracking abilities. *The Journal of Physiology* 601(1): 123.

Spring PA, et al. (2022) High coherence and low cross-talk in a tileable 3D integrated superconducting circuit architecture. *Science Advances* 8: eabl6698.

Sreedhar R, Vikstål P, Svensson M, Ask A, Johansson G, and García-Álvarez L (2022) The quantum approximate optimization algorithm performance with low entanglement and high circuit depth. *arXiv:2207.03404arXiv1*.

Stanisic S, Bosse JL, Gambetta FM, Santos RA, Mruczkiewicz W, O'Brien TE, Ostby E, and Montanaro A (2022) Observing ground-state properties of the Fermi-Hubbard model using a scalable algorithm on a quantum computer. *Nature Communications* 13(1): 5743.

Sugisaki K, Nakazawa S, Toyota K, Sato K, Shiomi D, and Takui T (2019) Quantum chemistry on quantum computers: A method for preparation of multiconfigurational wave functions on quantum computers without performing post-Hartree-Fock calculations. *ACS Central Science* 5: 167.

Sugisaki K, Kato T, Minato Y, Okuwaki K, and Mochizuki Y (2022) Variational quantum eigensolver simulations with the multireference unitary coupled cluster ansatz: A case study of the C2v quasi-reaction pathway of beryllium insertion into a H_2 molecule. *Physical Chemistry Chemical Physics* 24: 8439–8452.

Suzuki Y, Endo S, Fujii K, and Tokunaga Y (2022) Quantum error mitigation as a universal error reduction technique: Applications from the NISQ to the fault-tolerant quantum computing eras. *PRX Quantum* 3: 010345.
Svensson M, Andersson M, Grönkvist M, Vikstål P, Dubhashi D, Ferrini G, and Johansson G (2021) A hybrid quantum-classical heuristic to solve large-scale integer linear programs. *arXiv:2103.15433v2*.
Takagi R, Endo S, Minagawa S, and Gu M (2022) Fundamental limits of quantum error mitigation. *npj Quantum Information* 8: 114.
Tang E (2021) Quantum principal component analysis only achieves an exponential speedup because of its state preparation assumptions. *Physical Review Letters* 127: 060503.
Tang E (2022) Dequantizing algorithms to understand quantum advantage in machine learning. *Nature Reviews Physics* 4: 693.
Tang HL, Barnes E, Grimsley HR, Mayhall NJ, and Economou SE (2021) Qubit-ADAPT-VQE: An adaptive algorithm for constructing hardware-efficient ansätze on a quantum processor. *PRX Quantum* 2: 020310.
Temme K, Bravyi S, and Gambetta JM (2017) Error mitigation for short-depth quantum circuits. *Physical Review Letters* 119: 180509.
Tennant DM, et al. (2022) Low-frequency correlated charge-noise measurements across multiple energy transitions in a tantalum transmon. *PRX Quantum* 3: 030307.
Terhal BM (2015) Quantum error correction for quantum memories. *Reviews of Modern Physics* 87: 307.
Tilly J, et al. (2022) The variational quantum eigensolver: A review of methods and best practices. *Physics Reports* 986: 1–128.
Tkachenko NV, et al. (2021) Correlation-informed permutation of qubits for reducing ansatz depth in the variational quantum eigensolver. *PRX Quantum* 2: 020337.
Touil A and Deffner S (2020) Quantum scrambling and the growth of mutual information. *Quantum Science and Technology* 5: 035005.
Tranter A, et al. (2022) Benchmarking the performance of variational quantum eigensolvers (VQE) applied to the HCN molecule. *APS March Meeting* 67. abstract id.B01.010.
Tsuchimoto Y, et al. (2022) Large-bandwidth transduction between an optical single quantum dot molecule and a superconducting resonator. *PRX Quantum* 3: 030336.
van den Berg E, Minev ZK, Kandala A, and Temme K (2022) Probabilistic error cancellation with sparse Pauli-Lindblad models on noisy quantum processors. *arXiv:2201.09866v2*.
Vepsäläinen AP, et al. (2020) Impact of ionizing radiation on superconducting qubit coherence. *Nature* 584(7822): 551–556.
Verdon G, Broughton M, McClean JR, Sung KJ, Babbush R, Jiang Z, Neven H, and Mohseni M (2019) Learning to learn with quantum neural networks via classical neural networks. *arXiv:1907.05415v1*.
Vikstål P, Grönkvist M, Svensson M, Andersson M, Johansson G, and Ferrini G (2020) Applying the quantum approximate optimization algorithm to the tail-assignment problem. *Physical Review Applied* 14: 034009.
von Lüpke U, Yang Y, Bild M, Michaud L, Fadel M, and Chu Y (2022) Parity measurement in the strong dispersive regime of circuit quantum acoustodynamics. *Nature Physics* 18: 794.
Wack A, Paik H, Javadi-Abhari A, Jurcevic P, Faro I, Gambetta JM, and Johnson BR (2021) Scale, quality, and speed: Three key attributes to measure the performance of near-term quantum computers. *arXiv:2110.14108v2*.
Wang D, Higgott O, and Brierley S (2019) A generalised variational quantum eigensolver. *Physical Review Letters* 122: 140504.
Wang S, Fontana E, Cerezo M, Sharma K, Sone A, Cincio L, and Coles PJ (2021) Noise-induced barren plateaus in variational quantum algorithms. *Nature Communications* 12: 6961.
Wang C, Gonin I, Grassellino A, Kazakov S, Romanenko A, Yakovlev VP, and Zorzetti S (2022a) High-efficiency microwave-optical quantum transduction based on a cavity electro-optic superconducting system with long coherence time. *npj Quantum Information* 8: 149.
Wang C, et al. (2022b) Towards practical quantum computers: Transmon qubit with a lifetime approaching 0.5 milliseconds. *npj Quantum Information* 8: 3.
Warshel A (2014) Multiscale modeling of biological functions: From enzymes to molecular machines (nobel lecture). *Angewandte Chemie, International Edition* 53: 10020.
Wedelin D (1995) An algorithm for large scale 0–1 integer programming with application to airline crew scheduling. *Annals of Operations Research* 57: 283–301.
Weggemans JR, et al. (2022) Solving correlation clustering with QAOA and a Rydberg qudit system: A full-stack approach. *Quantum* 6: 687.
Wendin G (2017) Quantum information processing with superconducting circuits: A review. *Reports on Progress in Physics* 80: 106001.
Wendin, G., 2028. Five Years Later, What Happened? (In preparation).
Wendin G and Shumeiko VS (2022) Coherent manipulation of a spin qubit. *Science* 373: 390.
Wilen CD, et al. (2021) Correlated charge noise and relaxation errors in superconducting qubits. *Nature* 594(7863): 369–373.
Willsch M, Willsch D, Jin F, Raedt HD, and Michielsen K (2020) Benchmarking the Quantum Approximate Optimization Algorithm. *Quantum Information Processing* 19: 197.
Willsch D, Willsch M, Calaza CDG, Jin F, Raedt HD, Svensson M, and Michielsen K (2022) Benchmarking advantage and D-Wave 2000Q quantum annealers with exact cover problems. *Quantum Information Processing* 21: 141.
Wittler N, Roy F, Pack K, Werninghaus M, Roy AS, Egger DJ, Filipp S, Wilhelm FK, and Machnes S (2021) Integrated tool set for control, calibration, and characterization of quantum devices applied to superconducting qubits. *Physical Review Applied* 15: 034080.
Wollack EA, Cleland AY, Gruenke RG, Wang Z, Arrangoiz-Arriola P, and Safavi-Naeini AH (2022) Quantum state preparation and tomography of entangled mechanical resonators. *Nature* 604: 463.
Wu Y, et al. (2021) Strong quantum computational advantage using a superconducting quantum processor. *Physical Review Letters* 127: 180501.
Wurtz J and Love PJ (2022) Counterdiabaticity and the quantum approximate optimization algorithm. *Quantum* 6: 635.
Yan H, et al. (2022) Purification and protection in a superconducting quantum network. *Physical Review Letters* 128: 080504.
Yu J, Retamal JC, Sanz M, Solano E, and Albarrán-Arriagada F (2022) Superconducting circuit architecture for digital-analog quantum computing. *EPJ Quantum Technology* 9: 90.
Zhang B, Sone A, and Zhuang Q (2022a) Quantum computational phase transition in combinatorial problems. *npj Quantum Information* 8: 87.
Zhang P, et al. (2022b) Many-body Hilbert space scarring on a superconducting processor. *Nature Physics* 19(1): 120–125.
Zhang Y, et al. (2022c) Variational quantum eigensolver with reduced circuit complexity. *npj Quantum Information* 8: 96.
Zhao P, Linghu K, Li Z, Xu P, Wang R, Xue G, Jin Y, and Yu H (2022) Quantum crosstalk analysis for simultaneous gate operations on superconducting qubits. *PRX Quantum* 3: 020301.
Zhong Y, et al. (2021) Deterministic multi-qubit entanglement in a quantum network. *Nature* 590(7847): 571–575.
Zhou L, Wang S-T, Choi S, Pichler H, and Lukin MD (2020) Quantum approximate optimization algorithm: Performance, mechanism, and implementation on near-term devices. *Physical Review X* 10: 021067.
Zhu Q, et al. (2022) Quantum computational advantage via 60-qubit 24-cycle random circuit sampling. *Science Bulletin* 1667(3): 240–245.

Braids, motions and topological quantum computing

Eric C Rowell, Department of Mathematics, Texas A&M University, College Station, TX, United States

© 2024 Elsevier Ltd. All rights reserved.

Introduction **268**
Objectives 268
The braid group 269
Braids and knots in physics: An incomplete history 269
Topological quantum computation **270**
The origins of topological quantum computation 270
Modeling topological phases with categories 271
The role of the braid group in TQC **272**
Detecting non-abelian anyons via braiding 272
Braiding universality 273
Measurement assisted universality 274
Distinguishing anyons and anyon systems via braiding 274
Beyond braids **275**
Conclusion **276**
Appendix on categorical notions **276**
Acknowledgments **277**
References **278**

Abstract

The topological model for quantum computation is an inherently fault-tolerant model built on anyons in topological phases of matter. A key role is played by the braid group, and in this survey we focus on a selection of ways that the mathematical study of braids is crucial for the theory. We provide some brief historical context as well, emphasizing ways that braiding appears in physical contexts. We also briefly discuss the 3-dimensional generalization of braiding: motions of knots.

Introduction

Quantum computation is predicated upon the ability to create, manipulate and measure the states in quantum systems (Freedman et al., 2003). In the topological model for quantum computation (Freedman et al., 2003; Nayak et al., 2008) the quantum systems of interest are topological phases of matter. Typically, these are 2 dimensional systems harboring point-like excitations–anyons (Wilczek, 1990). This alternative to the more traditional quantum circuit model is theoretically robust against decoherence due to the topological nature of the states: the information is stable due to invariance of the states under small, local perturbations. On the other hand, in order to implement quantum gates more drastic evolution of the states must be employed. The most natural choice is particle exchange of the anyons, so that their trajectories in 2 + 1 dimensional space-time form braids. The corresponding transformations are the quantum gates, which are mathematically encoded in unitary representations of the braid group. The process of creating anyons, braiding them and then measuring form knots or links in (2 +1)-dimensional spacetime, which is interpreted as a (single run) of a topological quantum computation as illustrated in Fig. 1. Notice that the motions of the point-like excitations in the effectively two dimensional medium have a natural mathematical interpretation as the group of braids. Thus it comes as no surprise that the braid group $\mathcal{B}_n$ plays an outsized role in the development of topological quantum computation. In this article we will describe a selection of topics illustrating the connection between braids and topological quantum computation as well as some generalizations. We make no attempt to be exhaustive on the subject, nor will we provide a completely self-contained background. There are a number of much more complete treatments of topological quantum computation from various perspectives and for various tastes, a few of which we list here: (Wang, 2006, 2013, 2010; Delaney et al., 2016; Nayak et al., 2008; Pachos, 2012; Ogburn and Preskill, 1999; Freedman et al., 2003; Rowell, 2016; Rowell and Wang, 2018). For deeper and more complete mathematical details on the braid group and invariants of knots and links we suggest (Kassel and Turaev, 2008), while for the categorical background the text (Etingof et al., 2015) is an excellent resource. We provide a very brief tour of categorical notions in Appendix A.

Objectives

In the article we will:
- Introduce braids and the braid group, briefly discussing the history of braids in physics.
- Introduce topological quantum computation through a historical perspective.

https://doi.org/10.1016/B978-0-323-90800-9.00144-X

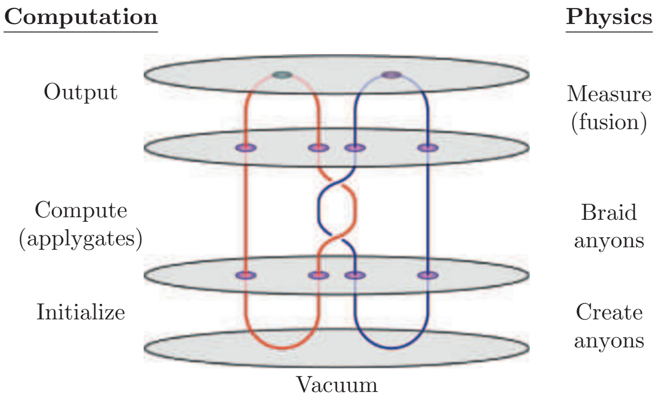

Fig. 1 A single iteration of a topological quantum computation via braiding.

- Discuss the categorical model for the relevant topological phases of matter.
- Elucidate the role of the braid group in topological quantum computation through a series of examples.
- Give a higher dimensional generalization of the braid group and speculate on its relevance to topological quantum computation.

The braid group

The braid group $\mathcal{B}_n$ on n strands is most concisely described using the abstract group presentation by generators and relations due to Artin (Artin, 1925):

$$\mathcal{B}_n = \langle \sigma_1, \sigma_2, \ldots, \sigma_{n-1} | \sigma_i\sigma_j = \sigma_j\sigma_i \text{ for } |i-j| \geq 2,$$
$$\sigma_i\sigma_{i+1}\sigma_i = \sigma_{i+1}\sigma_i\sigma_{i+1}, \text{ for } 1 \leq i, j \leq n-1\rangle$$

The first relation is referred to as far commutativity and the second is the braid relation.

For visualization purposes we display the generator σ_1 and its inverse σ_1^{-1} geometrically as members of $\mathcal{B}_4$:

$\sigma_1 =$ 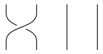 $\sigma_1^{-1} =$ 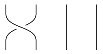

The composition in the group then corresponds to stacking, whereas the identity is clearly represented by unbraided strands.

Predating Artin's work on braids by 30 years is the work of Hurwitz (1891) on motions of points on the 2-dimensional sphere. This is much closer to their use in condensed matter physics: the world-lines of anyons under particle exchange can be viewed as trajectories of motions of points in the disk D^2. Connecting braids to knots and links are two key mathematical results: Alexander's theorem (Alexander, 1923) and Markov's theorem (Markov, 1936). The key consequence of Alexander's theorem is that any knot/link may be obtained the plat closure: capping off the strands of a braid in $\mathcal{B}_{2n}$ pairwise, on both the top and bottom. Birman's (1976) analogue of Markov's theorem establishes a way to determine if two distinct braids have the same plat closure.[1]

Braids and knots in physics: An incomplete history

Around the 7th century B.C.E. there was a debate between the natural philosopher Gārgī Vāchaknavī (daughter of Vachaknu) and the sage Yajnavalkya (Olivelle, 1998). She asks him:

> Since this whole world is woven back and forth on water, on what then is it woven back and forth?

To which he replies "On air, Gārgī." The exchange continues with Gārgī asking what air and the intermediate regions are woven upon, and eventually what the universe is woven upon. This could be the most ancient reference to braids in physics. That the universe consists of a sequence of braidings may seem quaint by today's scientific standards, but the similitude with topological quantum circuits is nonetheless intriguing.[2]

Many point to Gauss as the first person to study knots mathematically and suggest he was inspired by physical considerations such as magnetic potential, see, e.g., (Epple, 1998; Przytycki, 1998; Ricca and Nipoti, 2011). Maxwell himself (Maxwell, 1873) mentions Gauss' integral formula for the linking number of a two component link and its physical interpretation in electromagnetic induction.[3] Gauss' interest in braids goes back even earlier according to Epple (1998), as he drew the following braid sometime between 1815 and 1830:

---

[1] Both Alexander's and Markov's theorems actually deal with a different closure in which one glues the ends of top strands to the bottom strands. But the plat closure is more physically relevant.

[2] We thank Paul Martin for informing us of this ancient reference.

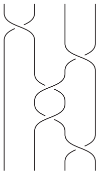

One might naturally surmise that Gauss' early interest in braids and knots were influential in his discovery of the linking number.

Yet another connection between physics and knots came some years later (see (Silver, 2014) for a full account) when Thompson (Lord Kelvin) learned of some experiments of Helmholtz in the 1850s producing knotted vortices of smoke. This led to the speculation by Thompson that matter was made up of knotted loops of luminiferous æther. This short-lived "vortex-atoms" theory suggested that different elements were distinguished by their knot-type. Yet again, we find an archaic theory resonating with a modern idea: in topological quantum computation information is stored in knotted world-lines of anyons. Mathematics reaped the benefit, as Tait produced the first reasonably comprehensive table of knots with few crossings, inspired by his friend Thompson's vortex-atom theory.

Topological quantum computation

Here we provide a historical perspective on topological quantum computation and set up the mathematical framework in terms of categories.

The origins of topological quantum computation

Topological quantum computation emerged as a confluence of ideas of Freedman, in topology, and Kitaev, in physics, (Freedman, 1998; Yu Kitaev, 2003) in the late 1990s. The framework was then laid out quickly in a series of papers of Freedman, Kitaev, Wang and Larsen (Freedman et al., 2002b,a, 2003).

Freedman postulated that physical systems described by topological quantum field theories (TQFTs) (Witten, 1989) could potentially be employed to perform certain Jones polynomial (Jones, 1985) evaluations. The Jones polynomial is a remarkably powerful invariant of knots and links. Its discovery in the early 1980s (Jones, 1985) precipitated the field of quantum topology. Although it is straightforward to compute for a given knot, the complexity of the competition grows quickly with the number of crossings. Indeed, evaluating the Jones polynomial at roots of unity is classically a #P-hard computation at most values (Jaeger et al., 1990). A clue to how physics could be useful for such computations is found in the original formulation of the Jones polynomial as the trace of the braid group representation associated with the $SU(2)$ Chern-Simons/Reshetikhin-Turaev TQFTs.

Meanwhile, Kitaev was interested in topological phases of matter harboring anyons for their potential use in fault-tolerant quantum computation. Topological phases of matter were studied going back to the 1970s and 1980s by the recipients of the 2016 Nobel Prize in Physics (Nobel Prize Committee, 2016): Kosterlitz, Thouless, and Haldane. Well-studied examples of include the fractional quantum Hall liquids (Moore and Read, 1991; Wen, 1991) that are expected to yield non-abelian anyons. Further examples include topological insulators (Nayak et al., 2008; das Sarma et al., 2015). More recently nanowires have been studied for their potential for harboring anyons (Mourik et al., 2012; Albrecht et al., 2016). The need for expensive error-correction due to decoherence continues to be a major hurdle for scaled up quantum computation. Kitaev's idea was that quantum gates could be implemented by braiding anyons, so that error-correction comes from the topological nature of the systems.

Remarkably, Freedman's and Kitaev's proposals are two sides of the same coin: 2D topological phases of matter are modeled by TQFTs! It is a rare instance when two essentially independent ideas converge yielding a powerful new paradigm.

To breathe life into this new paradigm some deep mathematics was needed from both quantum topology and group theory. The resulting proof-of-principle of topological quantum computation is found in Freedman et al. (2002b), Freedman et al. (2002a). There they show that (1) the topological model for quantum computation could be as powerful as the more standard quantum circuit model based on qubits and (2) it is not more powerful than the quantum circuit model. The second result is proved by showing that any topological quantum computation can be simulated on a universal qubit machine with polynomial overhead. The first result show that universal topological quantum computers exist, in principle. We will return to this below.

---

[3] There is some historical controversy here, which the reader may find in the references.

Modeling topological phases with categories

Anyons are topological quantum fields emerging as finite energy particle-like excitations in topological phases of matter. Like particles, they can be moved, but cannot be created or destroyed locally. To model them we consider the fusion and braiding structures of these elementary excitations in the plane. The anyon system is then modeled by a *unitary modular category* (UMC). For this reason we will use *anyon model* and *unitary modular category* synonymously.

There is a philosophical explanation for why category theory is suitable for describing some quantum physics. In quantum physics we appeal to measurements to "see" the elementary particles by analyzing their responses to measuring devices. Anyons are *defined* by how they interact with other particles, and their responses to measuring devices. According to Kapranov and Voevodsky (1994), the main principle in category theory is: "In any category it is unnatural and undesirable to speak about equality of two objects." In category theory an object X is determined by the vector spaces of morphisms $\mathrm{Hom}(X, Y)$ for all Y in the tensor category. Therefore, it is natural to treat objects as anyons, and the morphisms as models of the quantum processes between them. For a more complete treatment see the survey (Rowell and Wang, 2018).[4] The notion of a modular tensor category was invented by Moore and Seiberg using tensors (Moore and Seiberg, 1989), and its coordinate-free version: *modular category* was defined by Turaev (1992). In this model, an anyon X is a simple object in the category, while the vacuum is regarded as the monoidal unit $\mathbf{1}$. The Hilbert space of states of a system of anyons on a disk with prescribed boundary condition is modeled by the space of morphisms in the category so that the braiding of anyons provides unitary operators as the system evolves: the quantum gates in topological quantum computation. For example, the Hilbert space associated with n indistinguishable X anyons in the disk with boundary condition (total charge) Y is the space $\mathrm{Hom}(Y, X^{\otimes n})$. One assumption is that there are finitely many distinguishable indecomposable anyon types (including the vacuum type): $\{X_0 = \mathbf{1}, X_1, \ldots, X_r\}$, so that that every anyon corresponds to some fixed type $a \in \{0, \ldots, r\}$. A dictionary of terminologies between categories and anyons systems is given in Table 1, adapted from Wang (2010). The Hilbert space $V^c_{ab} = \mathrm{Hom}(a \otimes b, c)$ represents the span of the linearly independent ways of fusing anyons of type a and b to obtain the anyon of type c. In topological phases of matter the *ground state degeneracy* is typically encoded as the dimension of the spaces $\bigoplus_c V^c_{ab}$ where the sum is over all anyon types c. Most often this is consider for $a = b$ so that we can speak of the ground state degeneracy of a given anyon. In the vernacular one says a has non-trivial ground-state degeneracy if $\dim(\bigoplus_c V^c_{aa}) > 1$.

There are two basic local events that can occur during a topological quantum computation besides braiding, namely *splitting* and *fusion*. Fusion is when two anyons combine to produce another anyon, while splitting it the reverse. These events are conveniently represented using the diagrams in Fig. 2. A special case of fusion is *annihilation* when an anyon particle and its anti-particle fuse to the vacuum. Similarly *creation* is a special case of splitting in which a particle/anti-particle pair are drawn from the vacuum. We often depict the splitting/fusion involving the vacuum anyon type $\mathbf{1}$ by a dotted line, or sometimes we omit it entirely. This is justified as the vacuum anyon may be freely inserted/deleted in the system. Braiding is the isomorphism denoted $c_{X,Y} : X \otimes Y \mapsto Y \otimes X$.

As there are finitely many anyon types one may encode the fusion rules into a matrix: for a fixed type a, define $[N_a]_{c,b} := \dim(V^c_{ab})$. Running over all pairs (b, c) we obtain the fusion matrix N_a. An important invariant of an anyon is the *dimension* d_a of the corresponding anyon type: this is simply the largest eigenvalue of N_a, which is guaranteed to be real and positive by the Perron-Frobenius theorem. However, this dimension is not necessarily an integer–in general it is a real cyclotomic integer: a real number that can be expressed as a finite sum of roots of unity. We shall see later that the computational utility of anyons of type a in a given system is intimately intertwined with the value of d_a.

Table 1 A dictionary of categorical terms and their interpretations in anyonic systems.

Anyon model (UMC)	*Anyonic system*
Simple object	Anyon
Label	Anyon type or topological charge
Tensor product	Fusion
Triangular space V^c_{ab} or V^{ab}_c	Fusion/splitting space
Dual	Antiparticle
Birth/death	Creation/annihilation
Braid representation	Anyon statistics
Morphism	Physical process or operator
Braids	Anyon trajectories

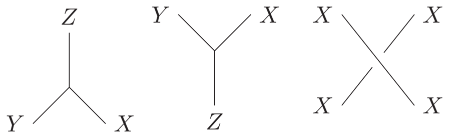

Fig. 2 Basic local events: fusion, splitting and braiding.

---

[4] We shall not need a full treatment here, we will introduce the key ideas as they become necessary.

We are now ready to describe the braid group representations associated with anyons of type a in a topological phase of matter. Suppose we have n type a anyons localized at positions $1, \dots, n$ in the system, whose total charge is b. Interchanging the anyons at positions i and $i+1$ induces a unitary operator $U_i(b)$ on the state space $\mathcal{H}(b;a,\dots,a) = \mathrm{Hom}(b, a^{\otimes n})$, which represents the braid group generator σ_i. Extending to all such interchanges and summing over all possible boundary conditions we obtain a representation

$$\rho_a : \mathcal{B}_n \to U\Big(\bigoplus_b \mathcal{H}(b;a,\dots,a)\Big) \quad \text{via} \quad \sigma_i \mapsto \bigoplus_b U_i(b).$$

With this formulation in hand, we can mathematically analyze topological gates. Note that dimension of the representation $\oplus_b \mathcal{H}(b;a,\dots,a)$ is asymptotic to d_a^n, so that the ground state degeneracy of n type a anyons in the disk can be approximated using the quantum dimension.

It is useful to keep in mind three examples: (1) the Fibonacci anyon τ with fusion rule $\tau^{\otimes 2} = \mathbf{1} + \tau$ and quantum dimension $d_\tau = \frac{1+\sqrt{5}}{2}$ (2) the Ising anyon σ with fusion rules $\sigma^{\otimes 2} = \mathbf{1} + \psi$, $\psi \otimes \sigma = \sigma$, and $\phi^{\otimes 2} = \mathbf{1}$ with $d_\sigma = \sqrt{2}$ and (3) the $\mathbb{Z}/3$ anyon ω with fusion rules $\omega^{\otimes 2} = \omega^*$, $\omega \otimes \omega^* = \mathbf{1}$ and $d_\omega = 1$. The ground state degeneracy of Fibonacci anyons in a disk is a Fibonacci number, while the $\mathbb{Z}/3$ has no disk ground state degeneracy and the Ising theory has disk ground state degeneracy of the form 2^n.

The role of the braid group in TQC

In this section we will review a number of ways that the braid group plays an essential role in topological quantum computation. The examples presented here are representative of the author's tastes and are by no means exhaustive.

Detecting non-abelian anyons via braiding

If the braid group representation ρ_a associated with an anyon of type a has abelian image, we say that a is an *abelian* anyon. Abelian anyons have been convincingly demonstrated in the laboratory, and can even be directly shown to admit braidings (Nakamura et al., 2020). Notice that anyons that have no ground state degeneracy are automatically abelian: if $\dim(V_{aa}^c) = 1$ for a *unique* anyon type c then it can be shown that $\mathrm{Hom}(b, a^{\otimes n})$ is 1-dimensional for a unique type b for each n, and 0-dimensional for all other types $c \neq b$. Thus the braid group representation ρ_a described above is 1 dimensional, hence has abelian image. In particular if $d_a = 1$, then a is an abelian anyon. On the other hand, non-abelian anyons are essential if one is to have any interesting (i.e., not phases) braiding gates. How can one detect if an anyon is non-abelian? In Rowell and Wang (2016) it is shown that if a is abelian then necessarily $d_a = 1$. The idea is the following where we assume that a is its own anti-particle type for convenience[5]:

Suppose that an anyon X of type a has $d_a > 1$, yet is abelian. This implies that there is some anyon Y of non-vacuum type $b \neq \mathbf{1}$ so that $\dim(V_{aa}^b) \geq 1$ by a simple eigenvector argument. We construct a non-zero state in $\mathrm{Hom}(a, a^{\otimes 3})$ by drawing a pair of type a anyons out of the vacuum (we have assumed that the splitting space $\mathrm{Hom}(\mathbf{1}, a^{\otimes 2})$ is non-trivial). Next we perform the braiding $\sigma_1\sigma_2\sigma_1^{-1}\sigma_2^{-1} \in \mathcal{B}_3$ on this state. Now $a^{\otimes 2}$ decomposes as a sum of simple objects that includes b, so that there is a non-zero vector in $\mathrm{Hom}(a, b \otimes a)$, which can be achieved as a consequence of a fusion of the left two type a anyons to a type b anyon Y. So the process yields the state in Fig. 3. Now if the X anyon were abelian, then the image of the braid $\sigma_1\sigma_2\sigma_1^{-1}\sigma_2^{-1}$ must be the identity, as illustrated in Fig. 4. Thus, since we cannot create a single anyon out of the vacuum, we obtain the zero state as illustrated in Fig. 5. This contradicts the assumption that $d_a > 1$.

Computing the quantum dimensions of the Fibonacci, Ising and $\mathbb{Z}/3$ anyons we get $\frac{1+\sqrt{5}}{2}$, $\sqrt{2}$ and 1, respectively. Thus the Fibonacci and Ising anyons are non-abelian, while the $\mathbb{Z}/3$ anyons are abelian.

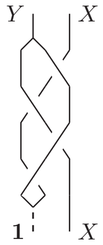

Fig. 3 A state achieved by creating a pair of X anyons from the vacuum, braiding, and then fusing two X anyons to an anyon Y. This is a non-zero state.

---

[5] This is not a crucial restriction: a slightly more complicated argument works for all types and in most examples one hopes to construct in the laboratory this is satisfied anyway.

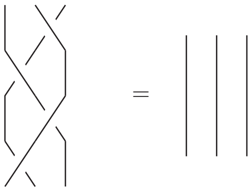

Fig. 4 If X is abelian, the sequence of braids has the same effect as the identity braid.

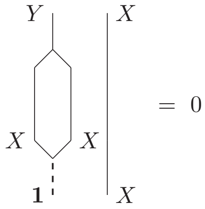

Fig. 5 Since $Y \neq \mathbf{1}$, the state on the left must be zero, and therefore the whole state must be 0.

Braiding universality

The foundational paper (Freedman et al., 2002b) exhibited the theoretical viability of topological quantum computers by showing that the so-called Fibonacci anyons are universal for quantum computation. This was achieved by demonstrating that one could efficiently approximately simulate a universal qubit computer on the Fibonacci topological model. Let us briefly recall the qubit model (Nielsen and Chuang, 2000). A qubit is a 2-dimensional vector space $V = \mathbb{C}^2$, typically modeled by some 2-level quantum system, e.g., a spin-system. One fixes a gate set $\mathcal{G}$ consisting of unitary operators $U_i \in U(V^{\otimes n_i})$. N-qubit quantum circuits are built as compositions of promotions of the U_i to $V^{\otimes N}$, i.e., $I_V^{\otimes a} \otimes U_i \otimes I_V^{\otimes b}$ where $N = a + n_i + b$. Each application of a gate is considered a single step, hence the length of the quantum circuit in an algorithm represents consumed time, and is a complexity measure. A gate set should be physically realizable and complicated enough to perform any computation given enough time.

Definition 3.1: The gate set $\mathcal{G}$ is said to be *universal* if any unitary operator $X \in U(V^{\otimes N})$ can be efficiently approximated (up to a phase) by a quantum circuit built from $\mathcal{G}$.

A typical choice of a universal gate set is

$$\mathcal{S} = \left\{H, \sigma_z^{1/4}, \text{CNOT}\right\}$$

consisting of the Hadamard, $\pi/8$ and CNOT gates:

$$H = \frac{1}{\sqrt{2}}\begin{pmatrix} 1 & 1 \\ 1 & -1 \end{pmatrix}, \quad \sigma_z^{1/4} = \begin{pmatrix} 1 & 0 \\ 0 & e^{\pi i/4} \end{pmatrix}, \quad \text{CNOT} = \begin{pmatrix} 1 & 0 & 0 & 0 \\ 0 & 1 & 0 & 0 \\ 0 & 0 & 0 & 1 \\ 0 & 0 & 1 & 0 \end{pmatrix}$$

Here the efficiency should be that the length of the quantum circuit is a polynomial in the desired accuracy. The Kitaev-Solovay theorem (see Freedman et al., 2002b for the most appropriate formulation) states that it is enough to show that the closure of the N-qubit circuits in the operator norm topology contains all unitaries in $U(V^{\otimes N})$ up to phases.

For the topological model with gates obtained from braiding as above, the following is the equivalent formulation of universality:

Definition 3.2: An anyon X is called *braiding universal* if, for some n_0, the images of $\mathcal{B}_n$ on the irreducible sub-representations $W \subset \text{End}(X^{\otimes n})$ are dense in $SU(W)$ for all $n \geq n_0$.

This is a mathematically precise definition, but in practice it can be quite difficult to verify universality (Freedman et al., 2002b). The Fibonacci anyon τ, which has quantum dimension $\frac{1+\sqrt{5}}{2}$ is universal, while the Ising anyon σ which has quantum dimension $\sqrt{2}$ is not. In fact the image of the braid group representations associated with the Ising anyon σ have *finite* groups as their images–very far from universal!

In practice this appears to be the dichotomy: either an anyon X is braiding universal, or the representations ρ_X have image a finite group, in which case we say X is a *property F* anyon. In principle, to determine if the image is finite or infinite requires fairly explicit descriptions of the representations, which are not always available. It would be useful to have an indirect way of detecting when an anyon X has associated braid group representations ρ_X with infinite image. The following gives a very concise conjectural condition:

Conjecture 3.1: (Naidu and Rowell, 2011) *An anyon X is braiding universal if and only* $d_x^2 \notin \mathbb{Z}$.

For simplicity we are conflating "infinite image" with "universality." But we do not lose too much by doing so: if an irreducible unitary braid group representation $\rho_X : \mathcal{B}_n \to U(V_n)$ has infinite image in $U(V_n)$ then its closure $\overline{\rho_X(\mathcal{B}_n)}$ is some infinite compact Lie group G. By analyzing the eigenvalues of the braid group generators' images one finds that G contains, with few exceptions, $SU(V_n)$, $SO(V_n)$ or $Sp(V_n)$ (see Larsen et al., 2005 for the general method).[6] To obtain universality on the nose one hopes for the first case, but one can typically lift the second two cases to special unitaries by taking n slightly larger.

This conjecture has been verified in numerous cases, see, e.g., (Etingof et al., 2008; Rowell, 2010; Rowell and Wenzl, 2017; Green and Nikshych, 2021; Larsen et al., 2005). In particular it is known to be true for anyon models obtained from quantum groups at roots of unity (equivalently, Kac-Moody algebras) as well as all so-called *weakly group-theoretical* braided fusion categories. This latter class includes the metaplectic anyons of Hastings et al. (2014).

Measurement assisted universality

Convincing laboratory confirmation of the existence of non-abelian anyons is still a major hurdle. The simplest model for non-abelian anyons correspond to the Ising categories, known as the Majorana zero modes (or more colloquially, Majorana fermions) (das Sarma et al., 2015). It would be a breakthrough to have such a confirmation for the Majorana zero modes. On the other hand, this could not be used for braiding universal topological quantum computation. The next simplest non-abelian anyons correspond to the $SU(2)_4$ model (certain metaplectic anyons (Hastings et al., 2014)), with some numerical evidence that this is realized by the fractional quantum Hall liquids at filling fraction $\nu = 8/3$[PWC+15]. But again, these are not braiding universal. If nature conspires against us (which she so often does) it might be the case that braiding universal anyons are out of reach. While disappointing, this does not mean that one cannot have topological quantum computers. In Cui et al. (2015), Cui and Wang (2015) protocols for recovering universality from metaplectic anyons are presented. The idea is to produce a universal gates set from braiding gates and one non-braiding gate achieved through a projective measurement of topological charge.

Specifically, the system modeled by the $SU(2)_4$ includes anyons $\mathbf{1}, Z, X$, and Y with the fusion rules $X^{\otimes 2} = \mathbf{1} + Y$ and $Y^{\otimes 2} = \mathbf{1} + Z + Y$, where Z is an abelian anyon satisfying $Z^{\otimes 2} = \mathbf{1}$ and $Z \otimes Y = Y$. A single qutrit is encoded as in Fig. 6.

The space is 3 dimensional, corresponding to the pairs (a, b) which can be $(\mathbf{1}, Y)$, $(Y, \mathbf{1})$, or (Y, Y). While braiding the four X-type anyons provides many gates, braiding alone is not universal. The additional measurement that must be performed is a projection of the left two X-type anyons onto the vacuum 1-type, and the orthogonal complement. If the left pair total charge is not $\mathbf{1}$ then the right pair total charge is in a coherent superposition of $(Y, \mathbf{1})$ and (Y, Y). This operation, together with the braiding gates *is* universal.

Distinguishing anyons and anyon systems via braiding

One of the key axioms of a modular category is the *non-degeneracy* of the braiding: this says that the only anyon type X so that the full exchange (double braid, see Fig. 7) with all anyon types Y is trivial is the vacuum type $\mathbf{1}$.

This turns out to be equivalent to the condition that the matrix with entries $S_{ab} := tr(c_{a,b} \circ c_{b,a})$ for all pairs of anyon types (a, b) has $\det(S) \neq 0$ (Bruguiéres, 2000).

This implies that, in principle, one may distinguish anyons X and Y by performing all exchanges of X and Y with an anyon of each other type. One would of course need to perform measurements–in this case the right computation is essentially the one illustrated

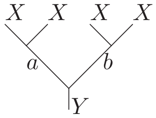

Fig. 6 One qutrit from $SU(2)_4$.

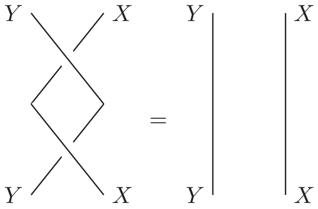

Fig. 7 If the full exchange is trivial for all Y, anyon X is transparent.

---

[6] These are the special unitary, special orthogonal and symplectic Lie groups.

in Fig. 1, creating two particle/anti-particle pairs and then projecting onto the vacuum-vacuum state. These are precisely the entries of the matrix S, in diagrams:

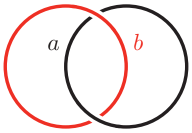

The S-matrix entries are the invariants of the Hopf link, with components "colored" by pairs of anyon types. Thus the non-degeneracy condition implies we may distinguish anyons by the set of double braidings.

The S-matrix records the traces of all double braidings, and hence gives an invariant of the anyon model. Suppose we wish to pin down precisely which modular category is the model for our anyon system. What computations/measurements must one perform? The quantum dimension d_a of each anyon type appears in the S-matrix: it corresponds to setting $b = 1$. Another invariant is obtained by taking the trace of a single braiding of X with itself, see Fig. 8: this yields the quantity $d_X\theta_X$ for a root of unity θ_X, known as the *topological spin* of X.

The S-matrix together with the twists θ_a for all anyon types a form the *modular data* of the theory. Is the modular data enough to determine the anyon model? The answer turns out to be "no" (Mignard and Schauenburg, 2017). It is possible for two inequivalent anyon models to have exactly the same modular data: known as *modular isotopes* (Delaney et al., 2021). By the philosophy that the anyon model should be determined by the topological measurements (mathematically, invariants) one might expect that there is a finite set of measurements that would determine the theory. That is, one seeks a set of knots and links, including the modular data, so that the invariants one obtains by "coloring" the components by anyon types completely determines the anyon model.

The two component Whitehead link is one candidate (see Fig. 9, left) which together with the modular data can be used to distinguish some modular isotopes Bonderson et al., 2019. The Whitehead link is named after the topologist J. C. Whitehead but predates him by about one millennium–it is found on Viking artifacts from around 1000C.E (Fig. 9, right). Interestingly, the Whitehead link has Gauss linking number 0.

Beyond braids

In the Gārgī-Yajnavalkya debate one finds the suggestion that the cosmos are braids upon braids upon braids. Lord Kelvin, in his the vortex-atom theory, proposed that all matter is built from knots. From our modern perspective these ideas are easily dismissed, but we see glimmers of them in topological phases of matter. Is there more to this?

So far we have focused on braids as trajectories of point-like excitations with 2-dimensional ambient space, and have seen that the braid group plays a key role. Many interesting computational and physical questions can be answered by studying braids. Can we push this theory to higher dimensions? Point-like excitations in 3 dimensions are not interesting: they must be bosons or fermions, and are thus abelian in the sense that braiding them has abelian image. But what about other kinds of excitations, such as loop-like vortices? Or, for that matter, knot-like vortices? At least mathematically, we can describe the dynamics of system in which knots are braided! The simplest example is known as the *loop braid group*: the motions of n oriented circles in S^3. It has two kinds of generators: the first by "leapfrogging" the ith circle through the $(i+1)$st σ_i and the second by loop interchanges s_i for $1 \leq i \leq n-1$. This group is denoted $\mathcal{LB}_n$ and has only been studied relatively recently (see Damiani, 2017 for a survey). Abstractly, $\mathcal{LB}_n$ is the

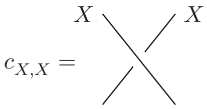

Fig. 8 The braiding of X with itself: the trace of this operator has value $d_X\theta_X$.

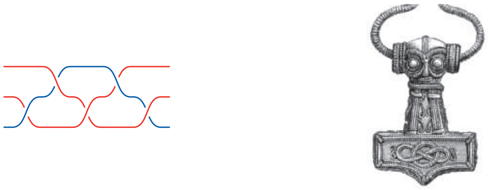

Fig. 9 Left: A braid with closure the Whitehead link colored to emphasize components. Right: Thor's hammer (Mjölnir) artifact featuring the Whitehead link, dating from around 1000 C.E.

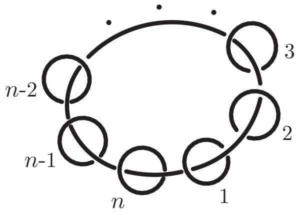

Fig. 10 The Necklace: motions include leapfrogging and moving each small circle by a rotation of $2\pi/n$ around the center point of the large circle.

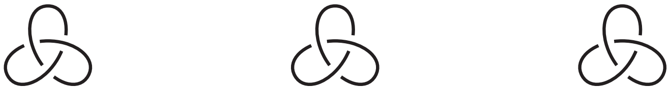

Fig. 11 Three trefoils: distinct motions could include passing one such knot through any of the four holes in a neighboring knot.

group generated by one copy of the n-strand braid group (generated by the σ_i) and one copy of the symmetric group (generated by the s_i) with the additional (mixed) relations:

$$\sigma_i\sigma_{i+1}s_i = s_{i+1}\sigma_i\sigma_{i+1}, \quad s_is_{i+1}\sigma_i = \sigma_{i+1}s_is_{i+1}, \quad 1 \le i \le n-2, \quad \sigma_i s_j = s_j\sigma_i \quad \text{if} \quad |i-j| > 1.$$

Other configurations are possible, such as "the necklace" as in Fig. 10. Representations of the motion group of the necklace, the *necklace braid group* have been studied, for example, in Bullivant et al. (2020).

A more complicated, but nonetheless intriguing example is the motions of three or more trefoil knots as in Fig. 11. One can imagine many different "leapfrog" motions between a pair of such knots.

Equipped with the mathematical description of these motions, one should be able to approach the theoretical analogues of those described above for 2-dimensional systems in topological phase, such as: *How do we model these systems?* and *What is the computational power of such a system?*

Conclusion

The landscape of topological quantum computation is still in flux as the goals of computer science and the realities of physics are reconciled within the bounds of engineering. It seems clear that on the mathematics side the braid group will continue to play a key role, with adjustments as dictated by the relevant models, as in the example of measurement-assisted universality. As new sources of quantum systems with topological features are found and our understanding of the extant systems is deepened, new ideas will be needed to find mathematical models and explore their utility in quantum technologies.

Appendix on categorical notions

We have used a number of standard notions from category theory that the reader may not be familiar with. Here we lay down some of the key ideas for the reader's convenience, always deferring to Etingof et al. (2015) for a comprehensive treatment.

A *category* consists of a collection of *objects* X, Y, … (not necessarily a set, and the objects have no assumed structure), together with a collection of *morphisms* $\mathrm{Hom}(X,Y)$ for each pair of objects, with a distinguished element $\mathrm{id}_X \in \mathrm{Hom}(X,X) = \mathrm{End}(X)$ for each object X. These morphisms can be composed when it makes sense to, and the composition is assumed to be associative. A basic idea in category theory is to axiomatize the notion of "sameness." Two objects X, Y are said to be isomorphic if there are morphisms $f \in \mathrm{Hom}(X,Y)$ and $g \in \mathrm{Hom}(Y,X)$ so that $f \circ g = \mathrm{id}_Y$ and $g \circ f = \mathrm{id}_X$. It is worth pointing out that while the objects have no structure (nor do the collection of objects), the morphisms do have structure.

In modern category theory one adds additional *structures* and requires additional *properties*. It can often be confusing to distinguish between structures and properties, but typically there are choices for a structure, while a property is either satisfied or isn't. For an instructive example from algebra, consider a set X with a binary operation $(x,y) \mapsto x \circ y \in X$. This is called a *magma* and it depends a structure–there are many choices for $\circ$. On the other hand, if the *property* that $(x \circ y) \circ z = x \circ (y \circ z)$ holds for all x, y, z then the magma $(X, \circ)$ is a called a semigroup. If there is an element $e \in X$ so that $e \circ x = x \circ e = x$ for all x, this is an additional property and the semigroup is called a *monoid*. If the property that $x \circ y = y \circ x$ for all x, y the monoid is called commutative, or abelian. To be a group the monoid must satisfy another property: every element should have an inverse. We could continue to build structures and insist on properties: a commutative group with an additional structure of scalar multiplication by the real numbers $\mathbb{R}$ satisfying several more properties defines a vector space, and so on. We are often interested in classifying categories with certain structures and properties. Moreover, many of the structures and properties are categorical generalizations of algebraic constructions we are already familiar with.

The categories we are concerned with are *modular categories*: concisely (albeit obfuscating), these are non-degenerate spherical braided fusion categories. Each of these adjectives carries with it some structure and/or assumes some properties hold. We will first unravel this definition in somewhat broad strokes before providing some examples.

(1) *Fusion* categories are modeled after the category of finite-dimensional complex representations $\mathrm{Rep}(G)$ for a finite group G. This axiomatizes notions like direct sum (additive structure), tensor product (monoidal structure $\otimes$) with proscribed associativity morphisms $\alpha_{X,Y,Z}$, trivial representation (monoidal unit $\mathbf{1}$), linearity ($\mathrm{Hom}(X,Y)$ is a finite dimensional vector space), duality (objects V^* for each V), irreducibility (simple objects), finiteness (finitely many simple objects up to isomorphism, among which is $\mathbf{1}$), and semisimplicity (all objects are sums of simples). *Sphericity* is a somewhat technical property having to do with choices ("pivotal" structure) of isomorphisms $V \cong V^{**}$ that lead to a notion of left and right traces for morphisms. Essentially, this structure is spherical if the ensuing left and right traces coincide. This trace is used to define the S-matrix in Section 3.4 for example.

(2) A *braiding* structure on a fusion category is a collection of morphisms $c_{X,Y} \in \mathrm{Hom}(X \otimes Y, Y \otimes X)$ that satisfy a version of the braid equation. This is of course crucial for our exposition above: the key fact is that

$$\sigma_i \mapsto \mathrm{id}_X^{\otimes i-1} \otimes c_{X,X} \otimes \mathrm{id}_X^{\otimes n-i-1}$$

can be modified to a braid group representation after employing appropriate re-coupling of the tensor factors. In practice one often assumes the category is *strict* so that the associativity constraints are identities. In the presence of a braiding the spherical structure is encoded in the topological twists $\Theta_X \in \mathrm{Hom}(X,X)$ for each object X. For simple objects we have $\Theta_X = \theta_X \cdot \mathrm{id}_X$ where θ_X is a root of unity. They satisfy the *balancing equation*: $\Theta_{X\otimes Y} = c_{Y,X} c_{X,Y} \Theta_X \otimes \Theta_Y$ which allows one to represent morphisms as labeled ribbons and manipulate them in a topologically consistent way (*graphical calculus*).

(3) The braiding has the property of being *non-degenerate* if the only simple object X such that $c_{Y,X} \circ c_{X,Y} = id_{X\otimes Y}$ for all Y is the monoidal unit $\mathbf{1}$. For a fixed spherical structure non-degeneracy can be encoded in terms of the invertibility of the S-matrix.

Three examples to keep in mind are the categories Fib, Ising and $\mathcal{C}(\mathbb{Z}/3)$ alluded to above. You may find further details on these categories in Rowell et al. (2009), Section 5.3, in which modular categories with at most four simple objects are classified.

Example A.1: The category Fib has 2 simple objects $\mathbf{1}$ and τ with fusion rules $\tau \otimes \tau = \tau \oplus \mathbf{1}$ as mentioned in the main text. The S-matrix is $\begin{pmatrix} 1 & \varphi \\ \varphi & -1 \end{pmatrix}$ where $\varphi = \frac{1+\sqrt{5}}{2}$. The twist of τ is $\theta_\tau = e^{4\pi i/5}$, while $\theta_{\mathbf{1}} = 1$ (for any category, in fact). The anyon τ is universal. We have $\tau^* \cong \tau$–the Fibonacci anyon is self-dual.

Example A.2: Ising has 3 simple objects $\mathbf{1}$, ψ and σ with the fusion rules described in the main text. The S-matrix is $\begin{pmatrix} 1 & \sqrt{2} & 1 \\ \sqrt{2} & 0 & -\sqrt{2} \\ 1 & -\sqrt{2} & 1 \end{pmatrix}$ while the non-trivial twists are $\theta_\psi = -1$ and $\theta_\sigma = e^{\pi i/8}$. The object ψ is a mathematical *fermion*: it is an abelian anyon with twist -1. The anyon σ is non-abelian, but non-universal. All of the objects in the Ising category are self-dual.

Example A.3: The category $\mathcal{C}(\mathbb{Z}/3)$ consists of abelian anyons 1, ω, ω^* with the fusion rules like the group $\mathbb{Z}/3$. In this case the object ω is not self-dual as $\omega \ncong \omega^*$. The S-matrix is $\begin{pmatrix} 1 & 1 & 1 \\ 1 & q & 1/q \\ 1 & 1/q & q \end{pmatrix}$ where $q = e^{2\pi i/3}$. and the twists are $\theta_\omega = \theta_{\omega^*} = q$.

We have introduced modular categories as a kind of axiomatization of various algebraic structures that some familiar categories have. Another perspective on modular categories is that it is the categorical structure underlying (2 + 1)-dimensional topological quantum field theory. As a fundamental level then modular categories may be thought of as the categorification of ribbon diagrams: essentially the various diagrams one may draw using the basic events in Fig. 2, interpreted as morphisms in some category, so that composition is stacking and the labels represent a finite set of colors for the ribbons. While we have drawn the ribbons as curves, it should be emphasized that these really have some width and a "framing" which is essentially the number of times the ribbon is twisted along its axis. The modularity condition is natural in the sense that it says we may distinguish the colors by means of braiding and traces.

Acknowledgments

Rowell is partially supported by NSF grants DMS-1664359 and DMS-2000331, and thanks Zhenghan Wang, Paul Martin and Xingshan Cui for helpful conversations.

References

Albrecht SM, Higginbotham AP, Madsen M, Kuemmeth F, Jespersen TS, Nygård J, Krogstrup P, and Marcus CM (2016) Exponential protection of zero modes in Majorana islands. *Nature* 531(7593): 206–209.

Alexander JW (1923) A lemma on systems of knotted curves. *Proceedings of the National Academy of Sciences of the United States of America* 9(3): 93–95.

Artin E (1925) Theorie der Zöpfe. *Abhandlungen aus dem Mathematischen Seminar der Universität Hamburg* 4(1): 47–72. MR 3069440.

Birman JS (1976) On the stable equivalence of plat representations of knots and links. *Canadian Journal of Mathematics* 28(2): 264–290. MR 402715.

Bonderson P, Delaney C, Galindo C, Rowell EC, Tran A, and Wang Z (2019) On invariants of modular categories beyond modular data. *Journal of Pure and Applied Algebra* 223(9): 4065–4088. MR 3944465.

Bruguiéres A (2000) Catégories prémodulaires, modularisations et invariants des variétés de dimension 3, (French). *Mathematische Annalen* 316(2): 215–236.

Bullivant A, Kimball A, Martin P, and Rowell EC (2020) Representations of the necklace braid group: topological and combinatorial approaches. *Communications in Mathematical Physics* 375(2): 1223–1247. MR 4083878.

Cui SX and Wang Z (2015) Universal quantum computation with metaplectic anyons. *Journal of Mathematical Physics* 56(3), 032202. 18. MR 3390917.

Cui SX, Hong S-M, and Wang Z (2015) Universal quantum computation with weakly integral anyons. *Quantum Information Processing* 14(8): 2687–2727. MR 3370675.

Damiani C (2017) A journey through loop braid groups. *Expositiones Mathematicae* 35(3): 252–285. MR 3689901.

Delaney C, Rowell EC, and Wang Z (2016) Local unitary representations of the braid group and their applications to quantum computing. *Revista Colombiana de Matemáticas* 50(2): 207–272. MR 3605648.

das Sarma S, Freedman M, and Nayak C (2015) Majorana zero modes and topological quantum computation. *Physical Review Letters* 94: 166802.

Delaney C, Kim S, Plavnik J (2021) Zesting produces modular isotopes and explains their topological invariants, Preprint.

Epple M (1998) Orbits of asteroids, a braid, and the first link invariant. *The Mathematical Intelligencer* 20: 45–52.

Etingof P, Rowell E, and Witherspoon S (2008) Braid group representations from twisted quantum doubles of finite groups. *Pacific Journal of Mathematics* 234(1): 33–41. MR 2375313.

Etingof P, Gelaki S, Nikshych D, and Ostrik V (2015) *Tensor categories, Mathematical Surveys and Monographs*. vol. 205. Providence, RI: American Mathematical Society.

Freedman MH (1998) P/NP, and the quantum field computer. *Proceedings. National Academy of Sciences. United States of America* 95(1): 98–101. MR 1612425.

Freedman MH, Kitaev A, and Wang Z (2002a) Simulation of topological field theories by quantum computers. *Communications in Mathematical Physics* 227(3): 587–603.

Freedman MH, Larsen M, and Wang Z (2002b) A modular functor which is universal for quantum computation. *Communications in Mathematical Physics* 227(3): 605–622.

Freedman MH, Kitaev A, Larsen MJ, and Wang Z (2003) Topological quantum computation. *American Mathematical Society* 40(1): 31–38. Mathematical challenges of the 21st century (Los Angeles, CA, 2000). MR 1943131.

Green J and Nikshych D (2021) On the braid group representations coming from weakly group-theoretical fusion categories. *Journal of Algebra and Its Applications* 20(1). Paper No. 2150210, 20. MR 4209972.

Hastings MB, Nayak C, and Wang Z (2014) On metaplectic modular categories and their applications. *Communications in Mathematical Physics* 330(1): 45–68. MR 3215577.

Hurwitz A (1891) Ueber Riemann'sche Flächen mit gegebenen Verzweigungspunkten. *Mathematische Annalen* 39(1): 1–60. MR 1510692.

Jaeger F, Vertigan DL, and Welsh DJA (1990) On the computational complexity of the Jones and Tutte polynomials. *Mathematical Proceedings of the Cambridge Philosophical Society* 108: 35–53. MR 1049758.

Jones VFR (1985) A polynomial invariant for knots via von Neumann algebras. *American Mathematical Society* 12(1): 103–111.

Kapranov MM and Voevodsky VA (1994) 2-categories and Zamolodchikov tetrahedra equations. *Algebraic Groups and Their Generalizations: Quantum and Infinite-Dimensional Methods (University Park, PA, 1991), Proc. Sympos. Pure Math.* vol. 56, pp. 177–259. Providence, RI: Amer. Math. Soc. MR 1278735.

Kassel C and Turaev V (2008) *Braid groups, Graduate Texts in Mathematics*. vol. 247. New York: Springer. With the graphical assistance of Olivier Dodane. MR 2435235.

Larsen MJ, Rowell EC, and Wang Z (2005) The N-eigenvalue problem and two applications. *International Mathematics Research Notices* (64): 3987–4018. MR 2206918.

Markov AA (1936) Uber die freie Aquivalenz der geschlossenen Zopfe. *Recueil Mathematique Moscou* 43(1): 73–78.

Maxwell JC (1873) *A Treatise on Electricity and Magnetism*. vol. 1. Oxford.

Mignard M and Schauenburg P (2017) Modular categories are not determined by their modular data. *Letters in Mathematical Physics* 111: preprint arXiv:1708.02796.

Moore G and Read N (1991) Nonabelions in the fractional quantum Hall effect. *Nuclear Physics B* 360(2): 362–396.

Moore G and Seiberg N (1989) Classical and quantum conformal field theory. *Communications in Mathematical Physics* 123(2): 177–254. MR 1002038.

Mourik V, Zuo K, Frolov SM, Plissard SR, Bakkers EPAM, and Kouwenhoven LP (2012) Signatures of Majorana fermions in hybrid superconductor-semiconductor nanowire devices. *Science* 336(6084): 1003–1007.

Naidu D and Rowell EC (2011) A finiteness property for braided fusion categories. *Algebr. Represent. Theory* 14(5): 837–855.

Nakamura J, Liang S, Gardner G, and Manfra MJ (2020) Direct observation of anyonic braiding statistics. *Nature Physics* 16(9): 931–936.

Nayak C, Simon SH, Stern A, Freedman M, and Sarma SD (2008) Non-abelian anyons and topological quantum computation. *Reviews of Modern Physics* 80(3): 1083.

Nielsen MA and Chuang IL (2000) *Quantum Computation and Quantum Information.* Cambridge: Cambridge University Press. MR 1796805.

Nobel Prize Committee (2016) *Topological phase transitions and topological phases of matter.* Tech. report .

Ogburn RW and Preskill J (1999) Topological quantum computation, Quantum computing and quantum communications (Palm Springs, CA, 1998). *Lecture Notes in Computer Science* 1509: 341–356. Springer, Berlin. MR 1750535.

Olivelle P (1998) *Upanisads.* Oxford University Press.

Pachos JK (2012) *Introduction to Topological Quantum Computation.* Cambridge University Press.

Przytycki JH (1998) Classical roots of knot theory. *Chaos, Solitons & Fractals* 9(4): 531–545. Knot Theory and Its Applications: Expository Articles on Current Research.

Ricca RL and Nipoti B (2011) Gauss' linking number revisited. *Journal of Knot Theory and its Ramifications* 20(10): 1325–1343. MR 2851711.

Rowell EC (2010) Braid representations from quantum groups of exceptional Lie type. *Revista de la Unión Matemática Argentina* 51(1): 165–175. MR 2681262.

Rowell EC (2016) An invitation to the mathematics of topological quantum computation. *Journal of Physics: Conference Series* 698: 012012. IOP Publishing.

Rowell EC and Wang Z (2016) Degeneracy and non-Abelian statistics. *Physical Review A* 93(3), 030102.

Rowell EC and Wang Z (2018) Mathematics of topological quantum computing. *Bulletin of the American Mathematical Society* 55(2): 183–238. MR 3777017.

Rowell E and Wenzl H (2017) $SO(N)_2$ braid group representations are Gaussian. *Quantum Topol.* 8(1): 1–33. MR 3630280.

Rowell E, Stong R, and Wang Z (2009) On classification of modular tensor categories. *Communications in Mathematical Physics* 292(2): 343–389.

Silver DS (2014) Knots in the nursery: (Cats) Cradle Song of James Clerk Maxwell. *Notices of the American Mathematical Society* 61(10): 1186–1194. MR 3241299.

Turaev VG (1992) Modular categories and 3-manifold invariants. *International Journal of Modern Physics B* 6(11–12): 1807–1824.

Wang Z (2006) Topologization of electron liquids with Chern-Simons theory and quantum computation. *Differential geometry and physics, Nankai Tracts Math.* vol. 10, pp. 106–120. Hackensack, NJ: World Scientific Publishing. MR 2322390.

Wang Z (2010) *Topological quantum computation.* no. 112. American Mathematical Soc.

Wang Z (2013) Quantum computing: A quantum group approach. *Symmetries and groups in contemporary physics, Nankai Ser. Pure Appl. Math. Theoret. Phys.* vol. 11, pp. 41–50. Hackensack, NJ: World Sci. Publ. MR 3221449.

Wen X-G (1991) Non-abelian statistics in the fractional quantum Hall states. *Physical Review Letters* 66(6): 802.

Wilczek F (1990) *Fractional statistics and anyon superconductivity*. vol. 5. World Scientific.

Witten E (1989) Quantum field theory and the Jones polynomial. *Communications in Mathematical Physics* 121(3): 351–399.

Yu Kitaev A (2003) Fault-tolerant quantum computation by anyons. *Annals of Physics* 303(1): 2–30.

Fibonacci anyon based topological quantum computer

Tapio Simula, Optical Sciences Centre, Swinburne University of Technology, Melbourne, VIC, Australia

© 2024 Elsevier Ltd. All rights reserved.

Introduction 279
Overview 279
Conventional two-level quantum computer 280
Fibonacci topological quantum computer 281
Fusion rules 281
Topological qubit 281
Braiding rules 282
Universality 283
Key issues 283
Leakage error 283
Quantum compilation error 283
Hardware error sources 283
Conclusion 284
Acknowledgments 284
References 284

Abstract

The idea of topological quantum computation with non-abelian anyons is presented using Fibonacci anyons as the building blocks of topological qubits. Using a single qubit conventional quantum computer as a reference, we outline how braiding Fibonacci anyons may be used for realizing fault tolerant topological qubit operations. We mention some key issues affecting topological quantum computers, and conclude with a brief discussion on the future prospects of topological quantum computing.

Objectives

- To introduce the idea of topological quantum computation by using the Fibonacci anyon model as an exemplar.
- To mention certain technicalities that affect the efficacy of braid-based topological quantum computers.
- To embed the Fibonacci anyon model within the broader context of nonabelian anyons and topological quantum computers.

Introduction

The material world around us is composed of two kinds of elementary particles, the bosons and the fermions (Leggett, 2005). This observation is formalized by the spin-statistics theorem, which essentially states that upon transporting a particle around another indistinguishable particle, the quantum state describing these particles must either remain unchanged (bosons) or change its sign (fermions). This is related to the fact that such a world line path can be contracted to a point. However, in systems where the (quasi) particles are constrained to move in two-dimensional plane, the mutual quasiparticle exchange statistics does not need to be bosonic or fermionic but can in principle be anything in between (Leinaas and Myrheim, 1977). Such quasiparticles are called anyons (Wilczek, 1982). The essence of the topological difference between the three and two dimensional systems is illustrated in Fig. 1. The topological richness afforded by two dimensional systems allows for an even more exotic possibility where an encirclement of one quasiparticle by another one may cause such a quasiparticle to become transmutated into an entirely different kind of quasiparticle! Such quasiparticles are called non-abelian anyons and they could be used as building blocks for constructing a topological quantum computer. For a comprehensive technical introduction to the topic of this encyclopedia entry on Fibonacci anyon based topological quantum computation, we refer the reader to Nayak et al. (2008), Trebst et al. (2008), Lahtinen and Pachos (2017), Field and Simula (2018).

Overview

It is useful to briefly outline some key concepts of conventional quantum computation before discussing the basics of a topological quantum computer. Note that, in addition to conventional and braid based topological quantum computers, several other kinds of quantum computer models also exist, such as a measurement-based one-way quantum computer, that will not be discussed here.

https://doi.org/10.1016/B978-0-323-90800-9.00072-X

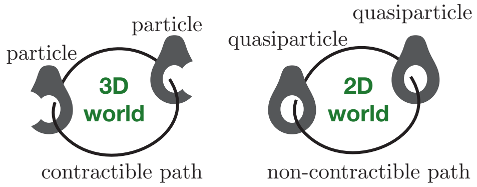

Fig. 1 Illustration of an exchange of two bosonic or fermionic particles along a contractible path (left) and two anyon quasiparticles along a non-contractible path (right). In the former case the particles can be "lifted off the world line," where as in the latter case this is not topologically allowed.

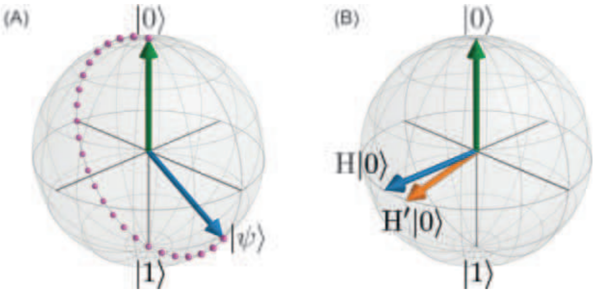

Fig. 2 Bloch sphere representation of single-qubit quantum computation. (a) the qubit is initialized in state $|0\rangle$. It is then rotated (dotted trajectory) using unitary quantum gates to the final superposition state $|\psi\rangle$. A projective measurement of the final state will yield the results $|0\rangle$ and $|1\rangle$ with probabilities $|\alpha|^2$ and $|\beta|^2$, respectively. (b) the initial state $|0\rangle$ is rotated using the Hadamard gate to a final state $H|0\rangle$. A noisy Hadamard gate H' leads to a deviation in the state vector and such errors rapidly accumulate during quantum computation.

Conventional two-level quantum computer

The "transistor" of a conventional quantum computer is called a qubit or an artificial two-level atom. The qubit has two possible states

$$|0\rangle = |\uparrow\rangle = \begin{pmatrix} 1 \\ 0 \end{pmatrix} \text{ and } |1\rangle = |\downarrow\rangle = \begin{pmatrix} 0 \\ 1 \end{pmatrix} \tag{1}$$

referred to as the spin-up and spin-down, respectively.[1] An arbitrary single qubit state may be expressed as a superposition

$$|\psi\rangle = \left(|0\rangle + e^{i\theta}|1\rangle\right)/\sqrt{2} \tag{2}$$

of the two possible qubit eigenstates, where θ determines the azimuthal phase angle of the state vector, and every one of such states can be visualized by a state vector on the Bloch sphere, shown in Fig. 2.[2] The state vectors can be rotated using unitary quantum gate operators U such as the Hadamard gate

$$\mathrm{H} = \frac{1}{\sqrt{2}} \begin{pmatrix} 1 & 1 \\ 1 & -1 \end{pmatrix} \tag{3}$$

to yield new state vectors $|\psi\rangle = U|\psi_0\rangle$ from the initial states $|\psi_0\rangle$. Quantum computation corresponds to sequential application of a predetermined set of unitary logic gates acting on a specified initial state $|\psi_0\rangle$, after which a probabilistic measurement of the final quantum state is made. In a single qubit quantum computer every logic gate operation rotates the quantum state vector on the Bloch sphere to a new location such that during the computation the state vector traces out a specific path on the Bloch sphere. After that a measurement yields either spin-up or spin-down outcome and to find out the respective probabilities the computation must be repeated very many times.

Gate fidelity is a major issue of conventional quantum computation. That is, how accurately the action of the quantum gates can be realized by the quantum hardware as any such errors rapidly accumulate in the course of the computation. In a single qubit quantum computer every imperfect unitary gate operation will rotate the state vector slightly off the target, see Fig. 2(b), and these errors add up such that after all gates have been applied the final state vector may be far away from its correct location such that the probability of repeated measurements will ultimately converge to the completely random classical 50/50 measurement outcome. To certain extent the adverse effects of a noisy environment may be mitigated by implementing sophisticated error correcting protocols.

To go beyond single qubit quantum computation, generic many qubit states can be constructed by summing up tensor products of single qubit states. The many-qubit state (Hilbert) space whose dimension is $2^N = e^{N\ln(2)}$ grows exponentially rapidly with the number N of added qubits.[3] An important resource in many-qubit quantum systems is entangled states, which cannot be expressed as a tensor product of any two quantum states. In addition to these rudiments, a practically useful quantum computer will need to satisfy a range of additional criteria such as scalability to very large numbers of qubits (Divincenzo, 2000).

---

[1] Eq. (1) uses the non-unique yet conventional representation of the two qubit basis states.

[2] On each point on the Bloch sphere there is also an attached fiber that accounts for the quantum mechanically unmeasurable global phase degree of freedom ϕ that amounts to transformation $|\psi\rangle = e^{i\phi}|\phi_0\rangle$.

[3] Note that also the number of possible configurations of classical two-state on-off switches is equal to 2^N, however, where as after the computation (pre-determined flicking of the switches) there is one and only one observable outcome, the state of a quantum computer may be in a state where all of the 2^N states can have a non-zero probability of being measured.

Fibonacci topological quantum computer

At the software level the operation of a topological quantum computer can be made to appear identical to that of a conventional quantum computer. The crucial difference occurs at the hardware level that enables the realization of fault tolerant qubits based on topology. Simplifying, the state vector rotations in a topological quantum computer can, in principle, be realized exactly even in the presence of noise sources that would cause the qubit rotations in a conventional quantum computer to be imprecise. In what follows, we will focus on the theoretical underpinnings of a braid group based topological quantum computer that uses Fibonacci anyons for its quantum logic operations.

Fusion rules

An anyon model that facilitates topological quantum computation is defined by its particle content and their fusion rules. The Fibonacci anyon model contains only one type of anyon, the non-abelian Fibonacci anyon τ in addition to the trivial vacuum state denoted by 1. The fusion rules of the Fibonacci anyon model are

$$\tau\otimes\tau = 1\oplus\tau; \qquad 1\otimes\tau = \tau\otimes 1 = \tau; \qquad \text{and} \qquad 1\otimes 1 = 1. \tag{4}$$

The first one of these is the most important one and states that when two Fibonacci anyons are brought together (fused) they may either annihilate each other yielding the vacuum 1 or combine to form a single Fibonacci anyon τ. This double valuedness of the fusion outcome can be used for defining a twolevel system—a topological qubit. It also means that the Fibonacci anyon may act as its own antiparticle. The latter two fusion rules correspond to "trivial" fusion outcomes.

When multiple Fibonacci anyons are fused sequentially, the possible fusion paths can be expressed using a fusion tree as illustrated in Fig. 3. The number of distinct fusion paths P_N as a function of the number N of anyons form a Fibonacci sequence, which gives the Fibonacci anyon its name. In the limit $\mathrm{N} \to \infty$ the ratio P_N/P_{N-1} converges to the golden ratio$\phi = \left(1+\sqrt{5}\right)/2$, which is also the so-called quantum dimension of the Fibonacci anyon model.

Topological qubit

A well defined topological qubit may be conveniently constructed out of an array of four Fibonacci anyons (τ_1, τ_2, τ_3, τ_4), where the subscript denotes their spatial position in the array, by creating them pairwise from the vacuum, which guarantees that the initial state satisfies $\tau_1 \otimes \tau_2 = 1$ and $\tau_3 \otimes \tau_4 = 1$. The conservation of the topological charge $\tau_1 \otimes \tau_2 \otimes \tau_3 \otimes \tau_4 = 1 \otimes 1 = 1$ thus means that there remains two possible fusion paths for these four anyons

$$\tau\otimes\tau\otimes\tau\otimes\tau \to 1\otimes\tau\otimes\tau \to \tau\otimes\tau \to 1 \cong |0\rangle$$

and

$$\tau\otimes\tau\otimes\tau\otimes\tau \to \tau\otimes\tau\otimes\tau \to \tau\otimes\tau \to 1 \cong |1\rangle$$

that can be used for the definition of a topological qubit. Measuring the state of the topological qubit may thus be determined solely by the fusion outcome of the first two anyons τ_1 and τ_2. In words, if $\tau_1 \otimes \tau_2 = 1$ the qubit state is $|0\rangle$ and if $\tau_1 \otimes \tau_2 = \tau$ the qubit state is $|1\rangle$.

The state of the topological qubit can be changed by braiding the world lines of the anyons, which physically corresponds to moving the anyons around in the two-dimensional plane. Shuffling around the anyons in the two-dimensional physical space thus realizes unitary qubit rotations of the quantum mechanical state vector in the abstract state space, which is equivalent to the Bloch sphere in the case of a single qubit.

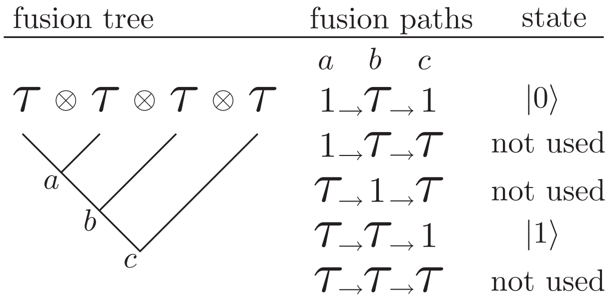

Fig. 3 Fusion of four Fibonacci anyons. Fusion of the four anyons sequentially from left to right leads to a fusion tree where the fusion outcome of the first two anyons is *a*, fusion of *a* with the third anyon yields *b* and fusion of *b* with the fourth anyon yields *c*. For four Fibonacci anyons there are five possible fusion paths that span the Hilbert space of possible state vectors. Topological charge conservation reduces the accessible state space from five to two, and these two fusion paths define a two level system (a topological qubit).

Braiding rules

When the anyons 1 and 2 are braided by moving them around each other counter-clockwise in the physical space to swap their positions, their world lines (string-like trajectories through space and time) become "knotted." This operation is denoted by σ_1. The inverse operation where the anyons are moved clockwise is denoted by σ_1^{-1}. If these two operations are performed one after another, the second operation undoes the first one such that $\sigma_1^{-1}\sigma_1 = \sigma_1\sigma_1^{-1} = 1$. Generally, braiding the anyons n and $n + 1$ is denoted by braid operators σ_n and σ_n^{-1}. The braid operators acting on n strands (anyons) generate a braid group B_n. For a single Fibonacci anyon topological qubit it is sufficient to braid anyons 1, 2 and 3, while the fourth anyon does not need to participate in braiding so that its sole purpose is to ensure topological charge conservation of the four anyons. The qubit transformations may therefore be mapped onto the braid group B_3. The two elementary braid operators of B_3 have explicit (truncated to a separable two-dimensional qubit subspace) matrix representations

$$\sigma_1 = \begin{pmatrix} e^{-i4\pi/5} & 0 \\ 0 & e^{i3\pi/5} \end{pmatrix} \tag{5}$$

and

$$\sigma_2 = \begin{pmatrix} \dfrac{e^{i4\pi/5}}{\phi} & \dfrac{e^{-i3\pi/5}}{\sqrt{\phi}} \\ \dfrac{e^{-i3\pi/5}}{\sqrt{\phi}} & -\dfrac{1}{\phi} \end{pmatrix} \tag{6}$$

and the operators $\sigma_1^{-1}=$ and σ_2^{-1} are the matrix inverses of σ_1 and σ_2, respectively. These representations may be derived by solving the so-called pentagon and heptagon equations. An elementary topological quantum computation operation with Fibonacci anyons may thus be compactly expressed using standard notation

$$|\psi\rangle = \sigma_2|0\rangle = \begin{pmatrix} \dfrac{e^{i4\pi/5}}{\phi} & \dfrac{e^{-i3\pi/5}}{\sqrt{\phi}} \\ \dfrac{e^{-i3\pi/5}}{\sqrt{\phi}} & -\dfrac{1}{\phi} \end{pmatrix} \begin{pmatrix} 1 \\ 0 \end{pmatrix} = \alpha|0\rangle + \beta|1\rangle \tag{7}$$

and it physically corresponds to braiding the second and third anyon by exchanging their positions in real space, see Fig. 4, which in the abstract two-dimensional Hilbert space corresponds to creating a superposition state $|\psi\rangle$ in Eq. (7). By fusing the anyons after this braiding, the topological qubit would be found to be in the state $|0\rangle$ with a probability $P_0 = |\langle 0|\psi\rangle|^2 = |\alpha|^2 = \phi^{-2} \approx 0.4$ and in the state $|1\rangle$ with a probability $P_1 = 1 - P_0 = |\beta|^2 = \phi^{-1} \approx 0.6$..

Any single-qubit operation can be realized by concatenating L elementary braids to form a braid word $W_L = \sigma_{iL}\ldots\sigma_{i2}\sigma_{i1}$ of length L and then acting with this braid word quantum gate on the initial state

$$|\psi\rangle = W_L|0\rangle. \tag{8}$$

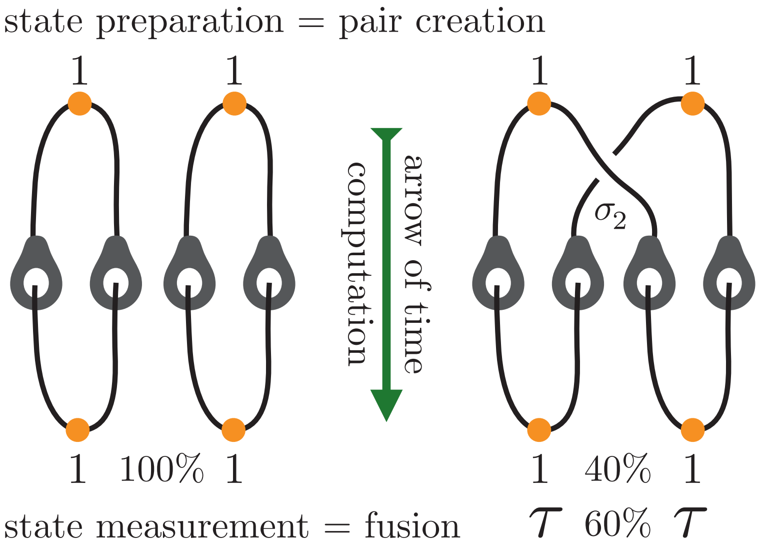

Fig. 4 Topological quantum computation is realized by braiding Fibonacci anyons. Four Fibonacci anyons are first spawned pairwise from the vacuum to create a topological qubit. Identity operator (left diagram) leaves the qubit intact and a fusion at the end of the computation will yield a definite outcome with a probability 1. If the anyons two and three are braided (acting on the qubit with a σ_2 operator) the qubit is rotated into a superposition state and final fusion will then have two possible outcomes with respective probabilities of occurrence that add up to one.

Universality

An important enabling feature of the Fibonacci anyon model is that it is universal for the purposes of quantum computation. In simple terms this means that every quantum state that may be expressed in terms of the available qubits may also be transformed to any other one by braiding the anyons and without requiring any other operations. In the single-qubit case this means that it is possible to construct all possible quantum gates as products of the elementary braid matrices, such that it is possible to connect any two state vectors (points on the Bloch sphere) by braiding the anyons. This property holds true also in the case of many qubits that may be constructed by sequencing the available anyons into groups of four. For instance, using eight anyons one may construct two logical topological qubits each of which is comprised of four Fibonacci anyons. Two-qubit gates may then be realized by braiding anyons belonging to the different logical qubits.

Key issues

Presently, by far the most serious issue regarding Fibonacci anyons is their (non-)existence. Although it has been suggested that certain quasiparticles in exotic fractional quantum-Hall states could potentially serve for realizations of Fibonacci anyons, proving or refuting this is beyond current experimental capabilities. Even if this most severe limitation would be overcome in the future, several other technical obstacles remain that would need to be resolved.

While topological quantum computers are often stated to be immune to the kinds of environmental noise that affects the conventional quantum computers, they nevertheless are susceptible to error sources and challenges of their own, both at the software and the hardware levels.

Leakage error

Even in the single-qubit case where only the first three anyons are being braided, the full Hilbert space representable by the anyons is five dimensional. However, the braiding only acts on the two dimensional qubit subspace. For two or more qubits, this is no longer the case. For instance, the braid operators of a two-qubit system involving eight anyons act on a 13 dimensional Hilbert space, only 4 of which are used for defining the two-qubit states, such that operators $\sigma_1(1,2)$ and $\sigma_2(2,3)$ are intrinsic to the first qubit and the operators $\sigma_4(5, 6)$ and $\sigma_5(6, 7)$ are intrinsic to the second qubit, where the numbers in the parenthesis enumerate the anyons. However, the inter-qubit braid operator $\sigma_3(3, 5)$ that braids the anyon τ_3 (in the first qubit) and the anyon τ_5 (in the second qubit) transfers population to some of the 9 so-called non-computational basis states. This is referred to as a leakage error as the probability leaks to quantum states not used for computational logic and this breaks the unitarity of the logic gates acting on the computational subspace. Although the amount of leakage can be mitigated by clever braiding protocols, this typically involves an additional computational overhead. This type of error could be completely avoided by making use of the full accessible Hilbert space and using multi-level qudits for computation instead of the more restricted two-level qubit basis and in this sense the leakage error is not a fundamental limitation of topological quantum computation.

Quantum compilation error

Another kind of error that affects topological quantum computers is the quantum compilation error. For instance, if one wishes to implement the Hadamard gate using a Fibonacci anyon based topological quantum computer, one must first compile the Hadamard gate. This means finding a braid word representation of H such that $W_L \approx \approx \mathrm{H}$. However, finding the optimal braid word of a fixed length L out of the exponentially, as a function of L, growing search space is a formidable task in its own right. Moreover, although universality of the Fibonacci anyon model guarantees that for every unitary U an arbitrarily good braidword approximation W_L may be obtained by increasing L, in practice for finite L, even the optimal W_L will only realize the target gate approximately. The compilation error thus has two parts, one due to the difficulty in finding the optimal braid word of given length L and another one due to the fact that even the optimal braid word will not in general be identical to the target gate.

As for the leakage error, the compilation error too could be mitigated by designing quantum computation algorithms that make direct use of the natural braid gates of the Fibonacci anyon model, rather than having to first compile a standard gate set from the elementary braids. The trade-off here is between computational efficiency and end-user convenience.

Hardware error sources

In addition to the error mitigation at the software level, topological quantum computers would also need to consider sources of errors originating from the hardware implementation of the anyons themselves such as the so-called quasiparticle poisoning. For instance, a pair of Fibonacci anyons could spontaneously form out of the vacuum and interfere with the braiding of the computational anyons. Material impurities or external causes could result in the appearance of patches of non-topological phases of matter, and in any physical realization there could exist so-far unidentified effects that could mimic braiding depending on how faithfully the physical system could be represented by the anyon model. These kinds of hardware level issues become important engineering considerations if non-abelian anyons will be proven to exist by experiments.

Conclusion

In summary, topological quantum computation is a form of quantum computation which is conducted using special kind of quantum hardware called non-abelian anyons. In a conventional quantum computer a rotation of a quantum state by a quantum gate is a continuous error prone operation in the sense that environmental noise may change the action of the quantum logic gate proportional to the strength of the noise leading to imprecise qubit rotations whose effects accumulate over the entire computation. By contrast, a topological quantum gate acts on the state vector either exactly or not at all, depending on the topology encoded in the world lines of the braided anyons. This special property could be harnessed to facilitate fault tolerant computations.

Here we have considered only one special kind of topological quantum computation model based on non-abelian Fibonacci anyons to illustrate some generic principles of topological quantum computation. Nevertheless, there exists a large variety of other types of anyon models. Perhaps the most promising one from the present day experimental physics perspective, the Ising anyon model, is based on Majorana fermion zero modes. Such non-abelian anyons are thought to be realizable by quantized vortices (Simula, 2019) in topological superfluids and at the end points of superconducting nano-wire structures.

Both the Fibonacci anyons and the Ising anyons belong to a broader (countably infinite) class of the so-called $SU(2)_k$ anyon models where the integer level $k = 3$ for the Fibonacci anyons and $k = 2$ for the Ising anyons. A major distinction between the $k = 2$ and $k = 3$ cases is that while the Fibonacci anyon model is universal for quantum computation, the Ising anyon model is not. This means that it is not possible to achieve full topological protection for the quantum computation in the $k = 2$ case, and that at least one quantum gate in the gate set of such a general purpose quantum computer must be implemented via non-topological means.

Another generic class of topological quantum computation models are the so called $D(H)$ quantum double models (de Wild Propitius and Bais, 1999). It has been suggested that such quantum double anyon models could potentially be realized by quantized vortices in spinor Bose–Einstein condensates (Mawson et al., 2019; Génetay Johansen and Simula, 2021). Such anyon models are based on representations of finite quantum groups and therefore, similarly to the Ising anyon models, they are not capable of universal quantum computation by braiding alone and need to be supplemented with non-topological gate operations.

At the time of writing, evolution of conventional quantum computers is still in its infancy and topological quantum computers do not yet exist. It will be exciting to see whether the future of scalable quantum computation will be based on topological or conventional qubits, or perhaps a combination of both?

Acknowledgments

This work was funded by the Australian Government through the Australian Research Council (ARC) Future Fellowship FT180100020.

References

de Wild Propitius M and Bais FA (1999) Discrete gauge theories. In: Semenoff G and Vinet L (eds.) *Particles and Fields*, p. 353. Springer-Verlag New York, Inc.

Divincenzo DP (2000) The physical implementation of quantum computation. *Fortschritte der Physik* 48: 771–783. https://doi.org/10.1002/1521-3978(200009)48:9/11<771::AID-PROP771>3.0.CO;2-E.

Field B and Simula T (2018) Introduction to topological quantum computation with non-Abelian anyons. *Quantum Science and Technology* 3: 045004. https://doi.org/10.1088/2058-9565/aacad2.

Génetay Johansen E and Simula T (2021) Fibonacci anyons versus Majorana fermions: A Monte Carlo approach to the compilation of braid circuits in $SU(2)_k$ anyon models. *PRX Quantum* 2: 010334. https://doi.org/10.1103/PRXQuantum.2.010334.

Lahtinen V and Pachos JK (2017) A Short introduction to topological quantum computation. *SciPost Physics* 3: 021. https://doi.org/10.21468/SciPostPhys.3.3.021.

Leggett A (2005) Quantum mechanics: Foundations. In: Bassani F, Liedl GL, and Wyder P (eds.) *Encyclopedia of Condensed Matter Physics*, pp. 51–56. Oxford: Elsevier. https://doi.org/10.1016/B0-12-369401-9/00616-1.

Leinaas JM and Myrheim J (1977) On the theory of identical particles. *Nuovo Cimento B Series* 37: 1–23. https://doi.org/10.1007/BF02727953.

Mawson T, Petersen TC, Slingerland JK, and Simula TP (2019) Braiding and fusion of non-abelian vortex anyons. *Physical Review Letters* 123: 140404. https://doi.org/10.1103/PhysRevLett.123.140404.

Nayak C, Simon SH, Stern A, Freedman M, and Das Sarma S (2008) Non-abelian anyons and topological quantum computation. *Reviews of Modern Physics* 80: 1083–1159. https://doi.org/10.1103/RevModPhys.80.1083.

Simula T (2019) *Quantised Vortices*. Morgan Claypool Publishers2053–2571. https://doi.org/10.1088/2053-2571/aafb9d.

Trebst S, Troyer M, Wang Z, and Ludwig AWW (2008) A short introduction to fibonacci anyon models. *Progress of Theoretical Physics Supplement* 176: 384–407. https://doi.org/10.1143/PTPS.176.384.

Wilczek F (1982) Quantum mechanics of fractionalspin particles. *Physical Review Letters* 49: 957–959. https://doi.org/10.1103/PhysRevLett.49.957.

Fractional quantum Hall effect in semiconductor systems

Zlatko Papić[a] and **Ajit C Balram**[b,c], [a]School of Physics and Astronomy, University of Leeds, Leeds, United Kingdom; [b]Institute of Mathematical Sciences, CIT Campus, Chennai, India; [c]Homi Bhabha National Institute, Mumbai, India

© 2024 Elsevier Ltd. All rights reserved.

Introduction **286**
Phenomenology of the FQH effect **287**
Incompressible fluids 289
Broken symmetry phases 290
Wigner crystals in the lowest Landau level 290
Stripes, nematics and bubble crystals in higher LLs 291
Laughlin states **291**
Laughlin's wave function 291
Charged excitations 292
Magnetoroton excitation 292
Edge excitations 292
Parent Hamiltonian and Haldane pseudopotentials 293
Hierarchy and composite fermions **293**
Haldane-Halperin hierarchy 293
Composite fermions 294
Half-filled Landau level **295**
Gapless composite fermion Fermi liquid in the half-filled Landau level 295
$\nu = 5/2$ state 295
Anti-Pfaffian 296
Non-Abelian states **296**
Non-Abelian anyons and topological quantum computation 296
$\nu = 12/5$ state 297
Other non-Abelian states 297
Multicomponent fractional quantum Hall effect **297**
Spinful systems 298
Bilayer systems 298
Recent developments **300**
Parton theory 300
Effective field theory 300
Entanglement-based approaches 301
Conclusion **302**
Acknowledgments **302**
References **302**

Abstract

The fractional quantum Hall (FQH) effect refers to the strongly-correlated phenomena and the associated quantum phases of matter realized in a two-dimensional gas of electrons placed in a large perpendicular magnetic field. In such systems, topology and quantum mechanics conspire to give rise to exotic physics that manifests via robust quantization of the Hall resistance. In this chapter, we provide an overview of the experimental phenomenology of the FQH effect in GaAs-based semiconductor materials and present its theoretical interpretations in terms of trial wave functions, composite fermion quasiparticles, and enigmatic non-Abelian states. We also highlight some recent developments, including the Parton theory and the Dirac composite fermion field theory of FQH states, the role of anisotropy and geometrical degrees of freedom, and quantum entanglement in FQH fluids.

Key points

- describe the rich phenomenology exhibited by two-dimensional electrons hosted in a semiconductor system placed in a perpendicular magnetic field;
- overview of different theoretical approaches for describing fractional quantum Hall (FQH) phases of matter;
- introduce the concept of non-Abelian FQH states and their potential applications in fault-tolerant topological quantum computation;
- summarize recent developments in the field, including parton theory of the FQH effect, geometric properties of FQH states, entanglement-based and field-theoretic approaches to understanding FQH systems.

https://doi.org/10.1016/B978-0-323-90800-9.00007-X

Notations and acronyms

$\boldsymbol{z = x - iy}$	Complex number representation of the electron coordinates (x, y) in the 2D plane
$\boldsymbol{\nu}$	Filling factor
$\boldsymbol{\Phi_1 \equiv \prod_{i<j}(z_i - z_j)}$	Laughlin-Jastrow factor
$\ell = \sqrt{\hbar/eB}$	Magnetic length
$\mathcal{P}_{\mathrm{LLL}}$	Projection to the lowest Landau level
$\boldsymbol{\Phi_n}$	Wave function of n filled Landau levels
2DEG	Two-dimensional electron gas
$\boldsymbol{B}$	Magnetic field strength
CF	Composite fermion
FQHE	Fractional quantum Hall effect
HLR	Halperin-Lee-Read
IQHE	Integer quantum Hall effect
LL	Landau level
LLL	Lowest Landau level
MR	Moore-Read
PH	Particle-hole
SLL	Second Landau level

Introduction

The fractional quantum Hall (FQH) effect occurs in a system of electrons confined to two spatial dimensions and a strong magnetic field perpendicular to the two-dimensional (2D) plane. In such systems, the kinetic energy is completely quenched by the magnetic field and Coulomb interaction exerts non-perturbative effects on the behavior of the electrons, typically without analogs in systems of weakly-interacting electrons encountered elsewhere in condensed matter physics. In this chapter, we do not aim to present a historical overview of the FQH effect, but rather highlight the key theoretical concepts for its understanding and to illustrate the connections between a variety of different approaches that have been deployed to tackle the problem. Perhaps most surprisingly, first-quantized wave functions have turned out to be highly valuable tools for understanding FQH phenomena, in contrast to the second-quantized field theories widely used in other areas of many-body physics. To emphasize this unique aspect of the FQH effect, our presentation will focus on introducing physics from the perspective of trial wave functions, motivated by experimental observations.

Before we dive into its fascinating experimental phenomenology, it is instructive to present a high-level description of the core of FQH physics. The following "Theory of Everything" Hamiltonian governing a FQH system should be familiar to most physicists:

$$\begin{aligned} H = &\sum_j \frac{1}{2m_\mathrm{b}}\left[\boldsymbol{p}_j + \frac{e}{c}\boldsymbol{A}\right]^2 + \sum_j U(\boldsymbol{r}_j) + g\mu_\mathrm{B}\boldsymbol{B}\cdot\boldsymbol{S} \\ &+ \frac{e^2}{4\pi\varepsilon}\sum_{j<k}\frac{1}{|\boldsymbol{r}_j - \boldsymbol{r}_k|}. \end{aligned} \tag{1}$$

The first line contains the one-body terms in the problem: the kinetic energy in the presence of a constant external magnetic field $\boldsymbol{B} = \nabla \times \boldsymbol{A}$; the potential U incorporating the lattice, disorder and confinement effects; finally, the Zeeman energy. The second line is the Coulomb interaction energy between (non-relativistic) electrons.

As a first step, let us simplify the problem down to its bare essentials. While disorder, confinement and lattice effects can be occasionally very important, we will neglect them here and set $U = 0$. Most FQH experiments discussed below are performed using GaAs-AlGaAs heterostructures, in which electrons have a band mass of $m_\mathrm{b} = 0.067m_\mathrm{e}$ (where m_e is the electron mass in vacuum), dielectric constant of $\varepsilon = 12.6\varepsilon_0$, and Landé g factor $g = -0.44$. From this, we can estimate the energy required to flip a spin – the Zeeman splitting – to be $E_Z = g\mu_\mathrm{B}B \approx 0.3B[\mathrm{T}]\mathrm{K}$, where the magnetic field $B[\mathrm{T}]$ is in units of Tesla. With the exception of Section "Multicomponent fractional quantum Hall effect," throughout this chapter, we will assume the electron spin is fully polarized due to a large magnetic field.

In order to diagonalize what's left of the Hamiltonian, the usual strategy is to first diagonalize the one-body part of H which gives rise to discrete Landau levels (LLs) of a single electron in a magnetic field. The Landau solution yields two important scales in the problem: the magnetic length

$$\ell = \left(\frac{\hbar}{eB}\right)^{1/2} \approx \frac{25}{\sqrt{B[\mathrm{T}]}}\mathrm{nm}, \tag{2}$$

and the cyclotron energy splitting between LLs

$$\hbar\omega_\mathrm{c} = \hbar\frac{eB}{m_\mathrm{b}} \approx 20B[\mathrm{T}]\mathrm{K}. \tag{3}$$

On the other hand, the Coulomb energy scale is set by

$$V_C \equiv \frac{e^2}{4\pi\varepsilon\ell} \approx 50\sqrt{B[\mathrm{T}]}\mathrm{K}. \tag{4}$$

The values on the rightmost side of Eqs. (3) and (4) are quoted for GaAs-based samples.

For the sake of convenience, throughout we shall use natural units where $\ell = 1$ and $e^2/(4\pi\varepsilon\ell) = 1$.

To render the many-body problem as tractable as possible, one often makes a further approximation by choosing $V_C \ll \hbar\omega_c$. In this limit, the Coulomb interaction is too weak to scatter particles across different LLs, i.e., entire dynamics is contained within a single LL and there is no "LL mixing." This assumption is not always warranted and its validity should be tested either numerically or experimentally. Nevertheless, under this approximation, the FQH Hamiltonian takes a remarkably simple form

$$H = \mathcal{P}\left(\frac{e^2}{4\pi\varepsilon}\sum_{j<k}\frac{1}{|\boldsymbol{r}_j - \boldsymbol{r}_k|}\right)\mathcal{P}, \tag{5}$$

i.e., the Hamiltonian is just the Coulomb interaction which must be diagonalized with the restriction of remaining in a single LL. The latter restriction is formally implemented by the global operator $\mathcal{P}$ which projects out all states that have a component outside the given LL. For most of our discussion below, the LL in question will be the lowest LL (LLL), although we will also mention the second LL (SLL) and higher LLs.

The model in Eq. (5) embodies the theoretical essence of the FQH effect: it is believed to capture universal physical properties of broad classes of correlated phases emerging in the regime of the FQH effect. However, despite its seemingly simple form, it is impossible to analytically diagonalize the Hamiltonian of Eq. (5). The difficulty stems from $\mathcal{P}$ being a global operator defined on a many-electron Hilbert space whose dimension grows exponentially with the number of electrons. Specifically, two main challenges are: (i) Eq. (5), has no parameters whatsoever, including no-small parameters that one might use to attempt a perturbative approach; (ii) If the Coulomb interaction is turned off, one ends up with an exponentially large degeneracy of any LL, again precluding an easy solution.

Broadly speaking, this chapter will focus on the following questions: (i) what are the possible phases of matter that arise from Eq. (5) as one varies the electron density (or, alternatively, the magnetic field)? (ii) what are the universal properties of such phases in the long-wavelength limit, e.g., the types of order and excitations that govern the low-energy physics? (iii) what are the fundamental principles that allow us to understand and microscopically model such phases?

Phenomenology of the FQH effect

In a typical FQH experiment, one measures the Hall resistance, extracted from the voltage drop perpendicular to the current flowing through a two-dimensional electron gas (2DEG) placed in a perpendicular magnetic field. The 2DEG should have sufficiently low concentration of impurities and high mobility of the electrons. The fabrication of such samples has required major technological advances that we will not touch upon. As found by Tsui et al. (1982), upon sweeping the magnetic field, the Hall resistance of such a 2DEG exhibits quantization at

$$R_{xy} = \frac{h}{\nu e^2}, \tag{6}$$

where ν was originally found to take the value 1/3. Subsequently, quantization was observed at other rational values of ν such as 2/3, 2/5, 3/7, etc. On the other hand, ν is related to the electron density ρ and is known as the *filling factor* or *filling fraction*,

$$\nu = \frac{\rho h}{eB}. \tag{7}$$

In an earlier work by Klitzing et al. (1980), similar resistance quantization had been observed for integral values of ν, i.e., in the regime of integer quantum Hall (IQH) effect. In both cases, the resistance was found to be quantized not only at the special value of ν but also in some neighborhood around the special value, which manifests as a resistance plateau in the experimental trace, as illustrated in the experimental data shown in Fig. 1A. Furthermore, when R_{xy} is pinned to a plateau, the longitudinal resistance (i.e., the one measured along the direction of the current) exhibits an Arrhenius behavior $R_{xx} \propto \exp(-\Delta/(2k_B T))$, where the energy scale Δ is interpreted as a gap to excitations. R_{xx} vanishes in the limit $T \to 0$, indicating dissipationless transport. A deep minimum in R_{xx} is often seen as a precursor of a developing FQH state, however, the definitive observation of a FQH state requires a quantized plateau in R_{xy}.

In both IQH and FQH cases, the R_{xy} quantization is remarkably accurate to about one part in a billion. This is a manifestation of quantum-mechanical coherence across a semiconductor material on mesoscopic length scales. Moreover, as seen from the appearance of the Planck constant, the quantization is not described by classical electrodynamics. The latter also predicts that the resistance should vary linearly with the magnetic field. One hint to a topological origin of the phenomenon is that the resistance is quantized, not the resistivity (they both have the same units in two dimensions). Moreover, the Hall quantization was found to be universal: it is independent of the sample type, geometry, and various materials parameters, such as the band mass of the electron or the dielectric constant of the background semiconductor, and is robust to sufficiently weak disorder.

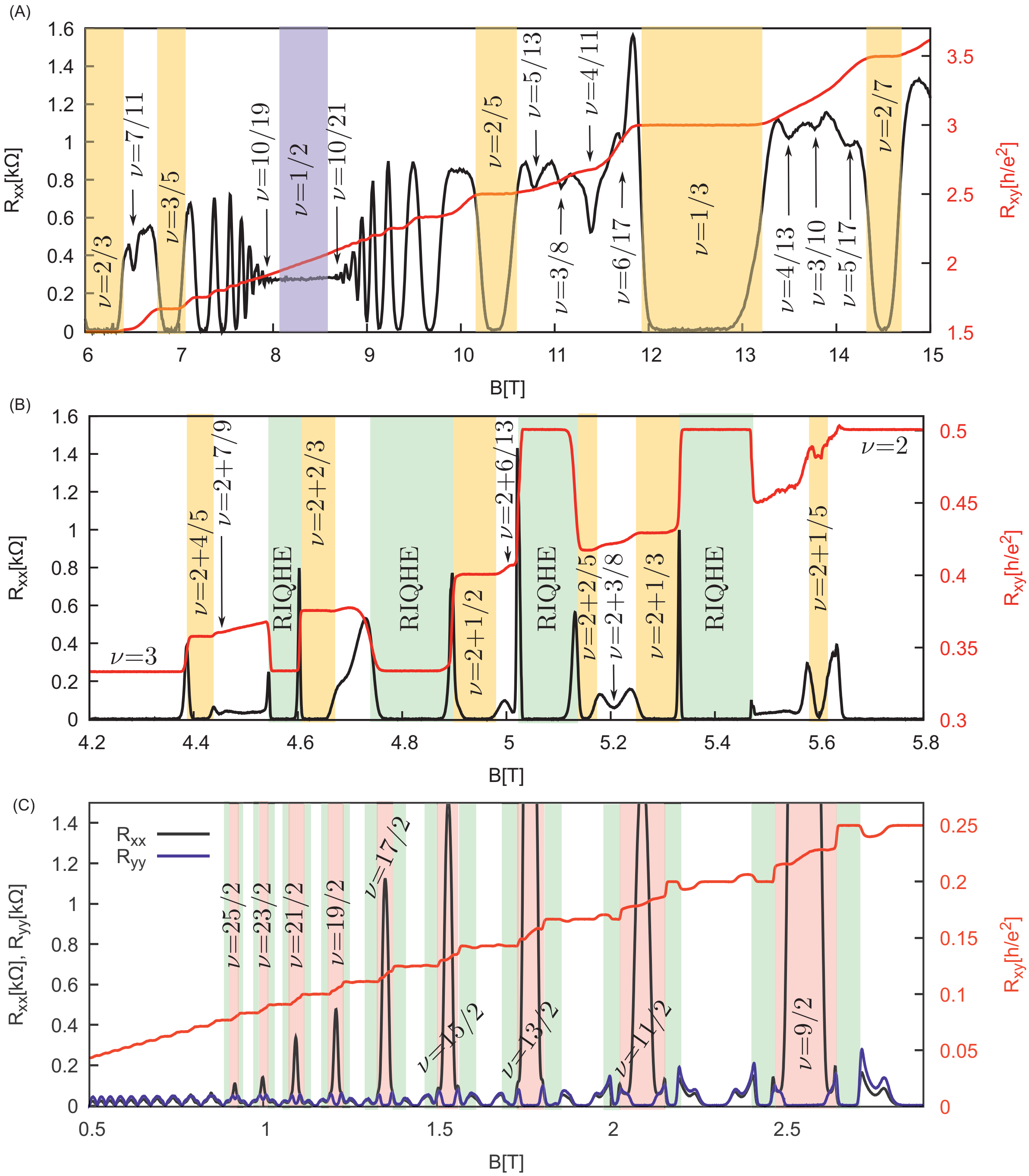

Fig. 1 Experimental measurements of the Hall resistance R_{xy} and the longitudinal resistance R_{xx} as a function of the magnetic field *B* applied perpendicularly to a 2DEG. (A) Resistance traces in the lowest Landau level from Ref. Pan et al. (2003). Prominent gapped states are shaded in yellow. Other weaker states (without fully developed minimum in R_{xx}) are also indicated. The composite Fermi liquid is shaded purple. (B) In the second Landau level, in addition to gapped states at odd-denominator filling factors, there are also even-denominator states at $\nu = 2 + 1/2$ and $\nu = 2 + 3/8$. Reentrant integer quantum Hall states are shaded in green. (C) In higher Landau levels, the FQH plateaus are replaced by states with strongly anisotropic transport, as revealed by the large difference between R_{xx} and R_{yy}. Examples are shaded in red and identified with stripe phases. Reentrant integer quantum Hall states are shaded in green. (A) From Pan W, Stormer HL, Tsui DC, Pfeiffer LN, Baldwin KW, and West KW (2003) Fractional quantum Hall effect of composite fermions. *Physical Review Letters* 90: 016801, doi: 10.1103/PhysRevLett.90.016801. (B) Data is reproduced from Ref. Kumar A, Csáthy GA, Manfra MJ, Pfeiffer LN, and West KW (2010) Nonconventional odd-denominator fractional quantum Hall states in the second Landau level. *Physical Review Letters* 105: 246808, doi: 10.1103/PhysRevLett.105.246808. (C) Data is taken from Ref. Ro D, Deng N, Watson JD, Manfra MJ, Pfeiffer LN, West KW, and Csáthy GA (2019) Electron bubbles and the structure of the orbital wave function. *Physical Review B* 99: 201111, doi: 10.1103/PhysRevB.99.201111.

Incompressible fluids

Performing the transport measurements described above, one obtains remarkable traces of R_{xy} and R_{xx} as a function of the magnetic field B, as we illustrate in Fig. 1 using current state-of-the-art experimental data. At sufficiently low temperatures (typically, in mK range) and very high magnetic fields, the trace is dominated by FQH states which display a quantized plateau in R_{xy} and vanishing R_{xx}. These are signatures of incompressible quantum fluids, which arise from strong Coulomb repulsion between the electrons residing in the partially-filled LLL, as the kinetic energy of the electrons is quenched. FQH fluids are unconventional in that they represent topological phases of matter. While a detailed theory of such topological quantum fluids will be presented in subsequent sections, here we briefly summarize some of their defining properties – see Fig. 2:

- FQH phases are quantum liquids that do not exhibit long-range order for any local order parameter. Thus, FQH phases cannot be described by a Landau-Ginzburg type theory based on spontaneous symmetry breaking Prange and Girvin (1987). For example, the (LL-projected) structure factor of a FQH state, shown in inset of Fig. 2B, takes the form characteristic of a liquid phase, indicating that the FQH state is uniform in the bulk and distinct from, say, a Wigner crystal.
- The bulk of a FQH fluid exhibits an energy gap Δ, i.e., there is a discontinuity in the chemical potential as one sweeps the magnetic field. Furthermore, there is also a gap for charge-neutral excitations at the fixed magnetic field, as seen in Fig. 2B. Near the system's boundary, however, there are *gapless* charged excitations which propagate chirally, in the direction determined by the external magnetic field, see Fig. 2A. In the semiclassical picture, these excitations can be visualized as "skipping orbits" Halperin (1982), which can also go around weak impurity potentials, avoiding dissipation.

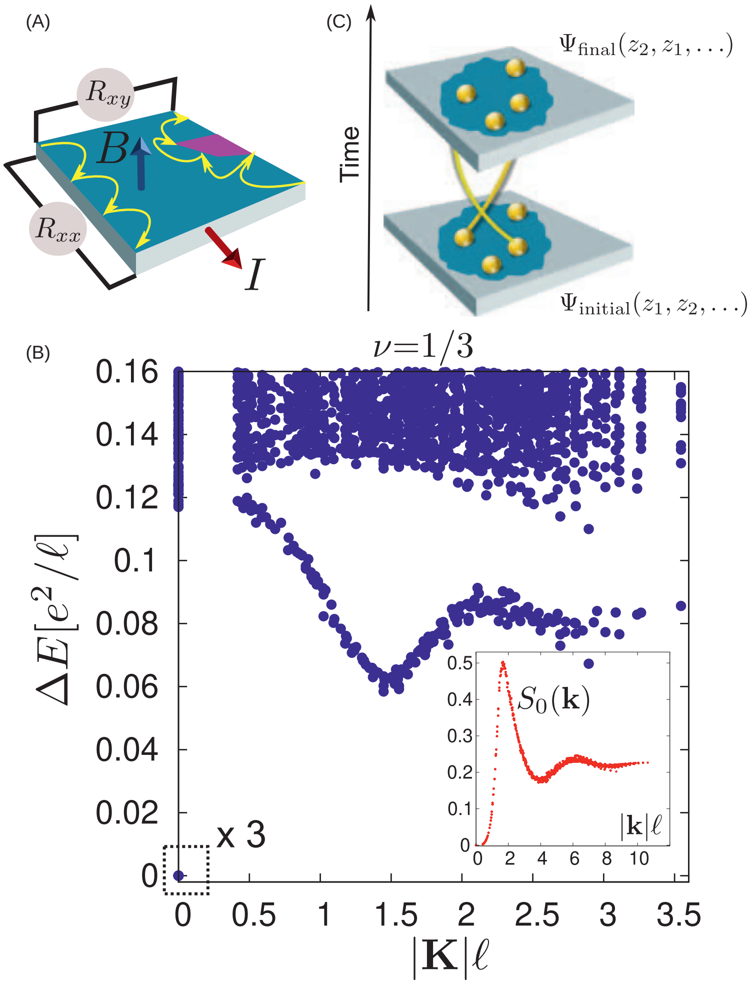

Fig. 2 Incompressible fluids and topological order. (A) Transport experiment probing a FQH state. Robust quantization of the Hall resistance is associated with a current-carrying edge state (yellow), which is insensitive to a low concentration of impurities (depicted in pink). In a semiclassical picture, the edge state forms a narrow one-dimensional channel that propagates ballistically in one direction. (B) On a torus, the $\nu = 1/3$ FQH ground state has a three-fold topological degeneracy and carries zero momentum $\mathbf{K} = 0$, while the rest of the energy spectrum is separated by a gap. Low energy charge-neutral excitations form a collective mode. Data is obtained using DiagHam open source package DiagHam for exact diagonalization of the Coulomb interaction projected to the lowest LL for $N \leq 12$ electrons. The same plot includes data for both square and hexagonal unit cells, illustrating the robustness of the low-energy physics to geometric details. Inset shows the projected guiding-center structure factor $S_0(\mathbf{k})$, which reveals a liquid ground state. (C) Elementary charged excitations of a FQH fluid behave as anyons: by taking two anyons around each other, the resulting wave function Ψ_{final} is not simply equal to $\pm\Psi_{\mathrm{initial}}$, as it would be for bosons or fermions.

- The 'topological' nature of the FQH fluid is manifested in its sensitivity to the topology of the manifold it lives in. For example, in the infinite plane or when wrapped around a sphere, the fluid has a unique ground state, but when it is placed on a torus or any higher genus surface, the ground state develops a degeneracy Wen and Niu (1990). At filling factor $\nu = p/q$, with p, q coprime positive integers, the ground state degeneracy is at least q Haldane (1985). For example, in the $\nu = 1/3$ state shown in Fig. 2B, the ground state is three-fold degenerate on the torus.
- By threading magnetic flux or, equivalently, by twisting the torus boundary conditions, the degenerate ground states can mix with one another but remain separated from other excited states by the energy gap Δ. The total Hall conductance carried by the ground state multiplet is proportional to the topological invariant called the Chern number C Thouless et al. (1982). This gives the Hall conductance for each member of the multiplet $\sigma_{xy} = \nu \frac{e^2}{h}$. The topological nature of the Hall conductance explains its robustness at sufficiently low temperatures $k_B T \ll \Delta$.
- Thermal Hall conductance of FQH fluids is given by Kane and Fisher (1997)

$$\kappa_{xy} = c_{\left[\pi^2 k_B^2/(3\hbar)\right]} T. \tag{8}$$

where the universal coefficient c_ is known as the chiral central charge. This expression holds at temperatures much smaller than the gap and under the assumption that edge modes are fully equilibrated.

- The excitations of incompressible FQH fluids are *anyons* Leinaas and Myrheim (1977) and Wilczek (1982): an exotic type of particle which carry a fraction of the electron charge and also have "fractional" exchange statistics Arovas et al. (1984). In particular, for states such as $\nu = 1/3$ depicted in Fig. 2C, the adiabatic exchange of the coordinates of two anyons results in a complex phase, $\Psi_{\text{final}}(z_2, z_1) = e^{i\theta}\Psi_{\text{initial}}(z_1, z_2)$ with $\theta = 2\pi/3$. Bosons and fermions are special cases with $\theta = 0$ and $\theta = \pi$, respectively, while Abelian anyons correspond to other real values of θ. Anyons with richer exchange statistics are also possible and will be discussed in Section "Non-Abelian states". We note that recent experiments have observed statistical properties of the simplest types of Abelian anyons in the $\nu = 1/3$ state using mesoscopic interferometry Nakamura et al. (2020) as well as anyon colliders Bartolomei et al. (2020).
- FQH fluids can be described by an emergent Chern-Simons gauge field **a**, which attaches magnetic fluxes to particles Zhang et al. (1989). This enables the transmutation of statistics and the existence of anyon excitations. The Chern-Simons field contributes a topological term to the effective action of FQH fluids,

$$\mathcal{L}_{\text{CS}} = \frac{1}{4\pi\nu} \varepsilon^{\mu\nu\lambda} a_\mu \partial_\nu a_\lambda, \tag{9}$$

where $\varepsilon^{\mu\nu\lambda}$ is the Levi-Civita tensor and we assumed the simplest FQH state is at filling $\nu = 1/q$, with Einstein summation convention implied. Thus, the effective low-energy theory of FQH fluids is a variant of topological quantum field theory (see Section "Effective field theory" for further discussion).

The properties summarized in this section are believed to be shared by all incompressible FQH states, which are primarily realized in the LLL and SLL, recall Fig. 1A and B. However, as we explain below, the microscopic mechanisms giving rise to these topological fluids can be very different. In particular, the FQH states in the LLL are markedly different from those in the SLL. In contrast to the majority of gapped FQH liquids presented in Fig. 1A, we note that there also exists a *gapless* liquid state which is similar to the Fermi liquid state in an ordinary 2DEG in zero magnetic field. This state occurs at $\nu = 1/2$ where one observes a smooth dependence of both the longitudinal and Hall resistances in Fig. 1A. Nevertheless, this Fermi-liquid-like state has many exotic properties of its own and it will be discussed separately in Section "Gapless composite fermion Fermi liquid in the half-filled Landau level".

We note here that FQH states extending on either side of $\nu = 1/2$ are related by an operation that maps electrons to holes and vice versa, i.e., it relates states at ν with $1 - \nu$. This particle-hole (PH) symmetry is exact in the limit $B \to \infty$. In this limit, any two-body interaction, like the Coulomb one, results in eigenstates that are perfectly PH symmetric. We will return to the consequences of PH symmetry in Sections "Anti-Pfaffian" and "Effective field theory".

Broken symmetry phases

In addition to incompressible liquids, other types of correlated phases of matter can occur in partially filled LLs, primarily in the regime of low filling factors or in higher LLs, see Fig. 1B and C (Ro et al., 2019). While interactions still underpin the formation of such phases, these phases spontaneously break the translation symmetry of the 2D plane by forming crystals or stripe patterns (Fig. 3). Such phases are typically weakly-correlated and they have been successfully understood using the more traditional methods, such as Hartree-Fock theory.

Wigner crystals in the lowest Landau level

"Classical" electrons at sufficiently low densities in 2D form a triangular Wigner crystal (WC) (see Fig. 3) to minimize the Coulomb repulsion between them. Strong magnetic field quenches the kinetic energy of the electrons, leaving only interactions to decide the fate of the system. This setting was believed to be ideal to stabilize the WC phase and provided one of the motivations for the Tsui-Stormer-Gossard experiment Tsui et al. (1982).

As it turned out, the FQH liquid has lower energy than WC at high filling factors Yoshioka et al. (1983). However, at very low filling factors, when the density of electrons is sufficiently small, a WC is expected to be stabilized. Recent studies suggest that the

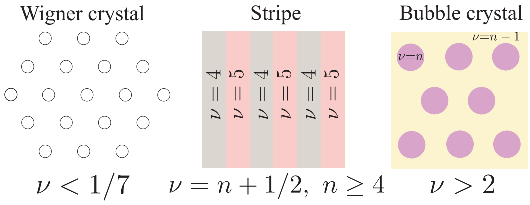

Fig. 3 Some examples of symmetry-broken phases realized in a two-dimensional electron gas placed in a strong perpendicular magnetic field.

FQH fluid can prevail over the WC at filling factors as low as $\nu = 1/7$ Pan et al. (2002), Chung et al. (2022). Furthermore, the WC that is stabilized at $\nu < 1/7$ is not that of electrons, but of electron-vortex composites called composite fermions (CFs) Archer et al. (2013) and Zuo et al. (2020), that we will introduce in Section "Composite fermions".

While direct signatures of the Wigner solid phase have remained elusive, experiments have observed a number of indirect signatures. The presence of a WC has been probed by studying the commensurability oscillations of CFs in a nearby layer Deng et al. (2016). Collective oscillations of the crystalline domains of the WC resulting from disorder give rise to "pinning resonances" in the frequency-dependent conductivity which have been detected experimentally (Williams et al., 1991; Zhu et al., 2010). The melting behavior of the magnetic-field-induced WC suggests that it harbors quantum correlations and is markedly different from the classical WC at zero-field Ma et al. (2020).

Stripes, nematics and bubble crystals in higher LLs

In higher LLs, interactions can also engender various phases that spontaneously break certain symmetries while exhibiting integral quantization of the Hall resistance, as seen in Fig. 1B and C. In the vicinity of integral fillings, if disorder is sufficiently weak, the additional electrons or holes are expected to form a WC. Using Hartree-Fock theory, Koulakov et al. (1996) and Fogler et al. (1996) predicted that the extra electrons or holes in a high LL have a tendency to form a WC, a "bubble" phase – a WC of bubbles of electrons, where each bubble hosts multiple electrons, or stripes of alternating fillings, depending on the filling factor (see Fig. 3). For example, when a high LL is nearly half full (i.e., the filling factor is $\nu = n + 1/2$ with n being a sufficiently large integer), strong transport anisotropy is observed, as shown in Fig. 1C, consistent with the formation of stripes (see Fig. 3) (Du et al., 1999; Lilly et al., 1999). The direction of the anisotropy aligns with one of the crystal axes, due to the explicit symmetry breaking via the host lattice. Moreover, the anisotropy can flip by 90° as a function of the in-plane magnetic field Lilly et al. (1999) or the density Zhu et al. (2002). Many re-entrant transitions are seen in higher LLs (Eisenstein et al., 2002; Xia et al., 2004), indicating competition between numerous approximately degenerate ground states Shibata and Yoshioka (2001) with a common feature of integral Hall resistance quantization.

Laughlin states

Laughlin's wave function

Soon after the experimental observation of the FQH plateau at $\nu = 1/3$, Laughlin constructed a novel ansatz to describe the electronic ground state at this filling Laughlin (1983). Laughlin's wave function is given by

$$\Psi^{\text{Laughlin}}_{\nu=1/(2p+1)} = \prod_{i<j} (z_i - z_j)^{2p+1} \exp\left[-\sum_k \frac{|z_k|^2}{4\ell^2}\right] \equiv \Phi_1^{2p+1}, \tag{10}$$

where $z_k = x_k - iy_k$ parametrizes the 2D coordinate of the k^{th} electron as a complex number, and p is a positive integer ($p = 1$ for $\nu = 1/3$). The $\nu = 1$ IQH wave function, $\Phi_1 = \prod_{i<j}(z_i - z_j)$, is referred to as the Laughlin-Jastrow factor. To simplify the notation, below we shall often drop the ubiquitous Gaussian factor and the subscript "$\nu =$" from the wave functions.

The high power of the Jastrow factor in the Laughlin wave function builds additional correlations in the many-body state (beyond those mandated by the Pauli principle) which keeps the electrons away from each other and thus minimizes their Coulomb repulsion. Because of this, one may expect the wave function in Eq. (10) to provide a good variational description of the exact ground state of the Hamiltonian in Eq. (5). Quite remarkably, it turned out that the overlap between the Laughlin wave function and the exact ground state of Eq. (5) for as many as $N = 15$ electrons is consistently above 98%, despite an exponential increase in the size of the Hilbert space with N and the lack of any variational parameters in Eq. (10). This suggests that the Laughlin wave function captures all the essential correlations of the $\nu = 1/3$ ground state even in the thermodynamic limit. Indeed, due to the "nice" form of the Laughlin wave function, many of its properties such as energy, density, pair-correlation function etc. have been studied in large systems using the Monte Carlo method Morf and Halperin (1986). The (projected) structure factor of the $\nu = 1/3$ state, shown in inset of Fig. 2B, confirms that the state describes an incompressible liquid.

Laughlin's theory furthermore predicts that the FQH effect can also occur at $\nu = 1/5$ and a quantized Hall plateau at this filling was observed in experiments. Subsequent numerical simulations have shown that the Laughlin wave functions have high overlaps with the exact LLL Coulomb ground state for small systems at $\nu = 1/3$, 1/5 and 1/7 Fano et al. (1986), d'Ambrumenil and Reynolds

(1988). For $\nu < 1/7$, a Laughlin liquid is expected to give way to a crystalline state Lam and Girvin (1984). By particle-hole conjugation in the LLL, Laughlin's theory also explains the plateaux observed at fractions $\nu = 1 - 1/(2p+1)$ which can be understood as a $1/(2p+1)$ Laughlin state of "holes."

Charged excitations

Laughlin also constructed wave functions for the charged excitations in this system. Laughlin's wave function for the positively charged excitation, referred to as a *quasihole* (qh), located at a position η, is given by:

$$\Psi^{\text{Laughlin,qh}}_{1/(2p+1)} = \prod_i (z_i - \eta)\Psi^{\text{Laughlin}}_{1/(2p+1)}, \tag{11}$$

while that of the negatively charged *quasiparticle* (qp) is:

$$\Psi^{\text{Laughlin,qp}}_{1/(2p+1)} = \prod_i (2\partial_{z_i} - \overline{\eta})\Psi^{\text{Laughlin}}_{1/(2p+1)}. \tag{12}$$

In Eq. (12) the derivatives only act on the polynomial part of the wave function and not on the Gaussian factor. To motivate these wave functions, consider the situation where $\eta = 0$. The polynomial factor $\prod_i z_i$ pushes electrons away from the origin (the wave function of Eq. (11) vanishes at η) thereby depleting the electron density at the origin resulting in the creation of a positively charged quasihole. The derivatives, on the other hand, pull electrons in towards the origin which leads to a build-up of an excess charge at the origin resulting in the creation of a negatively charged quasiparticle.

The probability density corresponding to Laughlin's ground state and quasihole wave functions can be interpreted as the partition function of a one-component classical plasma in 2D Laughlin (1987). Using this plasma analogy, Laughlin showed that the quasihole excitation carries a fractional charge of $e/(2p+1)$ (we denote the electronic charge by $-e$). Via PH conjugation, one can readily see that the quasiparticle excitation also carries a fractional charge of value $(-e)/(2p+1)$. Shot-noise experiments have verified the presence of $-e/3$ charged quasiparticles in the $\nu = 1/3$ state (Saminadayar et al., 1997; Dolev et al., 2008). Moreover, recent experiments Bartolomei et al. (2020) and Nakamura et al. (2020) have confirmed that the quasihole and quasiparticle excitations of the Laughlin state are Abelian anyons with a statistical phase $\theta = 2\pi/3$.

Magnetoroton excitation

Along with charged excitations, any FQH system, including the Laughlin states, also hosts "neutral" excitations which can be viewed as arising from a combination of an equal number of quasiparticles and quasiholes. Girvin, MacDonald, and Platzman (GMP) Girvin et al. (1985) proposed a general ansatz for the lowest-lying neutral excitation as a density wave riding on the ground state. The GMP wave function is written as $\Psi^{\text{GMP}}_{\nu,\mathbf{k}} = \overline{\rho}_{\mathbf{k}}\Psi_\nu$, where $\overline{\rho}_{\mathbf{k}}$ is the LLL projected density operator and Ψ_ν is the ground state wave function at filling ν. The GMP excitation is termed a *magnetoroton* since its dispersion has a characteristic minimum at a finite wavenumber reminiscent of the roton minimum in the excitation spectrum of liquid Helium. The GMP ansatz gives a reasonable account of the exact low-lying neutral excitation at wavenumbers near and below the roton minimum, $k\ell \lesssim 1$ He et al. (1994). Resonant inelastic light-scattering experiments have mapped out the magnetoroton branch of excitations at $\nu = 1/3$ Pinczuk et al. (1993).

Edge excitations

As we sketched in Fig. 2A, due to the insulating bulk, the conduction in FQH states occurs in the vicinity of the system's boundary via chiral edge channels. In the FQH effect, electron correlations are strong and one must model the edge channels using the Luttinger liquid description Wen (1990). Theoretical description of FQH edge states is provided by bosonization, which conveniently expresses the electronic degrees of freedom in terms of bosons. Due to chirality, backscattering in wide samples is minimized and the edge channels are found to propagate ballistically across long distances, with the dispersion $\varepsilon_k = \upsilon k$, where υ is the edge speed and k is the momentum along the edge.

In real samples, however, the edge may undergo a phenomenon of "reconstruction" Chklovskii et al. (1992), Chamon and Wen (1994) where instead of a single channel, the edge consists of compressible and incompressible stripes that form multiple parallel conducting channels, possibly counterpropagating. Unlike the insulating bulk, the physics of the edge is thus far more prone to non-universal effects due to the long-range tail of the Coulomb interaction and details of the confining potential near the boundary of the system.

The edge spectral function can be measured by tunneling an electron laterally into the edge. Wen's theory Wen (1990) predicts a nonlinear current-voltage, $I \propto V^m$, relation at zero temperature, with the edge exponent taking the quantized value $m = 2p+1$ for the $\nu = 1/(2p+1)$ Laughlin states. Thus, the quantized edge exponent distinguishes a FQH edge from an ordinary Luttinger liquid, whose edge exponent varies continuously with the strength of the interaction. The edge exponent was measured in experiments by Chang et al. (1996) who found its value to be reasonably close to 3 in the $\nu = 1/3$ state. However, various non-universal effects have also been observed in these experiments Chang (2003). This makes the study of FQH edges challenging even in the simplest fractions such as $\nu = 1/3$.

Parent Hamiltonian and Haldane pseudopotentials

An important step in validation of Laughlin's theory was Haldane's identification of a parent Hamiltonian for the state in Eq. (10) Haldane (1983). Any homogeneous and isotropic pairwise interaction potential $V(|z_i - z_j|)$, with the particles restricted to a single LL, can be written as Duncan Haldane (1990)

$$H_{\text{int}} = \sum_{i<j} V\left(|z_i - z_j|\right) = \sum_{m} \sum_{i<j} V_m \hat{P}_{ij}^{m}, \tag{13}$$

where $\hat{P}_{ij}^{m}$ projects onto a state in which particles i and j have relative angular momentum m. In the LLL, $\hat{P}_{ij}^{m}$ projects on the relative state $\psi_{\text{rel}} \sim (z_i - z_j)^m$ of any pair of particles. The numbers V_m are called the Haldane pseudopotentials and they represent an energy penalty for two particles to form a state with relative angular momentum m. For spinless electrons, only odd values of m can appear as ψ_{rel} must be fully antisymmetric in electrons' coordinates.

The parent Hamiltonian of the $\nu = 1/3$ Laughlin state is obtained by setting $V_1 > 0$ and all other $V_{m\geq 3} = 0$. This interaction assigns positive energy to any wave function that vanishes as $\psi_{\text{rel}} \sim (z_i - z_j)$, but it allows pairs of particles to form the state $\psi_{\text{rel}} \sim (z_i - z_j)^3$ for free. The latter is just the $p = 1$ Laughlin state in Eq. (10), which emerges as the unique and densest state with exactly zero energy for the V_1 pseudopotential interaction. The quasihole excitations of the Laughlin state, Eq. (11), similarly appear as exact zero-energy states of the same Hamiltonian. Numerics on finite systems show that any other state in the spectrum is separated by a gap on the order $\Delta \propto V_1$ but the persistence of this spectral gap in the thermodynamic limit has not been rigorously proven.

Haldane pseudopotentials greatly facilitate numerical modelling of FQH systems. For example, open-source libraries for exact diagonalization of FQH systems such as DiagHam DiagHam take full advantage of the pseudopotential formalism. On the analytical side, an arbitrary combination of pseudopotentials can be conveniently converted to a real space potential Trugman and Kivelson (1985), which enables systematic studies of parent Hamiltonian of more complex FQH states Simon et al. (2007a).

Hierarchy and composite fermions

Following the discovery of the $\nu = 1/3$ state, a zoo of more than a hundred FQH plateaux have been observed, many of which do not fit Laughlin's theory (see Fig. 1). These fractions predominantly belong to the sequence $\nu = n/(2pn \pm 1)$ [and their hole-conjugates at $1 - n/(2pn \pm 1)$], where n and p are positive integers (see Fig. 1). Consequently, new theoretical approaches had to be developed to describe such states. In this chapter we focus on two leading paradigms for understanding the various fractions observed the lowest LL: the Haldane-Halperin hierarchy and Jain's composite fermion theory.

Haldane-Halperin hierarchy

Haldane (1983) and Halperin (1984) proposed a hierarchical construction to obtain FQH states at arbitrary odd-denominator fractions. In the hierarchical construction, one starts with a nearby parent Laughlin state and views the filling factor difference from it as stemming from the presence of additional Laughlin quasiparticles/quasiholes. Assuming that interaction between the additional Laughlin quasiparticles/quasiholes is sufficiently strongly repulsive at short distances and weak in comparison to the parent Laughlin state, one condenses these excitations into Laughlin-like "daughter" FQH states. Iterating such a construction, one can produce candidate FQH states at all odd-denominator fractions – see Fig. 4 for the fractions originating from the $\nu = 1/3$ Laughlin state in the first three generations of a hierarchy.

A trial wave function for the first daughter state at filling factor $\nu = 1/(2p + 1 - q^{-1})$, where q is a positive even integer, with N electrons and N/q Laughlin quasiparticles is constructed as follows:

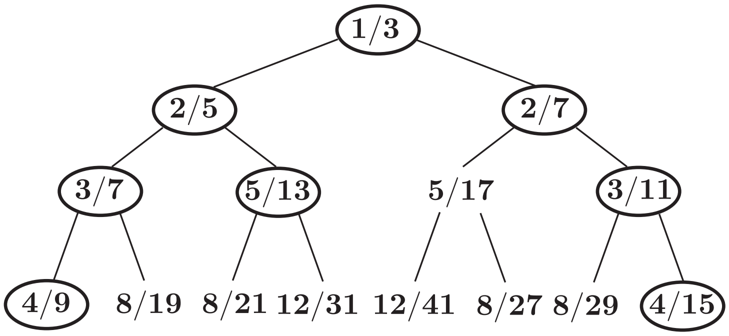

Fig. 4 Daughter fractions obtained from the Haldane-Halperin hierarchy originating from the parent Laughlin state at $\nu = 1/3$. Experimentally observed fractions in the lowest Landau level are circumscribed.

$$\int \left[\prod_{k=1}^{N/q} d^2\eta_k\right] \left[\Phi_1^*(\{\bar{\eta}_k\})\right]^q \Psi^{\text{Laughlin,qps}}_{1/(2p+1)}(\{z\};\{\eta_k\}), \tag{14}$$

where Φ_1 is the usual Laughlin-Jastrow factor and the term $\Psi^{\text{Laughlin, qps}}_{1/(2p+1)}$ is the Laughlin quasiparticle state of Eq. (12) generalized to multiple quasiparticles located at positions η_k. Analogous wave functions for the first daughter state at $\nu = 1/(2p+1+q^{-1})$ can be constructed from Laughlin's quasihole wave function of Eq. (11). The same idea can be used to construct wave functions for daughter states further down in the hierarchy.

For small systems at $\nu = 2/5$ and $3/7$, the hierarchical wave functions have been constructed numerically and these have high overlaps with the exact LLL Coulomb ground states Greiter (1994). Studies of larger systems and other filling factors are required to substantively test these wave functions. The order of fractions and their stability predicted by the hierarchy theory is not entirely consistent with experiments. For example, the 3/7 and 5/13 states appear at the same level in the hierarchy (see Fig. 4) but the FQH effect at 3/7 is much stronger than that at 5/13 as is evidenced from their gaps [see Fig. 1A]. Nonetheless, universal aspects, such as the charge and braiding statistics of the quasiparticles, predicted by the Haldane-Halperin construction are consistent with experiments.

Composite fermions

Jain's theory Jain (1989*a*) provides a conceptually different microscopic explanation of the $\nu = n/(2pn \pm 1)$ FQH states as IQH states of certain emergent topological particles called *composite fermions* (CFs). A composite fermion is a bound state of an electron and an even number ($2p$) of vortices. Due to the vortex-binding, the CFs see a reduced magnetic field $B^* = B - 2p\rho\phi_0$ compared to the external magnetic field B seen by the electrons [superscript * is used to denote CF quantities]. The + (parallel) and – (anti-parallel) signs in $\nu = n/(2pn \pm 1)$ indicate the direction of the residual magnetic field seen by the CFs with respect to the external magnetic field. In the zeroth-order approximation, the CFs are assumed to be non-interacting, and just like free electrons in a magnetic field, CFs form their own Landau-like levels, called *Lambda levels* (ΛLs). When an integer number $\nu^* = n$ of these ΛLs are fully filled, we get an FQH effect of electrons at $\nu = n/(2pn \pm 1)$. The existence of ΛLs has been established in experiment Kang et al. (1993). Recently, in an ultra-high mobility sample, FQH states all the way up to $n = 16$ in the $n/(2n \pm 1)$ Jain sequence have been observed Chung et al. (2021).

The mapping to an IQH effect leads to the Jain wave function for the FQH ground state at $\nu = n/(2pn \pm 1)$ Jain (1989*a*)

$$\Psi^{\text{Jain}}_{n/(2pn\pm1)} = \mathcal{P}_{\text{LLL}}\Phi_1^{2p}\Phi_{\pm n}. \tag{15}$$

Here Φ_n is the Slater determinant state of n filled LLs of electrons, while the Jastrow factor Φ_1^{2p} attaches $2p$ vortices to each of the electrons to convert them into CFs, see Fig. 5 for a schematic illustration. For $n = 1$ (with the + sign) the Jain wave function is identical to the Laughlin wave function of Eq. (10). For $n > 1$, the Jain wave function needs to be explicitly projected to the LLL, as denoted by $\mathcal{P}_{\text{LLL}}$..

Beyond ground state properties, the IQH mapping readily allows the construction of wave functions for the excitations as well, see Fig. 5. The positively charged quasihole called a CF hole is obtained by removing a CF from the topmost filled ΛL. The negatively charged quasiparticle, referred to as a CF particle, is obtained by adding a CF in the bottommost empty ΛL. The lowest-lying neutral excitation, called the CF-exciton, is obtained by combining a single CF particle and a CF hole. The excitations obtained using CF theory generally exceed the accuracy of other approaches, e.g., the Laughlin and GMP ansatz discussed in Section "Laughlin states," in describing the exact LLL Coulomb excited states.

We note here that although the Haldane-Halperin hierarchical states are topologically equivalent to CF states Read (1990), Wen (1995), the two theories propose different microscopic mechanisms for the origin of FQH effect Jain (2014). Unlike the hierarchy wave functions, the CF wave functions in Eq. (15) have proven amenable to large-scale numerical simulations Jain and Kamilla (1998). These studies have demonstrated that the CF theory provides a highly-accurate description of the majority of FQH states observed in the LLL. For example, neutral excitation spectrum observed using surface acoustic waves Kukushkin et al. (2009) is in good agreement with CF theory Scarola et al. (2000). Nevertheless, some quantitative discrepancy between the experimentally measured (Boebinger et al., 1985; Willett et al., 1988; Du et al., 1993; Pan et al., 2020; Villegas Rosales et al., 2021) and theoretically

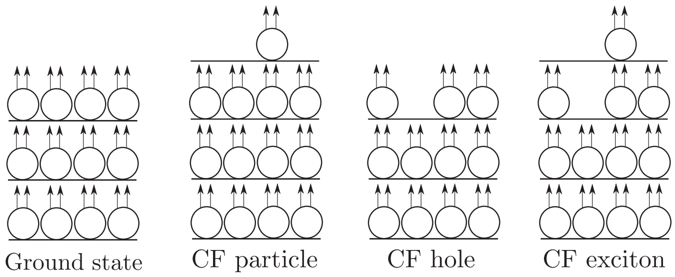

Fig. 5 Schematic representation of CF ground state, elementary charged and neutral excitations at $\nu = 3/7$.

predicted (Zhang and Das Sarma, 1986; Ortalano et al., 1997; Morf et al., 2002) charge gaps persists to this day. This likely arises from neglecting the effects of the disorder, interface roughening, and screening by gates in theoretical studies. Furthermore, theoretical calculations use simplified models to incorporate the effects of LL mixing and finite-width. More realistic calculations are needed to quantitatively explain the gaps obtained in experimental studies. Finally, certain delicate states, like those observed at $\nu = 4/11$ and $5/13$ (Samkharadze et al., 2015; Pan et al., 2015), Fig. 1A, and the states seen in the SLL, Fig. 1B, lie beyond the paradigm of *weakly-interacting* CFs presented in this section. To understand such states, one needs other approaches, as discussed in subsequent sections below.

Half-filled Landau level

The simplest fraction – half-filling of a LL – has remained in the focus of research since the early days of the FQH effect. The conundrum is that no quantized FQH plateau is observed when it is the LLL that is half-filled, i.e., at $\nu = 1/2$ – see Fig. 1A. Yet, when the *second* LL is half-filled, resulting in a total filling factor $\nu = 5/2$, a robust FQH plateau is seen instead (Fig. 1B). In this section, we discuss a novel kind of gapless Fermi-liquid like state that was introduced to describe the $\nu = 1/2$, and its pairing instability that is believed to give rise to the exotic gapped state at $\nu = 5/2$.

Gapless composite fermion Fermi liquid in the half-filled Landau level

The $\nu = 1/2$ state finds a natural interpretation in the CF theory since at half-filling CFs see no residual magnetic field. Therefore, like electrons at zero field, CFs can form a Fermi liquid state, called the composite Fermi liquid (CFL) (Kalmeyer and Zhang, 1992; Halperin et al., 1993), which is gapless and thus does not lead to a FQH effect. The CFL is a markedly different state from the ordinary Fermi sea: in the LLL, there is no kinetic energy and interactions alone conspire to create an emergent Fermi-liquid. The wave function for the CFL at even-denominator fillings $\nu = 1/(2p)$ is obtained as the $n \to \infty$ limit of the wave function in Eq. (15):

$$\Psi^{\mathrm{CFL}}_{1/(2p)} = \mathcal{P}_{\mathrm{LLL}} \Phi^{\mathrm{FL}} \Phi_1^{2p}, \Phi^{\mathrm{FL}} \equiv \det\left[e^{i\vec{k}_l \cdot \vec{r}_m}\right]. \tag{16}$$

Halperin, Lee, and Read (HLR) Halperin et al. (1993) evaluated many properties of the CFL using a Chern–Simons field theory in which flux quanta are bound to electrons to turn them into CFs. This description is in qualitative agreement with numerous experiments that have verified the presence of the CFL (Kang et al., 1993; Willett et al., 1993; Goldman et al., 1994). In Section "Effective field theory" we shall discuss one particular experiment, namely the measurement of the CF Fermi wave vector using geometric resonance (Willett et al., 1999; Kamburov et al., 2014; Hossain et al., 2020), which has renewed the interest in the CFL state.

$\nu = 5/2$ state

The observation of a FQH state at the even-denominator filling $\nu = 5/2$ Willett et al. (1987) indicated that not all FQH states can be described using the ideas discussed in Section "Hierarchy and composite fermions". Moore and Read Moore and Read (1991) identified conformal field theory (CFT) as an innovative tool for generating trial FQH wave functions (see Ref. Hansson et al. (2017) for an in-depth overview of this technique). Using a particular type of CFT, Moore and Read arrived at the following wave function for a state at $\nu = 1/2$:

$$\Psi^{\mathrm{MR\text{-}Pf}}_{1/2} = \mathrm{Pf}\left(\frac{1}{z_i - z_j}\right) \prod_{1 \le i < j \le N} (z_i - z_j)^2, \tag{17}$$

where the number of particles N is assumed to be even. The key component of this wave function is the Pfaffian – the antisymmetrized sum over pairs:

$$\mathrm{Pf}\left(\frac{1}{z_i - z_j}\right) = \mathbb{A}\left(\frac{1}{z_1 - z_2} \frac{1}{z_3 - z_4} \cdots\right), \tag{18}$$

where $\mathbb{A}$ represents the anti-symmetrization operator. The Pfaffian factor makes the overall wave function antisymmetric and therefore a valid trial state for electrons. As first suggested by Greiter et al. (1992), this wavefunction can provide a description of the experimental $\nu = 5/2$ resistance plateau, provided one assumes that the two lowest LLs of ↑ and ↓ spins are completely filled with electrons. Thus, Eq. (17) describes the correlations between fully spin-polarized electrons in the valence (half filled) SLL.

The Pffafian factor introduces weak pairing between the CFs Read and Green (2000). Indeed, in the antisymmetrized product over pairs, we recognize the real-space form of the wave function describing a 2D Bardeen-Cooper-Schrieffer (BCS) superconductor. Thus, we can view Eq. (17) as the FQH analog of a $p_x + ip_y$ superconductor. The physical origin of pairing is due to the effective Coulomb interaction being less repulsive at short distances in the SLL compared to LLL. Thus, forming CFs overscreens the Coulomb repulsion resulting in a weak residual attractive interaction between them which leads to a pairing instability of their CFL. One consequence of the electron pairing is an unconventional collective excitation on top of the Moore-Read ground state that was dubbed the "neutral fermion" mode (Bonderson et al., 2011; Möller et al., 2011).

The interest in the Moore-Read state was initially fueled by numerical simulations. Exact diagonalizations performed by Morf (1998) showed that the spin-polarized state at $\nu = 5/2$ had lower energy than any partially polarized or spin-singlet state, even in the absence of any Zeeman splitting. Furthermore, it was shown that the state was poised towards a compressible phase Rezayi and Haldane (2000) and can be easily pushed across the phase boundary by slightly varying the Hamiltonian in a way that mimics the effect of an in-plane magnetic field, accounting for experimental observations Eisenstein et al. (1990), Lilly et al. (1999), Pan et al. (1999). The correspondence between numerics and experiment has been made more quantitative by comparisons of the energy gap obtained from exact diagonalization Morf et al. (2002) and DMRG simulations Feiguin et al. (2008) with the one measured in experiments Kumar et al. (2010).

Anti-Pfaffian

While PH symmetry is exact for the FQH problem restricted to a single LL, the Moore-Read state in Eq. (17) is not invariant under PH transformation. The state obtained by PH conjugation applied to Eq. (17) is a topologically-distinct phase of matter that was named the "anti-Pfaffian" (aPf) (Levin et al., 2007; Lee et al., 2007). The two states have different thermal Hall responses and different edge excitations, which immediately leads to the question: which state describes the $\nu = 5/2$ ground state in the thermodynamic limit?

Distinguishing between the aPf and Moore-Read states has proven a considerable challenge. The key to discriminating between the two states is LL mixing, which explicitly breaks PH symmetry and lowers the energy of one of these states with respect to the other. Unfortunately, accurate modeling of LL mixing effects comes with many challenges, in particular its perturbative treatment Bishara and Nayak (2009), Sodemann and MacDonald (2013), Simon and Rezayi (2013), Pakrouski et al. (2015) cannot be rigorously justified. Nevertheless, as recently shown by Rezayi (2017), different theoretical approaches converge to the conclusion that LL mixing favors the aPf state.

On the other hand, experimental studies have detected signatures of $e/4$ quasiparticles at $\nu = 5/2$ using the interference of edge channels Willett et al. (2009). Shot noise measurements Dolev et al. (2010) and charge-sensing in the bulk using single-electron transistor Venkatachalam et al. (2011) have also reported evidence of $e/4$ quasiparticles. These results are consistent with both Moore-Read and aPf states. The dependence on voltage and temperature of the tunneling current was measured at a point contact in the $\nu = 5/2$ state and found to be consistent with the aPf state Radu et al. (2008). Furthermore, upstream neutral modes have been detected at $\nu = 5/2$ Bid et al. (2010), Dolev et al. (2011) which is consistent only with the aPf state.

Non-Abelian states

Contrasting the case of SLL with that of the LLL in Fig. 1A–B, one notices a few striking differences. One of the most prominent incompressible states in the SLL has an even denominator, $\nu = 2 + 1/2$ Willett et al. (1987) and its strength is roughly comparable with $\nu = 2 + 1/3$, which is expected to be analogous to the $\nu = 1/3$ Laughlin state in the LLL Balram et al. (2013). Moreover, FQH effect is also observed at $\nu = 2 + 3/8$ Xia et al. (2004), Kumar et al. (2010). Even the odd-denominator FQH states in the SLL appear out of order when compared with the LLL sequence: FQH effect has been observed at 1/3 and 2/5 in the LLL, but no FQH effect has been confirmed at 3/7, 4/9 and 5/11 but evidence for a plateau at 2 + 6/13 exists Kumar et al. (2010). To explain these unconventional fractions, different theoretical approaches have been put forward. A common theme in these approaches are quasiparticles with non-Abelian braiding statistics, qualitatively different from the Abelian anyons we encountered in Section "Incompressible fluids".

Non-Abelian anyons and topological quantum computation

Beyond the paired ground state wave function, the quasihole excitations of the Moore-Read state in Eq. (17) are particularly interesting: they must be created in pairs and they have non-Abelian braiding statistics. Imagine that $2n$ quasiholes have been added to the Moore-Read state by increasing the magnetic flux by n flux quanta. In non-Abelian FQH states, fixing the configuration of the quasiholes does not result in a unique quantum state – instead, there is a degenerate manifold of states. For example, in the Moore-Read state the $2n$-quasihole manifold is 2^{n-1}-fold degenerate and is spanned by some orthogonal basis $\{\psi_1, \psi_2, \cdots, \psi_{2^{n-1}}\}$. The braiding of two quasiholes, depicted in Fig. 2C, acts as a unitary transformation on this subspace, $\psi_\alpha = \mathcal{U}_{\alpha\beta}\psi_\beta$ Nayak and Wilczek (1996). As matrices $\mathcal{U}$ do not generally commute, the quasiholes in the Moore-Read state obey 'non-Abelian' braiding statistics.

The degenerate states ψ_α can be interpreted as basis states of a logical qubit, and the quasihole braiding operations $\mathcal{U}$ can be mapped to the action of quantum gates Freedman et al. (2003). These operations are topologically protected at sufficiently low temperatures $k_B T \lesssim \Delta_{\mathrm{MR}}$, where Δ_{MR} is the excitation gap of the Moore-Read state. This is because the qubit states are locally indistinguishable and any decoherence induced by local perturbations will be strongly suppressed. This idea of employing a topologically-protected manifold of non-Abelian FQH quasiholes to encode and manipulate a quantum bit is known as *topological quantum computation* Nayak et al. (2008).

While the prospect of avoiding the need for error correction in a quantum computer is of immense practical benefit, the particular system of Moore-Read anyons discussed above falls short of this goal as it is unable to perform so-called universal quantum computation. The simplest FQH system capable of universal topological quantum computation is discussed in Section "$\nu = 12/5$ state". At this stage, however, topological quantum computation with FQH states remains a theoretical concept, although recent progress in FQH interferometry Willett et al. (2021) and Nakamura et al. (2020) paves the way to a potential demonstration of an operating FQH qubit. We note that special types of one-dimensional nanowires can host boundary excitations with properties reminiscent of Moore-Read anyons Kitaev (2001), offering a potentially more practical realization of topological quantum computation. The efforts towards topological quantum computation will rely critically on better understanding and better control of FQH excitations, which may be aided by STM techniques (Papić et al., 2018).

$\nu = 12/5$ state

Universal quantum computation can be performed with more complex types of anyons that emerge in the Read-Rezayi (RR) sequence of states (Rezayi, 1999). These non-Abelian states generalize the notion of pairing between pairs of particles in the Moore-Read state to a clustering of larger groups (three or more particles). The RR states occur at filling factors $\nu = k/(k+2)$, with $k = 1, 2$ being the Laughlin and Moore-Read states, respectively. The $k = 3$ RR state is a qualitatively new non-Abelian state hosting the so-called Fibonacci anyons. This state is often referred to as $\mathbb{Z}_3$ RR state because its wavefunction was originally constructed using a $\mathbb{Z}_3$ parafermion conformal field theory (Rezayi, 1999).

Experimental observation of the $\nu = 12/5$ FQH plateau by Xia et al. (2004) and subsequently Kumar et al. (2010) has generated much excitement due to the possibility that it may be described by the PH conjugate of the $\mathbb{Z}_3$ RR state. Numerical work Rezayi (1999) indicated that the Coulomb ground state at $\nu = 12/5$ is close to a phase transition between the Abelian CF state and the PH conjugate of $\mathbb{Z}_3$ RR state. More recent studies using DMRG Mong et al. (2017) have found that the ground state at $\nu = 12/5$ is fully spin-polarized and in the vicinity to a charge-density-wave ordered phase. The latter was found to be much more sensitive to LL mixing at $\nu = 13/5$ than at $\nu = 12/5$ Pakrouski et al. (2016), accounting for the absence of a quantized plateau at $\nu = 13/5$. Due to a much smaller gap in the $\nu = 12/5$ state and the scarcity of its experimental realizations, the definitive determination of its nature remains much more challenging compared to $\nu = 5/2$.

Other non-Abelian states

Previously mentioned RR states are a small subset of a family of states associated with the so-called Jack polynomials Feigin et al. (2002). As first realized by Bernevig and Haldane (2008), the wave function of many FQH states at filling factors $\nu = k/(k+r)$ can be identified with a single Jack polynomial, parametrized by integers k, r and a so-called "root" state. In the case $r = 2$ the Jacks coincide with the RR states discussed in Section "$\nu = 12/5$ state". An interesting case with $k = 2$ and $r = 3$ corresponds to the socalled "Gaffnian" state Simon et al. (2007b), which has inspired much theoretical work as a potential example of a gapless non-Abelian state Read (2009a). The recursive properties of the Jack polynomials impose a great deal of analytical structure on FQH wave functions, a fact that has been fruitfully employed in numerical computations (Bernevig and Regnault, 2009).

Bonderson and Slingerland (2008) constructed trial wave functions for many of the filling factors where FQH states have been observed in the SLL. The Bonderson-Slingerland approach obtains FQH wave functions as a product of the bosonic version of the Moore-Read state and a composite fermion state. In particular, this approach yields a state that is competitive with the (PH conjugate of) $\mathbb{Z}_3$ RR state at $\nu = 12/5$ (Bonderson et al., 2012). On the other hand, the observed filling factor $2 + 6/13$ Kumar et al. (2010) is not a part of this sequence. Other constructions, based on condensing non-Abelian quasiparticles of the Moore-Read state Hermanns (2010) or by taking products of the bosonic RR states with the Laughlin state Jolicoeur (2007), have also been proposed. The hierarchical construction of Levin and Halperin (2009) may account for the FQH effect observed at filling $\nu = 2 + 6/13$. Somewhat surprisingly, the Levin-Halperin states turn out to be Abelian, even though they derive from a non-Abelian Moore-Read parent state. Most of these states, however, result in complicated wave functions that have not been systematically tested in numerical simulations.

Multicomponent fractional quantum Hall effect

Up to this point, our discussion was restricted to fully spin-polarized electrons, as is appropriate for the setting when the external magnetic field is large. It turns out that the Zeeman splitting E_Z (see Section "Introduction") is strongly suppressed in GaAs: the ratio of E_Z to the Coulomb energy scale for a typical magnetic field $B = 9$ T is $\xi = E_Z/(e^2/(4\pi\varepsilon\ell)) \approx 0.02$. Experimentally, it is possible to tune ξ by tilting the sample or introducing a parallel magnetic field, suppressing the g-factor using hydrostatic pressure (Leadley et al., 1997; Nicholas et al., 1998) or changing the 2DEG's density. Therefore, for certain parameter regimes, it could be favorable for a fraction of the electrons to flip their spin leading to the formation of unpolarized states Chakraborty and Zhang (1984), Chakraborty (2000). We now turn our attention to such "multicomponent" FQH states where the internal degree of freedom allows the electrons to form new kinds of correlated states without analogs in single-layer FQH systems.

Apart from ordinary spin, the valley degree of freedom could also lead to multi-component FQHE and this plays a particularly important role in materials such as graphene. Here, we just mention that multi-component FQHE has been also observed in multi-valley semiconductor systems such as AlAs (Bishop et al., 2007; Padmanabhan et al., 2009). Furthermore, it has also been possible to fabricate two single-layer 2DEGs in close proximity to each other, such that the two layers assume the role of ↑, ↓ spin states. The advantage of studying such bilayer FQH systems is the enhanced tunability of the interactions: one can vary both the tunneling Δ_{SAS} between the two layers, as well as the effective interlayer distance d/ℓ. Note that, conveniently, the physical distance d can be fixed and one varies ℓ by tuning the overall magnetic field (while also adjusting the electron density to remain at the same filling factor). The parameter d/ℓ directly modifies the interlayer Coulomb interaction, which has a strong effect on many-electron states. In experiment, two main architectures were pursued: wide single quantum wells in which electrostatic effects produce a ground subband wave function with a pronounced dumbbell shape Suen et al. (1992) and true double quantum wells consisting of two thin GaAs layers embedded in the alloy $\mathrm{Al}_x\mathrm{Ga}_{1-x}\mathrm{As}$ (Eisenstein et al., 1992).

Theoretical understanding of multicomponent FQH states is guided by Halperin's generalization of the Laughlin wave function in Eq. (10) to FQH systems with a discrete internal quantum number Halperin (1983). Halperin's states are parametrized by non-negative integers m, m' and n and their wave functions are given by

$$\Psi^{(m,m',n)} = \prod_{i<j}(z_i - z_j)^m \prod_{i<j}(w_i - w_j)^{m'} \prod_{i,j}(z_i - w_j)^n, \tag{19}$$

where $\{z_k\}$ and $\{w_k\}$ are the coordinates of the electrons in the "top" and "bottom" layer (or spin state), respectively. The exponents m and m' must be odd integers due to Pauli exclusion principle, while n does not have such a restriction. Moreover, because intra-species correlations are typically stronger than inter-ones we must have $m, m' \geq n$. The state in Eq. (19) corresponds to the filling factor $\nu_T = (m + m' - 2n)/(mm' - n^2)$. Most of the time, one is interested in the balanced case where the two layers or spin species are equivalent, i.e., $m = m'$, which can be physically interpreted as each layer forming a $\nu = 1/m$ Laughlin state, with interlayer correlations controlled by exponent n.

We note that the Halperin (m, m, n) states can be generalized to bilayer CF states, where the $\nu = 1/m$ Laughlin states in each layer are replaced by a Jain state Scarola and Jain (2001). Furthermore, in the case of spin, the CF wave function in Eq. (15) can be directly generalized to accommodate the spin degree of freedom by filling up $n_\uparrow$ LLs with $\uparrow$-spin electrons (and similarly $n_\downarrow$ LLs filled with electrons of opposite spin) Wu et al. (1993). Depending on $n_\uparrow$ and $n_\downarrow$, states with full or partial spin polarization can be readily constructed.

Spinful systems

In single-layer FQH systems, as ξ is varied, transitions between states with different spin polarization can take place and have been extensively studied in experiment, see an illustrative example in Fig. 6A. For example, at $\nu = 4/7$, three CF states can be constructed: (a) fully polarized with $n_\uparrow = 4$ and $n_\downarrow = 0$, (b) partially polarized with $n_\uparrow = 3$ and $n_\downarrow = 1$, and (c) spin-singlet with $n_\uparrow = 2 = n_\downarrow$. At large ξ, the ground state is fully polarized. As ξ is lowered, the fully polarized state transitions to a partially polarized state and eventually at small ξ goes into a spin-singlet state. At the Laughlin fractions, even at zero Zeeman splitting, the ground state is fully spin polarized due to exchange interactions, an effect that has been dubbed quantum Hall ferromagnetism Sondhi et al. (1993).

In the presence of spin, PH symmetry relates states at ν to $2 - \nu$. Experimentally in GaAs, spin transitions have predominantly been studied at fractions in the range $1 < \nu < 2$ (Clark et al., 1989; Du et al., 1995). The reason for this is at larger fillings, the magnetic field is smaller and thus the starting Zeeman energy is lower which allows access to the least polarized states. Then by tilting the sample, Zeeman energy can be increased and states with higher polarizations can be accessed. The spin phase diagram of the Jain fractions has been worked out in detail both theoretically (Park and Jain, 1998; Balram et al., 2015a) and experimentally (Du et al., 1995; Kukushkin et al., 1999; Liu et al., 2014) and these are in semi-quantitative agreement with each other.

In the presence of spin, the excitations of fully polarized ground states can also change character. In Sections "Magnetoroton excitation" and "Composite fermions" we discussed excitations which are spin-conserving. However, at low values of ξ, the lowest-lying excitation could involve a spin-flip. At the Laughlin fractions, this lowest-lying spin-flip mode, termed the spin-wave, has energy identical to the Zeeman splitting in the long-wavelength limit Kallin and Halperin (1984). In the fully polarized CF states the spin-wave mode has a roton minimum Mandal and Jain (2001) which lies below the ground state at zero-Zeeman splitting. The presence of these low-lying excitations is indicative of the fact that as ξ is lowered the fully polarized ground state could become unstable giving way to another state with lower polarization.

More exotic excitations involving spin-flip such as skyrmions (Sondhi et al., 1993; Fertig et al., 1994), that carry a topological spin texture, can also be stabilized at low values of ξ in the vicinity of a Laughlin fraction. These skyrmions can be viewed as CF particles or CF holes dressed by spin waves. The exchange interaction between CFs is much weaker than that between electrons, so it is a lot harder to realize and detect fractional skyrmions compared to their integer counterparts. Nevertheless, Zeeman-energy dependence of certain excitations does point to the existence of neutral spin-textures in the vicinity of $\nu = 1/3$ which have been interpreted as arising from pair(s) of skyrmions and anti-skyrmions Groshaus et al. (2008). More direct evidence for their existence has been obtained from the measurement of the binding energy of fractional skyrmions in the vicinity of $\nu = 1/3$ using light-scattering experiments (Balram et al., 2015b).

Bilayer systems

The first experimental evidence for unusual states in bilayer systems was the observation of a quantized Hall plateau at $\nu_T = 1/2$ in a bilayer system with $d/\ell \lesssim 3$, in stark contrast to a single-layer FQH system at the same filling (Suen et al., 1992; Eisenstein et al., 1992). Numerical calculations (Chakraborty and Pietiläinen, 1987; Yoshioka et al., 1989; He et al., 1993), verified the existence of an incompressible state and identified it with the (3,3,1) Halperin state in Eq. (19). More recently, there has been some renewed interest in the $\nu_T = 1/2$ two component systems Shabani et al. (2009, 2013) due to the possible transition into the Moore-Read state

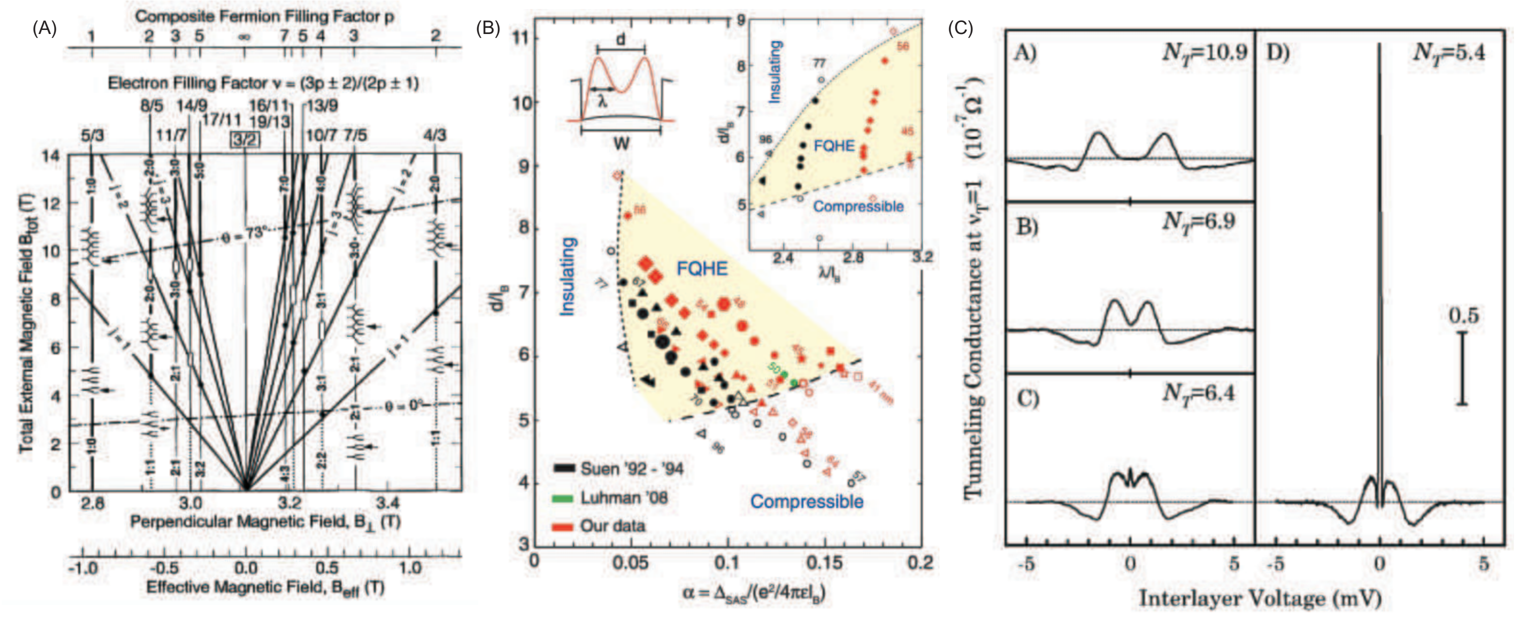

Fig. 6 Multicomponent FQH effects. (A) Transitions between CF states with different spin polarization (solid dots) as in-plane magnetic field is varied. The lines are fits from the free CF theory, with the g^* factor and the effective mass m^* treated as empirical parameters. B_{eff} is the effective magnetic field. (B) Phase diagram of GaAs wide quantum wells at $\nu_T = 1/2$ as a function of d/ℓ and $\alpha = \Delta_{\mathrm{SAS}}/(e^2/4\pi\varepsilon\ell)$. Region corresponding to an incompressible FQH state is shaded in yellow. The interlayer distance d and layer width λ are estimated numerically from the self-consistent charge distribution. (C) Exciton condensation in $\nu_T = 1$ bilayers. Tunneling conductance dI/dV vs interlayer voltage V for a range of total densities NT, corresponding to $1.6 \lesssim d/\ell \lesssim 2.3$. Trace *A*, at the highest density, shows a deep suppression of the tunneling near zero bias. By trace *D*, the lowest density of the four shown, this suppression has been replaced by a tall peak, signalling exciton condensation. The vertical scale is the same for all traces. (A) Data from Ref. Du RR, Yeh AS, Stormer HL, Tsui DC, Pfeiffer LN, and West KW (1995) Fractional quantum Hall effect around Composite fermions with a spin. *Physical Review Letters* 75: 3926–3929, doi: 10.1103/PhysRevLett.75.3926. (B) Figure reproduced from Ref. Shabani J, Liu Y, Shayegan M, Pfeiffer LN, West KW, and Baldwin KW (2013) Phase diagrams for the stability of the fractional quantum Hall effect in electron systems confined to symmetric, wide GaAs quantum wells. *Physical Review B* 88: 245413, doi: 10.1103/PhysRevB.88.245413. (C) Figure reproduced from Ref. Spielman IB, Eisenstein JP, Pfeiffer LN, and West KW (2000) Resonantly enhanced tunneling in a double layer quantum Hall ferromagnet. *Physical Review Letters* 84: 5808–5811, doi: 10.1103/PhysRevLett.84.5808.

as tunneling is increased Ho (1995), Peterson et al. (2010), Zhao et al. (2021). An example of the phase diagram in a wide quantum well at $\nu_T = 1/2$ is reproduced in Fig. 6B.

Perhaps the most remarkable bilayer quantum Hall phenomenon is the exciton condensation observed at total filling $\nu_T = 1$ (Spielman et al., 2000; Tutuc et al., 2004). The key to demonstrating the existence of excitons was the measurement of interlayer tunneling conductance at zero bias, which revealed a sharp change in the behavior depending on d/ℓ. When $d/\ell =$ is sufficiently small, one observes a pronounced Josephson-like peak Spielman et al. (2000), see Fig. 6C. The peak reflects the fact that there is no energy cost associated with the transfer of an electron from one layer to the other. Furthermore, one can also probe the system in a so-called "drag" configuration, where the current is driven through one of the layers and the voltage drop is measured in the other layer. In the exciton phase, the Hall drag resistance becomes accurately quantized (Kellogg et al., 2002; Tutuc et al., 2009).

Theoretical explanation of these experimental findings is provided by the Halperin (1,1,1) state of Eq. (19). In this state, each electron is a coherent linear superposition of the two layers Fertig (1989) where the relative phase ϕ is arbitrary and the same for all electrons. Such a state is ferromagnetically ordered in the $x-y$ plane, inclined by the angle ϕ relative to the x-axis and spontaneously chosen by the system. As a consequence of spontaneous U(1) symmetry breaking, the system acquires a gapless Goldstone mode – a linearly dispersing pseudospin wave Moon et al. (1995), which was detected in Ref. Spielman et al. (2001).

While the properties of the $\nu_T = 1$ bilayer have been well-understood in the limits of small and large d/ℓ, the nature of the transition at some critical d_c/ℓ and a possibility of intermediate phases remain the subject of on-going work (Möller et al., 2008; Milovanović et al., 2015; Zhu et al., 2017; Lian and Zhang, 2018; Wagner et al., 2021).

Recent developments

In recent years the interest in FQH phases has expanded beyond topology into broader investigations of geometric effects and quantum entanglement. Moreover, there has been a resurgence of interest in the parton description of FQH states and effective field theories that incorporate geometric effects and particle-hole symmetry. This section is an overview of these recent developments in the field.

Parton theory

Parton theory was initially introduced as a generalization of CF theory to describe a wider class of states Jain (1989*b*). In the Parton theory, one imagines splitting the electron into k (an odd integer) fictitious sub-particles called *partons*. To obtain an incompressible state, each of the partons is placed in an IQH state (or in general, any known incompressible state), resulting in the wave function:

$$\Psi_\nu^{n_1 n_2 \cdots n_k} = \mathcal{P}_{\mathrm{LLL}} \prod_{\beta=1}^{k} \Phi_{n_\beta}, \tag{20}$$

where β labels the parton species. The parton state described by the wave function given in Eq. (20) is referred to by the shorthand notation "$n_1 n_2 \cdots n_k$." The partons are unphysical entities so they need to be glued back together to recover the physical electrons. At the level of wave functions, this gluing procedure is implemented by setting the different parton species coordinates equal to the electron coordinate (each $\Phi_{n,\,\beta}$ in Eq. (20) is built up of all the electronic coordinates.). All the partons are exposed to the same external magnetic field as the underlying electrons and each parton species has the same density as that of the electrons. Therefore, the charge of the β parton $q_\beta = -e\nu/n_\beta$. The constraint that the sum of the parton charges should add to that of the electron relates the parton fillings to the electronic filling, i.e., $\sum_{\beta=1}^{k} q_\beta = -e \Rightarrow \nu = [\sum_{\beta=1}^{k} n_\beta^{-1}]^{-1}$.

Looking back at the wave functions in Eqs. (10) and (15), it follows that all of the Abelian Laughlin and Jain states are parton states. The parton theory can also describe non-Abelian states. In general, a parton state with a repeated factor of n, with $|n| \geq 2$ hosts non-Abelian excitations Wen (1991). The simplest non-Abelian parton state – the 221 state Jain (1989*b*) at $\nu = 1/2$ – can be interpreted as an f-wave superconductor of CFs Faugno et al. (2019). Recent identification of a parton state that lies in the same universality class as the aPf state but provides a better microscopic representation of the exact Coulomb ground state at 5/2 Balram et al. (2018) has led to a resurgence of interest in partons. Furthermore, it has been shown that certain high-energy excitations of the states in the Jain sequence lie beyond the scope of the CF theory Nguyen et al. (2022) while they lend themselves to a description in terms of partons Balram et al. (2022). At this stage, the parton theory promises to provide a unified framework for describing all of the quantum Hall effects.

Effective field theory

As we mentioned in Section "Incompressible fluids," many of the exotic properties of FQH states originate from the emergent Chern-Simons gauge field. Based on this idea, a field-theoretic approach to FQH systems was pioneered by Zhang et al. (1989) who showed, using a Cherns-Simons field theory, that the FQH effect at Laughlin fractions can be mapped onto a superfluid of composite bosons. Alternatively, the Chern-Simons field theory of CFs was introduced by Lopez and Fradkin (1991) and further developed by Halperin et al. (1993) and extended via a Hamiltonian formalism by Murthy and Shankar (2003). Detailed treatment of these theories is beyond the scope of the current chapter. Below we discuss two important recent developments in formulating an effective field theory of FQH systems: the role of PH symmetry and geometrical degrees of freedom.

The interest in the field-theoretic description of FQH systems, in particular in the role played by PH symmetry, has recently been renewed by geometric resonance experiments, which probe the radius of the cyclotron orbit of CFs. A series of measurements Kamburov et al. (2014) and Hossain et al. (2020) have shown that the CF Fermi wave vector k_F^* is determined by the density of minority carriers in the LLL, i.e., the CF Fermi wave vector is set by the electron density for $\nu \leq 1/2$ and by the hole density for $\nu > 1/2$. In other words, the quantity $k_F^* \ell$ is PH-symmetric. The state that underpins the HLR theory does not reside entirely in the LLL and thus it does not obey PH symmetry manifestly. This puzzle is resolved by going beyond the mean-field level, where it has been shown that the HLR theory produces results that are PH-symmetric and consistent with experiment (Wang et al., 2017).

In parallel, Son (2015) proposed a field theory that is valid in the vicinity of half-filling and has a built-in PH symmetry. In Son's theory, CFs are Dirac particles whose density is controlled by the external magnetic field as opposed to by the density of electrons. The PH symmetry of electrons acts as a time-reversal symmetry on Dirac CFs. This results in an absence of $2k_F$ back-scattering that was subsequently observed in DMRG simulations Geraedts et al. (2017), providing evidence in favor of Son's theory. One can ask how different are the predictions of Son's theory from that of the HLR theory? Surprisingly, it turns out that the refined version of HLR theory is consistent with Son's theory on many aspects (Wang et al., 2017).

Interestingly, Son's construction suggests a PH-symmetric gapped state at half-filling – dubbed the "PH symmetric Pfaffian" (PH-Pf). The PH-Pf state is topologically distinct from both the Moore-Read state and aPf state. Intriguingly, recent thermal Hall Banerjee et al. (2018) and heat transport measurements Dutta et al. (2021) at $\nu = 5/2$ appear to be consistent with only the PH-Pf order. Two candidate wave functions for the PH-Pfaffian phase have been considered in the literature Jolicoeur (2007) and Zucker and Feldman (2016), both with a high degree of PH symmetry. The two wave functions also have high overlaps with each other for small systems indicating that they likely describe the same phase. However, numerical studies find no evidence for the existence of the PH-Pf phase in clean systems (Balram et al., 2018; Mishmash et al., 2018). Understanding the heat transport measurements at $\nu = 5/2$ in light of the numerical results presents one of the foremost challenges in the field.

Apart from PH symmetry, it has recently become apparent that any effective field theory capable of capturing dynamical response of FQH phases must include the *geometric* degrees of freedom FQH systems, which are beyond the remit of purely topological field theories. An important example of a geometric property is the Wen-Zee shift Wen and Zee (1992), related to the response function known as Hall viscosity (Avron et al., 1995; Read, 2009b). This has highlighted the need for a deeper understanding of "quantum geometry" in FQH fluids Haldane (2011). The quantum geometry is associated with the magnetoroton (GMP) collective excitation of FQH fluids in the long-wavelength limit (cf. Section "Magnetoroton excitation"). In this limit, the GMP mode can be interpreted as a quadrupolar density-wave deformation of the ground state and it has been incorporated into a gravitational field theory in the form of a spin-2 field coupled to an ambient geometry (Gromov and Son, 2017). Occasionally, this emergent spin-2 degree of freedom is also referred to as "FQH graviton" (Yang et al., 2012a; Golkar et al., 2016; Liou et al., 2019). The dynamics of the spin-2 modes Liu et al. (2018) can be induced by mass anisotropy Yang et al. (2012b), Wang et al. (2012), and Ghazaryan and Chakraborty (2015) or by tilting the magnetic field (Chakraborty and Pietiläinen, 1989; Papić, 2013). In gapless CFL states, the geometric effects manifest through the shape of the Fermi contour (Gokmen et al., 2010; Jo et al., 2017). The investigation of geometric responses of FQH systems to the variations of ambient geometry represents an active research direction (You et al., 2014; Bradlyn and Read, 2015; Can et al., 2014).

Entanglement-based approaches

Quantum entanglement has recently emerged as a powerful probe of topological order. One characterizes entanglement by evaluating the system's reduced density matrix, obtained by partitioning the FQH system into two halves and tracing out one of the subsystems. As first shown by Li and Haldane Li and Haldane (2008), the spectrum of the reduced density matrix – the "entanglement spectrum" – contains information about the edge excitations of the system and it can be used to infer the CFT that governs the FQH state.

For FQH wave functions such as the Laughlin or Moore-Read, the number of levels in the entanglement spectrum as a function of momentum in the subsystem becomes universal as the subsystem size increases and it corresponds to the edge spectrum of the corresponding CFT. This "bulk-boundary" correspondence suggests that the bulk of the system and the physical edge are related to each other Dubail et al. (2012). On the other hand, the entanglement spectrum of a physical ground state of the Coulomb interaction is found to contain both a universal CFT part and a non-universal part. The latter is separated by a "entanglement gap" Thomale et al. (2010), which is argued to remain finite in a gapped FQH phase, signaling the robustness of topological order. The entanglement spectrum has found broad use as a tool for topological characterization of phases of matter beyond FQH states discussed in this chapter.

Finally, as first shown by Zaletel and Mong (2012), certain FQH wave functions that can be expressed as correlators of a CFT can also be turned into a matrix-product state (MPS) if one picks the basis of LL orbitals on a cylinder geometry. This leads to a significant advantage in extracting physical properties from FQH wave functions. Exact MPS representations have been found for many states discussed above Estienne et al. (2013). Beyond studies of FQH wave functions, the MPS method has been generalized into a variational density-matrix renormalization group scheme for approximating ground states of realistic systems with Coulomb interactions Zaletel et al. (2013).

Table 1 Summary of topological properties of main single-component FQH states considered in this chapter.

Filling, ν	*State*	*Shift,* S	*Chiral central charge,* $c\_$	*Quasiparticle charge,* Q_{qp}	*GSD*
$1/(2p+1)$	1^{2p+1}, Laughlin	$2p+1$	1	$1/(2p+1)$	$2p+1$
$n/(2pn \pm 1)$	$(\pm n)1^{2p}$, Jain	$(\pm n)+2p$	$1 \pm (n-1)$	$1/(2pn \pm 1)$	$2pn \pm 1$
$1/(2p)$	Moore-Read	$2p+1$	$3/2$	$1/(4p)$	$6p$
$1/(2p)$	$\bar{2}^2 1^{2p+1}$, anti-Pfaffian	$2p-3$	$-1/2$	$1/(4p)$	$6p$
$2/5$	$\bar{2}^3 1^4$, anti-$\mathbb{Z}_3$ Read-Rezayi	-2	$-4/5$	$1/5$	10

For the states captured by parton theory, we also show their parton label according to Eq. (20). Some of the quantities in this Table can be accessed experimentally: filling factor ν is related to the electrical Hall resistance R_{xy} via Eq. (6), chiral central charge $c\_$ is related to the thermal Hall conductance κ_{xy} via Eq. (8) (any filled LLs provide an additional contribution), Q_{qp} is the charge of fundamental quasiparticle in units of the electron charge which can be accessed via shot-noise experiments or by charge-sensing using a single-electron transistor, the shift S on the sphere is related to the Hall viscosity η_H. The ground state degeneracy (GSD) is quoted for the torus. The composite fermion Fermi liquid (CFL) is not expected to carry a quantized κ_{xy} since its bulk is gapless.

Conclusion

In this chapter we presented an introduction to the FQH effect observed in semiconductor systems. While it was impossible to give a historically exhaustive account of the entire field, we hope that the multitude of examples illustrates the great richness of emergent many-body phenomena and the diversity of approaches that have been developed over the years in order to understand the novel physics associated with the FQH effect. To emphasize this diversity, our presentation has focused on explaining the experimental observations through model states, which distil the essence of FQH physics into elegant wave functions that can be studied either analytically or in computer simulations. Thus, we conclude by presenting a summary of the properties of the main single-component FQH phases discussed above in Table 1. The table lists some key topological quantum numbers that can be used to characterize an FQH phase, as discussed in Section "Incompressible fluids". Some of these quantities are accessible in experiments and others in numerics.

Throughout this chapter, we have highlighted many open problems and research directions that remain particularly active at the time of writing (early 2022). We note in particular that the material realizations of the FQH effect continue to expand, most notably in the context of graphene and other van der Waals materials, fractional Chern insulators, as well as synthetic quantum simulators based on ultracold atoms and superconducting qubit arrays. We purposefully avoided discussing alternative material realizations of the FQH effect, as some of them are discussed in other chapters of this encyclopedia. These new material platforms may offer additional pathways to testing some of the theoretical ideas discussed above, while they will undoubtedly pose new puzzles to be understood. For a research field that is now four decades old, the FQH effect remains a remarkably active source of exciting new physics.

Acknowledgments

We would like to thank Gabor Csathy and Wei Pan for generously sharing their experimental data that we plotted in Fig. 1. The authors express their deep sense of gratitude to all of their collaborators over the years, without whom this chapter would not have been possible. A. C. B. acknowledges the Science and Engineering Research Board (SERB) of the Department of Science and Technology (DST) for financial support through the Start-up Grant SRG/2020/000154. A. C. B. and Z. P. thank the Royal Society International Exchanges Award IES\R2\202052 for funding support. Some of the numerical calculations reported in this work were carried out on the Nandadevi supercomputer, which is maintained and supported by the Institute of Mathematical Science's-High-Performance Computing Center. Z. P. acknowledges support by the Leverhulme Trust Research Leadership Award RL-2019-015.

References

Archer AC, Park K, and Jain JK (2013) Competing crystal phases in the lowest Landau level. *Physical Review Letters* 111: 146804.

Arovas D, Schrieffer JR, and Wilczek F (1984) Fractional statistics and the quantum Hall effect. *Physical Review Letters* 53: 722–723. https://doi.org/10.1103/PhysRevLett.53.722.

Avron JE, Seiler R, and Zograf PG (1995) Viscosity of quantum Hall fluids. *Physical Review Letters* 75: 697–700. https://doi.org/10.1103/PhysRevLett.75.697.

Balram AC, Wu Y-H, Sreejith GJ, Wójs A, and Jain JK (2013) Role of exciton screening in the $\nu = 7/3$ fractional quantum Hall effect. *Physical Review Letters* 110: 186801. https://doi.org/10.1103/PhysRevLett.110.186801.

Balram AC, Töke C, Wójs A, and Jain JK (2015a) Phase diagram of fractional quantum Hall effect of composite fermions in multicomponent systems. *Physical Review B* 91: 045109. https://doi.org/10.1103/PhysRevB.91.045109.

Balram AC, Wurstbauer U, Wojs A, Pinczuk A, and Jain JK (2015b) Fractionally charged skyrmions in fractional quantum Hall effect. *Nature Communications* 6. https://doi.org/10.1038/ncomms9981.

Balram AC, Barkeshli M, and Rudner MS (2018) Parton construction of a wave function in the anti-Pfaffian phase. *Physical Review B* 98: 035127. https://doi.org/10.1103/PhysRevB.98.035127.

Balram AC, Liu Z, Gromov A, and Papić Z (2022) Very high-energy collective states of partons in fractional quantum Hall liquids. *Physical Review X* 12: 021008. https://journals.aps.org/prx/abstract/10.1103/PhysRevX.12.021008.

Banerjee M, Heiblum M, Umansky V, Feldman DE, Oreg Y, and Stern A (2018) Observation of half-integer thermal hall conductance. *Nature* 559(7713): 205–210.

Bartolomei H, Kumar M, Bisognin R, Marguerite A, Berroir J-M, Bocquillon E, Plaçais B, Cavanna A, Dong Q, Gennser U, Jin Y, and Fève G (2020) Fractional statistics in anyon collisions. *Science* 368(6487): 173–177. https://science.sciencemag.org/content/368/6487/173.

Bernevig BA and Haldane FDM (2008) Model fractional quantum Hall states and jack polynomials. *Physical Review Letters* 100: 246802. https://doi.org/10.1103/PhysRevLett.100.246802.

Bernevig BA and Regnault N (2009) Anatomy of abelian and non-Abelian fractional quantum Hall states. *Physical Review Letters* 103: 206801. https://doi.org/10.1103/PhysRevLett.103.206801.

Bid A, Ofek N, Inoue H, Heiblum M, Kane CL, Umansky V, and Mahalu D (2010) Observation of neutral modes in the fractional quantum Hall regime. *Nature* 466(7306): 585–590.

Bishara W and Nayak C (2009) Effect of Landau level mixing on the effective interaction between electrons in the fractional quantum Hall regime. *Physical Review B* 80: 121302. https://doi.org/10.1103/PhysRevB.80.121302.

Bishop NC, Padmanabhan M, Vakili K, Shkolnikov YP, De Poortere EP, and Shayegan M (2007) Valley polarization and susceptibility of composite fermions around a filling factor $\nu = 3/2^{'}$. *Physical Review Letters* 98: 266404. https://doi.org/10.1103/PhysRevLett.98.266404.

Boebinger GS, Chang AM, Stormer HL, and Tsui DC (1985) Magnetic field dependence of activation energies in the fractional quantum hall effect. *Physical Review Letters* 55: 1606–1609. https://doi.org/10.1103/PhysRevLett.55.1606.

Bonderson P and Slingerland JK (2008) Fractional quantum Hall hierarchy and the second Landau level. *Physical Review B* 78: 125323. https://doi.org/10.1103/PhysRevB.78.125323.

Bonderson P, Feiguin AE, and Nayak C (2011) Numerical calculation of the neutral fermion gap at the $\nu = 5/2$ fractional quantum hall state. *Physical Review Letters* 106: 186802. https://doi.org/10.1103/PhysRevLett.106.186802.

Bonderson P, Feiguin AE, Möller G, and Slingerland JK (2012) Competing topological orders in the $\nu = 12/5$ quantum Hall state. *Physical Review Letters* 108: 036806. https://doi.org/10.1103/PhysRevLett.108.036806.

Bradlyn B and Read N (2015) Low-energy effective theory in the bulk for transport in a topological phase. *Physical Review B* 91: 125303. https://doi.org/10.1103/PhysRevB.91.125303.

Can T, Laskin M, and Wiegmann P (2014) Fractional quantum hall effect in a curved space: Gravitational anomaly and electromagnetic response. *Physical Review Letters* 113: 046803. https://doi.org/10.1103/PhysRevLett.113.046803.

Chakraborty T (2000) Electron spin transitions in quantum Hall systems. *Advances in Physics* 49(8): 959–1014. https://doi.org/10.1080/00018730050198161.

Chakraborty T and Pietiläinen P (1987) Fractional quantum Hall effect at half-filled Landau level in a multiple-layer electron system. *Physical Review Letters* 59: 2784–2787. https://doi.org/10.1103/PhysRevLett.59.2784.

Chakraborty T and Pietiläinen P (1989) Fractional quantum hall effect in tilted magnetic fields. *Physical Review B* 39: 7971–7973. https://doi.org/10.1103/PhysRevB.39.7971.

Chakraborty T and Zhang FC (1984) Role of reversed spins in the correlated ground state for the fractional quantum Hall effect. *Physical Review B* 29: 7032–7033. https://doi.org/10.1103/PhysRevB.29.7032.

Chamon CdC and Wen XG (1994) Sharp and smooth boundaries of quantum Hall liquids. *Physical Review B* 49: 8227–8241. https://doi.org/10.1103/PhysRevB.49.8227.

Chang AM (2003) Chiral Luttinger liquids at the fractional quantum Hall edge. *Reviews of Modern Physics* 75: 1449–1505. https://doi.org/10.1103/RevModPhys.75.1449.

Chang AM, Pfeiffer LN, and West KW (1996) Observation of chiral Luttinger behavior in electron tunneling into fractional quantum Hall edges. *Physical Review Letters* 77: 2538–2541. https://doi.org/10.1103/PhysRevLett.77.2538.

Chklovskii DB, Shklovskii BI, and Glazman LI (1992) Electrostatics of edge channels. *Physical Review B* 46: 4026–4034. https://doi.org/10.1103/PhysRevB.46.4026.

Chung YJ, Villegas Rosales KA, Baldwin KW, Madathil PT, West KW, Shayegan M, and Pfeiffer LN (2021) Ultra-high-quality two-dimensional electron systems. *Nature Materials*. https://doi.org/10.1038/s41563-021-00942-3.

Chung YJ, Graf D, Engel LW, Rosales KAV, Madathil PT, Baldwin KW, West KW, Pfeiffer LN, and Shayegan M (2022) Correlated states of 2D electrons near the Landau level filling $\nu = 1/7^{'}$. *Physical Review Letters* 128: 026802. https://doi.org/10.1103/PhysRevLett.128.026802.

Clark RG, Haynes SR, Suckling AM, Mallett JR, Wright PA, Harris JJ, and Foxon CT (1989) Spin configurations and quasiparticle fractional charge of fractional-quantum-Hall-effect ground states in the $N=0$ Landau level. *Physical Review Letters* 62: 1536–1539. https://doi.org/10.1103/PhysRevLett.62.1536.

d'Ambrumenil N and Reynolds AM (1988) Fractional quantum Hall states in higher Landau levels. *Journal of Physics C: Solid State Physics* 21(1): 119. http://stacks.iop.org/0022-3719/21/i=1/a=010.

Deng H, Liu Y, Jo I, Pfeiffer LN, West KW, Baldwin KW, and Shayegan M (2016) Commensurability oscillations of composite fermions induced by the periodic potential of a Wigner crystal. *Physical Review Letters* 117: 096601. https://doi.org/10.1103/PhysRevLett.117.096601.

DiagHam (n.d.), *https://www.nick-ux.org/diagham*

Dolev M, Heiblum M, Stern A, Umansky V, and Mahalu D (2008) Observation of a quarter of an electron charge at the $\nu = 5/2$ quantum Hall state. *Nature* 452: 829. EP https://doi.org/10.1038/nature06855.

Dolev M, Gross Y, Chung YC, Heiblum M, Umansky V, and Mahalu D (2010) Dependence of the tunneling quasiparticle charge determined via shot noise measurements on the tunneling barrier and energetics. *Physical Review B* 81: 161303. https://doi.org/10.1103/PhysRevB.81.161303.

Dolev M, Gross Y, Sabo R, Gurman I, Heiblum M, Umansky V, and Mahalu D (2011) Characterizing neutral modes of fractional states in the second Landau level. *Physical Review Letters* 107: 036805. https://doi.org/10.1103/PhysRevLett.107.036805.

Du RR, Stormer HL, Tsui DC, Pfeiffer LN, and West KW (1993) Experimental evidence for new particles in the fractional quantum Hall effect. *Physical Review Letters* 70: 2944–2947. https://doi.org/10.1103/PhysRevLett.70.2944.

Du RR, Yeh AS, Stormer HL, Tsui DC, Pfeiffer LN, and West KW (1995) Fractional quantum Hall effect around $\nu = 3/2$: Composite fermions with a spin. *Physical Review Letters* 75: 3926–3929. https://doi.org/10.1103/PhysRevLett.75.3926.

Du R, Tsui D, Stormer H, Pfeiffer L, Baldwin K, and West K (1999) Strongly anisotropic transport in higher two-dimensional Landau levels. *Solid State Communications* 109(6): 389–394. http://www.sciencedirect.com/science/article/pii/S003810989800578X.

Dubail J, Read N, and Rezayi EH (2012) Edge-state inner products and real-space entanglement spectrum of trial quantum Hall states. *Physical Review B* 86: 245310. https://doi.org/10.1103/PhysRevB.86.245310.

Duncan F and Haldane M (1990) The hierarchy of fractional states and numerical studies. In: *The Quantum Hall Effect*, pp. 303–352. Springer.

Dutta B, Yang W, Melcer R, Kundu HK, Heiblum M, Umansky V, Oreg Y, Stern A, and Mross D (2021) Distinguishing between non-abelian topological orders in a quantum Hall system. *Science* 375(6577), eabg6116 https://doi.org/10.1126/science.abg6116.

Eisenstein JP, Stormer HL, Pfeiffer LN, and West KW (1990) Evidence for a spin transition in the $\nu = 2/3$ fractional quantum Hall effect. *Physical Review B* 41: 7910–7913. https://doi.org/10.1103/PhysRevB.41.7910.

Eisenstein JP, Boebinger GS, Pfeiffer LN, West KW, and He S (1992) New fractional quantum Hall state in double-layer two-dimensional electron systems. *Physical Review Letters* 68: 1383–1386. https://doi.org/10.1103/PhysRevLett.68.1383.

Eisenstein JP, Cooper KB, Pfeiffer LN, and West KW (2002) Insulating and fractional quantum Hall states in the first excited Landau level. *Physical Review Letters* 88: 076801. https://doi.org/10.1103/PhysRevLett.88.076801.

Estienne B, Papić Z, Regnault N, and Bernevig BA (2013) Matrix product states for trial quantum hall states. *Physical Review B* 87: 161112. https://doi.org/10.1103/PhysRevB.87.161112.

Fano G, Ortolani F, and Colombo E (1986) Configuration-interaction calculations on the fractional quantum Hall effect. *Physical Review B* 34: 2670–2680. https://doi.org/10.1103/PhysRevB.34.2670.

Faugno WN, Balram AC, Barkeshli M, and Jain JK (2019) Prediction of a non-Abelian fractional quantum Hall state with *f*-wave pairing of composite fermions in wide quantum wells. *Physical Review Letters* 123: 016802. https://doi.org/10.1103/PhysRevLett.123.016802.

Feigin B, Jimbo M, Miwa T, and Mukhin E (2002) A differential ideal of symmetric polynomials spanned by Jack polynomials at r$\beta =$ - (r - 1)/(k + 1)',. *International Mathematics Research Notices* 2002(23): 1223–1237. https://doi.org/10.1155/S1073792802112050.

Feiguin AE, Rezayi E, Nayak C, and Das Sarma S (2008) Density matrix renormalization group study of incompressible fractional quantum hall states. *Physical Review Letters* 100: 166803. https://doi.org/10.1103/PhysRevLett.100.166803.

Fertig HA (1989) Energy spectrum of a layered system in a strong magnetic field. *Physical Review B* 40: 1087–1095. https://doi.org/10.1103/PhysRevB.40.1087.

Fertig HA, Brey L, Côté R, and MacDonald AH (1994) Charged spin-texture excitations and the hartree-fock approximation in the quantum Hall effect. *Physical Review B* 50: 11018–11021. https://doi.org/10.1103/PhysRevB.50.11018.

Fogler MM, Koulakov AA, and Shklovskii BI (1996) Ground state of a two-dimensional electron liquid in a weak magnetic field. *Physical Review B* 54: 1853–1871.

Freedman M, Kitaev A, Larsen M, and Wang Z (2003) Topological quantum computation. *Bulletin of the American Mathematical Society* 40(1): 31–38. https://www.ams.org/journals/bull/2003-40-01/S0273-0979-02-00964-3.

Geraedts SD, Repellin C, Wang C, Mong RSK, Senthil T, and Regnault N (2017) Emergent particle-hole symmetry in spinful bosonic quantum Hall systems. *Physical Review B* 96: 075148. https://doi.org/10.1103/PhysRevB.96.075148.

Ghazaryan A and Chakraborty T (2015) Aspects of anisotropic fractional quantum Hall effect in phosphorene. *Physical Review B* 92: 165409. https://doi.org/10.1103/PhysRevB.92.165409.

Girvin SM, MacDonald AH, and Platzman PM (1985) Collective-excitation gap in the fractional quantum Hall effect. *Physical Review Letters* 54: 581–583. https://doi.org/10.1103/PhysRevLett.54.581.

Gokmen T, Padmanabhan M, and Shayegan M (2010) Transference of transport anisotropy to composite fermions. *Nature Physics* 6: 621–624.

Goldman VJ, Su B, and Jain JK (1994) Detection of composite fermions by magnetic focusing. *Physical Review Letters* 72: 2065–2068. https://doi.org/10.1103/PhysRevLett.72.2065.

Golkar S, Nguyen DX, Roberts MM, and Son DT (2016) Higher-spin theory of the magnetorotons. *Physical Review Letters* 117: 216403. https://doi.org/10.1103/PhysRevLett.117.216403.

Greiter M (1994) Microscopic formulation of the hierarchy of quantized Hall states. *Physics Letters B* 336(1): 48–53. https://www.sciencedirect.com/science/article/pii/0370269394009570.

Greiter M, Wen XG, and Wilczek F (1992) Paired Hall states in double-layer electron systems. *Physical Review B* 46: 9586–9589. https://doi.org/10.1103/PhysRevB.46.9586.

Gromov A and Son DT (2017) Bimetric theory of fractional quantum hall states. *Physical Review X* 7: 041032. https://doi.org/10.1103/PhysRevX.7.041032.

Groshaus JG, Dujovne I, Gallais Y, Hirjibehedin CF, Pinczuk A, Tan Y-W, Stormer H, Dennis BS, Pfeiffer LN, and West KW (2008) Spin texture and magnetoroton excitations at $\nu =$ 1/3'. *Physical Review Letters* 100: 046804. https://doi.org/10.1103/PhysRevLett.100.046804.

Haldane FDM (1983) Fractional quantization of the Hall effect: A hierarchy of incompressible quantum fluid states. *Physical Review Letters* 51: 605–608. https://doi.org/10.1103/PhysRevLett.51.605.

Haldane FDM (1985) Many-particle translational symmetries of two-dimensional electrons at rational Landau-level filling. *Physical Review Letters* 55: 2095–2098. https://doi.org/10.1103/PhysRevLett.55.2095.

Haldane FDM (2011) Geometrical description of the fractional quantum Hall effect. *Physical Review Letters* 107: 116801. https://doi.org/10.1103/PhysRevLett.107.116801.

Halperin BI (1982) Quantized Hall conductance, current-carrying edge states, and the existence of extended states in a two-dimensional disordered potential. *Physical Review B* 25: 2185–2190. https://doi.org/10.1103/PhysRevB.25.2185.

Halperin BI (1983) Theory of the quantized Hall conductance. *Helvetica Physica Acta* 56(1–3): 75–102.

Halperin BI (1984) Statistics of quasiparticles and the hierarchy of fractional quantized Hall states. *Physical Review Letters* 52: 1583–1586. https://doi.org/10.1103/PhysRevLett.52.1583.

Halperin BI, Lee PA, and Read N (1993) Theory of the half-filled Landau level. *Physical Review B* 47: 7312–7343. https://doi.org/10.1103/PhysRevB.47.7312.

Hansson TH, Hermanns M, Simon SH, and Viefers SF (2017) Quantum hall physics: Hierarchies and conformal field theory techniques. *Reviews of Modern Physics* 89: 025005. https://doi.org/10.1103/RevModPhys.89.025005.

He S, Das Sarma S, and Xie XC (1993) Quantized Hall effect and quantum phase transitions in coupled two-layer electron systems. *Physical Review B* 47: 4394–4412. https://doi.org/10.1103/PhysRevB.47.4394.

He S, Simon SH, and Halperin BI (1994) Response function of the fractional quantized Hall state on a sphere. ii. exact diagonalization. *Physical Review B* 50: 1823–1831. https://doi.org/10.1103/PhysRevB.50.1823.

Hermanns M (2010) Condensing non-abelian quasiparticles. *Physical Review Letters* 104: 056803. https://doi.org/10.1103/PhysRevLett.104.056803.

Ho T-L (1995) Broken symmetry of two-component $\nu = 1/2$ quantum Hall states. *Physical Review Letters* 75: 1186–1189. https://doi.org/10.1103/PhysRevLett.75.1186.

Hossain MS, Mueed MA, Ma MK, Villegas Rosales KA, Chung YJ, Pfeiffer LN, West KW, Baldwin KW, and Shayegan M (2020) Precise experimental test of the Luttinger theorem and particle-hole symmetry for a strongly correlated fermionic system. *Physical Review Letters* 125: 046601. https://doi.org/10.1103/PhysRevLett.125.046601.

Jain JK (1989a) Composite-fermion approach for the fractional quantum Hall effect. *Physical Review Letters* 63: 199–202. https://doi.org/10.1103/PhysRevLett.63.199.

Jain JK (1989b) Incompressible quantum Hall states. *Physical Review B* 40: 8079–8082. https://doi.org/10.1103/PhysRevB.40.8079.

Jain JK (2014) A note contrasting two microscopic theories of the fractional quantum Hall effect. *Indian Journal of Physics* 88: 915–929. https://doi.org/10.1007/s12648-014-0491-9.

Jain JK and Kamilla RK (1998) Composite fermions: Particles of the lowest Landau level. In: *Composite Fermions*, pp. 1–90. Singapore: World Scientific Pub Co Inc. https://doi.org/10.1142/9789812815989_0001. chapter 1.

Jo I, Rosales KAV, Mueed MA, Pfeiffer LN, West KW, Bald-win KW, Winkler R, Padmanabhan M, and Shayegan M (2017) Transference of Fermi contour anisotropy to composite fermions. *Physical Review Letters* 119: 016402. https://doi.org/10.1103/PhysRevLett.119.016402.

Jolicoeur T (2007) Non-abelian states with negative flux: A new series of quantum Hall states. *Physical Review Letters* 99: 036805. https://doi.org/10.1103/PhysRevLett.99.036805.

Kallin C and Halperin BI (1984) Excitations from a filled Landau level in the two-dimensional electron gas. *Physical Review B* 30: 5655–5668. https://doi.org/10.1103/PhysRevB.30.5655.

Kalmeyer V and Zhang S-C (1992) Metallic phase of the quantum Hall system at even-denominator filling fractions. *Physical Review B* 46: 9889–9892. https://doi.org/10.1103/PhysRevB.46.9889.

Kamburov D, Liu Y, Mueed MA, Shayegan M, Pfeiffer LN, West KW, and Baldwin KW (2014) What determines the Fermi wave vector of composite fermions? *Physical Review Letters* 113: 196801. https://doi.org/10.1103/PhysRevLett.113.196801.

Kane CL and Fisher MPA (1997) Quantized thermal transport in the fractional quantum Hall effect. *Physical Review B* 55: 15832–15837. https://doi.org/10.1103/PhysRevB.55.15832.

Kang W, Stormer HL, Pfeiffer LN, Baldwin KW, and West KW (1993) How real are composite fermions? *Physical Review Letters* 71: 3850–3853. https://doi.org/10.1103/PhysRevLett.71.3850.

Kellogg M, Spielman IB, Eisenstein JP, Pfeiffer LN, and West KW (2002) Observation of quantized Hall drag in a strongly correlated bilayer electron system. *Physical Review Letters* 88: 126804. https://doi.org/10.1103/PhysRevLett.88.126804.

Kitaev AY (2001) Unpaired majorana fermions in quantum wires. *Physics-Uspekhi* 44(10S): 131–136. https://doi.org/10.1070/1063-7869/44/10S/S29.

Klitzing Kv, Dorda G, and Pepper M (1980) New method for high-accuracy determination of the fine-structure constant based on quantized Hall resistance. *Physical Review Letters* 45: 494–497. https://doi.org/10.1103/PhysRevLett.45.494.

Koulakov AA, Fogler MM, and Shklovskii BI (1996) Charge density wave in two-dimensional electron liquid in weak magnetic field. *Physical Review Letters* 76: 499–502.

Kukushkin IVv, Klitzing K, and Eberl K (1999) Spin polarization of composite fermions: Measurements of the Fermi energy. *Physical Review Letters* 82: 3665–3668. https://doi.org/10.1103/PhysRevLett.82.3665.

Kukushkin IV, Smet JH, Scarola VW, Umansky V, and von Klitzing K (2009) Dispersion of the excitations of fractional quantum Hall states. *Science* 324(5930): 1044–1047. http://www.sciencemag.org/content/324/5930/1044.abstract.

Kumar A, Csáthy GA, Manfra MJ, Pfeiffer LN, and West KW (2010) Nonconventional odd-denominator fractional quantum Hall states in the second Landau level. *Physical Review Letters* 105: 246808. https://doi.org/10.1103/PhysRevLett.105.246808.

Lam PK and Girvin SM (1984) Liquid-solid transition and the fractional quantum-Hall effect. *Physical Review B* 30: 473–475.

Laughlin RB (1983) Anomalous quantum Hall effect: An incompressible quantum fluid with fractionally charged excitations. *Physical Review Letters* 50: 1395–1398. https://doi.org/10.1103/PhysRevLett.50.1395.

Laughlin RB (1987) Elementary theory: The incompressible quantum fluid. In: *The Quantum Hall Effect*, pp. 233–301. Springer.

Leadley DR, Nicholas RJ, Maude DK, Utjuzh AN, Portal JC, Harris JJ, and Foxon CT (1997) Fractional quantum Hall effect measurements at zero $\sim g$ factor. *Physical Review Letters* 79: 4246–4249. https://doi.org/10.1103/PhysRevLett.79.4246.

Lee S-S, Ryu S, Nayak C, and Fisher MPA (2007) Particle-hole symmetry and the $\nu = 5/2$ quantum Hall state. *Physical Review Letters* 99: 236807. https://doi.org/10.1103/PhysRevLett.99.236807.

Leinaas J and Myrheim J (1977) On the theory of identical particles. *Il Nuovo Cimento B Series 11* 37(1): 1–23. https://doi.org/10.1007/BF02727953.

Levin M and Halperin BI (2009) Collective states of non-abelian quasiparticles in a magnetic field. *Physical Review B* 79: 205301. https://doi.org/10.1103/PhysRevB.79.205301.

Levin M, Halperin BI, and Rosenow B (2007) Particle-hole symmetry and the Pfaffian state. *Physical Review Letters* 99: 236806. https://doi.org/10.1103/PhysRevLett.99.236806.

Li H and Haldane FDM (2008) Entanglement spectrum as a generalization of entanglement entropy: Identification of topological order in non-abelian fractional quantum hall effect states. *Physical Review Letters* 101: 010504. https://doi.org/10.1103/PhysRevLett.101.010504.

Lian B and Zhang S-C (2018) Wave function and emergent su(2) symmetry in the $\nu_T = 1$ quantum hall bilayer. *Physical Review Letters* 120: 077601. https://doi.org/10.1103/PhysRevLett.120.077601.

Lilly MP, Cooper KB, Eisenstein JP, Pfeiffer LN, and West KW (1999) Evidence for an anisotropic state of two-dimensional electrons in high Landau levels. *Physical Review Letters* 82: 394–397. https://doi.org/10.1103/PhysRevLett.82.394.

Liou S-F, Haldane FDM, Yang K, and Rezayi EH (2019) Chiral gravitons in fractional quantum hall liquids. *Physical Review Letters* 123: 146801. https://doi.org/10.1103/PhysRevLett.123.146801.

Liu Y, Hasdemir S, Wójs A, Jain JK, Pfeiffer LN, West KW, Baldwin KW, and Shayegan M (2014) Spin polarization of composite fermions and particle-hole symmetry breaking. *Physical Review B* 90: 085301. https://doi.org/10.1103/PhysRevB.90.085301.

Liu Z, Gromov A, and Papić Z (2018) Geometric quench and nonequilibrium dynamics of fractional quantum hall states. *Physical Review B* 98: 155140. https://doi.org/10.1103/PhysRevB.98.155140.

Lopez A and Fradkin E (1991) Fractional quantum Hall effect and Chern-Simons gauge theories. *Physical Review B* 44: 5246–5262. https://doi.org/10.1103/PhysRevB.44.5246.

Ma MK, Villegas Rosales KA, Deng H, Chung YJ, Pfeiffer LN, West KW, Baldwin KW, Winkler R, and Shayegan M (2020) Thermal and quantum melting phase diagrams for a magnetic-field-induced wigner solid. *Physical Review Letters* 125: 036601. https://doi.org/10.1103/PhysRevLett.125.036601.

Mandal SS and Jain JK (2001) Low-energy spin rotons in the fractional quantum Hall effect. *Physical Review B* 63: 201310. https://doi.org/10.1103/PhysRevB.63.201310.

Milovanović MV, Dobardžić E, and Papić Z (2015) Meron deconfinement in the quantum hall bilayer at intermediate distances. *Physical Review B* 92: 195311. https://doi.org/10.1103/PhysRevB.92.195311.

Mishmash RV, Mross DF, Alicea J, and Motrunich OI (2018) Numerical exploration of trial wave functions for the particle-hole-symmetric Pfaffian. *Physical Review B* 98: 081107. https://doi.org/10.1103/PhysRevB.98.081107.

Möller G, Simon SH, and Rezayi EH (2008) Paired composite fermion phase of quantum hall bilayers at $\nu = \frac{1}{2} + \frac{1}{2}'$. *Physical Review Letters* 101: 176803. https://doi.org/10.1103/PhysRevLett.101.176803.

Möller G, Wójs A, and Cooper NR (2011) Neutral fermion excitations in the moore-read state at filling factor $\nu = 5/2'$. *Physical Review Letters* 107: 036803. https://doi.org/10.1103/PhysRevLett.107.036803.

Mong RSK, Zaletel MP, Pollmann F, and Papić Z (2017) Fibonacci anyons and charge density order in the 12/5 and 13/5 quantum Hall plateaus. *Physical Review B* 95: 115136. https://doi.org/10.1103/PhysRevB.95.115136.

Moon K, Mori H, Yang K, Girvin SM, MacDonald AH, Zheng L, Yoshioka D, and Zhang S-C (1995) Spontaneous interlayer coherence in double-layer quantum Hall systems: Charged vortices and kosterlitz-thouless phase transitions. *Physical Review B* 95: 5138. https://doi.org/10.1103/PhysRevB.51.5138.

Moore G and Read N (1991) Nonabelions in the fractional quantum Hall effect. *Nuclear Physics B* 360: 362–396. http://www.sciencedirect.com/science/article/pii/0550321391904070.

Morf RH (1998) Transition from quantum Hall to compressible states in the second Landau level: New light on the $\nu = 5/2$ enigma. *Physical Review Letters* 80: 1505–1508. https://doi.org/10.1103/PhysRevLett.80.1505.

Morf R and Halperin BI (1986) Monte Carlo evaluation of trial wave functions for the fractional quantized Hall effect: Disk geometry. *Physical Review B* 33: 2221–2246. https://doi.org/10.1103/PhysRevB.33.2221.

Morf RH, d'Ambrumenil N, and Das Sarma S (2002) Excitation gaps in fractional quantum Hall states: An exact diagonalization study. *Physical Review B* 66: 075408. https://doi.org/10.1103/PhysRevB.66.075408.

Murthy G and Shankar R (2003) Hamiltonian theories of the fractional quantum Hall effect. *Reviews of Modern Physics* 75: 1101–1158. https://doi.org/10.1103/RevModPhys.75.1101.

Nakamura J, Liang S, Gardner GC, and Manfra MJ (2020) Direct observation of anyonic braiding statistics. *Nature Physics* 16(9): 931–936.

Nayak C and Wilczek F (1996) 2n-quasihole states realize 2(n-1)-dimensional spinor braiding statistics in paired quantum Hall states. *Nuclear Physics B* 479(3): 529–553.

Nayak C, Simon SH, Stern A, Freedman M, and Das Sarma S (2008) Non-Abelian anyons and topological quantum computation. *Reviews of Modern Physics* 80: 1083–1159. https://doi.org/10.1103/RevModPhys.80.1083.

Nguyen DX, Haldane FDM, Rezayi EH, Son DT, and Yang K (2022) Multiple magnetorotons and spectral sum rules in fractional quantum Hall systems. *Physical Review Letters* 128: 246402. https://journals.aps.org/prl/abstract/10.1103/PhysRevLett.128.246402.

Nicholas RJ, Leadley DR, Maude DK, Portal JC, Harris JJ, and Foxon CT (1998) Skyrmions and composite fermions in the limit of vanishing zeeman energy. *Journal of Physics: Condensed Matter* 10: 11327–11335.

Ortalano MW, He S, and Das Sarma S (1997) Realistic calculations of correlated incompressible electronic states in GaAs-al$_x$ga$_{1-x}$as hetero-structures and quantum wells. *Physical Review B* 55: 7702–7714. https://doi.org/10.1103/PhysRevB.55.7702.

Padmanabhan M, Gokmen T, and Shayegan M (2009) Density dependence of valley polarization energy for composite fermions. *Physical Review B* 80: 035423. https://doi.org/10.1103/PhysRevB.80.035423.

Pakrouski K, Peterson MR, Jolicoeur T, Scarola VW, Nayak C, and Troyer M (2015) Phase diagram of the $\nu = 5/2$ fractional quantum Hall effect: Effects of Landau-level mixing and nonzero width. *Physical Review X* 5: 021004. https://doi.org/10.1103/PhysRevX.5.021004.

Pakrouski K, Troyer M, Wu Y-L, Das Sarma S, and Peterson MR (2016) Enigmatic 12/5 fractional quantum Hall effect. *Physical Review B* 94: 075108. https://doi.org/10.1103/PhysRevB.94.075108.

Pan W, Du RR, Stormer HL, Tsui DC, Pfeiffer LN, Baldwin KW, and West KW (1999) Strongly anisotropic electronic transport at landau level filling factor $\nu = 9/2$ and $\nu = 5/2$ under a tilted magnetic field. *Physical Review Letters* 83: 820–823. https://doi.org/10.1103/PhysRevLett.83.820.

Pan W, Stormer HL, Tsui DC, Pfeiffer LN, Baldwin KW, and West KW (2002) Transition from an electron solid to the sequence of fractional quantum Hall states at very low Landau level filling factor. *Physical Review Letters* 88: 176802.

Pan W, Stormer HL, Tsui DC, Pfeiffer LN, Baldwin KW, and West KW (2003) Fractional quantum Hall effect of composite fermions. *Physical Review Letters* 90: 016801. https://doi.org/10.1103/PhysRevLett.90.016801.

Pan W, Baldwin KW, West KW, Pfeiffer LN, and Tsui DC (2015) Fractional quantum Hall effect at Landau level filling $\nu = 4/11$'. *Physical Review B* 91: 041301. https://doi.org/10.1103/PhysRevB.91.041301.

Pan W, Kang W, Lilly MP, Reno JL, Baldwin KW, West KW, Pfeiffer LN, and Tsui DC (2020) Particle-hole symmetry and the fractional quantum hall effect in the lowest landau level. *Physical Review Letters* 124: 156801. https://doi.org/10.1103/PhysRevLett.124.156801.

Papić Z (2013) Fractional quantum Hall effect in a tilted magnetic field. *Physical Review B* 87: 245315. https://doi.org/10.1103/PhysRevB.87.245315.

Papić Z, Mong RSK, Yazdani A, and Zaletel MP (2018) Imaging anyons with scanning tunneling microscopy. *Physical Review X* 8: 011037. https://doi.org/10.1103/PhysRevX.8.011037.

Park K and Jain JK (1998) Phase diagram of the spin polarization of composite fermions and a new effective mass. *Physical Review Letters* 80: 4237–4240. https://doi.org/10.1103/PhysRevLett.80.4237.

Peterson MR, Papić Z, and Sarma SD (2010) Fractional quantum Hall effects in bilayers in the presence of interlayer tunneling and charge imbalance. *Physical Review B* 82(23) 235312.

Pinczuk A, Dennis BS, Pfeiffer LN, and West K (1993) Observation of collective excitations in the fractional quantum Hall effect. *Physical Review Letters* 70: 3983–3986. https://doi.org/10.1103/PhysRevLett.70.3983.

Prange RE and Girvin SM (eds.) (1987) *The Quantum Hall Effect*. New York: Springer-Verlag.

Radu IP, Miller JB, Marcus CM, Kastner MA, Pfeiffer LN, and West KW (2008) Quasi-particle properties from tunneling in the $\nu = 5/2$ fractional quantum Hall state. *Science* 320(5878): 899–902. https://science.sciencemag.org/content/320/5878/899.

Read N (1990) Excitation structure of the hierarchy scheme in the fractional quantum Hall effect. *Physical Review Letters* 65: 1502–1505. https://doi.org/10.1103/PhysRevLett.65.1502.

Read N (2009a) Conformal invariance of chiral edge theories. *Physical Review B* 79: 245304. https://doi.org/10.1103/PhysRevB.79.245304.

Read N (2009b) Non-abelian adiabatic statistics and Hall viscosity in quantum Hall states and $p_x + ip_y$ paired superfluids. *Physical Review B* 79: 045308. https://doi.org/10.1103/PhysRevB.79.045308.

Read N and Green D (2000) Paired states of fermions in two dimensions with breaking of parity and time-reversal symmetries and the fractional quantum Hall effect. *Physical Review B* 61: 10267–10297. https://doi.org/10.1103/PhysRevB.61.10267.

Read N and Rezayi E (1999) Beyond paired quantum Hall states: Parafermions and incompressible states in the first excited Landau level. *Physical Review B* 59: 8084–8092. https://doi.org/10.1103/PhysRevB.59.8084.

Rezayi EH (2017) Landau level mixing and the ground state of the $\nu = 5/2$ quantum hall effect. *Physical Review Letters* 119: 026801. https://doi.org/10.1103/PhysRevLett.119.026801.

Rezayi EH and Haldane FDM (2000) Incompressible paired Hall state, stripe order, and the composite fermion liquid phase in half-filled Landau levels. *Physical Review Letters* 84: 4685–4688. https://doi.org/10.1103/PhysRevLett.84.4685.

Ro D, Deng N, Watson JD, Manfra MJ, Pfeiffer LN, West KW, and Csáthy GA (2019) Electron bubbles and the structure of the orbital wave function. *Physical Review B* 99: 201111. https://doi.org/10.1103/PhysRevB.99.201111.

Saminadayar L, Glattli DC, Jin Y, and Etienne B (1997) Observation of the *e*/3 fractionally charged Laughlin quasiparticle. *Physical Review Letters* 79: 2526–2529. https://doi.org/10.1103/PhysRevLett.79.2526.

Samkharadze N, Arnold I, Pfeiffer LN, West KW, and Csáthy GA (2015) Observation of incompressibility at $\nu = 4/11$ and $\nu = 5/13$'. *Physical Review B* 91: 081109. https://doi.org/10.1103/PhysRevB.91.081109.

Scarola VW and Jain JK (2001) Phase diagram of bilayer composite fermion states. *Physical Review B* 64: 085313. https://doi.org/10.1103/PhysRevB.64.085313.

Scarola VW, Park K, and Jain JK (2000) Rotons of composite fermions: Comparison between theory and experiment. *Physical Review B* 61: 13064–13072. https://doi.org/10.1103/PhysRevB.61.13064.

Shabani J, Gokmen T, Chiu YT, and Shayegan M (2009) Evidence for developing fractional quantum Hall states at even denominator 1/2 and 1/4 fillings in asymmetric wide quantum wells. *Physical Review Letters* 103: 256802. https://doi.org/10.1103/PhysRevLett.103.256802.

Shabani J, Liu Y, Shayegan M, Pfeiffer LN, West KW, and Baldwin KW (2013) Phase diagrams for the stability of the $\nu = \frac{1}{2}$ fractional quantum Hall effect in electron systems confined to symmetric, wide GaAs quantum wells. *Physical Review B* 88: 245413. https://doi.org/10.1103/PhysRevB.88.245413.

Shibata N and Yoshioka D (2001) Ground-state phase diagram of 2d electrons in a high landau level: A density-matrix renormalization group study. *Physical Review Letters* 86: 5755–5758. https://doi.org/10.1103/PhysRevLett.86.5755.

Simon SH and Rezayi EH (2013) Landau level mixing in the perturbative limit. *Physical Review B* 87: 155426. https://doi.org/10.1103/PhysRevB.87.155426.

Simon SH, Rezayi EH, and Cooper NR (2007a) Pseudopotentials for multiparticle interactions in the quantum Hall regime. *Physical Review B* 75: 195306. https://doi.org/10.1103/PhysRevB.75.195306.

Simon SH, Rezayi EH, Cooper NR, and Berdnikov I (2007b) Construction of a paired wave function for spinless electrons at filling fraction $\nu = 2/5$'. *Physical Review B* 75: 075317. https://doi.org/10.1103/PhysRevB.75.075317.

Sodemann I and MacDonald AH (2013) Landau level mixing and the fractional quantum Hall effect. *Physical Review B* 87: 245425. https://doi.org/10.1103/PhysRevB.87.245425.

Son DT (2015) Is the composite fermion a Dirac particle? *Physical Review X* 5: 031027. https://doi.org/10.1103/PhysRevX.5.031027.

Sondhi SL, Karlhede A, Kivelson SA, and Rezayi EH (1993) Skyrmions and the crossover from the integer to fractional quantum Hall effect at small zeeman energies. *Physical Review B* 47: 16419–16426. https://doi.org/10.1103/PhysRevB.47.16419.

Spielman IB, Eisenstein JP, Pfeiffer LN, and West KW (2000) Resonantly enhanced tunneling in a double layer quantum Hall ferromagnet. *Physical Review Letters* 84: 5808–5811. https://doi.org/10.1103/PhysRevLett.84.5808.

Spielman IB, Eisenstein JP, Pfeiffer LN, and West KW (2001) Observation of a linearly dispersing collective mode in a quantum hall ferromagnet. *Physical Review Letters* 87: 036803. https://doi.org/10.1103/PhysRevLett.87.036803.

Suen YW, Engel LW, Santos MB, Shayegan M, and Tsui DC (1992) Observation of a $\nu = 1/2$ fractional quantum Hall state in a double-layer electron system. *Physical Review Letters* 68: 1379–1382. https://doi.org/10.1103/PhysRevLett.68.1379.

Thomale R, Sterdyniak A, Regnault N, and Bernevig BA (2010) En-tanglement gap and a new principle of adiabatic continuity. *Physical Review Letters* 104: 180502. https://doi.org/10.1103/PhysRevLett.104.180502.

Thouless DJ, Kohmoto M, Nightingale MP, and den Nijs M (1982) Quantized Hall conductance in a two-dimensional periodic potential. *Physical Review Letters* 49: 405–408. https://doi.org/10.1103/PhysRevLett.49.405.

Trugman SA and Kivelson S (1985) Exact results for the fractional quantum Hall effect with general interactions. *Physical Review B* 31: 5280–5284. https://doi.org/10.1103/PhysRevB.31.5280.

Tsui DC, Stormer HL, and Gossard AC (1982) Two-dimensional magnetotransport in the extreme quantum limit. *Physical Review Letters* 48: 1559–1562. https://doi.org/10.1103/PhysRevLett.48.1559.

Tutuc E, Shayegan M, and Huse DA (2004) Counterflow measurements in strongly correlated GaAs hole bilayers: Evidence for electron-hole pairing. *Physical Review Letters* 93: 036802. https://doi.org/10.1103/PhysRevLett.93.036802.

Tutuc E, Pillarisetty R, and Shayegan M (2009) Giant frictional drag in strongly interacting bilayers near filling factor one. *Physical Review B* 79: 041303. https://doi.org/10.1103/PhysRevB.79.041303.

Venkatachalam V, Yacoby A, Pfeiffer L, and West K (2011) Local charge of the [ngr] = 5/2 fractional quantum Hall state. *Nature* 469(7329): 185–188. https://doi.org/10.1038/nature09680.

Villegas Rosales KA, Madathil PT, Chung YJ, Pfeiffer LN, West KW, Baldwin KW, and Shayegan M (2021) Fractional quantum hall effect energy gaps: Role of electron layer thickness. *Physical Review Letters* 127: 056801. https://doi.org/10.1103/PhysRevLett.127.056801.

Wagner G, Nguyen DX, Simon SH, and Halperin BI (2021) s wave paired composite-fermion electron-hole trial state for quantum hall bilayers with $\nu = 1$ 2021. *Physical Review Letters* 127: 246803. https://journals.aps.org/prl/abstract/10.1103/PhysRevLett.127.246803.

Wang H, Narayanan R, Wan X, and Zhang F (2012) Fractional quantum hall states in two-dimensional electron systems with anisotropic interactions. *Physical Review B* 86: 035122. https://doi.org/10.1103/PhysRevB.86.035122.

Wang C, Cooper NR, Halperin BI, and Stern A (2017) Particle-hole symmetry in the fermion-Chern-Simons and Dirac descriptions of a half-filled Landau level. *Physical Review X* 7: 031029. https://doi.org/10.1103/PhysRevX.7.031029.

Wen XG (1990) Chiral Luttinger liquid and the edge excitations in the fractional quantum Hall states. *Physical Review B* 41: 12838–12844. https://doi.org/10.1103/PhysRevB.41.12838.

Wen XG (1991) Non-abelian statistics in the fractional quantum Hall states. *Physical Review Letters* 66: 802–805. https://doi.org/10.1103/PhysRevLett.66.802.

Wen X-G (1995) Topological orders and edge excitations in fractional quantum Hall states. *Advances in Physics* 44(5): 405–473. https://doi.org/10.1080/00018739500101566.

Wen XG and Niu Q (1990) Ground-state degeneracy of the fractional quantum hall states in the presence of a random potential and on high-genus riemann surfaces. *Physical Review B* 41: 9377–9396. https://doi.org/10.1103/PhysRevB.41.9377.

Wen XG and Zee A (1992) Shift and spin vector: New topological quantum numbers for the Hall fluids. *Physical Review Letters* 69: 953–956. https://doi.org/10.1103/PhysRevLett.69.953.

Wilczek F (1982) Quantum mechanics of fractional-spin particles. *Physical Review Letters* 49: 957–959. https://doi.org/10.1103/PhysRevLett.49.957.

Willett R, Eisenstein JP, Störmer HL, Tsui DC, Gossard AC, and English JH (1987) Observation of an even-denominator quantum number in the fractional quantum Hall effect. *Physical Review Letters* 59: 1776–1779. https://doi.org/10.1103/PhysRevLett.59.1776.

Willett RL, Stormer HL, Tsui DC, Gossard AC, and English JH (1988) Quantitative experimental test for the theoretical gap energies in the fractional quantum Hall effect. *Physical Review B* 37: 8476–8479. https://doi.org/10.1103/PhysRevB.37.8476.

Willett RL, Ruel RR, West KW, and Pfeiffer LN (1993) Experimental demonstration of a Fermi surface at one-half filling of the lowest Landau level. *Physical Review Letters* 71: 3846–3849. https://doi.org/10.1103/PhysRevLett.71.3846.

Willett RL, West KW, and Pfeiffer LN (1999) Geometric resonance of composite fermion cyclotron orbits with a fictitious magnetic field modulation. *Physical Review Letters* 83: 2624–2627. https://doi.org/10.1103/PhysRevLett.83.2624.

Willett RL, Pfeiffer LN, and West KW (2009) Measurement of filling factor 5/2 quasiparticle interference with observation of charge e/4 and e/2 period oscillations. *Proceedings of the National Academy of Sciences* 106(22): 8853–8858. http://www.pnas.org/content/106/22/8853.abstract.

Willett RL, Shtengel K, Nayak C, Pfeiffer LN, Chung YJ, Peabody ML, Baldwin KW, and West KW (2021) Interference measurements of non-abelian *e*/4 and abelian *e*/2 quasiparticle braiding. In: *arXiv:1905*, 10248. https://arxiv.org/abs/1905.10248.

Williams FIB, Wright PA, Clark RG, Andrei EY, Deville G, Glattli DC, Probst O, Etienne B, Dorin C, Foxon CT, and Harris JJ (1991) Conduction threshold and pinning frequency of magnetically induced Wigner solid. *Physical Review Letters* 66: 3285–3288. https://doi.org/10.1103/PhysRevLett.66.3285.

Wu XG, Dev G, and Jain JK (1993) Mixed-spin incompressible states in the fractional quantum Hall effect. *Physical Review Letters* 71: 153–156. https://doi.org/10.1103/PhysRevLett.71.153.

Xia JS, Pan W, Vicente CL, Adams ED, Sullivan NS, Stormer HL, Tsui DC, Pfeiffer LN, Baldwin KW, and West KW (2004) Electron correlation in the second Landau level: A competition between many nearly degenerate quantum phases. *Physical Review Letters* 93: 176809. https://doi.org/10.1103/PhysRevLett.93.176809.

Yang B, Hu Z-X, Papić Z, and Haldane FDM (2012a) Model wave functions for the collective modes and the magnetoroton theory of the fractional quantum Hall effect. *Physical Review Letters* 108: 256807. https://doi.org/10.1103/PhysRevLett.108.256807.

Yang B, Papić Z, Rezayi EH, Bhatt RN, and Haldane FDM (2012b) Band mass anisotropy and the intrinsic metric of fractional quantum Hall systems. *Physical Review B* 85: 165318. https://doi.org/10.1103/PhysRevB.85.165318.

Yoshioka D, Halperin BI, and Lee PA (1983) Ground state of two-dimensional electrons in strong magnetic fields and $\frac{1}{3}$ quantized Hall effect. *Physical Review Letters* 50: 1219–1222. https://doi.org/10.1103/PhysRevLett.50.1219.

Yoshioka D, MacDonald AH, and Girvin SM (1989) Fractional quantum Hall effect in two-layered systems. *Physical Review B* 39: 1932–1935. https://doi.org/10.1103/PhysRevB.39.1932.

You Y, Cho GY, and Fradkin E (2014) Theory of nematic fractional quantum hall states. *Physical Review X* 4: 041050. https://doi.org/10.1103/PhysRevX.4.041050.

Zaletel MP and Mong RSK (2012) Exact matrix product states for quantum Hall wave functions. *Physical Review B* 86: 245305. https://doi.org/10.1103/PhysRevB.86.245305.

Zaletel MP, Mong RSK, and Pollmann F (2013) Topological characterization of fractional quantum Hall ground states from microscopic Hamiltonians. *Physical Review Letters* 110: 236801. https://doi.org/10.1103/PhysRevLett.110.236801.

Zhang FC and Das Sarma S (1986) Excitation gap in the fractional quantum Hall effect: Finite layer thickness corrections. *Physical Review B* 33: 2903–2905. https://doi.org/10.1103/PhysRevB.33.2903.

Zhang SC, Hansson TH, and Kivelson S (1989) Effective-field-theory model for the fractional quantum Hall effect. *Physical Review Letters* 62: 82–85. https://doi.org/10.1103/PhysRevLett.62.82.

Zhao T, Faugno WN, Pu S, Balram AC, and Jain JK (2021) Origin of the $\nu = 1/2$fractional quantum Hall effect in wide quantum wells. *Physical Review B* 103: 155306. https://doi.org/10.1103/PhysRevB.103.155306.

Zhu J, Pan W, Stormer HL, Pfeiffer LN, and West KW (2002) Density-induced interchange of anisotropy axes at half-filled high landau levels. *Physical Review Letters* 88: 116803. https://doi.org/10.1103/PhysRevLett.88.116803.

Zhu H, Chen YP, Jiang P, Engel LW, Tsui DC, Pfeiffer LN, and West KW (2010) Observation of a pinning mode in a Wigner solid with $\nu = 1/3$ fractional quantum Hall excitations. *Physical Review Letters* 105: 126803. https://doi.org/10.1103/PhysRevLett.105.126803.

Zhu Z, Fu L, and Sheng DN (2017) Numerical study of quantum hall bilayers at total filling $\nu_T = 1$: A new phase at intermediate layer distances. *Physical Review Letters* 119: 177601. https://doi.org/10.1103/PhysRevLett.119.177601.

Zucker PT and Feldman DE (2016) Stabilization of the particle-hole Pfaffian order by Landau-level mixing and impurities that break particlehole symmetry. *Physical Review Letters* 117: 096802.

Zuo Z-W, Balram AC, Pu S, Zhao J, Jolicoeur T, Wójs A, and Jain JK (2020) Interplay between fractional quantum Hall liquid and crystal phases at low filling. *Physical Review B* 102: 075307. https://doi.org/10.1103/PhysRevB.102.075307.

From the integer to the fractional quantum hall effect in graphene

Mark O Goerbig, Laboratoire de Physique des Solides, CNRS - Université Paris-Saclay, Orsay, France

© 2024 Elsevier Ltd. All rights reserved.

Introduction 308
Landau levels and the integer quantum Hall effect in graphene 310
Electrons in a single Landau level 311
Correlated electronic phases in partially filled Landau levels in graphene 313
Spin-valley quantum Hall ferromagnets 314
Magnons 315
Skyrmions 316
Fractional quantum Hall states 317
The 1/3-family of fractional states in graphene 317
The particularity of the CF series p/(2sp + 1) in graphene 318
Even-denominator states 319
Electron crystals 319
Conclusion 320
References 321

Abstract

The fractional quantum Hall effect is a very particular manifestation of electronic correlations in two-dimensional systems in a strong perpendicular magnetic field. It arises as a consequence of a strong Coulomb repulsion between electrons in the same Landau level that conspires with a particular chirality of the electronic states. This chirality is inherited from the classical cyclotron motion, i.e., a particular sense of electronic rotation due to the orientation of the magnetic field. The specificity of the FQHE in graphene consists of a fourfold spin-valley degeneracy inherited from the electronic bands in the vicinity of the Fermi level. The relevant Coulomb interaction respects this SU(4) symmetry, and one is therefore confronted with a generic four-component fractional quantum Hall effect, as well as with other correlated four-component phases, such as spin-valley ferromagnetic states. The present article aims at a—mainly theoretical—discussion of these exotic phases, in comparison with experimental evidence for them.

Key points

- The fractional quantum Hall effect arises in partially filled degenerate Landau levels as a consequence of strong repulsive interactions.
- In graphene, the fractional quantum Hall effect reflects an approximate SU(4) symmetry because the twofold spin degeneracy is accompanied by a twofold valley degeneracy that is approximately respected by the relevant Coulomb repulsion between the electrons.
- In addition to its SU(4) symmetry, the effective interaction potential between electrons in graphene Landau levels is specific as compared to that in usual two-dimensional electron systems (semiconductor heterostructures) as a consequence of the overlap between the spinorial wave functions.
- The SU(4) symmetry of interacting electrons in graphene Landau levels is also relevant in the formation of generalized quantum-Hall ferromagnetic states at integer filling factors, as well as in the description of spin-valley skyrmions and magnons.
- Similarly to the generalized quantum-Hall ferromagnetic states, the fractional quantum Hall states in graphene are characterized by their (partial) spin-valley polarization, and some of them support magnon-type excitations and skyrmions due to a spontaneously broken spin-valley SU(4) symmetry.
- In higher Landau levels, the fractional quantum Hall effect coexists with other correlated electronic states (electronic crystals), and the alternation between fractional quantum Hall and crystalline states upon variation of the filling factor is at the origin of a reentrant integer quantum Hall effect.

Introduction

The quantum Hall effect is a universal phenomenon of two-dimensional (2D) electronic systems submitted to a strong magnetic field. First discovered in 1980 by Klitzing et al. (1980), who received the Nobel Prize in Physics for this discovery in 1985, the effect consists of the appearance of plateaus in the Hall resistance accompanied by a vanishing longitudinal resistance (for a sketch of the setup and a characteristic measurement, see Fig. 1, where the associated conductances are plotted). Most saliently, the plateaus in the

https://doi.org/10.1016/B978-0-323-90800-9.00106-2

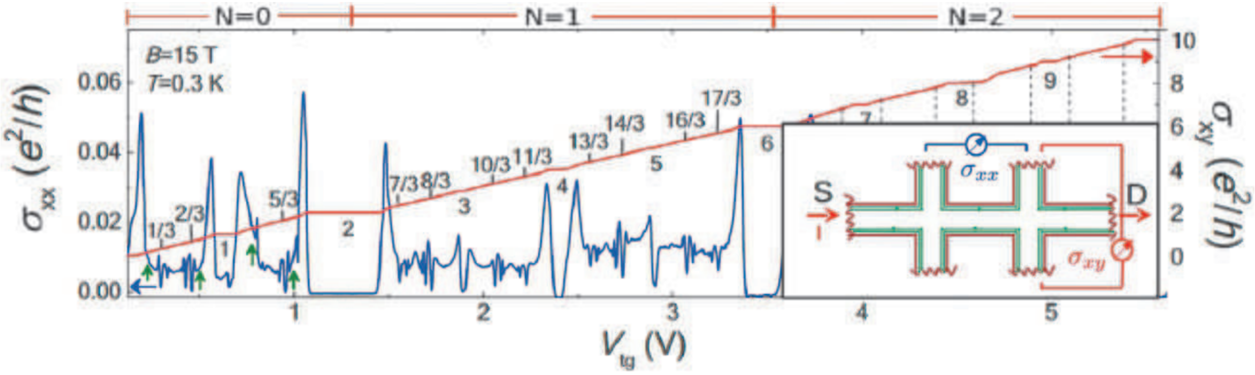

Fig. 1 Characteristic transport signatures of the quantum Hall effect in graphene. The Hall (blue) and the longitudinal (red) conductances are plotted as a function of the electronic density, which is proportional to the gate voltage V_{tg}, at fixed magnetic field ($B = 15$ T) and temperature $T = 0.3$ K. The inset shows the measurement setup in which a current is driven through the system via the contacts S (source) and D (drain). The longitudinal conductance is measured between the contacts connected by the blue line, while the Hall conductance is measured between the contacts connected by the red line. The numbers indicate the value j of the plateau in the Hall conductance $\sigma_{xy} = R_H^{-1} = e^2 j/h$. One clearly distinguishes the integer plateaus of the IQHE (integer numbers below the Hall-conductance curve) from the FQHE plateaus at fractional values of j (numbers above the Hall curve). Adapted from Ribeiro-Palau R, Chen S, Zeng Y, Watanabe K, Taniguchi T, Hone J, Dean CR (2019) High-quality electrostatically defined hall bars in monolayer graphene. *Nano Letters* 19: 2583–2587. https://doi.org/10.1021/acs.nanolett.9b00351.

Hall resistance indicate an extremely precise quantization, $R_H = h/e^2 j$, in terms of the inverse quantum of conductance $G_0 = e^2/h$ and an integer number j. It is the manifestation of the so-called Landau quantization according to which 2D electrons in a strong magnetic field have a discrete energy spectrum with highly degenerate energy levels (Landau levels, LLs). Soon after this discovery, D. Tsui and H. Störmer observed the fractional brother of the effect (Tsui et al., 1982): instead of an integer in the case of the so-called *integer quantum Hall effect* (IQHE), the number j can be a fractional one, whence the name *fractional quantum Hall effect* (FQHE). It became soon clear that the effect requires strong electronic interactions that govern the behavior of electrons inside a partially filled LL and that force the electrons to form an incompressible electron liquid at particular values of the filling factor $\nu = n_{\mathrm{el}}/n_B$, which denotes the filling of the LLs. It is the ratio between the electronic density n_{el} and the density of flux quanta $n_B = eB/h$ threading the 2D system. A first approach to describe the FQHE was provided by Laughlin (1983), who proposed trial wave functions for the electron liquids at odd-integer filling factors $\nu = 1/(2\,s + 1)$, in terms of the integer s. The in-built correlations of these wave functions turned out to be favorable for the minimization of the mutual Coulomb repulsion between the electrons, and he shared the 1998 Nobel Prize in Physics with Tsui and Störmer for the discovery and description of the FQHE. One of the most exotic aspects of these electron liquids is certainly that of their quasiparticle excitations, which have fractional charge as it was first theoretically shown by Laughlin (1983) and later experimentally proven in particular transport experiments. In the latter the so-called shot-noise was measured, which is proportional to the (fractional) charge (de Picciotto et al., 1997; Saminadayar et al., 1997). Associated with this fractional charge and the 2D nature of the system, these quasiparticles obey furthermore fractional statistics: they are anyons, i.e., neither bosons nor fermions, and the identification of fractional statistics remains an important topic of today's research in condensed quantum matter (see also the chapter by M. Greiter and F. Wilczek), with recent breakthrough both in interference (Nakamura et al., 2020) and transport measurements (Bartolomei et al., 2020).

While the observed states at $\nu = 1/3$ and $\nu = 1/5$ could indeed be understood in terms of Laughlin's wave function, a plethora of states at other partial filling factors has since been observed with the continuous increase of the sample quality in GaAs heterostructures. In order to account for those on a theoretical level, Laughlin's wave function has been generalized in several manners, the most noteworthy of which are Jain's composite fermion (CF) wave functions (Jain, 1989) that account for the observation of states at $\nu = p/(2sp + 1)$—the FQHE can then be seen as an IQHE of these CFs that populate p CF LLs—Halperin's wave functions (Halperin, 1983) which account for states that are not or only partially spin-polarized, as well as the Pfaffian wave function (Moore and Read, 1991; Greiter et al., 1991), which describes a FQHE in half-filled LLs that has been observed at $\nu = 5/2$ and 7/2 (Willett et al., 1987) in the first excited LL. Most interestingly, the quasiparticles of the Pfaffian state are a particular type of anyons: they are *non-Abelian* anyons, in which case exchanges of more than two quasiparticles do not commute, and they are expected to play a relevant role in possible quantum computation (Kitaev, 2003). (For more information about the FQHE in general, see the chapter by Z. Papić and A. C. Balram.)

The mechanical isolation of graphene in Novoselov et al. (2004) provided the condensed-matter-physics community with a novel 2D electronic system and has ever since been heavily studied because of its unexpected electronic properties and its remarkable relation with relativistic quantum mechanics. A milestone experiment in graphene research was the observation of a particular version of the IQHE in 2005 by two groups, that of A. K. Geim at Manchester University and that of P. Kim at Columbia University (Novoselov et al., 2005; Zhang et al., 2005). The relevance of this discovery is twofold. First, it confirmed the above-mentioned universality of the effect since graphene is a largely different 2D electron system as compared to the usual ones formed at semiconductor interfaces. Second, the particular filling-factor values $\nu = \pm 2(2n + 1)$, at which the effect manifests itself, is a fingerprint of the relativistic quantum-mechanical behavior of electrons in graphene that are described in terms of a Dirac rather than the usual Schrödinger equation of quantum mechanics. (For an introduction to the physics of graphene, see the chapter by E. McCann.)

As compared to the original discoveries of the quantum Hall effects in the 1980s, it took relatively longer to observe the FQHE in graphene, which was equally expected because of the universality of the phenomenon. First experimental indications of a FQHE at $\nu = \pm 1/3$ were found in 2009 in freestanding graphene, where the original substrate on which the graphene sheet had been posed was etched away (Du et al., 2009; Bolotin et al., 2009). A true breakthrough was achieved in 2011 with the use of clean hexagonal boron-nitride (h-BN) flakes as a substrate that increased considerably the electronic mobility in graphene. This increase of the mobility allowed for the observation of a large amount of FQHE states (Dean et al., 2011), similarly to the effect in the more conventional 2D electron systems in semiconductor heterostructures.

The present article mainly aims at responding at the following question: what are the main differences with respect to the FQHE in conventional 2D electron systems? In analogy with the IQHE, whose particular manifestation in graphene can be understood in terms of the relativistic nature of graphene's electrons, is there something such as a relativistic version of the FQHE? This was indeed a central issue in the theoretical discussions about the FQHE in graphene before its experimental discovery. After a short reminder of LL quantization in graphene and the IQHE in section "Landau levels and the integer quantum Hall effect in graphene", section "Electrons in a single Landau level" introduces the basic properties of the electron dynamics in a single LL from a theoretical point of view. It is the basis for understanding the appearance of correlated phases, as it is discussed in section "Correlated electronic phases in partially filled Landau levels in graphene", not only the FQHE states (section "Fractional quantum Hall states"), but also a particular form of spin-valley quantum Hall ferromagnetism the polarization in which does not only concern the usual electron spin but also another twofold (valley) degree of freedom (section "Spin-valley quantum Hall ferromagnets"), and electron crystalline phases (section "Electron crystals").

Landau levels and the integer quantum Hall effect in graphene

Landau quantization denotes the formation of discrete levels into which the kinetic energy of 2D electrons is quenched in the presence of a strong perpendicular magnetic field. It was first treated theoretically by L. Landau in 1930 for free non-relativistic particles with electric charge[1] $-e$ that, in the absence of a magnetic field, have a quadratic dispersion relation, i.e., a quadratic dependence of their energy on their wave vector $\mathbf{k}$. In a typical condensed-matter system, where one deals with electrons in a periodic potential created by the atoms forming the crystal, this situation arises generically in the vicinity of the bottom of an electronic band that is described by a Bloch Hamiltonian $H(\mathbf{k})$. Elementary band theory shows that in the vicinity of the band bottom, where the Fermi level resides, e.g., in the widely used semiconductor GaAs, the Bloch Hamiltonian is $H(\mathbf{k}) \simeq \hbar^2|\mathbf{k}|^2/2m$, i.e., precisely that of a free non-relativistic particle in terms of the band mass m. Landau quantization is then obtained by replacing the momentum $\mathbf{p} = \hbar\mathbf{k}$ by its gauge-invariant form $\mathbf{p} + e\mathbf{A}(\mathbf{r})$, where $\mathbf{A}(\mathbf{r})$ is the vector potential at the position $\mathbf{r}$, which yields the magnetic field $\mathbf{B} = \nabla \times \mathbf{A}(\mathbf{r})$. The usual quantum-mechanical non-commutativity of position and momentum, $[x, p_x] = [y, p_y] = i\hbar$, then gives the energy spectrum

$$E_n = \hbar\omega_C\left(n + \frac{1}{2}\right), n = 0,1,2,\ldots \tag{1}$$

of the harmonic oscillator, in terms of the cyclotron frequency $\omega_C = eB/m$. In contrast to the usual one-dimensional harmonic oscillator, the energy levels (the LLs) are highly degenerate because the system remains 2D. This degeneracy is related to translation symmetry in the case of a homogeneous magnetic field. Even if this symmetry is, strictly speaking, broken by the position-dependent vector potential entering in the Hamiltonian, translation symmetry is to some extent restored if we consider the electron dynamics from a (semi-)classical point of view. Indeed, the electrons are forced to perform a circular cyclotron motion around a position $\mathbf{R} = (X, Y)$—the *guiding center*—that is a constant of motion, in contrast to the momentum that constantly changes its direction. Most saliently, the two components of the guiding center do not commute, $[X, Y] = il_B^2\,\mathrm{sgn}\,(B)$, in terms of the magnetic length $l_B = \sqrt{\hbar/e|B|}$ and the orientation of the magnetic field, $\mathrm{sgn}(B) = B/|B|$. This has two consequences: first, each quantum state in a LL has a particular *chirality*, i.e., a rotational sense imposed by the orientation of the magnetic field; second, the position of the guiding center is not sharply defined, but submitted to a Heisenberg uncertainty relation—it is spread over a surface $2\pi l_B^2$ that can be viewed as the surface occupied by a quantum state in a particular LL. The total degeneracy N_B of each LL is therefore given by the total surface S divided by this minimal surface, $N_B = S/2\pi l_B^2 = SB/(h/e)$, which is nothing other than the total flux threading the 2D system, in units of the flux quantum h/e. As a consequence of the fermionic nature of the electrons and Pauli's exclusion principle, the filling of the LLs is therefore determined by the filling factor

$$\nu = \frac{N_{e1}}{N_B} = \frac{n_{\mathrm{el}}}{n_B}, \tag{2}$$

in terms of the total number of electron $N_{\mathrm{el}} = Sn_{\mathrm{el}}$.

The IQHE arises every time that an integer number of LLs is completely filled, i.e., at $\nu = j$. In this case, the Fermi level resides between the LLs $n-1$ and n, and the system is a bulk insulator. Strictly speaking, n should be an even integer due to the twofold spin degeneracy, but the latter is lifted either by the Zeeman effect or the formation of a ferromagnetic state due to exchange effects that favor a full spin polarization (see section "Spin-valley quantum Hall ferromagnets"). The conductance is then governed by j chiral ballistic edge channels the chirality of which is imposed by the orientation of the magnetic field, while additional electrons (or holes) that occupy adjacent LLs, if the filling factor is not precisely an integer, do not contribute to the electric transport due to their localization by the bulk impurities. It is noteworth to mention that this is a particular form of the bulk-edge correspondence that makes the IQHE a prototype of a topological insulator, where the bulk is insulating but the edges are necessarily conducting.

---

[1] Since we are interested, here, in electrons of negative charge, the following expressions are those for particles with charge $-e$, in terms of the elementary charge e, which we set to be positive.

As already mentioned, the graphene is special because the band dispersion is not quadratic in the vicinity of the Fermi level. In charge-neutral (i.e., undoped) graphene, the Fermi level is situated at the two inequivalent points K and K' in the first Brillouin zone, where the valence band touches the conduction band with a dispersion that is linear in the wave vector. This has two consequences. First, the low-energy spectrum in the vicinity of the Fermi level is *twofold valley-degenerate*; second, the Bloch Hamiltonian must account for both conduction and valence bands on equal footing, via the 2 × 2-matrix form

$$H(\mathbf{k}) = \hbar v_F \begin{pmatrix} 0 & (k_x - ik_y) \\ (k_x + ik_y) & 0 \end{pmatrix}. \tag{3}$$

This is precisely the 2D Dirac Hamiltonian of a massless particle in relativistic quantum mechanics, moving at the Fermi velocity v_F instead of the speed of light. Upon the same replacement of the wave vector by its gauge-invariant form as discussed above, $\hbar\mathbf{k} \rightarrow \mathbf{p} + e\mathbf{A}(\mathbf{r})$, to account for the magnetic field, one obtains the LL spectrum

$$E_n^G = \lambda\hbar \frac{v_F}{l_B}\sqrt{2n}, \tag{4}$$

where $\lambda = \pm$ denotes the two bands ($\lambda = +$ for the conduction and $\lambda = -$ for the valence band), and the ratio between the Fermi velocity and the magnetic length, v_F/l_B, plays the role of the cyclotron frequency here. It is clear from this spectrum that each LL in the conduction band has its counterpart in the valence band, apart from the $n = 0$ LL that is fixed at zero energy.

Similarly to LLs in non-relativistic 2D electron systems with a quadratic band dispersion, the LLs of graphene are highly degenerate, and the number of states per LL is again given by the number of flux quanta threading the 2D surface. Indeed, the argument invoked above—that the center of the cyclotron motion is a constant of motion and that there exists a minimal surface occupied by any quantum state in a LL—does not require a particular form of the electronic bands, but it is generally valid, regardless of the precise form of the LL spectrum. However, the internal degrees of freedom are not the same. While in a conventional 2D electron system, one is simply confronted with the twofold spin degeneracy, in the absence of the Zeeman effect, graphene LLs are fourfold degenerate. In addition to the usual spin, one has a twofold valley degeneracy as a consequence of the above-mentioned two inequivalent points K and K' where the Fermi level crosses the electronic bands. The electrons are therefore formally described within an SU(4) symmetry, which arises as a consequence of the possibility to make a quantum-mechanical superposition of the orbital wave functions of each for the four spin-valley combinations $|\uparrow, K\rangle$, $|\uparrow, K'\rangle$, $|\downarrow, K\rangle$, and $|\downarrow, K'\rangle$, where $s = \uparrow,\downarrow$ denotes the spin orientation. This particular SU(4) symmetry, which is respected to great extent in graphene LLs due to the smallness of the Zeeman effect and other valley-degeneracy lifting terms (Goerbig, 2011), turns out to be of great relevance for the understanding not only of the FQHE in graphene, but also for the formation of exotic quantum-Hall ferromagnetic phases that are discussed in the following sections. If one discards these phases for the moment, one therefore expects an IQHE in graphene at filling factors that are spaced in units of four due to the fourfold spin-valley degeneracy. This has indeed been observed experimentally (Novoselov et al., 2005; Zhang et al., 2005), but moreover the filling-factor series at which the IQHE occurs has an offset of two as compared to the IQHE in conventional 2D electron systems. This offset can be understood in the following manner. In contrast to non-relativistic systems, where the absence of any charge carriers at $\nu = 0$ leads to a completely empty lowest LL, charge neutrality in graphene ($\nu = 0$) means that the zero-energy LL $n = 0$ is globally half-filled; there are as many electrons as holes that occupy the $n = 0$ LL. Therefore, the Fermi level is situated inside this LL and not in the energy gap between two adjacent LLs, as it is required for the occurrence of the IQHE. The latter situation arises only at $\nu = 2$, when the $n = 0$ LL is completely filled, or at $\nu = -2$ when it is empty. In graphene, the IQHE thus occurs at the filling factors

$$\nu = \pm(4n + 2) = \pm 2(2n + 1), \tag{5}$$

as it has been demonstrated experimentally (Novoselov et al., 2005; Zhang et al., 2005). This particular filling-factor sequence of the IQHE is a fingerprint of the relativistic nature of the electrons in graphene.

Electrons in a single Landau level

In the preceding section, it was discussed that the IQHE arises as a consequence of Landau quantization every time that the Fermi level resides in between two adjacent LLs. As a consequence of the SU(2) spin symmetry in conventional 2D electron system, this is the case for $\nu = 2(n + 1)$, while the combination of (i) the relativistic nature of graphene electrons and (ii) their SU(4) spin-valley degeneracy yields an IQHE at $\nu = \pm 2(2n + 1)$ in graphene. In the present section, we discuss which of these two particularities are inherited by the FQHE in graphene. Because the FQHE phases occur at fractionally filled LLs, one needs to restrict the electronic dynamics to a single LL: the low-energy excitations are now those inside the same LL whereas excitations across LLs can be treated as belonging to high-energy degrees of freedom of a characteristic energy given by the LL separation, i.e., the energy scale $\hbar\omega_C$ in

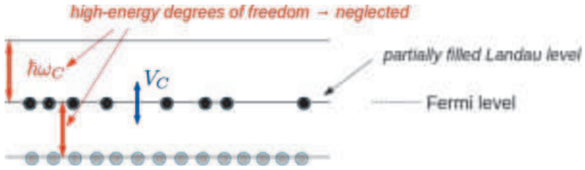
high-energy degrees of freedom → neglected
$\hbar\omega_C$
V_C
partially filled Landau level
Fermi level

Fig. 2 Sketch of the low-energy model of electrons restricted to a single LL. The Fermi level is situated in the partially filled LL (black circles represent the occupied states), while the LLs below are completely filled (gray circles) and those above completely empty. Excitations across LLs (red arrows) are associated with an energy given by the LL separation $\hbar\omega_C$ and belong to the neglected high-energy degrees of freedom, while excitations in the same LL are gouverned by the Coulomb interaction V_C.

conventional 2D electron systems or $\hbar v_F/l_B$ in graphene. This is depicted in Fig. 2. For the low-energy electronic excitations inside a single LL, the kinetic energy is therefore quenched, and the physical properties are governed by the Coulomb repulsion between the electrons.[2]

The low-energy electronic model finally appeals to the Coulomb interaction between the electronic densities $\rho_n(\mathbf{r})$ restricted to a single LL n,

$$H = \frac{1}{2}\int d^2r d^2r' \rho_n(\mathbf{r}) V(\mathbf{r} - \mathbf{r}')\rho_n(\mathbf{r}'), \tag{6}$$

where $V(\mathbf{r}) = e^2/\varepsilon\,|\,\mathbf{r}|$ is the usual Coulomb potential, which may eventually be screened due to a dielectric environment or the presence of gates. These screening properties are generically taken into account by the dielectric function ε. Let us now turn our attention in more detail to the LL-restricted densities $\rho_n(\mathbf{r})$, which are more conveniently described in reciprocal space, i.e., by Fourier transformation,

$$\rho_n(\mathbf{q}) = \int d^2r \rho_n(\mathbf{r}) e^{-i\mathbf{q}\cdot\mathbf{r}} = \left\langle \sum_j e^{-i\mathbf{q}\cdot\mathbf{r}_j} \right\rangle_n = F_n(\mathbf{q})\overline{\rho}(\mathbf{q}), \tag{7}$$

where $\langle \ldots \rangle_n$ indicates the restriction to the n-th LL, of the Fourier components $\sum_j \exp\left(-i\mathbf{q}\cdot\mathbf{r}_j\right)$ of the density operator in terms of the position operator $\mathbf{r}_j$ of the j-th particle. From a quantum-mechanical point of view, this restriction is necessary because the position operator has components in all LLs, and restricting the electron dynamics to a single LL amounts to replacing the position operator precisely be that of the guiding center $\mathbf{R}_j$. As mentioned above, $\mathbf{R}_j$ is a constant of motion and thus commutes with the kinetic Hamiltonian that gives rise to the LLs. The projected density operator in Eq. (7) is thus implicitly defined as $\overline{\rho}(\mathbf{q}) = \sum_j \exp\left(-i\mathbf{q}\cdot\mathbf{R}_j\right)$. The form factor $F_n(\mathbf{q})$ on the right-hand side of the expression (7) takes into account the LL wave functions that are system-dependent. In the case of the conventional 2D electron gaz (e.g., in GaAs heterostructures), it is given in terms of Laguerre polynomials,

$$F_n^{\text{2DEG}}(\mathbf{q}) = L_n\left(\frac{q^2 l_B^2}{2}\right) e^{-q^2 l_B^2/4}, \tag{8}$$

while in graphene one needs to distinguish the $n = 0$ LL from the other levels,

$$F_{n=0}^{\text{G}}(\mathbf{q}) = e^{-q^2 l_B^2/4} \text{and } F_{n\neq 0}^{\text{G}}(\mathbf{q}) = \frac{1}{2}\left[L_{n-1}\left(\frac{q^2 l_B^2}{2}\right) + L_n\left(\frac{q^2 l_B^2}{2}\right)\right] e^{-q^2 l_B^2/4}. \tag{9}$$

The form factors can be absorbed into an *effective interaction potential*

$$v_n(\mathbf{q}) = \frac{2\pi e^2}{\varepsilon(\mathbf{q})|\mathbf{q}|}\left[F_n(\mathbf{q})\right]^2, \tag{10}$$

so that the electronic properties in a partially filled LL and thus the correlated phases responsible for the FQHE are governed by the model

$$H = \frac{1}{2}\sum_{\mathbf{q}} v_n(\mathbf{q})\overline{\rho}(-\mathbf{q})\overline{\rho}(\mathbf{q}). \tag{11}$$

While this is a theoretical model that one would also start with for the description of electronic correlations in flat bands, the Hamiltonian (11) is quite special as a consequence of the magnetic field. Indeed, the magnetic field is still present via the guiding-center operators, which enter into the expressions for the restricted density operators, and its quantum-mechanical commutation relations impose a particular chirality on the electronic states. They induce highly unusual commutation relations for the density operators (Girvin et al., 1986)

---

[2] There is a second natural energy scale that is set by the inevitable impurities in the 2D systems. However, since the FQHE and other remarkable phases occur only in high-quality samples, the Coulomb repulsion is the leading energy scale and impurities should be treated perturbatively as a subordinate effect. Their main role is then to localize the quasiparticles of the FQHE liquid and thus to fix the Hall resistance over a certain filling-factor range, whence the appearance of the Hall plateau.

$$[\bar{\rho}(\mathbf{q}), \bar{\rho}(\mathbf{q}')] = 2i\,\mathrm{sgn}\,(B)\sin\left(\frac{\mathbf{q}\wedge\mathbf{q}' l_B^2}{2}\right)\bar{\rho}(\mathbf{q}+\mathbf{q}'), \tag{12}$$

where $\mathbf{q}\wedge\mathbf{q}' = q_x q_y' - q_x' q_y$ is the 2D vector product. The chirality is hidden in the expression on the right-hand side of Eq. (12), the sign of which is determined by the orientation of the magnetic field in the z-direction perpendicular to the 2D plane. This chirality is inherited from that of the guiding-center components, as discussed in the previous section.

To summarize this theoretical section on the basic model encoding the exotic physical properties of the FQHE, the correlated phases require

- flat degenerate levels (or bands), that are the LLs here, i.e., a quenched kinetic energy;
- repulsive interactions between the electronic density components inside this level, such as it is described by the Hamiltonians (6) and (11);
- a chirality of the quantum states that is encoded, here, in the commutation relation between the components of the guiding-center operator, $[X, Y] = il_B^2\,\mathrm{sgn}\,(B)$, and that yields a non-commutativity (12) to the Fourier components of the projected density operators;
- the precise form of the LL spectrum is irrelevant for the structure of this low-energy model, but it has an indirect effect via the effective interaction potential, which accounts for the LL wave functions.

This summary is noteworthy since recent theoretical and numerical studies have shown that the FQHE phases are not restricted to partially filled LLs in 2D systems in a strong magnetic field, but they can be found also in partially filled flat electronic 2D bands with a non-zero Chern number (Regnault and Bernevig, 2011), in which case one speaks of *fractional Chern insulators*. Indeed, in this case the low-energy model for interacting electrons in a flat band has the same structure as that of 2D electrons in a single LL if one uses an average Berry curvature that is homogeneous in reciprocal space over the first Brillouin zone (Parameswaran et al., 2012; Goerbig, 2011). Finally, one should retain from this discussion that the difference between the FQHE in conventional 2D electron systems and that in graphene stems not from the particular form of the LLs—be they relativistic or non-relativistic—but from (i) the different wave functions that yield slightly different effective interaction potentials and (ii) from the internal degrees of freedom, which turn out to be fourfold in the case of graphene because of the fourfold spin-valley degeneracy of its LLs. In contrast to the IQHE, there is thus nothing such as a relativistic version of the FQHE in graphene.[3] The (effective) Coulomb interaction in Eq. (10) respects this SU(4) symmetry; symmetry-breaking terms are suppressed algebraically in a/l_B, where $a = 0.14$ nm is the characteristic distance between nearest-neighbor carbon atoms in the graphene lattice, and the magnetic length is much larger at physically accessible magnetic fields, $l_B \simeq 24\text{ nm}/\sqrt{B[T]}$..

Correlated electronic phases in partially filled Landau levels in graphene

Based on the model presented in the previous section, we now describe the main electronic phases encountered in partially filled Landau levels. Quite generally, one might already mention that due to the flatness of the Landau levels, spin- and valley-polarized states are favored in order to minimize the exchange energy. This is reminiscent of the usual itinerant ferromagnetism, with the notable difference that in the case of LLs there is no cost in kinetic energy to fully polarize the electrons. This picture turns out to be the correct one in the description of quantum-Hall ferromagnetic (QHFM) states at integer filling factors other than the graphene sequence $\nu = \pm 2(2n+1)$, and, because of the conceptually simpler description, we present the particular physical properties of these states in section "Spin-valley quantum Hall ferromagnets" before the FQHE. However, this picture is more questionable in the theoretical description of the FQHE. As we discuss below, the *exchange energy* might be outcast in several situations by the *correlation energy*, which is intrinsically built into the trial wave functions such as the multi-component Halperin or Jain wave functions. In first exact-diagonalization studies that considered a completely polarized spin but a free valley polarization and that took into account the particular graphene LL form factors (9), the FQHE state at $\nu = 1/3-2$ turned out to be fully polarized while that at $\nu = 2/5-2$ is a valley singlet (Apalkov and Chakraborty, 2006). The strong variation of the spin-valley polarization of the various FQHE states has later been corroborated in theoretical studies that take into account the fourfold spin-valley degeneracy either in a four-component CF approach (Tőke and Jain, 2007) or in an approach that appeals to four-component generalizations of the Halperin wave function (Goerbig and Regnault, 2007).

From an experimental point of view, it is more difficult to obtain information about the spin-valley polarization of the various states. Signatures for the SU(4) nature of the 1/3-family of the FQHE have been obtained in transport measurements of graphene on h-BN (Dean et al., 2011) and later in compressibility measurements of the CF series at $\nu = p/(2sp+1)$ in different subbranches of the $n = 0$ LL in suspended graphene (Feldman et al., 2012). However, they are not based on a direct measurement of the spin or valley polarization but on a relative comparison between the gaps and visibilities of the various states.

---

[3] Notice that a relativistic description has been adopted with great success in the description of a half-filled LL that accounts naturally for the particle-hole symmetry manifest at this filling (Son, 2015). However, this particular description is by no means inherited from the original LLs since it has been used also in the context of conventional 2D quantum Hall systems, such as in GaAs heterostructures.

Spin-valley quantum Hall ferromagnets

The most straight-forward manifestation of the Coulomb repulsion is certainly the formation of QHFM states at integer fillings other than the characteristic IQHE series $\nu = \pm 2(2n+1)$ in graphene. This is easily understood in analogy with ferromagnetism of itinerant electrons: in order to minimize the Coulomb repulsion, the orbital part of the overall N-electron wave function should be as antisymmetric as possible such that the probability to find two electrons at the same position is decreased. Because of the fermionic global antisymmetry of the electronic wave function, the spin-valley part must therefore be symmetric, i.e., maximally spin-valley polarized, that is precisely the hallmark of an SU(4) ferromagnetic state. Because of the flatness of the LL, this polarization is not accompanied by a cost in kinetic energy as for itinerant electrons in dispersive energy bands.

Let us illustrate the particular SU(4) QHFM states in the LL $n = 0$. One needs to distinguish two cases, (i) $\nu = -1$, which is related by particle-hole symmetry to the case $\nu = +1$, and (ii) $\nu = 0$ at charge neutrality. At $\nu = -1$, one of the spin-valley components $\alpha = |\uparrow, K\rangle, |\uparrow, K'\rangle, |\downarrow, K\rangle, |\downarrow, K'\rangle$ is completely filled, and the associated wave function reads

$$\psi_{\nu=-1} = \prod_{k_\alpha < l_\alpha}^{N_B} \left(z_{k_\alpha} - z_{l_\alpha}\right) \exp\left(-\sum_{j_\alpha=1}^{N_B} \left|z_{j_\alpha}\right|^2 / 4 l_B^2 \right), \tag{13}$$

in terms of the complex position $z_{j_\alpha} = x_{j_\alpha} - i y_{j_\alpha}$ of the j_α-th electron in the component α. Because of the SU(4) symmetry of the Coulomb interaction, there is no spin-valley component favored over another one, and α could even represent an arbitrary quantum-mechanical superposition of the four components. Notice, however, that the SU(4) symmetry is eventually broken by interactions at the lattice scale (Alicea and Fisher, 2006; Herbut, 2007; Kharitonov, 2012), electron-phonon interactions (Fuchs and Lederer, 2007; Nomura et al., 2009) or simply the Zeeman effect. Generally, these effects are associated with energy scales that are one or two orders of magnitude smaller than the leading SU(4)-symmetric Coulomb repulsion (Goerbig, 2011), and we therefore consider the symmetric case first. Similarly, the QHFM wave function at charge neutrality ($\nu = 0$) can be written as

$$\psi_{\nu=0} = \prod_{k_\alpha < l_\alpha}^{N_B} \left(z_{k_\alpha} - z_{l_\alpha}\right) \prod_{k_\beta < l_\beta}^{N_B} \left(z_{k_\beta} - z_{l_\beta}\right) \exp\left(-\sum_{j_\alpha=1}^{N_B} \left|z_{j_\alpha}\right|^2 / 4 l_B^2 - \sum_{j_\beta=1}^{N_B} \left|z_{j_\beta}\right|^2 / 4 l_B^2 \right), \tag{14}$$

i.e., the two components α and β are now completely filled. As in the case $\nu = -1$, one may freely choose α and β among the four components, including quantum-mechanical superpositions of them, as long as the components α and β are orthogonal to one another.

Both at $\nu = -1$ and $\nu = 0$, the large variety of SU(4) polarizations is eventually fixed by the above-mentioned subleading symmetry-breaking terms, which are easily taken into account within a non-linear sigma model. In the conceptually simpler case $\nu = -1$, the energy due to these anisotropic terms can be written as (Nomura et al., 2009; Lian and Goerbig, 2017)

$$E_A = \frac{N_B}{2}\left[u_z M_{P_z}^2 + u_\perp \left(M_{P_x}^2 + M_{P_y}^2\right)\right] - N_B \Delta_Z M_{S_z}, \tag{15}$$

where $M_{S_\mu} = \langle F|\sigma_\mu|F\rangle$ is the spin polarization of a general superposition $|F\rangle$ of the four different spin-valley components, in terms of the Pauli matrices σ_μ acting on the spin components of $|F\rangle$. Similarly, $M_{P_\mu} = \langle F|\tau_\mu|F\rangle$ is the valley polarization of $|F\rangle$ in terms of the Pauli matrices τ_μ that now act on the valley components of $|F\rangle$. The usual Zeeman effect is taken into account by the energy scale Δ_Z, while u_z and $u_\perp$ act on the valley components. As mentioned above, they account for either lattice-scale interactions (Alicea and Fisher, 2006; Herbut, 2007; Kharitonov, 2012) or electron-phonon coupling.

The resulting phase diagram is shown in Fig. 3a, as a function of u_z/Δ_Z and $u_\perp/\Delta_Z$. It can be understood in the following manner. Apart from the *canted antiferromagnetic* (CAF) and the *antiferrimagnetic* (AFI) phases, the spin and valley polarizations are fully decoupled. Indeed, at $\nu = -1$, the system can be both fully spin- and fully valley-polarized, e.g., if all electrons occupy the state $|F\rangle = |\uparrow, K\rangle$. This is the case in the *charge-density-wave* (CDW) phase that is stabilized if $u_z < u_\perp < \Delta_Z$. The particular sublattice occupation, where only one sublattice is occupied, is a consequence of the particular nature of the one-particle wave functions in the

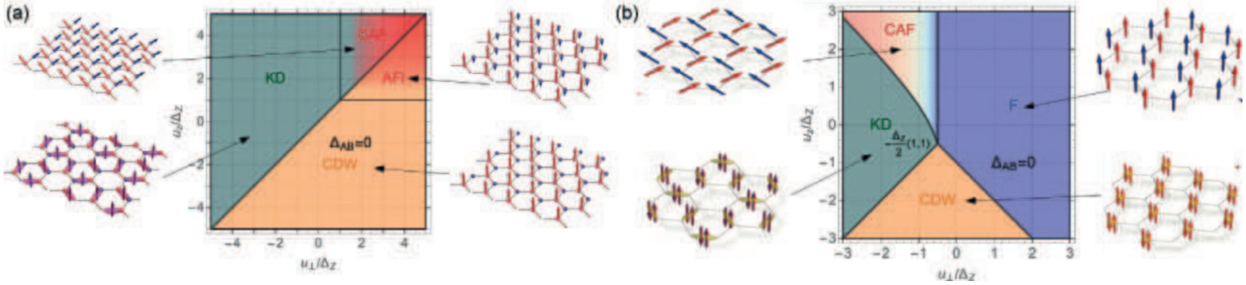

Fig. 3 Phase diagram for the QHFM phases at (a) $\nu = -1$ and (b) $\nu = 0$, as a function of the parameters u_z/Δ_Z and $u_\perp/\Delta_Z$. (a) At $\nu = -1$, the CDW and KD phases come along with a full spin polarization since the spin and valley degrees of freedom are decoupled. On the contrary, the AFI and CAF phases show spin-valley entanglement. The sketches indicate the lattice-resolved spin densities in the different phases. (b) At $\nu = 0$ the full valley polarization of the CDW and KD phases are spin-unpolarized, and the F phase with full spin polarization is therefore distinct from the former two phases. The CAF phase shows spin-valley entanglement.

graphene $n = 0$ LL, where sublattice and valley are identical: electrons of the valley K have a non-zero wave function only on one sublattice, while electrons of the valley K' solely occupy the other sublattice. Similarly, for $u_\perp < u_z < \Delta_Z$, the valley polarization is preferentially in a superposition of the valleys K and K', along with a full spin polarization in the z-direction. This superposition manifests itself in a particular lattice pattern in the form of a *kekulé distortion* (KD).

The phases CAF and AFI merit special attention. They are specific SU(4) ferromagnetic phases that have no counterpart in the usual SU(2) ferromagnetism since they are driven by an entanglement between the spin and valley degrees of freedom. Consider for example the AFI phase, which becomes antiferromagnetic in the limit of a vanishing Zeeman gap, $\Delta_Z \to 0$. From the above-mentioned perspective, it is perfectly admitted to construct an equal-weight superposition of the states $|\uparrow, \mathrm{K}\rangle$ and $|\downarrow, \mathrm{K}'\rangle$ of all electrons. In this case, the SU(4) QHFM consists only of spin-↑ electron in the K valley, i.e., on one sublattice, while the other sublattice (associated with the valley K') only hosts spin-↓ electrons. This would commonly be referred to as an *antiferromagnetic* state, but one must insist that it is an SU(4) *ferromagnetic* phase which can be transformed into one of the other QHFM phases by a global SU(4) rotation. This state is favored at positive values of u_z and $u_\perp$, which prefer to have a vanishing valley polarization in all directions, as one may see from Eq. (15). As a matter of fact, due to the spin-valley entanglement, a vanishing valley polarization comes along with a vanishing spin polarization (Douçot et al., 2008). However, a fully vanishing spin polarization can be achieved only in the limit of zero Zeeman effect, which otherwise prefers a non-zero value of the spin polarization in the z-direction, whence the term *antiferrimagnetic*. Similarly the CAF phase has a net spin polarization out of plane to account for the Zeeman effect, but an inplane antiferromagnetic pattern.

The phase diagram at $\nu = 0$ has similar phases (Kharitonov, 2012), but one needs to take into account the fact that now two components are fully occupied by electrons, as stipulated by the wave function (14). In this case, one cannot polarize fully both the spin and the valley, i.e., one now needs to make a distinction between the spin-polarized *ferromagnetic* (F) phase and the valley-polarized phases CDW and KD. The F phase comes along with a zero valley polarization while the CDW and KD phases are accompanied by a vanishing spin polarization. Again, it is possible to profit from spin-valley entanglement via special superpositions, such as in the CAF phase. The phase diagram (Kharitonov, 2012; Atteia et al., 2021) is shown in Fig. 3b for the same parameters u_z, $u_\perp$ and Δ_Z. The precise values of these parameters are yet unknown and they are likely to depend on the concrete physical system, e.g., the (dielectric) environment of the graphene sheet or its amount of disorder. Recent scanning-tunneling-spectroscopic measurements have found evidence for all four phases at $\nu = 0$ (Liu et al., 2022; Coissard et al., 2022), for graphene on different substrates.

Magnons

As a consequence of the spontaneously broken SU(4) symmetry in the formation of a QHFM, special low-energy collective excitations, called *Goldstone modes*, occur if one perturbs slightly the ground states. They are nothing other than generalized spin waves (magnons) that happen again to be special in graphene as a consequence of the relatively large SU(4) symmetry. In addition to the usual spin waves one has valley waves and mixed spin-valley magnons. This can be seen most easily again at $\nu = -1$, for which the situation is depicted in Fig. 4a. Indeed, a simple counting of the possible modes indicates that there are three magnon branches. In the case of an SU(4)-symmetric interaction all three branches have the same dispersion

$$E_{\mathbf{q}} = 2\sum_{\mathbf{k}} v_n(\mathbf{k}) \, \sin^2\left(\frac{\mathbf{q}\wedge\mathbf{k} l_B^2}{2}\right), \tag{16}$$

in terms of the effective interaction (10) and the pair wave vector $\mathbf{q}$. Indeed, a magnon can be viewed as a superposition at a specific wave vector $\mathbf{q}$ of a hole in the component α, which is fully occupied in the QHFM state $|F\rangle$, and an electron in the originally empty component β. Since the superposition is charge-neutral, the pair wave vector $\mathbf{q} = \Delta\mathbf{R} \times \mathbf{e}_z / l_B^2$, which is related to the spatial separation $\Delta\mathbf{R} = \mathbf{R} - \mathbf{R}'$ between the guiding center of the electron $\mathbf{R}$ and that of the hole $\mathbf{R}'$ and the orientation of the magnetic field $\mathbf{e}_z = \mathbf{B}/|B|$, remains a constant of motion even in the presence of a magnetic field, contrary to the wave vectors of the original (charged) constituents of the pair. In the central $n = 0$ LL, this yields the magnon dispersion (Kallin and Halperin, 1984; Yang et al., 2006; Doretto and Smith, 2007)

$$E_{\mathbf{q}} = \sqrt{\frac{\pi}{2}} \frac{e^2}{\varepsilon l_B} \left[1 - e^{-q^2 l_B^2/4} I_0\left(\frac{q^2 l_B^2}{2}\right)\right], \tag{17}$$

in terms of the modified Bessel function $I_0(x)$. The two limits for small and large wave vectors are readily understood; at small wave vectors, one retrieves the usual quadratic

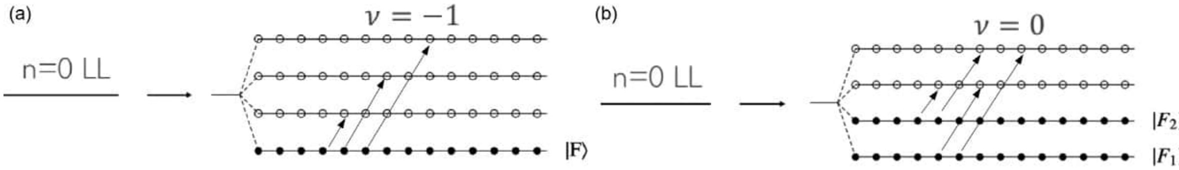

Fig. 4 Generic magnons at (a) $\nu = -1$ and (b) $\nu = 0$. The $n = 0$ LL hosts four spin-valley copies that are separated for illustration reasons while they remain degenerate in energy in the absence of explicit SU(4)-symmetry-breaking terms. At $\nu = -1$ (and its particle-hole-symmetric situation at $\nu = 1$) one of the spin-valley components is completely occupied and one obtains three magnon modes. At $\nu = 0$, two components are filled and one has four magnon modes.

$$E_{q\to 0} \simeq \frac{\rho_s}{2} q^2 l_B^2 \tag{18}$$

behavior of the Goldstone mode, in terms of the spin stiffness

$$\rho_s = \frac{1}{16\sqrt{2\pi}} \frac{e^2}{\varepsilon l_B}, \tag{19}$$

while at large wave vectors, the dispersion saturates at twice the exchange gap $E_X = \sqrt{\pi/8} e^2/\varepsilon l_B$,

$$E_{ql_B \gg 1} \simeq \left[2\sqrt{\frac{\pi}{8}} - \frac{1}{q l_B^2} \right] \frac{e^2}{\varepsilon l_B}. \tag{20}$$

Because the exchange gap E_X can be viewed as the energy to create a quasiparticle or a quasihole with a reversed spin, $2E_X$ is nothing other than the particle-hole dissociation energy, while at finite wave vectors with $ql_B > 1$ one needs to take into account the binding energy between the electron and the hole, which is given by the Coulomb energy $E_{\mathrm{Coul}} = e^2/\varepsilon \mid \Delta \mathbf{R} \mid \; = e^2/\varepsilon q l_B^2$ in the second term of the dispersion relation.

Similarly to the QHFM ground states, the magnon spectrum becomes modified when the anisotropic terms (15) are taken into account. Because the degeneracy between the SU(4) QHFM states is lifted, the magnons depend on the precise form of the chosen state. Furthermore, the magnons become generally gapped, e.g., by the Zeeman term for the spin magnons and the terms u_z and $u_\perp$ for the valley magnons (Atteia and Goerbig, 2021). Most saliently, the magnon dispersion may even change its wave-vector dependence, e.g., in the KD phase. Indeed, in this phase the energy functional, even in the presence of the anisotropic terms, remains U(1)-symmetric, while this symmetry is spontaneously broken by the intervalley coherence in the KD phase. This yields a particular gapless magnon with a dispersion that is linear in the wave vector.

Finally, the above energy arguments remain valid at charge neutrality ($\nu = 0$), but the counting of the possible modes is changed. Because there are now two fully occupied spin-valley components (and two empty ones), one finds four possible magnon modes (Yang et al., 2006; Lambert and Côté, 2013; Wu et al., 2015; Wei et al., 2021). However, for an SU(4)-symmetric Coulomb interaction, the magnon dispersion is still given by Eq. (17), and again some of the different magnon modes become gapped in the presence of an explicit spin-valley anisotropy (15).

Skyrmions

A very particular type of topological objects are formed on top of the QHFM when additional charges are added to the ground states at $\nu = -1$ or $\nu = 0$. Consider an electron added to a perfect QHFM state at $\nu = 0$. Naturally, this additional electron must occupy a spin-valley component that was initially completely empty. From an exchange-energy point of view it is however much more favorable that this *spin-valley flip* does not only concern the additional electron, but the latter encourages electrons in its vicinity to do likewise such as to minimize the overall exchange energy. This is depicted in Fig. 5 for a generic situation at $\nu = 0$. The skyrmion is a texture that appeals to one of the two originally occupied spin-valley components (here $|F_2\rangle$) and one of the unoccupied ones (here $|C_2\rangle$). As in the QHFM ground state, these components can be any type of superposition of the original spin-valley components, but all states, the occupied ones $|F_1\rangle$ and $|F_2\rangle$ as well as the unoccupied ones $|C_1\rangle$ and $|C_2\rangle$, must be mutually orthogonal. While the QHFM ground state fixes the states $|F_1\rangle$ and $|F_2\rangle$, there is yet a certain choice for the spinor $|C_2\rangle$ that describes the spin-valley polarization at the skyrmion core. Indeed, the skyrmion can be generically described by the field

$$\left| Z(x+iy) \right\rangle = \frac{1}{\sqrt{1 + (x^2+y^2)/|\lambda|^2}} \left(\left| C_2 \right\rangle + \frac{x+iy}{\lambda} \left| F_2 \right\rangle \right), \tag{21}$$

where $|\lambda|$ denotes the typical skyrmion size. As for the QHFM states, the lowest-energy skyrmion that is realized in the system depends on the SU(4)-symmetry-breaking terms (15), and both at $\nu = -1$ (Lian et al., 2016; Lian and Goerbig, 2017) and at $\nu = 0$ (Atteia et al., 2021), one finds a whole *skyrmion zoo* that is not presented here. However, it needs to be underlined that very recently there has been first spectroscopic evidence for the presence of skyrmions in graphene at $\nu = 0$ (Liu et al., 2022), in

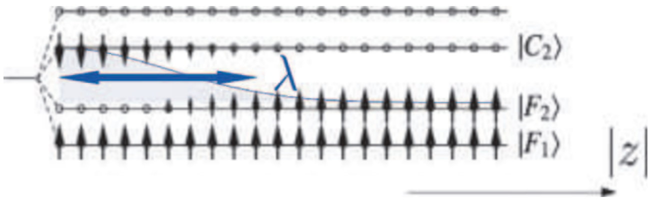

Fig. 5 Generic skyrmion at $\nu = 0$. The sublevels $|F_1\rangle$ and $|F_2\rangle$ are occupied in the QHFM ground state. The skyrmion consist of an electron that is promoted from the spin-valley component $|F_2\rangle$ to the initially unoccupied component $|C_2\rangle$ at the skyrmion core $z = 0$. Slightly away from the core, the electrons are in a superposition of $|C_2\rangle$ and $|F_2\rangle$, the relative weight of which changes upon increase of $|z|$. The typical size $|\lambda|$ indicates the equal-weight superposition of the two components, while at $|z| \to \infty$ the superposition converges to the QHFM background $|F_2\rangle$. At all distances, $|F_1\rangle$ remains unchanged as well as the unoccupied spectator component $|C_2\rangle$.

scanning-tunneling spectroscopy. While the QHFM is likely to be a KD phase, the spin-valley pattern at the skyrmion core is reminiscent of the CAF phase. Both phases have a particular signature in the sublattice occupation that has been precisely measured in the experiment.

Fractional quantum Hall states

In order to describe the four-component FQHE in graphene, one may start with a four-component generalization of Halperin's wave function (Goerbig and Regnault, 2007),

$$\psi_{m_1,\ldots,m_4;n_{\alpha\beta}} = \phi^{L}_{m_1,\ldots,m_4}\phi^{\text{inter}}_{n_{\alpha\beta}} \exp\left(-\sum_{\alpha=1}^{4}\sum_{j_\alpha=1}^{N_\alpha}\left|z_{j_\alpha}\right|^2/4l_B^2\right), \tag{22}$$

where

$$\phi^{L}_{m_1,\ldots,m_4} = \sum_{\alpha=1}^{4}\sum_{k_\alpha<l_\alpha}^{N_\alpha}\left(z_{k_\alpha} - z_{l_\alpha}\right)^{m_\alpha} \tag{23}$$

is the product of 4 Laughlin wave functions for each of the four components $\alpha, \beta = |\uparrow, K\rangle, |\uparrow, K'\rangle, |\downarrow, K\rangle$, and $|\downarrow, K'\rangle$. In the absence of inter-component correlations, which are taken into account in the term

$$\phi^{\text{inter}}_{n_{\alpha\beta}} = \prod_{\alpha<\beta}^{4}\prod_{k_\alpha}^{N_\alpha}\prod_{l_\beta}^{N_\beta}\left(z_{k_\alpha} - z_{l_\beta}\right)^{n_{\alpha\beta}}, \tag{24}$$

the exponents m_α are directly related to the component filling factors $\nu_\alpha = N_\alpha/N_B = 1/m_\alpha$, which enter the total filling factor

$$\nu = \sum_{\alpha}\nu_\alpha - 2, \tag{25}$$

in terms of the number of electrons per component N_α and the total number of electron N_{el}. The offset of 2 in the expression for the total filling factor is due to the fact that the $n = 0$ LL in graphene is completely empty (for $\nu_\alpha = 0$) at $\nu = -2$ because charge neutrality ($\nu = 0$) corresponds to a globally half-filled $n = 0$ LL, as mentioned in section "Landau levels and the integer quantum Hall effect in graphene". In general, however, the total filling factor for a four-component Halperin wave function depends not only on the exponents m_α but also on the inter-component correlations $n_{\alpha\beta}$, via the relation

$$1 = m_\alpha\nu_\alpha = \sum_{\beta\neq\alpha} n_{\alpha\beta}\nu_\beta. \tag{26}$$

Notice that the exponents m_α and $n_{\alpha\beta}$ induce correlations between the electrons. While the Pauli principle (i.e., the antisymmetry of the fermionic wave functions) only requires $m_\alpha = 1$ and does not constrain the inter-component correlations, the Halperin wave function (22) indicates that the electronic density of an electron of type α approaching another one of the same type is suppressed as $\sim r^{2m_\alpha}$, and it is suppressed as $\sim r^{2n_{\alpha\beta}}$ if an electron of type α approaches one of type β. These correlations are therefore globally favorable for the repulsive Coulomb interaction. However, not all combinations of exponents are eligible for physically relevant wave functions: if the inter-component correlations become stronger than the intra-component ones, the Halperin wave function no longer describes a spatially homogeneous electronic system but electrons in different components have a tendency to undergo a phase separation (de Gail et al., 2008). The four-component CF wave functions are more complex to write down, but the basic idea is to first rewrite a multi-component wave function of Halperin's type as a product

$$\psi = \phi_{\nu^*=1}\phi^{2s}_{\text{SU}(4)} \exp\left(-\sum_{\alpha=1}^{4}\sum_{j_\alpha=1}^{N_\alpha}\left|z_{j_\alpha}\right|^2/4l_B^2\right), \tag{27}$$

as a vortex part $\phi^{2s}_{\text{SU}(4)}$, and a wave function $\phi_{\nu^*=1}$ at a putative filling factor $\nu^* = 1$ for electrons of one, several or all components. In a second step, this wave function is then replaced by one for $\nu^* = p$ LLs that are called CF LLs (Tőke and Jain, 2007). Since this wave function has non-analytical components, i.e., components in LLs other than $n = 0$, the new wave function needs to be ultimately projected into this LL.

The 1/3-family of fractional states in graphene

The generalized Halperin wave functions (22) may be used as a first approach to understand the particular form of the 1/3-family of fractional states, which has been observed in graphene on a h-BN substrate and that has been interpreted as a manifestation of the particular SU(4) symmetry of the FQHE (Dean et al., 2011). Indeed, if the fourfold spin-valley degeneracy were lifted by external perturbations such as the Zeeman effect, which favors a particular spin orientation, all four subbranches of the LLs would be well separated in energy. In this case, one may argue that the electrons in each of the subbranches form correlated states independently of the other (completely filled or completely empty) subbranches. The latter would be electronically inert similarly to the other LLs that are remote in energy from the partially filled one, as we have discussed in section "Electrons in a single Landau level" where we constructed the low-energy model of electrons restricted to a single LL. In this case, one would expect to observe all spin-valley copies of the 1/3 Laughlin state at $\nu = \pm 5/3$, $\pm 4/3$, $\pm 2/3$, $\pm 1/3$ in the $n = 0$ LL. However, this was not observed in the experiment (Dean et al., 2011), where the $\pm 5/3$-states were almost absent in the measurement. In later experiments, at larger magnetic fields, the latter states became more pronounced (Polshyn et al., 2018), in line with the intuitive expectations that at higher magnetic field the subbranches are better separated in energy (due to a $\propto B$ scaling with the magnetic field, in contrast to the expected $\sqrt{B}$-scaling of the Coulomb interaction scale $e^2/\varepsilon l_B$) such that a one-component treatment in terms of Laughlin wave functions becomes more reliable.

In order to describe the $-5/3$-state (and its particle-hole symmetric one at $\nu = +5/3$), one can use the Halperin wave function (22), in which one sets all exponents $\mu_\alpha = n_{\alpha\beta} = 3$. In this case, one may interpret the state as an overall Laughlin wave function that is built up from all electrons regardless of the spin-valley components they occupy. In spite of its similarity with the usual one-component Laughlin state, one needs to emphasize that it is an intrinsic multi-component state with an internal SU(4) spin-valley symmetry, which allows one to distribute the electrons freely over the different spin-valley components. This freedom has consequences in the excitation spectrum in the form of generalized spin waves, similarly to the QHFM states at $\nu = \pm 1$ (see section "Spin-valley quantum Hall ferromagnets"): there are altogether three modes, a spin magnon, a valley magnon and a mixed spin-valley mode, while the usual one-component Laughlin wave function would not have such excitations. The presence of these modes is likely to be at the origin of the reduced robustness of the $\pm 5/3$ states as compared to the other ones of the 1/3 family.

The states at $\pm 1/3$ can also be understood in terms of the generalized Halperin wave functions (Papić et al., 2010). For illustration, consider a prominent Zeeman effect that favors a spin polarization over a valley polarization.[4] In this case, we have the exponents $m_\alpha = 1$ for $\alpha = |\uparrow, K\rangle$ and $|\uparrow, K'\rangle$, while we have $m_\alpha = 3$ for $\alpha = |\downarrow, K\rangle$ and $|\downarrow, K'\rangle$. Furthermore, there are no correlations between $|\uparrow, K\rangle$ and $|\uparrow, K'\rangle$ such that the corresponding exponent is $n_{12} = 0$, while it is $n_{34} = 3$ for the correlations between $|\downarrow, K\rangle$ and $|\downarrow, K'\rangle$. Finally, there are no correlations between states of different spin orientation, $n_{13} = n_{14} = n_{23} = n_{24} = 0$. Similarly to the $\pm 5/3$-states, this state has a residual symmetry in the $s = \downarrow$-spin branch since one can freely distribute the electrons of this spin orientation over the two valleys, i.e., one is confronted with a residual SU(2) symmetry that is spontaneously broken by the formation of the state and that supports thus a valley magnon. In addition to the number of generalized spin waves, there is an important difference between the Halperin states at $\nu = \pm 5/3$ and $\nu = \pm 1/3$: while the former is an eigenstate of the SU(4)-symmetric Hamiltonian, the latter is not. It therefore requires an explicit spin-valley SU(4) symmetry breaking, e.g., in the form of the above-mentioned Zeeman term Δ_Z, to stabilize this state. However, a term as small as $\Delta_Z/(e^2/\varepsilon l_B) \simeq 0.01$ is sufficient to stabilize the state (Papić et al., 2010). Because $e^2/\varepsilon l_B \simeq 109\sqrt{B[\mathrm{T}]}$ K for graphene on h-BN and $\Delta_Z \simeq 1.2B[\mathrm{T}]$ K, this condition is fulfilled for fields as small as $B \sim 1$ T, below the field values where the 1/3-states have been observed experimentally (Dean et al., 2011; Polshyn et al., 2018).

While numerical studies are less conclusive about their relevance at $\nu = \pm 2/3$ and $\pm 4/3$ (Wu et al., 2015; Le and Jolicoeur, 2022), Halperin wave functions may also be constructed for these filling factors, e.g., at $\nu = \pm 2/3$ with $m_1 = 1$, $m_2 = m_3 = m_4 = 3$, $n_{1\beta} = 0$ and $n_{\alpha\beta} = 3$ elsewise, which amounts to having one spin-valley subbranch completely filled, while the electrons in the other three subbranches form a Laughlin state with an SU(3) symmetry. As for the $\pm 1/3$-states, these states are not eigenstates of the SU(4)-symmetric Coulomb interaction and therefore require a (small) spin-valley degeneracy lifting. Similarly, the $\nu = \pm 4/3$ states may, in a first step, be approached in terms of a Lauglin state composed of electrons (or holes) in a single spin-valley subbranch, $m_1 = 3$, while the other intra-component exponents are $m_\alpha = 1$, and there are no inter-component correlations, i.e., $n_{\alpha\beta} = 0$. From this perspective, the $\nu = \pm 4/3$ states are those that are closest to the one-component Laughlin states.

However, it is noteworthy to mention that there are other candidate states for $\nu = \pm 4/3$, and it is unlikely that the ground state be described in terms of these Halperin wave functions. Indeed, exact-diagonalization studies at $\nu = 2/3 - 2 = -4/3$ in graphene have shown that the state is a singlet in one of the channels (spin or valley) and fully polarized in the other one (Apalkov and Chakraborty, 2006; Tőke and Jain, 2007; Goerbig and Regnault, 2007), and the spectra show magnon-type modes. Notice that, due to the large number of components, one may construct other Halperin wave functions for this filling factor, as for example a state with $m_\alpha = 3$ and $n_{\alpha\beta} = 1$, or else one with $m_\alpha = 3$, $n_{\alpha\beta} = n_{13} = n_{24} = 3$ for the correlations inside each valley and $n_{12} = n_{34} = n_{14} = n_{23} = 0$, i.e., no correlations for electrons in different valleys. While the latter trial state supports the numerically found magnon mode and has the correct ground-state degeneracy, there are no such modes in the former state in which the number of electrons is fixed in all components. Finally, one needs to emphasize that the different states are in competition with one another and that explicit subordinate spin-valley symmetry-breaking terms become relevant for the choice between these states, as it has just recently been shown in exact-diagonalization studies on the 1/3-family in graphene (Le and Jolicoeur, 2022), and in some cases trial states are required to be constructed beyond the Halperin or multi-component CF states (Wu et al., 2015).

The particularity of the CF series p/(2sp + 1) in graphene

The discussion of the 1/3-FQHE states in graphene has shown to what extent the spin-valley degrees of freedom are relevant in understanding the effect. While one might think, in view of these results, that generally the system chooses a maximal spin-valley polarization compatible with the total filling factor, numerical studies of the CF series at $\nu = p/(2sp + 1)$—2 have shown that the situation is more involved (Tőke and Jain, 2007). From an electronic point of view, one may always find a CF wave function with complete spin-valley polarization for these filling factors, in which the CFs occupy p CF LLs (Jain, 1989), as mentioned in the introduction. This, however, does not seem to be the scenario chosen by Nature. Instead, at $p = 2$ ($\nu = 2/5–2$), the electrons prefer to occupy another spin-valley branch instead of filling a second CF LL. This situation may either be described within an SU(4) spin-valley generalization of Jain's CF wave functions (Tőke and Jain, 2007) or in terms of the generalized Halperin wave function (22). It needs to be emphasized that both descriptions are equivalent for $p = 1, \ldots, 4$. Consider the situation of a small Zeeman effect that favors a spin over a valley polarization. In this case, the state at $\nu = 2/5–2$ may be described by the wave function (22) with $m_\alpha = 3$, $n_{\alpha\beta} = n_{13} = n_{24} = 3$ for all inter-component correlations inside each valley and $n_{\alpha\beta} = n_{12} = n_{34} = n_{14} = n_{23} = 2$. This state is a valley singlet, but the spin can be oriented freely for electrons inside each valley, i.e., the state has a residual $SU(2) \times SU(2)$ symmetry, and there are two spin-wave modes, one in each of the valleys.

---

[4] The argument does not depend on this choice, however, and one may exchange spin and valley or any two components.

A particularly interesting situation arises at $\nu = 4/9–2$, where all four components are filled such that the state is an SU(4) singlet with no magnon modes. This situation can be described in terms of the generalized Halperin wave function (22) with $m_\alpha = 3$ and $n_{\alpha\beta} = 2$ for all inter-component correlations, and numerical calculations show that this unpolarized state is indeed favored energetically over a completely polarized CF state (Tőke and Jain, 2007).

It is important to emphasize that such a completely unpolarized state or states with only partial polarization occur in this filling factor range of $-2 < \nu < -1$ (and by particle-hole symmetry in $1 < \nu < 2$). This is not in line with common expectations from the often used single-particle picture, where one is tempted to successively populate the different spin-valley branches separated in energy by Zeeman-type terms. As mentioned above, these terms are much smaller than the leading Coulomb interaction scale, and it is the latter that needs to be considered first. Also the picture of an exchange-driven maximal spin-valley polarization needs to be taken with care. While this picture is applicable at integer fillings such as $\nu = 0$ and ± 1 (and integer fillings different form the graphene IQHE series $\nu = \pm 2(2n + 1)$), where the exchange energy generates the QHFM states, the numerical studies of the CF series $p/(2sp + 1)$ in graphene indicate that the special correlation energy built in the FQHE wave functions generally outcasts the exchange energy and thus gives rise to an unexpected non-monotonic behavior of the spin-valley polarization if only the SU(4)-symmetric Coulomb repulsion is taken into account. However, as it has already been mentioned in the discussion of the 1/3-family, the precise nature of the CF states realized in a typical experimental situation may sensitively depend on the explicit symmetry-breaking terms. The energies of the different—polarized or unpolarized—trial states may be extremely close so that the latter subordinate terms are decisive in the choice of a particular type of states even if they are not the relevant scale in the formation of these states (Abanin et al., 2013; Le and Jolicoeur, 2022).

Even-denominator states

A particular FQHE state is the even-denominator state observed at $\nu = 5/2$ and 7/2 in 2D quantum-Hall systems in GaAs heterostructures (Willett et al., 1987). From an experimental point of view, it seems settled now that they are spin-polarized (Dean et al., 2008), as expected for the so-called Pfaffian state proposed by Moore and Read (Moore and Read, 1991). These states, however, observed in the $n = 1$ LL require a particular form of the effective interaction potential that is in line with that (10) for $n = 1$ in the usual 2D electron system.[5] Right from the beginning of graphene research, it was realized that the particular form of the effective interaction potential (10), if the appropriate form factors are taken into account, does not allow for the stabilization of the Moore-Read Pfaffian state (Goerbig et al., 2006). However, it is possible to construct a multicomponent Halperin wave function also for this filling factor, e.g., with $m_\alpha = 3$ and again $n_{\alpha\beta} = n_{13} = n_{24} = 3$ for all intercomponent exponents inside each valley and $n_{\alpha\beta} = n_{12} = n_{34} = n_{14} = n_{23} = 1$. Alternatively, if a valley-degeneracy lifting outcasts the Zeeman effect, one may exchange the role of the spin and valley indices. Recent capacitance measurements have shown that even-denominator states at $\nu = \pm 1/2$, $\pm 1/4$ can indeed be stabilized in the vicinity of a transition between two different spin-valley orders (Zibrov et al., 2018), which gives credit to the multi-component interpretation of the effect (Narayanan et al., 2018).

Electron crystals

While the FQHE states are certainly the most interesting correlated phases, due to their exotic quasiparticle excitations, they are, along with the QHFM phases, not the only correlated electronic phases that one encounters in partially filled LLs. Indeed, right after the discovery of the IQHE in the 1980s, some researchers proposed a Wigner crystal to be the ground state in partially filled LLs, in order to minimize the repulsive Coulomb potential. This classical state is indeed realized at low filling factors, in which case the magnetic length becomes much smaller than the average electronic spacing so that quantum-mechanical effects due to the electronic wave-function overlap can be neglected. From an experimental point of view, it is nevertheless difficult to identify an electronic solid in conventional transport measurements: the electronic crystals are collectively pinned by the underlying impurities and therefore yield an insulating response in the same manner as an individual electronic localization does.

From a theoretical point of view, electronic crystals become most interesting in higher LLs, where one does not only encounter the Wigner crystal but also more exotic bubble crystals, in which a lattice site is occupied by more than one electron, or stripe crystals. The phases have been theoretically predicted to arise in higher LLs in conventional GaAs heterostructures (Fogler et al., 1996; Moessner and Chalker, 1996), where e.g., the stripe crystals yield a highly anisotropic electronic transport in the LLs $n = 2$ (Lilly et al., 1999; Du et al., 1999). One of the most salient features of electronic crystals in higher LLs is the so-called reentrant IQHE, which was discovered in GaAs heterostructures (Cooper et al., 1999; Eisenstein et al., 2002). The effect consists of a non-monotonic behavior of the Hall resistance, in which a plateau corresponding to a FQHE is flanked by two plateaus at an

---

[5] From a technical point of view, this can be shown within an expansion of the effective interaction potential in Haldane's pseudopotentials (Haldane, 1983).

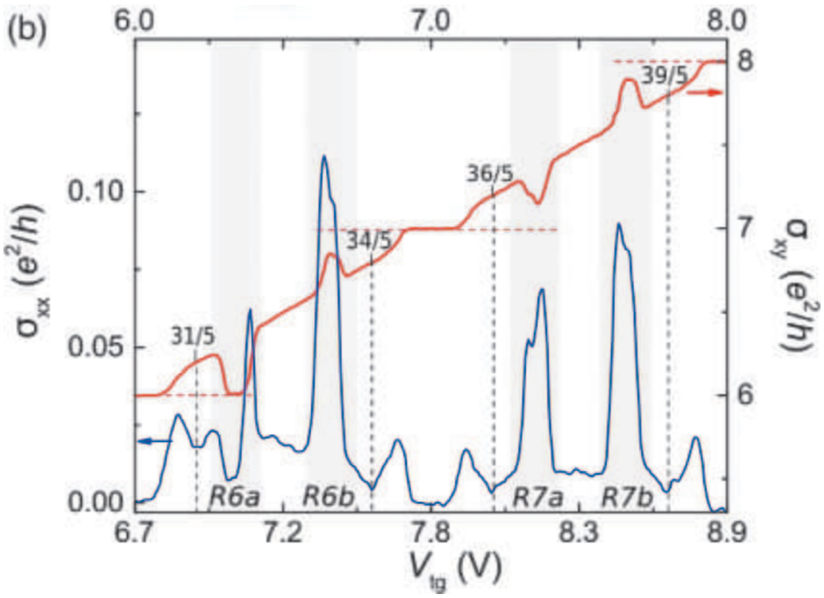

Fig. 6 Reentrant IQHE in graphene in the $n = 2$ LL. The non-monotonic behavior of the Hall conductance (red curve) as a function of the gate-voltage-induced electronic density is clearly visible at the four positions R6a, R6b, R7a, and R7b, where the conductances tend to their neighboring integer values at $j = 6$, 7 and 8 Adapted from Chen S, Ribeiro-Palau R, Yang K,Watanabe K, Taniguchi T, Hone J, Goerbig MO, Dean CR (2019) Competing fractional quantum hall and electron solid phases in graphene. *Physical Review Letters* 122: 026802. https://doi.org/10.1103/PhysRevLett.122.026802.

integer value of j. The corresponding effect in graphene, which has been observed in 2019 (Chen et al., 2019), is shown in Fig. 6, where e.g., the 31/5 state (at 1/5 filling of the $n = 2$ LL) is flanked by two plateaus at $j = 6$. While the plateau on the left-hand side can be understood in terms of single-particle localization of the few electrons occupying the lowest spin-valley branch of the $n = 2$ LL, this is unlikely the case on the right-hand side (around $V_{tg} \simeq 7$ V). Theoretical calculations (Knoester et al., 2016; Chen et al., 2019) indicate that the FQHE 1/5 Laughlin state competes with a Wigner crystal that is extremely close in energy at this filling factor. Precisely at $\nu = 31/5$, the FQHE state is lower in energy than the Wigner crystal, but once the filling factor is swept away from this precise value, the excited (gapped) quasiparticles or quasiholes raise the energy of the liquid states rapidly above that of the Wigner crystal, which becomes thus the ground state on both sides of the FQHE state and that gives rise to the insulating (IQHE) response there.

Conclusion

In conclusion, the observation of the FQHE and related correlated electronic phases in graphene corroborates the universality of the phenomenon: it is due to repulsive electronic interactions between electrons inside a single partially filled LL, in which the electrons' kinetic energy is frozen. In addition to this flat-band scenario, which one may encounter also in other situations in condensed-matter systems, the chirality of the quantum states, inherited from the classical cyclotron motion with a specific sense imposed by the orientation of the magnetic field, turns out to play an essential role in the formation of these exotic correlated states. The particularity of graphene is twofold: first, the states inherit the fourfold spin-valley degeneracy from the low-energy bands of graphene, and the associated SU(4) symmetry is to great extent respected by the leading Coulomb repulsion; second, the specific spinorial form of the wave functions of graphene electrons yields slightly different wave-function overlaps as compared to the more conventional (GaAs) semiconductor heterostructures. Similarly, bilayer graphene is yet another version of a multi-component quantum-Hall system; in addition to the fourfold spin-valley degeneracy, the LLs $n = 0$ and $n = 1$ are situated at zero energy, and one is therefore confronted with an eightfold degeneracy here (Novoselov et al., 2006). However, since the wave functions are different in the two LLs $n = 0$ and $n = 1$, the Coulomb interaction is not symmetric in this index so that there is no SU(8) symmetry as one might have expected at the beginning. Furthermore, the energy difference between the two layers and thus indirectly a *valley Zeeman effect* can be tuned by an electric field applied perpendicular to the 2D system such that there is an interesting controllable tunability in this system, as it has been proposed theoretically (Apalkov and Chakraborty, 2010) and measured experimentally (Maher et al., 2014). In this framework it is also interesting to notice that the situation between monolayer and bilayer graphene can to some extent be interpolated in layered systems where two graphene monolayers are separated by an insulating h-BN film of variable thickness. While for large thickness ($d \gg l_B$) the monolayers are essentially decoupled, and one would expect simply to measure twice a monolayer quantum Hall effect, the interlayer coupling becomes stronger in the opposite limit ($d \ll l_B$) of thin h-BN layers. In the latter limit, novel interlayer-correlated FQHE states have indeed been observed experimentally (Liu et al., 2019).

We have mainly explored, in this short review, the consequences of the SU(4) symmetry, which does not only impact in an unexpected manner the FQHE states in the form of highly non-monotonic spin-valley polarizations when increasing the filling factor in the zero-energy $n = 0$ LL, but also the QHFM states that are formed at integer fillings beyond the particular graphene-IQHE sequence $\nu = \pm 2(2n + 1)$. The QHFM phases, which are also relevant for many FQHE states that come along with certain forms of spin-valley polarization, host not only novel magnon types that are absent in conventional quantum-Hall systems with only the spin as an internal degree of freedom, but also a rich zoo of exotic skyrmions. While the theoretical classification of the QHFM states, as well as the spin-valley magnons and the skyrmions, is now rather complete, as a function of the subleading SU(4)-symmetry-breaking terms, the experimental investigation of these states has just started. As for the skyrmions, a promising first step has been made by scanning-tunneling-spectroscopic measurements that are capable of monitoring the particular sublattice occupation for valley-skyrmions with a spatially varying valley polarization (Liu et al., 2022; Coissard et al., 2022). In the case of magnons, a very interesting way of probing these collective excitations is that via non-local transport measurements with a high voltage bias between the source and the drain. While this non-local transport is expected to happen only at the edges (at low bias), it has been shown that at higher bias, above the Zeeman energy scale, magnons can be excited at the edges that propagate through the sample bulk and relax at another local gate tuned at $\nu = \pm 2$ (Stepanov et al., 2018; Wei et al., 2018; Assouline et al., 2021; Pierce et al., 2022). This opens the perspective for a resistively-detected means of probing magnons in quantum-Hall systems, namely in graphene.

It is also interesting to mention that in line with the discovery of graphene as a particular 2D electronic system, other 2D crystals with unexpected electronic properties have been isolated. Most importantly, one should mention the family of 2D transition-metal dichalcogenides (e.g., MoS_2, $MoSe_2$, WS_2 or WSe_2). Similarly to graphene, the low-energy electronic properties of these materials may be described in terms of Dirac fermions, albeit *massive* Dirac fermions now. Moreover, these materials show a significant spin-orbit interaction, most prominently in the valence band so that the spin-valley components are frozen there. Namely, the $n = 0$ LL happens to occur in a single spin-valley component over a large magnetic-field and density range. In contrast to graphene, this allows for the study of the FQHE and other correlated phases in the ideal single-component limit for which the original theoretical trial wave functions (Laughlin, 1983; Jain, 1989; Moore and Read, 1991; Greiter et al., 1991) have been constructed. Recent compressibility measurements on high-qualityWSe_2 samples have identified a large number of FQHE (Shi et al., 2020) and are a promising path to more detailed studies of the FQHE in these materials, corroborating both the universality of the phenomenon in 2D electronic systems in a strong magnetic field and the specificities of the different systems in terms of multi- vs. one-component manifestations of the effect.

References

Abanin DA, Feldman BE, Yacoby A, and Halperin BI (2013) Fractional and integer quantum hall effects in the zeroth landau level in graphene. *Physical Review B* 88: 115407. https://doi.org/10.1103/PhysRevB.88.115407.

Alicea J and Fisher MPA (2006) Graphene integer quantum hall effect in the ferromagnetic and paramagnetic regimes. *Physical Review B* 74: 075422. https://doi.org/10.1103/PhysRevB.74.075422.

Apalkov VM and Chakraborty T (2006) Fractional quantum hall states of dirac electrons in graphene. *Physical Review Letters* 97: 126801. https://doi.org/10.1103/PhysRevLett.97.126801.

Apalkov VM and Chakraborty T (2010) Controllable driven phase transitions in fractional quantum hall states in bilayer graphene. *Physical Review Letters* 105: 036801.

Assouline A, Jo M, Brasseur P, Watanabe K, Taniguchi T, Jolicoeur T, Glattli DC, Kumada N, Roche P, Parmentier FD, and Roulleau P (2021) Excitonic nature of magnons in a quantum hall ferromagnet. *Nature Physics* 17: 1369–1374. https://doi.org/10.1038/s41567-021-01411-z.

Atteia J and Goerbig MO (2021) Su(4) spin waves in the $\nu = \pm 1$ quantum hall ferromagnet in graphene. *Physical Review B* 103: 195413. https://doi.org/10.1103/PhysRevB.103.195413.

Atteia J, Lian Y, and Goerbig MO (2021) Skyrmion zoo in graphene at charge neutrality in a strong magnetic field. *Physical Review B* 103: 035403. https://doi.org/10.1103/PhysRevB.103.035403.

Bartolomei H, Kumar M, Bisognin R, Marguerite A, Berroir JM, Bocquillon E, Plaçais B, Cavanna A, Dong Q, Gennser U, Jin Y, and Fève G (2020) Fractional statistics in anyon collisions. *Science* 368: 173–177. https://doi.org/10.1126/science.aaz5601.

Bolotin KI, Ghahari F, Shulman MD, Stormer HL, and Kim P (2009) Observation of the fractional quantum hall effect in graphene. *Nature* 462: 196–199. https://doi.org/10.1038/nature08582.

Chen S, Ribeiro-Palau R, Yang K, Watanabe K, Taniguchi T, Hone J, Goerbig MO, and Dean CR (2019) Competing fractional quantum hall and electron solid phases in graphene. *Physical Review Letters* 122: 026802. https://doi.org/10.1103/PhysRevLett.122.026802.

Coissard A, Wander D, Vignaud H, Grushin AG, Repellin C, Watanabe K, Taniguchi T, Gay F, Winkelmann C, Courtois H, Sellier H, and Sacépé B (2022) Imaging tunable quantum Hall broken-symmetry orders in charge-neutral graphene. *Nature* 605: 51–56. https://doi.org/10.1038/s41586-022-04513-7.

Cooper KB, Lilly MP, Eisenstein JP, Pfeiffer LN, and West KW (1999) Insulating phases of two-dimensional electrons in high landau levels: Observation of sharp thresholds to conduction. *Physical Review B* 60: R11285–R11288. https://doi.org/10.1103/PhysRevB.60.R11285.

de Gail R, Regnault N, and Goerbig MO (2008) Plasma picture of the fractional quantum hall effect with internal SU(*k*) symmetries. *Physical Review B* 77: 165310. https://doi.org/10.1103/PhysRevB.77.165310.

de Picciotto R, Reznikov M, Heiblum M, Umansky V, Bunin G, and Mahalu D (1997) Direct observation of a fractional charge. *Nature* 389: 162–164. https://doi.org/10.1038/38241.

Dean CR, Piot BA, Hayden P, Das Sarma S, Gervais G, Pfeiffer LN, and West KW (2008) Intrinsic gap of the $\nu = 5/2$ fractional quantum hall state. *Physical Review Letters* 100: 146803. https://doi.org/10.1103/PhysRevLett.100.146803.

Dean CR, Young AF, Cadden-Zimansky P, Wang L, Ren H, Watanabe K, Taniguchi T, Kim P, Hone J, and Shepard KL (2011) Multicomponent fractional quantum hall effect in graphene. *Nature Physics* 7: 693–696. https://doi.org/10.1038/nphys2007.

Doretto RL and Smith CM (2007) Quantum hall ferromagnetism in graphene: Su(4) bosonization approach. *Physical Review B* 76: 195431. https://doi.org/10.1103/PhysRevB.76.195431.

Douçot B, Goerbig MO, Lederer P, and Moessner R (2008) Entanglement skyrmions in multicomponent quantum hall systems. *Physical Review B* 78: 195327. https://doi.org/10.1103/PhysRevB.78.195327.

Du R, Tsui D, Stormer H, Pfeiffer L, Baldwin K, and West K (1999) Strongly anisotropic transport in higher two-dimensional landau levels. *Solid State Communications* 109: 389–394. https://doi.org/10.1016/S0038-1098(98)00578-X.

Du X, Skachko I, Duerr F, Luican A, and Andrei EY (2009) Fractional quantum hall effect and insulating phase of dirac electrons in graphene. *Nature* 462: 192–195. https://doi.org/10.1038/nature08522.

Eisenstein JP, Cooper KB, Pfeiffer LN, and West KW (2002) Insulating and fractional quantum hall states in the first excited landau level. *Physical Review Letters* 88: 076801. https://doi.org/10.1103/PhysRevLett.88.076801.

Feldman BE, Krauss B, Smet JH, and Yacoby A (2012) Unconventional sequence of fractional quantum hall states in suspended graphene. *Science* 337: 1196–1199. https://doi.org/10.1126/science.1224784.

Fogler MM, Koulakov AA, and Shklovskii BI (1996) Ground state of a two-dimensional electron liquid in a weak magnetic field. *Physical Review B* 54: 1853–1871. https://doi.org/10.1103/PhysRevB.54.1853.

Fuchs JN and Lederer P (2007) Spontaneous parity breaking of graphene in the quantum hall regime. *Physical Review Letters* 98: 016803. https://doi.org/10.1103/PhysRevLett.98.016803.

Girvin SM, MacDonald AH, and Platzman PM (1986) Magneto-roton theory of collective excitations in the fractional quantum hall effect. *Physical Review B* 33: 2481–2494. https://doi.org/10.1103/PhysRevB.33.2481.

Goerbig MO (2011) Electronic properties of graphene in a strong magnetic field. *Reviews of Modern Physics* 83: 1193–1243. https://doi.org/10.1103/RevModPhys.83.1193.

Goerbig MO and Regnault N (2007) Analysis of a SU(4) generalization of halperin's wave function as an approach towards a SU(4) fractional quantum hall effect in graphene sheets. *Physical Review B* 75: 241405. https://doi.org/10.1103/PhysRevB.75.241405.

Goerbig MO, Moessner R, and Douçot B (2006) Electron interactions in graphene in a strong magnetic field. *Physical Review B* 74: 161407. https://doi.org/10.1103/PhysRevB.74.161407.

Greiter M, Wen XG, and Wilczek F (1991) Paired hall state at half filling. *Physical Review Letters* 66: 3205–3208. https://doi.org/10.1103/PhysRevLett.66.3205.

Haldane FDM (1983) Fractional quantization of the hall effect: A hierarchy of incompressible quantum fluid states. *Physical Review Letters* 51: 605–608. https://doi.org/10.1103/PhysRevLett.51.605.

Halperin BI (1983) Theory of the quantized hall conductance. *Helvetica Physica Acta* 56: 75.

Herbut IF (2007) Theory of integer quantum hall effect in graphene. *Physical Review B* 75: 165411. https://doi.org/10.1103/PhysRevB.75.165411.

Jain JK (1989) Composite-fermion approach for the fractional quantum hall effect. *Physical Review Letters* 63: 199–202. https://doi.org/10.1103/PhysRevLett.63.199.

Kallin C and Halperin BI (1984) Excitations from a filled landau level in the two-dimensional electron gas. *Physical Review B* 30: 5655–5668. https://doi.org/10.1103/PhysRevB.30.5655.

Kharitonov M (2012) Phase diagram for the $\nu=0$ quantum Hall state in monolayer graphene. *Physical Review B* 85: 155439. https://doi.org/10.1103/PhysRevB.85.155439.

Kitaev A (2003) Fault-tolerant quantum computation by anyons. *Annals of Physics* 303: 2–30. https://doi.org/10.1016/S0003-4916(02)00018-0.

Klitzing KV, Dorda G, and Pepper M (1980) New method for high-accuracy determination of the fine-structure constant based on quantized hall resistance. *Physical Review Letters* 45: 494–497. https://doi.org/10.1103/PhysRevLett.45.494.

Knoester ME, Papić Z, and Morais Smith C (2016) Electron-solid and electron-liquid phases in graphene. *Physical Review B* 93: 155141. https://doi.org/10.1103/PhysRevB.93.155141.

Lambert J and Côté R (2013) Quantum hall ferromagnetic phases in the landau level $n = 0$ of a graphene bilayer. *Physical Review B* 87: 115415. https://doi.org/10.1103/PhysRevB.87.115415.

Laughlin RB (1983) Anomalous quantum hall effect: An incompressible quantum fluid with fractionally charged excitations. *Physical Review Letters* 50: 1395–1398. https://doi.org/10.1103/PhysRevLett.50.1395.

Le ND and Jolicoeur T (2022) Spin and valley ordering of fractional quantum hall states in monolayer graphene. *Physical Review B* 105: 075203. https://doi.org/10.1103/PhysRevB.105.075203.

Lian Y and Goerbig MO (2017) Spin-valley skyrmions in graphene at filling factor $\nu = \pm 1$. *Physical Review B* 95: 245428. https://doi.org/10.1103/PhysRevB.95.245428.

Lian Y, Rosch A, and Goerbig MO (2016) SU(4) Skyrmions in the ν=Âś1 Quantum Hall State of Graphene. *Physical Review Letters* 117: 056806. https://doi.org/10.1103/PhysRevLett.117.056806.

Lilly MP, Cooper KB, Eisenstein JP, Pfeiffer LN, and West KW (1999) Evidence for an anisotropic state of two-dimensional electrons in high landau levels. *Physical Review Letters* 82: 394–397. https://doi.org/10.1103/PhysRevLett.82.394.

Liu X, Hao Z, Watanabe K, Taniguchi T, Halperin BI, and Kim P (2019) Interlayer fractional quantum hall effect in a coupled graphene double layer. *Nature Physics* 15: 893–897. https://doi.org/10.1038/s41567-019-0546-0.

Liu X, Farahi G, Chiu CL, Papic Z, Watanabe K, Taniguchi T, Zaletel MP, and Yazdani A (2022) Visualizing broken symmetry and topological defects in a quantum hall ferromagnet. *Science* 375: 321–326. https://doi.org/10.1126/science.abm3770.

Maher P, Wang L, Gao Y, Forsythe C, Taniguchi T, Watanabe K, Abanin D, Papić Z, Cadden-Zimansky P, Hone J, Kim P, and Dean CR (2014) Tunable fractional quantum hall phases in bilayer graphene. *Science* 345: 61–64. https://doi.org/10.1126/science.1252875.

Moessner R and Chalker JT (1996) Exact results for interacting electrons in high landau levels. *Physical Review B* 54: 5006–5015. https://doi.org/10.1103/PhysRevB.54.5006.

Moore G and Read N (1991) Nonabelions in the fractional quantum hall effect. *Nuclear Physics B* 360: 362.

Nakamura J, Liang S, Gardner GC, and Manfra MJ (2020) Direct observation of anyonic braiding statistics. *Nature Physics* 16: 931–936. https://doi.org/10.1038/s41567-020-1019-1.

Narayanan S, Roy B, and Kennett MP (2018) Incompressible even denominator fractional quantum hall states in the zeroth landau level of monolayer graphene. *Physical Review B* 98: 235411. https://doi.org/10.1103/PhysRevB.98.235411.

Nomura K, Ryu S, and Lee DH (2009) Field-induced kosterlitz-thouless transition in the $n = 0$ landau level of graphene. *Physical Review Letters* 103: 216801. https://doi.org/10.1103/PhysRevLett.103.216801.

Novoselov KS, Geim AK, Morozov SV, Jiang D, Zhang Y, Dubonos SV, Grigorieva IV, and Firsov AA (2004) Electric field effect in atomically thin carbon films. *Science* 306: 666–669. https://doi.org/10.1126/science.1102896.

Novoselov KS, Geim AK, Morozov SV, Jiang D, Katsnelson MI, Grigorieva IV, Dubonos SV, and Firsov AA (2005) Two-dimensional gas of massless dirac fermions in graphene. *Nature* 438: 197–200. https://doi.org/10.1038/nature04233.

Novoselov KS, McCann E, Morozov SV, Fal'ko VI, Katsnelson MI, Zeitler U, Jiang D, Schedin F, and Geim AK (2006) Unconventional quantum hall effect and berry's phase of 2π in bilayer graphene. *Nature Physics* 2: 177–180. https://doi.org/10.1038/nphys245.

Papić Z, Goerbig MO, and Regnault N (2010) Atypical fractional quantum hall effect in graphene at filling factor 1/3. *Physical Review Letters* 105: 176802. https://doi.org/10.1103/PhysRevLett.105.176802.

Parameswaran SA, Roy R, and Sondhi SL (2012) Fractional chern insulators and the W_∞ algebra. *Physical Review B* 85: 241308. https://doi.org/10.1103/PhysRevB.85.241308.

Pierce AT, Xie Y, Lee SH, Forrester PR, Wei DS, Watanabe K, Taniguchi T, Halperin BI, and Yacoby A (2022) Thermodynamics of free and bound magnons in graphene. *Nature Physics* 18: 37–41. https://doi.org/10.1038/s41567-021-01421-x.

Polshyn H, Zhou H, Spanton EM, Taniguchi T, Watanabe K, and Young AF (2018) Quantitative transport measurements of fractional quantum hall energy gaps in edgeless graphene devices. *Physical Review Letters* 121: 226801. https://doi.org/10.1103/PhysRevLett.121.226801.

Regnault N and Bernevig BA (2011) Fractional chern insulator. *Physical Review X* 1: 021014. https://doi.org/10.1103/PhysRevX.1.021014.

Saminadayar L, Glattli DC, Jin Y, and Etienne B (1997) Observation of the *e*/3 fractionally charged laughlin quasiparticle. *Physical Review Letters* 79: 2526–2529. https://doi.org/10.1103/PhysRevLett.79.2526.

Shi Q, Shih EM, Gustafsson MV, Rhodes DA, Kim B, Watanabe K, Taniguchi T, Papić Z, Hone J, and Dean CR (2020) Odd- and even-denominator fractional quantum hall states in monolayer wse2. *Nature Nanotechnology* 15: 569–573. https://doi.org/10.1038/s41565-020-0685-6.

Son DT (2015) Is the composite fermion a dirac particle? *Physical Review X* 5: 031027. https://doi.org/10.1103/PhysRevX.5.031027.

Stepanov P, Che S, Shcherbakov D, Yang J, Chen R, Thilahar K, Voigt G, Bockrath MW, Smirnov D, Watanabe K, Taniguchi T, Lake RK, Barlas Y, MacDonald AH, and Lau CN (2018) Long-distance spin transport through a graphene quantum Hall antiferro-magnet. *Nature Physics* 14: 907–911. https://doi.org/10.1038/s41567-018-0161-5.

Tőke C and Jain JK (2007) Su(4) composite fermions in graphene: Fractional quantum hall states without analog in gaas. *Physical Review B* 75: 245440. https://doi.org/10.1103/PhysRevB.75.245440.

Tsui DC, Stormer HL, and Gossard AC (1982) Two-dimensional magnetotransport in the extreme quantum limit. *Physical Review Letters* 48: 1559–1562. https://doi.org/10.1103/PhysRevLett.48.1559.

Wei DS, van der Sar T, Lee SH, Watanabe K, Taniguchi T, Halperin BI, and Yacoby A (2018) Electrical generation and detection of spin waves in a quantum Hall ferromagnet. *Science* 362: 229–233. https://science.sciencemag.org/content/362/6411/229. https://doi.org/10.1126/science.aar4061.

Wei N, Huang C, and MacDonald AH (2021) Scattering of magnons at graphene quantum-hall-magnet junctions. *Physical Review Letters* 126: 117203. https://doi.org/10.1103/PhysRevLett.126.117203.

Willett R, Eisenstein JP, Störmer HL, Tsui DC, Gossard AC, and English JH (1987) Observation of an even-denominator quantum number in the fractional quantum hall effect. *Physical Review Letters* 59: 1776–1779. https://doi.org/10.1103/PhysRevLett.59.1776.

Wu F, Sodemann I, MacDonald AH, and Jolicoeur T (2015) Su(3) and su(4) singlet quantum hall states at $\nu = 2/3$. *Physical Review Letters* 115: 166805. https://doi.org/10.1103/PhysRevLett.115.166805.

Yang K, Das Sarma S, and MacDonald AH (2006) Collective modes and skyrmion excitations in graphene *su*(4) quantum hall ferromagnets. *Physical Review B* 74: 075423. https://doi.org/10.1103/PhysRevB.74.075423.

Zhang Y, Tan YW, Stormer HL, and Kim P (2005) Experimental observation of the quantum hall effect and berry's phase in graphene. *Nature* 438: 201–204. https://doi.org/10.1038/nature04235.

Zibrov AA, Spanton EM, Zhou H, Kometter C, Taniguchi T, Watanabe K, and Young AF (2018) Even-denominator fractional quantum hall states at an isospin transition in monolayer graphene. *Nature Physics* 14: 930–935. https://doi.org/10.1038/s41567-018-0190-0.

Fractional quantum Hall effect at the filling factor $\nu = 5/2$

Ken KW Ma[a], **Michael R Peterson**[b], **VW Scarola**[c], **and Kun Yang**[d], [a]National High Magnetic Field Laboratory, Tallahassee, FL, United States; [b]Department of Physics & Astronomy, California State University Long Beach, Long Beach, CA, United States; [c]Department of Physics, Virginia Tech, Blacksburg, VA, United States; [d]Department of Physics and National High Magnetic Field Laboratory, Florida State University, Tallahassee, FL, United States

© 2024 Elsevier Ltd. All rights reserved.

Introduction 326
Theoretical background 327
Theory of composite fermions 328
Paired quantum Hall states 329
Pfaffian (Moore-Read) state 330
Conformal field theory description 330
Edge theory 331
Weak pairing of composite fermions 331
Anti-Pfaffian state 332
PH-Pfaffian state 332
Unified description: Kitaev's 16-fold way 333
Properties of anyons 334
Edge theory 334
Bulk collective excitations 335
Overview of numerical results 335
Numerical methods and geometries 335
Spin polarization 336
Excitation gaps 338
Transport gap 338
Neutral gap 338
Neutral fermion gap 338
Realistic effects on energy gaps 338
Evidence for pairing 339
Topological properties 340
Topological shift 340
Ground state degeneracy 340
Wave function overlaps 340
Entanglement entropy and spectra 340
Edge velocities 341
Non-Abelian quasiparticles 341
Adiabatic continuity 342
Competing phases and Landau level mixing 342
Perturbative LL mixing treatment I 343
Non-perturbative LL mixing treatment I 343
Perturbative LL mixing treatment II 343
Non-perturbative LL mixing treatment II 343
Perturbative LL mixing treatment III 344
Perturbative LL mixing treatment IV 345
Unexpected experimental results and the PH-Pfaffian 345
Summary of numerical results 345
Early experiments and evidence for/against non-Abelian states 346
Transport and optics: Bulk energy gap 346
Density dependence 346
Disorder, mobility, and sample design 347
In-plane magnetic field and sample tilt impacts the bulk gap 348
Optical probes of the bulk gap 348
Surface acoustic waves, geometric resonance transport, light scattering, and Knight shift: Spin polarization 348
Surface acoustic waves and geometric resonance 348
Transport 349
Light scattering 349
Knight shift 350

https://doi.org/10.1016/B978-0-323-90800-9.00135-9

Tunneling with QPCs and SETs: Quasiparticle charge and edge exponents 350
QPC tunneling 350
SETs 351
Edge exponents from tunneling conductance 351
Noise in QPCs: Upstream neutral mode 351
Interferometry: Quasiparticle charge and braiding 351
Interferometry and charge 351
Interferometry and braiding 351
Summary of early experimental findings 352
Recent surprises and puzzles 352
Experimental results 352
Possible interpretations 352
Bulk edge correspondence: PH-Pfaffian 353
Disorder induced Pf-APf domain walls 353
Partial equilibration on anti-Pfaffian edges 353
Recent and ongoing developments 354
Temperature dependence of ℓ_{eq} 354
Interface experiments 354
Summary of recent developments 355
Future directions 355
Noise measurements 355
Shot noise in dc transport 355
Thermal tunneling noise across a QPC 355
Local power measurement in multi-terminal thermal conductance experiment 355
Other interferometry experiments 356
Mach-Zehnder interferometry 356
Non-Abelian anyon collider 356
Bulk probes: Polarized Raman scattering and thermal power 356
Conclusion 357
Acknowledgments 357
References 357

Abstract

The fractional quantum Hall (FQH) effect at the filling factor $\nu = 5/2$ was discovered in GaAs heterostructures more than 35 years ago. Various topological orders have been proposed as possible candidates to describe this FQH state. Some of them possess non-Abelian anyon excitations, an entirely new type of quasiparticle with fascinating properties. If observed, non-Abelian anyons could offer fundamental building blocks of a topological quantum computer. Nevertheless, the nature of the FQH state at $\nu = 5/2$ is still under debate. In this chapter, we provide an overview of the theoretical background, numerical results, and experimental measurements pertaining to this special FQH state. Furthermore, we review some recent developments and their possible interpretations. Possible future directions toward resolving the nature of the 5/2 state are also discussed.

Key points

- The 5/2 fractional quantum Hall state was discovered more than 35 years ago but the nature of the physics underlying the state remains under intense debate.
- The exciting possibility of a paired 5/2 state hosting exotic excitations with non-Abelian braid statistics led to considerable effort to prove their existence.
- Strong numerical and experimental evidence suggests that the 5/2 state arises from pairing between composite fermions but the precise nature of the topological order defining the paired state remains unsettled.
- We review the culmination of experimental and theoretical studies on the 5/2 state and discuss possible future directions for further inquiry.

Notations and acronyms

$\mathscr{C}$	Chern number
$E_{\text{Coul}} = e^2/\varepsilon\ell_0$	Coulomb energy
$\hbar\omega_c = eB/mc$	Cyclotron energy
$J = \Pi_{1\le i\le j\le N}(z_i - z_j)$	Jastrow factor
$\kappa = E_{\text{Coul}}/\hbar\omega_c$	Landau level mixing parameter
$\phi_0 = h/e$	Magnetic flux quantum
$\ell_0 = \sqrt{\hbar/eB}$	Magnetic length
$\mathscr{P}_{\text{SLL}}$	Projection operator to the second electronic Landau level
CFT	Conformal field theory
DMRG	Density matrix renormalization group
FQH	Fractional Quantum Hall
K_H	Thermal Hall conductance
LL	Landau level
N	Number of electrons
Q	Monopole strength in the spherical geometry
QPC	Quantum point contact
S	Topological shift
SET	Single electron transistor
w	Quantum well thickness
$z_k = x_k - iy_k$	Position of k-th electron in the xy-plane
$\nu = \rho\phi_0/\text{B}$	Landau level filling factor
ν	Electron filling factor

Introduction

The discovery of the FQH effect in two-dimensional semiconductor heterostructures started a new chapter in condensed matter physics Tsui et al. (1982). For a recent review on the basic concepts in FQH physics, see Papić and Balram (2022). In contrast to the conventional wisdom from Landau-Ginzburg theory, different quantum Hall states cannot be distinguished by spontaneously broken symmetries Wen (2004). Furthermore, early theoretical work suggested that the low-energy excitations in a FQH liquid are neither bosons nor fermions. Instead, they possess fractional charges Laughlin (1983a) and fractional braiding statistics Arovas et al. (1984), Halperin (1984) [see also the review article by Feldman and Halperin, 2021], which are known as anyons Leinaas and Myrheim (1977), Wilczek (1982). This special type of excitation turns out to be the basic ingredient in the formulation of topological order, which provides an effective description of different FQH states and distinguishes them by specifying the sets of possible anyons the FQH states can support Wen (2004). Note that the existence of fractional statistics has received strong support from very recent experiments Bartolomei et al. (2020), Nakamura et al. (2020), Kundu et al. (2022).

Many FQH states at different filling factors have been observed in various materials. Nearly all of them have odd denominators. For a summary of the observed FQH states, readers may refer to the lists in Pan et al. (2008) and Hidalgo (2022). Among them, the FQH state at filling factor $\nu = 5/2$ (dubbed as the 5/2 state below) in GaAs-GaAlAs quantum wells has attracted a tremendous amount of attention since its discovery Willett et al. (1987). This historical result is shown in Fig. 1. The observation of the 5/2 state was surprising. It is a FQH state in the second LL (we define the lowest LL as the first LL). Also, it was the first FQH state with an even-denominator filling factor being observed in a single layer system.

The 5/2 state has been challenging to understand, as compared to other FQH states in the lowest LL which usually have odd-denominator filling factors. In particular, entirely new topological orders have been proposed as possible candidates to describe this special FQH state. Interestingly, some of them host non-Abelian anyons which may be useful in topological quantum computation Das Sarma et al. (2005), Kitaev (2003), Nayak et al. (2008).

Different types of experiments have been proposed and performed to probe the nature of the 5/2 state. Meanwhile, numerical simulation is another essential tool to study the problem. Evidence from both sources strongly suggests that the 5/2 state possesses non-Abelian topological order. Nevertheless, which one (or perhaps what combination of topological orders) is actually realized in real samples is still under considerable debate. A new twist on this 35-year old problem arose thanks to the exciting yet puzzling results from recent experiments Banerjee et al. (2018), Dutta et al. (2022a, 2022b) that we will discuss below. In order to resolve the apparent conflict between the recent experimental and existing numerical results, various scenarios have been proposed Asasi and Mulligan (2020), Feldman (2018), Lian and Wang (2018), Ma and Feldman (2019a), Mross et al. (2018), Simon (2018a), Simon (2018b), Simon and Rosenow (2020), Wang et al. (2018).

In this chapter, we provide an overview of the theoretical background, numerical studies, and experimental findings pertaining to the 5/2 state in GaAs heterostructures. Previous review articles on the same topic can be found in Jiang and Wan (2019), Lin et al. (2014), Peterson (2012), Schreiber and Csáthy (2020), Willett (2013). We will highlight recent developments in the past 5 years and outline possible future directions. Before diving into the details of the 5/2 state, it is worthwhile to mention that FQH states at

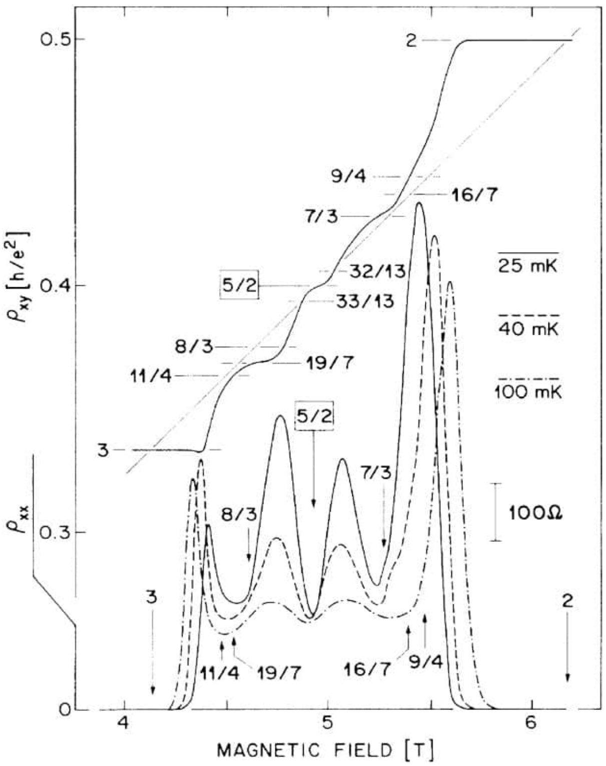

Fig. 1 The first experimental observation of the FQH state at $\nu = 5/2$ revealed by plotting both the Hall (ρ_{xy}) and longitudinal (ρ_{xx}) resistivity versus perpendicular magnetic field. The figure is taken from Willett R, Eisenstein JP, Störmer HL, Tsui DC, Gossard AC, and English JH (1987) Observation of an even-denominator quantum number in the fractional quantum Hall effect. *Physical Review Letters* 59: 1776–1779. https://doi.org/10.1103/PhysRevLett.59.1776 with permission.

Table 1 Summary of observed half-integer FQH states in different materials.

Material	*Filling factors*	*References*
Monolayer GaAs	5/2, 7/2	Willett et al. (1987), Pan et al. (1999b) Eisenstein et al. (2002), Liu et al. (2011b)
Bilayer GaAs	1/2	Suen et al. (1992), Eisenstein et al. (1992)
Monolayer ZnO	3/2, 5/2, 7/2, 9/2	Falson et al. (2015, 2018)
Monolayer WSe$_2$	3/2	Shi et al. (2020)
Monolayer graphene	−1/2, 1/2	Zibrov et al. (2018)
Bilayer graphene	−5/2, −1/2, 3/2, 5/2, 7/2	Ki et al. (2014), Kim et al. (2015) Zibrov et al. (2017), Li et al. (2017) Huang et al. (2022)

Note that additional half-integer FQH states have been observed in higher Landau levels in monolayer graphene Kim et al. (2019), which are not listed here.

different halfinteger filling factors have been observed in GaAs heterostructures and other materials. They are summarized in Table 1. For a recent review on half-integer FQH states in graphene-based systems, see Apalkov and Charkaborty (2023). Note that an anomalous quantized plateau at $\nu = 3/2$ has been observed in monolayer GaAs systems with gate-defined confined regions Fu et al. (2019), Hayafuchi et al. (2022), Yan et al. (2022). However, this plateau is believed to emerge from a larger filling factor in the bulk. Thus, its nature might be very different from a genuine half-integer FQH state.

We note the present chapter is different from (most) other chapters, as it covers a topic that is currently being studied very actively, and this ongoing research will likely continue for quite some time. We thus do not have the final word, but instead try to provide some balanced guidance to people who are interested in this subject, in particular those who may want to contribute to it in the future. An unintended consequence of this is the chapter is considerably longer than (most) other chapters.

Theoretical background

When a two-dimensional electron gas is placed under a strong perpendicular magnetic field, the electron kinetic energy is quantized into LLs. Consequently, the kinetic energy of electron is quenched, and the energetics is dominated by the strong correlation between electrons Girvin and Yang (2019). A minimal Hamiltonian for the FQH regime is Laughlin (1983b):

$$H = \frac{e^2}{\varepsilon \ell_0} \mathscr{P}_{\mathrm{SLL}} \sum_{i<j} \frac{1}{|z_i - z_j|} \mathscr{P}_{\mathrm{SLL}} \tag{1}$$

where $\mathscr{P}_{\mathrm{SLL}}$ projects the repulsive Coulomb interaction between electrons into a single LL, $z_j = x_j - iy_j$ denotes the complex coordinates of electrons in the xy-plane (we assume the magnetic field points upward), e is the electron charge, and ε is the dielectric constant of the host semiconductor. Eq. (1) assumes an infinitely thin plane and an infinite LL splitting (no LL mixing). The former can be easily fixed by including a finite extent of the electron wave function along the perpendicular direction (often referred to as sub-band wave function) when calculating the effective 2D Coulomb potential, while the latter can be corrected by modifying the form of the interaction Das Sarma and Pinczuk (1996), Jain (2007). Furthermore, Eq. (1) assumes no electron spin. If we include the spin degree of freedom we must also include a Zeeman term in Eq. (1). For a detailed discussion on different energy scales in FQH states in GaAs heterostructures, and the corresponding justification for Eq. (1), interested readers may refer to Papić and Balram (2022).

Eq. (1) contains only a single interaction term. As a result, standard perturbation theory becomes inapplicable in studying FQH physics, which is solely determined by ν (once the interaction is fixed). The seminal work by Jain introduced the theory of composite fermions which is particularly intuitive in revealing how ν controls the physics Jain (1989a).

Theory of composite fermions

In a first approximation, a composite fermion is formed by attaching an even number $2p$ of magnetic flux quanta to an electron Jain (2007). Here, we only focus on the situation in which each composite fermion carries two magnetic flux quanta ($p = 1$). The number density of electrons in the two-dimensional electron gas satisfies $\rho = \nu B/\phi_0$, where $\phi_0 = h/e$ is the magnetic flux quantum. Due to flux attachment, the composite fermions experience a reduced effective magnetic field B_{eff}. This is illustrated in Fig. 2. Under the mean field approximation,

$$B_{\mathrm{eff}} = B - 2\rho\phi_0 = B(1 - 2\nu). \tag{2}$$

Since B_{eff} and B are different but the number density of electrons equals that of the composite fermions, the effective filling factor of composite fermions differ from the filling factor of electrons. Then by analogy to the integer quantum Hall effect, the integer quantum Hall state of composite fermions filling n_{CF} effective LLs (or the so-called Λ levels) corresponds to the FQH state of electrons at $\nu = n_{\mathrm{CF}}/(2n_{\mathrm{CF}} \pm 1)$. Here, the sign $\pm$ denotes the direction of the residual magnetic field experienced by the composite fermions. If it is parallel (anti-parallel) to the original field B, then the sign is +(−).

At half filling of the lowest LL, $\nu = 1/2$, Eq. (2) predicts that the composite fermions experience a zero average magnetic field. This supports the absence of a FQH state at $\nu = 1/2$ in monolayer GaAs heterostructures. On the other hand, the ground state of electrons in a half-filled LL is a composite fermion Fermi liquid with a well-defined Fermi surface Halperin et al. (1993), Kalmeyer and Zhang (1992). Both the existence of composite fermions and the formation of a composite fermion Fermi surface at $\nu = 1/2$ have received strong experimental support Goldman et al. (1994), Hossain et al. (2020), Kamburov et al. (2014), Kang et al. (1993), Smet et al. (1996), Willett et al. (1993, 1999).

A possible starting point for studying FQH states at $\nu > 1$ is to simply focus on the partially filled LL(s). The above would then suggest that at $\nu = 5/2 = 2 + 1/2$ there would exist a gapless state and no FQH. But then how can we understand the presence of an energy gap to support the observed Hall plateau at $\nu = 5/2$? Previous approaches such as the hierarchical construction Haldane (1983), Halperin (1984) cannot directly explain gapped FQH states at even-denominator filling factors.

Wave function construction is central to the composite fermion ansatz and can be used to make progress. The microscopic flux attachment process defining the composite fermion wave function at total magnetic field B from an effective field at B_{eff} is given by Jain (1989a):

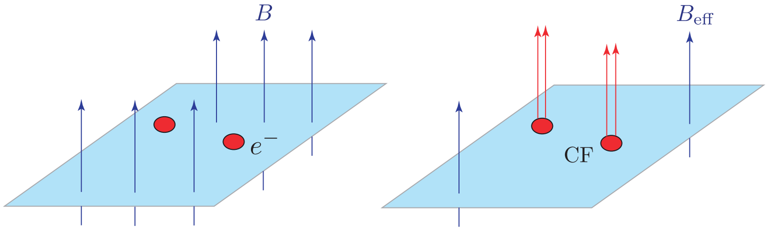

Fig. 2 Illustration of composite fermions (CFs). Left panel: Electrons in an external magnetic field B. Right panel: Composite fermions formed by attaching two magnetic flux quanta to each electron. The effective magnetic field experienced by the composite fermions is B_{eff}, which is different from B. The number of arrows indicates the number of magnetic flux quanta in the system.

$$\Psi^B = J^{2p}\psi^{B_{\text{eff}}} \tag{3}$$

where Ψ^B is an ansatz state of Eq. (1), J^{2p} is a Jastrow factor attaching an even number of vortices $(2p)$ to each electron, and $\psi^{B_{\text{eff}}}$ is a fermionic wave function at an effective field B_{eff} that results from projection into a single LL Jain and Kamilla (1997). In the symmetric gauge we have, for N particles:

$$J = \prod_{i<j}^{N} (z_i - z_j) \tag{4}$$

where we see that J vanishes if two particles occupy the same location. J implements vortex attachment Read (1989, 1994, 1996) which can be approximated by flux attachment in effective theories. Here we have used the terms vortex and flux attachment interchangeably with the understanding that they are not exactly equivalent Murthy and Shankar (2003), Jain (2007).

Ψ^B describes a large class of possible ansatz ground states because we are free to choose $\psi^{B_{\text{eff}}}$. In the simplest setting we assume that $\psi^{B_{\text{eff}}}$ describes weakly interacting fermions. For example, Eq. (3) reduces to the Laughlin wave function at $\nu = 1/(2p+1)$ Laughlin (1983a) if we set $\psi^{B_{\text{eff}}}$ to be an integer filled state of composite fermions at effective filling of $n_{\text{CF}} = 1$ Jain (1989a, 2007). We therefore see that the Laughlin states form a subset of states within the composite fermion wave function formalism.

A large class of states at half filling are also captured by Ψ^B. The composite fermion Fermi liquid Halperin et al. (1993) arises when we assume a filled Fermi sea at zero effective field ($n_{\text{CF}} \to \infty$) Rezayi and Read (1994) for $\psi^{B_{\text{eff}}}$. Here we have a gapless state that accurately captures the essential physics of the half-filled lowest LL Jain (2007). But in the following we discuss gapped examples of $\psi^{B_{\text{eff}}}$. relevant for even filling, specifically paired states, that yield energetically competitive ansatz wave functions for half filling of the second LL.

Paired quantum Hall states

The even denominator in the filling factor indicates that the 5/2 state may originate from bosonic entities formed by electrons or composite fermions. Different from the original description with strongly correlated electrons, the effective interaction between composite fermions is much weaker. Similar to the case of $\nu = 1/2$, a composite fermion Fermi liquid is formed when the system has filling factor 5/2. However, the effective interaction between composite fermions becomes weakly attractive at $\nu = 5/2$ and leads to a Cooper instability Scarola et al. (2000a). It is believed that the pairing between composite fermions gives rise to the gapped FQH state at $\nu = 5/2$ and other half-integer filling factors. This idea is illustrated in Fig. 3. This motivates ansatz states where $\psi^{B_{\text{eff}}}$ is an eigenstate of an effective pairing Hamiltonian Read and Green (2000).

The pairing Hamiltonian of Bardeen-Cooper-Schrieffer (BCS) takes the form:

$$H_{\text{BCS}} = \sum_{\boldsymbol{k}} \left[\left(\frac{\hbar^2 k^2}{2m^*} - \mu \right) c_{\boldsymbol{k}}^{\dagger} c_{\boldsymbol{k}} + \frac{1}{2} \left(\Delta_{\boldsymbol{k}}^{*} c_{-\boldsymbol{k}} c_{\boldsymbol{k}} + \Delta_{\boldsymbol{k}} c_{\boldsymbol{k}}^{\dagger} c_{-\boldsymbol{k}}^{\dagger} \right) \right]. \tag{5}$$

Here, $c_{\boldsymbol{k}}$ and $c_{\boldsymbol{k}}^{\dagger}$ are the second quantized operators for composite fermions, with the index $\boldsymbol{k}$ labeling the momentum. We assume the composite fermions are spin-polarized in this section and have thus suppressed the spin index. The symbols m^* and μ label the effective mass and chemical potential of composite fermions, respectively. Importantly, both m^* and μ are non-perturbative and due solely to the Coulomb interaction between electrons.

Knowing that composite fermions can form Cooper pairs does not completely determine the nature of the 5/2 state. Different pairing channels with different gap functions $\Delta_{\boldsymbol{k}}$ lead to different possible phases Read and Green (2000). Which one or what combination of these states are actually realized in a realistic experimental sample may depend sensitively on the microscopic details and experimental conditions. Notice that we use the terminologies, "states" and "topological orders" (sometimes abbreviated as orders) interchangeably in the following discussion.

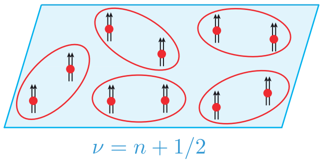

Fig. 3 Pairing of composite fermions in the $\nu = 5/2$ and other half-integer FQH states. The red dots are electrons. Each of them is attached to two magnetic flux quanta marked by black arrows and form a composite fermion. These composite fermions form Cooper pairs (grouped by the red ovals in the figure), that gives rise to a gapped phase at half-integer filling factors.

Pfaffian (Moore-Read) state

The Pfaffian state (also known as the Moore-Read state) has the following wave function Moore and Read (1991):

$$\Psi_{\mathrm{Pf}}(\{z_i\}) = J^2 \mathrm{Pf}\left(\frac{1}{z_i - z_j}\right) \exp\left(-\sum_i \frac{|z_i|^2}{4\ell_0^2}\right). \tag{6}$$

The attachment of two flux quanta to each electron is implemented by the Jastrow factor, which also fixes the filling factor to be $\nu = 1/2$. The Gaussian factor is ubiquitous in every quantum Hall wave function, which originates from the eigenfunctions of LLs in the symmetric gauge Prange and Girvin (1987). This factor will be dropped in the following discussion. Finally, the Pfaffian factor is defined as

$$\mathrm{Pf}\left(\frac{1}{z_i - z_j}\right) = \mathscr{A}\left(\frac{1}{z_1 - z_2}\frac{1}{z_3 - z_4}\cdots\right), \tag{7}$$

where $\mathscr{A}$ denotes anti-symmetrization over the set of coordinates z_i. This "explains" the name of the Pfaffian state.

The Pfaffian wave function has several important features. The right hand side of Eq. (7) can be understood as a real-space BCS paired state at zero effective magnetic field Read and Green (2000), Schrieffer (1999). Ψ_{Pf} is therefore gapped flowing to the composite fermion BCS gap. Ψ_{Pf} is also an exact zero energy ground state of an idealized three-body Hamiltonian Greiter et al. (1992), which will be further discussed in Section "Overview of numerical results".

Eq. (6) is an ansatz state for the incompressible (gapped) state of electrons half filling of the lowest LL. To describe the 5/2 state, we assume the electrons completely fill the lowest two LLs (one with spin up and another with spin down polarizations), and the Pfaffian wave function describes the fully polarized electrons in the half filled second LL only Greiter et al. (1992), Moore and Read (1991), Read and Green (2000). Note that wave functions for FQH states in higher LLs can be generated systematically by acting LL raising operators on a wave function defined in the lowest LL Girvin and Yang (2019). For this reason we can always represent a wave function in any LL by its lowest LL counterpart, which is what we do throughout this chapter unless noted otherwise.

Conformal field theory description

Historically, the wave function in Eq. (6) was introduced in Moore and Read (1991) via conformal field theory (CFT). CFT has since become a powerful tool in studying quantum Hall physics Hansson et al. (2017). For details on CFT, readers may refer to the textbook Francesco et al. (1997). Here, we will only outline the basic ideas and state the necessary results directly.

For the Pfaffian state, the CFT description actually involves two different CFTs. The first part is a compactified holomorphic boson $\phi(z)$, which is responsible for the correct filling factor at $\nu = 1/2$ for the half-filled LL. The second part is the holomorphic Ising CFT which has three different primary fields as summarized in Table 2. In particular, there is a holomorphic Majorana fermion field $\psi(z)$ which has the scaling dimension 1/2. The electron operator is defined as

$$\widehat{\Psi}_e(z_j) = \psi(z_j)\exp\left[2i\phi(z_j)\right], \tag{8}$$

which has scaling dimension 3/2 indicating that it indeed represents a fermion. The wave function in Eq. (6) can now be interpreted as the correlation function between electron operators:

$$\Psi_{\mathrm{Pf}}(\{z_j\}) = \prod_{j=1}^{N}\left\langle \widehat{\Psi}_e(z_j)\widehat{O}_{bg}(z_j)\right\rangle. \tag{9}$$

In the above equation, the background charge operator $\widehat{O}_{bg}(z_j)$ ensures that the correlation function does not vanish. It is also responsible for reproducing the correct Gaussian factor in the wave function.

Table 2 Primary fields in the holomorphic Ising CFT (top table) and their fusion rules (bottom table).

Primary field	*Scaling dimension*
I	0
ψ	1/2
σ	1/16

×	I	ψ	σ
I	I	ψ	σ
ψ	ψ	I	σ
σ	σ	σ	$\psi + I$

After defining the suitable electron operator in the CFT approach, all possible quasiparticles in the quantum Hall state can be deduced systematically. For example, consider the quasiparticle described by the CFT operator

$$\widehat{\Psi}_{\text{qp}}(z) = \sigma(z)e^{i\alpha\phi(z)}, \tag{10}$$

where α is a constant that needs to be determined. The operator product expansion between the quasi-particle and the electron operators must be single-valued (or without any branch cut). This condition leads to $\alpha = n' + 1/2$, with n' being an arbitrary integer. In particular, $n' = 0, -1$ corresponds to quasiparticles with charges $\pm e/4$. The corresponding CFT operator has scaling dimension 1/8, which is the most relevant operator among all possible operators for quasiparticles in the Pfaffian state. Interestingly, the fusion rule $\sigma \times \sigma = \psi + I$ indicates that these quasiparticles are non-Abelian anyons. This exciting feature has motivated many of the ongoing studies of 5/2 state, in the hope of finding its potential applications in topological quantum computation Kitaev (2003), Nayak et al. (2008).

Edge theory

FQH states that are gapped in the bulk must nonetheless become gapless at the edges Halperin (1982). Effective low-energy theories have been used to model gapless edge states Wen (2004). Also, the bulk-edge correspondence suggests that different bulk topological orders usually have correspondingly different edge structures Cano et al. (2014), Dubail and Read (2011), Qi et al. (2012), Swingle and Senthil (2012), Yan et al. (2019). The knowledge of edge physics can provide invaluable insight into the nature of the underlying quantum Hall states. Hence, various types of experiments have been proposed and performed to probe the edge structure of different quantum Hall states. For a review of these edge probes, see Heiblum and Feldman (2020).

For the Pfaffian state, its edge structure can be deduced from the aforementioned CFT approach. Similar to the Laughlin state, the Pfaffian edge possesses a chiral Bose mode ϕ_c. The subscript c indicates that it is a charge mode. Its chirality, which corresponds to the downstream direction of propagation, is fixed by the direction of the external magnetic field. In addition, the Pfaffian edge has a chiral Majorana fermion mode ψ that is copropagating with the Bose mode Milovanović and Read (1996), Wan et al. (2006), Wen (1993). As a result, the Pfaffian edge is described by the Lagrangian density,

$$\mathcal{L}_{\text{Pf}} = -\frac{2}{4\pi}\partial_x\phi_c(\partial_t + v_c\partial_x)\phi_c + i\psi(\partial_t + v_n\partial_x)\psi. \tag{11}$$

The symbols v_c and v_n denote the speeds of the charge Bose mode and neutral Majorana fermion mode, respectively. Notice that a chiral Bose field and a chiral Majorana fermion field are present in both the bulk and the edge of the Pfaffian state. This feature is a manifestation of the bulk edge correspondence. In numerical simulations, v_c and v_n were found to satisfy $v_c \gg v_n$ due to Coulomb interaction Wan et al. (2008)—see Section "Overview of numerical results". The charge density of the edge is completely governed by the Bose mode, given by $\rho(x) = -e\partial_x\phi_c/2\pi$. Its corresponding edge channel contributes to an electrical Hall conductance $\sigma_{xy} = e^2/2h$. At $\nu = 5/2$, there are actually two more edge channels originating from the two completely filled LLs. Both of them are described by chiral Bose modes different from ϕ_c. Each of these integer channels contributes $\sigma_{xy} = e^2/h$, so the electrical Hall conductance $5e^2/2\,h$ at $\nu = 5/2$ follows. Unless otherwise specified, we will ignore the two integer channels in this section. The edge structure for the Pfaffian state is shown in Fig. 4.

Weak pairing of composite fermions

As previously mentioned, the FQH state at $\nu = 5/2$ is believed to originate from the pairing between composite fermions. The Pfaffian state in particular postulates a weak pairing phase [i.e., $\mu > 0$ in Eq. (5)] of composite fermions in the p- wave angular momentum channel Read and Green (2000). The corresponding gap function in Eq. (5) takes the form $\Delta_{\boldsymbol{k}} = \Delta_0(k_x + ik_y)$. From this perspective, the Pfaffian factor in the wave function can be interpreted as the BCS wave function in position space representation. Furthermore, the Chern number of this weak pairing phase was evaluated to be $\mathscr{C} = 1$; an explicit calculation can be found in the Appendix A of Ma (2019). This indicates that the Pfaffian state is topologically nontrivial. It is reflected by the existence of a chiral Majorana fermion mode on the edge, which is also consistent with the breaking of time reversal symmetry in the p-wave BCS pairing channel.

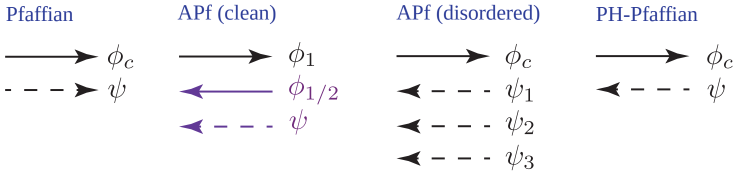

Fig. 4 Edge structures of the Pfaffian, anti-Pfaffian (abbreviated as APf in the figure), and PH-Pfaffian states. Here, solid lines and dashed lines denote Bose modes and Majorana fermion modes, respectively. The chirality of the overall charge mode ϕ_c is defined as the downstream direction (pointing to the right). In the anti-Pfaffian state, the description of its edge structure depends on disorder. In the case of clean edge, there are two Bose charge modes ϕ_1 (integer mode) and $\phi_{1/2}$ (fractional mode). These two modes can be coupled by disorder. For sufficiently strong disorder, the edge is driven to the disorder-dominated fixed point and being described by an overall charge mode and three upstream Majorana fermion modes. Note that we have neglected the two additional integer Bose modes due to the two lower LLs which are present in the actual edge of the 5/2 state.

Anti-Pfaffian state

When the effect of LL mixing is negligible, the particle-hole transformation is an exact symmetry in a half-filled LL. Thus, the particle-hole conjugate of the Pfaffian state provides another viable candidate to describe the 5/2 state. This motivated the introduction of the anti-Pfaffian state in Levin et al. (2007) and Lee et al. (2007). In principle, the wave function of the anti-Pfaffian state can be obtained systematically from particle-hole conjugating the Pfaffian wave function in Eq. (6) Lee et al. (2007). In fact, as discussed in Section "Overview of numerical results", since most numerical studies consider the limit where particle-hole symmetry is exact, both the Pfaffian and anti-Pfaffian states are trivially related—they are particle-hole conjugate states to one another. Nevertheless, more recent numerical work has undertaken studies of the anti-Pfaffian state under various conditions.

Using the parton theory introduced in Jain (1989b), the $\bar{2}\bar{2}111$ parton state was proposed to describe the 5/2 state (Balram et al., 2018a). It was discovered that the $\bar{2}\bar{2}111$ parton state describes the same phase, and has a high numerical overlap with the wave function of the anti-Pfaffian state Balram et al. (2018a). Meanwhile, the parton state is much easier to use in numerics.

The anti-Pfaffian state has a more complicated edge structure than the Pfaffian. First, there is an integer Bose mode circulating on the edge in the downstream direction. Due to the particle-hole transformation, the chiralities of the Bose mode and the Majorana fermion mode on the original Pfaffian edge are reversed. As a result, there are three different edge modes in the anti-Pfaffian state as illustrated in Fig. 4. In a real experimental sample, disorder exists and couples the edge modes. When this coupling is sufficiently strong, the anti-Pfaffian edge is driven to the disorder-dominated phase, which consists of a single downstream charge Bose mode and three upstream neutral Majorana fermion modes Lee et al. (2007), Levin et al. (2007). Furthermore, these Majorana fermion modes exhibit an emergent SO(3) symmetry and have the same velocity $\bar{v}_n$. As a result, the edge can be described by

$$\mathcal{L}_{\text{Apf}} = -\frac{2}{4\pi}\partial_x\phi_c(\partial_t + v_c\partial_x)\phi_c + i\sum_{j=1}^{3}\psi_j(\partial_t - \bar{v}_n\partial_x)\psi_j. \tag{12}$$

The anti-Pfaffian state also hosts non-Abelian anyons with charges $\pm e/4$. Since the edge is not maximally chiral, the scaling dimensions of CFT operators for quasiparticles are non-universal. The $e/4$ anyon has a minimum scaling dimension of 1/4, which is achieved in the aforementioned disorder-dominated phase. The scaling dimension is larger than the value of 1/8 in the Pfaffian state. This difference turns out to be important when one considers tunneling experiments discussed in Section "Early experiments and evidence for/against non-Abelian states".

In the weak pairing picture, the anti-Pfaffian state is interpreted as the superconducting phase arising from *f*-wave pairing between composite fermions. The gap function in Eq. (5) takes the form $\Delta_{\boldsymbol{k}} = \Delta_0(k_x - ik_y)^3$. Note that the corresponding Bogoliubov-de Gennes (BdG) Hamiltonian has Chern number $\mathscr{C} = -3$. This explains the difference between the numbers of chiral Majorana fermion edge modes in Pfaffian and anti-Pfaffian states.

PH-Pfaffian state

Recently, the particle-hole Pfaffian (PH-Pfaffian) state has attracted a considerable amount of attention as a candidate 5/2 state in GaAs heterostructures. It was originally introduced in the theory of Dirac composite fermions, which is a theory that preserves particle-hole symmetry explicitly in the half-filled LL Son (2015, 2016). In particular, the PH-Pfaffian state can be viewed as arising from *s*-wave pairing between Dirac composite fermions. This translates into a *p*-wave pairing (with the opposite chirality as the Pfaffian) between ordinary composite fermions, in which the corresponding BdG Hamiltonian has Chern number $\mathscr{C} = -1$. Different from the Pfaffian and anti-Pfaffian states, the PH-Pfaffian state is particle-hole symmetric. It is worth noting that a similar state known as the time-reversal symmetry preserving Pfaffian ($\mathscr{T}$-Pfaffian) was introduced to describe the $\mathscr{T}$-invariant surface state of topological insulators Bonderson et al. (2013), Fidkowski et al. (2013). Nevertheless, the realization of PH-Pfaffian order does not require the system itself to preserve particle-hole symmetry Zucker and Feldman (2016)—after all, LL mixing and other effects present in real experimental systems explicitly break particle-hole symmetry.

The edge structure of the PH-Pfaffian state can be deduced from its particle hole symmetry. After a particle hole transformation, the resulting edge theory has central charge $1-c$, with c being the central charge of the original edge theory. In order for the edge to be particle-hole symmetric, c needs to be 1/2. Furthermore, there must be a downstream Bose mode ϕ_c, such that its corresponding edge channel leads to the correct electrical Hall conductance of $\sigma_{xy} = e^2/2h$. Therefore, the remaining edge mode must be an upstream Majorana fermion mode ψ Hence, the PH-Pfaffian edge is described by the Lagrangian density,

$$\mathcal{L}_{\text{PH-Pf}} = -\frac{2}{4\pi}\partial_x\phi_c(\partial_t + v_c\partial_x)\phi_c + i\psi(\partial t - v_n\partial_x)\psi. \tag{13}$$

The edge structure is shown in Fig. 4.

After deducing the edge structure, it is straightforward to formulate the CFT description of the bulk. The electron operator with the appropriate chirality and scaling dimension is $\widehat{\Psi}_e(z) = \psi(\bar{z})\exp[2i\phi(z)]$. Here, $\bar{z}$ denotes the complex conjugation of z. Physically, the anti-holomorphicity of ψ originates from its upstream chirality at the edge. By evaluating the correlation function between electron operators, a possible wave function for the PH-Pfaffian state was written down explicitly in Zucker and Feldman (2016):

$$\Psi_{\text{PH-Pf}}(\{z_i\}) = J^2 \text{Pf}\left(\frac{1}{\bar{z}_i - \bar{z}_j}\right). \tag{14}$$

To be studied in numerics, one needs to project the wave function into a single LL, which turns out to be subtle. An alternative wave function can be obtained based on the argument of negative flux attachment Jolicoeur (2007). However, there is limited numerical support for either wave function to describe a gapped phase after the lowest LL projection. This issue will be discussed more in Section "Overview of numerical results".

Unified description: Kitaev's 16-fold way

Based on different approaches such as trial wave functions, CFT, parton theory, and particle-hole conjugation, other possible candidates for describing FQH states at half-integer filling factors were introduced. They are listed in Table 3. Some of them may be irrelevant to the 5/2 state in monolayer GaAs quantum wells, but they may describe different half-integer states in other materials listed in Table 1. For example, the spin-unpolarized version of Halperin-331 state is believed to describe the FQH state at $\nu = 1/2$ in bilayer systems and wide quantum wells. It has been studied widely numerically He et al. (1993), Peterson and Das Sarma (2010), Peterson et al. (2010), Scarola et al. (2010), Scarola and Jain (2001), Yoshioka et al. (1989). Also, the 221 parton state may describe

Table 3 Possible topological orders in the 16-fold way for the spin-polarized 5/2 state, and their predicted experimental signatures and topological shifts.

$\mathcal{C}$	*Name*	*References*	$g_e/4$	κ_H	*Even-odd effect?*	*Shift*
0	K = 8	(i, ii)	**1/8**	3	No	3
1	Pfaffian	(iii, iv)	**1/4**	3.5	Yes	3
–1	PH-Pfaffian	(v, vi)	**1/4**	2.5	Yes	1
2	331	(i)	**3/8**	4	Maybe	5
–2	113	(vii, viii)	**3/8**	2	Maybe	–1
3	221 parton/ $SU(2)_2$	(ix, x)	**1/2**	4.5	Yes	5
–3	Anti-Pfaffian/ $\bar{2}\bar{2}111$ parton	(ix, xi, xii, xiii)	**1/2**	1.5	Yes	–1
4	/	/	5/8	5	Maybe	/
–4	Anti-331	(xiv)	5/8	1	Maybe	/
5	/	/	3/4	5.5	Yes	7
–5	Anti-$SU(2)_2$	(xiv)	3/4	0.5	Yes	–3
6	/	/	7/8	6	Maybe	/
–6	/	/	7/8	0	Maybe	/
7	/	/	1	6.5	Yes	9
–7	/	/	1	–0.5	Yes	–5
8	/	/	9/8	7	Maybe	/

Here, the possibilities of edge reconstruction and Majorana gapping are ignored. The first column shows the Chern numbers of the topological orders. Topological orders with odd (even) are non-Abelian (Abelian). On the edges of these topological orders, there are chiral Majorana fermion modes. The orders with have upstream neutral modes. Since a pair of Majorana fermion modes can be combined into a neutral Bose mode, there is no unpaired Majorana fermion mode at even. In the second and third columns, we provide the usual names of the topological orders in the existing literature if any (see the end of this caption for the key of the references). The smallest possible charge anyon has the charge e/4. When the edge is in the disorder-dominated phase, the fourth column gives the tunneling exponents for the e/4 anyons. These values are boldfaced when the e/4 anyon is the most relevant quasiparticle. The fifth column lists the thermal Hall conductance in units of $\kappa_0 = \pi^2 k_B^2 T/3h$. They are half-integers (integers) for non-Abelian orders (Abelian orders). All non-Abelian orders should demonstrate the even-odd effect in a Fabry-Pérot interferometer. Abelian orders (except the K = 8 state) may also show the same effect if they possess flavor symmetry. These are listed in the sixth column. The last column shows the topological shifts for different topological orders, which are important for numerical studies performed on the spherical geometry. Note that the shifts for Abelian orders here are for the spin-polarized states. For the spin-unpolarized Halperin-331 state, the shift is 3 but not 5 Wen (1993). For Abelian orders with the shifts are unpublished. A brief overview of different experimental techniques are given in Section "Early experiments and evidence for/against non-Abelian states", "Transport and optics: Bulk energy gap", "Density dependence", "Disorder, mobility, and sample design", "In-plane magnetic field and sample tilt impacts the bulk gap", "Optical probes of the bulk gap", "Surface acoustic waves, geometric resonance transport, light scattering, and Knight shift: Spin polarization", "Surface acoustic waves and geometric resonance", "Transport", "Light scattering", "Knight shift", "Tunneling with QPCs and SETs: Quasiparticle charge and edge exponents", "QPC tunneling", "SETs", "Edge exponents from tunneling conductance", "Noise in QPCs: Upstream neutral mode", "Interferometry: Quasiparticle charge and braiding", "Interferometry and charge", "Interferometry and braiding", "Summary of early experimental findings", "Recent surprises and puzzles", "Experimental results", "Possible interpretations", "Bulk edge correspondence: PH-Pfaffian", "Disorder induced Pf-APf domain walls", "Partial equilibration on anti-Pfaffian edges", "Recent and ongoing developments", "Temperature dependence of ℓ_{eq}", "Interface experiments", "Summary of recent developments", "Future directions". For a detailed discussion, see Ma and Feldman (2019b). The labels for the references in which the topological orders were introduced are (i) Halperin (1983); (ii) Wen and Zee (1992a); (iii) Moore and Read (1991); (iv) Greiter et al. (1991); (v) Son (2015); (vi) Zucker and Feldman (2016); (vii) Yang and Feldman (2014); (viii) Yang (2015); (ix) Jain (1989b); (x) Jain (1990); (xi) Levin et al. (2007); (xii) Lee et al. (2007); (xiii) Balram et al. (2018a); (xiv) Yang and Feldman (2013).

half-integer states in graphene systems Kim et al. (2019), Wu et al. (2017). Given that these topological orders were introduced via different approaches, it is desirable to have a unified and systematic description.

The possible types of topological orders or phases in the paired quantum Hall state depend on the spin polarization of electrons and the associated composite fermions. Experimental results suggest that the 5/2 state observed in GaAs samples at the electron density $\rho \sim (2\text{–}3) \times 10^{11}\ \mathrm{cm}^{-2}$ are spin polarized (see Section "Early experiments and evidence for/against non-Abelian states"). This conclusion is also supported from numerical work (see Section "Overview of numerical results"). Furthermore, a recent geometric resonance measurement performed very close to $\nu = 5/2$ has provided strong evidence of a fully spin-polarized Fermi sea for composite fermions Hossain et al. (2018).

There are an infinite number of possible channels for pairing composite fermions which would, at first, appear to give an infinitely long list of possible topological orders for describing the 5/2 state. But the classification of possible theories is constrained. The classification of topological orders is based on the types of anyons they possess Wen (2004). When two topological orders have the same set of anyons (i.e., all fractional charges, braiding statistics, and fusion rules are the same), then they are equivalent. Following the above definition, there are only 16 possible topological orders from pairing spin-polarized composite fermions. This property is known as Kitaev's 16-fold way Kitaev (2006). Therefore, most of the existing candidates for describing the spin-polarized 5/2 state are particular members in the 16-fold way Ma and Feldman (2019b). The original work by Kitaev considered topological orders with neutral excitations only, however, charge excitations exist in the 5/2 state. It was shown that all of these topological orders can host charge $\pm e/4$ anyons. The Chern number $\mathscr{C}$ of the topological order carries important information, which will be discussed below. Based on the 16-fold way description, various experimental signatures for different topological orders were predicted and summarized in Table 3.

Properties of anyons

$\mathscr{C}$ can be identified as the Chern index in the original Kitaev's 16-fold way, such that the properties of anyons in each topological order can be inferred. The eight orders with even $\mathscr{C}$ are Abelian, whereas the eight with odd $\mathscr{C}$ are non-Abelian. In the latter case, quasiparticles with charges $(2m+1)e/4$ (where $m \in \mathbb{Z}$) are non-Abelian anyons. For the former case, there are two different types (or flavors) of Abelian anyons for quasiparticles with charges $(2m+1)e/4$. The scaling dimensions of the electron operator, and the operators for quasiparticles with charges $\pm e/4$ and $\pm\, e/2$ are Ma and Feldman (2019b)

$$\Delta_e = \frac{3}{2},\ \ \Delta_{e/2} = \frac{1}{4},\ \ \text{and}\ \ \Delta_{e/4} = \frac{|\mathscr{C}|+1}{16}. \tag{15}$$

These results are useful in analyzing quasiparticle tunneling conductance experiments. In particular, the low-temperature electrical conductance, in the idealized case, obeys $\sigma \sim T^{2g-2}$, where $g = 2\Delta$ is the tunneling exponent Wen (2004) and T is temperature. The value of g depends on the type of quasiparticles participating in the tunneling process, which can have different scaling dimension Δ for different candidate states for the 5/2 FQH state.

Edge theory

The Chern number $\mathscr{C}$ also specifies the number and chirality of the Majorana fermion modes on the edge of the topologically ordered phase. Suppose the edge is equilibrated by disorder, then its appropriate description consists of an overall charge mode ϕ_c and a collection of Majorana fermion modes ψ_j. Since a pair of counter propagating Majorana fermion modes can be gapped out or become localized due to electron tunneling on the edge, we can assume all ψ_j have the same chirality. In addition, these ψ_j exhibit an emergent SO($|\mathscr{C}|$) symmetry in the low temperature limit (i.e., the symmetry breaking terms are irrelevant in the renormalization group sense) and have the same velocity $\overline{v}_n$. For more details, see Yang and Feldman (2013, 2014). From the above discussion, the edge of a topologically ordered phase with Chern number $\mathscr{C}$ is described by Feldman and Halperin (2021), Ma and Feldman (2019b):

$$\mathscr{L} = -\frac{2}{4\pi}\partial_x\phi_c(\partial_x + v_c\partial_x)\phi_c + i\sum_{j=1}^{|\mathscr{C}|}\psi_j[\partial_t + \operatorname{sgn}(\mathscr{C})\overline{v}_n\partial_x]\psi_j. \tag{16}$$

Since a pair of ψ_j can be combined into a complex fermion mode and becomes a Bose mode upon bosonization, there are $|\mathscr{C}|/2$ neutral chiral Bose modes when $\mathscr{C}$ is even. Hence, Abelian orders such as the unpolarized Halperin-331 state do not have unpaired Majorana fermion modes on the edge. The existence or absence of unpaired Majorana fermion modes can be probed in the thermal Hall conductance experiments. The edge structures are different for topological orders with $\mathscr{C}$ and $\mathscr{C} + 16m$ (where $m \in \mathbb{Z}$), but the 16-fold way implies that they have the same set of anyons. Hence, they are equivalent.

Edge reconstruction and Majorana fermion gapping lead to additional candidates for describing the 5/2 edge state. These include the Majorana-gapped edge-reconstructed Pfaffian state and the Majorana gapped anti-Pfaffian state Overbosch and Wen (2008). However, their realization in real GaAs samples is not supported by tunneling conductance experiments or upstream noise measurements (see Section "Early experiments and evidence for/against non-Abelian states").

Bulk collective excitations

Incompressible FQH states must be gapped at all wavevectors. It turns out that lowest LL FQH states at filling $n_{\mathrm{CF}}/(2pn_{\mathrm{CF}} \pm 1)$ possesses a low-lying intra-LL branch of collective modes that were first identified numerically at 1/3 filling Haldane and Rezayi (1985). These modes are accurately captured by the composite fermion wave functions.

Quasiparticle-quasihole pairs inserted into $\psi^{B_{\mathrm{eff}}}$ define composite fermion magnetoexcitons. Composite fermion magnetoexcitons have a quasiparticle-quasihole spacing proportional to their wavevector. The ensuing collective mode dispersion reveals neutral roton modes at intermediate wavevectors and a well separated quasiparticle-quasihole pair at large wavevectors (Alternatively, they can be viewed as a density wave created on top of the otherwise uniform ground state.).

Composite fermion magnetoexciton wave functions have been systematically compared against unbiased numerical results and have been found to be essentially exact in the lowest LL Jain (2007). The gaps predicted from wave function energetics compare well with experiment as well Hirjibehedin et al. (2005), Kang et al. (2001), Kukushkin et al. (2009), Scarola et al. (2000b). These collective modes have also been incorporated as central features of composite fermion effective field theories of lowest LL FQH states Lopez and Fradkin (1993), Murthy and Shankar (2003). Unfortunately, accurate and well tested wave functions of the quasiparticle-quasihole excitations at 5/2 are still lacking.

A very useful approximation to FQH collective mode theory was originally formulated by Girvin, MacDonald and Platzman (GMP) Girvin et al. (1985). It only requires a ground state ansatz and captures the fact that these collective modes are akin to density waves. The GMP excitation is gapped and neutral as well. In the long-wavelength limit, the GMP mode behaves as a spin-2 mode analogous to a graviton Golkar et al. (2016a), Yang (2016), Yang et al. (2012). This graviton mode is chiral with its chirality (or polarization) depending on the FQH state Liou et al. (2019).

The GMP approximation was used to study the low lying excitations of the 5/2 state Park and Jain (2000), Wright and Rosenow (2012). Moreover, the GMP modes in Pfaffian, anti-Pfaffian, and PH-Pfaffian states have different polarizations Haldane et al. (2021), Nguyen and Son (2021). As reviewed in Section “Future directions”, this feature is useful in probing the nature of the 5/2 state. An additional type of collective excitation from Cooper-pair breaking was predicted for the Pfaffian state Greiter et al. (1991), which is dubbed as the neutral fermion mode Bonderson et al. (2011), Möller et al. (2011). It is gravitino-like and has spin 3/2 in the long-wavelength limit Yang et al. (2012). In the Pfaffian state, the GMP and neutral fermion modes can be viewed as superpartners Gromov et al. (2020). It is expected that neutral fermion modes also exist in other non-Abelian candidates in the 16-fold way. However, no related study has been reported.

Overview of numerical results

Numerical support for the Laughlin state and composite fermion theory of the FQH effect in the lowest LL was definitive and set an extremely high standard. For example, finite size effects are reduced due to the large energy gaps and fast spatial decay of correlations. Wave function overlaps between exact Coulomb ground states and the composite fermion states (including the Laughlin state) approach unity Jain (2007), Prange and Girvin (1987). Numerical support for the Pfaffian description of the FQH effect at 5/2, while impressive as reviewed in this section, is less conclusive.

Early numerical support for the Pfaffian description of the 5/2 state was provided in the seminal work by Morf (1998). Over the years, numerical work has continued to play an important role. Here we briefly discuss some technical details regarding the numerical approaches used in studies of the FQH effect before discussing important landmarks and results.

Numerical methods and geometries

The non-interacting basis states for the Hamiltonian consisting of only the electron-electron interaction, Eq. (1), are massively degenerate and there is no small parameter or normal state around which a perturbation theory can be formulated. An extremely useful parameterization, due to Haldane (1983) and discussed in more detail in Prange and Girvin (1987), reformulated the Hamiltonian into so-called Haldane pseudopotentials. Eq. (1) can be rewritten as

$$H = \sum_m V^{(n)}_{m,\text{two-body}} \sum_{i<j} \widehat{P}_{ij}(m), \tag{17}$$

where $\widehat{P}_{ij}(m)$ is a projection operator onto two particle states with relative angular momentum m and $V^{(n)}_{m,\text{two-body}}$ are the Haldane pseudopotentials in units of $e^2/\varepsilon\ell_0$. $V^{(n)}_{m,\text{two-body}}$ is the interaction energy between two electrons with relative angular momentum m projected into the n-th electronic LL (the $n = 1$ corresponds to the second LL, sometimes called the first excited LL).

To study the FQH effect at $\nu = 5/2$, the simplest model Hamiltonian is Eq. (17) with the $V^{(1)}_m$ corresponding to the Haldane pseudopotentials for the Coulomb interaction between electrons confined to the second LL. The pure Coulomb interaction is an idealized situation because the magnetic field strength is taken to infinity (or equivalently the electron mass going to zero), i.e., the case of infinite spacing between LLs or zero LL mixing.

It turns out that LL mixing Bishara and Nayak (2009), Peterson and Nayak (2013), Simon and Rezayi (2013), Sodemann and MacDonald (2013) and the finite thickness Peterson et al. (2008a, 2008b) of the quasi-two-dimensional electron system are important effects for second LL physics which must be taken into account. Finite thickness is typically parameterized by the width of the quantum well $w/\ell_0 \sim 2-3$ for GaAs samples [see Ando et al., 1982; Stern and Das Sarma, 1984; Zhang and Das Sarma, 1986] and LL mixing is parameterized by the ratio κ of the Coulomb interaction energy E_{Coul} to the cyclotron energy $\hbar\omega_c = eB/mc$ and depends inversely on the square root of the magnetic field strength:

$$\kappa = \frac{E_{\text{Coul}}}{\hbar\omega_c} \approx \frac{2.5}{\sqrt{B}}. \tag{18}$$

The second approximation is specific to GaAs heterostructures. Thus, when $\kappa \ll 1$, LL mixing can be ignored and the "pure" Coulomb Hamiltonian projected into the second LL is a good model. However, as discussed in Section "Early experiments and evidence for/against non-Abelian states" the FQH effect at 5/2 has been observed over a wide range of magnetic field strengths: 1 T $\lesssim$ B $\lesssim$ 30 T, corresponding to $2.5 \gtrsim \kappa \gtrsim 0.5$, hence, κ is never vanishingly small and is often sizable.

Besides the realistic (or idealized) Hamiltonian relevant for experimental systems mentioned above, there is a model Hamiltonian due to Greiter et al. (1992), which produces the Pfaffian as an exact zero-energy ground state. This (artificial) three-body Hamiltonian is written as

$$H_3 = \sum_{i<j<k} S_{ijk}\left\{\nabla_j^2[\delta(z_i - z_j)\nabla_k^4\delta(z_i - z_k)]\right\} \tag{19}$$

where S_{ijk} symmetrizes over all permutations of ijk. The form of H_3 is due to the fact that the Pfaffian vanishes whenever three electrons coincide Greiter et al. (1991), see Eqs. (6) and (7). Note that H_3 breaks particle-hole symmetry explicitly as does the Pfaffian wave function. The particle-hole conjugate of H_3, called $\overline{H}_3$, produces the anti-Pfaffian as an exact ground state Lee et al. (2007), Levin et al. (2007).

Three geometries are commonly utilized in numerical studies and pertinent details are discussed by Jain (2007). The experimental system is quasi-two-dimensional with edges created with confining potentials. For numerical convenience and simplicity this system is mapped to a quasi-two-dimensional one with periodic boundary conditions (the torus geometry), a rotationally symmetric system (the disk geometry), and a compact geometry where the electrons on the two-dimensional plane are mapped to the surface of a sphere with the perpendicular magnetic field produced by a magnetic monopole placed at the center (the spherical geometry). There is also the cylinder geometry (a torus with a cut) used primarily in DMRG calculations. Each geometry has pros and cons.

The torus geometry is perhaps the most straightforward Chakraborty and Pietiläinen (1995), Haldane (1985), Yoshioka (2002). The system is a parallelogram with periodic boundary conditions. The LL degeneracy per unit area is B/ϕ_0 and the filling factor is precisely defined as $\nu = \rho/(B/\phi_0)$. The energy eigenvalues are labeled by pseudo-momenta (k_x, k_y). This geometry has genus one (it has a single hole) and allows a topological ground state degeneracy greater than one that can be leveraged to identify the topological order of an exact ground state.

In the spherical geometry Wu and Yang (1976, 1977) the electrons are placed on the surface of a sphere of constant radius $R = \sqrt{Q}\ell_0$ where Q is the strength of the Dirac magnetic monopole at the center of the sphere. The total magnetic flux through the surface of the sphere is $2Q\phi_0$ and $2Q$ is an integer due to Dirac's quantization condition. The relationship between the number of electrons and the magnetic flux is given by

$$2Q = \nu^{-1}N - S \tag{20}$$

where S is an order-one number called the topological shift Wen and Niu (1990), Wen and Zee (1992b).

Different shifts S correspond to states with different topological orders. For example, the Pfaffian has $S = 3$ while the anti-Pfaffian has $S = -1$, see Table 3. The filling factor in this geometry is then defined as $\nu = \lim_{Q\to\infty} N/2|Q|$ and energy eigenstates are given as functions of total angular momentum L. This geometry has no edges and a finite degeneracy of $2(Q + n) + 1$ for the n-th LL. This makes the sphere especially convenient to study bulk physics, ground states and low-energy excitation spectra, and ansatz wave functions.

In the disk geometry, the single-particle states are especially simple Jain (2007). In fact, the disk geometry is utilized often when representing ansatz wave functions in real space and when calculating Haldane pseudopotentials of various interaction potentials. The disk geometry requires a confining potential to keep the electrons from repelling one another off to infinity. Since the disk geometry necessarily has an edge it can be used to study edge physics.

While all the numerical work has finite size effects due to the modest number of electrons that can be studied, i.e., up to about $N = 18$ for realistic Hamiltonians discussed in detail in Section "Competing phases and Landau level mixing" which has a total $L_z = 0$ subspace dimension of over 29 million states, the energy gap necessary for a FQH state to exist reduces the finite size effects substantially. See the Supplemental Materials of Balram and Wójs (2020) for the largest systems exactly diagonalized to date. We note that Monte Carlo simulations, which can treat on the order of hundreds of electrons, mostly involve the analysis of ansatz wave functions and not exact eigenstates.

Spin polarization

The FQH effect at 5/2 remained puzzling for a dozen years after its experimental discovery by Willett et al. (1987). Initial "tilt-field" experiments showed a disappearing FQH plateau upon tilting the sample with respect to the magnetic field direction while keeping the filling factor fixed. It was initially thought that the ground state at 5/2 was spin-unpolarized because of this which largely ruled out non-Abelian physics and the Pfaffian state, see Section "Surface acoustic waves, geometric resonance transport, light scattering, and Knight shift: Spin polarization". However, Morf (1998)'s seminal work changed the paradigm by providing substantial support for the Pfaffian description of 5/2.

Morf (1998) studied the pure Coulomb interaction via exact diagonalization in the spherical geometry for up to $N = 18$ electrons. As noted above, in the spherical geometry for electrons half-filling the second LL (the lowest spin-up and spin-down lowest LLs are taken to be fully occupied and inert) the relationship between Q and N for electrons in the second LL is $2Q = 2\,N\text{–}S$. In the limit of $Q \rightarrow \infty$ the filling factor is 1/2 in the second LL no matter the value of S. The Pfaffian has $S = 3$ but there is no a priori reason to fix S in exact diagonalization.[1] However, any FQH candidate state has to be a rotationally invariant state with $L = 0$ (uniform density) and a finite energy gap.

Morf (1998) showed three important things: fully spin polarized states had lower ground state energy than spin-unpolarized states, $S = 3$ had $L = 0$ ground states for all even N compared to other S, the state for $S = 3$ was found to have a finite energy gap in the thermodynamic limit (Fig. 5, top). In addition, it was shown that the wave function overlap between the exact ground state for $S = 3$ and the Pfaffian state was substantial (60–80%) and could be made nearly unity by increasing the $V_1^{(1)}$ pseudopotential by 10% compared to the bare value—the energy gap was also found to be maximum at this value of increased $V_1^{(1)}$.

A technically important point for numerical calculations is that H_3, which in the spherical geometry is written as

$$H_3 = \sum_{i<j<k} \widehat{P}_{ijk}(3Q - 3), \tag{21}$$

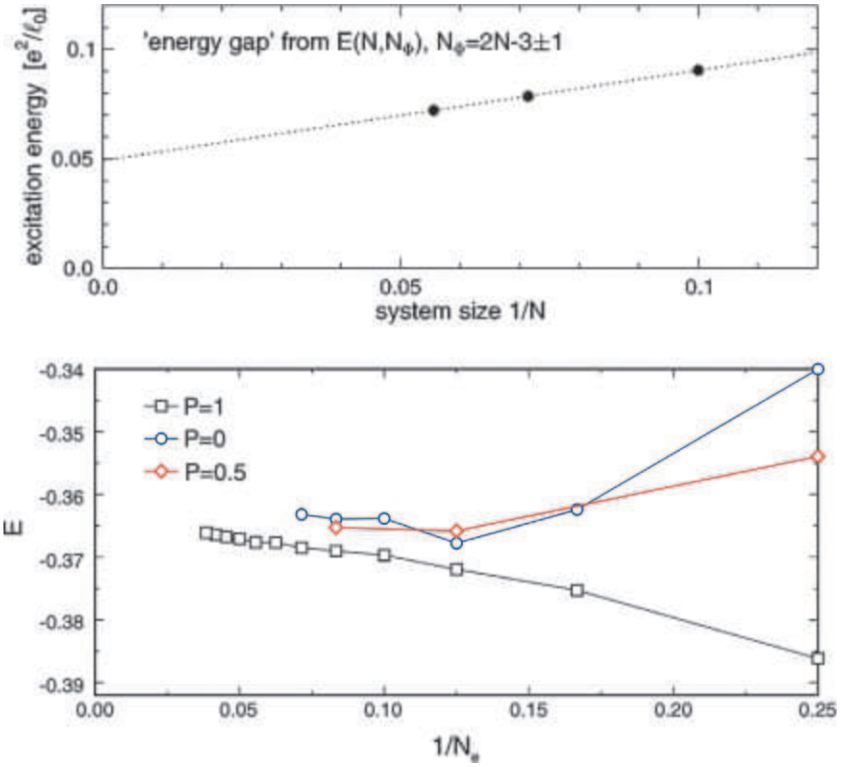

Fig. 5 (Top) Morf (1998) found the energy gap for the Pfaffian shift at $S = 3$ to be finite in the thermodynamic limit and that the low energy dispersion for fixed number of particles N displays a roton mode at finite wave vector (not shown). (Bottom) The ground state energy, obtained using density-matrix-renormalization-group techniques by Feiguin et al. (2009) for Eq. (1) in the second LL in the spherical geometry, versus inverse particle number. The thermodynamic limit is obtained for $1/N \rightarrow 0$. DMRG was able to study the largest systems to date and found the fully spin-polarized $P = 1$ ground state at the Pfaffian shift of $S = 3$ to be lower in energy than partially polarized states $P \neq 1$. This result significantly bolstered earlier results of Morf (1998). The figures are taken from Morf RH (1998) Transition from quantum Hall to compressible states in the second landau level: New light on the $\nu = 5/2$ enigma. *Physical Review Letters* 80: 1505–1508. https://doi.org/10.1103/PhysRevLett.80.1505 and Feiguin AE, Rezayi E, Yang K, Nayak C, and Das Sarma S (2009) Spin polarization of the $\nu = 5/2$ quantum Hall state. *Physical Review B* 79: 115322. https://doi.org/10.1103/PhysRevB.79.115322 with permission.

---

[1] We note a technical point in numerical studies on the sphere. From Table 3 some of the shifts for various candidate states can be up to $S = 9$. These large shifts are complicated to analyze due to an effect called "aliasing" where an instance of $(2Q, N)$ in Eq. (20) can correspond to a different filling factor ν' and a different shift S' or perhaps an excited state of an unrelated FQH state at yet another filing factor, see discussion in Morf et al. (2002).

where $\widehat{P}_{ijk}$ is a projection operator onto electron triplets with maximum angular momentum $L = 3Q–3$, can be solved to produce the Pfaffian state exactly in the second quantized representation. This greatly facilitates overlap calculations since the inner product can be calculated as a sum rather than a multi-dimensional integral. Furthermore, the energy spectrum of H_3 provides a model spectrum of a paired FQH state in a half-filled LL.

Note that Morf (1998) did not study the anti-Pfaffian with $S = –1$, which was not known at the time. Due to the particle-hole symmetry of the Hamiltonian, all the results would be identical[2] to $S = 3$ anyway.

The spin-polarization of the Coulomb interaction in the second LL is a numerically taxing problem to study, i.e., the Fock space is formidably large. While Morf (1998)'s early calculations strongly supported a spin-polarized ground state for $S = 3$, this result was more firmly established via DMRG for up to $N = 26$ particle Feiguin et al. (2008, 2009) (see Fig. 5, bottom). There is little numerical doubt that the FQH ground state at 5/2 is fully (or mostly) spin-polarized; see Biddle et al. (2013), Park et al. (1998) and Dimov et al. (2008) for more support using variational Monte Carlo techniques and Ginzburg-Landau theory, respectively. It is noteworthy that spin-polarization is maintained under realistic effects such as LL mixing and finite thickness of the quantum well Rezayi and Simon (2011).

Excitation gaps

There are several energy gaps relevant for the FQH effect at the 5/2 state. The transport gap, the "neutral" gap, and the neutral fermion gap. The thermodynamic stability of the FQH effect at 5/2 depends on all three.

Transport gap

The transport gap is the energy of a far separated quasiparticle/quasihole pair and is the gap experimentally measured by examining the longitudinal resistance; see Section "Early experiments and evidence for/against non-Abelian states". Here we discuss the transport gap calculated via exact diagonalization in the spherical geometry. The transport gap can be calculated two ways. One is to calculate the ground state energy for systems with $2Q = 2\,N–3$ and $2Q = 2\,N–3 \pm 1$, the ± 1 creates a two quasihole state or two quasiparticle state, respectively, with charges $\pm e/4$. The transport gap is the average of these excitation energies. Another method is to consider the low-energy dispersion at fixed N and take the gap between the lowest energy state for $L = N/2$ (for a paired state like the Moore-Read Pfaffian or $L = N$ for an unpaired state) and the $L = 0$ ground state.

Both of these methods for obtaining the transport gap are approximately the same. Morf (1998) found this transport gap to be approximately 0.05 $e^2/\varepsilon\ell_0$—the $\nu = 1/3$ Coulomb state in the lowest LL has a gap of about 0.1 $e^2/\varepsilon\ell_0$ for comparison Jain (2007). The gap calculations of Morf (1998) have been bolstered over the years, see Feiguin et al. (2008), Morf et al. (2002), Pakrouski et al. (2015). We note that Park and Jain (2000) used the GMP approximation to calculate the energy gap dispersion for the Pfaffian state finding similar results to Morf (1998) both qualitatively and quantitatively.

Neutral gap

The "neutral" gap is defined as the difference between the $L = 0$ ground state energy and the energy of the first excited state for any L. Morf (1998) calculated the neutral gap at $2Q = 2\,N–3$ and found it to be approximately 0.02 $e^2/\varepsilon\ell_0$. This gap is thought to be accessible experimentally via photoluminescence spectroscopy; see Section "Light scattering". In general, the neutral gap is smaller than, but of the same order of magnitude as, the transport gap.

Neutral fermion gap

The Pfaffian supports a neutral fermion excitation mode which is the gap for the Bogoliubov-de Gennes quasiparticles in the *p*-wave superconductor analogy for the Pfaffian state Bonderson et al. (2011), Greiter et al. (1991, 1992), Möller et al. (2011), Moore and Read (1991), Read and Green (2000)—this is not the "neutral" gap discussed above. This mode technically can be calculated in the spherical geometry by studying a system at $S = 3$ but for odd particle numbered systems instead of even required for pairing. Bonderson et al. (2011),(Sreejith et al., 2011), Hutzel et al. (2019), Möller et al. (2011) calculated the neutral fermion mode for the Pfaffian state and for the ground state of the second LL Hamiltonian corresponding to 5/2, see Fig. 6. Similar to the overlap and gap calculations of Morf (1998), increasing the $V_1^{(1)}$ Haldane pseudopotential by approximately 10% produced a result more in line with the Pfaffian expectation.

Realistic effects on energy gaps

Realistic effects such as LL mixing and/or finite thickness of the quantum well have been shown to generally reduce the size of the energy gaps by up to 50% Dean et al. (2008b), Luo et al. (2021), Morf et al. (2002), Pakrouski et al. (2015), Peterson et al. (2008a, 2008b). However, theoretical calculations still overestimate the experimentally measured energy gaps; see Section "Early experiments and evidence for/against non-Abelian states" below.

---

[2] For a particle-hole symmetric Hamiltonian in the spherical geometry in a half-filled LL, all spectra for S are identical to those with $S \rightarrow 2 — S$. Hence, the Pfaffian spectra for $S = 3$ is identical to the anti-Pfaffian spectra for $S = –1$.

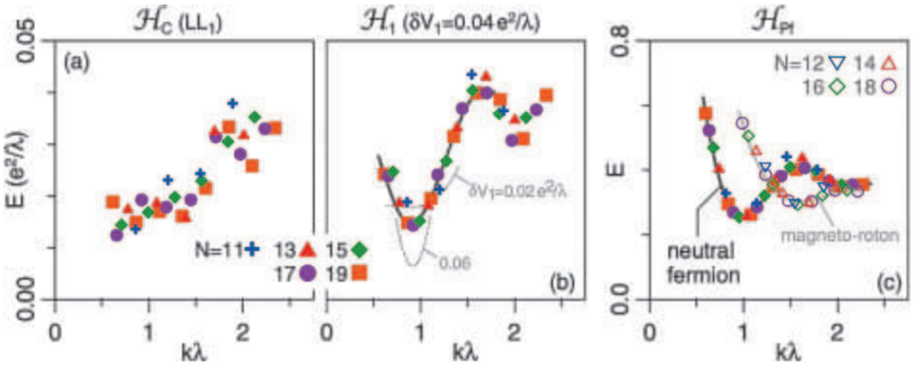

Fig. 6 Neutral fermion mode versus wave vector k in units of the magnetic length calculated using exact diagonalization in the spherical geometry by Möller et al. (2011). The right panel shows the mode for the Pfaffian state (in this work they denote the second LL Coulomb Hamiltonian H as $\mathcal{H}_C(\mathrm{LL}_1)$ and H_3 as $\mathcal{H}_{\mathrm{Pf}}$), whereas the left panel is the neutral fermion mode for the $n = 1$ Coulomb Hamiltonian. Increasing $V_1^{(1)}$ a little bit produces a mode closer qualitatively to that of the pure Pfaffian state, similar to overlaps and gaps found by Morf (1998). Note that Möller et al. (2011) denote λ as the magnetic length ℓ_0. The figure is taken from Möller G, Wójs A, and Cooper NR (2011) Neutral fermion excitations in the Moore-Read state at filling factor $\nu = 5/2$. *Physical Review Letters* 107: 036803. https://doi.org/10.1103/PhysRevLett.107.036803 with permission.

Evidence for pairing

An important physical aspect of the Pfaffian state is that the composite fermions form pairs analogous to a p-wave superconductor. Scarola et al. (2000a) used Monte Carlo with the composite fermion wavefunctions in the spherical geometry, showing that the residual interaction between the composite fermions in the second LL is attractive. This attractive interaction is not found for composite fermions in the half-filled lowest LL, see Fig. 7.

Lu et al. (2010) showed an even-odd effect in the ground state energy per particle for the second LL Coulomb Hamiltonian indicative of pairing. This effect was absent in the lowest LL and instead was qualitatively similar to the "shell" structure expected of a composite fermion Fermi sea. In addition, Lu et al. (2010) calculated a "superconducting order parameter", $\langle c_*^\dagger(\mathbf{r}) c_*^\dagger(\mathbf{0})\rangle$, where the

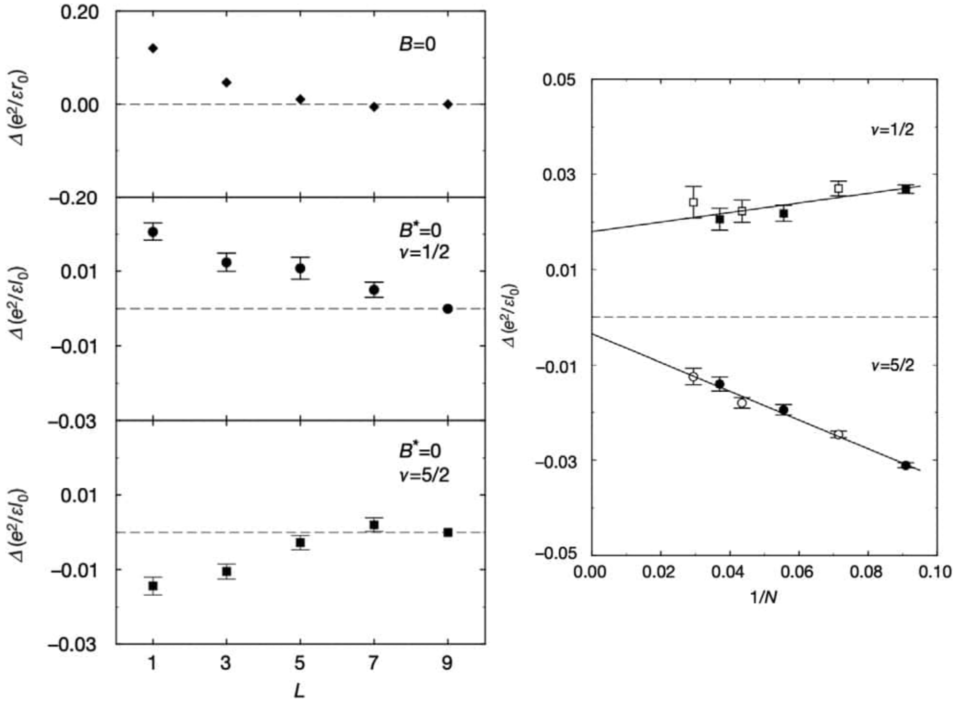

Fig. 7 (Left) The interaction energy for pairs of electrons ($B = 0$) and composite fermions ($B^* = 0$) in the lowest and second LL, respectively, versus angular momentum L, i.e., the pseudopotentials in the spherical geometry for $N = 27$ particles. Increasing L corresponds to increasing inter-particle separation when in a single LL. The short range composite fermion pseudopotentials are negative for 5/2 but not 1/2 where they are similar to those for electrons at $B = 0$. (Right) The binding energy Δ for a composite fermion pair in the second Landau level, compared to the lowest Landau level, extrapolates to a negative value as $1/N \to 0$ indicating a pairing instability in the $L = 1$ channel. Figures are taken from Scarola VW, Park K, and Jain JK (2000a) Cooper instability of composite fermions. *Nature (London)* 406: 863–865. http://www.nature.com/nature/journal/v406/n6798/abs/406863a0.html with permission.

creation operators $c_*^\dagger$ are composite fermion creation operators since they are the objects that pair in the Pfaffian state compared to electrons, see Fig. 3 in Lu et al. (2010). In addition to the above calculations, a small increase in the pair correlation function of the Pfaffian state, calculated via Monte Carlo, for small distances has been interpreted as evidence for real space pairing Park et al. (1998).

The relative stability of the Pfaffian phase and further evidence for pairing was demonstrated by Möller and Simon (2008), who considered a larger class of wave functions of the Pfaffian form, i.e.,

$$\Psi_{\text{CF}-\text{pairing}}(z_i) = J^2 \text{Pf}\left[g\left(z_i - z_j\right)\right] \tag{22}$$

where $g(z_i–z_j)$ is an antisymmetric pairing function for the composite fermions. The Pfaffian state has $g(z_i–z_j) = 1/(z_i–z_j)$, see Eq. (7). By varying the form of the interaction potential and using the pairing function as a variational parameter, it was shown through the calculation of wave function overlaps in the spherical geometry between $\Psi_{\text{CF}-\text{pairing}}$ and the exact ground state that the paring is maintained under realistic conditions, and the ground state remains in the Pfaffian phase. A similar conclusion was more recently obtained in the torus geometry by Sharma et al. (2021).

Topological properties

Any candidate for the FQH state at 5/2 must have an energy gap. There is also a consensus that some sort of pairing must be involved. However, the Pfaffian/anti-Pfaffian state has specific signatures related to yet another important property: non-Abelian topological order.

Topological shift

The shift S in the spherical geometry is a topological quantum number related to the topological order of the FQH state. The shift arises due to the orbital motion and the curvature of the sphere Wen and Niu (1990). Various candidate FQH states have an associated shift when represented in the spherical geometry. Incidentally the shift is related to the Hall viscosity Read (2009). As discussed above Morf (1998) found in the absence of LL mixing effects that $S = 3$ was rotationally invariant for all even N and had a finite energy gap. This is not necessarily true for other S.

The torus geometry does not have a shift. However, the so-called infinite-DMRG calculations done on an infinite cylinder can cleverly extract the shift from the quantum entanglement data of the ground state as the leading term of a theoretical object called the "momentum polarization" Tu et al. (2013), Zaletel et al. (2013, 2015).

Ground state degeneracy

In the torus geometry, the Pfaffian state displays an exact threefold ground state degeneracy at unique values of pseudomomenta. Note that we have factored out the (trivial) twofold center-of-mass degeneracy from the filling factor. This degeneracy can be understood analytically, see Greiter et al. (1992), and shows up numerically as well. Thus, if the second LL Coulomb interaction Hamiltonian is in the Pfaffian phase it should show this threefold (quasi)degeneracy. Peterson et al. (2008a, 2008b, 2010), Rezayi (2017), Wang et al. (2009) all found the threefold quasi-degeneracy manifest for the 5/2 system. In fact, Peterson et al. (2008a, 2008b) found that the realistic effect of finite thickness of the quantum well enhanced the degeneracy compared to the pure second LL Coulomb interaction.

Wave function overlaps

The numerical wave function overlap between the Pfaffian state and second LL Coulomb ground state was calculated by Morf (1998) and found to be nearly 80% and could be made nearly unity by increasing the short-range Haldane pseudopotential. We note that the interpretation of overlap calculations, while used widely in the study of FQH states, are subtle. Overlaps are necessarily calculated for finite size systems and vanish in the thermodynamic limit trivially. Thus, a high overlap should not be taken as evidence of the existence of a phase in isolation. Nonetheless, high overlaps between the exact ground state of second LL Coulomb interaction have been routinely calculated and have been shown to increase with moderate finite thickness of the quantum well before eventually decreasing at very wide quantum wells (Jeong and Park, 2015; Morf, 1998; Pakrouski et al., 2015; Papić et al., 2009; Peterson et al., 2008a,b; Rezayi, 2017; Rezayi and Simon, 2011; Tylan-Tyler and Lyanda-Geller, 2015; Wang et al., 2017).

Entanglement entropy and spectra

The overlap is not universal and vanishes in the thermodynamic limit. The entanglement entropy and spectrum provide a more universal signature. A wave function's entanglement entropy is calculated by dividing the system into two subsystems A and B, in orbital space,[3] and constructing the reduced density matrix ρ_A by taking a partial trace of all the degrees of freedom in the B subsystem, or vice-versa Srednicki (1993). The entanglement entropy is then the von Neumann entropy $S_E = -\text{Tr}[\rho_A \ln \rho_A]$ of ρ_A. For gapped ground states, S_E can be shown to generically scale with the length of the boundary between the two subsystems

---

[3] The division into subsystems can also be done in real space, see Sterdyniak et al. (2012). We consider only orbital cuts here.

Srednicki (1993). If a state has topological order, S_E will show a reduction by a universal constant, i.e., for a topological state the entanglement entropy is expected to obey

$$S_E = \alpha L - \gamma + \mathcal{O}(1/L) \tag{23}$$

where L is the length of the boundary, α is a system dependent non-universal constant, and γ is the so-called topological entanglement entropy Kitaev and Preskill (2006), Levin and Wen (2006). For a topologically ordered state $\gamma = \ln \mathcal{D}$ where $\mathcal{D}$ is the total quantum dimension of the theory, see Nayak et al. (2008). For the Pfaffian, $\gamma = \ln \sqrt{8}$ Dong et al. (2008), Fendley et al. (2007), Moore and Read (1991), Zozulya et al. (2007).

Consistent with energy gaps and overlaps, Friedman and Levine (2008) and Biddle et al. (2011) found that γ for ground state of the half-filled second LL Hamiltonian was consistent with the value for the Pfaffian state when finite thickness of the quantum well was included, see Fig. 3 in that work.

It turns out there is far more information in ρ_A than the entanglement entropy. Li and Haldane (2008) investigated the eigenvalues of ρ_A and defined corresponding entanglement "energies" ξ_n, whose spectrum is called entanglement spectrum. The entanglement spectrum can be used as a universal "fingerprint" to identify the topological order of a wave function. The low-lying levels are related quantitatively and qualitatively to the related CFT and its corresponding edge theory—the orbital cut is thought to create an edge of sorts and the edge excitations can be studied. Fig. 8 shows the entanglement spectra calculated by Li and Haldane (2008) for the ground state of the half-filled second LL for a system with $N = 16$ electrons in the spherical geometry. The inset shows the entanglement spectra for the Pfaffian wave function. For the Coulomb state there are several low-lying levels that match those of the Pfaffian and there is a so-called "topological entanglement gap" to non-universal levels protecting the topological properties.

The low-lying entanglement spectrum for the 5/2 system is maintained when finite thickness effects are included in addition to LL mixing effects (Section "Competing phases and Landau level mixing").

Edge velocities

While the entanglement spectrum is used to investigate the edge excitations by proxy, Wan et al. (2006) utilized the disk geometry to study the edge excitations of the Pfaffian state and the second LL Coulomb state directly. Chiral edge excitations were identified and fractionally charged excitations were consistent with the Pfaffian description. Additionally, the velocities for the fermionic and bosonic excitation branches v_b and v_f, respectively, were found to satisfy $v_b \gg v_f$. In a follow up work, Wan et al. (2008) mixed in the three-body H_3 term perturbatively to the analysis (similar to LL mixing discussed below) and suggested that a smooth edge confinement potential might favor the anti-Pfaffian state while a sharp edge favors the Pfaffian. As mentioned above, finite size effects arise more readily in the disk geometry and this work required particular care to choose a proper confining potential.

In contrast to edge studies in the disk geometry, Soulé et al. (2013) studied edge modes of the Pfaffian state (compared to the second LL Coulomb ground state) in a QPC-type geometry using an open cylinder. With a combination of exact diagonalization, using H_3 to generate the Pfaffian state exactly, and Monte Carlo, it was found that $v_b \approx v_f$.

Non-Abelian quasiparticles

Perhaps the most interesting aspect of non-Abelian FQH states is the braiding statistics of the excitations and their non-Abelian nature Moore and Read (1991), Nayak and Wilczek (1996), Prodan and Haldane (2009), Read and Rezayi (1996). Within the context of CFTs the non-Abelian braiding statistics are well-established as discussed above in Section "Theoretical background". In the spherical geometry the Pfaffian Hamiltonian in Eq. (19) produces a zero-energy 2^{n-1} degenerate manifold of states from

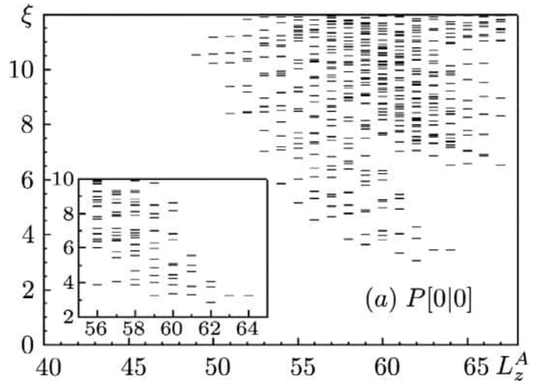

Fig. 8 The low-lying entanglement spectra ξ for the ground state of the half-filled second LL Coulomb interaction Hamiltonian for $N = 16$ electrons in the spherical geometry as a function of z-component of total angular momentum L_z^A in the A partition. The inset shows low-lying entanglement spectra for the Pfaffian state. The low-lying levels of both are in close correspondence and match the expectations from CFT for the Pfaffian. $P[0|0]$ corresponds to a particular orbital cut explained in detail by Li and Haldane (2008). The figure is taken from Li H and Haldane FDM (2008) Entanglement spectrum as a generalization of entanglement entropy: Identification of topological order in non-abelian fractional quantum Hall effect states. *Physical Review Letters* 101: 010504. https://doi.org/10.1103/PhysRevLett.101.010504 with permission.

$2n$ quasiholes, separated from the continuum by an energy gap, when exactly diagonalized at $2Q = 2N{-}3 + n$. The degeneracy 2^{n-1} is only obtained in the limit of $N \gg n$ and finite size effects produce more complicated degeneracies given in Table I of Read and Rezayi (1996)—an example of the non-Abelian zero-energy quasihole manifold is shown Fig. 3 of the same work for a system with $N = 10$ electrons. These quasihole excitations are analogous to the vortex excitations in the p-wave superconductor analogy of the Pfaffian state. Monte Carlo calculations were performed by Tserkovnyak and Simon (2003) confirming the CFT predictions of the Pfaffian quasihole wave functions Nayak and Wilczek (1996). Using the so-called bipartite composite fermion theory, (Sreejith et al., 2011a,b)constructed ansatz states for the non-Abelian quasiparticle excitations that accurately represent the non-abelian excitations of Eq. (19) and possibly are adiabatically connected to the low-energy states of the second LL Coulomb Hamiltonian.

However, a fair amount of numerical controversy continues regarding the question of whether non-Abelian excitations are manifest in a system with a realistic interaction appropriate for the FQH effect at 5/2. Generally, the Coulomb interaction, even when realistic effects such as LL mixing and finite thickness are included, does not show a zero-energy manifold of non-Abelian quasihole states separated from the continuum by an energy gap. Instead the quasihole degeneracy is strongly broken and the energy gap is not clearly discerned Peterson et al. (2008c), Tőke and Jain (2006), Wójs et al. (2010). Recently, Hutzel et al. (2019) showed that the zero-energy quasihole manifold is adiabatically connected to a degeneracy-broken set of states of a two-body Hamiltonian related more closely to the second LL Coulomb Hamiltonian than the three-body Hamiltonian of Eq. (19). Thus, it is possible that the broken quasihole degeneracy generally observed in two-body interacting systems is a consequence of finite-size effects and mutual quasihole interactions Nayak et al. (2008).

Finally, a recent parton wave function describing a half-filled FQH state, called the $\bar{2}\bar{2}111$ state was constructed based on the original idea in Jain (1989b). This wave function is constructed and analyzed in real space, via Monte Carlo for example, and was shown to be in the same phase as the anti-Pfaffian via an analysis of its entanglement spectra, wave function overlap, and pair correlation function Balram et al. (2018a). Since the anti-Pfaffian does not have a simple real space expression similar to Eq. (6) for the Pfaffian, the $\bar{2}\bar{2}111$ state is a particularly convenient representation. Beyond the convenience of the $\bar{2}\bar{2}111$ representation of the anti-Pfaffian, the parton theory of the half-filled second LL suggests a unique hierarchy of expected FQH states. In particular, the sequence of states from $\nu = 2 + 2/3$ to $2 + 1/2$ and $2 + 6/13$ discussed as possibly exotic in experiments Kumar et al. (2010). The $2 + 6/13$ state, which is topologically equivalent to the hierarchy state of Levin and Halperin (2009), is unexpected from weakly interacting composite fermion theory without the more robust observations of states at $\nu = 2 + n/(2n + 1)$ for $1 \leq n \leq 5$, see (Balram, 2021; Balram et al., 2018b, 2019). In fact, recent experimental work by Huang et al. (2022) in bilayer graphene used this method to investigate whether various half-filled FQH states arose from the anti-Pfaffian or the Pfaffian.

Adiabatic continuity

Historically, an important piece of numerical evidence supporting the Laughlin description of the FQH effect at $\nu = 1/3$ was that the Laughlin state was adiabatically connected to the Coulomb ground state. In this case the logic is straightforward. The Laughlin state for 1/3 is the exact ground state of Eq. (1) for which only $V^{(0)}_{1,\text{two-body}} \neq 0$ while all others are set to zero, the so-called hard-core potential. To show adiabatic continuity between the lowest LL Coulomb ground state and the Laughlin state, one calculates the energy spectrum for the Coulomb Hamiltonian and then "adiabatically" reduces all Haldane pseudopotentials other than $V^{(0)}_{1,\text{two-body}}$ to zero. If the energy gap remains finite throughout this process then the ground states for the "hardcore" potential and the lowest LL Coulomb Hamiltonian are equivalent.

For the FQH effect at 5/2, demonstrating adiabatic continuity is more complicated. Complications arise because H_3 (producing the Pfaffian) is a three-body interaction that is (i) artificial and (ii) breaks particle-hole symmetry. Nonetheless, one can construct a Hamiltonian that interpolates between the second LL Coulomb interaction and H_3, i.e., $H(\alpha) = (1{-}\alpha)H + \alpha H_3$. In Storni et al. (2010) [and a related calculation in Hutzel et al., 2019] it was shown that for the second LL Coulomb interaction the energy gap remained open as α was tuned from zero to one showing adiabatic continuity between the Pfaffian state and the ground state for 5/2, for finite sized systems. Interestingly, adiabatic continuity was not obtained for the lowest LL Coulomb interaction showing second LL physics is crucial for the formation of the Pfaffian state.

Competing phases and Landau level mixing

So far we have discussed a preponderance of evidence showing that the Pfaffian (and anti-Pfaffian) states are viable states to describe the FQH effect at 5/2 even in realistic systems with finite quantum well thickness. However, small changes in Hamiltonian parameters have demonstrated that transitions to other competing states are possible Peterson et al. (2008a, 2008b), Rezayi (2017), Wójs et al. (2010). For example, Rezayi (2017) performed exact diagonalization on both the sphere and torus and found a first-order quantum phase transition between the Pfaffian state and a compressible stripe (anisotropic) phase. Interestingly, the pure second LL Coulomb Hamiltonian was found to be barely on the compressible side of the phase transition but increasing the finite width of the quantum well was shown to drive the system into the Pfaffian phase.

Of particular interest are perturbations that can break the degeneracy between the Pfaffian and anti-Pfaffian. The system for the particle-hole symmetric second LL Coulomb Hamiltonian is right at the cusp of a (first-order) transition between these degenerate states without a particle-hole symmetry breaking term Peterson et al. (2008c), Wang et al. (2017). Realistic effects such as finite thickness soften the interaction generally, i.e., the Haldane pseudopotentials are reduced. LL mixing, however, not only softens the interaction, it also explicitly breaks particle-hole symmetry Bishara and Nayak (2009). Since the Pfaffian and anti-Pfaffian are related via particle-hole conjugation, LL mixing is an important effect.

LL mixing can be taken into account in essentially two ways. One way is to expand the Fock space to include higher and lower LLs, i.e., allow basis states with partially filled lower and higher LLs instead of projecting all the physics to the half-filled second LL. This increased Fock space must still be truncated to a finite size in order to do any calculations. Papić et al. (2012), Rezayi and Simon (2011), Zaletel et al. (2015) all analyzed the 5/2 FQH state using various non-perturbative methods that are not controlled or exact in any limit.

In contrast, Peterson and Nayak (2013), Simon and Rezayi (2013), Sodemann and MacDonald (2013), Wooten et al. (2013) constructed an effective Hamiltonian that included LL mixing perturbatively to lowest order in the LL mixing parameter κ. Hence, this approximation is exact for $\kappa \to 0$. Further, Peterson and Nayak (2013) constructed an effective Hamiltonian that included LL mixing and finite thickness. This latter effect is subtle since it requires LL and quantum well sub-band mixing. The form of the effective Hamiltonian is

$$H(w,\kappa) = \sum_m \left[V^{(1)}_{m,\text{two -body}}(w) + \kappa\ \delta V^{(1)}_{m,\text{two -body}}(w)\right] \sum_{i<j} \widehat{P}_{ij}(m) + \kappa \sum_m \tilde{V}^{(1)}_{m,\text{three -body}}(w) \sum_{i<j<k} \widehat{P}_{ijk}(m) \tag{24}$$

where $V^{(1)}_{m,\text{two-body}}(w)$ is the bare finite thickness dependent two-body Haldane pseudopotential, $\delta V^{(1)}_{m,\text{two-body}}(w)$ is its perturbative correction due to LL and sub-band mixing, and $\tilde{V}^{(1)}_{m,\text{three -body}}(w)$ is the emergent particle-hole symmetry breaking three-body pseudopotential Simon et al. (2007).

Perturbative LL mixing treatment I

Wójs et al. (2010) were the first to numerically investigate the particle-hole symmetry breaking effective LL mixing Hamiltonian constructed by Bishara and Nayak (2009). Assuming spin-polarized electrons, Wójs et al. (2010) studied the ground state and low-energy excitations of the realistic second LL Hamiltonian as a function of κ at $S = 3$ (for the Pfaffian) and $S = -1$ (anti-Pfaffian). It was found, primarily through wave function overlaps, that the Pfaffian and its low-energy excitations were favored compared to the anti-Pfaffian. We note, however, that the two-body pseudopotentials of the effective LL Hamiltonian calculated by Bishara and Nayak (2009) were incorrect due to a subtle normal-ordering error in the perturbation theory—this error was corrected by Peterson and Nayak (2013), Sodemann and MacDonald (2013).

Non-perturbative LL mixing treatment I

Rezayi and Simon (2011) did an exact diagonalization study in the torus geometry using a truncated Fock space that included LL mixing non-perturbatively. In particular, it was shown by comparing the size of the wave function overlap between the exact ground state and the Pfaffian or anti-Pfaffian that a model that included three LLs in the truncated Fock space, the Pfaffian was preferred. However, increasing the Fock space to include four and five LLs, the anti-Pfaffian was preferred.

We note that Wójs and Quinn (2006) studied the 5/2 FQH effect under LL mixing using a truncated Fock space similar to Rezayi and Simon (2011) finding chiefly that the energy gap is strongly reduced. However, they did not discuss the anti-Pfaffian since it had not been proposed yet.

Perturbative LL mixing treatment II

The effective Hamiltonian in Eq. (24) was analyzed via exact diagonalization in the spherical and toroidal geometry by Pakrouski et al. (2015). It is noteworthy that only the lowest $m \leq 8$ emergent three-body pseudopotentials $\tilde{V}^{(1)}_{m,\text{three -body}}$ were taken into account by Pakrouski et al. (2015)—above $m = 8$ some of the three-body terms become multi-valued and it is non-trivial to consider these types of terms in calculations. However, the $\tilde{V}^{(1)}_{m,\text{three -body}}$ decrease in value for increasing m and presumably have little effect, see Section "Perturbative LL mixing treatment III" below to revisit this aspect. By analyzing wave function overlaps, entanglement spectra, energy gaps, and an order parameter used to determine particle-hole symmetry breaking, it was found that the Pfaffian state edges out the anti-Pfaffian throughout parameter space. The approximate quantum phase diagram calculated by Pakrouski et al. (2015) is shown in Fig. 9. The stability of the Pfaffian phase was measured via the "neutral" energy gap. Sharp peaks in the entanglement entropy indicate phase transitions to a compressible state for $\kappa > 0.7$–1 (depending on w/ℓ_0). Between about $0.6 < \kappa < 0.7$ there was a hint of an intermediate FQH state. The entanglement spectra in this small window had low-lying levels with a slope opposite to the Pfaffian indicative of a state with edge modes opposite to the Pfaffian. However the entanglement and energy gaps were too small to reach a firm conclusion. Recent diagonalization and overlap calculations for $\kappa > 1$ suggest a reentrant anomalous quantized Hall state captured by Bose-Einstein condensates of composite bosons (Das et al., 2022).

Non-perturbative LL mixing treatment II

In contrast to the perturbative approach of Pakrouski et al. (2015), Zaletel et al. (2015) utilized infinite-DMRG to explore LL mixing effects within a truncated Fock space including up to five LLs. Starting at an experimentally relevant value of $\kappa = 1.38$, infinite-DMRG was performed on a truncated system, at zero quantum well thickness, with three LLs for decreasing values of κ toward the perturbative limit of $\kappa = 0$. The infinite-DMRG was performed by incorporating the matrix product form of either the Pfaffian or anti-Pfaffian on an infinite cylinder with a finite radius of approximately $20\ell_0$. By analyzing the energy splitting between the Pfaffian and anti-Pfaffian (see Fig. 10), they found the anti-Pfaffian phase dominates for all κ.

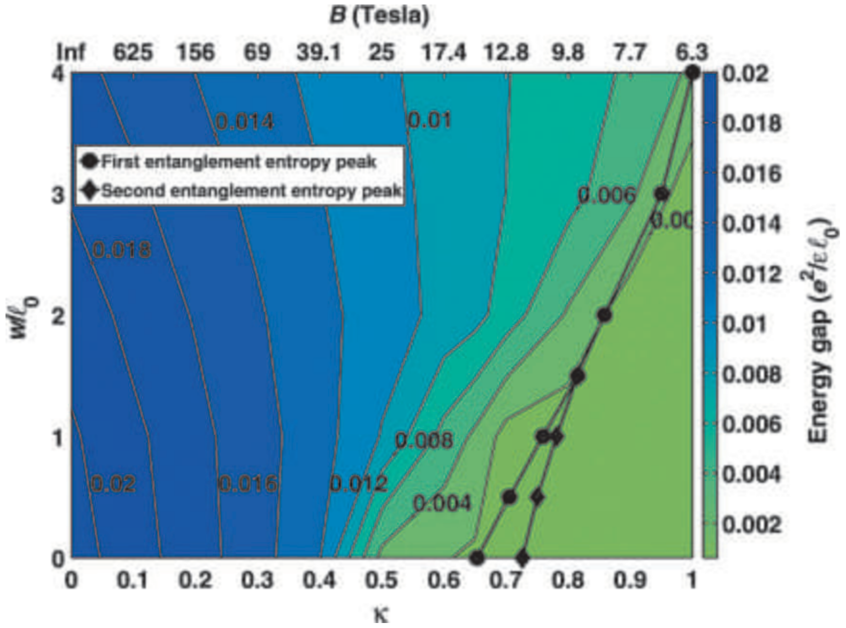

Fig. 9 Approximate quantum phase diagram for the FQH effect at 5/2 calculated by Pakrouski et al. (2015) as a function of quantum well width w/ℓ_0 and LL mixing parameter κ in the spherical geometry for a system of $N = 18$ electrons. The area left of the lines with black circles and diamonds corresponds to the Pfaffian state as determined by wave function overlap, entanglement spectrum, and a particle-hole symmetry breaking order parameter. The color indicates the strength of the "neutral" energy gap which indicates the stability of the phase. The magnetic field values in Tesla are shown on the upper ordinate $(\kappa \propto 1/\sqrt{B})$ The lines with the black circles and diamonds indicate peaks in the entanglement entropy marking phase transitions. The area to the right of the black diamonds is a non-FQH state. The small area in-between the circles and diamonds around $0.6 < \kappa < 0.7$ has a possible FQH ground state with edge modes moving opposite to the Pfaffian. The figure is taken from Pakrouski K, Peterson MR, Jolicoeur T, Scarola VW, Nayak C, and Troyer M (2015) Phase diagram of the $\nu = 5/2$ fractional quantum Hall effect: Effects of landau-level mixing and nonzero width. *Physical Review X* 5: 021004. https://doi.org/10.1103/PhysRevX.5.021004 with permission.

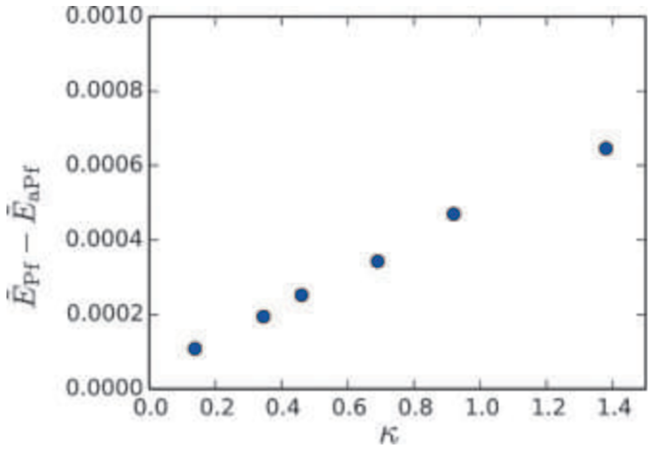

Fig. 10 Energy estimate from Zaletel et al. (2015) of the splitting between the Pfaffian and anti-Pfaffian states calculated via DMRG using a truncated Fock space simulating LL mixing as a function of κ. The positive value indicates the anti-Pfaffian is preferred from the experimentally relevant value of κ toward zero. The figure is taken from Zaletel MP, Mong RSK, Pollmann F, and Rezayi EH (2015) Infinite density matrix renormalization group for multicomponent quantum Hall systems. *Physical Review B* 91: 045115. https://doi.org/10.1103/PhysRevB.91.045115 with permission.

Perturbative LL mixing treatment III

Motivated by the contrasting results of Pakrouski et al. (2015) and Zaletel et al. (2015), Rezayi (2017) re-investigated the perturbative approach for zero quantum well width using the torus and spherical geometries for $N = 15$ and 16 electron systems. The torus geometry was utilized to directly compare the Pfaffian and anti-Pfaffian since there is no shift. The main difference between Rezayi (2017) and Pakrouski et al. (2015) was the inclusion of an approximate[4] $m = 9$ three-body LL mixing pseudopotential term in Eq. (24). As noted above, most of the emergent three-body pseudopotentials due to LL mixing above $m = 8$ are multi-component. Including this term tipped the balance toward the anti-Pfaffian as determined by wave function overlaps between the exact ground state and the Pfaffian or anti-Pfaffian, in both geometries, up to $\kappa \sim 1$ where the overlap with the anti-Pfaffian vanishes (the Pfaffian overlap collapsed early around $\kappa \sim 0.6$). The "neutral" energy gap was also shown to be larger for the anti-Pfaffian compared to the Pfaffian state. This result was found to be rather stable to changes in the value of the $m = 9$ three-body pseudopotential. However it is unknown to what extent quantum well sub-band mixing might affect the result.

---

[4] The multi-component $m = 9$ three-body term was diagonalized and the dominant term was taken as a single $m = 9$ term in Eq. (24).

Perturbative LL mixing treatment IV

In Tylan-Tyler and Lyanda-Geller (2015) a phase diagram was calculated via a perturbative LL mixing treatment and edge effects were analyzed in the disk geometry. Here both LL mixing and the neutralizing background break the Pfaffian/anti-Pfaffian degeneracy. It was found there was a quantum phase transition from anti-Pfaffian to Pfaffian as κ is increased from zero, qualitatively in contrast to what was found by Pakrouski et al. (2015). In the thermodynamic limit, the boundary effect (from the trapping potential) that breaks the Pfaffian/anti-Pfaffian degeneracy is negligible as compared to the LL mixing effect from the bulk. Meanwhile, the actual sample does have a finite size where the edge effect is present, which may play a role in breaking this degeneracy.

Unexpected experimental results and the PH-Pfaffian

Numerical work has demonstrated that the Pfaffian/anti-Pfaffian is a strong candidate for a realistic model for the FQH effect at 5/2 that includes finite thickness of the quantum well. LL mixing effects allow the possibility to determine whether a realistic system prefers the Pfaffian or anti-Pfaffian by explicitly breaking particle-hole symmetry. As discussed above, numerically that question remains unanswered as some calculations suggest the Pfaffian while others suggest the anti-Pfaffian. To some extent this question will have to be settled experimentally.

As discussed below in Section "Recent surprises and puzzles", thermal conductance experiments by Banerjee et al. (2018) were recently performed and did not settle the Pfaffian/anti-Pfaffian question. Instead, these experiments were consistent with a candidate state that is particle-hole symmetric known as the PH-Pfaffian Zucker and Feldman (2016); see Eq. (14) above. In the spherical geometry, this state has a shift of $S = 1$ (the particle-hole symmetric point) and has scant numerical support at this time. The second LL Coulomb interaction does not consistently obtain a rotationally invariant state with $L = 0$ for all N at $2Q = 2\,N{-}1$ with or without realistic effects of finite width and LL mixing. Furthermore, the overlap between the PH-Pfaffian and the exact second LL Coulomb ground state was shown by Balram et al. (2018a) to be nearly zero. On the other hand, the overlap with the lowest-lying $L = 0$ LLL Coulomb ground state is rather high leading Balram et al. (2018a) to speculate that the PH-Pfaffian is a critical state corresponding to a particle-hole symmetric pairing instability of the composite fermion Fermi sea [see also the theoretical discussion in Milovanović, 2017]. These results are consistent with those of Geraedts et al. (2016), Mishmash et al. (2018), Pakrouski (2021), Rezayi et al. (2021), Yutushui and Mross (2020).

There are theoretical suggestions by Antonić et al. (2018), Milovanović and Djurdjević (2021), Milovanović et al. (2020), Zucker and Feldman (2016) that LL mixing and/or disorder are needed to stabilize the PH-Pfaffian state. Recently, Zhu and Sheng (2019) studied disorder-driven transitions in the 5/2 FQH effect and found a transition from a pure Pfaffian/anti-Pfaffian phase, to an (unknown) intermediate phase, to a compressible composite fermion Fermi sea phase. The intermediate phase is consistent with either the PH-Pfaffian or the Pfaffian/anti-Pfaffian puddle state Lian and Wang et al. (2018), Mross et al. (2018), Wang et al. (2018), Zhu et al. (2020). Finally, Luo and Chakraborty (2017) found a positive gap (albeit less than the one for the Pfaffian shift of $S = 3$) for the PH-Pfaffian shift of $S = 1$ at finite κ via exact diagonalization on the sphere for $N = 10$ electrons. In this work they utilized yet another method of approximating LL mixing using an effective renormalized electron-electron interaction taking into account the polarizability of all the other Landau levels (random phase approximation) which preserves particle-hole symmetry.

Summary of numerical results

Extensive numerical work has been done since the discovery of the FQH effect at $\nu = 5/2$. The preponderance of evidence support the Pfaffian/anti-Pfaffian description for a realistic second LL Hamiltonian that takes into account the finite width of the quantum well. There is numerical support for the notion that the half-filled second LL Coulomb system is close to a first-order phase transition that breaks particle-hole symmetry between the Pfaffian and anti-Pfaffian. LL mixing is a realistic effect that explicitly breaks particle-hole symmetry. This effect has been incorporated into numerical studies in both the perturbative limit (exact as $\kappa \to 0$) and non-perturbative limit with mixed results. At the time of this writing, the (slim) majority of studies conclude the anti-Pfaffian is favored by LL mixing effects.

Meanwhile, thermal Hall conductance measurements at $\nu = 5/2$ yielded a result that was consistent with neither the Pfaffian nor anti-Pfaffian. Instead the result points toward either the PH-Pfaffian or disorder-induced Pfaffian/anti-Pfaffian puddle formation. The PH-Pfaffian has scant numerical support and disorder is notoriously difficult to include in numerical studies.

Early experiments and evidence for/against non-Abelian states

Theoretical developments in the quantum Hall effects walk hand-in-hand with experimental discovery and verification of hypotheses. Given the long list of possible candidates to describe the 5/2 state (Table 3), it is natural to rely on experiments to distinguish these candidate theories. Of central interest is whether or not experiments can verify the non-Abelian nature of the 5/2 state, and if so, which particular type. In this section, we summarize early experimental methods used to probe various properties of the 5/2 state. We review these results in the context of verification or exclusion of assumptions underlying certain candidate states. The next section focuses on reviewing more recent results from thermal Hall conductance measurements specifically. See also prior reviews of experimental progress in Das Sarma and Pinczuk (1996), Heiblum and Feldman (2020), Jiang and Wan (2019), Lin et al. (2014), Schreiber and Csáthy (2020), Willett et al. (2013).

Transport and optics: Bulk energy gap

Incompressibility in quantum Hall fluids requires a bulk energy gap. Larger gaps define more robust states and a vanishing of the gap defines phase boundaries in parameter space. Gaps at different momenta have acquired specific terminology.

The “transport gap” refers to the energy to create quasiparticle/quasihole pairs that are separated much further than their size, usually assumed to be directly related to gap inferred from the thermal activation transport measurements (in the following we refer to the activation gap measured in experiment as the “transport gap” to make connection with expectations from theory discussed in Section “Numerical methods and geometries”). The “neutral” bulk gap refers to the energy needed to create a quasiparticle-hole pair that are separated on the order of their size.

Numerical work shows that the quasiparticles at $\nu = 5/2$ can be as large as $\sim 10\ell_0$ Morf et al. (2002) and that the transport gap is expected to be much weaker than it is for filling factor 1/3 (see Section “Overview of numerical results”). The small gap obtained from theory is consistent with measurements showing precise quantization of the 5/2 plateau in the Hall resistance only at much lower temperatures than other fractions Pan et al. (1999b). The parameter dependence and size of these gaps offer a direct route to compare theory and experiment. Engineering a larger gap is an important goal for observing non-Abelian quasiparticles because many experiments become technically easier with large gaps.

Detailed transport measurements have been performed on the 5/2 state since its discovery. The transport gap was typically found to be less than ≈ 600 mK although a recent breakthrough set a record at ≈ 820 mK Chung et al. (2021). As discussed below, the gap depends on sample parameters. The measured transport gap of the 5/2 state is consistently found to be well below theory Choi et al. (2008), Dean et al. (2008a), Nuebler et al. (2010), Samkharadze et al. (2011) [as with the other FQH effect states Das Sarma and Pinczuk, 1996, Jain, 2007].

Several factors are known to lower the measured transport gap in comparison to the theoretical estimate of the charged gap. Finite thickness of the two-dimensional electron gas and LL mixing both soften the short range part of the Coulomb interaction and therefore lower the theoretical estimates Das Sarma and Pinczuk (1996), Jain (2007). But discrepancies still remain that are typically ascribed to disorder, which are seldom included in theoretical estimates of the gap Morf and d’Ambrumenil (2003), Wan et al. (2005).

Experimental parameters have shown a wide tun-ability of the transport gap. The following reviews experimental results showing the behavior of the transport gap at 5/2 as various parameters are tuned. These include density, in-plane fields, quantum well width, disorder, and other aspects of sample design.

Density dependence

Electronic gating of the two-dimensional electron gas allows tuning of its density, ρ. At fixed filling, increasing the density requires a linear increase in the magnetic field since $\rho = \nu B/\phi_0$. Since the Coulomb energy scales as $1/\ell_0 \propto \sqrt{B}$, increasing the density would therefore nominally increase the strength of the 5/2 energy gap in comparison to other energy scales, e.g., the temperature.

Early studies at 5/2 showed a smooth dependence of the transport gap on density Pan et al. (2001). But the role of density has been more widely explored Liu et al. (2011a), Pan et al. (2014), Reichl et al. (2014), Samkharadze et al. (2017) to reveal more complex behavior. It has been found that the transport gap of the 5/2 state is maximized at certain densities Liu et al. (2011a), Reichl et al. (2014) due to competing effects at high densities that include sub-band mixing. Furthermore, Samkharadze et al. (2017) found anomalous behavior in the transport gap and a possible topological phase transition at low densities, where LL mixing may play a role. At even lower densities, the gap was found to vanish in an apparent spin transition Pan et al. (2014) with later evidence for a nematic phase Samkharadze et al. (2016), Schreiber and Csáthy (2020), Schreiber et al. (2018) (see Section “In-plane magnetic field and sample tilt impacts the bulk gap”). Competing phases therefore also play an important role in the density dependence of transport gap measurements at 5/2.

Fig. 11 plots some of the measured transport gaps at 5/2 reported in the literature (before 2014) as a function of the density of the two-dimensional electron gas. The data do not show a clear increasing trend with density. While competing phases play a role, other important effects such as impurity screening also significantly impact gap measurements.

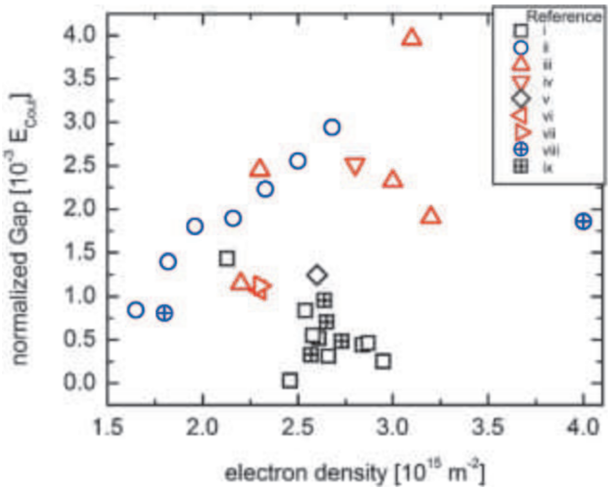

Fig. 11 Transport gaps measured at filling 5/2 normalized to Coulomb energy units ($E_{Coul} = e^2/\varepsilon\ell_0$) as a function of density of the two-dimensional electron gas as reported for various heterostructures in the literature. The symbols correspond to the following references: (i) Reichl et al. (2014), (ii) Nuebler et al. (2010), (iii) Pan et al. (2008), (iv) Choi et al. (2008), (v) Miller et al. (2007), (vi) Eisenstein et al. (1990), (vii) Pan et al. (1999a), (viii) Pan et al. (2011), and (ix) Gamez and Muraki (2013). The figure is taken from Reichl C, Chen J, Baer S, Rössler C, Ihn T, Ensslin K, Dietsche W, and Wegscheider W (2014) Increasing the $\nu = 5/2$ gap energy: An analysis of MBE growth parameters. *New Journal of Physics* 16: 023014. https://doi.org/10.1088/1367-2630/16/2/023014 with permission.

Disorder, mobility, and sample design

Disorder is believed to be responsible for a lowering of the transport gap. Disorder is typically parameterized by a constant shift Γ, where the measured transport gap is compared with $\Delta_A - \Gamma$ and Δ_A is the transport gap in the absence of disorder. The microscopic origin of Γ is not completely understood. Example scattering mechanisms include background impurities, interface roughness, alloys, or even phonons Ahn and Das Sarma (2022). Generally speaking, disorder which is in some way biased to lower the energy of spatially non-uniform excitations in comparison to otherwise uniform FQH ground states, would tend to lower the energy gap.

Mobility is often used as a proxy for sample quality because increases in zero-field sample mobility tend to, on average, increase the measured transport gap at 5/2 Choi et al. (2008), Chung et al. (2021), Dean et al. (2008b), Deng et al. (2014), Pan et al. (2011), Qian et al. (2017b), Reichl et al. (2014), Samkharadze et al. (2011, 2017), Shingla et al. (2018). But it is well known that the interplay of disorder, length scales, screening, and temperature leaves the zero-field sample mobility as only rather indirectly related to sample quality at it pertains to 5/2 Ahn and Das Sarma (2022), Das Sarma and Hwang (2014a, 2014b). This is consistent with a recent comparison between low field electron quantum lifetime measurements and 5/2 transport gaps which found a lack of correlation between these two quantities Qian et al. (2017a). The energy gap of the 5/2 state, however, was found to depend monotonically on the mobility in the regime in which only one scattering mechanism dominates, in this case alloy scattering Deng et al. (2014), Kleinbaum et al. (2020).

Screening of sample dopants and impurities can help increase the 5/2 transport gap. Fig. 11 shows a general increase in the gap with density (as nominally expected) but there is not a clear trend because many other factors impact the gap. For example, moving dopants far from the two-dimensional electron gas was reported to increase the 5/2 gap Reichl et al. (2014). Also, a nontrivial dependence was found depending upon the range of disorder in the type of sample used Pan et al. (2011). Furthermore, the FQH effect was observed at 5/2 at rather low mobility after illumination Gamez and Muraki (2013). These findings underscore the complex role of impurity screening on sample quality.

The non-trivial interplay of impurities and other parameters such as sub-band splitting led to work on the role of sample design itself to possibly engineer higher 5/2 transport gaps. It was found that samples designed to lower impurity concentrations while allowing a wide tuning of the electron density maximizes the 5/2 gap Chung et al. (2021), Liu et al. (2011a), Pan et al. (2011), Reichl et al. (2014), Watson et al. (2015). Furthermore, while it is usually expected that widening the width of quantum wells lowers the transport gap (due to a softening of the short range part of the effective Coulomb interaction; see Section "Overview of numerical results"), some experiments do show that widening the well width can increase the gap Xia et al. (2010), consistent with numerical simulations incorporating the trade off in competing phases Peterson (2012).

A recent breakthrough increased the 5/2 gap in GaAs-based quantum wells to a record 820 mK Chung et al. (2021). This significant (30%) improvement over the previous record Choi et al. (2008), Qian et al. (2017b) was achieved by reducing background impurities. A recent analysis by Ahn and Das Sarma (2022) points out that the new record brings the measured transport gap to within 40% of an ideal theoretical gap that includes only finite thickness (see Section "Numerical methods and geometries" for a discussion of finite thickness in numerics).

Confinement, pressure, and in-plane electric fields have also been explored as sample design parameters. Survival of the 5/2 state under lateral confinement in quantum point contacts (QPCs) is important for edge tunneling and braiding experiments. It was found that various confinement protocols can drive the formation of an even denominator FQH effect in the second LL Fu et al. (2016). But the direct application of a weak in-plane electric field in the Corbino geometry Zhu et al. (2018) did not show enhancement of the strength of the 5/2 state as expected Tylan-Tyler and Lyanda-Geller (2017). Pressure and strain can play a role in orientation of the nearby nematic phase Koduvayur et al. (2011) discussed below. They were found to reduce the gap at 5/2 and drive a transition to the nematic phase Samkharadze et al. (2016), Schreiber and Csáthy (2020), Schreiber et al. (2018).

In-plane magnetic field and sample tilt impacts the bulk gap

An in-plane field increases Zeeman energy in comparison to the Coulomb energy thus allowing a tuning of the ratio of these two energies. Increasing Zeeman energy would, in principal, favor states with higher spin polarization. Sample tilt in a fixed magnetic field was used to explore this ratio in the context of the important question of the polarization of the 5/2 state (see Section "Surface acoustic waves, geometric resonance transport, light scattering, and Knight shift: Spin polarization").

Sample tilt simultaneously alters several energy scales at once. For example, an in-plane field imposed by sample tilt can also alter the interaction by impacting finite thickness effects thus lowering the energy of competing ground states at 5/2 Peterson et al. (2008a, 2008b). As a result, experiments find differing behavior depending upon width, density, and tilt angle. For example, increasing tilt lowers the transport gap in some samples Dean et al. (2008a, 2008b), Eisenstein et al. (1988, 1990), Xia et al. (2010), Zhang et al. (2010), while others find weak dependence Csáthy et al. (2005),Wang et al. (2020) or even an enhancement Liu et al. (2012).

Sample tilt was found to introduce a competing anisotropic phase Du et al. (1999), Lilly et al. (1999), Pan et al. (1999a). The anisotropic phase is believed to be a compressible nematic (stripe) phase Fradkin et al. (2010), Koulakov et al. (1996), Moessner and Chalker (1996), Rezayi et al. (1999), Rezayi (2017), Schreiber and Csáthy (2020). The general trend found to date Csáthy et al. (2005), Dean et al. (2008a, 2008b), Eisenstein et al. (1988, 1990), Liu et al. (2012), Wang et al. (2020), Xia et al. (2010), Zhang et al. (2010) shows that increased tilt angles induce a transition from an isotropic incompressible state, to an anisotropic compressible state. For even larger tilt angles the anisotropy is observed to diminish with no transport gap observed.

Concomitant anisotropy and incompressibility have been reported as well. In addition to evidence reported in standard transport tilt experiments Liu et al. (2013), Xia et al. (2011), there is also evidence from optical methods Levy et al. (2016) and non-linear transport in the Corbino geometry Bennaceur et al. (2018) that there is concomitant FQH effect and charge density wave order even in the absence of tilt. Observation of FQH effect requires a gap. But charge density waves (assuming they cause anisotropy) tend to lead to compressibility. Concomitant FQH effect and anisotropy (and/or density wave order) is therefore at odds with the idea that the 5/2 FQH effect derives from a spatially uniform incompressible quantum Hall liquid. Observations of coexisting orders could also derive from domain formation Wan and Yang (2016).

Optical probes of the bulk gap

An incompressible FQH state requires a bulk collective-mode gap at all wavevectors. Optical studies of FQH states can be used to probe the bulk gap at many different wavevectors, not just the large wavevectors assigned to the transport gap. Since optical wavelengths are much smaller than the magnetic length, optical probes would be expected to create nearly zero-wavevector excitations. But the breakdown of translational invariance through, e.g., disorder, allows access to other wavevectors Das Sarma and Pinczuk (1996).

Several optics experiments at 5/2 reveal a uniform incompressible state as expected from transport experiments Du et al. (2019), Levy et al. (2016), Rhone et al. (2011), Stern et al. (2010b), Wurstbauer et al. (2013) [Note, however, that there is evidence of domain formation Rhone et al., 2011.]. Wurstbauer et al. (2013) report evidence of gapped low-lying excitations at 5/2 using resonant inelastic light scattering. The excitations observed here are reported to be consistent with spin-conserving roton-like neutral modes (see Section "Surface acoustic waves, geometric resonance transport, light scattering, and Knight shift: Spin polarization"). These results are also consistent with recent resonant inelastic light scattering experiments where the intra-LL plasmon spectrum characteristic of a nematic phase was observed to have a pronounced minimum at 5/2 Du et al. (2019). Du et al. (2019) argued that this was evidence for the strength of the uniform liquid paired state. Optical probes have also been used to infer spin polarization as discussed in the following section.

Surface acoustic waves, geometric resonance transport, light scattering, and Knight shift: Spin polarization

Anti-symmetry of the total electron wave function requires that odd l-wave chiral BCS pairing of composite fermions be in a symmetric spin state, e.g., full spin polarization. The Pfaffian wave function and other non-Abelian wave functions considered in the literature (see Table 3) usually assume full spin polarization. Full spin polarization is therefore believed to be an important condition for non-Abelian quasiparticle candidate states that have received the most attention in the literature. Although one can, in principle, construct non-Abelian states without full spin polarization, see, e.g., Barkeshli and Wen (2010a, 2010b), Faugno et al. (2019), Yang and Rezayi (2008). The following section reviews experimental findings regarding the assumption of full spin polarization.

Surface acoustic waves and geometric resonance

Pairing of composite fermions in a fully polarized state requires a fully polarized composite fermion Fermi sea Read and Green (2000) that can be thought of as originating from a composite fermion Cooper instability Scarola et al. (2000a). Surface acoustic wave measurements were used to deduce the existence of a composite fermion Fermi sea in the half-filled lowest LL ($\nu = 1/2$) Willett et al. (1993) and a later measurement Willett et al. (2002) at 5/2 revealed similar Fermi surface properties, although at 5/2 the temperature had to be tuned to be high enough to leave behind a gapless composite fermion Fermi sea at 5/2. Subsequent geometric resonance measurements Hossain et al. (2018), Mueed et al. (2017) went further to reveal evidence for a fully polarized Fermi sea near 5/2. These experiments thus provide evidence for an underlying polarized composite fermion Fermi sea that sets the stage for an instability to a fully polarized incompressible paired state at low temperatures at 5/2.

Transport

We now turn to transport experiments designed to infer the polarization of the gapped 5/2 state. Tilted field transport gap measurements were the first to be used to infer the ground state polarization Csáthy et al. (2005), Dean et al. (2008a, 2008b), Eisenstein et al. (1988, 1990), Liu et al. (2012), Wang et al. (2020), Xia et al. (2010), Zhang et al. (2010). But as discussed above, the presence of competing ground states with tilt complicates these interpretations. Early studies found a collapse of the transport gap upon tilt which was interpreted as evidence for an unpolarized (or partially polarized) state Eisenstein et al. (1988, 1990). However, the subsequent observation of a competing anisotropic phase at higher tilt Lilly et al. (1999), Pan et al. (1999a) shows that the reduction of the 5/2 transport gap was most likely due to competing phases for these parameters Dean et al. (2008a), Friess et al. (2014).

Density tuning, as opposed to sample tilt, was used as an alternate route to explore ground state polarization as inferred from the transport gap. Density and magnetic field dependence over a wide range initially showed Pan et al. (2001) no transition (in support of a full polarization). But subsequent studies Pan et al. (2014), Samkharadze et al. (2017) found evidence consistent with a spin transition from a fully polarized state at high density to an unpolarized state at low densities where LL mixing may play a strong role.

Light scattering

Light scattering has been used to probe the polarization and excitations of the 5/2 state. Polarization resolved photoluminescence spectroscopy at 5/2 exhibited a sharp drop near 5/2 which was initially interpreted as evidence for an unpolarized state Stern et al. (2010b). And a combination of elastic and inelastic resonant scattering reveals a spin-excitation continuum that suggests competing phases and possibly polarized/unpolarized domains slightly away from filling 5/2 Rhone et al. (2011). But later resonant inelastic light scattering revealed spin waves only very close to filling 5/2 Du et al. (2019), Levy et al. (2016), Wurstbauer et al. (2013) that were argued to reveal full (or nearly full) spin polarization.

Fig. 12 shows resonant inelastic light scattering data from Wurstbauer et al. (2013) performed at 5/2. Sample tilt is used to impart finite momentum transfer in photon backscattering [For a review of these methods see, e.g., Das Sarma and Pinczuk, 1996.].

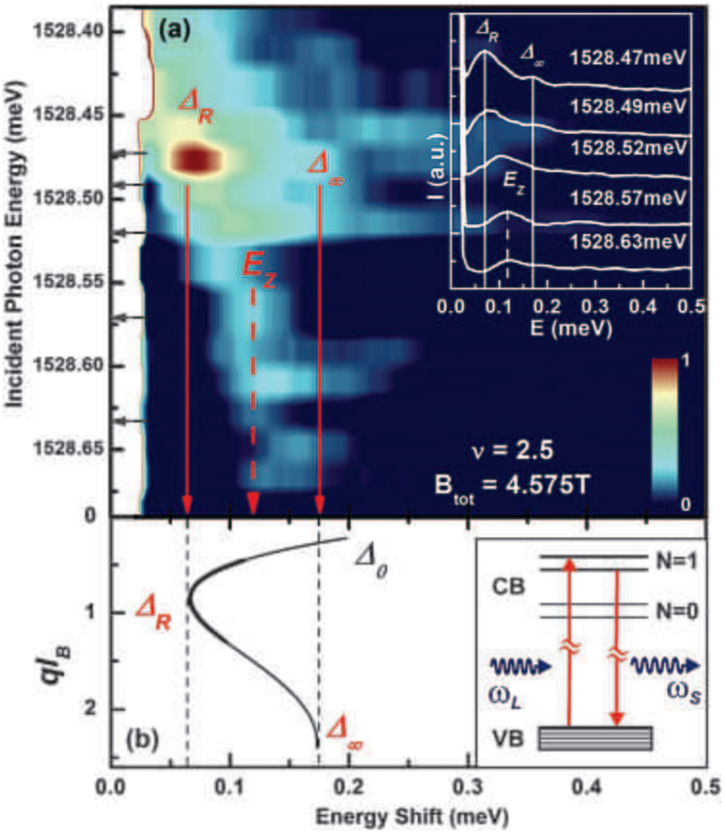

Fig. 12 (a) Resonant inelastic light scattering intensities measured at $\nu = 5/2$ as a function of the incoming photon energy. The inset shows spectra at energies marked by horizontal arrows in the color plot. E_Z labels the Zeeman energy to show evidence for spin-wave modes. (b) Empirical wavevector ($q\ell_0$) dispersion based on the observed resonant inelastic light scattering mode energies showing at least one deep roton minimum at energy Δ_R. Δ_0 and Δ_∞ label the small and large wavevector gaps, respectively. The inset shows a schematic of the optical transitions between the valence band (VB), conduction band (CB), and the LLs labeled by *N*. ω_L and ω_S label the incoming and scattered photon frequencies, respectively. The figure is taken from Wurstbauer U, West KW, Pfeiffer LN, and Pinczuk A (2013) Resonant inelastic light scattering investigation of low-lying gapped excitations in the quantum fluid at $\nu = 5/2$. *Physical Review Letters* 110: 026801. https://doi.org/10.1103/PhysRevLett.110.026801 with permission.

Fig. 12 reveals both a magnetoexciton collective mode (see Section "Overview of numerical results") and small wavevector spin wave modes excited near the Zeeman energy. The coexistence of these modes was interpreted to be consistent with a fully polarized state with a magnetoexciton, as expected for polarized candidate states such as the Pfaffian and anti-Pfaffian. A gapless mode was also found at fillings slightly away from 5/2, consistent with other optical experiments Rhone et al. (2011). These and other light scattering data therefore provide evidence for a gapped fully spin polarized state at fillings very close to 5/2 but a gapless mode (possibly due to domain formation or competing phases) slight away from filling 5/2 Du et al. (2019), Levy et al. (2016), Rhone et al. (2011), Stern et al. (2010b), Wurstbauer et al. (2013).

Knight shift

Strong evidence for full spin polarization at 5/2 also came from resistively detected nuclear magnetic resonance experiments Stern et al. (2012), Tiemann et al. (2012). These experiments rely on the hyperfine interaction between the electrons in the GaAs quantum well and the atomic nuclei. Shifts in the nuclear resonance frequency are used to infer the polarization of the electron gas (Knight shift).

Fig. 13 shows data from Tiemann et al. (2012). The data show that the ferromagnets expected at fillings $\nu = 1$ and $\nu = 1/3$ are nearly fully polarized whereas the data at and near $\nu = 5/2$ reveal full polarization (within error bars). These and other Knight shift data were interpreted as evidence for full spin polarization Stern et al. (2012), Tiemann et al. (2012) although some theory work suggests interpretation of full polarization is not always justified Chesi and Loss (2008).

Tunneling with QPCs and SETs: Quasiparticle charge and edge exponents

Candidate ground states at 5/2 all have dominant quasiparticle charges of $e/4$ (see Table 3). Experiments conclusively identifying bulk quasiparticle charge of $e/4$ are therefore crucial in confirming that the ground state at 5/2 is a paired state, a necessary condition before detecting their non-Abelian nature. Edge theories of various proposed states also rely on assumptions regarding quasiparticle charge. Many different edge tunneling exponents are predicted from these theories (Table 3). The tunneling exponent, g, is inferred from tunneling conductance measurements (see Section "Properties of anyons"). The following reviews experimental determination of quasiparticle charge and tunneling exponents with QPCs and SETs at filling 5/2.

QPC tunneling

Shot noise in tunneling across a QPC can be used to determine quasiparticle charge of a FQH liquid Girvin and Yang (2019). Initial work Dolev et al. (2008) found evidence for $e/4$, although subsequent work Dolev et al. (2010) finds the charge to be higher than expected when in a regime of very weak backscattering probability and sufficiently small excitation energies. Here the measured value of charge was found to vary with temperature and applied voltage. This puzzling result might be explained by the transport properties at low energies being dominated by agglomerate excitations with charge $e/2$, rather than the $e/4$ quasiparticles (Carrega et al., 2011). These two contributions may be distinguished by finite-frequency noise measurements (Carrega et al., 2012).

The quasiparticle charge can also be inferred from the detailed temperature and/or bias voltage dependence of QPC tunneling conductance. Here two parameters, the quasiparticle charge and the tunneling exponent are extracted. Several works Baer et al. (2014), Fu et al. (2016), Radu et al. (2008), Venkatachalam et al. (2011) extracted a quasiparticle charge consistent with

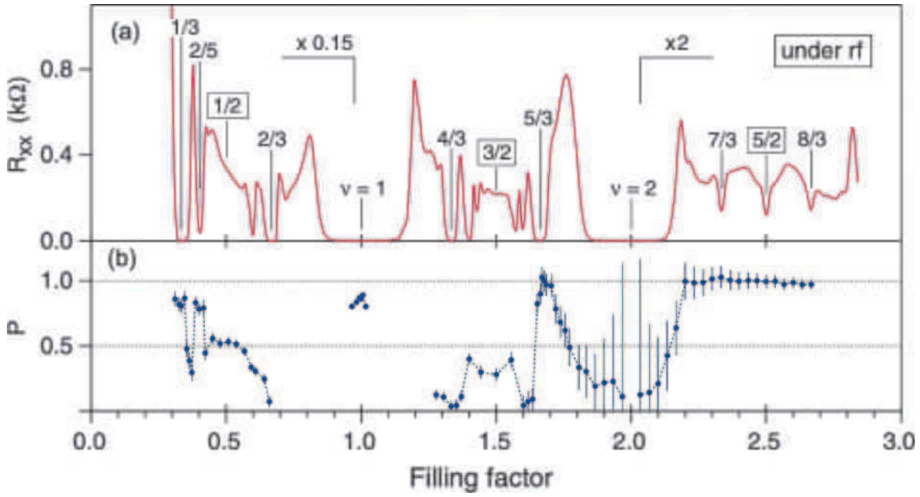

Fig. 13 (a) Longitudinal Hall resistance measured as a function of total filling factor in the presence of a radio frequency (rf) driving field. (b) The electron spin polarization (*P*) deduced from restively detected nuclear magnetic resonance plotted as a function of total filling factor. The figure is taken from Tiemann L, Gamez G, Kumada N, and Muraki K (2012) Unraveling the spin polarization of the $\nu = 5/2$ fractional quantum Hall state. *Science* 335: 828–831. https://doi.org/10.1126/science.1216697.

or below $e/4$. The non-universality of the observed charge at 5/2 is consistent with observations at other fractions Feldman and Halperin (2021).

SETs

SETs offered a method to extract local quasiparticle charge without relying on edge physics Venkatachalam et al. (2011). Here the inverse compressibility in a local region is measured and the quasiparticle charge is inferred from gate-tuned jumps. A value of $e/4$ was measured after disorder averaging. These experiments offer the most direct measurement of $e/4$ because they are local and avoid edge tunneling.

Edge exponents from tunneling conductance

Tunneling exponents extracted from tunneling conductance measurements can, unlike quasiparticle charge, be used to discern between various candidate states in Table 3. The tunneling exponent (Section "Properties of anyons") for the Majorana-gapped edge-reconstructed Pfaffian state is expected to be 0.5 Overbosch and Wen (2008). In weak backscattering tunneling conductance measurements Baer et al. (2014), Fu et al. (2016), Lin et al. (2012), Radu et al. (2008) the tunneling exponent was found to be smaller than 0.4, which is consistent with Abelian states. But confinement was found to alter the value of the tunneling exponents Fu et al. (2016). This is consistent with more recent work which finds tunneling exponents that are incompatible even with established theories of the lowest LL, e.g., the 1/3 state Hennel et al. (2018) [see also Section VIII in Feldman and Halperin, 2021 for further discussion].

Noise in QPCs: Upstream neutral mode

Some candidates for the 5/2 state possess topologically protected upstream neutral modes. These modes do not carry charge, so it is difficult to detect them in an electrical transport experiments. However, they carry energy and can generate excess upstream noise.

Noise in quantum point contact experiments have been used to detect the presence of upstream neutral modes at filling 5/2 Bid et al. (2010), Dolev et al. (2011), Gross et al. (2012). The detection of upstream neutral modes would appear to cast serious doubt on the Pfaffian state in real samples since only downstream modes are expected (see Fig. 4). On the other hand, it has been pointed out that edge reconstruction would allow an upstream neutral mode in a Pfaffian state Bid et al. (2010), Overbosch and Wen (2008).

Dolev et al. (2011) went on to explore the nature of the upstream neutral modes. They compared those found at 5/2 to those at 7/3 and 8/3 on the same device. They concluded that the neutral upstream modes are not due to edge reconstruction. Their conclusion casts doubt on the possibility of a Pfaffian ground state but supports an anti-Pfaffian state instead since it does possess an upstream neutral mode in the absence of edge reconstruction (Fig. 4).

Interferometry: Quasiparticle charge and braiding

Interferometry in the FQH regime relies on surface patterned gates to define multiple QPCs that guide edge currents in closed or open loops depending on gate voltages. The loops encircle Aharonov-Bohm fluxes to probe the accumulated phase of the wave function. The response of the device therefore depends on both the quasiparticle charge and the area enclosed. As a result, interference experiments can be used to measure both quasiparticle charge and quasiparticle braiding statistics. In this section we briefly review interferometry measurements of quasiparticle charge and braiding. More detailed discussion can be found in the reviews (Carrega et al., 2021) (Feldman and Halperin, 2021) and Willett et al., 2013.

Interferometry and charge

The Aharonov-Bohm phase depends on the quasiparticle charge. Interferometry measurements near 5/2 observed oscillations as a function of Aharonov-Bohm flux. The flux was tuned in two ways: magnetic field strength or area (tuned by a side gate). The observed oscillation patterns consistent with quasiparticle charge of both $e/4$ *and* $e/2$ were found Willett et al. (2009, 2010), but they coexist only at low temperatures. As temperature was increased, oscillations consistent with just $e/2$ charge survive. This was anticipated by Wan et al. (2008), who found the coherence length of the $e/4$ quasiparticles is much shorter than that of the $e/2$ quasiparticles, because the former involves the slow neutral mode velocity while the latter does not. As a result increasing temperature (which reduces coherence length) suppresses interference signal from the $e/4$ charge first.

Interferometry and braiding

We now review interferometry measurements that provide evidence for non-Abelian braiding statistics of quasiparticles in the 5/2 state. Interferometry experiments are expected to reveal topological properties of anyons through anomalies in the Ahoronov-Bohm effect Bonderson et al. (2006), Das Sarma et al. (2005), de Chamon et al. (1997), Fradkin et al. (1998), Nayak et al. (2008), Stern and Halperin (2006). A topological even-odd effect in interferometry was expected to lead to smoking-gun evidence of non-Abelian order (if present) derived from fusion rules summarized in Fig. 2. Nevertheless, it was later argued that some Abelian orders can also demonstrate the same effect under certain circumstances Stern et al. (2010a).

Several works went on to report evidence for non-Abelian excitations in interference experiments An et al. (2011), Willett et al. (2013, 2019). In these experiments resistance oscillations as a function of magnetic field were observed (similar to the oscillations used to infer quasiparticle charge). Here, however, periods consistent with the magnetic field needed to add one or more non-Abelian quasiparticles were observed as phase slips. The case for such oscillations were strengthened by controls done at filling 7/3 where only Abelian quasiparticles were expected. Willett et al. (2013) summarizes next steps and hurdles for operation of a device as described in Das Sarma et al. (2005). These include: phase stability, better control over device area, control of state changing current with time, and reproducibility in interference oscillations.

Summary of early experimental findings

We summarize early experimental support for assumptions underlying the possibility of candidate states hosting non-Abelian quasiparticles at filling 5/2. A culmination of experimental work finds that the bulk energy gaps measured in both optics and transport are consistent with theoretical models that account for finite thickness and LL mixing in a spin polarized state. It is expected that more realistic modeling that includes disorder would bring theory and experiment into better agreement. Furthermore, the culmination of evidence from both theory and experiment support the full polarization of the electrons in the half filled second LL, although there is some evidence of domain formation. All experiments tend to support a measured quasiparticle charge of $e/4$ with some evidence for an additional quasiparticle with charge $e/2$. Whereas results from quasiparticle edge tunneling, braiding, and shot noise have, so far, not been able to conclusively demonstrate sufficient conditions for non-Abelian quasiparticles.

Recent surprises and puzzles

The vast collection of experimental results reviewed in the previous section has provided invaluable insights into our understanding of the 5/2 state. Meanwhile, the underlying topological order remains elusive. This challenge can, in principle, be met by measuring the thermal Hall conductance,

$$K_H = c\left(\frac{\pi^2 k_B^2 T}{3h}\right) = ck_0 T. \tag{25}$$

Here, $c = c_d – c_u$ is the chiral central charge of the CFT describing the edge of the sample Cappelli et al. (2002), Kane and Fisher (1997), Read and Green (2000). Note that c_d and c_u are the total central charges for the downstream and upstream modes, respectively. When the edge of the quantum Hall system has counterpropagating edge modes, the interpretation of Eq. (25) becomes subtle. This issue will be discussed in Section "Partial equilibration on anti-Pfaffian edges".

Two types of edge modes are relevant to the 5/2 state. A Bose mode has central charge 1 or –1. This is independent of whether the mode is charged or neutral. A Majorana fermion mode has central charge 1/2 or –1/2. The positive/ negative value is adopted when the mode is downstream/ upstream in both cases. Therefore, each topological order in Table 3 has its predicted thermal Hall conductance at $v = 5/2$ given by

$$K_H = 3 + \frac{c}{2}. \tag{26}$$

The first term on the right hand side originates from the three Bose modes that exist in any topological order describing the 5/2 state. All of them are running downstream. Note that $K_H < 0$ indicates that heat (or energy) flow along the edge in the opposite direction as the flow of charges, but the sign of K_H cannot be resolved in the usual two-terminal setup.

Experimental results

The first set of experimental data of thermal conductance measurement in the 5/2 state was reported recently in Banerjee et al. (2018). The data is shown in Fig. 14.

At temperature around 20 mK, K_H was nearly quantized at $2.5\kappa_0$. This result is very exciting as the half-integer quantized value for K_H strongly supports the non-Abelian nature of the 5/2 state. Meanwhile, the result remains puzzling. It does not agree with the theoretical predicted values, namely either $K_H = 1.5\kappa_0$ for anti-Pfaffian state or $K_H = 3.5\kappa_0$ for Pfaffian state. A more detailed analysis of the data also reveals a very rapid increase of K_H at low temperature (below 18 mK). This growth is much faster than any other filling factors Banerjee et al. (2017).

Possible interpretations

Both the unusual growth of K_H at low temperature and its nearly quantized value at $2.5\kappa_0$ can be explained naturally if the sample has the PH-Pfaffian edge structure (see Section "Theoretical background"). However, the PH-Pfaffian state has not received much numerical support as the Pfaffian or anti-Pfaffian state (see Section "Overview of numerical results"). The apparent tension between experimental data and existing numerical results motivated various proposals (or scenarios), which we now turn to.

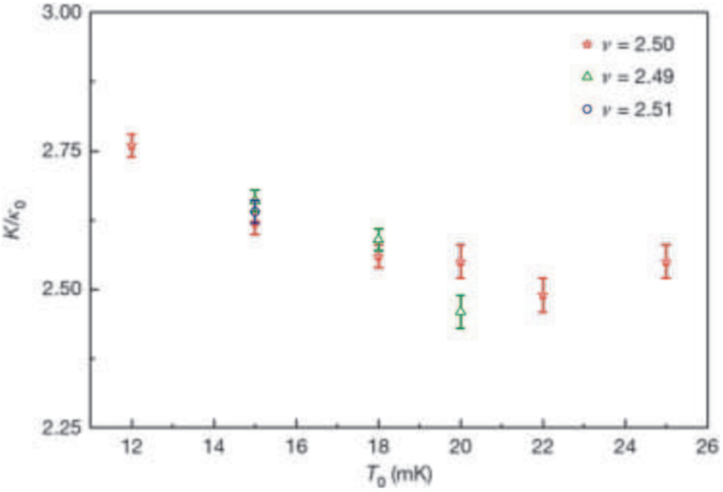

Fig. 14 Thermal conductance as a function of temperature for the 5/2 state in a GaAs heterostructure at electron number density $\rho \approx 3.0 \times 10^{10}$ cm^{-2}. Data is taken from Banerjee M, Heiblum M, Umansky V, Feldman DE, Oreg Y, and Stern A (2018) Observation of halfinteger thermal Hall conductance. *Nature (London)* 559: 205–210. https://www.nature.com/articles/s41586-018-0184-1 with permission.

Bulk edge correspondence: PH-Pfaffian

As already mentioned, the most straightforward interpretation is that the bulk possesses the PH-Pfaffian order. Then, one would need to understand how to reconcile with existing numerical studies, which largely ignored effects of disorder and LL mixing, although the latter has been treated perturbatively in some cases. It was first suggested that the PH-Pfaffian state may be stabilized by a combination of LL mixing and disorder effects Zucker and Feldman (2016). Meanwhile, the stabilization of PH-Pfaffian state by sufficiently strong LL mixing alone in uniform systems was also proposed Antonić et al. (2018), Milovanović et al. (2020). This idea is corroborated by demonstrating explicitly the possible emergence of the PH-Pfaffian state in translationally and rotationally invariant systems Sun et al. (2020). In particular, more than one LL needs to be involved in stabilizing the PH-Pfaffian state Milovanović and Djurdjević (2021).

Disorder induced Pf-APf domain walls

While it is challenging to include disorder directly in microscopic numerical studies, its effect can be studied in a more phenomenological manner. In the limit of zero LL mixing such that particle hole symmetry is preserved, the Pfaffian and anti-Pfaffian states are degenerate at $\nu = 5/2$. Disorder breaks the particle hole symmetry locally, and may induce Pfaffian and anti-Pfaffian domains. The domain walls are found to support gapless neutral (Majorana fermion) excitations, but have a charge gap Barkeshli et al. (2015), Wan and Yang (2016).

When the domain walls come close enough to each other, these neutral excitations can tunnel across the domain walls. The resulting percolation phase from the four copropagating Majorana fermions on each domain wall determines the thermal Hall conductance of the system. Using an effective network model, it was found that different phases can be realized in the system depending on the disorder strength (Lian and Wang, 2018; Mross et al., 2018; Wang et al., 2018). An effective field theory was further proposed in Hsin et al. (2020) to capture the qualitative features of the phase diagram found in Lian and Wang (2018). In principle, there is a phase with $K_H = 2.5\kappa_0$ and share the topological properties of the PH-Pfaffian state. Nevertheless, this phase is not favored for generic parameters in the network model analyzed by Wang et al. (2018). Its realization requires either the assumption that it is only a subdominant phase nucleated in the domain walls, or constraining the scattering events for Majorana fermion modes along domain walls by additional symmetry.

Using the technique of density matrix renormalization group, subsequent work studied the energetics of domain walls. It was originally concluded that the formation of domain wall is energetically unfavorable Simon et al. (2020). However, the later work Zhu et al. (2020) suggested that the intrinsic electric dipole moment emerging at the interface not taken into account in Simon et al. (2020) can stabilize the Pfaffian and anti-Pfaffian domains under experimental conditions.

The domain states discussed here are quite similar to the stripe state of Wan and Yang (2016) [proposed before the experiment Banerjee et al., 2018], where stripes (or domains) of Pfaffian and anti-Pfaffian states form spontaneously. Such a state restores particle-hole symmetry on average.

Partial equilibration on anti-Pfaffian edges

In the above two scenarios, one holds the view that the realistic sample has the PH-Pfaffian edge structure, although they have different bulk origins. This is reasonable because the value $2.5\kappa_0$ is only consistent with the PH-Pfaffian state (see Table 3). At the same time, this conclusion actually relies on the assumption that the edge of the sample is fully equilibrated. When the edge has downstream modes only, this assumption is always satisfied independent of the system size. Then, the thermal Hall conductance should agree with the theoretical predicted value in Eq. (25).

The situation becomes more subtle if the edge has counterpropagating modes. In this case the downstream and upstream modes along the same edge originate from two different sources at different temperatures Banerjee et al. (2018). The distance required for a pair of counterpropagating edge modes to reach thermal equilibration is known as the thermal equilibration length, denoted as ℓ_{eq}. In order to achieve a complete thermal equilibration on the edge, the length of the edge, denoted as L, needs to satisfy $L \gg \ell_{eq}$ Aharon-Steinberg et al. (2019), Banerjee et al. (2017).

The above subtlety gives rise to a possible reconciliation between the experimental data and the realization of anti-Pfaffian state in the sample (including the edge). When the edge is fully equilibrated, the anti-Pfaffian state has $K_H = 1.5\kappa_0$. This is because the net central charge of the edge theory is given by $c = 3–3(0.5) = 1.5$. On the other hand, the two central charges of a pair of counterpropagating edge modes should add instead of subtracting each other if these two modes do not equilibrate. Hence, K_H/κ_0 can be as large as $3 + 3(0.5) = 4.5$ in the anti-Pfaffian state, if all upstream modes do not thermally equilibrate with the downstream modes. For the measured value $K_H = 2.5\kappa_0$, it can be explained by partial thermal equilibration on the anti-Pfaffian edge. For the details of the mechanism, various proposals were introduced and debated Asasi and Mulligan (2020), Feldman (2018), Ma and Feldman (2019a), Simon (2018a, 2018b), Simon and Rosenow (2020).

Recent and ongoing developments

In an attempt to distinguish the above scenarios, several subsequent experimental and theoretical studies have been carried out.

Temperature dependence of ℓ_{eq}

Besides the value $2.5\kappa_0$, it is also important to explain the unusually rapid growth of K_H at low temperature. An increase of K_H at low temperature is actually reasonable because ℓ_{eq} is temperature dependent. Most of the topological orders (with both downstream and upstream edge modes) have $\ell_{eq} \sim T^{-2}$. For a sample edge with length L, the ratio L/ℓ_{eq} decreases as T is lowered. This can lead to a lack of thermal equilibration on the edge, and leads to an increase in K_H at low temperature Aharon-Steinberg et al. (2019), Banerjee et al. (2017).

The special structure of the PH-Pfaffian edge poses stringent constraints on possible interaction terms that couple the downstream Bose mode ϕ_c and the single upstream Majorana fermion mode ψ (see Fig. 4). The most relevant interaction is described by the operator,

$$\widehat{O}(x) = \eta(x)\partial_x\phi_c(\psi\partial_x\psi), \tag{27}$$

with $\eta(x)$ being a random variable in space. The scaling dimension of $\widehat{O}(x)$is $\Delta = 3$, which is larger than the usual operators that couple two counter-propagating Bose modes, or a downstream Bose mode and a pair of different upstream Majorana fermion modes. In the language of renormalization group, $\widehat{O}(x)$ describes a more irrelevant process and leads to $\ell_{eq}{\sim}T^{-4}$ in the PH-Pfaffian edge Ma and Feldman (2020). This exceptional dependence in temperature for the thermal equilibration length may explain the unusual rapid growth of K_H at low temperature, if the system has the PH-Pfaffian edge structure.

Interface experiments

One of the main differences among possible candidates for the 5/2 state is the number and chirality of neutral modes on the edge. Thus, it is desirable to probe them more directly. By placing a region with $\nu = 5/2$ close to another region with $\nu = 2$ or $\nu = 3$, a resulting 5/2–2 or 5/2–3 interface is formed. Some of the original edge modes are gapped out or become localized along the interface. For Pfaffian, anti-Pfaffian, and PH-Pfaffian edges, the modes that remain freely propagating along the interfaces are illustrated in Fig. 15. An important consequence is that these gapless modes dominate both charge and energy transport along the interface.

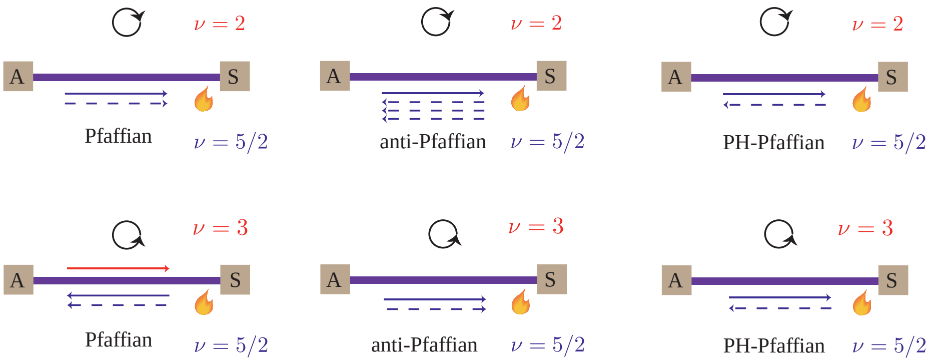

Fig. 15 Schematic diagram for the freely propagating (gapless) modes along the 5/2–2 and 5/2–3 interfaces when the 5/2 state has Pfaffian, anti-Pfaffian, or PH-Pfaffian edge. The solid lines and dashed lines label Bose charge modes and neutral Majorana fermion modes, respectively. The square with label A and S represent respectively the amplifier and source. The effective interface length is defined as the distance between A and S. A hot spot (denoted as the fire mark) is formed at the back of the source when a dc current is injected at the interface from *S*. Depending on the gapless modes' chirality, excess noise may be measured at the amplifier or not. Note that the direction of magnetic field was reversed in the experiment when switching from the 5/2–2 to the 5/2–3 interface, so that the positions of the source and amplifier needed not be interchanged.

By injecting a dc source current at the interface, a hot spot will be created at the back of the source. Relatively short interfaces (28 μm, 38 μm, 48 μm, and 58 μm) were employed in the experiment that realized thermally unequilibrated transport. In this regime, shot noise will be detected at the amplifier when there are gapless modes propagating away from the source to the amplifier. In the experiment, shot noise was observed in both 5/2–2 and 5/2–3 interfaces Dutta et al. (2022b). If one neglects the possibility of reconstruction along the interface, the experimental result is only achievable if the original 5/2 state has the PH-Pfaffian edge. This is because the PH-Pfaffian edge is the only one that remains unchanged under particle hole transformation. Furthermore, it has been theoretically proposed that electrical conductance measurement in a device that simultaneously contains both 5/2–2 and 5/2–3 interfaces could also identify the Pfaffian, anti-Pfaffian, and PH-Pfaffian edges uniquely Yutushui et al. (2022).

Another subsequent experiment was performed to measure the thermal conductance of the 5/2–2 and 5/2–3 interfaces Dutta et al. (2022a). In order to achieve thermal equilibration for a proper thermal conductance measurement, a much longer interface with length 160 μm was used. The measured values for the 5/2–2 and 5/2–3 interfaces were $(0.55 \pm 0.02)\kappa_0$ and $(0.53 \pm 0.02)\kappa_0$, respectively. For Pfaffian and anti-Pfaffian edges, either the resulting 5/2–2 or 5/2–3 interface will have a pair of copropagating Bose and Majorana fermion modes. These two modes are always equilibrated, so $K_H/\kappa_0 = 1.5$ is expected. Hence, the observed values in experiment favors the PH-Pfaffian edge in the original 5/2 state.

Summary of recent developments

To summarize, the results from recent experiments have provided increasing support for the realization of PH-Pfaffian edge in the 5/2 state. This edge structure is also consistent with previous results from tunneling experiments and the observation of upstream neutral modes. On one hand, the bulk-edge correspondence suggests that the bulk of the sample should be also described by the PH-Pfaffian state. On the other hand, the domain-wall picture hints at a possible difference between the bulk and the edge of the sample. Therefore, the underlying nature of the 5/2 state is still an open problem.

Future directions

In this section, some possible future research directions for the 5/2 state are listed.

Noise measurements

Besides the thermal conductance and interface experiments reviewed in the previous section, there are some recent theoretical proposals to identify the Pfaffian, anti-Pfaffian, and PH-Pfaffian edges via noise measurements. The corresponding results can further strengthen the support for or challenge the realization of PH-Pfaffian edges in real samples.

Shot noise in dc transport

It has been proposed that the combination of thermal conductance and shot noise measurements in dc transport can uniquely distinguish between the Pfaffian, anti-Pfaffian, and PH-Pfaffian edges. In addition to the edge modes coming from the second LL as shown in Fig. 4, all states at $\nu = 5/2$ have two additional edge modes originating from the lowest LL.

Depending on the sample edge length, it is possible that edge modes from the second LL equilibrate among themselves, but not with those from the lowest LL Ma and Feldman (2019a). In this scenario, both anti-Pfaffian and PH-Pfaffian edges will show $K_H = 2.5\kappa_0$. However, the predicted shot noises in dc measurement are distinct for these two edges. Only the anti-Pfaffian edge will generate a nonvanishing shot noise Park et al. (2020). For more details of the topological classification of noises in different types of edges, see Spånslätt et al. (2019). For the Pfaffian edge, it has no upstream modes. Thus, $K_H = 3.5\kappa_0$ independent of the sample edge length. At this moment, there is no proposal for the reconciliation between the thermal conductance data with the Pfaffian edge.

Thermal tunneling noise across a QPC

The scaling dimension of quasiparticles probed in tunneling experiments may help identify the edge structure of the 5/2 state. However, existing results depend sensitively on the device configuration and lead to ambiguous interpretations. It has been suggested that such an ambiguity could be removed by measuring the thermal tunneling noise across the QPC Schiller et al. (2022). This noise is generated due to quasiparticle tunneling, and should be defined as the excess noise away from the usual Nyquist-Johnson noise. In particular, the associated Fano factor will show different dependencies on the temperatures of the two edges and the voltage bias across the QPC, when the scaling dimension of the tunneling quasiparticle is changed. This feature allows one to distinguish between the anti-Pfaffian and PH-Pfaffian edges.

Local power measurement in multi-terminal thermal conductance experiment

The thermal conductance data reviewed in Section "Recent surprises and puzzles" was taken from a two-terminal setup, which cannot resolve the sign of K_H. Neither can it give a universal value of $|K_H|$ when the edge is not fully equilibrated. This leads to ambiguous interpretation of the experimental result. It is important to develop techniques for measuring K_H reliably, that should work independent of the equilibration on the sample edge.

In a very recent work, a multi-terminal measurement on thermal conductance was performed Melcer et al. (2022). Using the new setup, the power carried by the downstream and upstream edge modes can be measured separately. From this, K_H can be deduced properly from $K_H = K_d - K_u$, where K_d and K_u denote the thermal conductance for the downstream and upstream modes, respectively. At $\nu = 2/3$, the new setup gives $K_H = (0.04 \pm 0.03)\kappa_0$, which agrees with the theoretical predicted value, $K_H = 0$ for an equilibrated edge at $\nu = 2/3$. It would be natural to generalize the same kind of measurement to the 5/2 state. The result can provide another piece of information to help differentiate between the PH-Pfaffian and partially equilibrated anti-Pfaffian edges.

Other interferometry experiments

Direct measurement of braiding statistics of quasiparticles is an ideal probe of the topological order of a FQH liquid. While the Fabry-Pérot interferometer has become a commonly used device for detecting non-Abelian statistics, there are some caveats in this technique which were discussed in Section "Interferometry and braiding". The topological even-odd effect was originally proposed as a smoking-gun signal of non-Abelian nature of the 5/2 state Bonderson et al. (2006), Stern and Halperin (2006). However, it was later discovered that the Abelian 331 state Stern et al. (2010a), and all other Abelian states (except the $K = 8$ state) in the 16-fold way can mimic the same effect if the two types of $e/4$ anyons exhibit flavor symmetry Ma and Feldman (2019b). It will be important to include these caveats in future experimental designs to better delineate expected order at 5/2.

A recent breakthrough on interferometry at $\nu = 1/3$ in the lowest LL has significant implications for detection of non-Abelian excitations at $\nu = 5/2$ Nakamura et al. (2019). In Nakamura et al. (2020), Fabry-Pérot interferometry was used to directly observe Abelian anyon statistics at $\nu = 1/3$. Normally, such experiments are done in a regime where the strong Coulomb interaction between edge states and the bulk of the interferometer complicates interpretation of signals of anyonic phases. But samples used in Nakamura et al. (2020) incorporate epitaxially grown layers used to screen (and therefore soften) these interactions. The net result was a robust Aharonov-Bohm interference in the fractional quantum regime showing clear phase slips consistent with Abelian anyon fractional statistics. Application of these seminal developments to $\nu = 5/2$ is a logical next step.

Mach-Zehnder interferometry

Issues in discerning topological orders can be circumvented by employing the Mach-Zehnder interferometer Ji et al. (2003), Law et al. (2006), Ponomarenko and Averin (2007, 2010). Previous work discovered that the corresponding signatures (i.e., tunneling current and Fano factor) for each individual state in the 16-fold way are different Feldman and Kitaev (2006), Feldman et al. (2007), Ma and Feldman (2019b), Wang and Feldman (2010), Yang (2015), Zucker and Feldman (2016). Although it is much harder to fabricate an Mach-Zehnder interferometer than a Fabry-Pérot interferometer, the former was employed to yield evidence of fractional statistics of anyons in the FQH state at $\nu = 2/5$ Kundu et al. (2022). It will be highly desirable to perform the same experiment for the 5/2 state.

Non-Abelian anyon collider

Besides the result from the standard Fabry-Pérot interferometry Nakamura et al. (2020), fractional statistics of anyons in the Laughlin state at $\nu = 1/3$ was also observed in an anyon collider setup Bartolomei et al. (2020), Rosenow et al. (2016). In a recent preprint Lee and Sim (2022), it has been proposed that the latter technique may also differentiate among non-Abelian statistics of anyons in the Pfaffian, anti-Pfaffian, and PH-Pfaffian states. This may be achieved in future experiments.

Bulk probes: Polarized Raman scattering and thermal power

While the bulk edge correspondence is a very powerful tool in studying topological phases, there is the possibility of its breakdown in realistic samples due to various complications at the edge as discussed earlier. In fact the edge physics of the Laughlin 1/3 state is still not yet completely understood Chang (2003), most likely due (at least in part) to edge reconstruction Wan et al. (2002, 2003), Yang (2003). It would thus be highly desirable to go beyond edge physics and probe the 5/2 state (and other FQH states, Abelian or non-Abelian) in the bulk more directly in future experiments. We review some existing theoretical proposals below.

It was found that the graviton or magnetoroton in the Pfaffian state has a polarization −2 Liou et al. (2019), just like the Laughlin state. Since the chirality of the graviton is reversed under particle hole transformation Liou et al. (2019), Son (2019), the associated graviton in the anti-Pfaffian state has a polarization +2, as seen in numerics Haldane et al. (2021). The situation becomes more subtle in the PH-Pfaffian state. Due to particle hole symmetry, it is expected that gravitons (if they are present) should come with both polarizations (± 2).

In order to excite the graviton mode, a net angular momentum +2 or −2 needs to be transferred to the sample. This may be implemented by using Raman scattering with circularly polarized light Golkar et al. (2016b). Importantly, the absorption of a photon can occur only if the incoming photon has the correct polarization. For example, the incoming photon must have the polarization −1 in order to excite the graviton mode in the Pfaffian state Liou et al. (2019). On the other hand, the graviton mode in the anti-Pfaffian state requires an incoming photon with polarization +1. The emitted photon must have the opposite polarization such that the net angular momentum transfer is ± 2 for anti-Pfaffian and Pfaffian respectively. For the PH-Pfaffian state, roughly equal absorption of both kinds of polarized photons is expected Haldane et al. (2021), Nguyen and Son (2021). Suppose the sample contains Pfaffian and anti-Pfaffian domains, the same technique can also reveal this structure if the spatial resolution of the experiment is finer than the typical sizes of the domains. Since Raman scattering has already been performed in studying GMP modes in other quantum Hall states, it offers a huge potential in identifying the precise nature of the 5/2 state in future experiment, which goes beyond the knowledge from edge probes.

The polarized Raman scattering discussed above directly probes the chirality of the FQH state (namely, whether it is electron-like or hole like), but not the nature of its quasiparticles. The latter, on the other hand, can be probed using bulk thermoelectric and thermodynamic measurements Barlas and Yang (2012), Cooper and Stern (2009), Gervais and Yang (2010), Yang and Halperin (2009). More specifically, such experiments can (potentially) measure the logarithm of the quantum dimension of the non-Abelian quasiparticles, which is the topological entropy they carry (Abelian quasiparticles have quantum dimension one and thus carry no topological entropy). Subsequent thermal power experiments have yielded encouraging but not yet definitive results Chickering et al. (2010, 2013). It would be highly desirable to continue this line of work.

Conclusion

The physics of the 5/2 FQH state, most likely the first and only non-Abelian state of matter identified in nature at the time of writing, is extremely rich. This richness, revealed through enormous experimental, theoretical, and numerical effort, underlies the decades-long debate over the precise nature of the ground and excited states. Considerable progress has been made on all of these fronts, as we have reviewed here. The remaining unresolved puzzles that we have outlined in this chapter offer exciting opportunities for future research.

Acknowledgments

We would like to thank Ajit Balram, Matteo Carrega, Luca Chirolli, Gabor Csáthy, Sankar Das Sarma, Dima Feldman, Moty Heiblum, Jainendra Jain, Thierry Jolicoeur, Sudhansu Mandal, Michael Manfra, Kwon Park, Edward Rezayi, Ganesh Sreejith, and Steve Simon for helpful suggestions and comments. KKWM is supported by the Dirac postdoctoral fellowship in the National High Magnetic Field Laboratory. MRP acknowledges support from the Office of Research and Sponsored Programs at California State University Long Beach. VWS acknowledges support from AFOSR FA9550-18-1-0505, FA2386-21-1-4081. KY acknowledges support from NSF grant No. DMR-1932796. The work of KKWM and KY was performed at the National High Magnetic Field Laboratory, which is supported by National Science Foundation Cooperative Agreement No. DMR-1644779, and the State of Florida.

References

Aharon-Steinberg A, Oreg Y, and Stern A (2019) Phenomenological theory of heat transport in the fractional quantum Hall effect. *Physical Review B* 99: 041302. https://doi.org/10.1103/PhysRevB.99.041302.

Ahn S and Das Sarma S (2022) Density-dependent two-dimensional optimal mobility in ultra-high-quality semiconductor quantum wells. *Physical Review Materials* 6: 014603. https://doi.org/10.1103/PhysRevMaterials.6.014603.

An S, Jiang P, Choi H, Kang W, Simon SH, Pfeiffer LN, West KW, Baldwin KW (2011) *Braiding of Abelian and Non-Abelian Anyons in the Fractional Quantum Hall Effect.* arXiv:1112.3400. http://arxiv.org/abs/1112.3400.

Ando T, Fowler AB, and Stern F (1982) Electronic properties of two-dimensional systems. *Reviews of Modern Physics* 54: 437–672. https://doi.org/10.1103/RevModPhys.54.437.

Antonić L, Vučičević J, and Milovanović MV (2018) Paired states at 5/2: Particle-hole Pfaffian and particle-hole symmetry breaking. *Physical Review B* 98: 115107. https://doi.org/10.1103/PhysRevB.98.115107.

Apalkov V and Charkaborty T (2023) Interacting Dirac fermions and the rise of Pfaffians in graphene. In: *Encyclopedia of Condensed Matter Physics, 2e*. https://doi.org/10.1016/B978-0-323-90800-9.00102-5.

Arovas D, Schrieffer JR, and Wilczek F (1984) Fractional statistics and the quantum Hall effect. *Physical Review Letters* 53: 722–723. https://doi.org/10.1103/PhysRevLett.53.722.

Asasi H and Mulligan M (2020) Partial equilibration of anti-Pfaffian edge modes at $\nu = 5/2$. *Physical Review B* 102: 205104. https://doi.org/10.1103/PhysRevB.102.205104.

Baer S, Rössler C, Ihn T, Ensslin K, Reichl C, and Wegscheider W (2014) Experimental probe of topological orders and edge excitations in the second Landau level. *Physical Review B* 90: 075403. https://doi.org/10.1103/PhysRevB.90.075403.

Balram AC (2021) A non-Abelian parton state for the $\nu = 2 + 3/8$ fractional quantum Hall effect. *SciPost Physics* 10: 083. https://doi.org/10.21468/SciPostPhys.10.4.083.

Balram AC, Barkeshli M, and Rudner MS (2018a) Parton construction of a wave function in the anti-Pfaffian phase. *Physical Review B* 98: 035127. https://doi.org/10.1103/PhysRevB.98.035127.

Balram AC, Barkeshli M, and Rudner MS (2019) Parton construction of particle-hole-conjugate Read-Rezayi parafermion fractional quantum Hall states and beyond. *Physical Review B* 99: 241108(R). https://doi.org/10.1103/PhysRevB.99.241108.

Balram AC, Mukherjee S, Park K, Barkeshli M, Rudner MS, and Jain JK (2018b) Fractional quantum Hall effect at $\nu = 2 + 6/13$: The Parton paradigm for the second landau level. *Physical Review Letters* 121: 186601. https://doi.org/10.1103/PhysRevLett.121.186601.

Balram AC and Wójs A (2020) Fractional quantum Hall effect at $\nu = 2 + 4/9$. *Physical Review Research* 2: 032035(R). https://doi.org/10.1103/PhysRevResearch.2.032035.

Banerjee M, Heiblum M, Rosenblatt A, Oreg Y, Feldman DE, Stern A, and Umansky V (2017) Observed quantization of anyonic heat flow. *Nature (London)* 545: 75–79. https://www.nature.com/articles/nature22052.

Banerjee M, Heiblum M, Umansky V, Feldman DE, Oreg Y, and Stern A (2018) Observation of halfinteger thermal Hall conductance. *Nature (London)* 559: 205–210. https://www.nature.com/articles/s41586-018-0184-1.

Barkeshli M and Wen XG (2010a) Classification of Abelian and non-Abelian multilayer fractional quantum Hall states through the pattern of zeros. *Physical Review B* 82: 245301. https://doi.org/10.1103/PhysRevB.82.245301.

Barkeshli M and Wen XG (2010b) Non-Abelian two-component fractional quantum Hall states. *Physical Review B* 82: 233301. https://doi.org/10.1103/PhysRevB.82.233301.

Barkeshli M, Mulligan M, and Fisher MPA (2015) Particle-hole symmetry and the composite fermi liquid. *Physical Review B* 92: 165125. https://doi.org/10.1103/PhysRevB.92.165125.

Barlas Y and Yang K (2012) Thermopower of quantum Hall states in corbino geometry as a measure of quasiparticle entropy. *Physical Review B* 85: 195107. https://doi.org/10.1103/PhysRevB.85.195107.

Bartolomei H, Kumar M, Bisognin R, Marguerite A, Berroir JM, Bocquillon E, Plaçais B, Cavanna A, Dong Q, Gennser U, Jin Y, and Féve G (2020) Fractional statistics in anyon collisions. *Science* 368: 173–177. https://science.sciencemag.org/content/368/6487/173.

Bennaceur K, Lupien C, Reulet B, Gervais G, Pfeiffer LN, and West KW (2018) Competing Charge Density Waves Probed by Nonlinear Transport and Noise in the Second and Third Landau Levels. *Physical Review Letters* 120: 136801. https://doi.org/10.1103/PhysRevLett.120.136801.

Bid A, Ofek N, Inoue H, Heiblum M, Kane CL, Umansky V, and Mahalu D (2010) Observation of neutral modes in the fractional quantum Hall regime. *Nature (London)* 466: 585–590. https://www.nature.com/nature/journal/v466/n7306/full/nature09277.html.

Biddle J, Peterson MR, and Das Sarma S (2011) Entanglement measures for quasi-two-dimensional fractional quantum Hall states. *Physical Review B* 84: 125141. https://doi.org/10.1103/PhysRevB.84.125141.

Biddle J, Peterson MR, and Das Sarma S (2013) Variational Monte Carlo study of spin-polarization stability of fractional quantum Hall states against realistic effects in half-filled Landau levels. *Physical Review B* 87: 235134. https://doi.org/10.1103/PhysRevB.87.235134.

Bishara W and Nayak C (2009) Effect of landau level mixing on the effective interaction between electrons in the fractional quantum Hall regime. *Physical Review B* 80: 121302. https://doi.org/10.1103/PhysRevB.80.121302.

Bonderson P, Kitaev A, and Shtengel K (2006) Detecting non-abelian statistics in the $\nu = 5/2$ fractional quantum Hall state. *Physical Review Letters* 96: 016803. https://doi.org/10.1103/PhysRevLett.96.016803.

Bonderson P, Feiguin AE, and Nayak C (2011) Numerical calculation of the neutral fermion gap at the $\nu = 5/2$ fractional quantum Hall state. *Physical Review Letters* 106: 186802. https://doi.org/10.1103/PhysRevLett.106.186802.

Bonderson P, Nayak C, and Qi XL (2013) A timereversal invariant topological phase at the surface of a 3D topological insulator. *Journal of Statistical Mechanics* 3: P09016. http://iopscience.iop.org/article/10.1088/1742-5468/2013/09/P09016/meta.

Cano J, Cheng M, Mulligan M, Nayak C, Plamadeala E, and Yard J (2014) Bulk-edge correspondence in (2 + 1)-dimensional abelian topological phases. *Physical Review B* 89: 115116. https://doi.org/10.1103/PhysRevB.89.115116.

Cappelli A, Huerta M, and Zemba GR (2002) Thermal transport in chiral conformal theories and hierarchical quantum Hall states. *Nuclear Physics B* 636: 568–582. https://www.sciencedirect.com/science/article/pii/S0550321302003401.

Carrega M, Chirolli L, Heun S, and Sorba L (2021) Anyons in quantum Hall interferometry. *Nature Reviews Physics* 3: 698. https://doi.org/10.1038/s42254-021-00351-0.

Carrega M, Ferraro D, Braggio A, Magnoli N, and Sassetti M (2011) Anomalous charge tunneling in fractional quantum Hall edge states at a filling factor ν=5/2. *Physical Review Letters* 107: 146404. https://doi.org/10.1103/PhysRevLett.107.146404.

Carrega M, Ferraro D, Braggio A, Magnoli N, and Sassetti M (2012) Spectral noise for edge states at the filling factor ν= 5/2. *New Journal of Physics* 14: 023017. https://doi.org/10.1088/1367-2630/14/2/023017.

Chakraborty T and Pietiläinen P (1995) *The Quantum Hall Effects: Integral and Fractional*. Heidelberg, Germany: Springer-Verlag. https://doi.org/10.1007/978-3-642-79319-6.

Chang AM (2003) Chiral Luttinger liquids at the fractional quantum Hall edge. *Reviews of Modern Physics* 75: 1449–1505. https://doi.org/10.1103/RevModPhys.75.1449.

Chesi S and Loss D (2008) Quantum Hall ferromagnetic states and spin-orbit interactions in the fractional regime. *Physical Review Letters* 101: 146803. https://doi.org/10.1103/PhysRevLett.101.146803.

Chickering WE, Eisenstein JP, Pfeiffer LN, and West KW (2010) Thermopower of two-dimensional electrons at filling factors $\nu = 3/2$ and 5/2. *Physical Review B* 81: 245319. https://doi.org/10.1103/PhysRevB.81.245319.

Chickering WE, Eisenstein JP, Pfeiffer LN, and West KW (2013) Thermoelectric response of fractional quantized hall and reentrant insulating states in the $n = 1$ landau level. *Physical Review B* 87: 075302. https://doi.org/10.1103/PhysRevB.87.075302.

Choi HC, Kang W, Das Sarma S, Pfeiffer LN, and West KW (2008) Activation gaps of fractional quantum Hall effect in the second Landau level. *Physical Review B* 77: 081301. https://doi.org/10.1103/PhysRevB.77.081301.

Chung YJ, Villegas Rosales KA, Baldwin KW, Madathil PT, West KW, Shayegan M, and Pfeiffer LN (2021) Ultra-high-quality two-dimensional electron systems. *Nature Materials* 20: 632–637. http://www.nature.com/articles/s41563-021-00942-3.

Cooper NR and Stern A (2009) Observable bulk signatures of non-abelian quantum Hall states. *Physical Review Letters* 102: 176807. https://doi.org/10.1103/PhysRevLett.102.176807.

Csáthy GA, Xia JS, Vicente CL, Adams ED, Sullivan NS, Stormer HL, Tsui DC, Pfeiffer LN, and West KW (2005) Tilt-induced localization and delocalization in the second landau level. *Physical Review Letters* 94: 146801. https://doi.org/10.1103/PhysRevLett.94.146801.

Das Sarma S and Hwang EH (2014a) Mobility versus quality in two-dimensional semiconductor structures. *Physical Review B* 90: 035425. https://doi.org/10.1103/PhysRevB.90.035425.

Das Sarma S and Hwang EH (2014b) Short-range disorder effects on electronic transport in two-dimensional semiconductor structures. *Physical Review B* 89: 121413. https://doi.org/10.1103/PhysRevB.89.121413.

Das Sarma S and Pinczuk A (eds.) (1996) *Perspectives in Quantum Hall Effects*. New York: Wiley. https://onlinelibrary.wiley.com/doi/book/10.1002/9783527617258.

Das Sarma S, Freedman M, and Nayak C (2005) Topologically Protected Qubits from a Possible Non-Abelian Fractional Quantum Hall State. *Physical Review Letters* 94: 166802. https://doi.org/10.1103/PhysRevLett.94.166802.

Das S, Das S, and Mandal SS (2022) An anomalous reentrant 5/2 quantum hall phase at higher landau-level-mixing strength. arXiv:2206.04419.

de Chamon C, Freed DE, Kivelson SA, Sondhi SL, and Wen XG (1997) Two point-contact interferometer for quantum Hall systems. *Physical Review B* 55: 2331–2343. https://doi.org/10.1103/PhysRevB.55.2331.

Dean CR, Piot BA, Hayden P, Das Sarma S, Gervais G, Pfeiffer LN, and West KW (2008a) Contrasting behavior of the 5/2 and 7/3 fractional quantum Hall effect in a tilted field. *Physical Review Letters* 101: 186806. https://doi.org/10.1103/PhysRevLett.101.186806.

Dean CR, Piot BA, Hayden P, Das Sarma S, Gervais G, Pfeiffer LN, and West KW (2008b) Intrinsic gap of the $\nu = 5/2$ fractional quantum Hall state. *Physical Review Letters* 100: 146803. https://doi.org/10.1103/PhysRevLett.100.146803.

Deng N, Gardner GC, Mondal S, Kleinbaum E, Manfra MJ, and Csáthy GA (2014) $\nu = 5/2$ fractional quantum Hall state in the presence of alloy disorder. *Physical Review Letters* 112: 116804. https://doi.org/10.1103/PhysRevLett.112.116804.

Dimov I, Halperin BI, and Nayak C (2008) Spin order in paired quantum Hall states. *Physical Review Letters* 100: 126804. https://doi.org/10.1103/PhysRevLett.100.126804.

Dolev M, Heiblum M, Umansky V, Stern A, and Mahalu D (2008) Observation of a quarter of an electron charge at the $\nu = 5/2$ quantum Hall state. *Nature (London)* 452: 829–834. http://www.nature.com/nature/journal/v452/n7189/abs/nature06855.html.

Dolev M, Gross Y, Chung YC, Heiblum M, Umansky V, and Mahalu D (2010) Dependence of the tunneling quasi-particle charge determined via shot noise measurements on the tunneling barrier and energetics. *Physical Review B* 81: 161303. https://doi.org/10.1103/PhysRevB.81.161303.

Dolev M, Gross Y, Sabo R, Gurman I, Heiblum M, Umansky V, and Mahalu D (2011) Characterizing neutral modes of fractional states in the second landau level. *Physical Review Letters* 107: 036805. https://doi.org/10.1103/PhysRevLett.107.036805.

Dong S, Fradkin E, Leigh RG, and Nowling S (2008) Topological entanglement entropy in Chern-Simons theories and quantum Hall fluids. *Journal of High Energy Physics* 2008: 016. https://doi.org/10.1088/1126-6708/2008/05/016.

Du R, Tsui D, Stormer H, Pfeiffer L, Baldwin K, and West K (1999) Strongly anisotropic transport in higher two-dimensional Landau levels. *Solid State Communications* 109: 389–394. https://linkinghub.elsevier.com/retrieve/pii/S003810989800578X, arXiv:9812025.

Du L, Wurstbauer U, West KW, Pfeiffer LN, Fallahi S, Gardner GC, Manfra MJ, and Pinczuk A (2019) Observation of new plasmons in the fractional quantum Hall effect: Interplay of topological and nematic orders. *Science Advances* 5: eaav3407. https://www.science.org/doi/abs/10.1126/sciadv.aav3407.

Dubail J and Read N (2011) Entanglement spectra of complex paired superfluids. *Physical Review Letters* 107: 157001. https://doi.org/10.1103/PhysRevLett.107.157001.

Dutta B, Umansky V, Banerjee M, Heiblum M (2022a) *Isolated ballistic non-abelian interface channel*. arXiv:2109.11205. https://arxiv.org/abs/2109.11205.

Dutta B, Yang W, Melcer R, Kundu HK, Heiblum M, Umansky V, Oreg Y, Stern A, and Mross D (2022b) Distinguishing between non-abelian topological orders in a quantum Hall system. *Science* 375: 193. https://doi.org/10.1126/science.abg6116.

Eisenstein JP, Willett R, Stormer HL, Tsui DC, Gossard AC, and English JH (1988) Collapse of the even-denominator fractional Quantum Hall effect in tilted fields. *Physical Review Letters* 61: 997–1000. https://doi.org/10.1103/PhysRevLett.61.997.

Eisenstein J, Willett R, Stormer H, Pfeiffer L, and West K (1990) Activation energies for the even-denominator fractional quantum Hall effect. *Surface Science* 229: 31–33. https://linkinghub.elsevier.com/retrieve/pii/003960289090824R.

Eisenstein JP, Boebinger GS, Pfeiffer LN, West KW, and He S (1992) New fractional quantum Hall state in double-layer two-dimensional electron systems. *Physical Review Letters* 68: 1383–1386. https://doi.org/10.1103/PhysRevLett.68.1383.

Eisenstein JP, Cooper KB, Pfeiffer LN, and West KW (2002) Insulating and fractional quantum Hall states in the first excited landau level. *Physical Review Letters* 88: 076801. https://doi.org/10.1103/PhysRevLett.88.076801.

Falson J, Maryenko D, Friess B, Zhang D, Kozuka Y, Tsukazaki A, Smet JH, and Kawasaki M (2015) Even-denominator fractional quantum Hall physics in ZnO. *Nature Physics* 11: 347–351. https://www.nature.com/articles/nphys3259.

Falson J, Tabrea D, Zhang D, Sodemann I, Kozuka Y, Tsukazaki A, Kawasaki M, von Klitzing K, and Smet JH (2018) A cascade of phase transitions in an orbitally mixed half-filled Landau level. *Science Advances* 4: eaat8742. http://advances.sciencemag.org/content/4/9/eaat8742.

Faugno WN, Balram AC, Barkeshli M, and Jain JK (2019) Prediction of a Non-Abelian Fractional Quantum Hall State with *f*-Wave Pairing of Composite Fermions in Wide Quantum Wells. *Physical Review Letters* 123: 016802. https://doi.org/10.1103/PhysRevLett.123.016802.

Feiguin AE, Rezayi E, Nayak C, and Das Sarma S (2008) Density matrix renormalization group study of incompressible fractional quantum hall states. *Physical Review Letters* 100: 166803. https://doi.org/10.1103/PhysRevLett.100.166803.

Feiguin AE, Rezayi E, Yang K, Nayak C, and Das Sarma S (2009) Spin polarization of the $\nu = 5/2$ quantum Hall state. *Physical Review B* 79: 115322. https://doi.org/10.1103/PhysRevB.79.115322.

Feldman DE (2018) Comment on Interpretation of thermal conductance of the $\nu = 5/2$ edge. *Physical Review B* 98: 167401. https://journals.aps.org/prb/abstract/10.1103/PhysRevB.98.167401.

Feldman DE and Halperin BI (2021) Fractional charge and fractional statistics in the quantum Hall effects. *Reports on Progress in Physics* 84: 076501. https://iopscience.iop.org/article/10.1088/1361-6633/ac03aa.

Feldman DE and Kitaev A (2006) Detecting non-abelian statistics with an electronic Mach-Zehnder interferometer. *Physical Review Letters* 97: 186803. https://doi.org/10.1103/PhysRevLett.97.186803.

Feldman DE, Gefen Y, Kitaev A, Law KT, and Stern A (2007) Shot noise in an anyonic mach-zehnder interferometer. *Physical Review B* 76: 085333. https://doi.org/10.1103/PhysRevB.76.085333.

Fendley P, Fisher MPA, and Nayak C (2007) Topological entanglement entropy from the holographic partition function. *Journal of Statistical Physics* 126: 1111–1144. https://doi.org/10.1007/s10955-006-9275-8.

Fidkowski L, Chen X, and Vishwanath A (2013) Non-abelian topological order on the surface of a 3d topological superconductor from an exactly solved model. *Physical Review X* 3: 041016. https://doi.org/10.1103/PhysRevX.3.041016.

Fradkin E, Nayak C, Tsvelik A, and Wilczek F (1998) A Chern-Simons effective field theory for the Pfaffian quantum Hall state. *Nuclear Physics B* 516: 704–718. https://linkinghub.elsevier.com/retrieve/pii/S0550321398001114.

Fradkin E, Kivelson SA, Lawler MJ, Eisenstein JP, and Mackenzie AP (2010) Nematic fermi fluids in condensed matter physics. *Annual Review of Condensed Matter Physics* 1: 153–178. https://www.annualreviews.org/doi/10.1146/annurev-conmatphys-070909-103925.

Francesco PD, Mathieu P, and Senechal D (1997) *Conformal Field Theory*. New York: Springer-Verlag.

Friedman BA and Levine GC (2008) Topological entropy of realistic quantum Hall wave functions. *Physical Review B* 78: 035320. https://doi.org/10.1103/PhysRevB.78.035320.

Friess B, Umansky V, Tiemann L, von Klitzing K, and Smet JH (2014) Probing the microscopic structure of the stripe phase at filling factor $\nu = 5/2$. *Physical Review Letters* 113: 076803. https://doi.org/10.1103/PhysRevLett.113.076803.

Fu H, Wang P, Shan P, Xiong L, Pfeiffer LN, West K, Kastner MA, and Lin X (2016) Competing $\nu = 5/2$ fractional quantum Hall states in confined geometry. *PNAS* 113: 12386–12390. http://www.pnas.org/content/113/44/12386.

Fu H, Wu Y, Zhang R, Sun J, Shan P, Wang P, Zhu Z, Pfeiffer LN, West KW, Liu H, Xie XC, and Lin X (2019) 3/2 fractional quantum Hall plateau in confined two-dimensional electron gas. *Nature Communications* 10. https://doi.org/10.1038/s41467-019-12245-y.

Gamez G and Muraki K (2013) $\nu = 5/2$ fractional quantum Hall state in low-mobility electron systems: Different roles of disorder. *Physical Review B* 88: 075308. https://doi.org/10.1103/PhysRevB.88.075308. arXiv:1101.5856.

Geraedts SD, Zaletel MP, Mong RSK, Metlitski MA, Vishwanath A, and Motrunich OI (2016) The half-filled landau level: The case for Dirac composite fermions. *Science* 352: 197–201. https://doi.org/10.1126/science.aad4302.

Gervais G and Yang K (2010) Adiabatic cooling with non-abelian anyons. *Physical Review Letters* 105: 086801. https://doi.org/10.1103/PhysRevLett.105.086801.

Girvin SM and Yang K (2019) *Modern Condensed Matter Physics*. New York: Cambridge University Press.

Girvin SM, MacDonald AH, and Platzman PM (1985) Collective-excitation gap in the fractional quantum Hall effect. *Physical Review Letters* 54: 581–583. https://doi.org/10.1103/PhysRevLett.54.581.

Goldman VJ, Su B, and Jain JK (1994) Detection of composite fermions by magnetic focusing. *Physical Review Letters* 72: 2065–2068. https://doi.org/10.1103/PhysRevLett.72.2065.

Golkar S, Nguyen DX, Roberts MM, and Son DT (2016a) Higher-spin theory of the magnetorotons. *Physical Review Letters* 117: 216403. https://doi.org/10.1103/PhysRevLett.117.216403.

Golkar S, Nguyen DX, and Son DT (2016b) Spectral sum rules and magneto-roton as emergent graviton in fractional quantum Hall effect. *Journal of High Energy Physics* 21. https://doi.org/10.1007/JHEP01(2016)021.

Greiter M, Wen XG, and Wilczek F (1991) Paired Hall state at half filling. *Physical Review Letters* 66: 3205–3208. https://doi.org/10.1103/PhysRevLett.66.3205.

Greiter M, Wen XG, and Wilczek F (1992) Paired Hall states. *Nuclear Physics B* 374: 567–614. http://www.sciencedirect.com/science/article/pii/055032139290401V.

Gromov A, Martinec EJ, and Ryu S (2020) Collective excitations at filling factor 5/2: The view from superspace. *Physical Review Letters* 125: 077601. https://doi.org/10.1103/PhysRevLett.125.077601.

Gross Y, Dolev M, Heiblum M, Umansky V, and Mahalu D (2012) Upstream neutral modes in the fractional quantum Hall effect regime: Heat waves or coherent dipoles. *Physical Review Letters* 108: 226801. https://doi.org/10.1103/PhysRevLett.108.226801.

Haldane FDM (1983) Fractional quantization of the Hall effect: A hierarchy of incompressible quantum fluid states. *Physical Review Letters* 51: 605–608. https://doi.org/10.1103/PhysRevLett.51.605.

Haldane FDM (1985) Many-particle translational symmetries of two-dimensional electrons at rational landau-level filling. *Physical Review Letters* 55: 2095–2098. https://doi.org/10.1103/PhysRevLett.55.2095.

Haldane FDM and Rezayi EH (1985) Finite-size studies of the incompressible state of the fractionally quantized Hall effect and its excitations. *Physical Review Letters* 54: 237–240. https://doi.org/10.1103/PhysRevLett.54.237.

Haldane FDM, Rezayi EH, and Yang K (2021) Graviton chirality and topological order in the half-filled landau level. *Physical Review B* 104: L121106. https://doi.org/10.1103/PhysRevB.104.L121106.

Halperin BI (1982) Quantized Hall conductance, current-carrying edge states, and the existence of extended states in a two-dimensional disordered potential. *Physical Review B* 25: 2185–2190. https://doi.org/10.1103/PhysRevB.25.2185.

Halperin BI (1983) Theory of the quantized Hall conductance. *Helvetica Physica Acta* 56: 75–102.

Halperin BI (1984) Statistics of quasiparticles and the hierarchy of fractional quantized Hall states. *Physical Review Letters* 52: 1583–1586. https://doi.org/10.1103/PhysRevLett.52.1583.

Halperin BI, Lee PA, and Read N (1993) Theory of the half-filled landau level. *Physical Review B* 47: 7312–7343. https://doi.org/10.1103/PhysRevB.47.7312.

Hansson TH, Hermanns M, Simon SH, and Viefers SF (2017) Quantum Hall physics: Hierarchies and conformal field theory techniques. *Reviews of Modern Physics* 89: 025005. https://doi.org/10.1103/RevModPhys.89.025005.

Hayafuchi Y, Konno R, Noorhidayati A, Fauzi MH, Shibata N, Hashimoto K, and Hirayama Y (2022) Even-denominator fractional quantum Hall state in conventional triple-gated quantum point contact. *Applied Physics Express* 15: 025002. https://doi.org/10.35848/1882-0786/ac4c35.

He S, Das Sarma S, and Xie XC (1993) Quantized Hall effect and quantum phase transitions in coupled two-layer electron systems. *Physical Review B* 47: 4394–4412. https://doi.org/10.1103/PhysRevB.47.4394.

Heiblum M and Feldman DE (2020) Edge Probes of Topological Order. In: Halperin BI and Jain JK (eds.) *Fractional Quantum Hall Effects: New Developments*, pp. 183–230. Singapore: World Scientific. Also in *Int. J. Mod. Phys. A* 35: 2030009 (2020).

Hennel S, Scheidegger P, Kellermeier M, Hofmann A, Krähenmann T, Reichl C, Wegscheider W, Ihn T, and Ensslin K (2018) Quasiparticle tunneling in the lowest Landau level. *Physical Review B* 97: 245305. https://doi.org/10.1103/PhysRevB.97.245305.

Hidalgo M (2022) Quantum Hall effects in two-dimensional electron systems: A global approach. *The European Physical Journal Plus* 138: 137. https://doi.org/10.1140/epjp/s13360-021-02173-6.

Hirjibehedin CF, Dujovne I, Pinczuk A, Dennis BS, Pfeiffer LN, and West KW (2005) Splitting of Long-Wavelength Modes of the Fractional Quantum Hall Liquid at $\nu = 1/3$. *Physical Review Letters* 95: 066803. https://doi.org/10.1103/PhysRevLett.95.066803.

Hossain MS, Ma MK, Mueed MA, Pfeiffer LN, West KW, Baldwin KW, and Shayegan M (2018) Direct observation of composite fermions and their fully-spin-polarized fermi sea near $\nu = 5/2$. *Physical Review Letters* 120: 256601. https://doi.org/10.1103/PhysRevLett.120.256601.

Hossain MS, Mueed MA, Ma MK, Villegas Rosales KA, Chung YJ, Pfeiffer LN, West KW, Baldwin KW, and Shayegan M (2020) Precise experimental test of the Luttinger theorem and particle-hole symmetry for a strongly correlated fermionic system. *Physical Review Letters* 125: 046601. https://doi.org/10.1103/PhysRevLett.125.046601.

Hsin P-S, Lin Y-H, Paquette NM, and Wang J (2020) Effective field theory for fractional quantum Hall systems near $\nu = 5/2$. *Physical Review Research* 2: 043242. https://doi.org/10.1103/PhysRevResearch.2.043242.

Huang K, Fu H, Hickey DR, Alem N, Lin X, Watanabe K, Taniguchi T, and Zhu J (2022) Valley isospin controlled fractional quantum Hall states in bilayer graphene. *Physical Review X* 12: 031019. https://doi.org/10.1103/PhysRevX.12.031019.

Hutzel W, McCord JJ, Raum PT, Stern B, Wang H, Scarola VW, and Peterson MR (2019) Particle-hole-symmetric model for a paired fractional quantum Hall state in a half-filled landau level. *Physical Review B* 99: 045126. https://doi.org/10.1103/PhysRevB.99.045126.

Jain JK (1989a) Composite-fermion approach for the fractional quantum Hall effect. *Physical Review Letters* 63: 199–202. https://doi.org/10.1103/PhysRevLett.63.199.

Jain JK (1989b) Incompressible quantum Hall states. *Physical Review B* 40: 8079–8082. https://doi.org/10.1103/PhysRevB.40.8079.

Jain JK (1990) Theory of the fractional quantum Hall effect. *Physical Review B* 41: 7653–7665. https://doi.org/10.1103/PhysRevB.41.7653.

Jain JK (2007) *Composite Fermions*. New York: Cambridge University Press.

Jain JK and Kamilla RK (1997) Composite fermions in the Hilbert space of the lowest electronic landau level. *International Journal of Modern Physics B* 11: 2621–2660. https://doi.org/10.1142/S0217979297001301.

Jeong J-S and Park K (2015) Bilayer mapping of the paired quantum Hall state: Instability toward anisotropic pairing. *Physical Review B* 91: 195119. https://doi.org/10.1103/PhysRevB.91.195119.

Ji Y, Chung YC, Sprinzak D, Heiblum M, Mahalu D, and Shtrikman H (2003) An electronic Mach–Zehnder interferometer. *Nature (London)* 422: 415–418. https://www.nature.com/articles/nature01503.

Jiang N and Wan X (2019) Recent progress on the non-abelian $\nu = 5/2$ Quantum Hall state. *AAPPS Bulletin, Issue* 1(29): 58–64. http://aappsbulletin.org/myboard/read.php?Board=apctp&id=90.

Jolicoeur T (2007) Non-abelian states with negative flux: A new series of quantum Hall states. *Physical Review Letters* 99: 036805. https://doi.org/10.1103/PhysRevLett.99.036805.

Kalmeyer V and Zhang SC (1992) Metallic phase of the quantum Hall system at even-denominator filling fractions. *Physical Review B* 46: 9889–9892. https://doi.org/10.1103/PhysRevB.46.9889.

Kamburov D, Liu Y, Mueed MA, Shayegan M, Pfeiffer LN, West KW, and Baldwin KW (2014) What determines the fermi wave vector of composite fermions? *Physical Review Letters* 113: 196801. https://doi.org/10.1103/PhysRevLett.113.196801.

Kane CL and Fisher MPA (1997) Quantized thermal transport in the fractional quantum Hall effect. *Physical Review B* 55: 15832–15837. https://doi.org/10.1103/PhysRevB.55.15832.

Kang W, Stormer HL, Pfeiffer LN, Baldwin KW, and West KW (1993) How real are composite fermions? *Physical Review Letters* 71: 3850–3853. https://doi.org/10.1103/PhysRevLett.71.3850.

Kang M, Pinczuk A, Dennis BS, Pfeiffer LN, and West KW (2001) Observation of multiple magnetorotons in the fractional quantum Hall effect. *Physical Review Letters* 86: 2637–2640. https://doi.org/10.1103/PhysRevLett.86.2637.

Ki DK, Fal'ko VI, Abanin DA, and Morpurgo AF (2014) Observation of even denominator fractional quantum Hall effect in suspended bilayer graphene. *Nano Letters* 14: 2135–2139. https://doi.org/10.1021/nl5003922.

Kim Y, Lee DS, Jung S, Skákalová V, Taniguchi T, Watanabe K, Kim JS, and Smet JH (2015) Observation of even denominator fractional quantum Hall effect in suspended bilayer graphene. *Nano Letters* 15: 7445–7451. https://doi.org/10.1021/acs.nanolett.5b02876.

Kim Y, Balram AC, Taniguchi T, Watanabe K, Jain JK, and Smet JH (2019) Even denominator fractional quantum Hall states in higher Landau levels of graphene. *Nature Physics* 15: 154–158. https://www.nature.com/articles/s41567-018-0355-x.

Kitaev AY (2003) Fault-tolerant quantum computation by anyons. *Annals of Physics* 303: 2–30. https://www.sciencedirect.com/science/article/pii/S0003491602000180.

Kitaev AY (2006) Anyons in an exactly solved model and beyond. *Annals of Physics* 321: 2–111. http://www.sciencedirect.com/science/article/pii/S0003491605002381.

Kitaev A and Preskill J (2006) Topological entanglement entropy. *Physical Review Letters* 96: 110404. https://doi.org/10.1103/PhysRevLett.96.110404.

Kleinbaum E, Li H, Deng N, Gardner GC, Manfra MJ, and Csáthy GA (2020) Disorder broadening of even-denominator fractional quantum Hall states in the presence of a short-range alloy potential. *Physical Review B* 102: 035140. https://doi.org/10.1103/PhysRevB.102.035140.

Koduvayur SP, Lyanda-Geller Y, Khlebnikov S, Csathy G, Manfra MJ, Pfeiffer LN, West KW, and Rokhinson LP (2011) Effect of strain on stripe phases in the quantum Hall regime. *Physical Review Letters* 106: 016804. https://doi.org/10.1103/PhysRevLett.106.016804.

Koulakov AA, Fogler MM, and Shklovskii BI (1996) Charge density wave in two-dimensional electron liquid in weak magnetic field. *Physical Review Letters* 76: 499–502. https://doi.org/10.1103/PhysRevLett.76.499.

Kukushkin IV, Smet JH, Scarola VW, Umansky V, and von Klitzing K (2009) Dispersion of the excitations of fractional quantum Hall states. *Science* 324: 1044–1047. https://science.sciencemag.org/content/324/5930/1044.

Kumar A, Csáthy GA, Manfra MJ, Pfeiffer LN, and West KW (2010) Nonconventional odd-denominator fractional quantum Hall states in the second landau level. *Physical Review Letters* 105: 246808. https://doi.org/10.1103/PhysRevLett.105.246808.

Kundu HK, Biswas S, Ofek N, Umansky V, Heiblum M (2022) *Anyonic interference and braiding phase in a Mach-Zehnder Interferometer*. arXiv:1112.3400. https://arxiv.org/abs/2203.04205.

Laughlin RB (1983a) Anomalous quantum Hall effect: An incompressible quantum fluid with fractionally charged excitations. *Physical Review Letters* 50: 1395–1398. https://doi.org/10.1103/PhysRevLett.50.1395.

Laughlin RB (1983b) Quantized motion of three two-dimensional electrons in a strong magnetic field. *Physical Review B* 27: 3383–3389. https://doi.org/10.1103/PhysRevB.27.3383.

Law KT, Feldman DE, and Gefen Y (2006) Electronic Machzehnder interferometer as a tool to probe fractional statistics. *Physical Review B* 74: 045319. https://doi.org/10.1103/PhysRevB.74.045319.

Lee JYM and Sim HS (2022) *Non-Abelian Anyon Collider*. arXiv:2202.03649. https://arxiv.org/abs/2202.036493.

Lee SS, Ryu S, Nayak C, and Fisher MPA (2007) Particle-hole symmetry and the $\nu = 5/2$ quantum Hall state. *Physical Review Letters* 99: 236807. https://doi.org/10.1103/PhysRevLett.99.236807.

Leinaas J and Myrheim J (1977) *On the Theory of Identical Particles. Il Nuovo Cimento B Series*, vol. 11, 1. https://link.springer.com/article/10.1007/BF02727953.

Levin M and Halperin BI (2009) Collective states of non-abelian quasiparticles in a magnetic field. *Physical Review B* 79: 205301. https://doi.org/10.1103/PhysRevB.79.205301.

Levin M and Wen XG (2006) Detecting topological order in a ground state wave function. *Physical Review Letters* 96: 110405. https://doi.org/10.1103/PhysRevLett.96.110405.

Levin M, Halperin BI, and Rosenow B (2007) Particle-hole symmetry and the Pfaffian state. *Physical Review Letters* 99: 236806. https://doi.org/10.1103/PhysRevLett.99.236806.

Levy AL, Wurstbauer U, Kuznetsova YY, Pinczuk A, Pfeiffer LN, West KW, Manfra MJ, Gardner GC, and Watson JD (2016) Optical emission spectroscopy study of competing phases of electrons in the second landau level. *Physical Review Letters* 116: 016801. https://doi.org/10.1103/PhysRevLett.116.016801.

Li H and Haldane FDM (2008) Entanglement spectrum as a generalization of entanglement entropy: Identification of topological order in non-abelian fractional quantum Hall effect states. *Physical Review Letters* 101: 010504. https://doi.org/10.1103/PhysRevLett.101.010504.

Li JIA, Tan C, Chen S, Zeng Y, Taniguchi T, Watanabe K, Hone J, and Dean CR (2017) Even-denominator fractional quantum Hall states in bilayer graphene. *Science* 358: 648–652. https://science.sciencemag.org/content/358/6363/648.

Lian B and Wang J (2018) Theory of the disordered $\nu = 5/2$ quantum thermal Hall state: Emergent symmetry and phase diagram. *Physical Review B* 97: 165124. https://doi.org/10.1103/PhysRevB.97.165124.

Lilly MP, Cooper KB, Eisenstein JP, Pfeiffer LN, and West KW (1999) Anisotropic states of two-dimensional electron systems in high landau levels: Effect of an in-plane magnetic field. *Physical Review Letters* 83: 824–827. https://doi.org/10.1103/PhysRevLett.83.824.

Lin X, Dillard C, Kastner MA, Pfeiffer LN, and West KW (2012) Measurements of quasiparticle tunneling in the *upsilon* = 5/2 fractional quantum Hall state. *Physical Review B* 85: 165321. https://doi.org/10.1103/PhysRevB.85.165321.

Lin X, Du R, and Xie X (2014) Recent experimental progress of fractional quantum Hall effect: 5/2 filling state and graphene. *National Science Review* 1: 564–579. https://academic.oup.com/nsr/article/1/4/564/1514031.

Liou SF, Haldane FDM, Yang K, and Rezayi EH (2019) Chiral gravitons in fractional quantum Hall liquids. *Physical Review Letters* 123: 146801. https://doi.org/10.1103/PhysRevLett.123.146801.

Liu Y, Kamburov D, Shayegan M, Pfeiffer LN, West KW, and Baldwin KW (2011a) Anomalous robustness of the $\nu = 5/2$ fractional quantum Hall state near a sharp phase boundary. *Physical Review Letters* 107: 176805. https://doi.org/10.1103/PhysRevLett.107.176805.

Liu Y, Shabani J, Kamburov D, Shayegan M, Pfeiffer LN, West KW, and Baldwin KW (2011b) Evolution of the 7/2 fractional quantum Hall state in two-subband systems. *Physical Review Letters* 107: 266802. https://doi.org/10.1103/PhysRevLett.107.266802.

Liu G, Zhang C, Tsui DC, Knez I, Levine A, Du RR, Pfeiffer LN, and West KW (2012) Enhancement of the $\nu = 5/2$ fractional quantum Hall state in a small in-plane magnetic field. *Physical Review Letters* 108: 196805. https://doi.org/10.1103/PhysRevLett.108.196805.

Liu Y, Hasdemir S, Shayegan M, Pfeiffer LN, West KW, and Baldwin KW (2013) Evidence for a $\nu = 5/2$ fractional quantum Hall nematic state in parallel magnetic fields. *Physical Review B* 88: 035307. https://doi.org/10.1103/PhysRevB.88.035307.

Lopez A and Fradkin E (1993) Response functions and spectrum of collective excitations of fractional-quantum-Hall-effect systems. *Physical Review B* 47: 7080–7094. https://doi.org/10.1103/PhysRevB.47.7080.

Lu H, Das Sarma S, and Park K (2010) Superconducting order parameter for the even-denominator fractional quantum Hall effect. *Physical Review B* 82: 201303. https://doi.org/10.1103/PhysRevB.82.201303.

Luo W and Chakraborty T (2017) Pfaffian state in an electron gas with small landau level gaps. *Physical Review B* 96: 081108. https://doi.org/10.1103/PhysRevB.96.081108.

Luo W, Peng S, Wang H, Zhou Y, and Chakraborty T (2021) Stability of even-denominator fractional quantum Hall states in systems with strong landau-level mixing. *Physical Review B* 104: L161302. https://doi.org/10.1103/PhysRevB.104.L161302.

Ma KKW (2019) Identification of topological order in the fractional quantum Hall state at $\nu = 1/4$. *Physical Review B* 100: 205306. https://doi.org/10.1103/PhysRevB.100.205306.

Ma KKW and Feldman DE (2019a) Partial equilibration of integer and fractional edge channels in the thermal quantum Hall effect. *Physical Review B* 99: 085309. https://doi.org/10.1103/PhysRevB.99.085309.

Ma KKW and Feldman DE (2019b) The sixteenfold way and the quantum Hall effect at half-integer filling factors. *Physical Review B* 100: 035302. https://doi.org/10.1103/PhysRevB.100.035302.

Ma KKW and Feldman DE (2020) Thermal equilibration on the edges of topological liquids. *Physical Review Letters* 125: 016801. https://doi.org/10.1103/PhysRevLett.125.016801.

Melcer RA, Konyzheva S, Heiblum M, Umansky V (2022) *Direct Determination of the Topological Thermal Conductance via Local Power Measurement*. arXiv:2204.13431. https://arxiv.org/abs/2204.13431.

Miller JB, Radu IP, Zumbühl DM, Levenson-Falk EM, Kastner MA, Marcus CM, Pfeiffer LN, and West KW (2007) Fractional quantum Hall effect in a quantum point contact at filling fraction 5/2. *Nature Physics* 3: 561–565. https://www.nature.com/articles/nphys658.

Milovanović MV (2017) Paired states in half-filled Landau levels. *Physical Review B* 95: 235304. https://doi.org/10.1103/PhysRevB.95.235304.

Milovanović MV and Djurdjević S (2021) Particle-hole Pfaffian intracorrelations and intercorrelations in the quantum Hall bilayer. *Physical Review B* 104: 245303. https://doi.org/10.1103/PhysRevB.104.245303.

Milovanović M and Read N (1996) Edge excitations of paired fractional quantum Hall states. *Physical Review B* 53: 13559–13582. https://doi.org/10.1103/PhysRevB.53.13559.

Milovanović MV, Djurdjević S, Vučičević J, and Antonić L (2020) Pfaffian paired states for half-integer fractional quantum Hall effect. *Modern Physics Letters B* 34: 2030004. https://doi.org/10.1142/S0217984920300045.

Mishmash RV, Mross DF, Alicea J, and Motrunich OI (2018) Numerical exploration of trial wave functions for the particle-hole-symmetric Pfaffian. *Physical Review B* 98: 081107. https://doi.org/10.1103/PhysRevB.98.081107.

Moessner R and Chalker JT (1996) Exact results for interacting electrons in high Landau levels. *Physical Review B* 54: 5006–5015. https://doi.org/10.1103/PhysRevB.54.5006.

Möller G and Simon SH (2008) Paired composite-fermion wave functions. *Physical Review B* 77: 075319. https://doi.org/10.1103/PhysRevB.77.075319.

Möller G, Wójs A, and Cooper NR (2011) Neutral fermion excitations in the moore-read state at filling factor $\nu = 5/2$. *Physical Review Letters* 107: 036803. https://doi.org/10.1103/PhysRevLett.107.036803.

Moore G and Read N (1991) Nonabelions in the fractional quantum Hall effect. *Nuclear Physics B* 360: 362–396. http://www.sciencedirect.com/science/article/pii/0550321391904070.

Morf RH (1998) Transition from quantum Hall to compressible states in the second landau level: New light on the $\nu = 5/2$ enigma. *Physical Review Letters* 80: 1505–1508. https://doi.org/10.1103/PhysRevLett.80.1505.

Morf R and d'Ambrumenil N (2003) Disorder in fractional quantum Hall states and the gap at $\nu = 5/2$. *Physical Review B* 68: 113309. https://doi.org/10.1103/PhysRevB.68.113309.

Morf RH, d'Ambrumenil N, and Das Sarma S (2002) Excitation gaps in fractional quantum Hall states: An exact diagonalization study. *Physical Review B* 66: 075408. https://doi.org/10.1103/PhysRevB.66.075408.

Mross DF, Oreg Y, Stern A, Margalit G, and Heiblum M (2018) Theory of disorder-induced half-integer thermal Hall conductance. *Physical Review Letters* 121: 026801. https://doi.org/10.1103/PhysRevLett.121.026801.

Mueed MA, Kamburov D, Hossain MS, Pfeiffer LN, West KW, Baldwin KW, and Shayegan M (2017) Search for composite fermions at filling factor 5/2: Role of Landau level and subband index. *Physical Review B* 95: 165438. https://doi.org/10.1103/PhysRevB.95.165438.

Murthy G and Shankar R (2003) Hamiltonian theories of the fractional quantum Hall effect. *Reviews of Modern Physics* 75: 1101–1158. https://doi.org/10.1103/RevModPhys.75.1101.

Nakamura J, Fallahi S, Sahasrabudhe H, Rahman R, Liang S, Gardner GC, and Manfra MJ (2019) Aharonov-Bohm interference of fractional quantum Hall edge modes. *Nature Physics* 15: 563–569. https://www.nature.com/articles/s41567-019-0441-8.

Nakamura J, Liang S, Gardner GC, and Manfra MJ (2020) Direct observation of anyonic braiding statistics. *Nature Physics* 16: 931–936. https://www.nature.com/articles/s41567-020-1019-1.

Nayak C and Wilczek F (1996) $2n$-quasihole states realize 2^{n-1}-dimensional spinor braiding statistics in paired quantum Hall states. *Nuclear Physics B* 479: 529–553. http://www.sciencedirect.com/science/article/pii/0550321396004300.

Nayak C, Simon SH, Stern A, Freedman M, and Das Sarma S (2008) Non-abelian anyons and topological quantum computation. *Reviews of Modern Physics* 80: 1083–1159. https://doi.org/10.1103/RevModPhys.80.1083.

Nguyen DX and Son DT (2021) Probing the spin structure of the fractional quantum Hall magnetoroton with polarized Raman scattering. *Physical Review Research* 3: 023040. https://doi.org/10.1103/PhysRevResearch.3.023040.

Nuebler J, Umansky V, Morf R, Heiblum M, von Klitzing K, and Smet J (2010) Density dependence of the $\nu = 5/2$ energy gap: Experiment and theory. *Physical Review B* 81: 035316. https://doi.org/10.1103/PhysRevB.81.035316.

Overbosch BJ and Wen XG (2008) *Phase transitions on the edge of the $\nu = 5/2$ Pfaffian and anti-Pfaffian quantum Hall state*. arXiv:0804.2087. https://arxiv.org/abs/0804.2087.

Pakrouski K (2021) Approximate two-body generating Hamiltonian for the particle-hole Pfaffian wave function. *Physical Review B* 104: 245306. https://doi.org/10.1103/PhysRevB.104.245306.

Pakrouski K, Peterson MR, Jolicoeur T, Scarola VW, Nayak C, and Troyer M (2015) Phase diagram of the $\nu = 5/2$ fractional quantum Hall effect: Effects of landau-level mixing and nonzero width. *Physical Review X* 5: 021004. https://doi.org/10.1103/PhysRevX.5.021004.

Pan W, Du RR, Stormer HL, Tsui DC, Pfeiffer LN, Baldwin KW, and West KW (1999a) Strongly anisotropic electronic transport at landau level filling factor $\nu = 9/2$ and $\nu = 5/2$ under a tilted magnetic field. *Physical Review Letters* 83: 820–823. https://doi.org/10.1103/PhysRevLett.83.820.

Pan W, Xia JS, Shvarts V, Adams DE, Stormer HL, Tsui DC, Pfeiffer LN, Baldwin KW, and West KW (1999b) Exact quantization of the even-denominator fractional quantum Hall state at $\nu = 5/2$ Landau level filling factor. *Physical Review Letters* 83: 3530–3533. https://doi.org/10.1103/PhysRevLett.83.3530.

Pan W, Stormer H, Tsui D, Pfeiffer L, Baldwin K, and West K (2001) Experimental evidence for a spin-polarized ground state in the ν=5/2 fractional quantum Hall effect. *Solid State Communications* 119: 641–645. https://linkinghub.elsevier.com/retrieve/pii/S0038109801003118, arXiv:0103144.

Pan W, Xia JS, Stormer HL, Tsui DC, Vicente C, Adams ED, Sullivan NS, Pfeiffer LN, Baldwin KW, and West KW (2008) Experimental studies of the fractional quantum Hall effect in the first excited landau level. *Physical Review B* 77: 075307. https://doi.org/10.1103/PhysRevB.77.075307.

Pan W, Masuhara N, Sullivan NS, Baldwin KW, West KW, Pfeiffer LN, and Tsui DC (2011) Impact of disorder on the $\nu = 5/2$ fractional quantum Hall state. *Physical Review Letters* 106: 206806. https://doi.org/10.1103/PhysRevLett.106.206806.

Pan W, Serafin A, Xia JS, Yin L, Sullivan NS, Baldwin KW, West KW, Pfeiffer LN, and Tsui DC (2014) Competing quantum Hall phases in the second landau level in the low-density limit. *Physical Review B* 89: 241302. https://doi.org/10.1103/PhysRevB.89.241302.

Papić Z and Balram AC (2022) *Fractional quantum Hall effect in semiconductor systems*. arXiv:2205.03421. https://arxiv.org/abs/2205.03421.

Papić Z, Regnault N, and Das Sarma S (2009) Interaction-tuned compressible-to-incompressible phase transitions in quantum Hall systems. *Physical Review B* 80. https://doi.org/10.1103/PhysRevB.80.201303. 201303(R).

Papić Z, Haldane FDM, and Rezayi EH (2012) Quantum phase transitions and the ν=5/2 fractional Hall state in wide quantum wells. *Physical Review Letters* 109: 266806. https://doi.org/10.1103/PhysRevLett.109.266806.

Park K and Jain J (2000) Girvin–MacDonald–Platzman collective mode at general filling factors: Magneto-roton minimum at half-filled Landau level. *Solid State Communications* 115: 353–357. https://linkinghub.elsevier.com/retrieve/pii/S0038109800001812.

Park K, Melik-Alaverdian V, Bonesteel NE, and Jain JK (1998) Possibility of p-wave pairing of composite fermions at $\nu = 1/2$. *Physical Review B* 58: R10167–R10170. https://doi.org/10.1103/PhysRevB.58.R10167.

Park J, Spånslätt C, Gefen Y, and Mirlin AD (2020) Noise on the non-Abelian $\nu = 5/2$ fractional quantum Hall edge. *Physical Review Letters* 125: 157702. https://doi.org/10.1103/PhysRevLett.125.157702.

Peterson MR (2012) The fractional quantum Hall effect at filling factor 5/2: Numerically searching for non-abelian anyons. *Journal of Physics: Conference Series* 402: 012021. https://doi.org/10.1088/1742-6596/402/1/012021.

Peterson MR and Das Sarma S (2010) Quantum Hall phase diagram of half-filled bilayers in the lowest and the second orbital landau levels: Abelian versus non-abelian incompressible fractional quantum hall states. *Physical Review B* 81: 165304. https://doi.org/10.1103/PhysRevB.81.165304.

Peterson MR and Nayak C (2013) More realistic Hamiltonians for the fractional quantum Hall regime in gaas and graphene. *Physical Review B* 87: 245129. https://doi.org/10.1103/PhysRevB.87.245129.

Peterson MR, Jolicoeur T, and Das Sarma S (2008a) Finite-layer thickness stabilizes the Pfaffian state for the 5/2 fractional quantum Hall effect: Wave function overlap and topological degeneracy. *Physical Review Letters* 101: 016807. https://doi.org/10.1103/PhysRevLett.101.016807.

Peterson MR, Jolicoeur T, and Das Sarma S (2008b) Orbital landau level dependence of the fractional quantum Hall effect in quasi-two-dimensional electron layers: Finite-thickness effects. *Physical Review B* 78: 155308. https://doi.org/10.1103/PhysRevB.78.155308.

Peterson MR, Park K, and Das Sarma S (2008c) Spontaneous particle-hole symmetry breaking in the $\nu = 5/2$ fractional quantum Hall effect. *Physical Review Letters* 101: 156803. https://doi.org/10.1103/PhysRevLett.101.156803.

Peterson MR, Papić Z, and Das Sarma S (2010) Fractional quantum Hall effects in bilayers in the presence of interlayer tunneling and charge imbalance. *Physical Review B* 82: 235312. https://doi.org/10.1103/PhysRevB.82.235312.

Ponomarenko VV and Averin DV (2007) Mach-Zehnder interferometer in the fractional quantum Hall regime. *Physical Review Letters* 99: 066803. https://doi.org/10.1103/PhysRevLett.99.066803.

Ponomarenko VV and Averin DV (2010) Braiding of anyonic quasiparticles in charge transfer statistics of a symmetric fractional edge-state Mach-Zehnder interferometer. *Physical Review B* 82: 205411. https://doi.org/10.1103/PhysRevB.82.205411.

Prange RE and Girvin SM (eds.) (1987) *The Quantum Hall Effect*. New York: Springer-Verlag.

Prodan E and Haldane FDM (2009) Mapping the braiding properties of the moore-read state. *Physical Review B* 80: 115121. https://doi.org/10.1103/PhysRevB.80.115121.

Qi XL, Katsura H, and Ludwig AWW (2012) General relationship between the entanglement spectrum and the edge state spectrum of topological quantum states. *Physical Review Letters* 108: 196402. https://doi.org/10.1103/PhysRevLett.108.196402.

Qian Q, Nakamura J, Fallahi S, Gardner GC, Watson JD, Lüscher S, Folk JA, Csáthy GA, and Manfra MJ (2017a) Quantum lifetime in ultrahigh quality GaAs quantum wells: Relationship to $\Delta_{5/2}$ and impact of density fluctuations. *Physical Review B* 96: 035309. https://doi.org/10.1103/PhysRevB.96.035309.

Qian Q, Nakamura J, Fallahi S, Gardner GC, Watson JD, and Manfra MJ (2017b) High-temperature resistivity measured at $\nu = 5/2$ as a predictor of the two-dimensional electron gas quality in the $N = 1$ Landau level. *Physical Review B* 95: 241304. https://doi.org/10.1103/PhysRevB.95.241304.

Radu IP, Miller JB, Marcus CM, Kastner MA, Pfeiffer LN, and West KW (2008) Quasi-particle properties from tunneling in the $\nu = 5/2$ fractional quantum Hall state. *Science* 320: 899–902. http://science.sciencemag.org/content/320/5878/899.

Read N (1989) Order parameter and Ginzburg-landau theory for the fractional quantum Hall effect. *Physical Review Letters* 62: 86–89. https://doi.org/10.1103/PhysRevLett.62.86.

Read N (1994) Theory of the half-filled landau level. *Semiconductor Science and Technology* 9: 1859. https://doi.org/10.1088/0268-1242/9/11S/002.

Read N (1996) Recent progress in the theory of composite fermions near even-denominator filling factors. *Surface Science* 361-362: 7–12. https://www.sciencedirect.com/science/article/pii/0039602896003184.

Read N (2009) Non-Abelian adiabatic statistics and Hall viscosity in quantum Hall states and $p_x + ip_y$ paired superfluids. *Physical Review B* 79: 045308. https://doi.org/10.1103/PhysRevB.79.045308.

Read N and Green D (2000) Paired states of fermions in two dimensions with breaking of parity and time-reversal symmetries and the fractional quantum Hall effect. *Physical Review B* 61: 10267–10297. https://doi.org/10.1103/PhysRevB.61.10267.

Read N and Rezayi E (1996) Quasiholes and fermionic zero modes of paired fractional quantum Hall states: The mechanism for non-abelian statistics. *Physical Review B* 54: 16864–16887. https://doi.org/10.1103/PhysRevB.54.16864.

Reichl C, Chen J, Baer S, Rössler C, Ihn T, Ensslin K, Dietsche W, and Wegscheider W (2014) Increasing the $\nu = 5/2$ gap energy: An analysis of MBE growth parameters. *New Journal of Physics* 16: 023014. https://doi.org/10.1088/1367-2630/16/2/023014.

Rezayi EH (2017) Landau level mixing and the ground state of the $\nu = 5/2$ quantum Hall effect. *Physical Review Letters* 119: 026801. https://doi.org/10.1103/PhysRevLett.119.026801.

Rezayi E and Read N (1994) Fermi-liquid-like state in a half-filled Landau level. *Physical Review Letters* 72: 900–903. https://doi.org/10.1103/PhysRevLett.72.900.

Rezayi EH and Simon SH (2011) Breaking of particle-hole symmetry by landau level mixing in the $\nu = 5/2$ quantized Hall state. *Physical Review Letters* 106: 116801. https://doi.org/10.1103/PhysRevLett.106.116801.

Rezayi EH, Haldane FDM, and Yang K (1999) Charge-density-wave ordering in half-filled high landau levels. *Physical Review Letters* 83: 1219–1222. https://doi.org/10.1103/PhysRevLett.83.1219.

Rezayi EH, Pakrouski K, and Haldane FDM (2021) Stability of the particle-hole Pfaffian state and the 5/2-fractional quantum Hall effect. *Physical Review B* 104: L081407. https://doi.org/10.1103/PhysRevB.104.L081407.

Rhone TD, Yan J, Gallais Y, Pinczuk A, Pfeiffer L, and West K (2011) Rapid Collapse of Spin Waves in Nonuni-form Phases of the Second Landau Level. *Physical Review Letters* 106: 196805. https://doi.org/10.1103/PhysRevLett.106.196805.

Rosenow B, Levkivskyi IP, and Halperin BI (2016) Current correlations from a mesoscopic anyon collider. *Physical Review Letters* 116: 156802. https://doi.org/10.1103/PhysRevLett.116.156802.

Samkharadze N, Watson JD, Gardner G, Manfra MJ, Pfeiffer LN, West KW, and Csáthy GA (2011) Quantitative analysis of the disorder broadening and the intrinsic gap for the $\nu = 5/2$ fractional quantum Hall state. *Physical Review B* 84: 121305. https://doi.org/10.1103/PhysRevB.84.121305.

Samkharadze N, Schreiber KA, Gardner GC, Manfra MJ, Fradkin E, and Csáthy GA (2016) Observation of a transition from a topologically ordered to a spontaneously broken symmetry phase. *Nature Physics* 12: 191–195. http://www.nature.com/articles/nphys3523.

Samkharadze N, Ro D, Pfeiffer LN, West KW, and Csáthy GA (2017) Observation of an anomalous density-dependent energy gap of the $\nu = 5/2$ fractional quantum Hall state in the low-density regime. *Physical Review B* 96: 085105. https://doi.org/10.1103/PhysRevB.96.085105.

Scarola VW and Jain JK (2001) Phase diagram of bilayer composite fermion states. *Physical Review B* 64: 085313. https://doi.org/10.1103/PhysRevB.64.085313.

Scarola VW, Park K, and Jain JK (2000a) Cooper instability of composite fermions. *Nature (London)* 406: 863–865. http://www.nature.com/nature/journal/v406/n6798/abs/406863a0.html.

Scarola VW, Park K, and Jain JK (2000b) Rotons of composite fermions: Comparison between theory and experiment. *Physical Review B* 61: 13064–13072. https://doi.org/10.1103/PhysRevB.61.13064.

Scarola VW, May C, Peterson MR, and Troyer M (2010) Subband engineering even-denominator quantum Hall states. *Physical Review B* 82: 121304. https://doi.org/10.1103/PhysRevB.82.121304.

Schiller N, Oreg Y, and Snizhko K (2022) Extracting the scaling dimension of quantum Hall quasiparticles from current correlations. *Physical Review B* 105: 165150. https://doi.org/10.1103/PhysRevB.105.165150.

Schreiber KA and Csáthy GA (2020) Competition of pairing and nematicity in the two-dimensional electron gas. *Annual Review of Condensed Matter Physics* 11: 17–35. https://doi.org/10.1146/annurev-conmatphys-031119-050550.

Schreiber KA, Samkharadze N, Gardner GC, Lyanda-Geller Y, Manfra MJ, Pfeiffer LN, West KW, and Csáthy GA (2018) Electron–electron interactions and the paired-to-nematic quantum phase transition in the second Landau level. *Nature Communications* 9: 2400. http://www.nature.com/articles/s41467-018-04879-1.

Schrieffer JR (1999) *Theory of Superconductivity*. CRC Press. https://www.taylorfrancis.com/books/9780429964251.

Sharma A, Pu S, and Jain JK (2021) Bardeen-cooper-Schrieffer pairing of composite fermions. *Physical Review B* 104: 205303. https://doi.org/10.1103/PhysRevB.104.205303.

Shi Q, Shih EM, Gustafsson MV, Rhodes DA, Kim B, Watanabe K, Taniguchi T, Papić Z, Hone J, and Dean CR (2020) Odd- and even-denominator fractional quantum Hall states in monolayer WSe2. *Nature Nanotechnology*. https://doi.org/10.1038/s41565-020-0685-6.

Shingla V, Kleinbaum E, Kumar A, Pfeiffer LN, West KW, and Csáthy GA (2018) Finite-temperature behavior in the second Landau level of the two-dimensional electron gas. *Physical Review B* 97: 241105. https://doi.org/10.1103/PhysRevB.97.241105.

Simon SH (2018a) Interpretation of thermal conductance of the $\nu = 5/2$ edge. *Physical Review B* 97. https://doi.org/10.1103/PhysRevB.97.121406. 121406(R).

Simon SH (2018b) Reply to “Comment on ‘Interpretation of thermal conductance of the $\nu = 5/2$ edge’ ” *Physical Review B* 98: 167402. https://doi.org/10.1103/PhysRevB.98.167402.

Simon SH and Rezayi EH (2013) Landau level mixing in the perturbative limit. *Physical Review B* 87: 155426. https://doi.org/10.1103/PhysRevB.87.155426.

Simon SH and Rosenow B (2020) Partial equilibration of the anti-Pfaffian Edge due to Majorana disorder. *Physical Review Letters* 124: 126801. https://doi.org/10.1103/PhysRevLett.124.126801.

Simon SH, Rezayi EH, and Cooper NR (2007) Pseudopotentials for multiparticle interactions in the quantum Hall regime. *Physical Review B* 75: 195306. https://doi.org/10.1103/PhysRevB.75.195306.

Simon SH, Ippoliti M, Zaletel MP, and Rezayi EH (2020) Energetics of Pfaffian–anti-Pfaffian domains. *Physical Review B* 101: 041302. https://doi.org/10.1103/PhysRevB.101.041302.

Smet JH, Weiss D, Blick RH, Lütjering G, von Klitzing K, Fleischmann R, Ketzmerick R, Geisel T, and Weimann G (1996) Magnetic focusing of composite fermions through arrays of cavities. *Physical Review Letters* 77: 2272–2275. https://doi.org/10.1103/PhysRevLett.77.2272.

Sodemann I and MacDonald AH (2013) Landau level mixing and the fractional quantum Hall effect. *Physical Review B* 87: 245425. https://doi.org/10.1103/PhysRevB.87.245425.

Son DT (2015) Is the composite fermion a Dirac particle? *Physical Review X* 5: 031027. https://doi.org/10.1103/PhysRevX.5.031027.

Son DT (2016) The Dirac composite fermion of the fractional quantum Hall effect. *Progress of Theoretical and Experimental Physics* 12: 12C103. https://doi.org/10.1093/ptep/ptw133.

Son DT (2019) *Chiral metric hydrodynamics, kelvin circulation theorem, and the fractional quantum Hall effect*. arXiv:1907.07187. https://arxiv.org/abs/1907.07187.

Soulé P, Jolicoeur T, and Lecheminant P (2013) Many-body study of a quantum point contact in the fractional quantum Hall regime at $\nu = 5/2$. *Physical Review B* 88: 235107. https://doi.org/10.1103/PhysRevB.88.235107.

Spånslätt C, Park J, Gefen Y, and Mirlin AD (2019) Topological Classification of shot noise on fractional quantum Hall edges. *Physical Review Letters* 123: 137701. https://doi.org/10.1103/PhysRevLett.123.137701.

Srednicki M (1993) Entropy and area. *Physical Review Letters* 71: 666–669. https://doi.org/10.1103/PhysRevLett.71.666.

Sreejith GJ, Tőke C, and Jain JK (2011) Bipartite composite fermion states. *Physical Review Letters* 107: 086806. https://doi.org/10.1103/PhysRevLett.107.086806.

Sreejith GJ, Wójs A, and Jain JK (2011) Unpaired composite Fermion, topological exciton, and zero mode. *Physical Review Letters* 107: 136802. https://doi.org/10.1103/PhysRevLett.107.136802.

Sterdyniak A, Chandran A, Regnault N, Bernevig BA, and Bonderson P (2012) Real-space entanglement spectrum of quantum Hall states. *Physical Review B* 85: 125308. https://doi.org/10.1103/PhysRevB.85.125308.

Stern F and Das Sarma S (1984) Electron energy levels in gaas-ga$_{1-x}$al$_x$As heterojunctions. *Physical Review B* 30: 840–848. https://doi.org/10.1103/PhysRevB.30.840.

Stern A and Halperin BI (2006) Proposed experiments to probe the non-abelian $\nu = 5/2$ quantum Hall state. *Physical Review Letters* 96: 016802. https://doi.org/10.1103/PhysRevLett.96.016802.

Stern A, Rosenow B, Ilan R, and Halperin BI (2010a) Interference, coulomb blockade, and the identification of non-abelian quantum Hall states. *Physical Review B* 82: 085321. https://doi.org/10.1103/PhysRevB.82.085321.

Stern M, Plochocka P, Umansky V, Maude DK, Potemski M, and Bar-Joseph I (2010b) Optical probing of the spin polarization of the $\nu = 5/2$ quantum Hall state. *Physical Review Letters* 105: 096801. https://doi.org/10.1103/PhysRevLett.105.096801.

Stern M, Piot BA, Vardi Y, Umansky V, Plochocka P, Maude DK, and Bar-Joseph I (2012) NMR probing of the spin polarization of the ν=5/2 quantum Hall state. *Physical Review Letters* 108: 1–5. https://doi.org/10.1103/PhysRevLett.108.066810.

Storni M, Morf RH, and Das Sarma S (2010) Fractional quantum Hall state at $\nu = 5/2$ and the Moore-read Pfaffian. *Physical Review Letters* 104: 076803. https://doi.org/10.1103/PhysRevLett.104.076803.

Suen YW, Engel LW, Santos MB, Shayegan M, and Tsui DC (1992) Observation of a ν=1/2 fractional quantum Hall state in a double-layer electron system. *Physical Review Letters* 68: 1379–1382. https://doi.org/10.1103/PhysRevLett.68.1379.

Sun C, Ma KKW, and Feldman DE (2020) Particle-hole Pfaffian order in a translationally and rotationally invariant system. *Physical Review B* 102: 121303. https://doi.org/10.1103/PhysRevB.102.121303.

Swingle B and Senthil T (2012) Geometric proof of the equality between entanglement and edge spectra. *Physical Review B* 86: 045117. https://doi.org/10.1103/PhysRevB.86.045117.

Tiemann L, Gamez G, Kumada N, and Muraki K (2012) Unraveling the spin polarization of the $\nu = 5/2$ fractional quantum Hall state. *Science* 335: 828–831. https://doi.org/10.1126/science.1216697.

Tőke C and Jain JK (2006) Understanding the 5/2 fractional quantum Hall effect without the Pfaffian wave function. *Physical Review Letters* 96: 246805. https://doi.org/10.1103/PhysRevLett.96.246805.

Tserkovnyak Y and Simon SH (2003) Monte Carlo evaluation of non-abelian statistics. *Physical Review Letters* 90: 016802. https://doi.org/10.1103/PhysRevLett.90.016802.

Tsui DC, Stormer HL, and Gossard AC (1982) Two-dimensional magnetotransport in the extreme quantum limit. *Physical Review Letters* 48: 1559–1562. https://doi.org/10.1103/PhysRevLett.48.1559.

Tu HH, Zhang Y, and Qi XL (2013) Momentum polarization: An entanglement measure of topological spin and chiral central charge. *Physical Review B* 88: 195412. https://doi.org/10.1103/PhysRevB.88.195412.

Tylan-Tyler A and Lyanda-Geller Y (2015) Phase diagram and edge states of the $\nu = 5/2$ fractional quantum Hall state with landau level mixing and finite well thickness. *Physical Review B* 91: 205404. https://doi.org/10.1103/PhysRevB.91.205404.

Tylan-Tyler A and Lyanda-Geller Y (2017) In-plane electric fields and the $\nu = 5/2$ fractional quantum Hall effect in a disk geometry. *Physical Review B* 95: 121302. https://doi.org/10.1103/PhysRevB.95.121302.

Venkatachalam V, Yacoby A, Pfeiffer L, and West K (2011) Local charge of the $\nu = 5/2$ fractional quantum Hall state. *Nature (London)* 469: 185–188. https://www.nature.com/articles/nature09680.

Wan X and Yang K (2016) Striped quantum Hall state in a half-filled landau level. *Physical Review B* 93: 201303. https://doi.org/10.1103/PhysRevB.93.201303.

Wan X, Yang K, and Rezayi EH (2002) Reconstruction of fractional quantum Hall edges. *Physical Review Letters* 88: 056802. https://doi.org/10.1103/PhysRevLett.88.056802.

Wan X, Rezayi EH, and Yang K (2003) Edge reconstruction in the fractional quantum Hall regime. *Physical Review B* 68: 125307. https://doi.org/10.1103/PhysRevB.68.125307.

Wan X, Sheng DN, Rezayi EH, Yang K, Bhatt RN, and Haldane FDM (2005) Mobility gap in fractional quantum Hall liquids: Effects of disorder and layer thickness. *Physical Review B* 72: 075325. https://doi.org/10.1103/PhysRevB.72.075325.

Wan X, Yang K, and Rezayi EH (2006) Edge excitations and non-Abelian statistics in the Moore-read state: A numerical study in the presence of coulomb interaction and edge confinement. *Physical Review Letters* 97: 256804. https://doi.org/10.1103/PhysRevLett.97.256804.

Wan X, Hu ZX, Rezayi EH, and Yang K (2008) Fractional quantum Hall effect at $\nu = 5/2$: Ground states, non-abelian quasiholes, and edge modes in a microscopic model. *Physical Review B* 77: 165316. https://doi.org/10.1103/PhysRevB.77.165316.

Wang C and Feldman DE (2010) Identification of 331 quantum Hall states with Mach-Zehnder interferometry. *Physical Review B* 82: 165314. https://doi.org/10.1103/PhysRevB.82.165314.

Wang H, Sheng DN, and Haldane FDM (2009) Particle-hole symmetry breaking and the $\nu = 5/2$ fractional quantum Hall effect. *Physical Review B* 80: 241311. https://doi.org/10.1103/PhysRevB.80.241311.

Wang C, Cooper NR, Halperin BI, and Stern A (2017) Particle-hole symmetry in the Fermion-Chern-Simons and Dirac descriptions of a half-filled Landau Level. *Physical Review X* 7: 031029. https://doi.org/10.1103/PhysRevX.7.031029.

Wang C, Vishwanath A, and Halperin BI (2018) Topological order from disorder and the quantized Hall thermal metal: Possible applications to the $\nu = 5/2$ state. *Physical Review B* 98: 045112. https://doi.org/10.1103/PhysRevB.98.045112.

Wang P, Sun J, Fu H, Wu Y, Chen H, Pfeiffer LN, West KW, Xie XC, and Lin X (2020) Finite-thickness effect and spin polarization of the even-denominator fractional quantum Hall states. *Physical Review Research* 2: 022056. https://doi.org/10.1103/PhysRevResearch.2.022056.

Watson JD, Csáthy GA, and Manfra MJ (2015) Impact of heterostructure design on transport properties in the second Landau level of in situ back-gated two-dimensional electron gases. *Physical Review Applied* 3: 064004. https://doi.org/10.1103/PhysRevApplied.3.064004.

Wen XG (1993) Topological order and edge structure of $\nu = 1/2$ quantum Hall state. *Physical Review Letters* 70: 355–358. https://doi.org/10.1103/PhysRevLett.70.355.

Wen XG (2004) *Quantum Field Theory of Many-Body Systems: From the Origin of Sound to an Origin of Light and Electrons.* New York: Oxford University Press.

Wen XG and Niu Q (1990) Ground-state degeneracy of the fractional quantum Hall states in the presence of a random potential and on high-genus Riemann surfaces. *Physical Review B* 41: 9377–9396. https://doi.org/10.1103/PhysRevB.41.9377.

Wen XG and Zee A (1992a) Classification of Abelian quantum Hall states and matrix formulation of topological fluids. *Physical Review B* 46: 2290–2301. https://doi.org/10.1103/PhysRevB.46.2290.

Wen XG and Zee A (1992b) Shift and spin vector: New topological quantum numbers for the Hall fluids. *Physical Review Letters* 69: 953–956. https://doi.org/10.1103/PhysRevLett.69.953.

Wilczek F (1982) Quantum mechanics of fractional-spin particles. *Physical Review Letters* 49: 957–959. https://doi.org/10.1103/PhysRevLett.49.957.

Willett RL (2013) The quantum Hall effect at 5/2 filling factor. *Reports on Progress in Physics* 76: 076501. https://doi.org/10.1088/0034-4885/76/7/076501.

Willett R, Eisenstein JP, Störmer HL, Tsui DC, Gossard AC, and English JH (1987) Observation of an even-denominator quantum number in the fractional quantum Hall effect. *Physical Review Letters* 59: 1776–1779. https://doi.org/10.1103/PhysRevLett.59.1776.

Willett RL, Ruel RR, West KW, and Pfeiffer LN (1993) Experimental demonstration of a Fermi surface at one-half filling of the lowest Landau level. *Physical Review Letters* 71: 3846–3849. https://doi.org/10.1103/PhysRevLett.71.3846.

Willett RL, West KW, and Pfeiffer LN (1999) Geometric resonance of composite fermion cyclotron orbits with a fictitious magnetic field modulation. *Physical Review Letters* 83: 2624–2627. https://doi.org/10.1103/PhysRevLett.83.2624.

Willett RL, West KW, and Pfeiffer LN (2002) Experimental demonstration of fermi surface effects at filling factor $\nu = 5/2$. *Physical Review Letters* 88: 066801. https://doi.org/10.1103/PhysRevLett.88.066801.

Willett RL, Pfeiffer LN, and West KW (2009) Measurement of filling factor 5/2 quasiparticle interference with observation of charge *e*/4 and *e*/2 period oscillations. *Proceedings of the National Academy of Sciences of the United States of America* 106: 8853–8858. http://www.pnas.org/content/106/22/8853.

Willett RL, Pfeiffer LN, and West KW (2010) Alternation and interchange of e/4 and e/2 period interference oscillations consistent with filling factor 5/2 non-Abelian quasiparticles. *Physical Review B* 82: 205301. https://doi.org/10.1103/PhysRevB.82.205301.

Willett RL, Nayak C, Shtengel K, Pfeiffer LN, and West KW (2013) Magnetic-field-tuned Aharonov-Bohm oscillations and evidence for non-Abelian anyons at $\nu = 5/2$. *Physical Review Letters* 111: 186401. https://doi.org/10.1103/PhysRevLett.111.186401.

Willett R, Shtengel K, Nayak C, Pfeiffer L, Chung Y, Peabody ML, Baldwin K and West KW (2019) *Interference measurements of non-Abelian e/4 & Abelian e/2 quasiparticle braiding*. arXiv:1905.10248. https://arxiv.org/abs/1905.10248.

Wójs A and Quinn JJ (2006) Landau level mixing in the 5/2 fractional quantum Hall state. *Physical Review B* 74: 235319. https://doi.org/10.1103/PhysRevB.74.235319.

Wójs A, Tőke C, and Jain JK (2010) Landau-level mixing and the emergence of Pfaffian excitations for the 5/2 fractional quantum Hall effect. *Physical Review Letters* 105: 096802. https://doi.org/10.1103/PhysRevLett.105.096802.

Wooten RE, Macek JH, and Quinn JJ (2013) Including landau level mixing in numerical studies of the quantum Hall effect. *Physical Review B* 88: 155421. https://doi.org/10.1103/PhysRevB.88.155421.

Wright AR and Rosenow B (2012) Splitting of the roton minimum in the $\nu = 5/2$ Moore-Read state. *Physical Review B* 86: 115329. https://doi.org/10.1103/PhysRevB.86.115329.

Wu TT and Yang CN (1976) Dirac monopole without strings: Monopole harmonics. *Nuclear Physics B* 107: 365–380. https://linkinghub.elsevier.com/retrieve/pii/0550321376901437.

Wu TT and Yang CN (1977) Some properties of monopole harmonics. *Physical Review D* 16: 1018–1021. https://doi.org/10.1103/PhysRevD.16.1018.

Wu YH, Shi T, and Jain JK (2017) Non-Abelian Parton fractional quantum Hall effect in multilayer graphene. *Nano Letters* 17: 4643–4647. https://doi.org/10.1021/acs.nanolett.7b01080.

Wurstbauer U, West KW, Pfeiffer LN, and Pinczuk A (2013) Resonant inelastic light scattering investigation of low-lying gapped excitations in the quantum fluid at $\nu = 5/2$. *Physical Review Letters* 110: 026801. https://doi.org/10.1103/PhysRevLett.110.026801.

Xia J, Cvicek V, Eisenstein JP, Pfeiffer LN, and West KW (2010) Tilt-induced anisotropic to isotropic phase transition at ν=5/2. *Physical Review Letters* 105: 1–4. https://doi.org/10.1103/PhysRevLett.105.176807.

Xia J, Eisenstein JP, Pfeiffer LN, and West KW (2011) Evidence for a fractionally quantized Hall state with anisotropic longitudinal transport. *Nature Physics* 7: 845–848. http://www.nature.com/articles/nphys2118.

Yan B, Biswas RR, and Greene CH (2019) Bulk-edge correspondence in fractional quantum Hall states. *Physical Review B* 99: 035153. https://doi.org/10.1103/PhysRevB.99.035153.

Yan J, Wu Y, Yuan S, Liu X, Pfeiffer LN, West KW, Liu Y, Fu H, Xie XC, Lin X (2022) *Anomalous quantized plateaus in two-dimensional electron gas with gate confinement*. arXiv:2207.06701. https://arxiv.org/abs/2207.06701.

Yang K (2003) Field theoretical description of quantum Hall edge reconstruction. *Physical Review Letters* 91: 036802. https://doi.org/10.1103/PhysRevLett.91.036802.

Yang G (2015) Probing the $\nu = 5/2$ quantum Hall state with electronic Mach-Zehnder interferometry. *Physical Review B* 91: 115109. https://doi.org/10.1103/PhysRevB.91.115109.

Yang K (2016) Acoustic wave absorption as a probe of dynamical geometrical response of fractional quantum Hall liquids. *Physical Review B* 93: 161302. https://doi.org/10.1103/PhysRevB.93.161302.

Yang G and Feldman DE (2013) Inuence of device geometry on tunneling in the $\nu = 5/2$ quantum Hall liquid. *Physical Review B* 88: 085317. https://doi.org/10.1103/PhysRevB.88.085317.

Yang G and Feldman DE (2014) Experimental constraints and a possible quantum Hall state at $\nu = 5/2$. *Physical Review B* 90. https://doi.org/10.1103/PhysRevB.90.161306. 161306(R).

Yang K and Halperin BI (2009) Thermopower as a possible probe of non-abelian quasiparticle statistics in fractional quantum Hall liquids. *Physical Review B* 79: 115317. https://doi.org/10.1103/PhysRevB.79.115317.

Yang K and Rezayi EH (2008) Magnetization and spin excitations of non-abelian quantum Hall states. *Physical Review Letters* 101: 216808. https://doi.org/10.1103/PhysRevLett.101.216808.

Yang B, Hu ZX, Papić Z, and Haldane FDM (2012) Model wave functions for the collective modes and the Magne-toroton theory of the fractional quantum Hall effect. *Physical Review Letters* 108: 256807. https://doi.org/10.1103/PhysRevLett.108.256807.

Yoshioka D (2002) *The Quantum Hall Effect*. New York: Springer-Verlag.

Yoshioka D, MacDonald AH, and Girvin SM (1989) Fractional quantum Hall effect in two-layered systems. *Physical Review B* 39: 1932–1935. https://doi.org/10.1103/PhysRevB.39.1932.

Yutushui M and Mross DF (2020) Large-scale simulations of particle-hole-symmetric Pfaffian trial wave functions. *Physical Review B* 102: 195153. https://doi.org/10.1103/PhysRevB.102.195153.

Yutushui M, Stern A, and Mross DF (2022) Identifying the $\nu = 5/2$ topological order through charge transport measurements. *Physical Review Letters* 128: 016401. https://doi.org/10.1103/PhysRevLett.128.016401.

Zaletel MP, Mong RSK, and Pollmann F (2013) Topological characterization of fractional quantum Hall ground states from microscopic Hamiltonians. *Physical Review Letters* 110: 236801. https://doi.org/10.1103/PhysRevLett.110.236801.

Zaletel MP, Mong RSK, Pollmann F, and Rezayi EH (2015) Infinite density matrix renormalization group for multicomponent quantum Hall systems. *Physical Review B* 91: 045115. https://doi.org/10.1103/PhysRevB.91.045115.

Zhang FC and Das Sarma S (1986) Excitation gap in the fractional quantum Hall effect: Finite layer thickness corrections. *Physical Review B* 33: 2903–2905. https://doi.org/10.1103/PhysRevB.33.2903.

Zhang C, Knuuttila T, Dai Y, Du RR, Pfeiffer LN, and West KW (2010) $\nu = 5/2$ fractional quantum Hall effect at 10 t: Implications for the Pfaffian state. *Physical Review Letters* 104: 166801. https://doi.org/10.1103/PhysRevLett.104.166801.

Zhu W and Sheng DN (2019) Disorder-driven transition in the $\nu = 5/2$ fractional quantum Hall effect. *Physical Review Letters* 123: 056804. https://doi.org/10.1103/PhysRevLett.123.056804.

Zhu Z, Wang P, Fu H, Pfeiffer L, West K, Du RR, and Lin X (2018) Stability of the 5/2 fractional quantum Hall state in a Corbino disc sample with in-plane electric fields. *Physica E* 95: 1–5. https://linkinghub.elsevier.com/retrieve/pii/S1386947717306495.

Zhu W, Sheng DN, and Yang K (2020) Topological interface between Pfaffian and anti-Pfaffian order in $\nu = 5/2$ quantum Hall effect. *Physical Review Letters* 125: 146802. https://doi.org/10.1103/PhysRevLett.125.146802.

Zibrov AA, Kometter C, Zhou H, Spanton EM, Taniguchi T, Watanabe K, Zaletel MP, and Young AF (2017) Tunable interacting composite fermion phases in a half-filled bilayer-graphene Landau level. *Nature* 549: 360–364. https://doi.org/10.1038/nature23893.

Zibrov AA, Spanton EM, Zhou H, Kometter C, Taniguchi T, Watanabe K, and Young AF (2018) Even-denominator fractional quantum Hall states at an isospin transition in monolayer graphene. *Nature Physics* 14: 930–935. https://www.nature.com/articles/s41567-018-0190-0.

Zozulya OS, Haque M, Schoutens K, and Rezayi EH (2007) Bipartite entanglement entropy in fractional quantum Hall states. *Physical Review B* 76: 125310. https://doi.org/10.1103/PhysRevB.76.125310.

Zucker PT and Feldman DE (2016) Stabilization of the particle-hole Pfaffian order by landau-level mixing and impurities that break particle-hole symmetry. *Physical Review Letters* 117: 096802. https://doi.org/10.1103/PhysRevLett.117.096802.

Interacting Dirac fermions and the rise of Pfaffians in graphene

Vadym Apalkov[a] **and Tapash Chakraborty**[b,c], [a]Department of Physics and Astronomy, Georgia State University, Atlanta, GA, United States; [b]Department of Physics and Astronomy, University of Manitoba, Winnipeg, MB, Canada; [c]Department of Physics, Brock University, St. Catharines, ON, Canada

© 2024 Elsevier Ltd. All rights reserved.

Introduction **366**
Fractional quantum Hall effect **367**
Pfaffian function 369
Monolayer and bilayer graphene in a strong magnetic field **373**
Graphene monolayer 373
Bilayer graphene 374
Pfaffian states in graphene **377**
Graphene monolayer 377
Bilayer graphene 377
Finding the Pfaffians 380
Conclusion **380**
References **381**

Abstract

Fractional Quantum Hall effect (FQHE) is a unique many-body phenomenon, which was discovered in a two-dimensional electron system placed in a strong perpendicular magnetic field. It is entirely due to the electron-electron interactions within a given Landau level. For special filling factors of the Landau level, a many-particle incompressible state with a finite collective gap is formed. Among these states, when the Landau level is half filled, there is a special FQHE state that is described by the Pfaffian function and the state supports charged excitations that obey non-Abelian statistics. Such a 1/2-FQHE state can be realized only for a special profile of the electron-electron potential. For example, for conventional electron systems the 1/2-FQHE state occurs only in the second Landau level, while in a graphene monolayer, no 1/2-FQHE state can be found in the first and the second Landau levels. Another type of low-dimensional system is the bilayer graphene, which consists of two graphene monolayers coupled through the interlayer hopping. The system is quasi-two-dimensional, which makes it possible to tune the inter-electron interaction potential by applying either the bias voltage or the magnetic field that is applied parallel to the bilayer. Interestingly, in the bilayer graphene with AB stacking, there is one Landau level per valley where the 1/2-FQHE state can indeed be present. The properties of that 1/2-FQHE state have a nonmonotonic dependence on the applied magnetic field and this state can be even more stable than the one discovered in conventional electron systems.

Key points

- In two-dimensional electron systems an externally applied magnetic field results in the formation of highly discrete and degenerate Landau levels.
- In a strong enough magnetic field, the discrete nature of the energy spectrum of two-dimensional electrons results in the integer quantum Hall effect (IQHE), which happens when integer number of Landau levels are occupied.
- For a partially filled Landau levels, inter-electron interactions result in formation of incompressible liquids, which manifest themselves as the Fractional Quantum Hall Effect (FQHE).
- The conventional FQHE corresponds to filling factors of type p/q, where q is odd.
- The unconventional FQHE at half-filling ($\nu = 1/2$) of a given Landau level is described by the Pfaffian function as the wave function of the ground state and has excitations with the charge of $e/4$ and obey non-abelian statistics.
- For conventional 2D systems, 1/2-FQHE is realized only in the $n = 1$ Landau level.
- For graphene monolayer, there is no $\nu = 1/2$ incompressible liquid in the first and second Landau levels.
- For bilayer graphene there is a special Landau level in which the stability of the $\nu = 1/2$ incompressible state can be tuned by the magnitude and direction of the magnetic field and the bias voltage.

Introduction

A moving charge placed in an external magnetic field experiences a magnetic force, which can change only the direction of the charge velocity but not its magnitude. One of the manifestations of this property of the magnetic field is the Hall effect. The Hall effect occurs when the current flows through a solid and the magnetic field is applied perpendicular to the current. In this case the voltage

https://doi.org/10.1016/B978-0-323-90800-9.00102-5

difference, which is called the Hall voltage, is generated across the conductor in the direction transverse to both the current and the magnetic field. This effect was discovered by Edwin Hall in 1879 (Hall, 1879). If the electric current is in the x direction with the current density of j_x and magnetic field is in the z direction, then there is a Hall electric field generated in the y direction. The strength of the Hall effect is characterized by the Hall coefficient defined by the following expression (Ashcroft and Mermin, 1976; Hurd, 1972; Kittel, 2005)

$$R_H = \frac{E_y}{j_x B_z}. \tag{1}$$

It is possible to show that, within the classical approach, the Hall constant is related to the charge of the carriers, q, and their density, n,

$$R_H = \frac{1}{nq}. \tag{2}$$

One important property of this expression is that the Hall constant and correspondingly the Hall voltage depends on the sign of carrier's charge, q. For example, for semiconductors, when the carriers are negatively charged electrons or positively charged holes, the Hall constant can be negative or positive depending on the type of the major carriers.

The above expression for the Hall coefficient corresponds to the classical description of the electron dynamics in a magnetic field, or in the low magnetic field limit. With increasing magnetic field, the electron dynamics in the magnetic field becomes essentially quantum mechanical, which results in quantization of the corresponding energy spectrum and formation of highly degenerate and discrete Landau levels (Landau and Lifshitz, 1965). The energy distance between the Landau levels is proportional to the magnetic field. Due to discrete nature of the energy spectrum of carriers, the diagonal resistance of a solid as a function of the magnetic field shows oscillations, which are called the Shubnikov de Haas oscillations (Seiler and Stephens, 1991).

More interesting and unexpected phenomena occur in two-dimensional (2D) electron systems, such as in heterojunctions, atomic monolayers, or in quantum wells. If the magnetic field is applied perpendicular to the 2D layer, i.e., the (x, y) plane, then for weak magnetic fields there is the classical Hall effect, which can be also characterized by the Hall resistance R_{xy}

$$R_{xy} = \frac{E_y}{j_x} = R_H B_z. \tag{3}$$

Therefore in the classical regime, i.e., in a weak magnetic field, the Hall resistance is proportional to the magnetic field, B_z. At the same time, in stronger magnetic fields when the quantization of the in-plane electron dynamics results in Landau levels, there is another unique effect, which is the Integer Quantum Hall Effect (IQHE) (Chakraborty and Pietiläinen, 1995; von Klitzing et al., 2020; Klitzing, 2017; Klitzing et al., 1980; Prange and Girvin, 1987; Stone, 1992; Yoshioka, 2002). In this regime, the Hall resistance takes only quantized values of the form

$$R_{xy} = \frac{h}{e^2 \nu}, \tag{4}$$

where h is the Plank constant, e is the electron charge, and ν is an integer, $\nu = 1, 2, 3, \ldots$. The integer number ν corresponds to the number of completely filled Landau levels and whenever the Fermi energy is between the two Landau levels n and $n + 1$, the Hall resistance is constant, while the longitudinal resistance, R_{xx}, becomes zero. Strictly speaking, to understand the Quantum Hall Effect we also need to consider broadening of the Landau levels due to disorder and spatial localization of the in-gap electron states between the Landau levels (Chakraborty and Pietiläinen, 1995; Stone, 1992). However the main condition for the IQHE is the existence of the gaps in the energy spectrum which naturally occurs in 2D systems in a strong magnetic field.

The IQHE was discovered experimentally in 1980 and 2 years later another unexpected (and more spectacular) effect was observed in even stronger magnetic fields, and in better quality samples. This effect is known as the Fractional Quantum Hall Effect (FQHE) (Chakraborty and Pietiläinen, 1995; Tsui et al., 1982). In this case the filling factor ν in Eq. (4) is fractional and corresponds to partial occupation of a given Landau level, see Fig. 1. Since all levels within the Landau level are degenerate, the electron-electron interaction completely determines the properties of the system. At special fractional occupations of the Landau level, the interaction generates the incompressible ground states with gapped excitations, which finally results in the FQHE. The primary filling factors where the FQHE occur are $\nu = \frac{1}{3}, \frac{2}{3}, \frac{1}{5}, \frac{2}{5}, \frac{3}{5}, \frac{1}{7}$ etc. (Chakraborty and Pietiläinen, 1995; Halperin and Jain, 2020; Prange and Girvin, 1987). In all these cases the denominator is an odd number, which is due to the fermionic nature of electrons.

Fractional quantum Hall effect

First, we consider the conventional two-dimensional electron systems, such as the ones grown in heterojunctions or in a quantum well, for which the low-energy dispersion relation is parabolic. The Hamiltonian of such systems has the form

$$\mathcal{H}_c = \frac{\vec{p}^{\,2}}{2m^*}, \tag{5}$$

where $\vec{p}$ is the two-dimensional momentum and m^* is the electron effective mass. When the system is placed in a perpendicular external magnetic field, the Hamiltonian becomes

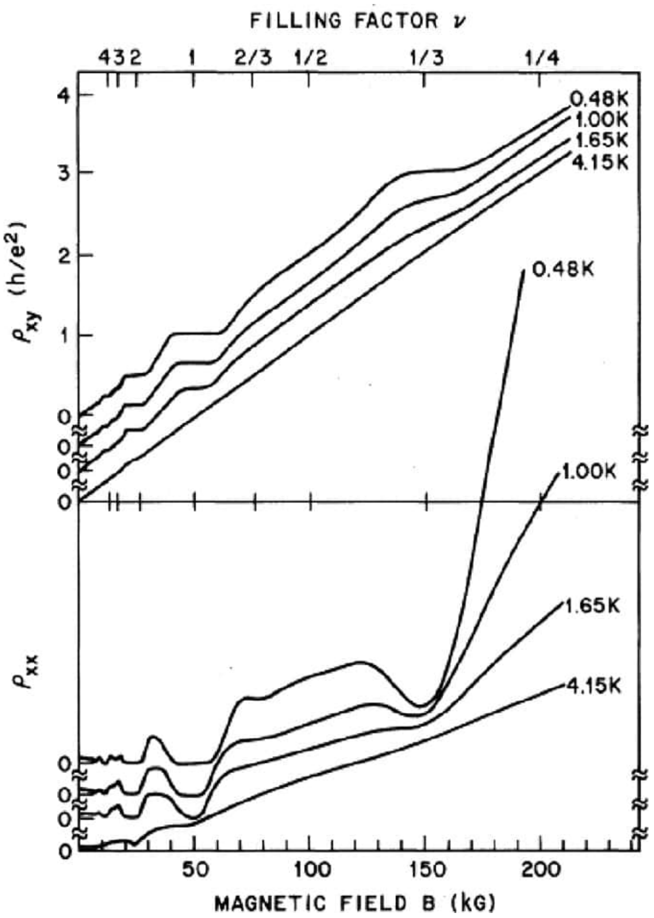

Fig. 1 Non-diagonal and diagonal resistivities, ρ_{xy} and ρ_{xx}, as a function of the magnetic field, B. The sample is GaAs—$Al_{0.3}Ga_{0.7}As$ with electron density of $n = 1.23 \times 10^{11}$ cm^{-2} and mobility $\mu = 90{,}000$ cm^2/Vs. Adapted from Tsui DC, Stormer HL, and Gossard AC (1982) Two-dimensional magnetotransport in the extreme quantum limit. *Physical Review Letters* 48: 1559–1562, doi:10.1103/PhysRevLett.48.1559.

$$\mathcal{H}_c = \frac{\vec{\pi}^2}{2m^*}, \tag{6}$$

where $\vec{\pi} = \vec{p} + e\vec{A}/c$ is the generalized momentum and $\vec{A}$ is the vector potential. The energy spectrum of the Hamiltonian (6) consists of highly degenerate discrete Landau levels (Landau and Lifshitz, 1965) with energy

$$\varepsilon_n = \hbar\omega_B\left(n + \frac{1}{2}\right), \tag{7}$$

where $\omega_B = eB/m^*$ is the cyclotron frequency and $n = 0, 1, 2, \ldots$ is the Landau level index. We write the corresponding Landau eigenfunctions as $\phi_{n,m}$, where the index m labels the degenerate wavefunctions within a given Landau level and is determined by the choice of the gauge. For example, in the Landau gauge, $A_x = 0$ and $A_y = Bx$, the index m is the y-component of the momentum, while in the symmetric gauge, $\vec{A} = \frac{1}{2}\vec{B} \times \vec{r}$, the index m is the z-component of electron angular momentum (Landau and Lifshitz, 1965). In what follows, we consider m as the z component of the angular momentum.

When a given Landau level is partially occupied by electrons, the properties of the system is completely determined by the electron-electron interactions. If the mixing of Landau levels due to the interactions is weak, then the interaction properties of electrons within a single Landau level are completely determined by the Haldane pseudopotentials $V_m^{(n)}$ (Haldane, 1983). The Haldane pseudopotential $V_m^{(n)}$ is the energy of two electrons with the relative angular momentum m and they can be found from the following expression (Haldane, 1987)

$$V_m^{(n)} = \int_0^\infty \frac{dq}{2\pi} qV(q)\,[F_n(q)]^2 L_m\left(q^2\right)e^{-q^2}, \tag{8}$$

where $L_m(x)$ are the Laguerre polynomials, $V(q) = 2\pi e^2/(\kappa\ell_0 q)$ is the Coulomb interaction in the momentum space, κ is the background dielectric constant, and $F_n(q)$ is the form factor of the n-th Landau level. The form factor is totally determined by the structure of the wavefunctions of the corresponding Landau level. Different two-dimensional systems, such as the graphene monolayer, transition-metal dichalcogenide monolayer, graphene bilayer, etc., have different form factors $F_n(q)$, but in all cases, the corresponding Haldane pseudopotentials are given by the same expression (8). For conventional two-dimensional electron systems with Landau wavefunctions $\phi_{n,m}$ the form factor is (Haldane, 1987)

$$F_n(q) = L_n\left(q^2/2\right). \tag{9}$$

If the electron system is fully spin polarized then the spatial component of the many-particle wavefunction is antisymmetric with respect to the particle exchange. In this case, only the Haldane pseudopotentials, $V_m^{(n)}$, with odd values of m, $m = 1, 3, 5, \ldots$, determine the properties of the system. The nature of the ground state mainly depends on the ratio of the first few pseudopotentials, $V_1^{(n)}/V_3^{(n)}$ and $V_3^{(n)}/V_5^{(n)}$.

At special values of the filling factor ν, which is defined as $\nu = N_e/N_0$, where N_e is the number of electrons in a given Landau level and N_0 is its degeneracy, the electron system becomes incompressible with a finite excitation gap. This incompressibility is entirely due to electron-electron interactions and is determined by the values of the Haldane pseudopotentials. Only for these filling factors the FQHE can be observed.

The conventional FQHE occurs at the filling factors of the form p/q, where q is odd, which is related to the antisymmetric property of a many-particle electron wavefunction when two particles are interchanged, i.e., $\Psi\left(\vec{r}_1, \vec{r}_2, \vec{r}_3, \ldots\right) = -\Psi\left(\vec{r}_2, \vec{r}_1, \vec{r}_3, \ldots\right)$. A prominent example of this type of FQHE is the $1/q$ sequence, i.e., 1/3, 1/5 etc. The corresponding many-particle wave function is well described by the Laughlin function (Laughlin, 1983) of the form

$$\Psi(z_1, z_2, z_3, \ldots) = \prod_{i<j} (z_i - z_j)^q \exp\left(-\sum_i \frac{z_i^2}{4\ell_0^2}\right), \tag{10}$$

where the positions of electrons are described in terms of complex variable $z = x - iy$, and $\ell_0 = \sqrt{h/eB}$ is the magnetic length. The Laughlin function (10) corresponds to the filling factor $1/q$ and is very close to the exact many-particle wave function of the system. The accuracy of the trial wave functions, for instance the Laughlin function, is tested through numerical calculations for a finite-size electron system. For a finite-size system placed in an external magnetic field, the many-particle basis is finite, which allows us to find both the ground state and the excitation spectrum of the system. Then, the overlap of the trial function with the exact ground state wave function of the many-particle system can be determined and that can be used to test the accuracy of the trial approximation. The incompressibility of the system is determined by the magnitude of the gap in the collective excitations of the system. Another interesting property of the $1/q$ FQHE, which is described by the Laughlin function, is that the charged excitations have fractional charge $e^* = e/q$. For example, for the 1/3-FQHE the quasiparticles carry a fractional charge $e^* = e/3$.

Our fundamental understanding of the origin of the odd-denominator FQHE is from the brilliant work of Laughlin which requires that we consider a *incompressible* fluid that has no long-range positional order. The incompressibility implies that all the excited states have a non-zero energy difference from the ground state. The ground state can be fully spin polarized or also have spin degree of freedom (Apalkov et al., 2001; Chakraborty et al., 1986; Chakraborty and Zhang, 1984) in the ground state and spin-reversed excitations. It is worth emphasizing that despite the torrent of ideas unleased by the Laughlin function, the origin of incompressibility in the Laughlin state still remains unresolved (Haldane, 2011).

In addition to the conventional FQHE set of type p/q, where q is odd, another type of FQHE corresponding to the filling 5/2 has been discovered experimentally (Willett et al., 1987; Willett, 2013). This filling factor implies that there are two completely occupied Landau levels, which correspond to spin-up and spin-down Landau levels with index $n = 0$, and the next Landau level is half-filled. It means that in the $n = 1$ Landau level the 1/2-FQHE occurs, i.e., the filling factor of the $n = 1$ Landau level is $\nu = 1/2$. This unusual FQHE cannot be described by the Laughlin function (10). This is because the many-particle wave function should be antisymmetric with respect to the particle interchange, because the corresponding electrons are fermions and therefore q must be an odd integer. But for $q = 2$, the Laughlin function is symmetric, and therefore describes a system of bosons. Another important property of the 1/2-FQHE is that the 1/2 incompressible liquid is realized only in higher Landau levels, for example, for $n = 1$ but not for the $n = 0$ level. Different wavefunctions (albeit a modification of the Laughlin state) have been proposed theoretically to describe this state. Among them are the Pfaffian (Moore and Read, 1991), anti-Pfaffian (Levin et al., 2007), particle-hole symmetric Pfaffian (Son, 2015), and the 221-parton (Wen, 1991) wavefunctions. The 1/2-FQHE is also sensitive to the inter-Landau level mixing (Rezayi, 2017) which modifies the electron-electron interaction potential (Peterson and Nayak, 2013) and opens up the possibility to observe the 1/2-FQHE in higher Landau levels (Kim et al., 2019) where the inter-Landau mixing becomes strong. Below we consider the properties of the 1/2-FQHE, which is described only by the Pfaffian wavefunction.

Pfaffian function

Some properties of the FQHE states can be understood by looking at the specially created composite objects, that are called the composite fermions. The composite fermion is an electron with an even number of flux quanta attached to it. These objects still have the same Fermi statistics as original electrons, but they feel a different magnetic field. To understand their properties, first, let us consider a fully filled Landau level. In this case, there is one magnetic flux quantum per each electron and under this condition we have the IQHE. Now let us consider a Landau level with the filling factor of $\nu = 1/3$, i.e., only 1/3 states within a given Landau level are occupied. For such a system, there are three magnetic flux quanta per electron and this state corresponds to the $\nu = 1/3$-FQHE. The composite fermions for this system are electrons bound to two magnetic flux quanta each. Therefore, for these composite fermions (one electron plus two flux quanta), there is one magnetic flux quanta per fermion, which corresponds to a fully occupied

Landau level and is therefore, the IQHE of composite fermions. Another way to state this is that, the FQHE for electrons is the IQHE for composite fermions. This correspondence exists only for the FQHE of type of p/q, where q is odd. As an example, for $\nu = 1/5$ the composite fermion is an electron plus four magnetic flux quanta and the composite fermions all occupy the first Landau level. It is important that the number of magnetic flux quanta attached to an electron is even. Only in this case the composite particles have the same Fermi statistics as electrons.

A unique situation occurs for the Landau level that is exactly half filled. For such a system, the composite fermion picture dictates that there are two magnetic flux quanta associated with each electron. In that case, a composite fermion comprise of an electron bound to two magnetic flux quanta and in a mean-field picture, the system of composite fermions does not experience a net magnetic field (Halperin et al., 1993). The properties of this composite fermion system are determined by the inter-fermion interaction, i.e., by the Haldane pseudopotentials. For the $n = 0$ Landau level, the composite fermions form a gapless composite Fermi liquid. A more interesting situation happens for the $n = 1$ Landau level, i.e., for the total filling factor $\nu = 5/2$. In this case, the theoretical and experimental results suggest that the system forms a gapped state which is due to pairing[*] of the composite fermions, i.e., by formation of Cooper pairs, similar to what we see in the superconductor systems. The pairing symmetry can then be different and below we consider only one type of symmetry, i.e., when the Cooper pairs of composite fermions have angular momentum −1. It was proposed that the corresponding ground state of the system expressed in terms of the coordinates of original electrons is described by the Pfaffian (Greiter et al., 1991, 1992; Moore and Read, 1991; Nayak et al., 2008) function, which has the following form

$$\Psi_{\mathrm{Pf}} = \mathrm{Pf}\left[\frac{1}{z_i - z_j}\right]\prod_{i<j}(z_i - z_j)^2 \exp\left(-\sum_i \frac{z_i^2}{4\ell_0^2}\right), \tag{11}$$

where the Pfaffian is defined as (Greiter, 2011; Moore and Read, 1991)

$$\mathrm{Pf}\;[\mathbf{M}] = \frac{1}{2^{N/2}(N/2)!}\sum_{\sigma\in S_N}\mathrm{sgn}\,\sigma\prod_{l=1}^{N/2} M_{\sigma(2l-1)\sigma(2l)}, \tag{12}$$

for an $N \times N$ antisymmetric matrix $\mathbf{M}$ whose elements are M_{ij}, where N is an even number. Here S_N is the group of permutations of N objects. The rest of the right-hand terms in (11) corresponds to a fully *spin-polarized* (Chakraborty and Pietiläinen, 1988) Laughlin state (10) for $q = 2$.

Historically, the concept of Pfaffians arose from a very surprising mathematical result: Consider the determinant of a $N \times N$ antisymmetric matrix $\mathbf{M} = [M_{ij}]$ written as $\det[M_{ij}]_{1\le i,j\le N}$ in which $M_{ij} = -M_{ji}$ for $i, j = 1, 2, \ldots, N$. If $\mathbf{M} = -\mathbf{M}^T$ is an antisymmetric matrix of order N then $\det[\mathbf{M}] = (-1)^N \det[\mathbf{M}]$ so that if the order is odd, then the determinant vanishes. However, when $N = 2\,m$, then the determinant is the square of a polynomial in coefficients of the given determinant. This result was first discovered by the British mathematician Arthur Cayley in 1847 (Cayley, 1847; Halton, 1966), who named this polynomial *Pfaffian* in honor of the great German mathematician Johann Pfaff, who discovered it in 1815, in the course of his work on differential equations.

For $N = 2$,

$$\det\begin{vmatrix} 0 & M_{12} \\ -M_{12} & 0 \end{vmatrix} = (M_{12})^2, \tag{13}$$

and the Pfaffian is $\mathrm{Pf}\;[\mathbf{M}] = M_{12}$. Similarly, for $N = 4$,

$$\det\begin{vmatrix} 0 & M_{12} & M_{13} & M_{14} \\ -M_{12} & 0 & M_{23} & M_{24} \\ -M_{13} & -M_{23} & 0 & M_{34} \\ -M_{14} & -M_{24} & -M_{34} & 0 \end{vmatrix} = (M_{12}M_{34} - M_{13}M_{24} + M_{14}M_{23})^2, \tag{14}$$

and the corresponding Pfaffian is

$$\mathrm{Pf}\;[\mathbf{M}] = M_{12}M_{34} - M_{13}M_{24} + M_{14}M_{23}. \tag{15}$$

There are three terms in the above expression. For a general antisymmetric matrix $N \times N$, the number of terms in the Pfaffian is $(N-1)!!$. The Pfaffians are sometimes referred to as triangular determinant or half-determinant (Crilly, 2016),

$$\mathrm{Pf}\;[\mathbf{M}] = \begin{vmatrix} M_{12} & M_{13} & M_{14} \\ & M_{23} & M_{24} \\ & & M_{34} \end{vmatrix}. \tag{16}$$

Moving on, one can obtain the following relation between the determinant of the matrix $\mathbf{M}$ and its Pfaffian (Cayley, 1847; Halton, 1966),

$$\det\,[\mathbf{M}] = (\mathrm{Pf}\;[\mathbf{M}])^2. \tag{17}$$

---

[*] Pairing of electrons in order to form a Laughlin state of bosons was first proposed by Halperin in his classic paper (Halperin, 1983).

This relation can be generalized for a special partially antisymmetric matrix of the form (Bajdich et al., 2008; Cayley, 1847)

$$\det\begin{bmatrix} 0 & b_{12} & b_{13} & \dots & b_{1N} \\ -a_{12} & 0 & a_{23} & \dots & a_{2N} \\ -a_{13} & -a_{23} & 0 & \dots & a_{3N} \\ \vdots & \vdots & \vdots & \vdots & \vdots \\ -a_{1N} & -a_{2N} & -a_{3N} & \dots & 0 \end{bmatrix} = \mathrm{Pf}\begin{bmatrix} 0 & a_{12} & a_{13} & \dots & a_{1N} \\ -a_{12} & 0 & a_{23} & \dots & a_{2N} \\ -a_{13} & -a_{23} & 0 & \dots & a_{3N} \\ \vdots & \vdots & \vdots & \vdots & \vdots \\ -a_{1N} & -a_{2N} & -a_{3N} & \dots & 0 \end{bmatrix} \times \mathrm{Pf}\begin{bmatrix} 0 & b_{12} & b_{13} & \dots & b_{1N} \\ -b_{12} & 0 & a_{23} & \dots & a_{2N} \\ -b_{13} & -a_{23} & 0 & \dots & a_{3N} \\ \vdots & \vdots & \vdots & \vdots & \vdots \\ -b_{1N} & -a_{2N} & -a_{3N} & \dots & 0 \end{bmatrix} \tag{18}$$

Other useful relations, involving Pfaffians of $N \times N$ matrices $\mathbf{M}$ and $\mathbf{A}$, are the following

$$\mathrm{Pf}\ \left[\mathbf{M}^T\right] = (-1)^{N/2}\mathrm{Pf}\ [\mathbf{M}] \tag{19}$$

$$\mathrm{Pf}\ [\lambda\mathbf{M}] = \lambda^{N/2}\mathrm{Pf}\ [\mathbf{M}] \tag{20}$$

$$\mathrm{Pf}\ \left[\mathbf{AMA}^T\right] = \det[\mathbf{A}]\ \mathrm{Pf}\ [\mathbf{M}]. \tag{21}$$

$$\mathrm{Pf}\begin{bmatrix} 0 & \mathbf{M} \\ -\mathbf{M}^{\mathrm{T}} & 0 \end{bmatrix} = (-1)^{N(N-1)/2}\det[\mathbf{M}] \tag{22}$$

$$\mathrm{Pf}\begin{bmatrix} \mathbf{M}_1 & 0 \\ 0 & \mathbf{M}_2 \end{bmatrix} = \mathrm{Pf}\ [\mathbf{M}_1]\ \mathrm{Pf}\ [\mathbf{M}_2] \tag{23}$$

There is also a special expression for the Pfaffian of skew-symmetric tridiagonal matrix,

$$\mathrm{Pf}\begin{bmatrix} 0 & a_1 & 0 & 0 & & & \\ -a_1 & 0 & 0 & 0 & & & \\ 0 & 0 & 0 & a_2 & & & \\ 0 & 0 & -a_2 & 0 & & & \\ & & & & \ddots & & \\ & & & & & 0 & a_{N/2} \\ & & & & & -a_{N/2} & 0 \end{bmatrix} = a_1 a_2 \dots a_{N/2} \tag{24}$$

Pfaffians actually describe a *pairing* state. In fact, the famous Bardeen-Cooper-Schrieffer (BCS) wave function that is the wavefunction for spin-singlet pairs can be expressed in terms of the Pfaffians or a determinant (Bajdich et al., 2008; Bouchaud et al., 1988).

The Pfaffian function (11) which determines the $\nu = 1/2$ state is defined only for *even* number of particles, which illustrates its fundamental property as a collective state of the Cooper pairs, i.e., the bound state of two electrons. Interestingly, while the Pfaffian itself, i.e., the first factor in Eq. (11), is singular when two electrons are at the same position ($z_i = z_j$), when multiplied by the second factor, the Pfaffian function (11) becomes regular. In other words, the Pfaffian state has a nonzero amplitude at the coincidence of two particles. As an example, for four electrons the Pfaffian function takes the following form

$$\Psi_{\mathrm{Pf}} = \left[\frac{1}{z_1 - z_2}\frac{1}{z_3 - z_4} - \frac{1}{z_1 - z_3}\frac{1}{z_2 - z_4} + \frac{1}{z_1 - z_4}\frac{1}{z_2 - z_3}\right] \times \\ (z_1 - z_2)^2 (z_1 - z_3)^2 (z_1 - z_4)^2 (z_2 - z_3)^2 (z_2 - z_4)^2 (z_3 - z_4)^2 \exp\left(-\sum_i \frac{z_i^2}{4\ell_0^2}\right). \tag{25}$$

One can see that the highest power of any z_i, e.g., z_1, in the above expression is 5. In general, for the number of electrons N_e, the highest power is $2N_e - 3$. In the thermodynamic limit, it gives the required filling factor 1/2.

The Pfaffian state has a very unique property in terms of the charged excitations. In fact, the function that describes creation of two positively charged holes has the following form

$$\Psi_{\mathrm{Pf}} = \mathrm{Pf}\left[\frac{(z_i - \eta_1)(z_j - \eta_2) + (z_j - \eta_1)(z_i - \eta_2)}{z_i - z_j}\right]\prod_{i<j}(z_i - z_j)^2 \exp\left(-\sum_i \frac{z_i^2}{4\ell_0^2}\right). \tag{26}$$

Here η_1 and η_2 are the coordinates of the holes. The charge of these excitations is fractional, $e^* = e/4$, and they obey the 'non-Abelian' statistics (Nayak et al., 2008; Stern, 2008; Stern and Halperin, 2006). The non-Abelian statistics means that when two excitations exchange their positions, it changes not only the phase of the wave function but also introduces an unitary transformation of the wave function itself. In general, those unitary transformations do not commute and the system of those excitations is called non-Abelian.

The charged excitations of the Pfaffian state also carry the signature of Majorana fermions (MFs) (Ivanov, 2001; Read and Green, 2000). The Majorana fermion is a special type of 'particle,' which can be seen as its own anti-particle. If γ_i is an operator corresponding to the Majorana fermion i, then it satisfies the relations

$$\{\gamma_i, \gamma_i\} = 2\delta_{ij} \tag{27}$$

$$\gamma_i^\dagger = \gamma_i, \tag{28}$$

where $\{\gamma_i, \gamma_i\}$ is the anti-commutator of γ_i and γ_j. The first relation determines that these particles are fermions and the second relation tells us that the particle is its own anti-particle. The Majorana particle can be formally expressed as a combination of the creation, $c_i^\dagger$, and annihilation, c_i, operators of regular fermions,

$$\gamma_i = c_i + c_i^\dagger. \tag{29}$$

It means that the Majorana operator creates simultaneously a particle, e.g., an electron with the negative charge $-e$, and an anti-particle, e.g., a hole with positive charge e. In conventional systems such an operation is impossible, but in systems such as the superconductors which support Cooper pairs and for which the electric charge is conserved mod 2, the Majorana fermions are possible. Superposition of two Majorana fermions correspond to a fermionic state where the constituent MFs are spatially separated. This intrinsic non-local nature of the fermionic state makes the state resilient against errors caused by local perturbations from the environment (Ivanov, 2001). This property and the associated non-abelian exchange statistics makes the MFs well suited for fault-tolerant quantum computing (Ayukaryana et al., 2021; Das Sarma et al., 2005; Kitaev, 2003).

Many numerical studies of the $\nu = 1/2$ state have been performed in the spherical geometry (see, e.g., Fano et al., 1986; Haldane, 1983; Haldane and Rezayi, 1985). In this geometry, the electrons are placed on a surface of a sphere and the magnetic field is created by a magnetic monopole placed at the center of the sphere. The strength of the magnetic field is characterized by the parameter S, where $2S$ is the number of magnetic fluxes through the sphere in units of the flux quantum. At the same time the parameter S is equal to the angular momentum of single-particle states. All single-particle states have the same energy and form the Landau level, where different states are distinguished by the z component of the angular momentum. Therefore, in spherical geometry, the total number of states in the Landau level is $2S + 1$. In a many-electron system the electron-electron interaction is introduced through the Haldane pseudopotentials and the number of electrons, N_e determines the filling factor of the Landau level. Here the $\nu = 1/2$ FQHE corresponds to the following condition: $2S = 2N_e - 3$. Although in this case the ratio of the number of electrons and the number of single-particle states is not 1/2, i.e., $N_e/(2S + 1) = N_e/(2N_e - 2) \neq 1/2$, for this value of S, the system has a gap and the ground state wave function is close to the Pfaffian function. In the thermodynamic limit, i.e., for $N_e \to \infty$, there is a correct identity $N_e/(2S + 1) = N_e/(2N_e - 2) \to 1/2$.

The position of an electron in spherical geometry can be described by either the two angles, ϕ and θ, or two components of a spinor, $u = \cos\theta \sin\phi$ and v. In terms of the variables u and v, the Pfaffian function takes the following form

$$\Psi_{\text{Pf}} = \text{Pf}\left[\frac{1}{u_i v_j - u_j v_i}\right] \prod_{i<j} (u_i v_j - u_j v_i)^2. \tag{30}$$

In the spherical geometry the Pfaffian function is an exact wave function of the ground state for the system with three-particle interaction defined as

$$H_{int} = \frac{e^2}{\kappa \ell_0} \sum_{i<j<k} P_{ijk}(3S - 3), \tag{31}$$

where P_{ijk} is the three-particle projection operator onto the state with the total angular momentum L.

In a planar geometry, the Pfaffian function is the exact ground state wave function of the system with the three-body interaction (Greiter et al., 1991, 1992) given by the following expression

$$H_{3B} = V_0 \sum_{i<j<k}^{N_{el}} S_{ijk} \nabla_i^2 \delta(i-j)\delta(i-k), \tag{32}$$

where $\delta(i-j) = \delta\left(\vec{r}_i - \vec{r}_j\right)$ is the δ function, ∇_i is the partial derivative with respect to $\vec{r}_i$, and S_{ijk} denotes symmetrization over permutations within (ijk): $S_{123} = f_{123} + f_{231} + f_{312}$, and f is symmetric in its first two indices. To understand why for the three-body interaction potential (32) the energy of the Pfaffian state is zero, we need to look at the structure of the Pfaffian wave function. For example, by looking at the four-particle system (see Eq. (25)) we can see that the terms with z_1 are of the type: $(z_1 - z_2)(z_1 - z_3)^2(z_1 - z_4)^2 \ldots$. Therefore, they have one factor with linear dependence on z_1, $(z_1 - z_2)$, and all other factors have quadratic dependence on z_1, $(z_1 - z_3)^2(z_1 - z_4)^2 \ldots$. Now let us consider the term in the three-particle Hamiltonian (32): $\nabla_1^2\delta(1-2)\delta(1-3)$. In order to find the contribution to the energy due to that term, we need to calculate the second derivative of $(z_1 - z_2)(z_1 - z_3)^2(z_1 - z_4)^2 \ldots$ with respect to z_1 and then set z_1 equals to z_2 and z_3, which finally gives us zero. Analyzing different terms both in the Hamiltonian (32) and the Pfaffian wave function, we can conclude that the energy of the Pfaffian state is zero and it is an eigenfunction of the three-particle Hamiltonian (32).

For the real two-body interaction, whether the Pfaffian function is the ground state wave function or not is determined by the values of Haldane pseudopotentials, mainly by the values of V_1/V_5 and V_3/V_5. The diagram, which shows under what values of these parameters the half-filled Landau level becomes incompressible and is described by the Pfaffian function, is shown in Fig. 2 (Storni et al., 2010). The diagram depicts the contour plot of the gap of the system, where for the compressible state the gap is zero. The gap also characterizes the stability of the corresponding 1/2-FQHE state. Here the blue region corresponds to the compressible state, which does not support the 1/2-FQHE. The maximum overlap of the ground state wave function with the Pfaffian function is marked by a solid black line.

The thick lines with dots correspond to the conventional electron system with parabolic energy dispersion and different thickness of the 2D layer. Here the thickness of the layer changes the Haldane pseudopotentials, resulting in the corresponding

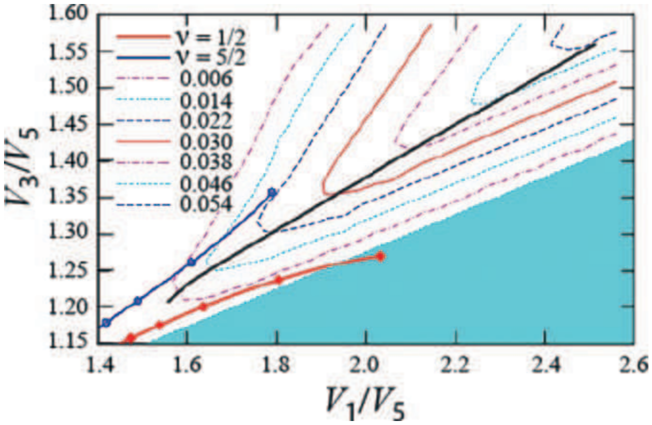

Fig. 2 Contour plot of the FQHE gap as a function of V_1/V_5 and V_3/V_5. The black line marks the maximum of the overlap of the ground state wave function and the Pfaffian function. The lines with dots depict the effect of the finite width of a 2D layer. Here the red line corresponds to filling factor $\nu = 5/2$, which is the same as $\nu = 1/2$ at the $n = 1$ Landau level, while the blue line corresponds to $\nu = 1/2$ at the $n = 0$ Landau level. The dots denote the width $w/\ell_0 = 0, 1, 2, 3, 4$ (from right to left). The compressible region is shaded blue. Reproduced with permission from Storni M, Morf RH, and Das Sarma S (2010) Fractional quantum hall state at $\nu = \frac{5}{2}$ and the Moore-read Pfaffian. *Physical Review Letters* 104: 076803, doi:10.1103/PhysRevLett.104.076803.

lines in the diagram. The results of Fig. 2 clearly show that, for the conventional system, the state in the half-filled $n = 0$ Landau level is compressible, while that for the half-filled $n = 1$ Landau level is incompressible and the overlap of the ground state wave function with the Pfaffian function is large. The half-filled $n = 1$ Landau level corresponds to the total filling factor of 5/2.

The diagram shown in Fig. 2 can be also used to analyze the properties of half-filled Landau levels for other systems, such as the graphene monolayer and the graphene bilayer. The Haldane pseudopotentials for these systems are different from the ones for the conventional electron system.

The effective electron-electron interaction potential also depends on the Landau level mixing. This mixing can be important for systems with small Landau level gaps, such as the ZnO quantum wells (Luo and Chakraborty, 2017). The strength of this mixing is determined by the ratio of the Coulomb interaction and the Landau level gap. When this ratio is varied, it was shown by numerical analysis (Luo and Chakraborty, 2017) that, in the ZnO quantum well systems the topological transitions can be observed for the half-filled Landau level. Further, in ZnO systems a stable Pfaffian state have been predicted at filling factors 5/2 and 7/2 (Luo and Chakraborty, 2017).

Monolayer and bilayer graphene in a strong magnetic field

Graphene monolayer

Graphene is a single layer of carbon atoms (Novoselov et al., 2004; Wallace, 1947), which form the 2D honeycomb crystal structure with two sublattices, say A and B [see Fig. 3A] (Abergel et al., 2010). The corresponding electron band structure has two valleys at two inequivalent points, $K = (2\pi/a)\left(\frac{1}{3}, \frac{1}{\sqrt{3}}\right)$ and $K' = (2\pi/a)\left(\frac{2}{3}, 0\right)$, in the reciprocal space [see Fig. 3B]. Here $a = 0.246$ nm is the lattice constant. The unique property of graphene is that the low-energy dispersion at each valley is determined by the massless Hamiltonian of the Dirac type (Dirac fermions) (Abergel et al., 2010; Castro Neto et al., 2009; Geim and Novoselov, 2007)

$$\mathcal{H}_\xi = \xi v_\mathrm{F} \begin{pmatrix} 0 & p_- \\ p_+ & 0 \end{pmatrix}, \tag{33}$$

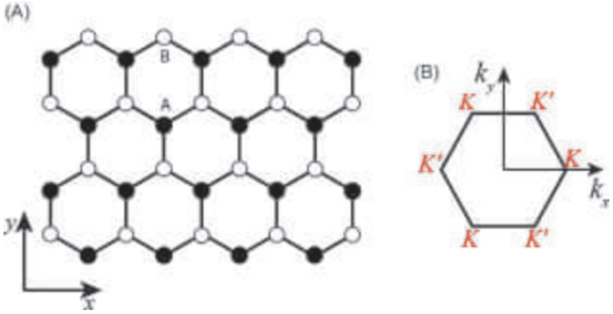

Fig. 3 (A) Honeycomb crystal structure of a graphene monolayer. Two equivalent sublattices A and B are marked by open and filled dots. (B) The first Brillouin zone of monolayer graphene. Two valleys K and K' are also shown.

where ξ is the valley index, which is 1 at the K valley and − 1 at the K' valley, $p_- = p_x - \mathrm{i}p_y$, $p_+ = p_x + \mathrm{i}p_y$, and $v_F \approx 10^6$ m/s is the Fermi velocity. The corresponding eigenfunctions of the Hamiltonian (33) have two components due to two sublattices, A and B, of the graphene honeycomb lattice. The wave functions are expressed as $(\psi_A, \psi_B)^T$ for valley K and $(\psi_B, \psi_A)^T$ for valley K', where ψ_A and ψ_B correspond to sublattices A and B, respectively.

The Landau level of electrons in graphene can be found from Hamiltonian (33) by replacing the electron momentum $\vec{p}$ with the generalized momentum $\vec{\pi} = \vec{p} + e\vec{A}/c$,

$$\mathcal{H}_\xi = \xi v_F \begin{pmatrix} 0 & \pi_- \\ \pi_+ & 0 \end{pmatrix}. \tag{34}$$

Then the eigenfunctions of the Hamiltonian (34) have the following form

$$\Psi^K_{n,m} = \begin{pmatrix} \psi_A \\ \psi_B \end{pmatrix} = C_n \begin{pmatrix} \mathrm{sgn}\,(n)\mathrm{i}^{|n|-1}\phi_{|n|-1,m} \\ \mathrm{i}^{|n|}\phi_{|n|,m} \end{pmatrix}, \tag{35}$$

for the valley K ($\xi = 1$) and

$$\Psi^{K'}_{n,m} = \begin{pmatrix} \psi_B \\ \psi_A \end{pmatrix} = C_n \begin{pmatrix} \mathrm{sgn}\,(n)\mathrm{i}^{|n|-1}\phi_{|n|-1,m} \\ \mathrm{i}^{|n|}\phi_{|n|,m} \end{pmatrix}, \tag{36}$$

for the valley K' ($\xi = -1$). Here $C_n = 1$ for $n = 0$ and $C_n = 1/\sqrt{2}$ for $n \neq 0$ and

$$\mathrm{sgn}\,(n) = \begin{cases} 0 & (n = 0) \\ 1 & (n > 0), \\ -1 & (n < 0) \end{cases} \tag{37}$$

where the positive and negative values of n correspond to the conduction and valence bands, respectively. The corresponding Landau energy spectrum takes the form (Castro Neto et al., 2009; Goerbig, 2011; McClure, 1956)

$$\varepsilon_n = \hbar\omega_B\,\mathrm{sgn}\,(n)\sqrt{|n|}, \tag{38}$$

where $\omega_B = \sqrt{2}v_F/\ell_0$.

Summarizing, we can say that there are two types of Landau levels in graphene. The first one corresponds to $n = 0$. In this case the wave function is

$$\Psi^K_{n=0,m} = \begin{pmatrix} 0 \\ \phi_{0,m} \end{pmatrix}. \tag{39}$$

This wave function consists of only the $\phi_{0,m}$ Landau function of a conventional system. The interacting electron system at $n = 0$ graphene Landau level is therefore identical to the interacting electron system in $n = 0$ Landau level of the conventional electron system.

The second class of graphene Landau levels correspond to $n \neq 0$. In this case the wave function is

$$\Psi^K_{n,m} = \frac{1}{\sqrt{2}} \begin{pmatrix} \mathrm{sgn}\,(n)\mathrm{i}^{|n|-1}\phi_{|n|-1,m} \\ \mathrm{i}^{|n|}\phi_{|n|,m} \end{pmatrix}. \tag{40}$$

Here the graphene wave function is the mixture of n and $n - 1$ Landau wave functions of a conventional electron system.

For Dirac fermions in graphene, the unique feature of the Landau levels (38) is their square-root dependence on both the magnetic field B and the Landau level index n. This behavior is different from that in conventional semiconductor 2D systems with the parabolic energy dispersion discussed above, where the Landau levels have linear dependence on both the magnetic field and the Landau level index [see Eq. 7]. The Landau level of graphene are shown in Fig. 4 as a function of the magnetic field. Here the positive and negative Landau level indices n correspond to the conduction and valence bands, respectively. These unique properties of the Landau levels of Dirac fermions in graphene result in the unconventional Quantum Hall Effect in graphene with quantum Hall plateaus at filling factors $4\left(n + \frac{1}{2}\right)$ (Novoselov et al., 2004; Zhang et al., 2005).

Bilayer graphene

The bilayer graphene consists of two coupled graphene monolayers (McCann and Falko, 2006; McCann and Koshino, 2013), which can be in two possible main stackings: (i) AA stacking and (ii) Bernal (AB) stacking, which are shown schematically in Fig. 5.

For bilayer graphene with AA stacking, there is a interlayer coupling between the Landau levels of two layers with the same Landau level indices. This coupling changes the energies of the Landau levels of graphene monolayers, but does not affect the wavefunctions of the layers. Therefore, the bilayer graphene Haldane pseudopotentials, which characterize the electron-electron interaction properties, are completely identical to the corresponding pseudopotentials of monolayer graphene.

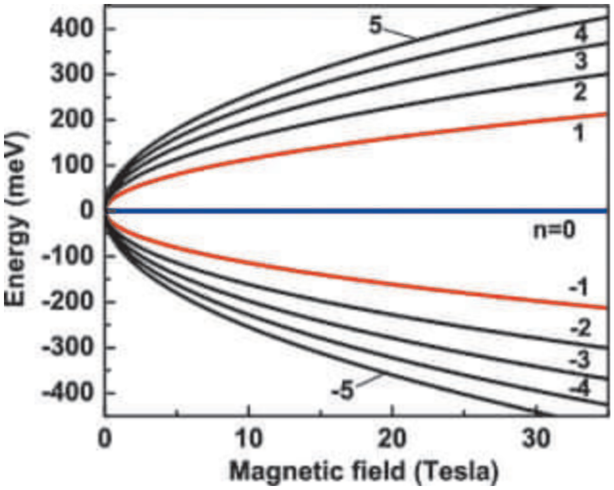

Fig. 4 The first few Landau levels of graphene monolayer as a function of perpendicular magnetic field. The Landau levels are labeled with integer index *n*, where positive and negative *n* correspond to the conduction and valence bands, respectively. The red and blue lines mark the Landau levels for which the FQHE can be observed.

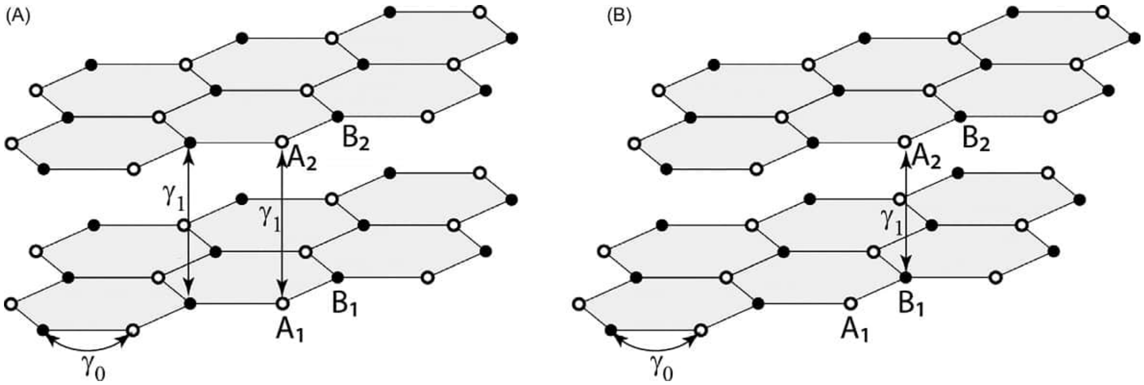

Fig. 5 (a) Bilayer graphene with AA stacking. Here the interlayer hopping couples sublattice A (B) in the top layer with sublattice A (B) in the bottom layer. (b) Bilayer graphene with AB stacking. For such stacking, sublattice A (B) in the top layer is coupled to sublattice B (A) in the bottom layer.

For bilayer graphene with Bernal (AB) stacking, the interlayer coupling strongly modifies the properties of the Landau level in the system. The corresponding Hamiltonian for valley $\xi = \pm 1$ has the form (McCann and Falko, 2006)

$$\mathcal{H}_{\xi}^{(AB)} = \xi \begin{pmatrix} \frac{U}{2} & v_{\mathrm{F}}\pi_{-} & 0 & 0 \\ v_{\mathrm{F}}\pi_{+} & \frac{U}{2} & \xi\gamma_1 & 0 \\ 0 & \xi\gamma_1 & -\frac{U}{2} & v_{\mathrm{F}}\pi_{-} \\ 0 & 0 & v_{\mathrm{F}}\pi_{+} & -\frac{U}{2} \end{pmatrix}, \tag{41}$$

where U is the inter-layer bias voltage and $\gamma_1 \approx 400$ meV is the interlayer hopping integral. The corresponding wave functions have the structure of $(\psi_{A_1}, \psi_{B_1}, \psi_{A_2}, \psi_{B_2})^T$, where A_1, B_1 correspond to the lower monolayer and A_2, B_2 correspond to the upper monolayer. From the Hamiltonian (41), the Landau level wave functions are

$$\Psi_{n,m}^{(\mathrm{bi})} = \begin{pmatrix} \xi C_1 \phi_{n-1,m} \\ C_2 \phi_{n,m} \\ C_3 \phi_{n,m} \\ \xi C_4 \phi_{n+1,m} \end{pmatrix}, \tag{42}$$

where C_1, C_2, C_3, and C_4 are constants. The wave functions in the bilayer graphene with AB stacking are therefore the mixtures of the conventional Landau wavefunctions with indices $n-1$, n, and $n+1$.

In Eq. (42) the Landau index n can take the following values: $n = -1, 0, 1, \ldots$. Here we assume that if the index of the Landau wave function, $\phi_{n,m}$, is negative then the function is identically zero, which means that $\phi_{-2,m} \equiv 0$ and $\phi_{-1,m} \equiv 0$. Hence, for $n = -1$, the wave function (42) is just $\Psi_{-1,\ m}^{(\mathrm{bi})} = (0, 0, 0, \phi_{0,\ m})$, i.e., the coefficients C_1, C_2, C_3 are zero. Therefore, there is only one energy level corresponding to $n = -1$. For $n = 0$, the wave function (42) has zero coefficient C_1 and, correspondingly, there are only three energy levels.

For $n > 0$, there are four eigenvalues of the Hamiltonian (41), corresponding to four Landau levels in a bilayer graphene at a given valley $\xi = \pm 1$. The eigenvalue equation, which determines the Landau levels is written as (Pereira et al., 2007)

$$\left[(\varepsilon + \xi u)^2 - 2n\right]\left[(\varepsilon - \xi u)^2 - 2(n+1)\right] = \tilde{\gamma}_1^2\left[\varepsilon^2 - u^2\right], \tag{43}$$

where ε is the energy of the Landau level in units of $\varepsilon_B, \varepsilon_B = \hbar v_F/\ell_0, \tilde{\gamma}_1 = \gamma_1/\varepsilon_B$, and $u = U/\varepsilon_B$.

The four Landau levels determined by Eq. (43) have two levels with negative energy (valence band) and two levels with positive energy (conduction band). It is then convenient to label these levels as follows: for a given value of n and a given valley ξ we label the levels as $n_i^{(\xi)}$, where $i = -2, -1, 1, 2$ in the ascending order and the negative and positive values of i correspond to the valence and conduction bands, respectively. Although for $n = 0$ there are only three Landau levels and for $n = -1$ there is only one Landau level, it is convenient to combine them in a single set of $n = 0$ Landau levels and label them as $0_i^{(\xi)}$, where $i = -2, -1, 1, 2$. Also, the Landau levels of different valleys are related as follows $\varepsilon(n_i^{(\xi)}) = -\varepsilon(n_{-i}^{(-\xi)})$. A few lowest Landau levels of bilayer graphene are shown in Fig. 6 as a function of the magnetic field.

With the known wave functions (42) of the bilayer graphene Landau levels, the form factor in Eq. (8) for Haldane pseudopotentials can be obtained from the following expression

$$F_n(q) = |C_1|^2 L_{n-1}\left(q^2/2\right) + \left(|C_2|^2 + |C_3|^2\right) L_n\left(q^2/2\right) + |C_4|^2 L_{n+1}\left(q^2/2\right). \tag{44}$$

There are two special Landau levels of bilayer graphene with almost zero energy (Apalkov and Chakraborty, 2011), see Fig. 6. The first one corresponds to $n = -1$ with the energy of $\varepsilon = -\xi u$ and the corresponding wave function

$$\Psi_{0_1^{(+)},m}^{(\mathrm{bi})} = \Psi_{0_{-1}^{(-)},m}^{(\mathrm{bi})} = \begin{pmatrix} 0 \\ 0 \\ 0 \\ \phi_{0,m} \end{pmatrix}. \tag{45}$$

The wave function consists of only the $n = 0$ conventional Landau level wave function. Therefore, the FQHE in this bilayer Landau level is exactly the same as the one in the 0-th conventional Landau level. For example, we can say that there is no FQHE in the half-filled $0_1^{(+)}$ Landau level.

In order to find the half-filled level with possible Pfaffian function as the ground state, the most interesting bilayer Landau level is $0_{-1}^{(+)}$ in the K valley and $0_1^{(-)}$ in the K' valley (Apalkov and Chakraborty, 2011). For small values of U, the energy of this state is almost zero, $\varepsilon \approx 0$. The wave function of $0_{-1}^{(+)}$ Landau level has the form

$$\Psi_{0_{-1},m}^{(\mathrm{bi})} = \frac{1}{\sqrt{\sim \gamma_1^2 + 2}} \begin{pmatrix} 0 \\ \sqrt{2}\phi_{0,m} \\ 0 \\ \sim \gamma_1 \phi_{1,m} \end{pmatrix} = \frac{1}{\sqrt{\gamma_1^2 + 2\varepsilon_B^2}} \begin{pmatrix} 0 \\ \sqrt{2}\varepsilon_B \phi_{0,m} \\ 0 \\ \gamma_1 \phi_{1,m} \end{pmatrix}. \tag{46}$$

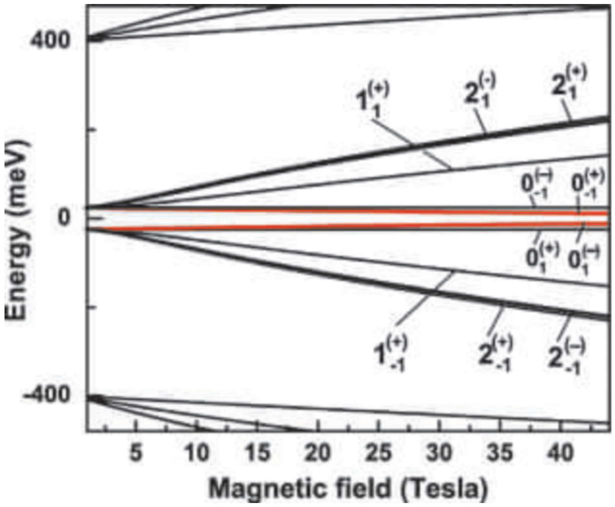

Fig. 6 A few lowest Landau levels of bilayer graphene as a function of the magnetic field. The bilayer graphene has the AB stacking. The Landau levels of both K and K' are shown. The red lines show special Landau levels, at which the $\nu = 1/2$ Pfaffian incompressible state can be realized. The bias voltage is 5 mV and interlayer hopping integral is $\gamma_1 = 400$ meV.

The wave function is the mixture of $\phi_{0,m}$ and $\phi_{1,m}$ states. For a relatively small magnetic field, $\varepsilon_B \ll \gamma_1$, the wave function becomes $(0, 0, 0, \psi_{1,m})^T$, i.e., it is completely identical to the $n = 1$ conventional Landau level. In a large magnetic field, $\varepsilon_B \gg \gamma_1$, the $0_{-1}^{(+)}$ Landau wave function becomes $(0, 0, \psi_{0,m}, 0)^T$, i.e., it is the same as $n = 0$ conventional Landau level. The interesting aspect of this is that, by varying the magnetic field the electron-electron interactions within the $0_{-1}^{(+)}$ Landau level transform from $n = 1$ to the conventional $n = 0$ case.

Pfaffian states in graphene

Graphene monolayer

The electron-electron interactions and correspondingly the nature of the ground state within a given Landau level are determined by the Haldane pseudopotentials, which are defined by the corresponding form factor $F(q)$. For the graphene monolayer there are two types of Landau levels: (i) the $n = 0$ Landau level and (ii) the $n \neq 0$ levels. For the $n = 0$ Landau level, the form factor is given by

$$F_0(q) = L_0\left(q^2/2\right) = 1. \tag{47}$$

This is exactly the same form factor as the one for the $n = 0$ conventional Landau level, for which there is no $\nu = 1/2$ FQHE state. We can then conclude that in the $n = 0$ graphene Landau level, there is no incompressible $\nu = 1/2$-FQHE state with the Pfaffian function as a ground state wave function. At the same time, all other FHQE states, such as p/q with odd q, have exactly the same properties, i.e., the same ground state wave functions and the same excitation gaps, as the ones for the $n = 0$ conventional Landau level. This suggests that, as long as there is no inter-Landau level mixing, the electron systems in the $n = 0$ graphene Landau level are identical to the systems in the $n = 0$ conventional Landau level.

On the other hand, for the $n \neq 0$ graphene Landau level, the form factor is

$$F_n(q) = \frac{1}{2}\left(L_{n-1}\left(q^2/2\right) + L_n\left(q^2/2\right)\right). \tag{48}$$

For example, for $n = 1$, $L_0(q^2/2) = 1$ and $L_0(q^2/2) = 1 - q^2/2$ and the form factor is $F_n(q) = 1 - q^2/4$. In this case the form factor is the mixture of the form factors of n and $n - 1$ conventional Landau levels. The electron-electron interactions in this case are completely different from those in conventional systems. One of these differences is related to stability, i.e., the magnitude of the excitation gaps of the conventional FQHE with the filling factor p/q, where q is odd. This means that, out of all the graphene Landau levels, including the $n = 0$ Landau level, the largest FQHE gaps are realized in the $n = 1$ Landau level (Apalkov and Chakraborty, 2006; Chakraborty and Apalkov, 2014). This is different from conventional systems, where the conventional FQHE states have the largest gaps for the $n = 0$ Landau level.

Our extensive numerical analyses have established that there is no incompressible $\nu = 1/2$ state of the Pfaffian type for $n = 0$ and $n = 1$ graphene Landau levels (Apalkov and Chakraborty, 2006). Here, the excitation gap is small and the overlap of the ground state wave function with the Pfaffian function is also small. This analysis has been done without considering any inter-Landau level mixing. This mixing can alter the properties of the half-filled Landau level, resulting in the formation of an incompressible state. For example, for conventional systems it was shown that the inter-Landau level mixing favors the anti-Pfaffian state over other type of ground states of the half-filled $n = 1$ Landau level (Rezayi, 2017). Also, both for conventional and graphene systems, the Landau level mixing crucially modifies for the 1/2-FQHE state the Haldane pseudopotentials V_1, V_3, and V_5 (Peterson and Nayak, 2013). The Landau level mixing is also more pronounced in higher Landau levels. It should be noted that, recent experimental results (Kim et al., 2019) indeed suggest that the incompressible $\nu = 1/2$ state may be realized in monolayer graphene, albeit in higher $n = 3$ Landau level. Here, the inter-Landau level mixing can be important and it can be the reason for the incompressible $\nu = 1/2$ state being present in the higher Landau level in graphene. Further, the even-denominator incompressible states have been observed experimentally in low Landau levels in graphene within some range of the magnetic fields (Zibrov et al., 2018), but the origin of those states is yet to be clearly determined and it can perhaps be related to multicomponent fractional quantum Hall states.

Bilayer graphene

For a Landau level of bilayer graphene, the form factor is given by the expression (44). Due to the bilayer nature of the system, there are extra parameters which can control the form factor and correspondingly the interaction strength. These parameters are the bias voltage and the direction of the magnetic field, i.e., the component of the magnetic field that is parallel to the bilayer. As we have mentioned above, in bilayer graphene there are two 'special' Landau levels $0_{-1}^{(+)}$ (K valley) and $0_1^{(-)}$ (K' valley) for which the Pfaffian function can be the ground state of the half-filled Landau level (Apalkov and Chakraborty, 2011; Chakraborty and Apalkov, 2013).

Extensive studies of the finite-size system of bilayer graphene have been performed by us in the spherical geometry (Apalkov and Chakraborty, 2010, 2011; Chakraborty and Apalkov, 2013, 2014). Those studies have revealed that for all bilayer Landau levels, except the ones $0_{-1}^{(+)}$ and $0_1^{(-)}$, the overlap of the $\nu = \frac{1}{2}$ ground state with the Pfaffian state is relatively small (less than 0.5). Therefore, for those Landau levels, the $\nu = \frac{1}{2}$ system is gapless and compressible. A different situation occurs for the Landau levels $0_{-1}^{(+)}$ and $0_1^{(-)}$. These levels belong to the K and K' valleys, respectively, and have exactly the same interaction properties. Hence, it is enough to consider only one of these levels, e.g., $0_{-1}^{(+)}$, as for the other Landau level, $0_1^{(-)}$, the results are exactly the same.

For the $0_{-1}^{(+)}$ Landau level the form factor is

$$F_{0_{-1}}(q) = \left[\frac{\gamma_1^2}{\gamma_1^2 + 2\varepsilon_B^2}\right] L_1\left(q^2/2\right) + \left[\frac{2\varepsilon_B^2}{\gamma_1^2 + 2\varepsilon_B^2}\right] L_0\left(q^2/2\right). \tag{49}$$

The strength of the magnetic field is determined by the parameter ε_B. With increasing magnetic field, i.e., with increasing ε_B, the form factor of the $0_{-1}^{(+)}$ level goes through the following main regions: (i) for small B, $\varepsilon_B \ll \gamma_1$, the form factor is $L_1(q^2/2)$ and identical to the one of the $n = 1$ conventional Landau level; (ii) at $\varepsilon_B = \gamma_1/\sqrt{2}$, the form factor is $\frac{1}{2}[L_0(q^2/2) + L_1(q^2/2)]$ and is the same as the one of the $n = 1$ Landau level of monolayer graphene; (iii) at $\varepsilon_B \gg \gamma_1$, the form factor is $L_0(q^2/2)$ and is the same as the one of the $n = 0$ conventional Landau level.

Since the $\nu = 1/2$ incompressible state is realized only in the $n = 1$ conventional Landau level, then for bilayer graphene, the $\nu = 1/2$ Pfaffian state should be observed only for relatively small values of the magnetic field. At the same time, it so happens that as a function of the magnetic field, the characteristics of the $\nu = 1/2$ system is not monotonic. In Fig. 7A the overlap of the $\nu = 1/2$ wave function with the Pfaffian function is shown as a function of the magnetic field. The calculations were done in a spherical geometry for $N_e = 14$ electron system. The overlap has a maximum at a finite magnetic field. The position of the maximum depends on the interlayer hopping integral, γ. For example, for $\gamma = 400$ meV, the maximum overlap occurs for ≈ 10 T. The profile of the overlap is also correlated with the gap of the collective excitation of the system [see Fig. 7B]. The energy gap also has a maximum at a finite magnetic field. Since in a small magnetic field, $B \to 0$, the $0_{-1}^{(+)}$ bilayer Landau system is equivalent to $n = 1$ conventional Landau systems, we are allowed to conclude that the stability of the Pfaffian $\nu = \frac{1}{2}$ state in bilayer graphene can be increased compared to that of the conventional systems.

The position of the maximum in Fig. 7 can be analyzed further by looking at some dimensionless quantities. For instance, in dimensionless units the maximum is achieved at $\gamma_1/\varepsilon_B \approx 4.9$. This means that, in terms of the magnetic field, the position of the maximum of the overlap is approximately proportional to γ_1, which is also seen in Fig. 7.

Using the phase diagram shown in Fig. 2, which characterizes the stability of the $\nu = 1/2$ state described by the Pfaffian function, we can illustrate how the interaction parameters in the $0_{-1}^{(+)}$ Landau level change with the magnetic field [see Fig. 8]. For a small magnetic field, the ground state of the system is well described by the Pfaffian function, while the overlap and the corresponding excitation gap reach their maximum at intermediate values of the magnetic field and finally, for a large magnetic field, > 100 T, the electron system becomes compressible.

Another parameter that can be used to control the stability of the Pfaffian ground state, is the magnetic field that is *parallel* to the 2D layer (Chakraborty and Apalkov, 2013). The reason why the parallel magnetic field changes the wave functions and the interaction potential is due to the bilayer nature of the system. In this case the system has extra dynamics in the z direction, which is described in the model as an inter-layer hopping. The parallel component of the magnetic field can be introduced into the Hamiltonian of bilayer graphene through a Peierls substitution as an extra position-dependent phase factor in the inter-layer hopping integral. The details of that study can be found elsewhere (Chakraborty and Apalkov, 2013).

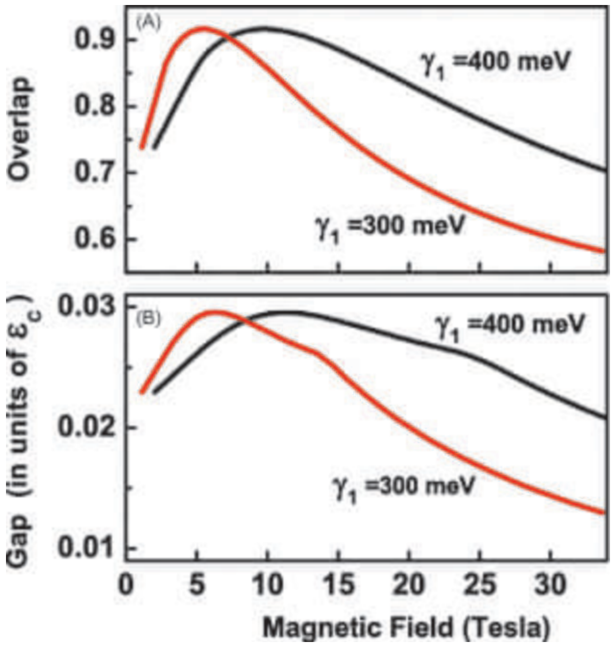

Fig. 7 Panel (A): Overlap of the ground state wave function of $\nu = 1/2$ state with the Pfaffian state as a function of the magnetic field. Panel (B): the collective excitation gap of the $\nu = 1/2$ state as a function of the magnetic field. The data are shown for the Landau level $0_{-1}^{(+)}$ of the bilayer graphene and for two values of the interlayer hopping integral, γ_1. Reproduced with permission from Apalkov VM, and Chakraborty T (2011) Stable Pfaffian state in bilayer graphene. *Physical Review Letters* 107: 186803, doi:10.1103/PhysRevLett.107.186803.

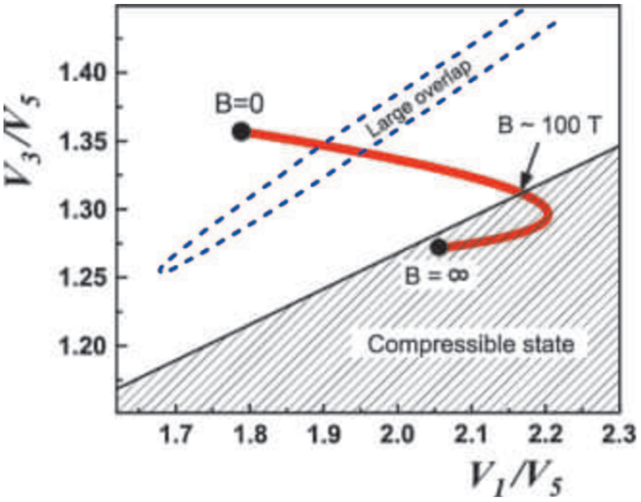

Fig. 8 Trajectory of the inter-electron interaction with varying magnetic field. The trajectory is shown by a solid red line in the plane $(V_1/V_5) - (V_3/V_5)$ for the Landau level $0_{-1}^{(+)}$ of the bilayer graphene. The initial point of the trajectory (at $B = 0$) corresponds to the conventional system at the $n = 1$ Landau level, while the final point (at $B = \infty$) corresponds to the conventional system at the $n = 0$ LL. The hatched region illustrates the compressible $\nu = 1/2$ state, while the blank region corresponds to the incompressible $\nu = 1/2$ state following the Ref. (Storni et al., 2010) and Fig. 2. The crossing of the boundary between the compressible and incompressible states occurs at $B \sim 100$ Tesla for the interlayer hopping integral $\gamma_1 = 400$ meV. The blue dashed line shows the region of large overlap of the ground state wave function with the Pfaffian function. Reproduced with permission from Apalkov VM and Chakraborty T (2011) Stable Pfaffian state in bilayer graphene. *Physical Review Letters* 107, 186803, doi:10.1103/PhysRevLett.107.186803.

The effect of the parallel component of the magnetic field is illustrated in Fig. 9, where the parameters V_1/V_5 and V_3/V_5 are shown as a function of the perpendicular component of the magnetic field and for different values of its parallel component. The most stable Pfaffian state is illustrated by the dashed lines. The results demonstrate that with increasing parallel component of the magnetic field the values of pseudopotentials, which correspond to the most stable Pfaffian state, are realized for smaller values of

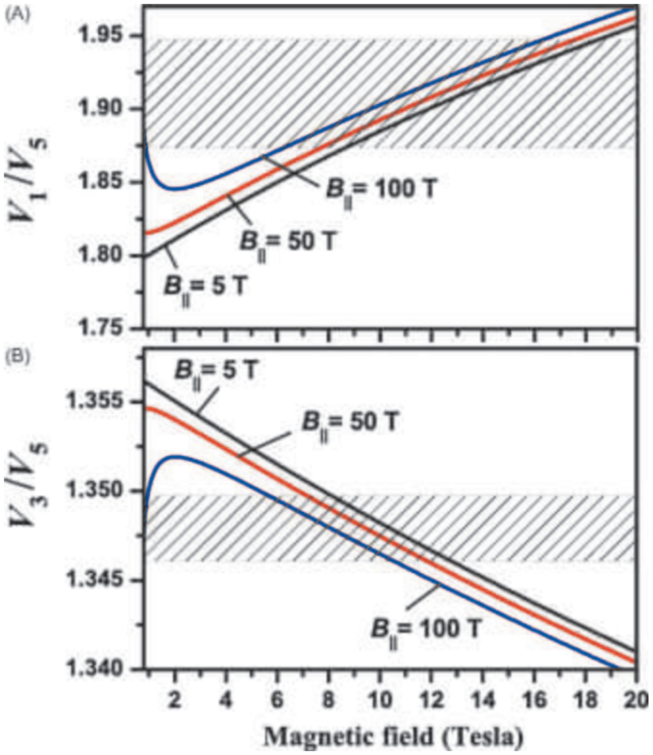

Fig. 9 Ratios of pseudopotentials at two values of angular momentum V_1/V_5 [panel (A)] and V_3/V_5 [panel (B)] are shown as the function of the perpendicular component of magnetic field and for different parallel components of magnetic field, $B_{\|} = 5$ T, 50 T, and 100 T. The data are shown for Landau level $0_{-1}^{(+)}$ of bilayer graphene. The hatched regions correspond to the values of pseudopotentials for which the large overlap of the ground state wave function with the Pfaffian function and large excitation gap of the incompressible ground state are achieved. Reproduced with permission from Chakraborty T and Apalkov VM (2013) Traits and characteristics of interacting dirac fermions in monolayer and bilayer graphene. *Solid State Communications* 175–176: 123–131, doi:10.1016/j.ssc.2013.04.002.

the perpendicular component of the magnetic field. Therefore, the parallel component of the magnetic field can be used to tune the stability of the Pfaffian state and the magnetic field where it can be realized.

Finding the Pfaffians

Even-denominator fractional quantum Hall effect has been observed experimentally in bilayer graphene (Li et al., 2017; Zibrov et al., 2017). It was found that the corresponding states were spin-polarized and it was suggested that they are Pfaffian or anti-Pfaffian states corresponding to the half-filled Landau level. Such states were observed at high energy bilayer Landau levels that are a mixture of the $n = 1$ and $n = 0$ conventional Landau levels. It was noted that the FQHE was observed only at the filling factor $\nu = 3/2$, but not at $\nu = 1/2$ and $5/2$ (Li et al., 2017). This observation illustrates the high sensitivity of the half-filled incompressible states to the structure of the electron wave functions which determine the electron-electron interaction potentials. Also the measured activation gap of the half-filled incompressible state was several times larger than the largest gaps measured in the GaAs systems (Zibrov et al., 2017), which also illustrates that the half-filled FHQE state is much more stable in bilayer graphene than in conventional electron systems. It was observed that the stability of the experimentally found 1/2-FQHE states is sensitive to both the magnitude of the magnetic field and the perpendicular component of the electric field. With variation of these parameters, transitions from the compressible to the incompressible states have been observed (Li et al., 2017). Such a behavior is in complete accord with our theoretical predictions elaborated in the previous section.

Conclusion

Two-dimensional electron systems placed in a strong magnetic field can support charged excitations with fractional charge and non-Abelian statistics. These excitations are possible only due to the nature of electron-electron interactions of a special type. An example of such a system is an electron gas in a given Landau level that is only half filled. Under a special profile of the interaction potential, the ground state of the $\nu = 1/2$-Landau level is described by the Pfaffian function. Here the profile of interaction potential is determined by the form factor of the corresponding Landau level. As a result, for the conventional electron systems, the incompressible $\nu = 1/2$-FQHE state is realized only in the $n = 1$ Landau level, but for the graphene monolayer which has the relativistic-like low-energy dispersion (that of the Dirac fermions), there is no incompressible $\nu = 1/2$ Pfaffian state in any Landau level. This theoretical conclusion is based on the properties of electrons within a given Landau level, without considering the admixture of other Landau levels. The Landau level mixing, which is especially relevant for higher Landau levels, can modify the properties of the half-filled Landau states [see Luo and Chakraborty, 2017; Pakrouski et al., 2015; Peterson and Nayak, 2013; Rezayi, 2017; Rezayi and Simon, 2011; Simon and Rezayi, 2013]. It can also open up the possibility to observe the $\nu = 1/2$-FQHE in higher Landau levels in graphene (Kim et al., 2019).

In this context, bilayer graphene is truly unique because for bilayer graphene with AB stacking, there are two special Landau levels: one in the K valley and another one in the K' valley, for which, there is a range of magnetic fields where the $\nu = 1/2$ ground state is determined by the Pfaffian function. Stability of such a ground state, i.e., its collective excitation gap, depends on the magnetic field and for a finite magnetic field, the $\nu = 1/2$-FQHE state becomes even more stable than the corresponding state in a conventional electron system. Another important property of bilayer graphene is that there are external parameters, such as the bias voltage and the in-plane magnetic field, that can alter the inter-electron interaction strength within a given Landau level and correspondingly change the properties of the $\nu = 1/2$ Pfaffian state.

In addition to the unique properties of the $\nu = 1/2$ Pfaffian state, the system with half filling of a given Landau level has another interesting feature. In particular, when the projection on a given Landau level is considered, i.e., only the states within this Landau level are taken into account with inter-landau level mixing, then the system itself has a particle-hole symmetry. It means that it can be described either as the $\nu = 1/2$ particle (electron) system or the $\nu = 1/2$ hole system. The Pfaffian function, which describes the $\nu = 1/2$ particle system, is not invariant under the exchange of particles and holes. When the particle-hole symmetry operation is applied to the Pfaffian function it generates the Pfaffian conjugated function, which is known as the anti-Pfaffian (Lee et al., 2007; Levin et al., 2007). The anti-Pfaffian function is given by

$$\Psi_{\mathrm{aPf}} = \mathrm{Pf}\left[\frac{z_i - z_j}{\left(z_i^* - z_j^*\right)^2}\right]\prod_{i<j}\left(z_i - z_j\right)^2 \exp\left(-\sum_i \frac{z_i^2}{4\ell_0^2}\right). \tag{50}$$

In addition to the Pfaffian and anti-Pfaffian functions, another type of function have been proposed in the literature. It is called the PH-Pfaffian and is symmetric with respect to the particle-hole symmetry operator (Son, 2015). The PH-Pfaffian is given by the following expression

$$\Psi_{\text{PH-Pf}} = \mathrm{Pf}\left[\frac{1}{z_i^* - z_j^*}\right]\prod_{i<j}\left(z_i - z_j\right)^2 \exp\left(-\sum_i \frac{z_i^2}{4\ell_0^2}\right). \tag{51}$$

All these functions, Pfaffian, anti-Pfaffian, and PH-Pfaffian, are of the superconductor-type with Cooper pairing but having different pairing symmetries. The corresponding charged excitations are non-Abelian anyons. Discussion of the conditions under which different Pfaffian-type functions are to be realized and their properties can be found in the literature (Antonić et al., 2018; Bonderson et al., 2011; Hsin et al., 2020; Pakrouski et al., 2015; Peterson and Nayak, 2013; Rezayi, 2017; Rezayi et al., 2021; Rezayi and Simon, 2011; Simon and Rezayi, 2013; Sodemann and MacDonald, 2013; Wójs et al., 2010; Zaletel et al., 2015). Confirmation of the presence of Pfaffian functions in half-filled FQHE will provide another open door to our understanding of this distinctive many-body phenomena, the FQHE, guided primarily by the Laughlin function, that have enthralled us for more than four decades. Additionally, it would be equally exciting to watch that the work of Cayley and Pfaff finally see the light of day through bilayer graphene.

References

Abergel DSL, Apalkov V, Berashevich J, Ziegler K, and Chakraborty T (2010) Properties of graphene: A theoretical perspective. *Advances in Physics* 59: 261–482. https://doi.org/10.1080/00018732.2010.487978.

Antonić L, Vučičević J, and Milovanović MV (2018) Paired states at 5/2: Particle-hole Pfaffian and particle-hole symmetry breaking. *Physical Review B* 98: 115107. https://doi.org/10.1103/PhysRevB.98.115107.

Apalkov VM and Chakraborty T (2006) Fractional quantum hall states of dirac electrons in graphene. *Physical Review Letters* 97: 126801. https://doi.org/10.1103/PhysRevLett.97.126801.

Apalkov VM and Chakraborty T (2010) Controllable driven phase transitions in fractional quantum Hall states in bilayer graphene. *Physical Review Letters* 105: 036801. https://doi.org/10.1103/PhysRevLett.105.036801.

Apalkov VM and Chakraborty T (2011) Stable pfaffian state in bilayer graphene. *Physical Review Letters* 107: 186803. https://doi.org/10.1103/PhysRevLett.107.186803.

Apalkov VM, Chakraborty T, Pietiläinen P, and Niemelä K (2001) Half-polarized quantum hall states. *Physical Review Letters* 86: 1311–1314. https://doi.org/10.1103/PhysRevLett.86.1311.

Ashcroft W and Mermin D (1976) *Solid State Physics*. Boston, MA: Cengage.

Ayukaryana NR, Fauzi MH, and Hasdeo EH (2021) The quest and hope of majorana zero modes in topological superconductor for fault-tolerant quantum computing: An introductory overview. *AIP Conference Proceedings* 2382: 020007. https://doi.org/10.1063/5.0059974.

Bajdich M, Mitas L, Wagner LK, and Schmidt KE (2008) Pfaffian pairing and backflow wavefunctions for electronic structure quantum monte carlo methods. *Physical Review B* 77: 115112. https://doi.org/10.1103/PhysRevB.77.115112.

Bonderson P, Gurarie V, and Nayak C (2011) Plasma analogy and non-abelian statistics for ising-type quantum hall states. *Physical Review B* 83: 075303. https://doi.org/10.1103/PhysRevB.83.075303.

Bouchaud J, Georges A, and Lhuillier C (1988) Pair wave functions for strongly correlated fermions and their determinantal representation. *Journal de Physique France* 49: 553–559. https://doi.org/10.1051/jphys:01988004904055300.

Castro Neto AH, Guinea F, Peres NMR, Novoselov KS, and Geim AK (2009) The electronic properties of graphene. *Reviews of Modern Physics* 81: 109–162. https://doi.org/10.1103/RevModPhys.81.109.

Cayley A (1847) Sur les de'terminants gauches. *Crelle's Journal* 38: 93.

Chakraborty T and Apalkov VM (2013) Traits and characteristics of interacting dirac fermions in monolayer and bilayer graphene. *Solid State Communications* 175-176: 123–131. https://doi.org/10.1016/j.ssc.2013.04.002.

Chakraborty T and Apalkov V (2014) *Aspects of the Fractional Quantum Hall Effect in Graphene.* Cham: Springer International Publishing, 251–300. https://doi.org/10.1007/978-3-319-02633-6_8.

Chakraborty T and Pietiläinen P (1988) Fractional quantum Hall effect at even-denominator filling fractions. *Physical Review B* 38: 19997(R). https://doi.org/10.1103/PhysRevB.38.10097.

Chakraborty T and Pietiläinen P (1995) *The Quantum Hall Effects*. New York: Springer.

Chakraborty T and Zhang FC (1984) Role of reversed spins in the correlated ground state for the fractional quantum hall effect. *Physical Review B* 29: 7032–7033. https://doi.org/10.1103/PhysRevB.29.7032.

Chakraborty T, Pietiläinen P, and Zhang FC (1986) Elementary excitations in the fractional quantum hall effect and the spin-reversed quasiparticles. *Physical Review Letters* 57: 130–133. https://doi.org/10.1103/PhysRevLett.57.130.

Crilly T (2016) Half-determinants: An historical note. *The Mathematical Gazette* 66: 316. https://www.cambridge.org/core/article/halfdeterminants-an-historical-note/FC1A9BB82E0DA1C074C181826E3E28F4https://doi.org/10.2307/3615529.

Das Sarma S, Freedman M, and Nayak C (2005) Topologically protected qubits from a possible non-abelian fractional quantum hall state. *Physical Review Letters* 94: 166802. https://doi.org/10.1103/PhysRevLett.94.166802.

Fano G, Ortolani F, and Colombo E (1986) Configuration-interaction calculations on the fractional quantum hall effect. *Physical Review B* 34: 2670–2680. https://doi.org/10.1103/PhysRevB.34.2670.

Geim AK and Novoselov KS (2007) The rise of graphene. *Nature Materials* 6: 183–191. https://doi.org/10.1038/nmat1849.

Goerbig MO (2011) Electronic properties of graphene in a strong magnetic field. *Reviews of Modern Physics* 83: 1193–1243. https://doi.org/10.1103/RevModPhys.83.1193.

Greiter M (2011) Landau level quantization on the sphere. *Physical Review B* 83: 115129. https://doi.org/10.1103/PhysRevB.83.115129.

Greiter M, Wen XG, and Wilczek F (1991) Paired hall state at half filling. *Physical Review Letters* 66: 3205–3208. https://doi.org/10.1103/PhysRevLett.66.3205.

Greiter M, Wen XG, and Wilczek F (1992) Paired hall states. *Nuclear Physics B* 374: 567–614. https://doi.org/10.1016/0550-3213(92)90401-V.

Haldane FDM (1983) Fractional quantization of the hall effect: A hierarchy of incompressible quantum fluid states. *Physical Review Letters* 51: 605–608. https://doi.org/10.1103/PhysRevLett.51.605.

Haldane FDM (1987) *The Quantum Hall Effect*. New York: Springer.

Haldane FDM (2011) Geometrical description of the fractional quantum hall effect. *Physical Review Letters* 107: 116801. https://doi.org/10.1103/PhysRevLett.107.116801.

Haldane FDM and Rezayi EH (1985) Finite-size studies of the incompressible state of the fractionally quantized hall effect and its excitations. *Physical Review Letters* 54: 237–240. https://doi.org/10.1103/PhysRevLett.54.237.

Hall EH (1879) On a new action of the magnet on electric currents. *American Journal of Mathematics* 2: 287–292. http://www.jstor.org/stable/2369245. https://doi.org/10.2307/2369245.

Halperin BI (1983) Theory of the quantized Hall conductance. *Helvetica Physica Acta* 56: 75–102. https://doi.org/10.5169/seals-115362.

Halperin B and Jain J (eds.) (2020) *Fractional Quantum Hall Effects: New Developments*. World Scientific.

Halperin BI, Lee PA, and Read N (1993) Theory of the half-filled landau level. *Physical Review B* 47: 7312–7343. https://doi.org/10.1103/PhysRevB.47.7312.

Halton JH (1966) A combinatorial proof of cayley's theorem on pfaffians. *Journal of Combinatorial Theory* 1: 224.

Hsin PS, Lin YH, Paquette NM, and Wang J (2020) Effective field theory for fractional quantum hall systems near $\nu = 5/2$. *Physical Review Research* 2: 043242. https://doi.org/10.1103/PhysRevResearch.2.043242.

Hurd CM (1972) *The Hall Effect in Metals and Alloys*. Plenum.

Ivanov DA (2001) Non-abelian statistics of half-quantum vortices in *p*-wave superconductors. *Physical Review Letters* 86: 268–271. https://doi.org/10.1103/PhysRevLett.86.268.

Kim Y, Balram AC, Taniguchi T, Watanabe K, Jain JK, and Smet JH (2019) Even denominator fractional quantum hall states in higher landau levels of graphene. *Nature Physics* 15: 154–158. https://doi.org/10.1038/s41567-018-0355-x.

Kitaev AY (2003) Fault-tolerant quantum computation by anyons. *Annals of Physics* 303: 2–30. https://doi.org/10.1016/S0003-4916(02)00018-0.

Kittel C (2005) *Introduction to Solid State Physics*. Hoboken, NJ: Wiley.

Klitzing KV (2017) Quantum hall effect: Discovery and application. *Annual Review of Condensed Matter Physics* 8: 13–30. https://doi.org/10.1146/annurevconmatphys-031016-025148.

Klitzing KV, Dorda G, and Pepper M (1980) New method for high-accuracy determination of the fine-structure constant based on quantized hall resistance. *Physical Review Letters* 45: 494–497. https://doi.org/10.1103/PhysRevLett.45.494.

Landau LD and Lifshitz EM (1965) *Quantum Mechanics: Non-Relativistic Theory*. Oxford and New York: Pergamon Press.

Laughlin RB (1983) Anomalous quantum hall effect: An incompressible quantum fluid with fractionally charged excitations. *Physical Review Letters* 50: 1395–1398. https://doi.org/10.1103/PhysRevLett.50.1395.

Lee SS, Ryu S, Nayak C, and Fisher MPA (2007) Particle-hole symmetry and the $\nu = \frac{5}{2}$ quantum hall state. *Physical Review Letters* 99: 236807. https://doi.org/10.1103/PhysRevLett.99.236807.

Levin M, Halperin BI, and Rosenow B (2007) Particle-hole symmetry and the pfaffian state. *Physical Review Letters* 99: 236806. https://doi.org/10.1103/PhysRevLett.99.236806.

Li JIA, Tan C, Chen S, Zeng Y, Taniguchi T, Watanabe K, Hone J, and Dean CR (2017) Even-denominator fractional quantum hall states in bilayer graphene. *Science* 358: 648–652. https://doi.org/10.1126/science.aao2521.

Luo W and Chakraborty T (2017) Pfaffian state in an electron gas with small landau level gaps. *Physical Review B* 96: 081108. https://doi.org/10.1103/PhysRevB.96.081108.

McCann E and Falko VI (2006) Landau-level degeneracy and quantum hall effect in a graphite bilayer. *Physical Review Letters* 96: 086805. https://doi.org/10.1103/PhysRevLett.96.086805.

McCann E and Koshino M (2013) The electronic properties of bilayer graphene. *Reports on Progress in Physics* 76: 056503. https://doi.org/10.1088/0034-4885/76/5/056503.

McClure JW (1956) Diamagnetism of graphite. *Physical Review* 104: 666–671. https://doi.org/10.1103/PhysRev.104.666.

Moore G and Read N (1991) Nonabelions in the fractional quantum hall effect. *Nuclear Physics B* 360: 362–396. https://doi.org/10.1016/0550-3213(91)90407-O.

Nayak C, Simon SH, Stern A, Freedman M, and Das Sarma S (2008) Non-abelian anyons and topological quantum computation. *Reviews of Modern Physics* 80: 1083–1159. https://doi.org/10.1103/RevModPhys.80.1083.

Novoselov KS, Geim AK, Morozov SV, Jiang D, Zhang Y, Dubonos SV, Grigorieva IV, and Firsov AA (2004) Electric field effect in atomically thin carbon films. *Science* 306: 666–669. `https://science.sciencemag.org/content/sci/306/5696/666.full.pdf.` https://doi.org/10.1126/science.1102896.

Pakrouski K, Peterson MR, Jolicoeur T, Scarola VW, Nayak C, and Troyer M (2015) Phase diagram of the $\nu = 5/2$ fractional quantum hall effect: Effects of landau-level mixing and nonzero width. *Physical Review X* 5: 021004. https://doi.org/10.1103/PhysRevX.5.021004.

Pereira JM, Peeters FM, and Vasilopoulos P (2007) Landau levels and oscillator strength in a biased bilayer of graphene. *Physical Review B* 76: 115419. https://doi.org/10.1103/PhysRevB.76.115419.

Peterson MR and Nayak C (2013) More realistic hamiltonians for the fractional quantum hall regime in gaas and graphene. *Physical Review B* 87: 245129. https://doi.org/10.1103/PhysRevB.87.245129.

Prange R and Girvin S (eds.) (1987) *The Quantum Hall Effect*. New York: Springer.

Read N and Green D (2000) Paired states of fermions in two dimensions with breaking of parity and time-reversal symmetries and the fractional quantum hall effect. *Physical Review B* 61: 10267–10297. https://doi.org/10.1103/PhysRevB.61.10267.

Rezayi EH (2017) Landau level mixing and the ground state of the $\nu = 5/2$ quantum hall effect. *Physical Review Letters* 119: 026801. https://doi.org/10.1103/PhysRevLett.119.026801.

Rezayi EH and Simon SH (2011) Breaking of particle-hole symmetry by landau level mixing in the $\nu = 5/2$ quantized hall state. *Physical Review Letters* 106: 116801. https://doi.org/10.1103/PhysRevLett.106.116801.

Rezayi EH, Pakrouski K, and Haldane FDM (2021) Stability of the particle-hole pfaffian state and the $\frac{5}{2}$-fractional quantum hall effect. *Physical Review B* 104: L081407. https://doi.org/10.1103/PhysRevB.104.L081407.

Seiler DG and Stephens AE (1991) *CHAPTER 18 - The Shubnikovde Haas Effect in Semiconductors: A Comprehensive Review of Experimental Aspects*. vol. 27, Elsevier1031–1133. https://doi.org/10.1016/B978-0-444-88873-0.50014-5.

Simon SH and Rezayi EH (2013) Landau level mixing in the perturbative limit. *Physical Review B* 87: 155426. https://doi.org/10.1103/PhysRevB.87.155426.

Sodemann I and MacDonald AH (2013) Landau level mixing and the fractional quantum hall effect. *Physical Review B* 87: 245425. https://doi.org/10.1103/PhysRevB.87.245425.

Son DT (2015) Is the composite fermion a dirac particle? *Physical Review X* 5: 031027. https://doi.org/10.1103/PhysRevX.5.031027.

Stern A (2008) Anyons and the quantum hall effect - pedagogical review. *Annals of Physics* 323: 204–249. https://doi.org/10.1016/j.aop.2007.10.008.

Stern A and Halperin BI (2006) Proposed experiments to probe the non-abelian $\nu = 5/2$ quantum hall state. *Physical Review Letters* 96: 016802. https://doi.org/10.1103/PhysRevLett.96.016802.

Stone M (1992) *Quantum Hall Effect*. World Scientific.

Storni M, Morf RH, and Das Sarma S (2010) Fractional quantum hall state at $\nu = \frac{5}{2}$ and the Moore-read Pfaffian. *Physical Review Letters* 104: 076803. https://doi.org/10.1103/PhysRevLett.104.076803.

Tsui DC, Stormer HL, and Gossard AC (1982) Two-dimensional magnetotransport in the extreme quantum limit. *Physical Review Letters* 48: 1559–1562. https://doi.org/10.1103/PhysRevLett.48.1559.

von Klitzing K, Chakraborty T, Kim P, Madhavan V, Dai X, McIver J, Tokura Y, Savary L, Smirnova D, Rey AM, Felser C, Gooth J, and Qi X (2020) 40 years of the quantum hall effect. *Nature Reviews Physics* 2: 397–401. https://doi.org/10.1038/s42254-020-0209-1.

Wallace PR (1947) The band theory of graphite. *Physics Review* 71: 622–634.

Wen XG (1991) Non-abelian statistics in the fractional quantum hall states. *Physical Review Letters* 66: 802–805. https://doi.org/10.1103/PhysRevLett.66.802.

Willett RL (2013) The quantum hall effect at 5/2 filling factor. *Reports on Progress in Physics* 76: 076501. https://doi.org/10.1088/0034-4885/76/7/076501.

Willett R, Eisenstein JP, Strmer HL, Tsui DC, Gossard AC, and English JH (1987) Observation of an even-denominator quantum number in the fractional quantum hall effect. *Physical Review Letters* 59: 1776–1779. https://doi.org/10.1103/PhysRevLett.59.1776.

Wójs A, Tőke C, and Jain JK (2010) Landau-level mixing and the emergence of pfaffian excitations for the 5/2 fractional quantum hall effect. *Physical Review Letters* 105: 096802. https://doi.org/10.1103/PhysRevLett.105.096802.

Yoshioka D (2002) *The Quantum Hall Effect*. New York: Springer.

Zaletel MP, Mong RSK, Pollmann F, and Rezayi EH (2015) Infinite density matrix renormalization group for multicomponent quantum hall systems. *Physical Review B* 91: 045115. https://doi.org/10.1103/PhysRevB.91.045115.

Zhang Y, Tan YW, Stormer HL, and Kim P (2005) Experimental observation of the quantum hall effect and berry's phase in graphene. *Nature* 438: 201–204. https://doi.org/10.1038/nature04235.

Zibrov AA, Kometter C, Zhou H, Spanton EM, Taniguchi T, Watanabe K, Zaletel MP, and Young AF (2017) Tunable interacting composite fermion phases in a half-filled bilayer-graphene landau level. *Nature* 549: 360–364. https://doi.org/10.1038/nature23893.

Zibrov AA, Spanton EM, Zhou H, Kometter C, Taniguchi T, Watanabe K, and Young AF (2018) Even-denominator fractional quantum hall states at an isospin transition in monolayer graphene. *Nature Physics* 14: 930–935. https://doi.org/10.1038/s41567-018-0190-0.

On the stability of Laughlin's fractional quantum hall phase

Nicolas Rougerie, Ecole Normale Supérieure de Lyon & CNRS, UMPA (UMR 5669), Lyon, France

© 2024 Elsevier Ltd. All rights reserved.

Introduction: Phenomenology of the FQHE **383**
Experimental facts 383
Theoretical road-map 385
Basic theory **385**
The many-body quantum Hamiltonian 385
Quantum Hall plateaux 385
Landau levels 386
The integer quantum Hall effect 386
The fractional quantum Hall effect 386
Restriction to the lowest Landau level 386
Killing the interaction's singularity 387
Laughlin quasi-holes 387
Stability of the Laughlin phase 388
Mathematical results and conjectures **388**
Haldane pseudo-potentials 388
The spectral gap conjecture 390
Stability of the Laughlin phase 390
Incompressibility estimates 391
Conclusion **392**
Acknowledgments **392**
References **392**

Abstract

The fractional quantum Hall effect in 2D electron gases submitted to large magnetic fields remains one of the most striking phenomena in condensed matter physics. Historically, the first observed signature is a Hall resistance quantized to the value $h/(e^2\nu)$ when the filling factor ν (electron density divided by magnetic flux quantum density) of a 2D electron gas is in the vicinity of an inverse odd integer $\nu \approx 1/(2m+1)$.This was one of the first observation of fractional quantum numbers. A large part of our basic theoretical understanding of this effect (and descendants) originates from Laughlin's theory of 1983, reviewed here from a mathematical physics perspective. We explain in which sense Laughlin's proposed ground and excited states for the system are rigid/incompressible liquids, and why this is crucial for the explanation of the effect.

Key points

- Discuss the basic phenomenology of the fractional quantum Hall effect (FQHE) in 2D electron gases (2DEG).
- Introduce Laughlin's theory of the effect at filling fraction $1/\ell$, ℓ an odd integer.
- Highlight two key incompressibility/rigidity properties the theory relies on.
- Explain the rigorous derivation of Haldane pseudo-potentials (whose ground eigenstates are generated from Laughlin's function) from first principles.
- State the (still open) spectral gap conjecture for said pseudo-potentials (first key rigidity property).
- State incompressibility estimates ensuring that the Laughlin phase is stable against external potentials and residual interactions (second key rigidity property). This essay is partially based on two previous review texts Rougerie (2018, 2022).

Introduction: Phenomenology of the FQHE

Experimental facts

The (fractional) (quantum) Hall effect (Jain, 2007 Girvin, 2004 Goerbig, 2009. Störmer et al., 1999 Laughlin, 1999) concerns the charge transport properties in 2D samples submitted to large magnetic fields. The Lorentz force exerted by the latter on moving charges leads to a non-trival transverse resistance $R_{xy} = V_y/I_x$ when a current I_x is applied in some direction x. The classical effect has historically served as a way of measuring the charge carriers' density in a given sample. It is however in the 1980's that dramatic, purely quantum signatures were discovered in this context: the quantum Hall effect (integer, then fractional). This lead to two Nobel prizes in physics (von Klitzing, 1985, Störmer-Tsui-Laughlin, 1998) and a half (Thouless-Haldane-Kosterlitz, 2016) and the advent of topology as a tool to classify phases in condensed matter physics.

https://doi.org/10.1016/B978-0-323-90800-9.00134-7

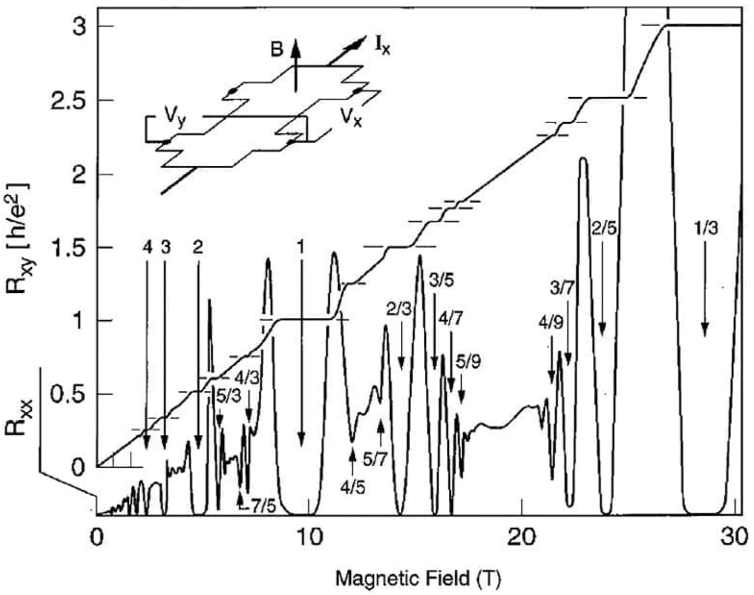

Fig. 1 The fractional quantum Hall effect (Störmer et al., 1999). Sketch of the experimental sample in top-left corner. Plots of the longitudinal $R_{xx} = V_x/I_x$ and transverse (Hall) $R_{xy} = V_y/I_x$ resistances as a function of the magnetic field.

We will limit our discussion to (some of the) most striking experimental findings as depicted on Fig. 1. Namely, consider a 2D gas of electrons submitted to a current and let the filling factor

$$\nu := \frac{hc}{e} \frac{\rho}{B} \tag{1}$$

with ρ the electrons' density, B the applied magnetic field and h, c, e respectively Planck's constant, the speed of light and the elementary charge. Around certain particular values of said factor:

- The direct resistance $R_{xx} = V_x/I_x$ exhibits sudden drops to almost 0 values.
- Simultaneously the Hall/transverse resistance $R_{xy} = V_y/I_x$ is very precisely quantized to the value $h/(e^2\nu)$, which stays stable for a certain window (plateau) of the applied field/filling factor.

Note that the value $h/(e^2\nu)$ taken by R_{xy} is precisely that one can derive from classical considerations. Thus the essence of the quantum effect is the plateau: that the measured resistance sticks on this value for a finite window of ν's around certain particular values.

The special values of ν at which the above happens are

- integers $\nu = 1,2,3\ldots$ This is the integer quantum Hall effect (IQHE).
- certain fractions, in particular $\nu = 1/m$, m odd. This is the fractional quantum Hall effect (FQHE).

The classification of all fractions at which the effect should occur is not a closed topic (as far as I know) but the most prominently observed are of the form

$$\nu = m + \frac{p}{2pn+1}, \quad m, p, n \text{ integers.} \tag{2}$$

This is certainly the case on Fig. 1, where actually one mostly sees the case $n = 1$. The particular case $p = 1$, n integer corresponds to Laughlin fractions, discussed below. For larger p one gets Jain fractions ($n = 1$, p integer corresponds to the principal Jain sequence, most prominent on the figure), explained in terms of the composite fermions theory (Jain, 2007), a generalization of Laughlin's picture we will not touch upon. Fractions of the form

$$m + 1 - \frac{p}{2pn+1}$$

correspond to a certain particle-hole transformation of those of the form (2), and their theory is thus the same.

Laughlin's theory and its' composite fermions generalization give a rationale for essentially all the features observed on Fig. 1. The most noteworthy unclear feature lies in the oscillations[1] in R_{xx} around $\nu = m + \frac{1}{2}, m = 0, 1$. Those however also have an explanation in terms of the composite fermions theory (Jain, 2007), that we will shall not discuss.

---

[1] Something different occurs at $\nu = 5/2$, see the chapter (Yngvason, 2022) "Quantum Hall states in higher Landau levels" by Jakob Yngvason.

Theoretical road-map

We will in the sequel give a mathematical physics perspective on the above facts, taking for granted the generally accepted hierarchization of energy scales leading to the effect, at least in its purest form:

(1) The perpendicular magnetic field is so large that the magnetic kinetic energy of electrons is by and large the main player.
(2) Next comes the repulsive interaction energy of electrons, due to Coulomb forces. The shortrange, singular, part is thought to be the most important.
(3) Finally all other energies are small compared to the previous ones. In particular, the temperature is neglected altogether. However, the electrostatic potential generated by impurities in the sample is crucial to the effect, and must be taken into account.

The essence of Laughlin's theory is that it provides a tentative ground state/vacuum for the system so that

- The magnetic kinetic energy is minimized exactly.
- The interaction energy is strongly reduced, in particular its' short range part.
- The filling factor is close to $1/m$, m an odd integer. This appears a posteriori after considering the first two points.
- The shape of the ground state is very robust, in particular in its' response to residual interactions and/or external fields.
- The response to external fields is to generate quasi-particles/holes of charge e/m, which serve as effective charge carriers in transport experiments.

The fourth point in particular is the aspect referred to in the title of this essay.

Basic theory

Before going into more precise statements regarding the rigidity/incompressibility of the Laughlin state, we explain its' basic, heuristic, derivation.

The many-body quantum Hamiltonian

We start from a basic Hamiltonian for the quantum 2D electron gas (in neologism form $\hbar = c = e = 2m = 1$)

$$H_N^{\text{QM}} = \sum_{j=1}^{N} \left[\left(-\mathrm{i}\nabla_{\mathbf{x}_j} - \frac{B}{2}\mathbf{x}_j^{\perp} \right)^2 + V(\mathbf{x}_j) \right] + \sum_{1 \le i < j \le N} W(\mathbf{x}_i - \mathbf{x}_j) \tag{3}$$

acting on $L^2_{\text{asym}}(\mathbb{R}^{2N})$, the Hilbert space for N 2D fermionic particles. Here $\mathbf{x}^{\perp}$ denotes the vector $\mathbf{x} \in \mathbb{R}^2$ rotated by $\pi/2$ counter-clockwise, so that

$$\operatorname{curl} \frac{B}{2}\mathbf{x}^{\perp} = B$$

and thus $\frac{B}{2}\mathbf{x}^{\perp}$ is the vector potential of a uniform magnetic field, expressed in symmetric gauge. In view of our choice of units, B is actually $\sqrt{\alpha}$ times the physical magnetic field, with $\alpha = e^2/(\hbar c) \sim 1/137$ the fine structure constant, see e.g. (Lieb and Seiringer, 2010, Section 2.17).

We take into account an external potential $V : \mathbb{R}^2 \mapsto \mathbb{R}$ modeling trapping and/or impurities in the sample, and repulsive pair interactions $W : \mathbb{R}^2 \mapsto \mathbb{R}$ between particles. Typically W should be the 3D Coulomb kernel (with α the fine structure constant again)

$$W(\mathbf{x} - \mathbf{y}) = \frac{\alpha}{|\mathbf{x} - \mathbf{y}|} \tag{4}$$

or some screened version. We have made the customary assumption that the magnetic field is strong enough to polarize all the electrons' spins.

Quantum Hall plateaux

The extremely precise quantization to particular values of R_{xy} (read on the vertical axis of Fig. 1) has an interpretation in terms of topological invariants of the system (Bellissard et al., 1994; Fröhlich, 1992, 1995), but that is not what we focus on here. Instead, looking at the horizontal axis of Fig. 1, we see that the particular features occur around special values (the numbers associated with arrows on the picture) of the filling factor (1) of the system.

In the sequel we (partially) address only the question "*why* does something special happen at these parameter values?" without touching much on the "*how* does the particular observed experimental signature emerge?" In a nutshell, the integer values found for R_{xy}^{-1} in the IQHE are Chern numbers associated to the ground state of free electrons in large magnetic fields. The fractional values of the FQHE can roughly be thought of as Chern numbers associated to the ground states of free quasi-particles generated on top of the strongly correlated FQH ground states.

Landau levels

The workhorse of the quantum Hall effect is the quantization of kinetic energy levels in the presence of a magnetic field. Namely, the appropriate kinetic energy operator for a 2D particle in a perpendicular magnetic field B is

$$H = \left(-\mathrm{i}\nabla_{\mathbf{x}} - \frac{B}{2}\mathbf{x}^{\perp}\right)^2 \tag{5}$$

acting on $L^2(\mathbb{R}^2)$.

The energy levels (eigenvalues) of the above are well-known (Rougerie and Yngvason, 2020, Jain, 2007) to be $2B(n+1/2)$ for integer n, since one can write

$$H = 2B\left(a^\dagger a + \frac{1}{2}\right)$$

for appropriate ladder operators a, $a^\dagger$ with $[a, a^\dagger] = 1$. The lowest eigenspace (lowest Landau level, corresponding to the eigenvalue B) can be represented as

$$\mathrm{LLL} = \left\{ f(z)e^{-\frac{B}{4}|z|^2} \in L^2(\mathbb{R}^2), f \text{ holomorphic} \right\} \tag{6}$$

and the n-th Landau level can be obtained as $(a^\dagger)^n$ LLL. Hence each energy level is infinitely degenerate when working on the full plane. Well-known arguments indicate that this degeneracy is reduced in finite regions, with a degeneracy $\propto B \times$ Area. One argument for this is that (5) can be restricted to a rectangle whose area is a multiple of $2\pi B^{-1}$, imposing magnetic-periodic boundary conditions see (Aftalion and Serfaty, 2007; Almog, 2006; Fournais and Kachmar, 2011; Périce, 2022; Nguyen and Rougerie, 2022) or (Jain, 2007, Sections 3.9 and 3.13). The energy levels are then the same as above, with degeneracy exactly $B(2\pi)^{-1}\times$ area of the rectangle.

The integer quantum Hall effect

Some plateaux (left of Fig. 1) in R_{xy}/drops in R_{xx} occur at integer values of ν and it is not surprising that something special should happen there (again, it is highly non-trivial to derive the specific signature of the "something special"). This can be understood in a non-interacting electrons picture, taking only the Pauli exclusion principle into account. One assumes that the magnetic kinetic energy, proportional to B, is the main player and that all other energy scales in (3) are negligible against it. By this we mean that W is dropped in (3) and that the only effect of V is to essentially confine the gas to a domain Ω.

As the name indicates, the filling factor measures the ratio of electron number to number of available one-body states $N_B(\Omega)$ in a given Landau level (see the above considerations, keeping in mind that $(2\pi)^{-1}h = c = e = 1$):

$$\nu = 2\pi\frac{\rho}{B} = 2\pi\frac{N}{|\Omega|B} \simeq \frac{N}{N_B(\Omega)}$$

if N electrons are confined to the region Ω with density $\rho = N/\mid\Omega\mid$. In the ground state of an independent electron picture (taking only the Pauli exclusion principle into account), one fills the eigenstates of (5) with one electron each, starting from the lowest one. At integer ν, the ν lowest Landau levels are thus completely filled, and the others completely empty, a very rigid and nondegenerate situation. This rigidity is actually important in order to treat the energy scales other than B perturbatively.

The fractional quantum Hall effect

Many plateaux however occur at particular *rational* filling factors and are impossible to explain in an independent electrons picture. Laughlin's groundbreaking theory (Laughlin, 1983, 1987, 1999) explains why something special ought to occur at

$$\nu = \frac{1}{\ell}, \ell \text{ an odd integer} \tag{7}$$

e.g. at the right-most plateau $\nu = 1/3$ of Fig. 1, but also at $\nu = 1/5$, a fraction also observed in experiments ($\nu = 1/9$ and lower is not observed, while $\nu = 1/7$ is borderline). The $\nu = 1/3$ fraction is the first to have been observed (Tsui et al., 1982), and the most stable. There are other, more exotic, fractions and features, but let us not get into that to focus on Laughlin's theory of the mother of all fractions, namely (7).

Restriction to the lowest Landau level

We henceforth restrict to filling factors $\nu < 1$. In the regime relevant to the quantum Hall effect, the gap B between the magnetic kinetic energy levels is so large that the first approximation we make is to project all the physics down to as few Landau levels as possible. With filling ratio $\nu \leq 1$, the lowest Landau level is vast enough (again, see the above heuristics) to accommodate all particles, and thus we restrict available many-body wave-functions to those made entirely of lowest Landau[2] levels orbitals (6). It is in fact convenient to work on the full space at first. The restrictions to finite area/density will actually be performed later, and we will have to make sure they are coherent with our aim: a thermodynamically large system with density $\rho \sim B\nu(2\pi)^{-1}$.

---

[2] Generalizations to larger filling factors, when one works in an excited Landau level, are discussed in (Rougerie and Yngvason, 2020).

Killing the interaction's singularity

The main energy scale, the magnetic kinetic energy, is now frozen by projecting all one-body states to (6). Laughlin's key idea is that the next energy scale to be considered is the pair interaction, and more precisely its singular short-range part. Any tentative ground state ought to belong to

$$\mathrm{LLL}_N = \left\{ A(z_1, \ \ldots, \ z_N) e^{-\frac{B}{4}\sum_{j=1}^N |z_j|^2}, \quad A \text{ analytic and antisymmetric} \right\} \tag{8}$$

and, for ℓ odd, the wave-function

$$\Psi_{\mathrm{Lau}}^{(\ell)}(z_1, \ \ldots, z_N) := c_{\mathrm{Lau}} \prod_{1 \le i < j \le N} \left(z_i - z_j\right)^{\ell} e^{-\frac{B}{4}\sum_{j=1}^N |z_j|^2} \tag{9}$$

is introduced in order to reduce as much as possible the probability of particle encounters. ${\Psi_{\mathrm{Lau}}}^{(\ell)}$ is designed to vanish when $z_i = z_j$ while preserving the anti-symmetry and analyticity. It may seem that ℓ is a free variational parameter. But so far we thought somewhat grand-canonically: we have not fixed the density of our system yet. It turns out that the one-particle density of Laughlin's function satisfies

$$\varrho_{\Psi_{\mathrm{Lau}}}(\mathbf{x}) \simeq \frac{B}{2\pi\ell} \mathbb{1}_{|\mathbf{x}| \le \sqrt{\frac{2N\ell}{B}}}. \tag{10}$$

That is, it lives on a thermodynamically large length scale (whose disk shape shall not bother us to determine bulk properties) and has filling factor $\nu = \ell^{-1}$ (recall the choice of units in (3)). This can be proved rigorously, see e.g. (Rougerie et al., 2013, 2014) and references therein. A common hand-waving heuristic is that in the construction of ${\Psi_{\mathrm{Lau}}}^{(\ell)}$, one needs $\ell\, N$ single particle orbitals

$$\varphi_k(z) = z^k e^{-\frac{B}{4}|z|^2}.$$

Hence the ratio of particle number to available states discussed above should indeed be ℓ^{-1}. One can also derive (Bernevig and Haldane, 2008) that the occupation number of each orbital is $\sim \ell^{-1}$.

Now we can answer our original question "what is special about filling factor $\nu = \ell^{-1}$?" The answer is that, at such parameter values, we may form a Laughlin state of exponent ℓ as approximate ground state of our system. It minimizes the magnetic kinetic energy exactly, and does a very good job at reducing the short-range part of the interaction.

Laughlin quasi-holes

So far we have argued that Laughlin's function is a good ansatz for the ground state of the system at the relevant filling factor, when neglecting the effect of the external potential V and the long-range part of the interaction W in (3). That is not the end of the story, for the latter ingredients do exist in actual experiments, in particular, the disorder landscape that impurities enforce in V is crucial to the quantum Hall effect. It leads to the finite width of the plateau by localizing charge carriers generated when the filling factor varies in the vicinity of a stable (incompressible) fraction (Laughlin, 1981).

The Laughlin state should in fact be seen as the "vacuum" of a theory explaining the FQHE experimental data. The next step is to construct the quasi-particles generated from said vacuum when suitably moderate external fields are applied, such as those generating the currents in experiments.

It is in fact easier to argue about quasi-holes, generated e.g. when the filling factor is lowered a little from the magic fraction ℓ^{-1}, as when moving toward the right on Fig. 1. The salient feature is that we stay on the same FQHE plateau for a while when doing so. It must hence be that the ground state of the system stays "Laughlin-like" for reasonably smaller ν. In fact, Laughlin's next key idea is two-fold:

- for smaller filling factors, the ground state is generated from (9) by adding uncorrelated quasi-holes. These are typically pinned by the impurities of the sample (modeled by V in (3)).
- when applying an external field at ν close to ℓ^{-1}, the current is carried by the motion of such quasi-holes.

The second idea in particular is quite far-reaching: it has by now been measured (Saminadayar et al., 1997; Martin et al., 2004; de Picciotto et al., 1997) that the current is carried in fractional lumps of $e\ell^{-1}$ and (Bartolomei et al., 2020; Nakamura et al., 2020) that the charge carriers obey fractional quantum statistics, i.e. are emergent anyons (Arovas et al., 1984; Halperin, 1984; Lundholm and Rougerie, 2016; Lambert et al., 2022; Zhang et al., 2014; Cooper and Simon, 2015).

To give a bit more mathematical flesh to these heuristics, observe that our considerations above (minimization of the magnetic kinetic energy, almost minimization of the interaction energy) generally suggest to look for states of the form

$$\Psi_F(z_1, \ \ldots, z_N) := c_F \Psi_{\mathrm{Lau}}^{(\ell)}(z_1, \ \ldots, z_N) F(z_1, \ \ldots, z_N) \tag{11}$$

with F analytic and symmetric, c_F a L^2-normalization constant. The next key steps has a "why go for complications if we can try something simple first" flavor. Namely we consider only a subset of the above possible states, those of the form

$$\Psi_f(z_1,\ \dots,z_N) := c_f \Psi^{(\ell)}_{\mathrm{Lau}}(z_1,\ \dots,z_N) \prod_{j=1}^{N} f(z_j) \tag{12}$$

where $f : \mathbb{C} \mapsto \mathbb{C}$ is analytic and c_f is a normalization constant. In some sense, we try not to add extra correlations on top of the already strongly correlated $\Psi_{\mathrm{Lau}}^{(\ell)}$.

It turns out that states of the form (12) give sufficient freedom to explain the effect. Namely, since f is essentially a polynomial, we write it in the manner

$$f(z) = \prod_{k=1}^{K} (z - a_k) \tag{13}$$

for points $a_1, \dots, a_K \in \mathbb{C}$. Since Ψ_f must vanish whenever any of the electrons coordinates approaches some a_k, those are interpreted as the (here, classical) locations of quasi-holes, whose role in the effect we discussed above.

Stability of the Laughlin phase

In the next section we discuss what is known/hoped for at a mathematical physics level of precision regarding two assumptions implicitly made above:

- The space of functions of the form (11) is indeed an approximate ground eigenspace for (at least the singular part of the) the interaction energy. It is separated from the rest of the spectrum by an energy gap, so that remaining energy scales can be treated perturbatively.
- When minimizing the remaining energy scales in the space (11) (in the spirit of degenerate perturbation theory), it is legitimate to restrict to the simpler form (12) of Laughlin plus quasi-holes wave-functions.

These two aspects are manifestations of the Laughlin state's rigidity/incompressibility. In fact the first one is most often referred to as incompressibility, so that we will refer to the second one as rigidity.

Mathematical results and conjectures

We now discuss in more mathematical details the two questions we mentioned last: (i) that the space (11) constructed from Laughlin's function almost minimizes the interaction energy, (ii) that the subset of Laughlin-plus-quasi-holes functions (12) is a stable subset of (11).

Haldane pseudo-potentials

In the case of true interactions, e.g. Coulombic (4), the Laughlin function is a good guess, but there is no obvious way of justifying this in a well-defined/controlled limit/approximation. However, the question can be given a clear mathematical meaning modulo simplifying the true interaction.

Namely, consider a toy Hamiltonian defined as follows. Let the fermionic lowest Landau level be

$$\mathrm{LLL}^N_{\mathrm{asym}} = \left\{ A(z_1,\ \dots,\ z_N) e^{-\frac{B}{4}\sum_{j=1}^{N}|z_j|^2}, \quad A \text{ analytic and antisymmetric} \right\} \tag{14}$$

where antisymmetric means "under exchange of the labels of the coordinates $z_1, \dots, z_N$." On this space, consider the action of the m-th Haldane pseudo-potential Hamiltonian

$$H(m, N) := \sum_{1 \le i < j \le N} |\varphi_m\rangle\langle\varphi_m|_{ij} \tag{15}$$

where $|\varphi_m\rangle\langle\varphi_m|_{ij}$ projects the relative coordinate[3] $\mathbf{x}_i - \mathbf{x}_j$ of particles i and j on the one-body state (c_m is a normalization constant)

$$\varphi_m(z) = c_m z^m e^{-\frac{B}{4}|z|^2}.$$

Note that, when acting on $\mathrm{LLL}^N_{\mathrm{asym}}$, only for odd m does $H(m, N)$ act non-trivially.

To motivate the above definition, we recall that the magnetic kinetic energy is the main energy scale, with discrete energy levels separated by huge gaps. Perturbation theory tells us that we should look for the ground state of the system by minimizing, in the ground eigenspace $\mathrm{LLL}^N_{\mathrm{asym}}$, the next main energy scale, namely the interaction. If one projects a bona-fide pair interaction Hamiltonian

---

[3] We identify points in the plane with complex numbers.

$$H_w = \sum_{1\le i<j\le N} w\left(x_i - x_j\right)$$

with *radial* potential $w \ge 0$ on the LLL, one obtains

$$H_w^{\mathrm{LLL}} := P_{\mathrm{LLL}^N_{\mathrm{sym/asym}}} H_w \quad P_{\mathrm{LLL}^N_{\mathrm{sym/asym}}} = \sum_{i<j}\sum_{m\ge 0} \langle \varphi_m | w | \varphi_m \rangle |\varphi_m\rangle\langle\varphi_m|_{ij}. \tag{16}$$

The coefficients $\langle \varphi_m | w | \varphi_m \rangle$ are called "Haldane pseudo-potentials" (Haldane, 1983; Bertsch and Papenbrock, 1999; Rougerie et al., 2014; Lieb et al., 2009; Lewin and Seiringer, 2009; Papenbrock and Bertsch, 2001; Girvin and Jach, 1984; Viefers, 2008). The toy Hamiltonian (15) above is obtained by discarding all terms from the sum but one, in order for the Laughlin state to be an exact ground state, and not just a very good approximation. Indeed, $\Psi_{\mathrm{Lau}}^{(\ell)}$ is clearly an exact ground state

$$H(\ell - 2, N)\Psi_{\mathrm{Lau}}^{(\ell)} = 0.$$

The rigorous justification of the expansion in Haldane pseudo-potentials and the truncation of the series is considered in (Lewin and Seiringer, 2009; Seiringer and Yngvason, 2020) (with techniques whose inspiration goes to back to (Dyson, 1957), see (Lieb et al., 2005; Rougerie, 2020)) in the limit of strong short-ranged potentials. One must be careful that for such singular potentials, the Haldane pseudo-potentials have to be modified to account for short-range correlations due to usual two-body scattering. This involves states outside the lowest Landau level.

Let $a > 0$ be a (small) length and (note that we subtract the LLL ground state energy for convenience)

$$H_a := \sum_{j=1}^{N} \left(\left(-\mathrm{i}\nabla_{\mathbf{x}_j} - \frac{B}{2}\mathbf{x}_j^{\perp} \right)^2 - B \right) + \sum_{1\le j<k\ne N} v_a\left(\mathbf{x}_j - \mathbf{x}_k\right) \tag{17}$$

where the potential

$$v_a(\mathbf{x}) = a^{-2} v\left(a^{-1}\mathbf{x}\right) \tag{18}$$

is scaled to be strong and short-range in the limit $a \to 0$. The convention is that the integral of v_a is fixed, so that the potential converges to a Dirac delta function. The following is proved in (Seiringer and Yngvason, 2020) (to which we refer for more comments):

Theorem 1: Derivation of Haldane pseudo-potentials.

Let ℓ be an odd number and the scattering coefficient

$$b_\ell := \frac{1}{4\pi\ell} \min\left\{ \int_{\mathbb{R}^2} |\mathbf{x}|^{2\ell}\left(|\nabla f(\mathbf{x})|^2 + \frac{1}{2} v(\mathbf{x}) |f(\mathbf{x})|^2 \right) d\mathbf{x},\, f(\mathbf{x}) \underset{|\mathbf{x}|\to\infty}{\to} 1 \right\}.$$

Set

$$c_\ell := 8\pi\ell\left(\pi 2^{\ell+1}\ell!\right)^{-1} b_\ell.$$

When $a \to 0$

$$a^{-2\ell} H_a \to c_\ell P_{\ell-2,N} H(\ell, N) P_{\ell-2,N}$$

in strong resolvent sense[4] *on $L^2_{\mathrm{asym}}(\mathbb{R}^{2N})$. Here $H(\ell, N)$ is as in (15) and $P_{\ell-2,\,N}$ projects on the kernel (11) of $H(\ell-2, N)$, with the convention $P_{\ell-2,\,N} = 1$ for $\ell = 1$.*

This says that the ℓ-th Haldane pseudo-potential is obtained at energies of order $a^{2\ell}$ in the limit of a potential of short range a. There is a multi-scale aspect: to reach such energies, one must first cancel the $\ell - 2$ first Haldane pseudo-potentials, whence the projection on their kernel. Note that for $\ell = 1$ there is no such lower Haldane pseudo-potential. Hence $a^{-2}H_a$ converges to $H(1,N)$ acting on the whole $\mathrm{LLL}^N_{\mathrm{asym}}$ (that one can identify with (11) for $\ell = 1$), with ground state space generated from $\Psi_{\mathrm{Lau}}^{(3)}$ as in (11). Noteworthily, one can identify $H(1, N)$ using derivatives of the delta- interaction potential,

$$H(1, N) = \pi \sum_{i<j} \Delta\delta\left(z_i - z_j\right)$$

where $\delta(z_i - z_j)$ acts as evaluation on the diagonal $z_i = z_j$ (which is a perfectly well-defined operation on the very regular LLL wave-functions).

Corollaries of the above result include that if a suitably small trapping term is added to $a^{2\ell}H_a$, its' ground state converges to $\Psi_{\mathrm{Lau}}^{(\ell)}$, see (Lewin and Seiringer, 2009; Seiringer and Yngvason, 2020) for more details.

---

[4] $H_n \to H$ in this sense if $(\mu + H_n)^{-1}\psi \to (\mu + H)^{-1}\psi$ for any state vector ψ and any $\mu > 0$.

The spectral gap conjecture

Hence, in a well-defined albeit idealized limit, the Laughlin state is a true ground state. However, the dependence on the particle number of the gap above the zero ground state energy is not known. Thus one cannot take the thermodynamic limit at the same time as the short-range limit, while precisely controlling the approximation.

The solution to this problem is an important conjecture. It says that the gap above the eigenvalue 0 does not close in the thermodynamic limit $N \to \infty$. To formulate this, observe first that $H(\ell - 2, N)$ commutes with the total angular momentum operator

$$\mathcal{L}_N := \sum_{j=1}^{N} z_j \partial z_j - \overline{z}_j \partial_{\overline{z}_j}, \tag{19}$$

and consider a joint diagonalization of the two operators on $\mathrm{LLL}^N_{\mathrm{asym}}$. The angular momentum of the Laughlin state (9) is

$$\mathcal{L}_N \Psi^{(\ell)}_{\mathrm{Lau}} = \frac{\ell}{2} N(N-1) \Psi^{(\ell)}_{\mathrm{Lau}}.$$

Conjecture 2: Spectral gap conjecture.

Consider the spectral gap of $H_{\ell-2,\,N}$ on the sector of angular momenta below that of the Laughlin state

$$\sigma(N, \ell) = \inf \left\{ \mathrm{spec}\Big(H(\ell-2,\, N)_{|\mathcal{L}_N \le \frac{\ell}{2} N(N-1)} \Big) \setminus \{0\} \right\}. \tag{20}$$

There exists a constant $c_\ell > 0$, independent of N, such that

$$\sigma(N, \ell) \ge c_\ell > 0.$$

The above is widely believed to be true (and has been advertised by experts) on the grounds that:

1. It is supported by numerical simulations (numerical diagonalizations of the Hamiltonian for small particle numbers, say up to $\sim$20, see for example (Jain, 2007, Viefers, 2008) and references therein).
2. Where it to be false, it would be extremely hard to make sense of the experimental data of the FQHE, obtained for thermodynamically large systems.

It should not actually be necessary to restrict the Hamiltonian to angular momenta below $\ell N(N-1)/2$ to obtain a lower bound to the spectral gap. It is likely that restricting to angular momenta below a larger value (but still of order N^2 when $N \to \infty$) would suffice. It is conceivable Yang et al., 2001 that the conjecture holds only for moderate values of ℓ.

There are other versions of the conjecture: for particles living on a sphere or a cylinder instead of in the plane, see (Jain, 2007, Sections 3.10 and 3.11) and references therein. The (appropriately modified) conjecture is known to hold (Nachtergaele et al., 2021, 2020; Warzel and Young, 2021a,b) in one such cases: particles confined to a thin torus, a limit in which the problem starts being reminiscent of a 1D quantum spin chain.

Stability of the Laughlin phase

We now take for granted that, in the FQHE regime around $\nu = \ell^{-1}$, leading energy considerations force us to restrict to trial states of the form (11), for they exhaust all the zero-energy eigenstates of the leading Haldane pseudo-potentials. As we discussed above, that is not the end of the story: we now need to justify the further restriction to the simpler states of the form (12).

We thus consider a Hamilton function

$$\mathbb{R}^{2N} \ni (\mathbf{x}_1, \ldots, \mathbf{x}_N) \mapsto \sum_{j=1}^{N} V(\mathbf{x}_j) + \lambda \sum_{1 \le i < j \le N} W(\mathbf{x}_i - \mathbf{x}_j) \tag{21}$$

where $V, W : \mathbb{R}^2 \mapsto \mathbb{R}$ are respectively a one-body and a two-body potential and $\lambda \in \mathbb{R}$ is a coupling constant. We shall discuss the following problem

$$E(N, \lambda) = \inf \left\{ \mathcal{E}_{N,\lambda}[\Psi_F] | \Psi_F \text{ of the form (3.9)}, \int_{\mathbb{R}^{2N}} |\Psi_F|^2 = 1 \right\} \tag{22}$$

where

$$\mathcal{E}_{N,\,\lambda}[\Psi_F] = \left\langle \Psi_F | \sum_{j=1}^{N} V(x_j) + \lambda \sum_{i<j} W(x_i - x_j) | \Psi_F \right\rangle_{L^2}. \tag{23}$$

In the spirit of degenerate perturbation theory (again), what the above means is that we minimize the remaining potential energy within the (approximate) ground eigenspace of the main energy scales. The two parts of the Hamilton function represent e.g. energies due to impurities in the sample and/or external fields, and the residual, long-range part of the interaction energy that is not killed by restricting to trial states of the form Ψ_F.

As discussed above, it is important in Laughlin's theory that one can further restrict variational states to the simpler form (12). This can be interpreted as the absence of superfluous correlations, and/or the emergence of quasi-holes generated by the action of external fields on the Laughlin "vacuum." To formulate this mathematically, define a restricted infimum by setting

$$e(N, \lambda) = \inf \left\{ \mathcal{E}_{N,\lambda}\left[\Psi_f\right] | \Psi_f \text{ of the form } (3.10), \int_{\mathbb{R}^{2N}} |\Psi_f|^2 = 1 \right\}. \tag{24}$$

Obviously $E(N, \lambda) \leq e(N, \lambda)$. What we would like to prove is that there is equality in the thermodynamic limit:

$$E(N, \lambda) \simeq e(N, \lambda) \quad \text{as } N \to \infty \text{ with } \lambda \text{ fixed.} \tag{25}$$

We now set the (presumably non-optimal, but illustrative) assumptions under which the above has been proved in (Lieb et al., 2018; Lieb et al., 2019; Rougerie and Yngvason, 2018; Olgiati and Rougerie, 2020). Since functions from our variational space (11) naturally live over thermodynamically large length scales $\sim \sqrt{N}$ it is natural to scale the potentials V and W accordingly. We thus set, for fixed functions v, w,

$$V(x) = v\left(N^{-1/2}x\right) \tag{26}$$

and (the N^{-1} pre-factor ensures that the potential and interaction energies stay of the same order when $N \to \infty$)

$$W(x) = N^{-1} w\left(N^{-1/2}x\right). \tag{27}$$

Theorem 3: Energy of the Laughlin phase.

Assume that v and w are smooth fixed functions. Assume that v goes to $+\infty$ polynomially at infinity, and that it has finitely many non-degenerate critical points. There exists $\lambda_0 > 0$ such that

$$\frac{E(N, \lambda)}{e(N, \lambda)} \underset{N \to \infty}{\to} 1$$

with $B > 0$ fixed, $\ell > 0$ a fixed integer and $|\lambda| \leq \lambda_0$.

In scaling the external potential as in (26) we make it live on the natural, thermodynamically large, length-scale of the Laughlin function. This is very reasonable for the trapping part of the potential, but much less so for the part modeling disorder, which typically lives on a much shorter length scale. We can in fact allow shorter length scales, but improving this to realistic values[5] remains an open problem. We prefer to use a single length scale, in order not to obscure the statement.

In Theorem 3 we assume the interaction to be smooth. This is because it is supposed to represent the long-range part only, the singular short-range part being taken care of by restricting to (11). Scaling W as in (27) has the merit of making the two terms in (23) of the same order of magnitude, as in a mean-field limit. This also simplifies statements a lot, but for interactions scaling like 3D Coulomb, this is actually the correct thing to do, see (Olgiati and Rougerie, 2020, Section 2.2).

Concerning the smallness assumption on λ in Theorem 3, it corresponds to the fact that the filling factor should stay close to ℓ^{-1} for the theorem to be true. Too large a deviation makes the system jump to a different FQHE plateau, e.g. a Laughlin state with higher exponent. Increasing the (repulsive) interaction strength has the net effect of spreading the system further, and hence lowering the filling factor (see again (Olgiati and Rougerie, 2020, Section 2.2) for more details). An upper bound, probably model-dependent and hard to estimate, on $|\lambda|$ is thus necessary for the statement to hold.

Incompressibility estimates

We will not go into the details of the proof of Theorem 3 (which also has corollaries regarding the optimal densities). We only mention that it mostly relies on a remarkable rigidity property shared by all states of the form (11). We coined this an "incompressibility estimate" in (Rougerie et al., 2014; Rougerie and Yngvason, 2015a, b) where partial results were obtained before the full result below was proved in (Lieb et al., 2019) and improved in (Olgiati and Rougerie, 2020). This notion of incompressibility should not be confused with that discussed in Section 4.1, that it complements (and of which it is logically independent).

Let

$$\varrho_{\Psi_F}(\mathbf{x}) := N \int_{\mathbb{R}^{2(N-1)}} |\Psi_F(\mathbf{x}, \mathbf{x}_2, \ldots, \mathbf{x}_N)|^2 d\mathbf{x}_2 \ldots d\mathbf{x}_N \tag{28}$$

be the one-particle density associated to Ψ_F of the form (11). We have the universal bound.

---

[5] The optimal assumption should be that the length scale be much larger than the magnetic length $B^{-1/2}$.

Theorem 4: Incompressibility estimate.

For any $\alpha > (\sqrt{5}-1)/4$, *any disk* D *of radius* N^α *and any (sequence of) states* Ψ_F *of the form* (11) *we have*

$$\int_D \varrho_{\Psi_F} \leq \frac{B}{2\pi\ell}|D|(1+o(1)) \tag{29}$$

where $|D|$ *is the area of the disk and* $o(1)$ *tends to zero as* $N \to \infty$.

What this says is that, in the sense of averages on sufficiently large length scales (which are allowed to be much smaller than the thermodynamic length scale $\sim \sqrt{N}$) and independently of F

$$\varrho_{\Psi_F} \lessapprox \frac{B}{2\pi\ell}.$$

I.e. the local filling factor can, in states of the form (11), nowhere be larger than the global filling factor of the Laughlin state.

We conjecture that the result only requires $N^\alpha \gg B^{-1/2}$ (i.e. that the bound holds in the sense of averages on any length scale larger than the magnetic length), but this remains an open problem. Its' solution would go a long way toward removing assumptions on length scales made in Theorem 3.

The proof of the above is based on Laughlin's plasma analogy, which maps the N-particle density of Ψ_F to Gibbs states of fictitious classical 2D electrostatic systems (somewhat contrived for non trivial F). Screening considerations valid in a large generality for these systems yield the result. The form of F can a priori be quite wild, but, being analytic, it leads to a repulsive electrostatic force in the plasma analogy. This can only lower the density compared to the case with no F. Most of the difficulties lie in vindicating this intuitive (but specific to Coulomb interactions) fact. One needs to show it for essentially any form of the corresponding charge distribution, which can be quite bizarre and correlated for general F.

Conclusion

We gave a very rough sketch of Laughlin's theory, the most basic building block of our theoretical understanding of the fractional quantum Hall effect. We argued that two crucial properties, assumed in the general theory, play a key role in making it an efficient description. From a mathematical physics point of view, the first property ("incompressibility") rests on Haldane pseudo-potentials and an open problem concerning their spectra, the spectral gap conjecture (partial results were however obtained recently (Nachtergaele et al., 2021; Nachtergaele et al., 2020; Warzel and Young, 2021a, b)). The second property ("rigidity") can be given the form of a stability question for Laughlin quasi-holes generated from the vacuum of the theory. This has been solved in some generality recently, although important questions remain on the optimal assumptions allowed in the current state of affairs. We did not mention at all extensions of the above considerations to other quantum Hall fractions than the inverse odd integers, simply because this remains a wide open problem.

Acknowledgments

Thanks to Tapash Chakraborty for inviting me to write this contribution and to Jakob Yngvason for helpful remarks. I am financially supported by the European Research Council (under the European Union's Horizon 2020 Research and Innovation Programme, Grant agreement CORFRONMAT No 758620).

References

Aftalion A and Serfaty S (2007) Lowest Landau level approach in superconductivity for the Abrikosov lattice close to H_{c_2}. *Selecta Mathematica* 13(2): 183–202.
Almog Y (2006) Abrikosov lattices in finite domains. *Communications in Mathematical Physics* 262: 677–702.
Arovas S, Schrieffer J, and Wilczek F (1984) Fractional statistics and the quantum Hall effect. *Physical Review Letters* 53(7): 722–723.
Bartolomei H, Kumar M, Bisognin R, Marguerite A, Berroir J-M, Bocquillon E, Plaçais B, Cavanna A, Dong Q, Gennser U, Jin Y, and Fève G (2020) Fractional statistics in anyon collisions. *Science* 368(6487): 173–177.
Bellissard J, Schulz-Baldes H, and Van Elst A (1994) The non commutative geometry of the quantum Hall effect. *Journal of Mathematical Physics* 35: 5373–5471.
Bernevig BA and Haldane FDM (2008) Model fractional quantum hall states and jack polynomials. *Physical Review Letters* 100: 246802.
Bertsch G and Papenbrock T (1999) Yrast line for weakly interacting trapped bosons. *Physical Review Letters* 83: 5412–5414.
Cooper NR and Simon SH (2015) Signatures of Fractional Exclusion Statistics in the Spectroscopy of Quantum Hall Droplets. *Physical Review Letters* 114: 106802.
de Picciotto R, Reznikov M, Heiblum M, Umansky V, Bunin G, and Mahalu D (1997) Direct observation of a fractional charge. *Nature* 389: 162–164.
Dyson FJ (1957) Ground-state energy of a hard-sphere gas. *Physics Review* 106(1): 20–26.
Fournais S and Kachmar A (2011) Nucleation of bulk superconductivity close to critical magnetic field. *Advances in Mathematics* 226: 1213–1258.
Fröhlich J (1992) Mathematical aspects of the quantum hall effect. In: *Proceedings of the First European Congress of Mathematics*, Basel: Birkäuser. S. C. (Ed.).
Fröhlich J (1995) The Fractional Quantum Hall Effect, Chern-Simons Theory, and Integral Lattices. In: *Proceedings of ICM'94*, Basel: Birkäuser. S. C. (Ed.).
Girvin S (2004) Introduction to the fractional quantum Hall effect. *Séminaire Poincaré* 2: 54–74.
Girvin S and Jach T (1984) Formalism for the quantum Hall effect: Hilbert space of analytic functions. *Physical Review B* 29(10): 5617–5625.
Goerbig MO (2009) *Quantum Hall effects*. arXiv:0909.1998.

Haldane FDM (1983) Fractional quantization of the Hall effect: A hierarchy of incompressible quantum fluid states. *Physical Review Letters* 51: 605–608.

Halperin BI (1984) Statistics of quasiparticles and the hierarchy of fractional quantized Hall states. *Physical Review Letters* 52: 1583–1586.

Jain JK (2007) *Composite Fermions*. Cambridge University Press.

Lambert G, Lundholm D, and Rougerie N (2022) *On quantum statistics transmutation via magnetic flux attachment*. 2201.03518. arXiv.

Laughlin RB (1981) Quantized Hall conductivity in two dimensions. *Physical Review B* 23: 5632.

Laughlin RB (1983) Anomalous quantum Hall effect: An incompressible quantum fluid with fractionally charged excitations. *Physical Review Letters* 50(18): 1395–1398.

Laughlin RB (1987) Elementary theory : The incompressible quantum fluid. In: Prange RE and Girvin SE (eds.) *The quantum Hall effect*. Heidelberg: Springer.

Laughlin RB (1999) Nobel lecture: Fractional quantization. *Reviews of Modern Physics* 71: 863–874.

Lewin M and Seiringer R (2009) Strongly correlated phases in rapidly rotating Bose gases. *Journal of Statistical Physics* 137(5–6): 1040–1062.

Lieb EH and Seiringer R (2010) *The Stability of Matter in Quantum Mechanics*. Cambridge University Press.

Lieb EH, Seiringer R, Solovej JP, and Yngvason J (2005) *The mathematics of the Bose gas and its condensation*. Birkhäuser: Oberwolfach Seminars.

Lieb EH, Seiringer R, and Yngvason J (2009) Yrast line of a rapidly rotating Bose gas: GrossPitaevskii regime. *Physical Review A* 79: 063626.

Lieb EH, Rougerie N, and Yngvason J (2018) Rigidity of the Laughlin liquid. *Journal of Statistical Physics* 172(2): 544–554.

Lieb EH, Rougerie N, and Yngvason J (2019) Local incompressibility estimates for the Laughlin phase. *Communications in Mathematical Physics* 365(2): 431–470.

Lundholm D and Rougerie N (2016) Emergence of fractional statistics for tracer particles in a Laughlin liquid. *Physical Review Letters* 116: 170401.

Martin J, Ilani S, Verdene B, Smet J, Umansky V, Mahalu D, Schuh D, Abstreiter G, and Yacoby A (2004) Localization of fractionally charged quasi-particles. *Science* 305: 980–983.

Nachtergaele B, Warzel S, and Young A (2020) Low-complexity eigenstates of a $\nu = 1/3$ fractional quantum Hall system. *Journal of Physics A: Mathematical and Theoretical 54,* 1: 01LT01.

Nachtergaele B, Warzel S, and Young A (2021) Spectral gaps and incompressibility in a $\nu = 1/3$ fractional quantum Hall system. *Communications in Mathematical Physics* 383: 1093–1149.

Nakamura J, Liang S, Gardner GC, and Manfra MJ (2020) Direct observation of anyonic braiding statistics. *Nature Physics* 16: 931–936.

Nguyen D-T and Rougerie N (2022) *Thomas-Fermi profile of a fast rotating Bose-Einstein condensate*. arXiv:2201.04418.

Olgiati A and Rougerie (2020) Stability of the Laughlin phase against long-range interactions. *Archive for Rational Mechanics and Analysis* **237**: 1475–1515. (2020) 237: 1475–1515.

Papenbrock T and Bertsch GF (2001) Rotational spectra of weakly interacting Bose-Einstein condensates. *Physical Review A* 63(2)023616.

Périce D (2022) *Multiple landau level filling for a large magnetic field limit of 2d fermions*. in preparation.

Rougerie N (2018) On the Laughlin function and its perturbations. *Séminaire Laurent Schwartz* 1–17.

Rougerie N (2020) Scaling limits of bosonic ground states, from many-body to nonlinear Schrödinger. *EMS Surveys in Mathematical Sciences* 7(2): 253–408.

Rougerie N (2022) *The classical Jellium and the Laughlin phase*. arXiv:2203.06952.

Rougerie N and Yngvason J (2015a) Incompressibility estimates for the Laughlin phase. *Communications in Mathematical Physics* 336: 1109–1140.

Rougerie N and Yngvason J (2015b) Incompressibility estimates for the Laughlin phase, part II. *Communications in Mathematical Physics* 339: 263–277.

Rougerie N and Yngvason J (2018) The Laughlin liquid in an external potential. *Letters in Mathematical Physics* 108(4): 1007–1029.

Rougerie N and Yngvason J (2020) Holomorphic quantum hall states in higher landau levels. *Journal of Mathematical Physics* 61: 041101.

Rougerie N, Serfaty S, and Yngvason J (2013) Quantum Hall states of bosons in rotating anharmonic traps. *Physical Review A* 87: 023618.

Rougerie N, Serfaty S, and Yngvason J (2014) Quantum Hall phases and plasma analogy in rotating trapped Bose gases. *Journal of Statistical Physics* 154: 2–50.

Saminadayar L, Glattli DC, Jin Y, and Etienne B (1997) Observation of the *e*/3 fractionally charged Laughlin quasiparticle. *Physical Review Letters* 79: 2526–2529.

Seiringer R and Yngvason J (2020) Emergence of Haldane pseudo-potentials in systems with short range interactions. *Journal of Statistical Physics* 181: 448–464.

Störmer H, Tsui D, and Gossard A (1999) The fractional quantum Hall effect. *Reviews of Modern Physics* 71: S298–S305.

Tsui DC, Stormer HL, and Gossard AC (1982) Two-dimensional magnetotransport in the extreme quantum limit. *Physical Review Letters* 48: 1559–1562.

Viefers S (2008) Quantum Hall physics in rotating Bose-Einstein condensates. *Journal of Physics C* 20: 123202.

Warzel S and Young A (2021a) *A bulk spectral gap in the presence of edge states for a truncated pseudopotential*. arXiv:2108.10794.

Warzel S and Young A (2021b) *The spectral gap of a fractional quantum Hall system on a thin torus*. arXiv:2112.13764.

Yang K, Haldane FDM, and Rezayi EH (2001) Wigner crystals in the lowest Landau level at low-filling factors. *Physical Review B* 64: 081301(R).

Yngvason J (2022) *Quantum Hall states in higher Landau levels*. arXiv:2209.14203.

Zhang Y, Sreejith GJ, Gemelke ND, and Jain JK (2014) Fractional angular momentum in cold atom systems. *Physical Review Letters* 113: 160404.

Fractional statistics in low-dimensional systems

Jon Magne Leinaas[a] **and Jan Myrheim**[b], [a]Department of Physics, University of Oslo, Oslo, Norway; [b]Department of Physics, The Norwegian University of Science and Technology, Trondheim, Norway

© 2024 Elsevier Ltd. All rights reserved.

Introduction 394
Fractional statistics in 2D 395
Fractional statistics in 1D 396
Anyons and the fractional quantum Hall effect 399
Conclusion 400
References 401

Abstract

We describe here the basic idea of fractional statistics in low dimensions. In quantum mechanics, multiplication of the wave function by a complex phase factor does not change the physical state described by the wave function. Another such physical identity transformation is a permutation of arguments in the wave function if they refer to identical particles. In three dimensions, a swapping of arguments gives rise to a phase factor of + 1 for two bosons and − 1 for two fermions. In two dimensions, fractional statistics appears as a possibility, where an interchange of two particles via a continuous path in the configuration space may give rise to a more general phase factor of $e^{\pm i\theta}$, with the sign of the phase depending on the direction of the path. In one dimension, two particles can be interchanged only by passing through each other. This introduces boundary conditions on the wave functions that may lead to other kinds of fractional statistics. Physical applications of these ideas are only briefly touched upon.

Key points

- Permutation of identical particles does not change the state of a physical system.
- This allows the identical particles to be bosons or fermions.
- A more careful analysis leads one to consider continuous interchange of particles instead of discrete permutations.
- In two dimensions this allows for anyons: particles with statistics between bosonic and fermionic.
- Anyons are observed as quasiparticles in the fractional quantum Hall effect.
- In one dimension the particle statistics appears as a boundary condition on the wave functions.
- The general boundary condition contains a parameter that may interpolate continuously between bosons and fermions.

Introduction

Quantum mechanics gives a unique characterization of both elementary and composite particles as being either *bosons* or *fermions*. This division into two types of particles follows from a simple symmetry argument. As was first noted by Heisenberg and Dirac, when a physical system consists of identical particles it means, by definition, that every observable is symmetric under permutations of the particles. Since symmetric operators preserve the symmetry or antisymmetry of the wave functions, it is possible to have two different quantum theories where the wave functions are restricted to be either symmetric or antisymmetric under permutation of particle coordinates. For two spinless particles, this symmetry is expressed through a sign factor which is associated with the swap of their positions,

$$\psi(\mathbf{r}_1, \mathbf{r}_2) = \pm\psi(\mathbf{r}_2, \mathbf{r}_1), \tag{1}$$

with + for bosons and − for fermions. From the symmetry constraint, when applied to a many-particle system, the statistical distributions of (noninteracting) particles over single particle states can be derived, and the completely different collective behavior of systems like electrons (fermions) and photons (bosons) can be understood.

The restriction to two possible kinds of quantum statistics, represented by the sign factor in (1), may seem almost obvious. On the one hand, the permutation of particle coordinates has no physical significance when the particles are identical, which means that the wave function can change at most by a complex phase factor $e^{i\theta}$. On the other hand, a double permutation seems to make no change at all, which further restricts the phase factor to be either + 1 or − 1. This is a standard argument used in textbooks like (Landau and Lifshitz, 1977).

However, there is little substance in this argument, as pointed out in Leinaas and Myrheim (1977), since the concept of particle interchange is not very precisely defined. We argued that the interchange should be defined as a continuous process rather than a discrete permutation. As a byproduct of this argument, it follows that if the dimension of space is reduced from three to two, the constraint on the phase factor is lifted and a continuum of possibilities appears that interpolates between the boson and fermion

https://doi.org/10.1016/B978-0-323-90800-9.00187-6

cases. In Leinaas and Myrheim (1977) these unconventional types of quantum statistics, often referred to as fractional statistics, were found by analysis of the wave functions defined on the many-particle configuration space. Other approaches by Goldin et al. (1981) and by Wilczek (1982a, b) lead to similar results, and Wilczek introduced the name *anyon* for these new types of particles.

The discovery of the fractional quantum Hall effect in 1982 gave a boost to the interest in anyons, and many new ideas for the application of the theory have followed. Recent experiments, with a direct observation of fractional statistics in the fractional quantum Hall effect, have also contributed to the continuing interest for this field of quantum physics. Our intention with the present contribution to the Encyclopedia is to discuss the basics of how fractional statistics has appeared as a possibility in two- and one-dimensional many-particle systems, while the interesting ideas of applications of anyons are only briefly commented on.

Fractional statistics in 2D

The difference between the two-dimensional and the three-dimensional cases is illustrated in Fig. 1, where, in two cases, the swapping of positions of two indistinguishable particles is shown as a continuous change of the particle positions in the plane. The curve drawn defines a continuous path in the configuration space, to be thought of as a mathematical object which does not represent a physical process. Assuming that the wave function is nowhere zero along the path, one may follow the continuous change of phase of the wave function. In the case of charged particles in a magnetic field there is a contribution to the phase from the electromagnetic vector potential; this is irrelevant here and should be subtracted.

Since the interchange of identical particles does not change the physical state, all that can happen is that the wave function as a whole will acquire a phase factor of $e^{i\theta}$, where $\theta \pmod{2\pi}$ is a real phase that is characteristic of a given species of particles. The superposition principle requires that the phase factor is the same for all wave functions. It is a reasonable assumption that θ does not change if the path is continuously deformed. Thus we must have $e^{i\theta} = 1$ for every path that can be continuously contracted to a point. An important point here is that we exclude singular points where two particles sit at the same point (these will often be singular points of the wave functions).

In two dimensions, the paths come with an orientation, and as a consequence, the counterclockwise and the clockwise paths are associated with phase factors $e^{i\theta}$ and $e^{-i\theta}$, which in principle may take any values on the complex unit circle. However, if a third dimension is introduced, counterclockwise and clockwise paths can be rotated into each other by use of the third dimension, implying that $e^{i\theta} = e^{-i\theta} = \pm 1$. In two dimensions this opens up for a continuum of intermediate statistics, while in three dimensions there are only two possibilities, bosons and fermions, as expressed in Eq. (1).

The condition on the wave function given in Eq. (1) is one way to express the indistinguishability of the particles in the quantum theory. It is needed because the mathematical points $(\mathbf{r}_1, \mathbf{r}_2)$ and $(\mathbf{r}_2, \mathbf{r}_1)$ represent the same physical situation. However, this double representation of the physics can be eliminated on the classical level, before quantization, thereby giving a new meaning to Eq. (1).

That is easy to demonstrate in the case of two particles in two dimensions. In Fig. 2A the four-dimensional configuration space is reduced to a two-dimensional flat space by removing the center of mass of the two particles. The coordinates of this two-dimensional plane then describe the relative position $\mathbf{r} = \mathbf{r}_1 - \mathbf{r}_2$, and due to the indistinguishability of the particles at $\mathbf{r}_1$ and $\mathbf{r}_2$, the full plane can be reduced to the half-plane, as shown in the figure. Furthermore, since pairs of points along the cut are identical, the full half-plane can be identified as a cone.

The different types of closed curves are determined by the number n of windings around the apex of the cone, where n can take both positive and negative integer values. In Fig. 2B two examples are shown. The first one has winding number $n = 0$, which means that it does not surround the apex, while the second one has winding number $n = 1$. In the quantum description the apex is a singular point of the wave functions, which usually are assumed to vanish at the apex. A wave function will thus under rotation around the apex pick up the phase factor $e^{in\theta}$, where n is the number of windings.

To illustrate this we consider the result for a two-particle case, earlier discussed in Leinaas and Myrheim (1977). The center of mass coordinate is neglected, for the reason already discussed, and the free-particle Hamiltonian is written as

$$H = -\frac{\hbar^2}{m}\left(\frac{\partial^2}{\partial r^2} + \frac{1}{r}\frac{\partial}{\partial r} + \frac{4}{r^2}\frac{\partial^2}{\partial \phi^2}\right), \tag{2}$$

where (r, ϕ) are the polar coordinates in relative space, defined such that

$$x = r\cos(\phi/2), \quad y = r\sin(\phi/2). \tag{3}$$

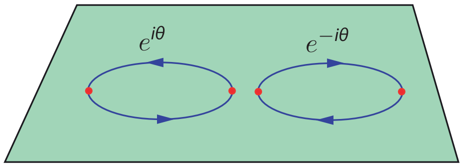

Fig. 1 Interchanging positions of pairs of indistinguishable particles in two dimensions. The difference between counterclockwise and clockwise interchange gives rise to quantum phase factors $e^{i\theta}$ and $e^{-i\theta}$ in the two cases, where $\theta \pmod{2\pi}$ can take any value between 0 and 2π (or equivalently between $-\pi$ and π). From Leinaas JM (2009) Anyons. In: Greenberger D, Hentschel K, and Weinert F (eds.) Compendium of Quantum Physics. Springer-Verlag Berlin Heidelberg, p. 10.

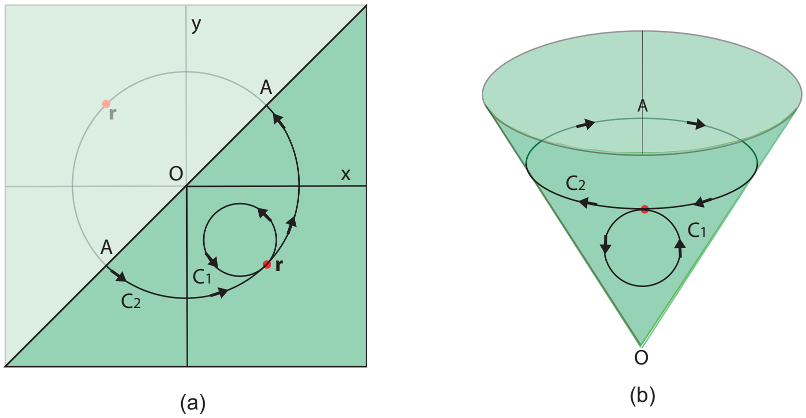

(a)

(b)

Fig. 2 The relative space of two identical particles in two dimensions. The relative position $\mathbf{r} = \mathbf{r}_1 - \mathbf{r}_2$ is physically identical to $-\mathbf{r} = \mathbf{r}_2 - \mathbf{r}_1$. To avoid this double counting, half the space in (A) can be removed, and identical points on the edge (such as the two points A) can be "glued" together. The result is the cone shown in (B). In (B) there are two circles, where C_1 does not enclose the apex of the cone, and C_2 which does so. In (A) the curve C_1 can be interpreted as change of positions that does not mix $\mathbf{r}_1$ and $\mathbf{r}_2$, while C_2 corresponds to a closed curve where $\mathbf{r}_1$ and $\mathbf{r}_2$ change positions.

Add to this Hamiltonian a harmonic oscillator potential

$$V(\mathbf{r}) = \frac{1}{4} m\omega^2 \mathbf{r}^2. \tag{4}$$

The eigenfunctions of the Hamiltonian, with V added, are written as

$$\psi(r,\phi) = \exp\left[i\left(l + \frac{\theta}{2\pi}\right)\phi\right]R(r), \quad l = 0, \pm 1, \pm 2, \ldots. \tag{5}$$

In this approach, the statistics phase θ appears explicitly in the wave function, but not in the Hamiltonian. Increasing the angle ϕ by 2π produces an anticlockwise interchange of the particles, and this operation multiplies the wave function by $e^{i\theta}$. Thus the wave functions are single-valued on the cone in Fig. 2 only if the particles are bosons, with $e^{i\theta} = 1$. In the fermion case in particular, with $e^{i\theta} = -1$, the wave functions are double-valued.

It is possible to remove θ from the wave function, by a gauge transformation which introduces a vector potential proportional to θ, but we do not discuss this here.

The radial function $R(r)$ is then determined by the equation

$$\left(\frac{d^2}{dr^2} + \frac{1}{r}\frac{d}{\partial r} - \frac{4}{r^2}\left(l + \frac{\theta}{2\pi}\right)^2 - \frac{1}{4}\frac{m^2\omega^2}{\hbar^2}r^2 + \frac{mE}{\hbar^2}\right)R = 0. \tag{6}$$

Except for the presence of θ this has the same form as the radial equation of the harmonic oscillator in two dimensions. With the solutions being nonsingular at the origin, the allowed energies are

$$E = 2\hbar\omega\left(n + \left|l + \frac{\theta}{2\pi}\right| + \frac{1}{2}\right), \quad n = 0, 1, 2, \ldots. \tag{7}$$

Fig. 3 shows how the energy spectrum changes from that of bosons to that of fermions when the parameter θ changes from 0 to π.

For two anyons in a harmonic oscillator well, the Schrödinger equation is exactly solvable for any value of the anyon variable θ. For more than two particles, however, that is not the case, and the relative configuration space is more complicated than the cone in Fig. 2B. However, if the continuous interchange of the particles is shown as a set of curves in the plane depending on a common time parameter, as in Fig. 4, this defines a pattern known as a braid. The total set of points is the same at the initial time and the final time, but at intermediate times the particle lines may intertwine. The set of all such braids with a given set of endpoints define a *braid group*. Each braid induces a phase factor $e^{in\theta}$ multiplying the anyon wave functions, where n is the total winding number of the braid. For bosons, $\theta = 0$, these phase factors define the trivial representation of the braid group, whereas for fermions, $\theta = \pi$, they define a representation of the braid group which is the antisymmetric representation of the symmetric group S_N. For this reason the fractional statistics, characterized by a more general value of the parameter θ, is often referred to as braiding statistics.

Fractional statistics in 1D

In one space dimension the identification of points in the relative space of two identical particles is

$$x = x_1 - x_2 \equiv -x \tag{8}$$

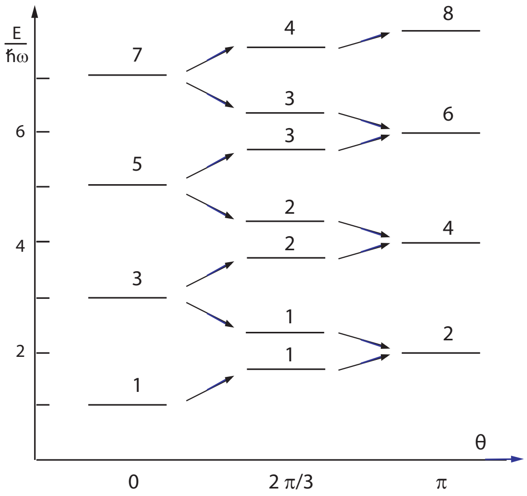

Fig. 3 The energy spectrum of a two-particle system, in two dimensions, with a harmonic–oscillator interaction, is here shown for three particular values of the parameter θ. The value $\theta = 0$ corresponds to the boson case and $\theta = \pi$ to the fermion case. The degeneracy of each energy level is given in the figure. As the figure indicates, the change of θ gives rise to a continuous transition from the boson to the fermion spectrum. From Leinaas JM and Myrheim J (1977) On the theory of identical particles. Il Nuovo Cimento 37: 1.

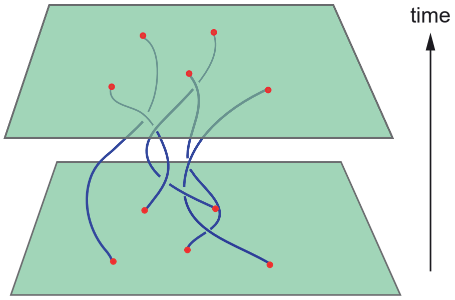

Fig. 4 When many particles interchange positions, the collection of continuous particle paths can be viewed as forming a braid, and the associated phase factor can be viewed as representing an element of the braid group. From Leinaas JM (2009) Anyons. In: Greenberger D, Hentschel K, and Weinert F (eds.) Compendium of Quantum Physics. Springer-Verlag Berlin Heidelberg, p. 10.

and it changes the full line to a half line. The singular configuration $x = 0$, which corresponds to the two particles located at the same position, is now a boundary point of the space. This is unique for one dimension, where two particles cannot interchange positions without actually passing through each other. For this reason the interchange operation is rather different here than in higher dimensions.

Since the singularity now has character of a boundary, it seems natural to represent the effect of the singularity by a boundary condition. A physically reasonable condition is to require the probability current to vanish at $x = 0$. If the Hamiltonian has the standard form, with a kinetic and a potential energy term, this condition has the general solution

$$\frac{\partial\psi}{\partial x}(x = 0) = \eta\psi(x = 0) \tag{9}$$

where η is a real parameter, independent of the center of mass coordinate and the function ψ. It can be interpreted as a statistics parameter, with $\eta = 0$ for bosons and $\eta = \pm\infty$ for fermions. Also in this case the effect of the statistics parameter can be transformed from a condition on the wave functions to a special type of interaction. If the wave functions are extended to symmetric functions on the full line, the effect of η can be expressed through a δ-function potential,

$$V_{\text{stat}} = 2\eta\frac{\hbar^2}{m}\delta(x), \tag{10}$$

where m is the mass of the particles. The effect of this interaction can be illustrated by the harmonic oscillator Hamiltonian,

$$H = \frac{\hbar^2}{m}\left(-\frac{\partial^2}{\partial x^2} + 2\eta\delta(x)\right) + \frac{1}{4}m\omega^2x^2. \tag{11}$$

The energy spectrum is given implicitly by the equation

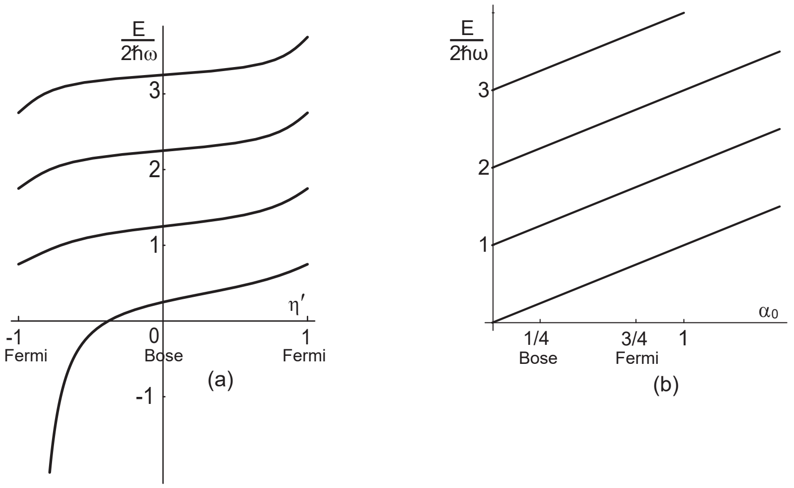

Fig. 5 The lowest energy eigenvalues in the two cases discussed in the text, with (A) as first case and (B) as the second case. In (A) the eigenvalues are functions of the statistics parameter η' and in (B) they are functions of α_0. Bosons have $\eta' = 0$ and $\alpha_0 = 1/4$, fermions have $\eta' = \pm 1$ and $\alpha_0 = 3/4$. From Leinaas JM and Myrheim J (1992) Heisenberg quantization for systems of identical particles. International Journal of Modern Physics 8: 3649.

$$\frac{\Gamma\left(\frac{3}{4} - (E/2\hbar\omega)\right)}{\Gamma\left(\frac{1}{4} - (E/2\hbar\omega)\right)} = -\eta\sqrt{\frac{\hbar}{2m\omega}}. \tag{12}$$

Solutions to this equation are shown in Fig. 5A. The spectrum is a periodic function of η in the interval $[-\infty, +\infty]$, in the sense that it is the same at both endpoints of the interval. But the periodic behavior is nontrivial in the sense that all levels move upward by one unit, while a new state appears from the infinite bottom and moves upward to take the place of the ground state.

The one-dimensional δ-function interaction between otherwise free bosons is known as the Lieb–Liniger model, and it was solved exactly in the general case of N particles in 1963 (Lieb and Liniger, 1963; Lieb, 1963).

The definition of one-dimensional anyons sketched above is not the only definition which is possible. While the former is based on the use of the wave function, another approach is possible, which is based on the observables x and p. For a single spinless particle, all observables are functions of these two. However, for two identical particles the relative position x and momentum p cannot be regarded as observables, since, if that was the case, they could be used to distinguish the two particles. Instead, the quadratic variables x^2, p^2, and xp, which are symmetric under interchange, can be used as the fundamental set of observables. They define a closed algebra under commutation, and if the following linear combinations are used,

$$\begin{aligned} A &= (1/4\omega)(p^2 + \omega^2 x^2), \\ B &= (1/4\omega)(p^2 - \omega^2 x^2), \\ C &= (1/4)(xp + px), \end{aligned} \tag{13}$$

where ω is arbitrary, the corresponding commutators are (with $\hbar = 1$)

$$[A, B] = iC, \quad [B, C] = -iA, \quad [C, A] = iB. \tag{14}$$

See Leinaas and Myrheim (1992). This is the noncompact version of the standard su(2) algebra.

Quantization of the system means defining an irreducible representation of the algebra. The operator A is then essentially the Hamiltonian of a harmonic oscillator, and $B_\pm = B \pm iC$ are raising and lowering operators in a ladder of eigenvalues of A. The commutator relations then imply for the eigenvectors of A,

$$A|\alpha_n\rangle = \alpha_n|\alpha_n\rangle, \quad B_\pm|\alpha_n\rangle = \beta_{n\pm}|\alpha_n \pm 1\rangle, \tag{15}$$

and the eigenvalues of A are

$$\alpha_n = \alpha_0 + n \tag{16}$$

where α_0 is a positive number and n is a nonnegative integer. Comparing with the standard description we find that bosons correspond to $\alpha_0 = \frac{1}{4}$ and fermions to $\alpha_0 = \frac{3}{4}$, but there is no obvious reason to restrict α_0 to these two values. So α_0 defines a continuous statistics parameter in the one-dimensional case, but this parameter, which is dimensionless, is not related to the dimensional parameter η, introduced before, in any simple way. However, as Eq. (12) shows, the expression $\eta\sqrt{\hbar/2m\omega} \equiv \tilde{\eta}$ is dimensionless, and in Fig. 5A, $\eta' \equiv (2/\pi)\arctan\tilde{\eta}$ is used as the variable corresponding to α_0 in Fig. 5B.

Thus, there are two different approaches to the quantization of the one-dimensional system and two different statistics parameters η' and α_0. To illustrate better the difference, we may consider the spectrum of the harmonic oscillator also in the wave function approach. In this case the effect of the statistics parameter can also be represented as a statistics interaction, but it has the form $1/x^2$ rather than a δ-function potential. The Hamiltonian of the relative motion is then

$$H = \frac{\hbar^2}{m}\left(-\frac{d^2}{dx^2} + \frac{\lambda}{x^2}\right) + \frac{1}{4}m\omega^2 x^2 \tag{17}$$

with

$$\lambda = 4\left(\alpha_0 - \frac{1}{4}\right)\left(\alpha_0 - \frac{3}{4}\right). \tag{18}$$

The spectrum is essentially the same as for the A operator,

$$E_n = 2\hbar\omega(\alpha_0 + n) \tag{19}$$

There is some resemblance with the spectrum depending on η', but in the present case the spectrum is only quasi-periodic in α_0 since no state moves in to replace the lowest energy state which is lost when α_0 is increased by one unit. However, the spectrum is simpler than with the δ-function potential since there is a constant difference between the neighboring levels for all values of the statistics parameter.

The one-dimensional inverse square interaction is another model which is exactly solvable for N particles, it is known as the Calogero (or Calogero–Sutherland) model (Calogero, 1971).

Anyons and the fractional quantum Hall effect

In our three-dimensional world the elementary particles are restricted to be either fermions or bosons. However, in condensed matter physics, the creation of quasi two-dimensional systems is possible, and in such systems anyons may emerge. They are then excitations of the quantum system with sharply defined particle properties, generally known as quasiparticles. The presence of anyons in such systems is not only a theoretical possibility, as was realized after the discovery in 1982 by D.C. Tsui, H.L. Stormer, and A.C. Gossard, of the *fractional* quantum Hall effect (Tsui et al., 1982). This effect is caused by the formation of a two-dimensional, incompressible electron fluid in a strong magnetic field.

The integer quantum Hall effect, Fig. 6, can be understood without taking electron–electron interactions into account. However, such interactions are crucial for the existence of a mobility gap in the case of partially filled Landau levels. In his pioneering paper (Laughlin, 1983), R.B. Laughlin concentrated on the filling fractions $\nu_m = 1/m$, with m as an odd integer, and introduced the following wave function for the ground state

$$\Psi_m = \Pi_{k<l}^{N}(z_k - z_l)^m e^{-\frac{1}{2}\sum_{i=1}^{N}|z_i|^2} \tag{20}$$

This function describes the expected properties of the ground state very well. The charge is distributed uniformly throughout the plane, with approximate radius $R = \sqrt{mN}$. Furthermore, as shown by Laughlin the state is incompressible and thereby gives the existence of the desired mobility gap.

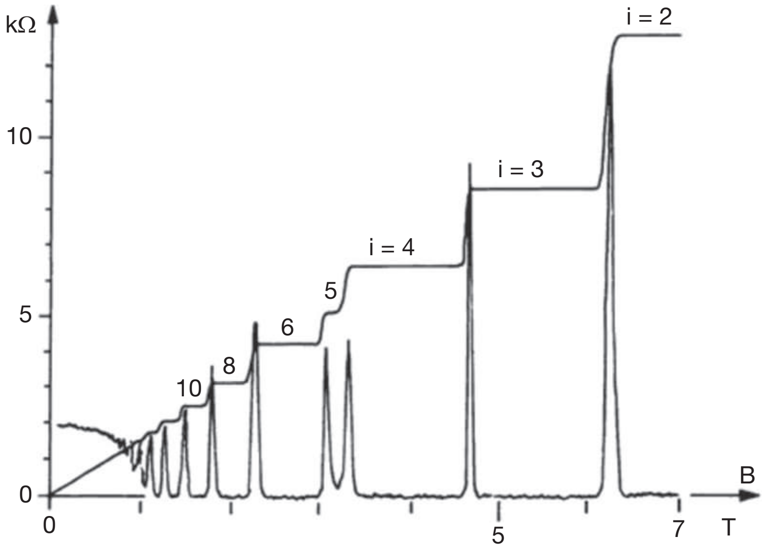

Fig. 6 The integer quantum Hall effect. The longitudinal and Hall resistivities are shown as functions of the magnetic field. The plateaus appear where a number of Landau levels are filled. In the *fractional* quantum Hall effect, new plateaus appear between those of the filled Landau levels. From https://www.nobelprize.org/prizes/physics/1998/press-release/.

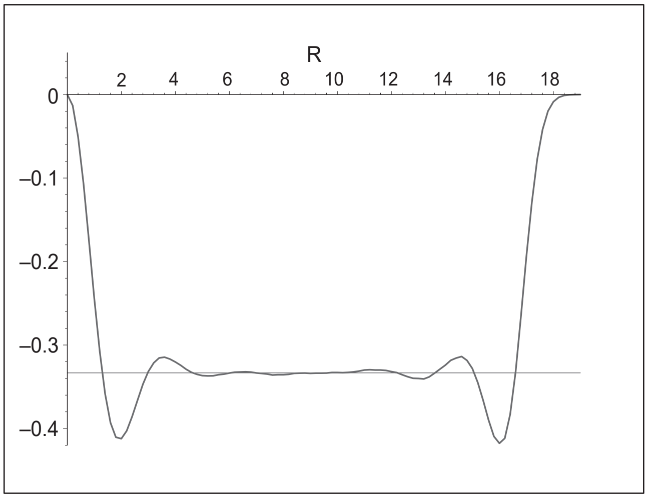

Fig. 7 The quasi-hole charge, in electron units, is measured within a variable radius *R*. The background system is composed of 100 electrons in the form of a circular droplet. For small *R*, there is a region where the charge builds up when *R* increases. In an intermediate region the charge seems to stabilize at a constant value, consistent with the expected value – 1/3, and for larger *R* there is a region where the charge again decreases to zero. From Kjønsberg H and Leinaas JM (1999) Charge and statistics of quantum Hall quasi-particles-numerical study of mean values and fluctuations. Nuclear Physics B 559: 705.

Laughlin also proposed the following functions for the quasi-hole and quasi-electron states,

$$\begin{aligned}\Psi_m^{qh} &= e^{-\frac{1}{2}\sum_{i=1}^{N}|z_i|^2}\Pi_{j=1}^{N}(z_j - z_0)\Pi_{k<l}^{N}(z_k - z_l)^m \\ \Psi_m^{qe} &= e^{-\frac{1}{2}\sum_{i=1}^{N}|z_i|^2}\Pi_{j=1}^{N}(\partial_{z_j} - z_0^*)\Pi_{k<l}^{N}(z_k - z_l)^m\end{aligned} \tag{21}$$

Numerical studies of the Laughlin states have later been performed (Kjønsberg and Myrheim, 1999; Kjønsberg and Leinaas, 1999), and the results for the Laughlin quasi-hole states are in good agreement with what is expected (see Fig. 7). However, in the case of the Laughlin quasi-electron state, the results are not equally good. Other proposed functions for the quasi-electron states, introduced by Jain (1989, 2020), show in this case better numerical results.

Not long after the Laughlin states were introduced, the anyon character of the quasiparticles in this system was demonstrated quite convincingly in theoretical studies by Halperin (1984) and Arovas et al. (1984). These observations were the starting point for the still ongoing interest in the physics of anyons, and later for the possible use of anyons in technological applications.

Although the theoretical results have strongly supported the idea of the presence of anyons in the fractional quantum Hall effect, a direct experimental evidence for the existence of anyons has, until recently, been lacking. However, in 2020, two teams of scientists, in Paris (Bartolomei et al., 2020) and at Purdue (Nakamura et al., 2020), announced experimental evidence for the existence of anyons. In the Paris group, presence of fractional statistics at filling factor $\nu = 1/3$ was demonstrated by measuring current correlations in collisions between anyons at a beam splitter. The Purdue group, on the other hand, used an electronic Fabry–Perot interferometer to demonstrate the presence of anyonic statistics, also in this case with a $\nu = 1/3$ fractional quantum Hall state. Experimental attempts had been done before, such as in Camino et al. (2005), but in these cases, clear signatures of anyons were missing due to possible interference with other sources. In the new experiments these problems were eliminated.

The anyons discussed so far are often referred to as *abelian* anyons. This means that the statistics phase factors are abelian representations of the braid group. This is so, since the wave functions of the anyons in the *in* and *out* configurations are assumed to be identical up to a phase factor, as a consequence of the particles being identical. However, nonabelian representations of the braid group exist, and they can be viewed as describing a new type of anyons, named nonabelian anyons, or simply *nonabelions*.

The additional degrees of freedom in this case are not associated with each anyon separately, and therefore they do not change the criteria of indistinguishability. Instead it is associated with the field of electrons which form the background of the anyons, and the change in the background is obtained by braiding of the anyons. This gives an extension of the simple identical particle picture of anyons, since new degrees of freedom in a sense are shared by the participants of the braid. In the rich physics of the quantum Hall effects there are indications that such nonabelions may indeed exist (Wen, 1991; Moore and Read, 1991), and theoretical ideas of exploiting such objects in the form of topological quantum computation (Kitaev, 2003) have gained much interest.

Conclusion

We have presented very briefly the reasoning leading to theories of fractional statistics in one and two dimensions. The two-dimensional case is most familiar, since it finds application to the fractional quantum Hall effect. The one-dimensional case is different, in that the particle statistics is expressed as a boundary condition on the wave function. We do not know of physical applications of the one-dimensional theory.

References

Arovas D, Schrieffer JR, and Wilzcek F (1984) Fractional statistics and the quantum Hall effect. *Physical Review Letters* 53: 722.
Bartolomei H, et al. (2020) Fractional statistics in anyon collisions. *Science* 368: 173.
Calogero F (1971) Solution of the one-dimensional N-body problem with quadratic and/or inversely quadratic pair potentials. *Journal of Mathematical Physics* 12: 419. Erratum ibidem (1996) 37: 3646.
Camino FE, Zhou W, and Goldman VJ (2005) Realization of a Laughlin quasiparticle interferometer: Observation of fractional statistics. *Physical Review B* 72: 075342.
Goldin GA, Menikoff R, and Sharp DH (1981) Representations of a local current algebra in nonsimply connected space and the Aharonov-Bohm effect. *Journal of Mathematical Physics* 22: 1664.
Halperin BI (1984) Statistics of quasiparticles and the hierarchy of fractional quantized Hall states. *Physical Review Letters* 52: 1583.
Jain JK (1989) Composite-fermion approach for the fractional quantum Hall effect. *Physical Review Letters* 63: 199.
Jain JK (2020) Thirty years of composite fermions and beyond. In: Halperin BI and Jain JK (eds.) *Fractional Quantum Hall Effects: New Developments*, p. 1. World Scientific.
Kitaev AY (2003) Fault-tolerant quantum computation by anyons. *Annals of Physics* 303: 2.
Kjønsberg H and Leinaas JM (1999) Charge and statistics of quantum Hall quasi-particles-numerical study of mean values and fluctuations. *Nuclear Physics B* 559: 705.
Kjønsberg H and Myrheim J (1999) Numerical study of charge and statistics of Laughlin quasiparticles. *International Journal of Modern Physics A* 14: 537.
Landau LD and Lifshitz LM (1977) *Quantum Mechanics: Non-Relativistic Theory*, 3rd edn. Elsevier Science.
Laughlin RB (1983) Anomalous quantum Hall effect: An incompressible quantum fluid with fractionally charged excitations. *Physical Review Letters* 50: 1395.
Leinaas JM and Myrheim J (1977) On the theory of identical particles. *Il Nuovo Cimento* 37: 1.
Leinaas JM and Myrheim J (1992) Heisenberg quantization for systems of identical particles. *International Journal of Modern Physics* 8: 3649.
Lieb EH (1963) Exact analysis of an interacting Bose gas. II. The excitation spectrum. *Physical Review* 130: 1616.
Lieb EH and Liniger W (1963) Exact analysis of an interacting Bose gas. I. The general solution and the ground state. *Physical Review* 130: 1605.
Moore G and Read N (1991) Nonabelions in the fractional quantum hall effect. *Nuclear Physics B* 360: 362.
Nakamura J, et al. (2020) Direct observation of anyonic braiding statistics. *Nature Physics* 16: 931.
Tsui DC, Stormer HL, and Gossard AC (1982) Two-dimensional magnetotransport in the extreme quantum limit. *Physical Review Letters* 48: 1559.
Wen X-G (1991) Non-Abelian statistics in the fractional quantum Hall states. *Physical Review Letters* 66: 802.
Wilczek F (1982) Magnetic flux, angular momentum and statistics. *Physical Review Letters* 48: 1144.
Wilczek F (1982) Quantum mechanics of fractional-spin particles. *Physical Review Letters* 49: 957.

Anyon collisions and fractional statistics

G Fève, Laboratoire de Physique de l'Ecole normale supérieure, ENS, Université PSL, CNRS, Sorbonne Université, Université Paris Cité, Paris, France;

© 2024 Elsevier Ltd. All rights reserved.

Introduction 403
Fermion and boson collisions 404
The collider with random sources 405
Random collisions of electrons 405
The anyon collider: Elements of theory 408
The anyon collider: Experimental results 411
Discussion of the results 413
Conclusion 414
References 415

Abstract

Quantum statistics refers to the properties of the wavefunction under the exchange of two particles. In three dimensions, there are two categories of particles depending on the value of the phase φ acquired by the wavefunction in the exchange process: bosons satisfy $\varphi = 0$ and fermions $\varphi = \pi$. In contrast, two-dimensional systems can host quasiparticles called anyons that obey intermediate, or fractional, statistics between fermions and bosons, with $0 \leq \varphi \leq \pi$. As a result, and contrary to fermions and bosons, anyons have non trivial braiding properties. It means that the phase factor $e^{2i\varphi}$ accumulated by the wavefunction when one anyon encircles another one is different from 1. The fractional quantum Hall effect, which occurs in high mobility two-dimensional electron gases placed in a strong perpendicular magnetic field, is one of the systems which hosts anyons. They carry a fractional charge and obey fractional statistics. The fractional charge of anyons was measured in the 1990s from the noise generated by partitioning an anyon beam at a beam splitter. We discuss here the recent demonstration of their fractional statistics in an anyon collider at the filling factor $\nu = 1/3$ of the fractional quantum Hall effect. In anyon collision experiments, two dilute beams of anyons generated randomly by two anyon sources collide on a beam splitter. For comparison with the anyon case, we present first bosonic and fermionic collisions. They are governed by boson bunching and fermion antibunching between two particles colliding simultaneously at the splitter. In the anyon case, specific mechanisms for charge transfer at the beam splitter occur, which are governed by the anyon braiding factor $e^{2i\varphi}$. In these mechanisms, a single anyon emitted at the splitter input may trigger the bunching of another anyon in the same output, leaving a hole in the other output. We discuss in this manuscript how these specific anyon transfer mechanisms, which lead to strong negative cross-correlations of the current fluctuations at the splitter output, are used to distinguish anyon collisions from the bosonic and fermionic cases. We also discuss how the dependence of the noise correlations in the anyon braiding phase is used to quantitatively investigate the fractional exchange phase φ of anyons in colliders.

Key points

- In three dimensions, particles are divided into two categories depending on the phase φ acquired by the wavefunction when two particles are exchanged. Bosons satisfy $\varphi = 0$ and tend to bunch together, fermions satisfy $\varphi = \pi$ and tend to exclude each other. The properties of particles with respect to particle exchange operations are called the quantum statistics
- In two dimensions, other particles with intermediate values of the exchange phase, $0 < \varphi < \pi$, may exist and are called anyons.
- In a braid operation one particle encircles another particle. In a braid operation, the many-body wavefunction acquires the phase 2φ. Bosons and fermions thus have trivial braid operations: $e^{i2\varphi} = 1$. Anyons have nontrivial braid operations: $e^{i2\varphi} \neq 1$.
- Colliders can characterize the quantum statistics of the colliding particles, bosons, fermions, and anyons. As no deterministic source of anyons is available at the moment, the direct comparison of bosonic, fermionic, and anyonic (also called fractional) statistics in collision experiments requires the use of random sources of particles.
- Boson collisions are characterized by boson bunching at the collider output, leading to negative cross-correlations of the current fluctuations. Fermion collisions are characterized by fermionic antibunching, resulting in the suppression of the current cross-correlations. In the two cases, boson bunching and fermion antibunching require one particle to be emitted at each input of the collider. As a consequence, the current cross-correlations show a characteristic dependence in the square of the probability to emit the particles.
- Specific charge transfers at the beam spitter need to be taken into account the anyon case. One specific mechanism is a backward tunneling process, where a single anyon emitted by the source drags with him another anyon in one output of the beam splitter, leaving a hole in the other output. This mechanism corresponds to the bunching of two anyons in a given output of the splitter and is thus associated with negative cross correlations of the current fluctuations, as in the bosonic

https://doi.org/10.1016/B978-0-323-90800-9.00188-8

case. However, contrary to the bosonic case, the emission of a single anyon in one input of the splitter is enough to trigger this bunching mechanism. The current cross correlations are thus directly proportional to the probability to emit the particles (contrary to its square in the bosonic and fermionic cases).

- The specific charge transfers in an anyon collision are directly mediated by the nontrivial braiding factor of anyons $e^{2i\varphi} \neq 1$ (and thus do not exist in the boson and fermion cases). Anyon collisions can thus be used to quantitatively measure the fractional statistics of anyons and their exchange phase φ. In particular the fractional statistics of anyons at the filling factor $\nu = 1/3$ of the fractional quantum Hall effect, with $\varphi = \pi/3$ has been demonstrated by several experiments.
- Anyon collisions can be extended, in principle, to the characterization of non-abelian anyons.

Introduction

In three-dimensional systems, there are only two categories of elementary excitations depending on the phase φ accumulated by the many-body wavefunction while exchanging two particles. Bosons, with $\varphi = 0$, tend to bunch together, whereas fermions, with $\varphi = \pi$, antibunch and follow Pauli's exclusion principle. In contrast, two-dimensional systems can host quasiparticles with quantum statistics intermediate between fermions and bosons (Leinaas and Myrheim, 1977; Wilczek, 1982b). As their exchange phase φ can take any value between 0 and π, these quasiparticles have been named anyons (Wilczek, 1982a). The fractional value of φ/π has important consequences when one performs a braiding operation, which consists in moving one particle around another one, thereby accumulating the phase 2φ. In the case of fermions ($\varphi = \pi$) or bosons ($\varphi = 0$), the accumulated braiding phase is trivial, with $e^{i2\varphi} = 1$. By contrast, anyons keep a memory of braiding operations as $e^{i2\varphi} \neq 1$. The stability of the braiding phase with local deformations of the anyon trajectories is at the origin of topologically protected quantum computing using non-abelian anyons (Kitaev, 2003; Nayak et al., 2008).

The fractional quantum Hall effect (Tsui et al., 1982; Laughlin, 1983), obtained by applying a strong magnetic field perpendicular to a high mobility two-dimensional electron gas, is one of the physical systems predicted to host anyons. We focus in this articles on the Laughlin series (Laughlin, 1983), of fractional quantum Hall states, where the filling ν of the first Landau level satisfies $\nu = 1/m$ where m is an odd integer. In this situation, anyons are predicted to carry a fractional charge $e^* = e/m$ (Laughlin, 1983) and to obey fractional statistics with a fractional value of the exchange phase $\varphi = \pi/m$ (Halperin, 1984; Arovas et al., 1984). For Laughlin states, a single topological number m thus describes the conductance quantization, the fractional charge, and the fractional statistics of anyons: $G/G_0 = e^*/e = \varphi/\pi = 1/m$, where $G_0 = e^2/h$ is the conductance quantum.

We discuss in this article charge transport experiments, where the properties of anyons are characterized from the fluctuations of the electrical currents flowing in a fractional quantum Hall sample. In the fractional quantum Hall effect, the bulk of the sample is insulating and charge transport occurs along gapless one-dimensional chiral channels located at the edge of the sample. For Laughlin states, the edge structure is simple with a single edge channel of conductance $G = G_0/m$ along which charge propagates ballistically on very long distances (larger than the characteristic size of samples). Backscattering between two counterpropagating edge channels can be induced by using a quantum point contact (QPC), see Fig. 1. It consists of two metallic split gates deposited on top of the electron gas and capacitively coupled to it. Applying a negative voltage to the split gates brings the two edge channels close to each other, allowing elementary excitations to tunnel from one edge channel to the other. In the integer quantum Hall effect, these elementary excitations are electrons. In contrast, when the backscattering probability T of the QPC is small ($T \ll 1$), anyons of fractional charge are randomly emitted by quantum point contacts in the fractional quantum Hall regime. The random generation of anyon currents by QPCs in the fractional quantum Hall effect was used to measure the anyon fractional charge e^*. The classical random partitioning of anyons leads to a current noise $S_{rp} = 2e^* I_T$ (Kane and Fisher, 1994; Chamon et al., 1995). Measuring

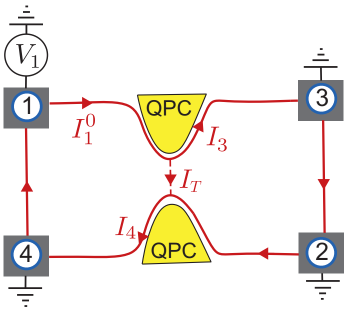

Fig. 1 Sketch of noise experiments using quantum point contacts. The two metallic split gates are represented in *gold* and the ballistic chiral edge channels in *red*. The *gray squares* are the ohmic contacts used as sources and drains of electrical currents. A dc voltage bias V_1 is applied to contact 1 to generate a noiseless current I_1^0 towards the QPC. The random transfer of anyons from one edge to the other is represented by the tunneling current I_T. The backscattering transmission of the QPC is defined as $T = \partial_{I_1^0} I_T$. The fluctuations of the currents at the output of the QPC are given by the random partition noise proportional to the charge e^*: $S_{rp} = 2e^* I_T$ where I_T is the average tunneling current (in this example, $I_4 = I_T$).

the slope of the current noise with the current tunneling through the QPC I_T (also called the backscattered current in these experiments) allowed for the measurement of the anyon fractional charge $e^* = e/3$ at filling factor $\nu = 1/3$ (de-Picciotto et al., 1997; Saminadayar et al., 1997).

These experiments can be seen as a demonstration of the existence of anyons, as the theory predicts consistently their fractional charge and their fractional statistics. However, it did not directly probe the fractional exchange phase $\varphi = \pi/m$ of anyons. Recent heat conduction measurements at the filling factor $\nu = 5/2$ showed evidence of a non-abelian state (Banerjee et al., 2018), though these results give only indirect evidences of the underlying quantum statistics. In 2020, two different experiments provided a direct probe of the fractional statistics of anyons at the filling factor $\nu = 1/3$. Nakamura et al. (2020) investigated manifestations of fractional statistics using single-particle Fabry–Perot interferometry (Chamon et al., 1997), whereas Bartolomei et al. (2020) investigated these manifestations using two-particle Hanbury Brown and Twiss interferometry (Safi et al., 2001; Vishveshwara, 2003; Kim et al., 2005; Vishveshwara and Cooper, 2010; Campagnano et al., 2012, 2013) in the geometry of the anyon collider (Rosenow et al., 2016). This article focuses on the description of anyon collision experiments. It starts with a review of fermion and boson collisions in order to highlight the differences with the anyonic case. It then turns to the anyon case, focusing on the Laughlin state $\nu = 1/3$ and discussing first elements of theory before presenting the experimental results.

Fermion and boson collisions

Two-particle interference experiments have been first introduced in the context of quantum optics by Hanbury Brown and Twiss (Hanbury Brown and Twiss, 1954, 1956). Contrary to single-particle interferometry where interferences are characterized by the measurement of the average current at the output of an interferometer, two-particle interferences are revealed by the measurement of current–current correlations at the output of a beam splitter. The geometry of a collision experiment is represented in Fig. 2A, where two sources are placed at the input of a beam splitter and one measures the cross-correlations of the current fluctuations at the splitter outputs S_{34}. In the context of optics, where such measurements have first been introduced, the correlations of the light intensity fluctuations are measured. In the context of quantum electronics, the electrical current plays the role of the light intensity in optics. Introducing $\delta I_3(t)$ and $\delta I_4(t)$ the electrical current fluctuations at time t in outputs 3 and 4, we discuss here the low-frequency correlations of the current fluctuations S_{34} defined by:

$$S_{34} = 2 \int d\tau \langle \delta I_3(t) \delta I_4(t+\tau) \rangle \tag{1}$$

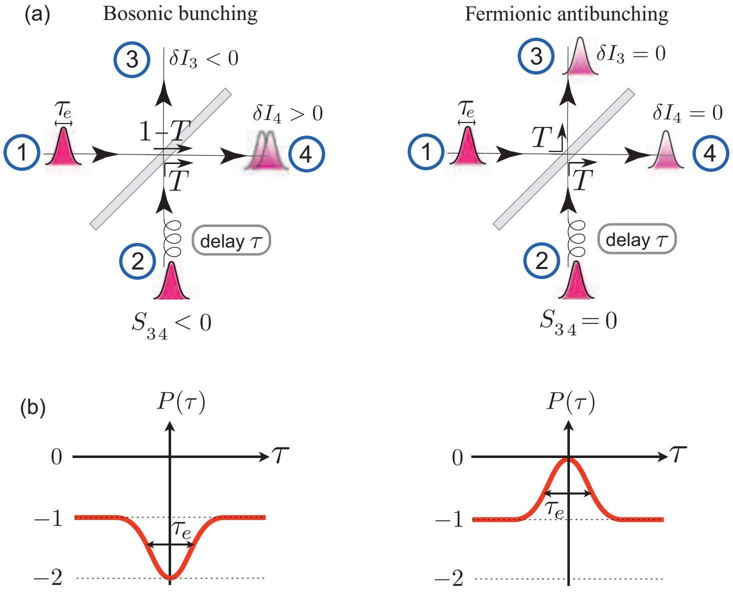

Fig. 2 (A) Collision experiment with single boson (left) and fermion (right) sources. Source 1 and source 2, placed at input 1 and 2 of a beam splitter with transmission T, emit single particle wave packet of temporal extension τ_e. One measures the output current cross-correlations S_{34} as a function of the time delay τ between the arrivals of particles emitted by source 1 and source 2 at the beam splitter. Left: boson bunching. Two particles exit in the same output of the splitter (output 4), leading to an excess current in 4 together with a deficit of current in 3. The current cross-correlations S_{34} are negative. Right: fermion antibunching. Two particles exit in different outputs of the splitter, leading to a suppression of the current fluctuations. The current cross-correlations S_{34} vanish. (B) Current cross-correlations S_{34} as a function of the time delay τ. For $\tau \gg \tau_e$, the cross-correlations are given by the classical random partitioning of particles on the splitter: $P(\tau \gg \tau_e) = -1$. For $\tau \leq \tau_e$; two-particle interferences take place. In the bosonic case (left), boson bunching leads to a dip in the cross-correlations, $P(\tau = 0) = -2$. In the fermionic case (right), fermion antibunching leads to a peak of the cross-correlations, which are suppressed, $P(\tau = 0) = 0$.

In the boson and fermion cases, collision experiments have been implemented using triggered single-photon (in the bosonic case) or single-electron (in the fermionic case) sources that periodically emit a single particle with unit probability. Considering first the case where a single source is plugged at input 1 of the collider, the random partitioning of particles at the beam splitter results in fluctuations of the output currents that can be computed from a classical binomial partitioning process $S_{34} = -S_{rp}$, with $S_{rp} = 2qT(1 - T)I_1$, where I_1 is the current generated by source 1, q is the charge of the emitted particles, and T is the backscattering probability of the beam splitter. Using $I_T = TI_1$, S_{rp} can be rewritten as $S_{rp} = 2qI_T(1 - T)$, which is identical to the expression introduced in the previous section in the weak-backscattering limit $T \ll 1$. Note that this calculation is obviously specific to the case of charged particles, such as electrons. It needs to be adapted in the photon case, replacing the electrical current by the light intensity.

In the case where two sources are plugged at inputs 1 and 2, one measures the output cross-correlations as a function of the time delay τ between the arrival time of both particles at the beam splitter. For long time delay τ, larger than the temporal width τ_e of the emitted wave packets, there is no overlap between particles emitted by source 1 and source 2 at the beam-splitter and two-particles interferences are suppressed. One then recovers the classical result, $S_{34} = -S_{rp}$ with $S_{rp} = 2qT(1 - T)I_+$, where I_+ is the sum of the currents generated by the two sources, $I_+ = I_1 + I_2$. Introducing the Fano factor $P(\tau)$ defined as the current cross-correlations normalized by the classical random partition noise, $P(\tau) = S_{34}(\tau)/S_{rp}$, one has $P(\tau \gg \tau_e) = -1$ independently of the bosonic or fermionic nature of the colliding particles. For short time delays, $\tau \leq \tau_e$, two-particle interferences occur leading to different results for bosons and fermions due to their different statistics. In the bosonic case (left panel of Fig. 2) the probability to have two bosons bunching together in the same output of the beam splitter is doubled compared to the classical case (where effects of quantum statistics would be absent). The formation of packets of two bosons in the same output leads to more negative cross-correlations with $P(\tau = 0) = -2$ (see left panel of Fig. 2B). This dip in the cross-correlations in the bosonic case for short time delays is called the Hong-Ou-Mandel (HOM) dip in reference to the seminal photon collision experiments (Hong et al., 1987). On the contrary for fermions (see right panel of Fig. 2), antibunching results in a suppression of the cross-correlations of the current fluctuations $P(\tau = 0) = 0$ (see right panel of Fig. 2B). As two electrons always exit in different outputs, the random fluctuations of the current are suppressed, resulting in a Pauli peak of the cross-correlations at short time delays. The suppression of the noise in electron collisions due to fermionic antibunching has first been observed using continuous stationary electron sources (Liu et al., 1998) and more recently using triggered single electron sources (Ol'Khovskaya et al., 2008; Bocquillon et al., 2013; Dubois et al., 2013) implementing the electronic analogue of the HOM experiment.

The collider with random sources

Contrary to the fermionic and bosonic cases, deterministic single anyon sources have not been developed at the present time. However, as used for the measurement of the fractional charge of anyons, QPCs tuned in the weak backscattering regime (regime where the backscattering probability T is much smaller than one) in the fractional quantum Hall effect can be used as random Poissonian emitters of anyons (Martin, 2005). In particular, at the filling factor $\nu = 1/3$, the backscattering of a stationary current I_0 by a QPC leads to the random emission of anyons with a fractional charge $e^* = e/3$ and a fractional exchange phase $\varphi = \pi/3$. By tuning the magnetic field to the regime of the integer quantum Hall effect, the same quantum point contact biased by a stationary current acts as a random source of electrons, which are the elementary excitations in the integer case. Comparing electrons and anyons in collisions thus requires to replace the deterministic sources of particles by random ones. This means that anyon collisions require the use of three QPCs, two QPCs being used as sources for anyon emission and another one as the beam splitter where particles collide.

The anyon collider has been introduced by Rosenow et al. (2016). It mimics the geometry of the electronic HOM experiments presented in the previous section, replacing the single electron emitters by QPCs used as random emitters of anyons. The sketch of the collider and the SEM picture of the device studied in Bartolomei et al. (2020) are represented on Fig. 3. Two noiseless currents I_1^0 and I_2^0 impinging on QPC1 and QPC2, tuned in the weak backscattering regime with emission probabilities T_1 and T_2, lead to the random generation of particles. The emitted particles then propagate toward a third QPC, cQPC, used as the beam splitter in the collision process. One measures the cross-correlations between the output currents, S_{34}, as a function of the experimental parameters: the input currents I_1 and I_2 and the backscattering probability T of cQPC. By changing the value of the magnetic field, two different types of collisions can be implemented. In the integer quantum Hall regime, the particles tunneling at QPC1 and QPC2 are electrons with fermionic statistics. In contrast, in the fractional quantum regime, the colliding particles are anyons with fractional statistics, offering the possibility to compare in the same setup the anyonic situation with the fermionic one. Two different configurations of the collider will be studied, differing by the imbalance between the currents I_1 and I_2 at the collider inputs. The balanced collider corresponds to symmetric bias of the collider inputs: $I_1^0 = I_2^0$ and $T_1 = T_2$. As both sources have the same emission probability in this case, we introduce the notation $T_S = T_1 = T_2$. The balanced configuration is thus characterized by a vanishing current difference between the inputs, $I_- = I_1 - I_2 = 0$, such that the current cross-correlations only depend on the total incoming current, $I_+ = I_1 + I_2$. The unbalanced case is obtained by increasing the imbalance ratio I_-/I_+. In particular, the fully unbalanced case corresponds to $I_- = I_+$, where one source (*e.g.*, source 2) has been switched off ($I_2 = 0$).

Random collisions of electrons

For comparison with the anyonic case, it is useful to discuss first the results of boson and fermion collisions described in Section "Fermion and boson collisions" in the case where random sources of particles replace the deterministic ones. The bosonic

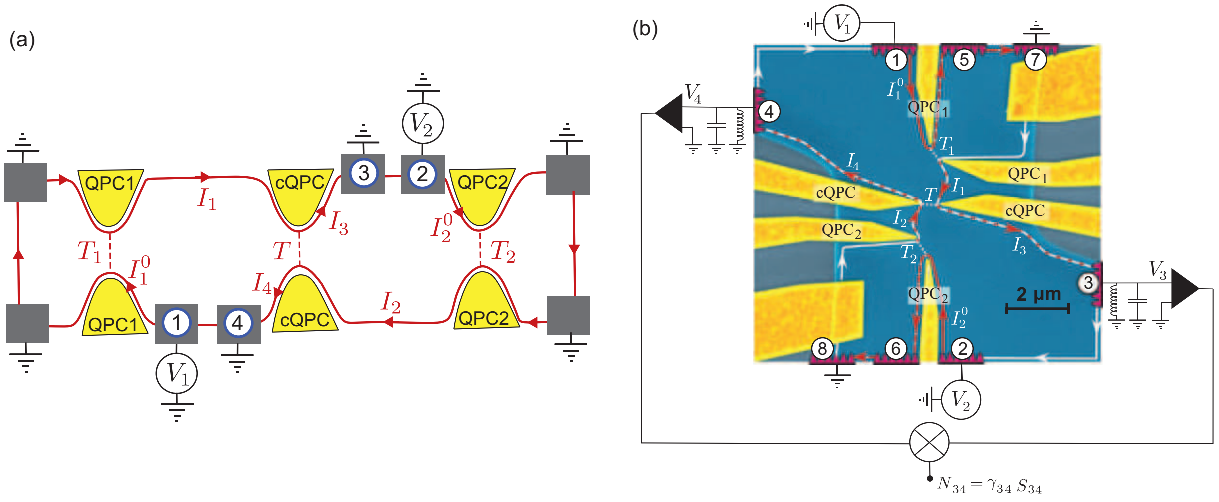

Fig. 3 (A) Sketch of the collider. Charge transport occurs along the ballistic and chiral edge channels represented in *red*. The voltage sources V_1 and V_2 generated the noiseless stationary currents I_1^0 and I_2^0. The partitioning of these currents by QPC1 and QPC2 leads to the random emission of particles (electrons for integer filling factor, anyons in the fractional case) with probabilities T_1 and T_2. The emitted particles propagate toward a third quantum point contact, cQPC, of backscattering transmission T, and which plays the role of the beam splitter in the collision. (B) Colored scanning electron microscope picture of the collider sample. The two-dimensional electron gas is represented in blue and edge channels in *red*. The metallic gates (QPC1, QPC2, and cQPC) are presented in *gold color*.

and fermionic situations can be described by a simple classical model (Rosenow et al., 2016), where source 1 (respectively source 2) emits one particle with probability T_1 (respectively T_2) at input 1 (respectively 2) of the collider. The probability that a source does not emit a particle is $1 - T_i$ ($i = 1, 2$) meaning that the probability that one source emits two particles is neglected (it is forbidden in the fermion case by the Pauli exclusion principle). In relation with the experiment, T_1 and T_2 are the backscattering probabilities of QPC1 and QPC2. In order to take into account the bosonic and fermionic statistics of particles, one can weigh the classical probability to have two particles in a given output (*e.g.* output 1), $P(2, 0) = T(1 - T)T_1T_2$, by a factor $1 - p$, where p encodes the effect of fermionic and bosonic statistics. $p = +1$ for fermions: due to Pauli exclusion principle, electrons are forbidden to exit in the same output and $P(2, 0) = 0$. $p = -1$ for bosons: bosons tend to bunch together such that the probability to have two particles in the same output is doubled compared to the classical case, $P(2, 0) = 2T(1 - T)T_1T_2$. Within this simple classical model, one can easily compute the current cross-correlations as a function of the incoming currents I_1 and I_2.

We focus first on the case of the balanced collider, $I_- = I_1 - I_2 = 0$. In this case, the current cross-correlations increase linearly with the total current $I_+ = I_1 + I_2$:

$$S_{34} = -2qT(1 - T)I_+(1 - p)T_S \tag{2}$$

$$P_{cl}(I_- = 0) = S_{34}/S_{rp} = -(1 - p)T_S, \tag{3}$$

where, as in Section "Fermion and boson collisions," the Fano factor P_{cl} is defined by normalizing the cross-correlations by the classical random partition noise $S_{rp} = 2qT(1 - T)I_+$. As can be seen in Eq. (3), this classical model, which correctly describes the bosonic and fermionic cases, predicts a Fano factor that varies linearly with the emission probability T_S. In particular, it vanishes in the Poissonian limit of particle emission, $T_S \ll 1$, both in the fermionic and bosonic cases. This can be understood by the suppression of two-particle interferences related to the statistics of particles when the probability to have one particle in each collider input becomes vanishingly small. The results of Eq. (3) also extend the results discussed in the deterministic case ($T_S = 1$) in Section "Fermion and boson collisions" to the case of arbitrary emission probability T_S. The balanced regime of the random collider, $I_- = 0$ corresponds to the regime $\tau \ll \tau_e$ in the case of deterministic particle emission. In particular, in the fermionic case ($p = 1$), one recovers the suppression of the cross-correlations, $P_{cl,f}(I_- = 0) = 0$ due to fermionic antibunching. In the bosonic case ($p = -1$), negative cross-correlations are enhanced by bosonic bunching, $P_{cl,b}(I_- = 0) = -2T_S$, which correspond to a factor 2 enhancement compared to the case of distinguishable particles ($p = 0$ and $P_{cl,d} = -T_S$). In the case of emission with unit probability, $T_S = 1$, one recovers $P_{cl,b}(I_- = 0) = P(\tau = 0) = -2$.

In the opposite limit of the completely unbalanced collider, $I_- = I_+$, the classical model predicts $P_{cl}(I_- = I_+) = -T_1$. This single source regime is the counterpart, for random sources, of the regime $\tau \gg \tau_e$ in the case of deterministic sources. Two-particle interferences are suppressed and the result does not depend on the fermionic or bosonic nature of particles. In particular, one recovers $P_{cl}(I_- = I_+) = -1$ in the regime of emission with unit probability, $T_1 = 1$. That means that negative cross-correlations are restored in the fermionic case when one increases the imbalance ratio I_-/I_+. Note that $P_{cl}(I_- = I_+) = -T_1$ can also be seen as a signature of a random Poissonian transfer of particles through cQPC in the limit $T \ll 1$. Introducing $S_{I_TI_T}$ the fluctuations of the tunneling current I_T at cQPC, S_{34} is related to $S_{I_TI_T}$ in the completely unbalanced regime by the relation $S_{34} = -S_{I_TI_T} + TS_{I_1I_1}$, where $S_{I_1I_1} = 2q(1 - T_1)I_1$ is the random partition noise resulting from the random particle emission at input 1 of cQPC. The first term in the expression of S_{34} results from the random partitioning of particles at cQPC. The second term represents the current fluctuations at input 1 of cQPC that are transmitted toward the outputs 3 and 4. One then immediately obtains, when $T \ll 1$:

$$S_{I_T I_T}(I_- = I_+) = 2qTT_1I_1 + 2qT(1 - T_1)I_1 = 2qI_T \tag{4}$$

$$F_{cl}(I_- = I_+) = \frac{S_{I_T I_T}}{2qI_T} = 1, \tag{5}$$

where one has introduced another Fano factor F_{cl} defined as the fluctuations of the tunneling current normalized by the Poissonian limit $2qI_T$ (Lee et al., 2022). Eq. (5) shows that, in the classical model and in the completely unbalanced case, where two-particle interferences are suppressed, the tunneling events at cQPC are completely uncorrelated. The regime of nonunit emission probability, $T_S \neq 1$, leads to an important hallmark of bosonic and fermionic collisions: $P_{cl}(I_-/I_+)$ is always proportional to the probability to emit particles. It means that $|P_{cl}(I_-/I_+)|$ decreases when T_S decreases. In particular, one has $P_{cl} \approx 0$ in the Poissonian limit for particle emission by sources 1 and 2: $T_1, T_2 \ll 1$. As shown by Eq. (3), P_{cl} is also proportional to T_S in the balanced case. It means that $P_{cl} \ll 1$ independently of the imbalance ratio I_-/I_+ in the regime $T_1, T_2 \ll 1$. As will be seen in Sections "The anyon collider: Elements of theory" and "The anyon collider: Experimental results," the results are completely different in the anyon case.

The predictions of the classical model in the fermionic case can be directly compared with experiments by setting the magnetic field at an integer filling factor. We plot on Fig. 4A the results for electron collisions in the balanced configuration at the integer filling factor $\nu = 3$ (similar results are obtained for $\nu = 2$). The observed results are in very good agreement with the predictions in the fermionic case. For all the emission probabilities T_S, one observes $S_{34} \approx 0$. For small values of T_S, one even observes slightly positive cross-correlations, with an increase of S_{34} at low current I_+ followed by a plateau of zero slope, $P \approx 0$. These residual positive cross-correlations might be related to residual effects of Coulomb interactions between electrons (Idrisov et al., 2022) which are not taken into account in this simple model. As discussed in the previous sections, this suppression of the cross-correlations in the fermion case is the signature of fermionic antibunching due to the Pauli exclusion principle. It is striking to compare the cross-correlations plotted on Fig. 4A with the auto-correlations of the current fluctuations $(S_{33} + S_{44})/2$, plotted on Fig. 4B. For $T_S = 1$ (*red empty circles*), the input currents I_1 and I_2 are noiseless and both the auto- and cross-correlations vanish. When decreasing the emission probability T_S, the noise of the currents I_1 and I_2 increases, as can be seen by the increase of the current auto-correlations. The observed increase of the auto-correlations when decreasing T_S is perfectly captured by the classical model which predicts $P_{cl,auto} = (S_{33} + S_{44})/(2S_{rp}) = (1 - T_S)/(2T(1 - T))$ (*red dashed line* for $T_S = 0.7$ and *orange dashed line* for $T_S = 0.2$ on Fig. 4B). For the lowest value of $T_S = 0.2$, the auto-correlations reach values more than ten times larger than the cross-correlations, reflecting the role of fermionic antibunching in the suppression of the cross-correlations.

The variation of $P(I_-/I_+)$ with the imbalance ratio I_-/I_+ at filling factor $\nu = 3$ is plotted in Fig. 5A. As expected in the electron case, increasing the imbalance between the collider inputs restores negative cross-correlations. In addition, $|P(I_- = I_+)|$ decreases when one decreases the emission probability T_S. For $T_S = 1$, the input QPCs play no role (as they transmit electrons with unit probability) and one effectively implements a single QPC experiment. In this case, the noise equals the random partition noise generated by the voltage difference $V_1 - V_2$ (or the current difference I_-) applied between the inputs of cQPC: $S_{34} = -S_{rp} = -2eT(1 - T)I_-$. Due to the definition of P, where S_{34} is normalized by the factor $2eT(1 - T)I_+$, the value $P_{cl}(I_-/I_+)$ in the single QPC regime ($T_S = 1$) is thus given by $P_{1QPC}(I_-/I_+) = -I_-/I_+$ (*black dashed line* in Fig. 5A). independently of the statistics of the particles. For $T_S < 1$, $|P(I_- = I_+)|$

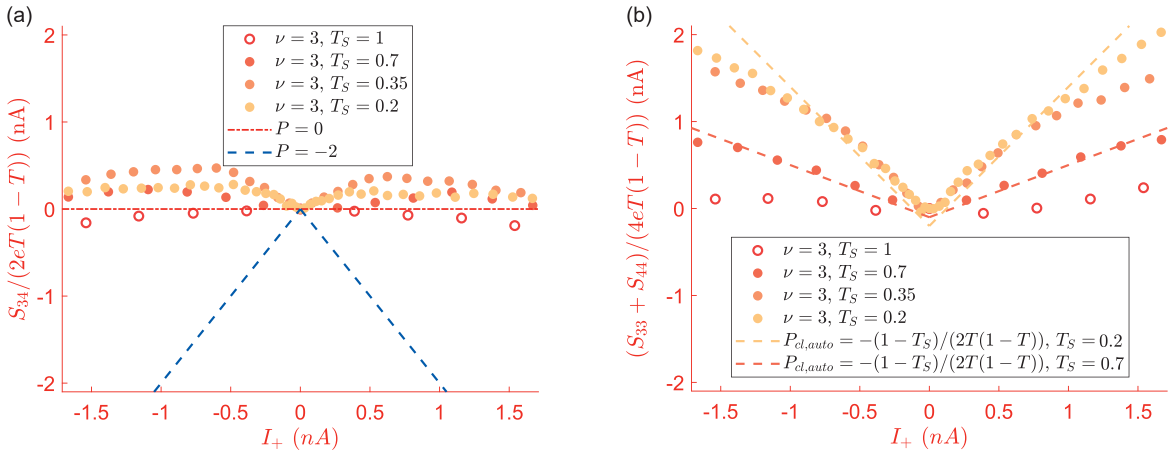

Fig. 4 Electron collisions, $\nu = 3$ and balanced configuration, $I_- = 0$. (A) Normalized cross-correlations, $S_{34}/(2eT(1 - T))$, as a function of the total emitted electron current I_+. Four different values of the electron emission probability are plotted: $T_S = 1$, $T_S = 0.7$, $T_S = 0.35$ and $T_S = 0.2$. (B) Normalized current auto-correlations, $(S_{33} + S_{44})/(4eT(1 - T))$, as a function of the total emitted electron current I_+ for the same values of T_S plotted in panel (A). The auto-correlations are suppressed for $T_S = 1$ (as the emitted current is noiseless) and increase when T_S decreases. The predictions from the classical model are represented in *red* (for $T_S = 0.7$) and *orange* (for $T_S = 0.2$) *dashed lines*.

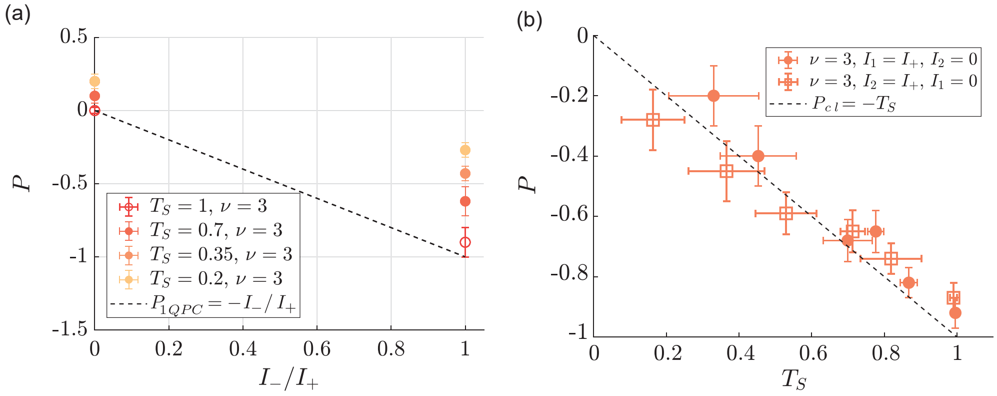

Fig. 5 Electron collisions, $\nu = 3$ as a function of the imbalance ratio I_-/I_+. (A) Measurement of $P(I_-/I_+)$. At $I_-/I_+ = 0$, $P \approx 0$ as a result of fermionic antibunching. For $I_-/I_+ = 1$, negative cross-correlations are restored and $|P(I_-/I_+)|$ decreases when one decreases the emission probability T_S. The *black dashed line* corresponds to $P_{1QPC}(I_-/I_+) = -I_-/I_+$, which is the expectation in a single QPC experiment (which is the limit obtained when $T_S = 1$). (B) $P(I_- = I_+)$ as a function of the source emission probability T_S. Data points follow the predictions from the classical model $P_{cl}(I_- = I_+) = -T_S$ (*black dashed line*), with $P(I_- = I_+ = 1)$ eventually going to zero for $T_S \ll 1$.

decreases, with vanishing values ($|P(I_- = I_+)| \ll 1$) in the Poissonian limit $T_S \ll 1$. Fig. 5B represents the evolution of $P(I_- = I_+)$ with T_S. The results agree very nicely with the prediction $P_{cl}(I_- = I_+) = -T_S$ from the classical model (*black dashed line* on Fig. 5B).

The anyon collider: Elements of theory

The case of anyon collisions cannot be described by the classical model presented in Section "The collider with random sources," as specific mechanisms occur for particles with nontrivial braiding properties: $e^{i2\varphi} \neq 1$. A full quantum model of anyon collisions was first developed in Rosenow et al. (2016), using nonequilibrium bosonization techniques (Levkivskyi and Sukhorukov, 2009; Gutman et al., 2010), for the calculation of the tunneling current I_T at cQPC and of its fluctuations $S_{I_T I_T}$. Identical results for I_T and $S_{I_T I_T}$ were obtained recently using nonequilibrium Keldysh theory (Morel et al., 2022; Lee and Sim, 2022; Mora, 2022). These works also pointed the specific role of nontrivial anyon braiding in the computation of the tunneling current and of its fluctuations. We present and discuss here the results obtained in these various publications.

We first introduce the operators $\Psi_i^\dagger(x)$, which create an anyon at position x of the chiral edge channels $i = 1$ or $i = 2$. At equilibrium ($V_1 = V_2 = 0$) and at zero temperature, the edge channels 1 and 2 are characterized by the temporal correlator $\langle \Psi_i^\dagger(x,t)\Psi_i(x,0)\rangle_{eq} = \frac{1}{(0^+ + it)^\delta}$, where $\delta/2$ is called the scaling dimension of the anyon creation operator $\Psi_i^\dagger$ and governs the power law of the temporal decay of the equilibrium correlation function. For a Laughlin state $\nu = 1/m$ with a simple edge structure, $\delta = 1/m$ is directly related to the topological order in the bulk. However, it may deviate from $1/m$ when edge reconstruction mechanisms leading to counterpropagating modes are present (Rosenow and Halperin, 2002).

In order to describe anyon transfers between edge channels 1 and 2 at cQPC, one introduces the anyon tunneling operator, H_T, at the location of cQPC assumed to be $x = 0$:

$$H_T = \mathcal{T} + \mathcal{T}^\dagger = \xi \Psi_2^\dagger(x=0)\Psi_1(x=0) + \xi^* \Psi_1^\dagger(x=0)\Psi_2(x=0), \tag{6}$$

where ξ is the tunneling amplitude. The calculation of the current cross-correlations at the output of the collider in the weak-backscattering limit for anyon tunneling at cQPC is then based on a perturbative calculation of the tunneling current and of its fluctuations at first order in the tunneling coupling $|\xi|^2$, when the conductor is driven out of equilibrium by the random Poissonian emission of anyons at inputs 1 and 2 of cQPC. As a result, the dominant contribution to the nonequilibrium correlations of the tunneling Hamiltonian, as well as the tunneling rates $W_{1\to 2}$ and $W_{2\to 1}$ describing anyon transfers between edge channel 1 and 2 are given by (Rosenow et al., 2016; Morel et al., 2022; Lee and Sim, 2022):

$$\langle \mathcal{T}^\dagger(0)\mathcal{T}(t)\rangle_{neq} = e^{-(1-e^{-2i\varphi})\frac{I_1}{q}t} e^{-(1-e^{2i\varphi})\frac{I_2}{q}t} \langle \mathcal{T}^\dagger(0)\mathcal{T}(t)\rangle_{eq} + \text{subleading terms}, \tag{7}$$

$$W_{1\to 2} = \int_{-\infty}^{+\infty} dt \langle \mathcal{T}^\dagger(0)\mathcal{T}(t)\rangle_{neq} = \alpha\, \Re\left[e^{i\pi\delta}\left(I_1(1 - e^{-2i\varphi}) + I_2(1 - e^{2i\varphi})\right)^{2\delta - 1}\right] \tag{8}$$

$$W_{2\to 1} = \int_{-\infty}^{+\infty} dt \langle \mathcal{T}(t)\mathcal{T}^\dagger(0)\rangle_{neq} = \alpha\, \Re\left[e^{i\pi\delta}\left(I_1(1 - e^{2i\varphi}) + I_2(1 - e^{-2i\varphi})\right)^{2\delta - 1}\right], \tag{9}$$

where α is a constant that will not play a role in the following. I_T and $S_{I_T I_T}$ can then be readily expressed as a function of the tunneling rates (Lee et al., 2022):

$$I_T = e^*(W_{1\to 2} - W_{2\to 1}) = -e^*\alpha\sin(\pi\delta)\Im\left[I_1(1-e^{-2i\varphi}) + I_2(1-e^{2i\varphi})\right]^{2\delta-1} \tag{10}$$

$$S_{I_T I_T} = 2e^{*^2}(W_{1\to 2} + W_{2\to 1}) = 2e^{*^2}\alpha\cos(\pi\delta)\Re\left[I_1(1-e^{-2i\varphi}) + I_2(1-e^{2i\varphi})\right]^{2\delta-1} \tag{11}$$

Eqs. (7), (8), and (9) show that, in the anyon case, the tunnel processes at cQPC explicitly depend on the braiding phase 2φ. Note that, although the phase 2φ is related to the braiding phase of bulk anyons by the bulk-edge correspondence, anyons at the edge are not protected by the gap that exists in the bulk. It means that 2φ may differ from the braiding phase of anyons in the bulk if, for example, the Coulomb interaction between several edge channels leads to charge fractionalization mechanisms (Safi and Schulz, 1995; Berg et al., 2009; Kamata et al., 2014; Inoue et al., 2014; Freulon et al., 2015). The resulting fractionalized charges may have different mutual fractional statistics (Lee et al., 2020), resulting in a modified value of the exchange phase φ at the output of the interedge interaction region (Levkivskyi, 2016; Idrisov et al., 2022). Note also that, in the case of bosonic or fermionic statistics discussed in the previous sections, the braiding phase is trivial, $2\varphi = 2n\pi$, such that $\langle \mathcal{T}^\dagger(0)\mathcal{T}(t)\rangle_{neq} = \langle \mathcal{T}^\dagger(0)\mathcal{T}(t)\rangle_{eq}$. One thus needs to compute the correlations of the tunneling Hamiltonian at the next leading order to capture its out of equilibrium contribution. It corresponds precisely to the classical model presented in Section "The collider with random sources," showing that the mechanisms involved in anyon collisions are fundamentally different from the ones involved in the bosonic and fermionic cases.

Let us discuss first these mechanisms in the completely unbalanced configuration, $I_- = I_+$, where source 2 has been switched off ($I_2 = 0$). In this case the natural forward tunneling process is $W_{1\to 2}$. It is represented in Fig. 6B: the random emission of anyons at input 1 of cQPC leads to the transmission of anyons from input 1 to input 2 at cQPC. However, in the anyon case, there is also a contribution of the reverse tunneling process, $W_{2\to 1}$, represented on Fig. 6A, where the random emission of anyons at input 1 of cQPC triggers the tunneling of another anyon from edge channel 2 to edge channel 1. $W_{2\to 1}$ is a bunching process which is specific to anyons, where two anyons bunch together in output 3 leaving an anti-anyon (or a hole) in output 4. $W_{2\to 1}$ involves the interferences between processes where the anyons emitted by source 1 are transmitted toward output 3 before the emission of the anyon/anti-anyon pair at cQPC (see Fig. 6A), and processes where anyons emitted by source 1 are transmitted toward output 3 after the creation of the anyon/anti-anyon pair (see Fig. 6C). As discussed in Morel et al. (2022) and Lee and Sim (2022), this interference term can be viewed, see Fig. 6D, as time-domain interferences involving the braiding of anyons emitted by source 1 by anyons tunneling at cQPC. This explains why $W_{2\to 1}$ and $W_{1\to 2}$ explicitly depend on the braiding phase 2φ and why the reverse process $W_{2\to 1}$ vanishes in the bosonic and fermionic cases.

In the balanced configuration $I_- = 0$, interference processes involving anyons emitted both by QPC1 and QPC2 need to be taken into account. Fig. 7A represents the interference term contributing to the tunneling rate $W_{2\to 1}$ when both sources are switched on: the braiding processes occur in opposite directions for the two sources. This explains why the braiding phases 2φ are weighted by different signs in Eqs. (7), (8), and (9). It means that the contribution of the two sources do not add up and that there is an interference contribution which directly depends on the imbalance ratio I_-/I_+.

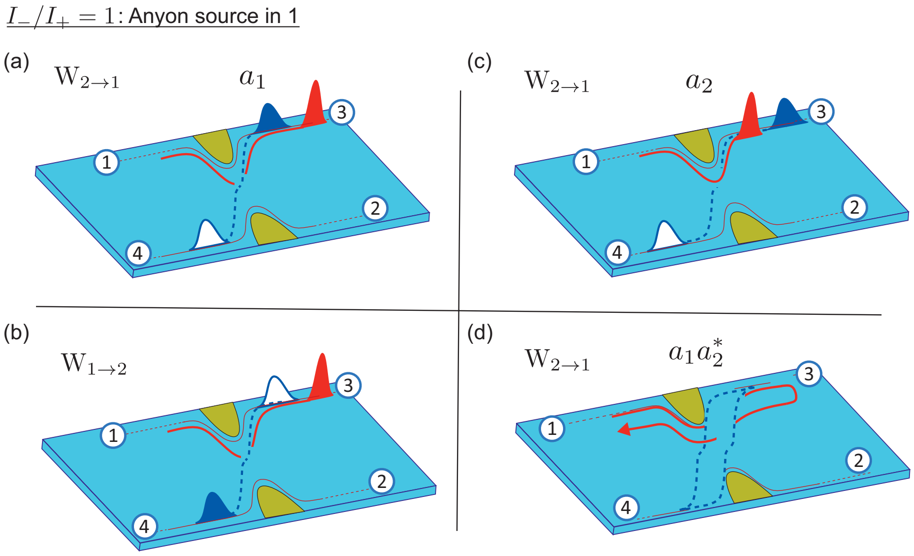

Fig. 6 (A) Reverse tunneling process $W_{2\to 1}$ at cQPC triggered by the emission of an anyon (represented in *red*) by source 1. In the reverse tunneling process, an anyon is created in edge channel 3 (represented in *blue*), leaving an anti-anyon (represented in *white*) in edge channel 4. In this process occurring with amplitude a_1, the anyon emitted by source 1 is transmitted in 3 before the creation of the anyon/anti-anyon pair. (B) Forward tunneling process $W_{1\to 2}$ at cQPC triggered by the emission of an anyon by source 1. In the forward tunneling process, an anyon is created in edge channel 4 (represented in *blue*), leaving an anti-anyon (represented in *white*) in edge channel 3. (C) Sketch of the reverse tunneling process occurring with amplitude a_2 where the transmission of the anyon emitted by source 1 toward output 3 and the creation of the anyon/anti-anyon pair are temporally exchanged compared to process a_1 (the *red* anyon is transmitted in 3 after the creation of the anyon/anti-anyon pair). (D) sketch of the interference term $a_1 a_2^*$ between process a_1 and process a_2. The process can be seen as a braiding in time-domain of the anyon emitted by source 1 by the anyon generated at cQPC.

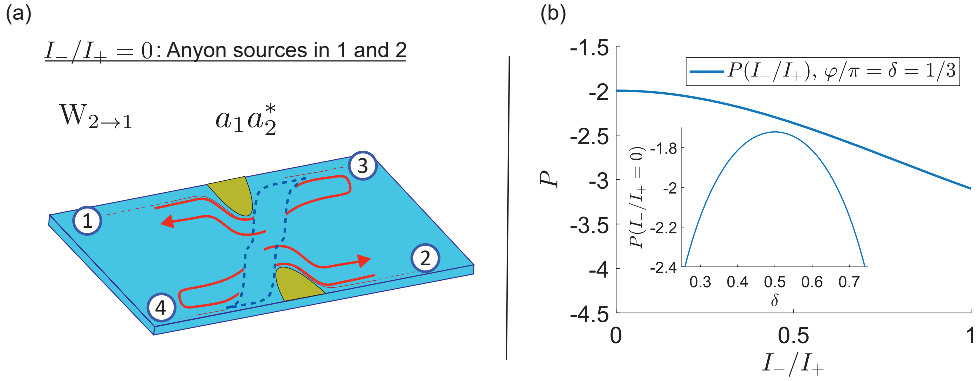

Fig. 7 (A) Sketch of the interference term $a_1a_2^*$ contributing to the reverse tunneling $W_{2\rightarrow1}$ in the case where both source 1 and source 2 emit anyons toward cQPC (balanced collider case, $I_- = 0$). As represented on the sketch the braiding of anyons emitted by source 1 and source 2 occurs in opposite directions. (B) Predictions from Rosenow et al. (2016) for $P(I_-/I_+)$ in the case $\varphi/\pi = \delta = 1/3$. As illustrated by the sketch of panel (A), as braiding for source 1 and source 2 anyons occurs in opposite directions, braiding effects are less important in the balanced case $I_- = 0$ compared to the unbalanced case $I_- = I_+$ and $|P(I_-/I_+)|$ decreases when I_-/I_+ increases. The inset shows the dependence of $P(I_- = 0)$ when varying δ, keeping $\varphi/\pi = 1/3$ constant. The variations of P are small (less than 10%) in the range $1/3 \leq \delta \leq 2/3$ showing that P is rather insensitive to the value of δ in a wide range.

The current correlations at the output of the collider S_{34} can then be expressed as a function of the fluctuations of the tunneling current: $S_{34} = -S_{I_TI_T} + 2e^*(I_+\partial_{I_-} + I_-\partial_{I_+})I_T$. As already discussed in Section "Random collisions of electrons," the second term entering the expression of S_{34} represents the transmission of the Poissonian noise generated by sources 1 and 2 from the inputs of cQPC toward outputs 3 and 4. In the balanced configuration, $I_- = 0$, it equals the classical random partition noise $2e^*TI_+$, where T is defined as $\partial_{I_-}I_T|_{I_T=0}$. The Fano factor P is then defined by the usual ratio: $P(I_-/I_+) = \frac{S_{34}}{2e^*TI_+}$. In the balanced configuration, a simple analytical expression for $P(I_- = 0)$ can be obtained (Rosenow et al., 2016):

$$P(I_- = 0) = 1 - \frac{\tan\varphi}{\tan\pi\delta}\frac{1}{1-2\delta} \tag{12}$$

Eq. (12) has two major differences with Eq. (3) in the classical case. First, it explicitly depends on the braiding phase φ of anyons. This stems from the role of time–domain interferences involving anyon braiding in the expression of the anyon tunneling rates. In particular, for a Laughlin state with $\varphi/\pi = \delta = 1/3$, one has $P(I_- = 0) = -2$, as experimentally observed in Bartolomei et al. (2020), see Section "The anyon collider: Experimental results." The cross-correlations are strongly negative, showing that anyons tend to form larger packets of charges at the outputs of the beam splitter, as described by the tunneling processes $W_{1\rightarrow2}$ and $W_{2\rightarrow1}$. As discussed above, braiding effects occur in opposite direction and compensate each other when two sources are switched on (balanced case). One thus expects $P(I_-/I_+)$ to be even more negative when increasing the imbalance ratio I_-/I_+. Fig. 7B shows the predictions for $P(I_-/I_+)$ as a function of I_-/I_+ in the Laughlin case $\varphi/\pi = \delta = 1/3$. Indeed $P(I_-/I_+)$ decreases when increasing I_-/I_+, reaching $P(I_- = I_+) \approx -3.1$ in the completely unbalanced case. One might also wonder how $P(I_-/I_+)$ is predicted to vary when one changes the value of δ. This is particularly relevant as nonlinear $I - V$ characteristics in quantum point contacts fail to reproduce the expected power laws, which exponent is related to δ (Wen, 1991; Fendley et al., 1995). As plotted on the inset of Fig. 7B, P is predicted to have a very weak dependence on δ in a rather broad range of values, with less than ± 10% variations in the range $0.3 \leq \delta \leq 0.7$. This shows that predictions for P are rather robust to the specific value of δ, which may deviate from $\delta = 1/3$ due to nonuniversal mechanisms.

There is a second important difference of Eq. (12) with the classical case. In the anyon case, $P(I_-/I_+)$ does not depend on the emission probabilities of source 1 and source 2. Indeed, in the classical case, boson bunching or fermion antibunching can only be present if both source 1 and source 2 emit particles, leading to a proportionality of the current cross-correlation to the product T_S^2, such that P_{cl} is proportional to T_S (as one factor T_S is absorbed by the normalization by the total input current I_+). In the anyon case, the mechanism governing anyon bunching is completely different. The emission of an anyon by source 1 may trigger the transfer of another anyon from channel 2 (leaving a hole behind) to channel 1, leading to the bunching of two anyons in the same output. This process is present even when a single anyon source is switched on, leading to cross-correlations S_{34} proportional to T_S and a Fano factor independent of T_S. This provides a way to clearly identify anyon collisions and distinguish them from the classical bosonic and fermionic cases.

Before turning to the presentation of the experimental results, it is worth discussing another possible definition of a Fano factor that was introduced in Lee et al. (2022) and already discussed in the electron case in Section "Random collisions of electrons." It is defined from the ratio of the fluctuations of the tunneling current $S_{I_TI_T}$ to the Poissonian limit for the noise:

$$F = \frac{S_{I_TI_T}}{2e^*I_T} = \frac{W_{1\rightarrow2} + W_{2\rightarrow1}}{W_{1\rightarrow2} - W_{2\rightarrow1}} \tag{13}$$

This second definition is more adapted to the study of the completely unbalanced case, $I_- = I_+$. In particular, it cannot be used in the balanced configuration as the tunneling current vanishes in this case, leading to diverging values of $F(I_- = 0)$. In the unbalanced case $(I_2 = 0)$, it illustrates the specific role of the bunching mechanisms, $W_{2\to1}$. When these bunching mechanisms are absent, $W_{2\to1} = 0$, one has immediately $F = 1$ which corresponds to classical Poissonian fluctuations of the tunneling current that are predicted by the classical model of collisions in the unbalanced configuration, see Eq. (5). In the case where the bunching mechanisms are present, $W_{2\to1} \neq 0$, one has immediately $F > 1$, showing super-Poissonian fluctuations of the tunneling current that are the counterpart of the strong negative values of $P(I_- = I_+)$. Similarly to $P(I_- = 0)$, a simple analytical expression for $F(I_- = I_+)$ can be obtained as a function of φ and δ: $F(I_- = I_+) = \cot(\pi\delta)\ \cot[(\pi - 2\varphi)(1/2 - \delta)]$. In particular, in the case of the Laughlin state $\varphi/\pi = \delta = 1/3$, one has $F(I_- = I_+) = 3.274$, as experimentally verified in Lee et al. (2022).

The anyon collider: Experimental results

We now discuss experimental results of Bartolomei et al. (2020) and Ruelle et al. (2022) for anyon collisions at the filling factor $\nu = 1/3$. We first present the results obtained in the balanced configuration ($I_- = 0$). QPC1 and QPC2 are tuned at equal transmissions T_S in the weak backscattering limit, $T_S \ll 1$, which is the regime for anyon emission. Fig. 8A represents the evolution of the normalized current cross-correlations $S_{34}/(2e^*T(1 - T))$ (with $e^* = e/3$) as a function of the total input anyon current I_+, for different values of the emission probability $T_S = 0.05$, $T_S = 0.15$ and $T_S = 0.25$. As can be seen on the figure, the normalized cross-correlations are strongly negative, and have a linear evolution with I_+.

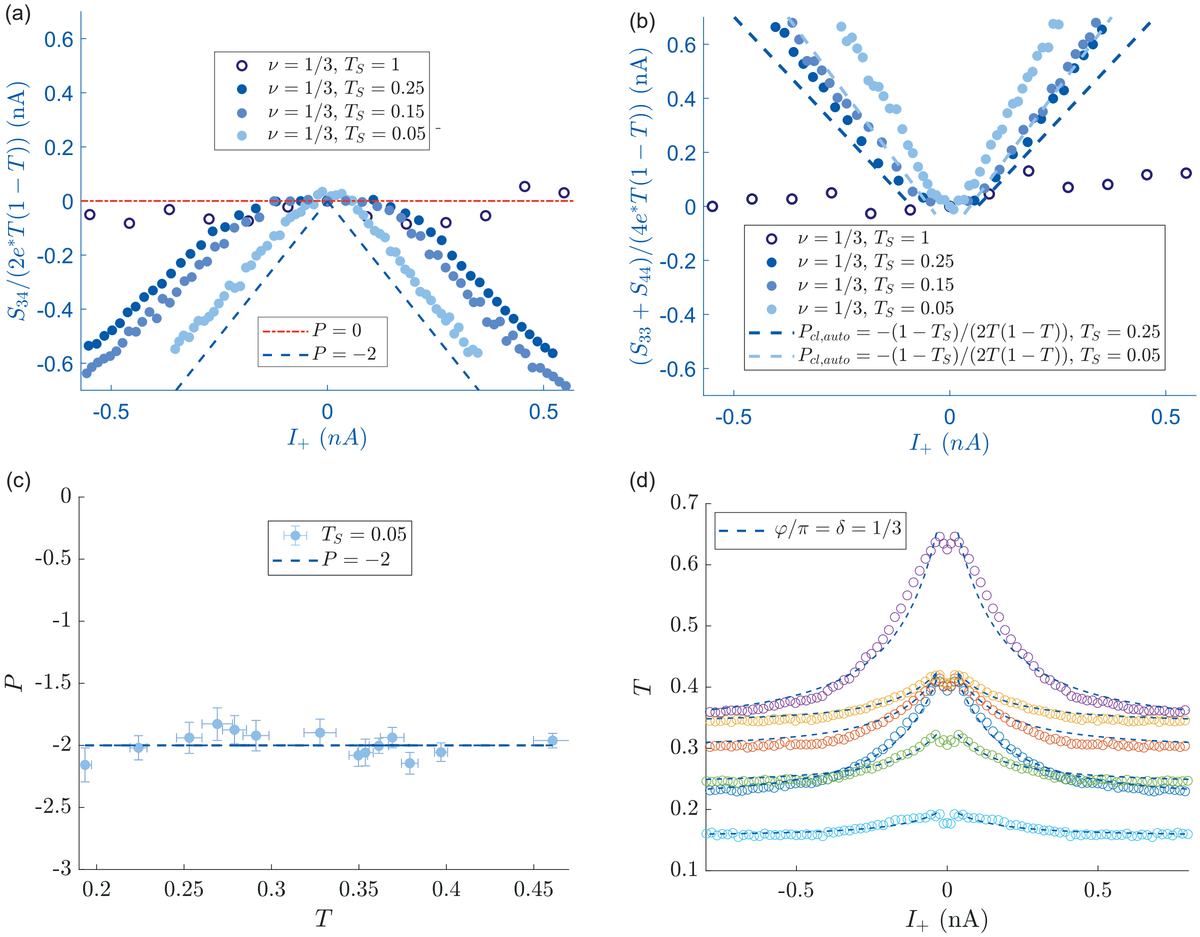

Fig. 8 Anyon collisions $\nu = 1/3$ and balanced configuration. (A) Normalized cross-correlations, $S_{34}/(2e^*T(1 - T))$, as a function of the total emitted anyon current I_+. Four different values of the emission probability are plotted: $T_S = 1$, $T_S = 0.25$, $T_S = 0.15$, and $T_S = 0.05$. The normalized cross-correlations are suppressed for $T_S = 1$ but strongly negative in the three other cases, with a slope close to $P = -2$ (*blue dashed line*). (B) Normalized current auto-correlations, $(S_{33} + S_{44})/(4e^* T(1 - T))$, as a function of the total emitted anyon current I_+ for the same values of T_S plotted in panel (A). The *blue* and *cyan dashed lines* represent the predictions of the classical model for $T_S = 0.25$ and $T_S = 0.05$. (C) Measurements of the slope P for $T_S = 0.05$ as a function of cQPC's backscattering probability T. All the measured values are close to the prediction $P = -2$. (D) Measurements of $\mathcal{T} = \partial_{I_-} I_T|_{I_-=0}$ as a function of the total input current I_+. The *blue dashed lines* represent the predictions of Eq. (15) with $\varphi/\pi = \delta = 1/3$.

The measured slope P is very close from the prediction $P = -2$ for anyons with an exchange phase $\varphi/\pi = \delta = 1/3$ (*blue dashed line* on Fig. 8A) . The measured slopes slightly decreases in absolute value when T_S increases, varying from $P = -1.9$ for $T_S = 0.05$ to $P = -1.6$ at $T_S = 0.25$. In the opposite limit, $T_S \approx 1$ (*empty blue circles* on Fig. 8A), one observes a completely different behavior: the cross-correlations are completely suppressed in this case, $S_{34} = 0$, which corresponds to the fermionic behavior. $T_S \approx 1$ is reached for a complete pinch off of QPC1 and QPC2, which is the regime of strong backscattering corresponding to electron emission instead of anyon emission. One thus does not expect to observe manifestations of anyon statistics in this case, but rather fermionic antibunching ($S_{34} = 0$). This result can also be understood from a gauge invariance argument. By closing completely QPC1 and QPC2 ($T_S = 1$), one effectively implements a single QPC experiment which cannot provide information on the anyon statistics. The balanced configuration corresponds to applying equal voltages $V_1 = V_2$ at the two inputs of cQPC. These voltages can be removed by a gauge transformation shifting all the potentials by the value $V_1 = V_2$, thereby removing the sources from the QPC inputs. Note that this gauge argument does not hold anymore as soon as T_S deviates from $T_S = 1$, as removing the voltage V_i from one input of QPCi would result in applying the voltage $-V_i$ to its other input.

Fig. 8B presents the measurement of the normalized auto-correlations $(S_{33} + S_{44})/(4e^*T(1 - T))$. The data for $T_S = 1$ shows zero noise: as there is no random emission of anyons for $T_S = 1$, the input currents I_1 and I_2 are noiseless. For the smaller values of $T_S = 0.25$, $T_S = 0.15$ and $T_S = 0.05$, one observes an increasing noise when T_S decreases, corresponding to more and more dilute beams of anyons. This qualitative behavior is similar to the electron case at filling factor $\nu = 3$. However, contrary to the electron case, the value of the auto-correlation is larger but comparable with the value of the cross-correlations. One can also see that, contrary to the electron case, the noise data is systematically above the predictions from the classical model for the auto-correlations (*blue* and *cyan dashed lines* on Fig. 8B). Predictions for the auto-correlations of the current fluctuations can be deduced from current conservation relations at cQPC: $I_1 + I_2 = I_3 + I_4$. This implies the following relation for the fluctuations: $S_{33} + S_{44} + 2S_{34} = S_{11} + S_{22}$, where $S_{11} + S_{22}$ is the noise generated by QPC1 and QPC2 at the inputs of cQPC: $S_{11} + S_{22} = 2e^*(1 - T_S)I_+$. The normalized auto-correlations are thus predicted to be given by:

$$\frac{S_{33} + S_{44}}{4e^* T(1 - T)} = -\frac{S_{34}}{2e^* T(1 - T)} + \frac{(1 - T_S)I_+}{2T(1 - T)} = -PI_+ + \frac{(1 - T_S)I_+}{2T(1 - T)} \tag{14}$$

In the Poissonian limit $T_S \ll 1$, the prediction from the anyon model is $P(I_- = 0) = -2$ compared to $P_{cl}(I_- = 0) = 0$ in the fermion case. It leads to the following prediction for the ratio of the slopes $P_{auto}/P_{cl,\ auto} = 1 + 2|P(I_- = 0)|T(1 - T) > 1$. The larger noise compared to the classical model is thus another manifestation of the anyon tunneling mechanisms $W_{1\to 2}$ and $W_{2\to 1}$ that lead both to strongly negative cross-correlations, and to an increase of the auto-correlation noise compared to the classical predictions. At the quantitative level, for $T \approx 0.3$ (used in the experiment), one expects an increase of 80% of the noise compared to a measured increase of 50%. However, it is not surprising that the determination of P from the auto-correlation noise is not as accurate as its determination from cross-correlation measurements as it is obscured by the larger contribution of the input noise generated by QPC1 and QPC2 in the balanced configuration (second term of Eq. 14).

Fig. 8C presents the robustness of the measurements of P extracted from the normalized cross-correlations when varying the transmission T of cQPC. The measurements are performed in the range $0.18 \leq T \leq 0.47$, for which anyon tunneling (with fractional charge $e^* = e/3$) occurs at cQPC. As can be seen in the figure, all the measured data agree nicely with the prediction $P = -2$ with a small scatter of $\pm$ 0.15 around the expected value in the full range of transmissions T.

The agreement of the measured value of P with the prediction for $\varphi/\pi = \delta = 1/3$ shows that the measured values of φ and δ agree with the values in the bulk. However, it is known that experiments investigating anyon tunneling in single QPC devices fail to observe the expected nonlinearities of the I–V characteristics, that are predicted to be related to the scaling dimension δ (Wen, 1991; Fendley et al., 1995). In the weak backscattering regime, the backscattering probability is expected to decrease down to zero with a characteristic power law dependence, $T \propto V^{2\delta-2}$, where V is the bias voltage across the QPC. In contrast with the expected behavior, experiments show a saturation of T at large voltage to a constant value, or offset, that is different from 0. Subtracting this offset, several experiments have observed a quantitative agreement with predictions for the dependence of T with the applied voltage. For example, in the $\nu = 5/2$ case, by fitting the experimental data (after removal of the offset) with the $T(V)$ dependence predicted by the model, several works (Radu et al., 2008; Lin et al., 2012; Baer et al., 2014; Fu et al., 2016) have been able to extract the anyon fractional charge e^* and the tunneling exponent δ, and to use these values to discriminate between different possible topological orders of the $\nu = 5/2$ state.

Eq. (10) shows that the quantum models of anyon collisions (Rosenow et al., 2016; Lee and Sim, 2022) also predict power laws for the evolution of the tunneling current. They differ from the nonlinear behavior predicted in single QPC experiments (in particular in collision experiments, T evolves nonlinearly with the input anyon current I_+, instead of the voltage V in single QPC experiments). However, they share common features, with T predicted to decrease down to zero at large current I_+ with a power law of the same exponent $2\delta - 2$. Interestingly, the exact dependence of T with I_+ is richer than the power law, as it depends on all the collision parameters e^*, φ, and δ (Ruelle et al., 2022):

$$T = \beta f(\delta, \xi_+) \tag{15}$$

$$f(\delta, \xi_+) = \frac{\Gamma(\delta + \xi_+)}{\Gamma(1 - \delta + \xi_+)} [\Psi(1 - \delta + \xi_+) - \Psi(\delta + \xi_+)] \tag{16}$$

$$\xi_+ = \frac{\hbar I_+}{2\pi e^* k_B T_{\rm el}} [1 - \cos(2\varphi)] \tag{17}$$

where Γ and Ψ are the gamma and digamma functions (with $\Psi(x) = \Gamma'(x)/\Gamma(x)$), and β is a constant which does not depend on I_+.

Fig. 8D shows the measurements of $T(I_+)$ in the balanced configuration of the collider. As shown in the figure, the data shows the expected decrease of T with I_+. However, as observed in single QPC experiments, T saturates at large currents at an offset value. Following the analysis performed in single QPC experiments (Roddaro et al., 2003, 2004; Radu et al., 2008; Lin et al., 2012; Baer et al., 2014; Fu et al., 2016), the experimental data can be compared with Eq. (15) subtracting an offset value T_0. The offset is extracted from a fit of the experimental data by a power law, $T(I_+) = T_0 + \alpha I_+^{\gamma}$, where T_0 , γ and α are the three fit parameters. Eq. (15) is also only valid for currents larger than the thermal limit ($I_+/e^* \geq k_B T_{\text{el}}/h$); therefore it cannot capture the thermal rounding observed on the experimental curves for $|I_+| \leq 35$ pA. In order to take into account these thermal effects, an offset of 35 pA is added to the values of I_+ in Eq. (15) (the same offset on I_+ is used on all the traces). Finally, the values of all the other parameters in Eq. (15) are fixed, with $\varphi/\pi = \delta = 1/3$, $T_{\text{el}} = 30$ mK, and $\beta = T(I_+ = 0)/f(\delta, \xi_+ = 0)$. The *blue dashed lines* on the figure represent the result of this analysis. As can be seen in Fig. 8D, the agreement with the data is excellent. Importantly, the data reproduces nicely the expected dependence on ξ_+ without adjusting parameter, taking into account braiding effects via the factor $(1 - \cos 2\varphi)$ in Eq. (17).

We finally discuss the results of anyon collisions in the unbalanced case ($I_- \neq 0$) at filling factor $\nu = 1/3$. As can be seen in Fig. 9, one observes a clear increase of P in absolute value when one increases the imbalance I_-/I_+. This is in agreement with the discussion developed in the previous section. As braiding effects occur with opposite signs for the two sources, they decrease when moving from the unbalanced case ($I_- = I_+$) to the balanced one ($I_- = 0$). As a result, and contrary to a naive expectation, the effects of braiding are quantitatively more important when a single anyon source is plugged at the input of the collider. Data points at the lowest transmission ($T_S = 0.05$) agree very well with the predictions for $P(I_-/I_+)$ of Rosenow et al. (2016) taking $\varphi/\pi = \delta = 1/3$ (*blue line*).

The results are completely different in the strong backscattering regime, $T_S \approx 1$ (*empty blue circles*), where anyon emission is suppressed. As discussed before, $P = 0$ in the balanced case, $I_- = 0$. For $T_S = 1$ in the unbalanced case, $I_- \neq 0$, as already discussed in Section "Random collisions of electrons" in the electron case, this configuration is identical to a single QPC experiment. The noise then equals the random partition noise generated by the current difference between the inputs I_- and one has $P_{1QPC}(I_-/I_+) = -I_-/I_+$ independently of the statistics of the particles, fermions or anyons. Indeed for $T_S \approx 1$, the results are identical for anyons at $\nu = 1/3$ (*open blue circle*) and for fermions at $\nu = 3$ (*open red circles*) with $P(I_- = I_+) \approx -1$. This confirms that single QPC experiments only probe the charge of the particles and not their statistics.

Finally, one can notice that $|P(I_-/I_+)|$ decreases when one increases the emission probability T_S. This contrasts with the electron case that shows the opposite behavior. This spectacularly illustrates the difference between fermions, with trivial braiding phase $e^{i2\varphi} = 1$, and which are very well described by the classical model of collisions, and the anyon case, with $e^{i2\varphi} \neq 1$, for which braiding mechanisms lead to a value of P that is predicted not to depend on T_S (in the limit where $T_S \ll 1$). This opposite dependence in the emission probability T_S is a signature of braiding mechanisms in anyon collisions compared to the electron case. As shown in Fig. 9, the measured values of P do depend on T_S in the anyon case ($|P|$ decreases when T_S increases). This evolution, which is not captured by the model, is expected as one deviates from the Poissonian emission regime, and one expects to reach $P = -1$ for $T_S = 1$. However, no theoretical prediction is available at this time to capture the evolution of P with T_S.

Discussion of the results

The results of anyon collisions at the filling factor $\nu = 1/3$ presented in this article have been reproduced recently in three different experiments (Lee et al., 2022; Glidic et al., 2022; Ruelle et al., 2022). Glidic et al. (2022) and Ruelle et al. (2022) carried a similar analysis as the one presented here, by measuring the cross-correlations of the current fluctuations at the output of the collider and by studying the evolution of P with the imbalance I_-/I_+ between the collider inputs. Their results at $\nu = 1/3$ reproduce those presented

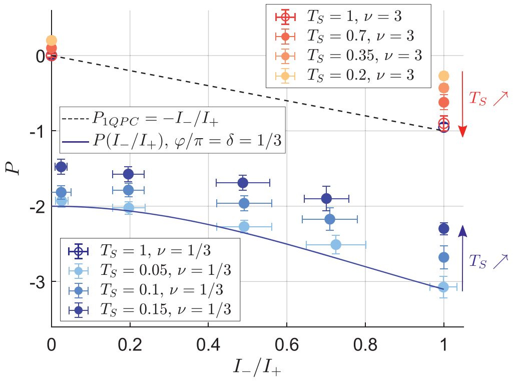

Fig. 9 Measurements of $P(I_-/I_+)$ for filling factors $\nu = 1/3$ (*blue points*) and $\nu = 3$ (*orange points*). The *blue line* represents predictions form Rosenow et al. (2016) with $\varphi/\pi = \delta = 1/3$. The *black dashed line* is the prediction for the single QPC experiment, $P_{1QPC}(I_-/I_+) = -I_-/I_+$. In the unbalanced case the anyon ($\nu = 1/3$) and fermion ($\nu = 3$) cases show opposite behaviors. $|P(I_- = I_+|$ increases when T_S decreases in the anyon case whereas $|P(I_- = I_+|$ decreases when T_S decreases in the fermion case.

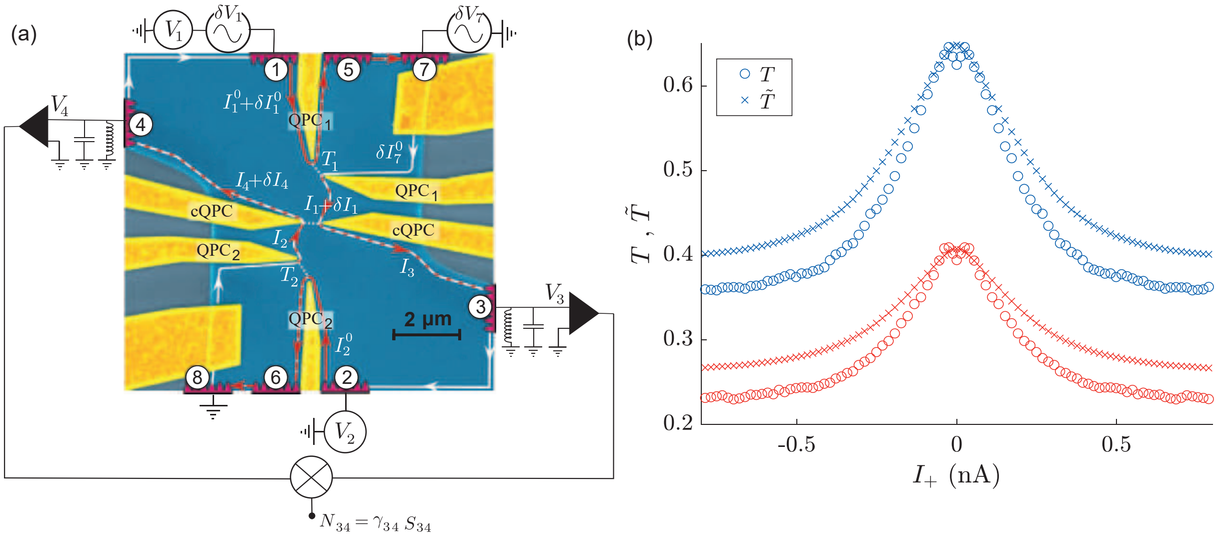

Fig. 10 (A) Sketch of the anyon collider device for the measurement of T and $\tilde{T}$ in the balanced configuration. For the measurement of T on applies a small a.c. bias δV_1 to contact 1 and one measures $T = \delta I_4/(T_1\delta I_1^0)$. For the measurement of $\tilde{T}$, the small a.c. bias is applied to contact 7 and one measures $\tilde{T} = \delta I_4/((1-T_1)\delta I_7^0)$. (B) Measurements of $T(I_+)$ and $\tilde{T}(I_+)$ for two different settings of cQPC.

here. Lee et al. (2022) focused on the completely unbalanced case, $I_- = I_+$, by switching off source 2 ($I_2 = 0$), and carried a different analysis by measuring the auto-correlations of the current fluctuations at output 4 of the collider, S_{44}, as a function of the tunneling current across cQPC I_T. Comparing the data with the predictions of the quantum model for the Fano factor F, Eq. (13), Lee et al. (2022) show a very nice agreement with $F = +3.27$, which is the prediction from the quantum model of anyon collisions for $\varphi/\pi = \delta = 1/3$ (whereas the classical model predicts $F_{cl} = 1$, see Eq. (5). All these experiments thus confirm the observation of fractional statistics at $\nu = 1/3$.

However, an open question remains regarding the measured dependence of the backscattering probability of cQPC T with the total anyon current I_+. First, as discussed in Section "The anyon collider: Experimental results," the measured evolution of $T(I_+)$ does not reproduce the predictions for its nonlinear behavior, even though a good agreement can be obtained when taking into account a possible offset of the transmission. More importantly, as originally discussed in Lee and Sim (2022), the measured value of T should show a dependence on the experimental configuration used for the measurement. T is defined as $\partial_{I_-} I_T|_{I_-=0}$. It is measured in the balanced configuration by generating a small a.c. current δI_1 at input 1 of cQPC and by measuring the resulting tunneling current δI_T in output 4, $T = \delta I_T/\delta I_1$. In configuration 1 (see Fig. 10A), which leads to the predictions of Eq. (15), the current δI_1 is an anyon current generated by a small a.c. voltage δV_1 applied to contact 1, $\delta I_1 = T_1 \delta I_1^0$, with $\delta I_1^0 = G_0/3\delta V_1$. In the second configuration (see Fig. 10A), a small a.c. current δI_7^0 is injected from contact 7, with $\delta I_1 = (1-T_1)\delta I_7^0$. δI_1 thus mostly consist of a direct propagation of charge from contact 7 to cQPC and not of anyons tunneling at QPC1. The backscattering transmission $\tilde{T}$ measured in this second configuration is given by $\tilde{T} = \delta I_T/((1-T_1)\delta I_7^0)$. As predicted in Lee and Sim (2022), this should lead to a ratio $T/\tilde{T} = \sin(2\varphi)/(2\pi e^*/e) < 1$. A difference between T and $\tilde{T}$ is indeed observed (Ruelle et al., 2022), see Fig. 10B, with $T < \tilde{T}$. However, the measured ratio of 0.85 is much larger than the prediction of $\sin(2\pi/3)/(2\pi/3) \approx 0.41$ for $\varphi = \pi/3$. This might be related to the observed saturation of both T and $\tilde{T}$ at large current I_+ that suppress the nonlinear dependence of T on I_+. As discussed in Glidic et al. (2022) and Ruelle et al. (2022), as P is defined from the normalization of the cross-correlations by T, a remarkable quantitative agreement with predictions of the quantum model is obtained using one definition of T, but would not be obtained using $\tilde{T}$. It is thus important to also test the agreement between data and theory using quantities that do not rely on the definition of T. This is precisely the advantage of using the definition of the Fano factor F as the ratio of the noise of the tunneling current on the tunneling current flowing through cQPC in the collision experiment (with the inconvenient that F can only be used in the unbalanced configuration as $I_T = 0$ in the balanced case). Measurement performed in Lee et al. (2022) for $I_- = I_+$ agree also perfectly with the predictions from the quantum model of anyon collisions, $F \approx 3.27$ showing that this agreement is robust to different analysis and to different quantities used for the normalization of the noise.

Conclusion

We have presented and compared collision experiments for different particles with different statistics: bosons and fermions, that can be described by a classical collision model, and anyons, for which specific mechanisms related to anyon braiding need to be taken into account by a quantum model. Boson and fermion collisions are governed by two-particle bunching (in the bosonic case) and antibunching (in the fermionic case). They lead respectively to negative current cross-correlations due to the formation of charge packets in a given output of the collider, or on the contrary to a suppression of the current cross-correlations when the two particles always exit in different outputs. Importantly, two-particle boson and fermion interferences are only present when one particle is emitted at each input of the collider, and are thus proportional to the emission probability squared: T_S^2. In the anyon case, specific anyon tunneling mechanisms occur at the beam splitter, which are governed by the anyon braiding factor $e^{i2\varphi}$. As a result, when one anyon is emitted at a given input of the beam-splitter, backward anyon tunneling may occur, where another anyon bunches together with the one generated by the anyon source in a given output of the beam splitter, leaving a hole in the other output. As in the bosonic case, this bunching mechanism leads to negative current cross-correlations. However, contrary to the bosonic case, it is present even when a single anyon is emitted at a given input of the beam splitter (and no anyon is emitted at the other input). As a result, the cross-correlations are proportional to T_S contrary to T_S^2 in the bosonic case (and in the fermionic one), providing a clear way to distinguish anyons from bosons (and fermions).

Regarding the quantitative analysis of anyon collisions, the explicit dependence of the anyon tunneling rates with the anyon braiding phase provides a way to directly measure the anyon fractional exchange phase φ. Different analysis can be performed by defining a Fano factor from the normalization of the noise, either by the incoming anyon current multiplied by the anyon backscattering probability at the beam splitter, TI_+, or by the tunneling current at the beam splitter I_T. Both analyses provide an excellent agreement with the predictions using $\varphi = \pi/3$, which is the expected exchange phase for anyons at the filling factor $\nu = 1/3$. However, the robustness of the measured values of P with respect to the defintion of the transmission T remains to be understood.

Anyon colliders can also be used to probe other varieties of anyons with different statistics obtained by varying the filling factor ν. In particular, experiments carried at the filling factor $\nu = 2/5$ (Ruelle et al., 2022; Glidic et al., 2022) on anyons with a fractional charge $e^* = e/5$ have demonstrated the ability of the anyon collider to distinguish between anyons of different statistics. Indeed, both experiments measure a smaller Fano factor $P(I_- = 0) \approx -0.6 \pm 0.1$ in Ruelle et al. (2022) (for the lowest value of T_S) and $P(I_- = 0) \approx -0.97 \pm 0.15$ in Glidic et al. (2022). Note that a large part of the difference between the two measured values of P may be understood from different normalizations. The normalization presented in this manuscript is used in Ruelle et al. (2022), $P = S_{34}/(2e^*T(1 - T)I_+)$, whereas P is defined as $S_{34}/(2e^*T(1 - T)(1 - T_S)I_+)$ in Glidic et al. (2022). The additional factor $1 - T_S$ may lead to nonnegligible differences (with an increase of P compared to the other definition) when T_S is not much smaller than one. Interestingly, both these values are close to the prediction for P for an exchange phase $\varphi = \pi/5$ which does not correspond to the simplest descriptions of anyons at filling factor $\nu = 2/5$ (but rather to the $\nu = 1/5$ case). Contrary to $\nu = 1/3$, where the edge structure is simple, $\nu = 2/5$ is also an example of a fractional quantum Hall state with a complex edge structure, with two copropagating edge channels. In this situation, one might expect that interchannel Coulomb interaction plays a role (Idrisov et al., 2022), for example, through the formation of charge and neutral eigenmodes. It will be important to characterize such interaction effects for fractional quantum Hall states with complex edge structure. It will be particularly relevant when investigating non-abelian anyons at the filling factor $\nu = 5/2$, where several copropagating channels are present. In this context, it is important to point that recent theory works have predicted the possibility to characterize non-abelian phases using the anyon collider, and to distinguish between different non-abelian topological orders (Lee and Sim, 2022).

Anyon collisions can also be extended to the time or frequency domains. In the first case, one can implement the anyon version of the Hong-Ou-Mandel experiment (Hong et al., 1987; Bocquillon et al., 2013) presented in Section "Fermion and boson collisions." In the anyon case (Rech et al., 2017; Jonckheere et al., 2022), one triggers the emission of pulses carrying a fractional charge and measures the variations of the current cross-correlations between the currents at the output of the beam splitter as a function of the time delay between the two sources. In the frequency domain, one generates a stationary flow of anyons, but measures the current cross-correlations at high frequency (instead of low frequency in the present experiment). It has already been shown that anyon properties could be directly measured from characteristic time or frequency scales, such as their fractional charge via the measurement of the Josephson frequency $f_J = e^*V/h$ (Ferraro et al., 2014; Roussel et al., 2016; Kapfer et al., 2019; Bisognin et al., 2019). Implementing similar experimental methods in the anyon collider geometry would provide direct measurements of anyon fractional statistics (Safi, 2020; Jonckheere et al., 2022), with a simplified analysis that would not rely on the simultaneous measurement of the backscattering transmission T or the tunneling current I_T at the central beam splitter, but rather directly from a characteristic time or frequency scale.

References

Arovas D, Schrieffer JR, and Wilczek F (1984) Fractional statistics and the quantum Hall effect. *Physical Review Letters* 53: 722.

Baer S, Rössler C, Ihn T, Ensslin K, Reichl C, and Wegscheider W (2014) Experimental probe of topological orders and edge excitations in the second Landau level. *Physical Review B* 90: 075403.

Banerjee M, Heiblum M, Umansky V, Feldman DE, Oreg Y, and Stern A (2018) Observation of half-integer thermal Hall conductance. *Nature* 559: 205.

Bartolomei H, Kumar M, Bisognin R, Marguerite A, Berroir J-M, Bocquillon E, Plaçais B, Cavanna A, Dong Q, Gennser U, Jin Y, and Fève G (2020) Fractional statistics in anyon collisions. *Science* 368: 173.

Berg E, Oreg Y, Kim EA, and Von Oppen F (2009) Fractional charges on an integer quantum hall edge. *Physical Review Letters* 102(23): 236402.

Bisognin R, Bartolomei H, Kumar M, Safi I, Berroir J-M, Bocquillon E, Plaçais B, Cavanna A, Gennser U, Jin Y, and Fève G (2019) Microwave photons emitted by fractionally charged quasiparticles. *Nature Communications* 10: 1708.

Bocquillon E, Freulon V, Berroir J-M, Degiovanni P, Plaçais B, Cavanna A, Jin Y, and Fève G (2013) Coherence and indistinguishability of single electrons emitted by independent sources. *Science* 339: 1054.

Campagnano G, Zilberberg O, Gornyi IV, Feldman DE, Potter AC, and Gefen Y (2012) Hanbury Brown-Twiss interference of anyons. *Physical Review Letters* 109: 106802.

Campagnano G, Zilberberg O, Gornyi IV, and Gefen Y (2013) Hanbury Brown and Twiss correlations in quantum Hall systems. *Physical Review B* 88: 235415.

Chamon CC, Freed DE, and Wen XG (1995) Tunneling and quantum noise in one-dimensional Luttinger liquids. *Physical Review B* 51: 2363.

Chamon CC, Freed DE, Kivelson SA, Sondhi SL, and Wen XG (1997) Two point-contact interferometer for quantum Hall systems. *Physical Review B* 55: 2331.

de-Picciotto R, Reznikov M, Heiblum M, Umansky V, Bunin G, and Mahalu D (1997) Direct observation of a fractional charge. *Nature* 389: 162.

Dubois J, Jullien T, Portier F, Roche P, Cavanna A, Jin Y, Wegscheider W, Roulleau P, and Glattli DC (2013) Minimal-excitation states for electron quantum optics using levitons. *Nature* 502: 659.

Fendley P, Ludwig AWW, and Saleur H (1995) Exact nonequilibrium transport through point contacts in quantum wires and fractional quantum Hall devices. *Physical Review B* 52: 8934.

Ferraro D, Roussel B, Cabart C, Thibierge E, Fève G, Grenier C, and Degiovanni P (2014) Real-time decoherence of Landau and Levitov quasiparticles in quantum Hall edge channels. *Physical Review Letters* 113: 166403.

Freulon F, Marguerite A, Berroir J-M, Plaçais B, Cavanna A, Jin Y, and Fève G (2015) Hong-Ou-Mandel experiment for temporal investigation of single-electron fractionalization. *Nature Communications* 6: 6854.

Fu H, Wang P, Shan P, Xiong L, Pfeiffer LN, West K, Kastner MA, and Lin X (2016) Competing $\nu = 5/2$ fractional quantum hall states in confined geometry. *Proceedings of the National Academy of Sciences* 113: 12386.

Glidic P, Maillet O, Aassime A, Piquard C, Cavanna A, Gennser U, Jin Y, Anthore A, and Pierre F (2023) Cross-correlation investigation of anyon statistics in the $\nu = 1/3$ and 2/5 fractional quantum Hall states. *Physical Review X* 13: 011030.

Gutman DB, Gefen Y, and Mirlin AD (2010) Bosonization of one-dimensional fermions out of equilibrium. *Physical Review B* 81: 085436.

Halperin BI (1984) Statistics of quasiparticles and the hierarchy of fractional quantized Hall states. *Physical Review Letters* 52: 1583.

Hanbury Brown R and Twiss RQ (1954) LXXIV. A new type of interferometer for use in radio astronomy. *The London, Edinburgh, and Dublin Philosophical Magazine and Journal of Science* 45: 663.

Hanbury Brown R and Twiss RQ (1956) Test of a new type of stellar interferometer on Sirius. *Nature* 178: 1046.

Hong CK, Ou ZY, and Mandel L (1987) Measurement of subpicosecond time intervals between two photons by interference. *Physical Review Letters* 59: 2044.

Idrisov EG, Levkivskyi IP, Sukhorukov EV, and Schmidt TL (2022) Current cross correlations in a quantum Hall collider at filling factor two. *Physical Review B* 106: 085405.

Inoue H, Grivnin A, Ofek N, Neder I, Heiblum M, Umansky V, and Mahalu D (2014) Charge fractionalization in the integer quantum Hall effect. *Physical Review Letters* 112: 166801.

Jonckheere T, Rech J, Grémaud B, and Martin T (2022) Anyonic statistics revealed by the Hong-Ou-Mandel dip for fractional excitations. *arXiv.* arXiv:2207.07172.

Kamata H, Kumada N, Hashisaka M, Muraki K, and Fujisawa T (2014) Fractionalized wave packets from an artificial Tomonaga-Luttinger liquid. *Nature Nanotechnology* 9: 177.

Kane CL and Fisher MPA (1994) Nonequilibrium noise and fractional charge in the quantum Hall effect. *Physical Review Letters* 72(724): 1994.

Kapfer M, Roulleau P, Santin M, Farrer I, Ritchie DA, and Glattli DC (2019) A Josephson relation for fractionally charged anyons. *Science* 363: 846–849.

Kim EA, Lawler M, Vishveshwara S, and Fradkin E (2005) Signatures of fractional statistics in noise experiments in quantum Hall fluids. *Physical Review Letters* 95: 176402.

Kitaev AY (2003) Fault-tolerant quantum computation by anyons. *Annals of Physics* 303: 2.

Laughlin RB (1983) Anomalous quantum Hall effect: An incompressible quantum fluid with fractionally charged excitations. *Physical Review Letters* 50: 1395.

Lee JYM and Sim HS (2022) Non-abelian anyon collider. *Nature Communications* 13: 6660.

Lee JYM, Han C, and Sim HS (2020) Fractional mutual statistics on integer quantum Hall edges. *Physical Review Letters* 125: 196802.

Lee JYM, Hong C, Alkalay T, Schiller N, Umansky V, Heiblum M, Oreg Y, and Sim HS (2022) Partitioning of diluted anyons reveals their braiding statistics. *arXiv.* arXiv:2209.15461.

Leinaas J and Myrheim J (1977) On the theory of identical particles. *Il Nuovo Cimento B (1971–1996)* 37: 1.

Levkivskyi IP (2016) Universal nonequilibrium states at the fractional quantum hall edge. *Physical Review B* 93: 165427.

Levkivskyi IP and Sukhorukov EV (2009) Noise-induced phase transition in the electronic Mach-Zehnder interferometer. *Physical Review Letters* 103: 085405.

Lin X, Dillard C, Kastner MA, Pfeiffer LN, and West KW (2012) Measurements of quasiparticle tunneling in the $\nu = 5/2$ fractional quantum Hall state. *Physical Review B* 85: 165321.

Liu RC, Odom B, Yamamoto Y, and Tarucha S (1998) Quantum interference in electron collision. *Nature* 391: 263.

Martin T (2005) Course 5 noise in mesoscopic physics. *Les Houches* 81: 283–359.

Mora C (2022) Anyonic exchange in a beam splitter. *arXiv.* arXiv:2212.05123.

Morel T, Lee JYM, Sim HS, and Mora C (2022) Fractionalization and anyonic statistics in the integer quantum Hall collider. *Physical Review B* 105: 075433.

Nakamura J, Liang S, Gardner GC, and Manfra MJ (2020) Direct observation of anyonic braiding statistics. *Nature Physics* 16: 931.

Nayak C, Simon SH, Stern A, Freedman M, and Das Sarma S (2008) Non-abelian anyons and topological quantum computation. *Reviews of Modern Physics* 80: 1083.

Ol'Khovskaya S, Splettstoesser J, Moskalets M, and Büttiker M (2008) Shot noise of a mesoscopic two-particle collider. *Physical Review Letters* 101: 166802.

Radu IP, Miller JB, Marcus CM, Kastner MA, Pfeiffer LN, and West KW (2008) Quasi-particle properties from tunneling in the $v = 5/2$ fractional quantum Hall state. *Science* 320: 899.

Rech J, Ferraro D, Jonckheere T, Vannucci L, Sassetti M, and Martin T (2017) Minimal excitations in the fractional quantum Hall regime. *Physical Review Letters* 118: 076801.

Roddaro S, Pellegrini V, Beltram F, Biasiol G, Sorba L, Raimondi R, and Vignale G (2003) Nonlinear quasiparticle tunneling between fractional quantum Hall edges. *Physical Review Letters* 90: 046805.

Roddaro S, Pellegrini V, Beltram F, Biasiol G, and Sorba L (2004) Interedge strong-to-weak scattering evolution at a constriction in the fractional quantum Hall regime. *Physical Review Letters* 93: 046801.

Rosenow B and Halperin BI (2002) Nonuniversal behavior of scattering between fractional quantum Hall edges. *Physical Review Letters* 88: 096404.

Rosenow B, Levkivskyi IP, and Halperin BI (2016) Current correlations from a mesoscopic anyon collider. *Physical Review Letters* 116: 156802.

Roussel B, Degiovanni P, and Safi I (2016) Perturbative fluctuation dissipation relation for nonequilibrium finite-frequency noise in quantum circuits. *Physical Review B* 93: 045102.

Ruelle M, Frigerio E, Berroir J-M, Plaçais B, Rech J, Cavanna A, Gennser U, Jin Y, and Fève G (2023) Comparing fractional quantum Hall Laughlin and Jain topological orders with the anyon collider. *Physical Review X* 13: 011031.

Safi I (2020) Fluctuation-dissipation relations for strongly correlated out-of-equilibrium circuits. *Physical Review B* 102: 041113.

Safi I and Schulz HJ (1995) Transport in an inhomogeneous interacting one-dimensional system. *Physical Review B* 52: R17040.

Safi I, Devillard P, and Martin T (2001) Partition noise and statistics in the fractional quantum Hall effect. *Physical Review Letters* 86: 4628.

Saminadayar L, Glattli DC, Jin Y, and Etienne B (1997) Observation of the e/3 fractionally charged Laughlin quasiparticle. *Physical Review Letters* 79: 2526.

Tsui DC, Stormer HL, and Gossard AC (1982) Two-dimensional magnetotransport in the extreme quantum limit. *Physical Review Letters* 48: 1559.

Vishveshwara S (2003) Revisiting the Hanbury Brown-Twiss setup for fractional statistics. *Physical Review Letters* 91: 196803.

Vishveshwara S and Cooper NR (2010) Correlations and beam splitters for quantum Hall anyons. *Physical Review B* 81: 201306.

Wen XG (1991) Edge transport properties of the fractional quantum hall states and weak-impurity scattering of a one-dimensional charge-density wave. *Physical Review B* 44: 5708.

Wilczek F (1982) Magnetic flux, angular momentum, and statistics. *Physical Review Letters* 48: 1144.

Wilczek F (1982) Quantum mechanics of fractional-spin particles. *Physical Review Letters* 49: 957.

Fractional statistics, gauge invariance and anomalies in condensed matter physics

Jürg Fröhlich, Institute for Theoretical Physics, ETH Zurich, Zurich, Switzerland

© 2024 Elsevier Ltd. All rights reserved.

Reproduced from *"Gauge invariance and anomalies in condensed matter physics,"* by Jürg Fröhlich, J. Math. Phys. **64**, 031903 (2023); https://doi.org/10.1063/5.0135142, published online 31 March 2023, with the permission of AIP Publishing.

Dedicated to the memory of *Krzysztof Gawędzki* and *Christopher King*—admired colleagues and dear friends.

Introduction: Gauge theory of states of matter **418**
Effective actions and their properties 420
The chiral anomaly **421**
A first application: Conduction quantization in quantum wires 424
What is fractional or braid statistics? **425**
The 2D quantum Hall effect **429**
The electrodynamics of 2D incompressible electron gases—Anomalous chiral edge currents 430
Classification of "abelian" Hall fluids 433
Induced Chern–Simons actions, dualities, and 2D chiral photonic wave guides **437**
Chiral spin currents in planar topological insulators **438**
Anomalous current commutators and the chiral magnetic effect **440**
A possible manifestation of the chiral magnetic effect in cosmology 441
A five-dimensional cousin of the Hall effect and axion electrodynamics **442**
A generalized chiral magnetic effect 443
3D Topological insulators and "axions" **444**
Weyl semimetals 445
Conclusion **446**
Acknowledgments **447**
References **447**

Abstract

A general formalism, dubbed "Gauge Theory of States/Phases of Matter," which serves to partially classify electronic states in systems of condensed matter physics, and the theory of fractional statistics in low-dimensional systems are reviewed. Applications to the quantum Hall effect, to 2D time-reversal invariant insulators, and to certain 2D wave guides with chiral edge modes are sketched. The theory of 3D topological insulators, including Halperin's 3D quantized Hall effect and axionic insulators, is discussed too. The chiral magnetic effect is recalled and applied to Weyl semimetals.

Key points

- To begin with, the so-called gauge theory of states/phases of matter is reviewed. This theory is a very useful tool in the study of systems of condensed matter without local order parameters so that Landau theory is not applicable.
- Concepts and facts from quantum field theory and, in particular, gauge theory are recalled. Some basic facts concerning the chiral anomaly are summarized. As a first application, conductance quantization in quantum wires is reviewed.
- The general theory of fractional (braid-group) statistics in one-dimensional and planar quantum systems is outlined.
- General features of the quantum Hall effect are summarized. The presence of anomalous chiral edge currents in planar incompressible electron gases (Hall fluids) is derived from general principles. It is shown that bulk transport properties of Hall fluids can be derived from Chern–Simons theory. A general classification of "abelian" Hall fluids is presented.
- A duality between insulators and superconductors and between Hall fluids and chiral photonic wave guides is recalled and applied.
- A general description of time-reversal invariant planar topological insulators realized in certain electron gases with spin–orbit interactions is presented.
- The so-called chiral magnetic effect is derived from explicit formulae for anomalous commutators. A five-dimensional analog of the quantum Hall effect is described and used to derive the basic equations of axion electrodynamics. These equations yield a generalization of the chiral magnetic effect useful in condensed matter physics and cosmology.

https://doi.org/10.1016/B978-0-323-90800-9.00257-2

- Three-dimensional topological insulators are considered. Halperin's 3D (quantum) Hall effect is derived from axion electrodynamics. The generalized chiral magnetic effect is applied to derive a formula for the conductivity of Weyl semimetals in the presence of a magnetic field.
- Some general conclusions and remarks on what is missing in this review are offered.

Introduction: Gauge theory of states of matter

This contribution is a gently altered and expanded version (with minor corrections implemented) of a review paper Fröhlich (2023) on the same subject that has appeared in the Journal of Mathematical Physics.[1]

Fröhlich (2023) includes material that was previously reviewed in Fröhlich and Studer (1993), Fröhlich et al. (1996), and Fröhlich (2018), and references given there. In particular, Fig. 2 first appeared in print in Fröhlich (2018), and Fig. 3 first appeared in Fröhlich et al. (1996). Both figures had previously been used on slides of lectures of mine. Besides showing substantial overlap with Fröhlich (2023) and with the present review, reference Fröhlich et al. (1996) contains quite a lot of material that is complementary to the one covered in the following. It is recommended to the attention of the reader.

This article is a survey of various developments in theoretical condensed matter physics, including ones that may not be generally known and appreciated yet. Many of the methods underlying the results discussed in the following and the style of this contribution are influenced by trends in particle physics and mathematical physics. This may make its reading somewhat challenging for readers not familiar with these fields. However, I am convinced that interactions between different fields of physics have always been fruitful and are likely to trigger interesting developments that would be missed without such interactions.

Some of the work on mathematical aspects of condensed matter physics carried out by my collaborators and myself during the period from the late 1980s until the late nineties of the past century (see Fröhlich and Studer, 1993; Fröhlich et al., 1996; Fröhlich, 2018), as well as a sketch of the theory of fractional- or braid statistics (see Klaiber, 1968; Streater and Wilde, 1970; Fröhlich, 1976, 1978; Fröhlich and Marchetti, 1988; Fröhlich and Gabbiani, 1990), which is relevant for understanding various features of condensed matter physics in two dimensions, form the core of this contribution. The findings described in Fröhlich and Studer (1993), Fröhlich and Marchetti (1988), and Fröhlich and Gabbiani (1990) have led to a general formalism, dubbed *"Gauge Theory of States/Phases of Matter,"* that has turned out to be very useful in characterizing properties of electron gases in a variety of systems of condensed matter physics, among them *"topological insulators."* This formalism complements the *Landau theory* of phases and phase transitions. For ideas and results somewhat related to those in Fröhlich and Studer (1993) and Fröhlich et al. (1996) see Hasan and Kane (2010a), Qi and Zhang (2011), Hasan and Moore (2011), and Sachdev (2019), and references given there.

One of the insights at the root of the efforts in Fröhlich and Kerler (1991), Fröhlich and Zee (1991), Fröhlich and Thiran (1994), Fröhlich (1995), Alekseev et al. (1998), and Fröhlich and Pedrini (2000), reviewed in (Fröhlich and Studer, 1993), Fröhlich et al. (1996), and Fröhlich (2018), was the realization that the *chiral anomaly*, discovered by particle theorists (see Jackiw et al. (1986) and references given there) can be used to predict the existence of chiral edge currents in two-dimensional interacting electron gases exhibiting the quantum Hall effect, and that these edge currents can be described using results from the theory of current (Kac–Moody) algebras; see Fröhlich and Kerler (1991). For the integer Hall effect observed in two-dimensional systems of noninteracting electrons in an external magnetic field, the existence of chiral edge currents had earlier been predicted by B. Halperin in a celebrated paper (Halperin, 1982). (See also Fröhlich et al. (2000) for some mathematical results on edge currents in noninteracting electron gases.) Independently of our efforts, the use of the chiral anomaly for the purpose of a general analysis of chiral edge currents in two-dimensional electron gases exhibiting the quantum Hall effect, including interacting gases, was advocated by Wen (1990) and Blok and Wen (1990).

The realization that the theory of fractional (braid) statistics may be put to use in analyses of the fractional quantum Hall effect was inspired by Laughlin's famous work (Laughlin, 1983a, b). The importance of this novel form of quantum statistics in the study of various systems of two-dimensional condensed matter physics may justify the inclusion of a brief outline of the theory of braid statistics in Section "What is fractional or braid statistics?" of this contribution. Applications to the theory of the fractional quantum Hall effect are sketched in Section "The 2D quantum Hall effect."

Numerous comments placing ideas presented in the following into a wider context, as well as plenty of references can be found in subsequent sections (but see also Fröhlich, 2023; Fröhlich and Studer, 1993; Fröhlich et al., 1996; Fröhlich, 2018). The subject covered in this contribution owes its advancement and its successes to the efforts of many colleagues. Some of their work will be referred to or is quoted in papers referred to in the text that follows. I wish to offer my apologies to colleagues whose contributions may not be properly highlighted in the following, due to my lack of knowledge of their work or oversights, or because their contributions are too recent to be included in this presentation. Results concerning topologically protected states of systems of *noninteracting* electron gases started with work of Laughlin (1981) and of Thouless et al. (1982) and Kohmoto (1985) and continued with Avron et al. (1990) and Avron et al. (1994). It cannot be reviewed in what follows; but see Kane and Mele

---

[1] I wish to thank AIP publishing for granting me the right to reproduce major portions of Fröhlich (2023) in this article.

(2005), Fu and Kane (2007), Kitaev (2009), Hasan and Kane (2010b), Graf and Porta (2013), Gawedzki (2015), Schulz-Baldes (2016), and Kennedy and Zirnbauer (2016) for plenty of references to more recent, important work in this direction.[2]

The analysis presented in this review is not meant to be mathematically rigorous, although the arguments described in the text or in the papers on which it is based are quite carefully constructed and, I think, convincing. It is hoped that this contribution may help its readers understand the relevance and usefulness of the *Gauge Theory of States/Phases of Matter* and of the theory of *fractional (braid) statistics* in various studies of condensed matter physics.

Here is a brief summary of the goals and the contents of this paper.

- In this introductory section, I will describe some basic concepts and results from gauge theory, current algebra, and general relativity, with the purpose to introduce the following important ingredients of the *Gauge Theory of States/Phases of Matter*.
  1. *Effective Actions* = generating functionals of connected current Green functions ⇔ formulae for transport coefficients, in particular *conductivities*.
  2. Implications of *gauge invariance* (⇔ current conservation, Ward–Takahashi identities), *locality*, and *power counting* (i.e., arranging different terms in an action functional according to their scaling dimensions) on the form of *Effective Actions*.
  3. *Gauge anomalies* and their cancellations (anomaly inflow) ⇔ cooperation between bulk- and edge/surface degrees of freedom ⇔ "holography."

The *Gauge Theory of States of Matter* takes the place of *Landau Theory* when the latter is not applicable, for example, because there are no local order parameters available to characterize physical states of a certain system of condensed matter of interest. The *Gauge Theory of States of Matter* yields information on current Green functions, whence on transport coefficients (conductivities), which, thanks to *Kubo formulae*, can be expressed as integrals over certain current Green functions.

Remark.

(i) A system of condensed matter physics with a *local order parameter* is one whose phase diagram can be described with the help of an order-parameter field, $\varphi(x)$, where x is a point in physical space. This field is most often a scalar or pseudo-scalar field with $N = 1, 2, \ldots$ components, whose expectation value, $\langle\varphi(x)\rangle_\xi$, in a ground state or equilibrium state $\langle(\cdot)\rangle_\xi$ corresponding to a pure phase labeled by ξ *uniquely* identifies this phase, and whose correlators (Green functions) in such states enable one to study physically interesting fluctuations in the system at large distance scales and low energies. The systems studied in this paper do *not* have local order parameters (in this sense of the expression). We will attempt to describe their ground states and equilibrium states by coupling their degrees of freedom to real or fictional external gauge fields. Special attention will be paid to *"topological insulators,"* which—it will turn out—can be described by *topological* gauge field theories, such as Chern–Simons theories and generalizations thereof. Some authors, see, for example, Wen, 1990; Blok and Wen, 1990, then speak of "topological order," a somewhat fuzzy notion.

(ii) I should mention that a "change of perspective" has recently been initiated in Gaiotto et al. (2015) and reviewed in McGreevy (2022) (and references given there) based on developing the idea of "higher-differential-form symmetry," which enables one to assign conserved charges to certain extended objects. With such generalizations of the concept of symmetry it appears to become possible to characterize most known equilibrium phases of matter by using an extended version of Landau theory derived from such generalized symmetries. I am not sufficiently knowledgeable to say much about the attempts alluded to here. But I tend to think that, when compared to the formalism described in this paper, the new perspective amounts mostly to a change of language.

- In Section "The chiral anomaly," I summarize some basic facts concerning the *chiral anomaly*. I will then sketch the derivation of the chiral anomaly in 2D theories of massless fermions making use of bosonization. As an application, conductance quantization in quantum wires will be discussed.
- Section "What is fractional or braid statistics?" is devoted to a summary of results concerning *fractional (braid) statistics*. These results are connected in a natural way to the material in Section "The chiral anomaly" and are relevant for the material reviewed in Section "The 2D quantum Hall effect" (quantum Hall effect).
- In Sections "The 2D quantum Hall effect," "Induced Chern–Simons actions, dualities, and 2D chiral photonic wave guides," and "Chiral spin currents in planar topological insulators," I present various applications of the Gauge Theory of States of Matter to the characterization and classification of "topologically protected" correlated *bulk- and surface states* of *interacting systems* of condensed matter in two dimensions, in particular of 2D electron gases/liquids, which do not have local order parameters. Among such applications, I will consider the following ones[3]:
  1. Theory of the Fractional Quantum Hall Effect (Section "The 2D quantum Hall effect")
  2. Theory of chiral states of light in certain planar wave guides (Section "Induced Chern–Simons actions, dualities, and 2D chiral photonic wave guides")
  3. Time-reversal invariant planar "topological" insulators and their chiral-edge spin currents (Section "Chiral spin currents in planar topological insulators")

---

[2] For lack of expertise, I will not be able to review any very recent results on topological states of matter.

[3] A fairly extensive list of references to relevant work will be given later in the text.

- In Section "Anomalous current commutators and the chiral magnetic effect," I sketch the derivation of the *chiral magnetic effect*. Some consequences of this effect in condensed matter physics are described in later sections.
- Subsequently, in Sections "A five-dimensional cousin of the Hall effect and axion electrodynamics" and "3D Topological insulators and "axions"," I discuss higher-dimensional cousins of the Quantum Hall Effect,[4] 3D topological insulators, and so called *Weyl semimetals* exhibiting the chiral magnetic effect.[5] Applications of related ideas and methods in other areas of physics, in particular in cosmology, should also, yet cannot be discussed in this paper; but see Alekseev et al. (1998), Fröhlich and Pedrini (2000), Boyarski et al. (2012), Brandenburg et al. (2017), and Schober et al. (2018).

Effective actions and their properties

In the remainder of this introduction, I explain how, under suitable assumptions, the general form of effective gauge-field actions, that is, generating functionals of connected current Green functions, can be determined, and I elucidate their properties and uses. My discussion follows the one in Fröhlich et al. (1996). Readers who may find it a little too abstract are encouraged to proceed to Section "A first application: Conduction quantization in quantum wires" and then to Section "The 2D quantum Hall effect."

We consider a quantum-mechanical system whose matter degrees of freedom are described by fields $\bar{\psi}, \psi, \ldots$ over a space-time region, Λ, equipped with a metric, $g_{\mu\nu}$, of signature $(-1, 1, 1, 1)$. The dynamics of the system is assumed to be derivable from an action functional

$$S(\bar{\psi}, \psi, \ldots; g_{\mu\nu}, A_\mu), \tag{1}$$

where $A = (A_\mu)$ is the electromagnetic vector potential describing an external electromagnetic field (or some other gauge potential describing an external gauge field) acting on the system. We assume that there is a conserved vector current (density) J^μ, with $\partial_\mu J^\mu = 0$. If the current J^μ is charged, that is, is carried by electrically charged degrees of freedom, then these degrees of freedom interact with the electromagnetic field. In the action functional (1) of the system, the charged fields are coupled to the electromagnetic field by "minimal substitution," that is, by replacing derivatives by covariant derivatives.

The *Effective Action* of the system at zero temperature on a space-time region Λ with metric $g_{\mu\nu}$ in an external electromagnetic field with vector potential A_μ can then be constructed with the help of, for example, functional integral methods.[6] We consider the formal functional integral

$$S_{eff}(g_{\mu\nu}, A_\mu) := -i\hbar \ \ln\left(\int \mathcal{D}\bar{\psi}\mathcal{D}\psi \ exp\left[\frac{i}{\hbar}S(\bar{\psi}, \psi, \ldots; g_{\mu\nu}, A_\mu)\right]\right) + \text{(divergent) const.} \tag{2}$$

A precise definition of the right side in (2) involves imposing "boundary conditions," initial and final field configurations, on the functional integral, for example, ones corresponding to ground states of the system (and renormalizing divergences when short-distance regularizations are removed). But in this review I will not present technical details concerning the precise definition of S_{eff} and the choice of boundary conditions in (2).

Next, I review some well-known, important *properties of effective actions*.

1. The variational derivatives of S_{eff} with respect to A_μ are given by connected current Green functions:

$$\frac{\delta S_{eff}(g_{\mu\nu}, A_\mu)}{\delta A_\mu(x)} = \langle J^\mu(x)\rangle_{g,A}, \tag{3}$$

and

$$\frac{\delta^2 S_{eff}(g_{\mu\nu}, A_\mu)}{\delta A_\mu(x)\ \delta A_\nu(y)} = \langle J^\mu(x) J^\nu(y)\rangle^c_{g,A}, \quad \text{for} \quad x \neq y, \tag{4}$$

where $\langle(\cdot)\rangle_{g,\,A}$ denotes a time-ordered expectation in the presence of external fields $g_{\mu\nu}$ and A_μ. Formally this follows from Eq. (2).
2. We consider the effect of a gauge transformation, $A_\mu \mapsto A_\mu + \partial_\mu\chi$, where χ is an arbitrary smooth function on Λ, on the effective action S_{eff}. Using (3) one finds that

$$\frac{\delta S_{eff}(g_{\mu\nu}, A_\mu + \partial_\mu\chi)}{\delta\chi(x)} = \partial_\mu\langle J^\mu(x)\rangle_{g,A} = 0 \tag{5}$$

vanishes, because J^μ is conserved. Thus, S_{eff} is *invariant under gauge transformations*.
3. We may also vary S_{eff} with respect to the metric $g_{\mu\nu}$:

---

[4] See Fröhlich and Pedrini (2000), Boyarski et al. (2012), Brandenburg et al. (2017), and Schober et al. (2018); they were later applied to studies in cold-atom physics—see Price et al. (2015) and Lohse et al. (2018) and references given there.

[5] An effect discovered in a preliminary form in Vilenkin (1980) and Fukushima (2013) and studied systematically in Alekseev et al. (1998).

[6] Functional- or path integral methods were originally introduced by Dirac (1933). An operator formalism to derive expressions for effective actions has been sketched elsewhere; see, e.g., Fröhlich and Kerler (1991); Fröhlich et al (1996), and references given there.

$$\frac{\delta S_{eff}(g_{\mu\nu}, A_\mu)}{\delta g_{\mu\nu}(x)} = \langle T^{\mu\nu}(x)\rangle_{g,A},$$

where $T^{\mu\nu}$ is the energy-momentum tensor of the system. Using local energy-momentum conservation, that is, $\nabla_\mu T^{\mu\nu} = 0$, we find that $S_{eff}(g_{\mu\nu}, A_\mu)$ is invariant under space-time coordinate transformations.

A general (possibly curved) metric $g_{\mu\nu}$ can be used to describe certain defects (disclinations) in a condensed matter system. Invariance of S_{eff} under Weyl rescalings of the metric implies that $\langle T^\mu_\mu(x)\rangle_{g,A} \equiv 0 \leftrightarrow$ *scale-invariance* (criticality) of the system.

4. In our analysis of ground-state properties of insulators, it will be assumed that the external fields $g_{\mu\nu}$ and A_μ vary very slowly in space and time so that an adiabatic theorem can be invoked in the description of the time-dependence of the state of the system under consideration, and that the Hamiltonians exhibit a spectral (or mobility) gap above the ground-state energy at all times. One may then argue that the zero-temperature connected current Green functions of such a system have good decay properties in space and time.In the *scaling limit,* that is, in the limit of very large distances and very low frequencies, its effective action can then be expected to approach a functional that is a space-time integral of *local, gauge-invariant polynomials* in A_μ and derivatives of A_μ, as well as curvature quantities only depending on the metric $g_{\mu\nu}$. These terms can be organized according to their scaling dimensions (power counting—I recall that a gauge potential and a space-time derivative scale like an inverse length). Among these terms, there may be *topological* (metric-independent) action functionals that can be indicative of "topological protection" (or "topological order") of the states in question.
5. *A generalization:* It is sometimes useful to consider more general effective actions involving *non-abelian gauge fields* and to analyze the associated currents, which are only covariantly conserved. Non-abelian gauge fields may represent physical external fields; but they may also represent "virtual" or "emergent" ones merely serving to develop the response theory needed to determine transport coefficients, such as conductivities, associated with the currents corresponding to those gauge fields. As an example of the relevance of non-abelian gauge fields in the study of condensed matter physics, I recall that, in nonrelativistic quantum theory, electron spin couples to $SU(2)$-gauge fields describing Zeeman interactions,[7] spin–orbit interactions and exchange interactions described by a *Weiss exchange field* (see Albert et al., 2006). The nonrelativistic quantum theory of electron gases/liquids turns out to be perfectly $U(1)_{em} \times SU(2)_{spin}$-gauge invariant (see Anandan, 1989; Fröhlich and Studer, 1993; Fröhlich et al., 1996). This observation is not only conceptually interesting; it can be used to, for example, analyze states of *time-reversal invariant planar topological insulators* (see Fröhlich, 2018 and Section "Chiral spin currents in planar topological insulators") and chiral spin liquids (see, e.g., Fröhlich et al., 1996).

It turns out that properties 1 through 5 enable us to determine the general form of bulk effective actions, S_{eff}, of (among other systems) *insulators* in the scaling limit and hence to derive formulae for transport coefficients, in particular certain conductivities, such as the Hall conductivity.

Example. We consider an insulator with broken parity (P) and time-reversal (T) symmetries confined to a region, Ω, of a flat 2D surface (e.g., an interface between an insulator and a semiconductor) embedded in physical space. The space-time of this system is defined to be $\Lambda = \Omega \times \mathbb{R}$. The effective action of the system can then be argued to tend to

$$S_{eff}(A) = \frac{\sigma_H}{2}\int_\Lambda A \wedge dA + \frac{1}{2}\int_\Lambda d^2x\, dt\, \left[\underline{E}(x) \cdot \varepsilon \underline{E}(x) - \mu^{-1}B(x)^2\right] + \cdots,$$

as the scaling limit is approached, where σ_H is the Hall conductivity, ε is the tensor of dielectric constants, μ is the magnetic permeability, and the dots stand for further less relevant terms. In the first term on the right side, A is viewed as a differential 1-form, d denotes exterior differentiation of differential forms, and $\wedge$ is the exterior product of differential forms. We note that the first term on the right side, that is, the *Chern–Simons action,* is *not* gauge-invariant if the space-time region Λ has a nonempty boundary, $\partial\Lambda = \partial\Omega \times \mathbb{R}$. This deficiency is cured by a boundary action. The cooperation of the Chern–Simons action and the boundary action in preserving gauge invariance may be viewed as an example of *"holography"* (see Section "The 2D quantum Hall effect").

The formalism sketched here can be generalized to become applicable to equilibrium states at positive temperature. For further details concerning the material reviewed here, see Fröhlich and Studer (1993), Fröhlich et al. (1996), and Fröhlich (2018).

The chiral anomaly

An excellent general reference for this section is Jackiw et al. (1986); (the original results can be found in Adler (1969) and Bell and Jackiw (1969), see also Fujikawa (1979, 1980)). We consider a system composed of relativistic, massless charged fermions in a (flat) space-time region, Λ, of dimension $2n, n = 1, 2, \ldots$. The (operator-valued, quantum-mechanical) vector current of this system is denoted by J^μ and the axial-vector current by J^μ_5. The vector current is conserved, that is,

$$\partial_\mu J^\mu = 0 \quad \leftrightarrow \quad \text{gauge invariance of theory.}$$

But the axial-vector current tends to be *anomalous.* In two space-time dimensions, for massless fermions,

---

[7] These are caused, for example, by an external magnetic field or by the vorticity of a velocity field that generates the motion of an ionic background.

$$\partial_\mu J_5^\mu = \frac{\alpha}{\pi}E, \quad \alpha := \frac{e^2}{\hbar}, \quad [J_5^0(\vec{y},t), J^0(\vec{x},t)] \;=\; -i\,\frac{\alpha}{\pi}\delta'(\vec{x}-\vec{y}), \tag{6}$$

where α is the finestructure constant and E is the external electric field.[8]

In four dimensions, for massless fermions,

$$\partial_\mu J_5^\mu = \frac{\alpha}{4\pi^2}\varepsilon^{\nu\lambda\kappa\rho}F_{\nu\lambda}F_{\kappa\rho} = \frac{\alpha}{2\pi^2}\vec{E}\cdot\vec{B}, \tag{7}$$

and

$$\left[J_5^0(\vec{y},t), J^0(\vec{x},t)\right] = i\frac{\alpha}{4\pi^2}\left(\vec{B}(\vec{y},t)\cdot\vec{\nabla}_{\vec{y}}\right)\,\delta(\vec{x}-\vec{y}), \tag{8}$$

where $\vec{E}$ is the electric field and $\vec{B}$ is the magnetic induction.[9] For massive fermions, there are terms proportional to fermion masses contributing to $\partial_\mu J_5^\mu$. The term $\vec{E}\cdot\vec{B}$ on the right side of (7), the "instanton density," is dual to $\frac{1}{2}F\wedge F$ (where F is interpreted as a 2-form) and $F\wedge F$ is the exterior derivative of the Chern–Simons 3-form, which expresses the *helicity* of the electromagnetic field.

For later purposes we also introduce the left and right chiral currents

$$J_\ell^\mu := \frac{1}{2}\left[J^\mu + J_5^\mu\right], \quad J_r^\mu := \frac{1}{2}\left[J^\mu - J_5^\mu\right]. \tag{9}$$

The commutation relations in (6) and (8) then imply that

$$\begin{aligned} \left[J_{\ell/r}^0(\vec{y},t), J^0(\vec{x},t)\right] &= \pm i\frac{\alpha}{2\pi}\delta'(\vec{x}-\vec{y}), && \text{in } d=2,\\ \left[J_{\ell/r}^0(\vec{y},t), J^0(\vec{x},t)\right] &= \pm i\frac{\alpha}{8\pi^2}\left(\vec{B}(\vec{y},t)\cdot\vec{\nabla}_{\vec{y}}\right)\,\delta(\vec{x}-\vec{y}), && \text{in } d=4. \end{aligned} \tag{10}$$

Remark. It is sometimes of interest to study systems of matter in a noninertially moving background—for example, electrons in a rotating metallic cylinder, a Bose gas in a rotating trap, or the Earth's atmosphere or oceans. Suppose the motion of the background is generated by a (possibly time-dependent) velocity field, $\vec{V}$, on physical space. Studying the matter currents of such a system, one finds that there is an anomalous axial vector current satisfying an inhomogeneous continuity equation analogous to (7) and exhibiting anomalous commutators analogous to (8), but with $M\vec{V}$ playing the role of $e\vec{A}$, hence $M\,\vec{\omega}$ playing the role of $e\vec{B}$, where M is a mass scale and $\vec{\omega} = \vec{\nabla}\times\vec{V}$ is the vorticity of the velocity field $\vec{V}$.[10] Effects observed in systems embedded in a moving background have been described in Fröhlich and Studer (1993) and Fröhlich et al. (1996). Some of them will be mentioned in Sections "The 2D quantum Hall effect" and "Anomalous current commutators and the chiral magnetic effect."

As a service to the reader we derive the formulae in (6), (setting $\hbar = 1$). We consider a system of massless fermions on 2D Minkowski space, Λ. Let $\imath$ be the 1-form dual to the vector current density J^μ. Then

$$\partial_\mu J^\mu = 0 \quad \Leftrightarrow \quad d\,\imath = 0.$$

Poincaré's lemma then implies that

$$\imath = \frac{Q}{\sqrt{2\pi}}d\varphi, \quad \text{where } \varphi \text{ is a pseudo} - \text{scalar field}$$

and Q is a quantity with the dimension of charge. Thus

$$J^\mu = \frac{Q}{\sqrt{2\pi}}\varepsilon^{\mu\nu}\partial_\nu\varphi \tag{11}$$

In two space-time dimensions (using the metric $g_{\mu\nu}$ to raise and lower indices), the axial-vector current of a system of massless Dirac fermions is given by

$$J_5^\mu = \varepsilon^{\mu\nu}J_\nu \overset{(11)}{=} \frac{Q}{\sqrt{2\pi}}\partial^\mu\varphi, \tag{12}$$

see Schwinger (1962) and Gattringer and Seiler (1994).

It is a general fact that, in two dimensions, the Hodge dual of the one-form $\imath$ is a one-form dual to an axial-vector current (and conversely). The following considerations apply to any system in two space-time dimensions with a conserved vector current $J^\mu$and an axial-vector current J_5^μ related to J^μ by Hodge duality. It follows from (12) that

---

[8] These formulae can be traced back to Tomonaga's work on 1D electron liquids; see Tomonaga (1950) and Luttinger (1963).

[9] The author cannot guarantee that, in this section and in Sections "Anomalous current commutators and the chiral magnetic effect," "A five-dimensional cousin of the Hall effect and axion electrodynamics," and "3D Topological insulators and "axions"," signs and factors of 1/2, 1/2π, … are accurate everywhere.

[10] In classical physics, the role of $e\vec{E}$ is played by $M\dot{\vec{V}} + \frac{M}{2}\vec{\nabla}|\vec{V}|^2$.

$$\partial_\mu J_5^\mu = \frac{Q}{\sqrt{2\pi}} \Box\, \varphi. \tag{13}$$

Unitarity of the quantum theory of the field φ suggests that it satisfies a field equation of the form

$$\Box\, \varphi = U'(\varphi, \partial_\mu \varphi, E),$$

where U' is the variational derivative with respect to φ of some functional U of φ, $\partial_\mu \varphi$ and the external electric field E (with U bounded below).

In the following, I consider systems in two space-time dimensions with the property that

$$U'(\varphi, \partial_\mu \varphi, E \equiv 0) = 0.$$

The field φ then describes noninteracting massless modes. It follows that J_5^μ is conserved as long as the external electric field vanishes. An example where this remark applies is a Tomonaga–Luttinger liquid (see Tomonaga, 1950; Luttinger, 1963) in the approximation where the dispersion law of the quasi-particles is linearized at the Fermi points. To summarize these remarks, we have that

$$\partial_\mu J_5^\mu = 0 \quad \overset{(12),\,(13)}{\Leftrightarrow} \quad \Box\, \varphi = 0, \tag{14}$$

provided that $E = 0$; that is, φ is a *massless free field*, which can be described by a Lagrangian quantum field theory with an action functional given by

$$S(\varphi) = \frac{1}{4\pi} \int_\Lambda d^2x\, \sqrt{-g(x)}\; \partial_\mu \varphi(x)\; \partial^\mu \varphi(x), \quad \text{with} \;\; x \equiv (t, \underline{x}) \in \Lambda. \tag{15}$$

Assuming for simplicity that Λ is flat, the "momentum," ϖ, canonically conjugate to φ is given by

$$\boldsymbol{\varpi}(x) = \frac{\delta S(\varphi)}{\delta(\partial_0 \varphi(x))} = \frac{1}{2\pi} \frac{\partial \varphi(x)}{\partial t} \; = \; -\frac{1}{\sqrt{2}Q} J^1(x).$$

By Eq. (12),

$$J_5^0 = \sqrt{2} Q \boldsymbol{\varpi}, \quad J_5^1 = \frac{Q}{\sqrt{2}\pi} \frac{\partial \varphi}{\partial \underline{x}}.$$

The usual equal-time canonical commutation relations on Fock space,

$$[\varphi(t, \underline{x}), \boldsymbol{\varpi}(t, \underline{y})] = i\, \delta(\underline{x} - \underline{y}),$$

then imply an "anomalous current commutator"

$$[J^0(t, \underline{x}), J_5^0(t, \underline{y})] = i \frac{Q^2}{\pi} \delta'(\underline{x} - \underline{y}), \tag{16}$$

see (6), with $Q^2 = \alpha$. We define so-called chiral vertex operators, $\psi_{\ell/r}^{(q)}(x)$, by setting

$$\psi_{\ell/r}^{(q)}(x) =: \exp i \frac{q}{\sqrt{2}} \left[\pm \varphi(x) + 2\pi \int_{\underline{x}}^\infty \boldsymbol{\varpi}(x^0, \underline{y}) d\underline{y} \right] :, \tag{17}$$

where the double colons indicate Wick ordering with respect to the free pseudo-scalar field with a *positive* mass (changing the mass used in the definition of Wick ordering just changes the fields $\psi_{\ell/r}^{(q)}(x)$ by a constant factor). When applied to a state in the Hilbert space of the system, the fields $\psi_{\ell/r}^{(q)}$ change the electric charge of the state by an amount $Q \cdot q$. The quantum statistics of the fields $\psi_{\ell/r}^{(q)}$ is determined by the phase factor $e^{\pm i \pi q^2}$ appearing in the Weyl relations of the vertex operator on the right side of (17). Thus, if $q = 1$ then $\psi_{\ell/r}^{(q)}$ is a *Fermi field*.

I hasten to add that the fields creating or annihilating *electrons* in an interacting Tomonaga–Luttinger liquid (Tomonaga, 1950; Luttinger, 1963) are in general not the ones given in (17); rather, they are composed of left-chiral and right-chiral vertex operators in a way determined by the strength of two-body interactions in the electron liquid (and by the requirements that they satisfy Fermi–Dirac statistics and create or annihilate an electric charge given by the elementary electric charge e).

To take into account the presence of an external electric field, E, the action functional $S(\varphi)$ in (15) must be replaced by

$$\begin{aligned} S(\varphi; A) :&= \frac{1}{4\pi} \int_\Lambda \partial_\mu \varphi \partial^\mu \varphi d^2x + \int\limits_\Lambda J^\mu A_\mu d^2x \\ &= \frac{1}{4\pi} \int_\Lambda \left\{ \partial_\mu \varphi \partial^\mu \varphi + 2\sqrt{2} Q \varepsilon^{\mu\nu} \partial_\nu \varphi A_\mu \right\} d^2x \\ &= \frac{1}{4\pi} \int_\Lambda \left\{ \partial_\mu \varphi \partial^\mu \varphi + 2\sqrt{2} Q \varphi E \right\} d^2x, \end{aligned} \tag{18}$$

where $E(x) = \varepsilon^{\mu\nu}(\partial_\mu A_\nu)(x)$. This formula can be derived from the theory of massless free Dirac fermions coupled to a vector potential A by convergent perturbation theory in the term $\int_\Lambda J^\mu A_\mu d^2x$ (see, e.g., Schwinger, 1962; Gattringer and Seiler, 1994). From expression (18) one easily derives the field equation for φ, which reads $\square\, \varphi(x) = \sqrt{2}Q\ E(x)$. Hence

$$\partial_\mu J_5^\mu = \frac{Q^2}{\pi} E(x), \tag{19}$$

which is the chiral anomaly in two space-time dimensions (interpreting Q^2 as the finestructure constant α).

Remarks on the chiral anomaly in four space-time dimensions will follow in Section "Anomalous current commutators and the chiral magnetic effect."

A first application: Conduction quantization in quantum wires

The material presented in this section is taken from Alekseev et al. (1997, 1998). We consider a physical system consisting of a very long wire that contains a 1D interacting electron gas described by a Tomonaga–Luttinger liquid (setting $Q = -e$ in (11)) connected to electron reservoirs on the left end and the right end of the wire. We assume that there are no back-scattering processes converting left-moving quasi-particles (charge-density fluctuations) into right-moving ones, or conversely. Very close to the Fermi points of the electron gas, the electron dispersion law can be linearized, and quasi-particles can be described as massless relativistic chiral field modes. This system has a conserved vector current, $J^\mu = \frac{e}{\sqrt{2}\pi}\varepsilon^{\mu\nu}\partial_\nu\varphi$, and, in the "relativistic" approximation and for a vanishing external electric field, a conserved axial-vector current, J_5^μ, as discussed above. In the presence of a nonvanishing external electric field, E, with vector potential A_μ the currents

$$\hat{J}^{\,\mu}_{\ell/r} := J^\mu_{\ell/r} \mp \frac{Q}{2\pi}\varepsilon^{\mu\nu}A_\nu$$

are conserved, $(\partial_\mu \hat{J}^\mu_{\ell/r} = 0)$, but *not* gauge-invariant. However, the chiral charges

$$N_{\ell/r} := \int \hat{J}^{\,0}_{\ell/r}(t,\underline{x})d\underline{x} \tag{20}$$

are *not only conserved*, but also *gauge-invariant*. It is important to observe (see Alekseev et al., 1998) that, if expressed in terms of the pseudo-scalar field φ introduced in (11) and (12), these charges are *independent* of the parameters describing the interactions in the Tomonaga–Luttinger liquid (Tomonaga, 1950; Luttinger, 1963).

Let H denote the Hamiltonian of the electron gas. The equilibrium state of this system at inverse temperature β is given by the density matrix

$$P_{\mu_\ell,\mu_r} := \Xi^{-1}_{\beta,\mu_\ell,\mu_r}\exp(-\beta H_{\mu_\ell,\mu_r}), \tag{21}$$

where $\Xi_{\beta,\mu_\ell,\mu_r}$ is the grand-canonical partition function, μ_ℓ and μ_r denote the chemical potentials of the electron reservoirs on the right end of the wire (injecting left-moving electrons into the wire) and on the left end of the wire, respectively, and

$$H_{\mu_\ell,\mu_r} := H - \mu_\ell N_\ell - \mu_r N_r.$$

Expectations with respect to P_{μ_ℓ,μ_r} are denoted by $\langle(\cdot)\rangle_{\mu_\ell,\mu_r}$. The electric current, I, flowing through the wire in the state $\langle(\cdot)\rangle_{\mu_\ell,\mu_r}$ is given by

$$I := \langle J^1(x)\rangle_{\mu_\ell,\mu_r} = -\frac{e}{\sqrt{2}\pi}\left\langle \frac{\partial\varphi(x)}{\partial t}\right\rangle_{\mu_\ell,\mu_r} = -i\frac{e}{\sqrt{2}\pi}\langle[H,\varphi(x)]\rangle_{\mu_\ell,\mu_r}, \tag{22}$$

where the last equation expresses the *Heisenberg equation of motion*. Formally, one has that

$$\langle[H,\varphi(x)]\rangle_{\mu_\ell,\mu_r} = \langle H\ \varphi(x) - \varphi(x)\ H\rangle_{\mu_\ell,\mu_r}. \tag{23}$$

Since the charges N_ℓ and N_r are conserved, one is tempted to conclude that the right side of this equation vanishes and, hence, that $I = 0$. This conclusion turns out to be *wrong* because the expression on the right of (23) is meaningless due to nontrivial zero modes of the field φ that can be present because φ is massless. In order to arrive at expressions that are meaningful, we replace the massless field φ used in the bosonization of the electron gas in the wire by a field with a small but *positive* mass that, at the end of our calculations, we will let approach 0. As long as this regularizing mass does not vanish, the Hamiltonian H does *not* commute with the charges N_ℓ and N_r, and hence (23) need *not* vanish. To find the correct expression for the current I passing through the wire, we use that

$$\begin{aligned} I &\overset{(23)}{=} -i\frac{e}{\sqrt{2}\pi}\langle[H,\varphi(x)]\rangle_{\mu\ell,\mu r} \\ &= -i\frac{e}{\sqrt{2}\pi}\left\langle\left[H_{\mu\ell,\mu r},\varphi(x)\right] + \left[\mu_\ell N_\ell + \mu_r N_r,\varphi(x)\right]\right\rangle_{\mu\ell,\mu r} \end{aligned} \tag{24}$$

As long as the mass of φ is positive, we have that

$$\langle [H_{\mu_\ell,\mu_r}, \varphi(x)] \rangle_{\mu_\ell,\mu_r} = \langle H_{\mu_\ell,\mu_r}\ \varphi(x) - \varphi(x)\ H_{\mu_\ell,\mu_r} \rangle_{\mu_\ell,\mu_r},$$

and the right side of this identity is meaningful and *does* vanish, as follows from (21) and the cyclicity of the trace. Using Eq. (20) and the anomalous commutator (16), we find that the remaining terms on the right side of expression (24) for the current I add up to

$$\begin{aligned} I &= -\frac{ie^2}{2\pi}(\mu_\ell - \mu_r) \int \left\langle \left[\boldsymbol{\varpi}\left(t, \underline{y}\right), \varphi(t, \underline{x}) \right] \right\rangle_{\mu_\ell,\mu_r} d\underline{y} \\ &= -\frac{e^2}{2\pi}(\mu_\ell - \mu_r), \end{aligned} \tag{25}$$

as follows from the canonical commutation relations between ϖ and φ. Eq. (25) remains true when the regularizing mass of φ tends to 0.

Notice that $-(\mu_\ell - \mu_r) =: \Delta V$ is the voltage drop through the wire. Re-installing Planck's constant $\hbar$, we find that

$$I = \sigma\ \Delta V, \qquad \text{with} \quad \sigma = \frac{e^2}{2\pi\hbar}.$$

Since electrons have spin $\frac{1}{2}$, there are actually *two* species of charged particles (electrons with "spin-up" and "spin-down") per nonempty band in the wire. Thus,

$$I = 2n\frac{e^2}{h}\Delta V, \quad \text{for a wire with } n \text{ nonempty bands.}$$

This equation implies that the conductance σ in a quantum wire is quantized in even multiples of e^2/h.

For general results on transport in 1D systems exhibiting conformal symmetry, see Gawedzki and Tauber (2015), Gawedzki et al. (2018), and Moosavi (2021) and references given there.

What is fractional or braid statistics?

I have been encouraged to include in this review an outline of some basic facts about fractional or braid statistics.[11] This exotic form of quantum statistics makes its appearance in quantum (field) theories in 1 + 1 and 2 + 1 space-time dimensions. Quasi-particles with fractional statistics will appear in my discussion of the fractional quantum Hall effect in Section "The 2D quantum Hall effect."

To start with, I propose to describe the exotic commutation relations between local quantum fields and certain fields localized on space-like rays, sometimes called *disorder fields,* in models of relativistic quantum field theory (rQFT) on two-dimensional (2D) Minkowski space, $\mathbb{M}^2$. This is the realm where *quantum fields* generalizing the well-known Bose and Fermi fields and giving rise to *fractional* or *braid statistics* were first discovered, at the beginning of the seventies of the past century (Klaiber, 1968; Streater and Wilde, 1970; Fröhlich, 1976, 1978); see also Fröhlich (1988b) (and Fredenhagen et al. (1989) for results inspired by Fröhlich (1988b)).

The Lorentz metric on $\mathbb{M}^2$ is given by

$$\left(\eta_{\mu\nu}\right) = \begin{pmatrix} 1 & 0 \\ 0 & -1 \end{pmatrix}.$$

Two space-time points, $x = (x^0, x^1)$ and $y = (y^0, y^1)$, in 2D Minkowski space are *space-like separated* iff

$$(x - y)^2 := \sum_{\mu,\nu} (x^\mu - y^\mu)\, \eta_{\mu\nu} (x^\nu - y^\nu) < 0.$$

If two space-time points x and y are space-like separated then to say that "*x is to the left of y*", namely $x^1 < y^1$, has an invariant meaning, that is, this statement is left unchanged by orthochronous Lorentz transformations of $\mathbb{M}^2$ of determinant 1.

The simplest rQFT on $\mathbb{M}^2$ is the theory of a free, massless scalar or pseudo-scalar field φ, which has been described in Section "The chiral anomaly," Eqs. (15) and (17). We consider the fields $\psi_\ell^{(q)}(\cdot)$ introduced in Eq. (17). Recalling the Weyl form of Heisenberg's canonical commutation relations, one easily verifies that

$$\psi_\ell^{(q_1)}(x) \cdot \psi_\ell^{(q_2)}(y) = e^{i\ \pi(q_1 \cdot\ q_2)} \psi_\ell^{(q_2)}(y) \cdot \psi_\ell^{(q_1)}(x), \tag{26}$$

provided x is to the left of y; if x is to the right of y then the sign in the exponent of the first factor on the right side of this equation changes. Note that if $q = 1$ then $\psi_{\ell/r}^{(q=1)}(\cdot)$ is a Fermi field (Klaiber, 1968; Streater and Wilde, 1970; Fröhlich, 1976, 1978). For future use we introduce the notation

---

[11] The present section is somewhat abstract and sketchy; readers may want to skip it in a first reading.

$$R_{q_1,q_2}(\pm) := e^{\pm i\ \pi(q_1 \cdot q_2)}. \tag{27}$$

The commutation relations in (26) show that, for $0 < q < \sqrt{2}$ and $q \neq 1$, the field $\psi_\ell^{(q)}$ is neither a Bose field nor a Fermi field, but something in between. More generally, there are hybrids between left-chiral ($\psi_\ell^{(q)}$) and right-chiral ($\psi_r^{(q)}$) fields that satisfy commutation relations intermediate between those of Bose and Fermi fields typical of fractional statistics. Fields with commutation relations intermediate between Bose and Fermi commutation relations (see also Eq. 30) may appear in models of certain one-dimensional quantum chains exhibiting fractionally charged quasi-particles. Examples of such systems are discussed in Goldstone and Jackiw (1975), Heeger (1977), and Su and Schrieffer (1981).

Next, we consider an interacting rQFT in 1 + 1 space-time dimensions, namely, a Lagrangian field theory of a two-component scalar field $\vec{\phi} = (\phi_1, \phi_2)$, whose action is given by

$$S(\vec{\phi}) = \int_{\mathbb{M}^2} dt\ d\underline{x} \Big\{ \partial_\mu \vec{\phi}(x) \cdot \partial^\mu \vec{\phi}(x) - U\Big(\vec{\phi}(x)\Big) \Big\}, \tag{28}$$

where U is a local self-interaction potential only depending on $\vec{\phi}$ which is invariant under the "clock transformations"

$$\begin{pmatrix} \phi_1 \\ \phi_2 \end{pmatrix} \to \begin{pmatrix} \cos\theta & \sin\theta \\ -\sin\theta & \cos\theta \end{pmatrix} \begin{pmatrix} \phi_1 \\ \phi_2 \end{pmatrix}, \qquad \text{with} \quad \theta = \{0, 2\pi/N, \ldots, 2\pi(N-1)/N\},$$

representing the group $\mathbb{Z}_N = \mathbb{Z}/N\mathbb{Z}$. Let $[N]$ be the smallest even integer strictly larger than N. It is straightforward to check (exercise) that one can choose U to be a polynomial of degree $[N]$ in ϕ_1 and ϕ_2 that is $\mathbb{Z}_N$-invariant and has deep minima along the rays

$$\big\{ \lambda \vec{e}_n \ \big|\ \lambda > 0, \vec{e}_n := (\cos(2\pi n/N), \sin(2\pi n/N)), n = 0, 1, \ldots, N-1 \big\}.$$

Under suitable assumptions on the depth of minima of U in the directions $\vec{e}_n$ this theory has N disjoint vacuum states, $\langle(\cdot)\rangle_n$, $n = 0, 1, \ldots, N-1$, with

$$\langle \vec{\phi}(0) \rangle_n = M \vec{e}_n \qquad n = 0, 1, \ldots, N-1, \ \text{for some} \ M > 0.$$

There exist unitary disorder (soliton/kink) fields, $s_k(x)$, interpolating between these vacua, which are quasi-local with respect to $\mathbb{Z}_N$-invariant Wick powers of $\vec{\phi}$ and are localized in a neighborhood of the point x, with the property that

$$\langle s_k(0, \underline{x})\ \phi(0, \underline{y})\ s_{-k}(0, \underline{x}) \rangle_n \to \begin{cases} M \cdot \vec{e}_n, & \text{as} \quad \underline{y} \to -\infty, \\ M \cdot \vec{e}_{n+k}, & \text{as} \quad \underline{x} \to +\infty. \end{cases} \tag{29}$$

Let $\varphi := \phi_1 + i\phi_2$; we introduce the fields

$$\Phi_k(x) :=: \varphi(x)^k : s_k(x), \qquad k = 1, 2, \ldots, N-1,$$

where the double colons indicate Wick ordering. We then find that if x and y are space-like separated

$$\Phi_k(x) \cdot \Phi_\ell(y) = e^{i\frac{k \cdot \ell}{2\pi N}}\ \Phi_\ell(y) \cdot \Phi_k(x), \qquad \text{for} \quad \underline{x} \ll \underline{y}, \tag{30}$$

the sign in the exponent of the first factor on the right side changing if $\underline{y} \ll \underline{x}$. Examples of such fields and their commutation relations were first considered in Fröhlich (1976); see also Fröhlich (1978). The ideas discussed in this paper (which triggered a little "industry") are closely related to ideas concerning order and disorder fields in statistical mechanics proposed in Kadanoff and Ceva (1971) and Schroer (1982).

In Fröhlich (1988b), these commutation relations were generalized as follows: We consider "quasi-local order-disorder fields," $\Phi_\alpha(x), x \in \mathbb{M}^2, \alpha = 1, \ldots, N,$ for some $N < \infty$, and suppose that they satisfy commutation relations of the type

$$\Phi_\alpha(x) \cdot \Phi_\beta(y) = R_{\alpha\beta}^{\gamma\delta}(\sigma) \Phi_\gamma(y) \cdot \Phi_\delta(x), \tag{31}$$

provided x and y are space-like separated, with $(x-y)^2 \ll 0$, and $\sigma = \text{sign}(\underline{y} - \underline{x})$. It was shown in that reference that the associativity of the product of field operators implies that the $N^2 \times N^2$-matrices $R(\sigma) = (R_{\alpha\beta}^{\gamma\delta}(\sigma))$ satisfy the *Yang-Baxter equations*, with $R(\sigma) \cdot R(-\sigma) = \mathbf{1}$. As the late *Vaughan Jones*[12] taught me in the spring of 1987, these R-matrices generate representations of the *braid groups* on an arbitrary number of strands.[13] Consider n strands in $\mathbb{R}^3$ connecting points $(0, \underline{x}_1), \ldots, (0, \underline{x}_n)$, with $\underline{x} = (x^1, x^2) \in \mathbb{R}^2$, to points $(t, \underline{x}_1), \ldots, (t, \underline{x}_n)$, for some $t > 0$. The braid group, B_n, on n strands has generators $\tau_{i,\ i+1}$ and $\tau_{i,i+1}^{-1}$, $i = 1, \ldots, n-1$, which can be defined graphically (Fig. 1):

---

[12] See Jones (1983), Jones (1986), and Jones (1987) for his seminal work.

[13] In the nonabelian case, the commutation relations between quasi-local fields described by Eq. (31) require some understanding of *quantum symmetries* acting on the state spaces of nontrivial superselection sectors; this has been studied in much detail in Fröhlich and Kerler (1993).

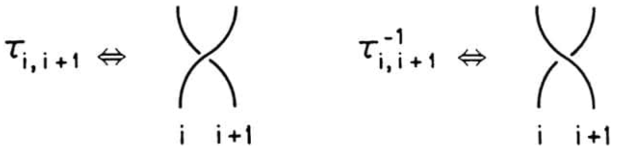

Fig. 1 Generators of the braid groups on an arbitrary number *n* of strands.

A representation of B_n on the vector space $V_1 \otimes \cdots \otimes V_n$, $\quad V_i \simeq \mathbb{C}^N, \forall\, i,$ is obtained by

$$\tau_{i,i+1} \mapsto R(+)\big|_{V_i \otimes V_{i+1}}, \qquad \tau^{-1}_{i,i+1} \mapsto R(-)\big|_{V_i \otimes V_{i+1}}, \qquad i = 1, \ldots, n-1,$$

with $R(\pm)$ as in Eq. (31).

Actually, these representations can also be derived from the monodromy of Euclidean Green functions of the fields Φ_α; (see Tsuchiya and Kanie, 1987; Fröhlich, 1988a; Kohno, 1987). The R-matrices appearing in Eqs. (26) and (30) determine *abelian* representations of the braid groups. As discussed at some length in my paper Fröhlich (1988b) (and references given there), besides plenty of examples of massive rQFT models there are certain 2D conformal field theories, such as the Wess–Zumino–Witten models (Witten, 1984), with chiral primary fields giving rise to R-matrices in commutation relations of the form of (31) that determine *non-abelian* representations of the braid groups. If one studies the conformal blocks of these fields, one finds that they exhibit nontrivial monodromy determining representations of the pure braid groups and braid groups.

We define the "n-point configuration space" M_n by

$$M_n := \big\{(z_1, \ldots, z_n) \mid z_i \in \mathbb{C}, i = 1, \ldots, n,\ z_i \neq z_j,\ \text{for } i \neq j\big\},$$

where each $z_j := x_j + iy_j$, with $(x_j, y_j) \in \mathbb{E}^2$, $\forall j = 1, \ldots, n$. The space M_n is not simply connected; its fundamental group is the pure braid group, P_n, on n strands. By $\widetilde{M}_n$ we denote the universal cover of M_n. We define $M_n^{sym} := M_n/S_n$, where S_n is the symmetric group on n objects; the fundamental group of M_n^{sym} is the braid group, B_n, on n strands. In the presence of order–disorder fields, the Euclidean Green functions of quantum field models in 1 + 1 dimensions,

$$G_n(z_1, \alpha_1, \ldots, z_n, \alpha_n), \qquad \alpha_j = 1, \ldots, N,\ \text{for}\ j = 1, \ldots, n,$$

are multivalued distributions on M_n that give rise to single-valued distributions on $\widetilde{M}_n$. In order to illustrate this fact, I consider the example of chiral primaries of the Wess–Zumino–Witten model with group $SU(M)$, $M \geq 2$, at level k. Let X_α, $\alpha = 1, \ldots, m \equiv M^2 - 1$, be a basis of the Lie algebra su(M), and let $d\pi$ be a representation of su(M) integrating to a representation π of $SU(M)$. The representation space of $d\pi$ is denoted by V. Let $V_1, \ldots, V_n$ be n copies of V. We define

$$\Omega_{ij} := \sum_{\alpha=1}^{m} \mathbf{1}|_{V_1} \otimes \cdots \otimes d\pi(X_\alpha)|_{V_i} \otimes \cdots \otimes d\pi(X_\alpha)|_{V_j} \otimes \cdots \otimes \mathbf{1}|_{V_n}, \quad 1 \leq i < j \leq n. \tag{32}$$

These matrices satisfy the so-called infinitesimal pure braid relations (see Fröhlich (1988b) and references given there). Let $G(z_1, v_1, \ldots, z_n, v_n), v_i \in V,\ \forall\, i = 1, \ldots, n$, be the conformal blocks of chiral primaries of the WZW model at level k transforming under the representation π of $SU(M)$. These are holomorphic functions on $\widetilde{M}_n$ satisfying the so-called *Knizhnik–Zamolodchikov* equations (Knizhnik and Zamolodchikov, 1984)

$$\frac{\partial}{\partial z_i} G(z_1, v_1, \ldots, z_n, v_n) = \frac{2}{k+2} \sum_{i \neq j} \frac{1}{z_i - z_j} \big(\Omega_{ij} G\big)(z_1, v_1, \ldots, z_n, v_n), \qquad i = 1, \ldots, n. \tag{33}$$

We note that the multivalued functions G are sections of a complex vector bundle with base space M_n and fiber $V^{\otimes n}$. The Knizhnik–Zamolodchikov equations (33) are nothing but the equations for parallel transport on this bundle determined by the flat connection ω given by

$$\omega = \frac{1}{k+2} \sum_{1 \leq i < j \leq n} \Omega_{ij}\ d \ln(z_i - z_j).$$

Flatness of ω is a consequence of the infinitesimal pure braid relations satisfied by the matrices Ω_{ij}, $1 \leq i < j \leq n$. The holonomies of this connection along noncontractible loops of M_n^{sym} determine a non-abelian representation of the braid group B_n, for arbitrary $n = 2, 3, \ldots$.

Of course one may also interpret M_n^{sym} as the configuration space of n identical point particles moving in the plane $\mathbb{C}$ that are required to stay away from the diagonal $D_n := \{(z_1, \ldots, z_n) \mid z_i = z_j,\ \text{for some}\ \ i \neq j\}$. Let us suppose that the particles have an internal degree of freedom with values in a vector space V that is not "observable." Quantum-mechanical wave functions of an n-particle system are then described by sections of a vector bundle with base space M_n^{sym} and fiber $V^{\otimes n}$ that is equipped with a flat connection $\omega = \sum_{1 \leq i < j \leq n} \Omega_{ij} d \ln(z_i - z_j)$, where the matrices Ω_{ij}, $1 \leq i < j \leq n$, satisfy the infinitesimal pure braid relations. The holonomies of ω along noncontractible loops in M_n determine a representation of the braid group B_n. Such wave functions come from single-valued functions on $\widetilde{M}_n$. With inspiration provided by the *Aharonov–Bohm* effect, the simplest examples of the quantum mechanics of such n-particle systems corresponding to nontrivial, but *abelian* representations of the braid groups B_n given by the matrices $R_{q_1,q_2}(\pm)$ in (26) (with $V = \mathbb{C}$) were discovered by Leinaas and Myrheim (1977). Their treatment was generalized by Goldin et al. (1980, 1981). In Wilczek (1982), Wilczek considered quantum field theories in 2 + 1 dimensions describing particles, called *"anyons,"* with fractional spin and abelian braid statistics (see also Wu, 1984a, b). These matters are reviewed in Lundholm (2023), and I don't have anything of great importance to add here. However, I propose to sketch how the braid statistics of superselection sectors, and of corresponding quasi-particles, appears in three-dimensional (3D) gauge theory. The results of Leinaas and Myrheim and of Wilczek can be viewed as special cases of such gauge theories.

I consider a 3D gauge theory with gauge group $G \overset{e.g.}{=} SU(M)$ on space-time $\mathbb{M}^3$. Let A denote the gauge potential of the theory, which is a 1-form on $\mathbb{M}^3$ with values in the Lie algebra, $\mathfrak{g}$, of the Lie group G, and let F_A denote the corresponding field strength, which is a 2-form on $\mathbb{M}^3$ with values in $\mathfrak{g}$. There may also be matter fields, $\Phi, \bar{\Phi}$, such as Higgs scalars, spinor fields, or nonrelativistic matter fields, transforming under certain finite-dimensional representations of G. The action functional, S, of the theory is given by

$$S(\Phi, \bar{\Phi}; A) := S_{matter}(\Phi, \bar{\Phi}; A) + g^{-2} \int_{\mathbb{M}^3} \mathrm{tr}\left[F_A \wedge \widetilde{F}_A\right] + CS(A), \tag{34}$$

where $\widetilde{F}_A$ is the dual field strength, and

$$CS(A) := \frac{k}{4\pi} \int_{\mathbb{M}^{(3)}} \mathrm{tr}\left[A \wedge dA + \frac{2}{3} A \wedge A \wedge A\right], \quad k \neq 0, \tag{35}$$

is the 3D Chern–Simons action. For $G = U(1)$, the constant k on the right side of (35) is an arbitrary real number, $dA = F_A$ is the electromagnetic field tensor, and the term $A \wedge A \wedge A$ vanishes. However, for $G = SU(M)$, the "level" k must be an integer; otherwise the integrand in the functional integral defining the theory would not be invariant under "large" gauge transformations. The example of a 3D abelian Higgs model ($G = U(1)$) has been treated in much detail in Fröhlich and Marchetti (1988), following the work in Wilczek (1982) and Wu (1984a, b). Among its "particles" this model describes magnetic vortices with fractional electric charge, fractional spin (given by a character, $s \in \mathbb{R}$, of the universal cover, $\widetilde{SO(2)} = \mathbb{R}$, of the group of space rotations in $\mathbb{M}^3$) and fractional statistics. The Euclidean Green functions of this model are described quite explicitly in Fröhlich and Marchetti (1988). Their monodromies determine abelian representations of the braid groups.

The results of Leinaas and Myrheim (see Leinaas and Myrheim, 1977) can be understood as arising from an abelian gauge theory with $G = U(1)$, where S_{matter} is the action of a system of an arbitrary number of conserved nonrelativistic particles coupled to a vector potential A, $g^{-2} = 0$ and k is an arbitrary real number. (The fields $\bar{\Phi}$ and Φ correspond to creation- and annihilation operators.)

An interesting special case of a 3D non-abelian gauge theory arises when we set

$$g^{-2} = 0, \quad S_{matter} = 0,$$

that is, *pure Chern–Simons theory*. This theory plays an important role in the theory of knots and links, as was recognized in Witten (1989) and Fröhlich and King (1989).

Pure Chern–Simons theory can be viewed as a Hamiltonian field theory, but with a vanishing Hamiltonian, exhibiting *static quasi-particles* that transform under finite-dimensional representations of the gauge group and satisfy non-abelian braid statistics. In a pure Chern–Simons theory with gauge group $SU(M)$ at level k, the wave functions of quasi-particles transforming under a representation π of $SU(M)$ on a finite-dimensional vector space V are given be the conformal blocks, $G(z_1, v_1, \ldots, z_n, v_n)$, $v_i \in V, \forall\, i$, of an $SU(M)$-WZW model at level k, which are solutions of the Knizhnik–Zamolodchikov equations displayed in Eq. (33). We choose coordinates $t := x^0$, $x_\perp := (x^+, x^-)$, on $\mathbb{M}^3$, with $x^+ = x^1 + ix^2$, $x^- = x^1 - ix^2$. In the Chern–Simons functional integral the conformal blocks $G(z_1, v_1, \ldots, z_n, v_n)$ appear as expectations of *networks of (open) Wilson lines* carrying the representation π of $SU(M)$ with end points, $(t, z_1 = x_1^+), \ldots, (t, z_n = x_n^+)$, in a plane at some fixed "time" t, provided one chooses the "light-cone gauge" to define the functional integral. The light-cone gauge is defined by

$$A = A_0 dt + A_+ dx^+ + A_- dx^-, \qquad \text{with} \quad A_- \equiv 0.$$

In this gauge, the action of Chern–Simons theory is quadratic in A, which enables one to "solve" the theory explicitly in terms of solutions of the Knizhnik–Zamolodchikov equations. This theme is developed in much detail in Fröhlich and King (1989), where, moreover, applications to pure mathematics (theory of knots and links) have been presented.

If one now assumes that the gauge coupling constant g in (34) is positive and finite and adds matter fields one is confronted with dynamical gauge theories with a positive mass gap and superselection sectors (and quasi-particles) satisfying fractional (braid) statistics. Such theories with gauge group $G = U(1)$ have been considered, for example, in Deser et al. (1982, 1988, 2000), Redlich (1984), and the fractionally charged magnetic vortices of these theories have been shown to satisfy abelian braid statistics in Wilczek (1982) and Fröhlich and Marchetti (1988). Dynamical gauge theories with non-abelian gauge groups, $G = SU(M), M = 2, 3, \ldots,$ have been studied, for example, in Pisarski and Rao (1985).

A general, mathematically rigorous analysis of braid statistics and of the connection between spin and (braid) statistics in 3D local quantum theory has been presented in Fröhlich and Gabbiani (1990). Among the main conclusions of this paper are the following ones: The charged fields of a local quantum theory in 2 + 1 space-time dimensions exhibit nontrivial fractional (braid) statistics *only* if (1) they are not localizable in bounded space-time regions (in fact, they are localized on space-like cones extending to infinity), which means, at least heuristically, that the theory is a *gauge theory*, (2) the charged states obtained by applying such fields to the vacuum state have fractional spin $s \notin \frac{1}{2}\mathbb{Z}$, and (3) the theory explicitly breaks the discrete symmetries of reflections in lines and time reversal (which, for a gauge theory, implies that its action contains a nontrivial Chern–Simons term). Well, there is *one* class of physical systems that can be studied in the laboratory which satisfy all these requirements: *2D electron gases in an external magnetic field exhibiting the fractional quantum Hall effect.* They are studied in the next section (see, in particular, the end of Section "Classification of "abelian" Hall fluids").

The 2D quantum Hall effect

In this section we outline some important elements of the *theory of the quantum Hall effect* (QHE) (see Prange and Girvin, 1990; Chakraborty and Pietiläinen, 1988, and references given there). We consider the idealized set-up, sketched in Fig. 2, for measurements of the Hall conductivity (= Hall conductance) and the longitudinal resistance (or conductance) of a two-dimensional electron gas formed at the interface of a semiconductor and an insulator when a gate voltage perpendicular to the interface is turned on. The two-dimensional electron gas is assumed to be confined to a compact region, Ω, contained in the xy-plane and is subjected to a magnetic field $\vec{B}_0 \perp \Omega$ (parallel to the z-axis). To observe the quantization of the Hall conductivity, σ_H, the filling factor $\nu := n_e/(eB_0/h)$ of the electron gas (where n_e is the density of the gas, and $B_0 := |\vec{B}_0|$) must be chosen in such a way that the longitudinal resistance, R_L, of the electron gas vanishes (Fig. 2). (If the Hall (transverse) conductivity, σ_H, does not vanish, then $R_L = 0$ is equivalent to a vanishing longitudinal conductance.) To show, mathematically, that, for an *interacting* two-dimensional electron gas in a uniform external magnetic field, one can choose the filling factor ν in such a way that $R_L = 0$ appears to be a very hard problem of quantum many-body theory that has not been solved under realistic assumptions about the electron gas but has been extensively studied numerically (see, e.g., Morf, 1992). In the following, we attempt to solve a much easier problem: *Assuming* that $R_L = 0$, what can one say about the properties of the electron gas and, in particular, about the possible values of the Hall conductivity σ_H (under the condition that the diameter of Ω is much larger than the magnetic length)? This question has a very elegant, general answer (see Fröhlich and Studer, 1993; Fröhlich et al., 1996; Fröhlich, 1995; Fröhlich et al., 2001). In order to find this answer, we have to study the response of a 2D electron gas confined to Ω to a small perturbing electromagnetic field $(\vec{E}, \vec{B})$, with $\vec{E} \parallel \Omega$ and $\vec{B} \perp \Omega$. We set

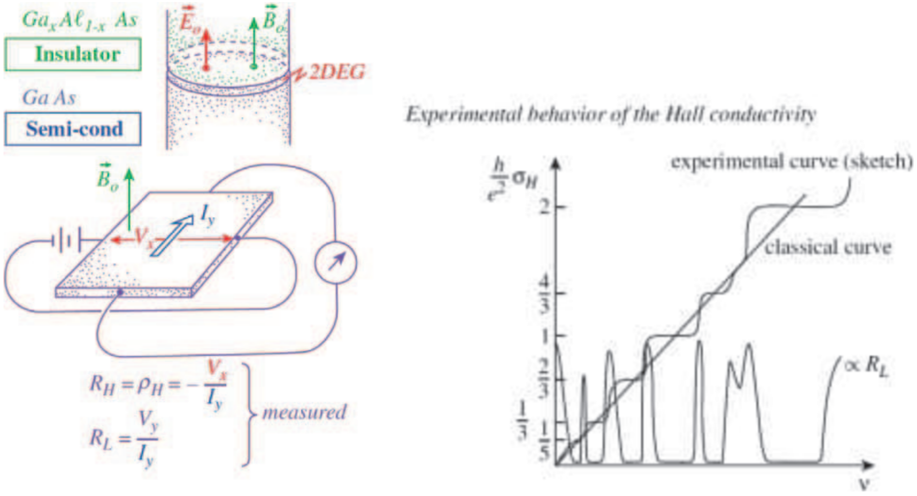

Fig. 2 Schematic representation of the experimental setup and of experimental results on the QHE. *Observations:* $R_L = 0 \leftrightarrow (\nu, \sigma_H) \in$ plateau; plateau heights $\in \frac{e^2}{h}\mathbb{Q}$; the cleaner the sample, the more numerous are the observed plateaux and the narrower they are; if $\frac{h}{e^2}\sigma_H \notin \mathbb{Z}$, then there appear to exist quasi-particles with fractional electric charges.

$$\vec{B}^{tot} := \vec{B}_0 + \vec{B}, \quad B := |\vec{B}|, \quad \underline{E} := (E_1, E_2).$$

It is helpful to review the electrodynamics of 2D "incompressible" ($R_L = 0$) electron gases. The electromagnetic field tensor, $F = (F_{\mu\nu}) = (\partial_\mu A_\nu - \partial_\nu A_\mu)$, $\mu, \nu = 0, 1, 2$, in 2 + 1 space-time dimensions is given by

$$F = \begin{pmatrix} 0 & E_1 & E_2 \\ -E_1 & 0 & -B \\ -E_2 & B & 0 \end{pmatrix}$$

The electric current density, j^μ, in the gas is given by

$$j^\mu(x) := \langle J^\mu(x) \rangle_A, \quad \mu = 0, 1, 2,$$

where $\langle (\cdot) \rangle_A$ denotes a (time-ordered) expectation in a very slowly varying external electromagnetic field with vector potential $A = (A_\mu)$.

The electrodynamics of 2D incompressible electron gases—Anomalous chiral edge currents

The basic equations of the (2 + 1)-dimensional electrodynamics of 2D incompressible electron gases (in units where the speed of light $c = 1$) are as follows:

(i) **Hall's Law**—*a phenomenological law*

$$j^k(x) = \sigma_H \varepsilon^{k\ell} E_\ell(x), \quad k, \ell = 1, 2, \quad \text{assuming that} \quad R_L = 0, \tag{36}$$

where $\varepsilon^{12} = -\varepsilon^{21} = 1$, $\varepsilon^{ii} = 0$, which shows that if $\sigma_H \neq 0$ the symmetries of reflections in lines (P) and time reversal (T) are broken. (Of course these symmetries are broken explicitly by the presence of an external magnetic field.)

(ii) **Charge conservation**—*a fundamental law*

$$\frac{\partial}{\partial t}\rho(x) + \underline{\nabla} \cdot \underline{j}(x) = 0. \tag{37}$$

(iii) **Faraday's induction law**—*a fundamental law*

$$\frac{\partial}{\partial t} B_3^{tot}(x) + \underline{\nabla} \wedge \underline{E}(x) = 0. \tag{38}$$

Combining Eqs. (i) through (iii), we obtain

$$\frac{\partial}{\partial t}\rho \overset{(ii)}{=} -\underline{\nabla} \cdot \underline{j} \overset{(i)}{=} -\sigma_H \underline{\nabla} \wedge \underline{E} \overset{(iii)}{=} \sigma_H \frac{\partial}{\partial t} B. \tag{39}$$

(iv) **Chern–Simons Gauss law**—(useful to determine the Hall conductivity)

Integrating (39) in time t, with integration constants chosen as follows

$$j^0(x) := \rho(x) + e \cdot n_e, \quad B(x) = B_3^{tot}(x) - B_0$$

we find the so called *Chern–Simons Gauss law* (see Eqs. (42) and (49))

$$j^0(x) = \sigma_H B(x). \tag{40}$$

As its derivation from (39) shows, this equation must be understood as saying that a small *change*, ΔB, of the external magnetic field transversal to the sample plane induces a small change, Δj^0, in the charge density of the sample. Eq. (40) is also known under the name of *Streda formula*; see Streda (1982). Integrating both sides of Eq. (39) in time from $t = t_i$ to $t = t_f$ and over sample space Ω, we conclude that

$$\Delta Q = \sigma_H \Delta\Phi, \tag{41}$$

where ΔQ is the change of the electric charge stored in the sample and $\Delta\Phi$ is the change of the magnetic flux through the sample during the time interval $[t_i, t_f]$.

Remark. For 2D incompressible gases of *noninteracting* electrons moving in a disordered potential landscape, relation (41) has been invoked in calculations of the Hall conductivity, σ_H, with the purpose to exhibit its topological character (see Laughlin, 1981; Avron et al., 1990, 1994). But this law, as well as Hall's law (36) can equally well be used to calculate the Hall conductivity for incompressible *interacting* 2D electron gases and to exhibit the topological nature of σ_H. For example, one may consider an electron gas confined to a 2D torus, $\mathcal{T}$, and thread a magnetic flux tube through the interior of $\mathcal{T}$ that does not cross/intersect $\mathcal{T}$ and is parallel to a noncontractible cycle, γ, of $\mathcal{T}$.[14] One may then ask how much electric charge, $\Delta Q_{\widetilde{\gamma}}$, crosses a cycle, $\widetilde{\gamma}$, on $\mathcal{T}$ conjugate to γ (i.e., γ and $\widetilde{\gamma}$ intersecting each other in a single point of $\mathcal{T}$) when the magnetic flux in the interior of the torus (parallel to γ) changes by an amount $\Delta\Phi$. A combination of Eq. (36) with Faraday's induction law (38) shows that the quotient $\Delta Q_{\widetilde{\gamma}}/\Delta\Phi$ is given by σ_H. Assuming that the electric charge of all charge carriers in the system is an integer multiple of the elementary electric charge e, and assuming that the longitudinal conductance vanishes, one can invoke the theory of the Aharonov–Bohm effect to conclude that the state of this system is unchanged if the magnetic flux in the interior of $\mathcal{T}$ is slowly increased by an integer multiple of the flux quantum h/e. This implies that, in the process of increasing $\Delta\Phi$ by h/e, an integer number of charge carriers with a total electric charge $Ne, N \in \mathbb{Z}$, must cross the cycle $\widetilde{\gamma}$. Hence

$$\Delta Q_{\widetilde{\gamma}} = Ne = \sigma_H (h/e) \quad \Leftrightarrow \quad \sigma_H = N \frac{e^2}{h}, \quad N \in \mathbb{Z}.$$

These considerations do not explain why the "Hall fraction," $\frac{h}{e^2}\sigma_H$, is often observed *not* to be an integer, but rather a *rational number* (most often with an odd denominator). It is plausible to imagine that if the Hall fraction is not an integer, then there must exist *fractionally charged quasi-particles*, as originally suggested by Tsui and Laughlin (see Section "Classification of "abelian" Hall fluids").

The sign of σ_H is determined by the nature of the quasi-particles carrying the Hall current, namely, whether these quasi-particles are electrons or holes. (Historically, this fact led to the discovery of holes in a nearly full conduction band of semiconductors.)

---

[14] Instead, we could consider a very large Corbino disk and study charge transport from the inner to the outer boundary circle when the magnetic flux threaded through its hole changes.

Hall's law (36) and the Chern–Simons Gauss law (40) yield the equation

$$j^{\mu}(x) = \sigma_H \varepsilon^{\mu\nu\lambda} F_{\nu\lambda}(x), \tag{42}$$

which is a *generally covariant* relation between the current density j^{μ} of the electron gas and the electromagnetic field tensor $F_{\nu\lambda}$.

Eq. (42) evokes to the following puzzle.

$$0 \overset{(ii)}{=} \partial_{\mu} j^{\mu} \overset{(iii),(42)}{=} \varepsilon^{\mu\nu\lambda}(\partial_{\mu}\sigma_H)F_{\nu\lambda}. \tag{43}$$

We observe that, while the left side of this equation vanishes by charge conservation, the right side does *not* vanish wherever the value of σ_H jumps, as, for example, at the boundary, $\partial\Omega$, of the sample region Ω. So, what is going on?

Solution of Puzzle: In Eq. (42), j^{μ} is the *bulk* current density, j^{μ}_{bulk}, which is apparently **not** conserved! The *conserved total electric current density*, j^{μ}_{tot}, can be decomposed into

$$j^{\mu}_{tot} = j^{\mu}_{bulk} + j^{\mu}_{edge}, \tag{44}$$

with

$$\partial_{\mu} j^{\mu}_{tot} = 0, \quad \text{but} \quad \partial_{\mu} j^{\mu}_{bulk} \overset{(43)}{\neq} 0.$$

We note that the support of the edge current density j^{μ}_{edge} coincides with the support of $\underline{\nabla}\sigma_H$,

$$\operatorname{supp} j^{\mu}_{edge} = \operatorname{supp}\{\underline{\nabla}\sigma_H\} \supseteq \partial\Omega, \qquad \text{with} \qquad \underline{j}_{edge} \perp \underline{\nabla}\sigma_H.$$

Combining (43) (setting $j^{\mu} = j^{\mu}_{bulk}$!) with (44), we find that

$$\partial_{\mu} j^{\mu}_{edge} \overset{(44)}{=} -\partial_{\mu} j^{\mu}_{bulk}\big|_{\operatorname{supp}\{\underline{\nabla}\sigma_H\}} \overset{(42)}{=} -\varepsilon^{\mu\nu}\partial_{\mu}\sigma_H E_{\nu}.$$

When restricted to the support of $\underline{\nabla}\sigma_H$, this equation becomes

$$\partial_{\mu} j^{\mu}_{edge} = -(\Delta\sigma_H)E_{\parallel}\big|_{\operatorname{supp}\{\underline{\nabla}\sigma_H\}}, \tag{45}$$

where $\Delta\sigma_H$ is the jump of the Hall conductivity across the edge in question. In the following, we assume that σ_H is constant throughout the interior of Ω and vanishes outside Ω (so that $\Delta\sigma_H = \sigma_H$ in (45)). This is not a realistic assumption; but it simplifies our discussion without introducing any misleading reasoning. Eq. (45) shows that j^{μ}_{edge} is an anomalous (chiral) current density in 1 + 1 dimensions. This equation can be viewed as a simple manifestation of "holography": The edge displays as much information about the Hall conductivity of the system as the bulk.

Here is a classical physics argument determining the chirality of j^{μ}_{edge}: At the edge of the sample, the Lorentz force acting on electrons must be canceled by the force confining them to the interior of the sample. Thus,

$$\frac{e}{c} B^{tot} v^{k}_{\parallel} = \varepsilon^{k\ell} \frac{\partial V_{edge}}{\partial x^{\ell}},$$

where V_{edge} is the potential of the force confining electrons to the interior of the sample region Ω. This enables us to find the equation for the chiral motion of degrees of freedom localized at the boundary, $\partial\Omega$, of the system ("skipping orbits"), and in particular for their propagation speed $v_{\parallel}$.

From the theory of the chiral anomaly in 1 + 1 dimensions, one may infer that, at the boundary $\partial\Omega$,

$$\partial_{\mu} j^{\mu}_{edge} = -\frac{e^2}{h}\left(\sum_{\text{species } \alpha} Q^2_{\alpha}\right) E_{\parallel} \overset{\text{with } (45)}{\Rightarrow} \sigma_H = \frac{e^2}{h} \sum_{\text{species } \alpha} Q^2_{\alpha} \tag{46}$$

where eQ_{α} is the "charge" (see 11) of the edge current, j^{μ}_{α}, corresponding to species α of clockwise-chiral edge modes; (similar contributions will come from counter-clockwise chiral edge modes, but with *reversed* sign).

Apparently, we have rediscovered *Halperin*'s chiral edge currents (Halperin, 1982), but only using very general arguments that are valid even for interacting electron gases. We observe that if $\sigma_H \notin \frac{e^2}{h}\mathbb{Z}$, then there must exist chiral edge currents, j_{α}, with *fractional charge*, that is, with $Q_{\alpha} \notin \mathbb{Z}$, propagating along edges.

A phenomenon in classical physics analogous to the anomalous edge currents of 2D electron gases is found in the physics of hurricanes:

$$\vec{B} \rightarrow \vec{\omega}_{earth}, \ \text{Lorentz force} \rightarrow \text{Coriolis force}, V_{edge} \rightarrow \text{air pressure}.$$

This shows (among other things) that hurricanes on the northern hemisphere always turn anticlockwise. Related phenomena are the equatorial winds and chiral coastal water waves, called *Kelvin waves* (after Lord Kelvin, who discovered them). The take-home message of this observation is that anomalies, anomaly inflow and anomaly cancellation, are effects that already appear in classical physics, in particular in the aerodynamics of the Earth's atmosphere and in the dynamics of fluids in noninertially moving containers, such as the Earth's oceans. (See Graf et al., 2021; Wiegmann and Abanov, 2022 for recent results on fluid dynamics.)

Next, we determine the (bulk and edge) effective action of 2D incompressible electron gases exhibiting the quantum Hall effect. As above, we consider a 2D electron gas in a neutralizing ionic background subject to a constant transversal magnetic field $\vec{B}_0$. The electrons are confined to a region Ω in the xy-plane. The space-time of the system is given by $\Lambda = \Omega \times \mathbb{R}$ (with $\mathbb{R}$ identified with the time axis). We suppose that the electrons are coupled to an external electromagnetic field with vector potential $A = A_0\,\mathrm{d}t + A_1\,\mathrm{d}x + A_2\,\mathrm{d}y$ describing a small, slowly varying perturbing electromagnetic field $(\underline{E}, B)$.

We assume that the 2D electron gas is an insulator, that is, that the longitudinal conductance vanishes. It is then easy to determine the form of the effective action, $S_{eff}(A)$, of this system as a functional of the external vector potential A in the limiting regime of very large distances and very low frequencies, that is, in the scaling limit; as alluded to in "Introduction: Gauge theory of states of matter" (see Fröhlich and Studer, 1993; Fröhlich et al., 1996 for details):

$$\begin{aligned} S_{eff}(A) = \frac{\sigma_H}{2}\int_\Lambda A \wedge [dA + K] + \text{boundary action} \\ + \frac{1}{2}\int_\Lambda \mathrm{d}^3x\left\{\underline{E}(x)\cdot\varepsilon\underline{E}(x) - \mu^{-1}B^2(x)\right\} + \cdots, \end{aligned} \tag{47}$$

where the first term on the right side is the topological Chern–Simons action (which is "marginal" in the infrared), and its coefficient, σ_H, turns out to be the *Hall conductivity*, K is the Gauss curvature 2-form on the sample space Ω, which gives rise to the famous "shift"; ε = tensor of dielectric constants, μ = magnetic permeability (and the first term on the second line of the right side of (47) is "irrelevant" in the infrared; the dots stand for further terms of even larger scaling dimension).

The presence of the Chern–Simons action on the right side of (47) can also be inferred from Eq. (42). Omitting curvature terms ($K = 0$),

$$\begin{aligned} \mathrm{j}^\mu_{bulk} = \langle J^\mu(x)\rangle_A \equiv \frac{\delta S_\Lambda(A)}{\delta A_\mu(x)} \\ \overset{(42)}{=} \sigma_H\,\varepsilon^{\mu\nu\lambda}F_{\nu\lambda}(x), \quad \text{for} \quad x \notin \partial\Lambda. \end{aligned} \tag{48}$$

Integrating Eq. (48), we find that the effective action $S_{eff}(A) \equiv S_\Lambda(A)$ is given by

$$S_\Lambda(A) = \frac{\sigma_H}{2}\int_\Lambda A \wedge dA + \text{ boundary action.} \tag{49}$$

That there *must* be a boundary action, denoted in the following by $\Gamma_{edge}(a)$, is a consequence of the fact that the Chern–Simons bulk action is *not* gauge-invariant on a space-time Λ with a nonempty boundary $\partial\Lambda$: Under a gauge transformation $A_\mu \to A_\mu + \partial_\mu\chi$, the Chern–Simons action changes by a boundary term

$$\frac{\sigma_H}{2}\int_{\partial\Lambda}[\chi dA]|_{\partial\Lambda} \tag{50}$$

This anomaly must be canceled by the anomaly of a boundary action.

Returning to Eqs. (45) and(46), we guess that the boundary action must be the generating functional of the connected Green functions of the (quantum-mechanical) anomalous chiral edge current density

$$\mathrm{j}^\mu_{edge} = \sum_\alpha \mathrm{j}^\mu_\alpha, \quad \alpha = 1, 2, \ldots,$$

where α labels the different species of charged chiral edge modes. The charge carried by j^μ_α has been denoted by eQ_α. Let v_α denote the propagation speed of the chiral modes that give rise to the edge current density j^μ_α. This propagation speed (which in general depends on the species α) plays the role of the "speed of light" in 2D current algebra. We introduce "light-cone coordinates," u^+, u^-, on $\partial\Lambda$. Let $a \equiv a_+du^+ + a_-du^- := A_\parallel$ denote the electromagnetic vector potential (which is a 1-form) restricted to the 1 + 1-dimensional boundary, $\partial\Lambda$, of the (2 + 1)-dimensional space-time.

The effective action of the chiral edge current density j^μ_α is given by

$$\frac{(eQ_\alpha)^2}{h}\Gamma^{(\alpha)}_{\partial\Lambda}(a), \text{ with } \quad \Gamma^{(\,\cdot\,)}_{\partial\Lambda}(a) := \frac{1}{2}\int_{\partial\Lambda}\left[a_+a_- - a_\pm\frac{\partial^2_\mp}{\Box}a_\pm\right]du^+\,du^-, \tag{51}$$

where $\Box := \partial_+\partial_-$, and the choice of subscripts "+" and "−" in the last term on the right side of (51) depends on the chirality of the modes giving rise to the edge current j^μ_α (the dependence of $\Gamma^{(\alpha)}_{\partial\Lambda}(a)$ on α is determined by the chirality of the mode α and its propagation speed v_α).

The reader is invited to verify that the anomaly (50) of the bulk effective action, namely, the term $\frac{\sigma_H}{2}\int_{\partial\Lambda}[\chi dA]|_{\partial\Lambda}$, is canceled by the anomaly of the edge effective action,

$$\Gamma_{edge}(a) := -\sum_{\text{species } \alpha} \frac{(eQ_\alpha)^2}{h} \Gamma^{(\alpha)}_{\partial\Lambda}(a), \tag{52}$$

under a gauge transformation $a \rightarrow a + d\chi|_{\partial\Lambda}$ if and only if

$$\partial_\mu \left(\delta\, \Gamma_{edge}(a)/\delta a_\mu(x)\right) = \partial_\mu j^\mu_{edge}(x) \equiv -\sigma^{edge}_H E_\parallel \overset{!}{=} -\sigma_H E_\parallel, \tag{53}$$

see (45); whence

$$\sigma^{edge}_H \overset{(52)}{=} \frac{e^2}{h} \sum_\alpha Q^2_\alpha = \sigma_H. \tag{54}$$

This shows that edge and bulk Hall conductivities must *coincide*, as already emphasized in Fröhlich and Studer (1993) and Fröhlich et al. (1996). Merely for simplicity, we have assumed here (and will continue to assume in the following) that all edge modes have the *same* chirality; otherwise, appropriate signs have to be introduced in these formulae.

Whatever has been said here about Hall insulators also applies to so called *Chern insulators*, which break reflection- and time-reversal invariance *even* in the absence of an external magnetic field; for example, because the bulk of the material is doped by magnetic impurities (as in the Haldane model Haldane (1988); see also Fröhlich and Kerler (1991)).

Classification of "abelian" Hall fluids

In this section, I sketch a general classification of 2D insulators with broken parity and time reversal invariance (Hall or Chern insulators) exhibiting quasi-particles with *abelian braid statistics*.[15] I will describe these systems in the limit of very large distance scales (i.e., I consider very large samples in units of the magnetic length) and of very low frequencies; that is, in the infrared *scaling limit*. Units will be used such that $\frac{e^2}{\hbar} = 1$. Let J denote the total operator-valued electric current density (bulk plus edge current density), which is conserved: $\partial_\mu J^\mu = 0$.

Ansatz:

$$J = \sum_{\alpha=1}^{N} Q_\alpha J_\alpha, \tag{55}$$

where the currents J_α are assumed to be canonically normalized and conserved, with charges $Q_\alpha \in \mathbb{R}$.

Comment. This ansatz has been criticized, a common objection being that there is no reason why there should be more than *one* conserved current density, namely, the total electric current density. To counter this objection, I first consider a gas of electrons confined to a planar region Ω with the topology of a disk and a smooth boundary; a uniform external magnetic field transversal to Ω is turned on, and it is assumed that there are no electron–electron interactions. This system can be understood by studying the one-electron Hamiltonian: its eigenvalues form Landau levels. The eigenvalues corresponding to eigenfunctions localized close to the boundary, $\partial\Omega$, of Ω, are shifted upward to rather high energies by the boundary potential that confines the electrons to the interior of Ω (a fact that can be verified in perturbation theory); that is, the Landau levels end in bands of energies corresponding to chiral modes with eigenfunctions localized near $\partial\Omega$ and extended along $\partial\Omega$. The *ground state* of the electron gas is obtained by filling *all* the eigenstates corresponding to energy levels below the Fermi energy, E_F. Assuming that E_F is such that a certain number, N, of Landau levels are partially filled, then there are N energy bands corresponding to chiral boundary modes that are partially filled up to an energy $\leq E_F$. These bands and the Landau levels they emerge from correspond to separately conserved current densities.

If the electrons move in a disordered potential landscape, the energy eigenvalues of the Landau levels are spread out in "Landau bands." Eigenvalues close to the edges of Landau bands correspond to localized eigenfunctions. But in the middle of each Landau band, there are eigenvalues corresponding to *extended* states. The eigenvalues corresponding to eigenfunctions localized near $\partial\Omega$ end in an energy band of chiral boundary modes that is close to the band found when the disorder potential vanishes (as follows from arguments similar to Halperin's (Halperin, 1982)). By dilating the region Ω, one may approach the *scaling limit*. In this limit, the extended states in the middle of a filled Landau band (labeled by α) together with the corresponding states of chiral boundary modes with energies $\leq E_F$ then give rise to a current density, $J^\mu_\alpha := J^\mu_{bulk,\alpha} + \mathrm{j}^\mu_\alpha$, which, at the very low frequencies that survive in the scaling limit, is *conserved.*

Thus, for noninteracting electron liquids, our ansatz appears to be justified in the scaling limit. (For finitely extended samples, there are corrections possibly describing some mixing of the currents, which, however, vanish in the scaling limit.)

For interacting electron liquids, the success of the **Ansatz** (55), which will be demonstrated below, appears to justify it. For an alternative ansatz, I refer to Fröhlich et al. (2001).

A topological field theory of conserved currents emerging in the scaling limit: On a 3D space-time $\Lambda = \Omega \times \mathbb{R}$, a conserved current J can be derived from a vector potential, B. If $\imath$ denotes the 2-form dual to J, then the continuity equation $\partial_\mu J^\mu = 0$ is equivalent to $d\imath = 0$. By Poincaré's lemma,

---

[15] States exhibiting quasi-particles with *non-abelian braid statistics* are discussed in my work, Fröhlich et al., 2001, with B. Pedrini, Chr. Schweigert, and J. Walcher.

$$\iota = \frac{1}{\sqrt{2\pi}} dB,$$

where the vector potential B is a 1-form, which is determined by ι up to the gradient of a scalar function, β: B and $B + d\beta$ yield the *same* 2-form ι.

For a gapped 2D insulator, the effective field theory of the currents $(J_\alpha)_{\alpha=1}^N$ must be *topological* in the scaling limit. If the symmetries of reflection in lines and time reversal are broken, the "most relevant" term in the action functional of the potentials, $\underline{B} := (B_\alpha)_{\alpha=1}^N$, of the currents J_α is the *Chern–Simons action*

$$S_\Lambda(\underline{B}, A) := \sum_{\alpha=1}^{N} \int_\Lambda \left\{ \frac{1}{2} B_\alpha \wedge dB_\alpha + A \wedge \frac{Q_\alpha}{\sqrt{2\pi}} dB_\alpha \right\} + \text{boundary terms} + \cdots, \tag{56}$$

where A is the electromagnetic vector potential, and the boundary terms must be added to cancel the anomalies of the bulk action under the "gauge transformations"

$$B_\alpha \to B_\alpha + d\beta_\alpha, \quad A \to A + d\chi.$$

Carrying out the oscillatory Gaussian integrals over the potentials B_α, we find

$$\begin{aligned} e^{iS_\Lambda(A)} \equiv \mathcal{N}^{-1}\ \mathcal{Z}_\Lambda(A) :&= \mathcal{N}^{-1} \int \exp(iS_\Lambda(\underline{B}, A)) \prod_{\alpha=1}^{N} \mathcal{D}B_\alpha \\ &= \exp\left(i\frac{\sigma_H}{2} \int_\Lambda A \wedge dA + \Gamma_{edge}(A_\parallel) \right), \end{aligned} \tag{57}$$

where $\mathcal{N}$ is a normalization factor independent of A, and it follows from (56) that

$$\sigma_H = \frac{1}{2\pi} \sum_{\alpha=1}^{N} Q_\alpha^2,$$

(compare to formula (46)).

Physical states of the Chern–Simons theory with action as in (56) can be constructed from *Wilson networks*, W, of Wilson lines and Wilson flux tubes contained in the half space Λ_-, where $\Lambda_{+/-} := \Omega \times \mathbb{R}_{+/-} = \Omega \times \{t \mid t \geq 0/t \leq 0\}$, whose open lines/flux tubes end in $\Omega_0 \equiv \Omega \times \{t = 0\}$. Given such a network W, let $|W\rangle$ denote the physical state corresponding to W (see "What is fractional or braid statistics?"). Let $\Theta(W)$ denote the network contained in Λ_+ arising from W by reflection in Ω_0, followed by complex conjugation. If W_1 and W_2 are two such networks with the property that their intersections with Ω_0, more precisely their *fluxes* through Ω_0, coincide we may consider the *gauge-invariant* network, $W_1 \circ \Theta(W_2)$, arising by multiplying W_1 with $\Theta(W_2)$; (graphically this amounts to concatenation at coinciding points/flux patches in Ω_0). Then the scalar product of the state $|W_1\rangle$ with the state $|W_2\rangle$ is given by

$$\langle W_2 \| W_1 \rangle := \mathcal{Z}_\Lambda(A)^{-1} \int (W_1 \circ \Theta(W_2))(\underline{B})\ \exp(iS_\Lambda(\underline{B}, A)) \prod_{\alpha=1}^{N} \mathcal{D}B_\alpha. \tag{58}$$

Fact: The Hamiltonian of a Hall insulator described by (56) through (58) vanishes. Thus, in the scaling limit, all excitations are *static*.

The operator, $\mathcal{Q}_\mathcal{O}$, measuring the electric charge stored in states corresponding to Wilson networks whose supports intersect the sample space Ω_0 in a region $\mathcal{O}$ can be constructed from the Wilson loops

$$\exp(i\varepsilon\mathcal{Q}_\mathcal{O}) := \exp\left(i\varepsilon \int_\mathcal{O} J^0 d^2x \right) = \exp\left(i \sum_{\alpha=1}^{N} \varepsilon \frac{Q_\alpha}{\sqrt{2\pi}} \int_{\partial\mathcal{O}} B_\alpha \right), \quad \varepsilon \in \mathbb{R}.$$

Because the ground-state energy of a Hall insulator is separated from the rest of the energy spectrum by a strictly *positive (mobility) gap*, *electric charge* is a good quantum number to label its physical states at zero temperature. In other words, the charge operators

$$\mathcal{Q}_\mathcal{O} \quad \text{and} \quad \mathcal{Q} := \lim\nolimits_{\mathcal{O} \nearrow \Omega} \mathcal{Q}_\mathcal{O}$$

are well defined on (zero-temperature) physical states.[16]

The electric charges, $q_{\mathcal{O},1}$ and $q_{\mathcal{O},2}$, contained in a region $\mathcal{O} \subset \Omega_0$ of two states $|W_1\rangle$, $|W_2\rangle$ with the property that $W_1 \circ \Theta(W_2)$ is gauge-invariant must be *identical*, that is, $q_{\mathcal{O},1} = q_{\mathcal{O},2} \equiv q_\mathcal{O}$. Their electric charge contained in $\mathcal{O}$, that is, the number $q_\mathcal{O}$, is given by

$$\exp(i\varepsilon q_\mathcal{O}) \langle W_2 \| W_1 \rangle = \mathcal{Z}_\Lambda(A)^{-1} \int (W_1 \circ \Theta(W_2))(\underline{B})\ \exp(i\varepsilon\mathcal{Q}_\mathcal{O})\ \exp(iS_\Lambda(\underline{B}, A)) \prod_{\alpha=1}^{N} \mathcal{D}B_\alpha, \tag{59}$$

---

[16] The same conclusion is reached by noticing that all Wilson loop expectations have perimeter decay and then invoking " 'tHooft duality."

with $\varepsilon \in \mathbb{R}$ arbitrary. If a Wilson network W creates a physical state $|W\rangle$ describing n electrons or holes located inside a region $\mathcal{O} \subset \Omega_0$ when applied to the ground state of a Hall insulator, then the charge, $q_{\mathcal{O}} \equiv q_{\mathcal{O}}(W)$, contained in $\mathcal{O}$ is given by $q_{\mathcal{O}}(W) = -n+2k$, where k is the number of holes in $\mathcal{O}$. If $-n+2k$ is odd, that is, if n is *odd*, then the excitation created by W inside $\mathcal{O}$ must have Fermi–Dirac statistics, and if n is *even* it must have Bose–Einstein statistics; that is, there is a *connection between electric charge and quantum statistics* of electron-hole excitations.

Digression: Let W and W' be two Wilson networks both creating excitations describing $n-k$ electrons and k holes ($k = 0, 1, \ldots, n$) located at *disjoint* points inside some region $\mathcal{O} \subset \Omega_0$, with $q_{\mathcal{O}}(W) = q_{\mathcal{O}}(W')$. Let $\widetilde{W}$ be an *arbitrary* Wilson network with the property that the networks $(W \cdot W') \circ \Theta(\widetilde{W})$ and $\mathcal{B}_{\mathcal{O}}(W \cdot W') \circ \Theta(\widetilde{W})$ are *gauge-invariant*, where $\mathcal{B}_{\mathcal{O}}(W \cdot W')$ arises from $W \cdot W'$ by braiding all lines of the two networks with endpoints inside $\mathcal{O}$, and *only* those, in such a way that the endpoints of all lines of W ending inside $\mathcal{O}$ are exchanged with the endpoints of all lines of W' ending in $\mathcal{O}$, but *without any lines twisted around or crossing each other*. Then (56) and (58) imply that

$$\langle \widetilde{W} \parallel \mathcal{B}_{\mathcal{O}}(W \cdot W')\rangle = \exp(i\pi n^2)\langle \widetilde{W} \parallel (W \cdot W')\rangle = (-1)^{q_{\mathcal{O}}}\langle \widetilde{W} \parallel (W \cdot W')\rangle.$$

This is the standard *connection between electric charge and statistics* of electron-hole excitations in a 2D incompressible electron gas. □

Consider a Wilson network W with support in Λ_- that has just a single line, γ_p, ending in a point p contained in a region $\mathcal{O} \subset \Omega_0$, and let $q := (q^\alpha)_{\alpha=1}^N$ denote the quantum numbers (fluxes) dual to the potentials B_α attached to the line γ_p. Then W is given by the Wilson line

$$\exp\left(i\sum_{\alpha=1}^{N}\sqrt{2\pi}q^\alpha\int_\gamma B_\alpha\right),$$

multiplied by lines or flux tubes contained in Λ_- that do *not* intersect Ω_0 in the region $\mathcal{O}$. It follows from Eq. (59) that

$$q_{\mathcal{O}}(W) = \sum_{\alpha=1}^{N} Q_\alpha\, q^\alpha \equiv Q \cdot q, \tag{60}$$

where $Q = (Q_1, \ldots, Q_N)$ and $q = (q^1, \ldots q^N)^T$. It is easy to argue that *quantum numbers, q, corresponding to multi-electron-hole excitations,* form a module, Γ, over $\mathbb{Z}$ of rank N, that is, *an integral lattice of rank N*, which we call a *"Hall lattice"* (to see this, consider the additivity of the electric charge and other "pseudo-charge" quantum numbers q under multiplication of Wilson line insertions creating such excitations). By (60), the "vector" $Q = (Q_1, \ldots, Q_N)$ must be an integer-valued, $\mathbb{Z}$-linear functional on Γ, that is, an element of the dual lattice, Γ^*.

The lattice Γ is equipped with an odd-integral quadratic form,

$$\langle q^{(1)}, q^{(2)}\rangle := \sum_\alpha q^{(1)\alpha} \cdot q^{(2)\alpha}, \quad q^{(1)}, q^{(2)} \in \Gamma.$$

That this defines an odd-integral quadratic form is shown as follows: Braiding two Wilson lines with quantum numbers $q^{(1)} = q^{(2)} = q \in \Gamma$ ending in Ω_0 yields a phase factor $\exp(i\pi\langle q, q\rangle)$, which must be $= 1$ if $Q \cdot q$ is even, and $= -1$ if $Q \cdot q$ is odd (connection between electric charge and quantum statistics).

If q is the vector of quantum numbers corresponding to a single electron/hole, then

$$Q \cdot q = \mp 1, \text{ and } \exp(i\pi\langle q, q\rangle) = -1. \tag{61}$$

It follows that $\langle\cdot,\cdot\rangle$ is odd-integral, and that Q is a visible vector in Γ^*. Since $Q \in \Gamma^*$ and Γ is an (odd-) integral lattice, we conclude that (reinstating e^2/h)

$$\frac{h}{e^2}\,\sigma_H = Q \cdot Q \equiv \sum_{\alpha=1}^{N} Q_\alpha^2 \quad \text{is a } \textit{rational} \text{ number.} \tag{62}$$

Our task is then to classify the pairs (Γ, Q) of an odd-integral lattice Γ and a visible vector $Q \in \Gamma^*$ encoding physical properties of the corresponding incompressible 2D electron gases, using *invariants* of these data. This rather nontrivial task has been carried out in collaboration with U. M. Studer and E. Thiran, during the period from 1992 till 1994; see Fröhlich and Thiran (1994), Fröhlich et al. (1996), and Fröhlich (1995). I will not go into any details here. Among the results of our efforts we have predicted the table of Hall fractions in the interval (0, 1] shown in Fig. 3; fractions indicated by a bullet (full dot) have been experimentally observed in incompressible electron gases exhibiting the quantum Hall effect. In Fig. 3, the Hall conductivity, $\sigma_H = \frac{e^2}{h} \cdot \frac{n_H}{d_H}$, is plotted horizontally (n_H and d_H are co-prime integers) and d_H is plotted vertically; units are chosen such that $e^2/h = 1$.

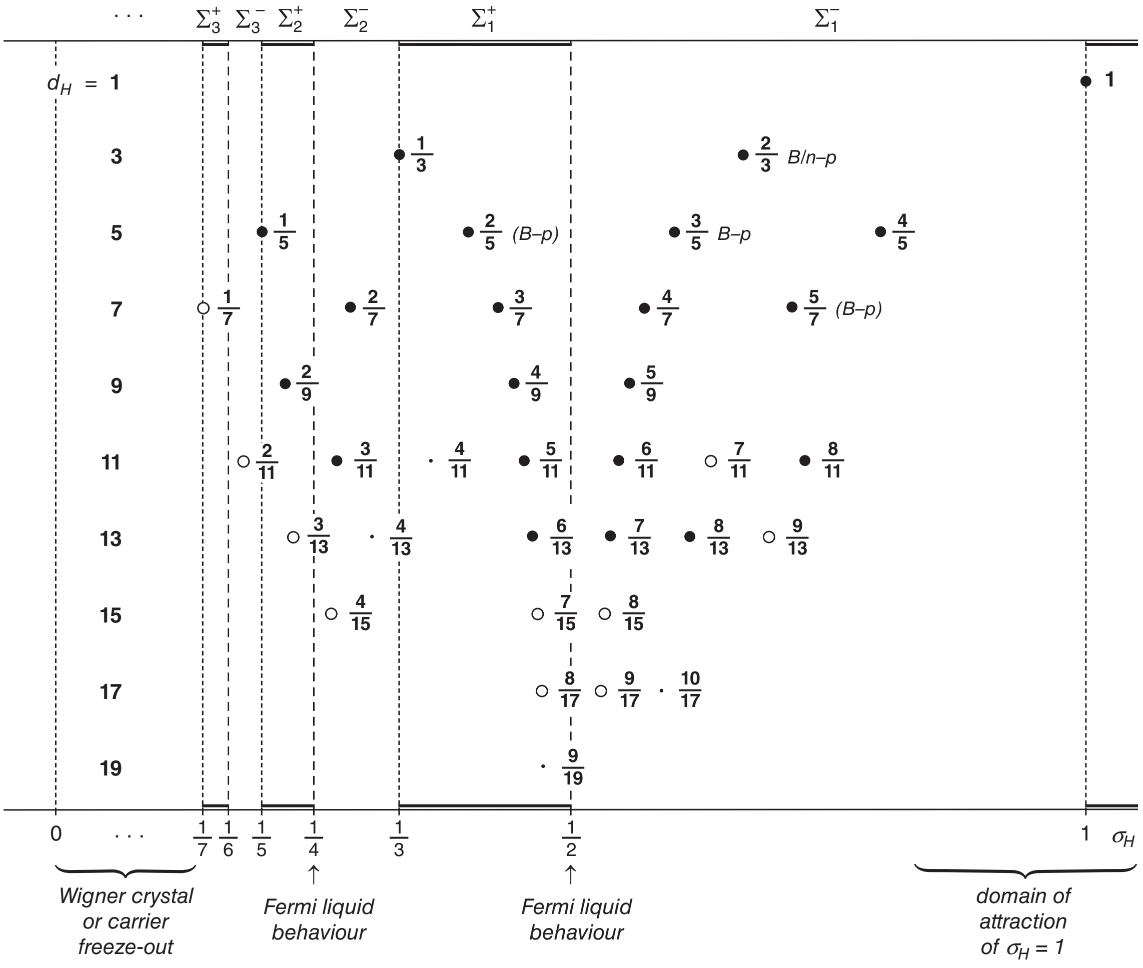
. . .
Σ_3^+
Σ_3^-
Σ_2^+
Σ_2^-
Σ_1^+
Σ_1^-
d_H = 1
3
5
7
9
11
13
15
17
19
1
$\frac{1}{3}$
$\frac{2}{3}$ B/n–p
$\frac{1}{5}$
$\frac{2}{5}$ (B–p)
$\frac{3}{5}$ B–p
$\frac{4}{5}$
$\frac{1}{7}$
$\frac{2}{7}$
$\frac{3}{7}$
$\frac{4}{7}$
$\frac{5}{7}$ (B–p)
$\frac{2}{9}$
$\frac{4}{9}$
$\frac{5}{9}$
$\frac{2}{11}$
$\frac{3}{11}$
$\frac{4}{11}$
$\frac{5}{11}$
$\frac{6}{11}$
$\frac{7}{11}$
$\frac{8}{11}$
$\frac{3}{13}$
$\frac{4}{13}$
$\frac{6}{13}$
$\frac{7}{13}$
$\frac{8}{13}$
$\frac{9}{13}$
$\frac{4}{15}$
$\frac{7}{15}$
$\frac{8}{15}$
$\frac{8}{17}$
$\frac{9}{17}$
$\frac{10}{17}$
$\frac{9}{19}$
0
. . .
$\frac{1}{7}$
$\frac{1}{6}$
$\frac{1}{5}$
$\frac{1}{4}$
$\frac{1}{3}$
$\frac{1}{2}$
1
σ_H
Wigner crystal or carrier freeze-out
Fermi liquid behaviour
Fermi liquid behaviour
domain of attraction of $\sigma_H = 1$

Fig. 3 Observed Hall fractions $\sigma_H = n_H/d_H$ in the interval $0 < \sigma_H < 1$, and their experimental status in single-layer 2D electron gases exhibiting the quantum Hall effect.

Comments. The Hall lattices Γ corresponding to fractions observed in the intervals $\Sigma_\ell^\pm, \ell = 2, 3, \dots,$ (see Fig. 3) are related to those corresponding to fractions in the intervals $\Sigma_1^\pm$ by the so called *shift map*; see Fröhlich and Thiran (1994) and Fröhlich (1995). The pattern of Hall fractions in Σ_ℓ^- is much richer than the pattern in Σ_ℓ^+: The Hall lattices Γ corresponding to the Hall fractions $\sigma_H = \frac{1}{3}, \frac{2}{5}, \frac{3}{7}, \dots$ contain the *A*- root lattices as their Witt sublattices[17] and are *unique*. Among the Witt sublattices of the Hall lattices corresponding to Hall fractions in Σ_1^- one also finds the *D*- and the *E*- root lattices. For some of the fractions, such as $\sigma_H = \frac{2}{3}, \frac{3}{5}$, possibly $\frac{5}{7}, \dots$, one finds two or more *distinct* pairs (Γ, *Q*) of a quantum Hall lattice and a *Q*-vector associated with one and the same value of σ_H. The *experimental* manifestation of this ambiguity is that, at each of these values of σ_H, *transitions* between *distinct* Hall insulator states with the *same* value of the Hall conductivity are observed that are driven by changing the in-plane component of the external magnetic field (Eisenstein et al., 1990; Clark et al., 1990; Engel et al., 1992; Sajoto et al., 1990), which may affect the spin polarization of the electron gas, as predicted and explored in Morf and Halperin (1986) and Chakraborty (1986). For $\sigma_H \overset{e.g.}{=} \frac{1}{2}$, such transitions may be driven by changing the density of charge carriers in a wide quantum well, accompanied by a change in the external magnetic field, as studied in Suen et al. (1994).

The story just told can also be presented from the point of view of edge degrees of freedom. The chiral anomaly (46) and expression (54) imply that there must exist several (*N*) species of gapless chiral quasi-particles propagating along the edge. They are described by *N* chiral scalar Bose fields $\{\varphi^\alpha\}_{\alpha=1}^N$ with propagation speeds $\{v_\alpha\}_{\alpha=1}^N$, with the properties that

1. the chiral electric edge current operator and the Hall conductivity are given by the formulae

$$j^\mu_{edge} = e\sum_{\alpha=1}^{N} \frac{Q_\alpha}{\sqrt{2\pi}}\, \varepsilon^{\mu\nu}\partial_\nu\varphi^\alpha, \quad \sigma_H^{edge} = \frac{e^2}{h} Q \cdot Q^T \overset{!}{=} \sigma_H, \quad \text{with} \quad Q := (Q_1, \dots, Q_N);$$

and

---

[17] See, for example, Conway and Sloane (1993) for information about integral lattices and their invariants.

2. multielectron/hole states localized at an edge are created by the vertex operators

$$: \exp i\left(\sum_{\alpha=1}^{N} \sqrt{\pi}\, q_\alpha \varphi^\alpha\right) : , \quad \text{where} \quad q = \begin{pmatrix} q_1 \\ \vdots \\ q_N \end{pmatrix} \in \Gamma. \tag{63}$$

The connection between electric charge and (quantum) statistics valid in 1D "chiral Luttinger liquids" implies that Γ must be an odd-integral lattice of rank N (which is seen by arguments identical to the ones described above for the bulk of the electron liquid). If the Witt sublattice of a Hall lattice Γ contains the root lattice of a Lie algebra $\mathfrak{g}$, then $\mathfrak{g}$ must belong to the A, D or E series; and one finds that the chiral Luttinger liquid describing the edge degrees of freedom gives rise to a Kac–Moody algebra of chiral edge currents $\hat{\mathfrak{g}}_{k=1}$ at level 1.

A large family of Hall insulators can be classified by the data encoded into an odd-integral lattice Γ and a visible vector Q in the dual lattice Γ^*. As already mentioned, this implies that the Hall conductivity of such systems has the property that $\frac{h}{e^2}\sigma_H \in \mathbb{Q}$.

Remarks.

I. It is expected that vectors q^* belonging to the dual lattice $\Gamma^*(\supset \Gamma)$ are the quantum numbers of quasi-particles with *fractional charge* and *fractional statistics*.

II. Fractional electric charges of quasi-particles propagating along the edges/boundaries of a 2D incompressible electron gas can and have been measured by using Mach–Zehnder interferometry (see Glattli (2005); and Fröhlich et al. (2010), Bieri and Fröhlich (2012) for theory).

III. The fractional quantum Hall effect might be observed in 2D-gapped electron gases with quasi-particles that obey *non-abelian braid statistics* (see Section "What is fractional or braid statistics?"; Moore and Read (1991), Fröhlich et al. (2001)). By dragging such quasi-particles adiabatically along nonintersecting world lines (braids) one could in principle realize quantum gates for quantum computation. This idea is described in Bonesteel et al. (2005).

Further details can be found in Fröhlich and Thiran (1994), Fröhlich et al. (1996), Fröhlich (1995), and Fröhlich et al. (2001).

Induced Chern–Simons actions, dualities, and 2D chiral photonic wave guides

We consider a model of 3D quantum electrodynamics (QED_3), namely, a relativistic quantum field theory of an odd number of Dirac fermions of electric charge e described by 2-component spinor fields, ψ_α, of masses $M_\alpha \neq 0$, $\alpha = 1, 2, \ldots, 2n+1$, propagating in a three-dimensional space-time, $\Lambda\ (= \Omega \times \mathbb{R})$, and minimally coupled to an electromagnetic vector potential A. This theory breaks the symmetries of time reversal and reflection in lines. Integrating over the degrees of freedom of the Dirac fermions, we find that the effective action of the vector potential A is given by

$$\begin{aligned} S_\Lambda(A) &= \sum_{\alpha=1}^{2n+1} \ell n\left[\det{}_{ren}\left(\left(\partial_\mu - eA_\mu\right)\gamma^\mu + M_\alpha\right)\right] \\ &= \sum_{\alpha=1}^{2n+1} Tr\ell n\left(1 - G_{M_\alpha} e A_\mu \gamma^\mu\right), \end{aligned} \tag{64}$$

where the matrices γ^μ, $\mu = 0, 1, 2$, are 2×2 Dirac matrices, and G_M is the propagator of a free 2-component Dirac spinor with mass $M \neq 0$ propagating in Λ; (constants are ignored on the right side of (64)). One may expand the logarithm on the right side of (64) in powers of A. For a large value of the mass M, the leading term in $Tr\ell n(\mathbf{1} + G_M e A_\mu \gamma^\mu)$ is the one quadratic in A, which can be calculated explicitly, as has been done by Deser et al. (1982, 1988, 2000) (see also Redlich (1984)).[18] The quadratic term is given by

$$sgn(M)\, \frac{e^2}{8\pi\hbar} \int_\Lambda A \wedge dA + \text{boundary term}, \tag{65}$$

that is, by a Chern–Simons term corresponding to a Hall conductivity $\sigma_H = \pm\frac{1}{2} \cdot \frac{e^2}{h}$. Terms of higher order in A tend to 0, as $M \to \infty$. I will not reproduce the calculations leading to (65); but see Deser et al. (1982, 1988, 2000) and Redlich (1984).

If the electromagnetic field is treated as a dynamical quantum field, one must add a Maxwell term to the induced Chern–Simons action appearing on the right side of (64). Thus the total effective action functional of QED_3 is given by

$$\begin{aligned} S_\Lambda(A) = &\sum_{\alpha=1}^{2n+1} sgn(M_\alpha)\left\{\frac{e^2}{8\pi\hbar}\int_\Lambda A \wedge dA + \Gamma_{\partial\Lambda}(A_\parallel)\right\} \\ &+ \int_\Lambda \left[\varepsilon \underline{E}^2 - \mu^{-1} B^2\right] d^3x + \text{less relevant terms}. \end{aligned} \tag{66}$$

Neglecting terms of higher than quadratic order in the electromagnetic vector potential A on the right side of (66), $S_\Lambda(A)$ is a quadratic form in the vector potential A. If Ω is a cube and periodic boundary conditions are imposed at $\partial\Omega$ (i.e., Ω is a torus), then this quadratic form can be diagonalized by Fourier transformation. This yields an explicit (momentum-space) expression for the 2-point functions of the electromagnetic field tensor; general n-point functions can be expressed as sums of products of 2-point functions by appealing to Wick's theorem. The denominators of the imaginary-time (Euclidean) 2-point functions of the components, $F_{\mu\nu}$, of the electromagnetic field tensor in Euclidean energy–momentum space are given by $[k^2 + \text{const.}e^2]$, where k is the energy–momentum variable. This shows that, in this model of QED_3, *photons* have a *strictly positive mass* proportional to e.

---

[18] This calculation also appeared in unpublished work on QED3 by J. Magnen, the late R. Sénéor, and myself.

If space-time Λ has a boundary then the effective action of the electromagnetic field has a boundary term given by the anomalous chiral action $\sigma_H \Gamma_{\partial\Lambda}(A_{\|})$ cancelling the anomaly of the Chern–Simons term in (66), as discussed in (51) and (57).

It is argued that, in certain planar systems of condensed matter, there exist charged quasi-particles with low-energy properties mimicking those of 2-component Dirac fermions. An example is "doped" graphene (see, e.g., Semenoff, 1984; Giuliani et al., 2012, and references given there). The low-energy properties of such systems can be described by a theory approaching the model of QED_3 introduced above in the infrared domain.

In planar systems (i.e., systems in three space-time dimensions), the electromagnetic vector potential, A, and the vector potential, B, of the conserved electric current density, $J = \nabla \wedge B$, play *dual roles*: Under the replacements

$$A \mapsto B, \quad B \mapsto A, \tag{67}$$

one finds that the (leading terms in the) effective actions of *conventional time-reversal invariant 2D insulators* are mapped to the (leading terms in the) effective actions of *2D superconductors*, and *electronic Hall- or Chern insulators* are mapped to *gapped photonic wave guides* exhibiting extended chiral electromagnetic surface waves; and *conversely* (see Fröhlich et al., 1996).

As an example we consider the duality between certain Hall or Chern insulators and gapped photonic wave guides. We define an action functional depending on the vector potential B of a conserved vector current in an insulator breaking time-reversal invariance by

$$\widetilde{S}_\Lambda(B) := \frac{1}{2\sigma_H}\int_\Lambda B \wedge dB + \text{boundary action} + \text{less relevant terms}, \qquad \sigma_H := \frac{e^2}{4\pi\hbar}. \tag{68}$$

In the infrared domain, *QED_3 with induced Chern–Simons action* and *the quantum theory of currents in Hall insulator* are then seen to be related by duality, that is, by the replacements in (67). This is elucidated by functional Fourier transformation:

$$e^{i\, S_\Lambda(A)} = \mathcal{N}^{-1}\int e^{i\widetilde{S}_\Lambda(B)}\, e^{i\int_\Lambda A\wedge dB}\mathcal{D}B, \tag{69}$$

where $\mathcal{N}$ is a normalization factor, and conversely. One may view the current driven through a planar wave guide with broken time-reversal invariance as a *classical control variable*, while the electromagnetic field is treated as a system of quantized *dynamical* degrees of freedom. The response equations of such a wave guide are then found to be given by

$$\langle F_{\mu\nu}(x)\rangle_B = \varepsilon_{\mu\nu\lambda}\frac{\delta\widetilde{S}_\Lambda(B)}{\delta B_\lambda(x)} = \sigma_H^{-1}\varepsilon_{\mu\nu\lambda}\, j^\lambda(x). \tag{70}$$

The boundary action on the right side of Eq. (68) is given by $\frac{1}{\sigma_H}\Gamma^{(\pm)}_{\partial\Lambda}(B|_{\partial\Lambda})$, with

$$\Gamma^{(\pm)}_{\partial\Lambda}(b) := \frac{1}{2}\int_{\partial\Lambda}\left[b_+ b_- - 2b_\pm \frac{\partial_\pm^2}{\Box} b_\pm\right] du^+\, du^-$$

in light-cone coordinates (u^+, u^-) on $\partial\Lambda$, with $B|_{\partial\Lambda} = b_+ du^+ + b_- du^-$. The sign of σ_H and the choice of "±" in $\Gamma^{(\pm)}_{\partial\Lambda}$ depend on the chirality of the electromagnetic edge waves. The boundary action $\Gamma^{(\pm)}_{\partial\Lambda}(b)$ is the generating functional of Green functions of *gapless edge modes of the quantized electromagnetic field* propagating chirally around the boundary of the wave guide. In the bulk of such wave guides, the electromagnetic field is gapped as remarked above.

It would be tempting to continue with a discussion of various further topics, such as the *theory of rotating Bose gases* in two dimensions and their Hall effects. This topic started with my work with U. M. Studer and E. Thiran (see Fröhlich et al., 1996). Much further work on 2D Bose gases has since been carried out in Cooper (2008) and Rougerie et al. (2014) (and references given there). The role of *gravitational anomalies* in an analysis of *heat transport* in 2D systems of condensed matter physics has been elucidated in Klevtsov and Wiegmann (2015) and Klevtsov et al. (2017).

Five-dimensional QED, a close cousin of the theory introduced in (64) through (66), will make a brief appearance in Section "A five-dimensional cousin of the Hall effect and axion electrodynamics" and might be of interest, for example, in cosmology.

Chiral spin currents in planar topological insulators

So far, we have ignored electron spin, in spite of the fact that there are 2D gapped electron gases exhibiting the fractional quantum Hall effect where electron spin plays an important role, as mentioned in Section "Classification of "abelian" Hall fluids." (We won't study these systems any further; but see Fröhlich and Studer (1993), Fröhlich and Thiran (1994), and Fröhlich et al. (1996), and references given there.)

In this section we consider **2D time-reversal invariant topological insulators** exhibiting chiral spin currents.[19] We start from the *Pauli equation* for the spinor wave function, Ψ_t, of a spinning electron

$$i\hbar D_0\Psi_t = -\frac{\hbar^2}{2m} g^{-1/2} D_k \left(g^{1/2} g^{kl}\, D_l \Psi_t\right), \tag{71}$$

where m is the effective mass of an electron, (g^{kl}) is the inverse of the Riemannian metric on sample space, Ω, an orthonormal frame bundle is introduced on space-time $\Omega \times \mathbb{R}$ enabling one to define 2-component *Pauli spinors*, Ψ, and, in particular, to introduce notions of spin-up, ↑, and spin-down, ↓:

$$\Psi_t(x) = \begin{pmatrix} \psi_t^{\uparrow}(x) \\ \psi_t^{\downarrow}(x) \end{pmatrix} \in L^2(\Omega, d\ vol.) \otimes \mathbb{C}^2.$$

Furthermore, the symbols $D_\mu,\ \mu = 0, \ldots, d, d = 2$ or $3,$ are covariant derivatives

$$i\hbar D_0 = i\hbar\partial_t + e\varphi - \vec{W}_0 \cdot \vec{\sigma}, \quad \vec{W}_0 = \mu c^2 \vec{B} + \cdots, \tag{72}$$

where φ is the electrostatic potential acting on the electrons, $\vec{W}_0 \cdot \vec{\sigma}$ is the Zeeman coupling of the spin of electrons to the zero-component, $\vec{W}_0$, of an $SU(2)$-gauge field; $\vec{W}_0$ describes an external magnetic field and/or a Weiss exchange field (Albert et al., 2006). Furthermore,

$$\frac{\hbar}{i} D_k = \frac{\hbar}{i}\nabla_k + eA_k - \vec{W}_k \cdot \vec{\sigma} + \cdots, \tag{73}$$

where $\vec{A}$ is the electromagnetic vector potential, and the dots stand for further terms present in a moving background (which we ignore in the following, but see Fröhlich et al., 1996); moreover, $\vec{W}_k$ is the k-component of an $SU(2)$-gauge field, which, for the systems considered in this section, describes spin–orbit interactions, hence is given by

$$\vec{W}_k \cdot \vec{\sigma} := \left[\left(-\widetilde{\mu}\vec{E} + \cdots \right) \wedge \vec{\sigma}\right]_k, \tag{74}$$

where $\widetilde{\mu} = \mu + \frac{e\hbar}{4mc^2}$; (the term $\frac{e\hbar}{4mc^2}$ is due to Thomas precession).

We observe that the Pauli equation (71) displays perfect $U(1)_{em} \times SU(2)_{spin}$ - gauge invariance. The $U(1)_{em}$- connection, A, is given in terms of the electromagnetic potentials $\varphi =: A_0$ and $\vec{A}$ by $A = A_0 dt + A_1 dx^1 + \cdots + A_d dx^d,$ while $\vec{W} = \vec{W}_0 dt + \vec{W}_1 dx^1 + \cdots \vec{W}_d dx^d$ is the $SU(2)_{spin}$- connection, with $x = (t \equiv x^0, x^1, \ldots, x^d), d = 2$ or $3,$ the space-time coordinates on $\Lambda = \Omega \times \mathbb{R}$. (See Fröhlich and Studer (1993) and Fröhlich et al. (1996) for a more detailed discussion.)

In the following, we consider an interacting electron gas confined to a planar region Ω, setting $d = 2$ and $x^1 \equiv x, x^2 \equiv y$. We assume that $\vec{B} \perp \Omega$ and $\vec{E} \equiv \underline{E}$ is parallel to Ω. Then the $SU(2)_{spin}$- connection, $\vec{W}_\mu$, is given by

$$W_\mu^3 \cdot \sigma_3, \quad \text{with } W_\mu^K \equiv 0, \text{ for } K = 1, 2, \tag{75}$$

with W_0^3 given by (72) and $W_k^3, k = 1, 2,$ given by (74). From (75), we conclude that, for the systems considered here, parallel transport of Pauli spinors splits into parallel transport for the spin-up (↑) and the spin-down (↓) components. The spin-up component, $\psi^{\uparrow}$, of a Pauli spinor Ψ couples to the *abelian* connection $a + w$, while $\psi^{\downarrow}$ couples to $a - w$, where

$$a_\mu = -eA_\mu, \quad \text{and} \quad w_\mu = W_\mu^3, \tag{76}$$

see (72) and (74). Under time reversal, T,

$$a_0 \to a_0,\ a_k \to -a_k, \quad \text{but} \quad w_0 \to -w_0,\ w_k \to w_k. \tag{77}$$

The dominant term in the effective action of a 2D time-reversal invariant topological insulator, with $\vec{W}$ as in (75), is given by a combination of Chern–Simons terms. If either $w \equiv 0$ or $a \equiv 0$ a Chern–Simons term in a or in w *alone* would *not* be time-reversal invariant. Hence, assuming time-reversal invariance and $w \equiv 0$, the dominant term would be given by

$$S_\Lambda(A) = \int_\Lambda dt\, d^2x \{\varepsilon \underline{E}^2 - \mu^{-1} B^2\}, \tag{78}$$

which is the effective action of a *conventional insulator*.

But, in the presence of both connections, a and w, a combination of *two* Chern–Simons actions **is** time-reversal invariant. The leading ("most relevant") contribution to the (bulk) effective action is given by

$$\begin{aligned} S_\Lambda(a, w) &= \frac{\sigma}{2}\int_\Lambda \{(a + w) \wedge d(a + w) - (a - w) \wedge d(a - w)\} \\ &= \sigma \int_\Lambda \{a \wedge dw + w \wedge da\}, \end{aligned} \tag{79}$$

---

[19] A general reference where the role of electron spin and spin currents and the spin Hall effect are analyzed is Dyakonov (2008).

where we have neglected the boundary (edge) actions.[20] The gauge fields a and w transform *independently* under gauge transformations preserving condition (75), and the action in (79) is *anomalous* under these gauge transformations, for a 2D sample space Ω with nonempty boundary. We have learned in Section "The 2D quantum Hall effect" that the anomalous boundary action,

$$\sigma\left[\Gamma^{+}_{\partial\Omega\times\mathbb{R}}\left((a+w)_{\parallel}\right)-\Gamma^{-}_{\partial\Omega\times\mathbb{R}}\left((a-w)_{\parallel}\right)\right], \tag{80}$$

cancels the anomalies of the bulk action; see Eqs. (50) and (51). This boundary action is the generating functional of connected Green functions of *two counter-propagating anomalous chiral edge currents*. One of the two counter-propagating edge currents is carried by electrons with spin up (↑), that is, spin polarization in the + 3-direction $\perp\Omega$, and the other one is carried by electrons with spin down (↓). These edge currents are exchanged by time reversal. A net *chiral spin current*, s^3_{edge}, can be excited to propagate along the edge of such a system. The bulk response equations (analogous to the Hall–Chern–Simons law (42)) are given by

$$j^k(x)=2\sigma\varepsilon^{k\ell}\partial_\ell B(x),\qquad s^\mu_3(x)=\frac{\delta S_\Lambda(a,w)}{\delta w_\mu(x)}=2\sigma\varepsilon^{\mu\nu\lambda}F_{\nu\lambda}(x), \tag{81}$$

where we have expressed the $SU(2)$-gauge field $\vec{W}$ in terms of the magnetic induction $\vec{B}=(0,0,B)$ and the electric field $\vec{E}=(\underline{E},0)=(E_1,E_2,0)$. As in Section "The 2D quantum Hall effect," Eqs. (43)–(45), (81) could again be used to deduce the existence of the edge spin currents discovered above.

We should ask what kinds of quasi-particles in the bulk of planar materials might produce the bulk Chern–Simons terms in (79). Given our findings in Section "Induced Chern–Simons actions, dualities, and 2D chiral photonic wave guides," it is tempting to argue that a 2D time-reversal invariant topological insulator with a bulk effective action as given in (79) must exhibit two species of charged quasi-particles in the bulk, with one species (spin-up, ↑) related to the other one (spin-down, ↓) by time reversal, and each species has two degenerate states per wave vector mimicking a two-component Dirac fermion at small energies, leading to the quantization of σ.

Materials of this kind have been produced and studied in the laboratory of L. Molenkamp in Würzburg (see Franz and Molenkamp, 2013). The experimental data are not very clean, the likely reason being that, due to magnetic impurities in the material and/or electric fields in the direction $\perp\Omega$, the condition in (75) is violated, that is, the $SU(2)$-gauge field $\vec{W}_\mu$ has nonvanishing components W^K_μ and is genuinely *non-abelian*. In this situation, the spin current is *not* conserved, anymore (but continues to be covariantly conserved, see Fröhlich and Studer, 1993), and time reversal invariance is broken.

The approach to 2D time-reversal invariant topological insulators sketched in this section can be generalized as follows: We consider a state of matter exhibiting a bulk spectrum of two species of quasi-particles related to one another by time reversal. In order to analyze the transport properties of such a state, one should study its response when one species is coupled to a (real or virtual, abelian or *non-abelian*) external gauge field W^+ and the other one to a gauge field W^- related to each other by time reversal according to

$$(W^+_0)^T=W^-_0,\quad (W^+_k)^T=-W^-_k.$$

If the leading term in the effective action for the gauge fields W^+ and W^- is given by the sum of two identical Chern–Simons terms, but with *opposite* signs, time-reversal invariance is manifestly preserved, and one concludes that there are *two counter-propagating chiral edge currents* generating current (Kac–Moody) algebras[21] based on a Lie group given by the gauge group of the gauge fields $W^\pm$. For noninteracting electrons, this group can be determined from band theory.

If one gives up the requirement of time-reversal invariance, one arrives at a general theory of *chiral states* in 2D (planar) systems of condensed matter physics. If $\vec{W}$ is an $SU(2)$-gauge field coupling to the spin of electrons, as in (72) and (74), one obtains a framework well suited to describe *chiral spin liquids* (see Fröhlich et al., 1996 and references given there).

Anomalous current commutators and the chiral magnetic effect

I recall the definition of left-handed and right-handed currents and the anomalous current commutators described in Section "The chiral anomaly" for theories in four space-time dimensions, namely

$$\begin{gathered}J^\mu_\ell:=\frac{1}{2}\left[J^\mu+J^\mu_5\right],\quad J^\mu_r:=\frac{1}{2}\left[J^\mu-J^\mu_5\right]\\ \left[J^0_{\ell/r}(\vec{y},t),J^0(\vec{x},t)\right]=\pm i\frac{\alpha}{8\pi^2}\left(\vec{B}(\vec{y},t)\cdot\vec{\nabla}_{\vec{y}}\right)\delta(\vec{x}-\vec{y});\end{gathered}\tag{82}$$

see Jackiw et al. (1986) and references given there, Faddeev (1984), and Fosco and Trinchero (1990) for a derivation using functional integrals.

I proceed to recall the *chiral magnetic effect* and its derivation from the anomalous commutator stated in (82). For this purpose I consider a theory of charged, massless Dirac fermions in four space-time dimensions. This theory has a conserved vector current, J^μ, satisfying the continuity equation

---

[20] Note that if $\vec{W}$ is expressed in terms of $\vec{B}$ and $\vec{E}$, as in (72), (74), (75), one recovers expression (78). The effective action in (79) first appeared in a paper with U. M. Studer (Fröhlich and Studer, 1993) in 1993!

[21] At level 1, for noninteracting electrons.

$$\partial_\mu J^\mu = 0.$$

This equation implies that there exist two vector fields, $\vec{\varphi}(x)$ and $\vec{\chi}(x)$, such that

$$J^0(x) = \frac{e}{2\pi}\vec{\nabla}\cdot\vec{\varphi}(x), \quad \vec{J}(x) = -\frac{e}{2\pi}\left\{\frac{\partial}{\partial t}\vec{\varphi}(x) + \vec{\nabla}\times\vec{\chi}(x)\right\}, \tag{83}$$

where e is the electric charge of the fermions. If H denotes the Hamiltonian of the system then the Heisenberg equations formally imply that

$$\frac{\partial}{\partial t}\vec{\varphi}(x) = \frac{i}{\hbar}[H, \vec{\varphi}(x)]. \tag{84}$$

We define chiral charges

$$N_{\ell/r} := \int d^3x\, \hat{J}^0_{\ell/r}(t, \vec{x}), \tag{85}$$

where

$$\hat{J}^\mu_{\ell/r} := J^\mu_{\ell/r} \mp \frac{e^2}{8\pi^2}\varepsilon^{\mu\nu\rho\lambda}A_\nu F_{\rho\lambda}.$$

The second term on the right side of this equation is dual to the Chern–Simons 3-form, $A\wedge dA$, that we are already familiar with. Since the fermions are assumed to be massless, the charges $N_{\ell/r}$ are *conserved*, as follows from Eq. (7) in Section "The chiral anomaly," and *gauge-invariant*.

Henceforth we suppose that all external fields, in particular the electromagnetic field, are *time-independent*. We may then consider an equilibrium state, $\langle(\,\cdot\,)\rangle_{\beta,\underline{\mu}}$, of the system with nonvanishing *chemical potentials*, $\underline{\mu} := (\mu_\ell, \mu_r)$, conjugate to the charges N_ℓ and N_r, respectively. Our aim is to calculate $\vec{j}(x) = \langle\vec{J}(x)\rangle_{\beta,\underline{\mu}}$, using arguments reminiscent of those in Section "A first application: Conduction quantization in quantum wires." By Eqs. (83) and (84),

$$\vec{j}(x) = -\frac{ie}{h}\langle[H, \vec{\varphi}(x)]\rangle_{\beta,\underline{\mu}} - \frac{e}{2\pi}\vec{\nabla}\times\langle\vec{\chi}(x)\rangle_{\beta,\underline{\mu}} \tag{86}$$

Formally, the term proportional to $\langle[H, \vec{\varphi}(x)]\rangle_{\beta,\underline{\mu}}$ vanishes because the equilibrium state is time-translation invariant. However, the field $\vec{\varphi}$ turns out to have ill-defined zero modes so that we cannot use the identity $[H, \vec{\varphi}(x)] = H\vec{\varphi}(x) - \vec{\varphi}(x)H$. We must regularize the right side of (86) by giving the field $\vec{\varphi}$ a small mass and then use that

$$\frac{\partial}{\partial t}\vec{\varphi}(x) = \frac{i}{h}\left[H - \mu_\ell N_\ell - \mu_r N_r, \vec{\varphi}(x)\right] + \frac{i}{h}\left[\mu_\ell N_\ell + \mu_r N_r, \vec{\varphi}(x)\right] \tag{87}$$

and that $\left\langle[H - \mu_\ell N_\ell - \mu_r N_r, \vec{\varphi}(x)]\right\rangle_{\beta,\underline{\mu}} = 0$. Combining this identity with (86) and (87), we find the *current sum rule*

$$\vec{j}(x) = -\frac{ie}{h}\left\langle\left[\mu_\ell N_\ell + \mu_r N_r, \vec{\varphi}(x)\right]\right\rangle_{\beta,\underline{\mu}} - \frac{e}{2\pi}\vec{\nabla}\times\langle\vec{\chi}(x)\rangle_{\beta,\underline{\mu}}. \tag{88}$$

Recalling formula (82) for the anomalous current commutators and (83), we conclude that

$$\left[\hat{J}^0_{\ell/r}(\vec{y}, t), \vec{\varphi}(\vec{x}, t)\right] = \mp i\frac{e}{4\pi}\vec{B}(\vec{y}, t)\,\delta(\vec{x} - \vec{y}) + \vec{\nabla}_x \wedge \vec{\Pi}_{\ell/r}(\vec{x}, \vec{y}; t), \tag{89}$$

for some $\vec{\Pi}_{\ell/r}$. Using (85), (88), and (89), we find that the current density $\vec{j}$ is given by the equation

$$\vec{j}(x) = \frac{e^2}{4\pi h}(\mu_\ell - \mu_r)\vec{B}(x) + \vec{\nabla}\times\vec{\mathfrak{B}}(x), \tag{90}$$

where the second term, proportional to $\vec{\mathfrak{B}}$, on the right side describes a persistent current not related to the magnetic induction $\vec{B}$, which we will not consider any further. Eq. (90) describes the *chiral magnetic effect* first considered in Vilenkin (1980) and Fukushima (2013) (see Alekseev et al. (1998) for a derivation along the lines of the arguments presented above). A more conceptual treatment of this effect is given in Section "A five-dimensional cousin of the Hall effect and axion electrodynamics."

An effect related to the chiral magnetic effect might be observed in systems of spinning particles propagating in a *rotating (noninertially moving) background*, such as leptons in a rapidly rotating star.

A possible manifestation of the chiral magnetic effect in cosmology

In this section, we sketch ideas concerning the evolution of magnetic fields in an expanding Universe, that is, with a Hubble constant $\mathcal{H} \geq 0$, filled with a plasma of charged particles, assuming that there exists an asymmetry between right-handed and left-handed fermions so that the chiral chemical potential $\mu_5 := \mu_\ell - \mu_r$ does not vanish. In the following we use units such that the speed of light $c = 1$.

Faraday's induction law and the absence of magnetic monopoles are encoded in the homogeneous Maxwell equations

$$\vec{\nabla} \wedge \vec{E} = -\dot{\vec{B}}, \quad \vec{\nabla} \cdot \vec{B} = 0.$$

Coulomb's law and the Ampère-Maxwell law are encoded in the inhomogeneous Maxwell equations

$$\vec{\nabla} \cdot \vec{E} = j^0, \qquad \vec{\nabla} \wedge \vec{B} = \dot{\vec{E}} + \mathcal{H}\vec{E} + \vec{j},$$

where $j = (j^0, \vec{j})$ is the vector current density of charged matter. We assume that the leading contribution to $\vec{j}$ is due to the *chiral magnetic effect*, besides a conventional contribution described by *Ohm's law*, that is,

$$\vec{j} = \frac{\alpha}{8\pi^2}\mu_5 \vec{B} + \sigma \vec{E}, \qquad \alpha = \frac{e^2}{\hbar}, \tag{91}$$

where σ is the *Ohmic conductivity* of the plasma. Taking the *curl* of the Ampère-Maxwell law, with $\vec{j}$ as in (91), and using Faraday's induction law we find that

$$\Box\, \vec{B} + \frac{\alpha}{8\pi^2}\mu_5 \vec{\nabla} \wedge \vec{B} + (\mathcal{H} + \sigma)\dot{\vec{B}} + \mathcal{O}(\dot{\mathcal{H}}, \sigma\mathcal{H}, \mathcal{H}^2) = 0, \tag{92}$$

where $\Box$ is the d'Alembert operator. The Hubble constant $\mathcal{H}$ is assumed to be slowly varying in time. From here on, the terms $\mathcal{O}(\dot{\mathcal{H}}, \sigma\mathcal{H}, \mathcal{H}^2)$ in this equation are neglected. We solve Eq. (92) by Fourier transformation, using the ansatz

$$\vec{B}(\vec{x}, t) = \vec{b}e^{i(kz-\omega t)}, \quad \text{with } \vec{b} \perp z\text{–}axis,$$

as required by the equation $\vec{\nabla} \cdot \vec{B} = 0$. Setting $\frac{\alpha}{8\pi^2}\mu_5 =: \widetilde{\mu}$, the frequency $\omega(k)$ is found to be given by

$$\omega(k) = -i(\mathcal{H} + \sigma) \pm \sqrt{-(\mathcal{H} + \sigma)^2 + k^2 \pm \widetilde{\mu}|k|}.$$

We observe that the assumptions that $\mathcal{H} \geq 0$ (expansion of the Universe) and $\sigma > 0$ (matter is a conducting plasma) lead to an *exponential damping* of $\vec{B}$ in time, *provided* that $|k| > \widetilde{\mu}$. But if $|k| < \widetilde{\mu}$ there exists a solution for which ω has a *positive* imaginary part, and the solution of (92) *grows exponentially*. This instability might be related to the growth of spatially very slowly varying primordial magnetic fields in the early Universe. Of course, the value of μ_5 is time-dependent, and it is expected that μ_5 tends to 0, as time t tends to ∞. The instability described here will therefore come to an end, and the magnetic induction $\vec{B}$ will cease to grow.

A thorough analysis of this mechanism can be found in Fröhlich and Pedrini (2000), Boyarski et al. (2012), and Brandenburg et al. (2017), and references given there.

A five-dimensional cousin of the Hall effect and axion electrodynamics

We consider a system of charged matter at zero temperature coupled to an external electromagnetic field. In our derivation of the chiral magnetic effect (see (87)–(90)) we have assumed that the external electromagnetic field is *time-independent*. This is usually not the case, and in applications to cosmology and condensed matter physics, it is unrealistic to assume that $\mu_5 := \mu_\ell - \mu_r$ is independent of space and time. It turns out that a *dynamical analog* of μ_5 is known in particle physics under the name of *"axion"*. A very natural way of introducing axions is to study a cousin of the *quantum Hall effect* for a class of systems on a five-dimensional (space-time) slab, $\Lambda = \Omega \times [0, L]$, with two four-dimensional "boundary branes," $\partial_\pm\Lambda \simeq \Omega$ parallel to the (x^0, x^1, x^2, x^3)-plane in five-dimensional Minkowski space, where x^0 is the time coordinate. The slab Λ is assumed to be filled with *very heavy four-component Dirac fermions* coupled to the 5D electromagnetic vector potential, $\hat{A}$ (viewed as a 1-form on Λ). Integration over the fermion degrees of freedom yields the effective action for $\hat{A}$, which has the form

$$\begin{aligned} S_\Lambda(\hat{A}) = \frac{1}{2L\alpha}\int_\Lambda d^5x\, \hat{F}_{MN}(x)\hat{F}^{MN}(x) + CS_\Lambda(\hat{A}) \\ + \Gamma_\ell(\hat{A}|_{\partial_+\Lambda}) + \Gamma_r(\hat{A}|_{\partial_-\Lambda}) + \cdots, \end{aligned} \tag{93}$$

where α is dimensionless, L is the width of the 5D slab Λ, and

$$CS_\Lambda(\hat{A}) := \frac{\kappa_H}{24\pi^2}\int_\Lambda \hat{A} \wedge \hat{F} \wedge \hat{F} \tag{94}$$

is the *5D Chern–Simons action*.[22] For the time being, the vector potential $\hat{A}$ is treated as a classical external field. The action (94) predicts an analog of the Hall current given by

---

[22] In this section we use units such that $\hbar = 1$.

$$j^M = \frac{\kappa_H}{8\pi^2}\, \varepsilon^{MNJKL} F_{NJ}\, F_{KL}, \tag{95}$$

where the dimensionless constant κ_H plays the role of the Hall fraction $\frac{h}{e^2}\sigma_H$. The constant κ_H, related to the number of species of massive four-component Dirac fermions in the bulk, must be an integer for the functional integral to be well defined (assuming that all fermionic degrees of freedom have electric charges that are integer multiples of the elementary electric charge e). In the following I will set $\kappa_H = 1$. Eq. (95) should be compared to Eq. (42) of Section "The 2D quantum Hall effect."

The action functional in Eqs. (93) and (94) describes the electrodynamics of a five-dimensional analog of the quantum Hall effect (5D QHE). Apparently, such 5D quantum Hall effects can be observed in certain systems of condensed-matter physics with virtual dimensions that play the role of space dimensions (see Price et al., 2015; Lohse et al., 2018 and references given there).

In (93), the functionals $\Gamma_{\ell/r}$ are the anomalous actions of left-handed/right-handed Dirac–Weyl fermions located on the boundary branes, $\partial_\pm\Lambda$. The action Γ_ℓ+Γ_r on the right side of (93) cancels the anomaly of the Chern–Simons action $CS_\Lambda(\hat{A})$; see Jackiw et al. (1986).

It is of interest to consider the *dimensional reduction* of the 5D theory with effective action given in (93) and (94) to a four-dimensional space-time, assuming that there is a gauge with the property that $\hat{A}_M$ is independent of x^4, for all $M = 0, 1, 2, 3$. We define a field φ of scaling dimension 0, henceforth called *axion* field, by setting

$$\varphi(x) := \int_{\gamma x} \hat{A}$$

where γ_x is a path parallel to the x^4-axis connecting $\partial_-\Lambda$ to $\partial_+\Lambda$ at constant values of $x = (x^0, x^1, x^2, x^3)$. Then the action functional in (93) becomes

$$\begin{aligned} S_\Omega(A;\varphi) = &\frac{1}{2\alpha}\int_\Omega d^4x \left[F_{\mu\nu}(x)F^{\mu\nu}(x) + \frac{1}{L^2}\partial_\mu\varphi(x)\partial^\mu\varphi(x)\right] \\ &+ \frac{1}{8\pi^2}\int_\Omega \varphi\,(F \wedge F) + \Gamma_\Omega(A) + \cdots, \end{aligned} \tag{96}$$

Under the present assumptions on the vector potential $\hat{A}$, the term $\Gamma_\Omega(A) = \Gamma_\ell(A) + \Gamma_r(A)$ is *not* anomalous and is ignored in the following.

Expression (96) shows that the pseudo-scalar field φ can be interpreted as an *axion* field, whence its name. One can add a self-interaction term, $U(\varphi)$, to the Lagrangian density in (96), requiring that $U(\varphi)$ be periodic in φ with period 2π. From (96) we derive the equations of motion for $F_{\mu\nu} = \partial_\mu A_\nu - \partial_\nu A_\mu$ and φ.

$$\partial_\mu F^{\mu\nu} = -\frac{\alpha}{4\pi^2}\partial_\mu\left(\varphi\widetilde{F}^{\mu\nu}\right), \qquad L^{-2}\,\Box\,\varphi = \frac{\alpha}{8\pi^2}F_{\mu\nu}\widetilde{F}^{\mu\nu} - \frac{\delta U(\varphi)}{\delta\varphi}, \tag{97}$$

where $\widetilde{F}^{\mu\nu}$ is the dual field tensor. These are the field equations of "axion-electrodynamics." In terms of the electric and magnetic fields, these equations take the form

$$\begin{aligned} \vec{\nabla}\cdot\vec{B} &= 0, \quad \vec{\nabla}\wedge\vec{E} + \dot{\vec{B}} = 0, \\ \vec{\nabla}\cdot\vec{E} &= \frac{\alpha}{4\pi^2}\left(\vec{\nabla}\varphi\right)\cdot\vec{B}, \\ \vec{\nabla}\wedge\vec{B} &= \dot{\vec{E}} - \frac{\alpha}{4\pi^2}\{\dot{\varphi}\vec{B} + \vec{\nabla}\varphi\wedge\vec{E}\}, \end{aligned} \tag{98}$$

and

$$L^{-2}\,\Box\,\varphi = \frac{\alpha}{4\pi^2}\vec{E}\cdot\vec{B} - \frac{\delta U(\varphi)}{\delta\varphi}. \tag{99}$$

A generalized chiral magnetic effect

If the axion field φ only depends on time then $\vec{\nabla}\varphi = 0$, and, comparing the right side of (98) with (90) and reinstating $\frac{e^2}{\hbar}$, we find that

$$\dot{\varphi} = \mu_\ell - \mu_r \equiv \mu_5, \tag{100}$$

and (98) reproduces the equation describing the chiral magnetic effect; see Hehl and Obukhov (2003) and Fröhlich and Pedrini (2000).

In condensed matter theory, the equation of motion for $\dot{\varphi} \equiv \mu_5$ can take the form of a *diffusion equation*, including a term $\tau^{-1}\mu_5$, where τ is a relaxation time associated with the *dissipation* of the asymmetry between left- and right-handed degrees of freedom. Thus

$$\dot{\mu}_5 + \tau^{-1}\mu_5 - D\,\triangle\,\mu_5 = L^2\frac{e^2}{2\pi h}\vec{E}\cdot\vec{B}, \tag{101}$$

where D is a *diffusion constant*, and it is assumed here that $U(\varphi) \equiv 0$. Eq. (101) implies that μ_5 approaches

$$\mu_5 \simeq \frac{\tau (Le)^2}{2\pi h} \vec{E} \cdot \vec{B}, \tag{102}$$

as time t tends to ∞ (assuming that $\vec{E} \cdot \vec{B}$ is very slowly varying in space and time). This expression for μ_5 can be plugged into Eq. (90) for the current density $\vec{j}$, which then yields an expression for a conductivity tensor, $\sigma = (\sigma_{k\ell})$, in the presence of an external magnetic field given by

$$\sigma_{k\ell} = \frac{\tau (L\alpha)^2}{4\pi^2} B_k B_\ell \tag{103}$$

This expression can be used in the study of transport properties of *Weyl semimetals*, to mention one example, which are considered in the next section.

Axion electrodynamics has intriguing applications not only in condensed-matter physics but also in the theory of heavy-ion collisions, in astrophysics, and in cosmology, where it may explain the growth of tiny, but highly uniform, cosmic magnetic fields extending over intergalactic distances, as mentioned in Section "A possible manifestation of the chiral magnetic effect in cosmology"; see Fröhlich and Pedrini (2000), Boyarski et al. (2012), Brandenburg et al. (2017), and Schober et al. (2018) and references given there.

For some purposes, it is of interest to assume that one boundary brane, for example, $\partial_-\Lambda$ (located at $x^4 = 0$), does not carry dynamical degrees of freedom, and that $\hat{A}|_{\partial_-\Lambda} = 0$ while $\hat{A}|_{\partial_+\Lambda} =: A$ is arbitrary. We then set

$$\hat{A}_M(x, x^4) := \frac{x^4}{L} A(x)_\mu, \quad M \equiv \mu = 0, 1, 2, 3, \quad \hat{A}_4(x, x^4) =: \frac{1}{L}\varphi(x).$$

The axion field φ then transforms under an electromagnetic gauge transformations like an angle. From the action functional (93) of 5D Chern–Simons electrodynamics we derive the expression for the *gauge-invariant* action functional on four-dimensional space-time Ω $(= \partial_+\Lambda)$

$$\begin{aligned} S_\Omega(A, \varphi) := & \frac{1}{4\alpha} \int_\Omega d^4x \Big[\frac{1}{3} F_{\mu\nu}(x) F^{\mu\nu}(x) \\ & + L^{-2}\big(\partial_\mu \varphi(x) - A_\mu(x)\big)\cdot\big(\partial^\mu \varphi(x) - A^\mu(x)\big)\Big] \\ & + \frac{1}{8\pi^2}\int_\Omega \varphi(F \wedge F) + \Gamma_\ell(A) + \text{"irrelevant" terms.} \end{aligned} \tag{104}$$

This is the effective action of an anomaly-free 4D theory of chiral fermions coupled to electromagnetism and to an axion-like field φ that is *not* gauge-invariant.

3D Topological insulators and "axions"

In this last section, we study 3D topological insulators and Weyl semimetals on a sample space-time $\Lambda := \Omega \times \mathbb{R}$, with a nonempty boundary $\partial\Omega \times \mathbb{R}$. We are interested in the general form of the effective action describing the response of such systems to turning on an external electromagnetic field. Until the mid-nineties, the effective action of a 3D insulator was thought to be given by

$$S_\Lambda(A) = \frac{1}{2}\int_\Lambda dt\, d^3x \{\vec{E} \cdot \varepsilon \vec{E} - \vec{B} \cdot \mu^{-1} \vec{B}\} + \text{"irrelevant" terms,} \tag{105}$$

where ε is the tensor of dielectric constants and μ is the magnetic permeability tensor. The action defined in (105) is dimensionless. In the seventies, particle theorists taught us that one could add another dimensionless term, namely

$$S_\Lambda(A) \to S_\Lambda^{(\theta)}(A) := S_\Lambda(A) + \theta\, I_\Lambda(A), \tag{106}$$

where I_Λ is a *"topological"* term given by

$$\begin{aligned} I_\Lambda(A) &= \frac{1}{4\pi^2}\int_\Lambda dt\, d^3x\, \vec{E}(\vec{x}, t) \cdot \vec{B}(\vec{x}, t) \\ &= \frac{1}{8\pi^2}\int_\Lambda F \wedge F \overset{Stokes}{=} \frac{1}{8\pi^2}\int_{\partial\Lambda} A \wedge dA. \end{aligned} \tag{107}$$

In particle physics, the parameter θ is called "vacuum angle." It is expected that the effective action of an insulator with broken parity and time reversal symmetries, after integration over all matter degrees of freedom, is given by the functional $S_\Lambda^{(\theta)}(A)$ introduced in (106) and (107). In the thermodynamic limit, $\Omega \nearrow \mathbb{R}^3$, $\exp[iS_\Lambda^{(\theta)}(A)]$ is periodic in θ with period 2π and invariant under time reversal iff $\theta = 0, \pi$. If $\theta = \pi$, on a space-time Λ with a nonempty boundary $\partial\Lambda$, the effective action $S_\Lambda^{(\theta)}(A)$ contains a contribution only depending on $a := A|_{\partial\Lambda}$ given by the Chern–Simons term

$$\Gamma^{CS}_{\partial\Lambda}(a) = \pm\frac{1}{8\pi}\int_{\partial\Lambda} a \wedge da, \tag{108}$$

which breaks time-reversal invariance. This term must be canceled by surface degrees of freedom[23] on $\partial\Lambda$ exhibiting a Hall conductivity of

$$\sigma_H = \mp\frac{1}{2}\cdot\frac{e^2}{h}. \tag{109}$$

We have encountered the action of Eq. (108) in Section "Induced Chern–Simons actions, dualities, and 2D chiral photonic wave guides" (see formulae (65), (66)). Up to further, "less relevant" and time-reversal invariant terms, it is the effective action of one species of 2-component Dirac fermions coupled to $a = A|_{\partial\Lambda}$. *Gapless quasi-particles with spin* $\frac{1}{2}$propagating along $\partial\Lambda$ could mimic such Dirac fermions and cancel (108). The design of 3D materials with surface degrees of this kind is an interesting challenge.

The vacuum angle θ might be the ground-state expectation of a dynamical "axion" field, φ. The topological term $\theta I_\Lambda(A)$ would have to be replaced by

$$I_\Lambda(A,\varphi) := \frac{1}{8\pi^2}\int_\Lambda \varphi(F\wedge F) + S_0(\varphi), \tag{110}$$

where $S_0(\varphi)$ is invariant under shifts $\varphi \mapsto \varphi + 2n\pi,\ n\in\mathbb{Z}$. We then enter the realm of *axion electrodynamics*, as reviewed in Section "A five-dimensional cousin of the Hall effect and axion electrodynamics."

Recalling the field equations (98), one rediscovers *Halperin's 3D quantum Hall effect*: From Eq. (98) we infer a formula for the current density $\vec{j}$ in an external electromagnetic field and an "axion" field, namely

$$\vec{j} = -\frac{e^2}{2\pi h}\left(\dot{\varphi}\cdot\vec{B} + \vec{\nabla}\varphi\times\vec{E}\right) \tag{111}$$

I now consider a 3D *spatially periodic* system of matter with an emergent "axion," φ. The underlying crystal lattice is denoted by $\mathfrak{L}$. I suppose that φ is time-independent, that is, $\mu_5 = 0$. Taking into account the periodicity of $\exp(iI_\Lambda(A,\varphi))$ under shifts, $\varphi\mapsto\varphi+2n\pi, n\in\mathbb{Z}$, invariance under lattice translations implies that

$$\varphi(\vec{x}) = 2\pi\left(\vec{K}\cdot\vec{x}\right) + \phi(\vec{x}), \tag{112}$$

where $\vec{K}$ belongs to the *dual lattice* $\mathfrak{L}^*$, and ϕ is invariant under lattice translations. Neglecting ϕ, we find that $\vec{\nabla}\varphi = 2\pi\vec{K}$ is "quantized," as $\vec{K}$ belongs to the *dual*, $\mathfrak{L}^*$, of the crystal lattice $\mathfrak{L}$. With (112) this implies that

$$\vec{j} = \frac{e^2}{h}\vec{K}\times\vec{E}, \qquad \vec{K}\in\mathfrak{L}^*.$$

This is Halperin's 3D *(quantum) Hall effect* (Halperin, 1987; Kohmoto et al., 1992).[24]

Next, I describe "axionic" effects in topological insulators with an effective action given by

$$S_\Lambda(A,\varphi) = S_\Lambda(A) + \frac{1}{8\pi^2}\int_\Lambda \varphi F\wedge F + S_0(\varphi), \tag{113}$$

see (110), where $S_0(\varphi)$ is now assumed to be invariant under shifts $\varphi\mapsto\varphi+n\pi,\ n\in\mathbb{Z}$. It is compatible with time-reversal invariance that $S_0(\varphi)$ has (well developed) minima at $\varphi = n\pi$. Then the material described by (113) is *not* an ordinary insulator. It may exhibit a *Mott transition*: At a positive temperature, the bulk of such a material contains *domain walls* across which the value of the axion field φ jumps by an integer multiple of π. Recalling the insight described after (108) and (109), we predict that such domain walls may carry gapless two-component Dirac-type fermions. At sufficiently high temperatures, some of these domain walls can be expected to become macroscopic, and this would then give rise to a *nonvanishing conductivity*; see Fröhlich and Werner (2013).

A curious effect somewhat related to the one described in Section "A possible manifestation of the chiral magnetic effect in cosmology" (see also Fröhlich and Pedrini, 2000) that could possibly be observed in materials with an effective axion has been pointed out in Ooguri and Oshikawa (2012): A time-independent external *electric field* $\vec{E}$ applied to an axionic magnetic material is *screened* once its strength exceeds a certain critical value, the excess energy being fed into the growth of a *magnetic field*.

Weyl semimetals

It may be argued that dynamical axions could emerge as effective degrees of freedom in

- certain *3D topological insulators* with anti-ferromagnetic short-range order, (magnetic fluctuations playing the role of a dynamical axion)[25]; and in
- crystalline *3D Weyl semimetals*,

---

[23] I am indebted to H.-G. Zirnstein for an instructive discussion of this point.

[24] I am indebted to Greg Moore for a very instructive discussion of this effect.

[25] A conjecture proposed by S.-C. Zhang and coworkers in Li et al. (2010), inspired by the work in Fröhlich and Pedrini (2000).

that is, in systems with two energy bands exhibiting two (or, more generally, an even number[26] of) double cones in quasi-momentum-frequency space corresponding to *chiral* quasi-particle states, assuming that the Fermi energy is close to the apices of those double cones; see Herring (1937) and Xu et al. (2015). At low frequencies, namely, near the apices of those double cones, the quasi-particle states of such systems are left- or right-handed Weyl fermions, respectively. In such systems, the time derivative, $\dot{\varphi} \equiv \mu_5$, of the "axion field" φ really has the meaning of a time-dependent *difference of chemical potentials* of left-handed and right-handed quasi-particles. It satisfies an equation of motion of the kind described in (101), that is,

$$\dot{\mu}_5 + \tau^{-1}\mu_5 - D \triangle \mu_5 = L^2 \frac{e^2}{2\pi h} \vec{E} \cdot \vec{B}. \tag{114}$$

A nonvanishing initial value of the chemical potential μ_5 may be triggered by strain applied to the system, leading to a left-right asymmetric population of the Fermi sea. Due to *inter-valley scattering processes*, a nonvanishing μ_5 will then relax toward 0, with a relaxation time corresponding to the parameter τ in Eq. (114). However, when applying a small external electric field $\vec{E}$ and a magnetic induction $\vec{B}$ to the system, with the property that $\vec{E} \cdot \vec{B} \neq 0$, one finds from (114) that μ_5 relaxes toward $\mu_5 \simeq \frac{\tau (Le)^2}{2\pi h} \vec{E} \cdot \vec{B}$. Thus, the conductivity tensor, $\sigma = (\sigma_{k\ell})_{k,\ell=1,2,3}$, is given by

$$\sigma_{k\ell} = \sigma_{k\ell}^{(0)} + \frac{\tau (L\alpha)^2}{4\pi^2} B_k B_\ell,$$

where the first term on the right side is the standard Ohmic conductivity (due to phonon and impurity scattering), and the second term is a manifestation of the *chiral magnetic effect*; see Eq. (103).

Conclusion

I conclude this contribution with some general remarks, including ones about what is missing in it and a few personal ones.

1. I hope that this review shows that the physics of systems of condensed matter in two and three dimensions, and in particular of (topological) insulators, is very rich. It has potential to find promising technological applications. Mathematical techniques ranging from abstract algebra over the topology of fiber bundles all the way to hard analysis have interesting and often surprising applications in the study of these fascinating states of matter. Electron gases, magnetic materials, Bose gases, etc. offer many challenges to experimentalists and theorists. General principles and interesting features of quantum theory, such as braid statistics, fractional spin and fractional electric charges (see Sections "What is fractional or braid statistics?" and "The 2D quantum Hall effect"), anomalies and their cancellation, current algebra, and holography enter the arena of condensed matter physics. Exotic species of quasi-particles, in particular, quasi-particles with braid statistics, two-component Dirac-like and Weyl fermions and Majorana fermions are encountered in the physics of various two- and three-dimensional systems of condensed matter explored, theoretically and experimentally, in recent years.
2. An important goal in this contribution has been to review some of the results in theoretical condensed matter physics that are *not* limited to non-interacting electron gases, but apply to correlated systems exhibiting interaction effects. I hope that I have reached this goal and that this review shows that concepts and methods from quantum field theory pioneered in particle physics can be used to one's advantage to study general features of *interacting* systems in condensed matter physics. In particular, these methods are very useful to characterize and classify plenty of examples of *topological states of matter*, in particular ones that do not have any local order parameters so that conventional Landau theory is not applicable. The best explored examples are 2D incompressible electron gases in an external magnetic field exhibiting the fractional quantum Hall effect; see Prange and Girvin (1990), Chakraborty and Pietiläinen (1988), Fröhlich and Thiran (1994), and Fröhlich et al. (1996) and references given there. In this review the emphasis is on showing how concepts from *quantum gauge theory*, such as effective actions, power counting, gauge invariance, the chiral anomaly and some of its consequences, such as the chiral magnetic effect, θ-ground states, axion electrodynamics, quasi-particles with braid statistics, etc. can be used to come up with nontrivial and often quite surprising insights into properties of states of systems of condensed matter that have attracted much interest in recent years. The general formalism reviewed in this paper can thus rightly be called *Gauge Theory of States/Phases of Matter*. The rather ambitious goals of the efforts reviewed in this article may explain why mathematical rigor has not been the main concern—the mathematical complexity of quantum-mechanical many-body theory of interacting/correlated systems is well known to be awesome. I hope that, in spite of its somewhat abstract style and in spite of employing concepts first developed in particle physics, this review will contribute to making efforts in theoretical condensed matter physics by my collaborators and myself and many other somewhat mathematically oriented colleagues a little more widely known and appreciated.[27]

---

[26] This follows from the celebrated Nielsen–Ninomiya theorem; see Friedan (1982) and references given there.

[27] To read, to mention but one example (see Landsteiner, 2022), that it is *only during the past decade* that the chiral anomaly has been used in the study of transport phenomena in condensed matter physics makes me wonder whether communication channels within the scientific community are congested (to put it politely). Of course, there are also plenty of examples of this congestion in the mathematical physics community.—In all modesty I claim some credit for my collaborators and myself for having developed a useful formalism, emphasizing connections to particle physics and quantum field theory including gauge theory and the chiral anomaly, for the study of "topological states of matter," starting more than thirty years ago.

3. What is clearly and most regrettably missing in this review is an account of the *bare-hands analysis* of spectral properties of many-body Hamiltonians describing "topological states of matter" at energies quite close to the ground-state energy and to derive properties of quasi-particles and of transport, using a variety of powerful analytical tools, such as multiscale analysis[28] and renormalization group methods. Colleagues who have devoted very substantial efforts extending over many years toward reaching results in this direction are T. Balaban, F. Dyson, J. Feldman, G. Gallavotti, A. Giuliani, H. Knörrer, E. H. Lieb, J. Magnen, V. Mastropietro, W. Pedra, A. Pizzo, M. Porta, V. Rivasseau, M. Salmhofer, B. Schlein, R. Seiringer, E. Trubowitz, J. Yngvason, and others. References to early work by some of these colleagues can be found in my Les Houches lectures Chen et al. (1994) of 1994; among a variety of recent contributions toward understanding analytical aspects of the quantum Hall effect are the papers quoted in Giuliani et al. (2012, 2017) and Mastropietro and Porta (2022). Further references to many important results in mathematical quantum many-body theory, due to colleagues mentioned in this paper and numerous other researchers, can easily be found on "arXiv" and "google scholar." I strongly recommend their papers to the attention of the reader. Obviously plenty of fascinating open problems remain to be tackled.

Acknowledgments

I am immensely grateful to my many collaborators who have joined me on our sometimes arduous journey through some provinces of condensed matter physics, including the following colleagues: C. Albert, A. Alekseev, S. Bieri, A. Boyarsky, V. Cheianov, T. Chen, L. Ferrari, R. Götschmann, G.-M. Graf, T. Kerler, A. Knowles, I. Levkivskyi, P.-A. Marchetti, B. Pedrini, A. Pizzo, O. Ruchayskiy, B. Schlein, Chr. Schweigert, T. Spencer, U. M. Studer, E. Sukhorukov, E. Thiran, J. Walcher, Ph. Werner, and A. Zee. I am very grateful to the late R. Morf for having introduced me to the miracles of the quantum Hall effect, for many discussions and for his criticism, to P. Wiegmann for very helpful discussions and encouragement, and to M. Zirnbauer for his kind interest, extending over many years, in my efforts and for having invited me to a workshop at the Schrödinger Institute in Vienna and for a series of lectures at Bad Honnef, on which this review is based. I am indebted to T. Chakraborty for giving me this opportunity to present my point of view on some topics in condensed matter physics and for suggesting some clarifications in this text. I have profited from what colleagues at ETH Zurich and elsewhere, too many to be listed here, have taught me in numerous discussions.

AIPP-Data Availability Statement: Data sharing is not applicable to this article as no new data were created or analyzed in this study.

References

Adler SL (1969) Axial-vector vertex in spinor electrodynamics. *Physics Review* 177: 2426–2438.
Albert C, Ferrari L, Fröhlich J, and Schlein B (2006) Magnetism and the Weiss exchange field—A theoretical analysis motivated by recent experiments. *Journal of Statistical Physics* 125: 77–124.
Alekseev A, Cheianov V, and Fröhlich J (1997) Comparing conductance quantization in quantum wires and quantum Hall systems. *Physical Review B* 54: R17320–R17322.
Alekseev A, Cheianov V, and Fröhlich J (1998) Universality of transport properties in equilibrium, the Goldstone theorem, and chiral anomaly. *Physical Review Letters* 81: 3503–3506.
Anandan J (1989) In: *Proceedings of the 3rd International Symposium on the Foundations of Quantum Mechanics, Tokyo*, p. 98. Tokyo: Phys. Soc. Jpn.
Avron J, Seiler R, and Simon B (1990) Quantum Hall effect and the relative index for projections. *Physical Review Letters* 65: 2185–2188.
Avron J, Seiler R, and Simon B (1994) The index of a pair of projections. *Journal of Functional Analysis* 120: 220–237.
Bell JS and Jackiw R (1969) A PCAC puzzle: $\pi^0\gamma$ in the σ-model. *Nuovo Cimento A* 60: 47–61.
Bieri S and Fröhlich J (2012) Effective field theory and tunnelling currents in the fractional quantum Hall effect. *Annals of Physics* 327: 959–993.
Blok B and Wen XG (1990) Effective theories of the fractional quantum Hall effect at generic filling fractions. *Physical Review B* 42: 8133–8144.
Bonesteel NE, Hormozi L, and Zikos G (2005) Braid topologies for quantum computation. *Physical Review Letters* 95. 140503–1-4.
Boyarski A, Fröhlich J, and Ruchayskiy O (2012) Self-consistent evolution of magnetic fields and chiral asymmetry in the early universe. *Physical Review Letters* 108.
Brandenburg A, Schober J, Rogachevskii I, Kahniashvili T, Boyarsky A, Fröhlich J, Ruchayskiy O, and Kleeorin N (2017) The turbulent chiral magnetic cascade in the early universe. *The Astrophysical Journal Letters* 845: L21–L27.
Chakraborty T (1986) Spin-reversed quasiparticles in the fractional quantum Hall effect: Many-body approach. *Physical Review B* 34: 2926–2928.
Chakraborty T and Pietiläinen P (1988) The fractional quantum Hall effect. In: *Springer Series in Solid-State Sciences*, vol. 85. Berlin, Heidelberg: Springer-Verlag.
Chen T, Fröhlich J, and Seifert M (1994) Renormalization group methods: Landau-Fermi liquid and BCS superconductor. In: David F, Ginsparg P, and Zinn-Justin J (eds.) *Géométries Fluctuantes en mécanique Statistique et en Théorie des Champs. Les Houches LXII*, pp. 771–912. Amsterdam: Elsevier Science B.V.
Glattli DChr (2005) Tunneling experiments in the fractional quantum Hall effect regime. In: Douçot B, Duplantier B, Pasquier V, and Rivasseau V (eds.) *The Quantum Hall Effect, Poincaré Seminar 2004. Progress in Mathematical Physics*, vol. 45, pp. 163–197. Basel, Boston, Berlin: Birkhäuser Verlag.
Clark RG, Haynes SR, Branch JV, Suckling AM, Wright PA, Oswald PMW, Harris JJ, and Foxon CT (1990) Spin configurations and quasiparticle fractional charge of fractional QHE ground-states in the $N = 0$ Landau level. *Surface Science* 229: 25–30.
Conway JH and Sloane NJA (1993) *Sphere Packings, Lattices and Groups*. New York: Springer-Verlag.
Cooper NR (2008) Rapidly rotating atomic gases. *Advances in Physics* 57: 539–616.
Deser S, Jackiw J, and Templeton S (1982) Topologically massive gauge theories. *Annals of Physics* 140: 372–411.
Deser S, Jackiw J, and Templeton S (1988) Topologically massive gauge theories. *Annals of Physics* 185: 406 (erratum).
Deser S, Jackiw J, and Templeton S (2000) Topologically massive gauge theories. *Annals of Physics* 281: 409–449.
Dirac PAM (1933) The Lagrangian in quantum mechanics. *Physikalische Zeitschrift der Sowjetunion* 3(1): 64–72.
Dyakonov M (2008) Spin Physics in Semiconductors. *Springer Series in Solid-State Sciences*, vol. 157. Springer-Verlag.
Eisenstein JP, Stormer HL, Pfeiffer LN, and West KW (1990) Evidence for a spin transition in the $\nu = \frac{2}{3}$ fractional quantum Hall effect. *Physical Review B* 41: 7910–7913.

---

[28] A technique that owes some of its early momentum to a paper Fröhlich and Spencer (1981) containing the first mathematically rigorous proof of existence of the Berezinskii–Kosterlitz–Thouless transition.

Engel LW, Hwang SW, Sajoto T, Tsui DC, and Shayegan M (1992) Fractional quantum Hall effect at $\nu = \frac{2}{3}$ and $\frac{3}{5}$ in tilted magnetic fields. *Physical Review B* 45: 3418–3425.

Faddeev LD (1984) Operator anomaly for the Gauss law. *Physics Letters B* 145: 81–84.

Fosco C and Trinchero RC (1990) Anomalous commutators and functional integration. *Physical Review D* 41: 1216–1226. And references given there.

Franz M and Molenkamp L (2013) Topological insulators. In: Burstein E, MacDonald AH, and Stiles PJ (eds.) *Contemporary Concepts of Condensed Matter Science*, vol. 6, pp. 125–143. Amsterdam: Elsevier.

Fredenhagen K, Rehren KH, and Schroer B (1989) Superselection sectors with braid group statistics and exchange algebras. *Communications in Mathematical Physics* 125: 201–226.

Friedan D (1982) A proof of the Nielsen-Ninomiya theorem. *Communications in Mathematical Physics* 85: 481–490.

Fröhlich J (1976) New super-selection sectors ("soliton-states") in two dimensional Bose quantum field models. *Communications in Mathematical Physics* 47: 269–310.

Fröhlich J (1978) Invariant Wave Equations. *Lecture Notes in Physics*, vol. 73. Berlin, Heidelberg, New York: Springer-Verlag.

Fröhlich J (1988a) Statistics and Monodromy in two- and three-dimensional quantum field theory. In: Bleuler K and Werner M (eds.) *Differential Geometrical Methods in Theoretical Physics*. Dordrecht: Kluwer Academic Publishers.

Fröhlich J (1988b) Statistics of fields, the Yang-Baxter equation, and the theory of knots and links. In: 't Hooft G, et al. (eds.) *Non-perturbative Quantum Field Theory*. New York: Plenum Press.

Fröhlich J (1995) The fractional quantum Hall effect, Chern-Simons theory, and integral lattices. In: Chatterji SD (ed.) *Proc. of ICM'94*, pp. 75–105. Basel, Boston, Berlin: Birkhäuser Verlag.

Fröhlich J (2018) Chiral anomaly, topological field theory, and novel states of matter. In: Ge M, Niemi A, Phua KK, and Takhtajan LA (eds.) *Ludwig Faddeev Memorial Volume: A Life in Mathematical Physics*. Singapore: World Scientific.

Fröhlich J (2023) Gauge invariance and anomalies in condensed matter physics. *Journal of Mathematical Physics* 64: 031903.

Fröhlich J and Gabbiani F (1990) Braid statistics in local quantum theory. *Reviews in Mathematical Physics* 2: 251–353.

Fröhlich J and Kerler T (1991) Universality in quantum Hall systems. *Nuclear Physics B* 354: 369–417.

Fröhlich J and Kerler T (1993) Quantum Groups, Quantum Categories and Quantum Field Theory. *Lecture Notes in Mathematics*, vol. 1542. Berlin, Heidelberg, New York: Springer-Verlag.

Fröhlich J and King C (1989) The Chern-Simons theory and knot polynomials. *Communications in Mathematical Physics* 126: 167–199.

Fröhlich J and Marchetti P-A (1988) Quantum field theory of anyons. *Letters in Mathematical Physics* 16: 347–358.

Fröhlich J and Pedrini B (2000) New applications of the chiral anomaly. In: Fokas A, Grigoryan A, Kibble T, and Zegarlinski B (eds.) *Mathematical Physics 2000*, pp. 9–47. London and Singapore: Imperial College Press.

Fröhlich J and Spencer T (1981) The Kosterlitz-Thouless transition in two-dimensional Abelian spin systems and the Coulomb gas. *Communications in Mathematical Physics* 81: 527–602.

Fröhlich J and Studer UM (1993) Gauge invariance and current algebra in non-relativistic many-body theory. *Reviews of Modern Physics* 65: 733–802.

Fröhlich J and Thiran E (1994) Integral quadratic forms, Kac-Moody algebras, and fractional quantum Hall effect. An ADE–*O* classification. *Journal of Statistical Physics* 76: 209–283.

Fröhlich J and Werner P (2013) Gauge theory of topological phases of matter. *Europhysics Letters* 101: 47007. P1-p6.

Fröhlich J and Zee A (1991) Large-scale physics of the quantum Hall fluids. *Nuclear Physics B* 364: 517–540.

Fröhlich J, Studer UM, and Thiran E (1996) Quantum theory of large systems of non-relativistic matter (Course 8, Part I). In: David F, Ginsparg P, and Zinn-Justin J (eds.) *Géométries Fluctuantes en Mécanique Statistique et en Théorie des Champs. Les Houches LXII, 1994*, pp. 771–912. Amsterdam: Elsevier Science B.V.

Fröhlich J, Graf GM, and Walcher J (2000) On the extended nature of edge states of quantum Hall Hamiltonians. *Annales Henri Poincaré* 1: 405–442.

Fröhlich J, Pedrini B, Schweigert Chr, and Walcher J (2001) Universality in quantum Hall systems: Coset construction of incompressible states. *Journal of Statistical Physics* 103: 527–567.

Fröhlich J, Levkivskyi IP, and Sukhorukov EV (2010) Theory of fractional quantum Hall interferometers. *Physical Review B* 86: 245105.

Fu L and Kane CL (2007) Topological insulators with inversion symmetry. *Physical Review B* 76: 045302.

Fujikawa K (1979) Path-integral measure for gauge-invariant fermion theories. *Physical Review Letters* 42: 1195–1198.

Fujikawa K (1980) Path integral for gauge theories with fermions. *Physical Review D* 21: 2848–2858.

Fukushima K (2013) Views of the Chiral magnetic effect. In: Kharzeev D, Landsteiner K, Schmitt A, and Ye H-U (eds.) *Strongly Interacting Matter in Magnetic Fields. Lecture Notes in Physics*, vol. 871, pp. 241–260. Berlin, Heidelberg: Springer-Verlag.

Gaiotto D, Kapustin A, Seiberg N, and Willet B (2015) Generalized global symmetries. *Journal of High Energy Physics* 2: 172–232.

Gattringer Chr and Seiler E (1994) Functional integral approach to the N-flavor Schwinger model. *Annals of Physics* 233: 97–124. And refs. given there.

Gawedzki K (2015) *Bundle Gerbes for Topological Insulators*. arXiv:1512.01028 [math-ph] 3 December 2015.

Gawedzki K and Tauber Chr (2015) Nonequilibrium transport through quantum-wire junctions and boundary defects for free massless bosonic fields. *Nuclear Physics B* 896: 138–199.

Gawedzki K, Langmann E, and Moosavi P (2018) Finite-time universality in nonequilibrium CFT. *Journal of Statistical Physics* 172: 353–378.

Giuliani A, Mastropietro V, and Porta M (2012) Universality of conductivity in interacting graphene. *Communications in Mathematical Physics* 311: 317–355.

Giuliani A, Mastropietro V, and Porta M (2017) Universality of the Hall conductivity in interacting electron systems. *Communications in Mathematical Physics* 349: 1107–1161.

Goldin GA, Menikoff R, and Sharp DH (1980) Particle statistics from induced representations of a local current group. *Journal of Mathematical Physics* 21: 650–664.

Goldin GA, Menikoff R, and Sharp DH (1981) Representations of a local current algebra in nonsimply connected space and the Aharonov-Bohm effect. *Journal of Mathematical Physics* 22: 1664–1668.

Goldstone J and Jackiw R (1975) Quantization of nonlinear waves. *Physical Review D* 11: 1486–1498.

Graf GM and Porta M (2013) Bulk-edge correspondence for two-dimensional topological insulators. *Communications in Mathematical Physics* 324: 851–895.

Graf GM, Jud H, and Tauber C (2021) Topology in shallow-water waves: A violation of bulk-edge correspondence. *Communications in Mathematical Physics* 383: 731–761.

Haldane FDM (1988) Model for a quantum Hall effect without Landau levels: Condensed-matter realization of the "parity anomaly". *Physical Review Letters* 61: 2015–2018.

Halperin B (1982) Quantized Hall conductance, current-carrying edge states, and the existence of extended states in a two-dimensional disordered potential. *Physical Review B* 25: 2185–2190.

Halperin BI (1987) Possible states for a three-dimensional electron gas in a strong magnetic field. *Japanese Journal of Applied Physics* 26(S3-3): 1913–1919.

Hasan MZ and Kane CL (2010a) Colloquium: Topological insulators. *Reviews of Modern Physics* 82: 3045–3067 (1002.3895).

Hasan MZ and Kane CL (2010b) Topological insulators. *Reviews of Modern Physics* 82: 3045–3067.

Hasan MZ and Moore JE (2011) Three-dimensional topological insulators. *Annual Review of Condensed Matter Physics* 2: 55–78. 1011.5462.

Heeger AJ (1977) Electrical conductivity in doped polyacetylene. *Physical Review Letters* 39: 1098–1101.

Hehl FW and Obukhov YN (2003) *Foundations of Classical Electrodynamics: Charge, Flux, and Metric*. Boston MA: Birkhäuser.

Herring WC (1937) Accidental degeneracy in the energy bands of crystals. *Physics Review* 52(4): 365–373.

Jackiw R, Gross D, and Treiman SB (1986) *Current Algebra and Anomalies*. Princeton NJ: Princeton University Press.

Jones VFR (1983) Index for subfactors. *Inventiones Mathematicae* 72: 1–25.

Jones VFR (1986) Braid groups, Hecke algebras and type II_1 factors. In: *Geometric Methods in Operator Algebras, Proc. US-Japan Seminar*, pp. 242–273.

Jones VFR (1987) Hecke algebra representations of braid groups and link polynomials. *Annals of Mathematics* 126: 335–388.

Kadanoff LP and Ceva H (1971) Determination of an operator algebra for the two-dimensional Ising model. *Physical Review B* 3: 3918–3939.

Kane CL and Mele EJ (2005) Z_2 Topological order and the quantum spin Hall effect. *Physical Review Letters* 95: 146802.

Kennedy R and Zirnbauer MR (2016) Bott periodicity for Z_2 symmetric ground states of gapped free-fermion systems. *Communications in Mathematical Physics* 342: 909–963.

Kitaev A (2009) Periodic table for topological insulators and superconductors. In: *Adv. Theor. Physics, "Landau Memorial Conference," AIP Conf. Proc*, vol. 1134, pp. 22–30. American Institute of Physics.
Klaiber B (1968) *Lectures in Theoretical Physics, Boulder 1967*, p. 141. New York: Gordon and Breach.
Klevtsov S and Wiegmann P (2015) Geometric adiabatic transport in quantum Hall states. *Physical Review Letters* 115: 086801-1-6.
Klevtsov S, Ma X, Marinescu G, and Wiegmann P (2017) Quantum Hall effect and Quillen metric. *Communications in Mathematical Physics* 349: 819–855.
Knizhnik VG and Zamolodchikov AB (1984) Current algebra and Wess-Zumino model in two dimensions. *Nuclear Physics B* 247: 83–103.
Kohmoto M (1985) Topological invariant and the quantization of the Hall conductance. *Annals of Physics* 160: 343–354.
Kohmoto M, Halperin BI, and Wu Y-S (1992) Diophantine equation for the three-dimensional quantum Hall effect. *Physical Review B* 45: 13488–13493.
Kohno T (1987) Monodromy representations of braid groups and Yang-Baxter equations. *Annales de l'institut Fourier de l'Univ. de Grenoble* 37: 139–160.
Landsteiner K (2022) Quantum anomalies (in) matter. *EPJ Web of Conferences* 258: 10003. p1-p8.
Laughlin RB (1981) Quantized Hall conductivity in two dimensions. *Physical Review B* 23: 5632–5633.
Laughlin RB (1983a) Anomalous quantum Hall effect: An incompressible quantum fluid with fractionally charged excitations. *Physical Review Letters* 50: 1395.
Laughlin RB (1983b) Quantized motion of three two-dimensional electrons in a strong magnetic field. *Physical Review B* 27: 3383–3389.
Leinaas JM and Myrheim J (1977) On the theory of identical particles. *Nuovo Cimento* 37: 1–23.
Li R, Wang J, Qi X-L, and Zhang S-C (2010) Dynamical axion field in topological magnetic insulators. *Nature Physics* 6: 284–288.
Lohse M, Schweizer C, Price HM, Zilberberg O, and Bloch I (2018) Exploring 4D quantum Hall physics with a 2D topological charge pump. *Nature* 553: 55–58.
Lundholm D (2023) Properties of 2D Anyon Gas. In: Chakraborty T (ed.). arXiv:2303.09544 [math-ph], March 2023, to appear in Encyclopedia of Condensed Matter Physics.
Luttinger JM (1963) An exactly soluble model of a many-fermion system. *Journal of Mathematical Physics* 4: 1154.
Mastropietro V and Porta M (2022) Multi-channel Luttinger liquids at the edge of quantum Hall systems. *Communications in Mathematical Physics* 395: 1097–1173 (and references given there).
McGreevy J (2022) Generalized symmetries in condensed matter. *arXiv:2204.03045v2*.
Moore G and Read N (1991) Nonabelions in the fractional quantum Hall effect. *Nuclear Physics B* 360: 362–396.
Moosavi P (2021) Inhomogeneous conformal field theory out of equilibrium. *Annales Henri Poincaré*. Publ. online. https://doi.org/10.1007/s00023-021-01118-0.
Morf RH (1992) Model calculations for the fractional quantum Hall effect. In: Landwehr G (ed.) *High Magnetic Fields in Semiconductor Physics III—Quantum Hall Effect, Transport and Optics. Springer Series in Solid-State Sciences*, vol. 101, pp. 207–216. Berlin, Heidelberg: Springer Verlag.
Morf R and Halperin BI (1986) Monte Carlo evaluation of trial wave functions for the fractional quantized Hall effect: Disk geometry. *Physical Review B* 33: 2221–2246.
Ooguri H and Oshikawa M (2012) Instability in magnetic materials with a dynamical axion field. *Physical Review Letters* 108: 161803. P1-p5.
Pisarski RD and Rao S (1985) Topologically massive chromodynamics in the perturbative regime. *Physical Review D* 32: 2081.
Prange RE and Girvin SM (eds.) (1990) The Quantum Hall Effect. In: *Graduate Texts in Contemporary Physics*, 2nd edn. New York: Springer-Verlag.
Price HM, Zilberberg O, Ozawa T, Carusotto I, and Goldman N (2015) Four-dimensional quantum Hall effect with ultracold atoms. *Physical Review Letters* 115: 195303.
Qi X-L and Zhang S-C (2011) Topological insulators and superconductors. *Reviews of Modern Physics* 83: 1057–1110 (1008.2026).
Redlich AN (1984) Parity violation and gauge noninvariance of the effective gauge field action in three dimensions. *Physical Review D* 29: 2366–2374.
Rougerie N, Serfaty S, and Yngvason J (2014) Quantum Hall phases and plasma analogy in rotating trapped Bose gases. *Journal of Statistical Physics* 154: 2–50.
Sachdev S (2019) Topological order, emergent gauge fields, and Fermi surface reconstruction. *Reports on Progress in Physics* 82: 014001.
Sajoto T, Suen YW, Engel LW, Santos MB, and Shayegan M (1990) Fractional quantum Hall effect in very-low-density $GaAs/Al_xGa_{1-x}As$ heterostructures. *Physical Review B* 41: 8449–8460.
Schober J, Rogachevskii I, Brandenburg A, Boyarsky A, Fröhlich J, Ruchayskiy O, and Kleeorin N (2018) Laminar and turbulent dynamos in chiral magnetohydrodynamics, II. Simulations. *The Astrophysical Journal* 858: 124–147.
Schroer B (1982) Functional integrals for order-disorder variables in terms of Bohm-Aharonov strings. *Nuclear Physics B* 210: 103–110.
Schulz-Baldes H (2016) Topological insulators from the perspective of noncommutative geometry and index theory. *Jahresbericht der Deutschen Mathematiker-Vereinigung* 118: 247–273.
Schwinger J (1962) Gauge invariance and mass. II. *Physical Review* 128: 2425–2429.
Semenoff GW (1984) Condensed-matter simulation of a three-dimensional anomaly. *Physical Review Letters* 53: 2449–2452.
Streater RF and Wilde IF (1970) Fermion states of a Boson field. *Nuclear Physics B* 24: 561–575. And references given there.
Streda P (1982) Theory of quantised Hall conductivity in two dimensions. *Journal of Physics C: Solid State Physics* 15: L717.
Su WP and Schrieffer JR (1981) Fractionally charged excitations in charge-density-wave systems with commensurability 3. *Physical Review Letters* 46: 738–741.
Suen YW, Manoharan HC, Ying X, Santos MB, and Shayegan M (1994) One-component to two-component transitions of fractional quantum Hall states in a wide quantum well. *Surface Science* 305: 13–17.
Thouless DJ, Kohmoto M, Nightingale MP, and Den Nijs M (1982) Quantized Hall conductance in a two-dimensional periodic potential. *Physical Review Letters* 49: 405–408.
Tomonaga S (1950) Remarks on Bloch's method of sound waves applied to many-fermion problems. *Progress in Theoretical Physics* 5: 544.
Tsuchiya A and Kanie Y (1987) Vertex operators in the conformal field theory of P_1, and monodromy representations of the braid group. *Letters in Mathematical Physics* 13: 303–312.
Vilenkin A (1980) Equilibrium parity violating current in a magnetic field. *Physical Review D* 22: 3080–3084.
Wen X-G (1990) Chiral Luttinger liquid and the edge excitations in the fractional quantum Hall states. *Physical Review B* 41: 12838–12844.
Wiegmann PB and Abanov AG (2022) Chiral anomaly in Euler fluid and Beltrami flow. *JHEP* 06: 038–054.
Wilczek F (1982) Quantum mechanics of fractional-spin particles. *Physical Review Letters* 49: 957–959.
Witten E (1984) Non-abelian bosonization in two dimensions. *Communications in Mathematical Physics* 92: 455–472.
Witten E (1989) Quantum field theory and the Jones polynomial. *Communications in Mathematical Physics* 121: 351–399.
Wu YS (1984a) General theory for quantum statistics in two dimensions. *Physical Review Letters* 52: 2103.
Wu YS (1984b) Multiparticle quantum mechanics obeying fractional statistics. *Physical Review Letters* 53: 111.
Xu S-Y, Belopolski I, Alidoust N, Neupane M, Bian G, Zhang C, Sankar R, Chang G, Yuan Z, Lee CC, Huang S-M, Zheng H, Ma J, Sanchez DS, Wang BK, Bansil A, Chou F-C, Shibayev PP, Lin H, Jia S, and Hasan MZ (2015) Discovery of a Weyl fermion semimetal and topological fermi arcs. *Science* 349(6248): 613–617.

Properties of 2D anyon gas

Douglas Lundholm, Department of Mathematics, Uppsala University, Uppsala, Sweden

© 2024 Elsevier Ltd. All rights reserved.

Introduction **451**
Brief historic overview 451
Three perspectives on anyons 451
Precursor ideas 452
Some remarks concerning one-dimensional anyons 452
Key points 453
The ideal anyon gas **453**
Quantum statistics 453
The braid group 455
Kinetic energy 456
Statistics transmutation in 2D 457
Exchange vs. exclusion 459
Toward density functionals for anyons 461
Local exclusion principle and degeneracy pressure for the ideal anyon gas 462
Some states of particular interest 465
The nonideal anyon gas **466**
The extended anyon gas 467
Almost-bosonic anyons 468
Almost-fermionic anyons 469
Magnetic TF theory 470
Point-interacting anyons 472
Other interactions and fields 472
Lowest Landau level (LLL) anyons 473
The non-abelian anyon gas **473**
Burau 475
Ising 475
Fibonacci 475
Emergence of the anyon gas **475**
The quantum Hall setting 476
Berry phases 476
Transmuted Hamiltonian 477
Impurities in the plane and polarons 478
Impurities on the sphere and angulons 480
Other emergent models for anyons 480
Conclusion **480**
Acknowledgments **481**
References **481**

Abstract

An overview is given of the 2D many-anyon gas, including its definition (both for ideal and certain less-than-ideal particles and for abelian and non-abelian braid group representations), its corresponding known properties starting out from the intricate relationship between exchange and exclusion, as well as its emergence from bosons and/or fermions in 3D.

Key points

- How can the 2D anyon gas be defined physically and modeled mathematically?
- What are the essential properties of the anyon gas? Does it admit some notion of exclusion statistics intermediate to bosons and fermions?
- How can an anyon gas emerge in a realistic physical system consisting of only bosons and/or fermions?

https://doi.org/10.1016/B978-0-323-90800-9.00260-2

Introduction

Quantum statistics refers to the symmetry and organizing principle assumed by the components of a quantum system. Primarily we think of particles, described by a joint state or wave function, which can fall into certain symmetry classes due to the fundamental constraints on the information that can be extracted from the system, such as those imposed by the uncertainty principle. **Bosons** and **fermions** are ensembles of identical such particle subsystems characterized by symmetry, respectively antisymmetry, with respect to particle exchange. In their ideal limits they manifest the statistical state distributions defined by Bose and Einstein, respectively Fermi and Dirac, with the latter subject to Pauli's exclusion principle. In a sense, whereas bosons unify, fermions individualize. **Anyons** are defined as identical quantum particles with an intermediate exchange symmetry characterized by representations of the braid group, which is the relevant group of continuous exchanges of particle configurations in 2D (two spatial dimensions). An **anyon gas** is a quantum system consisting of a large number of such particles subject to a fixed class of exchange symmetries, which is dependent on the specific underlying kinematics and dynamics of the quantum systems from which it emerged. The study of the behavior of the proper anyon gas presents a significant challenge to mathematics and physics. Our aim with this overview is to make these statements precise and to give an updated status report on some of the many facets of the topic.

Brief historic overview

For completeness and to set our reference point for this overview, we give a very brief account on the origins of the anyon gas, referring to Biedenharn et al. (1990), Fröhlich (1990), Leinaas and Myrheim (2022), and Goldin (2022) for further background.

Three perspectives on anyons

The discovery of anyons and intermediate quantum statistics in two spatial dimensions may be attributed to three independent research groups, working from three distinctly different perspectives (These three groups were initially unaware of each other's earlier contributions, and their initial works therefore lack the respective citations. There have subsequently been attempts to remedy this in the literature (Biedenharn et al., 1990).). Chronologically, these are (cf. Fig. 1):

1. **Geometric:** In 1977, Leinaas and Myrheim used geometric methods from gauge theory, fiber bundles, and extensions of the kinetic energy operator via boundary conditions (also known as **"Schrödinger quantization"**) to arrive at the possibility for what they termed **"intermediate statistics"** in 2D (as well as in 1D), and worked out some of its detailed consequences for two particles (Leinaas and Myrheim, 1977). They further pointed to the role of the fundamental group of the configuration space for arbitrary numbers of identical particles and the possibility for higher dimensional fibers (necessary for non-abelian representations, but they did not explicitly mention the braid group or its representation theory in their work).
2. **Algebraic:** In 1980–1981, starting out from the representation theory of the Lie algebra of local currents on $\mathbb{R}^d$ and the group of diffeomorphisms (akin to **"Heisenberg quantization"** and Dirac's canonical quantization scheme (Dirac, 1967)), Goldin, Menikoff, and Sharp found a kinematical derivation of the possibilities for quantum statistics with an unexpected dependence on the dimension d (Goldin et al., 1980, 1981). In Goldin et al. (1981) they also explored connections to the Aharonov–Bohm effect (in 3D) while subsequently in 1983, they highlighted the role of the one-dimensional unitary representations of the braid group (Goldin et al., 1983), and in 1985 pointed out that higher dimensional braid group representations induce inequivalent representations of the current algebra (Goldin et al., 1985). Such identical particles were later termed **"plektons"** (see, e.g., Dell'Antonio et al., 1997; Korff et al., 1999; Mund and Schrader, 1995) or simply **"non-abelian anyons"** (nowadays the more common term; cf., Nayak et al., 2008). It was also pointed out in Goldin et al. (1985) that nontrivial exchange phases in 2D do not require indistinguishability; the *colored* braid group serves as the fundamental group for configurations of *distinguishable* particles. The general algebraic (and potentially non-abelian) approach to quantum statistics was further developed in the field theory direction by Tsuchiya and Kanie (Tsuchiya and Kanie, 1987, 1988), Kohno (Kohno, 1987), as well as Fröhlich, Gabbiani, Kerler, and Marchetti (Fröhlich and Gabbiani, 1990; Fröhlich and Marchetti, 1988, 1989; Fröhlich, 1988, 1990; Fröhlich and Kerler, 1993), and Fredenhagen, Rehren, and Schroer (Fredenhagen et al., 1989).

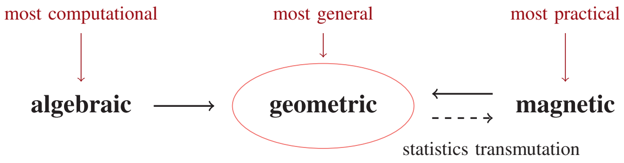

Fig. 1 Three different perspectives on anyons.

3. **Magnetic:** In 1982, motivated by topological gauge theory examples in higher dimensions ("θ-vacua" and "dyons"), Wilczek considered a composite of a 2D magnetic flux and a charged particle, coined for it the name **"anyon,"** as well as predicted its fractional spin and worked out the basic quantum mechanics for two such composite particles (Wilczek, 1982a, b). The same line of investigation was continued by Wu in 1984, who connected it to path integrals, extended it to arbitrary numbers of particles, and independently and explicitly invoked the braid group and its one-dimensional representations (Wu, 1984a, b). Further, Arovas, Schrieffer, Wilczek, and Zee considered in 1985 the statistical mechanics of a gas of such abelian anyons by means of its lowest order virial expansion (Arovas et al., 1985) (see also, Dowker, 1985).

The first concrete physical application of intermediate/fractional statistics and anyons came from the magnetic perspective and concerned the **fractional quantum Hall effect** (FQHE) (Laughlin, 1999; Stormer, 1999; Tsui, 1999), in which the emergent fractionally charged quasiparticles/holes introduced by Laughlin were proposed by Halperin to have such properties (Halperin, 1984). Arovas, Schrieffer, and Wilczek subsequently verified this (Arovas et al., 1984) (though under tacit assumptions of adiabaticity, Forte, 1991) by computing the corresponding Berry phase for quasiholes, thereby converging the geometric and magnetic (and eventually algebraic) perspectives. Further, the latent power of the algebraic perspective was brought to light in the new millennium as Kitaev proposed the usefulness of non-abelian anyons in topological quantum computation (Freedman et al., 2003; Kitaev, 2003, 2006). Most of the development of the field throughout this time span has been covered in the books and reviews (Canright and Johnson, 1994; Date et al., 2003; Forte, 1992; Fröhlich, 1990; Iengo and Lechner, 1992; Jackiw, 1990; Khare, 2005; Lerda, 1992; Myrheim, 1999; Nayak et al., 2008; Ouvry, 2007; Stern, 2008; Wilczek, 1990).

Precursor ideas

As is evident from the above, anyons and intermediate ("fractional") quantum statistics are the convergence of many central ideas and concepts in mathematical physics. The former notion (anyon) is more closely tied into the concepts of **exchange phases** and symmetry classes of wave functions while the latter (fractional statistics) to that of the **exclusion principle** and permissible probability distributions for particles. It has been—and still is—a nontrivial task to rigorously connect these two notions in the strictly intermediate case (see, e.g., the review, Canright and Johnson, 1994). Exploration of intermediate statistics from the latter approach of exclusion with a finite occupation number of one-body states was considered by Gentile already in 1940–1942 (Gentile, 1940, 1942), and—inspired by anyons—another, dimension-independent, approach allowing for **fractional exclusion statistics** was suggested by Haldane in 1991 (Haldane, 1991).

Ideas of charged particles encircling regions of magnetic flux were developed by Ehrenberg and Siday (Ehrenberg and Siday, 1949), Aharonov and Bohm (Aharonov and Bohm, 1959), and the more general concept of geometric phases by Pancharatnam (Pancharatnam, 1956), Berry (Berry, 1984), and Simon (Simon, 1983). Methods of geometric quantization were developed by Souriau around 1967–1970, and he pointed out that if the configuration space is not simply connected, then more than two different group characters could arise and this "would lead to prequantizations of a new type" (Souriau, 1970). Around the same time, homotopy classes of Feynman paths brought another topological perspective on quantum statistics (Dowker, 1972; Laidlaw and DeWitt, 1971; Schulman, 1968) (cf., e.g., Mouchet, 2021). For example, Laidlaw and DeWitt remarked that possibilities in two space dimensions are not limited to bosons and fermions, but they did not elaborate further (Laidlaw and DeWitt, 1971).

Foundations for non-abelian anyons were laid much earlier in the theory of parastatistics (non-abelian representations of the permutation group) (Green, 1953; Messiah and Greenberg, 1964). Further, the central idea employed by Leinaas and Myrheim that equivalent configurations of indistinguishable particles need to be identified goes back all the way to Gibbs (cf., Fröhlich, 1990; Leinaas and Myrheim, 1977).

The above shows that the essential ideas that were necessary for the discoveries of anyons were floating around at the time, and it is also of interest to remark that, while it took about half a century from the discovery of bosons and fermions to that of anyons, it took another half a century to see their experimental confirmation.

Some remarks concerning one-dimensional anyons

Although this article concerns anyons in the 2D setting, it is unavoidable to note the influence of ideas from generalized notions of quantum statistics in 1D (i.e., 1 + 1 spacetime dimensions). One of the first works in which generalized commutation relations for field operators can be found is Klaiber in 1968 (Klaiber, 1968), followed by Streater and Wilde (1970) and Fröhlich (1976). Transmutation of 1D hard-core bosons (studied classically by Tonks (1936)) into fermions and vice versa was considered by Girardeau (1960), who also noted topological and dimensional consequences for the configuration space (Girardeau, 1965). The Lieb–Liniger model (Lieb and Liniger, 1963) for point-interacting bosons in 1D constitutes the intermediate statistics found by Leinaas and Myrheim in 1D; however, exchange phases (thus "anyonic Lieb–Liniger") may also be added to that model (Kundu, 1999). Leinaas and Myrheim later considered a different approach to statistics in 1D (and in higher dimensions) akin to "Heisenberg quantization" (Leinaas and Myrheim, 1993), and found a relationship to the Calogero–Sutherland model (Calogero, 1969a, b; Polychronakos, 1989; Sutherland, 1971). 2D anyons that are forced into the lowest Landau level of a strong magnetic field may be understood using such 1D concepts (Ouvry, 2007).

Key points

We will in this overview focus on providing answers to the following key questions:

1. How can the 2D anyon gas be defined physically and modeled mathematically?
2. What are the essential properties of the anyon gas? Does it admit some notion of exclusion statistics intermediate to bosons and fermions?
3. How can an anyon gas emerge in a realistic physical system consisting of only bosons and/or fermions?

The first question is addressed in the first part of Section "The ideal anyon gas" for the case of the ideal abelian anyon gas, and in the first part of Section "The nonideal anyon gas" for the nonideal abelian gas. Section "The non-abelian anyon gas" introduces the non-abelian gas in brief. The second question is the subject of the later parts of Sections "The ideal anyon gas," "The nonideal anyon gas," and "The non-abelian anyon gas." The third and final question is addressed in Section "Emergence of the anyon gas." Conclusions and an outlook are given in Section "Conclusion."

The ideal anyon gas

Quantum statistics

The possibility for anyons in 2D boils down to the peculiar geometry and topology of the plane as compared to spaces of higher dimensions. Consider for simplicity two particles at positions $\mathbf{x}_1$ and $\mathbf{x}_2$ in the Euclidean plane $\mathbb{R}^2$, with a wave function Ψ encoding the probability density $|\Psi(\mathbf{x}_1, \mathbf{x}_2)|^2$ of observing the particles at these locations. An exchange of the two positions admits then a change in phase:

$$\Psi(\mathbf{x}_2, \mathbf{x}_1) = e^{\pm i\theta}\Psi(\mathbf{x}_1, \mathbf{x}_2),$$

where $\theta \in \mathbb{R}$. The sign is included above to specify the way in which the exchange is made, and if there is **orientation symmetry** then we cannot distinguish between clockwise and counterclockwise exchanges so that

$$e^{i\theta} = e^{-i\theta} \quad \Leftrightarrow \quad e^{2i\theta} = 1,$$

so $\theta/\pi \in \mathbb{Z}$ is either an even integer (bosons) or an odd integer (fermions). However, if we relax the assumption on orientation symmetry and consider a multivalued function for which we keep track of the number and orientation of elementary exchanges (the winding number), then we can allow *any* phase θ (anyons) to appear here. Conventionally, we write $\theta = \alpha\pi$ where α is known as the **statistics parameter** and can be either $\alpha \in \mathbb{R}$ (defined modulo periodicity 2) or in a suitable interval $\alpha \in (-1, 1]$ or $\alpha \in [0, 2)$; cf. Fig. 2.

More generally, we may consider a wave function Ψ for N **distinct particles** in d-dimensional Euclidean space $\mathbb{R}^d$ and its probability density:

$$|\Psi(\mathrm{x})|^2, \qquad \mathrm{x} = (\mathbf{x}_1, \mathbf{x}_2, \ldots, \mathbf{x}_N) \in \mathbb{R}^{dN} \setminus \triangle_N,$$

where, in order to indeed make them distinct, we have removed the (fat) **diagonal set** where any two or more particles overlap:

$$\triangle_N := \{\mathrm{x} \in \mathbb{R}^{dN} : \mathbf{x}_j = \mathbf{x}_k \text{ for some } j \neq k\}.$$

Our reason for considering distinct particles is that we, for simplicity at this stage, fix the particle number to N and assume that number to be certain and conserved (we shall return to possibilities of collisions on $\triangle_N$ later).

In the case where the particles are **identical** and thus **indistinguishable**, then we should reduce the configuration space further and ignore the (now artificial) labels:

$$X = \{\mathbf{x}_1, \mathbf{x}_2, \ldots, \mathbf{x}_N\} \in \mathcal{C}^N := (\mathbb{R}^{dN} \setminus \triangle_N)/S_N,$$

where the permutation group S_N acts on the labels j of $\mathrm{x} = (\mathbf{x}_j)_{j=1}^N$ while leaving the equivalence class (set) X subject to this action fixed. Indeed, our N-particle configuration space is identical to the manifold

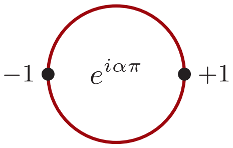

Fig. 2 The circle of abelian anyons, parametrized by the statistics parameter α. Note that any choice of proper anyons (i.e., neither bosons nor fermions) marks an additional point in this circle and thus breaks its orientation symmetry (mirror symmetry/complex conjugation).

$$\mathcal{C}^N = \{X = \{\mathbf{x}_1, \mathbf{x}_2, \ldots, \mathbf{x}_N\} \subset \mathbb{R}^d : |X| = N\}$$

of all N-point subsets of $\mathbb{R}^d$. If we now consider exchanges of particles, then we can no longer act by permutations since it has lost meaning on configurations X of identical particles; however, what we can consider instead is the *continuous* exchange of positions in $\mathcal{C}^N$. Namely, among the continuous paths from a point $X \in \mathcal{C}^N$ to another point $Y \in \mathcal{C}^N$ there are the *loops*, starting and ending at the same point $X = Y$, which we hereby take to represent **continuous physical exchanges** of identical particles (Leinaas and Myrheim, 1977). Given such **exchange loops** σ (continuous functions $[0,1] \to \mathcal{C}^N$ of a parameter, s.t. $\sigma(0) = \sigma(1)$), we may then consider lifting any wave function Ψ which has been assigned a value on a configuration $X \in \mathcal{C}^N$ to a multivalued function (More concretely, a section of a bundle with base space $\mathcal{C}^N$, or a ρ-equivariant function on the covering space of $\mathcal{C}^N$; see, for example, Dowker (1985), Fröhlich (1990), Mund and Schrader (1995), Dell'Antonio et al. (1997), Myrheim (1999), Lundholm (2019), and Lundholm and Qvarfordt (2020). The range/fiber is initially $\mathbb{C}$.) upon which the loops can act. Let us denote the action of a loop σ on Ψ at the point X by $\Psi(\sigma.X)$. Then we demand the **exchange conditions**

$$\Psi(\sigma.X) = \rho(\sigma)\Psi(X), \tag{1}$$

where $|\rho(\sigma)| = 1$ so that

$$|\Psi(\sigma.X)|^2 = |\Psi(X)|^2 \tag{2}$$

unambiguously defines a probability density at $X \in \mathcal{C}^N$. Further, $\rho(1) = 1$ for the trivial (constant) loop $\sigma = 1$, and if we compose two loops σ_1 and σ_2 into a new loop $\sigma_1\sigma_2$, then we demand the compatibility of the action,

$$\rho(\sigma_1\sigma_2) = \rho(\sigma_1)\rho(\sigma_2).$$

In other words, ρ is a group homomorphism and thus a **representation** of the group of exchange loops at X with composition.

In comparison, if we consider a single particle, $\mathcal{C}^{N=1} = \mathbb{R}^d$, charged and subject to magnetism, then the action of a path should be understood as the (parallel) transport of the charge along the path, and different loops σ may then give rise to different **holonomies** or phases given by the flux enclosed by the loop:

$$\rho(\sigma) = e^{i\Phi_\sigma}, \qquad \Phi_\sigma = \oint_\sigma \mathbf{A}\cdot d\mathbf{r} = \int_{\text{interior of } \sigma} B(\mathbf{x})\, d\mathbf{x},$$

where curl $\mathbf{A} = B$ is the magnetic field (viewed as a (pseudo)scalar field in $d = 2$ and appropriately projected in $d \geq 3$). However, for $N \geq 1$ and in the case that there is no external field so that $\rho(\sigma)$ should depend only on the topology of the loop σ, that is, if we require that $\rho(\sigma) = \rho(\sigma')$ for any two topologically equivalent loops $\sigma \sim \sigma'$ (connected by some continuous deformation), then we consider loops only up to homotopy and the relevant group of (equivalence classes of) loops is the **fundamental group** of the configuration space (Goldin et al., 1983, 1985; Wu, 1984a):

$$\sigma \in \pi_1(\mathcal{C}^N) = \begin{cases} \{1\}, & d = 1, \\ B_N, & d = 2, \\ S_N, & d \geq 3, \end{cases}$$

where B_N denotes the **braid group**, defined below. The group is trivial (Interesting statistics can still emerge as a choice of boundary condition on $\triangle_N$ (Leinaas and Myrheim, 1977).) in one dimension because particles then cannot exchange continuously without colliding, that is, hitting the diagonal set $\triangle_N$.

Now, if Ψ takes values in $\mathbb{C}$, then $\rho(\sigma)$ is a phase—the **exchange phase** corresponding to the exchange loop σ—and we may identify different **exchange quantum statistics** as symmetry classes of Ψ defined by ρ in (1):

Bosons $\rho(\sigma) = +1$, the trivial representation. Wave functions Ψ extend symmetrically from $\mathcal{C}^N$ to $\mathbb{R}^{dN}$ (L^2 denotes the Hilbert space of square-integrable functions with inner product $\langle \Psi, \Phi \rangle = \int \overline{\Psi(\mathrm{x})}\Phi(\mathrm{x})\, d\mathrm{x}$.),

$$L^2_{\text{sym}}(\mathbb{R}^{dN}) := \{\Psi \in L^2 : \Psi(\sigma.\mathrm{x}) = \Psi(\mathrm{x}),\ \sigma \in S_N\}$$

(the usual action of permutations, and with any missing data on $\triangle_N$ to be filled in, depending on our choice of Hamiltonian). For example, particles may be independent and identically distributed: $\Psi_0 = \otimes^N \psi_0 \in L^2_{\text{sym}}$,

$$\Psi_0(\mathrm{x}) = (\otimes^N \psi_0)(\mathrm{x}) = \prod_{j=1}^N \psi_0(\mathbf{x}_j),$$

corresponding to Bose–Einstein condensation in the single one-body state $\psi_0 \in L^2(\mathbb{R}^d)$.

Fermions $\rho(\sigma) = \mathrm{sign}(\sigma) \in \{-1, +1\}$, the signed representation on S_N (signature of permutation). In this case wave functions Ψ extend *anti*symmetrically from $\mathcal{C}^N$ to $\mathbb{R}^{dN}$,

$$L^2_{\text{asym}}(\mathbb{R}^{dN}) := \{\Psi \in L^2\ :\ \Psi(\sigma.\mathrm{x}) = \mathrm{sign}(\sigma)\Psi(\mathrm{x}),\ \sigma \in S_N\}$$

(in this case it is natural to require that Ψ vanishes on $\triangle_N$). We apparently obtain determinantal correlations and the **Pauli principle** since functions in L^2_{asym} are spanned by **Slater determinants**, such as $\Psi_0 = \psi_0 \wedge \psi_1 \wedge \cdots \wedge \psi_{N-1}$, where

$$\bigwedge_{k=0}^{N-1} \psi_k(\mathbf{x}_1, \ldots, \mathbf{x}_N) := \det \begin{bmatrix} \psi_0(\mathbf{x}_1) & \cdots & \psi_0(\mathbf{x}_N) \\ \vdots & & \vdots \\ \psi_{N-1}(\mathbf{x}_1) & \cdots & \psi_{N-1}(\mathbf{x}_N) \end{bmatrix}.$$

Anyons in $d = 2$ the most general ρ is a unitary representation of B_N. Proper anyons then correspond to those ρ which do not factor through S_N, that is, for which orientation symmetry is broken. Let us denote by L^2_ρ the Hilbert space of square-integrable multivalued wave functions Ψ based on the configuration space $\mathcal{C}^N$ and subject to the exchange conditions (1). A central question is, whether we can anticipate **intermediate or fractional exclusion statistics** in L^2_ρ? Actually, it turns out that the information at hand is not sufficient to decide this, and even the above conclusions for bosons and fermions can be misleading, as we will see below.

The braid group

For $d = 2$, the group of continuous loops in $\mathcal{C}^N$ modulo homotopy is conveniently visualized as a group of N-particle world lines that evolve in 2 + 1-dimensional spacetime, subject to composition via some arbitrary but fixed reference configuration $X_0 \in \mathcal{C}^N$. The resulting group, denoted B_N, is the **braid group on *N* strands** (Artin, 1925, 1947; Birman, 1974):

$$B_N = \left\langle \sigma_1, \ldots, \sigma_{N-1} \ : \ \sigma_j\sigma_{j+1}\sigma_j = \sigma_{j+1}\sigma_j\sigma_{j+1}, \sigma_j\sigma_k = \sigma_k\sigma_j \right\rangle_{k \neq j \pm 1}^{j,k=1\ldots N-1}$$

That is, the group generated by $N - 1$ elementary braids

σ_j :

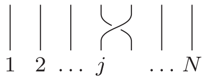

σ_j^{-1} :

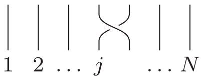

which are composed by stacking one on top of another. These elementary braids are subject to two sets of topological relations: one of which are known as the **Yang–Baxter relations**, and the other implement the commutativity of independent braids. In B_4 we have, for example,

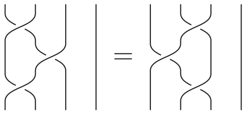

$\sigma_1\sigma_2\sigma_1 = \sigma_2\sigma_1\sigma_2$

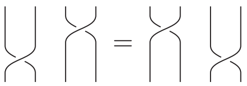

$\sigma_3\sigma_1 = \sigma_1\sigma_3$

If we add a third set of relations $\sigma_j^2 = 1\ \forall j$, or equivalently, $\sigma_j = \sigma_j^{-1}$, that is, clockwise and counterclockwise exchanges cannot be distinguished, then we obtain the **permutation group** S_N. This will be the case for $d \geq 3$ since an elementary exchange may be rotated out of the plane (continuously and homotopically). From now on, we shall stick to the anyonic case $d = 2$.

If one looks for irreducible abelian unitary representations, that is, **exchange phases**

$$\rho : B_N \to \mathrm{U}(1) = \{z \in \mathbb{C} : |z| = 1\},$$

then the Yang–Baxter relations single out a unique phase:

$$\rho(\sigma_j) = e^{i\alpha\pi}, \qquad \text{for all } j = 1, 2, \ldots, N-1; \tag{3}$$

cf. Figs. 2 and 3. The only representations that factor through S_N require either $\alpha = 0$ ($\alpha \in 2\mathbb{Z}$) or $\alpha = 1$ ($\alpha \in 2\mathbb{Z} + 1$), thus corresponding to bosons or fermions. We will return to the non-abelian case, and representations with higher rank than 1, in Section "The non-abelian anyon gas."

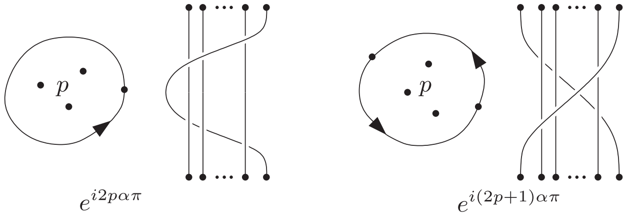

Fig. 3 Exchange loops for a single resp. a pair of particles with *p* other particles enclosed, and corresponding braid diagrams and phases. From Lundholm D and Solovej JP (2013a) Hardy and Lieb-Thirring inequalities for anyons. Communications in Mathematical Physics 322: 883–908

Kinetic energy

Above we considered wave functions $\Psi \in L^2_\rho$ that implement an exchange symmetry (1) by choice of a representation ρ of B_N. However, it turns out that this is only one part of the data that specifies an anyon model. The other, equally essential, part is the choice of a Hamiltonian or kinetic energy operator. Namely, in order to be able to consider continuous exchanges of particles we also need to resolve space and time at the appropriate energy scale.

Our starting point is the nonrelativistic (We remain nonrelativistic throughout this overview and likewise we will ignore spin; see however Jackiw (1990), Fröhlich (2009), and Mund (2009).) free kinetic energy for N particles with mass m:

$$T = \frac{1}{2m} \sum_{j=1}^{N} \mathbf{p}_j^2, \tag{4}$$

where $\mathbf{p}_j \in \mathbb{R}^2$ is the momentum of the particle with position $\mathbf{x}_j \in \mathbb{R}^2$. If the particles are all distinguishable, then the canonical quantization of this expression is obtained with momentum operators $\hat{\mathbf{p}}_j = -i\hbar\nabla_{\mathbf{x}_j}$ canonically conjugate to the position operators $\hat{\mathbf{x}}_j$, that is,

$$\hat{T}_{\text{dist}} := \frac{\hbar^2}{2m} \sum_{j=1}^{N} (-i\nabla_{\mathbf{x}_j})^2, \tag{5}$$

acting on (suitably regular) $\Psi \in L^2(\mathbb{R}^{2N})$.

In our case of identical anyons, we may consider the particles to be *locally* distinguishable. Namely, at any fixed point $X \in \mathcal{C}^N$, we may attach arbitrary labels to them:

$$\mathcal{C}^N \ni X = \{\mathbf{x}_1, \ldots, \mathbf{x}_N\} \ \leftrightarrow\ (\mathbf{x}_1, \ldots, \mathbf{x}_N) \in \mathbb{R}^{2N} \setminus \triangle_N,$$

and we can keep track of these labels along any paths from X in $\mathcal{C}^N$ as long as they cannot exchange nontrivially, that is, as long as any two possible paths do not compose to a topologically nontrivial loop. So in order to define free anyons, the idea is then that we should keep the kinetic energy operator as above whenever we consider wave functions Ψ supported on topologically trivial subsets of $\mathcal{C}^N$ (i.e., not encircling any of the holes in the manifold), which then can anyway be treated as subsets of the configuration space $\mathbb{R}^{2N} \setminus \triangle_N$ of distinguishable and distinct particles. Additional information must then be added to $\hat{T}_{\text{dist}}$ whenever we pass between different such subsets of $\mathcal{C}^N$ so as to complete topologically nontrivial loops $\sigma \in \pi_1(\mathcal{C}^N) = B_N$, $\sigma \neq 1$. One way to implement this concretely is to treat the exchange condition (1) as a topological boundary condition (Technically, Ψ is defined as a complex-valued function on the covering space of $\mathcal{C}^N$ subject to the ρ-equivariance condition (1), which is equivalent to regarding Ψ as a section of a complex line bundle over $\mathcal{C}^N$ with its geometry specified by $\rho\colon B_N \to \mathrm{U}(1)$ (locally flat, but globally curved by the holonomies specified by $\rho(\sigma)$ for $\sigma \in B_N$); see, for example Dowker (1985), Mund and Schrader (1995), and Lundholm and Qvarfordt (2020).) that Ψ must satisfy in order to be in the domain of the operator, which we denote by

$$\hat{T}_\rho := \frac{\hbar^2}{2m} \sum_{j=1}^{N} (-i\nabla^{(\rho)}_{\mathbf{x}_j})^2, \tag{6}$$

or simply by $\hat{T}_\alpha$ if $\rho(\sigma_j) = e^{i\alpha\pi}$. For convenience we also denote the Hilbert space L^2_ρ by L^2_α in this case. Again, we stress that $\hat{T}_\alpha$ acts *locally* as the standard Laplacian $\hat{T}_{\text{dist}} = \frac{\hbar^2}{2m}\sum_{j=1}^{N}(-\Delta_{\mathbf{x}_j})$ on (suitably regular) $\Psi \in L^2_\alpha$, thus *independently* of α, but *globally* we have also the exchange conditions to account for, such as **pair exchange**

$$\Psi(\mathbf{x}_1, \ldots, \mathbf{x}_k, \ldots, \mathbf{x}_j, \ldots, \mathbf{x}_N) = e^{i(2p+1)\alpha\pi}\Psi(\mathbf{x}_1, \ldots, \mathbf{x}_j, \ldots, \mathbf{x}_k, \ldots, \mathbf{x}_N), \tag{7}$$

where p is the number of other particles enclosed in the exchange loop as $\mathbf{x}_j$ and $\mathbf{x}_k$ are exchanged once in a counterclockwise manner (as well as other conditions; cf. Fig. 3).

As an example, consider the two-particle case $N = 2$ in center-of-mass and relative coordinates $\mathbf{X} = \frac{1}{2}(\mathbf{x}_1 + \mathbf{x}_2)$, $\mathbf{r} = \mathbf{x}_1 - \mathbf{x}_2$. Then the kinetic energy separates,

$$\hat{T}_\alpha = \frac{\hbar^2}{4m}(-\Delta_{\mathbf{X}}) + \frac{\hbar^2}{m}(-\Delta_{\mathbf{r}}), \tag{8}$$

and further, expressed in polar coordinates $(r = |\mathbf{r}|, \varphi)$:

$$-\Delta_{\mathbf{r}} = -\partial_r^2 - \frac{1}{r}\partial_r - \frac{1}{r^2}\partial_\varphi^2. \tag{9}$$

These operators act on functions $\Psi(\mathbf{X}, r, \varphi)$ (here with its proper multivaluedness on $\mathcal{C}^2$ incorporated in the winding of $\varphi \in \mathbb{R}$ over multiples of π) such that

$$\Psi(\mathbf{X}, r, \varphi + \pi) = e^{i\alpha\pi}\Psi(\mathbf{X}, r, \varphi), \quad r > 0, \tag{10}$$

corresponding to the exchange condition (7) (all braids in B_2 are generated by this simple exchange σ_1). The manifold $\mathcal{C}^2$ may be parametrized by the set in $\mathbb{R}^4$ given by the half-space

$$\Omega = \{\mathbf{X} \in \mathbb{R}^2,\ r > 0,\ 0 \leq \varphi < \pi\},$$

and its boundary

$$\partial\Omega = \{\mathbf{X} \in \mathbb{R}^2,\ r = 0 \text{ or } \varphi = 0 \text{ or } \varphi = \pi\}$$

relates the two points ($r > 0$, $\varphi = 0$) and ($r > 0$, $\varphi = \pi$) topologically to the same point in $\mathcal{C}^2$. An equivalent description is therefore (8) and (9) defined on $L^2(\Omega)$ and subject to the boundary condition

$$\Psi(\mathbf{X}, r, \varphi = \pi) = e^{i\alpha\pi}\Psi(\mathbf{X}, r, \varphi = 0), \quad r > 0.$$

The operator $\hat{T}_\rho$ as defined above is formally Hermitian but not self-adjoint (and not even necessarily *essentially* self-adjoint) since we have still not supplied any information at the diagonal set $\triangle_N$, which cuts out holes of codimension 2 in the manifold $\mathcal{C}^N$ (for $N = 2$ this set is $\triangle_2 = \{\mathbf{X} \in \mathbb{R}^2, r = 0\}$). There is however a canonical choice of a self-adjoint realization (known in the mathematical literature as the **Friedrichs extension**) obtained by considering the expectation value of the kinetic energy in its formal quadratic form expression (This is more appropriately defined on $\mathcal{C}^N$ and observed to extend unambiguously to the covering space (Lundholm and Qvarfordt, 2020).)

$$\langle\Psi, \hat{T}_\rho\Psi\rangle = \frac{\hbar^2}{2m}\int_{\mathbb{R}^{2N}}\sum_{j=1}^{N}|\nabla^{(\rho)}_{\mathbf{x}_j}\Psi|^2 dx \ \geq 0 \tag{11}$$

initially on (multivalued) wave functions Ψ that are smooth and compactly supported away from $\triangle_N$ and subject to the exchange conditions (7) resp. (1) (There is a natural extension (closure) of the energy form (11) to the largest subspace of the Hilbert space L^2_ρ upon which the energy is defined and finite, which is also the largest domain of the momentum operator $-i\nabla^{(\rho)}$. Denoting its adjoint $(-i\nabla^{(\rho)})^*$, one then defines $\hat{T}_\rho := \frac{\hbar^2}{2m}(-i\nabla^{(\rho)})^*(-i\nabla^{(\rho)})$, canonically self-adjoint on a corresponding smaller subspace of L^2_ρ. One might object that this approach seems to assume a **hard-core condition** on the anyons since functions are initially taken to vanish close to $\triangle_N$; however for bosons and fermions, this eventually yields exactly the standard free kinetic energy $\hat{T}_{\text{asym/sym}}$ (with the same expression as $\hat{T}_{\text{dist}}$) on the (Sobolev) spaces of anti/symmetric square-integrable functions with both one and two partial derivatives that are also square-integrable. It is in fact a peculiarity of dimensions $d \geq 2$ that any extra conditions at the diagonals disappear in this procedure so that our assumption on distinct particles is justified a posteriori; cf (Bourdeau and Sorkin, 1992; Lundholm and Solovej, 2014). This can also be understood by means of a more precise version of the Hardy inequality (34) discussed below (Lundholm and Qvarfordt, 2020).). For $N = 2$ the energy form (11) is

$$\langle\Psi, \hat{T}_\alpha\Psi\rangle = \frac{\hbar^2}{m}\int_{\mathbf{X}\in\mathbb{R}^2}\int_{r=0}^{\infty}\int_{\varphi=0}^{2\pi}\left(\frac{1}{4}|\nabla_{\mathbf{X}}\Psi|^2 + |\partial_r\Psi|^2 + \frac{1}{r^2}|\partial_\varphi\Psi|^2\right)d\varphi\, r dr\, d\mathbf{X}, \tag{12}$$

again subject to the exchange condition (10). In general then, this specific choice of a self-adjoint operator $\hat{T}_\rho$ resp. $\hat{T}_\alpha$ is what we take to mean precisely by ***free*** (noninteracting, as compared to point-interacting; see below) **ideal anyons**, by analogy with bosons and fermions.

Statistics transmutation in 2D

So far we have worked exclusively in the geometric perspective of anyons, but we will now be able to make the connection to the magnetic perspective.

Since we have fixed our attention on the plane $\mathbb{R}^2$, it is occasionally convenient to switch to complex notation:

$$\mathbb{R}^{2N} \ni \mathrm{x} = (\mathbf{x}_1, \ldots, \mathbf{x}_N) \ \leftrightarrow\ \mathrm{z} = (\mathrm{z}_1, \mathrm{z}_2, \ldots, \mathrm{z}_N) \in \mathbb{C}^N,$$

where the real (imaginary) part in $\mathbb{C}$ is canonically identified with the first (second) coordinate in $\mathbb{R}^2$.

Now, consider either a bosonic or a fermionic wave function $\Psi \in L^2_{\text{sym/asym}}(\mathbb{C}^N)$ restricted to the subset of distinct coordinates $\mathrm{z} \in \mathbb{C}^N \setminus \triangle_N$ and make there the gauge transformation $\Psi = U\tilde{\Psi}$, where

$$U(\mathrm{z}) := \prod_{j<k}\frac{z_j - z_k}{|z_j - z_k|} = \exp\left(i\sum_{j<k}\arg(z_j - z_k)\right), \tag{13}$$

the product of all relative phases of pairs of particles. One may verify that this expression is well defined and single valued on $\mathbb{C}^N \setminus \triangle_N$, unitary $|U(\mathrm{z})| = 1$, and antisymmetric w.r.t. permutations of labels in $\mathrm{z} = (z_j)_{j=1}^N$ so that if Ψ is symmetric, then $\tilde{\Psi} = U^{-1}\Psi$ is antisymmetric and vice versa. Thus, modulo the smaller set of diagonals $\triangle_N$ where it is not defined, the unitary transformation by U achieves a **statistics transmutation** $L^2_{\text{sym}} \leftrightarrow L^2_{\text{asym}}$ between bosons and fermions in 2D. This perhaps seems confusing, however, recall that the kinetic energy is equally important in defining the exchange statistics. Indeed, if we consider the momentum then this transmutation comes at the cost of a **gauge potential**:

$$-i\nabla_{\mathbf{x}_j}\Psi = U(-i\nabla_{\mathbf{x}_j} + \mathbf{A}_j)\tilde{\Psi}, \tag{14}$$

where we have defined the vector potentials

$$\mathbf{A}_j(\mathrm{x}) := -iU^{-1}\nabla_{\mathbf{x}_j}U = \sum_{k\neq j}\frac{(\mathbf{x}_j - \mathbf{x}_k)^{\perp}}{|\mathbf{x}_j - \mathbf{x}_k|^2}, \tag{15}$$

for $j = 1, \ldots, N$, and we denoted a $\pi/2$ rotation in $\mathbb{R}^2$

$$\mathbf{x} = (x, y) \quad \mapsto \quad \mathbf{x}^{\perp} = (-\mathrm{y}, \mathrm{x})$$

(or $z \mapsto iz$). In other words, if we had initially

$$\hat{T}_{\text{asym}} = \frac{\hbar^2}{2m}\sum_{j=1}^{N}(-i\nabla_{\mathbf{x}_j})^2 \quad \text{acting on } L^2_{\text{asym}},$$

then we now obtain

$$\hat{T}_{\text{sym}\to\text{asym}} := \frac{\hbar^2}{2m}\sum_{j=1}^{N}\left(-i\nabla_{\mathbf{x}_j} + \mathbf{A}_j\right)^2 \quad \text{acting on } L^2_{\text{sym}},$$

so that indeed fermions may be represented as bosons, although with an additional magnetic interaction. The magnetic field seen by particle j,

$$\operatorname{curl}_{\mathbf{x}_j}\mathbf{A}_j = 2\pi\sum_{k\neq j}\delta(\mathbf{x}_j - \mathbf{x}_k), \tag{16}$$

corresponds to the attachment of **Aharonov–Bohm point fluxes** of magnitude 2π to each of the other particles. The set where this field is singular is precisely $\triangle_N$.

Similarly, if we fix a statistics parameter $\alpha \in \mathbb{R}$ and consider $\Psi = U^{\alpha}\tilde{\Psi}$ (now typically a singular gauge transformation involving multivalued functions over $\mathbb{C}^N \setminus \triangle_N$), then

$$-i\nabla_{\mathbf{x}_j}\Psi = U^{\alpha}(-i\nabla_{\mathbf{x}_j} + \alpha\mathbf{A}_j)\tilde{\Psi}, \tag{17}$$

and thus if we originally had the anyonic kinetic energy

$$\hat{T}_{\alpha} = \frac{\hbar^2}{2m}\sum_{j=1}^{N}(-i\nabla_{\mathbf{x}_j})^2 \quad \text{acting on } \Psi \in L^2_{\alpha},$$

then we obtain an equivalent description in terms of bosons:

$$\hat{T}_{\text{sym}\to\alpha} := \frac{\hbar^2}{2m}\sum_{j=1}^{N}\left(-i\nabla_{\mathbf{x}_j} + \alpha\mathbf{A}_j\right)^2, \text{ acting on } \tilde{\Psi} \in L^2_{\text{sym}}.$$

If we instead consider the transformation $\Psi = U^{\alpha-1}\tilde{\Psi}$ where $\tilde{\Psi} \in L^2_{\text{asym}}$, then we arrive at a description in terms of fermions:

$$\hat{T}_{\text{asym}\to\alpha} := \frac{\hbar^2}{2m}\sum_{j=1}^{N}\left(-i\nabla_{\mathbf{x}_j} + (\alpha - 1)\mathbf{A}_j\right)^2,$$

acting on L^2_{asym}. The magnetic field of $\alpha\mathbf{A}_j$ corresponds to the attachment of Aharonov–Bohm fluxes of magnitude $2\pi\alpha$ to each of the other particles. In this way we have the freedom to treat anyons as either bosons or fermions with topological magnetic interactions. This tool can certainly be beneficial as we can trade a simple operator (the free kinetic energy) but on a complicated geometry (multivalued functions with appropriate exchange conditions), for a complicated operator (magnetic interactions) but on a simple geometry (symmetric or antisymmetric functions on $\mathbb{R}^{2N}$). The former choice is usually referred to as the **anyon gauge** while the latter is the **magnetic gauge**, and this connection also brings us from an idealized world of quantum statistics of point particles and closer to the various possibilities for emergent statistics transmutation phenomena.

The procedure we referred to above to ensure the self-adjointness of the kinetic energy operator by extending the energy form (Friedrichs extension) also applies in this magnetic gauge formulation of the problem so that indeed the operators $\hat{T}_{\text{sym/asym}\to\alpha}$ are self-adjoint on appropriate domains in $L^2_{\text{sym/asym}}$ where the energy is finite (Lundholm and Solovej, 2014). Further, we remark that multiples of the unitary multiplication operator

$$U^2 : L^2_{\text{sym/asym}/\alpha} \longrightarrow L^2_{\text{sym/asym}/(\alpha+2)}$$

may be used, together with complex conjugation symmetry, to obtain that the free ideal anyonic kinetic energies are unitarily equivalent w.r.t. the transformations

$$\alpha \mapsto \alpha + 2\mathrm{n},\ \mathrm{n} \in \mathbb{Z} \quad \text{and} \quad \alpha \mapsto -\alpha. \tag{18}$$

Exchange vs. exclusion

Now that we have managed to define more or less concrete but still hypothetical models for ideal abelian anyons, we come to the next question: How do such anyons actually behave? If we are ever to observe them in nature then we need to know their behavior. So, are they more like bosons or more like fermions, or something in between, like the terms "intermediate statistics" or "fractional statistics" suggest? In other words, can we in any way relate the intermediate (braid) **exchange statistics** encoded into anyons to some intermediate **exclusion statistics** concerning the occupation numbers of various states as seen from a one-body perspective. Of course, since the magnetic gauge picture clarifies that anyons are (possibly) at least as complicated as strongly interacting systems of bosons or fermions, it is a priori not at all obvious whether this is possible. The issue of exchange vs. exclusion was referred to as "α to β" by Canright and Johnson in their review (Canright and Johnson, 1994) on the matter.

Only in cases of very few particles, $N = 2, 3, 4$, are energy spectra for ideal anyons well understood because they have then been computed analytically (for $N = 2$ (Arovas et al., 1985; Leinaas and Myrheim, 1977; Wilczek, 1982b), also extending to a collective (Date and Murthy, 1993; Date et al., 2003) part of the spectrum for all N (Chou, 1991; Wu, 1984b)) or numerically (the remaining part of the spectrum (Murthy et al., 1991; Sporre et al., 1991, 1992)), in a few situations.

In order to lift the degeneracy of the spectrum and facilitate comparison, it is convenient to confine the particles in a harmonic trapping potential $V(\mathbf{x}) = \frac{1}{2}m\omega^2|\mathbf{x}|^2$. For N anyons in the magnetic gauge description w.r.t. bosons, we thus consider the Hamiltonian operator

$$\hat{H}_N = \hat{T}_{\mathrm{sym}\to\alpha} + \hat{V} = \sum_{j=1}^{N}\left[\frac{\hbar^2}{2m}\left(-i\nabla_{\mathbf{x}_j} + \alpha\mathbf{A}_j\right)^2 + V(\mathbf{x}_j)\right],$$

and its corresponding ground-state energy (g.s.e.)

$$E_N := \inf\operatorname{spec}\hat{H}_N = \inf_{0\neq\Psi\in L^2_{\mathrm{sym}}}\langle\hat{H}_N\rangle_\Psi, \tag{19}$$

where $\langle\hat{A}\rangle_\Psi := \langle\Psi,\hat{A}\Psi\rangle/\langle\Psi,\Psi\rangle$ denotes the expectation of any operator $\hat{A}$ in a state $\Psi \neq 0$. The spectrum of the 2D harmonic oscillator $\hat{H}_{N=1}$ is well known:

$$\operatorname{spec}\hat{H}_1 = \{\hbar\omega n\}_{n=1,2,3,\ldots}\ (\text{each with multiplicity } n),$$

and for bosons one thus obtains N times the lowest eigenvalue, $E_N(\alpha = 0) = \hbar\omega N$, while for (spinless) fermions, due to the Pauli principle, we must sum over the N first eigenvalues according to their multiplicity: $E_N(\alpha = 1) \sim \frac{\sqrt{8}}{3}\hbar\omega N^{3/2}$ as $N \to \infty$. Further, because of rotation symmetry, the Hamiltonian commutes with the total angular momentum operator

$$\hat{L}/\hbar = -i\sum_{j=1}^{N}\left[x_j\partial_{y_j} - y_j\partial_{x_j}\right] = \sum_{j=1}^{N}\left[z_j\frac{\partial}{\partial z_j} - \bar{z}_j\frac{\partial}{\partial\bar{z}_j}\right],$$

and its eigenvalues $L \in \mathbb{Z}$ can therefore be used to separate the energy spectrum further.

The spectrum of $\hat{H}_N$ for $N = 2$ and $N = 3$ is shown in Fig. 4, and while in the former case it manifests a strictly linear interpolation between bosons and fermions (Leinaas and Myrheim, 1977)

$$E_2(\alpha) = \hbar\omega\left(2 + \min_{q\in\mathbb{Z}}|2q + \alpha|\right), \tag{20}$$

in the latter case there are also nonlinearly interpolating states at various L, and such a state with $L \neq 0$ comes down from an excited level at $\alpha = 0$ to reach the Fermi energy at $\alpha = 1$. Similar features are also seen in the numerical spectrum for $N = 4$ (Sporre et al., 1992) and expected to occur for all $N \geq 3$ (Chitra and Sen, 1992).

Rough upper bounds for E_N at any α and N are obtained simply by considering trial states that localize the particles on separate domains in $\mathbb{R}^2$ so that their exchange statistics is not seen (in the magnetic gauge picture one may then gauge away all magnetic interactions while in the anyon gauge picture, one then stays within a domain of distinguishability). By balancing the localization energy and the spread into the potential one then finds that $E_N(\alpha) \lesssim \hbar\omega N^{3/2}$, that is, the energy is at most at the order of fermions. Note however that the fermionic energy does not provide a strict upper bound, as seen for $N = 3$ where $E_3(\alpha \approx 0.7) > E_3(\alpha = 1)$.

On the other hand, it is also useful to note that the bosonic energy, for which the g.s. Ψ_0 is a Gaussian at the origin $\mathrm{x} = 0$, always gives a rigorous lower bound:

$$E_N(\alpha) \geq E_N(0) = \hbar\omega N, \tag{21}$$

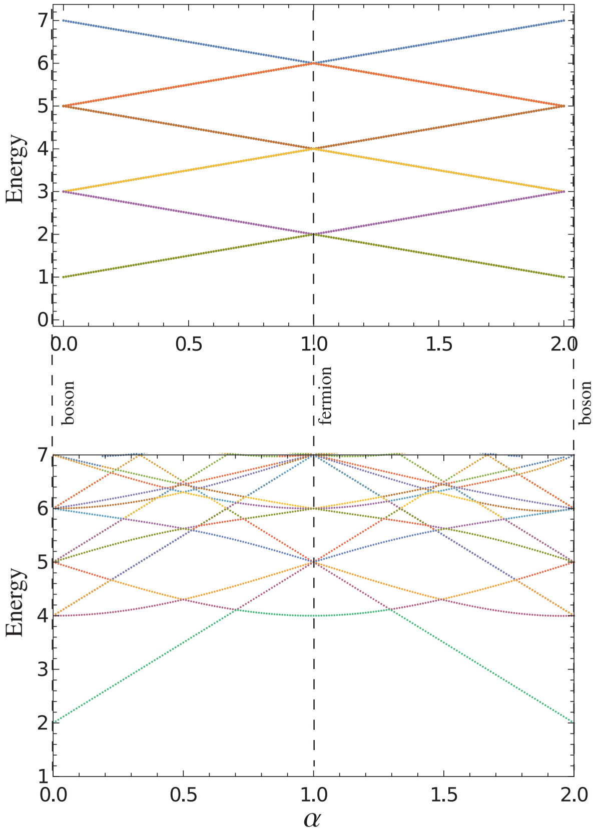

Fig. 4 Energy spectra for $N = 2$ (upper) and $N = 3$ (lower) anyons in a harmonic trap (minus the center of mass energy 1, and in suitable units). From Yakaboylu E, Ghazaryan A, Lundholm D, Rougerie N, Lemeshko M, and Seiringer R (2020) Quantum impurity model for anyons. Physical Review B 102: 144109; cf. also Leinaas JM and Myrheim J (1977) On the theory of identical particles. Nuovo Cimento B 37: 1–23; Murthy MVN, Law J, Brack M, and Bhaduri RK (1991) Quantum spectrum of three anyons in an oscillator potential. Physical Review Letters 67: 1817–1820; and Sporre M, Verbaarschot JJM, and Zahed I (1991) Numerical solution of the three-anyon problem. Physical Review Letters 67: 1813–1816

since the kinetic energy satisfies a **diamagnetic inequality** (Lundholm and Solovej, 2014)

$$\langle \hat{T}_\alpha \rangle_\Psi \geq \langle \hat{T}_{\mathrm{sym}} \rangle_{|\Psi|}. \tag{22}$$

This is observed by factoring Ψ into its modulus and phase, and dropping the phase contribution to the momentum $-i\nabla\,\Psi$.

Chitra and Sen (1992) provided a more interesting lower bound to the spectrum for any N, extending (20): for an arbitrary state Ψ with angular momentum L, it holds

$$\langle \hat{H}_N \rangle_\Psi \;\geq\; \hbar\omega\left(N + \left|L + \alpha\frac{N(N-1)}{2}\right|\right). \tag{23}$$

Combined with our a priori upper bound, this implies that in the ground state the angular momentum needs to be close to

$$L \approx -\alpha\binom{N}{2} \text{ since } \left|L + \alpha\binom{N}{2}\right| \lesssim O(N^{3/2}) \tag{24}$$

so that on the average, there needs to be an angular momentum $-\alpha$ for every pair of particles in order to cancel the shifted inherent/anyonic angular momentum (the number of attached units of magnetic flux per particle). This also means that as N grows large, there will be a large number $O(N^{1/2})$ of level crossings in the g.s. between different integer angular momenta because any fixed angular momentum L can only be good on a scale $\Delta\alpha = O(N^{-1/2})$. The situation is sketched in Fig. 5, where at fixed $N \gg 1$, one expects to find curves corresponding to families of states at fixed L that are smoothly varying with α, to eventually come down to an energy $O(N^{3/2})$ on a $O(N^{1/2})$-neighborhood around a suitable minimum $\alpha \approx \alpha_0(L)$, and then to again shoot upwards in energy with a slope $\gtrsim O(N^2)$.

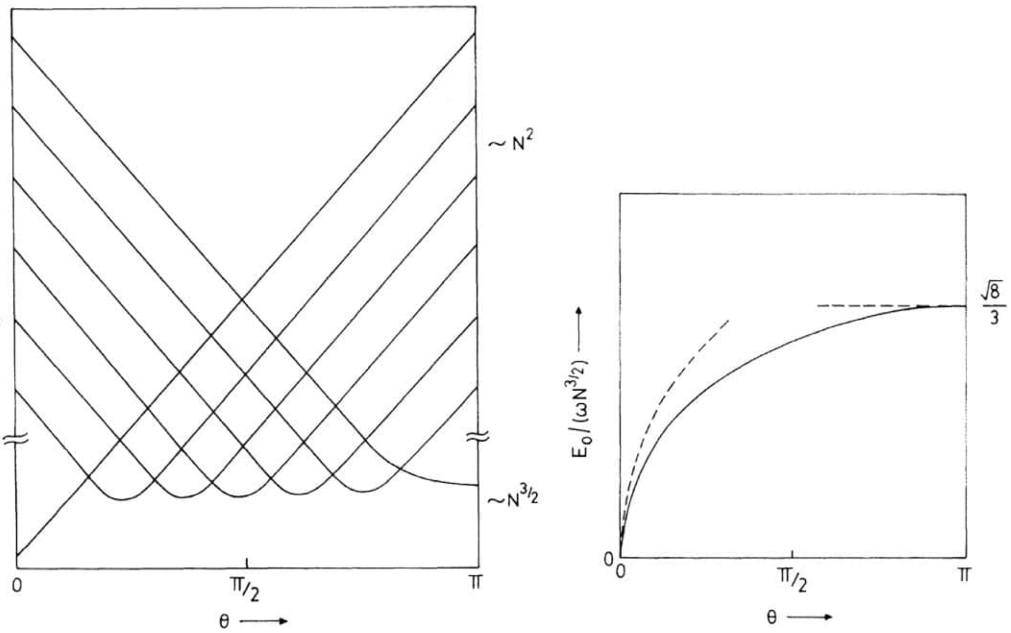

Fig. 5 Schematic energy spectrum for $N \gg 1$ (left) and estimates for the g.s.e. near bosons and fermions (right) for anyons with statistics $\alpha = \theta/\pi$ in a harmonic trap. From Chitra R and Sen D (1992) Ground state of many anyons in a harmonic potential. Physical Review B 46: 10923–10930

Chitra and Sen went on to estimate (again, see Fig. 5) the enveloping g.s.e. curve close to bosons (suggesting $E_N/(\hbar\omega N^{3/2}) \approx \frac{7\sqrt{3}}{9}\sqrt{\alpha}$) and to fermions (suggesting $E_N/(\hbar\omega N^{3/2}) \approx \frac{\sqrt{8}}{3}$), but left it as an open problem whether there are nonanalyticities in the limiting function

$$h(\alpha) := \liminf_{N\to\infty} E_N(\alpha)/(\hbar\omega N^{3/2}), \tag{25}$$

concluding that "This is an interesting but difficult question to answer."

Toward density functionals for anyons

The few-particle spectra led to some initial results on the thermodynamics of the anyon gas, by considering the high-temperature, low-density virial expansions (Arovas et al., 1985; Dowker, 1985) (see Khare, 2005; Mancarella et al., 2013b; Myrheim, 1999, for review). In the low-temperature regime, in order to make the many-anyon ground-state problem more manageable, we could wish for a limiting effective description with a relatively limited number of degrees of freedom that are sufficient to describe the collective state of the system at $N \to \infty$. Such a state might converge toward the minimizer of a suitable functional, that is, (taking some suitable scale $a > 0$ for normalization):

$$E_N/N^a \xrightarrow{N\to\infty} \text{minimum of } \mathcal{E}[\psi] \text{ or } \mathcal{E}[\varrho], \text{ and}$$

$$\text{some marginal of g.s. } \Psi_0 \text{ of } \hat{H}_N \xrightarrow{N\to\infty} \text{minimizer of } \mathcal{E},$$

where $\mathcal{E}$ is typically an energy functional of either one-body states $\psi \in L^2(\mathbb{R}^2)$ or of corresponding probability densities $\varrho = |\psi|^2 \in L^1(\mathbb{R}^2)$ (with mass 1 or N).

For example, for 2D fermions in a trapping potential V, one has the **Thomas–Fermi approximation** (Fermi, 1927; Thomas, 1927):

$$E_N = \inf_{0\neq\Psi\in L^2_{\text{asym}}} \langle \hat{T}_{\text{asym}} + \hat{V}\rangle_\Psi \approx \inf_{\varrho\geq 0:\, \int_{\mathbb{R}^2}\varrho = N} \mathcal{E}^{\text{TF}}[\varrho], \tag{26}$$

where the density $\varrho = \varrho^{\text{TF}} \approx \varrho_{\Psi_0}$ (one-body marginal of g.s.) minimizes the **Thomas–Fermi (TF) functional**

$$\mathcal{E}^{\text{TF}}[\varrho] := \int_{\mathbb{R}^2} \left[2\pi\varrho(\mathbf{x})^2 + V(\mathbf{x})\varrho(\mathbf{x})\right] d\mathbf{x}. \tag{27}$$

(**Note:** *To simplify our discussion, we shall now and in the remainder of this article assume that the physical constant* $\hbar^2/(2m) = 1$, *that is,* $T = \mathbf{p}^2$, *by an appropriate choice of units* $\hbar = 2m = c = e = 1$.) The kinetic energy density is here given by the energy per unit area of the **homogeneous 2D Fermi gas** at density $\varrho(\mathbf{x})$, obtained, for example, by confining N fermions in a box of area $L \times L$, summing the one-body eigenvalues and taking the thermodynamic limit:

$$E_N/L^2 \xrightarrow{N,L\to\infty} 2\pi\overline{\varrho}^2, \qquad \text{at fixed } \overline{\varrho} = N/L^2.$$

On the other hand, for bosons with sufficiently weak *scalar* interactions, one has the **Gross–Pitaevskii (GP) functional** (Gross, 1961; Pitaevskii, 1961):

$$\mathcal{E}^{\mathrm{GP}}[\psi] := \int_{\mathbb{R}^2} \left[|(-i\nabla + \mathbf{A}_{\mathrm{ext}})\psi|^2 + V|\psi|^2 + g|\psi|^4 \right], \tag{28}$$

describing approximate condensation into the state $\psi \in L^2(\mathbb{R}^2)$ as $E_N/N \to$ minimum of $\mathcal{E}^{\mathrm{GP}}$. In regimes where the interaction strength $g \in \mathbb{R}$ (related to the scattering length of the interaction potential) dominates over the kinetic term, one may neglect that term and keep only the last two terms, again leaving a functional of $\varrho = |\psi|^2$ of the Thomas–Fermi type with $g \leftrightarrow 2\pi N$ (this is only a formal analogy at the level of functionals since the two mechanisms of the approximations are very different).

In view of the above, could one then suggest the following interpolating functional for $0 < \alpha \leq 1$, describing an **"average-field" approximation** for anyons

$$\mathcal{E}^{\mathrm{af}}[\varrho] \approx \int_{\mathbb{R}^2} \left[2\pi\alpha\varrho(\mathbf{x})^2 + V(\mathbf{x})\varrho(\mathbf{x}) \right] d\mathbf{x} \quad ? \tag{29}$$

Indeed, in a mean-field (We differentiate between "average-field" and "mean-field," partly to distinguish the anyonic context but also because of more technical reasons that will be clarified below.) (**Hartree**) ansatz for the ground state in the bosonic representation, consider:

$$\Psi(\mathrm{x}) = \psi(\mathbf{x}_1)\psi(\mathbf{x}_2)\ldots\psi(\mathbf{x}_N), \tag{30}$$

and we may think of a single particle $\psi \in L^2(\mathbb{R}^2)$ in the magnetic field of the others (identically distributed):

$$B(\mathbf{x}) \approx 2\pi\alpha(N-1)|\psi(\mathbf{x})|^2 \approx 2\pi\alpha\varrho_\Psi(\mathbf{x}). \tag{31}$$

If the density $\varrho_\Psi = N|\psi|^2$ is approximately constant on an area $L \times L$ where N bosons condense into the lowest Landau level of the field B (cf. (64) below), then one indeed obtains an energy per unit area

$$E_N/L^2 \approx BN/L^2 \approx 2\pi\alpha\overline{\varrho}^2, \qquad \overline{\varrho} = N/L^2, \tag{32}$$

thus suggesting (29). For the ideal anyon gas, this argument is not rigorous, because one cannot apply such an ansatz in the singular magnetic field (it is not in the appropriate domain of $\hat{T}_\alpha$). This difficulty can be overcome using regularization, however, and we return to it in Section "Almost-bosonic anyons" in conjunction with the extended anyon gas. Thus, after accepting some refinements to the "average-field" approach in that context, it has been successfully applied in the limits $\alpha \to 0$ and $\alpha \to 1$ as $N \to \infty$.

To be precise, if we wish to refer to the approximation as above with an almost constant field (on the scale of a trap), then it is perhaps more appropriate to call it a **"constant-field" approximation**. We also note that if (29) would be a valid description for proper anyons, then it suggests that for the harmonic oscillator problem

$$E_N \overset{?}{\approx} \inf_{\substack{\varrho \geq 0 \\ \int \varrho = N}} \int_{\mathbb{R}^2} \left[\frac{\hbar^2\pi\alpha}{m}\varrho(\mathbf{x})^2 + \frac{m\omega^2}{2}|\mathbf{x}|^2\varrho(\mathbf{x}) \right] d\mathbf{x} = \frac{\sqrt{8}}{3}\sqrt{\alpha}\,\hbar\omega N^{3/2}, \qquad 0 < \alpha \leq 1. \tag{33}$$

Early applications of variants of **density functional theory** (DFT) to the anyon context were made by Chitra and Sen, who proposed the refinement as in Fig. 5 due to the bosons' hard core (Chitra and Sen, 1992), and by Li, Bhaduri and Murthy who considered an extension of TF theory to excited states in the spectrum (Li et al., 1992). Again, only some aspects have been rigorously justified, in the limits close to bosons and fermions.

Local exclusion principle and degeneracy pressure for the ideal anyon gas

An approach that has been successful for an increased qualitative understanding of the genuine ideal anyon gas at arbitrary α is to take a strictly *local* route to exclusion via the wider concept of **statistical repulsion**. Namely, one may note that statistical repulsion manifests itself in the anyon gas in (at least) three ways:

1. **Effective *scalar* pairwise repulsion.** The exchange conditions (7) for each pair of particles transpire to yield a pair repulsion between particles. Its simplest form can be stated as a lower bound (known in mathematics as a many-particle **Hardy inequality**, Hoffmann-Ostenhof et al., 2008; Lundholm and Solovej, 2013a) for the kinetic energy: for any N,

$$\hat{T}_\alpha \geq \frac{4\alpha_N^2}{N} \sum_{j<k} \frac{1}{|\mathbf{x}_j - \mathbf{x}_k|^2}, \tag{34}$$

interpreted in the sense of forms or expectation values, and where the so-called **N-fractionality of $\boldsymbol{\alpha}$**, defined

$$\alpha_N := \min_{p=0,1,\dots,N-2} \min_{q\in\mathbb{Z}} |(2p+1)\alpha - 2q|,$$

is the arcwise distance (in units of π) on the unit circle from the set $\{e^{i(2p+1)\alpha\pi}\}_{p=0,1,\dots,N-2}$ of all possible pair-exchange phases to the point +1 of bosons. Taking the limit as $N \to \infty$ one finds (see Fig. 6)

$$\alpha_{N\to\infty} = \begin{cases} \dfrac{1}{\nu}, & \text{if } \alpha = \dfrac{\mu}{\nu}\, odd\text{—numerator reduced rational,} \\ 0, & \text{otherwise,} \end{cases} \tag{35}$$

an odd variant of Thomae's "popcorn function."

The origin of the scalar lower bound (34) lies in the effective angular momentum barrier of each pair of particles at distance $r > 0$:

$$V_{\text{stat}}(r) = |(2p+1)\alpha - 2q|^2 \frac{1}{r^2} \geq \frac{\alpha_N^2}{r^2}. \tag{36}$$

Namely, in an exchange of two particles, as in (7) where p other particles happen to be ensnared, an anyonic phase shift $e^{i(2p+1)\alpha\pi} \neq 1$ leaves a residual angular momentum according to (36). Heuristically, we can anticipate this effect in the two-particle energy form (12), where the quantization condition (10) in the angular variable φ is appropriately modified to account for the presence of any extra particles, assuming all other position variables are fixed and the relative angular variable undergoes a full loop $\varphi \to \varphi + \pi$ in configuration space. The anyonic phase then shifts the relative angular momentum of the pair, which however is quantized over the even integers due to the half-circle symmetry for identical particles (The operator $\hat{\ell} = -i\partial_\varphi$ on $[0, \pi]$ with twisted boundary conditions $\psi(\pi) = e^{i\alpha\pi}\psi(0)$ has eigenvalues $\{\alpha - 2q\}_{q\in\mathbb{Z}}$. Therefore the minimum of $\hat{\ell}^2$ is $\min_{q\in\mathbb{Z}}|\alpha - 2q|^2 = \alpha_2^2$. Compare also (20).).

We expect the repulsive barrier (36) to be stronger than the r.h.s. on average as the number p fluctuates. Indeed, the coupling constant of the pair-interaction potential on the r.h.s. of (34) can be strengthened to a nearest-neighbor version, which only depends on the 2-fractionality α_2 (periodized α), if it is at the same time weakened by yet another factor of N (Lundholm and Qvarfordt, 2020; Rougerie and Yang, 2022). Anyway, the repulsion offered by the potential is strong enough to imply that $\Psi \to 0$ at $\triangle_N$ if $\alpha_2 \neq 0$, and can therefore be viewed as a **generalized Pauli principle** for anyons (Lundholm, 2017; Lundholm and Qvarfordt, 2020; Lundholm and Solovej, 2013b) (other variants were considered in Fröhlich and Marchetti (1988, 1989), Goldin and Sharp (1996), and Goldin and Majid (2004)).

2. **Local exclusion principle.** The bound (34) (with its various refinements Larson and Lundholm, 2018; Lundholm and Qvarfordt, 2020; Lundholm and Solovej, 2013a) can also be applied locally on subsets of the plane and is strong enough to yield a linear bound $E_N \gtrsim N - 1$ for the local (Neumann) energy (Lundholm and Seiringer, 2018; Lundholm and Solovej, 2013b). Again, this holds modulo a (positive) constant that either depends on α_N, or a typically weaker one (still positive) that only depends on α_2 (cf. Fig. 7).

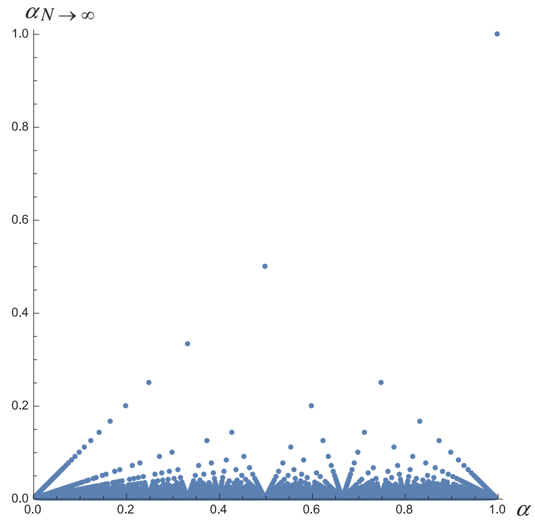

Fig. 6 ∞-Fractionality of α given by the odd popcorn function (35) (Lundholm, 2017; Lundholm and Solovej, 2013a).

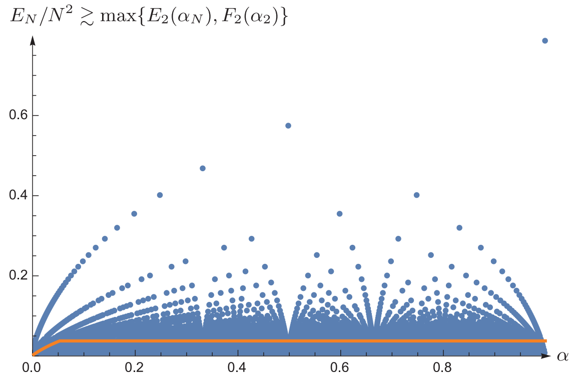

Fig. 7 Lower bounds to the homogeneous ideal anyon gas energy (Larson and Lundholm, 2018; Lundholm and Seiringer, 2018). The *blue points* are numerical lower bounds for $E_2(\alpha) = 4\pi\alpha + O(\alpha^{4/3})$ at $\alpha = \alpha_{N\to\infty}$ while the *orange curve* describes $F_2(\alpha_2) = \frac{1}{4}\min\{E_2(\alpha_2), 0.147\}$, correspondingly.

For comparison, take, for example, the unit square $Q = [0, 1]^2$ and consider fermions which there satisfy the bound

$$E_N(\alpha = 1, Q) \geq \pi^2(N - 1) \qquad \text{for } N \geq 1, \tag{37}$$

since each added particle is orthogonal to the ground state (the constant function) and thus adds at least the energy $E_2 = \pi^2$ of a first-excited state $\psi(x, y) \propto \cos(\pi x)$ or $\cos(\pi y)$.

For anyons, we denote the N-particle **Neumann energy on** $\boldsymbol{Q}$ by

$$E_N(\alpha, Q) := \inf_{0 \neq \Psi \in L^2_{\text{sym}}(Q^N)} \langle \hat{T}_{\text{sym}\to\alpha} \rangle_\Psi. \tag{38}$$

It is known that (Larson and Lundholm, 2018; Lundholm and Seiringer, 2018)

$$E_2(\alpha, Q) = 4\pi\alpha_2 + O(\alpha_2^{4/3}) \qquad \text{for any } \alpha, \tag{39}$$

and furthermore, all higher particle energies can be bounded uniformly in terms of this energy, or a suitable approximation ($\tilde{E}_2(\alpha) \approx 2\pi(j'_{\alpha_2})^2 \geq 4\pi\alpha_2$, where j'_α denotes the first zero of the derivative of the Bessel function J_α (Larson and Lundholm, 2018).) $\tilde{E}_2$ to it: for $N \geq 2$,

$$E_N \geq (N - 1)\tilde{E}_2(\alpha_N), \tag{40}$$

as well as

$$E_N/N \geq \frac{1}{4}\min\{E_2, E_3, E_4\} \geq \frac{1}{4}\min\{E_2(\alpha_2), 0.147\}. \tag{41}$$

This r.h.s. we denote by $F_2(\alpha_2)$; cf. Fig. 7. An interpretation of the above is that the nearest-neighbor energy E_2 is a relatively good approximation at every scale (at least as a lower bound) due to a balancing of uncertainty and exclusion in the gas.

3. **Degeneracy pressure.** Lastly, a combination of the above local exclusion principle and the uncertainty principle (also in a local formulation) yields a convenient measure of the degeneracy pressure in the anyon gas.

Compare the TF functional (27), which shows that the effect of the exclusion principle for fermions is a self-energy for the density that penalizes localization and thus forces a spread of the profile into the more expensive regions of the trapping potential. Indeed, the ideal Fermi gas satisfies the following kinetic energy inequality (known in mathematics as a **Lieb–Thirring inequality** (Lieb and Thirring, 1975)) which captures this type of degeneracy pressure: for any number N of particles and any N-fermion state $\Psi \in L^2_{\text{asym}}(\mathbb{R}^{2N})$,

$$\langle \hat{T}_{\text{asym}} \rangle_\Psi \gtrsim \int_{\mathbb{R}^2} \varrho_\Psi(\mathbf{x})^2 \, d\mathbf{x} \tag{42}$$

(modulo a universal constant (Deciding on the best constant in this inequality is a long-standing open problem, but it is conjectured (Lieb and Thirring, 1976) to be given by that of its restriction to $N = 1$ (a Sobolev constant) and is strictly smaller than the TF constant 2π. See Seiringer and Solovej (2023) for recent progress.)), where ϱ_Ψ is the one-body density associated to Ψ, obtained by marginalizing $N - 1$ particles. Inequalities of this type have been useful to prove qualitative properties of large fermionic systems such as their thermodynamic stability w.r.t. Coulomb interaction with a mixture of charges (Dyson and Lenard, 1967; Lieb and Seiringer, 2010; Lieb and Thirring, 1975). In the case that ν species of fermions or spin states are considered, the constant in (42) is weakened by a factor $1/\nu$.

The degeneracy pressure for anyons is measured by a similar inequality (Lundholm and Solovej, 2013a, b) (see Lundholm and Qvarfordt (2020) for review): for any number N of particles and any N-anyon state $\Psi \in L^2_\alpha$,

$$\langle \hat{T}_\alpha \rangle_\Psi \gtrsim \alpha_2 \int_{\mathbb{R}^2} \varrho_\Psi(\mathbf{x})^2 \, d\mathbf{x} \tag{43}$$

(again modulo a universal constant). Its strength thus depends on leading order of the 2-fractionality, that is, the nearest-neighbor exchange statistics α. It then follows, like for fermions, that charged anyonic systems (except bosons) with Coulomb interaction are also stable (Lundholm and Seiringer, 2018; Lundholm and Solovej, 2014).

Applied to the harmonic trap (19), the degeneracy pressure (43) yields the bound

$$E_N(\alpha, \text{harm.osc.}) \gtrsim \sqrt{\alpha_2}\, \hbar\omega N^{3/2}, \tag{44}$$

which indeed matches the constant-field approximation (33), and Fig. 5, up to the value of the universal constant.

On a disk geometry D with unit area, the analysis of Chitra and Sen again suggests a large number of level crossings as $N \to \infty$, and thus possibly nonanalyticities in the limiting g.s.e. per particle and unit density of the **homogeneous ideal anyon gas** (Although it has not been rigorously shown, we may expect the thermodynamic limit to be independent of the shape of the domain (and otherwise take the infimum over reasonable shapes).)

$$e(\alpha) := \liminf_{N\to\infty} E_N(\alpha, D)/N^2. \tag{45}$$

Most details about this function are still open, but from a further analysis of the homogeneous ideal anyon gas on the unit square Q (dividing it into smaller squares), one can at least derive the rigorous uniform bounds (cf. Fig. 7) (Lundholm and Seiringer, 2018)

$$\frac{1}{4}\max\{\tilde{E}_2(\alpha_N), F_2(\alpha_2)\} \le e(\alpha) \le 2\pi^2, \tag{46}$$

and

$$\alpha_2 \lesssim e(\alpha) \lesssim \alpha_2, \tag{47}$$

modulo lower and upper universal constants (certainly not optimal). Subject to the assumption that $e(\alpha)$ indeed has a fractal structure that captures universal aspects of planar geometry, a conjecture on its possible form can be given as in Fig. 8; cf. (Lankhorst et al., 2018).

Some states of particular interest

We saw above that there is a nontrivial and delicate balance between exclusion and uncertainty in the ground state energy. Certain types of states have been proposed (Lundholm, 2017; Lundholm and Solovej, 2013b) to minimize the kinetic energy $\hat{T}_{\text{sym}\to\alpha}$ at particular values of the statistics parameter: in the case of $\alpha = \mu/\nu \in [0, 1]$ being an *even*-numerator reduced fraction, and for $N = \nu K$, $K = 1, 2, \ldots$, a suitable sequence of particle numbers, let

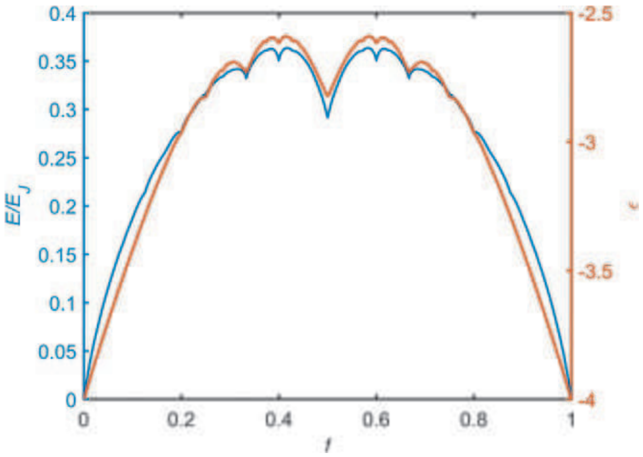

Fig. 8 Universal energy phenomena in 2D, from Lankhorst et al. (2018): lowest energy branch of a 100 × 100 square Josephson junction array (*left/blue*) resp. the Hofstadter butterfly (*right/orange*), which also is proportional to the critical temperature of a superconducting square network. (For comparison, $\alpha \sim 2f$.)

$$\Psi_\alpha := \prod_{j<k} |z_{jk}|^{-\alpha}\, \mathcal{S}\left[\prod_{q=1}^{\nu}\prod_{(j,k)\in\mathcal{E}_q} (\bar{z}_{jk})^{\mu}\right]\prod_{l=1}^{N}\psi_0(\mathbf{x}_l), \tag{48}$$

while for *odd* numerators μ, let

$$\Psi_\alpha := \prod_{j<k} |z_{jk}|^{-\alpha}\, \mathcal{S}\left[\prod_{q=1}^{\nu}\prod_{(j,k)\in\mathcal{E}_q} (\bar{z}_{jk})^{\mu} \bigwedge_{k=0}^{K-1} \psi_k\left(\mathbf{x}_{l\in\mathcal{V}_q}\right)\right]. \tag{49}$$

Here $z_{jk} := z_j - z_k$ are the pairwise relative complex coordinates and we have grouped, or "colored," the particles into ν different colors where $G_q = (\mathcal{V}_q, \mathcal{E}_q)$ denotes the complete graph over each such group of $|\mathcal{V}_q| = K$ vertices particles (see Fig. 9). The symmetrization $\mathcal{S}$ over all the particles then amounts to symmetrization over all such colorings and can be viewed as passing from a set of distinguishable particles (by color) to indistinguishable (cf., Regnault et al., 2008). The ψ_k, $k = 0, 1, 2, \ldots$, are the eigenstates (ordered by increasing energy) of the corresponding one-body Hamiltonian $\hat{H}_1$. The states Ψ_α are moderately singular and so we should actually consider $\Psi = \Phi\Psi_\alpha \in L^2_{\mathrm{sym}}(\mathbb{R}^{2N})$ with Φ a suitably chosen regularization factor to allow inclusion into the domain of $\hat{T}_{\mathrm{sym}\to\alpha}$.

Some of the reasons why these states appear to be of interest in the many-anyon problem include:

- They have the right average angular momentum (24) and are (for harmonic trap and certain K) homogeneous with a degree suitable to optimize the bound (23).
- They enjoy certain clustering properties that are beneficial to minimize the pair repulsion $V_{\mathrm{stat}}(r)$ on large scales r. States of the form (48) for $\mu = 2$, $\nu = 3, 5, \ldots$ are known in the FQHE context as Read–Rezayi states and are known to form clusters of ν particles bound to μ vortices (Cappelli et al., 2001; Read and Rezayi, 1999), while (49) for $\mu = 1$, $\nu = 2$ correspond to Dyson–Moore–Read/BCS/Pfaffian states subject to pairing (Dyson, 1967; Moore and Read, 1991). Further, excitations on top of these states appear to have non-abelian character (Bonderson et al., 2011; Nayak et al., 2008; Stern, 2008).
- They manifest certain structural stabilities with the smallness of $1 \le \mu \le \nu$, similar to the Laughlin states of the FQHE and indicative of a scale of robustness.
- Some of the states (48) are exact but moderately singular/generalized low-energy eigenfunctions of the Hamiltonian with singular boundary conditions (cf. point interactions below, Section "Point-interacting anyons") (Chou, 1991; Murthy et al., 1992).

The nonideal anyon gas

The "average(/constant)-field" approach, suggesting (29), leads to difficulties when applied to strictly ideal and pointlike particles, and it is both realistic and helpful to instead consider extended particles as well as other nonideal models of anyon gases that can more easily incorporate the average effects of exchange phases or flux. Heuristic approaches to ensure averaged influence of the statistics include a "self-consistency argument" wherein a typical cyclotron orbit of the generated field ought to contain a large number of particles, suggesting a better approximation if (Chen et al., 1989; Trugenberger, 1992b)

$$\alpha_2 \ll 1 \qquad \text{or} \qquad (1-\alpha_2)^2 \ll 1 \tag{50}$$

(i.e., slightly better around fermions due to Pauli repulsion) as well as a similar orbital argument but based instead on the scattering angles of combined Aharonov–Bohm and hard-disk interaction (Caenepeel and MacKenzie, 1994), again suggesting the conditions (50).

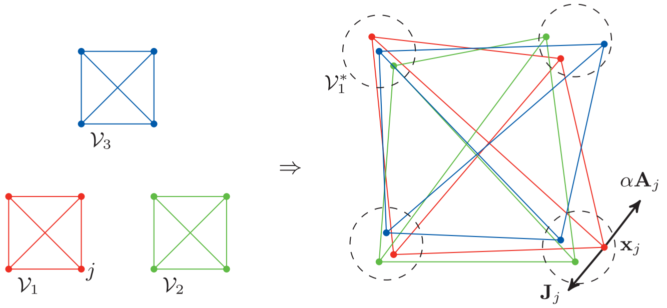

Fig. 9 A coloring of $N = 12$ particles with $\nu = 3$ colors into $K = 4$ 3-clusters V_q^*. Each colored edge $(j,k) \in E_q$ corresponds to one unit $-\mu$ of pairwise angular momentum. Also shown is the contribution to the magnetic potential $\alpha\mathbf{A}_j$ and the current $\mathbf{J}_j$ of particle j due solely to the 3-cluster V_1^*. From Lundholm D (2017) Many-anyon trial states. Physical Review A 96: 012116

The extended anyon gas

In the **extended anyon gas**, we work in the magnetic perspective and replace the point magnetic fluxes of ideal anyons by extended fluxes. For simplicity (and not completely ad hoc from the perspective of emergent models), we may consider the flux to be constantly spread over a disk-shaped magnetic field attached to each particle, with radius $R > 0$. We then replace the anyon magnetic potentials (15) by

$$\mathbf{A}_j^R(\mathrm{x}) := \sum_{k\neq j} \frac{(\mathbf{x}_j - \mathbf{x}_k)^{\perp}}{|\mathbf{x}_j - \mathbf{x}_k|_R^2}, \qquad |\mathbf{x}|_R := \max\{|\mathbf{x}|, R\}, \tag{51}$$

so that, if $\mathbb{1}_{\mathrm{D}(\mathbf{y},\,\mathrm{R})}$ denotes the indicator function on a disk of radius R centered at $\mathbf{y}$, the field is

$$\mathrm{curl}_{\mathbf{x}_j} \alpha \mathbf{A}_j^R = 2\pi\alpha \sum_{k\neq j} \frac{\mathbb{1}_{\mathrm{D}(\mathrm{x}_k,\,\mathrm{R})}(\mathbf{x}_j)}{\pi R^2} \xrightarrow{R\to 0} 2\pi\alpha \sum_{k\neq j} \delta_{\mathbf{x}_k}(\mathbf{x}_j).$$

The kinetic energy of the extended anyon gas with bosons as reference is then

$$\hat{T}^R_{\mathrm{sym}\to\alpha} := \frac{\hbar^2}{2m} \sum_{j=1}^{N} \left(-i\nabla_{\mathbf{x}_j} + \alpha \mathbf{A}_j^R\right)^2,$$

acting on L^2_{sym} while if we use fermions as reference then

$$\hat{T}^R_{\mathrm{asym}\to\alpha} := \frac{\hbar^2}{2m} \sum_{j=1}^{N} \left(-i\nabla_{\mathbf{x}_j} + (\alpha - 1) \mathbf{A}_j^R\right)^2,$$

acting on L^2_{asym}.

There is now an additional natural dimensionless parameter in the problem that can be defined as the ratio of the size of the magnetic flux disk to the average interparticle distance,

$$\bar{\gamma} := R\bar{\varrho}^{1/2}. \tag{52}$$

This density parameter has been called the **magnetic filling ratio** in Trugenberger (1992a, b) and Larson and Lundholm (2018). The limit $\bar{\gamma} = 0$ corresponds to ideal anyons while $\bar{\gamma} \sim 1$ is the "smearing" limit when particles typically begin to overlap, and $\bar{\gamma} \to \infty$ would describe the constant-field limit.

At any fixed choice of the two parameters $\alpha \in \mathbb{R}$, $\bar{\gamma} \geq 0$, the energy per particle and unit of density of the **homogeneous extended anyon gas** may thusly be defined via the thermodynamic limit

$$e_{\substack{\mathrm{sym}/\\ \mathrm{asym}}}(\alpha, \bar{\gamma}) := \liminf_{\substack{N,L\,\to\,\infty\\ N/L^2=\bar{\varrho}}} \frac{E_N(\alpha, R, LQ)}{\bar{\varrho}N}, \tag{53}$$

where $E_N(\alpha, R, LQ)$ denotes the g.s. energy of the respective operator $\hat{T}^R_{\mathrm{sym/asym}\to\alpha}$ on $L^2_{\mathrm{sym/asym}}(LQ^N)$. A corresponding TF-type functional for a **local-density approximation** within a trapping potential V is then

$$\mathcal{E}^{\alpha,R}_{\substack{\mathrm{sym}/\\ \mathrm{asym}}}[\varrho] := \int_{\mathbb{R}^2} \left[e_{\substack{\mathrm{sym}/\\ \mathrm{asym}}}\left(\alpha, R\varrho(\mathbf{x})^{1/2}\right)\varrho(\mathbf{x})^2 + V(\mathbf{x})\varrho(\mathbf{x}) \right] d\mathbf{x}, \tag{54}$$

with $\int_{\mathbb{R}^2}\varrho = N$.

The qualitative analysis of local exclusion effects of the ideal gas discussed in Section "Local exclusion principle and degeneracy pressure for the ideal anyon gas" has been extended to the extended gas, both in the bosonic and the fermionic references. Up to constants, one finds the qualitative bounds (Larson and Lundholm, 2018)

$$e_{\mathrm{sym}}(\alpha, \bar{\gamma}) \gtrsim \begin{cases} |\ln \bar{\gamma}|^{-1} + \alpha_{\infty}, & \bar{\gamma} \ll 1 \ (\alpha \text{ fixed}), \\ |\alpha|, & \bar{\gamma} \gtrsim 1, \end{cases}$$

where the first regime is a combination of a dilute 2D Bose gas (Lieb and Yngvason, 2001; Schick, 1971) and the strongest of the two lower bounds (46) for the ideal gas at odd numerators, $\tilde{E}_2(\alpha_\infty) \gtrsim \alpha_\infty$, while the second regime indeed captures the constant-field energy (29) for arbitrarily large α. The full regime $\bar{\gamma} \lesssim 1$ is more difficult to describe since it covers both soft-core and hard-core behaviors (see Section "Other interactions and fields"), and we should expect to replace α_∞ with α_2 in a suitable limit. Trugenberger (1992b) suggested that this gas with fixed extension parameter $R > 0$ will at low temperatures prefer to adjust its density to $\bar{\gamma} \gtrsim 1$, where the average field approximation is good and the gas becomes a superfluid, while for high temperatures the density drops, $\bar{\gamma} \ll 1$, the average-field loses validity and superfluidity is lost.

In the fermionic reference (Girardot and Rougerie, 2022)

$$e_{\text{asym}}(\alpha, \overline{\gamma}) \gtrsim \begin{cases} \alpha_2, & \overline{\gamma} \lesssim 1, \\ 1, & \overline{\gamma} \gtrsim 1. \end{cases}$$

In this case the inherent Pauli principle improves the dependence to nearest neighbor due to its scale independence. Note that both energies $e_{\text{sym/asym}}$ must be periodic in α at $\overline{\gamma} = 0$, but not at any finite $\overline{\gamma} > 0$, which therefore requires an interesting interpolation between the regimes.

Almost-bosonic anyons

The average field approach (29) can be made fully rigorous in the limit $N \to \infty$ close to bosons:

$$\alpha = \beta/N \to 0, \qquad \text{at fixed } \beta \in \mathbb{R},$$

in which the interaction may indeed be treated in a mean-field sense if anyons are also extended/smeared out to a finite size $R > 0$, as above. It is even possible to simultaneously take $R \sim N^{-\eta} \to 0$ at some sufficiently slow rate η (an "almost-ideal" limit). The idea is then as a final step to take $\beta = \alpha N$ (total flux) large (then "less bosonic") and study the appropriate ground-state energy functionals in this limit. Because of this particular order of limits, it is not completely clear whether this indeed describes the ideal anyon gas as defined above, or perhaps some nonideal model (see Section "Other interactions and fields"). We shall simply refer to it as **"almost-bosonic" anyons**.

In any case, the first steps above yield the seemingly *correct* **average-field functional** w.r.t. bosons for any fixed $\beta \in \mathbb{R}$ (Lundholm and Rougerie, 2015):

$$\mathcal{E}_{\beta}^{\text{af}}[\psi] = \int_{\mathbb{R}^2} \left[\left|(-i\nabla + \beta \mathbf{A}[|\psi|^2])\psi\right|^2 + V|\psi|^2 \right]. \tag{55}$$

The magnetic potential $\mathbf{A}[\varrho = |\psi|^2]$ is chosen such that it generates exactly the field $2\pi\varrho$:

$$\operatorname{curl} \beta \mathbf{A}[\varrho](\mathbf{x}) = 2\pi\beta\varrho(\mathbf{x}), \qquad \int_{\mathbb{R}^2} \varrho = 1. \tag{56}$$

Thus, the *scalar* self-interaction of the GP model (28) is here replaced with a *magnetic* self-interaction. This produces a peculiar new balancing problem, namely, in order to lower its energy in the self-generated magnetic field, as the coupling β (total number of flux units) grows, there needs to be an increasing phase and angular momentum in $\psi = |\psi|e^{i\phi}$ to cancel this magnetic field: (Due to the reasons described below, the cancellation is not complete, but both terms in (57) contribute an energy of order β.)

$$|(-i\nabla + \beta\mathbf{A})\psi|^2 = |\nabla|\psi||^2 + |\nabla\phi + \beta\mathbf{A}|^2|\psi|^2. \tag{57}$$

Further, in order to preserve regularity, any nontrivial such phase circulation must appear in the form of quantized vortices. On a typical disk $D(\mathbf{x}, R)$, the phase circulation

$$\Phi(\mathbf{x}, R) := \oint_{\partial D(\mathbf{x},R)} \beta\mathbf{A} \cdot d\mathbf{r} \approx -\int_{D(\mathbf{x},R)} \operatorname{curl} \nabla\phi \, d\mathbf{y} \tag{58}$$

then needs to minimize the residual angular momentum,

$$\int_0^{2\pi} \left|\partial_\varphi \phi + \beta A_\varphi\right|^2 d\varphi \geq \min_{q \in \mathbb{Z}} |q - \Phi(\mathbf{x}, R)|^2. \tag{59}$$

However, the amount of flux to be canceled by each vortex also depends on the typical value of the density ϱ there, which therefore sets a varying length scale for vortex formation (Correggi et al., 2017). It is thus expected (see also Chen et al. (1989) for an early conjecture) and indeed confirmed in numerical studies (Correggi et al., 2019; Girardot, 2021) that there is the formation of an Abrikosov-like vortex lattice. However, unlike in the Abrikosov setting with homogeneous rotation/field, the density of vortices here follows the average density profile in the trap V, which for $\beta \gg 1$ turns out to be given again by the minimizer of an effective **Thomas–Fermi-type functional** (Correggi et al., 2017):

$$\mathcal{E}_{\beta}^{\text{aTF}}[\varrho] := \int_{\mathbb{R}^2} \left[C_{\text{aTF}}|\beta|\varrho(\mathbf{x})^2 + V(\mathbf{x})\varrho(\mathbf{x}) \right] d\mathbf{x}. \tag{60}$$

Indeed, numerical simulations (Correggi et al., 2019; Girardot, 2021) (see Fig. 10) confirm the theoretical prediction of Correggi et al. (2017, 2018) that the g.s. ψ_{β}^{af} of (55) exhibits an approximately triangular vortex lattice distribution with scales set by the TF profile (minimizer) $\varrho_{\beta}^{\text{aTF}}$ of (60), and it is further estimated numerically that (Correggi et al., 2019)

$$C_{\text{aTF}} \approx 4\pi^{3/2}/3 \approx 1.18 \times 2\pi. \tag{61}$$

The fact that this constant is strictly bigger than the fermionic TF constant and constant-field prediction (Also in comparison to Fig. 5, Chitra and Sen, who estimated a substantially larger factor (Chitra and Sen, 1992), assumed rotational symmetry for the density to simplify their functional, plus added a hard-core delta regularization that itself amounts to the constant-field energy

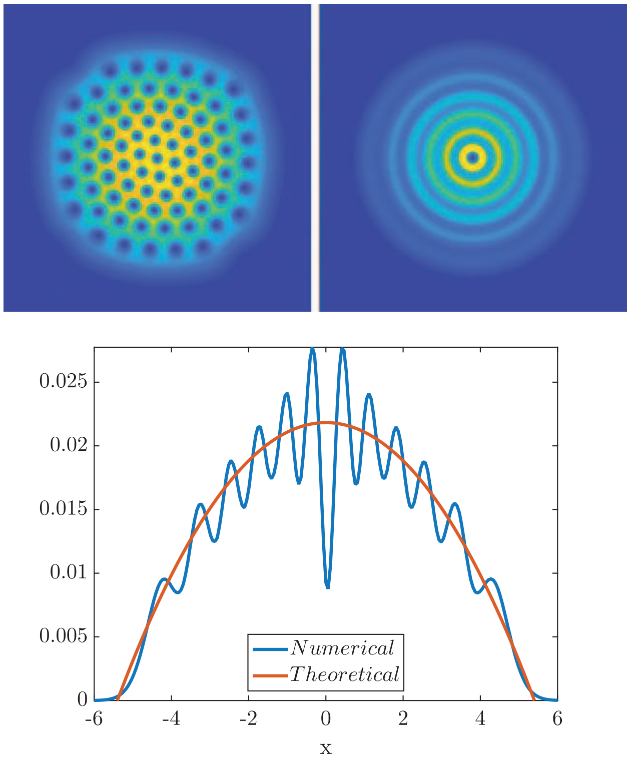

Fig. 10 Numerical simulation of the ground-state density $|\psi_\beta^{\mathrm{af}}|^2$ in the average-field functional (55) for $\beta = 90$ in a harmonic trap, averaged over rotations and then compared with the exact minimizer $\varrho_\beta^{\mathrm{aTF}}$ of (60). From Correggi M, Duboscq R, Lundholm D, and Rougerie N (2019) Vortex patterns in the almost-bosonic anyon gas. EPL (Europhysics Letters) 126: 20005

$2\pi|\beta|\varrho^2$.) 2π can be understood from the microscopic lattice inhomogeneity of $|\psi_\beta^{\mathrm{af}}|^2$ as compared to its average density $\varrho_\beta^{\mathrm{aTF}}$, which effectively raises the energy by a factor that is at least as big as the Abrikosov constant (≈ 1.1596; cf., Aftalion et al., 2006a, b).

Almost-fermionic anyons

A similar regularization approach can be taken close to fermions:

$$\alpha = 1 - \beta/\sqrt{N} \to 1, \qquad \beta, \hbar \text{ fixed},$$

for which the leading terms of the kinetic energy can be compared with the Fermi gas $E_N(\alpha = 1) \sim 2\pi N^2$, $N \to \infty$. By rescaling the parameters, it is equivalent to study a semiclassical mean-field limit

$$\alpha = 1 - \beta/N \to 1, \qquad \hbar \sim N^{-1/2} \to 0.$$

Also here we can allow "almost-ideal" or "virtually" extended anyons, $0 < R \sim N^{-\eta} \to 0$, if the rate η is small enough (The rate is better than for bosons because of the Pauli principle; cf. (50).).

This **almost-fermionic** approach takes us back to the actual TF functional for fermions (27), which remains correct for any finite β in this limit (Girardot, 2021; Girardot and Rougerie, 2021). More precisely, one obtains a semiclassical **Vlasov functional**:

$$\mathcal{E}_\beta^{\mathrm{Vla}}[\mu] := \frac{1}{(2\pi)^2}\int_{\mathbb{R}^4} |\mathbf{p} + \beta\mathbf{A}[\varrho]|^2 \mu(\mathbf{x}, \mathbf{p})\, d\mathbf{x}d\mathbf{p} + \int_{\mathbb{R}^2} V\varrho\, d\mathbf{x}$$

for $0 \le \mu(\mathbf{x}, \mathbf{p}) \le 1$ a measure on phase space $\mathbb{R}^4$, which is subject to the Pauli principle and normalized $\int_{\mathbb{R}^4}\mu = (2\pi)^2$. The minimizing measure μ of this functional is the corresponding filled Fermi sea:

$$\mu(\mathbf{x}, \mathbf{p}) = \mathbb{1}\{|\mathbf{p} + \beta\mathbf{A}[\varrho](\mathbf{x})|^2 \le 4\pi\varrho(\mathbf{x})\}, \tag{62}$$

with **spatial density** $\varrho = \varrho^{\mathrm{TF}}$ *independent* of β:

$$\varrho(\mathbf{x}) = \frac{1}{(2\pi)^2}\int_{\mathbb{R}^2} \mu(\mathbf{x}, \mathbf{p})\, d\mathbf{p} = (4\pi)^{-1}(\lambda^{\mathrm{TF}} - V(\mathbf{x}))_+.$$

The **momentum density** $t = t_\beta^{\mathrm{TF}}$,

$$t(\mathbf{p}) = \frac{1}{(2\pi)^2} \int_{\mathbb{R}^2} \mu(\mathbf{x}, \mathbf{p}) \, d\mathbf{x},$$

does depend on β, however, in a nonlocal way. The energy $\mathcal{E}_\beta^{\mathrm{Vla}}[\mu] = \mathcal{E}^{\mathrm{TF}}[\varrho^{\mathrm{TF}}]$ is locally a constant at $\alpha \approx 1$ in this approximation, thus confirming this aspect of Fig. 5.

The almost-fermionic regime was also studied numerically by Girardot (2021) using a **Hartree–Fock** approach, that is, on Slater determinants, and with a self-generated field $B = 2\pi\beta\varrho/N$ (total flux $2\pi\beta$), showing good agreements to the above. In fact, it can be interpreted as a multicomponent version of the bosonic functional (55) on orthogonal states ψ_k, $k = 1, 2, \ldots, N$. These are then able to complement each other's densities so as to fill in any holes left by vortices, and thus eventually smoothen out the overall density profile:

$$\varrho(\mathbf{x}) = \sum_{k=1}^{N} |\psi_k(\mathbf{x})|^2 \approx \varrho^{\mathrm{TF}}(\mathbf{x}), \tag{63}$$

thereby validating the "constant-field" (local density) approximation in this regime when β is not too large.

Magnetic TF theory

For higher ratios of the magnetic field to the density one may expect (Girardot, 2021) a **magnetic Thomas–Fermi theory** (Lieb et al., 1995; McEuen et al., 1992) to become valid. Namely, for a field $B(\mathbf{x})$, which is approximately constant on the scale of the trapping potential V, we can think of distributing the density

$$\varrho(\mathbf{x}) = \sum_{n=0}^{\infty} \varrho_n(\mathbf{x})$$

locally into the **Landau levels** (LLs) $\mathcal{H}_n$ of the corresponding one-body **Landau Hamiltonian** (In our units the cyclotron frequency is $\omega_c = 2|B|$.)

$$\hat{H}_1^{\mathrm{Lan}} = (-i\nabla_{\mathbf{x}} + B\mathbf{x}^{\perp}/2)^2 = \sum_{n=0}^{\infty} |B|(2n+1)\mathbb{1}_{\mathcal{H}_n}. \tag{64}$$

The degeneracy (per unit area) of each level is the number of flux units (per unit area), $d_B := |B|/(2\pi)$. Thus, defining the corresponding expected local magnetic energy at a given density ϱ,

$$j_B(\varrho) := \sum_{n=0}^{\infty} |B|(2n+1)\varrho_n, \qquad 0 \le \varrho_n \le d_B,$$

the **magnetic TF functional** for N fermions in a fixed *external* field $B > 0$ is then

$$\mathcal{E}^{\mathrm{mTF}}[\varrho] := \int_{\mathbb{R}^2} [j_B(\varrho(\mathbf{x})) + V(\mathbf{x})\varrho(\mathbf{x})] d\mathbf{x}, \qquad \int_{\mathbb{R}^2} \varrho = N. \tag{65}$$

At fixed B and ϱ, in order to minimize $j_B(\varrho)$ we fill all $N_B := \lfloor \varrho/d_B \rfloor$ lower Landau levels maximally:

$$\varrho_n = \begin{cases} d_B, & 0 \le n \le N_B - 1, \\ \varrho - N_B d_B, & n = N_B, \\ 0, & n \ge N_B + 1, \end{cases}$$

so that in the limit $B \to 0$, implying $d_B \to 0$,

$$j_B(\varrho) \approx \sum_{n=0}^{N_B - 1} |B|(2n+1)d_B = |B|N_B^2 d_B \approx |B|\varrho^2/d_B = 2\pi\varrho^2,$$

returning us to the usual TF for the free Fermi gas. On the other hand, if B is large enough that $d_B \ge \varrho$, then all particles will fit into the lowest Landau level (LLL):

$$j_B(\varrho) = |B|\varrho. \tag{66}$$

Now, considering a sufficiently extended anyon gas and formally taking the anyonic (average) magnetic field $B(\mathbf{x}) = 2\pi\beta\varrho(\mathbf{x})$, where $\beta = 1 - \alpha \in [0, 1]$ is the number of flux units per particle attached to fermions, we then obtain a **magnetic TF self-interaction functional** for anyons:

$$\tilde{\mathcal{E}}_\beta^{\mathrm{amTF}}[\varrho] := \int_{\mathbb{R}^2} \left[j_{B=2\pi\beta\varrho(\mathbf{x})}(\varrho(\mathbf{x})) + V(\mathbf{x})\varrho(\mathbf{x}) \right] d\mathbf{x}. \tag{67}$$

At any point $\mathbf{x} \in \mathbb{R}^2$ where $\varrho(\mathbf{x}) \neq 0$, let us consider there the fractions of density $f_n := \varrho_n(\mathbf{x})/\varrho(\mathbf{x})$ in the LLs:

$$\frac{j_B(\varrho)}{2\pi\varrho^2} = \sum_{n=0}^{\infty} \beta(2n+1) f_n, \qquad 0 \le f_n \le \beta \le 1,$$

which again is minimized by filling the lowest $N_B = \lfloor \beta^{-1} \rfloor$ levels:

$$f_n = \begin{cases} \beta, & 0 \le n \le \lfloor \beta^{-1} \rfloor - 1, \\ 1 - \beta \lfloor \beta^{-1} \rfloor, & n = \lfloor \beta^{-1} \rfloor, \\ 0, & n \ge \lfloor \beta^{-1} \rfloor + 1. \end{cases}$$

Hence, our minimum is

$$\frac{j_B(\varrho)}{2\pi\varrho^2} = \sum_{n=0}^{\lfloor \beta^{-1} \rfloor - 1} (2n+1)\beta^2 + \beta(2\lfloor \beta^{-1} \rfloor + 1)(1 - \beta\lfloor \beta^{-1} \rfloor),$$

which simplifies to

$$\frac{j_B(\varrho)}{2\pi\varrho^2} - 1 = \beta^2(1 - \{\beta^{-1}\})\{\beta^{-1}\} =: M(\beta) \in [0, \beta^2/4),$$

where $\{\beta^{-1}\} = \beta^{-1} - \lfloor \beta^{-1} \rfloor \in [0, 1)$ is the fractional part of β^{-1}. Therefore our proposed functional for the g.s. (a pointwise lower bound to (67)) takes the form

$$\tilde{\mathcal{E}}_\beta^{\mathrm{amTF}}[\varrho] := \int_{\mathbb{R}^2} \left[2\pi\varrho(\mathbf{x})^2 (1 + M(\beta)) + V(\mathbf{x})\varrho(\mathbf{x}) \right] d\mathbf{x}, \tag{68}$$

thus refining both the "constant-field" approximation (29) around fermions and the above almost-fermionic approximation.

The corresponding energy landscape (see Fig. 11) is now indicative of **stability** at the Fermi point $\beta = 0$. A possible interpretation for the gas is that the discretization of the Fermi sea into Landau levels imposes a more rigid structure in phase space, that is, as the attached flux β per particle increases, particles come from plane-wave states, which homogenize easily in space and then need to start organizing into the respective cyclotron orbits with decreasing radii as the field increases. Thus the Fermi sea becomes less fluid and more crystalline, with the most synergetic situation when a whole number of levels are approximately filled ($\{\beta^{-1}\} \approx 0$ or 1) so adjustments to the density can be accommodated at all levels in parallel while keeping the fractions f_n constant, and least synergetic when half a level is filled ($\{\beta^{-1}\} \approx 1/2$) and a larger fraction $\beta\{\beta^{-1}\}$ of particles need to organize their motion into that specific LL. However, we cannot expect this picture to be valid all the way to bosons at $\beta = 1$ (compare also (50)) because there will also be correlations across Landau levels, leading to effective attractions, clustering, and condensation, and for example, if the LLL is filled and there are only few particles in the first-excited LL, then one might consider the statistics transmutation situation discussed below where the excited particles would effectively rather be treated as bosons than fermions.

An analysis at these seemingly beneficial fractions $\alpha = 1 - 1/n$ was conducted by Chen et al. (1989) in the homogeneous setting (building on (Fetter et al., 1989)), where they indeed observed characteristics of **superfluidity**. For example, the energy there increases linearly when a small external magnetic field is applied in either direction, which is interpreted as a Meissner effect.

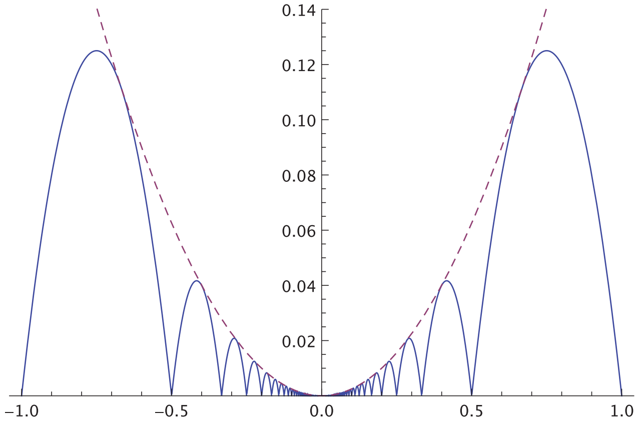

Fig. 11 The factor $M(\beta) = \beta^2(1 - \{\beta^{-1}\})\{\beta^{-1}\} \le \beta^2/4$ (r.h.s. *dashed*) in the magnetic TF functional (68) as a function of the relative statistics parameter $\beta = 1 - \alpha$ around fermions $\beta = 0$.

Recently another approach to a DFT for anyons, via Kohn–Sham theory with neglected exchange correlation (then similar to self-consistent Hartree–Fock) was taken by Hu et al. to study these effects (Hu et al., 2021). Their numerics agree well with the semiclassical TF approximation close to fermions and show significant deviations only when the magnetic field is strong enough that particles in the bulk occupy only the lowest few LLs. For trapped systems they also observe a boundary effect, which can compensate for the otherwise necessary fractional filling of LLs, but which vanishes in the thermodynamic limit. Indeed, due to the many parallels to the FQHE, Chen et al. suggested that "the physics of the anyon gas at general values of θ is likely to be quite rich and to depend quite strongly on 'number-theoretic' properties of θ."

Point-interacting anyons

Introducing **point or contact interactions** corresponds to specifying the behavior of wave functions at the diagonal (contact) set $\triangle_N$, that is, imposing boundary conditions there so as to render the Hamiltonian self-adjoint while allowing a different behavior than that of the canonical/free choice (Friedrichs; cf. Section "Kinetic energy"). This is equivalent to considering *all* of the possible boundary conditions, or **self-adjoint extensions**, of the operator $\hat{T}_\alpha$ starting from its initial definition on wave functions vanishing at $\triangle_N$ and having finite expected energy in the standard sense (11). For general N, this is difficult even for distinguishable particles, but one may reduce this problem significantly by adding assumptions such as translation and scale covariance. Our present understanding of general point-interacting (and pointlike, that is, nonextended) anyons is currently rather limited (cf., Dell'Antonio et al., 1997), however for $N = 2$ anyons, the situation is now well understood (Bourdeau and Sorkin, 1992; Correggi and Oddis, 2018; Coutinho et al., 1992; Grundberg et al., 1991; Manuel and Tarrach, 1991; Murthy et al., 1992; Oddis, 2020) and extends the corresponding analysis of the standard nonmagnetic two-body point-interaction problem in various dimensions (see, e.g., Albeverio et al., 2005).

For $\alpha_2 \neq 1$ (nonfermions), the problem admits a circle of different possibilities for point interaction, all of which are attractive and correspond to allowing wave functions with singularities at the diagonals. One simple way to understand this is via the form (12), which in the s-wave (radially symmetric) with $\Psi = r^{\pm\alpha_2}\phi(r)$ turns out to be equivalent to (Manuel and Tarrach, 1991; Oddis, 2020)

$$\int_0^\infty |\phi'(r)|^2 r^{d_\alpha - 1} dr, \tag{69}$$

for a parameter giving an effective **"intermediate dimension"**

$$2 \leq d_\alpha := 2 + 2\alpha_2 \leq 4. \tag{70}$$

Thus, for bosons the problem is indeed two-dimensional and has a circle of extensions, where a unique one $\hat{T}_{\text{sym}}$ (Friedrichs, $\Psi \sim 1$ as $r \to 0$) is nonnegative. For fermions, it is more akin to four dimensions where the corresponding bosonic problem is essentially self-adjoint, that is, has a unique extension $\hat{T}_{\text{asym}}$ (Friedrichs, $\Psi \sim r$). For proper anyons the situation is intermediate and actually closest akin to three dimensions. In this case there is again a circle of extensions, but the circle now splits into two halves (cf. Fig. 2): in one half one has negative extensions and a scale of increasingly negative bound states, and in the other, a scale of decreasingly-nonnegative (i.e., increasingly attractive) extensions. The largest (least attractive/"free") such extension is the usual free kinetic energy $\hat{T}_\alpha = \hat{T}_\alpha^{\mathrm{F}}$ (Friedrichs, $\Psi \sim r^{\alpha_2}$) while the smallest $\hat{T}_\alpha^{\mathrm{K}}$ (most attractive, $\Psi \sim r^{-\alpha_2}$, and known as the **Krein extension** (Alonso and Simon, 1980)) is also singled out as scale covariant while all the other intermediate extensions have scale.

If these observations extend to $N \geq 3$ particles, then it is reasonable to expect such **"kreinyons"** to be of interest in physics, and in fact may even correspond to some of the moderately singular "noninterpolating" exact eigenstates (Murthy et al., 1992) found in the harmonic oscillator problem (cf. Section "Some states of particular interest"). Other relevant connections of anyons to geometry and quantum mechanics on cone-like manifolds were reviewed in Jackiw (1990).

Other interactions and fields

One can obviously also include other (scalar) interactions into the magnetic models for anyons, as well as an external magnetic field (coupled by a charge $-q$), for example

$$\hat{H}_N := \frac{\hbar^2}{2m} \sum_{j=1}^{N} \left(-i\nabla_{\mathbf{x}_j} + q\mathbf{A}_{\text{ext}} + \alpha \mathbf{A}_j^R \right)^2 + \sum_{j=1}^{N} V(\mathbf{x}_j) + \sum_{j<k} W(\mathbf{x}_j - \mathbf{x}_k). \tag{71}$$

Reasonable external fields have been incorporated into some parts of the average-field theory (Girardot, 2020; Girardot and Rougerie, 2021), as well as point interactions (Correggi and Fermi, 2021; Oddis, 2020), and interacting anyons are certainly relevant in emergent models, as we will see below. Coulomb interactions and the thermodynamic stability of "anyonic matter" were addressed in Lundholm and Solovej (2014), Lundholm and Seiringer (2018), and Lundholm (2019). We note that since scalar interactions can show features akin to statistics, such as effective TF-type functionals and degeneracy pressure (Larson et al., 2021; Lieb et al., 2005; Lundholm, 2019; Lundholm et al., 2015, 2016), it is important to isolate the features that are due to the actual quantum statistics (cf., Lambert et al. (2022)).

Another way to view the effect of the magnetic flux disks in the average-field approximation is as an effective scalar potential

$$W(\mathbf{x}_j - \mathbf{x}_k) = \frac{2\pi|\alpha|}{\pi R^2} \mathbb{1}_{\mathrm{D}(\mathbf{x}_k,\, \mathrm{R})}(\mathbf{x}_j) \tag{72}$$

added to anyons (in the bosonic reference, this is indeed correct as a lower bound Larson and Lundholm, 2018). One may then consider the combination of parameters

$$\frac{|\alpha|}{\varrho R^2} = |\alpha|\overline{\gamma}^{-2}, \tag{73}$$

that is, the height of the potential compared to the average density, as a dimensionless measure of interaction strength, and for fixed α and $\overline{\gamma} \ll 1$, this then corresponds to a hard-core interaction, while if $|\alpha|\overline{\gamma}^{-2} \ll 1$, such as if $\sqrt{|\alpha|} \ll \overline{\gamma}$ where either side may be taken to grow or decline, then W instead corresponds to a weak soft-core interaction. With the convergence rates η currently allowed in the derivations of almost-bosonic and almost-fermionic models ($0 < \eta < 1/4$ (Girardot, 2020) resp. $0 < \eta < 1/3$ (Girardot and Rougerie, 2022)), we find that on a fixed homogeneous trap, $\overline{\gamma} \sim N^{1/2-\eta} \to \infty$ and $|\alpha|\overline{\gamma}^{-2} \sim N^{2\eta-2} \to 0$ resp. $|1 - \alpha|\overline{\gamma}^{-2} \sim N^{2\eta-3/2} \to 0$ as $N \to \infty$, that is a combined high-density and weak soft-core limit, indeed beneficial to the average-field approximation.

Lowest Landau level (LLL) anyons

If the anyons are ideal but in a strong external constant magnetic field, then all anyons fall into the LLL (cf. (66)), and the model actually becomes exactly solvable. The reason is that their wave function becomes (anti)analytic (modulo a Gaussian factor) and corresponds to changing the Jastrow factors in (48) and (49) from $|z_{jk}|^{-\alpha}$ to $(\bar{z}_{jk})^{\alpha}$, $\alpha \in [0, 1]$. It results in a description in terms of **fractional exclusion statistics** (cf., Haldane, 1991) with one-body occupation numbers (angular momenta) shifted by α, and a relation to Calogero–Sutherland models. We refer to Ouvry (2007) for an overview of this approach.

The non-abelian anyon gas

Let us now generalize our context further and consider an ideal ***N*-anyon wave function** as *locally* a map (Again, one way to concretize this is to regard the multivalued function Ψ as a ρ-equivariant function on the covering space of $\mathcal{C}^N$, or as a section of a vector bundle $E \to \mathcal{C}^N$ with fiber $\mathcal{F}$ (Lundholm and Qvarfordt, 2020).)

$$\Psi : \mathcal{C}^N \to \mathcal{F}, \quad \text{subject to} \quad \Psi(\sigma.X) = \rho(\sigma)\Psi(X), \tag{74}$$

where the **fiber** $\mathcal{F}$ is a Hilbert space of "internal" (nonspatial) degrees of freedom on which B_N acts unitarily (We can even let go of the unitarity condition on reps if one is willing to consider multivalued probability distributions (cf., Abramsky and Brandenburger, 2011).):

$$\rho : B_N \to \mathrm{U}(\mathcal{F}).$$

Now $\rho(\sigma)$ is an **exchange operator** on $\mathcal{F}$ corresponding to the braid $\sigma \in B_N$. There may be other observables of the considered system acting in $\mathcal{F}$, but for simplicity we here assume that it is finite dimensional, that is, $\mathcal{F} = \mathbb{C}^D$ for some $D \in \mathbb{N}$, and $\mathrm{U}(\mathbb{C}^D) = \mathrm{U}(D)$ is the group of $D \times D$ unitary matrices. We then identify three possibilities for these representations ("reps"):

1. **Irreducible abelian**: $\mathcal{F} = \mathbb{C}$, which is the case we treated above, with elementary exchange phase

$$\rho(\sigma_j) = e^{i\alpha\pi} \qquad \text{for all } j,$$

for a fixed statistics parameter α of abelian anyons.

2. **Reducible abelian**: $\mathcal{F} = \mathbb{C}^D$, $D > 1$, where all elementary exchange operators $\rho(\sigma_j)$ commute and thus are simultaneously diagonalizable (We write $A \cong B$ if two matrices or operators are similar, that is, unitarily equivalent.):

$$\rho(\sigma_j) \cong \mathrm{diag}(e^{i\alpha(1)\pi}, \ldots, e^{i\alpha(D)\pi}) \qquad \text{for all } j,$$

for statistics parameters $\alpha(k)$ corresponding to different sectors of particles that do not interact quantum statistically.

3. **Non-abelian**: $\mathcal{F} = \mathbb{C}^D$, $D > 1$, where not all elementary exchange operators commute:

$$\rho(\sigma_j)\rho(\sigma_k) \neq \rho(\sigma_k)\rho(\sigma_j) \qquad \text{for some } j \neq k.$$

Actually, it turns out that

$$D \geq N - 2 \qquad \text{if} \quad N \geq 7, \tag{75}$$

because otherwise the rep is necessarily abelian (this is a theorem in the rep theory of the braid group (Formanek, 1996); cf. (Weinberger, 2015), (Lundholm and Qvarfordt, 2020, Theorem 3.13)). Furthermore, if $N \geq 7$ and $D = N - 2$ or $D = N - 1$ then the rep is either abelian or, up to an abelian factor, the non-abelian (reduced) Burau representation. For any other reps, we need $D \geq N$. Because of this last remark, we cannot simply fix the fiber Hilbert space $\mathcal{F}$ or the rank of the representation $D = \dim \mathcal{F}$ and then study growing numbers N of anyons because they will then eventually abelianize. Further, in the non-abelian case it is, as far as this author is aware, not certain whether statistics transmutation is available, that is, whether one may always pass from the geometric to the magnetic perspective (this is a question in topology; see Lundholm and Qvarfordt (2020) and Maciazek and Sawicki (2019) for further discussion). Some models have magnetic formulations however (Kohno, 1987; Lee and Oh, 1994; Wen, 1991), but for simplicity in this overview we will remain in the geometric perspective and furthermore pull in a small sample of results from the **algebraic perspective** as well, where certain reps can be systematically and consistently constructed from elementary **fusion and braiding** rules, and exchange operators can be computed explicitly. The topic is quite complex and extends far outside the scope of this overview; instead we refer to Beer et al. (2018), Lundholm and Qvarfordt (2020), Stern (2008), Nayak et al. (2008), Lahtinen and Pachos (2017), and Masaki et al. (2023) for more detail on the algebraic and diagrammatic aspects of anyon models (and note that the representation theory of the braid group is a still incomplete and very active field of mathematics). Anyons with non-abelian braid group representations are generally called **"non-abelions"** or **"plektons."**

A **many-anyon model** is a sequence of fiber Hilbert spaces $\mathcal{F}_N$, $D_N = \dim \mathcal{F}_N$, and braid group representations

$$\rho_N : B_N \to \mathrm{U}(\mathcal{F}_N), \qquad N = 1, 2, 3, \ldots, \tag{76}$$

together with a sequence of kinetic energy operators

$$\hat{T}_{\rho_N} = \frac{\hbar^2}{2m} \sum_{j=1}^{N} \left(-i\nabla_{\mathbf{x}_j}^{(\rho_N)}\right)^2 \tag{77}$$

which implement these reps (by means of parallel transport) as the corresponding exchange operators in (74) (One might also require a compatibility between reps ρ_N w.r.t. the embedding sequence $B_{N-1} \boxtimes B_N$ of braid groups, which may be nontrivial (see Delaney et al., 2016; Rowell and Wang, 2012).).

The free kinetic energy operator $\hat{T}_{\rho_N}$ is again locally the same as the free Laplacian $\hat{T}_{\mathrm{dist}}$, supplemented with holonomies $\rho_N(\sigma) \in \mathrm{U}(D_N)$ w.r.t. any nontrivial exchange loops $\sigma \in B_N$. Instead of the abelian pair-exchange conditions (7), one now has

$$\Psi(\mathbf{x}_1, \ldots, \mathbf{x}_k, \ldots, \mathbf{x}_j, \ldots, \mathbf{x}_N) = U_{N,p}\Psi(\mathbf{x}_1, \ldots, \mathbf{x}_j, \ldots, \mathbf{x}_k, \ldots, \mathbf{x}_N), \tag{78}$$

with **pair-exchange operators** (Defined up to similarity; note, for example, that $\rho(\sigma_j) \cong \rho(\sigma_k)$ with similarities depending on j and k (Lundholm and Qvarfordt, 2020).)

$$U_{N,p} \cong \rho_N(\sigma_1\sigma_2 \ldots \sigma_p\sigma_{p+1}\sigma_p \ldots \sigma_2\sigma_1) \tag{79}$$

for any counterclockwise two-particle exchange loop in which $p \leq N - 2$ other particles are enclosed, corresponding to the second figure in Fig. 3. We denote their eigenvalues by

$$\operatorname{spec} U_{N,p} = \{e^{i\pi\gamma_k}\}_{k=1,2,\ldots,D_N},$$

where we normalize the full range of **statistics parameters** $\gamma_k = \gamma_k(N, p)$ in the interval $(-1, 1]$.

Non-abelions are still harder to treat as perturbations close to bosons or fermions since typically the eigenvalues of $U_{N,p}$ are separated from (or coincide with) ± 1. Also, because of a lack of general magnetic formulations, it is even more unclear what we should mean with an extended gas of non-abelions, except as derived from emergent models and Berry connections (see below). However, concerning the qualitative features and local exclusion properties for the ideal gas, somewhat analogous results as for the abelian gas may be obtained (Lundholm and Qvarfordt, 2020), as follows:

The N-**fractionality** is now replaced by

$$\alpha_{N,n} := \min_{p=0,\,1,\,\ldots,\,n-2} \beta_{N,p}, \qquad n \leq N, \tag{80}$$

where the **pair-exchange parameter** with $p \leq N - 2$ particles enclosed,

$$\beta_{N,p} := \min_{k=1,\,2,\,\ldots,\,D_N} |\gamma_k(N,p)| = \operatorname{dist}\big(\operatorname{spec}(U_{N,p}), +1\big),$$

is again the arcwise distance (in units of π) from the spectrum of $U_{N,p}$ to $+1$. Then, the statistical repulsion as given both by the Hardy inequality (34) (and its variants, depending on $\alpha_{N,n}$), the local exclusion principle (40) and (41), as well as the degeneracy pressure (43), generalize to the ideal non-abelion gas:

$$\langle \hat{T}_{\rho_N} \rangle_\Psi \gtrsim \alpha_{N,2} \int_{\mathbb{R}^2} \varrho_\Psi(\mathbf{x})^2 \, d\mathbf{x}. \tag{81}$$

Thus, it is again the nearest-neighbor pair exchange (in the rep ρ_N) that sets the main behavior of the gas w.r.t. fractional exclusion statistics.

Three classes of representations of special interest were considered in some detail in Lundholm and Qvarfordt (2020): Burau, Ising, and Fibonacci. Note that variations of these may arise by composing with abelian models. Some important features have been obtained also for other reps, such as scattering and dilute thermodynamics based on the nearest-neighbor pair exchange (Mancarella et al., 2013a, b; Verlinde, 1991; Wilczek and Wu, 1990).

Burau

The Burau rep (Burau, 1935) is a simple deformation of the defining rep of the permutation group, $S_N \to \mathrm{U}(N)$, that also must be reduced ($D_N = N - 1$ or $N - 2$) and unitarized to fit in the above framework. We are only aware of the simplest case $N = 3$, $\mathcal{F} = \mathbb{C}^2$ having been worked out explicitly so far (Weinberger, 2015), and then

$$\operatorname{spec} U_{3,0} = \{1, -w^2\}, \qquad \operatorname{spec} U_{3,1} = \{w^3, -w^3\}$$

for a parameter $w = e^{i\alpha\pi}$, $|\alpha| < 1/3$, of the representation. Here we find $\alpha_{3,\,2}(w) = 0$ for all such w and indeed there are states that do not vanish on the diagonal because of a lack of exclusion there (Lundholm and Qvarfordt, 2020).

Ising

Here $D_N = \dim \mathcal{F}_N$ grows roughly as $(\sqrt{2})^N$, which is related to reps of Clifford algebras (Nayak and Wilczek, 1996) (and there are distinctions between even/odd numbers of such anyons and of fermions which also appear in the models). The spectra of all pair-exchange operators have been computed (Lundholm and Qvarfordt, 2020):

$$\operatorname{spec} U_{N,p} = \begin{cases} \{e^{-i\pi/8}, e^{i\pi 3/8}\}, & \text{if } p = 0, \\ \{e^{-i\pi/8}, e^{i\pi 7/8}\}, & \text{if } p \geq 1 \text{ is odd}, \\ \{e^{-i\pi 5/8}, e^{-i\pi/8}, e^{i\pi 3/8}, e^{i\pi 7/8}\}, & \text{if } p \geq 2 \text{ is even}, \end{cases}$$

(in one rep, and their complex conjugates in another rep, and with multiplicities that grow with N). Thus,

$$\alpha_{N,n} = \beta_{N,0} = 1/8 \qquad \text{for all } N, n \geq 2,$$

so the Ising gas has an exclusion at the diagonals and a degeneracy pressure. Since these n-fractionalities are independent of n (and N), we do not see any benefits of clustering to minimize statistical repulsion, at this level of inquiry.

Fibonacci

Here $D_N = \dim \mathcal{F}_N$ grows with the Fibonacci sequence so that $D_{N+1}/D_N \xrightarrow{N\to\infty} \phi$, the golden ratio. Furthermore, the spectra of all pair-exchange operators have been computed (Qvarfordt, 2017):

$$\operatorname{spec} U_{N,p} = \begin{cases} \{e^{-i\pi 3/5}, e^{i\pi 4/5}\}, & \text{if } p = 0, \\ \{e^{-i\pi/5}, e^{i\pi/5}, e^{i\pi 4/5}\}, & \text{if } p = 1, \\ \{e^{-i\pi 3/5}, e^{-i\pi/5}, e^{i\pi/5}, e^{i\pi 4/5}\}, & \text{if } p \geq 2, \end{cases}$$

(in one rep, and their complex conjugates in another rep, and with multiplicities that grow with N, also along the Fibonacci sequence). Thus,

$$\alpha_{N,n} = \begin{cases} \beta_{N,0} = 3/5, & \text{if } n = 2, \\ \beta_{N,1} = 1/5, & \text{if } n \geq 3, \end{cases}$$

and therefore also the Fibonacci gas is subject to exclusion at the diagonals and a degeneracy pressure. Since $\alpha_{N,n} < \alpha_{N,2}$ for $n \geq 3$, this may be indicative of clustering in this gas in order to minimize statistical repulsion over long ranges.

Emergence of the anyon gas

In the study of emergent quantum statistics, we typically consider two distinct species of particle, one of which is numerous and numbered by, for example, $N \gg 1$, which we shall refer to as the **bath**, and another species, which is much less numerous, $1 \leq n \ll N$, which we refer to as **tracers** or **impurities**. These two species could be physically the same type of particle but effectively distinguished by some quantum number, such as their Landau level index for example. The bath forms a background and a collective coherence for the tracers so that its macroscopically well-defined state provides a limiting reference frame with respect to which tracers may transmute their properties.

The quantum Hall setting

In the quantum Hall (QH) setting, we assume that all particles are confined to a plane and subject to a large and approximately constant magnetic field $\mathbf{B} = -b\mathbf{e}_z$, $b > 0$, that is, the relevant one-body operator is again the Landau Hamiltonian (64)

$$\hat{H}_1^{\text{Lan}} = \frac{1}{2m}\left(-i\hbar\nabla_{\mathbf{x}} + qb\mathbf{x}^{\perp}/2\right)^2 = \hbar\omega_c(\hat{a}^{\dagger}\hat{a} + 1/2),$$

$\omega_c = |qb|/m$, and particles then distribute into the Landau levels (LLs) of this field. The lowest Landau level (LLL) is the kernel of $\hat{a}$ (let us now fix $\hbar = 1$ and $q = -1$):

$$LLL := \mathcal{H}_0 = \left\{\psi \in L^2(\mathbb{R}^2) : \psi(\mathbf{x}) = f(z)e^{-\frac{b}{4}|z|^2},\ f \text{ analytic}\right\} \tag{82}$$

and spanned by the orthonormal basis of Fock–Darwin states

$$\psi_l(z) = c_l z^l e^{-\frac{b}{4}|z|^2}, \qquad l = 0, 1, 2, \ldots,$$

for normalization constants $c_l > 0$. We assume electron spin is out of the picture due to the strong band separation, and also that there is a radial trapping potential centered at $z = 0$, penalizing higher angular momenta l.

The first concrete prediction of emergent anyonic statistics was made in the context of the *fractional* quantum Hall effect (FQHE) for electrons (Tsui et al., 1982), that is, fractional filling of the LLL, for which Laughlin proposed the following trial states in the electrons' coordinates $z_j \in \mathbb{C}$, $\mathrm{z} = (z_j)_{j=1,\ldots,N}$, to explain the effect (Laughlin, 1983, 1999) (Note that these also coincide with the anyonic trial states (48) and (49) if extended to $\alpha = \mu$ with trivial Jastrow factors (Lundholm, 2017).):

$$\Psi_{\mu}^{\text{Lau}}(\mathrm{z}) \propto \prod_{j<k} z_{jk}^{\mu} e^{-\frac{b}{4}|\mathrm{z}|^2}.$$

For electrons, μ is an odd integer so that $\Psi_{\mu}^{\text{Lau}} \in L^2_{\text{asym}}$. In the case that $\mu = 1$, suitable for an *integer* QH effect, the state corresponds to a Fermi sea filling of LLL with the least angular momentum: $\Psi_{\mu=1}^{\text{Lau}}(\mathrm{z})$ is proportional to

$$\bigwedge_{l=0}^{N-1} \psi_l(\mathrm{z}) \propto \det \begin{bmatrix} 1 & 1 & \ldots & 1 \\ z_1 & z_2 & \ldots & z_N \\ \vdots & \vdots & & \vdots \\ z_1^{N-1} & z_2^{N-1} & \ldots & z_N^{N-1} \end{bmatrix} e^{-\frac{b}{4}|\mathrm{z}|^2},$$

by Vandermonde's formula for the determinant. For fractional filling $1/\mu$, and to reduce Coulomb interaction energy among electrons, Laughlin thus proposed taking the determinant above to a power $\mu > 1$. On top of such states, Laughlin also considered states of quasiholes pinned to positions $w_k \in \mathbb{C}$, $\mathrm{w} = (w_k)_{k=1,\ldots,n}$:

$$\Psi_{\mu}^{\text{qh}}(\mathrm{w}; \mathrm{z}) \propto \prod_{k=1}^{n}\prod_{j=1}^{N}(w_k - z_j)\Psi_{\mu}^{\text{Lau}}(\mathrm{z})$$

(all states with appropriate normalization, and $\mathbf{y}_k \leftrightarrow w_k$, $\mathbf{x}_j \leftrightarrow z_j$ respective real and complex coordinates).

Berry phases

Halperin (1984) suggested that if the quasiholes are treated as quantum particles, then they ought to have fractional anyonic statistics, and Arovas, Schrieffer and Wilczek (Arovas et al., 1984) subsequently proposed a **Berry-phase approach** to determine their statistics. Namely, if we view Ψ_{μ}^{qh} as a map

$$\mathbb{C}^n \to L^2_{\text{asym}}(\mathbb{R}^{2N}), \qquad \mathrm{w} \mapsto \Psi_{\mu}^{\text{qh}}(\mathrm{w}; \cdot)$$

from the parameters w into the (fiber) Hilbert space of electrons, then Berry associates to such a geometry a canonical connection (Berry, 1984; Simon, 1983):

$$\tilde{\mathbf{A}}_j(\mathrm{y}) := \langle -i\nabla_{\mathbf{y}_j}\rangle_{\Psi^{\text{qh}}(\mathrm{y};\cdot)} = -i\int_{\mathbb{C}^N} \overline{\Psi_{\mu}^{\text{qh}}(\mathrm{y}; \mathrm{z})}\nabla_{\mathbf{y}_j}\Psi_{\mu}^{\text{qh}}(\mathrm{y}; \mathrm{z})\, d\mathrm{z}. \tag{83}$$

The holonomies of the connection w.r.t. loops on the parameters, $\sigma : [0, 1] \to \mathbb{C}^n$,

$$\rho(\sigma) = e^{i\Phi_{\sigma}}, \qquad \Phi_{\sigma} = \oint_{\sigma}\sum_{j=1}^{n}\tilde{\mathbf{A}}_j \cdot d\mathbf{y}_j, \tag{84}$$

are then interpreted to be the exchange phases (1) (now including an "external" field of constant curvature) effectively associated to the motion of the quasiholes in the bath of electrons. Thus, under the **adiabatic assumption** that the electrons move much faster than the holes, one can take statistical averages over $\mathrm{z} \in \mathbb{C}^N$ and use an analogy with a classical charged plasma to compute $|\Psi^{\mathrm{qh}}(\mathrm{y};\cdot)|^2$ and Φ_σ, and then indeed conclude that there is, on top of geometric holonomies corresponding to a constant field $B/\mu = -b/\mu$ (i.e., effectively coupled to a fractional charge $+\,1/\mu$ that *reduces* the field), also topological exchange phases corresponding to the localized (but somewhat extended) attachment of fractional flux $-\,2\pi/\mu$ to the quasiholes. For a relatively recent review of the approach, including possible extensions to non-abelian scenarios (for which the quasihole map Ψ^{qh} is multidimensional), see Bonderson et al. (2011).

Transmuted Hamiltonian

Forte (1991) argued that the above approach is not necessarily sufficient to determine the anyonic statistics because, as we have noted above with the freedom of statistics transmutation, the knowledge of the specific Hamiltonian for the quasiholes is essential since that is what ultimately sets the scale of validity of any adiabatic treatment. Thus, a different approach was suggested in Lundholm and Rougerie (2016) and Lambert et al. (2022) to remedy this situation and supply the missing dynamical information, by considering quasiholes pinned to already present quantum particles.

In brief, one may consider the following idealized situation (see Fig. 12):

1. large 2D bath of noninteracting *fermions*, $N \gg 1$,
2. n tracers/impurities (initially can be either bosons or fermions), $1 \leq n \ll N$,
3. strong external transverse magnetic field, $b \to \infty$,
4. strong short-range repulsive bath-tracer interaction, at coupling $g \to \infty$.

Taking the bath particles $\mathbf{x}_j$ to have unit mass and unit negative charge, the tracers $\mathbf{y}_k$ to have mass m and charge $-\,q$, and allowing for interaction and trapping of tracers in a joint potential W, the Hamiltonian of the joint system is

$$H_{n\oplus N} := \frac{1}{2}\sum_{j=1}^{N}\left(-i\nabla_{\mathbf{x}_j} - b\mathbf{x}_j^{\perp}/2\right)^2 + \frac{1}{2m}\sum_{k=1}^{n}\left(-i\nabla_{\mathbf{y}_k} - qb\mathbf{y}_k^{\perp}/2\right)^2 + g\sum_{j=1}^{N}\sum_{k=1}^{n}\delta(\mathbf{x}_j - \mathbf{y}_k) + W(\mathbf{y}_1, \ldots, \mathbf{y}_n),$$

acting on states

$$\Psi(\mathbf{y}_1, \ldots, \mathbf{y}_n; \mathbf{x}_1, \ldots, \mathbf{x}_N) \in L^2(\mathbb{R}^{2n}) \otimes L^2_{\mathrm{asym}}(\mathbb{R}^{2N}).$$

If one takes $b \sim N$ and $N \gg n$, and assumes the bath then sits entirely in the LLL, thus forming a disk-shaped QH droplet of size ~ 1, the Hilbert space is reduced to

$$\mathcal{H}^{n\oplus N}_{\mathrm{sym/asym}} := L^2_{\mathrm{sym/asym}}(\mathbb{R}^{2n}) \otimes \bigwedge\nolimits^{N} LLL$$

(allowing for either bosonic or fermionic tracers), with g.s.e.

$$E_{n\oplus N} := \inf_{0 \neq \Psi \in \mathcal{H}^{n\oplus N}_{\mathrm{sym/asym}}} \langle H_{n\oplus N}\rangle_\Psi.$$

For $g \to \infty$, we then take as our ansatz for the ground state of the system a state in the kernel of the interaction:

$$\Psi_\Phi(\mathrm{y};\mathrm{x}) := \Phi(\mathrm{w})c^{\mathrm{qh}}(\mathrm{w})\Psi^{\mathrm{qh}}(\mathrm{w};\mathrm{z}), \tag{85}$$

with $\Phi \in L^2_{\mathrm{sym/asym}}(\mathbb{C}^n)$, $c^{\mathrm{qh}} > 0$ and

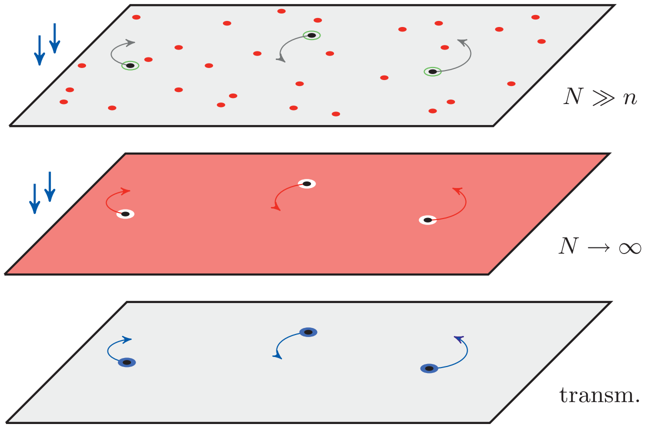

Fig. 12 Statistics transmutation in the QH setting. Bath particles (*red*) are repelled from tracers (*black*) by short-range interactions (*green*), and all particles move in an external homogeneous magnetic field (*blue arrows*). Subtracting the almost-homogeneous effective field generated by the bath as $b \sim N \gg 1$ then leaves a reduced/zero field plus remnant field (*blue disks*) at the holes punched in the bath by the tracers.

$$\int_{\mathbb{C}^n} |\Phi(\mathrm{w})|^2 \, d\mathrm{w} = 1, \quad c^{\mathrm{qh}}(\mathrm{w})^{-2} := \int_{\mathbb{C}^N} |\Psi^{\mathrm{qh}}(\mathrm{w}; \mathrm{z})|^2 dz,$$

ensuring the correct normalization $\int_{\mathbb{C}^{n+N}} |\Psi_\Phi|^2 dwdz = 1$.

The bath in LLL forces an *analytic* vanishing as $z_j \to w_k$, that is, $\mathbf{x}_j \to \mathbf{y}_k$. It suggests to take $\Psi^{\mathrm{qh}} = \Psi^{\mathrm{qh}}_\mu$ as above, corresponding to fractional filling $1/\mu$ of the LLL, or

$$\Psi^{\mathrm{qh}}_{\mu,p}(\mathrm{w}; \mathrm{z}) := \prod_{k=1}^{n} \prod_{j=1}^{N} (w_k - z_j)^p \, \Psi^{\mathrm{Lau}}_\mu(\mathrm{z}),$$

thus also allowing for nonsimple quasiholes if $p > 1$.

It was conjectured in Lundholm and Rougerie (2016) and Lambert et al. (2022) that in this ansatz

$$\langle H_{n \oplus N} \rangle_{\Psi_\Phi} = \frac{bN}{2} + \langle H^{\mathrm{eff}}_n \rangle_\Phi + \mathrm{error}_\Phi(n/N), \tag{86}$$

for an effective **statistics-transmuted Hamiltonian** for the tracers:

$$H^{\mathrm{eff}}_n := \frac{bn}{2m} \frac{p}{\mu} + \frac{1}{2m} \sum_{j=1}^{n} \left(-i\nabla_{\mathbf{y}_j} - \left(q - \frac{p}{\mu} \right) \frac{b}{2} \mathbf{y}_j^\perp - \frac{p^2}{\mu} \mathbf{A}_j \right)^2 + W(\mathrm{y}),$$

thus implying an effective renormalized charge $-q + p/\mu$ and shifted statistics parameter by $-p^2/\mu$.

In Lambert et al. (2022) it was proved mathematically that (86) is indeed a correct conclusion, with an error term of order $o(N)$ at fixed n and reasonable Φ, *if* $\mu = 1$ and $p = 1$, corresponding to transmutation of bosons into fermions and vice versa (cf. Section "Statistics transmutation in 2D"). Many crucial simplifications occur for these specific parameters, having to do with the Vandermonde structure of the state, and in the proof, it is also required that tracers have sufficient extra repulsion to not cluster too strongly at the diagonal set $\triangle_n$, which is ensured either by them being initially bosons and then eventually (free, if $q = 1$) fermions, or that W includes an additional and sufficiently strong intraspecies repulsion.

Impurities in the plane and polarons

Another route to statistics transmutation is to place tracers/impurities in a bath of bosons, such as the phonon vibrational modes of a crystal lattice, or photonic optical modes. Such systems are well known to enable transmutation of the impurities into **polarons**, that is, bound states of impurity particles and coherent states of phonons/photons (Fröhlich, 1954; Landau, 1933; Pekar, 1946). In Yakaboylu and Lemeshko (2018) and Yakaboylu et al. (2020), it was observed that, subject to suitable external fields and rotation of such systems, the polarons can also transmute their statistics.

As an illustrative toy model, we consider a single bosonic collective degree of freedom:

$$[\hat{a}, \hat{a}^\dagger] = 1, \quad \hat{N} := \hat{a}^\dagger \hat{a}, \quad \text{with eigenstates } |N\rangle, \ N \geq 0,$$

and an initial n-particle Hamiltonian

$$\hat{H}_0 = \sum_{j=1}^{n} (-i\nabla_{\mathbf{x}_j})^2 + W(\mathrm{x})$$

for bosons or fermions on $\mathcal{H}_0 = L^2_{\mathrm{sym/asym}}(\mathbb{R}^{2n})$. Let us then define the interaction Hamiltonian

$$\hat{H}_{\omega,\gamma} := \hat{H}_0 + \omega \hat{a}^\dagger \hat{a} + \gamma\omega(F\hat{a}^\dagger + F^{-1}\hat{a}) + \gamma^2\omega, \tag{87}$$

with two parameters $\omega > 0$ and $\gamma \in \mathbb{R}$. The interpretation of the terms added to $\hat{H}_0$ is that ω is the energy associated to an attachment or detachment of two units of flux or vorticity to each of the particles, which is done by the respective hopping terms with coupling $\gamma\omega$ and such that γ defines the ratio between these two effects. The last term is only a constant added for convenience.

We now denote $Z = \prod_{j<k} z_{jk}$, and consider two possible choices for F (or their complex conjugates, depending on which way the orientation symmetry is to be broken):

1. $F = (Z/|Z|)^2 = U^2$ corresponding to **flux attachment**,
2. $F = Z^2$ corresponding to **vortex attachment**.

By acting with $Fa^\dagger$ on the reference system $\mathcal{H}^0 = \mathcal{H}_0|0\rangle$, one obtains a ladder of Hilbert spaces of **composite bosons/fermions** (see Fig. 13):

$$\mathcal{H}^N := F^N \mathcal{H}_0 |N\rangle, \qquad N = 0, 1, 2, \ldots$$

Upon taking the "adiabatic limit" $\omega \to \infty$ at fixed γ, we claim that in the bottom of the spectrum of $\hat{H}_{\omega,\gamma}$ we then obtain a ladder of transmuted anyons with statistics parameter $\alpha = 2\gamma^2 + 2N$ (Yakaboylu et al., 2020). These anyons are either *interacting* by means of a

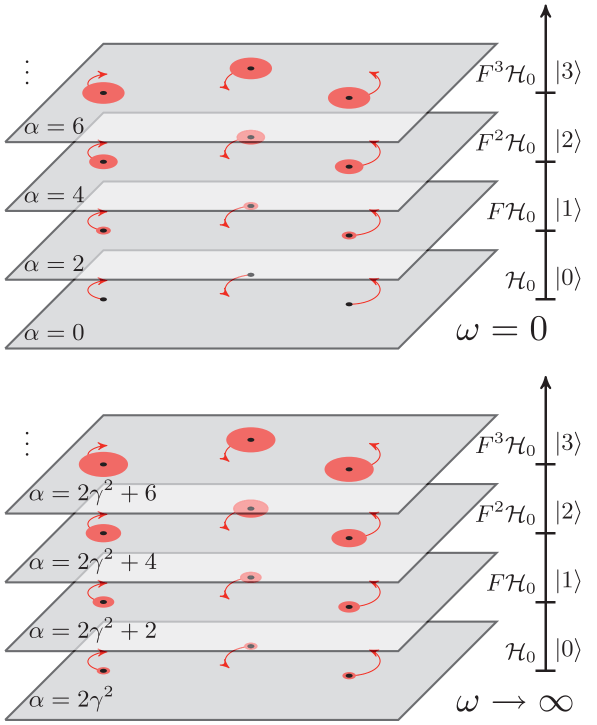

Fig. 13 Statistics transmutation in the polaron setting. An initial ladder of even-integer fluxes/vortices (composite bosons or fermions) is in the adiabatic limit transmuted into a ladder of fractional fluxes/vortices (anyons).

scalar potential $\sum_j \mathbf{A}_j^2$ (for the more realistic, unitary choice $F = U^2$) or *free* (for the more algebraic, nonunitary choice $F = Z^2$, yielding a non-Hermitian Hamiltonian with $i\mathbf{A}_j = \nabla_{\mathbf{x}_j} \log Z$). Namely, the transformations

$$\hat{S} = F^{\hat{N}} = e^{\hat{N}\log F}, \qquad \hat{U} = e^{-\gamma(\hat{a}^\dagger - \hat{a})}, \tag{88}$$

which diagonalize $\hat{H}_{\omega,\gamma}$,

$$\hat{U}^{-1}\hat{S}^{-1}\hat{H}_{\omega,\gamma}\hat{S}\hat{U} = \omega\hat{a}^\dagger\hat{a} + \sum_{j=1}^{N}\left[-i\nabla_{\mathbf{x}_j} + 2\mathbf{A}_j(\hat{a}^\dagger - \gamma)(\hat{a} - \gamma)\right]^2 + W(\mathbf{x}),$$

create coherent-state mixtures

$$\hat{S}\hat{U}|0\rangle = e^{-\gamma^2/2}\sum_{N=0}^{\infty}\frac{(-\gamma)^N}{\sqrt{N!}}F^N|N\rangle \tag{89}$$

over the initial ladder of integer composites and enable a shift of the expected amount of flux/vorticity by $\alpha_0 = 2\gamma^2 \geq 0$, possibly to noninteger values. This transmutation procedure has indeed been used (with the choice $F = Z^2$) to compute the numerical spectra seen in Fig. 4.

A possible plane polaron model with the above form is obtained upon applying a constant magnetic field $\mathbf{B}$ and shifting to a counter-rotating frame at half the cyclotron frequency $\Omega = B/(2m)$ (cf. Fig. 14, upper):

$$\hat{H}_N = \frac{1}{2m}\sum_{j=1}^{n}\hat{\mathbf{p}}_j^2 + W^\Omega(\mathbf{x}) + \sum_{\mathbf{k}}\omega_{\mathbf{k}}^\Omega\hat{b}_{\mathbf{k}}^\dagger\hat{b}_{\mathbf{k}} + \sum_{\mathbf{k}}\lambda_{\mathbf{k}}(\mathbf{x})\left(e^{-i\beta_{\mathbf{k}}(\mathbf{x})}b_{\mathbf{k}}^\dagger + e^{i\beta_{\mathbf{k}}(\mathbf{x})}b_{\mathbf{k}}\right),$$

for phonon vibration modes $b_{\mathbf{k}}$, $\mathbf{k} \in \mathbb{R}^2$ with dispersion $\omega_{\mathbf{k}}^\Omega$ (which is their bare dispersion shifted by their angular momentum coupled to Ω), and phonon-impurity interaction parameters $\lambda_{\mathbf{k}}$, $\beta_{\mathbf{k}}$. For $n = 2$ and a suitable interaction, realizable within the Fröhlich plane polaron model with quasi-2D Coulomb forces (Yakaboylu et al., 2020), the emergent gauge field

$$\alpha\mathbf{A}_j(\mathbf{x}) \approx \langle -i\nabla_{\mathbf{x}_j}\rangle_{\hat{S}\hat{U}|0\rangle} \approx -\sum_{\mathbf{k}}\left(\lambda_{\mathbf{k}}(\mathbf{x})/\omega_{\mathbf{k}}^\Omega\right)^2\nabla_{\mathbf{x}_j}\beta_{\mathbf{k}}(\mathbf{x}) \tag{90}$$

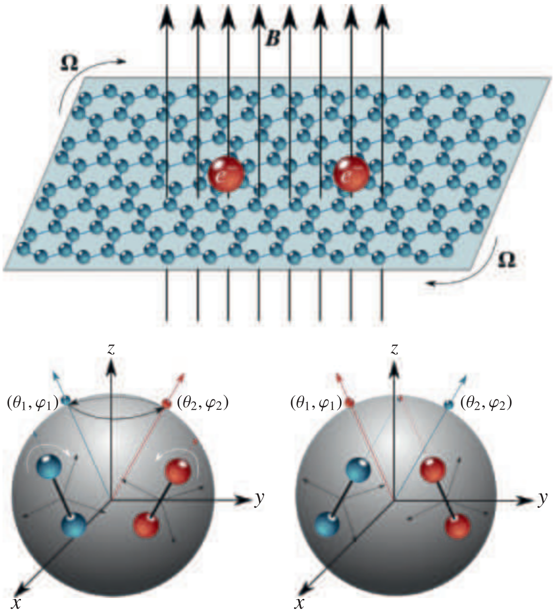

Fig. 14 Two possible experimental probes for emergent statistics transmutation: rotating plane in which Fröhlich polarons turn into anyons and the exchange of linear molecules. Upper, from Yakaboylu E, Ghazaryan A, Lundholm D, Rougerie N, Lemeshko M, and Seiringer R (2020) Quantum impurity model for anyons. Physical Review B 102: 144109; lower, from Brooks M, Lemeshko M, Lundholm D, and Yakaboylu E (2021b) Molecular impurities as a realization of anyons on the two-sphere. Physical Review Letters 126: 015301

is then approximately of the correct Aharonov–Bohm type and such as to transmute the statistics by $\alpha \approx \alpha(\Omega)$, ascertained by the system's correlations to the collective reference rotation/field.

Impurities on the sphere and angulons

A similar approach (Brooks et al., 2021a, b) can be taken for particles moving effectively on a sphere $\mathbb{S}^2$, namely, one may, for example, replace the planar kinetic energy (4) by the rotation energy

$$T_{\mathrm{rot}} = \sum_{j=1}^{n} \mathbf{L}_j^2 \tag{91}$$

(with units normalized suitably) of n identical linear molecules (cf. Fig. 14, lower). The resulting model for the Hamiltonian coupled to a bath of rotational angular momenta is called an **angulon** model (Schmidt and Lemeshko, 2015). This transmutation method has also been used to compute the energy spectrum of two anyons on a sphere (Brooks et al., 2021b); cf. (Ouvry and Polychronakos, 2019; Polychronakos and Ouvry, 2020) and see Einarsson (1992) concerning anyons in various topologies.

Other emergent models for anyons

Other approaches to investigate statistics transmutation in the QH setting include effects of anyonic shifted angular momentum on the energy spectrum (Cooper and Simon, 2015), and on pair correlation and other aspects of the density (Dubček et al., 2018; Graß et al., 2020; Morampudi et al., 2017; Umucalılar et al., 2018; Zhang et al., 2014), including non-abelian scenarios (Baldelli et al., 2021; Zhang et al., 2015). Emergent anyons can also be expected on spin networks and lattices (Bachmann, 2017; Bachmann et al., 2020, 2023). Certain classes of non-abelions have been proposed to emerge in the physics of neutrons and neutron stars (Masaki et al., 2023). Even in the quantum gravity context might we expect non-abelions, as they can capture the relevant degrees of freedom on the black-hole event horizon (Pithis and Ruiz Euler, 2015).

Conclusion

In light of recent experiments concerning anyons (Bartolomei et al., 2020; Fan et al., 2022; Google Quantum AI and Collaborators, 2022; Nakamura et al., 2020), it is increasingly important to gain a firm theoretical understanding of the basic properties of the anyon gas. We have here focused on its precise definition in typical ideal and nonideal contexts, its most basic physics as regards the connection between exchange and exclusion statistics, as well as its inevitable emergence in a few conceptually simple scenarios involving relatively well-understood bosonic and fermionic systems with manifest breaking of orientation symmetry, such as the rotated polaron and the quantum Hall setup.

In preparation for future experiments and theoretical research, one could make a few observations and highlight some potential obstacles. First, it is hoped that accurate density functional theories for large systems of anyons will provide more robust, detectable signatures, such as spatial and momentum density profiles, as compared to the typically extremely fragile phases probed by interferometry (cf., Camino et al., 2005; Nakamura et al., 2020). Second, the development of impurity models and the pinning of quasiholes, fluxes, and vortices to already well-understood quantum particles promises to eliminate some of the ambiguities inherent in conventional Berry phase and adiabatic treatments (cf., Forte, 1991; Jain, 2007; Lambert et al., 2022; Lundholm and Rougerie, 2016; Myrheim, 1999). Third, with the steadily growing literature on anyons and an increasing interest in their fascinating physics, even from the general public, it is important to be aware of potential confusion on how the term "anyon" is used. Hopefully, this overview has helped to clarify both the nontrivial relationship between exchange and exclusion statistics and the crucial differences between (a) the **choice or construction** of a concrete braid group representation $\rho_N : B_N \to \mathrm{U}(\mathcal{F}_N)$ (algebra, kinematics, or simply an action of a permutation on a system); (b) its **practical realization** such as by means of motion of classical parameters (magnetics, or computation using a classical or quantum computer; cf., Noh et al., 2020); and (c) **actual anyons** (or bosons or fermions) endowed with quantum kinetic energy $\hat{T}_{\rho_N}$ (geometrodynamics), uncertainty and exclusion.

Acknowledgments

The study of the magnetic TF functional for anyons was done in collaboration with Dinh Thi Nguyen, following helpful discussions with Nicolas Rougerie and Théotime Girardot. Further, I thank the editor Tapash Chakraborty for the timely invitation to write this overview, as well as Vincent Cavalier, Ask Ellingsen, Gerald Goldin, and Wolfgang Staubach for useful comments on the manuscript. I am thankful to numerous other colleagues for insightful discussions on this topic over the last 13 years, in particular Jan Philip Solovej, who raised my interest in it, as well as Eddy Ardonne, Morris Brooks, Michele Correggi, Romain Duboscq, Luca Fresta, Jürg Fröhlich, Thors Hans Hansson, Gaultier Lambert, Simon Larson, Jon Magne Leinaas, Tomasz Maciazek, Per Moosavi, Luca Oddis, Stéphane Ouvry, Viktor Qvarfordt, Robert Seiringer, Andrea Trombettoni, Susanne Viefers, and Enderalp Yakaboylu. The research project was funded by the Swedish Research Council (grant no. 2021-05328, "Mathematics of anyons and intermediate quantum statistics").

References

Abramsky S and Brandenburger A (2011) The sheaf-theoretic structure of non-locality and contextuality. *New Journal of Physics* 13(11): 113036.
Aftalion A, Blanc X, and Nier F (2006a) Lowest Landau level functional and Bargmann spaces for Bose-Einstein condensates. *Journal of Functional Analysis* 241(2): 661–702. MR2271933 (2008c:82052).
Aftalion A, Blanc X, and Nier F (2006b) Vortex distribution in the lowest Landau level. *Physical Review A* 73: 011601(R).
Aharonov Y and Bohm D (1959) Significance of electromagnetic potentials in the quantum theory. *Physical Review* 115: 485–491.
Albeverio S, Gesztesy F, Høegh-Krohn R, and Holden H (2005) Solvable Models in Quantum Mechanics. In: *With an Appendix by Pavel Exner*, 2nd edn. Providence, RI: AMS Chelsea Publishing. 2105735.
Alonso A and Simon B (1980) The Birman-Kreiˇn-Vishik theory of self-adjoint extensions of semibounded operators. *Journal of Operator Theory*: 251–270.
Arovas D, Schrieffer JR, and Wilczek F (1984) Fractional statistics and the quantum Hall effect. *Physical Review Letters* 53: 722–723.
Arovas DP, Schrieffer R, Wilczek F, and Zee A (1985) Statistical mechanics of anyons. *Nuclear Physics B* 251: 117–126.
Artin E (1925) Theorie der Zöpfe. *Abhandlungen aus dem Mathematischen Seminar der Universität Hamburg* 4(1): 47–72 (3069440).
Artin E (1947) Theory of braids. *Annals of Mathematics* 48(2): 101–126 (19087).
Bachmann S (2017) Local disorder, topological ground state degeneracy and entanglement entropy, and discrete anyons. *Reviews in Mathematical Physics* 29(6): 1750018.
Bachmann S, Bols A, De Roeck W, and Fraas M (2020) Many-body Fredholm index for ground-state spaces and abelian anyons. *Physical Review B* 101: 085138.
Bachmann S, Nachtergaele B, and Vadnerkar S (2023) Dynamical abelian anyons with bound states and scattering states. *arXiv e-prints*.
Baldelli N, Juliá-Díaz B, Bhattacharya U, Lewenstein M, and Graß T (2021) Tracing non-abelian anyons via impurity particles. *Physical Review B* 104: 035133.
Bartolomei H, Kumar M, Bisognin R, Marguerite A, Berroir J-M, Bocquillon E, Plaçais B, Cavanna A, Dong Q, Gennser U, Jin Y, and Fève G (2020) Fractional statistics in anyon collisions. *Science* 368(6487): 173–177.
Beer K, Bondarenko D, Hahn A, Kalabakov M, Knust N, Niermann L, Osborne TJ, Schridde C, Seckmeyer S, Stiegemann DE, et al. (2018) From categories to anyons: A travelogue. *arXiv e-prints*.
Berry MV (1984) Quantal phase factors accompanying adiabatic changes. *Proceedings of the Royal Society of London. Series A, Mathematical and Physical Sciences* 392: 45–57.
Biedenharn L, Lieb E, Simon B, and Wilczek F (1990) The ancestry of the 'Anyon'. *Physics Today* 43(8): 90.
Birman JS (1974) Braids, Links, and Mapping Class Groups. *Annals of Mathematics Studies, No. 82.* Princeton, N.J.: Princeton University Press. Tokyo: University of Tokyo Press.
Bonderson P, Gurarie V, and Nayak C (2011) Plasma analogy and non-abelian statistics for Ising-type quantum Hall states. *Physical Review B* 83: 075303.
Bourdeau M and Sorkin RD (1992) When can identical particles collide? *Physical Review D* 45: 687–696.
Brooks M, Lemeshko M, Lundholm D, and Yakaboylu E (2021a) Emergence of anyons on the two-sphere in molecular impurities. *Atoms* 9(4): 106.
Brooks M, Lemeshko M, Lundholm D, and Yakaboylu E (2021b) Molecular impurities as a realization of anyons on the two-sphere. *Physical Review Letters* 126: 015301.
Burau W (1935) Über Zopfgruppen und gleichsinnig verdrillte Verkettungen. *Abhandlungen aus dem Mathematischen Seminar der Universität Hamburg* 11(1): 179–186 (3069652).
Caenepeel D and MacKenzie R (1994) Parity violation, anyon scattering, and the mean field approximation. *Physical Review D* 50: 5418–5424.
Calogero F (1969a) Ground state of a one-dimensional N-body system. *Journal of Mathematical Physics* 10(12): 2197–2200.
Calogero F (1969b) Solution of a three-body problem in one dimension. *Journal of Mathematical Physics* 10(12): 2191–2196.
Camino FE, Zhou W, and Goldman VJ (2005) Realization of a Laughlin quasiparticle interferometer: Observation of fractional statistics. *Physical Review B* 72: 075342.
Canright GS and Johnson MD (1994) Fractional statistics: Alpha to beta. *Journal of Physics A: Mathematical and General* 27(11): 3579.

Cappelli A, Georgiev LS, and Todorov IT (2001) Parafermion Hall states from coset projections of abelian conformal theories. *Nuclear Physics B* 599(3): 499–530.

Chen YH, Wilczek F, Witten E, and Halperin BI (1989) On anyon superconductivity. *International Journal of Modern Physics B* 03: 1001–1067.

Chitra R and Sen D (1992) Ground state of many anyons in a harmonic potential. *Physical Review B* 46: 10923–10930.

Chou C (1991) Multianyon spectra and wave functions. *Physical Review D* 44: 2533–2547.

Cooper NR and Simon SH (2015) Signatures of fractional exclusion statistics in the spectroscopy of quantum Hall droplets. *Physical Review Letters* 114: 106802.

Correggi M and Fermi D (2021) Magnetic perturbations of anyonic and Aharonov-Bohm Schrödinger operators. *Journal of Mathematical Physics* 62: 032101.

Correggi M and Oddis L (2018) Hamiltonians for two-anyon systems. *Rendiconti di Matematica e Delle sue Applicazioni* 39: 277–292.

Correggi M, Lundholm D, and Rougerie N (2017) Local density approximation for the almost-bosonic anyon gas. *Analysis & PDE* 10: 1169–1200.

Correggi M, Lundholm D, and Rougerie N (2018) Local density approximation for almost-bosonic anyons. In: Bonetto F, Borthwick D, Harrell E, and Loss M (eds.) *Proceedings of QMath13, Atlanta, October 8–11, 2016. Mathematical Problems in Quantum Physics*, vol. 717, pp. 77–92. Contemp. Math.

Correggi M, Duboscq R, Lundholm D, and Rougerie N (2019) Vortex patterns in the almost-bosonic anyon gas. *EPL (Europhysics Letters)* 126: 20005.

Coutinho FAB, Nogami Y, and Fernando Perez J (1992) Self-adjoint extensions of the Hamiltonian for a charged particle in the presence of a thread of magnetic flux. *Physical Review A* 46: 6052–6055.

Date G and Murthy MVN (1993) Classical dynamics of anyons and the quantum spectrum. *Physical Review A* 48: 105–110.

Date G, Murthy MVN, and Vathsan R (2003) Classical and quantum mechanics of anyons. *arXiv e-prints*.

Delaney C, Rowell EC, and Wang Z (2016) Local unitary representations of the braid group and their applications to quantum computing. *Revista Colombiana de Matemáticas* 50(2): 207–272 (3605648).

Dell'Antonio G, Figari R, and Teta A (1997) Statistics in space dimension two. *Letters in Mathematical Physics* 40(3): 235–256 (1453763).

Dirac PAM (1967) Lectures on Quantum Mechanics. *Belfer Graduate School of Science Monographs Series.* vol. 2. New York: Belfer Graduate School of Science.

Dowker JS (1972) Quantum mechanics and field theory on multiply connected and on homogeneous spaces. *Journal of Physics A* 5(7): 936.

Dowker JS (1985) Remarks on nonstandard statistics. *Journal of Physics A* 18(18): 3521–3530 (822912).

Dubček T, Klajn B, Pezer R, Buljan H, and Jukić D (2018) Quasimomentum distribution and expansion of an anyonic gas. *Physical Review A* 97: 011601.

Dyson FJ (1967) Ground-state energy of a finite system of charged particles. *Journal of Mathematical Physics* 8(8): 1538–1545.

Dyson FJ and Lenard A (1967) Stability of matter. I. *Journal of Mathematical Physics* 8(3): 423–434.

Ehrenberg W and Siday RE (1949) The refractive index in electron optics and the principles of dynamics. *Proceedings of the Physical Society. Section B* 62(1): 8.

Einarsson, T., 1992. Anyons and Antiferromagnets: Two Two-Dimensional Topics. (Ph.D. thesis), Institute of Theoretical Physics, Chalmers University of Technology, Gothenburg.

Fan Y-a, Li Y, Hu Y, Li Y, Long X, Liu H, Yang X, Nie X, Li J, Xin T, et al. (2022) Experimental realization of a topologically protected Hadamard gate via braiding Fibonacci anyons. *arXiv e-prints*.

Fermi E (1927) Un metodo statistico per la determinazione di alcune priorieta dell'atome. *Rendiconti dell'Accademia Nazionale dei Lincei* 6: 602–607.

Fetter AL, Hanna CB, and Laughlin RB (1989) Random-phase approximation in the fractional-statistics gas. *Physical Review B* 39: 9679–9681.

Formanek E (1996) Braid group representations of low degree. *Proceedings of the London Mathematical Society 3* 73(2): 279–322 (1397691).

Forte S (1991) Berry's phase, fractional statistics and the Laughlin wave function. *Modern Physics Letters A* 6(34): 3152–3162.

Forte S (1992) Quantum mechanics and field theory with fractional spin and statistics. *Reviews of Modern Physics* 64: 193–236.

Fredenhagen K, Rehren K-H, and Schroer B (1989) Superselection sectors with braid group statistics and exchange algebras. I. General theory. *Communications in Mathematical Physics* 125(2): 201–226 (1016869).

Freedman MH, Kitaev A, Larsen MJ, and Wang Z (2003) Topological quantum computation. *Bulletin of the American Mathematical Society (N.S.)* 40(1): 31–38 (Mathematical challenges of the 21st century (Los Angeles, CA, 2000). 1943131).

Fröhlich H (1954) Electrons in lattice fields. *Advances in Physics* 3: 325–361.

Fröhlich J (1976) New super-selection sectors ("soliton-states") in two dimensional Bose quantum field models. *Communications in Mathematical Physics* 47(3): 269–310.

Fröhlich J (1988) Statistics of fields, the Yang-Baxter equation, and the theory of knots and links. In: *Nonperturbative Quantum Field Theory (Cargèse, 1987). NATO Advanced Science Institutes Series B: Physics*, vol. 185, pp. 71–100. New York: Plenum.

Fröhlich J (1990) Quantum statistics and locality. In: *Proceedings of the Gibbs Symposium (New Haven, CT, 1989)*, pp. 89–142. Providence, RI: American Mathematical Society.

Fröhlich J (2009) Spin, or actually: Spin and quantum statistics. In: Duplantier B, Raimond J-M, and Rivasseau V (eds.) *The Spin: Poincaré Seminar 2007*, pp. 1–60. Basel: Birkhäuser Basel.

Fröhlich J and Gabbiani F (1990) Braid statistics in local quantum theory. *Reviews in Mathematical Physics* 2(3): 251–353.

Fröhlich J and Kerler T (1993) *Quantum Groups, Quantum Categories and Quantum Field Theory*. Berlin-Heidelberg-New York: Springer-Verlag.

Fröhlich J and Marchetti PA (1988) Quantum field theory of anyons. *Letters in Mathematical Physics* 16(4): 347–358 (974482).

Fröhlich J and Marchetti PA (1989) Quantum field theories of vortices and anyons. *Communications in Mathematical Physics* 121(2): 177–223 (985396).

Gentile G (1940) Osservazioni sopra le statistiche intermedie. *Il Nuovo Cimento* 17(10): 493–497.

Gentile G (1942) Le statistiche intermedie e le proprietà dell'elio liquido. *Il Nuovo Cimento* 19(4): 109–125.

Girardeau M (1960) Relationship between systems of impenetrable bosons and fermions in one dimension. *Journal of Mathematical Physics* 1: 516–523. 0128913 (23 #B1950).

Girardeau MD (1965) Permutation symmetry of many-particle wave functions. *Physical Review* 139: B500–B508.

Girardot T (2020) Average field approximation for almost bosonic anyons in a magnetic field. *Journal of Mathematical Physics* 61(7): 071901 (23. 4123638).

Girardot, T., 2021. Mean-Field Approximation for the Anyon Gas (Ph.D. thesis), Université Grenoble Alpes & CNRS, l'École Doctorale Mathématiques, Sciences et technologies de l'information, Informatique.

Girardot T and Rougerie N (2021) Semiclassical limit for almost fermionic anyons. *Communications in Mathematical Physics* 387(1): 427–480.

Girardot T and Rougerie N (2022) A Lieb-Thirring inequality for extended anyons. *arXiv e-prints*.

Goldin GA (2022) The prediction of anyons: Its history and wider implications. *arXiv e-prints*.

Goldin GA and Majid S (2004) On the Fock space for nonrelativistic anyon fields and braided tensor products. *Journal of Mathematical Physics* 45(10): 3770–3787 (2095672).

Goldin GA and Sharp DH (1996) Diffeomorphism groups, anyon fields, and *q* commutators. *Physical Review Letters* 76: 1183–1187.

Goldin G, Menikoff R, and Sharp D (1980) Particle statistics from induced representations of a local current group. *Journal of Mathematical Physics* 21(4): 650–664.

Goldin GA, Menikoff R, and Sharp DH (1981) Representations of a local current algebra in nonsimply connected space and the Aharonov-Bohm effect. *Journal of Mathematical Physics* 22(8): 1664–1668.

Goldin GA, Menikoff R, and Sharp DH (1983) Diffeomorphism groups, gauge groups, and quantum theory. *Physical Review Letters* 51: 2246–2249.

Goldin GA, Menikoff R, and Sharp DH (1985) Comments on "general theory for quantum statistics in two dimensions". *Physical Review Letters* 54: 603. 603.

Google Quantum Collaborators AI (2022) Observation of non-abelian exchange statistics on a superconducting processor. *arXiv e-prints*.

Graß T, Juliá-Díaz B, Baldelli N, Bhattacharya U, and Lewenstein M (2020) Fractional angular momentum and anyon statistics of impurities in Laughlin liquids. *Physical Review Letters* 125: 136801.

Green HS (1953) A generalized method of field quantization. *Physical Review* 90: 270–273.

Gross E (1961) Structure of a quantized vortex in boson systems. *Nuovo Cimento* 20(3): 454–477.

Grundberg J, Hansson T, Karlhede A, and Leinaas J (1991) On singular anyon wavefunctions. *Modern Physics Letters B* 05(07): 539–546.

Haldane FDM (1991) "Fractional statistics" in arbitrary dimensions: A generalization of the Pauli principle. *Physical Review Letters* 67: 937–940.

Halperin BI (1984) Statistics of quasiparticles and the hierarchy of fractional quantized Hall states. *Physical Review Letters* 52: 1583–1586.

Hoffmann-Ostenhof M, Hoffmann-Ostenhof T, Laptev A, and Tidblom J (2008) Many-particle Hardy inequalities. *Journal of the London Mathematical Society* 77: 99–114.

Hu Y, Murthy G, Rao S, and Jain JK (2021) Kohn-Sham density functional theory of abelian anyons. *Physical Review B* 103: 035124.

Iengo R and Lechner K (1992) Anyon quantum mechanics and Chern-Simons theory. *Physics Reports* 213: 179–269.

Jackiw R (1990) Topics in planar physics. *Nuclear Physics B—Proceedings Supplements* 18A: 107–170. Integrability and quantization (Jaca, 1989). 1128794.

Jain JK (2007) *Composite Fermions*. Cambridge University Press.

Khare A (2005) *Fractional Statistics and Quantum Theory*. Singapore: World Scientific.

Kitaev AY (2003) Fault-tolerant quantum computation by anyons. *Annals of Physics* 303(1): 2–30 (1951039).

Kitaev A (2006) Anyons in an exactly solved model and beyond. *Annals of Physics* 321(1): 2–111 (2200691).

Klaiber B (1968) The Thirring model. In: Barut AO and Brittin WE (eds.) *Quantum Theory and Statistical Physics*. *Lectures in Theoretical Physics*, vol. X-A. New York: Gordon and Breach. Presented at the Theoretical Physics Institute, University of Colorado, Summer 1967, pp. 141–176.

Kohno T (1987) Monodromy representations of braid groups and Yang-Baxter equations. *Annales de l'institut Fourier (Grenoble)* 37(4): 139–160 (927394).

Korff C, Lang G, and Schrader R (1999) Two-particle scattering theory for anyons. *Journal of Mathematical Physics* 40(4): 1831–1869 (1683162).

Kundu A (1999) Exact solution of double δ function Bose gas through an interacting anyon gas. *Physical Review Letters* 83: 1275–1278.

Lahtinen V and Pachos J (2017) A short introduction to topological quantum computation. *SciPost Physics* 3(3): 021.

Laidlaw MGG and DeWitt CM (1971) Feynman functional integrals for systems of indistinguishable particles. *Physical Review D* 3: 1375–1378.

Lambert G, Lundholm D, and Rougerie N (2022) Quantum statistics transmutation via magnetic flux attachment. *arXiv e-prints*.

Landau L (1933) Über die Bewegung der Elektronen in Kristallgitter. *Physikalische Zeitschrift der Sowjetunion* 3: 644–645.

Lankhorst M, Brinkman A, Hilgenkamp H, Poccia N, and Golubov A (2018) Annealed low energy states in frustrated large square Josephson junction arrays. *Condensed Matter* 3: 19.

Larson S and Lundholm D (2018) Exclusion bounds for extended anyons. *Archive for Rational Mechanics and Analysis* 227: 309–365.

Larson S, Lundholm D, and Nam PT (2021) Lieb-Thirring inequalities for wave functions vanishing on the diagonal set. *Annales Henri Lebesgue* 4: 251–282.

Laughlin RB (1983) Anomalous quantum Hall effect: An incompressible quantum fluid with fractionally charged excitations. *Physical Review Letters* 50(18): 1395–1398.

Laughlin RB (1999) Nobel lecture: Fractional quantization. *Reviews of Modern Physics* 71: 863–874.

Lee T and Oh P (1994) Non-abelian Chern-Simons quantum mechanics and non-abelian Aharonov-Bohm effect. *Annals of Physics* 235(2): 413–434 (1297823).

Leinaas JM and Myrheim J (1977) On the theory of identical particles. *Nuovo Cimento B* 37: 1–23.

Leinaas JM and Myrheim J (1993) Heisenberg quantization for systems of identical particles. *International Journal of Modern Physics A* 8(21): 3649–3695.

Leinaas JM and Myrheim J (2022) Fractional statistics in low-dimensional systems. In: *Encyclopedia of Condensed Matter Physics*, 2nd.

Lerda A (1992) *Anyons*. Berlin-Heidelberg: Springer-Verlag.

Li S, Bhaduri RK, and Murthy MVN (1992) Thomas-fermi approximation for confined anyons. *Physical Review B* 46: 1228–1231.

Lieb EH and Liniger W (1963) Exact analysis of an interacting Bose gas. I. The general solution and the ground state. *Physical Review* 130(2): 1605–1616. 0156630 (27 #6551).

Lieb EH and Seiringer R (2010) *The Stability of Matter in Quantum Mechanics*. Cambridge University Press.

Lieb EH and Thirring WE (1975) Bound for the kinetic energy of fermions which proves the stability of matter. *Physical Review Letters* 35: 687–689.

Lieb EH and Thirring WE (1976) Inequalities for the moments of the eigenvalues of the Schrödinger Hamiltonian and their relation to Sobolev inequalities. In: *Studies in Mathematical Physics*, pp. 269–303. Princeton University Press.

Lieb EH and Yngvason J (2001) The ground state energy of a dilute two-dimensional Bose gas. *Journal of Statistical Physics* 103(3-4): 509–526. Special issue dedicated to the memory of Joaquin M. Luttinger. 1827922.

Lieb EH, Solovej JP, and Yngvason J (1995) Ground states of large quantum dots in magnetic fields. *Physical Review B* 51: 10646–10665.

Lieb EH, Seiringer R, Solovej JP, and Yngvason J (2005) *The Mathematics of the Bose Gas and Its Condensation*. Birkhäuser. Oberwolfach Seminars.

Lundholm D (2017) Many-anyon trial states. *Physical Review A* 96: 012116.

Lundholm D (2019) *Methods of Modern Mathematical Physics: Uncertainty and Exclusion Principles in Quantum Mechanics*. KTH and LMU Graduate Course Textbook (Latest version at http://www.mathematik.uni-muenchen.de//tilde/lundholm/methmmp.pdf).

Lundholm D and Qvarfordt V (2020) Exchange and exclusion in the non-abelian anyon gas. *arXiv e-prints*.

Lundholm D and Rougerie N (2015) The average field approximation for almost bosonic extended anyons. *Journal of Statistical Physics* 161(5): 1236–1267.

Lundholm D and Rougerie N (2016) Emergence of fractional statistics for tracer particles in a Laughlin liquid. *Physical Review Letters* 116: 170401.

Lundholm D and Seiringer R (2018) Fermionic behavior of ideal anyons. *Letters in Mathematical Physics* 108: 2523–2541.

Lundholm D and Solovej JP (2013a) Hardy and Lieb-Thirring inequalities for anyons. *Communications in Mathematical Physics* 322: 883–908.

Lundholm D and Solovej JP (2013b) Local exclusion principle for identical particles obeying intermediate and fractional statistics. *Physical Review A* 88: 062106.

Lundholm D and Solovej JP (2014) Local exclusion and Lieb-Thirring inequalities for intermediate and fractional statistics. *Annales Henri Poincaré* 15: 1061–1107.

Lundholm D, Portmann F, and Solovej JP (2015) Lieb-Thirring bounds for interacting Bose gases. *Communications in Mathematical Physics* 335(2): 1019–1056.

Lundholm D, Nam PT, and Portmann F (2016) Fractional Hardy-Lieb-Thirring and related inequalities for interacting systems. *Archive for Rational Mechanics and Analysis* 219(3): 1343–1382.

Maciazek T and Sawicki A (2019) Non-abelian quantum statistics on graphs. *Communications in Mathematical Physics* 371: 921–973.

Mancarella F, Trombettoni A, and Mussardo G (2013a) Statistical interparticle potential of an ideal gas of non-abelian anyons. *Journal of Physics A: Mathematical and Theoretical* 46(27): 275001.

Mancarella F, Trombettoni A, and Mussardo G (2013b) Statistical mechanics of an ideal gas of non-abelian anyons. *Nuclear Physics B* 867(3): 950–976.

Manuel C and Tarrach R (1991) Contact interactions of anyons. *Physics Letters B* 268(2): 222–226 (1131514).

Masaki Y, Mizushima T, and Nitta M (2023) Non-abelian anyons and non-abelian vortices in topological superconductors. In: *Encyclopedia of Condensed Matter Physics*, 2ndedn.

McEuen PL, Foxman EB, Kinaret J, Meirav U, Kastner MA, Wingreen NS, and Wind SJ (1992) Self-consistent addition spectrum of a coulomb Island in the quantum Hall regime. *Physical Review B* 45: 11419–11422.

Messiah AML and Greenberg OW (1964) Symmetrization postulate and its experimental foundation. *Physical Review* 136: B248–B267.

Moore G and Read N (1991) Nonabelions in the fractional quantum Hall effect. *Nuclear Physics B* 360(2): 362–396.

Morampudi SC, Turner AM, Pollmann F, and Wilczek F (2017) Statistics of fractionalized excitations through threshold spectroscopy. *Physical Review Letters* 118: 227201.

Mouchet A (2021) Path integrals in a multiply-connected configuration space (50 years after). *Foundations of Physics* 51(6): 107.

Mund J (2009) The spin-statistics theorem for anyons and plektons in d= 2+ 1. *Communications in Mathematical Physics* 286(3): 1159–1180.

Mund J and Schrader R (1995) Hilbert spaces for nonrelativistic and relativistic "free" plektons (particles with braid group statistics). In: *Advances in Dynamical Systems and Quantum Physics (Capri, 1993)*, pp. 235–259. River Edge, NJ: World Scientific.

Murthy MVN, Law J, Brack M, and Bhaduri RK (1991) Quantum spectrum of three anyons in an oscillator potential. *Physical Review Letters* 67: 1817–1820.

Murthy MVN, Law J, Bhaduri RK, and Date G (1992) On a class of noninterpolating solutions of the many-anyon problem. *Journal of Physics A: Mathematical and General* 25(23): 6163.

Myrheim J (1999) Anyons, topological aspects of low dimensional systems. In: Comtet A, Jolicœur T, Ouvry S, and David F (eds.) *Les Houches–Ecole d'Ete de Physique Theorique*, vol. 69, pp. 265–413. Berlin, Germany: Springer-Verlag.

Nakamura J, Liang S, Gardner GC, and Manfra MJ (2020) Direct observation of anyonic braiding statistics. *Nature Physics* 16: 931–936.

Nayak C and Wilczek F (1996) $2n$-Quasihole states realize 2^{n-1}-dimensional spinor braiding statistics in paired quantum Hall states. *Nature Physics B* 479(3): 529–553 (1418835).

Nayak C, Simon SH, Stern A, Freedman M, and Das Sarma S (2008) Non-abelian anyons and topological quantum computation. *Reviews of Modern Physics* 80: 1083–1159.

Noh J, Schuster T, Iadecola T, Huang S, Wang M, Chen KP, Chamon C, and Rechtsman MC (2020) Braiding photonic topological zero modes. *Nature Physics* 16(9): 989–993.
Oddis, L., 2020. Two-Anyon Schrödinger Operators (Ph.D. thesis), Università di Roma, Sapienza, Facoltà di Scienze Matematiche, Fisiche e Naturali.
Ouvry S (2007) Anyons and lowest Landau level anyons. *Séminaire Poincaré* 11: 77–107.
Ouvry S and Polychronakos AP (2019) Anyons on the sphere: Analytic states and spectrum. *Nuclear Physics B* 949: 114797.
Pancharatnam S (1956) Generalized theory of interference, and its applications: Part I. Coherent pencils. In: *Proceedings of the Indian Academy of Sciences-Section A*, vol. 44, pp. 247–262. New Delhi: Springer India.
Pekar S (1946) Local quantum states of electrons in an ideal ion crystal. *Zhurnal Eksperimentalnoi I Teoreticheskoi Fiziki* 16(4): 341–348.
Pitaevskii LP (1961) Vortex lines in an imperfect Bose gas. *Zhurnal Eksperimentalnoi I Teoreticheskoi Fiziki* 40(40): 646–651.
Pithis AGA and Ruiz Euler H-C (2015) Anyonic statistics and large horizon diffeomorphisms for loop quantum gravity black holes. *Physical Review D* 91: 064053.
Polychronakos AP (1989) Non-relativistic bosonization and fractional statistics. *Nuclear Physics B* 324(3): 597–622.
Polychronakos AP and Ouvry S (2020) Two anyons on the sphere: Nonlinear states and spectrum. *Nuclear Physics B* 951: 114906.
Qvarfordt, V., 2017. Non-Abelian Anyons: Statistical Repulsion and Topological Quantum Computation (Ph.D. thesis), KTH.
Read N and Rezayi E (1999) Beyond paired quantum Hall states: Parafermions and incompressible states in the first excited Landau level. *Physical Review B* 59: 8084–8092.
Regnault N, Goerbig MO, and Jolicoeur T (2008) Bridge between abelian and non-abelian fractional quantum Hall states. *Physical Review Letters* 101: 066803.
Rougerie N and Yang Q (2022) Dimensional reduction for a system of 2D anyons. *arXiv e-prints*.
Rowell EC and Wang Z (2012) Localization of unitary braid group representations. *Communications in Mathematical Physics* 311(3): 595–615 (2909757).
Schick M (1971) Two-dimensional system of hard-core Bosons. *Physical Review A* 3: 1067–1073.
Schmidt R and Lemeshko M (2015) Rotation of quantum impurities in the presence of a many-body environment. *Physical Review Letters* 114: 203001.
Schulman L (1968) A path integral for spin. *Physical Review* 176: 1558–1569.
Seiringer R and Solovej JP (2023) A simple approach to Lieb-Thirring type inequalities. *arXiv e-prints*.
Simon B (1983) Holonomy, the quantum adiabatic theorem, and Berry's phase. *Physical Review Letters* 51: 2167–2170.
Souriau J-M (1970) *Structure des Systèmes Dynamiques*. Dunod, Paris: Maîtrises de Mathématiques. English translation by Cushman RH and Tuynman GM (1997) Progress in Mathematics, vol. 149, Boston, MA: Birkhäuser Boston Inc.
Sporre M, Verbaarschot JJM, and Zahed I (1991) Numerical solution of the three-anyon problem. *Physical Review Letters* 67: 1813–1816.
Sporre M, Verbaarschot JJM, and Zahed I (1992) Four anyons in a harmonic well. *Physical Review B* 46: 5738–5741.
Stern A (2008) Anyons and the quantum Hall effect–a pedagogical review. *Annals of Physics* 323(1): 204–249. January Special Issue 2008.
Stormer HL (1999) Nobel lecture: The fractional quantum Hall effect. *Reviews of Modern Physics* 71: 875–889.
Streater RF and Wilde IF (1970) Fermion states of a Boson field. *Nuclear Physics B* 24(3): 561–575.
Sutherland B (1971) Quantum many-body problem in one dimension: Ground state. *Journal of Mathematical Physics* 12: 246–250.
Thomas LH (1927) The calculation of atomic fields. *Proceedings of the Cambridge Philosophical Society* 23(05): 542–548.
Tonks L (1936) The complete equation of state of one, two and three-dimensional gases of hard elastic spheres. *Physical Review* 50: 955–963.
Trugenberger C (1992a) The anyon fluid in the Bogoliubov approximation. *Physical Review D* 45: 3807–3817.
Trugenberger C (1992b) Ground state and collective excitations of extended anyons. *Physics Letters B* 288: 121–128.
Tsuchiya A and Kanie Y (1987) Vertex operators in the conformal field theory on p1 and monodromy representations of the braid group. *Letters in Mathematical Physics* 13: 303–312.
Tsuchiya A and Kanie Y (1988) Vertex operators in conformal field theory on p1 and monodromy representations of braid group. *Advanced Studies in Pure Math* 16: 297–372. Conformal Field Theory and Solvable Lattice Models.
Tsui DC (1999) Nobel lecture: Interplay of disorder and interaction in two-dimensional electron gas in intense magnetic fields. *Reviews of Modern Physics* 71: 891–895.
Tsui DC, Stormer HL, and Gossard AC (1982) Two-dimensional magnetotransport in the extreme quantum limit. *Physical Review Letters* 48: 1559–1562.
Umucalılar RO, Macaluso E, Comparin T, and Carusotto I (2018) Time-of-flight measurements as a possible method to observe anyonic statistics. *Physical Review Letters* 120: 230403.
Verlinde EP (1991) A note on braid statistics and the non-Abelian Aharonov-Bohm effect, modern quantum field theory: Proceedings. In: Das S, Dhar A, Mukhi S, Raina A, and Sen A (eds.) *Proc. of Conference: International Colloquium on Modern Quantum Field Theory, Bombay*, pp. 450–461. World Scientific.
Weinberger, O., 2015. The Braid Group, Representations and Non-Abelian Anyons (BSc thesis), KTH.
Wen XG (1991) Non-abelian statistics in the fractional quantum Hall states. *Physical Review Letters* 66: 802–805.
Wilczek F (1982a) Magnetic flux, angular momentum, and statistics. *Physical Review Letters* 48: 1144–1146.
Wilczek F (1982b) Quantum mechanics of fractional-spin particles. *Physical Review Letters* 49: 957–959.
Wilczek F (1990) *Fractional Statistics and Anyon Superconductivity*. Singapore: World Scientific.
Wilczek F and Wu Y-S (1990) Space-time approach to holonomy scattering. *Physical Review Letters* 65: 13–16.
Wu Y-S (1984a) General theory for quantum statistics in two dimensions. *Physical Review Letters* 52: 2103–2106.
Wu Y-S (1984b) Multiparticle quantum mechanics obeying fractional statistics. *Physical Review Letters* 53: 111–114.
Yakaboylu E and Lemeshko M (2018) Anyonic statistics of quantum impurities in two dimensions. *Physical Review B* 98: 045402.
Yakaboylu E, Ghazaryan A, Lundholm D, Rougerie N, Lemeshko M, and Seiringer R (2020) Quantum impurity model for anyons. *Physical Review B* 102: 144109.
Zhang Y, Sreejith GJ, Gemelke ND, and Jain JK (2014) Fractional angular momentum in cold atom systems. *Physical Review Letters* 113: 160404.
Zhang Y, Sreejith GJ, and Jain JK (2015) Creating and manipulating non-Abelian anyons in cold atom systems using auxiliary Bosons. *Physical Review B* 92: 075116.

Abelian and non-abelian anyons

Sumathi Rao, International Centre for Theoretical Studies, Tata Institute of Fundamental Research, Bangalore, India

© 2024 Elsevier Ltd. All rights reserved.

Introduction 485
Quantum statistics 485
Braiding and fusing of anyons 489
Anyons obey braid group statistics 489
Anyon composites or fusion rules 492
Non-abelian anyons 493
Generalities 493
Kitaev model in one dimension 494
Statistics of the Majorana modes 496
Conclusion 498
References 498
Further reading 498

Abstract

This is a pedagogical introduction to abelian and non-abelian anyons, where we discuss basic concepts in anyon physics, such as the idea of quantum statistics and introduce the idea of the braid group. We explain what is meant by braiding and fusing of anyons. We then briefly discuss non-abelian anyons where we use the one dimensional Kitaev model as a prototypical example to produce Majorana modes at the edge. We then explicitly show how braiding these Majoranas lead to rotations in the ground state manifold. We end with a brief discussion of the future prospects of the field.

Key points

- Phases of wavefunctions under adiabatic exchange
- Configuration space of a many-particle system
- Unitary representation for the group of inequivalent paths
- Braid group and Yang-Baxter relations
- Fusion rules
- Non-abelian anyons and ground state degeneracy
- Kitaev's one-dimensional model of Majoranas
- Statistics of Majorana modes

Introduction

What are anyons? While it is generally known that all particles in nature come in two classes, fermions and bosons, the name 'anyon' was coined by Wilczek (Wilczek, 1982) to indicate a new kind of particle that belongs to neither class. Fermions are particles with 1/2 integer spin obeying Fermi-Dirac statistics, which means that two or more identical fermions cannot co-exist at the same point in space or occupy the same energy level. Bosons, on the other hand, are integer spin particles obeying Bose-Einstein statistics, and can crowd together in the same space or occupy the same energy level. Unlike bosons and fermions, 'anyons' were initially just conjectured as theoretical possibilities (Leinaas and Myrrheim, 1977) as generalizations of what could happen when particles are intermediate between bosons and fermions, and obeyed a different kind of statistics. However, they shot into prominence in the 1980s when it was realized (Laughlin, 1983) that quasi-particle excitations in the fractional quantum Hall effect (Tsui et al., 1982) had fractional charges and most likely fractional statistics. The fractional charges were seen (De Picciotto et al., 1997) (in noise experiments in the 1990s, but it is only very recently that the fractional statistics obeyed by these quasi-particles have been convincingly seen (Nakamura et al., 2020).

Quantum statistics

Very naively, 'anyons' are particles obeying 'any' statistics. Clearly, this begs the question 'what are 'any' statistics? To answer this, we need to start with the notion of phases and statistics under exchange of identical or indistinguishable particles in quantum mechanics. The term 'exchange statistics' refers to the phase picked up by a wave-function when two identical particles are exchanged. But this definition is slightly ambiguous. Does statistics refer to the phase picked up by the wave-function when all

https://doi.org/10.1016/B978-0-323-90800-9.00033-0

the quantum numbers of the particles are exchanged (i.e., under permutation of the particles) or the actual phase that is obtained when two particles are adiabatically transported giving rise to the exchange? In three dimensions, these two definitions are equivalent but not in two dimensions. In quantum mechanics, we deal with interference of paths of particles and hence, it is the second definition which is more relevant, and we will show how it can be different from the first definition.

Recall that in quantum mechanics, the probability amplitude to go from one space-time point to another is given by

$$A = \sum_{paths} e^{i\mathcal{S}}, \tag{1}$$

where $\mathcal{S} = \int \mathcal{L}dt$ is the action for the particular trajectory or path. In other words, quantum mechanically, we need to include all possible paths between the initial and final points of the trajectory (See Fig. 1). But most of these paths will interfere destructively with each other and hence will not contribute to the probability amplitude. The only exception is the classical path and the paths close to it, which interfere constructively with the classical path i.e., the most important contribution will be from the classical path. So the amplitude for a system of two particles that moves from $(\mathbf{r}_1(t_1), \mathbf{r}_2(t_1))$to $(\mathbf{r}_1'(t_2), \mathbf{r}_2'(t_2))$ is given by

$$A = \sum_{paths} e^{i\int_{t_1}^{t_2} dt\mathcal{L}[\mathbf{r}_1(t),\ \mathbf{r}_2(t)]}. \tag{2}$$

Let us first consider the statistics under exchange of two particles in three dimensions. If the two particles are identical, then there are two classes of paths (see Fig. 2 where we have assumed that time runs vertically upwards). How do we see this? If we use the convention that we always refer to the position of the first particle first and the second particle second, then we see that the final configuration remains the same whether we have $(\mathbf{r}_1(t_2), \mathbf{r}_2(t_2))$ or$(\mathbf{r}_2(t_2), \mathbf{r}_1(t_2))$ because the two particles are identical. Even though the particles are exchanged in one path and not in the other, the final configuration is the same. Essentially, this means that the Hilbert space is halved as compared to the case of distinguishable particles. Another way of looking at this is to say that the configuration space (which is the name for the space of the states) has been split into topologically inequivalent sectors - one without exchange of the particles and one with exchange of the particles - which cannot be deformed into one another continuously.

To explain this further, and pictorially, let us think in terms of the center of mass $(\mathbf{R} = (\mathbf{r}_1 + \mathbf{r}_2)/2)$ and relative coordinates $(\mathbf{r} = \mathbf{r}_1 - \mathbf{r}_2)$. We note that the center of mass motion is the same for both the paths, but the relative coordinate changes for both the paths. Also, since the CM motion moves both the particles together, it is independent of any possible phase under exchange. So here, we will only focus on the relative coordinate $\mathbf{r}$. For convenience in visualizing the configuration space, let us keep $|\mathbf{r}|$ fixed and non-zero, i.e., the two particles do not intersect. Then, the vector r takes values on the surface of the sphere.

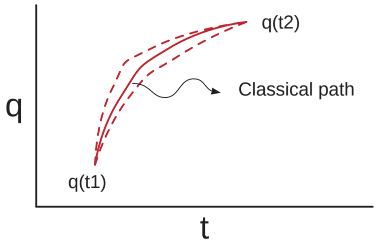

Fig. 1 Sum over paths from $q(t1)$ to $q(t2)$.

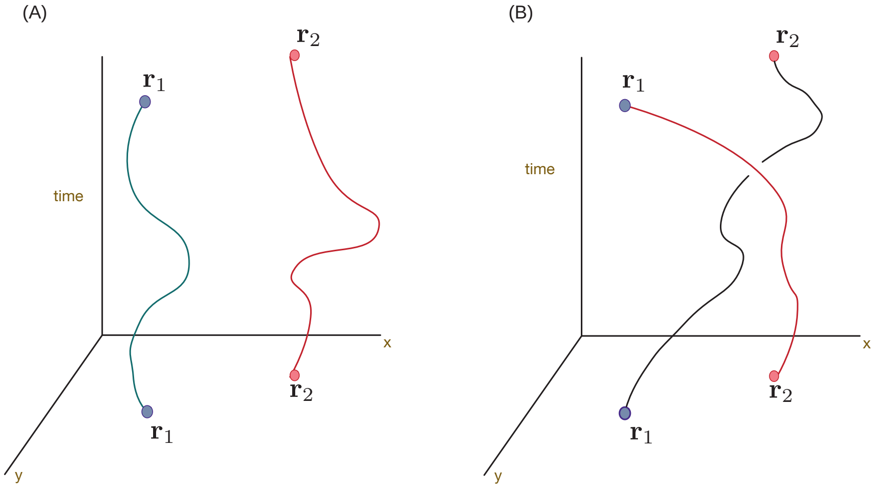

Fig. 2 Direct and exchange paths.

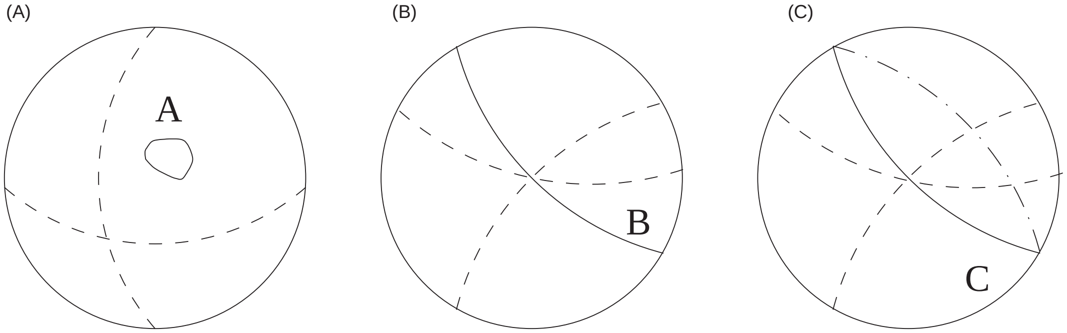

Fig. 3 Paths in three dimensional configuration space with fixed radius.

Now let us draw the paths in configuration space as shown in Fig. 3. It is clear that the paths can only move along the surface of the sphere as the two particles move, since $|\mathbf{r}|$ is fixed. But once they get back to their original positions or get exchanged, since they are indistinguishable, the path is closed. In other words, closed paths on the surface of the sphere are formed by the particles coming back to their original positions (no exchange) or going to the antipodal point ($\mathbf{r} \to -\mathbf{r}$ or getting exchanged). But if we exchange the particles once again, then r comes back to itself, after having gone around the sphere once. In terms of diagrams, this is shown in Fig. 3C. It can also retrace its path, but that will be trivially equivalent to no exchange like in Fig. 3A. Since we have eliminated coincident points, the wave-function is non-singular and well-defined at all points in the configuration space, and consequently on the surface of the sphere. So the phase picked up by the wave-function is also well-defined and does not change under continuous deformations of the path. Let us consider the possible phases of the wave-function when the motion of the particles is along each of the three paths, – A (no exchange), B (single exchange) and C (two exchanges) - depicted in Figs. 3A–C. Path A is a closed path which does not involve any exchange and can clearly be shrunk to a point. Hence, the wave-function cannot pick up any phase other than unity. Path B involves the exchange of the two particles and goes from a point on the sphere to its diametrically opposite point. Since the two end points are fixed, this path cannot be shrunk to a single point. So this exchange can have a non-trivial phase in the wave-function. However, path C which forms a closed loop on the surface and involves two exchanges can be continuously shrunk to a point by imagining the path to be a physical string looped around a sphere. So this again cannot pick up any phase. Let η be the phase picked up under a single exchange. Since two exchanges are equivalent to no exchange, $\eta^2 = +1 \Rightarrow \eta = \pm 1$. Hence, the only statistics possible in three dimensions are Fermi statistics or Bose statistics.

With slightly more mathematical rigor, one can say that the configuration space of relative coordinates is given by $(\mathbb{R}_3 \; -origin\,)/\mathbb{S}_2$. Here $\mathbb{R}_3$ is just the three dimensional Euclidean space spanned by the relative coordinate $\mathbf{r}$. We subtract out the origin because we have assumed that paths do not cross (which is true for all particles other than bosons, because of hard core repulsion and for bosons, it is irrelevant whether or not they cross, because the exchange phase is always unity). The division by $\mathbb{S}_2$ where $\mathbb{S}_2$ is the symmetric group or permutation group is because of the identification of $\mathbf{r}$ with $-\mathbf{r}$, which, in turn, is because the particles are indistinguishable. To study the phase picked up by the wave-function of a particle as it goes around another particle, we need to classify all paths in this configuration space. The claim, from the pictorial analysis above, is that there are just two classes of paths. Mathematically, this is expressed in terms of the first homotopy group Π_1 of the space, which is the group of inequivalent paths (paths not deformable to each other), passing through a given point in the space, with group multiplication being defined as traversing paths in succession and group inverse as traversing a path in the opposite direction. Thus

$$\Pi_1(\mathbb{R}_3 - origin\,)/\mathbb{Z}_2) = \Pi_1(\mathbb{RP}_2) = \mathbb{Z}_2 \tag{3}$$

where $\mathbb{RP}_2$ stands for real projective space and is the notation for the surface of the sphere with diametrically opposite points identified and $\mathbb{Z}_2 = (1, -1)$ is a group of just two elements.

In terms of the path integral, the amplitude (for 2 particles) can now be written as

$$A = \sum_{\text{regular paths}} e^{i\int_{t_1}^{t_2} dt\mathcal{L}[\mathbf{r}_1(t),\, \mathbf{r}_2(t)]} + e^{i\phi} \sum_{\text{exchange paths}} e^{i\int_{t_1}^{t_2} dt\mathcal{L}[\mathbf{r}_1(t),\, \mathbf{r}_2(t)]} \tag{4}$$

where we have introduced a phase between the regular and exchange paths. But since exchanging twice corresponds to a regular path, $e^{2i\phi} = 1$, with $\phi = 0$ corresponding to bosons and $\phi = \pi$ corresponding to fermions. This can now be easily generalized to N particles with

$$A = \sum_{g \in G} \rho(g) \sum_{\text{paths}} e^{i\int_{t_1}^{t_2} dt\mathcal{L}[\mathbf{r}_1(t),\, \mathbf{r}_2(t)]} \tag{5}$$

Here G is the fundamental group of paths, which, as explained above is just the group of inequivalent paths, which (in 3 + 1 dimensions) is just $\mathbb{S}_2$ for 2 particles, and generalizes to $\mathbb{S}_N$ for N particles. $\rho(g)$ is a unitary representation of G. It is easy to check that there are only two possible one-dimensional representations of G in 3 + 1 dimensions either $\rho(g) = 1$ for all g (bosons) or $\rho(g) = +1/-1$ for even or odd number of exchanges of the N particles (fermions). The story changes if we allow for higher dimensional representations of $\mathbb{S}_N$, but before we do that, let us see what happens in 2 + 1 dimensions.

What changes in two dimensions? The key point is that the topology of the configuration space is now different. In two spatial dimensions, the configuration space of the relative coordinates is given by $(\mathbb{R}_2 - origin\ )/\mathbb{S}_2$. Just as before, for ease of visualization, we can keep the magnitude of the relative coordinate fixed, so that configuration space can be represented by a circle, and since the particles are indistinguishable, diametrically opposite points are identified (see Figs. 4A–C). Here, however, several closed paths are possible. The path A that involves no exchanges can obviously be shrunk to a point, since it only moves along the circle and back. But path B that exchanges the two particles is non-contractible since the end-points are fixed. But even path C, where both the solid and dashed line are followed in the clock-wise direction (or anti-clockwise direction) cannot be contracted to a point. This is easily understood by visualizing the paths as physical strings looping around a cylinder. Thus, if η is the phase under single exchange, η^2 is the phase under two exchanges, η^3 is the phase under three exchanges and so on. All we can say is that since the modulus of the wave-function remains unchanged under exchange, η has to be a phase $-\eta = e^{i\theta}$ This explains why we can get 'any' statistics in two dimensions.

The distinction between the paths in two and three dimensions can also be seen as follows. In three dimensions, the loop that is formed by taking a particle all around another particle (two exchanges) can be lifted off the plane and shrunk to a point as shown in Fig. 5. This is not possible if the motion is restricted to a plane, as long as we disallow configurations where two particles are at the same point (removal of the origin).

The mathematical crux of the distinction between configuration spaces in two and three dimensions, is that the removal of the origin in two dimensional space, makes the space multiply connected (unlike in three dimensional space, where removal of the origin keeps it singly connected). So it is possible to define paths that wind around the origin. Mathematically, we can say that

$$\Pi_1((\mathbb{R}_2 - origin\ )/\mathbb{S}_2) = \Pi_1(\mathbb{RP}_1) = \mathbb{Z} \tag{6}$$

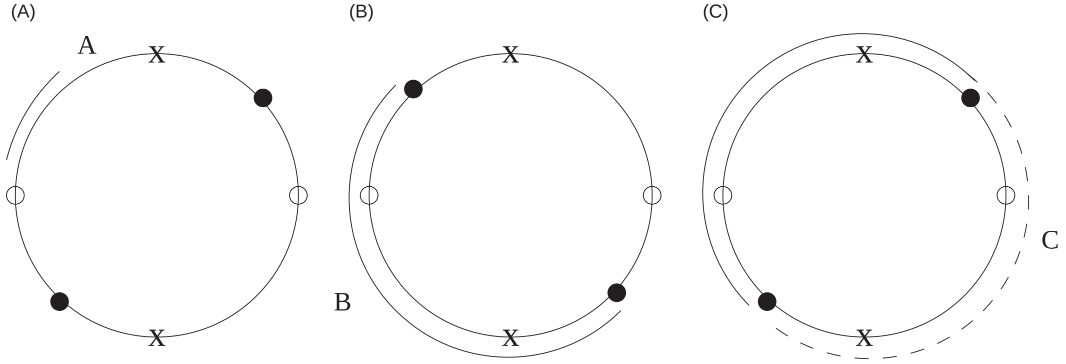

Fig. 4 Paths in two dimensional configuration space with fixed radius.

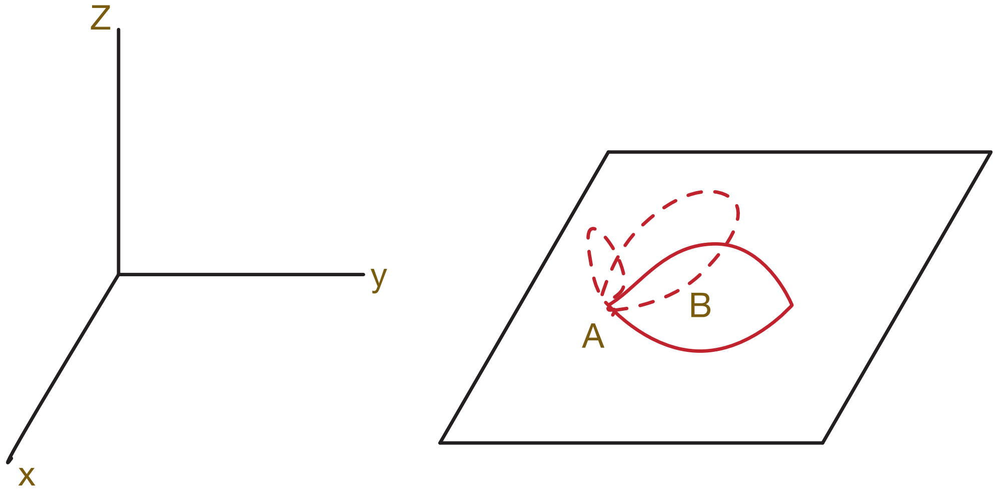

Fig. 5 Path of A around B being lifted off the surface and shrunk to a point.

where $\mathbb{Z}$ is the group of integers under addition. $\mathbb{RP}_1$ is just the notation for the circumference of a circle with diametrically opposite points identified. The different paths are labelled by integer winding numbers.

So in terms of path integrals, we now see that paths starting and ending at the same positions (up to exchanges due to indistinguishability) can be divided into an infinite number of classes, all distinct. So the path integral for the total amplitude is now given by

$$A = \sum_{g\in G}\rho(g)\sum_{paths} e^{i\int_{t_1}^{t_2} dt\mathcal{L}[\mathbf{r}_1(t),\ \mathbf{r}_2(t)]} \tag{7}$$

where G now is the group of inequivalent paths in 2 + 1 dimensions (called the braid group $\mathbb{B}_2$) and $\rho(g)$ now gives the possible unitary representations of $\mathbb{B}_2$ in 2 + 1 dimensions. Unlike in 3 + 1 dimensions, we can now get a different phase each time we exchange the particles, so that

$$A = \sum_{directpaths} e^{iS} + e^{i\phi}\sum_{sin\,gleexchange} e^{iS} + e^{2i\phi}\sum_{two\,exchangers} e^{iS} + \ldots \tag{8}$$

Here $\phi = 0, \pi$ give the usual bosons and fermions, but since in general, $e^{in\phi} \neq 1$ for any n, ϕ can be anything and as we said earlier, 'any' statistics of fractional statistics are possible in two dimensions. It is now easy to see that unlike for fermions and bosons, generalizing this to N particles is not trivial. At each time slice after the exchange of any two particles, the configuration depends on whether the particles have been exchanged in a clock-wise or counter clock-wise direction, or more generally, on the winding number of the exchange. So the entire history of the exchanges of every pair becomes relevant, and the problem of even free anyons becomes as complicated as the problem of particles, all of which are strongly interacting with one another.

Braiding and fusing of anyons

Anyons obey braid group statistics

The distinction between the phase of the wave-function when the quantum numbers of the particles are exchanged and the phase obtained under adiabatic transport of particles should now be clear. Under the former definition, the η^2 after two exchanges is always unity, whereas the phase under the latter definition has many more possibilities at least in two dimensions. Mathematically, the first definition classifies particle under the permutation group $\mathbb{S}_N$, whereas the second one classifies particles under the braid group$\mathbb{B}_N$. The permutation group $\mathbb{S}_N$ is the group formed by all possible permutations of N objects with group multiplication defined as successive permutations and group inverse as undoing the permutation. It is clear that permuting two objects twice brings the system back to the original configuration. Thus particles that transform as representations of the permutation group can only be bosons or fermions.

On the other hand, when we adiabatically exchange two particles, we can visualize the process as paths in space-time with time being the vertical axis and space being the horizontal axis as shown in Fig. 2. The particles can circle around each other and form closed paths by coming back to their original positions (up to permutations of the positions). The adiabatic exchange of particles classifies particles under the braid group. As we saw earlier, even under adiabatic exchange, in three spatial dimensions, we only have fermions or bosons, whereas in two dimensions, there are many other possibilities. Formally, the braid group $\mathbb{B}_N$ is the group of inequivalent paths that occur when adiabatically transporting N particles. Since they represent a configuration of N particles, at some particular time (say $t = 0$), evolving to a configuration of N particles at some later time $t = T$, the world lines cannot cross each other or form knots around each other or loop back. At each time, we want to have only N particles. Each history or set of trajectories of the N particles becomes a braid. For example, in Fig. 6, we show an example of some elements of the braid group $\mathbb{B}_4$, which is the braid group of 4 particles. (We have restricted the particles to be on a single line for ease of depiction). Exchanges of neighboring particles (by some counting rule, since the particles are in two dimensional space) form the generators of the group. For instance, the generators of the group $\mathbb{B}_4$ are given in Fig. 7 and are denoted as σ_j, $j = 1, 2, 3$. $\sigma_j$describes exchange of j^{th} particle with $(j+1)^{th}$ particle in a counter-clockwise direction (by definition), so that the clockwise exchange is denoted by $(\sigma_j)^{-1}$ The identity element is given by σ_0 where there is no exchange, and group inverse by the clockwise exchange $(\sigma_j)^{-1}$ as shown in Fig. 8. Group multiplication

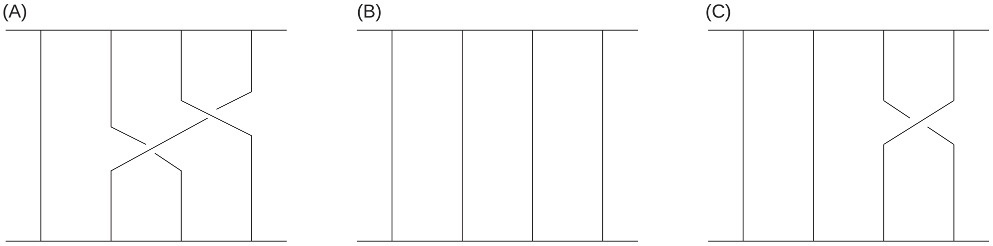

Fig. 6 Elements of the braid group $\mathbb{B}_4$.

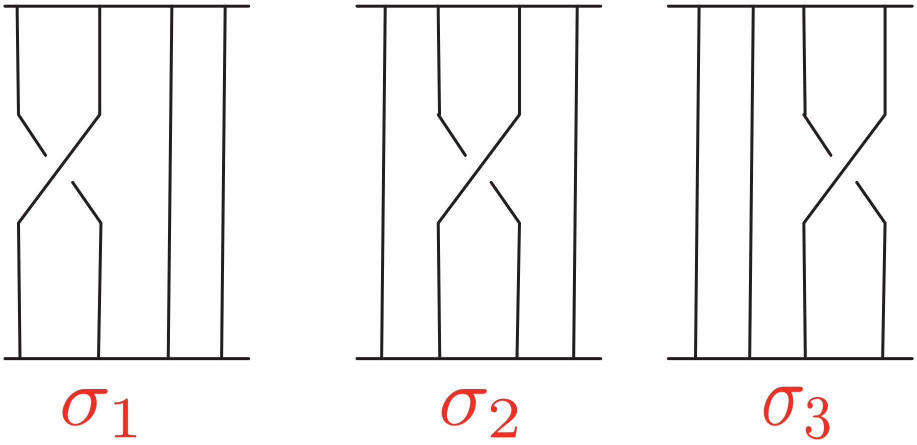

Fig. 7 The three generators of the braid group $\mathbb{B}_4$.

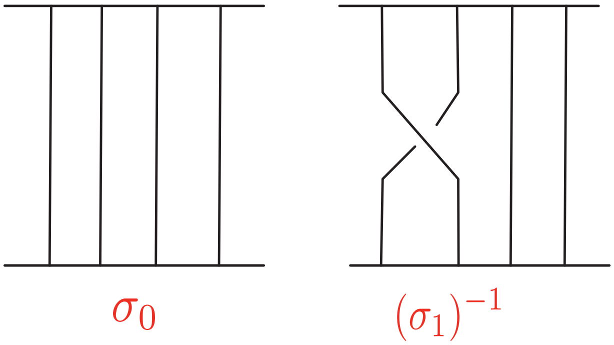

Fig. 8 The identity and the inverse of the generator σ_1.

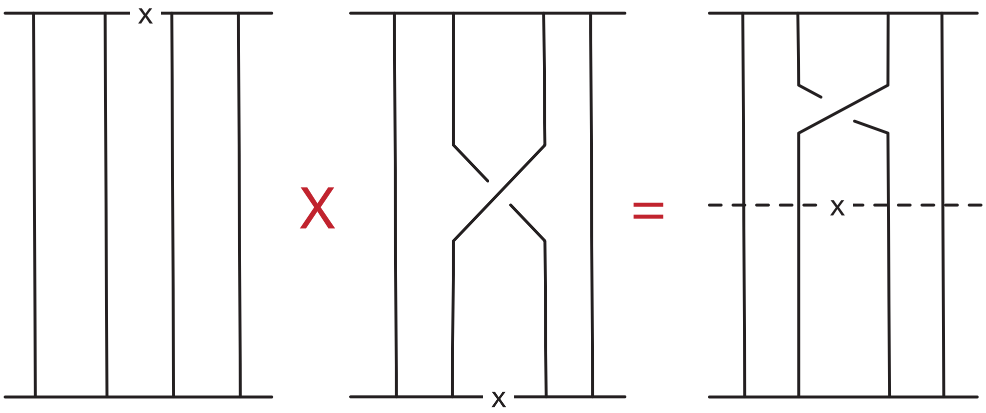

Fig. 9 Group multiplication.

is defined as following one trajectory by another in time as shown in Fig. 9. Note that we have put crosses on the time-lines which are identified (are at equal times) in the figure. It is now easy to check that $(\sigma_j)(\sigma_j)^{-1} = \sigma_0$ as shown in Fig. 10 (without the crosses). It is also easy to see that $(\sigma_1)^n \neq \sigma_0$ for any n, which is the reason that 'any' statistics are allowed in two dimensions. (See Fig. 11).

We will end this subsection by mentioning the two defining relations satisfied by the generators of the braid group.

$$\sigma_i\sigma_j = \sigma_j\sigma_i, \ |i-j| \geq 2$$

$$\sigma_j\sigma_{j+1}\sigma_j = \sigma_{j+1}\sigma_j\sigma_{j+1} \tag{9}$$

The second one is called the Yang-Baxter relation. Both these relations can be easily checked pictorially (as we show in Fig. 12 for the generators of $\mathbb{B}_4$).

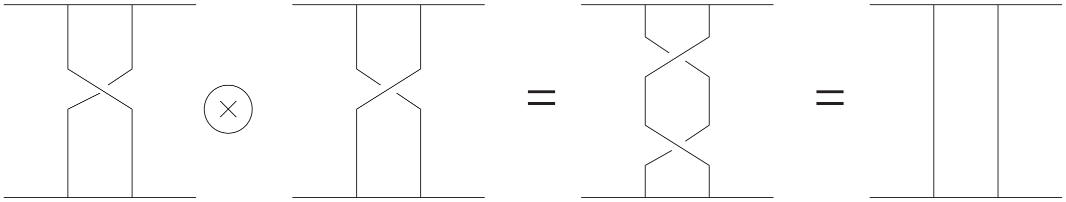

Fig. 10 Product of σ_1 and $(\sigma_1)^{-1}$ giving rise to identity.

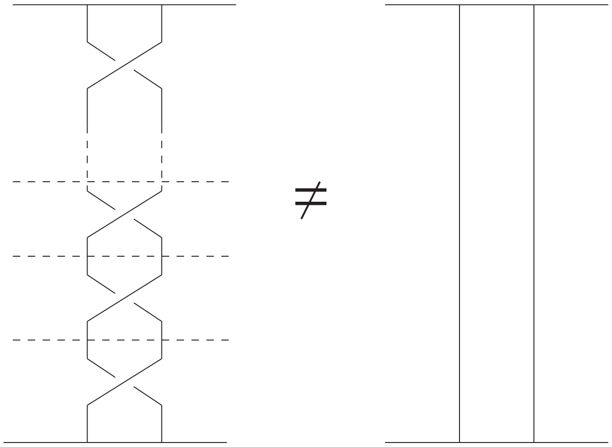

Fig. 11 $(\sigma_1)^n \neq \sigma_0$.

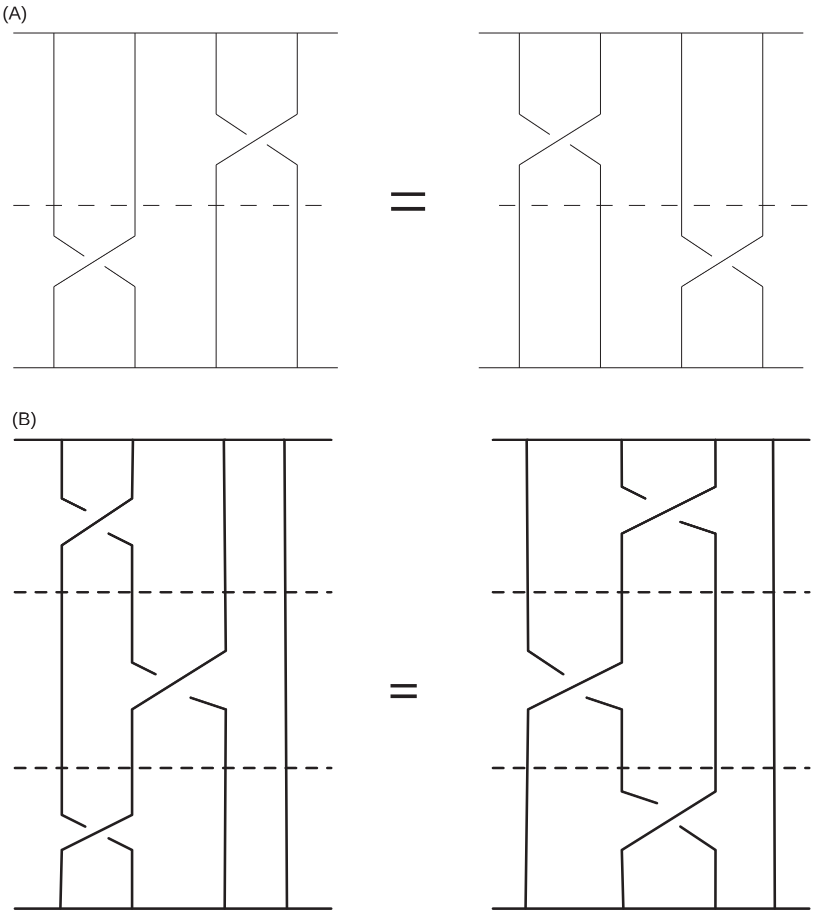

Fig. 12 Yang-Baxter relations.

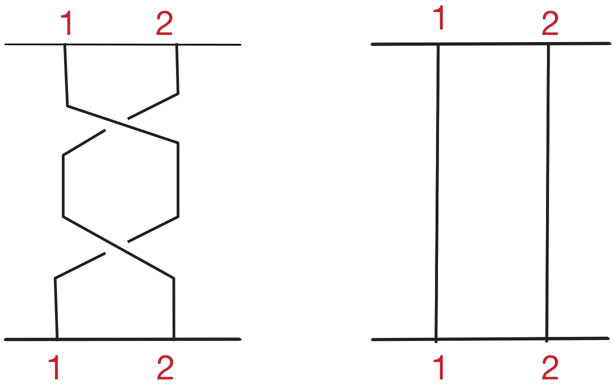

Fig. 13 Different elements of the braid group, but same element of the permutation group.

It should be clear by now that the braid group leads to a much finer classification than the permutation group. For instance, the two elements shown in Fig. 13 are different elements of the braid group, but the same element of the permutation group. So the quantum theory of anyons has the quantum states of the anyons transforming as unitary representations of the braid group. Abelian anyons form one-dimensional representations of the braid group. There are an infinite number of such representations, because under exchange, the phase that is picked up is $e^{i\theta}$ and θ can take any value $\theta = 0$ and $\theta = \pi$ represent bosons and fermions respectively. We will discuss non-abelian representations in the last section.

Note that if we do want to understand adiabatic exchange of particles in the Hamiltonian formulation without invoking path integral ideas, we need to pin down the particles by using a confining potential - i.e., by putting them in a box-.

$$H = \sum_i \frac{\mathbf{p}_i^2}{2m} + \sum_i V_{\text{box}}(\mathbf{x}_i - \mathbf{R}_i) \tag{10}$$

The particles can now be moved around by changing $\mathbf{R}_i$ as a function of time. Since the particles are identical, exchanges are equivalent to closed paths, and do not depend on the geometry of the paths $\mathbf{R}_i(t)$ involved. So the statistics of the particles under exchange can be found by computing the Berry phase when the particles are exchanged. However, here, we shall basically stick to the path integral formalism.

In recent times, the focus on the dimensionality of space-time has been reduced Instead, it has been realized that in any dimension, as long as constraints can be imposed to make every exchange of the paths in configuration space well-defined (as automatically happens in two dimensions), anyons are possible. The important point is that the particles transform as representations of the braid group.

Anyon composites or fusion rules

Before we go on to non-abelian anyons, we need to introduce one more concept and that is the idea of what happens when we bring two anyons close together. Does this form a new kind of composite particle? We know that a composite particle made of two bosons will still form a boson, but a composite particle made of two fermions will obey bosonic statistics and not fermionic statistics. What happens with anyons?

To understand this, the easiest way is to think of a physical model for the anyon. We imagine the anyon to be a charge bound to a very thin solenoid or flux-tube carrying a flux ϕ. Now we consider taking one such bound charge-flux particle around another. Due to the Aharonov-Bohm effect, (Aharonov and Bohm, 1959) we know that the phase acquired by the charge encircling a solenoid is given by $e^{iq\phi/\hbar}$ Equivalently, by the Aharonov-Casher effect (Aharonov and Casher, 1984), we know that the flux ϕ going around a charge q will also acquire a phase $e^{iq\phi/\hbar}$.So taking one-charge flux composite completely around the other gives rise to a phase of $e^{2iq\phi/\hbar}$ But since taking one particle completely around another is equivalent to two exchanges, we see that the phase acquired under an exchange of the charge-flux composite is $e^{iq\phi/\hbar}$ So the anyon parameter $\theta = q\phi/\hbar$ and is zero for bosons and π for fermions.

Now, we can try and see what happens when we bring two anyons together. The composite particle will now have a charge of $2q$ and a flux of 2ϕ. So the appropriate anyon that is formed will have a statistics parameter given by $4q\phi/\hbar$ since both the flux and the charge have been doubled. This is now a new or different kind of anyon with the sum of both the fluxes and the charges. This idea of bringing together anyons to form a new kind of particle is called fusion. Note that it is not really necessary for the two anyons to actually form a bound state. If they are brought close together and form a 'cluster,' then the cluster behaves like a single particle.

Non-abelian anyons

Generalities

Now let us consider higher dimensional representations of the braid group$\mathbb{B}_N$. Higher dimensional representations can occur typically when we have degeneracies in the system. Let us consider a set of M degenerate (orthonormal) states of N particles at fixed positions, $\psi_\alpha(\mathbf{r}_1, \ldots \mathbf{r}_N)$. In this basis, when we adiabatically exchange the position of two particles at $\mathbf{r}_1$ and $\mathbf{r}_2$, the original state gets unitarily rotated to another state in the same subspace. In other words,

$$\psi_\alpha(\mathbf{r}_1, \mathbf{r}_2, \ldots \mathbf{r}_N) \rightarrow U(\sigma_1)\psi_\alpha(\mathbf{r}_2, \mathbf{r}_1, \ldots \mathbf{r}_N) \tag{11}$$

where $U(\sigma_1)$ is an $M \times M$ unitary matrix acting in the space of degenerate states. U depends on the braiding operator σ_1 which exchanges particles 1 and 2. Similarly, we can get

$$\psi_\alpha(\mathbf{r}_j, \mathbf{r}_{j+1}) \rightarrow U(\sigma_j)\psi_\alpha(\mathbf{r}_{j+1}, \mathbf{r}_j) \tag{12}$$

for any other exchange of a pair of particles. Since, in general the $U(\sigma_j)$ for different values of j do not commute with each other, the particles obviously obey non-abelian braid group statistics. Clearly, we need at least a degeneracy of 2 to get non-abelian braiding; else, the U matrices are merely phases which commute with one other.

Non-abelian anyons were first introduced in the context of conformal field theory and the fractional quantum Hall effect (Moore and Read, 1991). The relevance to quantum computation comes from the fact that not only does braiding cause rotations in the degenerate subspace, the only way to go cause rotations in this subspace (at low enough energies, so that we cannot access any other high energy state) is via braiding. So the different states in the subspace are protected from local perturbations (as long as they do not have matrix elements within the degenerate subspace). You can go to another state in the system, only by braiding which is a non-local process, sensitive only to the topology of the trajectory and not to local geometry or dynamics. Hence, the system is decoherence free.

So how does one use non-abelian anyons for quantum computation? We first need to construct the qubit. Here, these are just the set of degenerate states - 2 for qubits, 3 for qutrits, etc. This is initialized by preparing it in a particular way, so that we know the initial state. We then perform unitary operations on the state by exchanging particles in some specified way. The resulting evolution is dependent only on the braiding and not on how the exchanges were carried out in detail. Then one can measure the state of the qubit at the end of the operation. We also do not need to worry about whether or not the particles were brought back to the exact positions, because often the initialization and measurement techniques involve creating, separating and bringing together quasi-particles, so that there are no open braids and the full process is completely topological. This is why generically, topological quantum computation using non-abelian anyons is called fault-tolerant.

With this motivation, let us continue with our study of non-abelian anyons. We first need a list of particles with their charges. Note that here by charges, we mean topological charges. In a condensed matter system, one can have quasi-particle excitations which are either local or which are topological. A simple example is that of spin flip excitations in an Ising model in one dimension as shown in Figs.14A and B. A single spin-flip (or even a few spin flips) is a local excitation and is equivalent to the identity as far as particle type is considered. But a domain wall is a topological excitation that is protected by the boundary conditions and cannot be removed by local perturbations. As long as the edge spins are kept fixed and opposite, there will be at least one domain wall or one topological charge in the system. In this example, a local excitation (where the edge spins are kept the same) can be considered as two domain walls. So here one can only get topological charges 0 or 1, because any two topological charges are considered equivalent if they differ by local charges (obtained by applying local operators). But more generally, even the number of types of topological charges that you can get in a theory is a topological property and is related to the number of degenerate states. (In the

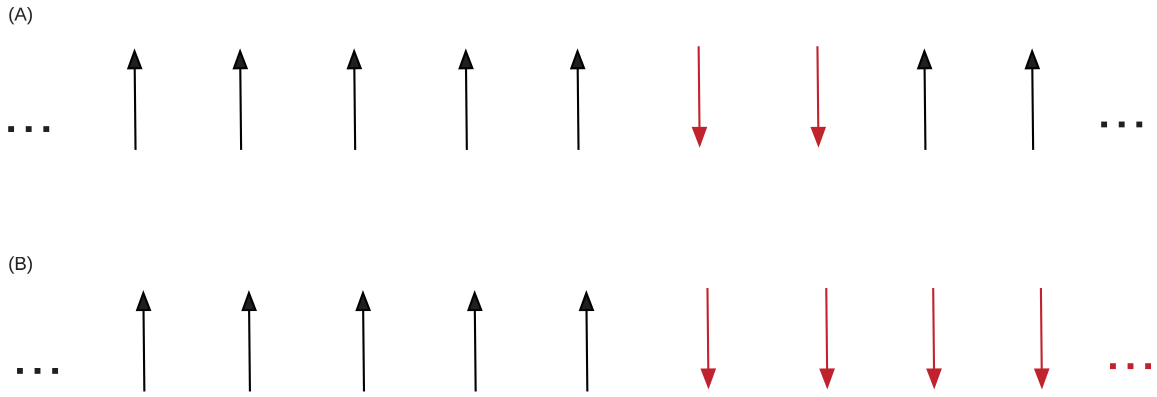

Fig. 14 The first denotes a local excitation, since it can be removed by flipping two spins locally, whereas the second one is a topological quasi-particle since it is protected by the boundary conditions which are fixed.

example, we have considered here, with a domain wall, the assumption is that, in the large system limit, the states with and without domain walls are approximately degenerate).

So to write down a theory of non-abelian anyons, the ingredients we require are the following (Preskill, 2004)

(a) a list of the topological charges
(b) fusion rules for fusing the topological charges (and its inverse, the splitting rules)
(c) braiding rules for exchanging two particles

So if we list the topological particles in our system as a, b, c . . ., then the fusion rules are given by

$$a \times b = \sum_c N_{ab}^c c \tag{13}$$

where $N_{ab}^c \geq 1$ This equation simply means that if $N_{ab}^c = 0$, then the particle c is not obtained and if $N_{ab}^c = 1$, then the particle c is obtained as a fusion product and if $N_{ab}^c > 1$, then c can be obtained in N_{ab}^c ways. Here, a, b, c are just labels of the different kinds of particles. For abelian anyons, an anyon with statistics parameter α_1 will fuse with an anyon with statistics parameter α_2 to yield a specific anyon with statistics parameter α_3 and ${N_{\alpha_1 \alpha_2}}^{\alpha_3} = 1$ and is otherwise zero. But this is not true for non-abelian anyons. The fusing of two anyons could lead to different types of particles with different probabilities. In that sense, fusion of particles is like a measurement. Given two abelian anyons a and b, their fusion is well-defined and leads to a unique answer. But for non-abelian anyons, it does not lead to a single answer. The integers N_{ab}^c define the probabilities of the outcome. The simplest non-abelian model will have $N_{ab}^c \neq 0$ for at least two distinct values of c. The Hilbert space of two (or more) dimensions formed from these distinct outcomes of fusing two particles is known as the topological Hilbert space of the pair of non-abelian anyons.

Now, let us consider what happens when we have many non-abelian anyons. For abelian anyons, each time you bring in a new particle, the fusion rules give you only one possible outcome. But for non-abelian anyons, since even two anyons can have more than one outcome, a third anyon can fuse with either of the outcomes and again give rise to more possible outcomes. So one can get many fusion paths, since fusion is not unique. Since sometimes, different paths can lead to the same outcomes, there are consistency conditions that need to be satisfied called pentagon equations. Once we also include braiding matrices in the game, there are also consistency conditions called hexagon equations which need to be satisfied.

However, instead of going further ahead with the abstract analysis, we will now change gears and study a concrete model with non-abelian excitations. The is the Kitaev one-dimensional toy model with unpaired Majorana fermions. We will explicitly show that these Majorana fermions obey non-abelian statistics under exchange.

Kitaev model in one dimension

The Hamiltonian for the Kitaev model in one dimension is given by (Kitaev, 2001)

$$H = -\mu \sum_{x=1}^{N} n_x - \sum_{x=1}^{N-1} \left(t c_x^{\dagger} c_{x+1} + \Delta c_x c_{x+1} + h.c. \right) \tag{14}$$

where c_x represents spinless fermions on site x, t is the amplitude of hopping to nearest neighbor sites, and Δ is the superconducting parameter and denotes p-wave pairing - p wave because the electrons are of the same kind (spinless or equivalently same projection of spin) - on nearest neighbor sites. μ is the chemical potential and $n_x = c_x^{\dagger} c_x$ is the density operator, so that $N = \sum_x n_x$. Since by a redefinition of the phase of the fermions, any phase in the superconducting order parameter can be absorbed, without loss of generality, we can take Δ to be real and positive.

Now, let us rewrite the Hamiltonian in terms of new operators called Majorana operators.

$$\begin{aligned} c_x &= \frac{1}{2} \left(\gamma_{A,x} - i \gamma_{B,x} \right) \\ c_x^{\dagger} &= \frac{1}{2} \left(\gamma_{A,x} - i \gamma_{B,x} \right) \end{aligned} \tag{15}$$

This implies that $\gamma_{A,\ x} = c_x + c_x^{\dagger}$ and $\gamma_{B,\ x} = i(c_x^{\dagger} - c_x)$ are hermitean (self-conjugate) operators. This is the definition of Majorana operators.

Now, let us look at some properties of these Majorana modes. We can check that they are fermions, in the sense that they anti-commute. More precisely, they satisfy the algebra given by

$$\left\{ \gamma_a, \gamma_b \right\} = \delta_{ab,}\ \gamma_a^2 = \gamma_b^2 = 1, \tag{16}$$

whereas genuine fermions satisfy

$$\left\{ c_a, c_b^{\dagger} \right\} = \delta_{ab,} \{ c_a,\ c_b \} = 0,\ c_a^2 = 0. \tag{17}$$

Pairs of Majorana fermions (γ_A and γ_B) can be combined to form genuine fermions which can form a single 2 level system, depending on whether the fermion state is occupied or unoccupied. The next step is to consider what happens when we have 2 N Majorana fermions. We can pair them up to make N ordinary fermions-

$$q_x = \frac{1}{2}\left(\gamma_{A,x} + i\gamma_{B,x}\right), \quad q_x^\dagger = \frac{1}{2}\left(\gamma_{A,x} - i\gamma_{B,x}\right) \tag{18}$$

(the same equations used to split the fermions into Majorana modes given in Eq. 15) with the number operators at each site x given as $N_x = q_x^\dagger q_x = 0,\ 1$. This gives a 2^N dimensional Fock space.

Why is it interesting to rewrite fermions in terms of pairs of Majorana fermions? Naively, this seems to be something which can always be done, and does not lead to anything new. But if a pair of Majoranas can be spatially separated, then the fermion made from them is delocalized. It is hence, protected from local changes that affect only one of them and hence protected from decoherence. This is why Majorana modes are expected to be relevant in quantum computation.

Now, let us get back to the Kitaev model. Let us first rewrite the Hamiltonian in terms of the Majorana operators to get

$$H = -\frac{\mu}{2}\sum_{N}^{x=1}\left(1 - i\gamma_{B,x}\gamma_{A,x}\right) + \sum_{N-1}^{x=1}\left[1\frac{t}{2}\left(\gamma_{B,x}\gamma_{A,x+1} - \gamma_{A,x}\gamma_{B,x+1}\right) + i\frac{\Delta}{2}\left(\gamma_{A,x}\gamma_{B,x+1} + \gamma_{B,x}\gamma_{A,x+1}\right)\right] \tag{19}$$

To understand the physics in a simple way, let us now consider two simple limits, where the Hamiltonian becomes particularly simple. First, consider the case when $\mu = 0$ and $t = \Delta$. Here, we get

$$H = -it\sum_{x=1}^{N-1}\gamma_{B,x}\gamma_{A,x+1} \tag{20}$$

In the other limit, we take $\mu < 0$ and $t = \Delta = 0$ and get

$$H = -\frac{\mu}{2}\sum_{x=1}^{N}\left(1 - i\gamma_{B,x}\gamma_{A,x}\right) \tag{21}$$

What do these two limits mean?

We first analyze the second case. Here, the fermion at each site is simply broken up into two Majorana fermions and the μ term simply couples them as shown in Fig. 15. In this case, there is a unique ground state corresponding to the vacuum state with no fermions. Adding a fermion to the system costs an energy μ, so the system is gapped.

The first limit, on the other hand, couples Majorana modes at adjacent sites. In terms of new fermions $d_x = (\gamma_{B,\,x} + i\gamma_{A,\,x+1})/2$, the Hamiltonian can be rewritten as

$$H = 2t\sum_{N-1}^{x=1} d_x^\dagger d_x \tag{22}$$

This clearly shows that the system has a gap and the cost of adding a fermion to the system is 2 t. But the interesting point to note is that the Hamiltonian is completely independent of the two Majorana modes $\gamma_{A,\,1}$ and $\gamma_{B,\,N}$ as shown in Fig. 16, at the two ends of the wire. These two Majorana modes can be combined to form a fermion as

$$c_M = \frac{1}{2}\left(\gamma_{A,1} + i\gamma_{B,N}\right) \tag{23}$$

But this is a highly non-local fermion, since $\gamma_{A,\,1}$ and $\gamma_{B,\,N}$ are localized at opposite ends of the chain. Moreover, since this fermion is absent from the Hamiltonian, the energy is the same whether or not this fermion state is occupied. So the ground state is degenerate. If $|0>$ is the ground state, then $c_M^\dagger\,|\,0>$ is also a ground state. Note that $\gamma_a^2 = 1$ implies that there is no Pauli principle for the

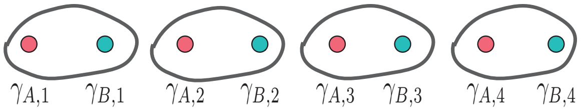

Fig. 15 Here, the bonds are between Majorana modes at the same site. The ground state is unique and the end Majorana modes do not play any special role.

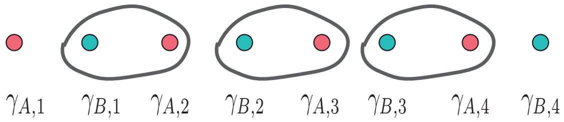

Fig. 16 Here, the bonds are between Majorana modes on adjacent sites. There are unpaired Majorana modes at the two ends. The ground state is doubly degenerate depending on whether the fermion state formed from the unpaired Majorana modes is occupied or unoccupied.

Majorana modes - in fact, as we saw earlier, there is no notion of occupation number for a single Majorana mode. Number operators only exist for fermions formed from pairs of Majorana modes. Depending on the occupation or not of the zero energy mode of the fermion - i.e., of C_M - there exists an odd or even number of fermions in the ground state referred to as 'fermion parity'. To change the parity, electrons have to be added or removed from the superconductor. This is unlike normal gapped superconductors, (e.g. the second limit), which have a unique ground state with even fermion parity.

In the more general case (Leinjse and Flensberg, 2012), when μ, t and Δ are non-zero, the general features of the topologically trivial case with a unique ground state, and the topologically non-trivial case with the Majorana edge states persist. Why do we call them topologically trivial and non trivial in the two cases? Well, in the trivial case there are no edge states and in the non-trivial case, there are edge states. In terms of the bulk properties of the Kitaev chain, one can find the bulk quasiparticle spectrum by going to momentum space (since the system is translationally invariant) and rewriting the Hamiltonian in Eq. (14) as

$$H = \sum_{k\in BZ} \zeta_k c_k^\dagger c_k + \sum_{k\in BZ}\left(e^{ik} c_k^\dagger c_{-k}^\dagger + e^{-ik} c_k c_{-k}\right) \tag{24}$$

$$= \sum_{k=0}^{\pi} \zeta_k \left(c_k^\dagger c_k + c_{-k}^\dagger c_{-k}\right) + \sum_{\pi}^{k=0}\left(\Delta_k c_k^\dagger c_{-k}^\dagger + \Delta_k^* c_{-k} c_k\right) \tag{25}$$

using $c_x = \frac{1}{\sqrt{N}}\sum_k e^{ikx} c_k$ and $c_x = c_{x+N}$, $\zeta_k = -2t\cos k - \mu$ and $\Delta_k = 2i\Delta \sin k$. This can be rewritten as

$$H = \sum_{k=0}^{\pi} \left(c_k^\dagger c_{-k}\right) \begin{pmatrix} \zeta_k & \Delta_k^* \\ \Delta_k & -\zeta_k \end{pmatrix} \begin{pmatrix} c_k \\ c_{-k}^\dagger \end{pmatrix} \tag{26}$$

We then introduce the Boguliobov-de Gennes quasiparticles $\eta_k = \cos\frac{\theta_k}{2} c_k + i\sin\frac{\theta_k}{2} c_{-k}^\dagger$ with $\cos\theta_k = (-\mu - 2t\cos k)/E_k$ and $\sin\theta_k = 2\Delta\sin k/E_k$ to obtain

$$H = \sum_{k\in BZ} E_k \eta_k^\dagger \eta_k \tag{27}$$

with $E_k = \sqrt{\left(\zeta_k^2 + 4\Delta^2 \sin k^2\right)}$.

Hence, the model is gapped, except when $\mu = -2t$ when $k = k_F = 0$ or when $\mu = +2t$ when $k = k_F = \pm\pi$. The lines $\mu = \pm 2t$ are where the system becomes gapless. For$\mu < 2t$, the system is topological and is adiabatically connected to the first limit with Majorana edge states. For $\mu < 2t$, the system is topologically trivial and is adiabatically connected to the second limit with no edge states. How do we see this? At first sight, it looks like both sides of the band-closing point at $\mu = 2t$ are identical. However, if we compute the bulk topological invariant, (which is beyond the scope of this article), for the system without boundaries (i.e., with periodic boundary conditions), and then cut the system to see what happens at the boundaries, then for $\mu = 2t$, we will find that the topological invariant has a certain value and no edge states when it is cut. On the other hand, when $\mu < 2t$, we will find that the topological invariant has a different value and that there are zero energy edge states when the system is cut. This shows us that there is a bulk topological invariant which distinguishes between topologically trivial and topologically non-trivial ground states. This analysis, in fact, also shows that there exists a bulk-boundary correspondence.

Statistics of the Majorana modes

Now, let us consider the statistics (Ivanov, 2001) of the Majorana modes. Let us start with the simplest case where $N = 1$. In this case, there are only two Majorana modes and the braid group only has a single generator τ As we saw in the first section, τ is the operator that exchanges the Majorana modes A and B (as shown in Fig. 17)

$$\gamma_A \rightarrow \gamma'_A = \tau^\dagger \gamma_A \tau = e^{i\phi}\gamma_B, \tag{28}$$

but it does not fix the phase ϕ which is arbitrary. We can choose it to be +1. But then the phase of

$$\gamma_B \rightarrow \gamma'_B = \tau^\dagger \gamma_B \tau = e^{i\phi}\gamma_A \tag{29}$$

is forced to be -1. This is because when there are only 2 Majorana modes, and the system is isolated, the fermion parity is forced to be conserved. The fermion state formed from the two Majorana modes is either occupied or unoccupied and we can check that

$$i\gamma_A\gamma_B = \left(1 - 2c_M^\dagger c_M\right) \tag{30}$$

So if the right hand side remains unchanged, then $i\gamma_A\gamma_B$ has to remain unchanged, which is only possible, if we choose the phases as shown above, since $\gamma_A\gamma_B = -\gamma_B\gamma_A$. Here, we can choose the exchange operator to be of the form

$$\tau = \frac{1}{\sqrt{2}}(1 + \gamma_A\gamma_B) \tag{31}$$

It is easy to check that τ defined this way is unitary and that it actually carries out the exchange by substituting for τ in Eq. (29). It is also easy to check that τ can be rewritten as $\exp(\pi\gamma_A\gamma_B/4)$. If we write it in terms of the fermion number operator,

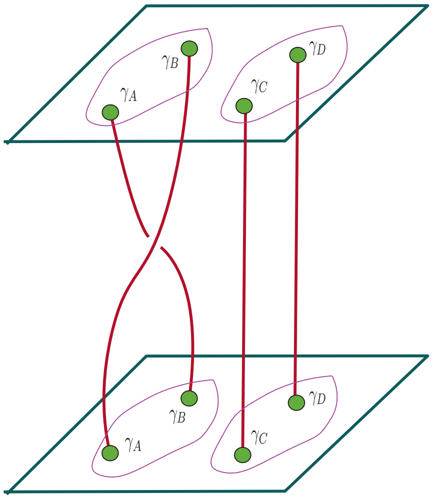

Fig. 17 Here, we exchange the Majorana modes belonging to the same fermion. This only gives rise to a phase and hence abelian statistics.

$$\tau = e^{i\pi(1-2n)/4}, \text{ where } n = c_M^\dagger c_M \tag{32}$$

Clearly, since n does not change, the statistics parameter is abelian and it cannot rotate states in the ground state manifold $(|0>, c_M^\dagger|0>)$.

Now, let us see what happens when $N = 2$. Here, we have 4 Majorana modes γ_i, $i = A\ldots D$ which can form 2 normal fermions

$$c_1 = \frac{1}{2}(\gamma_A + i\gamma_B),\ \ c_1^\dagger = \frac{1}{2}(\gamma_A - i\gamma_B)$$

$$c_2 = \frac{1}{2}(\gamma_C + i\gamma_D),\ \ c_2^\dagger = \frac{1}{2}(\gamma_C - i\gamma_D) \tag{33}$$

The degenerate states of the system are given by $|n_1, n_2> \ = c_1^\dagger c_2^\dagger|0, 0> \ = \{|0,0>, |1,0>, |0,1>, |1,1>\}$. Operator τ_{AB} exchanges the Majoranas γ_A and γ_B keeping γ_C, γ_D unchanged and operator τ_{CD} exchanges the Majoranas γ_C and γ_D keeping γ_A, γ_B unchanged. Similarly, we can define, τ_{AC}, τ_{BD}, etc.

It is now clear that analogous to the $N = 1$ case, if we exchange the two Majorana zero modes from the same fermion, as shown in Fig. 17, we will only get a phase - i.e.,

$$\tau_{AB}|n_1, n_2> = e^{i\pi(1-2n_1)/4}|n_1, n_2>$$

$$\tau_{CD}|n_1, n_2> = e^{i\pi(1-2n_2)/4}|n_1, n_2> . \tag{34}$$

In the first equation, n_2 comes along for a ride and in the second equation, n_1 comes along for a ride. So both these operators are abelian operators. But now, let us exchange one Majorana from one of the fermions with another Majorana from the other fermion, (as shown in Fig. 18)

$$\tau_{BC} = \frac{1}{\sqrt{2}}(1 + \gamma_B\gamma_C). \tag{35}$$

In terms of the fermions c_1 and c_2, this can be written as

$$\tau_{BC} = \frac{1}{\sqrt{2}}\left[1 - i\left(c_1 - c_1^\dagger\right)\left(c_2 + c_2^\dagger\right)\right]. \tag{36}$$

Now acting this on $|n_1, n_2>$ does not lead to a phase. Instead, it leads to a rotation in the space of degenerate states given by

$$\tau_{BC}|n_1, n_2> = \frac{1}{\sqrt{2}}[|n_1, n_2> + i(-1)^{n_1}|1 - n_1, 1 - n_2>]. \tag{37}$$

If we now consider sequential exchanges, it is clear that different exchanges will not commute with one another - the final state will depend on the order of the operations. This is what is meant by saying that the Majorana particles have non-abelian statistics under exchange.

The derivation of the non-abelian statistics is not dependent on the details of how the exchange between the particles is carried out, and hence it cannot be changed by disorder or local details. It is topologically stable.

To understand multiple non-abelian anyons, as we already mentioned, we need to understand fusion paths, since the fusion rules do not lead to unique results. These fusion paths represent a basis of the degenerate ground state manifold, and are most conveniently studied in terms of conformal blocks of the appropriate conformal field theory. But that is beyond the scope of this article and we will stop here.

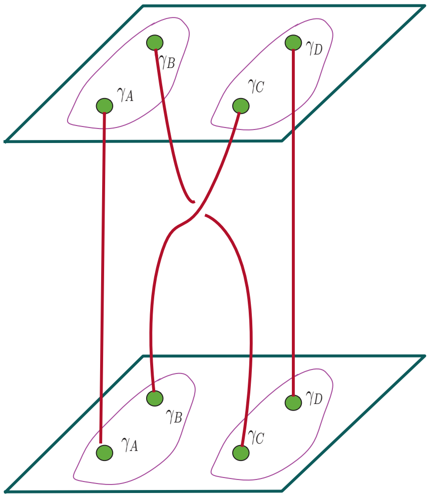

Fig. 18 Here, we exchange the Majorana modes belonging to two different fermions. This leads to a unitary rotation in the space of degenerate states and hence, to non-abelian statistics.

Conclusion

In this chapter, we have essentially given a detailed introduction to the idea of quantum statistics and how, in general, the wave-function of a many-particle system can pick up not only phases under exchanges of pairs of particles, but can also be rotated in a degenerate space, under exchange. More specifically, we have shown that abelian anyons transform as one-dimensional representations, and non-abelian anyons transform as higher dimensional representations of the braid group. We have introduced the concept of fusing or bringing together anyons to form new kinds of anyons. We have also discussed Kitaev's one-dimensional model of spinless fermions with nearest neighbor hopping as well as p-wave pairing to obtain end Majorana modes and have shown how the Majorana modes get rotated in the ground state manifold under exchange, as a specific example of non-abelian anyons.

The field of anyons, particularly, non-abelian anyons is still in its infancy. Majoranas are the simplest example of non-abelian anyons, and there has been a concerted effort all over the world to find them experimentally. Moreover, there has also been considerable amount of work, both in the theoretical and experimental arena to extend the work to more complex non-abelian anyons like Z_N parafermions (generalizations of the Majoranas which are also called Ising anyons, or Z_2 anyons) and Fibonacci anyons. The field is at the cross-roads of condensed matter physics and quantum information, and is expected not only to be of interest to researchers in both areas, but also benefit from the cross-fertilization of ideas from both fields.

References

Aharonov Y and Bohm D (1959) *Physics Review* 115: 485.
Aharonov Y and Casher A (1984) *Physical Review Letters* 53: 319.
De Picciotto R, Reznikov M, Heiblum M, Umansky V, Bunin G, and Mahalu D (1997) *Nature* 389: 162.
Ivanov DA (2001) *Physical Review Letters* 86: 268.
Kitaev AY (2001) Unpaired Majorana fermions in quantum wires. *Physics-Uspekhi* 44: 131.
Laughlin RB (1983) *Physical Review Letters* 50: 1395.
Leinaas JM and Myrrheim J (1977) *Il Nuovo Cimento B* 37: 1.
Leinjse M and Flensberg K (2012) *Semiconductor Science and Technology* 27: 124003.
Moore G and Read N (1991) *Nuclear Physics B* 360: 362.
Nakamura J, Liang S, Gardner GC, and Manfra MJ (2020) *Nature Physics* 16: 931–936.
Preskill J (2004) Lecture Notes for Physics 219: Quantum Computation. available at http://www.theory.caltech.edu/preskill/ph219/topological.pdf.
Tsui DC, Stormer HL, and Gossard AC (1982) *Physical Review Letters* 48: 1559.
Wilczek F (1982) *Physical Review Letters* 49: 957.

Further reading

Alicea J (2012) New directions in the pursuit of Majorana fermions in solid state systems. *Reports on Progress in Physics* 75: 076501.
Khare A (1998) *Fractional Statistics and Quantum Theory*. World Scientific.
Kitaev A (2003) Fault tolerant quantum computation by anyons. *Ann. Phys.* 321: 2.

Kitaev A and Laumann C (2008) Topological phases and quantum computation. In: *Les Houches Summer School 'Exact Methods in Low-Dimensional Physics and Quantum Computing'*.

Lerda A (1992) Anyons. In: *Lecture notes in Physics Monographs, Series 14*. Springer-Verlag Publications.

Nayak C, Simon SH, Freedman M, and Sarma SD (2008) Non-abelian anyons and topological quantum computation. *Reviews of Modern Physics* 80: 1083.

Rao S (1997) An anyon primer. In: Bhattacharjee SM (ed.) *Models and Techniques of Statistical Physics*. Narosa Publications.

Rao S (2017) Introduction to abelian and non-abelian anyons. In: Bhattacharjee SM, Mahan MJ, and Bandyopadhyay A (eds.) *Topology and Condensed Matter physics*. Hindustan Book Agency.

Simon SH (2020) Topological Quantum: Lecture Notes and Proto-Book. http://www-thphys.physics.ox.ac.uk/people/SteveSimon/topological2020/TopoBookOct27hyperlink.pdf.

Stern A (2008) Anyons and the quantum Hall effect - A pedagogical review. *Annals of Physics* 323: 204.

Wilczek F (1990) *Fractional Statistics and Anyon Superconductivity*. *Series on Directions in Condensed Matter Physics*World Scientific Publications.

Statistical anyons

Nathan M Myers, Department of Physics, Virginia Tech, Blacksburg, VA, United States

© 2024 Elsevier Ltd. All rights reserved.

Introduction **500**
“Statistical” anyons **502**
Statistical anyon wavefunction 504
Statistical anyons in the second quantization 505
Statistical anyons and generalized exclusion statistics 506
Equilibrium thermodynamics of statistical anyons **507**
1D Statistical anyons 508
2D Statistical anyons 509
2D FES anyons 510
Thermodynamic equivalence **511**
Conclusion **512**
Summary 512
Impacts and future directions 512
References **512**

Abstract

In general, the term anyons is applied to describe quasiparticles that display behavior that falls on a continuum between that of bosons and fermions. Two primary constructions of anyons exist: generalized exclusion statistics (GES), which extends the Pauli exclusion principle to allow a continuum of state occupancy, and fractional exchange statistics (FES), which generalizes the phase picked up by the wave function under particle exchange. In this chapter, we outline an alternative framework for simulating anyonic behavior called statistical anyons. Under this framework, anyonic features emerge from the average behavior of a statistical mixture of bosons and fermions. We demonstrate that statistical anyons are equivalent to GES anyons and can replicate the thermodynamic behavior of FES anyons.

Key points

- In the statistical anyon framework, the averaged behavior of an ensemble of bosons and fermions is used to simulate anyonic properties.
- Ideal statistical anyons are equivalent to interacting particles obeying Haldane’s generalized exclusion statistics, but do not replicate the topological exchange behavior of anyons obeying fractional exchange statistics.
- Statistical anyons can replicate the thermodynamic behavior of fractional exchange statistics anyons through a parameter-dependent choice of the fraction of the ensemble that are bosons.

Introduction

A primary distinguishing feature of quantum particles, in comparison to classical descriptions, is that they are truly indistinguishable. This indistinguishability does not arise from insufficient measurement precision, but rather is a fundamental property of the particles themselves. Quantum mechanics, as a linear theory, presents us with a method of accounting for this indistinguishability. The quantum state of a system of indistinguishable particles must be expressed as a superposition of all possible permutations of the individual particle states. However, such a composition is not unique. A family of possible solutions exists, with each solution distinguished by the phase picked up when two of the constituent particles are exchanged. In three spatial dimensions, the constraint that two sequential exchanges must leave the wave function unchanged leaves only two possibilities for this phase factor: positive and negative one. Particles with a wave function that is symmetric under exchange, corresponding to a phase factor of +1, are bosons, while particles with a wave function that is antisymmetric under exchange, corresponding to a phase factor of −1, are fermions.

Rather than being purely a concern of mathematical record keeping, this wave function symmetry has profound physical consequences. The antisymmetry of fermionic wave functions leads to vanishing probability that any two fermions will be found in the same quantum state (the Pauli exclusion principle), while no such restriction exists for bosons. Furthermore, a straightforward

https://doi.org/10.1016/B978-0-323-90800-9.00217-7

examination of the average separation distance between a pair of indistinguishable particles shows that bosons are more likely to be found closer together while fermions are more likely to be found farther apart, in comparison to classical, distinguishable particles. This phenomenon, commonly called exchange forces, leads to an effective attraction between bosons and an effective repulsion between fermions.

While in three dimensions topological considerations limit the phase factor picked up under particle exchange to positive and negative one, this restriction does not apply in two-dimensional systems, as first demonstrated by Leinaas and Myrheim (1977). In 2D, there can exist a continuum of fractional statistics solutions, represented by a general phase factor of $e^{i\pi\nu}$ picked up under particle exchange (braiding). For $\nu = 2n$, where $n = 0, 1, 2, \ldots$, bosonic behavior is recovered, while for $\nu = 2n + 1$, fermionic behavior is recovered. Shortly thereafter, Wilczek proposed that these anyons could exist as composite particles formed from a charged particle orbiting a tube of magnetic flux (Wilczek, 1982). Under this implementation particle exchange is accomplished by successive half-rotations of each quasiparticle around the other with the anyonic phase resulting from the Aharonov–Bohm effect. It was later proven by Arovas, Schrieffer, and Wilczek that quasiparticles entering the fractional quantum Hall regime also obey fractional exchange statistics (Arovas et al., 1984).

Anyons have been the subject of much recent interest due to the potential for non-Abelian anyons (Moore and Read, 1991) to serve as the basis of fault-tolerant topological quantum computers (Kitaev, 2003; Nayak et al., 2008). The non-Abelian nature of the braid group can be used to implement sequences of braids in multianyon systems that result in unitary transformations on the system state, analogous to quantum logic gates. As small, local perturbations do not change the braiding properties of the anyons, this method of quantum computation is, in principle, very robust against noise (Kitaev, 2003). While non-Abelian anyons have been the focus of much theoretical study, experimental detection remains a challenge and so far only indirect evidence of non-Abelian anyonic states has been found (Clarke et al., 2013; Kasahara et al., 2018; Banerjee et al., 2018).

As previously noted, the concept of fractional exchange statistics is only valid under the restriction to two dimensions. Thus, extending the concept of anyons to arbitrary dimensions requires a different approach. A dimension independent formulation of anyons is provided through the concept of *generalized exclusion statistics* (GES), first introduced by Haldane (1991). Based on a generalization of the Pauli exclusion principle, under GES particle nature is quantified by a statistical interaction that determines the degree to which two identical particles can occupy the same state. In practice, bosons or fermions subject to particular interparticle interactions can be treated as noninteracting particles obeying GES. Two well-studied interactions that can manifest GES are the inverse square law interaction of the Calogero–Sutherland (CS) model gas (Calogero, 1969; Sutherland, 1988; Murthy and Shankar, 1994b; Dasnières de Veigy and Ouvry, 1995; Bytsko and Fring, 1998; Meljanac et al., 2004; Comtet et al., 2007; del Campo, 2016) and the contact interactions of the 1D Lieb–Liniger model gas (Lieb and Liniger, 1963), with the distinctions that the statistical interaction occurs between particles of different momenta (Bernard and Wu, 1994; Isakov et al., 1996; Aneziris et al., 1991; Batchelor and Guan, 2007) and that the coupling constant of the interaction cannot be directly identified with the parameter controlling the statistics, except in the bosonic and fermionic limits (Ouvry and Polychronakos, 2009).

Despite the differences between their approaches, with FES generalizing the exchange behavior and GES generalizing the state occupancy of the exclusion principle, the two concepts of anyons are conceptually linked. When first proposing GES, Haldane noted that FES anyons confined to the lowest Landau level can be identified as obeying GES (Haldane, 1991). The two approaches can be combined, and it has been demonstrated that dimensionally confined, interacting FES anyons can be mapped to ideal FES anyons that obey GES (Kundu, 1999; Batchelor et al., 2006; Batchelor and Guan, 2006; Batchelor et al., 2007; Calabrese and Mintchev, 2007; Pâţu et al., 2007; Batchelor et al., 2008; Hao et al., 2008; del Campo, 2008; Pâţu et al., 2008a, b; Santachiara and Calabrese, 2008).

The differences in statistical behavior between bosons and fermions provide the foundation of quantum statistical mechanics. With this being the case, it is not surprising that much attention has been paid to studying the statistical mechanics of both FES and GES anyons. For GES anyons, much of this work has focused on analyzing the distribution function (Wu, 1994; Isakov, 1994b; Khare, 2005; Rovenchak, 2014; Joyce et al., 1996; Anghel, 2013), partition functions (Murthy and Shankar, 1994b; Dasnières de Veigy and Ouvry, 1995; Comtet et al., 2007; Ouvry and Polychronakos, 2021), virial coefficients (Murthy and Shankar, 1994a; Isakov et al., 1996; Rovenchak, 2014), equation of state (Wu, 1994; Dasnières de Veigy and Ouvry, 1995; Isakov et al., 1996; Ouvry and Polychronakos, 2021), and deriving thermodynamic behavior using the thermodynamic Bethe ansatz (Bernard and Wu, 1994; Isakov, 1994a, b; Guan and Chen, 2016). Similarly, the partition function (Bhaduri et al., 1991; Myrheim, 1999) and the virial coefficients (Arovas et al., 1985; Sen, 1992; Sporre et al., 1993; Giacconi et al., 1996; Lerda, 1992; Myrheim, 1999; Polychronakos, 2000; Khare, 2005) for FES anyons have been studied, along with their relativistic thermodynamics (Chen, 1995) and phase transitions (Nasu and Motome, 2015).

Despite significant theoretical analysis, the difficulty of accessing anyons had led to comparatively fewer experimental studies. A typical approach to detecting FES anyons arising in the fractional quantum Hall regime is through the use of quasiparticle interferometers whose interference effects are sensitive to the anyonic phase (de Chamon et al., 1997; Ji et al., 2003; Law et al., 2006; Bonderson et al., 2006). This method has seen experimental implementation (Camino et al., 2005; Ofek et al., 2010; McClure et al., 2012; Willett et al., 2013; Nakamura et al., 2019; Willett et al., 2019); however distinguishing signatures of the anyonic phase from interference effects arising from Coulomb blockading and Aharonov–Bohm interference makes this approach challenging (Bartolomei et al., 2020).

In this chapter we detail an alternative framework for anyons, in which the anyonic behavior arises from a statistical mixture of boson and fermion pairs. This approach is referred to as "statistical anyons" (Myers and Deffner, 2021). In Section “"Statistical" anyons" we motivate the main idea behind statistical anyons using the Hong-Ou-Mandel (HOM) effect first observed in photonic interferometry (Hong et al., 1987). Then in Section "Equilibrium thermodynamics of statistical anyons" we demonstrate how the statistical anyon framework is equivalent to the GES formulation of anyons. In Section "Thermodynamic equivalence" we examine the equilibrium thermodynamic properties of statistical anyons in comparison to FES anyons. We show that, with a parameter-dependent choice of the anyonic phase, statistical anyons can mimic the thermodynamics of FES anyons. Finally, in Section "Conclusion" we conclude with a summary and perspective on future research directions.

"Statistical" anyons

To motivate the main concept behind statistical anyons, we begin with a brief overview of the typical HOM effect. Consider a pair of entangled photons incident symmetrically on a two-port 50/50 beamsplitter. The initial bosonic spatial state is described by a symmetric superposition of each input,

$$\left|\psi_{\mathrm{i}}^{\mathrm{B}}\right\rangle=\frac{1}{\sqrt{2}}\left(|a\rangle_1|b\rangle_2+|b\rangle_1|a\rangle_2\right). \tag{1}$$

The operation of the beamsplitter evolves state $|a\rangle \rightarrow \frac{1}{\sqrt{2}}(|c\rangle+i|d\rangle)$ and state $|b\rangle \rightarrow \frac{1}{\sqrt{2}}(i|c\rangle+|d\rangle)$ with the imaginary component denoting the phase shift of π picked up upon reflection. The final state after the beamsplitter is then

$$\left|\psi_{\mathrm{f}}^{\mathrm{B}}\right\rangle=\frac{i}{\sqrt{2}}\left(|c\rangle_1|c\rangle_2+|d\rangle_1|d\rangle_2\right). \tag{2}$$

Remarkably, we see that the only possible output states are those in which both photons exit the same port of the beamsplitter. This "boson bunching" can be interpreted as a consequence of the effective attraction between bosons arising from the exchange forces (Hong et al., 1987).

It is important to note that the above analysis assumes that all other degrees of freedom of the photons (such as frequency and polarization) are identical. However, it is straightforward to extend the HOM analysis to the case in which this is no longer the case (Zeilinger, 1998). Consider a case in which the incident photons are prepared in one of the maximally entangled Bell states in the polarization basis. The four possible Bell pairs are

$$\begin{aligned}
|\Phi_A\rangle &= \frac{1}{\sqrt{2}}(|00\rangle+|11\rangle),\\
|\Phi_B\rangle &= \frac{1}{\sqrt{2}}(|00\rangle-|11\rangle),\\
|\Phi_C\rangle &= \frac{1}{\sqrt{2}}(|01\rangle+|10\rangle),\\
|\Phi_D\rangle &= \frac{1}{\sqrt{2}}(|01\rangle-|10\rangle),
\end{aligned} \tag{3}$$

where $|0\rangle$ and $|1\rangle$ denote orthogonal polarization states. Three of these states are symmetric under exchange ($|\Phi_A\rangle$, $|\Phi_B\rangle$, and $|\Phi_C\rangle$) while one of them ($|\Phi_D\rangle$) is antisymmetric. Since photons are bosons, their overall wave function must still be symmetric. This can be accomplished by either pairing a symmetric spatial state with one of the three symmetric polarization states, or by pairing an antisymmetric spatial state with the antisymmetric polarization state. For the latter case, the overall wave function for the incident photon pair is,

$$\left|\Psi_{\mathrm{i}}^{\mathrm{F}}\right\rangle=\frac{1}{\sqrt{2}}\left(|a\rangle_1|b\rangle_2-|b\rangle_1|a\rangle_2\right)\otimes|\Phi_D\rangle. \tag{4}$$

Assuming it is nonpolarizing, the beamsplitter acts only on the spatial portion of the wavefunction resulting in the output state

$$\left|\psi_{\mathrm{f}}^{\mathrm{F}}\right\rangle=\frac{1}{\sqrt{2}}\left(|c\rangle_1|d\rangle_2-|d\rangle_1|c\rangle_2\right). \tag{5}$$

We see that now, unlike the previous case, the only possible output states are those in which both photons exit opposite ports of the beamsplitter. Despite the fact that photons are fundamentally bosons, since the beamsplitter only acts on the antisymmetric portion of the overall state, the photons behave like fermions. This guarantee that the photons exit opposite ports of the beamsplitter can be seen as a manifestation of the Pauli exclusion principle. In Fig. 1A we illustrate the outcomes for both the spatially symmetric and antisymmetric initial states.

In a sense, the additional degree of freedom provided by the polarization can be thought of as a quantum substrate on which the desired statistics can be constructed. Notably, both bunching and antibunching behaviors vanish if the photons become distinguishable. A simple means of accomplishing this is to introduce a difference in the flight time between the two ports of the beamsplitter (Zeilinger, 1998).

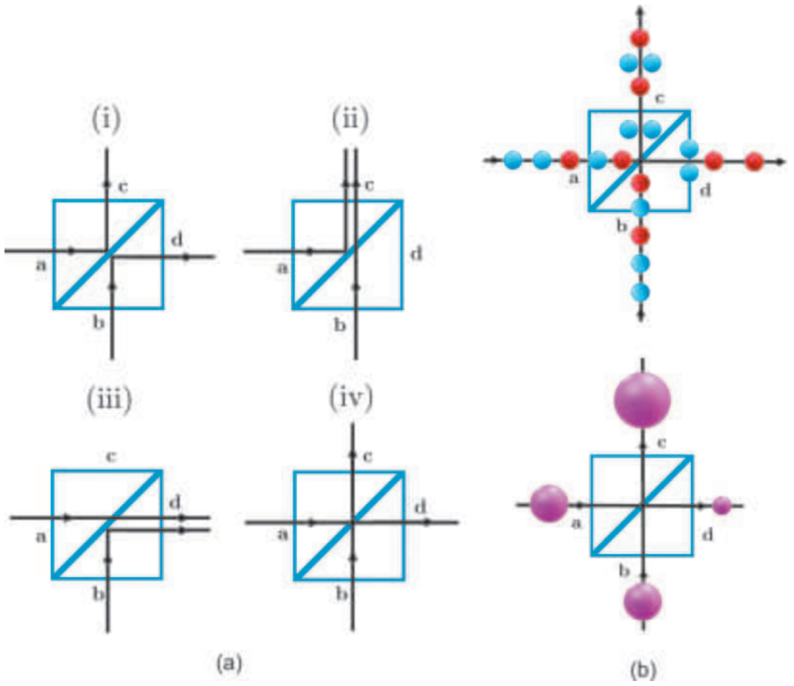

Fig. 1 (A) Possible transmission and reflection combinations for two photons incident on a two-port 50/50 beamsplitter. For photon pairs with symmetric (bosonic) spatial states possibilities (i) and (iv) interfere deconstructively while for photons with antisymmetric (fermionic) spatial states (i) and (iv) interfere constructively. (B) Example of statistical anyons for $N = 5$ photon pairs. Top figure: The particle pairs are incident on opposite ports of the beamsplitter. *Blue particles* represent pairs with symmetric entanglement and *red particles pairs* with antisymmetric entanglement. At the output, the *blue pairs* always exit at the same port, and the *red pairs* at opposite ports. Bottom figure: The statistical anyonic representation of the same process. Here particle size represents the normalized probability density of finding a particle at that port.

The HOM bunching and antibunching can be extended to anyonic statistics through the introduction of a phase that tunes between the symmetric and antisymmetric Bell states. This phase can be introduced in a number of ways, including using a rotated polarization beamsplitter (Matthews et al., 2013), adjusting path length (Rarity et al., 1990; Michler et al., 1996), or introducing phase plates (Wang et al., 2007). In the statistical anyon framework, this phase is effectively introduced by averaging over the behavior of a statistical mixture of symmetrically and antisymmetrically entangled photon pairs. Consider an incident anyonic wave function of the form

$$|\psi_{\mathrm{i}}^{\mathrm{A}}\rangle = \frac{1}{\sqrt{2}}(|a\rangle_1|b\rangle_2 + e^{i\pi v}|b\rangle_1|a\rangle_2). \tag{6}$$

After the beamsplitter, the probability of finding both photons in the same output port is

$$P_{\text{same}} = \frac{1}{2}(1 + \cos[\pi v]). \tag{7}$$

By varying v, we see that the probability of finding both photons at the same port can be tuned between the bosonic and fermionic limits of 1 and 0, respectively. Now let us consider the case of N photon pairs incident on the beam splitter, of which some fraction are symmetrically entangled and the rest are antisymmetrically entangled. We can replicate the same probability of finding both photons of a pair at the same port *on average* by varying the ratio of symmetrically to antisymmetrically entangled pairs in the ensemble. In this framework the anyonic phase parameter v is associated with the probability that any given pair in the mixture is symmetrically entangled, $v = v(p_B)$. This behavior is shown pictorial in Fig. 1B.

We refer to this implementation as "statistical anyons" in contrast to FES anyons and GES anyons. Each formulation of anyons displays behavior interpolating between that of fermions and bosons. However, in the statistical anyon framework this behavior is a result of averaging over a large number of particles, while for FES anyons it is a property of the quasiparticles themselves and for GES anyons it is a product of the interparticle interactions.

Topologically, statistical anyons are akin to GES anyons and distinct from FES anyons. The two-dimensional nature of FES anyons means that two repeated exchanges is a topologically distinct from doing nothing and does not necessarily result in an unchanged wave function (Leinaas and Myrheim, 1977; Lerda, 1992). Since the configuration space of FES anyons is represented by the braid group, the *direction* of the exchange is significant. Two exchanges in the same direction will result in a wavefunction different from the original by a phase of $e^{2i\pi v}$. Like GES anyons, two repeated exchanges of statistical anyons will always return the original wave function, since each element of the statistical anyon ensemble is fundamentally a boson or fermion. For statistical anyons the anyonic phase is an average over the bosonic and fermionic phases of the constituent particles and thus will always fall between negative one and one. Thus the statistical anyon mixture corresponding to a FES anyon phase of $e^{i\pi v}$ will be weighted such

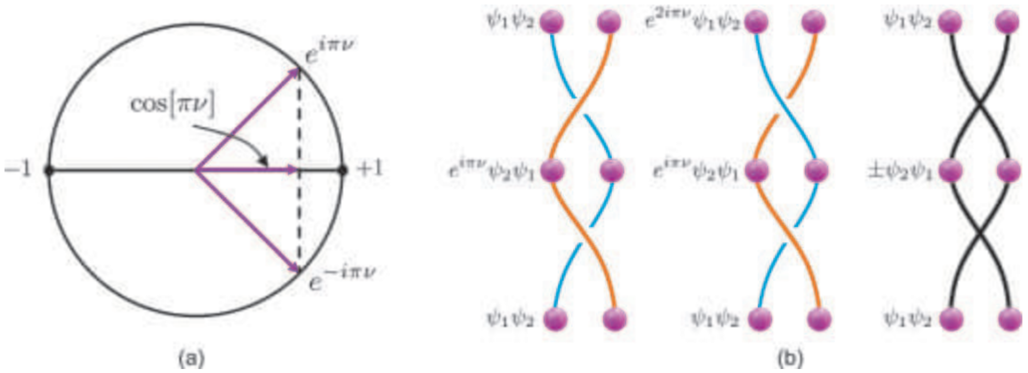

Fig. 2 (A) Comparison between the exchange phase of FES and statistical anyons. For FES anyons, the direction of the exchange determines the sign of the anyonic phase parameter ν. Thus the space of possible FES anyonic phases can be represented by a unit circle in the complex plane with the bosonic and fermionic phases lying on the intercepts with the real axis at ± 1. For statistical anyons, the anyonic phase parameter is given by the probability that a given pair of particles in the ensemble will be bosons. As such, the space of possible statistical anyon phases is confined to the real axis between positive and negative one. This leads to reduced complexity, as the sign of the phase (direction of exchange) is irrelevant. (B) Comparison between 2D FES and statistical anyons undergoing two exchanges. For FES anyons two exchanges in opposite directions leaves the wavefunction unchanged (left diagram), while two exchanges in the same direction results in the original wavefunction with a phase of $e^{2i\pi\nu}$ (middle diagram). For statistical anyons the direction of the exchange is irrelevant, with two exchanges always resulting in an unchanged wavefunction (right diagram).

that the average phase of the mixture is $\cos[\pi\nu]$. Note that the since the direction of exchange is irrelevant for statistical anyons, the FES anyonic phases of $e^{i\pi\nu}$ and $e^{-i\pi\nu}$ are both identified with the same statistical anyon phase. These differences between the FES and statistical anyon phases are illustrated graphically in Fig. 2.

Statistical anyon wavefunction

Let us now consider how to treat statistical anyons outside of the framework of quantum optics. In general, the symmetric spatial wave function for a pair of bosons is

$$\Psi_{\mathrm{B}}(\mathbf{x}) = \frac{1}{\sqrt{2(1+\delta_{n_1,n_2})}}\left[\psi_{n_1}(x)\psi_{n_2}(y) + \psi_{n_1}(y)\psi_{n_2}(x)\right], \tag{8}$$

where $\psi_n(x)$ is the normalized single-particle eigenstate corresponding to quantum number n. Note that the normalization coefficient for bosons depends on whether the particles occupy the same state. Conversely, the antisymmetric spatial wave function for a pair of fermions is

$$\Psi_{\mathrm{F}}(\mathbf{x}) = \frac{1}{\sqrt{2}}\left[\psi_{n_1}(x)\psi_{n_2}(y) - \psi_{n_1}(y)\psi_{n_2}(x)\right]. \tag{9}$$

In this case no delta function is required in the normalization, as the fermionic wave function vanishes if both fermions ever occupy the same state.

Now we consider a case in which we have N independent pairs of particles, of which N_{B} are bosons and $N_{\mathrm{F}} = N - N_{\mathrm{B}}$ are fermions. The total wave function is then

$$\Psi(\mathbf{x}_1, \mathbf{x}_2, \ldots, \mathbf{x}_N) = \prod_{j=1}^{N_{\mathrm{B}}} \Psi_{\mathrm{B}}(\mathbf{x}_j) \prod_{k=N_{\mathrm{B}}+1}^{N} \Psi_{\mathrm{F}}(\mathbf{x}_k), \tag{10}$$

where $\mathbf{x} = (x, y)$. This wave function can be equivalently represented in the framework of statistical anyons as

$$\Psi(\mathbf{x}_1, \mathbf{x}_2, \ldots, \mathbf{x}_N) = \prod_{j=1}^{N} \Psi_{\mathrm{A}}(\mathbf{x}_j), \tag{11}$$

where

$$\Psi_{\mathrm{A}}(\mathbf{x}_j) = \frac{1}{\sqrt{2(1+\delta_{n_1,n_2})}}\left[\psi_{n_1}(x_j)\psi_{n_2}(y_j) + e^{i\pi\nu_j}\psi_{n_1}(y_j)\psi_{n_2}(x_j)\right]. \tag{12}$$

We note here a significant difference between the statistical anyon wave function in Eq. (11) and the wave function for FES anyons. From Eqs. (11) and (12), it is clear that the statistical anyon wave function can always be constructed from a product of superpositions of the single particle wave functions. This is *not* generally true for the wave function of FES anyons, outside of the bosonic and fermionic limits (Lerda, 1992; Myrheim, 1999; Khare, 2005).

Since Eqs. (11) and (10) must match, we select the anyonic phase parameter in Eq. (12) to be $v_j = \Theta(j - N_B - 1)$, where $\Theta(\cdot)$ is the Heaviside step function, using the convention $\Theta(0) = 1$. This way, the anyonic factor in Eq. (12) gives the 'average' phase picked up under exchange for any one of the N pairs of particles. For a large ensemble of particles ($N \gg 1$), we can express the number of bosonic and fermionic particle pairs as $N_B = Np_B$ and $N_F = Np_F = N(1 - p_B)$ where p_B (p_F) is the probability of a particle pair having bosonic (fermionic) symmetry.

In the limit of a single two-particle system, the anyonic wave function becomes

$$\Psi_A(\mathbf{x}) = \frac{1}{\sqrt{2(1 + \delta_{n_1,n_2})}}[\psi_{n_1}(x)\psi_{n_2}(y) \pm \psi_{n_1}(y)\psi_{n_2}(x)], \tag{13}$$

with the sign determined by whether p_B is zero or one. This is a reflection of the fact that each individual pair of particles in the ensemble is, in reality, either bosonic or fermionic.

Statistical anyons in the second quantization

To understand the how to extend the framework of statistical anyons to the second quantization we must determine the appropriate commutation relations. Let us first consider the case of FES anyons. The creation and annihilation operators for FES anyons can be determined from the bosonic or fermionic operators via the Jordan–Wigner transformation, and obey the following commutation relations (Lerda and Sciuto, 1993):

$$\begin{aligned}
a(\mathbf{x}_\mathcal{C})a(\mathbf{y}_\mathcal{C}) - e^{-i\pi v}a(\mathbf{y}_\mathcal{C})a(\mathbf{x}_\mathcal{C}) &= 0,\\
a(\mathbf{x}_\mathcal{C})a^\dagger(\mathbf{y}_\mathcal{C}) - e^{i\pi v}a^\dagger(\mathbf{y}_\mathcal{C})a(\mathbf{x}_\mathcal{C}) &= 0,\\
a^\dagger(\mathbf{x}_\mathcal{C})a(\mathbf{y}_\mathcal{C}) - e^{i\pi v}a(\mathbf{y}_\mathcal{C})a^\dagger(\mathbf{x}_\mathcal{C}) &= 0.\\
a^\dagger(\mathbf{x}_\mathcal{C})a^\dagger(\mathbf{y}_\mathcal{C}) - e^{-i\pi v}a^\dagger(\mathbf{y}_\mathcal{C})a^\dagger(\mathbf{x}_\mathcal{C}) &= 0.
\end{aligned} \tag{14}$$

The direction-dependent nature of the FES phase factor is incorporated through the dependence of the commutators on the curve $\mathcal{C}$, which indicates the direction of the exchange rotation. We see that taking the limit of $v \to 0$ and $v \to 1$ in Eq. (14) restores the bosonic commutation and fermionic anticommutation relations, respectively.

For particles at the same location ($\mathbf{x}_\mathcal{C} = \mathbf{y}_\mathcal{C}$), the canonical commutation relation reduces to (Lerda and Sciuto, 1993; Khare, 2005)

$$a(\mathbf{x}_\mathcal{C})a^\dagger(\mathbf{x}_\mathcal{C}) \pm a^\dagger(\mathbf{x}_\mathcal{C})a(\mathbf{x}_\mathcal{C}) = 1, \tag{15}$$

with the (+) occurring if the anyonic operators are constructed from transformed fermionic operators, and the (−) if they are constructed from transformed bosonic operators. An important feature of FES anyons is the fact that they obey an exclusion principle for all $v \neq 0$. As is the case for GES anyons, the anyonic phase parameter can be thought of as quantifying the degree of repulsion between two identical particles (Khare, 2005).

For the case of statistical anyons, we follow a similar approach to the construction of the statistical anyon wave function in the first quantization. Let us consider an N-particle Fock state, consisting of N_B bosons and $N_F = N - N_B$ fermions. This state can be constructed from the vacuum state by applying N_B bosonic and N_F fermionic creation operators

$$|1\rangle_1|1\rangle_2 \ldots |1\rangle_N = \prod_{j=1}^{N_B} b_j^\dagger|0\rangle_j \prod_{k=N_B+1}^{N} f_k^\dagger|0\rangle_k. \tag{16}$$

We can construct an identical state by applying a statistical anyon creation operator to the vacuum state N times,

$$|1\rangle_1|1\rangle_2 \ldots |1\rangle_N = \prod_{j=1}^{N} s_j^\dagger|0\rangle_j. \tag{17}$$

The statistical anyon creation operator, $s_j^\dagger$, must reduce to the bosonic creation operator for $j \leq N_B$ and to the fermionic creation operator for $j > N_B$. This condition allows us to construct the statistical anyon commutation relations,

$$\begin{aligned}
s_j^\dagger s_j - e^{i\pi\Theta(j-N_B-1)}s_j s_j^\dagger &= 1,\\
s_j s_j^\dagger - e^{i\pi\Theta(j-N_B-1)}s_j^\dagger s_j &= 1,\\
s_j^\dagger s_j^\dagger - e^{i\pi\Theta(j-N_B-1)}s_j^\dagger s_j^\dagger &= 0,\\
s_j s_j - e^{i\pi\Theta(j-N_B-1)}s_j s_j &= 0.
\end{aligned} \tag{18}$$

Note the similar form of the statistical anyon phase to the case of the statistical anyon phase in the first quantization wave function.

In the single-particle limit, the canonical commutation reduces to

$$s_j s_j^\dagger \pm s_j^\dagger s_j = 1, \tag{19}$$

as in reality the particle is either a boson or a fermion. This echoes Eq. (15), where the form of the commutation relation depends on whether the anyonic operators are constructed from transformed fermionic or bosonic operators.

Statistical anyons and generalized exclusion statistics

In the previous sections, we have outlined the framework of statistical anyons and repeatedly compared it to the case of FES anyons. In this section, we now compare statistical anyons to GES anyons.

Previously, we noted that, outside the bosonic limit, FES anyons obey the exclusion principle (Khare, 2005). Statistical anyons, on the other hand, only obey the exclusion principle in the fermionic limit. Outside of this limit, statistical anyons admit "partially occupied" states that arise from averaging over the occupancy of all N systems. This behavior is more akin to that of GES anyons.

GES is constructed by extending the Pauli exclusion principle through the definition of a parameterized differential relation that quantifies the change in the dimension of the Hilbert space of a discrete-state system upon a change in the particle number (Haldane, 1991)

$$\Delta d_{\mathrm{GES}} = -g\Delta N. \tag{20}$$

Since infinitely many bosons can occupy the same state, for bosons the dimension is independent of the particle number, thus $g = 0$. As only a single fermion can occupy each state, the dimension scales directly with the total particle number, thus $g = 1$.

Physical systems known to host GES anyons include the CS model gas (Murthy and Shankar, 1994b; Bytsko and Fring, 1998; Meljanac et al., 2004; del Campo, 2016), which can also be mapped to FES anyons confined to the lowest Landau level (Wu, 1994; Dasnières de Veigy and Ouvry, 1994, 1995; Ouvry and Polychronakos, 2018; Ouvry, 2001; Ouvry and Polychronakos, 2021). Under this condition, the thermodynamic potential for a gas of particles with a discrete one-body spectrum obeying GES can be constructed from a generalization of the relation found for Calogero model GES anyons or lowest Landau level topological anyons (Ouvry and Polychronakos, 2021). GES can also manifest in Lieb–Liniger and hard core Tonks–Girardeau gasses with δ-function potentials (Kundu, 1999; Batchelor et al., 2006; Girardeau, 2006; Batchelor et al., 2007; Calabrese and Mintchev, 2007; Pâţu et al., 2007; Batchelor et al., 2008; Hao et al., 2008; del Campo, 2008; Pâţu et al., 2008a, b; Santachiara and Calabrese, 2008) as well as Hubbard chains (Vitoriano and Coutinho-Filho, 2009; Tang et al., 2015). The anyonic behavior of the latter can be simulated using ultracold gasses (Yannouleas and Landman, 2019). In general, GES can be connected with a class of integrable models solvable by the thermodynamic Bethe ansatz (Bernard and Wu, 1994; Isakov, 1994a, b; Bytsko and Fring, 1998; Guan and Chen, 2016).

We can follow a similar approach for statistical anyons. In this case the change in the Hilbert space dimension will be the weighted average over the change for bosons and fermions

$$\Delta d_{\mathrm{SA}} = p_{\mathrm{B}}\Delta d_{\mathrm{B}} + p_{\mathrm{F}}\Delta d_{\mathrm{F}}. \tag{21}$$

Using $\Delta d_{\mathrm{B}} = 0$ and $\Delta d_{\mathrm{F}} = -\Delta N$ this simplifies to

$$\Delta d_{\mathrm{SA}} = -p_{\mathrm{F}}\Delta N. \tag{22}$$

We see here that Eq. (22) is equivalent to Eq. (20) with the statistical parameter, g, replaced by the fermion probability.

The fact that GES anyons could be described in terms of bosons and fermions was first noted by Murthy and Shankar (1994b) in the context of the CS model gas. They showed that partition function for the GES anyons could be factored into bosonic and fermionic components raised to the power of the GES parameter g and $g-1$, respectively. Motivated by these results, we will explicitly demonstrate the equivalence of the statistical and GES anyon frameworks for the CS model.

The two-particle CS Hamiltonian is (Calogero, 1971)

$$H = \sum_{i=1}^{2}\left(-\frac{\hbar^2}{2m}\frac{\partial^2}{\partial x_i^2} + \frac{1}{2}m\omega^2 x_i^2\right) + \sum_{j<i}^{2}\frac{\hbar^2 g(g-1)}{2m(x_i - x_j)^2}. \tag{23}$$

The wavefunction corresponding to this Hamiltonian can be written as (Polychronakos, 1989; Brink et al., 1992; Isakov, 1994a; Gurappa and Panigrahi, 1999)

$$\Psi(x_1, x_2) = (x_2 - x_1)^g \Phi^+(x_1, x_2) \tag{24}$$

where the $(x_2 - x_1)^g$ term is the two-particle simplification of the Jastrow product and $\Phi^+(x_1, x_2)$ is a completely symmetric wave function. For the case of $g = 0$ we restore the wavefunction of two bosons in a pure harmonic potential, and for $g = 1$ we restore the wavefunction of two fermions in a pure harmonic potential. Now consider a large ensemble of N identical systems of which $N_B = Np_B$ consist of bosons and $N_F = Np_F$ consist of fermions. The global wavefunction can then be expressed as

$$\Psi_N(x_1, x_2) = \prod_{i=1}^{N_B}\Psi_i^B(x_1, x_2)\prod_{j=N_B+1}^{N}\Psi_j^F(x_1, x_2). \tag{25}$$

Replacing $\Psi_i^B(x_1,x_2)$ and $\Psi_j^F(x_1,x_2)$ in Eq. (25) with the bosonic and fermionic limits of Eq. (24) we have

$$\begin{aligned}\Psi_N(x_1, x_2) &= \prod_{i=1}^{N_B}\Phi_i^+(x_1, x_2)\prod_{j=N_B+1}^{N}(x_2 - x_1)^{N_F}\Phi_j^+(x_1, x_2)\\ &= \left[\Phi^+(x_1, x_2)\right]^{N_B}\left[(x_2 - x_1)\Phi^+(x_1, x_2)\right]^{N_F}.\end{aligned} \tag{26}$$

Using $N_F + N_B = N$ and $N_F = Np_F$ this simplifies to

$$\Psi_N(x_1, x_2) = \left[(x_2 - x_1)^{p_F}\Phi^+(x_1, x_2)\right]^N. \tag{27}$$

Thus we see that Eq. (25) can be equivalently expressed as

$$\Psi_N(x_1, x_2) = \prod_{i=1}^{N} \Psi_i^A(x_1, x_2), \tag{28}$$

where $\Psi^A(x_1, x_2) = (x_2 - x_1)^{p_F}\Phi^+(x_1, x_2)$ can be considered the *average* wavefunction across all N systems. This is identical to (24) with g replaced by p_F.

Let us now consider the spectrum. It is well established that the Calogero model can be mapped to a system of noninteracting oscillators with a shifted energy via similarity or canonical transformations (Polychronakos, 1989; Brink et al., 1992; Brzeziński et al., 1999; Gurappa and Panigrahi, 1999, 2000; Polychronakos, 2006; Chen, 2018). In the relative and center of mass coordinate system, the eigenenergies corresponding to relative motion of (23) are (Brink et al., 1992; Brzeziński et al., 1999; Gurappa and Panigrahi, 1999; Polychronakos, 2006)

$$E_n = \hbar\omega\left(2n + g + \frac{1}{2}\right), \tag{29}$$

where $n = (0, 1, 2, \ldots)$. Considering now a system of two noninteracting bosons or fermions in a harmonic potential. The eigenenergies corresponding to the relative coordinate are identical to those of the harmonic oscillator

$$E_{n_r} = \hbar\omega\left(n_r + \frac{1}{2}\right), \tag{30}$$

where the quantum symmetry is encoded in the fact that n_r consists of even integers for the case of bosons, and odd integers for the case of fermions. Using this we can rewrite (30) as

$$E_B = \hbar\omega\left(2n + \frac{1}{2}\right) \quad \text{and} \quad E_F = \hbar\omega\left(2n + 1 + \frac{1}{2}\right) \tag{31}$$

where now $n = (0, 1, 2, \ldots)$. The spectrum of N identical systems, of which N_B are bosons and N_F are fermions, is then

$$E_N = N_B E_B + N_F E_F = N\hbar\omega\left[\left(2n + \frac{1}{2}\right)(p_B + p_F) + p_F\right] = N\hbar\omega\left(2n + p_F + \frac{1}{2}\right). \tag{32}$$

The *average* spectrum for the relative coordinate of any given pair of particles in the mixture is then

$$E_n = \hbar\omega\left(2n + p_F + \frac{1}{2}\right) \tag{33}$$

which is identical to Eq. (29).

In this section we have demonstrated explicitly that GES can be constructed from the average behavior of an ideal statistical mixture of bosons and fermions, and identified the GES parameter with the statistical weights of the mixture. We conclude the section with Table 1, which summarizes the important distinctions between the three anyon frameworks, FES, GES, and statistical anyons.

Equilibrium thermodynamics of statistical anyons

As a branch of physics, thermodynamics was expressly developed to study the average behavior of systems consisting of a large number of microscopic constituents. As the anyonic behavior of statistical anyons arises from averaging over the behavior of a large ensemble of bosons and fermions, the statistical anyon framework is particularly suited to the study of thermodynamic behavior. In this section we will derive the equilibrium thermodynamic quantities for one- and two-dimensional statistical anyons, and compare this behavior to FES anyons. Ultimately, we will demonstrate how a particular choice of the statistical anyon phase (determined by the statistical weights of the Bose–Fermi mixture) can be used to mimic the thermodynamic behavior of FES anyons.

Table 1 Comparison of FES, GES, and statistical anyons

	Dim.	*Rep. group*	*Exclusion principle*	*Origin of anyonic behavior*
FES	2D	Braid	Hard core for all $\nu \neq 0$	Complex phase introduced by exchange
GES	Arbitrary	Permutation	Generalized exclusion	Generalization of state occupancy arising from interparticle interactions
Statistical	Arbitrary	Permutation	Generalized exclusion	Statistical average of bosonic and fermionic behavior

1D Statistical anyons

The first step in determining equilibrium thermodynamic quantities, such as internal energy, entropy, and heat capacity, is deriving the appropriate partition function. Motivated by the manifestation of GES in trapped, interacting gasses, as well as the verification of statistical and GES anyon equivalence for the CS model given in the previous section, let us consider two statistical anyons in a 1D harmonic potential. However, unlike the CS model GES, we will consider *noninteracting* particles. There is particular precedent for studying trapped boson–fermion mixtures both theoretically (Fang et al., 2011; Dehkharghani et al., 2017; Decamp et al., 2017) and experimentally (Fukuhara et al., 2009; Onofrio, 2016; Sowiński and García-March, 2019). This work has focused primarily on effects on the ground state configurations that arise from interactions between the boson and fermion species. In the statistical anyon framework we instead consider the average collective behavior that arises in the ideal gas limit of such a mixture.

The Hamiltonian for two harmonically confined noninteracting statistical anyons is

$$H = \frac{p_1^2 + p_2^2}{2m} + \frac{1}{2} m\omega^2 \left(x_1^2 + x_2^2\right). \tag{34}$$

For N independent pairs of particles, the partition function is given by

$$Z_{\mathrm{A}}^N = \operatorname{tr}\left\{e^{-\beta H}\right\} = \prod_{j=1}^{N} \int dx_j \int dy_j \left\langle x_j y_j \middle| e^{-\beta H_j} \middle| x_j y_j \right\rangle \tag{35}$$

Inserting the identity in the energy basis twice yields

$$Z_{\mathrm{A}}^N = \prod_{j=1}^{N} \int dx_j \int dy_j \sum_{n_1^{(j)}, n_2^{(j)}=0}^{\infty} \; \sum_{m_1^{(j)}, m_2^{(j)}=0}^{\infty} \Psi_{\mathrm{A}}^*(x_j, y_j) \Psi_{\mathrm{A}}(x_j, y_j) \times e^{-\beta\hbar\omega(m_1^{(j)}+m_2^{(j)}+1)} \left\langle n_1^{(j)} n_2^{(j)} | m_1^{(j)} m_2^{(j)} \right\rangle \tag{36}$$

where $\Psi_{\mathrm{A}}(x_j, y_j)$ is given by Eq. (12) with

$$\psi_n(x) = \frac{1}{\sqrt{2^n n!}} \left(\frac{m\omega}{\pi\hbar}\right)^{1/4} e^{-\frac{m\omega x^2}{2\hbar}} H_n\left(\sqrt{\frac{m\omega}{\hbar}} x\right). \tag{37}$$

Evaluating the integral in Eq. (36) results in

$$Z_{\mathrm{A}}^N = \prod_{j=1}^{N} \sum_{n_1^{(j)}, n_2^{(j)}=0}^{\infty} \frac{1}{4} e^{-\beta\hbar\omega\left(n_1^{(j)}+n_2^{(j)}+1\right)} \left(2 + e^{-i\pi\Theta(j-N_{\mathrm{B}}+1)} \delta_{n_1^{(j)}, n_2^{(j)}} + e^{i\pi\Theta(j-N_{\mathrm{B}}+1)} \delta_{n_1^{(j)}, n_2^{(j)}}\right), \tag{38}$$

where δ_{n_1,n_2} is the Kronecker delta. The step functions in Eq. (38) can be evaluated by separating the product into two, one from 1 to N_{B} and a second from $N_{\mathrm{B}} + 1$ to N

$$Z_{\mathrm{A}}^N = \prod_{j=1}^{N_{\mathrm{B}}} \sum_{n_1^{(j)}, n_2^{(j)}=0}^{\infty} \frac{1}{2} e^{-\beta\hbar\omega\left(n_1^{(j)}+n_2^{(j)}+1\right)} \left(1 + \delta_{n_1^{(j)}, n_2^{(j)}}\right) \times \prod_{j=N_{\mathrm{B}}+1}^{N} \sum_{n_1^{(j)}, n_2^{(j)}=0}^{\infty} \frac{1}{2} e^{-\beta\hbar\omega\left(n_1^{(j)}+n_2^{(j)}+1\right)} \left(1 - \delta_{n_1^{(j)}, n_2^{(j)}}\right). \tag{39}$$

Eq. (39) can be rewritten in the simple form

$$Z_{\mathrm{A}}^N = \prod_{j=1}^{N_{\mathrm{B}}} Z_{\mathrm{B}}^{(j)} \prod_{k=1}^{N_{\mathrm{F}}} Z_{\mathrm{F}}^{(k)} = Z_{\mathrm{B}}^{N_{\mathrm{B}}} Z_{\mathrm{F}}^{N_{\mathrm{F}}}, \tag{40}$$

where Z_{B} and Z_{B} are the individual partition functions for two bosons and two fermions in harmonic potential

$$\begin{aligned} Z_{\mathrm{B}} &= \sum_{n_1, n_2=0}^{\infty} \frac{1}{2}\left(1 + \delta_{n_1,n_2}\right) e^{-\beta\hbar\omega(n_1+n_2+1)} \\ Z_{\mathrm{F}} &= \sum_{n_1, n_2=0}^{\infty} \frac{1}{2}\left(1 - \delta_{n_1,n_2}\right) e^{-\beta\hbar\omega(n_1+n_2+1)}. \end{aligned} \tag{41}$$

Finally, using the fact that for large N we can express the number of bosonic and fermionic particle pairs as $N_{\mathrm{B}} = Np_{\mathrm{B}}$ and $N_{\mathrm{F}} = Np_{\mathrm{F}} = N(1 - p_{\mathrm{B}})$ where p_{B} (p_{F}) is the probability of a particle pair having bosonic (fermionic) symmetry, the statistical anyon partition function can be expressed as

$$Z_{\mathrm{A}}^N = \left(Z_{\mathrm{B}}^{p_{\mathrm{B}}} Z_{\mathrm{F}}^{p_{\mathrm{F}}}\right)^N. \tag{42}$$

Thus the partition function for a single pair of statistical anyons is

$$Z_{\mathrm{SA}} = \left(Z_{\mathrm{B}}\right)^{p_{\mathrm{B}}} \left(Z_{\mathrm{F}}\right)^{1-p_{\mathrm{B}}}. \tag{43}$$

As expected, Eq. (43) is identical to that of a GES CS model gas (Murthy and Shankar, 1994b), with the GES parameter g replaced by $1 - p_{\mathrm{B}}$. However, we see that in the statistical anyon framework the anyonic behavior arises purely out of the average properties, rather than from an interaction term in the Hamiltonian.

From Eq. (43) we can determine the internal energy, free energy, entropy, and heat capacity by taking the appropriate derivatives

$$\begin{aligned} E &= -\frac{\partial}{\partial\beta}\ln(Z_{\mathrm{SA}}), & F &= -\frac{1}{\beta}\ln(Z_{\mathrm{SA}}), \\ S &= k_{\mathrm{B}}\beta^2\frac{\partial F}{\partial\beta}, & C &= -k_{\mathrm{B}}\beta^2\frac{\partial E}{\partial\beta}, \end{aligned} \tag{44}$$

where β is the inverse temperature and k_{B} is Boltzmann's constant. For 1D ideal statistical anyons in a harmonic potential we find,

$$\begin{aligned} E &= \frac{1}{2}\hbar\omega[3\coth(\beta\hbar\omega) + \operatorname{csch}(\beta\hbar\omega) - 2p_{\mathrm{B}} + 1] \\ F &= \frac{1}{\beta}\ln\left[\frac{1}{8}\operatorname{csch}^2\left(\frac{\beta\hbar\omega}{2}\right) - \frac{1}{4}\operatorname{csch}(\beta\hbar\omega)\right] - p_{\mathrm{B}}\hbar\omega \\ S &= \frac{1}{2}k_{\mathrm{B}}\beta\hbar\omega[3\coth(\beta\hbar\omega) + \operatorname{csch}(\beta\hbar\omega) + 1] \\ &\quad + k_{\mathrm{B}}\ln\left[\frac{1}{8}\operatorname{csch}^2\left(\frac{\beta\hbar\omega}{2}\right) - \frac{1}{4}\operatorname{csch}(\beta\hbar\omega)\right] \\ C &= \frac{1}{2}k_{\mathrm{B}}\beta^2\hbar^2\omega^2\operatorname{csch}^2(\beta\hbar\omega)[\cosh(\beta\hbar\omega) + 3] \end{aligned} \tag{45}$$

Examining Eq. (45) we see that the internal energy and free energy are shifted by a constant proportional to p_{B}. This shift is a manifestation of the generalized exclusion principle for statistical anyons. As p_{B} varies from one to zero the lowest energy state of the system shifts from the bosonic limit, with both particles in the ground state of the oscillator, to the fermionic limit, with one particle in the ground state and the other in the first excited state. Notably both the entropy and heat capacity are independent of the statistics. Physically, this is a consequence of the fact that in the thermal equilibrium state both fermions and bosons have an equivalent, countably infinite, number of available states. Plots of the one-dimensional equilibrium thermodynamic quantities as a function of temperature are shown in Fig. 3.

2D Statistical anyons

If we ultimately wish to compare the thermodynamic behavior of statistical anyons with FES anyons, we must extend our thermodynamic analysis to two dimensions. Repeating the same approach for the case of a two-dimensional harmonic potential we find

$$\begin{aligned} E &= \hbar\omega\left[2\coth\left(\frac{1}{2}\beta\hbar\omega\right) + \tanh\left(\frac{1}{2}\beta\hbar\omega\right) - p_{\mathrm{B}}\tanh(\beta\hbar\omega)\right] \\ F &= -\frac{1}{\beta}\ln\left\{\frac{1}{8}[\cosh(\beta\hbar\omega)]^{p_{\mathrm{B}}}\operatorname{csch}^2\left(\frac{1}{2}\beta\hbar\omega\right)\operatorname{csch}^2(\beta\hbar\omega)\right\} \\ S &= k_{\mathrm{B}}\beta\hbar\omega\left[2\coth\left(\frac{1}{2}\beta\hbar\omega\right) + \tanh\left(\frac{1}{2}\beta\hbar\omega\right) - p_{\mathrm{B}}\tanh(\beta\hbar\omega)\right]. \\ &\quad + k_{\mathrm{B}}\ln\left\{\frac{1}{8}[\cosh(\beta\hbar\omega)]^{p_{\mathrm{B}}}\operatorname{csch}^2\left(\frac{1}{2}\beta\hbar\omega\right)\operatorname{csch}^2(\beta\hbar\omega)\right\} \\ C &= \frac{1}{2}k_{\mathrm{B}}\beta^2\hbar^2\omega^2\left[2\operatorname{csch}^2\left(\frac{1}{2}\beta\hbar\omega\right) - \operatorname{sech}^2\left(\frac{1}{2}\beta\hbar\omega\right) + 2p_{\mathrm{B}}\operatorname{sech}^2(\beta\hbar\omega)\right] \end{aligned} \tag{46}$$

In contrast to the one-dimensional case, we see that now the entropy and heat capacity now depend on p_{B}. The origin of this difference is clear if we think of the behavior of the entropy for two indistinguishable particles in the zero-temperature limit. For bosons there is only one available configuration, consisting of both particles in the ground state. In contrast, the fermion ground state is degenerate. The Pauli exclusion principle requires that one particle must be in the ground state and the other in the first excited state, but the excited state can be in either dimension. This degeneracy results in nonzero entropy in the limit $T \to 0$. Thus, for

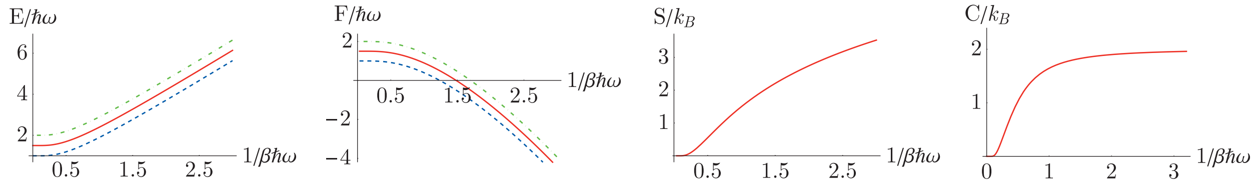

(a) (b) (c) (d)

Fig. 3 Equilibrium (A) internal energy, (B) free energy, (C) entropy, and (D) heat capacity for two statistical anyons in a one-dimensional harmonic potential with $p_{\mathrm{B}} = 1$ (*blue, dashed*), $p_{\mathrm{B}} = 1/2$ (*red, solid*), and $p_{\mathrm{B}} = 0$ (*green, dot-dashed*).

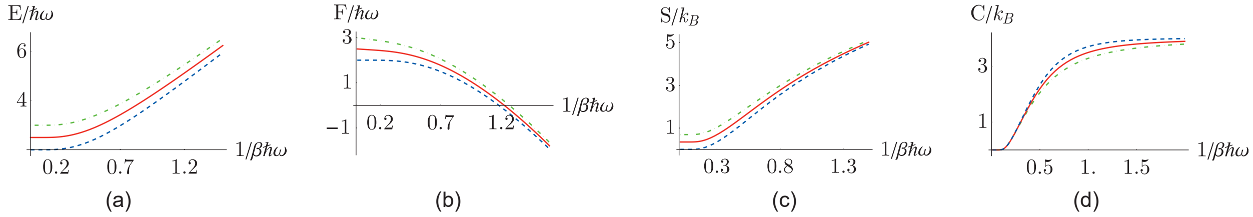

(a) (b) (c) (d)

Fig. 4 Equilibrium (A) internal energy, (B) free energy, (C) entropy, and (D) heat capacity for two statistical anyons in a two-dimensional harmonic potential with $p_B = 1$ (*blue*, *dashed*), $p_B = 1/2$ (*red*, *solid*), and $p_B = 0$ (*green*, *dot-dashed*).

statistical anyons the entropy varies smoothly between the boson and fermion limits as p_B changes from one to zero. Plots of the two-dimensional equilibrium thermodynamic quantities as a function of temperature are shown in Fig. 4.

2D FES anyons

For the case of two FES anyons in a harmonic potential the partition function has the following analytical form (Lerda, 1992; Myrheim, 1999)

$$Z_{\mathrm{TA}} = \frac{e^{-\beta\hbar\omega(2+v)} + e^{-\beta\hbar\omega(4-v)}}{\left(1-e^{-\beta\hbar\omega}\right)^2\left(e^{-2\beta\hbar\omega}\right)^2}, \tag{47}$$

where v is the anyonic phase parameter. Unlike the statistical anyon partition function, the FES partition function cannot be expressed as a function of the boson and fermion partition functions. In the two anyon problem, the anyonic phase can be interpreted as shifting the value of the relative motion angular momentum (Khare, 2005). Unlike GES and statistical anyons, the direction of rotation matters. Accounting for both possible exchange directions results in a multivalued wave function and leads to the two separate anyonic phase-dependent terms seen in the numerator of Eq. (47) (Myrheim, 1999).

As before, we determine the equilibrium internal energy, free energy, entropy, and heat capacity for the two FES anyon system by plugging Eq. (47) into Eq. (44) which yields

$$\begin{aligned}
E &= \hbar\omega\left[\coth\left(\frac{1}{2}\beta\hbar\omega\right) + 2\coth(\beta\hbar\omega)+(v-1)\tanh(\beta\hbar\omega(1-v))\right]\\
F &= \frac{1}{\beta}\ln\left[8\,\mathrm{sech}(\beta\hbar\omega(v-1))\sinh^2\left(\frac{1}{2}\beta\hbar\omega\right)\sinh^2(\beta\hbar\omega)\right]\\
S &= k_B\beta\hbar\omega\left[\coth\left(\frac{1}{2}\beta\hbar\omega\right) + 2\coth(\beta\hbar\omega)+(v-1)\tanh(\beta\hbar\omega(1-v))\right]\\
&\quad + k_B\ln\left[\frac{1}{8}\cosh(\beta\hbar\omega(v-1))\mathrm{csch}^2\left(\frac{1}{2}\beta\hbar\omega\right)\mathrm{csch}^2(\beta\hbar\omega)\right]\\
C &= \frac{1}{2}k_B\beta^2\hbar^2\omega^2\left[\mathrm{csch}^2\left(\frac{1}{2}\beta\hbar\omega\right) + 4\,\mathrm{csch}^2(\beta\hbar\omega)+2(v-1)^2\mathrm{sech}^2(\beta\hbar\omega(v-1))\right]
\end{aligned} \tag{48}$$

In Fig. 5, we plot each thermodynamic quantity as a function of temperature. Qualitatively, the behavior is similar to that of statistical anyons. However, there are some notable differences. First, we see that the entropy for FES anyons converges to zero as $T \rightarrow 0$. This indicates the existence of a unique ground state configuration for all values of v except $v = 1$. Furthermore, we see that at intermediate values of the anyonic phase parameter the heat capacity exceeds the bosonic value at low temperatures. Significantly, this indicates that the thermodynamic behavior of FES anyons is not confined to fall between that of bosons and fermions, as is the case for statistical anyons.

Comparing Figs. 4 and 5, we see that for the statistical anyons the line corresponding to $p_B = 1/2$ always remains evenly spaced between the bosonic and fermionic limits. This is expected as the statistical anyon energy spectrum is a weighted average over the bosonic and fermionic spectrums which, in turn, leads to thermodynamic behavior that is evenly spaced between the bosonic and fermionic limits over all temperatures for $p_B = 1/2$. Conversely, for FES anyons the line corresponding to $v = 1/2$ bends more toward

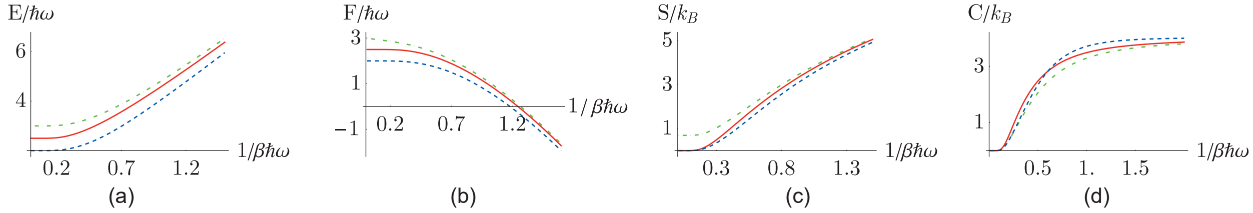

(a) (b) (c) (d)

Fig. 5 Equilibrium (A) internal energy, (B) free energy, (C) entropy, and (D) heat capacity for two FES anyons in a two-dimensional harmonic potential with anyon phase parameters $v = 0$ (*blue*, *dashed*), $v = 1/2$ (*red*, *solid*), and $v = 1$ (*green*, *dot-dashed*).

the fermionic limit as temperature increases. A consequence of this difference in thermodynamic behavior is that statistical anyons will retain their intermediate properties in higher temperature regimes.

Physically, the thermodynamic behavior of the FES anyons' has its roots in their hard-core nature and multivalued wave function. For harmonically confined FES anyons the energy, degeneracy, and level spacing all depend on ν (Myrheim, 1999; Khare, 2005). In the ground state, the energy eigenvalues corresponding to the two branches of the wave function only coincide in the fermionic limit, making $\nu = 1$ the only situation under which the ground state is degenerate and giving rise to the zero-temperature limit of the entropy observed in Fig. 5. At finite temperature the hard-core nature of FES anyons biases their thermodynamic behavior more toward the fermionic limit.

The behavior observed in the FES anyon heat capacity has similar physical origins. In the zero-temperature limit, the internal energy of FES anyons interpolates linearly between the bosonic and fermionic ground states, while at higher temperatures it converges to the fermionic behavior. This transition between an even average of the bosonic and fermionic behavior at zero temperature to near-fermionic behavior at higher temperatures necessitates a steeper positive slope of the internal energy at low temperatures than either bosons or fermions. This, in turn, leads to a heat capacity at intermediate values of ν that exceeds both bosons and fermions in this low-temperature transition region.

Thermodynamic equivalence

The previous results show that statistical and FES anyons display notably different thermodynamic behavior. However, with a parameter-dependent choice of the statistical mixture weights, it is possible to simulate the richer behavior of the FES anyons using the theoretically straightforward framework of statistical anyons.

The previously-examined thermodynamic behavior was derived entirely from the statistical and FES anyon partition functions. Setting the two partition functions (Eqs. 43 and 47) and solving for the statistical anyon parameter, p_{B}, yields

$$p_{\mathrm{B}} = \frac{\ln[\cosh((\nu - 1)\beta\hbar\omega)]}{\ln[\cosh(\beta\hbar\omega)]}. \tag{49}$$

We immediately see that this relationship between p_{B} and ν is dependent on the other physical parameters, namely, the inverse temperature and trapping frequency. However, if we take the high-temperature limit of Eq. (49), we find a simpler, parameter-independent relation,

$$p_{\mathrm{B}} = (\nu - 1)^2. \tag{50}$$

This approximation is exact in the limits of $\nu \to 0$ and $\nu \to 1$, which is expected as both statistical and FES anyons must converge to the same bosonic and fermionic limits. Eq. (50) is reminiscent of previous comparisons between Haldane's GES parameter and the topological anyon phase using the second Virial coefficient which also determined a quadratic polynomial relation (Murthy and Shankar, 1994a).

In Fig. 6, we plot the internal energy, free energy, entropy, and heat capacity for FES anyons, in comparison to statistical anyons with p_{B} chosen as given by Eq. (50). We see that the statistical and FES anyon behavior rapidly converges as temperature increases. However, the simplified relation between the anyon phase parameters does not capture the low-temperature behavior of the FES anyon heat capacity. To fully imitate this behavior, we must use Eq. (49). By plugging Eq. (49) into Eq. (44) we see that the equations of state for statistical and FES anyons become identical.

Detecting and manipulating FES anyons in two-dimensional materials is extremely challenging, which makes probing their thermodynamics difficult. Mimicking the thermodynamic behavior of FES anyons using statistical anyons provides a straightforward alternative approach, both as a model to test thermodynamic control of FES anyons or as a replacement in applications that would rely on their thermodynamics properties.

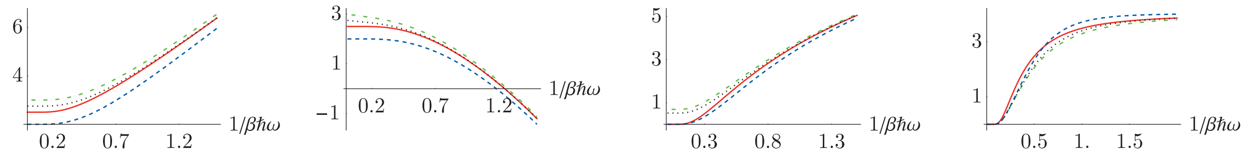

(a) (b) (c) (d)

Fig. 6 Comparison of (A) internal energy, (B) free energy, (C) entropy, and (D) heat capacity of two FES anyons with phase parameter ν, against two statistical anyons using phase parameter $p_{\mathrm{B}} = (\nu - 1)^2$ for $\nu = 0$, $p_{\mathrm{B}} = 1$ (*blue, dashed*), $\nu = 1$, $p_{\mathrm{B}} = 0$ (*green, dot-dashed*), $\nu = 1/2$ (red, solid), and $p_{\mathrm{B}} = 1/4$ (*black, dotted*).

Conclusion

Summary

In this chapter we have presented a dimension-independent formulation of anyons, "statistical anyons," in which the anyonic properties arise from averaging over the behavior of a statistical mixture of bosons and fermions. We began by outlining an optical implementation of statistical anyons where the anyonic behavior manifests through a generalization of the HOM effect. Moving beyond quantum optics, we showed that the statistical anyon framework is equivalent to Haldane's GES. Motivated by the statistical origins of the anyonic behavior, we compared the equilibrium thermodynamics of statistical and FES anyons. We demonstrated that, with a parameter-dependent choice of the anyonic phase, statistical anyons can exactly imitate the thermodynamic behavior of FES anyons.

Impacts and future directions

The framework of statistical anyons provides a tractable theoretical tool for studying anyonic behavior. It extends GES to a range of new experimental settings, including Bose–Fermi mixtures (Fang et al., 2011; Dehkharghani et al., 2017; Decamp et al., 2017; Fukuhara et al., 2009; Onofrio, 2016; Sowiński and García-March, 2019), optimechanical systems (Holmes et al., 2020), and surface plasmonics (Chen et al., 2018).

Statistical anyons, like the GES anyons they replicate, lack the non-Abelian properties necessary for implementing topological quantum computation. However, as demonstrated in Section "Thermodynamic equivalence," they do provide an accessible tool for simulating the thermodynamic behavior of FES anyons. From a device-oriented standpoint, the role of anyonic behavior in the performance of quantum thermal machines has been studied both in the context of GES (Jaramillo et al., 2016; Beau et al., 2016) and statistical anyons (Myers and Deffner, 2021; Myers et al., 2021). Other thermodynamic properties of statistical anyons, such as the impact of anyonic statistics in Gibbs mixing (Yadin et al., 2020), remain to be explored. The framework of statistical anyons itself provides a range of possible new directions. The relationship between statistical anyons and other methods of generating anyonic behavior, including N00N states subject to Bloch oscillations (Lebugle et al., 2015), quasi-holes in Bose–Einstein condensates (Paredes et al., 2001), and black hole gasses (Strominger, 1993; Medvedev, 1997) is unknown. Finally, we note that the statistical anyon framework has only been applied for the case of an ensemble of noninteracting particles. In analogy to how the addition of an interparticle interaction can manifest GES in ideal bosons and fermions, it is possible that incorporating interactions may expand the state space of possible anyonic phases accessible to statistical anyons.

References

Aneziris C, Balachandran AP, and Sen D (1991) Statistics in one dimension. *International Journal of Modern Physics A* 06(26): 4721. https://doi.org/10.1142/S0217751X91002240.

Anghel D-V (2013) From fractional exclusion statistics back to Bose and Fermi distributions. *Physics Letters A* 377(41): 2922. https://doi.org/10.1016/j.physleta.2013.09.007.

Arovas D, Schrieffer JR, and Wilczek F (1984) Fractional statistics and the quantum Hall effect. *Physical Review Letters* 53(7): 722. https://doi.org/10.1103/PhysRevLett.53.722.

Arovas DP, Schrieffer R, Wilczek F, and Zee A (1985) Statistical mechanics of anyons. *Nuclear Physics B* 251: 117. https://doi.org/10.1016/0550-3213(85)90252-4. https://www.sciencedirect.com/science/article/pii/0550321385902524.

Banerjee M, Heiblum M, Umansky V, Feldman DE, Oreg Y, and Stern A (2018) Observation of half-integer thermal Hall conductance. *Nature* 559(7713): 205–210. https://doi.org/10.1038/s41586-018-0184-1.

Bartolomei H, Kumar M, Bisognin R, Marguerite A, Berroir J-M, Bocquillon E, Plaçais B, Cavanna A, Dong Q, Gennser U, Jin Y, and Fève G (2020) Fractional statistics in anyon collisions. *Science* 368(6487): 173. https://doi.org/10.1126/science.aaz5601. https://science.sciencemag.org/content/368/6487/173.

Batchelor MT and Guan X-W (2006) Generalized exclusion statistics and degenerate signature of strongly interacting anyons. *Physical Review B* 74(19): 195121. https://doi.org/10.1103/PhysRevB.74.195121.

Batchelor MT and Guan X-W (2007) Fermionization and fractional statistics in the strongly interacting one-dimensional Bose gas. *Laser Physics Letters* 4(1): 77. https://doi.org/10.1002/lapl.2006100681.

Batchelor MT, Guan X-W, and Oelkers N (2006) One-dimensional interacting anyon gas: Low-energy properties and Haldane exclusion statistics. *Physical Review Letters* 96(21): 210402. https://doi.org/10.1103/PhysRevLett.96.210402.

Batchelor MT, Guan X-W, and He J-S (2007) The Bethe ansatz for 1D interacting anyons. *Journal of Statistical Mechanics: Theory and Experiment* 2007(03): P03007. https://doi.org/10.1088/1742-5468/2007/03/p03007.

Batchelor MT, Guan X-W, and Kundu A (2008) One-dimensional anyons with competing δ-function and derivative δ-function potentials. *Journal of Physics A* 41(35): 352002. https://doi.org/10.1088/1751-8113/41/35/352002.

Beau M, Jaramillo J, and del Campo A (2016) Scaling-up quantum heat engines efficiently via shortcuts to adiabaticity. *Entropy* 18(5): 168. https://doi.org/10.3390/e18050168.

Bernard D and Wu Y-S (1994) *A note on statistical interactions and the thermodynamic Bethe ansatz.* arXiv:cond-mat/9404025.

Bhaduri RK, Bhalerao RS, Khare A, Law J, and Murthy MVN (1991) Semiclassical two- and three-anyon partition functions. *Physical Review Letters* 66(5): 523. https://doi.org/10.1103/PhysRevLett.66.523.

Bonderson P, Kitaev A, and Shtengel K (2006) Detecting non-Abelian statistics in the $\nu = 5/2$ fractional quantum Hall state. *Physical Review Letters* 96(1): 016803. https://doi.org/10.1103/PhysRevLett.96.016803.

Brink L, Hansson TH, and Vasiliev MA (1992) Explicit solution to the N-body Calogero problem. *Physics Letters B* 286(1): 109. https://doi.org/10.1016/0370-2693(92)90166-2.

Brzeziński T, Gonera C, and Maślanka P (1999) On the equivalence of the rational Calogero-Moser system to free particles. *Physics Letters A* 254(3): 185. https://doi.org/10.1016/S0375-9601(99)00149-8. https://www.sciencedirect.com/science/article/pii/S0375960199001498.

Bytsko AG and Fring A (1998) Thermodynamic Bethe ansatz with Haldane statistics. *Nuclear Physics B* 532(3): 588. https://doi.org/10.1016/S0550-3213(98)00531-8. https://www.sciencedirect.com/science/article/pii/S0550321398005318.

Calabrese P and Mintchev M (2007) Correlation functions of one-dimensional anyonic fluids. *Physical Review B* 75(23): 233104. https://doi.org/10.1103/PhysRevB.75.233104.

Calogero F (1969) Solution of a three-body problem in one dimension. *Journal of Mathematical Physics* 10(12): 2191. https://doi.org/10.1063/1.1664820.

Calogero F (1971) Solution of the one-dimensional N-body problems with quadratic and/or inversely quadratic pair potentials. *Journal of Mathematical Physics* 12(3): 419. https://doi.org/10.1063/1.1665604.

Camino FE, Zhou W, and Goldman VJ (2005) Realization of a Laughlin quasiparticle interferometer: Observation of fractional statistics. *Physical Review B* 72(7): 075342. https://doi.org/10.1103/PhysRevB.72.075342.

Chen W (1995) Thermodynamics of an anyon system. *Physical Review D* 52(10): 6122. https://doi.org/10.1103/PhysRevD.52.6122.

Chen Z (2018) Mapping quantum many-body system to decoupled harmonic oscillators: General discussions and examples. *Physics Letters A* 382(37): 2613. https://doi.org/10.1016/j.physleta.2018.07.043. https://www.sciencedirect.com/science/article/pii/S037596011830820X.

Chen Y, Lee C, Lu L, Liu D, Wu Y-K, Feng L-T, Li M, Rockstuhl C, Guo G-P, Guo G-C, Tame M, and Ren X-F (2018) Quantum plasmonic N00N state in a silver nanowire and its use for quantum sensing. *Optica* 5(10): 1229. https://doi.org/10.1364/OPTICA.5.001229. http://www.osapublishing.org/optica/abstract.cfm?URI=optica-5-10-1229.

Clarke DJ, Alicea J, and Shtengel K (2013) Exotic non-Abelian anyons from conventional fractional quantum Hall states. *Nature Communications* 4(1). https://doi.org/10.1038/ncomms2340.

Comtet A, Majumdar SN, and Ouvry S (2007) Integer partitions and exclusion statistics. *Journal of Physics A: Mathematical and Theoretical* 40(37): 11255. https://doi.org/10.1088/1751-8113/40/37/004.

Dasnières de Veigy A and Ouvry S (1994) Equation of state of an anyon gas in a strong magnetic field. *Physical Review Letters* 72(5): 600. https://doi.org/10.1103/PhysRevLett.72.600.

Dasnières de Veigy A and Ouvry S (1995) One-dimensional statistical mechanics for identical particles: The Calogero and anyon cases. *Modern Physics Letters B* 09(05): 271. https://doi.org/10.1142/S0217984995000267.

de Chamon CC, Freed DE, Kivelson SA, Sondhi SL, and Wen XG (1997) Two point-contact interferometer for quantum Hall systems. *Physical Review B* 55(4): 2331. https://doi.org/10.1103/PhysRevB.55.2331.

Decamp J, Jünemann J, Albert M, Rizzi M, Minguzzi A, and Vignolo P (2017) Strongly correlated one-dimensional Bose–Fermi quantum mixtures: Symmetry and correlations. *New Journal of Physics* 19(12): 125001. https://doi.org/10.1088/1367-2630/aa94ef.

Dehkharghani AS, Bellotti FF, and Zinner NT (2017) Analytical and numerical studies of Bose-Fermi mixtures in a one-dimensional harmonic trap. *Journal of Physics B* 50(14): 144002. https://doi.org/10.1088/1361-6455/aa7797.

del Campo A (2008) Fermionization and bosonization of expanding one-dimensional anyonic fluids. *Physical Review A* 78(4): 045602. https://doi.org/10.1103/PhysRevA.78.045602.

del Campo A (2016) Exact quantum decay of an interacting many-particle system: The Calogero-Sutherland model. *New Journal of Physics* 18(1): 015014. https://doi.org/10.1088/1367-2630/18/1/015014.

Fang B, Vignolo P, Gattobigio M, Miniatura C, and Minguzzi A (2011) Exact solution for the degenerate ground-state manifold of a strongly interacting one-dimensional Bose-Fermi mixture. *Physical Review A* 84(2): 023626. https://doi.org/10.1103/PhysRevA.84.023626.

Fukuhara T, Sugawa S, Takasu Y, and Takahashi Y (2009) All-optical formation of quantum degenerate mixtures. *Physical Review A* 79(2): 021601(R). https://doi.org/10.1103/PhysRevA.79.021601.

Giacconi P, Maltoni F, and Soldati R (1996) Second virial coefficient for contact-interacting anyons. *Physical Review B* 53(15): 10065. https://doi.org/10.1103/PhysRevB.53.10065.

Girardeau MD (2006) Anyon-fermion mapping and applications to ultracold gases in tight waveguides. *Physical Review Letters* 97(10): 100402. https://doi.org/10.1103/PhysRevLett.97.100402.

Guan X-W and Chen Y-Y (2016) Yang-Yang equilibrium statistical mechanics: A brilliant method. *60 Years of Yang-Mills Gauge Field Theories*, pp. 399–414. https://doi.org/10.1142/9789814725569_0024.

Gurappa N and Panigrahi PK (1999) Equivalence of the Calogero-Sutherland model to free harmonic oscillators. *Physical Review B* 59(4): R2490. https://doi.org/10.1103/PhysRevB.59.R2490.

Gurappa N and Panigrahi PK (2000) Free harmonic oscillators, Jack polynomials, and Calogero-Sutherland systems. *Physical Review B* 62(3): 1943. https://doi.org/10.1103/PhysRevB.62.1943.

Haldane FDM (1991) Fractional statistics" in arbitrary dimensions: A generalization of the Pauli principle. *Physical Review Letters* 67(8): 937. https://doi.org/10.1103/PhysRevLett.67.937.

Hao Y, Zhang Y, and Chen S (2008) Ground-state properties of one-dimensional anyon gases. *Physical Review A* 78(2): 023631. https://doi.org/10.1103/PhysRevA.78.023631.

Holmes Z, Anders J, and Mintert F (2020) Enhanced energy transfer to an optomechanical piston from indistinguishable photons. *Physical Review Letters* 124(21): 210601. https://doi.org/10.1103/PhysRevLett.124.210601.

Hong CK, Ou ZY, and Mandel L (1987) Measurement of subpicosecond time intervals between two photons by interference. *Physical Review Letters* 59(18): 2044. https://doi.org/10.1103/PhysRevLett.59.2044.

Isakov SB (1994a) Fractional statistics in one dimension: Modeling by means of $1/x^2$ interaction and statistical mechanics. *International Journal of Modern Physics A* 09(15): 2563–2582. https://doi.org/10.1142/S0217751X94001023.

Isakov SB (1994b) Statistical mechanics for a class of quantum statistics. *Physical Review Letters* 73(16): 2150. https://doi.org/10.1103/PhysRevLett.73.2150.

Isakov SB, Arovas DP, Myrheim J, and Polychronakos AP (1996) Thermodynamics for fractional exclusion statistics. *Phys. Lett. A* 212(6): 299. https://doi.org/10.1016/0375-9601(96)00157-0. http://www.sciencedirect.com/science/article/pii/0375960196001570.

Jaramillo J, Beau M, and del Campo A (2016) Quantum supremacy of many-particle thermal machines. *New Journal of Physics* 18(7): 075019. https://doi.org/10.1088/1367-2630/18/7/075019.

Ji Y, Chung Y, Sprinzak D, Heiblum M, Mahalu D, and Shtrikman H (2003) An electronic Mach-Zehnder interferometer. *Nature* 422(6930): 415. https://doi.org/10.1038/nature01503.

Joyce GS, Sarkar S, Spalek J, and Byczuk K (1996) Thermodynamic properties of particles with intermediate statistics. *Physical Review B* 53(3): 990. https://doi.org/10.1103/PhysRevB.53.990.

Kasahara Y, Ohnishi T, Mizukami Y, Tanaka O, Ma S, Sugii K, Kurita N, Tanaka H, Nasu J, Motome Y, Shibauchi T, and Matsuda Y (2018) Majorana quantization and half-integer thermal quantum Hall effect in a Kitaev spin liquid. *Nature* 559(7713): 227. https://doi.org/10.1038/s41586-018-0274-0.

Khare A (2005) *Fractional Statistics and Quantum Theory*, second ed. World Scientific. https://doi.org/10.1142/5752.

Kitaev A (2003) Fault-tolerant quantum computation by anyons. *Annals of Physics* 303(1): 2. https://doi.org/10.1016/s0003-4916(02)00018-0.

Kundu A (1999) Exact solution of double δ function Bose gas through an interacting anyon gas. *Physical Review Letters* 83(7): 1275. https://doi.org/10.1103/PhysRevLett.83.1275.

Law KT, Feldman DE, and Gefen Y (2006) Electronic Mach-Zehnder interferometer as a tool to probe fractional statistics. *Physical Review B* 74(4): 045319. https://doi.org/10.1103/PhysRevB.74.045319.

Lebugle M, Gräfe M, Heilmann R, Perez-Leija A, Nolte S, and Szameit A (2015) Experimental observation of N00N state Bloch oscillations. *Nature Communications* 6(1): 8273. https://doi.org/10.1038/ncomms9273.

Leinaas JM and Myrheim J (1977) On the theory of identical particles. *Il Nuovo Cimento B* 37(1): 1. https://doi.org/10.1007/BF02727953.

Lerda A (1992) *Anyons: Quantum Mechanics of Particles with Fractional Statistics*. Springer Berlin Heidelberg. https://doi.org/10.1007/978-3-540-47466-1.

Lerda A and Sciuto S (1993) Anyons and quantum groups. *Nuclear Physics B* 401(3): 613. https://doi.org/10.1016/0550-3213(93)90316-H.

Lieb EH and Liniger W (1963) Exact analysis of an interacting Bose gas. I. The general solution and the ground state. *Physics Review* 130(4): 1605. https://doi.org/10.1103/PhysRev.130.1605.

Matthews JCF, Poulios K, Meinecke JDA, Politi A, Peruzzo A, Ismail N, Wörhoff K, Thompson MG, and O'Brien JL (2013) Observing fermionic statistics with photons in arbitrary processes. *Scientific Reports* 3(1): 1539. https://doi.org/10.1038/srep01539.

McClure DT, Chang W, Marcus CM, Pfeiffer LN, and West KW (2012) Fabry-Perot interferometry with fractional charges. *Physical Review Letters* 108(25): 256804. https://doi.org/10.1103/PhysRevLett.108.256804.

Medvedev MV (1997) Properties of particles obeying ambiguous statistics. *Physical Review Letters* 78(22): 4147. https://doi.org/10.1103/PhysRevLett.78.4147.

Meljanac S, Mileković M, and Samsarov A (2004) Generalized Calogero model in arbitrary dimensions. *Physics Letters B* 594(1): 241. https://doi.org/10.1016/j.physletb.2004.05.034. http://www.sciencedirect.com/science/article/pii/S0370269304007816.

Michler M, Mattle K, Weinfurter H, and Zeilinger A (1996) Interferometric Bell-state analysis. *Physical Review A* 53(3): R1209. https://doi.org/10.1103/PhysRevA.53.R1209.

Moore G and Read N (1991) Nonabelions in the fractional quantum hall effect. *Nuclear Physics B* 360(2): 362. https://doi.org/10.1016/0550-3213(91)90407-O. http://www.sciencedirect.com/science/article/pii/055032139190407O.

Murthy MVN and Shankar R (1994a) Haldane exclusion statistics and second virial coefficient. *Physical Review Letters* 72(23): 3629. https://doi.org/10.1103/PhysRevLett.72.3629.

Murthy MVN and Shankar R (1994b) Thermodynamics of a one-dimensional ideal gas with fractional exclusion statistics. *Physical Review Letters* 73(25): 3331. https://doi.org/10.1103/PhysRevLett.73.3331.

Myers NM and Deffner S (2021) Thermodynamics of statistical anyons. *PRX Quantum* 2(4): 040312. https://doi.org/10.1103/PRXQuantum.2.040312.

Myers NM, McCready J, and Deffner S (2021) Quantum heat engines with singular interactions. *Symmetry* 13(6): 978. https://doi.org/10.3390/sym13060978. https://www.mdpi.com/2073-8994/13/6/978.

Myrheim J (1999) Anyons. In: Comtet A, Jolicœur T, Ouvry S, and David F (eds.) *Topological Aspects of Low Dimensional Systems*, p. 265. Springer Berlin Heidelberg. https://doi.org/10.1007/3-540-46637-1.

Nakamura J, Fallahi S, Sahasrabudhe H, Rahman R, Liang S, Gardner GC, and Manfra MJ (2019) Aharonov-Bohm interference of fractional quantum Hall edge modes. *Nature Physics* 15(6): 563. https://doi.org/10.1038/s41567-019-0441-8.

Nasu J and Motome Y (2015) Thermodynamics of chiral spin liquids with Abelian and non-Abelian anyons. *Physical Review Letters* 115(8): 087203. https://doi.org/10.1103/PhysRevLett.115.087203.

Nayak C, Simon SH, Stern A, Freedman M, and Das Sarma S (2008) Non-Abelian anyons and topological quantum computation. *Reviews of Modern Physics* 80(3): 1083. https://doi.org/10.1103/RevModPhys.80.1083.

Ofek N, Bid A, Heiblum M, Stern A, Umansky V, and Mahalu D (2010) Role of interactions in an electronic Fabry-Perot interferometer operating in the quantum Hall effect regime. *Proceedings of the National Academy of Sciences* 0027-8424. 107(12): 5276. https://doi.org/10.1073/pnas.0912624107. https://www.pnas.org/content/107/12/5276.

Onofrio R (2016) Cooling and thermometry of atomic Fermi gases. *Physics-Uspekhi* 59(11): 1129. https://doi.org/10.3367/ufne.2016.07.037873.

Ouvry S (2001) On the relation between the anyon and Calogero models. *Physics Letters B* 510(1): 335. https://doi.org/10.1016/S0370-2693(01)00601-3.

Ouvry S and Polychronakos AP (2009) The Lieb–Liniger model in the infinite coupling constant limit. *Journal of Physics A* 42(27): 275302. https://doi.org/10.1088/1751-8113/42/27/275302.

Ouvry S and Polychronakos AP (2018) Mapping the Calogero model on the anyon model. *Nuclear Physics B* 936: 189. https://doi.org/10.1016/j.nuclphysb.2018.09.011.

Ouvry S and Polychronakos AP (2021) *Exclusion statistics for particles with a discrete spectrum.* arXiv:2105.14042.

Paredes B, Fedichev P, Cirac JI, and Zoller P (2001) $\frac{1}{2}$-anyons in small atomic Bose-Einstein condensates. *Physical Review Letters* 87(1): 010402. https://doi.org/10.1103/PhysRevLett.87.010402.

Pâţu OI, Korepin VE, and Averin DV (2007) Correlation functions of one-dimensional Lieb-Liniger anyons. *Journal of Physics A* 40(50): 14963. https://doi.org/10.1088/1751-8113/40/50/004.

Pâţu OI, Korepin VE, and Averin DV (2008a) One-dimensional impenetrable anyons in thermal equilibrium: I. Anyonic generalization of Lenard's formula. *Journal of Physics A* 41(14): 145006. https://doi.org/10.1088/1751-8113/41/14/145006.

Pâţu OI, Korepin VE, and Averin DV (2008b) One-dimensional impenetrable anyons in thermal equilibrium: II. Determinant representation for the dynamic correlation functions. *Journal of Physics A* 41(25): 255205. https://doi.org/10.1088/1751-8113/41/25/255205.

Polychronakos AP (1989) Non-relativistic bosonization and fractional statistics. *Nuclear Physics B* 324(3): 597. https://doi.org/10.1016/0550-3213(89)90522-1. https://www.sciencedirect.com/science/article/pii/0550321389905221.

Polychronakos AP (2000) Virial coefficients of non-Abelian anyons. *Physical Review Letters* 84(6): 1268. https://doi.org/10.1103/PhysRevLett.84.1268.

Polychronakos AP (2006) The physics and mathematics of Calogero particles. *Journal of Physics A* 39(41): 12793. https://doi.org/10.1088/0305-4470/39/41/s07.

Rarity JG, Tapster PR, Jakeman E, Larchuk T, Campos RA, Teich MC, and Saleh BEA (1990) Two-photon interference in a Mach-Zehnder interferometer. *Physical Review Letters* 65(11): 1348. https://doi.org/10.1103/PhysRevLett.65.1348.

Rovenchak A (2014) Two-parametric fractional statistics models for anyons. *European Physical Journal B* 87(8): 175. https://doi.org/10.1140/epjb/e2014-50171-8.

Santachiara R and Calabrese P (2008) One-particle density matrix and momentum distribution function of one-dimensional anyon gases. *Journal of Statistical Mechanics: Theory and Experiment* 2008(06): P06005. https://doi.org/10.1088/1742-5468/2008/06/p06005.

Sen D (1992) Spectrum of three anyons in a harmonic potential and the third virial coefficient. *Physical Review Letters* 68(20): 2977. https://doi.org/10.1103/PhysRevLett.68.2977.

Sowiński T and García-March MÁ (2019) One-dimensional mixtures of several ultracold atoms: A review. *Reports on Progress in Physics* 82(10): 104401. https://doi.org/10.1088/1361-6633/ab3a80.

Sporre M, Verbaarschot JJM, and Zahed I (1993) Anyon spectra and the third virial coefficient. *Nuclear Physics B* 389(3): 645. https://doi.org/10.1016/0550-3213(93)90357-U.

Strominger A (1993) Black hole statistics. *Physical Review Letters* 71(21): 3397. https://doi.org/10.1103/PhysRevLett.71.3397.

Sutherland B (1988) Exact solution of a lattice band problem related to an exactly soluble many-body problem: The missing-states problem. *Physical Review B* 38(10): 6689. https://doi.org/10.1103/PhysRevB.38.6689.

Tang G, Eggert S, and Pelster A (2015) Ground-state properties of anyons in a one-dimensional lattice. *New Journal of Physics* 17(12): 123016. https://doi.org/10.1088/1367-2630/17/12/123016.

Vitoriano C and Coutinho-Filho MD (2009) Fractional statistics and quantum scaling properties of the Hubbard chain with bond-charge interaction. *Physical Review Letters* 102(14): 146404. https://doi.org/10.1103/PhysRevLett.102.146404.

Wang Q, Zhang Y-S, Huang Y-F, and Guo G-C (2007) Simulating the fourth-order interference phenomenon of anyons with photon pairs. *European Physical Journal D* 42(1): 179. https://doi.org/10.1140/epjd/e2007-00003-3.

Wilczek F (1982) Quantum mechanics of fractional-spin particles. *Physical Review Letters* 49(14): 957. https://doi.org/10.1103/PhysRevLett.49.957.

Willett RL, Nayak C, Shtengel K, Pfeiffer LN, and West KW (2013) Magnetic-field-tuned Aharonov-Bohm oscillations and evidence for non-Abelian anyons at $\nu = 5/2$. *Physical Review Letters* 111(18): 186401. https://doi.org/10.1103/PhysRevLett.111.186401.

Willett RL, Shtengel K, Nayak C, Pfeiffer LN, Chung YJ, Peabody ML, Baldwin KW, and West KW (2019) *Interference measurements of non-Abelian e/4 and Abelian e/2 quasiparticle braiding.* arXiv:1905.10248.

Wu Y-S (1994) Statistical distribution for generalized ideal gas of fractional-statistics particles. *Physical Review Letters* 73(7): 922. https://doi.org/10.1103/PhysRevLett.73.922.

Yadin B, Morris B, and Adesso G (2020) Extracting work from mixing indistinguishable systems: A quantum Gibbs "paradox. *arXiv:2006.12482*.

Yannouleas C and Landman U (2019) Anyon optics with time-of-flight two-particle interference of double-well-trapped interacting ultracold atoms. *Physical Review A* 100(1): 013605. https://doi.org/10.1103/PhysRevA.100.013605.

Zeilinger A (1998) Quantum entanglement: A fundamental concept finding its applications. *Physica Scripta* T76(1): 203. https://doi.org/10.1238/physica.topical.076a00203.

Recent developments in fractional Chern insulators

Zhao Liu[a] and **Emil J Bergholtz**[b], [a]Zhejiang Institute of Modern Physics, Zhejiang University, Hangzhou, China; [b]Department of Physics, Stockholm University, AlbaNova University Center, Stockholm, Sweden

© 2024 Elsevier Ltd. All rights reserved.

Introduction **515**
Microscopic model **517**
Tight-binding formalism 517
Effective continuum model 518
Conditions of the existence of FCIs **519**
Requirements for the band 519
Requirements for the interaction 520
Particle-hole asymmetry 520
Numerical diagnosis of FCIs **521**
Basic identifications 521
Competing phases 522
FCIs in twisted bilayer graphene **523**
Microscopic model of TBG 523
Numerical evidence of FCIs 524
Numerical evidence of competing phases 526
FCIs in Bloch bands with high Chern numbers **527**
Experimental observation of FCIs **528**
Experiment in Bernal-stacked bilayer graphene 528
Experiment in twisted bilayer graphene 529
FCIs in cold-atom systems **530**
Conclusion **531**
Acknowledgments **531**
References **532**

Abstract

Fractional Chern insulators (FCIs) are lattice generalizations of the conventional fractional quantum Hall effect (FQHE) in two-dimensional (2D) electron gases. They typically arise in a 2D lattice without time-reversal symmetry when a nearly flat Bloch band with nonzero Chern number is partially occupied by strongly interacting particles. Band topology and interactions endow FCIs exotic topological orders which are characterized by the precisely quantized Hall conductance, robust ground-state degeneracy on high-genus manifolds, and fractionalized quasiparticles. Since in principle FCIs can exist at zero magnetic field and be protected by a large energy gap, they provide a potentially experimentally more accessible avenue for observing and harnessing FQHE phenomena. Moreover, the interplay between FCIs and lattice-specific effects that do not exist in the conventional continuum FQHE poses new theoretical challenges. In this chapter, we provide a general introduction of the theoretical model and numerical simulation of FCIs, then pay special attention on the recent development of this field in moiré materials while also commenting on potential alternative implementations in cold atom systems. With a plethora of exciting theoretical and experimental progress, topological flat bands in moiré materials such as magic-angle twisted bilayer graphene on hexagonal boron nitride have indeed turned out to be a remarkably versatile platform for FCIs featuring an intriguing interplay between topology, geometry, and interactions.

Introduction

Restricting electrons in a two-dimensional (2D) plane penetrated by a uniform magnetic field and cooling the system to low temperature seems like a simple setup. However, it provides one of the most significant discoveries in condensed matter physics over the past half century. Remarkably, the Hall resistance R_H of this 2D electron gas (2DEG) has a novel dependence on the magnetic field B. Instead of increasing linearly with B as predicted by the classical theory, R_H develops multiple plateaus near proper rational filling ν, on which its value is precisely quantized at $R_H = h/(\nu e^2)$. Here h is the Planck constant, $-e$ is the electron charge, and $\nu = N/N_\phi$ with N and N_ϕ the number of electrons and magnetic flux quanta, respectively. This phenomenon is known as the quantum Hall effect (QHE). The plateaus near integer $\nu = n$, called the integer QHE (IQHE), were first discovered in 1980 by K. von Klitzing (Klitzing et al., 1980). These IQHE states can be understood in a single-particle picture: they result from the Landau quantization of an electron in the magnetic field, and correspond to n fully filled Landau levels (LLs). On the boundary, these n LLs come with n chiral edge modes. The precisely quantized R_H originates from a topological invariant—the Chern number $\mathcal{C}$ which is one for each LL (Thouless et al., 1982; Avron et al., 1983; Niu et al., 1985). This Chern number cannot change so long as the energy

https://doi.org/10.1016/B978-0-323-90800-9.00136-0

gap in the bulk, which is the LL spacing in this case, does not close. This gives rise to the robustness of the IQHE plateaus. In this sense, the IQHE states are the first observed topological band insulators. By contrast, the QHE near fractional $\nu = f$, observed by Tsui and Störmer in 1983 (Tsui et al., 1982) and dubbed the fractional quantum Hall effect (FQHE), has a very different origin. As the single-particle states in each LL are exactly degenerate, it must be the electron-electron interaction that lifts the huge degeneracy in the partially filled LL and stabilize the FQHE. While this strongly correlated nature makes the FQHE notoriously difficult to study, it also endows the FQHE an exotic order: the intrinsic topological order (Wen, 1990), as characterized by non-trivial ground-state degeneracies depending on the genus of the manifold on which the FQH states reside (Wen and Niu, 1990), long-range entanglement (Kitaev and Preskill, 2006; Levin and Wen, 2006), and fractionalized quasiparticle excitations (Laughlin, 1983; Moore and Read, 1991; Feldman and Halperin, 2021). Motivated by understanding and utilizing exotic topological orders, the FQHE has grown to become one of the arguably most exuberant fields of modern condensed matter physics.

With more FQHE plateaus discovered in 2DEGs and deeper understanding obtained about the nature of observed states, relaxing the limitations of the strong magnetic field and ultralow temperature required to realize the FQHE remains a long-standing dream. In conventional 2DEG setups, $B \sim 15$ T and $T \lesssim 1$ K are necessary for the robust $\nu = 1/3$ plateau (Tsui et al., 1982). We need stronger magnetic fields to reach smaller fillings, and temperature of at least one order of magnitude lower and cleaner samples to see more fragile FQH states. Hence, a natural question arises: can we realize the FQHE at zero (at least much weaker) magnetic fields and higher temperature? Intuitively the solution to this question calls for a platform change. The first important step in this direction was provided by Haldane in his seminal work in 1988, where he constructed a simple tight-binding model on the honeycomb lattice and showed that the IQHE can exist in the lattice at zero net magnetic field (Haldane, 1988). In this model, the time-reversal symmetry (TRS) breaking caused by the magnetic field in the conventional IQHE is achieved by complex hopping which can be emulated by spin-orbit coupling in the lattice, and isolated Bloch bands carrying $\mathcal{C} = \pm 1$ play the role of LLs. Such lattice versions of the conventional IQHE are now called Chern insulators, which were first reported in 2013 in thin films of chromium-doped $(\mathrm{Bi, Sb})_2\mathrm{Te}_3$ (Chang et al., 2013) and later also in cold-atom systems (Jotzu et al., 2014).

Haldane's construction of Chern insulators raises the possibility of obtaining the FQHE in 2D lattice systems with broken TRS, dubbed fractional Chern insulators (FCIs), down to zero magnetic field. Of course, a lattice model should satisfy several conditions in order to host FCIs. The most natural requirement is a nearly flat Bloch band with nonzero Chern number, i.e., a nearly flat topological (Chern) band which can mimic an exactly flat LL in a 2DEG. The weak band dispersion enhances the interaction effect, so that intuitively interacting particles have a chance to form FQHE-like states when they partially occupy the band. Despite of important early work on FCIs, including the construction of a parent Hamiltonian in lattices containing only short range interactions and an exponentially decaying tail of hopping terms (Kapit and Mueller, 2010), the research in this direction became mainstream only in 2011 when it was emphasized that nearly flat Chern bands can exist in tight-binding models with strictly short-ranged hopping (Tang et al., 2011; Sun et al., 2011; Neupert et al., 2011). Subsequent numerical works indeed confirmed the existence of FCIs in various $|\mathcal{C}| = 1$ flat bands as lattice analogs of conventional FQH states, including the Laughlin state, Moore-Read state, and hierarchy-composite-fermion series (Sheng et al., 2011; Regnault and Andrei Bernevig, 2011; Wang et al., 2011, 2012b; Wu et al., 2012a; Läuchli et al., 2013; Liu et al., 2013a). The adiabatic continuity between these FCIs and the corresponding conventional FQH states (Scaffidi and Möller, 2012; Wu et al., 2012b; Liu and Bergholtz, 2013; Wu et al., 2013) was established via mapping single-particle states in a Chern band to those in a LL (Qi, 2011; Wu et al., 2012b; Jian and Qi, 2013; Wu et al., 2013, 2014). Crucially, the energy gap protecting these FCIs may be greatly increased compared to conventional FQH states in 2DEGs, as it is determined by Coulomb interaction on the lattice scale rather than the magnetic length in 2DEGs which is typically two orders of magnitude larger. In fact, a naive estimate does not rule out FCIs at room-temperature (Tang et al., 2011).

The benefit of studying FCIs soon exceeds just finding lattice analogs of the already known conventional FQH states. The remarkable distinctions between a Chern band and a LL raise possibilities of new physics and meanwhile pose new challenges. Unlike for LLs, the quantum geometry (Berry curvature, Fubini-Study metric, etc.) of a Chern band is in general fluctuating in the Brillouin zone. Shortly after the first numerical identifications of FCIs, the key role played by this inhomogeneous quantum geometry on the stability of FCIs was noticed (Parameswaran et al., 2012; Roy, 2014; Jackson et al., 2015). Geometry might sound less important than topology, because under deformation of the band it is not invariant like Chern number even if the band keeps isolated. However, analytical and numerical analysis has unveiled it as a crucial criterion to judge how good a Chern band is for hosting FCIs. Thanks to the studies on FCIs, now we are understanding more about the effect of fluctuating band geometry on the many-body physics (Claassen et al., 2015; Wang et al., 2021; Parker et al., 2021; Varjas et al., 2022; Abouelkomsan et al., 2022), which is absent in the conventional FQHE due to the uniform geometry of a LL. Apart from the non-uniform quantum geometry, a Bloch band can support high Chern number $|\mathcal{C}| > 1$ (Wang and Ran, 2011; Trescher and Bergholtz, 2012; Yang et al., 2012), while each LL can only carry $|\mathcal{C}| = 1$. This lattice-specific feature implies qualitatively new FCI states beyond the FQH paradigm. Excitingly, plethora of such states have been confirmed in high Chern number bands (Liu et al., 2012; Wang et al., 2012a; Sterdyniak et al., 2013; Wu et al., 2013; Möller and Cooper, 2015; Wu et al., 2015; Bergholtz et al., 2015; Behrmann et al., 2016), but the complete understanding of them still needs more effort. Moreover, lattice defects in these high-$\mathcal{C}$ FCIs may act as worm-hole-like objects, suitably dubbed "genons", that effectively change the genus of space and obey non-Abelian exchange statistics (Barkeshli and Qi, 2012; Barkeshli et al., 2013; Liu et al., 2017; Knapp et al., 2019; Liu and Bergholtz, 2019). This could lead to a new scheme of topological quantum computation.

The field of FCI has flourished over the last decade, motivated by its potential to manifest higher-temperature FQHE-like phenomena at much weaker magnetic fields and novel physics beyond the conventional FQHE. A main trend in the development of this field is to gather inspiration from other research fields, like material science and ultracold atoms, such that we can find suitable lattice platforms to really produce FCIs in experiments. Remarkably, exciting progress has been made along this direction in recent years. The first experimental observation of FCI states was reported in 2018 for Bernal-stacked bilayer graphene, which, however, still needs a strong magnetic field of $B \sim 30$ T to create the required topological flat bands (Spanton et al., 2018). The rapid development of techniques to fabricate van-der-Waals heterostructures with moiré patterns (Geim and Grigorieva, 2013; Novoselov et al., 2016) provides new materials that can harbor intrinsic flat Chern bands at zero magnetic field (Zhang et al., 2019a), in which recent numerical works have identified the existence of zero-field FCIs (Abouelkomsan et al., 2020; Repellin and Senthil, 2020; Liu et al., 2021a; Parker et al., 2021). Consistent with earlier theoretical predictions (Abouelkomsan et al., 2020; Repellin and Senthil, 2020; Ledwith et al., 2020), multiple FCI states were indeed experimentally observed in 2021 with twisted bilayer graphene (TBG) (Bistritzer and MacDonald, 2011; Andrei and MacDonald, 2020) aligned with hexagonal boron nitride at weak magnetic fields down to 5 T (Xie et al., 2021b), in which the weak magnetic field was used only to improve the band geometry such that FCIs became favored. This experiment paves the way toward real zero-field FCIs, and meanwhile reports some exotic FCIs which need further investigation. Currently, the research on a broad range of moiré materials and the strongly-correlated phases thereof is making FCI an active field.

This chapter will provide a general introduction to the basic concepts, the methodology and the experimental observation of FCIs, mainly responding to the following questions: (i) what is the appropriate theoretical microscopic model to study FCIs? (ii) what conditions should this model satisfy to favor FCIs? (iii) how to identify FCIs and their competing phases in numerical simulations and experiments? (iv) how different FCIs are from the conventional FQHE? Meanwhile we will focus on the very recent development through our introduction. It is impossible to cover everything in this field within a chapter. For topics that are not discussed in detail, we recommend the readers to refer to earlier review articles (Parameswaran et al., 2013; Bergholtz and Liu, 2013; Neupert et al., 2015) and references therein.

Microscopic model

Here we present the general microscopic model for studying FCIs in 2D lattices with broken TRS. In most cases, we need to get a many-body Hamiltonian projected to a partially filled Bloch band to capture the low-energy physics within the band, in analogy to the LL projection in 2DEGs. There are two typical ways to achieve this in the literature, which we will describe below.

Tight-binding formalism

Tight-binding formalism is a common method to model particles in lattice systems. It is practical especially when the underlying lattice is not too complicated (i.e., only a few sites in each unit cell), and is highly relevant to cold atoms in optical lattices. This formalism has been used to study FCIs in various toy lattice models, like the kagome, checkerboard, and honeycomb lattice (Sheng et al., 2011; Regnault and Andrei Bernevig, 2011; Wang et al., 2011, 2012b; Wu et al., 2012a; Läuchli et al., 2013). Under the tight-binding scenario, it is natural to consider a many-body Hamiltonian of the form

$$H = \sum_{n,m}\sum_{\alpha,\beta} t^{\alpha\beta}_{nm} c^{\dagger}_{n,\alpha} c_{m,\beta} + \sum_{n,m}\sum_{\alpha,\beta} V^{\alpha\beta}_{nm} c^{\dagger}_{n,\alpha} c^{\dagger}_{m,\beta} c_{m,\beta} c_{n,\alpha}, \tag{1}$$

where $n,\ m = 1,\ \cdots,\ N_u$ label the unit cells of the lattice at positions $\mathbf{R}_n$ and $\mathbf{R}_m$, $\alpha,\ \beta = 1,\ \cdots,\ N_b$ label the internal states (for example, inequivalent sites) in each unit cell, and $c^{\dagger}_{n,\alpha}(c_{n,\alpha})$ creates (annihilates) a particle in unit cell $\mathbf{R}_n$ and state α. In Eq. (1), the first term is the single-particle Hamiltonian describing the hopping of particles in the lattice, and the second term is the two-body Hubbard-like interaction between particles. Translation invariance of both the hopping and the interaction is usually assumed, that is, $t^{\alpha\beta}_{nm}$ and $V^{\alpha\beta}_{nm}$ only depend on $\mathbf{R}_n - \mathbf{R}_m$. Then we can switch to the reciprocal space by the Fourier transform $c^{\dagger}_{\mathbf{k},\alpha} = \frac{1}{\sqrt{N_u}}\sum_n e^{i\mathbf{k}\cdot\mathbf{R}_n} c^{\dagger}_{n,\alpha}$, which creates a particle in state α with crystal momentum $\mathbf{k} = (k_x, k_y)$ restricted in the first Brillouin zone (1BZ) of the lattice. This reexpresses Eq. (1) as

$$H = \sum_{\mathbf{k}\in 1\mathrm{BZ}}\sum_{\alpha,\beta} \mathcal{H}^{\alpha\beta}_0(\mathbf{k}) c^{\dagger}_{\mathbf{k},\alpha} c_{\mathbf{k},\beta} + \sum_{\{\mathbf{k}_i\}\in 1\mathrm{BZ}}\sum_{\alpha,\beta} V^{\alpha\beta}_{\mathbf{k}_1\mathbf{k}_2\mathbf{k}_3\mathbf{k}_4} c^{\dagger}_{\mathbf{k}_1,\alpha} c^{\dagger}_{\mathbf{k}_2,\beta} c_{\mathbf{k}_3,\beta} c_{\mathbf{k}_4,\alpha}. \tag{2}$$

In Eq. (2), the single-particle and interaction matrix elements are

$$\mathcal{H}^{\alpha\beta}_0(\mathbf{k}) = \sum_n t^{\alpha\beta}_{n0} e^{-i\mathbf{k}\cdot\mathbf{R}_n} \tag{3}$$

and

$$V^{\alpha\beta}_{\mathbf{k}_1\mathbf{k}_2\mathbf{k}_3\mathbf{k}_4} = \frac{1}{N_u}\delta'_{\mathbf{k}_1+\mathbf{k}_2,\mathbf{k}_3+\mathbf{k}_4}\sum_n V^{\alpha\beta}_{n0} e^{-i(\mathbf{k}_1-\mathbf{k}_4)\cdot\mathbf{R}_n}, \tag{4}$$

respectively, where we have set $\mathbf{R}_m = \mathbf{0}$ and $\delta'_{\mathbf{k},\mathbf{k}'}$ is the 2D periodic Kronecker delta function with period of primitive reciprocal lattice vectors.

The single-particle band structure of the system can be extracted by diagonalizing the $N_b \times N_b$ matrix $\mathcal{H}_0^{\alpha\beta}(\mathbf{k})$ for each $\mathbf{k} \in 1\mathrm{BZ}$ separately. The resulting eigenvalues $\{\in_s(\mathbf{k})\}$ are just the band energies, and the eigenvector $\psi_s(\mathbf{k})$ gives the Bloch state of the s-th band as $|\psi_s(\mathbf{k})\rangle = \sum_\alpha \psi_s^\alpha(\mathbf{k}) c_{\mathbf{k},\alpha}^\dagger|\mathrm{vacuum}\rangle$. With the band eigenvectors at hand, one can define a new set of operators $\gamma_{\mathbf{k},s}^\dagger$ that create a particle with crystal momentum $\mathbf{k}$ in a specific band s, such that

$$\gamma_{\mathbf{k},s}^\dagger = \sum_\alpha \psi_s^\alpha(\mathbf{k}) c_{\mathbf{k},\alpha}^\dagger, c_{\mathbf{k},\alpha}^\dagger = \sum_s \left[\psi_s^\alpha(\mathbf{k})\right]^* \gamma_{\mathbf{k},s}^\dagger. \tag{5}$$

In terms of $\gamma_{\mathbf{k},s}^\dagger$ and $\gamma_{\mathbf{k},s}$, one finds the many-body Hamiltonian Eq. (2) is rewritten as

$$H = \sum_{\mathbf{k}\in 1\mathrm{BZ}} \sum_s \epsilon_s(\mathbf{k}) \gamma_{\mathbf{k},s}^\dagger \gamma_{\mathbf{k},s} + \sum_{\{\mathbf{k}_i\}\in 1\mathrm{BZ}} \sum_{\{s_i\}} \sum_{\alpha,\beta} V_{\mathbf{k}_1\mathbf{k}_2\mathbf{k}_3\mathbf{k}_4}^{\alpha\beta} \left[\psi_{s_1}^\alpha(\mathbf{k}_1)\right]^* \left[\psi_{s_2}^\beta(\mathbf{k}_2)\right]^* \psi_{s_3}^\beta(\mathbf{k}_3) \psi_{s_4}^\alpha(\mathbf{k}_4) \gamma_{\mathbf{k}_1,s_1}^\dagger \gamma_{\mathbf{k}_2,s_2}^\dagger \gamma_{\mathbf{k}_3,s_3} \gamma_{\mathbf{k}_4,s_4}. \tag{6}$$

The transform of the many-body Hamiltonian from Eq. (1) to Eq. (6) makes it convenient to deal with a situation that we are primarily interested in, that is, a single isolated band is partially filled by interacting particles while other bands are either fully occupied or empty. In this case, it makes sense to project the whole Hamiltonian to the partially filled band—this is where all the low-energy actions are expected to take place. Naively one may think this is valid only when the interaction strength is much smaller than the band gap such that band mixing is absent. However, the band projection actually works far beyond this limit as particles often prefer to restrict the low-energy actions in the partially filled band even if the interaction strength exceeds the band gap (Kourtis et al., 2014), similar to the situation in the conventional FQHE.

To do the band projection, we restrict the band indices in Eq. (6) to the partially filled band, reaching the projected Hamiltonian

$$H = \sum_{\mathbf{k}\in 1\mathrm{BZ}} \epsilon(\mathbf{k}) \gamma_{\mathbf{k}}^\dagger \gamma_{\mathbf{k}} + \sum_{\{\mathbf{k}_i\}\in 1\mathrm{BZ}} \overline{V}_{\mathbf{k}_1\mathbf{k}_2\mathbf{k}_3\mathbf{k}_4} \gamma_{\mathbf{k}_1}^\dagger \gamma_{\mathbf{k}_2}^\dagger \gamma_{\mathbf{k}_3} \gamma_{\mathbf{k}_4}, \tag{7}$$

where we have dropped the band index for simplicity and

$$\bar{V}_{\mathbf{k}_1\mathbf{k}_2\mathbf{k}_3\mathbf{k}_4} = \sum_{\alpha,\beta} V_{\mathbf{k}_1\mathbf{k}_2\mathbf{k}_3\mathbf{k}_4}^{\alpha\beta} [\psi^\alpha(\mathbf{k}_1)]^* \left[\psi^\beta(\mathbf{k}_2)\right]^* \psi^\beta(\mathbf{k}_3) \psi^\alpha(\mathbf{k}_4). \tag{8}$$

Eq. (7) is the starting point in most literatures to investigate FCIs and other correlated phases occurring in lattice systems. In the flat-band limit where the band dispersion is sufficiently weak, we can even only keep the interaction term in Eq. (7). In this case, the band-projected Hamiltonian has almost the same form as the LL-projected Hamiltonian of the conventional FQHE, for which $\mathbf{k}$ is replaced by the orbital index of the LL.

Although majority of reported FCI states is captured by Eq. (7), exceptions beyond the single-band description exist. First, projection to multiple bands is necessary if an isolated set of bands is partially occupied, leading to multicomponent FCI states (Repellin et al., 2014; Zeng and Sheng, 2018; Zeng et al., 2019; Zeng, 2021; Zeng et al., 2022; Zeng and Zhu, 2022). The generalization of Eq. (7) to this case is straightforward. Second, sometimes strong interactions may dramatically modify the non-interacting band structure and produce an emergent Chern band in which FCIs can develop, even if the non-interacting band has zero Chern number or even not isolated (Simon et al., 2015; Zhu et al., 2016). We cannot rely on the single-band projection to study these states. For simplicity, we will not discuss these situations in this chapter.

Effective continuum model

Unlike in toy lattice models, realistic solid-state materials are often too complicated to be formulated as a simple tight-binding Hamiltonian. This is the case in moiré materials where a unit cell contains a few hundreds sites. For moiré systems, theorists usually rely on first-principle calculations to construct an effective continuum single-particle Hamiltonian H_0 in the reciprocal space to describe the low-energy bands (for instance, see Refs. Bistritzer and MacDonald, 2011; Zhang et al., 2019a,b; Lee et al., 2019; Haddadi et al., 2020; Chebrolu et al., 2019). We will give a concrete example of H_0 for twisted bilayer graphene in Section "FCIs in twisted bilayer graphene," but here we give some general statements.

Like in the tight-binding formalism, the effective H_0 is also expressed in terms of the particle's creation and annihilation operators $-c_{\mathbf{k},\alpha}^\dagger$ and $c_{\mathbf{k},\alpha}$, where α labels internal degrees of freedom of a particle. Similar to Eq. (5), $c_{\mathbf{k},\alpha}^\dagger$ and $c_{\mathbf{k},\alpha}$, can in turn be related to the band operators $\gamma_{\mathbf{k},s}^\dagger$ and $\boldsymbol{\gamma}_{\mathbf{k},s}$ after diagonalizing H_0. Regarding the two-body interaction in continuum, we can write it by the standard second-quantization formula as

$$H_{\mathrm{int}} = \frac{1}{2} \sum_{\mathbf{q}\in R^2} \tilde{V}(\mathbf{q}) : \rho(\mathbf{q}) \rho(-\mathbf{q}) : , \tag{9}$$

where the summation of $\mathbf{q}$ is in the whole reciprocal space R^2 instead of only the 1BZ, $\tilde{V}(\mathbf{q}) = \frac{1}{A} \int V(\mathbf{r}) e^{-i\mathbf{q}\cdot\mathbf{r}} d\mathbf{r}$ is the Fourier transform of the interaction potential $V(\mathbf{r})$ with A the area of the 2D system, $\rho(\mathbf{q}) = \sum_\alpha c_{\mathbf{k}+\mathbf{q},\alpha}^\dagger c_{\mathbf{k},\alpha}$ is the density operator, and:: is the normal ordering. Then we can project the many-body Hamiltonian $H = H_0 + H_{\mathrm{int}}$ to the partially filled band by the relation between $c_{\mathbf{k},\alpha}^\dagger$, $c_{\mathbf{k},\alpha}$ and $\gamma_{\mathbf{k},s}^\dagger$, $\gamma_{\mathbf{k},s}$ and restricting the band index s to the partially filled band. The obtained band-projected Hamiltonian has exactly the same form as Eq. (7).

Conditions of the existence of FCIs

Given the Hamiltonian Eq. (7) of interacting particles partially occupying a single isolated band, whether FCIs are favored as the ground states strongly depends on the system details, including the filling factor, the shape of the finite lattice, and properties of the band and the interaction. Insight of proper filling factors can be obtained in analogy to the conventional FQHE. For a finite lattice, we expect that its shape should be close to the 2D isotropic limit. In the following, we will summarize the known conditions which the band and the interaction should satisfy to harbor FCIs.

Requirements for the band

For a partially filled isolated band s, numerical works and analytical studies have identified three of its properties—bandwidth, topology, and quantum geometry, that are highly relevant to the existence of FCIs. The bandwidth W is determined by the band energies via $W = \max_{\mathbf{k},\mathbf{k}' \in 1\mathrm{BZ}}[\epsilon_s(\mathbf{k}) - \epsilon_s(\mathbf{k}')]$. By contrast, the topology and quantum geometry are encoded in band eigenstates (Cheng, 2010; Roy, 2014; Jackson et al., 2015; Ozawa and Mera, 2021). Denoting the cell periodic part of $|\psi_s(\mathbf{k})\rangle$ as $|u_s(\mathbf{k})\rangle$, the quantum geometric tensor of band s is defined as

$$\mathcal{Q}_s^{ab}(\mathbf{k}) = \left\langle \partial_{\mathbf{k}}^a u_s(\mathbf{k}) \middle| \partial_{\mathbf{k}}^b u_s(\mathbf{k}) \right\rangle - \left\langle \partial_{\mathbf{k}}^a u_s(\mathbf{k}) \middle| u_s(\mathbf{k}) \right\rangle \left\langle u_s(\mathbf{k}) \middle| \partial_{\mathbf{k}}^b u_s(\mathbf{k}) \right\rangle \equiv g_s^{ab}(\mathbf{k}) - \frac{i}{2}\Omega_s^{ab}(\mathbf{k}) \tag{10}$$

with $a, b = x, y$. Up to a constant factor $-1/2$, the imaginary part of $\mathcal{Q}_s^{ab}(\mathbf{k})$ is just the Berry curvature

$$\Omega_s^{ab}(\mathbf{k}) = i\left[\langle \partial_{\mathbf{k}}^a \mathrm{u}_s(\mathbf{k}) | \partial_{\mathbf{k}}^b u_s(\mathbf{k}) \rangle - \langle \partial_{\mathbf{k}}^b \mathrm{u}_s(\mathbf{k}) | \partial_{\mathbf{k}}^a u_s(\mathbf{k}) \rangle\right] \tag{11}$$

which resembles the effect of magnetic field in reciprocal space. The band topology is then characterized by the integral of Berry curvature over the 1BZ, called Chern number

$$\mathcal{C}_s = \frac{1}{2\pi}\int_{1\mathrm{BZ}} \Omega_s^{xy}(\mathbf{k}) dk_x dk_y, \tag{12}$$

which must be an integer. Chern number is a topological invariant in the sense that it cannot be changed by modifying the band dispersion unless the band gap is closed. On the other hand, the real part of the quantum geometric tensor is the Fubini-Study (FS) metric

$$g_s^{ab}(\mathbf{k}) = \frac{1}{2}\left(\langle \partial_{\mathbf{k}}^a u_s(\mathbf{k}) | \partial_{\mathbf{k}}^b u_s(\mathbf{k}) \rangle - \langle \partial_{\mathbf{k}}^a u_s(\mathbf{k}) | u_s(\mathbf{k}) \rangle \langle u_s(\mathbf{k}) | \partial_{\mathbf{k}}^b u_s(\mathbf{k}) \rangle + a \leftrightarrow b\right) \tag{13}$$

of the band. As $|\langle u_s(\mathbf{k}) | u_s(\mathbf{k} + d\mathbf{k}) \rangle| \approx 1 - \frac{1}{2} g_s^{ab}(\mathbf{k}) dk_a dk_b$, the FS metric measures the distance between two $|u_s\rangle$ states at different $\mathbf{k}$ points. Moreover, the Berry curvature and the FS metric are related by two important inequalities (Parameswaran et al., 2013; Roy, 2014; Jackson et al., 2015; Claassen et al., 2015; Wang et al., 2021)

$$\mathrm{tr} g_s^{ab}(\mathbf{k}) \geq |\Omega_s(\mathbf{k})|, \ \det g_s^{ab}(\mathbf{k}) \geq \frac{1}{4}|\Omega_s(\mathbf{k})|^2, \tag{14}$$

the saturations of which are referred to as the trace condition and the determinant condition, respectively. In fact, the second inequality can be derived from the first one (Roy, 2014; Wang et al., 2021), thus the determinant condition is definitely satisfied when the trace condition is.

Considering the formation of the conventional FQHE in LLs, we naturally expect that the existence of FCIs builds on how well a Bloch band can reproduce the physics of a LL. In Table 1, we compare a Bloch band with a LL. Based on their differences in aspects of

Table 1 The comparison between a Landau level and a Bloch band from aspects of band dispersion, topology, quantum geometry, and PH asymmetry of the projected two-body interaction. Here we assume no disorder or boundary effects.

	Landau level	*Bloch band*
Dispersion	No dispersion, i.e., all single-particle states within each LL is perfectly degenerate.	Finite bandwidth in general.
Topology	Chern number $\lvert C\rvert = 1$ for each LL. The sign is determined by the direction of the magnetic field.	Chern number of a Bloch band can be an arbitrary integer. Apart from $C = 0$ and $\lvert C\rvert = 1$, there are also Bloch bands with higher Chern number $\lvert C\rvert > 1$.
Quantum geometry	Uniform ($\mathbf{k}$-independent) nonzero Berry curvature and FS metric. In particular, both inequalities in Eq. (14) are saturated for the lowest LL.	In general, both the Berry curvature and FS metric fluctuate in the 1BZ. While the trace and determinant conditions in Eq. (14) are satisfied for all two-band models at any $\mathbf{k}$ (Claassen et al., 2015; Wang et al., 2021), in general this does not hold for multiband models.
PH asymmetry of projected two-body interactions	No	Yes

dispersion, topology and quantum geometry, the following conditions appear to be necessary for a Bloch band to mimic a LL and host FQHE-like phenomena.

- *Bandwidth*. The bandwidth W should be smaller than the interaction strength V, such that the interaction dominates the physics. Otherwise, the ground state is expected to be a usual Fermi liquid of electrons or pile of bosons in the band bottom. Given a typical interaction scale in the system, it is easier to satisfy $W \ll V$ if the band is tuned to be flatter.
- *Band topology*. Typically we require that the band should carry nonzero Chern number, although this is not a fundamental necessity if strong interactions can induce an emergent Chern band (Simon et al., 2015; Kourtis, 2018). To get nonzero Chern number, we need to break the TRS, which can be achieved by complex hopping via spin-orbit coupling, ferromagnetism, artificial gauge fields, or interaction-induced spontaneous TRS breaking.
- *Band geometry*. The Berry curvature and FS metric should not strongly fluctuate in the 1BZ. Meanwhile, the trace and determinant conditions in Eq. (14) should be approximately satisfied if we need to mimic the lowest LL (LLL). The key role of band geometry on the stability of FCIs has been demonstrated in various lattice models, for instance, see Refs. Jackson et al. (2015), Wilhelm et al. (2021), Bauer et al. (2022) and Abouelkomsan et al. (2022).

One should note that, for a given lattice model, in general the smallest bandwidth, nonzero Chern number, and the most ideal band geometry cannot be achieved simultaneously by optimizing the model parameters. In fact, it has been proven that one cannot get topological bands with zero bandwidth by finite-range hopping (Chen et al., 2014). Even if one introduces infinite-range hopping to get an exactly flat topological band (Kapit and Mueller, 2010), its Berry curvature still fluctuates (Liu et al., 2013b). While perfectly flat band with exactly constant Berry curvature and finite Chern number can exist in multiband models (three or more bands) with infinite-range hopping, the trace and determinant conditions in Eq. (14) are not satisfied meanwhile (Varjas et al., 2022). For two-band models, both inequalities in Eq. (14) are saturated (Claassen et al., 2015; Wang et al., 2021), but the possibility of realizing exactly constant Berry curvature has been ruled out (Varjas et al., 2022). Therefore, we need to reach a compromise between the band dispersion, topology, and geometry when seeking "good" models to host FCIs. Over-optimizing one of those band properties does not always improve the stability of FCIs.

Requirements for the interaction

Generally speaking, interactions which decay fast with distance, like the onsite interaction (for bosons), Hubbard-like interactions between the nearest neighboring (NN) or next NN sites, long-range Coulomb and dipolar interactions, often work well to stabilize Abelian FCIs. However, for non-Abelian FCIs, one need to tune the interaction carefully, or even use less realistic multibody interactions. More rigorously, in analogy to what is done in the FQH case, we can use the lattice version of Haldane's pseudopotentials (Haldane, 1983) to predict what kind of interactions may stabilize a specific FCI state. These pseudopotentials on the lattice can be evaluated through the two-particle energy spectrum of the interaction (Läuchli et al., 2013; Bergholtz and Liu, 2013; Liu et al., 2013b) or the mapping between the LLL and the lattice Wannier functions (Lee et al., 2013).

Particle-hole asymmetry

Having stated the requirements for the band and the interaction separately, we now turn to another key condition for the emergence of FCI states, whose satisfaction is determined jointly by the band and interaction properties. This condition originates from different behavior of the projected Hamiltonian Eq. (7) under particle-hole (PH) transformation in a Bloch band from that in a LL. Under the standard PH transformation of fermions $\gamma_{\mathbf{k}}^{\dagger} \leftrightarrow \gamma_{\mathbf{k}}$, Eq. (7) transforms to

$$H \longrightarrow \sum_{\mathbf{k}\in 1BZ} \epsilon_h(\mathbf{k})\gamma_{\mathbf{k}}^{\dagger}\gamma_{\mathbf{k}} + \sum_{\{\mathbf{k}_i\}\in 1\mathrm{BZ}} \overline{V}^{*}_{\mathbf{k}_1\mathbf{k}_2\mathbf{k}_3\mathbf{k}_4}\gamma_{\mathbf{k}_1}^{\dagger}\gamma_{\mathbf{k}_2}^{\dagger}\gamma_{\mathbf{k}_3}\gamma_{\mathbf{k}_4} \tag{15}$$

up to a constant, which includes a hole-hole interaction term similar to that of electrons and a single-hole dispersion

$$\epsilon_h(\mathbf{k}) = -\epsilon(\mathbf{k}) + \sum_{\mathbf{k}'\in 1\mathrm{BZ}} \left(\overline{V}_{\mathbf{k}\mathbf{k}'\mathbf{k}\mathbf{k}'} + \overline{V}_{\mathbf{k}'\mathbf{k}\mathbf{k}'\mathbf{k}} - \overline{V}_{\mathbf{k}\mathbf{k}'\mathbf{k}'\mathbf{k}} - \overline{V}_{\mathbf{k}'\mathbf{k}\mathbf{k}\mathbf{k}'}\right) \equiv -\epsilon(\mathbf{k}) + \epsilon_h^i(\mathbf{k}). \tag{16}$$

Remarkably, apart from the contribution from the band dispersion $\epsilon(\mathbf{k})$ of electrons, holes experience an additional dispersion $\epsilon_h^i(\mathbf{k})$ originating from the interaction. In a LL, one can prove that ϵ_h^i is simply a constant shift (chemical potential) for two-body interactions (Möller and Simon, 2005), which, together with the exact degeneracy of LL orbitals, means both electrons and holes in a LL experience the same zero dispersion (although this does not hold for multi-body interactions). However, $\epsilon_h^i(\mathbf{k})$ generically varies with $\mathbf{k}$ in a Bloch band even for two-body interactions (Läuchli et al., 2013; Liu et al., 2013b), because the interaction matrix element $\overline{V}_{\mathbf{k}_1\mathbf{k}_2\mathbf{k}_3\mathbf{k}_4}$ in general lacks translational invariance in the reciprocal space of the lattice. This PH asymmetry, i.e., electrons and holes experience different dispersions, is a lattice-specific feature of the projected Hamiltonian in a Bloch band. As the strength of the PH asymmetry is quantified by the bandwidth of $\epsilon_h^i(\mathbf{k})$, we need a weakly dispersive $\epsilon_h^i(\mathbf{k})$ to simulate the LL physics on the many-body level. In fact, the bandwidth of $\epsilon_h^i(\mathbf{k})$ is also closely related to the homogeneity of FS metric via

$$\epsilon_h^i(\mathbf{k}) \approx \sum_{\mathbf{q}} \tilde{V}(\mathbf{q}) e^{-\sum_{ab} q_a q_b g^{ab}(\mathbf{k})} \tag{17}$$

when the product of the interaction $\tilde{V}(\mathbf{q})$ and the band form factor $\langle \psi(\mathbf{k}) | \psi(\mathbf{k}-\mathbf{q}) \rangle$ decay fast with $|\mathbf{q}|$ (Abouelkomsan et al., 2022).

We can see the importance of uniform band geometry and weakly dispersive $\epsilon_h^i(\mathbf{k})$ from Eq. (17). Similar to FQH states in a LL, FCIs prefers nearly uniform particle density and Berry curvature in the 1BZ, so that all particles can feel an approximately constant effective magnetic field. In narrow bands, the distribution of particles in the 1BZ is greatly affected by $\epsilon_h^i(\mathbf{k}) : \mathbf{k}$ points with small (large) $\epsilon_h^i(\mathbf{k})$ tend to be occupied by holes (electrons). Therefore, if the FS metric is sufficiently uniform in a narrow band, the particles have no priorities to occupy the 1BZ, which, together with an approximately constant Berry curvature, should stabilize FCIs. Otherwise, strongly fluctuating FS metric will distribute electrons to regions with larger $\epsilon_h^i(\mathbf{k})$ even when the bandwidth of $\epsilon(\mathbf{k})$ is small. Such non-uniform density can destabilize the FCI phase, and can even completely destroy it if the Berry curvature happens to be weak in these regions (Wilhelm et al., 2021; Abouelkomsan et al., 2022). We will discuss phases competing against FCIs caused by this mechanism in Section "Competing phases." The crucial dependence of the many-body ground state on the band geometry is absent in LLs due to the uniform geometry there. In fact, flattening band geometry is one of the main challenges for realizing FCIs in experiments.

Numerical diagnosis of FCIs

The conditions listed in the previous section serve as guiding principles to search for suitable candidate lattice models harboring FCIs. However, to quantitatively judge whether a candidate model is really good, we need to extract the low-energy physics of Eq. (7) by numerical techniques such as exact diagonalization (ED) and density matrix renormalization group (DMRG). In this section, we will discuss how to diagnose FCIs by numerical simulations. We will give numerical identifications not only for FCIs, but also for some competing phases. A concrete example in twisted bilayer graphene will be presented in the next section.

Basic identifications

The standard numerical approach to explore the low-energy physics of Eq. (7) is to diagonalize the many-body Hamiltonian for a partially filled band of a finite system, consisting of N particles and N_1 and N_2 unit cells in the two primary directions of the lattice, then extract information from the obtained low-lying energy levels and eigenstates. Here the band filling is defined as $\nu \equiv N/(N_1 N_2)$, and interacting particles can either be electrons in solid materials or bosons in cold-atom setups. Some common methods for identifying FCIs' topological orders from numerical data are listed below. Depending on the method, the finite system is often put on the torus or the cylinder geometry.

- *Topological degeneracy*. The most obvious numerical evidence of FCIs is the topological degeneracy of incompressible (i.e., gapped) ground states on the torus, i.e., in a 2D system with periodic boundary conditions in both directions. This can be directly examined in the low-lying energy spectrum returned by numerical diagonalization, thus is usually the first thing to confirm in most literatures. In analogy to the conventional FQHE, at least q approximately degenerate ground states are expected for FCIs at band filling $\nu = p/q$, where p and q are coprime (multicomponent and non-Abelian FCIs have ground-state degeneracies larger than q). These ground states should carry momenta that match the Haldane statistics characterizing the candidate FCIs (Regnault and Andrei Bernevig, 2011; Andrei Bernevig and Regnault, 2012; Wu et al., 2014). In general, the FCI ground-state degeneracies are not exact for finite systems due to the symmetry reduction compared to the conventional FQHE. However, the ground-state manifold should be separated from excited levels by a many-body gap that does not vanish in the thermodynamic limit and, ideally, the ground state splitting should vanish exponentially with the increasing of system size. Moreover, The ground-state degeneracy should be insensitive to the boundary conditions, which can be demonstrated by calculating the spectral flow under insertion of magnetic flux through the handle of the torus. Typically, the FCI ground states evolve into each other in the spectral flow for an appropriate flux insertion but do not mix with higher excited levels.
- *Entanglement measures*. Besides energetic evidence, one can rely on entanglement spectroscopies for more insights into the nature of the ground states. Such entanglement information is entirely extracted from the numerically obtained ground-state wavefunctions. For a bipartition of a 2D topologically ordered state in real space, the entanglement entropy between the two subsystems obeys an area law, with a subleading term encoding the quantum dimensions of quasiparticles (Kitaev and Preskill, 2006; Levin and Wen, 2006). Numerical evaluation of this subleading term, dubbed topological entropy, for the ground state can distinguish FCIs from trivial phases (Grushin et al., 2015; Gerster et al., 2017; Andrews et al., 2021a; Andrews and Soluyanov, 2020). Moreover, the entanglement spectrum (ES) (Li and Haldane, 2008) of the ground state, i.e., the whole spectrum of the reduced density matrix of one subsystem, contains more information than the entanglement entropy. For the real-space bipartition, the counting structure in the low-lying ES (Liu et al., 2013c; Andrews et al., 2021a; Zhu et al., 2016; Motruk et al., 2016; Luo et al., 2020, 2021; Andrews et al., 2021b; Andrews and Soluyanov, 2020) is the same as that of edge excitations (He et al., 2020; Luo et al., 2013; Kjäll and Moore, 2012), thus providing a fingerprint of the underlying topological order according to the bulk-edge correspondence. One can also bipartite the system by dividing all particles into two parts. The corresponding particle-cut ES (PES) (Sterdyniak et al., 2011) encodes the physics of bulk quasihole excitations in its low-lying part, which has been extensively used to identify FCIs (Regnault and Andrei Bernevig, 2011; Scaffidi and Möller, 2012; Sterdyniak et al., 2012; Andrei Bernevig and Regnault, 2012; Wu et al., 2012a; Liu et al., 2013a, 2012; Sterdyniak et al., 2013; Li et al., 2014; Wang et al., 2013; Repellin et al., 2014; Behrmann et al., 2016; Simon et al., 2015; Sterdyniak et al., 2015; Abouelkomsan et al., 2020; Liu et al., 2021a; Kupczyński et al., 2021; Wang and Liu, 2022).

- *Hall conductance*. As another hallmark, the quantized fractional Hall conductance is achieved when the ground state is in the FCI phase. The Hall conductance is proportional to the ground-state Chern number (Thouless et al., 1982; Niu et al., 1985), which can be evaluated by twisting the boundary conditions on the torus (Wang et al., 2011, 2012b; Gerster et al., 2017; Zeng and Sheng, 2018; Zeng et al., 2019; Zeng, 2021; Zeng et al., 2022; Zeng and Zhu, 2022; Okamoto et al., 2022). Alternatively, for systems on the cylinder surface one can perform a numerical flux insertion through the hole of the cylinder and determine the Hall conductance by measuring the charges pumped from one edge to the other edge of the cylinder, which can be easily implemented in DMRG simulations (Zaletel et al., 2014; Grushin et al., 2015; Andrews et al., 2021a; Zhu et al., 2016; Motruk et al., 2016; Andrews et al., 2021b; Wang et al., 2022; Zeng and Sheng, 2018; Zeng et al., 2019; Zeng, 2021; Zeng et al., 2022; Luo et al., 2021; Zeng and Zhu, 2022; Andrews and Soluyanov, 2020).
- *Quasiparticle statistics*. The fractional statistics of quasiparticles is a characterizing feature of FCI states. One can directly simulate the generation and braiding of quasiparticles to demonstrate their fractional statistics (Liu et al., 2015; Rodríguez and Nielsen, 2015; Mantas Račiūnas et al., 2018; Manna et al., 2018; Jaworowski et al., 2019; Macaluso et al., 2020; Srivatsa et al., 2021; Wang et al., 2022). Alternatively, the statistics is encoded in the so called modular matrix (Verlinde, 1988; Wen, 1990). We can numerically evaluate these matrices from the ground-state wavefunctions by constructing the minimally entangled states in the ground-state manifold for bipartitions of the lattice along different directions (Zhang et al., 2012; Zhu et al., 2013, 2014, 2016; Liu and Bergholtz, 2019).

Competing phases

FCI is only one possibility among various phases that can potentially exist in a Chern band. Competing phases prevail when the microscopic details of the system disfavor FCIs, which often happens when the conditions listed in Section "Conditions of the existence of FCIs" are not satisfied. Studying the competition of FCIs with other candidate phases is crucial for determining the stable regions of FCIs in experiments. In the following, we discuss two common competing phases and their features which can be observed in numerical simulations.

- *Crystalline phases*. The competition in 2DEGs between conventional FQH states and charge density waves (CDWs), like Wigner crystals and stripe phases, has been known for long (Fukuyama et al., 1979; Yoshioka and Lee, 1983; Moessner and Chalker, 1996; Rezayi et al., 1999; Haldane et al., 2000; Yang et al., 2001). Both CDWs and FQH states rely on the presence of strong interactions, however, the formers spontaneously break the translational symmetry. Similarly, when the interaction dominates in topological flat bands, the competition between CDWs and FCIs is also typically expected at fillings that are commensurate with the lattice. Indeed, such competition has been confirmed in various flat-band models (Wang et al., 2011; Varney et al., 2010; Kourtis et al., 2012; Grushin et al., 2012; Li et al., 2014; Kourtis and Daghofer, 2014; Kourtis et al., 2017; Kourtis, 2018; Luo et al., 2020; Wilhelm et al., 2021; Jaworowski et al., 2018; Kupczyński et al., 2021; Parker et al., 2021; Abouelkomsan et al., 2022; Hu and Liu, 2022). Apparently, the formation of these states requires proper filling factor, interaction, and lattice shape. Recently, the studies of FCIs in moiré systems found that strongly fluctuating quantum geometry also facilitates the formation of CDWs by distributing particles to specific regions of the 1BZ (Wilhelm et al., 2021; Parker et al., 2021; Abouelkomsan et al., 2022).

CDWs are characterized by their specific charge orders. In numerical simulations, this order can be revealed most prominently by calculating the structure factor

$$S(\mathbf{q}) = \frac{1}{N_1 N_2}\left(\langle\rho(\mathbf{q})\rho(-\mathbf{q})\rangle - N^2\delta_{\mathbf{q},\mathbf{0}}\right), \tag{18}$$

which is the Fourier transform of the static density-density correlation function. Here the average $\langle\rangle$ is over the ground state. When the charge order develops, $S(\mathbf{q})$ should manifest pronounced peaks at the order momenta.

These order momenta are reciprocal vectors of the real-space modulation of charge density. By contrast, $S(\mathbf{q})$ of FCI states is expected to be featureless due to the absence of charge order. Regarding the low-energy many-body spectra, the CDW phase is accompanied by the ground-state degeneracy that corresponds to all possible charge configurations for a given charge order. Unlike the FCIs, the momenta of degenerate CDW states are separated by the order momenta instead of being determined by the Haldane statistics (occasionally these may coincide such that further diagnostics are needed to settle the nature of the states).

- *Fermi liquids*. Generally speaking, there are two types of Fermi liquid (FL) that can emerge in a partially filled Bloch band. The first one is usual, caused by the strong dispersion of electron band $\epsilon(\mathbf{k})$. This type of state can be identified by the Fermi surface structure in the dependence of electron's ground-state occupation $n(\mathbf{k})$ on $\epsilon(\mathbf{k})$ at momentum point $\mathbf{k}$, that is, $n(\mathbf{k})$ suddenly drops from ≈ 1 to ≈ 0 at some critical $\epsilon(\mathbf{k})$. The possibility of this usual FL phase can be ruled out when the electron band is very flat.

The second type of FL phase is much less intuitive. As we showed in Eqs. (15) and (16), holes experience an additional dispersion $\epsilon_h^i(\mathbf{k})$ induced by interactions, which may be strongly dispersive even in a narrow electron band. If $\epsilon_h^i(\mathbf{k})$ dominates over the hole-hole interaction in a narrow electron band, FL becomes a good candidate for the ground state of holes, which still renders FL a natural ground-state candidate for electrons even if they do not feel strong band dispersion. Unlike the usual FL, this new FL is a correlated phase, as $\epsilon_h^i(\mathbf{k})$ is contributed by the interaction in flat bands. It should be characterized by a strong correlation between $n(\mathbf{k})$ and $\epsilon_h^i(\mathbf{k})$: $n(\mathbf{k})$ is small (large) at $\mathbf{k}$ points with small (large) $\epsilon_h^i(\mathbf{k})$ which tend to be occupied (unoccupied) by holes. Also, the

Fermi sea structure is expected to appear in the $n(\mathbf{k}) - \epsilon_h^i(\mathbf{k})$ curve, which provides a fingerprint for the this unusual FL phase in numerical simulations.

Intuitively, one may expect that the interaction-driven FL phase in narrow electron bands dominates over FCIs at high electronic band fillings. Indeed, this was confirmed in several toy models, where FCIs are replaced by the FL states at band filling $\nu \gtrsim 2/3$ (Läuchli et al., 2013; Bergholtz and Liu, 2013). However, in some moiré flat bands this unusual FL phase was found to prevail in a much wider range of ν down to $\nu = 1/3$, where FCIs are totally absent (Abouelkomsan et al., 2020, 2022). This can be understood by the very strong $\epsilon_h^i(\mathbf{k})$ originating from the far-from-flat quantum geometry of these bands, as shown in Eq. (17).

FCIs in twisted bilayer graphene

After a general discussion of numerical identifications of FCI states and their competing phases, we now use twisted bilayer graphene (TBG) as a concrete example to show how these identifications work. Recent developments have picked moiré flat bands in TBG as promising platforms to host FCIs.

Microscopic model of TBG

TBG consists of two sheets of monolayer graphene with a twist angle θ in between (Andrei and MacDonald, 2020). At small twist angles $\theta \lesssim 10°$, the difference between commensurate and incommensurate structures can be ignored, and the twisting leads to a moiré pattern of spatial periodicity $a_M = a/(2\sin(\theta/2)) \gg a$ (Fig. 1(a)), where $a = 0.246$ nm is the lattice constant of monolayer graphene. The enlargement of the spatial periodicity corresponds to folding of original graphene 1BZ into much smaller moiré BZ (MBZ) (Fig. 1(b)). The low-energy states reside in the MBZs near the Dirac points $\mathbf{K}^{\pm}$ of monolayer graphene, called as two valleys of TBG which are related by time-reversal conjugation. At small twist angles, weak effects like intervalley scattering and spin-orbit coupling are negligible, leading to valley and spin degeneracy of each moiré band. The non-interacting low-energy band structure near the charge neutrality point (CNP) thus consists of four degenerate valence bands and four degenerate conduction bands, labeled by their valley index +, – and spin index ↑, ↓ . By convention the filling is chosen as $\nu = 0$ at CNP, such that $\nu = -4$ ($\nu = +4$) when these eight bands are all empty (occupied). At a set of magic angles (Bistritzer and MacDonald, 2011; Tarnopolsky et al., 2019), valence and conduction bands become flat (Bistritzer and MacDonald, 2011; Lopes dos Santos et al., 2012, 2007; Tarnopolsky et al., 2019), however, still touch each other. This Dirac band touching is protected by the combination of C_{2z} rotation symmetry and time-reversal ($\mathcal{T}$) symmetry. On the single-particle level, the band gap can be opened by alignment with hexagonal boron nitride (hBN) which breaks the $C_{2z}\mathcal{T}$ symmetry. In this case, the valence and conduction bands for each fixed valley and spin flavors are isolated and may carry opposite Chern numbers $C = \pm 1$ in opposite valleys (Hunt et al., 2013; Jung et al., 2015; Song et al., 2019; Liu et al., 2019; Po et al., 2019; Zhang et al., 2019a,b), however, the valley and spin degeneracies of band energies remain. While it is complicated to predict how electrons occupy these degenerate bands when ν changes from –4 to +4 (Kang and Vafek, 2019; Liu and Dai, 2021; Repellin et al., 2020b; Xie et al., 2021a), recent theoretical studies found that interactions are able to lift the valley and spin degeneracies under suitable circumstances (Repellin et al., 2020b; Bultinck et al., 2020; Liu and Dai, 2021; Xie et al., 2021a). When this happens, we have a simple picture in which the eight spin and valley polarized bands are sequentially filled, giving rise to Chern insulating states at integer fillings. These Chern insulators at integer ν are indeed observed in experiments down to zero magnetic field (Zondiner et al., 2020; Nuckolls et al., 2020; Wu et al., 2021; Saito et al., 2021; Das et al., 2021; Choi et al., 2021; Park et al., 2021; Stepanov et al., 2021; Serlin et al., 2020; Pierce et al., 2021).

The above results motivate the investigation of interactions within a single band of TBG with fixed spin and valley flavors (Abouelkomsan et al., 2020; Repellin and Senthil, 2020; Wilhelm et al., 2021; Parker et al., 2021). To proceed, we assume that the top and bottom graphene layers are rotated by, $\pm\theta/2$, respectively, and hBN is aligned with the top layer. We focus on the valence

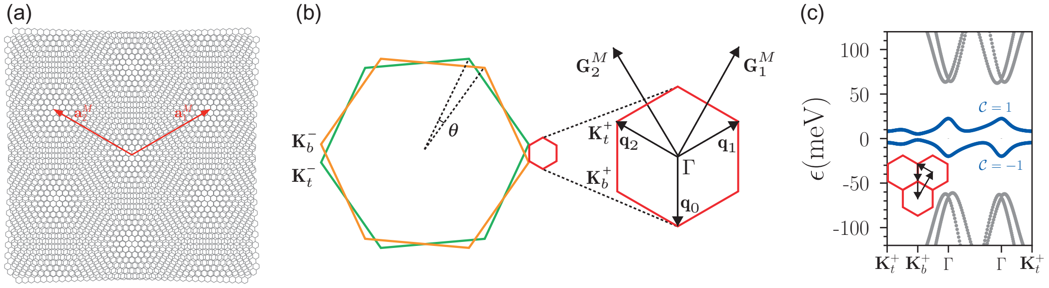

Fig. 1 (a) TBG moiré pattern in real space, whose periodicity is given by vectors $\mathbf{a}_1^M = a_M\left(\sqrt{3}/2, 1/2\right)$ and $\mathbf{a}_2^M = a_M\left(\sqrt{3}/2, 1/2\right)$. (b) The moiré Brillouin zone (MBZ) of TBG. Two large hexagons (green and orange) are original first Brillouin zones of top and bottom graphene layers. The small red hexagon represents the MBZ resulting from twist. The $\mathbf{K}_{+,-}^{t,b}$ points, the vectors $\mathbf{q}_{0,1,2}$ and the MBZ reciprocal lattice vectors $\mathbf{G}_1$ and $\mathbf{G}_2$ are given. (c) Low-energy band structure of TBG-hBN for $\theta = 1.30°$, $M = 20$ meV along a trajectory in the reciprocal space shown as the inset. The valence and conduction band (blue) near CNP carries Chern number $C = -1$ and $C = 1$, respectively.

band of valley $\mathbf{K}^{+}$. At small twist angles ($a_M \gg a$), the band information is encoded in an effective single-particle continuum Hamiltonian (Bistritzer and MacDonald, 2011; Zhang et al., 2019a,b)

$$\begin{aligned} H_0 = &\sum_{\mathbf{k}} \mathbf{c}_t^{\dagger}(\mathbf{k}) h_{-\theta/2}\left(\mathbf{k} - \mathbf{K}_t^{+}\right) \mathrm{c}_t(\mathbf{k}) + \sum_{\mathbf{k}} \mathbf{c}_B^{\dagger}(\mathbf{k}) h_{\theta/2}\left(\mathbf{k} - \mathbf{K}_b^{+}\right) \mathbf{c}_b(\mathbf{k}) \\ &+ \sum_{\mathbf{k}} \sum_{j=0}^{2} \left(\mathbf{c}_t^{\dagger}\left(\mathbf{k} - \mathbf{q}_0 + \mathbf{q}_j\right) T_j \mathbf{c}_b(\mathbf{k}) + h.c.\right) + M \sum_{\mathbf{k}} \mathbf{c}_t^{\dagger}(\mathbf{k}) \sigma_z \mathbf{c}_t(\mathbf{k}), \end{aligned} \tag{19}$$

where $\mathbf{c}_{t/b}(\mathbf{k}) = \begin{pmatrix} c_{A_t/b}(\mathbf{k}) \\ c_{B_t/b}(\mathbf{k}) \end{pmatrix}$ are spinors of annihilation operators for electrons with momentum $\mathbf{k}$ in top (t) and bottom (b) graphene layers, respectively, and A and B label the two sublattices of single-layer graphene. Note that $\mathbf{k}$ in H_0 is near the $\mathbf{K}^{+}$ valley, but not restricted in the MBZ. The first two terms in H_0 are just the standard Dirac Hamiltonians of top and bottom graphene layers, for which $h_\theta(\mathbf{k}) = h(R_\theta \mathbf{k})$ with $h(\mathbf{k}) = -\left(\sqrt{3} a t_0/2\right)\left(k_x \sigma_x + k_y \sigma_y\right)$,$t_0 = 2.62$ eV, and R_θ the counter-clockwise rotation around the z-axis in the momentum space. To the lowest order of approximation, the alignment of hBN induces an onsite potential of strength M (the last term in H_0) on the top graphene layer, where we have neglected the weaker effect from the moiré pattern formed between the top layer graphene and hBN (Zhang et al., 2019b). A rough estimation gives $M \approx 15$ meV (Zhang et al., 2019b), however, larger values like $M = 30$ meV were also used in theoretical studies (Xie et al., 2021b; Parker et al., 2021), so we choose $M = 20$ meV throughout this section. The moiré tunneling between two graphene layers (the third term in H_0) is given by $T_j = w_0 - w_1 e^{i(2\pi/3)j\sigma_z} \sigma_x e^{-i(2\pi/3)j\sigma_z}$ with $\mathbf{q}_0 = \mathbf{k}_t^{+} - \mathbf{k}_b^{+}$, $\mathbf{q}_1 = R_{2\pi/3}\mathbf{q}_0$ and $\mathbf{q}_2 = R_{-2\pi/3}\mathbf{q}_0$ (Fig. 1(b)), where w_0 and w_1 are the interlayer tunneling strengths between AA and AB sites, respectively. w_0 is smaller than w_1 because of lattice relaxation (Popov et al., 2011; Nam and Koshino, 2017; Uchida et al., 2014; van Wijk et al., 2015; Koshino et al., 2018). Theoretical calculations and experimental measurements suggest $w_0/w_1 = 0.5$–0.8 (Koshino et al., 2018; Xie et al., 2019; Guinea and Walet, 2019; Das et al., 2021), hence we choose $w_0 = 0.7 w_1$ in this section, where w_1 is fixed as 110 meV according to *ab initio* numerics (Jung et al., 2014). For each $\mathbf{k}_0 \in$ MBZ, the moiré band structure in the MBZ can be obtained by writing $\mathbf{k}$ in H_0 as $\mathbf{k} = \mathbf{k}_0 + m\mathbf{G}_1 + n\mathbf{G}_2$ with integers $m, n = -d, \ldots, d$ then diagonalizing H_0, where $\mathbf{G}_1$ and $\mathbf{G}_2$ are the MBZ primitive reciprocal lattice vectors (Fig. 1(b)) and d is a cutoff typically set as $d = 5$–9. In Fig. 1(c), we show the low-energy band structure at $\theta = 1.30°$, where the flat valence and conduction bands near CNP have Chern number $\mathcal{C} = \mp 1$, respectively.

Regarding the interaction, we consider a dual-gate setup to mimic experiments, in which electrons experience the gate-screened Coulomb interaction, whose Fourier transform reads

$$\tilde{V}(\mathbf{q}) = \frac{e^2}{4\pi\varepsilon A} \frac{2\pi \tanh(\xi q/2)}{q}, \tag{20}$$

where ε is the dielectric constant of the material and ξ is the distance between the top and bottom gates. Based on typical parameters in TBG experiments, we choose $\varepsilon = 4\varepsilon_0$ (Bessler et al., 2019; Guinea and Walet, 2018) with ε_0 the vacuum dielectric constant and scan ξ between a_M and $2a_M$ (Saito et al., 2020; Stepanov et al., 2020).

The total Hamiltonian projected to the valence band has the same form as Eq. (7), in which $\mathbf{k}$'s should be now restricted in the MBZ and $\epsilon_{\mathbf{k}}$ is the valence band dispersion. The matrix elements of the projected interaction are

$$\overline{V}_{\mathbf{k}_1\mathbf{k}_2\mathbf{k}_3\mathbf{k}_4} = \frac{1}{2} \delta'_{\mathbf{k}_1+\mathbf{k}_2, \mathbf{k}_3+\mathbf{k}_4} \sum_{\mathbf{G}} \tilde{V}(\mathbf{k}_1 - \mathbf{k}_4 + \mathbf{G}) \langle \psi(\mathbf{k}_1) | \psi(\mathbf{k}_4 - \mathbf{G}) \rangle \langle \psi(\mathbf{k}_2) | \psi(\mathbf{k}_3 + \mathbf{G} + \delta\mathbf{G}) \rangle, \tag{21}$$

where $\mathbf{G}$ is summed over the entire reciprocal space instead of MBZ only, $\delta\mathbf{G} = \mathbf{k}_1 + \mathbf{k}_2 - \mathbf{k}_3 - \mathbf{k}_4$, and $|\psi(\mathbf{k})\rangle$ is the valence band eigenvector. One may further account the effects of remote bands in the mean-field level by adding extra single-particle terms (Andrei Bernevig et al., 2021; Xie et al., 2021a; Parker et al., 2021), however, we neglect this issue to avoid technical complexity in this tutorial introduction.

Numerical evidence of FCIs

With the microscopic many-body Hamiltonian projected to the valence band of the $\mathbf{K}^{+}$ valley, we can run extensive ED calculations on the torus geometry to search for numerical identifications of FCI states, as discussed in Section "Numerical diagnosis of FCIs." We do this in the parameter space spanned by $\theta \in [1.0°, 1.6°]$ and $\xi/a_M \in [1,2]$, in which the valence band is always isolated and carries Chern number $\mathcal{C} = -1$. The system has a finite size, consisting of N electrons on the $N_1 \times N_2$ moiré lattice. Considering that robust FCIs at one-third band filling were observed in various $|\mathcal{C}| = 1$ flat bands (Sheng et al., 2011; Regnault and Andrei Bernevig, 2011; Wu et al., 2012a; Läuchli et al., 2013), we choose $\overline{\nu} \equiv N/(N_1 N_2) = 1/3$ filling of the valence band and expect the emergence of lattice analogs of the Laughlin FQH state (Laughlin, 1983).

First of all, provided all eigenvalues $\{E_n\}$ of the many-body Hamiltonian returned by ED have been sorted in ascending order, the threefold degeneracy of incompressible FCI ground states can be probed by the FCI gap $\Delta_{\mathrm{FCI}} \equiv E_4 - E_1$ and the FCI splitting $W_{\mathrm{FCI}} \equiv E_3 - E_1$. If the lowest three eigenstates are not in momentum sectors predicted by the Haldane statistics of the Laughlin state, we simply set $\Delta_{\mathrm{FCI}} = 0$. The numerical data of scanning Δ_{FCI} and Δ_{FCI} $\Delta_{\mathrm{FCI}}/W_{\mathrm{FCI}}$ in the (θ, ξ) parameter space for $N = 10$ electrons are demonstrated in Fig. 2(a) and (b), from which we can identify a wide range of parameters supporting nice threefold degeneracies

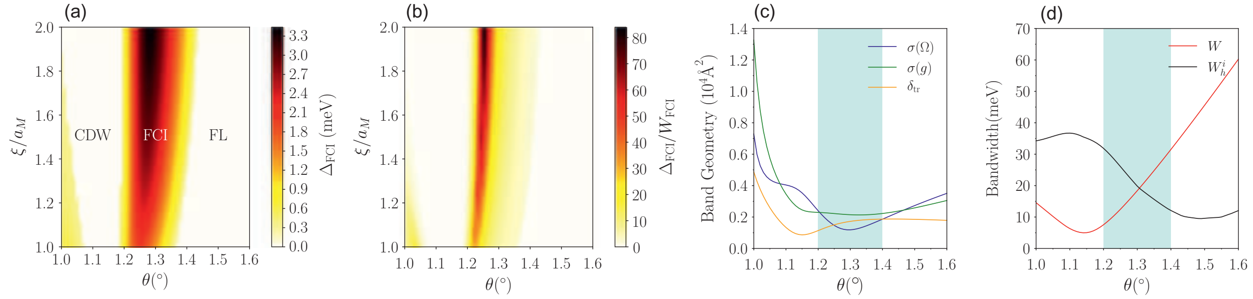

Fig. 2 Numerical data in the $\theta - \xi$ parameter space of TBG-hBN. (a) The FCI gap $\Delta_{\rm FCI}$ and (b) the quality of FCI degeneracy $\Delta_{\rm FCI}/W_{\rm FCI}$ for $N = 10$ electrons in the valence band of $N_1 \times N_2 = 5 \times 6$ moiré lattice. (c) Band geometry of the valence band, including the Berry curvature fluctuation $\sigma(\Omega)$, the FS metric fluctuation $\sigma(g)$, and the deviation $\delta_{\rm tr}$ from the saturated trace condition. (d) Bandwidths of the valence band (W) and the interaction-induced hole dispersion (W_h^i). The shades in (c) and (d) indicates the range of twist angle in which robust FCIs exist. In (a), we give a tentative phase diagram. As shown later, the CDW phase is identified by the structure factor, and the usual Fermi liquid (FL)-like phase is characterized by the step structure in the $n(\mathbf{k}) - \epsilon(\mathbf{k})$ curve.

in the momentum sectors of the Laughlin state. This region slightly expands in the θ direction from $\theta \in [1.20°, 1.35°]$ to $\theta \in [1.20°, 1.40°]$ with the increasing of ξ from a_M to $2a_M$ (weaker screening).

Having obtained the threefold degeneracy for $N = 10$ electrons as preliminary evidence of the $\bar{\nu} = 1/3$ FCI, we analyze the numerical data more carefully at a representative parameter point $(\theta, \xi) = (1.27°, 2a_M)$ in this region (Fig. 3). First, the dependence of the degeneracy on the system size and the boundary condition should be examined. The energy spectra of different system sizes, plotted vs the many-body momentum (K_1, K_2), are presented in Fig. 3(a), in which the threefold degeneracy in the momentum sectors predicted for the Laughlin state appear for all system sizes. Moreover, this degeneracy persists under magnetic flux insertion through the handles of the toroidal system (Fig. 3(c)). A finite-size scaling of $\Delta_{\rm FCI}$ and $W_{\rm FCI}$ suggests that both the threefold degeneracy and the groundstate gap are very likely to survive in the thermodynamic limit (Fig. 3(b)). Note that the gap extrapolating to the $1/N \to 0$ limit goes to $\sim$2 meV, corresponding to a temperature which is an order of magnitude higher than required by the conventional FQHE in 2DEGs. The nontrivial topological properties of the ground state can be further corroborated by the PES, whose levels $\{\lambda_n\}$ are labeled by the total momentum $({K_1}^A, {K_2}^A)$ of the subsystem with N_A electrons. Strikingly, an entanglement gap appears in the PES (Fig. 3(d)), the number of levels below which exactly matches the counting of quasihole excitations in the Laughlin state (Regnault and Andrei Bernevig, 2011).

Both the low-energy spectrum and entanglement spectroscopy strongly indicate that lattice analogs of the continuum $\nu = 1/3$ Laughlin state exist in the valence band of TBG-hBN. We can even establish their adiabatic continuity by using the mapping between single-particle states in a Chern band and in the LLL. Such mapping has been constructed either between lattice Wannier states and LLL orbitals in the Landau gauge (Qi, 2011; Wu et al., 2012b; Jian and Qi, 2013; Wu et al., 2014), or between lattice Bloch states and LLL Bloch-like basis (Wu et al., 2013). In fact, TBG in the so called chiral limit (Tarnopolsky et al., 2019) allows to build a more explicit correspondence between $|\mathcal{C}| = 1$ Chern bands with *ideal geometry* and the LLL. To reach this limit, we need to set $w_0 = 0$ such that the single-particle Hamiltonian possesses chiral symmetry $\sigma_z H_0 \sigma_z = -H_0$, where σ_z is the Pauli matrix acting on the sublattice. While it is a drastic approximation to decrease w_0 to zero even in the presence of lattice relaxation, the magic angle phenomena of TBG can already be well captured in the chiral limit: the entire valence and conduction bands near CNP become perfectly flat at a set of twist angles when $w_0 = 0$, which is the origin of the nearly flat bands observed at magic angles with finite w_0 (Tarnopolsky et al., 2019). In the presence of chiral symmetry, the magic-angle TBG (MATBG) flat bands gains ideal quantum geometry (Ledwith et al., 2020), that is, the Berry curvature does not change sign and varies in sync with the FS metric via

$$g^{ab}(\mathbf{k}) = \frac{1}{2}\delta^{ab}|\Omega(\mathbf{k})|, \tag{22}$$

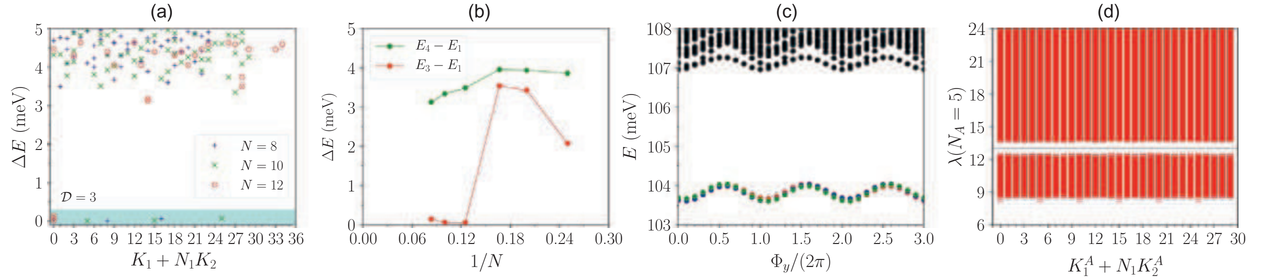

Fig. 3 Numerical evidence of the $\bar{\nu} = 1/3$ FCI in the valence band of TBG-hBN at a representative parameter point $(\theta, \xi) = (1.27°, 2a_M)$. (a) The low-lying energy spectra for $N = 8$, 10, 12 electrons on the $N/2 \times 6$ lattice. The shade indicates the threefold ($\mathcal{D} = 3$) topological degeneracy of the ground states. (b) The finite-size scaling of the energy gap $E_4 - E_1$ and the ground-state splitting $E_3 - E_1$ for $N = 4$, 5, 6, 8, 10, 12 electrons. (c) The spectral flow for $N = 10$, $N_1 \times N_2 = 5 \times 6$, where Φ_y is the magnetic flux insertion in the $\mathbf{a}_2^M$ direction. (d) The particle entanglement spectrum for $N = 10$, $N_1 \times N_2 = 5 \times 6$ and $N_A = 5$, with 23,256 levels below the entanglement gap (the dashed line).

in the entire MBZ, where δ^{ab} is the identity matrix. In this situation, both inequalities in Eq. (14) are saturated, just like in the LLL (see (Mera and Ozawa, 2021) for a systematic method to construct bands with ideal quantum geometry). Moreover, the real-space forms $\psi_{\mathbf{k}}(\mathbf{r})$ of flat-band wave functions in chiral MATBG are fixed by the ideal quantum geometry as (Wang et al., 2021)

$$\psi_{\mathbf{k}}(\mathbf{r}) = \mathcal{N}_{\mathbf{k}}\mathcal{B}(\mathbf{r})\varphi_{\mathbf{k}}(\mathbf{r}), \tag{23}$$

where $\mathcal{N}_{\mathbf{k}}$ is the normalization factor, $\mathcal{B}(\mathbf{r})$ is a $\mathbf{k}$-independent function, and $\varphi_{\mathbf{k}}(\mathbf{r})$ is the Bloch-like basis in the LLL. Remarkably, Eq. (23) does not only hold for chiral MATBG, but is valid for all $|\mathcal{C}| = 1$ bands with the ideal quantum geometry (Wang et al., 2021). Starting from this relation in the single-particle level, one can also generalize Haldane pseudopotentials from the LLL to ideal $|\mathcal{C}| = 1$ flat bands and construct model FCIs as zero-energy ground states of short-ranged interactions (Ledwith et al., 2020; Wang et al., 2021). Zero-energy FCIs were also observed in other models (Kapit and Mueller, 2010; Liu et al., 2013b; Behrmann et al., 2016, which implies that the band geometry is also ideal there. The ideal band geometry and model FCIs are also expected in chiral MATBG at a finite magnetic field (Sheffer and Stern, 2021).

Back to our numerical results in TBG-hBN, the stabilization of the $\overline{\nu} = 1/3$ FCI phase is closely related to whether the conditions listed in Section "Conditions of the existence of FCIs" are satisfied. To see this, we characterize quantum geometry of the valence band by fluctuations of the Berry curvature $\Omega(\mathbf{k})$ and FS metric $g^{ab}(\mathbf{k})$ and the violation of the saturated trace condition, as quantified by

$$\begin{aligned}
\sigma(\Omega) &= \sqrt{\langle \Omega^2(\mathbf{k})\rangle - \langle \Omega(\mathbf{k})\rangle^2},\\
\sigma(g) &= \sqrt{\sum_{a,b=x,y} \left(\langle g^{ab}(\mathbf{k}) g^{ba}(\mathbf{k})\rangle - \langle g^{ab}(\mathbf{k})\rangle\langle g^{ba}(\mathbf{k})\rangle\right)},\\
\delta_{\mathrm{tr}} &= \left\langle \mathrm{tr} g^{ab}(\mathbf{k}) - |\Omega(\mathbf{k})|\right\rangle,
\end{aligned} \tag{24}$$

respectively, where $\langle O(\mathbf{k})\rangle = \frac{1}{A_{\mathrm{MBZ}}}\int_{\mathrm{MBZ}} O(\mathbf{k}) dk_x dk_y$ is the average of quantity O in the MBZ, with A_{MBZ} the area of MBZ. We plot $\sigma(\Omega)$, $\sigma(g)$, δ_{tr}, together with the bandwidth W of the electron's valence band and the bandwidth W_h^i of interaction-induced hole dispersion $\epsilon_h^i(\mathbf{k})$ in Fig. 2(c) and (d) as a function of twist angle θ. Remarkably, the most robust FCI states indeed appear when all of these quantities are sufficiently small. Nevertheless, the minima of these quantities, are not located at the same θ, so over-minimizing one quantity does not necessarily improve the stability of the FCI phase. In particular, the robust FCIs appear at twist angles slightly above the TBG magic angle. These numerical results are consistent with the requirements listed in Section "Conditions of the existence of FCIs."

Numerical evidence of competing phases

As we discussed before, competing phases will prevail when properties of the microscopic model disfavor FCI states. In our numerical data, the FCI phase obviously breaks down when the twist angle is either reduced or increased out of the optimal range in Fig. 2. On the left side of the FCI phase (with smaller θ), there is a pronounced sensitivity of the energy spectrum to the lattice size. In particular, when both N_1 and N_2 are divisible by three, we observe a new kind of threefold ground-state degeneracy appearing in equally spaced momentum sectors rather than in $\overline{\nu} = 1/3$ Laughlin FCI sectors. For example, at a representative parameter point $(\theta, \xi) = (1.10°, 2a_M)$ in this region, the three ground states of $N = 12$, $N_1 \times N_2 = 6 \times 6$ appear in the $(K_1, K_2) = (0, 0)$, $(2, 2)$ and $(4, 4)$ sectors (Fig. 4(a)). By contrast, the ground states in the FCI phase of the same system size are all located in the $(K_1, K_2) = (0, 0)$ sector (Fig. 3(a)).

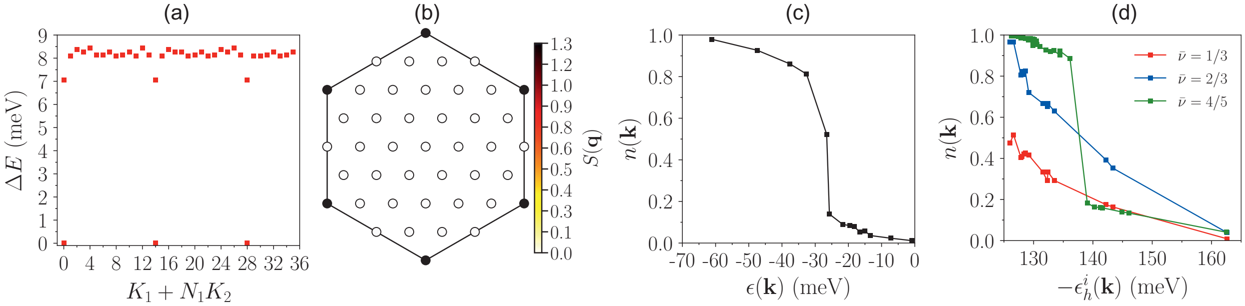

Fig. 4 Numerical evidence of competing phases in the valence band of TBG-hBN. (a) The low-lying energy spectrum of the CDW phase at a representative parameter point $(\theta, \xi) = (1.10°, 2a_M)$. The three ground states at separated by the order momenta $\Delta\mathbf{K} = (2, 2)$ and $(4, 4)$. (b) The structure factor $S(\mathbf{q})$ of the CDW state at the same parameter point as in (a). (c) The ground-state occupation $n(\mathbf{k})$ of electrons vs the electron band dispersion in the usual FL phase at a representative parameter point $(\theta, \xi) = (1.60°, 2a_M)$. We choose $N = 12$ electrons at $\overline{\nu} = 1/3$ in the $N_1 \times N_2 = 6 \times 6$ lattice in (a)–(c). (d) The ground-state occupation $n(\mathbf{k})$ of electrons vs the interaction-induced hole dispersion $\epsilon_h^i(\mathbf{k})$ at the parameter point $(\theta, \xi) = (1.10°, 2a_M)$ for fillings $\overline{\nu} = 1/3$,$2/3$ and 4/5. The corresponding system sizes are $N = 12$, $N_1 \times N_2 = 6 \times 6$, $N = 24$, $N_1 \times N_2 = 6 \times 6$, and $N = 28$, $N_1 \times N_2 = 5 \times 7$, respectively.

Distribution of degenerate ground states over equally spaced momenta is a signal of CDWs. As we discussed in Section "Competing phases," this can be further confirmed by the structure factor $S(\mathbf{q})$. Indeed, pronounced peaks of $S(\mathbf{q})$ exist at the corners of the MBZ (Fig. 4(b)), revealing the underlying phase is the CDW with the order momentum $\mathbf{K}^+_{t,b}$. These order momenta are indeed those separating the degenerate ground states, by noting $\Delta\mathbf{K} = (2,2) = (\mathbf{G}_1 + \mathbf{G}_2)/3 \sim \mathbf{K}^+_b$ and $\Delta\mathbf{K} = (4,4) = 2(\mathbf{G}_1 + \mathbf{G}_2)/3 \sim \mathbf{K}^+_t$. Here $\sim$ means "equal to" up to a MBZ primitive reciprocal lattice vector. The order momenta suggest a tripled unit cell of charge modulation compared to the original moiré lattice (Wilhelm et al., 2021). The identification of order momenta also explains the absence of the CDW phase when either N_1 or N_2 are indivisible by three. Remember that the single-electron momentum $\mathbf{k}$ can only take $\mathbf{k} = \frac{m_1}{N_1}\mathbf{G}_1 + \frac{m_2}{N_2}\mathbf{G}_2$ for a finite periodic system. Hence both N_1 and N_2 must be divisible by three if $\mathbf{K}^+_{t,b}$ belong to this set of allowed $\mathbf{k}$.

On the other hand, on the right side of the FCI phase (larger θ), neither the FCI degeneracy nor the CDW degeneracy appears in the low-energy spectra, no matter what the lattice size is. Note that in this region the electron bandwidth dramatically increases while the interaction-induced hole bandwidth remains small (Fig. 2(d)), implying that the ground state is a usual FL. Indeed, we find a sharp step in the electronic occupation number $n(\mathbf{k})$ at some critical $\epsilon(\mathbf{k})$, as shown in Fig. 4(c).

To see the unusual interaction-induced FL phase, we need to check the region in which the interaction-induced hole dispersion is much stronger than electron dispersion. Therefore, we choose the parameter point $(\theta, \xi) = (1.10°, 2a_M)$ where this condition is satisfied (Fig. 2(d)). Remarkably, we do find the emergence of a Fermi-surface structure in the $n(\mathbf{k}) - \epsilon^i_h(\mathbf{k})$ with the increasing of the filling factor from 1/3 to 4/5 (Fig. 4(d)). This means the $\mathbf{K}$-CDW phase at $\bar{\nu} = 1/3$ is replaced by the unusual FL phase at large fillings.

FCIs in Bloch bands with high Chern numbers

As listed in Table 1, a significant qualitative difference of a Chern band from a LL is that it can support higher Chern number $|\mathcal{C}| > 1$. In general, one can add longer-range hopping in a $|\mathcal{C}| = 1$ model or appropriately stack multilayers of $|\mathcal{C}| = 1$ models to get $|\mathcal{C}| > 1$ bands (Wang and Ran, 2011; Zhang et al., 2011; Trescher and Bergholtz, 2012; Yang et al., 2012; Sticlet and Piéchon, 2013; Wu et al., 2015; Behrmann et al., 2016; Zhang et al., 2019a; Chittari et al., 2019; Lee et al., 2019). This strategy also works for moiré materials. One can systematically construct $|\mathcal{C}| = n$ bands near the CNP by twisting two sheets of Bernal-stacked n graphene layers (Wang and Liu, 2022; Ledwith et al., 2022). TBG corresponds to the $n = 1$ case. $n = 2$ gives the twisted double bilayer graphene (TDBG), for which $|\mathcal{C}| = 2$ flat bands near the CNP have been confirmed (Zhang et al., 2019a; Lee et al., 2019; Chebrolu et al., 2019). Strikingly, the model constructed in this way gains chiral symmetry for any $n \geq 1$ if only intersublattice couplings are kept. At magic angles, these chiral models all possess perfectly flat valence and conduction bands with ideal band geometry.

FCIs can be diagnosed in high-Chern number bands by the same identifications as in $|\mathcal{C}| = 1$ models. Excitingly, series of high-$\mathcal{C}$ FCI states have been numerically discovered in realistic moiré bands (Liu et al., 2021a; Wang and Liu, 2022) inspired by earlier numerical findings in tight-binding toy models (Yang et al., 2012; Wang et al., 2012a; Liu et al., 2012; Wang et al., 2013; Sterdyniak et al., 2013; Wu et al., 2013; Bergholtz et al., 2015; Wu et al., 2015; Behrmann et al., 2016; Möller and Cooper, 2015; Andrews and Moller, 2018). These FCIs appear at band fillings, for instance,

$$\nu = \frac{k}{|\mathcal{C}|(m-1)+1} \tag{25}$$

with integer $k \geq 1$ and $m \geq 2$. Here $k = 1$ and $k > 1$ correspond to Abelian and non-Abelian states, respectively, and m is even (odd) for bosons (fermions). Further fillings of high-$\mathcal{C}$FCIs can be predicted by applying the composite-fermion theory to Hofstadter bands (Möller and Cooper, 2015). Some of the observed high-$\mathcal{C}$FCIs are even model states occurring as the zero-energy ground states of proper short-ranged interactions (Behrmann et al., 2016; Wang and Liu, 2022).

Ample attention has been directed toward understanding these high-$\mathcal{C}$FCIs. Intuitively, they may have a relation with the conventional FQH states in $|\mathcal{C}|$ copies of the LLL, which also carry Chern number $\mathcal{C}$ as a whole. However, an obvious discrepancy exists between a single Chern number $\mathcal{C}$ band and $|\mathcal{C}|$ copies of the LLL: the number of single-particle orbitals in the latter must be divisible by $|\mathcal{C}|$ as each LLL contains an integer number of orbitals, while the number of single-particle states in the former does not necessarily to be a multiple of $|\mathcal{C}|$. To resolve this discrepancy, a new type of $|\mathcal{C}|$-component LLL was proposed. Here component refers to internal degrees of freedom of particles, like spin or physical layer. In contrast to the usual multicomponent LLL where the $|\mathcal{C}|$ components are decoupled, a new set of boundary conditions, called "color-entangled" boundary conditions, is adopted to connect different components, i.e., a particle can change its component index when crossing the boundary of the system (Wu et al., 2013, 2014). Under this scenario, one can construct a single manifold of Bloch-like states with Chern number $\mathcal{C}$, rather than $|\mathcal{C}|$ separate Chern-number-one manifolds, such that the number of orbitals per LLL does not need to be an integer. Diagonalizing Haldane's pseudopotentials in the "color-entangled" LLL basis produces unconventional FQH states, which were found to have high overlaps and the same PES countings with high-$\mathcal{C}$FCIs in lattice models (Wu et al., 2013). However, the analytical ansatz wavefunctions of the high-$\mathcal{C}$FCIs are still unknown, and it remains unclear whether the color-entangled boundary conditions lead to new topological orders compared with conventional $|\mathcal{C}|$-component FQH states.

Experimental observation of FCIs

We have seen that FCIs arise from the interplay between interactions and the dispersion, topology, and geometry of the partially filled band. Therefore, their experimental realizations likely require highly controllable platforms in which band properties and interactions can be easily tuned to the suitable regime. Given this, van-der-Waals heterostructures with moiré patterns (Geim and Grigorieva, 2013; Novoselov et al., 2016) naturally emerge as a promising candidate to host FCIs. There are many experimental knobs in this kind of setups that can affect band properties and interactions, including the twist angle, the external fields, the dielectric environment, and even the material itself. In the past few years, rapid progress has been made on manufacturing van-der-Waals heterostructures and investigating the exotic correlated phases thereof.

Experiment in Bernal-stacked bilayer graphene

The first observation of FCI states was reported in a van-der-Waals heterostructure made of Bernal-stacked bilayer graphene aligned with hBN (BLG-hBN), penetrated by a perpendicular magnetic field $B \sim 30\,\mathrm{T}$ (Spanton et al., 2018). In this system, electrons experience a moiré superlattice potential from the mismatched graphene and hBN lattices. The interplay between the magnetic field and the moiré potential creates topological Harper-Hofstadter bands that act as parents of potential FCI states. By determining the compressibility of the system via measuring the penetration field capacitance for variable electron density n_e and magnetic flux density n_ϕ per moiré superlattice cell, multiple incompressible states are identified along trajectories obeying Streda formula

$$n_e = t n_\phi + s, \tag{26}$$

where $t = \sigma_{xy} h / e^2$ is the dimensionless Hall conductance and s is the zero-field filling factor Streda (1982); MacDonald (1983).

The observed incompressible states can be distinguished by their values of t and s (see Table 2): non-integer t signals intrinsic topological order whereas fractional s may originate from either topological order or translational symmetry (TS) breaking. Remarkably, apart from the trivial states, QHE states in LLs, and Chern insulators in Hofstadter bands, clear evidence of states with fractional s and fractional t was observed in the experiment, which correspond to FCIs. These FCI states develop from electron/hole doping the nearby parent Chern insulating states with an effective filling $\overline{\nu}$ in the partially filled band. Some of them exist in a $\mathcal{C} = -1$ band at $\overline{\nu} = 1/3, 2/3, 2/5, 3/5$, falling into the odd-denominator Laughlin and composite fermion sequence. Notably, several other states exist in a $\mathcal{C} = 2$ band, for instance, at $\overline{\nu} = 1/3$ and $\overline{\nu} = 1/6$. The $\mathcal{C} = 2, \overline{\nu} = 1/3$ state, with $(t, s) = (8/3, -1/3)$, preserves TS of the moiré superlattice and belongs to the sequence predicted in Ref. Möller and Cooper (2015). However, the $\mathcal{C} = 2, \overline{\nu} = 1/6$ state carries $(t, s) = (7/3, -1/6)$, which means that only half fundamental charge $e/3$ is bound to each moiré unit cell. This feature suggests doubling of unit cell in the electron density distribution which spontaneously breaks TS of the moiré superlattice. The TS-broken FCI, as well as the observed TS-broken Chern insulators, imply an intriguing hybridization of conventional CDW and topological phase. Such combination of CDW and topological features is also numerically discovered in $\mathcal{C} = 0, \pm 1, 2$ bands of several toy tight-binding models (Kumar et al., 2014; Kourtis and Daghofer, 2014; Kourtis, 2018) and experimentally observed in other moiré materials (Pierce et al., 2021; Polshyn et al., 2022). The hybrid states in $|\mathcal{C}| = 2$ bands may originate from ferromagnetism of internal degree of freedoms and their entanglement with real-space translation in high Chern number bands (Kumar et al., 2014; Polshyn et al., 2022).

Table 2 The observed incompressible states in Refs. Spanton et al. (2018) and Xie et al. (2021b) classified by their values of t and s. While some of the observed Chern insulators and FCIs preserve translational symmetry (TS) of the moiré superlattice, others spontaneously break this symmetry with an expanded unit cell of electron density distribution, implying an intriguing combination of conventional charge density wave and topological features. Those exotic fractional Chern insulators in the last row are neither simple TS preserving nor TS broken states, and may originate from the interplay between the multicomponent nature of the material and the spatial symmetry.

Incompressible states	*Values of* t *and* s
Trivial correlated insulator	$t = 0$ and integer $s \neq 0$
Charge density wave	$t = 0$ and fractional s
Integer quantum Hall states in LLs	Integer $t \neq 0$ and $s = 0$
TS-preserving Chern insulators	Integer $t \neq 0$ and integer $s \neq 0$
TS-broken Chern insulators (also observed in Refs. Pierce et al. (2021) and Polshyn et al. (2022))	Integer $t \neq 0$ and fractional s
Fractional quantum Hall states in LLs	Fractional t and $s = 0$
TS-preserving fractional Chern insulators	Fractional t and fractional s, t and s have the same denominator
TS-broken fractional Chern insulators	Fractional t and fractional s, denominator of s is a multiple of that of t
Exotic fractional Chern insulators	Fractional t and fractional s, t and s have coprime denominators

Experiment in twisted bilayer graphene

While the experiment above realizes the FCI states in the sense that they have no direct LL counterparts, a quite high magnetic field is still needed to produce the topological band structure. Therefore, to turn the dream of zero-field FCI into reality, we must find systems hosting intrinsic topological flat bands in the absence of (or at least with weak) external magnetic fields. As predicted by theoretical works (Zhang et al., 2019a; Song et al., 2019; Liu et al., 2019; Po et al., 2019; Zhang et al., 2019b), TBG appears as a promising candidate to satisfy this requirement. A plethora of recent experiments down to zero field (Zondiner et al., 2020; Nuckolls et al., 2020; Wu et al., 2021; Saito et al., 2021; Das et al., 2021; Choi et al., 2021; Park et al., 2021; Stepanov et al., 2021; Serlin et al., 2020; Pierce et al., 2021) have confirmed the existence of Chern insulating states at integer band fillings, thus indeed raising the possibility of realizing zero-field FCIs in TBG systems.

A significant progress was made in this direction in which FCI states were observed in TBG aligned with hBN at weak magnetic fields as low as $\sim$5 T (Xie et al., 2021b). In this experiment, TBG devices were prepared near the magic twist angle $\theta \sim 1.06^\circ$, then a perpendicular magnetic field is applied. Local electronic compressibility measurements were preformed using a scanning single-electron transistor. Similar to the BLG-hBN experiment (Spanton et al., 2018), the dependence of this compressibility on the electron density and magnetic field, as shown in Fig. 5(a), reveals a large number of incompressible states (Table 2) satisfying Eq. (26), in which multiple FCI states with fractional t and s are identified. Remarkably, the first two FCI states appear in the range of $3 < \nu < 4$ at a weak magnetic field of only $\sim$5 T [state 1 with $(t, s) = (2/3, 10/3)$ and state 2 with $(t, s) = (1/3, 11/3)$ in Fig. 5(b)]. According to their (t, s) values, these two states are formed at $\overline{\nu} = 1/3$ and $\overline{\nu} = 2/3$ filling of a $\mathcal{C} = -1$ band and preserve the TS of the moiré superlattice, thus they can be interpreted as lattice analogs of the $\nu = 1/3$ Laughlin FQH state and its particle-hole conjugate. The energy gaps for both states are estimated as $\sim$0.6 K, which is comparable to the typical temperature required to realize Laughlin states in 2DEGs. Notably, these two FCI states are suddenly replaced by CDWs with the decreasing of the magnetic field. Numerical simulations in Refs. Xie et al. (2021b) and Parker et al. (2021) interpreted this phenomenon in terms of quantum geometry of the partially filled band: the applied magnetic field flattens the band Berry curvature, such that favorable band geometry conditions for the emergence of FCIs are created. However, unlike in the BLG-hBN experiment where the whole Chern band is created by the

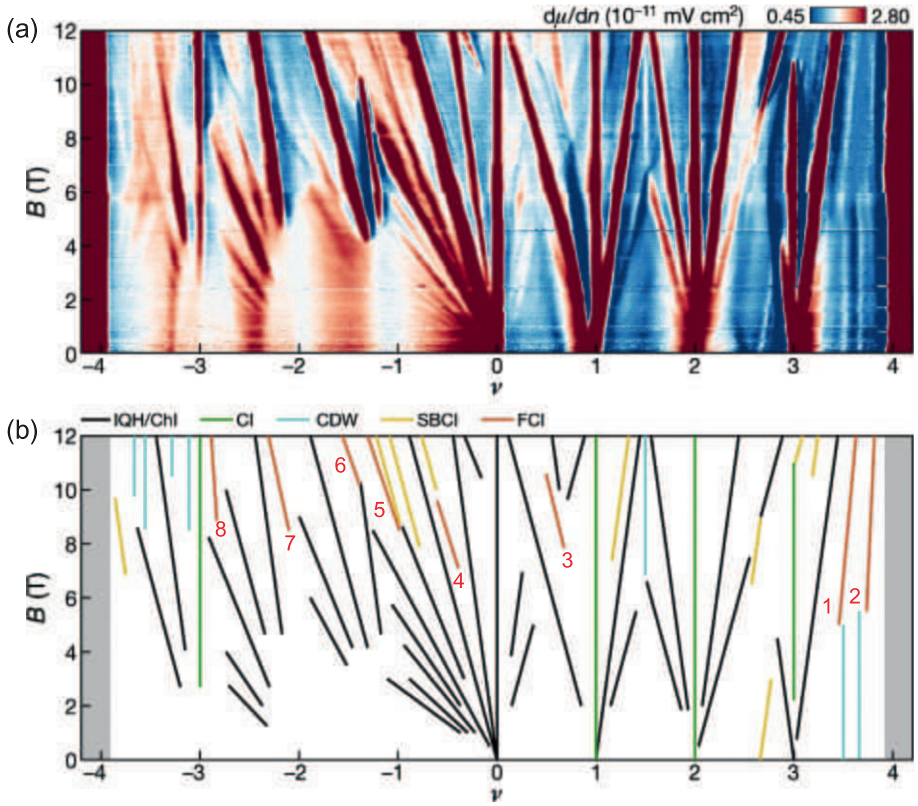

Fig. 5 Incompressible states observed in TBG-hBN. (a) Local inverse compressibility $d\mu/dn$ as a function of electron filling ν and the magnetic field B. Those red trajectories correspond to incompressible states. (b) Wannier diagram extracted from the experimental data in (a). Black lines correspond to integer quantum Hall states/TS-preserving Chern insulators (IQH/ChI); green lines correspond to trivial correlated insulators (CI); blue lines correspond to charge density waves (CDW); yellow lines correspond to TS-broken Chern insulators (SBCI); and orange lines correspond to (both TS-preserving and TS-broken) fractional Chern insulators (FCI). The detailed definitions of these states can be found in Table 2. The red numbers 1–8 indicate the eight observed FCI states. Modified from Ref. Xie Y., Pierce A.T., Park J.M., Parker D.E., Khalaf E., Ledwith P., Cao Y., Lee S.H., Chen S., Forrester P.R., Watanabe K., Taniguchi T., Vishwanath A., Jarillo-Herrero P., Yacoby A. (2021b). Fractional chern insulators in magic-angle twisted bilayer graphene. *Nature* 600(7889):439–443. doi: 10.1038/s41586-021-04002-3.

magnetic field, here the Berry curvature stems from the zero-field topological band of TBG-hBN and the role of the magnetic field is merely to redistribute Berry curvature. Once the Berry curvature can be flattened by other effects, the magnetic field will probably become unnecessary and these $\bar{\nu} = 1/3$ and $\bar{\nu} = 2/3$ FCIs are expected to survive at zero field. Indeed, zero-field $\bar{\nu} = 1/3$ FCIs in TBG-hBN were first numerically predicted at weaker $w_1 = 90$ meV (Abouelkomsan et al., 2020), where the Berry curvature is flatter. Alternatively, a reduction of w_0/w_1 or slightly increasing the twist angle can also improve the band geometry (Parker et al., 2021).

Apart from the weak-field FCI states 1 and 2, additional FCIs were also observed in TBG-hBN away from $3 < \nu < 4$ at slightly stronger magnetic fields, including TS-preserving states [state 6 with $(t, s) = (-13/5, -2/5)$ and state 7 with $(t, s) = (-4/3, -5/3)$] and TS-broken states [state 3 with $(t, s) = (-8/5, 11/10)$ and state 4 with $(t, s) = (-7/3, 2/9)$]. More intriguingly, there are also FCI states with coprime denominators of t and s, like state 5 with $(t, s) = (-5/2, -1/5)$ and state 8 with $(t, s) = (-1/2, -8/3)$, which are neither simple TS-preserving nor TS-broken states. These exotic FCIs may originate from complex interplay between the multicomponent nature of TBG and spatial symmetry.

FCIs in cold-atom systems

Beside solid-state moiré systems, the high microscopic control and precision that are achievable in ultracold atoms make them also among the most promising candidates to realize rich correlated physics. In fact, there is a long-standing interest to realize the FQHE via cold atoms. The key task is to achieve a tight-binding model with complex hopping. Theoretical works along this direction have proposed several schemes, such as dipole systems (Weber et al., 2022; Yao et al., 2012) and bosons in optical flux lattice (Cooper, 2011; Cooper and Moessner, 2012; Cooper and Dalibard, 2013; Sterdyniak et al., 2015), and predicted FCIs therein. In particular, tremendous effort is made to study onsite-interacting bosons confined in a square optical lattice penetrated by a uniform effective magnetic field. This system is described by the 2D Harper-Hofstadter-Hubbard (HHH) Hamiltonian

$$H = -J\sum_{m,n}\left(a^{\dagger}_{m,n+1}a_{m,n} + e^{i2\pi\phi n}a^{\dagger}_{m+1,n}a_{m,n} + \text{H.c.}\right) + \frac{U}{2}\sum_{m,n}\widehat{n}_{m,n}(\widehat{n}_{m,n} - 1), \tag{27}$$

where J is the nearest-neighboring hopping strength, $a^{\dagger}_{m,n}(a_{m,n})$ creates (annihilates) a boson on the lattice site (m, n), ϕ is the effective magnetic flux through each elementary square of the lattice, U is the magnitude of onsite repulsion, and $\widehat{n}_{m,n} = a^{\dagger}_{m,n}a_{m,n}$ is the occupation number operator on site (m, n). A plethora of numerical works find bosonic Abelian and non-Abelian FCIs as ground states of the HHH model at rational flux density $\phi \leq 1/3$ when the interaction is sufficiently strong and the lowest band is partially filled (Palmer and Jaksch, 2006; Sørensen et al., 2005; Hafezi et al., 2007; Hormozi et al., 2012; Gerster et al., 2017; Möller and Cooper, 2015; Hudomal et al., 2019; Palm et al., 2021; Boesl et al., 2022). The introduction of longer-range hopping and reduction of flux density may further stabilize these states. Fine-tuned exponentially decaying hopping can even perfectly flatten the lowest band and support model FCIs as the zero-energy ground states (Kapit and Mueller, 2010; Liu et al., 2013b).

The FCI states found in the HHH model can be prepared quasi-adiabatically, that is, one begins with a trivial state with low entropy, then slowly ramps the system to the desired final state (Popp et al., 2004; Grusdt et al., 2014; Barkeshli et al., 2015; He et al., 2017; Motruk and Pollmann, 2017; Palm et al., 2021). This protocol replies on continuous phase transitions between FCIs and other competing phases like CDW and superfluid. While dissipation is often thought of being harmful to the success of state preparation, some protocols suggest using special dissipative mechanism to pumping bosons from higher bands to the lowest band to make the state closer to FCIs (Liu et al., 2021b).

Theoretical works are further encouraged by the rapid development of experimental techniques on artificial gauge field and quantum gas microscope, which make the HHH Hamiltonian a paradigmatic model that has been realized in cold-atom experiments. Once bosons are trapped in an optical lattice, the effective magnetic field can be achieved by generating an artificial gauge field through lattice shaking techniques (Aidelsburger et al., 2013; Miyake et al., 2013). The nontrivial band topology in the HHH model has been confirmed by measuring the transverse deflection of the atomic cloud in response to an optical gradient (Aidelsburger et al., 2015). Further, the model has been pushed into the strong-interaction regime (Eric Tai et al., 2017), such that FCIs of ultracold atomic gases may potentially be within reach in the not too distant future.

Motivated by the encouraging theoretical and experimental progress, recent research focuses on how to detect FCI states once they are ready in cold-atom systems. In particular, such detection should be experimentally feasible and valid for those few-particle settings limited by the current technology. One way of detection is to probe the Hall conductance. However, because the transport measurements akin to those in solid state systems cannot be straightforwardly adopted into the cold-atom setting, alternative schemes have to be designed to extract Hall conductance. There have been several protocols on this aspect. One can apply a weak external force to the atomic cloud and track its center of mass drift (Repellin et al., 2020a; Motruk and Na, 2020). It is also possible to evaluate Hall conductance using interferometric protocols (Grusdt et al., 2016), randomized measurement scheme (Cian et al., 2021), or through circular-dichroic measurement (Tran et al., 2017; Repellin and Goldman, 2019). Apart from Hall conductance measurements, other promising schemes include probing fractionalized quasiholes through density measurement (Mantas Račiūnas et al., 2018; Umucalılar, 2018; Macaluso et al., 2020; Wang et al., 2022) and detecting chiral edge excitation (Kjäll and Moore, 2012; Dong et al., 2018). All of these proposals have been examined by numerical simulations in small cold-atom systems. Yet, it remains unclear which protocol is the most experimentally feasible before FCIs of cold atoms really turn to reality.

Conclusion

In this chapter, we have presented an introduction to fractional Chern insulators in topological flat bands. While FCIs share key features with conventional FQH states, the significant discrepancies between a Chern band and a Landau level make FCIs an ideal stage to realize the FQH physics under more general experimental conditions, to explore in the pursuit for qualitatively new topologically ordered states, and for unveiling the profound interplay between interaction, topology and geometry. Although it is impossible to provide a fully comprehensive account of the entire field here, we hope that our introduction has demonstrated the major methodology that has been used to understand FCIs and the new research trends which are emerging recently in this field.

The enthusiasm of studying FCIs has lasted over the past decade, and is now gaining renewed and extended interest due to their direct relevance in moiré materials. We would like to close this chapter by listing several directions which in our opinion are important for the development of this field in near future.

- *Exploring new platforms*. The recent trend of studying FCIs in moiré materials has clearly demonstrated the intimate relation between FCI and material science. Searching for new solid-state platforms that can host FCIs will significantly stimulate further development of this field. The research in this direction will need contributions from material calculations via, for instance, density functional theory. In fact, progress is already being made in this direction. In addition to more graphene based materials (Park et al., 2020; Rademaker et al., 2020; Chen et al., 2021), moiré systems built on transition metal dichalcogenides (TMD) are found to support topological flat bands (Wu et al., 2019; Pan et al., 2020; Li et al., 2021b; Zhang et al., 2021; Devakul et al., 2021; Pan et al., 2021; Zhou et al., 2022). Excitingly, a few numerical works have identified FCIs in twisted TMD homobilayers, like twisted bilayer $MoTe_2$ (Li et al., 2021a) and WSe_2 (Crépel and Fu, 2022). It requires more effort to thoroughly investigate FCI states and their competing phases in these new materials. These theoretical explorations will be greatly helpful to accelerate the experimental realization of zero-field FCIs.
- *Experimental realization of high-temperature zero-field FCIs*. Despite of the encouraging experimental observation of FCI states in TBG-hBN at weak magnetic fields down to ~ 5 T (Xie et al., 2021b), how to stabilize these states at further reduced fields remains a crucial challenge for really achieving zero-field FCIs. Theoretical works have suggested to probe TBG-hBN at twist angles above the magic angle, which could improve the band geometry such that the magnetic field might become unnecessary (Parker et al., 2021). Alternatively, one can also try other materials like twisted bilayer TMD. These proposals should be examined by experiments, then the optimal setups which facilitate the realization of zero-field FCIs the most can be selected. Moreover, apart from the compressibility measurement used in current experiments, transport features, which directly show the characterizing Hall conductance plateaus, is in an ideal situation a preferable method to identify FCIs in the future.

In addition to the static realization of zero-field FCIs, one may also consider the dynamic preparation of these states in periodically driven systems. Recently, there have been a series of works studying the photon-dressed band structure of moiré materials driven by an external laser light field (Topp et al., 2019; Katz et al., 2020; Vogl et al., 2020; Li et al., 2020; Rodriguez-Vega et al., 2020; Assi et al., 2021; Topp et al., 2021; Vogl et al., 2021; Benlakhouy et al., 2022). Based on these Floquet band structures, numerical simulations have demonstrated the possibility of Floquet FCIs (Grushin et al., 2014; Anisimovas et al., 2015) in light-driven TBG (Hu and Liu, 2022).

The energy gaps of the observed $\bar{\nu} = 1/3$ FCIs in TBG-hBN are about 0.6 K (Xie et al., 2021b), which are still close to that of the conventional Laughlin state in 2DEGs. Considering the expectation that FCIs can in principle exist at much higher temperature than conventional FQH states, it is definitely worthy of seeking a way to further increase the gap.

- *Searching and understanding new states*. With more theoretical and experimental explorations in various platforms, we should pay special attention on searching and understanding new states. Clearly, non-Abelian FCI states are still absent in experimental observation. In fact, it is difficult to get them even in numerical simulations, where multi-body interactions are often required (Wang et al., 2012b; Andrei Bernevig and Regnault, 2012; Wu et al., 2012a; Sterdyniak et al., 2013; Behrmann et al., 2016). Considering the potential application of non-Abelian anyons in topological quantum computation, it is a challenging albeit urgent task to find schemes that can provide non-Abelian FCIs by realistic two-body interactions.

The valley and spin degrees of freedom in moiré systems make it interesting to probe novel multicomponent FCI states. On the other hand, the symmetry-broken and other exotic FCI states (Table 2) found in the recent TBG-hBN experiment (Xie et al., 2021b) fall beyond the scope of conventional translational-symmetry-preserving FCIs. Apparently they have no analog in continuum FQH states. More theoretical and experimental effort is needed to understand these enigmatic states. Crucial open questions include: (i) Can these states survive at zero magnetic field? (ii) Can numerical simulations probe these states and extract their topological orders? (iii) Can experiments further identify the nature of these states, for example, their quasihole charges?

Motivated by seeking solutions of the questions above, we are convinced that the study of FCIs will remain an active field providing exciting and beautiful new physics.

Acknowledgments

Z. L. is supported by the National Key Research and Development Program of China through Grant No. 2020YFA0309200.

References

Abouelkomsan A, Liu Z, and Bergholtz EJ (2020) Particle-hole duality, emergent fermi liquids, and fractional chern insulators in moiré flatbands. *Physical Review Letters* 124: 106803. https://doi.org/10.1103/PhysRevLett.124.106803.

Abouelkomsan A, Yang K, and Bergholtz EJ (2022) *Quantum Metric Induced Phases in Moiré Materials*. https://doi.org/10.48550/ARXIV.2202.10467.

Aidelsburger M, Atala M, Lohse M, Barreiro JT, Paredes B, and Bloch I (2013) Realization of the hofstadter hamiltonian with ultracold atoms in optical lattices. *Physical Review Letters* 111: 185301. https://doi.org/10.1103/PhysRevLett.111.185301.

Aidelsburger M, Lohse M, Schweizer C, Atala M, Barreiro JT, Nascimbène S, Cooper NR, Bloch I, and Goldman N (2015) Measuring the chern number of hofstadter bands with ultracold bosonic atoms. *Nature Physics* 11(2): 162–166. https://doi.org/10.1038/nphys3171.

Andrei Bernevig B and Regnault N (2012) Emergent many-body translational symmetries of abelian and non-abelian fractionally filled topological insulators. *Physical Review B* 85: 075128. https://doi.org/10.1103/PhysRevB.85.075128.

Andrei Bernevig B, Song Z-D, Regnault N, and Lian B (2021) Twisted bilayer graphene. iii. Interacting hamiltonian and exact symmetries. *Physical Review B* 103: 205413. https://doi.org/10.1103/PhysRevB.103.205413.

Andrei EY and MacDonald AH (2020) Graphene bilayers with a twist. *Nature Materials* 19(12): 1265–1275. https://doi.org/10.1038/s41563-020-00840-0.

Andrews B and Soluyanov A (2020) Fractional quantum hall states for moiré superstructures in the hofstadter regime. *Physical Review B* 101: 235312. https://doi.org/10.1103/PhysRevB.101.235312.

Andrews B, Mohan M, and Neupert T (2021a) Abelian topological order of $\nu = 2/5$ and 3/7 fractional quantum hall states in lattice models. *Physical Review B* 103: 075132. https://doi.org/10.1103/PhysRevB.103.075132.

Andrews B and Möller G (2018) Stability of fractional Chern insulators in the effective continuum limit of Harper-Hofstadter bands with Chern number $|C|>1$. *Physical Review B* 97(3): 035159. https://doi.org/10.1103/PhysRevB.97.035159.

Andrews B, Neupert T, and Möller G (2021b) Stability, phase transitions, and numerical breakdown offractional chern insulators in higher chern bands of the hofstadter model. *Physical Review B* 104: 125107. https://doi.org/10.1103/PhysRevB.104.125107.

Anisimovas E, Žlabys G, Anderson BM, Juzeliūnas G, and Eckardt A (2015) Role of real-space micromotion for bosonic and fermionic floquet fractional chern insulators. *Physical Review B* 91: 245135. https://doi.org/10.1103/PhysRevB.91.245135.

Assi IA, LeBlanc JPF, Rodriguez-Vega M, Bahlouli H, and Vogl M (2021) Floquet engineering and nonequilibrium topological maps in twisted trilayer graphene. *Physical Review B* 104: 195429. https://doi.org/10.1103/PhysRevB.104.195429.

Avron JE, Seiler R, and Simon B (1983) Homotopy and quantization in condensed matter physics. *Physical Review Letters* 51: 51–53. https://doi.org/10.1103/PhysRevLett.51.51.

Barkeshli M and Qi X-L (2012) Topological nematic states and non-abelian lattice dislocations. *Physical Review X* 2: 031013. https://doi.org/10.1103/PhysRevX.2.031013.

Barkeshli M, Jian C-M, and Qi X-L (2013) Twist defects and projective non-abelian braiding statistics. *Physical Review B* 87: 045130. https://doi.org/10.1103/PhysRevB.87.045130.

Barkeshli M, Yao NY, and Laumann CR (2015) Continuous preparation of a fractional chern insulator. *Physical Review Letters* 115: 026802. https://doi.org/10.1103/PhysRevLett.115.026802.

Bauer D, Talkington S, Harper F, Andrews B, and Roy R (2022) Fractional chern insulators with a non-landau level continuum limit. *Physical Review B* 105: 045144. https://doi.org/10.1103/PhysRevB.105.045144.

Behrmann J, Liu Z, and Bergholtz EJ (2016) Model fractional chern insulators. *Physical Review Letters* 116: 216802. https://doi.org/10.1103/PhysRevLett.116.216802.

Benlakhouy N, Jellal A, Bahlouli H, and Vogl M (2022) Chiral limits and effect of light on the hofstadter butterfly in twisted bilayer graphene. *Physical Review B* 105: 125423. https://doi.org/10.1103/PhysRevB.105.125423.

Bergholtz EJ and Liu Z (2013) Topological flat band models and fractional chern insulators. *International Journal of Modern Physics B* 27(24): 1330017. https://doi.org/10.1142/S021797921330017X.

Bergholtz EJ, Zhao Liu M, Trescher RM, and Udagawa M (2015) Topology and interactions in a frustrated slab: Tuning from weyl semimetals to $C > 1$ fractional chern insulators. *Physical Review Letters* 114: 016806. https://doi.org/10.1103/PhysRevLett.114.016806.

Bessler R, Duerig U, and Koren E (2019) The dielectric constant of a bilayer graphene interface. *Nanoscale Advances* 1: 1702–1706. https://doi.org/10.1039/C8NA00350E.

Bistritzer R and MacDonald AH (2011) Moiré bands in twisted double-layer graphene. *Proceedings of the National Academy of Sciences of the United States of America* 00278424108(30): 12233–12237. https://doi.org/10.1073/pnas.1108174108.

Boesl J, Dilip R, Pollmann F, and Knap M (2022) Characterizing fractional topological phases of lattice bosons near the first mott lobe. *Physical Review B* 105: 075135. https://doi.org/10.1103/PhysRevB.105.075135.

Bultinck N, Chatterjee S, and Zaletel MP (2020) Mechanism for anomalous hall ferromagnetism in twisted bilayer graphene. *Physical Review Letters* 124: 166601. https://doi.org/10.1103/PhysRevLett.124.166601.

Chang C-Z, Zhang J, Feng X, Shen J, Zhang Z, Guo M, Li K, Yunbo O, Wei P, Wang L-L, Ji Z-Q, Feng Y, Ji S, Chen X, Jia J, Dai X, Fang Z, Zhang S-C, He K, Wang Y, Li L, Ma X-C, and Xue Q-K (2013) Experimental observation of the quantum anomalous hall effect in a magnetic topological insulator. *Science* 340(6129): 167–170. https://doi.org/10.1126/science.1234414.

Chebrolu NR, Chittari BL, and Jung J (2019) Flat bands in twisted double bilayer graphene. *Physical Review B* 99: 235417. https://doi.org/10.1103/PhysRevB.99.235417.

Chen L, Mazaheri T, Seidel A, and Tang X (2014) The impossibility of exactly flat non-trivial chern bands in strictly local periodic tight binding models. *Journal of Physics A: Mathematical and Theoretical* 47(15): 152001. https://doi.org/10.1088/1751-8113/47/15/152001.

Chen S, He M, Zhang Y-H, Hsieh V, Zaiyao Fei K, Watanabe TT, Cobden DH, Xiaodong X, Dean CR, and Yankowitz M (2021) Electrically tunable correlated and topological states in twisted monolayer–bilayer graphene. *Nature Physics* 17(3): 374–380. https://doi.org/10.1038/s41567-020-01062-6.

Cheng R (2010) *Quantum Geometric Tensor (Fubini-Study Metric) in Simple Quantum System: A Pedagogical Introduction*. https://doi.org/10.48550/ARXIV.1012.1337.

Chittari BL, Chen G, Zhang Y, Wang F, and Jung J (2019) Gate-tunable topological flat bands in trilayer graphene boronnitride moiré superlattices. *Physical Review Letters* 122: 016401. https://doi.org/10.1103/PhysRevLett.122.016401.

Choi Y, Kim H, Peng Y, Thomson A, Lewandowski C, Polski R, Zhang Y, Arora HS, Watanabe K, Taniguchi T, Alicea J, and Nadj-Perge S (2021) Correlation-driven topological phases in magic-angle twisted bilayer graphene. *Nature* 589(7843): 536–541. https://doi.org/10.1038/s41586-020-03159-7.

Cian Z-P, Dehghani H, Elben A, Vermersch B, Zhu G, Barkeshli M, Zoller P, and Hafezi M (2021) Many-body chern number from statistical correlations of randomized measurements. *Physical Review Letters* 126: 050501. https://doi.org/10.1103/PhysRevLett.126.050501.

Claassen M, Lee CH, Thomale R, Qi X-L, and Devereaux TP (2015) Position-momentum duality and fractional quantum hall effect in chern insulators. *Physical Review Letters* 114: 236802. https://doi.org/10.1103/PhysRevLett.114.236802.

Cooper NR (2011) Optical flux lattices for ultracold atomic gases. *Physical Review Letters* 106: 175301. https://doi.org/10.1103/PhysRevLett.106.175301.

Cooper NR and Dalibard J (2013) Reaching fractional quantum hall states with optical flux lattices. *Physical Review Letters* 110: 185301. https://doi.org/10.1103/PhysRevLett.110.185301.

Cooper NR and Moessner R (2012) Designing topological bands in reciprocal space. *Physical Review Letters* 109: 215302. https://doi.org/10.1103/PhysRevLett. 109.215302.

Crépel V and Fu L (2022) *Anomalous Hall Metal and Fractional Chern Insulator in Twisted Transition Metal Dichalcogenides*. https://doi.org/10.48550/ARXIV.2207.08895.

Das I, Xiaobo L, Herzog-Arbeitman J, Song Z-D, Watanabe K, Takashi Taniguchi B, Bernevig A, and Efetov DK (2021) Symmetry-broken chern insulators and rashba-like landau-level crossings in magic-angle bilayer graphene. *Nature Physics* 17(6): 710–714. https://doi.org/10.1038/s41567-021-01186-3.

Devakul T, Crépel V, Zhang Y, and Liang F (2021) Magic in twisted transition metal dichalcogenide bilayers. *Nature Communications* 12(1): 6730. https://doi.org/10.1038/s41467-021-27042-9.

Dong X-Y, Grushin AG, Motruk J, and Pollmann F (2018) Charge excitation dynamics in bosonic fractional chern insulators. *Physical Review Letters* 121: 086401. https://doi.org/10.1103/PhysRevLett.121.086401.

Eric Tai M, Lukin A, Rispoli M, Schittko R, Menke T, Borgnia D, Preiss PM, Grusdt F, Kaufman AM, and Greiner M (2017) Microscopy of the interacting harper–hofstadter model in the two-body limit. *Nature* 546(7659): 519–523. https://doi.org/10.1038/nature22811.

Feldman DE and Halperin BI (2021) Fractional charge and fractional statistics in the quantum hall effects. *Reports on Progress in Physics* 84(7)076501. https://doi.org/10.1088/1361-6633/ac03aa.

Fukuyama H, Platzman PM, and Anderson PW (1979) Two-dimensional electron gas in a strong magnetic field. *Physical Review B* 19: 5211–5217. https://doi.org/10.1103/PhysRevB.19.5211.

Geim AK and Grigorieva IV (2013) Van der Waals heterostructures. *Nature* 00280836499(7459): 419–425. https://doi.org/10.1038/nature12385.

Gerster M, Rizzi M, Silvi P, Dalmonte M, and Montangero S (2017) Fractional quantum hall effect in the interacting hofstadter model via tensor networks. *Physical Review B* 96: 195123. https://doi.org/10.1103/PhysRevB.96.195123.

Grusdt F, Letscher F, Hafezi M, and Fleischhauer M (2014) Topological growing of laughlin states in synthetic gauge fields. *Physical Review Letters* 113: 155301. https://doi.org/10.1103/PhysRevLett.113.155301.

Grusdt F, Yao NY, Abanin D, Fleischhauer M, and Demler E (2016) Interferometric measurements of many-body topological invariants using mobile impurities. *Nature Communications* 7(1): 11994. https://doi.org/10.1038/ncomms11994.

Grushin AG, TitusNeupert CC, and Mudry C (2012) Enhancing the stability of a fractional chern insulator against competing phases. *Physical Review B* 86: 205125. https://doi.org/10.1103/PhysRevB.86.205125.

Grushin AG, Gómez-León Á, and Neupert T (2014) Floquet fractional chern insulators. *Physical Review Letters* 10797114112(15): 1–5. https://doi.org/10.1103/PhysRevLett.112.156801.

Grushin AG, Motruk J, Zaletel MP, and Pollmann F (2015) Characterization and stability of a fermionic $\nu = 1/3$ fractional chern insulator. *Physical Review B* 91: 035136. https://doi.org/10.1103/PhysRevB.91.035136.

Guinea F and Walet NR (2018) Electrostatic effects, band distortions, and superconductivity in twisted graphene bilayers. *Proceedings of the National Academy of Sciences of the United States of America* 115(52): 13174–13179. https://doi.org/10.1073/pnas.1810947115.

Guinea F and Walet NR (2019) Continuum models for twisted bilayer graphene: Effect of lattice deformation and hopping parameters. *Physical Review B* 99: 205134. https://doi.org/10.1103/PhysRevB.99.205134.

Haddadi F, QuanSheng W, Kruchkov AJ, and Yazyev OV (2020) Moiréflat bands in twisted double bilayer graphene. *Nano Letters* 20(4): 2410–2415. https://doi.org/10.1021/acs.nanolett.9b05117.

Hafezi M, Sørensen AS, Demler E, and Lukin MD (2007) Fractional quantum hall effect in optical lattices. *Physical Review A* 76: 023613. https://doi.org/10.1103/PhysRevA.76.023613.

Haldane FDM (1983) Fractional quantization of the hall effect: A hierarchy of incompressible quantum fluid states. *Physical Review Letters* 51: 605–608. https://doi.org/10.1103/PhysRevLett.51.605.

Haldane FDM (1988) Model for a quantum hall effect without landau levels: Condensed-matter realization of the “parity anomaly” *Physical Review Letters* 61: 2015–2018. https://doi.org/10.1103/PhysRevLett.61.2015.

Haldane FDM, Rezayi EH, and Yang K (2000) Spontaneous breakdown of translational symmetry in quantum hall systems: Crystalline order in high landau levels. *Physical Review Letters* 85: 5396–5399. https://doi.org/10.1103/PhysRevLett.85.5396.

He Y-C, Grusdt F, Kaufman A, Greiner M, and Vishwanath A (2017) Realizing and adiabatically preparing bosonic integer and fractional quantum hall states in optical lattices. *Physical Review B* 96: 201103. https://doi.org/10.1103/PhysRevB.96.201103.

He A-L, Luo W-W, Yao H, and Wang Y-F (2020) Non-abelian fractional chern insulator in disk geometry. *Physical Review B* 101: 165127. https://doi.org/10.1103/PhysRevB.101.165127.

Hormozi L, Möller G, and Simon SH (2012) Fractional quantum hall effect of lattice bosons near commensurate flux. *Physical Review Letters* 108: 256809. https://doi.org/10.1103/PhysRevLett.108.256809.

Hu P-S and Liu Z (2022) *Floquet Fractional Chern Insulators and Competing Phases in Twisted Bilayer Graphene*. https://doi.org/10.48550/ARXIV.2207.07314.

Hudomal A, Regnault N, and Vasić I (2019) Bosonic fractional quantum hall states in driven optical lattices. *Physical Review A* 100: 053624. https://doi.org/10.1103/PhysRevA.100.053624.

Hunt B, Sanchez-Yamagishi JD, Young AF, Yankowitz M, LeRoy BJ, Watanabe K, Taniguchi T, Moon P, Koshino M, Jarillo-Herrero P, and Ashoori RC (2013) Massive dirac fermions and hofstadter butterfly in a van der waals heterostructure. *Science* 340(6139): 1427–1430. https://doi.org/10.1126/science.1237240.

Jackson TS, Möller G, and Roy R (2015) Geometric stability of topological lattice phases. *Nature Communications* 6(1): 8629. https://doi.org/10.1038/ncomms9629.

Jaworowski B, Güçlü AD, Kaczmarkiewicz P, Kupczyński M, Potasz P, and Wójs A (2018) Wigner crystallization in topological flat bands. *New Journal of Physics* 20(6): 063023. https://doi.org/10.1088/1367-2630/aac690.

Jaworowski B, Regnault N, and Liu Z (2019) Characterization of quasiholes in two-component fractional quantum hall states and fractional chern insulators in $|C| = 2$ flat bands. *Physical Review B* 99: 045136. https://doi.org/10.1103/PhysRevB.99.045136.

Jian C-M and Qi X-L (2013) Crystal-symmetry preserving wannier states for fractional chern insulators. *Physical Review B* 88: 165134. https://doi.org/10.1103/PhysRevB.88.165134.

Jotzu G, Messer M, Desbuquois R, Lebrat M, Uehlinger T, Greif D, and Esslinger T (2014) Experimental realization of the topological haldane model with ultracold fermions. *Nature* 515(7526): 237–240. https://doi.org/10.1038/nature13915.

Jung J, Raoux A, Qiao Z, and MacDonald AH (2014) Ab initio theory of moiré superlattice bands in layered two-dimensional materials. *Physical Review B* 89: 205414. https://doi.org/10.1103/PhysRevB.89.205414.

Jung J, DaSilva AM, MacDonald AH, and Adam S (2015) Origin of band gaps in graphene on hexagonal boron nitride. *Nature Communications* 6: 6308. https://doi.org/10.1038/ncomms7308.

Kang J and Vafek O (2019) Strong coupling phases of partially filled twisted bilayer graphene narrow bands. *Physical Review Letters* 122: 246401. https://doi.org/10.1103/PhysRevLett.122.246401.

Kapit E and Mueller E (2010) Exact parent hamiltonian for the quantum hall states in a lattice. *Physical Review Letters* 105: 215303. https://doi.org/10.1103/PhysRevLett.105.215303.

Katz O, Refael G, and Lindner NH (2020) Optically induced flat bands in twisted bilayer graphene. *Physical Review B* 24699969102(15): 155123. https://doi.org/10.1103/PhysRevB.102.155123.

Kitaev A and Preskill J (2006) Topological entanglement entropy. *Physical Review Letters* 96: 110404. https://doi.org/10.1103/PhysRevLett.96.110404.

Kjäll JA and Moore JE (2012) Edge excitations of bosonic fractional quantum hall phases in optical lattices. *Physical Review B* 85: 235137. https://doi.org/10.1103/PhysRevB.85.235137.

Klitzing KV, Dorda G, and Pepper M (1980) New method for high-accuracy determination of the fine-structure constant based on quantized hall resistance. *Physical Review Letters* 45: 494–497. https://doi.org/10.1103/PhysRevLett.45.494.

Knapp C, Spanton EM, Young AF, Nayak C, and Zaletel MP (2019) Fractional Chern insulator edges and layer-resolved lattice contacts. *Physical Review B* 99(8): 081114. https://doi.org/10.1103/PhysRevB.99.081114.

Koshino M, Yuan NFQ, Koretsune T, Ochi M, Kuroki K, and Fu L (2018) Maximally localizedwannier orbitals and the extended hubbard model for twisted bilayer graphene. *Physical Review X* 216033088(3): 31087. https://doi.org/10.1103/PhysRevX.8.031087.

Kourtis S (2018) Symmetry breaking and the fermionic fractional chern insulator in topologically trivial bands. *Physical Review B* 97: 085108. https://doi.org/10.1103/PhysRevB.97.085108.

Kourtis S and Daghofer M (2014) Combined topological and landau order from strong correlations in chern bands. *Physical Review Letters* 113: 216404. https://doi.org/10.1103/PhysRevLett.113.216404.

Kourtis S, Venderbos JWF, and Daghofer M (2012) Fractional chern insulator on a triangular lattice of strongly correlated t_{2_g} electrons. *Physical Review B* 86: 235118. https://doi.org/10.1103/PhysRevB.86.235118.

Kourtis S, Neupert T, Chamon C, and Mudry C (2014) Fractional chern insulators with strong interactions that far exceed band gaps. *Physical Review Letters* 112: 126806. https://doi.org/10.1103/PhysRevLett.112.126806.

Kourtis S, Neupert T, Mudry C, Sigrist M, and Chen W (2017) Weyl-type topological phase transitions in fractional quantum hall like systems. *Physical Review B* 96: 205117. https://doi.org/10.1103/PhysRevB.96.205117.

Kumar A, Roy R, and Sondhi SL (2014) Generalizing quantum hall ferromagnetism to fractional chern bands. *Physical Review B* 90: 245106. https://doi.org/10.1103/PhysRevB.90.245106.

Kupczyński M, Jaworowski BŻ, and Wójs A (2021) Interaction-driven transition between the wigner crystal and the fractional chern insulator in topological flat bands. *Physical Review B* 104: 085107. https://doi.org/10.1103/PhysRevB.104.085107.

Läuchli AM, Liu Z, Bergholtz EJ, and Moessner R (2013) Hierarchy of fractional chern insulators and competing compressible states. *Physical Review Letters* 111: 126802. https://doi.org/10.1103/PhysRevLett.111.126802.

Laughlin RB (1983) Anomalous quantum hall effect: An incompressible quantum fluid with fractionally charged excitations. *Physical Review Letters* 50: 1395–1398. https://doi.org/10.1103/PhysRevLett.50.1395.

Ledwith PJ, Tarnopolsky G, Khalaf E, and Vishwanath A (2020) Fractional chern insulator states in twisted bilayer graphene: An analytical approach. *Physical Review Research* 2: 023237. https://doi.org/10.1103/PhysRevResearch.2.023237.

Ledwith PJ, Vishwanath A, and Khalaf E (2022) Family of ideal chern flatbands with arbitrary chern number in chiral twisted graphene multilayers. *Physical Review Letters* 128: 176404. https://doi.org/10.1103/PhysRevLett.128.176404.

Lee CH, Thomale R, and Qi X-L (2013) Pseudopotential formalism for fractional chern insulators. *Physical Review B* 88: 035101. https://doi.org/10.1103/PhysRevB.88.035101.

Lee JY, Khalaf E, Liu S, Liu X, Hao Z, Kim P, and Vishwanath A (2019) Theory of correlated insulating behaviour and spin-triplet superconductivity in twisted double bilayer graphene. *Nature Communications* 10(1): 5333. https://doi.org/10.1038/s41467-019-12981-1.

Levin M and Wen X-G (2006) Detecting topological order in a ground state wave function. *Physical Review Letters* 96: 110405. https://doi.org/10.1103/PhysRevLett.96.110405.

Li H and Haldane FDM (2008) Entanglement spectrum as a generalization of entanglement entropy: Identification of topological order in non-abelian fractional quantum hall effect states. *Physical Review Letters* 101: 010504. https://doi.org/10.1103/PhysRevLett.101.010504.

Li W, Liu Z, Yong-Shi W, and Chen Y (2014) Exotic fractional topological states in a two-dimensional organometallic material. *Physical Review B* 89: 125411. https://doi.org/10.1103/PhysRevB.89.125411.

Li Y, Fertig HA, and Seradjeh B (2020) Floquet-engineered topological flat bands in irradiated twisted bilayer graphene. *Physical Review Research* 2: 043275. https://doi.org/10.1103/PhysRevResearch.2.043275.

Li H, Kumar U, Sun K, and Lin S-Z (2021a) Spontaneous fractional chern insulators in transition metal dichalcogenide moiré superlattices. *Physical Review Research* 3: L032070. https://doi.org/10.1103/PhysRevResearch.3.L032070.

Li T, Jiang S, Shen B, Zhang Y, Li L, Tao Z, Devakul T, Watanabe K, Taniguchi T, Liang F, Shan J, and Mak KF (2021b) Quantum anomalous hall effect from intertwined moirébands. *Nature* 600(7890): 641–646. https://doi.org/10.1038/s41586-021-04171-1.

Liu Z and Bergholtz EJ (2013) From fractional chern insulators to abelian and non-abelian fractional quantum hall states: Adiabatic continuity and orbital entanglement spectrum. *Physical Review B* 87: 035306. https://doi.org/10.1103/PhysRevB.87.035306.

Liu Z and Bergholtz EJ (2019) Fractional quantum hall states with gapped boundaries in an extreme lattice limit. *Physical Review B* 99: 195122. https://doi.org/10.1103/PhysRevB.99.195122.

Liu J and Dai X (2021) Theories for the correlated insulating states and quantum anomalous hall effect phenomena in twisted bilayer graphene. *Physical Review B* 103: 035427. https://doi.org/10.1103/PhysRevB.103.035427.

Liu Z, Bergholtz EJ, Fan H, and Läuchli AM (2012) Fractional chern insulators in topological flat bands with higher chern number. *Physical Review Letters* 109: 186805. https://doi.org/10.1103/PhysRevLett.109.186805.

Liu T, Repellin C, Bernevig BA, and Regnault N (2013a) Fractional chern insulators beyond laughlin states. *Physical Review B* 87: 205136. https://doi.org/10.1103/PhysRevB.87.205136.

Liu Z, Bergholtz EJ, and Kapit E (2013b) Non-abelian fractional chern insulators from long-range interactions. *Physical Review B* 88: 205101. https://doi.org/10.1103/PhysRevB.88.205101.

Liu Z, Kovrizhin DL, and Bergholtz EJ (2013c) Bulk-edge correspondence in fractional chern insulators. *Physical Review B* 88: 081106. https://doi.org/10.1103/PhysRevB.88.081106.

Liu Z, Bhatt RN, and Regnault N (2015) Characterization of quasiholes in fractional chern insulators. *Physical Review B* 91: 045126. https://doi.org/10.1103/PhysRevB.91.045126.

Liu Z, Möller G, and Bergholtz EJ (2017) Exotic non-abelian topological defects in lattice fractional quantum hall states. *Physical Review Letters* 119: 106801. https://doi.org/10.1103/PhysRevLett.119.106801.

Liu J, Liu J, and Dai X (2019) Pseudo landau level representation of twisted bilayer graphene: Band topology and implications on the correlated insulating phase. *Physical Review B* 99: 155415. https://doi.org/10.1103/PhysRevB.99.155415.

Liu Z, Abouelkomsan A, and Bergholtz EJ (2021a) Gate-tunable fractional chern insulators in twisted double bilayer graphene. *Physical Review Letters* 126: 026801. https://doi.org/10.1103/PhysRevLett.126.026801.

Liu Z, Bergholtz EJ, and Budich JC (2021b) Dissipative preparation of fractional chern insulators. *Physical Review Research* 3: 043119. https://doi.org/10.1103/PhysRevResearch.3.043119.

Lopes dos Santos JMB, Peres NMR, and Castro Neto AH (2007) Graphene bilayer with a twist: Electronic structure. *Physical Review Letters* 99: 256802. https://doi.org/10.1103/PhysRevLett.99.256802.

Lopes dos Santos JMB, Peres NMR, and Castro Neto AH (2012) Continuum model of the twisted graphene bilayer. *Physical Review B* 86: 155449. https://doi.org/10.1103/PhysRevB.86.155449.

Luo W-W, Chen W-C, Wang Y-F, and Gong C-D (2013) Edge excitations in fractional chern insulators. *Physical Review B* 88: 161109. https://doi.org/10.1103/PhysRevB.88.161109.

Luo W-W, He A-L, Zhou Y, Wang Y-F, and Gong C-D (2020) Quantum phase transitions in a $\nu=1/2$ bosonic fractional chern insulator. *Physical Review B* 102: 155120. https://doi.org/10.1103/PhysRevB.102.155120.

Luo W-W, He A-L, Wang Y-F, Zhou Y, and Gong C-D (2021) Bosonic fractional chern insulating state at integer fillings in a multiband system. *Physical Review B* 104: 115126. https://doi.org/10.1103/PhysRevB.104.115126.

Macaluso E, Comparin T, Umucalılar RO, Gerster M, Montangero S, Rizzi M, and Carusotto I (2020) Charge and statistics of lattice quasiholes from density measurements: A tree tensor network study. *Physical Review Research* 2: 013145. https://doi.org/10.1103/PhysRevResearch.2.013145.

MacDonald AH (1983) Landau-level subband structure of electrons on a square lattice. *Physical Review B* 28: 6713–6717. https://doi.org/10.1103/PhysRevB. 28.6713.

Manna S, Wildeboer J, Sierra G, and Nielsen AEB (2018) Non-abelian quasiholes in lattice moore-read states and parent hamiltonians. *Physical Review B* 98: 165147. https://doi.org/10.1103/PhysRevB.98.165147.

Mantas Račiūnas F, Ünal N, Anisimovas E, and Eckardt A (2018) Creating, probing, and manipulating fractionally charged excitations of fractional chern insulators in optical lattices. *Physical Review A* 98: 063621. https://doi.org/10.1103/PhysRevA.98.063621.

Mera B and Ozawa T (2021) Engineering geometrically flat Chern bands with Fubini-Study Kähler structure. *Physical Review B* 104(11): 115160. https://doi.org/10.1103/PhysRevB.104.115160.

Miyake H, Siviloglou GA, Kennedy CJ, Burton WC, and Ketterle W (2013) Realizing the harper hamiltonian with laser-assisted tunneling in optical lattices. *Physical Review Letters* 111: 185302. https://doi.org/10.1103/PhysRevLett.111.185302.

Moessner R and Chalker JT (1996) Exact results for interacting electrons in high landau levels. *Physical Review B* 54: 5006–5015. https://doi.org/10.1103/PhysRevB.54.5006.

Möller G and Cooper NR (2015) Fractional chern insulators in harper-hofstadter bands with higher chern number. *Physical Review Letters* 115: 126401. https://doi.org/10.1103/PhysRevLett.115.126401.

Möller G and Simon SH (2005) Composite fermions in a negative effective magnetic field: A monte carlo study. *Physical Review B* 72: 045344. https://doi.org/10.1103/PhysRevB.72.045344.

Moore G and Read N (1991) Nonabelions in the fractional quantum hall effect. *Nuclear Physics B* 0550-3213360(2): 362–396. https://doi.org/10.1016/0550-3213(91)90407-O.

Motruk J and Na I (2020) Detecting fractional chern insulators in optical lattices through quantized displacement. *Physical Review Letters* 125: 236401. https://doi.org/10.1103/PhysRevLett.125.236401.

Motruk J and Pollmann F (2017) Phase transitions and adiabatic preparation of a fractional chern insulator in a boson cold-atom model. *Physical Review B* 96: 165107. https://doi.org/10.1103/PhysRevB.96.165107.

Motruk J, Zaletel MP, Mong RSK, and Pollmann F (2016) Density matrix renormalization group on a cylinder in mixed real and momentum space. *Physical Review B* 93: 155139. https://doi.org/10.1103/PhysRevB.93.155139.

Nam NNT and Koshino M (2017) Lattice relaxation and energy band modulation in twisted bilayer graphene. *Physical Review B* 2469996996(7): 1–12. https://doi.org/10.1103/PhysRevB.96.075311.

Neupert T, Santos L, Chamon C, and Mudry C (2011) Fractional quantum hall states at zero magnetic field. *Physical Review Letters* 106: 236804. https://doi.org/10.1103/PhysRevLett.106.236804.

Neupert T, Chamon C, Iadecola T, Santos LH, and Mudry C (2015) Fractional (chern and topological) insulators. *Physica Scripta* T164: 014005. https://doi.org/10.1088/0031-8949/2015/t164/014005.

Niu Q, Thouless DJ, and Wu Y-S (1985) Quantized hall conductance as a topological invariant. *Physical Review B* 31: 3372–3377. https://doi.org/10.1103/PhysRevB.31.3372.

Novoselov KS, Mishchenko A, Carvalho A, and Castro Neto AH (2016) 2D materials and van der Waals heterostructures. *Science* 10959203353(6298). https://doi.org/10.1126/science.aac9439.

Nuckolls KP, Myungchul O, Wong D, Lian B, Watanabe K, Takashi Taniguchi B, Bernevig A, and Yazdani A (2020) Strongly correlated chern insulators in magic-angle twisted bilayer graphene. *Nature* 588(7839): 610–615. https://doi.org/10.1038/s41586-020-3028-8.

Okamoto S, Mohanta N, Dagotto E, and Sheng DN (2022) Topological flat bands in a kagome lattice multiorbital system. *Communications Physics* 5(1): 198. https://doi.org/10.1038/s42005-022-00969-1.

Ozawa T and Mera B (2021) Relations between topology and the quantum metric for Chern insulators. *Physical Review B* 104(4): 045103. https://doi.org/10.1103/PhysRevB.104.045103.

Palm FA, Buser M, Léonard J, Aidelsburger M, Schollwöck U, and Grusdt F (2021) Bosonic pfaffian state in the hofstadter-bose-hubbard model. *Physical Review B* 103: L161101. https://doi.org/10.1103/PhysRevB.103.L161101.

Palmer RN and Jaksch D (2006) High-field fractional quantum hall effect in optical lattices. *Physical Review Letters* 96: 180407. https://doi.org/10.1103/PhysRevLett.96.180407.

Pan H, Wu F, and Sarma SD (2020) Band topology, hubbard model, heisenberg model, and dzyaloshinskii-moriya interaction in twisted bilayer wse$_2$. *Physical Review Research* 2: 033087. https://doi.org/10.1103/PhysRevResearch.2.033087.

Pan H, Xie M, Wu F, and Sarma SD (2021) *Topological Phases in ab-Stacked mote$_2$/wse$_2$:* $\mathbb{Z}_2$ Topological Insulators, Chern Insulators, and Topological Charge Density Waves. https://doi.org/10.48550/ARXIV.2111.01152.

Parameswaran SA, Roy R, and Sondhi SL (2012) Fractional chern insulators and the W_∞ algebra. *Physical Review B* 85: 241308. https://doi.org/10.1103/PhysRevB.85.241308.

Parameswaran SA, Roy R, and Sondhi SL (2013) Fractional quantum hall physics in topological flat bands. *Comptes Rendus Physique* 1631-070514(9): 816–839. https://doi.org/10.1016/j.crhy.2013.04.003. Topological insulators/Isolants topologiques.

Park Y, Chittari BL, and Jung J (2020) Gate-tunable topological flat bands in twisted monolayer-bilayer graphene. *Physical Review B* 102: 035411. https://doi.org/10.1103/PhysRevB.102.035411.

Park JM, Cao Y, Watanabe K, Taniguchi T, and Jarillo-Herrero P (2021) Flavour hund's coupling, chern gaps and charge diffusivity in moirégraphene. *Nature* 592(7852): 43–48. https://doi.org/10.1038/s41586-021-03366-w.

Parker D, Ledwith P, Khalaf E, Soejima T, Hauschild J, Xie Y, Pierce A, Zaletel MP, Yacoby A, and Vishwanath A (2021) *Field-Tuned and Zero-Field Fractional Chern Insulators in Magic Angle Graphene*. https://doi.org/10.48550/ARXIV. 2112.13837.

Pierce AT, Xie Y, Park JM, Khalaf E, Lee SH, Cao Y, Parker DE, Forrester PR, Chen S, Watanabe K, Taniguchi T, Vishwanath A, Jarillo-Herrero P, and Yacoby A (2021) Unconventional sequence of correlated chern insulators in magic-angle twisted bilayer graphene. *Nature Physics* 17(11): 1210–1215. https://doi.org/10.1038/s41567-021-01347-4.

Po HC, Zou L, Senthil T, and Vishwanath A (2019) Faithful tight-binding models and fragile topology of magic-angle bilayer graphene. *Physical Review B* 99: 195455. https://doi.org/10.1103/PhysRevB.99.195455.

Polshyn H, Zhang Y, Kumar MA, Soejima T, Ledwith P, Watanabe K, Taniguchi T, Vishwanath A, Zaletel MP, and Young AF (2022) Topological charge density waves at half-integer filling of a moirésuperlattice. *Nature Physics* 18(1): 42–47. https://doi.org/10.1038/s41567-021-01418-6.

Popov AM, Lebedeva IV, Knizhnik AA, Lozovik YE, and Potapkin BV (2011) Commensurate-incommensurate phase transition in bilayer graphene. *Physical Review B* 1098012184(4): 1–6. https://doi.org/10.1103/PhysRevB.84.045404.

Popp M, Paredes B, and Cirac JI (2004) Adiabatic path to fractional quantum hall states of a few bosonic atoms. *Physical Review A* 70: 053612. https://doi.org/10.1103/PhysRevA.70.053612.

Qi X-L (2011) Generic wave-function description of fractional quantum anomalous hall states and fractional topological insulators. *Physical Review Letters* 107: 126803. https://doi.org/10.1103/PhysRevLett.107.126803.

Rademaker L, Protopopov IV, and Abanin DA (2020) Topological flat bands and correlated states in twisted monolayer-bilayer graphene. *Physical Review Research* 2: 033150. https://doi.org/10.1103/PhysRevResearch.2.033150.

Regnault N and Andrei Bernevig B (2011) Fractional chern insulator. *Physical Review X* 1: 021014. https://doi.org/10.1103/PhysRevX.1.021014.

Repellin C and Goldman N (2019) Detecting fractional chern insulators through circular dichroism. *Physical Review Letters* 122: 166801. https://doi.org/10.1103/PhysRevLett.122.166801.

Repellin C and Senthil T (2020) Chern bands of twisted bilayer graphene: Fractional chern insulators and spin phase transition. *Physical Review Research* 2: 023238. https://doi.org/10.1103/PhysRevResearch.2.023238.

Repellin C, Andrei Bernevig B, and Regnault N (2014) $\mathbb{Z}_2$ fractional topological insulators in two dimensions. *Physical Review B* 90: 245401. https://doi.org/10.1103/PhysRevB.90.245401.

Repellin C, Léonard J, and Goldman N (2020a) Fractional chern insulators of few bosons in a box: Hall plateaus from center-of-mass drifts and density profiles. *Physical Review A* 102: 063316. https://doi.org/10.1103/PhysRevA.102.063316.

Repellin C, Dong Z, Zhang Y-H, and Senthil T (2020b) Ferromagnetism in narrow bands of moiré superlattices. *Physical Review Letters* 124: 187601. https://doi.org/10.1103/PhysRevLett.124.187601.

Rezayi EH, Haldane FDM, and Yang K (1999) Charge-density-wave ordering in half-filled high landau levels. *Physical Review Letters* 83: 1219–1222. https://doi.org/10.1103/PhysRevLett.83.1219.

Rodríguez ID and Nielsen AEB (2015) Continuum limit of lattice models with laughlin-like ground states containing quasiholes. *Physical Review B* 92: 125105. https://doi.org/10.1103/PhysRevB.92.125105.

Rodriguez-Vega M, Vogl M, and Fiete GA (2020) Floquet engineering of twisted double bilayer graphene. *Physical Review Research* 2: 033494. https://doi.org/10.1103/PhysRevResearch.2.033494.

Roy R (2014) Band geometry of fractional topological insulators. *Physical Review B* 90: 165139. https://doi.org/10.1103/PhysRevB.90.165139.

Saito Y, Ge J, Watanabe K, Taniguchi T, and Young AF (2020) Independent superconductors and correlated insulators in twisted bilayer graphene. *Nature Physics* 16(9): 926–930. https://doi.org/10.1038/s41567-020-0928-3.

Saito Y, Ge J, Rademaker L, Watanabe K, Taniguchi T, Abanin DA, and Young AF (2021) Hofstadter subband ferromagnetism and symmetry-broken chern insulators in twisted bilayer graphene. *Nature Physics* 17(4): 478–481. https://doi.org/10.1038/s41567-020-01129-4.

Scaffidi T and Möller G (2012) Adiabatic continuation of fractional chern insulators to fractional quantum hall states. *Physical Review Letters* 109: 246805. https://doi.org/10.1103/PhysRevLett.109.246805.

Serlin M, Tschirhart CL, Polshyn H, Zhang Y, Zhu J, Watanabe K, Taniguchi T, Balents L, and Young AF (2020) Intrinsic quantized anomalous hall effect in a moiré heterostructure. *Science* 367(6480): 900–903. https://doi.org/10.1126/science.aay5533.

Sheffer Y and Stern A (2021) Chiral magic-angle twisted bilayer graphene in a magnetic field: Landau level correspondence, exact wave functions, and fractional chern insulators. *Physical Review B* 104: L121405. https://doi.org/10.1103/PhysRevB.104.L121405.

Sheng DN, Zheng-Cheng G, Sun K, and Sheng L (2011) Fractional quantum hall effect in the absence of landau levels. *Nature Communications* 2(1): 389. https://doi.org/10.1038/ncomms1380.

Simon SH, Harper F, and Read N (2015) Fractional chern insulators in bands with zero berry curvature. *Physical Review B* 92: 195104. https://doi.org/10.1103/PhysRevB.92.195104.

Song Z, Wang Z, Shi W, Li G, Fang C, and Bernevig BA (2019) All magic angles in twisted bilayer graphene are topological. *Physical Review Letters* 123: 036401. https://doi.org/10.1103/PhysRevLett.123.036401.

Sørensen AS, Demler E, and Lukin MD (2005) Fractional quantum hall states of atoms in optical lattices. *Physical Review Letters* 94: 086803. https://doi.org/10.1103/PhysRevLett.94.086803.

Spanton EM, Zibrov AA, Zhou H, Taniguchi T, Watanabe K, Zaletel MP, and Young AF (2018) Observation of fractional chern insulators in a van der waals heterostructure. *Science* 360(6384): 62–66. https://doi.org/10.1126/science.aan8458.

Srivatsa NS, Li X, and Nielsen AEB (2021) Squeezing anyons for braiding on small lattices. *Physical Review Research* 3: 033044. https://doi.org/10.1103/PhysRevResearch.3.033044.

Stepanov P, Das I, Xiaobo L, Fahimniya A, KenjiWatanabe TT, Koppens FHL, Lischner J, Levitov L, and Efetov DK (2020) Untying the insulating and superconducting orders in magic-angle graphene. *Nature* 583(7816): 375–378. https://doi.org/10.1038/s41586-020-2459-6.

Stepanov P, Xie M, Taniguchi T, Watanabe K, Xiaobo L, MacDonald AH, Andrei Bernevig B, and Efetov DK (2021) Competing zero-field chern insulators in superconducting twisted bilayer graphene. *Physical Review Letters* 127: 197701. https://doi.org/10.1103/PhysRevLett.127.197701.

Sterdyniak A, Regnault N, and Bernevig BA (2011) Extracting excitations from model state entanglement. *Physical Review Letters* 106: 100405. https://doi.org/10.1103/PhysRevLett.106.100405.

Sterdyniak A, Regnault N, and Möller G (2012) Particle entanglement spectra for quantum hall states on lattices. *Physical Review B* 86: 165314. https://doi.org/10.1103/PhysRevB.86.165314.

Sterdyniak A, Repellin C, Andrei Bernevig B, and Regnault N (2013) Series of abelian and non-abelian states in $c > 1$ fractional chern insulators. *Physical Review B* 87: 205137. https://doi.org/10.1103/PhysRevB.87.205137.

Sterdyniak A, Andrei Bernevig B, Cooper NR, and Regnault N (2015) Interacting bosons in topological optical flux lattices. *Physical Review B* 91: 035115. https://doi.org/10.1103/PhysRevB.91.035115.

Sticlet D and Piéchon F (2013) Distant-neighbor hopping in graphene and haldane models. *Physical Review B* 87: 115402. https://doi.org/10.1103/PhysRevB.87.115402.

Streda P (1982) Theory of quantised hall conductivity in two dimensions. *Journal of Physics C: Solid State Physics* 15(22): L717–L721. https://doi.org/10.1088/0022-3719/15/22/005.

Sun K, Zhengcheng G, Katsura H, and Sarma SD (2011) Nearly flatbands with nontrivial topology. *Physical Review Letters* 106: 236803. https://doi.org/10.1103/PhysRevLett.106.236803.

Tang E, Mei J-W, and Wen X-G (2011) High-temperature fractional quantum hall states. *Physical Review Letters* 106: 236802. https://doi.org/10.1103/PhysRevLett.106.236802.

Tarnopolsky G, Kruchkov AJ, and Vishwanath A (2019) Origin of magic angles in twisted bilayer graphene. *Physical Review Letters* 122: 106405. https://doi.org/10.1103/PhysRevLett.122.106405.

Thouless DJ, Kohmoto M, Nightingale MP, and den Nijs M (1982) Quantized hall conductance in a two-dimensional periodic potential. *Physical Review Letters* 49: 405–408. https://doi.org/10.1103/PhysRevLett.49.405.

Topp GE, Jotzu G, McIver JW, Xian L, Rubio A, and Sentef MA (2019) Topological floquet engineering of twisted bilayer graphene. *Physical Review Research* 1: 023031. https://doi.org/10.1103/PhysRevResearch.1.023031.

Topp GE, Eckhardt CJ, Kennes DM, Sentef MA, and Törmä P (2021) Light-matter coupling and quantum geometry in moiré materials. *Physical Review B* 104: 064306. https://doi.org/10.1103/PhysRevB.104.064306.

Tran DT, Dauphin A, Grushin AG, Zoller P, and Goldman N (2017) Probing topology by heating: Quantized circular dichroism in ultracold atoms. *Science Advances* 3(8)e1701207. https://doi.org/10.1126/sciadv.1701207.

Trescher M and Bergholtz EJ (2012) Flat bands with higher chern number in pyrochlore slabs. *Physical Review B* 86: 241111. https://doi.org/10.1103/PhysRevB.86.241111.

Tsui DC, Stormer HL, and Gossard AC (1982) Two-dimensional magnetotransport in the extreme quantum limit. *Physical Review Letters* 48: 1559–1562. https://doi.org/10.1103/PhysRevLett.48.1559.

Uchida K, Furuya S, Iwata J-I, and Oshiyama A (2014) Atomic corrugation and electron localization due to moiré patterns in twisted bilayer graphenes. *Physical Review B* 90: 155451. https://doi.org/10.1103/PhysRevB.90.155451.

Umucalılar RO (2018) Real-space probe for lattice quasiholes. *Physical Review A* 98: 063629. https://doi.org/10.1103/PhysRevA.98.063629.

van Wijk MM, Schuring A, Katsnelson MI, and Fasolino A (2015) Relaxation of moiré patterns for slightly misaligned identical lattices: Graphene on graphite. *2D Materials* 2(3): 034010. https://doi.org/10.1088/2053-1583/2/3/034010.

Varjas D, Abouelkomsan A, Yang K, and Bergholtz EJ (2022) Topological lattice models with constant berry curvature. *SciPost Physics* 12: 118. https://doi.org/10.21468/SciPostPhys.12.4.118.

Varney CN, Sun K, Rigol M, and Galitski V (2010) Interaction effects and quantum phase transitions in topological insulators. *Physical Review B* 82: 115125. https://doi.org/10.1103/PhysRevB.82.115125.

Verlinde E (1988) Fusion rules and modular transformations in 2d conformal field theory. *Nuclear Physics B* 0550-3213300: 360–376. https://doi.org/10.1016/0550-3213(88)90603-7.

Vogl M, Rodriguez-Vega M, and Fiete GA (2020) Effective floquet hamiltonians for periodically driven twisted bilayer graphene. *Physical Review B* 101: 235411. https://doi.org/10.1103/PhysRevB.101.235411.

Vogl M, Rodriguez-Vega M, Flebus B, MacDonald AH, and Fiete GA (2021) Floquet engineering of topological transitions in a twisted transition metal dichalcogenide homobilayer. *Physical Review B* 103: 014310. https://doi.org/10.1103/PhysRevB.103.014310.

Wang J and Liu Z (2022) Hierarchy of ideal flatbands in chiral twisted multilayer graphene models. *Physical Review Letters* 128: 176403. https://doi.org/10.1103/PhysRevLett.128.176403.

Wang F and Ran Y (2011) Nearly flat band with chern number $c = 2$ on the dice lattice. *Physical Review B* 84: 241103. https://doi.org/10.1103/PhysRevB.84.241103.

Wang Y-F, Gu Z-C, Gong C-D, and Sheng DN (2011) Fractional quantum hall effect of hard-core bosons in topological flat bands. *Physical Review Letters* 107: 146803. https://doi.org/10.1103/PhysRevLett.107.146803.

Wang Y-F, Yao H, Gong C-D, and Sheng DN (2012a) Fractional quantum hall effect in topological flat bands with chern number two. *Physical Review B* 86: 201101. https://doi.org/10.1103/PhysRevB.86.201101.

Wang Y-F, Yao H, Zheng-Cheng G, Gong C-D, and Sheng DN (2012b) Non-abelian quantum hall effect in topological flat bands. *Physical Review Letters* 108: 126805. https://doi.org/10.1103/PhysRevLett.108.126805.

Wang D, Liu Z, Cao J, and Fan H (2013) Tunable band topology reflected by fractional quantum hall states in two-dimensional lattices. *Physical Review Letters* 111: 186804. https://doi.org/10.1103/PhysRevLett.111.186804.

Wang J, Cano J, Millis AJ, Liu Z, and Yang B (2021) Exact landau level description of geometry and interaction in a flatband. *Physical Review Letters* 127: 246403. https://doi.org/10.1103/PhysRevLett.127.246403.

Wang B, Dong X-Y, and Eckardt A (2022) Measurable signatures of bosonic fractional Chern insulator states and their fractional excitations in a quantum-gas microscope. *SciPost Physics* 12: 95. https://doi.org/10.21468/SciPostPhys.12.3.095.

Weber S, Bai R, Makki N, Mögerle J, Lahaye T, Browaeys A, Daghofer M, Lang N, and Büchler HP (2022) Experimentally accessible scheme for a fractional Chern insulator in Rydberg atoms. *arXiv.* 2202.00699. https://doi.org/10.48550/ARXIV.2202.00699.

Wen XG (1990) Topological orders in rigid states. *International Journal of Modern Physics B* 04(02): 239–271. https://doi.org/10.1142/S0217979290000139.

Wen XG and Niu Q (1990) Ground-state degeneracy of the fractional quantum hall states in the presence of a random potential and on high-genus Riemann surfaces. *Physical Review B* 41: 9377–9396. https://doi.org/10.1103/PhysRevB.41.9377.

Wilhelm P, Lang TC, and Läuchli AM (2021) Interplay of fractional chern insulator and charge density wave phases in twisted bilayer graphene. *Physical Review B* 103: 125406. https://doi.org/10.1103/PhysRevB.103.125406.

Wu Y-L, Bernevig BA, and Regnault N (2012a) Zoology of fractional chern insulators. *Physical Review B* 85: 075116. https://doi.org/10.1103/PhysRevB.85.075116.

Wu Y-L, Regnault N, and Andrei Bernevig B (2012b) Gauge-fixed wannier wave functions for fractional topological insulators. *Physical Review B* 86: 085129. https://doi.org/10.1103/PhysRevB.86.085129.

Wu Y-L, Regnault N, and Bernevig BA (2013) Bloch model wave functions and pseudopotentials for all fractional chern insulators. *Physical Review Letters* 110: 106802. https://doi.org/10.1103/PhysRevLett.110.106802.

Wu Y-L, Regnault N, and Bernevig BA (2014) Haldane statistics for fractional chern insulators with an arbitrary chern number. *Physical Review B* 89: 155113. https://doi.org/10.1103/PhysRevB.89.155113.

Wu Y-H, Jain JK, and Sun K (2015) Fractional topological phases in generalized hofstadter bands with arbitrary chern numbers. *Physical Review B* 91: 041119. https://doi.org/10.1103/PhysRevB.91.041119.

Wu F, Lovorn T, Tutuc E, Martin I, and MacDonald AH (2019) Topological insulators in twisted transition metal dichalcogenide homobilayers. *Physical Review Letters* 122: 086402. https://doi.org/10.1103/PhysRevLett.122.086402.

Wu S, Zhenyuan Zhang K, Watanabe TT, and Andrei EY (2021) Chern insulators, van hove singularities and topological flat bands in magic-angle twisted bilayer graphene. *Nature Materials* 20(4): 488–494. https://doi.org/10.1038/s41563-020-00911-2.

Xie Y, Lian B, Jäck B, Liu X, Chiu C-L, Watanabe K, Takashi Taniguchi B, Bernevig A, and Yazdani A (2019) Spectroscopic signatures of many-body correlations in magic-angle twisted bilayer graphene. *Nature* 572(7767): 101–105. https://doi.org/10.1038/s41586-019-1422-x.

Xie F, Cowsik A, Song Z-D, Lian B, Bernevig BA, and Regnault N (2021a) Twisted bilayer graphene. vi. an exact diagonalization study at nonzero integer filling. *Physical Review B* 103: 205416. https://doi.org/10.1103/PhysRevB.103.205416.

Xie Y, Pierce AT, Park JM, Parker DE, Khalaf E, Ledwith P, Cao Y, Lee SH, Chen S, Forrester PR, Watanabe K, Taniguchi T, Vishwanath A, Jarillo-Herrero P, and Yacoby A (2021b) Fractional chern insulators in magic-angle twisted bilayer graphene. *Nature* 600(7889): 439–443. https://doi.org/10.1038/s41586-021-04002-3.

Yang K, Haldane FDM, and Rezayi EH (2001) Wigner crystals in the lowest landau level at low-filling factors. *Physical Review B* 64: 081301. https://doi.org/10.1103/PhysRevB.64.081301.

Yang S, Zheng-Cheng G, Sun K, and Sarma SD (2012) Topological flat band models with arbitrary chern numbers. *Physical Review B* 86: 241112. https://doi.org/10.1103/PhysRevB.86.241112.

Yao NY, Laumann CR, Gorshkov AV, Bennett SD, Demler E, Zoller P, and Lukin MD (2012) Topological flat bands from dipolar spin systems. *Physical Review Letters* 109: 266804. https://doi.org/10.1103/PhysRevLett.109.266804.

Yoshioka D and Lee PA (1983) Ground-state energy of a two-dimensional charge-density-wave state in a strong magnetic field. *Physical Review B* 27: 4986–4996. https://doi.org/10.1103/PhysRevB.27.4986.

Zaletel MP, Mong RSK, and Pollmann F (2014) Flux insertion, entanglement, and quantized responses. *Journal of Statistical Mechanics: Theory and Experiment* 2014(10): P10007. https://doi.org/10.1088/1742-5468/2014/10/p10007.

Zeng T-S (2021) Fractional quantum hall effect of bose-fermi mixtures. *Physical Review B* 103: L201118. https://doi.org/10.1103/PhysRevB.103.L201118.

Zeng T-S and Sheng DN (2018) SU(n) fractional quantum hall effect in topological flat bands. *Physical Review B* 97: 035151. https://doi.org/10.1103/PhysRevB.97.035151.

Zeng T-S and Zhu W (2022) Chern-number matrix of the non-abelian spin-singlet fractional quantum hall effect. *Physical Review B* 105: 125128. https://doi.org/10.1103/PhysRevB.105.125128.

Zeng T-S, Sheng DN, and Zhu W (2019) Topological characterization of hierarchical fractional quantum hall effects in topological flat bands with su(n) symmetry. *Physical Review B* 100: 075106. https://doi.org/10.1103/PhysRevB.100.075106.

Zeng T-S, Liangdong H, and Zhu W (2022) Bosonic halperin (441) fractional quantum hall effect at filling factor $\nu = 2/5$. *Chinese Physics Letters* 39(1)017301. https://doi.org/10.1088/0256-307x/39/1/017301.

Zhang F, Jung J, Fiete GA, Niu Q, and MacDonald AH (2011) Spontaneous quantum hall states in chirally stacked few-layer graphene systems. *Physical Review Letters* 106: 156801. https://doi.org/10.1103/PhysRevLett.106.156801.

Zhang Y, Grover T, Turner A, Oshikawa M, and Vishwanath A (2012) Quasiparticle statistics and braiding from ground-state entanglement. *Physical Review B* 85: 235151. https://doi.org/10.1103/PhysRevB.85.235151.

Zhang Y-H, Mao D, Cao Y, Jarillo-Herrero P, and Senthil T (2019a) Nearly flat chern bands in moiré superlattices. *Physical Review B* 99: 075127. https://doi.org/10.1103/PhysRevB.99.075127.

Zhang Y-H, Mao D, and Senthil T (2019b) Twisted bilayer graphene aligned with hexagonal boron nitride: Anomalous hall effect and a lattice model. *Physical Review Research* 1: 033126. https://doi.org/10.1103/PhysRevResearch.1.033126.

Zhang Y, Devakul T, and Liang F (2021) Spin-textured chern bands in ab-stacked transition metal dichalcogenide bilayers. *Proceedings of the National Academy of Sciences* 118(36): e2112673118. https://doi.org/10.1073/pnas.2112673118.

Zhou BT, Egan S, and Franz M (2022) Moiré flat chern bands and correlated quantum anomalous hall states generated by spinorbit couplings in twisted homobilayer mos_2. *Physical Review Research* 4: L012032. https://doi.org/10.1103/PhysRevResearch.4.L012032.

Zhu W, Sheng DN, and Haldane FDM (2013) Minimal entangled states and modular matrix for fractional quantum hall effect in topological flat bands. *Physical Review B* 88: 035122. https://doi.org/10.1103/PhysRevB.88.035122.

Zhu W, Gong SS, Haldane FDM, and Sheng DN (2014) Identifying non-abelian topological order through minimal entangled states. *Physical Review Letters* 112: 096803. https://doi.org/10.1103/PhysRevLett.112.096803.

Zhu W, Gong SS, and Sheng DN (2016) Interaction-driven fractional quantum hall state of hard-core bosons on kagome lattice at one-third filling. *Physical Review B* 94: 035129. https://doi.org/10.1103/PhysRevB.94.035129.

Zondiner U, Rozen A, Rodan-Legrain D, Cao Y, Queiroz R, Taniguchi T, Watanabe K, Oreg Y, von Oppen F, Ady Stern E, Berg PJ-H, and Ilani S (2020) Cascade of phase transitions and dirac revivals in magic-angle graphene. *Nature* 582(7811): 203–208. https://doi.org/10.1038/s41586-020-2373-y.

Quantum Hall states in higher Landau levels

Jakob Yngvason, Fakultät für Physik, Universität Wien, Vienna, Austria; Erwin Schrödinger Institute for Mathematics and Physics, Vienna, Austria

© 2024 Elsevier Ltd. All rights reserved.

Introduction **540**
The magnetic Hamiltonian and its Eigenfunctions **540**
The Landau levels 540
The two oscillators 541
Complex notation 542
Eigenfunctions 543
Factorization 543
The lowest Landau level as a Bargmann space of holomorphic functions 543
Unitary maps between Landau levels **544**
Many body states and ℓ-particle densities **545**
Mapping Hamiltonians to the LLL **546**
Another proof of 546
Coherent state representations **547**
Coherent states 547
Integral kernels 548
Recap of the different expressions for the unitary maps **548**
Some special states **549**
Laughlin states 549
Filling factor $\nu = 5/2$ 550
Conclusion **551**
Acknowledgments **551**
References **551**

Abstract

The unitary correspondence between Quantum Hall states in higher Landau levels and states in the lowest Landau level is discussed together with the resulting transformation formulas for particle densities and interaction potentials. This correspondence leads in particular to a representation of states in arbitrary Landau levels in terms of holomorphic functions. Some important special Quantum Hall states in higher Landau levels are also briefly discussed.

Key points

- Describe the emergence of Landau levels from for the quantized two-dimensional motion of charged particles in a perpendicular magnetic field.
- Introduce non-commutative guiding center and cyclotron variables and the associated two commuting harmonic oscillators.
- Discuss the description of states in higher Landau levels in terms of holomorphic wave functions in the lowest Landau level.
- Derive formulas that express particle densities and interaction potentials in an arbitrary Landau level in terms of corresponding quantities in the lowest Landau level.
- Discuss briefly Laughlin states in higher Landau levels and recent investigations of states with filling factor 5/2.

Notations

ℓ_B Magnetic length
LLL Lowest Landau level (single particle)
$\mathbf{LLL}^N$ Lowest Landau level (N particles)
n**LL** n-th Landau level (single particle)
$n\mathbf{LL}^N$ n-th Landau level (N particles)
$\mathbf{\Pi_0}$ Projector on LLL
$\mathbf{\Pi}_n$ Projector on nLL

https://doi.org/10.1016/B978-0-323-90800-9.00062-7

Introduction

The quantum states of charged particles moving in a plane orthogonal to a homogeneous magnetic field are naturally grouped into Landau levels which correspond to quantization of the cyclotron motion of the particles in the magnetic field. The interplay of this motion with external electric fields and impurities as well as Coulomb interactions between the particles is the subject of Quantum Hall Physics which has developed into a major subfield of condensed matter physics since the discovery of the integer and fractional Quantum Hall Effects in Klitzing et al. (1980) and Störmer et al. (1982) respectively. These developments are extensively discussed in many monographs and review articles, see, e.g., (Chakraborty and Pietiläinen, 1988; Chakraborty and Pietiläinen, 1995; Goerbig, 2009; Fradkin, 2013; Laughlin, 1987, 1999; Prange and Girvin, 1987; Störmer et al., 1999; Goerbig and Lederer, 2006; Greiter, 2011; Jain, 2007; Tong, 2016). The present chapter focuses on one particular theoretical aspect, namely the relations between some basic properties of Quantum Hall states in different Landau levels.

In strong magnetic fields the lowest Landau level, corresponding to the smallest of the discrete values for the cyclotron radius, plays a special role. The fractional quantum Hall effect was first discovered in strongly correlated states within this level and the celebrated Laughlin wave function (Laughlin, 1983), describing a quantum liquid at filling factor 1/3 (more generally $1/q$ with small odd values of q), turned out to be very successful in describing ground state properties as well as excitations.

An important mathematical feature of wave functions in the lowest Landau level is the fact that they form a Bargmann space of *holomorphic* functions when the position coordinates are expressed as complex numbers in the symmetric gauge. The holomorphy has been used for derivations of some basic properties of the states, for examples bounds on the local particle density (Lieb et al., 2018; Lieb et al., 2019). Wave functions in higher Landau levels, on the other hand, involve also powers of the complex conjugate position variables in the standard representation and at first sight it might appear that the advantage of holomorphic representations gets lost.

It was, however, noted early (MacDonald, 1984) that, due to a unitary correspondence between states in different Landau levels, wave functions in higher Landau levels can also be represented by holomorphic functions. In particular, there are Laughlin states in any Landau level. The physical picture behind this correspondence is based on the fact that the position variable has a natural decomposition into two sets of non-commutative variables, one associated with the cyclotron motion and the other with the *guiding centers* around which the cyclotron motion takes place. Mathematically, these correspond to two sets of mutually commuting harmonic oscillators. For a given Landau level, the cyclotron motion can be thought of as fixed, while the physics takes place in the guiding center degrees of freedom where holomorphic wave functions appear naturally.

In this chapter the mathematical implementation of this idea is presented in two versions, one employing ladder operators and another one based on coherent states. Each brings different aspects of the unitary correspondence between states in higher Landau levels with those in the lowest Landau level into focus. Furthermore we derive formulas that relate effective potentials in higher Landau levels to their counterparts in the lowest Landau level.

In the last section we discuss some important special states in higher Landau levels and their relation to states in the lowest Landau level.

The magnetic Hamiltonian and its Eigenfunctions

The Landau levels

The magnetic Hamiltonian of a single spinless (or spin-polarized) particle of charge q and effective mass m^*, moving in a plane with position variables $\mathbf{r} = (x, y)$, is

$$H = \frac{1}{2m^*}\left(\pi_x^2 + \pi_y^2\right) \tag{1}$$

where

$$\boldsymbol{\pi} = \left(\pi_x, \pi_y\right) = \mathbf{p} - q\mathbf{A} \tag{2}$$

is the gauge invariant kinetic momentum with

$$\mathbf{p} = -i\hbar\left(\partial_x, \partial_y\right) \tag{3}$$

the canonical momentum and $\mathbf{A}$ the magnetic vector potential. We assume a homogeneous magnetic field of strength B perpendicular to the plane and choose the symmetric gauge

$$\mathbf{A} = \frac{B}{2}(-y, x). \tag{4}$$

Moreover, we choose units and signs such that $|q| = 1$, $qB \equiv B > 0$, $\hbar = 1$ and $m^* = 1$. Then

$$\pi_x = -\mathrm{i}\partial_x + \frac{1}{2}By, \quad \pi_y = -\mathrm{i}\partial_y - \frac{1}{2}Bx \tag{5}$$

and the kinetic momentum components satisfy the canonical commutation relations (CCR)

$$[\pi_x, \pi_y] = \mathrm{i}\ell_B^{-2} \tag{6}$$

with

$$\ell_B = B^{-1/2} \tag{7}$$

the *magnetic length*.

In terms of the creation and annihilation operators

$$a^\dagger = \frac{\ell_B}{\sqrt{2}}(-\pi_y - \mathrm{i}\pi_x), \quad a = \frac{\ell_B}{\sqrt{2}}(-\pi_y + \mathrm{i}\pi_x) \tag{8}$$

with $[a, a^\dagger] = 1$ one can write (1) as

$$H = 2B\left(a^\dagger a + \frac{1}{2}\right) \tag{9}$$

which is the Hamiltonian of a harmonic oscillator with eigenvalues

$$\varepsilon_n = \left(n + \frac{1}{2}\right)2B, n = 0, 1, \ldots . \tag{10}$$

The Gaussian

$$\varphi_0(\mathbf{r}) = \frac{1}{\sqrt{\pi}} e^{-(x^2+y^2)/4\ell_B^2} \tag{11}$$

with $a\varphi_0 = 0$ is a ground state for H with energy $\varepsilon_0 = B$.

The discrete energy values (10) result from the quantization of the classical *cyclotron motion* of a charged particle around *guiding centers* as discussed below. Every energy eigenvalue is infinitely degenerate due to the different possible positions of the guiding centers. The degeneracy per unit area is $(2\pi\ell_B^2)^{-1}$.

The eigenspace in $L^2(\mathbb{R}^2)$ to the eigenvalue ε_n is called the *n-th Landau level* and denoted by nLL. The *lowest Landau level*, corresponding to $n = 0$ will be denoted by LLL. The corresponding fermionic spaces for N electrons, denoted by $n\mathrm{LL}^N$ and LLL^N respectively, are the antisymmetric tensor powers

$$\mathrm{LLL}^N = \mathrm{LLL}^{\otimes_a N}, \quad n\mathrm{LL}^N = n\mathrm{LL}^{\otimes_a N}. \tag{12}$$

For bosons the antisymmetric tensor product is replaced by the symmetric one; this is e.g. relevant for cold atomic gases in rapid rotation, where the rotational velocity takes over the role of the magnetic vector potential (Cooper, 2008).

The *filling factor* ν in a given Landau level is by definition the ratio of the particle density in that level to the degeneracy $(2\pi\ell_B^2)^{-1}$ per unit area. In a sample with area A a completely filled Landau level of fermions (filling factor $\nu = 1$) thus contains $N = (2\pi\ell_B^2)^{-1}A$ particles.

Remark. In the whole chapter, with the exception of the last Section 8.2, we focus on the orbital motion of the charged particles, ignoring spin and the accompanying Zeeman energy $\sum_i g^* \mu_B \mathbf{B} \cdot \mathbf{S}_i$ (with $\mathbf{S}_i$ the spin operator for particle i, $\mathbf{B}$ the magnetic field, μ_B the Bohr magneton and g^* the effective Landé g-factor). This is justified if the particles are either spinless, or their spin is fully polarized due to a strong magnetic field. Moreover, in semiconductors the Zeeman energy is typically much smaller than the gap between Landau levels because the effective g-factor is small. See, e.g., (Tong, 2016, p. 16).

The two oscillators

Quantum mechanically the dynamics of the guiding centers is described by another harmonic oscillator commuting with the cyclotron oscillator (1). While the latter determines the Landau energy spectrum (10), the quantization of the guiding center oscillator parametrizes the degeneracy creating a natural basis of states in each Landau level.

One arrives at this picture by splitting the (gauge invariant) position operator $\mathbf{r}$ into a guiding center part $\mathbf{R}$ and the cyclotron part

$$\tilde{\mathbf{R}} = \ell_B^2 \mathbf{n} \times \pi, \tag{13}$$

with $\mathbf{n}$ the unit normal vector to the plane. Both $\mathbf{R}$ and $\tilde{\mathbf{R}}$ are gauge invariant and they commute with each other. On the other hand the two components (R_x, R_y) of $\mathbf{R}$ do not commute and likewise for the components of $\tilde{\mathbf{R}}$. More precisely, we have

$$\mathbf{r} = \mathbf{R} + \tilde{\mathbf{R}} \tag{14}$$

with

$$R_x = x + \ell_B^2 \pi_y = \frac{1}{2}x - \mathrm{i}\ell_B^2 \partial_y, \quad R_y = y - \ell_B^2 \pi_x = \frac{1}{2}y + \mathrm{i}\ell_B^2 \partial_x, \tag{15}$$

$$\tilde{R}_x = -\ell_B^2 \pi_y = \frac{1}{2}x + \mathrm{i}\ell_B^2 \partial_y, \quad \tilde{R}_y = \ell_B^2 \pi_x = \frac{1}{2}y - \mathrm{i}\ell_B^2 \partial_x \tag{16}$$

and the commutation relations

$$\left[\mathbf{R}, \tilde{\mathbf{R}}\right] = \mathbf{0}, \quad \left[R_x, R_y\right] = -\mathrm{i}\ell_B^2, \quad \left[\tilde{R}_x, \tilde{R}_y\right] = \mathrm{i}\ell_B^2. \tag{17}$$

The creation and annihilation operators for $\tilde{\mathbf{R}}$ are the same as (8), namely

$$a^\dagger = \frac{1}{\sqrt{2}\ell_B}\left(\tilde{R}_x - \mathrm{i}\tilde{R}_y\right), \quad a = \frac{1}{\sqrt{2}\ell_B}\left(\tilde{R}_x + \mathrm{i}\tilde{R}_y\right). \tag{18}$$

Those for the guiding centers, on the other hand, are

$$b^\dagger = \frac{1}{\sqrt{2}\ell_B}\left(R_x + \mathrm{i}R_y\right), \quad b = \frac{1}{\sqrt{2}\ell_B}\left(R_x - \mathrm{i}R_y\right). \tag{19}$$

with $[b, b^\dagger] = 1$ and $[a^\#, b^\#] = 0$. Note the different signs compared to (18) due to the different signs in (17).

Complex notation

The two-dimensional configuration space $\mathbb{R}^2$ can be identified with the complex plane $\mathbb{C}$. Defining complex coordinates and derivatives by

$$z = x + \mathrm{i}y, \quad \bar{z} = x - \mathrm{i}y, \quad \partial_z = \frac{1}{2}\left(\partial_x - \mathrm{i}\partial_y\right), \quad \partial_{\bar{z}} = \frac{1}{2}\left(\partial_x + \mathrm{i}\partial_y\right) \tag{20}$$

we can write

$$a^\dagger = \frac{1}{\sqrt{2}\ell_B}\left(\frac{1}{2}\bar{z} - 2\ell_B^2 \partial_z\right), \quad a = \frac{1}{\sqrt{2}\ell_B}\left(\frac{1}{2}z + 2\ell_B^2 \partial_{\bar{z}}\right). \tag{21}$$

Choosing units so that $B = 2$, or equivalently, defining $z = \frac{1}{\sqrt{2}\ell_B}(x + \mathrm{i}y)$, this simplifies to

$$a^\dagger = \frac{1}{2}\bar{z} - \partial_z, \quad a = \frac{1}{2}z + \partial_{\bar{z}}. \tag{22}$$

Also, the gaussian factor $e^{-(|x|^2+|y|^2)/4\ell_B^2}$ becomes $e^{-|z|^2/2}$. We note that besides the standard definition $z = x + \mathrm{i}y$, other complexifications of $\mathbb{R}^2$ are possible and can be useful, as stressed in Haldane (2018).

For computations it is often convenient to use instead of (22) the operators $\hat{a}^\dagger$, $\hat{a}$ which act only on the pre-factors to the gaussian and are defined by

$$a^\#\left[f(z,\bar{z})e^{-|z|^2/2}\right] = \left[\hat{a}^\# f(z,\bar{z})\right]e^{-|z|^2/2}. \tag{23}$$

These are

$$\hat{a}^\dagger = \bar{z} - \partial_z, \quad \hat{a} = \partial_{\bar{z}}. \tag{24}$$

In the sequel we shall generally use the hat ˆ on operators and functions to indicate that gaussian normalization factors are dropped from the notation.

The creation and annihilation operators for the guiding center oscillator are in complex notation

$$b^\dagger = \frac{1}{\sqrt{2}\ell_B}\left(\frac{1}{2}z - 2\ell_B^2 \partial_{\bar{z}}\right), \quad b = \frac{1}{\sqrt{2}\ell_B}\left(\frac{1}{2}\bar{z} + 2\ell_B^2 \partial_z\right). \tag{25}$$

For $B = 2$

$$b^\dagger = \frac{1}{2}z - \partial_{\bar{z}}, \quad b = \frac{1}{2}\bar{z} + \partial_z \tag{26}$$

and

$$\hat{b}^\dagger = z - \partial_{\bar{z}}, \quad \hat{b} = \partial_z. \tag{27}$$

The splitting (14) corresponds to

$$(z, \bar{z}) = \left(b^\dagger, b\right) + \left(a, a^\dagger\right). \tag{28}$$

While the operators $a^\dagger$, a increases or decrease the Landau level index, the operators $b^\dagger$, b leave each Landau level invariant. Pictorially speaking we can say that operators $a^\#$ associated with the cyclotron oscillator are ladder operators moving states "vertically" on the energy scale, while the ladder operators $b^\#$ associated with the guiding center oscillator move states "horizontally", keeping the energy fixed.

Eigenfunctions

With the gaussian $\varphi_{0,0} \coloneqq \varphi_0$ (11) as the common, normalized lowest energy state for the two oscillators the states

$$\varphi_{n,m} = \frac{1}{\sqrt{n!m!}} \left(a^\dagger\right)^n \left(b^\dagger\right)^m \varphi_{0,0} = \frac{1}{\sqrt{n!m!}} \left(b^\dagger\right)^m \left(a^\dagger\right)^n \varphi_{0,0}, \quad n, m = 0, 1, \ldots \tag{29}$$

form a basis of eigenstates of the Hamiltonian (1). For fixed n the states $\varphi_{n,m}$, $m = 0, 1, \ldots$ generate the Hilbert space nLL of the n'th Landau level with $n = 0$ corresponding to the lowest Landau level LLL.

In complex coordinates the wave functions with $n = 0$ respectively $m = 0$, are

$$\varphi_{0,m}(\mathbf{r}) = \frac{1}{\sqrt{\pi m!}} z^m e^{-|z|^2/2}, \quad \varphi_{n,0}(\mathbf{r}) = \frac{1}{\sqrt{\pi n!}} \bar{z}^n e^{-|z|^2/2}. \tag{30}$$

More generally, one can write

$$\varphi_{n,m}(\mathbf{r}) = \frac{1}{\sqrt{\pi n!m!}} [(z - \partial_{\bar{z}})^m \bar{z}^n] e^{-|z|^2/2} = \frac{1}{\sqrt{\pi n!m!}} [(\bar{z} - \partial_z)^n z^m] e^{-|z|^2/2}. \tag{31}$$

These functions can be written in polar coordinates in terms of associated Laguerre polynomials (Landau and Lifschitz, 1977; Gradshteyn and Ryzhik, 1994). They are simultaneous eigenfunctions of the Hamiltonian (1) and the angular momentum operator $\mathbf{L} = \mathbf{r} \times \mathbf{p}$ in the symmetric gauge. Its action on the pre-factor of the gaussian is

$$\widehat{L} = z\partial_z - \bar{z}\partial_{\bar{z}} \tag{32}$$

with eigenvalues $M = m - n$, $m = 0, 1, \ldots$ in the nLL. The operators $b^\dagger$ and b shift the angular momentum within each Landau level.

Factorization

The mutual commutativity of the two oscillators has an important consequence:

Lemma 2.1: (Factorization). If *A is a function of* $a^\dagger$, *a and B of* $b^\dagger$, *b, then*

$$\langle \varphi_{n',m'} | AB | \varphi_{n,m} \rangle = \langle \varphi_{n',0} | A | \varphi_{n,0} \rangle \langle \varphi_{0,m'} | B | \varphi_{0,m} \rangle. \tag{33}$$

The proof follows from the fact that the two commuting harmonic oscillators (8) and (19) can be represented, in a unitarily equivalent way, in the tensor product of two spaces with basis vectors $\varphi_{n,0}$ and $\varphi_{0,m}$ respectively. In this representation $\varphi_{n,m} \simeq \varphi_{n,0} \otimes \varphi_{0,m}$ and the operators A and B act independently on each of the tensor factors. (Alternatively, one can choose A, B to be polynomials in the creation and annihilation operators and use the CCR to prove (33) directly.) Note, however, that in the representation (31) the functions $\varphi_{n,m}(z, \bar{z})$ are not simply products of the functions $\varphi_{n,0}(z)$ and $\varphi_{0,m}(\bar{z})$. Indeed, the variables z and $\bar{z}$ do not act independently in the tensor factors because they involve sums of $a^{\#}$'s and $b^{\#}$'s, cf. Eq. (28). The lemma, however, is in accord with the intuitive picture stressed in Haldane (2013) that in a given Landau level all the non-trivial structure is in the guiding center degrees of freedom while the cyclotron motion just produces a decoration by a fixed factor in matrix elements.

The lowest Landau level as a Bargmann space of holomorphic functions

Wave functions ψ in the lowest Landau level LLL are characterized by the equation

$$a\psi = 0 \tag{34}$$

which by (24) means that

$$\psi(\mathbf{r}) = f(z) e^{-|z|^2/2} \tag{35}$$

with f satisfying the Cauchy-Riemann equation $\partial_{\bar{z}} f = 0$, i.e., f is a *holomorphic* function of z. Holomorphic functions that are square integrable on $\mathbb{R}^2$ with respect to the Lebesgue measure with the gaussian weight factor $e^{-|z|^2}$ form a *Bargmann space* (Bargmann, 1961).

In the same way, N-particle fermionic wave functions in LLL^N have the form

$$\Psi(\mathbf{r}_1 \ldots, \mathbf{r}_N) = F(z_1, \ldots, z_N) e^{-\left(|z_1|^2 + \cdots + |z_N|^2\right)/2} \tag{36}$$

with a holomorphic, antisymmetric function F of the N variables $z_1, \ldots, z_N$.

In the sequel we shall show that representations of states by holomorphic functions are not limited to the lowest Landau level.

Unitary maps between Landau levels

The structure of the eigenfunctions (29) with the mutually commuting sets of creation and annihilation operators $a^\#$ and $b^\#$ for the two oscillators leads immediately to a unitary correspondence nLL ↔ LLL. In fact, the operator

$$U_n = (n!)^{-1/2} a^n \quad \text{restricted to } n\text{LL} \tag{37}$$

maps $\varphi_{n,m} \mapsto \varphi_{0,m}$ because a commutes with $b^\dagger$, and the inverse

$$U_n^{-1} = (n!)^{-1/2} \left(a^\dagger\right)^n \quad \text{restricted to LLL} \tag{38}$$

takes $\varphi_{0,m} \mapsto \varphi_{n,m}$. Hence U_n is a unitary map nLL → LL.

The wave functions in nLL are by (31) polynomials in $\bar{z}$ of order n with coefficients that are holomorphic functions of z. Using the representations (24) for the creation and annihilation operators we conclude that the following holds:

Proposition 3.1: (Unitary map between nLL and LLL)

Let $\psi_n \in n$LL have wave function

$$\psi_n(\mathbf{r}) = \sum_{k=0}^{n} \bar{z}^k f_k(z) e^{-|z|^2/2}, \tag{39}$$

with f_k holomorphic for $k = 0, \ldots, n$. Then $\psi_0 = U_n \psi_n \in$ LLL has the wave-function

$$\psi_0(\mathbf{r}) = \sqrt{n!} f_n(z) e^{-|z|^2/2}. \tag{40}$$

Conversely, the wave function of $\psi_n = U_n^{-1}\psi_0 \in n$LL is

$$\begin{aligned} \psi_n(\mathbf{r}) &= [(\bar{z} - \partial_z)^n f_n(z)] e^{-|z|^2/2} \\ &= \left[\bar{z}^n f_n(z) + \sum_{k=1}^{n} (-1)^k \binom{n}{k} \bar{z}^{n-k} \partial^k f_n(z)\right] e^{-|z|^2/2}. \end{aligned} \tag{41}$$

Note that Eq. (41) implies in particular that the holomorphic factor $f_n(z)$ to the highest power n of $\bar{z}$ determines uniquely the factors to the lower powers $\bar{z}^k$:

$$f_k(z) = (-1)^{n-k} \binom{n}{k} f_n^{(n-k)}(z). \tag{42}$$

A wave function in nLL is thus *completely fixed by the holomorphic function* f_n *and the Landau level index* n.

These considerations lead also to a formula for projecting functions into the lowest Landau level:

Proposition 3.2: (LLL projection).

Let ϕ be a state in $\oplus_{k=0}^{n} k$LL with wave function

$$\phi(\mathbf{r}) = \sum_{k=0}^{n} \bar{z}^k g_k(z) e^{-|z|^2/2} \tag{43}$$

with holomorphic functions g_k. It's orthogonal projection into LLL is

$$\Pi_0 \phi(z) = \sum_{k=0}^{n} \partial^k g_k(z) e^{-|z|^2/2}. \tag{44}$$

This is known as the recipe "move all $\bar{z}$ factors to the left and replace them by derivatives in z", see e.g. (Jain, 2007).

Proof. The previous considerations lead by induction to a splitting of the state (43) into its components in the different kLL, $k = 0, \ldots, n$: Start with a wave function as in (43). It's component ψ_n in the nLL is given by (41) with $f_n := g_n$ and f_k for $0 \le k \le n-1$ defined by (42). The difference $\tilde{\phi} = \phi - \psi_n$ is now in $\oplus_{k=0}^{n-1} k$LL and we can repeat the procedure with n replaced by $n-1$, ϕ by $\tilde{\phi}$ etc. until we obtain the splitting $\phi = \sum_{k=0}^{n} \psi_k$ with $\psi_k \in k$LL. By induction over n, using that $\sum_{k=0}^{n} \binom{n}{k} (-1)^k = (1-1)^n = 0$, this procedure implies (44).

Many body states and ℓ-particle densities

The considerations of the previous sections carry in a straightforward manner over to many-body states in symmetric or anti-symmetric tensor powers $n\mathrm{LL}^N \equiv n\mathrm{LL}^{\otimes \mathrm{s,a}N}$ of single-particle states by applying the single-particle formulas to each tensor factor.

Let Ψ_n be a state in $n\mathrm{LL}^N$ with wave function

$$\Psi_n(\mathbf{r}_1, \ldots, \mathbf{r}_N) = \widehat{\Psi}_n(\mathbf{r}_1, \ldots, \mathbf{r}_N) e^{-\left(|z_1|^2 + \cdots + |z_N|^2\right)/2}. \tag{45}$$

Expanding in powers of $\bar{z}_i$ we can write

$$\widehat{\Psi}_n(\mathbf{r}_1, \ldots, \mathbf{r}_N) = \prod_{i=1}^{N} \bar{z}_i^n f_n(z_1, \ldots, z_N) + \sum \prod_{i=1}^{N} \bar{z}_i^{k_i} f_{k_1,\ldots,k_N}(z_1, \ldots, z_N). \tag{46}$$

The sum is here over N-tuples $(k_1, \ldots k_N)$ such that $k_i < n$ for at least one i. The functions f_n and $f_{k_1, \ldots, k_N}$ are holomorphic and the latter ones are, in fact, derivatives of f_n, cf. (42).

Consider now the state $\Psi_0 = \mathcal{U}_{N,n}\Psi_n$ in LLL^N where

$$\mathcal{U}_{N,n} = U_n \otimes \cdots \otimes U_n \quad \text{with } U_n \text{ defined by (37)}. \tag{47}$$

Its wave function is

$$\Psi_0(\mathbf{r}_1, \ldots, \mathbf{r}_N) = \widehat{\Psi}_0(z_1, \ldots, z_N) e^{-\left(|z_1|^2 + \cdots + |z_N|^2\right)/2} \tag{48}$$

with the holomorphic function

$$\widehat{\Psi}_0(z_1, \ldots, z_N) = (n!)^{-N/2} \prod_{i=1}^{N} \partial_{\bar{z}_i}^n \widehat{\Psi}_n(z_1, \bar{z}_1; \ldots; z_N, \bar{z}_N) = (n!)^{N/2} f_n(z_1, \ldots, z_N). \tag{49}$$

Now $\Psi_n = \mathcal{U}_{N,n}^{-1}\Psi_0$ so the wave function $\widehat{\Psi}_n$ can by (38) and (24) be expressed in terms of the holomorphic function f_n:

$$\widehat{\Psi}_n(z_1, \bar{z}_1; \ldots; z_N, \bar{z}_N) = (n!)^{-N/2} \prod_{i=1}^{N} (\bar{z}_i - \partial_{z_i})^n \widehat{\Psi}_0(z_1, \ldots, z_N) = \prod_{i=1}^{N} (\bar{z}_i - \partial_{z_i})^n f_n(z_1, \ldots, z_N). \tag{50}$$

Next we consider *ℓ-particle densities*, $\ell = 1, 2, \ldots$, which for a general N-particle wave function Ψ are defined by

$$\rho_{\Psi}^{(\ell)}(\mathbf{r}_1, \ldots, \mathbf{r}_\ell) = \binom{N}{\ell} \int_{\mathbb{R}^{2(N-\ell)}} \left|\Psi\left(\mathbf{r}_1 \cdots \mathbf{r}_\ell; \mathbf{r}'_{\ell+1} \cdots \mathbf{r}'_N\right)\right|^2 \mathrm{d}\mathbf{r}'_{\ell+1} \cdots \mathrm{d}\mathbf{r}'_N. \tag{51}$$

Theorem 4.1: (Particle densities in the n-th Landau level)

The ℓ-particle densities of $\Psi_n \in n\mathrm{LL}^N$ and $\Psi_0 = \mathcal{U}_{N,n}\Psi_n \in \mathrm{LLL}^N$ are connected by

$$\rho_{\Psi_n}^{(\ell)}(\mathbf{r}_1, \ldots, \mathbf{r}_\ell) = \prod_{i=1}^{\ell} L_n\left(-\frac{1}{4}\Delta_{\mathbf{r}_i}\right) \rho_{\Psi_0}^{(\ell)}(\mathbf{r}_1, \ldots, \mathbf{r}_\ell) \tag{52}$$

where L_n is the n-th Laguerre polynomial

$$L_n(t) = \sum_{l=0}^{n} \binom{n}{l} \frac{(-t)^l}{l!}. \tag{53}$$

The proof is a simple consequence of the following Lemma:

Lemma 4.2: (Reshuffling differentiations)

Let f be a holomorphic function. Then

$$(n!)^{-1} \overline{[(\bar{z} - \partial_z)^n f(z)]}[(\bar{z} - \partial_z)^n f(z)] e^{-z\bar{z}} = L_n(-\partial_{\bar{z}}\partial_z)\left[\overline{f(z)} f(z) e^{-z\bar{z}}\right]. \tag{54}$$

Proof. This is a straightforward computation by induction over n, using the recursion relation for the Laguerre polynomials,

$$(n+1)L_{n+1}(u) = (2n+1)L_n(u) - nL_{n-1}(u) - uL_n(u). \tag{55}$$

To compute

$$\partial_{\bar{z}}\partial_z\left[\overline{[(\bar{z} - \partial_z)^n f(z)]}[(\bar{z} - \partial_z)^n f(z)] e^{-z\bar{z}}\right], \tag{56}$$

starting with $n = 0$ and $L_0 = 1$, one uses the commutation relations

$$\partial_{\bar{z}}(\bar{z} - \partial_z)^n = (\bar{z} - \partial)^n \partial_{\bar{z}} + n(\bar{z} - \partial_z)^{n-1}, \quad \partial_z(\bar{z} - \partial_z)^n = (\bar{z} - \partial)^n \partial_z, \tag{57}$$

and the fact that $\partial_{\bar{z}} f(z) = \partial_z \overline{f(z)} = 0$ for holomorphic f.

Theorem 4.1 follows by applying the Lemma to the first ℓ variables of Ψ_0, noting that $\partial_{\bar{z}}\partial_z = \frac{1}{4}\Delta$.

Mapping Hamiltonians to the LLL

Consider an N-body Hamiltonian of the form

$$H_{V,w} = \sum_{i=1}^{N} \left[H^{(i)} + V(\mathbf{r}_i)\right] + \sum_{i<j} w\left(\mathbf{r}_i - \mathbf{r}_j\right) \tag{58}$$

where $H^{(i)}$ is the 1-particle Landau Hamiltonian (1) for particle i, V is an external potential, and w a translationally invariant two-body interaction potential.

A common situation in Quantum Hall physics is that the first $n - 1$ Landau levels are filled with electrons and can be regarded as "inert" while the interesting phenomena take place in the tensor factor of the state in the n-th Landau level. The formulas of the last section, which establish a unitary correspondence between states and densities in different Landau levels, make it possible to reduce the study of the Hamiltonian in the n-the level to a unitarily equivalent Hamiltonian in the lowest Landau level where states are described by holomorphic wave functions. This reduction is accompanied by a transformation of the potentials V and w. The precise statement is as follows:

Theorem 5.1: (Effective Hamiltonians in different LL's).

Let $H_{V,w}$ be given by (58) and define

$$H^{n\mathrm{LL}}_{V,w} = \Pi_n^N H_{V,w} \Pi_n^N \tag{59}$$

where Π_n^N is the orthogonal projector from $L^2_{\mathrm{asym}}(\mathbb{R}^{2N})$ to $n\mathrm{LL}^N$. Then, for any n,

$$H^{n\mathrm{LL}}_{V,w} - n\cdot 2BN \tag{60}$$

is unitarily equivalent to

$$H^{\mathrm{LLL}}_{V^{(n)},w^{(n)}} = \Pi_0^N H_{V^{(n)},w^{(n)}} \Pi_0^N \tag{61}$$

with Π_0^N the projector onto the lowest Landau level LLL^N and the effective potentials

$$V^{(n)}(\mathbf{r}) = L_n\left(-\frac{1}{4}\Delta\right) V(\mathbf{r}) \tag{62}$$

$$w^{(n)}(\mathbf{r}) = L_n\left(-\frac{1}{4}\Delta\right)^2 w(\mathbf{r}) \tag{63}$$

where Δ is the Laplacian and L_n the Laguerre polynomial (53). More generally, one can consider interactions beyond the two-body case: For an ℓ particle interaction the $L_n\left(-\frac{1}{4}\Delta\right)^2$ in (63) is replaced by a product of $L_n\left(-\frac{1}{4}\Delta_i\right), i = 1, \dots, \ell$.

Proof. The proof follows directly from a comparison of expectation values of $H^{n\mathrm{LL}}_{V,\,w}$ in a state $\Psi_n \in n\mathrm{LL}^N$ with the corresponding state $\Psi_0 = \mathcal{U}^{-1}_{N,n}\Psi_n \in \mathrm{LLL}^N$, using the transformation formula (52) for one- and two-particle densities (more generally, ℓ-particle densities).

Remark. This is the basic result that allows to study interaction in higher LL's in terms of effective interactions in the LLL. It can be found in different guises in a number of sources, in particular (Haldane, 2018; Chen and Biswas, 2020; Tong, 2016; Jain, 2007; MacDonald and Girvin, 1986; Ciftja and Quintanilla, 2010).

Another proof of Theorem 5.1

An alternative approach to (62) and (63) is based on the splitting (14) of the position variables in guiding centers and cyclotron motion and the factorization $\exp(\mathrm{i}\mathbf{q}\cdot\mathbf{r}) = \exp(\mathrm{i}\mathbf{q}\cdot\mathbf{R})\exp\left(\mathrm{i}\mathbf{q}\cdot\tilde{\mathbf{R}}\right)$. This factorization carries over to matrix elements by Lemma 2.1.

Lemma 5.2: (Plane waves projected in different Landau levels).

For any $\mathbf{q} \in \mathbb{R}^2$, identify $e^{\mathrm{i}\mathbf{q}\cdot\mathbf{r}}$ with the corresponding multiplication operator on $L^2(\mathbb{R}^2)$, where $\mathbf{r}$ is the spatial variable. Let $\mathbf{R}$ be the guiding center operator defined in Section "The two oscillators", Π_n the orthogonal projector on nLL and $U_n : n\mathrm{LL} \rightarrow \mathrm{LLL}$ the unitary map (37). Then, in the LLL,

$$U_n \Pi_n e^{i\mathbf{q}\cdot\mathbf{r}} \Pi_n U_n^{-1} = L_n\left(\frac{|\mathbf{q}|^2}{4}\right) e^{-\frac{|\mathbf{q}|^2}{8}} \Pi_0 e^{i\mathbf{q}\cdot\mathbf{R}} \Pi_0 = L_n\left(\frac{|\mathbf{q}|^2}{4}\right) \Pi_0 e^{i\mathbf{q}\cdot\mathbf{r}} \Pi_0 \tag{64}$$

with L_n the Laguerre polynomial (53).

The equality of the left-hand and the right-hand sides of (64) can be seen as a Fourier transformed version of (52) (with $\ell = 1$).

The proof of the Lemma is a simple computation using the commutation relations (17) and the Baker-Campbell-Hausdorff formula

$$e^{X+Y} = e^X e^Y e^{-\frac{1}{2}[X,Y]} \tag{65}$$

for operators such that $[X,[X,Y]] = [Y,[X,Y]] = 0$. The computation can be found in Rougerie and Yngvason (2020), p. 12 and also in Jain (2007) (proof of Theorem 3.2 in that reference) and in Goerbig and Lederer (2006). Eqs. (62) and (63) follow from (64) by the Fourier decompositions

$$V(\mathbf{r}) = \int_{\mathbb{R}^2} \widehat{V}(\mathbf{q}) e^{i\mathbf{q}\cdot\mathbf{r}} d\mathbf{q} \tag{66}$$

and

$$w(\mathbf{r}_1 - \mathbf{r}_2) = \int_{\mathbb{R}^2} \widehat{w}(\mathbf{q}) e^{i\mathbf{q}\cdot\mathbf{r}_1} e^{-i\mathbf{q}\cdot\mathbf{r}_2} d\mathbf{q} \tag{67}$$

using the Fourier representation of the Laplacian, $-\Delta = |\mathbf{q}|^2$.

Coherent state representations

The considerations so far, in particular the holomorphic representation of states in any Landau level via the formulas (40) and (41), are based on the use of the ladder operators $a^{\#}$ which connect higher Landau levels with the LLL. We now discuss an alternative approach which offers additional insights. It relies on a representation of states in nLL in terms of coherent states for the guiding center oscillator.

Coherent states

A coherent state in nLL with parameter $Z \in \mathbb{C}$ associated with the guiding center oscillator is defined in a standard way (Klauder and Skagerstam, 1985; Combescure and Robert, 2021) as

$$|Z,n\rangle = e^{\left(Zb^\dagger - \overline{Z}b\right)} \varphi_{n,0} = \sum_{m=0}^{\infty} \frac{Z^m}{\sqrt{m!}} \varphi_{n,m} e^{-|Z|^2/2}. \tag{68}$$

The overlap of two coherent states is

$$\langle Z,n|Z',n'\rangle = \delta_{n,n'} e^{\left(2\overline{Z}Z' - |Z|^2 - |Z'|^2\right)/2} = \delta_{n,n'} e^{-|Z-Z'|^2/2} e^{i\mathrm{Im}\left(\overline{Z}Z'\right)} \tag{69}$$

and

$$\int |Z,n\rangle\langle Z,n| \frac{\mathrm{d}^2 Z}{\pi} = \sum_{m=0}^{\infty} |\varphi_{n,m}\rangle\langle\varphi_{n,m}| = \Pi_n \tag{70}$$

is the projector on nLL, where $\mathrm{d}^2 Z := \frac{i}{2}\, \mathrm{d}Z \wedge \mathrm{d}\overline{Z}$ is the Lebesgue measure on the plane.

The coherent states lead directly to an interpretation of nLL as a Bargmann space of holomorphic functions of the coherent state variable Z: If $\psi \in n$LL then

$$\widehat{\Psi}(Z) := \langle \overline{Z}, n|\psi\rangle e^{|Z|^2/2} = \sum_{m=0}^{\infty} \langle \varphi_{n,m}|\psi\rangle \frac{Z^m}{\sqrt{m!}} \tag{71}$$

is analytic in Z and

$$\Psi\left(Z,\overline{Z}\right) = \widehat{\Psi}(Z) e^{-|Z|^2/2} \tag{72}$$

has the same L^2 norm as ψ because of (70). Thus the map

$$U_n : \psi \mapsto \Psi \tag{73}$$

is isometric from the nLL to the LLL. From the definition it is clear that

$$U_n \varphi_{n,m} = \varphi_{0,m} \quad \text{and} \quad U_n|Z, n\rangle = |Z, 0\rangle \tag{74}$$

with the inverse

$$U_n^{-1} \varphi_{0,m} = \varphi_{n,m} \quad \text{and} \quad U_n^{-1}|Z, 0\rangle = |Z, n\rangle. \tag{75}$$

Thus U_n is identical to the unitary defined by ladder operators in (37) and (38). In particular the holomorphic function (71) is mathematically identical to the function $\widehat{\psi}_0(z) = \sqrt{n!} f_n(z)$ in (40) if $\psi = \psi_n$ and Z is identified with the complex position variable $z = x + \mathrm{i}y$. Note, however, that Z is associated with the (non-commutative) components of the guiding center operator $\mathbf{R}$ rather than the (commutative) position operator $\mathbf{r}$.

Remark. By the definition (71) Ψ depends linearly on ψ; the alternative definition $\Psi(Z) = \langle \psi | Z, n \rangle$, that is used in some references, leads to an anti-unitary correspondence.

Integral kernels

The unitary map $\psi \mapsto \Psi$ defined by (71) can also be achieved using the integral kernel

$$G_n\left(Z, \overline{Z}; z, \overline{z}\right) = \frac{1}{\sqrt{\pi n!}} (z - Z)^n e^{-\left(|Z|^2 + |z|^2 - 2Z\overline{z}\right)/2} = \frac{1}{\sqrt{\pi n!}} (z - Z)^n e^{-|z-Z|^2/2} e^{-\mathrm{i} Im(\overline{z}Z)}. \tag{76}$$

Namely, we have

$$\Psi\left(Z, \overline{Z}\right) = \int G_n\left(Z, \overline{Z}; z, \overline{z}\right) \psi(z, \overline{z}) \mathrm{d}^2 z. \tag{77}$$

The inverse map is given by

$$\psi(z, \overline{z}) = \int \overline{G}_n\left(z, \overline{z}; Z, \overline{Z}\right) \Psi\left(Z, \overline{Z}\right) \mathrm{d}^2 Z \tag{78}$$

with

$$\overline{G}_n\left(z, \overline{z}; Z, \overline{Z}\right) = \frac{1}{\sqrt{\pi n!}} \left(\overline{z} - \overline{Z}\right)^n e^{-\left(|Z|^2 + |z|^2 - 2\overline{Z}z\right)/2} = \frac{1}{\sqrt{\pi n!}} \left(\overline{z} - \overline{Z}\right)^n e^{-|z-Z|^2/2} e^{-\mathrm{i}\,\mathrm{Im}\left(z\overline{Z}\right)}. \tag{79}$$

The (short) proof can be found in Rougerie and Yngvason (2020), p. 8 and also (with a slightly different notation) in Champel and Florens (2007), Eq. (34). See also Champel and Florens (2009) and Champel et al. (2008).

Note that G_n can be written as

$$g_n(z - Z) e^{-2\mathrm{i}\;\mathrm{Im}(\overline{z}Z)} \tag{80}$$

where g_n is essentially concentrated in a disc of radius $\sim \sqrt{n+1}$ and the factor is a phase factor. Recall also that the length unit is $\sqrt{2}\ell_B \sim B^{-1/2}$.

A further remark is that G_0 is the reproducing kernel for the Bargmann space, confirming again that in the LLL Ψ and ψ are the same function on $\mathbb{C}$ just with different names for the variables. The phase factor in G_n is essential for this to hold.

Recap of the different expressions for the unitary maps

In the previous sections we have displayed three equivalent ways to represent a state $\psi \in n$LL by holomorphic functions in Bargmann space:

1. Apply the differential operator $\partial_{\overline{z}}$ n-times to the pre-factor of the Gaussian, cf. Eqs. (37) and (38). Equivalently: Expand the pre-factor in powers of $\overline{z}$ and keep only the highest power. The inverse mapping, LLL → nLL, is achieved by applying the differential operator $(\overline{z} - \partial_z)^n$ to the analytic function representing the state in the LLL.
2. Take the scalar product $\langle \overline{Z}, n | \psi \rangle$ with a coherent state, cf. (71).
3. Use Eq. (77) with the integral kernel (76).

The three methods generalize in all cases to many body states in $n\mathrm{LL}^N \equiv n\mathrm{LL}^{\otimes_{\mathrm{s,a}} N}$ by applying the prescriptions to each tensor factor.

Computationally the first method is usually the simplest, but the two others are sometimes more illuminating from the physics point of view since they bring the pivotal role of the guiding center variables into focus.

Some special states

Laughlin states

Consider an N-body Hamiltonian (58) with a rotationally symmetric interaction potential w but without an external potential. Its projection onto the LLL can be written as[1]

$$H_w^{\mathrm{LLL}} = \sum_{i<j}\sum_{m\geq 0}\langle\varphi_{0,m}|w|\varphi_{0,m}\rangle\left(|\varphi_{0,m}\rangle\langle\varphi_{0,m}|\right)_{ij}. \tag{81}$$

The matrix elements

$$w_m := \langle\varphi_{0,m}|w|\varphi_{0,m}\rangle = \frac{1}{\pi m!}\int_{\mathbb{R}^2}|w(\mathbf{r})|r^{2m}e^{-Br^2}d^2\mathbf{r} \tag{82}$$

are usually called "Haldane pseudo-potentials"[2] cf. (Haldane, 1983). If the sum is truncated at $m = q-1$ for some natural number q then the *Laughlin wave function*

$$\Psi_N^{\mathrm{Lau}}(z_1, \ldots, z_N) = c_N\prod_{i<j}(z_i - z_j)^q e^{-\sum_{j=1}^N |z_j|^2/2} \tag{83}$$

is an exact ground state of (81) (L^2-normalized by the constant in front).

The Laughlin state in LLL^N can also be written as

$$\Psi_N^{\mathrm{Lau}} = c_N\prod_{i<j}(b_i - b_j)^q\varphi_{0,0}^{\otimes N} \tag{84}$$

and its counterpart in $n\mathrm{LL}^N$, obtained by applying the unitary transformation $\mathcal{U}_{N,n}^{-1}$ defined by (47) to Ψ_N^{Lau}, is

$$\Psi_{n,N}^{\mathrm{Lau}} = c_N\prod_{i<j}\left(b_i^\dagger - b_j^\dagger\right)^q\varphi_{n,0}^{\otimes N} = c_N\prod_{i<j}\left(b_i^\dagger - b_j^\dagger\right)^q\prod_{i=1}^N\left[\left(a_i^\dagger\right)^n\varphi_{0,0}\right] \tag{85}$$

with wave function (cf Proposition 3.1)

$$\Psi_{n,N}^{\mathrm{Lau}}(\mathbf{r}_1, \ldots, \mathbf{r}_N) = c_N\left[\frac{1}{(n!)^{N/2}}\prod_{i=1}^N(\bar{z}_i - \partial_{z_i})^n\prod_{i<j}(z_i - z_j)^q\right]e^{-\left(|z_1|^2+\cdots+|z_N|^2\right)/2}. \tag{86}$$

This is, in *electronic position variables*, the exact ground state of a Hamiltonian obtained by

- Projecting the Hamiltonian (58) onto $n\mathrm{LL}^N$.
- Unitarily mapping the result down to an effective Hamiltonian on LLL^N using Theorem 5.1.
- Neglecting the one-body potential $V^{(n)}$ and truncating the Haldane pseudo-potential series (82) for the interaction potential $w^{(n)}$ at $m = q - 1$..

Note that the pseudopotentials $w_m^{(n)}$ now depend on n because w is replaced by the effective interaction (63).

If the wave function (86) is transformed back to LLL^N using the representation of $\mathcal{U}_{N,n}^{-1}$ in terms of the integral kernel (76), we obtain again the function (83) but with the z_i replaced by the coherent state *guiding center variables* Z_i. Since the integral kernel is essentially concentrated in a disc of radius $\sim\sqrt{n+1}\ell_B$, one can expect that for large B and not too large n the particle densities of (83) and (86) are essentially the same in extended systems. This is indeed vindicated by the more detailed analysis mentioned below.

According to Laughlin's plasma analogy (Laughlin, 1983) the density profile of (83) is for large N well approximated by a droplet of radius $(\ell N)^{1/2}$ and fixed density $(\pi q)^{-1}$,

$$\varrho_N^{\mathrm{flat}}(\mathbf{r}) := \begin{cases}\dfrac{1}{\pi q}\,\mathrm{if}\,|z| \leq \sqrt{qN}\\ 0\ \text{otherwise.}\end{cases} \tag{87}$$

By a rigorous mean-field analysis it can be proved (Rougerie et al., 2014) that this approximation holds in the sense of averages over discs of radius N^α with $1/2 > \alpha > 1/4$. More generally, the k-particle densities are well approximated in this sense by the k-fold tensor power of the flat density if $N \to \infty$. The more refined analysis of classical Coulomb systems in Leblé and Serfaty (2018), Bauerschmidt et al. (2017) and Serfaty (2020) leads to an extension of this result down to mesoscopic scales N^α for all $\alpha > 0$.

---

[1] Note that fermionic wave-functions do not see the even m terms of (81).

[2] For very strong interaction potentials of range much smaller than the magnetic length $\sim B^{-1/2}$, in particular if there is a hard core, an expansion of the interaction in terms of moments as in (81) is not adequate. This situation is analysed in Seiringer and Yngvason (2020) which generalizes the paper (Lewin and Seiringer, 2009). It is shown that in an appropriate scaling limit the pseudo-potential operators $|\varphi_m\rangle\langle\varphi_m|$ also emerge, but with renormalized pre-factors involving the scattering lengths of the interaction potentials in the different angular momentum channels, rather than expectation values as in (81).

Using the transformation formula (52) and the fact that the Laguerre polynomial $L_n(t)$ is close to unity for small values of the argument then allows to conclude the same result for fixed n and large N. The precise statement can be found as Theorem 8.1 in Rougerie and Yngvason (2020).

In order to adapt to an external potential V a natural modification of the Laughlin state is to insert *quasi-holes*, i.e., to consider states of the form

$$\Psi(z_1, \ldots, z_N) = C'_N \Psi_N^{\mathrm{Lau}}(z_1, \ldots, z_N) \prod_{i=1}^{N} f(z_i) \tag{88}$$

where $f(z) = c\prod_{j=1}^{M}(z - a_j)$ with $a_j \in \mathbb{C}$. In Rougerie and Yngvason (2018) it is discussed how such states minimize the potential energy in an external potential among all states in the LLL which vanish like $(z_i - z_j)^q$ when two points come close. This result generalizes to higher Landau levels for large N by an analogous arguments as for pure Laughlin states, the intuition being again that in higher Landau levels position coordinates should be replaced by guiding center coordinates and the potential V by the effective potential $V^{(n)} = L_n\left(-\frac{1}{4}\Delta\right)V$.

Filling factor $\nu = 5/2$

A Quantum Hall state with a clear signature for filling factor $\nu = 5/2$ was first observed in Willett et al. (1987). It is thought to consist of *two* completely filled lowest Landau levels (i.e., with $n = 0$) but with opposite spin polarizations, combined with a spin polarized state with $n = 1$ and half filling. This state is unusual since the great majority of observed plateaus in the Quantum Hall conductance correspond to filling factors with an odd denominator as seemingly natural for fermions. Moreover, there is no sign of a plateau in the Hall resistance at $\nu = 1/2$ for $n = 0$ alone.

Since its discovery the $\nu = 5/2$ state has been extensively studied experimentally, see (Willett, 2013) for a comprehensive review. It is also very interesting theoretically because quasi-hole excitations of the principal candidates for describing this state may show *non-abelian* braid statistics. In brief, the reason is that the manifold of states with 2 k quasiholes is 2^{k-1} degenerate and the braiding of two quasiholes defines a unitary map on the space spanned by this manifold. The unitaries corresponding to different braidings do not commute in general. An adequate discussion of these aspects would go well beyond the scope of the present chapter but a concise account with further references can be found in Tong (2016) as well as in Greiter (2011). A detailed discussion of non-abelian anyons and potential applications for quantum computation is given in Nayak et al. (2008). The recent review of Ma et al. (2022) discusses both theoretical and experimental aspects at filling factor $\nu = 5/2$. See also Greiner and Wilczek (2022) for a general review of fractional statistics.

The main candidates for the quantum Hall state at $\nu = 5/2$ are a *Moore-Read state* (Moore and Read, 1991) as well as its variant obtained by particle hole conjugation. A Moore-Read state in the LLL for an even particle number N and has the form

$$\Psi_{\mathrm{MR}}(z_1, \ldots, z_N) = \mathrm{Pf}\left(\frac{1}{z_i - z_j}\right) \prod_{i<j}^{N} (z_i - z_j)^q \prod_{i=1}^{N} e^{-|z_i|^2/2} \tag{89}$$

with the Pfaffian

$$\mathrm{Pf}\left(\frac{1}{z_i - z_j}\right) = \mathcal{A}\left\{\frac{1}{z_1 - z_2} \cdots \frac{1}{z_{N-1} - z_N}\right\} \tag{90}$$

where $\mathcal{A}$ stands for anti-symmetrization over all possible pairings of the coordinates. It has filling fraction $1/q$ and is antisymmetric for *even* values of q. It is also holomorphic because singular factors in the Pfaffian are compensated by the factors $(z_i - z_j)^q$. In contrast to the Laughlin wave function and its quasi-hole descendants the Moore-Read wave functions do not vanish when two particles come together, but may vanish when more particles become coincident. In particular for $q = 1$ it is a ground state of the formal 3-body Hamiltonian

$$H = \sum_{i<j<k} \delta(z_i - z_j)\delta(z_i - z_k). \tag{91}$$

The anti-Pfaffian state (Lee et al., 2007) is the particle-hole conjugate version of (89). The concept of particle hole conjugation is thoroughly discussed in Zirnbauer (2021), see also (Girvin, 1984). In the present case it means replacing the creation operators b_i^* by the annihilation operators b_i and applying the result to a fully occupied LLL state (the Fermi sea) rather than the gaussian ground state $\varphi_{0,0}^{\otimes N}$, cf. Eq. (3.1) in Zirnbauer (2021). The Fermi sea in the LLL is a Slater determinant and has a wave function as in (83) with $q = 1$. The explicit formula for the anti-Pfaffian state, given in Lee et al. (2007), is

$$\Psi_{\mathrm{aPf}}(z_1, \ldots, z_N) = \prod_{i<j}^{N} (z_i - z_j) \prod_{i=1}^{N} e^{-|z_i|^2/2} \times \int \prod_{\alpha=1}^{N} \mathrm{d}^2\eta_\alpha \prod_{i,\,\alpha}(z_i - \eta_\alpha) e^{-|\eta_\alpha|^2/2} \prod_{\beta<\gamma}\left(\eta_\beta - \eta_\gamma\right) \Psi_{\mathrm{MR}}(\overline{\eta}_1, \ldots \overline{\eta}_N). \tag{92}$$

Yet another candidate for the quantum Hall state at $\nu = 5/2$ is a particle-hole symmetric state suggested in Son (2015).

All the states mentioned are specified in the lowest Landau level, where they are given by holomorphic wave functions. The general procedure of Sections "Unitary maps between Landau levels", "Many body states and l-particle densities", "Mapping Hamiltonians to the LLL", "Remark", "Another proof of Theorem 5.1", "Coherent state representations" then takes care of lifting them up to any Landau level $n\mathrm{LL}^N$. In the $\nu = 5/2$ case one takes $n = 1$ and assumes a fully spin polarized state. An important point is now that the effective interaction depends on the Landau level as described in Eq. (63). For instance, a Coulomb potential is more repulsive at short distances for $n = 1$ than for $n = 0$, (cf. Fig. 1 in Ciftja and Quintanilla, 2010). This may explain why, e.g. a Moore-Read state with $q = 2$ can have an energy gap in the $n = 1$ level and exhibit a FQHE plateau, while being a gapless Fermi liquid in the LLL.

The nature of the true ground state at $\nu = 5/2$ is, however, still a matter of considerable debate. The issues of spin polarization and the possibility of *Landau level mixing* play an important role here. In this chapter so far it has always been assumed that a single spin polarized Landau level, namely the highest partially filled one, is the arena for the phenomena under consideration while all lower levels are completely filled and can be regarded as inert. Landau level mixing means that the projection of the interaction Hamiltonian into a single Landau level is not adequate and processes where interactions induce transitions between different levels become relevant. Mathematically this means that it is not sufficient to consider states that are simply a tensor product of a state in a partially filled level with filled lower levels but one must consider states which are linear combinations of states with partial filling in more than one level.

Effective Hamiltonians to account for Landau level mixing at $\nu = 5/2$ were derived in Peterson and Nayak (2013), Simon and Rezayi (2013) and Sodemann and MacDonald (2013), and in Rezayi (2017) it was concluded that when mixing is allowed, an anti-Pfaffian state is favored. The effects of mixing may depend, however, on the size and shape of samples, and clear-cut answers for the thermodynamic limit are hard to come by. Moreover, the strength of the mixing depends on the material with e.g., ZnO showing stronger effects that GaAs. The paper (Luo et al., 2021) deals in particular with systems with strong mixing and the question of stability for incompressible ground states.

Conclusion

In this chapter it has been explained how quantum Hall states for many-body systems in arbitrary Landau levels can be mapped unitarily onto states in the lowest Landau level. The basis for this mapping is a splitting of the two-dimensional position variables into two sets of non-commutative variables associated respectively with the guiding centers and the cyclotron motion of the particles in the magnetic field. In a fixed Landau level the cyclotron variables play the role of bystanders while the state for the guiding center variables can be described by holomorphic wave functions independently of the Landau level. As a consequence, it is possible to treat particle densities and interactions in higher Landau levels in terms of suitably transformed densities and interactions in the lowest Landau level.

These insights are applied to Laughlin states in arbitrary Landau levels as well as to Pfaffian and anti-Pfaffian states that have been proposed for explaining pronounced quantum Hall plateaus at filling fraction 5/2 and may exhibit non-abelian braid statistics of excitations. Their discussion in this chapter is quite brief, however, but detailed treatments of these matters are presented in other chapters of the Encyclopedia (Ma et al., 2022; Greiner and Wilczek, 2022).

Acknowledgments

Thanks are due to Nicolas Rougerie for collaboration on the review (Rougerie and Yngvason, 2020) which is the basis for the present chapter.

References

Bargmann V (1961) On a Hilbert space of analytic functions and an associated integral transform. *Communications on Pure and Applied Mathematics* 14: 187–214.

Bauerschmidt R, Bourgade P, Nikula M, and Yau H-T (2017) Local density for twodimensional one-component plasma. *Communications in Mathematical Physics* 356: 189–230.

Chakraborty T and Pietiläinen P (1988) *The Fractional Quantum Hall Effect*. New York: Springer.

Chakraborty T and Pietiläinen P (1995) *The Quantum Hall Effects*, 2nd edn. New York: Springer.

Champel T and Florens S (2007) Quantum transport properties of two-dimensional electron gases under high magnetic fields. *Physical Review B* 75: 245326.

Champel T and Florens S (2009) Local density of states in disordered two-dimensional electron gases at high magnetic field. *Physical Review B* 80: 161311.

Champel T, Florens S, and Canet L (2008) Microscopics of disordered two-dimensional electron gases under high magnetic fields: Equilibrium properties and dissipation in the hydrodynamic regime. *Physical Review B* 78: 125302.

Chen Y and Biswas RR (2020) Gauge-invariant variables reveal the quantum geometry of fractional quantum Hall states. *Physical Review B* 102: 165313.

Ciftja O and Quintanilla J (2010) Effective interaction potentials in the uppermost landau level. *Journal of Low Temperature Physics* 159: 189–192.

Combescure M and Robert D (2021) *Coherent States and Applications in Mathematical Physics*, 2nd edn. New York: Springer.

Cooper NR (2008) Rapidly rotating atomic gases. *Advances in Physics* 57(6): 539–616.

Fradkin E (2013) *Field Theories of Condensed Matter Systems*. Cambridge University Press.

Girvin SM (1984) Particle-hole symmetry in the anomalous quantum Hall effect. *Physical Review B* 29: 6012–6013.

Goerbig MO (2009) Quantum Hall effects. arXiv:0909.1998.

Goerbig MO and Lederer P (2006) *Introduction to the Quantum Hall Effects*. https://webspace.science.uu.nl/~duine102/qfinqm08/LedererQHE.pdf (Retrieved April 11, 2022).

Gradshteyn IS and Ryzhik IM (1994) *Table of Integrals, Series and Products*, 5th edn. Academic Press.

Greiner M and Wilczek F (2022) Fractional Statistics. ArXiv: 2210.02530.

Greiter M (2011) *Mapping of Parent Hamiltonians—From non-Abelian Quantum Hall States to Exact Models of Critical Spin Chains*. New York: Springer.

Haldane D (1983) Fractional quantization of the hall effect: A hierarchy of incompressible quantum fluid states. *Physical Review Letters* 51: 605–608.

Haldane FDM (2013) *Geometry, Topology and Entanglement in the FQHE*. http://wwwphy.princeton.edu/∼haldane/talks/ictp20130705-haldane.pdf (Retrieved April 7, 2022).

Haldane FDM (2018) The origin of holomorphic states in Landau levels from non-commutative geometry, and a new formula for their overlaps on the torus. *Journal of Mathematical Physics* 59: 081901.

Jain JK (2007) *Composite Fermions*. Cambridge University Press.

Klauder J and Skagerstam B (1985) *Coherent States, Applications in Physics and Mathematical Physics*. Singapore: World Scientific.

Klitzing VK, Dorda G, and Pepper M (1980) New method for high-accuracy determination of the fine-structure constant based on quantized hall resistance. *Physical Review Letters* 45: 494–497.

Landau LD and Lifschitz EM (1977) *Quantum Mechanics*, 3rd edn. Oxford: Pergamon.

Laughlin RB (1983) Anomalous quantum Hall effect: An incompressible quantum fluid with fractionally charged excitations. *Physical Review Letters* 50: 1395–1398.

Laughlin RB (1987) Elementary theory: The incompressible quantum fluid. In: Prange RE and Girvin SE (eds.) *The Quantum Hall Effect. Graduate Texts in Contemporary Physics*. New York, NY: Springer.

Laughlin RB (1999) Nobel lecture: Fractional quantization. *Reviews of Modern Physics* 71: 863–874.

Leblé T and Serfaty S (2018) Fluctuations of two-dimensional Coulomb gases. *Geometric and Functional Analysis* 28: 443–508.

Lee S-S, Ryu S, Nayak C, and Fisher MPA (2007) Particle-Hole Symmetry and the $\nu = 5/2$ Quantum Hall State. *Physical Review Letters* 99: 236807.

Lewin M and Seiringer R (2009) Strongly correlated phases in rapidly rotating bose gases. *Journal of Statistical Physics* 137: 1040–1062.

Lieb EH, Rougerie N, and Yngvason J (2018) Rigidity of the laughlin liquid. *Journal of Statistical Physics* 172: 544–554.

Lieb EH, Rougerie N, and Yngvason J (2019) Local incompressibility estimates for the Laughlin phase. *Communications in Mathematical Physics* 365: 431–470.

Luo W, Peng S, Wang H, Zhou Y, and Chakraborty T (2021) Stability of even-denominator fractional quantum Hall states in systems with strong Landau-level mixing. *Physical Review B* 104: L161302.

Ma K, Peterson MR, Scarola VW, and Yang K (2022) Fractional quantum Hall effect at the filling factor $\nu = 5/2$. ArXiv: 2208.07908.

MacDonald AH (1984) Laughlin states in higher landau levels. *Physical Review B* 30: 3350–3353.

MacDonald AH and Girvin SM (1986) Collective excitations of fractional Hall states and Wigner crystallization in higher Landau levels. *Physical Review B* 33: 4009–4013.

Moore G and Read M (1991) Non abelions in the fractional quantum hall effect. *Nuclear Physics* B360: 362–396.

Nayak C, Simon SH, Stern A, Friedman M, and Das Sarma S (2008) Non-Abelian anyons and topological quantum computation. *Reviews of Modern Physics* 80: 1083–1159.

Peterson MR and Nayak C (2013) More realistic Hamiltonians for the fractional quantum Hall regime in GaAs and graphene. *Physical Review B* 87: 245129.

Prange RE and Girvin SE (eds.) (1987) *The Quantum Hall Effect*. Springer.

Rezayi EH (2017) Landau Level Mixing and the Ground State of the $\nu = 5/2$ Quantum Hall Effect. *Physical Review Letters* 119: 026801.

Rougerie N and Yngvason J (2018) The Laughlin liquid in an external potential. *Letters in Mathematical Physics* 108: 1007–1029.

Rougerie N and Yngvason J (2020) Holomorphic quantum Hall states in higher Landau levels. *Journal of Mathematical Physics* 61: 041101.

Rougerie N, Serfaty S, and Yngvason J (2014) Quantum Hall phases and plasma analogy in rotating trapped Bose gases. *Journal of Statistical Physics* 154: 2–50.

Seiringer R and Yngvason J (2020) Emergence of haldane pseudo-potentials in systems with short range interactions. *Journal of Statistical Physics* 281: 448–464.

Serfaty S (2020) *Gaussian Fluctuations and Free Energy Expansion for 2D and 3D Coulomb Gases at Any Temperature*. ArXiv:2003.11704, 2020.

Simon SH and Rezayi EH (2013) Landau level mixing in the perturbative limit. *Physical Review B* 87: 155426.

Sodemann I and MacDonald AH (2013) Landau level mixing and the fractional quantum Hall effect. *Physical Review B* 87: 245425.

Son DT (2015) Is the composite fermion a dirac particle? *Physical Review X* 5: 031027.

Störmer HL, Tsui DC, and Gossard AC (1982) Two-dimensional magnetotransport in the extreme quantum limit. *Physical Review Letters* 48: 1559–1562.

Störmer HL, Tsui DC, and Gossard AC (1999) The fractional quantum Hall effect. *Reviews of Modern Physics* 71: S298–S305.

Tong D (2016) *Lectures on the quantum Hall effect*. http://damtp.cam.ac.uk/user/tong/qhe.html (Retrived April 11, 2022).

Willett R (2013) The quantum Hall effect at 5/2 filling factor. *Reports on Progress in Physics* 76: 076501. 39pp.

Willett R, Eisenstein JP, Störmer HL, Tsui DC, Gossard AC, and English H (1987) Observation of an even-denominator quantum number in the fractional quantum hall effect. *Physical Review Letters* 59: 15.

Zirnbauer MR (2021) Particle-Hole symmetries in condensed matter. *Journal of Mathematical Physics* 62: 021101.

Quantum Hall effect[☆]

Jürgen Weis, Max Planck Institute for Solid State Research, Stuttgart, Germany

© 2024 Elsevier Ltd. All rights reserved.

This is an update of J. Weis, Quantum Hall Effect, Editor(s): Franco Bassani, Gerald L. Liedl, Peter Wyder, Encyclopedia of Condensed Matter Physics, Elsevier, 2005, Pages 22–29, ISBN 9780123694010, https://doi.org/10.1016/B0-12-369401-9/00730-0.

Introduction **555**
Hall effect **555**
Two-dimensional charge carrier system **556**
Hall effect on two-dimensional charge carrier system—Quantum Hall effect **557**
Theoretical models for the quantum Hall effect **559**
Integer quantum Hall effect **559**
The single-particle energy spectrum—Landau levels 559
Dissipationless current flow 560
Compressible and incompressible regions within a two-dimensional electron system 560
Current distribution in real samples 561
Role of metal contacts 563
Breakdown 563
Localization 564
Fractional quantum Hall effect **564**
Conclusion **565**
References **565**

Abstract

Measurement of the Hall effect on a two-dimensional charge carrier system at low temperatures and high magnetic fields leads to the observation of well-defined Hall resistance values which remain constant against variation of the applied magnetic field or the charge carrier density—the quantum Hall effect (QHE). The quantized Hall resistance values depend only on the Planck constant h, the elementary charge e, and either an integer or a fractional valued number. The QHE has enabled in 2019 the redefinition of the International System of Units (SI), based now on five fundamental constants of nature. As described here, the robustness of the QHE is related to the evolution of an electrical compressible/incompressible landscape inside the naturally inhomogeneous charge carrier system with varying magnetic field/charge carrier density. The incompressibility has its origin in the formation of energy gaps, which arise—besides the formation of Landau levels—also by strong correlation effects between the charge carriers.

Key points

- The quantum Hall effect is observed, usually at high magnetic fields and low temperatures, on two-dimensional charge carrier systems in various materials, even with different band structures.
- The values of the quantized Hall resistance plateaus depend only on fundamental constants - the Planck constant h and elementary charge e, and an integer or fractional valued number ν.
- The quantum Hall resistance has been used as reference in metrology and has been a key to revise the International System of Units, now based on five fundamental constants of nature.
- If a certain relation between the charge carrier density and the magnetic flux density is fulfilled, an energy gap opens up, i.e., electrical incompressibility appears within the charge carrier system. As no states are present at the Fermi level, the local longitudinal conductivity becomes zero—the charge carrier system behaves locally as an insulator. However, local Hall conductivity exists and takes the value $\nu\, e^2/h$ where ν is an integer or a rational fraction, respectively.
- The formation of quantum Hall plateaus relies on inhomogeneities within the two-dimensional charge carrier density, either due to the natural depletion towards the edges or variations in the bulk due to disorder and imperfections.
- Due to these inhomogeneities, an electrically compressible/incompressible landscape is formed within the two-dimensional charge carrier system that evolves with varying either the magnetic field or the charge carrier density. Pathes of incompressibility might be present along the Hall bar over a larger range in magnetic field/charge carrier density.

[☆] Change History: September 2022. J Weis updated the chapter. Key points added, Figure 6 replaced. Figure 7 added. Sections on 'Role of Metal Contacts' and 'Breakdown' added. All Sections updated and extended. References added to the text.

- In the quantum Hall plateau regime, the bias voltage, applied to the Hall bar ends, is carried by the compressible regions along the Hall bar edges into the Hall bar and is then present as a Hall voltage over the Hall bar cross-section. In consequence, the local Hall voltage drop drives a dissipationless Hall current in the incompressible regions along the Hall bar.
- A well-defined quantized Hall resistance is measured if the Hall voltage in that cross-section drops only over incompressible regions of same integer or fractional v.

Abbreviations

B	Magnetic flux density
c	Speed of light in vacuum
$D(\varepsilon)$	Energy density of states
E	Electrical field
$-e$	Electron charge
e	Elementary charge
g^*	Effective Landé factor
g_s	Spin degeneracy
I	Current
i, f, ν	Integer or fractional valued number, respectively
j	Current density
k	Wavevector
l	Magnetic length
m^*	Effective mass
m_0	Free electron mass
n	Charge carrier concentration
N	Electron number
n	Landau level index
n_L	Landau level degeneracy
n_s	Sheet charge carrier density
q	Charge
r	Location vector
R_H	Hall resistance
R_K	von Klitzing constant
$R_{K\text{-}90}$	Conventional von Klitzing constant
R_{xx}, R_{xy}	Resistance
s_z	Spin quantum number
V	Voltage
w	Hall bar witdh
x, y, z	Spatial coordinates
α	Sommerfeld fine-structure constant
ε	Single-particle energy
ε_F	Fermi energy
λ	de Broglie wavelength
λ_F	Fermi wavelength
μ	Charge carrier mobility
μ_0	Permeability of vacuum
μ_B	Bohr magneton
μ_{ch}	Chemical potential
μ_{elch}	Electrochemical potential
ν_L	(Landau level) Filling factor
σ	Electical conductivity
Φ	Magnetic flux
Φ_0	Magnetic flux quantum
$\hbar = h/2\pi$	Planck constant
$\hbar\omega_c$	Cyclotron energy

Introduction

The quantum Hall effect (QHE) and its relation to fundamental physical constants was discovered in 1980 by von Klitzing et al. (1980), and was honored by the Nobel prize in 1985 (von Klitzing, 1986). The Hall resistance R_H (Hall voltage divided by the applied current), measured on a two-dimensional charge carrier system at low temperatures (typically at liquid Helium temperature $T = 4.2$ K) and high magnetic fields (typically several Tesla) which is applied perpendicularly to the plane of the charge carrier system, shows well-defined constant values for wide magnetic field or charge carrier density variations. These plateau values are described by $|R_H| = h/(i\, e^2)$ where h is the Planck constant, e is the elementary charge and i an integer value with $i = \{1,2,3, \ldots\}$. Nowadays this effect is denoted as integer quantum Hall effect (IQHE) since, beginning with the year 1982, plateaus have been found in the Hall resistance of two-dimensional electron systems of higher quality and at lower temperature which are described by $|R_H| = h/(f\, e^2)$ where f is a fractional number (Tsui et al., 1982; Laughlin, 1983). The fractions $f = \{1/3,\ 2/3\}$ are the most prominent ones. For the discovery of these unexpected new quantum states in 1982, manifesting themselves in the fractional quantum Hall effect (FQHE), Dan C. Tsui, Horst L. Störmer, and Robert B. Laughlin were honored by the Nobel prize in 1998.

The important implication of the integer quantum Hall effect was its application in metrology where the effect is used to represent a resistance standard. Due to the small standard uncertainty in reproducing the value of the quantized Hall resistance (few parts of 10^{-9}), its value was fixed in 1990 for resistance calibration purpose to 25812.807 Ohm and has been denoted as conventional von Klitzing constant $R_{K\text{-}90}$ (Taylor and Witt, 1989). Recent developments try to establish the IQHE, measured under ac current modulation of few kilohertz (ac-QHE), even as primary standard reference for electrical impedances (Schurr et al., 2011).

It is generally accepted that the von Klitzing constant R_K agrees to h/e^2. As in 1980 the speed of light c in vacuum and the permeability of vacuum μ_0 were fixed physical constants in the International System of Units (SI), R_K was directly related to the Sommerfeld fine-structure constant $\alpha = (\mu_0\, c/2)\ (e^2/h) = (\mu_0\, c/2)\ (R_K)^{-1}$, which is a measure for the strength of the interaction between electromagnetic fields and elementary particles. Therefore, it was also pointed out (von Klitzing et al., 1980) that the integer quantum Hall effect allows to determine the fine-structure constant α with high precision, simply based on magneto-resistance measurements on a solid-state device.

The most important impact in metrology however happened recently: The precision and the link of the QHE to the fundamental physical constant h—the fundamental constant of quantum mechanics—has enabled the redefinition of the International System of Units (SI) where the kilogram prototype (Davis, 2003) is replaced by a fixed value for the Planck constant. To ensure a smooth transition, a final value of h in the old SI base unit system was determined by Kibble balance experiments (Robinson and Schlamminger, 2016) where mechanical and electrical power are compared, taking use of the quantum Hall effect and the Josephson effect (Josephson, 1962). The revised SI unit system, effective since 20 May 2019, is now based on five exactly defined values for natural physical constants—the speed of light c, the elementary charge e, the Planck constant h, the Boltzmann constant and the Avogadro constant. By that, the von Klitzing constant R_K is fixed too—with an infinite number of digits in units of Ohm. The direct link to the Sommerfeld fine-structure constant α is lost as μ_0 became uncertain (von Klitzing, 2019).

Not only the application in metrology but mostly questions in fundamental physics have pushed the interest in the quantum Hall effect up to now. The fractional quantum Hall effect is a manifestation of strong correlation effects among the charge carriers interacting in the two-dimensional system that lead to the formation of new quantum states. With improving the quality and reaching lower temperatures for the charge carrier system, more and more quantum Hall states have been found, and even more might be discovered in the future. Quantum Hall systems are, therefore, used as model systems for studying the formation of strongly correlated many-particle states, developing theory for their description, and identifying, probably, their simpler description in terms of the formation of new quasi-particles, for instance, the so-called ‘composite fermions’ or ‘anyons’ (see further Contributions in this Encyclopedia).

Since 2007 the citations of the original QHE publication by von Klitzing et al. (1980) have risen significantly. The type of samples showing the QHE are nowadays considered as a special class of topological insulators, derived from the material’s band structure properties, widening also the material base for observing the QHE and related effects (see further Contributions in this Encyclopedia).

Hall effect

An electrical charge moving with constant velocity in a homogenous magnetic field feels the Lorentz force acting in a direction perpendicular to both the magnetic field orientation and the direction of motion. Driving a current through an electrical conductor (an experimental setup is shown in Fig. 1) leads to the Hall effect discovered by Hall (1879). As can be derived within the Drude model (Drude, 1900), the free charge carriers in the conductor accumulate due to the Lorentz force on one side and deplete on the opposite side leading to an electrical field (Hall field) in the conductor which in back-action compensates for the Lorentz force so that, under stationary conditions, the charge carriers drift straight through the sample. If only one type of charge carrier is present, the related Hall voltage V_H, that is, the difference in the electrochemical potentials between two contacts at opposite sample edges, where the connection line between these two contacts lies perpendicular to the current direction, is simply described by $V_H = V_y = R_H\, I_x$ with the Hall resistance R_H given by

$$R_H \equiv R_{x\,y} = B_z/(q\, n\, d)$$

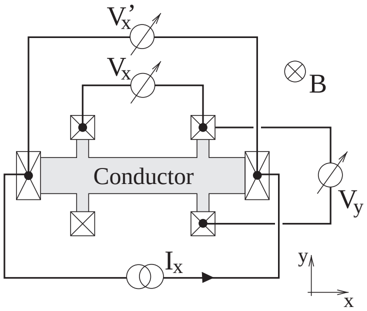

Fig. 1 Setup for measuring the Hall resistance $R_{xy} = V_y/I_x$, the (four-terminal) longitudinal resistance $R_{xx} = V_x/I_x$, and the (two-terminal) longitudinal resistance $R'_{xx} = V'_x/I_x$.

for the orientation of the arrangement shown in Fig. 1. The Hall resistance is positive or negative depending on the type of charge carriers which are either electrons ($q = -e$) or missing electrons/holes at top of an else filled electronic band ($q = +e$). Its magnitude increases linearly with the homogenously applied magnetics flux density B_z and the slope of the increase is given by the concentration n of these carriers and the thickness d of the conducting layer. That is why the Hall effect is used as an important diagnostic tool to determine essential properties of electrical conductors—free charge carrier concentration n and sign of q. Hall devices find various applications as magnetic field sensors.

Two-dimensional charge carrier system

The quantum Hall effect is observed in two-dimensional charge carrier systems, belonging to the class of so-called low-dimensional charge carrier systems. Simplified, the charge carriers in a bulk conductor can be considered as independent charged quasi-particles moving with an effective mass m^* freely in the three-dimensional space of the crystal. Such a charge carrier system is treated as the Sommerfeld fermion gas, that is, the wavefunctions of these quasi-particles are described by plane waves and their eigenenergies by $\varepsilon = |\hbar \boldsymbol{k}|^2 / (2\, m^*)$, where $\boldsymbol{k}$ denotes the wavevector and $\hbar = h/2\pi$. The de Broglie wavelength $\lambda = 2\pi/|\boldsymbol{k}|$ of the charge carriers at their Fermi level in the bulky conductor (= Fermi wavelength λ_F) is given by $\lambda_F = h/\sqrt{(2\, m^*\, \varepsilon_F)}$. Confining the charge carriers to spatial dimensions of the length of the Fermi wavelength λ_F, the charge carriers are restricted in their motion: Only certain eigenenergies are allowed in the confined direction, and the distance between these eigenenergies increases with narrowing the spatial width of the confinement, until only the lowest eigenenergy is still lying below the Fermi level. Two-dimensional charge systems allow motion only in a plane, one-dimensional charge systems—denoted as quantum wires—only along a line, and in a zero-dimensional system—denoted as quantum dots or 'artificial atoms'—the charge carriers are confined in a cage allowing them overall only a discrete set of eigenenergies.

The Fermi wavelength $\lambda_F = h/\sqrt{(2\, m^*\, \varepsilon_F)}$ of charge carriers in a bulky conductor is large in case of a low Fermi energy ε_F, achieved by a low charge carrier concentration n, and a low effective mass m^*. Therefore, semiconductors and especially the III–V compound semiconductor materials are preferred to define the low-dimensional charge carrier systems by confining conduction band electrons or valence band holes in one or more directions to few tens of nanometers or less. In this regard, the gallium arsenide (GaAs) stands out as in this case the band structure of the conduction band exhibits a single absolute minimum at the Γ point, and the dispersion relation is isotropic, described by a single effective mass $m^* = 0.067\, m_0$ (where m_0 is the free electron mass).

The first two-dimensional charge carrier systems were realized in **m**etal-**o**xide-**s**emiconductor **f**ield **e**ffect **t**ransistors (MOSFETs) in the thin conducting channel at the insulator-semiconductor interface. Silicon-MOSFETs are used as electronic switches of which nowadays billions are integrated in modified design on a single microprocessor die. The quantum Hall effect was originally discovered on such a Si-MOSFET device (von Klitzing et al., 1980). Two-dimensional charge carrier systems of higher quality are obtained in layers or at interfaces of III–V compound semiconductor heterostructures which are fabricated by **m**olecular **b**eam **e**pitaxy (MBE) or **m**etal **o**rganic **c**hemical **v**apor **d**eposition (MOCVD). III–V semiconductor heterostructures find various applications as base material for low-noise and high-frequency transistors, as optoelectronic devices like light-emitting diodes and laser-diodes, or even integrated photonic circuits which belong nowadays to key elements in modern communication technology.

Highest quality two-dimensional electron systems are obtained in GaAs/$Al_xGa_{1-x}As$ heterostructures based on modulation-doping (Dingle et al., 1978). The quality of conductors is usually characterized by the charge carrier mobility μ which relates, without an applied magnetic field, the drift velocity $\boldsymbol{v}_D$ of the free charge carriers to the applied electric field $\boldsymbol{E}$ by $\boldsymbol{v}_D = \mu\, \boldsymbol{E}$. As derived from the Drude model, the mobility is obtained from measuring the electrical conductivity σ via $\sigma = q\, \mu\, n$. The larger the absolute value of the mobility μ, the larger the distance a charge carrier can move without being scattered. Due to the spatial separation of dopants and free charge carriers in modulation-doped heterostructures, the scattering of the charge carriers on the ionized dopants is strongly reduced. At temperatures below 1 K, electron mobilities of more than 3×10^3 $m^2/(Vs) = 3000$ 1/T have been reported in electron systems at such a heterojunction, allowing free mean paths of several 100 μm (Pfeiffer et al., 1989; Umansky et al., 2009). At room temperature such devices are used as **h**igh-**e**lectron **m**obility **t**ransistors (HEMT) in communication technology.

As shown in Fig. 2, for modulation doping, the donors are located in an $Al_xGa_{1-x}As$ layer which has a conduction band bottom lying higher than that of bulk GaAs. The band offset is tunable by the ratio x by which gallium atoms are replaced by aluminum

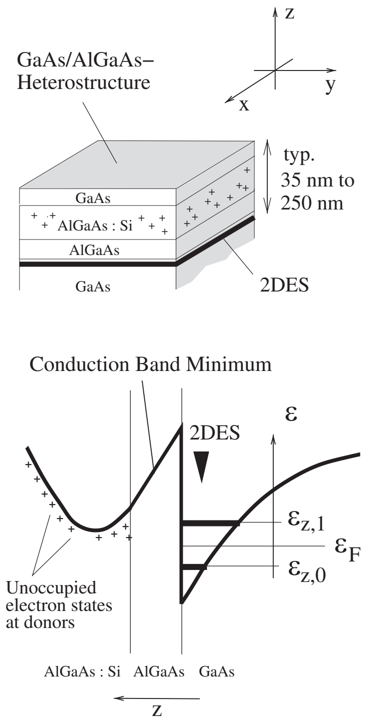

Fig. 2 AlGaAs/GaAs heterostructure with a two-dimensional electron system (2DES) at the heterojunction in GaAs. Below: Sketch of the respective profile of the conduction band edge in *z* direction, and the two lowest subband energies $\varepsilon_{z,0}$ and $\varepsilon_{z,1}$ due to the triangular-shaped confining potential in *z* direction.

atoms on their crystal lattice sites. The electrons separate from their donors and accumulate in the GaAs at the heterojunction, because they are still attracted by the positively charged donor ions. Each electron feels a triangular shaped confining potential which restricts the electron motion to a free motion parallel to the heterojunction plane. If the electron density and the temperature are low enough, then only the lowest subband with energy $\varepsilon_{z,0}$ is occupied and the possible eigenenergies are described by

$$\varepsilon = \left| \hbar \boldsymbol{k}_{\|} \right|^2 / \left(2\, m^*\right) + \varepsilon_{z,0},$$

where $\boldsymbol{k}_{||}$ denotes the wavevector of the charge carrier in the plane of the 2D system. For the two-dimensional charge system with such a parabolic dispersion relation, the density of states $D_{2\mathrm{D}}(\varepsilon)$ is constant,

$$D_{2\mathrm{D}}(\varepsilon) = g_s\, m^* / 2\pi\hbar^2,$$

where the factor $g_s = 2$ takes into account the two possible spin orientations for each plane wave state characterized by the wavevector $\boldsymbol{k}_{||}$.

In 2004 Andre Geim and Konstantin Novoselov (Nobel prize in 2010) introduced a fundamentally new type of two-dimensional charge carrier system—graphene, a single 2D crystal layer of carbon exfoliated from graphite as found in pencils (Novoselov et al., 2004). The type of charge carriers can be tuned electrostatically directly from electrons to holes by a gate electrode. Due to the linear dispersion relation in the band structure, the charge carriers behave as mass-less Dirac fermions. Meanwhile more 2D crystals have been realized, for instance from exfoliating transition metal dichalogenides, and artificially staking such layers leads to so-called van der Waals heterostructures (Ajayan et al., 2016).

Hall effect on two-dimensional charge carrier system—Quantum Hall effect

In Fig. 3, Hall resistance curves versus magnetic flux density are shown as they are measured on two-dimensional electron systems of different quality, embedded in (Al,Ga)As heterostructures as sketched in Fig. 1. At low magnetic fields, the Hall resistance is linearly increasing with the magnetic flux density B_z,

$$|R_{\mathrm{H}}| = |R_{x\,y}| = |\, V_y / I_x \,| = |\, B_z / (\, -e\, n_{\mathrm{s}}) \,|, \tag{1}$$

and allows to determine the respective *sheet* charge carrier density n_{s} of the two-dimensional electron system. At higher magnetic field, the Hall effect on the two-dimensional charge system shows, in certain magnetic field ranges, values which are independent of the magnetic field. The values of these plateaus are perfectly described by

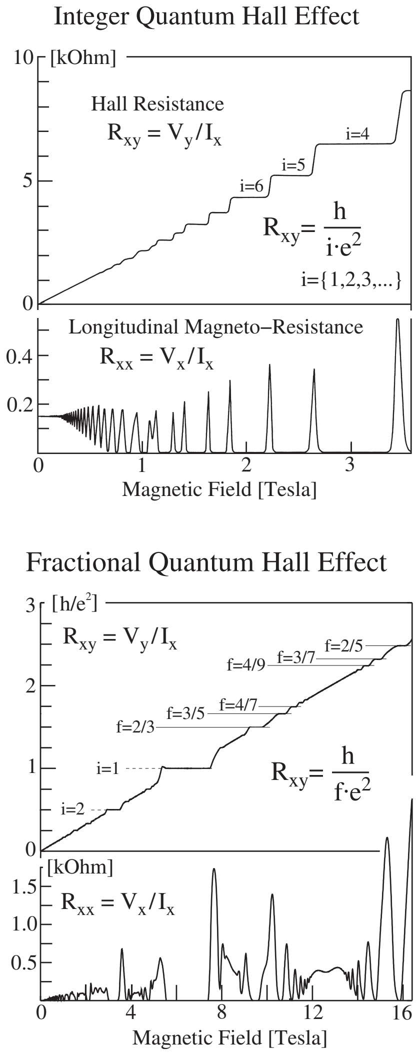

Fig. 3 Quantum Hall effect: Hall resistance R_{xy} and longitudinal resistance R_{xx} measured on a two-dimensional electron system embedded in (Al,Ga)As heterostructures of different quality as a function of the applied magnetic field. In certain magnetic field regions plateaus are observed in R_{xy}, and at the same time R_{xx} vanishes.

$$|R_H| = h/(\nu\, e^2) \tag{2}$$

where ν is equal to an integer number $i = \{1,2,3, \ldots\}$ or a certain fractional number f which seems to follow $f = p/q$ with $p = \{1,2,3, \ldots\}$ and $q = \{3,5,7, \ldots\}$, with exceptions like $f = 5/2$. The same plateaus are found by keeping the magnetic flux density B_z constant and varying the sheet electron concentration n_s. Therefore, varying the ratio n_s/B_z in certain ranges allows to observe Hall resistance plateaus described by Eq. (2).

Such Hall resistance values are expected due to the comparison between Eqs. (1) and (2) only for certain well-defined ratios $n_s/B_z = \nu\ e/h$. The meaning of this ratio can be expressed slightly differently: Taking a certain area A out of a homogeneous two-dimensional electron system enclosing the integer number $N = n_s\, A$ of electrons, the magnetic flux penetrating this area is given by $\Phi = A\, B_z$. The ratio between electron number N and magnetic flux Φ in units of the magnetic flux quantum $\Phi_0 = e/h$ is then

$$\nu = N/(\Phi/\Phi_0), \tag{3}$$

that is, for each electron, ν^{-1} magnetic flux quanta are present.

Whenever in the Hall resistance a plateau is found, the (four-terminal) longitudinal resistance $R_{xx} = V_x/I_x$ vanishes, that is, $R_{xx} = 0$, – the occurrence of the Hall plateau is accompanied by a dissipation less current flowing along the sample. However, this does not mean that there is no dissipation at all: in the plateau regimes, the (two-terminal) resistance $R' = V_x'/I_x$ measured between the current biased contacts (see Fig. 1) is about the Hall resistance $|R_H|$, that is, the electrical power $|R_H|\, I_x^2$ is dissipated. The heat is created in two spot-like regions, one located close to each current biased contact. Along the sample away from the hot spot regions, dissipation is absent, indicated by the absence of a voltage drop along the sample. In the transition regimes between Hall plateaus, dissipation occurs along the whole sample, measurable by $R_{xx} \neq 0$.

The Hall plateau values for $i = 2$ and $i = 4$ are reproducible to the standard uncertainty of 10^{-9}, independent of the sheet charge carrier density, the sample geometry and further properties of the material in which the two-dimensional charge carrier system is embedded. That is why the quantum Hall resistance has been used since 1990 as a resistance standard. Si-MOSFET, but mostly (Al, Ga)As-HEMT devices have been applied for this purpose (Delahaye and Jeckelmann, 2003). In future, graphene-based quantum Hall devices might replace them due to moderate requirement on operation temperature and strength of magnetic field. Graphene shows signature of QHE even at room temperature at very high magnetic field (45 T) (Novoselov et al., 2007). Large areas of graphene are obtained on the surface of silicon carbide by thermal deposition, and seems to be the choice to realize a quantum resistance standard (Tzalenchuk et al., 2010). All these materials differ significantly in their band structure, but all show the QHE with high precision.

To trust in the plateau values obtained on a certain sample for metrological application, the flatness of the Hall plateau, the vanishing of the longitudinal resistance $R_{xx} = 0$, and the invariance of the Hall resistance with changing the temperature are checked (Delahaye and Jeckelmann, 2003). Increasing the quality of the samples, the Hall plateaus get smaller. In consequence, a certain amount of disorder is required to obtain well-defined Hall resistance plateaus and therefore accuracy in the quantized Hall resistance value. For metrological application, the sheet density n_s of the two-dimensional electron system in a GaAs/Al$_x$Ga$_{1-x}$As heterostructure is typically in the range of 3–6 × 10^{15} m^{-2} with a mobility μ of 40–80 T^{-1} and the measurements are done at the temperature $T = 1.5$ K. For high-precision measurements, it is desirable to have the current level as high as possible. However, the current level is limited for the respective sample, since the quantum Hall effect breaks suddenly down with increasing the current beyond of a certain critical current level, denoted as electrically induced breakdown. The typical critical sheet current density I_x/w is in the order of 0.5–1.5 A m^{-1}. For metrology, typically Hall bar samples of several 100 μm width are used. Also a significant increase of the working temperature degrades the Hall plateau, and the plateaus finally disappear.

Theoretical models for the quantum Hall effect

A complete microscopic theory still does not exist which allows to determine the quantum Hall plateau accuracy, flatness and width in real samples. However, the current distribution within the two-dimensional electron system for a robust quantum Hall plateau has been understood. It is commonly accepted that the integer quantum Hall effect can be described within a model of independent charge carriers, whereas for the fractional quantum Hall effect, many-particle correlations due to strong electron-electron interaction are of importance.

Integer quantum Hall effect

Starting at the late 1990s (McCormick et al., 1999; Weitz et al., 2000), spatially resolved measurements of the Hall potential profile with low-temperature scanning probe microscopes on two-dimensional electron systems embedded in GaAs-AlGaAs heterostructure devices have revealed the following microscopic picture of the integer quantum Hall effect (Weis and von Klitzing, 2011).

The single-particle energy spectrum—Landau levels

The magnetic field forces the electrons on cyclotron orbits. Quantum mechanically, the possible eigenenergies cluster in discrete Landau levels described by

$$\varepsilon = \varepsilon_{z,0} + (n + ½)\,\hbar\omega_c + s_z\, g^*\, \mu_B\, B \tag{4}$$

with the Landau level index $n = \{0,1,2,\ldots\}$, and the spin quantum number $s_z = \{-½, ½\}$. The gaps between the Landau levels are either given by the cyclotron energy $\omega_c = \hbar\, eB/m^*$ minus the Zeeman energy $g^*\ \mu_B\ B$, or the Zeeman energy (μ_B denotes the Bohr magneton $\mu_B = e\,\hbar/(2\,m_0)$ and g^* the effective Landé factor). The degeneracy $n_L = e\,B/h$ of each (spin-resolved) Landau level and the cyclotron energy ω_c increase with B. Therefore with increasing magnetic field, the electrons are redistributed to lower Landau levels leading to a sawtooth-like variation of the chemical potential $\mu_{ch}(n_s, B)$ for fixed sheet electron density n_s with increasing magnetic field (see Fig. 4). The ratio between the sheet electron density n_s and Landau level degeneracy n_L is denoted Landau level filling factor ν_L (or shortly filling factor),

$$\nu_L = n_s/n_L \tag{5}$$

Whenever the filling factor ν_L takes an integer value, the chemical potential lies energetically between two Landau levels, and in the homogenous electron system the respective fraction $\nu^{-1} = \{1,1/2,1/3,1/4,\ \ldots.\}$ of a magnetic flux quantum is present for each electron, consistent with relation (3). For integer filling factors, the electron system behaves incompressible, that is, the compressibility κ becomes zero due to the jump in $\mu_{ch}(n_s, B)$ with increasing n_s,

$$\kappa \propto (\partial\mu_{ch}/\partial n_s)^{-1} \rightarrow 0 \tag{6}$$

We will see, that the incompressibility, manifesting in relation (6), is a key to understand not only the IQHE, but also the FQHE.

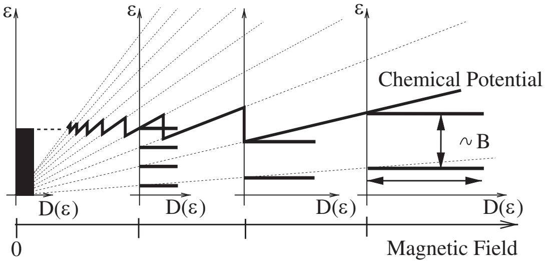

Fig. 4 For an infinite homogeneous electron gas, the single-particle eigenenergy spectrum splits up into Landau levels with applying a strong magnetic field (in this sketch, the spin is neglected). The chemical potential varies in a sawtooth-like manner with increasing magnetic field.

Dissipationless current flow

For an infinite two-dimensional electron system with applied magnetic field in z direction and a homogeneous electric field in y direction, all Landau level states undergo a drift in x direction, so that the local sheet current density j_x in the x direction is given by

$$j_x = \nu_L \, e/h^2 \, E_y. \tag{7}$$

This Hall current flows without dissipation since this drift is a property of the eigenfunctions solving the respective Hamiltonian. To emphasize this, all occupied Landau levels contribute to the Hall conductivity $\sigma_H = \nu_L \, e/h^2$.

In fact, for any smoothly varying electrical field $E_y\,(y)$, the relation (7) remains locally valid (MacDonald et al., 1983). Integrating the sheet current density $j_x(y)$ over a certain width w in y direction, the integral current $I_x = \int_0^w j_x(y)\,\mathrm{d}y$ is given by the voltage drop $V_y = \int_0^w E_y(y)\,\mathrm{d}y$ over this width

$$I_x = \nu_L \, e/h^2 \, V_y, \tag{8}$$

and is therefore independent of the details of the Hall voltage drop along the y direction as long as ν_L is constant where the Hall field E_y is nonzero within the width w. For integer values of the ν_L, that is, whenever the electron system is incompressible, the Hall resistance values for Eq. (2) are obtained.

However, this does not explain Hall resistance plateaus. Here the theoretical models refer to disorder and inhomogeneity being present in real two-dimensional electron systems. Especially the edges of the sample and static potential fluctuations all over the sample lead to variations of the local filling factor within the two-dimensional electron system. Scanning probe experiments on (Al,Ga)As quantum Hall samples have shown (for a review see Weis, 2007) that the evolution of the electrical compressible/incompressible landscape due to these natural inhomogeneities inside the two-dimensional electron system allows for robust quantum Hall plateaus.

Compressible and incompressible regions within a two-dimensional electron system

A natural inhomogeneity, being present even in very clean samples, exists along the edges of the two-dimensional electron system. Within the depletion regions, the sheet electron density changes from zero to its bulk value over a typical distance of a few µm. Within this depletion region, the electrons have to rearrange themselves due to the electrostatic boundary conditions and due to the electrostatic interaction among them (electrostatic screening).

In thermodynamical equilibrium, the electron density profile can be calculated within a Thomas-Fermi approximation by (1) the constraint that the electrochemical potential μ_{elch}, that is, the sum of local chemical potential $\mu_{\mathrm{ch}}(n_s(\boldsymbol{r}))$ plus the electrostatic energy $-e\phi\,(\boldsymbol{r})$, is constant within the whole two-dimensional electron system, and (2) by the Poisson equation which relates the local electrostatic potential $\phi\,(\boldsymbol{r})$ to the local sheet electron density $n_s(\boldsymbol{r})$, taking into account the adequate boundary condition for $\phi\,(\boldsymbol{r})$ which are due to the respective sample. The problem can self-consistently be solved if (3) the chemical potential $\mu_{\mathrm{ch}}(n_s,B)$ of the two-dimensional electron system is known as a function of the sheet electron density n_s. Here the situation without and with high magnetic field differs. This Thomas-Fermi approach is suitable for high magnetic fields where the magnetic length, $l = \sqrt{\,}(\hbar/eB) \approx 25\ \mathrm{nm}/\sqrt{\,}(\mathrm{B}/[\mathrm{T}])$, becomes small (Lier and Gerhardts, 1994).

Without the applied magnetic field, the density of states is constant and therefore the chemical potential increases linearly with n_s, and the electron concentration rises smoothly at the edge towards the bulk (see Fig. 5). In contrast, with an applied high magnetic field, the density of states is discrete, the chemical potential increases in a step-like manner with increasing n_s, and therefore it is energetically favorable that the electron density profile shows regions of varying and of constant electron density. A strip-like structure is found along the edges (Chklovskii et al., 1992; Lier and Gerhardts, 1994), where the strips of constant electron density behave as a locally incompressible electron system whereas the regions of varying electron density are compressible. In compressible regions, occupied and unoccupied electronic states exist at the Fermi level, whereas in incompressible regions the Fermi level lies in an energy gap. They act insulating, that is, they suppress electron scattering between compressible regions. In the incompressible regions, the local Landau level filling factor $\nu_L(\boldsymbol{r})$ takes an integer value.

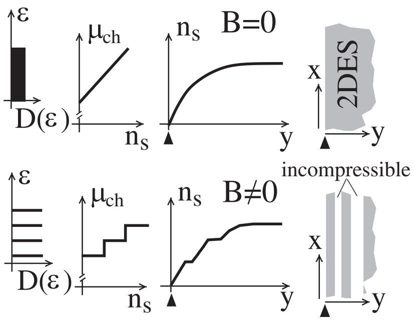

Fig. 5 Formation of compressible and incompressible strips within the depletion region along the edges of the two-dimensional electron system for a strong applied magnetic field.

In simplified terms, the position of an incompressible strip at a certain magnetic field can be identified within the electron density profile $n_s\ (\boldsymbol{r}, B = 0)$ without magnetic field by searching for the local electron density $n_s(\boldsymbol{r})$ for which the incompressibility at that magnetic field is expected. The width of the incompressible strip at that position is larger, (1) the smaller is the gradient in $n_s(\boldsymbol{r}, B = 0)$ at that position, and (2) the larger is the gap energy of the incompressibility. The electron density profile at the edges depends on the electron density in the bulk, and especially on the (electrostatic) boundary conditions at the edges, which are even affected by details of the device fabrication.

The gap energy of the incompressibility (cyclotron energy and Zeeman energy) rises with the magnetic field. Therefore, with increasing magnetic field, the strips shift away from the edges into the bulk as the same incompressibility is obtained for higher magnetic fields at larger electron density. They get broader as the electron density profile gets smoother towards the bulk. The strongest move is found for the respective innermost incompressible strip which merge from all depletion regions to an incompressible bulk at integer values of n_s/n_L (Chklovskii et al., 1992; Lier and Gerhardts, 1994). With further increase of the magnetic field, the next innermost incompressible strip with lower integer-valued filling factor takes the same evolution. This repeats down to filling factor one for the bulk.

The steeper the electron density profile, the smaller the width of the incompressible strip at the edges, that is, the outermost incompressible strips might become too small (below magnetic length) and therefore do not exist. It depends on the details of the sample. The energy gap due to the cyclotron motion is larger than that due to the Zeeman splitting in GaAs, which means that the incompressible strips with odd integer filling factor are narrower than those of even filling factor at the same position in the depletion region. Therefore, it is worth noting that the number of well-expressed compressible/incompressible strips at the respective edge is not strictly linked to the Landau level filling factor in the bulk. However, with increasing magnetic field, a widening innermost incompressible strip will appear in the depletion region before the bulk will become incompressible.

Increasing the magnetic field further, the bulk would switch immediately from the incompressible state to the compressible state. However, due to potential fluctuations within the bulk region of the real two-dimensional electron system, the local electron density $n_s(\boldsymbol{r})$ varies—a landscape of compressible and incompressible regions is formed also there which reshapes with varying the mean sheet electron density n_s or the magnetic field. Around integer values of n_s/n_L, the bulk is mainly incompressible with compressible droplets embedded. The range in magnetic field for which this regime exists depends on the sample quality—the cleaner the sample is, the smaller the magnetic field range. In case of large inhomogeneity, incompressible regions might appear already in the bulk while still an incompressible strip evolves from the edges.

Fig. 6 shows in sketches how the compressible/incompressible landscape within a two-dimensional electron system evolves over the range of a quantum Hall plateau. It turns out (Ahlswede et al., 2002) that even in front of ohmic contacts the electron concentration is slightly reduced (presumable due to the work function difference between GaAs and the metal contacts), so that an incompressible strip might not only exist along the edges of the Hall sample but also in front of contacts. This evolution of the compressible/incompressible landscape inside the two-dimensional electron system governs how the biased current distributes inside the sample.

Current distribution in real samples

With these ingredients, the integer quantum Hall effect in (AlGa)As samples is roughly described by the following qualitative picture which repeats with rising magnetic field for the different quantum Hall plateaus.

With the application of an electrochemical potential difference between the source and drain contact, the electrochemical potential of source is carried by the compressible strips along one edge, the potential of drain by the compressible strips along the opposite edge into the sample (Fig. 6). A Hall voltage is present in the cross section over the Hall bar width. As a consequence, the Landau level bending in the respective cross section of the Hall bar width is affected. In Fig. 7 the Landau level bending with and without the Hall voltage is sketched for different situations along a quantum Hall plateau.

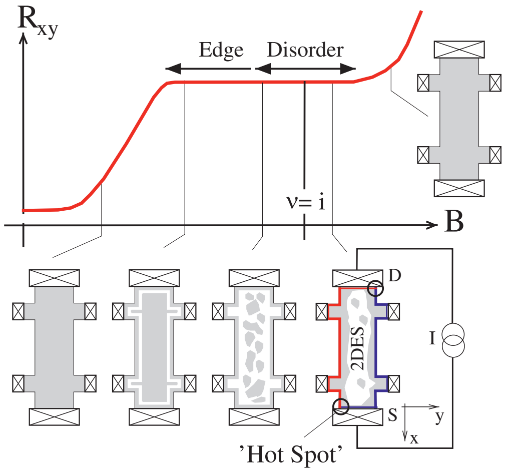

Fig. 6 Schematic evolution of the compressible/incompressible landscape within the two-dimensional electron system over a quantum Hall plateau. On low magnetic field side of a QH plateau, a well-expressed incompressible strip might exist along the edges of the quantum Hall sample, while at the higher magnetic field side the bulk is incompressible with embedded compressible droplets. Taken from Weis J, von Klitzing K (2011) Metrology and microscopic picture of the integer quantum Hall effect. *Philosophical Transactions of the Royal Society A* 369: 3954–3974.

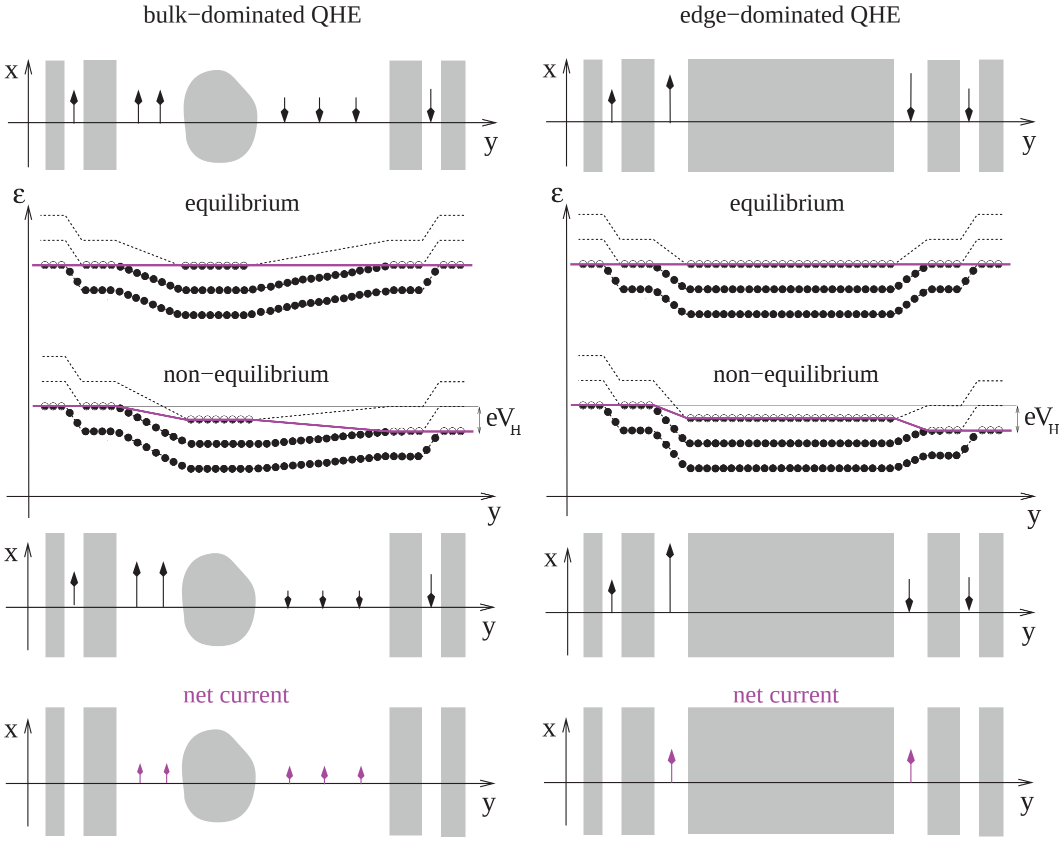

Fig. 7 Bending of Landau levels in a Hall bar cross section in the bulk-dominated (a) and edge-dominated (b) quantum Hall regime without and with Hall voltage. Top and below: Respective current densities in the incompressible regions due to the local electric field, leading net to the distribution of biased current sketched at bottom. Adapted from Weis J, von Klitzing K (2011) Metrology and microscopic picture of the integer quantum Hall effect. *Philosophical Transactions of the Royal Society A* 369: 3954–3974.

In the situation sketched in Fig. 7a, the bulk is mainly incompressible with the local filling factor $\nu_L = i$. Due to the inhomogeneities within the electron density ('disorder'), compressible droplets are embedded. Already in thermal equilibrium, that is, equal electrochemical potential within the 2DES, the electrostatic potential varies owing to these inhomogeneities. Due to relation (7), local current densities encircle the compressible droplets, leading by integration within a cross section over the sample width to zero net current. This is also true for the current densities present owing to the electrostatic potential rises towards the edges:

the current densities on the left and right edges are oriented in opposite directions and compensate for each other. With a Hall voltage, that is, with an electrochemical potential difference between the edges, the compressible/incompressible landscape is affected: compressible droplet might rearrange, but the Hall voltage drops appear still as electrostatic potential drops only in the incompressible regions of $\nu_L = i$. Integrated over the whole sample width, a net current $I_x = (i\, e/h^2)\, V_y$ is obtained. Any variations in the compressible droplet landscape, for instance, by varying the applied magnetic field, affect the local current densities in the incompressible regions; however, they are not visible in the integral current. The relation between the integral current and the Hall voltage is stabilized. The current is driven in this cross section widely spread in the 2DES bulk as a Hall current without dissipation, carried by locally all occupied Landau level states, giving the well-defined Hall conductance. The amount of inhomogeneity of the bulk dominate the range in magnetic field stabilizing the situation, that is why this regime is denoted as bulk-dominated quantum Hall regime.

Towards the lower magnetic field side of the quantum Hall plateau, the compressible/incompressible landscape changes significantly. The bulk of the two-dimensional electron system becomes compressible, and incompressible regions are shifted into the depletion regions at the edges. Well-expressed incompressible strip might still exist along both edges of the Hall bar (Fig. 7b). In thermal equilibrium, current densities are present in the incompressible strips due to the rise in the electrostatic potential at the edges, however, as they are counterpropagating, they compensate for each other within the cross section. However, with a Hall voltage, the electrostatic potential drop inside the incompressible strip on one edge gets steeper, and on the other edge flatter. It means, compared to thermal equilibrium, the current densities are enhanced on one side and reduced on the other side, so that in net the biased non-equilibrium current flows equally distributed in the innermost incompressible strip along both edges of the Hall bar. As long as the Hall voltage drop happens only within these two incompressible strips of same filling factor, the relation $I_x = (i\, e/h^2)\, V_y$ is valid. This is the edge-dominated quantum Hall regime, usually extending the quantum Hall plateau to lower magnetic fields. Important is here, that the respective incompressible strips also exists in front of the metal contacts (Ahlswede et al., 2002), otherwise this edge-dominated quantum Hall regime is suppressed as compressible edge and compressible bulk are locally equilibrated (electrically shorten).

With further lowering of the magnetic field, the incompressible strips move closer to the respective edge, get smaller, and finally are no longer able to withstand a Hall voltage drop. Electrons scatter from the compressible edge into the compressible bulk. Although the quantum Hall plateau regime breaks down, the Hall voltage drop might still strongly be confined to the edges; however, also in the bulk an increasing fraction of the drop is found. Before entering the regime of the next quantum Hall plateau at lower magnetic field, the drop is almost homogeneously distributed over the whole 2DES width (Ahlswede et al., 2001).

Using the self-consistent evolution of the compressible/incompressible landscape in a narrow 2DES cross section, Siddiki and Gerhardts was able to calculate quantitatively a Hall resistance curve with quantum Hall plateaus for a two-dimension electron system which is constricted in the y direction and translation-invariant in the x direction (Siddiki and Gerhardts, 2004).

Role of metal contacts

Metal contacts to the 2DES are needed to bias the 2DES with a current and to probe the electrochemical potential at different positions along the Hall bar. From those, the Hall resistance and longitudinal resistance are determined.

In case of the bulk-dominated quantum Hall regime, the biased current distributes in the connected incompressible bulk. As the current flow is dissipationless, the compressible edge strips along the Hall bar form equipotential lines carrying the potential of the source or drain contact, respectively. It requires the longitudinal conductivity of the compressible strips to carry the respective electrochemical potential. To obtain the quantized Hall resistance value it is important that the Hall voltage drop happens only over incompressible regions of same integer-valued filling factor. If additional well-expressed incompressible strips of different filling factor exists in the depletion regions, the metal contacts have to suppress any Hall voltage drop over these incompressible strips. They have to ensure that the electrochemical potentials of all the compressible strips along the same edge are equilibrated by electrically shortening them. For (Al,Ga)As quantum Hall samples it is known that this depends on how the borderline between 2DES and alloyed metal is oriented relatively to the crystal orientation of the (AlGa)As heterostructure (Dahlem et al., 2010).

In case of the edge-dominated quantum Hall regime, well-expressed incompressible strips exists along the edges while the bulk is compressible. This regime is only measurable when the incompressible strips pass by in front of the metal contacts. It requires a partial depletion of the electron density, that is, an electron density profile to a lower $n_s > 0$ in front of the contacts which is indeed observed for (AlGa)As devices (Ahlswede et al., 2002). Such a depletion can also be mimicked by electrostatic depletion due to a voltage-biased gate electrodes on top of the Hall bar finger towards the metal contact. To observe the expected well-defined Hall resistance value, the Hall voltage has to drop only over the innermost incompressible strip at both edges in a cross section. Again, here the metal contacts can ensure this.

Breakdown

At elevated temperatures, thermal excitations of electrons via the energy gap diminish the incompressibility. It leads to the thermally induced breakdown of the quantum Hall effect, that is, the longitudinal resistance rises and the quantum Hall resistance gets lost. The application of the QHE in metrology requires a high current level to ensure that current and voltages reach a level so that they are measurable with high accuracy. The level is limited by the electrically induced breakdown of the QHE.

In the edge-dominated quantum Hall regime, the width of the incompressible strips on both edges changes with rising Hall voltage (Gerhardts et al., 2013; Panos et al., 2014). This is due to the self-consistent rearrangement of electrons, reacting on the additional voltage. With increasing Hall voltage, an asymmetry in the Hall potential drop—and therefore in the current distribution—arises continuously between the left and right edges of the Hall bar. This results in a dominant incompressible strip with enhanced electric field on one edge. A strong electric field bends the Landau levels, reducing also spatially their distance so that electron tunneling between the Landau levels might become possible (Eaves and Sheard, 1986). The insulating property of the incompressible strip is lost. On the other edge, that is, on the positive Hall voltage side, the possible Hall potential drop is limited by the quantization energy (Landau level or Zeeman energy gap). The width of the incompressible strip shrinks to zero. In consequence, electrons from the bulk may relax into the outer compressible edge by phonon and/or photon emission (Ikushima et al., 2004). As in the edge-dominated quantum Hall regime the 2DES bulk is compressible, its width of the bulk does not matter for the breakdown threshold, that is, the threshold in Hall voltage does not scale with Hall bar width (Haremski et al., 2020).

In the bulk-dominated quantum Hall regime, the Hall voltage drop is widely distributed over the bulk. Rising the Hall voltage leads to a rearrangement of the compressible droplets and affects therefore the incompressible paths along the Hall bar. The additional electrical fields within the incompressible regions scale with the Hall bar width for a given Hall voltage (Haremski et al., 2020). Therefore, wide Hall bars lead to high breakdown thresholds. The bulk-dominated quantum Hall regime is robust for metrological applications.

Localization

Since a certain amount of disorder is required to explain the occurrence of plateaus in the Hall resistance, the quantum Hall effect has been addressed from the beginning as a localization-delocalization phenomena of charge carriers in a random disorder potential (von Klitzing, 1986). The model of an incompressible and compressible landscape within the bulk region as depicted above is applicable in case of a smooth varying disorder potential, and takes electron-electron interaction self-consistently in an electrostatic manner into account. Other common models investigate the universality of the localization/delocalization phenomenon and the possibility of quantum phase transitions in such a quantum Hall system. The system is then discussed in terms of the density of states in energy where each Landau level is broadened in energy due to the static potential fluctuations. It turns out that states in the tails of the broadened Landau levels correspond to localized states, that is, they are not extended beyond a certain typical length under the respective conditions. Extended states exist only in the energetical center of broadened Landau levels. Localized states cannot contribute to Hall and longitudinal conductivity, that is, varying the Fermi level in the range of localized states, these states can be filled or emptied without affecting the transport properties—ingredients for the observation of plateaus in the Hall resistance.

Fractional quantum Hall effect

With increasing magnetic field, electrons finally end in the lowest Landau level. Here the electron-electron interaction becomes dominant leading to many-electron correlations, that is, their motions are not independent of each other. For certain fractional filling factors $\nu_L = \nu$, it has been found that the many-electron quantum state behaves incompressible and the respective charge excitations in the electron system are quasi-particles of fractional charge. In a later theoretical description, the electrons and flux quanta present in the system have been combined to new quasi-particles—so-called composite particles which have either fermionic or bosonic character depending whether the number of flux quanta attached to an electron is even or odd. This has simplified the picture of the fractional quantum Hall effect: Around fractional ν of even denominators, like $\nu = \{1/2, 3/2, 1/4, 3/4, 5/4, \ldots\}$ composite fermions are formed which do not see any effective magnetic field at the respective filling factor ν. The larger the denominator, the more fragile are these composite fermions.

With varying magnetic field, these composite fermions survive and they feel now an effective magnetic field which enforce them to a cyclotron motion. Therefore, within the picture of composite fermions, the series of fractional quantum Hall states which lie symmetrically around $\nu = \frac{1}{2}$ are interpreted as the integer quantum Hall effect of composite fermions consisting of an electron with two flux quanta attached (Stormer, 1999). This symmetry is also visible in the data for the FQHE in Fig. 3 around 12.6 T which corresponds to $\nu = \frac{1}{2}$ in that sample: At $\nu = \frac{1}{2}$, the composite fermion does not see any magnetic flux, i.e., $(\nu_{CF})^{-1} = 0$, whereas at $\nu \neq \frac{1}{2}$, $(\nu_{CF})^{-1} = |\nu^{-1} - 2|$ flux quanta are present for the composite fermion. An integer filling factor $\nu_{CF} = \nu/|1 - 2\nu|$ is reached for the fractional filling factors $\nu = \{1/3, 2/5, 3/7, 4/9, 5/11, \ldots\}$ and $\nu = \{1, 2/3, 3/5, 4/7, 5/9, \ldots\}$. The fractional quantum Hall states $\nu = 2/3$ and $\nu = 2/5$ are therefore the integer quantum Hall states $i_{CF} = 2$ of this composite fermion. This picture gives a hierarchy to certain fractional quantum Hall states been observed.

Meanwhile, fractional states at higher Landau levels have been observed. The observed exotic fractional quantum Hall state $\nu = 5/2$ is interpreted as a pairing of composite fermions into a novel many-particle ground state. Although the experimental findings support the composite fermion picture, the theoretical foundation for this description is still under debate. A further discussion of correlated states at certain fractional filling factors is done by Papic and Balram within this Encyclopedia.

It is common to the fractional quantum Hall states that they are electrically incompressible due to strong electron-electron correlations. There exists an energy gap stabilizing the correlated electron state which appears for a certain fraction of the ratio between the numbers of electrons and magnetic flux quanta sharing a certain area. Scanning probe investigations have recently shown (Gauß, 2019) that the same evolution of Hall potential profiles and therefore current distribution is observed along a quantum Hall plateau as for the IQHE described above. Edge- and bulk-dominated quantum Hall regimes are identified also for the FQHE.

IQHE and FQHE have in common the appearance of an incompressible state for certain electron densities at given magnetic field. As the property $(\partial\mu_{\mathrm{ch}}/\partial n_{\mathrm{s}})^{-1} \to 0$ is valid in both cases, incompressible strips might be present in the depletion region along the edges. These incompressible strips with fractional filling factor evolve similarly to those with integer filling factor (Gauß, 2019): starting from the edges, with rising magnetic field, they shift towards the bulk, get wider and finally merge into an incompressible bulk. The strong electron-electron interaction in these incompressible states leads to correlations in the relative motion of the electrons, the common center-of-mass motion is still given by the group velocity of the single-particle states. The correlated state gets a drift velocity by the local Hall field, and as a well-defined number of occupied Landau level states contribute, the local current density is given by $j_x = \nu_{\mathrm{L}}\, e/h^2\, E_y$. Hall voltage drop only over incompressible region of same fractional valued filling factor leads to the quantized Hall resistance relation (2).

Conclusion

Self-consistent electrostatic screening, especially in the depletion regions at the edges, plays a very important role in the formation of quantum Hall plateaus in two-dimensional electron systems embedded in (Al,Ga)As Hall bar samples.

At the low magnetic field side of quantum Hall plateaus, well-expressed incompressible strips are present offering dissipationless pathes for the biased current along both edges of the Hall bar. With increasing magnetic field, the innermost incompressible strips at the edges shifts and widens until they merge into an incompressible bulk. Due to inhomogeneity of the electron density, compressible droplets are embedded which stabilize this incompressible/compressible landscape for a certain magnetic field range, until at higher magnetic fields the bulk becomes compressible, thus ending the quantum Hall regime. Such evolution has been found by scanning probe experiments both for integer and fractional quantum Hall plateaus.

The quantized Hall resistance is obtained whenever the Hall voltage drops within a Hall bar cross section exclusively over incompressible regions of same well-defined Landau level filling factor. That is why especially the Hall voltage drop over incompressible regions at the edges with lower filling factor have to be suppressed. Here the potential-probing metal contacts play a very important role to equilibrate the compressible strips along the respective edge. Samples for metrological application have to rely on inhomogeneity (=disorder) where the Hall potential drop and the current distribution are widely spread over the 2DES bulk. Here too, the contacts have to suppress any Hall voltage drop over incompressible strips of different filling factors at the edges.

Not only for the formation of a quantum Hall plateau but also for the electrically induced breakdown of the QHE, the electrostatic self-consistent evolution of the incompressible/incompressible landscape plays the key role. In case of the bulk-dominated quantum Hall regime, the threshold level scales with the Hall bar width, whereas in the edge-dominated quantum Hall regime, the threshold is indeed independent of the width.

The quantum Hall effect has been observed on two-dimensional charge carrier systems in materials with more complex band structures—such as graphene. Incompressibility is seen for different range of charge carrier densities and magnetic field than described by Eq. (5) (Novoselov et al., 2005; Zhang et al., 2005). Similar evolution of a compressible/incompressible landscape is expected and has indeed been seen (Panos, 2014) in forming quantum Hall plateaus.

References

Ahlswede E, Weitz P, Weis J, von Klitzing K, and Eberl K (2001) Hall potential profiles in the quantum Hall regime measured by a scanning force microscope. *Physica B* 298: 562–566.

Ahlswede E, Weis J, von Klitzing K, and Eberl K (2002) Hall potential distribution in the quantum Hall regime in the vicinity of a potential probe contact. *Physica E* 12: 165–168.

Ajayan P, Kim P, and Banerjee K (2016) Two-dimensional van der Waals materials. *Physics Today* 69: 38–44.

Chklovskii DB, Shklovskii BI, and Glazman LI (1992) Electrostatics of edge channels. *Physical Review B* 46: 4026.

Dahlem F, Ahlswede E, Weis J, and von Klitzing K (2010) Cryogenic scanning force microscopy of quantum Hall samples: Adiabatic transport originating in anisotropic depletion at contact interfaces. *Physical Review B* 82: 121305.

Davis R (2003) The SI unit of mass. *Metrologia* 40: 299–305.

Delahaye F and Jeckelmann B (2003) Revised technical guidelines for reliable dc measurements of the quantized Hall resistance. *Metrologia* 40: 217–233.

Dingle R, Stormer HL, Gossard AC, and Wiegmann W (1978) Electron mobilities in modulation-doped semiconductor heterojunction superlattices. *Applied Physics Letters* 33: 665–667.

Drude P (1900) Zur Elektronentheorie der Metalle. *Annalen der Physik* 306: 566–613.

Eaves L and Sheard FW (1986) Size-dependent quantised breakdown of the dissipationless quantum Hall effect in narrow channels. *Semiconductor Science and Technology* 1: 346.

Gauß AW (2019) *A Scanning Single-Electron Transistor Array Microscope Probes the Hall Potential Profile in the Fractional Quantum Hall Regime.* PhD Thesis Germany: University of Stuttgart. https://doi.org/10.18419/opus-10422.

Gerhardts RR, Panos K, and Weis J (2013) Current-induced asymmetries of incompressible stripes in narrow quantum Hall systems. *New Journal of Physics* 15: 073034.

Hall EH (1879) On a new action of the magnet on electric currents. *American Journal of Mathematics* 2: 287–292.

Haremski P, Mausser M, Gauß A, von Klitzing K, and Weis J (2020) Electrically induced breakdown of the quantum Hall effect at different Hall bar widths: Visualizing the edge- and bulk-dominated regimes within a quantum Hall plateau. *Physical Review B* 102: 205306.

Ikushima K, Sakuma H, Komiyama S, and Hirakawa K (2004) Imaging of cyclotron emission from edge channels in quantum Hall conductors. *Physical Review Letters* 93: 146804.

Josephson BD (1962) Possible new effects in superconductive tunneling. *Physics Letters* 1: 251.

Laughlin R (1983) Anomalous quantum hall effect: An incompressible quantum fluid with fractionally charged excitations. *Physical Review Letters* 50: 1395–1398.

Lier K and Gerhardts RR (1994) Self-consistent calculations of edge channels in laterally confined two-dimensional electron systems. *Physical Review B* 50: 7757.

MacDonald AH, Rice TM, and Brinkman WF (1983) Hall voltage and current distributions in an ideal two-dimensional system. *Physical Review B* 28: 3648–3650.

McCormick KL, Woodside MT, Huang M, Wu M, McEuen PL, Duruoz C, and Harris JS (1999) Scanned potential microscopy of edge and bulk currents in the quantum Hall regime. *Physical Review B* 59: 4654.

Novoselov KS, Geim AK, Morozov SV, Jiang D, Zhang Y, Dubonos SV, Grigorieva IV, and Firsov AA (2004) Electric field effect in atomically thin carbon films. *Science* 306: 666–669.

Novoselov KS, Geim AK, Morozov SV, Jiang D, Katsnelson MI, Grigorieva IV, Dubonos SV, and Firsov AA (2005) Two-dimensional gas of massless Dirac fermions in graphene. *Nature* 438: 197–200.

Novoselov KS, Jiang Z, Zhang Y, Morozov SV, Stormer HL, Zeitler U, Maan JC, Boebinger GS, Kim P, and Geim AK (2007) Room-temperature quantum Hall effect in graphene. *Science* 315: 1379.

Panos K (2014) *Current Distribution and Hall Potential Landscape within the Quantum Hall Effect in Graphene and towards the Breakdown in a (Al,Ga)As Heterostructure*. PhD Thesis Germany: University of Stuttgart. https://doi.org/10.18419/opus-6851.

Panos K, Gerhardts RR, Weis J, and von Klitzing K (2014) Current distribution and Hall potential landscape towards breakdown of the quantum Hall effect: A scanning force microscopy investigation. *New Journal of Physics* 16: 113071.

Pfeiffer L, West KW, Stormer HL, and Baldwin KW (1989) Electron mobilities exceeding 10^7 cm^2/Vs in modulation-doped GaAs. *Applied Physics Letters* 55: 1888–1890.

Robinson A and Schlamminger S (2016) The watt or Kibble balance: A technique for implementing the new SI definition of the unit of mass. *Metrologia* 53: A46.

Schurr J, Kucera J, Pierz K, and Kibble B (2011) The quantum Hall impedance standard. *Metrologia* 48: 47.

Siddiki A and Gerhardts RR (2004) Incompressible strips in dissipative Hall bars as origin of quantized Hall plateaus. *Physical Review B* 70: 195335.

Stormer HL (1999) Nobel Lecture: The fractional quantum Hall effect. *Reviews of Modern Physics* 71: 875.

Taylor BN and Witt TJ (1989) New international electrical reference standards based on the Josephson and quantum Hall effects. *Metrologia* 26: 47.

Tsui D, Stormer H, and Gossard A (1982) Two-dimensional magnetotransport in the extreme quantum limit. *Physical Review Letters* 48: 1559–1562.

Tzalenchuk A, Lara-Avila S, Kalaboukhov A, Paolillo S, Syvajarvi M, Yakimova R, Kazakova O, Janssen TJBM, Fal'ko V, and Kubatkin S (2010) Towards a quantum resistance standard based on epitaxial graphene. *Nature Nanotechnology* 5: 186–189.

Umansky V, Heiblum M, Levinson Y, Smet J, Nübler J, and Dolev M (2009) MBE growth of ultra-low disorder 2DEG with mobility exceeding 35 x 10^6 cm^2/Vs. *Journal of Crystal Growth* 311: 1658–1661.

von Klitzing K (1986) The quantized hall effect. *Reviews of Modern Physics* 58: 519–531.

von Klitzing K (2019) Essay: Quantum Hall effect and the new international system of units. *Physical Review Letters* 122: 200001.

von Klitzing K, Dorda G, and Pepper M (1980) New method for high-accuracy determination of the fine-structure constant based on quantized Hall resistance. *Physical Review Letters* 45: 494–497.

Weis J (2007) Hall potential profiles in quantum Hall samples measured by a low-temperature scanning force microscope. *International Journal of Modern Physics B* 21: 1297–1306.

Weis J and von Klitzing K (2011) Metrology and microscopic picture of the integer quantum Hall effect. *Philosophical Transactions of the Royal Society A* 369: 3954–3974.

Weitz P, Ahlswede E, Weis J, von Klitzing K, and Eberl K (2000) Hall-potential investigations under quantum Hall conditions using scanning force microscopy. *Physica E* 6: 1.

Zhang Y, Tang Y-W, Stormer HL, and Kim P (2005) Experimental observation of the quantum Hall effect and Berry's phase in graphene. *Nature* 438: 201–204.

The network model and the integer quantum Hall effect

JT Chalker, Theoretical Physics, University of Oxford, Oxford, United Kingdom

© 2024 Elsevier Ltd. All rights reserved.

Introduction 567
Anderson localization and the integer quantum hall effect 568
The network model 570
Generalizations of the network model 572
Conclusion 573
References 573

Abstract

We review the network model for the integer quantum Hall effect. The model provides a simplified description of Anderson localization in this context. It represents non-interacting electrons moving in two dimensions under the combined influence of a strong magnetic field and a smooth disordered potential. In this setting, electron eigenstates form disorder-broadened Landau levels and their character varies with energy across the Landau level. States in both the low-energy and the high-energy tails of the Landau level are localized, with a spatial extent characterized by the localization length. At the center of the Landau level there is a transition between phases with different quantized values of the Hall conductance and the localization length is divergent. The network model captures universal features of this transition.

Key points

- The integer quantum Hall effect is a localization phenomenon.
- Transitions between states with different quantized values of Hall conductance are quantum phase transitions.
- The network model represents these transitions in a simple way.

Introduction

Soon after the discovery of the integer quantum Hall effect (IQHE) (Klitzing et al., 1980) it was realized that Anderson localization plays a central role in understanding what is observed (Aoki and Ando, 1981; Laughlin, 1981). More specifically, within a single-particle description, Anderson localization of electron eigenstates at some energies in a sample provides a way to understand the observation of plateaus in Hall conductance. This in turn implies that Anderson delocalization of eigenstates at other energies is responsible for transitions between different quantized values of Hall conductance as magnetic field strength or electron density are varied.

While quantization of Hall conductance was immediately acknowledged as a very significant discovery, appreciation of its broader importance has grown in dramatic ways since then. Three key developments are the TKNN topological interpretation of quantization (Thouless et al., 1982), the identification of the so-called 10-fold way for symmetry classes in Anderson localization (Altland and Zirnbauer, 1997), and the recognition of IQHE plateau phases as members of the broader class of topological insulators (Hasan and Kane, 2010).

Single-particle models for Anderson localization in the context of the IQHE can be formulated in a variety of ways (Huckestein, 1995). The essential ingredients that must be included are the effects of a strong magnetic field and of scattering by impurities. In addition, since computer simulation is the main tool for determining behavior, it is necessary to define a model in a way that facilitates numerical studies. There are three routes to the required discretization. One is to consider a tight-binding model with magnetic field included via the Peierls substitution, and impurities represented by random site energies. A second is to consider a strong-field limit in which impurity scattering can be restricted to states within a single Landau level. A third route starts from a scattering potential that is a smooth function of position. It leads, as we describe in this article, to the network model (sometimes referred to as the Chalker-Coddington model) (Chalker and Coddington, 1988). The model has the advantage of omitting details of the problem that turn out to be inessential, while retaining what is believed to be essential to capture the features of the quantum Hall plateau transition that are universal within a single-particle treatment.

The remainder of the article is organized as follows. In the section "Anderson localization and the integer quantum hall effect" we discuss the relation between Anderson localization and the IQHE. In the section "The network model" we formulate the network model, and summarize results of numerical studies of its properties. In the section "Generalizations of the network model" we introduce two generalizations of the network model. These represent plateau transitions in systems with symmetries that are different from those of the IQHE and that arise in certain superconductors. Finally, in the section "Conclusion" we summarize this discussion and point out some further related directions.

https://doi.org/10.1016/B978-0-323-90800-9.00080-9

Anderson localization and the integer quantum hall effect

An outline of behavior observed in the integer quantum Hall effect is as follows. The experimental system consists of a two-dimensional electron gas in a strong per-pendicular magnetic field and at low temperature. Electron eigenstates form a series of Landau levels and the most important control parameter is the Landau level filling factor ν. This indicates the number (not in general an integer) of Landau levels occupied by electrons and is given by the ratio of the electron density to the magnetic flux density. The behavior of the electron gas is probed by measurement of the diagonal and off-diagonal components of the conductivity tensor, σ_{xx} and σ_{xy}, with results of the form sketched in Fig. 1.

The Hall conductivity σ_{xy} as a function of ν exhibits a staircase, taking an accurately quantized value ne^2/h (with e the electron charge and h Planck's constant) over a range of filling factors around each integer filling n and rising rapidly from one quantized value to the next for ν mid-way between integer values. The behavior of the dissipative conductivity σ_{xx} is also distinctive: it is small within each Hall plateau and has peaks at the filling factors where the Hall conductance steps between quantized values.

This behavior can be understood on the basis of the picture shown in Fig. 2 for localization properties of single-particle eigenstates as a function of energy. Landau levels are broadened in energy by a disordered potential arising from randomly located donors in the sample, and the nature of eigenstates varies with energy across each Landau level. States in both the low-energy and the high-energy tails of each Landau level are localized with a size characterized by the localization length ξ, which is a function of energy. It is small in the tails of the Landau level but divergent at an energy near its center. In the simplest discussion, electron-electron scattering is represented by an inelastic scattering length ℓ_{in} which increases as temperature is reduced. States with $\xi < \ell_{\text{in}}$ are assumed not to contribute to transport, so that at low temperature only electrons in the small fraction of electrons near the center of each Landau level are mobile.

The form of the density of states is characterized by two energy scales: the width of a Landau level due to disorder, and the cyclotron energy $\hbar\omega_c$, which (omitting consideration of electron spin) is the separation between Landau levels. Standard conditions for the observation of the IQHE are, first, that the magnetic field should be strong enough for the cyclotron energy to exceed the Landau level width, and second, that the temperature should be low enough for the thermal energy to be less than the Landau level width.

Given the localization properties of electron eigenstates we have described, some of the main features in the dependence of the conductivity tensor on filling factor follow naturally. If ν is close to an integer value, the chemical potential lies within a band of localized states. In this case, small variations in ν alter the occupation only of localized states and not of current-carrying ones. The Hall conductivity is therefore independent of ν within this range: it exhibits a plateau. Moreover, under these conditions electron scattering can occur only between localized states within a thermal window around the chemical potential. Such scattering cannot cause dissipation and so σ_{xx} is small. By contrast, if ν is mid-way between two integers, the chemical potential lies near a Landau level

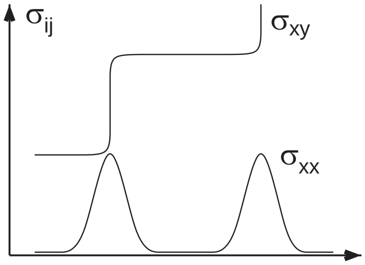

Fig. 1 Schematic illustration of the dependence of the Hall conductivity σ_{xy} and dissipative conductivity σ_{xx} on filling factor ν in an integer quantum Hall system.

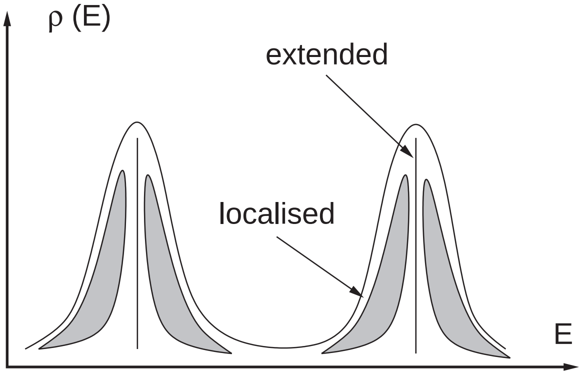

Fig. 2 Properties of single-particle eigenstates in a model for the IQHE. The density of states $\rho(E)$ as a function of energy E forms a series of disorder-broadened Landau levels (two in this illustration). The nature of the eigenstates varies with energy across each Landau level as indicated: states in the low and high-energy tails are Anderson localized, but there is an energy near each Landau level centre where states are extended.

center and electrons in states close to the chemical potential are mobile. In this case, the Hall conductivity varies with ν, as is observed in the risers between Hall plateaus. In addition, scattering of electrons close to the chemical potential can give rise to dissipation, and so σ_{xx} displays a peak.

The discussion so far has been in terms of bulk properties of a system. It is also useful to take a complementary view by considering a system with a boundary, such as the Hall bars used experimentally. Modelling the boundary by a confining potential at the edge of the system, Landau levels rise in energy close to the sample boundary, as shown in Fig. 3. Then each Landau level that is filled in the bulk of the sample can be associated with an edge state at the boundary, where the level passes through the chemical potential (Halperin, 1982). These edge states are chiral, carrying current only in one direction along the boundary—behavior that is already apparent at a classical level from consideration of a skipping trajectory for a charged particle moving under the combined influence of a magnetic field and a confining potential.

At energies for which bulk states are localized, each edge state is isolated from its oppositely directed counterpart at the far side of the sample. Because electrons in isolated edge states cannot be backscattered by disorder, they evade Anderson localization. Instead, each edge state forms a perfectly transmitting channel. Applying this picture to a sample in which a current is flowing, the presence of a Hall voltage implies that there is a chemical potential difference between edge states on opposite edges of the sample. Moreover, the Landauer value for the conductance of a perfectly transmitting channel ensures that each occupied edge state contributes e^2/h to the Hall conductance (Büttiker, 1988). The absence of backscattering means that the chemical potential is constant along the length of each edge. In the geometry of a Hall bar, this means there is no voltage drop in the direction of current flow and hence no dissipation.

In summary, for a finite system with a boundary, the IQHE has an interpretation in terms of edge states. The value of the Hall conductance counts the number of edge states, and this number changes at quantum Hall plateau transitions. At energies for which bulk states are extended, edge states loose their identity because they mix with extended states in the bulk. In the absence of perfectly transmitting channels at the sample boundaries, the Hall conductance of a sample is unquantized and dissipation is not suppressed. Note that even when focusing on edge states in a discussion of the IQHE, the existence of localized bulk states in Landau levels tails is crucial. Specifically, for quantum Hall plateaus to have a finite width in ν, we require the chemical potential to remain between Landau level energies over a range of values of ν. This happens because small variations in ν change the occupation of localized states, so moving the chemical potential over a limited interval.

A framework for discussing transitions between quantum Hall plateau transitions is provided by scaling theory. Such a theory relies on an identification of the appropriate coupling constants that characterize behavior of a system across the transition. It aims to describe how these coupling constants evolve if a system is probed on an increasing length scale ℓ. It is justified if this evolution depends only the values of coupling constants themselves, and not on other properties of the system. For the plateau transition, these coupling constants are taken (on the basis of the field-theoretic formulation of the Anderson localization problem (Levine et al., 1982)) to be the two independent components of the conductivity tensor. A change in scale can be arranged experimentally by varying temperature (and hence ℓ_{in}) or in other ways, and in simulations by varying sample size.

The IQHE scaling flow (Kheml'nitskii, 1983) is shown in Fig. 4. For sufficiently small ℓ, the variation of the conductivity components with ν is smooth, as indicated by the dashed line in Fig. 4. Following the scaling flow, this smooth variation evolves with increasing ℓ into the sharp features of Fig. 1, since all trajectories lead to fixed points at large ℓ, and trajectories that are nearby initially may end at distinct fixed points. The fixed points are of two kinds, both labelled by integer n. Those at $(\sigma_{xx}, \sigma_{xy}) = (0, ne^2/h)$ represent quantum Hall plateau states and are stable in both directions. Those at $(\sigma_{xx}, \sigma_{xy}) = (\sigma_{xx}^*, [n+1/2]e^2/h)$ represent transition points and are unstable to small deviations $\delta\sigma_{xy} = \sigma_{xy} - [n+1/2]e^2/h$. The growth rate

$$\ell \frac{d\delta\sigma_{xy}}{d\ell} = \frac{1}{\overline{\nu}} \delta\sigma_{xy} \tag{1}$$

parameterized by $\overline{\nu}$ is a crucial property of the scaling flow. In particular, within a single-particle description of Anderson localization in quantum Hall systems, it follows from Eq. (1) that the localization length is a function of energy E, diverging at a critical energy E_c near the center of a Landau level as

$$\xi(E) \propto |E - E_c|^{-\overline{\nu}}. \tag{2}$$

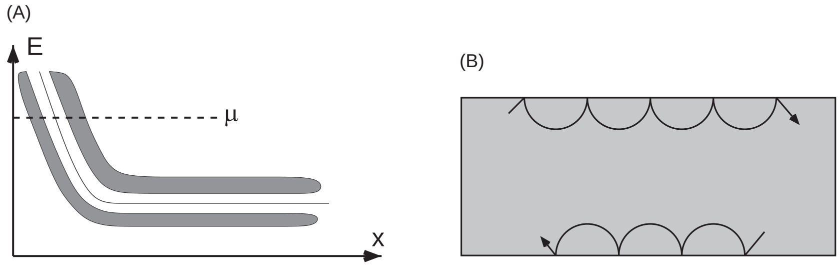

Fig. 3 Edge states in the IQHE. Left: energy E of states in a disorder-broadened Landau level as a function of distance x from a sample boundary. For the indicated value of chemical potential μ, an extended edge state appears at the boundary. Right: classical skipping trajectory and directions of propagation of edge states at opposite boundaries of a sample displaying the IQHE.

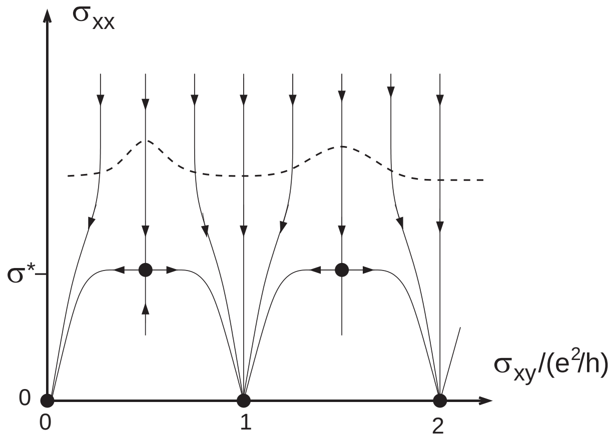

Fig. 4 Scaling flow diagram for the IQHE. Each curve shows the trajectory followed by the coupling constants σ_{xx} and σ_{xy} with increasing ℓ. Different curves represent systems under different conditions (e.g. different ν) and the dashed line indicates how the coupling constants change as a function of ν for small ℓ. See main text for further discussion.

Some of the objectives in modelling the IQHE are to test whether the scaling flow diagram shown in Fig. 4 is correct and to determine the value of $\overline{\nu}$. The unstable fixed points of interest lie at strong coupling (simulations suggest $\sigma^* \approx 0.5e^2/h$), presenting a challenge for analytical calculations, and so much of the information available is from numerical studies. The network model provides a starting point for these studies and potentially for analytical treatments. As we discuss in the section "The network model", it also makes explicit the interplay between the idea of edges states and the formulation of the localization problem.

The network model

The network model gives a simplified representation of the Anderson localization problem for an IQHE system in which the potential due to disorder is smooth. More precisely, it is appropriate in the limit in which the characteristic length scale λ for fluctuations in the random potential energy representing impurities is much larger than the magnetic length ℓ_B, related to the magnetic flux density B by $\ell_B \equiv \sqrt{\hbar/eB}$. The ratio λ/ℓ_B is in fact the only dimensionless parameter that can be varied over a wide range without leaving the IQHE regime, since the other candidate, the ratio of the energy width of Landau levels to the cyclotron energy, is required to be small in order that Landau levels do not overlap in energy. We expect that critical behavior at the IQHE plateau transition is independent of the length ratio, so that the choice $\ell_B \ll \lambda$ is just one of convenience.

To study this localization problem we must find eigenstates of the Hamiltonian $H = H_0 + V(\mathbf{r})$, where H_0 is the usual kinetic energy for a charged particle moving in two dimensions with uniform magnetic flux density B, and V(r) is a random function of position r. If $V(\mathrm{r})$ is smooth, it is natural to start from a Taylor expansion of the potential, with the aim of finding local solutions to the Schrödinger equation that can subsequently be stitched together to form eigenstates in a large system. The network model is a representation of this matching process.

As a preliminary, it is useful to consider an equivalent classical problem in which a charged particle with cyclotron radius $r_c \ll \lambda$ moves in the same potential landscape. Its trajectory can be decomposed into a fast component, consisting of cyclotron orbits around a guiding center, and a slow component, consisting of drift of this guiding center along a contour of the potential. Correspondingly, the total energy is a sum of a kinetic contribution from the cyclotron motion and a potential contribution fixed by the drift contour. These two energies are separately conserved in a smooth potential, because in the smooth limit they are adiabatic invariants.

In the quantum-mechanical treatment, quantization of the fast component of motion yields a sequence of Landau levels, and states at different energies within a Landau level are associated with different contours of the potential. In this way, an eigenstate from the n th Landau level at energy $E = (n + 1/2)\hbar\omega_c + V$ has its probability density confined to a strip around the contour of the potential on which $V(\mathrm{r}) = V$, with the strip width set by the cyclotron radius $R_c = \sqrt{2n+1}\ell_B$. This state carries probability current along the contour, mirroring the classical guiding center drift. Current conservation ensures that this probability current (integrated across the width of the strip) is independent of position along the length of any segment of the contour that is well separated from other segments of the same potential contour. On the other hand, near a saddlepoint in the potential where two segments come close together on the scale of R_c, quantum tunnelling is possible between them.

To formulate a model based on these ingredients, we divide the contour into individual segments that meet near saddlepoints, as illustrated in Fig. 5. These segments form links or edges of a graph that has saddlepoints as its nodes or vertices. The graph is a directed one, since each link has a unique direction for current flow, and it is generically fourfold coordinated, with two ingoing and two outgoing links at each node, since this is the description of a generic potential saddlepoint.

The features of the wavefunction that are relevant for localization are all contained in a set of complex scalar current amplitudes z_i, defined on the links i of the network. The value of $|z_i|^2$ gives the probability current carried by this link, and the phase of z_i is chosen equal to that of the wavefunction at a convenient reference point on the corresponding segment of contour. Other details of the state (such as the dependence of the wavefunction on the transverse coordinate) are unimportant in our context.

Amplitudes on links that meet at a node are related by a scattering matrix S, which is constrained by current conservation to be unitary. Using the labelling given in Fig. 5, we can write

$$\begin{pmatrix} z_3 \\ z_4 \end{pmatrix} = \begin{pmatrix} e^{i\varphi_3} & \\ & e^{i\varphi_4} \end{pmatrix} \begin{pmatrix} \cos\alpha & \sin\alpha \\ -\sin\alpha & \cos\alpha \end{pmatrix} \begin{pmatrix} e^{i\varphi_1} & \\ & e^{i\varphi_2} \end{pmatrix} \begin{pmatrix} z_1 \\ z_2 \end{pmatrix}. \tag{3}$$

Here α, lying in the range $0 \leq \alpha \leq \pi/2$, is the key parameter, since (referring to Fig. 5) the probabilities for a particle incident on the node to turn either left or right are respectively $p = \sin^2\alpha$ and $1 - p = \cos^2\alpha$. Moreover, (again referring to Fig. 5) α is a monotonically increasing function of the energy V of the contour under consideration, since if V lies far below the energy of the saddlepoint, $p \to 0$, while if V lies far above this energy, $p \to 1$. At the saddlepoint, symmetry implies that $\alpha = \pi/4$ and $p = 1/2$.

The parameters φ_1, φ_2, φ_3 and φ_4 represent phases accumulated by electrons as they propagate between saddlepoints of the potential. Individually these phases are dependent on the choice of gauge, but the net phase accumulated around the boundary of any plaquette of the graph is gauge-invariant and equal to $2\pi(\Phi/\Phi_0)$, where Φ is the magnetic flux passing through this plaquette and Φ_0 is the flux quantum. Since $\Phi/\Phi_0 \sim (\lambda/\ell_B)^2$ is much larger than one in a smooth potential and varies with the area of the plaquette, it is natural to take the phases to be independent random variables uniformly distributed between zero and 2π. It remains to specify the the graph made up from these links and nodes. This is determined by the form of the potential energy $V(\mathrm{r})$ and an obvious choice would be a random geometry, following an underlying continuum percolation problem. It is more convenient, however, to consider a checkerboard potential that has maximum and minima regularly arranged on the plaquettes of a square lattice, with only a small additional random component. Then the graph likewise forms a square lattice, and we can take the value of the scattering parameter α to be the same at every node, so that randomness appears exclusively in the values of the phases φ_i. We expect from general notions of universality at a critical point that these simplifications will be unimportant as far as critical behavior of the IQHE plateau transition is concerned. With this choice, as illustrated in Fig. 6, directed links circulate in opposite senses around alternate plaquettes of the lattice: (say) clockwise around minima in the potential and anticlockwise around maxima.

We can now discuss how the network model gives a representation of quantum states for a system consisting of many links and nodes. In essence, we want to choose amplitudes z_i on each link i so that the scattering relations of Eq. (3) are satisfied at every node. There are differences in the logic required according to whether we are treating an eigenstate of a closed system or a stationary scattering state of an open system.

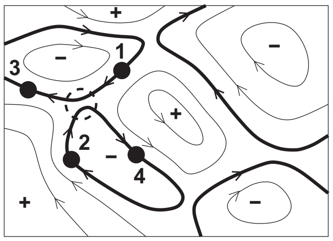

Fig. 5 Contours of a disordered potential $V(\mathrm{r})$. Local maxima and minima are labelled + and −. Arrows indicate direction of drift of cyclotron guiding centers in classical motion, and of current carried in quantum eigenstates. Points on four contour segments that meet at a saddlepoint are labelled 1, 2, 3 and 4 as in Eq. (3). The saddlepoint is marked with a dashed circle.

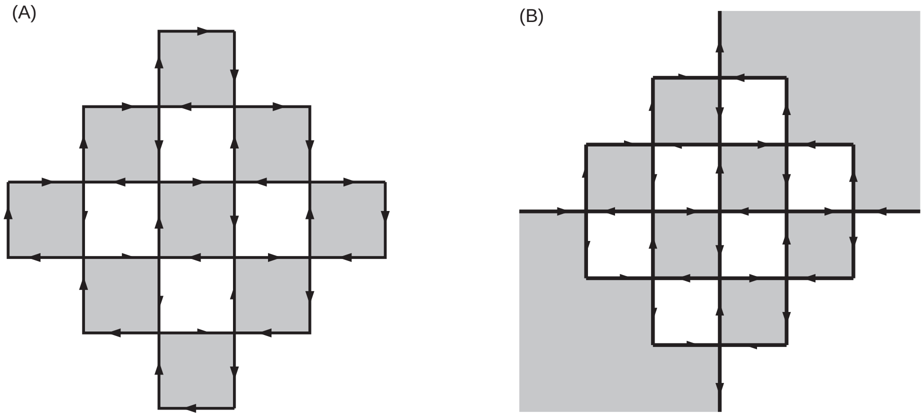

Fig. 6 Choice of square lattice graph for the network model, showing circulation in opposite senses around adjacent plaquettes of the lattice, which are respectively shaded and unshaded to indicate regions of low and high potential $V(\mathrm{r})$. Left: with closed boundary conditions. Right: with open boundary conditions.

For a closed system, the right-hand side of Eq. (3) at each node defines a 2×2 block of a unitary matrix $\mathcal{U}$. This matrix is of size $\mathcal{N} \times \mathcal{N}$, and acts on an $\mathcal{N}$-component vector $\mathcal{Z}$ that has entries made up of the amplitudes z_i on all incoming links. The vector $\mathcal{U}\mathcal{Z}$ consists of the amplitudes on outgoing links that are compatible with these incoming amplitudes. Moreover, each link that is outgoing from a given node is also incoming at another node, and so the condition for a stationary state is that $\mathcal{U}\mathcal{Z} = \mathcal{Z}$. A closed finite system has a discrete spectrum, and at an energy not in the spectrum, there is no stationary state and so none of the eigenvalues of $\mathcal{U}$ are unity. Adjusting energy to locate eigenstates will change the positions of potential contours and hence the values of φ_i. We can represent this in a simple way by taking $\varphi_i \to \varphi_i + \phi$ with ϕ a function of energy. Then $\mathcal{U} \to e^{i\phi}\mathcal{U}$ and an eigenvector of $\mathcal{U}$ represents a stationary state at the energy for which the corresponding eigenvalue of $e^{i\phi}\mathcal{U}$ is unity. Note that although the scattering parameter α also varies with energy, it does so much more slowly by a factor $(\lambda/\ell_{\mathrm{B}})^2$ than the phases φ_i, and it is therefore appropriate to regard it simply as a parameter in $\mathcal{U}$.

In an open system, links can be divided into three groups: links that are internal; links that incoming from outside the system; and links that are outgoing. For example, in Fig. 6B there are two incoming and two outgoing links. The amplitudes on incoming links determine other all amplitudes, on both internal and outgoing links. These internal and outgoing amplitudes are the unique solution to the set of equations obtained by applying Eq. (3) at every node.

Edge states arise naturally within the network model when we consider the dependence of the system on the value of α. As discussed above, in the low energy tail of the Landau level $\alpha \to 0$, and in the high-energy tail $\alpha \to \pi/2$. In the first limit, the network model decomposes into a set of disconnected loops around minima in the potential. In the second limit there is a similar decomposition, but with loops around maxima in the potential and with the addition of an edge state at a sample boundary, as illustrated in Fig. 7. This evolution of geometry with α is precisely what is required to capture the edge state interpretation of the IQHE, introduced in the section "Anderson localization and the integer quantum hall effect".

Our knowledge of behavior for intermediate values of α comes mainly from numerical calculations. These indicate that stationary states are indeed localized away from the critical point at the Landau level centre, where $\alpha = \alpha_c \equiv \pi/4$. The localization length ξ diverges as $\xi \sim |\alpha - \alpha_c|^{-\bar{\nu}}$ on approaching the critical point (Chalker and Coddington, 1988), while states at the critical point $\alpha = \alpha_c$ have a multifractal distribution of amplitudes z_i (Evers et al., 2008; Klesse and Metzler, 1995). Estimates of the value of the localization length exponent have improved in precision, from the initial result $\bar{\nu} = 2.5 \pm 0.5$ (Chalker and Coddington, 1988) to more recent studies yielding $\bar{\nu} = 2.62 \pm 0.06$ (Obuse et al., 2012; Slevin and Ohtsuki, 2009).

Generalizations of the network model

An obvious generalization of the network model described in the section "The network model" is to a version in which each link carries a number N of chiral channels with $N > 1$, so that the amplitudes z_k become N-component spinors. Then the random phase factors $e^{i\varphi_k}$ appearing in Eq. (3) should be replaced with random $N \times N$ unitary matrices V_k. Without any restrictions, this extended model exhibits transitions at N distinct values of α in the range $0 < \alpha < \pi/2$, each having the same critical behavior as in the model

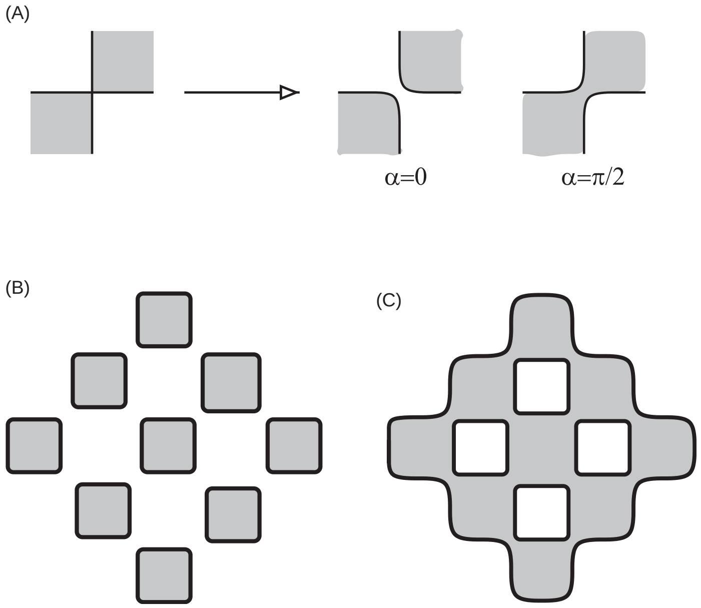

Fig. 7 Limiting behavior in the low and high energy tails of a Landau level. Top: scattering at a node, for $\alpha = 0$ (low energy) and $\alpha = \pi/2$ (high energy). Bottom: network model as in Fig. 6A for $\alpha = 0$ (left) and $\alpha = \pi/2$ (right), showing appearance of edge state in second case.

with $N = 1$. At every transition, the number of edge states changes by one, as expected from the scaling flow diagram of Fig. 4 (Lee and Chalker, 1994).

Versions of the model with different critical behavior may arise if constraints are imposed on the choice of the unitary scattering matrices V_k on links. These constraints appear in treatments of quasiparticle scattering in gapless superconductors, starting from the Bogoliubov de Gennes equations, and fall within an overall classification scheme known as the 10-fold way (Altland and Zirnbauer, 1997). The specific possibilities of interest are termed class C and class D. In this physical situation, charge transport is short-circuited by the superfluid condensate and so quasiparticle properties must be probed via heat transport, or spin transport in systems for which spin is conserved.

Class C arises for superconductors in which time reversal symmetry is broken for orbital motion but spin rotation symmetry is preserved. To describe this situation, N is required to be even and V_k are SP(N) matrices, with $N = 2$ and $\mathrm{Sp}(2) \sim \mathrm{SU}(2)$ as the simplest version (Kagalovsky et al., 1999). A notable feature in this case is that many disorder-averaged properties of this version of the quantum Hall plateau transition can be computed exactly via a mapping to models of classical percolation (Gruzberg et al., 1999).

Class D represents superconductors with neither time reversal nor spin-rotation symmetry. In this case the V_k are orthogonal matrices, reducing in the simplest version to signs ± 1 for $N = 1$. For models of this type, depending on details of the disorder, both localized and metallic phases are possible, as well as a distinct version of the quantum Hall plateau transition (Chalker et al., 2001).

Like the original model, these generalizations all capture transitions between localized phases that are topological in the sense that they are distinguished by the number of edge states they support.

Conclusion

In summary, we have described how the concept of Anderson localization is central to understanding the existence of the integer quantum Hall effect and the nature of transitions between quantum Hall plateau phases with different values of Hall conductance. For a sample with boundaries, the idea of edge states is also key in our description of the quantization of the Hall conductance. The network model uses the notation of edge states for internal regions of a sample as a way of formulating the localization problem in the language of scattering theory.

The discussion leading to the network model, as presented in the section "The network model", can be supported by more detailed treatments of edge states (Halperin, 1982) and of scattering in a potential with a quadratic saddlepoint (Fertig and Halperin, 1987). In addition, for a smooth potential that has finite-range correlations in place of the checkerboard form discussed so far, the potential contours are cluster boundaries in a continuum percolation problem (Trugman, 1983). This raises a question of what the interplay is between such classical critical behavior and the IQHE plateau transition, and the answer depends on the regime. For such a potential at any fixed energy away from the Landau level center, behavior in the limit $\lambda/\ell_{\mathrm{B}} \to \infty$ is governed by the classical description, because in this case the probability p of tunnelling takes the value either 0 or 1 at every node. On the other hand, for any large fixed value of λ/ℓ_B we expect crossover of critical behavior from classical, far from the transition, to quantum, close to the transition, with quantum critical behavior captured by the network model.

We have limited this article to consideration of the single-particle problem, with the consequences of electron-electron interactions summarized in terms of an inelastic scattering length, ℓ_{in}. For a more complete view of the quantum Hall plateau transition, one should regard it as a quantum critical point, with interactions and disorder treated on an equal footing at the outset: see for example (Sondhi et al., 1997).

While results for the critical behavior of network model have so far been derived mainly from numerical simulations, it is natural to hope that it can also be a starting point for an analytical treatment of the IQHE plateau transition. One avenue is provided by a mapping from the model to a form of quantum spin chain, in which disorder in a two-dimensional single-particle problem is traded for many-body interactions in a system in one space dimension (Bondesan et al., 2017). See (Zirnbauer, 2021) for a discussion of difficulties and recent progress.

References

Altland A and Zirnbauer MR (1997) Nonstandard symmetry classes in mesoscopic normalsuperconducting hybrid structures. *Physical Review B* 55: 1142–1161.

Aoki H and Ando T (1981) Effect of localization on the hall conductivity in the two-dimensional system in strong magnetic fields. *Solid State Communications* 38(11): 1079–1082.

Bondesan R, Wieczorek D, and Zirnbauer MR (2017) Gaussian free fields at the integer quantum hall plateau transition. *Nuclear Physics B* 918: 52–90.

Büttiker M (1988) Absence of backscattering in the quantum hall effect in multiprobe conductors. *Physical Review B* 38: 9375–9389.

Chalker JT and Coddington PD (1988) Percolation, quantum tunnelling and the integer hall effect. *Journal of Physics C: Solid State Physics* 21(14): 2665–2679.

Chalker JT, Read N, Kagalovsky V, Horovitz B, Avishai Y, and Ludwig AWW (2001) Thermal metal in network models of a disordered two-dimensional superconductor. *Physical Review B* 65: 012506.

Evers F, Mildenberger A, and Mirlin AD (2008) Multifractality at the quantum hall transition: Beyond the parabolic paradigm. *Physical Review Letters* 101: 116803.

Fertig HA and Halperin BI (1987) Transmission coefficient of an electron through a saddle-point potential in a magnetic field. *Physical Review B* 36: 7969–7976.

Gruzberg IA, Ludwig AWW, and Read N (1999) Exact exponents for the spin quantum hall transition. *Physical Review Letters* 82: 4524–4527.

Halperin BI (1982) Quantized hall conductance, currentcarrying edge states, and the existence of extended states in a two-dimensional disordered potential. *Physical Review B* 25: 2185–2190.

Hasan MZ and Kane CL (2010) Colloquium: Topological insulators. *Reviews of Modern Physics* 82: 3045–3067.

Huckestein B (1995) Scaling theory of the integer quantum hall effect. *Reviews of Modern Physics* 67: 357–396.

Kagalovsky V, Horovitz B, Avishai Y, and Chalker JT (1999) Quantum hall plateau transitions in disordered superconductors. *Physical Review Letters* 82: 3516–3519.

Kheml'nitskii DE (1983) Quantization of hall conductivity. *JETP Letters* 38: 552–556.

Klesse R and Metzler M (1995) Universal multifractality in quantum hall systems with long-range disorder potential. *Europhysics Letters (EPL)* 32(3): 229–234.

Klitzing KV, Dorda G, and Pepper M (1980) New method for high-accuracy determination of the fine-structure constant based on quantized hall resistance. *Physical Review Letters* 45: 494–497.

Laughlin RB (1981) Quantized hall conductivity in two dimensions. *Physical Review B* 23: 5632–5633.

Lee DKK and Chalker JT (1994) Unified model for two localization problems: Electron states in spin-degenerate landau levels and in a random magnetic field. *Physical Review Letters* 72: 1510–1513.

Levine H, Libby SB, and Pruisken AMM (1982) Electron delocalization by a magnetic field in two dimensions. *Physical Review Letters* 51: 1915–1918.

Obuse H, Gruzberg IA, and Evers F (2012) Finite-size effects and irrelevant corrections to scaling near the integer quantum hall transition. *Physical Review Letters* 109: 206804.

Slevin K and Ohtsuki T (2009) Critical exponent for the quantum hall transition. *Physical Review B* 80: 041304.

Sondhi SL, Girvin SM, Carini JP, and Shahar D (1997) Continuous quantum phase transitions. *Reviews of Modern Physics* 69: 315–333.

Thouless DJ, Kohmoto M, Nightingale MP, and den Nijs M (1982) Quantized hall conductance in a twodimensional periodic potential. *Physical Review Letters* 49: 405–408.

Trugman SA (1983) Localization, percolation, and the quantum hall effect. *Physical Review B* 27: 7539–7546.

Zirnbauer MR (2021) Marginal cft perturbations at the integer quantum hall transition. *Annals of Physics* 431: 168559.

Photonic quantum Hall effects

Daniel Leykam[a] **and Daria Smirnova**[b,*], [a]Centre for Quantum Technologies, National University of Singapore, Singapore, Singapore;
[b]Nonlinear Physics Centre, Research School of Physics, Australian National University, Canberra, ACT, Australia

© 2024 Elsevier Ltd. All rights reserved.

Introduction 575
Overview 576
Historical background 576
Pre-quantum Hall era (1938–1980) 576
Quantum Hall era (1980–2011) 576
Topological photonics era (2011–present) 577
Theoretical and experimental approaches 577
Schrödinger formalism for electromagnetism 578
Routes to topological bands 578
Key issues 580
Are photonic quantum Hall effects genuinely robust? 580
Losses and non-Hermitian topological phases 580
Symmetry-breaking perturbations 580
Optical nonlinearities 581
Potential device applications 581
Topological waveguides and cavities 581
Topological lasers 582
Making photonic quantum Hall effects quantum 583
Theoretical proposals 583
Experiments 583
Conclusion 584
References 585

Abstract

This article reviews the development of photonic analogues of quantum Hall effects, which have given rise to broad interest in topological phenomena in photonic systems over the past decade. We cover early investigations of geometric phases, analogies between electronic systems and the spectra of periodic photonic media including photonic crystals, efforts to generalize topological band theory to open, dissipative, and nonlinear wave systems, pursuit of useful device applications, and ongoing studies of photonic Hall effects in classical nonlinear optics and the quantum regime of strong photon-photon interactions.

Key points

- Review theoretical and experimental work on topological phases of light
- Emphasize similarities and differences compared to electronic quantum Hall effects
- Discuss possible device applications of photonic quantum Hall effects, including robust waveguides and lasers
- Outline new developments in the study of classical and quantum photonic topological systems

Introduction

The quantum Hall (QH) phase discovered in 1980, which arises in two-dimensional electron gases under a strong applied external out-of-plane magnetic field, represents the first example of a topological insulating phase of matter (von Klitzing et al., 2020). Such materials are distinguished by bulk band gaps in their band structures with gapless chiral edge states which propagate unidirectionally along the boundaries with a built-in topological immunity to backscattering from disorder.

The use of topological concepts to explain robust physical observables originated with the seminal works of Thouless et al. (Thouless et al., 1982; Kohmoto, 1985) connecting the experimentally observed quantized Hall conductance with a topological invariant, namely, the Chern number, defined in the momentum space. Studies of related topological insulating materials have attracted enormous interest from the mid 2000s until the present day.

---

[*] Corresponding author: e-mail address: daria.smirnova@anu.edu.au

https://doi.org/10.1016/B978-0-323-90800-9.00125-6

Interestingly, topological phases are not limited to fermionic systems and can be translated to classical wave phenomena. Unusual manifestations inherent to topologically nontrivial states, including the ability of edge modes to overcome structural imperfections without back-reflection, drive general interest in topological and quantum Hall effects of classical waves, especially within photonics and optical communications (Ozawa et al., 2019; Smirnova et al., 2020).

Topological photonics has recently emerged as a novel approach to robust waveguiding and routing of light. It exploits engineered photonic structures (Lu et al., 2016) with properties analogous to electronic topological insulators (Hasan and Kane, 2010), which are insulating in their bulk but exhibit conducting states at their surfaces.

While discussions of photonic topological phases are usually framed as being inspired by and analogous to more widely-known electronic topological phases, closer inspection of the history of electronic and photonic topological effects reveals they are in fact closely intertwined. For example, the explanation of the quantum Hall effect in terms of the Chern number was quickly found to be related to geometric phases anticipated decades earlier in optics.

Here we will attempt to present a complete history of the study of photonic quantum Hall effects from its surprisingly early origins up to ongoing research. To keep this Chapter concise we will focus on two-dimensional photonic quantum Hall and spin-Hall effects, mentioning related topological phenomena (e.g. one-dimensional edge states, higher-order topological phases) only in passing and directing the interested reader to relevant in-depth reviews.

Overview

Historical background

The study of photonic quantum Hall effects can be loosely divided into three eras:

1. A pre-quantum Hall era of foundational theoretical and experimental works on optical beam and polarization shifts, now understood in terms of geometric phases.
2. A period of growing interest in analogies between condensed matter physics and photonics, culminating in the first observation of topological photonic edge states at microwave frequencies.
3. The topological photonics era, sparked by the crucial breakthrough that symmetry protection could circumvent the need for magneto-optic materials, opening up the exploration of topological phenomena to a wider variety of photonic systems.

Pre-quantum Hall era (1938–1980)

The Chern number underlying the quantum Hall effect is closely related to the parallel transport properties of quantum states, which form rays in Hilbert space. Already in 1938 Rytov found that classical rays of light undergo a polarization rotation under non-planar propagation (Rytov, 1938), shown in Fig. 1 for the case of light propagation in a twisted optical fiber. The polarization rotation is determined purely by the area enclosed by the trajectory, being an example of a geometric phase (Vladimirskii, 1941; Pancharatnam, 1956). Another foundational discovery was the Imbert-Fedorov shifts of reflected light beams (Fedorov, 1955; Imbert, 1972), which are now recognized as an example of spin Hall effects of light (Bliokh and Aiello, 2013).

Quantum Hall era (1980–2011)

Shortly after Thouless and collaborators explained the quantum Hall effect in terms of a topological invariant (Thouless et al., 1982), Simon (1983) showed how the invariant was related to the quantum geometric phase studied by Berry (Berry, 1984). While the first experimental observation of Berry's geometric phase as polarization rotation in a twisted optical fiber loop (Tomita and Chiao, 1986) argued it was a genuinely quantum mechanical effect that survives in the classical limit (Chiao and Wu, 1986), Haldane (1986) emphasized that this and earlier polarization rotation experiments by Ross (1984) could be understood purely classically using differential geometry. Nevertheless, these geometric phase experiments and theoretical proposals for photonic

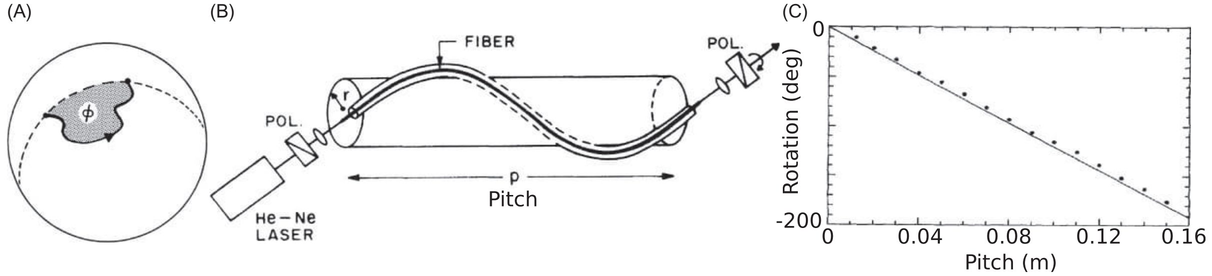

Fig. 1 Geometric phase in twisted optical fibers. (A) The geometric polarization rotation is determined by the solid angle ϕ subtended by the fiber trajectory. (B) Experimental setup for measuring the geometric polarization rotation. (C) Polarization rotation induced by a single twist as a function of its pitch. Points are experimental measurements and the solid line is the prediction from theory. (A) Modified from Haldane FDM (1986) Path dependence of the geometric rotation of polarization in optical fibers. *Optics Letters* 11(11): 730–732. (B) Modified from Tomita A and Chiao RY (1986) Observation of Berry's topological phase by use of an optical fiber. *Physical Review Letters* 57: 937–940. (C) Modified from Ross JN (1984) The rotation of the polarization in low birefringence monomode optical fibres due to geometric effects. *Optical and Quantum Electronics* 16(5): 455–461.

crystals inspired by electronic band gaps (Yablonovitch, 1987; John, 1987) demonstrate the increasing cross-fertilization of ideas between quantum condensed matter physics and optics.

Haldane (1988) presented a condensed matter lattice model exhibiting a quantum Hall effect in the absence of a magnetic field, demonstrating how time reversal symmetry-breaking, not magnetic flux, underlies the quantum Hall effect. While the broad importance of this finding was not widely appreciated at the time (the article attracted only a few dozen citations over the next decade), Haldane's model formed the basis for the surge in interest in topological materials in the 2000s (Hasan and Kane, 2010).

The 1990s saw continued interest in geometric phase effects, including their influence on the semiclassical dynamics of wavepackets in periodic potentials studied by Niu – a former PhD student of Thouless – and his collaborators (Chang and Niu, 1995; Xiao et al., 2010). The semiclassical formalism showed how weak intrinsic Hall and spin Hall effects could be strongly enhanced in certain periodic potentials, inspiring further studies of spin Hall effects of electrons (Murakami et al., 2003; Kato et al., 2004) and photons (Onoda et al., 2004, 2006; Bliokh and Bliokh, 2004a, 2004b; Kavokin et al., 2005; Leyder et al., 2007).

Kane and Mele (2005a) showed that strong spin-orbit coupling may imitate the effect of a magnetic field in time-reversal invariant electronic systems, giving rise to a quantum spin Hall effect. Its simplest form constitutes essentially two time-reversed copies of the quantum Hall phase, where up and down spin electrons are decoupled and experience opposite effective magnetic fields. Remarkably, the quantum spin Hall effect is robust to coupling between the two spin sectors, forming a distinct topological phase of matter protected by time-reversal symmetry (Kane and Mele, 2005*b*).

Also in 2005, Haldane and Raghu proposed a photonic analogue of the quantum Hall effect in time reversal symmetry-breaking photonic crystals in a preprint that was only published in Physical Review Letters 3 years later (Haldane and Raghu, 2008). While potential applications as a basis for broadband unidirectional optical waveguiding were compelling, the weak strength of magnetic effects at optical frequencies suggested this proposal would be challenging to implement in practice. Wang et al. (2008) predicted that, even if an optical frequency realization might be impractical, the effect could be readily observed at microwave frequencies. Their seminal experiments using a magneto-optical photonic crystal shown in Fig. 2 demonstrated for the first time that robust quantum Hall-like edge states could be observed in photonic systems (Wang et al., 2009).

Topological photonics era (2011–present)

Present broad interest in topological bands and quantum Hall effects for photons was sparked by the discovery of several alternatives to weak magneto-optical effects:

1. Spin-selective excitations that effectively break the time-reversal symmetry of all-dielectric structures (Hafezi et al., 2011).
2. Suitably-designed temporal modulation of the coupling in optical resonator lattices that creates effective magnetic fields for light (Fang et al., 2012).
3. Waveguiding geometries with longitudinal refractive index modulations, where the propagation axis plays the role of "time" (Rechtsman et al., 2013).
4. Metamaterials that emulate the electronic spin-orbit coupling underlying quantum spin Hall phases (Khanikaev et al., 2013).

While these proposals each had their own limitations, (e.g. being limited to weakly-coupled cavity or waveguide lattices), more general and accessible designs soon followed, including all-dielectric topological photonic crystals (Wu and Hu, 2015; Ma and Shvets, 2016; Barik et al., 2016). There now exists a wide variety of approaches for generating quantum Hall-like edge states in photonic systems.

Theoretical and experimental approaches

To put photonic quantum Hall effects on a solid theoretical footing it is necessary to demonstrate a correspondence with the models of topological phases studied in condensed matter physics. On the other hand, the differences between Maxwell's equations for electromagnetism and the Schrödinger equation provide the opportunity to explore novel classes of topological phenomena inaccessible in electronic condensed matter systems.

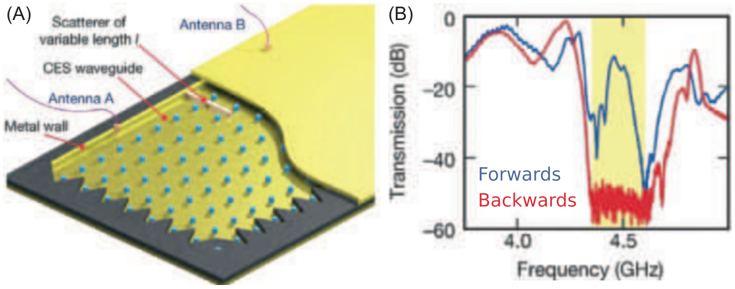

Fig. 2 (A) Schematic of two-dimensional magneto-optic photonic crystal including a pair of antennas to measure the transmission of the photonic quantum Hall edge state past a strong scatterer. (B) Measured transmission spectrum from A to B (forward; blue) and from B to A (backward; red). Yellow shaded region denotes the topological band gap exhibiting strong unidirectional transmission. Modified from Wang Z, Chong Y, Joannopoulos JD, and Soljačić M (2009) Observation of unidirectional backscattering-immune topological electromagnetic states. *Nature* 461: 772–775.

Schrödinger formalism for electromagnetism

Consider the source-free Maxwell's equations for time t and space $\boldsymbol{r}$-dependent electromagnetic fields $\boldsymbol{E}(\boldsymbol{r}, t)$, $\boldsymbol{D}(\boldsymbol{r}, t)$, $\boldsymbol{B}(\boldsymbol{r}, t)$, $\boldsymbol{H}(\boldsymbol{r}, t)$, in units with speed of light $c = 1$,

$$\nabla \times \boldsymbol{E} = -\partial_t \boldsymbol{B}, \quad \nabla \times \boldsymbol{H} = \partial_t \boldsymbol{D}, \quad \nabla \cdot \boldsymbol{D} = 0, \quad \nabla \cdot \boldsymbol{B} = 0, \tag{1}$$

$$\boldsymbol{D} = \varepsilon_0 \boldsymbol{E} + \boldsymbol{P}, \quad \mu_0 \boldsymbol{H} = \boldsymbol{B} - \mu_0 \boldsymbol{M}, \tag{2}$$

where ε_0 and μ_0 are the permittivity and permeability of free space, respectively, and $\boldsymbol{P}(\boldsymbol{r}, t)$ and $\boldsymbol{M}(\boldsymbol{r}, t)$ are the local polarization and magnetization densities of the material. A Schrödinger-like wave equation can be obtained by introducing the "wavefunction" $(\boldsymbol{E}, \boldsymbol{H})^T$ and assuming a linear constitutive relation between the fields, $(\boldsymbol{D}, \boldsymbol{B})^T = \widehat{W}(\boldsymbol{E}, \boldsymbol{H})^T$, corresponding to $\boldsymbol{P}$ and $\boldsymbol{M}$ being proportional to the local $\boldsymbol{E}$ and $\boldsymbol{B}$ fields,

$$i\partial_t \widehat{W} \begin{pmatrix} \boldsymbol{E} \\ \boldsymbol{H} \end{pmatrix} = \begin{pmatrix} 0 & i\nabla\times \\ -i\nabla\times & 0 \end{pmatrix} \begin{pmatrix} \boldsymbol{E} \\ \boldsymbol{H} \end{pmatrix}. \tag{3}$$

Assuming monochromatic fields with frequency ω, i.e. $(\boldsymbol{E}(\boldsymbol{r}, t), \boldsymbol{H}(\boldsymbol{r}, t))^T = e^{-i\omega t}\Psi$, and letting $\widehat{\mathcal{H}} = (-\nabla\times) \otimes \widehat{\sigma}_y$, we obtain the generalized electromagnetic eigenvalue problem

$$\omega \widehat{W} \Psi = \widehat{\mathcal{H}} \Psi. \tag{4}$$

If the constitutive matrix $\widehat{W}$ is positive definite the generalized eigenvalue problem is Hermitian and supports a complete set of modes Ψ_n orthonormal with respect to the modified inner product,

$$\langle \Psi_m | \Psi_n \rangle = \int \Psi_m^* \widehat{W} \Psi_n \, d\boldsymbol{r} = \delta_{m,n}, \tag{5}$$

where $\delta_{m,n}$ is the Kronecker delta function. Therefore periodic electromagnetic media can be studied using standard tools from electronic condensed matter, including the decomposition of the spectrum into a band structure using Bloch's theorem.

There do however exist some peculiar differences between Schrödinger and electromagnetic waves. For example, the physical $\boldsymbol{E}$ and $\boldsymbol{H}$ fields are real-valued, demanding a particle-hole symmetry between positive and negative frequency modes of Eq. (4); this means the spectrum of $\widehat{\mathcal{H}}$ is unbounded for both positive and negative frequencies, in contrast to the spectrum of the usual Schrödinger equation, which has a ground state. Moreover, the response of a material to an electromagnetic field is in general non-instantaneous; causality (Kramers-Kronig relations) requires the components of the constitutive matrix to be frequency-dependent and complex, i.e. $\widehat{W} = \widehat{W}(\boldsymbol{r}, \omega) = \widehat{W}^*(\boldsymbol{r}, -\omega)$. For further more rigorous discussion on the Schrödinger formalism for electromagnetism and implications for topological band theory, we recommend the article by De Nittis and Lein (2018).

Routes to topological bands

A spatially-periodic constitutive relation plays the role of a periodic potential in the electronic Schrödinger equation; appropriate choices of $\widehat{W}$ can therefore be used to create topological band gaps supporting photonic quantum Hall states. Different approaches are possible depending on the wavelength of interest λ and the scale of structural modifications a, summarized in Fig. 3.

The most ubiquitous topological phases, in terms of characteristic topological invariants, are the Chern insulators characterized by the first Chern number. For a particular energy band, the Chern number is defined as an integral of the Berry curvature over the

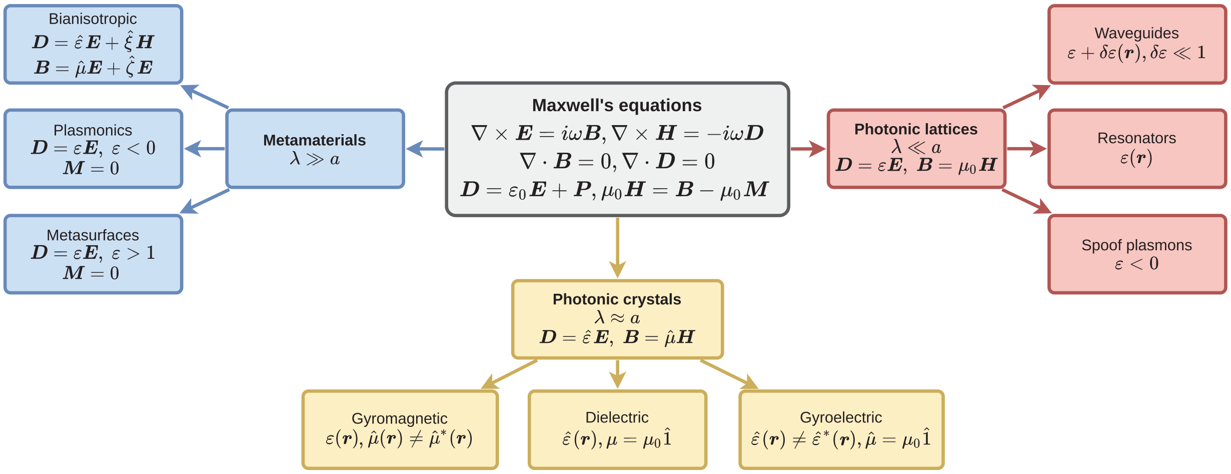
Bianisotropic
$\boldsymbol{D} = \hat{\varepsilon}\boldsymbol{E} + \hat{\xi}\boldsymbol{H}$
$\boldsymbol{B} = \hat{\mu}\boldsymbol{E} + \hat{\zeta}\boldsymbol{E}$
Plasmonics
$\boldsymbol{D} = \varepsilon\boldsymbol{E},\ \varepsilon < 0$
$\boldsymbol{M} = 0$
Metasurfaces
$\boldsymbol{D} = \varepsilon\boldsymbol{E},\ \varepsilon > 1$
$\boldsymbol{M} = 0$
Metamaterials
$\lambda \gg a$
Maxwell's equations
$\nabla \times \boldsymbol{E} = i\omega\boldsymbol{B}, \nabla \times \boldsymbol{H} = -i\omega\boldsymbol{D}$
$\nabla \cdot \boldsymbol{B} = 0, \nabla \cdot \boldsymbol{D} = 0$
$\boldsymbol{D} = \varepsilon_0\boldsymbol{E} + \boldsymbol{P}, \mu_0\boldsymbol{H} = \boldsymbol{B} - \mu_0\boldsymbol{M}$
Photonic lattices
$\lambda \ll a$
$\boldsymbol{D} = \varepsilon\boldsymbol{E},\ \boldsymbol{B} = \mu_0\boldsymbol{H}$
Waveguides
$\varepsilon + \delta\varepsilon(\boldsymbol{r}), \delta\varepsilon \ll 1$
Resonators
$\varepsilon(\boldsymbol{r})$
Spoof plasmons
$\varepsilon < 0$
Photonic crystals
$\lambda \approx a$
$\boldsymbol{D} = \hat{\varepsilon}\boldsymbol{E},\ \boldsymbol{B} = \hat{\mu}\boldsymbol{H}$
Gyromagnetic
$\varepsilon(\boldsymbol{r}), \hat{\mu}(\boldsymbol{r}) \neq \hat{\mu}^*(\boldsymbol{r})$
Dielectric
$\hat{\varepsilon}(\boldsymbol{r}), \mu = \mu_0\hat{1}$
Gyroelectric
$\hat{\varepsilon}(\boldsymbol{r}) \neq \hat{\varepsilon}^*(\boldsymbol{r}), \hat{\mu} = \mu_0\hat{1}$

Fig. 3 Summary of different approaches for realizing photonic quantum Hall and spin Hall effects, grouped according to the ratio of the operating wavelength λ to the modulation scale a. Note that generally a is less than structure periodicity *d*.

first Brillouin zone, $C_n = \frac{1}{2\pi}\int_{BZ} d^2\boldsymbol{k}\Omega_n(\boldsymbol{k})$. A non-zero Chern number implies a discontinuity of Berry connection and emergence of the topological charge, which leads to the non-vanishing geometric phase term in an eigenvector. For finite systems, the bulk Chern number accounts for the number of unidirectional topologically protected edge modes (Hasan and Kane, 2010).

In two-dimensional Chern insulators the TR symmetry is necessarily broken, for example, by the magnetic field bias, and in finite Chern insulators the propagation direction of topological edge states is controlled by the sign of the total magnetic flux.

The original experiments of Wang et al. (2009) broke time-reversal symmetry by applying a magnetic field to a square-lattice photonic crystal of gyromagnetic ferrite rods confined vertically between two metallic plates to mimic the TM-polarized modes in infinitely long cylinders, shown in Fig. 2A. The resultant band structure hosts a gapless chiral edge state that propagates around defects with back scattering significantly suppressed and, by contrast, high transmittance within the band gap shaded yellow in Fig. 2B. Theoretically, the system is described by periodically-modulated scalar permittivity $\varepsilon(\boldsymbol{r})$ and inverse permeability tensor

$$\widehat{\mu}^{-1}(\boldsymbol{r}) = \begin{pmatrix} \tilde{\mu}^{-1} & i\eta & 0 \\ -i\eta & \tilde{\mu}^{-1} & 0 \\ 0 & 0 & \mu_0^{-1} \end{pmatrix}, \tag{6}$$

where the time reversal symmetry-breaking off-diagonal terms $\pm i\eta$ are induced by an external out-of-plane magnetic field. Eliminating the magnetic field $\boldsymbol{H}$ from Maxwell's equations Eq. (1) and introducing the "wavefunction" $\psi = E_z\sqrt{\tilde{\mu}}$, the eigenvalue problem reduces to (Wang et al., 2008)

$$-|\nabla + i\boldsymbol{A}(\boldsymbol{r})|^2\psi + V(\boldsymbol{r})\psi = 0, \tag{7}$$

where

$$\boldsymbol{A} = \frac{\tilde{\mu}}{2}\widehat{z} \times \nabla\eta, \quad V = \frac{1}{4}\left(|\nabla \ln \tilde{\mu}|^2 + |\tilde{\mu}\nabla\eta|^2\right) - \frac{1}{2}\nabla^2 \ln \tilde{\mu} - \tilde{\mu}\varepsilon\omega^2. \tag{8}$$

Thus, the gyrotropic response produces an effective vector potential for light, which breaks time-reversal symmetry and can create topological band gaps with nonzero Chern number.

Unfortunately gyrotropic response is very weak at optical frequencies, severely limiting the size of any topological band gap. Therefore alternate approaches suitable for time reversal-symmetric dielectric materials are preferred. Synthetic gauge fields for light can also be introduced by periodic modulation of photonic crystal parameters in time or space. The effective magnetic field, associated with the complex phase accumulation, can thus force unidirectional propagation of photons without the use of magnetic materials at optical frequencies, in a way similar to electrons moving along skipping orbits along the edge in a two-dimensional magnetically-biased electron gas.

For example, light propagation in waveguide lattices formed by a weak modulation δn of the refractive index $n(\boldsymbol{r}) = \sqrt{\varepsilon(\boldsymbol{r})} = n_0 + \delta n(\boldsymbol{r})$ is described by the paraxial wave equation (Rechtsman et al., 2013)

$$i\partial_z\psi(\boldsymbol{r}_\perp, z) = -\frac{1}{2k_0}\nabla_\perp^2\psi - \frac{k_0\delta n(\boldsymbol{r}_\perp, z)}{n_0}\psi(\boldsymbol{r}_\perp, z), \tag{9}$$

where $\boldsymbol{r}_\perp = (x, y)$ are the transverse coordinates, z is the propagation direction, and $k_0 = 2\pi n_0/\lambda$ is the wavelength of light in the medium. Since z plays the role of "time" in the paraxial equation, broken inversion symmetry $\delta n(\boldsymbol{r}_\perp, z) \neq \delta n(\boldsymbol{r}_\perp, -z)$ can be used to obtain nonzero Chern numbers for light propagating through the waveguide array.

The second most important class of topological phase is the quantum spin Hall or Z_2 topological insulator, which can be considered (loosely) as consisting of two copies of Chern topological insulators with gauge fields acting on opposite spins (Hasan and Kane, 2010). In fact, it is the time-reversal symmetry that ensures the topological stability of the edge states supported by quantum spin Hall topological insulators, with spin-orbital coupling, in the absence of spin-flipping processes. However, one should keep in mind that while time-reversal symmetry alone is sufficient to guarantee the presence of degenerate spin-1/2 states in condensed-matter physics, owing to Kramers' theorem for fermions, this is not the case for photons because they obey the bosonic quantum statistics. Therefore, additional deliberately-engineered symmetries related to pseudotime-reversal operators $\widehat{\mathcal{C}}_\mathrm{b}$, $\widehat{\mathcal{C}}_\mathrm{b}^2 = -1$, $\widehat{\mathcal{C}}_\mathrm{b}\widehat{\mathcal{H}}\widehat{\mathcal{C}}_\mathrm{b}^{-1} = \widehat{\mathcal{H}}$ are required in photonics to mimic the fermionic property of electrons $\widehat{\mathcal{T}}_\mathrm{f}^2 = -1$, with time-reversal operator $\widehat{\mathcal{T}}_\mathrm{f} = i\widehat{\sigma}_y\widehat{K}$, and achieve time-reversal-invariant topological order (Ozawa et al., 2019). They include internal symmetry of the electromagnetic field inside a photonic structure or crystalline symmetries of a photonic lattice. Such symmetries can produce modal degeneracies in a band structure, generating doublet states to emulate the pseudospin degree of freedom, thus enabling photonic analogues of the quantum spin-Hall effect (Khanikaev and Shvets, 2017).

For example, metamaterials formed through subwavelength modifications to the material properties can be used to engineer constitutive relations not found in natural materials, including negative refractive indices and strong coupling between electric and magnetic field components. Khanikaev et al. (2013) exploited this tunability to engineer two-dimensional metamaterials with bianisotropic coupling between transverse electric (TE; H_z) and transverse magnetic (TM; E_z) field components,

$$\left(k_0^2\mu_{zz} + \nabla_\perp \frac{1}{\varepsilon_\perp}\nabla_\perp\right)H_z = \left[\nabla_\perp\left(\frac{-i\chi_{xy}}{\varepsilon_\perp\mu_\perp}\right) \times \nabla_\perp E_z\right]_z, \tag{10}$$

$$\left(k_0^2\varepsilon_{zz} + \nabla_\perp \frac{1}{\mu_\perp}\nabla_\perp\right) E_z = \left[\nabla_\perp\left(\frac{-i\chi_{xy}}{\varepsilon_\perp\mu_\perp}\right)\times\nabla_\perp H_z\right]_z. \tag{11}$$

By engineering the metamaterial parameters such that $\mu_{zz} = \varepsilon_{zz}$ and $\mu_\perp = \varepsilon_\perp$, the electric and magnetic field components become degenerate. Consequently, bianisotropic coupling $\chi_{xy} \neq 0$ then gives rise to new eigenmodes $\psi_\pm = E_z \pm H_z$ emulating the quantum spin Hall phase.

Key issues

Are photonic quantum Hall effects genuinely robust?

The exact correspondence between electronic and photonic quantum Hall effects only holds under certain idealized conditions, including the absence of losses and optical nonlinearities. Remarkably, studies of the robustness of topological photonic edge states under non-ideal conditions have lead to the discovery of new kinds of topological phenomena in both photonic and condensed matter systems.

Losses and non-Hermitian topological phases

Early works on photonic topological edge states already recognized that unavoidable absorption, radiation, and scattering losses in photonic systems would place practical limits on their robustness and lifetime (Wang et al., 2009).

Material absorption is a fundamental property of optical media that cannot be eliminated via collective (band structure) effects. In fact, topological band structures typically emerge from confinement or multiple scattering, slowing down light propagation and enhancing absorption compared to homogeneous systems (Baba, 2008).

Radiation and scattering losses occur because there is no topological robustness of two-dimensional photonic quantum Hall effects against out-of-plane propagation. Modes of quasi-two-dimensional slabs with momenta above the light line will couple into the continuum of free space, resulting in radiative decay (Gorlach et al., 2018). Nominally-bound modes below the light line can still couple to radiation modes and acquire a finite lifetime in the presence of fabrication defect-induced scattering, such as roughness at boundaries between different materials comprising the slab (Sauer et al., 2020). To avoid out-of-plane scattering it is necessary to embed the planar photonic crystal in a three-dimensional photonic crystal supporting a complete omnidirectional band-gap at the frequency of interest.

Generally losses are manageable at microwave frequencies, where metals are good conductors and can provide perfect in-plane confinement and low-loss dielectric materials exist. At higher frequencies (terahertz and above) losses typically increase and feasible refractive index contrasts are weaker, making in-plane confinement harder. One way losses can be managed is by introducing optical gain (amplification), but this often brings about separate issues including amplification of noise and instabilities.

Regardless of their microscopic origin, the influence of loss and gain can be modelled by non-Hermitian effective Hamiltonians. Initial theoretical studies of the one-dimensional Su-Schrieffer-Heeger model suggested topologically-protected bulk (Rudner and Levitov, 2009) and edge (Schomerus, 2013) phenomena could still persist in non-Hermitian systems, subsequently observed using optical waveguide arrays (Zeuner et al., 2015) and microwave resonator chains (Poli et al., 2015). Later studies have generalized these ideas to two-dimensional topological phases (Ozawa and Carussoto, 2014) and observed non-Hermitian topological phenomena in a variety of systems including photonic crystal slabs (Zhen et al., 2015; Zhou et al., 2018) and microring resonator lattices (Zhao et al., 2019). Bergholtz et al. (2021) provide a more comprehensive review of non-Hermitian topological band theory.

Symmetry-breaking perturbations

Even if losses can be perfectly eliminated or compensated, disorder and imperfections can still spoil the robustness of most photonic quantum Hall effects; only systems that break time-reversal symmetry can be genuinely robust to all kinds of (Hermitian) perturbations.

The time reversal-symmetric systems supporting spin Hall effects most widely used in photonics do not share the robustness of their electronic counterparts; the robustness of the electronic quantum spin Hall effect is due to backscattering suppression protected by the $\widehat{\mathcal{T}}_\mathrm{f}^2 = -1$ fermionic time-reversal symmetry. As noted in Section "Theoretical and Experimental Approaches," the photonic time-reversal symmetry ordinarily obeys $\widehat{\mathcal{T}}_\mathrm{b}^2 = +1$; fermionic $\widehat{\mathcal{C}}_\mathrm{b}^2 = -1$ requires introduction of auxiliary spin-like degrees of freedom, such as valley or polarization (Khanikaev et al., 2013). Since this spin is not intrinsic but emerges due to structural properties, certain structural imperfections and lattice terminations can spoil the protection and induce backscattering (Saba et al., 2020).

For example, the valley Hall photonic crystals only support robust edge states in the absence of coupling between their two valleys. Short-scale structural deformations can induce inter-valley scattering that localizes the edge states. Similarly, topological crystalline phases such as the shrunken-expanded hexagonal photonic crystal design of Wu and Hu (2015) are protected by crystalline rotational symmetries. Typically, the symmetry is broken locally at domain walls or edges, inducing small gaps in the spectra of the interface states (Xu et al., 2016).

Therefore topological robustness of symmetry-protected photonic quantum Hall effects only holds to the extent that the underlying symmetries can be preserved. This poses a challenge because fabrication disorders will typically not preserve any spatial symmetries.

Optical nonlinearities

What is remarkable about electronic quantum Hall effects is that, even though the basic physics can be captured by simple single particle band structures, they are robust to electron-electron interactions and other many-body effects, giving rise to robust quantized transport. It is thus interesting to ask whether similar robustness can hold for classical waves in the presence of nonlinear interactions. This is another frontier of studies of photonic quantum Hall effects, reviewed by Smirnova et al. (2020).

Theoretical works have predicted that nonlinearities can lead to self-focusing (Leykam and Chong, 2016), instabilities (Lumer et al., 2016), and nonlinear localization (Lumer et al., 2013), potentially destroying robust transport. Nonlinearities also induce coupling between different linear modes of the system, potentially channeling energy between robust edge states into non-robust bulk modes (Xia et al., 2020). On the other hand, nonlinear pumps can be used to break time-reversal symmetry (Bardyn et al., 2016) and induce robust transport of weak probe beams (Peano et al., 2016).

Experimental studies on the effect of nonlinearities on photonic quantum Hall edge phases have observed a variety of effects, including frequency conversion (Mittal et al., 2018; Smirnova et al., 2019), bulk soliton generation (Mukherjee and Rechtsman, 2020), nonlinearity-induced edge states (Maczewsky et al., 2020; Mukherjee and Rechtsman, 2021), and nonlinearity-induced higher-order topological phases (Kirsch et al., 2021).

Since the dynamics of nonlinear systems cannot be completely characterized in terms of a unique spectrum or band structure, and are sensitive to the initial state and input intensity, rigorously demonstrating topological robustness in nonlinear wave systems is quite challenging. One notable example of where nonlinear robustness has been predicted and observed is in quantized Thouless pumping induced by periodic modulation of system parameters (Jürgensen et al., 2021), as shown in Fig. 4. Following a complete modulation cycle the soliton solutions must be identical up to translation invariance, thus solitons must be pumped a quantized integer number of unit cells. This number can change as the input power is varied due to nonlinear bifurcations.

Potential device applications

Electronic quantum Hall effects are useful as the electrical resistance standard, thanks to their unexpectedly extreme robustness (von Klitzing et al., 2020). On the other hand, photonic quantum Hall edge states have required clever and careful designs to observe, with claims of robustness typically based on the introduction of specific controlled perturbations. Will photonic quantum Hall effects also see useful applications? A few directions are currently being pursued.

Topological waveguides and cavities

Robust broadband non-reciprocal optical waveguiding was the first key application proposed for photonic quantum Hall effects (Haldane and Raghu, 2008), however, practical implementations competitive with the best conventional waveguide designs remain out of reach, in part due to the limitations to topological robustness leading to enhanced losses and nonzero backscattering (Sauer et al., 2020) discussed in Section "Are photonic quantum Hall effects genuinely robust?."

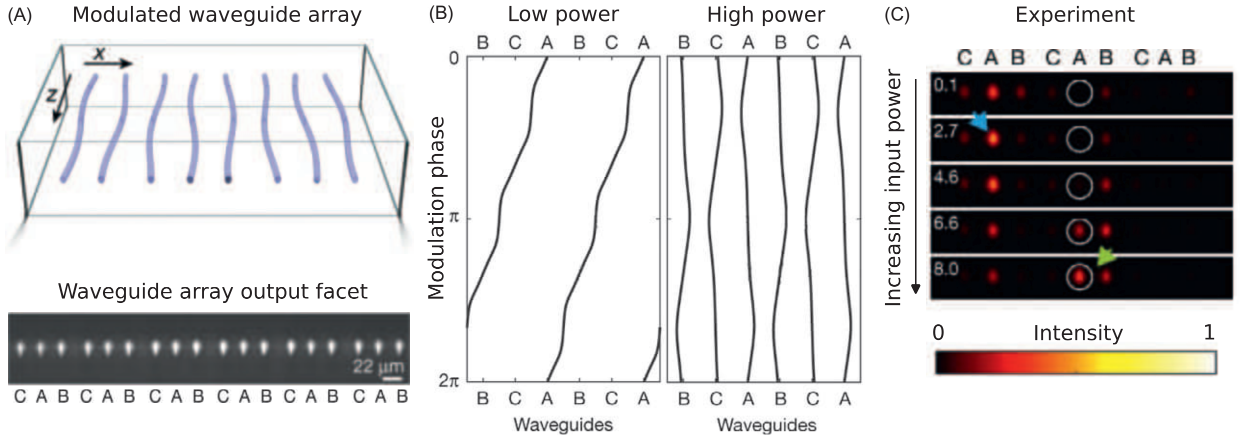

Fig. 4 (A) One-dimensional periodically-modulated waveguide array implementing a Thouless pump. (B) Instantaneous nonlinear spectra during one modulation cycle. Low power solitons are pumped one unit cell per modulation cycle, whereas high power solitons remain pinned to the initial unit cell. (C) Experimental observation of quantized Thouless pumping of solitons. Low power output profile is displaced one unit cell with respect to the input waveguide (white circles), while output becomes pinned to input unit cell at high powers. Modified from Jürgensen M, Mukherjee S, and Rechtsman MC (2021) Quantized nonlinear Thouless pumping. Nature 596(7870): 63–67.

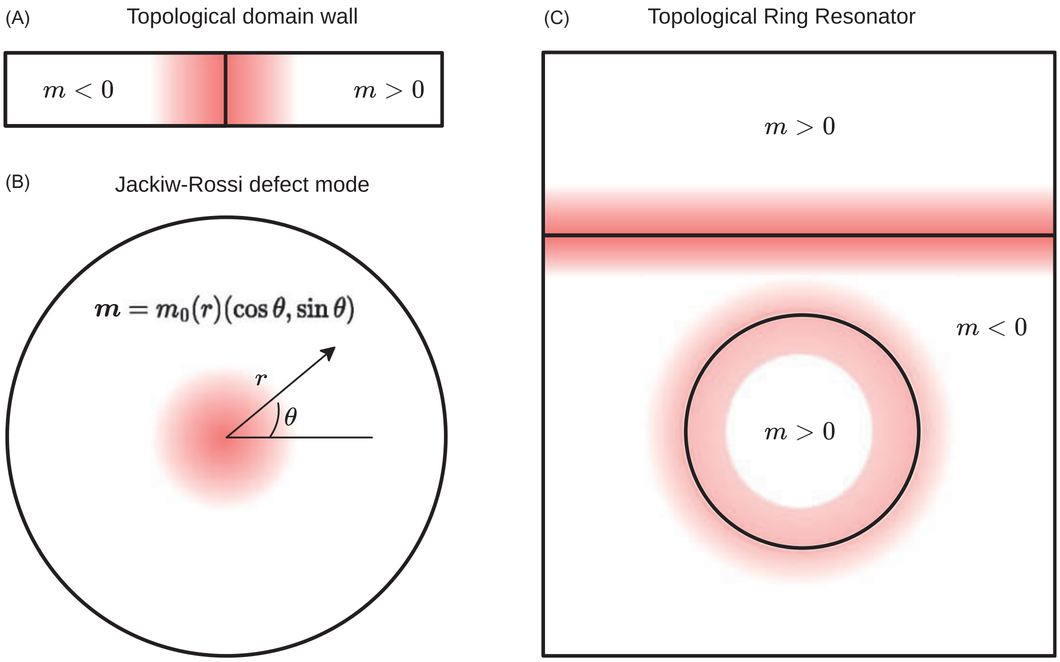

Fig. 5 Examples of topological waveguides and cavities. (A) A domain wall between inequivalent topological phases (denoted by $m < 0$ and $m > 0$) results in a localized mid-gap mode in 1D systems and a unidirectional edge state in 2D systems. (B) Generation of robust 2D localized mode using a vortex-like modulation of the topological gap parameter **m**. (C) Topological ring resonator coupled to a waveguide using topological domain walls in a 2D system.

Topological phases have also been considered as a way to create robust localized modes and resonators for light, with some examples illustrated in Fig. 5. The simplest approach is based on mid-gap localized modes appearing in one-dimensional photonic crystals (Malkova et al., 2009). Subsequently, topological resonators based on rings of valley Hall edge states (Ma et al., 2019b), topological corner modes (Mittal et al., 2019), and topological vortex defect modes (Gao et al., 2020) have been investigated. Kim et al. (2020) provide a more in-depth review.

One issue of vital importance to the design of waveguides and cavities is the device footprint. For example, in the case of two-dimensional quantum Hall edge states, robustness against backscattering is provided by the two-dimensional bulk. If one attempts to minimize the device footprint by reducing the size of the bulk, coupling between opposite edges will spoil the topological protection. Thus, topological waveguides and resonators tend to have a larger physical size (constrained by the size of the topological band gap) compared to conventional waveguides and resonators. This limitation needs to be taken into account when comparing the performance of topological and non-topological designs.

A more comprehensive overview on the design of topological photonic crystal waveguides and cavities is given by Iwamoto et al. (2021).

Topological lasers

Lasers are arguably one of the most important inventions of the 20th century and are now ubiquitous in a range of communication, sensing, and fabrication technologies. Naturally there has been tremendous interest in studying whether photonic quantum Hall edge states or other topological phases can serve as the basis for new and improved laser designs with better performance.

The first experiments combining optical gain media with topological photonic systems considered mid-gap modes of one-dimensional lattices (St-Jean et al., 2017; Zhao et al., 2018; Parto et al., 2018). Bahari et al. (2017) observed lasing of quantum Hall edge states using the magneto-optic photonic crystal shown in Fig. 6, exploiting the fact that light emission from a continuous wave laser is intrinsically narrowband, which makes the weak magneto-optic response at optical frequencies sufficient to resolve localized edge states.

The first observation of lasing of quantum spin Hall states by Bandres et al. (2018) employed ring resonator lattices. Lasing in the spin Hall phase was observed to spontaneously break time-reversal symmetry, resulting in chiral light emission. Since lasing modes based on two-dimensional edge states appear to be insensitive to the shape of the boundary, they offer a potential route towards designing large cavities robust to fabrication disorders.

Since these seminal experiments numerous follow-up theoretical and experimental studies have been performed, considering different cavity designs and dimensions and various pumping schemes, reviewed by Ota et al. (2020). Efforts now focus on two complementary directions: (1) How to maximize the modal volume while preserving stable single mode lasing, and (2) how to reduce the mode volume and increase the quality factor to design highly efficient, low power lasers.

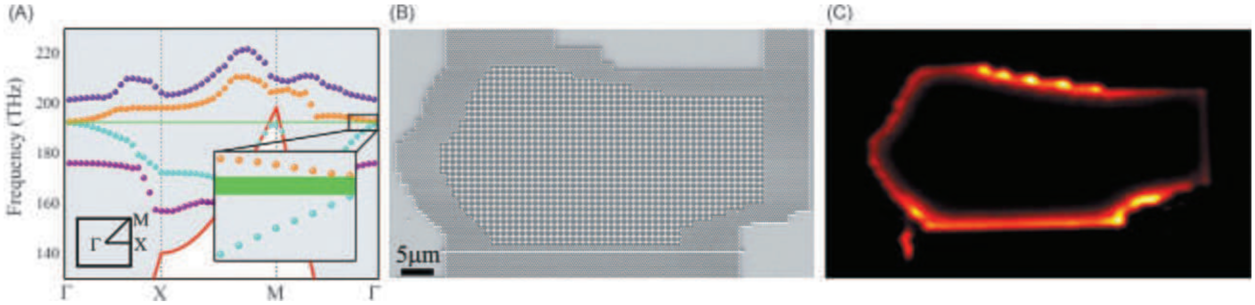

Fig. 6 First two-dimensional topological laser. (A) Band structure of the InGaAsP-YIG photonic crystal. Under an applied magnetic field, the YIG gyrotropic response breaks time-reversal symmetry, opening a small topological band gap with nonzero Chern number (green shaded region in inset). (B) Topological cavity formed by irregular boundary between inner topological photonic crystal and outer trivial photonic crystal. (C) Image of the device under high power optical pumping, revealing emission from the topological edge mode. Modified from Bahari B, Ndao A, Vallini F, Amili AE, Fainman Y, and Kanté B (2017) Nonreciprocal lasing in topological cavities of arbitrary geometries. *Science* 358(6363): 636–640.

The best route towards maximizing the modal volume remains under debate. Competing approaches include 2D quantum Hall-like edge states (Bandres et al., 2018), valley-Hall modes at domain walls (Zeng et al., 2020), bulk modes (Shao et al., 2020), vortex defect modes (Gao et al., 2020; Yang et al., 2022), and Dirac point modes of gapless band structures (Contractor et al., 2022). On the other hand, one obstacle against small modal volumes is that topological effects are a collective lattice property; protection is provided by having a sufficiently large bulk. It seems difficult to reduce the modal volumes below that achievable using a single isolated resonator or defect cavity; the main benefit of the topology may be in achieving a robustness to disorder at the expense of a larger modal volume.

On the theory side, research on understanding the mechanisms for stable lasing in topological systems is ongoing. For example, it is commonly assumed that stable edge state lasing requires the optical gain to be localized to the edge of the system. On the other hand, even though the experiments shown in Fig. 6 employed uniform optical pumping, no lasing of bulk modes was observed. Seclì et al. (2021) proposed a mechanism for this surprising observation based on excess gain occurring in the topologically-trivial cladding medium. Research on this topic including the interplay with non-Hermitian topological phenomena remains ongoing.

Making photonic quantum Hall effects quantum

A long-standing challenge has been to integrate topological band structure effects with strong (single photon level) interactions to generate many-body bosonic quantum Hall effects. This is hard because nonlinear optical effects are typically very weak, requiring intricate schemes involving resonant nonlinearities (Imamoğlu et al., 1997), ultra-high quality factor cavities, and pumping to compensate for losses. Comprehensive reviews on this subject and the quantum simulation of other strong interaction phenomena using photons are given by Noh and Angelakis (2016) and Carusotto et al. (2020).

Theoretical proposals

Early works proposed bosonic analogues of fractional quantum Hall states using atoms trapped in optical lattices and cavity arrays, using modulated couplings to induce effective magnetic fields for neutral particles (Sørensen et al., 2005; Hafezi et al., 2007; Cho et al., 2008; Hayward et al., 2012). These proposals were then generalized to photonic systems with strong photon-photon interactions (Koch et al., 2010; Nunnenkamp et al., 2011; Umucalılar and Carusotto, 2011; Hafezi et al., 2011).

An important question specific to the photonic schemes is how to reliably generate (fractional) quantum Hall states. Early proposals predicted that in the presence of strong interactions and sufficiently weak losses, two-photon Laughlin states of light could be excited using a coherent pump tuned to the state's energy (Umucalılar and Carusotto, 2012; Hafezi et al., 2013; Umucalılar et al., 2014).

However, uniform driving approaches cannot be easily scaled to larger systems where topological robustness is expected to emerge due to inevitable losses. Losses lead to spectral broadening of the modes, resulting in excitation of multiple modes in larger systems. Moreover, higher photon number states will be exponentially suppressed by losses. Subsequent studies proposed solutions based on two-photon driving designed to restore lost photons (Kapit et al., 2014), and local driving combined with topological pumping Grusdt et al. (2014).

Experiments

Experimentally, strong single photon-level interactions have been demonstrated at microwave frequencies using superconducting qubits (Chen et al., 2014) and at optical frequencies using Rydberg atoms (Firstenberg et al., 2013). In both these platforms, the main difficulty is to maintain the strong interactions while scaling up the system size and number of particles, while using fine-tuning to compensate for and minimize inevitable disorder effects.

Roushan et al. (2017a) were the first to combine strong interactions with a synthetic magnetic field using the three-site lattice of superconducting microwave qubits shown in Fig. 7A, observing a photon number-dependent chirality of the dynamics. Subsequent

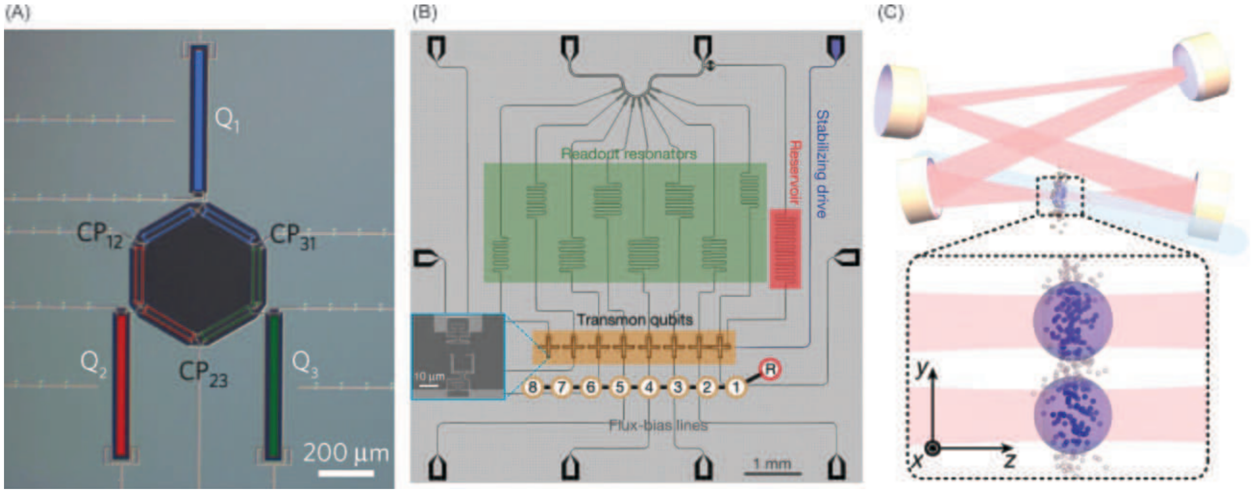

Fig. 7 Experimental platforms for many-body bosonic quantum Hall effects. (A) Superconducting transmon qubits Q_i connected via adjustable couplers CP_{ij} which are periodically modulated in time to induce an effective magnetic flux. (B) Array of superconducting transmon qubits, where two-photon driving combined with coupling to a lossy auxiliary resonator reservoir is used to stabilize a photonic Mott insulator. (C) Twisted four-mirror optical cavity used to generate photonic Landau levels, with strong photon-photon interactions mediated using trapped Rydberg atoms (inset). (A) Modified from Roushan P et al. (2017a) Chiral ground-state currents of interacting photons in a synthetic magnetic field. *Nature Physics* 13(2): 146–151. (B) Modified from Ma R, Saxberg B, Owens C, Leung N, Lu Y, Simon J, and Schuster DI (2019a) A dissipatively stabilized Mott insulator of photons. *Nature* 566(7742): 51–57. (C) Modified from Clark LW, Schine N, Baum C, Jia N, and Simon J (2020) Observation of Laughlin states made of light. *Nature* 582(7810): 41–45.

work observed a Hofstadter butterfly spectrum in a quasiperiodically-modulated one-dimensional lattice (Roushan et al., 2017b). Ma et al. (2019a) implemented two-photon driving to prepare a Mott insulator state of photons in the eight-site lattice shown in Fig. 7B. Implementation of fractional quantum Hall states in this platform remains an outstanding challenge, requiring the combination of a two-dimensional lattice geometry with precise control over the qubit couplings and frequencies.

Parallel efforts targeted at optical frequencies started by generating a continuum Landau level spectrum for photons using the twisted ring resonator (Schine et al., 2016) shown in Fig. 7C. This platform can be combined with strong single photon-level interactions by placing ultra-cold Rydberg atoms within the resonator (Clark et al., 2019), enabling generation of two-photon Laughlin states of light (Clark et al., 2020), detected by measuring angular two-photon correlations. Future work aims to combine this platform with dissipative preparation schemes to assemble many-body quantum Hall states of light.

Conclusion

Over the past decade the emulation of topological phenomena in condensed matter physics including quantum Hall effects has captured the imagination of researchers in photonics. In this Chapter we have attempted to provide a broad overview of this active and still-developing field from its early origins up to topics of ongoing research. While it remains unclear as to whether photonic quantum Hall effects will remain a curiosity among researchers or will form the basis for new and improved devices, there is no doubt that this elegant formalism completes the band theory describing periodic photonic media including photonic crystals (Joannopoulos et al., 2008).

There are numerous future directions for research. On the fundamental side, there are ongoing efforts towards understanding the properties of recently-discovered topological phenomena including higher-order topological phases, topological defect modes, non-Hermitian topological phases, and the role of topology in nonlinear and strongly-interacting systems, as well as observing these phenomena in experiments. At the same time, one (valid) criticism of the ongoing tremendous interest in topological photonic systems is that they are exotica; a solution in search of a problem. Existing approaches towards generating photonic quantum Hall effects have been largely based on clever and intricate designs. To realize the dream of useful device applications we need to develop new approaches to achieve improved figures of merit compared to conventional design approaches.

Photonic quantum Hall effects are one of many examples of how ideas from other research fields can inspire new approaches towards the design and understanding of photonic systems. It is natural to ask where the next big inspiration will come from. One leading candidate is machine learning, a topic which has seen tremendous progress over the past decade and has now started to capture the attention of physicists (Carleo et al., 2019). Not only can ideas from machine learning be applied towards analysis of photonic systems, but concepts from topological photonics might be useful as a means for designing photonic hardware for machine learning including neuromorphic computing (Tan, 2021) and image processing (Zhang and Zhang, 2019; Zhu et al., 2019, 2021) with ultrafast speed and low energy consumption.

References

Baba T (2008) Slow light in photonic crystals. *Nature Photonics* 2(8): 465–473.

Bahari B, Ndao A, Vallini F, Amili AE, Fainman Y, and Kanté B (2017) Nonreciprocal lasing in topological cavities of arbitrary geometries. *Science* 358(6363): 636–640.

Bandres MA, Wittek S, Harari G, Parto M, Ren J, Segev M, Christodoulides DN, and Khajavikhan M (2018) Topological insulator laser: Experiments. *Science* 359: eaar4005.

Bardyn C-E, Karzig T, Refael G, and Liew TCH (2016) Chiral Bogoliubov excitations in nonlinear bosonic systems. *Physical Review B* 93: 020502.

Barik S, Miyake H, DeGottardi W, Waks E, and Hafezi M (2016) Two-dimensionally confined topological edge states in photonic crystals. *New Journal of Physics* 18(11), 113013.

Bergholtz EJ, Budich JC, and Kunst FK (2021) Exceptional topology of non-Hermitian systems. *Reviews of Modern Physics* 93: 015005.

Berry MV (1984) Quantal phase factors accompanying adiabatic changes. *Proceedings of the Royal Society of London A. Mathematical and Physical Sciences* 392(1802): 45–57.

Bliokh KY and Aiello A (2013) Goos–Hänchen and Imbert–Fedorov beam shifts: An overview. *Journal of Optics* 15(1), 014001.

Bliokh K and Bliokh Y (2004a) Topological spin transport of photons: The optical Magnus effect and Berry phase. *Physics Letters A* 333(3): 181–186.

Bliokh KY and Bliokh YP (2004b) Modified geometrical optics of a smoothly inhomogeneous isotropic medium: The anisotropy, Berry phase, and the optical Magnus effect. *Physical Review E* 70: 026605.

Carleo G, Cirac I, Cranmer K, Daudet L, Schuld M, Tishby N, Vogt-Maranto L, and Zdeborová L (2019) Machine learning and the physical sciences. *Reviews of Modern Physics* 91: 045002.

Carusotto I, Houck AA, Kollár AJ, Roushan P, Schuster DI, and Simon J (2020) Photonic materials in circuit quantum electrodynamics. *Nature Physics* 16(3): 268–279.

Chang M-C and Niu Q (1995) Berry phase, hyperorbits, and the Hofstadter spectrum. *Physical Review Letters* 75: 1348–1351.

Chen Y, Neill C, Roushan P, Leung N, Fang M, Barends R, Kelly J, Campbell B, Chen Z, Chiaro B, Dunsworth A, Jeffrey E, Megrant A, Mutus JY, O'Malley PJJ, Quintana CM, Sank D, Vainsencher A, Wenner J, White TC, Geller MR, Cleland AN, and Martinis JM (2014) Qubit architecture with high coherence and fast tunable coupling. *Physical Review Letters* 113: 220502.

Chiao RY and Wu Y-S (1986) Manifestations of Berry's topological phase for the photon. *Physical Review Letters* 57: 933–936.

Cho J, Angelakis DG, and Bose S (2008) Fractional quantum Hall state in coupled cavities. *Physical Review Letters* 101: 246809.

Clark LW, Jia N, Schine N, Baum C, Georgakopoulos A, and Simon J (2019) Interacting Floquet polaritons. *Nature* 571(7766): 532–536.

Clark LW, Schine N, Baum C, Jia N, and Simon J (2020) Observation of Laughlin states made of light. *Nature* 582(7810): 41–45.

Contractor R, Noh W, Redjem W, Qarony W, Martin E, Dhuey S, Schwartzberg A, and Kanté B (2022) Scalable single-mode surface emitting laser via open-Dirac singularities. *Nature* 608(7924): 692–698.

De Nittis G and Lein M (2018) The Schrödinger formalism of electromagnetism and other classical waves – How to make quantum-wave analogies rigorous. *Annals of Physics* 396: 579–617.

Fang K, Yu Z, and Fan S (2012) Realizing effective magnetic field for photons by controlling the phase of dynamic modulation. *Nature Photonics* 6(11): 782–787.

Fedorov FI (1955) K teorii polnogo otrazheniya. *Doklady Akademii Nauk SSSR* 105(3): 465–468.

Firstenberg O, Peyronel T, Liang Q-Y, Gorshkov AV, Lukin MD, and Vuletić V (2013) Attractive photons in a quantum nonlinear medium. *Nature* 502(7469): 71–75.

Gao X, Yang L, Lin H, Zhang L, Li J, Bo F, Wang Z, and Lu L (2020) Dirac-vortex topological cavities. *Nature Nanotechnology* 15(12): 1012–1018.

Gorlach MA, Ni X, Smirnova DA, Korobkin D, Zhirihin D, Slobozhanyuk AP, Belov PA, Alù A, and Khanikaev AB (2018) Far-field probing of leaky topological states in all-dielectric metasurfaces. *Nature Communications* 9(1): 909.

Grusdt F, Letscher F, Hafezi M, and Fleischhauer M (2014) Topological growing of Laughlin states in synthetic gauge fields. *Physical Review Letters* 113: 155301.

Hafezi M, Sørensen AS, Demler E, and Lukin MD (2007) Fractional quantum Hall effect in optical lattices. *Physical Review A* 76: 023613.

Hafezi M, Demler EA, Lukin MD, and Taylor JM (2011) Robust optical delay lines with topological protection. *Nature Physics* 7(11): 907–912.

Hafezi M, Lukin MD, and Taylor JM (2013) Non-equilibrium fractional quantum Hall state of light. *New Journal of Physics* 15(6): 063001.

Haldane FDM (1986) Path dependence of the geometric rotation of polarization in optical fibers. *Optics Letters* 11(11): 730–732.

Haldane FDM (1988) Model for a quantum Hall effect without Landau levels: Condensed-matter realization of the "parity anomaly" *Physical Review Letters* 61: 2015–2018.

Haldane FDM and Raghu S (2008) Possible realization of directional optical waveguides in photonic crystals with broken time-reversal symmetry. *Physical Review Letters* 100(1), 013904.

Hasan MZ and Kane CL (2010) Colloquium: Topological insulators. *Reviews of Modern Physics* 82(4): 3045–3067.

Hayward ALC, Martin AM, and Greentree AD (2012) Fractional quantum Hall physics in Jaynes-Cummings-Hubbard lattices. *Physical Review Letters* 108: 223602.

Imamoḡlu A, Schmidt H, Woods G, and Deutsch M (1997) Strongly interacting photons in a nonlinear cavity. *Physical Review Letters* 79: 1467–1470.

Imbert C (1972) Calculation and experimental proof of the transverse shift induced by total internal reflection of a circularly polarized light beam. *Physical Review D* 5: 787–796.

Iwamoto S, Ota Y, and Arakawa Y (2021) Recent progress in topological waveguides and nanocavities in a semiconductor photonic crystal platform. *Optical Materials Express* 11(2): 319–337.

Joannopoulos JD, Johnson SG, Winn JN, and Meade RD (2008) *Photonic Crystals: Molding the Flow of Light*, 2nd edn. Princeton University Press.

John S (1987) Strong localization of photons in certain disordered dielectric superlattices. *Physical Review Letters* 58: 2486–2489.

Jürgensen M, Mukherjee S, and Rechtsman MC (2021) Quantized nonlinear Thouless pumping. *Nature* 596(7870): 63–67.

Kane CL and Mele EJ (2005a) Quantum spin Hall effect in graphene. *Physical Review Letters* 95: 226801.

Kane CL and Mele EJ (2005b) Z_2 topological order and the quantum spin Hall effect. *Physical Review Letters* 95: 146802.

Kapit E, Hafezi M, and Simon SH (2014) Induced self-stabilization in fractional quantum Hall states of light. *Physical Review X* 4: 031039.

Kato YK, Myers RC, Gossard AC, and Awschalom DD (2004) Observation of the spin Hall effect in semiconductors. *Science* 306(5703): 1910–1913.

Kavokin A, Malpuech G, and Glazov M (2005) Optical spin Hall effect. *Physical Review Letters* 95: 136601.

Khanikaev AB and Shvets G (2017) Two-dimensional topological photonics. *Nature Photonics* 11(12): 763–773.

Khanikaev AB, Hossein Mousavi S, Tse W-K, Kargarian M, MacDonald AH, and Shvets G (2013) Photonic topological insulators. *Nature Materials* 12: 233–239.

Kim M, Jacob Z, and Rho J (2020) Recent advances in 2D, 3D and higher-order topological photonics. *Light: Science & Applications* 9(1): 130.

Kirsch MS, Zhang Y, Kremer M, Maczewsky LJ, Ivanov SK, Kartashov YV, Torner L, Bauer D, Szameit A, and Heinrich M (2021) Nonlinear second-order photonic topological insulators. *Nature Physics* 17(9): 995–1000.

Koch J, Houck AA, Hur KL, and Girvin SM (2010) Time-reversal-symmetry breaking in circuit-QED-based photon lattices. *Physical Review A* 82: 043811.

Kohmoto M (1985) Topological invariant and the quantization of the Hall conductance. *Ann. Phys.* 160(2): 343–354.

Leyder C, Romanelli M, Karr JP, Giacobino E, Liew TCH, Glazov MM, Kavokin AV, Malpuech G, and Bramati A (2007) Observation of the optical spin Hall effect. *Nature Physics* 3(9): 628–631.

Leykam D and Chong YD (2016) Edge solitons in nonlinear-photonic topological insulators. *Physical Review Letters* 117: 143901.

Lu L, Joannopoulos JD, and Soljačić M (2016) Topological states in photonic systems. *Nature Physics* 12(7): 626–629.

Lumer Y, Plotnik Y, Rechtsman MC, and Segev M (2013) Self-localized states in photonic topological insulators. *Physical Review Letters* 111: 243905.

Lumer Y, Rechtsman MC, Plotnik Y, and Segev M (2016) Instability of bosonic topological edge states in the presence of interactions. *Physical Review A* 94: 021801.

Ma T and Shvets G (2016) All-Si valley-Hall photonic topological insulator. *New Journal of Physics* 18(2): 025012.

Ma R, Saxberg B, Owens C, Leung N, Lu Y, Simon J, and Schuster DI (2019a) A dissipatively stabilized Mott insulator of photons. *Nature* 566(7742): 51–57.

Ma J, Xi X, and Sun X (2019b) Topological photonic integrated circuits based on valley kink states. *Laser & Photonics Reviews* 13(12): 1900087.

Maczewsky LJ, Heinrich M, Kremer M, Ivanov SK, Ehrhardt M, Martinez F, Kartashov YV, Konotop VV, Torner L, Bauer D, and Szameit A (2020) Nonlinearity-induced photonic topological insulator. *Science* 370(6517): 701–704.

Malkova N, Hromada I, Wang X, Bryant G, and Chen Z (2009) Observation of optical Shockley-like surface states in photonic superlattices. *Optics Letters* 34(11): 1633–1635.

Mittal S, Goldschmidt EA, and Hafezi M (2018) A topological source of quantum light. *Nature* 561(7724): 502–506.

Mittal S, Orre VV, Zhu G, Gorlach MA, Poddubny A, and Hafezi M (2019) Photonic quadrupole topological phases. *Nature Photonics* 13(10): 692–696.

Mukherjee S and Rechtsman MC (2020) Observation of Floquet solitons in a topological bandgap. *Science* 368(6493): 856–859.

Mukherjee S and Rechtsman MC (2021) Observation of unidirectional solitonlike edge states in nonlinear Floquet topological insulators. *Physical Review X* 11: 041057.

Murakami S, Nagaosa N, and Zhang S-C (2003) Dissipationless quantum spin current at room temperature. *Science* 301(5638): 1348–1351.

Noh C and Angelakis DG (2016) Quantum simulations and many-body physics with light. *Reports on Progress in Physics* 80(1), 016401.

Nunnenkamp A, Koch J, and Girvin SM (2011) Synthetic gauge fields and homodyne transmission in Jaynes–Cummings lattices. *New Journal of Physics* 13(9): 095008.

Onoda M, Murakami S, and Nagaosa N (2004) Hall effect of light. *Physical Review Letters* 93: 083901.

Onoda M, Murakami S, and Nagaosa N (2006) Geometrical aspects in optical wave-packet dynamics. *Physical Review E* 74: 066610.

Ota Y, Takata K, Ozawa T, Amo A, Jia Z, Kante B, Notomi M, Arakawa Y, and Iwamoto S (2020) Active topological photonics. *Nanophotonics* 9(3): 547–567.

Ozawa T and Carussoto I (2014) Anomalous and quantum Hall effects in lossy photonic lattices. *Physical Review Letters* 112: 133902.

Ozawa T, Price HM, Amo A, Goldman N, Hafezi M, Lu L, Rechtsman MC, Schuster D, Simon J, Zilberberg O, and Carusotto I (2019) Topological photonics. *Reviews of Modern Physics* 91: 015006.

Pancharatnam S (1956) Generalized theory of interference and its applications. *Proceedings of the Indian Academy of Sciences - Section A* 44(6): 398–417.

Parto M, Wittek S, Hodaei H, Harari G, Bandres MA, Ren J, Rechtsman MC, Segev M, Christodoulides DN, and Khajavikhan M (2018) Edge-mode lasing in 1D topological active arrays. *Physical Review Letters* 120(11): 113901.

Peano V, Houde M, Marquardt F, and Clerk AA (2016) Topological quantum fluctuations and traveling wave amplifiers. *Physical Review X* 6: 041026.

Poli C, Bellec M, Kuhl U, Mortessagne F, and Schomerus H (2015) Selective enhancement of topologically induced interface states in a dielectric resonator chain. *Nature Communications* 6(1): 6710.

Rechtsman MC, Zeuner JM, Plotnik Y, Lumer Y, Podolsky D, Dreisow F, Nolte S, Segev M, and Szameit A (2013) Photonic Floquet topological insulators. *Nature* 496(7444): 196–200.

Ross JN (1984) The rotation of the polarization in low birefringence monomode optical fibres due to geometric effects. *Optical and Quantum Electronics* 16(5): 455–461.

Roushan P, et al. (2017a) Chiral ground-state currents of interacting photons in a synthetic magnetic field. *Nature Physics* 13(2): 146–151.

Roushan P, et al. (2017b) Spectroscopic signatures of localization with interacting photons in superconducting qubits. *Science* 358(6367): 1175–1179.

Rudner MS and Levitov LS (2009) Topological transition in a non-Hermitian quantum walk. *Physical Review Letters* 102: 065703.

Rytov S (1938) On transition from wave to geometrical optics. *Doklady Akademii Nauk SSSR* 18: 263–266.

Saba M, Wong S, Elman M, Oh SS, and Hess O (2020) Nature of topological protection in photonic spin and valley Hall insulators. *Physical Review B* 101: 054307.

Sauer E, Vasco JP, and Hughes S (2020) Theory of intrinsic propagation losses in topological edge states of planar photonic crystals. *Physical Review Research* 2: 043109.

Schine N, Ryou A, Gromov A, Sommer A, and Simon J (2016) Synthetic Landau levels for photons. *Nature* 534(7609): 671–675.

Schomerus H (2013) Topologically protected midgap states in complex photonic lattices. *Optics Letters* 38(11): 1912–1914.

Seclì M, Ozawa T, Capone M, and Carusotto I (2021) Spatial and spectral mode-selection effects in topological lasers with frequency-dependent gain. *APL Photonics* 6(5), 050803.

Shao Z-K, Chen H-Z, Wang S, Mao X-R, Yang Z-Q, Wang S-L, Wang X-X, Hu X, and Ma R-M (2020) A high-performance topological bulk laser based on band-inversion-induced reflection. *Nature Nanotechnology* 15(1): 67–72.

Simon B (1983) Holonomy, the quantum adiabatic theorem, and Berry's phase. *Physical Review Letters* 51: 2167–2170.

Smirnova D, Kruk S, Leykam D, Melik-Gaykazyan E, Choi D-Y, and Kivshar Y (2019) Third-harmonic generation in photonic topological metasurfaces. *Physical Review Letters* 123: 103901.

Smirnova D, Leykam D, Chong Y, and Kivshar Y (2020) Nonlinear topological photonics. *Applied Physics Reviews* 7(2), 021306.

Sørensen AS, Demler E, and Lukin MD (2005) Fractional quantum Hall states of atoms in optical lattices. *Physical Review Letters* 94: 086803.

St-Jean P, Goblot V, Galopin E, Lemaître A, Ozawa T, Gratiet LL, Sagnes I, Bloch J, and Amo A (2017) Lasing in topological edge states of a one-dimensional lattice. *Nature Photonics* 11(10): 651.

Tan DTH (2021) Topological silicon photonics. *Adv. Photonics Res.* 9: 2100010.

Thouless DJ, Kohmoto M, Nightingale MP, and den Nijs M (1982) Quantized Hall conductance in a two-dimensional periodic potential. *Physical Review Letters* 49(6): 405–408.

Tomita A and Chiao RY (1986) Observation of Berry's topological phase by use of an optical fiber. *Physical Review Letters* 57: 937–940.

Umucalılar RO and Carusotto I (2011) Artificial gauge field for photons in coupled cavity arrays. *Physical Review A* 84: 043804.

Umucalılar RO and Carusotto I (2012) Fractional quantum Hall states of photons in an array of dissipative coupled cavities. *Physical Review Letters* 108: 206809.

Umucalılar RO, Wouters M, and Carusotto I (2014) Probing few-particle Laughlin states of photons via correlation measurements. *Physical Review A* 89: 023803.

Vladimirskii V (1941) The rotation of a polarization plane for curved light ray. *Doklady Akademii Nauk SSSR* 21: 222–225.

von Klitzing K, Chakraborty T, Kim P, Madhavan V, Dai X, McIver J, Tokura Y, Savary L, Smirnova D, Rey AM, Felser C, Gooth J, and Qi X (2020) 40 years of the quantum Hall effect. *Nature Physics* 2(8): 397–401.

Wang Z, Chong YD, Joannopoulos JD, and Soljačić M (2008) Reflection-free one-way edge modes in a gyromagnetic photonic crystal. *Physical Review Letters* 100(1): 013905.

Wang Z, Chong Y, Joannopoulos JD, and Soljačić M (2009) Observation of unidirectional backscattering-immune topological electromagnetic states. *Nature* 461: 772–775.

Wu L-H and Hu X (2015) Scheme for achieving a topological photonic crystal by using dielectric material. *Physical Review Letters* 114(22): 223901.

Xia S, Jukić D, Wang N, Smirnova D, Smirnov L, Tang L, Song D, Szameit A, Leykam D, Xu J, Chen Z, and Buljan H (2020) Nontrivial coupling of light into a defect: the interplay of nonlinearity and topology. *Light: Science & Applications* 9(1): 147.

Xiao D, Chang M-C, and Niu Q (2010) Berry phase effects on electronic properties. *Reviews of Modern Physics* 82: 1959–2007.

Xu L, Wang H-X, Xu Y-D, Chen H-Y, and Jiang J-H (2016) Accidental degeneracy in photonic bands and topological phase transitions in two-dimensional core-shell dielectric photonic crystals. *Optics Express* 24(16): 18059–18071.

Yablonovitch E (1987) Inhibited spontaneous emission in solid-state physics and electronics. *Physical Review Letters* 58: 2059–2062.

Yang L, Li G, Gao X, and Lu L (2022) Topological-cavity surface-emitting laser. *Nature Photonics* 16(4): 279–283.

Zeng Y, Chattopadhyay U, Zhu B, Qiang B, Li J, Jin Y, Li L, Davies AG, Linfield EH, Zhang B, Chong Y, and Wang QJ (2020) Electrically pumped topological laser with valley edge modes. *Nature* 578(7794): 246–250.

Zeuner JM, Rechtsman MC, Plotnik Y, Lumer Y, Nolte S, Rudner MS, Segev M, and Szameit A (2015) Observation of a topological transition in the bulk of a non-Hermitian system. *Physical Review Letters* 115: 040402.

Zhang W and Zhang X (2019) Backscattering-immune computing of spatial differentiation by nonreciprocal plasmonics. *Physical Review Applied* 11: 054033.

Zhao H, Miao P, Teimourpour MH, Malzard S, El-Ganainy R, Schomerus H, and Feng L (2018) Topological hybrid silicon microlasers. *Nature Communications* 9(1): 981.

Zhao H, Qiao X, Wu T, Midya B, Longhi S, and Feng L (2019) Non-Hermitian topological light steering. *Science* 365(6458): 1163–1166.

Zhen B, Hsu CW, Igarashi Y, Lu L, Kaminer I, Pick A, Chua S-L, Joannopoulos JD, and Soljačić M (2015) Spawning rings of exceptional points out of Dirac cones. *Nature* 525(7569): 354–358.

Zhou H, Peng C, Yoon Y, Hsu CW, Nelson KA, Fu L, Joannopoulos JD, Soljačić M, and Zhen B (2018) Observation of bulk Fermi arc and polarization half charge from paired exceptional points. *Science* 359(6379): 1009–1012.

Zhu T, Lou Y, Zhou Y, Zhang J, Huang J, Li Y, Luo H, Wen S, Zhu S, Gong Q, Qiu M, and Ruan Z (2019) Generalized spatial differentiation from the spin Hall effect of light and its application in image processing of edge detection. *Physical Review Applied* 11: 034043.

Zhu T, Guo C, Huang J, Wang H, Orenstein M, Ruan Z, and Fan S (2021) Topological optical differentiator. *Nature Communications* 12: 680.

The Anomalous Hall Effect

Dimitrie Culcer, School of Physics, The University of New South Wales, Sydney, NSW, Australia

© 2024 Elsevier Ltd. All rights reserved.

Introduction 587
Overview 588
Key issues 590
A very brief picture of ferromagnetism 590
Spin-orbit coupling 592
Topological materials 593
Charge transport description of the anomalous Hall effect 594
Anomalous Hall effects in topological materials 598
Conclusion 600
Acknowledgments 600
References 600

Abstract

This article reviews the main contributions to the anomalous Hall effect and its resurgence in the past three decades, which has been accompanied by the rise of topological phenomena and topological materials. I will show that the anomalous Hall effect stems from the interplay of magnetism, spin-orbit coupling, disorder scattering and driving electric fields, it spans the classical, quantum and relativistic worlds, and has generated controversy for nearly one and a half centuries. It has become the smoking gun for detecting magnetic order and, extraordinarily, it continues to reveal new physics, with several novel varieties reported in the past decade.

Key points

- Review experimental and theoretical work on the anomalous Hall effect.
- Elucidate the vital role played by the spin-orbit interaction.
- Demonstrate the interplay of topological quantities and scattering processes.
- Outline new developments in topological materials.

Introduction

In 1879 Edwin Hall discovered the effect that bears his name (Hall, 1879). When a non-ferromagnetic metallic sample is exposed to a perpendicular external magnetic field B, the Lorentz force acting on the current carriers gives rise to a transverse voltage in the plane of the sample. The transverse component of the resistivity, ρ_{xy}, depends on the magnetic field through the relationship $\rho_{xy} = R_0 B$, where $R_0 = 1/(ne)$ is known as the Hall coefficient, n is the carrier density, and $-e$ is the electron charge. This phenomenon, whose explanation is entirely classical, is known as the ordinary Hall effect and is well understood. Determining the Hall coefficient R_0 has become the tool of choice for measuring carrier densities in conducting materials.

The following year Hall noticed that in many ferromagnets the transverse resistivity acquires an additional term independent of the magnetic field, which is often proportional to the magnetization M of the sample, and becomes constant once the sample has reached its saturation magnetization (Hall, 1881). The effect is referred to as the anomalous Hall effect (AHE). Whereas the ordinary Hall effect of classical physics requires an external magnetic field, the anomalous Hall effect requires only a magnetization, and it was soon realized that ferromagnets display a spontaneous Hall conductivity in the absence of an external magnetic field. The effect has been subsequently observed in a multitude of systems, including transition metals and their oxides, in materials which exhibit colossal magnetoresistance, ferromagnetic semiconductors, topological insulators and a host of other topological materials (Nagaosa et al., 2010).

The anomalous Hall effect stems from the fact that, when a current passes through a magnetic material, electrons are predominantly deflected in one direction. This results in an additional current perpendicular to the driving current, which vanishes if the material is non-magnetic. The mechanisms responsible for this deflection have been the subject of substantial controversy ever since Hall's experimental work. Whereas several mechanisms are known to be responsible, the principal actors are united by the spin-orbit interaction—magnetism by itself is usually not sufficient to give rise to an anomalous Hall current. Furthermore, spin-orbit coupling effects are conventionally divided into intrinsic processes, stemming from a material's band structure, and extrinsic processes, related to scattering events. Recent research has shown that intrinsic spin-orbit coupling effects are intertwined with the topological properties of a material's band structure, and that the interplay of intrinsic and extrinsic processes is highly non-trivial.

https://doi.org/10.1016/B978-0-323-90800-9.00006-8

This review attempts to present a unified picture of our current understanding of the anomalous Hall effect, of its rich history, and of the tremendous excitement generated by developments over the past two decades. I will begin with a brief historical overview focusing on experimental results and on the theoretical controversy that emerged in the 1950s concerning the relative roles of intrinsic and extrinsic processes in the steady state established in an electric field. I will then cover the key physical aspects of the effect: a brief review of ferromagnetism and inhomogeneous magnetic textures, followed by a discussion of the spin-orbit interaction and its manifestation in the solid state, topological materials, semiclassical dynamics and the quantum kinetic equation, band structure spin-orbit coupling and the topological contribution to the anomalous Hall effect, the role of scalar scattering, and the effect of spin-orbit coupling on scattering potentials leading to skew scattering and side jump scattering. Next I will discuss modern developments in the field, spanning the last 20 years, including the quantized anomalous Hall effect in topological insulators, the distinct roles of bulk and edge transport in topological materials, the planar Hall effect and its offshoots, and the non-linear anomalous Hall effect. I will end with a brief summary and discussion of future directions.

Overview

The anomalous Hall effect has a lengthy and controversial history and remains incompletely understood. At its heart lie the physical concepts of ferromagnetism and spin-orbit coupling, on which I will concentrate in the next section. To facilitate the exposition I will identify a *Classic Period*, spanning the time from the discovery of the anomalous Hall effect to the last decade of the twentieth century, and a *Modern Era* spanning the last decade of the twentieth century and the first decade of the twenty-first, and a or *Topological Era*, from the rise of topological materials to the present day. The Classic Period was characterized by initial experimental observations followed by a lengthy fundamental debate, and we can place its end approximately after the discovery of the quantum Hall effects. The Modern Period has been characterized by a surge in interest in topological quantities and a persistent effort to understand the parameter ranges in which different mechanisms dominate. The Topological Period has been shaped by the discovery of topological materials and the emergence of a variety of new anomalous Hall effects.

Classic Period. Following Hall's original work, experiments focused on the anomalous Hall effect in transition metals, and on its exact relationship to the magnetization M. It was determined empirically that the Hall resistivity follows the relationship $\rho_{xy} = R_0B + R_sM$, with the constant R_s referred to as the anomalous Hall coefficient (Pugh and Lippert, 1932). Frequently $R_s \gg R_0$ (Pugh et al., 1950). It was established that a spontaneous Hall current indeed exists in the absence of a magnetic field, as shown in Fig. 1. In due course this spontaneous current became the smoking gun for the identification of ferromagnetic order, considering that such a transport test is much easier to perform experimentally than optical techniques based on dichroism or on the Kerr and Faraday effects.

The controversy surrounding the origins of the anomalous Hall effect began after decades of experimental work. The theory of the AHE was pioneered by Karplus and Luttinger in the 1950s (Karplus and Luttinger, 1954), who found that the spin splitting of bands can give rise to a Hall conductivity in the presence of spin-orbit coupling, identifying a contribution to the AHE which was independent of scattering, or intrinsic. The controversy emerged when Smit countered that in a perfectly periodic lattice the AHE

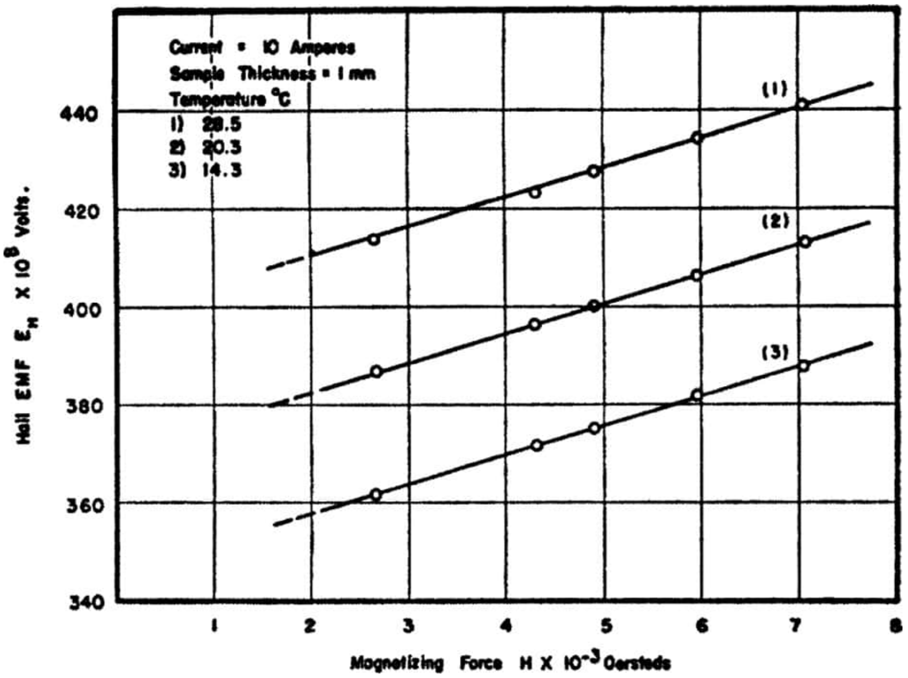

Fig. 1 Hall electromotive force as a function of the applied magnetic field in a Ni sample which has reached its saturation magnetization. The slope of the lines gives the ordinary Hall coefficient while the *y*-intercepts give the anomalous Hall coefficients. From Pugh EM, Rostoker N and Schindler A (1950) On the Hall Effect in Ferromagnetics. *Physical Review* **80**: 688.

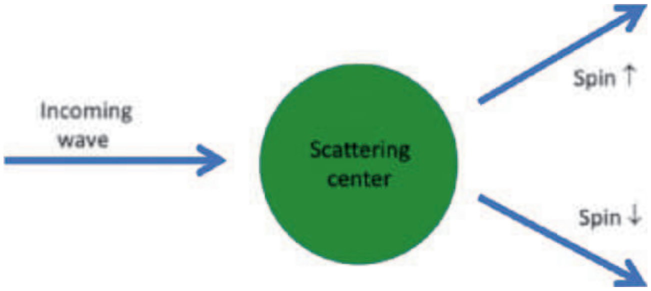

Fig. 2 Skew scattering. Spin-up and spin-down electrons are scattered preferentially in different directions.

could not occur without scattering from impurities (Smit, 1955). To explain the AHE Smit introduced the extrinsic skew scattering mechanism, which consists of asymmetric scattering of up and down spins by an impurity potential modified by the spin-orbit interaction: an electron is scattered at an angle to its original direction, while spin-up electrons are predominantly scattered in one direction, and spin-down electrons are predominantly scattered in the other. This is illustrated in Fig. 2. Note that spin-orbit coupling is vital in Smit's argument as well: although magnetic impurities cause up and down spins to be scattered in different directions, they will not give AHE by themselves. In response to Smit, in a more complete treatment Luttinger found a term corresponding to skew scattering, which depends on the details of the scattering potential, but maintained that the scattering free contribution to the AHE remains (Luttinger and Kohn, 1955; Kohn and Luttinger, 1957; Luttinger, 1958; Luttinger and Kohn, 1958; Adams and Blount, 1959).

Luttinger's finding was revolutionary, since transport effects known at the time relied on scattering to establish a steady state and give rise to dissipation: both the longitudinal resistivity and the ordinary Hall resistivity depend on scattering. It touched on a fundamental point: the Hall conductivity itself can be non-dissipative, even though for a Hall effect linear in the electric field to occur time reversal needs to be broken, which in the AHE is accomplished by the presence of magnetic order. This can be seen if we think of power dissipation as $\vec{F}\cdot\vec{v}$, the scalar product of the external force with the net velocity. The force in this case comes from the electric field, so that the scalar product vanishes for velocity components transverse to the electric field. The only constraint on the Hall response is the Onsager relation, which states that the transverse conductivity $\sigma_{xy}\left(\vec{B}\right) = \sigma_{yx}\left(-\vec{B}\right)$, or if only a magnetisation is present $\sigma_{xy}\left(\vec{M}\right) = \sigma_{yx}\left(-\vec{M}\right)$. The transverse resistivity likewise satisfies $\rho_{xy}\left(\vec{M}\right) = \rho_{yx}\left(-\vec{M}\right)$.

The skew scattering mechanism introduced by Smit gives a contribution to ρ_{xy} which is proportional to ρ_{xx}, the longitudinal resistivity. Later, a new mechanism, called the side jump was introduced by Berger to explain the observed $\rho_{xy} \propto \rho_{xx}^2$ dependence in certain parameter regimes, to be elaborated below (Berger, 1970). Side jump represents a transverse shift in a wave-packet's center of mass in the course of scattering, which is also asymmetric between spin up and spin down, as shown in Fig. 3. The electron incident into the area of influence of the potential emerges parallel to its original direction but displaced perpendicular to it. The side jump has become the source of much debate, including confusion in terminology (Lyo and Holstein, 1972; Nozieres and Lewiner, 1973; Chazalviel, 1975; Sinitsyn, 2008). The subtle discussion surrounding the side-jump is covered extensively in Nagaosa et al. (2010). Complicating matters is the fact that the intrinsic mechanism leads to the same $\rho_{xy} \propto \rho_{xx}^2$ dependence as Berger's side jump.

Modern Period. One fundamental insight of modern research into the AHE is that the intrinsic, scattering-free contribution of Luttinger and Karplus is related to the Berry curvature of Bloch electrons. It is associated with a deflection of particle trajectories under the action of the spin-orbit interaction in the band structure of the material. This insight first emerged from semi-classical analyses of wave-packet dynamics and has been confirmed by rigorous derivations based on the Kubo formula and the density matrix. At the same time, it is now understood that skew scattering and side-jump, which were originally introduced for electrons with a scalar dispersion scattering off a spin-dependent potential, are qualitatively similar for electrons with spin-dependent dispersions in the presence of scalar potentials.

Much of the recent work has focused on transition metals and transition metal oxides, some of which are itinerant ferromagnets. An important aim has been elucidating the roles of distinct AHE contributions in different parameter regimes, since it is understood that in principle all mechanisms are present concomitantly, and two types of contributions exist which have different dependencies on ρ_{xx}, and therefore on the scattering time τ. Three resistivity regimes have been identified: a high mobility regime in which skew scattering dominates because τ is large (Majumdar and Berger, 1973), a good metal regime in which the dominant contribution is

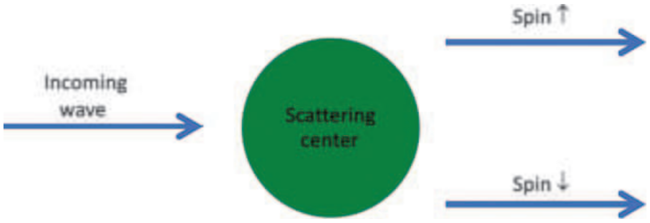

Fig. 3 Side-jump. Spin-up and spin-down electrons undergo a lateral shift in different directions during a scattering process.

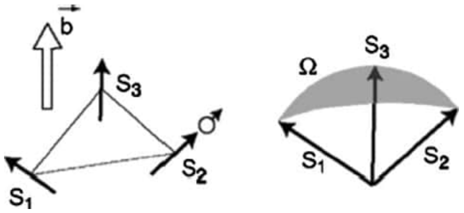

Fig. 4 Spin chirality, as illustrated in Nagaosa et al. (2010). An electron spin circulated around three local spins, with which it interacts via exchange coupling, feels the effect of a fictitious magnetic field, whose magnitude is determined by the solid angle subtended by the local spins. From Nagaosa N et al. (2010) Anomalous Hall effect. *Reviews of Modern Physics* **82**: 1539.

independent of τ (Miyasato et al., 2007), and may be intrinsic or side-jump or both, and a low-mobility regime where conduction occurs primarily by hopping, where the overall picture remains unclear (Nagaosa et al., 2010).

Considerable attention was devoted in the 2000s to ferromagnetic semiconductors, which are III–V semiconductors doped with transition metals, the textbook case being (Ga, Mn)As (Jungwirth et al., 2006). Ferromagnetism is mediated by the delocalized conduction holes through the Ruderman-Kittel-Kasuya-Yosida (RKKY) interaction. It was established early on that the scattering-independent contribution $\rho_{xy} \propto \rho_{xx}^2$ dominates the AHE, and nowadays it is strongly believed the intrinsic contribution is responsible. This topological contribution was evaluated for (Ga, Mn)As with magnetic interactions accounted for in a mean field theory, yielding excellent agreement with experiments (Jungwirth et al., 2002). Yet interest in ferromagnetic semiconductors dipped when avenues for pushing the critical temperature to room temperature appeared to be exhausted.

Additional developments in AHE paralleled developments in magnetic materials, notably the discovery of giant and colossal magneto-resistances. Much of the work in this direction has been on complex oxide ferromagnets, and has revealed a novel AHE mechanism termed spin chirality, which also has a geometrical origin, associated with the real-space magnetic texture (Matl et al., 1998). This is shown in Fig. 4. It occurs in manganites, in which transport mainly involves electrons hoping between Mn sites, which leads to colossal magneto-resistance. An electron spin hopping between three or more Mn sites with non-coplanar spin orientations acquires a geometric phase, which can be regarded as stemming from a fictitious magnetic field with magnitude determined by the solid angle subtended by the localized spins. This fictitious magnetic field is coupled to the magnetization through the spin-orbit interaction, and this coupling leads to an anomalous Hall current. A realization of such an inhomogeneous magnetic texture is a topological defect called a skyrmion, and spin chirality reflects an excess of e.g., positive skyrmions over negative skyrmions at finite temperature. The spin chirality mechanism can thus be related to a Berry phase acquired in real space (Ye et al., 1999; Lyanda-Geller et al., 2001). It also leads to an anomalous Hall effect in antiferromagnets (Shindou and Nagaosa, 2001). Spin chirality may occur in the ground state of pyrochlore ferromagnets under the influence of anisotropy, frustration and spin fluctuations but experimental results are inconclusive (Ohgushi et al., 2000; Onoda and Nagaosa, 2003a, 2003b). Indeed the AHE remains poorly understood in many classes of materials with complex spin structures, such as spin glasses with random order, MnSi with spiral spin order, spinels and Heusler alloys.

Topological Period. The last 15 years have been shaped by the rise of topological materials, including topological insulators, Weyl semimetals, transition metal dichalcogenides, and van der Waals heterostructures. The band structures of many of these materials are reminiscent of relativistic dispersions with non-trivial topological structures, and they possess complex surface and edge states. The materials are often quite dirty, making disorder effects important. Topological materials have brought with them a new understanding of the AHE. It was shown that the anomalous Hall effect can be quantized in undoped topological insulators and Weyl semimetals, and it can switch sign in doped topological insulators. In transition metal dichalcogenides the AHE has different signs in the two valleys, leading to a valley Hall effect. Most recently, non-linear and planar versions of the anomalous Hall effect have been identified. The AHE in topological materials is one of the most vibrant research areas today.

Key issues

A very brief picture of ferromagnetism

Since the AHE occurs in ferromagnets, understanding it requires a succinct review of a few key concepts. Ferromagnetism is a consequence of the Coulomb interaction and the Pauli exclusion principle and is intimately connected with the notion of exchange. Based on their relative spin orientations, two electrons can be in either a singlet or a triplet state. The singlet is spatially symmetric and spin anti-symmetric, while the triplet is spin symmetric and spatially anti-symmetric. Due to their different spatial configurations the singlet and triplet states are split by an energy referred to as the exchange energy J, which takes the form

$$J = \int d^3r\, \phi^*(\overrightarrow{r_1})\psi^*(\overrightarrow{r_2})V_{ee}\phi(\overrightarrow{r_2})\psi(\overrightarrow{r_1}), \tag{1}$$

where ϕ, ψ are the two spatial wave functions, V_{ee} is the Coulomb interaction and (1), (2) denote the two electrons. J may have either sign. In the convention used here positive exchange leads to a triplet ground state. In terms of spin operators this interaction may be written as $H_{2e} = -J\overrightarrow{S}_1\cdot\overrightarrow{S}_2$. For an array of atoms interacting via exchange the above Hamiltonian is generalised to the Heisenberg Hamiltonian, appropriate to some insulating systems.

$$H_{He} = -\sum_{ij} J_{ij} \vec{S}_i \cdot \vec{S}_j. \tag{2}$$

Very often the parameters J_{ij} are approximated by a single exchange constant J. It is easily checked that the ground state of the Heisenberg Hamiltonian with positive exchange has all spins pointing in the same direction. The system has the freedom to choose the direction, and when it does so both time reversal and rotational symmetry are broken.

Exchange leads to magnetic order in many different forms, and the situation in real materials is far more complex than the above. For example, magnetism in manganites is mediated by double exchange, which involves different atomic orbitals, while magnetism in spinels occurs due to super-exchange, which involves an intermediate atom. Ferromagnetism can also leak from one material into another material adjacent to it via a ferromagnetic proximity effect.

Conducting ferromagnets are often itinerant, with a notable example being provided by ferromagnetic semiconductors (Dietl et al., 2001). In the simplest picture, a local Mn moment interacts with an itinerant hole. That interaction is in fact anti-ferromagnetic, so their spins tend to align anti-parallel to each other. The hole, being delocalized, travels through the sample and interacts anti-ferromagnetically with a second local Mn moment. The hole thus mediates an interaction between the two local moments, which end up aligning parallel to each other, so the net interaction between them is ferromagnetic. This is the basis of the Ruderman-Kittel-Kasuya-Yosida (RKKY) interaction. In topological insulators doped with ferromagnetic ions the situation is similar in spirit except magnetism is mediated by band electrons through the van Vleck mechanism. These electrons may reside in the valence band and the mechanism is active even when the system is insulating.

Due to the complexity of a fully quantum mechanical description in terms of spin operators, magnetism is most often thought of in a *mean field* picture. Each spin is assumed to interact with the net effective magnetization M produced by all the other spins. For itinerant ferromagnets the simplest theory is the Stoner description, which considers the charge carriers to be quasiparticles in spontaneously split bands. Thus a spin travelling through a ferromagnetic material interacts with the average magnetization, while fluctuations in the magnetization play an analogous role to spin-dependent scattering off an impurity.

In general the magnetization $\vec{M} = \vec{M}\left(\vec{r}\right)$ is inhomogeneous and has a strong position dependence. Real samples are fragmented into domains, whose magnetizations point in different directions, and which are separated by domain walls. Magnetizations can vary in space in other ways, exhibiting topological defects referred to as skyrmions, which are akin to vortices (Göbel et al., 2001). An example of a magnetic skyrmion is shown in Fig. 5. These are prominent in correlated oxides and dilute magnetic semiconductors. Magnetic skyrmions are small swirling topological magnetic excitations with particle-like properties, in which the spin at the core and the spin at the perimeter point in opposite directions. They result from the competition between the Dzyaloshinskii-Moriya and exchange interactions, and give rise to a nonzero Berry curvature in real space, which plays the role of an effective or *emergent* magnetic field, and can reach the equivalent of thousands of Teslas in very small skyrmions, that is, smaller than 10 nm. This emergent magnetic field deflects conduction electrons and causes a topological Hall effect, a relative of the anomalous Hall effect that does involves neither a magnetic field nor spin-orbit coupling (Bruno et al., 2004). At the same time the formation of magnetic skyrmions reduces an average magnetization and makes it somewhat challenging experimentally to differentiate the topological Hall effect from the anomalous Hall effect.

The simplest textbook models tend to assume tacitly that the temperature is absolute zero. Ferromagnetism occurs below the Curie temperature T_c. The critical temperature at which ferromagnetism occurs is determined by a number of parameters, including the exchange and the size of the ionic spins. As ferromagnetism vanishes above T_c the anomalous Hall effect vanishes with it, making it a useful tool for measuring the transition temperature. Below T_c several temperature-dependent mechanisms come into play, including the temperature-dependence of the magnetisation, which dominates in $SrRuO_3$ (Allen et al., 1996; Izumi et al., 1997; Fang et al., 2003), the variation of scattering times with temperature and contributions from spin waves. Their interplay makes the AHE temperature dependence exceedingly complex, and it remains an active research area.

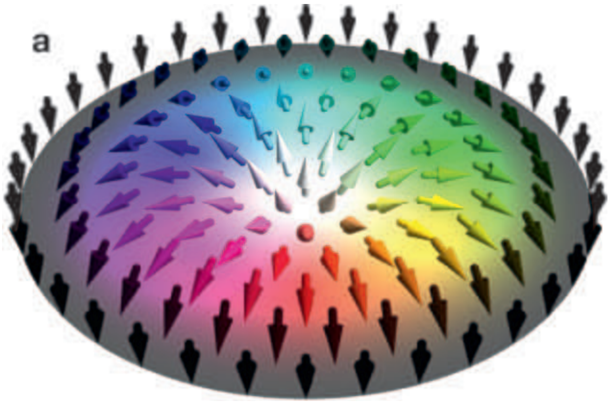

Fig. 5 An example of a magnetic skyrmion. From Göbel B, Mertig I and Tretiakov OA (2001) Beyond skyrmions: Review and perspectives of alternative magnetic quasiparticles. *Physics Reports* 895: 1.

Spin-orbit coupling

At the heart of the anomalous Hall effect lies the spin-orbit interaction. Since all contributions to AHE are traced back to spin-orbit coupling, we shall discuss this interaction and its consequences for transport in solid state systems in some detail. The spin-orbit interaction appears in quantum mechanics as a relativistic effect, emerging explicitly when one transitions from the Dirac equation to the Pauli equation. For free electrons with charge $-e$ a natural separation of energy scales can be made into small terms (momentum) and large terms (mass), which leads to a decomposition of the resulting Hamiltonian into the kinetic energy, the electrostatic potential contribution eV, the Zeeman term and spin-orbit coupling, which takes the form: (Messiah, 2014)

$$H_{SO} = \frac{\hbar}{4m^2c^2}\,\vec{\sigma}\cdot\vec{\nabla}V \times \vec{p}. \tag{3}$$

The potential V is the full potential acting on the electron. For a free electron the spin-orbit interaction is typically negligible. In an atom $\vec{\nabla}V$ is the central potential and the spin-orbit interaction is $\propto \vec{L}\cdot\vec{S}$, where $\vec{L}$ denotes the orbital angular momentum and $\vec{S}$ the electron spin, which accounts for the name of the interaction. Atomic spin-orbit coupling can be very strong and, since the atomic potential appears in Eq. (3), it is clear that the spin-orbit coupling increases with atomic number and becomes stronger as one advances down the periodic table.

For electrons in a crystal V contains: (i) an *intrinsic* contribution arising from the periodic potential and applied electric fields, the latter encompassing both electrostatic gates and driving electric fields; and (ii) an *extrinsic* contribution from the random disorder potential and phonons.

In the effective mass picture the overall form of the band structure spin-orbit interaction around a particular band extremum can be determined from symmetry considerations. To obtain the relevant pre-factors one typically adds the spin-orbit term of Eq. (3) to the general crystal Hamiltonian and projects out bands until we find an effective model for the bands of interest, which tend to be the conduction band or the valence band. It is worth noting the similarity between Eq. (3) and the Zeeman effect. To understand we recall that electrons in the conduction bands of many materials behave as quasiparticles with an effective spin-1/2, in other words their behavior is very similar to that of free electrons. As a consequence, the intrinsic band-structure contribution to the spin-orbit interaction is very similar to that for free electrons. It can be represented as the interaction between the spin and a momentum-dependent effective Zeeman field whose form is determined by the symmetry of the crystal. This effective field is odd in momentum and integrates to zero over the crystal since spin-orbit coupling does not break time-reversal. For terms odd in the momentum to be allowed the structure must break inversion symmetry. In 3D the crystal itself must break inversion symmetry, a property known as bulk inversion asymmetry (BIA). To describe the spin-orbit interaction in confined systems one needs to add the confinement potential. Confinement to 2D can be modelled analytically by a square or parabolic well for the symmetric case, or by a triangular well for the asymmetric case, and by more sophisticated Schrodinger-Poisson methods when electron-electron interactions need to be taken into account. In the context of Eq. (3), gate fields are usually taken into account within the device confinement model, while driving electric fields, and their accompanying spin-orbit effects, are treated perturbatively, most often within a linear-response framework. In a 2D structure an additional spin-orbit mechanism is present. For an effective spin-1/2 such interactions have the general form of Eq. (3), with the pre-factor replaced by a material- and structure-specific parameter. In a 2D electron gas we need to consider the contribution from the confinement potential, which generates an electric field along the z-direction perpendicular to the interface, so that, setting $\vec{\nabla}V \parallel \hat{z}$ in Eq. (3), we obtain the well-known Rashba interaction (Bychkov and Rashba, 1984),

$$H_R = \alpha\left(\sigma_x k_y - \sigma_y k_x\right). \tag{4}$$

Spin-orbit coupling provides a wave vector-dependent quantization direction for the charge carriers' spins. For the Rashba interaction to be nonzero the 2D electron gas needs to be asymmetric, a feature referred to as structure inversion asymmetry (SIA). It increases linearly with the gate electric field for known electron systems.

In analogy with the Rashba interaction, the spin-orbit interaction for electron systems in conducting materials can very frequently be written in the form $\vec{\sigma}\cdot\vec{B}_{\vec{k}}$, where $\vec{B}_{\vec{k}}$ can be thought of as an effective magnetic field that depends on the electron momentum (Winkler, 2003). This picture, which remains very common, is intimately linked to one of the main spin relaxation mechanisms in conductors, the Dyakonov-Perel mechanism (D'yakonov and Perel, 1971; Pikus and Titkov, 1984). The spin-orbit interaction in these materials is accompanied by the scalar kinetic energy $H_{kin} = \frac{\hbar^2k^2}{2m}$, which is much larger than it. The total Hamiltonian has two eigenstates which correspond to two spin-split sub-bands. The spin precesses between scattering events under the action of the band structure spin-orbit effective field $\vec{B}_{\vec{k}}$. During ordinary scalar scattering events, the wave vector changes from $\vec{k}$ to $\vec{k}'$, and the spin now precesses about a different field $\vec{B}_{\vec{k}'}$. If the scattering rate is much larger than the precession frequency the spin does not have time to precess between scattering events and preserves its orientation, leading to the counter-intuitive conclusion that more momentum scattering increases the spin lifetime. If we associate momentum scattering with a relaxation time τ, the product $\vec{B}_{\vec{k}}\tau/\hbar$, with $\vec{k}$ usually evaluated at the Fermi energy, determines two qualitatively different regimes. The Dyakonov-Perel regime corresponds to $\frac{\vec{B}_{\vec{k}}\tau}{\hbar} \ll 1$, while in the weak scattering regime $\frac{\vec{B}_{\vec{k}}\tau}{\hbar} \gg 1$, and momentum scattering leads to a reduction in the spin lifetime. In the past, especially at the time of the debate between Luttinger, Smit and Berger, the Dyakonov-Perel regime was the only experimentally accessible regime. Whether referring explicitly to spin relaxation or not, early calculations of the anomalous Hall effect almost invariably assumed the Dyakonov-Perel regime. In the past two decades, as a result of substantial increases in sample quality, the weak scattering regime is routinely accessed.

Another contribution to the potential in Eq. (3) is the random disorder potential $U\left(\vec{r}\right)$, which, in momentum space, gives rise to the following term, which causes spin-dependent scattering:

$$H_{ss} = -i\,\lambda\,U_{\vec{k}\vec{k}'}\,\vec{\sigma}\cdot\vec{k}\times\vec{k}'. \tag{5}$$

It can be thought of as a random effective magnetic field, which depends on an electron's incident and scattered wave vectors. In two-dimensional systems, in which $\vec{k}$ and $\vec{k}'$ are both in the plane, the effective magnetic field points out of the plane. In the older literature it was common to associate the additional term in the potential with a fictitious coordinate shift, so that the position operator would be modified from $\vec{r}$ to $\vec{r}+\lambda\,\vec{\sigma}\times\vec{k}$. When the potential $U\left(\vec{r}\right)$ becomes $U\left(\vec{r}+\lambda\,\vec{\sigma}\times\vec{k}\right)$ and is expanded in λ Eq. (5) emerges (Sinitsyn, 2008).

Skew scattering and side jump are both a consequence of Eq. (5). In skew scattering spin-up electrons are predominantly scattered in one direction, and spin-down electrons in the other. Side jump consists of a transverse displacement of the outgoing electron trajectory with respect to its incoming path, which again has the opposite sign for up and down spins. Eq. (5) is also at the heart of the second most common spin relaxation mechanism, referred to as the Elliott-Yafet mechanism, in which the electron spin flips during scattering events as a result of the λ-dependent term in the potential (Elliott, 1954; Yafet, 1963). This mechanism is important in materials that have a center of inversion, so that $\vec{B}_{\vec{k}} = 0$ and there is no spin precession.

Topological materials

Another set of materials in which spin precession is generally absent, albeit for qualitatively different reasons, is that of topological materials. The term topological materials encompasses a broad range of structures that exhibit phases characterized by a topological invariant that remains unchanged by deformations in the system Hamiltonian. This can be the Chern number or the Z_2 invariant, or the discussion can be phrased more generically in terms of the Berry curvature, whose integral over the Brillouin zone yields the Chern number. Topological materials include topological insulators, Weyl and Dirac semimetals, and topological superconductors. The distinction is not always clear cut, since some categories overlap. For example, certain transition metal dichalcogenides can become topological insulators under appropriate circumstances, while others, such as WTe_2, can be Weyl semimetals.

The surface states of topological insulators are described by the Hamiltonian (Liu et al., 2010):

$$H_{TI} = \hbar v_F\left(\sigma_x k_y - \sigma_y k_x\right) + w\sigma_z\left(k_x^3 - 3k_x k_y^2\right), \tag{6}$$

where v_F and lambda are material-specific parameters and σ_i are the Pauli spin matrices. The hexagonal warping term is particularly strong in Bi_2Te_3. These states reside on opposite surfaces of a three-dimensional slab, yet usually all surfaces have topological states, which in Hall transport in particular mean that current can flow around the edges. The Hamiltonian H_{TI} can be thought of as the limit of the Rashba Hamiltonian without the kinetic energy term $H_{kin} = \frac{\hbar^2 k^2}{2m}$. This distinction is illustrated in Fig. 6. In this case we no longer have a conduction band consisting of two spin-split sub-bands, but the two eigenvalues of the Hamiltonian correspond to the surface conduction and valence bands. Only the surface conduction band crosses the Fermi surface and there can be no spin precession, since that involves the electron switching between two sub-bands. In fact in equilibrium the direction of the momentum fully determines the direction of the spin, which is referred to as spin-momentum locking. For Hamiltonians of the Rashba form, where the spin is transverse to the momentum, spin-momentum locking leads to chirality, as opposed to helicity, which characterizes Hamiltonians of the form $\vec{\sigma}\cdot\vec{k}$, where the spin is parallel or anti-parallel to the momentum. Because of spin-momentum locking, when the wave vector changes in a scattering process the spin also changes, and if the wave vector is reversed the spin must be flipped, which breaks time reversal. It follows that time-reversal invariant perturbations such as charged impurities and phonons cannot lead to back-scattering in topological insulators.

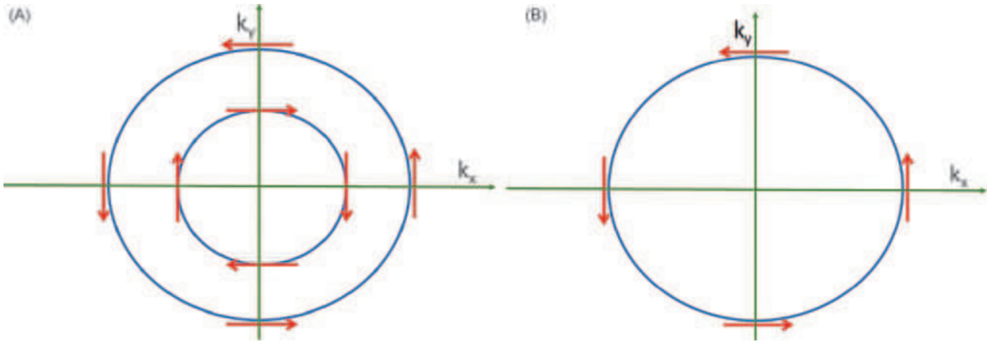

Fig. 6 Effective fields representing the spin-orbit interaction in (A) Rashba semiconductors and (B) topological insulators.

Dirac and Weyl semimetals are different cases of the following Hamiltonian (Armitage et al., 2018)

$$H_{DW} = \hbar v_F \tau_x \, \vec{\sigma}\cdot\vec{k} + m\tau_z + b\sigma_z + b'\tau_z\sigma_x, \tag{7}$$

where the vector $\vec{\sigma}$ of Pauli spin matrices here represents a pseudo-spin degree of freedom, $\vec{\tau}$ the valleys or nodes, m is a mass parameter, and b and b' are effective Zeeman fields due to various internal degrees of freedom. Dirac semimetals have a single node and correspond to $m = b = b' = 0$, while the simplest model of a Weyl semimetal has two nodes when $|b| > |m|$ and $b' = 0$, that act as source and sink of Berry curvature. Known materials typically possess many pairs of nodes. Weyl semimetals break inversion symmetry or time reversal symmetry or both. The materials that break time reversal tend to have a magnetization built into the system and exhibit an anomalous Hall effect, which will be discussed below.

Transition metal dichalcogenides are described by the Hamiltonian (Xiao et al., 2012):

$$H_{TMD} = \hbar v_F\left(\tau\sigma_x k_x + \sigma_y k_y\right) + \frac{\Delta}{2}\sigma_z - \frac{\gamma\tau}{2}(\sigma_z - I)s_z + \frac{\kappa}{2}\left(\sigma_+ k_+^2 + \sigma_- k_-^2\right) \tag{8}$$

where s_i represents spin, $\tau = \pm$ is the valley, $\vec{\sigma}$ is an orbital pseudospin index, analogous to the sublattice pseudospin encountered in graphene, I represents the identity matrix in two dimensions, and $\sigma_\pm = \sigma_x \pm i\sigma_y$. The spin splitting at the valence band top caused by the spin-orbit coupling is denoted by 2γ. Additional terms encapsulate the spin splitting of the conduction band, the electron-hole asymmetry and the trigonal warping of the spectrum. There is always a gap between the valence and conduction bands, which is manifested in the mass appearing in each of the copies of the Dirac Hamiltonian. Consequently, to satisfy time reversal invariance, the materials have two valleys, which are related by time reversal. The valleys are spin polarized with opposite polarizations. Even when spin-orbit coupling is strong there is no spin precession, but only a tilting of the spin quantization axis.

Charge transport description of the anomalous Hall effect

We are now ready to introduce a dynamical description of the anomalous Hall effect in terms of charge transport under the action of an electric field. Considerable insight can be gleaned from the conceptually simplest transport theory, which consists of the semi-classical model of carrier dynamics combined with the Boltzmann equation. Before discussing the semi-classical model some preliminary considerations are necessary.

In a non-trivial multi-band system, the energy and thus the Hamiltonian of the electron depend not only on the average position of the electron in the crystal but also its wave momentum in the Brillouin Zone. We can regard this as a situation where the Hamiltonian is adiabatically changed via a parameter, in this case the momentum. In quantum mechanics, the wave function acquires a dynamical phase factor due to energetic oscillation of the eigenstates. This has the form $e^{-i\varepsilon_n t/\hbar}$, where where ε_n is the energy dispersion of band n. Aside from this, Berry studied the effect of a slowly changing Hamiltonian and found that an additional geometric phase is accumulated, known as the Berry phase (Berry, 1984). The wave function acquires local phases in momentum space, which manifest themselves in the Berry connection $\vec{\mathcal{A}}_n = i\langle \mathrm{u_n}|\frac{\partial \mathrm{u_n}}{\partial \vec{\mathrm{k}}}\rangle$, where $|u_n\rangle$ is the lattice-periodic part of the Bloch wave. The Berry connection $\vec{\mathcal{A}}_n$ is a gauge field, that is, a device to account for the local phases that arise from the band structure. It is gauge-dependent, but the phase acquired by the wave function can also be expressed in terms of the gauge-invariant Berry curvature $\vec{\Omega}_n = \vec{\nabla}_{\vec{k}} \times \vec{\mathcal{A}}_n$. This relationship between the Berry connection and Berry curvature is analogous to the one connecting the magnetic vector potential and magnetic field. Therefore, $\vec{\mathcal{A}}_n$ has a gauge freedom arising from the choice of basis, whereas the curvature $\vec{\Omega}_n$ is a gauge invariant physically meaningful quantity. The Berry curvature can be identified with a monopole in momentum space. An alternative way to look at it is by noting that the expectation value of the position operator in Bloch bands contains a term analogous to that for free electrons, plus a correction that depends on the Berry connection. Due to this correction different components of the electron position, when restricted to a single band, do not commute. If we denote the position expectation value in band n by $\vec{R}_n$, then $\vec{R}_n \times \vec{R}_n = \vec{\Omega}_n$, in exact analogy to the non-commutativity of different components of the momentum in the presence of a magnetic field.

The semi-classical model describes the dynamics of wave-packets between scattering events, while the Boltzmann equation, to be discussed in due course, captures the change in occupation induced by electric fields and scattering. A wave packet has a finite width about its center of mass $\vec{r}_n$in real space, and a finite width in momentum space about its average wave momentum $\vec{k}_n$. The widths in real and momentum space must be consistent with the uncertainty principle. The wave packet starts in a band n and is assumed to remain in this band. The wave momentum and position evolve in time according to the semiclassical equations of motion (Sundaram and Niu, 1999):

$$\hbar\dot{\vec{k}}_n = -e\left(\vec{E} + \dot{\vec{r}}_n \times \vec{B}\right) \tag{9}$$

$$\hbar\dot{\vec{r}}_n = \frac{\partial\varepsilon_n}{\partial\vec{k}} - \hbar\dot{\vec{k}}_n \times \vec{\Omega}_n. \tag{10}$$

and $\vec{\Omega}_n$, as above, is the Berry curvature. The first equation is familiar: it simply encapsulates the combined effect of the electrostatic force and the Lorentz force acting on the electron. The second equation shows that the geometric phase must be taken into account in calculating the velocity of a wave packet through the Berry curvature term $\vec{\Omega}_n$. With this term the equations for the velocity and acceleration look similar, where the Berry curvature is analogous to a magnetic field defined in momentum space. In the systems we are interested in the Berry curvature usually arises from band structure spin-orbit coupling. Importantly, if we turn off the magnetic field the second equation simplifies to

$$\hbar \dot{\vec{r}}_n = \frac{\partial \varepsilon_n}{\partial \vec{k}} + e\vec{E} \times \vec{\Omega}_n. \tag{11}$$

The second term represents a sideways displacement of charge carriers even in the absence of scattering. This displacement is responsible for a transverse current, in other words a Hall effect, and since there is no magnetic field this is an anomalous Hall effect. Given that the change in the wave packet position is already first order in the electric field the expectation value of the current involves only the equilibrium distribution, i.e., the Fermi-Dirac function. Scattering does not enter this expression. This is the intrinsic topological contribution to the AHE (Onoda and Nagaosa, 2002).

Let us examine the symmetry considerations for the Berry curvature and for its integral over filled states. The semiclassical equations must be invariant under time reversal, therefore $\vec{\Omega}_n$ must be odd under this transformation, $\vec{\Omega}_n\left(-\vec{k}\right) = -\vec{\Omega}_n\left(\vec{k}\right)$. A geometric argument can also be made by noting that the Berry phase is a path dependent quantity. Under time reversal, both the path along which the wavefunction is transported and the orientation of the wave vector $\vec{k}$ are reversed. A clockwise path spanning a set of wave vectors $\vec{k}$ becomes an anticlockwise path spanning the set of wave vectors $-\vec{k}$. This implies that the Berry phase changes sign under time reversal and the Berry curvature satisfies the above constraint.

If time reversal symmetry is present, Kramers degeneracy must also be present, imposing $\varepsilon_n\left(\vec{k}\right) = \varepsilon_n\left(-\vec{k}\right)$. Therefore, if the state at wave vector $\vec{k}$ is occupied then so is the state at wavevector $-\vec{k}$. This, together with the condition $\vec{\Omega}_n\left(-\vec{k}\right) = -\vec{\Omega}_n\left(\vec{k}\right)$ implies that the integral of $\vec{\Omega}_n\left(\vec{k}\right)$ over all filled states vanishes. Therefore, in general it is always necessary for the system to lack time reversal symmetry in order for the AHE to occur. This requirement is fulfilled by the magnetisation. In the systems we are interested in the Berry curvature usually arises from the band structure spin-orbit coupling. Therefore the interplay of band structure spin-orbit interaction, adiabatic change in the wave vector in the external electric field, and out-of-plane magnetization leads to a nonzero AHE through the Berry curvature. We can think of the effect as a dynamical process. A driving electric field accelerates the electron, changing its momentum, and from Eq. (3) it is apparent that a change in momentum results in a spin rotation. The spin rotation in turn causes a change in the wave vector, and this change results in a displacement transverse to the original direction, leading to a Hall current. We can take as an example a two-dimensional system spanning the xy-plane with a Hamiltonian of the form

$$H_{2D} = \frac{\hbar^2\left(k_x^2 + k_y^2\right)}{2m} + \alpha\left(\sigma_x k_y - \sigma_y k_x\right) + M\sigma_z, \tag{12}$$

where M is the perpendicular magnetisation (Culcer et al., 2003). The dispersion is sketched in Fig. 7 and the Berry curvature in Fig. 8. The intrinsic anomalous Hall conductivity takes the form

$$\sigma_{xy} = -\frac{e^2}{h}\int \frac{d^2k}{2\pi}\sum_n f_{FD}^n \Omega_{n,z}, \tag{13}$$

where f_{FD}^n is the Fermi-Dirac distribution for band n and $\Omega_{n,z}$ is the z-component of the Berry curvature of the band. If conduction involves more than one band or sub-band one needs to sum over all n. The Fermi-Dirac function ensures this term in the conductivity contains an integral over filled states, hence it originates from the entire Fermi sea. At zero temperature, when the Fermi-Dirac distribution is a Heaviside function the conductivity is given by the integral of the Berry curvature over occupied states. Formally the conductivity will be quantized if the integral involves one band and covers the entire Brillouin zone. The integral of the Berry curvature over the Brillouin Zone is referred to as the Chern number. This is a topological invariant, meaning that

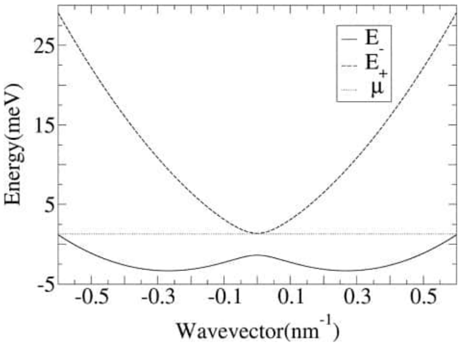

Fig. 7 Energy dispersion as a function of wave vector for the model of Eq. (12). The chemical potential μ in this example has been placed in the gap between the spin-split sub-bands opened by the magnetization. Adapted from Culcer D, MacDonald AH and Niu Q (2003) Anomalous Hall effect in paramagnetic two-dimensional systems. *Physical Review B* **68**: 045327.

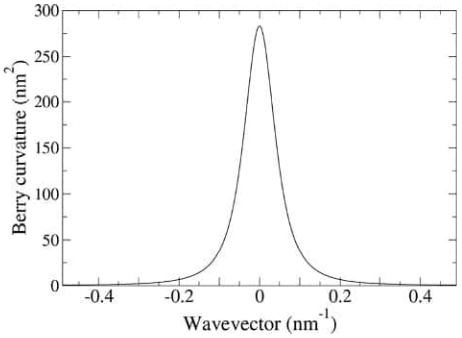

Fig. 8 Berry curvature as a function of wave vector for Eq. (12). Adapted from Culcer D, MacDonald AH and Niu Q (2003) Anomalous Hall effect in paramagnetic two-dimensional systems. *Physical Review B* **68**: 045327.

perturbations to the bands do not change it unless the band structure is re-ordered and band crossing points are created or destroyed, in which case it changes by an integer.

The quantized value depends on the specifics of the Berry curvature: for the Rashba interaction it is ½. The integral may be close to its quantized value if a single band is occupied and the Fermi wave vector is large enough. Yet it should be noted that in systems in which spin-orbit coupling leads to spin precession, which essentially means all known metal and semiconductor structures, conduction involves at least two spin-split sub-bands. The Berry curvatures of these sub-bands invariably have opposite signs. If the Fermi energy is such that only one sub-band is occupied then the Fermi wave vector tends to be relatively small, so that the integral in Eq. (13) is considerably less than the quantized value. Therefore in systems exhibiting spin precession it is virtually impossible for the topological contribution to the AHE to be quantized. This possibility exists, however, in systems displaying spin-momentum locking, such as topological insulators.

To visualize the connection between a quantum mechanical phase and a conductivity note that the spin orbit interaction couples the spin up and spin down bands. This coupling transfers the time reversal violation from the spin degree of freedom to the orbital motion, which is responsible for the Berry curvature. Spin-orbit coupling provides a wave vector-dependent quantization direction for the spin, so that as the wave vector is displaced the spin is rotated and it is possible to obtain a nonzero Berry curvature. For example, for the Rashba interaction, the spins prefer to lie in the xy-plane and be perpendicular to the wave vector. As a result, when the wave vector sweeps a circle around the origin, the spins are rotated by a solid angle of 2π, and acquire a Berry phase of π. Since this phase is independent of the area enclosed, it follows that the Berry curvature is singular at the origin and is zero everywhere else. A perpendicular magnetization will tilt the spins out of the xy-plane. The amount of tilting depends on the competition between the Rashba term and the magnetization. The solid angle swept by the spins is different from 2π and depends on the size of $\vec{k}$, tending to zero as the radius of the circle tends to zero. This implies that the Berry curvature is now spread out and is finite at the origin.

Disorder contributions to the AHE are exceedingly complex. The full disorder potential is

$$H^{dis}_{\vec{k}\vec{k'}} = U_{\vec{k}\vec{k'}}\left(1 - i\,\lambda\,\vec{\sigma}\cdot\vec{k} \times \vec{k'}\right) \tag{14}$$

where the first term represents scalar, spin-independent scattering, due to e.g., Coulomb impurities, roughness, dislocations, and the second term is the spin-orbit correction to it, causing spin-dependent scattering. The disorder potential is a random function, therefore in determining expectation values one deals only with averages over impurity configurations, expressing final results in terms of a parameter quantifying the disorder strength. Here this parameter is chosen to be the impurity density n_i.

We consider first the case when the AHE is purely extrinsic. There is no spin-orbit coupling in the band structure and spin is conserved between scattering events. In this case skew scattering and side jump are captured by the Boltzmann equation. They arise from the spin-dependent part of the scattering potential $\propto \lambda$, as was originally discussed for ferromagnetic metals. We consider as a pedagogical model the simplest example of a 2D system, so that $\vec{k} \times \vec{k'}$ points out of the plane, and $\vec{\sigma} \to \sigma_z$. In this case one may write down separate Boltzmann equations for the non-equilibrium distributions $f_{\vec{k}s} \equiv f_{\vec{k}\uparrow}, f_{\vec{k}\downarrow}$ for the up and down spins. In a spatially uniform system in the steady state, where the time dependence drops out, these take the form:

$$J\left(f_{\vec{k}s}\right) = \frac{e\vec{E}}{\hbar} \cdot \frac{\partial f_{FD,s}}{\partial \vec{k}}. \tag{15}$$

Working to linear order in the electric field, the right hand side contains the equilibrium Fermi-Dirac distribution, which differs for the two spin species only through the presence of the magnetization in the energy. $J\left(f_{\vec{k}s}\right)$ denotes the scattering term. The leading term in $J\left(f_{\vec{k}s}\right)$, corresponding to the Born approximation and Fermi's Golden Rule, contains the absolute value $\left|H^{dis}_{\vec{k}\vec{k'}}\right|^2$, whence it is immediately seen that the imaginary, spin-dependent term $\propto \lambda$ drops out when the absolute value is taken. It follows that for a scalar band structure there is no skew scattering in the Born approximation. The expansion in the scattering potential must be continued up to third order, and the resulting transition rate will be asymmetric in the incident and scattered wave vectors: for any one spin species the amplitude for scattering from $\vec{k}$ to $\vec{k'}$ is not the same as the amplitude for scattering from $\vec{k'}$ to $\vec{k}$, in other words, we have asymmetric scattering of up and down spins.

For $\lambda = 0$ for an isotropic band structure Eq. (15) is easily solved to yield

$$f_{\vec{k}s} = \frac{e\vec{E}\tau_s}{\hbar} \cdot \frac{\partial f_{FD,s}}{\partial \vec{k}}, \tag{16}$$

where $\tau_s \propto 1/n_i$ is the momentum relaxation time for each spin species. Since the magnetisation is invariably a small fraction of the Fermi energy, $\tau_\uparrow \approx \tau_\downarrow \approx \tau$, and we may speak of a single momentum relaxation time evaluated at the Fermi surface. The distribution function in this case leads to the familiar Drude term for the conductivity, $\sigma_{xx} \propto \tau$, and the resistivity $\rho_{xx} \propto 1/\tau$. Noting that $\frac{\partial f_{FD}}{\partial \vec{k}}$ at absolute zero is a delta function at the Fermi energy, the Drude term is due to the electrons at the Fermi surface. For $\lambda \neq 0$ an additional term linear in λ appears in each distribution, with opposite signs for the two spins. There is a difference in the transport of up and down spins, and a full analysis reveals that up spins and down spins are displaced in different directions perpendicular to their direction of travel. The additional, skew scattering, contribution to the conductivity is a Hall term σ_{xy} linear in λ, linear in the magnetisation, proportional to τ, and attributed to the electrons at the Fermi surface.

Experimentally one measures the resistivity rather than the conductivity. Inverting the conductivity tensor we obtain $\rho_{xy} = \frac{\sigma_{xy}}{\sigma_{xx}^2 + \sigma_{xy}^2} \approx \frac{\sigma_{xy}}{\sigma_{xx}^2}$, since $\sigma_{xx} \gg \sigma_{xy}$. For skew scattering the Hall conductivity $\sigma_{xy} \propto \tau$ meaning $\rho_{xy} \propto 1/\tau$ in other words $\rho_{xy} \propto \rho_{xx}$. In contrast, for the intrinsic topological term σ_{xy} is independent of τ, hence $\rho_{xy} \propto 1/\tau^2$ that is $\rho_{xy} \propto \rho_{xx}^2$.

The side-jump term in the AHE appears in the Born approximation provided some modifications are made. To begin with, in Eq. (3) we need to include the contribution to V due to the external electric field, and this gives rise to an additional, spin-dependent term in the interaction of an electron with the field. It is tantamount to a spin- and electric field-dependent modification of the electron energy. Aside from this, in the derivation of Fermi's Golden Rule, the quantum mechanical time evolution operator must include the interaction with the electric field—physically, one must account for the fact that electrons are accelerated by the external field during collisions. Solving the resulting Boltzmann equation including these new terms one finds the side-jump contribution, which is linear in λ, linear in the magnetisation, apparently independent of τ due to the cancellation of terms $\propto \tau$ and $\propto 1/\tau$, and due to the Fermi surface. Being independent of τ it leads to $\rho_{xy} \propto \rho_{xx}^2$, exactly the same as the intrinsic term.

The appearance of disorder terms to order zero in τ is simply a reflection of the fact that (i) the non-equilibrium correction to the electron distribution is an expansion in powers of the disorder strength, which can be cast as an expansion in the parameter $1/\tau$; and (ii) the leading term in this expansion is $\propto \tau$, linear in the transport time that is needed to keep the Fermi surface near equilibrium. The next-to-leading term is thus of order $\tau^0 \to 1$.

What happens when spin-orbit coupling is present in the band structure, and scattering off impurities is purely scalar? For this we need the full kinetic equation, which is beyond the scope of this review. The main conclusions are as follows. Physically, the combination of band structure spin-orbit coupling and scalar scattering can be understood in the same language as extrinsic spin-orbit scattering: there are contributions to the AHE that can be understood as skew scattering and side-jump. Importantly, in this case the side-jump contribution is of the same order of magnitude as the topological contribution, and for certain models and in certain regimes cancels it altogether (Inoue et al., 2006; Nunner et al., 2007). In the Rashba model of semiconductor nanostructures the AHE cancels altogether when the Fermi energy is deep in the upper sub-band. In doped topological insulators the skew scattering and side-jump terms induced by the band structure spin-orbit coupling ultimately cancel the topological contribution to the AHE, leaving terms that explicitly depend on the magnetization. These disorder effects have also been incorporated into the semiclassical equations (Burgos Atencia et al., 2022). The case of magnetic impurities is qualitatively different, and relatively less studied (Nunner et al., 2008).

In the final analysis one needs to account for spin-orbit coupling both in the band structure and in the scattering potential, and for the interplay of the band structure spin-orbit coupling with scalar and spin-dependent disorder (Onoda et al., 2006; Borunda et al., 2007; Kovalev et al., 2009). In multi-band systems, where the spin precesses, this precession reduces the contributions of the extrinsic terms, and in certain cases causes them to vanish, as in a 2D electron gas. Asymmetric scattering of up and down spins takes place, but after scattering the spins precess and are randomized before reaching the boundary, and as they are randomized the resulting contributions to the AHE disappear. In single-band systems such as topological insulators the contributions due to extrinsic spin-orbit scattering are expected to be much smaller than the surviving terms from the band structure and scalar scattering discussed above.

To complete our discussion of scattering effects that are formally of zeroth order in the disorder strength we need to consider coherent backscattering. This refers to interference between the time-reversed incident and back-scattered paths in a scattering event. It is contained in the Cooperon, the sum of maximally crossed diagrams, which classically represents the probability that a particle will return to its starting position after scattering. The time over which the electron wave function retains its phase is determined by dynamic perturbations such as electron-electron, electron-phonon and electron-magnon scattering. In the absence of spin-orbit coupling coherent backscattering reduces the conductivity leading to weak localization. Spin-orbit coupling in the impurity potential or in the band structure leads to weak anti-localization and an increase in the conductivity. A magnetic field destroys phase coherence due to the difference in the Aharonov-Bohm phases of the two paths and with it coherent backscattering. At weak magnetic fields coherent backscattering is present in the ordinary Hall effect but does not affect the Hall coefficient. Magnetic impurities reduce coherent backscattering but do not eliminate it.

In two dimensions coherent backscattering leads to a logarithmic dependence of the conductivity on the transport time τ, and a corresponding logarithmic temperature-dependence. It is predicted to affect the anomalous Hall conductivity. Theory concentrated on the role of extrinsic spin-orbit scattering, identifying a logarithmic τ- and temperature-dependence in the AHE (Dugaev et al., 2002; Wölfle and Muttalib, 2006). Being zeroth order in τ this is of the same order of magnitude to topological effects and their disorder corrections. Experiments on ferromagnetic thin films to date have have reported a logarithmic temperature dependence of the AHE, believed to be due to weak localisation. The complex case of coherent backscattering in topological insulators, with strong band structure spin-orbit coupling, has not been studied theoretically or experimentally.

Anomalous Hall effects in topological materials

The revolutionary role of topological materials became apparent when it was demonstrated that the anomalous Hall effect in topological insulators can be quantized (Yu et al., 2010), with the conductivity

$$\sigma_{xy}^{QAHE} = \frac{e^2}{h}. \tag{17}$$

Four years after its theoretical prediction the quantized anomalous Hall was observed in a Bi_2Se_3 thin film (Chang et al., 2013), followed by studies reporting precise quantization (Bestwick et al., 2015). Results from the latter experiment are shown in Fig. 9. Although the possibility of quantization had been discussed in two-dimensional ferromagnets (Onoda and Nagaosa, 2003a, 2003b), the prediction and observation of this effect in topological insulators marks a cornerstone of modern physics (Liu et al., 2016).

The effect can be explained using either a surface state picture or an edge state picture. In the former we resort to the topological mechanism discussed above. The sample is a thin TI film doped with magnetic impurities in which ferromagnetic order occurs through the van Vleck mechanism. The chemical potential lies in the magnetization-induced gap between the surface valence and conduction bands, hence the material is in the insulating state. We envisage one surface, for example the top, of such a topological insulator and integrate the Berry curvature over the entire valence band, which yields a quantized conductivity $\sigma_{xy}^{2D} = \frac{e^2}{2h}$ due to the Berry curvature monopole at the top of the valence band. The bottom surface makes the same contribution once we take into account the fact that the normal to it points in the opposite direction. Altogether thus we have $\sigma_{xy}^{QAHE} = \frac{e^2}{h}$. Mathematically, the Hamiltonian describing the states on the top and bottom surfaces can be broken up into two blocks, and a sufficiently large magnetization gives rise to a difference in Chern number of one between the two blocks. Alternatively one can demonstrate that, when the Fermi energy is in the gap between the surface valence and conduction bands, a topological insulator possesses spin polarized edge states, which travel ballistically and may be described using a Landauer-Buttiker picture. The presence of a single channel results in a quantized conductivity of $\frac{e^2}{h}$. Remarkably, the quantized result holds even in the presence of disorder and electron-electron interactions.

A recurring problem in topological insulators is the presence of unintentional bulk carriers, which may place the Fermi energy in the bulk conduction band. Interestingly, the same physics leading to the quantized anomalous Hall effect causes a topological insulator thin film weakly coupled to a ferromagnet to exhibit strong magneto-optical Kerr and Faraday effects, which are less likely to be affected by unintentional bulk carriers (Tse and MacDonald, 2010). At low frequencies the Faraday rotation angle has a universal value, which is determined by the vacuum fine structure constant, when the Fermi energy lies in the Dirac gap for both

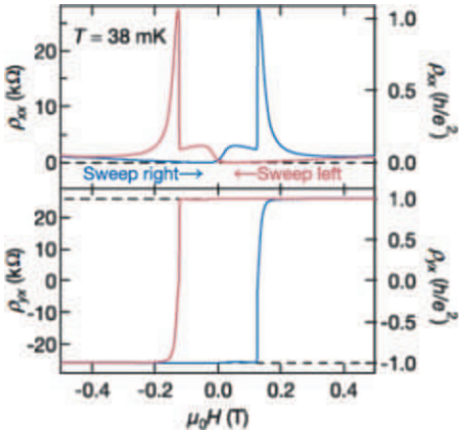

Fig. 9 Quantized anomalous Hall effect in $(Cr_{0.12}\ Bi_{0.26}\ Sb_{0.62})_2Te_3$. From Bestwick AJ et al. (2015) Precise quantization of the anomalous Hall effect near zero magnetic field. *Physical Review Letters* **114**: 187201.

surfaces. The Kerr rotation angle in this regime is universal and equal to $\pi/2$, hence the nomenclature of a giant Kerr rotation. The giant Kerr effect explicitly involves both surfaces and reflects the interplay between the chiral nature of the topological surface states and interference between waves reflected off the top surface and waves scattered off the bottom surface. The surface Hall response creates a splitting between the reflected left-handed and right-handed circularly polarized fields along the transverse direction. The left-handed and right-handed circularly polarized fields each acquire a phase of approximately $\pi/2$ in opposite directions, leading to a $\pi/2$ Kerr rotation.

If the topological insulator surface states are metallic, that is if the conduction band is occupied, the physical situation is quite different due to the presence of Berry curvature monopoles of opposite polarities at the top of the valence band and the bottom of the conduction band. When the chemical potential is in the gap one expects one TI surface to contribute $\sigma_{xy}^{TI} = \frac{e^2}{h}$ to the anomalous Hall conductivity. As soon as the chemical potential passes the bottom of the conduction band this topological contribution is cancelled by the Berry curvature monopole in the conduction band (Nomura and Nagaosa, 2011). What remains is the Fermi surface contribution, which depends on the magnetization and on the disorder profile (Sinitsyn et al., 2007). This dependence is rather subtle, and capturing it correctly requires including crossed diagrams, which are of higher order in the disorder strength (Ado et al., 2015; Ado et al., 2017). Interestingly, the anomalous Hall conductivity in doped topological insulators has been observed to have different signs under nominally identical conditions. Such a sign change could be explained by the correlation between the charge and spin part of the potential characterizing magnetic impurities (Keser et al., 2019).

The anomalous Hall effect in time-reversal breaking Weyl semimetals can be understood straightforwardly. We recall that the anomalous Hall conductivity of 2D massive Dirac fermions is $\sigma_{xy}^{2D} = \frac{e^2}{2h}$ when the chemical potential lies in the gap. In the 3D case of Weyl semimetals the anomalous Hall conductivity is nonzero only in the region $-k_0 < k_z < k_0$, hence the relevant part of the 3D phase space is an infinite collection of 2D planes spanning this interval, each plane contributing the 2D conductivity quantum. This is equivalent to integrating the 2D conductivity over the interval $-k_0 < k_z < k_0$, yielding (Burkov, 2014)

$$\sigma_{xy}^{3D} = \frac{e^2}{2\pi^2}. \tag{18}$$

The anomalous Hall effect in Weyl semimetals is also quantized when the chemical potential lies near the bottom of the conduction band. Due to the presence of the node wave vector k_0 the quantised value is extremely large, and overwhelms any additional contributions that may arise from a finite electron density in the conduction band. Remarkably, corrections due to scalar disorder vanish altogether (Sekine et al., 2017).

Topological materials have been instrumental in revealing a series of close relatives of the AHE. To begin with transition metal dichalcogenides have two degenerate valleys, which are related by time reversal, so that the masses in the two valleys have opposite signs. Unlike graphene they typically have sizable spin-orbit interactions. Given that the spin is essentially locked to the valleys it is not clear that the two can be manipulated independently, yet accessing the elusive valley degree of freedom is fascinating from a fundamental standpoint. The analogue of the anomalous Hall effect in doped transition metal dichalcogenide monolayers is the valley Hall effect, which has been detected in MoS_2 (Mak et al., 2014). Physically it corresponds to an anomalous Hall effect with different signs for different valleys. There is no net charge current, because the anomalous Hall currents from the two valleys cancel each other out, but electrons from different valleys flow to different sides of the sample generating a valley polarization, which can be detected using circularly polarized light. The valley Hall effect generates a non-local resistance, which has a non-trivial dependence on the longitudinal resistivity.

The past decade has witnessed a surge in interest in Hall effects in two-dimensional systems in response to an in-plane magnetic field. In the classical theory a Hall effect is not expected when the magnetic field is in the plane of the sample: the ordinary Hall effect occurs because the Lorentz force causes electrons to move in cyclotron orbits perpendicular to it. Nevertheless an in-plane magnetic field can induce a planar Hall effect in topological materials, since protection from backscattering is removed for spins perpendicular to the magnetic field, but is retained for spins parallel to it (Taskin et al., 2017). The planar Hall effect has contributions from the Berry phase and orbital magnetic moment, and an anomalous planar Hall effect has likewise been predicted, driven by topological mechanisms (Zyuzin, 2020; Cullen et al., 2021; Battilomo et al., 2021; Tan et al., 2021). These investigations reveal that topological effects can influence the response to a magnetic field, blurring the boundary between ordinary and anomalous Hall effects.

Non-linear electrical effects are enabled by a lack of inversion symmetry, the application of a magnetic field, or the presence of a valley polarization. The quantity of interest in the second-order response is the next term in perturbation theory beyond the linear response to an electric field. The relevant signal can be detected by scanning higher harmonics of the applied frequency. The second-order response is not constrained by Onsager relations (Tokura and Nagaosa, 2018), thus non-linear Hall effects are allowed in time-reversal symmetric systems (Sodemann and Fu, 2015), and have been found to be particularly strong in transition metal dichalcogenides. Two papers have reported a non-linear anomalous Hall effect in bilayer/few-layer WTe_2 (Ma et al., 2019; Kang et al., 2019). In the former the non-linear anomalous Hall effect results in a much larger transverse than longitudinal voltage. The effect is generally extrinsic in time-reversal invariant systems, but can be intrinsic if time-reversal symmetry is broken. The static non-linear Hall conductivity contains an intrinsic contribution proportional to the Berry curvature dipole in reciprocal space, that is, the term $k\vec{\Omega}_n$, where we recall $\vec{\Omega}_n$ is the Berry curvature. The non-linear anomalous Hall effect is a new area of research, where significant developments are likely in the coming years.

Conclusion

The anomalous Hall effect has become a mainstay of modern condensed matter physics. Indispensable for its occurrence are ferromagnetism and spin-orbit coupling. Magnetic interactions contribute to the AHE either through the magnetization or through spin chirality, while spin-orbit coupling gives rise to a momentum-dependent effective magnetic field in the band structure, as well as to spin dependent scattering. The combination of an effective magnetic field and a magnetization is responsible for Berry curvature monopoles, and these generate a strong intrinsic topological contribution to the AHE, associated with the Fermi sea of electrons. In addition to this one may distinguish several extrinsic contributions due to scattering, associated with the Fermi surface, and stemming either from the spin dependence of the scattering potential, or from scalar scattering combined with the effective spin-orbit field in the band structure. Systems where both intrinsic and extrinsic effects are strong are complex, with various terms occasionally vanishing altogether: intrinsic processes may be cancelled out by scattering terms independent of the disorder concentration, while extrinsic effects are reduced by spin precession and in extreme cases vanish.

Many unanswered questions remain, and elucidating these will no doubt preoccupy researchers in the coming years, if not decades. Determining and understanding the temperature dependence of the AHE in all classes of materials in which it is observed, including the effect of magnetic excitations, is a major long term challenge for experiment as well as theory. At the fundamental level, the role of disorder in the AHE remains incompletely understood, in particular in dirty materials and in the hopping regime, while the role of localization effects has not been settled. In inhomogeneous ferromagnets disentangling the topological and anomalous Hall effects has emerged as a significant experimental hurdle. Designing devices that can harness the quantized AHE is a challenge for technological applications.

It is natural to expect relatives of the AHE to emerge in anti-ferromagnets, in particular topological anti-ferromagnets, and potentially in the non-linear regime. In this context we note that the same fundamental questions must be answered for the non-linear AHE—determining the relative sizes of intrinsic and disorder contributions, and of the Fermi surface and Fermi sea contributions. Moreover, the non-linear response is intensively studied at optical frequencies, where non-linear anomalous Hall effects and related phenomena exist both in the AC second-harmonic response and in the DC photo-current response, for example as part of rectification, shift and injection currents. Considerable growth is expected in this area, especially given the potential for applications in solar cells and opto-electronic devices.

Research on the anomalous Hall effect shows no sign of abating. One and a half centuries after its discovery we are not achieving closure but entering uncharted territory.

Acknowledgments

DC is supported by the Australian Research Council Future Fellowship FT190100062.

References

Adams E and Blount E (1959) Formalisms of band theory. *Journal of Physics and Chemistry of Solids* 10: 286.
Ado IA, Dmitriev IA, Ostrovsky PM, and Titov M (2015) Anomalous Hall effect with massive Dirac fermions. *Europhysics Letters* 111: 37004.
Ado IA, Dmitriev IA, Ostrovsky PM, and Titov M (2017) Sensitivity of the anomalous Hall effect to disorder correlations. *Physical Review B* 96: 235148.
Allen PB, et al. (1996) Transport properties, thermodynamic properties, and electronic structure of $SrRuO_3$. *Physical Review B* 53: 4393.
Armitage NP, Mele EJ, and Vishwanath A (2018) Weyl and Dirac semimetals in three-dimensional solids. *Reviews of Modern Physics* 90: 015001.
Battilomo R, Scopigno N, and Ortix C (2021) Letter open access Anomalous planar Hall effect in two-dimensional trigonal crystals. *Physical Review Research* 3: L012006.
Berger L (1970) Side-Jump mechanism for the hall effect of ferromagnets. *Physical Review B* 2: 4559.
Berry MV (1984) Quantal phase factors accompanying adiabatic changes. *Proceedings of the Royal Society of London A* 392: 45.
Bestwick AJ, et al. (2015) Precise quantization of the anomalous Hall effect near zero magnetic field. *Physical Review Letters* 114: 187201.
Borunda M, et al. (2007) Absence of skew scattering in two-dimensional systems. *Physical Review Letters* 99: 066604.
Bruno P, Dugaev VK, and Taillefumier M (2004) Topological hall effect and berry phase in magnetic nanostructures. *Physical Review Letters* 93: 096806.
Burgos Atencia R, Niu Q, and Culcer D (2022) Semiclassical response of disordered conductors: Extrinsic carrier velocity and spin and field-corrected collision integral. *Phys. Rev. Research* 4: 013001.
Burkov AA (2014) Chiral anomaly and diffusive magnetotransport in weyl metals. *Physical Review Letters* 113: 247203.
Bychkov YA and Rashba EI (1984) Oscillatory effects and the magnetic susceptibility of carriers in inversion layers. *Journal of Physics C* 17: 6039.
Chang C-Z, et al. (2013) Experimental observation of the quantum anomalous Hall effect in a magnetic topological insulator. *Science* 340: 167.
Chazalviel JN (1975) Spin-dependent Hall effect in semiconductors. *Physical Review B* 11: 3918.
Culcer D, MacDonald AH, and Niu Q (2003) Anomalous Hall effect in paramagnetic two-dimensional systems. *Physical Review B* 68: 045327.
Cullen JH, et al. (2021) Generating a topological anomalous Hall effect in a nonmagnetic conductor: An in-plane magnetic field as a direct probe of the berry curvature. *Physical Review Letters* 126: 256601.
D'yakonov MI and Perel VI (1971) Spin orientation of electrons associated with the interband absorption of light in semiconductors. *Journal of Experimental and Theoretical Physics* 33: 1053.
Dietl T, Ohno H, and Matsukura F (2001) Hole-mediated ferromagnetism in tetrahedrally coordinated semiconductors. *Physical Review B* 63: 195205.
Dugaev VK, Crépieux A, and Bruno P (2002) Weak localization corrections to the anomalous Hall effect. *Journal of Magnetism and Magnetic Materials* 240: 159.
Elliott RJ (1954) Theory of the effect of spin-orbit coupling on magnetic resonance in some semiconductors. *Physics Review* 96: 266.
Fang Z, et al. (2003) The anomalous Hall effect and magnetic monopoles in momentum space. *Science* 302: 92.
Göbel B, Mertig I, and Tretiakov OA (2001) Beyond skyrmions: Review and perspectives of alternative magnetic quasiparticles. *Physics Reports* 895: 1.

Hall EH (1879) On a new action of the magnet on electric currents. *American Journal of Mathematics* 2(3): 287.
Hall EH (1881) On the “Rotational Coefficient” in nickel and cobalt. *Philosophical Magazine* 12: 157.
Inoue J, et al. (2006) Vertex corrections to the anomalous Hall effect in spin-polarized two-dimensional electron gases with a rashba spin-orbit interaction. *Physical Review Letters* 97: 046604.
Izumi M, et al. (1997) Magnetotransport of $SrRuO_3$ Thin Film on $SrTiO_3$(001). *Journal of the Physical Society of Japan* 66: 3893.
Jungwirth T, Niu Q, and MacDonald AH (2002) Anomalous Hall effect in ferromagnetic semiconductors. *Physical Review Letters* 88: 207208.
Jungwirth T, et al. (2006) Theory of ferromagnetic (III,Mn)V semiconductors. *Reviews of Modern Physics* 78: 809.
Kang K, et al. (2019) Nonlinear anomalous Hall effect in few-layer WTe_2. *Nature Materials* 18: 324.
Karplus R and Luttinger JM (1954) Hall effect in ferromagnetics. *Physics Review* 95: 1154.
Keser AC, Raimondi R, and Culcer D (2019) Sign change in the Anomalous Hall effect and strong transport effects in a 2D Massive Dirac metal due to spin-charge correlated disorder. *Physical Review Letters* 123: 126603.
Kohn W and Luttinger JM (1957) Quantum theory of electrical transport phenomena. *Physics Review* 108: 590.
Kovalev AA, Tserkovnyak Y, Vyborny K, and Sinova J (2009) Transport theory for disordered multiple-band systems. *Physical Review B* 79: 195129.
Liu C-X, et al. (2010) Model Hamiltonian for topological insulators. *Physical Review B* 82: 045122.
Liu C-X, Zhang S-C, and Qi X-L (2016) The quantum anomalous Hall effect: Theory and experiment. *Annual Reviews of Condensed Matter Physics* 7: 301.
Luttinger JM (1958) Theory of the hall effect in ferromagnetic substances. *Physics Review* 112: 739.
Luttinger JM and Kohn W (1955) Motion of electrons and holes in perturbed periodic fields. *Physics Review* 97: 868.
Luttinger JM and Kohn W (1958) Quantum theory of electrical transport phenomena. II. *Physics Review* 109: 1892.
Lyanda-Geller Y, et al. (2001) Charge transport in manganites: Hopping conduction, the anomalous Hall effect, and universal scaling. *Physical Review B* 63: 184426.
Lyo SK and Holstein T (1972) Side-Jump mechanism for ferromagnetic hall effect. *Physical Review Letters* 29: 423.
Ma Q, et al. (2019) Observation of the nonlinear Hall effect under time-reversal-symmetric conditions. *Nature* 565: 337.
Majumdar A and Berger L (1973) Hall effect and magnetoresistance in pure iron, lead, Fe-Co, and Fe-Cr dilute alloys. *Physical Review B* 7: 4203.
Mak KF, McGill KL, Park J, and McEuen PL (2014) The valley Hall effect in MoS_2 transistors. *Science* 344: 1489.
Matl P, et al. (1998) Hall effect of the colossal magnetoresistance manganite $La_{1-x}Ca_xMnO_3$. *Physical Review B* 57: 10248.
Messiah A (2014) *Quantum Mechanics*. New York: Dover Publications.
Miyasato T, et al. (2007) Crossover behavior of the anomalous Hall effect and anomalous nernst effect in itinerant ferromagnets. *Physical Review Letters* 99: 086602.
Nagaosa N, et al. (2010) Anomalous Hall effect. *Reviews of Modern Physics* 82: 1539.
Nomura K and Nagaosa N (2011) Surface-quantized anomalous Hall current and the magnetoelectric effect in magnetically disordered topological insulators. *Physical Review Letters* 106: 166802.
Nozieres P and Lewiner C (1973) A simple theory of the anomalous Hall effect in semiconductors. *Journal of Physiology, Paris* 34: 901.
Nunner TS, et al. (2007) Anomalous Hall effect in a two-dimensional electron gas. *Physical Review B* 76: 235312.
Nunner TS, Zarand G, and von Oppen F (2008) Anomalous Hall effect in a two dimensional electron gas with magnetic impurities. *Physical Review Letters* 100: 236602.
Ohgushi K, Murakami S, and Nagaosa N (2000) Spin anisotropy and quantum Hall effect in the kagomé lattice: Chiral spin state based on a ferromagnet. *Physical Review B* 62: 6065.
Onoda M and Nagaosa N (2002) Topological nature of anomalous Hall effect in ferromagnets. *Journal of the Physical Society of Japan* 71: 19.
Onoda S and Nagaosa N (2003a) Spin chirality fluctuations and anomalous Hall effect in itinerant ferromagnets. *Physical Review Letters* 90: 196602.
Onoda M and Nagaosa N (2003b) Quantized anomalous Hall effect in two-dimensional ferromagnets: Quantum hall effect in metals. *Physical Review Letters* 90: 206601.
Onoda S, Sugimoto N, and Nagaosa N (2006) Intrinsic versus extrinsic anomalous Hall effect in ferromagnets. *Physical Review Letters* 97: 126602.
Pikus GE and Titkov AN (1984) Spin relaxation under optical orientation in semico. In: Meier F and Zakharchenya BP (eds.) *Optical Orientation*, pp. 73–131. Amsterdam: Elsevier.
Pugh EM and Lippert TW (1932) Hall e.m.f. and intensity of magnetization. *Physics Review* 42: 709.
Pugh EM, Rostoker N, and Schindler A (1950) On the hall effect in ferromagnetics. *Physics Review* 80: 688.
Sekine A, Culcer D, and MacDonald AH (2017) Quantum kinetic theory of the chiral anomaly. *Physical Review B* 96: 235134.
Shindou R and Nagaosa N (2001) Orbital ferromagnetism and anomalous Hall effect in antiferromagnets on the distorted fcc lattice. *Physical Review Letters* 87: 116801.
Sinitsyn NA (2008) Semiclassical theories of the anomalous Hall effect. *Journal of Physics: Condensed Matter* 20: 023201.
Sinitsyn NA, et al. (2007) Anomalous Hall effect in a two-dimensional Dirac band: The link between the Kubo-Streda formula and the semiclassical Boltzmann equation approach. *Physical Review B* 75: 045315.
Smit J (1955) The spontaneous hall effect in ferromagnetics I. *Physica (Amsterdam)* 21: 877.
Sodemann I and Fu L (2015) Quantum Nonlinear Hall effect induced by berry curvature dipole in time-reversal invariant materials. *Physical Review Letters* 115: 216806.
Sundaram G and Niu Q (1999) Wave-packet dynamics in slowly perturbed crystals: Gradient corrections and Berry-phase effects. *Physical Review B* 59: 14915.
Tan H, Liu Y, and Yan B (2021) Unconventional anomalous Hall effect from magnetization parallel to the electric field. *Physical Review B* 103: 214438.
Taskin AA, et al. (2017) Planar Hall effect from the surface of topological insulators. *Nature Communications* 8: 1340.
Tokura Y and Nagaosa N (2018) Nonreciprocal responses from non-centrosymmetric quantum materials. *Nature Communications* 9: 3740.
Tse WK and MacDonald AH (2010) Giant magneto-optical kerr effect and universal faraday effect in thin-film topological insulators. *Physical Review Letters* 105: 057401.
Winkler R (2003) *Spin-Orbit Coupling Effects in Two-Dimensional Electron and Hole systems*. Berlin: Springer.
Wölfle P and Muttalib KA (2006) Anomalous Hall effect in ferromagnetic disordered metals. *Annals of Physics* 15: 508.
Xiao D, et al. (2012) Coupled spin and valley physics in monolayers of MoS_2 and other Group-VI dichalcogenides. *Physical Review Letters* 108: 196802.
Yafet Y (1963) G-factors and spin-lattice relaxation of conduction electrons. In: Seitz F and Turnbull D (eds.) *Solid State Physics*. vol. 14, pp. 1–98. New York: Academic Press.
Ye J, et al. (1999) Berry phase theory of the anomalous Hall effect: Application to colossal magnetoresistance manganites. *Physical Review Letters* 83: 3737.
Yu R, et al. (2010) Quantized anomalous Hall effect in magnetic topological insulators. *Science* 329: 61.
Zyuzin VA (2020) In-plane Hall effect in two-dimensional helical electron systems. *Physical Review B* 102: 241105.

Monolayer and bilayer graphene

Edward McCann, Physics Department, Lancaster University, Lancaster, United Kingdom

© 2024 Elsevier Ltd. All rights reserved.

Introduction **603**
Graphene 603
History 603
Fabrication 603
Properties 603
Applications 604
Electrical properties of monolayer graphene **604**
Crystal structure 604
Band structure and tight-binding model 605
Dirac effective-mass model, pseudospin and chirality 606
Symmetries 606
Berry phase π 607
Trigonal warping and other tight-binding parameters 607
Ambipolar electric field effect 608
Klein tunneling 608
Integer quantum Hall effect 610
Landau levels 610
Semiclassical quantization and Berry phase 610
Integer quantum Hall effect 611
Electronic properties of Bernal-stacked bilayer graphene **611**
Crystal structure 612
Electronic band structure and tight-binding model 612
Effective-mass model, pseudospin and chirality 613
Symmetries 615
Berry phase 2π 615
Trigonal warping and other tight-binding parameters 615
Band gap tunable with an electric field 616
Band structure with a band gap 616
Self-consistent screening 617
Integer quantum Hall effect 618
Electronic properties of AA-stacked bilayer graphene **618**
Crystal structure 618
Electronic band structure and tight-binding model 618
Conclusion **620**
References **620**

Abstract

This chapter presents the electronic properties of monolayer and bilayer graphene. It begins with an overview of graphene including its history, fabrication methods, properties, and current and potential applications. We then detail the tight-binding model in order to describe the emergence of the Dirac equation near the Fermi level in monolayer graphene and its consequences including massless charge carriers with a linear electronic dispersion, pseudospin and chirality, Berry phase π, Klein tunneling, and an unusual sequence of plateaus in the integer quantum Hall effect. We explain how this is generalized in Bernal-stacked bilayer graphene as characterized by a novel Hamiltonian describing massive chiral charge carriers and in AA-stacked bilayer graphene which displays two shifted copies of the monolayer bands at low energy.

Key points

- An overview of graphene including its history, fabrication methods, properties, and current and potential applications.
- The tight-binding model of electrons in monolayer and bilayer graphene.
- The emergence of the Dirac equation near the Fermi level in monolayer graphene.
- Consequences including massless charge carriers with a linear electronic dispersion, pseudospin and chirality, Berry phase π, Klein tunneling, and an unusual sequence of plateaus in the integer quantum Hall effect.

https://doi.org/10.1016/B978-0-323-90800-9.00019-6

- Bernal-stacked bilayer graphene as characterized by a novel Hamiltonian describing massive chiral charge carriers.
- AA-stacked bilayer graphene which displays two copies of the monolayer bands at low energy.

Introduction

Graphene

Graphene is a two-dimensional material consisting of a single layer of carbon atoms arranged on a honeycomb lattice (Castro Neto et al., 2009). It was isolated by Andre Geim, Konstantin Novoselov and colleagues at the University of Manchester in 2004 (Novoselov et al., 2004), and the Nobel Prize in Physics 2010 was awarded to Geim and Novoselov 'for groundbreaking experiments regarding the two-dimensional material graphene'. A closely-related material is graphite (Dresselhaus and Dresselhaus, 2002) which is a three-dimensional stack of parallel, weakly-coupled layers of graphene. The phrase 'graphene' usually refers to a single layer, but is sometimes used more generally to refer to a quasi-two-dimensional very thin film of graphite, as in 'few-layer graphene' or 'multilayer graphene'; the phrase 'monolayer graphene' can be used specifically for a single layer to avoid ambiguity.

History

Prior to the 2004 isolation of graphene by Geim, Novoselov and colleagues (Novoselov et al., 2004), very thin films of graphite had been fabricated by various methods including reduction of graphene oxide, epitaxial growth, and mechanical cleavage (Geim, 2012). The 2004 paper (Novoselov et al., 2004) was a major step forward in the preparation of atomically-thin layers, but it also unearthed two amazing properties of graphene (Geim, 2012): the ambipolar electric field effect in which an applied gate voltage can tune the electronic density and related electronic properties, and remarkably high electrical mobility $\sim 10{,}000\ \mathrm{cm}^2\,\mathrm{V}^{-1}\,\mathrm{s}^{-1}$ at room temperature. Independent papers published in 2005 by Geim, Novoselov and colleagues (Novoselov et al., 2005), and Philip Kim and colleagues (Zhang et al., 2005) observed the integer quantum Hall effect with an unusual sequencing of quantized plateaus which confirmed predictions based on a low-energy theory of Dirac-like fermions (with linear dispersion) instead of the usual Schrödinger picture (with quadratic dispersion).

Theoretically, graphene has been studied for many years as a building block of graphite (DiVincenzo and Mele, 1984; Dresselhaus and Dresselhaus, 2002; McClure, 1956; Slonczewski and Weiss, 1958; Wallace, 1947), buckyballs (González et al., 1992) and carbon nanotubes (Ajiki and Ando, 1993; Ando et al., 1998; Kane and Mele, 1997; McEuen et al., 1999; Saito et al., 1998). Remarkably, this includes a description of the electronic band structure by Wallace in 1947 (Wallace, 1947) and the energy spectrum in a quantizing magnetic field (Landau level spectrum) by McClure in 1956 (McClure, 1956). In the 1980s, it was realised that the effective low-energy theory is that of Dirac fermions (DiVincenzo and Mele, 1984; Semenoff, 1984). Graphene also played a role in the understanding of topological insulators: the Haldane model (Haldane, 1988) and the Kane-Mele model (Kane and Mele, 2005a,b) are based on graphene and exemplify Chern insulators and spin-Hall insulators, respectively (Cayssol and Fuchs, 2021).

Fabrication

The fabrication of graphene by Geim, Novoselov and colleagues (Novoselov et al., 2004) was by mechanical exfoliation, informally known as the 'Scotch tape' or 'sticky tape' method. This generally yields high quality samples, but is labor intensive and low yield. It involves manually cleaving a piece of graphite along the in-plane direction, possibly using sticky tape. The resulting collection of smaller samples is placed on a substrate (such as silicon) and identified using optical microscopy (Orlita and Potemski, 2010). A possible way to accelerate this process is to employ ultrasonic exfoliation.

There are many other methods to fabricate graphene (Ferrari et al., 2015; Zhu et al., 2010). In chemical reduction of graphene oxide (Pei and Cheng, 2012), graphite oxide is prepared by oxidation of graphite and is subsequently broken up using ultrasonic exfoliation in water to create graphene oxide; this can then be chemically reduced to produce graphene. Graphene can be grown by chemical vapor deposition (CVD) growth on metallic substrates (Bae et al., 2010; Kim et al., 2009; Li et al., 2009a), allowing for large area samples, but often containing grain boundaries. Graphene can also be grown epitaxially on SiC whereby, at high temperature, silicon sublimes leaving a carbon-rich surface which forms graphene (de Heer et al., 2011).

Properties

Graphene is extremely strong with an instrinsic strength ~ 130 GPa (Lee et al., 2008a) and it is very rigid when tension is applied in the in-plane direction with Young's modulus ~ 1 TPa (Lee et al., 2008a). However, it is flexible and can bend in response to an out-of-plane force, with bending stiffness ~ 1 eV (Han et al., 2020). It is chemically stable at room temperature when exposed to air, but graphene begins to react with oxygen gas above 200 °C (Liu et al., 2008; Yamada et al., 2014).

The Dirac-like low energy electronic dispersion yields a linear electronic dispersion over an energy scale of the order of 1 eV with zero band gap between the conduction and valence bands. Graphene is almost transparent, absorbing about 2.3% of incoming light across the whole visible spectrum, and this fraction is equal to $\pi\alpha$ where α is the fine structure constant (Nair et al., 2008; Orlita and Potemski, 2010). Graphene is an excellent electrical conductor with room temperature mobility in excess of $100{,}000\ \mathrm{cm}^2\,\mathrm{V}^{-1}\,\mathrm{s}^{-1}$

reported for high quality samples (typically suspended above a substrate (Bolotin et al., 2008; Du et al., 2008) or encapsulated in boron nitride (Mayorov et al., 2011)). This corresponds to ballistic transport over a distance more than 1 μm at room temperature (Mayorov et al., 2011). It is also an excellent thermal conductor, with thermal conductivity up to $\sim 5000\ \mathrm{W\,m^{-1}\,K^{-1}}$ at room temperature (Balandin et al., 2008).

Applications

Graphene is used as conductive ink for printed electronics, as heat sinks in electronic devices including mobile phones and computer components, and graphene composites are employed in advanced sportswear and equipment. In addition, graphene is being studied for its possible use in a wide range of other applications (Ferrari et al., 2015; Novoselov et al., 2012).

In electronics, there is potential as a flexible and transparent conductive coating for touch screen displays, electronic paper, and organic light-emitting diodes (Avouris, 2010; Ferrari et al., 2015; Novoselov et al., 2012; Zhu et al., 2010). There is research into the use of graphene-based transistors, although the absence of an electronic band gap tends to compromise the on/off ratio, limiting the use of graphene in logic transistors (Avouris, 2010). However graphene may still be useful in high-frequency applications (Avouris, 2010; Ferrari et al., 2015; Gayduchenko et al., 2021). There is also interest in applications to thermal management (Fu et al., 2020) and interconnects in integrated circuits (Ferrari et al., 2015). Owing to weak spin-orbit coupling in graphene, it may have applications in spintronic devices as a non-magnetic channel with a long spin-relaxation time (Ferrari et al., 2015; Pesin and MacDonald, 2012).

The gapless, linear dispersion of electrons results in almost constant absorption of light over a wide range from infrared to ultraviolet. Coupled with the high electronic mobility, this suggests use in photonic devices including photodetectors, optical modulators, and saturable absorbers for lasers (Avouris, 2010; Ferrari et al., 2015; Peng and Yan, 2021; Yamashita, 2019). Owing to its two-dimensional nature, strength, and ability to be functionalized by various chemical species, the use of graphene is being explored in a wide range of sensors (e.g., for gas, strain, electromagnetic waves, biosensors) (Ferrari et al., 2015; Schedin et al., 2007). As well as biosensors, there are potential bioapplications in areas such as drug delivery and tissue engineering (Ferrari et al., 2015; Wang et al., 2011). It also has possible application in energy generation and storage including solar cells, supercapacitors, batteries and hydrogen storage (Bonaccorso et al., 2015; Ferrari et al., 2015; Zhu et al., 2010). Graphene promises a new resistance standard (Ferrari et al., 2015; Janssen et al., 2013) based on the large gap between energy levels in an external magnetic field (Landau levels), as manifested in the integer quantum Hall effect.

Electrical properties of monolayer graphene

Crystal structure

Carbon has atomic number 6. Two of its electrons are core electrons in the first shell, the other four are valence electrons in the second shell. In crystals, the latter occupy $2s$, $2p_x$, $2p_y$ and $2p_z$ orbitals, and the mixing of the $2s$ orbital with $n = 1$, 2 or 3 of the p orbitals gives rise to sp^n hybridization. This enables the existence of different allotropes of carbon. For example, diamond is an example of sp^3 hybridization, whereas graphite and graphene have sp^2 hybridization (Saito et al., 1998).

Typically, graphene is considered to lie in the x-y plane, with mixing of the $2s$ orbital with the $2p_x$ and $2p_y$ orbitals. Such mixing results in very strong σ bonds between each carbon atom and its three neighbors, creating a honeycomb lattice as shown in Fig. 1. The corresponding σ electronic energy bands are gapped, and lie a few electron volts away from the Fermi level (Saito et al., 1998). However, the remaining $2p_z$ orbital on each atom forms relatively weak π bonds with neighboring atoms, resulting in π bands at the Fermi level. The resulting electronic states are extended over the system, causing metallic behavior.

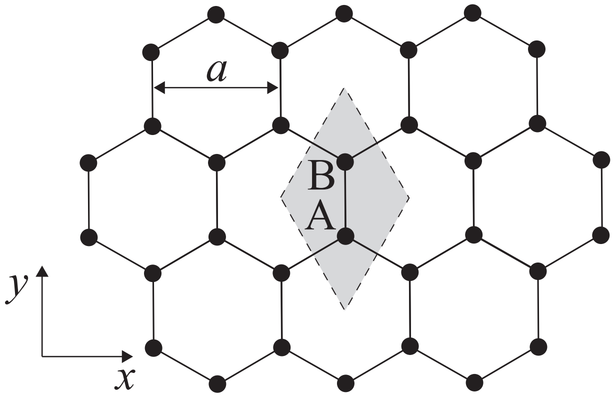

Fig. 1 Schematic of the honeycomb lattice of graphene with black circles indicating carbon atoms and solid straight lines representing covalent σ bonds between neighboring atoms. The shaded rhombus represents a unit cell containing two atomic positions, labeled A and B, and a is the lattice constant.

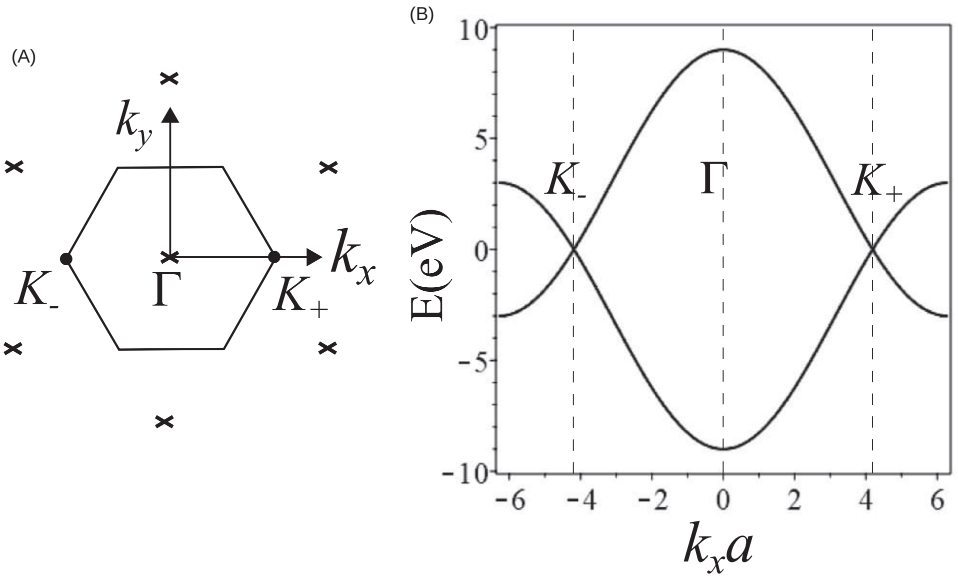

Fig. 2 (A) Schematic of the reciprocal lattice (crosses) and the first Brillouin zone (hexagon) showing symmetry points Γ at the origin, and K_+ and K_- at the corners of the first Brillouin zone. (B) Electronic band structure according to Eq. (3) with $\gamma_0 = 3$ eV plotted along the line $k_y = 0$. Vertical dashed lines show the positions of the symmetry points Γ, K_+ and K_-.

The honeycomb lattice, Fig. 1, is not a Bravais lattice because there are two nonequivalent atomic positions A and B, i.e., the honeycomb lattice consists of a hexagonal Bravais lattice with a basis of two atoms per unit cell. With lattice constant $a = 2.46$ Å, the interatomic separation is $a/\sqrt{3} = 1.42$ Å. If one would consider only A atoms, they would lie on a hexagonal Bravais lattice, likewise the B atoms. Hence one speaks of A and B sublattices.

Band structure and tight-binding model

The honeycomb lattice consists of a hexagonal Bravais lattice with a basis of two atoms per unit cell, denoted A and B, Fig. 1. Electronic energy bands at the Fermi level are π bands arising from the mixing of one $2p_z$ electronic orbital per atom. With one $2p_z$ orbital per atom and two atoms per unit cell, there are two orbitals per cell which yield two energy bands. Assuming translational invariance within the graphene plane, it is possible to derive a Bloch Hamiltonian $H(\mathbf{k})$ as a two-component matrix in the basis of Bloch orbitals on A and B sites, where $\mathbf{k} = (k_x, k_y)$ is the wave vector (Saito et al., 1998). The reciprocal lattice is a hexagonal Bravais lattice, and the first Brillouin zone is a hexagon, as shown in Fig. 2A.

Including only coupling between nearest-neighbor A and B sites, and assuming atomic orbitals on adjacent atoms are orthogonal, the tight-binding Bloch Hamiltonian is

$$H(\mathbf{k}) = \begin{pmatrix} 0 & -\gamma_0 f(\mathbf{k}) \\ -\gamma_0 f^*(\mathbf{k}) & 0 \end{pmatrix}, \tag{1}$$

$$f(\mathbf{k}) = e^{ik_y a/\sqrt{3}} + 2e^{-ik_y a/(2\sqrt{3})}\cos(k_x a/2), \tag{2}$$

where a is the lattice constant and $\gamma_0 \approx 3$ eV (Dresselhaus and Dresselhaus, 2002; Saito et al., 1998) is the nearest-neighbor hopping parameter. The two energy bands are given by

$$E_\pm(\mathbf{k}) = \pm\gamma_0 |f(\mathbf{k})|, \tag{3}$$

and are plotted in Fig. 2B along the line $k_y = 0$.

Given twofold spin degeneracy, graphene is at half filling at charge neutrality (i.e., when the system isn't doped or exposed to external gating). In this case the Fermi level will lie at $E = 0$. Fig. 2 indicates notable symmetry points in the first Brillouin zone, namely Γ at the origin, and K_+ and K_- at the corners of the first Brillouin zone. Note that we only discuss two distinct corners (K_+ and K_-) because the other corners are equivalent (to either K_+ or K_-) via a translation by a reciprocal lattice vector. From the band structure, Fig. 2B, it can be seen that there is no band gap between the two bands, and that there is band degeneracy at the two K points (K_+ and K_-) at $E = 0$. Moreover, the electronic dispersion is approximately linear near these points over a large energy scale ~ 1 eV. Note that the K points are also referred to as the two valleys of graphene. The degeneracy at the valley centers arises because $f(\mathbf{k}) = 0$ there. It means that the A and B sublattices have no coupling between them, but, being identical hexagonal Bravais lattices consisting of carbon atoms, they support two degenerate electronic states.

Dirac effective-mass model, pseudospin and chirality

The two valley centers, K_+ and K_-, are located at wave vectors $\mathbf{k}_\xi = \xi(4\pi/(3a), 0)$ where the valley index $\xi = \pm 1$ is used to distinguish them. Since $f(\mathbf{k}_\xi) = 0$, it is possible to derive a continuum effective-mass model by expanding the function $f(\mathbf{k})$, Eq. (2), near the valley centers $\mathbf{k}_\xi$ using $\mathbf{k} = \mathbf{k}_\xi + \mathbf{q}$ where $|\mathbf{q}|a \ll 1$. To linear order in $|\mathbf{q}|a$, this is $\gamma_0 f(\mathbf{k}_\xi + \mathbf{q}) = -\hbar v(\xi q_x - iq_y)$ where $v = \sqrt{3}a\gamma_0/(2\hbar) \approx 10^6 \,\mathrm{m\,s^{-1}}$ has physical dimensions of velocity. Then, the Hamiltonian $H(\mathbf{k})$, Eq. (1), may be approximated as

$$H_\xi(\mathbf{q}) = \begin{pmatrix} 0 & \hbar v\left(\xi q_x - iq_y\right) \\ \hbar v\left(\xi q_x + iq_y\right) & 0 \end{pmatrix}. \tag{4}$$

The subscript ξ is used to stress that this is valid near each valley K_ξ.

The effective mass model $H_\xi(\mathbf{q})$ describes the linear dispersion of the gapless energy bands near the valleys and the Fermi level ($E = 0$),

$$E_\pm(\mathbf{q}) = \pm\hbar v|\mathbf{q}|. \tag{5}$$

Corresponding eigenstates can be conveniently written as

$$\psi_\pm = \frac{1}{\sqrt{2}}\begin{pmatrix} 1 \\ \pm\xi e^{-i\xi\phi} \end{pmatrix}, \tag{6}$$

where ϕ is the polar angle of the wave vector, $q_x = |\mathbf{q}| \cos\phi$, $q_y = |\mathbf{q}| \sin\phi$. Taking into account twofold spin degeneracy and twofold valley degeneracy, the isotropic dispersion Eq. (5) yields a density of states per unit energy per unit area given by

$$g(E) = \frac{2}{\pi}\frac{|E|}{\hbar^2 v^2}, \tag{7}$$

and Fermi velocity $v_\mathrm{F} = v$.

Effective mass models often have the form of a Schrödinger equation yielding quadratic energy $E = \hbar^2 k^2/(2\, m_*)$ with effective mass m_*. Here, instead, the dispersion is linear, reminiscent of relativistic dynamics, with velocity $v \approx 10^6$ ms^{-1} significantly less than the speed of light in vacuum. Although Eq. (4) is written near a single valley, if one explicitly included both valleys the effective mass model would have four components and it would be the massless Dirac equation in two spatial dimensions. The dispersion Eq. (5) describes a Dirac cone at each valley, and the valley center is often referred to as a Dirac point. Note that the two components of $H_\xi(\mathbf{q})$, Eq. (4), are not electron spin (we assume twofold spin degeneracy), but the A, B sublattice degree of freedom, which is known as pseudospin.

The pseudospin may be represented using Pauli spin matrices in the A, B sublattice space so that

$$H_\xi(\mathbf{q}) = \hbar v\left(\xi q_x \sigma_x + q_y \sigma_y\right). \tag{8}$$

For a vector of Pauli spin matrices $\boldsymbol{\sigma} = (\sigma_x, \sigma_y, \sigma_z)$, its expectation value with respect to the eigenstates Eq. (6) is $\langle\psi_\pm|\boldsymbol{\sigma}|\psi_\pm\rangle = \pm\hat{\mathbf{n}}_1$ where the unit vector $\hat{\mathbf{n}}_1$ is

$$\hat{\mathbf{n}}_1 = (\xi\cos\phi,\ \sin\phi,\ 0). \tag{9}$$

Thus the Hamiltonian may be further written as

$$H_\xi(\mathbf{q}) = \hbar v|\mathbf{q}|\boldsymbol{\sigma}\cdot\hat{\mathbf{n}}_1, \tag{10}$$

which emphasizes that electrons in graphene are chiral. Energy eigenstates $\psi_\pm$ with $E_\pm(\mathbf{q}) = \pm\hbar v|\mathbf{q}|$ also have eigenvalues $\boldsymbol{\sigma}\cdot\hat{\mathbf{n}}_1 = \pm 1$ for measurement of pseudospin along the direction $\hat{\mathbf{n}}_1$. The pseudospin direction is linked to that of the electronic wave vector (e.g., at valley $\xi = 1$, they are parallel for the conduction band and antiparallel for the valence band).

Symmetries

In the absence of external perturbations, graphene satisfies space and time inversion symmetries. Both of these involve inversion of the wave vector $\mathbf{k}$ so that, when applied to electronic states in the vicinity of a valley as described by $H_\xi(\mathbf{q})$, the valley index must be inverted $\xi \to -\xi$:

$$\text{space inversion}: \qquad \sigma_x H_\xi(\mathbf{q})\sigma_x = H_{-\xi}(-\mathbf{q}), \tag{11}$$

$$\text{time inversion}: \qquad H_\xi^*(\mathbf{q}) = H_{-\xi}(-\mathbf{q}). \tag{12}$$

Note that some authors discuss an additional fictitious time inversion symmetry which acts at one valley as $\sigma_y H_\xi^*(\mathbf{q})\sigma_y = H_\xi(-\mathbf{q})$ without inverting the valley index.

Chiral, or sublattice, symmetry is described by the Pauli matrix σ_z in the A, B sublattice space (Cayssol and Fuchs, 2021) and acts as

$$\text{chiral}: \qquad \sigma_z H_\xi(\mathbf{q})\sigma_z = -H_\xi(\mathbf{q}). \tag{13}$$

Chiral symmetry ensures electron-hole symmetry of the electronic spectrum, as shown in Fig. 2B. Chiral symmetry may be combined with time-inversion symmetry to give charge conjugation symmetry $\sigma_z H_\xi^*(\mathbf{q})\sigma_z = -H_{-\xi}(-\mathbf{q})$. Note that the preservation of chiral symmetry (and charge conjugation) is only approximately correct at low energy, due to approximations made in deriving the tight-binding model Eq. (1). For example, introducing non-orthogonality of adjacent $2p_z$ orbitals will break electron-hole symmetry of the band structure (Saito et al., 1998).

Berry phase π

Graphene satisfies space and time inversion symmetries, so Berry curvature is zero everywhere (Cayssol and Fuchs, 2021; Xiao et al., 2010). Nevertheless, it is possible to accumulate non-zero Berry phase along a closed trajectory in reciprocal space which encloses a valley center. Consider, for example, states $\psi_\pm$ near a valley center as described by Eq. (6), and a closed circular trajectory C at constant energy and a constant radial distance $|\mathbf{q}|$ from the valley center. The Berry connection $\mathbf{A}_\pm(\mathbf{q})$ is defined (Berry, 1984) as

$$\mathbf{A}_\pm(\mathbf{q}) = i\langle\psi_\pm|\nabla_\mathbf{q}|\psi_\pm\rangle, \tag{14}$$

which may be evaluated as $\mathbf{A}_\pm(\mathbf{q}) = -\xi\hat{\mathbf{e}}_\phi/(2|\mathbf{q}|)$ where $\hat{\mathbf{e}}_\phi$ is the unit vector of polar angle ϕ. The Berry phase is

$$\gamma_\pm = \oint_C \mathbf{A}_\pm(\mathbf{q})\cdot d\mathbf{q} = -\xi\pi. \tag{15}$$

This is somewhat analogous to a winding number because the accumulated Berry phase is nonzero only when the path encloses the valley center. Note that the Berry connection is not gauge invariant, and that the Berry phase is only defined modulo 2π. Whatever gauge is chosen for the eigenstates $\psi_\pm$, they should be single-valued around the trajectory C for the calculation of Berry phase to be valid.

It is possible to imagine breaking inversion symmetry in graphene by introducing asymmetry between the A and B onsite energies, modifying the effective mass model (Semenoff, 1984) as

$$H_\xi(\mathbf{q}) = \hbar v\left(\xi q_x\sigma_x + q_y\sigma_y\right) + \Delta\sigma_z, \tag{16}$$

where Δ is a real parameter characterizing the asymmetry as $E_A - E_B = 2\Delta$. It opens a gap in the energy spectrum, $E_\pm(\mathbf{k}) = \pm\sqrt{\Delta^2 + \hbar^2 v^2|\mathbf{q}|^2}$, and leads to non-zero Berry curvature (Xiao et al., 2007, 2010),

$$\Omega_\pm(\mathbf{q}) = \mp\frac{\xi\Delta\hbar^2 v^2}{2\left(\hbar^2 v^2|\mathbf{q}|^2 + \Delta^2\right)^{3/2}}. \tag{17}$$

The Berry curvature is strongly peaked near the valley center, but with opposite signs at the two valleys. Hence, the contributions of the valleys cancel to give zero Chern number for the filled valence bands (as expected because time-inversion symmetry is preserved). Although the Chern number is zero, the Dirac effective mass model of graphene is an important example of a two-band model, and it played a role in the understanding of topological insulators. Particularly, the Haldane model (Haldane, 1988) and the Kane-Mele model (Kane and Mele, 2005a,b) are based on graphene and exemplify Chern insulators and spin-Hall insulators, respectively (Cayssol and Fuchs, 2021).

Trigonal warping and other tight-binding parameters

The Dirac-like effective mass model Eq. (4) is linear in the wavevector $\mathbf{q}$ measured from the valley center, and this is generally a good approximation when $|\mathbf{q}|$ is small, i.e., $|\mathbf{q}|a \ll 1$. It gives the isotropic electronic dispersion $E_\pm(\mathbf{q}) = \pm\hbar v|\mathbf{q}|$, Eq. 5. Corrections emerge at larger $|\mathbf{q}|$ values, and they may be included by expanding $f(\mathbf{k}_\xi + \mathbf{q})$ to higher powers in $|\mathbf{q}|$. For example, to quadratic order (Ando et al., 1998),

$$H_\xi(\mathbf{q}) = \begin{pmatrix} 0 & \hbar v\left(\xi q_x - iq_y\right) \\ \hbar v\left(\xi q_x + iq_y\right) & 0 \end{pmatrix} - \frac{\gamma_0 a^2}{8}\begin{pmatrix} 0 & \left(\xi q_x + iq_y\right)^2 \\ \left(\xi q_x - iq_y\right)^2 & 0 \end{pmatrix}. \tag{18}$$

The corresponding energy eigenvalues are

$$E_\pm(\mathbf{q}) = \pm\hbar v|\mathbf{q}|\sqrt{1 - \frac{\xi|\mathbf{q}|a\cos(3\phi)}{2\sqrt{3}} + \frac{|\mathbf{q}|^2 a^2}{48}}. \tag{19}$$

With the dependence on $\cos(3\phi)$ where ϕ is the polar angle of the wavevector, this describes a triangular-shaped distortion to the otherwise circular Fermi surface known as 'trigonal warping'. It is illustrated in Fig. 3 for valley K_+; note that the orientation of trigonal warping is reversed at the other valley K_-. Even at a rather large energy (e.g., $E \approx 1.2$ eV in Fig. 3), the perturbation due to

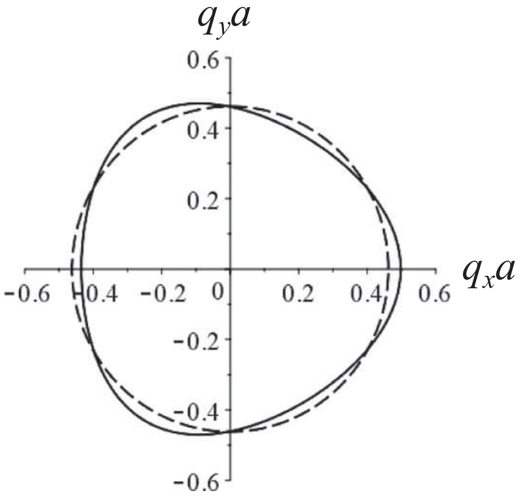

Fig. 3 Trigonal warping in graphene at the K_+ valley showing a constant energy contour $E = 0.4\gamma_0 \approx 1.2$ eV. The solid line shows the influence of trigonal warping Eq. (19) as compared to its absence in the isotropic dispersion $E = \hbar v|\mathbf{q}|$ (dashed line).

trigonal warping is relatively slight. The Hamiltonian with trigonal warping Eq. (18) satisfies chiral symmetry Eq. (13), so electron-hole symmetry of the energy spectrum is maintained.

It is possible to consider tight-binding parameters in addition to the nearest-neighbor hopping γ_0. One example is to take into account non-orthogonality of $2p_z$ orbitals on adjacent sites (Saito et al., 1998), another is to include next-nearest neighbor hopping (Johnson and Dresselhaus, 1973; Peres et al., 2006; Sasaki et al., 2006; Wallace, 1947). Both of these break chiral symmetry Eq. (13) and, thus, introduce electron-hole asymmetry in the band structure. However, they are both quadratic in $\mathbf{q}$ corrections to the Dirac-like effective mass model so are very small at low energy.

Ambipolar electric field effect

The carrier density n in graphene may be tuned using an external gate potential, and this allows the measurement of the density-dependence of many physical observables (Novoselov et al., 2004). Graphene has a gapless band structure with degeneracy at the valley centers, Fig. 2B. As measured from the valley center, for a partially-filled conduction band, the carrier density n is given by

$$n = \frac{q_F^2}{\pi} = \frac{E_F^2}{\pi \hbar^2 v^2}, \tag{20}$$

where q_F (E_F) is the magnitude of the Fermi wavevector (energy), and this expression includes fourfold band degeneracy (for spins and valleys). The density n may be tuned (Novoselov et al., 2004) using a gate parallel to the graphene of voltage V_g, separated at a distance d by a spacer with dielectric constant ε_g. Modeling the gate and graphene as two surfaces of a parallel plate capacitor, the carrier density is

$$n = \frac{\varepsilon_0 \varepsilon_g}{ed} V_g, \tag{21}$$

where we use SI units and denote electronic charge as $-e$ with $e > 0$.

Klein tunneling

Klein tunneling is a process in which chiral electrons in graphene display perfect transmission at normal incidence on a potential barrier (Ando et al., 1998; Beenakker, 2008; Castro Neto et al., 2009; Cheianov and Fal'ko, 2006; Katsnelson et al., 2006; McEuen et al., 1999). It is the result of a continuous, gapless energy spectrum between the conduction and valence bands, and of conservation of pseudospin as a particle travels between the states in those bands.

To demonstrate this effect, we consider a potential $V(x)$ with translational invariance in the transverse direction y, but with a step dependence in the longitudinal x direction (Katsnelson et al., 2006) such that $V(x) = 0$ for $x < 0$ and for $x > L$, and $V(x) = V_0$ for $0 < x < L$, as shown in Fig. 4. The low energy Hamiltonian Eq. (4) in real space is written as

$$H_\xi = \begin{pmatrix} V(x) & v\left(\xi p_x - i p_y\right) \\ v\left(\xi p_x + i p_y\right) & V(x) \end{pmatrix}, \tag{22}$$

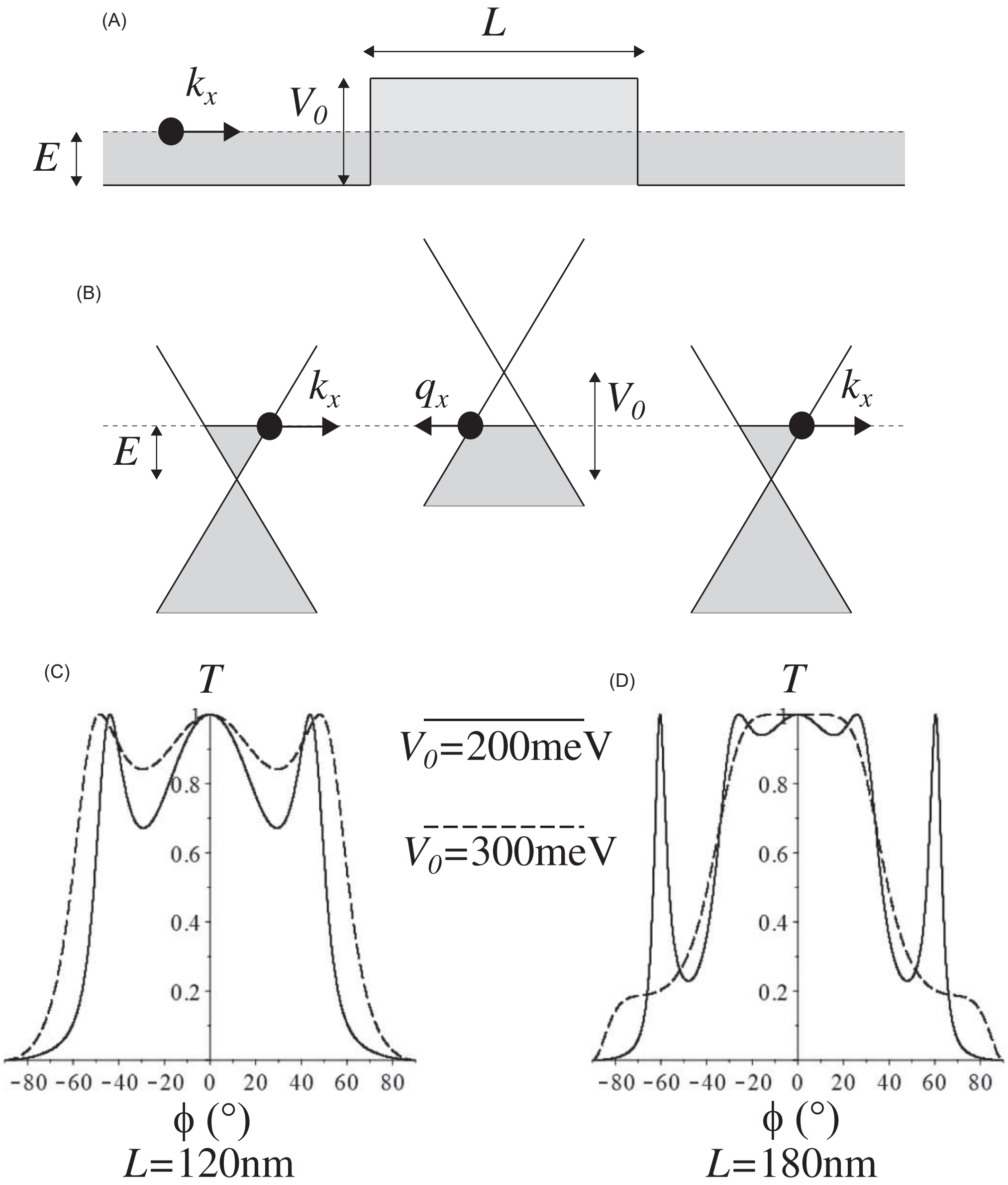

Fig. 4 Klein tunneling in graphene. (A) Schematic of an incoming electron of energy E and longitudinal wavevector component k_x incident on a square potential barrier of height V_0 and length L. (B) Schematic of the relative positions of the graphene energy bands for the case $V_0 > E > 0$. A normally incident electron on the left with wavevector k_x in the conduction band transfers to a state in the valence band under the barrier with wavevector $-q_x$, which then transfers to an outgoing state on the right with wavevector k_x in the conduction band. (C) Transmission probability $T(\phi)$ as a function of incident angle ϕ for incoming electrons of energy $E = 70$ meV ($\lambda = 59$ nm), barrier length $L = 120$ nm and barrier heights $V_0 = 200$ meV (solid) and $V_0 = 300$ meV (dashed). (D) Transmission probability $T(\phi)$ for incoming electrons of energy $E = 70$ meV ($\lambda = 59$ nm), barrier length $L = 180$ nm and barrier heights $V_0 = 200$ meV (solid) and $V_0 = 300$ meV (dashed). Plots were made with velocity $v = 1.0 \times 10^6$ m s^{-1}.

where p_x, p_y are components of the momentum operator. For an incoming wave of unit flux from the left side, we determine solutions to the Hamiltonian on the left $x < 0$, ψ_{L}, in the center $0 < x < L$, ψ_{C}, and on the right $x > L$, ψ_{R}. Then, we use wave matching to determine the transmission probability, assuming planar interfaces at the boundaries $x = 0$ and $x = L$ such that the transverse component k_y of the wave vector is conserved. The states can be written as

$$\psi_{\mathrm{L}} = \left[\begin{pmatrix} 1 \\ s\xi e^{-i\xi\phi} \end{pmatrix} e^{ik_x x} + r \begin{pmatrix} 1 \\ -s\xi e^{-i\xi\phi} \end{pmatrix} e^{-ik_x x}\right] e^{ik_y y},$$

$$\psi_{\mathrm{C}} = \left[C \begin{pmatrix} 1 \\ s_{\mathrm{C}}\xi e^{i\xi\theta} \end{pmatrix} e^{iq_x x} + D \begin{pmatrix} 1 \\ -s_{\mathrm{C}}\xi e^{-i\xi\theta} \end{pmatrix} e^{-iq_x x}\right] e^{ik_y y},$$

$$\psi_{\mathrm{R}} = t \begin{pmatrix} 1 \\ s\xi e^{i\xi\phi} \end{pmatrix} e^{ik_x x + ik_y y},$$

where r, t, C, and D are constants to be determined by the wave matching (r and t are reflection and transmission amplitudes, respectively). On the left and the right, the energy is $E = s\hbar v\sqrt{k_x^2 + k_y^2}$ where $s = \mathrm{sign}(E)$, and ϕ is the polar angle, $\tan\phi = k_y/k_x$. In the center, $E = V_0 + s_{\mathrm{C}}\hbar v\sqrt{q_x^2 + k_y^2}$ where $s_{\mathrm{C}} = \mathrm{sign}(E - V_0)$, and θ is the polar angle, $\tan\theta = k_y/q_x$.

As the Hamiltonian Eq. (22) is linear in momentum, it is sufficient to match the sublattice components of the states at $x = 0$ and at $x = L$, not their spatial derivatives. This process yields the reflection $R = |r|^2$ and transmission $T = |t|^2$ probabilities, where $R + T = 1$, as (Castro Neto et al., 2009; Katsnelson et al., 2006)

$$R = \frac{(\sin\phi - ss_{\mathrm{C}}\sin\theta)^2\sin^2 q_xL}{\cos^2\phi\cos^2\theta\cos^2 q_xL + (ss_{\mathrm{C}} - \sin\phi\sin\theta)^2\sin^2 q_xL},$$

$$T = \frac{\cos^2\phi\cos^2\theta}{\cos^2\phi\cos^2\theta\cos^2 q_xL + (ss_{\mathrm{C}} - \sin\phi\sin\theta)^2\sin^2 q_xL}.$$

They are both independent of the valley index ξ. These expressions show that there are resonances at $q_xL = \pi N$, for integer N, when $R = 0$ and $T = 1$. In addition, there is also perfect transmission $R = 0$ and $T = 1$ at normal incidence $\phi = \theta = 0$. Plots of the transmission probability T as a function of the polar angle ϕ of incoming electrons are shown in Fig. 4C and D for different parameter values, illustrating the perfect transmission at normal incidence and the parameter-dependent resonances at other angles.

Perfect transmission at normal incidence $\phi = \theta = 0$ is illustrated in Fig. 4B. In this case, with $V_0 > E > 0$, $s = 1$, $s_{\mathrm{C}} = -1$, $r = C = 0$ and $|t| = |D| = 1$: as the potential $V(x)$ is diagonal in the A/B sublattice space, it is unable to change the direction of pseudospin which must be conserved as a particle crosses the barrier. In this case, the pseudospin points in the direction of positive x and all the non-zero states have the form $\psi^T \sim (1\ 1)$ in the A/B sublattice space.

Integer quantum Hall effect

Landau levels

In the presence of a perpendicular magnetic field, the energy spectrum consists of a series of discrete energy levels known as Landau levels. Off-diagonal elements of the Dirac effective-mass model, Eq. (4), act on magnetic oscillator states as raising or lowering operators (Castro Neto et al., 2009). With magnetic field $\mathbf{B} = (0, 0, -B)$ (in Cartesian coordinates) and the Landau gauge for vector potential $\mathbf{A} = (0, -Bx, 0)$, then, at the first valley,

$$H_+ = \frac{\sqrt{2}\hbar v}{\lambda_B}\begin{pmatrix} 0 & ia^\dagger \\ -ia & 0 \end{pmatrix}, \tag{23}$$

where $\lambda_B = \sqrt{\hbar/(eB)}$ is the magnetic length, and $a^\dagger$, a are raising and lowering operators which act on magnetic operator states ϕ_ℓ as

$$a^\dagger\phi_\ell = \sqrt{\ell + 1}\,\phi_{\ell+1}, \tag{24}$$

$$a\phi_\ell = \sqrt{\ell}\,\phi_{\ell-1}, \tag{25}$$

where ℓ is an integer with $\ell \geq 0$ and $a\phi_0 = 0$. Two-component eigenstates $\psi_{\ell,\pm}$ for $\ell \geq 1$ are given by

$$\psi_{\ell,\pm} = \frac{1}{\sqrt{2}}\begin{pmatrix} \phi_\ell \\ \mp i\phi_{\ell-1} \end{pmatrix}, \tag{26}$$

corresponding to a positive and negative series of Landau levels with energies $E_\pm$ given by McClure (1956)

$$E_{\ell,\pm} = \pm\frac{\hbar v}{\lambda_B}\sqrt{2\ell}; \quad \ell \geq 1. \tag{27}$$

In graphene, the energy levels depend on the square root of the magnetic field B and the index ℓ, unlike a conventional two-dimensional semiconductor where the dependences are linear. In addition, there is a zero energy state with weight on the A sublattice only,

$$\psi_0 = \begin{pmatrix} \phi_0 \\ 0 \end{pmatrix}; \quad E_0 = 0. \tag{28}$$

At the second valley, K_-, the spectrum is degenerate with that of K_+, but the role of the A and B sublattices is reversed. In particular, the zero energy state has weight only on the B sublattice.

Semiclassical quantization and Berry phase

The Landau level spectrum may be understood in terms of the Onsager semiclassical quantization (Xiao et al., 2010),

$$S(E) = \frac{2\pi}{\lambda_B^2}\left(\ell + \frac{1}{2} - \frac{\gamma}{2\pi}\right), \tag{29}$$

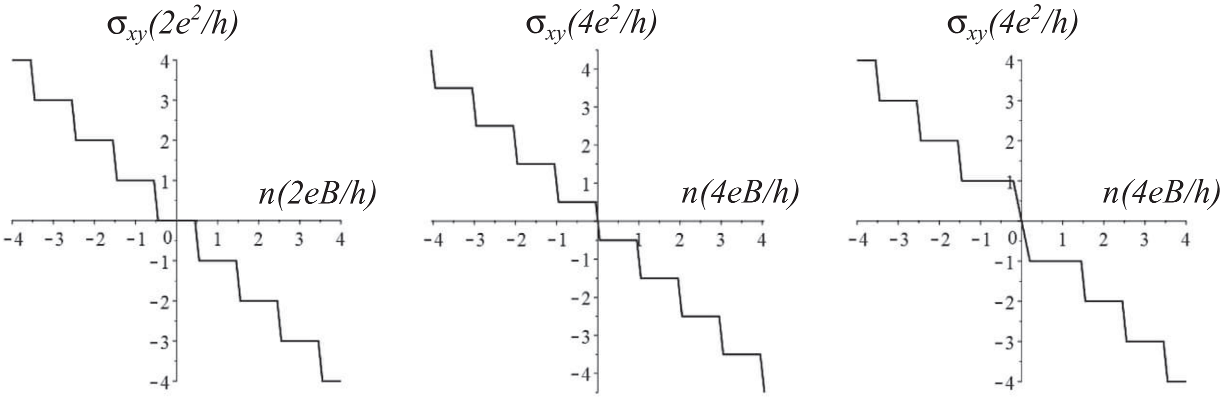

Fig. 5 Schematic of the Hall conductivity σ_{xy} vs carrier density n showing the integer quantum Hall effect for (A) a conventional two-dimensional semiconductor with zero Berry phase and twofold spin degeneracy, (B) monolayer graphene, (C) Bernal-stacked bilayer graphene.

where $S(E)$ is the area in reciprocal space enclosed by a contour at constant energy E, γ is Berry phase, and integer $\ell \geq 0$. For a conventional two-dimensional semiconductor with quadratic dispersion $E = \hbar^2 k^2/(2\, m_*)$, effective mass m_*, then $S(E) = \pi k^2 = 2\pi m_* E/\hbar^2$. With zero Berry phase $\gamma = 0$, Eq. (29) then gives the usual harmonic oscillator relation, $E_\ell = \hbar\omega_c(\ell + 1/2)$, where the cyclotron frequency is $\omega_c = eB/m_*$.

For graphene, with $E = \pm\hbar v k$, then $S(E) = \pi k^2 = \pi E^2/(\hbar^2 v^2)$. Berry phase $\gamma = \pi$ cancels the factor of 1/2 on the right side of Eq. (29), giving $E_{\ell,\pm} = \pm(\hbar v/\lambda_B)\sqrt{2\ell}$, in agreement with the fully quantum calculation Eq. (27). The spectrum of levels, without the zero point energy $\hbar\omega_c/2$, but with a level fixed with $E_0 = 0$, can be interpreted as a manifestation of Berry phase π.

Integer quantum Hall effect

In a conventional two-dimensional semiconductor with zero Berry phase, the Landau level spectrum is $E_\ell = \hbar\omega_c(\ell + 1/2)$ where $\omega_c = eB/m_*$ is the cyclotron frequency and integer $\ell \geq 0$. In the integer quantum Hall effect, quantized plateaus in the Hall conductivity σ_{xy} occur values of $M(2e^2/h)$ for twofold spin degeneracy, quantum of conductance e^2/h, and integer M. This is plotted in Fig. 5A showing σ_{xy} as a function of carrier density n. Each step as a function of density n correponds to the crossing of a Landau level, and, as the capacity per level is $2eB/h$, the separation of plateaus on the density axis is $2eB/h$.

In monolayer graphene there is fourfold degeneracy due to twofold spin and twofold valley degeneracy, so quantized plateaus in the Hall conductivity are separated by steps of height $4e^2/h$. However, the plateaus occur at half-integer values of $4e^2/h$ (Gusynin and Sharapov, 2005; Haldane, 1988; Peres et al., 2006; Zheng and Ando, 2002), rather than the conventional integer ones,

$$\text{quantization}: \quad \sigma_{xy} = -\frac{2M+1}{2}\left(\frac{4e^2}{h}\right), \tag{30}$$

for integer M, as observed experimentally (Novoselov et al., 2005; Zhang et al., 2005). This is plotted in Fig. 5B, where the plateaus are separated by the Landau level capacity $4eB/h$ on the density axis. This unusual sequencing of plateaus is sometimes called the 'half-integer' quantum Hall effect. It may be interpreted in terms of the level fixed with $E_0 = 0$ (as a manifestation of Berry phase π) which requires a step of height $4e^2/h$ in σ_{xy} as the density crosses zero between the electron and hole sides. Here we assumed that any splitting of the levels, due to breaking of spin or valley degeneracy, say, is negligible in comparison to temperature and level broadening.

Electronic properties of Bernal-stacked bilayer graphene

Bilayer graphene (or 'graphene bilayers') refers to two parallel monolayers of graphene. This might be two layers either side of a dielectric spacer (Gorbachev et al., 2012; Schmidt et al., 2008) or two layers in direct contact with weak atomic bonding between them. In the latter case, there are different possible ways to orient, or stack, the two layers with respect to each other. One option is twisted bilayer graphene (Cao et al., 2016; Kim et al., 2016; Rozhkov et al., 2016) resulting in either a periodic overall lattice with a very large unit cell, or a system with no periodicity. There are also two common ways which result in a periodic lattice with a small unit cell of lattice constant a, the same as that of a single layer. These are called Bernal stacking (or AB-stacking) (Bernal, 1924; McCann and Koshino, 2013; Novoselov et al., 2006; Rozhkov et al., 2016) and AA stacking (Lee et al., 2008b; Rozhkov et al., 2016), and Bernal stacking is the most energetically favorable of the two (Lebedeva et al., 2011; Mostaani et al., 2015).

If we consider each monolayer to lie in the horizontal (x-y) plane, then Bernal-stacked bilayer graphene (also known as AB-stacked bilayer graphene) is when half of the atoms are situated directly above or below an atom in the other layer. For AA stacking, every atom is directly above or below an atom in the other layer.

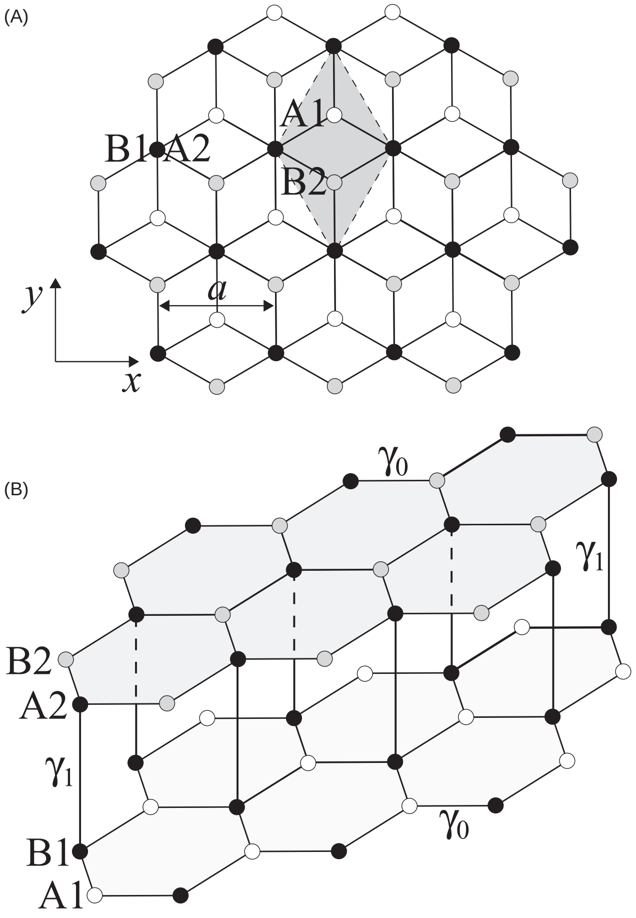

Fig. 6 Schematic of the lattice of Bernal-stacked bilayer graphene with A1 (white) and B1 (black) atomic sites on the lower layer, and A2 (black) and B2 (grey) atomic sites on the upper layer. (A) is a plan view, and the shaded rhombus represents a unit cell. (B) is a side view, indicating intralayer nearest-neighbor tight-binding parameter γ_0 and interlayer nearest-neighbor tight-binding parameter γ_1.

Crystal structure

With A1, B1 atomic sites on the lower layer and A2, B2 sites on the upper layer, Bernal stacking (Bernal, 1924) describes the case when B1 and A2 sites lie directly below and above each other, but A1 and B2 have no such counterpart; they lie below or above the center of a hexagon in the other layer, Fig. 6. The result is a periodic lattice in the horizontal (x-y) plane with unit cell of the same area as that of monolayer graphene, Fig. 6A, but the unit cell now contains four atomic sites A1, B1, A2, B2. The interlayer spacing is about 3.35 $\AA$.

Electronic band structure and tight-binding model

As with monolayer graphene, the electronic band structure near the Fermi level can be described by considering one $2p_z$ orbital per atom, i.e., four orbitals per unit cell for bilayer graphene. These yield four electronic bands. Assuming translational invariance within the graphene plane, it is possible to derive a Bloch Hamiltonian $H(\mathbf{k})$ as a four-component matrix in the basis of Bloch orbitals on A1, B1, A2, B2 sites, where $\mathbf{k} = (k_x, k_y)$ is the wave vector. The reciprocal lattice is the same as that of monolayer graphene: a hexagonal Bravais lattice with a hexagonal first Brillouin zone, as shown in Fig. 2A.

The ‘minimal model’ includes only coupling between nearest-neighbor intralayer sites (A1-B1 and A2-B2) with tight-binding parameter $\gamma_0 \approx 3$ eV (Dresselhaus and Dresselhaus, 2002; Saito et al., 1998), coupling between nearest-neighbor interlayer sites (B1-A2) with tight-binding parameter $\gamma_1 \approx 0.4$ eV (Dresselhaus and Dresselhaus, 2002; Kuzmenko et al., 2009; Li et al., 2009b; Zhang et al., 2008), and assuming atomic orbitals on adjacent atoms are orthogonal, the tight-binding Bloch Hamiltonian in basis A1, B1, A2, B2 (McCann and Fal’ko, 2006) is

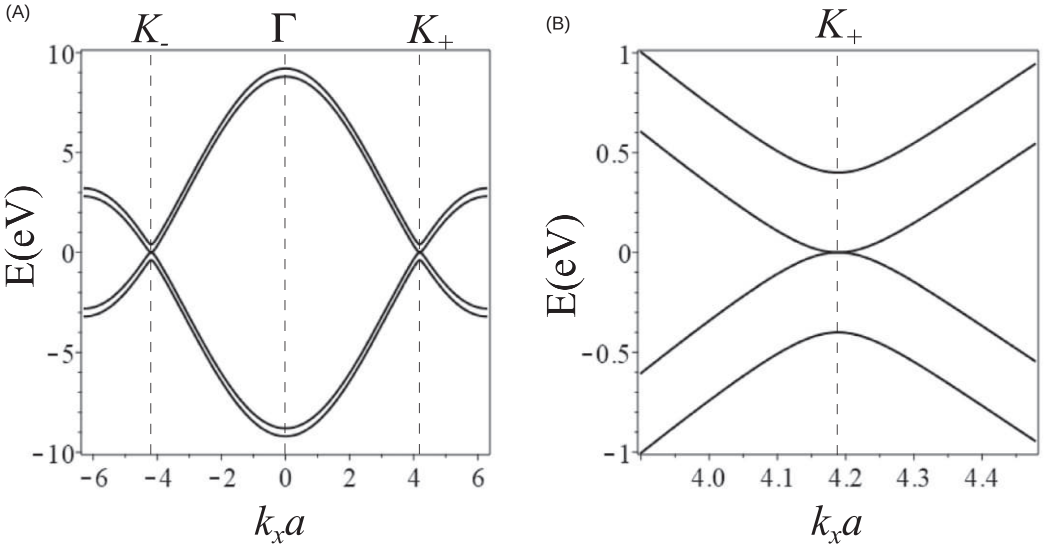

Fig. 7 (A) Electronic band structure of Bernal-stacked bilayer graphene according to Eq. (31) with $\gamma_0 = 3$ eV, $\gamma_1 = 0.4$ eV, plotted along the line $k_y = 0$. Vertical dashed lines show the positions of the symmetry points Γ, K_+ and K_-. (B) Scaled up plot of the bands near the K_+ point, showing touching conduction and valence bands with quadratic dispersion at the valley center, and linear dispersion further away.

$$H(\mathbf{k}) = \begin{pmatrix} 0 & -\gamma_0 f(\mathbf{k}) & 0 & 0 \\ -\gamma_0 f^*(\mathbf{k}) & 0 & \gamma_1 & 0 \\ 0 & \gamma_1 & 0 & -\gamma_0 f(\mathbf{k}) \\ 0 & 0 & -\gamma_0 f^*(\mathbf{k}) & 0 \end{pmatrix},$$

where $f(\mathbf{k})$ is defined in Eq. (2). Each 2×2 block on the diagonal describes intralayer hopping, the off-diagonal 2×2 blocks account for interlayer coupling. The four energy bands are given by

$$E_{\pm}^{(\beta)}(\mathbf{k}) = \pm\frac{\gamma_1}{2}\left(\sqrt{1+\frac{4\gamma_0^2|f(\mathbf{k})|^2}{\gamma_1^2}}+\beta\right), \tag{31}$$

where $\beta = \pm 1$. They are plotted in Fig. 7 along the line $k_y = 0$. In general, Fig. 7A, the bands are two copies of the monolayer bands, Fig. 2B, split by the interlayer coupling parameter γ_1. As in monolayer, there is no band gap, but a degeneracy at the Fermi level at the two K points (K_+ and K_-), Fig. 7B.

At the two valley centers, K_+ and K_-, $f(\mathbf{k}_\xi) = 0$. At these points, Eq. (31) shows that two bands with $\beta = 1$ are $E_\pm{}^{(1)}(\mathbf{k}_\xi) = \pm\gamma_1$ and split away from the Fermi level, whereas the two bands with $\beta = -1$ are $E_\pm{}^{(-1)}(\mathbf{k}_\xi) = 0$, touching at the Fermi level. Near the valley centers $\mathbf{k} = \mathbf{k}_\xi + \mathbf{q}$, for $|\mathbf{q}|a \ll 1$, then $\gamma_0|f(\mathbf{k})| \approx \hbar v|\mathbf{q}|$ and Eq. (31) interpolates between quadratic dispersion at the valley center to linear dispersion at larger energy,

$$E_{\pm}^{(-1)} \approx \begin{cases} \pm\hbar^2|\mathbf{q}|^2/(2m_*) & \text{for } 2\hbar v|\mathbf{q}| \ll \gamma_1 \\ \pm\hbar v|\hbar\mathbf{q}| & \text{for } 2\hbar v|\mathbf{q}| \gg \gamma_1 \end{cases}, \tag{32}$$

where the effective mass is very light, $m_* = \gamma_1/(2v^2) \approx 0.04 m_e$ where m_e is the free electron mass. Interlayer coupling γ_1 introduces an additional energy scale as compared to monolayer graphene. There is a corresponding length scale $\ell_\perp = \hbar v/\gamma_1$ with value $\ell_\perp = \sqrt{3}\gamma_0 a/(2\gamma_1) \approx 21$ Å so that $\ell_\perp \approx 9a$. Hence the quadratic dispersion at long wavelength described by Eq. (32) occurs for $\ell_\perp|\mathbf{q}| \ll 1$.

Effective-mass model, pseudospin and chirality

Near the valley center, two bands $E_\pm{}^{(1)}(\mathbf{k}_\xi) = \pm\gamma_1$ are split away from $E = 0$. They arise predominantly from the interlayer coupling γ_1 between orbitals on the B1 and A2 sites, creating a dimer with a bonding and anti-bonding pair of energies.

The two bands that touch at the valley center at $E = 0$ arise from orbitals on the A1 and B2 sites (the ones without a counterpart in the other layer directly above or below), and the quadratic dispersion near the valley center may be understood as effective coupling between these orbitals. An electron hopping from A1 to B2 involves a path via the strongly coupled B1-A2 dimer: intralayer hopping on each layer (e.g., A1 to B1 and A2 to B2) gives a quadratic dispersion with the interlayer hopping (B1 to A2) contributing to the effective mass $m_* = \gamma_1/(2v^2)$. This process may be described by an effective 2×2 Bloch Hamiltonian in the basis of orbitals of A1 and B2 sites only. It is obtained by eliminating the B1 and A2 components (the matrix equation $H(\mathbf{k})\psi_\pm{}^{(\beta)}(\mathbf{k}) = E_\pm{}^{(\beta)}(\mathbf{k})\psi_\pm{}^{(\beta)}(\mathbf{k})$ may be viewed as four simultaneous equations) and using the substitution $\gamma_0 f(\mathbf{k}_\xi + \mathbf{q}) = -\hbar v(\xi q_x - iq_y)$ with $\ell_\perp |\mathbf{q}| \ll 1$.

Hence, in the A1-B2 basis, the low-energy effective Hamiltonian (McCann and Fal'ko, 2006) is

$$H_\xi^{(2)}(\mathbf{q}) = -\frac{\hbar^2}{2m_*}\begin{pmatrix} 0 & \left(\xi q_x - iq_y\right)^2 \\ \left(\xi q_x + iq_y\right)^2 & 0 \end{pmatrix}, \tag{33}$$

where the superscript (2) is used to stress that this is for bilayer graphene. The effective mass model $H_\xi^{(2)}(\mathbf{q})$ describes the quadratic dispersion of the gapless energy bands near the valleys and the Fermi level ($E = 0$),

$$E_\pm(\mathbf{q}) = \pm\frac{\hbar^2|\mathbf{q}|^2}{2m_*}. \tag{34}$$

Corresponding eigenstates can be conveniently written as

$$\psi_\pm = \frac{1}{\sqrt{2}}\begin{pmatrix} 1 \\ \mp e^{2i\xi\phi} \end{pmatrix}, \tag{35}$$

where ϕ is the polar angle of the wave vector, $q_x = |\mathbf{q}|\cos\phi$, $q_y = |\mathbf{q}|\sin\phi$. Taking into account twofold spin degeneracy and twofold valley degeneracy, the isotropic dispersion Eq. (5) yields a density of states per unit energy per unit area at low energy given by

$$g(E) = \frac{2m_*}{\pi\hbar^2}, \tag{36}$$

which is independent of energy E, and Fermi velocity $v_F = \hbar q_F/m_*$ where q_F is the magnitude of the Fermi wavevector measured from the valley center.

The effective mass model Hamiltonian Eq. (33) is a generalization of the Dirac effective-mass model of monolayer graphene Eq. (4), and there is a pseudospin related to the A1, B2 sublattice degree of freedom. With Pauli matrices in the sublattice space, the low-energy effective Hamiltonian Eq. (33) may be written as

$$H_\xi^{(2)}(\mathbf{q}) = -\frac{\hbar^2}{2m_*}\left[\left(q_x^2 - q_y^2\right)\sigma_x + 2\xi q_x q_y \sigma_y\right]. \tag{37}$$

For a vector of Pauli spin matrices $\boldsymbol{\sigma} = (\sigma_x, \sigma_y, \sigma_z)$ in the A1, B2 space, its expectation value with respect to the eigenstates Eq. (35) is $\langle\psi_\pm|\boldsymbol{\sigma}|\psi_\pm\rangle = \pm\hat{\mathbf{n}}_2$ where the unit vector $\hat{\mathbf{n}}_2$ is

$$\hat{\mathbf{n}}_2 = -(\cos 2\phi, \xi\sin 2\phi, 0). \tag{38}$$

Hence the Hamiltonian may be further written as

$$H_\xi^{(2)}(\mathbf{q}) = \frac{\hbar^2|\mathbf{q}|^2}{2m_*}\boldsymbol{\sigma}\cdot\hat{\mathbf{n}}_2, \tag{39}$$

which emphasizes that electrons in bilayer graphene are chiral with the pseudospin direction linked to that of the electronic wave vector. However, in bilayer the pseudospin Eq. (38) turns twice as quickly in the plane as the wave vector.

The two-component effective Hamiltonians Eqs. (4 and 33) can be generalized for arbitary positive integer $N \geq 1$ (Novoselov et al., 2006) as

$$H_\xi^{(N)}(\mathbf{q}) = -\gamma_1(-\ell_\perp)^N\begin{pmatrix} 0 & \left(\xi q_x - iq_y\right)^N \\ \left(\xi q_x + iq_y\right)^N & 0 \end{pmatrix}, \tag{40}$$

where $\ell_\perp = \hbar v/\gamma_1$. This Hamiltonian occurs as a contribution to the low-energy description of surface states in rhombohedral graphite with a finite number of layers N (Guinea et al., 2006; Koshino and McCann, 2009; Mañes et al., 2007; Min and MacDonald, 2008; Slizovskiy et al., 2019). Its eigenstates, with energy $E_\pm(\mathbf{q}) = \pm\gamma_1(\ell_\perp|\mathbf{q}|)^N$, have expectation of pseudospin given by $\langle\psi_\pm|\boldsymbol{\sigma}|\psi_\pm\rangle = \pm\hat{\mathbf{n}}_N$ where the unit vector $\hat{\mathbf{n}}_N$ is

$$\hat{\mathbf{n}}_N = (-\xi)^{N+1}(\xi\cos N\phi, \sin N\phi, 0). \tag{41}$$

Hence the Hamiltonian may be written (McCann and Fal'ko, 2006; Novoselov et al., 2006) as

$$H_\xi^{(N)}(\mathbf{q}) = \gamma_1(\ell_\perp|\mathbf{q}|)^N\boldsymbol{\sigma}\cdot\hat{\mathbf{n}}_N, \tag{42}$$

describing chiral electrons where the pseudospin turns N times more quickly than the wavevector in the graphene plane.

Symmetries

In the absence of external perturbations, bilayer graphene satisfies space and time inversion symmetries. For the low-energy effective Hamiltonian Eq. (33), these are expressed as

$$\text{space inversion}: \quad \sigma_x H_\xi^{(2)}(\mathbf{q})\sigma_x = H_{-\xi}^{(2)}(-\mathbf{q}), \tag{43}$$

$$\text{time inversion}: \quad \left(H_\xi^{(2)}(\mathbf{q})\right)^* = H_{-\xi}^{(2)}(-\mathbf{q}). \tag{44}$$

In the minimal model, with nearest-neighbor intralayer and interlayer hopping, the low-energy Hamiltonian also satisfies chiral symmetry,

$$\text{chiral}: \quad \sigma_z H_\xi^{(2)}(\mathbf{q})\sigma_z = -H_\xi^{(2)}(\mathbf{q}), \tag{45}$$

which ensures electron-hole symmetry of the electronic spectrum, as shown in Fig. 7. Chiral symmetry may be combined with time-inversion symmetry to give charge conjugation symmetry $\sigma_z (H_\xi^{(2)}(\mathbf{q}))^* \sigma_z = -H_{-\xi}^{(2)}(-\mathbf{q})$.

Berry phase 2π

For bilayer graphene, the eigenstates Eq. (35) have Berry connection $\mathbf{A}_\pm(\mathbf{q}) = -\xi\hat{\mathbf{e}}_\phi/|\mathbf{q}|$ where $\hat{\mathbf{e}}_\phi$ is the unit vector of polar angle π. The Berry phase for a closed path in reciprocal space around a single valley is

$$\gamma_\pm = \oint_C \mathbf{A}_\pm(\mathbf{q})\cdot d\mathbf{q} = -\xi 2\pi, \tag{46}$$

and, hence, bilayer graphene is sometimes described as having Berry phase 2π (McCann and Fal'ko, 2006; Novoselov et al., 2006). Berry phase, however, is only gauge invariant modulo 2π so the Berry phase in bilayer graphene is zero. Nevertheless, the factor of $N = 2$ is used to describe the degree of chirality in bilayer as demonstrated by the pseudospin vector Eq. (38). In the same way, the Hamiltonian Eq. (40) is said to have Berry phase $N\pi$, reflecting the behavior of the pseudospin in Eq. (41).

Trigonal warping and other tight-binding parameters

The Hamiltonians Eqs. (31 and 33) are written in the minimal model which includes only nearest-neighbor intralayer γ_0 and interlayer γ_1 coupling. However, the presence of two layers with interlayer coupling allows for more tight-binding parameters than in monolayer graphene. Authors often adopt the Slonczewski-Weiss-McClure model (Dresselhaus and Dresselhaus, 2002; McClure, 1957, 1960; Slonczewski and Weiss, 1958) which is a seven-parameter model of bulk Bernal-stacked graphite. With only two layers, Bernal-stacked bilayer does not allow for all seven parameters (such as those describing next-nearest layer hopping), but the 'skew' interlayer hoppings parameterized by γ_3 and γ_4 can be important.

Parameter γ_3 (Dresselhaus and Dresselhaus, 2002; McCann and Fal'ko, 2006) describes interlayer coupling between $A1$ and $B2$ orbitals which form the basis for the low-energy Hamiltonian Eq. (33). As it connects them directly, it gives a contribution at linear order in $\mathbf{q}$ to Eq. (33),

$$H_\xi^{(2)}(\mathbf{q}) = -\frac{\hbar^2}{2m_*}\begin{pmatrix} 0 & \left(\xi q_x - iq_y\right)^2 \\ \left(\xi q_x + iq_y\right)^2 & 0 \end{pmatrix} + \hbar v_3 \begin{pmatrix} 0 & \left(\xi q_x + iq_y\right) \\ \left(\xi q_x - iq_y\right) & 0 \end{pmatrix}, \tag{47}$$

where $v_3 = \sqrt{3}a\gamma_3/(2\hbar)$ has physical dimensions of velocity, and $|v_3| \approx 10^5$ m s^{-1}. Corresponding eigenvalues are

$$E_\pm(\mathbf{q}) = \pm\sqrt{(\hbar v_3|\mathbf{q}|)^2 - \frac{\xi\hbar^3 v_3|\mathbf{q}|^3}{m_*}\cos(3\phi) + \left(\frac{\hbar^2|\mathbf{q}|^2}{2m_*}\right)^2}. \tag{48}$$

The factor of $\cos(3\phi)$ introduces trigonal warping of a constant energy contour (which would be circular otherwise, Eqs. (32 and 34)). Since the γ_3 term in the Hamiltonian is linear in wavevector $\mathbf{q}$, the trigonal warping tends to be pronounced at low energy (as opposed to trigonal warping in monolayer graphene). As the energy is reduced, the trigonal distortion increases. At energy $E_\mathrm{L} = (\gamma_1/4)(\gamma_3/\gamma_0)^2 \approx 1$ meV, there is a Lifshitz transition in which the Fermi surface at each K point breaks into four separate contours: a central contour at the valley center with three elliptically-shaped contours at distance $|\mathbf{q}| \approx \gamma_1 v_3/(\hbar v^2)$ and separated by angles of $2\pi/3$. The orientation of trigonal warping depends on the sign of the product $\gamma_1\gamma_3$, and scanning tunneling microscope measurements (Joucken et al., 2020) have determined that $\gamma_3 = -0.3$ eV. This means that the orientation of trigonal warping at low energy, due to γ_3, is opposite to that of monolayer graphene, Fig. 3. At high energy, e.g., $E \gg \gamma_1$, the orientation of trigonal warping will be the same as that in monolayer, because the cause is the same (higher order in $\mathbf{q}$ terms in the expansion of $f(\mathbf{k}_\xi + \mathbf{q})$).

Parameter γ_4 (Dresselhaus and Dresselhaus, 2002) describes interlayer coupling between $A1$ and $A2$ orbitals, and between $B1$ and $B2$ orbitals. It gives a contribution to the $A1$-$B2$ low-energy Hamiltonian of the form

$$H_{\gamma_4}(\mathbf{q}) = \frac{\gamma_4 \hbar^2 |\mathbf{q}|^2}{\gamma_0 m_*} \begin{pmatrix} 1 & 0 \\ 0 & 1 \end{pmatrix}. \tag{49}$$

Taken with the minimal model low-energy Hamiltonian Eq. (33), this gives eigenvalues as

$$E_{\pm}(\mathbf{q}) = \frac{\gamma_4 \hbar^2 |\mathbf{q}|^2}{\gamma_0 m_*} \pm \frac{\hbar^2 |\mathbf{q}|^2}{2m_*}. \tag{50}$$

Since γ_4 connects A atoms to other A atoms, and B atoms to other B atoms, H_{γ_4} is diagonal in the sublattice space, and it breaks chiral symmetry Eq. (45). Thus, the energy spectrum Eq. (50) breaks electron-hole symmetry. However, for $\gamma_4 \approx 0.1$ eV (Kuzmenko et al., 2009; Malard et al., 2007; Zhang et al., 2008), the factor $\gamma_4/\gamma_0 \approx 0.03$, so the influence of γ_4 is generally quite small.

Band gap tunable with an electric field

Band structure with a band gap

As with monolayer graphene, an external gate voltage may be used to tune the carrier density in bilayer graphene. However, such an external potential will also introduce asymmetry between the electrostatic potentials of the two layers, and this asymmetry creates a tunable band gap in the bilayer energy spectrum (Castro et al., 2007; McCann, 2006; McCann and Fal'ko, 2006; McCann and Koshino, 2013; Min et al., 2007; Ohta et al., 2006; Oostinga et al., 2008).

If we parameterize the difference in energy between the layers as U, then the lower layer is at energy $-U/2$ and the upper layer at $U/2$. Then, the low-energy effective Hamiltonian in the $A1$, $B2$ basis Eq. (33) is modified (McCann and Fal'ko, 2006) as

$$H_{\xi}^{(2)}(\mathbf{q}) = -\frac{\hbar^2}{2m_*} \begin{pmatrix} 0 & \left(\xi q_x - i q_y\right)^2 \\ \left(\xi q_x + i q_y\right)^2 & 0 \end{pmatrix} - \frac{U}{2} \begin{pmatrix} 1 & 0 \\ 0 & -1 \end{pmatrix}, \tag{51}$$

with energies

$$E_{\pm}(\mathbf{q}) = \pm \sqrt{\frac{U^2}{4} + \left(\frac{\hbar^2 |\mathbf{q}|^2}{2m_*}\right)^2}, \tag{52}$$

and band gap $E_g = E_+(0) - E_-(0) = |U|$. Corresponding eigenstates are

$$\psi_{\pm} = \sqrt{\frac{E_{\pm} - U/2}{2E_{\pm}}} \begin{pmatrix} 1 \\ -\dfrac{\hbar^2 |\mathbf{q}|^2}{2m_*(E_{\pm} - U/2)} e^{2i\xi\phi} \end{pmatrix}, \tag{53}$$

The first component of the eigenstates Eq. (53) describes the amplitude on site A1 in the first layer, the second component describes the amplitude on site B2 in the second layer. Thus, the presence of the asymmetry parameter U in the eigenstates Eq. (53) accounts for different carrier densities n_1 and n_2 on the two layers, where the total carrier density is $n = n_1 + n_2$. As the energy spectrum is isotropic around the valley center Eq. (52), the densities on each layer may be determined by integrating over a circular Fermi surface,

$$n_{1(2)} = \frac{2}{\pi} \int \left|\psi_{A1(B2)}(q)\right|^2 q dq \tag{54}$$

where q is the magnitude of the wavevector, and $\psi_{A1(B2)}$ is the component of the eigenstate on the $A1$ ($B2$) site. A factor of four is included to account for spin and valley degeneracy.

If we consider a partially filled conduction band, then we can integrate Eq. (54) for $0 < q < q_F$, where q_F is the magnitude of the Fermi wavevector. The filled valence band can be included by integrating for $0 < q < q_{\max}$, where $q_{\max} = \gamma_1/(\hbar v)$ is an ultraviolet cutoff, equivalent to a large density $n_\perp$. Then, the layer densities (Fogler and McCann, 2010; McCann, 2006; McCann and Koshino, 2013) are

$$n_{1(2)} \approx \frac{n}{2} \mp \frac{n_\perp U}{4\gamma_1} \ln\left(\frac{|n|}{2n_\perp} + \frac{1}{2}\sqrt{\left(\frac{n}{n_\perp}\right)^2 + \left(\frac{U}{2\gamma_1}\right)^2}\right), \tag{55}$$

where the minus (plus) sign is for the first (second) layer, n is the total carrier density (as measured from the Dirac point), and $n_\perp$ is a characteristic density scale,

$$n = \frac{q_F^2}{\pi}; \quad n_\perp = \frac{\gamma_1^2}{\pi \hbar^2 v^2}. \tag{56}$$

With $\gamma_1 = 0.4$ eV and $v = 1.0 \times 10^6$ m s^{-1}, then $n_\perp = 1.2 \times 10^{13}$ cm^{-2}. The dependence of the layer densities on the asymmetry parameter, Eq. (55), is illustrated in Fig. 8A.

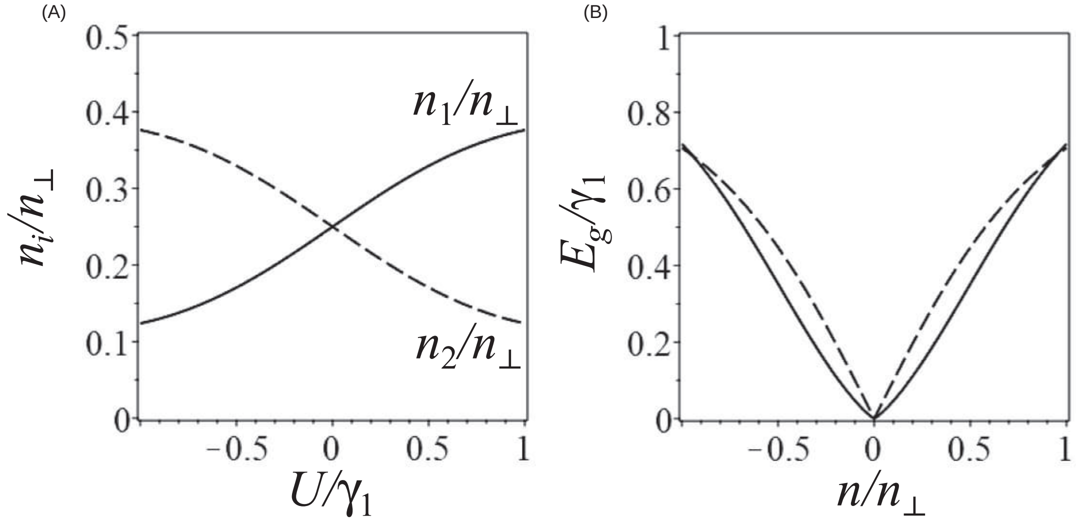

Fig. 8 (A) Layer densities n_1 (solid line) and n_2 (dashed) as a function of the asymmetry parameter U for fixed total density $n = n_1 + n_2 = n_\perp/2$ according to Eq. (55). (B) Band gap $E_g = |U|\gamma_1/\sqrt{\gamma_1^2 + U^2}$ as a function of total density n with asymmetry parameter U determined by numerical solution of Eq. (61) with screening parameter $\Lambda = 1$ (solid line). The dashed line shows E_g with $U = U_{\mathrm{ext}}$ neglecting screening. Note that n is proportional to the external gate voltage V_g, Eq. (57).

Self-consistent screening

The layer carrier densities n_1, n_2, Eq. (55), are dependent on the total carrier density n, and the difference in layer energies U. External gate potentials will modify n and U, and hence n_1, n_2, but, at the same time, the layer charge densities $\sigma_1 = -en_1$ and $\sigma_2 = -en_2$ will screen the gate potentials. This screening may be modeled simply using a Hartree approximation (i.e., neglecting exchange and correlations between electrons), and the resulting equations solved self-consistently to determine the dependence of the layer densities and band gap on the external potentials.

We consider the situation with a back gate, voltage V_g, of infinite extent in the x-y plane and located at $z = -d$. Bilayer graphene is modeled as two narrow layers, of infinite extent in the x-y plane and located at $z = \pm c_0/2$, where c_0 is the layer separation and $c_0 \ll d$. Using Gauss's law, the gate voltage V_g is related to the layer carrier densities and interlayer asymmetry (McCann, 2006) as

$$n = \frac{\varepsilon_0 \varepsilon_g}{ed} V_g, \tag{57}$$

$$U = \frac{e^2 c_0}{\varepsilon_0 \varepsilon_r} n_2, \tag{58}$$

where we use SI units and denote electronic charge as $-e$ with $e > 0$. The dielectric constant of the space between the gate and bilayer is ε_g, that of the space between the two bilayer layers is ε_r. Eq. (57) shows that the total density n is proportional to the gate voltage V_g, as in monolayer, Eq. (21). Eq. (58) relates the asymmetry parameter U to the density n_2 on the layer furthest from the gate; by Gauss's law, the charge density $\sigma_2 = -en_2$ accounts for the interlayer electric field $U/(ec_0)$.

We rewrite the expression for the interlayer asymmetry (McCann and Koshino, 2013) as

$$U = U_{\mathrm{ext}} + \Lambda \gamma_1 \frac{(n_2 - n_1)}{n_\perp}, \tag{59}$$

where the first term, U_{ext}, describes the value of U in the absence of screening, i.e., as if $n_2 = n_1 = n/2$, and the second term describes screening where Λ is the dimensionless screening parameter,

$$U_{\mathrm{ext}} = \frac{e\varepsilon_g c_0}{2\varepsilon_r d} V_g, \quad \Lambda = \frac{e^2 c_0 n_\perp}{2\gamma_1 \varepsilon_0 \varepsilon_r}. \tag{60}$$

With interlayer spacing $c_0 = 3.35\,Å$ and $\varepsilon_r \sim 1$, then $\Lambda \sim 1$ which indicates that screening is important. Substiting the expression for layer densities, Eq. (55), into that for asymmetry U, Eq. (59), gives the density dependence of the asymmetry parameter (and band gap) (Fogler and McCann, 2010; McCann and Koshino, 2013) as

$$\frac{U}{U_{\mathrm{ext}}} \approx \left[1 - \frac{\Lambda}{2} \ln\left(\frac{|n|}{2n_\perp} + \frac{1}{2}\sqrt{\left(\frac{n}{n_\perp}\right)^2 + \left(\frac{U}{2\gamma_1}\right)^2}\right)\right]^{-1}. \tag{61}$$

With $U_{\text{ext}} = \Lambda\gamma_1 n/n_\perp$, and using $|U| \gg \gamma_1$ for density that is not too small, then this may be simplified to give an explicit formula (McCann, 2006),

$$U \approx \frac{\Lambda\gamma_1 n}{n_\perp}\left[1 - \frac{\Lambda}{2}\ln\left(\frac{|n|}{n_\perp}\right)\right]^{-1}. \tag{62}$$

At low density $|n| \ll n_\perp$, the logarithmic term is large, indicating the important role of screening. At high density $|n| \sim n_\perp$, however, the logarithm is small and $U \approx U_{\text{ext}} = \Lambda\gamma_1 n/n_\perp$ is linear in density (and gate voltage). Here we only used the low-energy two-component Hamiltonian Eq. (51); use of the full four-component model Eq. (31) shows that the band gap E_g depends on the asymmetry U as $E_g = |U|\gamma_1/\sqrt{\gamma_1^2 + U^2}$. Then the band gap saturates, $E_g \to \gamma_1$, for large asymmetry $|U| \gg \gamma_1$. The dependence of E_g on n is illustrated in Fig. 8B (where n is proportional to V_g, Eq. (57)).

Integer quantum Hall effect

In the presence of a perpendicular magnetic field $\mathbf{B} = (0, 0, -B)$ with vector potential $\mathbf{A} = (0, -Bx, 0)$, the low-energy Hamiltonian Eq. (33) at the first valley may be written (McCann and Fal'ko, 2006) as

$$H_+^{(2)} = \hbar\omega_c\begin{pmatrix} 0 & \left(a^\dagger\right)^2 \\ a^2 & 0 \end{pmatrix}, \tag{63}$$

where $\omega_c = eB/m_*$, and $a^\dagger$, a are raising and lowering operators Eqs. (24 and 25). Eigenvalues and eigenstates are given by

$$\begin{aligned} \ell \ge 2: \quad & E_{\ell,\pm} = \pm\hbar\omega_c\sqrt{\ell(\ell-1)}, \quad & \psi_{\ell,\pm} = \frac{1}{\sqrt{2}}\begin{pmatrix} \phi_\ell \\ \pm\phi_{\ell-2} \end{pmatrix}, \\ \ell = 1: \quad & E_1 = 0, & \psi_1 = \begin{pmatrix} \phi_1 \\ 0 \end{pmatrix}, \\ \ell = 0: \quad & E_0 = 0, & \psi_0 = \begin{pmatrix} \phi_0 \\ 0 \end{pmatrix}. \end{aligned}$$

The Landau levels depend linearly on magnetic field and, for $\ell \gg 1$, linearly on the index ℓ, in contrast to monolayer graphene where there are square root dependences. In bilayer, however, there are two zero energy levels, E_1 and E_0, with states having weight on the A1 sublattice only at valley K_+. At the second valley, K_-, the spectrum is degenerate with that of K_+, but the role of the A1 and B2 sublattices is reversed, so that the zero energy states have weight only on the B2 sublattice.

The presence of two zero energy levels, E_1 and E_0, gives eightfold degeneracy of levels at zero energy, including spin and valley degeneracy. This is manifested in the integer quantum Hall effect, shown in Fig. 5C. Landau levels at nonzero energy are fourfold degenerate, due to spin and valley, and quantized plateaus in the Hall conductivity occur at integer values of $4e^2/h$,

$$\text{quantization}: \sigma_{xy} = -M\left(\frac{4e^2}{h}\right), \tag{64}$$

where M is integer, but $M \neq 0$ (McCann and Fal'ko, 2006), as observed experimentally (Novoselov et al., 2006). The eightfold degenerate levels with $E_1 = E_0 = 0$ require a step of height $8e^2/h$ in σ_{xy} as the density crosses zero between the electron and hole sides. Here we assumed that any splitting of the levels, due to breaking of spin or valley degeneracy, say, is negligible in comparison to temperature and level broadening.

Electronic properties of AA-stacked bilayer graphene

Crystal structure

With A1, B1 atomic sites on the lower layer and A2, B2 sites on the upper layer, AA stacking (Lee et al., 2008b; Rozhkov et al., 2016) describes the case when the two lattices are exactly aligned, i.e., A1 and A2 sites lie directly below and above each other, and B1 and B2 sites lie directly below and above each other, Fig. 9. The result is a periodic lattice in the horizontal (x-y) plane with unit cell of the same area as that of monolayer graphene, Fig. 9A. The unit cell now contains four atomic sites A1, B1, A2, B2.

Electronic band structure and tight-binding model

The electronic band structure near the Fermi level can be described by considering one $2p_z$ orbital per atom, i.e., four orbitals per unit cell for AA-stacked bilayer graphene. These yield four electronic bands. Assuming translational invariance within the graphene plane, it is possible to derive a Bloch Hamiltonian $H(\mathbf{k})$ as a four-component matrix in the basis of Bloch orbitals on A1, B1, A2, B2

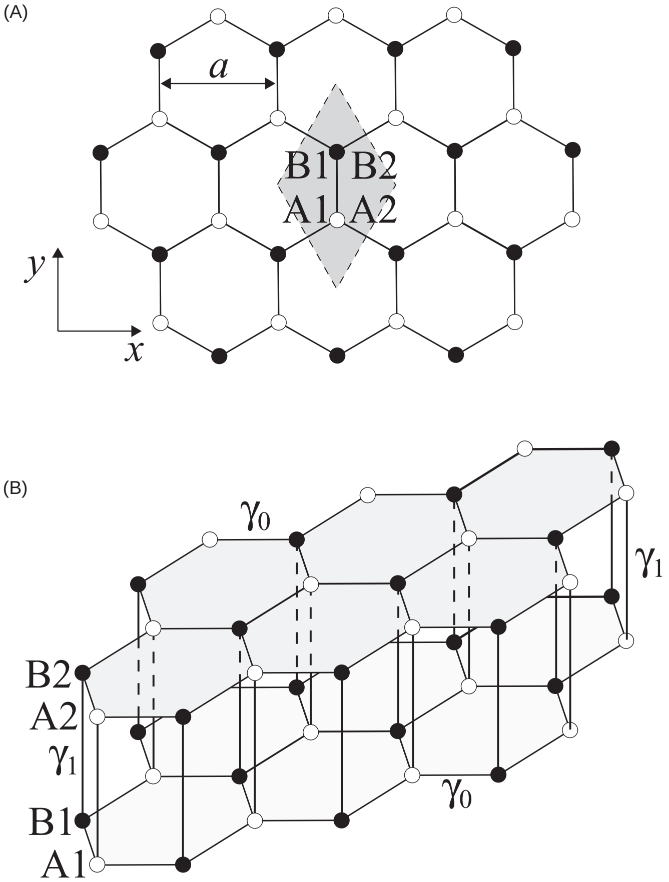

Fig. 9 Schematic of the lattice of AA-stacked bilayer graphene with A1 (white) and B1 (black) atomic sites on the lower layer, and A2 (white) and B2 (black) atomic sites on the upper layer. (A) is a plan view, with the atoms of the second layer lying directly above their counterparts in the first layer, and the shaded rhombus represents a unit cell. (B) is a side view, indicating intralayer nearest-neighbor tight-binding parameter γ_0 and interlayer nearest-neighbor tight-binding parameter γ_1.

sites, where $\mathbf{k} = (k_x, k_y)$ is the wave vector. The reciprocal lattice is the same as that of monolayer graphene: a hexagonal Bravais lattice with a hexagonal first Brillouin zone, as shown in Fig. 2A.

Including only coupling between nearest-neighbor intralayer sites (A1-B1 and A2-B2) with tight-binding parameter $\gamma_0 \approx 3$ eV, coupling between nearest-neighbor interlayer sites (A1-A2 and B1-B2) with tight-binding parameter $\gamma_1 \approx 0.3$ eV, and assuming atomic orbitals on adjacent atoms are orthogonal, the tight-binding Bloch Hamiltonian in basis A1, B1, A2, B2 is (Rozhkov et al., 2016)

$$H(\mathbf{k}) = \begin{pmatrix} 0 & -\gamma_0 f(\mathbf{k}) & \gamma_1 & 0 \\ -\gamma_0 f^*(\mathbf{k}) & 0 & 0 & \gamma_1 \\ \gamma_1 & 0 & 0 & -\gamma_0 f(\mathbf{k}) \\ 0 & \gamma_1 & -\gamma_0 f^*(\mathbf{k}) & 0 \end{pmatrix},$$

where $f(\mathbf{k})$ is defined in Eq. (2).

The basis can be rewritten as a pair of two-component bases, $(A1 + \alpha A2)/\sqrt{2}$, $(B1 + \alpha B2)/\sqrt{2}$, with $\alpha = 1$ or $\alpha = -1$. Then, the Hamiltonian is split into two independent 2×2 blocks,

$$H^{(\alpha)}(\mathbf{k}) = \begin{pmatrix} \alpha\gamma_1 & -\gamma_0 f(\mathbf{k}) \\ -\gamma_0 f^*(\mathbf{k}) & \alpha\gamma_1 \end{pmatrix}, \tag{65}$$

with energy bands given by

$$E_{\pm}^{(\alpha)}(\mathbf{k}) = \alpha\gamma_1 \pm \gamma_0 |f(\mathbf{k})|. \tag{66}$$

They are plotted in Fig. 10 along the line $k_y = 0$. The bands are two exact copies of the monolayer bands, Fig. 2B, split by the interlayer coupling parameter γ_1, and the split linear bands are evident near the Fermi level at the two K points (K_+ and K_-),

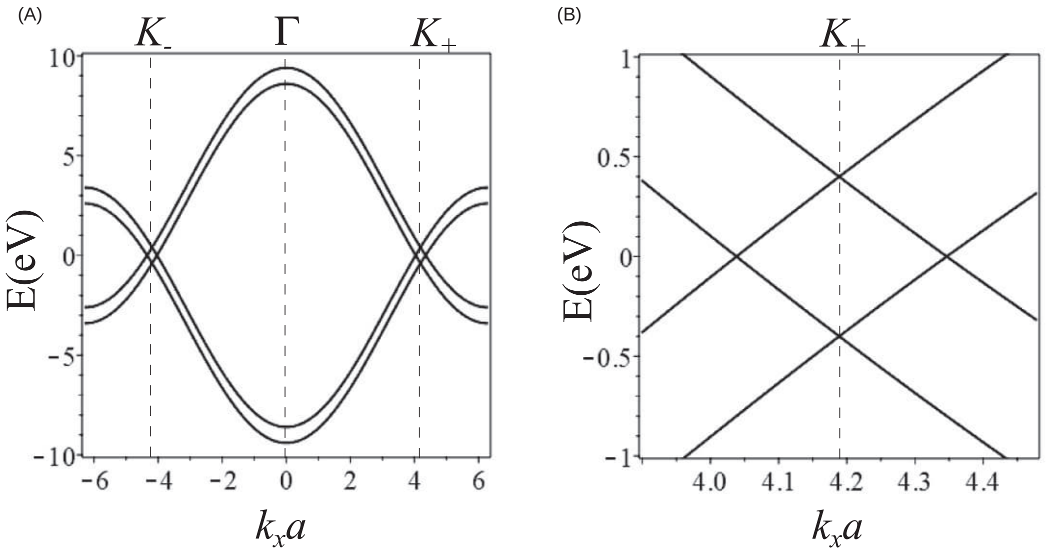

Fig. 10 (A) Electronic band structure of AA-stacked bilayer graphene according to Eq. (66) with $\gamma_0 = 3$ eV, $\gamma_1 = 0.4$ eV, plotted along the line $k_y = 0$. Vertical dashed lines show the positions of the symmetry points Γ, K_+ and K_-. (B) Scaled up plot of the bands near the K_+ point, showing crossing of linear bands near the valley center.

Fig. 10B. This means that many properties of AA-stacked bilayer graphene may be related to those of monolayer graphene, at least in the approximation that uses only nearest-neighbor tight-binding parameters.

Conclusion

This chapter focused on the electronic properties of graphene, including Dirac-like chiral charge carriers with a linear electronic dispersion in monolayer graphene, and massive chiral charge carriers with a quadratic dispersion in bilayer graphene. Since the isolation of graphene by Geim, Novoselov and colleagues in 2004 (Novoselov et al., 2004), it has been the subject of intense research. Some of the topics not covered here, with references for further reading, are spectroscopy and imaging including Raman spectroscopy, scanning tunneling microscopy, photoemission and optical spectroscopy (Andrei et al., 2012; Basov et al., 2014; Ferrari, 2007; Malard et al., 2009; Orlita and Potemski, 2010), phonons and strain (Castro Neto et al., 2009), electronic transport (Castro Neto et al., 2009; Das Sarma et al., 2011; Peres, 2010), quantum dots and nanoribbons (Abergel et al., 2010; Castro Neto et al., 2009), disorder (Abergel et al., 2010; Castro Neto et al., 2009), magnetism (Yazyev, 2010), spintronics and pseudospintronics (Pesin and MacDonald, 2012), orbital magnetism (Castro Neto et al., 2009; Koshino and Ando, 2007), Andreev reflection (Beenakker, 2008), and, finally, many-body effects (Abergel et al., 2010; Basov et al., 2014; Castro Neto et al., 2009).

References

Abergel DSL, Apalkov V, Berashevich J, Ziegler K, and Chakraborty T (2010) Properties of graphene: A theoretical perspective. *Adv. Phys.* 59: 261–482.

Ajiki H and Ando T (1993) Electronic states of carbon nanotubes. *J. Phys. Soc. Jpn.* 62: 1255–1266.

Ando T, Nakanishi T, and Saito R (1998) Berry's phase and absence of back scattering in carbon nanotubes. *J. Phys. Soc. Jpn.* 67: 2857–2862.

Andrei EY, Li G, and Du X (2012) Electronic properties of graphene: A perspective from scanning tunneling microscopy and magnetotransport. *Rep. Prog. Phys.* 75: 056501.

Avouris P (2010) Graphene: Electronic and photonic properties and devices. *Nano Lett.* 10: 4285–4294.

Bae S, Kim H, Lee Y, Xu X, Park J-S, Zheng Y, Balakrishnan J, Lei T, Kim HR, Song YI, Kim Y-J, Kim KS, Özyilmaz B, Ahn J-H, Hong BH, and Iijima S (2010) Roll-to-roll production of 30-inch graphene films for transparent electrodes. *Nat. Nanotechnol.* 5: 574–578.

Balandin AA, Ghosh S, Bao W, Calizo I, Teweldebrhan D, Miao F, and Lau CN (2008) Superior thermal conductivity of single-layer graphene. *Nano Lett.* 8: 902–907.

Basov DN, Fogler MM, Lanzara A, Wang F, and Zhang Y (2014) Colloquium: Graphene spectroscopy. *Rev. Mod. Phys.* 86: 959–994.

Beenakker CWJ (2008) Colloquium: Andreev reflection and Klein tunneling in graphene. *Rev. Mod. Phys.* 80: 1337–1354.

Bernal JD (1924) The structure of graphite. *Proc. Roy. Soc. A* 106: 749–773.

Berry MV (1984) Quantal phase factors accompanying adiabatic changes. *Proc. R. Soc. Lond. A* 392: 45–57.

Bolotin KI, Sikes KJ, Hone J, Stormer HL, and Kim P (2008) Temperature-dependent transport in suspended graphene. *Phys. Rev. Lett.* 101: 096802.

Bonaccorso F, Colombo L, Yu GH, Stoller M, Tozzini V, Ferrari AC, Ruoff RS, and Pellegrini V (2015) Graphene, related two-dimensional crystals, and hybrid systems for energy conversion and storage. *Science* 347: 1246501.

Cao Y, Luo JY, Fatemi V, Fang S, Sanchez-Yamagishi JD, Watanabe K, Taniguchi T, Kaxiras E, and Jarillo-Herrero P (2016) Superlattice-induced insulating states and valley-protected orbits in twisted bilayer graphene. *Phys. Rev. Lett.* 117: 116804.

Castro EV, Novoselov KS, Morozov SV, Peres NMR, Lopes dos Santos JMB, Nilsson J, Guinea F, Geim AK, and Castro Neto AH (2007) Biased bilayer graphene: Semiconductor with a gap tunable by the electric field effect. *Phys. Rev. Lett.* 99: 216802.

Castro Neto AH, Guinea F, Peres NMR, Novoselov KS, and Geim AK (2009) The electronic properties of graphene. *Rev. Mod. Phys.* 81: 109–162.

Cayssol J and Fuchs J-N (2021) Topological and geometrical aspects of band theory. *J. Phys. Mater.* 4: 034007.

Cheianov VV and Fal'ko VI (2006) Selective transmission of Dirac electrons and ballistic magnetoresistance of n-p junctions in graphene. *Phys. Rev. B* 74: 041403(R).

Das Sarma S, Adam S, Hwang EH, and Rossi E (2011) Electronic transport in two-dimensional graphene. *Rev. Mod. Phys.* 83: 407–470.

de Heer WA, Berger C, Ruan M, Sprinkle M, Li X, Hu Y, Zhang B, Hankinson J, and Conrad E (2011) Large area and structured epitaxial graphene produced by confinement controlled sublimation of silicon carbide. *PNAS* 108: 16900–16905.

DiVincenzo DP and Mele EJ (1984) Self-consistent effective-mass theory for intralayer screening in graphite intercalation compounds. *Phys. Rev. B* 29: 1685–1694.

Dresselhaus MS and Dresselhaus G (2002) Intercalation compounds of graphite. *Adv. Phys.* 51: 1–186.

Du X, Skachko I, Barker A, and Andrei EY (2008) Approaching ballistic transport in suspended graphene. *Nat. Nanotechnol.* 3: 491–495.

Ferrari AC (2007) Raman spectroscopy of graphene and graphite: Disorder, electron–phonon coupling, doping and nonadiabatic effects. *Solid State Commun.* 143: 47–57.

Ferrari AC, et al. (2015) Science and technology roadmap for graphene, related two-dimensional crystals, and hybrid systems. *Nanoscale* 7: 4598–4810.

Fogler MM and McCann E (2010) Comment on "Screening in gated bilayer graphene" *Phys. Rev. B* 82: 197401.

Fu Y, Hansson J, Liu Y, Chen S, Zehri A, Samani MK, Wang N, Ni Y, Zhang Y, Zhang Z-B, Wang Q, Li M, Lu H, Sledzinska M, Sotomayor Torres CM, Volz S, Balandin AA, Xu X, and Liu J (2020) Graphene related materials for thermal management. *2D Mater.* 7: 012001.

Gayduchenko I, Xu SG, Alymov G, Moskotin M, Tretyakov I, Taniguchi T, Watanabe K, Goltsman G, Geim AK, Fedorov G, Svintsov D, and Bandurin DA (2021) Tunnel field-effect transistors for sensitive terahertz detection. *Nat. Commun.* 12: 543.

Geim AK (2012) Graphene prehistory. *Phys. Scr.* T146: 014003.

González J, Guinea F, and Vozmediano MAH (1992) Continuum approximation to fullerene molecules. *Phys. Rev. Lett.* 69: 172–175.

Gorbachev RV, Geim AK, Katsnelson MI, Novoselov KS, Tudorovskiy T, Grigorieva IV, MacDonald AH, Morozov SV, Watanabe K, Taniguchi T, and Ponomarenko LA (2012) Strong Coulomb drag and broken symmetry in double-layer graphene. *Nat. Phys.* 8: 896–901.

Guinea F, Castro Neto AH, and Peres NMR (2006) Electronic states and Landau levels in graphene stacks. *Phys. Rev. B* 73: 245426.

Gusynin VP and Sharapov SG (2005) Unconventional integer quantum Hall effect in graphene. *Phys. Rev. Lett.* 95: 146801.

Haldane FDM (1988) Model for a quantum Hall effect without Landau levels: Condensed-matter realization of the "parity anomaly" *Phys. Rev. Lett.* 61: 2015–2018.

Han E, Yu J, Annevelink E, Son J, Kang DA, Watanabe K, Taniguchi T, Ertekin E, Huang PY, and van der Zande AM (2020) Ultrasoft slip-mediated bending in few-layer graphene. *Nat. Mater.* 19: 305–309.

Janssen TJBM, Tzalenchuk A, Lara-Avila S, Kubatkin S, and Falko VI (2013) Quantum resistance metrology using graphene. *Rep. Prog. Phys.* 76: 104501.

Johnson JG and Dresselhaus G (1973) Optical properties of graphite. *Phys. Rev. B* 7: 2275–2285.

Joucken F, Ge Z, Quezada-López EA, Davenport JL, Watanabe K, Taniguchi T, and Velasco J Jr. (2020) Determination of the trigonal warping orientation in Bernal-stacked bilayer graphene via scanning tunneling microscopy. *Phys. Rev. B* 101: 161103(R).

Kane CL and Mele EJ (1997) Size, shape, and low energy electronic structure of carbon nanotubes. *Phys. Rev. Lett.* 78: 1932–1935.

Kane CL and Mele EJ (2005a) Quantum spin Hall effect in graphene. *Phys. Rev. Lett.* 95: 226801.

Kane CL and Mele EJ (2005b) Z_2 topological order and the quantum spin Hall effect. *Phys. Rev. Lett.* 95: 146802.

Katsnelson MI, Novoselov KS, and Geim AK (2006) Chiral tunneling and the Klein paradox in graphene. *Nat. Phys.* 2: 620–625.

Kim KS, Zhao Y, Jang H, Lee SY, Kim JM, Kim KS, Ahn J-H, Kim P, Choi J-Y, and Hong BH (2009) Large-scale pattern growth of graphene films for stretchable transparent electrodes. *Nature* 457: 706–710.

Kim Y, Herlinger P, Moon P, Koshino M, Taniguchi T, Watanabe K, and Smet JH (2016) Charge inversion and topological phase transition at a twist angle induced van Hove singularity of bilayer graphene. *Nano Lett.* 16: 5053–5059.

Koshino M and Ando T (2007) Diamagnetism in disordered graphene. *Phys. Rev. B* 75: 235333.

Koshino M and McCann E (2009) Trigonal warping and Berry's phase $N\pi$ in ABC-stacked multilayer graphene. *Phys. Rev. B* 80: 165409.

Kuzmenko AB, Crassee I, van der Marel D, Blake P, and Novoselov KS (2009) Determination of the gate-tunable band gap and tight-binding parameters in bilayer graphene using infrared spectroscopy. *Phys. Rev. B* 80: 165406.

Lebedeva IV, Knizhnik AA, Popov AM, Lozovik YE, and Potapkin BV (2011) Interlayer interaction and relative vibrations of bilayer graphene. *Phys. Chem. Chem. Phys.* 13: 5687–5695.

Lee C, Wei X, Kysar JW, and Hone J (2008a) Measurement of the elastic properties and intrinsic strength of monolayer graphene. *Science* 321: 385–388.

Lee J-K, Lee S-C, Ahn J-P, Kim S-C, Wilson JIB, and John P (2008b) The growth of *AA* graphite on (111) diamond. *J. Chem. Phys.* 129: 234709.

Li X, Cai W, An J, Kim S, Nah J, Yang D, Piner R, Velamakanni A, Jung I, Tutuc E, Banerjee SK, Colombo L, and Ruoff RS (2009a) Large-area synthesis of high-quality and uniform graphene films on copper foils. *Science* 324: 1312–1314.

Li ZQ, Henriksen EA, Jiang Z, Hao Z, Martin MC, Kim P, Stormer HL, and Basov DN (2009b) Band structure asymmetry of bilayer graphene revealed by infrared spectroscopy. *Phys. Rev. Lett.* 102: 037403.

Liu L, Ryu S, Tomasik MR, Stolyarova E, Jung N, Hybertsen MS, Steigerwald ML, Brus LE, and Flynn GW (2008) Graphene oxidation: Thickness-dependent etching and strong chemical doping. *Nano Lett.* 8: 1965–1970.

Malard LM, Nilsson J, Elias DC, Brant JC, Plentz F, Alves ES, Castro Neto AH, and Pimenta MA (2007) Probing the electronic structure of bilayer graphene by Raman scattering. *Phys. Rev. B* 76: 201401(R).

Malard LM, Pimenta MA, Dresselhaus G, and Dresselhaus MS (2009) Raman spectroscopy in graphene. *Phys. Rep.* 473: 51–87.

Mañes JL, Guinea F, and Vozmediano MA (2007) Existence and topological stability of Fermi points in multi-layered graphene. *Phys. Rev. B* 75: 155424.

Mayorov AS, Gorbachev RV, Morozov SV, Britnell L, Jalil R, Ponomarenko LA, Blake P, Novoselov KS, Watanabe K, Taniguchi T, and Geim AK (2011) Micrometer-scale ballistic transport in encapsulated graphene at room temperature. *Nano Lett.* 11: 2396–2399.

McCann E (2006) Asymmetry gap in the electronic band structure of bilayer graphene. *Phys. Rev. B* 74: 161403(R).

McCann E and Fal'ko VI (2006) Landau-level degeneracy and quantum Hall effect in a graphite bilayer. *Phys. Rev. Lett.* 96: 086805.

McCann E and Koshino M (2013) The electronic properties of bilayer graphene. *Rep. Prog. Phys.* 76: 056503.

McClure JW (1956) Diamagnetism of graphite. *Phys. Rev.* 104: 666–671.

McClure JW (1957) Band structure of graphite and de Haas-van Alphen effect. *Phys. Rev.* 108: 612–618.

McClure JW (1960) Theory of diamagnetism of graphite. *Phys. Rev.* 119: 606–613.

McEuen PL, Bockrath M, Cobden DH, Yoon Y-G, and Louie SG (1999) Disorder, pseudospins, and backscattering in carbon nanotubes. *Phys. Rev. Lett.* 83: 5098–5101.

Min H, Sahu BR, Banerjee SK, and MacDonald AH (2007) Ab initio theory of gate induced gaps in graphene bilayers. *Phys. Rev. B* 75: 155115.

Min H and MacDonald AH (2008) Chiral decomposition in the electronic structure of graphene multilayers. *Phys. Rev. B* 77: 155416.

Mostaani E, Drummond ND, and Fal'ko VI (2015) Quantum Monte Carlo calculation of the binding energy of bilayer graphene. *Phys. Rev. Lett.* 115: 115501.

Nair RR, Blake P, Grigorenko AN, Novoselov KS, Booth TJ, Stauber T, Peres NMR, and Geim AK (2008) Fine structure constant defines visual transparency of graphene. *Science* 320: 1308.

Novoselov KS, Geim AK, Morozov SV, Jiang D, Zhang Y, Dubonos SV, Grigorieva IV, and Firsov AA (2004) Electric field effect in atomically thin carbon films. *Science* 306: 666–669.

Novoselov KS, Geim AK, Morozov SV, Jiang D, Katsnelson MI, Grigorieva IV, Dubonos SV, and Firsov AA (2005) Two-dimensional gas of massless Dirac fermions in graphene. *Nature* 438: 197–200.

Novoselov KS, McCann E, Morozov SV, Fal'ko VI, Katsnelson MI, Zeitler U, Jiang D, Schedin F, and Geim AK (2006) Unconventional quantum Hall effect and Berry's phase of 2π in bilayer graphene. *Nat. Phys.* 2: 177–180.

Novoselov KS, Fal'ko VI, Colombo L, Gellert PR, Schwab MG, and Kim K (2012) A roadmap for graphene. *Nature* 490: 192–200.

Ohta T, Bostwick A, Seyller T, Horn K, and Rotenberg E (2006) Controlling the electronic structure of bilayer graphene. *Science* 313: 951–954.
Oostinga JB, Heersche HB, Liu X, Morpurgo AF, and Vandersypen LMK (2008) Gate-induced insulating state in bilayer graphene devices. *Nat. Mater.* 7: 151–157.
Orlita M and Potemski M (2010) Dirac electronic states in graphene systems: Optical spectroscopy studies. *Semi-cond. Sci. Technol.* 25: 063001.
Pei SF and Cheng HM (2012) The reduction of graphene oxide. *Carbon* 50: 3210–3228.
Peng X and Yan Y (2021) Graphene saturable absorbers applications in fiber lasers. *J. Eur. Opt. Soc.-Rapid Publ.* 17: 16.
Peres NMR, Guinea F, and Castro Neto AH (2006) Electronic properties of disordered two-dimensional carbon. *Phys. Rev. B* 73: 125411.
Peres NMR (2010) Colloquium: The transport properties of graphene: An introduction. *Rev. Mod. Phys.* 82: 2673–2700.
Pesin D and MacDonald AH (2012) Spintronics and pseudospintronics in graphene and topological insulators. *Nat. Mater.* 11: 409–416.
Rozhkov AV, Sboychakov AO, Rakhmanov AL, and Nori F (2016) Electronic properties of graphene-based bilayer systems. *Phys. Rep.* 648: 1–104.
Saito R, Dresselhaus MS, and Dresselhaus G (1998) *Physical Properties of Carbon Nanotubes.* London: Imperial College Press.
Sasaki K, Murakami S, and Saito R (2006) Stabilization mechanism of edge states in graphene. *Appl. Phys. Lett.* 88: 113110.
Schedin F, Geim AK, Morozov SV, Hill EW, Blake P, Katsnelson MI, and Novoselov KS (2007) Detection of individual gas molecules adsorbed on graphene. *Nat. Mat.* 6: 652–655.
Schmidt H, Lüdtke T, Barthold P, McCann E, Fal'ko VI, and Haug RJ (2008) Tunable graphene system with two decoupled monolayers. *Appl. Phys. Lett.* 93: 172108.
Semenoff GW (1984) Condensed-matter simulation of a three-dimensional anomaly. *Phys. Rev. Lett.* 53: 2449–2452.
Slizovskiy S, McCann E, Koshino M, and Fal'ko VI (2019) Films of rhombohedral graphite as two-dimensional topological semimetals. *Commun. Phys.* 2: 164.
Slonczewski JC and Weiss PR (1958) Band structure of graphite. *Phys. Rev.* 109: 272–279.
Wallace PR (1947) The band theory of graphite. *Phys. Rev.* 71: 622–634.
Wang Y, Li Z, Wang J, Li J, and Lin Y (2011) Graphene and graphene oxide: Biofunctionalization and applications in biotechnology. *Trends Biotechnol.* 29: 205–212.
Xiao D, Yao W, and Niu Q (2007) Valley-contrasting physics in graphene: Magnetic moment and topological transport. *Phys. Rev. Lett.* 99: 236809.
Xiao D, Chang M-C, and Niu Q (2010) Berry phase effects on electronic properties. *Rev. Mod. Phys.* 82: 1959–2007.
Yamada Y, Murota K, Fujita R, Kim J, Watanabe A, Nakamura M, Sato S, Hata K, Ercius P, Ciston J, Song CY, Kim K, Regan W, Gannett W, and Zettl A (2014) Subnanometer vacancy defects introduced on graphene by oxygen gas. *J. Am. Chem. Soc.* 136: 2232–2235.
Yamashita S (2019) Nonlinear optics in carbon nanotube, graphene, and related 2D materials. *APL Photon.* 4: 034301.
Yazyev OV (2010) Emergence of magnetism in graphene materials and nanostructures. *Rep. Prog. Phys.* 73: 056501.
Zhang Y, Tan Y-W, Stormer HL, and Kim P (2005) Experimental observation of the quantum Hall effect and Berry's phase in graphene. *Nature* 438: 201–204.
Zhang LM, Li ZQ, Basov DN, Fogler MM, Hao Z, and Martin MC (2008) Determination of the electronic structure of bilayer graphene from infrared spectroscopy. *Phys. Rev. B* 78: 235408.
Zheng Y and Ando T (2002) Hall conductivity of a two-dimensional graphite system. *Phys. Rev. B* 65: 245420.
Zhu Y, Murali S, Cai W, Li X, Suk JW, Potts JR, and Ruoff RS (2010) Graphene and graphene oxide: Synthesis, properties, and applications. *Adv. Mater.* 22: 3906–3924.

Relevant website

The Nobel Prize in Physics. https://www.nobelprize.org/prizes/physics/2010/summary/.

Quantum spin Hall effect

Shoushu Gong[a] **and DN Sheng**[b], [a]Department of Physics, Beihang University, Beijing, China; [b]Department of Physics and Astronomy, California State University Northridge, Los Angeles, CA, United States

© 2024 Elsevier Ltd. All rights reserved.

Introduction and overview 623
Topological insulator and quantum spin Hall effect 624
Z_2 characterization of topological insulators 625
Many-body Chern number matrix 625
The fractional quantum spin Hall effect 626
Fractionalized spin Hall transport in frustrated spin systems 627
Conclusion 627
References 628

Abstract

This article is an introduction to the nontrivial topological properties associated with the special band structure in the electron systems with strong spin-orbital coupling, where a new topological phase known as topological insulator emerges. A Z_2 topological invariant can distinguish a topological insulator from a trivial band insulator in time-reversal invariant systems. The theoretically predicted quantum spin Hall effect and three dimensional topological insulators have been discovered experimentally. We provide an introduction to the understandings of topological insulating state, interaction effect and fractional quantum spin Hall effect, as well as their numerical identification.

Key points

- A new topological state emerges in the time-reversal invariant system with spin-orbital coupling.
- A Z_2 topological index provides a topological characterization of the topological insulator.
- A quantum spin Hall effect naturally emerges for topological insulators.
- A topological insulator has a nonzero spin Chern number and a projected spin gap for the occupied bands.
- A fractional topological insulator can emerge in interacting system.
- A chiral system liquid is an example of the bosonic fractional quantum Hall effects in spin systems, which can be detected by spin pumping and quantized Chern number.

Introduction and overview

The quantum Hall effect is one of the most remarkable phenomena discovered in two-dimensional (2D) electron systems subject to a strong perpendicular magnetic field. The GaAs/AlGaAs heterojunction grown by molecular beam epitaxy is a typical example of material realization of this system. If made sufficiently pure, such systems can exhibit both integer and fractional quantum Hall effects (IQHE/FQHE) at low enough temperature (Prange and Girvin, 1990; Klitzing et al., 1980; Tsui et al., 1982), which conduct quantized Hall currents without any dissipation. Both IQHE and FQHE can be characterized by the topological Chern number associated with either energy band or many-body ground state. The charge Hall conductance is found to be determined by the Chern number of the filled bands (or many-body Chern number), which is known as the Thouless-Kohmoto-Nightingaleden Nijs (TKNN) integer (Thouless et al., 1982; Qian Niu et al., 1985).

While the IQHE is usually observed in a strong magnetic field, Haldane first proposed a lattice model of spinless fermion with the complex hoppings breaking time-reversal symmetry, which has nontrivial topological bands carrying nonzero Chern numbers that can lead to the IQHE without a magnetic field (Haldane, 1988). Interestingly, when considering spin degrees of freedom, the two-component Haldane model can be more naturally realized in realistic systems, where the complex hoppings can be induced by the intrinsic spin-orbital coupling and such systems also recover time-reversal symmetry.

In such electron systems with strong spin-orbital coupling, a new class of nontrivial insulators has been theoretically identified as a time-reversal invariant 2D electronic phase (Kane and Mele, 2005a,b; Andrei Bernevig and Zhang, 2006; Andrei Bernevig et al., 2006; Sheng et al., 2006, 2005; Qi et al., 2006a,b; Liang and Kane, 2006; Congjun et al., 2006; Roy, 2009; Moore and Balents, 2007), which has a bulk energy gap generated by spin-orbital coupling. It is known as the topological insulator with a Z_2 topological invariant (Kane and Mele, 2005a; Qi et al., 2006a; Liang and Kane, 2006; Roy, 2009; Moore and Balents, 2007), which is distinguished from trivial insulator by the fact that the edge of a topological insulator contains a time-reversal symmetry protected pair of gapless edge modes with opposite chiralities. Such protected edge modes and the resulting quantum spin Hall effect (QSHE) have been observed in the HgTe quantum wells (König et al., 2007) and many other systems (Hasan and Kane, 2010). Graphene

https://doi.org/10.1016/B978-0-323-90800-9.00060-3

and other electron systems with intrinsic spin-orbital coupling have been used as examples for illustrating the nontrivial topological insulator with dissipationless QSHE (Andrei Bernevig and Zhang, 2006; Kane and Mele, 2005b; Sheng et al., 2005; Qi et al., 2006a,b), where the spin-orbital coupling induces a spin-dependent effective magnetic field.

In this chapter, we will introduce the lattice model, the bulk topological characterization and its connection with the edge spin polarization. We will also discuss the robustness of the QSHE against the effect of disorder and Rashba spin coupling. We will further discuss the fractional quantum spin Hall effect (FQSHE) (Levin and Stern, 2009; Maciejko et al., 2010; Swingle et al., 2011; Neupert et al., 2011; Chen and Yang, 2012; Ghaemi et al., 2012) and FQHE in spin systems (Kalmeyer and Laughlin, 1987; Wen et al., 1989; He et al., 2014; Gong et al., 2014; Bauer et al., 2014), both can be characterized by many-body Chern numbers (Thouless et al., 1982; Qian Niu et al., 1985; Sheng et al., 2006, 2003a).

Topological insulator and quantum spin Hall effect

We begin with a single-particle Hamiltonian with spin-orbital couplings and on-site random disorder on the honey-comb lattice (Haldane, 1988; Kane and Mele, 2005a; Sheng et al., 2006):

$$\begin{aligned} H_0 = & -t\sum_{\langle ij\rangle} c_i^\dagger c_j + \frac{2i}{\sqrt{3}} V_{SO} \sum_{\langle\langle ij\rangle\rangle} c_i^\dagger \sigma\cdot\left(\mathbf{d}_{kj}\times\mathbf{d}_{ik}\right) c_j \\ & + iV_R \sum_{\langle ij\rangle} c_i^\dagger \hat{\mathbf{z}}\cdot\left(\sigma\times\mathbf{d}_{ij}\right) c_j + \sum_i w_i c_i^\dagger c_i, \end{aligned} \tag{1}$$

where $c_i^\dagger = (c_{i\uparrow}^\dagger, c_{i\downarrow}^\dagger)$ denotes electron creation operators for spin up and spin down, and σ is the Pauli matrix. The first term is the nearest-neighbor (NN) hopping, and the second term is the intrinsic spin-orbital coupling between the next-nearest-neighbor (NNN) sites i, j with k being their shared NN site, where $\mathbf{d}_{ik} = \mathbf{R}_i - \mathbf{R}_k$ is the displacement vector. The third term stands for the Rashba spin-orbital coupling, and the last term is an on-site random disorder with strength uniformly distributed within $|w_i| \leq W/2$.

We first discuss the physics of this two-component Haldane model without the Rashba spin-orbital coupling ($V_R = 0$). In this case, each spin component is subject to the complex NNN hoppings as illustrated in Fig. 1(a), where the hoppings are complex conjugate of each other for the two spin components. Therefore, the energy spectrum is gapped with Chern number $C^{up} = 1$ ($C^{down} = -1$) for the lower band of spin up (spin down), leading to the IQHE for each spin component. The Chern number of a band can be obtained as (Thouless et al., 1982):

$$C = \frac{i}{2\pi}\int d^2k\left[\left\langle \frac{\partial u_k}{\partial k_x}\middle|\frac{\partial u_k}{\partial k_y}\right\rangle - \left\langle \frac{\partial u_k}{\partial k_y}\middle|\frac{\partial u_k}{\partial k_x}\right\rangle\right], \tag{2}$$

where u_k is the single-particle wave function of an energy band at a given momentum $\mathrm{k} = (k_x, k_y)$. The IQHE can be characterized by the topological Chern number associated with each band, and the Hall conductance of the system is proportional to the total Chern number of all the occupied bands (Thouless et al., 1982). If we consider the Fermi energy $E_F = 0$, there are two occupied bands with opposite spins and opposite Chern numbers, which give rise to the vanished total Hall conductance $\sigma_H = 0$. However, following the simple version of spin Chern number $C^s = C^{up} - C^{down} = 2$, the spin Hall conductance is nonzero, $\sigma_H^s = e/(2\pi)$. For the two bands with nonzero Chern numbers, there are corresponding gapless edge modes carrying opposite currents and opposite spins.

In the presence of the Rashba coupling ($V_R \neq 0$), each eigenstate has mixed spins. We can explicitly compute the spin polarization $P_m^z = \frac{\hbar}{2}\langle m|\sum_i c_i^\dagger \sigma^z c_i|m\rangle$ along the $\hat{z}$-direction with $|m\rangle$ as the m-th single-particle eigenstate. Spin polarizations along the $\hat{x}$- and $\hat{y}$-directions are found much smaller. Interestingly, all the eigenstates form Kramers degenerate pairs and each pair carry zero total spin due to time-reversal symmetry before we insert flux into the system. However, if a small flux is inserted into the system (or using the twisted boundary condition), a nonzero spin polarization will be quickly developed for each edge state (Sheng et al., 2006). The spin polarization is finite only for the edge states within the bulk energy gap and insensitive to disorder configuration and sample size, which clearly demonstrates that the current-carrying edge states have finite spin polarization and thus lead to the QSHE.

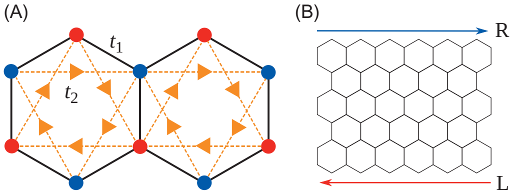

Fig. 1 Haldane honeycomb-lattice model and illustration of the edge states. (a) The Haldane model has the nearest-neighbor hopping t_1 and next-nearest-neighbor hopping t_2. t_2 is complex and denotes the charge hopping along the arrow direction. (b) Illustration of the chiral edge currents along the opposite directions in the open boundaries.

Z_2 characterization of topological insulators

The nonzero Z_2 topological index characterizes the time-reversal invariant topological insulators with symmetry protected edge transport (Kane and Mele, 2005a; Andrei Bernevig et al., 2006; Liang and Kane, 2006; Roy, 2009; Moore and Balents, 2007). The Z_2 topological insulator has an odd number of Kramers pairs of gapless edge modes. In the original work of Kane and Mele (2005a), the Z_2 invariant is obtained based on the K-theory by calculating the Pffafian of the matrix of time reversal operator. Later, other methods are introduced, including using the non-Abelian Berry connection (Fukui and Fujiwara, 2009; Rui et al., 2011), the Berry curvature and Chern number in the effective Brillouin zone (EBZ) (Liang and Kane, 2006; Roy, 2009; Moore and Balents, 2007), and spin Chern number (Sheng et al., 2006; Prodan, 2009, 2011). The spin Chern number for a time-reversal invariant system with a projected spin gap can be connected to the Z_2 invariant through the relation $Z_2 = \mathrm{mod}(C^s/2, 2)$.

Time-reversal symmetry connects the quantum states in the EBZ with the states in other half Brillouin zone. By mapping the EBZ to the space of the Bloch Hamiltonian, a Chern number associated with the EBZ can be defined, which classifies the energy band structure into two topological classes, namely a nontrivial (trivial) topological class characterized by an odd (even) Chern number as demonstrated by Moore and Balents (2007). The obtained topological invariants in 2D are multiple copies of the Z_2 invariant, and there are four such invariants per band pair in three dimensions, which characterize three-dimensional topological insulators (Moore and Balents, 2007; Liang et al., 2007; Fukui and Hatsugai, 2007).

Fu and Kane defined a Z_2 pump characterized by a Z_2 topological invariant (Liang and Kane, 2006). For an isolated system, a single cycle of the pumping process can effectively pump spins between the open edges even when the spin of the system is not conserved due to spin-orbital interaction. When the system is coupled to leads, it is demonstrated that the Z_2 pump works as a spin pump, which transmits spins at a finite rate and leads to a robust QSHE.

Many-body Chern number matrix

To generalize the Chern number definition of an energy band to multi-component systems, we introduce many-body Chern number (Sheng et al., 2003a), which can effectively characterize the bulk topological nature of quantum systems with spin coupling and electron-electron interaction. Because electrons can have both charge and spin responses, we can consider spin-dependent boundary phases to obtain the generalized topological Chern number matrix (Sheng et al., 2006). We start from applying a boundary condition for a two-dimensional many-body wave-function: $\Phi(\ldots, \mathbf{r}_{i_\alpha} + \mathbf{L}_j, \ldots) = e^{i\theta_j^\alpha}\Phi(\ldots, \mathbf{r}_{i_\alpha}, \ldots)$, where $j = x$ or y, the system length vectors are $\mathbf{L}_x, \mathbf{L}_y$, and $\alpha = \uparrow$ and $\downarrow$ denotes spin index. Through a unitary transformation $\Psi = \exp\left[-i\sum_\alpha \sum_{i_\alpha}\left(\frac{\theta_x^\alpha}{L_x}x_{i_\alpha} + \frac{\theta_y^\alpha}{L_y}y_{i_\alpha}\right)\right]\Phi$, where the summation runs over all electrons, Ψ becomes periodic on a torus. One can now define the topological Chern numbers as:

$$C^{\alpha,\beta} = \frac{i}{2\pi}\int\int d\theta_x^\alpha d\theta_y^\beta \left[\left\langle \frac{\partial\Psi}{\partial\theta_x^\alpha}\middle|\frac{\partial\Psi}{\partial\theta_y^\beta}\right\rangle - \left\langle \frac{\partial\Psi}{\partial\theta_y^\beta}\middle|\frac{\partial\Psi}{\partial\theta_x^\alpha}\right\rangle\right], \tag{3}$$

where the area integration is over a unit cell $0 \leq \theta_x^\alpha, \theta_y^\beta \leq 2\pi$. With $\alpha, \beta = \uparrow, \downarrow$, $C^{\alpha,\beta}$ form a 2×2 Chern number matrix. Each element of the Chern number matrix is exactly quantized as an integer for a gapped insulating state following the argument of Thouless et al. (1982).

We calculate the topological Chern number matrix numerically by dividing the unit cell of the boundary phases into N_{mesh} mesh points such that the integration in Eq. (3) is replaced by the sum of the solid angle $\Omega_j : C^s = \sum_j \frac{\Omega_j}{2\pi}$. Here, $\Omega_j = \arg \Pi_i \langle \Psi_{ji} | \Psi_{ji+1} \rangle$ where $i = 1$–4 (with $j_5 \equiv j_1$) denote the four parameter points in the boundary phase space around the j-th square of mesh patches. The Chern number matrix obtained by this way is well converged and insensitive to mesh sizes.

In the case without Rashba coupling ($V_R = 0$), only the diagonal matrix elements are nonzero: $C^{\alpha,\alpha} = \pm 1$ (for positive V_{SO}) with $\alpha = 1$ and 2 representing spin up and down, respectively. This matrix describes the IQHE in decoupled subsystems. The total charge Chern number $C^c \equiv \sum_{\alpha,\beta} C^{\alpha,\beta}$ (corresponding to the total charge Hall conductance) cancels out, while the total spin-related Chern number is quantized to $C^s \equiv \sum_{\alpha,\beta} \alpha C^{\alpha,\beta} = 2$, which represents the spin Hall response when a common electric field for both spin components is imposed along the $\widehat{y}$ direction. In this spin decoupled limit, the quantized spin Chern number C^s is associated with the spin Hall conductance $\sigma_H^s = C^s = 2$ in units of $\frac{e}{4\pi}$.

Now we turn on the Rashba coupling and discuss how to numerically determine C^s. This can be done by calculating each $C^{\alpha,\beta}$ first as discussed above. One can also carry out the integration in Eq. (3) for opposite boundary condition along the $\widehat{x}$ direction (spin twist $\theta_x^\uparrow = -\theta_x^\downarrow = \theta_x$) and common one along the $\widehat{y}$ direction ($\theta_y^\uparrow = \theta_y^\downarrow = \theta_y$) to directly obtain C^s. We choose the latter method in the following. One finds that C^s always remains quantized at $C^s = 2$ before the band gap collapses. In Fig. 2(a), we show the energy spectrum for $V_R = 0{:}1\ t$ and $V_{SO} = 0{:}3\ t$, where a gap appears between the two lower bands and the two upper bands. With Rashba coupling, the two lower bands are spin entangled. The relation between the QSHE, spin pumping through edge states and spin Chern number has been addressed by our previous work and the work by Prodan (2009, 2011). One can obtain the spin spectrum for the occupied states by defining the matrix $M\ (s_z) = P\_\sigma_z P\_$ with $P\_$ being the projection operator to the occupied eigenstates. This allows us to analyze the spin spectrum for the occupied states by diagonalizing the matrix $M\ (s_z)$. Because Hamiltonian is block-diagonalized for pure system without considering disorder scattering, we can do the similar block diagonalization for $M\ (s_z)$. The obtained spin spectrum is shown in Fig. 2(b). Interestingly, the spin information of the eigenstates is revealed by the

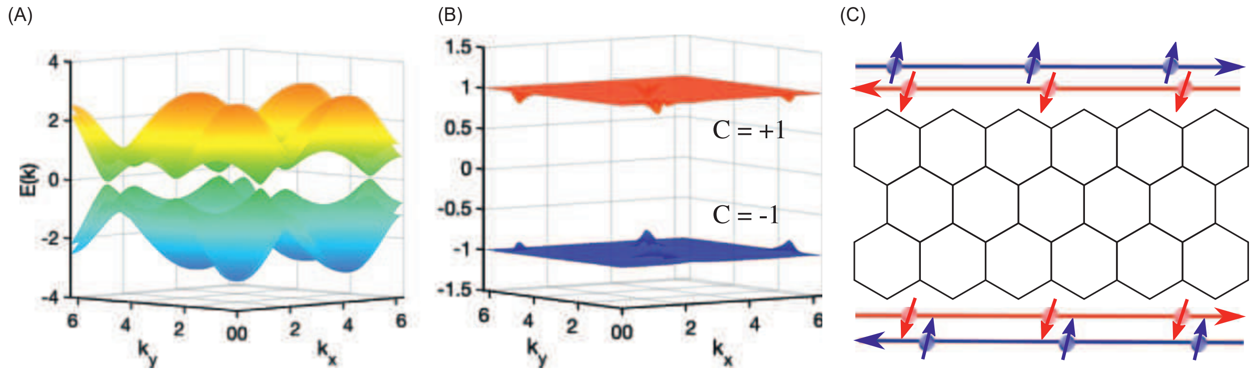

Fig. 2 (a) Energy spectrum for the two-component Haldane model with intrinsic spin-orbital coupling. (b) The spin eigenvalues for the projected spin S_z operator, where a spin gap is identified between the spin states with different polarizations. These states with near opposite spin polarizations also have opposite Chern numbers. (c) The helical edge states for such a system with nonzero spin Chern number is illustrated.

spin spectrum, which separates into two disentangled bands, with near quantized spin quantum numbers $\sigma_z \approx \pm 1$ (here we use Pauli matrix for spin operator). Physically, these two projected bands carry opposite Chern numbers and near oppositely polarized spins, which contribute to the quantized spin Chern number. The exactly quantized spin Chern number is protected simultaneously by the energy spectrum gap and project spin spectrum gap. The helical edge states corresponding to the nonzero spin Chern number is illustrated in Fig. 2(c), which is responsible for the nearly quantized spin Hall conductance (Sheng et al., 2006). The gapless feature is protected by time-reversal symmetry or nonzero Z_2 topological invariant. Such a topologically nontrivial phase also survives for very small V_{SO}, so long as V_R is not much larger than V_{SO}. With the increase of the Rashba coupling, at a larger $V_R = 0{:}33\ t$ with a fixed $V_{SO} = 0{:}1\ t$, the energy gap is about to collapse, and spin gap also closes around a similar critical point, signaling a topological transition from topological insulator to a metallic state (Sheng et al., 2006).

The fractional quantum spin Hall effect

What is the effect of interaction in topological insulators? It has been shown that topological insulators are also robust against not too strong interaction (Cenke and Moore, 2006; Lee and Ryu, 2008; Rachel, 2018). Interestingly, for strongly interacted systems, there may be a new class of topological insulators, characterized by counterpropagating edge states and fractionalized spin Hall effect as suggested by theoretical studies (Levin and Stern, 2009; Swingle et al., 2011; Neupert et al., 2011; Chen and Yang, 2012; Ghaemi et al., 2012). The basic physical picture is simple, as fractionalized quantum phases can emerge when electrons fractionally fill the effective Landau levels generated by spin-orbital couplings. Because interaction effect is competing with kinetic energy, the topological insulator with relatively flat energy band is a desired condition for hosting fractional quantum spin Hall effect (FQSHE).

We first consider a simple model of two-component system with electrons of the opposite spins or pseudospins (valley or layer degrees of freedom) subjected to spin-dependent magnetic fields opposite to each other (Ghaemi et al., 2012), with a non-interacting Hamiltonian

$$H_0 = \frac{1}{2m}\left(\mathbf{p} - \sigma_z \frac{e\mathbf{A}}{c}\right)^2. \tag{4}$$

Due to the applied magnetic fields, Landau levels are realized for each spin species. We can consider the effects of two-particle interactions $H_{int} = V(\mathbf{r}_1, \mathbf{r}_2)$, which can be projected into the lowest Landau levels or partially occupied excited Landau levels. In the absence of any coupling between two spin degrees of freedom but only interactions within each spin component, uncoupled fractional quantum Hall states are realized for each spin component, which will contribute to a FQSHE. However, this is a trivial case as it belongs to the same universality class as the FQHE. Our goal is to discuss the nontrivial FQSHE in which two spins are effectively coupled by spin-orbital coupling or Coulomb interaction. To proceed, we project the Hamiltonian into the lowest Landau level for each spin. The inter-spin Coulomb term is different from the intra-spin interaction as it couples the two components with opposite vector potentials as well as different center of cyclotron orbits.

The numerical results are presented in Fig. 3 to illustrate the ground state degeneracy for an electron system with total filling number 2/3 (each layer is at 1/3 filling). We show the energy spectrum as a function of layer separation d and assume that the inter-layer Coulomb interaction decays with the layer separation and there is no tunneling (Sheng et al., 2003a). The lowest level has nine near-degenerate states (each level shown here has a threefold degeneracy) at large d side, which is well separated from the excited levels by an energy gap. The gap closes near a finite layer separation $d_c \sim 1.2\ l$ (l is the magnetic length), where a transition to a metallic state takes place. Similar physics was first identified by Chen and Yang (Chen and Yang, 2012).

What is the nature of the quantum phase at large d side? When two spin components are only coupled by the Coulomb interaction, the spin (or pseudospin) S_z is conserved. The Chern number matrix can fully characterize the topological properties of the state (Sheng et al., 2003a,b). The charge Chern number is zero because of time-reversal symmetry. The combined Chern number which has the one-to-one relation to the quantum spin Hall effect is the spin Chern number, $C^s = \sum_{\alpha,\beta}$

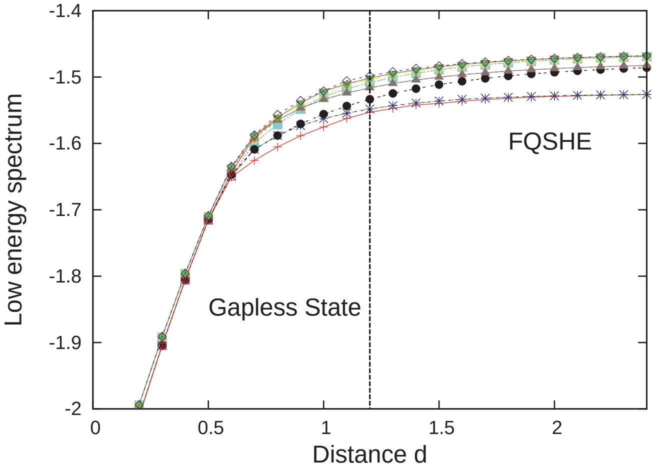

Fig. 3 The low-energy spectrum of the 1/3 + 1/3 system as a function of the layer separation *d* with zero Rashba coupling. The excitation gap is shown to be robust at large *d* side, separating the ground state manifold (only three levels in the ground state manifold are shown, each representing three degenerating levels) from higher excited states until $d_c \sim 1.2\ l$ (l is magnetic length). At $d > 1.2\ l$ side, the FQSHE remains to be robust characterized by a quantized spin Chern number $C^s = \frac{2}{3}$ and fractional quantized spin Hall conductance $\frac{2}{3}e/4\pi$ for this spin conserved system.

$\alpha C^{\alpha\beta} = C^{1,1} + C^{1,2} - C^{2,1} - C^{2,2}$. Physically, the spin Chern number represents a spin-Hall response of the system to the common electric field. For a pure system without disorder, we find that $C^s = 2/3$ for each energy level in the ground state manifold (Ghaemi et al., 2012). This is a nontrivial result since each of the many-body state has a spin lying in the $x - y$ plane with total spin $S_z = 0$. In other words, this new quantum phase belongs to a new class of fractional topological insulator (Levin and Stern, 2009) similar to its integer partner which has the Z_2 invariant (Kane and Mele, 2005a).

How robust is the FQSHE state? We first discuss the effect of the disorder. With the presence of disorder scattering, the spin Chern number carried by each eigenstate immediately becomes integer quantized similar to the one in the 1/3 FQHE (Sheng et al., 2003b). Remarkably, the total spin Chern number of each three states are conserved, which is quantized at $C^s_{tot} = \sum_{i=1}^{3} C^s_i = 2$ just like in the pure limit. Thus the FQSHE remains robust as the spin Chern number averaged for each state remains to be 2/3. Furthermore, we address the issue of Rashba coupling. With a finite Rashba coupling, the spins are free to flip, which induces an effective tunneling between two layers (or two spin components). The low-energy spectrum and the spin Chern number quantization will remain robust for small Rashba coupling.

The strained honeycomb lattices are promising platforms to realize fractional topological phase in the absence of any magnetic field. The strain-induced pseudomagnetic fields are oppositely oriented in the two valleys which are readily hosting FQHE in each valley. However, for realistic Coulomb interactions, the coupling between two valleys are too strong for inducing FQSHE. Motivated by artificial graphene systems, Ghaemi *et al.* considered tuning the short-range part of interactions and showed that exotic valley fractional topological insulator can be induced through attractive neighboring interactions in additional to the repulsive Coulomb interactions.

Fractionalized spin Hall transport in frustrated spin systems

Another interesting direction for observing topological phase is two-dimensional frustrated spin systems, where transverse spin transport may emerge when time-reversal symmetry is spontaneously broken. The observed state is known as the chiral spin liquid (CSL) with gapless chiral edge modes, which is an analog of the bosonic FQHE. The CSL was first proposed in 1987 (Kalmeyer and Laughlin, 1987; Wen et al., 1989), and in recent years the Kalmeyer-Laughlin CSL corresponding to the $\nu = 1/2$ FQHE state has been identified in different frustrated spin systems (He et al., 2014; Gong et al., 2014; Bauer et al., 2014; Kumar et al., 2015).

The chiral edge states in CSL can be probed by spin transport and associated Chern number. As an example, we consider a spin-1/2 system on a cylinder geometry. If a flux is inserted in the cylinder, the spin flip terms along the circumference direction have an additional phase. By increasing the flux adiabatically, spin transport can be detected by measuring the accumulated spin on the open edges. For the Kalmeyer-Laughlin CSL, a quantized Chern number 1/2 will be obtained with the flux increasing from zero to 2π, corresponding to a pumped fractionalized spinon with spin-1/2.

Conclusion

The topological insulator is one of great discoveries in recent 20 years. There are many experimental realizations in real materials for rich varieties of topological phases in two and three dimensional systems (Hasan and Kane, 2010). The interplay between the nontrivial band topology and interaction remains to be one of the most challenging issues to be fully understood, which will also bring more exciting discoveries including fractional quantum spin Hall effect and bosonic topological insulators (Vishwanath and Senthil, 2013), and topological superconductivity in complex materials (Liang and Kane, 2008; Qi and Zhang, 2011).

References

Andrei Bernevig B and Zhang S-C (2006) Quantum spin hall effect. *Physical Review Letters* 96: 106802.

Andrei Bernevig B, Hughes TL, and Zhang S-C (2006) Quantum spin Hall effect and topological phase transition in HgTe quantum wells. *Science* 314: 1757.

Bauer B, Cincio L, Keller BP, Dolfi M, Vidal G, Trebst S, and Ludwig AWW (2014) Chiral spin liquid and emergent anyons in a Kagome lattice Mott insulator. *Nature Communications* 5: 5137.

Cenke X and Moore JE (2006) Stability of the quantum spin Hall effect: Effects of interactions, disorder, and F_2 topology. *Physical Review B* 73: 045322.

Chen H and Yang K (2012) Interaction-driven quantum phase transitions in fractional topological insulators. *Physical Review B* 85: 195113.

Congjun W, Bernevig BA, and Zhang S-C (2006) Helical liquid and the edge of quantum spin hall systems. *Physical Review Letters* 96: 106401.

Prange RE and Girvin SM (eds.) (1990) *For a Review See, The Quantum Hall Effect*. Berlin: Springer-Verlag.

Fukui T and Fujiwara T (2009) Quantization of non-abelian berry phase for time-reversal-invariant systems. *Journal of the Physical Society of Japan* 78: 093001. https://doi.org/10.1143/JPSJ.78.093001.

Fukui T and Hatsugai Y (2007) Quantum spin hall effect in three dimensional materials: Lattice computation of z2 topological invariants and its application to bi and sb. *Journal of the Physical Society of Japan* 76: 053702. https://doi.org/10.1143/JPSJ.76.053702.

Ghaemi P, Cayssol J, Sheng DN, and Vishwanath A (2012) Fractional topological phases and broken time-reversal symmetry in strained graphene. *Physical Review Letters* 108: 266801.

Gong S-S, Zhu W, and Sheng DN (2014) Emergent chiral spin liquid: fractional quantum hall effect in a kagome heisen-berg model. *Scientific Reports* 4: 6317.

Haldane FDM (1988) Model for a quantum hall effect without landau levels: Condensed-matter realization of the "parity anomaly" *Physical Review Letters* 61: 2015–2018.

Hasan MZ and Kane CL (2010) Colloquium: Topological insulators. *Reviews of Modern Physics* 82: 3045–3067.

He Y-C, Sheng DN, and Chen Y (2014) Chiral spin liquid in a frustrated anisotropic kagome heisenberg model. *Physical Review Letters* 112: 137202.

Kalmeyer V and Laughlin RB (1987) Equivalence of the resonating-valence-bond and fractional quantum hall states. *Physical Review Letters* 59: 2095–2098.

Kane CL and Mele EJ (2005a) Z_2 topological order and the quantum spin hall effect. *Physical Review Letters* 95: 146802.

Kane CL and Mele EJ (2005b) Quantum spin hall effect in graphene. *Physical Review Letters* 95: 226801.

Klitzing KV, Dorda G, and Pepper M (1980) New method for high-accuracy determination of the fine-structure constant based on quantized hall resistance. *Physical Review Letters* 45: 494–497.

König M, Wiedmann S, Brüne C, Roth A, Buhmann H, Molenkamp LW, Qi X-L, and Zhang S-C (2007) Quantum spin hall insulator state in HgTe quantum wells. *Science* 318: 766.

Kumar K, Sun K, and Fradkin E (2015) Chiral spin liquids on the kagome lattice. *Physical Review B* 92: 094433.

Lee S-S and Ryu S (2008) Many-body generalization of the Z_2 topological invariant for the quantum spin hall effect. *Physical Review Letters* 100: 186807.

Levin M and Stern A (2009) Fractional topological insulators. *Physical Review Letters* 103: 196803.

Liang F and Kane CL (2006) Time reversal polarization and a Z_2 adiabatic spin pump. *Physical Review B* 74: 195312.

Liang F and Kane CL (2008) Superconducting proximity effect and majorana fermions at the surface of a topological insulator. *Physical Review Letters* 100: 096407.

Liang F, Kane CL, and Mele EJ (2007) Topological insulators in three dimensions. *Physical Review Letters* 98: 106803.

Maciejko J, Qi X-L, Karch A, and Zhang S-C (2010) Fractional topological insulators in three dimensions. *Physical Review Letters* 105: 246809.

Moore JE and Balents L (2007) Topological invariants of time-reversal-invariant band structures. *Physical Review B* 75: 121306.

Neupert T, Santos L, Ryu S, Chamon C, and Mudry C (2011) Fractional topological liquids with time-reversal symmetry and their lattice realization. *Physical Review B* 84: 165107.

Prodan E (2009) Robustness of the spin-chern number. *Physical Review B* 80: 125327.

Prodan E (2011) Disordered topological insulators: A non-commutative geometry perspective. *Journal of Physics A: Mathematical and Theoretical* 44: 113001.

Qi X-L and Zhang S-C (2011) Topological insulators and superconductors. *Reviews of Modern Physics* 83: 1057–1110.

Qi X-L, Yong-Shi W, and Zhang S-C (2006a) General theorem relating the bulk topological number to edge states in two-dimensional insulators. *Physical Review B* 74: 045125.

Qi X-L, Wu Y-S, and Zhang S-C (2006b) Topological quantization of the spin hall effect in two-dimensional paramagnetic semiconductors. *Physical Review B* 74: 085308.

Qian Niu D, Thouless J, and Wu Y-S (1985) Quantized hall conductance as a topological invariant. *Physical Review B* 31: 3372–3377.

Rachel S (2018) Interacting topological insulators: A review. *Reports on Progress in Physics* 81: 116501.

Roy R (2009) Z_2 classification of quantum spin hall systems: An approach using time-reversal invariance. *Physical Review B* 79: 195321.

Rui Y, Qi XL, Bernevig A, Fang Z, and Dai X (2011) Equivalent expression of z_2 topological invariant for band insulators using the non-abelian berry connection. *Physical Review B* 84: 075119.

Sheng DN, Balents L, and Wang Z (2003a) Phase diagram for quantum hall bilayers at $\nu = 1$. *Physical Review Letters* 91: 116802.

Sheng DN, Xin Wan EH, Rezayi KY, Bhatt RN, and Haldane FDM (2003b) Disorder-driven collapse of the mobility gap and transition to an insulator in the fractional quantum hall effect. *Physical Review Letters* 90: 256802.

Sheng L, Sheng DN, Ting CS, and Haldane FDM (2005) Nondissipative spin hall effect via quantized edge transport. *Physical Review Letters* 95: 136602.

Sheng DN, Weng ZY, Sheng L, and Haldane FDM (2006) Quantum spin-hall effect and topologically invariant chern numbers. *Physical Review Letters* 97: 036808.

Swingle B, Barkeshli M, McGreevy J, and Senthil T (2011) Correlated topological insulators and the fractional magnetoelectric effect. *Physical Review B* 83: 195139.

Thouless DJ, Kohmoto M, Nightingale MP, and den Nijs M (1982) Quantized hall conductance in a two-dimensional periodic potential. *Physical Review Letters* 49: 405–408.

Tsui DC, Stormer HL, and Gossard AC (1982) Two-dimensional magnetotransport in the extreme quantum limit. *Physical Review Letters* 48: 1559–1562.

Vishwanath A and Senthil T (2013) Physics of three-dimensional bosonic topological insulators: Surface-deconfined criticality and quantized magnetoelectric effect. *Physical Review X* 3: 011016.

Wen XG, Wilczek F, and Zee A (1989) Chiral spin states and superconductivity. *Physical Review B* 39: 11413–11423.

Quantum hall and synthetic magnetic-field effects in ultra-cold atomic systems

Philipp Hauke[a] **and Iacopo Carusotto**[b], [a]INO-CNR BEC Center and Department of Physics, University of Trento, Italy and INFN-TIFPA, Trento Institute for Fundamental Physics and Applications, Trento, Italy; [b]Pitaevskii BEC Center, CNR-INO and Dipartimento di Fisica, Università di Trento, Trento, Italy

© 2024 Elsevier Ltd. All rights reserved.

Introduction **629**
Synthetic magnetic fields **630**
Integer quantum Hall effect **631**
IQH in cold atoms 631
Extensions 632
Fractional quantum hall effect in cold atoms **633**
Dynamical synthetic gauge fields **633**
Dynamical vector potentials and Peierls phases 633
Lattice gauge theories 635
Conclusion **636**
References **636**

Abstract

In this Chapter, we give a brief review of the state of the art of theoretical and experimental studies of synthetic magnetic fields and quantum Hall effects in ultracold atomic gases. We focus on integer, spin, and fractional Hall effects, indicate connections to topological matter, and discuss prospects for the realization of full-edged gauge field theories where the synthetic magnetic field has its own dynamics. The advantages of these systems over traditional electronic systems are highlighted. Finally, interdisciplinary comparisons with other synthetic matter platforms based on photonic and trapped-ion systems are drawn. We hope this chapter to illustrate the exciting progress that the field has experienced in recent years.

Key points

This chapter aims to

- illustrate how synthetic magnetic fields can effectively be generated in neutral matter;
- highlight breakthroughs in realizing integer and spin quantum Hall effect;
- showcase steps toward strongly interacting systems displaying the fractional quantum Hall effect;
- illustrate some of the rich physics that can be achieved when the atoms act back on the synthetic gauge fields;
- emphasize the fascinating progress of the field and the outstanding main challenges.

Introduction

The discovery of the quantum Hall (QH) effects in two-dimensional electron gases subject to a strong magnetic field has revolutionized our view of quantum condensed-matter physics and has opened a new field of research at the crossroad with quantum information and topology (Tong, 2016). While usual phase transitions such as ferromagnetism or even Bose–Einstein condensation are described within the Landau–Ginzburg theory by the onset of a macroscopic order parameter, topological states of matter cannot be revealed by the measurement of any local observable and instead are characterized by subtle quantum correlations between the constituent particles (Kitaev and Preskill, 2006; Levin and Wen, 2006; Wen, 1995, 2013). The most direct signature of integer and fractional quantum Hall states is the quantized value of the transverse conductivity in units of e^2/h. Besides opening windows into novel physical phenomena of fundamental interest, such states have been also anticipated for practical applications in quantum information processing, e.g., as a promising platform to transmit quantum information and protect it from decoherence (Nayak et al., 2008).

Beyond the traditional observation of quantum Hall effects in electron gases in solid-state devices, a strong activity is presently being devoted to synthetic quantum matter systems (Ozawa and Price, 2019) such as gases of ultracold atoms (Cooper, 2008; Pitaevskiĭ and Stringari, 2016), spin and phonon systems realized in trapped ions (Bermudez et al., 2011; Geier et al., 2021b; Manovitz et al., 2020; Nigg et al., 2014), or fluids of strongly interacting photons in nonlinear topological photonics devices (Carusotto and Ciuti, 2013; Carusotto et al., 2020). In all these systems, the charge neutrality of the constituent particles requires introducing a so-called synthetic magnetic field in order to observe QH physics (Dalibard, 2016; Dalibard et al., 2011; Goldman et al., 2014); at the same time, such systems allow for a broader range of techniques for the manipulation and diagnostics well

https://doi.org/10.1016/B978-0-323-90800-9.00061-5

beyond the standard transport and optical probes of solid state systems (Yoshioka, 2002), which opens exciting new perspectives to experimental studies. While a number of phenomena related to the integer quantum Hall (IQH) effect have been observed in the last years for non-interacting particles in suitably designed band structures for either atoms or photons, fractional quantum Hall (FQH) effects require strong interactions among particles and low temperatures, and are still a subject of intense work.

In what follows, we give a timely account of the state of the art of experimental and theoretical research toward the realization of FQH liquids of ultracold atoms. We also discuss relatively novel directions, where the magnetic vector potential acquires its own dynamics, leading to interesting backaction effects of matter particles onto the synthetic magnetic field and even to full-edged gauge theories reminiscent of quantum electrodynamics. This chapter thus complements other reviews on synthetic gauge fields (Dalibard, 2016; Dalibard et al., 2011; Goldman et al., 2014), on rotating atomic clouds (Cooper, 2008), and on topological effects in synthetic quantum matter (Cooper et al., 2019; Ozawa and Price, 2019; Zhang et al., 2018). While the main focus of our discussion here will be on ultracold atoms, connections to other promising platforms such as trapped ions or photonic devices will also be drawn.

This review chapter is organized as follows. In Section "Synthetic magnetic fields," we recapitulate approaches to imbuing ultracold atomic gases with synthetic magnetic fields, a key prerequisite for observing QH physics. Sections "Integer quantum Hall effect" and "Fractional quantum hall effect in cold atoms" discuss recent advances in cold atom systems in observing the IQH and FQH, respectively. In Section "Dynamical vector potentials," we highlight some recent developments in inducing backaction of the matter system onto the synthetic magnetic field, leading to the generation of dynamical Peierls phases and even to pioneering steps in the creation of lattice gauge theories. Section "Conclusion" contains our conclusions and some further outlooks.

Synthetic magnetic fields

The motion of quantum mechanical particles of mass m and charge q in a classical background magnetic field is described via the minimal coupling Hamiltonian

$$H_{\mathrm{kin}} = \frac{\left(\mathbf{P} - \frac{q}{c}\mathbf{A}\right)^2}{2m} \tag{1}$$

in terms of the vector potential $\mathbf{A}(\mathbf{r})$, related to the magnetic field by $\mathbf{B} = \mathrm{rot}\mathbf{A}$. In a discrete, spatially-periodic lattice geometry, this Hamiltonian can be reformulated in terms of a non-trivial hopping phase in the tight-binding Hamiltonian,

$$H_{\mathrm{kin}} = -J\sum_{\langle i,\ j\rangle}\Psi_i^{\dagger}U_{i,j}\Psi_j, \tag{2}$$

where J is the bare hopping amplitude, $\psi_i^{\dagger}$ and ψ_i are fermionic or bosonic creation and annihilation operators at lattice site i, respectively, and $U_{i,j} = \exp\left(i\frac{q}{c}\int_{\mathbf{r}_i}^{\mathbf{r}_j}\mathrm{d}\mathbf{r}\cdot\mathbf{A}(\mathbf{r})\right)$ is the Peierls phase, corresponding to the Aharonov–Bohm phase accumulated by the particle when moving from site i to site j. Starting from these formulations, it is straightforward to derive the celebrated features of quantum mechanical motion in magnetic fields, such as cyclotron motion and Landau levels (Girvin, 1999; Tong, 2016).

Since atoms are charge neutral ($q = 0$), it is impossible to observe this physics using standard magnetic fields, whose effect on atoms typically reduces to Zeeman shifts of the internal levels. More subtle manipulations are therefore necessary to generate effective vector potentials affecting the orbital atomic motion along the lines of Eqs. (1) or (2). Over the years, a number of strategies to generate such *synthetic magnetic fields* have been developed. Here, we will briefly review the most promising and/or physically transparent ones (Dalibard, 2016; Dalibard et al., 2011; Goldman et al., 2014). As the basic object realized in the experiments is typically the vector potential, gauge-invariance of the framework raises interesting subtleties in the conceptual analysis of the experiments (LeBlanc et al., 2015). Though synthetic gauge fields give rise also to other intriguing effects, e.g., supersolid behavior (Geier et al., 2021a; Li et al., 2017; Putra et al., 2020), our attention in this review will be focused on the family of integer and fractional Quantum Hall effects.

Historically, the first strategy was based on the mathematical analogy between the Coriolis force $\mathbf{F} = \mathbf{v} \times \mathbf{\Omega}$ in a rotating frame and the Lorentz force $\mathbf{F} = q\frac{\mathbf{v}}{c} \times \mathbf{B}$ in a magnetic field. By putting the atom trap into mechanical rotation around some axis, the atomic cloud gets to equilibrate in a rotating frame where the angular speed plays the role of the magnetic field. Over the years, this approach has led to pioneering advances for weakly interacting Bose–Einstein condensates, such as the observation of periodic arrays of quantized vortices (Abo-Shaeer et al., 2001; Bretin et al., 2004; Schweikhard et al., 2004) resembling the Abrikosov vortex arrays generated by magnetic fields in type-II superconductors.

A conceptually different approach to generate a synthetic magnetic field is based on the Berry phase that moving atoms experience when they are dressed by a suitable combination of optical, micro- and radio-wave, and static electromagnetic fields (Dum and Olshanii, 1996; Juzeliunas and Öhberg, 2004; Ruseckas et al., 2005): in this framework, the roles of the vector potential and of the magnetic field are played by the Berry connection and the Berry curvature, respectively. Remarkable outcomes of this approach include the nucleation of quantized vortices under the effect of strong enough synthetic fields (Lin et al., 2009), as highlighted in Fig. 1.

Discrete, spatially periodic geometries realized by imposing optical lattice potentials offer additional tools to generate synthetic magnetic fields via non-trivial hopping phases. Complex hopping phases induced by inter-site Raman processes were first proposed in Jaksch and Zoller (2003), Mueller (2004), Osterloh et al. (2005), Sorensen et al. (2005) and then implemented to realize, e.g., an atomic Harper–Hofstadter model (Aidelsburger et al., 2013; Miyake et al., 2013).

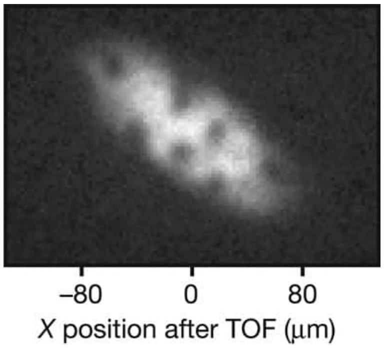

Fig. 1 Quantized vortices nucleated in an atomic BEC under the effect of a synthetic magnetic field. Reprinted by permission from Lin, Y-J, Compton, RL, Jiménez-García, K, Porto, JV and Spielman, IB (2009) Synthetic magnetic fields for ultracold neutral atoms. *Nature* 462(7273): 628–632. Copyright Springer Nature Ltd. 2009.

Alternatively, non-trivial band geometries and topologies have been realized in a Floquet framework based on periodic shaking or time-modulation of the lattice potential (Bukov et al., 2015; Eckardt and Anisimovas, 2015). By suitably choosing the shaking protocol, e.g., such that the periodic shaking function explicitly breaks time-reversal symmetry, one can obtain—in a time-averaged or stroboscopic Floquet description—an effective Hamiltonian that has a non-trivial Peierls phase (Goldman and Dalibard, 2014; Hauke et al., 2012; Kitagawa et al., 2010, 2011; Kolovsky, 2011; Oka and Aoki, 2009; Struck et al., 2012). This approach has led to the realization of the Haldane (Jotzu et al., 2014) and the Harper–Hofstadter model (Aidelsburger et al., 2015).

An exciting new frontier of these investigations is to combine the internal and orbital dynamics of atoms into a single geometric entity so to realize configurations with a larger number of effective spatial dimensions than the usual three spatial ones (Celi et al., 2014), where to observe new magnetic and topological effects that are peculiar of high dimensionalities (Price et al., 2015). Pioneering steps in the direction of realizing such *synthetic dimensions* were reported in the experiments of Mancini et al. (2015), Stuhl et al. (2015).

Integer quantum Hall effect

In electronics, the main signature of the Integer Quantum Hall (IQH) effect consists in a quantized value of the transverse conductance to integer multiples of e^2/h whenever electrons completely fill an integer number of Landau levels (Tong, 2016). Soon after the discovery of the IQH, it was realized that the quantized conductance can be related to integer-valued topological invariants characterizing the geometry of the electronic bands (Thouless et al., 1982). In a modern understanding, IQH systems are then interpreted as an example of the wider class of topological insulators, where the bulk-boundary correspondence translates topological properties of the bands of the insulating bulk into chiral currents around the edges of the sample (Hasan and Kane, 2010), see Fig. 2(a). Since these features are related to integer-valued topological invariants, they are resilient against disorder and similar types of small perturbations.

Based on such insights, the IQH effect could be studied in a number of atomic systems: even though conductivity experiments analogous to electronic ones are not naturally performed in atomic systems, many other observables are available to obtain an even deeper information on the properties of this state of matter.

IQH in cold atoms

Anomalous Hall effects were first predicted in the atomic context in Dudarev et al. (2004) and experimentally observed in honeycomb-like lattices in Jotzu et al. (2014) as a lateral displacement of the atoms whenever their k-space distribution is pushed

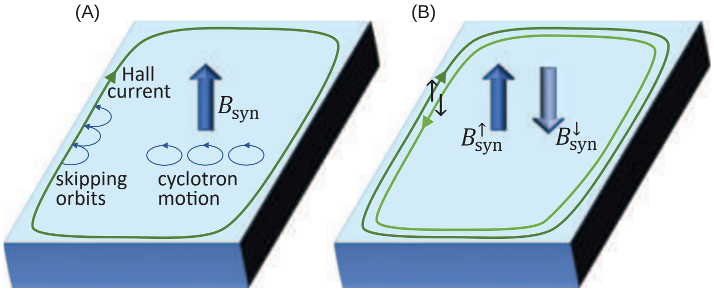

Fig. 2 (a) Integer Quantum Hall effect. A synthetic magnetic field pierces a cloud of ultracold neutral atoms, induced, e.g., by trap rotation, Berry phase imprinting, or lattice shaking. Within the bulk, this leads to cyclotron motion. The corresponding skipping orbits at the boundary add up to a chiral edge current, which is protected by the topology of the sample. (b) Spin Hall effect. Two (pseudo-)spin states (e.g., two atomic hyperfine states) see an opposite synthetic magnetic field. As a result, the system has vanishing net charge transport, but the presence of helical edge states results in a topologically protected spin current around its boundaries.

across a finite-Berry-curvature region. A quantized displacement analogous to the IQH was then observed for an atomic cloud uniformly filling a band (Aidelsburger et al., 2015). A precursor of this was the measurement of the Zak phase characterizing topological Bloch bands in a one-dimensional optical lattice (Atala et al., 2013).

While chiral edge states have been the major workhorse to characterize topological photonic systems (Ozawa et al., 2019), a relatively limited number of experiments have investigated edge currents in atomic systems. On the one hand, this is due to the difficulty of directly measuring currents in cold-atom systems, though significant theoretical and experimental advances have been achieved in recent years (Brown et al., 2019; Geier et al., 2021b; Hauke et al., 2014; Jepsen et al., 2020; Keßler and Marquardt, 2014; Krinner et al., 2015; Laflamme et al., 2017; Nichols et al., 2019; Scherg et al., 2018). On the other hand, an obstacle is the absence of sharp boundaries in standard, harmonically trapped atomic clouds. Also for this reason, the remarkable studies of edge transport in Mancini et al. (2015), Stuhl et al. (2015) illustrated in Fig. 3 made use of a synthetic dimension set-up combining a spatially one-dimensional lattice with an additional dimension formed by the internal spin degrees.

A great advantage of atomic systems is the possibility of combining macroscopic transport measurements with a direct microscopic insight into the quantum many-body wavefunction (Gebert et al., 2020). In the IQH context, a remarkable example in this direction was the experimental tomography of the Berry phase (Fläschner et al., 2016; Hauke et al., 2014), with follow-ups such as the identification of dynamical topological invariants in the time evolution of an atomic system (Tarnowski et al., 2019).

Extensions

An important extension of the IQH effect is obtained when a spin degree of freedom of the particles is included, $\sigma = \uparrow, \downarrow$, such that Eq. (2) becomes $H_{\text{kin}} = -J\sum_{\langle i,j\rangle} \sum_\sigma \psi_{i,\sigma}^\dagger U_{i,j}^\sigma \psi_{j,\sigma}$. In the so-called spin-Hall effect (Hasan and Kane, 2010), particles with different spin orientations see opposite magnetic fields, $(U_{i,j}^\uparrow)^\dagger = U_{i,j}^\downarrow$ and time-reversal symmetry is restored. The result is a system without any net charge current but chiral spin edge currents that run around the sample in opposite directions, see Fig. 2(b). Pioneering proposals have been based on extending schemes for light-induced vector potentials to several hyperfine levels (Zhu et al., 2006) and on state-dependent, slowly time-varying magnetic potentials engineered in an atom chip on a micron scale (Goldman et al., 2010). The spin Hall effect has been observed in free space, where spin-dependent Lorentz forces have been measured using a spatially inhomogeneous spin-orbit coupling field (Beeler et al., 2013), as well as in an optical lattice using laser-assisted tunneling induced in a tilted optical lattice via periodic driving (Aidelsburger et al., 2013).

This physics can be generalized even further by replacing the spin-dependent Peierls phase by a matrix, $H_{\text{kin}} = -J\sum_{\langle i,j\rangle}\sum_{\sigma,\sigma'} \psi_{i,\sigma}^\dagger U_{i,j}^{\sigma,\sigma'} \psi_{j,\sigma'}$, where $U_{i,j}^{\sigma,\sigma'}$ mixes the different spin states during hopping. Genuinely non-Abelian effects occur if the product of the $U_{i,j}^{\sigma,\sigma'}$ around a closed path (the non-Abelian Wegner–Wilson loop) does not reduce to a simple phase factor $e^{i\phi}\mathbb{1}$. Such a situation can be obtained through periodically shaken optical superlattices where an internal degree of freedom of the atoms plays the role of the (pseudo-) spin (Hauke et al., 2012). As a striking consequence of the non-Abelian Hall effect, novel fractal features have been predicted to appear in the phase diagram (Bermudez et al., 2010; Goldman et al., 2009).

Another exciting direction of research concerns the extension of IQH effects to higher-dimensional, 4 + 1 geometries as first proposed in Price et al. (2015) using the concept of synthetic dimensions mentioned above. Pioneering experimental evidence of

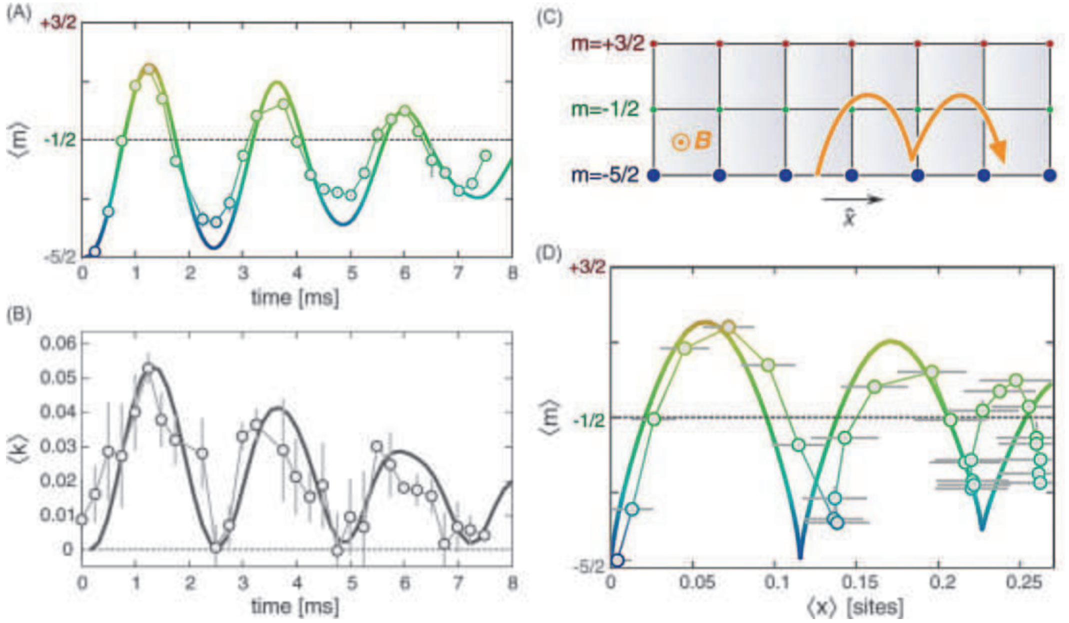

Fig. 3 Experimental observation of edge-cyclotron orbits in a synthetic three-leg ladder system based on a spatial *x* dimension and a synthetic dimension encoded in the atomic spin. From Mancini, M, Pagano, G, Cappellini, G, Livi, L, Rider, M, Catani, J, Sias, C, Zoller, P, Inguscio, M, Dalmonte, M et al. (2015) Observation of chiral edge states with neutral fermions in synthetic hall ribbons. *Science* 349(6255): 1510–1513. Reprinted with permission from AAAS.

the role of higher-dimensional topological invariants in the atomic transport properties under crossed synthetic-electric and magnetic fields in 4-dimensional models was reported in Lohse et al. (2018).

Fractional quantum hall effect in cold atoms

In the previous section, we have seen the intriguing effects that appear in the presence of completely occupied Landau levels or topological bands, but where interactions play at most a subdominant role. Even more subtle physics occurs when the macroscopic degeneracy of partially filled Landau levels is lifted by strong inter-particle interactions and the lowest energy state acquires a non-trivial topology for the many-body wavefunction (Kitaev and Preskill, 2006; Levin and Wen, 2006; Wen, 1995, 2013).

One of the most celebrated examples of such topological many-body phases of matter is the so-called fractional quantum Hall (FQH) effect, first detected in two-dimensional electron gases under strong magnetic fields as a precise quantization of the transverse conductivity at rational values proportional to the electron filling, i.e., the number of electrons per unit magnetic flux piercing the system (Girvin, 1999; Tong, 2016; Yoshioka, 2002). As even more intriguing signatures of the many-body topology of the FQH state, excitations with a fractional charge and fractional statistics have been anticipated for these systems, the so-called *anyons* (Stern, 2008). While fractionally charged edge excitations have been observed in shot-noise measurements (De-Picciotto et al., 1998; Saminadayar et al., 1997), the observation of fractional statistical properties interpolating between bosonic and fermionic behaviors is still the subject of intense experimental work (Bartolomei et al., 2020; Nakamura et al., 2020).

First steps towards the realization of FQH fluids using ultracold atomic clouds were made by pushing the rotation frequency toward the trapping frequency, so that the atomic cloud expands in space under the effect of the centrifugal potential and reaches the required magnetic flux per particle values. For sufficiently low temperatures, it is then predicted to enter a FQH state (Cooper, 2008). In spite of early concerns about heating due to spurious asymmetries of the trap potential and the need for a fine tuning of the rotation speed, remarkable advances on condensates in rotating traps have been recently reported (Fletcher et al., 2021; Mukherjee et al., 2022). Besides these works on a mean-field-interacting dynamics, hints of correlated FQH physics have been reported in small atomic clusters trapped at the rotating minima of a temporally modulated optical lattice potential (Gemelke et al., 2010). A different strategy to realize a strongly interacting Harper–Hofstadter lattice using a combination of optical lattice potentials and Raman transitions was adopted in Tai et al. (2017) and led to the observation of a correlated two-particle dynamics, a precursor of fractional quantum Hall effects, see Fig. 4. In the meanwhile, an intense theoretical activity has been devoted to the study of alternative protocols to realize FQH states using, e.g., adiabatic ramps along suitably designed paths in parameter space (Popp et al., 2004; Sorensen et al., 2005) or sequences of adiabatic flux insertion and hole replenishing (Grusdt et al., 2014).

The main advantage of FQH fluids of ultracold atoms over solid-state systems is the much wider variety of manipulation and diagnostics tools compared to the transport and optical probes traditionally available for electronic systems. While waiting for macroscopic FQH clouds to be experimentally realized, theoretical proposals to investigate their intriguing properties include interferometric techniques (Grusdt et al., 2016; Paredes et al., 2001), quasi-hole dynamics in response to external potentials (Grass et al., 2012), microscopic imaging of the density profile of a quasi-hole (Macaluso et al., 2020), quantum mechanics of anyonic molecules formed by an impurity bound to a FQH quasi-hole (Baldelli et al., 2021; De Las Heras et al., 2020; Zhang et al., 2014; Lundholm and Rougerie, 2016; Yakaboylu et al., 2020), the center of mass motion of the cloud (Repellin et al., 2020), its circular-dichroic response to circular excitations in the bulk (Repellin and Goldman, 2019), or the linear and nonlinear response of the edge modes (Nardin and Carusotto, 2022).

Together with direct measurements of the entanglement entropy (Jiang et al., 2012; Li and Haldane, 2008) as experimentally pioneered in Islam et al. (2015), we anticipate that these proposals will eventually be a most valuable tool to obtain a deeper insight in the basic physics of FQH fluids and synthetic topological matter, and to exploit the benefits of their atomic implementation in view of quantum information tasks (Nayak et al., 2008).

Dynamical synthetic gauge fields

In all of the above discussions, the vector potential appearing in Eqs. (1) and (2) was assumed to have a constant value, corresponding to a classical, externally imposed background field. Entirely new effects can appear once the vector potential is imbued with its own dynamics.

Dynamical vector potentials and Peierls phases

In the first proposal for continuum systems (Edmonds et al., 2013), a density-dependent vector potential was anticipated to arise from interaction-induced energy shifts of the internal atomic states involved in the optical transitions generating the Berry phase. Among the observable consequences, density-dependent persistent currents in ring geometries and chiral solitons were pointed out. Along similar lines, Ballantine et al. (2017) proposed to replace one of the optical fields generating the Berry phase by a multimode cavity field. The density of the atoms can then act back on the cavity field, which—due to its multimode character—can acquire a spatial dependence. In this way, the equivalent of the celebrated Meissner effect can be generated, whereby a magnetic field is expelled from the atom-cloud sample, see Fig. 5.

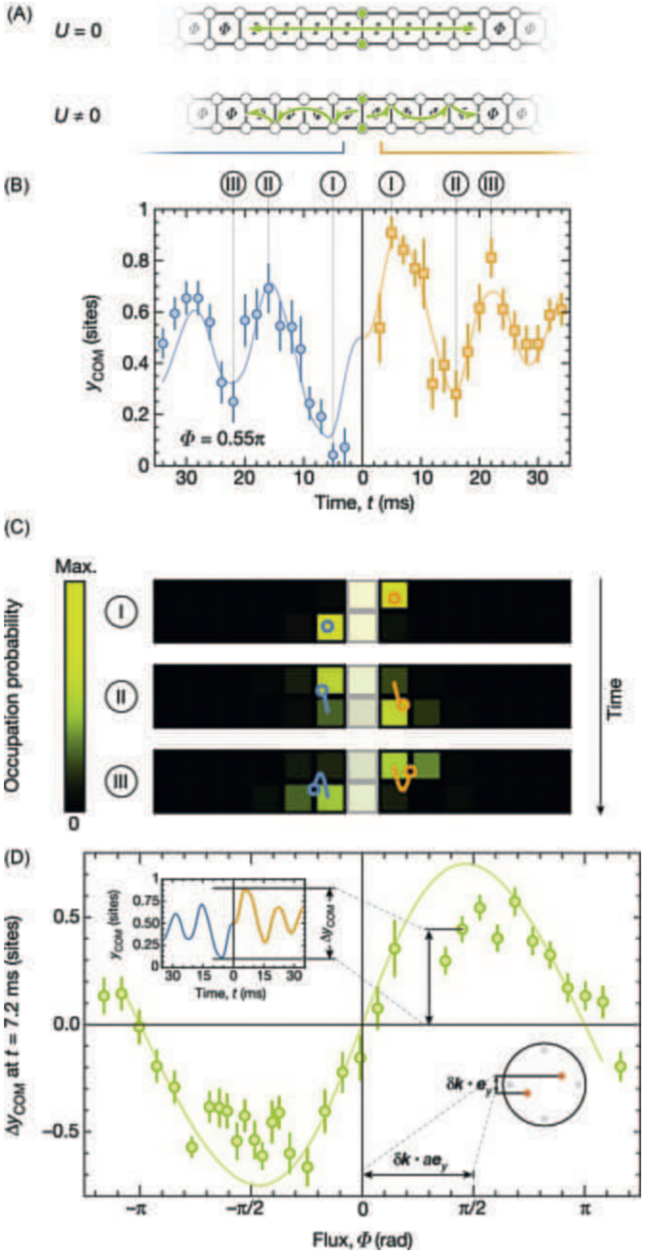

Fig. 4 Chiral motion of two interacting atoms in a Harper–Hofstadter ladder, where each plaquette is pierced by a synthetic magnetic flux Φ. Upper panel: sketch of the trajectories for non-interacting ($U = 0$) and interacting ($U \neq 0$) atoms. Lower panel: temporal dynamics along y displaying the chiral motion of the so-called skipping orbits. Reprinted by permission from Tai, ME, Lukin, A, Rispoli, M, Schittko, R, Menke, T, Borgnia, D, Preiss, PM, Grusdt, F, Kaufman, AM and Greiner, M (2017) Microscopy of the interacting harper–hofstadter model in the two-body limit. *Nature* 546(7659): 519–523. Copyright Springer Nature Ltd. 2017.

In lattice systems, a complementary direction is taken by turning the Peierls phase into a quantum-mechanical operator. This can happen, e.g., through density-dependent tunneling, where the complex hopping phase $U_{i,j}$ becomes a function $U_{i,j}(\hat{n}_i,\ \hat{n}_j)$ of the atom number operators $\hat{n}_\ell = a_\ell^\dagger a_\ell$ at adjacent sites $\ell = i,\ j$. Such a situation can be generated by Floquet engineering (Meinert et al., 2016), as experimentally demonstrated in Görg et al. (2019), and it can naturally appear in regimes of very strong interactions or high occupation numbers (Dutta et al., 2011). Such a density-dependent tunneling has been proposed to lead to deformations of phase diagrams and the generation of novel phases such as pair superfluids (Dutta et al., 2011; Johnstone et al., 2019; Maik et al., 2013; Suthar et al., 2020) as well as to topological transitions in the ground state (Raventos et al., 2016).

In other schemes, the role of the Peierls phase can also be taken over by a second, independent atomic species. E.g., in an atomic mixture, an itinerant species can be coupled to the (pseudo-)spin degree of freedom of a second, kinetically frozen species (Kasper et al., 2021; Mil et al., 2020). By replacing the static hopping matrix by an additional quantum mechanical spin degree of freedom,

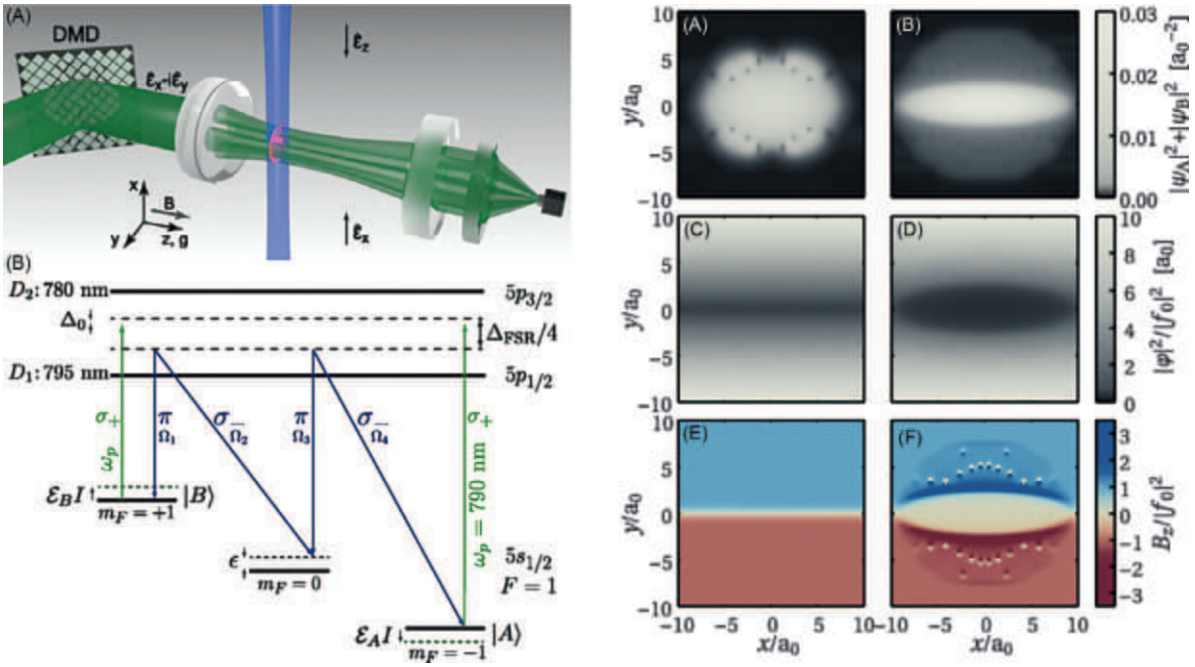

Fig. 5 Left: By suitably coupling the internal levels of ultracold atoms to a multi-mode cavity, a backaction from atoms onto the synthetic magnetic field can be engineered, where the spatial profile of the synthetic magnetic field varies depending on the atomic density. Right: Simulations of the atom-cavity system without (panels a,c,e) and with backaction (b,d,f). The backaction leads to an analog of the Meissner effect, where the magnetic field is expelled from the sample, leading to an extended region with $B = 0$. Reprinted figure with permission from Ballantine, KE, Lev, BL and Keeling, J (2017) Meissner-like effect for a synthetic gauge field in multimode cavity qed. *Physical Review Letters* 118: 045302. doi:10.1103/PhysRevLett.118.045302. Copyright 2017 by the American Physical Society.

$U_{i,j} \rightarrow S^{\alpha}_{i,j}$, $\alpha = x, y, z$, backaction phenomena between two different fields can lead, e.g., to topological and fractionalization effects such as a Peierls transition where an alternating pattern of strong and weak bonds dynamically emerges similar to polyacetylene (González-Cuadra et al., 2019, 2020). The additional possibilities offered by these experiments with atomic mixtures also enabled the observation of a Lamb shift effect in the atomic self energy. Similarly to the Lamb shift experienced by QED electrons due to their interaction with the quantum mechanical vector potential, an energy shift is induced here on one atomic species by their interactions with a second one (Rentrop et al., 2016).

Lattice gauge theories

In these approaches, the "vector potential" acquires its own dynamics, but the combined system of "particles" and "vector potential" does not necessarily respect the fundamental laws of QED, making it necessary to take similarities to magnetic fields with a grain of salt. To recover a full-edged system of charged matter moving in a quantum mechanical electromagnetic field, additional care needs to be taken to enforce the $U(1)$ gauge symmetry that interlinks the two different types of dynamical degrees of freedom. In particular, the dynamics of the system needs to conserve the local symmetry that underpins QED, given by Gauss' law, at all spatial coordinates and throughout the entire evolution time.

Although this task is highly challenging, groundbreaking experiments with local gauge symmetry have already been realized in Rydberg quantum simulators (Bernien et al., 2017; Surace et al., 2020), using Floquet techniques in optical lattices (Schweizer et al., 2019), exploiting angular momentum conservation in atomic mixtures (Mil et al., 2020) (proposed, e.g., in Stannigel et al., 2014; Zache et al., 2018; Zohar et al., 2013), as well as with energy penalties in optical superlattices (Halimeh et al., 2021; Yang et al., 2020; Zhou et al., 2021). Pioneering realizations have also been demonstrated in other platforms, in particular trapped ions (Kokail et al., 2019; Martinez et al., 2016; Nguyen et al., 2021), superconducting qubits (Klco et al., 2018, 2020; Mildenberger et al., 2022; Wang et al., 2022), and even classical electronic circuits (Riechert et al., 2021).

Most of these implementations focused on salient physical phenomena in one spatial dimension, and it is a current challenge to advance ultracold-atom lattice gauge theories into higher spatial dimensions (Zohar, 2022). In the future, these may enable, e.g., the investigation of strong-field effects on anomalous currents (Ott et al., 2020) as well as a range of new anomalous transport phenomena including the chiral magnetic effect (Fukushima et al., 2008; Kharzeev, 2014), the chiral vortical effect (Son and Zhitnitsky, 2004), or the conformal magnetic edge effect (Chernodub et al., 2019; Chu and Miao, 2018).

Conclusion

This review chapter summarized our point of view on the rich physics that can be obtained by synthetic static and dynamical gauge fields in cold-atom setups. We have reviewed the way synthetic magnetic fields can be engineered in such systems, discussed progress in controlled implementations of the integer, spin, and fractional quantum Hall effects, as well as some of the fascinating phenomena that appear when the atoms act back on the synthetic magnetic fields, without or with respecting gauge symmetry given by Gauss's law. These are, however, just some of the many facets of ongoing research in the broad context of synthetic gauge fields.

Promising implementations have been designed and realized in other synthetic quantum matter platforms. For example, topological photonic systems are presently one of the most active fields of research in optics, with potential technological applications such as efficient optical isolation and large-area, fabrication-disorder-robust topological lasers (Price et al., 2022). Synthetic magnetic field for photons are one of the key building blocks in this context and, analogously to the atomic case, can be realized in many different ways, from twisted optical cavities leading to an effective overall rotation (Schine et al., 2016), to static or time-dependent complex hopping phases (Hafezi et al., 2013; Roushan et al., 2017), to Floquet-like temporal modulations (Rechtsman et al., 2013). In combination with sizable photon-photon interactions arising from the optical nonlinearity of the underlying optical medium, a synthetic magnetic field for light may lead to the generation of novel states of photonic matter (Carusotto et al., 2020): baby versions of a quantum Hall fluid of light of a few photons have been recently realized (Clark et al., 2020). Other promising platforms are, e.g., analog implementations in trapped ions, where techniques similar to those for optical lattices have been developed to imprint Peierls phases (Bermudez et al., 2011; Manovitz et al., 2020), as well as universal quantum computers, where proposals for realizing fractional quantum Hall states (Rahmani et al., 2020) as well as experimental realizations of topological matter exist (Nigg et al., 2014; Satzinger et al., 2021; Semeghini et al., 2021).

All together, the examples discussed in this review illustrate the on-going exciting progress in the study of quantum Hall effects in cold atomic fluids as well as in related synthetic quantum matter platforms (Ozawa and Price, 2019). Beyond the remarkable achievements obtained so far, there are a lot of equally exciting open questions ahead of the community, as well as a number of potentially game-changing applications in quantum technologies (Nayak et al., 2008).

References

Abo-Shaeer JR, Raman C, Vogels JM, and Ketterle W (2001) Observation of vortex lattices in bose-einstein condensates. *Science* 292(5516): 476–479.

Aidelsburger M, Atala M, Lohse M, Barreiro JT, Paredes B, and Bloch I (2013) Realization of the hofstadter hamiltonian with ultracold atoms in optical lattices. *Physical Review Letters* 111(18), 185301.

Aidelsburger M, Lohse M, Schweizer C, Atala M, Barreiro JT, Nascimbène S, Cooper N, Bloch I, and Goldman N (2015) Measuring the chern number of hofstadter bands with ultracold bosonic atoms. *Nature Physics* 11(2): 162–166.

Atala M, Aidelsburger M, Barreiro JT, Abanin D, Kitagawa T, Demler E, and Bloch I (2013) Direct measurement of the Zak phase in topological bloch bands. *Nature Physics* 9: 795.

Baldelli N, Juliá-Díaz B, Bhattacharya U, Lewenstein M, and Grass T (2021) Tracing non-Abelian anyons via impurity particles. *Physical Review B* 104: 035133. https://doi.org/10.1103/PhysRevB.104.035133.

Ballantine KE, Lev BL, and Keeling J (2017) Meissner-like effect for a synthetic gauge field in multimode cavity qed. *Physical Review Letters* 118: 045302. https://doi.org/10.1103/PhysRevLett.118.045302.

Bartolomei H, Kumar M, Bisognin R, Marguerite A, Berroir J-M, Bocquillon E, Placais B, Cavanna A, Dong Q, Gennser U, et al. (2020) Fractional statistics in anyon collisions. *Science* 368(6487): 173–177.

Beeler MC, Williams RA, Jiménez-García K, LeBlanc LJ, Perry AR, and Spielman IB (2013) The spin hall effect in a quantum gas. *Nature* 498: 201–204.

Bermudez A, Goldman N, Kubasiak A, Lewenstein M, and Martin-Delgado M (2010) Topological phase transitions in the non-Abelian honeycomb lattice. *New Journal of Physics* 12: 033041.

Bermudez A, Schaetz T, and Porras D (2011) Synthetic gauge fields for vibrational excitations of trapped ions. *Physical Review Letters* 107: 150501. https://doi.org/10.1103/PhysRevLett.107.150501.

Bernien H, Schwartz S, Keesling A, Levine H, Omran A, Pichler H, Choi S, Zibrov AS, Endres M, Greiner M, Vuletić V, and Lukin MD (2017) Probing many-body dynamics on a 51-atom quantum simulator. *Nature* 551(7682): 579–584. https://doi.org/10.1038/nature24622.

Bretin V, Stock S, Seurin Y, and Dalibard J (2004) Fast rotation of a bose-einstein condensate. *Physical Review Letters* 92(5), 050403.

Brown PT, Mitra D, Guardado-Sanchez E, Nourafkan R, Reymbaut A, Hébert C-D, Bergeron S, Tremblay A-MS, Kokalj J, Huse DA, Schauß P, and Bakr WS (2019) Bad metallic transport in a cold atom Fermi–Hubbard system. *Science* 363(6425): 379–382. URL https://science.sciencemag.org/content/363/6425/379.

Bukov M, D'Alessio L, and Polkovnikov A (2015) Universal high-frequency behavior of periodically driven systems: From dynamical stabilization to floquet engineering. *Advances in Physics* 64(2): 139–226. https://doi.org/10.1080/00018732.2015.1055918.

Carusotto I and Ciuti C (2013) Quantum fluids of light. *Reviews of Modern Physics* 85(1): 299.

Carusotto I, Houck AA, Kollár AJ, Roushan P, Schuster DI, and Simon J (2020) Photonic materials in circuit quantum electrodynamics. *Nature Physics* 16(3): 268–279.

Celi A, Massignan P, Ruseckas J, Goldman N, Spielman IB, Juzeliūnas G, and Lewenstein M (2014) Synthetic gauge fields in synthetic dimensions. *Physical Review Letters* 112(4), 043001.

Chernodub M, Goy V, and Molochkov A (2019) Conformal magnetic effect at the edge: A numerical study in scalar qed. *Physics Letters B* 789: 556–561. URL https://www.sciencedirect.com/science/article/pii/S0370269319300152.

Chu C-S and Miao R-X (2018) Weyl anomaly induced current in boundary quantum field theories. *Physical Review Letters* 121: 251602. https://doi.org/10.1103/PhysRevLett.121.251602.

Clark LW, Schine N, Baum C, Jia N, and Simon J (2020) Observation of laughlin states made of light. *Nature* 582(7810): 41–45.

Cooper NR (2008) Rapidly rotating atomic gases. *Advances in Physics* 57(6): 539–616.

Cooper NR, Dalibard J, and Spielman IB (2019) Topological bands for ultracold atoms. *Physical Review Letters* 91: 015005. https://doi.org/10.1103/RevModPhys.91.015005.

Dalibard J (2016) Introduction to the physics of artificial gauge fields. In: Inguscio M, Ketterle W, and Stringari S (eds.) *Quantum Matter at Ultralow Temperatures. Proceedings of the International School of Physics "Enrico Fermi"*, vol. 191. IOS Press.

Dalibard J, Gerbier F, Juzeliūnas G, and Öhberg P (2011) Colloquium: Artificial gauge potentials for neutral atoms. *Reviews of Modern Physics* 83(4): 1523.

De Las Heras AM, Macaluso E, and Carusotto I (2020) Anyonic molecules in atomic fractional quantum hall liquids: A quantitative probe of fractional charge and anyonic statistics. *Physical Review X* 10(4), 041058.

De-Picciotto R, Reznikov M, Heiblum M, Umansky V, Bunin G, and Mahalu D (1998) Direct observation of a fractional charge. *Physica B: Condensed Matter* 249: 395–400.

Dudarev AM, Diener RB, Carusotto I, and Niu Q (2004) Spin-orbit coupling and berry phase with ultracold atoms in 2d optical lattices. *Physical Review Letters* 92(15), 153005.

Dum R and Olshanii M (1996) Gauge structures in atom-laser interaction: Bloch oscillations in a dark lattice. *Physical Review Letters* 76(11): 1788.

Dutta O, Eckardt A, Hauke P, Malomed B, and Lewenstein M (2011) Bose–hubbard model with occupation-dependent parameters. *New Journal of Physics* 13: 023019.

Eckardt A and Anisimovas E (2015) High-frequency approximation for periodically driven quantum systems from a floquet-space perspective. *New Journal of Physics* 17: 093039.

Edmonds MJ, Valiente M, Juzeliunas G, Santos L, and Ohberg P (2013) Simulating an interacting gauge theory with ultracold Bose gases. *Physical Review Letters* 110: 085301.

Fläschner N, Rem B, Tarnowski M, Vogel D, Lühmann D-S, Sengstock K, and Weitenberg C (2016) Experimental reconstruction of the berry curvature in a floquet bloch band. *Science* 352(6289): 1091–1094.

Fletcher RJ, Shaffer A, Wilson CC, Patel PB, Yan Z, Crépel V, Mukherjee B, and Zwierlein MW (2021) Geometric squeezing into the lowest Landau level. *Science* 372(6548): 1318–1322.

Fukushima K, Kharzeev DE, and Warringa HJ (2008) Chiral magnetic effect. *Physical Review D: Particles and Fields* 78: 074033. https://doi.org/10.1103/PhysRevD.78.074033.

Gebert U, Irsigler B, and Hofstetter W (2020) Local chern marker of smoothly confined hofstadter fermions. *Physical Review A* 101: 063606. https://doi.org/10.1103/PhysRevA.101.063606.

Geier KT, Martone GI, Hauke P, and Stringari S (2021a) Exciting the goldstone modes of a supersolid spin-orbit-coupled bose gas. *Physical Review Letters* 127: 115301. https://doi.org/10.1103/PhysRevLett.127.115301.

Geier KT, Reichstetter J, and Hauke P (2021b) *Noninvasive Measurement of Currents in Analog Quantum Simulators*. arXiv:2106.12599 [quant-ph].

Gemelke N, Sarajlic E, and Chu S (2010) *Rotating Few-Body Atomic Systems in the Fractional Quantum Hall Regime*. arXiv preprint arXiv:1007.2677.

Girvin SM (1999) The quantum hall effect: Novel excitations and broken symmetries. In: Comtet A, Jolicœur T, Ouvry S, and David F (eds.) *Aspects Topologiques de la Physique en basse Dimension. Topological Aspects of Low Dimensional Systems*, pp. 53–175. Berlin, Heidelberg: Springer Berlin Heidelberg.

Goldman N and Dalibard J (2014) Periodically driven quantum systems: Effective hamiltonians and engineered gauge fields. *Physical Review X* 4(3), 031027.

Goldman N, Kubasiak A, Gaspard P, and Lewenstein M (2009) Ultracold atomic gases in non-abelian gauge potentials: The case of constant wilson loop. *Physical Review A* 79: 023624. https://doi.org/10.1103/PhysRevA.79.023624.

Goldman N, Satija I, Nikolic P, Bermudez A, Martin-Delgado MA, Lewenstein M, and Spielman IB (2010) Realistic time-reversal invariant topological insulators with neutral atoms. *Physical Review Letters* 105: 255302. https://doi.org/10.1103/PhysRevLett.105.255302.

Goldman N, Juzeliūnas G, Öhberg P, and Spielman IB (2014) Light-induced gauge fields for ultracold atoms. *Reports on Progress in Physics* 77(12), 126401.

González-Cuadra D, Bermudez A, Grzybowski PR, Lewenstein M, and Dauphin A (2019) Intertwined topological phases induced by emergent symmetry protection. *Nature Communications* 10: 2694. https://doi.org/10.1038/s41467-019-10796-8.

González-Cuadra D, Dauphin A, Grzybowski PR, Lewenstein M, and Bermudez A (2020) Dynamical solitons and boson fractionalization in cold-atom topological insulators. *Physical Review Letters* 125: 265301. https://doi.org/10.1103/PhysRevLett.125.265301.

Görg F, Sandholzer K, Minguzzi J, Desbuquois R, Messer M, and Esslinger T (2019) Realization of density-dependent peierls phases to engineer quantized gauge fields coupled to ultracold matter. *Nature Physics* 15(11): 1161–1167. https://doi.org/10.1038/s41567-019-0615-4.

Grass T, Juliá-Díaz B, and Lewenstein M (2012) Quasihole dynamics as a detection tool for quantum Hall phases. *Physical Review A* 86: 053629. https://doi.org/10.1103/PhysRevA.86.053629.

Grusdt F, Letscher F, Hafezi M, and Fleischhauer M (2014) Topological growing of laughlin states in synthetic gauge fields. *Physical Review Letters* 113: 155301. https://doi.org/10.1103/PhysRevLett.113.155301.

Grusdt F, Yao NY, Abanin D, Fleischhauer M, and Demler E (2016) Interferometric measurements of many-body topological invariants using mobile impurities. *Nature Communications* 7(1): 1–9.

Hafezi M, Mittal S, Fan J, Migdall A, and Taylor J (2013) Imaging topological edge states in silicon photonics. *Nature Photonics* 7(12): 1001–1005. http://www.nature.com/nphoton/journal/v7/n12/full/nphoton.2013.274.html.

Halimeh JC, Lang H, Mildenberger J, Jiang Z, and Hauke P (2021) Gauge-symmetry protection using single-body terms. *PRX Quantum* 2: 040311. https://doi.org/10.1103/PRXQuantum.2.040311.

Hasan MZ and Kane CL (2010) Colloquium: Topological insulators. *Reviews of Modern Physics* 82(4): 3045.

Hauke P, Tieleman O, Celi A, Ölschläger C, Simonet J, Struck J, Weinberg M, Windpassinger P, Sengstock K, Lewenstein M, and Eckardt A (2012) Non-abelian gauge fields and topological insulators in shaken optical lattices. *Physical Review Letters* 109: 145301. https://doi.org/10.1103/PhysRevLett.109.145301.

Hauke P, Lewenstein M, and Eckardt A (2014) Tomography of band insulators from quench dynamics. *Physical Review Letters* 113: 045303. https://doi.org/10.1103/PhysRevLett.113.045303.

Islam R, Ma R, Preiss PM, Eric Tai M, Lukin A, Rispoli M, and Greiner M (2015) Measuring entanglement entropy in a quantum many-body system. *Nature* 528(7580): 77–83.

Jaksch D and Zoller P (2003) Creation of effective magnetic fields in optical lattices: The hofstadter buttery for cold neutral atoms. *New Journal of Physics* 5(1): 56.

Jepsen PN, Amato-Grill J, Dimitrova I, Ho WW, Demler E, and Ketterle W (2020) Spin transport in a tunable Heisenberg model realized with ultracold atoms. *Nature (London)* 588(7838): 403–407.

Jiang H-C, Wang Z, and Balents L (2012) Identifying topological order by entanglement entropy. *Nature Physics* 8(12): 902–905.

Johnstone D, Westerberg N, Duncan CW, and Öhberg P (2019) Staggered ground states in an optical lattice. *Physical Review A* 100: 043614. https://doi.org/10.1103/PhysRevA.100.043614.

Jotzu G, Messer M, Desbuquois R, Lebrat M, Uehlinger T, Greif D, and Esslinger T (2014) Experimental realization of the topological haldane model with ultracold fermions. *Nature* 515(7526): 237–240.

Juzeliunas G and Öhberg P (2004) Slow light in degenerate fermi gases. *Physical Review Letters* 93: 033602. https://doi.org/10.1103/PhysRevLett.93.033602.

Kasper V, González-Cuadra D, Hegde A, Xia A, Dauphin A, Huber F, Tiemann E, Lewenstein M, Jendrzejewski F, and Hauke P (2021) Universal quantum computation and quantum error correction with ultracold atomic mixtures. *Quantum Science and Technology* 7(1), 015008. https://doi.org/10.1088/2058-9565/ac2d39.

Keßler S and Marquardt F (2014) Single-site-resolved measurement of the current statistics in optical lattices. *Physical Review A* 89: 061601. https://doi.org/10.1103/PhysRevA.89.061601.

Kharzeev DE (2014) The chiral magnetic effect and anomaly-induced transport. *Progress in Particle and Nuclear Physics* 75: 133–151. https://www.sciencedirect.com/science/article/pii/S0146641014000039.

Kitaev A and Preskill J (2006) Topological entanglement entropy. *Physical Review Letters* 96: 110404. https://doi.org/10.1103/PhysRevLett.96.110404.

Kitagawa T, Berg E, Rudner M, and Demler E (2010) Topological characterization of periodically driven quantum systems. *Physical Review B* 82: 235114. https://doi.org/10.1103/PhysRevB.82.235114.

Kitagawa T, Oka T, Brataas A, Fu L, and Demler E (2011) Transport properties of nonequilibrium systems under the application of light: Photoinduced quantum hall insulators without landau levels. *Physical Review B* 84: 235108. https://doi.org/10.1103/PhysRevB.84.235108.

Klco N, Dumitrescu EF, McCaskey AJ, Morris TD, Pooser RC, Sanz M, Solano E, Lougovski P, and Savage MJ (2018) Quantum-classical computation of schwinger model dynamics using quantum computers. *Physical Review A* 98: 032331. https://doi.org/10.1103/PhysRevA.98.032331.

Klco N, Savage MJ, and Stryker JR (2020) Su(2) non-abelian gauge field theory in one dimension on digital quantum computers. *Physical Review D: Particles and Fields* 101: 074512. https://doi.org/10.1103/PhysRevD.101.074512.

Kokail C, Maier C, van Bijnen R, Brydges T, Joshi MK, Jurcevic P, Muschik CA, Silvi P, Blatt R, Roos CF, and Zoller P (2019) Self-verifying variational quantum simulation of lattice models. *Nature* 569(7756): 355–360. https://doi.org/10.1038/s41586-019-1177-4.

Kolovsky AR (2011) Creating artificial magnetic fields for cold atoms by photon-assisted tunneling. *Europhysics Letters* 93: 20003.

Krinner S, Stadler D, Husmann D, Brantut J-P, and Esslinger T (2015) Observation of quantized conductance in neutral matter. *Nature (London)* 517(7532): 64–67.

Laflamme C, Yang D, and Zoller P (2017) Continuous measurement of an atomic current. *Physical Review A* 95: 043843.

LeBlanc LJ, Jiménez-García K, Williams RA, Beeler MC, Phillips WD, and Spielman IB (2015) Gauge matters: observing the vortex-nucleation transition in a bose condensate. *New Journal of Physics* 17(6), 065016. https://doi.org/10.1088/1367-2630/17/6/065016.

Levin M and Wen X-G (2006) Detecting topological order in a ground state wave function. *Physical Review Letters* 96(11), 110405.

Li H and Haldane FDM (2008) Entanglement spectrum as a generalization of entanglement entropy: Identification of topological order in non-abelian fractional quantum hall effect states. *Physical Review Letters* 101(1), 010504.

Li J-R, Lee J, Huang W, Burchesky S, Shteynas B, Top FC, Jamison AO, and Ketterle W (2017) A stripe phase with supersolid properties in spin–orbit-coupled bose–einstein condensates. *Nature (London)* 543: 91.

Lin Y-J, Compton RL, Jiménez-García K, Porto JV, and Spielman IB (2009) Synthetic magnetic fields for ultracold neutral atoms. *Nature* 462(7273): 628–632.

Lohse M, Schweizer C, Price HM, Zilberberg O, and Bloch I (2018) Exploring 4d quantum hall physics with a 2d topological charge pump. *Nature* 553(7686): 55–58.

Lundholm D and Rougerie N (2016) Emergence of fractional statistics for tracer particles in a laughlin liquid. *Physical Review Letters* 116(17), 170401.

Macaluso E, Comparin T, Umucalılar RO, Gerster M, Montangero S, Rizzi M, and Carusotto I (2020) Charge and statistics of lattice quasiholes from density measurements: A tree tensor network study. *Physical Review Research* 2(1), 013145.

Maik M, Hauke P, Dutta O, Zakrzewski J, and Lewenstein M (2013) Density dependent tunneling in the extended bose-hubbard model. *New Journal of Physics* 15: 113041. https://doi.org/10.1088/1367-2630/15/11/113041.

Mancini M, Pagano G, Cappellini G, Livi L, Rider M, Catani J, Sias C, Zoller P, Inguscio M, Dalmonte M, et al. (2015) Observation of chiral edge states with neutral fermions in synthetic hall ribbons. *Science* 349(6255): 1510–1513.

Manovitz T, Shapira Y, Akerman N, Stern A, and Ozeri R (2020) Quantum simulations with complex geometries and synthetic gauge fields in a trapped ion chain. *PRX Quantum* 1: 020303. https://doi.org/10.1103/PRXQuantum.1.020303.

Martinez EA, Muschik CA, Schindler P, Nigg D, Erhard A, Heyl M, Hauke P, Dalmonte M, Monz T, Zoller P, and Blatt R (2016) Real-time dynamics of lattice gauge theories with a few-qubit quantum computer. *Nature* 534(7608): 516–519. https://doi.org/10.1038/nature18318.

Meinert F, Mark MJ, Lauber K, Daley AJ, and Nägerl H-C (2016) Floquet engineering of correlated tunneling in the bose-hubbard model with ultracold atoms. *Physical Review Letters* 116: 205301. https://doi.org/10.1103/PhysRevLett.116.205301.

Mil A, Zache TV, Hegde A, Xia A, Bhatt RP, Oberthaler MK, Hauke P, Berges J, and Jendrzejewski F (2020) A scalable realization of local u(1) gauge invariance in cold atomic mixtures. *Science* 367(6482): 1128–1130. https://science.sciencemag.org/content/367/6482/1128.

Mildenberger J, Mruczkiewicz W, Halimeh JC, Jiang Z, and Hauke P (2022) Probing Confinement in a z_2 Lattice Gauge Theory on a Quantum Computer. https://arxiv.org/abs/2203.08905.

Miyake H, Siviloglou GA, Kennedy CJ, Burton WC, and Ketterle W (2013) Realizing the harper hamiltonian with laser-assisted tunneling in optical lattices. *Physical Review Letters* 111(18), 185302.

Mueller EJ (2004) Artificial electromagnetism for neutral atoms: Escher staircase and Laughlin liquids. *Physical Review A* 70: 041603. https://doi.org/10.1103/PhysRevA.70.041603.

Mukherjee B, Shaffer A, Patel PB, Yan Z, Wilson CC, Crépel V, Fletcher RJ, and Zwierlein M (2022) Crystallization of bosonic quantum Hall states in a rotating quantum gas. *Nature* 601(7891): 58–62.

Nakamura J, Liang S, Gardner GC, and Manfra MJ (2020) Direct observation of anyonic braiding statistics. *Nature Physics* 16(9): 931–936.

Nardin A and Carusotto I (2022) *Linear and Nonlinear Edge Dynamics of Trapped Fractional Quantum Hall Droplets Beyond the Chiral Luttinger Liquid Paradigm*. arXiv preprint arXiv:2203.02539.

Nayak C, Simon SH, Stern A, Freedman M, and Das Sarma S (2008) Non-abelian anyons and topological quantum computation. *Reviews of Modern Physics* 80: 1083–1159. https://doi.org/10.1103/RevModPhys.80.1083.

Nguyen NH, Tran MC, Zhu Y, Green AM, Alderete CH, Davoudi Z, and Linke NM (2021) Digital Quantum Simulation of the Schwinger Model and Symmetry Protection With Trapped Ions. URL https://arxiv.org/abs/2112.14262.

Nichols MA, Cheuk LW, Okan M, Hartke TR, Mendez E, Senthil T, Khatami E, Zhang H, and Zwierlein MW (2019) Spin transport in a Mott insulator of ultracold fermions. *Science* URL https://science.sciencemag.org/content/early/2018/12/05/science.aat4387.

Nigg D, Mueller M, Martinez EA, Schindler P, Hennrich M, Monz T, Martin-Delgado MA, and Blatt R (2014) Quantum computations on a topologically encoded qubit. *Science* 345: 302–305.

Oka T and Aoki H (2009) Photovoltaic hall effect in graphene. *Physical Review B* 79: 081406. https://doi.org/10.1103/PhysRevB.79.081406.

Osterloh K, Baig M, Santos L, Zoller P, and Lewenstein M (2005) Cold atoms in non-Abelian gauge potentials: From the Hofstadter "Moth" to lattice gauge theory. *Physical Review Letters* 95: 010403. https://doi.org/10.1103/PhysRevLett.95.010403.

Ott R, Zache T, Mueller N, and Berges J (2020) Non-cancellation of the parity anomaly in the strong-field regime of qed2+1. *Physics Letters B* 805: 135459. https://www.sciencedirect.com/science/article/pii/S037026932030263X.

Ozawa T and Price HM (2019) Topological quantum matter in synthetic dimensions. *Nature Reviews Physics* 1(5): 349–357.

Ozawa T, Price HM, Amo A, Goldman N, Hafezi M, Lu L, Rechtsman MC, Schuster D, Simon J, Zilberberg O, et al. (2019) Topological photonics. *Reviews of Modern Physics* 91(1), 015006.

Paredes B, Fedichev P, Cirac J, and Zoller P (2001) 1 2-anyons in small atomic bose-einstein condensates. *Physical Review Letters* 87(1), 010402.

Pitaevskiĭ L and Stringari S (2016) *Bose-Einstein Condensation and Superfluidity. International series of monographs on physics.* Oxford University Press. https://books.google.it/books?id=k_ZGCwAAQBAJ.

Price HM, Zilberberg O, Ozawa T, Carusotto I, and Goldman N (2015) Four-dimensional quantum hall effect with ultracold atoms. *Physical Review Letters* 115(19), 195303.

Popp M, Paredes B, and Cirac JI (2004) Adiabatic path to fractional quantum Hall states of a few bosonic atoms. *Physical Review A* 70: 053612. https://doi.org/10.1103/PhysRevA.70.053612.

Price H, Chong Y, Khanikaev A, Schomerus H, Maczewsky LJ, Kremer M, Heinrich M, Szameit A, Zilberberg O, Yang Y, et al. (2022) Roadmap on topological photonics. *Journal of Physics: Photonics* 4: 032501.

Putra A, Salces-Cárcoba F, Yue Y, Sugawa S, and Spielman IB (2020) Spatial coherence of spin-orbit-coupled bose gases. *Physical Review Letters* 124: 053605. https://doi.org/10.1103/PhysRevLett.124.053605.

Rahmani A, Sung KJ, Putterman H, Roushan P, Ghaemi P, and Jiang Z (2020) Creating and manipulating a laughlin-type $\nu = 1/3$ fractional quantum hall state on a quantum computer with linear depth circuits. *PRX Quantum* 1: 020309. https://doi.org/10.1103/PRXQuantum.1.020309.

Raventos D, Grass T, Juliá-Díaz B, Santos L, and Lewenstein M (2016) Topological phases of lattice bosons with a dynamical gauge field. *Physical Review A* 93: 033605. https://doi.org/10.1103/PhysRevA.93.033605.

Rechtsman MC, Zeuner JM, Plotnik Y, Lumer Y, Podolsky D, Dreisow F, Nolte S, Segev M, and Szameit A (2013) Photonic floquet topological insulators. *Nature* 496(7444): 196–200. http://www.nature.com/nature/journal/v496/n7444/full/nature12066.html.

Rentrop T, Trautmann A, Olivares FA, Jendrzejewski F, Komnik A, and Oberthaler MK (2016) Observation of the phononic lamb shift with a synthetic vacuum. *Physical Review X* 6: 041041. https://doi.org/10.1103/PhysRevX.6.041041.

Repellin C and Goldman N (2019) Detecting fractional chern insulators through circular dichroism. *Physical Review Letters* 122(16), 166801.

Repellin C, Leonard J, and Goldman N (2020) Fractional chern insulators of few bosons in a box: Hall plateaus from center-of-mass drifts and density profiles. *Physical Review A* 102(6), 063316.

Riechert H, Halimeh JC, Kasper V, Bretheau L, Zohar E, Hauke P, and Jendrzejewski F (2021) Engineering a u(1) Lattice Gauge Theory in Classical Electric Circuits. URL https://arxiv.org/abs/2108.01086.

Roushan P, Neill C, Megrant A, Chen Y, Babbush R, Barends R, Campbell B, Chen Z, Chiaro B, Dunsworth A, et al. (2017) Chiral ground-state currents of interacting photons in a synthetic magnetic field. *Nature Physics* 13(2): 146. URL https://www.nature.com/articles/nphys3930.

Ruseckas J, Juzeliunas G, Öhberg P, and Fleischhauer M (2005) Non-Abelian gauge potentials for ultracold atoms with degenerate dark states. *Physical Review Letters* 95: 010404. https://doi.org/10.1103/PhysRevLett.95.010404.

Saminadayar L, Glattli D, Jin Y, Etienne B, and c.-m. (1997) Observation of the e/3 fractionally charged laughlin quasiparticle. *Physical Review Letters* 79(13): 2526.

Satzinger KJ, Liu Y-J, Smith A, Knapp C, Newman M, Jones C, Chen Z, Quintana C, Mi X, Dunsworth A, Gidney C, Aleiner I, Arute F, Arya K, Atalaya J, Babbush R, Bardin JC, Barends R, Basso J, Bengtsson A, Bilmes A, Broughton M, Buckley BB, Buell DA, Burkett B, Bushnell N, Chiaro B, Collins R, Courtney W, Demura S, Derk AR, Eppens D, Erickson C, Faoro L, Farhi E, Fowler AG, Foxen B, Giustina M, Greene A, Gross JA, Harrigan MP, Harrington SD, Hilton J, Hong S, Huang T, Huggins WJ, Ioffe LB, Isakov SV, Jeffrey E, Jiang Z, Kafri D, Kechedzhi K, Khattar T, Kim S, Klimov PV, Korotkov AN, Kostritsa F, Landhuis D, Laptev P, Locharla A, Lucero E, Martin O, McClean JR, McEwen M, Miao KC, Mohseni M, Montazeri S, Mruczkiewicz W, Mutus J, Naaman O, Neeley M, Neill C, Niu MY, O'Brien TE, Opremcak A, Pató B, Petukhov A, Rubin NC, Sank D, Shvarts V, Strain D, Szalay M, Villalonga B, White TC, Yao Z, Yeh P, Yoo J, Zalcman A, Neven H, Boixo S, Megrant A, Chen Y, Kelly J, Smelyanskiy V, Kitaev A, Knap M, Pollmann F, and Roushan P (2021) Realizing topologically ordered states on a quantum processor. *Science* 374(6572): 1237–1241. https://doi.org/10.1126/science.abi8378.

Scherg S, Kohlert T, Herbrych J, Stolpp J, Bordia P, Schneider U, Heidrich-Meisner F, Bloch I, and Aidelsburger M (2018) Nonequilibrium mass transport in the 1D Fermi–Hubbard model. *Physical Review Letters* 121: 130402.

Schine N, Ryou A, Gromov A, Sommer A, and Simon J (2016) Synthetic landau levels for photons. *Nature* 534(7609): 671–675.

Schweikhard V, Coddington I, Engels P, Mogendorff VP, and Cornell EA (2004) Rapidly rotating bose-einstein condensates in and near the lowest landau level. *Physical Review Letters* 92(4), 040404.

Schweizer C, Grusdt F, Berngruber M, Barbiero L, Demler E, Goldman N, Bloch I, and Aidelsburger M (2019) Floquet approach to Z_2 lattice gauge theories with ultracold atoms in optical lattices. *Nature Physics* 15(11): 1168–1173. https://doi.org/10.1038/s41567-019-0649-7.

Semeghini G, Levine H, Keesling A, Ebadi S, Wang TT, Bluvstein D, Verresen R, Pichler H, Kalinowski M, Samajdar R, Omran A, Sachdev S, Vishwanath A, Greiner M, Vuletić V, and Lukin MD (2021) Probing topological spin liquids on a programmable quantum simulator. *Science* 374(6572): 1242–1247. https://doi.org/10.1126/science.abi8794.

Son DT and Zhitnitsky AR (2004) Quantum anomalies in dense matter. *Physical Review D: Particles and Fields* 70: 074018. https://doi.org/10.1103/PhysRevD.70.074018.

Sorensen A, Demler E, and Lukin MD (2005) Fractional quantum hall states of atoms in optical lattices. *Physical Review Letters* 94: 086803. https://doi.org/10.1103/PhysRevLett.94.086803.

Stannigel K, Hauke P, Marcos D, Hafezi M, Diehl S, Dalmonte M, and Zoller P (2014) Constrained dynamics via the zeno effect in quantum simulation: Implementing non-abelian lattice gauge theories with cold atoms. *Physical Review Letters* 112: 120406. https://doi.org/10.1103/PhysRevLett.112.120406.

Stern A (2008) Anyons and the quantum hall effect—A pedagogical review. *Annals of Physics* 323(1): 204–249.

Struck J, Ölschläger C, Weinberg M, Hauke P, Simonet J, Eckardt A, Lewenstein M, Sengstock K, and Windpassinger P (2012) Tunable gauge potential for neutral and spinless particles in driven optical lattices. *Physical Review Letters* 108: 225304. https://doi.org/10.1103/PhysRevLett.108.225304.

Stuhl B, Lu H-I, Aycock L, Genkina D, and Spielman I (2015) Visualizing edge states with an atomic bose gas in the quantum hall regime. *Science* 349(6255): 1514–1518.

Surace FM, Mazza PP, Giudici G, Lerose A, Gambassi A, and Dalmonte M (2020) Lattice gauge theories and string dynamics in rydberg atom quantum simulators. *Physical Review X* 10: 021041. https://doi.org/10.1103/PhysRevX.10.021041.

Suthar K, Kraus R, Sable H, Angom D, Morigi G, and Zakrzewski J (2020) Staggered superfluid phases of dipolar bosons in two-dimensional square lattices. *Physical Review B* 102: 214503. https://doi.org/10.1103/PhysRevB.102.214503.

Tai ME, Lukin A, Rispoli M, Schittko R, Menke T, Borgnia D, Preiss PM, Grusdt F, Kaufman AM, and Greiner M (2017) Microscopy of the interacting harper–hofstadter model in the two-body limit. *Nature* 546(7659): 519–523.

Tarnowski M, Unal FN, Flaeschner N, Rem BS, Eckardt A, Sengstock K, and Weitenberg C (2019) Measuring topology by dynamics: Chern number from linking number. *Nature Communications* 10: 1728.

Thouless DJ, Kohmoto M, Nightingale MP, and den Nijs M (1982) Quantized hall conductance in a two-dimensional periodic potential. *Physical Review Letters* 49(6): 405.

Tong D (2016) *Lectures on the Quantum Hall Effect*. ArXiv e-prints.

Wang Z, Ge Z-Y, Xiang Z, Song X, Huang R-Z, Song P, Guo X-Y, Su L, Xu K, Zheng D, and Fan H (2022) Observation of emergent Z_2 gauge invariance in a superconducting circuit. *Physical Review Research* 4: L022060.

Wen X-G (1995) Topological orders and edge excitations in fractional quantum hall states. *Advances in Physics* 44(5): 405–473.

Wen X-G (2013) Topological order: From long-range entangled quantum matter to a unified origin of light and electrons. *ISRN Condensed Matter Physics*, 198710.

Yakaboylu E, Ghazaryan A, Lundholm D, Rougerie N, Lemeshko M, and Seiringer R (2020) Quantum impurity model for anyons. *Physical Review B* 102(14), 144109.

Yang B, Sun H, Ott R, Wang H-Y, Zache TV, Halimeh JC, Yuan Z-S, Hauke P, and Pan J-W (2020) Observation of gauge invariance in a 71-site bose–hubbard quantum simulator. *Nature* 587(7834): 392–396. https://doi.org/10.1038/s41586-020-2910-8.

Yoshioka D (2002) *The Quantum Hall Effect. Physics and Astronomy Online Library.* Springer.https://books.google.it/books?id=hFpOcAgCviQC.

Zache TV, Hebenstreit F, Jendrzejewski F, Oberthaler MK, Berges J, and Hauke P (2018) Quantum simulation of lattice gauge theories using wilson fermions. *Quantum Science and Technology* 3(3), 034010. https://doi.org/10.1088/2058-9565/aac33b.

Zhang Y, Sreejith GJ, Gemelke ND, and Jain JK (2014) Fractional angular momentum in cold-atom systems. *Physical Review Letters* 113: 160404. https://doi.org/10.1103/PhysRevLett.113.160404.

Zhang D-W, Zhu Y-Q, Zhao YX, Yan H, and Zhu S-L (2018) Topological quantum matter with cold atoms. *Advances in Physics* 67(4): 253–402. https://doi.org/10.1080/00018732.2019.1594094.

Zhou Z-Y, Su G-X, Halimeh JC, Ott R, Sun H, Hauke P, Yang B, Yuan Z-S, Berges J, and Pan J-W (2021) Thermalization dynamics of a gauge theory on a quantum simulator. *Science* 377: 311–314.

Zhu S-L, Fu H, Wu C-J, Zhang S-C, and Duan L-M (2006) Spin hall effects for cold atoms in a light-induced gauge potential. *Physical Review Letters* 97: 240401. https://doi.org/10.1103/PhysRevLett.97.240401.

Zohar E (2022) Quantum simulation of lattice gauge theories in more than one space dimension—Requirements, challenges and methods. *Philosophical Transactions of the Royal Society of London. Series A* 380(2216): 20210069.

Zohar E, Cirac JI, and Reznik B (2013) Quantum simulations of gauge theories with ultracold atoms: Local gauge invariance from angular-momentum conservation. *Physical Review A* 88: 023617. https://doi.org/10.1103/PhysRevA.88.023617.

Quantum Hall phases of cold Bose gases

Nicolas Rougerie[a] **and Jakob Yngvason**[b,c], [a]Ecole Normale Supérieure de Lyon & CNRS, UMPA (UMR 5669), Lyon, France; [b]Fakultät für Physik, Universität Wien, Vienna, Austria; [c]Erwin Schrödinger Institute for Mathematics and Physics, Vienna, Austria

© 2024 Elsevier Ltd. All rights reserved.

Introduction 641
The basic Hamiltonian 641
Confinement to the lowest Landau level 642
The 1-particle case 642
Complex notation and Bargmann space 642
The *N*-particle case, contact interaction 643
The yrast curve 644
Spectral gaps 644
The uncorrelated (Gross-Piaevskii) regime 645
Passage to the Laughlin state 646
Adding an anharmonic potential 646
Fully correlated states 647
The N-particle density as a Gibbs measure 648
Plasma analogy and mean field limit 648
Formulas for the mean field density 649
Conclusion 650
Acknowledgments 650
References 650

Abstract

Cold atomic gases of interacting bosons subject to rapid rotation and confined in anharmonic traps can theoretically exhibit analogues of the fractional quantum Hall effect for electrons in strong magnetic fields. In this setting the Coriolis force due to the rotation mimics the Lorentz force on charged particles but artificial gauge fields can also be obtained by coupling the internal structure of the atoms to light fields. The chapter discusses mathematical aspects of transitions to different strongly correlated phases that appear when the parameters of a model Hamiltonian are varied.

Key objectives

- Define a model Hamiltonian for trapped, interacting bosons in rapid rotation.
- Describe the confinement to the lowest Landau level for the kinetic part of the Hamiltonian.
- Discuss the yrast curve and the transition from an uncorrelated ground state in the lowest Landau level to fractional quantum Hall states.
- Discuss transitions from a Laughlin state to other strongly correlated states including giant vortex states in anharmonic traps.
- Derive density profiles of the strongly correlated states by means of Laughlin's plasma analogy and rigorous mean field theory.

Notations and acronyms

$\boldsymbol{\Omega}_{\mathbf{rot}}$:	rotational frequency
$\boldsymbol{\omega} = \boldsymbol{\Omega}_{\mathbf{trap}} - \boldsymbol{\Omega}_{\mathbf{rot}}$:	frequency difference
$\boldsymbol{\Omega}_{\mathbf{trap}}$:	frequency of a harmonic trap
$e^{\parallel}$:	spectral gap of the transverse confinement
$\mathcal{L} = \mathbf{e}_3 \cdot \mathbf{L}$:	transverse component of angular momentum
$V^{\parallel}$:	transverse confining potential
L:	angular momentum
LLL	lowest Landau level

https://doi.org/10.1016/B978-0-323-90800-9.00154-2

Introduction

Since the early 1990's it has been possible to isolate ultra-cold atomic gases of bosons in magneto-optical traps and maintain them in metastable states that can be modeled as ground states of many-body Hamiltonians with repulsive short range interactions. At sufficiently low temperatures the gas forms a Bose-Einstein condensate (BEC) (Ketterle and van Druten, 1996; Cornish et al., 2000) with all the atoms in the same state that can for dilute gases be described by an effective single particle equation of Gross-Pitaevskii type (Pethick and Smith, 2008; Pitaevskii and Stringari, 2016).

The atoms usually have no electric charge, but an artificial magnetic field can be imposed on them by a steady rotation of the trap. The analogy between the Lorentz and Coriolis forces implies that the Hamiltonian for neutral atoms in a rotating trap is formally identical to that of charged particles in a uniform magnetic field, apart from the centrifugal potential associated with the rotation. The analogy shows up, in particular, in the emergence of quantized vortices in cold rotating Bose gases (Bretin et al., 2004; Aftalion, 2006; Cooper, 2008; Fetter, 2009; Correggi et al., 2011), similar to those appearing in type II superconductors submitted to external magnetic fields.

An even more striking possibility is to employ rapid rotation to create phases with the characteristics of the fractional quantum Hall effect (FQHE) for electrons in very large magnetic fields (Prange and Girvin, 1987; Chakraborty and Pietiläinen, 1988, 1995; Störmer et al., 1999; Jain, 2007). In this regime, the Bose gas is no longer a condensate and mean-field theories fail to capture this phenomenon. A truly many-body description is required and strongly correlated states, such as the celebrated Laughlin state (Laughlin, 1983), may theoretically occur. This requires, however that the Coriolis force is very strong which inevitably means that the centrifugal force is also strong and may outweigh the trapping force. This can lead to an instability of the system unless special countermeasures are taken (Bretin et al., 2004; Schweikhard et al., 2004; Viefers, 2008; Fetter, 2009). In fact, the competing demands of a large rotation speed on the one hand, necessary for entering the FQHE regime, and of a sufficiently stable system on the other hand, have so far left the FQHE regime in rotating gases unattainable with current technology. Alternative methods to create artificial gauge fields have therefore been proposed and even partly realized in experiments (Dalibard et al., 2011; Roncaglia et al., 2011; Clark et al., 2020; Hauke and Carusotto, 2022).

From a theoretical point of view, however, the use of an anharmonic trapping potential to beat the destabilizing effect of the Coriolis force in a rotating trap remains a conceptually simple road to strongly correlated phases of Bosons with short range interactions. In this chapter, which is partly based on the lecture notes (Yngvason, 2014), we shall discuss how different phases may be produced by varying the parameters in this set-up. The same conclusions will apply to other experimental realizations of the Hamiltonian whenever they can be achieved.

The basic Hamiltonian

We consider first the following many-body Hamiltonian for N bosons of unit mass with position vectors $\mathbf{x}_{(1)}, \ldots \mathbf{x}_{(N)}$ in a rotating frame of reference:

$$H_N = \sum_{i=1}^{N} \left(-\frac{1}{2}\nabla_{(i)}^2 + V\left(\mathbf{x}_{(i)}\right) - \mathbf{L}_{(i)} \cdot \boldsymbol{\Omega} \right) + \sum_{1 \le i < j \le N} v\left(\left| \mathbf{x}_{(i)} - \mathbf{x}_{(j)} \right| \right). \tag{1}$$

Here $\boldsymbol{\Omega} = \Omega_{\text{rot}} \mathbf{e}_3$ is the angular velocity, with $\mathbf{e}_3$ the unit vector in the 3-direction and with $\Omega_{\text{rot}} \ge 0$, $\mathbf{L} = -\mathrm{i}\mathbf{x} \times \nabla$ the angular momentum operator,

$$V(\mathbf{x}) = \frac{1}{2} \Omega_{\text{trap}}^2 r^2 + V^{\|}(x_3) \tag{2}$$

with $\mathbf{x} = (x_1, x_2, x_3)$, $r^2 = (x_1)^2 + (x_2)^2$, a quadratic trapping potential in the 12-plane, $V^{\|}$a confining positive potential in the 3-direction, and v the pair interaction potential, assumed to be ≥ 0. Units have been chosen so that Planck constant $\hbar$ as well as the particle mass is 1.

It is convenient to define the gauge field as

$$\mathbf{A}(\mathbf{x}) = \Omega_{\text{trap}}(x_2, -x_1, 0) \tag{3}$$

and write the Hamiltonan (1) as

$$H_N = \sum_{j=1}^{N} \left\{ \frac{1}{2} \left(\mathrm{i}\nabla_{(j)} + \mathbf{A}\left(\mathbf{x}_{(j)}\right) \right)^2 + \omega\, \mathbf{e}_3 \cdot \mathbf{L}_{(j)} + V^{\|}(x_3) \right\} + \sum_{i<j} v\left(\left| \mathbf{x}_{(i)} - \mathbf{x}_{(j)} \right| \right) \tag{4}$$

with[1]

$$\omega = \Omega_{\text{trap}} - \Omega_{\text{rot}}. \tag{5}$$

We are interested in the case that $\omega > 0$ is small and Ω_{rot} (hence also Ω_{trap}) is large.

---

[1] Alternatively, one can define $\mathbf{A}(\mathbf{x}) = \Omega_{\text{rot}}(-x_2, x_1, 0)$ in which case $\omega \mathbf{e}_3 \cdot \mathbf{L}$ is replaced by $\frac{1}{2}\left(\Omega_{\text{trap}}^2 - \Omega_{\text{rot}}^2\right) r^2$.

Confinement to the lowest Landau level

The 1-particle case

The single-particle Hamiltonian

$$H_1 = \frac{1}{2}(\mathrm{i}\nabla_\perp + \mathbf{A}(\mathbf{x}))^2 + \omega\mathcal{L} - \frac{1}{2}\partial_3^2 + V^{\|}(x_3) \tag{6}$$

with the notation $\mathcal{L} = \mathbf{e}_3 \cdot \mathbf{L}$ and $\nabla_\perp = (\partial_1, \partial_2)$, is a sum of three commuting operators,

$$\frac{1}{2}(\mathrm{i}\nabla_\perp + \mathbf{A}(\mathbf{x}))^2 \tag{7}$$

$$\omega\mathcal{L} \tag{8}$$

$$-\frac{1}{2}\partial_3^2 + V^{\|}(x_3). \tag{9}$$

The first operator, $\frac{1}{2}(\mathrm{i}\nabla_\perp + \mathbf{A}(\mathbf{x}))^2$, has the form of a magnetic Hamiltonian with the *Landau spectrum*

$$\left(n + \frac{1}{2}\right)2\Omega_{\mathrm{trap}}, \quad n = 0,1,2, \ldots, . \tag{10}$$

The spectrum of $\omega\mathcal{L}$ is

$$\ell\omega, \quad \ell = 0, \pm 1, \pm 2 \ldots \tag{11}$$

and $-\frac{1}{2}\partial_3^2 + V^{\|}(x_3)$ has a spectral gap, $e^{\|} > 0$, above its ground state.

The energy of (6) is minimized in states with $n = 0$, i.e., in the lowest Landau level (LLL) of the magnetic Hamiltonian. Moreover, in the lowest energy state the motion in the x_3-direction is 'frozen' in the ground state of $h^{\|}$. Confinement to the LLL in the N-particle context, taking the repulsive interaction into account, is discussed in Subsection 'The N-particle case, contact interaction' below.

From now on we focus on the 2-dimensional motion in the 12-plane and choose units so that $\Omega_{\mathrm{trap}} = 1$.

Complex notation and Bargmann space

It is convenient to adopt complex notation for the position variables. Replacing (x_1, x_2) by the complex coordinate $z = x_1 + \mathrm{i}x_2$ and denoting $\partial = \frac{1}{2}(\partial_1 - \mathrm{i}\partial_2)$, $\bar{\partial} = \frac{1}{2}(\partial_1 + \mathrm{i}\partial_2)$ we can write

$$\frac{1}{2}(\mathrm{i}\nabla_\perp + \mathbf{A}(\mathbf{x}))^2 = 2\left(\hat{a}^\dagger\hat{a} + \frac{1}{2}\right) \tag{12}$$

with

$$\hat{a}^\dagger := \frac{1}{2}(-2\partial + \bar{z}), \quad \hat{a} := \frac{1}{2}(2\bar{\partial} + z). \tag{13}$$

These operators satisfy the canonical commutation relations

$$\left[\hat{a}, \hat{a}^\dagger\right] = 1. \tag{14}$$

The operators

$$\hat{b}^\dagger := \frac{1}{2}(-2\bar{\partial} + z), \quad \hat{b} := \frac{1}{2}(2\partial + \bar{z}) \tag{15}$$

also satisfy the canonical commutation relations and commute with $\hat{a}$ and $\hat{a}^\dagger$. They correspond to a replacement $\mathbf{A} \to -\mathbf{A}$:

$$\frac{1}{2}(\mathrm{i}\nabla_\perp - \mathbf{A}(\mathbf{x}))^2 = 2\left(\hat{b}^\dagger\hat{b} + \frac{1}{2}\right). \tag{16}$$

Moreover,

$$\hat{b}^\dagger\hat{b} - \hat{a}^\dagger\hat{a} = z\partial - \bar{z}\bar{\partial} = \mathcal{L}. \tag{17}$$

Hence the eigenvalues of $\hat{a}^\dagger\hat{a}$ are infinitely degenerate and the degenerate eigenstates can be labeled by eigenvalues of either $\hat{b}^\dagger\hat{b}$ or $\mathcal{L}$.

The lowest eigenvalue of $\hat{a}^\dagger\hat{a}$ is zero so the eigenfunctions $\psi(z, \bar{z})$ in the LLL are solutions of the equation $\hat{a}\psi = 0$, i.e.,

$$\bar{\partial}\psi(z, \bar{z}) = -\frac{1}{2}z\psi(z, \bar{z}). \tag{18}$$

This means that

$$\psi(z, \bar{z}) = \varphi(z)\exp\left(-|z|^2/2\right) \tag{19}$$

with $\bar{\partial}\varphi(z) = 0$, i.e., φ is an analytic (holomorphic) function of z.

The LLL can thus be regarded as the Bargmann space B (Bargmann, 1961; Girvin and Jach, 1984) of analytic functions φ such that

$$\langle\varphi,\varphi\rangle := \int |\varphi(z)|^2 \exp\left(-|z|^2\right)\mathrm{d}^2 z < \infty \tag{20}$$

where $\mathrm{d}^2 z$ denotes the Lebesgue measure on $\mathbb{C}$ (regarded as $\mathbb{R}^2$).

The Bargmann space is a Hilbert space with scalar product

$$\langle\varphi\psi\rangle := \int \bar{\varphi}(z)\psi(z)\exp\left(-|z|^2\right)\mathrm{d}^2 z. \tag{21}$$

On $\mathcal{B}$ the angular momentum operator is $\mathcal{L} = z\partial$. Moreover, for $\varphi \in \mathcal{B}$,

$$\langle\varphi,\mathcal{L}\varphi\rangle = \int \left(|z|^2 - 1\right)|\varphi(z)|^2 \exp\left(-|z|^2\right)\mathrm{d}^2 z. \tag{22}$$

The eigenvalues of $\mathcal{L}$ restricted to $\mathcal{B}$ are $\ell = 0, 1, 2, \ldots$ with corresponding normalized eigenfunctions

$$\varphi_\ell(z) = (\pi\ell!)^{-1/2} z^\ell. \tag{23}$$

By (22) the probability density $|\varphi_\ell(z)|^2 e^{-|z|^2}$ is localized around $|z| = \sqrt{\ell + 1}$.

The N*-particle case, contact interaction*

For N bosons in the LLL the relevant Hilbert space is

$$\mathcal{B}_N = \mathcal{B}^{\otimes^N_{\mathrm{symm}}}, \tag{24}$$

i.e., it consists of symmetric, analytic functions ψ of $z_1, \ldots, z_N$ such that

$$\int_{\mathbb{C}^N} |\psi(z_1, \ldots z_N)|^2 \exp\left(-\sum_{j=1}^N |z_j|^2\right)\mathrm{d}^2 z_1 \cdots \mathrm{d}^2 z_N < \infty. \tag{25}$$

As next we take the interaction $\sum_{1\le i<j\le N} \upsilon(|\mathbf{x}_i - \mathbf{x}_j|)$ into account.

For short range, nonnegative interaction potentials υ it was proved in (Lewin and Seiringer, 2009) that under suitable conditions on N, υ and ω:

- The ground state of (6) is effectively confined to the LLL in the 12-variables and in the 3-direction to the ground state of (9).
- The interaction potential υ can be replaced by a contact interaction (pseudopotential) in the 12-variables of the form $g\delta(z_i - z_j)$ with a coupling constant

$$g = a \cdot \sqrt{e^{\|}} \int |\chi|^4 \tag{26}$$

where a is the s-wave scattering length of the potential υ and χ the ground state wave function of (9).

Precise statements are contained in Theorems 1 and 2 in Lewin and Seiringer (2009). For the emergence of the pseudopotential see also (Seiringer and Yngvason, 2020), Theorem 2. Since wave functions in the Bargmann space $\mathcal{B}_N$ are analytic, the 2-body contact potential $\delta(z_i - z_j)$ is well defined and, in fact, given by a bounded operator: Defining δ_{12} on $\mathcal{B}_2$ by

$$\delta_{12}\varphi(z_1, z_2) = \frac{1}{2\pi}\varphi\left(\frac{1}{2}(z_1 + z_2), \frac{1}{2}(z_1 + z_2)\right), \tag{27}$$

a simple computation, using the analyticity of φ, shows that

$$\langle\varphi, \delta_{12}\varphi\rangle = \int_{\mathbb{C}} |\varphi(z,z)|^2 \exp\left(-2|z|^2\right)\mathrm{d}^2 z. \tag{28}$$

Thus the formal $\delta(z_i - z_j)$ can be replaced by the projection operator δ_{ij}. The effective Hamiltonian on the LLL can be written as.

$$H_N^{\mathrm{LLL}} = \omega\mathcal{L}_N + g\mathcal{I}_N \tag{29}$$

with

$$\mathcal{L}_N = \sum_{i=1}^N z_i \partial_i \quad \mathcal{I}_N = \sum_{i<j} \delta_{ij}. \tag{30}$$

We denote its ground state energy by $E_N^{\mathrm{LLL}}(\omega, g)$.

Writing $v(\mathbf{x}) = v_a(\mathbf{x}) = a^{-2} v_1(\mathbf{x}/a)$ and keeping v_1 fixed while varying a, we denote by $E_N(\omega, a)$ the ground state energy of (1) with $N\times$ the lowest energy of (7) and (9) subtracted. Then Theorem 1 in Lewin and Seiringer (2009) states that

$$\lim \frac{E_N(\omega, a)}{E_N^{\mathrm{LLL}}(\omega, g)} = 1 \tag{31}$$

in a limit where

$$(Ng\omega)^{1/2} \ll \min\left\{\Omega_{\mathrm{trap}}, e^{\|}\right\}. \tag{32}$$

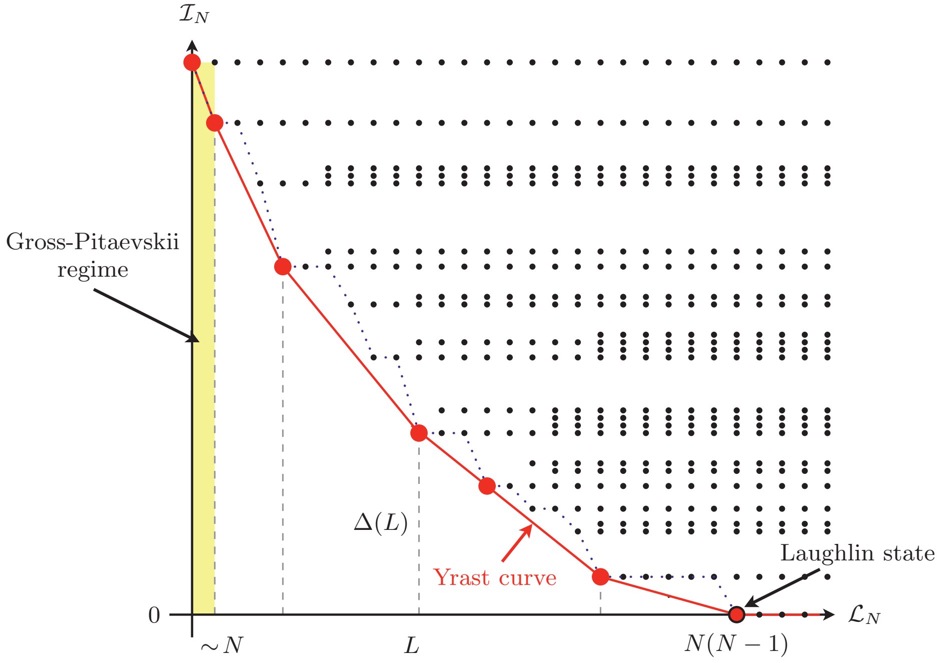

Fig. 1 The joint spectrum of $\mathcal{L}_N$ and $\mathcal{I}_N$. Adapted from Lewin M, Seiringer R (2009) Strongly correlated phases in rapidly rotating Bose gases. *Journal of Statistical Physics* 137: 1040–1062.

Moreover, in the same limit also the ground state converges to its projection onto the LLL (Theorem 2 in Lewin and Seiringer (2009)).

The yrast curve

An important property of the Hamiltonian (29) is that the operators $\mathcal{L}_N$ and $\mathcal{I}_N$ commute. The lower boundary of (the convex hull of) their joint spectrum in a plot with angular momentum as the horizontal axis is called the yrast curve. See Fig. 1 and Viefers (2008) for its qualitative features.

As a function of the eigenvalues L of $\mathcal{L}_N$ the yrast curve $I(L)$ is decreasing from $I(0) = (4\pi)^{-1}N(N-1)$ to $I(N(N-1)) = 0$. The monotonicity follows from the observation that if a simultaneous eigenfunction of $\mathcal{L}_N$ and $\mathcal{I}_N$ is multiplied by the center of mass, $(z_1 + \cdots + z_N)/N$, the interaction is unchanged while the angular momentum increases by one unit.

For a given ratio ω/g the ground state of (29) (in general not unique) is determined by the point(s) on the yrast curve where a supporting line of the curve has slope $-\omega/g$. The ground state energy is

$$E(N, \omega, g) = \min_L (\omega L + gI(L)). \tag{33}$$

The filling factor of a state with angular momentum L is defined as

$$\nu = \frac{N(N-1)}{2L} = \frac{N}{N_v} \tag{34}$$

where $N_v = 2L/(N-1)$ is called the number of vortices see Cooper (2008), Sec. 2.4. The filling factor of the ground state depends on the ratio ω/g and varies from ∞ to 0 as the ratio decreases and the angular momentum increases. Note the difference to the fermionic case, where the maximal filling factor in a fixed Landau level is 1.

Spectral gaps

For every value of the angular momentum L the interaction operator $\mathcal{I}_N$ has a nonzero spectral gap above 0

$$\Delta_N(L) = \inf\{spec\, \mathcal{I}_N \vdash_{\mathcal{L}_N=L} \setminus \{0\}\} > 0. \tag{35}$$

This follows simply from the fact that states with a given eigenvalue L correspond to the finite dimensional space of symmetric homogeneous polynomials of degree L and contains states with strictly positive interaction energy. (Take for example, (const.) $\sum_j z_j^L$.) The gap, and hence the Yrast curve $I(L)$, are monotonously decreasing with L for the reason already mentioned: The angular momentum of an eigenstate of $\mathcal{I}_N$ can be increased by one unit by multiplying the wave function with the center of mass coordinate

$(z_1 + \cdots + z_N)/N$. This does not change the interaction energy and leads to a family of ‘daughter states’ for each state on the yrast curve. There is numerical (see e.g., Viefers et al., 2000; Regnault et al., 2006) and some theoretical evidence that

$$\Delta_N(L) \geq \Delta_N(N(N-1)-N) = \min_{L' \leq N(N-1)} \Delta_N(L') =: \Delta > 0 \tag{36}$$

for all L with Δ independent of N but this is still not proved. (Proofs in a simplified setting can be found in Nachtergaele et al. (2020); Warzel and Young (2021a,b)) We shall call the validity of (36) *the spectral gap conjecture*.

The uncorrelated (Gross-Piaevskii) regime

A rough estimate for the radius R of the system, assuming that the kinetic and interaction energy of (29) are of the same order of magnitude, gives

$$R \sim (Ng/\omega)^{1/4} \quad \text{and} \quad L \sim N\Omega R^2 \sim N(Ng/\omega)^{1/2}. \tag{37}$$

Thus, if $\omega/g \gg N^{-1}$ then $L \ll N^2$ and $\nu \gg 1$. In this case the ground state can be shown to be well described by an uncorrelated product state $(\varphi^{\text{GP}})^{\otimes N}$ where $N^{1/2}\varphi^{\text{GP}}$ minimizes the Gross-Piitaevskii energy functional on Bargmann space (Aftalion et al., 2006; Aftalion and Blanc, 2008)

$$\mathcal{E}^{\text{GP}}[\varphi] = \omega\langle\varphi, \mathcal{L}\varphi\rangle + \frac{g}{2}\int_{\mathbb{C}} |\varphi(z)|^4 \exp\left(-2|z|^2\right) d^2z \tag{38}$$

under the condition $\int |\varphi|^2 \exp(-|z|^2) d^2z = N$ with energy

$$E_N^{\text{GP}}(\omega, g) = NE_1^{\text{GP}}(\omega, Ng). \tag{39}$$

More precisely, the following holds (Lieb et al., 2009):

Theorem 1 (GP limit theorem in LLL). *For every $c > 0$ there is a $C < \infty$ such that*

$$E_N^{\text{GP}}(\omega, g) \geq E_N(\omega, g) \geq E_N^{\text{GP}}(\omega, g)\left(1 - C(g/N\omega)^{1/10}\right) \tag{40}$$

$$\textit{provided } gN/\omega > c.$$

The lower bound covers the whole regime $L \ll N^2$, i.e., $\nu \gg 1$, but the GP description might have a wider range of applicability, see Fetter (2009) Section V C.

The proof of (1) uses similar techniques as in Lieb and Seiringer (2006) for the 3D GP limit theorem at fixed Ω and $N\,a$, in particular coherent states.

The analysis of the GP problem defined above is of interest in its own right (Aftalion and Blanc, 2008; Aftalion et al., 2006; Gérard et al., 2019). It is expected (see Aftalion, 2006; Viefers, 2008; Cooper, 2008; Fetter, 2009 and references therein) that for $\omega \to 0$ a vortex lattice is nucleated in the condensate. Namely, the zeroes of the analytic part of the GP minimizer in Bargmann space arrange on a triangular lattice in the bulk of the condensate, with a deformation at the edge (Aftalion et al., 2005; Ho, 2001; Aftalion and Blanc, 2008; Aftalion et al., 2006). Taking this fact into consideration in a local density approximation, one expects that

$$E_1^{\text{GP}}(\omega Ng) \sim E^{\text{TF}}(\omega Ng) \text{ in the limit } \omega \to 0 \text{ with } \omega \ll Ng \ll \omega^{-1} \tag{41}$$

where

$$E^{\text{TF}}(\omega, Ng) = \min\left\{\int_{\mathbb{R}^2} \left((\omega|x|^2 - 1)\rho(x) + \frac{Ng}{2}e^{\text{Ab}}\rho(x)^2\right)dx \mid \rho \geq 0, \int \rho = 1\right\} \tag{42}$$

with

$$e^{\text{Ab}} \approx 1.16 \tag{43}$$

the Abriskosov constant (Abrikosov, 1957; Aftalion et al., 2006), i.e., the energy per area of a homogeneous vortex lattice. One also expects for the corresponding density of the GP minimizer

$$|u^{\text{GP}}|^2 \simeq \rho^{\text{TF}} = \frac{1}{Nge^{\text{Ab}}}\left(\lambda - \omega|x|^2\right)_+ \tag{44}$$

in the same regime, where λ is a chemical potential ensuring normalization. The above expectations were rigorously proven in Nguyen and Rougerie (2022) (under the restricted assumption that $Ng \ll \omega^{-3/5}$).

These results suggest a formula distribution of quantized vortices in the condensate. Indeed,[2] writing the GP minimizer in the lowest Landau level in the manner

$$u^{\text{GP}}(z) = c\prod_{j=1}^{m}\left(z - a_j\right)e^{-\frac{|z|^2}{2}} \tag{45}$$

---

[2] Putting the following discussion on the same level of mathematical rigor as (44) remains a challenging open problem.

one finds (Aftalion et al., 2005; Ho, 2001)

$$\sum_{j=1}^{m} \delta_{a_j} = \frac{1}{4\pi}\left(4 + \Delta \log |u^{\mathrm{GP}}|^2\right) \tag{46}$$

for the empirical distribution of the zeroes of u^{GP}, i.e., the locations of quantized vortices. Inserting the approximation (44) one finds

$$\sum_{j=1}^{m} \delta_{a_j} \simeq \frac{1}{\pi} + \frac{1}{4\pi}\Delta \log\left(\left(\lambda - \omega |x|^2\right)_+\right). \tag{47}$$

The first term, corresponding to a uniform density of vortices, dominates the asymptotics. The second one is a inhomogeneous correction, manifest mostly at the edge of the atomic cloud, see Aftalion et al. (2005), Aftalion and Blanc (2008), Aftalion et al. (2006) for more details.

The breakdown of the GP approximation is indicated by the number of vortices nucleated in the gas exceeding the total particle number. The above considerations indicate that this takes place when $g \gtrsim N\omega$, which marks the transition to a series of correlated many-body states, ending with a bosonic Laughlin function, as we discuss next.

Passage to the Laughlin state

As the filling factor decreases the ground state becomes increasingly correlated. The exact ground states are largely unknown (except for $L \leq N$ Papenbrock and Bertsch, 2001), but candidates of states with various rational filling factors (*composite fermion states, Moore-Read states, Read-Rezayi states*, ...) for energy upper bounds have been suggested and studied as discussed in the review article Cooper (2008).

If $\omega/g < \Delta/N^2$ one reaches the *Laughlin state* with filling factor $\frac{1}{2}$ whose wave function in Bargmann space is

$$\psi_{\mathrm{Laughlin}}(z_1, \ldots, z_N) = c \prod_{i<j} (z_i - z_j)^2. \tag{48}$$

It has interaction energy 0 and angular momentum $L = N(N-1)$. For an intuitive picture of the Laughlin state the following analogy may be helpful: The density $|\Psi_{\mathrm{Laugh}}(z_1, \ldots z_N)|^2$ assigns probabilities to the possible configurations of N points moving in the plane. The points like to keep a distance at least of order 1 from each other because the factors $|z_i - z_j|^4$ strongly reduce the probability when the particles are close. On the other hand the damping due to the gaussian favors a tight packing of the 'balls' of size $O(1)$ around the individual particles. The motion is strongly correlated in the sense that if one ball moves, all the other have also to move in order to satisfy these constraints.

Adding an anharmonic potential

The limit $\omega \to 0$, keeping $\omega > 0$, is experimentally very delicate. For stability, but also to study new effects, we consider now a modification of the Hamiltonian (29) by adding a small anharmonic term:

$$H_N^{\mathrm{LLL}} \to H_{k,N}^{\mathrm{LLL}} := H_N^{\mathrm{LLL}} + k \sum_{i=1}^{N} |z_i|^4 \tag{49}$$

with a new parameter $k > 0$. The potential $|z|^4$ can be expressed through $\mathcal{L}$ and $\mathcal{L}^2$ on Bargmann space, because with $\mathcal{L} = z\partial$ we have by partial integration, using the analyticity of φ:

$$\langle \varphi, \mathcal{L}\varphi \rangle = \int |\varphi(z)|^2 \left(|z|^2 - 1\right) \exp\left(-|z|^2\right) \mathrm{d}^2 z \tag{50}$$

and

$$\left\langle \varphi, \mathcal{L}^2 \varphi \right\rangle = \int \left(|z|^4 - 3|z|^2 + 1\right) |\varphi(z)|^2 \exp\left(-|z|^2\right) \mathrm{d}^2 z. \tag{51}$$

Thus the modified Hamiltonian, denoted again by H_N^{2D}, can be written (up to an unimportant additive constant)

$$H_{k,N}^{\mathrm{LLL}} = (\omega + 3k)\mathcal{L}_N + k \sum_{i=1}^{N} \mathcal{L}_{(i)}^2 + g\mathcal{I}_N \tag{52}$$

Fully correlated states

The Bargmann space $\mathcal{B}^N$ with the scalar product (25) is naturally isomorphic to the Hilbert space $\mathcal{H}^N_{\rm LLL} \subset L^2(\mathbb{C}^{\otimes_s N}, \mathrm{d}^{2N}z)$ consisting of wave functions of the form

$$\Psi(z_1, \ldots, z_N) = \psi(z_1, \ldots, z_N) \exp\left(-\sum_j |z_j|^2/2\right), \quad \psi \in \mathcal{B}_N \tag{53}$$

with the standard L^2 scalar product. The energy can accordingly be considered as a functional on this space,

$$\mathcal{E}[\Psi] = \int V_{\omega,k}(z)\rho^{(1)}_\Psi(z) + \langle \Psi, \mathcal{I}_N \Psi\rangle, \tag{54}$$

where $\rho^{(1)}_\Psi$ is the one-particle density of $\Psi \in \mathcal{H}^N_{\rm LLL}$ with the normalization $\int \rho_\Psi^{(1)}(z)\mathrm{d}^2z = N$ and the potential is

$$V_{\omega,k}(z) = \omega|z|^2 + k|z|^4. \tag{55}$$

Note that now $\omega < 0$ is allowed, provided $k > 0$.

We shall call states with vanishing interaction energy, i.e., $\Psi \in \ker \mathcal{I}_N$ fully correlated, because the particles stay away from each other in the sense that the wave function vanishes if $z_i = z_j$ for some pair $i \neq j$, in sharp contrast to a fully *un*correlated Hartree state. The fully correlated states in $\mathcal{H}^N_{\rm LLL}$ are of the form

$$\Psi(z_1, \ldots z_N) = \phi(z_1, \ldots, z_N)\Psi_{\rm Laugh}(z_1, \ldots z_N) \tag{56}$$

with ϕ symmetric and analytic, and the Laughlin state

$$\Psi_{\rm Laugh}(z_1, \ldots z_N) = c\prod_{i<j}(z_i - z_j)^2 e^{-\sum_{j=1}^{N}|z_j|^2/2}. \tag{57}$$

For the Hamiltonian *without* the anharmonic addition to the potential the Laughlin state is an *exact* fully correlated ground state with energy 0 and angular momentum $L_{\rm Laugh} = N(N-1)$. This is not true for $k \neq 0$ because $\sum_{i=1}^N \mathcal{L}^2_{(i)}$ does not commute with $\mathcal{I}_N$. Note, however, that $\mathcal{L}_N$ still commutes with the Hamiltonian.

We now address the following question: Under what conditions is it possible to tune the parameters ω, g and k so that a ground state Ψ_0 of (52) becomes fully correlated for $N \to \infty$? The following theorem, proved in Rougerie et al. (2013) (see also Rougerie et al., 2014), gives sufficient conditions for this to happen. In order to state it as simply as possible we shall assume the 'spectral gap conjecture' of Subsection 'Spectral gaps.' This conjecture is not really needed, however, because is possible to replace the assumed universal gap Δ by other gaps depending on N, ω and k, cf. Eq. (IV.5) in Rougerie et al. (2013).

Theorem 2 (Criteria for full correlation). *With $P_{(Ker\,\mathcal{I}_N)^\perp}$ the projector onto the orthogonal complement of* Ker $\mathcal{I}_N$ *we have*

$$\left\| P_{(Ker\,\mathcal{I}_N)^\perp}\Psi_0 \right\| \to 0 \tag{58}$$

in the limit $N \to \infty$, ω, $k \to 0$ if one of the following conditions holds:

- $\omega \geq 0$ and $\omega N^2 + kN^3 \ll g\Delta$.
- $0 \geq \omega \geq -2kN$ and $N(\omega^2/k) + \omega N^2 + kN^3 \ll g\Delta$.
- $\omega \leq -2kN$, $|\omega|/k \lesssim N^2$ and $kN^3 \ll g\Delta$
- $\omega \leq -2kN$, $|\omega|/k \gg N^2$ and $|\omega|N \ll g\Delta$

Note: For $k = 0$ the first item is just the sufficient condition for the passage to the Laughlin state, $\omega/g < \Delta/N^2$, while the other conditions are void because $\omega < 0$ is only allowed if $k > 0$.

A proof of the Theorem is given in Section V of Rougerie et al. (2013). It is based on two estimates:

- A lower bound for the ground state energy at fixed angular momentum L:

$$E_0(L) \geq (\omega + 3k)L + k\frac{L^2}{N}. \tag{59}$$

- An upper bound for the energy of suitable trial functions.

The first bound (59) is quite simple; it follows essentially from the inequality

$$\sum_i \mathcal{L}_{(i)}^2 \geq \frac{1}{N}\left(\sum_i \mathcal{L}_{(i)}\right)^2 \tag{60}$$

that holds because $\mathcal{L}_{(\mathrm{i})}$ and $\mathcal{L}_{(\mathrm{j})}$ commute for any i, j.

The upper bound is achieved by means of trial states of the form 'giant vortex times Laughlin,' namely, with $m \geq 0$ and $c_{m,\,N}$ a normalization constant,

$$\Psi_{\mathrm{gv}}^{(m)}(z_1,\,\ldots,z_N) = c_{m,N}\prod_{j=1}^{N} z_j^m \prod_{i<j}(z_i - z_j)^2 e^{-\sum_{j=1}^{N}|z_j|^2/2} \tag{61}$$

These are special 'quasi hole' states (Laughlin, 1983) but for $m \gtrsim N$, i.e., $mN \gtrsim N^2$, the label 'giant vortex' appears more appropriate.[3]

The energy of a trial state of the form (61) can be estimated using properties of the angular momentum operators and the radial symmetry in each variable of the gaussian measure with the pre-factor $\prod_{j=1}^{N}|z_j|^{2m}$. The computation is presented in Eqs. (V3)–(V7) in Rougerie et al. (2013). Optimizing the estimate over m leads to

$$m_{\mathrm{opt}} = \begin{cases} 0 & \text{if}\,\omega \geq -2kN \\ \dfrac{|\omega|}{2k} - N & \text{if}\,\omega < -2kN. \end{cases} \tag{62}$$

This is consistent with the picture that the Laughlin state is an approximate ground state in the first two cases of Theorem 1, in particular for negative ω as long as $|\omega|/k \lesssim N$. The angular momentum remains $O(N^2)$ in these cases.

When $\omega < 0$ and $|\omega|/(kN)$ becomes large the angular momentum is approximately

$$L_{\mathrm{qh}} := N|\omega|/k \gg N^2, \tag{63}$$

much larger than for the Laughlin state. A further transition at $|\omega|/k \sim N^2$ is manifest through the change of the subleading contribution to the energy of the trial functions. Its order of magnitude changes from $O(kN^3)$ to $O(|\omega|N)$ at the transition.

To gain further insights into the physics of the transition we consider the particle density of the trial wave functions. This analysis (Rougerie et al., 2014) is based on Laughlin's 'plasma analogy' where the N-particle density is written as a Gibbs distribution of a 2D Coulomb gas Laughlin (1983). This distribution can be studied in a rigorous mean field limit which brings out the essential features of the single particle density for large N.

The N-particle density as a Gibbs measure

We denote $(z_1,\ldots,z_N)$ by Z for short and consider the scaled N particle density (normalized to 1)

$$\rho_{N,m}(Z) := N^N|\Psi_{\mathrm{gv}}^{(m)}\left(\sqrt{N}Z\right)|^2. \tag{64}$$

We can write

$$\begin{aligned}\rho_{N,m}(Z) &= \mathcal{Z}_{N,m}^{-1}\exp\left(\sum_{j=1}^{N}\left(-N|z_j|^2 + 2m\log|z_j|\right) + 4\sum_{i<j}\log|z_i - z_j|\right)\\ &= \mathcal{Z}_{N,m}^{-1}\exp\left(-\frac{1}{T}\mathscr{H}_{N,m}(Z)\right),\end{aligned}$$

with $T = N^{-1}$ and

$$\mathscr{H}_{N,m}(Z) = \sum_{j=1}^{N}\left(|z_j|^2 - \frac{2m}{N}\log|z_j|\right) - \frac{4}{N}\sum_{i<j}\log|z_i - z_j| \tag{65}$$

Plasma analogy and mean field limit

The Hamilton function $\mathcal{H}_{N,m}(Z)$ is that of a classical 2D Coulomb gas ('plasma,' one-component 'jellium') in a uniform background of opposite charge and with a point charge $(2m/N)$ at the origin, corresponding respectively to the $|z_i|^2$ and the $-\frac{2m}{N}\log|z_j|$ terms.

The probability measure $\rho_{N,\,m}(Z)$ minimizes the free energy functional

---

[3] Note that mathematically and physically these states are quite different from the *uncorrelated* giant vortex states in the GP theory of rotating Bose gases discussed in Correggi et al. (2011).

$$\mathcal{F}(\rho) = \int_{\mathbb{R}^{2N}} \mathscr{H}_{N,m}(Z)\rho(Z) + T\int_{\mathbb{R}^{2N}} \rho(Z)\log\rho(Z) \tag{66}$$

for this Hamiltonian at $T = N^{-1}$.

The $N \to \infty$ limit is in this interpretation a mean field limit where at the same time $T \to 0$. It is thus not unreasonable to expect that for large N, and in an appropriate sense,

$$\rho_{N,m} \approx \rho^{\otimes N} \tag{67}$$

with a one-particle density ρ minimizing a mean field free energy functional.

The mean field free energy functional is defined as

$$\mathcal{E}^{\mathrm{MF}}_{N,m}[\rho] := \int_{\mathbb{R}^2} W_m\rho - 2\int_{\mathbb{R}^2}\int_{\mathbb{R}^2} \rho(z)\log|z-z'|\rho(z') + N^{-1}\int_{\mathbb{R}^2}\rho\log\rho \tag{68}$$

with

$$W_m(z) = |z|^2 - 2\frac{m}{N}\log|z|. \tag{69}$$

It has a minimizer $\rho^{\mathrm{MF}}_{N,m}$ among probability measures on $\mathbb{R}^2$ and this minimizer is in Rougerie et al. (2014) proved to be a good approximation for the scaled 1-particle density of the trial wave function, i.e., for

$$\rho^{(1)}_{N,m}(z) := \int_{\mathbb{R}^{2(N-1)}} \rho_{N,m}(z, z_2, \ldots, z_N)\mathrm{d}^2z_2\ldots\mathrm{d}^2z_N.$$

(Recall the scaling: This density in the scaled variables z is normalized so that its integral is 1. The corresponding density in the physical, unscaled variables $\zeta = \sqrt{N}z$ has total mass N.)

Formulas for the mean field density

The picture of the 1-particle density that arises from asymptotic formulas for the mean-field density, valid for large N, is as follows:

If $m \le N^2$, then ρ^{MF}_m is well approximated by a density $\hat{\rho}^{\mathrm{MF}}_m$ that minimizes the mean field functional without the entropy term $N^{-1}\int_{\mathbb{R}^2}\rho\log\rho$. This density takes a constant value $(2\pi)^{-1}$ on an annulus with inner and outer radii (in the scaled variables!)

$$R_- = (m/N)^{1/2}, \quad R_+ = (2 + m/N)^{1/2}$$

and is zero otherwise. The constant value is a manifestation of the incompressibility of the density of the trial state.[4]

For $m \gtrsim N^2$ the entropy term becomes important and may dominate the electrostatic interaction term $\iint\rho(z)\log|z-z'|\rho(z')$. The density is well approximated by a gaussian profile $\rho^{\mathrm{th}}(z) \sim |z|^{2m}\exp(-N|z|^2)$ that is centered around $(m/N)^{-1/2}$ but has maximal value $\sim N/m^{1/2} \ll 1$ for $m \gg N^2$.

Thus, as the parameters ω and k tend to zero and N is large, the qualitative properties of the optimal trial wave functions exhibit different phases:

- For positive ω, more generally for $\omega/k > -2N$, the Laughlin state is the ground state.
- When ω is negative and $|\omega|$ exceeds $2kN$ the state changes from a pure Laughlin state to a modified Laughlin state with a 'hole' in the density around the center.
- A further transition occurs at $|\omega| \sim kN^2$. The density profile changes from being 'flat' to an annulus with a Gaussian shape in the radial variable.

The qualitative features of these three phases are indicated in Fig. 2. An intuitive understanding of the transitions may be obtained by employing the previous picture of the points z_i as being the centers of essentially non overlapping balls of size $O(1)$. From the point of view of the plasma analogy the particles stay away from each other because of the repulsive Coulomb potential between them, while the attractive external potential due to the uniformly charged background keeps them as close together as possible. Modifying the wave function by a factor $\prod_j z_j^m$ has the effect of a repulsive charge of magnitude m at the origin that pushes the particles (collectively!) away from the origin, creating a 'hole.' The effect of such a hole on the energy of the wave function in the trap potential is to increase the energy if ω is positive. Hence the ground state will not have a hole. If $\omega < 0$ the effective trapping potential has a Mexican hat shape with a minimum away from the origin, but since no ball can move without 'pushing' all the other balls, it is too costly for the system to take advantage of this as long as k stays above the critical value $|\omega|/2N$. For smaller k a hole is formed. The balls remain densely packed until the minimum of the Mexican hat potential moves so far from the origin that an annulus of width $O(1)$ at the radius of the minimum can accommodate all N balls. This happens for $k \lesssim |\omega|/N^2$. For smaller k (larger radius) the balls need not be tightly packed in the annulus and the average local density decreases accordingly.

---

[4] Note that these is a statement about the mean field density that is a good approximation, suitably averaged, to the true 1– particle density for large N. See Ciftja (2006) for numerical calculations of the true density of the Laughlin state for $N = 400$.

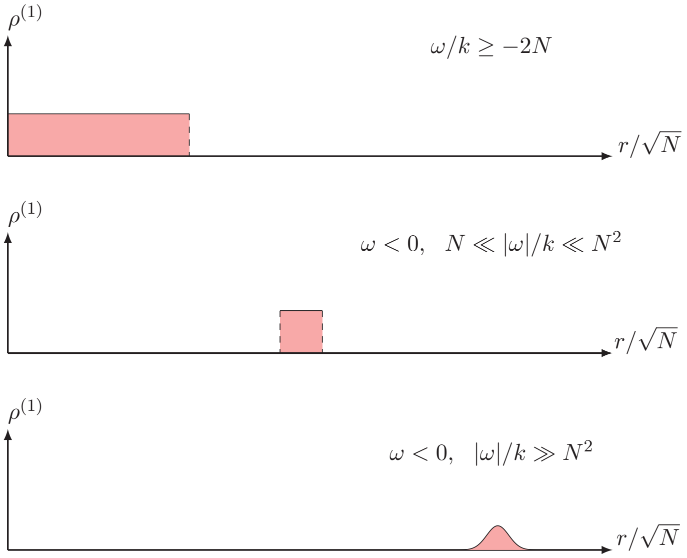

Fig. 2 The three phases of the density $\rho_{N,\,m}^{(1)}$ (not to scale).

Conclusion

The main conclusion from the analysis presented above of the ground states in the lowest Landau level generated by rapid rotation can be summarized as follows:

- For the Hamiltonan (29) the parameter regime $g \ll N\omega$, i.e., $L \ll N^2$, can be described by Gross-Piaevskii theory in the LLL.
- To enter the 'fully correlated' regime with $L \geq N(N-1)$ we have studied the Hamiltonian (52) with a quadratic plus quartic trap where the rotational frequency can exceed the frequency of the quadratic part of the trap, i.e., the frequency difference ω can be negative.
- Through the analysis of trial states for energy upper bounds, and simple lower bounds, we have obtained criteria for the ground state to be fully correlated in an asymptotic limit. The lower bounds, although not sharp, are of the same order of magnitude as the upper bounds.
- The particle density of the trial wave functions can be analyzed using Laughlin's plasma analogy combined with rigorous mean field limits. The character of the ground state density changes at $|\omega\,|\,/k = O(N)$ and again at $|\omega\,|\,/k = O(N^2)$.

Acknowledgments

Funding from the European Research Council (ERC) under the European Union's Horizon 2020 Research and Innovation Programme (Grant agreement CORFRONMAT No 758620) is gratefully acknowledged.

References

Abrikosov AA (1957) The magnetic properties of superconducting alloys. *Journal of Physics and Chemistry of Solids* 2: 199–208.

Aftalion A (2006) *Vortices in Bose-Einstein Condensates, Progress in Nonlinear Differential Equations and their Applications 67*. Basel: Birkhäuser.

Aftalion A and Blanc X (2008) Reduced energy functionals for a three dimensional fast rotating Bose- Einstein condensate. *Annales de l'Institut Henri Poincaré C, Analyse Non Linéaire* 25: 339–355.

Aftalion A, Blanc X, and Dalibard J (2005) Vortex patterns in a fast rotating Bose-Einstein condensate. *Physical Review A* 71: 023611.

Aftalion A, Blanc X, and Nier F (2006) Lowest landau level functionals and Bargmann Spaces for Bose- Einstein condensates. *Journal of Functional Analysis* 241: 661–702.

Bargmann V (1961) On a Hilbert space of analytic functions and an associated integral transform. *Communications on Pure and Applied Mathematics* 14: 187–214.

Bretin V, Stock S, Seurin Y, and Dalibard J (2004) Fast rotation of a Bose-Einstein condensate. *Physical Review Letters* 92: 050403.

Chakraborty T and Pietiläinen P (1988) *The Fractional Quantum Hall Effect*. New York: Springer.

Chakraborty T and Pietiläinen P (1995) *The Quantum Hall Effects*, 2nd ed. New York: Springer.

Ciftja O (2006) Monte Carlo study of Bose Laughlin wave function for filling factors 1/2, 1/4 and 1/6. *Europhysics Letters* 74: 486–492.

Clark LW, Schine N, Baum C, Jia N, and Simon J (2020) Observation of Laughlin states made of light. *Nature* 582: 41–45.

Cooper NR (2008) Rapidly rotating atomic gases. *Advances in Physics* 57: 539–616.

Cornish SL, Claussen NR, Roberts JL, Cornell EA, and Wieman CE (2000) Stable ^{85}Rb Bose-Einstein condensates with widely tunable interactions. *Physical Review Letters* 85: 1795–1798.

Correggi M, Pinsker F, Rougerie N, and Yngvason J (2011) Rotating superfluids in anharmonic traps: From vortex lattices to giant vortices. *Physical Review A* 84: 053614.

Dalibard J, Gerbier F, Juzeliūnas G, and Öhberg P (2011) Artificial gauge potentials for neutral atoms. *Reviews of Modern Physics* 83: 1523.
Fetter AL (2009) Rotating trapped Bose-Einstein condensates. *Reviews of Modern Physics* 81: 647–691.
Gérard P, Germain P, and Thomann L (2019) On the cubic lowest Landau level equation. *Archive for Rational Mechanics and Analysis* 231: 1073–1128.
Girvin S and Jach T (1984) Formalism for the quantum Hall effect: Hilbert space of analytic functions. *Physical Review B* 29: 5617–5625.
Hauke P and Carusotto I (2022) Quantum hall and synthetic magnetic-field effects in ultra-cold atomic systems. In: *Encyclopedia of Condensed Matter Physics*, 2nd ed. Elsevier.
Ho TL (2001) Bose-Einstein condensates with large number of vortices. *Physical Review Letters* 87: 060403.
Jain JK (2007) *Composite Fermions*. Cambridge University Press.
Ketterle W and van Druten NJ (1996) Evaporative cooling of trapped atoms. *Advances in Atomic, Molecular and Optical Physics*. vol. 37, pp. 181–236. Academic Press.
Laughlin RB (1983) Anomalous quantum Hall effect: An incompressible quantum fluid with fractionally charged excitations. *Physical Review Letters* 50: 1395–1398.
Lewin M and Seiringer R (2009) Strongly correlated phases in rapidly rotating Bose gases. *Journal of Statistical Physics* 137: 1040–1062.
Lieb EH and Seiringer R (2006) Derivation of the Gross-Pitaevskii equation for rotating Bose gases. *Communications in Mathematical Physics* 264: 505–537.
Lieb EH, Seiringer R, and Yngvason J (2009) The yrast line of a rapidly rotating Bose gas: The Gross- Pitaevskii regime. *Physical Review A* 79: 063626.
Nachtergaele B, Warzel S, and Young A (2020) Low-complexity eigenstates of a $\nu = 1/3$ fractional quantum Hall system. *Journal of Physics A: Mathematical and Theoretical* 1: p. 01LT01.
Nguyen D-T and Rougerie N (2022) Thomas-Fermi profile of a fast rotating Bose-Einstein condensate. Pure and applied analysis, to appear. *ArXiv* . 2201.04418.
Papenbrock T and Bertsch GF (2001) Rotational spectra of weakly interacting Bose-Einstein condensates. *Physical Review A* 63: 023616.
Pethick C and Smith H (2008) *Bose-Einstein Condensation of Dilute Gases*, 2nd edition Cambridge University Press.
Pitaevskii L and Stringari S (2016) *Bose-Einstein Condensation*, 2nd ed. Oxford: Oxford Science Publications.
Prange RE and Girvin SE (eds.) (1987) *The Quantum Hall Effect*. Springer.
Regnault N, Chang CC, Jolicoeur T, and Jain JK (2006) Composite fermion theory of rapidly rotating two-dimensional bosons, 2006. *Journal of Physics B: Atomic, Molecular and Optical Physics* 39: S89–S99.
Roncaglia M, Rizzi M, and Dalibard J (2011) From rotating atomic rings to Quantum Hall States. *Scientific Reports* 1: 43.
Rougerie N, Serfaty S, and Yngvason J (2013) Quantum Hall phases and plasma analogy in rotating trapped Bose gases. *Physical Review A* 87: 023618.
Rougerie N, Serfaty S, and Yngvason J (2014) Quantum hall phases and plasma analogy in rotating trapped Bose gases. *Journal of Statistical Physics* 154: .
Schweikhard V, Coddington I, Engels P, Mogendorff VP, and Cornell EA (2004) Rapidly rotating Bose-Einstein condensates in and near the lowest landau level. *Physical Review Letters* 92: 040404.
Seiringer R and Yngvason J (2020) Emergence of Haldane Pseudo-potentials in systems with short range interactions. *Journal of Statistical Physics* 281: 448–464.
Störmer HL, Tsui DC, and Gossard AC (1999) The fractional quantum Hall effect. *Reviews of Modern Physics* 71: S298–S305.
Viefers S (2008) Quantum Hall physics in rotating Bose-Einstein condensates. *Journal of Physics C* 12: 123202.
Viefers S, Hansson TH, and Reimann SM (2000) Bose condensates at high angular momenta. *Physical Review A* 62: 053604.
Warzel S and Young A (2021a) The spectral gap of a fractional quantum Hall system on a thin torus. *ArXiv* . 2112.13764.
Warzel S and Young A (2021b) A bulk spectral gap in the presence of edge states for a truncated pseudopotential. *ArXiv* 2108: 10794.
Yngvason J (2014) Topics in the mathematical physics of cold bose gases. *ArXiv* 1402.0706.

Valley Currents in Graphene

Satoshi Moriyama[a] **and Yoshifumi Morita**[b], [a]Department of Electrical and Electronic Engineering, School of Engineering, Tokyo Denki University, Tokyo, Japan; [b]Faculty of Engineering, Gunma University, Kiryu, Japan

© 2024 Elsevier Ltd. All rights reserved.

Introduction 652
Overview 652
Key issues 655
Conclusion 656
Acknowledgments 657
References 657

Abstract

In several solid-state systems, (charge) neutral currents originating from different "valleys" of an energy band can flow in different spatial directions and lead to long-ranged "valley currents." Graphene (Gr), a monolayer of carbon atoms with broken time-reversal symmetry (T) and/or inversion symmetry (P), is a promising stage for this phenomenon, where (2 + 1)-dimensional Dirac fermion with an internal degree of freedom ("flavor") plays a crucial role in the low-energy limit. Based on experiments, such a neutral current can be realized and detected by all-electrical nonlocal measurements in hexagonal-boron-nitride (hBN)/Gr superlattices, which are investigated herein.

Key points

- Valley currents are novel charge-neutral currents in solid states.
- Graphene superlattice is an ideal stage for manipulating and detecting valley currents.
- Dirac fermions emerge in graphene in the low-energy limit as quasiparticles.
- The transport properties of graphene and its variants are described by Dirac fermion models.
- Nonlocal transport is an effective probe of charge-neutral currents.

Introduction

A valley is a quantum-mechanical degree of freedom built into electrons for several solid-state systems. A valley in an energy band is a degenerate local minimum (maximum) in the conduction (valence) band, referred to as *K* and *K*′ in the case of graphene (Gr), corresponding to valley pseudospin states (Xiao et al., 2007).

Graphene, a monolayer of carbon atoms, is the "parent" of the novel promising class of quantum metamaterials, e.g., the emergence of "topological" current associated with a valley degree of freedom (Xiao et al., 2007; Xiao et al., 2010). Graphene is distinguished from its family members/two dimensional (2D) materials by its "relativistic" energy dispersion, rendering its quasiparticle identical to "(2 + 1)-dimensional Dirac fermion." It has two valley pseudospin states ("flavors"), which transform into each other under spatial inversion. The broken inversion symmetry (P) induces valley-contrasted physics through the emergence of a "hot spot" for each valley where Berry curvatures accumulate (Xiao et al., 2007; Xiao et al., 2010). Nonlocal transport could be a Berry-phase-sensitive probe for detecting such a hot spot in hexagonal boron nitride (hBN)/Gr superlattices (Gorbachev et al., 2014; Komatsu et al., 2018; Lensky et al., 2015). Quantum valley current was also detected through nonlocal resistance in the quantum limit (Komatsu et al., 2018). This is based on the quantum Hall effect (QHE) but without magnetic-field/time-reversal symmetry (T) breaking (Haldane, 1988; Laughlin, 1981; Thouless et al., 1982).

The emergence of such "hot spot" and "valley current" in graphene needs a broken T and/or P. This can be achieved by applying a magnetic field and/or fabricating a heterostructure, such as hBN/Gr heterostructures, which are discussed below.

Overview

Graphene has attracted intense interest, especially in electronic systems, where charge carriers have a nodal/"Dirac-cone" shape with linear energy dispersion (Geim and Novoselov, 2007). Graphene exhibits novel charge carrier transport properties, including bipolar QHE, minimum metallic conductivity, and Klein tunneling. Typical data are shown in Fig. 1. Fig. 1A shows a sharp peak of the longitudinal resistance near zero gate bias, corresponding to the Dirac point (DP), which reflects the "Dirac-cone" of the energy dispersion. Bipolar QHE is also detected as magnetic field evolution of the resistance, as shown in Fig. 1B.

Graphene was discovered early in this century when it was exfoliated on SiO_2 (Geim and Novoselov, 2007). Graphene-based devices on SiO_2 are generally disordered, and their characteristics are inferior to those of the intrinsic ones. The quality of SiO_2-supported graphene has remained basically unchanged since its discovery. Although the exact nature of the scattering that

https://doi.org/10.1016/B978-0-323-90800-9.00008-1

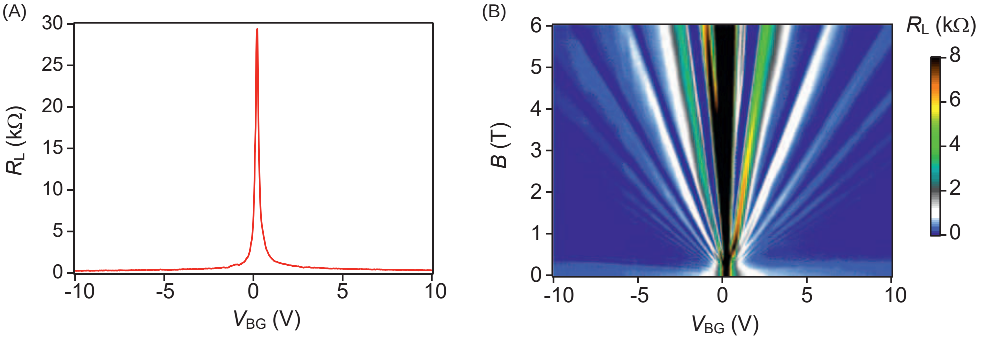

Fig. 1 Typical electron transport in single-layer graphene (SLG). (A) Longitudinal (local) resistance (R_L) as a function of back-gate voltage (V_{BG}) without magnetic fields at $T = 6$ K. (B) R_L as a function of V_{BG} and magnetic field (B) applied perpendicular to the graphene sheet at $T = 6$ K. Reproduced with the permission of Ahmad NF, Komatsu K, Iwasaki T, Watanabe K, Taniguchi T, Mizuta H, Wakayama Y, Hashim AM, Morita Y, Moriyama S, Nakaharai S (2019) Fabry-Perot resonances and a crossover to the quantum Hall regime in ballistic graphene quantum point contacts. *Scientific Reports* **9**: 3031, copyright 2019, Springer Nature Limited.

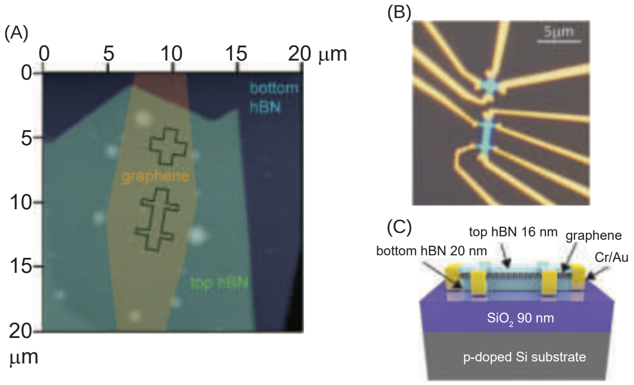

Fig. 2 (A) False-color atomic force microscopy (AFM) image of a hexagonal-boron-nitride (hBN)/SLG/hBN stack after thermal annealing. We carefully aligned SLG and the top/bottom hBN flakes by aligning the long edges of each flake. The thermal annealing process could also improve the alignment of the layers. The shape shown with a black line represents the Hall-bar part of the device. (B) Optical microscope image of an hBN/SLG/hBN superlattice device fabricated from the stack in (A). (C) Schematic of the cross-section of the device. Reactive ion etching (RIE) using SF_6 was performed to form Hall-bar geometry and made one-dimensional edge metal contacts of Cr/Au. Reproduced with the permission of Komatsu K, Morita Y, Watanabe E, Tsuya D, Watanabe K, Taniguchi T, Moriyama S (2018) Observation of the quantum valley Hall state in ballistic graphene superlattices. *Science Advances* **4**: eaaq0194, copyright 2018, AAAS.

characterizes graphene devices remains unclear, an underlying substrate should play a crucial role. On SiO_2, for example, the carrier mobility is limited by scattering from the charged surface state, impurities, substrate surface roughness, ripples, and SiO_2 surface optical phonons combined with fabrication residue on and/or under the graphene layer. Around the nodes of "Dirac cone"/DP, 2D electron gas (2DEG) has been broken up into the so-called "electron-hole" puddles due to substrate-induced disorder. Furthermore, charged impurities in the substrate or graphene–substrate interface can cause "self-doping" of 2DEG, resulting in a shift in the Dirac point. Therefore, there is a need for alternatives to SiO_2.

Although suspension of graphene improves device quality (Bolotin et al., 2008), its geometry highly limits the architecture of the device, and this challenge needs to be overcome. Graphene superlattice structures, hBN/Gr(/hBN), can overcome the above-mentioned challenge. Heterostructures based on hBN and graphene are a novel class of quantum metamaterials and devices.

hBN is a promising and ideal substrate dielectric (Watanabe et al., 2004). BN is an insulating analog of graphite, where boron (B) and nitrogen (N) atoms occupy the inequivalent sublattice sites in the Bernal structure. The difference in the onsite energies of the B and N atoms results in a large bandgap (~6 eV) and a small lattice mismatch (1.7%) with graphite. Due to the strong, in-plane, ionic bonding of the planar hBN structure, hBN is inert and expected to be free of dangling bonds or surface charge traps. Furthermore, the dielectric properties of hBN ($\varepsilon \sim 3$–4 and $V_{\text{BreakDown}} \sim 1$ V/nm) and the surface optical phonon modes (twice larger in energy than the corresponding modes SiO_2) are also idealistic compared with those of SiO_2.

hBN/Gr superlattices have the so-called "moiré superlattice" with a long-wavelength moiré pattern and inversion-symmetry (P) breaking, which is associated with the energy gap/hot spot at the charge-neutral point (CNP), and satellites of CNP emerge. This CNP corresponds to the DP introduced above, and the satellites to "higher-generation" DP. The moiré superlattice also induces an intriguing energy spectrum under a magnetic field, which is referred to as "Hofstadter's butterfly." When subject to a magnetic field, the resistance peaks result in first- and second-generation Landau fans, which are demonstrated below. The first generation corresponds to CNP, and the second generation is attributed to inversion-symmetry breaking and corresponds to the satellites of CNP.

Fig. 2 shows hBN/Gr(/hBN) moiré superlattices, where single-layer graphene (SLG) and top/bottom hBN flakes are set by aligning the long edges of each flake.

In Fig. 3, the quantum Hall effect of the hBN/SLG superlattice is shown near DP (Fig. 3C), and the Landau-fan diagrams of Hofstadter's butterfly are observed (Figs. 3A and B). CNP is near $V_g = 0$, and the satellites are away from there. The satellite shows a clear (second-generation) Landau fan in the hole side (negative V_g) (Figs. 3A and B). The emergence of "massive" Dirac fermion is confirmed by the Arrhenius plots (Fig. 3D), which show the temperature dependence of the local resistance at DP and second satellites of CNP shown as a secondary Dirac point (SDP). In Fig. 3D, the gaps at DP and SDP were estimated as 32 meV and 14 meV, respectively, by linear fitting in the high-temperature region, which corresponds to the emergence of "massive" Dirac fermions with a "hot spot."

Generally, nonlocality in electronic devices refers to the emergence of a voltage across contacts "far away" from the path through which an excitation (charge) current is expected to flow. The first "giant" nonlocal resistance was detected in graphene under a magnetic field (Abanin et al., 2011), which faded out under zero magnetic fields. The origin of this phenomenon is still controversial. Herein, we focus on graphene device with a broken P (and unbroken T). This is realized in the graphene superlattice with hBN.

Inversion symmetry is broken by hBN, resulting in finite Berry curvature and bandgap in the momentum space (Xiao et al., 2007; Xiao et al., 2010). Analogous to a magnetic field controlling electron motion in real space, the Berry curvature can be interpreted as a finite magnetic field in momentum space, which also modifies the motion of electrons. The Berry curvature has opposite signs for the two valleys; thus, electrons belonging to different valleys flow in opposite directions under an electric field, even under a zero magnetic field. This is the origin of the bulk valley current.

In moiré superlattices, a long-wavelength moiré pattern develops, resulting in Hofstadter's butterfly under a magnetic field (Dean et al., 2013; Ponomarenko et al., 2013) (Fig. 3), where the hot spot emerges in the momentum space due to the broken inversion symmetry. The electrical current induced at one end of the H-bar induces a topological valley current in the transverse direction because of the hot spot, and this current is converted to a voltage drop at the other end of the H-bar through the inverse effect (Figs. 4–6). Recently, graphene superlattices due to the moiré structure have been intensively studied. Since the work of Bistritzer and MacDonald (2011a), Bistritzer and MacDonald (2011b) in particular, moiré bands/butterflies in bilayer graphene (BLG) have been extensively studied. They are analogous to those of SLG (Ponomarenko et al., 2013). BLG has a unique electronic structure quite different from that of SLG, and its bandgap can be tuned by applying an electric field perpendicular to the system. The two layers in BLG generally exhibit AB (Bernal) stacking. An example is shown in Fig. 6, where a long-wavelength moiré pattern stems from the small lattice mismatching as in the SLG case.

Herein, we analyze the experimental setting based on our device in Komatsu et al. (2018) (Fig. 4). Here, the Hall bar geometry and nonlocal resistance measurement setup were applied. Local and nonlocal resistances were measured using a low-frequency lock-in technique with minimized AC excitation. ρ_{xx} is the longitudinal resistivity for the current terminal (1, 4, shown as $I14$) and

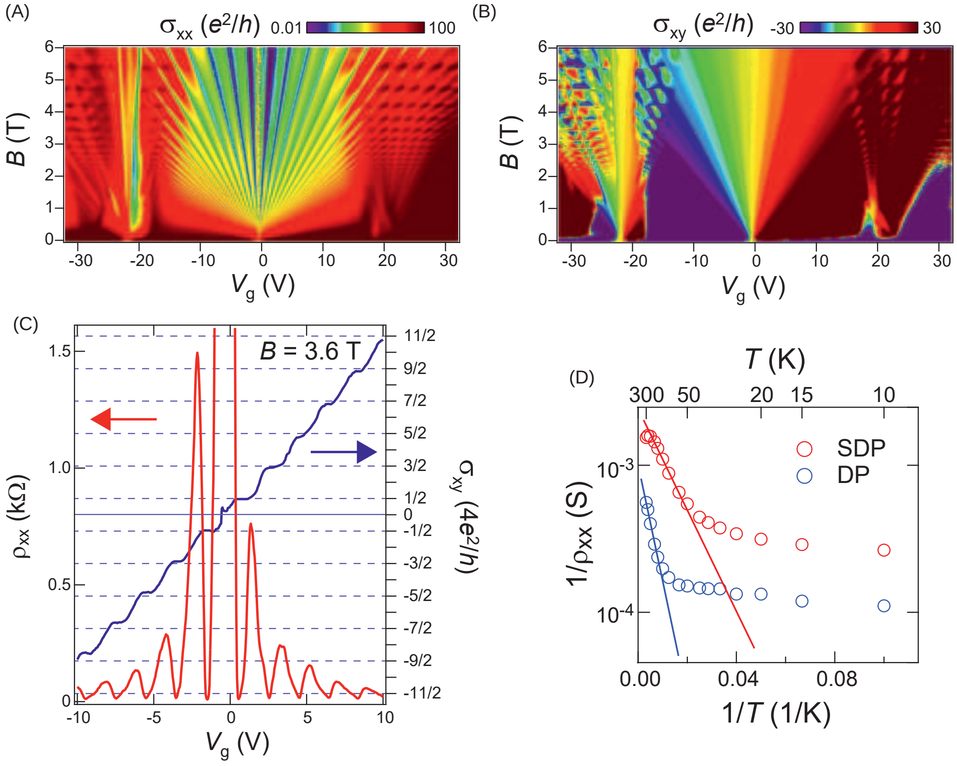

Fig. 3 Quantum transport in hBN/SLG superlattices. (A) Longitudinal conductivity (σ_{xx}) and (B) Hall conductivity (σ_{xy}) as functions of V_g and B at $T = 5$ K. (C) Longitudinal resistivity (ρ_{xx}) and σ_{xy} as functions of V_g at a fixed B of 3.6 T. (D) Arrhenius plot of the resistivity at the Dirac point (DP) and secondary Dirac point (SDP). (A) and (D) are reproduced with the permission of Komatsu K, Morita Y, Watanabe E, Tsuya D, Watanabe K, Taniguchi T, Moriyama S (2018) Observation of the quantum valley Hall state in ballistic graphene superlattices. *Science Advances* **4**: eaaq0194, copyright 2018, AAAS.

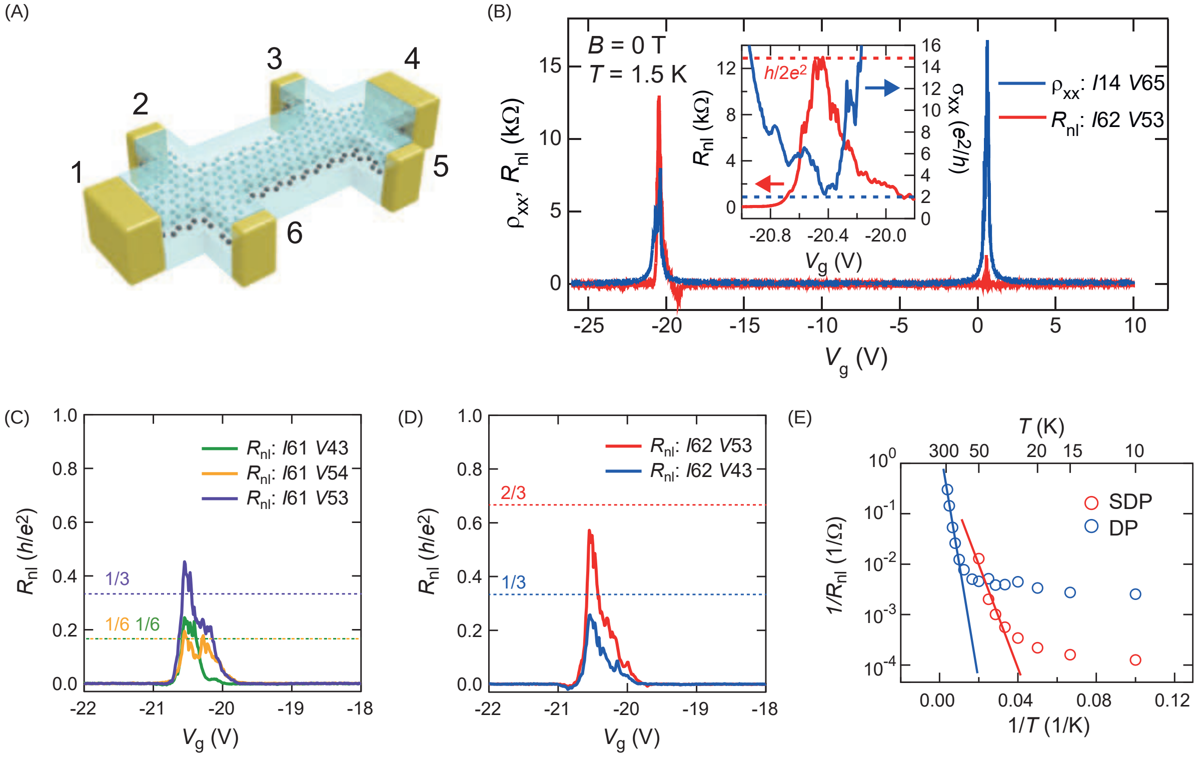

Fig. 4 Valley current in hBN/SLG superlattices. (A) Six-terminal Hall-bar device with terminal numbers. (B) Local resistivity (ρ_{xx}) and nonlocal resistance (R_{nl}) as a function of V_g at $T = 1.5$ K and $B = 0$ T. Inset: Zoomed in longitudinal conductivity (σ_{xx}) and R_{nl} near SDP. (C) and (D) R_{nl} with different terminal configurations with a channel length of 2.5 μm. Horizontal dotted lines show theoretical values of the resistance based on the minimal edge-state model. (E) Arrhenius plot of R_{nl} at DP and SDP. (A), (C), (D), and (E) are adapted from Komatsu K, Morita Y, Watanabe E, Tsuya D, Watanabe K, Taniguchi T, Moriyama S (2018) Observation of the quantum valley Hall state in ballistic graphene superlattices. *Science Advances* **4**: eaaq0194, copyright 2018, AAAS.

the voltage terminal (6, 5, shown as V65), and R_{nl} is a nonlocal resistance for the current terminal (I62) and voltage terminal (V53) in Figs. 4A and B. In the nonlocal measurements, the charge current on the left (terminals 6 and 2) generates a valley current in its transverse direction, which is converted into a voltage on the right (terminals 5 and 3). The nonlocal resistance R_{nl} is defined as the voltage divided by the current. Fig. 4B shows ρ_{xx} (blue curve) and R_{nl} (red curve) as functions of V_g at 1.5 K and 0 T. Figs. 4C and D show the resistances with different terminal configurations of a six-terminal sample. The horizontal dotted lines show the theoretical values of the resistance based on the minimum edge-state model. As shown in Fig. 4E, the nonlocal resistance shows a thermally-activated behavior as in the conventional longitudinal resistance in Fig. 3D.

Li et al. (2020), reported R_{nl} of the order of the quantum resistance near DP. Fig. 5A shows an optical microscope image of hBN/SLG/hBN superlattice devices reported by Li et al. (2020), and Fig. 5B shows the local and nonlocal transport near DP. Graphene is aligned with both the top and bottom hBN layers in device I. In contrast, it is aligned with the top layer of hBN ($\theta \approx 0°$) but misaligned ($\theta \approx 30°$) with the bottom hBN in device II. R_{nl} approaches the quantum resistance in device I, but it is much smaller (60 Ω) in device II. Therefore, device I should correspond to the experiment in Komatsu et al. (2018), which was reconfirmed here in Li et al. (2020). Fig. 5C shows the resistance with different terminal configurations.

Figs. 4 and 5 show nonlocal transport in hBN/SLG/hBN superlattices. To check the universality of this phenomenon, we studied hBN/BLG/hBN superlattices (Endo et al., 2019). Fig. 6 shows hBN/BLG/hBN superlattices. In both cases, R_{nl} of the order of kilo-Ohms (I14 V23) was observed. Fig. 6A shows an optical image of the hBN/BLG/hBN superlattice device, and the inset shows a schematic of the four-terminal device structure with the terminal numbers.

Key issues

In generic setting, nonlocality is conventionally attributed to the "Ohmic contribution" due to "stray charge currents," which is expressed by the van der Pauw formula. In this study, the Ohmic contribution is much smaller than R_{nl}; thus, is not the main factor influencing our observation. Furthermore, the scaling relation between ρ_{xx} and R_{nl} indicates the emergence of a bulk topological current (Abanin et al., 2009; Endo et al., 2019; Gorbachev et al., 2014; Komatsu et al., 2018). Such nonlocal resistance cannot be detected without a superlattice structure in the absence of a magnetic field.

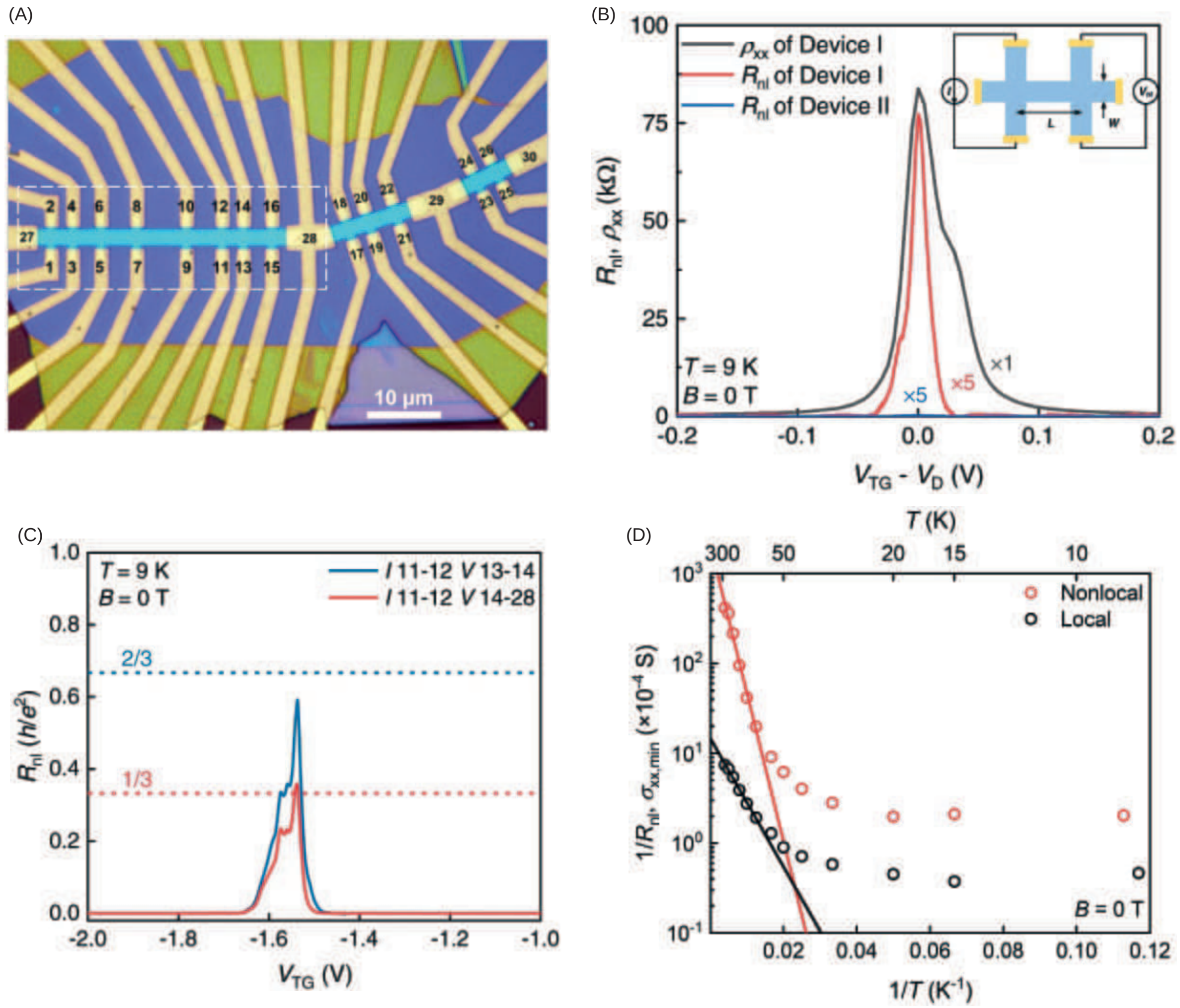

Fig. 5 Valley current in hBN/SLG superlattices of another device. (A) Optical microscope image of the device. Device I is shown in the dotted white square. (B) ρ_{xx} and R_{nl} as functions of the gate-voltage (V_{TG}—V_G) at $T = 9$ K and $B = 0$ T. (C) R_{nl} with different terminal configurations for a channel length of 3 μm. Horizontal dotted lines show theoretical values of the resistance based on the minimal edge-state model. (D) Arrhenius plot of the ρ_{xx} and R_{nl} at DP. Reproduced with the permission of Li Y, Amado M, Hyart T, Mazur GP, Robinson JWA (2020) Topological valley currents via ballistic edge modes in graphene superlattices near the primary Dirac point. *Communications on Physics* **3**: 224, copyright 2020, Springer Nature Limited.

A moiré superlattice with broken inversion symmetry causes the accumulation of hot spots with Berry curvature at CNP and harbors the satellites of CNP. We observed nonlocal resistance of the order of kilo-Ohms, which obeys a scaling relation (Abanin et al., 2009). This nonlocal resistance evolves from the quantum Hall effect but without magnetic field/time-reversal symmetry breaking, which is associated with the hot-spot-induced topological valley current. In other words, the nonlocal resistance is a Berry-phase-sensitive probe to detect hot spots in gapped Dirac materials with inversion-symmetry breaking.

At the low-temperature limit, on the other hand, a clear deviation from the scaling relationship was observed. Komatsu et al. (2018) attributed this to edge-mode conduction, which was also reconfirmed by Li et al. (2020). The detailed nature of this edge mode would be investigated in future studies.

Conclusion

Valley currents, particularly in graphene superlattices, are promising. There is a need for hybrid devices with quantum dots on such monolithic 2D materials as they have many application potentials. The profound nonlocality in hBN/Gr devices, which are sensitive probes for such a neutral degree of freedom as valleys, provides key information that cannot be obtained using conventional approaches.

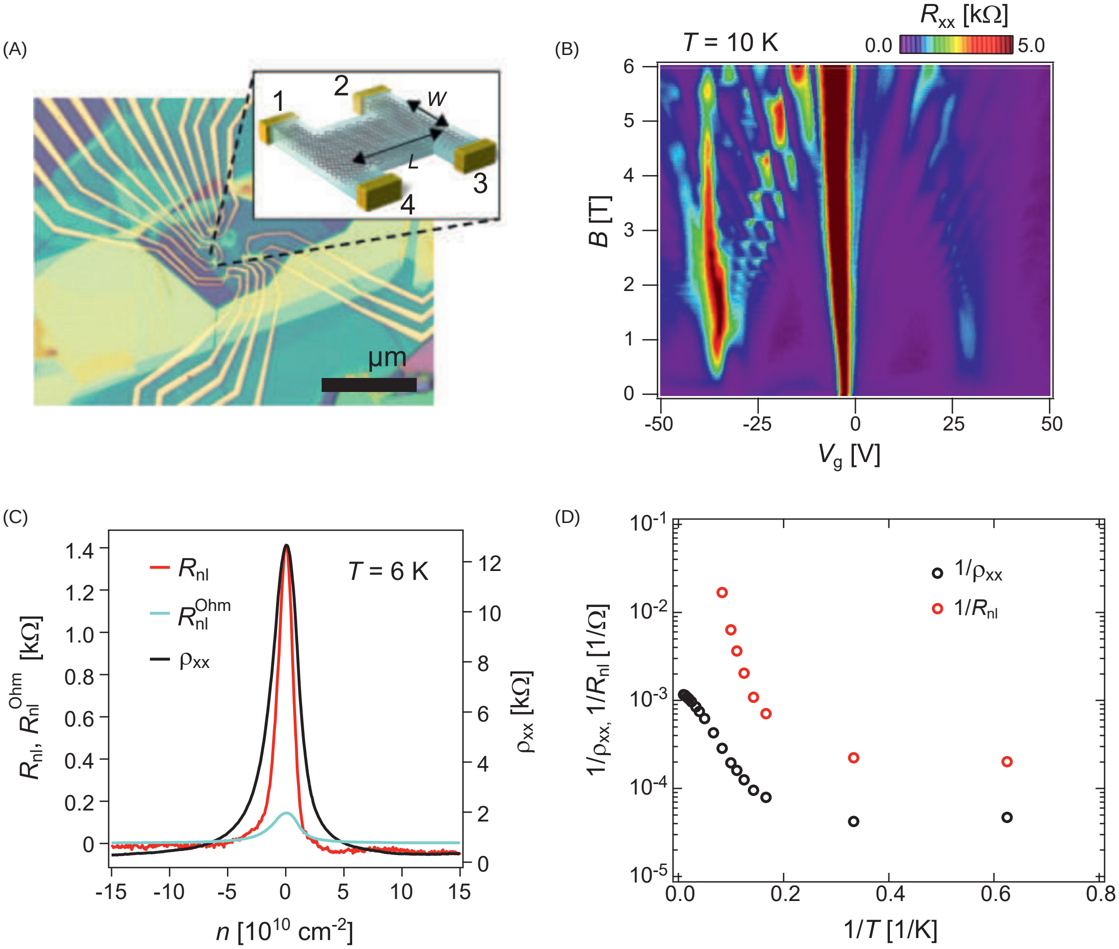

Fig. 6 Valley current in hBN/BLG superlattices. (A) Optical image of an hBN/BLG/hBN superlattice device. The inset shows a schematic of the four-terminal device structure with terminal numbers, where the characteristic length of $L = 1.5$ μm and $W = 1.0$ μm. (B) R_{xx} (I12 V43) as a function of V_g and B at $T = 10$ K. (C) ρ_{xx} ($= R_{xx}(W/L)$) and R_{nl} (I14 V23) with Ohmic contribution R_{nl}^{Ohm} as a function of V_g at $T = 6$ K and $B = 0$ T. (D) Arrhenius plot of ρ_{xx} and R_{nl} at CNP. Reproduced with the permission of Endo K, Komatsu K, Iwasaki T, Watanabe E, Tsuya D, Watanabe K, Taniguchi T, Noguchi Y, Wakayama Y, Morita Y, Moriyama S (2019) Topological valley currents in bilayer graphene/hexagonal boron nitride superlattices. *Applied Physics Letters* **114**: 243105, copyright 2019, AIP Publishing.

Acknowledgments

We thank all our collaborators who helped in the experiments. Although we do not list all of them here (see, for example, Ahmad et al., 2019; Endo et al., 2019; Komatsu et al., 2018), we acknowledge Katsuyoshi Komatsu, who played a key role in this project.

References

Abanin DA, Shytov AV, Levitov LS, and Halperin BI (2009) Nonlocal charge transport meditated by spin diffusion in the spin Hall effect regime. *Physical Review B* 79: 035304.
Abanin DA, Morozov SV, Ponomarenko LA, Gorbachev RV, Mayorov AS, Katsnelson MI, Watanabe K, Taniguchi T, Novoselov KS, Levitov LS, and Geim AK (2011) Giant nonlocality near the dirac point in graphene. *Science* 332: 328–330.
Ahmad NF, Komatsu K, Iwasaki T, Watanabe K, Taniguchi T, Mizuta H, Wakayama Y, Hashim AM, Morita Y, Moriyama S, and Nakaharai S (2019) Fabry-Perot resonances and a crossover to the quantum Hall regime in ballistic graphene quantum point contacts. *Scientific Reports* 9: 3031.
Bistritzer R and MacDonald AH (2011a) Moiré bands in twisted double-layer graphene. *Proceedings. National Academy of Sciences. United States of America* 108: 12233–12237.
Bistritzer R and MacDonald AH (2011b) Moiré butterflies in twisted double-layer graphene. *Physical Review B* 84: 035440.
Bolotin KI, Sikes KJ, Jiang Z, Klima M, Fudenberg G, Hone J, Kim P, and Stormer HL (2008) Ultrahigh electron mobility in suspended graphene. *Solid State Communications* 146: 351–355.
Dean CR, Wang L, Maher P, Forsythe C, Ghahari F, Gao Y, Katoch J, Ishigami M, Moon P, Koshino M, Taniguchi T, Watanabe K, Shepard KL, Hone J, and Kim P (2013) Hofstadter's butterfly and the fractal quantum Hall effect in moiré superlattices. *Nature* 497: 598–602.
Endo K, Komatsu K, Iwasaki T, Watanabe E, Tsuya D, Watanabe K, Taniguchi T, Noguchi Y, Wakayama Y, Morita Y, and Moriyama S (2019) Topological valley currents in bilayer graphene/hexagonal boron nitride superlattices. *Applied Physics Letters* 114: 243105.
Geim AK and Novoselov KS (2007) The rise of graphene. *Nature Materials* 6: 183–191.

Gorbachev RV, Song JCW, Yu GL, Kretinin AV, Withers F, Cao Y, Mishchenko A, Grigorieva IV, Novoselov KS, Levitov LS, and Geim AK (2014) Detecting topological currents in graphene superlattices. *Science* 346: 448–451.

Haldane FDM (1988) Model for a quantum Hall effect without Landau levels: Condensed-matter realization of the "parity anomaly" *Physical Review Letters* 61: 2015–2018.

Komatsu K, Morita Y, Watanabe E, Tsuya D, Watanabe K, Taniguchi T, and Moriyama S (2018) Observation of the quantum valley Hall state in ballistic graphene superlattices. *Science Advances* 4: eaaq0194.

Laughlin RB (1981) Quantized Hall conductivity in two dimensions. *Physical Review B* 23: 5632–5633.

Lensky YD, Song JC, Samutpraphoot P, and Levitov LS (2015) Topological valley currents in gapped Dirac materials. *Physical Review Letters* 114: 256601.

Li Y, Amado M, Hyart T, Mazur GP, and Robinson JWA (2020) Topological valley currents via ballistic edge modes in graphene superlattices near the primary Dirac point. *Communications on Physics* 3: 224.

Ponomarenko LA, Gorbachev RV, Yu GL, Elias DC, Jalil R, Patel AA, Mishchenko A, Mayorov AS, Woods CR, Wallbank JR, Mucha-Kruczynski M, Piot BA, Potemski M, Grigorieva IV, Novoselov KS, Guinea F, Fal'ko VI, and Geim AK (2013) Cloning of Dirac fermions in graphene superlattices. *Nature* 497: 594–597.

Thouless DJ, Kohmoto M, Nightingale MP, and Den Nijs M (1982) Quantized Hall conductance in a two-dimensional periodic potential. *Physical Review Letters* 49: 405–408.

Watanabe K, Taniguchi T, and Kanda H (2004) Direct-bandgap properties and evidence for ultraviolet lasing of hexagonal boron nitride single crystal. *Nature Materials* 3: 404–409.

Xiao D, Yao W, and Niu Q (2007) Valley-contrasting physics in graphene: Magnetic moment and topological transport. *Physical Review Letters* 99: 236809.

Xiao D, Chang M-C, and Niu Q (2010) Berry phase effects on electronic properties. *Reviews of Modern Physics* 82: 1959–2007.

Bulk-edge correspondence

Yasuhiro Hatsugai, Department of Physics, University of Tsukuba, Tsukuba, Japan

© 2024 Elsevier Ltd. All rights reserved.

Introduction 659
Quantum Hall effects 660
Laughlin argument and edge states 660
Role of edge states 661
TKNN integer 661
Bulk-edge correspondence 662
Quantum Hall effect to Chern insulators 662
Universality of the bulk-edge correspondence 665
Short-range entangled states, symmetry protection and edge states 666
Conclusion 668
References 668

Abstract

Topological phase is a new concept, that is independent of the standard phase classification by symmetry breaking, and is characterized by quantized quantities (topological numbers) of the gapped bulk which may not be always experimentally observable. Physical quantities to be measured are gapless excitations (edge states) near the boundaries of the systems. These low energy modes are stable against local perturbations protected by the bulk gap. This is the topological stability. The relation between the topological number of the bulk and the edge states is the bulk-edge correspondence. It has been first established for quantum Hall states. Today not only quantum but also many classical phenomena are recognized as under the control of the bulk-edge correspondence. Universality of the bulk-edge correspondence is extending rapidly over different areas. We also mentioned on the unique feature of the bulk-edge correspondence in topological pump and the extension for symmetry protected topological phases.

Key points

- Bulk-edge correspondence, that is a fundamental concept for topological phases, is explained.
- TKNN numbers, Chern numbers and a topological number of edge states are defined for integer quantum Hall effect and discussed.
- Topological pump and symmetry protected topological phases are mentioned from the bulk-edge correspondence.

Introduction

According to the standard characterization of physical phases, the order parameter, which is an experimental observable and reflecting specific symmetry breaking, is a key quantity. Finite magnetization due the rotational symmetry breaking in spin space is a typical example. The order parameter is extensive, that is, its value per volume (density) is finite when the system size is sufficiently large (in the thermodynamic limit). This naturally implies that its value as a density is independent of local perturbations such as effects of boundaries and finite number of local impurities.

On the other hand, as for the topological phase, which is a new way of description for material phases, there is no fundamental order parameter associated with the symmetry breaking that any experiments may access. Experimental observables for the topological phases are *localized states* (generic edge states) as we explain here. A surface sensitive experiment such as the angle resolved photoemission spectroscopy (ARPES) is a typical technique that has been effective for experimental characterization of topological phases (topological insulators). The edge states reflect topologically non-trivial bulk. Conversely bulk without any boundaries with non-trivial topological number implies edge states when one makes boundaries by dividing the system. This relation is the bulk-edge correspondence that has been realized as a key concept for the study of the topological phases for the decades.

Let us define the word "*localized*" for a open-particle state $\psi(x)$. It is localized if and only if it is normalizable as $\int d^d x |\psi_{\rm loc}(x)|^2 < +\infty$ where x is a spatial coordinate in d-dimension. Otherwise it is extended (unnormalized) such as plane waves. If one considers a system with its spatial size L, total norm of the state $\int_{L^d} d^d x |\psi_{\rm ext}(x)|^2$ diverges for the extended state $\psi_{\rm ext}(x)$ in the limit $L \to \infty$. Or if one uses a system dependent normalization $\psi_L(x) = N^{-1/2}\psi_{\rm ext}(x)$ ($N = \int_{L^d} d^d x |\psi_{\rm ext}(x)|^2$), $\psi_L(x) \to 0$ everywhere ($L \to \infty$). Then $\psi_L(x)$ is useless, which is a physical meaning of *unnormalizability*. As is clear by this discussion, whether

https://doi.org/10.1016/B978-0-323-90800-9.00158-X

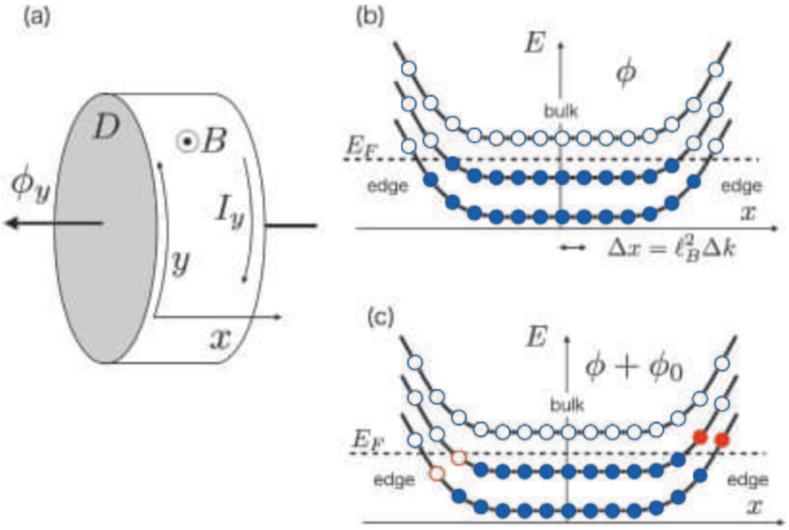

Fig. 1 (a) Setup of Laughlin argument. (b), (c) Edge states on a cylinder. In this example, the unknown integer of the Laughlin argument is explicitly fixed as +2. Two states are passing through the system during the adiabatic process.

the state is extended or localize is well defined only in the infinite system. The bulk-edge correspondence is used for the infinite system with/without edges.[1]

Although the bulk-edge correspondence is, in principle, independent of the translation symmetry, let us assume translation symmetry to make the discussion simple. By writing the translation by a as T_a, the translation invariance for the Hamiltonian implies $[T_a, H] = 0$ and all eigenstates of the Hamiltonian are also simultaneous eigenstate of T_a as $T_a\psi = \rho\psi$. Further the unitarity of the translation (conservation of the norm) implies $|\rho| = 1$. For an one-particle state ψ with energy ϵ, this is the Bloch theorem, that is, all states of the translation invariant system have to be extended since $|\psi(x)| = |\psi(y)|(x - y = na)$ for any integer n. Its energy ϵ belongs to energy bands. It is then also true, as a contrapositive, that localized states exist only for systems without translation invariance and its energy needs to be in the energy gaps (complement of the energy bands). Typical cases can be systems with boundaries or with impurities. Formally the bulk-edge correspondence is a relation between the states with different boundary conditions since the Bloch condition implies the periodic boundary condition and a system with boundary implies vanishing its value at the edges. It reminds us well-known Levinson's theorem in quantum mechanics and Friedel's sum rule where phase shifts of the scattering states (bulk) govern the number of bound states. This is one of the physical backgrounds of the bulk-edge correspondence.

Quantum Hall effects

Laughlin argument and edge states

Since the Laughlin argument (Laughlin, 1981) using a gauge invariance associated with a vector potential $\boldsymbol{A}$ (gauge field) to explain the integer quantum Hall effect (Klitzing et al., 1980) is fundamentally important for the bulk-edge correspondence, let us discuss it carefully. Conceptually the argument is also applied for various topological phases by introducing fictitious gauge field $\boldsymbol{A}_f$ and charge e_f associated with the minimum coupling for a spatial derivative $-i\hbar\nabla \to -i\hbar\nabla - e_f \boldsymbol{A}_f$.

The setup of the Laughlin argument itself is topologically non trivial as putting two-dimensional electrons (charge $-e$) in a magnetic field on a cylinder (periodic boundary condition in y-direction) and open one in x-direction. Introducing the Aharonov-Bohm (AB) flux ϕ_y passing through the cylinder implies a shift of the vector potential $\bar{\boldsymbol{A}} = \boldsymbol{A} + \delta\boldsymbol{A}$, $\delta\boldsymbol{A} = \left(0, \frac{\phi_y}{L_y}, 0\right)$ as shown in Fig. 1. Note that $\int_D \, d\boldsymbol{S} \cdot \mathrm{rot}\,\delta\boldsymbol{A} = \int_{\partial D} \, d\boldsymbol{r} \cdot \delta\boldsymbol{A} = \phi_y$. Since the velocity of electrons in y-direction is written as $v_y = \partial_{\delta A_y} h/e$ where the one-particle Hamiltonian $h = \frac{(\boldsymbol{p} + e\boldsymbol{A})^2}{2m} = -\frac{\hbar^2}{2m}\left(\nabla + i\frac{2\pi}{\phi_0}\boldsymbol{A}\right)^2$, $\mathrm{rot}\,\boldsymbol{A} = (0, 0, B)$ and $\phi_0 = \frac{h}{e}$ is a flux quantum, the current density j_y in x-y plane per unit width is written by the many particle Hamiltonian (without interaction) $H = \sum_j h(r_j)$ as $j_y = -\frac{1}{L_x L_y}\sum_j e v_y(r_j) = -\frac{1}{L_x}\partial_{\phi_y} H$ where $\boldsymbol{r}_j$ is a coordinate of the j-th electron. It implies the Hall current in $-y$ direction I_y (Fig. 1) is written as $I_y \equiv -L_x\langle j_y\rangle_\Psi = \langle \partial_{\phi_y} H\rangle_\Psi$ where the expectation value is taken for a many particle state Ψ of the system (constructed from one-particle state ψ's). Assuming the AB flux ϕ_y is adiabatically modified, it is given by the Feynman's theorem as

---

[1] To distinguish the (localized) edge states from the extended states, one needs to take a limit $L \to \infty$ even with the open boundary condition. This is the infinite system with edges.

$$I_y = \frac{\partial E}{\partial \phi_y} \tag{1}$$

where $E = \langle H\rangle_\Psi$ is the energy of the snapshot many-particle ground state $\Psi(\phi_y)$, $H(\phi_y)\Psi(\phi_y) = \Psi(\phi_y)E(\phi_y)$.

The AB flux is locally gauged out by the (large) gauge transformation

$$Uh(\bar{\boldsymbol{A}})U^\dagger = h(\boldsymbol{A}),\ U = e^{i2\pi \frac{\phi_y}{\phi_0}\frac{y}{L_y}}$$
$$\psi = U\bar{\psi} = e^{i2\pi \frac{\phi_y}{\phi_0}\frac{y}{L_y}}\bar{\psi}$$

where $h(\bar{\boldsymbol{A}})\bar{\psi} = \bar{\psi}\epsilon$ and $h(\boldsymbol{A})\psi = \psi\epsilon$ with a one-particle energy ϵ. However, the periodic boundary condition for $\bar{\psi}$ implies a twisted boundary condition for ψ as $\psi(x, y) = e^{i\theta}\psi(x, y + L_y)$ with $\theta = 2\pi\frac{\phi}{\phi_0}$. It implies the wave function is generically discontinuous at $y = 0$ $(y = L_y)$ where the system is glued to form a cylinder. It costs extra energy. Only when $\phi = \phi_0$, this mismatch vanishes and the effect of the Aharonov-Bohm ϕ_y is completely gauged out. It implies the system remains the same, or goes back to the initial state.

When the system size is sufficiently large $(L_y \to \infty)$, one may replace the derivative in Eq. (1) as $\frac{\partial E}{\partial \phi} \to \frac{\Delta E}{\Delta \phi_0}$ noting that $\delta A_y \sim \frac{\phi_0}{L_y}$ is sufficiently small. According to Laughlin, the energy cost ΔE for this adiabatic process should be then followed by some number of states, say, (unknown) n states, are carried from the right to the left boundaries. Assuming the potential difference between the boundaries due to the external field as V_x, $\Delta E = -neV_x$. It simply results in

$$I_y = -\frac{neV_x}{\phi_0} = \sigma_{yx}V_x.$$

This implies the quantization of the Hall conductance as $\sigma_{xy} = -\sigma_{yx} = n\frac{e^2}{h}$ where the integer n is not fixed by the present gauge invariance argument.

Role of edge states

Although, the quantization of the Hall conductance is clear, its value n is not specified in the Laughlin argument. Actually it is given by *the number of edge states passing through the Fermi energy*, which was first pointed out by Halperin (Halperin, 1982). Let us repeat it in the cylindrical geometry. Taking a Landau gauge, $\boldsymbol{A} = \left(0, Bx + \frac{\phi_y}{L_y}, 0\right)$, the one-particle wave function after the large gauge transformation is written as $\psi = U\bar{\psi} = e^{-ik_y y}\varphi\left(x - x_{k_y}\right)$. It is a plane wave in y-direction and φ is a solution of the Schrödinger equation of the harmonic oscillator in x-direction localized near $x_{k_y} = \ell_B^2 k_y$ (if the system is infinite) where $\ell_B = \sqrt{\frac{\hbar}{eB}}$ is a magnetic length. The periodic boundary condition of $\bar{\psi}$ implies the quantization of the shifted momentum as $k_y = \frac{2\pi}{L_y}\left(n - \frac{\phi}{\phi_0}\right), n \in \mathbb{Z}$.

With boundaries in x-direction, let us consider soft boundaries to discuss the situation of the cylinder qualitatively. Then one needs to expand the wave function by those of the harmonic oscillator for each momentum k_y. Since the one-particle energies of the states centered far away outside from the position of the (soft boundaries) should be far above the Fermi energy, one may expect the one-particle energies of the states specified by the preserved momentum k_y are raised from the Landau levels as shown in Fig. 1 (b) and (c). Here we assume the continuity of the energy of the one-particle state as a function of k_y. Then the carried states among the adiabatic process by increasing the Aharonov-Bohm flux by ϕ_0 in the Laughlin argument is specified by the number of the states localized near each boundary (pairs of particle-hole excitations separated far away by bulk). These are the edge states. Also the continuity of the effective Landau levels as shown in the Fig. 1, implies that this number is the same as that of the number of the Landau levels below the Fermi energy at bulk (far away from the boundaries). Since the number of the filled Landau levels is stable for local perturbation, it is a topological number. We may then consider this relation as *an implicit bulk-edge correspondence*.

TKNN integer

Here let us consider lattice fermions on a two-dimensional square lattice

$$H = \sum_{i,j}(c_i^\dagger h_{i,j}c_j + V_{i,j}\hat{n}_i\hat{n}_j), \hat{n}_j = c_j^\dagger c_j$$

where c_j is an annihilation operator of a fermion at the site $j = (m_j, n_j)$ and $\hat{n}_j$ is its number operator. We assume the hopping matrix elements $h_{i,j}$ and particle-particle interaction $V_{i,j}$ are short-ranged. By identifying the sites j and those at $j + (L_x, 0)$ and $j + (0, L_y)$, $j = 1, \ldots, L_y$, the system is a torus of the size $L_x \times L_y$.

We further assume the many-particle ground state is gapped and unique. A typical case is an non-interacting gapped system such as the integer quantum Hall state and topologically non trivial band insulators (Chern insulators (Haldane, 1988)).

It respects a local $U(1)$ gauge invariance

$$UH(\bar{h}_{i,j})U^\dagger = H(h_{i,j}),\ U = e^{i\sum_j \Omega_j \hat{n}_j},$$
$$h_{i,j} = e^{i(\Omega_i - \Omega_j)}\bar{h}_{i,j}$$

where $Uc_j^\dagger U^\dagger = e^{i\Omega_j} c_j^\dagger$. It induces a large gauge transformation, $\Omega_j^g = \theta_x x_j + \theta_y y_j$, $U = U_x U_y$, $U_x = e^{i\theta_x \sum_j x_j \hat{n}_j}$, $U_y = e^{i\theta_y \sum_j y_j \hat{n}_j}$, $x_i = \frac{m_i}{L_x}$ and $y_i = \frac{m_i}{L_y}$.

As for a one-particle state, $|\psi\rangle = \sum_j c_j^\dagger \psi_j |0\rangle$, the Schrödinger equation $H|\psi\rangle = \epsilon|\psi\rangle$ is written as $\sum_j h_{i,j}\psi_j = \psi_i \epsilon$. The large gauge transformation implies

$$|\psi\rangle = U|\bar{\psi}\rangle, \psi_j = e^{i\Omega_j^g}\bar{\psi}_j.$$

Assuming $|\bar{\psi}\rangle$ is defined on a torus of the size $L_x L_y$, it satisfies a periodic boundary condition $\bar{\psi}_j = \bar{\psi}_{j+(L_x,0)} = \bar{\psi}_{j+(0,L_y)}$. It induces a twisted boundary condition for $|\psi\rangle$ as $\psi_j = e^{i\theta_x}\psi_{j+(L_x,0)} = e^{i\theta_y}\psi_{j+(0,L_y)}$, which can be compared with the effects of the Aharonov-Bohm flux in the Laughlin argument.

We may assume the phase factors $\theta_{x,y} = 2\pi\phi_{x,y}/\phi_0$ as the external vector potential, $\delta\boldsymbol{A} = \left(\frac{\phi_x}{L_x}, \frac{\phi_y}{L_y}\right) = \frac{\phi_0}{2\pi}\left(\frac{\theta_x}{L_x}, \frac{\theta_y}{L_y}\right)$. Then the current operator in y-direction is given by

$$\hat{I}_y = 2\pi\phi_0^{-1}\partial_y \bar{H}, \bar{H} = H(\bar{h}_{ij}),$$

where $\partial_\alpha = \frac{\partial}{\partial\theta_\alpha}$ $(\alpha = x, y)$. Noting the electric field written by the vector potential as $\boldsymbol{E} = -\partial_t \boldsymbol{A}$, the external electric field in x-direction E_x is expressed by $\delta A_x = -E_x t$, which induces adiabatic time dependence of the system by $\partial_t = -L_x E_x \frac{2\pi}{\theta_0}\partial_x = -V_x \frac{2\pi}{\theta_0}\partial_x$ where $V_x = L_x E_x$ may be understood as a potential difference across the system in x-direction although we assume the system is periodic.

Since *the system is gapped*, the time-dependent ground state $|G\rangle$ is written by the adiabatic approximation as (Thouless, 1983)

$$|G\rangle = e^{i\Gamma}\left(|g\rangle + i\hbar \sum_{\alpha \neq g} \frac{|\alpha\rangle\langle\alpha|\partial_t g\rangle}{E_\alpha - E_g}\right)$$

where $|\alpha\rangle$ is a many-particle eigenstate of the Hamiltonian $\bar{H}$ as $\bar{H}|\alpha\rangle = |\alpha\rangle E_\alpha$, $\Gamma \in \mathbb{R}$ and $|G(0)\rangle = |g(0)\rangle$ where $|g\rangle$ is a ground state of $\bar{H}$. After a few algebra, one obtains a compact form for the Hall conductance $\sigma_{yx} = I_y/V_x$, $I_y = \langle G|\hat{I}_y|G\rangle$ as

$$\sigma_{yx} = \frac{e^2}{h}\mathcal{C}, \quad \mathcal{C} = \frac{1}{2\pi i}\int_{T^2} d^2\theta\, \mathcal{B}_z$$
$$\mathcal{B} = \mathrm{rot}\,\mathcal{A}, \quad \mathcal{A} = \langle g|\boldsymbol{\nabla} g\rangle,$$

where $\boldsymbol{\nabla} = (\partial_x, \partial_y, \partial_z)$, $T^2 = \{(\theta_x, \theta_y) | 0 \leq \theta_{x,y} \leq 2\pi\}$ is a two dimensional torus and $\mathcal{C}$ is the (first) Chern number of the Berry connection $\mathcal{A}$ (Avron et al., 1983; Kohmoto, 1985). This is the Niu-Thuoless-Wu formula (Niu et al., 1985).

As for the non-interacting system, the Chern number C^ℓ is written by that of the one-particle state $|\psi^\ell\rangle$,

$$\mathcal{C} = \sum_{\ell=1}^{M} C^\ell, \quad C^\ell = \frac{1}{2\pi i}\int_{T^2_{\mathrm{BZ}}} d^2k\, b_z^\ell(\boldsymbol{k}),$$
$$\boldsymbol{b}^\ell(\boldsymbol{k}) = \mathrm{rot}\,\boldsymbol{a}^\ell, \quad \boldsymbol{a}^\ell(\boldsymbol{k}) = \langle\psi^\ell(\boldsymbol{k})|\boldsymbol{\nabla}_k \psi^\ell(\boldsymbol{k})\rangle$$

where $h(\boldsymbol{k})|\psi^\ell(\boldsymbol{k})\rangle = |\psi^\ell(\boldsymbol{k})\rangle\epsilon^\ell(\boldsymbol{k})$ is a Bloch function of the ℓ-th band and T^2_{BZ} is the Brillouin zone. We assume the system is a band insulator where the Fermi energy is in the M-th energy gap. This is the celebrated TKNN formula (Thouless et al., 1982; Kohmoto, 1985) written by the Berry connection $\boldsymbol{a}$ of the Bloch state.[2] Although explicit calculations of the Chern number are tricky due to the phase ambiguity of the eigenstate (gauge freedom of the Berry connection, $\mathcal{A}$ and $\boldsymbol{a}$), today, a well-established numerically stable and efficient method is known (Fukui et al., 2005).

Bulk-edge correspondence

Quantum Hall effect to Chern insulators

The TKNN integer is determined without any mention to the boundaries. It implies that the TKNN integer as a topological invariant is a bulk property. According to the Laughlin argument, the Hall conductance is also determined by the consideration of the edge states. Here let us discuss the edge states associated with the TKNN integers, which induces a new topological invariant.

When the system is in a uniform magnetic field, effects of magnetic field are included by the Peierls phase for the hopping h_{ij}. On a square lattice with nearest-neighbor hopping, it is given in the Landau gauge as $h_{j+(1,0),j} = h_{j,j+(1,0)} = -t$ and $h_{j+(0,1),j} = h^*_{j,j+(0,1)} = -te^{i2\pi\phi m}$, $(j = (m,n), t \in \mathbb{R})$ where $2\pi\phi\phi_0$ is a flux per plaquette and $\phi = p/q$ with mutually prime integers p and q. By assuming that $\psi_j = e^{ik_y n}\varphi_m$ (analogs to the discussion of the Landau gauge in the continuum), the one-particle Schrödinger equation, $H|\psi\rangle = |\psi\rangle E$ reduces to the Harper equation, that is a lattice analog of that of the harmonic oscillator,

---

[2] Historically the TKNN formula was first discovered based on the linear response theory and extended to the Niu-Thouless-Wu formula (Niu et al., 1985).

$$\varphi_{m+1} + \varphi_{m-1} + 2\cos(k_y - 2\pi\phi m)\varphi_m = -\epsilon\varphi_m,$$

where $\epsilon = E/t$. Here we consider two cases. The first one is a periodic infinite system (without boundaries). It is for a bulk which gives the TKNN integer. The other is an open-boundary condition, $\varphi_0 = \varphi_{L_x} = 0$, that is for a cylindrical system (Hatsugai, 1993a). This is with edges.

The translation invariance of the Harper equation, $m \to m + q$, implies the Bloch condition

$$\varphi_{m+q} = \rho\varphi_m.$$

The translation invariance further requires that the state is extended as $\rho(k_x) = e^{ik_x}$, $|\rho| = 1$. They define q energy bands for the spectrum, $\epsilon_\ell(k_x, k_y)$, $\ell = 1, \cdots, q$. With boundaries, there appear $g = q - 1$ localized states near the boundaries of the cylinder whose energies μ_j's ($j = 1, \ldots g$) are in each of the j-th band gap, $\epsilon_\ell(k_x, k_y) \le \mu_j(k_y) \le \epsilon_{\ell+1}(k_x, k_y)$, $\ell = 1, \cdots, g$ for each k_y, if $L_x = qL'_x$, $L'_x \in \mathbb{N}$ for the Harper equation.[3] See Fig. 2 for an example. In this case, the unknown integer in the Laughlin argument is $I_\ell = +1$ ($\ell = 2$), that is a number of the edge states connecting the bands below and above the ℓ-th gap where the Fermi energy lies. It is denoted here by I_ℓ.

As for the Hall conductance, we have two different expressions, $\sigma_{yx}^{\text{bulk}} = \frac{e^2}{h}C$, by bulk due to TKNN and $\sigma_{yx}^{\text{edge}} = \frac{e^2}{h}I_\ell$ for cylindrical system by the Laughlin argument. Then we expect the following physically natural relation which was proved for the system that reduces to the Harper equation (Hatsugai, 1993b)

$$\sigma_{yx}^{\text{bulk}} = \sigma_{yx}^{\text{edge}}. \tag{2}$$

This is the bulk-edge correspondence (Hatsugai, 1993b, 1997). This is a relation for a many-particle state and should be valid not only for the non-interacting system but also for a system with interaction as far as the energy gap of the many particle state does not close. In the non-interacting case, it reduces to the relation for the one-particle states (energy bands) as $\sum_{j=1}^{\ell} C_j = I_\ell$, ($I_0 = 0$). Then by shifting the Fermi energy to the (ℓ−1)-th gap, it implies a fundamental formula for a relation for one-particle states (Hatsugai, 1993b) with and without edges

$$C_\ell = I_\ell - I_{\ell-1}. \tag{3}$$

If the Chern number of the band is non-zero, there exist necessarily edge states in the energy gap above or below the energy band for the system with edges. One can predict the existence of the edge states without any calculation with edges. Only a calculation with the Bloch condition is enough. As pointed out later, this formula is applicable not only for quantum Hall systems but also for various systems including classical analogs.

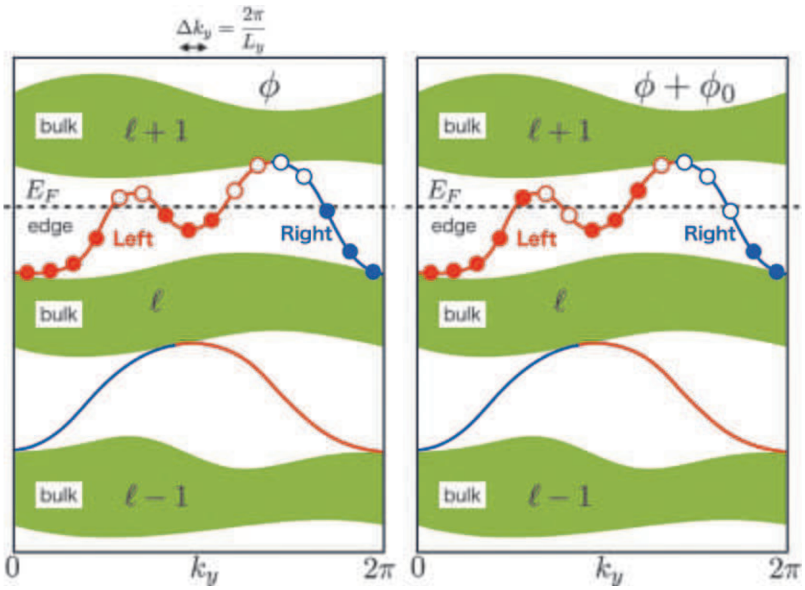

Fig. 2 Schematic energy spectrum of the Harper equation ($q = 3$ and $\ell = 2$ here) as a function of k_y ($L_x = qL'_x, L'_x \in \mathbb{N}$). Green areas are energy bands and the lines in the gaps are energies of the edge states. The dotted line is the Fermi energy. The ground state of the left system is (adiabatically) connected to that of the right by the increase of the AB flux by ϕ_0 where the system size is sufficiently large and the hybridization between the right and left edge states is neglected.

---

[3] Due to the Laughlin argument, the behavior of the edge states is independent of the details of the boundaries, although their explicit behavior depends on them. Then we can safely discuss its topological behavior for the special parameters.

As for the cylindrical system that reduces to the Harper equation, we may go further topologically. The integer I_j that appears in the Laughlin argument has an independent topological meaning. By the suitable analytical continuation of the energy, $\epsilon \to z \in \mathbb{C}$, of the Bloch state $\varphi_j(z)$, the Bloch state satisfies the open boundary condition (Hatsugai, 1993a) $\varphi_0(\mu) = 0$ and $\varphi_{L_x}(\mu) = \rho^{L'_x} = 0$. It implies that the energies of the edge states, μ_j, are zeros of the Bloch function $\varphi_0(z) = 0$ on the extended complex energy surface, that is a genus $g = q - 1$ Riemann surface Σ_g. See Fig. 3 and its caption for the construction and an example, $q = 3$ and $g = 2$. Note that the energy bands are the branch cuts and the energy gaps form loops inside the g holes and the energies of the edge states, μ_j, locate on it.

On the Riemann surface, the positions of the edge states are specified by the location of μ_j. When the edge state is localized near the left(right) boundary of the cylinder, μ_j is on the Riemann surface R_+ (R_-).[4] This construction of the Riemann surface is for a fixed momentum k_y. Assuming the energy gap is finite for all momentum k_y, each of the Riemann surface is topologically equivalent and identified as Σ_g. The periodicity of the Harper equation for $k_y \in \{0, 2\pi\}$ implies that the edge state energies μ_j form oriented loops denoted by $\mathcal{L}_j$ which define winding numbers $w(\mathcal{L}_j)$. Noting that the position of the edge state on the Riemann surface and that of the real space behavior is related, these winding numbers of the loops $\mathcal{L}_j$ is the unknown integer in the Laughlin argument as $I_j = w(\mathcal{L}_j)$, that is, I_j is a topological number of the edge states.

Although the Chern numbers are gauge independent, that is, independent of the phase of the Bloch state, the gauge fixing of the Bloch state is fundamental. It was first pointed out in ref. Kohmoto (1985) and the general scheme of the gauge fixing is given in ref. Hatsugai (2004). For example, the derivative by parameters is not defined without gauge fixing. Simplest gauge fixing, the convention for the phase of the Bloch state is assuming the q-th component of the Bloch state φ_q to be real positive (Kohmoto, 1985; Hatsugai, 1993b, 2004). However, this convention does not work if $\varphi_q = 0$. This is the gauge singularities. It also implies that the Bloch state also satisfies the condition with edges since $\varphi_q = \rho\varphi_0 = 0$. As shown in the Fig. 3, the loop $\mathcal{L}_j$ of the j-th gap cuts the energy bands (branch cuts) above and below the gap I_j times, that gives gauge singularities of the Berry connections for the j-th and ($j + 1$)-th bands. It results in the bulk-edge correspondence of the one-particle Chern number Eq. (3) (See ref. Hatsugai, 1993b of the details of the mathematical proof).

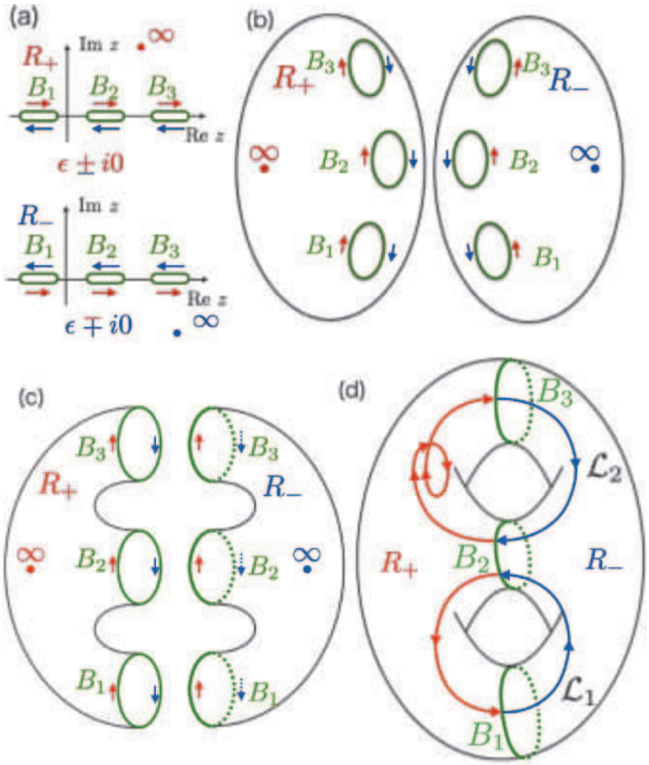

Fig. 3 The Riemann surface Σ_g (complex energy surface) of the Bloch function for the Harper equation ($q = 3$ and $g = q - 1 = 2$ here) (Hatsugai, 1993a). (a) Make branch cuts along the energy bands $\epsilon \pm i0$ for the two complex energy planes $R_\pm$. (b) Make 2 Riemann spheres by identifying ∞ to a point for each. (c) Glue 2 Riemann spheres by the branch cuts along the red (blue) arrows. (d) The Riemann surface with $g = q - 1$ holes and the zeros of the Bloch function φ_j, μ_j, are on the real axes inside the holes. When the edge state is localized near the left (right) boundary of the cylinder, it is on the Riemann surface R_+ (R_-). The g energies of the edge states μ_j form oriented loops associated with change of the momentum k_y: $0 \to 2\pi$ that wind I_j times around the holes. In this example, $I_1 = +1$ and $I_2 = -1$. The loops $\mathcal{L}_j$ cuts the energy bands B_{j-1} and B_j. These crossings give gauge singularities for each bands, that is the origin of non-zero Chern numbers, $C_1 = -1$, $C_2 = +1$ and $C_3 = -1$ respectively. It establishes the bulk-edge correspondence Eq. (3) (Hatsugai, 1993b).

---

[4] One may see analogy of the standard discussion of the behavior of the localized state e_{ikx} as localized near $x \sim 0$ if Im $k > 0$ ($x \sim L \gg 1$ if Im $k < 0$).

Universality of the bulk-edge correspondence

Although physical motivation of the original bulk-edge relation, Eq. (3) is for an integer quantum Hall effect and the proof is for the Harper equation, this relation is applicable for various situations universally where a linear partial differential equation with/without edges. This bulk-edge correspondence has been also focused and discussed from mathematical view points as well (Schulz-Baldes et al., 1999; Kellendonk et al., 2002; Graf and Porta, 2013; Hayashi, 2017).

Discovery of the two-dimensional quantum spin Hall state (Kane and Mele, 2005; Bernevig and Zhang, 2006; König et al., 2007) has triggered the universal use of the bulk-edge correspondence (Kane and Mele, 2005; Qi et al., 2006). It is a layered Haldane model (Haldane, 1988) with spins associated with reversed magnetic fields. The Haldane model breaks the time-reversal symmetry and its gapped ground state is characterized by non-zero TKNN integers (Chern numbers). Today there are various such a class of materials, which is known as the Chern insulators where the edge states associated with the bulk-edge correspondence are observed. The quantum spin Hall state preserves the time-reversal symmetry and their Chern number is zero. They are characterized by the non-zero *spin* Chern numbers (if the spin is conserved) which are not physical observables. What should be observed experimentally are localized *spin* edge states due to the bulk-edge correspondence (Kane and Mele, 2005). This is true even if the spin is not conserved assuming the gap is finite and adiabatically connected to the spin conserved system. The bulk is hidden. Nontrivial topology of the bulk is reflected by the localized degrees of freedom as the edge states. As for topological insulators as three dimensional analog (Fu et al., 2007) of the quantum spin Hall states, the situation is the same. The bulk is hidden and the non-trivial topology of the bulk has never been (at least not easily) measured directly. What can be experimentally measured are surface states governed by the non-trivial topology of the bulk. Angle resolved photoemission spectroscopy (ARPES) experiments have been successfully performed and the surface states predicted by the bulk topology are confirmed in various topological insulators (Moore, 2009; Hasan and Kane, 2010; Qi and Zhang, 2011).

The bulk-edge correspondence governs not only quantum systems but also some of classical analogs. The first such an example is photonic crystal with time-reversal symmetry breaking (Haldane and Raghu, 2008; Wang et al., 2008). Electromagnetic fields in material with periodic structures obeying the Maxwell equation possess energy bands and gaps (photonic gaps). Associated with the time-reversal breaking, there exist topological edge states as one-way going (chiral) modes localized near the system boundaries as a complete analog to that of the integer quantum Hall effect (Halperin, 1982; Hatsugai, 1993a). Such edge states are predicted by the bulk-edge correspondence Eq. (3) (Hatsugai, 1993b) by the non-zero TKNN integers (Chern numbers), although these bulk topological numbers do not have any physical meaning such as the quantized Hall conductance. However, these one-way going edge states are experimentally observed (Wang et al., 2009). The bulk is really hidden and the experimental observables are localized edge states where the bulk-edge correspondence plays a crucial role. This is the fundamental concept of the topological photonics (Ozawa et al., 2019).

Now the classical analogs of the quantum Hall states exist in various fields. Topological mechanics and chiral edge states in classical mechanics (Prodan and Prodan, 2009; Kariyado and Hatsugai, 2015; Huber, 2016). A coupled resonator with time-reversal symmetry breaking also possess chiral edge states (Hafezi et al., 2011). Coupled LC circuits are also described by the bulk-edge correspondence and there exist chiral edge states (Ningyuan et al., 2015) (topological circuit). One of the recent surprises is a topological origin of equatorial waves as chiral edge states associated with finite Chern numbers on earth (Delplace et al., 2017). Well known equatorial waves in geophysics as the Kelvin wave and the Yanai wave are due to the bulk-edge correspondence where the Coriolis force on earth breaks the time-reversal symmetry. The equator is a boundary since the Coriolis force vanishes. The bulk-edge correspondence is further applied for phenomena in different fields. Chiral edge states exist in a spatially coupled macroscopic system described by the evolutionary game theory (Yoshida et al., 2021) and active nematic cells (topological biology) (Yamauchi et al., 2020).

Looking back the discussion up to this point, the topological number of bulk, the Chern number and the TKNN integer are defined by the Berry connection associated with the twisted boundary condition. The twist is originated by the large gauge transformation. This gauge invariance needs not be physical one since it may not be directly related to the physical observables. The fictitious gauge invariance mentioned at the beginning of the section "Laughlin argument and edge states" is written as $\nabla \to \nabla - i\frac{A_f}{\phi_f}$ where $\phi_f = \frac{h}{e_f}$ is a flux quantum for the fictitious gauge field. It implies the discussion is not restricted to the quantum mechanics since $\hbar$ is hidden. One may use the topological argument by suitable interpretation of the fictitious flux quantum ϕ_f for the (classical) problem as well. This fictitious gauge invariance also allows to use the Laughlin argument which requires edge states governed by the bulk topological number. This conceptually justifies the bulk-edge correspondence for the various non-quantum problems.

Since the conceptual background of the bulk-edge correspondence is a formal analogy to the quantum Hall effects, it is directly applied for two-dimensional problems. When the momentum along the boundary is conserved, one may apply the bulk-edge correspondence for three dimensional problems by slicing the system with a section with fixed such a momentum. The three dimensional quantum Hall effects is a typical and historical example (Halperin, 1987). Assuming the energy gap for fixed momentum, say k_z, one may consider 3-dimensional system as a set of 2-dimensional systems parameterized by k_z. Three dimensional Weyl semi-metals (Wan et al., 2011) can be understood in this way. One may define a Chern number for each section specified by k_z. If this Chern number (section Chern number (Oono et al., 2016)) is non-zero, there exist an edge state due to the bulk-edge correspondence for a system with/without edges specified by k_z. This edge state is the Fermi-arc. The section Chern number may change by changing k_z associated with the gap closing (topological phase transition), which is the Weyl point. It implies that the Fermi-arc are connecting the Weyl points.

Another physical system where the bulk-edge correspondence plays a fundamental role is a one-dimensional topological (adiabatic) pump originally proposed by Thouless (Thouless, 1983) in 1980s. The word, "pump," implies the system is periodic in time. Assuming the adi-abaticity, the time can be considered as a periodic parameter such as a conserved momentum along the cylinder in the Laughlin argument. The momentum k_y in Fig. 2 can be reinterpreted as a time, t, as $k_y \to 2\pi \frac{t}{T}$ where T is a period of the pump (Hatsugai and Fukui, 2016). Then one may apply the bulk-edge correspondence for a one-dimensional adiabatic pump. After more than several decades studies, this theoretical idea has been experimentally realized in synthetic systems of cold atoms (Nakajima et al., 2016; Lohse et al., 2016). The role of edge state has been discussed motivated by the experimental realization (Hatsugai and Fukui, 2016). It is quite special since the physical observable of the topological pump is a center of mass due to bulk and the edge states cannot be directly measured since gapless nature of the edge states implies that effects of the edge states are hardly observed experimentally. Instead, a topological origin of the topological pump (physical reason for the quantization of the pumped charge) is clear by the argument of the edge state (See ref. Hatsugai and Fukui, 2016). Contrary to the standard topological phases, the edges are hidden and the bulk induces physical observables. This is a unique feature of the topological pump. Still the bulk-edge correspondence plays a fundamental role. As for the topological pump of correlated systems such as interacting fermions and quantum spins, reinterpretation of the time, as a synthetic dimension of the two dimensional topological phases, is impossible. It opens a new area of topological physics. The gap closing of the symmetry protected phases is an origin of the non-trivial topology associated with the symmetry breaking perturbation specified by the time. The bulk-edge correspondence is a key ingredient of the topological pump of the correlated systems (Kuno and Hatsugai, 2020, 2021a,b; Hatsugai and Kuno, 2023).

As discussed, the concept of the bulk-edge correspondence is quite universal. Let us here mention on the effective field theory of the QHE where the gauge invariance of the system with boundaries requires extra boundary action to be gauge invariant as a whole (Wen, 1990). It is a bulk-edge correspondence from a different point, which supports its universality.

Short-range entangled states, symmetry protection and edge states

The bulk-edge correspondence in two-dimensional phenomena as discussed is topologically stable and physically strong against small but finite perturbation unless the energy gap collapses. One may extend the bulk-edge correspondence for wider class of phenomena as generic bulk-edge correspondence (bulk-boundary correspondence) by imposing an additional symmetry restriction. This is the idea of symmetry protection (Hatsugai, 2006; Pollmann et al., 2012; Chen et al., 2013).[5] A topological order parameter of the symmetry protected topological phases can be a quantized Berry phase (Hatsugai, 2006). Instead of the Chern number that is intrinsically quantized, the Berry phase takes any value in modulo 2π due to the gauge ambiguity (Berry, 1984; Wilczek and Zee, 1984). It has been discussed in momentum space in relation to the polarization (King-Smith and Vanderbilt, 1993). With the symmetry protection, the Berry phase is quantized and works as a topological order parameter (Hatsugai, 2006).

Let us define a short-range entangled state as a set of clusters coupled with each other adiabatically by a short-range interaction without gap closing (Hatsugai, 2006; Kariyado and Hatsugai, 2014) (See Fig. 4). "Adiabatically coupled" implies that the gapped decoupled clusters are coupled to each other without gap closing. In other words, the short-range entangled state is adiabatically

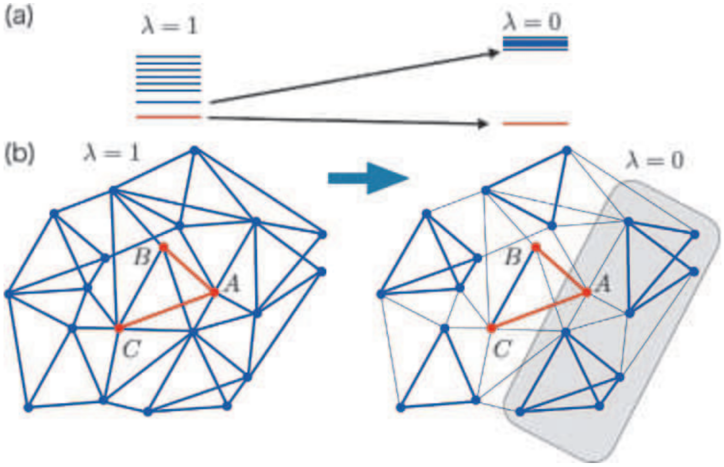

Fig. 4 Adiabatic deformation of a short-range entangled state and edge states. This adiabatic deformation is specified by $\lambda \in [0, 1]$. (a) Many-particle energy spectrum. (b) Cluster decomposition and a system with an edge state (gray region). We assume the system is a collection of the decoupled clusters when $\lambda = 0$.

---

[5] The symmetry protection by the time-reversal symmetry has been fundamentally important for quantum spin Hall effects and topological insulators (Kane and Mele, 2005).

deformed to a collection of clusters. The former way of the construction is trivial if the coupling is small. This weak coupling ansatz may not be necessary. The interaction between the clusters can be comparable to the one inside. Then the latter way of the construction is a highly non-trivial statement since the distribution of the couplings of the final system does not necessarily reflect the original set of the clusters. It is highly non-trivial task to find the set of clusters for a generic short-range entangled state. An $S = 1/2$ Heisenberg quantum spin chain with alternating exchange interaction due to Hida (Hida, 1992) is a typical example where a set of dimers are coupled with each other by the ferromagnetic Heisenberg interaction J_F. Collection of decoupled dimers is trivially gapped but the system is adiabatically deformed (without gap closing) to the highly non-trivial $S = 1$ Haldane spin chain by taking an infinite coupling limit ($J_F \to \infty$) where the Berry phase associated with the dimers characterizes the system, which is the Haldane spin chain (Hatsugai, 2006, 2007). On the other hand, one of the examples, that is not short-ranged entangled state, is a non-trivial Chern insulator. Since the Chern number of the decoupled clusters for any kind of boundary twists is vanishing, a system with a finite Chern number is not short-range entangled.

To be specific, let us consider a fermionic system. Quantum spin systems can be also discussed similarly. As for a decoupled limit, we further assume that the filling of the site we focus, say, the site A is rational as $\rho_A = P/Q$, $P,\ Q \in \mathbb{N}$, $(P, Q) = 1$ where $\rho_j = \langle g_0|\hat{n}_j|g_0\rangle$ with a fermion annihilation operator c_j, its number operator $\hat{n}_j = c_j^\dagger c_j$, the many-particle ground state $|g_0\rangle$ of the whole system and the Hamiltonian $H_0(\lambda)$. Let us introduce a local gauge twist θ by $H_A(0) = U_A(\theta)H_0U_A^\dagger(\theta)$, $U_A = e^{i\theta\hat{n}_A}$ and consider a Berry phase $\gamma_A = -i\int_0^{2\pi}d\theta\ \langle g|\partial_\theta\ g\rangle$ where $H_A(0)|g\rangle = |g\rangle E$. Since $|g\rangle = U_A(\theta)|g_0\rangle$, the Berry phase is fractionally quantized as $\gamma_A = 2\pi\frac{P}{Q}$.

As for the decoupled system, the twists appear in the Hamiltonian H_A as a modified couplings along the red lines in Fig. 4(b) due to the gauge transformation at the site A. Using the same twisted couplings, let us further consider a modified Hamiltonian $H_A(\lambda)$, $(\lambda > 0)$. Note that the twist is not gauged out when $\lambda \neq 0$. Then the Berry phase γ_A may take any value and is not quantized in general. Here we further assume the quantization of the Berry phase γ_A for any λ due to some symmetry (*symmetry protection*). Z_2 quantization of the Berry phase for the Bloch function was discussed in the pioneering work of Zak (Zak phase) (Zak, 1989). This Z_2 quantized Berry phase is used for the proposal of topological order parameter for many particle states and quantum spins (Hatsugai, 2006). This symmetry assisted quantization is extended to define Z_Q $(Q = 2, 3, \ldots)$ Berry phases associated with the Z_Q symmetry (Hatsugai and Maruyama, 2011). Z_Q sub-groups of crystal symmetries are typical examples (See Fig. 5). It includes order 2 unitary/anti-unitary symmetries such as the time-reversal symmetry and the particle hole symmetry of lattice fermions on a bipartite lattice (reduced to the chiral symmetry of one-particle state). We can define Q independent Berry phases, γ_j, $j = 1, \ldots, Q$ and impose physical constraints

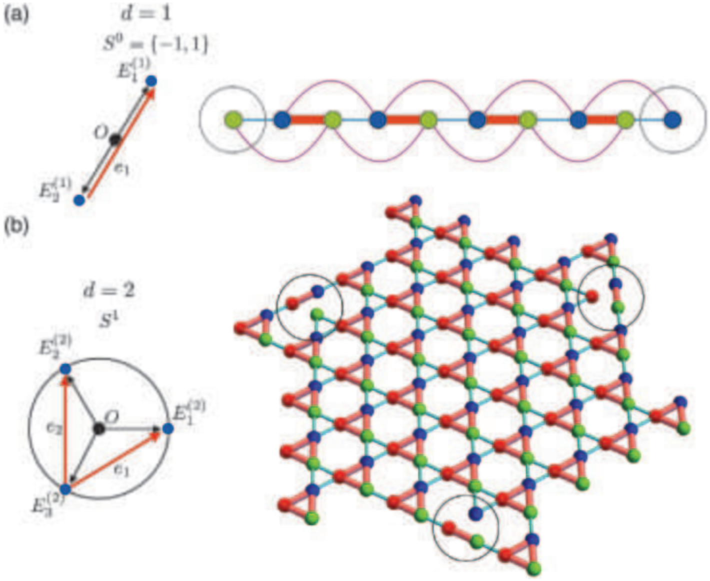

Fig. 5 Z_Q symmetries of the hyper-pyrochlore lattice with edges/defects. $(Q = d + 1)$ Unit vectors on a $(d - 1)$-dimensional sphere, $E_j^{(d)}$, $(j = 1, \cdots Q)$ are shown. d independent translation vectors are specified by $e_j^{(d)} = E_j^{(d)} - E_Q^{(d)}$, $(j = 1, \cdots d)$. Examples for $d = 1$ and $d = 2$ are shown. The black circles are the origins for $d = 1$ and 2. The white circles are uniformly distributed Q points, $E_j^{(d)}$, on the d-dimensional spheres S^d. The colored circles (spheres) of Q species are atomic sites at $\frac{1}{2}E_j^{(d)} + \sum_k n_k E_j^{(d)}$ $(j = 1, \cdots, Q)$ where $^\exists n_k \in \mathbb{Z}$, $\sum_k n_k = 0$. For a suitable shape of the finite system, all atomic sites are connected by the strong bonds (red) except on the boundary (edge/corner/defect) sites (enclosed by thin circles). The weak bonds are shown in pink and cyan. The system with/without boundaries are Z_Q symmetric. Z_Q symmetry is generated by the shift of the colors, $\sigma : E_j^{(d)} \to E_{j+1(\mathrm{mod}\ Q)}^{(d)}$, $\sigma^Q = 1$ (See ref. Hatsugai and Maruyama, 2011 for the definitions of $E_j^{(d)}$ and the details). (a) the dimerized one-dimensional chains $(d = 1)$ and (b) breezing Kagome lattice $(d = 2)$. The Berry phase of the gapped systems with periodic boundary condition is quantized in $\frac{2\pi}{Q}$. The system with the edges/defects has Q degenerate one particle states (with exponential accuracy as for the distance between the corners) which induce $1/Q$ fractionalization.

$$Z_1 \equiv Z_2 \equiv \cdots \equiv Z_Q, \text{mod } 2\pi$$
$$0 = Z_1 + \cdots + Z_Q$$

noting that the Berry phase has a 2π ambiguity (Berry, 1984). It implies the Z_Q quantization as ($n \in \mathbb{Z}$)

$$\gamma_A(\lambda) = 0,\ \ 2\pi\frac{n}{Q},\ \ (\text{mod } 2\pi).$$

This Z_Q-Berry phase is used as a topological order parameter of the short-range entangled states. If the system is a gray region with boundary as shown in Fig. 4, there exists an edge/corner/defect state at the site A. It is clear that the breaking of the cluster induces the localized edge states (corner states and defect states) (Hatsugai, 2011). If the system is fermionic, existence of a single isolated edge/corner/defect site of the multiple decoupled clusters implies degenerate zero energy one-particle states (zero modes) (Ryu and Hatsugai, 2002). One may consider the other fermionic degrees of the bulk freedom are gapped out away from the zero energy. We assume the zero modes are macroscopically separated such as boundaries of the chain. By the adiabatic inclusion of the interaction between the clusters, the energies of the localized one-particle states may deviate from zero due to the local interaction between the defect and surrounding clusters. Still the Q-fold degeneracy is preserved due to the Z_Q symmetry up to exponentially accuracy as for the system size. It results in the $1/Q$ fractionalization (Jackiw and Rebbi, 1976; Ryu and Hatsugai, 2002) (see Fig. 5).

A typical and historical example is a soliton of polyacetylene (Su et al., 1979; Ryu and Hatsugai, 2002) and the localized spin 1/2 degrees of freedom for the $S = 1$ Haldane chain (Kennedy's triplet (Kennedy, 1990; Pollmann et al., 2012)). Majorana bound states of the anomalous superconductor are also due to the similar idea (Kitaev, 2001). Localized states at corners of 2D and 3D systems of higher-order topological insulators have been focused as edges of edges (Benalcazar et al., 2017; Hashimoto et al., 2017; Schindler et al., 2018; Hayashi, 2018; Ezawa, 2018), which are also symmetry protected localized modes in this class. The Z_Q quantized Berry phases are the topological order parameter of the bulk and the relation between the localized modes are considered as *generalized* bulk-edge correspondence (bulk-boundary correspondence) (Araki et al., 2020; You et al., 2020). The Haldane spin chain is a typical correlated system. We do have similar counterparts in electronic systems as a higher-order topological Mott insulator (Kudo et al., 2019; Otsuka et al., 2021).

Slicing the system with conserved momentum as parameters, that works for the discussion of the Weyl semimetal and Fermi-arc, is also effective for the short-range entangled states in higher dimensions. The Fujita states (Fujita et al., 1996; Hatsugai and Aoki, 2014) of the zigzag boundary of graphene and the Andreev bound states of d-wave superconductors in two-dimensions are understood both as one-dimensional edge states with symmetry protection where conserved momentum as a parameter (Ryu and Hatsugai, 2002). In these examples, experimentally observed local boundary magnetization (Okada and Oshiyama, 2001) and local flux generation (symmetry breaking) of the d-wave superconductor are associated with its symmetry breaking (Ryu and Hatsugai, 2004; Matsumoto and Shiba, 1995).

Conclusion

As for the topological phases, the topological number of the bulk and the edge states as localized gapless modes near the boundaries are intimately related. This is the bulk-edge correspondence, which is established for the quantum Hall effect and its lattice analog. Recently the notion of the bulk-edge correspondence is applied not only for quantum but also for many classical phenomena such as gyromagnetic photonic crystals, equatorial waves on earth and, etc. The gauge invariance associated with charge conservation is fundamental. It justifies the universality of the bulk-edge correspondence.

References

Araki H, Mizoguchi T, and Hatsugai Y (2020) Z_Q Berry phase for higher-order symmetry-protected topological phases. *Physical Review Research* 2: 012009.

Avron JE, Seiler R, and Simon B (1983) Homotopy and quantization in condensed matter physics. *Physical Review Letters* 51: 51–53.

Benalcazar WA, Bernevig BA, and Hughes TL (2017) Quantized electric multipole insulators. *Science* 357(6346): 61–66.

Bernevig BA and Zhang S-C (2006) Quantum Spin Hall effect. *Physical Review Letters* 96: 106802.

Berry MV (1984) *Proceedings of the Royal Society* A392: 45.

Chen X, Gu Z-C, Liu Z-X, and Wen X-G (2013) Symmetry protected topological orders and the group cohomology of their symmetry group. *Physical Review B* 87: 155114.

Delplace P, Marston JB, and Venaille A (2017) Topological origin of equatorial waves. *Science* 358(6366): 1075–1077.

Ezawa M (2018) Higher-order topological insulators and semimetals on the breathing kagome and pyrochlore lattices. *Physical Review Letters* 120: 026801.

Fu L, Kane CL, and Mele EJ (2007) Topological insulators in three dimensions. *Physical Review Letters* 98: 106803.

Fujita M, Wakabayashi K, Nakada K, and Kusakabe K (1996) Peculiar localized state at zigzag graphite edge. *Journal of the Physical Society of Japan* 65(7): 1920–1923.

Fukui T, Hatsugai Y, and Suzuki H (2005) Chern numbers in discretized brillouin zone: Efficient method of computing (spin) Hall conductances. *Journal of the Physical Society of Japan* 74: 1674.

Graf GM and Porta M (2013) Bulk-edge correspondence for two-dimensional topological insulators. *Communications in Mathematical Physics* 324(3): 851–895.

Hafezi M, Demler EA, Lukin MD, and Taylor JM (2011) Robust optical delay lines with topological protection. *Nature Physics* 7(11): 907–912.

Haldane FDM (1988) Model for a quantum Hall effect without landau levels: Condensed-matter realization of the "parity anomaly". *Physical Review Letters* 61: 2015–2018.

Haldane FDM and Raghu S (2008) Possible realization of directional optical waveguides in photonic crystals with broken time-reversal symmetry. *Physical Review Letters* 100: 013904.

Halperin BI (1982) Quantized Hall conductance, current-carrying edge states, and the existence of extended states in a two-dimensional disordered potential. *Physical Review B* 25: 2185.

Halperin BI (1987) Possible states for a three-dimensional electron gas in a strong magnetic field. *Japanese Journal of Applied Physics* 26(S3–3): 1913.

Hasan MZ and Kane CL (2010) Colloquium: Topological insulators. *Reviews of Modern Physics* 82: 3045–3067.
Hashimoto K, Wu X, and Kimura T (2017) Edge states at an intersection of edges of a topological material. *Physical Review B* 95: 165443.
Hatsugai Y (1993a) Chern number and edge states in the integer quantum Hall effect. *Physical Review Letters* 71: 3697–3700.
Hatsugai Y (1993b) Edge states in the integer quantum Hall effect and the Riemann surface of the Bloch function. *Physical Review B* 48: 11851–11862.
Hatsugai Y (1997) Topological aspects of the quantum Hall effect. *Journal of Physics: Condensed Matter* 9(12): 2507–2549.
Hatsugai Y (2004) Explicit gauge fixing for degenerate multiplets: A generic setup for topologicalorders. *Journal of the Physical Society of Japan* 73: 2604.
Hatsugai Y (2006) Quantized Berry phases as a local order parameter of a quantum liquid. *Journal of the Physical Society of Japan* 75(12): 123601.
Hatsugai Y (2007) Quantized Berry phases for a local characterization of spin liquids in frustrated spin systems. *Journal of Physics: Condensed Matter* 19(14): 145209.
Hatsugai Y (2011) Symmetry, dirac cones & berry connection for frustrated fermions: Characterization of short-range entangled states. In: *Invited Talk, The 26th Nishinomiya-Yukawa Memorial International Workshop: Novel Quantum States in Condensed Matter (NQS2011)*.
Hatsugai Y and Aoki H (2014) Graphene: Topological properties, chiral symmetryand their manipulation. In: Aoki H and Dresselhaus MS (eds.) *Physics of Graphene*, pp. 213–250. Springer.
Hatsugai Y and Fukui T (2016) Bulk-edge correspondence in topological pumping. *Physical Review B* 94: 041102.
Hatsugai Y and Kuno Y (2023) Topological pump of *SU(Q)* quantum chain and Diophantine equation. *Physical Review B* 107: 235106.
Hatsugai Y and Maruyama I (2011) Z_Q topological invariants for polyacetylene, kagome and pyrochlore lattices. *Europhysics Letters* 95(2): 20003.
Hayashi S (2017) Bulk-edge correspondence and the cobordism invariance of the index. *Reviews in Mathematical Physics* 29: 1750033.
Hayashi S (2018) Topological invariants and corner states for hamiltonians on a three-dimensional lattice. *Communications in Mathematical Physics* 364(1): 343–356.
Hida K (1992) Crossover between the haldane gap phase and the dimer phase in the s1/2 alternating h chain. *Physical Review B* 45: 2207.
Huber SD (2016) Topological mechanics. *Nature Physics* 12(7): 621–623.
Jackiw R and Rebbi C (1976) Solitons with fermion number $\frac{1}{2}$. *Physical Review D* 13: 3398–3409.
Kane CL and Mele EJ (2005) Z_2 topological order and the quantum spin Hall effect. *Physical Review Letters* 95: 146802.
Kariyado T and Hatsugai Y (2014) Fractionally quantized Berry phase, adiabatic continuation, and edge states. *Physical Review B* 90: 085132.
Kariyado T and Hatsugai Y (2015) Manipulation of dirac cones in mechanical graphene. *Scientific Reports* 5(1): 18107.
Kellendonk J, Richter T, and Schulz-Baldes H (2002) Edge current channels and Chern numbers in the integer quantum Hall effect. *Reviews in Mathematical Physics* 14: 87.
Kennedy T (1990) Exact diagonalisations of open spin-1 chains. *Journal of Physics. Condensed Matter* 2: 5737.
King-Smith RD and Vanderbilt D (1993) Theory of polarization of crystalline solids. *Physical Review B* 47: 1651–1654.
Kitaev AY (2001) Unpaired majorana fermions in quantum wires. *Physics-Uspekhi* 44(10S): 131.
Klitzing Kv, Dorda G, and Pepper M (1980) New method for high-accuracy determination of the fine-structure constant based on quantized Hall resistance. *Physical Review Letters* 45: 494–497.
Kohmoto M (1985) Topological invariant and the quantization of the Hall conductance. *Annals of Physics* 160(2): 343–354.
König M, Wiedmann S, Brüne C, Roth A, Buhmann H, Molenkamp LW, Qi X-L, and Zhang S-C (2007) Quantum spin Hall insulator state in hgte quantum wells. *Science* 318(5851): 766–770.
Kudo K, Watanabe H, Kariyado T, and Hatsugai Y (2019) Many-body Chern number without integration. *Physical Review Letters* 122: 146601.
Kuno Y and Hatsugai Y (2020) Interaction-induced topological charge pump. *Physical Review Research* 2. 042024(R).
Kuno Y and Hatsugai Y (2021a) Plateau transitions of a spin pump and bulk-edge correspondence. *Physical Review B* 104: 045113.
Kuno Y and Hatsugai Y (2021b) Topological pump and bulk-edge-correspondence in an extended Bose-Hubbard model. *Physical Review B* 104: 125146.
Laughlin RB (1981) Quantized Hall conductivity in two dimensions. *Physical Review B* 23. 5632(R).
Lohse M, Schweizer C, Zilberberg O, Aidelsburger M, and Bloch I (2016) A Thouless quantum pump with ultracold bosonic atoms in an optical superlattice. *Nature Physics* 12(4): 350–354.
Matsumoto M and Shiba H (1995) Coexistence of different symmetry order parameters near a surface in d-wave superconductors i. *Journal of the Physical Society of Japan* 64(9): 3384–3396.
Moore J (2009) The next generation. *Nature Physics* 5(6): 378–380.
Nakajima S, Tomita T, Taie S, Ichinose T, Ozawa H, Wang L, Troyer M, and Takahashi Y (2016) Topological Thouless pumping of ultracold fermions. *Nature Physics* 12(4): 296–300.
Ningyuan J, Owens C, Sommer A, Schuster D, and Simon J (2015) Time- and site-resolved dynamics in a topological circuit. *Physical Review X* 5: 021031.
Niu Q, Thouless DJ, and Wu Y-S (1985) Quantized Hall conductance as a topological invariant. *Physical Review B* 31: 3372.
Okada S and Oshiyama A (2001) Magnetic ordering in hexagonally bonded sheets with first-row elements. *Physical Review Letters* 87: 146803.
Oono S, Kariyado T, and Hatsugai Y (2016) Section Chern number for a three-dimensional photonic crystal and the bulk-edge correspondence. *Physical Review B* 94: 125125.
Otsuka Y, Yoshida T, Kudo K, Yunoki S, and Hatsugai Y (2021) Higher-order topological mott insulator on the pyrochlore lattice. *Scientific Reports* 11(1): 20270.
Ozawa T, Price HM, Amo A, Goldman N, Hafezi M, Lu L, Rechtsman MC, Schuster D, Simon J, Zilberberg O, and Carusotto I (2019) Topological photonics. *Reviews of Modern Physics* 91: 015006.
Pollmann F, Berg E, Turner AM, and Oshikawa M (2012) Symmetry protection of topological phases in one-dimensional quantum spin systems. *Physical Review B* 85: 075125.
Prodan E and Prodan C (2009) Topological phonon modes and their role in dynamic instability of microtubules. *Physical Review Letters* 103: 248101.
Qi X-L and Zhang S-C (2011) Topological insulators and superconductors. *Reviews of Modern Physics* 83: 1057–1110.
Qi X-L, Wu Y-S, and Zhang S-C (2006) General theorem relating the bulk topological number to edge states in two-dimensional insulators. *Physical Review B* 74: 045125.
Ryu S and Hatsugai Y (2002) Topological origin of zero-energy edge states in particle-hole symmetric systems. *Physical Review Letters* 89: 077002.
Ryu S and Hatsugai Y (2004) Zero-energy edge states and chiral symmetry breaking at edges of graphite sheets. *Physica E: Low-dimensional Systems and Nanostructures* 22(1): 679–683.
Schindler F, Cook AM, Vergniory MG, Wang Z, Parkin SSP, Bernevig BA, and Neupert T (2018) Higher-order topological insulators. *Science Advances* 4(6): eaat0346.
Schulz-Baldes H, Kellendonk J, and Richter T (1999) Simultaneous quantization of edge and bulk Hall conductivity. *Journal of Physics A: Mathematical and General* 33(2): L27–L32.
Su WP, Schrieffer JR, and Heeger AJ (1979) Solitons in polyacetylene. *Physical Review Letters* 42: 1698–1701.
Thouless DJ (1983) Quantization of particle transport. *Physical Review B* 27: 6083–6087.
Thouless DJ, Kohmoto M, Nightingale MP, and den Nijs M (1982) Quantized Hall conductance in a two-dimensional periodic potential. *Physical Review Letters* 49: 405–408.
Wan X, Turner AM, Vishwanath A, and Savrasov SY (2011) Topological semimetal and fermi-arc surface states in the electronic structure of pyrochlore iridates. *Physical Review B* 83: 205101.
Wang Z, Chong YD, Joannopoulos JD, and Soljačić M (2008) Reflection-free one-way edge modes in a gyromagnetic photonic crystal. *Physical Review Letters* 100: 013905.
Wang Z, Chong Y, Joannopoulos JD, and Soljačić M (2009) Observation of unidirectional backscattering-immune topological electromagnetic states. *Nature* 461(7265): 772–775.
Wen XG (1990) Electrodynamical properties of gapless edge excitations in the fractional quantum Hall states. *Physical Review Letters* 64: 2206–2209.
Wilczek F and Zee A (1984) Appearance of gauge structure in simple dynamical systems. *Physical Review Letters* 52: 2111–2114.
Yamauchi L, Hayata T, Uwamichi M, Ozawa T, and Kawaguchi K (2020) Chirality-driven edge flow and non-Hermitian topology in active nematic cells. *arXiv*. 2008.10852.
Yoshida T, Mizoguchi T, and Hatsugai Y (2021) Chiral edge modes in evolutionary game theory: A kagome network of rock-paper-scissors cycles. *Physical Review E* 104: 025003.
You Y, Bibo J, and Pollmann F (2020) Higher-order entanglement and many-body invariants for higher-order topological phases. *Physical Review Research* 2: 033192.
Zak J (1989) Berry's phase for energy bands in solids. *Physical Review Letters* 62: 2747.

Berry phase and geometrical observables

Raffaele Resta, Istituto Officina dei Materiali IOM-CNR, Trieste, Italy; Donostia International Physics Center, Donostia-San Sebastián, Spain

© 2024 Elsevier Ltd. All rights reserved.

This is an update of R. Resta, Geometrical Phase and Polarization in Solids, Editor(s): Franco Bassani, Gerald L. Liedl, Peter Wyder, Encyclopedia of Condensed Matter Physics, Elsevier, 2005, Pages 267–273, ISBN 9780123694010, https://doi.org/10.1016/B0-12-369401-9/01137-2.

Introduction **670**
Bloch geometry **671**
Class I observables **673**
Generalities 673
Polarization 673
Polarization as a topological observable 673
Magnetoelectric response and the “axion” 674
Class II observables **675**
Generalities 675
Time-reversal odd observables 675
Anomalous Hall conductivity 675
Magneto-optical sum rule 676
Orbital magnetization 676
Time-reversal even observables 677
Longitudinal conductivity 677
Souza-Wilkens-Martin sum rule 677
Drude weight 678
Conclusion **679**
Acknowledgments **679**
References **679**

Abstract

Intensive observables in condensed matter have a microscopic formulation in terms of the electronic ground state. In some cases—such e.g., macroscopic electrical polarization and orbital magnetization—such formulation did not exist until relatively recent times; no expression, computationally implementable within band-structure theory, was available. The turning point occurred in 1993 when the theory of polarization (called “modern” at the time) was founded: it was discovered that polarization is a Berry phase, i.e. a geometrical property of the manifold of the occupied Bloch states. Over the following years a few other observables became accessible to electronic-structure theory and revealed their geometrical nature: most notably orbital magnetization in 2006. The present work thoroughly reviews, in the framework of band-structure theory, all the geometrical observables known to the author at the time of writing. Among the observables addressed, there are common features but also outstanding differences, both formal and phenomenological.

Key points

- Crystalline solids addressed via band-structure theory.
- Bloch geometry in reciprocal space.
- Physical observables having their expression in the ground-state geometry.
- Multiple-valued bulk observables versus single-valued ones.
- Observables related to electrostatics, magnetostatics, and electron transport.

Introduction

Electronic structure has undergone a genuine revolution since the early 1990s, when it was found that macroscopic polarization is a geometric phase (Berry phase) of the electronic wavefunction. The geometrical and/or topological nature of several other ground-state intensive observables was elucidated over the following years; the common archetype of these developments is the celebrated discovery, by Thouless et al. (1982), of the topological nature of the quantum Hall effect.

The present review attempts at a taxonomy of the geometrical/topological observables known so far. We address here only crystalline systems of noninteracting electrons (Hartree-Fock or Kohn-Sham), whose ground state is described in terms of occupied Bloch orbitals, and where all intensive observables obtain for insulators as Brillouin-zone (BZ) integrals, and for metals as

https://doi.org/10.1016/B978-0-323-90800-9.00075-5

Fermi-volume integrals. An observable is called geometrical when the essential entries of the integrand are **k**-derivatives of the Bloch states; more precisely of the *lattice-periodical factors* of the Bloch states. In some special cases a geometrical observable may become topological.

As it will become clear below, the known geometrical observables can be sharply partitioned in two classes, which in the following we will address as class I and II. The formal expression of class I observables has an odd number of **k**-derivatives (i.e. one or three) in the integrand, while class II observables are expressed by means of an even number of derivatives (i.e. two). This mathematical difference is at the root of outstanding differences in the physical nature of the observables. For instance observables in class I are defined for insulators only (both formally and phenomenologically), while those in class II may be defined for metals as well.

The overwhelming importance of the number of **k**-derivatives entering the geometrical integrand is best illustrated if we address three paradigmatic observables in their "natural" minimal dimension: polarization is one-dimensional (1D), in the sense that it can it be defined even for a 1D system; anomalous Hall conductivity requires at least two dimensions, and the so-called "axion" (defined in Section "Magnetoelectric response and the "axion"") at least three. When addressed in their minimal dimension, each of these observables obtains as a universal constant times the integral of a dimensionless differential form: 1-form, 2-form, and 3-form, respectively. The coefficients of the 1-form (nowadays called the Berry connection) contains one **k**-derivative, the one of the 2-form (nowadays called the Berry curvature) contains two **k**-derivatives, and those of the 3-form three **k**-derivatives. A basic tenet of differential geometry is that spaces of even and odd dimensions behave quite differently, particularly when considering antisymmetric forms (time-reversal odd in condensed-matter physics). Chern-Simons forms are defined only in odd dimensions, while in dimension $2n$ one may define the n-th Chern form, which is (locally) the generalized curl of the corresponding $2n{-}1$ Chern-Simons form. The three forms listed above are, in mathematical speak, a Chern-Simons 1-form, a first Chern form, and a Chern-Simons 3-form, respectively. The outstanding qualitative difference between the observables of class I and those of class II are ultimately rooted in the different mathematical features of the corresponding differential forms in odd vs. even dimensions.

In our 3D world the expression of a geometrical observable becomes—as said above—a 3D **k**-integral; the number of **k**-derivatives in the integrand is, for a given observable, D-independent. As an explicit example, polarization in 3D is proportional to the BZ integral of a 3D Berry connection, where only one **k**-derivative appears: Eqs. (7) and (15) below.

As for class I, the only observables known so far are those mentioned above: macroscopic polarization and the axion; the latter is a term which originally appeared as a geometrical contribution to magnetoelectric response, but whose role in electronic-structure theory transcends magnetoelectricity. Both class I observables make sense for insulators only, where they obtain as an integral over the BZ, and both are multivalued, defined modulo 2π in dimensionless units: the modulo 2π ambiguity is fixed only after the termination of a bounded insulating sample is specified. Furthermore in presence of some protecting symmetry only the values zero or π (mod 2π) are allowed: this has clearly a one-to-one mapping to the additive group of the integers modulo 2: the $\mathbb{Z}_2$ group. The observable becomes then a topological index: a $\mathbb{Z}_2$-odd crystalline insulator cannot be "continuously deformed" into a $\mathbb{Z}_2$-even one without closing the gap and/or breaking the symmetry protection.

Several ground-state geometrical observables are instead known in class II; differently from class I, all of them are single-valued, and some exist even for metals (both phenomenologically and formally). In the following synoptic table we partition them into time-reversal (T) odd and even; in the former case they can be nonzero only if the solid spontaneously breaks T-symmetry.

Time-reversal odd	*Time-reversal even*
Anomalous Hall conductivity	Souza-Wilkens-Martin sum rule
Magneto-optical sum rule	??
Orbital magnetization	Drude weight

All these observables will be defined and discussed below in Section "Class II observables"; here I only comment about the inclusion of a couple of sum rules in the table. A sum rule is a frequency integration, hence not a ground-state property; nonetheless, even if the experiment probes the excitations of the solid, the measured quantity is uniquely determined by its electronic ground state.

In Section "Bloch geometry" we define the main quantities which formally address the geometry of the occupied Bloch manifold: Bloch projector, Berry connection, Berry curvature, quantum metric. In Section "Class I observables" we provide the formal expressions for the only known geometrical observables in class I: macroscopic electric polarization and the axion.; we also discuss their topological implication in presence of a protecting symmetry. In Section "Class II observables" we provide the formal expression and a brief discussion for all the five class-II observables in the synoptic table. For each of them, the geometrical integrand is explicitly displayed twice: once in the standard gauge (the Hamiltonian gauge, defined below) and one gauge-invariant in form. Some general conclusions are drawn in Section "Conclusion".

Bloch geometry

The electronic ground-state properties of an independent-electron system are embedded in the one-particle density matrix; for a singlet ground state it equals twice the (spinless) ground state projector $\mathscr{P}$. In a crystalline solid the orbitals assume the Bloch form: $|\psi_{j\mathbf{k}}\rangle = e^{i\mathbf{k}\cdot\mathbf{r}} \mid u_{j\mathbf{k}}\rangle$; here we normalize them to one over the unit cell of volume V_{cell}. The $|u_{j\mathbf{k}}\rangle$ orbitals are eigenstates of $\mathscr{H}_{\mathbf{k}} = \mathrm{e}^{-i\mathbf{k}\cdot\mathbf{r}}\mathscr{H}\,\mathrm{e}^{i\mathbf{k}\cdot\mathbf{r}}$ with eigenvalues $\varepsilon_{j\mathbf{k}}$. The $|\psi_{j\mathbf{k}}\rangle$ at different $\mathbf{k}$ values are orthogonal, hence they belong to different Hilbert spaces; one considers instead the quantum geometry of the $|u_{j\mathbf{k}}\rangle$ state vectors, defined in the Hilbert space of the lattice-periodical functions.

A unitary transformation of the occupied $|u_{j\mathbf{k}}\rangle$ among themselves leaves the many-body wavefunction, and all ground-state observables, unchanged. Mixing the **k** vectors yields the Wannier functions (in insulators). Here we only consider transformations at fixed **k**:

$$|u_{j\mathbf{k}}\rangle \to |\tilde{u}_{j\mathbf{k}}\rangle = \sum_{\varepsilon_{j'\mathbf{k}}<\mu} U_{jj'}(\mathbf{k})\, |u_{j'\mathbf{k}}\rangle; \tag{1}$$

in mathematical language the unitary matrix $U(\mathbf{k})$ is an element of the nonAbelian gauge group. Even for metals we aim at formula which are gauge-invariant in the sense of Eq. (1). It is customary to dub "Hamiltonian gauge" any gauge where the Hamiltonian eigenstates are *not* unitarily transformed (Vanderbilt, 2018).

The ground-state projector is by definition

$$\mathscr{P} = V_{\text{cell}} \sum_j \int_{\text{BZ}} [d\,\mathrm{k}]\; \theta(\mu - \varepsilon_{j\mathbf{k}}) |\psi_{j\mathbf{k}}\rangle\langle\psi_{j\mathbf{k}}|, \tag{2}$$

where the integration is over $[d\,\mathrm{k}] = d\mathbf{k}/(2\pi)^d$, d is the dimension, and μ is the Fermi level. For $d = 1{,}2$ the cell volume V_{cell} must be understood as length and area, respectively; $\mathscr{P}$ is a lattice-periodical operator, commuting with the translation group. We cast $\mathscr{P}$ in terms of gauge-invariant Bloch projectors $\mathscr{P}_{\mathbf{k}}$, defined as follows:

$$\langle \mathbf{r}|\mathscr{P}|\mathbf{r}'\rangle = V_{\text{cell}} \int_{\text{BZ}} [d\mathrm{k}]\; e^{i\mathbf{k}\cdot(\mathbf{r}-\mathbf{r}')} \langle \mathbf{r}|\mathscr{P}_{\mathbf{k}}|\mathbf{r}'\rangle \tag{3}$$

$$\mathscr{P}_{\mathbf{k}} = \sum_j \theta\left(\mu - \varepsilon_{j\mathbf{k}}\right) |u_{j\mathbf{k}}\rangle\langle u_{j\mathbf{k}}|. \tag{4}$$

In order to establish a differential geometry in the space of the parameter **k** we choose a gauge which makes the $|u_{j\mathbf{k}}\rangle$ smooth (i.e. C^∞) throughout the whole BZ; this is always possible, even in topologically nontrivial materials. This allows us to write the **k**-derivatives of $\mathscr{P}_{\mathbf{k}}$:

$$\begin{aligned} \partial_{\mathbf{k}} \mathscr{P}_{\mathbf{k}} = & -\sum_j \delta(\mu - \varepsilon_{j\mathbf{k}}) \partial_{\mathbf{k}} \varepsilon_{j\mathbf{k}} |u_{j\mathbf{k}}\rangle\langle u_{j\mathbf{k}}| \\ & + \sum_j \theta(\mu - \varepsilon_{j\mathbf{k}}) \left(|u_{j\mathbf{k}}\rangle\langle \partial_{\mathbf{k}} u_{j\mathbf{k}}| + |\partial_{\mathbf{k}} u_{j\mathbf{k}}\rangle\langle u_{j\mathbf{k}}|\right). \end{aligned} \tag{5}$$

The δ-like singularity at the Fermi surface vanishes in insulators; as for the remaining contributions, they are smooth in insulators and piecewise smooth in metals. We anticipate that the gauge-invariant derivative $\partial_{\mathbf{k}} \mathscr{P}_{\mathbf{k}}$ will be the main entry of class II geometrical observables.

We focus, for the time being, on an insulator with n occupied bands, where

$$\partial_{\mathbf{k}} \mathscr{P}_{\mathbf{k}} = \sum_{j=1}^{n} \left(|u_{j\mathbf{k}}\rangle\langle \partial_{\mathbf{k}} u_{j\mathbf{k}}| + |\partial_{\mathbf{k}} u_{j\mathbf{k}}\rangle\langle u_{j\mathbf{k}}|\right). \tag{6}$$

Each of the two terms in parenthesis is gauge-dependent; and in fact the trace $\langle u_{j\mathbf{k}}|\, \partial_{\mathbf{k}} u_{j\mathbf{k}}\rangle$, summed over the occupied states and multiplied by i, is the Berry connection entering the theory of polarization, Eq. (15):

$$\mathscr{A}_\alpha(\mathbf{k}) = i \sum_{j=1}^{n} \langle u_{j\mathbf{k}}|\partial_{\mathbf{k}_\alpha} u_{j\mathbf{k}}\rangle. \tag{7}$$

Its curl is by definition the Berry curvature, and is gauge invariant:

$$\Omega_{\alpha\beta}(\mathbf{k}) = i \sum_{j=1}^{n} \left(\langle \partial_{k_\alpha} u_{j\mathbf{k}}|\partial_{k_\beta} u_{j\mathbf{k}}\rangle - \langle \partial_{k_\beta} u_{j\mathbf{k}}|\partial_{k_\alpha} u_{j\mathbf{k}}\rangle\right). \tag{8}$$

In the 2D case the Chern-Gauss-Bonnet theorem states that the dimensionless integral of the curvature (i.e. of the first Chern form) over the BZ (a "compact orientable manifold") is quantized:

$$\frac{1}{2\pi} \int_{\text{BZ}} d\mathbf{k}\;\; \Omega_{xy}(\mathbf{k}) = C_1, \tag{9}$$

where the integer $C_1 \in \mathbb{Z}$ is known as the first Chern number.

In order to establish a metric, one may define a gauge-invariant (squared) distance $D^2_{\mathbf{k},\mathbf{k}+\kappa}$ between the two sets of n occupied states at **k** and $\mathbf{k} + \kappa$, which for infinitesimal κ yields the metric tensor:

$$D^2_{\mathbf{k},\mathbf{k}+d\mathbf{k}} = g_{\alpha\beta}(\mathbf{k}) dk_\alpha dk_\beta, \tag{10}$$

where the sum over repeated Cartesian indices is understood (here and throughout). Its expression is

$$g_{\alpha\beta}(\mathbf{k}) = \operatorname{Re} \sum_{j=1}^{n} \langle \partial_{k_\alpha} u_{j\mathbf{k}} | \partial_{k_\beta} u_{j\mathbf{k}} \rangle - \sum_{jj'=1}^{n} \langle \partial_{k_\alpha} u_{j\mathbf{k}} | u_{j'\mathbf{k}} \rangle \langle u_{j'\mathbf{k}} | \partial_{k_\beta} u_{j\mathbf{k}} \rangle. \tag{11}$$

This metric made its first appearance in electronic structure in the theory of the maximally localized Wannier functions (Marzari and Vanderbilt, 1997). We notice that the second term in Eq. (11) is real, ergo the metric and the curvature can be cast as the real and imaginary (times −2) parts, respectively, of the metric-curvature tensor

$$F_{\alpha\beta}(\mathbf{k}) = \sum_{j=1}^{n} \langle \partial_{k_\alpha} u_{j\mathbf{k}} | \partial_{k_\beta} u_{j\mathbf{k}} \rangle - \sum_{jj'=1}^{n} \langle \partial_{k_\alpha} u_{j'\mathbf{k}} | u_{j\mathbf{k}} \rangle \langle u_{j'\mathbf{k}} | \partial_{k_\beta} u_{j\mathbf{k}} \rangle. \tag{12}$$

The tensor $F_{\alpha\beta}(\mathbf{k})$ is gauge-invariant, but not gauge-invariant *in form*: Eq. (12) is cast in the Hamiltonian gauge. Nonetheless it can be identically recast directly in terms of $\mathscr{P}_\mathbf{k}$, ergo as gauge-invariant by inspection:

$$F_{\alpha\beta}(\mathbf{k}) = \operatorname{Tr}\{\mathscr{P}_\mathbf{k}(\partial_{k_\alpha}\mathscr{P}_\mathbf{k})(\partial_{k_\beta}\mathscr{P}_\mathbf{k})\}, \tag{13}$$

where "Tr" indicates the trace over the Hilbert space. We are going to show that an analogous orbital-free expression holds for the geometrical integrands at the root of all the class II observables in the previous table.

Class I observables

Generalities

The observables in class I—defined for insulators only—obtain as the BZ integral of a gauge-dependent integrand, which therefore cannot be *directly* expressed in terms of $\mathscr{P}_\mathbf{k}$. It has been anticipated above that, in the case of polarization, the relevant ingredient is one of the two terms in Eq. (6), and not their sum. The BZ-integrated quantity is instead gauge-invariant, although modulo 2π (in dimensionless units); the modulo ambiguity in the corresponding observable is fixed for a bounded sample only after its termination is specified. An essential condition is that even the sample surface is insulating, besides its bulk (Vanderbilt, 2018).

It is expedient to define the nonAbelian Berry connection as

$$\mathscr{A}_{jj',\alpha}(\mathbf{k}) = i\langle u_{j\mathbf{k}} | \partial_{k_\alpha} u_{j'\mathbf{k}} \rangle, \tag{14}$$

which for any Cartesian coordinate α is an Hermitian matrix in the (occupied) band indices jj'. The Abelian Berry connection of the occupied Bloch manifold is the trace of the matrix, Eq. (7): it is clearly a vector function of $\mathbf{k}$, and is the main quantum-mechanical entry in the theory of polarization, Eq. (15) below. The nonAbelian Berry connection is instead needed in the axion theory (Section "Magnetoelectric response and the "axion"").

Polarization

The electrical dipole of a bounded sample is well defined only for a globally neutral system; analogously, the macroscopic polarization of a solid is well defined only after the electronic and nuclear contributions are summed.

The—by now famous—Berry phase theory of polarization, first established by King-Smith and Vanderbilt (1993), yields the macroscopic polarization of a crystalline insulator with n doubly occupied bands as (Vanderbilt, 2018)

$$\mathbf{P} = -2ie\sum_{j=1}^{n}\int_{\mathrm{BZ}}[d\mathbf{k}]\langle u_{j\mathbf{k}}|\partial_\mathbf{k} u_{j\mathbf{k}}\rangle + \mathbf{P}^{(\mathrm{nucl})}, \qquad \mathbf{P}^{(\mathrm{nucl})} = \frac{e}{V_{\mathrm{cell}}}\sum_{\ell} Z_\ell \mathbf{R}_\ell, \tag{15}$$

where $\mathbf{R}_\ell$ are the nuclear coordinates in the unit cell, and Z_ℓ the corresponding atomic numbers. The electronic contribution to $\mathbf{P}$ is the BZ integral of the Abelian Berry connection, Eq. (7), times $-2e$. Each of the two contributions separately depends on the (arbitrary) choice of the origin in the unit cell, while their sum is invariant.

A basic tenet of polarization theory holds that—insofar as an unbounded crystalline solid is addressed within band-structure theory—bulk polarization is ambiguous modulo a "quantum", whose value is $e\mathbf{R}/V_{\mathrm{cell}}$, where $\mathbf{R}$ is any lattice vector (Vanderbilt and King-Smith, 1993). This is kind of obvious looking at the nuclear term in Eq. (15): by adding $\mathbf{R}$ to any $\mathbf{R}_\ell$ this term changes by a multiple of the quantum; as for the electronic term, its origin from a Berry phase makes it also arbitrary modulo (twice) the quantum.

In solid state physics it is often legitimate to choose a crystal cell which is a multiple of the primitive cell; this is instead forbidden when addressing $\mathbf{P}$, because the "quantum"—and the multivalued observable—would change. It is therefore worth stressing that, whenever a material is crystalline, a *uniquely defined* lattice is associated with the real sample: the previous statement can even be regarded as an unambiguous definition of "crystallinity". The actual wavefunction might require a supercell in cases e.g., with correlation, quantum nuclei, finite temperature, chemical disorder (i.e. crystalline alloys). … Even in these cases the lattice is a mathematical construction uniquely defined (by means of an appropriate average), and $\mathbf{P}$ is a uniquely defined multivalued observable.

Polarization as a topological observable

It is expedient to switch from the three Cartesian components of $\mathbf{P}$ to the three dimensionless quantities $\gamma_s = V_{\mathrm{cell}}\,\mathbf{G}_s \cdot \mathbf{P}/e$, where $\mathbf{G}_s$ are the fundamental reciprocal-lattice vectors: each of the γ_s is clearly an angle, defined modulo 2π. In presence of inversion

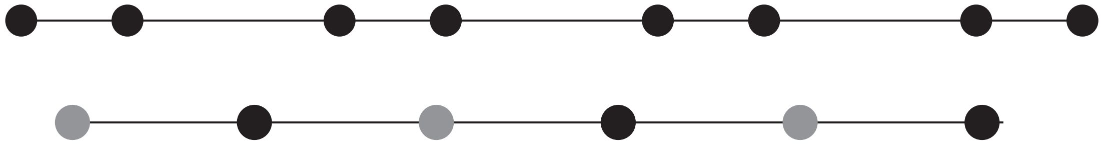

Fig. 1 Two paradigmatic inversion-symmetric lattices in 1d.

(I) symmetry $\mathbf{P} = -\mathbf{P}$, ergo γ_s is either 0 modulo 2π or π modulo 2π: each of the γ_s becomes then a topological $\mathbb{Z}_2$ index, "protected" by I-symmetry (Resta, 2018b).

In 1D the "quantum" is equal to e, and

$$P = \frac{e}{2\pi}\gamma; \tag{16}$$

in the I-symmetric case the two topological classes (i.e. $\mathbb{Z}_2$-even and $\mathbb{Z}_2$-odd) are easily illustrated by means of a toy model Hamiltonian.

The top sketch in Fig. 1 refers to an idealized molecular crystal, or to an alternant polymer, like polyacetylene; the bottom sketch refers to an idealized ionic crystal. Both systems are I-symmetric and can be described at the simplest level by an extreme tight-binding model Hamiltonian, whose only parameters are the first-neighbor hoppings t and the onsite energies ε. The top chain has alternating t's and constant ε; the bottom chain has constant t and alternating ε's. At half filling the system is a one-band insulator (except in the non-alternating case); if we consider spinful electrons, charge neutrality requires +1 classical charges on each site for both chains.

It is simple to show that the top chain in Fig. 1 has $P = 0 \bmod e$: it is $\mathbb{Z}_2$-even; the bottom chain has $P = e/2 \bmod e$, and is $\mathbb{Z}_2$-odd. It is also a straightforward exercise to show that one cannot "continuously deformate" the Hamiltonian (and its ground state) from one case into the other without closing the gap, while conserving I-symmetry. Instead, one could imagine to continuously deformate the I-symmetric Hamiltonian from the model one to a realistic one: as a basic tenet of topology, P cannot change insofar the gap does not close.

If—instead of considering unbounded chains within periodic boundary conditions—we address finite chains, i.e. bounded realizations of the same toy-model Hamiltonians, then P (trivially evaluated as the dipole over the length) converges to its topological value in the long-chain limit, independently of the values of the model parameters.

Magnetoelectric response and the "axion"

In insulators where T-symmetry and I-symmetry are both spontaneously broken a magnetic field $\mathbf{B}$ may linearly induce polarization $\mathbf{P}$ and an electric field $\mathbf{E}$ may induce magnetization $\mathbf{M}$:

$$\alpha_{\beta\gamma} = \frac{\partial P_\beta}{\partial B_\gamma} = \frac{\partial M_\gamma}{\partial E_\beta}; \tag{17}$$

the response tensor $\overleftrightarrow{\alpha}$ is dimensionless (in Gaussian units). A simple magnetoelectric crystal is Cr_2O_3, antiferromagnetic and non-centrosymmetric.

The magnetoelectric tensor $\overleftrightarrow{\alpha}$ is the sum of several terms; here we consider solely the orbital magnetoelectric polarizability, i.e. the clamped-nuclei orbital response only. The tensor obtains from the appropriate Kubo formula and therefore is *not* a ground-state property; nonetheless besides Kubo, an additional purely geometrical term enters the response (Malashevich et al., 2010). This term is a pseudoscalar: it accounts for a component of magnetization parallel to the electric field, or equivalently for a component of polarization parallel to the magnetic field. We are going to focus on this component only, called the "axion", and indicated with the scalar α. This ground-state geometrical term deserves much attention per se, well beyond its actual contribution to Eq. (17) (Vanderbilt, 2018).

Looking back at Eq. (16), we recognize that P in 1D obtains as a universal constant, times the phase angle γ, and divided by 2π. The electronic contribution to γ is a Berry phase, i.e. the BZ integral of a Chern-Simons 1-form: the 1D Abelian Berry connection, which in turn is the trace of the nonAbelian one, Eq. (14). The axion α has a very similar form:

$$\alpha = \frac{1}{4\pi^2}\frac{e^2}{\hbar c}\theta = \frac{e^2}{hc}\frac{\theta}{2\pi}, \tag{18}$$

where one recognizes the fine-structure constant. The angle θ obtains as the BZ integral of a Chern-Simons 3-form, i.e. of the trace (over the band indices) of an expression whose only entry is the 3D nonAbelian connection, Eq. (14), and where three $\mathbf{k}$-derivatives appear. Therefore θ can be interpreted as the 3D generalization of the Berry phase in 1D. Both γ and θ are defined modulo 2π, hence both P and α are multivalued observables.

The Chern-Simons 3-form and the angle θ have a simple and elegant expression in the compact mathematicians' notations, based on wedge products and exterior differentiations. When translated into the prolix notations of electronic-structure theory, θ has the following (rather formidable) expression in terms of the nonAbelian connection matrices $\mathcal{A}_\alpha(\mathbf{k})$, Eq. (14):

$$\theta = -\frac{1}{4\pi}\varepsilon_{\alpha\beta\gamma}\int_{\mathrm{BZ}} d\mathbf{k}\,\mathrm{tr}\left[\mathcal{A}_\alpha(\mathbf{k})\partial_{k_\beta}\mathcal{A}_\gamma(\mathbf{k}) - \frac{2i}{3}\mathcal{A}_\alpha(\mathbf{k})\mathcal{A}_\beta(\mathbf{k})\mathcal{A}_\gamma(\mathbf{k})\right], \tag{19}$$

where $\varepsilon_{\alpha\beta\gamma}$ is the antisymmetric tensor, and the symbol "tr" indicates the trace of the matrix (over the band indices), not to be confused with the symbol "Tr" used elsewhere.

In presence of either T-symmetry or I-symmetry $\theta = -\theta$, therefore either $\theta = 0$ or $\theta = \pi$ (modulo 2π): even in this case we have a topological, symmetry-protected, $\mathbb{Z}_2$ index. The T-invariant insulators where $\theta = \pi$ (i.e. $\mathbb{Z}_2$-odd) are called "strong topological insulators" (Vanderbilt, 2018). The evaluation of Eq. (19) would allow the detection of topological order; first-principle calculations are challenging, though.

We have said above that a nonzero magnetoelectric response requires absence of both T-and I-symmetry, while instead here we are discussing the T-symmetric case. In a topological ($\mathbb{Z}_2$-odd) insulator two remarkable things happen. (1) All Kubo terms are symmetry forbidden and disappear: the axion is the only surviving term. (2) Because of the same symmetry reasons, the magnetoelectric response of a bounded sample is zero, even though α (a bulk property) is nonzero: ergo the surface must be metallic. And in fact the topologically protected metallic surfaces are experimentally probed in order to detect topological order (Hasan and Kane, 2010; paradigmatic strong topological insulators are Bi_2Se_3 and Bi_2Te_3).

Class II observables

Generalities

The five class II geometrical observables known to the author are reported in the synoptic table displayed in the Introduction. They all obtain from **k**-integration (over the BZ in insulators, over the Fermi-volume in metals) of an integrand where two **k**-derivatives of the $|u_{j\mathbf{k}}\rangle$ Bloch states appear. Loosely speaking, one says that they obtain from integrating a 2-form, even when the integral is in 1D or in 3D.

All class II observables share the following properties, which make them very different from those in class I: the observables are single-valued; the integrand defining them is gauge-invariant; their actual value for a bounded sample does not depend on sample termination; because of this, they admit a "density" and are locally well defined even in inhomogeneous systems (e.g., heterostructures).

The reason behind the tabular arrangement is that the observables on the same row obtain from **k** integration of the same geometrical integrand: its imaginary antisymmetric part yields the left side (T-odd observable), while its symmetrical real part yields the right side (T-even observable). The first row is the simplest case: the integrand is the metric-curvature tensor $\mathcal{F}_{\alpha\beta}(\mathbf{k})$, Eqs. (12) and (13); for the other rows the integrand is a modifications of $\mathcal{F}_{\alpha\beta}(\mathbf{k})$, whose entries include the Hamiltonian besides the $|u_{j\mathbf{k}}\rangle$ derivatives.

The observables in the left column exist for 2D and 3D systems; those on the right column are well defined even in 1D. At variance with those on the right column, those in the left columns are phenomenologically defined for both insulators and metals, and obtain from integrating the same integrand (over either the BZ or the Fermi volume). This fundamental difference between T-odd and T-even observables owes to the singular Fermi-surface term in Eq. (5), which disappears after anti-symmetrization and therefore does not affect the T-odd observables, while instead it has a huge effect on the T-even observables. The Souza-Wilkens-Martin (SWM) sum rule—defined below—is formally infinite in all metals, and is a material-dependent geometrical ground-state property in insulators. The Drude weight, instead, is trivially zero in all insulators and is a material-dependent property in metals, which admits a geometrical expression.

Time-reversal odd observables

When T-symmetry is absent the spin-up bands are generally different from the spin-down ones. Therefore the expressions of the T-odd observables are given below per spin channel, or equivalently for "spinless electrons".

Anomalous Hall conductivity

Edwin Hall discovered the eponymous effect in 1879; 2 years later he discovered the anomalous Hall effect in ferromagnetic metals. The latter is, by definition, the Hall effect in absence of a macroscopic **B** field. In the normal Hall effect T-symmetry is broken by the applied **B** field; in the anomalous one it is spontaneously broken, for instance by the development of ferromagnetic order. The theory of anomalous Hall conductivity in metals has been controversial for many years; since the early 2000s it became clear that, besides extrinsic effects, there is also an intrinsic contribution, which can be expressed as a geometrical property of the occupied Bloch manifold in the pristine crystal (Nagaosa et al., 2010). We address this term only in the following.

The transverse dc conductivity is quantized in insulators, and topological in 2D: this is indeed the Thouless et al. (1982) result, celebrated by the Nobel prize in 2016. Notice however that, in presence of a macroscopic **B** field, the present formulation needs to be modified because the Hamiltonian is not lattice-periodical in the usual sense. The topological nature of the observable rules out any extrinsic effect, insofar as the system remains insulating. The metallic case is different: therein extrinsic mechanisms are needed to warrant Ohm's law; in absence of T-symmetry, extrinsic mechanisms also affect transverse conductivity.

We generalize the Berry curvature, Eq. (8) to include the metallic case as well:

$$\Omega_{\alpha\beta}(\mathbf{k}) = i\sum_j \theta(\mu - \varepsilon_{j\mathbf{k}})\left(\langle \partial_{k_\alpha} u_{j\mathbf{k}} | \partial_{k_\beta} u_{j\mathbf{k}}\rangle - \langle \partial_{k_\beta} u_{j\mathbf{k}} | \partial_{k_\alpha} u_{j\mathbf{k}}\rangle\right); \tag{20}$$

$$= i\,\mathrm{Tr}\left\{\mathscr{P}_{\mathbf{k}}\left[\partial_{k_\alpha}\mathscr{P}_{\mathbf{k}}, \partial_{k_\beta}\mathscr{P}_{\mathbf{k}}\right)\right]\right\}, \tag{21}$$

where the second line owes to Eq. (13). As said above, the Fermi-surface singularity in $\partial_{\mathbf{k}}\mathscr{P}_{\mathbf{k}}$ disappears after anti-symmetrization.

The geometrical/topological term in the antisymmetric component of the dc conductivity tensor is

$$\mathrm{Re}\,\sigma^{(-)}_{\alpha\beta}(0) = -\frac{e^2}{\hbar}\int_{\mathrm{BZ}}[d\mathrm{k}]\ \Omega_{\alpha\beta}(\mathbf{k}), \tag{22}$$

and it holds as written for either insulators or metals, either in 2D or 3D; in the metallic case the integrand is piecewise continuous.

In the special case of a 2D insulator the anomalous Hall conductivity—as said above—is quantized: in fact it is proportional to the Chern number, Eq. (9):

$$\mathrm{Re}\,\sigma^{(-)}_{xy}(0) = -\frac{e^2}{\hbar}\int_{\mathrm{BZ}}\frac{d\mathbf{k}}{(2\pi)^2}\,\Omega_{xy}(\mathbf{k}) = --\frac{e^2}{h}\frac{1}{2\pi}\int_{\mathrm{BZ}}d\mathbf{k}\,\Omega_{xy}(\mathbf{k}) = -\frac{e^2}{h}C_1; \tag{23}$$

Notice that h/e^2 is the natural resistance unit: one klitzing, equal to about $2.6\cdot 10^4\ \Omega$. The possible existence of 2D insulators with nonzero transverse conductivity was pointed out by Haldane in 1988 (co-laureate of the 2016 Nobel prize); actual synthesis of materials which realize the QAHE (quantum anomalous Hall effect) was first achieved in 2013.

Magneto-optical sum rule

Circularly polarized light from a synchrotron source is a very powerful probe for investigating spontaneous T-breaking in the orbital degrees of freedom of a given material, whose great virtue is of being element, structure, and site specific: this kind of spectroscopy goes under the acronym XMCD (X-ray magnetic circular dichroism). An incorrect belief, widespread in the synchrotron-physics community, holds that the XMCD sum-rule (defined below) probes the ground-state orbital magnetization in a given material. It is instead well established that XMCD quantitatively probes T-breaking in a different ground-state observable (Kunes and Oppeneer, 2000; Resta, 2020).

XMCD experiments measure the frequency integral of the imaginary part of the antisymmetric term in the conductivity tensor

$$I_{\alpha\beta} = \mathrm{Im}\int_0^\infty d\omega\ \sigma^{(-)}_{\alpha\beta}(\omega); \tag{24}$$

or even partial integrals over selected frequency ranges. A kind of fluctuation-dissipation theorem guarantees that $I_{\alpha\beta}$ is a ground-state property of the given T-breaking solid although—as stressed above—the property defined by Eq. (24) does *not* coincide with orbital magnetization. The geometrical ground-state expression for $I_{\alpha\beta}$ in the Hamiltonian gauge is

$$I_{\alpha\beta} = -\frac{\pi e^2}{\hbar^2}\mathrm{Im}\sum_j\int_{\mathrm{BZ}}[d\mathrm{k}]\ \theta(\mu - \varepsilon_{j\mathbf{k}})\langle \partial_{k_\alpha} u_{j\mathbf{k}}|(\mathscr{H}_{\mathbf{k}} - \varepsilon_{j\mathbf{k}})|\partial_{k_\beta} u_{j\mathbf{k}}\rangle, \tag{25}$$

clearly the Fermi-volume (or BZ) integral of an antisymmetric 2-form.

In order to arrive at the equivalent—gauge-invariant in form—expression we define the geometrical tensor field

$$\tilde{G}_{\alpha\beta}(\mathbf{k}) = \mathrm{Tr}\left\{(\mathscr{H}_{\mathbf{k}} - \mu)(\partial_{k_\alpha}\mathscr{P}_{\mathbf{k}})(\partial_{k_\beta}\mathscr{P}_{\mathbf{k}})\right\}, \tag{26}$$

whose antisymmetric imaginary part yields the XMCD sum-rule:

$$I_{\alpha\beta} = \frac{\pi e^2}{\hbar^2}\mathrm{Im}\int_{\mathrm{BZ}}[d\mathrm{k}]\ \tilde{G}_{\alpha\beta}(\mathbf{k}). \tag{27}$$

Orbital magnetization

Magnetization is comprised of two terms: a spin and an orbital one, which can be experimentally resolved. As for the former term, it is trivial within electronic-structure theory: simply proportional to the cell-averaged spin density. The latter term accounts (in common materials) for 5–10% of the total, and is a nontrivial geometrical ground-state property. We address here the orbital term only, indicated with **M**; the ultimate formula which defines it in a crystalline solid was arrived at in 2006. Its γ-component is, in the Hamiltonian gauge (Ceresoli et al., 2006; Vanderbilt, 2018),

$$M_\gamma = -\frac{e}{\hbar c}\varepsilon_{\gamma\alpha\beta}\mathrm{Im}\sum_j\int_{\mathrm{BZ}}[d\mathrm{k}]\ \theta(\mu - \varepsilon_{j\mathbf{k}})\langle \partial_{k_\alpha} u_{j\mathbf{k}}|(2\mu - \mathscr{H}_{\mathbf{k}} - \varepsilon_{j\mathbf{k}})|\partial_{k_\beta} u_{j\mathbf{k}}\rangle; \tag{28}$$

it is the integral of a gauge-invariant 2-form, clearly different from the one entering the XMCD sum-rule, Eq. (25). The expression holds as it stands in trivial insulators, topological insulators, and metals, in either 2D or 3D.

The insulating case deserves a brief discussion. Suppose we choose an arbitrary μ value within the bulk gap: then Eq. (28) has a term linear in μ. It is easily seen that the μ-derivative of **M** is proportional to the BZ integral of the Berry curvature: this is zero in the trivial case (as one would expect), but nonzero in the topological case. The reason for a μ-dependent $\mathbf{M}$ can be understood by addressing a 2D bounded sample, which is insulating in the bulk but has metallic states at the boundary, topologically protected: these states contribute—according to their filling—to $\mathbf{M}$. Eq. (28) is formulated for an unbounded sample within periodic boundary conditions; nonetheless the μ-dependence of $\mathbf{M}$ therein accounts for the analogous phenomenon in a bounded sample.

In order to display the equivalent expression, gauge-invariant in form, we define the tensor field

$$G_{\alpha\beta}(\mathbf{k}) = \mathrm{Tr}\left\{|\mathcal{H}_{\mathbf{k}} - \mu|\left(\partial_{k_\alpha}\mathcal{P}_{\mathbf{k}}\right)\left(\partial_{k_\beta}\mathcal{P}_{\mathbf{k}}\right)\right\}, \tag{29}$$

where the operator $|\mathcal{H}_{\mathbf{k}} - \mu|$ is diagonal on the Hamiltonian eigenstates:

$$|\mathcal{H}_{\mathbf{k}} - \mu||u_{j\mathbf{k}}\rangle = |\varepsilon_{j\mathbf{k}} - \mu||u_{j\mathbf{k}}\rangle. \tag{30}$$

A somewhat lengthy calculation proves that Eq. (28) is equivalent to

$$M_\gamma = -\frac{e}{\hbar c}\varepsilon_{\gamma\alpha\beta}\,\mathrm{Im}\int_{\mathrm{BZ}}[d\mathrm{k}]\; G_{\alpha\beta}(\mathbf{k}),. \tag{31}$$

This elegant gauge-invariant form can be equivalently rewritten (for both insulators and metals) as:

$$\mathbf{M} = \frac{ie}{2\hbar c}\int_{\mathrm{BZ}}[d\mathrm{k}]\;\mathrm{Tr}\{|\mathcal{H}_{\mathbf{k}} - \mu|(\partial_{\mathbf{k}}\mathcal{P}_{\mathbf{k}}) \times (\partial_{\mathbf{k}}\mathcal{P}_{\mathbf{k}})\}. \tag{32}$$

Time-reversal even observables

Longitudinal conductivity

The two geometrical observables on the right side of the synoptic table are both related to longitudinal conductivity: therefore some general considerations are in order. Longitudinal conductivity is by definition the symmetric part of the frequency-dependent conductivity tensor, whose real and imaginary parts are related by causality (Kramers-Kronig relationships). Its general form is

$$\sigma^{(+)}_{\alpha\beta}(\omega) = D_{\alpha\beta}\left[\delta(\omega) + \frac{i}{\pi\omega}\right] + \sigma^{(\mathrm{regular})}_{\alpha\beta}(\omega), \tag{33}$$

where the constant $D_{\alpha\beta}$ goes under the name of Drude weight (also known as charge stiffness); it vanishes in insulators. In the metallic case the singular first term in Eq. (33) accounts for the fact that—in absence of dissipation—a dc electric field induces free acceleration in the many-electron system; the $D_{\alpha\beta}$ value measures its inverse inertia (Resta, 2018a).

Within band-structure theory (i.e. for crystalline systems of noninteracting electrons) the regular term obtains by an interband Kubo formula. It is gapped in both insulators and metals: $\sigma_{\alpha\beta}^{(\mathrm{regular})}(\omega) = 0$ for $\omega < \varepsilon_{\mathrm{gap}}/\hbar$, where $\varepsilon_{\mathrm{gap}}$ is the minimum direct gap. The Drude weight can instead be regarded as the intraband linear response: see Eq. (41) below.

In the special case of free electrons (i.e. noninteracting electrons in a flat potential) the second term in Eq. (33) vanishes and

$$D_{\alpha\beta} = D_{\mathrm{free}}\delta_{\alpha\beta}. \qquad D_{\mathrm{free}} = \frac{\pi e^2 n}{m}, \tag{34}$$

where n is the electron density.

Longitudinal conductivity obeys the f-sum rule:

$$\int_0^\infty d\omega\;\mathrm{Re}\,\sigma_{\alpha\beta}(\omega) = \frac{D_{\alpha\beta}}{2} + \int_{\varepsilon_{gap}/\hbar}^\infty d\omega\;\mathrm{Re}\,\sigma^{(\mathrm{regular})}_{\alpha\beta}(\omega) = \frac{D_{\mathrm{free}}}{2}\delta_{\alpha\beta}. \tag{35}$$

Therefore the switching on of the periodic potential has the effect of transferring some spectral weight from the Drude peak into the regular term; as said above, in the case of insulators the Drude peak vanishes and the regular term by itself saturates the f-sum rule.

An important subtlety must be stressed: if the ω-integration includes the ultraviolet and x-ray regions of the spectrum, then the density n in D_{free} must include the core electrons. When the focus is instead on dc transport and optical properties the core contributions to the f-sum rule must be discounted: this happens by construction in a pseudopotential framework.

Souza-Wilkens-Martin sum rule

The so-called gauge-invariant quadratic spread, defined for insulators only, is the BZ-integral of the trace of the metric tensor, Eqs. (11) and (13):

$$\Omega_{\mathrm{I}} = V_{\mathrm{cell}}\sum_\alpha\int_{\mathrm{BZ}}[d\mathrm{k}]\; g_{\alpha\alpha}(\mathbf{k}) = V_{\mathrm{cell}}\sum_\alpha\int_{\mathrm{BZ}}[d\mathrm{k}]\;\mathrm{Re}\;\;\mathcal{F}_{\alpha\alpha}(\mathbf{k}). \tag{36}$$

Since the diagonal elements are real, the “Re” will be omitted in the following.

The quantity Ω_{I} entered electronic-structure theory as a formal quantity in the theory of maximally localized Wannier functions (Marzari and Vanderbilt, 1997; Marzari et al., 2012; Vanderbilt, 2018). Such quantity was not defined originally by means of a physical observable; nonetheless any gauge-invariant property of the electronic ground state corresponds—at least in principle—to a measurable quantity, and therefore some experiment should ideally yield the $\Omega_{\rm I}$ value. It was discovered by Souza et al. (2000) that $\Omega_{\rm I}$ is proportional to a sum rule for longitudinal conductivity.

The key SWM integral is

$$I^{(\rm SWM)} = \int_0^\infty \frac{d\omega}{\omega} \sum_\alpha \sigma^{(+)}_{\alpha\alpha}(\omega), \tag{37}$$

and was introduced as the main discriminant between metals and insulators. The integral was mostly aimed at nontrivial insulators, including e.g., Anderson insulators, Mott insulators, and more; $I^{(\rm SWM)}$ has the virtue of being divergent in all metals and convergent to a finite value in all insulators (Souza et al., 2000; Resta, 2018c). In the present review we limit ourselves throughout to band-structure theory, i.e. the special case of crystalline systems of noninteracting electrons: therein the metallic divergence is obvious from the first (Drude) term in Eq. (33).

In the insulating case $I^{(\rm SWM)}$ is instead finite and material-dependent; a kind of fluctuation-dissipation theorem relates it indeed to $\Omega_{\rm I}$. The SWM sum rule reads

$$\frac{\hbar}{\pi e^2} \int_{\varepsilon_{\rm gap}/\hbar}^\infty \frac{d\omega}{\omega} \sum_\alpha \sigma^{(+)}_{\alpha\alpha}(\omega) = \frac{\Omega_{\rm I}}{V_{\rm cell}} = \sum_\alpha \int_{\rm BZ} [d\mathbf{k}]\, \mathcal{F}_{\alpha\alpha}(\mathbf{k}), \tag{38}$$

where $\mathcal{F}_{\alpha\alpha}(\mathbf{k})$ is a diagonal element of the metric-curvature tensor, Eqs. (12) and (13).

Drude weight

For a crystalline metal with double band occupancy the Drude weight obtains as a the Fermi-volume integral (Resta, 2018a):

$$D_{\alpha\beta} = 2\pi e^2 \sum_j \int_{\rm BZ} [d\mathbf{k}]\, \theta(\mu - \varepsilon_{j\mathbf{k}}) m^{-1}_{j,\,\alpha\beta}(\mathbf{k}), \tag{39}$$

where the effective inverse mass tensor of band j is

$$m^{-1}_{j,\alpha\beta}(\mathbf{k}) = \frac{1}{\hbar^2} \frac{\partial^2 \varepsilon_{j\mathbf{k}}}{\partial k_\alpha \partial k_\beta}. \tag{40}$$

Only partially occupied bands contribute to $D_{\alpha\beta}$; in insulators Eq. (39) vanishes altogether.

Eq. (39) can be equivalently expressed as a Fermi-surface integral, by means of an integration by parts: it acquires then the meaning of an "intraband" term:

$$D_{\alpha\beta} = -2\pi e^2 \sum_j \int_{\rm BZ} [d\mathbf{k}]\; f'(\varepsilon_{j\mathbf{k}}) v_{j\alpha}(\mathbf{k}) v_{j\beta}(\mathbf{k}), \qquad v_{j\alpha}(\mathbf{k}) = \frac{1}{\hbar} \frac{\partial \varepsilon_{j\mathbf{k}}}{\partial k_\alpha}, \tag{41}$$

where at zero temperature the Fermi occupation function is $f(\varepsilon) = \theta(\mu - \varepsilon)$. The formula as given is for a simple Fermi surface; in general there may be multiple bands that cross the Fermi level and Fermi surfaces having complex topology, for example including disconnected sections. Actual integration by parts requires then some care.

The Fermi-surface expression shows explicit agreement with the spirit of Landau's Fermi-liquid theory, which holds that charge transport in metals involves only quasiparticles with energies within $k_{\rm B}T$ of the Fermi level. Indeed, Eq. (41) can be alternatively derived in a purely semiclassical framework (Ashcroft and Mermin, 1976).

Both Eqs. (39) and (41) do not look "geometrical"; nonetheless there is an alternative and very meaningful expression equivalent to Eq. (40), where the deviation of $m^{-1}_{j,\alpha\beta}(\mathbf{k})$ from its free-electron value appears as a geometrical term in reciprocal space. We remind that the orbitals $|u_{j\mathbf{k}}\rangle$ are eigenstates of $\mathcal{H}_{\mathbf{k}} = {\rm e}^{-i\mathbf{k}\cdot\mathbf{r}} \mathcal{H}\, {\rm e}^{i\mathbf{k}\cdot\mathbf{r}}$, hence the identity $\langle u_{j\mathbf{k}}|(\mathcal{H}_{\mathbf{k}} - \varepsilon_{j\mathbf{k}})|u_{j\mathbf{k}}\rangle \equiv 0$ holds. Taking two derivatives, one arrives at

$$m^{-1}_{j,\alpha\beta}(\mathbf{k}) = \frac{1}{m}\delta_{\alpha\beta} - \frac{2}{\hbar^2} \,{\rm Re}\, \langle \partial_{k_\alpha} u_{j\mathbf{k}}|(\mathcal{H}_{\mathbf{k}} - \varepsilon_{j\mathbf{k}})|\partial_{k_\beta} u_{j\mathbf{k}}\rangle, \tag{42}$$

$$D_{\alpha\beta} = \frac{\pi e^2 n}{m}\delta_{\alpha\beta} - \frac{4\pi e^2}{\hbar^2} \sum_j \int_{\rm BZ} [d\mathbf{k}]\, \theta(\mu - \varepsilon_{j\mathbf{k}})\, {\rm Re}\, \langle \partial_{k_\alpha} u_{j\mathbf{k}}|(\mathcal{H}_{\mathbf{k}} - \varepsilon_{j\mathbf{k}})|\partial_{k_\beta} u_{j\mathbf{k}}\rangle; \tag{43}$$

therein the first term on the r.h.s. is the free-electron Drude weight $D_{\rm free}\delta_{\alpha\beta}$, while the second one is a geometrical correction due to the periodic potential; for free electrons the $|u_{j\mathbf{k}}\rangle$ are $\mathbf{k}$-independent, ergo the correction vanishes.

Eq. (43) is formulated in the Hamiltonian gauge. In order to cast it as gauge-invariant in form we remind that $\partial_{\mathbf{k}}\mathcal{P}_{\mathbf{k}}$, Eq. (5) comprises a singular Fermi-surface term, which needs to be discounted here. We therefore define the regular term in Eq. (5) as

$$\partial^{(\rm r)}_{\mathbf{k}} \mathcal{P}_{\mathbf{k}} = \sum_j \theta(\mu - \varepsilon_{j\mathbf{k}}) \left(|u_{j\mathbf{k}}\rangle\langle \partial_{\mathbf{k}} u_{j\mathbf{k}}| + |\partial_{\mathbf{k}} u_{j\mathbf{k}}\rangle\langle u_{j\mathbf{k}}|\right),$$

and we notice that—owing to anti-symmetrization—the difference between $\partial^{(\rm r)}_{\mathbf{k}}\mathcal{P}_{\mathbf{k}}$ and $\partial_{\mathbf{k}}\mathcal{P}_{\mathbf{k}}$ is irrelevant in all the previous expressions for the T-odd observables. It is expedient to redefine the gauge-invariant tensor field $G_{\alpha\beta}(\mathbf{k})$, Eq. (29), as

$$G_{\alpha\beta}(\mathbf{k}) = \mathrm{Tr}\left\{ |\mathscr{H}_{\mathbf{k}} - \mu| \left(\partial^{(\mathrm{r})}_{k_\alpha} \mathscr{P}_{\mathbf{k}} \right) \left(\partial^{(\mathrm{r})}_{k_\beta} \mathscr{P}_{\mathbf{k}} \right) \right\}, \tag{44}$$

whose imaginary antisymmetric part defines the orbital magnetization, Eqs. (31) and (32). A somewhat lengthy calculation shows that Eq. (43) can be identically recast as

$$D_{\alpha\beta} = D_{\mathrm{free}}\delta_{\alpha\beta} - \frac{4\pi e^2}{\hbar^2} \int_{\mathrm{BZ}} [d\mathrm{k}]\ \mathrm{Re}\ G_{\alpha\beta}(\mathbf{k}). \tag{45}$$

Conclusion

We have provided here the quantum-mechanical formulations for seven ground-state observables which enter very different physical phenomena: three of them belong to electrostatics/magnetostatics (polarization, orbital magnetization, magnetoelectric coupling); two concern dc conductivity (anomalous Hall conductivity and Drude weight); and two are conductivity sum rules. Despite being so different from the phenomenology viewpoint, all these observables are related by the common fil rouge of Bloch geometry.

For all these seven observables the microscopic formal expression is geometrical, although—as stressed throughout—such expressions are sharply partitioned in two classes, called here I and II. Such formal difference has a strong qualitative implication on phenomenological features of the corresponding observables, in particular about their multiple-valued versus single-valued bulk nature.

Macroscopic polarization **P** and orbital magnetization **M** are two paradigmatic observables which deserve some further comments. When a bounded sample is addressed, the definitions of the two observables are very similar: **P** is the dipole over the volume, **M** is the orbital moment over the volume (large-sample limit thereof). Furthermore the formal expression for the dipole (of the microscopic charge density) and for the orbital moment (of the microscopic current density) are also very similar. The corresponding expressions for unbounded samples within band-structure theory became available in 1993 for **P** and in 2006 for **M**. Contrary to some expectations, it was immediately realized that geometry-wise the two observables are extremely different: according to the present partition **P** is in class I, **M** in class II. We have emphasized here the profound reason for such difference: at bare bones **P** is a one-dimensional phenomenon while **M** is a two-dimensional one; at the root of their difference is algebraic geometry, which displays very different features in odd vs. even dimensions.

Observables in class I are defined for insulators only, and the geometrical integrands entering them are gauge-dependent. Only the BZ integral is gauge-invariant, although modulo 2π (in dimensionless units). The observables in class II may be defined for metals as well, and the geometrical integrand entering them is gauge-invariant. For each of the five class II observables a double expression is provided here: the first one is given in the Hamiltonian gauge (as in most of the existing literature); the second one is gauge-invariant by inspection.

The presence/absence of a Fermi surface in the metallic/insulating band structure has an overwhelming effect on class II observables: when they are further partitioned in T-odd and T-even ones (left and right column in the synoptic table) a general trend becomes perspicuous.

The three known T-odd observables obtain in either metals or insulators by integrating the same geometrical integrand (a 2-form) on either the Fermi volume or on the BZ; the presence of a Fermi surface plays essentially no role, and this owes in turn to the fact that the 2-forms are antisymmetric in the T-odd cases. Instead in the T-even cases the geometrical integrands are symmetrical and the presence/absence of a Fermi surface has outstanding consequences: the SWM sum rule defines a material-dependent ground-state property for insulators only, while opposedly the Drude weight defines a material-dependent ground-state property for metals only.

Finally, some considerations on the special cases where a geometrical observable may become topological: even in this respect the difference between class I and class II observables is extreme. In class I the observable becomes topological only when "protected" by a given symmetry (either T or I), in which case the invariant is a two-valued index, i.e. $\mathbb{Z}_2$. In class II, instead, only one of the observables dealt with above becomes topological: anomalous Hall conductivity in a 2D insulator. It does not require any protecting symmetry; quite on the contrary, it requires T-symmetry to be absent. The topological invariant is a Chern number, i.e. a $\mathbb{Z}$ index (not $\mathbb{Z}_2$).

Acknowledgments

Work supported by the U.S. Office of Naval Research through grant N00014-20-1-2847.

References

Ashcroft NW and Mermin ND (1976) *Solid State Physics*. Philadelphia: Saunders.

Ceresoli D, Thonhauser T, Vanderbilt D, and Resta R (2006) Orbital magnetization in crystalline solids, Multi-band insulators, Chern insulators, and metals. *Physical Review B* 74: 024408.

Hasan MZ and Kane CL (2010) Topological insulators. *Reviews of Modern Physics* 82: 3045.
King-Smith RD and Vanderbilt D (1993) Theory of polarization of crystalline solids. *Physical Review B* 47: 1651.
Kunes J and Oppeneer M (2000) Exact many-body sum rule for the magneto-optical spectrum of solids. *Physical Review B* 61: 15774.
Malashevich A, Souza I, Coh S, and Vanderbilt D (2010) Theory of orbital magnetoelectric response. *New Journal of Physics* 12: 053032.
Marzari N and Vanderbilt D (1997) Maximally localized generalized Wannier functions for composite energy bands. *Physical Review B* 56: 12847.
Marzari N, et al. (2012) Maximally localized Wannier functions, Theory and applications. *Reviews of Modern Physics* 84: 1419.
Nagaosa N, et al. (2010) Anomalous Hall effect. *Reviews of Modern Physics* 82: 1539.
Resta R (2018a) Drude weight and superconducting weight. *Journal of Physics. Condensed Matter* 30: 414001.
Resta R (2018b) Polarization in Kohn-Sham density-functional theory. *European Physics Journal B* 91: 100.
Resta R (2018c) Theory of the insulating state. *La Rivista del Nuovo Cimento* 41: 463.
Resta R (2020) Magnetic circular dichroism versus orbital magnetization. *Physical Review Research* 2: 023139.
Souza I, Wilkens T, and Martin RM (2000) Polarization and localization in insulators, Generating function approach. *Physical Review B* 62: 1666.
Thouless DJ, Kohmoto M, Nightingale MP, and den Nijs M (1982) Quantized Hall conductance in a two-dimensional periodic potential. *Physical Review Letters* 49: 405.
Vanderbilt D (2018) *Berry Phases in Electronic Structure Theory*. Cambridge: Cambridge University Press.
Vanderbilt D and King-Smith RD (1993) Electric polarization as a bulk quantity and its relation to surface charge. *Physical Review B* 48: 4442.

Topological properties of Dirac and Weyl semimetals☆

AA Burkov, Department of Physics and Astronomy, University of Waterloo, Waterloo, ON, Canada; Perimeter Institute for Theoretical Physics, Waterloo, ON, Canada

© 2024 Elsevier Ltd. All rights reserved.

Introduction 681
Magnetic Weyl semimetal 682
Chiral anomaly 684
Topological magnetotransport phenomena in semimetals 685
Conclusion 689
Further reading 689

Abstract

This chapter describes topological (Dirac and Weyl) semimetals from the viewpoint of their observable electromagnetic response. We argue that this response may be represented by topological terms with unquantized (non-integer) coefficients and make a connection with the Luttinger's theorem, which relates the size of the Fermi surface of an ordinary metal to the number of electrons per unit cell. We discuss observable transport phenomena, associated with this topological response.

Key points

- Topological semimetals are intermediate phases between insulators with different electronic structure topology.
- Topological response of Dirac and Weyl topological semimetals may be viewed as a consequence of the chiral anomaly.
- Observable manifestations are intrinsic anomalous Hall effect with a noninteger Hall conductance in units of e^2/h per atomic plane, negative longitudinal magnetoresistance, scale-dependent quasiballistic transport and extra low-frequency peak in the optical conductivity.

Introduction

Solid crystalline materials are typically categorized as either metals or insulators. Metals have a finite conductivity in the limit of zero temperature, while in insulators the conductivity tends to zero in this limit. The existence of metals and insulators is a fundamental consequence of quantum mechanics and is one of the basic macroscopic quantum phenomena. Whether a given material is a metal or an insulator is determined by a single parameter: the number of valence electrons per unit cell per spin, or filling, denoted as ν henceforth. If ν is not an integer, the material is a metal (unless electron-electron interactions are so strong that a Mott insulator state is formed). The main characteristic of a conventional metal is the existence of a Fermi surface: a surface in the crystal momentum space, separating filled and empty states, whose volume is directly proportional to the fractional part of the filling, a statement known as the Luttinger's theorem. On the other hand, if ν is an integer, the material is either an insulator or a compensated semimetal, which has a number of electron and hole pockets, whose total volume in momentum space, weighted by the sign of the charge carrier (i.e. negative for electrons and positive for holes), sums up to zero. Since the existence of a compensated semimetal is not required by the Luttinger's theorem, it may be viewed as accidental, in the sense that it may be deformed to an insulator without changing ν. We may then say that a noninteger ν always corresponds to a metal, while integer ν always means an insulator.

This simple picture, which has been around for many decades, was significantly enriched and modified by the recent developments in understanding the role of topology in condensed matter physics. In particular, it has been understood that a (semi)metallic state may arise for topological reasons in situations when the Luttinger parameter is an integer, which would normally correspond to an insulator. The simplest example of this are the metallic surface states of topological insulators, which arise inevitably as a consequence of the bulk insulator electronic structure topology. Topological semimetals may also exists in stand-alone bulk systems, most naturally in three spatial dimensions (3D). Just as ordinary metals may be viewed as intermediate phases between two band insulators, corresponding to different integer values of ν, topological semimetals arise as intermediate phases between insulators with different electronic structure topology at a fixed integer value of ν. For example, a magnetic Weyl semimetal is an intermediate phase between an ordinary 3D insulator and an integer quantum Hall insulator with the Hall conductance of e^2/h per atomic plane. A time-reversal (TR) invariant Weyl semimetal is an intermediate phase between an ordinary insulator and a 3D TR-invariant topological insulator (TI), which has an odd number of two-dimensional (2D) Dirac cone surface

---

☆*Change History*: July 2022. AA Burkov updated the chapter.

https://doi.org/10.1016/B978-0-323-90800-9.00052-4

states. A (type-I) Dirac semimetal is an intermediate phase between an ordinary insulator and a weak topological crystalline insulator, protected by a combination of TR, inversion, and crystal rotation symmetries. A nodal line semimetal is an intermediate phase between an ordinary insulator and a topological crystalline insulator, protected by mirror symmetry.

Just as an ordinary metal may be characterized by a fractional value of the filling parameter ν, which determines the size of its Fermi surface, topological semimetals may be characterized by topological invariants, which, although not integer, not quantized, and continuously tunable, are otherwise robust to interactions and disorder. Integer values of these invariants correspond to insulators, while fractional values correspond to topological semimetal phases, intermediate between the insulators. In the simplest case of the magnetic Weyl semimetal, this tunable invariant is the Hall conductance per atomic plane in units of e^2/h. Any noninteger value of this invariant requires Weyl band-touching nodes to be present when the Luttinger parameter ν is an integer (otherwise the Hall conductance can take any value due to the contribution of the Fermi surface). In other types of topological semimetals, the invariants are more subtle, but the idea remains the same: a noninteger value of the invariant requires gapless band-touching points or lines to be present.

Magnetic Weyl semimetal

This section explains the connection between unquantized topological invariants and the existence of gapless band-touching points in the Brillouin zone (BZ) on the simplest example of a topological semimetal: a magnetic Weyl semimetal with only a pair (the minimal number) of band-touching nodes. Such a Weyl semimetal arises as an intermediate phase between a quantum anomalous Hall and an ordinary insulator in 3D.

A 3D quantum anomalous Hall insulator may be obtained by making a stack of 2D quantum Hall insulators. 2D quantum anomalous Hall effect (QAHE) arises naturally in a very thin film of a 3D TI material, doped with magnetic impurities. A 3D TR-invariant TI is a bulk insulator with nontrivial electronic structure topology, which leads to gapless metallic surface states, described by a 2D massless Dirac Hamiltonian of the general form

$$H = \hbar v_F(\widehat{z} \times \sigma) \cdot \mathrm{k}, \tag{1}$$

where σ is the spin degree of freedom, v_F is the Fermi velocity, and $\widehat{z}$ is the normal to the surface. The gaplessness of the spectrum of Eq. (1) is protected by TR symmetry, which prohibits the “mass” term in the 2D Dirac Hamiltonian. If time reversal symmetry is violated, which may be accomplished by doping the surface with magnetic impurities, the “mass” term will be allowed and a gap in the 2D Dirac surface state dispersion will be opened.

A thin film of magnetically-doped 3D TI, shown in Fig. 1, may be modeled by focusing only on the low-energy degrees of freedom, which are simply the 2D Dirac surface states of Eq. (1) on the top and bottom surfaces of the film. The corresponding Hamiltonian reads

$$H = \hbar v_F \tau^z(\widehat{z} \times \boldsymbol{\sigma}) \cdot \mathbf{k} + \Delta_S \tau^x + b\sigma^z. \tag{2}$$

Here the eigenvalues of τ^z refer to the top or bottom surface degree of freedom, Δ_S is the probability amplitude for tunneling between the top and bottom surfaces of the film, and b is the exchange spin-splitting, which arises due to the presence of magnetized impurities. Note that $b\sigma^z$ acts as a “mass term” for the individual 2D Dirac surface states, as mentioned above. A unitary transformation brings this to the form

$$H = \hbar v_F(\widehat{z} \times \boldsymbol{\sigma}) \cdot \mathbf{k} + (\Delta_S \tau^x + b)\sigma^z, \tag{3}$$

which may be further brought to a block-diagonal form by diagonalizing the $\Delta_S \tau^x$ matrix

$$H_r = \hbar v_F(\hat{z} \times \boldsymbol{\sigma}) \cdot \mathbf{k} + (b + r\Delta_S)\sigma^z, \tag{4}$$

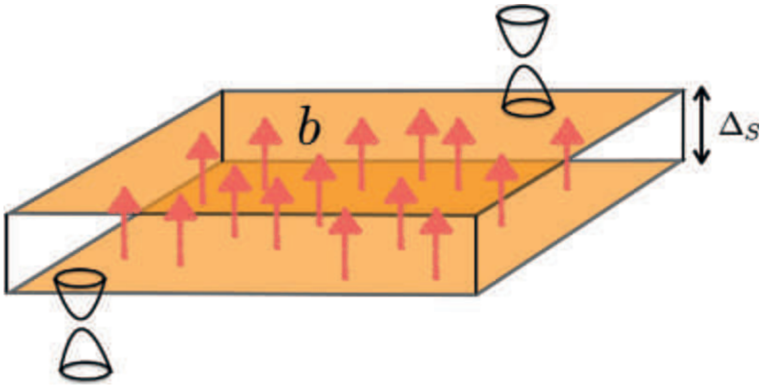

Fig. 1 Thin film of magnetically doped 3D TI. Δ_S is the tunneling amplitude between the top and bottom 2D Dirac surface states and b is the spin splitting due to magnetized impurities. When $b > \Delta_S$, the film is a quantum anomalous Hall insulator with $\sigma_{xy} = e^2/h$. When $b < \Delta_S$, it is an ordinary insulator with zero Hall conductivity.

where $r = \pm$. Each of the 2 × 2 blocks of Eq. (4) is the Hamiltonian of a 2D Dirac fermion with a "mass" $m_r = b + r\Delta_S$. The 2D Dirac fermion possesses an important property, which is known as the "parity anomaly." In our context this means that $H_\pm$ is associated with a Hall conductivity

$$\sigma_{xy}^r = \frac{e^2}{2h}\,\mathrm{sign}(m_r), \tag{5}$$

when the Fermi energy is in the gap between the positive and negative energy bands, obtained by diagonalizing H_r

$$\varepsilon_{rs}(\mathbf{k}) = s\sqrt{\hbar^2 v_F^2 \mathbf{k}^2 + m_r^2}, \tag{6}$$

with $s = \pm$. This implies that this system exhibits a quantum Hall plateau transition from $\sigma_{xy} = 0$ to $\sigma_{xy} = e^2/h$ as the ratio of b/Δ_s is varied and taking both b and Δ_S to be positive for concreteness. In other words, in 2D there exists a direct transition between a topological insulator with $\sigma_{xy} = e^2/h$ and a normal insulator with $\sigma_{xy} = 0$. The critical point between the two is described by a massless 2D Dirac Hamiltonian.

Suppose we now make a stack of such 2D layers, exhibiting QAHE, as shown in Fig. 2. Let individual layers be separated by insulating spacers, such that the amplitude for tunneling between the adjacent surfaces of neighboring QAHE layers is Δ_D, which we will also take to be positive. The Hamiltonian, that describes this system, takes the form.

$$\begin{aligned} H = {} & \hbar v_F \tau^z (\hat{z} \times \boldsymbol{\sigma}) \cdot \mathbf{k} + [\Delta_S + \Delta_D \cos(k_z d)]\tau^x \\ & -\Delta_D \sin(k_z d)\tau^y + b\sigma^z, \end{aligned} \tag{7}$$

where d is the period of the resulting superlattice heterostructure in the z-direction. Making the same unitary transformation as above and partially diagonalizing the resulting Hamiltonian, we obtain

$$H_r = \hbar v_F (\hat{z} \times \boldsymbol{\sigma}) \cdot \mathbf{k} + m_r(k_z)\sigma^z, \tag{8}$$

where $m_r(k_z) = b + r\sqrt{\Delta_S^2 + \Delta_D^2 + 2\Delta_S\Delta_D \cos(k_z d)} \equiv b + r\Delta(k_z)$. Now we see that the quantum Hall plateau transition we discussed before as a function of b/Δ_S, may now happen in momentum space as k_z is swept through the BZ. Indeed $m\_(k_z)$ will change sign at $k_z^\pm = \pi/d \pm Q$, where

$$Q = \frac{1}{d}\arccos\left(\frac{\Delta_S^2 + \Delta_D^2 - b^2}{2\Delta_S\Delta_D}\right). \tag{9}$$

At $\mathbf{k} = (0, 0, k_z^\pm)$, the two nondegenerate bands, corresponding to the eigenvalue $r = -$ touch each other, i.e. these are locations of two Weyl nodes, see Fig. 3.

The nodes exist as long the spin splitting b is in the interval between two critical values $b_{c1} < b < b_{c2}$, where $b_{c1} = |\Delta_S - \Delta_D|$ and $b_{c2} = \Delta_S + \Delta_D$. When $b < b_{c1}$ the system is an ordinary insulator with $\sigma_{xy} = 0$, while when $b > b_{c2}$ it is a 3D quantum anomalous Hall insulator with $\sigma_{xy} = e^2/hd$. In between the heterostructure is in the intermediate Weyl semimetal phase with

$$\sigma_{xy} = \frac{2Q}{2\pi}\frac{e^2}{h}, \tag{10}$$

which depends only on the distance between the Weyl nodes in momentum space and varies continuously between 0 and e^2/hd. Thus, unlike in 2D, in 3D a direct transition between a TI with nonzero quantized Hall conductivity and a normal insulator with zero Hall conductivity does not exist. The transition instead proceeds through an intermediate gapless Weyl semimetal phase. The system, described above, constitutes the simplest potential realization of a topological semimetal. Most of the properties of Weyl and Dirac semimetals may be understood by studying this system.

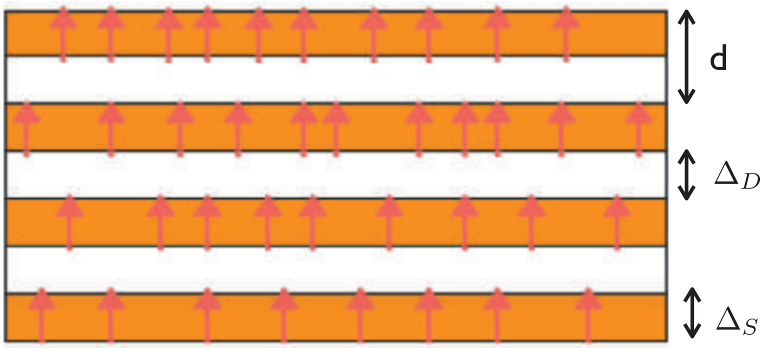

Fig. 2 Coupled-layer construction of an elementary Weyl semimetal. Magnetically-doped TI layers are coupled through insulating spacers. The tunneling amplitude between neighboring TI layers is Δ_D.

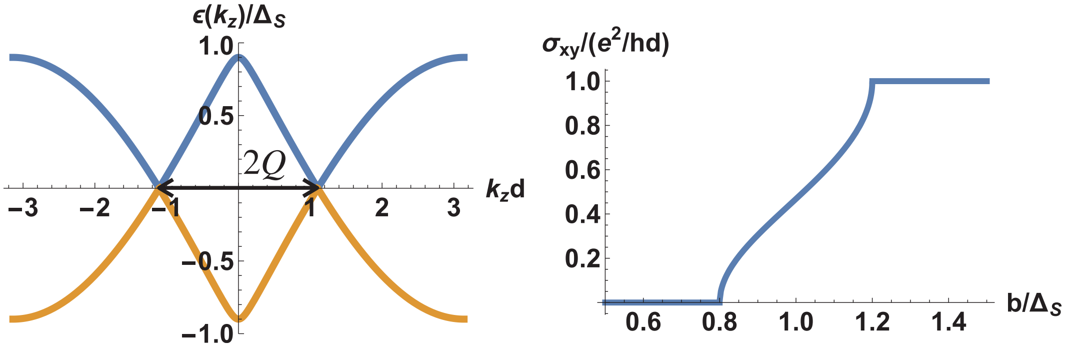

Fig. 3 (A) Electronic structure of the simplest Weyl semimetal, with two nodes of opposite chirality, separated by a distance of $2Q$ along the z-axis in momentum space. (B) The corresponding anomalous Hall conductivity as a function of b/Δ_S, showing a broadened plateau transition. Weyl semimetal is an intermediate gapless phase between the quantum anomalous Hall and ordinary insulators.

Chiral anomaly

This section describes basics of the topological response of Weyl and other point node semimetals. This response may be viewed as a consequence of the chiral anomaly, a phenomenon, originally discovered in the particle physics context by Adler, Bell and Jackiw. To understand the connection to the chiral anomaly, let us note that the Hall conductivity of a magnetic Weyl semimetal Eq. (10) may be expressed as the following contribution to the imaginary-time action of the electromagnetic field

$$S = i\frac{2Q}{4\pi}\frac{e}{\Phi_0}\int drd^3r\varepsilon_{z\nu\alpha\beta}A_\nu\partial_\alpha A_\beta, \tag{11}$$

where A_μ is the gauge potential of the electromagnetic field, $\Phi_0 = h/e$ is the magnetic flux quantum, and the Hall conductivity is obtained by varying S with respect to A_x

$$j_x = -\frac{\delta S}{\delta A_x} = \frac{2Q}{2\pi}\frac{e^2}{h}E_y. \tag{12}$$

To make a connection with the chiral anomaly, we need to first remind ourselves of some basic notions of the crystal elasticity theory. A perfect 3D crystal may be described in terms of three families of crystal planes, defined by the relation

$$\theta^i(\mathbf{R}, t) = \mathbf{b}^i \cdot \mathbf{R} = 2\pi n^i, \tag{13}$$

where $i = 1, 2, 3$, $\mathbf{R}$ are the Bravais lattice vectors, $\mathbf{b}^i$ are the three primitive reciprocal lattice vectors and n^i are integers. In a distorted crystal, $\theta^i(\tilde{\mathbf{R}}, t) = 2\pi n^i$ continues to hold, where $\tilde{\mathbf{R}}$ are the actual lattice site positions, but $\partial_j\theta^i = b^i_j$ no longer holds. Instead $\partial_j\theta^i$ may be viewed as components of local coordinate basis vectors of the reciprocal space in a distorted crystal. It is then useful to view

$$e^i_\mu = \frac{1}{2\pi}\partial_\mu\theta^i, \tag{14}$$

which may have temporal in addition to spatial components, as crystal translational symmetry "gauge fields." In a crystal without dislocations, $de^i = \frac{1}{2}\left(\partial_\mu e^i_\nu - \partial_\nu e^i_\mu\right)dx^\mu dx^\nu = 0$, as follows from Eq. (14). If a dislocation with a Burgers vector along $\mathbf{b}^i$ is present, the integral around a loop, enclosing the dislocation line, is $\oint e^i = 1$. Everywhere outside of the dislocation line, however, we may still take $de^i = 0$, which will be assumed henceforth.

The point of this exercise in the crystal elasticity theory, is that Eq. (11) may now be rewritten as

$$\begin{aligned} S &= i\frac{1}{2}\frac{e}{\Phi_0}\frac{2Q}{2\pi/d}\int d\tau d^3r\varepsilon_{\mu\nu\alpha\beta}e^z_\mu A_\nu\partial_\alpha A_\beta \\ &= i\frac{\lambda}{2}\frac{e}{\Phi_0}\int e^z \wedge A \wedge dA. \end{aligned} \tag{15}$$

Here $\lambda = 2Q/(2\pi/d)$ is the dimensionless magnitude of the separation between the Weyl nodes in units of the reciprocal lattice vector. This looks like a standard topological term, since it involves only gauge fields and a universal coefficient, except for the fact that the coefficient is not quantized, since λ is not an integer and is continuously tunable. This is exactly analogous to the noninteger value of the Luttinger filling parameter ν in metals, which requires Fermi surface of gapless modes to be present. In a Weyl semimetal ν is integer, but a noninteger value of the parameter λ still requires gapless modes to be present, but in the form of point band-touching nodes rather that a Fermi surface.

To connect Eq. (15) with the standard chiral anomaly we now note the following. If we focus only on the low-energy modes, Weyl semimetal appears to have a larger symmetry group than it actually has. Its true microscopic symmetry group is $U(1) \times \mathbb{Z}$, where U (1) corresponds to the electric charge conservation and $\mathbb{Z}$ to lattice translations (other discrete crystal symmetries, such as rotations, are irrelevant here). At low energies, however, the symmetry group appears to be $U(1)_L \times U(1)_R$, which corresponds to separate conservation of Weyl fermions of left (L) and right (R)-handed chirality. This symmetry group, if it were a true microscopic symmetry, would be anomalous, in the sense that it could not be realized in any 3D lattice model, but could only appear on the surface of a four-dimensional (4D) topological insulator, described by the following topological field theory

$$S = \frac{i}{6}\frac{e}{\Phi_0^2}\int (A_R \wedge dA_R \wedge dA_R - A_L \wedge dA_L \wedge dA_L), \tag{16}$$

where $A_{R,L}$ are $U(1)$ gauge fields, corresponding to the separate U $(1)_{R,L}$ symmetries. We now write $A_R = A + \tilde{Q}\tilde{A}$ and $A_L = A - \tilde{Q}\tilde{A}$, where $\tilde{A}$ is a chiral U (1) gauge field, which couples antisymmetrically to fermions of opposite chirality and $\tilde{Q}$ is the corresponding "charge." This gives

$$S = i\tilde{Q}\frac{e}{\Phi_0^2}\int \tilde{A} \wedge dA \wedge dA. \tag{17}$$

On the 3D boundary of this 4D topological insulator, Eq. (17) becomes

$$S = i\tilde{Q}\frac{e}{\Phi_0^2}\int \tilde{A} \wedge A \wedge dA. \tag{18}$$

If we now identify $\tilde{Q} = Qd = \pi\lambda$, i.e. the dimensionless magnitude of the momentum of the two Weyl points (i.e. translational symmetry charge) and $\tilde{A} = e^z\Phi_0/2\pi$, we get precisely Eq. (15), which describes topological response of the physical 3D Weyl semimetal. The reason Eq. (15) can exist in a stand-alone 3D system, rather than a boundary of a 4D topological insulator, is that the physical translational symmetry group is $\mathbb{Z}$ rather than $U(1)$ and, moreover, translation is not a truly "internal" symmetry, like chiral charge conservation. Nevertheless, formally Eq. (15) and (18) are identical, which does lead to a number of unique observable phenomena in topological semimetals, which are usually described as consequences of the chiral anomaly. These are discussed in the following section.

Topological magnetotransport phenomena in semimetals

This section describes some of the observable phenomena, which are encoded in Eq. (15). If we vary the action with respect to A_x, A_y and e_z^z, this gives the Hall conductance per atomic plane

$$G_{xy} = \lambda\frac{e^2}{h}, \tag{19}$$

which in a perfect crystal is equivalent to the Hall conductivity, given by Eq. (10). Expressing this in terms of conductance per atomic plane eliminates the dependence on a nonuniversal lattice constant d, leaving only the pure number λ. A noninteger value of the Hall conductance per atomic plane in units of e^2/h is impossible in a gapped insulator (unless it has topological order), which is another way to see that gapless modes must be present in a Weyl semimetal.

The noninteger Hall conductance of Eq. (19) is a property that is specific to magnetic Weyl semimetals with broken TR symmetry. A more universal property, common, in some form, to all point-node topological semimetals, is revealed by looking at Eq. (15) from a different angle. Suppose a straight magnetic flux tube along the z-direction, carrying a quantum of flux Φ_0, is inserted into the sample. Eq. (15) tell us that the action, describing this one-dimensional (1D) magnetic flux tube, is given by

$$S = ie\lambda\int e^z \wedge \mathsf{A}. \tag{20}$$

This action describes a 1D metal, which has a noninteger charge per unit cell of

$$\rho d = i\frac{\delta S}{\delta A_0 \delta e_z^z} = e\lambda, \tag{21}$$

where ρ is the charge density. The Fermi momentum of this metal is

$$k_F = \pi\rho = \frac{\pi\lambda}{d} = Q, \tag{22}$$

which means that the 1D band dispersion crosses zero energy at the locations of the band-touching nodes of the 3D Weyl semimetal.

This is a simple demonstration of a fundamental property, shared (with some modifications) by all 3D point-node topological semimetals, namely the existence of a special Landau level, or more generally levels, which cross the Fermi energy at the locations of the band-touching nodes, see Fig. 4. In a magnetic Weyl semimetal, discussed above, a magnetic field B, applied along the z-direction, generates

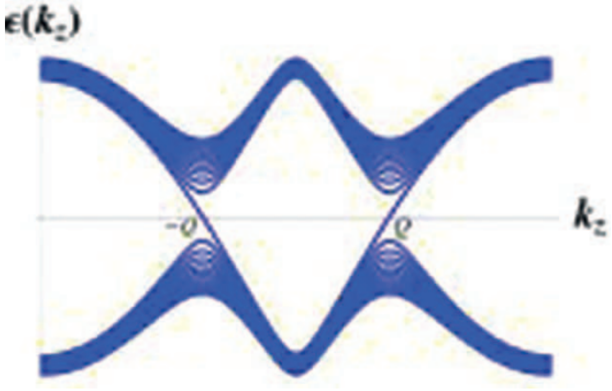

Fig. 4 Landau levels of a Weyl semimetal with a pair of Weyl nodes at $k_z = \pm Q$.

$$N_\Phi = \frac{BL^2}{\Phi_0}, \tag{23}$$

1D channels, i.e. one per every flux quantum, which corresponds to a magnetic-field-dependent charge density of

$$\rho = \frac{e\lambda}{d}\frac{B}{\Phi_0}. \tag{24}$$

According to the Streda formula, this corresponds to the Hall conductivity

$$\sigma_{xy} = \frac{\partial\rho}{\partial B} = \frac{e^2}{h}\frac{\lambda}{d}, \tag{25}$$

which agrees with Eq. (10).

Aside from the Hall conductivity of magnetic Weyl semimetals, this Landau level is responsible for all the special magnetotransport phenomena in 3D point-node topological semimetals. Consider diffusive transport equations for a Weyl semimetal with a single pair of opposite-chirality nodes, for simplicity. There are two conserved quantities: total electron density $n = n_R + n_L$ and chiral electron density $n_c = n_R — n_L$, where $n_{R\,L}$ are the densities of right (R) and left (L)-handed electrons. The transport equations for n and n_c are given by

$$\begin{aligned}\frac{\partial n}{\partial t} &= D\nabla^2(n + gV) + \mathbf{\Gamma}\cdot\nabla n_c,\\ \frac{\partial n_c}{\partial t} &= D\nabla^2 n_c - \frac{n_c}{\tau_c} + \mathbf{\Gamma}\cdot\nabla(n + gV).\end{aligned} \tag{26}$$

Here V is the external electrostatic potential, $D \sim v_F^2\tau$ is the diffusion constant, τ is the momentum relaxation time, which depends on the density of states g and the strength of the impurity scattering. $\tau_c \gg \tau$ is the chirality relaxation time, which is assumed to be much longer than the momentum relaxation time. The density of states g is taken to be finite even in the absence of the external magnetic field $\mathbf{B}$. This may be due to the Fermi energy not exactly coinciding with the location of the Weyl nodes, which will generically be the case in the presence of impurities. In this case $g = \varepsilon_F{}^2/(\pi^2\hbar^3 v_F{}^3) = k_F{}^2/(\pi^2\hbar v_F)$ for a pair of Weyl nodes. A finite density of states may also be directly induced by strong enough disorder even when $\varepsilon_F = 0$.

$\mathbf{\Gamma}$ is a new transport coefficient, related to the chiral anomaly, given by

$$\mathbf{\Gamma} = \frac{\widehat{B}}{2\pi^2\hbar\ell_B^2 g} \sim \frac{v_F}{(k_F\ell_B)^2}\widehat{B}, \tag{27}$$

where $\ell_B = \sqrt{\hbar/eB}$ is the magnetic length and $\widehat{B}$ is a unit vector in the direction of the magnetic field. Since the total electron number is exactly conserved, we may read off the expression for the electric current from the first of Eq. (26)

$$\mathbf{j} = \frac{\sigma}{e}\nabla\mu + eg\mu_c\mathbf{\Gamma}, \tag{28}$$

where $\sigma = e^2 gD$ is the diagonal conductivity and μ, μ_c are the electrochemical potentials, associated with the total and chiral particle densities. The first term in Eq. (28) is the standard Ohm's law. The second term describes an extra contribution to the electrical conductivity, which arises from the chiral anomaly, namely the N_Φ 1D conduction channels, which are opened up by the applied field. It is clear that this additional contribution to the current can have a dramatic effect in transport, since it is associated with first derivative terms in the transport equations Eq. (26), while the standard drift-diffusion terms which involve second derivatives.

To quantify this effect, it is useful to find the eigen-modes of the transport equations, which are given by

$$\omega_{\pm} = \pm\omega_0 - i\left(Dq^2 + 1/2\tau_c\right), \tag{29}$$

where

$$\omega_0 = \sqrt{(\Gamma q)^2 - 1/4\tau_c^2}. \tag{30}$$

We now note that the frequency ω_0 is purely imaginary at the smallest momenta when

$$q < \frac{1}{2\Gamma\tau_c} = \frac{L_a}{2L_c^2} \equiv \frac{1}{L_*}, \tag{31}$$

where we have introduced two length scales

$$L_c = \sqrt{D\tau_c}, \tag{32}$$

which has the meaning of the chiral charge diffusion length, and

$$L_a = \frac{D}{\Gamma} \sim \ell(k_F\ell_B)^2, \tag{33}$$

where $\ell = v_F\tau$ is the mean free path. L_a is a magnetic-field-related length scale, distinct from the magnetic length, which arises from the chiral anomaly. It is a long hydrodynamic length scale in the weak magnetic field regime, in the sense that $L_a \gg \ell$, but it may still be much smaller that either the chiral charge diffusion length L_c or the sample size L. In fact, the ratio L_c/L_a quantifies the strength of the chiral-anomaly-related transport phenomena, as will be seen below.

Thus when $q < 1/L_*$ the eigenfrequencies of the transport equations are purely imaginary, which corresponds to ordinary diffusion (nonpropagating) modes. However, when $q > 1/L_*$ (which may be a very small momentum when the ratio L_c/L_a is large), ω_0 is real, which signals the emergence of a pair of propagating modes in this regime. The modes are only weakly damped as long as

$$\omega_0 \approx \Gamma q > Dq^2, \tag{34}$$

which defines the upper limit on the wavevector $q = 1/L_a$, above which the propagating modes disappear. The propagating modes thus exist in the interval

$$1/L_* < q < 1/L_a. \tag{35}$$

This interval is significant when $L_c/L_a \gg 1$. On the other hand, when $L_a > L_c$, propagating modes do not exist for any q and one obtains a pair of standard diffusion modes

$$\omega_+ = -iDq^2, \omega_- = -iDq^2 - i/\tau_c, \tag{36}$$

which corresponds to independent diffusion of the total and the chiral charge densities.

The propagating mode of Eq. (34) signals the emergence of quasiballistic transport at long enough length scales. This may be seen explicitly by solving Eq. (26) in the steady state, assuming a uniform sample of linear size L, attached to metallic leads in the z-direction (i.e. the current flows along the magnetic field). One obtains the following expression for the scale-dependent sample conductance

$$G(L) = \frac{e^2N_\phi}{h}F(L/L_a, L/L_c), \tag{37}$$

where the scaling function $F(x,y)$ is given by

$$F(x, y) = \frac{(1 + y^2/x^2)^{3/2}}{\frac{y^2}{2x}\sqrt{1 + y^2/x^2} + \tanh\left(\frac{x}{2}\sqrt{1 + y^2/x^2}\right)}. \tag{38}$$

This scaling function exhibits crossover behaviors which exactly match the corresponding crossovers in the wavevector dependence of the diffusion modes, found above.

Indeed, when $x \ll y$, which means $L_a \gg L_c$, we have $F(x,y) \approx 2/x$, which gives

$$G(L) \approx e^2gDL = \sigma L, \tag{39}$$

which is simply the standard Ohmic conductance, with a small magnetic-field dependent correction, which goes as $(L_c/L_a)^2$, and which we have ignored here for the sake of brevity. This arises in the regime, in which we have two independent diffusion modes, given by Eq. (36), corresponding to independent diffusion of the total and the chiral charges.

On the other hand, when $L_a \ll L_c$, or $x \gg y$, we obtain

$$F(x, y) \approx \frac{1}{y^2/2x + \tanh(x/2)}. \tag{40}$$

This exhibits a regime of quasiballistic conductance with

$$G(L) \approx \frac{e^2 N_\phi}{h}, \tag{41}$$

which is realized when

$$L_a < L < L_*. \tag{42}$$

This corresponds precisely to the range of the wavevectors q in Eq. (35), for which propagating modes exist when $L_a \ll L_c$. Thus, one of the observable manifestations of the existence of quasi-1D propagating modes in a topological semimetal is the quasiballistic conductance, given by Eq. (41). Upon further increase of the sample size, a crossover back into the diffusive regime happens when $y^2 > x$, or equivalently when the sample size exceeds the length L_*

$$L > L_* \gg L_c. \tag{43}$$

In this regime the conductance is dominated by the field-dependent chiral anomaly contribution, but with $\propto B^2$, instead of $\propto B$, dependence

$$G(L) = \sigma(L_c/L_a)^2 L. \tag{44}$$

When $L_a > L_c$ this result still holds in the infinite sample limit, but with Eq. (44) only representing a subdominant correction to the Ohmic conductance.

Perhaps the clearest evidence for the chiral anomaly can come from the measurement of the optical magneto-conductivity. This may be evaluated using the full frequency and wavevector-dependent density response function $\chi(q, \omega)$, with ladder impurity vertex corrections

$$\sigma_{zz}(\omega) = -e^2 \lim_{q \to 0} \frac{i\omega}{q^2} \chi(q, \omega). \tag{45}$$

A straightforward calculation then gives

$$\sigma_{zz}(\omega) = \frac{\sigma}{1 - i\omega\tau} \frac{1 - i\omega\tau_c + (L_c/L_a)^2}{1 - i\omega\tau_c}. \tag{46}$$

Evaluating the real part, one obtains

$$\mathrm{Re}\, \sigma_{zz}(\omega) = \frac{\sigma}{1 + \omega^2\tau^2} \left[1 + \left(\frac{L_c}{L_a} \right)^2 \frac{1 - \omega^2 \tau\tau_c}{1 + \omega^2 \tau_c^2} \right]. \tag{47}$$

The prefactor in Eq. (47) is the standard Drude expression for the optical conductivity of a metal. The part in the square brackets is a correction that arises in a topological semimetal as a consequence of the chiral anomaly. This correction represents transfer of the spectral weight from high frequencies into a new low-frequency peak, whose width scales with the chiral charge relaxation rate $1/\tau_c$, while height is proportional to the ratio $(L_c/L_a)^2$. Importantly, Eq. (47) satisfies the exact f-sum rule

$$\int_0^\infty d\omega\, \mathrm{Re}\, \sigma_{zz}(\omega) = \frac{\pi\sigma}{2\tau}, \tag{48}$$

which means that the appearance of the new low-frequency peak indeed represents spectral weight transfer, as it should, see Fig. 5. The extra zero-frequency peak in the optical conductivity is a direct evidence of the opening up of a new transport channel (the zeroth Landau level) by the applied magnetic field.

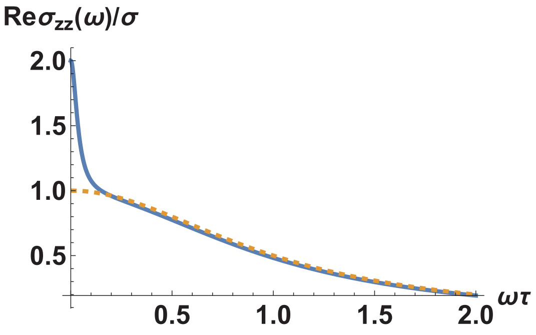

Fig. 5 Frequency-dependent conductivity for $L_c/L_a = 1$ (solid line) and $L_c/L_a = 0$ (dashed line), and $\tau/\tau_c = 0.04$.

Conclusion

In conclusion, we have described topological properties of Dirac and Weyl semimetals. These may be viewed as a consequence of the chiral anomaly and manifest in observable phenomena: intrinsic anomalous Hall effect with a non-integer Hall conductance per atomic plane; negative longitudinal magnetoresistance and scale-dependent quasiballistic transport; extra magnetic-field-dependent low-frequency peak in the optical conductivity, whose width is determined by the chirality relaxation rate.

Further reading

Altland A and Bagrets D (2016) Theory of the strongly disordered Weyl semimetals. *Physical Review B* 93: 075113.
Armitage NP, Mele EJ, and Vishwanath A (2018) Weyl and Dirac semimetals in three-dimensional solids. *Reviews of Modern Physics* 90: 015001.
Burkov AA (2018) Dynamical density response and optical conductivity in topological metals. *Physical Review B* 98: 165123.
Burkov AA and Balents L (2011) Weyl semimetal in a topological insulator multilayer. *Physical Review Letters* 107: 127205.
Cheng B, Schumann T, Stemmer S, and Armitage NP (2021) Probing charge pumping and relaxation of the chiral anomaly in a Dirac semimetal. *Science Advances* 7: eabg0914.
Gioia L, Wang C, and Burkov AA (2021) Unquantized anomalies in topological semimetals. *Physical Review Research* 3: 043067.
Li Q, Kharzeev DE, Zhang C, Huang Y, Pletikosic I, Fedorov AV, Zhong RD, Schneeloch JA, Gu GD, and Valla T (2016) Chiral magnetic effect in $ZrTe_5$. *Nature Physics* 12: 550.
Nissinen J and Volovik GE (2019) Elasticity tetrads, mixed axial-gravitational anomaly and $(3 + 1) - d$ quantum Hall effect. *Physical Review Research* 1: 023007.
Son DT and Spivak BZ (2013) Chiral anomaly and classical negative magnetoresistance of Weyl metals. *Physical Review B* 88: 104412.
Xiong J, Kushwaha SK, Liang T, Krizan JW, Hirschberger M, Wang W, Cava RJ, and Ong NP (2015) Evidence for the chiral anomaly in the Dirac semimetal Na_3Bi. *Science* 350: 413.

Topological insulators

Yoichi Ando, Physics Institute II, University of Cologne, Cologne, Germany

© 2024 Elsevier Ltd. All rights reserved.

Introduction 690
Historical perspective 691
Theory of topological insulators 692
Model Hamiltonian of A 3D topological insulator 694
Representative topological insulator materials 695
Topological crystalline insulators 696
Higher-order topological insulators 696
Experimental confirmation of TIs 696
Syntheses of TI materials 697
Interesting phenomena derived from TIs 697
Topological superconductivity and Majorana zero modes 697
Quantum anomalous Hall effect 697
Conclusion 698
Acknowledgments 698
References 698
Further reading 699

Abstract

Topological insulators are characterized by insulating bulk and conducting surface, the latter is a necessity consequence of the nontrivial topology of the wavefunctions forming the valence band. This chapter gives a historical overview of the discovery of topological insulators and a concise description of the Z_2 topology which defines them. The concept of topological insulators have been extended to various other topologies, giving rise to the recognition of further topological states of matter such as topological crystalline insulators and higher-order topological insulators. Representative materials of topological insulators, their synthesis techniques, and the ways for the experimental confirmation of the topological nature are introduced. Among the interesting phenomena derived from topological insulators, topological superconductivity, Majorana zero modes, and quantum anomalous Hall effect are briefly discussed.

Key points

- Bulk-boundary correspondence guarantees the appearance of gapless boundary states in a topological material.
- Topological insulators are defined by the Z_2 topology that was theoretically discovered in 2005.
- Spin-momentum locking is a key characteristic of the boundary states of topological insulators, allowing for topological superconductivity to show up in proximity to a conventional superconductor.
- Most topological-insulator materials are not really insulating in the bulk, but bulk-insulating samples can be obtained for Bi_2Te_2Se, $Bi_{2-x}Sb_xTe_3$, $Bi_{2-x}Sb_xTe_{3-y}Se_y$, HgTe, and $WeTe_2$.
- Quantum anomalous Hall effect can be realized in ferromagnetic topological insulators.

Introduction

Topological insulators (TIs) are a class of insulators whose occupied states are characterized by a nontrivial topological invariant. In the widest sense of the term, a two-dimensional (2D) electron gas in high magnetic fields showing the quantum Hall effect can be considered a TI, because such a system is characterized by a non-zero Chern number, which is a prototypical topological invariant for a time-reversal-breaking system. However, the term TI is most commonly used for time-reversal-invariant insulators that are characterized by a non-zero Z_2 index. Both 2D and three-dimensional (3D) systems can be TIs, and a 2D TI may also be called a quantum spin Hall insulator for historical reasons. While a 2D TI is characterized by a single Z_2 index, a combination of four Z_2 indices is necessary to fully characterize 3D TIs, which can be subdivided into strong TIs and weak TIs based on the Z_2 indices. New types of TIs characterized by different topological invariants, such as topological crystalline insulators or higher-order TIs, have been discovered with concrete materials realizations.

An important consequence of the nontrivial topology of TIs is that a gapless boundary state necessarily shows up when the material is physically terminated. This is because the nontrivial topology is a discrete characteristic of the gapped energy states,

https://doi.org/10.1016/B978-0-323-90800-9.00005-6

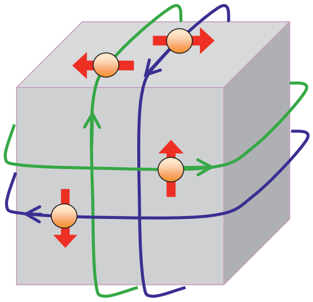

Fig. 1 Schematic picture of the spin-momentum locking in the topological surface states of a 3D TI. Electrons moving in opposite directions (depicted by green or blue lines with arrows) have opposite spin directions (red arrows); note that spins are perpendicular to the momentum.

which cannot change as long as the energy gap remains open. Since the vacuum (i.e. outside of the TI) is also gapped and is topologically trivial, there is a collision of different topologies at the boundary. In order for the topology to change across the boundary, the gap must close there. Therefore, 3D TIs are always associated with gapless surface states, and so are two-dimensional 2D TIs with gapless edge states. Furthermore, the resulting gapless states always reflect the topological character of the bulk states, which is called bulk-boundary correspondence.

In 2D and 3D TIs, their nontrivial topology is protected by time-reversal symmetry (TRS). There are special points in the Brillouin zone called time-reversal-invariant momenta, at which the momentum **k** is invariant upon time reversal. The Kramers theorem dictates that the gapless boundary states of a TI must be degenerate at a time-reversal-invariant momentum; as a result, the energy dispersion of the boundary states of a TI takes the form of a massless Dirac cone located at one of the time-reversal-invariant momenta. This massless Dirac cone is spin-non-degenerate, and the requirement of TRS means that the direction of the spin must be opposite between the states with **k** and −**k**. This relationship is called spin-momentum locking (see Fig. 1), which is one of the most important characteristics of TIs. In a 2D TI, the spin-momentum locking in the 1D edge state leads to the quantum spin Hall effect. When the TRS is broken, the gapless (or massless) nature of the Dirac cone is no longer protected by the topology and a gap may open at the Dirac point, but it does not mean that the Dirac cone disappears altogether upon TRS breaking.

Historical perspective

The quantum Hall effect (QHE) was discovered in 1980 by von Klitzing et al. in a high-mobility 2D semiconductor under high magnetic fields (Klitzing et al., 1980). In 1982, Thouless, Kohmoto, Nightingale, and den Nijs (TKNN) (Thouless et al., 1982) calculated the Hall conductance σ_{xy} of a Landau-quantized 2D system and showed that, when the chemical potential lies in a gap between Landau levels, $\sigma_{xy} = \nu(e^2/h)$ with an integer ν. This integer ν, often called TKNN invariant, was later shown to be nothing but the first Chern number of a 2D TRS-breaking topological system (Kohmoto, 1985). Therefore, the importance of topology in condensed matter was already recognized in the QHE system in 1980s.

Another important event preceding TIs was the discovery in 2004 of the spin Hall effect (Kato et al., 2004), the appearance of transverse spin current in response to longitudinal electric field. The spin Hall effect in nonmagnetic systems is fundamentally related to the anomalous Hall effect in ferromagnets (Nagaosa et al., 2010) and it can have both intrinsic and extrinsic origins. The intrinsic mechanism stems from the Berry curvature of the valence-band Bloch wavefunctions integrated over the Brillouin zone. Since such an integral can be non-zero even in an insulator, Murakami, Nagaosa, and Zhang proposed the idea of spin Hall insulator (Murakami et al., 2004), which is a gapped insulator with a finite spin Hall conductivity. Although this idea was later shown to be unrealistic as a bulk property (Onoda and Nagaosa, 2005), this triggered the subsequent proposal of the quantum spin Hall insulator in 2005 by Kane and Mele (Kane and Mele, 2005a, 2005b), who considered the edge states associated with an insulating 2D bulk. The ingenious proposal by Kane and Mele provided a concrete model (graphene with spin-orbit coupling) to realize the bulk band gap and gapless edge states in zero magnetic field (Kane and Mele, 2005a). More importantly, Kane and Mele recognized that the electronic states of their quantum spin Hall insulator is characterized by a novel topology specified by a Z_2 index (Kane and Mele, 2005b). This theoretical discovery of the Z_2 topology in insulators was an important step in our understanding of topological phases of matter. Experimentally, since the spin-orbit coupling in graphene is very weak, it is unfortunately difficult to observe the quantum spin Hall effect predicted in the Kane-Mele model. However, in 2006 Bernevig, Hughes, and Zhang proposed another 2D model to produce a Z_2 topological phase based on the band structure of HgTe, and they predicted that a CdTe/HgTe/CdTe quantum well should be a quantum spin Hall insulator (Bernevig et al., 2006). This prediction was verified in 2007 by Konig et al. (2007), who observed the quantization of the longitudinal conductance to $2e^2/h$ in zero magnetic field, giving evidence for the gapless edge states in the insulting regime.

In parallel with the experimental verification of the Z_2 topology in 2D, the topological classification of time-reversal-invariant insulators was extended to 3D systems. It was shown in 2006–2007 that four Z_2 indices are needed to fully characterize the topology for 3D (Fu et al., 2007; Moore and Balents, 2007; Roy, 2009). The term "topological insulator" was coined by Moore and Balents when they proposed the existence of topological systems in 3D (Moore and Balents, 2007). Fu and Kane made a concrete prediction that the $\mathrm{Bi}_{1-x}\mathrm{Sb}_x$ alloy in the insulating composition should be a 3D TI, and they further proposed that the nontrivial topology can be verified with the angle-resolved photoemission spectroscopy (ARPES) by counting the number of times the surface states cross the Fermi energy between two time-reversal-invariant momenta (Fu and Kane, 2007). The proposed experiment was conducted by Hsieh et al. who reported in 2008 that $\mathrm{Bi}_{1-x}\mathrm{Sb}_x$ is indeed a 3D TI (Hsieh et al., 2008).

Before the $\boldsymbol{Z}_2$ topology was theoretically discovered by Kane and Mele, a time-reversal-invariant topological state was conceived for four-dimensional (4D) systems, for which the topological invariant is an integer (Zhang and Hu, 2001). The effective field theory constructed for such 4D topological systems (Bernevig et al., 2002) was shown to be useful for 3D and 2D TIs (Qi et al., 2008), leading to interesting predictions regarding topological magnetoelectric effects (Qi et al., 2008).

Theory of topological insulators

The Berry connection of the Bloch wavefunctions in the momentum space plays the key role in the theory of topological insulators. Let us consider a band insulator described by a Bloch Hamiltonian $H(\boldsymbol{k})$ with the crystal momentum $\boldsymbol{k}$. The eigenstates are given by the solutions of the Bloch equation,

$$H(\boldsymbol{k})|u_n(\boldsymbol{k})\rangle = E_n(\boldsymbol{k})|u_n(\boldsymbol{k})\rangle. \tag{1}$$

The Berry connection $\boldsymbol{\mathcal{A}}^{(n)}(\boldsymbol{k})$ is defined by

$$\boldsymbol{\mathcal{A}}^{(n)}(\boldsymbol{k}) \equiv i\langle u_n(\boldsymbol{k})|\partial_{\boldsymbol{k}} u_n(\boldsymbol{k})\rangle, \tag{2}$$

which measures the rate of change in the wavefunction $|u_n(\boldsymbol{k})\rangle$ in the momentum space.

A gauge-invariant quantity constructed from $\boldsymbol{\mathcal{A}}^{(n)}(\boldsymbol{k})$ is the Berry phase, which is defined by

$$\gamma_n[C] \equiv \oint_C d\boldsymbol{k}\cdot\boldsymbol{\mathcal{A}}^{(n)}(\boldsymbol{k}), \tag{3}$$

where the line integral is performed along a closed path C in the momentum space and the gauge is chosen so that $\boldsymbol{\mathcal{A}}^{(n)}(\boldsymbol{k})$ is non-singular on C. Note that $\gamma_n[C]$ has a freedom of $2\pi N$ with integer N and is not strictly gauge-invariant, but $e^{i\gamma_n[C]}$ is.

Another gauge-invariant quantity that can be constructed from $\boldsymbol{\mathcal{A}}^{(n)}(\boldsymbol{k})$ is the field strength defined by

$$\mathcal{F}_{ij}^{(n)}(\boldsymbol{k}) \equiv \partial_{k_i}\mathcal{A}_{k_j}^{(n)}(\boldsymbol{k}) - \partial_{k_j}\mathcal{A}_{k_i}^{(n)}(\boldsymbol{k}). \tag{4}$$

For a 2D system, the Chern number of the n-th band is defined as the integral of the field strength $\mathcal{F}_{ij}^{(n)}(\boldsymbol{k})$ over the 2D Brillouin zone:

$$Ch^{(n)} = \frac{1}{2}\int_{\mathrm{2D\ BZ}} dk_x dk_y \mathcal{F}_{xy}^{(n)}(\boldsymbol{k}). \tag{5}$$

This integral vanishes if $\boldsymbol{\mathcal{A}}^{(n)}(\boldsymbol{k})$ has no singularity over the Brillouin zone. But if $\boldsymbol{\mathcal{A}}^{(n)}(\boldsymbol{k})$ has a singularity at $\boldsymbol{k}_0$, the gauge transformation

$$\boldsymbol{\mathcal{A}}^{(n)'}(\boldsymbol{k}) = \boldsymbol{\mathcal{A}}^{(n)}(\boldsymbol{k}) - \partial_{\boldsymbol{k}}\phi_n(\boldsymbol{k}) \tag{6}$$

in the region R including $\boldsymbol{k}_0$ can make $\boldsymbol{\mathcal{A}}^{(n)'}(\boldsymbol{k})$ to have no singularity in R. Using the Stokes' theorem, Eq. (5) becomes

$$Ch^{(n)} = \frac{1}{2}\int_{\partial R} d\boldsymbol{k}\cdot\partial_{\boldsymbol{k}}\phi_n(\boldsymbol{k}), \tag{7}$$

where ∂R is the boundary of R. Because $e^{i\phi_n(\boldsymbol{k})}$ is a unique function on ∂R, this $Ch^{(n)}$ must be an integer. For a 2D insulator, the total Chern number Ch of the occupied bands is given by

$$Ch = \sum_{E_n<E_{\mathrm{F}}} Ch^{(n)}. \tag{8}$$

Note that Ch can be finite only when the time-reversal symmetry is broken, because $Ch = -Ch$ under time-reversal symmetry.

The key insight of Kane and Mele (2005b) was that the Kramers degeneracy makes it possible to define a new topological invariant (i.e. the $\boldsymbol{Z}_2$ index) for 2D time-reversal-invariant systems. The time reversal operator $\mathcal{T}$ obeys $\mathcal{T}^2 = -1$ for spin-$\frac{1}{2}$ electrons, and the anti-unitarity of $\mathcal{T}$ yields

$$\langle\mathcal{T}u|\mathcal{T}v\rangle = \langle v|u\rangle \tag{9}$$

for any states $|u\rangle$ and $|v\rangle$. This leads to the conclusion that a state $|u\rangle$ is orthogonal to its time-reversal partner $\mathcal{T}|u\rangle$, i.e. $\langle u|\mathcal{T}u\rangle = 0$, because $\langle u|\mathcal{T}u\rangle = \langle\mathcal{T}^2u|\mathcal{T}u\rangle = -\langle u|\mathcal{T}u\rangle$. In a time-reversal-invariant system, $|u\rangle$ and $\mathcal{T}|u\rangle$ have the same energy, and hence their orthogonality means a guaranteed two-fold degeneracy, which is the essence of the Kramers degeneracy.

The time-reversal invariance makes the Bloch Hamiltonian $H(\boldsymbol{k})$ in Eq. (1) to have the following property:

$$\mathcal{T}H(\boldsymbol{k})\mathcal{T}^{-1} = H(-\boldsymbol{k}). \tag{10}$$

Hence, for an eigenstate $|u_n(\boldsymbol{k})\rangle$ of $H(\boldsymbol{k})$, its Kramers partner $\mathcal{T}|u_n(\boldsymbol{k})\rangle$ is an eigenstate of $H(-\boldsymbol{k})$. The orthogonality between $|u_n(\boldsymbol{k})\rangle$ and $\mathcal{T}|u_n(\boldsymbol{k})\rangle$ means that the latter can also be written by using a different eigenstate $|u_{n'}(\boldsymbol{k})\rangle$ of $H(\boldsymbol{k})$ as $|u_{n'}(-\boldsymbol{k})\rangle$. Hereafter, we write such a Kramers pair $(|u_n(\boldsymbol{k})\rangle, |u_{n'}(\boldsymbol{k})\rangle)$ as $(|u_n^{\mathrm{I}}(\boldsymbol{k})\rangle, |u_n^{\mathrm{II}}(\boldsymbol{k})\rangle)$. Due to the phase ambiguity of the eigenstates, there is a general relation

$$|u_n^{\mathrm{II}}(\boldsymbol{k})\rangle = e^{i\varphi_n(\boldsymbol{k})}\mathcal{T}|u_n^{\mathrm{I}}(-\boldsymbol{k})\rangle, \tag{11}$$

with $\varphi_n(\boldsymbol{k})$ the gauge degree of freedom.

The $\boldsymbol{Z}_2$ index was originally provided in the form of a Pfaffian (Kane and Mele, 2005b), but here we derive it as a variant of the spin Chern number (Sheng et al., 2006), which is well-defined when a 2D system has a fixed spin orientation, say S_z. In the diagonal basis of S_z, the Bloch Hamiltonian is written as

$$H(\boldsymbol{k}) = \begin{pmatrix} H_\uparrow(\boldsymbol{k}) & 0 \\ 0 & H_\downarrow(\boldsymbol{k}) \end{pmatrix}, \tag{12}$$

where $H_\uparrow(\boldsymbol{k})$ and $H_\downarrow(\boldsymbol{k}))$ are for the $S_z = 1/2$ and $S_z = -1/2$ sector, respectively. With this separation of $H(\boldsymbol{k})$, the spin Chern number $Ch_\uparrow$ and $Ch_\downarrow$ are defined as the Chern number of $H_\uparrow(\boldsymbol{k})$ and $H_\downarrow(\boldsymbol{k})$, respectively. Since each spin sector breaks time-reversal symmetry, the spin Chern number can be nonzero even for a time-reversal-invariant system, although the total Chern number must always vanish (i.e. $Ch_\uparrow + Ch_\downarrow = 0$) due to time-reversal symmetry.

In general, spin-orbit coupling breaks spin conservation, and thus the spin Chern number is not well-defined in a spin-orbit coupled system. However, in the presence of time-reversal symmetry, one can derive an analogous topological number as follows: Instead of the spin eigen-sectors, we use Kramers pairs $(|u_n^{\mathrm{I}}(\boldsymbol{k})\rangle, |u_n^{\mathrm{II}}(\boldsymbol{k})\rangle)$ to divide the Hilbert space into two subspaces, and then introduce the Chern numbers in those subspaces,

$$\begin{aligned} Ch_{\mathrm{I}} &= \frac{1}{2\pi}\int_{2\mathrm{D\ BZ}} dk_x dk_y \mathcal{F}_{xy}^{\mathrm{I}(-)}(\boldsymbol{k}), \\ Ch_{\mathrm{II}} &= \frac{1}{2\pi}\int_{2\mathrm{D\ BZ}} dk_x dk_y \mathcal{F}_{xy}^{\mathrm{II}(-)}(\boldsymbol{k}), \end{aligned} \tag{13}$$

where $\mathcal{F}_{xy}^{\mathrm{I}(-)}(\boldsymbol{k})$ and $\mathcal{F}_{xy}^{\mathrm{II}(-)}(\boldsymbol{k})$ are the field strengths of the Berry connections $\boldsymbol{\mathcal{A}}^{\mathrm{I}(-)}(\boldsymbol{k})$ and $\boldsymbol{\mathcal{A}}^{\mathrm{II}(-)}(\boldsymbol{k})$, which are defined for the occupied states as

$$\begin{aligned} A^{\mathrm{I}(-)}(\boldsymbol{k}) &= i\sum_{E_n<E_{\mathrm{F}}} \langle u_n^{\mathrm{I}}(\boldsymbol{k})|\partial_{\boldsymbol{k}} u_n^{\mathrm{I}}(\boldsymbol{k})\rangle, \\ A^{\mathrm{II}(-)}(\boldsymbol{k}) &= i\sum_{E_n<E_{\mathrm{F}}} \langle u_n^{\mathrm{II}}(\boldsymbol{k})|\partial_{\boldsymbol{k}} u_n^{\mathrm{II}}(\boldsymbol{k})\rangle. \end{aligned} \tag{14}$$

These Chern numbers share the same property as the spin Chern numbers: they take integer numbers, and $Ch_{\mathrm{I}} + Ch_{\mathrm{II}} = 0$ due to time-reversal symmetry. However, Ch_{I} and Ch_{II} themselves are not really well-defined, because the superscripts I and II do not have any physical meaning, and hence they can be exchanged; such an exchange leads to $Ch_{\mathrm{I}} \to Ch_{\mathrm{II}}$ $(=- Ch_{\mathrm{I}})$ and $Ch_{\mathrm{II}} \to Ch_{\mathrm{I}}$ $(=- Ch_{\mathrm{II}})$, and thus the Chern numbers Ch_{I} and Ch_{II} cannot be unique.

Nevertheless, by considering only the parity of these Chern numbers, i.e. $(-1)^{Ch_{\mathrm{I}}}$ and $(-1)^{Ch_{\mathrm{II}}}$, this ambiguity can be avoided; namely, because of the constraint $Ch_{\mathrm{I}} = -Ch_{\mathrm{II}}$, the parity satisfies $(-1)^{Ch_{\mathrm{I}}} = (-1)^{-Ch_{\mathrm{II}}} = (-1)^{Ch_{\mathrm{II}}}$, making them robust against the exchange of the superscripts. As a result, we have a unique $\boldsymbol{Z}_2$ index $(-1)^{\nu_{2D}}$ which is defined as

$$(-1)^{\nu_{2D}} \equiv (-1)^{Ch_{\mathrm{I}}} = (-1)^{Ch_{\mathrm{II}}}. \tag{15}$$

An insulator with $(-1)^{\nu_{2D}} = -1$ is topologically distinct from an ordinary insulator and such a system is called a 2D TI or a quantum spin Hall insulator. ν_{2D} is called $\boldsymbol{Z}_2$ topological invariant and takes the value 0 or 1.

The time-reversal invariance allows us to introduce $\boldsymbol{Z}_2$ indices in three dimensions (Moore and Balents, 2007). A time-reversal-invariant momentum Γ_i is defined as a momentum-space point satisfying $-\Gamma_i = \Gamma_i + \boldsymbol{G}$ for a reciprocal lattice vector $\boldsymbol{G}$. In a 3D Brillouin zone, there are a total of eight such Γ_i's and they can be indexed by using three integers n_a $(a = 1, 2, 3)$ taking the value of 0 or 1 as

$$\Gamma_{i=(n_1,n_2,n_3)} = \frac{1}{2}(n_1\boldsymbol{b}_1 + n_2\boldsymbol{b}_2 + n_3\boldsymbol{b}_3) \tag{16}$$

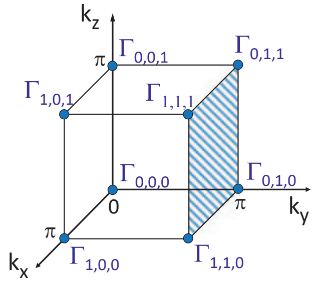

Fig. 2 The eight time-reversal-invariant momenta Γ_i $[i = (n_1, n_2, n_3)]$ in the 3D Brillouin zone having tetragonal symmetry. The time-reversal-invariant plane $\Sigma^a_{n_a}$ for $a = 2$ and $n_a = 1$ is hatched as an example.

with the primitive reciprocal lattice vectors $\boldsymbol{b}_i$ (see Fig. 2). Fixing one of the three n_a's gives a group of four time-reversal-invariant momenta. For example, by fixing n_2 to be 1, one obtains four time-reversal-invariant momenta $\Gamma_{(n_1,1,n_3)}$ with $n_1 = 0, 1$ and $n_3 = 0, 1$. These four time-reversal-invariant momenta specifies a distinct time-reversal-invariant plane ${\Sigma^a}_{n_a}$ in the 3D Brillouin zone (see Fig. 2 for the example of ${\Sigma^a}_{n_a}$ for $a = 2$ and $n_a = 1$). One can easily see that there are six distinct time-reversal-invariant planes in the 3D Brillouin zone.

It is easy to see that each time-reversal-invariant plane ${\Sigma^a}_{n_a}$ has its own Z_2 index $(-1)^{Ch_{\mathrm{I}}(\Sigma a_{na})}$. Hence, there are a total of six Z_2 indices that are defined in this manner, but they are not completely independent and the following constraints exist (Moore and Balents, 2007):

$$\begin{aligned}(-1)^{Ch_{\mathrm{I}}\left(\Sigma_1^1\right)-Ch_{\mathrm{I}}\left(\Sigma_0^1\right)} &= (-1)^{Ch_{\mathrm{I}}\left(\Sigma_1^2\right)-Ch_{\mathrm{I}}\left(\Sigma_0^2\right)} \\ &= (-1)^{Ch_{\mathrm{I}}\left(\Sigma_1^3\right)-Ch_{\mathrm{I}}\left(\Sigma_0^3\right)}.\end{aligned} \tag{17}$$

As a result, only the following four Z_2 indices are independent (Moore and Balents, 2007):

$$\begin{aligned}(-1)^{{\nu_{2\mathrm{D}}}^a} &\equiv (-1)^{Ch_{\mathrm{I}}\left(\Sigma_1^a\right)}, \quad (a = 1, 2, 3) \\ (-1)^{\nu_{3\mathrm{D}}} &\equiv (-1)^{Ch_{\mathrm{I}}\left(\Sigma_1^1\right)-Ch_{\mathrm{I}}\left(\Sigma_0^1\right)} = (-1)^{Ch_{\mathrm{I}}\left(\Sigma_1^1\right)}(-1)^{Ch_{\mathrm{I}}\left(\Sigma_0^1\right)}.\end{aligned} \tag{18}$$

The first three Z_2 indices becomes nontrivial (i.e. –1) if the system is just a stack of 2D TIs, and these three are called weak indices. On the other hand, the last Z_2 index $(-1)^{\nu_{3\mathrm{D}}}$ is intrinsic to 3D and this is called strong Z_2 index. An insulator with nontrivial strong Z_2 index is called a strong 3D TI, while those having only nontrivial weak indices are called weak 3D TIs. The set of four parameters $(\nu_{3\mathrm{D}}; \nu_{2\mathrm{D}}^1, \nu_{2\mathrm{D}}^2, \nu_{2\mathrm{D}}^3)$ constitutes the 3D Z_2 topological invariants to fully characterize the Z_2 topology of a 3D insulator.

When an insulator has inversion symmetry, the evaluation of the Z_2 indices becomes simple (Fu and Kane, 2007). The inversion operator P has the property $P^2 = 1$ and the Bloch Hamiltonian $H(\boldsymbol{k})$ of a centrosymmetric system satisfies

$$PH(\boldsymbol{k})P^{-1} = H(-\boldsymbol{k}). \tag{19}$$

From this relation, one can conclude that an eigenstate of $H(\boldsymbol{k})$ at $\boldsymbol{k} = \Gamma_i$ is simultaneously an eigenstate of P. Furthermore, because of the relation $[\mathcal{T}, P] = 0$, a Kramers pair have a common eigenvalue $\xi_i = \pm 1$ of P:

$$\begin{aligned}P|u_n^{\mathrm{I}}(\Gamma_i)\rangle &= \xi_i|u_n^{\mathrm{I}}(\Gamma_i)\rangle, \\ P|u_n^{\mathrm{II}}(\Gamma_i)\rangle &= \xi_i|u_n^{\mathrm{II}}(\Gamma_i)\rangle.\end{aligned} \tag{20}$$

The Z_2 index in 2D is evaluated by using these ξ_i as

$$(-1)^{\nu_{2\mathrm{D}}} = \prod_i \xi_i, \tag{21}$$

where the product is taken for all inequivalent Γ_i's in 2D (there are 4 of them). The Z_2 indices for 3D systems are given by

$$(-1)^{{\nu_{2\mathrm{D}}}^a} = \prod_{n_a=1;\, n_{b\neq a}} \xi_{i=(n_1 n_2 n_3)} \tag{22}$$

and

$$(-1)^{\nu_{3\mathrm{D}}} = \prod_i \xi_i, \tag{23}$$

where the product for the strong index is taken for all eight Γ_i's in the 3D Brillouin zone.

Model Hamiltonian of A 3D topological insulator

The nontrivial electronic structure of TIs stems from strong spin-orbit coupling. As an example, here we consider a prototypical topological insulator, Bi_2Se_3. Its bulk bands near the Fermi energy are mainly derived from the p_z orbitals of two inequivalent Se atoms in the unit cell, which makes the effective Hamiltonian to have a 4 × 4 matrix form (Zhang et al., 2009)

$$H_{\mathrm{TI}}(\boldsymbol{k}) = \left(m_0 - m_1\boldsymbol{k}^2\right)\sigma_x + v_z k_z \sigma_y + v\sigma_z\left(k_x s_y - k_y s_x\right), \tag{24}$$

with σ_i denoting the Pauli matrices in the orbital space and s_i the Pauli matrices in the spin space. Note that the eigenstates of σ_z (i.e. $\sigma_z = \pm 1$) correspond to the two p_z orbitals. The third term is a result of strong spin-orbit coupling. Since the inversion operation exchanges the p_z orbitals, one can see that the inversion operator P is given by σ_x. The $H_{\mathrm{TI}}(\boldsymbol{k})$ is invariant under the inversion P, i.e.

$$PH_{\mathrm{TI}}(-\boldsymbol{k})P^{-1} = H_{\mathrm{TI}}(\boldsymbol{k}). \tag{25}$$

The model Hamiltonian Eq. (24) focuses on the physics near the Γ point (i.e. $\boldsymbol{k}=0$), and the strong $\boldsymbol{Z}_2$ index given by Eq. (23) can be evaluated by taking the multiple of the parity of the occupied states at $\boldsymbol{k}=0$ and at the Brillouin zone boundary ($k \to \infty$ in this model).

Let us now consider the case $m_0 > 0$ and $m_1 > 0$ and examine if the system is topological. At $\boldsymbol{k}=0$ we have $H_{\mathrm{TI}}(k=0)=m_0\sigma_x$, and hence the eigenstate with odd parity ($\sigma_x = -1$) becomes the occupied state when $m_0 > 0$. On the other hand, since we have $H_{\mathrm{TI}}(\boldsymbol{k} \to \infty) \sim - m_1 k^2 \sigma_x$ at large k, the even-parity eigenstate becomes occupied when $m_1 > 0$. Thus, in this case, the strong $\boldsymbol{Z}_2$ index (i.e. the multiple of the parity of the occupied states at $\boldsymbol{k}=0$ and at $k \to \infty$) is –1, meaning that the system is topological. More generally, one can infer that the system becomes topological when m_0 and m_1 have the same sign, which is expressed as

$$(-1)^{\nu_{3D}} = -\operatorname{sgn}\ (m_0 m_1). \tag{26}$$

Physically, the condition for the system to become topological is that the parity of the occupied state switches at somewhere in the Brillouin zone between $\boldsymbol{k}=0$ and $k \to\ \infty$; such a switching is called band inversion, and the above discussion shows that it is the band inversion which makes Bi_2Se_3 to be topological.

Let us now derive the topological surface states from $H_{\mathrm{TI}}(\boldsymbol{k})$. We consider a surface at $z=0$ with the insulator occupying the positive z region. The wavefunction at the surface has the form

$$\psi_{k_x,k_y}(z) = \left(e^{-\kappa_- z} - e^{-\kappa_+ z}\right)\begin{pmatrix}0\\1\end{pmatrix}_\sigma \otimes u_s(k_x k_y), \tag{27}$$

with

$$\kappa_\pm = -\frac{v_z}{2m_1} \pm \sqrt{\left(\frac{v_z}{2m_1}\right)^2 + k_x^2 + k_y^2 - \frac{m_0}{m_1}}. \tag{28}$$

Substituting $\psi_{k_x,k_y}(z)$ into the Schrödinger equation

$$H_{\mathrm{TI}}(k_x, k_y, -i\partial_z)\psi_{k_x,k_y}(z) = E\psi_{k_x,k_y}(z), \tag{29}$$

one obtains a 2D Dirac equation

$$-v(k_x s_y - k_y s_x)u_s(k_x, k_y) = E u_s(k_x, k_y). \tag{30}$$

The term $k_x s_y - k_y s_x$ dictates the spin-momentum locking of the 2D Dirac fermions; namely, the spin is perpendicular to the surface momentum $\boldsymbol{k}_{2D}$ and lies within the surface plane.

Representative topological insulator materials

Usually, the TI materials become topological due to a band inversion, as one sees in the example in the previous section. The ultra-thin layer of HgTe is the most studied 2D TI. In the bulk HgTe, an inversion between *p*- and *s*-orbital bands gives the system a potential to be a TI, but these two bands are degenerate at the Γ point. The quantum-confinement effect in a thin layer opens a gap and makes the system to be a 2D TI (Bernevig et al., 2006). Applying an epitaxial strain to a thick layer of HgTe can also open a gap and make the system to be a 3D TI (Bruene et al., 2011). Both TI phases have been experimentally confirmed. The highest mobility for the topological surface states of a 3D TI ($\sim 3 \times 10^4$ cm^2/Vs) has been obtained in strained HgTe, although the bulk band gap attainable in strained HgTe would be limited to ~22 meV (Bruene et al., 2011). The HgTe system has not gained a wide popularity in the TI research, because the growth of HgTe films requires elaborate facilities.

The quantum well of AlSb/InAs/GaSb/AlSb realizing an inverted band alignment was theoretically predicted (Liu et al., 2008) and experimentally confirmed (Knez et al., 2011) to be a 2D TI. The valence-band top of GaSb lies above the conduction-band bottom of InAs, so when thin layers of InAs and GaSb are in direct contact and they are both quantum confined, the resulting hole subband in GaSb may lie above the electron subband in InAs, realizing the band inversion necessary for a TI. However, it has been reported that the 2D TI phase in this system is very fragile against disorder and it is difficult to utilize the edge transport in this system (Shojaei et al., 2018).

The monolayer of WTe_2 has recently emerged as a promising 2D TI (Qian et al., 2014). WTe_2 is a van-der-Waals material and a monolayer flake can be obtained by exfoliation. It was shown that the quantized conductance due to the 1D edge states persists up to ~100 K in WTe_2 (Wu et al., 2018).

The first material that was confirmed (Hsieh et al., 2008) to be a 3D TI, $Bi_{1-x}Sb_x$, has a relatively high 2D carrier mobility of $\sim 10^4$ cm^2/Vs (Taskin and Ando, 2009). Also, it is relatively easy for this system to reduce the bulk carrier density to the 10^{16} cm^{-3} level in high-quality single crystals, making it possible, for example, to perform Landau level spectroscopy of the surface states via magneto-optics (Schafgans et al., 2012). The bulk band gap is up to ~30 meV, which is large enough to detect the 2D transport properties at 4 K.

The most widely used 3D TIs for various studies of the topological phenomena are the family of materials having the tetradymite structure, Bi_2Se_3, Bi_2Te_3, Sb_2Te_3, and their relatives. Their 3D TI nature was predicted in 2009 (Zhang et al., 2009), followed by experimental confirmations of the existence of the topological surface states (Chen et al., 2009; Xia et al., 2009). Their crystal structure consists of covalently bonded quintuple layers (QLs), e.g. Se—Bi—Se—Bi—Se, that are stacked and weakly bonded by the van der Waals force, making it easily to cleave between QLs. High-quality single crystals and thin films of the binary compounds (Bi_2Se_3, Bi_2Te_3, Sb_2Te_3) can be relatively easily grown, which is one of the reasons for the popularity of these 3D TIs. It should be noted that those binary compounds are always conducting in the bulk and they are not really insulators, because bulk carrier doping due to naturally-occurring defects is unavoidable for entropy reasons. In 2010, the ternary compound Bi_2Te_2Se was discovered to be the first bulk-insulating 3D TI material (Ren et al., 2010), where the concealment of Se in the middle of the QL plays a key role in achieving bulk insulation. It is also possible to synthesize bulk-insulating samples by employing the concept of compensation, namely, balancing donors and acceptors so that they cancel each other. A series of compositions to realize bulk-insulation have been identified for $Bi_{2-x}Sb_xTe_{3-y}Se_y$ which can be grown as high-quality bulk single crystals (Ren et al., 2011); for example, $Bi_{1.5}Sb_{0.5}Te_{1.7}Se_{1.3}$ shows a particularly low bulk conductivity (Taskin et al., 2011). Also, it has been shown that bulk-insulating thin films can be obtained by optimizing the growth condition of $Bi_{2-x}Sb_xTe_3$ (Zhang et al., 2011).

A less studied materials family of 3D TIs is $TlBiSe_2$ and its variants ($TlBiTe_2$, $TlSbTe_2$, $TlBiSe_{2-x}S_x$, etc.). In the solid solution $TlBiSe_{2-x}S_x$, one can access the topological phase transition between the TI and non-TI phases by tuning the x value (Sato et al., 2011; Xu et al., 2011). Bulk-insulating single crystals can be grown by tuning the composition in $TlBi_xSb_{1-x}Te_2$ (Breunig et al., 2017), in which the compensation similar to that in $Bi_{2-x}Sb_xTe_3$ can be achieved.

An interesting material in the context of 3D TIs is SmB_6, which may be a topological Kondo insulator in which the band gap originates from strong electron correlations (Dzero et al., 2010). There is strong evidence for surface-dominated transport at low temperature, but its topological nature remains controversial. Note that the surface-dominated transport can be observed in trivial insulators due to the formation of an accumulation or inversion layer, as reported for pure Te (von Klitzing and Landwehr, 1971).

Topological crystalline insulators

The Z_2 topology protected by time-reversal symmetry is not the only possible topological classification of band insulators. Another topology protected by point-group symmetries of the crystal lattice can also classify insulators, and a material that is nontrivial with such a topology is called a topological crystalline insulator (TCI) (Fu, 2011). Concrete topological invariants have been constructed for systems possessing four-fold (C_4) or six-fold (C_6) rotation symmetry (Fu, 2011) and also for systems having mirror symmetry (Hsieh et al., 2012).

In this context, SnTe is a TCI protected by mirror symmetry, even though it is trivial in the Z_2 topology. Here, the topology is specified by the topological invariant called mirror Chern number $n_{\mathcal{M}}$, which evaluates the Chern number in only one of the two Hilbert subspaces divided according to the mirror eigenvalues (Teo et al., 2008). SnTe is characterized by $n_{\mathcal{M}} = -2$, and its surface states on the {001} surface present a peculiar double-Dirac-cone structure near the $\overline{X}$ points, which was theoretically predicted (Hsieh et al., 2012) and experimentally confirmed (Tanaka et al., 2012). Interestingly, the surface states on the {111} surface have a different structure consisting of two different Dirac cones at $\overline{\Gamma}$ and $\overline{M}$ points (Tanaka et al., 2013b). The TCI phase has also been reported for $Pb_{0.77}Sn_{0.23}Se$, in which a transition to a topologically-trivial phase was observed upon increasing temperature (Dziawa et al., 2012). The topological phase transition also occurs as a function of the composition in $Pb_{1-x}Sn_xTe$, in which the TCI phase is realized for x_c ⊠ 0.25 (Tanaka et al., 2013a; Xu et al., 2012).

The mirror Chern number $n_{\mathcal{M}}$ can also be used for time-reversal-invariant 3D TIs to further classify them (Teo et al., 2008). For example, $Bi_{1-x}Sb_x$ is a TI with Z_2 invariant (1;111), and it can have $n_{\mathcal{M}} = \pm 1$. The sign of $n_{\mathcal{M}}$ is called mirror chirality, which is related to the sign of the g factor. It was experimentally elucidated that $Bi_{1-x}Sb_x$ has the mirror chirality –1 (Nishide et al., 2010).

Higher-order topological insulators

It has been shown that 3D insulators can have a topology that leaves the surface to be gapped but some of their hinges or corners to accommodate symmetry-protected gapless states. The topological corner states may have fractional charge (Benalcazar et al., 2017). Such topological materials are called higher-order topological insulators — a 2nd-order 3D TI has gapless hinge states, and a 3rd-order 3D TI or a 2nd-order 2D TI has gapless corner states (Benalcazar et al., 2017; Schindler et al., 2018a, b). For example, in the presence of time-reversal and mirror symmetries, a 2nd-order 3D TI with helical hinge modes can be conceived, and SnTe has been proposed to be such a higher-order TI (Schindler et al., 2018a). Recently, Bi was elucidated to be a 2nd-order 3D TI in which the topology is protected by three-fold rotation and inversion symmetries, with the experimental proof of the existence of helical hinge states on the (111) surface (Schindler et al., 2018b).

Experimental confirmation of TIs

In the case of 2D TIs, the existence of helical 1D edge states should be probed, which is possible only through quantum transport experiments using device structures. The existence of edge states can be confirmed through conductance quantization when the Fermi level is gate-tuned into the bulk band gap (Konig et al., 2007). Also, the helical spin polarization of the edge states may be detected by transport experiments using spin Hall effect (Bruene et al., 2012).

For 3D TIs, observation of the Dirac-cone surface states by ARPES experiments is the most straightforward. To firm up the identification of a TI, spin-resolved ARPES should be employed to detect the helical spin polarization of the Dirac cone (Hsieh et al., 2009; Nishide et al., 2010). In transport experiments, it is necessary to prepare a sufficiently bulk-insulating sample to observe Shubnikov-de Haas (SdH) oscillations coming from high-mobility surface carriers, but if it is successful, the 2D Dirac nature of the topological surface states can be elucidated by the dependence of the SdH-oscillation frequency on the direction of the applied magnetic fields as well as by the π Berry phase that can be identified via the Landau-level fan-diagram analysis (Taskin and Ando, 2011). The 2D Dirac nature may also be confirmed by scanning tunneling epectroscopy (STS) experiments in magnetic fields, through the observation of the peculiar Landau quantization in which the level spacing changes as $\sqrt{N}$ and the zero-energy Landau level is pinned to the Dirac point (Cheng et al., 2010).

Syntheses of TI materials

The synthesis of bulk single crystals of the chalcogenide 3D TI materials (Bi_2Se_3, Bi_2Te_2Se, SnTe, etc.) are done in sealed evacuated quartz-glass tubes, because chalcogen atoms are volatile. The necessity of containment limits the range of applicable growth techniques, and the Bridgman method or vapor transport method are usually employed. In the Bridgman method, stoichiometric amounts of raw materials are first melted and then gradually cooled down in the presence of a temperature gradient, so that the crystallization starts at the cold end of the tube and the crystal grows as the solidification proceeds from this end. In the vapor transport technique, a chunk of polycrystalline material is put on the hot end of a sealed quartz-glass tube and the tube is kept for a long time in a furnace with a certain temperature gradient, during which the polycrystalline material sublimates and crystallizes at somewhere in the colder part.

For the growth of high-quality epitaxial thin films of TI materials, molecular beam epitaxy (MBE) technique is usually employed, in which the constituent elements are co-evaporated with suitable flux ratios. Although the lattice matching between the substrate and the grown material is usually very important for an epitaxial growth, in the case of the TI materials having the tetradymite structure, the lattice matching with the substrate is not crucial and the epitaxial growth proceeds in the so-called van-der-Waals epitaxy mode. For example, epitaxial growths of Bi_2Se_3 is possible on various substrates including Si(111), graphene-terminated 6H-SiC(0001), $SrTiO_3$(111), GaAs(111), sapphire(0001), and InP(111).

Nanowires and nanoribbons of 3D TI materials are of interest because of the peculiar quantum-confined 1D states realized in those structures (Breunig and Ando, 2021). Nanowires of Bi_2Te_3 or similar compounds are usually synthesized by gold-catalyzed vapor liquid solid (VLS) technique (Peng et al., 2010). In this technique, heated Au nanoparticles (typically $\sim$20 - nm diameter) are exposed to a flow of the vaporized material, which is absorbed at the top of the melted Au nanoparticles (liquid) and crystalizes at their bottom (solid), resulting in a forest of standing nanowires having a Au nanoparicle at their top.

Interesting phenomena derived from TIs

Topological superconductivity and Majorana zero modes

The spin-momentum locking in the topological surface states of 3D TIs makes them a promising platform to realize topological superconductivity hosting Majorana zero modes (MZMs), which are emergent zero-energy states described by a real creation operator γ. When the creation operator γ of a particle is real, it is self-conjugate, i.e. $\gamma = \gamma^{\dagger}$, and there is no distinction between creation and annihilation of the particle; in such a situation, one can say that the particle is its own antiparticle, which is the key characteristics of a Majorana particle and γ is called Majorana operator. Importantly, a fermion creation operator $f^{\dagger}$ can be constructed by using two Majorana operators as $f^{\dagger} = (\gamma_1 + i\gamma_2)/2$. One can easily see that the number operator of this fermion is written as $f^{\dagger}f = (1 - i\gamma_1\gamma_2)/2$, which means that $-i\gamma_1\gamma_2$ is 1 (−1) when the fermionic state is occupied (unoccupied). This operator $-i\gamma_1\gamma_2$ is called parity operator, and it signifies the occupancy of the zero-energy fermionic state f by an electron. This situation allows to encode quantum information in terms of the fermion parity by using two MZMs, which is the basis of topological quantum computation (Nayak et al., 2008).

Fu and Kane showed (Fu and Kane, 2008) that when superconductivity is induced in the topological surface states by using the superconducting proximity effect from a conventional *s*-wave superconductor in contact with a 3D TI, the resulting 2D superconducting state is topological and a MZM will show up in the vortex core. In usual *s*-wave superconductors, the spin-singlet Cooper pairs always leads to spin degeneracy in the in-gap states created in the superconducting condensate, and the spin degeneracy prohibits in-gap states to have the Majorana character. In the topological surface states, however, the spin-momentum locking removes this degeneracy, and further breaking of time-reversal symmetry in the vortex core leads to the MZM. Nanowires of 3D TIs are also an interesting platform to host MZMs. In this case, the quantum confinement of the topological surface states leads to spin-degenerate 1D subbands, but their degeneracy can be lifted by a parallel magnetic field to recover the spin-momentum locking. When superconductivity is induced in such subbands, 1D topological superconductivity is realized and MZMs will show up at the ends of the nanowire (Cook and Franz, 2011). Further breaking inversion symmetry by electrostatic gating is predicted to give rise to stable MZMs (Legg et al., 2021).

Quantum anomalous Hall effect

The quantum anomalous Hall effect (QAHE) occurs without Landau quantization and it signifies the Chern number of the occupied states of a 2D ferromagnetic insulator. The surface states of 3D TIs can be gapped when time-reversal symmetry is broken by a ferromagnetic order, which can be induced in 3D TIs by doping magnetic elements. When such a ferromagnetic 3D TI is made into an ultra-thin film (thickness $\lesssim$ 10 nm) and the Fermi level is tuned into the gap opened at the Dirac point, the QAHE can be realized. In the QAHE, the electrical current is carried by the spin-polarized 1D chiral edge state, which causes the Hall conductance σ_{xy} to be quantized to e^2/h and the longitudinal conductance σ_{xx} to vanish. Experimentally, the QAHE has been observed in the bulk-insulating TI material $(Bi_{1-x}Sb_x)_2Te_3$ doped with Cr or V (Chang et al., 2013, 2015). It can also be achieved in thin exfoliated flakes of $MnBi_2Te_4$ (Deng et al., 2020).

When a TI presenting the QAHE is in contact with a conventional *s*-wave superconductor, the combination of electron doping from the superconductor to the TI surface and the superconducting proximity effect is expected to lead to a time-reversal-breaking 2D topological superconductivity (Qi et al., 2010). The existence of ferromagnetism in the TI surface makes the situation different from the case of the proximitization of a pristine TI. Due to the TRS breaking, the proximitized TI surface is expected to be accompanied by chiral Majorana edge states (Qi et al., 2010), which are a dispersive 1D edge mode having the Majorana character (i.e. this mode is self-conjugate) and may also be called chiral Majorana fermions. Experimentally, the generation of chiral Majorana fermions is yet to be achieved.

Conclusion

The discovery of TIs has caused a paradigm shift in our understanding of how quantum mechanics governs the properties of materials. It has become recognized that the topological nature of the quantum-mechanical wavefunctions realized in a material has sharply observable consequences. The search for new topological invariants in materials and classifications of materials based on new topological classes are an active forefront of the current condensed matter physics. Also, this new viewpoint for materials has triggered the search for similar topological nature in other systems, such as cold atoms, photonic crystals, mechanical metamaterials, qubit arrays, etc.

The concept of topological superconductors is related to topological insulators, because both materials have a gap at the Fermi energy – the superconducting gap in the former and the band gap in the latter. Because of the existence of the gap, the same bulk-boundary correspondence applies to topological superconductors and they must be accompanied by gapless boundary states, which often (but not always) bear the Majorana character. When a 2D topological superconductor breaks time reversal symmetry and has no spin degeneracy, its edge harbors chiral Majorana fermions and the vortex core accommodates a MZM. The 3D TI material Bi_2Se_3 becomes a superconductor upon doping of Cu, Sr, or Nb; the resulting 3D superconductivity has been elucidated to be topological and presents peculiar nematic superconductivity (Yonezawa, 2019). The Majorana physics realized in topological superconductors is a very interesting topic in the future, and TIs provide a useful platform to address topological superconductivity.

Acknowledgments

The author has been supported by the European Research Council (ERC) under the European Union's Horizon 2020 research and innovation programme (grant agreement No 741121) and by the Deutsche Forschungsgemeinschaft (DFG, German Research Foundation) under CRC 1238 - 277146847 (Subproject A04) as well as under Germany's Excellence Strategy - Cluster of Excellence Matter and Light for Quantum Computing (ML4Q) EXC 2004/1 - 390534769.

References

Benalcazar WA, Bernevig BA, and Hughes TL (2017) *Science* 357(6346): 61.
Bernevig BA, Chern CH, Hu JP, Toumbas N, and Zhang SC (2002) *Ann. Phys.* 300(2): 185.
Bernevig BA, Hughes TL, and Zhang S-C (2006) *Science* 314(5806): 1757.
Breunig O and Ando Y (2021) *Nature Reviews Physics*. https://doi.org/10.1038/s42254-021-00402-6.
Breunig O, Wang Z, Taskin AA, Lux J, Rosch A, and Ando Y (2017) *Nature Communications* 8: 15545.
Bruene C, Liu CX, Novik EG, Hankiewicz EM, Buhmann H, Chen YL, Qi XL, Shen ZX, Zhang SC, and Molenkamp LW (2011) *Physical Review Letters* 106(12), 126803.
Bruene C, Roth A, Buhmann H, Hankiewicz EM, Molenkamp LW, Maciejko J, Qi X-L, and Zhang S-C (2012) *Nature Physics* 8(6): 485.
Chang C-Z, Zhang J, Feng X, Shen J, Zhang Z, Guo M, Li K, Ou Y, Wei P, Wang L-L, Ji Z-Q, Feng Y, Ji S, Chen X, Jia J, Dai X, Fang Z, Zhang S-C, He K, Wang Y, Lu L, Ma X-C, and Xue Q-K (2013) *Science* 340(6129): 167.
Chang C-Z, Zhao W, Kim DY, Zhang H, Assaf BA, Heiman D, Zhang S-C, Liu C, Chan MHW, and Moodera JS (2015) *Nature Materials* 14(5): 473.
Chen YL, Analytis JG, Chu JH, Liu ZK, Mo SK, Qi XL, Zhang HJ, Lu DH, Dai X, Fang Z, Zhang SC, Fisher IR, Hussain Z, and Shen ZX (2009) *Science* 325(5937): 178.
Cheng P, Song C, Zhang T, Zhang Y, Wang Y, Jia J-F, Wang J, Wang Y, Zhu B-F, Chen X, Ma X, He K, Wang L, Dai X, Fang Z, Xie X, Qi X-L, Liu C-X, Zhang S-C, and Xue Q-K (2010) *Physical Review Letters* 105(7): 076801.
Cook A and Franz M (2011) *Physical Review B* 84(20), 201105.
Deng Y, Yu Y, Shi MZ, Guo Z, Xu Z, Wang J, Chen XH, and Zhang Y (2020) *Science* 367(6480): 895.
Dzero M, Sun K, Galitski V, and Coleman P (2010) *Physical Review Letters* 104(10): 106408.
Dziawa P, Kowalski BJ, Dybko K, Buczko R, Szczer-bakow A, Szot M, Lusakowska E, Balasubramanian T, Wojek BM, Berntsen MH, Tjernberg O, and Story T (2012) *Nature Materials* 11(12): 1023.
Fu L (2011) *Physical Review Letters* 106: 106802.
Fu L and Kane CL (2007) *Physical Review B* 76: 045302.
Fu L and Kane CL (2008) *Physical Review Letters* 100(9): 096407.

Fu L, Kane CL, and Mele EJ (2007) *Physical Review Letters* 98(10): 106803.
Hsieh D, Qian D, Wray L, Xia Y, Hor YS, Cava RJ, and Hasan MZ (2008) *Nature* 452(7190): 970.
Hsieh D, Xia Y, Wray L, Qian D, Pal A, Dil JH, Os-terwalder J, Meier F, Bihlmayer G, Kane CL, Hor YS, Cava RJ, and Hasan MZ (2009) *Science* 323(5916): 919.
Hsieh TH, Lin H, Liu J, Duan W, Bansil A, and Fu L (2012) *Nature Communications* 3: 982.
Kane CL and Mele EJ (2005a) *Physical Review Letters* 95(22): 226801.
Kane CL and Mele EJ (2005b) *Physical Review Letters* 95(14): 146802.
Kato YK, Myers RC, Gossard AC, and Awschalom DD (2004) *Science* 306(5703): 1910.
Klitzing Kv, Dorda G, and Pepper M (1980) *Physical Review Letters* 45(6): 494.
Knez I, Du R-R, and Sullivan G (2011) *Physical Review Letters* 107(13): 136603.
Kohmoto M (1985) *Ann. Phys.* 160: 343.
Konig M, Wiedmann S, Brune C, Roth A, Buhmann H, Molenkamp LW, Qi XL, and Zhang SC (2007) *Science* 318(5851): 766.
Legg HF, Loss D, and Klinovaja J (2021) *Physical Review B* 104(16): 165405.
Liu C, Hughes TL, Qi X-L, Wang K, and Zhang S-C (2008) *Physical Review Letters* 100(23): 236601.
Moore JE and Balents L (2007) *Physical Review B* 75(12): 121306.
Murakami S, Nagaosa N, and Zhang SC (2004) *Physical Review Letters* 93(15): 156804.
Nagaosa N, Sinova J, Onoda S, MacDonald AH, and Ong NP (2010) *Reviews of Modern Physics* 82(2): 1539.
Nayak C, Simon SH, Stern A, Freedman M, and Das Sarma S (2008) *Reviews of Modern Physics* 80: 1083.
Nishide A, Taskin AA, Takeichi Y, Okuda T, Kak-izaki A, Hirahara T, Nakatsuji K, Komori F, Ando Y, and Matsuda I (2010) *Physical Review B* 81(4), 041309.
Onoda M and Nagaosa N (2005) *Physical Review Letters* 95(10): 106601.
Peng H, Lai K, Kong D, Meister S, Chen Y, Qi X-L, Zhang S-C, Shen Z-X, and Cui Y (2010) *Nature Materials* 9(3): 225.
Qi X-L, Hughes TL, and Zhang S-C (2008) *Physical Review B* 78: 195424.
Qi X-L, Hughes TL, and Zhang S-C (2010) *Physical Review B* 82(18): 184516.
Qian X, Liu J, Fu L, and Li J (2014) *Science* 346(6215): 1344.
Ren Z, Taskin AA, Sasaki S, Segawa K, and Ando Y (2010) *Physical Review B* 82(24): 241306.
Ren Z, Taskin AA, Sasaki S, Segawa K, and Ando Y (2011) *Physical Review B* 84(16): 165311.
Roy R (2009) *Physical Review B* 79(19): 195322.
Sato T, Segawa K, Kosaka K, Souma S, Nakayama K, Eto K, Minami T, Ando Y, and Takahashi T (2011) *Nature Physics* 7(11): 840.
Schafgans AA, Post KW, Taskin AA, Ando Y, Qi X-L, Chapler BC, and Basov DN (2012) *Physical Review B* 85(19): 195440.
Schindler F, Cook AM, Vergniory MG, Wang Z, Parkin SSP, Bernevig BA, and Neupert T (2018a) *Science Advances* 4(6): eaat0346.
Schindler F, Wang Z, Vergniory MG, Cook AM, Murani A, Sengupta S, Kasumov AY, Deblock R, Jeon S, Drozdov I, Bouchiat H, Guéron S, Yazdani A, Bernevig BA, and Neupert T (2018b) *Nature Physics* 14(9): 918.
Sheng DN, Weng ZY, Sheng L, and Haldane FDM (2006) *Physical Review Letters* 97: 036808.
Shojaei B, McFadden AP, Pendharkar M, Lee JS, Flatté ME, and Palmstrøm CJ (2018) *Physical Review Materials* 2(6): 064603.
Tanaka Y, Ren Z, Sato T, Nakayama K, Souma S, Takahashi T, Segawa K, and Ando Y (2012) *Nature Physics* 8(11): 800.
Tanaka Y, Sato T, Nakayama K, Souma S, Takahashi T, Ren Z, Novak M, Segawa K, and Ando Y (2013a) *Physical Review B* 87(15): 155105.
Tanaka Y, Shoman T, Nakayama K, Souma S, Sato T, Takahashi T, Novak M, Segawa K, and Ando Y (2013b) *Physical Review B* 88(23), 235126.
Taskin AA and Ando Y (2009) *Physical Review B* 80(8): 085303.
Taskin AA and Ando Y (2011) *Physical Review B* 84(3): 035301.
Taskin AA, Ren Z, Sasaki S, Segawa K, and Ando Y (2011) *Physical Review Letters* 107(1): 016801.
Teo JCY, Fu L, and Kane CL (2008) *Physical Review B* 78(4): 045426.
Thouless DJ, Kohmoto M, Nightingale MP, and Dennijs M (1982) *Physical Review Letters* 49(6): 405.
von Klitzing K and Landwehr G (1971) *Solid State Communications* 9(24): 2201.
Wu S, Fatemi V, Gibson Quinn D, Watanabe K, Taniguchi T, Cava Robert J, and Jarillo-Herrero P (2018) *Science* 359(6371): 76.
Xia Y, Qian D, Hsieh D, Wray L, Pal A, Lin H, Bansil A, Grauer D, Hor YS, Cava RJ, and Hasan MZ (2009) *Nature Physics* 5(6): 398.
Xu S-Y, Xia Y, Wray LA, Jia S, Meier F, Dil JH, Osterwalder J, Slomski B, Bansil A, Lin H, Cava RJ, and Hasan MZ (2011) *Science* 332(6029): 560.
Xu S-Y, Liu C, Alidoust N, Neupane M, Qian D, Be-lopolski I, Denlinger JD, Wang YJ, Lin H, Wray LA, Landolt G, Slomski B, Dil JH, Marcinkova A, Morosan E, Gibson Q, Sankar R, Chou FC, Cava RJ, Bansil A, and Hasan MZ (2012) *Nature Communications* 3: 1192.
Yonezawa S (2019) *Condensed Matter* 4(1): 2.
Zhang SC and Hu JP (2001) *Science* 294(5543): 823.
Zhang H, Liu C-X, Qi XL, Dai X, Fang Z, and Zhang S-C (2009) *Nature Physics* 5: 438.
Zhang J, Chang C-Z, Zhang Z, Wen J, Feng X, Li K, Liu M, He K, Wang L, Chen X, Xue Q-K, Ma X, and Wang Y (2011) *Nature Communications* 2: 574.

Further reading

Ando Y (2013) Topological insulator materials. *Journal of the Physical Society of Japan* 82: 102001.
Ando Y and Fu L (2015) Topological crystalline insulators and topological superconductors: From concepts to materials. *Annual Review of Condensed Matter Physics* 6: 361.
Bernevig BA and Hughes TL (2013) *Topological Insulators and Topological Superconductors*. Princeton University Press.
Sato M and Ando Y (2017) Topological superconductors: A review. *Reports on Progress in Physics* 80: 076501.
Hasan MZ and Kane CL (2010) Colloquium: Topological insulators. *Reviews of Modern Physics* 82: 3045.
Qi X-L and Zhang S-C (2011) Topological insulators and superconductors. *Reviews of Modern Physics* 83: 1057.
Tokura Y, Yasuda K, and Tsukazaki A (2019) Magnetic topological insulators. *Nature Reviews Physics* 1: 126.

Bloch electrons in a magnetic field

Jean Bellissard, School of Mathematics, Georgia Institute of Technology, Atlanta, GA, the United States

© 2024 Elsevier Ltd. All rights reserved.

Introduction 700
Low magnetic fields 700
Semiclassical methods and magnetic oscillations 702
Strong magnetic fields in 2*D* 703
Semiclassical methods at strong magnetic field 705
References 710

Abstract

This article provides a review of methods and results concerning the computation of electronic spectrum for a conductor submitted to a magnetic field.

Key points

- de Haas–van Alphen and Schubnikov–de Haas effects
- Peierls substitution and small magnetic fields
- Harper model and Hofstadter butterfly
- Rotation algebra and analysis tools thereon
- Semiclassical expansion for periodic potentials and strong magnetic fields
- Magnetic operators on triangular and hexagonal lattices
- Helffer and Sjöstrand's semiclassical spectral renormalization scheme

Introduction

A magnetic field applied to the electron gas of a solid breaks the time reversal symmetry giving access to information at the atomic scale that are inaccessible otherwise. The de Haas–van Alphen (de Haas and van Alphen, 1930) oscillations of the magnetic susceptibility or the Shubnikov–de Haas (Schubnikov and de Haas, 1930) oscillations of the conductivity are one of the classical experimental tools used in High Magnetic Fields facilities worldwide to investigate the structure of the Fermi surface. The Hall effect gives access to the type of the charge carriers, electrons, or holes. The cyclotron resonance frequency can also be measured through radio wave oscillations and gives access to the electron effective mass or various relaxation times. At last nuclear magnetic resonance (NMR) experiments give local information on the local density of states.

In most situations, the magnetic field can be considered as uniform at least on the scale of the electron mean free path. In much the same way, it is only at frequencies in the TeraHertz range and beyond, namely, of the order of the inverse of the inelastic collision time, that the magnetic field must be considered as non constant in time. Hence a magnetic field of up to $500T$ applied during a microsecond (explosion) can still be considered as constant in time.

The energy spectrum of independent electrons in a periodic potential and submitted to a magnetic field was immediately recognized by theoretical Physicists as very difficult to compute. This problem was investigated more systematically from the early 1950s onward. As a consequence of the Peierls approach (Peierls, 1933, 1956), Harper (1955) designed in 1955 a simplified model which is the paradigm of this problem (see Eq. 6). The calculation of the band spectrum of this model was investigated in several papers later on until Hofstadter (Hofstadter, 1976) in 1976 made a numerical computation and showed that it is a remarkable Cantor set (see Fig. 1), at a time when even the word *fractal* had not been coined by Mandelbrot yet. Since then, this *Hofstadter butterfly* has never ceased to fascinate physicists and mathematicians alike, even though it is still difficult to fully observe it in realistic experiments (Ponomarenko et al., 2013; Weiss, 2013). This butterfly has *zero Lebesgue measure*, namely, it cannot fly (Zero Lebesgue measure means that it surface area is zero. Therefore if it were realized by engineers, the total aerodynamic force acting on the wings would vanish as well, and the butterfly would just not take off.)!

Low magnetic fields

In the simplest approximation, the electron gas in a metal can be seen as a perfect Fermi gas of independent free electrons (or holes) with mass m_* (the effective mass in the medium) and charge $q = \mp e$. Let $\vec{R} = (R_1, R_2, R_3)$ be the position operators and let

https://doi.org/10.1016/B978-0-323-90800-9.00264-X

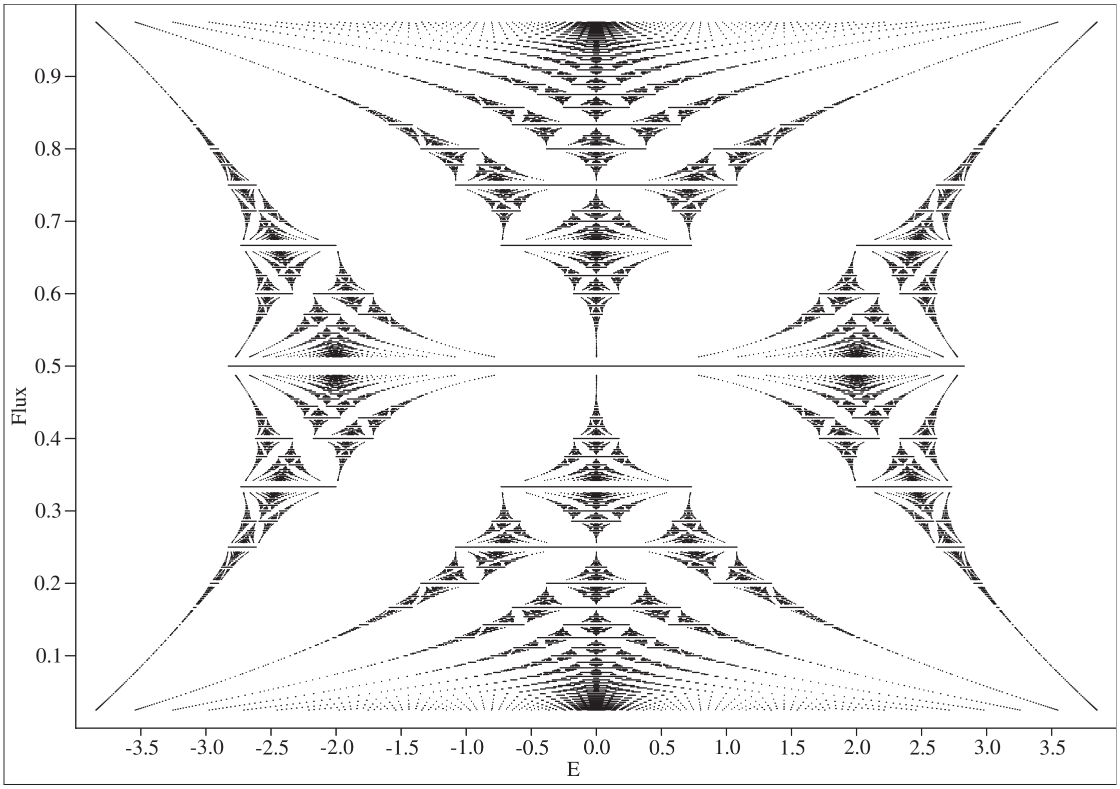

Fig. 1 Band spectrum for the Harper model describing a 2*D*-Bloch electron in a uniform magnetic field (Bellissard, 1994b)(ii).

$\vec{P} = (P_1, P_2, P_3)$ be the momentum operator so that $[R_i, P_j] = \imath\hbar\delta_{ij}$. The free Hamiltonian is given by $H = \vec{P}^2/2m_*$. Adding a uniform constant magnetic field $\vec{B} = (0, 0, B)$ can be done through the substitution $\vec{P}\mapsto\vec{P} - q\vec{A}$ if $\vec{A} = (A_1, A_2, A_3)$ is the vector potential, depending upon the position and defined by

$$\partial_1 A_2 - \partial_2 A_1 = B, \quad \partial_2 A_3 - \partial_3 A_2 = 0 = \partial_3 A_1 - \partial_1 A_3.$$

The quasimomentum operator is defined by $\vec{K} = (\vec{P} - q\vec{A})/\hbar = (K_1, K_2, K_3)$ and satisfies the following commutation rules

$$[K_1, K_2] = -\imath\frac{qB}{\hbar}, \quad [K_2, K_3] = [K_1, K_3] = 0. \tag{1}$$

The Hamiltonian for the free particle in a magnetic field becomes

$$\hat{H}_B = \frac{\hbar^2}{2m_*}\left(K_1^2 + K_2^2 + K_3^2\right) = H_B + \frac{\hbar^2}{2m_*}K_3^2.$$

Since K_3 commutes to K_1 and K_2, it is sufficient to compute the spectrum of H_B. H_B is called the *Landau Hamiltonian* (Landau, 1930) and represents the electronic motion in the plane perpendicular to $\vec{B}$. Thanks to the commutation rules (1), H_B can be seen as an harmonic oscillator with *effective* Planck's constant $\hbar_{eff} = qB/\hbar$. In particular, its spectrum is made of isolated eigenvalues (called Landau levels)

$$E_n = \hbar\omega_c(n + 1/2), \qquad n = 0, 1, 2, \ldots \qquad \omega_c = qB/m_*.$$

ω_c is called the *cyclotron frequency*. Thanks to the translation invariance of the problem, each such eigenvalue has, however, an infinite multiplicity given by 2π times the number of flux quanta per unit area, namely, $eB/\hbar$.

If the electron gas is now put in a periodic potential $V(\vec{R})$, such as what happens in a real metal, the one-particle Hamiltonian is $\hat{H}_B + V$. Then there are three vectors $\{\vec{a}_1, \vec{a}_2, \vec{a}_3\}$ in $\mathbb{R}^3$ such that $V(\vec{R} + \vec{a}) = V(\vec{R})$ whenever $\vec{a} = m_1\vec{a}_1 + m_2\vec{a}_2 + m_3\vec{a}_3$ and $m_i \in \mathbb{Z}$. If $B = 0$, Bloch's theory (1928) shows that the energy spectrum is made of *bands* described by functions $E_j(\vec{k})$ depending upon the *quasimomentum* $\vec{k}$ and periodic with respect to the reciprocal lattice defined as the set of $\vec{b} \in \mathbb{R}^3$ such that $\vec{a}_i{\cdot}\vec{b} \in 2\pi\mathbb{Z}$ for $i = 1, 2, 3$. Here, j is the band index and runs in a countable set. If $B \neq 0$ is small enough, the effective Hamiltonian describing electrons can be obtained from the band functions by substituting $\vec{K}$ to $\vec{k}$ (Peierls substitution Peierls, 1933). Using the periodicity, each band function can be expanded into a Fourier series

$$E_j(\vec{k}) \;=\; \sum_{m\in\mathbb{Z}^3} E_{j,m}\, e^{\imath\vec{k}\cdot(m_1\vec{a}_1+m_2\vec{a}_2+m_3\vec{a}_3)}, \qquad \Rightarrow \qquad H_{Peierls} = \sum_{m\in\mathbb{Z}^3} E_{j,m}\, e^{\imath\vec{K}\cdot(m_1\vec{a}_1+m_2\vec{a}_2+m_3\vec{a}_3)}, \tag{2}$$

Actually this substitution is only the lowest order contribution to an expansion in powers of B, but the following theorem holds.

Theorem 1 (Bellissard, 1986). *Let $\hat{H}_{B=0} + V$ have an interval $I \subset \mathbb{R}$ in its spectrum that is disconnected from the rest I^c of the spectrum and let I be generated by a finite family $E_1(\vec{k}), \ldots, E_N(\vec{k})$ of band functions. Then as $B \neq 0$ is small enough, the gaps separating I from I^c does not close. Moreover, the spectrum of $\hat{H}_B + V$ inside this region is described by an effective operator $H_{Peierls}$ of the form given by Eq. (2) where the Fourier coefficients are now $N \times N$ matrices depending continuously of the magnetic field.*

This theorem gives an effective Hamiltonian in terms of a *noncommutative Fourier* expansion using the three unitary operators

$$U_i = e^{\imath\vec{K}\cdot\vec{a}_1} = \left(U_i^{-1}\right)^*, \qquad U_iU_j = e^{\imath\theta_{ij}}U_jU_i, \qquad \theta_{ij} = -\theta_{ji} = 2\pi\frac{e}{h}\vec{B}\cdot\vec{a}_i \times \vec{a}_j.$$

The angle θ_{ij} represents 2π times the ratio of the magnetic flux through the parallelogram defined by vectors $\vec{a}_i$ and $\vec{a}_j$ by the flux quantum $\phi_0 = h/e$. To complete the analogy with Fourier series, let $\mathcal{T}$ be the linear map defined on the set of polynomials in the U_i's such that

$$\mathcal{T}(U_1^{m_1}U_2^{m_2}U_3^{m_3}) \;=\; 0 \qquad \text{if } |m_1|+|m_2|+|m_3| \neq 0 \quad \mathcal{T}(\mathbf{1}) \;=\; 1. \tag{3}$$

It can be checked that if A, B are two such polynomials, then (a) $\mathcal{T}(A^*A) \geq 0$ (state property), and (b) $\mathcal{T}(AB) = \mathcal{T}(BA)$ (*trace property*). Moreover it can be shown that $\mathcal{T}$ coincides with the *trace per unit volume* (Bellissard, 1986), meaning this map generalizes the integration over $\vec{k}$.

For most values (modulus and directions) of the magnetic field $\vec{B}$, the three angles θ_{ij} are incommensurate so that the algebra generated by the U_i's becomes *simple*, namely, it cannot be decomposed into a direct sum of simpler algebras, making the explicit computation of the energy spectrum a very difficult problem. However, the $\theta_{ij}/2\pi$'s can be seen as dimensionless effective Planck's constant and for a realistic crystal with $|\vec{a}_i| = 1$Å and a magnetic field $B = 1T$ their values is $O(10^{-5})$, thus justifying the use of semiclassical methods.

Semiclassical methods and magnetic oscillations

The semiclassical methods go back to the early days of the old theory of quanta, with the Bohr–Sommerfeld (1912–16) quantization formula. The use of such methods for electrons in magnetic fields was the basis of the Onsager argument (1952) (Onsager, 1952) to explain the de Haas–van Alphen (dHvA) (de Haas and van Alphen, 1930) and Shubnikov–de Hass (SdH) (Schubnikov and de Haas, 1930) oscillations (Lifshitz and Kosevich, 1955; Shoenberg, 1984).

As explained in Section "Low magnetic fields," the magnetic field B quantizes the quasimomentum space with an effective Planck constant proportional to B. Moreover, if a periodic potential is added, the relevant dimensionless Planck constant is so small as to make the problem semiclassical. In particular, the Heisenberg equations of motions for the effective Peierls Hamiltonian (2) gives

$$\frac{d\vec{K}}{dt} = \frac{\imath}{\hbar}[H_{Peierls}, \vec{K}].$$

Since K_3 commutes with K_1 and K_2, it follows that $dK_3/dt = 0$ so that the motion takes place in the plane perpendicular to $\vec{B}$. Moreover, using the commutation rules (1) leads to the following approximate equation of motion

$$\frac{dk_1}{dt} = -\frac{qB}{\hbar^2}\frac{\partial E_j}{\partial k_2}, \qquad \frac{dk_2}{dt} = \frac{qB}{\hbar^2}\frac{\partial E_j}{\partial k_1}, \qquad \frac{dk_3}{dt} = 0,$$

implying that $E_j(\vec{k})$ is conserved. Thus the classical orbit associated with conduction electrons in the limit of zero temperature lies on the Fermi surface $E_j = E_F$ in a plane perpendicular to the magnetic field corresponding to $k_3 = \vec{k}\cdot\vec{B} = const$. Each such plane plays the role of a phase space for one degree of freedom, where k_2 is equivalent to the position and k_1 to the momentum, while the band function $E(k_1, k_2)$ plays the role of the Hamiltonian. Thanks to the Bohr–Sommerfeld quantization formula, only orbits with quantized action do survive quantum interferences, leading to

$$\oint_{orb} k_1 dk_2 = -2\pi e\frac{B}{\hbar}(n + \nu) \qquad n \in \mathbb{Z}, \quad \nu = \text{Maslov index}, \tag{4}$$

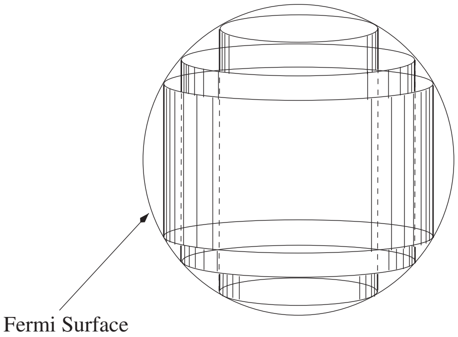

Fig. 2 Landau cylinders inside the Fermi surface.

where the contour integral is computed on the classical orbit. By the Stokes formula the *l.h.s.* is the area A enclosed by the classical orbit. The usual argument is now to compute the free energy F of such an electron gas and to remark that it takes into account these orbits with all possible values of k_3 provided $\vec{k}$ stays inside the Fermi surface. The Bohr–Sommerfeld condition (4) select cylinders indexed by n with areas depending on the magnetic field (see Fig. 2).

As the magnetic field increases, the radius of each such cylinders increases as well until it gets out of the Fermi surface. Then the cylinder with index n has an area equal to the maximum area A_{max} of a section of the Fermi surface with a plane perpendicular to the magnetic field. As B increases again, the cylinder with index $n - 1$ dominates leading to oscillations of the free energy with periods given by the Onsager formula

$$\Delta\left(\frac{1}{B}\right) = \frac{2\pi e}{hA_{max}}$$

By tilting the direction of the magnetic field, this formula gives access to measuring the maximal area of the Fermi surface in the plane perpendicular to B. In addition, since the magnetization is given by the thermodynamical relation $M = \mu_0(\partial F/\partial B)_\mu$, it also exhibits oscillations at the same period and this is what experiments are measuring giving access to the size of the Fermi surface. Extensions of this theory (the Lifshitz and Kosevich formula (Lifshitz and Kosevich, 1955) and magnetic breakdown) can be found in Shoenberg (1984).

Strong magnetic fields in 2*D*

If the magnetic field is oriented along one of the crystal axis, the operator U_3 commutes with the others, so the model can be reduced to the 2D plane perpendicular to $\vec{B}$. On the other hand, modern devices that are effectively two-dimensional are currently available in labs. Such is the case for interfaces between the semiconductor and the oxide of a MOSFET or between the two parts of an heterojunction used in meso- or nanoscale technology.

Then, if only one band contributes, two unitaries suffice to express the effective Hamiltonian as

$$H = \sum_{m_1, m_2} h_{m_1,m_2} e^{\imath\theta m_1 m_2/2} U_1^{m_1} U_2^{m_2}, \quad U_1 U_2 = e^{\imath\theta} U_2 U_1, \tag{5}$$

where $\bar{h}_{m_1,m_2} = h_{-m_1,-m_2}$ (selfadjointness of H) are called the *Fourier coefficients* of H. The simplest example is the *Almost–Mathieu model* (if $t_1 \neq t_2$) or *Harper model* (if $t_1 = t_2$) given by

$$H_{Harper} = t_1(U_1 + U_1^{-1}) + t_2(U_2 + U_2^{-1}), \tag{6}$$

where $t_1, t_2 > 0$ are called the *hopping parameters*. A numerical calculation of the band spectrum is possible if $\theta = 2\pi p/q$, where p/q is a fraction. Here is the recipe

(i) replace U_1 and U_2 by $U_i(k_1, k_2) = e^{\imath k_i} u_i$, where

$$u_1 = \begin{bmatrix} 0 & 1 & 0 & \cdots & 0 \\ 0 & 0 & 1 & \cdots & 0 \\ \vdots & \vdots & \vdots & \ddots & \vdots \\ 0 & 0 & 0 & \cdots & 1 \\ 1 & 0 & 0 & \cdots & 0 \end{bmatrix}, \qquad u_2 = \begin{bmatrix} 1 & 0 & 0 & \cdots & 0 \\ 0 & e^{2\imath\pi p/q} & 0 & \cdots & 0 \\ \vdots & \vdots & \vdots & \ddots & \vdots \\ 0 & 0 & 0 & \cdots & 0 \\ 1 & 0 & 0 & \cdots & e^{2\imath\pi(p-1)p/q} \end{bmatrix}.$$

Then H becomes a $q \times q$ Hermitian matrix depending periodically on $k = (k_1, k_2)$ with period 2π. Then k is called the *quasimomentum*.

(ii) For each value of (k_1, k_2), compute the eigenvalues $e_1(k_1, k_2) \leq \cdots \leq e_q(k_1, k_2)$ of $H(k_1, k_2)$. The spectrum is obtained as the union of all these values. In practice the e_j's are computed for only a finite number of values of (k_1, k_2). Then, as in the case of band theory, use the symmetries of the model to choose the relevant (k_1, k_2)'s. In the Harper or in the Almost–Mathieu models, the values $(k_1, k_2) = (0, 0)$ or (π, π) gives the band edges.

Fig. 1 represents the energy spectrum of the Harper model (see Eq. 6), which was obtained for the first time in 1976 by D. R. Hofstadter in his Ph.D. thesis (Hofstadter, 1976) as a numerical calculation following the previous algorithm. The vertical axis represents the values of $\theta/2\pi$ between 0 and 1 while the horizontal one represents the values of the energies in unit of $t_1 = t_2$ varying from − 4 to + 4. The picture obtained suggests that the gap edges are continuous with respect to θ even though a closer look shows that these functions have discontinuous derivative at each rational point. This has been proved rigorously (Rammal and Bellissard, 1990; Bellissard, 1994b, a)

Theorem 2. *Let H be given by Eq. (5) with Fourier coefficients depending smoothly on θ and decreasing fast enough as (m_1, m_2) increase to infinity. Then the gap edges of the spectrum of H are continuous functions of θ. Moreover, these functions are differentiable almost everywhere. At each rational value of θ, the right and left derivatives of such function exist but are not necessarily equal. The discontinuity of the derivative at a rational point p/q at the edge of the band j, represented by the band function $e_j(k_1, k_2)$, can be computed through the following formula:*

$$\Delta = |\det \partial_\mu \partial_\nu e_j(k^{(j)})|^{1/2}$$

where $k^{(j)} = (k_1^{(j)} k_2^{(j)})$ is the value of the quasimomentum corresponding to the gap edge of the band j.

In the specific case of the Almost–Mathieu operator (see Eq. 6), additional properties have been proved over the years by several theoretical physicists and mathematicians (The number of articles on this subject is too large for being cited here. The main contributors are S. Aubry, D. Thouless, B. Simon, Y. Last, S. Jitomirskaya, and J. Puig.).

Theorem 3. *Let H be given by Eq. (6). Then*

(i) *for all irrational values of $\theta/2\pi$ and for $t_1 \neq t_2$, the Lebesgue measure of the spectrum of H is equal to $4|t_1 - t_2|$ (Aubry's conjecture).*
(ii) *For almost all irrational values of $\theta/2\pi$ and for $t_1 = t_2$, the spectrum of H has zero Lebesgue measure. For a* large *set of such θ's, the Hausdorff dimension of the spectrum is less than or equal to 1/2.*
(iii) *If $\theta/2\pi$ satisfies a* diophantine condition, *then the spectrum of H is a Cantor set (* i.e., *its complement is a dense open set and it has no isolated points).*

Let $\mathcal{T}$ be the *trace* defined in Eq. (3). Then the *integrated density of states* (IDoS) $\mathcal{N}(E)$ is defined as the number of eigenvalues of H per unit volume smaller than or equal to E. The *Shubin* formula asserts that (Bellissard, 1994b)

$$\mathcal{N}(E) = \mathcal{T}(\chi(H \leq E))$$

where $\chi(H \leq E)$ is the projection on the space spanned by eigenstates of H with eigenvalues smaller than or equal to E. Then

Theorem 4. *Let H be given by Eq. (5). Then*

(i) *its IDoS is a nondecreasing function of* E *varying from 0 to 1. It is constant of spectral gaps, and it values on spectral gaps are given by the fractional part of* nθ/2π *form some integer n (gap labeling theorem).*
(ii) *If H is the Almost–Mathieu model and if $\theta/2\pi$ is irrational, then for any integer n there is a gap with IDoS equal to the fractional part of $n\theta/2\pi$.*

The previous class of model can be seen as a tight-binding representation for the effective Hamiltonian representing the charge carrier motion on a perfect 2*D* lattice. Other models can be constructed by considering that U_1 and U_2 represent translation along the basis vectors of a 2*D* crystal. Examples of models are the following:

(i) The Harper model on a triangular lattice: there are three translations U_1, U_2, and U_3 with $U_1 U_2 U_3 = e^{2\imath\pi\eta}$ and $U_1^{-1} U_2^{-1} U_3^{-1} = e^{2\imath\pi(\gamma - \eta)}$ if η and $\gamma - \eta$ are the dimensionless fluxes in the two types of triangles (see Fig. 3). The Hamiltonian becomes

$$H_\Delta = t\left(U_1 + U_1^{-1} + U_2 + U_2^{-1} + U_3 + U_3^{-1}\right).$$

(ii) The corresponding model for the honeycomb lattice takes into account the existence of two sublattices A and B (see Fig. 4). Each site in A has its neighbors in B in directions $\vec{e}_1$, $\vec{e}_2$, and $\vec{e}_3$, where these three vectors add up to zero and make angle of 120° and vice versa. Hence a wave packet can be seen as a spinor with components $|\psi_A\rangle$ and $|\psi_B\rangle$ and the Hamiltonian becomes a 2 × 2 matrix with coefficients depending on the U_i's as follows

$$H_{\text{hexa.}} = t\begin{bmatrix} 0 & U_1 + U_2 + U_3 \\ U_1^{-1} + U_2^{-1} + U_3^{-1} & 0 \end{bmatrix},$$

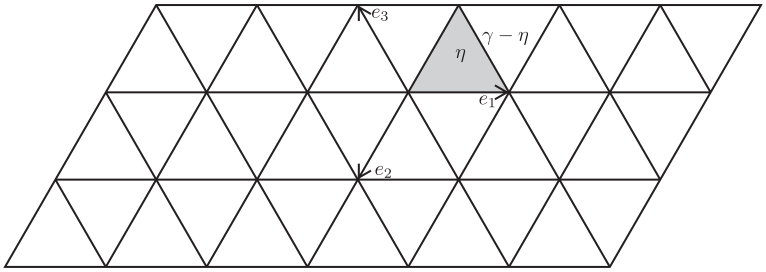

Fig. 3 Triangular lattice, its basis, and two types of triangles.

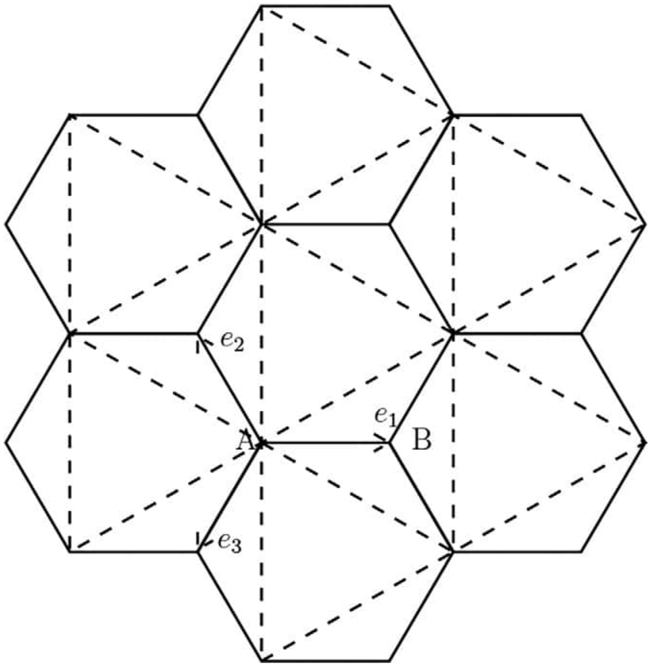

Fig. 4 The honeycomb and its basis.

Here, γ represents the dimensionless flux through the cell generated by $\vec{e}_1$ and $\vec{e}_2$, namely, it is the third of the flux through the unit cell given by an hexagon and $\eta = \gamma/2$.

Various compounds admit a honeycomb structures, such as graphite monolayers built on the surface of silicon carbide *SiC*. More generally for quasi 2D systems, the previous construction can be used to build the effective Hamiltonian. It has been applied for instance to the magnetic breakdown observed in organic conductors of type (BEDT-TTF), which are mainly a stack of weakly coupled 2D layers (Fortin and Ziman, 1998).

Semiclassical methods at strong magnetic field

It is remarkable then that semiclassical methods could be used at strong magnetic field as well. For indeed, the stronger the magnetic field, the bigger $\hbar_{eff}$. In the eighties, the works by Helffer and Sjöstrand (1987a,b, 1988, 1989, 1990) and Rammal and Bellissard (1990) (Rammal and Bellissard, 1990; Bellissard, 1994b) on the Harper model and its extensions have shown the method.

If θ is close to a rational multiple of 2π, say $\theta = 2\pi p/q + \delta$, with $\delta > 0$ small, then the two unitaries U_1 and U_2 can be taken as $U_i = e^{\imath k_i} u_i \otimes \hat{U}_i$ with $\hat{U}_1 \hat{U}_2 = e^{\imath\delta} \hat{U}_2 \hat{U}_1$ implying $U_1 U_2 = e^{\imath\theta} U_2 U_1$. These unitary operators are $q \times q$ matrices with operator coefficients. The phase factor $e^{\imath k_i}$ can be chosen arbitrarily, without changing the spectrum. This substitution is the rigorous version of the Peierls one. The following representation is used

$$\hat{U}_i = e^{\imath\sqrt{\delta}K_i}, \quad K_i = K_i^*, \quad [K_1, K_2] = -\imath\mathbf{1}.$$

Let now $|j\rangle$ denotes an eigenvector of the Hamiltonian obtained by setting $\delta = 0$. Then using the Feshbach method (also called Schur complement or Green function method), the $q \times q$ Hamiltonian H is transformed into a 1×1 effective one given by

$$H_{eff}(z) = \langle j|H|j\rangle + \langle j|HQ_j \frac{1}{z - Q_j H Q_j} Q_j H|j\rangle, \quad Q_j = \mathbf{1}_q - |j\rangle\langle j|.$$

For $\delta = 0$, the Hamiltonian becomes a $q \times q$-matrix valued function of k denoted by $\mathcal{H}$ while for $\delta \neq 0$, its matrix elements depend on $\hat{U}_1$ and $\hat{U}_2$. It is possible to expand the Hamiltonian in powers of $\sqrt{\delta}$, leading to a generalization of the semiclassical expansion. However here, the Hamiltonian being a $q \times q$ matrix, some complication occurs depending upon what point of the spectrum is considered. The simplest expansion corresponds to expanding near a band edge. Then $k = (k_1, k_2)$ is chosen to correspond to this band edge in the eigenvalue e_j of the Hamiltonian at $\delta = 0$. Moreover, let $|j\rangle$ be the q-dimensional eigenvector of the Hamiltonian for eigenvalue e_j at k. The eigenvalue equation is then $E|\psi\rangle = H_{eff}(E)|\psi\rangle$, which is nonlinear in E. Expanding this operator in powers of $\sqrt{\delta}$ to lowest order gives again an harmonic oscillator as lowest order contribution which can be interpreted as a Landau Hamiltonian.

Using the Landau spectrum, this gives eigenvalues in the following form (see Figs. 5 and 6).

$$E_{n,j}(\delta) = e_j(k) + |\delta|(n + 1/2)\left(\det D^2 e_j(k)\right)^{1/2} + \delta\, \frac{\partial e_j(k)}{\partial \delta} + \delta\sigma + O\left(\delta^{3/2}\right),$$

where

$$\sigma = \frac{\imath}{2} \sum_{\ell:\neq j} \frac{\langle j|\partial_1 \mathcal{H}|\ell\rangle\langle \ell|\partial_2 \mathcal{H}|j\rangle - \langle j|\partial_2 \mathcal{H}|\ell\rangle\langle \ell|\partial_1 \mathcal{H}|j\rangle}{e_j - e_\ell}$$

The very same formula holds if $\delta < 0$ using a similar method. This formula gives rise to the discontinuity of the derivative of the band edges as stated in Theorem 2. It is remarkable that a systematic higher order expansion gives right corrections to the Landau levels, as long as the level width is ignored.

If two bands are touching (see Fig. 7) for $\delta = 0$, the previous analysis fails. The degeneracy of the eigenvalues e_j and say, e_{j-1} at k for $\delta = 0$ requires using a degenerate perturbation theory. The lowest order in the $\sqrt{\delta}$ expansion is given by a 2*D-Dirac* operator of the form

$$H_{Dirac} = C, \sqrt{\delta} \begin{bmatrix} 0 & K_1 + \imath K_2 \\ K_1 - \imath K_2 & 0 \end{bmatrix} + O(\delta), \quad \Rightarrow \quad E_n^{\pm} = \pm C\sqrt{n\delta}\,(1 + O(\delta)),$$

where C is a model-dependent constant, the $E_n^{\pm}$'s are the eigenvalues, and $n = 0, 1, 2, \ldots$ is an integer (see Fig. 8).

As can be seen in Figs. 1, 6, and 8, the Landau–Dirac level broadens into a band as δ gets too large. This is a general phenomena due to *tunneling* in phase space. A spectacular illustration of tunneling effect is the braiding seen in Fig. 9 in the following model:

$$H_2 = t\left(U_1 + U_1^{-1} + U_2 + U_2^{-1} + \tau\left(U_1^2 + U_1^{-2} + U_2^2 + U_2^{-2}\right)\right). \tag{7}$$

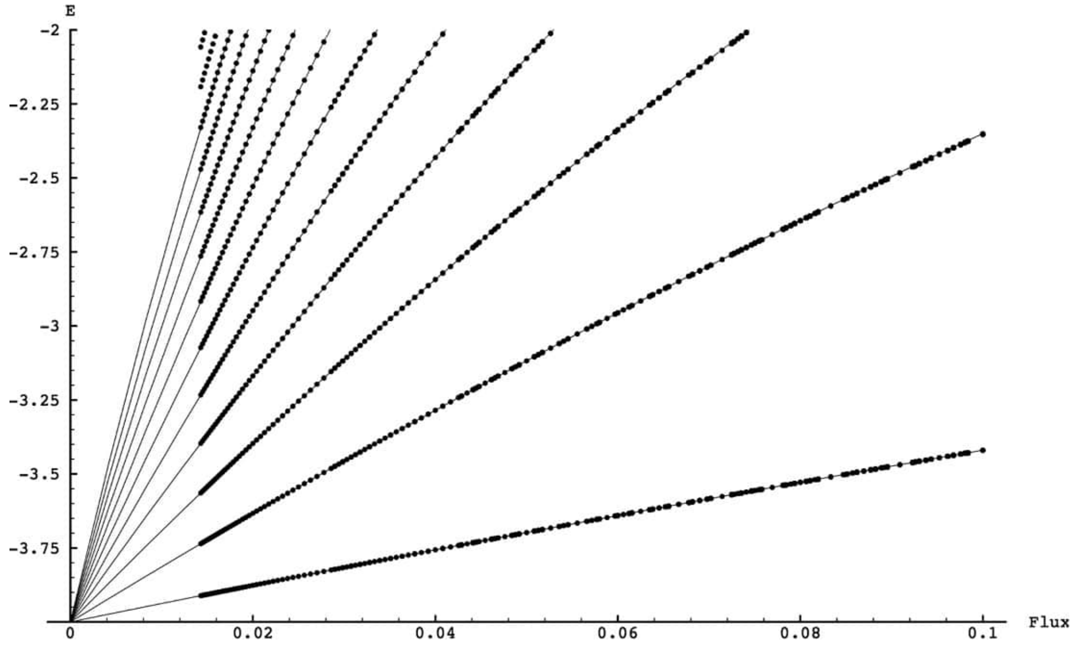

Fig. 5 Comparison between semiclassical calculations (continuous lines) and exact numerical spectrum (points) for Landau levels in the Harper model (6) on the square lattice near the band edge at $\theta = 0$ (Bellissard, 1994b)(ii).

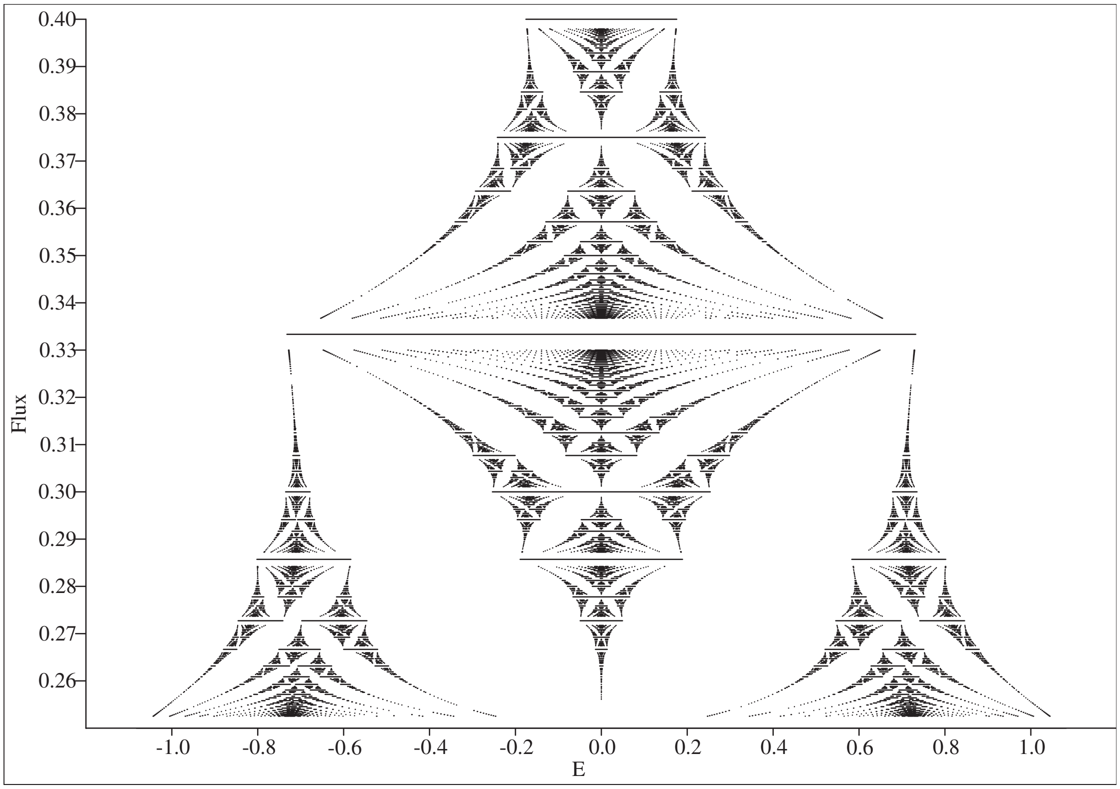

Fig. 6 Discontinuity of derivatives of the band edge near the magnetic flux $\alpha = \theta/2\pi \approx 1/3$ for the Harper model on the square lattice (Bellissard, 1994b) (ii).

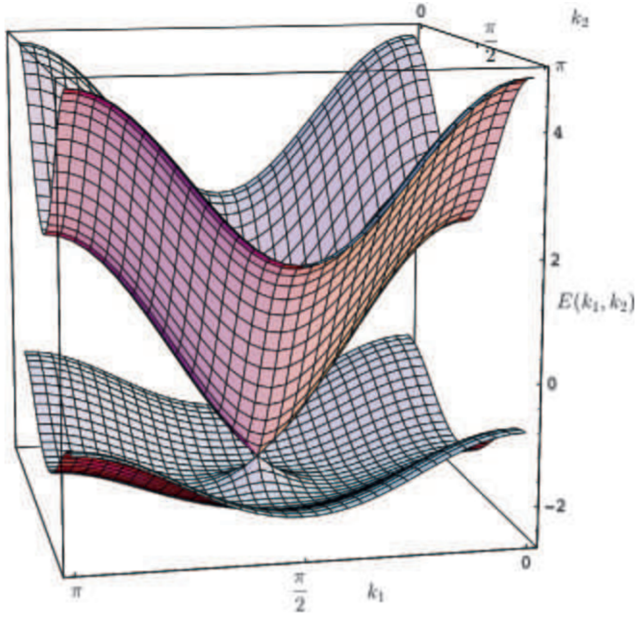

Fig. 7 Band-touching and bandoverlapping near half-flux in the model $H = U_1 + U_2 + 1/2(U_1^2 + U_2^2) + h.c.$ (Bellissard, 1994b)(ii).

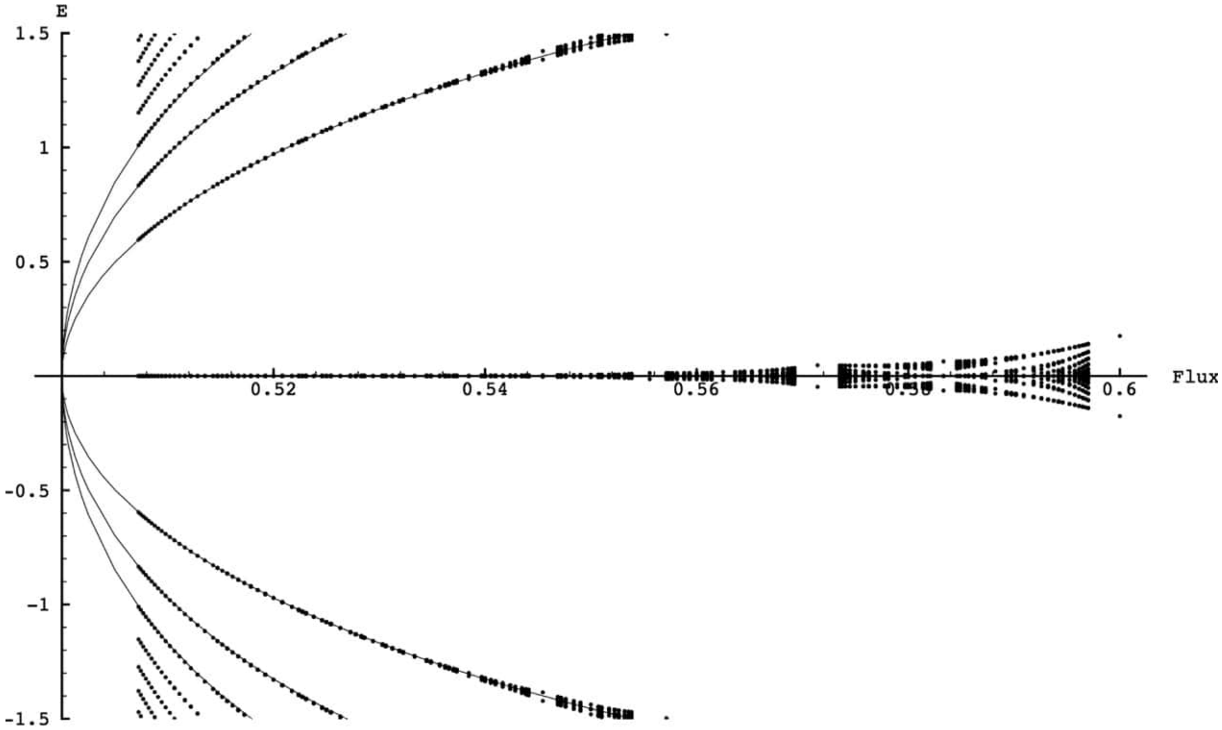

Fig. 8 Comparison between semiclassical calculations (full curves) and exact numerical spectrum (points) for Dirac levels in the Harper model near half flux (Bellissard, 1994b)(ii).

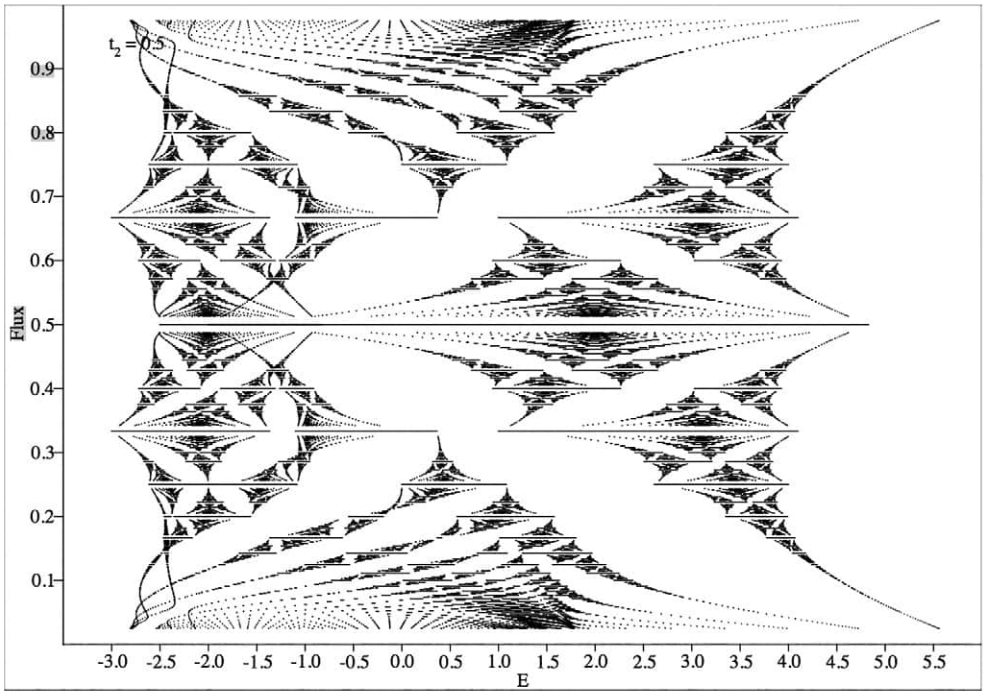

Fig. 9 Spectrum of a Harper-like model (7) for $t_2 = 1/2$. In the left corners, braids are due to tunneling effect (magnetic breakdown) (Bellissard, 1994b; Barelli and Kreft, 1991).

As τ passes beyond the critical value 1/4, the minimum of energy at zero flux bifurcates to become a local maximum and gives four degenerate minima. If τ is close enough to 1/4, these four minima are so close that the tunneling effect between then becomes enormous. The semiclassical analysis for the tunneling effect consists in extending the classical motion into the complex values of (k_1, k_2). Then the classical (complex) action is given by

$$S = \oint_{\gamma} k_1 dk_2,$$

where γ is any path joining two such minima in the complex energy surface $E(k + \imath k') = E_0$ (if E_0 is the minimum of the energy). Cohomology arguments (Stokes theorem) show that the value of S depends only upon the homotopy class of γ provided it stays in the energy surface. In the previous case, $S = S' + \imath S''$ with $S' \neq 0$ and $S'' > 0$. Then the splitting between the four-level consecutive to tunneling between the classical minima is proportional to $\Re(\exp \imath(\phi + S/\delta))$, for some phase ϕ depending upon what splitting is considered, leading to (i) a damping of the amplitude as $\delta \downarrow 0$ given by $e^{-S''/\delta}$ and (ii) an oscillation of the amplitude due to the term $e^{\imath S'/\delta}$. This is illustrated in Fig. 10 (Barelli and Kreft, 1991).

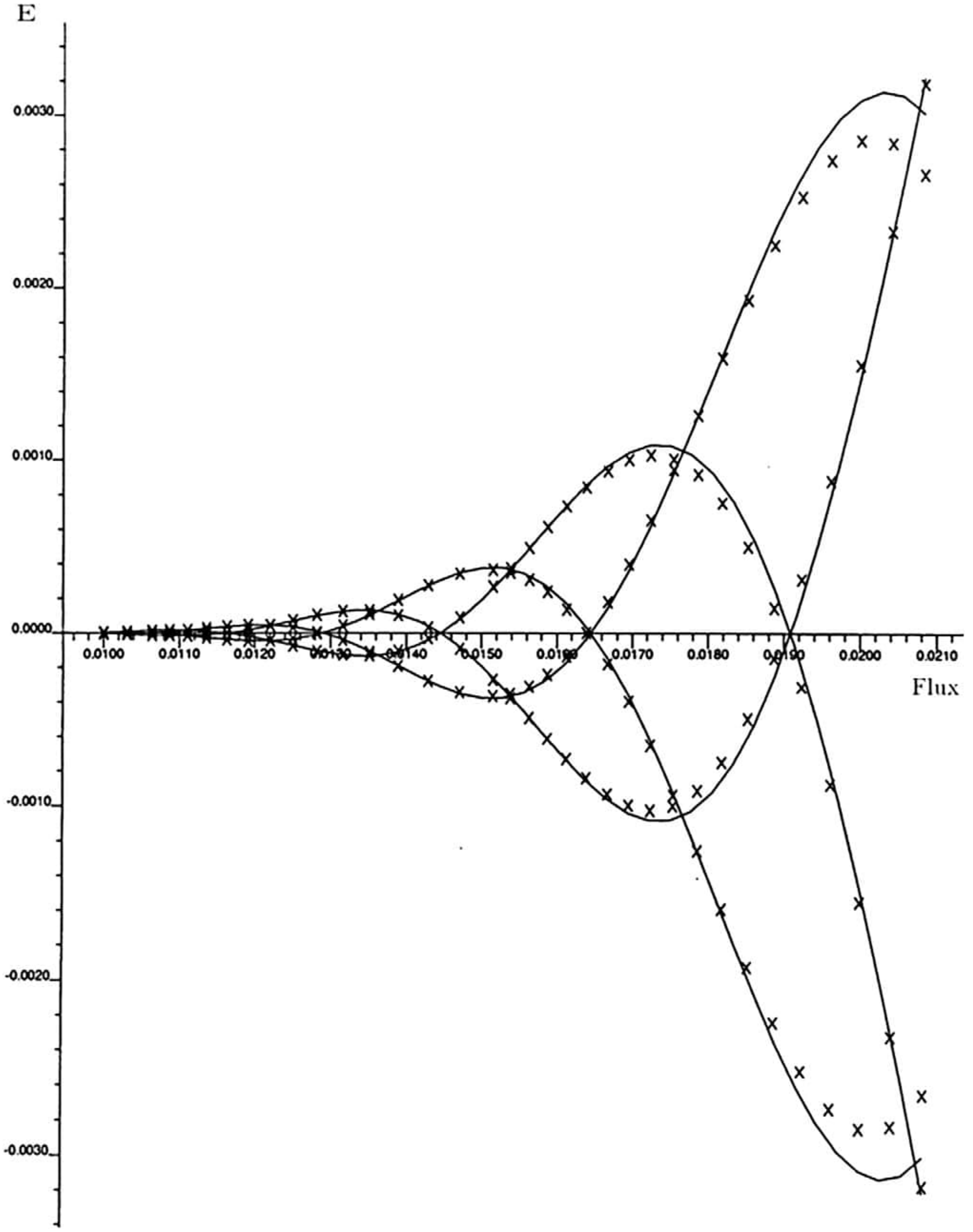

Fig. 10 Comparison between semiclassical calculations (full curves) and exact numerical spectrum (crosses) for Landau braids of model (7) (Barelli and Kreft, 1991).

Tunneling also explains the broadening of the Landau subbands. For indeed the classical *effective* Hamiltonian obtained for $\delta = 0$ (or for $\theta = 0$ when $p/q = 0$) is a periodic function of the quasi momenta k_1 and k_2. Thus any band edge occurring at k also occurs at $k + 2\pi(m_1, m_2)$ for all $m_i \in \mathbb{Z}$. Hence, each classical orbit is infinitely degenerate in phase space. Each such orbit represents an approximate eigenstate that can be in principle computed semiclassically and called a *quasimode*. Hence the Hilbert space corresponding to these semiclassical eigenvalues is infinite dimensional, and the tunneling effect between the quasimodes produces a broadening of the Landau or Landau–Dirac levels. As usual with tunneling effect, this broadening is exponentially small in the effective Planck constant (here given by δ). Such a calculation is difficult and many attempts where proposed in the 1960s. Eventually, Helffer and Sjöstrand (1987a,b) carried it out for the special case of the Harper model (Helffer and Sjöstrand, 1988, 1989, 1990) based upon Wilkinson's analysis (Wilkinson, 1984).

The main result of this analysis is that Landau *subbands* are well described by an effective Hamiltonian of the form

$$H_{subbband} \overset{\delta\downarrow 0}{=} E(\delta) + \left(e^{\imath S/\delta}\left(\tilde{U}_1 + \tilde{U}_2\right)e^{-\imath\bar{S}/\delta}\left(\tilde{U}_1^{-1} + \tilde{U}_2^{-1}\right)\right) + O\left(e^{-S_1/\delta}\right),$$

where $E(\delta)$ is the semiclassical value of the eigenvalue computed by the previous method, t is a model-dependent constant (computable by semiclassical methods), and S is the classical action between two nearest neighboring repetitions of the corresponding band edge in the complex energy surface, $S_1 > |\mathrm{I}S|$ and

$$\tilde{U}_1\tilde{U}_2 = e^{\imath 4\pi^2/\delta}\,\tilde{U}_2\tilde{U}_1.$$

Hence the spectrum of the subband is itself approximately the same as the Harper spectrum but for a *renormalized* value of the dimensionless flux, namely, $\alpha = \delta/2\pi \mapsto 1/\alpha = 2\pi/\delta$. Since this new flux arises in a phase adding or subtracting an integer to $1/\alpha$ does not change the phase, so that the map becomes $\alpha \in (0, 1) \mapsto G(\alpha) = \{1/\alpha\} \in (0, 1)$, where $\{x\}$ denotes the fractional part of x. G is called the Gauss map and is known to generate the continuous fraction expansion of the number α, namely, if $[x]$ denotes the integer part of x

$$\alpha = \cfrac{1}{a_1 + \cfrac{1}{a_2 + \cdots \cfrac{1}{a_n + \cdots}}}, \quad a_n = \left[G^{n-1}(\alpha)\right].$$

This rule does not work near a band center though. Then the analysis is more complicated because the classical Hamiltonian associated with the Harper equation has a *saddle point*. Then tunneling between periodic equivalent quasimodes is enhanced by the proximity near a saddle point. Helffer and Sjöstrand showed that depending on the subband considered, there are three types of *normal forms* for the effective Hamiltonian describing them. Moreover, the rule for the new flux might not be given by the Gauss map as was shown by Hofstadter. They also showed that each of them can be analyzed in the same way as the Harper equation so that at each step of the renormalization procedure, the effective subband Hamiltonian takes on one of the four normal forms previously considered: Harper or the three ones occurring at saddle points. Such an analysis explains why the Hofstadter spectrum shown in Fig. 1 (see an enlargement in Fig. 6) looks like a fractal set, namely, it is self-reproducing at any scale.

References

Barelli A and Kreft C (1991) Braid-structure in a Harper model as an example of phase space tunneling. *Journal de Physique I* 1(9): 1229–1249. ISSN: 1155-4304. https://doi.org/10.1051/jp1:1991203.

Bellissard J (1986) K-theory of C*—Algebras in solid state physics. In: *Statistical Mechanics and Field Theory: Mathematical Aspects*, pp. 99–156. Berlin, Heidelberg: Springer Berlin Heidelberg. https://doi.org/10.1007/3-540-16777-3_74.

Bellissard J (1994a) Lipshitz continuity of gap boundaries for Hofstadter-like spectra. *Communications in Mathematical Physics* 160(3): 599–613. ISSN: 0010-3616. https://doi.org/10.1007/BF02173432.

Bellissard J (1994b) Non commutative methods in semiclassical analysis. In: *Transition to Chaos in Classical and Quantum Mechanics*, pp. 1–64. Springer. https://doi.org/10.1007/BFb0074074.

de Haas WJ and van Alphen PM (1930) Note on the dependance of the susceptibility of diamagnetic metals on the field. In: *Communications From the Physical Laboratory of the University of Leiden*, vol. 208d. University of Leiden.

Fortin JY and Ziman T (1998) Frequency mixing of magnetic oscillations: Beyond Falicov-Stachowiak theory. *Physical Review Letters* 80(14): 3117–3120. ISSN: 10797114. https://doi.org/10.1103/PhysRevLett.80.3117.

Harper PG (1955) Single band motion of conduction electrons in a uniform magnetic field. *Proceedings of the Physical Society. Section A* 68(10): 874–878. ISSN: 0370-1298. https://doi.org/10.1088/0370-1298/68/10/304. (1955) The general motion of conduction electrons in a uniform magnetic field, with application to the diamagnetism of metals, Proceedings of the Physical Society. Section A, 68: 879–892.

Helffer B and Sjöstrand J (1987a) Équation de Schrödinger avec champ magnétique et équation de Harper. In: Helffer B and Sjöstrand J (eds.) *Schrödinger Equation With a Magnetic Field and the Harper Equation.* Palaiseau: École Polytechnique, Centre de Mathématiques. Exp. No. VI, 9 pp., ISBN: 2-7302-0159-9.

Helffer B and Sjöstrand J (1987b) Analyse semi-classique pour l'équation de Harper. In: Helffer B and Sjöstrand J (eds.) *Semiclassical Analysis for the Harper Equation.* Palaiseau: École Polytechnique, Centre de Mathématiques. Exp. No. XVII, 13 pp. ISBN: 2-7302-0160-2.

Helffer B and Sjöstrand J (1988) Analyse semi-classique pour l'équation de Harper (avec application à l'équation de Schrödinger avec champ magnétique). *Mémoires de la Société Mathématique de France* 1: 1–113. ISSN: 0249-633X. https://doi.org/10.24033/msmf.335. http://www.numdam.org/item?id=MSMF_1988_2_34__1_0.

Helffer B and Sjöstrand J (1989) Semiclassical analysis for Harper's equation. III. Cantor structure of the spectrum. *Mémoires de la Société Mathématique de France* 39(39): 1–124. ISSN: 0249-633X. https://doi.org/10.24033/msmf.346. http://www.numdam.org/item?id=MSMF_1989_2_39__1_0.

Helffer B and Sjöstrand J (1990) Analyse semi-classique pour l'équation de Harper. II: Comportement semi-classique près d'un rationnel. *Mémoires de la Société Mathématique de France* 1: 1–139. ISSN: 0249-633X. https://doi.org/10.24033/msmf.347. http://www.numdam.org/item?id=MSMF_1990_2_40__1_0.

Hofstadter DR (1976) Energy levels and wave functions of Bloch electrons in rational and irrational magnetic fields. *Physical Review B* 14(6): 2239–2249. ISSN: 01631829. https://doi.org/10.1103/PhysRevB.14.2239.

Landau L (1930) Diamagnetismus der Metalle. *Zeitschrift für Physik* 64(9–10): 629–637. ISSN: 14346001. https://doi.org/10.1007/BF01397213.

Lifshitz IM and Kosevich AM (1955) Zhurnal Eksperimental'noi i Teoreticheskoi Fiziki 29 (in Russian); English translation: Lifshitz IM and Kosevich AM (1956) Theory of magnetic susceptibility in metals at low temperatures. Soviet Physics JETP 2 (4), 730.

Onsager L (1952) Interpretation of the de Haas-van Alphen effect. *The London, Edinburgh, and Dublin Philosophical Magazine and Journal of Science* 43(344): 1006–1008. ISSN: 1941-5982. https://doi.org/10.1080/14786440908521019.

Peierls R (1933) Zur Theorie des Diamagnetismus von Leitungselektronen. *Zeitschrift für Physik* 80(11–12): 763–791. ISSN: 1434-6001. https://doi.org/10.1007/BF01342591.

Peierls RE (1956) *Quantum Theory of Solids*. Oxford: Oxford University.

Ponomarenko LA, Gorbachev RV, Yu GL, Elias DC, Jalil R, Patel AA, Mishchenko A, Mayorov AS, Woods CR, Wallbank JR, Mucha-Kruczynski M, Piot BA, Potemski M, Grigorieva IV, Novoselov KS, Guinea F, Fal'Ko VI, and Geim AK (2013) Cloning of Dirac fermions in graphene superlattices. *Nature* 497(7451): 594–597. ISSN: 0028-0836. https://doi.org/10.1038/nature12187.

Rammal R and Bellissard J (1990) An algebraic semi-classical approach to Bloch electrons in a magnetic field. *Journal de Physique* 51(17): 1803–1830. ISSN: 0302-0738. https://doi.org/10.1051/jphys:0199000510170180300.

Schubnikov L and de Haas WJ (1930) Magnetische Widerstandsvergrösserung in Einkristallen von Wismut bei tiefen Temperaturen. *Proceedings of the Royal Netherlands Academy of Arts and Science* 33: 433–439.

Shoenberg D (1984) *Magnetic Oscillations in Metals*. Cambridge University Press, ISBN: 9780521224802. https://doi.org/10.1017/CBO9780511897870. https://www.cambridge.org/core/books/magnetic-oscillations-in-metals/56C41223B4CDE32E43BD3109BFD74722.

Weiss D (2013) The butterfly emerges. *Nature Physics* 9(7): 395–396. ISSN: 1745-2473. https://doi.org/10.1038/nphys2680.

Wilkinson M (1984) Critical properties of electron eigenstates in incommensurate systems. *Proceedings of the Royal Society of London. A. Mathematical and Physical Sciences* 391(1801): 305–350. ISSN: 00804630. https://doi.org/10.1098/RSPA.1984.0016.

The Ten Martini problem

Jean Bellissard, School of Mathematics, Georgia Institute of Technology, Atlanta, GA, the United States

© 2024 Elsevier Ltd. All rights reserved.

Introduction	**712**
The Harper and Almost Mathieu models	**713**
Numerical solution	**715**
Transfer matrix	715
Matrix formulation	716
Gap opening	716
A toolbox for solving the Ten Martini problem	**717**
Rational approximation	718
Spectral continuity	718
Transfer matrices and gaps	719
Rotation number	719
Floquet–Bloch solutions	719
Reducibility to constant coefficients	720
The miracle	720
Solving the Ten Martini problem	**721**
The Diophantine regime	721
The Liouville regime	721
Conclusion	**722**
References	**722**

Abstract

The Ten Martini problem proves, with mathematical rigor, that the energy spectrum for electron on a square or rectangular lattice in a uniform magnetic field is actually a Cantor set whenever the dimensionless magnetic flux per plaquette is irrational. Its enhanced version, sometimes called the Dry Ten Martini problem, is to prove as rigorously that all gaps that may open according to the gap labeling theorem are actually opened. The problem with its main challenges is explained, and its potential relevance in Physics is discussed. Main references for various proofs are provided.

Key points

- Harper model with irrational magnetic fields
- Almost Mathieu operator and Aubry’s duality
- Transfer matrix and estimates on gap sizes
- Spectral edges and their continuity
- Cantor nature of the spectrum
- Continued fraction expansions as rational approximations
- Diophantine and Liouville regimes

Introduction

The Ten Martini Problem concerns the simplified, paradigmatic Harper model, representing the movement of a charged quantum particle on a square lattice in the presence of a uniform magnetic field perpendicular to the plane of the lattice. Whenever the flux per unit cell is an irrational multiple of the flux quantum, the numerical calculation performed in 1976 by Hofstadter (1976) (see Fig. 1) suggests that its spectrum is a Cantor set, meaning, in this precise case, that any energy in the spectrum can be approximated by a sequence of energies belonging to a spectral gap, namely, outside the spectrum. This was formulated by Mark Kac as an open problem for mathematicians and made an offer, which is why it was named *Ten Martini*, by Simon (see Simon, 2000, Problem 4):

> *Prove or disprove that the energy spectrum of the Harper model is a Cantor set for irrational magnetic fields.*

https://doi.org/10.1016/B978-0-323-90800-9.00261-4

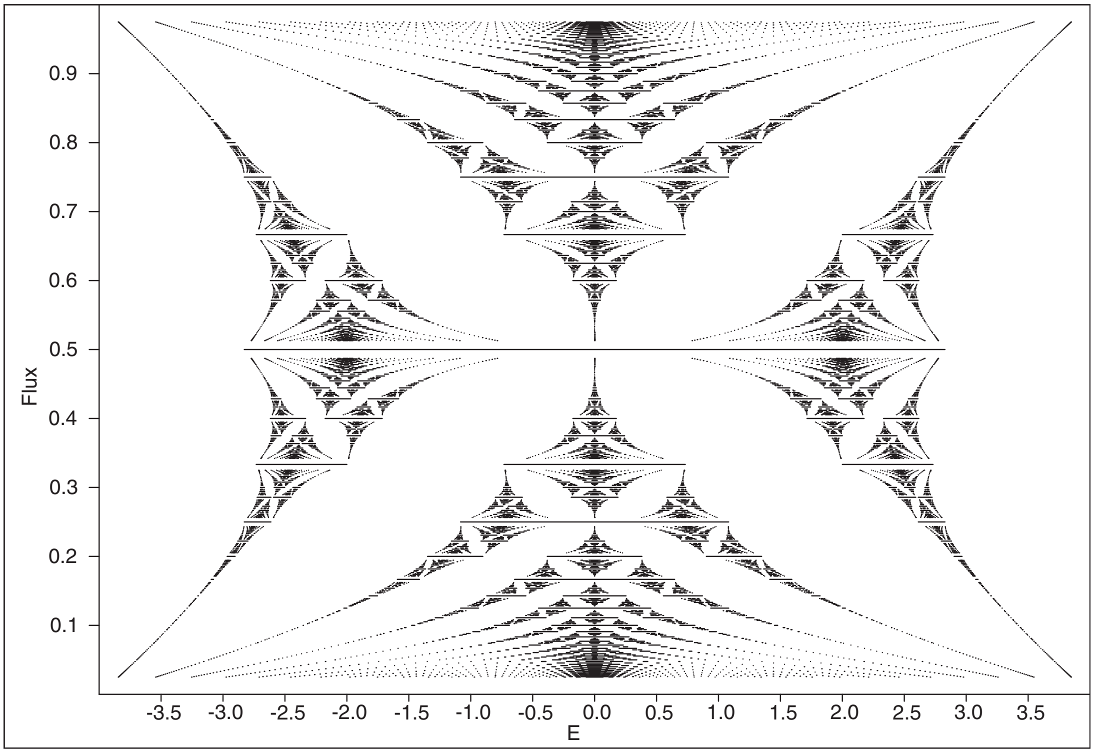

Fig. 1 Energy spectrum of the Harper model describing a 2*D*-Bloch electron in a uniform magnetic field as a function of the dimensionless magnetic flux per unit cell (see Bellissard (1994)(ii)).

The first result was obtained in 1982 (Bellissard and Simon, 1982), but was incomplete. Possible issues showed up with some categories of irrational numbers, and with possible mechanism for gap closing. Several contributions brought critical techniques. The first complete result, described in Section "The Harper and Almost Mathieu models," was announced in 2006, by Svetlana Jitomirskaya and Artur Avila (Avila and Jitomirskaya, 2006) and published in 2009 (Avila and Jitomirskaya, 2009) in the prestigious journal Annals of Mathematics. It took a quarter of a century to solve this difficult problem.

Is this problem relevant for physicists? This was a question posed by Philippe Nozières to the author in the early 1980s during a seminar: *"Why should we, physicists, be concerned by the difference between rational and irrational numbers? Isn't it true that after all, all relevant numbers we use in practice are simple fractions?."* It expressed a deep skepticism toward the content of the talk. The answer is related to the concept of limit, as each irrational number can be seen as a limit of a convergence (or Cauchy) sequence of fractions. There are global (or qualitative) properties seen in the limit that cannot easily be seen before taking the limit. As an analogy, in Statistical Mechanics, one cannot prove the existence of a phase transition without taking the thermodynamic limit, namely, letting the volume of the system be infinite. Only in this limit do we see and classify the phase diagram. Another analogy concerns the distinction between finite sums and integrals: while an integral is defined as a limit of large sum with small summands (Riemann sums), the algebraic treatment of the limit is far easier than treating the sums before taking the limits.

The Harper and Almost Mathieu models

To express the Harper model in a language easily understood by condensed matter physicists, one consider first a 2D-plane and a uniform magnetic field B perpendicular to this plane. A charged particle of charge e and mass m has a kinetic energy $H_L = \hbar^2\left(K_1^2 + K_2^2\right)/2m$ where $K_i = (p_i - eA_i)/\hbar$ is the wave vector, p_i is the particle momentum operator, and A_i is the magnetic vector potential in the direction $i = 1, 2$. The vector potential is any solution of the equation $(\partial_1 A_2 - \partial_2 A_1) = B$ and the choice of a solution is called a *gauge*. The quantum commutation rule implies

$$[K_1, K_2] = \imath\frac{eB}{\hbar}, \quad \hbar = \frac{h}{2\pi}. \tag{1}$$

If this particle is forced to stay on a square lattice (in the so-called *tight binding representation*), the translation operators, known as the *magnetic translations* (Zak, 1964a,b), in each of the two directions, are $U_i = \exp(K_i a)$, leading to the tight binding representation

$$H_{AM} = t_1\left(U_1 + U_1^{-1}\right) + t_2\left(U_2 + U_2^{-1}\right), \tag{2}$$

where t_1 and t_2 are the hopping energies in each direction. The square symmetric case corresponds to $t_1 = t_2$ and is due to Harper (1955a,b) while the rectangular symmetry $t_1 \neq t_2$ will be called the *Almost Mathieu* model here. By a rotation of $\pi/2$, the roles of t_1, t_2 are interchanged while $U_1 \to U_2$ and $U_2 \to U_1^{-1}$, but the energy spectrum is unchanged, which will lead to *Aubry's duality*. The remarkable fact is that the two magnetic translations U_1 and U_2 do not commute

$$U_1 U_2 = e^{2\imath\pi\alpha}\, U_2 U_1, \quad \alpha = \frac{eBa^2}{h} \quad (\alpha = \textbf{dimensionless flux}). \tag{3}$$

Indeed, α is the ratio of the magnetic flux Ba^2 through the unit cell and the flux quantum h/e making it a dimensionless parameter.

Definition 1.

(i) The rotation algebra $\mathcal{A}_\alpha$ is the set of operators that can be approximated by polynomials in U_1 and U_2 for the operator norm.
(ii) An $*$-automorphism of $\mathcal{A}_\alpha$ is a linear invertible map $\rho : \mathcal{A}_\alpha \to \mathcal{A}_\alpha$ respecting the product and taking the adjoint.
(iii) The spectrum of an element A of $\mathcal{A}_\alpha$ is the set of complex numbers z such that $z - A$ has no bounded inverse. The spectrum is invariant by automorphisms.

It follows that changing U_i into $\epsilon_i U_i$ for $i = 1, 2$ and $\epsilon_i = \pm 1$ does not change the commutation rules, so it defines a $*$-automorphism that does not change the spectrum of H_{AM}. In particular

The energy spectrum of the Almost Mathieu operator is symmetric around $E = 0$. In addition, it is enough to consider the situation where t_1 and t_2 are nonnegative.

Since the early times of Quantum Mechanics, physicists and mathematicians are usually more comfortable with the Schrödinger equation than dealing with operator algebras. To express it though, the choice of a gauge is required. Two such choices are usually made: the Landau gauge where $A_1 = -By$, $A_2 = 0$ or the symmetric gauge $a_1 = -By/2$, $A_2 = Bx/2$, where (x, y) are the two position coordinates. To take into account the underlying lattice, it will be convenient to write the two coordinates as $x = am$, $y = an$ where m and n are integers (positive or not). The advantage of the Landau gauge comes from its translation invariance in the x-direction. The Schrödinger equation $H\psi = \mathcal{E}\psi$ (where $\mathcal{E}$ is the energy) becomes

$$\mathcal{E}\psi(m,n) = t_1\left(e^{2\imath\pi\alpha n}\psi(m+1,n) + e^{-2\imath\pi\alpha n}\psi(m-1,n)\right) + t_2(\psi(m,n+1) + \psi(n-1)) \tag{4}$$

An immediate consequence is that if S_1 and S_2 are defined by $S_1\psi(m,n) = (-1)^m\psi(m,n)$ and $S_2\psi(m,n) = (-1)^n\psi(m,n)$, then $S_1 H_{AM}(t_1,t_2)S_1^{-1} = H_{AM}(-t_1,t_2)$ and similarly for S_2. This shows in a more familiar way that t_1 and t_2 can be chosen positive. Moreover, applying S_1S_2 shows that *the energy spectrum is invariant by $\mathcal{E} \to -\mathcal{E}$*.

Due to the translation invariance in the x-direction, it is possible to decompose any eigenstate into plane waves solution of the form $\psi(m,n) = e^{2\imath\pi\theta m}\phi(n)$, where θ becomes a parameter, leading to

$$E\phi(n) = \phi(n+1) + \phi(n-1) + 2\lambda\cos 2\pi(\alpha n + \theta)\,\phi(n), \quad \lambda = \frac{t_1}{t_2}, \quad E = \frac{\mathcal{E}}{t_2}. \tag{5}$$

The latter expression explains the name *Almost Mathieu* given to the model (a suggestion of Barry Simon): it is a discrete and almost periodic version of the Mathieu equation (second-order differential equation with a periodic cosine potential). Indeed here, the ratio α measures the incommensurability between the periodicity of the cosine potential and the periodicity of the 1D-lattice labeled by n. It ought to be remarked also that both E and λ are dimensionless parameters that will nevertheless be called *energy* and *coupling constant*, respectively. At last by imposing a rotation of $\pi/2$ in the original lattice, exchanging the roles of t_1 and t_2, it leads to Aubry (1978) and Aubry and André (1980).

Proposition 1 (Aubry's duality). *The energy spectrum of the Almost Mathieu operator is unchanged under the transformation of (λ, E) into ($1/\lambda$, E/λ).*

The main result obtained by Avila and Jitomirskaya requires the concept of Cantor set. Mathematically it is defined as a topological compact set completely disconnected with no isolated point. For physicists, compactness is not a familiar concept; it actually means that a compact set can be approximated by a finite number of points. More precisely if, for instance, the topology is defined by a metric, then given any $\varepsilon > 0$, there is a finite family of points $\{x_1, x_2, \ldots, x_n\}$ such that the balls of radius ε centered at these points cover the set.

More concretely, if K is a Cantor subset of the real line $\mathbb{R}$, then (i) it is closed, namely, any convergent sequence of real numbers in K converges, in K, (ii) it is contained into a closed interval of finite length, (iii) its complement $\mathbb{R}\backslash K$, which is open, is dense in $\mathbb{R}$, namely, any real number can be approximated by a sequence of numbers outside K (iv) for all points x in K and any $\varepsilon > 0$, the interval $(x - \varepsilon, x + \varepsilon)$ intersects K (namely no point is isolated).

With this in mind, the main result can be phrased as follows:

Theorem 1 (Ten Martini **(Avila and Jitomirskaya, 2009)**). *The energy spectrum of the Almost Mathieu operator is a Cantor set for any irrational value of α and non zero value of λ.*

The following sections will describe more about the sources of difficulties and the strategy of the proof.

Numerical solution

In order to solve Eq. (5), the first step consists in assuming α rational, namely, of the form $\alpha = p/q$ where p and q are integers prime to each other (irreducible fraction). Then, the potential part has period q. Therefore, following Bloch's theory, one searches for solutions satisfying $\phi(n+q) = e^{\imath k_1}\phi(n)$ for any n. The set of such sequences becomes a Hilbert space of finite dimension q when endowed with the inner product $\langle\psi|\phi\rangle = \sum_{n=0}^{q-1}\overline{\psi(n)}\phi(n)$. Hence, the problem is amenable to numerical calculation as the Hamiltonian becomes a finite dimensional matrix. At that point there are two ways of seeing this problem: (i) by writing down this $q \times q$ matrix and finding solution of the characteristic polynomial and (ii) by exploiting the two-term recursion character of Eq. (5) and use transfer matrix. Numerically the method (ii) is faster while method (i) gives useful qualitative and quantitative information.

Transfer matrix

For numerical efficiency, it is actually more convenient to use the transfer matrix formulation. Namely, the wave function ϕ is written through a 2D vector $\Phi(n)$ with components $\phi(n)$, $\phi(n-1)$. Then Eq. (5) becomes

$$\Phi(n+1) = S(n)\Phi(n), \quad S(n) = S(E,\lambda; n\alpha+\theta) = \begin{bmatrix} E - 2\lambda\cos 2\pi(\alpha n+\theta) & -1 \\ +1 & 0 \end{bmatrix}. \tag{6}$$

An important property is $\det S(n) = 1$, in particular $S(n)$ is invertible. For $\alpha = p/q$, an irreducible fraction, S, is periodic, namely, $S(n+q) = S(n)$. Bloch's theory leads to searching solutions such that $\Phi(n+q) = e^{\imath k}\Phi(n) = T(n)\Phi(n)$, using the recursion formula with $T(n) = \prod_{m=0}^{q-1} S(m+n)$ (ordered product: m increases from right to left). Hence $e^{\imath k}$ is an eigenvalue of the 2×2 matrix $T(n)$. Since $\det T(n) = 1$, it follows that the other eigenvalue is $e^{-\imath k}$ so that $\mathrm{Tr}(T(n)) = 2\cos k \in [-2, +2]$. Such a condition is satisfied only if E belongs to the energy spectrum Σ. The trace of $T(n)$ is a monic polynomial of degree q with respect to E (namely, its highest degree coefficient is 1). Moreover, since all $S(n)$s are invertible, it follows that $T(n+1)$ is similar to $T(n)$ so that $\mathrm{Tr}(T(n))$ is independent of n. However, changing n into $n+1$, is equivalent to changing θ into $\theta + p/q$. Consequently $\mathrm{Tr}(T(n))$ is periodic of period $1/q$ with respect to θ so that it is a Fourier series in the variable $e^{2\imath\pi q\theta}$. But each matrix $S(n)$ is a trigonometric polynomial of degree ± 1 in $e^{2\imath\pi\theta}$ so that $T(n)$ has degree ± 1 in $e^{2\imath\pi q\theta}$, leading to the first *Chambers formula* (see Chambers, 1965, Appendix)

$$\mathrm{Tr}(T(n)) = P_\lambda(E) + (-1)^q 2\lambda^q \cos 2\pi q\theta. \quad (\textbf{Chambers '65}) \tag{7}$$

It follows that eigenvalues are given by the equation

$$P_\lambda(E) = 2\cos(qk) - (-1)^q 2\lambda^q \cos 2\pi q\theta. \tag{8}$$

Varying k and θ gives the band spectrum. In particular $E \in \Sigma$ if and only if $P_\lambda(E) \in [-2(1+\lambda^q), +2(1+\lambda^q)]$. This is seen in Fig. 2 for q even. It follows that the band edges are given by the values $(qk, 2\pi(q\theta + 1/2)) = (0, 0)$ or (π, π) so that numerically there is no need to explore all these values. This is the algorithm used since the work of Hofstadter (1976).

Fig. 1 is obtained this way with α on the vertical axis and E on the horizontal axis for the value $\lambda = 1$ corresponding to the square symmetry.

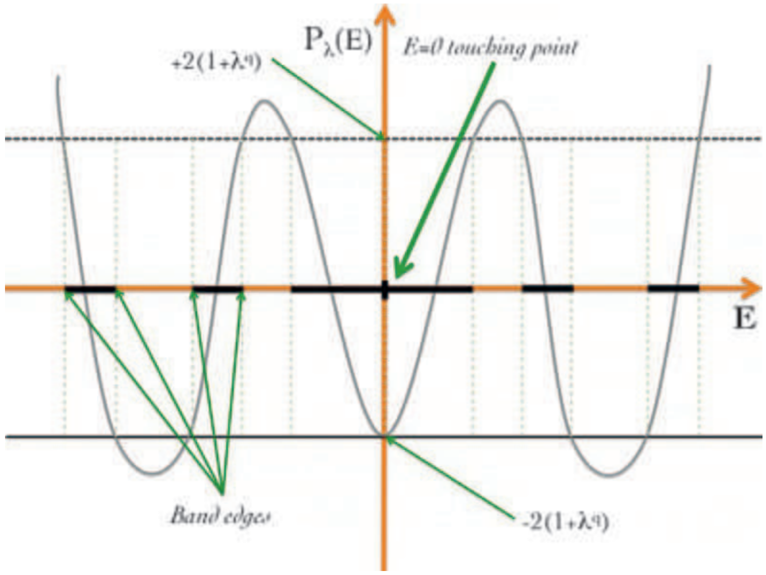

Fig. 2 Construction of the band spectrum from Chamber's formula.

Studying the mathematical properties of the transfer matrix was a central theme for Avila and Jitomirskaya. Their proof of the Ten Martini problem is based upon this point of view.

From these arguments, it follows that the transfer matrix method gives all useful spectral information on the Almost Mathieu model. It is important to notice though, that for this method to be useful, the Schrödinger equation must be reducible to a 2-term recursion formula. However, for the purpose of physical applications, it is inconvenient. Indeed, the effective Hamiltonian describing an electron on a square lattice defined by a periodic potential, once expressed in the tight binding representation, is never the Almost Mathieu model, but a small perturbation of it, including higher powers of u_1 and u_2. In such a case, the transfer matrix formulation is no longer appropriate.

Matrix formulation

Looking back at the Schrödinger point of view, it is convenient to set $\varphi(n) = e^{-\imath k_1}\phi(n)$, with $k_1 = k$, so that φ is periodic with period q. Hence ϕ can be seen as a complex vector with q components. In addition, it is convenient to write $k_2 = 2\pi\theta$. With such notations, let u_1 denote the translation operator $u_1\varphi(n) = \varphi(n-1)$ and let u_2 denote the multiplication operator $u_2\varphi(n) = e^{2\imath\pi np/q}\varphi(n)$. Then u_1 and u_2 can be seen as $q \times q$ matrices such that the monomials $u_1^{m_1}u_2^{m_2}$ make up a basis of the space of $q \times q$ matrices. Then

$$u_1 u_2 = e^{2\imath\pi p/q} u_2 u_1, \quad u_i^{-1} = u_i^*, \quad u_1^q = u_2^q = \mathbf{1}. \tag{9}$$

In addition, using the Hilbert–Schmidt inner product of two $q \times q$ complex matrices $\mathfrak{a}$ and $\mathfrak{b}$ defined by

$$\langle \mathfrak{a}|\mathfrak{b}\rangle = \frac{1}{q}\mathrm{Tr}(\mathfrak{a}^*\mathfrak{b}), \tag{10}$$

the basis $\{u_1^{m_1}u_2^{m_2}\ ;\ 0 \le m_i \le q-1\}$ is *orthonormal* and *complete* in the set of $q \times q$ complex matrices (this can be called *noncommutative Fourier expansion*).

Using these notations, it follows that Eq. (5) becomes

$$H(k_1,k_2)\varphi = E\varphi, \quad H(k_1,k_2) = e^{\imath k_1}u_1 + e^{-\imath k_1}u_1^{-1} + \lambda\left(e^{\imath k_2}u_2 + e^{-\imath k_2}u_2^{-1}\right). \tag{11}$$

Then the eigenvalues of $H(k_1, k_2)$ are the roots of $z \to P(z, k_1, k_2) = \det(z - H(k_1, k_2))$, which is a monic polynomial of degree q in z, and trigonometric polynomial of degree at most q and at least $-q$ in each of the k_i's. Using the commutation rules given in Eq. (9), and the invariance of the determinant under unitary transformation u_i's, it follows that P is actually periodic of period $2\pi p/q$ in each of the k_i, namely, periodic of period $2\pi/q$ since p/q is irreducible. Using the Fourier expansion in the k_i's, a simple calculation leads to (see Chambers, 1965, Appendix; Chambers used the transfer matrix formulation)

$$P(z,k_1,k_2) = P_\lambda(z) - 2(\cos(qk_1) + \lambda^q\cos(qk_2)), (\textbf{Chambers '65}) \tag{12}$$

where P_λ is also a monic polynomial of degree q in z and a polynomial in λ of degree q as well. Comparing with Eq. (8), it is clear that the two polynomial P_λ must be the same. Since $H(k_1, k_2)$ is Hermitian, the equation $P(z, k_1, k_2) = 0$ has q real roots in z for each value of k_1 and k_2. In particular, it follows that the band spectrum is defined by the values of z (automatically on the real line) for which $-2(1+\lambda^q) \le P_\lambda(z) \le +2(1+\lambda^q)$. It follows that P_λ is monotonous on each band.

If q is *odd*, changing k_i into $k_i + \pi$ changes the sign of $H(k_1, k_2)$. From this it follows that $P_\lambda(-z) = -P_\lambda(z)$ is odd. Therefore $P_\lambda(0) = 0$. In particular if k_1 and k_2 are chosen such that $2\cos(qk_1) + \lambda^q 2\cos(qk_2) = 0$, it follows that 0 is an eigenvalue. Thus 0 belongs to the spectrum of the Almost Mathieu operator for any odd value of q.

If q is *even*, the unitary matrix $S = u_1^{q/2}u_2^{q/2}$ gives $SH(k_1, k_2)S^{-1} = -H(k_1, k_2)$. From this it follows that the set of eigenvalues of $H(k_1, k_2)$ is invariant under $E \to -E$. Moreover $P_\lambda(-z) = P_\lambda(z)$ follows from this symmetry. It follows that when q is a multiple of 4, $z = 0$ is a maximum of P_λ; therefore it is enough to look at k_i's such that $qk_i = 0 \ (\mathrm{mod} 2\pi)$. If $q-2$ is a multiple of 4, it is a minimum of P_λ instead, and it is enough to look at k_i's such that $qk_i = \pi \ (\mathrm{mod} 2\pi)$. In addition the symmetry $R\varphi(n) = \varphi(-n)$ leaves the matrices $H(k_1, k_2)$ invariant for the values of (k_1, k_2) at these extrema. By decomposing the space into the direct sum of subspaces of symmetric or antisymmetric eigenvectors of R, a simple counting leads to

Proposition 2 (see Bellissard and Simon, 1982). *The spectrum of the Almost Mathieu operator is symmetric around $E = 0$ and $E = 0$ always belongs to this spectrum for any fractional value of α. The band edges are given by the eigenvalues of $H(k_1, k_2)$ for which $k_i = 0 \ (\mathrm{mod}\pi)$. In addition if $\alpha = p/q$ with q odd, $E = 0$ is the center of the middle spectral band while if q even, the central gap is closed, namely, the two neighboring spectral bands are touching.*

Gap opening

Even for $\alpha = p/q$ is an irreducible fraction, the question of showing that the spectral bands are separated by a gap is nontrivial. It boils down to showing that for the edges, values of (k_1, k_2) the roots of $P_\lambda(z) = \pm 2(1+\lambda^q)$ are simple. Let then Σ_λ denote the set of pairs (z, λ) such that $P(z, 0, 0) = 0$ or $P(z, \pi, \pi) = 0$. Since P depends polynomially on λ as well, Σ is a finite union of (algebraic) curves. The condition of $z = a$ being a double root of this equation boils down, thanks to Eq. (12) to add the condition $dP_\lambda/dz(z = a) = 0$. In the curve $\Sigma - \lambda$, such a condition is satisfied only at a finite number of isolated points because of the polynomial character of all these equations (Bellissard and Simon, 1982). In particular, the complement of the union of these points in the plane (z, λ), which corresponds to gap opening, is a dense open set $\mathcal{O}(\alpha)$. The intersection $\mathcal{O} = \cap_{p/q}\mathcal{O}(p/q)$ might not be open but is called a G_δ-set (countable intersection of open sets). Using a fundamental standard result of Baire, since each term of the intersection is dense, the set $\mathcal{O}$ is dense as well. Mathematicians are calling a property *generic* whenever it holds true on a dense G_δ-set. Using this argument, and extending it to include irrational values of α, a first weak form of the Ten Martini problem was proved in Bellissard and Simon (1982)

Proposition 3. *For a generic set of values of* $(\alpha, \lambda) \in \mathbb{R}^2$, *the spectrum of the Almost Mathieu model is a Cantor set.*

As it turns out, Choi, Eliott, and Yui proved a stronger result in a remarkable paper (Choi et al., 1990), using a purely algebraic method.

Theorem 2 (see Choi et al., 1990). *For* $\alpha = p/q$, *an irreducible fraction, and* $\lambda \neq 0$ *there are constants* $c_0(\lambda) > 0$ *and* $1 > c_1 > 0$ *such as all gaps of* H_{AM}, *except at* $E = 0$, *have width at least* $c_0(\lambda)\ (c_1\lambda)^{q/2}$. *In particular all gaps but for* $E = 0$ *are open.*

In particular this proves that all gaps but the central one are open, and it gives a quantitative estimate. The method relies upon a remarkable Gaussian formula, namely

$$(u_1 + \lambda u_2)^n = \sum_{j=0}^{n} \frac{[n]_\zeta}{[j]_\zeta [n-j]_\zeta}\ \lambda^j\ u_1^{n-j} u_2^j, \text{where } [n]_\zeta = \prod_{j=1}^{n} (1 - \zeta^j), \zeta = e^{2\imath\pi\alpha}. \tag{13}$$

The first main result consists in evaluating the Gaussian binomial coefficient for $n = 2j$ and they proved, using an easy computation, that because $\zeta^q = 1$,

$$\left| \frac{[2j]_\zeta}{[j]_\zeta^2} \right| \geq 1. \tag{14}$$

Next step: If f is any monic polynomial of degree $2m < q$, the development of $f(H(k_1, k_2))$ in powers of u_1 and u_2 (noncommutative Fourier expansion), the term $u_1^m u_2^m$ can only come from the expression $(e^{\imath k_1} u_1 + \lambda e^{\imath k_2} u_2)^m$ the coefficient of which is the product of λ^m by the Gaussian binomial coefficient corresponding to $n = 2m$, $j = m$. Using the inequality (14), this coefficient is larger than or equal to λ^m. On the other hand, this coefficient is given by (see Eq. (10) and the following comment)

$$\lambda^m e^{\imath m(k_1+k_2)} \frac{[2m]_\zeta}{[m]_\zeta^2} = \frac{1}{q} \mathrm{Tr}\left(u_2^{-m} u_1^{-m} f(H(k_1, k_2))\right) \tag{15}$$

The right-hand side is bounded from above by $\|f(H(k_1, k_2)\|$ while the left hand side is bounded from below by λ^m, leading to

$$\| f(H(k_1, k_2)) \| \geq \lambda^m. \tag{16}$$

The next and last step consists in applying this result to various f's. For instance, if $\lambda \leq 1$ and $q = 2m + 1$ then choose $1 \leq j \leq q$. Set $f_j(x) = \prod_{i;i \neq j}(x - E_i)$ whenever $E_1 \leq E_2 \leq \cdots \leq E_q$ denotes the eigenvalues of $H(k_1, k_2)$ (see Fig. 2). Then f_j is monic of degree $2m < q$ and $f_j(H(k_1, k_2)) = \prod_{i;i \neq j}(E_j - E_i) \times |j\rangle\langle j|$ where $|j\rangle$ is the eigenstate of $H(k_1, k_2)$ for the energy E_j. Since $|E_j - E_i| \leq 4(1 + \lambda^q) \leq 8$, combining with Eq. (16), this gives

$$|E_{j+1} - E_j| \geq \frac{\lambda^{(q-1)/2}}{8^{q-2}}. \tag{17}$$

A similar bound is obtained for $\lambda \geq 1$ using Aubry's duality. For $q = 2m + 2$, a similar strategy can be used, exploiting the fact that each eigenvalue E has also $-E$ as an eigenvalue. However the eigenvalues of the two central bands are to be excluded from the polynomial f since the central gap is actually closed.

A toolbox for solving the Ten Martini problem

The main problem with the Hofstadter spectrum shown in Fig. 1 is that even if it looks like having global properties of a fractal, with gap boundaries looking regular as a function of α, it is computed only for a finite number of rational values of α. Does it guarantee that this picture still holds for irrational values? So far there is no finite algorithm allowing to compute the energy spectrum of the Almost Mathieu model with α irrational. Physicists are pragmatic: if irrational values of α were showing unexpected properties, it would be seen for rational numbers p/q with large q's. They just let Mathematicians play with the problem. As it turns out, going from fractions to irrational numbers is technically very demanding. No wonder that it took a quarter of a century (Avila and Jitomirskaya, 2006, 2009) to solve this problem entirely. It required the contributions of two of the finest analysts in the world, one of whom is a Fields medalist, to achieve such a difficult task. But several contributions brought some key arguments used in the final proof, the list of which can be found in Last (2005).

The main steps leading to the final result are

1. controlling the rational approximations of α,
2. controlling the gap edges continuity as a function of α,
3. evaluating the size of gaps for rational values of α.

Rational approximation

The traditional description of numbers by decimal expansion gives approximation by decimal fractions. Binary expansion achieves similar results but with only two digits. However these expansions are not necessarily optimal to control the approximation of a number by fraction. The continued fraction expansion described in this section was introduced a long time ago in history, but two names emerge who provided substantial general results, namely, Euler in 1737 and Gauss in 1813. Both used continued fractions to express special functions from which a formula for special numbers can be derived. A classical introduction, actually easy to read, can be found in the book (Hardy and Wright, 2008), by Hardy and Wright (see Chapters 10 and 11).

Given a real number $0 < \alpha \leq 1$, it has a positive inverse $1/\alpha > 1$ so that it can be written in a unique way as $1/\alpha = a_1 + \alpha_1$ where $a_1 = [1/\alpha]$ is a natural integer (in particular $a_1 \geq 1$) called the *integer part* and $0 \leq \alpha_1 = \{1/\alpha\} < 1$ is the *fractional part* of $1/\alpha$. This means

$$\alpha = \frac{1}{a_1 + \alpha_1}.$$

If $\alpha_1 \neq 0$, applying the same procedure with α_1 and iterating leads to the continued fraction $\alpha = [a_1, a_2, a_3, \ldots]$ where

$$\alpha = \cfrac{1}{a_1 + \cfrac{1}{a_2 + \cfrac{1}{a_3 + \cdots}}} \qquad \text{denoted by} \qquad \alpha = [a_1, a_2, a_3, \ldots], \tag{18}$$

where a_i are all natural integers. If α is a fraction, this procedure stops after a finite number of steps. In any case, stopping the fraction at level n gives a fraction denoted as $p_n/q_n = [a_1, a_2, a_3, \ldots, a_n]$ which satisfies $q_{n+1} = a_{n+1}q_n + q_{n-1}$, $p_{n+1} = a_{n+1}p_n + p_{n-1}$ with initial conditions $q_0 = p_1 = 1$. It is easy to check by induction that $q_{2m}p_{2m-1} - q_{2m-1}p_{2m} = 1$ for m a natural integer and that

$$\frac{p_{2m}}{q_{2m}} < \alpha < \frac{p_{2m-1}}{q_{2m-1}}, \text{for} \quad m \geq 1 \qquad \Rightarrow \qquad \left|\alpha - \frac{p_n}{q_n}\right| < \frac{1}{q_n q_{n+1}}, \quad \forall n \geq 1.$$

In particular, since $q_{n+1} \geq q_n + q_{n-1}$, it implies that the q_n's increase exponentially fast in n and that the continued fraction actually converges. One can then classify numbers according to how fast this expansion converges.

If one endows the interval [0, 1] with uniform probability, the following holds:

1. If $\alpha = [a_1, a_2, \ldots, a_n, \ldots]$, the sequence $(a_n)_{n\geq 1}$ is unbounded with probability one.
2. Given $\eta > 0$, with probability one, there is $c > 0$ such that $|\alpha - p/q| \geq c/q^{2+\eta}$, which implies that $q_{n+1} \leq c^{-1} q_n^{1+\eta}$. Such numbers are called *Diophantine*.

Among the non-Diophantine numbers, there are two categories, the ones slowly approximated by rationals and the ones that are extremely well approximated by rationals which are called *Liouville numbers*. Hence, numbers $0 \leq \alpha \leq 1$ with bounded sequence of a_n (such as the golden mean $\sigma = (\sqrt{5} - 1)/2$ for which $a_n = 1$ for all n's) are those that are the most difficult to approximate by fractions. Their set has zero probability, but is nevertheless a dense G_δ, namely, it is uncountably infinite or they are *generic*. Similarly, numbers such that $q_{n+1} \geq f(q_n)$ for infinitely many n's for some function f increasing faster than any polynomial at infinity have also zero probability even if they make a G_δ-set.

In their seminal work (Avila and Jitomirskaya, 2006), Jitomirskaya and Avila used the following measure of the speed of convergence, namely, they define

$$\beta = \limsup_{n\to\infty} \frac{\ln q_{n+1}}{q_n}.$$

If $0 < \beta < \infty$, then it means roughly that given $0 < \beta' < \beta$, the inequality $q_{n+1} \geq e^{\beta' q_n}$ holds for infinitely many n's. Moreover, if $\beta'' > \beta$ then there is an integer N such that $q_{n+1} \leq e^{\beta'' q_n}$ for $n \geq N$. Such numbers are Liouville.

Indeed Liouville proved in the mid-19th century that if α is algebraic and irrational, namely, if it is the root of a polynomial of degree l with integer coefficients, then there is a constant $C > 0$ such that $|\alpha - p/q| \geq C/q^l$ for any fraction. In particular algebraic numbers are Diophantine and have $\beta = 0$. This theorem allowed Liouville to exhibit nonalgebraic irrational numbers, namely, transcendental numbers, for the first time. His method was used, improved and optimized over the decades, and permitted eventually to prove that both numbers e and π were transcendental.

Spectral continuity

Looking back at the Hofstadter spectrum in Fig. 1, it seems that the gap edges vary continuously with α. But it cannot be a proof since the bands represented in this figure correspond to rational values of α. Mathematicians must prove that property. The earliest result goes back to 1982 (Elliot, 1982) and 1983 (Avron and Simon, 1983), showing that the gap edges are continuous indeed. However to make sure that the gap width does not change wildly, simple continuity is insufficient.

In order to describe the main result, let f be a function defined on the real line with real values. Let also $0 < r \leq 1$. The function f is called r-Hölder continuous on an interval (a, b) if there is a constant $C > 0$ such that for any pair of points $a < x, y < b$ in this interval, $|f(x) - f(y)| \leq C|x - y|^r$. If $r = 1$ the function f is called Lipschitz continuous. The best result known so far is the following:

Theorem 3. *For* $0 \le \alpha \le 1$, *let* $H_\alpha = U_1 + U_1^{-1} + \lambda(U_2 + U_2^{-1})$ *denote the Almost Mathieu operator (see Eq. 2 with* $t_1 = 1$, $t_2 = \lambda$*), where* U_1 *and* U_2 *generate the irrational rotation algebra* $\mathcal{A}_\alpha$ *(see Eq. 3).*

(i) *If* $\mathfrak{g}_\alpha = (E_-(\alpha), E_+(\alpha))$ *is a gap in the spectrum of* H_α, *the gap edges* $E_\pm(\alpha)$ *are Lipschitz continuous functions of* α *on every interval where the gap does not close. The same holds for the spectral boundaries.*

(ii) *In the vicinity of a value* α_0 *for which the gap closes, namely,* $E_+(\alpha_0) = E_-(\alpha_0)$, *the gap edges are* $1/2$*-Hölder continuous.*

Several proofs are available in the literature, all technical. In particular, a general argument valid for any self-adjoint operator can be found in Beckus and Bellissard (2016). But the reference used by Avila and Jitomirskaya is (Avron et al., 1991) the oldest. This result is actually optimal: Lipschitz continuity cannot be replaced by differentiability. Indeed the right and left derivatives exist everywhere, but they do not coincide at any rational value of α (Rammal and Bellissard, 1990). In addition, the central gap of the Almost Mathieu operator for $\alpha = p/q$ with q even is closed. A semiclassical expansion of the gap edge (Rammal and Bellissard, 1990) confirms that the nonvanishing gap edges are proportional $\sqrt{\alpha - p/q}$ in the vicinity of $\alpha_0 = p/q$ (see Fig. 1 especially at $\alpha_0 = 1/2$).

Transfer matrices and gaps

Avila and Jitomirskaya used the transfer matrix method. They followed a strategy initiated by Puig (2004) and Eliasson (1999). Here are few hints about how to use it to prove that all but the central gap of the Almost Mathieu spectrum are open.

Rotation number

As described in Eq. (6), the Schrödinger equation for the Almost Mathieu model can be expressed as

$$\Phi(n+1) = \begin{bmatrix} \phi(n+1) \\ \phi(n) \end{bmatrix} = S(E, \lambda; \alpha n + \theta)\, \Phi(n)$$

where $S(E, \lambda; x)$ is a 2×2 matrix with real coefficients and determinant 1. It is a trigonometric polynomial in x of period 1. Since $\Phi(1) \neq 0$, the vector $\Phi(n)$ never vanishes as n varies. Therefore the straight line passing through 0 and $\Phi(n)$ rotates in the 2D plane. This straight line is the same after a rotation by π of course. After N such rotations, if $\pi\theta_N$ denotes the total angle between $n = 1$ and $n = N$ seen as a real number defines a rotation angle per step namely

$$\rho(E, \lambda) = \lim_{N\to\infty} \frac{\theta_N}{N}, \quad (\textbf{rotation number}) \tag{19}$$

Actually, at each rotation of π, the wave function $\phi(n)$ changes its sign so that this rotation number coincides with the number of sign changes of ϕ per unit length. This is a critical concept exhibited in the 19th century, known as the Sturm–Liouville theory, for second-order differential equations, permitting to relate the rank of excited states energies, ranked in increasing order starting at 0 for the ground state to the number of zeroes of the corresponding wave eigenfunction. Using this method for the Almost Mathieu operator restricted to a finite interval with N sites permits to define the number of eigenstates below some energy E per unit length to give the *integrated density of states* (IDS) $\mathcal{N}(E, \lambda)$. By a classical argument using the Sturm–Liouville theory, the rotation number and the IDS are simply related by

$$\rho(E, \lambda) = \mathcal{N}(E, \lambda).$$

In particular if E belongs to a spectral gap, these numbers do not depend upon where in this gap E is located since changing E in this gap does not add any new eigenstate. Using various arguments, topological (K-theory) or analytical, each with different flavor (see Bellissard, 1982; Johnson and Moser, 1983; Elliot, 1982), it can be shown that

Theorem 4 (Gap Labeling Theorem). *Given a spectral gap* $\mathfrak{g}$ *of the Almost Mathieu operator, there is an integer m such that* $N(E, \lambda) = m\alpha - [m\alpha]$ *for* $E \in \mathfrak{g}$.

This result is not surprising for a physicist. Indeed, it is sufficient to consider the fractional situation with $\alpha = p/q$. Gaps separate Bloch bands. Therefore if E belongs to such a gap, the number of eigenstates per period below this energy is one per band below this gap and each band count for the fraction $1/q$ of the total number of eigenstates per period. Since p/q is irreducible, this number is a multiple of $\alpha = p/q$ modulo 1. Unsurprisingly, the Gap Labeling Theorem extends this result to irrational values of the dimensionless magnetic flux per unit cell. But as usual, the proof requires more than just such an argument.

Floquet–Bloch solutions

The next step is to find solutions of Bloch type, called *Floquet solutions* in Mathematics. In general a Floquet–Bloch solutions should have the form $\phi(n) = e^{-\imath kn}\varphi(n\alpha + \theta)$, where k is equal to the parameters k_1 in Eq. (11). Whenever α is irrational, the Almost Mathieu spectrum does not depend upon these parameters so that k can be chosen to be zero. Hence a Bloch wave solution has the form $\phi(n) = \varphi(n\alpha + \theta)$ with φ a smooth function with period 1. The Schrödinger equation takes the form

$$\varphi(x - \alpha) + \varphi(x + \alpha) + 2\lambda \cos x\, \varphi(x) = E\varphi(x) \tag{20}$$

By Fourier's expansion, the Fourier coefficients $\hat{\varphi}(l)$ satisfy the *dual equation* (Aubry and André, 1980) called *Aubry's duality*

$$\hat{\varphi}(l-1)+\hat{\varphi}(l+1)+\frac{2\cos(2\pi l\alpha)}{\lambda}\hat{\varphi}(l)=\frac{E}{\lambda}\hat{\varphi}(l) \tag{21}$$

At this point if we impose to search φ to be only square integrable in x over intervals of length 1, the Fourier series must be square summable, implying that $\hat{\varphi}(l)\to 0$ as $l\to\pm\infty$. The following Wronskian argument implies that if such an L^2 Floquet–Bloch solution exists, it must be unique, up to a scaling factor: assume that $\hat{\varphi},\hat{\psi}$ are to square-summable solutions of Eq. (21). Then the Wronskian is given by

$$W(n)=\begin{bmatrix}\hat{\varphi}(n) & \hat{\psi}(n)\\ \hat{\varphi}(n-1) & \hat{\psi}(n-1)\end{bmatrix}.$$

It clearly satisfies

$$S(n)W(n)=W(n+1),\quad S(n)=\begin{bmatrix}E/\lambda-2\cos(2\pi l\alpha) & -1\\ 1 & 0\end{bmatrix}.$$

The property $\det S(n)=1$ implies $\det W(n)=\det W(n-1)=const$. As both $\hat{\varphi}$ and $\hat{\psi}$ decay to zero as $n\to\pm\infty$, by assumption, it follows that $\det W(n)=0$ for all n's implying that $\hat{\varphi}=c\hat{\psi}$ are proportional, c being a scalar independent of n.

Reducibility to constant coefficients

Reducibility was introduced by Eliasson (1999). It consists in finding a constant 2×2 matrix B of determinant 1, called the *Floquet matrix* and an x dependent smooth 2×2 matrix Z, of period 1 and determinant 1, such that

$$S(E,\lambda;x)=Z(x+\alpha)BZ(x)^{-1}.\quad(\textbf{reducibility}) \tag{22}$$

If a smooth Floquet solution exists then the vector $\Phi(n)$ can be written as $\Phi(n)=\Psi(n\alpha+\theta)$ for $\Psi(x)$ smooth and periodic of period 1. Then setting $\hat{\Psi}(x)=Z(x)^{-1}\Psi(x)$ leads to

$$\hat{\Psi}(x+\alpha)=B\hat{\Psi}(x).$$

Iterating implies, since $\hat{\Psi}$ is smooth and periodic, that B^n must stay bounded as $n\to\pm\infty$. In particular its two eigenvalues must have modulus smaller than or equal to one. Since the determinant is 1, the eigenvalues are inverse of each other so that they must be of the form $e^{\pm\gamma}$ for some angle γ. In particular if $\gamma\notin\{0,\pi\}$, it would give two coexisting Floquet solutions, which has been already excluded by Aubry's duality. So the eigenvalues are both equal to either +1 or −1. To exclude coexisting solutions, B can only be reduced to an upper triangular matrix by change of basis, namely

$$B=\pm\begin{bmatrix}1 & c\\ 0 & 1\end{bmatrix},\quad\text{with}\quad c\neq 0.$$

The miracle

In his paper Puig (2004) reports the following: if φ is a Bloch wave solution of Eq. (20), then it can be chosen to be real valued and the following matrix

$$Z(x)=\begin{bmatrix}\varphi(x) & -\varphi(x-\alpha)/N(x)\\ \varphi(x-\alpha) & +\varphi(x)/N(x)\end{bmatrix},\quad N(x)=\varphi(x)^2+\varphi(x-\alpha)^2,$$

has determinant 1 and obey the following equation

$$S(x)Z(x)=Z(x+\alpha)B(x), S(x)=\begin{bmatrix}E-2\lambda\cos(x) & -1\\ 1 & 0\end{bmatrix}, B(x)=\begin{bmatrix}1 & b(x)\\ 0 & 1\end{bmatrix}, \tag{23}$$

where $b(x)$ is a periodic function of x with same the same regularity as φ. Now, if there is a solution $g(x)$ of the following equation (called *cocycle equation*)

$$g(x+\alpha)-g(x)=b(x)-\bar{b},\quad(\textbf{cocycle equation}) \tag{24}$$

then $B(x)$ is *similar* to the constant matrix B obtained by replacing $b(x)$ by $\bar{b}$. Integrating both sides over one period, *such a solution exist only if* $\bar{b}=\int_0^1 b(x)dx$. The term *similar* means that $B(x)G(x)=G(x+\alpha)B$ if $G(x)$ is defined as

$$G(x)=\begin{bmatrix}1 & g(x)\\ 0 & 1\end{bmatrix}$$

The main result at this point is Eliasson (1992, 1999) and Puig (2004).

Proposition 4. *A Floquet–Bloch solution exists if and only if the transfer matrix* $S(E,\lambda;x)$ *is reducible as in Eq. (23). A gap at the energy* E *is open if and only if the matrix* $B(x)$ *is similar to a constant matrix distinct from the identity* $\mathbf{1}$.

Solving the Ten Martini problem

To solve the Ten Martini Problem, Avila and Jitomirskaya distinguish two regimes. The first regime, called Liouville, deals with numbers with $\beta > \ln\lambda$ and the other regime, called Diophantine, looks at numbers with $\beta < \ln\lambda$. Actually there is a special treatment to be done for $\beta \le \ln\lambda \le 2\beta$. The treatment of this delicate regime will be skipped. This article is devoted to make the main ideas accessible to physicists.

The Diophantine regime

While the Diophantine Regime is most technical and requires fine analysis, it has been considered since the earliest work by Dinaburg and Sinai (1975) on the Almost Mathieu equation. The strategy they used was inspired by the method of the KAM Theorem, proposed first by Kolmogorov in 1952 and then by Arnold and Moser in 1962–1963 to treat perturbation theory in Classical Mechanics. The main difficulty comes from what astronomers of the 19th century called *secular terms* and called today *the small divisor problem*. Such a situation is already contained in the solution of the cocycle equation (see Eq. 24). Indeed, to solve this equation, let $g(x)$ be expanded in Fourier series

$$g(x) = \sum_{m=-\infty}^{m=+\infty} e^{2\imath\pi mx}\,\hat{g}_m,\; b(x) = \sum_{m=-\infty}^{m=+\infty} e^{2\imath\pi mx}\,\hat{b}_m,\; \hat{b}_0 = \int_0^1 b(x)dx = \bar{b}.$$

Thus

$$\hat{g}_m = \frac{\hat{b}_m}{e^{2\imath\pi m\alpha}-1}, \quad \forall m \neq 0.$$

If α is irrational, the Fourier coefficients of g are all well defined apart from $\hat{g}_0$, which can be chosen arbitrarily. The problem comes from numbers m's such that $m\alpha$ is very close to a rational number. For instance if $m = q_n$, one of the continued fraction rational approximations, then $|q_n\alpha - p_n| \le 1/q_{n+1}$. Therefore, using the definition of β this gives

$$|e^{2\imath\pi q_n\alpha} - 1| \le 2\pi e^{-\beta q_n},$$

which can be very small, leading the Fourier series for g to diverge. To solve this problem, the trick is to use functions $b(x)$ that can be analytically continued in the complex plane replacing x by $z = x + \imath y$ with $|y| < \delta$ for a suitable $\delta > 0$. Then this is possible provided $|\hat{b}_m| \le const.e^{-\delta|m|}$ for all m. In this case as long as $\beta < \delta$, the cocycle equation can be solved with g analytic in $|y| = |\mathrm{I}z| < \delta - \beta$.

Why is this relevant? Because, as guessed by Aubry and André (1980), the decay of the wave functions solution of the dual equation (21) is given by the *Lyapunov exponent* γ, namely, the behavior at infinity of the transfer matrix between the sites N and $N + n$ as $n \to \pm\infty$. A beautiful argument from Herman (1983) using the properties of subharmonic function leads to

$$\gamma = \begin{cases} 0 & \text{if } 0 \le \lambda \le 1 \\ \ln\lambda & \text{if } \lambda \ge 1 \end{cases}.$$

Consequently, as proved by Sinai (see Puig, 2004)

Theorem 5. *If $0 < \lambda < 1$, the dual equation (21) admits a unique solution $\hat{\varphi}$ such that, for some $C > 0$*

$$\frac{\hat{\varphi}(l+1)^2 + \hat{\varphi}(l)^2}{\hat{\varphi}(1)^2 + \hat{\varphi}(0)^2} \le C\, e^{-2|\ln\lambda||l|}, \quad |l| \to \infty.$$

Equivalently the Almost Mathieu equation (20) admits a unique Floquet–Bloch solution that can be extended by analyticity to $z = x + \imath y$ in the complex plane, in the strip defined by $|\Im z| < |\ln\lambda|$.

Corollary 1. *If $0 < \lambda < 1$, the cocycle equation (24) admits a solution if α satisfies $\beta(\alpha) < |\ln\lambda|$, analytic in the strip $|\Im z| < |\ln\lambda| - \beta(\alpha)$. In particular, all spectral gaps of the Almost Mathieu operator, but at $E = 0$, are open.*

Proof. Indeed the function $b(x)$ obtained in Eq. (23) is a function computable in terms of the Floquet–Bloch solution φ and is analytic in the same trip as φ. From Theorem 5, this domain is the strip $|\Im z| < |\ln\lambda|$. From solving the cocycle equation, the function g is analytic in $|\Im z| < |\ln\lambda| - \beta(\alpha)$. At last if $E \neq 0$ due to the uniqueness of the solution of the dual equation, the constant $\bar{b}$ cannot vanish, proving that all gaps, but $E = 0$ are open for such αs.

The Liouville regime

If $\beta(\alpha)$ is large enough though, a different strategy can be used, which was initiated in the seminal paper of Choi et al. (1990). Indeed, the Hölder continuity of the gap edges can be used to estimate the gap size near a rational approximation of α to prove that the gap stay open. The main difference brought by Avila and Jitomirskaya is the use of the improved Hölder estimate proved at about the same time by Avron et al. (1991). This improved estimate permits to extend the arguments to irrational numbers with $\beta(\alpha) > 2|\ln\lambda|$.

The argument (with many details skipped) goes as follows: let $\mathfrak{g}_\alpha = (E_-(\alpha), E_+(\alpha))$ be a spectral gap for the Almost Mathieu operator. Thanks to Avron et al. (1991), there is a constant $C_H > 0$ such that $|E_\sigma(\alpha) - E_\sigma(\alpha')| \leq C_H\sqrt{|\alpha - \alpha'|}$ for $\sigma = \pm 1$. If p_n/q_n is a rational approximation of α obtained from the continued fraction expansion, it follows that $|\alpha - p_n/q_n| \leq c_1 e^{-\beta q_n}$ if $\beta > \beta(\alpha)$ and if n large enough while c_1 is some positive constant. Therefore

$$\left|E_\sigma(\alpha) - E_\sigma\left(\frac{p_n}{q_n}\right)\right| \leq C_H\left|\alpha - \frac{p_n}{q_n}\right|^{1/2} \leq c_1 e^{\beta q_n/2}.$$

It follows that for the gap width this leads to the following inequality

$$|E_-(\alpha) - E_+(\alpha)| \geq \left|E_-\left(\frac{p_n}{q_n}\right) - E_+\left(\frac{p_n}{q_n}\right)\right| - 2c_1 e^{-\beta q_n/2}.$$

Thanks to Choi et al. (1990), the gap width for p_n/q_n is bounded from below by

$$\left|E_-\left(\frac{p_n}{q_n}\right) - E_+\left(\frac{p_n}{q_n}\right)\right| \geq c_0(\lambda)(c_1\lambda)^{q_n/2}, \quad 0 < c_1 < 1.$$

where $c_1 > 0$ is some numerical constant (see Eq. 17 valid for q_n odd, for instance). As $n \to \infty$, one can choose β sufficiently close to $\beta(\alpha)$. From this it follows that if $\beta(\alpha) > |\ln \lambda| + |\ln D|$, the gap $\mathfrak{g}_\alpha$ is open.

So, there might still be a gap in the range of values of $\beta(\alpha)$ for which the sketch of the proof presented above might fail to show that the gaps stay open. The paper by Avila and Jitomirskaya fills the gap in between.

Conclusion

This article is aimed at explaining to an audience of nonexpert scientists the strategy required to solve the Ten Martini Problem. Nevertheless entering into some technical details is unavoidable. Many contributions were necessary, which spread over a quarter of a century to clarify each point until a synthesis of all the arguments could lead to the solution. Several contributions were appreciated as major steps, so much so as to be published by the highest rated Mathematical or Mathematical Physics journals.

References

Aubry S (1978) The new concept of transitions by breaking of analyticity in a crystallographic model. In: *Solitons and Condensed Matter Physics. Springer Series Solid-State Science*, vol. 8. Berlin-New York: Springer-Verlag. xi+341 pp. ISBN: 3-540-09138-6.

Aubry S and André G (1980) Analyticity breaking and Anderson localization in incommensurate lattices. *Annals of the Israel Physical Society* 3(133): 18.

Avila A and Jitomirskaya S (2006) Solving the Ten Martini problem. In: Asch J and Joye A (eds.) *Mathematical Physics of Quantum Mechanics. Lecture Notes in Physics*, vol. 690, pp. 5–16. Springer, Berlin, Heidelberg.

Avila A and Jitomirskaya S (2009) The ten Martini problem. *Annals of Mathematics* 170(1): 303–342. ISSN: 0003486X. https://doi.org/10.4007/annals.2009.170.303.

Avron J and Simon B (1983) Almost periodic Schrödinger operators, II. The density of states. *Duke Mathematical Journal* 50: 369–391.

Avron JE, van Mouche P, and Simon B (1991) On the measure of the spectrum for the Almost Mathieu operator. *Communications in Mathematical Physics* 139(1): 215. ISSN: 0010-3616. https://doi.org/10.1007/BF02102736. 215.

Beckus S and Bellissard J (2016) Continuity of the spectrum of a field of self-adjoint operators. *Annales Henri Poincaré* 17(12): 3425–3442. ISSN: 1424-0637. https://doi.org/10.1007/s00023-016-0496-3.

Bellissard J (1982) Schrödinger operators with almost periodic potential: An overview. In: *Mathematical Problems in Theoretical Physics*, pp. 356–363. Springer Berlin Heidelberg.

Bellissard J (1994) Non commutative methods in semiclassical analysis. In: *Transition to Chaos in Classical and Quantum Mechanics*, pp. 1–64. Berlin: Springer.

Bellissard J and Simon B (1982) Cantor spectrum for the almost Mathieu equation. *Journal of Functional Analysis* 48(3): 408–419. ISSN: 0022-1236. https://doi.org/10.1016/0022-1236(82)90094-5.

Chambers WG (1965) Linear-network model for magnetic breakdown in two dimensions. *Physical Review* 140(1A): A135–A143. ISSN: 0031899X. https://doi.org/10.1103/PhysRev.140.A135.

Choi MD, Elliott GA, and Yui N (1990) Gauss polynomials and the rotation algebra. *Inventiones Mathematicae* 99(1): 225–246. ISSN: 00209910. https://doi.org/10.1007/BF01234419.

Dinaburg EI and Sinai YG (1975) The one-dimensional Schrodinger equation with quasi-periodic potential. *Functional Analysis and Its Applications* 9(4): 8–21.

Eliasson LH (1992) Floquet solutions for the 1-dimensional quasi-periodic Schrödinger equation. *Communications in Mathematical Physics* 146(3): 447–482. ISSN: 0010-3616. https://doi.org/10.1007/BF02097013.

Eliasson LH (1999) On the discrete one-dimensional quasi-periodic Schrödinger equation and other smooth quasi-periodic skew products. *Hamiltonian Systems With Three or More Degrees of Freedom* 1995: 55–61. https://doi.org/10.1007/978-94-011-4673-9_6.

Elliot GA (1982) Gaps in the spectrum of an almost periodic Schrodinger operator. *Comptes Rendus des Seances de l'Academie des Sciences, Serie A: Sciences Mathematiques Canada* IV(5): 255–259.

Hardy GH and Wright EM (2008) *An Introduction to the Theory of Numbers*, 6th. Clarendon: Oxford. https://www.ams.org/bull/1929-35-06/S0002-9904-1929-04793-1/. 1938.

Harper PG (1955a) The general motion of conduction electrons in a uniform magnetic field, with application to the diamagnetism of metals. *Proceedings of the Physical Society. Section A* 68(10): 879. ISSN: 0370-1298. https://doi.org/10.1088/0370-1298/68/10/305.

Harper PG (1955b) Single band motion of conduction electrons in a uniform magnetic field. *Proceedings of the Physical Society. Section A* 68(10): 874–878. ISSN: 0370-1298. https://doi.org/10.1088/0370-1298/68/10/304.

Herman MR (1983) Une méthode pour minorer les exposants de Lyapounov et quelques exemples montrant le caractère local d'un théorème d'Arnold et de Moser sur le tore de dimension 2. *Commentarii Mathematici Helvetici* 58(1): 453–502. ISSN: 0010-2571. https://doi.org/10.1007/BF02564647.

Hofstadter DR (1976) Energy levels and wave functions of Bloch electrons in rational and irrational magnetic fields. *Physical Review B* 14(6): 2239–2249. ISSN: 01631829. https://doi.org/10.1103/PhysRevB.14.2239.

Johnson R and Moser J (1983) The rotation number for almost periodic potentials. *Communications in Mathematical Physics* 90(2): 317–318. ISSN: 00103616. https://doi.org/10.1007/BF01205510.

Last Y (2005) Spectral theory of Sturm-Liouville operators on infinite intervals: A review of recent developments. In: *Sturm-Liouville Theory*, pp. 99–120. Basel: Birkhäuser-Verlag.

Puig J (2004) Cantor spectrum for the Almost Mathieu operator. *Communications in Mathematical Physics* 244(2): 297–309. ISSN: 00103616. https://doi.org/10.1007/s00220-003-0977-3.

Rammal R and Bellissard J (1990) An algebraic semi-classical approach to Bloch electrons in a magnetic field. *Journal de Physique* 51(17): 1803–1830. ISSN: 0302-0738. https://doi.org/10.1051/jphys:0199000510170180300.

Simon B (2000) Schrödinger operators in the twenty-first century. In: *Mathematical Physics 2000*, pp. 283–288. Published by Imperial College Press and Distributed by World Scientific Publishing Co.

Zak J (1964a) Magnetic translation group. *Physical Review* 134(6A): A1602. ISSN: 0031899X. https://doi.org/10.1103/PhysRev.134.A1602.

Zak J (1964b) Magnetic translation group. II. Irreducible representations. *Physical Review* 134(6A): A1607. ISSN: 0031899X. https://doi.org/10.1103/PhysRev.134.A1607.

Hofstadter butterfly in graphene

Wei Yang and Guangyu Zhang, Institute of Physics, Chinese Academy of Sciences, Beijing, China

© 2024 Elsevier Ltd. All rights reserved.

Introduction 724
Graphene superlattices 725
Hofstadter butterfly in graphene/hBN superlattice 726
Hofstadter butterfly in twisted bilayer graphene 727
Conclusion 729
References 729

Abstract

This chapter reports recent progresses on the observation of Hofstadter butterfly in graphene, and organized as follows. We first briefly introduce the concept of Hofstadter butterfly, including the theoretical model of Bloch electrons in the magnetic field, the resulting Harper's equation and its solution, and its realizations in non-graphene systems. Then, we discuss the ways to realize the fractal Hofstadter spectra in graphene, and introduce three types of graphene superlattice structure, including graphene/hBN, twisted graphene layers, nanofabricated graphene superlattice. In particular, details about the fractal Hofstadter spectrum in graphene will be focused and discussed in the graphene/hBN superlattice and the twisted bilayer graphene.

Key points

- Introduction of Hofstadter Butterfly and the realization in non-graphene systems
- Graphene superlattices: graphene/hBN, twisted graphene layers, nanofabricated graphene superlattice
- The realization of fractal Hofstadter butterfly in Graphene/hBN superlattice
- Topological Chern insulators and Hofstadter butterfly in Twisted bilayer graphene

Introduction

Hofstadter butterfly refers to the energy spectrum of two-dimensional (2D) electrons being subjected to both the periodic electrostatic potential and a perpendicular magnetic field (B), which leads to a self-similar recursive Landau level spectrum resembling a butterfly. It is named after D. Hofstadter who first obtained the fractal energy spectrum mathematically for a square lattice in 1976 (Hofstadter, 1976). He assumed that the tight-binding Bloch energy has the form of $2E_0(\cos k_x\lambda + \cos k_y\lambda)$, where E_0 is an empirical parameter, λ is the electrostatic potential period, and $\mathbf{k}$ is the wave vector. He then replaced the momentum by doing a Peierls substitution, i.e., $\hbar\mathbf{k} \rightarrow \hbar\mathbf{k} - e\mathbf{A}$, where e is the electron charge and $\mathbf{A}$ is the vector potential with $\mathbf{B} = \nabla \times \mathbf{A}$. By solving the time-independent Schrodinger equation with the ansatz of $\psi(x, y) = g_n e^{i\alpha m}$, where $x = n\lambda$ and $y = m\lambda$ (n and m the integers) with α depends on energy, one could obtain Harper's equation:

$$g_{n+1} + g_{n-1} + 2\cos(2\pi n\phi/\phi_0 - \alpha)g_n = \varepsilon g_n,$$

with $\phi = B\lambda^2$ is the magnetic flux through the unit cell, $\phi_0 = h/e$ is the magnetic quantum flux with h the Planck constant, and $\varepsilon = 2E/E_0$ with E the energy. At rational fillings with $\phi/\phi_0 = p/q$, where p and q are co-prime integers, the solution of the Harper's equation reveals that the Bloch band would split into q distinct energy subbands, resulting in a recursive fractal energy diagram as shown Fig. 1, the so called Hofstadter butterfly.

In 1978, Wannier (1978) took the density of state into account and transformed the fractal energy spectrum into a linear trajectory of density-field diagram, so called Wannier diagram. In this representation, the Hofstadter butterfly is described by the Diophantine relation:

$$n/n_0 = t(\phi/\phi_0) + s$$

Here n is the carrier density and n_0 is the carrier density of a unit cell. The first quantum number t corresponds to the topological properties of Landau level flat band and the second quantum number s is the Bloch band filling index. Later on, the fractal spectrum was also calculated for triangular lattices (Claro and Wannier, 1979) and honeycomb lattices (Rammal, 1985).

To experimentally observe the Hofstadter butterfly is rather challenging. The minigaps of the fractal spectrum is considerable when magnetic flux is comparable to the quantum flux, in other words, the magnetic length $l_B = \sqrt{\hbar/eB}$ is of the same order as λ, the period of electrostatic potential of the Bloch band. For a real crystal, the period is the lattice constant, which is of the order of

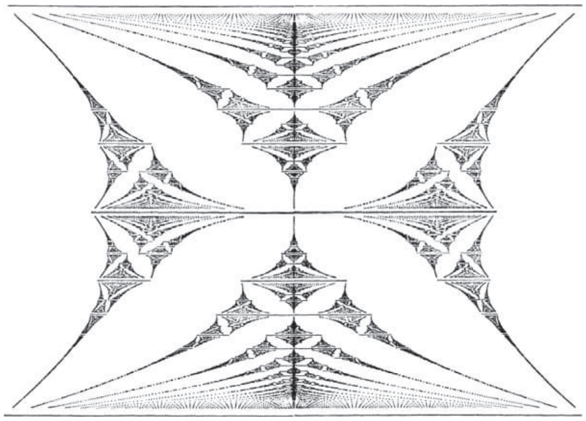

Fig. 1 Calculated Fractal spectrum in a unit cell by D. Hofstadter. Reproduced from Hofstadter D.R. (1976) Energy levels and wave functions of Bloch electrons in rational and irrational magnetic fields. *Physical Review B* 14, 2239–2249.

sub-nanometer, and thus it usually requires an extremely large magnetic field over 1000T that is experimentally inaccessible in the lab. Back in the 1990s, electrostatic periods much larger than its lattice constant were achieved by fabricating lateral superlattices for 2D electron gas in GaAs/AlGaAs heterostructures (Schlösser et al., 1996; Albrecht et al., 1999, 2001, 2003; Geisler et al., 2004). Although signatures of Hofstadter spectrum were observed in these artificial superlattices, the device quality degradation due to nanofabrication as well as the difficulty in tuning carrier density hindered the revelation of the fractal structure.

The fractal Hofstadter spectrum was vividly realized in a microwave waveguide with a periodic arrangement of scatterers (Kuhl and Stöckmann, 1998). In this photonic system, the transmission matrix mimics the Hamiltonian of Bloch electrons in the magnetic field, and equivalently leads to the Harper equation and a fractal Hofstadter butterfly. Similar realizations of the Hofstadter Hamiltonian were also reported in optical lattices with ultracold atoms (Aidelsburger et al., 2013) and in superconducting qubits (Roushan et al., 2017).

Graphene superlattices

Being atomically thin, graphene is an ideal 2D electron system. Soon after the discovery of quantum Hall effect in graphene (Novoselov et al., 2005; Zhang et al., 2005), calculations of the fractal Hofstadter spectrum were carried out in monolayer graphene (Hasegawa and Kohmoto, 2006) and bilayer graphene (Nemec and Cuniberti, 2007). Yet, the problem is obvious as the graphene lattice constant is small, $a = 0.246$ nm, thus requiring a superlattice structure.

One solution is to realize graphene superlattice structures with external periodic potentials, whose band structure was calculated by Park et al. (2008), revealing an emergence of secondary Dirac point at the superlattice Brillouin zone boundary. Similar calculations were also done by Brey and Fertig, 2009, and Barbier et al., 2010. The first and also the best experimental demonstration is the moiré superlattice structure on graphene/hexagonal boron nitride (hBN) heterostructure, formed due to their lattice mismatch as illustrated in Fig. 2A. The graphene/hBN superlattice was initially observed in a scanning tunneling microscope/spectrum (STM/STS) study by Yankowitz et al. (2012). Perfect twist angle control with the $\theta = 0^{\circ}$ was realized via direct epitaxy of graphene on hBN with a superlattice period of $\sim$15.6 nm (Yang et al., 2013). Note that the twist angle between graphene

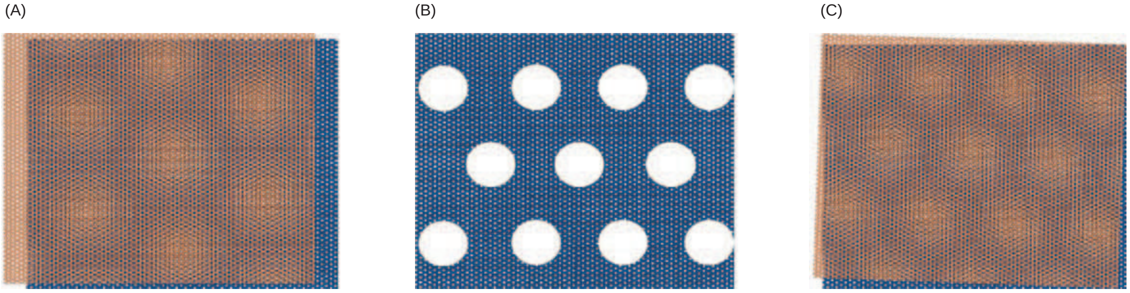

Fig. 2 Sketches of graphene superlattice structures formed by lattice constant mismatch (A), nanofabrication (B), and twisting between graphene layers (C).

and hBN could also be tuned by thermal annealing (Wang et al., 2016) and AFM tip manipulation (Koren et al., 2016; Wang et al., 2016; Ribeiro-Palau et al., 2018). The fractal Hofstadter spectrum was realized in transferred graphene/hBN superlattices (Dean et al., 2013; Hunt et al., 2013; Ponomarenko et al., 2013; Yu et al., 2014; Wang et al., 2015; Krishna Kumar et al., 2017, 2018; Spanton et al., 2018), in epitaxial graphene/hBN superlattices (Yang et al., 2013, 2016; Chen et al., 2017; Lu et al., 2020), and in ABC-trilayer graphene/hBN superlattice (Chen et al., 2020a). Soon after the experimental observations, the fractal Hofstadter spectrum were calculated in graphene/hBN superlattice (Chen et al., 2014).

Besides, there are also other graphene superlattices based on nanofabrication, such as one-dimensional (1D) superlattices with a comb-like gate (Dubey et al., 2013; Drienovsky et al., 2014), etched graphene antidots (Sandner et al., 2015; Yagi et al., 2015), and patterned dielectric superlattice (Forsythe et al., 2018), as sketched in Fig. 2B. However, the results are not promising. The 1D gated superlattices suffered from serious p-n junction effects, and the graphene antidots were limited by its big superlattice size and thus dominated by classic commensurate effect between the superlattice period and the cyclotron orbits. The patterned dielectric superlattices with a reduced period of ~40 nm and a stronger tunability of the periodic potential revealed signatures of the fractal spectrum; however, the quality was still limited as it suffered from similar problems as those of lateral superlattices of the 2D electron gas in GaAs/AlGaAs heterostructures.

Another strategy in this effort is a moiré butterfly by rotating two graphene layers with the period of $\lambda = a/(2\sin(\theta/2))$ at a twisted angle (θ) (Fig. 2C). This was firstly proposed in (Bistritzer and MacDonald, 2011b), where fractal spectrum at a strong field limit ($\phi/\phi_0 > 1$) was investigated. Later, calculations of the fractal spectrum at a weak field limit ($1 > \phi/\phi_0 > 0$) were carried out in twisted bilayer graphene (TBG) for different twist angles by Moon and Koshino (2012) and Wang et al. (2012). In fact, the moiré superlattice structure of the TBG were observed in a series of the STM experiments (Li et al., 2010; Luican et al., 2011; Brihuega et al., 2012). In the early works of quantum transport on TBG prepared either by CVD growth on *SiC* (Lee et al., 2011) or by folded graphene (Schmidt et al., 2014), the device quality was much limited and no signature of the fractal band was observed. Thanks to the development of "pick-up" transfer technique (Wang et al., 2013) and subsequent "tear and stack" technique using the same graphene flake (Kim et al., 2016a), accurate control of twist angle in TBG and high-quality devices were possible. In 2016, realizations of TBG with $\theta \sim 2^o$ (corresponding to $\lambda \sim 7$nm) were reported by Kim et al. (2016b) and Cao et al. (2016), where two sets of LLs were observed; one stemming from the main charge neutral point (CNP) and the other from the superlattice gaps (or called full filling $n = 4n_0$). However, the two LLs intersect each other without revealing the recurring fractal structures. Then, the magic angle TBG with $\theta \sim 1.1^o$ (corresponding to $\lambda \sim 12.8$ nm) was firstly realized by Cao et al. (2018a,b), where the LLs are observed to fan out of the main CNP and superlattice gaps, and later by (Lu et al., 2019; Yankowitz et al., 2019) with the LLs developed from half filling and quarter fillings. The fractal Hofstadter spectrum was also observed in other twisted graphene multilayer moiré systems including but not limited to the twisted double bilayer graphene (TDBG) (Burg et al., 2019; Cao et al., 2020; Liu et al., 2020; Shen et al., 2020), twisted monolayer bilayer graphene (TMBG) (Chen et al., 2020b; Polshyn et al., 2020, 2021; He et al., 2021; Xu et al., 2021), and twisted trilayer graphene (TTG) (Hao et al., 2021; Park et al., 2021b; Siriviboon et al., 2021).

Hofstadter butterfly in graphene/hBN superlattice

In graphene/hBN heterostructure, graphene and hBN share a similar triangular lattice with a mismatch of $\delta = \sim 1.7\%$, which gives a triangular moiré superlattice with a period of $\lambda = (1+\delta)a/\sqrt{2(1+\delta)(1-cos\theta)+\delta^2}$ at a given twist angle (θ). The area of the superlattice unit cell $A = \sqrt{3}\lambda^2/2$ defines the number of electron states per area of a fully filled Bloch band $n_0 = 1/A$. Here, the carrier density n can be largely tuned by gating $n = C_G V_G/e$, where C_G (V_G) is the geometrical capacitance (gate voltage), and the magnetic flux is defined by $\phi = BA$. Then, the measured Landau fan diagram, a mapping of longitudinal resistance (R_{xx}) or Hall resistance (R_{xy}) to the change of V_G and B, could be transformed into the Wannier diagram of the fractal Hofstadter butterfly spectrum, as shown in Fig. 3, following the Diophantine relation: $n/n_0 = t(\phi/\phi_0) + s$, where both t and s are integers in the single-particle picture.

At zero magnetic field, i.e., $\phi/\phi_0 = 0$, the R_{xx} peak at $s = 0$ corresponds to the charge neutral point (CNP) of graphene, while two satellite peaks developed at $s = \pm 4$ are referred to the gap openings at the moiré mini-Brillouin zone boundary (or called secondary Dirac points in some literatures), and the number 4 also means the fourfold degeneracy (spin and valley) of the Bloch band, i.e., 4 electrons/holes to fully filled one moiré unit cell. There is electron-hole asymmetry, and usually the superlattice effect is stronger for holes than that for electrons.

At $s = 0$, the Diophantine relation is simplified to $n/n_0 = t(\phi/\phi_0)$. This is exactly the case of 2D free electrons/holes subjected to a perpendicular magnetic field, and the quantum number t has the same physical meaning as the filling factors of Landau levels in graphene where the Hall conductance is quantized to te^2/h. Let us take the monolayer (bilayer) graphene/hBN superlattice as an example. The states developed at $t = 4N+2$ (4N for bilayer graphene) means that the Landau quantization gaps with fourfold symmetry, while those at other integers are corresponding to the gaps with broken symmetry, with $N = 0, 1, 2\ldots$ Landau level index ($N = 1, 2, 3\ldots$ for bilayer graphene).

At $s = \pm 4$, the Diophantine relation can be modified as $(n/n_0 \mp 4) = t(\phi/\phi_0)$. At a small magnetic field before the Landau quantization, the sign of R_{xy} changes at $s = \pm 4$, which is exactly the same as sign change of R_{xy} at CNP. As the magnetic field increases further, features of the Landau level states are found fanning out from $s = \pm 4$ with a slop of $t = (\phi/\phi_0)/(n/n_0 \mp 4)$, similar

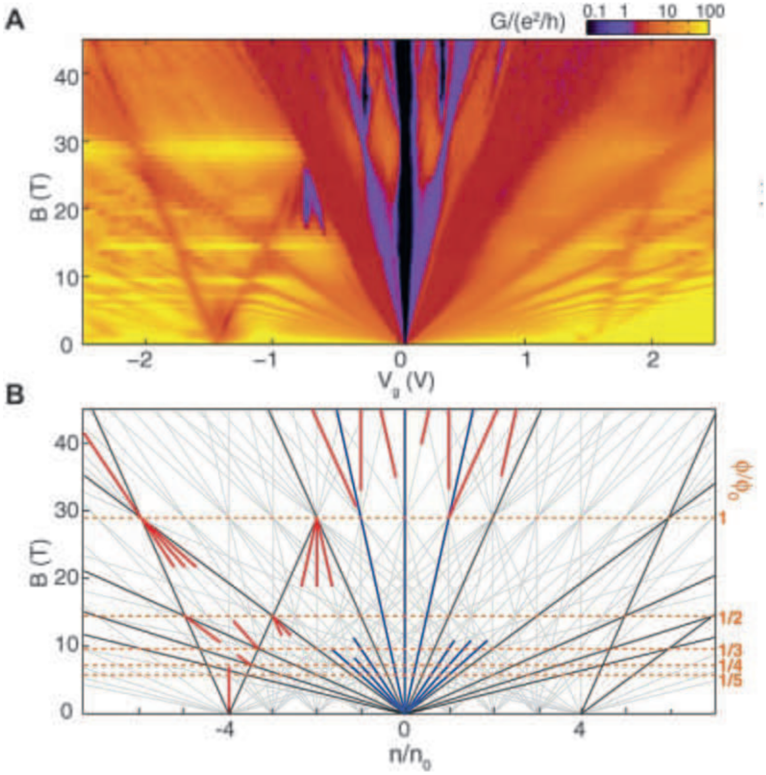

Fig. 3 Fractal Hofstadter butterfly revealed in a color mapping of conductance to magnetic field B and gate voltage Vg (A) and corresponding Wannier diagram (B) in graphene/hBN superlattice. Reproduced from Hunt B., Sanchez-Yamagishi J.D., Young A.F., Yankowitz M., LeRoy B.J., Watanabe K., Taniguchi T., Moon P., Koshino M., Jarillo-Herrero P., et al. (2013) Massive Dirac Fermions and Hofstadter butterfly in a van der Waals heterostructure. *Science* 340, 1427–1430.

to those fanning out from CNP with a slope of $t=(\phi/\phi_0)/(n/n_0)$. The whole spectra stemming at $s = \pm 4$ is like a replica of those at CNP, a signature of fractal Hofstadter butterfly. Note that the LLs stemmed from $s = -4$ show up at almost the same magnetic field as those at the CNP.

The most intriguing evidence of the fractal Hofstadter spectrum is revealed at the fractional filling $\phi/\phi_0 = p/q$. If $p = 1$ as in most cases, the LLs from $s = -4$ and those from $s = 0$ intersect at $\phi/\phi_0 = 1/q$. For instance, the LLs with $t = 2$ from $s = -4$ will meet those with $t = -2$, -6, and -10 from $s = 0$ at $q = 1$, 2, and 3, respectively, as shown in Fig. 3B (Hunt et al., 2013). At these crossing points, mini Hofstadter gaps open at $\phi/\phi_0 = 1/q$, and moreover LLs with different t are developed at an effective magnetic field $B_{\text{eff}} = \pm |B - B_{1/q}|$, whose traces at B = 0 could be any integer s between 0 and −4. In principle, similar recursive fractal gaps should be found at other crossing points in the Wannier diagram, and the whole spectrum constructs the fractal Hofstadter butterfly. Note that the fractional s with an integer t (also named symmetry broken Chern insulator) as well as a fractional t with $s = 0$ (fractional quantum Hall insulator) are observed in graphene/hBN superlattice (Wang et al., 2015). Moreover, gaps with both fractional s and fractional t (also named fractional Chern insulator) are revealed in bilayer graphene/hBN superlattices (Spanton et al., 2018), indicating fractional Hofstadter butterfly spectra in the many-body picture.

The fractal Hofstadter spectrum can be probed in conductance measurement (Dean et al., 2013; Hunt et al., 2013; Ponomarenko et al., 2013; Wang et al., 2015; Yang et al., 2016; Chen et al., 2017; Krishna Kumar et al., 2017) and also in capacitance measurements (Hunt et al., 2013; Yu et al., 2014; Spanton et al., 2018). Note that the fractal Hofstadter butterfly spectra can survive at elevated temperature up to 100 K (Krishna Kumar et al., 2017, 2018), even though the fractal Hofstadter butterfly spectra are thermally smeared into Brown-Zak oscillations, i.e., the conductance oscillations in ϕ_0/ϕ.

Hofstadter butterfly in twisted bilayer graphene

The situation in TBG are more complicated and interesting, because now the twisted angle (θ) determines not only the size of the moiré superlattice $\lambda = a/(2\sin(\theta/2))$, but also the interlayer coupling. At a magic angle of ~1.05°, the resulting moiré bands are extremely flat with a bandwidth of ~10 meV, implying a reduced Fermi velocity (Bistritzer and MacDonald, 2011a). The moiré flat band in the magic angle TBG gives rise to the strong electron correlation effects, including the correlated insulators at half fillings and superconductivity nearby (Cao et al., 2018a,b), as well as correlator insulators at quarter fillings (Lu et al., 2019; Yankowitz et al., 2019). In TBG, it is convenient to define the moiré band filling factor ($\nu = n/n_0$), corresponding to the number of carriers filled in the moiré conduction/valence band, with $n_0 = 1/A$ and $A = \sqrt{3}\lambda^2/2$. As a result, the resistance peaks at $\nu = \pm 1$ (± 3), ± 2, ± 4 in the transfer curve are corresponding to the correlated insulators at quarter (three quarters) fillings, half fillings, and moiré band insulators, respectively.

The fractal Hofstadter butterfly spectrum in TBG is also revealed in the Wannier diagram, following the Diophantine relation: $n/n_0 = t(\phi/\phi_0) + s$, where both t and s are integers in the single-particle picture. The strong electron-electron interactions in TBG could substantially reshape the fractal Hofstadter spectrum. Usually, the correlated insulators are quite robust against the magnetic field, and the replica of the LLs emerges at these integer fillings ν, unlike the dominating LLs at $\nu = 0$ and ± 4 in graphene/hBN superlattice. Note that the LL filling factor ν_{LL} in the replica spectrum at non-zero integer ν is usually twofold or even onefold degenerate, and the filling factors ν_{LL} have the same sign as those of ν. In addition, the quantum oscillations in TBG are usually much weaker than those in the graphene/hBN superlattice. This is due to the reduced Fermi velocity of the flat band, especially for MATBG, and therefore the Landau quantization gaps as well as the fractal Hofstadter gaps are smaller compared to the dispersive moiré bands in the graphene/hBN superlattice.

Additionally, these moiré flat bands in TBG are topological with non-trivial Berry curvatures (Liu et al., 2019a,b) at zero magnetic fields. The zero-field topological bands are mathematically the same as those LLs or fractal LLs at finite magnetic fields. Note that the quantum Hall insulator is in principle a Chern insulator where the LL filling factor corresponds to the Chern number, and here we use "Chern" specifically for the moiré Chern bands to avoid confusion. Considering spin, valley, and the moiré valley, the moiré bands are eightfold degenerate at the Dirac point, protected by the C_2T symmetry where C_2 is the inversion symmetry and T is time reversal symmetry.

If C_2T symmetry is unbroken, then the total Chern number is zero since the moiré bands with opposite Chern numbers touches at the Dirac point, even though each of the moiré bands are topological with $C = \pm 1$. This can be related to the fragile topology (Ahn et al., 2019; Po et al., 2019; Song et al., 2019; Lian et al., 2020), whose signature is revealed in the observation of the $C = 0$ band gaps being intersected by the non-zero LLs at $\phi/\phi_0 = 2$ ($B \sim 9T$) in the TBG with $\theta \sim 0.45^\circ$ (Lu et al., 2021).

If the inversion symmetry is broken by a staggered potential mass while the T symmetry is preserved, it leads to $C = +1$ at the K valley and $C = -1$ at the K′ valley in the moiré conduction band, and $C = -1$ at the K valley and $C = +1$ at the K′ valley in the moiré valence band. As a result, the Chern insulator with $C = +1$ or -1 emerge when the odd number of carriers is filled in the moiré band. The breaking of the C_2 symmetry happens when the TBG is aligned with the hBN lattice, first realized by A. Sharpe (Sharpe et al., 2019) with the observations of ferromagnetism and Chern insulator with $C = 1$ at $\nu = 3$, and then by Serlin et al. (2020) with the observation of quantized anomalous Hall effect (QAH) with $C = 1$ at $v = 3$, as shown Fig. 4A. Similar observations have also been observed in ABC-trilayer graphene/hBN superlattice (Chen et al., 2020a), twisted monolayer bilayer graphene (Chen et al., 2020b; Polshyn et al., 2020). These observations are in stark contrast to the conventional fractal Hofstadter butterfly that strongly depends on the magnetic flux in the moiré superlattice.

If the T symmetry is broken by the electron-electron interaction induced Haldane mass (Haldane, 1988), it leads to $C = +1$ at both the K and K′ valley in the moiré conduction band, and $C = -1$ at the K and K′ valley in the moiré valence band. As a result, it gives a Chern insulator with Chern number depending on a sequential filling of carriers, i.e., $C = -4 - \nu$ for holes and $C = 4 - \nu$ for electrons (as shown Fig. 4B). The Chern insulators with the T symmetry-broken are observed in various experiments, for instance in

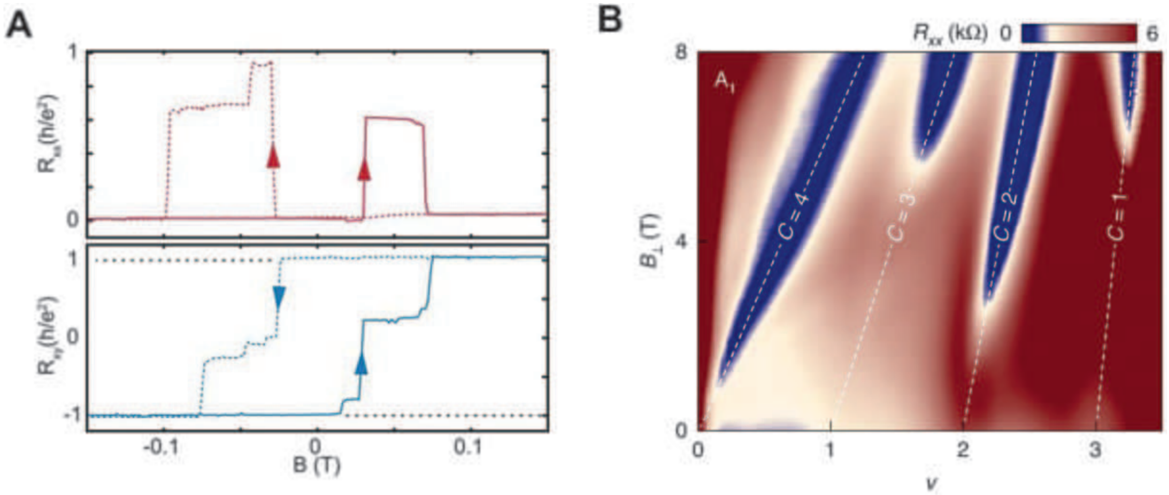

Fig. 4 (A) Observation of quantized anomalous Hall effect in hBN aligned TBG, i.e., $R_{xy} = h/(Ce^2)$ and $R_{xx} = 0\ h/e^2$ with Chern number $C = 1$. (B) Observation of sequential filled Chern insulator with $C = 4 - \nu$. Panel (a): Reproduced from Serlin, M., Tschirhart C.L., Polshyn H., Zhang Y., Zhu J., Watanabe K., Taniguchi T., Balents L., Young A.F. (2020) Intrinsic quantized anomalous Hall effect in a moire heterostructure. *Science* 367, 900–903. Panel (b): Reproduced from Das I., Lu X., Herzog-Arbeitman J., Song Z.-D., Watanabe K., Taniguchi T., Bernevig B.A., Efetov D.K. (2021) Symmetry-broken Chern insulators and Rashba-like Landau-level crossings in magic-angle bilayer graphene. *Nature Physics* 17, 710–714.

transport measurements (Das et al., 2021; Park et al., 2021a; Saito et al., 2021; Shen et al., 2021; Wu et al., 2021b) and scanning spectroscopic measurements (Nuckolls et al., 2020; Choi et al., 2021; Pierce et al., 2021). These Chern insulators are found to compete with the zero-field ground states in MATBG (Stepanov et al., 2021). These Chern insulators are also observed for the non-magic angle TBG fractal Hofstadter spectra at finite magnetic fields (Choi et al., 2021; Shen et al., 2021).

Moreover, fractional Chern insulators with fractional C and ν (referred to the fractional t and fractional s in the Diophantine language), symmetry-broken Chern insulators (non-zero integers t and fractional s), and charge density waves ($t = 0$ and fractional s) are observed in local compressibility measurements (Xie et al., 2021), and are also studied in the numerical calculations (Andrews and Soluyanov, 2020; Wang and Santos, 2020). Similar topological phases with a fractional ν are also observed in the twisted monolayer-bilayer graphene (Polshyn et al., 2021) and twisted trilayer graphene (Siriviboon et al., 2021).

All these Chern insulators as well as CDW phases are weakly dependent on the filling of the magnetic flux, unlike the fractal and fractional fractal Hofstadter spectra in graphene/hBN superlattices. In fact, it is also possible to suppress the Chern insulators and recover the conventional fractal Hofstadter spectrum by twisting away from the magic angle (Shen et al., 2021). Because the moiré bands are more dispersive for the non-magic angle, which leads to stronger Landau quantization (bigger fractal Hofstadter gaps) and weaker electron interactions (smaller Chern gaps). Also note that the moiré bands in TBG at a non-magical angle might be topologically trivial. Besides, it is also possible to reveal the fractal Hofstadter spectra in the MATBG by tuning the Fermi level from the flat moiré bands to the dispersive remote bands (Das et al., 2021). Last but not least, aside from TBG, other twisted graphene multilayer system offers a good opportunity to study the electrical field tunable Hofstadter spectrum. Take the TDBG for example, the Landau fan diagram of the Hofstadter butterfly spectrum is strongly displacement field tunable (Liu et al., 2022a) and stacking order dependent (Crosse et al., 2020; Wu et al., 2021a), and the valley polarized correlated insulators at half fillings in TDBG are observed topological (Liu et al., 2022b) and could host insulating quantum oscillations (Liu et al., 2022a). These observations suggest a rich interplay among the moiré flat band topology, symmetry, Landau quantization and others.

Conclusion

Graphene is an ideal platform to experimentally realize the fractal Hofstadter butterfly. The development of van der Waals stacking techniques allows the realizations of high-quality graphene superlattice structures, including the graphene/hBN superlattice and the TBG and other twisted graphene multilayers. In a graphene/hBN superlattice, the recursive nature of the fractal Hofstadter spectra has been vividly revealed at rational fillings of ϕ/ϕ_0. In TBG, the fractal Hofstadter spectra is strongly twist-angle dependent. In particular, the magic angle TBG reveals abundant topological Chern insulators including the quantized anomalous Hall effect at zero magnetic field, which is distinct from the conventional fractal Hofstadter spectrum.

References

Ahn J, Park S, and Yang B-J (2019) Failure of Nielsen-Ninomiya theorem and fragile topology in two-dimensional systems with space-time inversion symmetry: Application to twisted bilayer graphene at magic angle. *Physical Review X* 9: 021013.

Aidelsburger M, Atala M, Lohse M, Barreiro JT, Paredes B, and Bloch I (2013) Realization of the Hofstadter Hamiltonian with ultracold atoms in optical lattices. *Physical Review Letters* 111: 185301.

Albrecht C, Smet J, Weiss D, Von Klitzing K, Hennig R, Langenbuch M, Suhrke M, Rössler U, Umansky V, and Schweizer H (1999) Fermiology of two-dimensional lateral superlattices. *Physical Review Letters* 83: 2234.

Albrecht C, Smet JH, von Klitzing K, Weiss D, Umansky VV, and Schweizer H (2001) Evidence of Hofstadter's fractal energy spectrum in the quantized hall conductance. *Physical Review Letters* 86: 147–150.

Albrecht C, Smet JH, von Klitzing K, Weiss D, Umansky V, and Schweizer H (2003) Evidence of Hofstadter's fractal energy spectrum in the quantized Hall conductance. *Physica E: Low-dimensional Systems and Nanostructures* 20: 143–148.

Andrews B and Soluyanov A (2020) Fractional quantum Hall states for moir\'e superstructures in the Hofstadter regime. *Physical Review B* 101: 235312.

Barbier M, Vasilopoulos P, and Peeters FM (2010) Extra Dirac points in the energy spectrum for superlattices on single-layer graphene. *Physical Review B* 81: 075438.

Bistritzer R and MacDonald AH (2011a) Moire bands in twisted double-layer graphene. *Proceedings of the National Academy of Sciences of the United States of America* 108: 12233–12237.

Bistritzer R and MacDonald AH (2011b) Moiré butterflies in twisted bilayer graphene. *Physical Review B* 84: 035440.

Brey L and Fertig HA (2009) Emerging zero modes for graphene in a periodic potential. *Physical Review Letters* 103: 046809.

Brihuega I, Mallet P, González-Herrero H, Trambly de Laissardière G, Ugeda MM, Magaud L, Gómez-Rodríguez JM, Ynduráin F, and Veuillen JY (2012) Unraveling the intrinsic and robust nature of Van Hove singularities in twisted bilayer graphene by scanning tunneling microscopy and theoretical analysis. *Physical Review Letters* 109: 196802.

Burg GW, Zhu J, Taniguchi T, Watanabe K, MacDonald AH, and Tutuc E (2019) Correlated insulating states in twisted double bilayer graphene. *Physical Review Letters* 123: 197702.

Cao Y, Luo JY, Fatemi V, Fang S, Sanchez-Yamagishi JD, Watanabe K, Taniguchi T, Kaxiras E, and Jarillo-Herrero P (2016) Superlattice-induced insulating states and valley-protected orbits in twisted bilayer graphene. *Physical Review Letters* 117: 116804.

Cao Y, Fatemi V, Demir A, Fang S, Tomarken SL, Luo JY, Sanchez-Yamagishi JD, Watanabe K, Taniguchi T, Kaxiras E, et al. (2018a) Correlated insulator behaviour at half-filling in magic-angle graphene superlattices. *Nature* 556: 80–84.

Cao Y, Fatemi V, Fang S, Watanabe K, Taniguchi T, Kaxiras E, and Jarillo-Herrero P (2018b) Unconventional superconductivity in magic-angle graphene superlattices. *Nature* 556: 43–50.

Cao Y, Rodan-Legrain D, Rubies-Bigorda O, Park JM, Watanabe K, Taniguchi T, and Jarillo-Herrero P (2020) Tunable correlated states and spin-polarized phases in twisted bilayer–bilayer graphene. *Nature* 583: 215–220.

Chen X, Wallbank JR, Patel AA, Mucha-Kruczyński M, McCann E, and Fal'ko VI (2014) Dirac edges of fractal magnetic minibands in graphene with hexagonal moiré superlattices. *Physical Review B* 89: 075401.

Chen G, Sui M, Wang D, Wang S, Jung J, Moon P, Adam S, Watanabe K, Taniguchi T, Zhou S, et al. (2017) Emergence of tertiary dirac points in graphene moire superlattices. *Nano Letters* 17: 3576–3581.

Chen G, Sharpe AL, Fox EJ, Zhang Y-H, Wang S, Jiang L, Lyu B, Li H, Watanabe K, Taniguchi T, et al. (2020a) Tunable correlated Chern insulator and ferromagnetism in a moire superlattice. *Nature* 579: 56–61.

Chen S, He M, Zhang Y-H, Hsieh V, Fei Z, Watanabe K, Taniguchi T, Cobden DH, Xu X, Dean CR, et al. (2020b) Electrically tunable correlated and topological states in twisted monolayer–bilayer graphene. *Nature Physics* 17: 374–380.

Choi Y, Kim H, Peng Y, Thomson A, Lewandowski C, Polski R, Zhang Y, Arora HS, Watanabe K, Taniguchi T, et al. (2021) Correlation-driven topological phases in magic-angle twisted bilayer graphene. *Nature* 589: 536–541.

Claro FH and Wannier GH (1979) Magnetic subband structure of electrons in hexagonal lattices. *Physical Review B* 19: 6068–6074.

Crosse JA, Nakatsuji N, Koshino M, and Moon P (2020) Hofstadter butterfly and the quantum Hall effect in twisted double bilayer graphene. *Physical Review B* 102: 035421.

Das I, Lu X, Herzog-Arbeitman J, Song Z-D, Watanabe K, Taniguchi T, Bernevig BA, and Efetov DK (2021) Symmetry-broken Chern insulators and Rashba-like Landau-level crossings in magic-angle bilayer graphene. *Nature Physics* 17: 710–714.

Dean CR, Wang L, Maher P, Forsythe C, Ghahari F, Gao Y, Katoch J, Ishigami M, Moon P, Koshino M, et al. (2013) Hofstadter's butterfly and the fractal quantum Hall effect in moire superlattices. *Nature* 497: 598–602.

Drienovsky M, Schrettenbrunner F-X, Sandner A, Weiss D, Eroms J, Liu M-H, Tkatschenko F, and Richter K (2014) Towards superlattices: Lateral bipolar multibarriers in graphene. *Physical Review B* 89: 115421.

Dubey S, Singh V, Bhat AK, Parikh P, Grover S, Sensarma R, Tripathi V, Sengupta K, and Deshmukh MM (2013) Tunable superlattice in graphene to control the number of Dirac points. *Nano Letters* 13: 3990–3995.

Forsythe C, Zhou X, Watanabe K, Taniguchi T, Pasupathy A, Moon P, Koshino M, Kim P, and Dean CR (2018) Band structure engineering of 2D materials using patterned dielectric superlattices. *Nature Nanotechnology* 13: 566–571.

Geisler MC, Smet JH, Umansky V, von Klitzing K, Naundorf B, Ketzmerick R, and Schweizer H (2004) Detection of a Landau band-coupling-induced rearrangement of the Hofstadter butterfly. *Physical Review Letters* 92: 256801.

Haldane FDM (1988) Model for a quantum hall effect without Landau levels: Condensed-matter realization of the "parity anomaly". *Physical Review Letters* 61: 2015–2018.

Hao Z, Zimmerman A, Ledwith P, Khalaf E, Najafabadi DH, Watanabe K, Taniguchi T, Vishwanath A, and Kim P (2021) Electric field–tunable superconductivity in alternating-twist magic-angle trilayer graphene. *Science* 371: 1133–1138.

Hasegawa Y and Kohmoto M (2006) Quantum Hall effect and the topological number in graphene. *Physical Review B* 74: 155415.

He M, Zhang YH, Li Y, Fei Z, Watanabe K, Taniguchi T, Xu X, and Yankowitz M (2021) Competing correlated states and abundant orbital magnetism in twisted monolayer-bilayer graphene. *Nature Communications* 12: 4727.

Hofstadter DR (1976) Energy levels and wave functions of Bloch electrons in rational and irrational magnetic fields. *Physical Review B* 14: 2239–2249.

Hunt B, Sanchez-Yamagishi JD, Young AF, Yankowitz M, LeRoy BJ, Watanabe K, Taniguchi T, Moon P, Koshino M, Jarillo-Herrero P, et al. (2013) Massive Dirac Fermions and Hofstadter butterfly in a van der Waals heterostructure. *Science* 340: 1427–1430.

Kim K, Yankowitz M, Fallahazad B, Kang S, Movva HCP, Huang S, Larentis S, Corbet CM, Taniguchi T, Watanabe K, et al. (2016a) van der Waals heterostructures with high accuracy rotational alignment. *Nano Letters* 16: 1989–1995.

Kim Y, Herlinger P, Moon P, Koshino M, Taniguchi T, Watanabe K, and Smet JH (2016b) Charge Inversion and topological phase transition at a twist angle induced van hove singularity of bilayer graphene. *Nano Letters* 16: 5053–5059.

Koren E, Leven I, Lortscher E, Knoll A, Hod O, and Duerig U (2016) Coherent commensurate electronic states at the interface between misoriented graphene layers. *Nature Nanotechnology* 11: 752–757.

Krishna Kumar R, Chen X, Auton G, Mishchenko A, Bandurin DA, Morozov SV, Cao Y, Khestanova E, Ben Shalom M, Kretinin A, et al. (2017) High-temperature quantum oscillations caused by recurring Bloch states in graphene superlattices. *Science* 357: 181–184.

Krishna Kumar R, Mishchenko A, Chen X, Pezzini S, Auton GH, Ponomarenko LA, Zeitler U, Eaves L, Fal'ko VI, and Geim AK (2018) High-order fractal states in graphene superlattices. *Proceedings of the National Academy of Sciences of the United States of America* 115: 5135–5139.

Kuhl U and Stöckmann H-J (1998) Microwave realization of the Hofstadter butterfly. *Physical Review Letters* 80: 3232.

Lee DS, Riedl C, Beringer T, Castro Neto AH, von Klitzing K, Starke U, and Smet JH (2011) Quantum Hall effect in twisted bilayer graphene. *Physical Review Letters* 107: 216602.

Li G, Luican A, Lopes dos Santos JMB, Castro Neto AH, Reina A, Kong J, and Andrei EY (2010) Observation of Van Hove singularities in twisted graphene layers. *Nature Physics* 6: 109–113.

Lian B, Xie F, and Bernevig BA (2020) Landau level of fragile topology. *Physical Review B* 102: 041402.

Liu J, Liu J, and Dai X (2019a) Pseudo Landau level representation of twisted bilayer graphene: Band topology and implications on the correlated insulating phase. *Physical Review B* 99: 155415.

Liu J, Ma Z, Gao J, and Dai X (2019b) Quantum valley Hall effect, orbital magnetism, and anomalous hall effect in twisted multilayer graphene systems. *Physical Review X* 9: 031021.

Liu X, Hao Z, Khalaf E, Lee JY, Ronen Y, Yoo H, Haei Najafabadi D, Watanabe K, Taniguchi T, Vishwanath A, et al. (2020) Tunable spin-polarized correlated states in twisted double bilayer graphene. *Nature* 583: 221–225.

Liu L, Chu Y, Yang G, Yuan Y, Wu F, Ji Y, Tian J, Yang R, Watanabe K, and Taniguchi T (2022a) Quantum oscillations in correlated insulators of a moir\'e superlattice. *arXiv*. preprint arXiv:2205.10025.

Liu L, Zhang S, Chu Y, Shen C, Huang Y, Yuan Y, Tian J, Tang J, Ji Y, Yang R, et al. (2022b) Isospin competitions and valley polarized correlated insulators in twisted double bilayer graphene. *Nature Communications* 13: 3292.

Lu X, Stepanov P, Yang W, Xie M, Aamir MA, Das I, Urgell C, Watanabe K, Taniguchi T, Zhang G, et al. (2019) Superconductors, orbital magnets and correlated states in magic-angle bilayer graphene. *Nature* 574: 653–657.

Lu X, Tang J, Wallbank JR, Wang S, Shen C, Wu S, Chen P, Yang W, Zhang J, Watanabe K, et al. (2020) High-order minibands and interband Landau level reconstruction in graphene moiré superlattices. *Physical Review B* 102: 045409.

Lu X, Lian B, Chaudhary G, Piot BA, Romagnoli G, Watanabe K, Taniguchi T, Poggio M, MacDonald AH, Bernevig BA, et al. (2021) Multiple flat bands and topological Hofstadter butterfly in twisted bilayer graphene close to the second magic angle. *Proceedings of the National Academy of Sciences of the United States of America* 118: e2100006118.

Luican A, Li G, Reina A, Kong J, Nair RR, Novoselov KS, Geim AK, and Andrei EY (2011) Single-layer behavior and its breakdown in twisted graphene layers. *Physical Review Letters* 106: 126802.

Moon P and Koshino M (2012) Energy spectrum and quantum Hall effect in twisted bilayer graphene. *Physical Review B* 85: 195458.

Nemec N and Cuniberti G (2007) Hofstadter butterflies of bilayer graphene. *Physical Review B* 75: 201404.

Novoselov KS, Geim AK, Morozov SV, Jiang D, Katsnelson MI, Grigorieva IV, Dubonos SV, and Firsov AA (2005) Two-dimensional gas of massless Dirac fermions in graphene. *Nature* 438: 197–200.

Nuckolls KP, Oh M, Wong D, Lian B, Watanabe K, Taniguchi T, Bernevig BA, and Yazdani A (2020) Strongly correlated Chern insulators in magic-angle twisted bilayer graphene. *Nature* 588: 610–615.

Park CH, Yang L, Son YW, Cohen ML, and Louie SG (2008) New generation of massless Dirac fermions in graphene under external periodic potentials. *Physical Review Letters* 101: 126804.

Park JM, Cao Y, Watanabe K, Taniguchi T, and Jarillo-Herrero P (2021a) Flavour Hund's coupling, Chern gaps and charge diffusivity in moire graphene. *Nature* 592: 43–48.

Park JM, Cao Y, Watanabe K, Taniguchi T, and Jarillo-Herrero P (2021b) Tunable strongly coupled superconductivity in magic-angle twisted trilayer graphene. *Nature* 590: 249–255.

Pierce AT, Xie Y, Park JM, Khalaf E, Lee SH, Cao Y, Parker DE, Forrester PR, Chen S, Watanabe K, et al. (2021) Unconventional sequence of correlated Chern insulators in magic-angle twisted bilayer graphene. *Nature Physics* 17: 1210–1215.

Po HC, Zou L, Senthil T, and Vishwanath A (2019) Faithful tight-binding models and fragile topology of magic-angle bilayer graphene. *Physical Review B* 99: 195455.

Polshyn H, Zhu J, Kumar MA, Zhang Y, Yang F, Tschirhart CL, Serlin M, Watanabe K, Taniguchi T, MacDonald AH, et al. (2020) Electrical switching of magnetic order in an orbital Chern insulator. *Nature* 588: 66–70.

Polshyn H, Zhang Y, Kumar MA, Soejima T, Ledwith P, Watanabe K, Taniguchi T, Vishwanath A, Zaletel MP, and Young AF (2021) Topological charge density waves at half-integer filling of a moiré superlattice. *Nature Physics* 18: 42–47.

Ponomarenko LA, Gorbachev RV, Yu GL, Elias DC, Jalil R, Patel AA, Mishchenko A, Mayorov AS, Woods CR, Wallbank JR, et al. (2013) Cloning of Dirac fermions in graphene superlattices. *Nature* 497: 594–597.

Rammal R (1985) Landau level spectrum of Bloch electrons in a honeycomb lattice. *Journal de Physique* 46: 1345–1354.

Ribeiro-Palau R, Zhang C, Watanabe K, Taniguchi T, Hone J, and Dean CR (2018) Twistable electronics with dynamically rotatable heterostructures. *Science* 361: 690–693.

Roushan P, Neill C, Tangpanitanon J, Bastidas VM, Megrant A, Barends R, Chen Y, Chen Z, Chiaro B, Dunsworth A, et al. (2017) Spectroscopic signatures of localization with interacting photons in superconducting qubits. *Science* 358: 1175–1179.

Saito Y, Ge J, Rademaker L, Watanabe K, Taniguchi T, Abanin DA, and Young AF (2021) Hofstadter subband ferromagnetism and symmetry-broken Chern insulators in twisted bilayer graphene. *Nature Physics* 17: 478–481.

Sandner A, Preis T, Schell C, Giudici P, Watanabe K, Taniguchi T, Weiss D, and Eroms J (2015) Ballistic transport in graphene antidot lattices. *Nano Letters* 15: 8402–8406.

Schlösser T, Ensslin K, Kotthaus JP, and Holland M (1996) Landau subbands generated by a lateral electrostatic superlattice-chasing the Hofstadter butterfly. *Semiconductor Science and Technology* 11: 1582.

Schmidt H, Rode JC, Smirnov D, and Haug RJ (2014) Superlattice structures in twisted bilayers of folded graphene. *Nature Communications* 5: 5742.

Serlin M, Tschirhart CL, Polshyn H, Zhang Y, Zhu J, Watanabe K, Taniguchi T, Balents L, and Young AF (2020) Intrinsic quantized anomalous Hall effect in a moire heterostructure. *Science* 367: 900–903.

Sharpe AL, Fox EJ, Barnard AW, Finney J, Watanabe K, Taniguchi T, Kastner MA, and Goldhaber-Gordon D (2019) Emergent ferromagnetism near three-quarters filling in twisted bilayer graphene. *Science* 365: 605–608.

Shen C, Chu Y, Wu Q, Li N, Wang S, Zhao Y, Tang J, Liu J, Tian J, Watanabe K, et al. (2020) Correlated states in twisted double bilayer graphene. *Nature Physics* 16: 520–525.

Shen C, Ying J, Liu L, Liu J, Li N, Wang S, Tang J, Zhao Y, Chu Y, Watanabe K, et al. (2021) Emergence of chern insulating states in non-magic angle twisted bilayer graphene. *Chinese Physics Letters* 38: 047301.

Siriviboon P, Lin J-X, Scammell HD, Liu S, Rhodes D, Watanabe K, Taniguchi T, Hone J, Scheurer MS, and Li J (2021) Abundance of density wave phases in twisted trilayer graphene on WSe $ _2$. *arXiv*. preprint arXiv:2112.07127.

Song Z, Wang Z, Shi W, Li G, Fang C, and Bernevig BA (2019) All magic angles in twisted bilayer graphene are topological. *Physical Review Letters* 123: 036401.

Spanton EM, Zibrov AA, Zhou H, Taniguchi T, Watanabe K, Zaletel MP, and Young AF (2018) Observation of fractional Chern insulators in a van der Waals heterostructure. *Science* 360: 62–66.

Stepanov P, Xie M, Taniguchi T, Watanabe K, Lu X, MacDonald AH, Bernevig BA, and Efetov DK (2021) Competing zero-field chern insulators in superconducting twisted bilayer graphene. *Physical Review Letters* 127: 197701.

Wang J and Santos LH (2020) Classification of topological phase transitions and van hove singularity steering mechanism in graphene superlattices. *Physical Review Letters* 125: 236805.

Wang ZF, Liu F, and Chou MY (2012) Fractal Landau-level spectra in twisted bilayer graphene. *Nano Letters* 12: 3833–3838.

Wang L, Meric I, Huang P, Gao Q, Gao Y, Tran H, Taniguchi T, Watanabe K, Campos L, Muller D, et al. (2013) One-dimensional electrical contact to a two-dimensional material. *Science* 342: 614–617.

Wang L, Gao Y, Wen B, Han Z, Taniguchi T, Watanabe K, Koshino M, Hone J, and Dean CR (2015) Evidence for a fractional fractal quantum Hall effect in graphene superlattices. *Science* 350: 1231–1234.

Wang D, Chen G, Li C, Cheng M, Yang W, Wu S, Xie G, Zhang J, Zhao J, Lu X, et al. (2016) Thermally induced graphene rotation on hexagonal boron nitride. *Physical Review Letters* 116: 126101.

Wannier G (1978) A result not dependent on rationality for Bloch electrons in a magnetic field. *Physica Status Solidi* 88: 757–765.

Wu Q, Liu J, Guan Y, and Yazyev OV (2021a) Landau levels as a probe for band topology in graphene Moir\'e superlattices. *Physical Review Letters* 126: 056401.

Wu S, Zhang Z, Watanabe K, Taniguchi T, and Andrei EY (2021b) Chern insulators, van Hove singularities and topological flat bands in magic-angle twisted bilayer graphene. *Nature Materials* 20: 488–494.

Xie Y, Pierce AT, Park JM, Parker DE, Khalaf E, Ledwith P, Cao Y, Lee SH, Chen S, Forrester PR, et al. (2021) Fractional Chern insulators in magic-angle twisted bilayer graphene. *Nature* 600: 439–443.

Xu S, Al Ezzi MM, Balakrishnan N, Garcia-Ruiz A, Tsim B, Mullan C, Barrier J, Xin N, Piot BA, Taniguchi T, et al. (2021) Tunable van Hove singularities and correlated states in twisted monolayer–bilayer graphene. *Nature Physics* 17: 619–626.

Yagi R, Sakakibara R, Ebisuoka R, Onishi J, Watanabe K, Taniguchi T, and Iye Y (2015) Ballistic transport in graphene antidot lattices. *Physical Review B* 92: 195406.

Yang W, Chen G, Shi Z, Liu C-C, Zhang L, Xie G, Cheng M, Wang D, Yang R, Shi D, et al. (2013) Epitaxial growth of single-domain graphene on hexagonal boron nitride. *Nature Materials* 12: 792–797.

Yang W, Lu X, Chen G, Wu S, Xie G, Cheng M, Wang D, Yang R, Shi D, and Watanabe K (2016) Hofstadter butterfly and many-body effects in epitaxial graphene superlattice. *Nano Letters* 16: 2387–2392.

Yankowitz M, Xue J, Cormode D, Sanchez-Yamagishi JD, Watanabe K, Taniguchi T, Jarillo-Herrero P, Jacquod P, and LeRoy BJ (2012) Emergence of superlattice Dirac points in graphene on hexagonal boron nitride. *Nature Physics* 8: 382–386.

Yankowitz M, Chen S, Polshyn H, Zhang Y, Watanabe K, Taniguchi T, Graf D, Young AF, and Dean CR (2019) Tuning superconductivity in twisted bilayer graphene. *Science* 363: 1059–1064.

Yu GL, Gorbachev RV, Tu JS, Kretinin AV, Cao Y, Jalil R, Withers F, Ponomarenko LA, Piot BA, Potemski M, et al. (2014) Hierarchy of Hofstadter states and replica quantum Hall ferromagnetism in graphene superlattices. *Nature Physics* 10: 525–529.

Zhang Y, Tan Y-W, Stormer HL, and Kim P (2005) Experimental observation of the quantum Hall effect and Berry’s phase in graphene. *Nature* 438: 201–204.

Tight-binding method in electronic structure[☆]

DA Papaconstantopoulos[a], **MJ Mehl**[b], **AG Chronis**[c], **and MM Sigalas**[c], [a]Department of Computational and Data Sciences, George Mason University, Fairfax, VA, United States; [b]Department of Mechanical Engineering and Materials Sciences, Duke University, Durham, NC, United States; [c]Department of Materials Science, University of Patras, Patras, Greece

© 2024 Elsevier Ltd. All rights reserved.

This is an update of D.A. Papaconstantopoulos, M.J. Mehl, Tight-Binding Method in Electronic Structure, Editor(s): Franco Bassani, Gerald L. Liedl, Peter Wyder, Encyclopedia of Condensed Matter Physics, Elsevier, 2005, Pages 194–206, ISBN 9780123694010, https://doi.org/10.1016/B0-12-369401-9/00452-6.

Introduction 732
NRL tight-binding method 734
Technical procedure 735
Ground-state behavior and phase stability 735
Elastic constants 738
Vacancies 740
Surfaces 742
Stacking faults 742
Phonons 742
Point defects 745
Finite temperature properties from molecular dynamics 746
Multicomponent systems 746
One- and two-dimensional structures 748
Conclusion 754
Acknowledgments 754
References 754

Abstract

The Slater-Koster (SK) method was originally developed as a technique for interpolating first-principles energy bands from a limited number of k-points to a large one, for the purpose of accurately determining Fermi surfaces and densities of states. Numerous applications of the SK method have been made and extensions to include total energy determinations. One extension of the SK approach is the Naval Research Laboratory Tight-Binding (NRL-TB) method which has been very successful in fitting a set of first-principles electronic structure results and in addition being capable to predict properties that were not fitted and to also perform molecular dynamics simulations. This review presents a summary of applications using the NRL-TB scheme which covers most of the elements in the periodic Table and examples for multi-component systems.

Key points

- The NRL tight-binding method uses the Slater-Koster method to reproduce first-principles results.
- The resulting parameters can predict results not included in the database.
- The reduced size of the Hamiltonian allows rapid evaluation of systems containing hundreds of atoms.
- Phonon spectra as well as defect, stacking fault, and surface energies can be computed.
- Finite-temperature molecular dynamics simulations can compute thermodynamic properties.
- One- and two-dimensional systems, as well as nanoparticles, can be modeled.

Introduction

In the linear combination of atomic orbitals (LCAO) method, the one-electron wave function is expressed as a linear combination of Bloch sums. When such an expansion is made to the wave function in the Schrödinger equation, one obtains a set of simultaneous linear equations that has a nonzero solution if the determinant of the coefficients vanishes, that is,

$$\tilde{H} - \varepsilon \tilde{S} = 0 \qquad (1)$$

[☆] *Change History*: September 2022. DA Papaconstantopoulos and MJ Mehl updated all sections with minor changes. New figures have been added and changes made in tables.

https://doi.org/10.1016/B978-0-323-90800-9.00103-7

The matrix elements in this equation have the form

$$H_{nm} = \sum_{R_j} \exp\left[\mathrm{i}\boldsymbol{k}\cdot\left(\boldsymbol{R}_j - \boldsymbol{R}_i\right)\right] \times \int \phi_n^*(\boldsymbol{r}-\boldsymbol{R}_i)\tilde{H}\phi_m\left(\boldsymbol{r}-\boldsymbol{R}_j\right)\mathrm{d}^3 r \tag{2}$$

and

$$S_{nm} = \sum_{R_j} \exp\left[\mathrm{i}\boldsymbol{k}\cdot\left(\boldsymbol{R}_j - \boldsymbol{R}_i\right)\right] \times \int \phi_n^*(\boldsymbol{r}-\boldsymbol{R}_i)\phi_m\left(\boldsymbol{r}-\boldsymbol{R}_j\right)\mathrm{d}^3 r \tag{3}$$

where $\boldsymbol{R}_i$ and $\boldsymbol{R}_j$ denote the positions of atoms located on orbitals ϕ_n and ϕ_m, respectively. The integrals in the above equations can, in principle, be calculated directly, however the most common practice has been to follow Slater and Koster (SK) (Slater and Koster, 1954). They suggested replacing these integrals by adjustable parameters that could be estimated from experiment, but which are generally determined by fitting to more elaborate electronic structure calculations. The size of the matrices $\sim H$ and $\sim S$ is determined by the number of atoms in the unit cell and the number of atomic orbitals on each site. So, for face-centered cubic (f.c.c.), body-centered cubic (b.c.c.), and simple cubic (s.c.) lattices with one atom per unit cell, $\sim H$ and $\sim S$ are 9×9 matrices representing one s-function, three *p*-functions, and five *d*-functions. The *f*-states have been omitted in most works, although there have been papers that provide extensions of the SK scheme that include *f*-orbitals (Durgavich et al., 2016). For diatomic lattices, such as hexagonal close-packed (h.c.p.) and diamond and in binary compounds the *spd* model will result in an 18×18 matrix. Often in semiconductors such as Si and Ge the *d*-states are not included and hence the size of the Hamiltonian is 8×8. The full SK Hamiltonian for a monatomic material could require the determination of 81 parameters between each pair of atoms; however, SK showed that these parameters are related by symmetry operations that considerably reduce their actual number. The resulting independent matrix elements may be found in the tables given by SK. The reader is cautioned that some obvious typographical errors appear in these tables which have been corrected by users. Since the above summations are over the interatomic distances R_j, the number of parameters increases for calculations that include more than first nearest neighbors. In practice, no more than the third nearest neighbors are included. The integrals in [2] are three-centered since they are the product of an atomic wave function $\phi^*(\boldsymbol{r}-\boldsymbol{R}_i)$ centered on the atom at position $\boldsymbol{R}_i$, an atomic wave function $\phi(\boldsymbol{r}-\boldsymbol{R}_j)$ located on the atom at position $\boldsymbol{R}_j$, and a potential function inside the Hamiltonian H, centered on a third atom. These three-center integrals can be reduced to two-center integrals by approximating the potential energy as a sum of spherical potentials located on the same two atoms where the atomic orbitals are located. For the relationships between three-and two-center integrals, see Papaconstantopoulos (2015). Although working in three-center formalism has the advantage of fitting band structures more accurately, the two-center approximation has the distinct advantage that its parameters are transferable from one structure to another. This property of the two-center scheme makes it suitable to introduce bond-length dependence in the parameters which leads one to implementing a total energy capability in the SK method.

Since the 1960s there have been numerous applications of tight-binding (TB) theories, in particular the SK approach, to calculate electronic energy bands, densities of states, and, more recently, total energies, forces, and molecular dynamics simulations (Cleri and Rosato, 1993; Cohen et al., 1994; Gross et al., 1999; Groß et al., 2003; Haftel et al., 2004; Harrison, 1989; Mehl et al., 2000; Mehl and Papaconstantopoulos, 2002; Papaconstantopoulos and Mehl, 2003; Silayi et al., 2018; Shi and Papaconstantopoulos, 2004; Yang et al., 1998). There are two main uses of the TB theory. One is to determine a small number of parameters with the aim of providing a physical insight into the electronic structure without the necessity of going beyond a qualitative description. A classic example of this approach is the universal TB parameters of Harrison (1989). Harrison's TB theory has been of great educational value for a whole generation of scientists. More recently, extensions to this theory have been provided that greatly improve its accuracy. The other approach is to place emphasis on accurately reproducing the results of first-principles calculations by applying a least-squares procedure using a large number of parameters. The authors of this article have generally followed the second approach. A handbook by Papaconstantopoulos (2015) provides TB parameters for all elements in the periodic table, except for those with *f*-states. The handbook provides TB parameters in both two-center and three-center bases as well as in orthogonal and nonorthogonal representations, however these parameters are fitted to the ground state of each element and have very limited transferability to other volumes and structures. In addition, these TB Hamiltonians are not designed to compute total energies. The NRL-TB scheme (Cohen et al., 1994; Mehl and Papaconstantopoulos, 1996), on the other hand, which is discussed in the next section, is a two-center nonorthogonal TB method that uses environment-dependent parameters that capture the volume dependence of both the energy bands and the total energy.

To complete this introduction, the attention of the reader is drawn to a simple level of the TB theory, known as the second moment approximation (SMA), which originates from the Friedel model of rectangular density of states for the *d*-bands. The SMA method does not account for the band structure but, at least for the f.c.c. metals, reproduces well the total energy which has led to its wide use in molecular dynamics simulations. This method contains four adjustable parameters fitted to reproduce either experimental quantities or the total energies from first-principles calculations.

NRL tight-binding method

In the (Naval Research Laboratory) NRL-TB scheme, the on-site terms h_{il} are written as a polynomial

$$h_{il} = a_l + b_l\rho_i^{2/3} + c_l\rho_i^{4/3} + d_i\rho_i^2, \tag{4}$$

where i labels the atom and l the angular momentum of s, p, and d characters in the present form of the method.

The quantity ρ_i that appears in [4] is an embedded-atom-like "density" per atom given by the expression

$$\rho_i = \sum \exp\left(-\lambda^2 R_{ij}\right)F\left(R_{ij}\right), \tag{5}$$

where R_{ij} denotes the position of neighboring atoms from a central atom i, and $F(R_{ij})$ is the cutoff function. The quantities a_l, b_l, c_l, d_l, and λ are 13 parameters to be determined by a least-squares fit to the first-principles results. It is possible, within this scheme, for example, to split the d-onsite parameters to t_{2g} and e_g, or going even further, to have different parameters for the three p-orbitals and the five d-orbitals. It is also to be noted that this scheme has the flexibility of adding more terms in [4] to describe the density contributions from atom A to atom B (and vice versa) in the case of a binary material.

It was shown by SK that the two-center (spd) hopping integrals can be constructed from ten independent parameters $H_{ll'm}$, where

$$\begin{aligned}(ll'm) &= ss\sigma, sp\sigma, pp\sigma, pp\pi, sd\sigma,\\ &\quad pd\sigma, pd\pi, dd\sigma, dd\pi, \text{and}\, dd\delta.\end{aligned}$$

One notes that in the case of a binary material AB, there will be a set of four additional parameters

$$(ll'm) = ps\sigma, ds\sigma, dp\sigma, \text{and } dp\pi.$$

In the NRL-TB, each of these parameters is expressed in the form of a second-order polynomial-times an exponential function

$$\begin{aligned}H_{ll'm}(r) &= \left(e_{ll'm} + f_{ll'm}r + g_{ll'm}r^2\right)\\ &\quad\times \exp\left(-t_{ll'm}^2 r\right)F(r)\end{aligned}, \tag{6}$$

where r is the distance between atoms, $F(r)$ the cutoff function as in [5], and $e_{ll'm}$, $f_{ll'm}$, $g_{ll'm}$, and $t_{ll'm}$ are an additional set of 40 parameters (or 56 for the, A-B interactions) to be determined by fitting to the first-principles results. Since one usually fits to a nonorthogonal Hamiltonian, an additional set of 40 parameters is used (56 for A-B) for the overlap matrix following [6]. In cases where the validity of the parameters for interatomic distances much smaller than those in the original databases needs to be extended, one finds that the following form of overlap parameters is more successful

$$\begin{aligned}S_{ll'm}(r) &= \left(\delta_{ll'} + p_{ll'm}r + q_{ll'm}r^2 + r_{ll'm}r^3\right)\\ &\quad\times \exp\left(-s_{ll'm}^2 r\right)F(r)\end{aligned}, \tag{7}$$

where $p_{ll'm}$, $q_{ll'm}$, $r_{ll'm}$, and $S_{ll'm}$ are the corresponding parameters of the overlap matrix and $\delta_{ll'}$ is the Kronecker delta.

In most TB approaches (Cleri and Rosato, 1993; Harrison, 1989), as well as in all the so-called "glue" potential atomistic methods (Finnis and Sinclair, 1984), one writes the total energy as a sum of a band energy term (sum of eigenvalues) and a repulsive potential $G[n(r)]$ that can be viewed as replacing all the charge density-dependent terms appearing in the total energy expression of the density-functional theory. The NRL-TB method has the unique feature that eliminates G by the following ansatz: a quantity V_0 is defined as

$$V_0 = G[n(r)]/N_e, \tag{8}$$

where N_e is the number of valence electrons and $n(r)$ is the charge density. All the first-principles eigenvalues $\varepsilon_i(\boldsymbol{k})$ are then shifted by the constant V_0, and the shifted eigenvalue is defined as

$$\varepsilon_i'(\boldsymbol{k}) = \varepsilon_i(\boldsymbol{k}) + V_0 \tag{9}$$

The result of this manipulation is that the first-principles total energy E is given by the expression

$$E = \sum \varepsilon_i'(\boldsymbol{k}) \tag{10}$$

where the sum is over all occupied bands and all k-points in the Brillouin zone. It is noted that the constant V_0 is different for each volume and structure of the first-principles database. The reader should recognize that each band structure has been shifted by a constant, retaining the exact shape of the first-principles bands. It should also be stressed that all this is done to the first-principles database before one proceeds with the fit that will generate the TB Hamiltonian. The next step is to use a least-squares procedure to fit this database with the shifted eigenvalues ε_i to the TB Hamiltonian.

A typical database in the NRL-TB method contains, for example, in a transition metal, five volumes each for the f.c.c. and b.c.c. structures and often the s.c. lattice to achieve better transferability to other periodic structures or defect structures.

The TB method can also be extended to cover magnetism. In this case, a set of spin-polarized parameters are constructed by fitting to spin-polarized linearized augmented plane wave (LAPW) calculations. Common hopping [6] and overlap [7] parameters are used for the majority and minority spin cases, but separate onsite [4] parameters for each channel are developed. Each channel is then diagonalized separately. A set of paramagnetic TB parameters is constructed by averaging the majority and minority spin onsite parameters. Next the pressure-induced ferromagnetic-to-paramagnetic transitions are studied by noting whether the spin-polarized or paramagnetic parameters produce lower energies. Currently well-tested parameters for Fe, Co, and Ni are available (Bacalis et al., 2001; Mehl and Papaconstantopoulos, 2005).

The parameters are fit to reproduce the first-principles total energies and eigenvalues by using the Levenberg-Marquardt algorithm to minimize the mean square error of the expression (McGrady and Papaconstantopoulos, 2021)

$$M = \sum_{i}^{j} w_E(i)\left|E_{LAPW}(i) - E_{TB}(i)\right|^2 + \sum_{i,j,n} w_B(i,k,n)\left|\epsilon_{LAPW}(i,\ k,\ n) - \epsilon_{TB}(i,\ k,\ n)\right|^2 \tag{11}$$

In Eq. 11, w_E is the weighting factor for the total energy for structure i, w_B the weight for the bands, E_{LAPW} and E_{TB} are the respective first-principles and TB total energies for the i^{th} structure and ε_{LAPW} and ε_{TB} are the eigenvalues for the nth band and the k^{th} k-point of the i^{th} structure.

Technical procedure

The first-principles calculations were done either with the muffin-tin potential augmented plane wave (APW) method or with the full-potential LAPW method. The small differences between these two approaches, especially for closed packed structures, are within the error one makes after fitting to the TB Hamiltonian.

For the f.c.c., b.c.c., and s.c. structures uniform *k*-point meshes that include the origin and contain 89, 55, and 35*k*-points in the irreducible part of the Brillouin zone, respectively, are used. In most cases, the Hedin-Lundqvist parametrization of the local density approximation (LDA) to the density-functional theory (DFT) is used. In some cases, such as for spin-polarized iron (Bacalis et al., 2001), the generalized gradient approximation (GGA) has been used. Spin-polarized calculations were performed for the appropriate metals in the 3*d* transition series. For a typical transition metal, there are ~4000 eigenvalues and energies in the database. An IMSL package is used, based on a finite-difference Levenberg-Marquardt algorithm, to adjust the 93 parameters involved to reproduce this database by means of a nonlinear least-squares fit, with the total energies typically weighted ~200 times larger than the eigenvalues in a single band. Starting parameters are selected guided by those found in the previous work and it is ensured that the symmetry of the eigenstates is taken into account. This is an important issue because a block-diagonalization of the Hamiltonian avoids the possibility of incorrectly aligning the bands and preserves the angular momentum character of the states. For details of this symmetrization procedure, refer to (Mehl and Papaconstantopoulos, 1996).

Another issue is the number of bands per *k*-point used in the fit. Both occupied and empty states are fitted. For example, in the transition metals, the lowest six bands for all *k*-points are fitted but the bands 7–9 are also included for the four high-symmetry points. With this choice, one obtains reliable values for the SK parameters that correspond to the *p*-orbitals. The fitting RMS errors are in the range 1–5 mRy for six bands and ~0.5 mRy for the total energies. For the semiconductors, eight bands, divided into four valence and four conduction bands in an *s-p* basis are fitted. Here, the RMS error is ~5 mRy for the valence bands but much higher for the conduction bands. There is a very significant improvement in the conduction bands upon inclusion of the *d*-orbitals. However, the *s-p* basis gives a very good fit to the total energy with an RMS error not exceeding 0.5 mRy.

Fig. 1 shows an example of the accuracy of the TB fit: we show a comparison between the TB and LAPW energy bands for hcp beryllium (McGrady and Papaconstantopoulos, 2021). Clearly the TB Hamiltonian accurately reproduces the first-principles results.

Ground-state behavior and phase stability

The NRL-TB Hamiltonians have been tested to give the correct ground state for all materials for which TB parameters have been generated. The results are summarized in Tables 1 and 2. Table 1 shows the equilibrium lattice constants and bulk moduli for all the materials studied, comparing them to first-principles LDA calculations and to experiment. The equilibrium lattice constant is typically within 1–2% of the LDA value and correspondingly very close to the measured values. In this table, the magnetic elements are spin-polarized in a manner consistent with the observed magnetic structure. Thus, one can find that the ground state of chromium is an anti-ferromagnetic CsCl phase, which is a good approximation to the experimentally observed spin density wave.

Similarly, the equilibrium bulk moduli are in good agreement with the first-principles results, within 10% for most elements. Except for Ti, the h.c.p. phases were not fit to first-principles results, but instead predicted as an output of the TB scheme. As a result, the equations of state predicted by the TB model are not as accurate as for the cubic lattices. The largest error is for zirconium, where *a* is 7% smaller than experiment and *c* is 8% larger. Yttrium and hafnium also show large discrepancies between the TB model and experiment. The lattice constants for the other elements are within 2% of experiment, consistent with the errors one would find in first-principles calculations. The discrepancies from experiment found in Zr, Y, and Hf can be removed by including h.c.p. and, if necessary, the simple cubic lattice.

For Ti, the GGA calculations were fitted with the h.c.p. and s.c. lattices (Mehl and Papaconstantopoulos, 2005). In this more elaborate fit, it was possible to improve on the lattice constants and differentiate between the h.c.p. and ω phases. This TB method

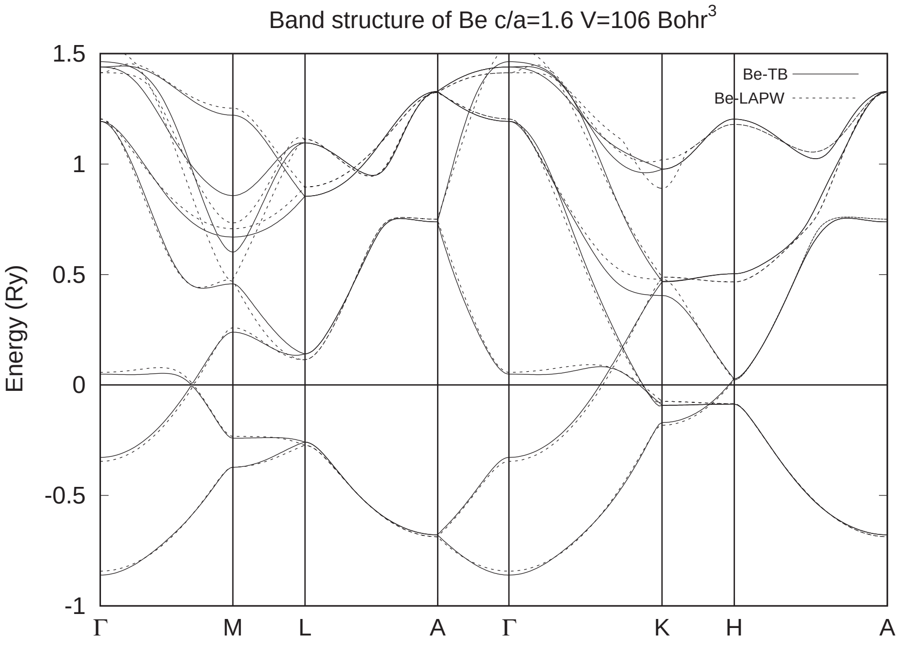

Fig. 1 Comparison of the bands from the NRL-TB and LAPW methods for the HCP Be structure with c/a = 1.6 and a volume of 106 Bohr^3 (McGrady and Papaconstantopoulos, 2021). The LAPW bands are shown with a dashed line and the NRL-TB results are shown with a solid line. The Fermi energy is at 0 Ry.

Table 1 Equilibrium lattice constants and bulk moduli for the experimentally observed ground-state structures of the elements, comparing the results of the TB parametrization (Bernstein et al., 2000, 2002; Gotsis et al., 2002; McGrady et al., 2014; McGrady and Papaconstantopoulos, 2021; Mehl and Papaconstantopoulos, 1996; Wang et al., 2003; Yang et al., 1998), first-principles DFT, where available, and experiment

Element	*Structure*	*a (Å)*			*c (Å)*			*B₀ (GPa)*		
		TB	*DFT*	*Expt.*	*TB*	*DFT*	*Expt.*	*TB*	*DFT*	*Expt.*
Li*	b.c.c.	3.40	3.39	3.49	*a*	*a*	*a*	26	30	12
Be*	h.c.p.	4.25	4.28	4.32	6.80	6.72	6.78	115	124	127
B*	rhomb	4.90		12.43	4.91		12.57	250	226	
C	dia	3.52	3.53	3.57	*a*	*a*	*a*	480	468	443
Mg	h.c.p.	3.22	3.16	3.21	5.26	5.02	5.21	34	39	35
Al	f.c.c.	4.00	3.99	4.05	*a*	*a*	*a*	80	70	72
Si	dia	5.43	5.40	5.43	*a*	*a*	*a*	108	96	99
Ca	f.c.c.	5.35	5.28	5.58	*a*	*a*	*a*	16	19	15
Ca*	f.c.c.	5.51	5.55	5.58	*a*	*a*	*a*	15	16	15
Sc	h.c.p.	3.26	3.21	3.31	4.91	5.01	5.27	63	65	44
Ti	h.c.p.	2.94	2.94	2.95	4.56	4.65	4.68	112	112	107
V	b.c.c.	2.94	2.93	3.03	*a*	*a*	*a*	211	196	162
Cr	CsCl	2.79		2.88	*a*	*a*	*a*	305		190
Mn	αMn	8.64		8.91	*a*	*a*	*a*	248		60
Fe	b.c.c.	2.84	2.83	2.87	*a*	*a*	*a*	180	197	168
Co	h.c.p.	2.54		2.51	4.01		4.07	237		191
Ni	f.c.c.	3.43	3.52	3.52	*a*	*a*	*a*	264	200	186
Cu	f.c.c.	3.54	3.56	3.61	*a*	*a*	*a*	106	195	137
Zn	h.c.p	4.87		5.03	8.89		9.35	41		66
Ga	αGa	4.63	4.38	4.51	4.52	4.35	4.52	651	669	613
		7.63	7.39	7.64						
Ge	dia	5.60	5.61	5.66	*a*	*a*	*a*	67	78	77
Sr	f.c.c.	5.73	5.74	6.08	*a*	*a*	*a*	15	16	12
Sr*	f.c.c.	6.09	6.05	6.08	*a*	*a*	*a*	11.5	11	12
Y	h.c.p.	3.59	3.52	3.65	5.35	5.61	5.73	46	48	37
Zr	h.c.p.	2.99	3.17	3.23	5.57	5.14	5.15	108	119	83
Nb	b.c.c.	3.25	3.25	3.30	*a*	*a*	*a*	185	193	170
Mo	b.c.c.	3.12	3.12	3.15	*a*	*a*	*a*	283	291	272

Table 1 (Continued)

Element	*Structure*	*a (Å)*			*c (Å)*			*B_0 (GPa)*		
		TB	*DFT*	*Expt.*	*TB*	*DFT*	*Expt.*	*TB*	*DFT*	*Expt.*
Tc	h.c.p.	2.72		2.74	4.34		4.40	304		297
Ru	h.c.p.	2.68		2.71	4.26		4.28	360		321
Rh	f.c.c.	3.77	3.76	3.80	*a*	*a*	*a*	306	309	270
Pd	f.c.c.	3.85	3.85	3.89	*a*	*a*	*a*	212	220	181
Ag	f.c.c.	4.02	4.00	4.09	*a*	*a*	*a*	109	154	132
Cd	h.c.p.	5.51		5.63	10.37	10.62		53		52
In	b.c.t.	4.29	4.60	5.10	*a*	*a*	*a*			
Sn	dia	6.48	6.47	6.49	*a*	*a*	*a*	45	45	53
Ba	b.c.c.	4.82	4.80	5.02	*a*	*a*	*a*	10	11	10
La*	d.h.c.p.	3.62	3.62	3.77	11.68	11.68	12.1	28.0	30.0	24.3
Yb	f.c.c.	5.40	5.40	5.48	*a*	*a*	*a*	26.4	16	13.3
Hf	h.c.p.	3.07	3.18	3.19	5.08	5.15	5.05	111	110	109
Ta	b.c.c.	3.30	3.24	3.30	*a*	*a*	*a*	185	224	200
W	b.c.c.	3.14	3.14	3.16	*a*	*a*	*a*	319	333	323
Re	h.c.p.	2.78	2.77	2.76	4.39	4.50	4.46	371	388	372
Os	h.c.p.	2.75	2.73	2.74	4.31	4.39	4.32	441	440	418
Ir	f.c.c.	3.86	3.82	3.84	*a*	*a*	*a*	389	401	355
Pt	f.c.c.	3.90	3.90	3.92	*a*	*a*	*a*	318	305	278
Au	f.c.c.	4.06	4.06	4.08	*a*	*a*	*a*	181	198	169
Pb	f.c.c.	4.88	4.88	4.95	*a*	*a*	*a*	50	54	45
Po	s.c.	3.26	3.34	3.35	*a*	*a*	*a*	59	44	26
Ac	f.c.c.	5.52	5.50	5.31	*a*	*a*	*a*	25.9	27.6	
Th*	f.c.c.	5.08	5.08	5.08	*a*	*a*	*a*	47.3	57.7	54.0

First-principles calculations were done within the LDA except for those rows marked with an asterisk, which have GGA calculations.

The "CsCl" structure given for Cr is described in the text. Note that gallium has an orthorhombic structure, so values for lattice constants *a* and *b* are both given in the *a* columns.

Table 2 TB energies discussed in the text.

Struct.	*f.c.c.*	*b.c.c.*	*h.c.p.*	*dia*	*βSn*	*b.c.t.*	*gra.*	*αMn*	*s.c.*
Struk.	*A1*	*A2*	*A3*	*A4*	*A5*	*A6*	*A9*	*A12*	*A_h*
Li*	–0.7	0.0	–0.4	–	–	–	–	–	9.5
Be*	6.2	6.6	0.0	118.					73.5
B*	108.7	135.9			44.9	107.6			93.1
C	306.6	302.3	307.4	1.1	1.1	120.2	0.0	41.7	206.0
Mg	0.8	3.6	0.0	74.5	19.9	2.7	68.0	5.0	28.3
Al	0.0	8.1	2.0	61.0	22.5	5.2	42.2	4.2	29.4
Si	36.4	34.8	36.6	0.0	26.5	34.8	58.6	32.2	20.4
Ca	0.0	2.2	0.8	144.1	28.2	2.3	85.9	6.0	39.9
Ca*	0.0	1.4	2.8	70.1	–	–	–	–	29
Sc	4.7	8.6	0.0	101.1	13.5	7.8	49.8	10.3	35.5
Ti	5.1	7.5	0.0	171.6	26.9	7.0	73.8	14.1	57.9
V	19.7	0.0	20.9	180.3	48.2	13.5	112.3	11.8	76.7
Cr	28.7	0.0	30.6	228.2	78.6	26.7	134.4	20.4	119.3
Mn	7.4	14.3	2.8	171.3	60.4	7.4	80.9	0.0	90.0
Fe	9.8	0.0	11.8	76.7	34.0	8.4	61.4	8.0	47.6
Co	2.7	13.1	0.0	92.4	28.0	11.1	48.4	3.4	57.8
Ni	0.0	8.1	2.3	89.7	33.7	5.4	53.9	3.8	55.7
Cu	0.0	2.6	0.4	81.3	27.2	2.6	59.0	6.1	39.3
Zn	3.2	8.4	0.0	40.4	14.0	–	30.8	5.2	15.9
Ge	17.3	20.7	19.6	0.0	15.5	19.4	48.1	19.8	12.4
Sr	0.0	16.4	15.3	87.2	30.6	14.9	59.1	24.4	36.2
Sr*	0.0	0.2	0.2	71.8	–	–	–	–	26
Y	2.3	8.8	0.0	97.9	16.7	8.0	46.9	8.6	34.3
Nb	29.6	0.0	28.8	187.7	42.8	14.0	111.6	15.4	74.1
Mo	29.7	0.0	30.6	147.0	48.4	24.9	90.8	17.2	68.8

(*Continued*)

Table 2 (Continued)

Struct. *Struk.*	*f.c.c.* *A1*	*b.c.c.* *A2*	*h.c.p.* *A3*	*dia* *A4*	*βSn* *A5*	*b.c.t.* *A6*	*gra.* *A9*	*αMn* *A12*	*s.c.* *A_h*
Tc	6.1	23.4	0.0	72.9	43.4	21.8	53.3	0.2	56.8
Ru	7.5	50.9	0.0	134.5	80.8	42.0	124.8	16.4	106.2
Rh	0.0	31.6	5.0	159.7	68.0	17.2	120.5	16.2	96.2
Pd	0.0	10.2	2.6	148.8	60.9	8.6	109.1	9.3	85.0
Ag	0.0	2.8	0.6	66.1	18.2	2.5	50.2	6.0	24.6
Cd	2.5	8.5	0.0	45.5	17.0	–	35.1	4.2	21.8
Ba	0.8	0.0	0.0	12.0	14.1	0.8	52.4	2.8	23.9
Hf	0.9	7.1	0.0	380.3	73.8	6.9	203.9	22.9	115.9
Ta	24.6	0.0	25.4	188.7	39.8	11.8	107.4	9.0	64.6
W	35.8	0.0	38.1	159.3	76.5	31.7	124.8	18.2	115. 0
Re	9.1	28.1	0.0	38.8	35.1	26.2	35.1	0.2	55.3
Os	7.9	66.0	0.0	11.8	44.4	47.5	65.5	17.8	59.0
Ir	0.0	49.9	8.3	83.7	57.7	20.2	96.6	23.9	83.4
Pt	0.0	10.0	4.8	169.0	54.8	5.0	131.9	14.5	79.1
Au	0.0	1.0	0.7	70.6	15.4	0.5	55.4	8.1	20.4
Ac	0.0	10.0	2.0	125.					49
Th*	0.0	15.	7.	149.					66
Pb	0.0	4.6	2.2	14.6	13.3	2.5	24.2	1.2	19.1
Po	21.3	14.4	5.7	23.9	7.4	22.0	14.5	1.3	0.0

The energy of the experimental ground-state structure is arbitrarily set to zero. Energies for boron are relative to the R105 ground state (McGrady et al., 2014). All energies are calculated at the equilibrium volume found by the TB fit and are expressed in mRy. Below the common name of each phase is its *Strukturbericht* designation. The fit was made using LDA first-principles results except for those rows marked with an asterisk, which were fit to GGA results (Mehl and Papaconstantopoulos, 1996; Bernstein et al., 2000, 2002; Gotsis et al., 2002; McGrady et al., 2014, McGrady and Papaconstantopoulos, 2021; Sha et al., 2011; Durgavich et al., 2016)

succeeds in predicting the correct ground state for all materials presented here. Fig. 2 shows the energy volume curves for a representative sample of materials that crystallize in different structures. The results for all the elements are summarized in Table 2, which shows the equilibrium energy of each of these phases expressed as the difference in energy between that phase and the equilibrium energy of the experimental ground state. The energy of each crystal structure is computed by doing a conjugate-gradient minimization of the total energy with respect to all the parameters in the lattice, internal (atomic positions) as well as external (a, c, etc.). The TB method correctly predicts the ground-state structure for all metals including the ferromagnetic metals iron, cobalt, and nickel. The results are also consistent with the accepted crystal structure for the semiconductors Si and Ge, and with the more complex structures of Mn, Ga, and In.

As a further example, Fig. 3 shows the energy/volume behavior of boron (McGrady et al., 2014) in a variety of structures. The low energy states of boron are all consist of differing arrangements of regular icosahedra, a structure not seen in other elements. Tight-binding parameters were fit to DFT results for the f.c.c., b.c.c., s.c., and dhcp and boron R12 structure, the simplest of the boron structures. These parameters correctly predict the R105 structure to be lower in energy than the other known boron structures, however the R105 + vacancy structure is found to be the ground state. There is some uncertainty in the R105 structure, with some models only partially filling some sites. The prediction of a vacancy structure may be a reflection of these models.

The fact that this method finds the correct ground states of the h.c.p. metals and the other complex structures that were not included in the fit of the TB parameters should be emphasized.

The robustness of the TB parameters has also been established by studying crystal structures of lower symmetry such as the volume-conserving tetragonal strain, the so-called Bain path. The Bain path of Mo at the experimentally observed equilibrium volume of the b.c.c. phase is shown in Fig. 4 (Mehl and Papaconstantopoulos, 1996). The energy is properly a minimum for the b.c.c. lattice, where $c/a = 1$, and attains a local maximum at the f.c.c. structure ($c/a = \sqrt{2}$). This shows that the f.c.c. elastic constant associated with tetragonal shear, $C_{11} - C_{12}$, is negative; hence, the f.c.c. structure is unstable.

Elastic constants

Elastic constants measure the proportionality between strain and stress in a crystal, provided that the strain is not so large as to violate Hook's law. Computationally, the elastic constant is determined by applying a strain to a crystal, measuring the energy versus strain, and determining the elastic constant from the curvature of this function at zero strain (Mehl et al., 1994). A given strain is associated with a certain linear combination of elastic constants. For cubic systems, including diamond, there are three independent elastic constants, C_{11}, C_{12}, and C_{44}. One linear combination of the elastic constants is obtained from the bulk modulus

$$B(V) = VE''(V) = 1/3(C_{11} + 2C_{12}) \tag{11}$$

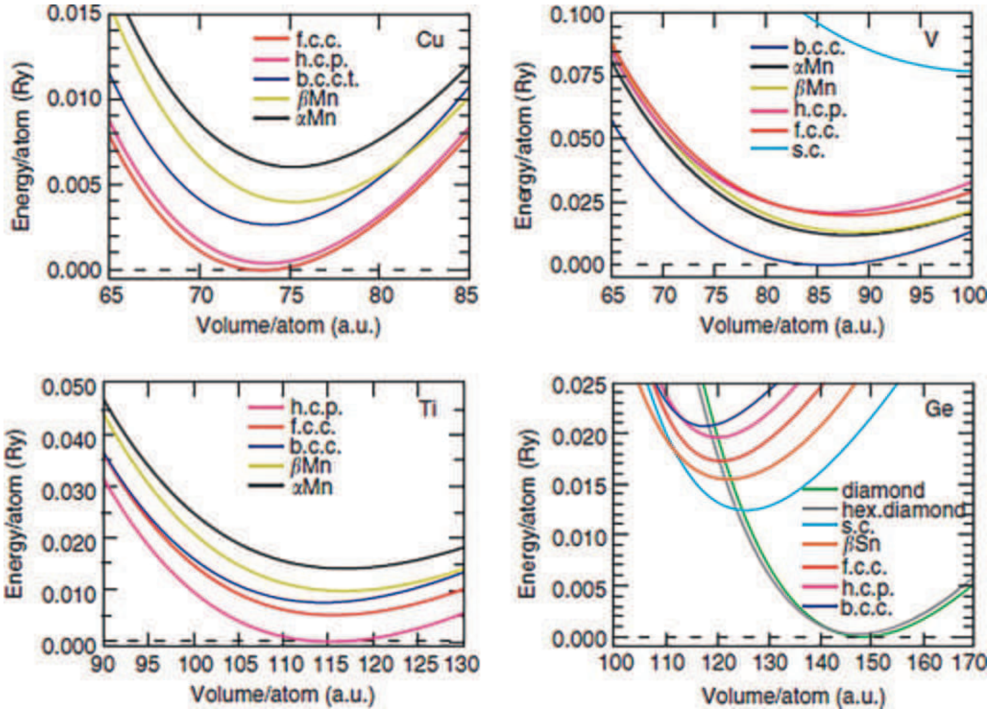

Fig. 2 Energy vs. volume curves for various phases of (clockwise from the top left) copper, vanadium, germanium, and titanium, using the NRL-TB parameters described in the text. Note that the method correctly predicts the equilibrium structure (Bernstein et al., 2002; Mehl and Papaconstantopoulos, 1996, 2002).

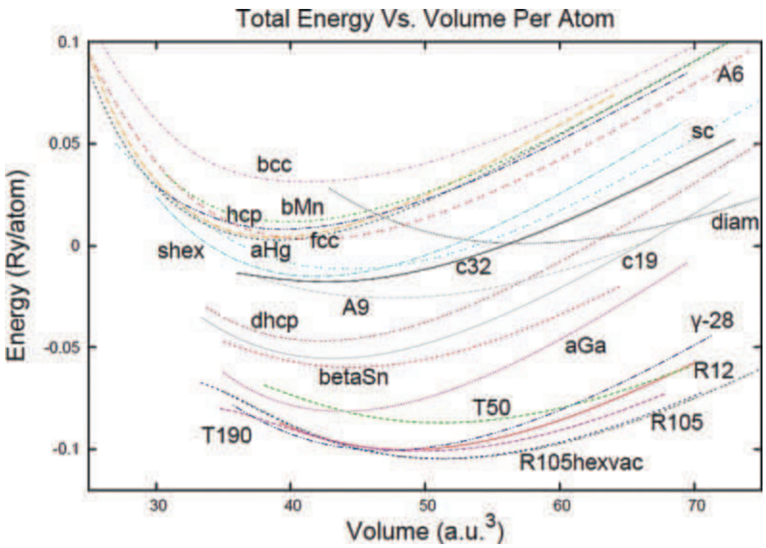

Fig. 3 Energy per atom versus volume per atom for possible structures of boron using the NRL tight-binding fit (McGrady et al., 2014). The R105$_{\text{hexvac}}$ structure is the minimum energy of the R105 structure with one vacancy. The R12 structure was included in the tight-binding fit along with the standard structures. The energies of the remaining boron structures (R105, R105$_{\text{hexvac}}$, T190, T50, γ-28) are predicted from this fit.

where V is the unit cell volume. A second combination is most easily obtained by straining the crystal in the (1 0 0) direction while simultaneously compressing it in the (0 1 0) direction to conserve the volume, with lengths in the (0 0 1) direction remaining fixed. If x is the fractional change in the (10 0) direction, then,

$$E(x) = E_0 + V\,(C_{11} - C_{12})\,x^2 + O(x^4) \tag{12}$$

where the function, $E(x)$ measures the energy as a function of strain. Finally, one finds C_{44} by straining the crystal in the (1 1 0) direction and fixing the volume by compressing in the $(1\bar{1}0)$ direction. In this case,

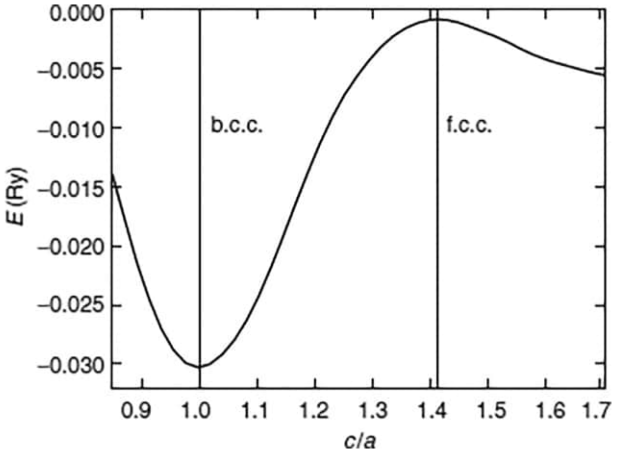

Fig. 4 TB calculation of the energy of molybdenum, at the experimental equilibrium volume, under a tetragonal strain, as a function of *c/a*. The vertical lines denote the positions of the b.c.c. and f.c.c. lattices (Mehl and Papaconstantopoulos, 1996).

$$E(x) = E_0 + \frac{1}{2} V C_{44} x^2 + O(x^4) \tag{13}$$

Note that for diamond the calculation of C_{44} requires the minimization of the total energy with respect to an internal parameter at each strain.

The calculation of elastic constants assesses the ability of the method to determine properties not included in the fitting database. The elastic constants of the cubic materials calculated by the NRL-TB approach are compared to the experimental values in Table 3. These calculations were performed at the experimental volume and therefore they are not consistent with the equilibrium value of B found in Table 1. The deviation of the calculated C_{11} and C_{12} from the measured values is within 10–15% which is very close to the error one finds when comparing with a direct evaluation from first-principles calculations.

An inspection of Table 3 reveals somewhat larger errors for C_{44}. A solution to this problem is to fit C_{44} either to LAPW calculations or to experiment. It should be noted here that calculations of C_{ij} in the alkaline-earth metals is problematic because the lattice is extremely soft. One can also note that the method correctly reproduces the sign of the elastic constant difference $C_{12}-C_{44}$, even in the metals rhodium and iridium, and the semiconductors Si and Ge where it is negative. It is worth mentioning that this negative sign cannot be obtained from the standard embedded-atom method, and that a model with only central forces would have $C_{12} = C_{44}$, the Cauchy relationship.

The elastic constants for the h.c.p. structure are C_{11}, C_{12}, C_{13}, C_{33}, and C_{44} (Mehl et al., 1994). The elastic constants found by the NRL-TB method show larger relative deviations from experiment than found in the cubic crystals. These were found from TB parameters fitted only to cubic lattices. It is shown, in the case of Ti, that if one extends the fitting database to include the h.c.p. lattice as well, there is a dramatic improvement in the comparison of TB and measured elastic constants.

Vacancies

Vacancy formation energies have been calculated by a supercell method. One atom in the supercell is removed and neighboring atoms are allowed to relax around this vacancy while preserving the symmetry of the lattice. The great advantage of the NRL-TB method over first-principles approaches is that one can do the calculation in a very large supercell, in a computationally efficient manner, including relaxation. It is found that a supercell containing 128 atoms is sufficient to eliminate the vacancy-vacancy interaction. The vacancy formation energy is given by

$$E_{\text{vac}}(N) = E(N-1) - (N-1)\, E(N, 0)/N \tag{14}$$

where $E(M, Q)$ is the total energy of a supercell containing $M + Q$ sites, where M are occupied by atoms and Q are vacant, whence $E(N,0)$ is N times the energy of one atom in its bulk crystal structure. The experimental lattice constant is used to set the volume of the system, since under experimental conditions the lattice constant of a metal containing isolated vacancies will be the lattice constant of the bulk metal.

Calculated values of the vacancy formation energy of the metals (Mehl and Papaconstantopoulos, 1996) (in eV) are shown in Table 4. (Note that vacancy formation energies for Si and Ge are shown in Table 6). Relaxation around the vacancy was included via a conjugate gradient procedure but it introduced, not unexpectedly, a small effect. Where available, it is compared to both first-principles calculations and experiment (Schaefer, 1987). The results for niobium, silver, tantalum, and iridium are in excellent agreement with experiment. The vacancy formation energies for rhodium, tungsten, and platinum do not compare well with

Table 3 Elastic constants for cubic elements (in GPa).

		TB			*Exp.*		
Element	*Structure*	C_{11}	C_{12}	C_{44}	C_{11}	C_{12}	C_{44}
Li*	b.c.c.	36.7	20.7	8.2			
C	dia	1036	48	601	1076	125	576
Al	f.c.c.	125	58	26	103	53	28
Si	dia	179	73	95	166	64	80
Ca	f.c.c.	15	10	14	16	12	8
Ca*	f.c.c.	18.	12.7	17.	16	12	8
V	b.c.c.	224	106	92	228	119	43
Fe	b.c.c.	223	95	78	237	141	69
Cu	f.c.c.	146	86	76	168	122	75
Ge	dia	133	20	107	131	49	68
Sr	f.c.c.	8	3	−3	15	6	10
Sr*	f.c.c.	13.8	10.3	11.3	15	6	10
Nb	b.c.c.	277	139	37	246	139	29
Mo	b.c.c.	453	147	120	450	173	125
Rh	f.c.c.	491	171	260	433	185	206
Pd	f.c.c.	233	163	63	227	176	72
Ag	f.c.c.	150	87	48	130	90	46
Sn	dia	68	30	38	67	36	30
Yb	f.c.c.	36.3	21.42	36.17			
Ta	b.c.c.	275	140	78	261	157	82
W	b.c.c.	529	170	198	523	203	160
Ir	f.c.c.	694	260	348	590	249	262
Pt	f.c.c.	380	257	71	347	251	76
Au	f.c.c.	195	174	40	189	159	42
Ac	f.c.c.	41.21	18.2	22.68			
Th*	f.c.c.	91.50	25.20	33.82	95.93	33.04	31.0
Pb	f.c.c.	53	35	19	47	39	14
Po	s.c.	128	13	6			

All calculations were fit to LDA first-principles results except for those rows marked with an asterisk, which were fit to GGA calculations (Bernstein et al., 2000, 2002; McGrady et al., 2014; McGrady and Papaconstantopoulos, 2021; Mehl and Papaconstantopoulos, 1996, 2002; Papaconstantopoulos et al., 1998; Wang et al., 2003; Durgavich et al., 2016).

All elements for which a set of TB parameters have been constructed and for which one has a cubic ground state (except manganese) are presented here. A comparison is made between the results of the TB parametrization and experiment. Calculations were performed at the experimental volume.

Table 4 TB vacancy formation energies compared to first-principles calculations and experiment.

	TB			
Element	*Fixed*	*Relaxed*	*DFT*	*Exp.*
Al	0.49	0.40	0.56, 0.84	0.66
Ca*	–	0.66	EAM 0.95	
Cu	1.29	1.18	1.41, 1.29	1.28–1.42
Sr*		1.03	EAM 0.97	
Nb	2.84	2.82		2.62 ± 0.03
Mo	2.63	2.46		3.0–3.6
Rh	3.39	3.35	2.26	1.71
Pd	2.46	2.45	1.57	1.85 ± 0.25
Ag	1.31	1.24	1.20, 1.06	1.11–1.31
Ta	3.17	2.95		2.9 ± 0.4
W	6.86	6.43		4.6 ± 0.8
Ir	2.19	2.17		1.97
Pt	2.79	2.79		1.35 ± 0.09
Au	1.24	1.12		0.89 ± 0.04
Ac		1.68		
Th*		1.71		0.95
Pb	0.76	0.64		0.54

The LDA density functional was used for fitting and comparisons, except for those rows marked with an asterisk, which use GGA. All energies are in eV (Mehl and Papaconstantopoulos, 1996).

Energies were computed using a 128-atom supercell. Calculations with the atoms at the primitive lattice sites in the crystal (fixed) and allowing relaxation around the vacancy (relaxed) are shown. First-principles calculations of the vacancy formation energy are given in the column labeled "LDA." The experimental column shows a range of energies if several experiments have been tabulated. Otherwise, the estimated error in the experiment is given. TB results are from Mehl and Papaconstantopoulos (1996). Experimental data are from Schaefer (1987).

experiment. Aluminum is an intermediate case. It is possible that the measured values are not reliable. Otherwise, there may be a need to check these results against first-principles data and perhaps fit to DFT calculations.

Surfaces

Surface energies are also calculated by a supercell technique (Haftel et al., 2004; Lekka et al., 2003a, 2003b; Mehl and Papaconstantopoulos, 1996). A slab of metal is formed by cleaving the crystal along the desired plane, creating two identical free surfaces. The distance between the two surfaces is increased, creating a set of slabs that repeat periodically in the direction perpendicular to the surfaces. The slabs are separated by a large region of vacuum so that the electrons on one slab cannot hop to a neighboring slab. In addition, the slabs must be thick enough so that the atoms at the center of the slab have the electronic properties of atoms in the bulk material and the two surfaces on the same slab cannot interact with each other. It is found that these criteria are met if slabs containing 25 atomic layers and 7–13 layers between slabs depending on the direction of the surface are used. Care should be taken with respect to the *k*-point mesh convergence. Depending on the surface and underlying bulk structure, this requires ~200*k*-points in the two-dimensional Brillouin zone. The surface energy, expressed as the energy required to create a unit area of new surface, is then given by the formula

$$E_{\mathrm{surf}} = (E_{\mathrm{slab}} - N\,E_{\mathrm{bulk}})/(2\,A), \tag{15}$$

where A is the area occupied by one unit cell on the surface of the slab, E_{slab} is the total energy of the slab, N is the number of atoms in the unit cell, and E_{bulk} is the energy of one atom in the bulk at the lattice constant of the atoms in the interior of the slab. In the first surface calculations, the bulk equilibrium lattice parameters with no relaxation or reconstruction at the surface were used. These calculations showed reasonable agreement with experiment indicating that relaxation does not seriously affect the surface energy. However, recently calculations with all atoms completely relaxed were performed, including charge self-consistency. The new results for Nb (Lekka et al., 2003b) and several f.c.c. metals (Haftel et al., 2004) show significant differences in the interlayer separations and reconstruction.

The results for the f.c.c. metals are particularly gratifying. For the f.c.c. metals, it is found that $E(1\ 1\ 1) < E\ (1\ 0\ 0) < E\ (1\ 1\ 0)$, which means that close-packed surfaces are the most stable for the f.c.c. metals. For the b.c.c. metal surface energies, the opposite inequality is satisfied, $E(1\ 1\ 0) < E(1\ 0\ 0) < E\ (1\ 1\ 1)$.

Stacking faults

Stacking faults are introduced in a crystal by cutting a perfect crystal block along a plane and shifting the upper part with respect to the lower part by a vector f, defining the generalized stacking fault energy surface (Mehl et al., 2000). Local energy minima on this surface are called stable intrinsic stacking faults. In f.c.c. systems and for the (111) slip plane, the stable stacking fault corresponds to a slip of $a/\sqrt{6}$ in the $<1\ 2\ 1>$ direction. The $<1\ 2\ 1>$ slip is modeled on a (1 1 1) slip plane by a supercell consisting of nine close-packed (1 1 1) planes of atoms. The primitive vectors of the supercell are

$$\begin{aligned}\boldsymbol{a}_1 &= \frac{1}{2}a\hat{y} + \frac{1}{2}a\hat{z}\\ \boldsymbol{a}_2 &= \frac{1}{2}a\hat{x} + \frac{1}{2}a\hat{z}\\ \boldsymbol{a}_3 &= \left(3 + \frac{q}{6}\right)a\hat{x} + \left(3 + \frac{q}{6}\right)a\hat{y} - \left(3 - \frac{q}{3}\right)a\hat{z}\end{aligned} \tag{16}$$

where q is the stacking fault displacement of the atoms in the boundary layer along the vector f in the $<1\ 1\ 2>$ direction. At $q = 0$, the atoms are in f.c.c. positions and at $q = 1$, at the h.c.p. positions. Since the calculations are computationally intensive because of the nine planes of atoms and the 4730*k*-points used in the irreducible part of the Brillouin zone, the NRL-TB method proves to be very efficient. The results of the stacking fault energy as a function of the displacement q are shown in Fig. 5. The results correctly predict the qualitative effect that the energies for Ir are much larger than that for the noble metals and they also agree with full-potential linearized muffin-tin orbital (FLMTO) results for Al, Ag and Ir. Finally, the value at the maximum energy in Fig. 5 has been used to extract the unstable stacking fault energy γ_{us}, which is used together with the surface energy γ_{surf} to establish the Rice criterion for ductility,

$$D = 0.3\,\gamma_{\mathrm{us}}/\gamma_{\mathrm{surf.}} \tag{17}$$

One finds, in agreement with experiment, that the noble metals have the largest values of D.

Phonons

Phonon frequencies at high-symmetry points in the Brillouin zone computed with the NRL-TB model using the frozen phonon approximation are compared with experimentally measured values in Table 5. In this table, results from metals and semiconductors

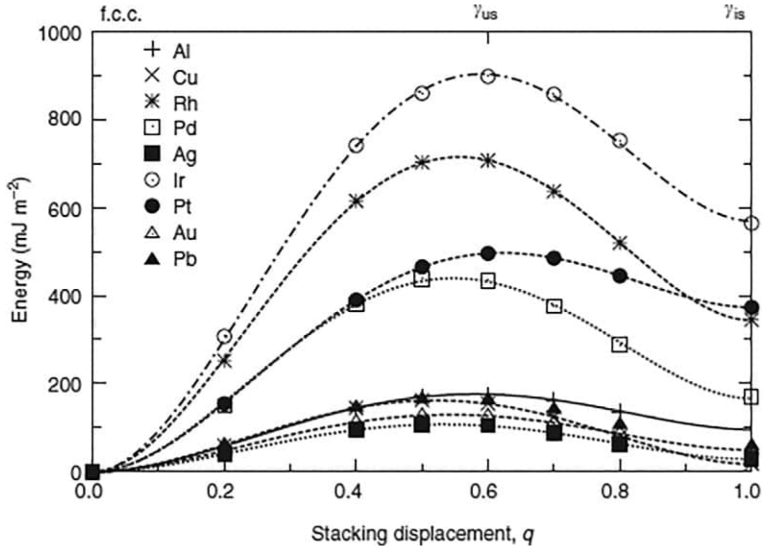

Fig. 5 Stacking fault energy as a function of the parameter *q* in [16] for the elemental f.c.c. metals, as determined by the NRL-TB method. The labels γ_{us} and γ_{is} indicate the positions of the unstable and intrinsic stacking faults, respectively, while the f.c.c. label on the left vertical axis indicates the position of the ground-state bulk structure (Mehl et al., 2000).

Table 5 Phonon frequencies (in THz) at high symmetry points for various elements (Gotsis et al., 2002; Mehl and Papaconstantopoulos, 2002; Papaconstantopoulos et al., 1998).

	Sym.	*TB*	*Exp.*
C	Γ_{25}'	39.3	39.9
(dia)	X_1	34.2	35.5
	X_3	29.8	32.1
	X_4	24.7	24.2
	L_1	39.3	36.6
	L_2'	36.5	31.0
	L_3^+	17.6	16.9
	L_3^-	35.3	36.2
Mg	Γ_3^+	12.1	7.3
(h.c.p.)	Γ_5^+	4.3	3.7
	A_1	7.1	2.9
	A_3	3.9	5.2
Si	Γ_{25}'	15.9	15.5
(dia)	X_1	12.1	12.3
	X_3	15.2	13.9
	X_4	4.8	4.5
	L_3^+	3.8	3.4
	L_3^-	16.0	14.7
Ca	X_3	3.45	4.52
(f.c.c)	X_5	3.12	3.63
	L_2’	4.26	4.61
	L_3	2.17	2.36
	W_2’	2.62	3.66
	W_3	3.20	4.61
	Δ_1	3.17	3.66
	Δ_5	2.55	2.36
Ti	Γ_3^+	5.7	5.5
(h.c.p.)	Γ_5^+	4.2	4.1
	A_1	5.3	5.7
	A_3	2.9	3.0
Cu	X_3	7.2	7.3
(f.c.c.)	X_5	4.4	5.1

(*Continued*)

Table 5 (Continued)

	Sym.	*TB*	*Exp.*
	L_2	7.9	7.3
	L_3	3.5	3.4
Ge	Γ_{25}'	9.7	9.1
(dia)	X_1	6.4	7.2
	X_3	8.9	8.3
	X_4	3.2	2.4
	L_1	9.3	8.7
	L_2'	5.2	6.7
	L_3^+	2.5	1.9
	L_3^-	7.3	7.3
Sr	X_3	3.56	3.17
(f.c.c.)	X_5	2.32	2.48
	L_2'	3.52	3.08
	L_3	1.49	1.74
	W_2'	2.31	2.57
	W_3	3.04	–
	Δ_1	2.32	1.90
	Δ_5	1.62	1.50
	Σ_1	2.92	2.70
	Σ_2	1.46	1.40
	Σ_3	2.49	2.40
Nb	H	6.3	6.5
(b.c.c.)	P	5.7	5.0
	N_2	4.9	5.1
	N_3	5.9	5.7
	N_4	4.4	3.9
Mo	H	4.1	5.5
(b.c.c.)			
Au	X_3	5.3	4.6
(f.c.c.)	X_5	2.9	2.7
	L_2	5.5	4.7
	L_3	1.9	2.0
Ac	X_3	2.35	
(f.c.c.)	X_5	1.84	
	L_2'	1.35	
	L_3	0.53	
	W_2'	1.83	
	W_3	1.58	
	Δ_1	1.56	
	Δ_5	1.04	
	Σ_1	1.71	
	Σ_2	1.12	
	Σ_3	1.35	
Th*	X_3	2.03	3.47
(f.c.c.)	X_5	3.34	2.26
	L_2'	2.78	3.24
	L_3	1.94	1.28
	W_2'	2.34	2.88
	W_3	3.35	2.22
	Δ_1	2.95	2.42
	Δ_5	1.97	1.59
	Σ_1	3.39	3.06
	Σ_2	1.94	2.24
	Σ_3	2.65	1.50
Pb	X_3	1.9	1.8
(f.c.c.)	X_5	1.0	0.9
	L_2	2.2	2.2
	L_3	1.0	0.9

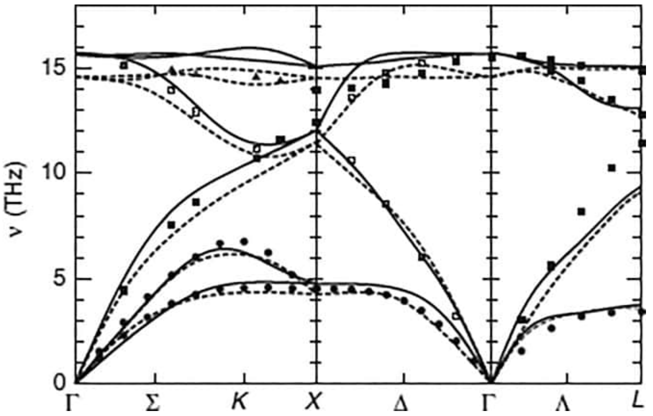

Fig. 6 Phonon dispersion curves for diamond-structured Si computed from the velocity-velocity correlation function found during a molecular-dynamics simulation at 300 K (solid line) and 1500 K (dashed line) (Bernstein et al., 2000). Dots are taken from experimental data (Tubino et al., 1972).

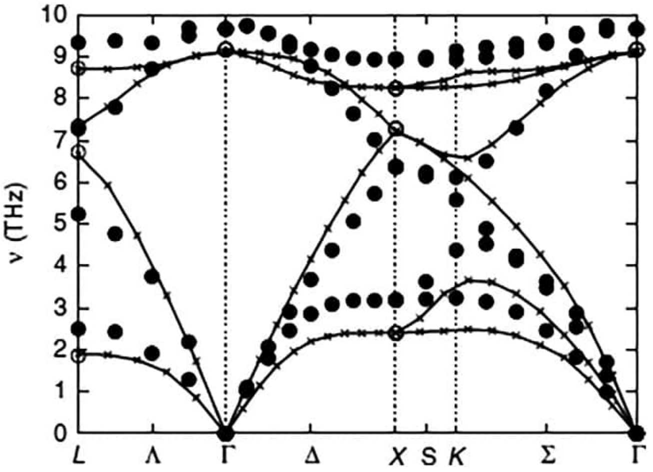

Fig. 7 Phonon frequencies along high symmetry lines in Ge using the *sp*^{3} basis TB parameters (Bernstein et al., 2002) (solid symbols) compared to DFT/LDA results (Giannozzi et al., 1991) (open symbols) and experiment (crosses) at 80 K (Nelin and Nilsson, 1972).

have been included. The agreement with experiment is similar to that with elastic constants. For most modes the TB results are within 15–20% of experiment, which is also comparable to phonon frequencies obtained directly from first-principles calculations. For some materials, larger errors as for the L_1, and W_2 modes in silicon, and the P and N modes in niobium have been found. This issue has been addressed for Nb (Lekka et al., 2003b) whereby augmenting the first-principles database by including the energies at displacement of 0.005 lattice coordinates for the high symmetry points P and N, the overall fit of the phonon spectrum has been drastically improved. Figs. 6 and 7 show the phonon dispersion curves of Si and Ge that indicate a good agreement with the measured spectra.

Point defects

Point defects in the semiconductors Si (Bernstein et al., 2000) and Ge (Bernstein et al., 2002) have been calculated. Point defects are a major source of disorder in semiconductors since they are thermodynamically favored to occur at finite concentrations and temperatures. Because they are far more mobile than perfectly bonded atoms, they dominate diffusion. The formation energy of such defects strongly influences their concentrations and is, therefore, an important material property.

Table 6 lists the formation energies of three interstitial configurations: the tetrahedral, hexagonal, and 110 split, for Si and Ge. These defect energies were computed using a cubic supercell at the equilibrium lattice constant with 216 atoms, sampling the Brillouin zone at the Γ point. The relaxed configurations were obtained by a conjugate-gradient algorithm using as a criterion the force on each atom to be less than 3 meVA^{-1}. The formation and relaxation energies of all three interstitial configurations are within 10% of the range of LDA calculations for Si but not as good for Ge. On the other hand, the relaxed geometries show more serious discrepancies from *ab initio* results.

Table 6 Formation energies E_f (ideal) and relaxation energies ΔE_f (relaxed), in eV, for point defects computed using the TB model and comparison to DFT/LDA results (Bernstein et al., 2000, 2002).

	TB		*LDA*		*TB*		*LDA*
	E_f^0	E_f	E_f^0	E_f	E_f^0	E_f	E_f
V	Si 4.2	3.2	3.3–4.3	2.9–3.7	Ge 4.6	3.6	1.9
I_t	4.8	4.5	3.7–4.8	3.6–4.6	3.1	2.5	3.2
I_h	5.6	5.1	4.3–5.0	3.7–3.9	5.6	4.4	2.9
⟨110⟩	3.7		3.3		4.3	3.3	2.3

Since the structure of the ideal split interstitial is not uniquely defined, the energy listed under ideal is actually the relaxed formation energy.

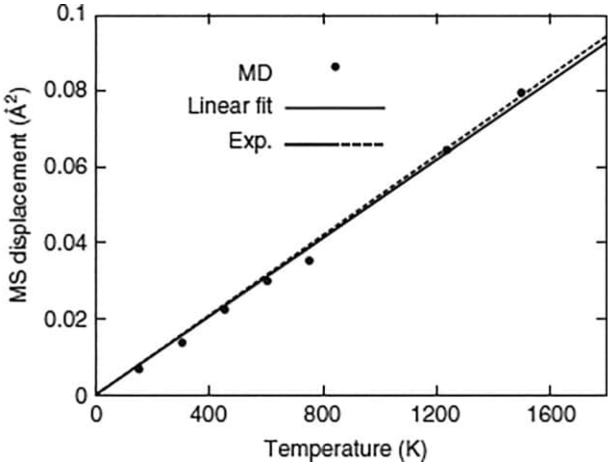

Fig. 8 Mean-squared displacement of atoms in diamond-structured silicon as a function of temperature, as determined by TBMD (Bernstein et al., 2000). The dots represent the TBMD data, and the lines are linear (solid) and higher-order representations of the experimental data. From Batterman BW and Chipman DR (1962) Vibrational amplitudes in germanium and silicon. *Physical Review* **127**: 690.

Finite temperature properties from molecular dynamics

The TB method described above can be used with the NRL-TB molecular dynamics (TBMD) package developed by Kirchhoff et al. (2001) to determine thermodynamic properties. For example, the TBMD package can be used to describe computed mean square displacements, and pair correlation functions as a function of temperature, as well as thermal expansion, in silicon, germanium, and gold. It is also possible to extract phonon-dispersion curves from the velocity autocorrelation function determined in an MD simulation.

As an example of the power of the method, one can describe the calculation of the mean-squared displacement of diamond structure silicon as a function of temperature (Bernstein et al., 2000). The calculation used a 512-atom unit cell, evolving at constant energy with fixed initial kinetic energy for 2000 timesteps of length 2.0 fs. As seen in Fig. 8, results are compared with the experimentally determined values, computed from the experimental measurements of the temperature dependence of broadening of the X-ray diffraction peak. The agreement is excellent.

The TBMD code can also determine the change in pressure versus temperature at constant volume. Coupled with the bulk modulus found in Table 1, we can determine the linear coefficient of thermal expansion,

$$\alpha = \frac{1}{3V}\left(\frac{\partial V}{\partial T}\right)_P = \frac{1}{3B}\left(\frac{\partial P}{\partial T}\right)_V \tag{18}$$

Table 7 compares the results for selected elements to experiment.

da Silva et al. (2001) used the NRL-TB parameters for Au to present a very interesting simulation of the formation, evolution, and breaking of Au nanowires.

Multicomponent systems

The above work was confined to single-component systems. The method is extendable to systems with more than one atomic species by making two modifications. First, one adds additional terms to the onsite energies which couple the density from atoms of type *i* to atoms of type *j*. Second, one notes that the SK parameters $ps\sigma$, $ds\sigma$, $dp\sigma$, and $dp\pi$, which in the single-atom case are

Table 7 Linear thermal expansion coefficient α (in K^{-1}) calculated using the TBMD with the NRL-TB parameters for selected elements.

Element	*Calculated*	*Experiment*
Ca*	3.07×10^{-5}	2.23×10^{-5}
Sr*	2.45×10^{-5}	2.25×10^{-5}
Be*	1.52×10^{-5}	1.20×10^{-5}
Cu	2.50×10^{-5}	1.80×10^{-5}
Ag	1.07×10^{-5}	2.00×10^{-5}
Au	1.43×10^{-5}	1.40×10^{-5}

The parameters were fit to first-principles LDA calculations except for those elements marked with an asterisk, which are GGA (Chellathurai et al., 2020; McGrady and Papaconstantopoulos, 2021; Silayi et al., 2018).

equivalent (within a sign) to *spσ*, *sdσ*, *pdσ*, and *pdπ*, respectively, are now independent parameters. These complications raise the total number of parameters from 93 in the single-atom case, to 330 for two-atom type systems.

This method has been applied to several compounds, including Nb—C, Nb—Mo, Pd—H, Fe—Al, Pt—O, CuZr, Cu—Ag, and Cu—Au (Mehl and Papaconstantopoulos, 1996; Lekka et al., 2009; Silayi et al., 2020). For Cu—Au, the energy of a variety of structures was computed, and it was found that the expected ordered phases (the $L1_2$, Cu_3Au, and $L1_0$ CuAu) were stable, while other structures were not. However, the advantage of the TB model is that one can compared to structures which are not found experimentally, allowing one to explore configurations that might occur locally in an alloy, but which do not form long-range ordered states. To check the correctness of the Cu—Au parameters in this case, it is compared to the cluster-expansion and first-principles calculations of Ozoliņš et al. Fig. 9 shows formation energies computed for several ordered phases in the Cu_xAu_{1-x} system and compares them to the energies obtained by Ozoliņš et al. (1998). It is found that the agreement is excellent.

We have also applied the NRL-TB method to understanding the electronic structure of the high-temperature superconductor SH_3 (Drozdov et al., 2015; Papaconstantopoulos et al., 2015). The tight-binding Hamiltonian is a 12×12 matrix including the s, p, and d orbitals of sulfur and three hydrogen s-orbitals. We have simultaneously fitted the energy bands and total energies as a function of volume for the Im3m (superconducting), A15 and $L1_2$ structures. The total energy (or formation energy) for these three structures is shown in Fig. 10 as a function of volume. The agreement between TB and LAPW is excellent. The energy bands and DOS are shown in Fig. 11 for the bcc-like Im3m structure at the lattice constant $a = 5.6$ Bohr, corresponding to a pressure of 200 GPa where high temperature superconductivity of $Tc = 190$ K has been computationally predicted and observed experimentally. The excellent agreement between TB and LAPW for both bands and DOS is also noted. Table 8 summarizes the DOS at the Fermi level at its decomposition per site and angular momentum the superconducting Im3m structure at a lattice constant of 5.6 Bohr. The strongest contributions to $N(E_f)$ are from the sulfur p- and hydrogen s-states, with a significant contribution from the sulfur d-states.

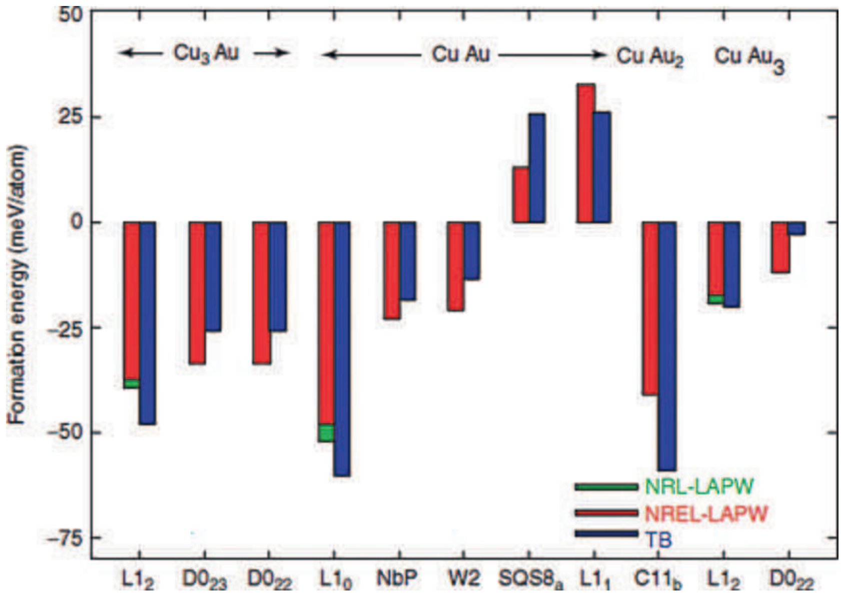

Fig. 9 Formation energy of several ordered phases in the Cu_xAu_{1-x} system, calculated using the TB parameters (blue bars), and compared to first-principles calculations performed by Ozoliņš et al. (1998) (red bars). On this scale, the cluster-expansion energies are indistinguishable from the corresponding LAPW results. For comparison, the first-principles LAPW results (green bars), which were used in the Cu-Au TB fitting process are also plotted.

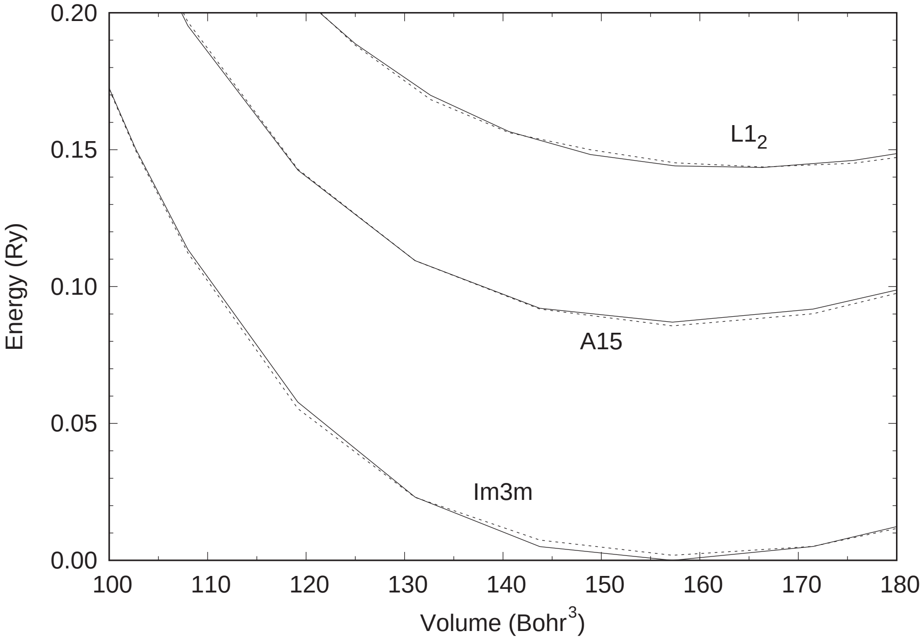

Fig. 10 Comparison of tight-binding (dashed lines) and LAPW (solid lines) total energies for three phases of SH_3. Energies and volumes are for one formula unit of each compound.

One- and two-dimensional structures

The NRL-TB method was applied to one- and two-dimensional structures of Cu and Au in conjunction with the conjugate gradient method to study nanoparticles. The TB parameters used (Silayi et al., 2018) were derived by fitting to LAPW calculations of periodic f.c.c., b.c.c., and simple cubic structures. It is impressive that this TB Hamiltonian works well for one- and two-dimensional structures. These TB results are in good agreement with binding energies and bond lengths found by independent first-principles DFT calculations which were not included in the fit. The conjugate gradient method is used to relax the clusters.

Nanoparticles with elongated geometries were made by cutting atoms from the f.c.c. crystalline structure. There are four categories of structures which we labeled A, B, C and D. In category (A) the elongation grows along the [100] direction. In category (B) the elongation is in the [011] direction. In category C the elongation starts with the atoms placed as in (B) and then grows in the [0–11] direction. In category (D) the structure is similar to (A) but it continues along the [1–10] axis. The TB results for binding energy and bond lengths were compared with DFT results for Cu and Au nanoparticles of small number of atoms (between 40 and 60 atoms) where DFT calculations can be done within reasonable computer times. The TB v. DFT comparison was good, motivating us to use the NRL-TB method to perform calculations in larger structures where, due to computational time and memory issues, DFT calculations are problematic. Our TB calculations were able to simulate structures with up to 800 atoms efficiently. The calculation times show that TB is at least three orders of magnitude faster than DFT.

For each category we started with a small structure (for example in category (A), we started with a structure with 40 atoms). Next, we cut the structure in half, moving the two parts in opposite directions. Finally, we add the corresponding atoms to create the largest structure (in this case the structure with 50 atoms, next the structure with 60 atoms, etc.). An important issue in this process was that the nearest neighbor distance of the initial structure must be reasonable (2.6 Ångstrom or smaller) to prevent structure breaking.

The binding energies (BE) per atom for Cu and Au NPs, as calculated with the TB method, are shown in Fig. 12. By comparing with the DFT results for both Cu and Au we find that the TB results follow the same trend as the DFT results. That is, the BE of category (B) has the lowest values, the category (D) follows, and the category (A) has the highest values of all categories. Specifically, the BE energies for Cu with 200 atoms we have: category (A) BE 3.94 eV, category (D) 3.90 eV and category (B) 3.72 eV. The corresponding values for Au are: category (A) 3.29 eV, category (D) 3.27 eV and category (B) 3.22 eV. Furthermore, we observe that the TB BE difference between smaller and larger 0D structures are 1.50 eV for Cu and 1.03 eV for Au. The corresponding results for DFT are 1.20 eV and 0.88 eV for Cu and Au, respectively; a quantitative difference but with the same trend.

After establishing that the TB results for small systems are in good agreement with the DFT ones, larger structures were considered. Fig. 13 shows TB results for Cu NPs of the (D) category. The lengths along the longest direction are 5.18, 7.73, 10.27, 14.39 and 19.26 nm respectively for Cu_{205}, Cu_{304}, Cu_{403} Cu_{601} and Cu_{808}. Similarly, Au NPs have lengths of 4.79 and 9.78 nm for Au_{205} and Au_{403} respectively. The BE per atom of Cu NPs (with 300 atoms), converge to values of 3.97, 3.92 and 3.84 eV for the (A), (D) and (B) categories respectively. The corresponding saturated BE values for Au NPs (with 300 atoms), are 3.284, 3.287 and 3.220 eV for the (A), (D) and (B) categories.

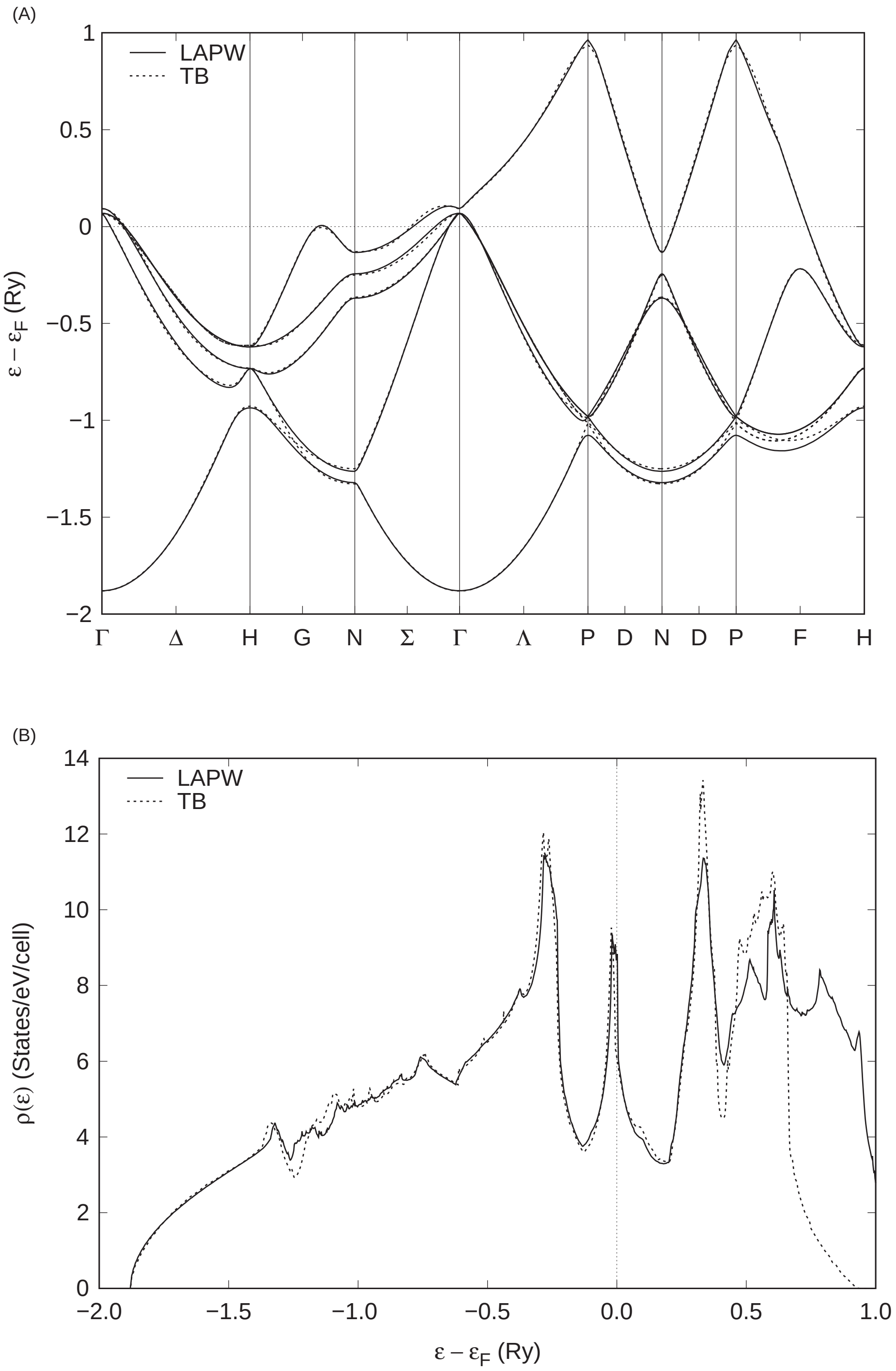

Fig. 11 Comparison of the LAPW (solid lines) and tight-binding (dashed lines) electronic structure (a) and density of states (b) for the high-temperature superconductor SH_3 at the cubic lattice constant 5.60 Bohr.

Table 8 Total electronic density of states and the orbital contributions to the DOS at the Fermi level of the Im3m superconducting phase of SH_3.

N(E$_f$)	*S-s*	*S-p*	*S-d*	*H-s*
6.05	0.30	2.07	1.62	2.06

This data was extracted from the tight-binding fit at the lattice constant of 5.6 Bohr. The DOS is given in units of states/Rydberg/cell for both spins. The hydrogen s value includes the contributions from all three atoms.

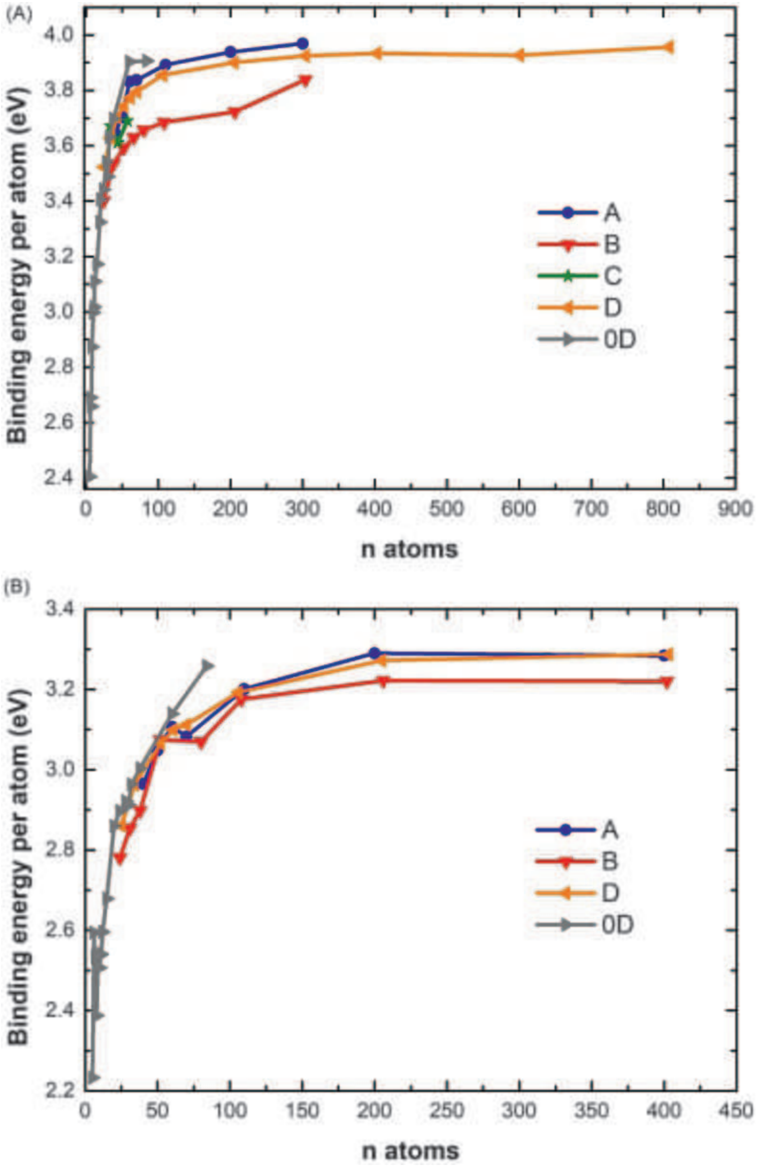

Fig. 12 The Binding Energy per atom of (a) Cu and (b) Au structures, using Tight Binding.

We have also calculated the HOMO-LUMO (HL) Gap and the Density of States (DOS). The TB results are compared with the corresponding DFT results in Fig. 14 for the HL gap and Fig. 13 for the DOS showing good agreement. We note that the HL gap for the smaller structures have higher values compared to the HL gap for the larger structures. This happens due to the transition from semiconductor to metallic behavior. This transition occurs at about 30–50 atoms systems. Generally, the HL gap of DFT has somewhat lower values compared to TB. For DFT, the values of the HL gap for Cu_{25} (category D) and Cu_{80} (category B) structures are 0.69 eV and 0.10 eV, respectively. The corresponding values for TB are 0.75 eV and 0.18 eV. This discrepancy is probably due to the following two factors: (a) the TB parameters used result from a fit to LAPW results from periodic cubic structures where the exchange and correlation functional (Hedin-Lundqvist) is different than that in the DFT code, and (b) different temperature broadening parameters used in the respective methods for calculating the DOS.

In Fig. 15 we show the per one atom DOS for different sizes of Cu and Au systems (24 and 108 atoms). The per one atom DOS shown are similar, characterized by the dominant d- states of Cu and Au, below the Fermi level and very small s-like DOS values at E_f reminiscent of the DOS of bulk periodic Cu. The DOS for small number of atoms shows a gap at the Fermi level (see Cu_{24} and Au_{24} in Fig. 14). For larger systems like Cu_{108} and Au_{108}, this gap is filled by s-like states. Furthermore, we calculate the per one atom DOS for the Cu_{601} and Cu_{808} cases. The graphs for those cases are similar to the corresponding Cu_{108} graph.

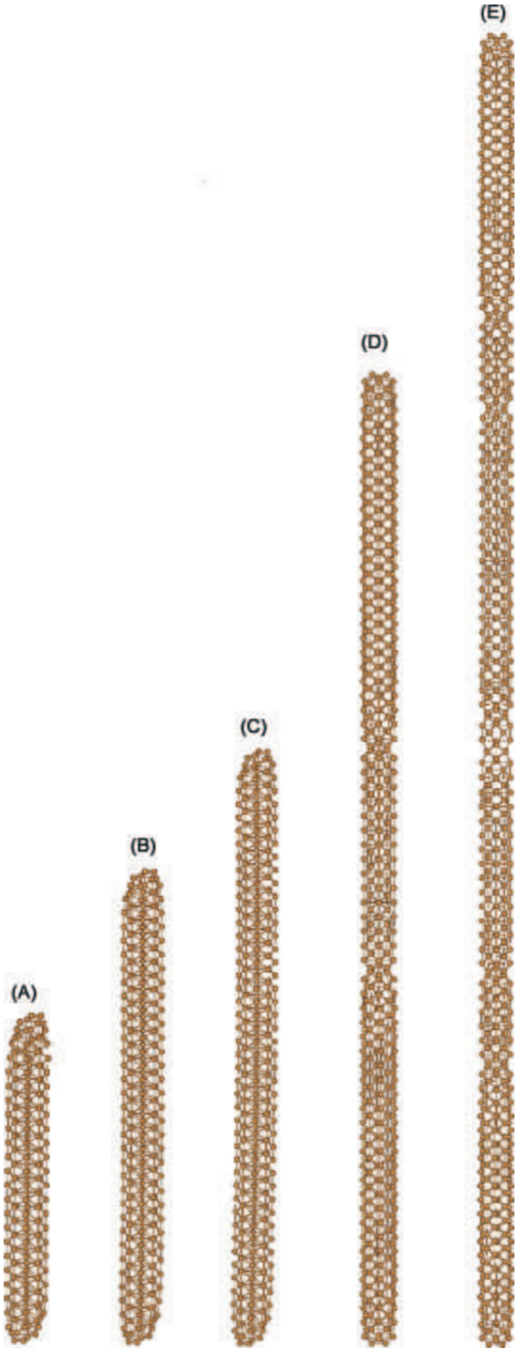

Fig. 13 The Copper structures over 200 atoms, that grow along the [110] direction (category D), using Tight Binding. More specifically, (a) Cu_{205}, (b) Cu_{304}, (c) Cu_{403}, (d) Cu_{601} and Cu_{808}.

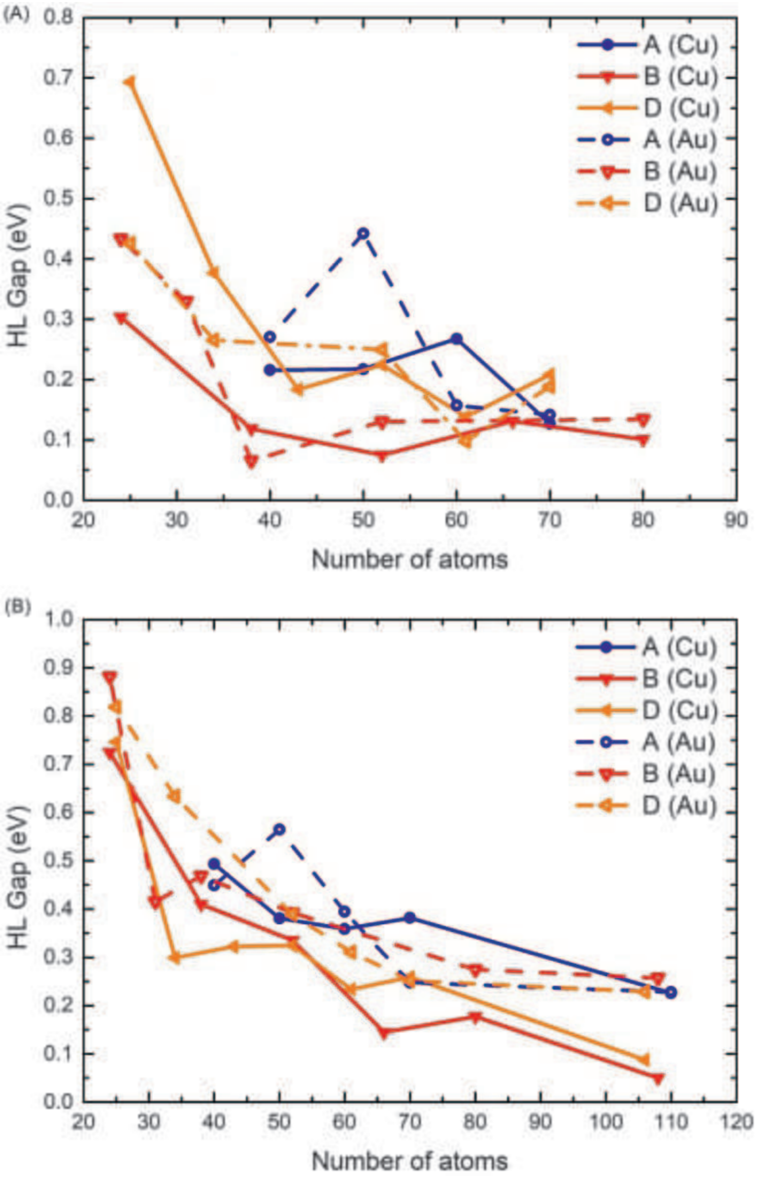

Fig. 14 The HOMO-LUMO Gap of the Cu (solid lines) and Au (dashed lines) structures (A, B and D categories), calculated with (a) DFT and (b) Tight Binding method.

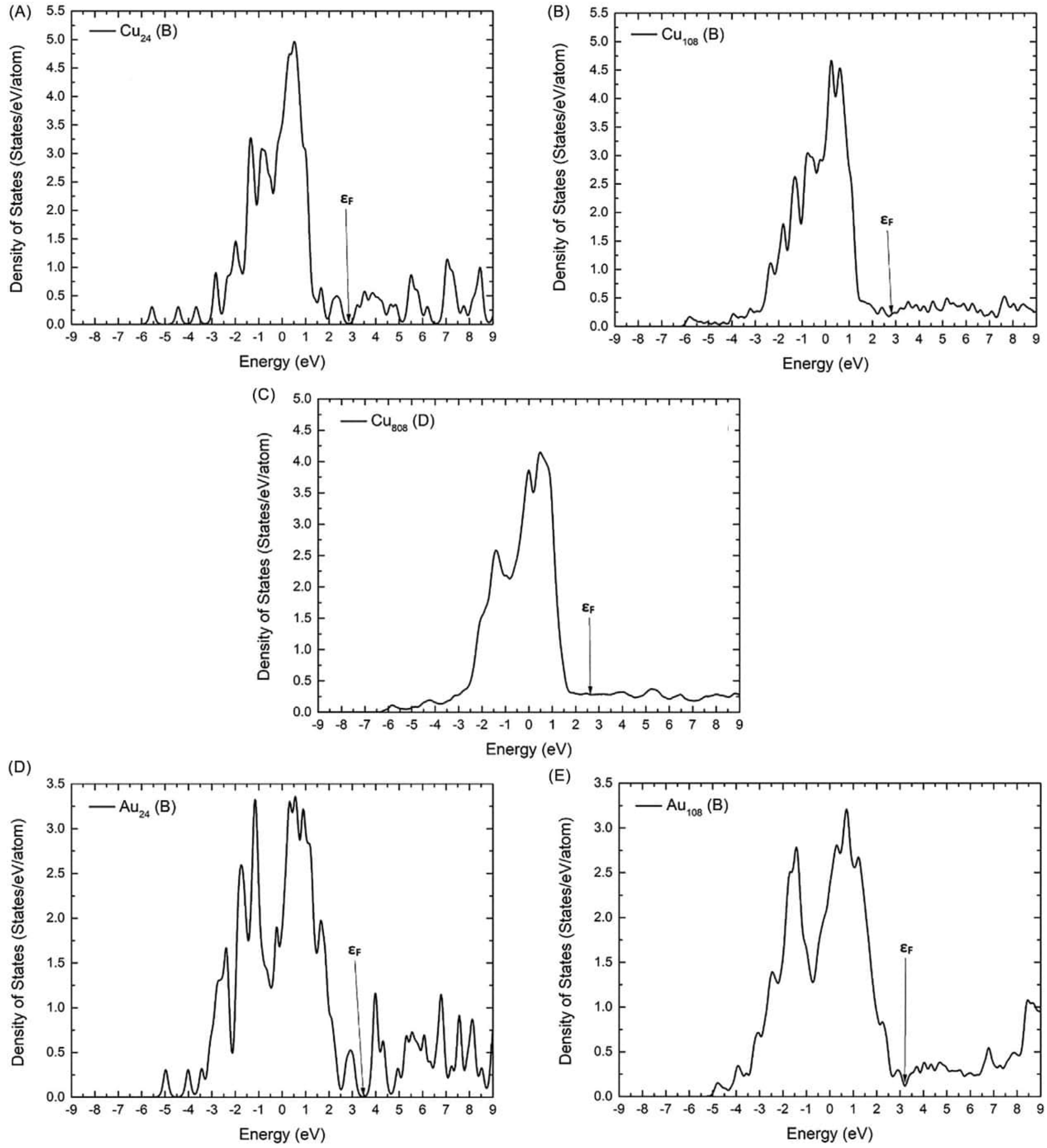

Fig. 15 The DOS per one atom for (a) Cu_{24}—category B, (b) Cu_{108}—category B, (c) Cu_{808}—category D, (d) Au_{24}—category B and (e) Au_{108}—category B.

Conclusion

We have shown that the NRL-TB method generates TB Hamiltonians that fit very well first-principles electronic structure results such as LAPW energy bands, density of states and total energies for most elements in the periodic Table and several compounds. This scheme accurately determines the ground state and the equilibrium lattice parameter of the system and positions well the total energies of other structures that were not included in the fit. Also, mechanical properties like elastic constants and bulk moduli as well as phonon frequencies are found in good agreement with experiment without being included in the database of the original fit. Large scale molecular dynamics simulations give a good account of mean-squared displacements, vacancy formation energies and the coefficient of thermal expansion, with a much smaller computational cost than most first-principles calculations. It should be emphasized that the NRL-TB approach is successful in obtaining a wide spectrum of properties unlike other TB or empirical potential schemes which usually have a restricted range of applications.

Acknowledgments

The authors thank the collaborators in this work. This work was supported by the US Office of Naval Research and the US Department of Energy.

References

Bacalis NC, Papaconstantopoulos DA, Mehl MJ, and Lach-hab M (2001) Transferable tight-binding parameters for ferromagnetic and paramagnetic iron. *Physica B: Condensed Matter* 296: 125.

Bernstein N, Mehl MJ, Papaconstantopoulos DA, Papanicolaou NI, Bazant MZ, et al. (2000) Energetic, vibrational, and electronic properties of silicon using a nonorthogonal tight-binding model. *Physical Review B* 62: 4477. Erratum: Physical Review B 65: 249002(E).

Bernstein N, Mehl MJ, and Papaconstantopoulos DA (2002) Nonorthogonal tight-binding model for germanium. *Physical Review B* 66: 075212.

Chellathurai M, Gogovi GK, and Papaconstantopoulos DA (2020) Electronic structure and tight-binding molecular dynamics simulations for calcium and strontium. *Materialia* 14: 100915.

Cleri F and Rosato V (1993) Tight-binding potentials for transition metals and alloys. *Physical Review B* 48: 22.

Cohen RE, Mehl MJ, and Papaconstantopoulos DA (1994) Tight-binding total-energy method for transition and noble metals. *Physical Review B* 50: 14694.

da Silva EZ, da Silva JR, and Fazzio A (2001) How do gold nanowires break? *Physical Review Letters* 87: 256102.

Drozdov AP, Eremets MI, Troyan IA, Ksenofontov V, and Shylin SI (2015) Conventional superconductivity at 203 Kelvin at hi pressures in the sulfur hydride system. *Nature* 525: 73.

Durgavich J, Sayed S, and Papaconstantopoulos D (2016) Extension of the NRL tight-binding method to include f orbitals and applications in Th, Ac, La and Yb. *Computational Materials Science* 112: 395.

Finnis MW and Sinclair JE (1984) A simple empirical N-body potential for transition metals. *Philosophical Magazine A* 50: 45.

Giannozzi P, de Gironcoli S, Pavone P, and Baroni S (1991) *Ab Initio* calculation of phonon dispersions in semiconductors. *Physical Review B* 43: 7231.

Gotsis HJ, Papaconstantopoulos DA, and Mehl MJ (2002) Tight-binding calculations of the band structure and total energies of the various phases of magnesium. *Physical Review B* 65: 134101.

Gross A, Scheffler M, Mehl MJ, and Papaconstantopoulos DA (1999) *Ab initio* based tight-binding Hamiltonian for the dissociation of molecules at surfaces. *Physical Review Letters* 82: 1209.

Groß A, Eichler A, Hafner J, Mehl MJ, and Papaconstantopoulos DA (2003) Unified picture of the molecular adsorption process: O_2/Pt (111). *Surface Science* 539: L542.

Haftel MI, Bernstein N, Mehl MJ, and Papaconstantopoulos DA (2004) Interlayer surface relaxations and energies of fcc metal surfaces by a tight-binding method. *Physical Review B* 70: 125419.

Harrison WA (1989) *Electronic Structure and the Properties of Solids: The Physics of the Chemical Bond*. New York: Dover.

Kirchhoff F, Mehl MJ, Papanicolaou NI, Papaconstantopoulos DA, and Khan FS (2001) Dynamical properties of Au from tight-binding molecular-dynamics simulations. *Physical Review B* 63: 195101.

Lekka CE, Bernstein N, Mehl MJ, and Papaconstantopoulos DA (2003a) Electronic structure of the Cu_3Au (111) surface. *Applied Surface Science* 219: 158.

Lekka CE, Mehl MJ, Bernstein N, and Papaconstantopoulos DA (2003b) Tight-binding simulations of Nb surfaces and surface defects. *Physical Review B* 68: 035422.

Lekka CE, Papaconstantopoulos DA, Mehl MJ, Finkenstadt D, and Evangelakis G (2009) Static and dynamic tight-binding simulations of the binary NbMo and CuZr alloys. *Journal of Alloys and Compounds* 483: 627.

McGrady JW and Papaconstantopoulos DA (2021) Tight-binding study of beryllium. *Computational Materials Science* 188: 110142.

McGrady JW, Papaconstantopoulos DA, and Mehl MJ (2014) Tight-binding study of boron structures. *Journal of Physics and Chemistry of Solids* 75: 1106.

Mehl MJ and Papaconstantopoulos DA (1996) Applications of a tight-binding total-energy method for transition and noble metals: Elastic constants, vacancies, and surfaces of monatomic metals. *Physical Review B* 54: 4519.

Mehl MJ and Papaconstantopoulos DA (2002) Tight-binding study of high-pressure phase transitions in titanium: Alpha to omega and beyond. *Europhysics Letters* 60: 248.

Mehl MJ and Papaconstantopoulos DA (2005) Tight-binding total energy methods for magnetic materials and multi-element systems. In: Yip S (ed.) *Handbook of Materials Modeling*, pp. 275–305. The Netherlands: Springer. ch. 1.14.

Mehl MJ, Klein BM, and Papaconstantopoulos DA (1994) First-principals calculation of elastic properties. In: Westbrook JH and Fleischer RL (eds.) *Intermetallic Compounds—Principles and Practice*. vol. 1, pp. 195–210. London: Wiley. ch. 9.

Mehl MJ, Papaconstantopoulos DA, Kioussis N, and Herbranson M (2000) Tight-binding study of stacking fault energies and the Rice criterion of ductility in the fcc metal. *Physical Review B* 61: 4894.

Nelin G and Nilsson G (1972) Phonon density of states in germanium at 80 K measured by neutron spectrometry. *Physical Review B* 5: 3151.

Ozoliņš V, Wolverton C, and Zunger A (1998) Cu-Au, Ag-Au, Cu-Ag, and Ni-Au intermetallics: First-principles study of temperature-composition phase diagrams and structures. *Physical Review B* 57: 6427.

Papaconstantopoulos DA (2015) *Handbook of the Band Structure of Elemental Solids*. New York: Springer.

Papaconstantopoulos DA and Mehl MJ (2003) The Slater-Koster tight-binding method: A computationally efficient and accurate approach. *Journal of Physics. Condensed Matter* 15: R413.

Papaconstantopoulos DA, Mehl MJ, Erwin SE, and Pederson MR (1998) Tight-binding Hamiltonians for carbon and silicon. *Materials Research Bulletin* 491: 221.

Papaconstantopoulos DA, Klein BM, Mehl MJ, and Pickett WE (2015) Cubic H_3S around 200 GPa: An atomic hydrogen superconductor stabilized by sulfur. *Physical Review B* 91: 184511.

Schaefer H-E (1987) Investigation of thermal equilibrium vacancies in metals by positron annihilation. *Physica Status Solidi* 102: 47.

Sha XW, Papaconstantopoulos DA, Mehl MJ, and Bernstein N (2011) Tight-binding study of hcp Zn and Cd. *Physical Review B* 84(18): 184109. https://doi.org/10.1103/PhysRevB.84.184109.

Shi L and Papaconstantopoulos DA (2004) Modifications and extensions to Harrison's tight-binding theory. *Physical Review B* 70: 205101.

Silayi S, Papaconstantopoulos DA, and Mehl MJ (2018) A tight-binding molecular dynamics study of the noble metals Cu, Ag, and Au. *Computational Materials Science* 146: 278.

Silayi S, Chang P-H, and Papaconstantopoulos DA (2020) Electronic structure and dynamics analysis of the Cu-Ag binary alloy by a tight-binding parameterization. *Computational Materials Science* 173: 109454.

Slater JC and Koster GF (1954) Simplified LCAO method for the periodic potential problem. *Physical Review* 94: 1498.

Tubino R, Piseri L, and Zerbi G (1972) Lattice dynamics and spectroscopic properties by a valence force potential of diamondlike crystals: C, Si, Ge, and Sn. *Journal of Chemical Physics* 56: 1022.

Wang GM, Papaconstantopoulos DA, and Blaisten-Barojs E (2003) Pressure induced transitions in calcium: A tight-binding approach. *Journal of Physics and Chemistry of Solids* 64: 185.

Yang SH, Mehl MJ, and Papaconstantopoulos DA (1998) Application of a tight-binding total-energy method for Al, Ga, and In. *Physical Review B* 57: R2013.

Electronic Structure Calculations: Plane-Wave Methods

ML Cohen, University of California at Berkeley, Berkeley, CA, USA

© 2005 Elsevier Ltd. All rights reserved.

This is an update of M.L. Cohen, Electronic Structure Calculations: Plane-Wave Methods, Editor(s): Franco Bassani, Gerald L. Liedl, Peter Wyder, Encyclopedia of Condensed Matter Physics, Elsevier, 2005, Pages 85–93, ISBN 9780123694010, https://doi.org/10.1016/B0-12-369401-9/00449-6.

Introduction **756**
The Standard Model of Solids 756
Pseudopotentials **757**
Total Energy Calculations and Structural Properties **759**
Superconductors, Optical Properties, and Novel Materials 761
Conclusion **764**
Acknowledgments **764**
Further Reading **764**

Introduction

Understanding the electronic structure of solids is basic to explaining and predicting solid-state properties, but what is an appropriate description of electronic states in solids?

Although it is clear that solids are made of atoms and that one can think of the gas-to-liquid-to-solid transitions as a process in which atoms just get closer together, the electronic properties of solids often differ significantly from what one would expect from a collection of isolated atoms. In cases where the interactions between the atoms are weak, as in the case of rare gas solids, it is reasonable to consider these interactions as perturbations of atomic states. However, when atoms are close to each other in a solid, sometimes they can give up their outermost electrons easily, and it is even possible to end up with a sea of nearly free electrons. In fact, a nearly free-electron model is appropriate for metals such as the alkali metals, aluminum, and many others.

It is also fortunate and useful that this nearly free-electron model applies to a wider class of solids when a few modifications are added. A totally free electron is described by a plane-wave wave function. Hence, if one assumes that the electrons describing a metal behave as if they are nearly free, then a plane-wave position-dependent wave function $\Psi(\boldsymbol{r})$ confined to a box of volume Ω, having a wave vector $(\mathbf{k})$ which can be written as

$$\psi(\boldsymbol{r}) = \frac{1}{\sqrt{\Omega}} \mathrm{e}^{\mathrm{i}\boldsymbol{k}\cdot\boldsymbol{r}}$$

may be a good starting point for describing the electrons in metals such as sodium. If one examines the resulting electronic density corresponding to a plane-wave wave function, it is constant since it is proportional to $\psi^*(\boldsymbol{r})\psi(\boldsymbol{r})$. Therefore, the collection of atoms with localized wave function on each atomic site and peaked electronic density yields a valence electron density which is vastly different.

What about bonds? For example, covalent bonds arise because electrons tend to concentrate in certain regions between atoms. Can the bonds and charge modulation known to exist in metals and especially in covalent semiconductors be described using plane waves as a starting point? The answer is yes for a broad class of solids. A plane wave is a solution to Schrödinger's equation when the electron–ion and electron–electron potentials are zero. However, when these potentials are included (and if they are not too strong and if the electrons are not strongly correlated), a perturbative scheme can be used to modify the free-electron picture, and this is the "nearly free-electron model" which is described in many textbooks. However, more generally, Schrödinger's equation is solved by diagonalizing a Hamiltonian matrix with appropriate potentials and a basis set composed of plane waves to describe the wave function.

What about alternatives to the nearly free-electron model? The opposite approach to using plane waves is the utilization of atomic wave functions for the basis set. There are tight-binding methods where linearized combinations of atomic orbitals form the basis. This description is also very useful especially when the solid-state wave functions are not too different from the atomic wave functions forming them. If done correctly with sufficient orbitals in the basis set, both the above methods work and are useful.

In the following discussion, the plane-wave basis is featured. In particular, a pseudopotential-density functional approach is described which has been applied successfully to a large number of solids, clusters, nanostructures, and molecules.

The Standard Model of Solids

In Figure 1, a schematic picture of a solid is presented where the nuclei and core electrons for the atoms are represented as positive cores and the stripped-off valence electrons are contributed to the electron sea which flows through the periodic array of cores. In this model, the solid system is viewed as having two types of particles: cores and valence electrons. The interaction between the positive cores is taken to be a standard Coulomb interaction describable by Madelung sums. The electron–core and electron–electron interactions are essential inputs to this model. As mentioned above, the form of the standard model of solids, represented by Figure 1, which is focused here, will model the electron–core interaction using pseudopotentials and the electron–electron interaction using the density-functional theory – in particular, the local density approximation (LDA).

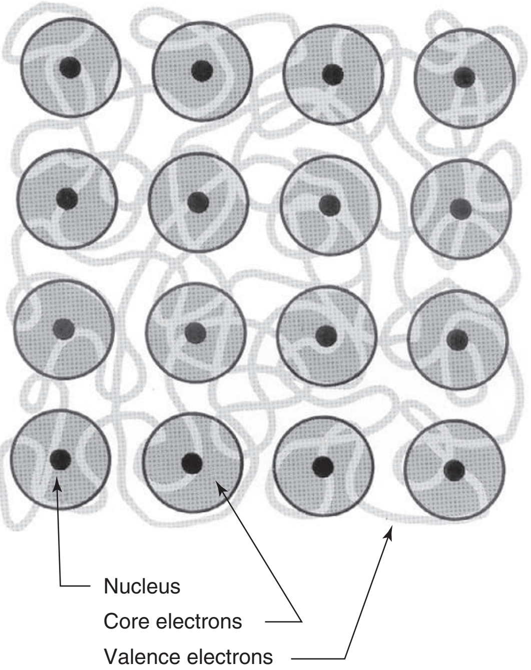

Figure 1 Schematic view of a solid with positive cores at fixed lattice positions in a periodic array and a sea of relatively free valence electrons moving through the lattice.

Pseudopotentials

Arguments for the use and/or appropriateness of a weak electron–core potential have been made since the 1930s. In 1934, Fermi constructed a pseudopotential to describe highly excited electronic states of alkali atoms. His weak potential was designed to yield an accurate description of the outer portions of the wave function and to avoid the more difficult calculation of the properties of the oscillations of the wave function near the core. This would require a strong potential. Since solid-state effects are dominated by the outer portions of atomic wave functions, this is a viable approach for constructing pseudopotentials for solids. As shown in Figure 2,

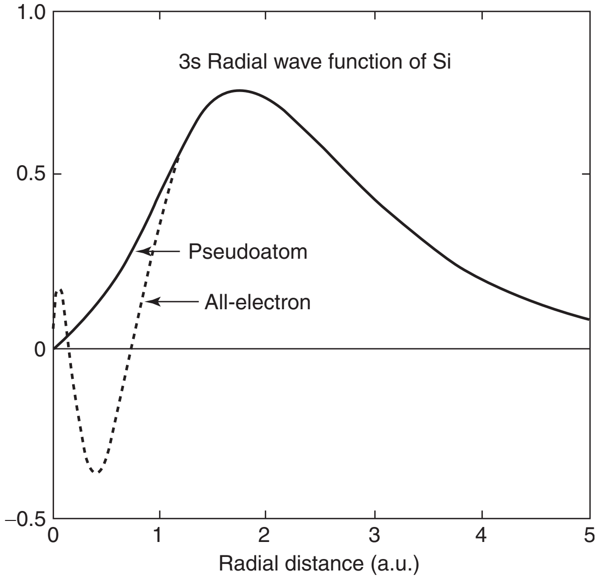

Figure 2 The solid line represents the Si 3*s* pseudo-wave-function resulting from the use of a pseudopotential. The dashed line results from an “all electron” calculation.

a "pseudoatom" wave function is generated which is identical to an "all-electron" 3*s* radial wave function for Si away from the core and smooth near the core. The weak pseudopotential which produced the pseudoatom wave function can be computed from first principles using only the atomic number as input. There are many schemes available for producing these *ab initio* pseudopotentials, which in principle can be constructed for all atoms.

The electron–electron interactions can be approximated using the electronic density. This density-functional approach represents the Hartree and exchange-correlation potentials as functionals of the electronic density. Hence, a self-consistent calculation can be done with a plane-wave basis set, pseudopotentials, and the LDA to density-functional theory. The calculated electronic density can be used to produce LDA potentials which in turn can produce updated wave functions and subsequently, new LDA potentials. This scheme and variants using pseudopotentials and plane waves are often referred to as the "plane-wave pseudopotential method" (PWPM). In general, the method has been extremely successful for determining the electronic structure and many other properties of solids.

Although most modern pseudopotential calculations use *ab initio* pseudopotentials of the type described above, the pseudopotential method went through a semi-empirical stage of development where experimental input was used to generate a potential representing the total valence electron potential (electron–core plus electron–electron). This approach, called the empirical pseudopotential method (EPM), used plane waves and a few Fourier coefficients of the potential which were fit to experimental data. In addition to explaining the origin of the optical structure in the visible and UV in terms of interband electronic transitions and many other properties of solids, the EPM set the stage for the first-principles methods and the standard model.

A schematic real space potential is illustrated in Figure 3. The strong ionic Coulomb potential is "cut off" in the core region. The physical origin of the cancelation of the ionic potential in the core region was attributed by Phillips and Kleinman to a repulsive potential arising because of the Pauli exclusion principle preventing the valence electrons from occupying core states. The result is again a weak net potential describable by a few Fourier form factors and a wave function which can be expanded in a plane-wave basis set. Usually, three pseudopotential form factors per atom gave highly accurate electronic band structures.

The EPM was the first successful plane-wave method for real materials with applications to metals, semiconductors, and insulators. Dozens of band structures and optical response functions were calculated with high precision for the first time. The optical spectra of semiconductors were interpreted in terms of critical points in the electronic band structure, and when the wave functions were used to compute the electronic density, the covalent and ionic bonds were pictorially displayed – again for the first time.

In Figure 4, a plot of the predicted electronic density for Si is displayed and compared with results based on subsequent X-ray studies. In addition to the striking agreement between theory and experiment, these plots reveal the nature of the covalent bond. It is particularly satisfying to see the local build-up of charge in the Si–Si bond region even though the basis set is composed of plane waves which yield a constant density before the potential is "turned on." There is no prior prejudice for this pile-up of charge in the bond region built into the basis set.

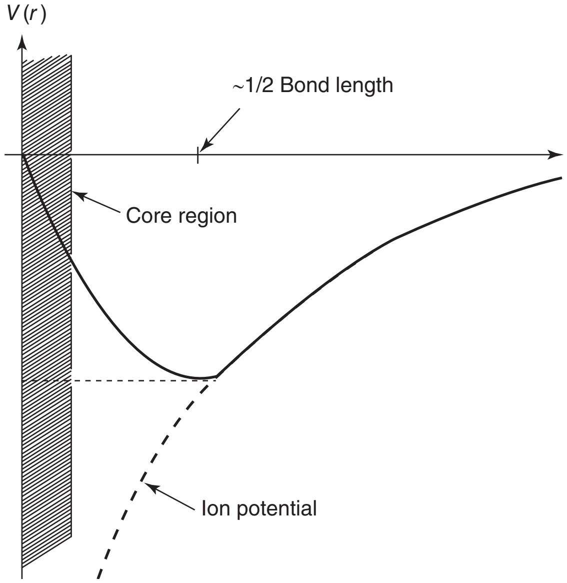

Figure 3 Schematic drawing of a pseudopotential (solid curve) compared to a Coulomb ion potential (dashed line).

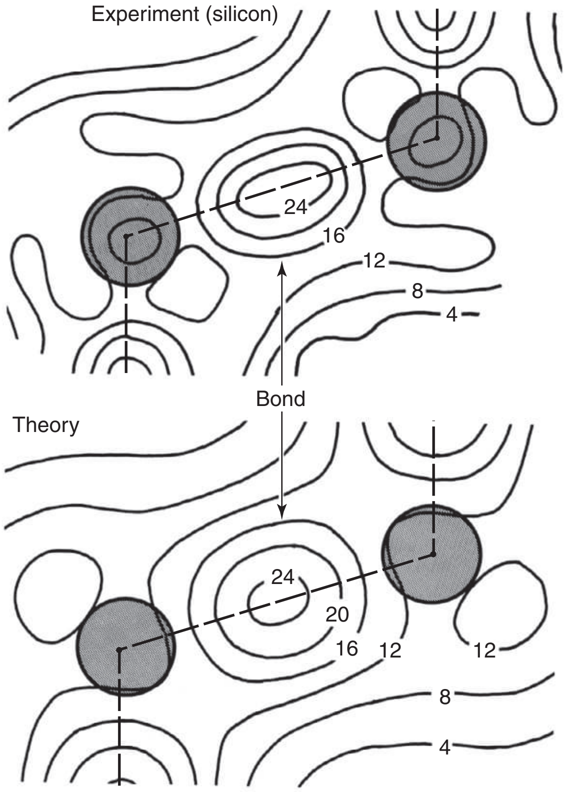

Figure 4 Valence electron density for silicon. The contour spacings are in units of electrons per unit cell volume. The shaded disks represent atomic cores.

Total Energy Calculations and Structural Properties

The EPM calculations were constructed to deal with bulk crystals which were not terminated. Standard techniques, described in textbooks, use periodic boundary conditions to avoid having surfaces or interfaces. The EPM pseudopotential V($\boldsymbol{r}$) has the periodicity of the lattice so it could be expressed as an expansion using reciprocal lattice vectors $\boldsymbol{G}$:

$$V(\boldsymbol{r}) = \sum_{G} S(\boldsymbol{G})V(\boldsymbol{G})e^{iG.r}$$

where S($\boldsymbol{G}$) is the structure factor that locates the atoms relative to a lattice point. It is the form factors V($\boldsymbol{G}$) which are fit to experiment in the EPM scheme.

In order to deal with surfaces and interfaces, one has to allow charge to redistribute at a surface or interface and break translational invariance. To do this, the EPM evolved into a scheme where the electron–core and the electron–electron potentials were separated. As in modern calculations, the electron–core potential is referred to as the "pseudopotential" and the electron–electron potential was expressed in terms of the density. In early calculations, the Slater and Wigner approximations were used. This allowed the charge density to readjust to a surface or interface and because of self-consistency, so did the potentials. The surface or interface was modeled by introducing a supercell which contained the geometric configuration of interest. For example, a (1 1 1) Si surface was modeled using a slab containing 12 atomic layers separated from the next slab by an equivalent space with no atoms. The surface of the slab represented the surface of the Si crystal and self-consistency required the rearrangement of the electronic density to correspond to the new geometry. Figure 5 shows this rearrangement of electron density on an ideal Si (1 1 1) surface in one of the first calculations done with this method. Later calculations used supercells to examine Schottky barriers, heterojunctions, and reconstructions at surfaces and interfaces.

The evolution of the use of the LDA was straightforward since in this approach the electron–electron potentials are expressed as functionals of the electron density. Hence, surfaces, interfaces, and localized configurations in general could be dealt with using supercells and by letting the charge density adjust to the geometric constraints. The use of the PWPM and the LDA also allowed the exploration of other solid-state properties.

Important applications became possible once a scheme was developed to calculate the total structural energy$E_S$of the solids for given configurations of the atomic cores. Once$E_S$is evaluated for a series of candidate structures, a comparison of their structural energies immediately reveals the lowest energy structure for the group. At a given volume, this lowest energy structure would be the

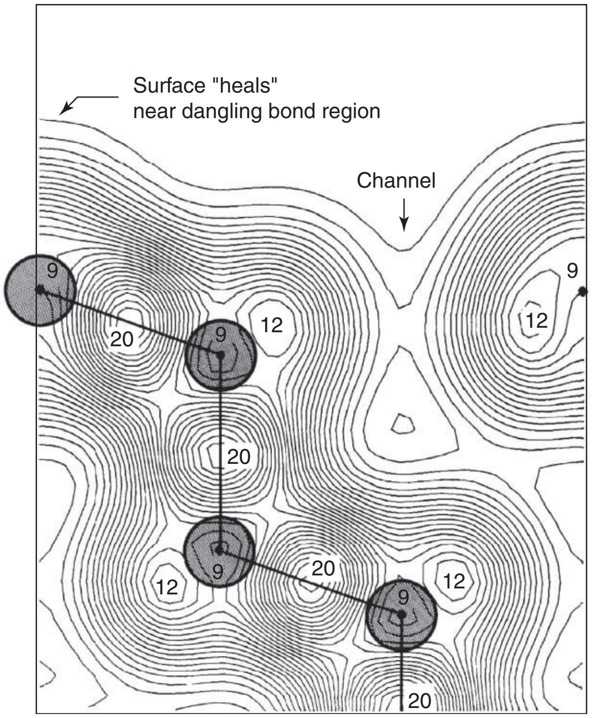

Figure 5 Valence electron density for the ideal Si (1 1 1) surface. Contours are plotted in the perpendicular (1 1 0) plane with units corresponding to one electron per primitive cell. The shaded disks represent atomic cores.

most stable structure if all possible structures are considered. Since it is not possible to test all structures, a limitation on this method is the possible omission of the most stable structure. However, in practice, it has often been possible to choose the most likely structures, and the success rate of the PWPM is high for predicting new structures and structural properties. Because E_{S} depends on volume (or lattice separations), changes induced by pressure can cause solid–solid phase transitions where crystal structures can change. Therefore, calculations of the dependence of on volume can predict transition pressures and volumes for the structural phase changes. Similar calculations for lattice constant changes caused by strains or alloying can yield elastic constants and even vibrational spectra.

Using the standard model with cores and valence electrons as illustrated in Figure 1, the total structural energy of the solid can be expressed as

$$E_{\mathrm{S}} = E^{\mathrm{cc}} + E^{\mathrm{ec}} + E^{\mathrm{e}}_{\mathrm{k}} + E^{\mathrm{ee}}_{\mathrm{c}} + E^{\mathrm{ee}}_{\mathrm{x}}$$

and all the energy components can be evaluated using the PWPM. The core–core Coulomb energy E^{cc} can be calculated from point–ion sums as discussed earlier, E^{ec} is evaluated using the pseudopotential, and both the Hartree (Coulomb) electron–electron energy $E^{\mathrm{ee}}_{\mathrm{c}}$ and the exchange-correlation energy $E^{\mathrm{ee}}_{\mathrm{x}}$ can be approximated using the electron density. The electron kinetic energy $E^{\mathrm{c}}_{\mathrm{k}}$ is obtained once the wave function is computed. Therefore, with pseudopotentials and the LDA approximation, the total energy E_{S} and many ground-state properties can be determined for different structural configurations.

It is convenient to evaluate the above energy contributions to E_{S} using expressions for the potentials and energies in reciprocal space. An early application was the examination of the ground-state properties of Si. Figure 6 contains the results for calculations of E_{S} as a function of volume for seven candidate structures. The volume is normalized by the experimental volume of the diamond phase at atmospheric pressure. Therefore, when the volume is unity, this corresponds to ambient pressure and the diamond structure has the lowest energy. As the pressure increases and the volume decreases, it is noted that the hexagonal diamond-structured material is always at a higher energy than the diamond (cubic) structure; therefore, diamond is the more stable phase. At smaller volumes (higher pressures), the β-tin phase has a lower energy than diamond-structured Si, and β-tin is therefore the stable phase. If one views the transition as occurring along the dashed line (Figure 6) which is the common tangent between the diamond and β-tin curves, the transition volumes (points 2 and 3) can be evaluated along with the transition pressure which is the slope of the common tangent. These values are all found to be in good agreement with the measured data. In addition, the minimum energy volume for the diamond structure yields a calculation of the equilibrium lattice constant while the curvature of E_{S} as a function of volume near the minimum energy point yields the bulk modulus or compressibility for Si. In all the calculations, it is assumed that the temperature is zero.

Using the above method, the lattice constants and bulk moduli have been calculated for many solids. Typical accuracies are less than 1% for lattice constants and less than 5% for bulk moduli. Discrepancies between theory and experiment for transition volumes and pressures are normally in the few percent range. In addition, modifications of structures at interfaces and surfaces can

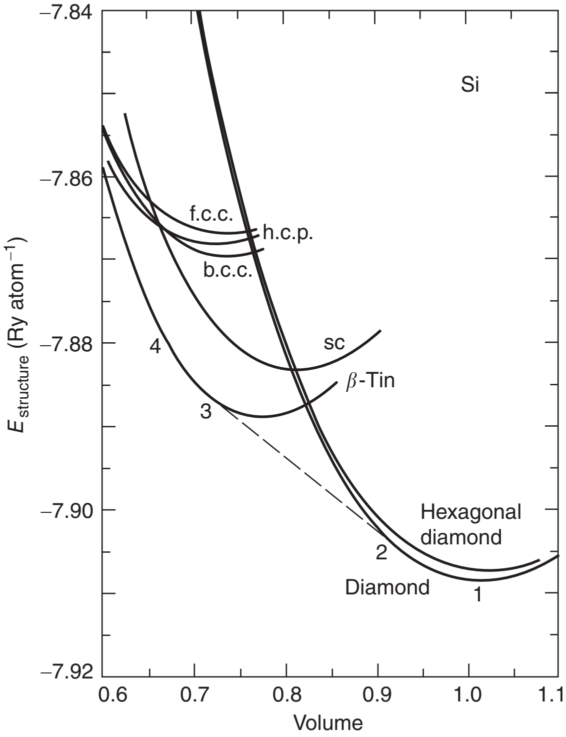

Figure 6 Structural energies for seven structures of Si as a function of volume normalized to the experimental volume at ambient pressure (solid lines). The common tangent represented by the dashed line illustrates the structural transition between the diamond and β-tin structures.

also be addressed with this approach. By calculating the changes in energy with movements of specific atoms or by computing Hellmann–Feynman forces, it is possible to determine reconstructions of surfaces and interfaces. In the calculations described above, the only input is the atomic number of the constituent atoms to calculate the pseudopotential and the candidate structure.

Another important application of this method is the determination of vibrational spectra. The method often used within the PWPM is called the "frozen phonon" approach, where the crystal structure is distorted to represent the displaced atoms associated with a particular phonon mode. By comparing the energies of the undistorted and distorted structures or by directly calculating the forces on the atoms, the phonon spectrum can be determined. Here, one needs to input the atomic masses of the constituent atoms as well as their atomic numbers. Again, agreement with experiment is excellent.

Superconductors, Optical Properties, and Novel Materials

A particularly striking success of this approach is its application to superconductivity. The systems considered are expected to be "BCS electron–phonon superconductors." A variation on the frozen phonon method allows a determination of the electron–phonon coupling constants. As described above, the PWPM within the LDA yields ground-state properties with high precision. Since the superconducting transition temperature in the BCS description is extremely sensitive to the strength of the electron–phonon parameter λ and, to a lesser extent, the Coulomb parameter μ^*, it is imperative that the normal-state properties of the material studied be known with high precision. Only a few first-principles calculations of μ^* are available; however, this parameter does not vary a great deal for different materials, and it scales reasonably well with the density of states at the Fermi energy. In contrast, λ can have a much larger variation and therefore the focus for first-principles calculations for superconducting materials has been on the determination of λ.

The enhancement of the effective mass is also related to λ:

$$m^* = m_{\text{b}}(1 + \lambda)$$

where m_{b} is the band mass calculated without including the electron–phonon interactions. The strong dependence on λ for the superconducting transition temperature, T_{c}, can be illustrated by equations such as the McMillan equation which have the generic form

$$T_{\text{c}} = AT_{\text{D}}\exp\left(\frac{1}{\lambda^* - \mu^*}\right)$$

where A is a constant, T_{D} is the Debye temperature, and $\lambda^* = \lambda/(1 + \lambda)$.

The PWPM formulation for the calculation of λ had as its first application a study of high-pressure phases of Si. The results were dramatic because the existence of the two high-pressure solid metallic phases, simple (or primitive) hexagonal (s.h.) and hexagonal close packed (h.c.p.) were predicted by PWPM calculations. In addition to predicting the transition pressures needed to obtain these phases, their electronic, structural, vibrational, and superconducting properties were successfully predicted. The input information was only the atomic number and atomic mass of Si, the candidate structures, and an estimate of μ^*.

Although the PWPM has limited use for highly correlated materials, it is sometimes used as a starting point to obtain the electronic structure before correlation effects, such as a Hubbard *U* parameter, are considered to estimate the expected changes when correlation is considered. However, when new superconductors are found, it is common to apply the approach described above as a test of whether one is dealing with a conventional superconductor or not. Superconducting doped C_{60} materials, nanotubes, and MgB_2 are good representatives of materials in this category.

The case of MgB_2 serves as an excellent example of what can be done now with the PWPM and Eliashberg theory, which is an extension of the BCS theory. The method yielded the electronic and vibrational properties of MgB_2 and demonstrated that the strongest electron–phonon coupling was associated with a particular phonon mode. By considering phonon anharmonicity and including the anisotropy of the superconducting energy gap which was found to be important when doing the calculation, it was possible to reproduce the experimental data and predict new properties. The results were consistent with the proposal that MgB_2 is a BCS superconductor with electron pairing caused by electron–phonon coupling and that the superconducting energy gap was multivalued. The results for MgB_2 are particularly striking since this PWPM calculation had no experimental input except for the estimate of μ^* and the known structure of MgB_2.

The optical properties of solids are of particular interest when one is describing a method for computing an electronic structure. The interplay between the development of quantum mechanics and the study of atomic optical spectra was extremely important to the evolution of both fields. However, identifying peaks in optical response functions for solids appeared to be a formidable task. Unlike atomic spectra that contained very sharp peaks which could be interpreted in terms of electronic transitions between narrow electronic states, solid-state spectra were broad and featureless.

The challenge remained in essence until the 1960s, and, for the most part, it was the use of the EPM which provided the tools to deal with these spectra, particularly for semiconductors. An important feature is the fact that peaks in optical response functions, such as reflectivity, arise from interband transitions between states where the bands are parallel. For example, if an electron in a valence band *n* at point k in the Brillouin zone with energy $E_n(\boldsymbol{k})$ is excited to an empty state *m* with energy $E_m(\boldsymbol{k})$, this requires a photon having energy $\hbar\omega = E_m(\boldsymbol{k}) - E_n(\boldsymbol{k})$. This transition will result in a more prominent structure or "signature" in the reflectivity if the initial occupied and final unoccupied bands are parallel at the point k. The condition is $\nabla_{\boldsymbol{k}} E_n(\boldsymbol{k}) = \nabla_{\boldsymbol{k}} E_m(\boldsymbol{k})$, and this is the requirement for a "critical point" to occur in the band structure. It can be shown that this critical point is associated with the structure in the joint density of states between the two bands. This structure, referred to as a Van Hove singularity, in turn, appears in the optical response functions such as the reflectivity or frequency-dependent dielectric function. It was the analysis of these critical points in semiconductor spectra that yielded the energy separations used to fit the pseudopotential form factors for the EPM. A typical result is shown in Figure 7 where the modulated or derivative reflectivity spectrum of Ge is displayed. Derivative spectroscopy is used to accentuate the Van Hove structures, and the zeros and peaks arise because of the nature of the critical points. As discussed before, the positions of these are related to the energies of the critical points. In Figure 7, near the 2 eV region, it is noted that although there is reasonable agreement between theory and experiment for the critical point energies, the magnitudes of the curves differ considerably. This arises because of electron–hole attraction effects which are not included in the calculation. These are discussed later.

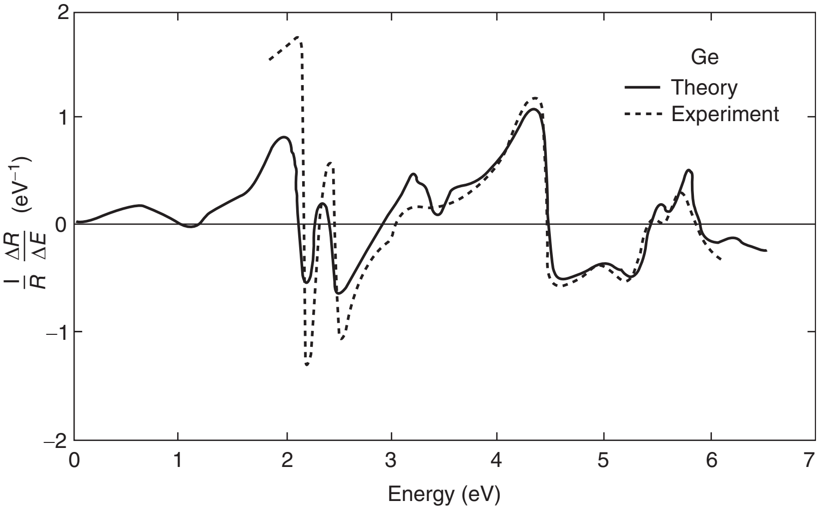

Figure 7 The modulated or derivative reflectivity spectrum for Ge. A comparison is made between the experimental spectrum and the theoretical calculation.

Although the transition from the EPM to *ab initio* PWPM applications was fairly straightforward, there were particularly interesting problems associated with the calculations of energy-band separations, the minimum bandgap, optical spectra, and the role of electron–hole effects described above. The most dramatic signal that one could not just apply the LDA and the PWPM to obtain experimental band structures was the fact that researchers using this approach were consistently underestimating bandgaps. The specific focus was on Si where the measured and EPM values for the minimum gap were 1.1 eV, while the PWPM–LDA gap was half this value. The EPM was fit to give the correct result, but the *ab initio* method had as its input the LDA, the pseudopotential, and the plane-wave bases. It was soon found that other methods using the LDA gave similar results. Hence, it was concluded that it was the use of the LDA which resulted in calculations which underestimated the bandgap. Since it was emphasized by the inventors of the LDA that, in principle, this approximation should not be applicable for bandgap determination, this result came as no surprise. However, because of the ease of use of the LDA and its success for determining ground-state properties, it was hoped that modifications could be made to standard LDA methods to allow the computation of bandgaps and optical spectra.

A successful practical solution to this dilemma that was often referred to as "the bandgap problem" involved the use of the "GW" method. In this approach, the quasiparticle energies appropriate to excited electron and hole states are calculated starting with LDA calculations. In this scheme, the electron self-energy is computed using the Green's function G and a screened Coulomb potential W. When the resulting self-energy is included in the LDA calculation, the electronic states are renormalized and yield bandgaps in excellent agreement with experiment for a broad class of materials. An analysis of the results of applying the GW method reveals that two important physical features are mainly responsible for the success of the method. First, by using an appropriate dielectric function which includes local field effects, the variations in the charge density arising because of bonding effects are correctly included. Second, the renormalization of the electronic energies because of their interactions with plasmons and electron–hole excitations is included to produce appropriate quasiparticle states produced because of the excitations.

Hence with the inclusion of GW modifications to the LDA, the calculations employing the PWPM can yield bandgaps and band structures in agreement with experiment on a level of accuracy found for the experimentally fit EPM results. In addition, these *ab initio* calculations have been extended further and have addressed the problems of the effects on the optical response functions arising from electron–hole interactions. This problem was raised earlier when discussing the results shown in Figure 7. Modifications of spectra of this kind are sometimes referred to as exciton enhancements of oscillator strengths near band edges. However, even when excitons, which are bound states of electron–hole pairs, are not formed, the electron–hole interactions in the excited state can still modify the oscillator strengths and in turn the optical response functions. Applications of the Bethe–Salpeter approach for two-particle interactions to this problem with electron and hole wave functions computed using the PWPM have been successful. At this point, applications of the GW approximation including electron–hole effects have been done for several materials. The computational requirements are somewhat heavy, but the results in all cases tested yield excellent spectra.

A major and important component of condensed matter physics is the research focused on the development of new and novel materials. In the past two or three decades, new systems have revealed new physical properties, new physics, and important application. Systems such as superlattices, fullerenes, nanotubes, and high-temperature superconductors have broadened the horizons. Often novel materials are complex, structurally or electronically, and they offer new challenges for theoretical methods such as the PWPM. In particular, the number of atoms in a unit cell or supercell is a constraint on this method. Usually, complex materials or configurations of materials can only be modeled with a large number of atoms, and this may require a very large number of plane waves in the basis set. If the electronic structure results in very localized configurations as might be appropriate for complex molecules, again many plane waves may be required. A further and interesting aspect of most novel systems on the nanoscale level is that there are effects of confinement. These effects can be dominant for lower-dimensional or very small structures, and they must be accounted for in the calculational scheme.

A typical example is the case of research on nanocrystals where there have been significant advances in recent years. Here, supercells can be employed along with the PWPM. Other techniques which start out with plane waves have had success. One such approach is to use the EPM to generate Bloch functions for a bulk crystal and then convert these itinerant states into more localized states represented by Wannier functions. If the nanocrystal is then modeled using a potential which is bulk-like inside the nanocrystal and zero outside, the Wannier functions can be used to solve the resulting Hamiltonian appropriate to the nanocrystal. One example of the application of this method is a study of the bandgap of InAs as a function of the nanocrystal radius. The results are in excellent agreement with experiment.

Many applications of the PWPM to C_{60} and nanotubes have appeared in the literature. Electronic structure calculations for C_{60} were used to interpret optical, photoemission, superconducting, and other properties. For nanotubes, the explorations have been even more extensive. For carbon nanotubes, calculations of the properties of semiconductor and metal nanotubes have revealed interesting aspects of their electronic structure for interpreting transport and optical properties. Theoretical predictions of Shottky barrier and heterojunction systems composed of semimetallic and semiconductor nanotubes have been verified. There is even evidence of superconductivity which is consistent with semi-empirical calculations based on PWPM results. No completely *ab initio* calculations of the superconducting properties of fullerenes or nanotubes as in the case of MgB_2 have as yet been done.

A dramatic success of applications of the methods described here to this area is the successful prediction of compound nanotubes. In particular, the prediction of BN nanotubes was verified. In this case, unlike the situation for carbon nanotubes, all BN nanotubes without defects or impurities are semiconducting independent of their "chirality." Theory also suggests that when doped, BN nanotubes will have interesting behavior. An example is the nature of the free electron-like wave function associated with the lowest conduction band for this system. It is predicted that when doped appropriately, the electron density for this state will reside in the center of the BN nanotube. It is expected that this system will resemble a tube with electrons filling its center. Other interesting predictions are that, for BC_2N nanotubes, doping can result in electrons traveling along a spiral path producing effects resembling a nanocoil. For BC_3N, it is expected that each tube will behave as if it were a semiconductor, but a collection of these tubes would be metallic. Although the existence of these predicted compound nanotubes has been established, in general, their transport properties have not been measured, so tests for these unusual predicted properties will have to wait until the appropriate experimental techniques become available.

Conclusion

Summarizing, the history of the use of plane-wave methods for electronic structure calculations has many components. As was discussed, the physical justifications came in different forms, and the development of the techniques required physical interpretation. For example, the major changes in the development of the PWPM were motivated by the desire to answer new questions or to broaden the application of the method. Although the advances in computer hardware had a large effect, the largest impact came from the knowledge gained from doing the calculations. It is important to know what is important, or as Linus Pauling said, "The secret to having good ideas is to have many ideas and the judgment to know which ones should be discarded."

Acknowledgments

This work was supported by National Science Foundation Grant No. DMR00-87088 and by the Director, Office of Science, Office of Basic Energy Sciences, Division of Materials Sciences and Engineering, US Department of Energy under Contract No. DE-AC03-76SF00098.

Further Reading

Balkanski M and Walis RF (2000) *Semiconductor Physics and Applications*. Oxford: Oxford University Press.
Bassani F and Pastori Parravicin G (1975) *Electronic States and Optical Transitions in Solids*. Oxford: Pergamon Press.
Cohen ML (1982) Pseudopotentials and total energy calculations. *Physica Scripta* , vol. T1, 5–10.
Cohen ML and Chelikowsky JR (1988) *Electronic Structure and Optical Properties of Semiconductors*. Berlin: Springer-Verlag.
Kittel C (1996) *Introduction to Solid State Physics*, 7th edn. New York: Wiley.
Phillips JC (1973) *Bonds and Bands in Semiconductors*. New York: Academic Press.
Yu PY and Cardona M (1996) *Fundamentals of Semiconductors*. Berlin: Springer.

Plasmons in monolayer and bilayer graphene

Xue-Feng Wang[a] **and Tapash Chakraborty**[b,c], [a]School of physical science and technology, Soochow University, Suzhou, China; [b]Department of Physics and Astronomy, University of Manitoba, Winnipeg, MB, Canada; [c]Department of Physics, Brock University, St. Catharines, ON, Canada

© 2024 Elsevier Ltd. All rights reserved.

Introduction 765
Plasmons in monolayer graphene 766
Plasmons in bilayer graphene 769
Plasmon in biased bilayer graphene 771
Conclusion 776
References 777

Abstract

The collective oscillations of electrons in monolayer and bilayer graphene show different characteristics from those in ordinary two-dimensional Fermi gases. The chirality of the electrons in graphene sets up extra selection rules to their dynamics. The unconventional energy dispersion relation in graphene modifies the electron movement. The narrow gap encourages the carrier exchange between the conduction and the valence bands. The competition between the intra- and the inter-band interactions may introduce extra plasmon branches. The potential bias between the sublattices in monolayer graphene and the monolayers in bilayer graphene opens gap in the electron-hole single particle continuum. Undamped plasmon modes with almost zero group velocity may appear in the gap.

Key points

- Coulomb screening and collective excitations of electrons in monolayer and bilayer graphene are studied in the random phrase approximation.
- Physical mechanism behind the evolution of plasmon spectra in parameter spaces are described.
- Approaches to manipulating the plasmon spectra in graphene are proposed.
- Optimized conditions for undamped plasmon modes with low group velocity are discussed.

Introduction

Mobile electrons in a charge neutral solid material may be a plasma system with negative charges immersed in a uniform background of equal and opposite positive charges. An external charge therein redistributes the negative charges and result in an electric field different from that in vacuum. This Coulomb screening effect can be described by the dielectric function $\varepsilon(\omega)$ which relates the modified electric field E and the electric field in vacuum or the electric displacement D by $E = D/\varepsilon$ at frequency ω. Collective plasma oscillations may be excited spontaneously at some specific plasma frequency ω_p if $\varepsilon(\omega_p) = 0$. As in the case of a simple harmonic oscillator, the energy of each plasma oscillation is quantized into units of $\hbar\omega_p$ according to the quantum mechanics. The corresponding quasi particles with the energy unit are known as plasmons Yu and Cardona (2003). In an ordinary two-dimensional electronic Fermi gas (2DEG), an effective mass m^* can be used to describe the energy dispersion of the electrons as $E = \hbar^2k^2/2m^*$, and $\omega_p^{2D} = [ne^2q/2\varepsilon_0\varepsilon_b m^*]^{\frac{1}{2}}$ in the long wavelength limit $q \sim 0$ (Ando et al., 1982). Here k is the electronic wave vector, n is the sheet density of the electron gas, q is the wave vector of plasmon, ε_0 is the permittivity of vacuum, and ε_b is the background high-frequency dielectric constant. An electron gas in graphene may differ from the normal Fermi gases in at least three aspects, the energy dispersion, the chirality, and the energy gap between the conduction and the valence bands. The random phase approximation (RPA) for many-body Coulomb interaction can be employed to describe approximately the screening effect and understand the behavior of plasmons in graphene as in normal Fermi gas (Castro Neto et al., 2009; Abergel et al., 2010; Das Sarma et al., 2011; Goerbig, 2011; Kotov et al., 2012; Vafek, 2006; Wang and Chakraborty, 2007a, b, 2010; You and Wang, 2012; Hwang and Das Sarma, 2008).

The RPA Coulomb interaction in the Fourier space $V(q,\omega)$ obeys the equation

$$V(q, \omega) = v_0 + v_0\hat{\Pi}_0(\mathbf{q}, \omega)V(q, \omega) \tag{1}$$

with the electron-hole propagator

https://doi.org/10.1016/B978-0-323-90800-9.00063-9

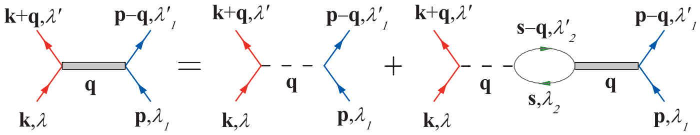

Fig. 1 Diagrammatic illustration of the RPA dressed Coulomb interaction.

$$\hat{\Pi}_0(\mathbf{q},\omega) = 4\sum_{\lambda,\lambda',\boldsymbol{k}}\left|g_{\boldsymbol{k}}^{\lambda,\lambda'}(\mathrm{q})\right|^2 \frac{f\left[E_{\boldsymbol{k+q}}^{\lambda'}\right]-f\left[E_{\boldsymbol{k}}^{\lambda}\right]}{\omega+E_{\boldsymbol{k+q}}^{\lambda'}-E_{\boldsymbol{k}}^{\lambda}+i\delta}, \tag{2}$$

as illustrated by the Feynmann diagram in Fig. 1. Here the factor 4 comes from the degenerate two spins and two nonequivalent valleys K and K' of honeycomb lattice in graphene, $f(E)$ is the Fermi-Dirac distribution function for electrons of energy E, $v_0 = e^2/(2\varepsilon_0\varepsilon_b q)$ is the two-dimensional bare Coulomb interaction (in Fourier space) (Peres et al., 2005), the index $\lambda = \pm$ marks the conduction and valence bands, $g_{\boldsymbol{k}}^{\lambda,\ \lambda'}(\boldsymbol{q})$ is the Coulomb interaction vertex factor which depends on the electron wave functions. The plasmon spectrum can be obtained by finding the zeros of the real part of the dielectric function

$$\hat{\varepsilon}(q,\omega) = 1 - v_0(q)\hat{\Pi}_0(\mathbf{q},\omega). \tag{3}$$

The imaginary part of the dielectric function gives the damping rate of the collective excitations to the electronhole single-particle excitations (Mahan, 2000).

Plasmons in monolayer graphene

Monolayer graphene (MLG) has a honeycomb lattice of carbon atoms with two sublattices A and B. The two sublattices are displaced from each other along an edge of the hexagons by a distance of $a_0 = 1.42$Å. Its energy band can be calculated by the tight-binding model and an intrinsic graphene is a semimetal with the Fermi energy located at the nonequivalent K and K' points at opposite corners of its hexagonal Brillouin zone (Wallace, 1947; Slonczewski and Weiss, 1958; Zunger, 1978; Ando, 2002). In the effective mass approximation, the Hamiltonian of electrons near the Fermi energy is expressed by a 8 × 8 matrix. In the case of spin and valley degeneracies, the matrix can be reduced to four independent 2 × 2 blocks. In the representation of the two sublattices, the Hamiltonian of a spin-up electron near the K point of the reciprocal space reads

$$H^{mg} = v_{mg}\boldsymbol{p}\cdot\boldsymbol{\sigma} + \Delta\sigma_z = \begin{bmatrix} \Delta & v_{mg}p_- \\ v_{mg}p_+ & -\Delta \end{bmatrix}, \tag{4}$$

with $\boldsymbol{\sigma} = (\sigma_x, \sigma_y, \sigma_z)$ the Pauli matrices in the pseudospin space of the two sublattices and $p_\pm = -i\hbar(\partial/\partial x \pm i\partial/\partial y)$ (Kane and Mele, 2005;DiVincenzo and Mele, 1984; Sinitsyn et al., 2006). Here $v_{mg} = 10^6$ m/s is the 'light' velocity of the Dirac electron gas in MLG. 2Δ is the potential bias between the two sublattices, which is zero in intrinsic graphene but can be nonzero in graphene grown on substrates like boron nitride.

The eigenenergy and eigenfunction of the above Hamiltonian read

$$E_{\boldsymbol{k}}^{\lambda} = \lambda\sqrt{\Delta^2 + \hbar^2 v_{mg}^2 k^2}, \tag{5}$$

$$\Psi_{\boldsymbol{k}}^{\lambda} = e^{i\boldsymbol{k}\cdot\mathbf{r}}\begin{pmatrix} \sin\left[\alpha_{\boldsymbol{k}}/2 + (1+\lambda)\pi/4\right] \\ -\cos\left[\alpha_{\boldsymbol{k}}/2 + (1+\lambda)\pi/4\right]e^{i\phi_{\boldsymbol{k}}} \end{pmatrix} \tag{6}$$

with $\tan\phi_{\boldsymbol{k}} = k_y/k_x$, $\tan\alpha_{\boldsymbol{k}} = \hbar vk/\Delta$, and $k = \sqrt{k_x^2 + k_y^2}$. The interaction vertex factor reads $|g_{\boldsymbol{k}}^{\lambda,\ \lambda'}(\boldsymbol{q})|^2 = [1 + \lambda\lambda'\cos\alpha_{\boldsymbol{k+q}}\cos\alpha_{\boldsymbol{k}} + \lambda\lambda'\sin\alpha_{\boldsymbol{k+q}}\sin\alpha_{\boldsymbol{k}}(k + q\cos\theta)/|\boldsymbol{k}+\boldsymbol{q}|]/2$ with θ being the angle between $\boldsymbol{k}$ and $\boldsymbol{q}$. Since the intra-band backward scattering at $\boldsymbol{q} = 2\,\boldsymbol{k}$ and the inter-band vertical transition at $\boldsymbol{q} = 0$ are not allowed under Coulomb interaction in the system, we have $|g_{\boldsymbol{k}}^{\lambda,-\lambda}(0)|^2 = |g_{\boldsymbol{k}}^{\lambda,\ \lambda}(2\boldsymbol{k})|^2 = 0$.

In intrinsic MLG, the net electron density is equal to zero and $E_F = 0$. There exists no plasmon mode at zero temperature. Fig. 2A and B show the real (ε_r) and imaginary (ε_i) parts of the dielectric function at temperature $T = 0$ for $\Delta = 0$ (solid), 0.08 (dashed), and 0.1 meV (dotted) at a wave vector $q = 0.05 \times 10^5$ cm^{-1}. At zero temperature, only inter-band transitions are allowed for electrons. The electron-hole propagator for $\Delta = 0$ is given by $\hat{\Pi}_0(\mathbf{q},\omega) = -q^2/\left[4\sqrt{\hbar^2 v_{mg}^2 q^2 - \omega^2}\right]$ (J. González et al., 1994, 1999, 2001; Khveshchenko, 2006). Therefore we have $\varepsilon_r = 1$ (for $\omega > \hbar v_{mg} q$) above the interband electron-hole continuum (EHC) edge and $\varepsilon_i = 0$ (for $\omega < \hbar v_{mg} q$) below it. With increasing Δ, the peaks of ε_r and ε_i, which are located at the edge of the interband EHC, $\omega_H = 2\sqrt{\Delta^2 + \hbar^2 v_{mg}^2 q^2/4}$, shift to higher energies. At the same time, for $\omega > \omega_H$, ε_r increases continuously with Δ and remains positive.

At a finite temperature, the intra-band transitions are allowed and contribute to the electron-hole propagator of Eq. (2) and a ε_r dip at the intra-band EHC edge $\omega_L = \hbar v_{mg} q$ is formed as shown in Fig. 2C. For $\Delta = 0$ where $\omega_L = \omega_H$, two plasmon modes may

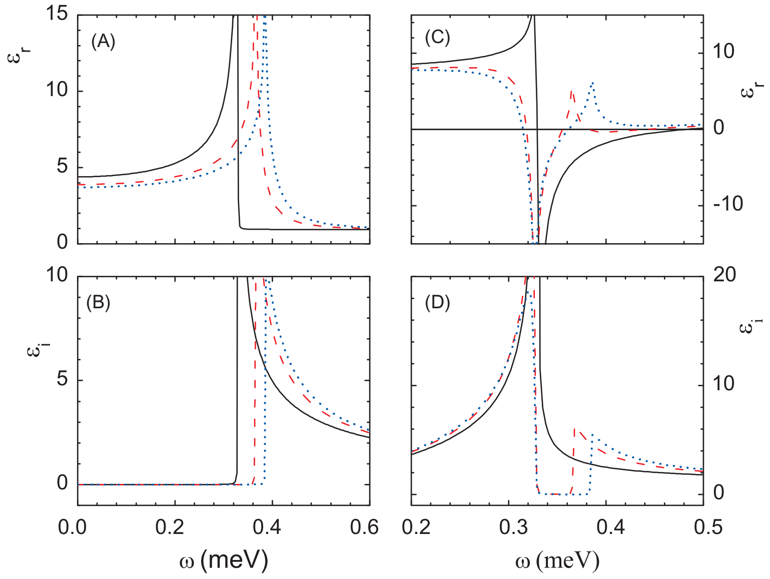

Fig. 2 Real (ε_r) and imaginary (ε_i) parts of the dielectric function vs ω in MLG at $T = 0$ (left panels) and $T = 2$ K (right panels) for $E_F = 0$ and $\Delta = 0$ (solid), 0.08 meV (dashed), and 0.1 meV (dotted). The wave vector is $q = 0.05 \times 10^5$ cm^{-1}.

appear, one strongly Landau damped at $\omega = \hbar v_{mg} q$ and another weakly damped at a higher energy. The damping rates of the plasmon modes are indicated in Fig. 2D by ε_i at the corresponding energies. Comparing the curves in Fig. 2D with those in (B), at finite temperatures a finite ε_i at $\omega < \omega_L$ is introduced by the intra-band transition and a decreased ε_i for $\omega > \omega_L$ due to the weakening of the inter-band transitions, a result of the electronic occupation of the conduction band. With increasing Δ, the ε_r peak shifts with ω_H to higher energy while the ε_r dip stays with ω_L. Since the ε_r peak has a lower energy than the ε_r dip initially at $\Delta = 0$, the peak and the dip merge at first and split again. As a result, at temperature $T = 2$ K as shown in Fig. 2C, the ε_r curve for $\Delta = 0.08$ meV is deformed in such a way that two extra zeros of ε_r or two new plasmon modes emerge. Corresponding to the separation of the ε_r peak from its dip, the ε_i curve evolves a gap between ω_L and ω_H as illustrated in Fig. 2D. One of the plasmon modes is located in this ε_i gap or the EHC gap and is undamped, and so it can be observed experimentally. For $\Delta = 0.1$ meV, there is no damped plasmon mode in the inter-band EHC.

The appearance of the undamped plasmon mode in the existence of energy gap is a result of the interplay between intra- and inter-band correlations which can be adjusted by varying the temperature of the system in experiments. For an MLG of $\Delta = 0.08$ meV, with increasing temperature from $T = 0$, the ratio of the intrato the inter-band correlation increases and ε_r in the EHC gap ($\omega_L \leqslant \omega \leqslant \omega_H$) decreases and crosses zero. There is no plasmon mode when inter-band correlation dominates at $T \leq 1.1$ K and only two damped modes exist when the intra-band correlation dominates at $T \geq 3.3$ K. In the temperature regime 1.1 K $\leq T \leq 3.3$ K or $T \approx 2\Delta$ when the intra- and inter-band correlations can match with each other, however, $\varepsilon_r(\omega_L) < 0$ while $\varepsilon_r(\omega_H) > 0$ and one undamped plasmon mode exists. Furthermore, in the upper end of this regime at 1.9 K $\leq T \leq 3.3$ K, one undamped mode and three damped modes exists.

The ω versus q spectrum of the plasmon modes at $T = 2$ K is plotted by thick solid curves for $\Delta = 0$ in Fig. 3A and for $\Delta = 0.08$ meV in Fig. 3B. The weakly damped plasmon mode in the $\Delta = 0$ case has an approximate dispersion of $\omega \propto \sqrt{q}$ at small q. A finite Δ separates ω_H from ω_L and opens a gap between the intraand inter-band EHC's. As a result, the formerly weakly damped plasmon mode becomes undamped near $q = 0$ because it is now located in the gap. When it approaches the inter-band EHC edge, the dispersion curve of this mode is squeezed to a lower energy by the ε_r peak near the inter-band EHC edge as shown in Fig. 2C and then is split into three plasmon modes, viz., two new plasmon modes emerge near the inter-band EHC edge. One of the modes remain undamped in the EHC gap and the other Landau damped two are located inside the inter-band EHC. The latter two modes merge and disappear at q near 0.07×10^5 cm^{-1} for $\Delta = 0.08$ meV. The undamped mode survives in larger wavevectors until it merges with the strongly damped mode to the intra-band EHC edge when the inter-band correlation dominates and ε_r becomes positive in the all frequency regime. The insets of Fig. 3 show the excitation spectral weight or the dynamical structure factor $S(\mathbf{q}, \omega) = -(1/nv_0(q))\mathrm{Im}[1/\hat{\varepsilon}(q, \omega)]$ at $q = 0.05 \times 10^5$ cm^{-1} (Mahan, 2000; Hwang and Das Sarma, 2008). The damped plasmon spectra is hidden in the EHC's while the undamped plasmon spectra appears as a sharp peak in the EHC spectral gap and should be observable in experiments (Grimes and Adams, 1976).

As discussed above, dominant intra-band correlation results in the appearance of the plasmon mode with dispersion $\omega \propto \sqrt{q}$ at small q in Dirac gases as well as in Fermi gases (Stern, 1967). Different from 2DEGs, Dirac gases of $E_F = 0$ show only inter-band correlation at zero temperature and there is a strong competition between intra- and inter-band correlations as the parameters of the system vary. Controlling the sublattice bias and the carrier density can change significantly the ratio between intra- and inter-band many-body correlations of the Dirac electron gas and may introduce undamped plasmon modes (Novoselov et al., 2005; Zhang et al., 2005).

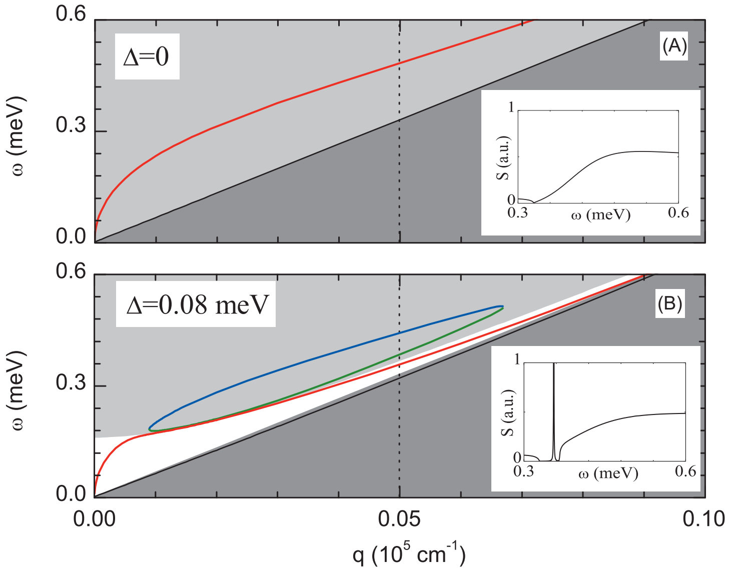

Fig. 3 Plasmon spectrum (thick curves) of MLG ($E_F = 0$) at temperatures $T = 2$ K with $\Delta = 0$ in (A) and 0.08 meV in (B). Intra- (dark shaded) and inter- (light shaded) band single-particle continuums are also shown. ω_L and ω_H are the lower and upper borders separating the white (EHC gap) and shaded areas respectively in (B). The vertical dotted lines indicate the q values for which excitation intensity is shown in the insets and the dielectric function is shown in Fig. 2C.

Due to the symmetry of the band structure, MLG having the same density of electrons or holes are similar and the result can be shown by a system with a net electron density and positive Fermi energy E_F. For a Dirac gas in a MLG, the extra electrons in the conduction band reduce the inter-band scattering rate but enhances the intra-band one by increasing the length of the Fermi ring. Similar to the case of finite temperature, a plasmon mode with an approximate dispersion $\omega \propto \sqrt{q}$ at small q appears even at zero temperature as shown in Fig. 4A. For $\Delta = 0$ and at $T = 0$, a EHC gap of width $2\hbar v_{mg}(k_F - q)$ is opened above the intra-band EHC edge in the range $0 < q < k_F$. This EHC gap at finite Fermi energy lets the $\omega \propto \sqrt{q}$ plasmon mode undamped near $q = 0$. Another character of this mode at finite fermi energy is its flat dispersion slope as shown by the dashed curve in Fig. 4A, compared with the case at finite temperature as shown in Fig. 3A, near its entrance into the interband EHC. Furthermore, in contrast to the emergence of new plasmon modes occurred when its dispersion curve enters the inter-band EHC from a EHC gap, the dispersion curve enters the inter-band EHC smoothly here. We can characterize the carrier density by the Fermi energy to emphasize the interesting energy regime in the existence of energy gap. The corresponding carrier density can be estimated with the help of their simple relation at zero temperature $n = (E_F^2 - \Delta^2)/(\pi v_{mg}^2)$. For example, the carrier density of a system with $E_F = 1$ meV is $n = 7.34 \times 10^7$ cm^{-2}.

The presence of the energy gap changes the physical scenario of the excitation spectrum in the $\Delta = 0$ case described above. At $T = 0$, the intraband EHC edge deviates from $\omega = \hbar v_{mg} q$ to a lower energy $\sqrt{\Delta^2 + \hbar^2 v_{mg}^2 (k_F + q)^2} - \sqrt{\Delta^2 + \hbar^2 v_{mg}^2 k_F^2}$; the inter-band EHC edge shifts to a higher energy $\sqrt{\Delta^2 + \hbar^2 v_{mg}^2 k_F^2} + \sqrt{\Delta^2 + \hbar^2 v_{mg}^2 (k_F - q)^2}$ for $q < 2k_F$ while remains ω_H when $q > 2k_F$.

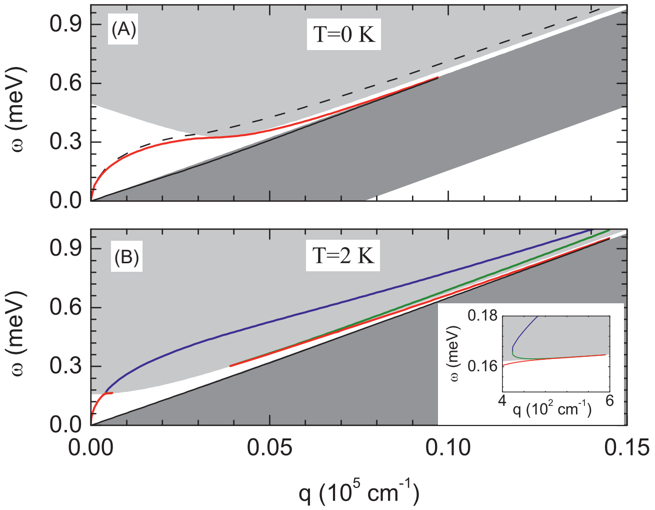

Fig. 4 The same as in Fig. 3 with $E_F = 0.25$ meV at $T = 0$ (A) and $T = 2$ K (B). The solid curves are for $\Delta = 0.08$ meV and the dashed in (A) for $\Delta = 0$. The inset of (B) shows the zoomed area where the $\sqrt{q}$ plasmon mode enters the interband EHC and splits into three modes.

More interestingly, the sublattice bias may shift the plasmon mode in the interband EHC to the EHC gap and makes it undamped. For a system of $E_F = 0.25$ meV, the plasmon mode at $q = 0.05 \times 10^5$ cm^{-1} becomes undamped if $\Delta > 0.02$ meV. In a MLG of $\Delta = 0.08$ meV, the plasmon mode remains undamped up to $q = 0.1 \times 10^5$ cm^{-1} where it merges with the mode in the intra-band EHC as illustrated by the solid curves in Fig. 4A.

At higher temperature the restriction to single-particle transitions by the Fermi energy is relaxed and the EHC is independent of the Fermi energy as shown by the shades in Fig. 3B and Fig. 4B. However, the collective excitation spectrum changes as the ratio of intra- to interband correlation increases with the net electron density. The relative weakening of inter-band correlation when $E_F > \Delta$ lowers the ε_r peak at the inter-band EHC edge, shown in Fig. 2C, and consequently changes the number or shifts the position of the zeros of ε_r for different q. Comparing the resulting plasmon spectrum plotted in Fig. 4B with that in Fig. 3B, we find that for q between 0.006 – 0.04 × 10^5 cm^{-1} the undamped mode disappears because the ε_r peak becomes lower than zero and for q bigger than 0.07×10^5 cm^{-1} two damped modes exist in the inter-band EHC.

Plasmons in bilayer graphene

The bilayer graphene (BLG) is formed by stacking two graphene monolayers in the same way as the stacking occurs in graphite, i.e., the Bernal stacking (McCann and Fal'ko, 2006; Koshino and Ando, 2006; Nilsson et al., 2006; Ohta et al., 2006). The two graphene monolayers are arranged in such a way that the A sublattice is exactly on top of the sublattice $B^{'}$ with a vertical separation of $b_0 = 3.4$ Å (Trickey et al., 1992). The system can be described by a tight-binding model characterized by three coupling parameters, $\gamma_0 = 3.16$ eV between the atoms A and B or $A^{'}$ and $B^{'}$ (intra-layer coupling), $\gamma_1 = 0.39$ eV between A and $B^{'}$ (the direct inter-layer coupling), and $\gamma_3 = 0.315$ eV between $A^{'}$ and B, A and $A^{'}$, or B and $B^{'}$ (the indirect inter-layer coupling) (Koshino and Ando, 2006).

In the k space, the BLG has the same hexagonal Brillouin zone as that of a monolayer. Its physical properties are mainly determined by the energy spectrum and the wavefunction near the two inequivalent corners of the Brillouin zone K and $K^{'}$, where the π^* conduction band and the π valence band meet at the Fermi surface (Wallace, 1947). Due to the strong interlayer coupling (the π orbit overlap) both the conduction band and the valence band in a bilayer are split by an energy of ~0.4 eV near the K and $K^{'}$ valleys (Trickey et al., 1992; Yoshizawa et al., 1996; Ohta et al., 2006). Since this energy splitting is larger than the energy range we are interested in from the bottom of the energy band, we take into account only the upper valence band and the lower conduction band. The BLG cannot be treated as two independent graphenes monolayer with the interlayer coupling as a perturbation because of the strong interlayer overlap of the π orbits. In contrast, the perturbation treatment of the interlayer coupling is valid for a normal double quantum well system or in an intercalated graphite (Wang, 2005; Shung, 1986; Visscher and Falicov, 1971).

In the effective-mass approximation (McCann and Fal'ko, 2006; Koshino and Ando, 2006), the electrons in the K valley are described by a Hamiltonian with a mixture of the linear and the quadratic terms of p

$$H^{bg} = \frac{\hbar^2}{2m^*}\begin{pmatrix} 0 & p_-^2 \\ p_+^2 & 0 \end{pmatrix} - \frac{\hbar^2 k_{bg}}{2m^*}\begin{pmatrix} 0 & p_+ \\ p_- & 0 \end{pmatrix}. \tag{7}$$

The effective mass of the quadratic term is $m^* = 2\hbar^2\gamma_1/(3a_0\gamma_0)^2 \approx 0.033m_0$ with m_0 the free electron mass and the 'light' velocity of the linear term is $v_{bg} = \hbar k_{bg}/2m^* = 3a_0\gamma_3/2\hbar \approx 10^5$ m/s with $k_{bg} \approx 10^8/\sqrt{3}$ m^{-1}.

The eigenenergy and eigenfunction of the above Hamiltonian read

$$E_{\boldsymbol{k}}^{\lambda} = \lambda\hbar^2 k\sqrt{k^2 - 2k_{bg}k\cos 3\phi + k_{bg}^2}/2m^*, \tag{8}$$

$$\Psi_{\boldsymbol{k}}^{\lambda}(\boldsymbol{r}) = \frac{e^{i\boldsymbol{k}\cdot\boldsymbol{r}}}{\sqrt{2}}\begin{pmatrix} e^{i\varphi_{\boldsymbol{k}}} \\ \lambda \end{pmatrix}. \tag{9}$$

with the pseudospin angle $\lambda\varphi_{\boldsymbol{k}} = \lambda \arg(ke^{-2i\phi} - k_{bg}e^{i\phi})$. Here $\arg(z)$ is the argument θ of a complex $z = |z|e^{i\theta}$.

For $k \gg k_{bg}$ the electron states are chiral with $\varphi = -2\phi$ and have an approximately isotropic parabolic energy dispersion $E_{\boldsymbol{k}}^{\lambda} = \lambda\hbar^2k^2/2m^*$. Near $k = k_{bg}$, the energy dispersion becomes highly anisotropic as shown in Fig. 5A and B. The corresponding characteristic energy is $E_0 = \hbar^2k_{bg}^2/2m^* = 3.9$ meV. At $E = 0$, where the Fermi energy is located in the undoped BLG, there are four contact points between the conduction and the valence bands: One at $k = 0$, the center of the valley and the three satellites at $k = k_{bg}$ in the directions of $\phi = 0$, $2\pi/3$, and $4\pi/3$. They can be treated as four Dirac points because the electronic states near each point have a linear energy dispersion and have the same chirality as those near a Dirac point in the monolayer graphene. However, compared to the monolayer graphene, the energy dispersion here is anisotropic and the 'light' velocity is about 10 times slower. As illustrated in Fig. 5A and B, there is an energy pocket with a depth of about $E_0/4$ at each Dirac point. The above peculiar characteristics of the BLG makes it quite different from the MLG in their Coulomb screening properties as described in the following.

The Coulomb interaction vertex factor reads $|g_{\boldsymbol{k}}^{\lambda,\lambda'}(\boldsymbol{q})|^2 = [1 + \lambda\lambda'\cos(\varphi_{\boldsymbol{k}} - \varphi_{\boldsymbol{k}+\boldsymbol{q}})]/2$. Near the central Dirac point at $k = 0$, the intraband backward scattering and interband vertical Coulomb scattering are forbidden and $|g_{\boldsymbol{k}}^{\lambda,-\lambda}(0)|^2 = |g_{\boldsymbol{k}}^{\lambda,\lambda}(-2\boldsymbol{k})|^2 = 0$. The same rules also hold for the three satellite Dirac points. For a large $k(k \gg k_{bg})$, $|g_{\boldsymbol{k}}^{\lambda,-\lambda}(0)|^2 = |g_{\boldsymbol{k}}^{\lambda,-\lambda}(-2\boldsymbol{k})|^2 = 0$ but $|g_{\boldsymbol{k}}^{\lambda,\lambda}(-2\boldsymbol{k})|^2 = 1$, i.e. the intraband backward transition is allowed but both the interband backward and vertical transitions are forbidden. The above selection rules together with the energy dispersion of the carriers in the BLG indicate that the electrons (holes) close to the bottom (top) of the conduction (valence) band have very different behaviors from those away from the bottom (top).

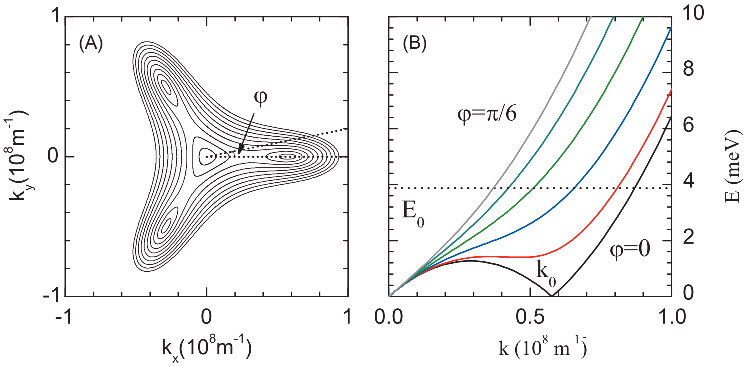

Fig. 5 (A) The contour lines of the energy in the $k_x - k_y$ plane near the K point in BLG. The corresponding energies, starting with the innermost curve are $0.1E_0$ to E_0 with an increment of $0.1E_0$. (B) The energy spectrum for equally separated ϕ from 0 to $\pi/6$ (curves with increasing energy).

Note that in a MLG the dielectric function $\hat{\varepsilon}$ is invariant if all the parameters with the energy unit, ω, E_F, and k_BT, and with the wavevector unit, $\boldsymbol{k}$ and $\boldsymbol{q}$, vary proportionally because of the linear energy dispersion of the Dirac gas (Wang and Chakraborty, 2007a). As a result, the dielectric function and the plasmon dispersion is uniform for systems with proportional parameters. In a BLG, however, this is not true anymore because of the nonlinear energy dispersion.

The static dielectric function at zero temperature versus q is plotted in Fig. 6A. Its long wavelength limit is given by the properties of the four Dirac points. The central point has an isotropic 'light' velocity v_{bg} while the satellite ones have the elliptic form of equi-energy lines with a minimum 'light' velocity equal to v_{bg} along their radical direction and a maximum of $3v_{bg}$ along the azimuthal direction. The static dielectric constant at $q = 0$ is estimated to be $\varepsilon_s = 1 + 3e^2/(8\varepsilon_0\hbar v_{bg}) \approx 105$. This value is much bigger than that of the MLG (4.5) (Wang and Chakraborty, 2007a). This means that the long-range Coulomb interaction is much more strongly screened for the bilayer system, thanks to a much bigger density of states near the Fermi energy in a BLG.

Another characteristic of the BLG is its screening anisotropy, especially for scattering at a distance range of about 10 nm. This is shown by the difference between the solid and the dotted curves in Fig. 6, corresponding to the directions of $\boldsymbol{q}$ pointing to any satellite from the central Dirac points ($\alpha = 0$) or connecting any two satellites ($\alpha = \pi/6$) respectively. Here α is the angle between $\boldsymbol{q}$ and the x-axis. At $q = \sqrt{3}k_{bg} = 10^8$ m^{-1}, the wavevector distance between any two satellite Dirac points, the anisotropy of ε_s reaches its maximum with a mismatch of 20% along the different directions. The shoulder near $q = k_{bg} = 0.58 \times 10^8$ m^{-1} in the solid curve reflects the strong scattering between the carriers in the central and the $\phi = 0$ satellite Dirac points. At a finite temperature, the energy pockets near the Dirac points are partially occupied and the intraband scattering strength is greatly enhanced. As a result, the static dielectric function near $q = 0$ increases rapidly, as shown in Fig. 6B at $T = 4.2$ K. The real and imaginary parts of the dynamic dielectric function versus the energy for a small wavevector $q = 0.005$ along $\alpha = 0$ at $T = 0$ and at $T = 4.2$ K are shown in Fig. 6C and Fig. 5D.

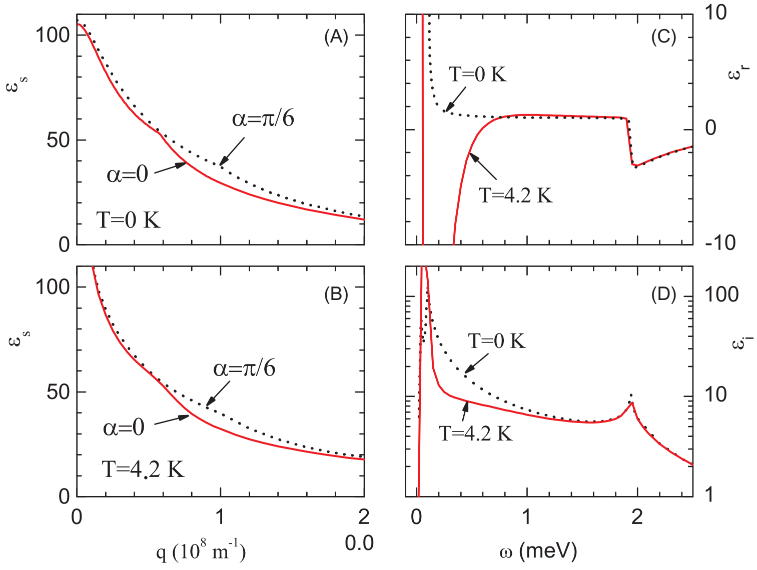

Fig. 6 (A) The static dielectric function ε_s vs the wavevector q in BLG along the direction $\alpha = 0$ (solid) and $\pi/6$ (dotted) at $T = 0$. (B) The same as (A) but at $T = 4.2$ K. (C) The real part of the dielectric function ε_r vs frequency ω at $T = 0$ (dotted) and at $T = 4.2$ K (solid). (D) The imaginary part of the dielectric function ε_i vs ω at $T = 0$ (dotted) and at $T = 4.2$ K (solid). In (C) and (D), $q = 0.005 \times 10^8$ m^{-1} and $\alpha = 0$. In the limit $\omega \to \infty$, ε_r gradually approaches to one while ε_i approaches to zero.

For $\omega > E_0/2$, the dielectric function of a BLG is similar to that of a normal Fermi gas and its temperature dependence is weak. The step of ε_r and the peak of ε_i near $\omega = E_0/2 = 2$ meV correspond to the single-particle excitation coupling states with a vanishing group velocity and having wavevectors located near the middle between the central and the satellite Dirac points. For small ω, however, the dielectric function becomes more sensitive to the temperature and shows characteristics of the Dirac gas. One sign of the Dirac gas is the lack of Coulomb screening ($\varepsilon_r \approx 1$) in the energy window between 1 and 2 meV. Another sign is that a low-energy plasmon mode appears only at a finite temperature. As shown in Fig. 6C, the ε_r has no negative value for the energy $\omega < E_0/2$ at $T = 0$ but evolves into a deep negative dip at a finite temperature $T = 4.2$ K, when the energy pockets near the Dirac points is partially occupied. As a result, one observes a weakly Landau damped plasmon mode of dispersion $\omega \sim \sqrt{q}$ at T = 0 and may observe two such weakly damped modes at finite temperatures.

Fig. 7A presents the plasmon spectrum of an intrinsic BLG ($E_F = 0$). The dispersion of the weakly Landau damped mode is indicated by the thick curve and has a $\sqrt{q}$ dependence. Interestingly, the plasmon mode exists only at the energy higher than $E_0/2$, i.e., double the depth of the energy pockets in the Dirac points. At a finite temperature $T = 4.2$ K, another weakly damped plasmon mode appears at the energy lower than $E_0/2$ and also has a dispersion of $\sqrt{q}$ near $q = 0$, as illustrated in Fig. 7B. The plasmon mode of higher energy that exists at $T = 0$ is not sensitive to the temperature. This temperature dependence of the low and high energy plasmon spectra represents the marked difference between the electron gases having linear (without the collective excitation) and quadratic (with the collective excitation) energy dispersion at $T = 0$. We have established earlier that the collective excitations appear only at a finite temperature for the Dirac gas (Wang and Chakraborty, 2007a). The electronic states in a BLG are similar to the Fermi type at the high energies but reverts to a Dirac type at the low energy.

The carrier density of the system can be changed by doping. For a typical doping density of 10^{12} cm^{-2}, the Fermi energy is high enough from the conduction bottom and the linear k term in the Hamiltonian can be neglected (Koshino and Ando, 2006; Ohta et al., 2006). The electrons then have a quadratic dispersion but with chirality and $\varphi = -2\phi$. Near $q = 0$, the plasmon dispersion in a doped BLG has again a $\sqrt{q}$ dispersion as shown by the solid curve in Fig. 8 and shares the same dispersion with a normal 2DEG. The effect of the chirality is shown by the dotted curve for the plasmon dispersion of a normal two-dimensional Fermi gas with two valleys, for comparison. The two curves overlap for the small q but separate as q increases. The maximum difference in the dispersion appears near $q = \sqrt{2}k_F$ when $\boldsymbol{k}$ and $\boldsymbol{k} + \boldsymbol{q}$ form a right angle in the Fermi plane and the corresponding transition is forbidden in the BLG due to its chirality.

Plasmon in biased bilayer graphene

Under a perpendicular electric field, an energy gap opens between the conduction and the valence bands in BLG (McCann and Fal'ko, 2006), when an electrostatic potential bias U exists between the two graphene layers. In the effective-mass approximation, the Hamiltonian describing electrons of moderate energies in the K valley of a biased BLG reads

$$H^{bbg} = \frac{\hbar^2}{2m^*}\begin{pmatrix} 0 & p_-^2 \\ p_+^2 & 0 \end{pmatrix} + \frac{U}{2}\begin{pmatrix} 1 & 0 \\ 0 & -1 \end{pmatrix}. \tag{10}$$

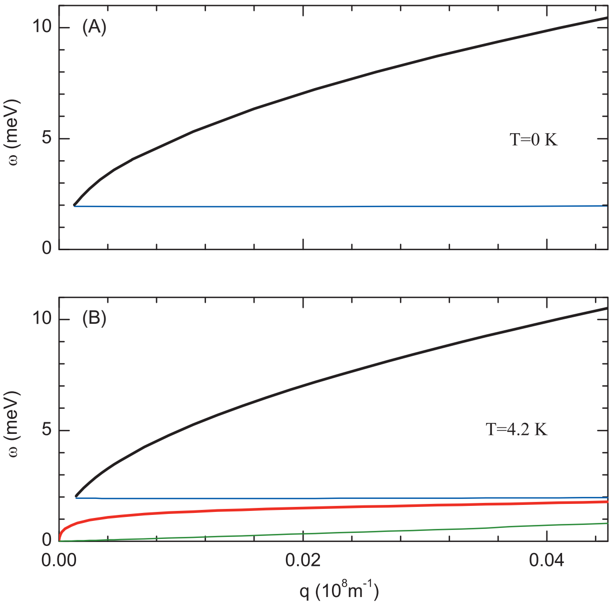

Fig. 7 The plasmon spectrum of intrinsic BLG at $T = 0$ (A) and at $T = 4.2$ K (B). The thick curves indicate the weakly Landau damped modes while the thin curves represent the strongly damped modes.

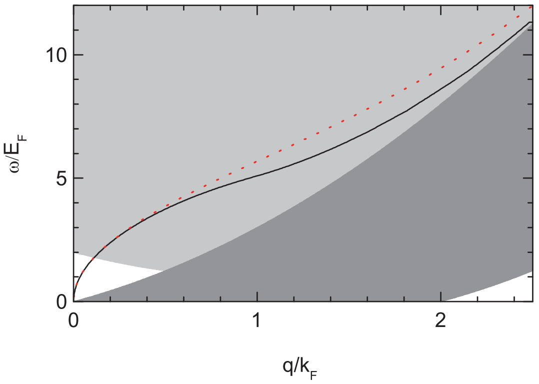

Fig. 8 The plasmon spectrum of a doped BLG (solid curve) with a typical carrier density of 10^{12} cm^{-2}, corresponding to $E_F = 36.3$ meV and $k_F = 1.77 \times 10^8$ m^{-1}. The plasmon spectrum in the same system but without chirality is plotted as a dotted curve for comparison. Intra- (dark shaded) and inter- (light shaded) band single-particle continuums are also shown.

The indirect inter-layer coupling is neglected since it affects only the energy band in the range of less than 2 meV from the middle of the conduction-valence band gap. The eigenenergy and eigenfunction of the above Hamiltonian read

$$E_{\boldsymbol{k}}^{\lambda} = \lambda \sqrt{\left(\frac{\hbar^2 k^2}{2m^*}\right)^2 + \left(\frac{U}{2}\right)^2}, \tag{11}$$

$$\Psi_{\boldsymbol{k}}^{\lambda} = e^{i\boldsymbol{k}\cdot\mathbf{r}} \begin{pmatrix} \sin\left[\beta_{\boldsymbol{k}}/2 + (1+\lambda)\pi/4\right] \\ -\cos\left[\beta_{\boldsymbol{k}}/2 + (1+\lambda)\pi/4\right] e^{i2\phi_{\boldsymbol{k}}} \end{pmatrix}. \tag{12}$$

Here $\beta_{\boldsymbol{k}}$ indicates the ratio of the kinetic energy to the potential bias with $\tan\beta_{\boldsymbol{k}} = \hbar^2 k^2/(m^* U)$. For such an energy dispersion the DOS of the system is

$$D(E) = \frac{1}{(\pi)^2} \int \frac{dS}{|\nabla_{\boldsymbol{k}} E|} = \frac{m^*}{\pi\hbar^2} \frac{E}{\sqrt{E^2 - \left(\frac{U}{2}\right)^2}}, \tag{13}$$

Under finite bias U, the DOS of the BLG diverges on the edge of the energy gap $E = |U/2|$. The vertex factor reads

$$\left|g_{\boldsymbol{k}}^{\lambda,\lambda'}(\mathbf{q})\right|^2 = \left|\left\langle \boldsymbol{k}+\mathbf{q},\ \lambda' \right| e^{i\mathbf{q}\cdot\mathbf{r}} \left| \boldsymbol{k},\ \lambda \right\rangle\right|^2 = \frac{1}{2}\left[1 + \lambda\lambda' \cos\beta_{\boldsymbol{k}} \cos\beta_{\boldsymbol{k}+\mathbf{q}} + \lambda\lambda' \sin\beta_{\boldsymbol{k}} \sin\beta_{\boldsymbol{k}+\mathbf{q}} \cos\left(2\phi_{\boldsymbol{k}} - 2\phi_{\boldsymbol{k}+\mathbf{q}}\right)\right].$$

When $\mathbf{q} = 0$ and $\mathbf{q} = -2\boldsymbol{k}$, $\left|g_{\boldsymbol{k}}^{\lambda,\lambda'}(\mathbf{q})\right|^2 = \frac{1}{2}\left(1 + \lambda\lambda'\right)$. Similar to unbiased BLG, the interband vertical and back scatterings are both forbidden but the intraband back scattering is allowed in biased BLG. For intraband scattering with $\boldsymbol{k} \perp \mathbf{k} + \mathbf{q}$, we have $\left|g_{\boldsymbol{k}}^{\lambda,\lambda'}(\mathbf{q})\right|^2 = \frac{1}{2}\left[1 + \cos\left(\beta_{\boldsymbol{k}} + \beta_{\boldsymbol{k}+\mathbf{q}}\right)\right]$, which becomes zero in unbiased BLG.

The intraband component ($\lambda = \lambda'$) of the electronhole propagator is expected to be similar to that in normal 2DEG except the effect of chirality and deformation of energy band. The interband one ($\lambda = -\lambda'$), which can be manipulated by the bias voltage, modifies qualitatively the screening properties of the system. Since the approximate energy spectrum we use in this study is isotropic, the obtained properties are also isotropic and we use $q \equiv |\mathbf{q}|$ and $k \equiv |\boldsymbol{k}|$ in the following discussion.

Fig. 9 shows the negative intraband propagator in unit of $N_0 = 2m^*/\pi$ (the DOS of intrinsic BLG) versus frequency ω for three typical wavevector q values. Similar to the 2DEG result at zero temperature, the imaginary part is nonzero in the single-particle continuum $0 < \omega < \omega_u$ for $0 < q < 2k_F$ and $\omega_l < \omega < \omega_u$ for $q > 2k_F$, with $\omega_l = |E_{k_F-q}^{1} - E_{k_F}^{1}|$ and $\omega_u = E_{k_F+q}^{1} - E_{k_F}^{1}$. The derivative of the imaginary part is not continuous at the continuum edges and for $0 < q < 2k_F$ is also not continuous at $\omega = \omega_l$ besides $\omega = 0$ and ω_u. When the bias U increases, the structures of the curves shift to lower energy because the energy band is narrowed and the group velocity of electrons at the bottom of the conduction band decreases. When the temperature increases, the sharp edges become smoother and the nonzero range gets wider as expected.

Different from the 2DEG result, as illustrated in Fig.9C for $q > k_F$ at $U = 0$ and $T = 0$, the imaginary part has a sharp dip with a derivative discontinuity at $\omega_m = q^2/2m^*$ between the edges due to the chiral nature of the wave functions (Sensarma et al., 2010). The dip and discontinuity persist at finite temperature but become softened and disappear under finite bias voltage.

The real part, presented in the lower panels of Fig.9, shows a sharp peak at ω_l and a sharp dip at ω_u with an extra peak near ω_m for $q > k_F$ and moves in a similar way as the imaginary part with bias and temperature. However, the structure near ω_m for both the imaginary and real part develops in a different way from those at ω_l and ω_u when U and T increase. It remains at high temperature and removes off with the bias voltage while those at ω_l and ω_u decay with temperature. On average, the variation range of the propagator decreases with q.

Fig.11 illustrates the negative interband propagator in unit of N_0 versus ω for the same three q values as in Fig.10. Its imaginary part and the single-particle continuum have a minimal energy limit $\omega_1 = E_{k_F}^{1} - E_{k_F-q}^{-1}$ at zero temperature or $\omega_2 = 2E_{q/2}^{1}$ at finite

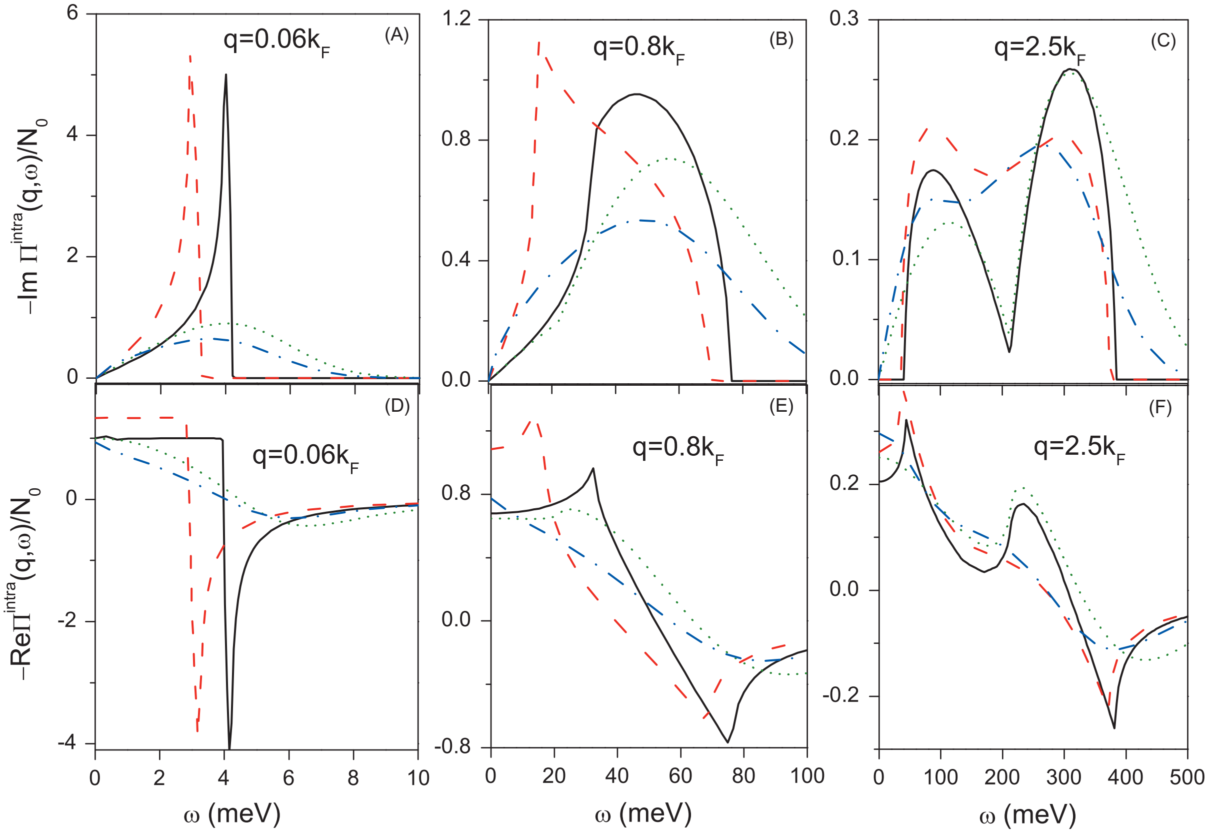

Fig. 9 The negative intraband electron-hole propagator in unit of N_0 versus frequency ω in unbiased/biased BLG at zero/room temperature. The imaginary part for q = 0.06, 0.8, and 2.5k_F is plotted in panel (A), (B), and (C), respectively, and the corresponding real part in (D), (E), and (F). The electron density is $n = 10^{12}$ cm^{-2} with the Fermi wavevector $k_F = 1.77 \times 10^8$ m^{-1}. The corresponding Fermi energy is $E_F = 34$ meV at $U = 0$ and $E_F = 45.4$ meV at $U = 60$ meV. Solid curves are for $T = 0$, $U = 0$; dashed $T = 0$, $U = 60$ meV; dotted $T = 300$ K, $U = 0$; dash-dotted $T = 300$ K, $U = 60$ meV.

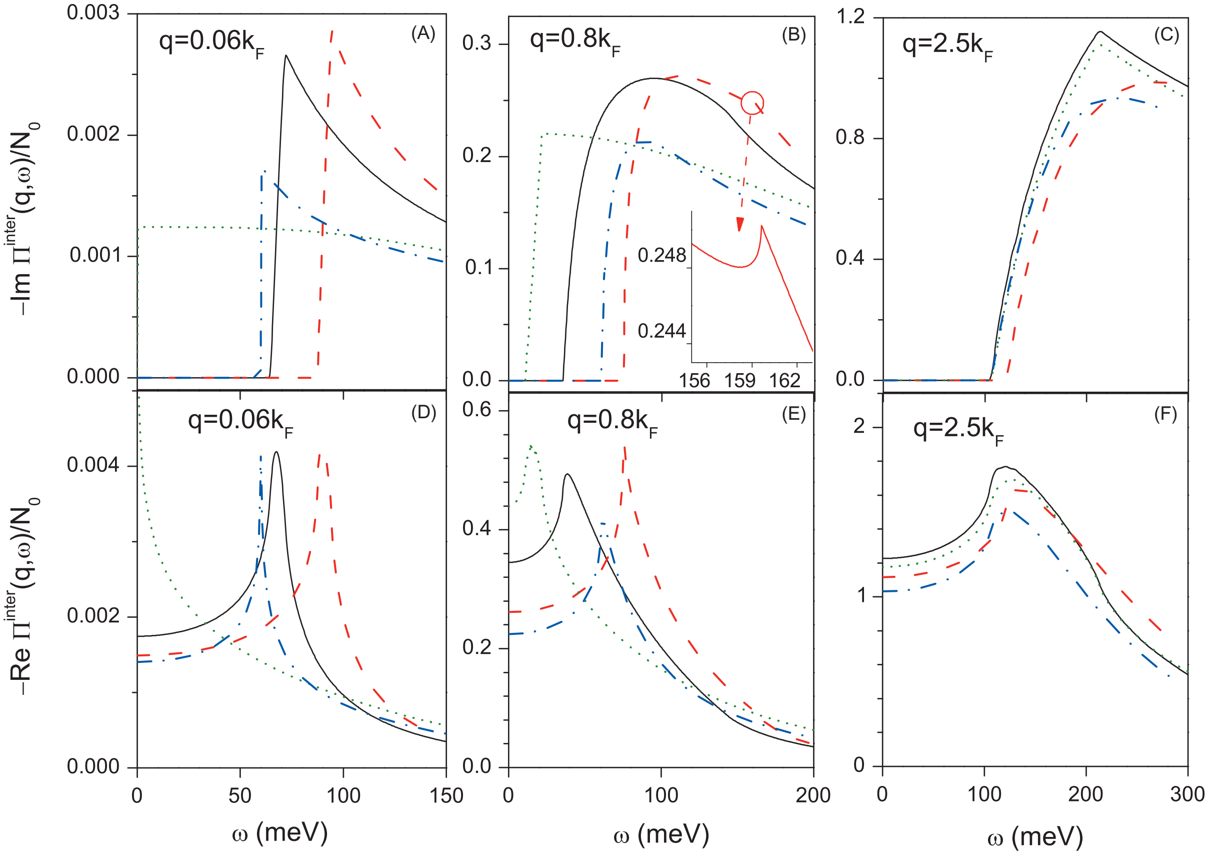

Fig. 10 The negative interband electron-hole propagator of BLG in unit of N_0 versus frequency ω is plotted for the same parameters set and arrangement as in Fig.9.

temperature. For small q [Fig.10A] the imaginary part increases sharply and reaches a peak before decreases in a way $\sim 1/\omega$. For mediate $q = 0.8k_F$ [Fig.10B] the main peak becomes round and smooth while a sharp peak near $\omega_3 = E_{k_F}{}^1 - E_{k_F+q}^{-1}$ appears under bias as shown in the inset of Fig.10B. This latter peak grows and becomes more visible as U increases. For $q > k_F$ a peak with discontinuity appears near $\omega_m = q^2/2m^*$ at zero temperature in both biased and unbiased BLG as shown in Fig.10C (Sensarma et al., 2010).

Corresponding to the continuum edges of the imaginary part, on the curve of the real part as shown in the lower panels of Fig.10, there is a peak near $\omega_1(\omega_2)$ at low (high) temperature when the electron system is degenerate (nondegenerate). The peak near ω_2 may become very sharp for small q in biased BLG because the bottom (top) of the conduction (valence) band becomes flat and the DOS diverges on the edge of energy gap. The overal1 contribution of interband excitation to the propagator increases with q and in a way $\sim q^2$ at small q.

The electron-hole propagator reflects the electric polarizability of a many-body system screening a Coulomb potential. After being reduced by the background dielectric constant ε_b, it determines the dielectric function $\varepsilon(q,\omega) = \varepsilon_r + i\varepsilon_i$. The zero of the real part ε_r gives the collective excitation of the system in the absence of external electromagnetic field. The imaginary part ε_i gives the spectrum of the single-particle excitation. In the presence of only intraband single particle excitation as in conventional 2DEG, there exist maximally two plasmon modes, one acoustic mode of frequency ω_A within the single-particle excitation and another optical mode ω_O, because $-Re\,[\Pi(q,\omega)]$ has only one dip below zero as shown in Fig.9. The acoustic mode is thus always overdamped with little spectral weight and not experimentally relevant. The contribution from interband excitation introduces fine structures to ε_r near zero and at least two extra modes, ω_3^p and ω_4^p may emerge.

Fig. 10 displays ε_r versus ω for various temperature T (A), bias voltage U (B), electron density n (C), and wavevector q (D). In the high frequency limit, the effect of polarization vanishes and $\varepsilon_b = 1$. For intrinsic BLG where $n = 0$, the intraband polarization is negligible and $\varepsilon_r > 0$ at $T = 0$. There is no collective mode. In other cases, the ε_r versus ω curve has a deep dip at ω_u and a peak at ω_1 or/and ω_2. The competition among value one, the intra-, and the inter-band contributions to the polarizability determine its fine features. For typical parameters, as illustrated in Figs. 9 and 10, the effect of the intra-(inter-) band polarization decreases (increases) with q so we expect that ε_r mainly shows intra- (inter-) band characteristics for long (short) wavelength. In this study we are mostly interested in the screening and collective excitation properties of long wavelength in the system, and in Fig.11 we present the details only for $q \ll k_F$ near $\varepsilon_r = 0$.

The result for a system of $U = 30$ meV, $n = 10^{12}\text{cm}^{-2}$, and $q = 0.1 \times 10^8\ \text{m}^{-1}$ is exhibited in Fig.11A. At low temperature $T = 4$ K (solid) when the system is degenerate, the intraband contribution dominates and a peak appear near $\omega_1 = E_{k_F}{}^1 - E_{k_F-q}^{-1} \simeq 2E_{k_F}{}^1 = 74.4$ meV which is out of the panel. When the temperature increases to 200 K (dashed) and the system becomes nondegenerate, a sharp peak emerge near $\omega_2 = 2E_{q/2}^1 \simeq 30$ meV. Since this interband peak is located just below the optical

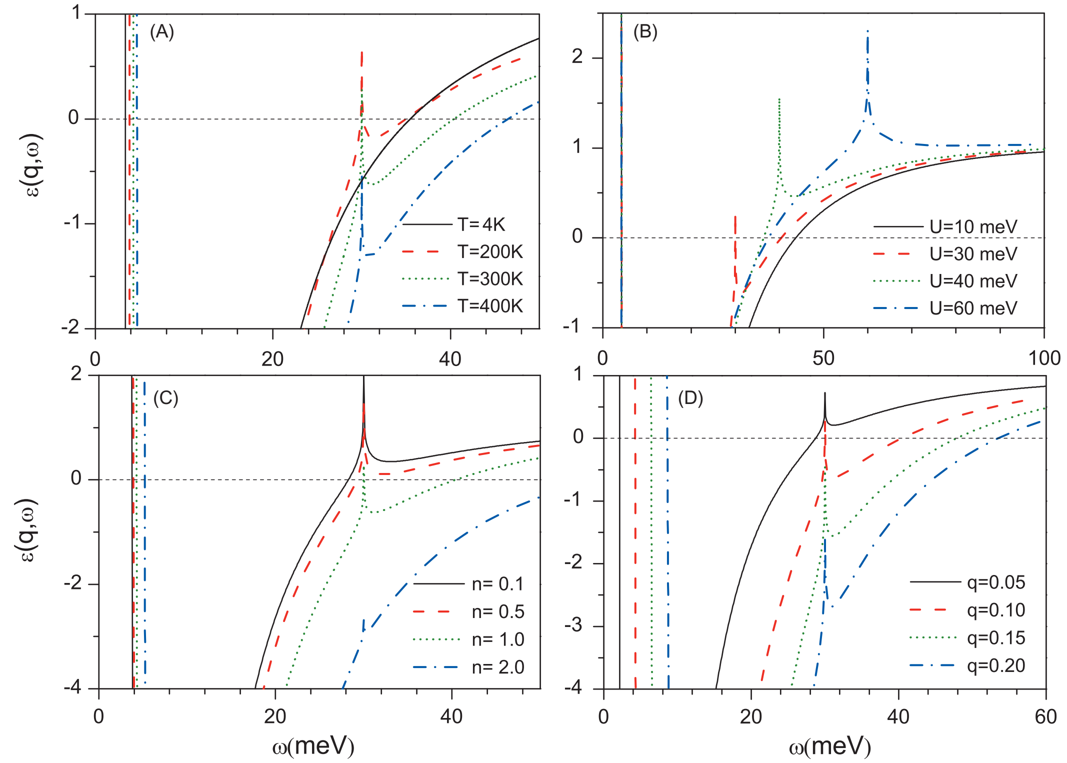

Fig. 11 The real part of the dielectric function ε_r vs frequency ω when $\varepsilon_b = 1$ in variety of the BLG bias U, temperature T, electron density $n(\times 10^{12}\ \text{m}^{-2})$, and wavevector $q(\times 10^8\ \text{m}^{-1})$ is plotted in (A)–(D), respectively. Parameters U = 30 meV $n = 10^{12}\ \text{m}^{-2}$, $q = 0.1 \times 10^8\ \text{m}^{-1}$, $T = 300$ K are used if not specified in the panels.

plasmon energy ω_O, it can introduce two extra roots ω_3^p and ω_4^p to the equation $\varepsilon_r = 0$, i.e., two extra plasmon modes in the system. The extra plasmon mode of lower energy ω_3^p is out of the interband single-particle continuum and can be only weakly damped. When the temperature increases further (dotted and dash-dotted) the enhanced intraband contribution shifts the peak below zero and the extra plasmon modes disappear. In the same time, ω_O increases with the temperature as more electrons (holes) exist in the conduction (valence) band.

As shown in Fig.11B, the bias voltage can sensitively shift the interband peak and control the emergence of the extra plasmon modes. These modes have energies (frequencies) proportional to the bias voltage and group velocities close to zero. The increase of the electron density enhances the degeneracy of the system and reduces the amplitude of the interband peak at $\omega_2 = 2E^1_{q/2}$ as plotted in Fig.11C. The enhanced intraband contribution at higher density also increases the frequency of the optical plasmon mode ω_O.

Fig.1D illustrates how the $\varepsilon_r - \omega$ curve develops with q at room temperature $T = 300$ K. Overall the intra-(inter-) band contribution to ε simply decreases (increases) with q as shown previously in Figs.10 and 11, but their effect on the plasmon spectrum is more complicated due to their competition with each other. When q increases, the intraband introduced ε_r dip becomes wide which usually results in the increase of the plasmon frequency. The interband peak of ε_r is located at the fixed energy $\omega_2 \simeq 30$meV and its amplitude increases with q. As a result, only when ω_2 is close to ω_O, the interband contribution can affect significantly the plasmon spectrum.

The plasmon spectrum in intrinsic BLG (unbiased and undoped) depicted in Fig.12 at various temperatures T (A) and for various background dielectric constant ε_b (B). At zero temperature, there is no carrier and no plasmon mode in the system. At finite temperature, electrons (holes) are excited in the conduction (valence) band and two plasmon modes emerge. In the long-wavelength limit, their frequencies are proportional to $\sqrt{T}$ at high temperature. Similar to the 2DEG result, we also observe a dispersion $\omega_O \propto \sqrt{q}$ and $\omega_A \propto q$. The background dielectric constant can also be employed to modify the plasmon frequency as shown in Fig.12B. The acoustic mode is not sensitive with ε_b but the frequency of optical mode decreases quickly with ε_b.

In Fig. 13, the plasmon spectrum for various electron densities at zero temperature is illustrated in unbiased BLG (A) and in biased one with $U = 60$ meV (B). In the long-wave limit, $q \sim 0$, the dielectric function is dominated by the intraband contribution. The properties of the system at zero temperature is mainly determined by the group velocity of electrons at the Fermi energy. The plasmon spectrum of unbiased system is similar to that of 2DEG. If the electron density is not high, e.g. $n \lesssim 10^{12}\text{cm}^{-2}$ for $U = 60$ meV as shown in Fig.13B, the Fermi group velocity of electrons decreases when the external electric field is turned on, due to the band deformation, and the plasmon mode is softened. With increasing q the interband contribution becomes more important, which reduces the group velocity of the optical plasmon mode. In some cases, the group velocity of plasmon can be close

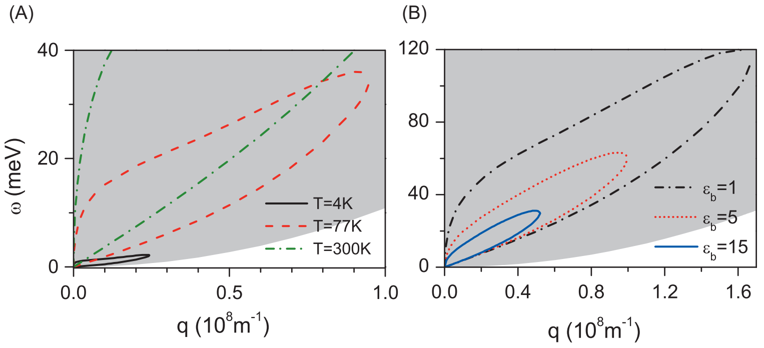

Fig. 12 Plasmon spectrum of intrinsic BLG (A) in vacuum with $\varepsilon_b = 1$ at various temperature and (B) with various dielectric constant at room temperature $T = 300$ K. The shadow shows the electron-hole single-particle continuum at zero temperature.

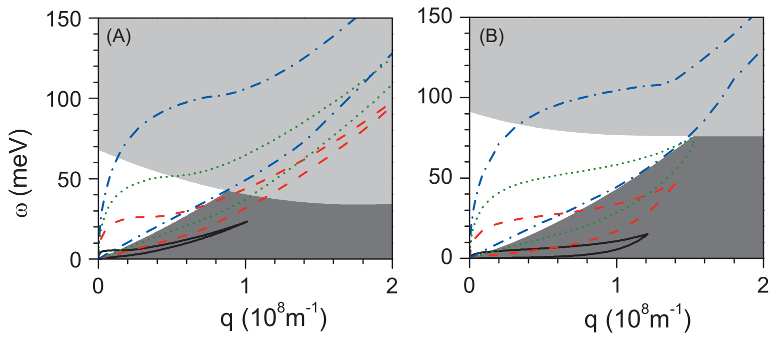

Fig. 13 Plasmon spectrum at zero temperature of (A) unbiased (B) U = 60 meV biased BLG in vacuum for density $n = 0.1$ (solid), 0.5 (dashed), 1.0 (dotted), and 2.0 (dash-dotted) $\times 10^{12}$ cm^{-2}. The single-particle continuum at $n = 10^{12}$ cm^{-2} is also present (light/dark shadow for the inter−/intra-band part).

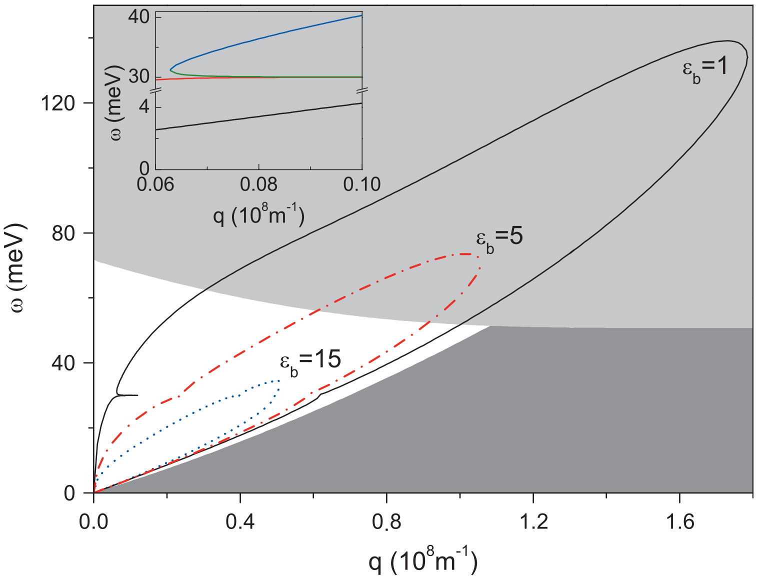

Fig. 14 Plasmon spectrum of biased and doped BLG with $U = 30$ meV and $n = 10^{12}$ cm^{-2} at room temperature $T = 300$ K in environment of different background dielectric constants ε_b. The inset shows the zoomed spectrum of the plasmon branches ω_O, ω_3^p, ω_4^p, and ω_A for $\varepsilon_b = 1$ at small q. The light (dark) shadow shows the interband (intraband) single-particle continuum at zero temperature.

to zero, a favorite situation for the stimulated plasmon emission (Rana, 2008). For large q, when the optical plasmon branch enters the interband single-particle continuum, i.e. $\omega_O > \omega_1$, the effect of interband contribution decreases and the plasmon spectrum has a long tail in unbiased system or when the carrier density is high. However, in biased systems with low carrier density, the effect of the interband contribution can be significant due to the flat band and the plasmon spectrum ends near where the intra- and inter-band single-particle continua meet at $\omega_u = \omega_1$.

The competition between the intra- and inter-band contributions may result in two extra plasmon modes for proper U at finite temperature when thermal excitation becomes important as previously discussed in Fig.11. This is an interesting phenomenon because those modes have unique properties and might be used in nanotechnology. In Fig.14, we plot the plasmon spectra of a biased system with $U = 30$ meV at $T = 300$ K and $n = 10^{12}$cm^{-2} for background dielectric constant $\varepsilon_b = 1$ (solid), 5 (dash-dotted), and 15 (dotted). At room temperature $T = 300$ K, the electronic system is not degenerate and the plasmon spectrum is in general similar to the one of intrinsic BLG as shown in Fig.12B. However, as shown in Figs.10 and 11, the interband contribution adds a sharp peak at ω_2 which is around U for small q. As a result, the plasmon spectra are deformed at ω_2 and bifurcate in some cases where two extra plasmon modes ω_3^p and ω_4^p emerge as shown in the inset of Fig.14.

The emerged two plasmon modes have almost zero group velocities and their frequencies are proportional to the bias voltage. In addition, their energies are in the gap of the zero-temperature single particle continuum and the lower one is below the lower limit of single-particle excitation, ω_2, at high temperature. This suggests that the modes are undamped or weakly damped and have long lifetime. These undamped plasmon modes are similar to those in MLG but have lower group velocity. Their energies can be easily manipulated by the bias voltage. These undamped modes with almost zero group velocities.

Conclusion

The Coulomb screening properties and the collective excitation modes in monolayer and bilayer graphene are discussed in the random phase approximation. In intrinsic monolayer graphene there is no collective excitation at zero temperature. A potential bias between the sublattices transfers the semimetal to a narrow gap semiconductor system and opens a gap between the intra- and the inter-band electron-hole continuum (EHC). At finite temperature or under the gate voltage, the switch-on of intra-band correlation introduces plasmon modes to the system and the interplay between the intra- and interband correlations play an important role in determining the plasmon spectrum. Undamped plasmon modes exist in the EHC gap. In addition, in a gated graphene with net electrons or holes, a EHC gap is formed for $q < k_F$ and an undamped plasmon mode of frequency $\omega \propto \sqrt{q}$ exist in monolayer graphene gas even at zero temperature, similar to the situation in a normal Fermi gas.

In semimetal intrinsic bilayer graphene, the static dielectric constant is much bigger than that in monolayer graphene, due to the existence of four Dirac points in each energy valley and the much lower 'light' velocity of the Dirac points than the one in monolayer graphene. The Coulomb screening also shows a strong anisotropy. The dynamic Coulomb screening has the characteristics of a Dirac gas on the low energy side and those of a normal Fermi gas on the high energy side. This transition from the Dirac to a Fermi gas is also reflected in the plasmon dispersion as the wavevector or the energy increases from zero. In doped bilayer graphene, the long wavevector limit of plasmon spectrum is the same as in normal two-dimensional Fermi gas with two valleys.

A potential bias between the two monolayer in bilayer graphene opens a gap between the conduction and valence bands and increases the DOSs at the band edges. As a result, the bias modifies the dielectric function greatly. In the long-wave limit, a sharp and controllable dielectric peak might appear at the energy equal to the band gap at high temperature when the system is nondegenerate or at the energy of double the Fermi energy at low temperature when the system is degenerate. In some cases, two extra undamped plasmon modes appear at energies close to the band gap energy and have almost zero group velocities.

References

Abergel DSL, et al. (2010) Properties of graphene: A theoretical perspective. *Advances in Physics* 59: 261–482.

Ando T (2002) Electronic states and transport in carbon nanotubes. In: Chakraborty T, et al. (ed.) *Nanophysics & Bio-electronics: A new Odyssey*, pp. 2–59. Amsterdam, New York: Elsevier.

Ando T, et al. (1982) Electronic properties of twodimensional systems. *Reviews of Modern Physics* 54: 437–672.

Castro Neto AH, et al. (2009) The electronic properties of graphene. *Reviews of Modern Physics* 81: 109–162.

Das Sarma S, et al. (2011) Electronic transport in twodimensional graphene. *Reviews of Modern Physics* 83: 407–470.

DiVincenzo DP and Mele EJ (1984) Self-consistent effective-mass theory for intralayer screening in graphite intercalation compounds. *Physical Review B* 29: 1685–1694.

Goerbig MO (2011) Electronic properties of graphene in a strong magnetic field. *Reviews of Modern Physics* 83: 1193–1243.

González J, et al. (1994) Non-Fermi liquid behaviour of electrons in the half-filled honeycomb lattice (a renormalization group approach). *Nuclear Physics B* 424: 595–618.

González J, et al. (1999) Electronic structure: Wideband, narrow-band, and strongly correlated systems-Marginal-Fermi-liquid behavior from two-dimensional Coulomb interaction. *Physical Review B* 59: R2474.

González J, et al. (2001) Electron-electron interactions in graphene sheets. *Physical Review B* 63: 134421.

Grimes CC and Adams G (1976) Observation of two-dimensional plasmons and electron-ripplon scattering in a sheet of electrons on liquid helium. *Physical Review Letters* 36: 145–148.

Hwang EH and Das Sarma S (2008) Screening, kohn anomaly, friedel oscillation, and RKKY interaction in bilayer graphene. *Physical Review Letters* 101: 156802.

Kane CL and Mele EJ (2005) Quantum spin hall effect in graphene. *Physical Review Letters* 95: 226801.

Khveshchenko DV (2006) Coulomb-interacting Dirac fermions in disordered graphene. *Physical Review B* 74: 161402(R).

Koshino M and Ando T (2006) Transport in bilayer graphene: Calculations within a self-consistent Born approximation. *Physical Review B* 73: 245403.

Kotov VN, et al. (2012) Electron-electron interactions in graphene: Current status and perspectives. *Reviews of Modern Physics* 84: 1067–1125.

Mahan GD (2000) *Many-Particle Physics*, 3rd edn. Kluwer Academic/Plenum Publishers.

McCann E and Fal'ko VI (2006) Landau-level degeneracy and quantum hall effect in a graphite bilayer. *Physical Review Letters* 96: 086805.

Nilsson J, et al. (2006) Electron-electron interactions and the phase diagram of a graphene bilayer. *Physical Review B* 73: 214418.

Novoselov KS, et al. (2005) Two-dimensional gas of massless Dirac fermions in graphene. *Nature* 438: 197–200.

Ohta T, et al. (2006) Controlling the electronic structure of bilayer graphene. *Science* 313: 951–954.

Peres NMR, et al. (2005) Coulomb interactions and ferromagnetism in pure and doped graphene. *Physics Review* 72: 174406.

Rana F (2008) Graphene terahertz plasmon oscillators. *IEEE Transactions on Nanotechnology* 7: 91–99.

Sensarma R, et al. (2010) *Physical Review B* 82: 195428.

Shung KWK (1986) Dielectric function and plasmon structure of stage-1 intercalated graphite. *Physical Review B* 34: 979–993.

Sinitsyn NA, et al. (2006) Charge and spin hall conductivity in metallic graphene. *Physical Review Letters* 97: 106804.

Slonczewski JC and Weiss PR (1958) The band structure of graphite. *Physics Review* 109: 272–279.

Stern F (1967) Polarizability of a two-dimensional electron gas. *Physical Review Letters* 18: 546–548.

Trickey SB, et al. (1992) Interplanar binding and lattice relaxation in a graphite delayer. *Physical Review B* 45: 4460–4468.

Vafek O (2006) Thermoplasma polariton within scaling theory of single-layer graphene. *Physical Review Letters* 97: 266406.

Visscher PB and Falicov LM (1971) Dielectric screening in a layered electron gas. *Physics Review* 3: 2541–2547.

Wallace PR (1947) The band structure of graphite. *Physics Review* 71: 622–634.

Wang XF (2005) Semiconductors II: Surfaces, interfaces, microstructures, and related topics-Plasmon spectrum of two-dimensional electron systems with Rashba spin-orbit interaction. *Physical Review B* 72: 85317.

Wang XF and Chakraborty T (2007a) Collective excitations of Dirac electrons in a graphene layer with spinorbit interactions. *Physical Review B* 75: 033408.

Wang XF and Chakraborty T (2007b) Coulomb screening and collective excitations in a graphene bilayer. *Physical Review B* 75: 041404(R).

Wang XF and Chakraborty T (2010) Coulomb screening and collective excitations in biased bilayer graphene. *Physical Review B* 81: 081402(R).

Yoshizawa K, et al. (1996) Interlayer interactions in two-dimensional systems: Second-order effects causing ABAB stacking of layers in graphite. *The Journal of Chemical Physics* 105: 2099–2105.

You WL and Wang XF (2012) Dynamic screening and plasmon spectrum in bilayer graphene. *Nanotechnology* 23: 505204.

Yu PY and Cardona M (2003) *Fundamentals of Semiconductors: Physics and Materials Properties*, 3rd edn. Springer.

Zhang Y, et al. (2005) Experimental observation of the quantum Hall effect and Berry's phase in graphene. *Nature* 438: 201–204.

Zunger A (1978) Self-consistent LCAO calculation of the electronic properties of graphite. I. The regular graphite lattice. *Physical Review B* 17: 626–641.

Electron gas (theory)

G Vignale[a] **and MP Tosi**[b,*], [a]Department of Physics and Astronomy, University of Missouri, Columbia, MO, United States; [b]Scuola Normale Superiore, Pisa, Italy

© 2024 Elsevier Ltd. All rights reserved.

Introduction 779
Ideal Fermi gas and Fermi liquid theory 780
Weakly interacting electron gas: Exchange effects 782
Electron correlations: Calculation of the ground state energy 783
Electron gas and density functional theory 785
Static screening 785
Dynamical screening and plasmons 787
Wigner crystallization 789
Electron gas in reduced dimensionality 789
Two-dimensional electron gas in graphene 790
Two-dimensional electron gas at high magnetic field 793
Transport coefficients 794
Spin-orbit interaction 795
Conclusion 796
References 796

Abstract

This article provides an overview of the uniform electron gas model (also known as jellium model) for electrons in solid matter. Historically, this model has provided the basis for the understanding of electron-electron interaction effects in metals and semiconductors and it currently plays a crucial role at the foundations of Density Functional Theory. We review the basic properties of the model, such as the existence of the Fermi surface, the exchange and correlation energy, static and dynamic screening, quasiparticles and plasmons and the possibility of electron crystallization and magnetic phases. The two-dimensional electron gas in systems such as quantum wells and graphene and in the presence of spin-orbit interactions and magnetic fields is also discussed.

Key points

- An electron gas pervades all known materials and is responsible for many of their observed properties
- Electrons in metals are described by Fermi liquid theory, whereby each electron behaves essentially like a free particle, dressed by interactions.
- The energy of the electron gas is controlled by the so-called "exchange-correlation" hole, arising in part from the Pauli exclusion principle, in part from the Coulomb interaction, whereby the average electrons density is reduced in the vicinity of an electron pinned at a given position.
- Electrons in metals rearrange around an external charged impurity in such a way that the impurity is "screened," i.e., it becomes essentially invisible at large distance from the impurity. This screening effect is very effective in three dimensions, less so in lower dimension.
- The electron gas supports collective excitations of the charge density known as plasmons. Collective oscillation dominate the high-frequency response of the electron gas and give a large contribution to the correlation energy.
- Besides the liquid phases, other phases of the electron gas are possible, including crystalline and magnetic ones, and have been investigated by numerical Quantum Monte Carlo methods.
- The electron gas in two and one-dimensional structures may present non Fermi liquid behavior, such as the Luttinger liquid in one dimension and the quantum Hall liquid in two dimensions.

---

[*] Deceased.

https://doi.org/10.1016/B978-0-323-90800-9.00167-0

Notations and Acronyms

$\epsilon(q)$	Dielectric function
ϵ_F	Fermi energy
a_B	Bohr radius
B	Bulk modulus
e	Electron charge
$g(r)$	Pair distribution function
H	Magnetic field
h	Planck constant
$\hbar$	Planck constant h-crossed (h divided by 2π)
K	Compressibility
k_B	Boltzmann constant
k_F	Fermi wave number
ℓ	Magnetic length
m	Electron mass
m_c	Cyclotron mass
n	Electron density
p_F	Fermi momentum
q	Wave number
QMC	Quantum Monte Carlo
r	Distance
r_s	Dimensionless electron-electron coupling strength
S	Shear modulus
T	Temperature
α_{ee}	Electron-electron interaction coupling constant in graphene
λ	de Broglie wavelength
λ_{TF}	Thomas-Fermi screening length
ν_F	Density of states at the Fermi surface
$\chi(q)$	Density response function
$\chi_0(q)$	Static density susceptibility
χ_S	Spin susceptibility
ω_c	Cyclotron frequency
ω_P	Plasma frequency $v(q)$: Fourier transform of the Coulomb interaction

Introduction

The homogeneous gas of electrons (also known as jellium) is one of the most important basic models in the physics of condensed matter. It was introduced by Drude in 1900 to account for the electromagnetic properties of plasmas and was used by the pioneers of quantum mechanics in the early 1930s to model the sea of interacting valence electrons in a metal. The valence electrons are the outer electrons of an atom and determine how it interacts with its surroundings, but in a metal they are released by the atoms into a collective state. In the early studies, the ions of the crystalline lattice in the metal were smeared into a rigid uniform background of positive charge, which exactly balances the negative charge associated with the distribution of outer electrons. More generally, the background charge can be endowed with an ability to deform under pressure leading to a less widely known, but very useful "deformable jellium model." Following the explosive growth of density-functional theory in the 1980s, the electron gas has become the basic reference system in most calculations of electronic structure not only for metallic or insulating solids and liquids, but also for atomic-scale systems and biomolecules.

In metals the density of valence (or conduction) electrons is high enough that many of their properties can be understood in terms of a picture in which they move almost independently of each other, forming a paramagnetic fluid made of equal numbers of up and down spins. The success of this counterintuitive single-electron picture of metals rests on the work carried out in the 1950s by Landau in developing the theory of Fermi liquids, as will be discussed in the next section. With decreasing density the potential energy associated with the Coulomb interactions between the electrons grows to dominate over their kinetic energy and ultimately at very low density the electron gas freezes into the "Wigner crystal," in which the electrons become localized on lattice sites. This behavior is just the opposite of what happens with classical systems, where it is high density that favors a lattice structure. It has long been believed that crystallization of the electron gas in the jellium model is preceded, in an intermediate range of density, by the stabilization of a spin-polarized state in which the spins spontaneously align into a ferromagnetic state of order. This possibility was foreseen by Bloch in 1929 in the context of the Hartree-Fock approximation, and was initially confirmed by accurate calculations of the ground state energy based on quantum Monte Carlo (QMC) methods implemented on modern computers. The traditional

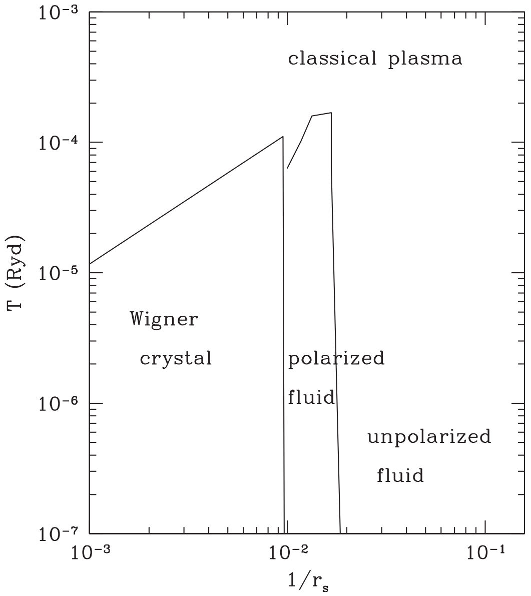

Fig. 1 The traditional QMC phase diagram for a three dimensional electron gas (Ceperley, 2004) Recent studies suggest that the narrow "polarized fluid" region is a computational artifact and does not exist in reality. Ceperley DM (2004) Introduction to quantum Monte Carlo methods applied to the electron gas. Proceedings of the International School of Physics Enrico Fermi, Course CLVII, edited by Giuliani GF and Vignale G. Amsterdam: IOS Press used with permission.

phase diagram of the electron gas in three dimensions is shown in Fig. 1 (Ceperley, 2004). However, more recent studies, also based on quantum Monte Carlo, have cast serious doubts on the existence of the ferromagnetic phase both in two-dimensions (Drummond and Needs, 2009) and in three dimensions (Holzmann and Moroni, 2020).

The electron gas framework, when widened to include artificial semiconductor heterostructures in which the electronic carriers are constrained to move in a plane (as in a quantum well) or on a line (as in a quantum wire) or under three-dimensional confinement (as in a quantum dot), provides much of the basic understanding that is necessary for modern condensed matter physics and nanotechnology. However, it is appropriate to note at this point that some more exotic properties of the valence-electron gas have come to the fore during the last few decades. These developments started with the idea of Cooper pairs in the BCS theory of superconductivity in metals and have been stimulated by discoveries of novel materials, such as the cuprate high-T_c superconductors and other oxides, or of novel physical effects such as the Kondo scattering against magnetic impurities and the fractional quantum Hall effect. The quantum theory of solids is now no longer confined to the electron as the quasiparticle of a Fermi liquid carrying an elementary charge and a spin, but in special situations the system of valence electrons reconstructs to produce quasiparticles that may behave like fragments of an electron, or more complicated objects such as composite fermions, composite bosons, holons and spinons. Also spin-orbit interaction effects, and linearly dispersing electrons in novel two-dimensional materials consisting of a single atomic layer (e.g., graphene) have been intensively studied. A complete discussion of electron gas theory up to 2005 can be found in the monograph by G. F. Giuliani and G. Vignale (Giuliani and Vignale, 2005). More recent topics will be briefly covered later in this article.

Ideal Fermi gas and Fermi liquid theory

Conduction electrons in normal metals under ordinary laboratory conditions form a highly degenerate Fermi fluid, in which the mean interparticle spacing a is a small fraction of the characteristic de Broglie wavelength $\lambda = h/p_{th}$ (here h is the Planck constant and p_{th} is the momentum of a particle of mass m having kinetic energy equal to the thermal energy $k_B \boldsymbol{T}$, with k_B the Boltzmann constant and $\boldsymbol{T}$ the temperature). If for the moment one neglects all interactions, one can write the energy levels $\boldsymbol{E}$ of the gas in terms of the single-particle kinetic energies ε_k and of the number n_k of electrons in a single-particle state at energy $\varepsilon_k : E = \sum_k n_k \varepsilon_k$. Here k is a label specifying the momentum and the spin of each electron and $\varepsilon_k = \frac{\hbar^2 k^2}{2m}$ (with $\hbar = \frac{h}{2\pi}$) is the kinetic energy of each such electron. The Pauli exclusion principle restricts the values that n_k may take for particles of half-integer spin to $n_k = 0$ or 1. A cell of volume h^3 in phase space can thus contain at most two electrons with opposite spins, so that in the ground state at $\boldsymbol{T} = 0$ the electrons must have a spread of momenta in a range up to a maximum momentum p_F (the "Fermi momentum"). For N electrons with up and down spins inside a volume V and defining $k_F = p_F/\hbar$ (the Fermi wave number), one can write the density $n = N/V$ as $n = k_F^3/3\pi^2$ (The expression for the Fermi wave number becomes $(2\pi n)^{1/2}$ in two dimensions and $\pi n/2$ in one dimension, where n is given by N/A and N/L respectively). The Fermi wave number k_F is the radius of a spherical surface in wave number space

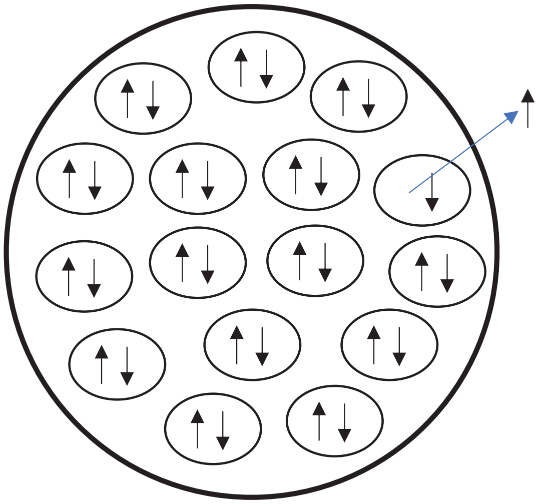

Fig. 2 Schematic representation of a section of the Fermi sphere for a paramagnetic electron gas, showing also a process of excitation of an electron-hole pair.

(the "Fermi surface") and the energy of an electron at the Fermi surface is, by definition, the Fermi energy $\varepsilon_F = \hbar^2 k_F^2/2m$. This also is the lowest energy cost at which one may add a further electron to the gas (i.e., ε_F is the chemical potential of the gas at $T = 0$) and evidently increases with the electron density, since $k_F = (3\pi^2 n)^{1/3}$.

The notion of a spherical Fermi surface allows a vivid picture of ground state and excitations in a normal Fermi fluid. At $T = 0$, the single-particle states inside the Fermi sphere are fully occupied by the fermions and the states outside of it are empty. The momentum distribution (i.e., the occupation number of an electron state of given momentum and spin) thus takes a discontinuous change from 1 to 0 as the momentum crosses the Fermi surface. Thermal excitations at finite temperature bring fermions from states inside to states outside the Fermi surface, leaving "holes" behind and lowering the chemical potential of the gas (see the schematic picture in Fig. 2).

It is somewhat surprising that a number of properties of normal metals are observed to behave as predicted by the ideal Fermi-gas model, in spite of the electron-electron and electron-ion interactions that may be expected to lead to substantial departures from ideality. In particular, the electronic contribution to the specific heat of a metal increases linearly with temperature and the paramagnetic spin susceptibility is independent of temperature, both quantities being proportional to the density of electronic states at the Fermi surface, denoted by ν_F. These results are in agreement with the noninteracting electron gas model. The explanation of these behaviors was first given by Landau in what is now known as the "Landau theory of Fermi liquids." Landau realized that at low temperature electrons with momenta close to the Fermi surface have limited opportunity to scatter against each other and thus change their state of motion. This is due to the combined constraints of energy conservation and the Pauli exclusion principle. These electrons therefore behave as if they were essentially free and their individual momentum is almost exactly conserved: such "almost free" particles are appropriately termed "quasiparticles." Once one deals with quasiparticles rather than with "bare" electrons, the excitations of the fluid can be described as an almost ideal gas of quasiparticles. A crucial point in Landau's theory is that the quasiparticles obey Fermi statistics, so that at low temperature the low-lying excitations of the interacting system are in one-to-one correspondence with those of the ideal noninteracting system, i.e., they are quasi-electron/quasi-hole pairs across the sharply defined Fermi surface. The correct behavior of the electronic specific heat and spin susceptibility follows at once.

There are, however, some major differences to be emphasized between quasiparticles and bare particles. First of all, a quasiparticle can be visualized as a bare particle "dressed" by a cloud of surrounding particles: the effect of this "dressing" is to rescale the relation between energy and momentum, introducing an effective mass m^* that depends on the strength of the electron-electron interaction. Thus, while the energy of a bare particle, relative to the chemical potential, is $\varepsilon_k - \mu \simeq \hbar k_F(k - k_F)/m$ for $k \simeq k_F$ (with m the bare mass of the electron), the energy of a quasiparticle is $\varepsilon_k^* - \mu \simeq \hbar k_F(k - k_F)/m^*$ where m^* is the effective mass. m^*/m is usually of order 1 in the electron gas at metallic densities, but it can rise into the hundreds for electrons in strongly correlated materials (heavy-fermion materials). Second, there are residual interactions between the quasiparticles, which cause the energy of a quasiparticle to change in proportion to the density of quasiparticle excitations already present in the system as a result of finite temperature and/or external excitation. These interactions are described by an (in principle, infinite) set of numbers known as "Landau parameters." Third, the lifetime τ of a quasiparticle is not really infinite: its inverse goes to zero in the low-energy limit as $\hbar/\tau \propto (\varepsilon_k - \varepsilon_F)^2/\varepsilon_F$ (for $T = 0$) or in the low-temperature limit as $\hbar/\tau \propto (k_B T)^2/\varepsilon_F$ (for $\varepsilon_k = \varepsilon_F$). While this is much smaller than either $\varepsilon_k - \varepsilon_F$ or $k_B T$, justifying a posteriori the validity of the quasiparticle concept, it cannot be entirely neglected because it plays an important role in the calculation of the transport coefficients, when the system is driven out of equilibrium.

The effective mass of quasiparticles causes a shift in the density of states at the Fermi surface, $\nu_F^*/\nu_F = m^*/m$, which affects the values of the thermodynamic properties of the interacting electron gas relative to the ideal Fermi gas. For example, the low-temperature heat capacity of the interacting electron gas in three dimensions is given by $C_v = (\pi^2/3)k_B^2 T \nu_F^*$, which is still linear in T but is modified by a factor m^*/m relative to its noninteracting counterpart. Remarkably, the interaction between quasiparticles

(Landau parameters) does not enter this result. In contrast, the bulk modulus $n^2 d\,\mu/d\,n$ and the spin susceptibility (defined as the derivative of the spin magnetization with respect to an applied magnetic field) are affected both by the effective mass and by the quasiparticle interaction. In the electron gas these interactions reduce the bulk modulus and increase the spin susceptibility: the second effect can be seen as a consequence of interactions favoring the alignment of neighboring electron spins in a parallel configuration (see below). Theoretical calculations and experimental measurements of the effective mass and the quasiparticle interaction parameters in the electron gas are reviewed in Chapter 8 of Ref. (Giuliani and Vignale, 2005), to which we refer the reader.

Weakly interacting electron gas: Exchange effects

As a start to a calculation of the ground-state energy of the interacting electron gas, one might ask what is the distribution of electron pairs in the ideal Fermi gas as a function of their relative distance r. The pair distribution function, which is written in general as $g(r)$, is defined by computing the average number of electrons that lie within a spherical shell of radius r and thickness dr centered on any given electron and equating this to the quantity $ng(r)(4\pi r^2 dr)$. For the electron gas with equal numbers of up and down spins it can be written as $g(r) = [g_{\uparrow\uparrow}(r) + g_{\uparrow\downarrow}(r)]/2$, the average of the values for pairs of electrons with parallel spins and antiparallel spins. Whereas $g(r) = 1$ in a classical ideal gas, the probability of finding two electrons with the same spin at a distance r vanishes exactly as $r \to 0$. This property derives from the symmetry imposed by the Pauli exclusion principle, according to which the wave function of a Fermi fluid changes sign under the operation of exchange of two identical fermions. That is, the many-body wave function of the electron gas has a zero whenever two parallel-spin electrons overlap in space. The property $g_{\uparrow\uparrow}(0) = 0$ is an exact result and implies, by continuity, that each electron of given spin induces a local depletion of the density of electrons with the same spin in its surroundings. If we bear in mind that the Coulomb interactions between electrons are repulsive, it is seen that the presence of the "Pauli hole" that was introduced above is accompanied by a gain in potential energy of the electron gas. Exchange effects keep apart electrons with parallel spins and therefore reduce on average the Coulomb repulsion energy of parallel-spin pairs. In the ideal Fermi gas $g(r)$ is given by the expression

$$g_{ideal}(r) = 1 - \frac{9}{2}\,[j_1(k_F r)/(k_F r)]^2 \quad , \tag{1}$$

where $j_1(x) = (\sin x - x\cos x)/x^2$ is a spherical Bessel function. The shape of this function, which describes the Pauli hole in the ideal Fermi gas, is shown in Fig. 3.

Of course, no correlations exist at this level between pairs of electrons with antiparallel spins, therefore $g_{\uparrow\downarrow}(r) = 1$. The expression for $g_{ideal}(r)$ can be used to evaluate the ground-state energy in first-order perturbation theory. This calculation corresponds to the energy of the electron gas in the Hartree-Fock approximation, since by translational symmetry the self-consistent Hartree-Fock single-particle orbitals must be the plane-wave orbitals of the ideal gas. The result (in three dimensions) is

$$\begin{aligned} E_g^{HF}(r_s) &= \left(\frac{3}{5\alpha^2 r_s^2} - \frac{3}{2\pi\alpha r_s}\right)\text{Ryd} \\ &\simeq \left(\frac{2.21}{r_s^2} - \frac{0.916}{r_s}\right)\text{Ryd} \end{aligned}$$

per electron, with $\alpha = (9\pi/4)^{-1/3}$ and in units of the Rydberg ($1\ \text{Ryd} = e^2/(2a_B)$, with $a_B = \hbar^2/(me^2)$ being the Bohr radius). Here, we have introduced the crucial density parameter r_s by the definition $4\pi(r_s a_B)^3 = n^{-1}$, that is to say, r_s represents the mean distance between electrons in units of the Bohr radius. Electronic densities that are usually found in metals (metallic densities) have values of r_s ranging from $\simeq 2$ for Al to $\simeq 6$ for Cs. Much smaller as well as much higher values of r_s, corresponding to higher and lower densities respectively, can be found in semiconductors and semiconductor heterostructures.

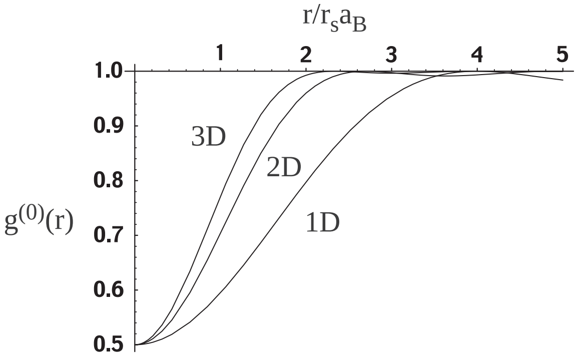

Fig. 3 The Pauli hole surrounding an electron of given spin in the ideal Fermi gas in three, two, and one dimension.

The two terms in $E_g^{HF}(r_s)$ are the average kinetic energy and the average potential energy per electron, respectively, and their ratio is evidently proportional to $1/r_s$. This shows that the role of the electron-electron interactions becomes progressively more important as r_s increases, that is, as the density of the electron gas decreases. This counterintuitive fact, already noted in the Introduction, is now clearly seen to be a consequence of the Pauli exclusion principle which forces the electrons to occupy states of higher and higher momentum, and therefore higher kinetic energy, as their density increases. This is reflected in the behavior of the kinetic energy, which increases as $1/r_s^2$. The Coulomb interaction energy, on the other hand, scales as $1/r_s$, as expected from the $1/r$ behavior of the Coulomb potential, and therefore becomes negligible in comparison with the kinetic energy for $r_s \to 0$. Thus, the electron gas becomes effectively noninteracting in the limit of very high density.

Electron correlations: Calculation of the ground state energy

Naturally, the expression for the energy presented above (Eq. 2) is valid only when the effect of interactions is weak, i.e., in the high-density limit. Going beyond the Hartree-Fock expression requires the full machinery of many-body theory. This has been done in several steps, starting with the celebrated Random Phase Approximation (RPA) in the 1950s (Bohm and Pines, 1953; Gell-Mann and Brueckner, 1957) and continuing with semi-analytical theories such as the STLS theory (Singwi et al., 1968) (an extension of the RPA based on the Hubbard concept of "local field factor," see below) and culminating with the essentially exact quantum Monte Carlo calculations by Ceperley et al. in 1980 (Ceperley and Alder, 1980). All these calculations take into account, with varying degrees of accuracy, the Coulomb correlations between electrons, i.e., the correlations that are caused by the Coulomb interaction in addition to the ones that are required by the Pauli principle.

It has been already remarked that no correlations between antiparallel spins are present in the ideal Fermi gas. This is no longer true in the presence of Coulomb interaction. The main effect is that the motions of opposite-spin electrons, which were completely uncorrelated in the ideal case, start to be correlated, and the depletion of the local electron density around each electron deepens since pairs of electrons with antiparallel spins are now kept apart by the Coulomb repulsion (The depletion of parallel-spin electrons is also somewhat deepened, but this is a relatively small effect since those electrons were already kept apart by the Pauli exclusion principle).

Fig. 4 shows the "Pauli-Coulomb hole," calculated from QMC for increasing values of the coupling strength r_s (Ortiz and Ballone, 1994). An exact property of this function (also shared by the ideal pair correlation function of Eq. (1)) is that the total local depletion of electron density around the electron at the origin corresponds to taking away exactly one electron from its neighborhood. This ensures that the central electron plus the "exchange-correlation" (xc) hole surrounding it is an overall charge-neutral object. Within this constraint strong Coulomb interactions at low density cause a deepening of the xc hole and also a diminished contrast between parallel- and antiparallel-spin correlations (i.e., the Pauli exclusion principle becomes less important in the

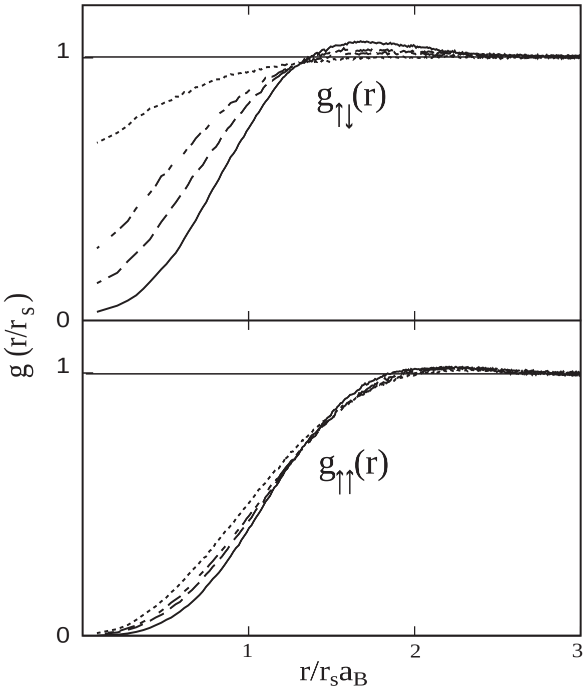

Fig. 4 The Pauli-Coulomb hole in the interacting spin-unpolarized electron gas for various values of the coupling strength r_s: $r_s = 1$ (dotted line), $r_s = 3$ (dash-dotted line), $r_s = 5$ (dashed line), and $r_s = 10$ (full line). Adapted from Ref. Ortiz G and Ballone P (1994) *Physical Review B* 50: 1391.

presence of strong Coulomb repulsion). The diminished contrast between parallel and antiparallel spins plays a crucial role in keeping the electron gas paramagnetic, rather than ferromagnetic, at metallic densities.

Besides deepening the exchange-correlation (xc) hole, correlations also affect the kinetic energy of the electron gas by modifying the occupation numbers n_k of momentum states. In the ideal gas these occupation numbers are distributed according to a step function: $n_k = 1$ for $k < k_F$ and $n_k = 0$ for $k > k_F$. In the interacting electron gas the occupation numbers are reduced below 1 for $k > k_F$ and do not vanish for $k > k_F$ resulting in an increased kinetic energy (see Fig. 4). However a discontinuity in n_k persists at $k = k_F$, being a key signature of the existence of Landau quasiparticle. The discontinuity Z, known as quasiparticle renormalization constant, is loosely speaking, a measure of the fraction of the spectral weight of single-particle excitations that fall under the description of quasiparticles.

The calculation of the ground state energy of the electron gas requires both the pair correlation function and the momentum space occupation numbers. Alternatively, the energy can be calculated from the pair correlation function alone if the latter is known as a function of the coupling constant r_s' in the range $0 < r_s' < r_s$ (this is denoted by $gr_s'(r)$). Then the formula for the total ground state energy is

$$\frac{E_g}{N} = \varepsilon_{kin}(r_s) + \frac{1}{r_s}\int_0^{r_s} dr_s' \int d\mathbf{r}\frac{e^2}{r}\, n\left[g_{r_s'}(r) - 1\right] \tag{2}$$

where $\varepsilon_{kin}(r_s) \simeq 2.21/r_s^2$ Ryd in 3D is the noninteracting energy per particle. In the early stages of the electron gas theory the pair correlation functions was obtained either perturbatively, or from approximate theories of the density response function which were developed to describe the phenomenon of *screening* (described in the next section). Modern approaches, like QMC, extract $g(r)$ directly from the many-body wave function. The results of these calculations have been cast in convenient parametrized form, which can be found, for example, in Chapter 1 of Ref. (Giuliani and Vignale, 2005) (Fig. 5).

Fig. 6 shows the energy per electron of the electron gas in 3D and 2D obtained from analytic fits to the QMC results. Qualitatively, its behavior is not very different from that of the Hartree-Fock approximation (Eq. 2), but of course it lies considerably below Hartree-Fock in the low density limit, going in 3D as $\simeq -1.8/r_s$ Ryd rather than $-0.916/r_s$ Ryd. Both energy curves shows a minimum, followed by and an inflection point (change in the sign of the curvature) at a slightly higher value of r_s. These two special points are marked by arrows in Fig. 6. The minimum indicates vanishing pressure $\boldsymbol{P}$, and the inflection point is associated with a vanishing bulk modulus $\boldsymbol{B}$.

One may wonder why negative values of $\boldsymbol{P}$ and $\boldsymbol{B}$, occurring for values of r_s larger than the minimum and the inflection point respectively, are allowed at all. Normally, such negative values would indicate a thermodynamic instabilities of the system. The reason why these apparently unphysical values of $\boldsymbol{P}$ and $\boldsymbol{B}$ are allowed is that the jellium model includes a rigid background of positive charge. This rigid background fixes the density of the electron gas, which is therefore not allowed nor required to adjust its density to the minimum of the energy vs density curve. Likewise, the rigid background neutralizes any tendency of the electron gas to spontaneously contract or expand.

Fig. 7 shows the inverse bulk modulus $\boldsymbol{K} = 1/\boldsymbol{B}$ (also known as compressibility) and the spin susceptibility of the three-dimensional electron gas as calculated from QMC. Both quantities are plotted in units of their ideal-gas (i.e., noninteracting) counterparts. We also plot the same quantities obtained from the Hartree-Fock approximation. It is evident from these plots that while interactions generally enhance both the compressibility and the spin susceptibility, the specific effect of correlations (primarily correlations between antiparallel spin electrons) as revealed by the difference between Hartree-Fock and fully interacting results, is to further enhance the effect of exchange on the compressibility but at the same time to suppress the effect of exchange on the spin susceptibility. The second effect is the reason why ferromagnetism does not occur at metallic densities, and most likely at no density.

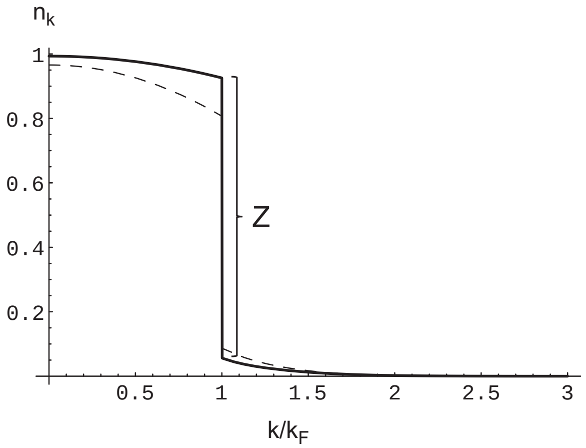

Fig. 5 Occupation numbers in momentum space for the three dimensional electron gas from Ref. (Senatore et al., 1996) for $r_s = 2$ (solid line) and $r_s = 5$ (dashed line). The occupation number discontinuity Z is shown.

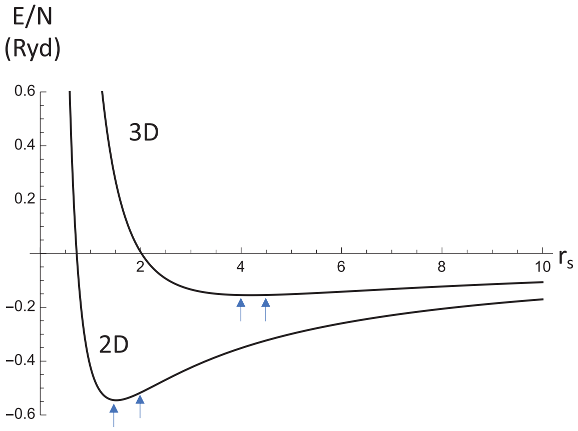

Fig. 6 Energy vs r_s curves of a three- and two-dimensional electron gas. The arrows at the lower value of r_s indicate the points where the energy has a minimum (zero pressure), while the arrows at the higher values of r_s indicate the inflection points in the energy vs density relation (zero bulk modulus).

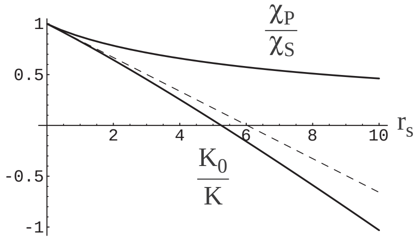

Fig. 7 Plot of the dimensionless compressibility ***K*** and spin susceptibility χ of a three-dimensional electron gas as a function of r_s. $\boldsymbol{K_0}$ is the non-interacting compressibility and χ_P is the non-interacting spin susceptibility. In the Hartree-Fock approximation, which includes only exchange, both ***K*** and χ are enhanced relative to their non-interacting values. Correlations between opposite spin electron cause ***K*** to be even more enhanced, while χ is reduced.

Electron gas and density functional theory

The ground state energy of the uniform electron gas can be written as

$$E_g/N = \varepsilon_{kin}(n) + \varepsilon_{xc}(n), \tag{3}$$

where $\varepsilon_{kin} \simeq 2.21/r_s^2$ Ryd is the noninteracting energy per electron in 3D. The remainder $\varepsilon_{xc}(n)$ is known as the *exchange-correlation* (xc) energy (per particle): it includes the interaction contribution to the kinetic energy.

The xc energy has found widespread use in density functional theory. According to this theory, the effect of the electron-electron interaction on the ground state of an electronic system can be mimicked by a local exchange-correlation potential, $v_{xc}(r)$, which is added to the external potential and to the classical electrostatic potential of the charge distribution, so that interactions do not need to be taken into account explicitly. In the local density approximation the xc potential is given by

$$v_{xc}(r) = \frac{d}{dn}\left[n\varepsilon_{xc}(n)\right]\Big|_{n=n(r)} \tag{4}$$

i.e., it is the derivative of the uniform xc energy density with respect to density, evaluated at the local density of the system. Several parametrized expression of $\varepsilon_{xc}(r_s)$ (where r_s is a proxy for the density) are available in the literature (see Chapter 7 in Ref. (Giuliani and Vignale, 2005)).

Static screening

When a foreign charged particle (impurity) is inserted in the electron gas, the electrons respond by rearranging their density around the impurity in such a way that, at large distance from the impurity, the electric field created by the impurity is largely cancelled by the electric field created by the displaced electrons. This phenomenon is known as *screening*. To be more precise, let us denote by $V_{ext}(q)$ the Fourier transform of the potential created by the impurity. Then in the linear response approximation (valid at large distance from the impurity, where the potential is weak) the Fourier transform of the induced electronic density is

$$\delta n(q) = \chi(q)V_{ext}(q). \tag{5}$$

The static density response function $\chi(q)$ is a fundamental property of the electron gas. It allows us to calculate the net electric potential from the impurity and the displaced electrons as

$$\begin{aligned} V_{sc}(q) &= V_{ext}(q) + v(q)\delta n(q) \\ &= [1 + v(q)\chi(q)]V_{ext}(q) \\ &= \frac{V_{ext}(q)}{\varepsilon(q)} \end{aligned} \tag{6}$$

where $v(q)$ is the Fourier transform of the Coulomb interaction ($v(q) = 4\pi e^2/q^2$ in three dimensions), and $\varepsilon(q) \equiv [1 + v(q)\chi(q)]^{-1}$ is known as the *static dielectric function* of the electron gas.

The calculation of $\chi(q)$ and $\varepsilon(q)$ is a classic problems in electron gas theory. For the ideal noninteracting gas one has

$$\chi_0(q) = -\nu_F\left[\frac{1}{2} - \frac{q^2 - 4k_F^2}{8k_F}\ \ln\left|\frac{q - 2k_F}{q + 2k_F}\right|\right], \tag{7}$$

in three dimensions (similar analytical results are obtained in two and one dimension, see Fig. 8).

Here ν_F is the density of states at the Fermi surface which for a three-dimensional ideal gas is given by $\nu_F = 3n/(2\varepsilon_F)$. For the interacting electron gas one has

$$\chi(q) = \frac{\chi_s(q)}{1 - v(q)\,\chi_s(q)}, \tag{8}$$

where $\chi_s(q)$, is known as the *proper* density response function and describes the response of the electronic density to the screened potential, i.e., $\delta n(q) = \chi_s(q)V_{sc}(q)$. The exact form of $\chi_s(q)$ is not known. The most popular approximation for $\chi_s(q)$ is the *random phase approximation*, which simply posits $\chi_s(q) = \chi_0(q)$. That is to say, the random phase approximation assumes that the electron gas responds as an ideal gas to the self-consistently screened potential. This leads to the widely used expression

$$\chi_{RPA}(q) = \frac{\chi_0(q)}{1 - v(q)\chi_0(q)}. \tag{9}$$

The corresponding dielectric function

$$\varepsilon_{RPA}(q) = 1 - v(q)\chi_0(q) \tag{10}$$

is easily seen to go to infinity as $1/q^2$ for $q \to 0$ (since $\chi_0(q) \to -\nu_F$ in this limit). This demonstrates the screening property described at the beginning of this section. The screened potential is suppressed by a diverging dielectric function in the limit of $q \to 0$, which physically corresponds to large distances from the impurity. Indeed, in this limit the RPA dielectric function reduces to $\varepsilon_{TF}(q) = 1 + (q\lambda_{TF})^{-2}$ where $\lambda_{TF} = (4\pi e^2 \nu F)^{-1/2}$ is the Thomas-Fermi screening length. The Fourier transform of the screened potential $v(q)/\varepsilon_{TF}(q)$ is easily seen to decay exponentially as $e^{-r/\lambda_{TF}}$, where r is the distance from the impurity. However, this result is not quite accurate. A careful consideration of the logarithmic singularity of $\chi_0(q)$ at $q = 2k_F$ (see Eq. 7) reveals that the electronic density at a distance r from the impurity is asymptotically described by the expression

$$n(r) - n \propto \frac{\cos(2k_F r + \phi)}{r^3} \quad . \tag{11}$$

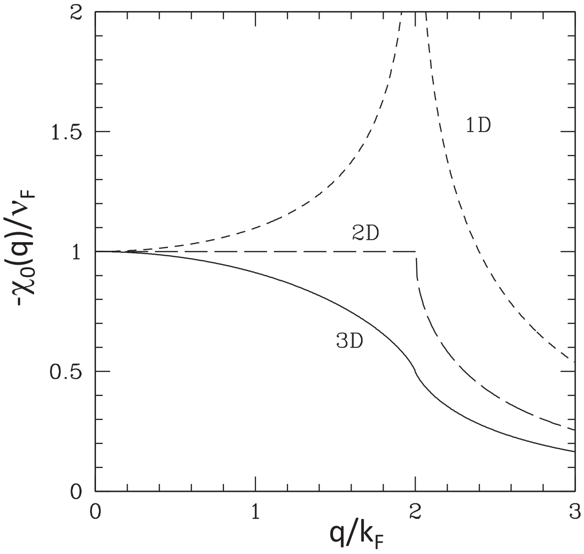

Fig. 8 Static susceptibility of the Fermi gas in dimensions 1,2, and 3, as a function of wave number q; the vertical dashes show the position $q = 2k_F$.

The presence of the Fermi surface induces microscopic "Friedel oscillations" of wavelength π/k_F in the electron density. This result should be contrasted with the monotonic decay of the screened potential in a classical plasma, as found for instance in the Debye-Hückel theory of electrolytic solutions. Instead the effective potential created by an ion inserted in the electron gas, as well as the effective potential with which each electron interacts with the other electrons, are oscillating functions of distance showing both repulsive and attractive regions.

These results of the random phase approximation are essentially confirmed by more accurate many-body theories of the density response function. In these theories one often assumes that the electron gas responds as an ideal gas not to the self-consistently screened electrostatic potential, but to an effective self-consistent potential that is modified to take into account short-range exchange-correlation effects. In other words, one posits

$$\delta n(q) = \chi_0(q)[V_{ext}(q) + v(q)\delta n(q) - v(q)G(q)\delta n(q)] \tag{12}$$

where the second term in the brackets is the electrostatic potential created by the charge density distribution and the last term, containing the so-called local-field factor $G(q)$, generates the additional exchange-correlation potential (this is the term that is neglected in the RPA). Different many-body theories propose different approximate forms for $G(q)$, beginning with the first and perhaps most famous one, due to Hubbard, which goes as $G(q) \simeq (q^2/2)/(q^2 + k_F^2)$. In all cases $G(q)$ tends to zero as q^2 for $q \to 0$ reflecting the short-range nature of the xc effects. In these theories the density response takes the form

$$\chi(q) = \frac{\chi_0(q)}{1 - v(q)[1 - G(q)]\ \chi_0(q)}, \tag{13}$$

and the finite $q \to 0$ limit of $v(q)G(q)$ amounts to a many-body renormalization of the density of states at the Fermi surface, hence of the screening length.

Fast-forwarding over many years of theoretical development (the interested reader can find a review in Ref. Giuliani and Vignale, 2005). Fig. 9 shows the plot of an analytical fit (Corradini et al., 1998) to the local field factor calculated directly from QMC by applying a periodic potential to electrons in the simulation box. More recent calculations and parametrization of $G(q)$ are also available (Chen and Haule, 2019; Ruzsinszky et al., 2020).

The local field factor (also known in the literature through its alias, the exchange correlation kernel $f_{xc}(q) = -v(q)G(q)$), and its spin-dependent and frequency-dependent generalizations $G_{\sigma\sigma'}(q)$ and $G_{\sigma\sigma'}(q,w)$ respectively (where σ and σ' are spin indices), plays a crucial role in density functional theory and in many real-world applications of the electron gas model. In particular, the effective interaction between two electrons in the electron gas (Kukkonen and Overhauser, 1979; Kukkonen and Chen, 2021; Dornheim et al., 2022), which is constructed in terms of local field factors and differs from the effective interaction between two impurities embedded in the electron gas can be used to analyze the possibility of superconductivity in electronic systems (Kukkonen and Chen, 2021).

Dynamical screening and plasmons

While the low energy excitations of the electron gas are fermionic quasi-particles, the spectrum of long-wavelength density fluctuations is overwhelmingly dominated by high-frequency collective oscillations known as "plasmons." The physical origin of plasmons is very simple. When the density of the electron gas is locally perturbed (say increased) electrons from neighboring regions move to screen the charge inhomogeneity, but in doing so they tend to overshoot the mark. Then they are pulled back toward the original disturbance and overshoot again, setting up an oscillation that decays slowly in time. The process is very similar to the one giving rise to sound waves in an ordinary gas, but there is an important difference: the restoring force responsible for the oscillation is the average long-range field created by all the electrons as opposed to, in the case of sound, the force arising from frequent

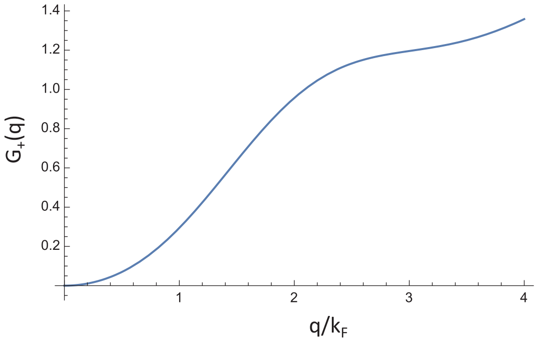

Fig. 9 Analytical fit to the local field factor calculated from QMC at $r_s = 2$ (Corradini et al., 1998). Notice that, unlike earlier approximations, this local field factor appears to grow indefinitely for large wave vector q.

short-range collisions between particles. Because of the long-range nature of the Coulomb interaction, the frequency of oscillations at wave vector q, denoted by $\omega_p(q)$, tends to be high and is given in the long-wavelength limit by

$$\omega_p(q \to 0) = \sqrt{nq^2 v(q)/m} = \sqrt{4\pi ne^2/m} \tag{14}$$

for the three-dimensional electron gas. The possibility of such oscillations was anticipated by Langmuir in 1928, long before the central importance of plasmons in the theory of the electron gas was recognized in the seminal work of Bohm and Pines in the 1950s. Notice that in Eq. (14) m is the bare electron mass in vacuum, *not* the quasiparticle effective mass. This simple long-wavelength result is exact, regardless of the relative strength of the electron-electron interaction, because a long-wavelength plasmon can be viewed as a rigid motion of the center of mass of the entire system, which does not involve the complex exchange and correlation effects that dress the motion of individual electron quasiparticles. Plasmon excitations are observed in inelastic scattering experiments on metals, using either a beam of fast electrons in electron energy loss spectroscopy or a beam of X-rays.

The simplest way to calculate the plasmon frequency is to look for the poles of the density response function, properly generalized to accommodate periodic potentials oscillating at a frequency ω, as a function of ω. This is easily understood by considering the definition of the dynamical density response function $\chi(q, \omega)$:

$$\delta n(q,\omega) = \chi(q,\omega) V_{ext}(q,\omega) \tag{15}$$

where $\delta n(q, \omega)$, $V_{ext}(q, \omega)$are Fourier transforms of δn and V_{ext} in both space and time. The existence of a self-sustained plasma oscillation implies the possibility of a finite density fluctuation δn in the absence of an external field V_{ext}. This can only happen if $\chi(q, \omega)$ is infinite at the plasmon frequency. The general theory of the linear response guarantees that poles of $\chi(q, \omega)$ can only occur in the lower half of the complex frequency plane, but nothing prevents these poles from coming arbitrarily close to the real frequency axis. When this happens, the real part of the frequency is the plasmon frequency, while the imaginary part (small and negative) is related to the damping rate of the oscillation.

These general features are clearly brought out by the simplest approximation, the RPA, in which one has (with obvious generalization of Eq. (16))

$$\chi_{RPA}(q,\omega) = \frac{\chi_0(q,\omega)}{1 - v(q)\chi_0(q,\omega)} \ , \tag{16}$$

where $\chi_0(q, \omega)$ is the frequency-dependent response function of the ideal electron gas, which is known analytically and usually referred to as the *Lindhard function (*Giuliani and Vignale, 2005*)*. The plasmon frequency is then obtained by the solution of the equation

$$1 - v(q)\chi_0(q,\omega) = 0, \tag{17}$$

which, in view of the exact result $\chi_0(q, \omega) \to nq^2/(m\omega^2)$ for $q \to 0$ and finite ω leads directly to Eq. (14). It is worth noting that the solution is purely real, i.e. the plasmon is not damped in the RPA, The situation is illustrated in Fig. 10A, where we see that plasmons

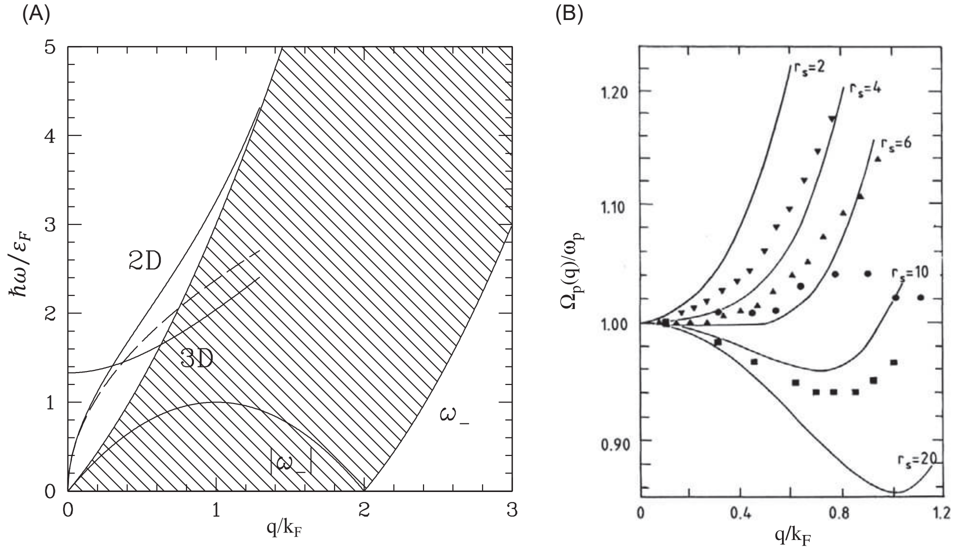

Fig. 10 (A) Plasmon dispersion in three and two dimensional electron gas (full lines) for $r_s = 2$. The dashed line represents the approximate two dimensional dispersion given by Eq. (17). Notice that both in three and two dimensions the long wavelength plasmons lie well above the edge of the particle hole continuum (shaded region), which protects them from decay into single electron-hole pairs. (B) Plasmon dispersion normalized to the plasmon frequency at q = 0. The symbols represent the experimental data for Na ($r_s = 3.93$, downward triangles), K (rs = 4.86, upward triangles), Rb ($r_s = 5.20$, dots) and Cs ($r_s = 5.62$, squares). The solid lines give the theoretical plasmon dispersions obtained with the use of the STLS static local field factor.

oscillations being much higher in frequency than electron-hole pair excitations at the same wave vector, have no viable mechanism for decaying into single electron-hole pairs while obeying the conservation of momentum and energy. The situation changes, however, when one consider more sophisticated many-body theories beyond the RPA. In these theories the plasmon can decay by emitting *two* electron-hole pairs with large but nearly opposite momenta, so that the total energy and momentum match those of the plasmons. But even these more sophisticated theories predict plasmon damping to vanish as q^2 for $q \rightarrow 0$ in agreement with the general physical argument outlined above, namely the decoupling of the center of mass motion from the internal degrees of freedom of the electron gas (Kohn's theorem).

Fig. 10B shows the plasmon dispersion $\omega_p(q)$ for the three dimensional electron gas at various densities. These results are obtained using the STLS theory, which includes xc local field factors beyond the RPA. At high density (small r_s) the frequency increases with increasing q until a critical q is reached where the plasmon merges with the continuum of electron-hole excitations and is no longer a well-defined excitation. Here the RPA is qualitatively correct. But, as the density decreases, the plasmon dispersion flattens and even bends downward. This effect cannot be reproduced within the RPA and reflects the increasing importance of correlations at low density. A vanishing plasmon frequency at finite q would in principle indicate an instability of the uniform electron gas and the emergence of a highly correlated phase such as the Wigner crystal (see below).

Wigner crystallization

It has already been remarked that as the dimensionless electron spacing r_s increases (i.e., as the electron density decreases) the kinetic energy becomes less and less important relative to the potential energy associated with the Coulomb repulsions. In the 1930s Wigner had noticed that an optimal value is obtained for the potential energy of jellium if the electrons are placed on the sites of a body-centered cubic lattice structure. Localization of the electrons raises their kinetic energy and an electron crystal may become favored only at very low density, where the potential energy becomes dominant. Of course, in the crystal the electrons are not strictly localized on the lattice sites but execute vibrational motions around them. But the kinetic energy associated with this zero-point motion scales as $r_s^{-3/2}$ and becomes negligible compared to the interaction energy r_s^{-1} in the low density limit. At the same time, the amplitude of the zero-point oscillations scales as $r_s^{3/4}$ which is much smaller than r_s when r_s is large, justifying the picture of well-localized electrons in the limit under consideration. Of course, strong anharmonicity and high concentrations of lattice defects will be present in this quantum crystal near the transition density, or even at lower densities as the temperature is raised and the melting point is approached.

The problem of "Wigner crystallization" has become a classic in many-body physics, from both the theoretical and the experimental point of view. Quantum Monte Carlo studies have indicated that the ground state of three-dimensional (3D) jellium undergoes a first-order transition to a body-centered-cubic crystal around $r_s \simeq 100$, which is probably beyond the reach of experiments. In two dimensions, however, a first-order transition between the paramagnetic liquid and a triangular Wigner crystal is predicted to occur at a much lower value of $r_s \simeq 35$. The search for Wigner crystallization in the laboratory has therefore focused on quasi-2D assemblies of electronic carriers, mostly in artificial semiconductor heterostructures. The first unambiguous observation of Wigner crystallization was reported by Grimes and Adams in 1979 for electrons floating on top of a substrate of liquid ^{4}He in a quasi-classical regime. Metal-insulator transitions have subsequently been reported in quasi-2D systems of carriers subject to very strong magnetic fields in the fractional quantum Hall effect regime or in the presence of disorder and also in high-purity quasi-2D samples having exceptionally high carrier mobility. The observation of shear phonon modes, pinning-depinning transitions, and, more recently, geometric resonances occurring when the cyclotron radius of electrons becomes commensurate with the lattice constant, have been considered "smoking gun" evidence for Wigner crystallization.

Electron gas in reduced dimensionality

Electron gases in reduced dimensionalities present strong fundamental interest and high technological relevance. A general consequence of reducing the dimensionality is an increasing role of the electron-electron correlations at each given value of the dimensionless coupling strength r_s. This is ultimately a consequence of the modified topology of the electronic motions as the electrons are constrained to move in a plane or along a line or inside a quantum dot. This profoundly modifies the excitation spectrum of the ideal Fermi gas and often enhances the susceptibility to external perturbations.

Two-dimensional electron gases (2DEGs) are typically realized in semiconductor heterostructures at the interface between two different semiconductors. Typical examples are the inversion layer that forms at the surface of *p*-type Si in a metal-oxide-semiconductor (MOS) heterostructure with M = polycrystalline highly doped Si, I=SiO_2, S = *p*-type Si, and GaAs-AlGaAs-GaAs quantum wells, where the electrons reside in the AlGaAs region. These system are two-dimensional in the sense that the motion of electrons in one direction (perpendicular to the heterostructure) is strongly quantized (i.e., all the electrons reside in the lowest quantized state of motion, which is separated from other states by a large energy gap) but the electrons move freely in the remaining two directions. What makes the systems particularly attractive is (i) the possibility of changing the electronic density by orders of magnitude by electrostatic gating (whereas the electron density in traditional metallic systems is essentially fixed by the ionic background) and (ii) the possibility of spatially separating the electrons from sources of disorder such as donor impurities, resulting in much higher mobilities. In recent years a new class of two-dimensional materials has emerged, which are based on single atomic layers, such as a single layer of C atom (known as graphene) where the electronic density can be controlled by doping and by electrostatic gating. Within this family of systems many variations are possible, such as double electronic layers, multiple layers, and periodic superlattices. Recently, it has also become possible to twist two adjacent atomic layers relative to each other, thus generating incommensurate patterns known as moiré superlattices.

The Landau theory of Fermi liquids remains generally applicable to 2DEGs, in spite of some subtle differences. For example, the inverse lifetime of Landau quasiparticle in 2D varies as $(\varepsilon_k - \varepsilon_F)^2 \ln \mid \varepsilon_k - \varepsilon_F \mid /\varepsilon_F$ as a function of energy and as $(k_B \boldsymbol{T})^2 \ln |k_B \boldsymbol{T}/\boldsymbol{E}_F|/\boldsymbol{E}_F$ as a function of temperature. The logarithmic terms, which are absent in three dimensions, tend to decrease the lifetime of quasiparticles in 2D. 2DEGs are also much more sensitive to impurity scattering than their 3D counterparts. For example in the *non-interacting* 2DEG it is widely believed that all electronic states are localized in the presence of disorder. Electron-electron interactions restore the metallic state, but the inverse lifetime of quasiparticles now scales as $k_B\boldsymbol{T}$, which is much larger that $k_B\boldsymbol{T})^2 \ln \boldsymbol{T}$, making these systems *marginal Fermi liquids*.

Static screening is greatly reduced in two dimensions as the electric field created by, say, an impurity can escape out of the plane and reach far away electrons in spite of the presence of compensating charge in the plane. Plasmon excitation are similarly reduced in frequency, their long-wavelength dispersion going as

$$\omega_p^{2D}(q \to 0) = \left(2\pi n e^2 q/m\right)^{1/2}, \tag{18}$$

which goes to zero for $q \to 0$ but still lies much above the energies of electron-hole pairs (linear in q). The above formula, incidentally, is exactly what one gets from Eq. (14), provided one takes care to use the correct form of the Fourier transform of the Coulomb potential in two dimensions, namely $v^{2\mathrm{D}}(q) = 2\pi e^2/q$. Thus, Eq. (14) is valid for the Galilean-invariant electron gas in any number of dimensions.

Similarly, the formula for the Friedel oscillations in the static screening density is modified due to the fact that the static density response function has a cusp at $q = 2k_F$ (see Fig. 6): this causes the amplitude of the oscillations to decay more slowly as a function of distance, v.i.z., as $1/r^2$ rather than as $1/r^3$.

Some of the most impressive examples of 2DEG physics have emerged in the presence of high magnetic field (quantum Hall effect) and in graphene where a peculiar band structure causes the free particle dispersion to be linear in k (mass less Dirac fermions). We will say more about these in the next two sections.

Consider now a system in which the conduction electrons are restricted to move along a line. The "Fermi surface" reduces to two points located at $k = \pm k_F$ and only forward or backward scattering processes are allowed at the "Fermi surface". Here the Landau theory of Fermi liquid breaks down completely even in the absence of disorder. In fact, one can show that the Landau quasiparticles are no longer well-defined, as their inverse lifetime becomes comparable to or larger than their energy. Fermionic quasiparticles are superseded by linearly dispersing collective excitation (similar to plasmons) with bosonic character. This leads to a new paradigm of interacting electrons known as the "Luttinger liquid". Characteristics of the Luttinger liquid are (i) There are no single-particle excitations: sharp peaks in the one-particle spectral function at $k = k_F$ are replaced by power-law singularities (ii) there is no Fermi surface: the discontinuity in the momentum distribution across the Fermi surface is replaced by a different type of nonanalytic behavior, (iii) Correlation functions between observables at different points in space decay with power laws with fractional exponents that depend on the strength of the interaction (iv) spin-charge separation occurs, i.e., spin-carrying collective excitations and charge-carrying collective excitations propagate with different velocities (in a normal Fermi liquid both spin and charge reside in the Landau quasiparticle and travel with the same velocity).

Even a simple look at the density response function of the noninteracting 1D Fermi gas shows how unusual this system can be. We have

$$\chi_0^{1D}(q) = -\frac{2m}{\pi\hbar^2 q}\ln\left|\frac{q+2k_F}{q-2k_F}\right|. \tag{19}$$

In Fig. 6 this density response function is plotted visa-vis its counterparts in 2 and 3 dimensions. In all cases there is a singularity at $|q| = 2k_F$, but the singularity gains strength as dimensionality is reduced, going from a logarithmic divergence in the derivative of $\chi_0(q)$ in 3D, to a discontinuity in the derivative of $\chi_0(q)$ in 2D, and finally to a logarithmic divergence in $\chi_0(q)$ itself in 1D. The divergence of the response means that the system is on the verge of an instability which will cause a massive reconstruction of the ground state as soon as additional interactions are turned on. For example, a monoatomic 1D conductor with a half-filled conduction band (one electron per atom) will gain electronic energy as soon as the electron-lattice coupling is turned on. The system undergoes a lattice distortion which opens a gap at the Fermi level through the formation of dimers. This is known as "Peierls instability". Similarly, electron-electron interactions, even in the absence of electron-lattice coupling, lead to the formation of a Luttinger liquid.

Two-dimensional electron gas in graphene

In its pristine state graphene – a single layer of C atoms arranged in a honeycomb lattice – is a semimetal. Its valence and conduction bands touch at two points in the Brillouin zone (Dirac points) and the band dispersion is near these points with the two bands being mirror images of each other (see Fig. 11). This unusual form of the energy-momentum relation arises from the fact that the

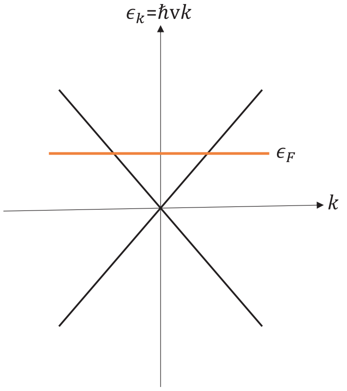

Fig. 11 Band dispersion for massless Dirac fermions in the vicinity of the crossing point (Dirac point). In pristine graphene the Fermi level cuts the bands at the crossing point, so that there are no free carriers at zero temperature. Doping and/or electrostatic doping can shift the Fermi level away from the crossing point, as shown in this figure, creating a two-dimensional gas of massless Dirac electrons (case shown) or holes.

honeycomb lattice has two inequivalent sites in each unit cell, thus endowing the electron with an additional degree of freedom, formally equivalent to a spin, which has eigenvalues 1 or −1 depending on whether the electron is on or the other site. Under these conditions the electron wave function can no longer be described by a scalar plane wave: it becomes instead a two-component spinor, similar to the spinors that occur in the theory of massless relativistic Dirac fermions, but, of course, in a completely non-relativistic context. The pseudospin degree of freedom plays a crucial role in the calculation of the electronic properties of graphene. For a detailed review see Ref. (Castro Neto et al., 2009).

This system can host a 2DEG if we add electrons to the conduction band by doping or by electrostatic gating. Or it can host a two-dimensional hole gas if we remove electrons from the valence band. We will focus on the former case. Let us set the zero of the energy at one of the Dirac points, and let us also choose that point as the origin of momentum space. The main differences between this and the ordinary 2DEG stem from (i) the linearity of the conduction band dispersion $\varepsilon_k = \hbar v k$ (notice the energy vanishing at the Dirac point $k = 0$) and (ii) the presence of occupied valence band states which are separated from empty conduction band states by energies of the order of the Fermi energy.

Concerning point (i) we notice that the linear dispersion breaks Galilean invariance, which mandates a quadratic relation between energy and momentum. On the contrary, this is the dispersion of massless relativistic particles (e.g., photons) which move with a preassigned speed v ($v =$ speed of light in the case of photons) independent of the momentum. For electrons in graphene, v is about 1/300 the speed of light. As usual, we introduce the Fermi wave number k_F, which separates occupied from empty states within the conduction band (see Fig. 4): it is related to the two-dimensional electron density by $k_F = (\pi n)^{1/2}$, where we have taken into account not only the spin degeneracy but also the existence of two degenerate states associated with the same k in the vicinity of two different Dirac points. The Fermi energy is then $\varepsilon_F = \hbar v k_F = \hbar v(\pi n)^{1/2}$..

An important difference between the 2DEG in graphene and the ordinary 2DEG emerges immediately from the above. Namely, the kinetic energy per particle $\sim\varepsilon_F \propto \hbar v n^{1/2}$ and the potential energy per particle $e^2/r \propto e^2 n^{1/2}$ scale with the same power of density and the ratio of the second to the first is $\alpha_{ee} = e^2/(\hbar v) \sim 2$ in graphene. Thus, the electron gas in graphene does not seem to become "more ideal" as the density is increased, or "less ideal" as it is decreased – rather it presents us with an intermediate-coupling scenario at all densities (the actual value of α_{ee} is strongly affected by the dielectric environment of the graphene sheet, and can be larger or smaller than 2. The value quoted above is for a graphene sheet in vacuum). However, there is now another measure of the importance of interaction effects, and that is Λ/k_F where Λ is an cutoff wave vector, which determines the largest momentum of the occupied states for which the linear band model is still valid. The precise value of this cutoff wave vector is somewhat fuzzy, but is expected to be of order $1/a$, where a is the lattice constant. So even though α_{ee} is constant, interaction effects become stronger as k_F tends to zero, which is similar to the familiar situation, but leads to very different phenomenology in this case. For example it can be shown that the bulk modulus, proportional to $\partial\mu/\partial n$, is increased by interactions rather than decreased (Polini et al., 2007). This happens because when the electronic density is increased the Fermi level in the upper band moves farther away from the lower band: the negative exchange energy that is lost due to this effect outweighs the negative exchange energy that is gained by having more electrons in the upper band. The same phenomenon is observed for the spin susceptibility, which is now reduced, rather than enhanced, by interactions.

The existence of a finite k_F allows one to define an effective mass, even though the underlying particles are massless. To do this notice that in the ordinary electron gas the energy of a particle near the Fermi level can be approximated as $\varepsilon_k - \varepsilon_F = \hbar k_F(k - k_F)/m$, where m is the mass of the particles. Comparing this with the corresponding expression for massless fermions $\varepsilon_k - \varepsilon_F = \hbar v(k - k_F)$ one is led to the identification of an effective mass $m_c = \hbar k_F/v$, which is also known as the *cyclotron mass*. Thus, massless electrons in the vicinity of the Fermi surface behave like ordinary massive electrons with an effective mass $\hbar k_F/v$. This would seem a rather uninteresting story until we realize that this effective mass is density-dependent, because k_F is, and does indeed tend to zero in the limit of low carrier density.

These differences are duly reflected in the calculation of the ideal-gas linear response functions $\chi_0\,(q)$ and $\chi_0\,(q,\,\omega)$. For example in the ordinary 2DEG one has $\chi_0\,(q,\,\omega) \to nq^2/(m\omega^2)$ for $q \to 0$ and finite ω. For electrons in graphene this relation is replaced by $\chi_0(q,\omega) \to \varepsilon_F q^2/(\pi\hbar^2\omega^2)$, which follows directly from the replacement of m by the cyclotron mass. Making use of this limiting form the plasmon dispersion for electrons in graphene is found to be

$$\omega_p(q \to 0) \simeq \left(2e^2\varepsilon_F q\right)^{1/2}/\hbar, \tag{20}$$

which is qualitatively different from Eq. (18) because the coefficient of $q^{1/2}$ scales with density as $n^{1/4}$ rather than $n^{1/2}$. More importantly, the coefficient of $q^{1/2}$ is no longer "universal", in the sense of being independent of the electron-electron interaction strength. In the Galilean-invariant electron gas, that universality stems from the fact that long-wavelength plasmons correspond to a rigid motion of the center of mass of the electron gas, and the center of mass is decoupled from the internal degrees of freedom. This is no longer the case for the electron gas in graphene. The center of mass motion does not decouple from internal degrees of freedom and the coefficient of $q^{1/2}$ in Eq. (18) (also known as *Drude weight*) is found to depend on the strength of the electron-electron interaction (i.e., the value of the coupling constant α_{ee}).

Additional differences between ordinary 2DEG and graphene 2DEG emerge when one consider the structure of the electron-hole excitation spectrum (see Fig. 12A), which now contains an entirely new branch in which electrons are promoted from a valence band state to a conduction band state with excitation energies comparable to the Fermi energy. Also plotted in Fig. 12B is the static density response function $\chi_0\,(q)$, which is distinctly different from the one plotted in Fig. 6, rising linearly, rather than decreasing, as a function of q, for $q > 2k_F$. The different form of the singularity at $q = 2k_F$ is reflected in a different form of the Friedel oscillations induced by an impurity. The amplitude of these oscillations decays as $\cos(2k_F r)/r^3$, at variance with the 2DEG result $\cos(2k_F r)/r^2$.

Coming to electron-electron interaction effects, we point out that, as the Fermi level approaches the crossing point with decreasing density, the Fermi liquid concept remains in force as long as $k_F > 0$, but the effective mass of quasi-particles is found to be logarithmically suppressed relative to the noninteracting cyclotron mass (Kotov et al., 2012). Another way of saying this is that the Fermi velocity v is renormalized to $v^*(k_F) > v$ where $v^*(k_F)$ diverges logarithmically in first order perturbation theory as $k_F \to 0$:

$$\frac{v^*(k_F)}{v} = 1 + \frac{\alpha_{ee}}{4}\ln\left(\frac{\Lambda}{k_F}\right). \tag{21}$$

While an increase of the velocity, leading to a reshaping of the bands near the Dirac point, has been experimentally observed, the divergence of $v^*(k_F)$ poses a problem of legitimacy for the microscopic perturbation theory on which this prediction is based. A non-perturbative approach is needed to analyze the $k_F \to 0$ limit. This approach is provided by the renormalization group, which is reviewed in Ref. (Kotov et al., 2012), and generally confirms the predictions of the weak coupling theory.

What is the effect of the interaction of the compressibility and the spin susceptibility of a the electron gas in graphene? In an ordinary 2DEG both are strongly enhanced by the interaction because the exchange energy becomes larger in absolute value (i.e., actually more negative) when the electron gas is spin polarized (spin susceptibility) or when the Fermi energy is pushed toward higher values. Surprisingly, the situation is reversed in the case of graphene 2DEG: detailed microscopic calculations (Polini et al., 2007) reveal that both the spin susceptibility and the compressibility are reduced by electron interaction. The explanation of this counterintuitive result lies in the fact that the exchange energy has a large contribution from the "spectator"

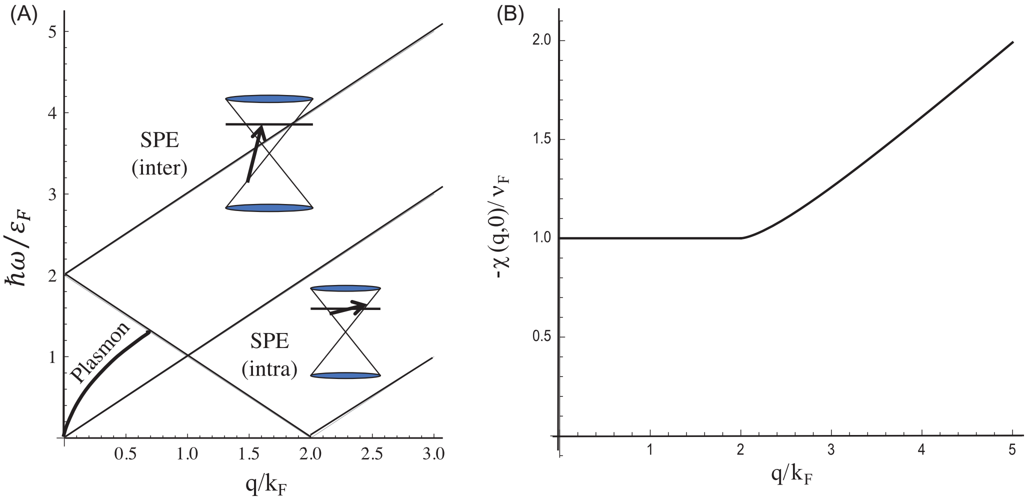

Fig. 12 (A) Schematic diagram of electron-hole pairs and collective excitations in graphene. Notice that the electron-hole pair excitation spectrum now contains transitions from the valence to the conduction band, as well as the usual transitions within the conduction band (B) The static density response function of the 2DEG in graphene. Notice the rapid linear increase as a function of q for $q > 2k_F$. This unusual behavior is a consequence of interband transitions which contribute to the polarizability of the electron gas in graphene.

electrons in the valence band. At first sight, it may seem that the distribution of electrons in the valence band should not be affected by the position of an electron in the conduction band for the same reason that the distribution of spin-down electrons is not affected by the presence of a spin-up electron in an ideal electron gas. But this is not true because valence and conduction band states of the same spin orientation (unlike states of opposite spin orientations) are not completely distinguishable at a given point in space: this gives rise to an inter-band exchange energy. When the chemical potential in the conduction band is raised, it turns out that the familiar gain in intra-band exchange is more than compensated by the loss of inter-band exchange (due to decreased overlap of the electron wave function at the Fermi level with valence band wave functions). Hence the sign of the effect is reversed.

Two-dimensional electron gas at high magnetic field

One of the most spectacular effects in the two-dimensional electron gas is the Quantum Hall Effect, which occurs when the gas is exposed to a strong perpendicular magnetic field $\boldsymbol{H}$ of the order of several Teslas and sufficiently low temperatures (von Klitzing et al., 1980; Tsui et al., 1982). The effect can be described as the quantization of the Hall conductance (i.e., the ratio $\boldsymbol{I_H}/\boldsymbol{V_L}$, where $\boldsymbol{I_H}$ is the transverse current and V_L is the longitudinal voltage) in multiples of the fundamental quantum of conductance $e^2/h \simeq 10^{-4}$S. Thus one has $\boldsymbol{I_H} = \nu(e^2/h)V_L$ where ν is an integer in the integer quantum Hall effect or an odd-denominator fraction in the fractional quantum Hall effect. (The two versions of the effect, integral and fractional, have different physical origins, as we will see). The quantization is spectacularly accurate (one part in 10^10), in stark contrast with ordinary conductances, with or without magnetic fields, which depend strongly on the preparation of the sample, the level of purity, the temperature, and so on.

To explain this effect, we recall that the energy levels of an electron in 2D in the presence of a perpendicular magnetic field are the so-called Landau levels

$$\varepsilon_j = \left(j + \frac{1}{2}\right)\hbar\omega_c \tag{22}$$

where $\omega_c = e\boldsymbol{H}/m$ is the cyclotron frequency and j is a nonnegative integer. These discrete levels replace the continuous distribution of energies $\varepsilon_k = \hbar^2k^2/(2m)$ of a free particle. However, since the number of states must be conserved, each of the Landau levels is macroscopically degenerate, i.e., for a particle confined to a 2D box of area A the number of degenerate states in each Landau level is

$$D = \frac{HA}{\Phi_0}, \tag{23}$$

where $\Phi_0 = h/e$ is the quantum of magnetic flux. Notice that this degeneracy is the same for all Landau levels, regardless of j.

We note in passing that the situation is qualitatively similar in graphene, except for the fact that the "mass" m is no longer a constant but scales with the square root of the electronic density. And since the electronic density, for a fixed number of occupied Landau levels, is proportional to $\boldsymbol{H}$, as follows from the degeneracy of Landau levels, Eq. (23), it is quite plausible that the effective cyclotron frequency, which determines the energy of the Landau levels in Eq. (22) should become proportional to $\sqrt{H}$ rather than $\boldsymbol{H}$. Indeed, the correct formula for the cyclotron frequency in graphene is v/ℓ, where $\ell = \hbar/(e\boldsymbol{H})$ is the magnetic length, related to the radius of a semiclassical orbit and described more precisely below.

The integer quantum Hall effect occurs whenever the Fermi level falls in the gap between two Landau levels, so that one has an integer number of fully occupied Landau levels. In a perfectly clean electron gas this situation would require an extremely accurate tuning of the electronic density, impossible to achieve in practice. Fortunately, the 2DEG in semiconductor heterostructures is sufficiently dirty to allow a significant density of localized electronic states to exist in the gap between Landau levels. These localized states do not contribute to the Hall effect, but play an essential role in allowing the Fermi level to remain inside the gap over a finite range of densities. According to conventional wisdom, this system should be an insulator, since all the states at the Fermi level are localized and unable to conduct electricity. Nevertheless, it is observed that the Hall conductance is ne^2/h where n is the number of occupied Landau levels. The apparent contradiction can be resolved in two ways.

The first approach is to recognize that the gap exists only in the bulk of the 2DEG. As the edges of the Hall bar are approached the Landau levels rise under the action of a confinement potential, and the n fully occupied ones eventually cross the Fermi level, thus closing the gap and generating conducting states on each edge. These "edge states" are like a one way street, allowing electrons to propagate only in one direction, with no possibility of backscattering. It is then shown that each pair of perfectly conducting edge channels (one state on each edge, with a potential difference between the two edges) contributes exactly a quantum of a conductance, e^2/h, so that the total conductance equals ne^2/h.

The second approach focuses on the bulk of the sample, which is now bent in the shape of an annulus (the so-called Corbino disk). In this description, one notices that the nominally insulating electron in the occupied Landau levels can still transport a current if they all move together in rough analogy with bags on a conveyor belt. The electromotive force is generated by a varying magnetic flux threading the annulus and is directed tangentially along the annulus. At the same time, the varying magnetic flux causes the centers of the electronic states in each Landau level to slowly drift in the radial direction, thus creating the Hall current. The precise quantization of the current follows from the fact that each additional flux quantum threaded through the annulus causes an integer number of electron to be transported from the inner to the outer edge.

The precise relation between the edge and bulk descriptions of the quantum Hall effect is still somewhat unsettled to date, particularly with regard to the spatial distribution of the Hall current. What is certain is that the effect has a topological origin, related to the existence of exactly n bundles of extended states (the Landau levels) below the Fermi level.

In contrast to the integral QHE, the fractional QHE occurs when the Fermi level falls in a gap created by electron-electron interactions within the lowest Landau level. The many-body origin of this gap has attracted tremendous attention from many-body theorists. A microscopic theory of the gap responsible for the 1/3 effect was first proposed by Laughlin (Laughlin, 1983), who proposed that the state of the 2DEG in the 1/3 quantum Hall state could be described by the elegant wave function

$$\psi(z_1, \ldots, z_N) = \prod_{i<j}^{N} \left(z_i - z_j\right)^3 e^{-\sum_{i=1}^{N} |Z_i|^2/4\ell^2} \tag{24}$$

where $z_i = x_i + iy_i$ is a complex variable that combines to the coordinates x_i and y_i of each electron, and $\ell = \hbar/(e\boldsymbol{H})$ is the magnetic length for magnetic field $\boldsymbol{H}$ (the magnetic length is the radius of a disk that encloses one quantum of magnetic flux). This is a highly correlated wave function in which the electrons avoid each other very efficiently (and thus keep their energy low) thanks to deep (third order) zeroes that occur when $z_i = z_j$. This wave function stands out because it associates three flux quanta to each particle. A similar wave function can be constructed with fifth, or seventh order zeroes, corresponding to 1/5 and 1/7 quantum Hall states, but not for even denominator states, since an even exponent would violate the required antisymmetry of the wave function under interchange of two particles. Starting from the state described by Eq. (24) any attempt to insert an extra electron in the system incurs a high energy cost (the gap) because this extra electron is not protected by the powerful zeroes of the ground state wave function and is therefore able to come closer to any of the pre-existing electrons. In addition, Laughlin showed that this extra electron would locally carry a fractional charge of $e/3$ – the remaining $2e/3$ being delocalized at the system's boundary.

Perhaps the simplest way to understand the physics of the Laughlin wave function is the *composite fermion theory* developed by Jainendra Jain (Jain, 1989). In this theory one assumes that each electron captures *two* magnetic flux quanta, thus forming what Jain calls a composite fermion. In the 1/3 quantum Hall state each composite fermion sees an effective magnetic field arising from the remaining one flux quantum per electron that has not been used in the construction of the composite fermion. Thus the composite fermion in the 1/3 quantum Hall state behaves like a regular electron in a completely filled Landau level. From this point of view, the fractional quantum Hall effect is nothing more than the integer quantum Hall effect of composite Fermions. This qualitative picture has been confirmed by many detailed calculations based on microscopic wave functions which were constructed starting from the composite fermion picture.

The collective excitations of the 2DEG at high magnetic field have also received a great deal of attention.

The most prominent excitation at $q = 0$, analogous to the plasmon, is the cyclotron resonance, corresponding to an excitation of the center of mass of the system, which rotates at the cyclotron frequency ω_c. Just as for the ordinary plasmon, the frequency of this motion is not affected by electron-electron interactions – a statement that goes under the name of Kohn's theorem.

Besides the center of mass mode, there are also intra-Landau level collective excitations, which have no analog at $\boldsymbol{H} = 0$ and correspond to quadrupolar deformations of the wave function within the lowest Landau level. These excitations exhibit a many-body gap at $q = 0$ and have been observed in Raman scattering experiments.

Transport coefficients

The transport of charge, spin, energy and momentum in electronic systems is largely controlled by extrinsic agents such as impurities and lattice vibrations (phonons) and as such does not fall entirely within the realm of electron gas theory. But, if the system is extremely clean (no impurities) and the temperature in neither too high (so that phonons can be neglected) nor too low (to ensure frequent collisions between quasiparticles) then the intrinsic transport coefficients can be calculated entirely within electron gas theory. The intrinsic transport coefficients are (i) the spin diffusion constant D_s (proportional to the spin conductivity σ_s), which relates the spin current to the gradient of the spin density (ii) the thermal conductivity, κ, which relates the heat current to the gradient of the temperature, and (iii) the shear and bulk viscosities η and ζ respectively, which relate the traceless and traceful components of the momentum current (also known as stress tensor) to the corresponding components of the time derivative of the strain tensor. Notably, in a homogeneous electron gas there is no intrinsic transport coefficient for charge, i.e. no intrinsic electric conductivity or diffusion constant, since these quantities would be infinite by momentum conservation (one may say that the transport of charge in a perfectly clean electron gas proceeds by the emission of plasmons rather than by diffusion). The remaining three coefficients are finite even in the absence of impurity and phonon scattering because none of the three currents considered (the spin current, the heat current, and the momentum current) is conserved by the electron-electron interaction.

Quasiparticle collisions, which are responsible for the finite quasiparticle lifetime, are absolutely essential to calculate the intrinsic transport coefficient. In fact, these coefficients would all be infinite if collisions between the quasiparticles were completely neglected, which of course becomes a better and better approximation as the temperature is reduced. This counterintuitive result (divergence of the intrinsic transport coefficients for $\boldsymbol{T} \to 0$) follows from the "asymptotic freedom" of the Landau quasiparticles in the low-temperature limit. Indeed, one can show that the transport coefficient are qualitatively described by the following formulas

$$D_s \sim v_F^2 \tau_s, \quad \eta \sim S\tau_\eta, \quad \zeta \sim B\tau_\zeta, \quad \kappa = nc_v v_F^2 \tau_q, \tag{25}$$

where ***S*** and ***B***, are, respectively, the high-frequency shear modulus and the bulk modulus (both on the order of $n\varepsilon_F$) and c_v is the heat capacity (per particle) of the Fermi liquid. Here τ_s, τ_η etc.. . . are transport relaxation times which are similar but not identical to the quasiparticle lifetime. All these scattering times diverge in the limit of zero temperature as $1/\boldsymbol{T}^2$ in three dimensions. In two dimensions the situation is more complicated as the scattering times associated with spin diffusion and thermal conductivity diverge as $1/(\boldsymbol{T}^2 \ln \boldsymbol{T})$, while the scattering time associated with the viscosity continues to diverge as $1/\boldsymbol{T}^2$ (Hui-Hsing and Ebner, 1974). This is due to the fact that the scattering processes that are responsible for the $\ln \boldsymbol{T}$ term are associated with zero momentum transfer and therefore do not contribute to the transfer of momentum in the liquid. Disregarding impurities and phonons, the divergence of the transport coefficients is cut off when the quasiparticle mean free path becomes comparable to the macroscopic size of the system, at which point the coefficients lose their hydrodynamic significance.

Explicit formulas for the calculation of transport coefficients were worked out in three dimensions in the works of Abrikosov and Khalatnikov (Abrikosov and Khalatnikov, 1959) and their formulas, originally developed for liquid ^{3}He, can be adapted to the electron gas. Similar formulas can be found in the literature for the Galilean-invariant 2DEG (Hui-Hsing and Ebner, 1974). For the 2DEG in graphene the transport coefficients were recently calculated in Refs. (Principi and Vignale, 2015; Principi et al., 2016)

Compensated semimetals, such as graphene itself at the charge neutrality point, offer the possibility of defining an intrinsic electric conductivity. This is because these systems contain equal numbers of electrons and holes, which drift in opposite directions under the action of the electric field. The relative motion of electrons and holes is hindered by electron-hole collisions, which tends to equalize the velocities of electrons and holes. This phenomenon is known as Coulomb drag and results in an intrinsic mechanism of resistance for compensated semimetals.

Spin-orbit interaction

We have until now neglected the possible coupling between the orbital motion and the spin of the electrons. This can be quite strong in three-dimensional heavy metals such Pt, and is responsible for important effects, such as the spin Hall effect and its inverse. If inversion symmetry is broken it is also possible to have an interesting phenomenon known as current-induced spin polarization, whereby a static spin polarization appears in response to an electric current. The inverse of this process, whereby an optically created spin polarization is converted to charge current, is known as "spin-galvanic effect" and has also been observed experimentally.

Starting in the first decade of the 2000 increasing attention has been paid to spin-orbit interaction effects in the 2DEG in semiconductor heterostructures and in graphene, with an eye to potential applications in the field of spintronics. In particular, several theoretical works have appeared, which combine the traditional jellium model with spin-orbit coupling.

Here we present the two most commonly used forms of spin-orbit coupling. The first, known as the Bychkov-Rashba interaction is most directly connected with the familiar spin-orbit interaction in atoms. It occurs in two-dimensional heterostructures in the presence of a perpendicular electric field ***E*** which breaks inversion symmetry along the z-axis. Its form is

$$H_{\boldsymbol{BR}} = \alpha_{\boldsymbol{BR}}(\mathbf{p} \times \widehat{\mathbf{z}})\cdot\sigma \tag{26}$$

where $\mathbf{p}$ is the two-dimensional momentum σ is the Pali matrix representative of the spin, and α_{BR} is a velocity proportional to the magnitude of the electric field in the z direction.

The second form is known as the Dresselhaus spin-orbit coupling and its structure is quite different from that of an atomic spin-orbit coupling. This interaction arises from the projection of a three-dimensional band structure lacking inversion symmetry (for example the band structure of GaAs) over the two dimensions of a quantum well derived from the same material. Its form is

$$\boldsymbol{H}_D = \alpha_D\left(p_x\sigma_x - p_y\sigma_y\right) \tag{27}$$

where again α_D has the dimensions of a velocity but now it does not arise from an external electric field but from the broken inversion symmetry of a three-dimensional solid.

A very interesting effect that arises from the Bychkov-Rashba and Dresselhaus spin-orbit interactions is known as "spin-momentum locking." This simply means that, in the absence of electron-electron interactions, the orientation of the spin of an electron is uniquely determined by its momentum, being either parallel or antiparallel to the direction of an appropriate linear combination of the Bychkov-Rashba field $\alpha_{BR}(p_y,-p_x)$ or the Dresselhaus field $\alpha_D(p_x,-p_y)$, where (a, b) denotes a two-dimensional vector with components a along the x axis and b along the y axis. The two possible orientations of the spin have different energies and, if the spin-orbit coupling is sufficiently large, it is quite possible to have a situation in which electrons at the Fermi level are entirely locked in a single orientation, say parallel to the effective field, which however depends on the momentum $\mathbf{p}$ and therefore changes around the Fermi surface. The intriguing magnetic response properties of the resulting spin-textures in momentum space, as well as their effect on electronic transport are a rapidly evolving area of research.

Adding the Rashba-Bychkov and/or the Dresselhaus interactions to the conventional electron gas Hamiltonian creates an open field for theoretical investigations of the spin-orbit coupled electron gas. The Landau theory of Fermi liquid has been generalized to include spin-orbit coupling. Microscopic calculations of the correlation energy are lagging behind, mostly due to the numerical challenge of implementing accurate QMC calculations with spin-dependent wave functions. Such calculations will play an important role in the development of spin-density functional theory for system with strong spin-orbit interaction and non-collinear spins.

Conclusion

The electron gas is the universal glue that binds together all known materials. While the properties of materials vary dramatic from one realization to the other, the properties of the underlying electron gas are fairly universal and provide the basis for a universal treatment of Coulomb interaction effect in materials as demonstrated by the widespread use of Density Functional Theory in materials science. In addition, the electron gas theory underlies the modern technology of semiconductor-based electronic devices. The study of novel phase of the electron gas, assisted by spin-orbit interaction, magnetic fields, and low dimensionality, is an extremely active field of fundamental research in which new discoveries are being made at a fast pace.

References

Abrikosov AA and Khalatnikov IM (1959) Reports on progress in physics. *The Physical Society of London* 22: 329–367.
Bohm D and Pines D (1953) *Physical Review* 92: 609.
Castro Neto AH, Guinea F, Peres NMR, Novoselov KS, and Geim AK (2009) *Reviews of Modern Physics* 81: 109.
Ceperley DM (2004) Introduction to quantum Monte Carlo methods applied to the electron gas. In: Giuliani GF and Vignale G (eds.) Proceedings of the International School of Physics Enrico Fermi, Course CLVII, Amsterdam: IOS Press.
Ceperley DM and Alder (1980) *Physical Review Letters* 45: 566.
Chen K and Haule K (2019) *Nature Communications* 10: 3725.
Corradini M, Del Sole R, Onida G, and Palummo M (1998) *Physical Review B* 57: 14569.
Dornheim T, Tolias P, Moldabekov ZA, Cangi A, and Vorberger J (2022) *The Journal of Chemical Physics* 156: 244113.
Drummond ND and Needs RJ (2009) *Physical Review Letters* 102: 126402.
Gell-Mann M and Brueckner KA (1957) *Physical Review* 106: 364.
Giuliani GF and Vignale G (2005) *Quantum Theory of the Electron Liquid*. Cambridge University Press.
Holzmann M and Moroni S (2020) *Physical Review Letters* 124: 206404.
Hui-Hsing F and Ebner C (1974) *Physical Review A* 10: 338.
Jain JK (1989) *Physical Review Letters* 63: 199.
Kotov VN, Uchoa B, Pereira VM, Guinea F, and Castro Neto AH (2012) *Reviews of Modern Physics* 84: 1067.
Kukkonen CA and Chen K (2021) *Physical Review B* 104: 195142.
Kukkonen CA and Overhauser A (1979) *Physical Review B* 20: 550.
Laughlin RB (1983) *Physical Review Letters* 50: 1395.
Ortiz G and Ballone P (1994) *Physical Review B* 50: 1391.
Polini M, Asgari R, Barlas Y, Pereg-Barnea T, and MacDonald AH (2007) *Solid State Communications* 143: 58.
Principi A and Vignale G (2015) *Physical Review B* 91: 205423.
Principi A, Vignale G, Carrega M, and Polini M (2016) *Physical Review B* 93: 125410.
Ruzsinszky A, Nepal NK, Pitarke JM, and Perdew JP (2020) *Physical Review B* 101: 245135.
Senatore G, Moroni S, and Ceperley DM (1996) In: Kraeft WD and Schlanges M (eds.) *Proceedings of the International Conference on the Physics of Strongly Coupled Plasmas*, p. 429. Singapore: World Scientific.
Singwi KS, Tosi MP, Land RH, and Sjölander A (1968) *Physical Review* 176: 589.
Tsui DC, Störmer HL, and Gossard AC (1982) *Physical Review Letters* 48: 1559.
von Klitzing K, Dorda G, and Pepper M (1980) *Physical Review Letters* 45: 494.

The Jahn-Teller effects

IB Bersuker, The University of Texas at Austin, Austin, TX, United States

© 2024 Elsevier Ltd. All rights reserved.

This is an update of E.E. Vogel, Jahn–Teller Effect, Editor(s): Franco Bassani, Gerald L. Liedl, Peter Wyder, Encyclopedia of Condensed Matter Physics, Elsevier, 2005, Pages 53–60, ISBN 9780123694010, https://doi.org/10.1016/B0-12-369401-9/00475-7.

Introduction **797**
Four modification of the JTEs. Adiabatic potentials vs observables **798**
JTEs in local properties of solids. Examples **801**
Ultrasonic exploration 801
Qubits for spintronics in quantum information devices 804
Cooperative properties in crystals. Ferroelectricity, multiferroicity, and orientational polarization **805**
Cooperative PJTE, ferroelectricity 805
Multiferroicity 807
Orientational polarization of solids 808
Flexoelectricity 808
Enhanced permittivity 809
Giant electrostriction 810
Manipulation of solids and 2D systems by influencing their JTEs parameters **810**
Inducing the JTE in crystal sublattices 810
Planarization of puckered two-dimensional systems 811
Conclusion **812**
References **812**

Abstract

In a brief review, the definitions and the main features of the four so-called Jahn-Teller effects (JTEs) in atomic matter are illustrated by the cross sections of their adiabatic potential energy surfaces (APES). They characterize the four specific cases of electronic structures of polyatomic systems that lead to spontaneous symmetry breaking, termed as proper JTE, *pseudo*-JTE (PJTE), *hidden*-JTE, and *hidden*-PJTE, respectively. The latter two of them, the "*hidden*" versions, are also appended with examples of electronic structure calculations for clarity. Then follows the warning that APES are not direct observables: although they serve well for some important qualitative predictions of possible (virtual) properties, further considerations may be necessary to reveal them. A recently developed experimental method of investigation of local JTEs in solids by means of ultrasonic measurements is described. The novel properties of matter induced by the underlying JTEs are inexhaustible; several examples of more recent achievements in this field are presented exploring the role of the JTEs in local properties (e.g., in qubits), and cooperative effects in crystals, including the PJTE origin of ferroelectricity, multiferroicity, and orientational polarization of perovskite crystals. A novel trend of manipulating polyatomic properties via influencing their JTEs parameters is developing, applied so far to changing crystal sublattices by specific doping, and planarization of two-dimensional systems by coordination to external groups.

Key points

- The Jahn-Teller effects (JTEs) describe the fundamental property of atomic matter to undergo spontaneous symmetry breaking (SSB), and the conditions of its occurrence.
- There are (presently known) four modifications of the JTEs: the proper JTE, pseudo-JTE, and more recently revealed *hidden*-JTE and *hidden*-PJTE. Examples of the hidden versions are shown.
- The induced by these SSB observable properties of polyatomic systems are vast, but their widespread attribution to just the form of the adiabatic potential energy surface (APES) may be inadequate (or even misleading), as the APES are not directly observable properties.
- Latest achievements in this field, especially in relevance to condensed matter, include revealing the APES of local centers in crystals with JTEs by means ultrasonic investigations, magnetic field induced tunneling between orthogonal JTE formations in solids, the role of the JTEs in the properties of qubits, demonstrated using the SiV(0) center in diamond as an example.
- A series of effects due to cooperative JTEs in crystals, including ferroelectricity, multiferroicity, and orientational polarization leading to giant flexoelectricity and permittivity, shows the way of continuous further developments in this field.
- The knowledge of the origin of SSB in polyatomic systems as due to the JTEs is used to work out procedures for manipulating their properties by external influence targeting the underlying JTEs parameters. Examples include modification of crystal sublattices and planarization of two-dimensional systems.

https://doi.org/10.1016/B978-0-323-90800-9.00053-6

Introduction

The series of four Jahn-Teller effects (JTEs), formulated below, emerges from the fundamental property of polyatomic systems to undergo spontaneous symmetry breaking (SSB), subject to electronic degeneracy and pseudodegeneracy. It was formulated first in 1934 by L. Landau in a discussion with Teller (1972), by stating that *the configuration of nonlinear polyatomic systems in electronic degenerate states undergoes spontaneous distortion that removes the degeneracy*, later proved and published by Jahn and Teller (1937). Since the first formulation, this background idea underwent tremendous evolution, directly influencing the theory of molecular and solid state structures and their properties (see, e. g., Bersuker, 1966; Englman, 1972; Köppel et al., 1984; Bersuker and Polinger, 1989; Chancey and O'Brien, 1997; Bersuker, 2006, 2021, and references therein). First, it was shown that the spontaneous distortion may take place also when the degenerate energy level is slightly split (pseudodegenerate) (Öpik and Pryce, 1957). This, at first sight not very significant enlargement of the JTE subjects, later on served as a trigger for a similar, but much more important conclusion that sufficiently strong vibronic coupling between any two electronic states (often ground and excited) with any energy gap between them, under certain conditions leads to instability and distortion of the polyatomic configuration. This is the pseudo JTE (PJTE) (Bersuker, 1966, 2006, 2013a,b, 2021). More recently, the Landau idea of SSB was extended to polyatomic structures with neither degeneracy, nor pseudodegeneracy in the ground state of their high-symmetry configuration, but with strong JTE or PJTE in their low-lying excited state, which penetrate the ground state producing global distorted configurations; these SSB were termed as *hidden*-JTE (*h*-JTE) and *hidden*-PJTE (*h*-PJTE), respectively (Bersuker, 2009, 2020a).

With the PJTE, *h*-JTE and *h*-PJTE added to the original JTE, we conclude that there are no configurations of polyatomic systems that can a priori be excluded from the possibility of SSB. Moreover, it was proved that the JTE and the PJTE are the only source of instability and spontaneous distortions of high-symmetry configurations of polyatomic systems (see Bersuker et al., 1984; Bersuker and Polinger, 1989; Bersuker, 2006, and references therein). And, more general, degeneracy and pseudodegeneracy are the only source of SSB in the whole spectrum of transformations in matter from elementary particles to nuclei, to atoms, molecules and solids (Bersuker, 2016).

In what follows in this brief review of the subject, we introduce the JTEs in a general, mostly qualitative view, with more recent examples of their influence on observable local and cooperative properties in solids. In so doing, we try to avoid the mathematical deductions of the underlying nonadiabaticity and vibronic coupling effects, which can be easily find in the reference literature.

Four modification of the JTEs. Adiabatic potentials vs observables

The definitions of the four modifications of the JTEs are illustrated in Fig. 1. They all are consequences of the vibronic coupling interactions in the ground or low-lying excited states, and are given here in terms of the cross-sections of the adiabatic potential

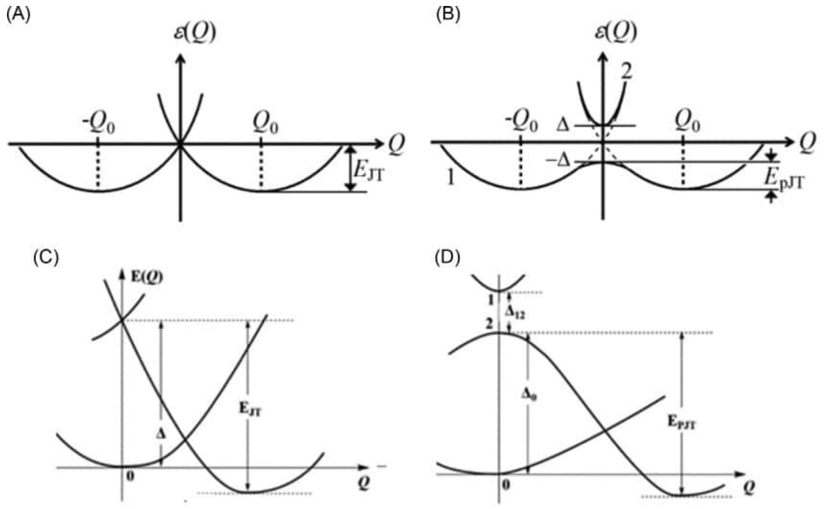

Fig. 1 Illustration to the definition of the four types of electronic configurations causing the four kinds of Jahn-Teller effects; for simplicity, in all four cases only one symmetrized coordinate Q of the low-symmetry nuclear displacements from the reference high-symmetry configuration at $Q = 0$ is shown; E_{JT} and E_{PJT} are the JTE stabilization energies, and Δ denotes energy gaps. (*a*) In the case of *proper JTE* the system is unstable, it has no minimum of the APES at the point of electronic degeneracy $Q = 0$, but it may be stable in the distorted configurations at $\pm Q_0$; (*b*) The *pseudo-JTE* (PJTE) case: there is no degeneracy at $Q = 0$, but the system is unstable due to the pseudodegeneracy when $\Delta < F^2/K_0$ (see the text); (*c*) *Hidden-JTE*: there is neither degeneracy nor pseudodegeneracy in the ground state of the system, but there is a relatively low-lying excited state that has a JTE, which is so strong, $E_{JT} > \Delta$, that it penetrates the high-symmetry ground state, producing a global minimum with a distorted configuration; (*d*) *Hidden-PJTE*: the same situation as in the *hidden*-JTE, but the intervening excited state has a strong PJTE with $E_{PJT} > \Delta_0$, instead of the JTE.

energy surfaces (APES), showing only one distortion coordinate of the system. In all the four cases the APES has no global minimum in the high-symmetry configuration, meaning possible SSB, as in the original Landau formulation for the JTE.

This simplified, one-dimensional presentation of the four JTEs is for visual demonstration only, allowing one to get a glimpse on the rich variety of the specific vibronic coupling effects in polyatomic systems, which lead to SSB. We see that while the JTE, nominally, takes place in all the cases of electronic degeneracy, the other three cases are rather limited by the energy gaps and the vibronic coupling strength between the involved electronic states. In particular, the condition of pseudodegeneracy leading to the PJTE is as follows:

$$\Delta < F^2/K_0 \tag{1}$$

where 2Δ is the energy gap between the coupled electronic states, F is the vibronic coupling constant, and K_0 is primary force constant (the stiffness of the systems with respect to the Q displacements). The analytical conditions for the *h*-JTE ($E_{JT} > \Delta$) and *h*-PJTE ($E_{PJT} > \Delta_0$), graphically seen in Fig. 1, are slightly more complicated (Bersuker, 2009, 2020*a*). In reality, the APES and the consequent effects are multidimensional with many ramifications and particular cases, including (most important) strong dependence on external perturbations.

The picture as a whole for the JTE and PJTE, their modifications and applications, are well presented in books and reviews, cited in the Introduction (see, e.g., Bersuker, 2006, 2021 and references therein). The present brief account of the subject is just to review the latest achievements in the evolution of understanding of these effects and their general applications, allowing the reader to find the necessary details and proofs (most important, mathematical proofs and deduction of these effects based on first principles) in the cited literature. The hidden modifications, *h*-JTE and *h*-PJTE, are relatively new, much less studied, and so far not widely applied to relevant local properties in solids. Therefore, we bring here some examples that further illustrate their physical meaning.

For illustration of the *h*-JTE, consider the ozone molecule O_3, which is unstable in its high-symmetry D_{3h} configuration. Its full APES has three equivalent minima, in each of which the regular triangular configuration is distorted to an obtuse triangle. The distortion could not be explained, neither by the JTE, as its ground state in the high-symmetry configuration is nondegenerate, nor by the PJTE, because of the very high energy of the relevant excited state, which does not follow the condition of pseudodegeneracy (1). Fig. 2 illustrates the results of ab initio calculations of the energy profiles of the O_3 APES in the cross-section along one of the coordinates of the e type displacements from the high-symmetry configuration, in the ground and the lowest excited state (Garcia-Fernandez et al., 2006). It shows convincingly that the instability of the high-symmetry configuration in the ground state is due to the very strong JTE in its excited E state, which penetrates the ground state to produce the three distorted configuration of the JTE in the $E \otimes e$ problem, exactly following the above definition of the *h*-JTE (Fig. 1c).

As for the *h*-PJTE, a series of demonstrative examples emerged from a class of molecular systems and local centers in crystals with electronic configurations e^2 and t^3 half-occupied by 2 and 3 electrons with parallel spins, respectively (half-filled closed shells), which take place, for example, in systems with at least one threefold (or higher) symmetry axis (Garcia-Fernandez and Bersuker, 2011). For instance, the CuF_3 molecule (and any similar local formation in crystals) falls in this category. The electronic configuration of the Cu^{3+} ion in this molecule (or cluster) is $(t_{2g})^6e^2$, occupied by 8 electrons, two in the e^2 configuration. Its

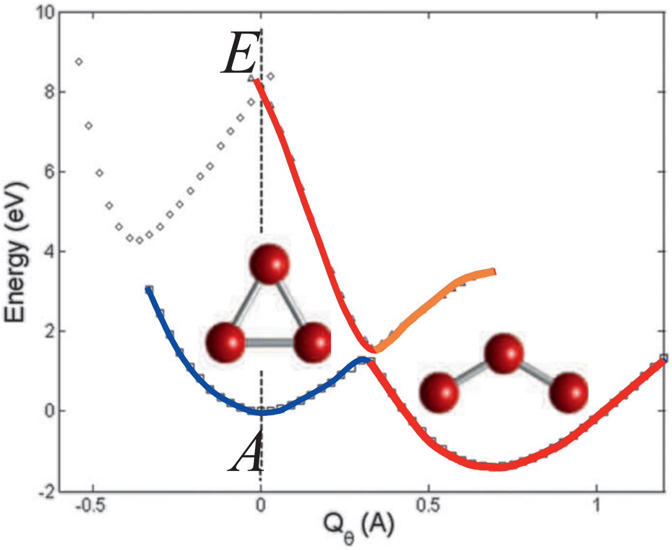

Fig. 2 Cross-section of the APES of the ozone molecule along the Q_θ component of the double degenerate e mode (one of the three equivalent distortions in the $E \otimes e$ problem of the JTE), obtained by numerical ab initio calculations including the highly excited E state (at $\Delta \sim 9$ eV), explicitly demonstrating that the ground state distorted configurations are due to the JTE in the excited state. The global minimum is at $Q_\theta = 0.69$ Å and the E-A avoided crossing takes place at $Q_\theta \sim 0.35$ Å. Reprinted from Bersuker I.B. (2020a) *Hidden Jahn-Teller and Pseudo-Jahn-Teller Effects*, *Encyclopedia*, *General & Theoretical Physics*, *Topic Review*. https://encyclopedia.pub/4283. Copyright (2020) MDPI.

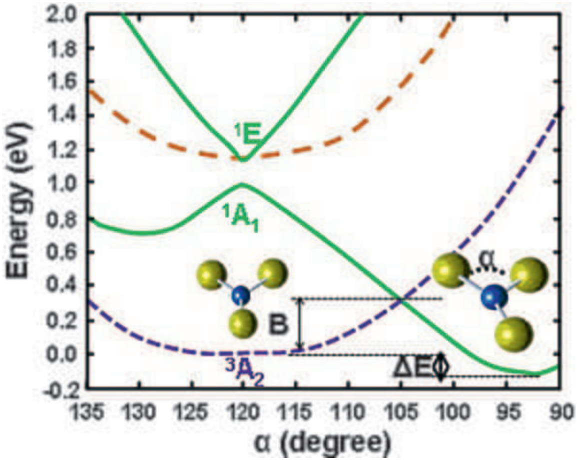

Fig. 3 Ab initio calculated energy profiles of the planar CuF_3 molecule (cluster) in the ground and lowest excited states as a function of the angle α (*e* mode distortion of the D_{3h} configuration), showing the formation of two equilibrium geometries with the lower energy one distorted at $\alpha \sim 93^\circ$, induced by the PJTE on two excited states. The distorted and undistorted configurations have different spin multiplicity (magnetic moments) and different dipole moments. Reproduced from Bersuker I.B. (2020a) *Hidden Jahn-Teller and Pseudo-Jahn-Teller Effects, Encyclopedia, General & Theoretical Physics, Topic Review*. https://encyclopedia.pub/4283. Copyright 2020 MDPI.

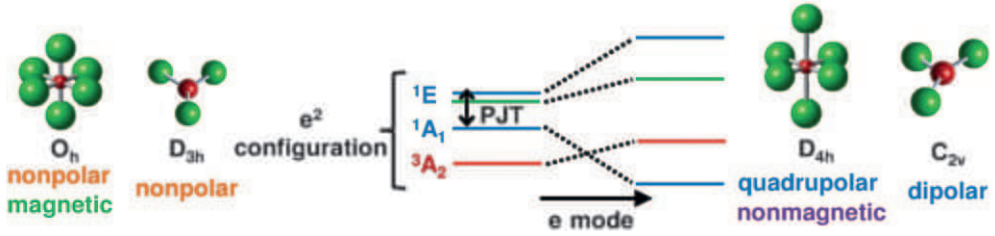

Fig. 4 The e^2 electronic configuration spans the states $^3A_2$, $^1A_1$, and ^1E. While the magnetic $^3A_2$ state is lowest in energy and stable in the high-symmetry configuration (left), the excited two states are coupled via the PJTE leading to a lower-energy non-magnetic and distorted equilibrium configuration (right). Reprinted from: Bersuker I.B. (2020a) *Hidden Jahn-Teller and Pseudo-Jahn-Teller Effects, Encyclopedia, General & Theoretical Physics, Topic Review*. https://encyclopedia.pub/4283. Copyright 2020 MDPI.

calculated energy level scheme is shown in Fig. 3. We see that the ground state of the undistorted regular triangular configuration of this system is a spin triplet, $^3A_2$, but a strong PJTE mixing of two excited singlet states, $^1A_1$, and ^1E, produces an additional lower-energy state with a distorted configuration. The latter becomes the global minimum of the APES when the stabilization energy E_{PJT} is larger than the energy gap Δ to the ground state. This example is of special interest also because it leads to an interesting molecular magnetic-dielectric dualism (Garcia-Fernandez and Bersuker, 2011; Bersuker, 2020b). Indeed, the distorted configuration has a non-zero dipole moment, but a zero magnetic moment (zero spin), whereas the undistorted configuration has no dipole moment, but a nonzero magnetic moment of the spin-triplet electronic state.

As mentioned above, the *h*-PJTE may take place in any system with half-filled e^2 or t^3 electronic configurations. Fig. 4 shows the general scheme of the energy level states of systems with e^2 configurations (similar schemes are available for t^3 systems). The CO_3 molecule may serve as an example of *h*-JTE combined with *h*-PJTE (Liu et al., 2009).

An important feature of the JTEs is that they are defined in a general way by the specifics of their APES. However, APES are not directly observable properties of the system. Ignoring this circumstance played as a difficulty in finding the first experimental confirmation of the original JTE, and continues to be an impediment in correctly understanding of what observable changes in the properties of polyatomic systems, caused by these effects, are expected. The situation is aggravated by its being continuously ignored in many books, reviews, academic lecturing, and even in some scientific publication, leading to erroneous conclusions in prediction of observable properties, induced by the JTEs.

Nevertheless, serving as the potential energy in the Schrödinger equation for observables, the specific APES features of the JTEs may allow for qualitative predictions of some of the expected properties. First, we note that for any given high-symmetry configuration, there are several (or an infinite number of) equivalent low-symmetry distortions that satisfy the JTE requirement of SSB. This means that the APES should be an equivalent-multiminimum surface, or a trough of continuing minima. In other words, the JTEs, in general, predict a multiminimum potential with a complicated picture of nuclear dynamics and observables that depends of the form of this potential. However, again, the multiminimum potentials of the APES, by themselves, are not directly observable experimentally.

The consequences for observable properties of the system induced by its JTEs are inexhaustible, they are considered in many books, reviews, and original publications. In general, without additional consideration, they cannot be reduced to observable distortion of space configuration of free polyatomic systems, as it is stated in "primitive" definitions in some literature on the JTEs. More important, the form of the APES is sometimes erroneously taken as the direct observable property of the system. For instance, in some recent publications devoted to the influence of spin-orbital coupling (SOC) on the JTE, the authors calculated the changes of the APES by SOC perturbation, assuming that this is the observable effect. Excluding the possibility of exact solution, the correct approximate calculations would get first the energy levels and wave functions with the APES of the JTE system, and then include the SOC as a perturbation (if it is sufficiently small), which would yield the vibronic reduction of the SOC (Ham, 1972).

It follows that, strictly speaking, we cannot define the observable properties of the system with JTEs just based on their APES, without further investigation. The direct way to do this is to solve the relevant Schrödinger equation including the nuclear dynamics. In overcoming the difficulties in solving the problem with arbitrary APES of JTEs, we explore, as usual, approximations and limiting cases (see in: Englman, 1972, Bersuker and Polinger, 1989, Bersuker, 2006, Köppel et al., 1912, etc.). In condensed matter problems, the most important way to reveal the observable properties in the JTEs is to involve external perturbations (see below).

JTEs in local properties of solids. Examples

As mentioned above, exploration of the observable JTEs in molecular systems and condensed matter is presently well developed and continuing, presented in a series of books, reviews, and original papers, cited in the Introduction (for more citations, see Bersuker, 1984; Perlin and Wagner, 1984; Bersuker, 2021). As it is clearly seen from the definitions in section "Four modification of the JTEs. Adiabatic potentials vs observables," all JTEs are of local origin, grounded in the specifics of the local interactions between electronic states and nuclear displacements (vibronic coupling); they define the local properties of solids directly. Note that in the overwhelming majority of cases, point defects (local impurity, dopant, and vacancy centers), as well as the bulk local centers in crystals, have degenerate or pseudodegenerate electronic ground and/or excited states (both explicit and hidden), subject to the JTEs, which influence all their properties. Below are several examples of the latest achievements in this field. Obviously, in condensed matter, the local JTEs distortions may interact strongly, resulting in cooperative effects, discussed in the next section.

With regard to JTEs, local properties in solids (inherent to neutral molecules, ions, clusters, impurity and vacancy centers in solids, qubits, quantum dots, thin films, etc.) are studied by a variety of spectroscopies, including optical, electron spin resonance (ESR), X-ray, EXAFS, and other related methods, and also with the same methods under influence of external fields and pressure. Cooperative interactions in crystals with JTEs lead to structural, magnetic, ferroelectric, multiferroic, etc., phase transitions. The study of the JTEs shows also how we can manipulate condensed matter properties by employing external perturbations that directly influence the underlying JTEs parameters. Below we show examples from the latest achievements on these topics.

Ultrasonic exploration

Recently developed studies based on measurements of ultrasonic attenuation and velocity change induced by JTEs impurities in crystals (Gudkov and Bersuker, 2012; Averkiev et al., 2017a,b; Gudkov et al., 2020), demonstrated high efficiency in obtaining important information about the structure and properties of the system. Distinguished from ESR, optical, and other similar experimental methods, in which the measurement perturbation engages primarily with the electronic subsystem, ultrasound interacts directly with the nuclear arrangement, thus determining the main features of the APES of the JTEs centers. When propagating through the crystal containing the latter, and dependent on direction of propagation and polarization, the ultrasonic wave unequally shifts the minima of the multiminimum APES, making them nonequivalent, thus creating a non-equilibrium distribution of the JT complexes over their energy levels (Fig. 5). This non-equilibrium state relaxes to equilibrium during a characteristic relaxation time τ. The relaxation process introduces an additional channel of energy loss, which results in the ultrasonic wave attenuation, velocity change, and dispersion (Gudkov and Bersuker, 2012; Averkiev et al., 2017a).

It follows that in relation to ultrasonic experiments the subsystem of JT centers in crystals is very special: due to their well-defined local multiminimum APES and strong anisotropy with respect to the polarized ultrasound wave, it produces specific anomalies in the ultrasound propagation that are absent in other ultrasound absorbers (the latter thus can be easily excluded). Ultrasonic experiments with doped crystals directly reveal the symmetry properties and the local APES parameters, including the JT active modes (trigonal, tetragonal, and orthorhombic JTE distortions, respectively), linear and quadratic vibronic coupling constants, extrema point positions on the APES, including minima positions and energy barriers between them. In other words, ultrasonic investigations provide for a unique possibility to reveal the whole APES of JTE centers in crystals and consequent properties. Below we show an example that illustrates this statement.

The dopant Cr^{2+} center in a fluorite crystal, SrF_2:Cr, is subject to the JTE problem $T \otimes (e + t_2)$, which (with the quadratic vibronic coupling terms included) yields the predicted by the theory six-dimensional APES in the space of two tetragonal and three trigonal symmetrized atomic displacements around the Cr^{2+} center (Bersuker and Polinger, 1989; Bersuker, 2006). It includes six equivalent orthorhombic global minima with four trigonal and three tetragonal saddle-points between them. This most complicated APES of a JTE system was fully reconstructed experimentally based on ultrasonic measurements, thus demonstrating their unique possibilities (Averkiev et al., 2017a). The temperature-dependent relaxation attenuation of the longitudinal ultrasonic waves (propagating along

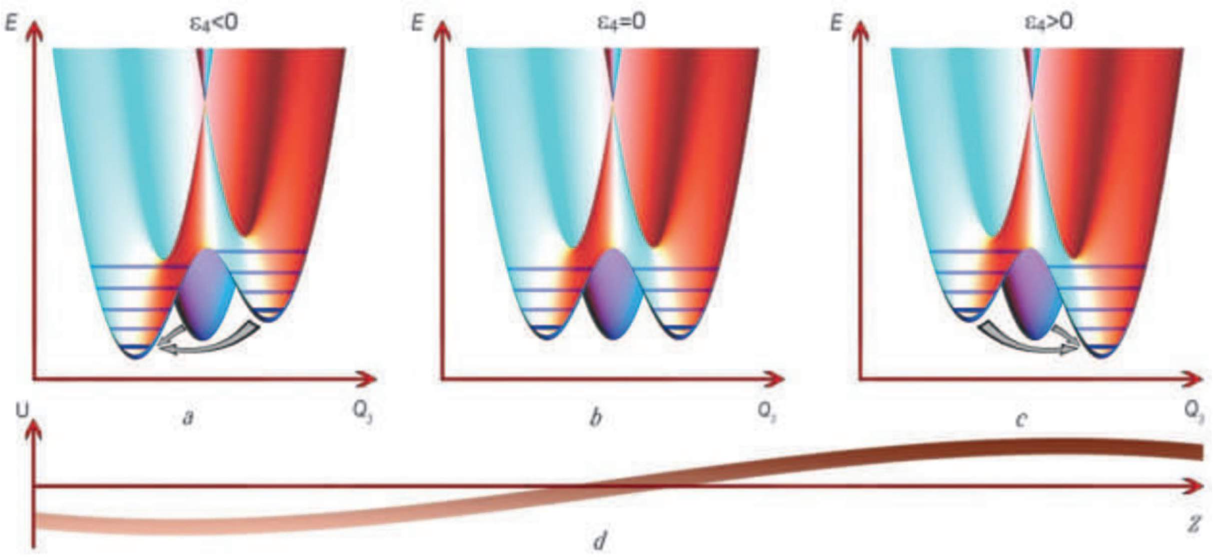

Fig. 5 Distortions of the APES of a JTE center in crystals (subject to the $E \otimes e$ problem), produced by the ε_4-type ultrasonic mode deformations, which violate the equivalency of the minima and the equilibrium conditions within the JT subsystem. Panels (a), (b), (c) show the APES distortions in accordance with the wave's profile shown in panel (d) (U_y is the instant displacement of the atoms perpendicular to the propagation direction z axis at $t = t_0$). Gray arrows indicate the relaxation process. Reproduced from Gudkov V.V., Sarychev M.N., Zherlitsyn S., Zhevstovskikh I.V., Averkiev N.S., Vinnik D.A., Gudkova S.A., Niewa R., Dressel M., Alyabyeva L.N., Gorshunov B.P., Bersuker I.B. (2020) Sub-lattice of Jahn-Teller centers in hexaferrite crystal. *Nature Scientific Reports* 10: 7076–7091. Copyright 2020 Nature Scientific Reports.

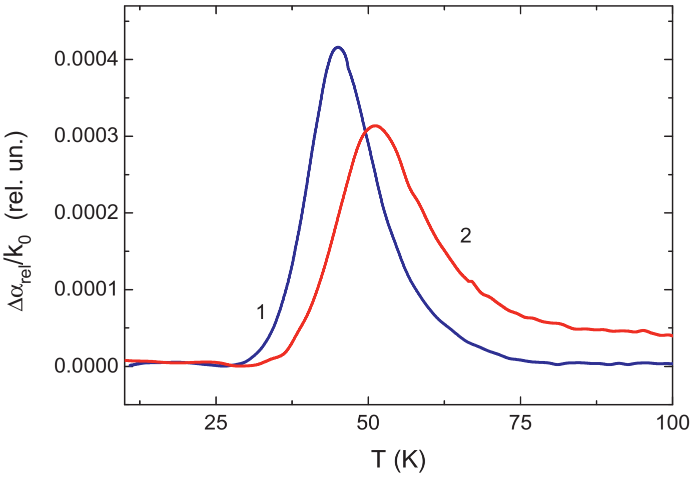

Fig. 6 Temperature dependence of the relaxation attenuation of the longitudinal ultrasonic wave propagating along the [110] axis of the SrF_2:Cr crystal, at the wave frequencies of 52 MHz (curve 1), and 162 MHz (curve 2). Reproduced from Averkiev NS, Bersuker IB, Gudkov V, Zhevstovskikh IV, Sarychev MN, Zherllitsyn S, Yasin S, Shakurov GS, Ulanov VA, Surikov VT (2017) Manifestation of the Jahn-Teller effect in elastic moduli of strontium fluorite crystals doped with chromium ions. Journal of Physics Conference Series 833: 012003. Copyright 2017 IOP Publishing.

the [110] axis of this crystal), induced by the JTE distortions, is shown in Fig. 6. It allows extracting the relaxation time τ as a function of temperature (Fig. 7) using well-established relations (Averkiev et al., 2017a).

The relaxation attenuation of the shear ultrasonic wave is directly determined by the linear vibronic coupling constants in tetragonal F_E and trigonal F_T distortions: $|F_T| = 3.66 \cdot 10^{-5}$ dyn and $|F_E| = 0.63 \cdot 10^{-5}$ dyn (Averkiev, 2017a). On the other hand, the temperature dependence of the relaxation time in Fig. 7 shows that there are two barriers of relaxation. At low temperatures, first the lower barrier between the tetragonal distortions ($V_0 = 45.6$ cm^{-1}) is overcome, followed by the barrier between the larger trigonal distortions ($V_0 = 271$ cm^{-1}) at higher temperatures. The two barrier heights give us also the energy positions of the tetragonal and trigonal saddle-points, respectively. Involving the more complicated part of the JTE theory for a T term with the quadratic terms of the vibronic coupling included (Bersuker and Polinger, 1989) and some additional considerations about the elastic properties and local low-frequency vibrations of this crystal, the authors revealed also the stabilization energy of the orthorhombic minima

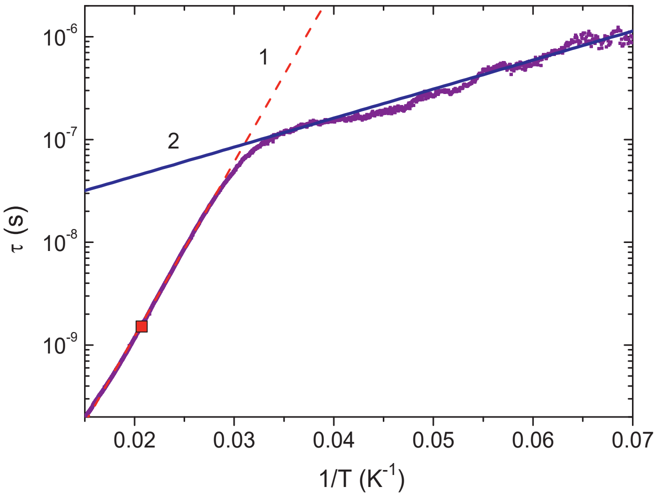

Fig. 7 Temperature dependence of the relaxation time obtained from the attenuation of the c_{44} normal mode at the frequency of $\omega = 105$ MHz. The square symbol corresponds to the condition $\omega\tau = 1$. The lines represent two exponential functions $\tau = \tau_0^{(i)} \exp (V_0^{(i)}/\kappa T)$ overcoming tetragonal (Curve 1, $\tau_0^{(1)} = 5 \times 10^{-11}$ s, $V_0^{(1)} = 390$ K $= 271$ cm^{-1}) and trigonal (curve 2, $\tau_0^{(2)} = 0.5 \times 10^{-8}$ s, $V_0^{(2)} = 65$ K $= 45.2$ cm^{-1}) potential barriers. Reproduced from Averkiev N.S., Bersuker I.B., Gudkov V., Zhevstovskikh I.V., Sarychev M.N., Zherllitsyn S., Yasin S., Shakurov G.S., Ulanov V.A., Surikov V.T. (2017a) Manifestation of the Jahn-Teller effect in elastic moduli of strontium fluorite crystals doped with chromium ions. *Journal of Physics Conference Series* 833: 012003. Copyright 2017 IOP publishing.

$E_{JT}^{or} = 562$ cm^{-1}, the quadratic vibronic coupling constant $W_{E,T} = -2.1 \times 10^{-4}$ dyn/cm, the primary force constants K_{0E} and K_{0T}, and the symmetrized coordinates of the tetragonal, trigonal, and orthorhombic extrema points of the six-dimensional APES, as well as the splitting of the lowest vibrational states in the minima produced by the tunneling between the six equivalent orthorhombic minima, $\Gamma \sim 19$ cm^{-1}. Thus the first full description of a rather complicated APES created by the JTE in a crystal center was obtained experimentally by means of ultrasonic investigation (Averkiev, 2017a).

Another example of ultrasound investigation of JTEs in local properties of crystals illustrates its efficiency in combination with *magnetic field influence* (Averkiev et al., 2017b), which is important in view of possible applications in electronics and spintronics. It was shown that in some JTE systems, an external magnetic field induces tunneling transitions between local configurations in polyatomic systems with orthogonal electronic states, for which no tunneling is expected, the tunneling levels being produced by the magnetic field. In a variety of impurity and vacancy centers in cubic crystals and similar molecular systems with cubic and icosahedral symmetry in different aggregate states (including thin films and quantum dots) the ground or excited electronic state may be threefold degenerate T state, subject to the $T \otimes e$ problem of the JTE. In these cases (ignoring the SOC reduced by the vibronic coupling), the APES has three equivalent minima along the three tetragonal distortions, in which, distinguished from the $E \otimes e$ problem, the three electronic functions of the three distorted configurations in the minima are orthogonal, so no tunneling or direct relaxation transitions between them are allowed. This is one of the JTE problems where tunneling between the equivalent minima in the ground state is forbidden.

It was shown that an external magnetic field removes this prohibition, producing a new channel of tunneling and direct relaxation transitions between the distorted orthogonal configurations (Averkiev, 2017b). The theory of the JTE $T \otimes e$ problem in magnetic fields, and in interaction with ultrasound, and the ultrasonic experimental observations of the novel effect were carried out using the Cr^{2+} impurities in the crystal ZnSe:Cr^{2+} as a typical example. In this impurity center the ground state is electronically threefold degenerate with three orbital wave functions of a hole in the closed-shell $3d^5$ configuration, transforming as vectors. They can be described by an orbital momentum operator with $L = 1$, hence being subjects to magnetic field influence. Experimental data show that the JTE distortions in the impurity center under consideration are tetragonal, thus evidencing for the $T \otimes e$ problem.

Tunneling effects in JTE systems, in general, were predicted in 1961–1962 (Bersuker, 1961, 1962) and observed in optical, ESR, and ultrasonic experiments in a variety of systems with non-orthogonal minima states. In ultrasonic experiments tunneling manifests itself in the temperature dependence of relaxation time τ_{rel}, where, by lowering the temperature, the function $\tau_{rel}(1/T)$ changes from $\tau_{rel} \approx (\nu_0)^{-1} \exp (V_0/k_B T)$ in the activation mechanism with over-the-barrier transitions to the tunneling mechanism with vanishing temperature dependence. The analysis of the temperature dependence of the relaxation time in zero magnetic field shows the absence of tunneling in the JT system of Cr^{2+} centers in the ZnSe crystal. When a weak magnetic field is applied to the system at low temperatures, a sharp increase in the attenuation of ultrasound is observed, illustrated in Fig. 8 (Averkiev, 2017b).

A microscopic theory was developed showing that the magnetic field produces a new relaxation channel associated with tunneling between the orthogonal distorted configurations, made possible due to magnetic-induced coupling between their (otherwise orthogonal) orbital states (Averkiev, 2017b). The rather cumbersome deductions carried out for the ultrasound attenuation in magnetic fields in ZnSe:Cr^{2+} can be concluded as follows. In zero magnetic field there is a relaxation attenuation of ultrasound driven by the relaxation time, which is determined by one-phonon processes in the absence of tunneling between

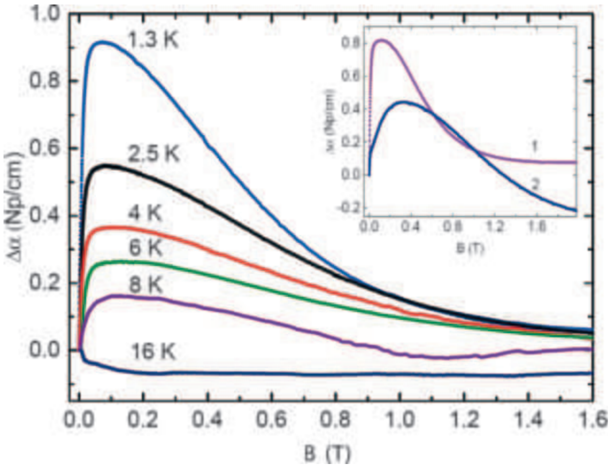

Fig. 8 Magnetic field dependence of ultrasound attenuation $\Delta\alpha = \alpha(B) - \alpha(0)$ at different temperatures, for the ultrasound frequency $\omega/2\pi = 33$ MHz and magnetic field induction **B**‖[110]. Inset: the peak of attenuation in magnetic fields at $T = 1.3$ K at the same frequency, but different directions of **B**: curve 1, **B**‖[110]; curve 2, **B**‖ [001]. Reproduced with permission from ref. Averkiev N.S., Bersuker I.B., Gudkov V.V., Zhevstovskikh I.V., Baryshnikov K.A., Sarychev M.N., Zherlitsyn S., Yasin S., Korostelin Yu.V. (2017b) Magnetic field induced tunneling and relaxation between orthogonal configurations in solids and molecular systems. *Physical Review B* 96: 094431. Copyright 2017 American Physical Society.

equivalent JTE configurations. In weak magnetic fields up to 0.1 T (up to 3 mT for B‖ [001]) the ultrasonic attenuation is still determined by the relaxation mechanism, but due to magnetic field induced tunneling there is a sharp increase in relaxation rate, which leads to a sharp increase of attenuation. Finally in magnetic fields above 0.1 T there is a transition to a quasi-resonance mechanism of attenuation with a smooth decrease of attenuation up to the fields of 2 T (Averkiev, 2017b).

Qubits for spintronics in quantum information devices

Investigations are continuously developing in application of the JTE and PJTE theory to revealing the structure and properties of specific defect centers in diamond and similar crystals (impurity, dopant and vacancy centers and their combinations), which are promising candidates as quantum bits (qubits) for a wide variety of quantum technologies, including quantum sensors to repeater nodes for long-range quantum networks. The studied qubit centers include a large variety of neutral atoms as impurities plus a vacancy, denoted as XV0 (X = N, Si, Ge, Sn, Pb, etc.), or a charged atom plus vacancy (e.g., NV−), as well as many other combinations.

As could be expected, all of these artificial defects in diamond, potential qubits for spintronics, are strongly affected by the JTE, and many of them are also influenced by the PJTE (the possibility of the hidden JTEs was not explored as yet). The JTEs essentially alter the energy level positions and their ordering, including the spin-orbit splitting, as well as optical transitions between them with intersystem crossing and zero-phonon lines, making electronic structure calculations without the JTEs absolutely unreliable. For instance, one of the most important features of such qubits, the presence of an excited spin state with a sufficiently long lifetime, strongly depends on the spin-orbit coupling (SOC). As mentioned above, the dynamic JTE may reduce the SOC by orders of magnitude (Ham, 1972). With regard to qubits, this was confirmed by direct calculations in exploring the active electronic ^3E state of the NV(−) center in diamond: the calculation of the SOC without the JTE yields it equal to 15.8 GHz, which is about three times larger than the measured one (Thiering and Gali, 2017). The idea was further developed by more accurate calculations of the JTE and SOC simultaneously (non-perturbatively) for a series of qubit centers in diamond, GeV0, SnV0 and PbV0, which show that the JTE reduces the SOC by an order of magnitude (Ciccarino et al., 2020). These fine structure details reveal the new physics of color center qubits in diamond, and present a pathway to identify them experimentally.

To show the JTE implication in these problems in somewhat more technical detail, we bring here a brief demonstration of the JTE in the XV0 (X = Si, Ge, Sn, Pb) centers in diamond with numerical results for SiV0 (Thiering and Gali, 2019). The JTE in these centers is produced by multi-electron states, in which the JTE stabilization energy E_{JT} is larger than (or of the same order of magnitude of) the interelectron repulsion that leads to the multiplet term formation. In such cases it is more convenient to consider first the vibronic coupling in the separate one-electron molecular-orbital (MO) states, and then their interelectron interaction. This leads to the product-JTE (see in: Bersuker, 2006); in the case under consideration, it yields (in the excited state) two orbital degenerate MOs, e_g and e_u, coupled via E_g displacements, denoted as the $(e_g \otimes e_u) \otimes E_g$ product-JTE, which, upon interelectron interaction, results in two triplet terms, $^3\hat{A}'_{2u}$ and $^3\hat{E}'_u$. Fig. 9 illustrates the results of the calculations performed for the SiV0 center in diamond (Thiering and Gali, 2019).

Similar in trend (but different in detail) APES with ground and excited energy levels and transitions between them, showing the defining role of the JTE or PJTE (or both), were found in all the other candidates for qubits in quantum information systems, that were explored theoretically; there are no known defects in diamond and other similar systems with no JTE or PJTE implications.

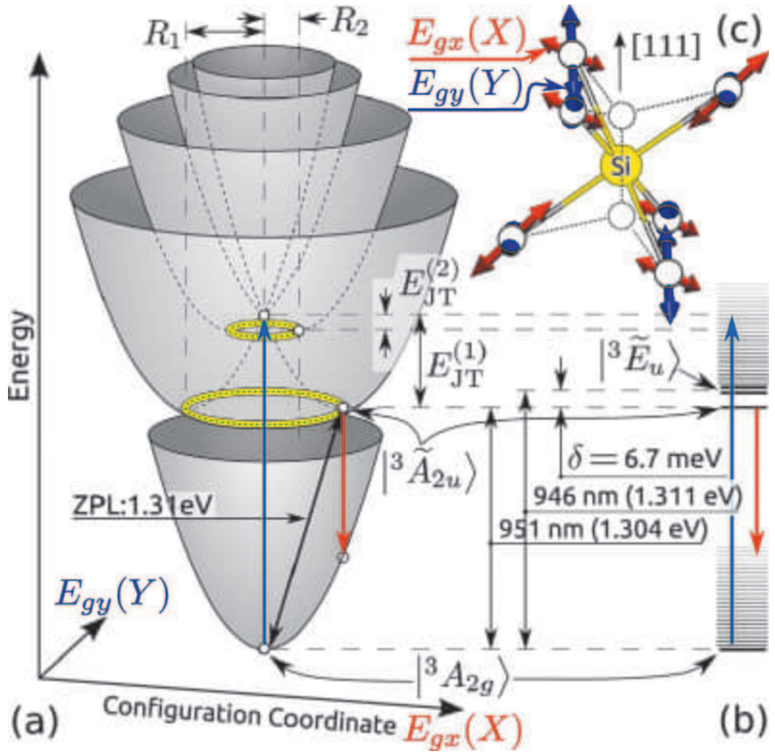

Fig. 9 (a) Adiabatic potential energy surface of the SiV(0) center in diamond that shows the ($e_g \otimes e_u$) $\otimes$ E_g product JTE in the excited state. The separate JTE in the two MOs, e_g and e_u, produce two “Mexican hat”-type surfaces with stabilization energies $E_{JT}^{(1)}$ and $E_{JT}^{(2)}$; (b) Their resulting electronic triplet terms $^3\hat{A}_{2u}$ and $^3\hat{E}_u$, respectively, with an energy gap of 6.7 meV. The vertical absorption, luminescence, and zero-phonon lines are shown by blue, red, and black arrows, respectively; (c) geometry of the undistorted SiV(0) center with D_{3d} symmetry, showing also the carbon-localized *X* and *Y* coordinates of the JTE active normal mode E_g (Bersuker, 2006). Reproduced from Thiering G., Gali A. (2019) The (eg$\otimes$eu)$\otimes$Eg product Jahn–Teller effect in the neutral group-IV vacancy quantum bits in diamond. *Nature Computational Materials* 5: 1–6. Copyright 2019 Nature Computational Materials.

Cooperative properties in crystals. Ferroelectricity, multiferroicity, and orientational polarization

As mentioned above, cooperative interactions between crystal centers with JTEs lead to important observable properties. The first investigations of cooperative JTE were performed on rare-years orthovanadates and similar systems (Ghering and Ghering, 1975; for more details, see Bersuker and Polinger, 1989; Polinger, 2009; Kaplan and Vekhter, 1995), showing their rich influence on solid state properties, leading to structural phase transitions. Before that, the cooperative PJTE as leading to ferroelectricity was suggested (Bersuker, 1966), its full theory being developed in more recent times. We bring here an outlook of its latest achievements (Bersuker, 2017a, 2018; Bersuker and Polinger, 2020; Polinger and Bersuker, 2018).

Cooperative PJTE, ferroelectricity

Actually, the explanation of the origin of ferroelectricity in perovskite type crystals (like $BaTiO_3$) as triggered by the local PJTE was the first application of this effect to solving a major solid state problem (Bersuker, 1966). It was shown that in the centrosymmetric configuration of the perovskite crystals, local dipolar distortions in the metal centers may occur due to the PJTE. Without the latter, the existing theories implied that the spontaneous polarization of such crystals is due to a self-consistent cooperative mechanism, in which the local (repulsive) dipolar displacements are compensated by their long-range dipole-dipole attractions. However, all the experimental data, accumulated in years, show unambiguously that the instant local dipolar distortions are there in all the phases of the crystal, including the paraelectric phase, before the phase transition to the ferroelectric one (see, e.g., Ravel et al., 1998; Stern, 2004). The PJTE theory solves this problem (Bersuker, 1966, 2018, 2019; Bersuker and Polinger, 2020).

Fig. 10 shows the local electronic structure of the octahedral $[TiO_6]^{8-}$ cluster in the paraelectric phase of $BaTiO_3$. Very briefly, the local PJTE emerges from the vibronic mixing of the ground state A_{1g}, formed by the fully populated highest occupied (HO) six molecular orbitals (HOMO) t_{1u} and t_{2u} (mostly oxygen 2*p* orbitals), with three lowest unoccupied MO (LUMO) t_{2g} (mostly titanium 3*d* orbitals), a total of 9 MO’s, by the polar t_{1u} type normal coordinates Q_x, Q_y, and Q_z. This PJTE $(A_{1g} + T_{1u}) \otimes t_{1u}$ problem results in a 9 × 9 secular equation. Its solution yields the following APES of the TiO_6^{8-} cluster, obtained already in the first paper on the subject (Bersuker, 1966, 2018):

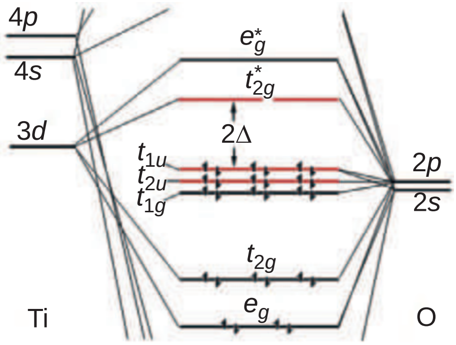

Fig. 10 The energy-level correlation diagram (not to scale) for the octahedral cluster $[TiO_6]$. HOMO t_{1u} and t_{2u} (of mostly oxygen origin) and LUMO t_{2g} (mostly titanium) are one-electron energy levels of the orbitals that are coupled in the PJTE. The shown electron populations correspond to the particular case of $[TiO_6]^{8-}$. Reprinted from Bersuker I.B. (2006) *The Jahn-Teller Effect*. Cambridge, UK: Cambridge University Press. Copyright 2006 I. B. Bersuker.

$$U(Q) = \frac{1}{2}K_0Q^2 - 2\left[\sqrt{\Delta^2 + 2F^2\left(Q^2 - Q_x^2\right)} + \sqrt{\Delta^2 + 2F^2\left(Q^2 - Q_y^2\right)} + \sqrt{\Delta^2 + 2F^2\left(Q^2 - Q_z^2\right)}\right] \tag{2}$$

where $Q^2 = Q_x^2 + Q_y^2 + Q_z^2$, 2Δ is the energy gap between the mixing electronic states, K_0 is the primary force constant for the Q displacements (stiffness of the crystal without the vibronic coupling), and F is the vibronic coupling constant (H is the Hamiltonian),

$$F = \left\langle 2p_z(\mathrm{O}) \middle| \left(\frac{\partial H}{\partial Q_x}\right)_0 \middle| 3d_{xz}(\mathrm{Ti}) \right\rangle \tag{3}$$

In a more rigorous treatment by the Green's functions approach (Polinger et al., 2015), the local PJTE in the cluster unit was appended with the bulk crystal properties by taking into account the interaction of the Ti ion with the whole crystal via its electronic and vibrational bands. It improved the results by yielding appropriately band-averaged parameters instead of the local cluster ones.

The three-dimensional APES (2) has a specific form. Under the condition.

$$\Delta < 8F^2/K_0 \tag{4}$$

the surface (2) has a maximum (meaning instability) when the Ti ion is in the center of the octahedron, eight equivalent minima placed along the four trigonal axes, in which the Ti ion is displaced toward three oxygen ions (away from the other three); higher-in-energy 12 equivalent saddle points along the six C_{2v} axes, at which the Ti ion is displaced toward two oxygen ions (at the top of the lowest barrier between two near-neighbor minima); and next six higher-in-energy equivalent saddle points, at which the Ti ion is displaced to one of the oxygen ions along the fourfold axes (Bersuker, 1966, 2018).

With additional two experimentally determined structural constants, the band-averaged energy gap $2\Delta = 2.8$ eV and the vibrational frequency at the bottom of the trigonal minimum $\hbar\omega_E = 193\ \mathrm{cm}^{-1}$, all the main parameters of this APES, shown in Table 1, were estimated, including K_0, F, the positions of the minima $Q_x = Q_y = Q_z = Q_0$ and first saddle points $Q_x = Q_y = q_0$, $Q_z = 0$, their PJTE stabilization energies, and the tunneling splitting Γ. The latter is a characteristic measure of the energy barrier between the near-neighbor minima of the APES.

The four phases of $BaTiO_3$ emerge directly from this APES by gradually populating the states in the minima with temperature and stepwise overcoming its barriers (Bersuker, 1966; Polinger, 2013; Polinger et al., 2015). Of particular interest is also the prediction of disorder in the orthorhombic and tetragonal ferroelectric phases and in the cubic paraelectric phase. As mentioned above, it was confirmed later together with a variety of other predictions of the theory that have no explanation in displacive theories (see in: Bersuker, 2018). Using the numerical estimates of Table 1, the interaction between the PJTE induced local dipole moments in $BaTiO_3$ was taken into account in a mean-field approximation, in which both the local off-center displacement and the mean field of the environment are interdependent in a self-consistent way (Polinger, 2013). It yields the experimentally observed phase transitions in $BaTiO_3$ with reasonable values of Curie temperatures.

Table 1 Numerical values of the PJTE vibronic coupling and APES parameters of the Ti active centers in the $BaTiO_3$ crystal (Polinger et al., 2015).

K_0	2Δ	F	$\hbar\omega_E$	Q_0	q_0	$E_{JT}[111]$	$E_{JT}[110]$	Γ
55 eV/$Å^2$	2.8 eV	3.42 eV/Å	193 cm^{-1}	0.14 Å	0.16 Å	–1250 cm^{-1}	–1130 cm^{-1}	35 cm^{-1}

Multiferroicity

The PJTE theory was extended to formulate the necessary condition of coexisting magnetic and ferroelectric (multiferroicity) properties in ABO_3 perovskite crystals with B as a transition metal ion in a d^n configuration, $n = 1, 2, \ldots 10$ (Bersuker, 2012, 2013b), that found already confirmation in experiments (Domracheva et al., 2013; Raymond et al., 2014; Weston et al., 2016) and ab initio calculations. Multiferroicity implies that the ferroelectric crystal, which is a dielectric, has also a nonzero magnetic moment, meaning unpaired electrons. In the ferroelectric $BaTiO_3$ with perovskite ABO_3 structure the d^0 configuration of the Ti^{4+} ion has no unpaired electrons, and attempts to obtain ferroelectricity in perovskites with d^n, $n > 0$, configurations of the transition metals B ions were unsuccessful for a long time (Barone and Picozzi, 2015). The PJTE origin of ferroelectricity not only explains how the possible ferroelectric properties of perovskite crystal may coexist with unpaired electrons, but it shows also when this coexistence may take place. Moreover, for d^n ions with $n = 3, 4, 5, 6$, and 7, which are directly influenced by the well-known transition metal high-spin/low-spin crossover, one may expect the coexistence of three phenomena: ferroelectricity (FE), magnetism (M), and spin crossover (SCO). This, in turn, leads to a quite novel phenomenon: magnetic-ferroelectric (multiferroics) crossover (MFCO), creating a rich variety of possible magnetoelectric and related effects (Bersuker, 2012, 2013b). The vibronic (PJTE) theory, exclusively, reveals the role of spin in spontaneous polarization of crystals.

The above MO energy scheme for an octahedral cluster BO_6^{8-} in Fig. 10 shows the MO electron population of the d^0 transition metal ion, e.g., when $B \equiv Ti$, with the HOMO electron configuration $(t_{1u})^6 = (t_{1u}\downarrow)^3(t_{1u}\uparrow)^3$, where the arrows up and down indicate the two spin states. The energy term of this configuration is $^1A_{1g}$. The excited state with opposite parity is formed by the one-electron, $(t_{1u}\uparrow) \rightarrow (t_{2g}\uparrow)$ or $(t_{1u}\uparrow) \rightarrow (e_g\uparrow)$, excitation, resulting in the lowest excited ungerade term $^1T_{1u}$ at the energy gap 2Δ. In this case, the PJTE at the B center, under the condition of instability $\Delta < 8F^2/K_0$ (Eq. 4), produces a polar displacements of the B atom along [111]-type directions, which triggers the ferroelectric polarization (see section "Cooperative PJTE, ferroelectricity").

For the d^1 configuration of the B ion instead of the d^0, the HOMO becomes $(t_{1u}\downarrow)^3(t_{1u}\uparrow)^3(t_{2g}\uparrow)^1$ with the term $^2T_{2g}$, and the LUMO, taking into account Hund's rule, is $(t_{1u}\downarrow)^2(t_{1u}\uparrow)^3(t_{2g}\uparrow)^2$ with the lowest excited ungerade term $^4T_{1u}$. Hence the two closest terms of different parity, *possess different spin multiplicity*, and hence *they do not mix by the vibronic coupling*; the latter does not contain spin operators. In principle, there may be higher in energy electronic configurations of opposite parity with the same spin as the ground state one, but they are at much larger energy gaps Δ, and therefore less appropriate to satisfy the condition of instability (4) (numerical estimates show that the condition (4) may be very restricting). A similar picture emerges for d^2 configurations for which the two lowest terms of opposite parity are $^2T_{2g}$ and $^5T_{1u}$.

The situation changes for d^3. Indeed, in this case the HOMO is $(t_{1u}\downarrow)^3(t_{1u}\uparrow)^3(t_{2g}\uparrow)^3$ with the ground state term $^4A_{1g}$, and in the low-spin conditions of the strong ligand fields (large t_{2g}-e_g separation in Fig. 10), the LUMO is $(t_{1u}\downarrow)^2(t_{1u}\uparrow)^3(t_{2g}\uparrow)^3(t_{2g}\downarrow)^1$ with the lowest ungerade term $^4T_{1u}$. Therefore, for d^3 configurations (e.g., Mn^{4+}) in sufficiently strong ligand fields the situation becomes again favorable for the PJTE and polar distortions, but in this case, distinguished from the d^0 case, the system possess also a magnetic moment created by three unpaired electrons. However, if the ligand field is weak and the separation t_{2g}-e_g is small, the high-spin arrangement of the excited electronic configuration takes place, and the excitation electron occupies the $e_g\uparrow$ orbital instead of $t_{2g}\downarrow$; the LUMO configuration under Hund's rule becomes $(t_{1u}\downarrow)^2(t_{1u}\uparrow)^3(t_{2g}\uparrow)^3(e_g\uparrow)^1$ with the lowest ungerade state $^6T_{1u}$. Here again there is no PJTE on dipolar distortions and no ferroelectric instability. This is one of the examples, which shows explicitly how the spin states interfere directly into the possible local polar displacement and ferroelectricity.

In this way all the d^n configurations with $n = 0, 1, 2, \ldots 10$, were explored (Bersuker, 2012) showing that in perovskite ABO_3 crystals, only B ions with configurations d^0, d^3-low-spin, d^4-low-spin, d^5-low-spin and high-spin, d^6-high-spin and intermediate-spin, d^7-high-spin, d^8, and d^9 can, in principle, produce multiferroics, provided the criterion of instability (4) is satisfied. If the (in general, hardly significant) contribution of higher excited states can be ignored, transition metal ions B with configurations d^1, d^2, d^3-high-spin d^4-high-spin, d^6-low-spin, d^7-low-spin, and d^{10} are not expected to produce multiferroics under this mechanism of proper ferroelectricity. Experimentally observed multiferroics with such B ions, for example, $Mn^{4+}(d^3)$, $Cr^{3+}(d^3)$, $Mn^{3+}(d^4)$, $Fe^{3+}(d^5)$, $Fe^{2+}(d^6)$, $Co^{2+}(d^7)$, etc., fit well with this conclusion; there are no perovskite multiferroics with d^0, d^1, d^2, and d^{10} configurations.

Of special importance is also the fact that some d^n ions with $n = 3, 4, 5, 6$, and 7, dependent on the ligands of the octahedral environment, may produce two types of magnetic centers, high-spin (HS) and low-spin (LS), and in d^6 case there maybe also intermediate spin (IS) states (d^3 has two spin configurations in the one-electron excitation). According to the analysis (Bersuker, 2012), only d^5 systems follow the necessary condition of potential multiferroics in both spin states, but the PJTE condition of instability and the magnetic moments are different in these two cases. For d^3, d^4, d^6, and d^7 ions only one of the two spin states may serve as a candidate of potential multiferroics. On the other hand, in many cases the two spin states are close in energy, producing the mentioned above well-known phenomenon of transition metal *spin crossover* (SCO), in which case the system can be relatively easily transferred from one spin state to another by external perturbations like heat, light, and magnetic fields. Since, as shown above, the change of the spin state also changes the possibility of ferroelectric polarization, the SCO in some perovskite crystals is simultaneously a magnetic-ferroelectric (multiferroic) crossover (MFCO). This coexisting magnetic, ferroelectric, and spin-crossover phenomena opens a variety of new possibilities to manipulate the properties of the system with exciting novel functionalities to electronics and spintronics.

In addition to many examples that confirm the (outlined by the PJTE theory) necessary conditions of multiferroicity (see, e.g., Barone and Picozzi, 2015), several papers reported observing also the predicted magnetic-ferroelectric spin-crossover effect (Domracheva et al., 2013; Raymond et al., 2014; Weston et al., 2016), and it was also shown that in $BiCoO_3$ the ferroelectric polarization is greatly enhanced when the Co^{3+} ion is in the high-spin state, as compared to the nonmagnetic state with the Co^{3+} ion in the low-spin configuration (Weston et al., 2016). The authors demonstrated also the predicted *electric magnetization* (Bersuker, 2012, 2013b), when by means of induced polarization the spin state changes from low-spin ($S = 0$) to high-spin ($S = 2$). They concluded that in contrary to the widespread belief, "*unpaired electron spins actually drive ferroelectricity*, rather than inhibit it, which represents a shift in the understanding of how ferroelectricity and magnetism interact in perovskite oxides" (Weston et al., 2016). This conclusion follows directly (and exclusively) from the above PJTE theory of ferroelectricity and multiferroicity.

Orientational polarization of solids

If the interactions between the JTEs centers in crystals are not sufficiently strong (at temperatures above the structural phase transitions to the cooperative effects), and in the absence of external perturbations, the local distortions at each center are not fully correlated with the others, and they resonate between the different equivalent orientations controlled by the local multiminimum APES. If the barriers between the minima are not very high, the picture as a whole looks like the local dipole moments performing hindered rotations. Under a uniaxial external perturbation (e.g., strain, stress, or electric field E) the equivalency between the minima of the APES is violated, and the system becomes trapped in one of the minima, or in an orientational controlled linear combination of two or several minima that remain equivalent in the external field, in the same direction for all the PJTE centers under the same perturbation.

In other words, under external perturbations, the induced by the PJTE local dipole moments rotate to adjust along the external field, resulting in *orientational polarization of solids*. It is an essentially novel property, which, similar to orientational polarization of liquids, results in drastically enhanced polarization susceptibility in terms of orders of magnitude (Bersuker, 2015a,b; Polinger and Bersuker, 2017; Bersuker and Polinger, 2020). Remarkably, the possible existence of dielectric crystals with randomly oriented dipole moments (similar to ferromagnetics), which may behave like a polar liquid above its freezing point, was first suggested by P. Debye more than a century ago (Debye, 1912), but not discovered till the recent works (Bersuker, 1966, 2015a,b). Below follow several examples of experimentally observable orientational polarization of solids.

Flexoelectricity

There are many consequences of this orientational effect induced by the multiminimum nature of the APES of systems with JTEs. We show here several examples beginning with polarization of centrosymmetric dielectric solids under a strain gradient, called flexoelectricity. The physical origin of flexoelectricity is, in general, quite transparent: a strain gradient removes the inversion symmetry of the lattice in at least one direction, thus inducing a polar distortion of the charge distribution (see, e.g., Tagantsev and Yudin, 2017). Without JTEs the polarization under the flexoelectric effect in usual ionic crystals is expected to be small, of the order of nCm^{-1}, but the experimental measurements of the flexoelectricity effect in ferroelectric systems show that it can be much larger than the theoretical predictions by 3–4 orders of magnitude (Ma and Cross, 2006; Ma, 2010; Nguyen et al., 2013; Zubko et al., 2013). The largest effect is obtained in the paraelectric phase of $BaTiO_3$, but it is much smaller in the similar $SrTiO_3$ crystal, while it approximately follows the theoretical predictions in the majority of other non-ferroelectric crystals. For $BaTiO_3$ the flexoelectric coefficient f (the component of the tensor coefficient of proportionality between the polarization and strain gradient in the one-dimensional model) decreases significantly when moving from the paraelectric phase to its ferroelectric phases of consequent lower symmetry and becomes "normal" (of the order of magnitude predicted by the theory) in the rhombohedral phase. In essence, the publications on this subject based on displacive theories give no reasonable explanation of this controversy beyond the unproved assumption of different crystal imperfections.

The essential controversies in the origin of flexoelectricity with several orders of magnitude in the difference between its calculated and measured values disappear when the JTE or PJTE leading to orientational polarization, are taken into account. As outlined above, these effects under certain conditions, produce a local dipolar instability and dipolar distortions, which in the free system are of dynamic nature, but become oriented by the gradient of strain. The latter restores a static orientation of the dipoles, in the same direction for all the centers, thus polarizing the centrosymmetric system. This explains the (by-orders-of-magnitude) bigger flexoelectric effect in perovskite crystals as due to the PJTE: restoring a resonating dipole moment (stopping its tunneling between equivalent minima by violating their equivalency) is much easier than separating opposite charges (polarizing) a rigid ionic lattice.

For a demonstration of the orientational polarization, we bring here some numerical estimates of the flexoelectric properties of the $BaTiO_3$ crystal, for which numerical values of the PJTE induced APES parameters are given in Table 1 (Bersuker, 2015a,b; for a more rigorous treatment, see Polinger and Bersuker, 2017). In the paraelectric $BaTiO_3$ the Ti ions are (instantly) dipolar displaced in one of the eight equivalent trigonal minima, with tunneling between them (see section "Cooperative PJTE, ferroelectricity"). Any small perturbation in the form of strain gradient makes these PJTE minima nonequivalent, thus violating the conditions of tunneling between them and restoring some of the local dipole moments; the strain gradient acts as a "stop-flow" terminating a part of the tunnelings. Since the strain gradient has the same direction for all the unit cells, this leads to the polarization of the crystal. A rough (qualitative) estimate of the flexoelectric coefficient f in the paraelectric phase of $BaTiO_3$, employing the vibronic coupling parameters of Table 1, yields the following relation:

$$f = (d_0/a)(20K_0/\Gamma)^{1/2} \tag{5}$$

where we used the expression for the polarization produced by the dipole moments in the minima $P = d_0/a^3$. The dipolar minimum position from Table 1 is $x_0 = \sqrt{3}Q_0$ and the effective (Born) charge of the Ti ion is $Z^* = 8.7e$, hence $d_0 = -\sqrt{3}Z^*eQ_0$. With numerical values of the parameters and K_0 from Table 1 we get the following estimate: $f = -0.43 \cdot 10^{-6}$ Cm^{-1}.

Thus instead of (and in addition to) producing a polar charge redistribution in a rigid cubic crystal of the order of nCm^{-1} the strain gradient in the paraelectric phase of a PJTE ferroelectric in an orientational polarization recovers the virtual local dipole moments (suppresses their dynamical averaging) inducing the ferroelectric polarization of the order of $\mu\mathrm{Cm}^{-1}$. This removes the main controversy in the theory of flexoelectricity explaining the origin of the 3–4 orders of magnitude larger flexoelectric coefficient f in paraelectric $BaTiO_3$ as compared with nonferroelectric crystals. As the dynamic JTE and the PJTE are of local origin, the enhanced flexoelectric effect takes place everywhere these effects produce local dipolar distortions, and the density of such JTE or PJTE centers is high enough for experimental observation.

Enhanced permittivity

Similar to flexoelectricity, permittivity of ferroelectric crystals is strongly influenced by the orientational polarization of the dipolar distortions produced by the JTE or PJTE (Bersuker, 2015b). A more rigorous treatment of permittivity of crystals with these effects is given in (Polinger and Bersuker, 2017), but a rough estimation, yielding orders of magnitude, can be obtained directly from the data in Table 1. In the case of permittivity the equivalency between the minima of the APES is violated by an external electric field $\boldsymbol{E}$, due to which the dynamic polar distortions become trapped in one of the minima (or in an orientational controlled linear combination of the two or several minima that remain equivalent in the field $\boldsymbol{E}$), in the same direction for all the JTE or PJTE centers. In case of polar distortions this results in polarization of the system, $P_o = \chi_o E$, where χ_o is the contribution to the dielectric susceptibility, which is thus of orientational nature: the virtual dipole moment that resonates between the equivalent minima becomes real, oriented along the field. In addition to this orientational effect there is also the usual displacive susceptibility χ_d. The orientational contribution to the polarization is always much larger than the displacive one, provided there are orientational degrees of freedom in the system (for example, in water $\chi_o = 72$, whereas $\chi_d = 5$). This is quite understandable: similar to the case of flexoelectricity, discussed above, it is much easier to rotate a ready-made dipole along the electric field, than to displacive-polarize a stable polyatomic formation.

Similar to the above rough estimate for the coefficient of flexoelectricity in $BaTiO_3$, we get the following relation for the orientational dielectric susceptibility χ_o in the relation $P_o = \chi_o E$, based on the vibronic PJTE theory (Bersuker, 2015b):

$$\chi_o = 2d_0^2/k\Gamma a^3 \tag{6}$$

where $k = 0.1$–1.0 is an adaptive coefficient. By using the numerical data for the $BaTiO_3$ crystal in Table 1 we can estimate the numerical value of the susceptibility: $\chi_o = 0.45 \times 10^3$–$0.45 \times 10^4$. This agrees well by orders of magnitude with experimental measurements of permittivity in this system.

On the other hand, ignoring the PJTE, the displacive polarization of the unit cell P_d is limited by its stiffness (force constant) K_0 with respect to the polar distortions along the above normal coordinate Q. Hence the electric force $2|e|Z^*E$, producing the dipole moment $|e|Z^*Q$, is compensated by the elastic force K_0Q. Thus, $2|e|Z^*E = K_0Q$ and $P_d = \frac{|e|Z^*Q}{a^3} = \chi_d E$, which leads us to the expression:

$$\chi_d = 2(eZ^*)^2/a^3K_0 \tag{7}$$

Using the same numerical values as above and the K_0 value from Table 1 we get the following estimate: $\chi_d = 1.22$. This yields a typical value expected for permittivity in ionic crystals with just displacive (no orientational) contribution (and in the paraelectric region far from the phase transition). Compared with the value $\chi_o = 0.45 \times 10^3 - 0.45 \times 10^4$, obtained above for the orientational contribution, we see that *by taking into account the dynamic PJTE the calculated permittivity of* $BaTiO_3$ *increases by more than three orders of magnitude*.

In fact the whole permittivity in the field E up to the orientational saturation at $E = E_m$ is of PJTE origin, acquiring a less-significant displacive-only addition in higher fields. The value of E_m can be estimated from the above expression $E_m \cong k\Gamma/2d_0$. For $BaTiO_3$ $E_m \cong k \times 1.15 \times 10^7$ V/m. It follows that up to this voltage the permittivity is strongly enhanced by the orientational contribution of the dynamic PJTE, reaching the value of polarization $P = d_0/a^3 \cong 0.47$ Cm^{-2} which coincides approximately with that of the ferroelectric phase.

The estimates above demonstrate qualitatively the strong effect of orientational polarization in the properties of crystals with JTEs centers. In a more rigorous consideration (Polinger and Bersuker, 2017) the orientational effect is strongly dependent on the speed of the inter-minima dipoles orientation, characterized by the tunneling splitting parameter Γ in comparison with the local dipole moment d_0 in the minima of the APES, the relative strength of the applied electric field, and even its direction with respect of perovskite crystal axes, illustrated in Fig. 11 (Polinger and Bersuker, 2017).

The enhanced polarization may take place in any dielectric polyatomic formation in the presence of dynamic JTE or PJTE, and the number of such systems in solid, liquid, and gas phases is innumerable. If the centers of the system with local trigonal symmetry are in a degenerate electronic E state, the local $E \otimes e$ type JTE results in three dipolar minima or a trough of dipolar distortions of the Mexican-hat type (Bersuker, 2006). As in the $BaTiO_3$ case, their contribution to the polarization in electric fields is expected to strongly enhance the permittivity. Similarly, enhancement is expected when the centers with trigonal symmetry are subject to a PJTE.

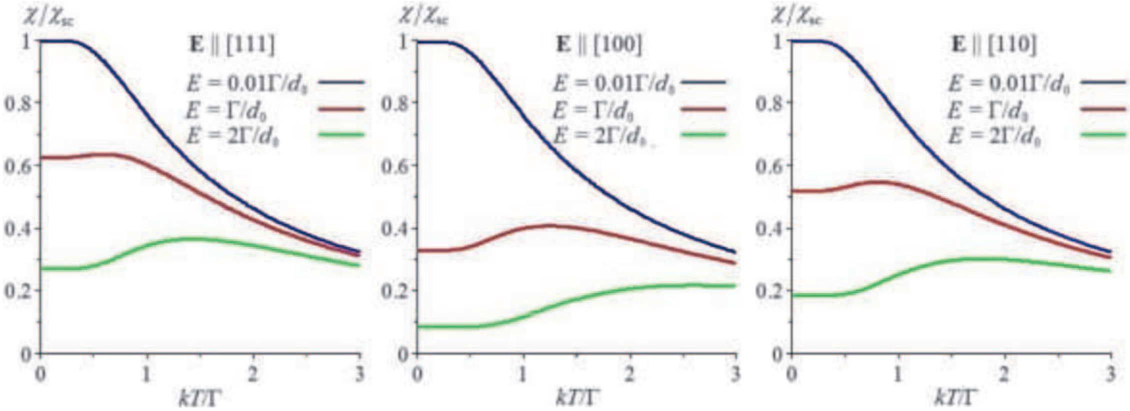

Fig. 11 Temperature dependence of the dielectric susceptibility χ of the cluster [BO_6] in perovskite crystals at three directions of the external electric field, E || [111], E || [100] and E || [110], and three absolute values, $E = 0.01\Gamma/d_0$, Γ/d_0, and $2\Gamma/d_0$, [in units of $\chi_{sc} = d_0^2/(3\Gamma\varepsilon_0 a^3)$ with ε_0 ss the vacuum constant]. The temperature is given in dimensionless units kT/Γ. Reprinted from Polinger V.Z., Bersuker I.B. (2017) Pseudo Jahn-Teller effect in permittivity of ferroelectric perovskites. *Journal of Physics Conference Series* 833: 012012. Copyright 2017 IOP publishing.

Giant electrostriction

Since the electric field along the trigonal axis of $BaTiO_3$ suppresses the tunneling between the dipolar minima of the APES, trapping all the units of the system in the same kind of trigonal minimum along the whole crystal, the latter will be not only polarized, but also strained in this direction. Similar to permittivity and flexoelectricity, the change in the dimensions of the unit cell in the electric field E, the electrostriction, can be estimated for the $BaTiO_3$ crystal (Bersuker, 2015b). In fact the electrostriction problem is closely related to the inverse of flexoelectricity: instead of polarization P induced by strain gradient G in flexoelectricity, electrostriction is the strain S (not strain gradient) induced by the polarization. In the one-dimensional model with the electric field and strain along the same trigonal axis of the crystal we have: $S = \gamma P^2$, where γ is the coefficient of electrostriction. More convenient is to measure the strain as a function of the electric field intensity E, $S = \eta E^2$. As shown above, at $E_m \sim (10^6\text{–}10^7)\ \text{Vm}^{-1}$ in the trigonal direction the full orientational ordering of the local unit cell dipoles is reached resulting in the strain $S = Q/a \cong \sqrt{3}Q_0/4 \cong 0.05$. Without the orientational contribution of the dynamic PJTE, from the data above we have: $2|e|Z^*E = K_0Q$ which at $E = E_m$ yields the strain $S \sim 10^{-5}$, a typical value for a regular ionic crystal. Again, as for permittivity and flexoelectricity, the orientational polarization induces giant electrostriction of paraelectric $BaTiO_3$, about three orders of magnitude bigger than that in similar systems without the dynamic PJTE, and this effect is in accord with experimental measurements.

Manipulation of solids and 2D systems by influencing their JTEs parameters

The knowledge that the structural instability and distortions of high-symmetry configurations of molecular systems and solids are induced by the JTEs allows one to restore the symmetry of the system by suppressing these effects with external perturbations that influence (modify) the JTEs (vibronic coupling) parameters. Conversely, specific external perturbations can induce the JTEs, producing polyatomic structures with distorted configurations and novel properties. Manipulation of atomic systems by influencing their features induced by the vibronic coupling effects is a novel trend (see in: Bersuker, 2017b, 2019, Gorinchoy et al., 2011, Gorinchoy and Bersuker, 2017, Gudkov et al., 2020); below are several examples.

Inducing the JTE in crystal sublattices

There are two possibilities to manipulate JTE-induced properties of the system by means of external influence targeting the corresponding JTE parameters: (1) destroying the high-symmetry configuration that produces the degeneracy of the electronic state by means of lower-symmetry perturbations; (2) adding or removing valence electrons in a redox process that removes or installs the degeneracy of the state under consideration (without destroying the reference symmetry of the configuration). Low-symmetry external perturbations (e.g., strain, crystal field environment, coordination to lower symmetry groups, electric or magnetic fields, etc.), at first sight, may produce the same kind of distortions, as expected from the JTE, but actually they are essentially different: external perturbation produce *fixed* local distortions without the local JTE dynamics. Obviously, the degeneracies can be manipulated also by adding or removing electronic charge in oxidation, reduction, excitation, coordination, and via other fractional charge transfers (Gorinchoy et al., 2011).

One of these possibilities was recently realized by inducing the JTE in a crystal sublattice of the hexaferrite $BaFe_{12}O_{19}$ crystal (Gudkov, 2020). In this crystal structure, all iron ions are in the $Fe^{3+}(d^5)$ oxidation state with the high-spin configuration ($S = 5/2$), and they occupy five different crystallographic locations with octahedral, tetrahedral, and bi-pyramidal coordination. In all of them the electronic ground state is orbitally non-degenerate, $^6A_1(t_2^3e^2)$, and hence there is no JTE. The authors (Gudkov, 2020) suggested and realized a doping procedure that targets the nondegenerate Fe^{3+} centers, reducing them to $Fe^{2+}(d^6)$, with the ground state electronic term $^5T_2(t_2^4e^2)$ in the octahedral, and $^5E(t_2^3e^3)$ in the tetrahedral coordination, both becoming subjects of the JTE. This process was achieved by doping the crystal with electron-donor Ti atoms. It cames out that the dopants target first a tetrahedral site (which is in an easier way of reduction). Therefore, by regulating the concentration of dopants, a whole tetrahedral sublattice of the crystal was transformed in a sublattice with the JTE (the $E \otimes e$ problem) on each of its centers.

Actually, by inducing the JTE in a whole sublattice of the host lattice, we get a modified crystal with properties different from that of the parent crystal. In particular, if the JT centers in the transformed sublattice are sufficiently close to each other, their interaction may lead to the cooperative JTE (see section "Cooperative PJTE, ferroelectricity") with thermally controlled structural phase transitions within the JTE-modified sublattice. Such a (quite novel) phenomenon with sublattice phase transitions in a complex crystal remains to be explored in more detail. By comparing the properties of the JT modified crystal with the parental crystal, one gets important information about the crystal structure in both of them (Gudkov, 2020).

The formation of the JTE sublattice in the tetrahedral sites of the hexaferrite crystal by means of Ti doping was confirmed by ultrasonic and terahertz-infrared experiments performed at temperatures 2–200 K in external magnetic fields up to 13 T. The vibronic coupling in the tetrahedral $E \otimes e$ type JTE, was analyzed by ultrasound experiments, employing the mentioned above methodology (see section "Ultrasonic exploration"). Using terahertz-infrared spectroscopy made also possible to determine the crystallographic sites of the induced JT centers. The realization of the modified sublattice in a complex crystal seems to be the first case of such manipulation of the JTE by targeted external influence.

Planarization of puckered two-dimensional systems

The origin of instability and distortions of high-symmetry configurations of molecular systems in nondegenerate states as due to the PJTE is already well established with many examples well studied (Bersuker, 2006, 2013a), but manipulation of their structural features based on this knowledge is relatively new and so far applied mainly to planar and quasi planar (two-dimensional (2D) and quasi 2D) systems and their extended forms (see, e.g., Bersuker, 2017b, 2021; Gorinchoy and Bersuker, 2020, and references therein). The enhanced attention to these systems is due to their special structural feature, their out-of-plane distortions in the form of puckering or buckling, which influence all their properties, notably the chemical reactivity, charge mobility, and band gaps. It raises the importance of manipulating this structural feature by means of external implications (perturbations). Many attempts to influence the planarity of 2D systems employ the considerations of atomic orbital hybridization, which correctly illustrates the origin of the out-of-plane distortion effect in some particular cases, but it is insufficient to explain the origin of puckering or buckling in more complicated situations, which cannot be reduced to just hybridizations.

Based on the general proof that all the deviations from high-symmetry configuration of polyatomic systems in nondegenerate states are of PJTE origin, we can find out the main features of the planar configuration of 2D systems that are responsible for the out-of-plan instability and try to influence them by external perturbations. The procedure starts with electronic structure calculations of the ground and low-lying excited states in the planar configuration, their energy, symmetry, MO origin, and the numerical values of the parameters in the condition of instability (1). This gives us the necessary insight on how we can enhance or suppress the distortions, meaning manipulate the puckering or buckling of the system.

In case of the PJTE induced distortions the following manipulation possibilities were suggested: (1) increasing the energy gap Δ between the PJTE active electronic states, e.g., by means of weak coordination with outside systems (van-der-Waals or polarizing external influence); (2) changing the symmetries of the active ground or excited states by removing electrons from, or adding electrons to targeted orbitals, that would nullify the vibronic coupling for the distortion under consideration; (3) changing the numerical value of the constant of the vibronic coupling between the active electronic states by means of partial charge transfer via coordination to outer groups; (4) making targeted chemical substitutions that change the planarity, but do not violate the quasi-2D character of the system; (5) by spectroscopic excitations.

All these possibilities were realized (see: Bersuker, 2017b, and references therein). For illustration, we show here the example of the carbon nitride g-C_3N_4, where the procedure of planarization was realized by influencing the vibronic coupling parameters via charge transfer by coordination. Graphitic carbon nitride g-C_3N_4 is a 2D system, which is similar to graphene in many aspects, but unlike graphene, g-C_3N_4 is not regular planar, it is buckled as shown in Fig. 12.

The PJTE origin of the buckling in this system was studied in detail with the goal to influence it by external perturbations (Ivanov et al., 2015). It was shown that its planar configuration is unstable along the e'' symmetrized displacements for which the coupled HOMO and LUMO responsible for the PJTE instability were revealed by ab initio calculations. With these data and previous experience, the authors suggested suppressing the PJTE and restoring the planar configuration of this system by adding Be^{2+} ions below and above the fragment unit in an inverse sandwich arrangement. The calculations show indeed that the electron acceptor ions change the HOMO-LUMO positions thus quenching the PJTE and flattening the system. Fig. 13 shows the optimized structures of both the fragment unit and the extended sheet of g-C_3N_4 with appropriately positions of the Be^{2+} ions, which restore the planar configuration, showing also the electronic band structure. Similar planarization procedures involving appropriate external influencing the PJTE parameters were carried out on a series of other 2D systems (see: Bersuker, 2017b, and references therein).

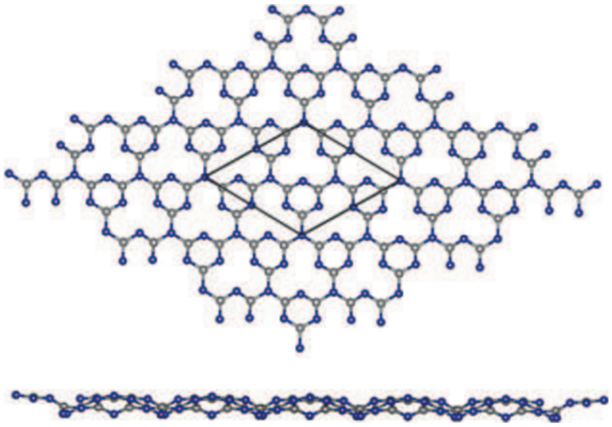

Fig. 12 Buckled 2D structure of graphitic carbon nitride *g*-C_3N_4 shown in top and side view. Here and below the gray, blue, and white spheres represent carbon, nitrogen, and hydrogen atoms, respectively. Reprinted with permission from Ivanov AS, Miller E, Boldyrev AI, Kameoka Y, Sato T, and Tanaka K (2015) Pseudo Jahn – Teller origin of buckling distortions in two-dimensional triazine-based graphitic carbon nitride (g-C3N4) sheets. *Journal of Physical Chemistry C* 119: 12008–12015. Copyright 2015 American Chemical Society.

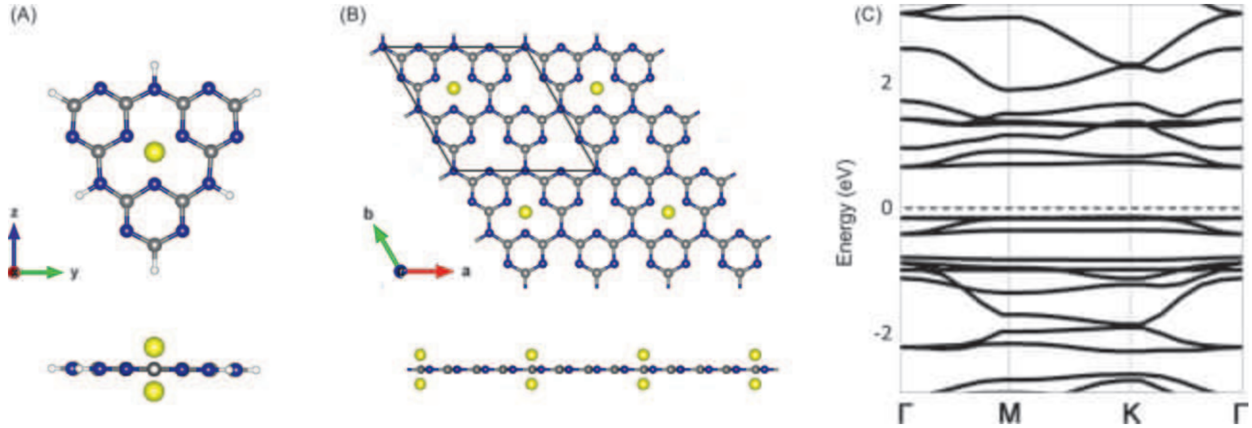

Fig. 13 Top and side views of the optimized complex of the graphitic carbon nitride, *g*-C_3N_4, local unit with two Be^{2+} ions in an inverse sandwich arrangement (a), the corresponding extended 2D sheet (b) and its electronic band structure (c). Reprinted with permission from Ivanov AS, Miller E, Boldyrev AI, Kameoka Y, Sato T, and Tanaka K (2015) Pseudo Jahn – Teller origin of buckling distortions in two-dimensional triazine-based graphitic carbon nitride (g-C3N4) sheets. *Journal of Physical Chemistry C* 119: 12008–12015. Copyright 2015 American Chemical Society.

Conclusion

The definition of the JTEs, followed by illustrative examples of some of their more recent applications to the study of structure and properties of polyatomic systems, with examples of applications to local and cooperative properties of solids shows that presently these effects are unalienable features of condensed matter. The theory of JTEs continues developing, and their implication in observable properties is rapidly expanding. All the four JTEs are of local origin, steaming from the specifics of the electron-nuclear (vibronic) interactions. Of them, the best known is the JTE, less known, but already in wider use, is the PJTE, while the exploration of the hidden effects, *h*-JTE and *h*-PJTE, just started. From the most novel applications to condensed matter, local and cooperative properties of crystals are most influenced, the latter including ferroelectricity, multiferroicity, and a novel property of solids, orientational polarization. Quite new is also the developing trend of manipulation of polyatomic properties via influencing their JTEs parameters by means of external perturbations.

References

Averkiev NS, Bersuker IB, Gudkov V, Zhevstovskikh IV, Sarychev MN, Zherllitsyn S, Yasin S, Shakurov GS, Ulanov VA, and Surikov VT (2017a) Manifestation of the Jahn-Teller effect in elastic moduli of strontium fluorite crystals doped with chromium ions. *Journal of Physics Conference Series* 833: 012003.

Averkiev NS, Bersuker IB, Gudkov VV, Zhevstovskikh IV, Baryshnikov KA, Sarychev MN, Zherlitsyn S, Yasin S, and Korostelin YV (2017b) Magnetic field induced tunneling and relaxation between orthogonal configurations in solids and molecular systems. *Physical Review B* 96: 094431.

Barone P and Picozzi S (2015) Mechanisms and origin of multiferroicity. *Comptes Rendus Physique* 16: 143–152.

Bersuker IB (1961) Hindered motions in transition metal complexes. *Optics and Spectroscopy* 11: 319–324.

Bersuker IB (1962) Inversion splitting of energy levels in free transition metal complexes. *Zhurnal Éksperimental'noĭ i Teoreticheskoĭ Fiziki* 43: 1315–1322. [English translation: 1963. Sov. Phys. JETP 17, 933–938].

Bersuker IB (1966) On the origin of ferroelectricity in perovskite type crystals. *Physics Letters* 20: 589–591.

Bersuker IB (ed.) (1984) *The Jahn-Teller Effect. A Bibliographic Review*, pp. 1–590. New York: IFI/Plenum.

Bersuker IB (2006) *The Jahn-Teller Effect*. Cambridge (UK): Cambridge University Press.

Bersuker IB (2009) Recent developments in the Jahn-Teller effect theory. The hidden Jahn-Teller effect. In: Köppel H, Yarkony DR, and Barentzen H (eds.) *The Jahn-Teller Effect. Fundamentals and Implications for Physics and Chemistry, Springer Series of Chemical Physics*. vol. 97, pp. 3–23. Heidelberg: Springer.

Bersuker IB (2012) Pseudo Jahn-Teller origin of perovskite multiferroics, magnetic-ferroelectric crossover, and magnetoelectric effects. The d^0-d^{10} problem. *Physical Review Letters* 108: 137202.

Bersuker IB (2013a) The pseudo Jahn-Teller effect—A two-state paradigm in formation, deformation, and transformation of molecular systems and solids. *Chemical Reviews* 113: 1351–1390.

Bersuker IB (2013b) A local approach to solid state problems: Pseudo Jahn-Teller origin of ferroelectricity and multiferroicity. *Journal of Physics Conference Series* 428: 012028.

Bersuker IB (2015a) Pseudo Jahn-Teller effect in the origin of enhanced flexoelectricity. *Applied Physics Letters* 107: 202904.

Bersuker IB (2015b) Giant permittivity and electrostriction induced by dynamic Jahn-Teller and pseudo Jahn-Teller effects. *Applied Physics Letters* 107: 202904.

Bersuker IB (2016) Spontaneous symmetry breaking in matter induced by degeneracy and pseudodegeneracy. In: Rice S and Dinner R (eds.) *Advances in Chemical Physics*. vol. 160, pp. 159–208. New York: Wiley.

Bersuker IB (2017a) The Jahn-Teller and pseudo Jahn-Teller effect in materials science. *Journal of Physics Conference Series* 833: 01200.

Bersuker IB (2017b) Manipulation of structure and properties of two-dimensional systems employing the pseudo Jahn-Teller effect. *FlatChem* 6: 11–27.

Bersuker IB (2018) The vibronic (pseudo-Jahn-Teller) theory of ferroelectricity. Novel aspects and applications. *Ferroelectrics* 536: 1–59.

Bersuker IB (2019) The Jahn-Teller and pseudo Jahn-Teller effect in materials science. In: Lind PR (ed.) *Recent Studies in Materials Science*, pp. 1–95. Nova Science Publishers.

Bersuker IB (2020a) Hidden Jahn-Teller and Pseudo-Jahn-Teller effects, Encyclopedia, General & Theoretical Physics, Topic Review. https://encyclopedia.pub/4283.

Bersuker IB (2020b) Spin crossover and magnetic-dielectric bistability induced by hidden pseudo-Jahn-Teller effect. *Magnetochemistry* 6(4): 64.

Bersuker IB (2021) Jahn–Teller and pseudo-Jahn–Teller effects: From particular features to general tools in exploring molecular and solid state properties. *Chemical Reviews* 121: 1463–1512.

Bersuker IB and Polinger VZ (1989) *Vibronic Interactions in Molecules and Crystals*. Berlin-Heidelberg: Springer-Verlag.

Bersuker IB and Polinger V (2020) Perovskite crystals: Unique pseudo-Jahn-Teller origin of ferroelectricity, multiferroicity, permittivity, flexoelectricity, and polar nanoregions. *Condensed Matter* 5(4): 68.

Bersuker IB, Gorinchoy NN, and Polinger VZ (1984) On the origin of dynamic instability of molecular systems. *Theoretica Chimica Acta* 66: 161–172.

Chancey CC and O'Brien MCM (1997) *The Jahn-Teller effect in C_{60} and other icosahedral complexes*. Princeton, New Jersey: Princeton University Press.

Ciccarino CJ, Flick J, Harris IB, Trusheim ME, Englund DR, and Narang P (2020) Strong spin–orbit quenching via the product Jahn–Teller effect in neutral group IV qubits in diamond. *npj Quantum Materials* 5: 75. https://doi.org/10.1038/s41535-020-00281-7.

Debye P (1912) Eine Resultate einer Kinetischen Theorie der Isolatoren. *Physikalische Zeitschrift* 13: 97–100.

Domracheva NE, Pyataev AV, Vorobeva VE, and Zueva EM (2013) Detailed EPR study of spin-crossover dendrimeric iron(III) complex. *The Journal of Physical Chemistry B* 117: 7833–7842.

Englman R (1972) *The Jahn-Teller Effect in Molecules and Crystals*. London: Wiley1972.

Garcia-Fernandez P and Bersuker IB (2011) A class of molecular and solid state systems with correlated magnetic and dielectric bistabilities induced by the pseudo Jahn-Teller effect. *Physical Review Letters* 106: 246406.

Garcia-Fernandez P, Bersuker IB, and Boggs JE (2006) Lost topological (Berry) phase factor in electronic structure calculations. Example: The ozone molecule. *Physical Review Letters* 96: 163005.

Ghering GA and Ghering KA (1975) Cooperative Jahn-Teller effect. *Reports on Progress in Physics* 38: 1–89.

Gorinchoy NN and Bersuker IB (2017) Pseudo Jahn-Teller effect in control and rationalization of chemical transformations in two-dimensional compounds. *Journal of Physics Conference Series* 833: 012010.

Gorinchoy NN, Balan I, and Bersuker IB (2011) Jahn-Teller, pseudo Jahn-Teller, and Renner-Teller effects in systems with fractional charges. *Computational & Theoretical Chemistry* 976: 113–119.

Gorinchoy N and Bersuker IB (2020) Origin of puckering (buckling) of planar heterocycles and methods of its suppression. In: Danielsen JM (ed.) *Heterocycles: Synthesis, Reactions and Applications*, pp. 129–188. Nova Science Publishers.

Gudkov VV and Bersuker IB (2012) Experimental evaluation of the Jahn-Teller parameters by means of ultrasonic measurements. Application to impurity centers in crystals. In: Atanasov M, Daule C, and Tregenna-Pigot P (eds.) *Vibronic Interactions and the Jahn-Teller Effect: Theory and Applications; Progress in Theoretical Chemistry and Physics*. vol. 23, pp. 143–161. Heidelberg: Springer.

Gudkov VV, Sarychev MN, Zherlitsyn S, Zhevstovskikh IV, Averkiev NS, Vinnik DA, Gudkova SA, Niewa R, Dressel M, Alyabyeva LN, Gorshunov BP, and Bersuker IB (2020) Sub-lattice of Jahn-Teller centers in hexaferrite crystal. *Nature Scientific Reports* 10: 7076–7091.

Ham FS (1972) Jahn-Teller effect in electron paramagnetic resonance spectra. In: Geschwind S (ed.) *Electron Paramagnetic Resonance*, p. 1972. New York: Plenum Press.

Ivanov AS, Miller E, Boldyrev AI, Kameoka Y, Sato T, and Tanaka K (2015) Pseudo Jahn – Teller origin of buckling distortions in two-dimensional triazine-based graphitic carbon nitride (g-C3N4) sheets. *Journal of Physical Chemistry C* 119: 12008–12015.

Jahn HA and Teller E (1937) Instability of polyatomic molecules in degenerate electronic states. I. Orbital degeneracy. *Proceedings of the Royal Society of London. Series A* 161: 220–235.

Kaplan MD and Vekhter BG (1995) *Cooperative Phenomena in Jahn-Teller Crystals*. New York: Plenum Press1995.

Köppel H, Domcke W, and Cederbaum LS (1984) Multimode molecular dynamics beyond the Born-Oppenheimer approximation. *Advances in Chemical Physics* 57: 59–246.

Köppel H, Yarkony DR, and Barentzen H (1912) *The Jahn-Teller Effect. Fundamentals and Implications for Physics and Chemistry. Springer Series of Chemical Physics* 97: Heidelberg: Springer.

Liu Y, Bersuker IB, Zou W, and Boggs JE (2009) Combined Jahn-Teller and pseudo Jahn-Teller effects in the CO_3 molecule: a seven-state six-mode problem. *Journal of Chemical Theory and Computation* 5: 2679–2686.

Ma W (2010) Flexoelectric charge separation and size dependent piezoelectricity in dielectric solids. *Physica Status Solidi B* 247: 213–218.

Ma W and Cross LE (2006) Flexoelectricity in barium titanate. *Applied Physics Letters* 88: 232902.

Nguyen TH, Mao S, Yeh Y-W, Purohit PK, and McAlpine MC (2013) Nanoscale flexoelectricity. *Advanced Materials* 25: 946–974.

Öpik U and Pryce MHL (1957) Studies of the Jahn-Teller effect I. A survey of the static problem. *Proceedings of the Royal Society of London. Series A* 238: 425–447.

Perlin YE and Wagner M (eds.) (1984) *Dynamical Jahn-Teller Effect in Localized Systems*. Amsterdam: Elsevier.

Polinger VZ (2009) Orbital ordering versus the traditional approach in the cooperative Jah-Teller effect: A comparative study. In: Köppel H, Yarkony DR, and Barentzen H (eds.) *The Jahn-Teller Effect. Fundamentals and Implications for Physics and Chemistry, Springer Series of Chemical Physics*. vol. 97, pp. 685–725. Heidelberg: Springer.

Polinger VZ (2013) Ferroelectric phase transitions in cubic perovskites. *Journal of Physics Conference Series* 428: 012026.

Polinger VZ and Bersuker IB (2017) Pseudo Jahn-Teller effect in permittivity of ferroelectric perovskites. *Journal of Physics Conference Series* 833: 012012.

Polinger V and Bersuker IB (2018) Origin of polar nanoregions and relaxor properties of ferroelectrics. *Physical Review B* 98: 214102.

Polinger VZ, Garcia-Fernandez P, and Bersuker IB (2015) Pseudo Jahn-Teller origin of ferroelectric instability in $BaTiO_3$ type perovskites. The green's function approach and beyond. *Physica B: Condensed Matter* 457: 296–309.

Ravel B, Stern EA, Vedrinskii RI, and Kraisman V (1998) Local structure and the phase transitions of $BaTiO_3$. *Ferroelectrics* 206–207: 407–430.

Raymond O, Ostos C, Font R, Curiel M, Bueno-Baques D, Machorro R, Mestres L, Portelles J, and Siqueiros JM (2014) Multiferroic properties and magnetoelectric coupling in highly textured $Pb(Fe_{0.5}Nb_{0.5})O_3$ thin films obtained by RF sputtering. *Acta Materialia* 66: 184–191.

Stern E (2004) Character of order-disorder and displacive components in barium titanate. *Physical Review Letters* 93: 037601.

Tagantsev AK and Yudin PV (2017) *Flexoelectricity in Solids. From Theory to Applications*. Singapore: World Scientific.

Teller E (1972) An historical note. In: Englman R (ed.) *The Jahn-Teller Effect in Molecules and Crystals*. London, Foreword: Wiley.

Thiering G and Gali A (2017) *Ab initio* calculation of spin-orbit coupling for an NV center in diamond exhibiting dynamic Jahn-Teller effect. *Physical Review B* 96: 81115(R).

Thiering G and Gali A (2019) The $(e_g \otimes e_u) \otimes E_g$ product Jahn–Teller effect in the neutral group-IV vacancy quantum bits in diamond. *Nature Computational Materials* 5: 1–6.

Weston L, Cui XY, Ringer SP, and Stampfl C (2016) Multiferroic crossover in perovskite oxides. *Physical Review B* 93: 165210.

Zubko P, Catalan G, and Tagantsev AK (2013) Flexoelectric effect in solids. *Annual Review of Materials Research* 43: 387–421.

Fermi surface measurements[☆]

SB Dugdale, H.H. Wills Physics Laboratory, University of Bristol, Bristol, United Kingdom

© 2024 Elsevier Ltd. All rights reserved.

This is an update of C. Bergemann, Fermi Surface Measurements, Editor(s): Franco Bassani, Gerald L. Liedl, Peter Wyder, Encyclopedia of Condensed Matter Physics, Elsevier, 2005, Pages 185–192, ISBN 9780123694010, https://doi.org/10.1016/B0-12-369401-9/00456-3.

Introduction **815**
Quantum oscillations **816**
Experimental realization 817
Angle-resolved photoemission **819**
Experimental realization 820
Angle-dependent magnetoresistance oscillations **821**
Types of oscillation 821
Experimental realization 822
The electron momentum distribution—Compton scattering and positron annihilation **822**
Compton scattering 824
Positron annihilation 826
Spin-resolved measurements 828
Strengths and weaknesses of the various techniques **828**
Sensitivity to correlations 828
Sample purity 828
Temperature 828
Dimensionality 828
k-space resolution 828
Bulk sensitivity 829
Other techniques **829**
Anomalous skin effect 829
Cyclotron resonance 829
Kohn anomalies, RKKY and Friedel oscillations 829
Conclusion **830**
Acknowledgments **830**
References **830**

Abstract

The Fermi surface separates occupied from unoccupied states in momentum space at zero temperature. For free electrons, the Fermi surface is a sphere, but those of real metals exhibit a spectacular range of topologies. Knowledge of those Fermi surface topologies is the key to understanding the dynamical properties of electrons in metals. An arsenal of ingenious experimental techniques has been developed to reveal the Fermi surfaces of a wide range of materials. This article explores some of these methods, providing a theoretical background and an overview of how the experiments are carried out. The strengths and weaknesses of the different experimental approaches are summarized.

Key points

- Motivate the experimental determination of the Fermi surface.
- Describe the techniques which are able to measure the Fermi surface, with examples.
- Discuss the strengths and weaknesses of those techniques.

Introduction

An isolated atom can meaningfully be thought of as being composed of a positively charged ion core (comprising the nucleus of neutrons and protons as well as the most tightly bound electrons) surrounded by a small number of more loosely bound valence electrons (Chambers, 1966). The atoms in a crystalline solid are sufficiently close together for the wavefunctions of valence

---

[☆] *Change History*: October 2022. SB Dugdale uodated the chapter.

electrons, on one ion core, to overlap with those of its neighbors, allowing the electrons in a metal to move from one ion to the next. These mobile electrons are the conduction electrons of the metal, and one can get a surprisingly good description of the motion of these electrons by only considering the motion of a single electron in the average distribution of all the other electrons in the solid. Perhaps even more surprisingly, substantial insight can be gained by solving the simplest quantum mechanical model of electrons confined to a box (with periodic boundary conditions) in which the energy eigenfunctions are plane waves with eigenvalues which depend quadratically on the (crystal) momentum of the electron. Since electrons are fermions, the Pauli exclusion principle permits each discrete momentum state allowed by the periodic boundary conditions to be filled by (at most) two electrons of opposite spin. Once all the electrons in the crystal have been accommodated, the resulting surface in reciprocal space which separates occupied from unoccupied momentum states at zero temperature is called the Fermi surface (Dugdale, 2016). For free electrons the Fermi surface is simply a sphere. When the interaction between the electrons and the lattice of ion cores, and indeed the correlations between electrons are taken into account, the Fermi surface continues to exist, but, in general will not be spherical and the electrons will behave as though they have masses different from the free-electron mass.

The significance of the Fermi surface lies in the fact that the electrical and thermal properties of a metal are essentially determined by a tiny fraction of its electrons, namely those that lie at or very close to the Fermi surface. The dynamical properties of those electrons depend on where the electron is on the Fermi surface, which means determining the shape of the Fermi surface is a crucial step in understanding the properties of a metal (Dugdale, 2016).

The development of density functional theory (DFT), and its practical implementation in widely available computer codes, has facilitated the calculation of electronic band structure. Theoretical predictions for the topologies of Fermi surfaces have been able to provide great insight. Nevertheless, the experimental determination of Fermi surface remains vitally important as a test of the predictive capability of those calculations, particularly when the presence of strong electron correlations precludes a conventional DFT description.

Quantum oscillations

The phenomenon of quantum oscillations is most easily understood within a semi-classical picture. The classical motion of a charged particle in the presence of a magnetic field B, will be helical in real space. Thus in reciprocal (momentum) space the electron will trace out a circular path. The angular frequency of the motion, ω_c, is called the cyclotron frequency and is given by

$$\omega_c = \frac{eB}{m^*}, \tag{1}$$

where e is the charge on the electron and m^* is the cyclotron mass (which for a free electron is the same as the free-electron mass, m_e). While any cyclotron radius is classically allowed, the necessity of the quantum mechanical wavefunction to be single-valued means that only a discrete set of orbits are permitted. The Bohr-Sommerfeld quantization of the motion of the electron restricts the areas of real space orbits, in the plane perpendicular to the magnetic field, to those which contain an integer multiple of the flux quantum. The area of the n^{th} allowed orbit in real space, A_n, is given by

$$A_n = \left(n + \frac{1}{2}\right) \frac{h}{eB}, \tag{2}$$

where e is the charge on the electron and h is Planck's constant.

The circular orbits in reciprocal space will be similarly quantized; they are called 'Landau levels' and will have areas A_n^*, given by

$$A_n^* = \left(n + \frac{1}{2}\right) \frac{2\pi eB}{\hbar}. \tag{3}$$

Since there is no additional quantization of the orbits parallel to the magnetic field, in three dimensions these semi-classical orbits lie on 'Landau tubes', as shown in Fig. 1. The Fermi surface, which was quasi-continuous in zero magnetic field, is now constrained to lie on these Landau tubes.

The density of states will be a set of sharp δ-function-like peaks, separated in energy by $\hbar\omega_c^*$. If the energy of an electron state on one of these Landau tubes is below the chemical potential, the state will be occupied. As the magnetic field B is changed, the separation of the Landau levels will change, and as a Landau level passes through the chemical potential μ, the density of states at the chemical potential will change. The chemical potential is identical to the Fermi energy at zero temperature, but at low temperature in a metal the Fermi energy is a very good approximation to the chemical potential (and the two are often used interchangeably, even if this is not strictly correct).

Consider a two-dimensional free-electron gas of non-interacting electrons at low temperature and in zero magnetic field. The Fermi surface will be a circle with a radius equal to the Fermi wavevector, k_F, enclosing an area $A_{\text{FS}}^*(=\pi k_F^2)$ containing occupied states. In the presence of a magnetic field B, the allowed electron states will coalesce onto Landau levels, the energy separation of which will increase with B such that successive Landau levels will pass through the chemical potential when they have an area A_{FS}^*. As each Landau level is depopulated, electrons will be transferred to and accommodated in lower Landau levels, this being permitted since the degeneracy of each level is proportional to B. Consider a situation in which at some magnetic field, B_n, the n^{th} Landau level is coincident with the Fermi surface i.e., it has an area A_{FS}^*. If the magnetic field is changed so that the separation between Landau levels changes then at some new magnetic field, B_{n+1}, the next $((n+1)^{\text{th}})$ Landau level will also have the same area, A_{FS}^*. For that to be true, then

$$A_{\text{FS}}^* = \left(n + \frac{1}{2}\right) \frac{2\pi eB_n}{\hbar} \tag{4}$$

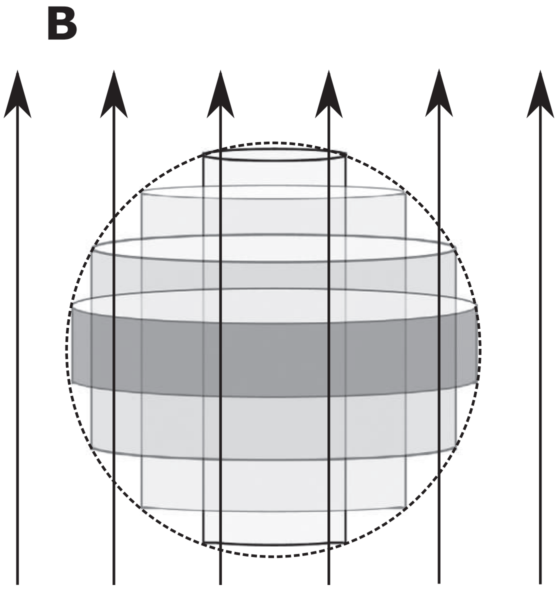

Fig. 1 A spherical Fermi surface (dashed line) in a magnetic field together with some Landau tubes.

and

$$A^*_{\text{FS}} = \left(n + 1 + \frac{1}{2}\right) \frac{2\pi e B_{n+1}}{\hbar}. \tag{5}$$

It follows that

$$A^*_{\text{FS}} \left(\frac{1}{B_{n+1}} - \frac{1}{B_n}\right) = \frac{2\pi e}{\hbar}, \tag{6}$$

and therefore the change in (inverse) magnetic field ($\Delta(1/B)$) needed to make two consecutive Landau levels have areas which coincide with the Fermi surface is

$$\Delta \left(\frac{1}{B}\right) = \frac{2\pi e}{\hbar A^*_{\text{FS}}}. \tag{7}$$

If measurements of $\Delta \left(\frac{1}{B}\right)$ can be made by determining the period of oscillations as a function of inverse magnetic field as B is changed, then Eq. (7) (the so-called 'Onsager relation' (Onsager, 1952)) can be used to infer the area of the Fermi surface, A^*_{FS}. Almost all of the physical properties of a metal are sensitive to the density of states at the chemical potential and therefore it is to be expected that there will be modulation of these physical properties as successive Landau levels pass through the chemical potential.

Moving from two to three dimensions, it can be shown using the stationary phase approximation that the contributions of different non-extremal areas will cancel such that the signal is dominated by the extremal areas. The extremal areas are usually identified as distinct frequencies (and their harmonics) in the Fourier transform of the measured oscillations. In a three-dimensional metal, a measurement will provide information about extremal (maximal and minimal) Fermi surface cross-sectional areas in planes perpendicular to the magnetic field. For a spherical Fermi surface, such a measurement immediately provides the equatorial area of the Fermi surface and measurements with the magnetic field aligned along different crystallographic directions would always yield the same extremal cross-sectional area. For a cylindrical Fermi surface (Fig. 2), the extremal area will increase like $1/\cos\theta$ as the magnetic field is moved away from the cylindrical axis. For more complicated topologies (e.g. Fig. 3), or when more than one sheet of Fermi surface exists (owing to more than one band crossing the Fermi energy), it is necessary to try and solve the inverse problem of extracting the Fermi surface topology from the set of measured extremal areas as a function of the magnetic field direction (Mueller and Priestley, 1966). In practice, the experimentally extracted extremal areas are compared with predictions of DFT calculations (Rourke and Julian, 2012). For example, in their measurement of the Fermi surface of the nodal-line semi-metal CaAgAs, Kwan et al. (2020) were able to match their quantum oscillations measurements as a function of angle to the geometry of a toroid.

Experimental realization

In practice, many measurable quantities will exhibit quantum oscillations, including the magnetic susceptibility (de Haas-van Alphen effect) (Shoenberg, 1984), resistivity (Shubnikov-de Haas effect), specific heat and magnetostriction (lattice deformation in

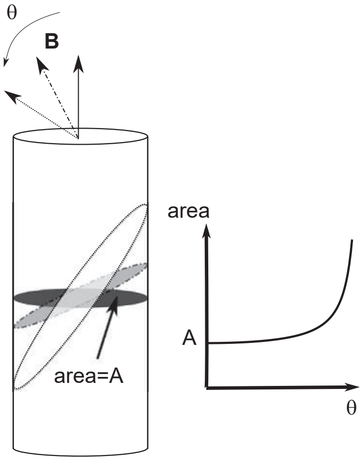

Fig. 2 For a cylindrical Fermi surface with cross-sectional area *A*, the extremal area increases as $\frac{A}{\cos\theta}$ the magnetic field is rotated by θ away from the cylindrical axis.

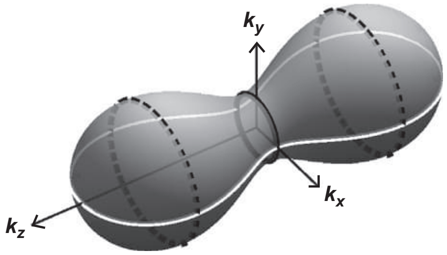

Fig. 3 Extremal orbits on the Fermi surface. The white orbit shows the single extremal orbit when the magnetic field parallel to k_y. When the field is parallel to k_z there will be both a maximum orbit (dashed black line) and a minimum orbit (solid black line).

the presence of magnetization). The observation of quantum oscillations in metals relies on very low temperatures (typically less than 1 K), very large magnetic fields (typically greater than 10 T) and for the electron mean-free-path to be very long (typically greater than 1000 Å, implying a residual resistivity of less than 1 μ Ω cm). The development of several laboratories around the world which are dedicated to providing high magnetic field environments (both DC and pulsed) has meant that the restriction on sample purity can be less stringent.

De Haas-van Alphen oscillations are usually measured using a field modulation technique in which a modulation field of a few mT and a frequency of a few Hz is applied on top of a background field (Bergemann et al., 2003). This is combined with torque cantilever magnetometery in which the sample is attached to one end of a cantilever which acts as one plate of a capacitor (Sheikin et al., 2003). The torque in the magnetic field bends the cantilever with respect to the fixed capacitor plate, changing the capacitance. By using a capacitance bridge, such an arrangement can detect changes to less than one part in a million (Hall et al., 2001). Piezo-resistive cantilevers (Rossel et al., 1996), combined with resistance bridges have also been used (Cooper et al., 2003).

Given that the energy separation of two neighboring Landau levels is $\hbar\omega_c^* = \frac{\hbar eB}{m^*}$, if k_BT becomes comparable with that separation then the amplitude of the oscillations will be strongly suppressed. One term in the Lifshitz-Kosevich formula describes the temperature damping of the oscillations by a factor $\left(\frac{X}{\sinh X}\right)$, where $X = \left(\frac{2\pi^2 k_B T m^*}{\hbar eB}\right)$ (Lifshitz and Kosevich, 1956; Shoenberg, 1984). By tracking the amplitude of the oscillations as a function of temperature, very accurate quasiparticle effective masses can be determined. The effective mass m^* measured in a quantum oscillations experiment will be renormalized by both electron-electron and electron-phonon interactions (Kohn, 1961; Quader et al., 1987). The presence of disorder (for example from impurities) will introduce a finite relaxation time, τ, to the quasiparticles which will broaden the Landau levels. This broadening in energy can be estimated from the Heisenberg Uncertainty Principle as being of the order of $\hbar/\tau$. A full treatment shows that owing to a finite τ, the amplitude of the oscillations will be reduced by a factor proportional to $e^{(-\pi/\omega_c\tau)}$, and when its full form is considered in the Lifshitz-Kosevich formula, it is known as the 'Dingle factor' (Shoenberg, 1984). This factor enables the relaxation time τ to be extracted. There will be a further reduction in the amplitude of the oscillations due to electron spin. In the presence of a magnetic field, the spin-up and spin-down electrons will have separate Landau tubes. This will lead to interference between oscillations coming from electrons of opposite spin which reduces the amplitude of the signal. Further details can be found in Shoenberg (1984).

The observation of 'giant' orbits in de Haas-van Alphen measurements of Mg which were larger than the cross-sectional area of the Brillouin zone (Priestley and Shoenberg, 1963) were explained by Cohen and Falicov (1961) in terms of electrons tunneling from one orbit on one section of the Fermi surface to another separated from it by a small energy gap, ε_g. This was referred to as 'magnetic breakdown'. It was subsequently shown that the criterion for magnetic breakdown to occur is that $\hbar\omega_c \geq \varepsilon_g^2/E_F$, where E_F is the Fermi energy (Blount, 1962). In practice, this means that magnetic breakdown could occur in magnetic fields of the order of 1 T (Shoenberg, 1984).

Shubnikov-de Haas oscillations of the (magneto)resistivity in metals are often weak (Shoenberg, 1984) and challenging to observe and the theory is quite complicated (Adams and Holstein, 1959). The effect is easier to observe in semiconductors and semimetals. As an example, the observation of Shubnkiov-de Haas oscillations in 'magic-angle' twisted bilayer graphene have confirmed the presence of a small Fermi surfaces which emerges from the correlated insulating state (Cao et al., 2018). In sample geometries where there is limited scope for pick-up coils, such as inside pressure cells, measurements of Shubnikov-de Haas oscillations are favored. Putzke et al. (2016) were able to follow the behavior of the effective mass m^* in $YBa_2Cu_4O_8$ under hydrostatic pressure (up to about 0.8 GPa) and correlate this with the superconducting critical temperature.

Angle-resolved photoemission

Angle-resolved photoemission spectroscopy (ARPES) can measure the single-particle spectral function, $A(\mathbf{k}, \omega)$, which contains information not only about the band structure and Fermi surface, but also about the self-energy $\Sigma(\mathbf{k}, \omega)$, since the real part of the self-energy will change the centers of the bands and the imaginary part will broaden them. In the last 30 years, ARPES has developed into a powerful tool for revealing Fermi surfaces and providing significant insight into the impact of electron correlations on electronic structure (Sobota et al., 2021).

In the photoelectric effect, the energy of a photon which is incident on the surface of a material is absorbed by an electron which then escapes from the material's surface. In an ARPES experiment, by measuring properties of the electron outside the material, the kinematics of photoemission can be used to infer the binding energy, E_B, and the crystal momentum $\hbar\mathbf{k}$ of the electron prior to its emission.

An ARPES experiment requires a monochromatic source of photons, typically in the UV regime which then impinge on the surface of a single-crystal sample, as shown in Fig. 4. Some fraction of the photoelectrons, which are emitted in all directions, are then detected by an analyzer. The two-dimensional detector of the popular hemispherical analyzer chromatically disperses the electron beam such that the kinetic energy, E_{kin} can be recorded along one spatial dimension and the angular distribution along the other (Mårtensson et al., 1994). The emission angle (θ, ϕ) is defined such that the polar angle θ is described with respect to the surface normal, and the azimuthal angle ϕ is usually defined relative to a crystallographic direction. Two important relationships can be derived by considering the conservation of energy and momentum

$$E_B = h\nu - \Phi - E_B - E_{\text{kin}}, \tag{8}$$

where Φ is the work function, and

$$\hbar\mathbf{k}_{\parallel} = \sqrt{2mE_{\text{kin}}}\sin\theta, \tag{9}$$

where $\hbar\mathbf{k}_{\parallel}$ is the crystal momentum parallel to the surface in the extended zone scheme and where the photon momentum (negligible in the UV regime) has been neglected in Eq. (9). The parallel component, $\hbar\mathbf{k}_{\parallel}$ is conserved (up to an in-plane reciprocal lattice vector $\mathbf{G}_{\parallel}$, due to the discrete in-plane translational invariance). Although the crystal momentum perpendicular to the surface, $\hbar\mathbf{k}_{\perp}$, is not conserved, it is usually possible to infer it if one assumes that the final-state dispersion of the photoelectron inside the crystal can be parameterized using a free-electron dispersion shifted by a so-called 'inner potential'. It should be noted that in truly 2D materials, $\hbar\mathbf{k}_{\perp}$ is not relevant.

Spin-resolved ARPES measurements are also feasible (Osterwalder, 2006). If a spin detector (e.g., a Mott polarimeter) is coupled to the analyzer, spin- and angle-resolved photoemission spectroscopy is possible. For example, in the 3D topological insulator $Bi_{1-x}Sb_x$, the spin-polarized nature of the surface states has been observed using such a Mott detector (Hsieh et al., 2010).

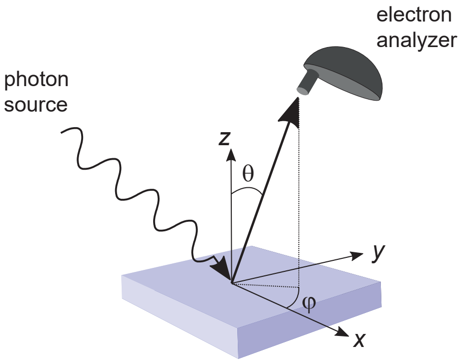

Fig. 4 An ARPES experiment. Photons, typically from a synchrotron source impinge on a sample, ejecting a photoelectron which is emitted at polar and azimuthal angles (θ, ϕ), respectively. The electron is detected by the hemispherical analyzer.

Experimental realization

Synchrotron sources provide photon energies which are continuously tunable from the vacuum ultraviolet (VUV) through to hard X-rays (although not on the same synchrotron beamline). This is an important advantage of a synchrotron photon source, since it permits measurements to be made at different energies and polarizations, both of which influence the matrix elements for the photoemission process (Bansil and Lindroos, 1999). A tunable photon source also allows the k_z dispersion to be investigated. Photoemission is surface sensitive, the escape of the photoelectron being limited by its inelastic mean-free-path. This is strongly dependent on the incident photon energy, but only varies weakly from one material to another, giving rise to the so-called 'universal curve' shown in Fig. 5 (Seah and Dench, 1979). At typical photon energies from UV sources, the inelastic mean-free-path is less than 1 nm. In order to obtain bulk information, a necessary, but not sufficient condition, is that the sample surface is atomically flat and clean. The presence of surface states and/or surface reconstruction would still prevent a bulk measurement. Therefore surface preparation is key and treatments such as sputtering and annealing are often employed if the crystal cannot be cleaved in situ to expose a pristine surface. Measurements at temperatures of ~10 K are commonplace, and ARPES has even successfully been performed below 1 K (Borisenko et al., 2010). Once the surface has been prepared, it needs to be kept at pressures of the order of 10^{-9} Pa. An estimate of the time (in seconds) for a monolayer of a highly reactive gas (e.g., oxygen) to form on a clean transition metal surface under a pressure of p Pa is of the order of $t_m(s) \approx 2 \times 10^{-4}/p$; this is only ~2 days at $p \sim 10^{-9}$ Pa (Hofmann, 2013).

In practice, higher cross-sections and better resolution for a given resolving power mean that the majority of experiments are conducted in the VUV range. The typical beam spot size is between 10 μm and 100 μm, although by focusing the photon beam onto an area of the sample of the order of a 100 nm wide, recent advances in so-called nano-ARPES offer the possibility of probing the electronic structure of nano-scale samples, single domains within a crystal, and permitting spatially resolved measurements by raster scanning across the surface of a sample (Avila and Asensio, 2014).

UV lasers can also be used to produce high photon fluxes with great energy stability and energy/momentum resolutions, with spot sizes smaller than 5 μm having been achieved. Gas discharge lamps combined with a monochromator can also be used as a photon source, with spot sizes typically of about 1 mm, although smaller sizes down to about 200 μm are possible.

The ability of ARPES to rapidly deliver great insight into the Fermi surface topologies of new classes of material in the form of beautiful images and multi-dimensional datasets which contain a wealth of information about the nature of their electronic structure is most certainly one of its great strengths. Such has been its success that it has become almost commonplace to expect that ARPES can deliver many important answers to questions about the underlying physics at play in a material. The recent exposition of the Fermi surface of the Kagome-lattice superconductor KV_3Sb by Luo et al. (2022) showcases how such experiments can reveal not only the Fermi surface in exquisite detail, but also evidence of charge-density-wave reconstruction including the extraction of the size and anisotropy of the induced gaps, signatures of electron-phonon coupling such as kinks in the band dispersions, and self-energy effects in the electronic structure. In another topological Kagome metal, CsV_3Sb_5, ARPES measurements have been able to probe the role of van-Hove singularities in electronic symmetry breaking (Kang et al., 2022). Being able to follow electronic structure through phase transitions governed by some control parameter other than temperature is a highly desirable objective. By subjecting a sample of Pr-doped Ca_2RuO_4 to uniaxial strain, Riccò et al. (2018) were able to suppress the Mott-insulating phase and induce metallicity as evidenced by the appearance of a Fermi surface.

Time- and angle-resolved photoemission spectroscopy (trARPES) can provide new insights into the dynamics and out-of--equilibrium behaviors of electrons in solids. This pump-probe approach typically uses a femtosecond infra-red laser pulse to first excite the sample which is subsequently probed by the UV pulse at some time delay with respect to the excitation. An example of this approach is a study of the dynamics associated with the melting and recovery of a charge-density wave (CDW) (Zong et al., 2019). The investigation revealed the re-appearance (upon melting) of the nested parts of the Fermi surface of $LaTe_3$ and their subsequent disappearance as both the CDW coherence and the gap are re-established. In a spin, time and angle-resolved study, the pump-probe measurements of Jozwiak et al. (2016) were able to reveal spin texture in the unoccupied bands above the Fermi energy in Bi_2Se_3.

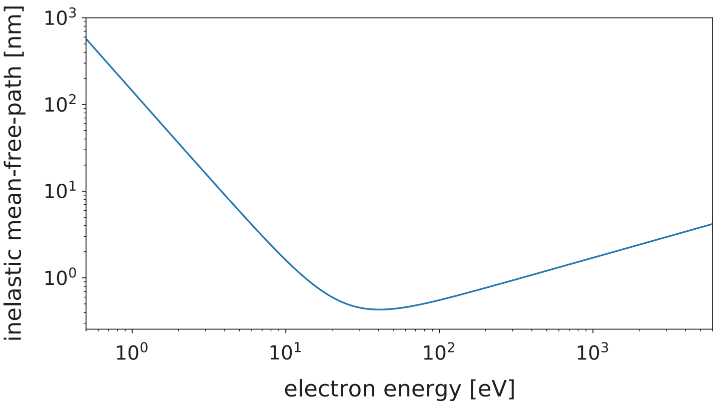

Fig. 5 The depth from which a photoelectron can escape is limited by its inelastic mean-free-path. This 'universal curve' as a function of electron's kinetic energy is based on data from Seah and Dench (1979).

ARPES measurements are usually made by rotating the sample with respect to a fixed analyzer. In order to scan the sample surface in real space to locate regions which are of interest (for example, a particular domain) before performing ARPES, either the sample has to be moved with respect to the photons which are confined to a small spot size, or by using an instrument which permits the both real space and *k*-space to be imaged using strong electric fields to extract the electrons (Cattelan and Fox, 2018). However, there is another category of instrument which is generally referred to as an energy-filtered photoemission electron microscope (EF-PEEM), or more succinctly as a 'momentum microscope'. Here, the photoelectrons are accelerated into a column containing electron optical elements, as well as apertures in the image plane which can be used to select μm-sized regions of a sample. The optical elements can be adjusted to image either in real-space or reciprocal space. This means that interesting regions of the sample in real space can be selected before switching to reciprocal space where ARPES is carried out by acquiring images of the available portion of *k*-space at a series of different kinetic energies. The Fermi surface can be mapped by acquiring images of the spectral weight at the Fermi energy (Cattelan and Fox, 2018). One clear advantage of EF-PEEM instruments over conventional ARPES for FS measurements is that all of the available $\mathbf{k}_{\parallel} = (k_x, \ k_y)$ momentum space is measured simultaneously (this sometimes being referred to as 'full wavevector ARPES') i.e., a 2D image of the FS is acquired at once.

Many more details about instrumentation and the current capabilities of ARPES, can be found in the review by Iwasawa (2020).

Angle-dependent magnetoresistance oscillations

In materials whose electronic structure is quasi one- or two-dimensional, the magnetoresistivity (which describes the change in the resistivity in an external magnetic field) for currents along the high-resistivity axis, is particularly sensitive to the direction of the applied magnetic field. In the previous section, Shubnikov-de Haas quantum oscillations in the resistivity and the connection between the period of those oscillations (in inverse magnetic field) and the extremal area of the Fermi surface has been described. The non-extremal orbits, while not contributing to the oscillations, do generate a non-oscillatory background magnetoresistance which can be quite sensitive to the direction of the magnetic field (Blundell and Singleton, 1996a, 1996b). In some cases, very large angle-dependent magnetoresistance oscillations (AMROs) can be found at fixed magnetic field.

AMROs can be measured experimentally by rotating the sample in a fixed magnetic field. They can provide complementary information to quantum oscillations since the signal comes from all electrons on the Fermi surface, not just those associated with the extremal orbits. Since AMROs don't come from Landau levels passing through the chemical potential, they should be observable at much higher temperatures and much lower magnetic fields than quantum oscillations. Scattering from impurities will, however, suppress the oscillations. AMROs should be visible if $\omega_c\tau \gg 1$, where τ is the relaxation time (inverse scattering rate). In practice, however, the usefulness of this powerful technique is limited to lower dimensional electronic structures (1D and 2D) and to metals with only one or two sheets of Fermi surface since analysis becomes difficult when there are contributions from more than one.

Types of oscillation

In general, the different kinds of oscillations that can be found in quasi-1D and quasi-2D materials have been given different names (for example, the 'Danner-Kang-Chaikin' oscillations seen in quasi-1D metals (Danner et al., 1994)). A description of the types of oscillations associated with some of these can names can be found in Goddard et al. (2004) and an excellent description of AMROs in quasi-one-dimensional metals can be found in Blundell and Singleton (1996a, 1996b).

As an example, considered a quasi-2D Fermi surface such as a warped cylinder, as shown in Fig. 6. On the simplest level, for such a Fermi surface there will be a maximum in the magnetoresistance whenever the magnetic field is oriented such that the Fermi surface cross-sectional areas in the plane perpendicular to the field are all the same. The phenomenon can be understood from a semi-classical perspective within the relaxation time approximation in which oscillations as a function of the angle of the magnetic

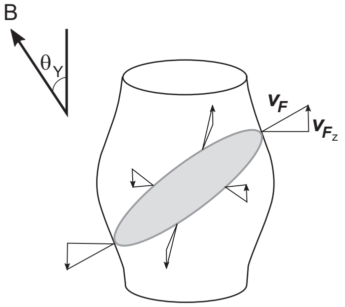

Fig. 6 When the magnetic field B is rotated away from the cylindrical *c*-axis by a Yamaji angle (θ_Y), the *c*-axis conductivity disappears because the *c*-axis component of the Fermi velocity v_{F_z} averages to zero over the cyclotron orbit. Adapted from Bergemann C, Mackenzie AP, Julian SR, Forsythe D, Ohmichi E (2003) Quasi-two-dimensional fermi liquid properties of the unconventional superconductor Sr_2RuO_4. *Advances in Physics* **52**: 639–725. https://doi.org/10.1080/00018730310001621737.

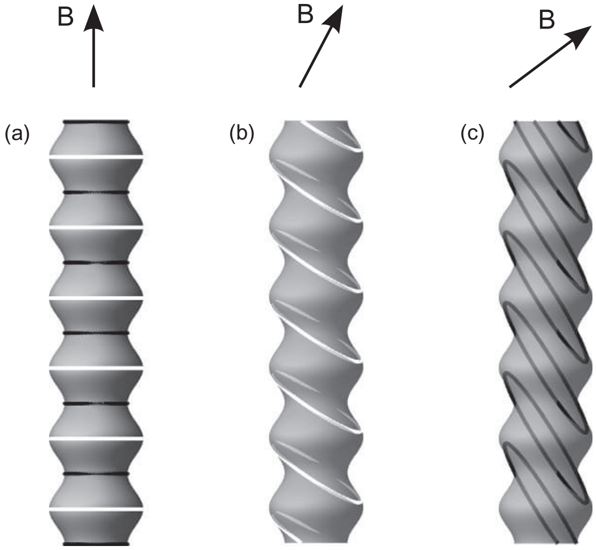

Fig. 7 When the magnetic field *B* is parallel to the cylindrical *c*-axis, all the cyclotron orbits are different, as indicated by the extremal black and white orbits shown in (a). When the field is rotated to a Yamaji angle, as shown in (b) and (c), all the Fermi surface cross-sections perpendicular to the magnetic field have the same area.

field originate from the way the components of the quasiparticle velocity is averaged over the cyclotron orbits which occur at a particular orientation of the magnetic field, θ_Y, known as a 'Yamaji angle', as indicated in Fig. 6.

Consider the warped cylindrical Fermi surface shown repeated over several Brillouin zones in Fig. 7. The applied magnetic field *B* will make the electrons execute cyclotron orbits on the Fermi surface in planes perpendicular to the field. When the magnetic field is rotated away from the high-resistivity axis then at certain angles θ_Y, determined by the shape of the Fermi surface, the areas of *all* orbits will be equal. In such cases, the component of the velocity parallel to the high-resistivity axis will average to zero, and there will be a maximum in the resistivity. These Yamaji 'magic' angles are periodic in tan θ.

Experimental realization

The *c*-axis resistivity is measured as a function of the direction of the magnetic field. The analysis of AMROs involve the fitting of the experimental data to a parameterization of the underlying Fermi surface. A description of how this can be done efficiently can be found in Bergemann et al. (2003). The measurement of a coherent 3D Fermi surface in a cuprate superconductor by Hussey et al. (2003) is an excellent example of how AMROs can provide important insight. The Fermi surface of $Tl_2Ba_2CuO_{6+\delta}$ was revealed by fitting the oscillations, measured using a single-axis rotator in a magnetic fields of 45 T (provided by a hybrid magnet) and a temperature of 4.2 K, to a parameterized Fermi surface. These AMRO results for the Fermi surface topology were subsequently confirmed by ARPES (Platé et al., 2005), and quantum oscillations (both Shubnikov-de Haas and de Haas-van Alphen) (Vignolle et al., 2008).

The electron momentum distribution—Compton scattering and positron annihilation

Within the one-electron approximation, the electron momentum distribution (EMD) can be expressed in terms of the one-electron wavefunction $\psi(\mathbf{r})$ as

$$\rho(\mathbf{p}) = \left(\frac{1}{2\pi\hbar}\right)^3 \sum_{\text{occ}} \left| \int \psi(\mathbf{r}) \exp\left(-i\mathbf{p}\cdot\mathbf{r}/\hbar\right) \right|^2 d\mathbf{r}. \tag{10}$$

The EMD contains information about the occupied states in momentum space and therefore in a metal will possess signatures associated with the presence of the Fermi surface due to the sum being over the occupied momentum states. Experimentally, the EMD can be accessed using Compton scattering and positron annihilation. The main advantage of these experimental techniques is that they are bulk probes which can be used at elevated temperatures and which are not limited by the electron mean-free-path (meaning, for example, that the Fermi surfaces of disordered alloys can be measured (Dugdale et al., 2006)). Compton scattering is a unique probe of the many-body ground state wavefunction.

One significant strength of both techniques is that measurements can be made at elevated temperature, including above room temperature which is required to probe the Fermi surface of paramagnetic Cr (Fretwell et al., 1995). Positrons are susceptible to being trapped by open-volume defects such as vacancies (resulting in a partial or complete suppression of any anisotropy in the measured distributions (Dugdale and Laverock, 2014)). Compton scattering has no such restriction. Although both techniques measure a projection of the momentum distribution (rather than the distribution itself, as described below), it is straightforward (if time consuming because of the number of projections which must be measured) to tomographically recover the full three-dimensional momentum distribution by combining measurements made along different crystallographic directions (Kontrym-Sznajd and Samsel-Czekała, 2000; Kontrym-Sznajd, 1990).

Both positron annihilation and Compton scattering experiments measure the real momentum $\mathbf{p}$ (as opposed to the crystal momentum $\mathbf{k}$) of the electrons in the material. In the presence of a Fermi surface (such as that of Li whose Fermi surface, calculated from DFT in the non-interacting zero-temperature limit, is shown in Fig. 8), the discontinuities in the momentum distribution arise when the contribution of a band appears or disappears as the band passes through the Fermi energy (at $\mathbf{k} = \mathbf{k}_F$) (see Fig. 9). These will appear not only at $\mathbf{p} = \mathbf{k}_F$, but also at all $\mathbf{p} = \mathbf{k}_F + \mathbf{G}$, where $\mathbf{G}$ is a reciprocal lattice vector. This is illustrated in Fig. 10 in which the EMD, $\rho(\mathbf{p})$, is plotted along the [100] direction. At $\mathbf{p} = \mathbf{k}_F$, the contribution of the 2 *s* band drops to zero, before reappearing in what would be the second Brillouin zone in the extended zone scheme. The two insets in Fig. 10 show these so-called 'higher momentum components'.

However, it is straightforward to restore the discrete translational invariance of $\mathbf{k}$-space by bringing the measured densities back into the first Brillouin zone (using the reciprocal lattice vectors) by taking the contributions in higher Brillouin zones and adding them to that in the first Brillouin zone (in a process known as 'LCW folding' (Lock et al., 1973)). The discontinuities associated with the partially occupied bands will reinforce constructively, and the contributions from fully occupied bands will combine to give a constant background. In this LCW procedure, the momentum density in $\mathbf{p}$-space becomes an occupation number in $\mathbf{k}$-space. Returning to our Li example, the resulting occupation number can be seen in Fig. 11. The Fermi surface will then be visible as a

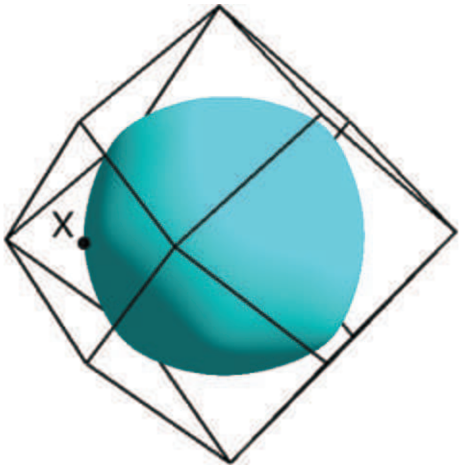

Fig. 8 The Fermi surface of Li is almost spherical. The X symmetry point on the Brillouin zone is indicated. The program FermiSurfer was used to plot the Fermi surface (Kawamura, 2019).

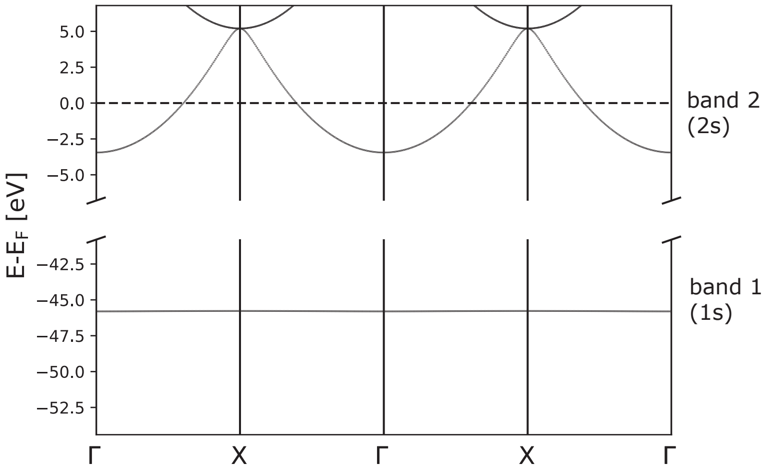

Fig. 9 The band structure of Li, plotted along the [100] direction in the repeated zone scheme. The tightly-bound lower band is due to the core-like 1 *s* electrons and as such is almost flat (dispersionless). The upper band is due to the (much larger) overlap of 2*s* electron wavefunctions, resulting in a much more dispersive band. Note that the energy scale has been split since the 1*s* is a long way below the Fermi energy.

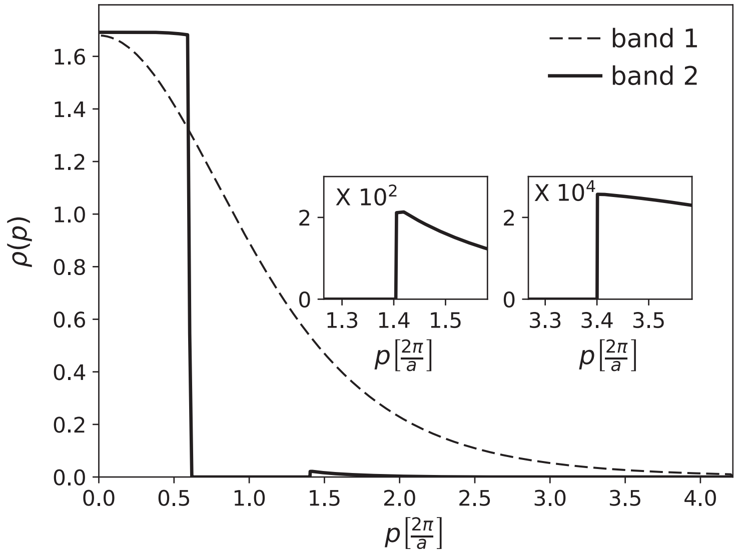

Fig. 10 The electron momentum distribution of Li resolved along the [100] direction. Note that 1 atomic unit (a.u.) of momentum is equal to $1.99285191410 \times 10^{-24}$ kg m s^{-1}. The two insets (with their ordinate axes scaled by 10^2 and 10^4, respectively) show how the momentum density for band 2, which decreases to zero at $p = k_F$, reappears to make contributions in the second and third Brillouin zones.

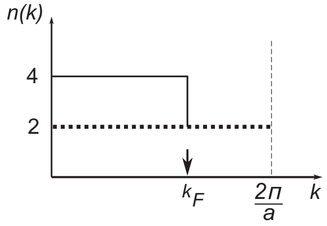

Fig. 11 Occupation number for Li along the [100] direction obtained by LCW folding (Lock et al., 1973) the EMD back into the first Brillouin zone. At the origin (the Γ point), both bands are occupied giving four electrons. The completely occupied 1*s* band sums to a constant, but the partially occupied 2*s* exhibits a discontinuity at the Fermi wavevector k_F as the occupation number for that band drops to zero. Note that the Brillouin zone boundary at the symmetry point X is at $\left(\frac{2\pi}{a}\right)$ in the body-centered cubic lattice of Li.

change in the occupation number. An example of fitting several Fermi surface breaks to an occupation number reconstruction from several high-resolution Compton profiles measured on the high-entropy alloy NiFeCoCr can be found in Robarts et al. (2020). Since the Fermi surface is highly smeared due to the extreme compositional disorder (the atoms are randomly distributed on an underlying face-centered cubic lattice), the smeared Fermi breaks can be clearly resolved, and the local contributions to the electron mean-free-path determined across the Fermi surface from the degree of smearing.

Compton scattering

Following Schülke (2007), the basic kinematics of an inelastic scattering experiment are shown in Fig. 12. A photon of energy $\hbar\omega_1$, wavevector $\mathbf{K}_1$, and (unit) polarization vector $\mathbf{e}_1$ scatters at an angle θ off a target which is characterized by a state vector $|i\rangle$ and energy E_i, resulting in a photon of energy $\hbar\omega_2$, wavevector $\mathbf{K}_2$ and polarization vector $\mathbf{e}_2$. The target is left in a final state $|f\rangle$ with an energy E_f. Conservation of energy and momentum imply that an energy $\hbar\omega$, given by $\hbar\omega \equiv \hbar(\omega_1 - \omega_2) = E_f - E_i$, and a momentum $\hbar\mathbf{q} \equiv \mathbf{K}_1 - \mathbf{K}_2$ are transferred to the target. As long as $\omega \ll \omega_1$, $q \approx 2\, K_1 \sin(\theta/2)$ (Schülke, 2007).

In a Compton scattering experiment, monoenergetic incident photons are scattered by the electrons in the sample and the energy distribution of the scattered photons is measured to a resolution $d\hbar\omega_2$ within some solid angle $d\Omega_2$. This is the double differential scattering cross-section, which can be expressed in the non-relativistic limit as (Schülke, 2007):

$$\frac{d^2\sigma}{d\Omega_2 d\hbar\omega_2} = r_0^2 \left|\mathbf{e}_1 \cdot \mathbf{e}_2^*\right|^2 \left(\frac{\omega_2}{\omega_1}\right) \sum_{i,f} p_i \left| \left\langle f \middle| \sum_j e^{i\mathbf{q}\cdot\mathbf{r}_j} \middle| i \right\rangle \right|^2 \delta\left(E_f - E_i - \hbar\omega\right), \tag{11}$$

where p_i is the probability of the initial state $|i\rangle$ and r_0 is the classical electron radius. The sum over j is over all the electrons in the system.

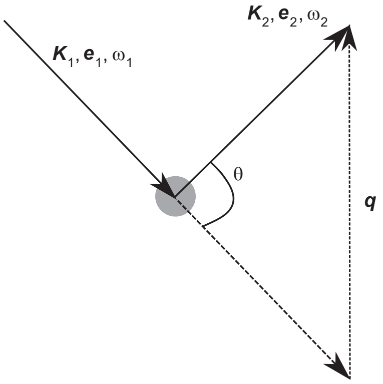

Fig. 12 Compton scattering of a photon with wavevector $\mathbf{K}_1$, unit polarization vector $\mathbf{e}_1$ and frequency ω_1 by an angle θ by a moving electron in an initial state $|i\rangle$, leaving it in a final state $|f\rangle$.

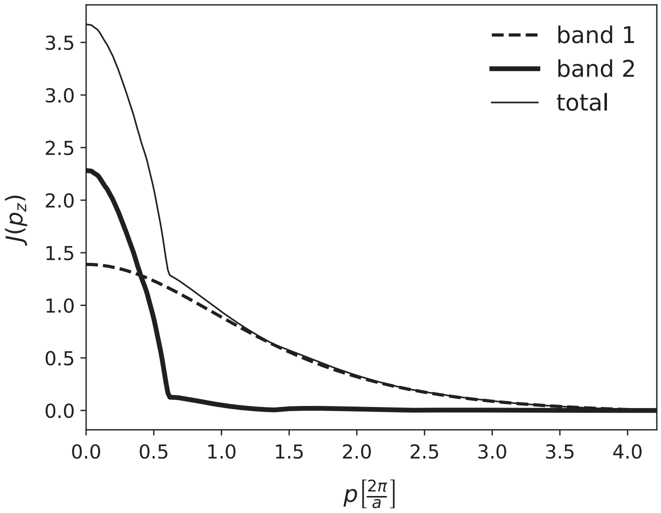

Fig. 13 The Compton profile $J(p_z)$ of Li, resolved along the [100] direction.

In order to probe single-particle properties (rather than their collective behavior), q^{-1} must be much smaller than the distance between the electrons. For the properties to be representative of the ground state, the scattering process should be fast such that the energy transfer $\hbar(\omega_1 - \omega_2)$ is sufficiently high to prevent the remaining system of electrons from rearranging itself. This is usually described within the so-called 'impulse approximation' which is valid when the energy transferred in the scattering process is much larger than the binding energies of any electrons involved; the other electrons are mere spectators since the scattering occurs on a very short timescale on the order of 10^{-19} s.

If the photons were scattering off stationary electrons then the scattered photons would all have the same energy given by the usual Compton formula Compton (1923). However, the electrons have finite momentum and therefore the photon energies will be Doppler-broadened and the distribution of energies recorded at that fixed angle can be related to the momentum distribution of the electrons along the scattering vector integrated over the two orthogonal momentum components. It can be shown that

$$\frac{d^2\sigma}{d\Omega_2 d\hbar\omega_2} \propto \int\int \rho(\mathbf{p})dp_x dp_y, \tag{12}$$

where $\rho(\mathbf{p})$ is the momentum density. The quantity

$$J(p_z) \equiv \int\int \rho(\mathbf{p})dp_x dp_y \tag{13}$$

is called the Compton profile; it is the projection of the momentum density along the scattering vector. A detailed description of the theoretical background can be found in Refs. (Cooper et al., 2004; Eisenberger and Platzman, 1970; Eisenberger and Reed, 1974; Ribberfors, 1975a, 1975b).

Revisiting the Li example, its Compton profile along the [100] direction is shown in Fig. 13. In this case, the fully occupied first band gives rise to a broad, smooth, Gaussian-like distribution, whereas the almost spherical Fermi surface contributes an inverted

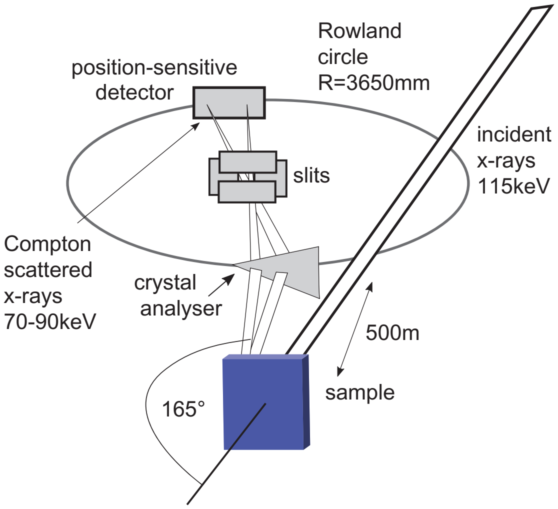

Fig. 14 Schematic of a Cauchois-type high-resolution Compton spectrometer, based on Itou et al. (2001).

parabola when it is integrated over two momentum components. However, the Fermi break k_F can still be identified (in Fig. 13 at about $p \sim 0.6\ (2\pi/a)$) and the higher momentum components are just visible as bumps at momenta outside the first Brillouin zone. If the LCW procedure were applied to the Compton profile, a projected occupation number would be obtained.

The two 'lost' momentum components can be reconstructed tomographically, typically by measuring 10—30 Compton profiles along different crystallographic directions. With reconstruction techniques based on polynomial expansions, the number of profiles required for a faithful reconstruction can be reduced by carefully choosing the directions.

Experiments are usually performed at synchrotron sources. As an example of an experimental geometry, the Cauchois-type high-resolution Compton spectrometer at SPring-8 (shown in Fig. 14) offers a typical momentum resolution of 0.1 a.u. (Itou et al., 2001) and a photon energy of 115 keV. At these kinds of photon energies, it is clear that it is the bulk being probed. The Compton-scattered photons are dispersed by a bent crystal analyzer and registered on a position-sensitive detector. In some spectrometers, a trade-off can be made between count rate and resolution, and ultra-high resolution measurements (with a momentum resolution of about 0.02 a.u.) measurements have been performed (Schülke et al., 2001).

An excellent example of the kind of information that Compton scattering can provide can be found in Tanaka et al. (2001). Since bcc Li has a martensitic transformation at 75 K (Smith, 1987), quantum oscillatory probing of the Fermi surface is challenging (Hunt et al., 1989). By reconstructing the full 3D EMD from high-resolution Compton profiles, the small anisotropy (~4%) in its Fermi surface has been revealed (Schülke et al., 1996; Tanaka et al., 2001). Moreover, both studies were able to show electron correlation substantially reducing the size of the break Z_k in the momentum density (sometimes called the 'quasiparticle residue') at the Fermi surface. Compton scattering has also been able to map out the evolution of the Fermi surface of $La_{2-x}Sr_xCuO_4$ as a function of doping (Sakurai et al., 2011) and expose the possible role of nematicity in the CuO_2 planes in deforming the Fermi surface in the underdoped regime (Yamase et al., 2021).

Positron annihilation

The electron momentum distribution can also be probed using positrons. In this case, it is the electron momentum distribution *as seen by* the positron which is measured, and it is often called the electron-positron momentum distribution or the 'two-photon momentum distribution' (TPMD, where the 'two-photon' refers to the pair of annihilation γ-photons which are experimentally measured).

Within the independent particle model (in which the electron and positron are treated as non-interacting independent particles), the TPMD can be expressed as

$$\rho^{2\gamma}(\mathbf{p}) = \sum_{\text{occ}} \left(\frac{1}{2\pi\hbar}\right)^3 \left| \int \psi(\mathbf{r})\psi_+^*(\mathbf{r}) \exp\left(-i\mathbf{p}\cdot\mathbf{r}/\hbar\right) \right|^2 d\mathbf{r}, \tag{14}$$

where $\psi_+{}^*(\mathbf{r})$ represents the (complex conjugate of the) positron wavefunction.

The technique is commonly known as 2D angular correlation of annihilation radiation (2D-ACAR). Positrons, usually obtained from a ^{22}Na source, are implanted into the sample being studied. The positrons have a typical β energy spectrum with a maximum energy of about 0.5 MeV, and thus penetrate into the bulk of the sample. Typical source activity and annihilation rates mean that there will only ever be one positron in the sample at any time. After thermalization, which happens on a timescale of several picoseconds in a metal (Kubica and Stewart, 1975), the positron will propagate in its own Bloch state (at the bottom of its own positronic band) for ~100 ps before annihilation with an electron which proceeds predominantly through the creation of two

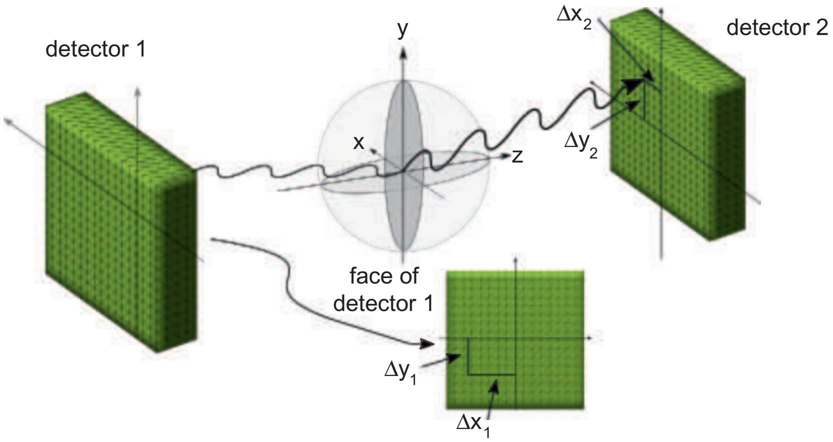

Fig. 15 Geometry of a 2D-ACAR experiment. A pair of γ photons resulting from electron-positron annihilation are detected in coincidence on a pair of position-sensitive detectors. The angular deviation from being back-to-back can then be calculated from the positions ΔX and ΔY on the two detectors.

γ-photons which, owing to conservation of energy and momentum will be emitted back-to-back in the center-of-momentum frame. However, in the laboratory frame, in which the electron and positron have a finite momentum, there will be a small angle (~mrad) between the γs.

Since the positron has only a thermal momentum, the combined momentum of the pair is completely dominated by that of the electron. Two components of the momentum can be directly inferred by measuring the angular deviation of the two γ from being back-to-back by recording where they hit position-sensitive detectors (Dugdale et al., 2013) typically located about 10 m away on either side of the sample, as shown in Fig. 15.

If the momentum of the pair has components (p_x, p_y, p_z), then

$$p_x \approx mc\theta_x, \tag{15}$$

and

$$p_y \approx mc\theta_y, \tag{16}$$

where m is the electron rest mass, c is the speed of light and θ_x and θ_y can be calculated from the detected γ positions if the distance of each detector from the sample is L.

$$\theta_x = \frac{\Delta x_1 + \Delta x_2}{L}, \tag{17}$$

and

$$\theta_y = \frac{\Delta y_1 + \Delta y_2}{L}. \tag{18}$$

The remaining momentum component, which would be encoded in a Doppler shift in the energy of the photons, cannot be measured with the same precision. This means that this third component is integrated over, and the resulting spectrum is a projection of the underlying momentum distribution. Tomographic reconstruction is necessary to regain the third momentum component, and this is achieved by measuring down a small number (typically fewer than six) crystallographic directions. However, in many cases, an excellent understanding of the Fermi surface topology can be gained from a single high-symmetry projection. The momentum resolution is normally dominated (at least at low temperatures) by the precision with which the coordinates of γ-photons can be recorded on the two position-sensitive detectors as well as uncertainty in the origin of annihilation due to the source spot on the sample. The latest generation of detectors offer sub-mm position resolutions Dugdale et al. (2013), which at typical distances from the sample means momentum resolutions of a few percent of the Brillouin zone of Cu.

Not all electrons are *seen* by the positron equally, since the positron's positive charge means that it is strongly repelled by the nucleus. This results in a smaller overlap between the positron's wavefunction and those of the most tightly bound electrons. Their contribution is therefore strongly suppressed, but that from electrons at the Fermi surface is enhanced since annihilation is more likely to occur with one from among the screening cloud of electrons at the Fermi surface. While many-body electron-positron correlations can modulate the shape of the momentum density, the position of the discontinuity is not affected (Majumdar, 1965) meaning that the Fermi surface can be clearly identified. Although the TPMD is sensitive to electron-positron correlations (for example, see Laverock et al. (2010)), it is still possible to study the effect of electron correlation on the occupation numbers in **k**-space (Harris-Lee et al., 2021). Positron annihilation experiments have been used to investigate the impact of electron correlation on the Fermi surface of vanadium (Weber et al., 2017). This was achieved by comparing the densities calculated using a combination of DFT and dynamical mean-field theory with experimental measurements.

Spin-resolved measurements

Both Compton scattering and positron annihilation can be operated in a spin-resolved mode. In the case of Compton scattering, magnetic measurements exploit the spin-dependent term in the scattering cross-section for circularly polarized photons (Duffy, 2013). Magnetic Compton scattering experiments are typically performed using a solid-state detector which has a relatively poor energy resolution corresponding to a momentum resolution which is comparable to the size of the Brillouin zone, making any sensible study of the Fermi surface impossible. However, high-resolution magnetic Compton profiles with a resolution acceptable for Fermi surface studies have been measured (Sakurai et al., 1994). Spin-resolved positron annihilation relies on the parity violation in beta decay which manifests as a preferential positron spin parallel to its velocity vector. It is possible to extract a spin-resolved Fermi surface (Hanssen et al., 1990; Weber et al., 2015) by making measurements with a magnetic field in different directions, since two-photon annihilation relies on the electron and positron having opposite spins.

Strengths and weaknesses of the various techniques

There is a great deal of complementarity between the techniques which have been discussed. All have their advantages and disadvantages, their strengths and weaknesses.

Sensitivity to correlations

Through their ability to measure the effective mass, quantum oscillations can probe electron correlation on the low energy (<0.1 meV) scale. ARPES can provide complementary information about correlation through the self-energy, for example, directly imaging the renormalization of the bandwidth and revealing the presence of Hubbard bands. Since these are on a larger energy scale (~ 1 eV), these two techniques provide complementary information. AMROs, however, are insensitive to many-body correlations. Both positron annihilation and Compton scattering are sensitive probes of electron correlation.

Sample purity

To observe quantum oscillations and AMROs, high-quality crystals with low residual resistivities are required to give a high relaxation time, τ, such that $\omega_c \tau \gg 1$. For bulk-representative measurements, ARPES requires clean, ordered surfaces. While positron annihilation does not require purity, it is the concentration of open-volume defects (such as vacancies) which is important as positrons will be trapped resulting in isotropic momentum distributions. Vacancy concentrations as low as one part-per-million can be enough to trap every positron. Compton scattering is insensitive to both the purity of the sample or vacancies.

Temperature

To observe quantum oscillations, the condition $k_B T < \hbar\omega_c$ must be satisfied which implies both large magnetic fields and low temperatures (often in the mK regime requiring ^{3}He cryostats or dilution refrigerators). For AMROs, oscillations are observable until the scattering due to temperature reduces the relaxation time such that $\omega_c \tau \gg 1$ is no longer satisfied, also restricting the technique to low temperatures. ARPES can be carried out at elevated temperatures, but resolution will be degraded. Both Compton scattering and positron annihilation can be carried out at elevated temperatures, but for positron annihilation increased temperature degrades the resolution since the thermal energy of the positron contributes to the overall momentum resolution.

Dimensionality

Quantum oscillations, positron annihilation and Compton scattering are all capable of delivering full three-dimensional Fermi surface geometries, but the latter two do require tomographic resolution. Although ARPES is well-suited to 2D materials, it can also provide three-dimensional Fermi surface information. AMROs are only observable in quasi-1D and quasi-2D materials.

k-space resolution

In the following discussion, the resolution is compared to the size of the Brillouin zone of Cu (for lattice constant a, Brillouin zone size of a real-space face-centered cubic lattice is $4\pi/a = 3.47\ \text{Å}^{-1}$). The k-space resolution of quantum oscillations is excellent, reaching up to 10 ppm of the Brillouin zone in the most favorable situations, although a typical experiment with a carefully calibrated magnetic field might deliver a precision of 0.1% of the Brillouin zone (Bergemann, 2005). ARPES experiments operate typically at the level of 1% of that Brillouin zone. A similar resolution can be achieved in AMRO experiments (where the resolution crucially depends on the number of oscillations which can be observed), with $\sim$1% being possible for Yamaji oscillations in a good crystal (Bergemann, 2005). Positron annihilation experiments can routinely achieve a resolution of about 4% of the Brillouin zone, and Compton scattering is typically about 5%.

Bulk sensitivity

Quantum oscillations, AMROs, positron annihilation and Compton scattering all probe the bulk electronic structure. ARPES is sensitive to the surface, but different degrees of bulk sensitivity can be achieved by varying the photon energy.

Other techniques

There are several other techniques, some of which have played an important role in the history of Fermi surface determination. Some of these are discussed below.

Anomalous skin effect

A high-frequency (radio frequency) field will induce currents to flow in the surface of a metal, preventing the field penetrating into the bulk. However, the depth of the penetration, known as the 'skin depth', depends on the (frequency dependent) electrical conductivity of the metal. At very high frequencies, for a pure specimen at low temperature (such that the conductivity is very high), the skin depth can be less than the electron mean-free-path. In such a case, only electrons which are travelling parallel to the surface (and thus stay within the skin layer) can interact significantly with the field. The consequence of this is a so-called 'anomalous skin depth' which depends on the ratio of the conductivity to the mean-free-path (Ziman, 1962). For a free-electron metal, this ratio is a constant which depends on the velocity of the electrons on the Fermi surface, and not on any scattering mechanism. Since only electrons parallel to the surface contribute, if the Fermi surface is not a sphere then samples with cut surfaces in different orientations should behave differently. A detailed analysis shows that measurements of the surface impedance can provide information about the radius of curvature of the Fermi surface in a plane normal to the sample surface and parallel to the direction in which the impedance is being measured. Through measurements of the anomalous skin effect Pippard was able to demonstrate that the Fermi surface of Cu was very distorted, and that it most likely touched the boundary of the Brillouin zone (Pippard, 1957).

Cyclotron resonance

In the Azbel'-Kaner geometry (Azbel' and Kaner, 1958), the magnetic field is aligned exactly parallel to the surface of the metal such that the electrons will execute helical paths in planes perpendicular to the field. If the sample is exposed to a microwave electromagnetic field, although most of the electron's helical path will be below the skin depth (and thus preserved from the microwave field), during the part of the path which is within the skin depth, the electron will be able to interact with, and rapidly absorb energy from the field. Resonances will therefore occur when the microwave frequency coincides with the cyclotron frequency (or its harmonics). In an experiment, the microwave frequency is fixed while the magnetic field is increased, leading to a series of peaks in the measured signal (the derivative of the surface resistance with respect to magnetic field) equally spaced in inverse magnetic field. As in the quantum oscillatory experiments, the signal will be dominated by extremal orbits on the Fermi surface. It should be emphasized that this does not deliver the geometry of the Fermi surface, but rather the *dynamical* cyclotron mass which, to first order, is only renormalized by electron-phonon interactions. This means that when combined with a quantum oscillations measurement, electron-phonon effects can be separated from those of electron-electron correlation (Singleton et al., 1992). However, as well as being able to compare these masses with theoretical predictions, the measured cyclotron frequencies deliver the derivatives of the band structure in **k**-space (Ziman, 1962).

Kohn anomalies, RKKY and Friedel oscillations

The wavevector-dependent screening properties of the electrons in a metal are governed by the shape of the Fermi surface (Dugdale, 2016). Kohn suggested that singularities arising from the geometry of the Fermi surface could manifest themselves in phonon spectra (Kohn, 1959), pointing out that the shape of the Fermi surface could be inferred from the locations of singularities in the vibrational spectra. These 'images of the Fermi surface' (as they were described) in the phonon spectra of Pb were measured soon afterwards (Woll and Kohn, 1962; Brockhouse et al., 1962). The electron-phonon coupling is particularly strong in Pb; in practice these anomalies are quite weak for most metals. However, the idea of mapping out the Fermi surface from these Kohn anomalies was subsequently explored in Al (Weymouth and Stedman, 1970). The conclusion, however, was that in general any sensible interpretation on a hitherto unknown Fermi surface would rely heavily on additional information and would at best be a complementary Fermi surface probe. More recently, the thermal diffuse scattering of x-rays has been used to image the Fermi surface of Zn (Bosak et al., 2009). By combining their measurements with both an inelastic X-ray scattering study and ab initio DFT calculations, they were able to show that diffuse scattering is connected to the phonons, and that an image of the Fermi surface can be obtained owing to the electron-phonon coupling.

A similar case could be made about exploiting the Ruderman-Kittel-Kasuya-Yosida (RKKY) interaction to understand the Fermi surface (Roth et al., 1966). And just as the RKKY interaction concerns the screening of spins, Friedel oscillations arise from the screening of charge impurities (Friedel, 1958). The Fermi surface of a Cu (111) surface (that is, the *surface* Fermi surface, as opposed to the bulk) is a circle of radius $k_F = 0.215$ Å^{-1} (Winkelmann et al., 2012). Oscillations with a spatial period of π/k_F or $\approx$15 Å, have been observed around point defects on a Cu (111) surface in scanning-tunneling microscope (STM) images (Crommie et al., 1993). Fourier transforms of such 'quantum interference' can provide images of the Fermi surface. An insightful comparison of the Fermi surfaces of Sr_2RhO_4 obtained from ARPES, STM and quantum oscillations can be found in Battisti et al. (2020).

Conclusion

For as long as the technological exploitation of new metallic materials depends on understanding their electronic structure, determining the topologies of their Fermi surface will continue to be vital. Progress continues to be made through the ingenuity of new tools and improvements in the precision and efficiency of more established ones. Fermi surface measurements continue to demand approaches which challenge our expertise in harnessing large magnetic fields, ultra-low temperatures and high pressures, which take advantage of large-scale national and international scientific facilities, which push our theoretical and computational abilities to new limits. And the excitement of contributing to the solution of some of the biggest problems in physicists awaits a new generation of Fermiologists.

Acknowledgments

I am indebted to Jude Laverock for many years of sage advice. And to my Dad, for sparking and nurturing my passion for physics.

References

Adams E and Holstein T (1959) Quantum theory of transverse galvano-magnetic phenomena. *Journal of Physics and Chemistry of Solids* 10: 254–276. https://doi.org/10.1016/0022-3697(59)90002-2.

Avila J and Asensio MC (2014) First nanoarpes user facility available at soleil: An innovative and powerful tool for studying advanced materials. *Synchrotron Radiation News* 27: 24–30. https://doi.org/10.1080/08940886.2014.889549.

Azbel' M and Kaner E (1958) Cyclotron resonance in metals. *Journal of Physics and Chemistry of Solids* 6: 113–135. https://doi.org/10.1016/0022-3697(58)90086-6.

Bansil A and Lindroos M (1999) Importance of matrix elements in the arpes spectra of bisco. *Physical Review Letters* 83: 5154–5157. https://doi.org/10.1103/PhysRevLett.83.5154.

Battisti I, Tromp WO, Riccò S, Perry RS, Mackenzie AP, Tamai A, Baumberger F, and Allan MP (2020) Direct comparison of arpes, stm, and quantum oscillation data for band structure determination in Sr_2RhO_4. *NPJ Quantum Materials* 5: 91. https://doi.org/10.1038/s41535-020-00292-4.

Bergemann C (2005) Fermi surface measurements. In: Bassani F, Liedl GL, and Wyder P (eds.) *Encyclopedia of Condensed Matter Physics*, pp. 185–192. Oxford: Elsevier. https://doi.org/10.1016/B0-12-369401-9/00456-3.

Bergemann C, Mackenzie AP, Julian SR, Forsythe D, and Ohmichi E (2003) Quasi-two-dimensional fermi liquid properties of the unconventional superconductor Sr_2RuO_4. *Advances in Physics* 52: 639–725. https://doi.org/10.1080/00018730310001621737.

Blount EI (1962) Bloch electrons in a magnetic field. *Physics Review* 126: 1636–1653. https://doi.org/10.1103/PhysRev.126.1636.

Blundell SJ and Singleton J (1996a) Semiclassical description of angle-dependent magnetoresistance oscillations in quasi-one-dimensional metals. *Physical Review B* 53: 5609–5619. https://doi.org/10.1103/PhysRevB.53.5609.

Blundell SJ and Singleton J (1996b) Angle-dependent magnetoresistance in organic metals. *Journal de Physique* 6: 1837–1847. https://doi.org/10.1051/jp1:1996191.

Borisenko SV, Zabolotnyy VB, Evtushinsky DV, Kim TK, Morozov IV, Yaresko AN, Kordyuk AA, Behr G, Vasiliev A, Follath R, and Büchner B (2010) Superconductivity without nesting in lifeas. *Physical Review Letters* 105: 067002. https://doi.org/10.1103/PhysRevLett.105.067002.

Bosak A, Hoesch M, Krisch M, Chernyshov D, Pattison P, Schulze-Briese C, Winkler B, Milman V, Refson K, Antonangeli D, and Farber D (2009) 3d imaging of the fermi surface by thermal diffuse scattering. *Physical Review Letters* 103: 076403. https://doi.org/10.1103/PhysRevLett.103.076403.

Brockhouse BN, Arase T, Caglioti G, Rao KR, and Woods ADB (1962) Crystal dynamics of lead. i. dispersion curves at 100°k. *Physics Review* 128: 1099–1111. https://doi.org/10.1103/PhysRev.128.1099.

Cao Y, Fatemi V, Fang S, Watanabe K, Taniguchi T, Kaxiras E, and Jarillo-Herrero P (2018) Unconventional superconductivity in magic-angle graphene superlattices. *Nature* 556: 43–50. https://doi.org/10.1038/nature26160.

Cattelan M and Fox NA (2018) A perspective on the application of spatially resolved arpes for 2d materials. *Nanomaterials* 8. https://doi.org/10.3390/nano8050284.

Chambers RG (1966) The fermi surface. *Science Progress* 54: 163–191. http://www.jstor.org/stable/43419533.

Cohen MH and Falicov LM (1961) Magnetic breakdown in crystals. *Physical Review Letters* 7: 231–233. https://doi.org/10.1103/PhysRevLett.7.231.

Compton AH (1923) A quantum theory of the scattering of x-rays by light elements. *Physics Review* 21: 483–502. https://doi.org/10.1103/PhysRev.21.483.

Cooper J, Carrington A, Meeson P, Yelland E, Hussey N, Balicas L, Tajima S, Lee S, Kazakov S, and Karpinski J (2003) De haas–van alphen effect in MgB_2 crystals. *Physica C: Superconductivity* 385: 75–84. https://doi.org/10.1016/S0921-4534(02)02318-3.

Cooper M, Mijnarends P, Shiotani N, Sakai N, and Bansil A (2004) *X-Ray Compton Scattering. Oxford Series on Synchrotron Radiation*Oxford University Presshttps://doi.org/10.1093/acprof:oso/9780198501688.001.0001.

Crommie M, Lutz C, and Eigler D (1993) Imaging standing waves in a two-dimensional electron gas. *Nature* 363: 524.

Danner GM, Kang W, and Chaikin PM (1994) Measuring the fermi surface of quasi-one-dimensional metals. *Physical Review Letters* 72: 3714–3717. https://doi.org/10.1103/PhysRevLett.72.3714.

Duffy JA (2013) What we can learn from magnetic compton scattering: application to the determination of spin polarization. *Journal of Physics: Conference Series* 443: 012011. https://doi.org/10.1088/1742-6596/443/1/012011.

Dugdale SB (2016) Life on the edge: A beginner's guide to the fermi surface. *Physica Scripta* 91: 053009. https://doi.org/10.1088/0031-8949/91/5/053009.

Dugdale SB and Laverock J (2014) Recovering the fermi surface with 2d-ACAR spectroscopy in samples with defects. *Journal of Physics: Conference Series* 505: 012046. https://doi.org/10.1088/1742-6596/505/1/012046.

Dugdale SB, Watts RJ, Laverock J, Major Z, Alam MA, Samsel-Czekała M, Kontrym-Sznajd G, Sakurai Y, Itou M, and Fort D (2006) Observation of a strongly nested fermi surface in the shape-memory alloy $Ni_{0.62}Al_{0.38}$. *Physical Review Letters* 96: 046406. https://doi.org/10.1103/PhysRevLett.96.046406.

Dugdale SB, Laverock J, Utfeld C, Alam MA, Haynes TD, Billington D, and Ernsting D (2013) The bristol HIDAC 2d-ACAR spectrometer. *Journal of Physics: Conference Series* 443: 012083. https://doi.org/10.1088/1742-6596/443/1/012083.

Eisenberger P and Platzman PM (1970) Compton scattering of x rays from bound electrons. *Physical Review A* 2: 415–423. https://doi.org/10.1103/PhysRevA.2.415.

Eisenberger P and Reed WA (1974) Relationship of the relativistic compton cross section to the electron's velocity distribution. *Physical Review B* 9: 3237–3241. https://doi.org/10.1103/PhysRevB.9.3237.

Fretwell HM, Dugdale SB, Alam MA, Biasini M, Hoffmann L, and Manuel AA (1995) Reconstruction of 3d electron-positron momentum densities from 2d projections: Role of maximum-entropy deconvolution prior to reconstruction. *Europhysics Letters (EPL)* 32: 771–776. https://doi.org/10.1209/0295-5075/32/9/012.

Friedel J (1958) Metallic alloys. *IL Nuovo Cimento (1955-1965)* 7: 287–311. https://doi.org/10.1007/BF02751483.

Goddard PA, Blundell SJ, Singleton J, McDonald RD, Ardavan A, Narduzzo A, Schlueter JA, Kini AM, and Sasaki T (2004) Angle-dependent magnetoresistance of the layered organic superconductor κ—(ET)$_2$Cu(NCS)$_2$: Simulation and experiment. *Physical Review B* 69: 174509. https://doi.org/10.1103/PhysRevB.69.174509.

Hall D, Palm EC, Murphy TP, Tozer SW, Fisk Z, Alver U, Goodrich RG, Sarrao JL, Pagliuso PG, and Ebihara T (2001) Fermi surface of the heavy-fermion superconductor CeCoIn$_5$: The de haas–van alphen effect in the normal state. *Physical Review B* 64: 212508. https://doi.org/10.1103/PhysRevB.64.212508.

Hanssen KEHM, Mijnarends PE, Rabou LPLM, and Buschow KHJ (1990) Positron-annihilation study of the half-metallic ferromagnet NiMnSb: Experiment. *Physical Review B* 42: 1533–1540. https://doi.org/10.1103/PhysRevB.42.1533.

Harris-Lee EI, James ADN, and Dugdale SB (2021) Sensitivity of the fermi surface to the treatment of exchange and correlation. *Physical Review B* 103: 235144. https://doi.org/10.1103/PhysRevB.103.235144.

Hofmann S (2013) *Introduction and Outline*. Berlin, Heidelberg: Springer1–10. https://doi.org/10.1007/978-3-642-27381-0_1.

Hsieh D, Wray L, Qian D, Xia Y, Dil JH, Meier F, Patthey L, Osterwalder J, Bihlmayer G, Hor YS, Cava RJ, and Hasan MZ (2010) Direct observation of spin-polarized surface states in the parent compound of a topological insulator using spin- and angle-resolved photoemission spectroscopy in a mott-polarimetry mode. *New Journal of Physics* 12: 125001. https://doi.org/10.1088/1367-2630/12/12/125001.

Hunt MB, Reinders PHP, and Springford M (1989) A de haas-van alphen effect study of the fermi surface of lithium. *Journal of Physics: Condensed Matter* 1: 6589–6602. https://doi.org/10.1088/0953-8984/1/37/007.

Hussey NE, Abdel-Jawad M, Carrington A, Mackenzie AP, and Balicas L (2003) A coherent three-dimensional fermi surface in a high-transition-temperature superconductor. *Nature* 425: 814–817. https://doi.org/10.1038/nature01981.

Itou M, Hiraoka N, Ohata T, Mizumaki M, Deb A, Sakurai Y, and Sakai N (2001) Present status of the cauchois-type compton scattering spectrometer at spring-8. *Nuclear Instruments and Methods in Physics Research Section A: Accelerators, Spectrometers, Detectors and Associated Equipment* 467-468: 1109–1112. https://doi.org/10.1016/S0168-9002(01)00592-7. Proceedings of the 7th International Conference on Synchrotron Radiation Instru Mentation.

Iwasawa H (2020) High-resolution angle-resolved photoemission spectroscopy and microscopy. *Electronic Structure* 2: 043001. https://doi.org/10.1088/2516-1075/abb379.

Jozwiak C, Sobota JA, Gotlieb K, Kemper AF, Rotundu CR, Birgeneau RJ, Hussain Z, Lee DH, Shen ZX, and Lanzara A (2016) Spin-polarized surface resonances accompanying topological surface state formation. *Nature Communications* 7: 13143. https://doi.org/10.1038/ncomms13143.

Kang M, Fang S, Kim JK, Ortiz BR, Ryu SH, Kim J, Yoo J, Sangiovanni G, Di Sante D, Park BG, Jozwiak C, Bostwick A, Rotenberg E, Kaxiras E, Wilson SD, Park JH, and Comin R (2022) Twofold van hove singularity and origin of charge order in topological kagome superconductor CsV$_3$Sb$_5$. *Nature Physics* 18: 301–308. https://doi.org/10.1038/s41567-021-01451-5.

Kawamura M (2019) Fermisurfer: Fermi-surface viewer providing multiple representation schemes. *Computer Physics Communications* 239: 197–203. https://doi.org/10.1016/j.cpc.2019.01.017.

Kohn W (1959) Image of the fermi surface in the vibration spectrum of a metal. *Physical Review Letters* 2: 393–394. https://doi.org/10.1103/PhysRevLett.2.393.

Kohn W (1961) Cyclotron resonance and de haas-van alphen oscillations of an interacting electron gas. *Physics Review* 123: 1242–1244. https://doi.org/10.1103/PhysRev.123.1242.

Kontrym-Sznajd G (1990) Three-dimensional image reconstruction with application in positron annihilation. *Physica Status Solidi* 117: 227–240. https://doi.org/10.1002/pssa.2211170124.

Kontrym-Sznajd G and Samsel-Czekała M (2000) New reconstruction method of electron momentum densities from compton profiles. *Applied Physics A* 70: 89–92. https://doi.org/10.1007/s003390050017.

Kubica P and Stewart AT (1975) Thermalization of positrons and positronium. *Physical Review Letters* 34: 852–855. https://doi.org/10.1103/PhysRevLett.34.852.

Kwan YH, Reiss P, Han Y, Bristow M, Prabhakaran D, Graf D, McCollam A, Parameswaran SA, and Coldea AI (2020) Quantum oscillations probe the fermi surface topology of the nodal-line semimetal caagas. *Physical Review Research* 2: 012055. https://doi.org/10.1103/PhysRevResearch.2.012055.

Laverock J, Haynes TD, Alam MA, and Dugdale SB (2010) Experimental determination of the state-dependent enhancement of the electron-positron momentum density in solids. *Physical Review B* 82: 125127. https://doi.org/10.1103/PhysRevB.82.125127.

Lifshitz I and Kosevich A (1956) Theory of magnetic susceptibility in metals at low temperature. *Soviet Physics - JETP* 2: 636–645.

Lock DG, Crisp VHC, and West RN (1973) Positron annihilation and Fermi surface studies: A new approach. *Journal of Physics F: Metal Physics* 3: 561. http://stacks.iop.org/0305-4608/3/i=3/a=014.

Luo H, Gao Q, Liu H, Gu Y, Wu D, Yi C, Jia J, Wu S, Luo X, Xu Y, Zhao L, Wang Q, Mao H, Liu G, Zhu Z, Shi Y, Jiang K, Hu J, Xu Z, and Zhou XJ (2022) Electronic nature of charge density wave and electron-phonon coupling in kagome superconductor Kv$_3$Sb$_5$. *Nature Communications* 13: 273. https://doi.org/10.1038/s41467-021-27946-6.

Majumdar CK (1965) Two contributions to the theory of annihilation of positrons in metals. i. determination of the true fermi surface. *Physics Review* 140: A227–A236. https://doi.org/10.1103/PhysRev.140.A227.

Mårtensson N, Baltzer P, Brühwiler P, Forsell JO, Nilsson A, Stenborg A, and Wannberg B (1994) A very high resolution electron spectrometer. *Journal of Electron Spectroscopy and Related Phenomena* 70: 117–128. https://doi.org/10.1016/0368-2048(94)02224-N.

Mueller FM and Priestley MG (1966) Inversion of cubic de haas-van alphen data, with an application to palladium. *Physics Review* 148: 638–643. https://doi.org/10.1103/PhysRev.148.638.

Onsager L (1952) Interpretation of the de haas-van alphen effect. *The London, Edinburgh, and Dublin Philosophical Magazine and Journal of Science* 43: 1006–1008. https://doi.org/10.1080/14786440908521019.

Osterwalder J (2006) *Spin-Polarized Photoemission*. Berlin, Heidelberg: Springer95–120. https://doi.org/10.1007/3-540-33242-1_5.

Pippard AB (1957) An experimental determination of the fermi surface in copper. *Philosophical Transactions of the Royal Society of London. Series A, Mathematical and Physical Sciences* 250: 325–357. https://doi.org/10.1098/rsta.1957.0023.

Platé M, Mottershead JDF, Elfimov IS, Peets DC, Liang R, Bonn DA, Hardy WN, Chiuzbaian S, Falub M, Shi M, Patthey L, and Damascelli A (2005) Fermi surface and quasiparticle excitations of overdoped Tl$_2$Ba$_2$CuO$_{6+\delta}$. *Physical Review Letters* 95: 077001. https://doi.org/10.1103/PhysRevLett.95.077001.

Priestley MG and Shoenberg D (1963) An experimental study of the fermi surface of magnesium. *Proceedings of the Royal Society of London. Series A: Mathematical and Physical Sciences* 276: 258–277. https://doi.org/10.1098/rspa.1963.0205.

Putzke C, Malone L, Badoux S, Vignolle B, Vignolles D, Tabis W, Walmsley P, Bird M, Hussey NE, Proust C, and Carrington A (2016) Inverse correlation between quasiparticle mass and T_c in a cuprate high-T_c superconductor. *Science Advances* 2: e1501657. https://doi.org/10.1126/sciadv.1501657.

Quader KF, Bedell KS, and Brown GE (1987) Strongly interacting fermions. *Physical Review B* 36: 156–167. https://doi.org/10.1103/PhysRevB.36.156.

Ribberfors R (1975a) Relationship of the relativistic compton cross section to the momentum distribution of bound electron states. *Physical Review B* 12: 2067–2074. https://doi.org/10.1103/PhysRevB.12.2067.

Ribberfors R (1975b) Relationship of the relativistic compton cross section to the momentum distribution of bound electron states. II. Effects of anisotropy and polarization. *Physical Review B* 12: 3136–3141. https://doi.org/10.1103/PhysRevB.12.3136.

Riccò S, Kim M, Tamai A, McKeown Walker S, Bruno FY, Cucchi I, Cappelli E, Besnard C, Kim TK, Dudin P, Hoesch M, Gutmann MJ, Georges A, Perry RS, and Baumberger F (2018) In situ strain tuning of the metal-insulator-transition of Ca$_2$RuO$_4$ in angle-resolved photoemission experiments. *Nature Communications* 9: 4535. https://doi.org/10.1038/s41467-018-06945-0.

Robarts HC, Millichamp TE, Lagos DA, Laverock J, Billington D, Duffy JA, O'Neill D, Giblin SR, Taylor JW, Kontrym-Sznajd G, Samsel-Czekała M, Bei H, Mu S, Samolyuk GD, Stocks GM, and Dugdale SB (2020) Extreme fermi surface smearing in a maximally disordered concentrated solid solution. *Physical Review Letters* 124: 046402. https://doi.org/10.1103/PhysRevLett.124.046402.

Rossel C, Bauer P, Zech D, Hofer J, Willemin M, and Keller H (1996) Active microlevers as miniature torque magnetometers. *Journal of Applied Physics* 79: 8166–8173. https://doi.org/10.1063/1.362550.

Roth LM, Zeiger HJ, and Kaplan TA (1966) Generalization of the ruderman-kittel-kasuya-yosida interaction for nonspherical fermi surfaces. *Physics Review* 149: 519–525. https://doi.org/10.1103/PhysRev.149.519.

Rourke P and Julian S (2012) Numerical extraction of de haas–van alphen frequencies from calculated band energies. *Computer Physics Communications* 183: 324–332. https://doi.org/10.1016/j.cpc.2011.10.015.

Sakurai Y, Tanaka Y, Ohata T, Watanabe Y, Nanao S, Ushigami Y, Iwazumi T, Kawata H, and Shiotani N (1994) The high-resolution magnetic compton profile of Fe-5.8 at.% Si. *Journal of Physics: Condensed Matter* 6: 9469–9475. https://doi.org/10.1088/0953-8984/6/44/025.

Sakurai Y, Itou M, Barbiellini B, Mijnarends PE, Markiewicz RS, Kaprzyk S, Gillet JM, Wakimoto S, Fujita M, Basak S, Wang YJ, Al-Sawai W, Lin H, Bansil A, and Yamada K (2011) Imaging doped holes in a cuprate superconductor with high-resolution compton scattering. *Science* 332: 698–702. https://doi.org/10.1126/science.1199391.

Schülke W (2007) Electron Dynamics by Inelastic X-Ray Scattering. *Oxford Series on Synchrotron Radiation*Oxford University Press.

Schülke W, Stutz G, Wohlert F, and Kaprolat A (1996) Electron momentum-space densities of li metal: A high-resolution compton-scattering study. *Physical Review B* 54: 14381–14395. https://doi.org/10.1103/PhysRevB.54.14381.

Schülke W, Sternemann C, Kaprolat A, and Döring G (2001) Ultra-high resolution compton scattering of li metal: Evaluation with respect to the correlation corrected occupation number density. *Zeitschrift für Physikalische Chemie* 215: 1353. https://doi.org/10.1524/zpch.2001.215.11.1353.

Seah MP and Dench WA (1979) Quantitative electron spectroscopy of surfaces: A standard data base for electron inelastic mean free paths in solids. *Surface and Interface Analysis* 1: 2–11. https://doi.org/10.1002/sia.740010103.

Sheikin I, Gröger A, Raymond S, Jaccard D, Aoki D, Harima H, and Flouquet J (2003) High magnetic field study of $CePd_2Si_2$. *Physical Review B* 67: 094420. https://doi.org/10.1103/PhysRevB.67.094420.

Shoenberg D (1984) *Magnetic Oscillations in Metals*. *Cambridge Monographs on Physics*Cambridge University Presshttps://doi.org/10.1017/CBO9780511897870.

Singleton J, Pratt FL, Doporto M, Janssen TJBM, Kurmoo M, Perenboom JAAJ, Hayes W, and Day P (1992) Far-infrared cyclotron resonance study of electron dynamics in $(BEDT\text{-}TTF)_2KH_G(SCN)_4$. *Physical Review Letters* 68: 2500–2503. https://doi.org/10.1103/PhysRevLett.68.2500.

Smith HG (1987) Martensitic phase transformation of single-crystal lithium from bcc to a 9r-related structure. *Physical Review Letters* 58: 1228–1231. https://doi.org/10.1103/PhysRevLett.58.1228.

Sobota JA, He Y, and Shen ZX (2021) Angle-resolved photoemission studies of quantum materials. *Reviews of Modern Physics* 93: 025006. https://doi.org/10.1103/RevModPhys.93.025006.

Tanaka Y, Sakurai Y, Stewart AT, Shiotani N, Mijnarends PE, Kaprzyk S, and Bansil A (2001) Reconstructed three-dimensional electron momentum density in lithium: A compton scattering study. *Physical Review B* 63: 045120. https://doi.org/10.1103/PhysRevB.63.045120.

Vignolle B, Carrington A, Cooper RA, French MMJ, Mackenzie AP, Jaudet C, Vignolles D, Proust C, and Hussey NE (2008) Quantum oscillations in an overdoped high-tc superconductor. *Nature* 455: 952–955. https://doi.org/10.1038/nature07323.

Weber JA, Bauer A, Böni P, Ceeh H, Dugdale SB, Ernsting D, Kreuzpaintner W, Leitner M, Pfleiderer C, and Hugenschmidt C (2015) Spin-resolved fermi surface of the localized ferromagnetic heusler compound Cu_2MnAl measured with spin-polarized positron annihilation. *Physical Review Letters* 115: 206404. https://doi.org/10.1103/PhysRevLett.115.206404.

Weber JA, Benea D, Appelt WH, Ceeh H, Kreuzpaintner W, Leitner M, Vollhardt D, Hugenschmidt C, and Chioncel L (2017) Electronic correlations in vanadium revealed by electron-positron annihilation measurements. *Physical Review B* 95: 075119. https://doi.org/10.1103/PhysRevB.95.075119.

Weymouth JW and Stedman R (1970) Fermi surface of aluminum from kohn anomalies. *Physical Review B* 2: 4743–4751. https://doi.org/10.1103/PhysRevB.2.4743.

Winkelmann A, Tusche C, Akin Ünal A, Ellguth M, Henk J, and Kirschner J (2012) Analysis of the electronic structure of copper via two-dimensional photoelectron momentum distribution patterns. *New Journal of Physics* 14: 043009.

Woll EJ and Kohn W (1962) Images of the fermi surface in phonon spectra of metals. *Physics Review* 126: 1693–1697. https://doi.org/10.1103/PhysRev.126.1693.

Yamase H, Sakurai Y, Fujita M, Wakimoto S, and Yamada K (2021) Fermi surface in la-based cuprate superconductors from compton scattering imaging. *Nature Communications* 12: 2223. https://doi.org/10.1038/s41467-021-22229-6.

Ziman JM (1962) Electrons in metals: A short guide to the fermi surface. *Contemporary Physics* 4: 1–14. https://doi.org/10.1080/00107516208205824.

Zong A, Kogar A, Bie YQ, Rohwer T, Lee C, Baldini E, Ergeçen E, Yilmaz MB, Freelon B, Sie EJ, Zhou H, Straquadine J, Walmsley P, Dolgirev PE, Rozhkov AV, Fisher IR, Jarillo-Herrero P, Fine BV, and Gedik N (2019) Evidence for topological defects in a photoinduced phase transition. *Nature Physics* 15: 27–31. https://doi.org/10.1038/s41567-018-0311-9.

Pseudopotential methods[☆]

James R Chelikowsky, Center for Computational Materials, Oden Institute of Computational Engineering and Sciences, Departments of Physics and Chemical Engineering, University of Texas at Austin, Austin, TX, United States

© 2024 Elsevier Ltd. All rights reserved.

This is an update of A. Filippetti, G.B. Bachelet, Pseudopotential Method, Editor(s): Franco Bassani, Gerald L. Liedl, Peter Wyder, Encyclopedia of Condensed Matter Physics, Elsevier, 2005, Pages 431–440, ISBN 9780123694010, https://doi.org/10.1016/B0-12-369401-9/00453-8.

Introduction 833
Early pseudopotentials 834
The Phillips-Kleinman cancellation theorem 834
Model potentials 836
The empirical pseudopotential method 838
First principles pseudopotentials using density-functional theory 840
Conclusion 846
References 847

Abstract

After the inception of quantum mechanics, workers recognized that an exact solution for electronic structure of interacting atoms was intractable. Over the past century, this situation has prompted a search for *practical methods* to accurately approximate atomic systems. One of the most successful practical methods centers on the creation of *pseudopotentials*, which only reproduce the chemically active states. Since the energy and length scales are set by the valence states, these potentials dramatically simplify the problem. We outline the construction of pseudopotentials with some example applications to condensed matter systems.

Introduction

A long sought goal of condensed matter physics centers on the ability to the predict the properties of materials solely based on the atomic species present. Before the turn of the twentieth century, such a goal was not in the realm of possibility. Quantum mechanics had not been invented, much less applied to materials. Moreover, as the rudimentary quantum theory evolved, e.g., the Bohr theory of the hydrogen atom, the arguments at the time were often focused on the structure of an individual atom. Workers did not dream of addressing problems of materials containing a large number of atoms. However, as quantum mechanics became accepted for atoms, interest in applying quantum theory to materials grew.

Indeed, once the predictive power of quantum mechanics for atoms and simple molecules became clear, the notion of predicting materials properties by solving the quantum mechanical behavior of the system of interest, did not seem so outlandish. One of the first visionaries was P.A.M. Dirac (Dirac, 1929). In 1930 he stated: *The underlying physical laws necessary for the mathematical theory of a large part of physics and the whole of chemistry are thus completely known, and the difficulty is only that the exact application of these laws leads to equations much too complicated to be soluble. It therefore becomes desirable that approximate practical methods of applying quantum mechanics should be developed, which can lead to an explanation of the main features of complex atomic systems without too much computation.*

The implication of this statement was clear. A solution of the quantum mechanical problem would yield the "whole of chemistry." One could predict properties of the chemical bond and the corresponding materials properties of matter without resort to laboratory work. Chemistry and materials properties could be predicted by computation. However, the equations in question were much too complicated to be solved when Dirac made this statement. In fact, they are much too complicated to be solved today, even with state of the art computational platforms.

As Dirac anticipated, the key to progress in this area is to develop "approximate practical methods." Today, we have a number of such practical methods that allow us to access some properties in a manner Dirac suggested. The first successes appeared some 30 or 40 years after Dirac's statement and were led by the development of the *pseudopotential* concept.

The pseudopotential model of a solid provided a practical model to address the quantum mechanical problem and advances in computers provided the means to overcome numerical hurdles.

One notable attribute of a pseudopotential is that it allows one to address directly chemically active valence states of an atom and remove from consideration inert core states. This decomposition between active and inactive states is readily done for most atoms, e.g., in a silicon atom the $1s^2 2s^2 2p^6$ core states are tightly bond compared to the $3s^2 3p^2$ valence states. The physical nature of this decomposition is confirmed by the content of the periodic table in which chemical properties are grouped into columns of elements with similar valence electron configurations.

In Fig. 1, we illustrate the pseudopotential model for a crystalline solid. In this case, the core electrons and nucleus of an atom are treated as an inert, transferable ion core; the valence electrons are treated as an electron sea moving under the influence of the ion cores.

[☆] *Change History*: October 2022. JR Chelikowsky updated the chapter.

https://doi.org/10.1016/B978-0-323-90800-9.00122-0

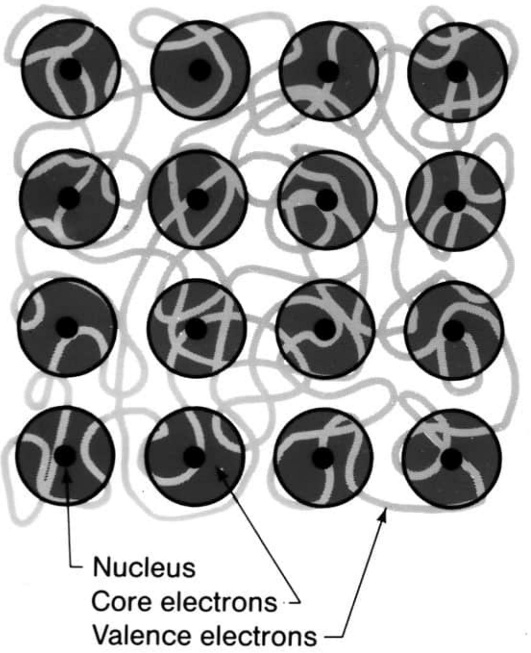

Fig. 1 Pseudopotential model of a crystal. The nucleus and core electrons form a chemically inert ion core, which can be replaced by a pseudopotential.

This pseudopotential picture sets the *length and energy* scale to the problem that is determined by the valence states. Consider a heavy metal atom like Pb. When compared to the outermost electrons, the energies of the innermost electron states are a factor of $\sim 10^4$ more tightly bound. The length scale of these states are also highly localized when compared to the valence states, typically by a factor of $\sim 10^2$. Without the pseudopotential approximation, any description of the electronic states in Pb would need to span orders of magnitude differences in energy and length scales.

Early pseudopotentials

The pseudopotential idea is not new. Several key elements were identified after the advent of quantum mechanics. Both Enrico Fermi and Hans Hellmann contributed seminal papers in the mid-1930s (Fermi, 1934; Hellman, 1935). Interestingly, they recognized somewhat different, but important elements of pseudopotential theory. Fermi's turned his focus on determining the phase shift in wave functions of high lying alkali atoms subject to perturbations from foreign atoms. He correctly argued that if one were interested in the long range behavior of the wave function, it was not necessary to get the details correct near the nucleus. It should be possible to replace the true potential near the nucleus with a simple potential, or pseudopotential, that yields a similar value for the long range part. Fermi also established the importance of a scattering length within this paper.

Hellmann's work is probably closer to our contemporary picture (Schwarz et al., 1999a,b). Hellmann recognized that the valence orbitals for many electron atoms contained pronounced oscillations, *a nodal structure*, within the atomic core. Determining an accurate description of the oscillating behavior near the core and the long range behavior in the chemical relevant region would render the problem computationally difficult. Hellmann also observed that these core electron did not play an important role in determining the chemical bond.

Today, we would argue that the valence electrons experience an additional kinetic energy contribution in the core region because of the orthogonality requirement, i.e., the valence state of an atom is orthogonal to a core state by nodal structure in the core region. In his 1935 paper, Hellmann proposed that this kinetic energy term could be quantified using the Thomas-Fermi expression for the kinetic energy of a free electron gas, which depends only on the electron density (Hellman, 1935). When this term was added to the attractive Coulomb part of the valence electron interacting with the ion core, he argued that the resulting potential was "weak and constant." An example of a pseudopotential similar to those Hellmann suggested is schematically illustrated in Fig. 2.

The Phillips-Kleinman cancellation theorem

While the work of Hellmann and Fermi established the elementary ideas associated with pseudopotentials, a rigorous transcription of an "all electron" potential to a pseudopotential was lacking. One of the earliest transcriptions is based on the ideas of Phillips and Kleinman (Phillips and Kleinman, 1959; Kleinman and Phillips, 1960a,b; Phillips and Kleinman, 1962). Although their

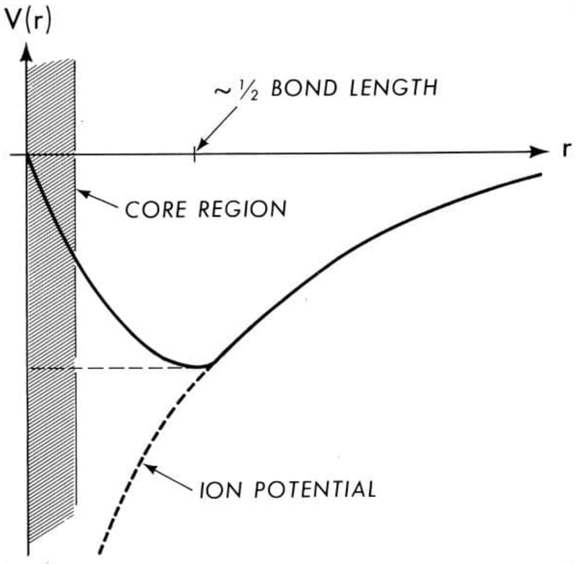

Fig. 2 Schematic of an ion core pseudopotential. The "all electron" potential and the pseudopotential ion core potential are similar outside of the core region.

conclusions are more far reaching, we will focus on solving the electronic structure problem for an isolated atom. We will make the "one-electron" approximation, i.e., the Schrödinger equation for the atomic orbitals can be written as

$$H\Psi_n\left(\vec{r}\right) = \left[\frac{-\hbar^2\nabla^2}{2m} + V\left(\vec{r}\right)\right]\Psi_n\left(\vec{r}\right) = E_n\Psi_n\left(\vec{r}\right), \tag{1}$$

where m is the electron mass, $\hbar$ is Planck's constant divided by 2π, V is the all electron potential and (E_n, Ψ_n) are the eigen pairs: the energy levels and corresponding wave functions. Here we assume both core and valence states exist. We express the wave function for the valence state, Ψ_v, as

$$\Psi_v\left(\vec{r}\right) = \Phi_v^p\left(\vec{r}\right) + \sum_c a_{v,c}\Psi_c\left(\vec{r}\right). \tag{2}$$

The sum is over the core states, Ψ_c, and Φ_v^p represents the pseudopotential wave function. This form of the wave function recognizes that near the nucleus the valence wave function should appear atomic like. Away from the nucleus, we expect: $\Psi_v\left(\vec{r}\right) \approx \Phi_v^p\left(\vec{r}\right)$. Moreover, we expect $\Phi_v^p\left(\vec{r}\right)$ outside of the core region to be nodeless and slowly varying.

To determine the admixture of the core state with the pseudo wave function, we demand the following condition

$$\int \Psi_c^*\left(\vec{r}\right)\Psi_v\left(\vec{r}\right)\, d^3r = \langle\Psi_c|\Psi_v\rangle = 0, \tag{3}$$

where we use the "bra-ket" notation. The valence state must be orthogonal to the core state, owing to the nature of the eigenvalue problem. The orthogonality requirement yields

$$a_{v,c} = -\left\langle\Psi_c|\Phi_v^p\right\rangle. \tag{4}$$

This form of the wave function was first proposed by Conyers Herring (Herring, 1940) in a different context. Herring proposed describing electronic states in crystals using "orthogonalized plane waves." In this model, the valence states in a solid were replicated using plane waves that were orthogonalized to the core levels.

If we apply the Hamiltonian in Eq. (1) to the valence wave function, we obtain

$$H\Phi_v^p + \sum_c \left\langle\Psi_c|\Phi_v^p\right\rangle\ (E_v - E_c)\Psi_c = E_v\Phi_v^0. \tag{5}$$

We have used $H\Psi_c = E_c\Psi_c$. We can define a pseudopotential Hamiltonian, H^p, as

$$H^p = H + \mathcal{V}_R, \tag{6}$$

where we define a potential operator, $\mathcal{V}_R$, as

$$\mathcal{V}_R = \sum_c \langle\Psi_c|\ldots\rangle\ (E_v - E_c)\Psi_c. \tag{7}$$

The empty "ket" given by | . . . > requires an operation wherein the wave function is projected on Ψ_c and the functional dependence now corresponds to Ψ_c. If we define a pseudopotential as $V_p = V + \mathcal{V}_R$ we now have now transformed the one-electron Schrödinger equation to

$$H_p \Phi_v^p = \left[\frac{-\hbar^2 \nabla^2}{2m} + V_p \right] \Phi_v^p = E_v \Phi_v^p. \tag{8}$$

This description of an atom has a number of advantages. The repulsive part of the potential, $\mathcal{V}_R$, largely cancels the attractive part of the all electron potential in the core region. The pseudo wave function is smooth as the core oscillations have been removed and the eigenvalue, E_v, is identical to the all electron potential. While the wave function is now amenable to a simple basis, the pseudopotential within this construction is more complex than the all electron potential. The potential is weak and only binds the valence state, but it is also energy dependent, state dependent and involves a nonlocal, non-Hermitian operator. Owing to these complexities, the Phillips-Kleinman potential is rarely, if ever, used for calculating pseudopotentials. However, the cancellation theorem is useful in demonstrating the essential features of a pseudopotential.

Model potentials

For many purposes, a model pseudopotential can be used to capture the essential physics and advance the essential understanding of the system of interest. As a starting point, we consider a simple model for the ion-core pseudopotential. This potential is expected to be transferable since it depends only on the nuclear and core states. In a vein similar to what Hellmann proposed, we write

$$V_c^p(r) = \begin{cases} 0 & r \le r_c, \\ -Z_v e^2/r & r > r_c. \end{cases} \tag{9}$$

Within the core, this potential is defined as an "empty core." r_c is defines the size of the core region of the potential. The electron charge is e, and Z_v is the number of valence electrons.

In most cases, the number of valence electrons is simply given by the column of the periodic table. Some issues arise in the presence of loosely bound core states. An example is the $3d$ state in Cu, which can be taken as a valence state or a core state. This issue can be tested by considering both cases and assessing any differences.

To form a solution for the electronic structure of a crystal, we need to input the structure of the crystal and account for the interactions of the valence electrons. This is often handled by expressing the wave functions in terms of a plane wave basis, which requires an expression of the potential in Fourier-space characterized by an atomic form factor, $V_c^p(q)$

$$V_c^p(q) = \frac{1}{\Omega_a} \int V_c^p(r) \ \exp\left(i \vec{q} \cdot \vec{r}\right) \, d^3 r. \tag{10}$$

where Ω_a is the atomic volume. The atomic form factor for empty core pseudopotential is given by

$$V_c^p(q) = \frac{-4\pi Z_v e^2}{\Omega_a q^2} \ \cos \ (q r_c). \tag{11}$$

The long range nature of the Coulomb tail requires special handling in executing this integral when $q \to 0$. Also, the form factor "rings", i.e., the form factor oscillators as a cosine function owing to the discontinuity in the potential at r_c.

The ion core pseudopotential needs to be screened by the valence electrons. For simplicity, Thomas-Fermi screening is often used for this purpose (Kittel, 2005)

$$V_a^p(q) = \frac{V_c^p(q)}{\varepsilon_{TF}(q)}, \tag{12}$$

where the screening is characterized by a dielectric function given by

$$\varepsilon_{TF}(q) = 1 + \frac{K_s^2}{q^2}, \tag{13}$$

where $1/K_s$ is the Thomas-Fermi screening length $K_s^2 = 6\pi n e^2/E_F$, which depends on the valence electron density, ($n = Z_v/\Omega_a$) and E_F is the Fermi energy for a free electron gas of density, n. The atomic form factor is now given by

$$V_a^p(q) = \frac{-4\pi e^2 \ n}{q^2 + K_s^2} \ \cos \ (q r_c). \tag{14}$$

A common practice is to set the potential to zero outside of the second node to remove the oscillatory or ringing behavior of the $\cos(q r_c)$ term. This simple potential is characterize by only one parameter, r_c and the electron density, n.

An interesting consequence of Thomas-Fermi screening is that the potential now has a well defined value when $q = 0$,

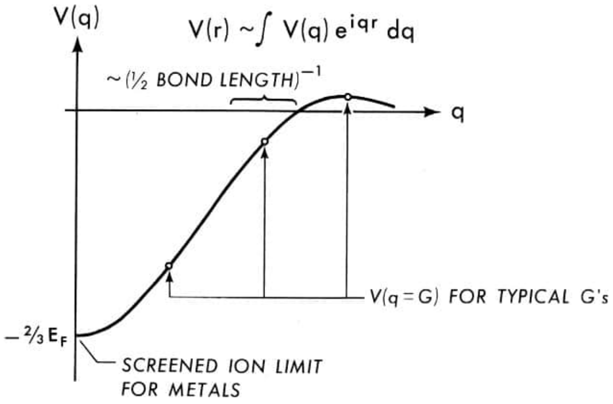

Fig. 3 Model of an atomic pseudopotential. The required form factors can be extracted from this model. Note the limiting case of $G=0$ for a metallic system.

$$V_a^p(0)=\frac{-4\pi e^2\, n}{K_s^2}=-\frac{2}{3}E_F. \tag{15}$$

The $q=0$ term corresponds to the average of the crystalline potential. This limiting case from Thomas-Fermi screening is not a very good approximation for a semiconductor like silicon and is more appropriate for a metal. This is expected as the Thomas-Fermi expression works best for a "free electron" gas, which is likely to be a better model for a simple metal as opposed to a semiconductor.

We have considered a general value, q, in Fourier space, but symmetry restricts the value of q to be a reciprocal space vector, determined by the crystal lattice (Kittel, 2005). This is depicted in Fig. 3 where a schematic of a screened atomic potential is illustrated.

We can write the total crystalline potential as

$$V^p\left(\vec{r}\right)=\sum_{\vec{R},\vec{\tau}}V_a^p\left(\vec{r}-\vec{R}-\vec{\tau}\right), \tag{16}$$

where the position of the lattice point are given by the lattice vector, $\vec{R}$, and the atomic positions associated with the lattice point by the basis vector, $\vec{\tau}$. Using the atomic form factors, we can express this pseudopotential as

$$V^p\left(\vec{r}\right)=\sum_{\vec{G},\vec{\tau}}V_a^p(G)S\left(\vec{G}\right)\exp\left(i\,\vec{G}\cdot\vec{r}\right), \tag{17}$$

where $S\left(\vec{G}\right)$ is the structure factor:

$$S\left(\vec{G}\right)=\frac{1}{N_a}\sum_{\tau}\exp\left(i\vec{G}\cdot\vec{\tau}\right). \tag{18}$$

$\vec{G}$ is a reciprocal lattice vector and N_a is the number of atoms in the unit cell (Kittel, 2005). This expression assumes an elemental crystal, but generalizing the potential to a crystal with different atomic species present is straightforward. The total pseudopotential is determined by the atomic structure factor, which represents the screened ion core potential, and the crystal structure determined by the reciprocal lattice and the atomic positions.

This simple pseudopotential is called a "local" pseudopotential as the ion core is a simple function of position. The potential does not reflect elements present in the Phillips-Kleinman cancellation theorem wherein the potential depends on the nature of the core states. For example, in carbon there is no $1p$ core state and the valence $2p$ is not required to be orthogonal to the core. This is not true for silicon in which both s and p states exist in the core, both the s and p valence states experience a repulsive term. Historically, this difference has been used to explain why silicon and carbon chemistry are different, the former representing "geology" and the later "biology" (Kittel, 2005).

The empty core model potential can be modified to reflect the state dependence

$$V_{c,l}^p(r)=\begin{cases}A_l & r\le r_{c,l},\\ -Z_v e^2/r & r>r_{c,l}.\end{cases} \tag{19}$$

This potential is not a simple function of position, but rather acts on the l-component present in the wave function (Cohen and Chelikowsky, 1982, 1989; Chelikowsky and Cohen, 1992). This can be accomplished by using a projection operator as will be discussed later. There are additional parameters to be determined as the well depth and size must be fixed for each l-component.

A common practice in the early days of pseudopotential involved estimating the well depths and sizes (A_l, $r_{c,l}$) to replicate optical data of ionized atoms. For example, to construct an ion core pseudopotential for an Al atom, one needs to consider the optical excitations for an Al^{+2} ion. In some cases, this is relatively easy, e.g., treating the Na atom does not involve an ionized atom.

However, determining such parameters for an O atom requires the examination of an O^{+5} ion. The experimental task of multiply ionizing atoms and measuring the resulting atomic levels is difficult. Often the potentials were estimated by extrapolation from lighter atoms to heavier ones. Another issue concerns using more accurate dielectric functions screening the potentials. Both issues were the subject of a number of studies. By the mid 1960s an inventory of such model potentials existed (Animalu and Heine, 1965; Cohen and Heine, 1970) with some success.

The empirical pseudopotential method

One of the most significant advances in applying pseudopotential theory was the development of the empirical pseudopotential method (EPM). The intuitive picture of Fermi and Hellmann was greatly advanced by Phillips and Kleinman; however, a practical method of predicting accurate energy band structures was not achieved until the EPM. This method developed in the late 1960s was based on fixing an energy band so that a measured response function, such as the reflectivity of a solid, was reproduced (Cohen and Bergstresser, 1965). To accomplish this feat, one had to develop a framework of translating an energy band solution to a response function.

Determining the energy band structure for a simple pseudopotential is not difficult. If we are given the crystalline potential, we can solve the corresponding eigenvalue problem (Eq. 1) using a variety of approaches. Since the pseudopotential is weak compared to the all electron potential, we can write the wave function in terms of a plane wave basis, which are expected to converge quickly

$$\psi_{n,\vec{k}}\left(\vec{r}\right)=\sum_{\vec{G}}\alpha_n\left(\vec{k},\ \vec{G}\right)\ \exp\left(i\left(\vec{k}+\vec{G}\right)\cdot r\right). \tag{20}$$

n is a band index, $\vec{k}$ is the wave vector. The sum is over all reciprocal lattice vectors, $\left\{\vec{G}\right\}$, but in principle the sum is truncated for $|\vec{k}+\vec{G}|>G_{max}$. This form of the wave function is consistent with the Bloch form of the wave function for a periodic potential. The Bloch form of the wave function allows one to express the corresponding periodicity of the wave function, save a phase factor determined by the wave vector

$$\psi_{n,\vec{k}}\left(\vec{r}+\vec{R}\right)=\exp\left(i\vec{k}\cdot\vec{R}\right)\ \psi_{n,\vec{k}}\left(\vec{r}\right). \tag{21}$$

Inserting the crystalline potential (Eq. 17) and the plane wave basis (Eq. 20) in the one-electron Schrödinger equation, yields the following:

$$\sum_{\vec{G}'}\left\{\left[\frac{\hbar^2}{2m}\left(\vec{K}+\vec{G}\right)^2-E_n\left(\vec{k}\right)\right]\delta_{\vec{G}\vec{G}'}+V_a^p\left(|\vec{G}'-\vec{G}|\right)S\left(|\vec{G}'-\vec{G}|\right)\right\}\alpha_n\left(\vec{k}\vec{G}'\right)=0, \tag{22}$$

which corresponds to a set of linear equations, one for each $\vec{G}$-vector in the set. For a non-trivial solution, we require the following:

$$\det\left|\left[\frac{\hbar^2}{2m}\left(\vec{k}+\vec{G}\right)^2-E_n\left(\vec{k}\right)\right]\delta_{\vec{G}\vec{G}'}+V_a^p\left(|\vec{G}'-\vec{G}|\right)\ S\ \left(|\vec{G}'-\vec{G}|\right)\right|=0, \tag{23}$$

The diagonal elements of this determinant contain the kinetic energy contribution; the off diagonal elements contain the form factors for the pseudopotential and the structure factor. This is an eigenvalue problem and a standard mathematical problem, which is easily handled, save for large systems, i.e., the matrix is large and dense (Saad et al., 2010). Owing to the rapid convergence of the pseudopotentials in Fourier space for common semiconductors or simple metals, one needs only a few hundred plane waves to obtain a converged result.

As a specific example, consider the energy band structure of germanium as computed by pseudopotentials. The band structure is shown in Fig. 4. The energy at point $\vec{k}$ and band n, $E_n\left(\vec{k}\right)$, is plotted along different high symmetry directions, e.g., the energy band along Γ to X is plotted from $\vec{k}=(2\pi/a)(0,0,0)$ to $\vec{k}=(2\pi/a)(1,0,0)$ along the $\langle 100\rangle$ or Δ direction. The input required to compute the energy band includes the crystal structure of germanium, which occurs in a diamond structure, and the form factors required to construct the pseudopotential for the crystal.

As indicated in Fig. 3, only three form factors are required for this case. The empirical pseudopotential method treats these form factors as adjustable parameters. The form factors are not linearly independent, so the information required to fix the form factors is not great. Three or four band structure features are sufficient. As a starting point, one can use a model pseudopotential based on optical spectra for atoms. The form factors are then refined by using optical or photoemission data for the crystal of interest.

Given the energy band of a crystal, one can compute the complex index of refraction and the reflectivity. The first such computations were based on simplified dielectric theories that excluded electron-hole interactions (Cohen and Chelikowsky, 1989). Four ingredients are included: conservation of energy, conservation of crystal momentum, wave function symmetry and the number of states accessible. Energy conservation requires a photon energy sufficient to excite an electron from an occupied

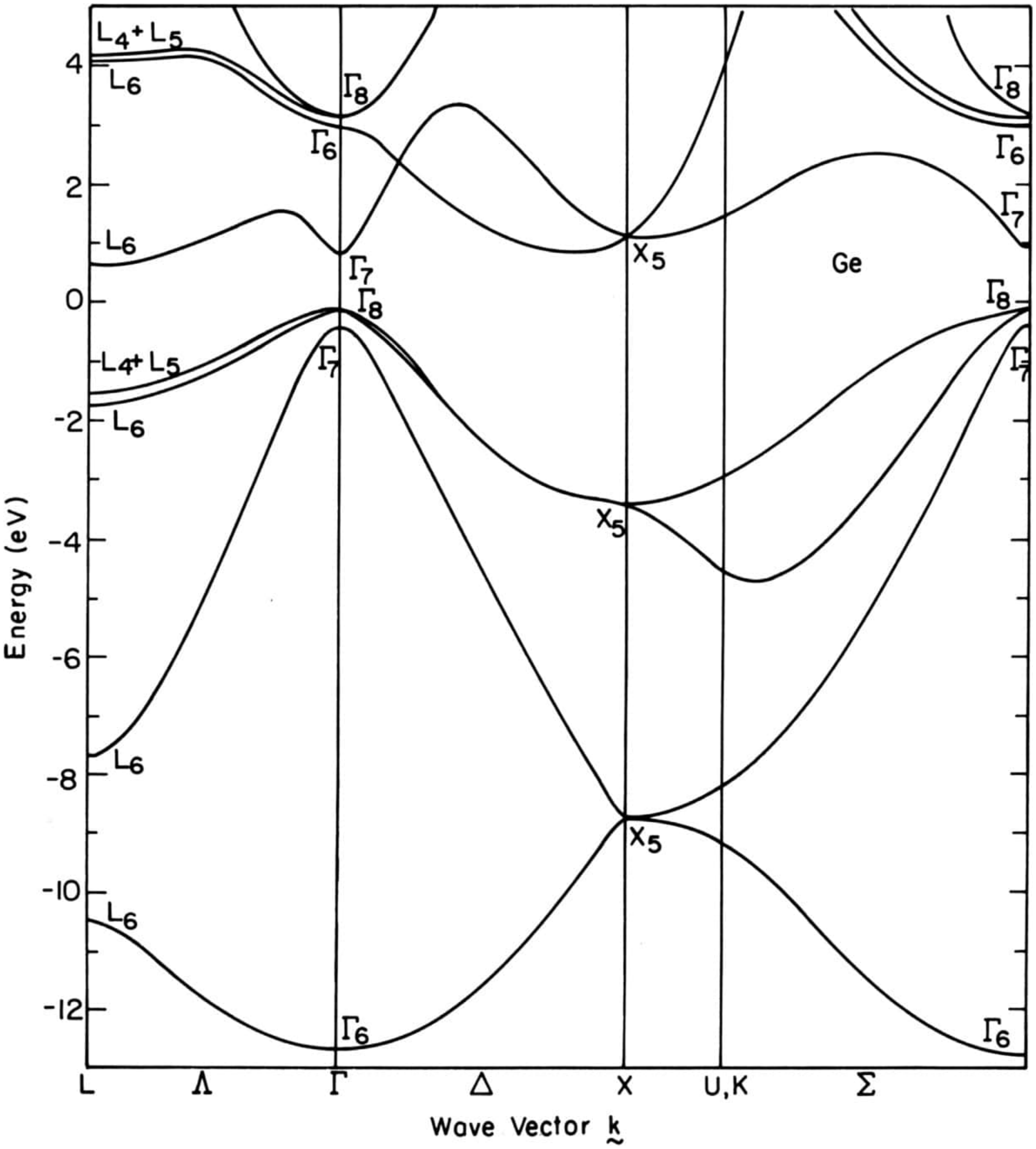

Fig. 4 Band structure of germanium using pseudopotentials (Cohen and Chelikowsky, 1989). The valence band maximum is set to zero.

valence band to an empty conduction band. Such transitions are direct, i.e., the wave vector of the valence band and conduction bands are the same so that crystal momentum is conserved. Just as in an atomic state, the overlap of initial and final states should have a dipole component to couple to the electric field of the photon. Finally, for a given energy difference and wave vector, one can compute the number of possible valence and conduction band states accessible. The larger the number of states, the more probable is an optical excitation.

The computed reflectivity of germanium is given in Fig. 5. The agreement between experiment and theory is sufficient to identify features in the reflectivity spectrum that can be associated with energy band features. For example, the reflectivity peak around 2 eV can be identified with transitions occurring between the top of the valence band and lowest conduction bands near the *L*-high symmetry point. If the theoretical reflectivity for this part of the spectrum does not agree with experiment, we know that the energy band structure is incorrect. If the theoretical reflectivity agrees with experiment, we can be reasonably confident that the energy band structure is correct.

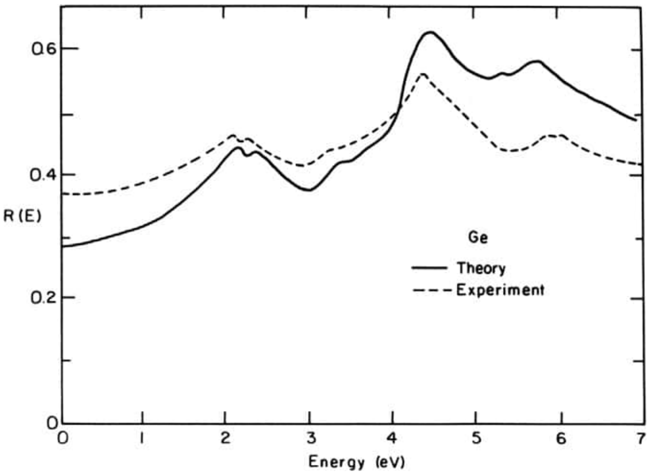

Fig. 5 Experimental (Philipp and Ehrenreich, 1963) and theoretical reflectivity of crystalline germanium (Cohen and Chelikowsky, 1989).

The empirical pseudopotential method provided the first realistic energy band structures for many simple metals and semiconductors (Cohen and Chelikowsky, 1989). Most of our knowledge of the electronic structure of these materials was pioneered by this type of pseudopotential.

However, the empirical pseudopotential method is somewhat limited for several reasons. The potential requires experimental input and this input can bias the pseudopotential. For example, suppose we fit the optical properties of GaSb and extract a Ga potential, we must be careful in trying to use this fit Ga potential in a different crystal. This potential might work fine in GaAs, which has a similar bonding configuration when compared to GaSb, but the potential may fail to describe GaN, which is considerably more ionic than GaSb.

A related problem concerns how the form factors are fit. For high symmetry systems, only a small subset of reciprocal lattice vectors come into play. If the crystal volume or structure changes, one must extrapolate to a new subset of vectors. The required set of data may notably exceed the available experimental data. This problem can occur at a surface or at a defect. In crystalline GaAs, each Ga atom is surrounded by four As atoms. For the cleavage plane, the (110) surface, the Ga atom is bonded to three As atoms. Given the coordination change, the surface Ga atom cannot be expected to retain a" bulk-like" screening potential. There is no reason to be confident that the Ga pseudopotential extracted from the crystalline environment will be very accurate at the surface. Of course, this problem is made worse if one wants to examine a material where the structure is not known as for an amorphous solid or a structure varying in time such as in a liquid state, where the coordination around an atom may continuously change.

First principles pseudopotentials using density-functional theory

A key issue is how to account for the valence charge density screening the ion core pseudopotential. We can consider the form factors to be composed of two interactions: the "ion core-valence electron" interaction and the "valence electron-valence electron" interaction. A fundamental postulate of the pseudopotential method is that the ion core pseudopotential is not dependent on the chemical environment. We assume that this part of the potential can be transferred from one environment to another with no loss in accuracy. A notable problem is the determination of the total pseudopotential by including interactions between the valence electrons. We illustrated the use of Thomas-Fermi dielectric screening in model potentials, which can be used as a first pass for empirical potentials.

A better approach constructs a self-consistent potential by using the valence charge density within density functional theory. Let us assume a one-electron Hamiltonian, which can be based on density functional theory (Hohenberg and Kohn, 1964; Kohn and Sham, 1965)

$$\left[\frac{-\hbar^2\nabla^2}{2m} + V_{ion}^{p}\left(\vec{r}\right) + V_H\left(\vec{r}\right) + V_{xc}\left(\vec{r}\right)\right]\Psi_n\left(\vec{r}\right) = E_n\Psi_n\left(\vec{r}\right). \tag{24}$$

The ion-core pseudopotential, V_{ion}^{p}, can be taken as a linear superposition of ion core atomic potentials. Determining the ionic potential can be accomplished by resort to atomic structure calculations. The potential arising from the valence-electron interactions can be divided into two parts. One part represents the "classical" electrostatic terms, named the Hartree or Coulomb potential

$$\begin{aligned} \nabla^2 V_H\left(\vec{r}\right) &= -4\pi e\rho\left(\vec{r}\right), \\ \rho\left(\vec{r}\right) &= e\sum_{n,\,occup}\left|\Psi_n\left(\vec{r}\right)\right|^2. \end{aligned} \tag{25}$$

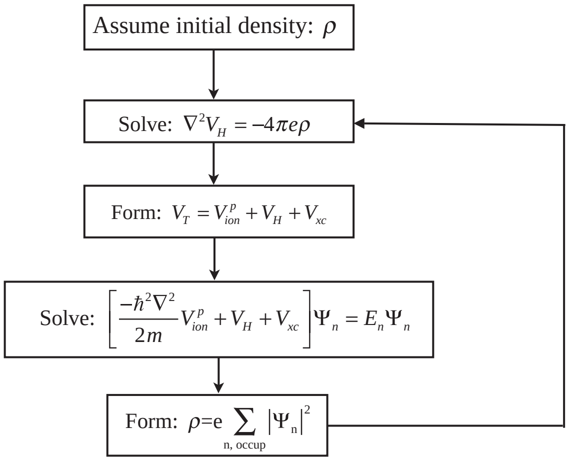
Assume initial density: ρ
Solve: $\nabla^2 V_H = -4\pi e\rho$
Form: $V_T = V_{ion}^p + V_H + V_{xc}$
Solve: $\left[\frac{-\hbar^2\nabla^2}{2m} V_{ion}^p + V_H + V_{xc}\right]\Psi_n = E_n\Psi_n$
Form: $\rho = e\sum_{n,\,occup}|\Psi_n|^2$

Fig. 6 Self-consistent field loop. The loop is repeated until the "input" and "output" charge densities are equal to within some specified tolerance.

where ρ is the valence electron charge density. The second part of the screening potential, the effective "exchange-correlation" part of the potential, V_{xc}, is quantum mechanical in nature.

A common approximation for this part of the potential is the local density approximation. The potential depends only on the charge density at the point of interest, $V_{xc}\left(\vec{r}\right) = V_{xc}\left[\rho\left(\vec{r}\right)\right]$. In principle, density functional theory is exact, provided one can obtain an exact functional for V_{xc}. One productive approach is to assume that the functional extracted for a homogeneous electron gas (Ceperley and Alder, 1980) is "universal" and can be applied to an inhomogeneous gas. The procedure for generating a self-consistent field (SCF) potential is given in Fig. 6. The SCF cycle is initiated with a potential constructed by a superposition of atomic densities. These densities are then used to solve a Poisson equation for the Hartree potential and a density functional is used to obtain the exchange-correlation potential. A screening potential composed of the Hartree and exchange-correlation potentials is then added to the fixed ion-core pseudopotential, after which the one-electron Schrödinger equation, or Kohn-Sham equation, is solved. The resulting wave functions from this solution are then employed to construct a new potential and the cycle is repeated. In practice, the "output" and "input" potentials are mixed using a scheme that accounts for the history of the previous iterations (Broyden, 1965; Chelikowsky and Cohen, 1992).

Methods for constructing ion core pseudopotentials can be based on this density functional framework. The first step is to consider an electronic structure calculation for a free *atom*, including all the electrons. This is an easy numerical calculation as the atomic densities are assumed to possess spherical symmetry and the problem reduces to a one dimensional radial integration.

Once we know the solution for an "all electron" potential, we can *invert* the Kohn-Sham equation and find the total pseudopotential, i.e., one can "unscreen" the total potential and extract the ion core pseudopotential. This ion core potential, which arises from tightly bound core electrons and the nuclear charge, is not expected to change from one environment to another. It should be transferable from the atom to a molecular state to a solid state or liquid state. The issue of this transferability must be addressed according to the system of interest. An immediate issue focuses on the pseudo-wave functions, which can be used to define the corresponding ion core pseudopotential.

Suppose we insist that the pseudo-wave function be identical to the all-electron wave function outside of the core region. As a specific example, let us consider the 3*s* state for a silicon atom. We want the pseudo-wave function to be identical to the all electron state outside the core region

$$\phi_{3s}^p(r) = \psi_{3s}(r) \qquad r > r_c, \tag{26}$$

where ϕ_{3s}^p is a pseudo-wave function and r_c defines the core size. This assignment will guarantee that the pseudo-wave function will possess properties identical to the all electron wave function, ψ_{3s} in the region away from the ion core.

For $r < r_c$, we alter the all-electron wave function. We are free to do this as we do not expect the valence wave function within the core region to affect the chemical properties of the system. We can make the pseudo-wave function smooth and nodeless in the core region. This will provide rapid convergence with simple basis functions. One other criterion is mandated. Namely, the integral of the pseudocharge density within the core should be equal to the integral of the all-electron charge density. Without this condition, the normalized pseudo wave function differs by a scaling factor from the all-electron wave function. Pseudopotentials constructed with this constraint are called "norm conserving" (Hamann et al., 1979). Since we expect the bonding in a solid to be highly dependent on the tails of the valence wave functions, it is imperative that the normalized pseudo wave function be identical to the all-electron wave functions.

There are many ways of constructing "norm conserving" pseudopotentials as within the core the pseudo wave function is not unique. One of the most straightforward construction procedures places conditions on the pseudo-wave functions and then inverts a density functional solution for the atom (Kerker, 1980; Troullier and Martins, 1991).

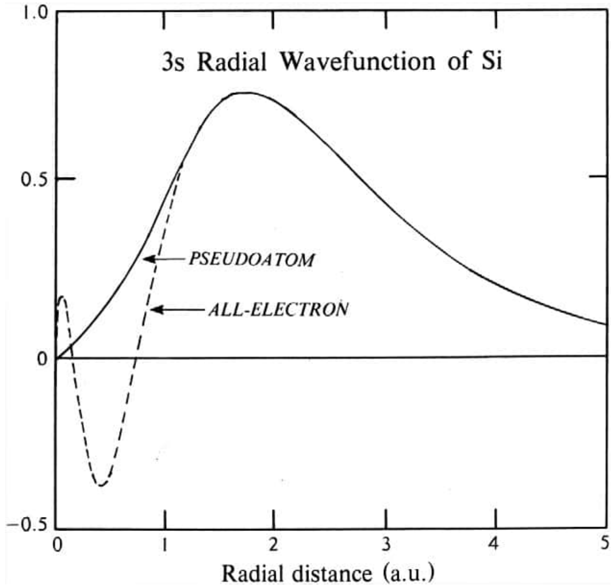

Fig. 7 An all electron and a pseudo-wave function for the silicon 3 *s* radial wave function.

Suppose one assumes the pseudo-wave function, $\phi_l^p(r)$ has the following properties:

$$\phi_l^p(r) = \begin{cases} r^l \exp\left(p(r)\right) & r \le r_c, \\ \psi_l(r) & r > r_c. \end{cases} \tag{27}$$

$p(r)$ is taken to be a polynomial of the form:

$$p(r) = c_0 + \sum_{n=1}^{6} c_{2n} r^{2n}. \tag{28}$$

This form assures us that the pseudo-wave function is nodeless and by taking even powers in the polynomial there is no cusp associated with the pseudo-wave function. The parameters, c_{2n}, are fixed by the following criteria: (a) The all-electron and pseudo-wave functions have the same valence eigenvalue. (b) The pseudo-wave function is nodeless and be identical to the all-electron wave function for $r > r_c$. (c) The pseudo-wave function must be continuous as well as the first four derivatives of the wave function at r_c. (d) The pseudopotential has zero curvature at the origin.

This approach to pseudopotential construction is easy to implement and to include other possible constraints. An example of an atomic pseudo-wave function for Si is given in Fig. 7 where it is compared to an all-electron wave function. Unlike the 3*s* all electron wave function, the pseudo-wave function has no nodes.

Once the pseudo-wave function is constructed, then the Kohn-Sham equation can be inverted to arrive at the ion-core pseudopotential

$$V_{ion,\,l}^{p}(r) = \frac{\hbar^2 \nabla^2 \phi_l^p}{2m\phi_l^p} - E_{n,\,l} - V_H(r) - V_{xc}[\rho(r)]. \tag{29}$$

The ion core pseudopotential is well behaved as ϕ^p has no nodes and does not vanish. However, the potential is state dependent and energy dependent. The energy dependence is usually weak. For example, the 4*s* state in silicon computed by the pseudopotential constructed from the 3*s* state is usually accurate. Physically this happens because the 4 *s* state is extended and experiences the potential in a region where the ion core potential has assumed a simple $-Z_v e^2/r$ behavior. However, the state dependence through *l* is an issue, the difference between a potential generated via a 3*s* state and a 3*p* can be significant. In particular, for first row elements such as C or O, the nonlocality or state dependence is quite large as there are no *p* states within the core region. For the first row transition elements for such as Fe , this is also an issue as again there are no *d*-states within the core.

An additional advantage of the norm conserving potential concerns the logarithmic derivative of the pseudo-wave function (Bachelet et al., 1982). An identity exists

$$-2\pi \left((r\phi)^2 \frac{d^2 \ln \phi}{dE\, dr} \right)_R = 4\pi \int_0^R \phi^2 r^2\, dr = Q(R). \tag{30}$$

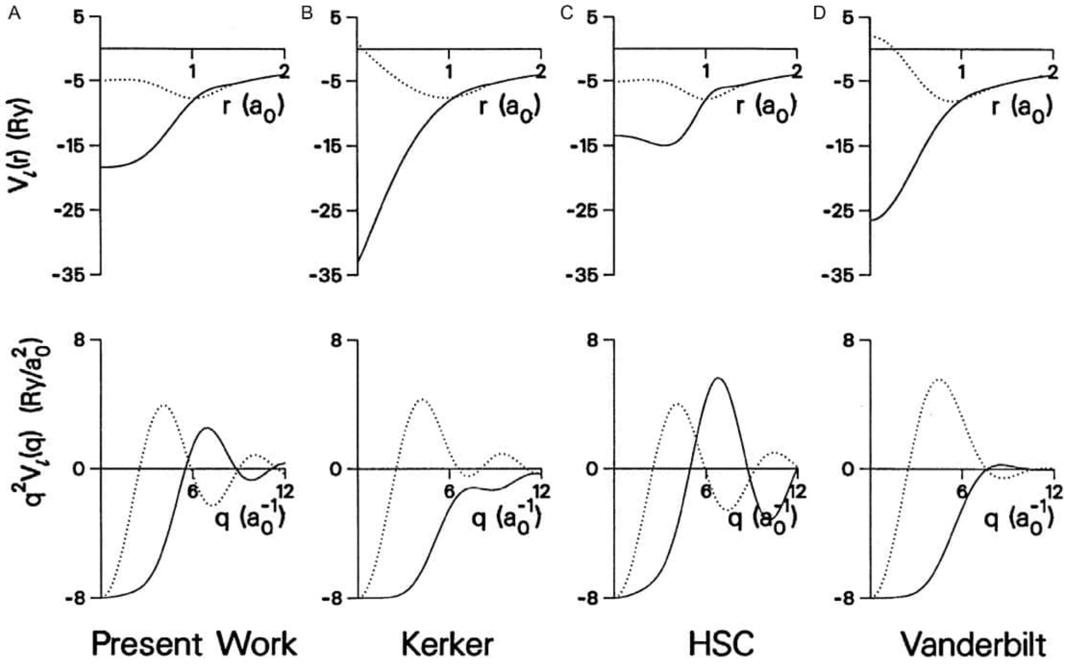

Fig. 8 Ion core pseudopotentials for carbon generated by four different methods in real and reciprocal space: (A) Troullier and Martins (1991), (B) Kerker (1980), (C) Hamann et al. (1979) and (D) Vanderbilt (1985). The dotted and solid lines correspond to the *s* and *p* pseudopotentials, respectively.

The energy derivative of the logarithmic derivative of the pseudo-wave function is fixed by the amount of charge, Q, within a radius, R. The radial derivative of the wave function ϕ is related to the scattering phase shift from elementary quantum mechanics. For a norm-conserving pseudopotential, the scattering phase shift at $R = r_c$ and at the eigenvalue of interest is identical to the all-electron case as Q is the same for the all-electron potential and the pseudopotential. As a consequence, the scattering properties of the pseudopotential and the all-electron potential have the same energy variation to first order when transferred to other systems.

The pseudo wave function is not unique. This property was recognized early in its inception. For example, within the Phillips-Kleinman formulation, one can always add a function, f, to the pseudo-wave functions without altering the pseudopotential provided f is orthogonal to the core states. Consider the matrix element in Eq. 5. If one changes Φ_v^p to $\Phi_v^p + f$, then $\langle \Psi_c | \Phi_v^p + f \rangle = \langle \Psi_c | \Phi_v^p \rangle + \langle \Psi_c | f \rangle = \langle \Psi_c | \Phi_v^p \rangle$. Nothing is changed in the Phillips-Kleinman pseudopotential by this addition.

The non-uniqueness of the pseudopotential can be exploited to optimize the convergence of the pseudopotentials for the basis of interest. Much effort has been made to construct "soft" pseudopotentials. By "soft," one means a "rapidly" convergent calculation using plane waves as a basis. Such potentials are characterized by a "large" core size, i.e., a large value for r_c. However, as the core becomes larger, the "goodness" of the pseudo-wave function can be compromised as the transferability of the pseudopotential becomes more limited. In Fig. 8, the ion core pseudopotential for carbon is plotted in real space and in reciprocal space. Although the potentials look quite different in the core region, they all give reliable electronic structure properties for carbon.

Pseudopotentials constructed within density functional theory are inherently nonlocal as they depend on the all electron state of the atom. This feature can also be included in empirical pseudopotentials using parameterized potentials (Cohen and Chelikowsky, 1989).

In setting up the eigenvalue problem, we need to include an additional matrix element in Eq. (22). One can consider a local potential as a reference potential. For example, we can write $\Delta V_l = V_{local} - V_l$, where V_{local} can be any local potential, but is often chosen to a specific component. As an example, suppose we have a carbon atom. We can find a pseudopotential for the *s*-state and take this as a local component. The *p* potential is then referenced as $V_s + \mathcal{P}_p^{\dagger}\left(V_p - V_s\right)\mathcal{P}_p$ where $\mathcal{P}_p$ is a projection operator that only acts on the $l = 1$ component of the wave function. In general, the nonlocal elements are very short ranged in real space as the size of the ion core is determined by r_c. Outside of the core the potential components converge to the same limit.

A major strength of density functional pseudopotentials is that they can be employed for systems with many atoms of low symmetry, e.g., clusters, liquids, and surfaces, without having to fit any form factors. However, a plane wave basis will require a large cutoff for such systems. In this case, the nonlocal matrix elements can be difficult to evaluate as elements depend on both $\vec{k} + \vec{G}$ and $\vec{k} + \vec{G}'$. An efficient form for the required nonlocal matrix elements (Kleinman and Bylander, 1982) is given by

$$\begin{aligned}\Delta V_l^{KB}\left(\vec{k}+\vec{G},\vec{k}+\vec{G}'\right) &= \frac{\sum\limits_m Y_{lm}^*\left(\widehat{\vec{k}+\vec{G}}\right) Y_{lm}\left(\widehat{\vec{k}+\vec{G}'}\right)}{4\pi\Omega_a \int \Phi_l^p(r)\,\Delta V_l(r)\,\Phi_l^p(r)\,dr} \\ &\times \int \Phi_l^p(r)\,\Delta V_l(r) j_l\left(|\vec{k}+\vec{G}'|r\right) r^2\,dr \\ &\times \int \Phi_l^p(r)\,\Delta V_l(r) j_l\left(|\vec{k}+\vec{G}|r\right) r^2 dr,\end{aligned} \tag{31}$$

where Φ_l^p is the atomic reference pseudo-wave function and Y_{lm}^* is a spherical harmonic with the angles determined by the unit vector: $\widehat{\vec{k}+\vec{G}}$. This matrix element form has a great advantage as the integrals are separable in that they are solely a function of $\vec{k}+\vec{G}$ or a function of $\vec{k}+\vec{G}'$. The individual integrals can be stored and retrieved as required in setting up the matrix.

The Kohn-Sham problem can also be solved directly in real space (Chelikowsky et al., 1994). In this case the nonlocal matrix elements can be cast as

$$\begin{aligned}\Delta V_l^{KB}(x,y,z)\phi^p\ (x,y,z) &= \sum_{lm} G_{lm}\, u_{lm}^p\ (x,y,z)\ \ \Delta V_l(x,y,z) \\ G_{lm} &= \frac{\int\ u_{lm}^p\ \ \Delta V_l \phi^p\ \ dx\ \ dy\ \ dz}{\int\ u_{lm}^p\ \ \Delta V_l\ \ u_{lm}^p\ \ dx\ \ dy\ \ dz},\end{aligned} \tag{32}$$

where u_{lm}^p are the reference atomic pseudo-wave functions. The nonlocal nature of the pseudopotential is apparent from the definition of G_{lm}, the value of these coefficients are dependent on the pseudo-wave function, ϕ^p, acted on by the operator ΔV_l.

While our focus has been on "norm conserving" pseudopotentials, one can generalize the pseudopotential method. It is possible to make the pseudopotentials even weaker by relaxing this condition. (Vanderbilt, 1990) proposed such a method for constructing *ultra soft pseudopotentials*, which are constructed as a generalized eigenvalue problem. The norm conservation constraint is relaxed, and the charge density within the ion core is not explicitly considered as part of the pseudo-wave function. The relaxation of the norm conservation constraint allows one to consider a much larger core radius and a much softer potential.

One issue which is relevant for pseudopotential constructions, regardless of whether the potential is intended for use with a plane wave basis or not, concerns the issue of unbound, or weakly bound, atomic states. If an atom does not bind a state of interest, then the atomic wave function corresponding to this state is clearly not normalizable. Nonetheless, the pseudopotential corresponding to this state might be of some interest, e.g., in a crystal such diverging wave functions are "captured" by the potentials of neighboring atoms. For example, Ba has a strong *f*-component resonance. However, these *f*-states are not bound for neutral Ba atom. In order to bind such states, one must consider highly ionized atomic states, which result in very strong pseudopotentials. Sometimes these potentials are so strong as to be useless for a plane wave basis, or so far removed from the chemical environment of interest that their transferability may be suspect. Hamann (1989) has suggested a method for handling such cases by integrating out the Kohn-Sham equation to a large distance and at that point terminating the pseudo-wave function. The corresponding "terminated" wave function is then used to generate a pseudopotential for the component of interest.

Empirical pseudopotentials provide effective tools in understanding the optical and dielectric properties of semiconductor crystals (Cohen and Chelikowsky, 1989); however, to understand structural properties, we need to employ a different approach. Since the form factors in the empirical pseudopotential have been fit to optical transitions, there is no reason to believe that they will be very accurate for structural properties such as the phase stability, the equilibrium bond length, and the bulk modulus of a crystal. Pseudopotentials constructed within density functional theory can serve this purpose.

Evaluating the total energy of a crystal can be a difficult task. The total energy of the system contains terms that individually diverge, e.g., the repulsive Coulomb terms between the ion cores and the electron-electron interactions. These terms can be handled in Fourier or momentum space using a plane wave basis (Ihm et al., 1979). The total energy of the system can be written as

$$E_T = E_{kin} + E_{ec} + E_H + E_{xc} + E_{cc}. \tag{33}$$

E_T is the total electronic energy, E_{kin} represents the electronic kinetic energy, the electron-ion core interaction energy is given by E_{ec}, the electrostatic coulomb energy is given by the Hartree energy, E_H, the non-classical exchange-correlation energy is given by E_{xc} and the ion core-ion core classical term is given by E_{cc}. The momentum-space expressions for the electronic energy terms are as follows:

$$E_{kin} = \frac{1}{N}\sum_{n,\vec{k},\vec{G}} \left|\phi_n^p\left(\vec{k}+\vec{G}\right)\right|^2 \frac{\hbar^2\left|\vec{k}+\vec{G}\right|^2}{2m}, \tag{34}$$

$$E_{ec} = \frac{1}{N} \sum_{n,\vec{k},\vec{G}} \phi_n^{p*}\left(\vec{k} + \vec{G}\right) \phi_n^p\left(\vec{k} + \vec{G}'\right) \times \left(V_c^p\left(\vec{k} + \vec{G}, \vec{k} + \vec{G}'\right) + \delta_{\vec{G},\vec{G}'} \frac{1}{\Omega_c} \int \frac{Ze^2}{r} d^3r \right), \tag{35}$$

$$E_H = \frac{\Omega_c}{2} \sum_{\vec{G}, G \neq 0} \frac{4\pi e^2}{G^2} |\rho\left(\vec{G}\right)|^2, \tag{36}$$

$$E_{xc} = \frac{\Omega_c}{2} \sum_{\vec{G}} \rho^*\left(\vec{G}\right) \varepsilon_{xc}\left(\vec{G}\right), \tag{37}$$

$$E_{cc} = \frac{e^2}{2} \sum_{s,s'} Z_{v,s} Z_{v,s'} \left\{ \frac{4\pi}{\Omega_c} \sum_{\vec{G}, G \neq 0} \left[\frac{1}{G^2} \cos\left(\vec{G} \cdot \left(\vec{\tau}_s - \tau_{s'}\right)\right) \times \exp\left(\frac{-G^2}{4\eta^2}\right)\right] - \frac{\pi}{\Omega_c \eta^2} + \sum_{\vec{R}, R \neq 0} \left[\frac{\operatorname{erfc}\left(\eta\left|\vec{R} - \vec{\tau}_s + \vec{\tau}_{s'}\right|\right)}{\left|\vec{R} - \vec{\tau}_s + \vec{\tau}_{s'}\right|} \right] - \frac{2\eta}{\sqrt{\pi}} \delta_{s,s'} \right\}. \tag{38}$$

Each term yields the energy per cell; N is the total number of cells, Ω_c is the cell volume, $\vec{R}$ is a lattice vector, $\vec{G}$ is a reciprocal lattice vector, Z is the total core charge, which is a sum of the individual core charges Z_v, $\vec{\tau}$ is the basis vector, $\vec{k}$ is the crystal momentum and ϕ_n^p is wavefunction for state n. $\rho\left(\vec{G}\right)$ $V_c^p\left(\vec{k} + \vec{G}, \vec{k} + \vec{G}'\right)$, and $\phi_n^p\left(\vec{k} + \vec{G}\right)$ represent the Fourier components of the charge, ion core potential and the pseudo-wave function. The sums involving the pseudo-wave functions run only over the occupied states. η is parameter that controls the convergence of the Ewald summation in real space versus momentum space (Ihm et al., 1979).

In practice, it is easier to make use of the eigenvalue explicitly and subtract off the "double counting terms," i.e., one can write the total energy as

$$E_T = \frac{1}{N} \sum_{n,\vec{k}} E_n\left(\vec{k}\right) - E_H + \Delta E_{xc} + E_{cc}. \tag{39}$$

The sum is over all occupied states. The eigenvalue term contains the exchange-correlation term whereas the total energy should contain the exchange-correlation energy. This term can be written as

$$\Delta E_{xc} = \Omega_c \sum_{\vec{G}} \rho^*\left(\vec{G}\right) \left[\varepsilon_{xc}\left(\vec{G}\right) - V_{xc}\left(\vec{G}\right)\right], \tag{40}$$

where ε_{xc} is related to the exchange-correlation via a functional derivative:

$$\Delta V_{xc} = \frac{\delta(\rho\, \varepsilon_{xc}[\rho])}{\delta \rho}, \tag{41}$$

In the local density approximation (Kohn and Sham, 1965)

$$E_{xc}[\rho] = \int \rho\left(\vec{r}\right) \varepsilon_{xc}\left[\rho\left(\vec{r}\right)\right] d^3r. \tag{42}$$

In the simplest formalism, ε_{xc} is extracted from a homogeneous electron gas (Kohn and Sham, 1965).

The total energy, E_T, for a crystal structure can be calculated using Eq. (39) as a function of the lattice constant and any internal structural parameters. This calculation can be used to find the equation of state for a given phase (Yin and Cohen, 1980). This approach represents a seminal point in condensed matter physics, e.g. it demonstrated a workable scheme for examining structural properties of solids and its extension led to molecular dynamics using quantum forces (Car and Parrinello, 1985).

The first application of phase stability using pseudopotential-density functional theory centered on a number of silicon crystal structures: face centered cubic, body centered cubic, hexagonal close packed, hexagonal diamond, cubic diamond, white tin and simple cubic. For each structure, the energy was minimized for a given volume by optimizing the internal coordinates, e.g., for a hexagonal structure the c/a ratio was optimized. Depending on the system studied the range of volumes considered is varied.

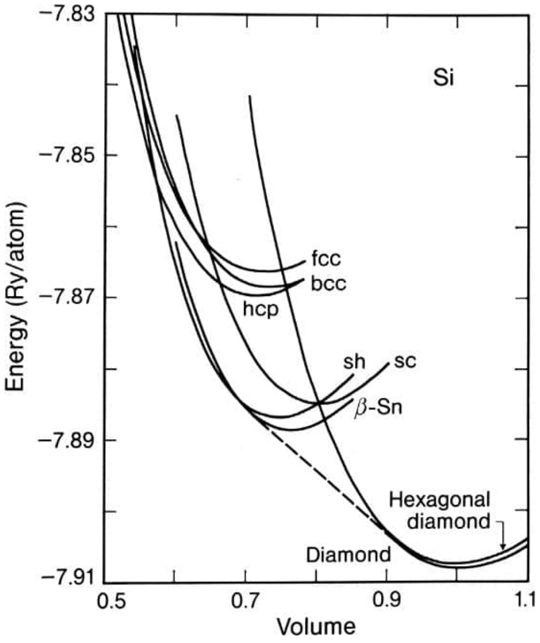

Fig. 9 Total electronic energy for seven phases of crystalline silicon as function of the atomic volume (Yin and Cohen, 1980). The volume has been normalized to the measure value of diamond. The dashed line is a common tangent of the energy curves for the diamond and β-tin phases. The total energy reference is the energy per pseudo Si atom.

The results are impressive when one considers that this is a calculation requiring only the atomic number and crystal structure as input. Generally, the pseudopotential-density functional method yields lattice constants and bulk moduli to an accuracy of about 1% and 5%, respectively. The cohesive energy can be calculated by comparing the total energy at the equilibrium lattice constant with the energy of the isolated atoms. Spin polarization effects (von Barth and Hedin, 1972; Gunnarsson et al., 1974) and zero point vibrational energy need to be considered. Early results computed within the local density approximation gave reasonable estimates of the cohesive energies; however, in general the generalized gradient approximation yields more accurate cohesive energies (Becke, 1992).

The total energy versus volume curves for seven crystal phases of silicon and are shown in Fig. 9. The lowest energy state corresponds to the diamond structure, which is observed experimentally under ambient conditions. As with any such calculation, there is no guarantee that there is an untried structure with a lower energy state.

For small volumes other structural phases are lower in energy than the diamond phase, hence pressure induced solid-solid structural phase transitions are predicted. As hydrostatic pressure is applied the path indicated in the figures, $1 \rightarrow 2 \rightarrow 3 \rightarrow 4$, illustrates the change from diamond at 1 to β-tin at 4, with the transformation occurring along the $2 \rightarrow 3$ segment of the path where both structures can coexist. The predicted phase transition pressure for the diamond → β-tin phase is 99 kbar; the measured values are 125 and 100 kbar, respectively (Yin and Cohen, 1982).

The successful prediction of high pressure structural phases such as hexagonal forms of Si and Ge and fcc Si are one of the impressive results of the pseudopotential-density functional theory calculations (Chang and Cohen, 1984). Moreover, these high pressure phases are metallic and predicted to be superconductors (Chang et al., 1985). Since these calculations, total energy computations using pseudopotentials constructed within density functional theory have become routine for a wide variety of materials.

As with any computational approach, an accurate solution is limited by the least accurate approximation. In the case of density functional pseudopotentials, the weakest aspect centers on the nature of the exchange-correlation functional. For example, computations for highly correlated systems are likely to fail. A pseudopotential constructed within a given functional will accurately reproduce a solution of the functional, but if the functional is flawed the pseudopotential will reflect his flaw.

In contrast to density functional theory, the accuracy of the pseudopotential can be validated by replacing it with an all electron potential and assessing any differences. What cannot be done is to take an approximate density functional and replace it with an exact functional, as an exact functional does not exist, save in limiting cases like a homogeneous electron gas.

Conclusion

The pseudopotential concept has had a profound impact on our understanding of the electronic structure of semiconductors. In this chapter, both empirical and density functional pseudopotential concepts were outlined and some central applications discussed.

Empirical pseudopotentials provided a means for understanding the optical and dielectric properties of semiconductors and the underlying energy band structures. It is sometimes stated that the empirical pseudopotential method (EPM) established the validity of the energy band concept for solids in general. There is truth to this statement. In the 1950s, there were extended discussions about the validity of the one electron picture and whether it could be applied to solids and specifically to semiconductors such as silicon. Some workers thought that the electron-hole interactions for a optical excitation would be so strong as to obscure any attempt at understanding such excitations using energy band theory. Given that the EPM allowed adjustments to the one electron potential, if the EPM had failed to work with the flexibility of choosing a potential, one would have questioned whether it was possible to construct a meaningful one-electron potential and corresponding energy band structure. The consequences of this failure would have been very damaging to prospects for using energy bands to interpret optical, dielectric, photoemission, and transport properties of semiconductors.

Fortunately, this was not the case, the EPM provided a simple and effective way to couple band structure theory to experimental work and its impact was immediate. While much of this effort took place in the 1960s and 1970s, the EPM still serves as an effective means to interpret optical data for semiconductors. While more sophisticated methods now exist to examine optical properties, few of the conclusions of the EPM have been overturned by these methods.

The coupling of density functional theory with pseudopotentials in the early 1980s resulted in another impressive advance for understanding the electronic structure of materials. The accuracy of density functional theory for predicting electronic and structural energies was problematic at that time. However, the direct numerical application to structural energies to problems involving bond lengths, compressibilities, phonon modes, and phase stabilities showed conclusively the applicability of pseudopotential methods to these problems. Over the last 10 years, more than 10,000 papers have appeared with pseudopotentials in the title or abstract and these papers have been cited over 100,000 times.

The future of pseudopotentials constructed within density functional theory clearly depend on advances in creating more accurate functionals. One proposed advance centers on mixing exact exchange with local density functionals (Perdew et al., 1996). These so called hybrid functionals should capture nonlocal contributions and result in a more accurate description of the many electron problem. Of course, such approaches can be computationally complex to implement. As these difficulties are overcome (Boffi et al., 2016), pseudopotentials constructed within hybrid functionals will become more commonplace.

The vitality and future of the pseudopotential method is without question. The method is now used to examine new and exciting materials systems. These systems include nanoscale systems, amorphous solids, glasses, and liquids. Moreover, owing to strong advances in both hardware and software (algorithms) it is now possible to address systems with thousands of atoms on an almost routine basis (Liou et al., 2021).

References

Animalu AOE and Heine V (1965) The screened model for 25 elements. *Philosophical Magazine* 12: 1249.

Bachelet G, Hamann DR, and Schlüter M (1982) Pseudopotentials that work: From hydrogen to plutonium. *Physical Review B* 26: 4199.

Becke AD (1992) Density-functional thermochemistry 1. The effect of the exchange-only gradient correction. *The Journal of Chemical Physics* 96:2155.

Boffi NM, Jain M, and Natan A (2016) Efficient computation of the Hartree–Fock exchange in real-space with projection operators. *Journal of Chemical Theory and Computation* 12: 3614.

Broyden CG (1965) A class of methods for solving nonlinear simultaneous equations. *Mathematics of Computation* 19: 577.

Car R and Parrinello M (1985) Unified approach for molecular dynamics and density-functional theory. *Physical Review Letters* 55: 2471.

Ceperley DM and Alder BJ (1980) Ground state of the electron gas by a stochastic method. *Physical Review Letters* 45: 566.

Chang KJ and Cohen ML (1984) Structural and electronic properties of the high-pressure hexagonal phases of silicon. *Physical Review B* 30: 5376.

Chang KJ, Dacorogna MM, Cohen ML, Mignot JM, Chouteau G, and Martinez G (1985) Superconductivity in high-pressure metallic phases of Si. *Physical Review Letters* 54: 2375.

Chelikowsky JR and Cohen ML (1992) *Ab initio* pseudopotentials for semiconductors. In: Moss TS and Landsberg PT (eds.) *Handbook of Semiconductors*, p. 59. Amsterdam: Elsevier.

Chelikowsky JR, Troullier N, and Saad Y (1994) The finite-difference-pseudopotential method: Electronic structure calculations without a basis. *Physical Review Letters* 72: 1240.

Cohen M and Chelikowsky J (1982) Pseudopotentials for semiconductors. In: Paul W (ed.) *Handbook on Semiconductors*, vol. 1, p. 219. Amsterdam, North Holland.

Cohen ML and Bergstresser TK (1965) Band structures and pseudopotential form factors for fourteen semiconductors of the diamond and zinc-blende structures. *Physics Review* 141: 789.

Cohen ML and Chelikowsky JR (1989) *Electronic Structure and Optical Properties of Semiconductors*, 2nd edn. Berlin: Springer-Verlag.

Cohen ML and Heine V (1970) The fitting of pseudopotentials to experimental data and their subsequent application. In: Ehrenreich H, Seitz F, and Turnbull D (eds.) *Solid State Physics*. vol. 24, p. 37. New York: Academic Press.

Dirac PAM (1929) Quantum mechanics of many elecrton systems. *Proceed Royal Soc London A* 123: 714.

Fermi E (1934) Sullo spostamento per pressione dei termini elevati delle serie spettrali (on the pressure displacement of higher terms in spectral series). *Nuovo Cimento* 11: 157.

Gunnarsson O, Lundqvist BI, and Wilkins JW (1974) Cohesive energy of simple metals. Spin-dependent effect. *Phys Rev B* 10: 1319.

Hamann DR (1989) Generalized norm-conserving pseudopotentials. *Physical Review B* 40: 2980. https://doi.org/10.1103/PhysRevB.40.2980.

Hamann DR, Schlüter M, and Chiang C (1979) Norm-conserving pseudopotentials. *Physical Review Letters* 43: 1494.

Hellman H (1935) A new approximation method in the problem of many electrons. *Journal of Chemical Physics* 3: 61.

Herring C (1940) A new method for calculating wave functions in crystals. *Physics Review* 57: 1169. https://doi.org/10.1103/PhysRev.57.1169.

Hohenberg P and Kohn W (1964) Inhomogeneous electron gas. *Physics Review* 136: B864. https://doi.org/10.1103/PhysRev.136.B864.

Ihm J, Zunger A, and Cohen ML (1979) Momentum-space formalism for the total energy of solid. *Journal of Physics C* 12: 4409.

Kerker GP (1980) Nonsingular atomic pseudopotentials for solid state applications. *Journal of Physics C* 13: L189.

Kittel C (2005) *Introduction to Solid State Physics*, 8th edn. New York: Wiley.

Kleinman L and Bylander DM (1982) Efficacious form for model pseudopotentials. *Physical Review Letters* 48: 1425.

Kleinman L and Phillips JC (1960a) Crystal potential and energy bands of semiconductors. II. Self-Consistent calculations for cubic boron nitride. *Physics Review* 117: 460. https://doi.org/10.1103/PhysRev.117.460.

Kleinman L and Phillips JC (1960b) Crystal potential and energy bands of semiconductors. III. Self-Consistent calculations for silicon. *Physics Review* 118: 1153. https://doi.org/10.1103/PhysRev.118.1153.

Kohn W and Sham LJ (1965) Self-consistent equations including exchange and correlation effects. *Physical Review A* 140: 1133. https://doi.org/10.1103/PhysRev.140.A1133.

Liou KH, Biller A, Kronik L, and Chelikowsky J (2021) Space-filling curves for real-space electronic structure calculations. *Journal of Chemical Theory and Computation* 17: 4039.

Perdew JP, Ernzerhof M, and Burke K (1996) Rationale for mixing exact exchange with density functional approximations. *The Journal of Chemical Physics* 105: 9982.

Philipp HR and Ehrenreich H (1963) Optical properties of semiconductors. *Physics Review* 129: 1550.

Phillips JC and Kleinman L (1959) New method for calculating wave functions in crystals and molecules. *Physics Review* 116: 287.

Phillips JC and Kleinman L (1962) Crystal potential and energy bands of semiconductors. IV. Exchange and correlation. *Physics Review* 128: 2098. https://doi.org/10.1103/PhysRev.128.2098.

Saad Y, Chelikowsky J, and Shontz S (2010) Numerical methods for electronic structure calculations of materials. *SIAM Review* 52: 3.

Schwarz W, Andraea D, Arnold S, Heidberg J, Hellmann H Jr, Hinze J, Karachalios A, Kovner M, Schmidtand P, Zülicke L, and Hans GA (1999a) Hellmann (1903-1938): Part I. A pioneer of quantum chemistry. *Bunsen-Magazin* 1: 10.

Schwarz W, Andraea D, Arnold S, Heidberg J, Hellmann H Jr, Hinze J, Karachalios A, Kovner M, Schmidtand P, Zülicke L, and Hans GA (1999b) Hellmann (1903-1938): Part II. A German pioneer of quantum chemistry in Moscow. *Bunsen-Magazin* 2: 60.

Troullier N and Martins J (1991) Efficient pseudopotentials for plane-wave calculations. *Physical Review B* 43: 1993.

Vanderbilt D (1985) Optimally smooth norm-conserving pseudopotentials. *Physical Review B* 32: 8412.

Vanderbilt D (1990) Soft self-consistent pseudopotentials in a generalized eigenvalue formalism. *Physical Review B* 41: 7892.

von Barth U and Hedin L (1972) Local exchange-correlation potential for the spin-polarized case. I. *Journal of Physics C* 5: 1629.

Yin MT and Cohen ML (1980) Microscopic theory of the phase transformation and lattice dynamics of Si. *Physical Review Letters* 45: 1004.

Yin MT and Cohen ML (1982) Ab initio calculation of the phonon dispersion relation: Application to silicon. *Physical Review B* 25: 4317.

Effective masses☆

Jeanlex Soares de Sousa, Departamento de Física, Universidade Federal do Ceará, Fortaleza, Brazil

© 2024 Elsevier Ltd. All rights reserved.

This is an update of A.L. Wasserman, Effective Masses, Editor(s): Franco Bassani, Gerald L. Liedl, Peter Wyder, Encyclopedia of Condensed Matter Physics, Elsevier, 2005, Pages 1–5, ISBN 9780123694010, https://doi.org/10.1016/B0-12-369401-9/00457-5.

Introduction **849**
Electron dynamics 850
Band curvature and types of charge carriers 850
Parabolic band approximation 851
Effective mass theory 852
Heterostructures 852
Density of states and carriers concentration 853
Two-dimensional materials 854
Measurement methods 854
Conclusion **855**
References **855**

Abstract

The effective mass of a particle in an energy band is its inertia due to the interaction with the lattice during its motion through the crystal. Effective masses are important quantities to parameterize the band structure of materials and their electronic properties like the intrinsic carrier concentrations as function of temperature, electrical conductivity, speed of integrated circuits or the efficiency of solar cells. This chapter aims to review the basic principles and quantum theory behind the concept of effective mass in solid state physics.

Key points

- Parabolic band approximation
- Effective mass theory
- Envelope function approximation
- Density-of-states effective mass
- Effective mass in Dirac cones

Introduction

Electrons move very differently in a periodic lattice than when they are free in space. In vacuum, the electron mass is a fundamental constant of nature given by $m_0 = 9,66 \times 10^{-31}$ kg. In crystalline solids, electrons sense the environment and interact with (i) the lattice atoms, (ii) other electrons moving around the lattice, and (iii) with vibrations of the lattice. As a consequence of all these interactions, electrons move as if their mass was different from m_0. This is the most fundamental idea behind the concept of effective masses.

The well-known single particle energy of free electrons is

$$E\left(\vec{k}\right) = \frac{\hbar^2 k^2}{2m_o}, \tag{1}$$

where $\vec{k}$ is the electron wave vector (Ashcroft and Mermin, 1976). In a crystal close to an energy band extremum, the single particle energy of electrons including the effect of all interactions with the surroundings can be described as

$$E\left(\vec{k}\right) = \frac{\hbar^2 k^2}{2m^*}, \tag{2}$$

☆*Change History*: September 2022. JS de Sousa updated sections Abstract, Introduction, Electron dynamics, Band curvature and types of charge carriers, Parabolic band approximation, Effective mass theory, Heterostructures, Density of states and carriers concentration, Two-dimensional materials, Measurement methods, Conclusions and 2 figures.

https://doi.org/10.1016/B978-0-323-90800-9.00089-5

where m* is the effective mass of the electron in the crystal. Such a surprisingly simple result is successful in describing many physical phenomena in crystalline condensed matter. In fact, effective masses provide a very useful and powerful way to parameterize solid state materials like semiconductors and insulators.

Electron dynamics

In a crystalline solid, electrons occupy electronic states characterized by their wave vector $\vec{k}$ and a band index n. The energy in any band is a quasi-continuous function $E_n(\vec{k})$, and the ensemble of functions $E_n(\vec{k})$ constitutes the energy band structure of a given crystal. Due to the periodicity of the lattice, a quantum state may be described by a Block function $\psi_{n,\vec{k}}(\vec{r}) = u_{n,\vec{k}}(\vec{r})e^{i\vec{k}\cdot\vec{r}}$, that satisfies the Schrödinger equation $\left[\hat{p}^2/2m + V(\vec{r})\right]\psi_{n,\vec{k}}(\vec{r}) = E_n(\vec{k})\psi_{n,\vec{k}}(\vec{r})$, where $V(\vec{r})$ is the periodic potential energy created by the crystalline lattice.

As the electronic states $\psi_{n,\vec{k}}(\vec{r})$ extend over the whole crystal with the same periodicity as the lattice, it may not be very insightful to describe the dynamics of electrons. Instead, one constructs a moving wavepacket localized in space, whose group velocity is given by

$$\vec{v}_n = \frac{1}{\hbar}\nabla_k E_n(\vec{k}), \tag{3}$$

where the index n indicates that the wavepacket was constructed with $\psi_{n,\vec{k}}(\vec{r})$ states belonging to a single energy band (it will be dropped in the following analysis). The acceleration of this wavepacket is then given by:

$$\vec{a} = \frac{d\vec{v}}{dt} = \frac{1}{\hbar}\frac{d}{dt}\nabla_k E(\vec{k}) = \frac{1}{\hbar}\left(\frac{d\vec{k}}{dt}\cdot\nabla_k\right)\nabla_k E(\vec{k}) = \frac{1}{\hbar^2}H_E(\vec{k})\frac{d(\hbar\vec{k})}{dt}, \tag{4}$$

where $H_E(\vec{k})$ is the Hessian matrix, whose elements are given by $H_E^{(i,\,j)}(\vec{k}) = \partial^2 E(\vec{k})/\partial k_i \partial k_j$. An external force acting on the wavepacket is given by $\vec{F} = d(\hbar\vec{k})/dt$, where $\vec{p} = \hbar\vec{k}$ is the electron momentum. Comparing Eq. (4) with Newton's second law $\vec{a} = \vec{F}/m$, one obtains that the electron mass is replaced by an effective mass tensor m^*, whose elements are given by:

$$m^*_{i,j} = \left(\frac{1}{\hbar^2}\frac{\partial^2 E(\vec{k})}{\hbar^2 \partial k_i \partial k_j}\right)^{-1}. \tag{5}$$

Eq. (5) indicates that the effective mass is inversely proportional to the curvature of the band structure. Large curvatures imply small effective masses, and vice-versa. The importance of this result is paramount: It indicates that despite the complexity of the multiple interactions undergone by electrons across the crystal, they all can be accounted for by a single parameter in their dynamics. The tensor nature of the effective mass indicates that materials can be anisotropic, i.e., their properties depend on orientation of the material's body.

Band curvature and types of charge carriers

In a typical band structure, shown in Fig. 1, there are many energy bands for which curvatures vary as function of $\vec{k}$. Hence, near the bottom of any band the curvature is positive, whereas near the top of any band the curvature is negative. This indicates that the effective masses can be either positive or negative.

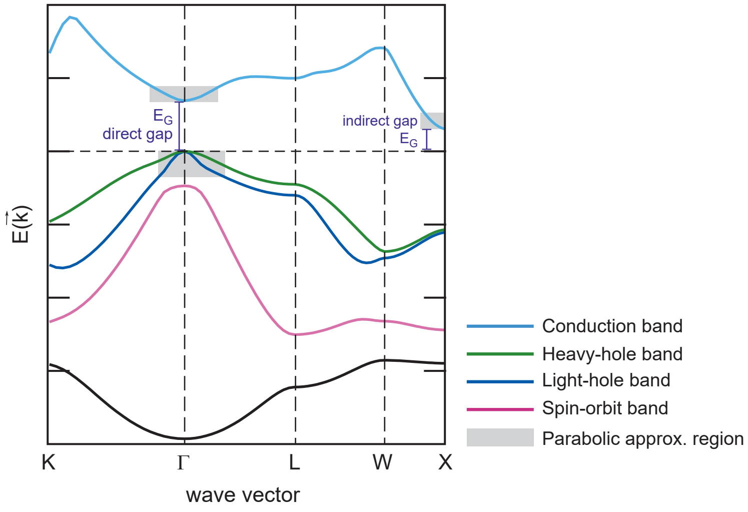

Fig. 1 Schematics of a semiconductor energy band structure.

In pure dielectric materials at $T = 0$ K, there are just enough electrons to fill the valence band, and no electrons to occupy the conduction band. The band gap E_G provides a primary indication of the metallic, semiconductor, or insulator character of materials. $E_G \geq 3.5$ eV are representative of insulators, $E_G \approx 0$ eV are found in metallic materials and E_G ranging between 0.3 eV and 3.5 eV are typical of semiconductor materials. One important feature of the band structure of real materials is that the maximum of the valence band (VBM) and the minimum of the conduction band (CBM) may be located at distinct $\vec{k}$ points in the reciprocal space. If so, they are called indirect gap materials, otherwise they are called direct gap materials.

At finite temperatures, some of those electrons occupying the top of the valence band are transferred across the band gap to the bottom of the conduction band, leaving unoccupied states behind in the valence band. Particles occupying conduction band states exhibit positive effective mass, and are called electrons. On the other hand, particle occupying valence band states are called holes, and exhibit negative effective mass. This means that holes act as if they were positively charged and are accelerated by an external electric field in the reverse direction expected for electrons. Usually, the top of the valence band is degenerate exhibiting energy bands with different curvatures, giving rise to the heavy-hole (smaller curvature) and light-hole (larger curvature bands). There is even a third type of hole band called spin-orbit split-off band, which arises from the spin-orbit interaction. In general, the effective masses of electrons and holes are different.

Parabolic band approximation

Near band edges, like the top of the valence band and/or bottom of the conduction band, $E\left(\vec{k}\right)$ can be expanded into Taylor series. For simplicity, we temporarily assume that $\vec{k}$ is a scalar

$$E(k) = E(k_0) + (k - k_0)\frac{dE}{dk}\bigg|_{k_0} + \frac{(k - k_0)^2}{2}\frac{d^2E}{dk^2}\bigg|_{k_0} + O\left[(k - k_0)^3\right], \tag{6}$$

where k_0 is the position of the band edge in the reciprocal space. We keep in mind that the energy bands at the band edges are extrema ($[dE(k)/dk]_{k_0} = 0$), and that the energy states above/below few k_BT of the band edges are hardly occupied at finite temperatures. We can disregard high order terms $O[(k-k_0)^3]$ in the above expansion to obtain the well-known parabolic band approximation

$$E(k) - E(k_0) = \frac{(k - k_0)^2}{2}\frac{d^2E}{dk^2}\bigg|_{k_0} = \frac{\hbar^2 (k - k_0)^2}{2m^*}, \tag{7}$$

where we used the definition of the effective mass in terms of the band curvature near $k = k_0$. One should note that the parabolic band approximation is similar to the energy dispersion of the free electrons replacing m_0 by m^* in Eq. (1). Recovering the vector form of $\vec{k}$, the parabolic band approximation becomes:

$$E\left(\vec{k}\right) = E\left(\vec{k}_0\right) + \frac{\hbar^2}{2}\left(\vec{k} - \vec{k}_0\right)\cdot\left(\frac{1}{m^*}\right)\cdot\left(\vec{k} - \vec{k}_0\right), \tag{8}$$

where the effective mass is written in the tensor form whose elements are given by Eq. (5).

We are now in position to describe some few cases of energy bands in terms of effective masses. The simplest possible case is for isotropic direct gap materials (e.g., GaAs, InAs) whose band edges are located at Γ point $\left(\vec{k}_0 = 0\right)$ in the Brillouin zone. In this case, the conduction, light-hole, heavy hole, and split-off bands are respectively given by:

$$E_c\left(\vec{k}\right) = \mathrm{E}_c(0) + \frac{\hbar^2 k^2}{2m_c^*}, \tag{9}$$

$$E_{lh}\left(\vec{k}\right) = \mathrm{E}_v(0) + \frac{\hbar^2 k^2}{2m_{lh}^*}, \tag{10}$$

$$E_{hh}\left(\vec{k}\right) = \mathrm{E}_v(0) + \frac{\hbar^2 k^2}{2m_{hh}^*}. \tag{11}$$

$$E_{so}\left(\vec{k}\right) = \mathrm{E}_v(0) + \frac{\hbar^2 k^2}{2m_{so}^*}. \tag{12}$$

In the above equations, m_e^*, m_{hh}^*, m_{lh}^* and m_{SO}^* represent the effective masses of electrons, heavy-holes, light-holes and split-off band, respectively. Δ_0 is the spin–orbit split-off energy, and the band gap is given by $E_G = E_c(0) - E_v(0)$.

For indirect gap materials (e.g., Si, Ge), the VBM is located at the Γ point, but the CBM is located away from the Brillouin zone center. In this case, the light-hole and heavy-hole bands are considered reasonably isotropic, and can be described in the same way of Eqs. (10) and (11). However, the CBM is degenerated, highly anisotropic and can be written as

$$E_c\left(\vec{k}\right) = \mathrm{E}_c\left(\vec{k}_0\right) + \frac{\hbar^2 k_{x'}^2}{2m_l^*} + \frac{\hbar^2\left(k_{y'}^2 + k_{z'}^2\right)}{2m_t^*} \tag{13}$$

where $\vec{k}_0$ is located near the X of the Brillouin zone for Si, and at L point for Ge. Those are symmetric points with six degenerated equivalent directions. $k_{x'}$ is measured from the CBM and it is oriented along the ΓX direction for Si, and along ΓL direction for Ge.

Table 1 Effective masses of some of the most common semiconductors.

Material	m_e^*/m_0	m_{hh}^*/m_0	m_{lh}^*/m_0	m_{SO}^*/m_0
Si	0.91 (0.19)	0.49	0.16	0.24
Ge	1.58 (0.082)	0.33	0.043	0.084
C	1.40 (0.36)	2.12	0.7	1.06
GaAs	0.063	0.51	0.082	0.15
InAs	0.023	0.41	0.026	0.16
InP	0.008	0.60	0.089	0.17
GaP	1.12 (0.22)	0.79	0.14	0.83
GaSb	0.041	0.40	0.05	0.14
InSb	0.014	0.43	0.015	0.19

$k_{y',z'}$ lie along perpendicular directions with respect to $k_{x'}$. m_l^* and m_t^* refer to longitudinal and transverse effective masses with respect to direction connecting Γ point and the position $\vec{k}_0$ of the CBM. Table 1 lists the effective masses of some of the most common elemental and compound semiconductors.

Effective mass theory

Although we have described the concept of effective masses phenomenologically so far, there is a solid theoretical framework behind it. Consider the general Schrödinger equation for a Bloch state $H(\vec{r})\Psi_{n,\vec{k}}(\vec{r}) = \mathrm{E}_n(\vec{k})\Psi_{n,\vec{k}}(\vec{r})$, where $\psi_{n,\vec{k}}(\vec{r}) = u_{n,\vec{k}}(\vec{r})e^{i\vec{k}\cdot\vec{r}}$. Written in terms of$u_{n,\vec{k}}(\vec{r})$, it becomes

$$\left[H_0 + \frac{\hbar^2}{m_0}\vec{k}\cdot\vec{p}\right]u_{n,\vec{k}}(\vec{r}) = \left[E_n(\vec{k}) - \frac{\hbar^2 k^2}{2m_0}\right]u_{n,\vec{k}}(\vec{r}). \tag{14}$$

where $H_0 = \frac{p^2}{2m_0} + V(\vec{r})$ is the unperturbed crystal Hamiltonian, and $H_1 = (\hbar^2/m_0)\vec{k}\cdot\vec{p}$ is a perturbation. The unperturbed problem obeys $H_0 u_{n,0}(\vec{r}) = \mathrm{E}_n(0)u_{n,0}(\vec{r})$. The time-independent perturbation theory gives the energy to 2nd order in perturbation:

$$E_n(\vec{k}) = \mathrm{E}_n(0) + \frac{\hbar^2 k^2}{2m_0} + \frac{\hbar^2}{m_0^2}\sum_{n'\neq n}\frac{\left|\vec{k}\cdot\vec{p}_{n,n'}\right|^2}{E_n(0) - E_{n'}(0)}, \tag{15}$$

where $\vec{p}_{n,m} = \left\langle u_{n,0}|\vec{p}|u_{m,0}\right\rangle$ is the momentum matrix element. The first order correction $E_n^{(1)}(\vec{k}) = (\hbar/\mathrm{m}_0)\vec{\mathrm{k}}\cdot\vec{p}_{n,n}$ vanishes because $\vec{p}_{n,n} = 0$ due to symmetry considerations. This equation can be written as:

$$E_n(\vec{k}) = E_n(0) + \frac{\hbar^2}{2}\sum_{\alpha,\beta}\left(\frac{1}{m^*}\right)_{\alpha\beta}k_\alpha k_\beta, \tag{16}$$

where

$$\left(\frac{1}{m^*}\right)_{\alpha\beta} = \frac{1}{m_0}\delta_{\alpha\beta} + \frac{2}{m_0^2}\sum_{n'\neq n}\frac{p^{\alpha}_{n,n'}p^{\beta}_{n',n}}{E_n(0) - E_{n'}(0)}. \tag{17}$$

Although the above expression was developed for a band whose edge is located at $\vec{k} = 0$, it is valid for any location $\vec{k}_0$.

The above theory is based on non-degenerated time-independent perturbation theory, and it needs modification in order to accurately include the light-hole, heavy-hole and spin-orbit bands. Further accuracy can be obtained by noticing that the functions $u_{m,\vec{k}_0}$ (for a given $\vec{k}_0$) deliver a complete set of eigenfunctions. The eigenfunctions $u_{n,\vec{k}}$ can be expressed as linear combination of $u_{m,\vec{k}_0}$, for a proper choice of $\vec{k}_0$, and the Eq. (14) can be solved using this basis set. This approach gave rise to widely used models in the literature as Kane and Luttinger-Kohn models (Chuang, 1995; Kane, 1966; Luttinger and Kohn, 1956).

Heterostructures

One of the most important consequences of the effective mass theory is the *envelope function approximation* to study the electronic properties of heterostructures (e.g., quantum wells, wires and dots). In this approach, the single band effective Schrödinger equation for the whole heterostructure is written as (Bastard, 1988; Burt, 1992):

$$\left[-\frac{\hbar^2}{2}\nabla\left(\frac{1}{m^*\left(\vec{r}\right)}\right)\nabla+U\left(\vec{r}\right)\right]F\left(\vec{r}\right)=EF\left(\vec{r}\right) \tag{18}$$

where $U\left(\vec{r}\right)$ is the heterostructure potential constructed from the alignment of band gaps at the interfaces of different materials and/or an external potentials, $m^*\left(\vec{r}\right)$ is the position-dependent effective mass, E is measured from the band edge of the quantum well (QW) region, and $F\left(\vec{r}\right)$ is known as envelope wavefunction. In the envelope function approximation, the atomistic description of the different materials in the heterostructure are embedded in their effective masses. The approximate atomistic wavefunction is linked to the envelope wavefunction as $\psi\left(\vec{r}\right)=F\left(\vec{r}\right)u_{n,\vec{k}_0}\left(\vec{r}\right)$,where $\vec{k}_0$ is the position of the band edge for which the envelope function description is being constructed. The presence of boundaries between materials demands the application of continuity boundary conditions in the envelope function $F\left(\vec{r}\right)$ and in the quantity $\left[m^*\left(\vec{r}\right)\right]^{-1}\nabla F\left(\vec{r}\right)$ at the interfaces between materials.

Fig. 2 shows an example of how the alignment of band structures in the assembly of a QW heterostructure gives rise to a position-dependent effective mass. If the QW is thin enough (up to few tens of nanometers), discrete energy states in the conduction and valence bands appear in the QW region in the direction of confinement. Assuming infinite confinement barriers, those energy states measured from the bottom of their respective band edges, are given by:

$$E_n^v=\frac{\hbar^2}{2m_v^*}\frac{\pi^2}{L^2}n^2. \tag{19}$$

where $v=e$, hh, lh, and L is the QW width.

Density of states and carriers concentration

The concentration of mobile carriers in the conduction (n) and valence (p) bands are given by:

$$n=\int_{E_c}^{\infty}g_c(E)f(E)dE, \tag{20}$$

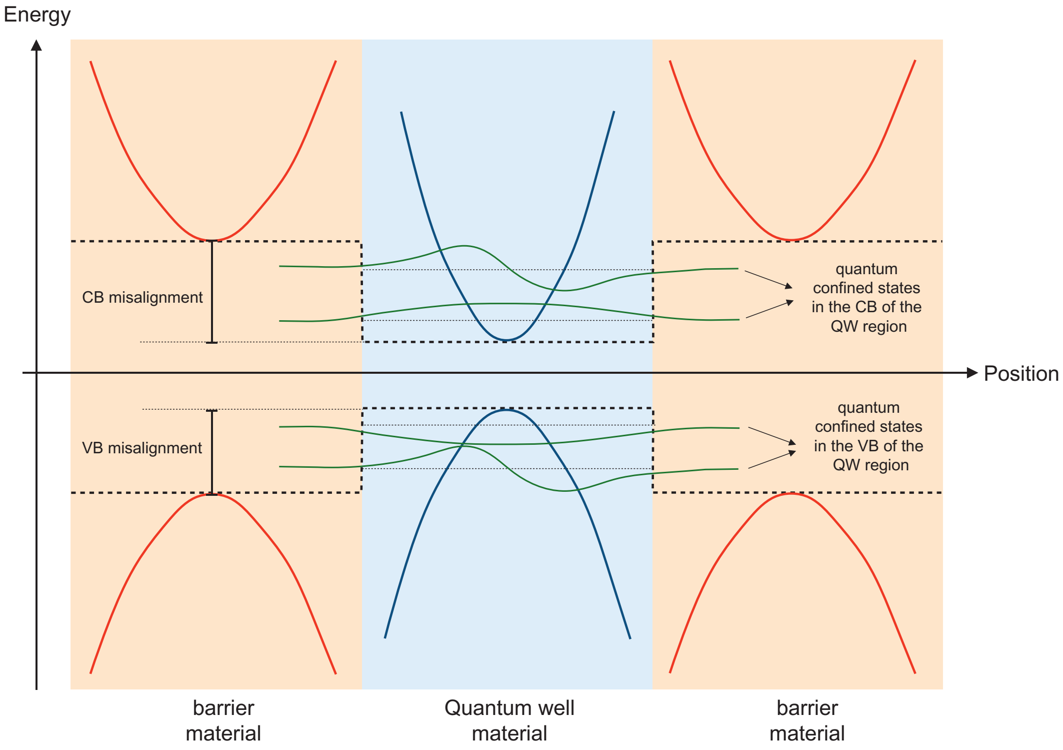
Energy
Position
CB misalignment
VB misalignment
quantum confined states in the CB of the QW region
quantum confined states in the VB of the QW region
barrier material
Quantum well material
barrier material

Fig. 2 Schematics of band alignment and position-dependent effective mass in heterostructures.

$$p = \int_{-\infty}^{E_v} g_v(E)[1 - f(E)]\mathrm{d}E, \tag{21}$$

where $g_{c,v}(E)$ are the density of states in the conduction and valence bands, respectively. $f(E) = 1/1 + e^{-(E-E_f)/e_B^T}$ is the Fermi-Dirac distribution, E_f is the Fermi energy, k_B is the Boltzmann constant, and T the absolute temperature. The density of states $g_v(E)$ $(v = c, v)$ represents the number of states per unit volume per unit energy in ν band, and it is obtained by counting all states in the reciprocal space for each energy band. Assuming the parabolic band approximation, the respective densities of states (DOS) are given by:

$$g_c(E) = \frac{1}{2\pi^2}\left(\frac{2m_e^*}{\hbar^2}\right)^{3/2}\sqrt{E - E_c}\,(E > E_c), \tag{22}$$

$$g_v(E) = \frac{1}{2\pi^2}\left(\frac{2m_h^*}{\hbar^2}\right)^{3/2}\sqrt{E_v - E}\,(E < E_v). \tag{23}$$

For anisotropic materials, m_e^* and m_h may be slightly different from the values obtained from the curvatures of the band structure. For Si, for example, the DOS effective mass becomes $m_e^* = (m_l m_t^2)^{1/3}$. Solving Eqs. (20) and (21) for nondegenerate semiconductors i.e., $(E_c - E_f) \geq 3k_BT$ and $(E_f - E_v) \geq 3k_BT$, one obtains

$$n = N_c e^{-(E_c - E_f)/k_BT}, \tag{24}$$

$$p = N_v e^{-(E_v - E_f)/k_BT}. \tag{25}$$

N_v $(v = c, v)$ is known as the effective density of states in each band, and they are given by:

$$N_v = 2\left(\frac{m_v^* k_B T}{2\pi\hbar^2}\right)^{3/2} \tag{26}$$

In intrinsic (pure) materials, for every electron in the conduction band there is a hole in the valence band. This equilibrium condition is commonly written as $n = p = n_i$, where n_i is the intrinsic carrier concentration. Applying the condition $np = n_i^2$ (that holds even for doped materials), one obtains:

$$n_i = \sqrt{N_c N_v}\, e^{-E_g/2k_BT}. \tag{27}$$

The above quantities provide a drastically simplified method to parameterize carriers concentrations of solid state materials in terms of their effective masses, energy gap and temperature.

Two-dimensional materials

The recent discovery of graphene and other two dimensional (2D) materials (e.g., phosphorene, transition metal dichalcogenides, boron nitride just to mention a few) motivated huge efforts to investigate their electronic properties and to develop practical applications with those materials. Nowadays, there is a plethora of reported 2D materials with a wide variety of properties, ranging from metallic to semiconductors (Miró et al., 2014).

In 2D materials, the definition of effective masses in terms of band curvature (Eq. 5) still holds with a few important differences. The most intriguing difference is found in graphene, whose band structure exhibit linear dispersion, i.e., $E\left(\vec{k}\right) \propto k$ near the Fermi energy forming the so called Dirac cones, for which the absence of band curvature clearly results in an infinite effective mass. On the other hand, electrons in graphene are said to be *massless* in a clear contradiction with the conventional solid state definition of effective mass. This confusion is explained if we consider electrons in graphene as relativistic particles, for which the energy-momentum relationship is given by $E^2 = (pc)^2 + (m_0c^2)^2 = (\hbar kc)^2 + (m_0c^2)^2$, where m_0 is the rest mass of the particle. For *massless* particle we simply obtain $E = \pm \hbar kc$. Such a linear energy dispersion of *massless* relativistic is similar to the band structure of graphene at low energies.

In practice, cyclotron resonance measurements have shown that the electrons in graphene are not massless (Novoselov et al., 2005), and the electronics properties of graphene are better described by Dirac equation rather than Schrödinger equation. Thus, the alternative definition of effective mass for materials exhibiting linear band structure is (Ariel and Natan, 2012)

$$m^* = \hbar^2 k\left(\frac{dE(k)}{dk}\right)^{-1}. \tag{28}$$

As for 2D materials with non-diverging effective masses defined by Eq. (5), the most important difference is the absence of heavy-hole, light-hole and spin-orbit split-off bands as compared to three-dimensional materials.

Measurement methods

Effective masses have been traditionally measured using cyclotron resonance (Dresselhaus et al., 1955). In this method, the microwave absorption of an electron moving in an orbit perpendicular to a static magnetic field exhibits a peak at $\omega_c = \frac{eB}{m^*}$, where e is the electron charge, and B is the magnetic field intensity. The effective mass can be also determined by methods that directly measure the band structure $E\left(\vec{k}\right)$ like low energy angular-resolved photoemission spectroscopy (ARPES) (Damascelli, 2004).

Measurements of specific heat C_v in Fermi systems can be also used to determine the effective mass. At very low temperatures, the phonons contribution to C_v becomes negligible, and C_v becomes dominated by the electronic contribution. At this regime, one has $C_v = \pi^2 k_B^2 g(E_f)T/3$, where $g(E_f)$ is the density of states at the Fermi energy (Ashcroft and Mermin, 1976). Using Eq. (22), one obtains $C_v = k_B^2 k_f m_e^* T/3\hbar^2$, where k_f is the radius of the Fermi sphere in the reciprocal space. However, thermodynamic experiments are not able to distinguish directional effective masses, and the values estimated from C_v represent the DOS effective mass.

Effective masses are also helpful for the analysis of other experiments associated to electronic properties:

- The electrical conductivity σ is given by

$$\sigma = \frac{ne^2\tau}{m_e^*}, \tag{29}$$

where n is the density of mobile electrons, τ is a transport relaxation time. An electrical conductivity for holes can also be determined by replacing m_e^* by $m_h^*$and n by p, where p is the density of mobile holes. In the most general case where electrons and holes contribute to the charge transport, the total conductivity is $\sigma = \sigma_e + \sigma_h$.For anisotropic materials, the electrical conductivity assumes a tensor form.

- Plasma oscillation is a collective excitation of all available mobile electrons whose oscillation frequency (also known as plasma frequency) is:

$$\omega_p^2 = \frac{ne^2}{m_e^*\varepsilon} \tag{30}$$

where e is the electron charge, and ε is the dielectric permittivity of the material.

- Excitons are fundamental electronic excitations associated to bound states of e-h pairs acting as a hydrogen-like atom. The exciton binding energy is given by:

$$E_b = \frac{\mu}{m_0}\frac{\varepsilon_0^2}{\varepsilon^2}\frac{R_y}{n^2}\ \ (n = 1, 2, 3, \ldots) \tag{31}$$

where $R_y = 13.6$ eV is the Rydberg energy, and $\mu = m_e^* m_h^*/(m_e^* + m_h^*)$ is the reduced effective mass of the exciton.

Conclusion

In conclusion, effective mass is a cornerstone concept of condensed matter physics whose importance and applicability is far greater than what it is possible to cover in such a short chapter. The beauty of the effective mass theory relies on the fact that it provides a rather simple method to describe materials in terms of a reduced number of parameters (e.g., band gap energy and band curvatures at high symmetry points of the Brillouin zone). Perhaps its most important practical consequence is the envelop function approximation that allows to accurately model the electronic and transport properties of quantum heterostructures, which are ubiquitous in modern technologies.

References

Ariel V and Natan A (2012) Electron effective mass in graphene.
Ashcroft NW and Mermin ND (1976) *Solid State Physics*. Saunders College.
Bastard G (1988) *Wave Mechanics Applied to Semiconductor Heterostructures, Monographies de physique*. Les Editions de Physique.
Burt MG (1992) The justification for applying the effective-mass approximation to microstructures. *Journal of Physics: Condensed Matter* 4(32): 6651–6690.
Chuang SL (1995) *Physics of Optoelectronic Devices*. New York: Wiley.
Damascelli A (2004) Probing the electronic structure of complex systems by ARPES. *Physica Scripta* T109: 61.
Dresselhaus G, Kip AF, and Kittel C (1955) Cyclotron resonance of electrons and holes in silicon and germanium crystals. *Physical Review* 98(2): 368–384.
Kane EO (1966) The k.p method. In: Willardson RK and Beer AC (eds.) *Semiconductor and Semimetals*. vol. 1, pp. 193–217. New York: Academic Press.
Luttinger JM and Kohn W (1956) Quantum theory of cyclotron resonance in semiconductors: General theory. *Physics Review* 102: 1030–1041.
Miró P, Audiffred M, and Heine T (2014) An atlas of two-dimensional materials. *Chemical Society Reviews* 43(18): 6537–6554.
Novoselov KS, Geim AK, Morozov SV, Jiang D, Katsnelson MI, Grigorieva IV, Dubonos SV, and Firsov AA (2005) Two-dimensional gas of massless dirac fermions in graphene. *Nature* 438(7065): 197–200.

Electronic structure: Impurity and defect states in insulators[☆]

AM Stoneham, J Strand, and AL Shluger, Department of Physics and Astronomy, University College London, London, United Kingdom

© 2024 Elsevier Ltd. All rights reserved.

This is an update of A.M. Stoneham, A.L. Shluger, Insulators, Impurity and Defect States in, Editor(s): Franco Bassani, Gerald L. Liedl, Peter Wyder, Encyclopedia of Condensed Matter Physics, Elsevier, 2005, Pages 380–388, ISBN 9780123694010, https://doi.org/10.1016/B0-12-369401-9/00471-X.

Introduction 856
Theoretical methods for defect electronic structure 858
Coupling of electrons and lattice deformation 860
Self-trapping and localization 862
Defects in disordered materials 863
Surfaces and interfaces 863
Conclusion 865
References 865

Abstract

Defects in insulators control properties of materials and devices. We first define the main issues and describe the theoretical methods for calculating defect electronic structure. Then we describe the main point defect types and consider how defect electrons couple to the motion of nearby ions. The concepts of electron and hole localization and self-trapping of polarons and excitons are introduced next. Properties of defects in disordered systems are briefly outlined and key points concerning defects at surfaces and interfaces are discussed including the dependence of the defect charge state on the position of the system Fermi energy. Finally, a short outlook is provided.

Key points

- Outline the main issues pertaining to defects in materials and defect types
- Define the main structure parameters of interest
- Outline the main theoretical models and methods used to study defect properties
- Introduce the electron-lattice coupling
- Describe intrinsic and extrinsic polaron and exciton localization and self-trapping
- Outline properties of defects in disordered materials
- Describe the main defect-induced properties of surfaces and interfaces

Introduction

Serious studies of materials are often serious studies of defects, for control of properties of materials implies control of defects or impurities. Understanding the electronic structure of defects in insulators has helped the development of microelectronic and quantum devices, the photographic process, solid electrolytes, and the applied surface physics of sensors and catalyst substrates (Crawford and Slifkin, 1972; Fleetwood et al., 2009; Hayes and Stoneham, 1985; Lannoo and Bourgoin, 1981; Stoneham, 1975). Here we will focus mainly on *point defects*, but dislocations and grain boundaries are very important too. The understanding of defect properties is based on a synthesis of theories, modelling, and experiment.

Defining the issues. Some of the common point defects are shown schematically in Fig. 1. They can be created in different charge states and undergo transformations during the lifetime of materials and devices. When a new material is created, which defects are important? Will there be vacancy-interstitial pairs (Frenkel defects) or just vacancies of several types (Schottky defects)? Will there be non-standard ionic charge states, like 3+ Fe ions in FeO? Could one species move on to the sites of another, e.g. As antisites on Ga sites in GaAs? Can the material be doped with electrically-active impurities? Are there understandable trends of properties from material to material in some class, like II-VI compounds? Electronic structure is subtle and varied, with the key ideas identified by a mix of theory and experiment.

In most insulators Coulomb energies dominate, so antisite defects are not energetically easy, and charge transfer across sublattices is difficult, instead non-stoichiometry is common. Thus vacant lattice sites (*vacancies*), ions placed at normally unoccupied sites (*interstitial ions*), foreign ions present as impurity or dopant, and ions with charges different from those of the

---

[☆] *Change History*: September 2022. J Strand and AL Shluger prepared the update. Figs. 1, 3, 5, 7, 8 are new. All chapters and figures have been updated.

https://doi.org/10.1016/B978-0-323-90800-9.00031-7

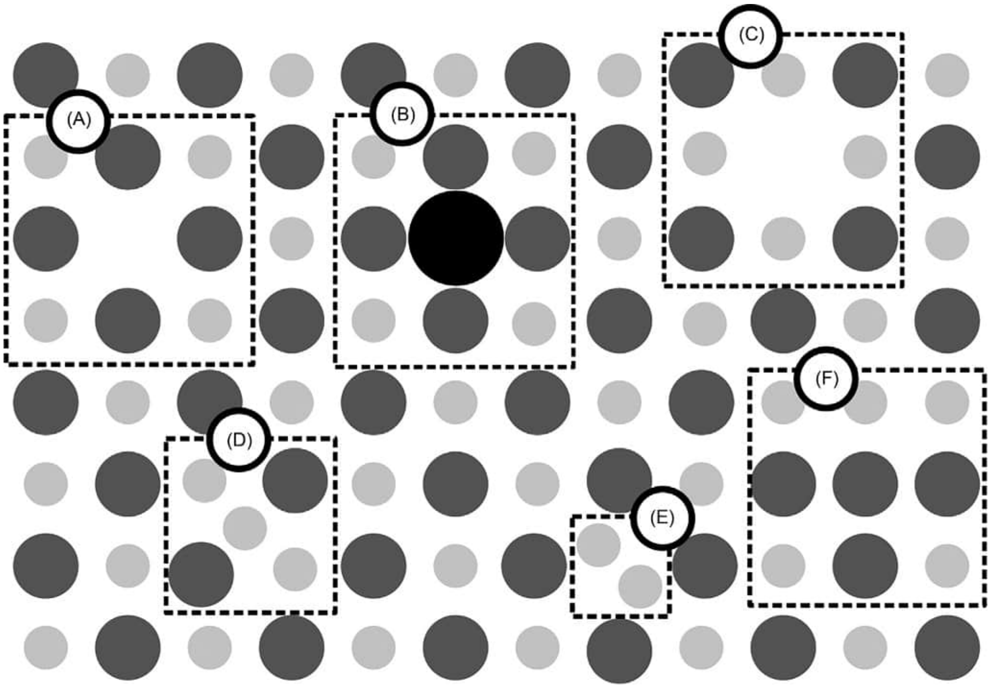

Fig. 1 Schematic of basic defect types in a binary insulator AB. (A) and (C) are vacancies of atoms type A and B, respectively. (B) An impurity atom on the site of atom A. (D) and (E) are two types of interstitial configurations of atom A: (D) – self-interstitial and (E) dumbbell interstitial. A pair of vacancy and interstitial defects, such as (A) + (D) or (A) + (E), is called a Frenkel pair. A pair of vacancies of atoms A and B, such as (A) + (C), is called a Schottky pair. (F) is a pair of anti-site defects, where the atom of type B occupies the site of the atom type A and the atom of type A occupies the site of the atom type B.

host ions are prevalent defect types (Fig. 1). Electronic defects may arise either as ions with charges deviating from those on lattice ions, or from excitation of electrons from filled valence bands to empty conduction bands. When a valence-band electron is missing, one has an electron hole (*hole*) and its behavior can be compared with that of an electron in a normally empty conduction band. Electron and hole together can form a transient neutral species, the *exciton*. In the absence of macroscopic electric fields or irradiation, ionic lattices must be electrically neutral overall, implying that one charged defect must be compensated by another charged defect or defects to satisfy the electro-neutrality condition locally or over the whole sample. The charges of defects and of the regular lattice particles, defined with respect to the neutral ideal lattice, are called *effective charges*.

Complexity is the norm for advanced materials. When solid-state lasers degrade, when mechanical properties change under irradiation, defect processes occur in parallel on timescales from femtoseconds upwards. In a composite material, defect phenomena may happen in the matrix, the fiber or at the interface. When a metal is oxidized, interfacial, diffusional and impurity processes co-exist. Separating these processes by experiment alone may not be feasible. The electronic structure theory establishes priorities, and is used to organize and analyze massive amounts of data, to identify what is novel and point to significant issues.

Which electronic structure parameters are of interest? Defects control the properties and performance of materials and devices in various ways. For luminescence, whether of rare earths in oxides or sulfides or CsI:Na, the spectroscopic properties of impurities, optical *absorption and luminescence energies*, are of the utmost importance. Bragg grating formation in silica fibers is associated with the optical absorption of induced defects. Defect species in gate dielectrics, such as oxygen vacancies, impurities and hydrogen, influence device performance. In microelectronic devices these defects may initiate degradation, trap charge, or create fixed charge, which scatters carriers in the Si substrate. Their *electron and hole trapping energies and cross-sections* are of main interest. Many radiation-induced processes in insulators involve forming self-trapped excitons and holes, so the electron coupling to lattice deformation plays a crucial role. Designing *qubit* formation in wide band gap insulators requires deep defect states which can be initialized, manipulated, and measured with high fidelity at room temperature. Among other criteria, they should possess *optical transitions* that do not introduce interference from the electronic states of the host. In photovoltaic materials, except for selected dopants, defects often have detrimental effects and should be eliminated to minimize *charge recombination*. On the other hand, in photocatalysis defects often play an active role by stabilizing *charge separation* and mediating rate-limiting catalytic steps.

Experimental *defect characterization* is vital for our understanding which defects influence the optical, magnetic and electrical properties of materials. A broad range of characterization techniques includes vibrational spectroscopy, electron paramagnetic resonance (EPR), optical techniques, e.g. photoluminescence spectroscopy, and electrical techniques, such as deep-level transient spectroscopy (DLTS), as well as optoelectrical techniques, e.g. photocurrent spectroscopy (Bassani and Pastori Parravicini, 1975; Fleetwood et al., 2009; Spaeth and Overhof, 2003; Toyozawa, 2003; Weil and Bolton, 2007). Each method has its advantages and disadvantages. Therefore, the different methods complement each other as there is not a single method to fully characterize any defect. The raw data of defect studies describe spectroscopic observations and their dependence on time and other parameters, such

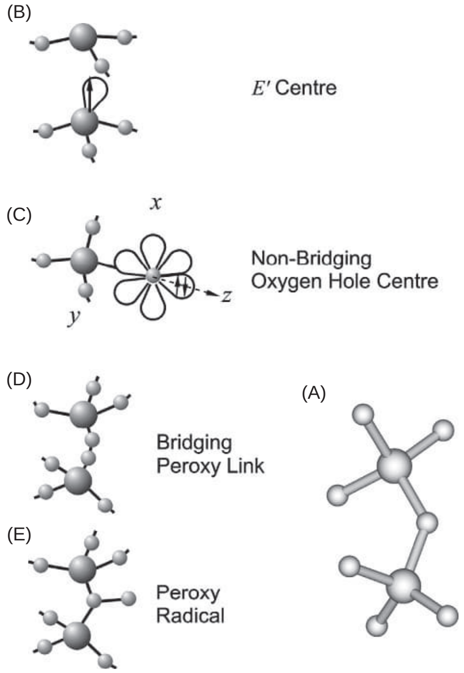

Fig. 2 Schematics of defect models developed for amorphous silica. (A) A fragment of perfect SiO_2 lattice showing two tetrahedral SiO_4 units connected via a common oxygen ion; smaller balls are oxygen ions. (B) An oxygen vacancy with an unpaired electron on a dangling bond of a three-coordinated Si atom. (C) A non-bridging oxygen atom trapping a hole; the partially filled *p*-orbitals of the oxygen atom are shown. (D) A bridging peroxy linkage center formed by incorporation of an oxygen atom at a regular Si – O – Si bond. (E) A peroxy radical center formed by attachment of an oxygen ion to a regular oxygen site.

as dopant concentration, temperature, pressure, irradiation power and dose. Carefully-obtained data provide the basis for formulating *defect models*. Fig. 2 shows several such models for major paramagnetic defects in irradiated fused silica. The most reliable models knit together the best-available experimental data from many sources with solid-state physics theory, often aided by detailed calculations. Some of the key ideas underpinning modern calculations of the electronic structure of point defects in insulators are reviewed here. We start from outlining some of the theoretical methods used to study defect electronic structure. Then we review some of the concepts necessary for understanding the electronic properties of point defect in crystalline and disordered solids and at interfaces.

Theoretical methods for defect electronic structure

Even simple answers can be useful answers. At one level, electrons and holes can be treated implicitly only. Born's model of ionic solids as *polarizable point ions*, interacting through transferable inter-atomic potentials, was the basis for describing cohesion, dielectric and vibrational properties of perfect solids. The large Coulomb energies are the reason why accurate defect studies were first practical for ionic crystals. Yet polarization energies are large too (for an ion of charge $Z + 2$ substituting for a $2+$ Mg ion in MgO, Madelung terms are about $24 \times Z$ eV and polarization about $6 \times Z^2$ eV) and explain why so many charge states of impurities can be stable. Mott and Littleton's systematic way of calculating the Coulomb and polarization contributions to defect formation energies in ionic solids forms the basis of many current state-of-the art codes (Hayes and Stoneham, 1985; Stoneham, 1975).

Modelling simple one-electron systems: For non-polar semiconductors, *effective mass theory* is superb, often working well beyond its justification using empirical bulk properties. For ionic crystals, point ions are a surprisingly good start, but *pseudo-potential methods* were necessary to explain why, and to give the "ion-size corrections" needed for accurate trends over the whole series of alkali halides and oxides. The F center (electron at an anion vacancy) was the first deep trap to be predicted well over a very wide range of halide and oxide hosts, and the same techniques were successful in early modelling states of self-trapped excitons.

For most systems, however, the *many-electron treatment* is essential. Here both first-principles and empirical theories are often used. Empirical methods help most in new situations where what is important is still not certain, for more complex systems, where computer power and technique has yet to be sufficient for the best methods, or for extrapolation across a broad range of materials. Many of the problems addressed empirically today will be solved by far better methods tomorrow.

By choosing *first-principles methods* one is not reliant on parametrized theories or fitting possibly inaccurate experiments (Martin, 2004). These theories can be applied more reliably to hypothetical materials, defects for which data are not available, or for extreme temperature, pressure and irradiation conditions. Computational techniques for modelling defects in solids exist in a form of computer codes implementing a *model of a solid with a defect* and *methods* for calculation of defect structure and properties (Freysoldt et al., 2014).

Most first-principles *methods* are based on *Hartree-Fock* and *Density Functional Theory* (DFT) approximations. DFT states that the ground state properties of a system are given by the charge density, and state-of-the-art methods allow us to compute the charge density and energy self-consistently using various effective exchange-correlation potentials that account for the quantum mechanical interactions between electrons. The local density approximation (LDA) takes the exchange-correlation potential from uniform electron gas theory at the density for each point in the material. The generalized gradient approximation (GGA) includes the effects of local gradients in the density. DFT's success is facilitated by the computational efficiency of these approximations, which made it applicable to studies of complex materials and defects. The continuous development of more sophisticated density functionals as well as Quantum Monte Carlo methods significantly improved the accuracy of predicted defect properties. As computing power has increased, hybrid DFT functionals have also been employed, which combine DFT estimation of exchange with a percentage of Hartree-Fock exchange (called "exact" exchange). Hybrid DFT has been successful in predicting band gaps and describing the behavior of localized states.

The main computational *models* of a point defect in a crystal include a periodic model, an embedded cluster, and molecular cluster models, illustrated in Fig. 3. They differ by the boundary conditions imposed on a system wave-function. The *periodic model* was first developed for calculating electronic structure and properties of ideal crystals (Kantorovich, 2004; Kittel, 2004), whereas the cluster model evolved from molecular calculations (Grimes et al., 1992). They are compared in Table 1. Within the periodic model a unit cell with a defect is periodically translated. It is ideal if one is interested in the properties of large concentration of neutral defects, which weakly perturb the surrounding lattice. Many molecular cluster models treat a defect with surrounding atoms simply as a molecule or *cluster*. They disregard the effects of the rest of the atoms outside the cluster, but apply semi-empirical fixes to the atoms at the cluster surface to diminish their adverse effect. This major problem is addressed and partially solved in "embedded

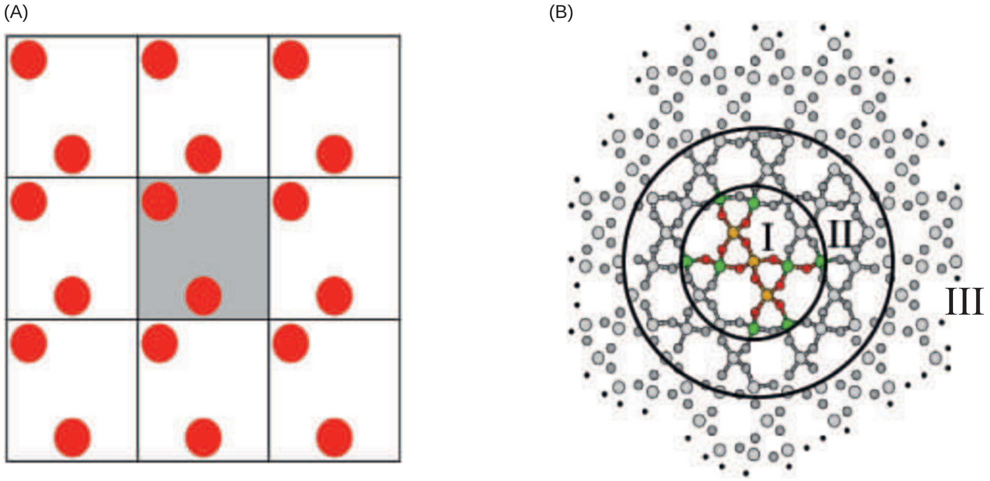

Fig. 3 Schematic of two prevalent computational models used for simulations of defects. (A) A periodic model, where each rectangle represents a periodic cell. (B) An embedded cluster model, where a cluster of atoms in the region I is treated using a high level quantum-mechanical theory (DFT, Coupled Cluster, GW); the surrounding region II is treated on a more approximate level of theory (semi-empirical quantum chemistry, atomistic simulations using a polarizable ion model to treat atomic polarizations); the region III is a polarizable continuum representing the rest of the infinite solid. The boundary between regions I and II is represented by link atoms or embedding potential to provide a seamless link between the two regions.

Table 1 Comparison of computational methods used in defect calculations.

Models	*Methods*	*Properties*
Molecular cluster: molecule represents local defect environment in a solid	Density Functional Theory and ab initio and semi-empirical Hartree-Fock Theory in localized basis sets	Can predict local defect structure, vibrational, optical and EPR properties providing intermediate and long-range order are not important.
Embedded cluster: local defect environment is treated quantum-mechanically and the rest of the solid structure treated classically	Density Functional Theory and ab initio and semi-empirical Hartree-Fock Theory in localized basis sets	Can predict local defect structure, ionization energies and electron and hole affinities, vibrational, optical and EPR properties and diffusion parameters. Can treat infinite amorphous structures.
Periodic: defects are repeated periodically in a lattice	Density Functional Theory, Hartree-Fock Theory, tight-binding methods in plane wave and localized basis sets.	Can predict local defect structure, electrical levels, vibrational and EPR properties and diffusion parameters providing the interaction between periodically translated defects is small. Treats amorphous structures as periodic arrangement of disordered cells.

cluster" models, where a cluster with a defect is embedded in an infinite solid (Fig. 3B). This model works well in ionic insulators, such as MgO, however, for insulators with ionic-covalent character of bonding, such as SiO_2 or Ga_2O_3, an accurate embedding is challenging to achieve. It is ideal for modelling individual defects and allows one to self-consistently include the effect of polarizable environment into predicting the defect characteristics, which is particularly important for charged defects in insulators.

Both static Hartree-Fock and DFT methods are ground state theories, in the form of an effective one-particle Schrödinger equation (the Kohn-Sham equation in the case of DFT). The eigenvalues of these equations are often interpreted as electron energies and their differences as optical excitation energies. This interpretation is linked to an intuitive picture of independent electrons occupying well-defined energy levels. However, this is a gross simplification: the electrons are not independent, and when, for example, an electron is removed to form a hole, all remaining electrons respond by changing their electronic states. This electron relaxation and other quantum-mechanical contributions must be taken into account for energy differences to be calculated correctly. This can be achieved using advanced methods of quantum chemistry, such as Coupled Cluster, as well as other techniques often implemented in periodic boundary conditions, such as GW (Golze et al., 2019). The improved efficiency of GW facilitated accurate predictions of electronic excitations in materials and defects as well as of charged excitations as measured in direct or inverse photoemission spectroscopy. One can retain the picture of one-particle energy levels, but these particles are quasi-electrons and quasi-holes, which embody the effects of interaction with all the other particles.

The concept of *quasi-particles* is often used to represent the electronic states of an insulator with a defect schematically, as shown in Fig. 4. Such energy diagrams usually include the highest valence band and the lowest conduction band of the system (Freysoldt et al., 2014). Point defects and impurities may induce occupied and unoccupied states in the gap and so-called resonant states in the valence and conduction bands of the system. The wavefunctions of defect states are often strongly localized in the defect area (Fig. 5) and the corresponding quasi-electron energies are located in the band gap of the solid. The resonant states differ from the ordinary band states in that they are localized in the defect region with the major wavefunction component decaying exponentially from the defect, but their quasi-electron energies are located within the occupied or unoccupied bands. Quasi-particle energy diagrams similar to that shown in Fig. 4 are used to summarize pictorially the electronic structure and processes involving optical excitation, luminescence, ionization and energy transfer between defects.

Coupling of electrons and lattice deformation

One of the issues crucial for the understanding defect properties is how defect electrons couple to the motion of nearby ions or, alternatively, the way defect electrons apply forces to host ions (Hayes and Stoneham, 1985; Itoh and Stoneham, 2001; Song and Williams, 1993; Stoneham, 1975). The static polarization and distortion of the host lattice affects defect formation and transition energies; the dynamics leads to transitions between electronic states and to defect diffusive motion. Optical spectra change qualitatively: the optical line width, the existence of a zero-phonon line, and the Stokes shift, the energy difference between optical absorption and emission energies, give direct measures of this coupling. Although any of a large number of atomic displacements might influence a defect in a solid, often a very specific combination of displacements is especially important. For example, the radial displacement of the nearest neighbors to the defect can be represented by a single *configuration coordinate* Q, as illustrated in Fig. 6. We note that it is most unlikely that the coordinate Q will be one of the dynamically-independent *normal vibrational modes* **q**. It is almost certain that normal modes of many different frequencies will be needed to make up Q. Moreover, the precise mode combinations making up Q will depend on the defect electronic state (it will be different in the excited state of defects shown in

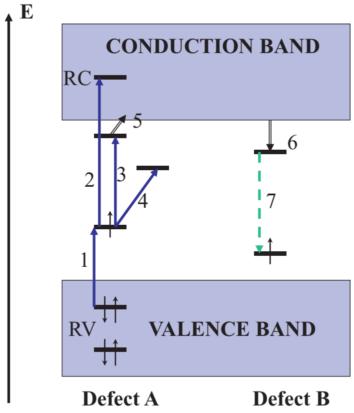

Fig. 4 The quasi-particle energy diagram representing total energies of a solid with two defects A and B. The defect A produces local single-occupied and unoccupied states within the band gap, and resonant states (denoted RV and RC) in the valence and conduction band, respectively. The defect B is characterized only by two local states in the gap. The arrows 1–4 correspond to optical transitions between states in the defect A. The arrow 5 corresponds to thermal ionization of an electron from the excited state of the defect A into the conduction band. Process 6 is non-radiative trapping of an electron from the conduction band on an empty state of the defect B. Process 7 is the de-excitation of the defect B which may be either radiative or non-radiative.

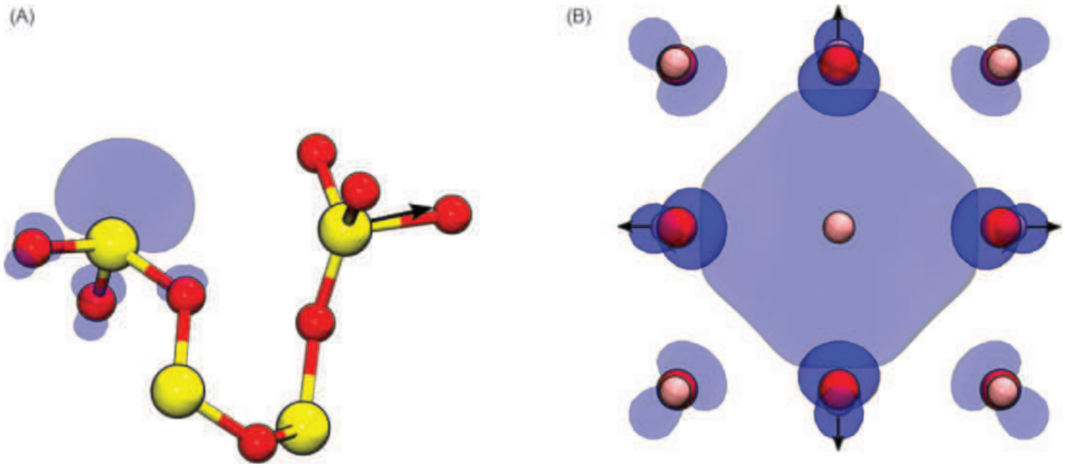

Fig. 5 The geometric configurations and electronic states of positively charged oxygen vacancies in oxides. (A) The relaxed configuration of the positively charged oxygen vacancy, E'_1 center, in α-quartz; red are oxygen ions. The envelope of the density of the unpaired electron mostly localized on a p-orbital of one Si ion is shown pointing into the vacancy. The arrow indicates the direction of the displacement of the second Si ion of the vacancy. This is the so-called "puckered" configuration of the E'_1 center. (B) The relaxed configuration of the positively charged oxygen vacancy, F^+ center, in MgO; red are oxygen ions. The envelope of the density of the unpaired electron localized on an s-orbital inside the vacancy is shown. Note the electron density of the unpaired electron propagates much further out from the vacancy. Depressions in the envelope show that the unpaired electron avoids the core electrons of surrounding Mg ions. The arrows indicate the symmetric displacements of the six nearest-neighbor Mg ions surrounding the vacancy. This radial displacement of the six Mg ions is often used as a configuration coordinate, Q, in considering the spectroscopic properties of the F^+ center.

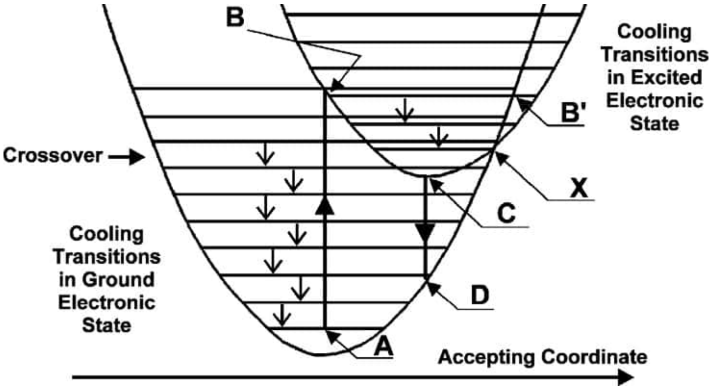

Fig. 6 Configuration coordinate diagram. The figure shows the main characteristic energies and transitions, both radiative and non-radiative. Accepting coordinate represents one of the configuration coordinates effective in vibrational energy dissipation. The vertical arrow A – B corresponds to a vertical (so called Franck-Condon) transition between the ground and excited states of the system represented by two harmonic energy surfaces. Horizontal lines indicate vibrational energy levels with small arrows showing transitions between these levels (cooling transitions) dissipating the excess vibrational energy (relaxation energy). The transition C – D between the lowest vibrational state in the excited state back to the ground state energy surface corresponds to the Franck-Condon de-excitation with photon emission (luminescence or phosphorescence). It is accompanied by further cooling transitions in ground electronic state. The area near the crossing point X is where the system can cross nonradiatively from the excited to the ground state. In this case the relaxation energy, which is the energy difference between X and A or between C and A, is dissipated into lattice vibrations. The zero-phonon transition energy is the energy difference between C and A.

Fig. 4). Yet this configuration coordinate model is surprisingly effective, giving an invaluable tool for showing what happens after electronic excitation, and a simple language for describing defect processes. An example of such a diagram is given in Fig. 6.

A central issue for optical and electronic materials is how they recover after excitation. A good X-ray phosphor emits the most visible light after excitation and degrades least from defect production. A solid-state laser needs both population inversion and a lack of wasteful competing processes; carrier capture in semiconductors determines what defects and materials are acceptable; photographic (not to mention the photosynthetic) processes have their own demands. In such cases, non-radiative transitions are central, a role evident from over half a century of theory.

In *nonradiative decay*, excitation energy is transformed into heat, defect production, or to excitation of other electrons, the so-called Auger processes which are especially important at higher carrier densities. The recombination of carriers in semiconductors and insulators is governed mainly by nonradiative processes often described by the Shockley-Read-Hall model. The probability of this process decreases when the number of the emitted phonons increases. Therefore, recombination is facilitated by the presence of deep impurity or other defect states (recombination centers), because this makes it possible to reduce the number of phonons emitted in one event. Hence, the rate of recombination is governed by the nature and concentration of recombination centers in a crystal. For deep centers, the nonradiative carrier capture occurs via multiphonon emission. Another common manifestation of nonradiative decay of an excited state concerns suppression of luminescence. Can one tell from optical absorption data alone whether or not luminescence will occur? Huang and Rhys's (1950) seminal study showed one possible criterion: the larger the excitation energy, the faster the optical transition and the slower the non-radiative decay, since larger numbers of phonons would be needed (see Fig. 6). Dexter et al. (1956) developed other criteria relating to the final state energy achieved by optical excitation and the energy at which the ground and excited electronic states intersected on the configuration coordinate diagram: the energy surfaces, rather than some matrix element, controlled the result. This led Bartram & Stoneham to show that simple expressions could be given for branching ratios at critical steps, and that these ideas - which could be applied to much more complex cases - correctly predicted behavior over a wide range of systems.

Self-trapping and localization

Landau made the remarkable suggestion of *self-trapping:* an electron could be so strongly coupled to the lattice that, even without a defect, it would lead to lattice distortion and be effectively immobilized. The suggestion was the basis of the important ideas of small polarons (incoherent hopping of localized carriers, as in some transition metal oxides, rather than the long mean-free-path motion of carriers in Si or metals), and even of the recently-observed barrier to self-trapping (Itoh and Stoneham, 2001; Song and Williams, 1993). The observed small polarons (e.g. self-trapped holes in halides in Fig. 7) show both the soundness of Landau's idea and (since naive belief in band theory appears to be violated) the importance of theorists learning from experiment too. Hole polarons are ubiquitous in oxides and halides, but electron polarons are less common. If a polaron can trap two electrons (or holes) with the second bound more strongly than the first, it has *negative-U* properties (where pairing of two electrons and two holes in a localized region is favored against single polaron formation), as originally suggested by Anderson (1975). Distortion and polarization dominate too in negative-U behavior of defects, where a charge disproportionation is exothermic (so the

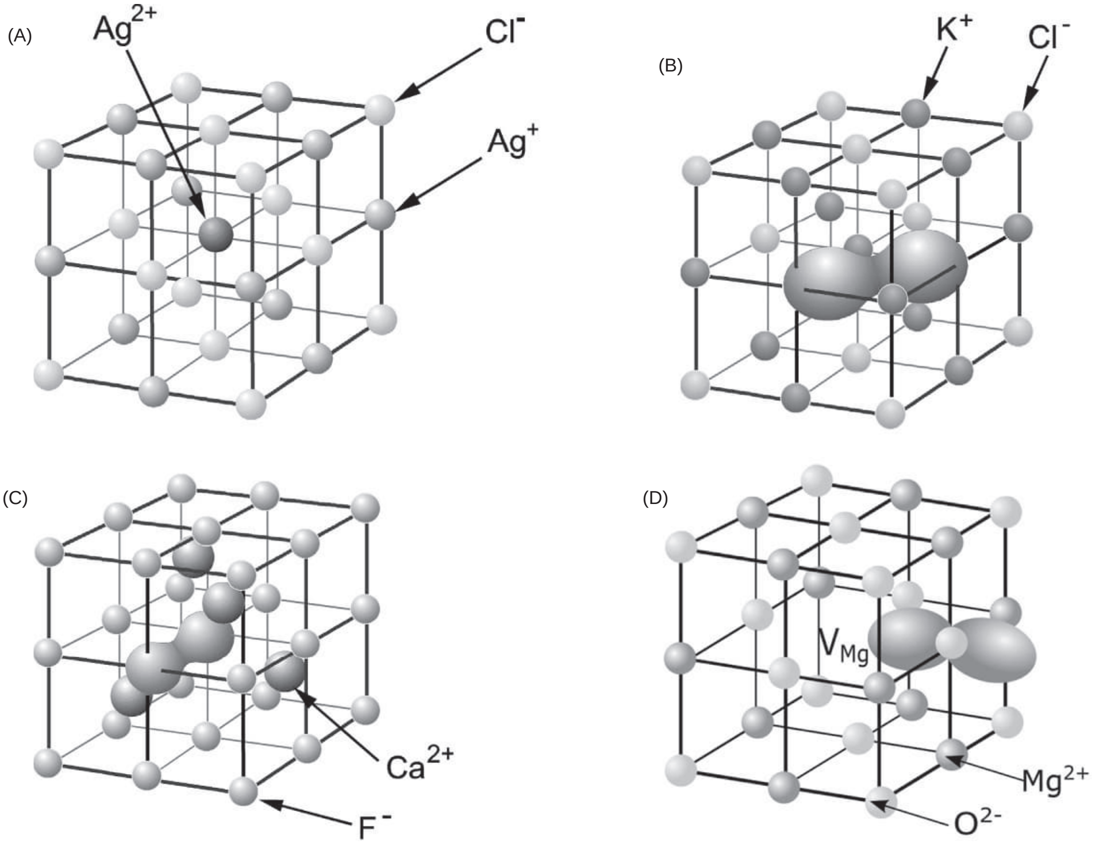

Fig. 7 Atomic structure of the trapped hole centers in halides and MgO: (A) AgCl – the hole is localized on a silver ion; (B) alkali halides of NaCl structure – the hole is localized on two halogen ions forming a Cl_2^- molecule; (C) CaF_2 – the hole is localized on two fluorine ions forming a F_2^- molecule. Note that in (B) – (C) the X_2^- (X = F, Cl) molecular ion occupies two nearest anion lattice sites. (D) The hole localized on an O^- ion neighboring the Mg vacancy (V_{Mg}) in MgO (the so-called V^- center). In all cases, the hole localization is accompanied by a strong distortion of the surrounding lattice (not shown in the figure).

positive vacancies in Si decay from 2 V^+ to $V^0 + V^{2+}$ as well as H^+ and H^- are the preferred thermodynamic states of hydrogen in the bulk of many oxides).

Localization can correspond to carrier or exciton trapping by an isolated defect (*extrinsic trapping*). If there is an attractive perturbation ΔV at a defect site, then, for large enough ΔV, a bound state emerges for the extra electron, hole or exciton. Both impurity-induced potentials and electron-phonon interaction play crucial roles in this localization. Extrinsic electron trapping near defects is quite rare in insulators because electron polarons are not easily formed in these materials. However, exciton trapping by impurities is very common in most insulators.

As well-established examples of extrinsic hole trapping, one can consider holes trapped near cation vacancies in MgO (so called V^o and V^- centers) and holes trapped near Ge and Al impurities in α-quartz (Schirmer, 2006). In particular, cation vacancies in MgO have an effective negative charge of −2e with respect to the lattice and therefore attract positive holes. When one hole is trapped, a paramagnetic V^- center is formed, well-studied experimentally using Electron Paramagnetic Resonance and optical spectroscopy (Fig. 7D). Similar centers occur in CaO, SrO and BaO, in the fourfold coordinated oxides like BeO and ZnO and in related sulfides, selenides and tellurides. In MgO, at low temperatures the hole is strongly localized on one of the six oxygen ions surrounding the vacancy. As the temperature rises, the hole moves more and more rapidly among the equivalent oxygens until it appears delocalized at room temperature. The nature of optical transitions in this center is characteristic to many other hole centers in oxides: there are two types of optical transitions. One is internal to the O^- ion on which the hole is localized. This is a crystal-field transition, since the transition energy is largely determined by the electrical field at the O^- ion due to the Mg^{2+} vacancy. The other, more important, transitions involve charge transfer of the hole to other neighbors of the vacancy. These are analogous to electron excitation from resonant states in the valence band into the unoccupied hole state shown in Fig. 4. Similar charge transfers are important in determining the color of gemstones.

Extensive experimental and theoretical studies show that excitons self-trap in both α-quartz (the most stable crystalline polymorph of SiO_2) and amorphous SiO_2. However, EPR studies show that holes and electrons do not self-trap in α-quartz. Yet, in high-purity Ge-doped quartz, low-temperature irradiation leads to the formation of a hole center localised at an oxygen site next to Ge. This formation of the localized hole centers associated with Ge impurity can be described as "extrinsic self-trapping," where both impurity-induced potential and electron-phonon interaction play crucial roles in the hole localization. In amorphous SiO_2, two types of localized hole centers have been determined that are free from pre-existing lattice defects such as vacancies, interstitials, or impurities, and are trapped by some precursor states induced by *disorder* of amorphous structure. This example demonstrates that the mechanisms of localization processes in amorphous solids are more complicated than in crystalline materials due to co-existence of electron-phonon interaction, structural defects and static potential fluctuations. It is not straightforward to distinguish experimentally the polaron self-trapping due to strong electron-phonon interaction from charge trapping by structural defects in amorphous structure.

Defects in disordered materials

Defect structures and processes in amorphous materials have been studied extensively, partly as fundamental research on model amorphous materials, and partly to understand their extremely important role in technology (Catlow, 1994; Mott and Davis, 1979; Pacchioni et al., 2000). For example, the mechanisms and kinetics of relaxation of electronic excitations in SiO_2 are crucial in micro- and opto-electronics applications (Pacchioni et al., 2000). There are at least four basic fallacies concerning amorphous systems. First, it is wrong to assume there is only a single amorphous structure for a given composition, since the method of preparation can have significant effects. Secondly, it is wrong to think that the *mean* energies of defect formation or of trap ionization in an amorphous structure are sufficient to understand the behavior: the form and tails of the distribution are equally important. Thirdly, one should not assume that crystals and amorphous systems of the same composition have the same values for defect and trap energies. Finally, amorphous systems may have several accessible metastable states, leading to easy reorganization of the structure when the system is perturbed by defect processes, such as carrier trapping and detrapping.

Structural disorder in amorphous materials generally means that all sites are different. In most experimental studies the effect is hidden in broadening of the spectral features and only rarely has disorder been implicated in formation of different structural types of the same defect. Predicting defect properties and relative abundance of different defect configurations generally requires considering not one or several, as in crystals, but a statistical ensemble of structural sites. Additional factors include the sample history and the mechanism of defect formation. This provides new challenges for both theoretical and experimental analysis of defects in amorphous materials.

Surfaces and interfaces

No discussion of defects could be complete without mention of interfaces. Their structures are rarely, if ever, the ideal terminations of perfect crystal structures, and the variety of reconstructions is becoming clearer as microscopies (e.g. the *Transmission Electron Microscope*, *Scanning Tunnelling Microscope* and *Atomic Force Microscope*) develop (Carter and Williams, 2016; Hofer et al., 2003). Defects or impurities at surfaces and interfaces are especially important for most applications. It is impurities close to grain boundaries, which are most strongly involved in the operation of solid-state gas sensors, and the framework of Debye-Hückel theory is central (Maier, 2004). The *space-charge* in silver halides relates to their photographic effectiveness; the Mott and Gurney theory provided the basic framework. Space-charge layers play significant role in the overall performance of electrochemical cells and ionic conduction. Defects at the interface between silicon and gate dielectrics control the reliability of microelectronic devices. Ceramists recognize the importance of segregation in oxides, where experiment shows Mg in alumina gives dramatic improvements in sintering.

Defects also influence adhesion. What controls the variation from one oxide to another of the adhesion of a non-reactive metal? Why (a related question) does liquid Cu wet some oxides (NiO, urania, chromia) but not other similar oxides (MgO, thoria, alumina)? The answer lies largely in the defect populations and basic electrostatics: charged defects close to the highly-polarizable metal have lower energy; those close to the unpolarizable vacuum have higher energy. The operation of gas sensors relies on electron transfer across interfaces, as does the operation of contacts to semiconductors (whether conventional or organic) and electrodes.

Yet another issue, specific for microelectronics applications, is that the dielectric of interest can be in contact with the electrode(s) - semiconducting (e.g. silicon) or metallic - which provides a source of extra electrons. Also, a dielectric film can be placed in the electric field between the two electrodes, which may alter the defect charge states. Charged defects can cause substantial random fields, which may alter breakdown thresholds locally. Typically, for 100 ppm of charged defects, there will be random fields of order 10^5 V/cm. Defects can be involved in stress-induced leakage currents (SILC) and *dielectric breakdown*. In such cases, the defect offers a channel for electron transfer across the dielectric: an electron tunnels from one electrode into an oxide defect; there are then relaxation processes or a sequence of defect processes, and the electron can then tunnel to the other electrode (Fleetwood et al., 2009). What can we say about the defects responsible, their electrical energy levels and relaxation energies (differences in energy for electron capture and emission)? Can we give useful estimates of electron and hole trapping cross-sections? Will there be any field-stimulated diffusion of defects?

To define which charge state of an intrinsic defect (e.g. vacancy) or incorporated defect species is favored, assuming the common case of oxide film grown on silicon, the source or sink of electrons is the bottom of silicon conduction band at the Si/SiO_2 interface. Hence the *chemical potential* of the electron can be chosen at the bottom of Si conduction band or at the silicon midgap energy. Electrons are assumed to be able to tunnel elastically or inelastically from/to these states to/from defect states in the oxide and create charged species as illustrated in Fig. 8. Most calculations use experimental information to estimate the energy of an electron at the bottom of the conduction band of Si with respect to the defect states.

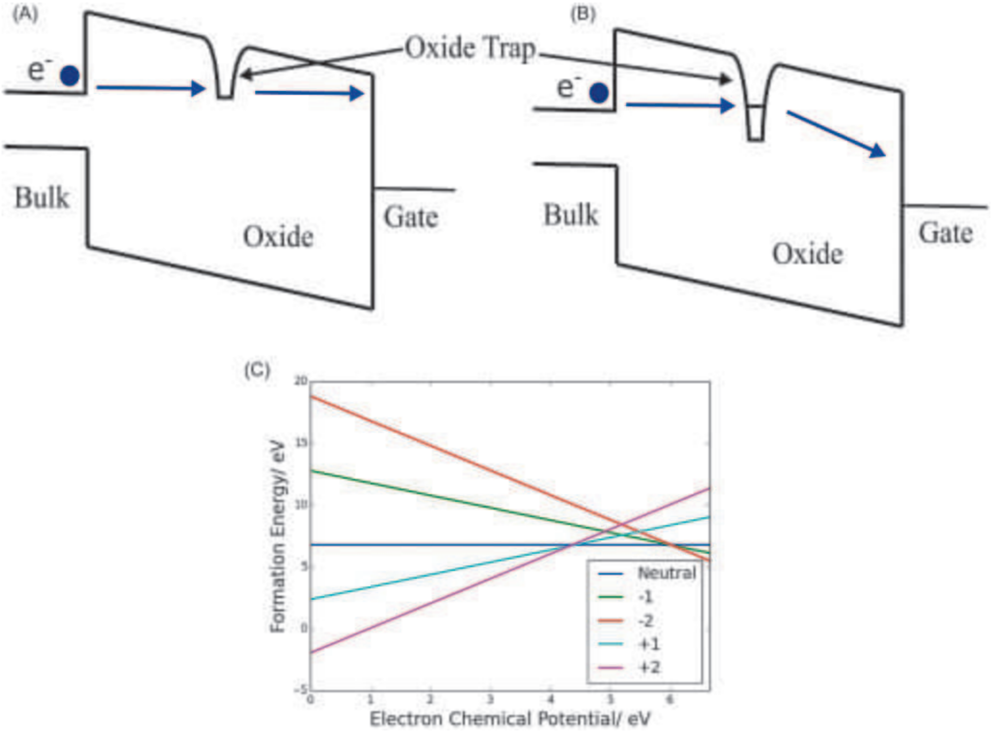

Fig. 8 Potential energy diagrams of an electronic device with a defect. (A) Illustrates an elastic tunnelling of an electron from the bottom of the conduction band of the left electrode (Si, Ge) into the gate metal electrode; electron scatters on the oxide trap. (B) Inelastic tunnelling of an electron from the bottom of the conduction band of the left electrode (Si, Ge) into the gate metal electrode. The electron first tunnels into the localized state of the oxide trap and, after vibrational relaxation, tunnels into the metal electrode. This type of process is also called multi-phonon trap assisted tunnelling. (C) Diagram showing the formation energies of O vacancies in the monoclinic phase of HfO_2 as a function of the Fermi level position (electron chemical potential) in the band gap calculated using DFT in a periodic model. Lines show the dependence of the defect formation energy in different charge states on the electron chemical potential. Crossing points are the charge transition energies. They correspond to chemical potential above/below which the existence of the defect in the different charge state is becoming more energetically favorable. One can see that positively charged vacancy states dominate up to about 4.3 eV.

The key point about defect states in dielectrics from a device point of view is to control the dependence of the defect charge state on the position of the system Fermi energy (Fleetwood et al., 2009; Freysoldt et al., 2014). It is useful to distinguish two charge transition levels: the thermodynamic level, E_{th}, and the transient level, E_{tr}. The thermodynamic charge transition level corresponds to the system Fermi energy for which a defect changes its charge in thermal equilibrium. E_{th} is defined as a difference of total energies of systems of N and N + 1 electrons, each in its fully relaxed ground state: $E_{th} = E(N + 1) - E(N)$. Thus, if E_F is the energy required to remove an electron from some electron reservoir (e.g. Si at the Si/SiO$_2$ interface), $E_{th} - E_F$ is the energy required to add an electron from the reservoir to the lowest unoccupied charge-state level. The position of the defect charge transition levels indicates whether the defect is a deep or shallow donor or an acceptor. Furthermore, if the defect charge transition level is in the same position as the electrode Fermi level (said to be in resonance), then tunnelling rates between the defect and electrode will be very high, provided the defect is close enough to the interface (typically up to 3 nm). An example of defect formation energy diagram showing charge transition levels is shown in Fig. 8C.

Taking into account that the electrical measurements and the electronic processes are often fast compared with the time needed for the system to come to equilibrium, another, transient, level is introduced, which is consistent with the Frank-Condon principle. E_{tr} is defined as the energy required for trapping an electron or a hole in the geometry of the system as it was prior to the trapping. Thus E_{tr} are obtained as the differences of the total energies of the system with N and N + 1 electron, but in the local atomic geometries, which correspond to one of these systems. For example, $E_{tr}(0/-) = E(-) - E(0)$ denotes the energy required to add an electron to the neutral defect calculated using the neutral defect geometry.

Once the charge-transition levels are calculated, the dependence of the defect charge state on the electrode Fermi energy can be introduced via a correction term $q \times E_F$, where E_F is varied in the energy range from the maximum of the last valence band of the oxide to the bottom of the first conduction band. The results are presented as plots of E_{th} vs. E_F or E_{tr} vs. E_F calculated for different values of E_F (Fig. 8C). The crossing points of the corresponding lines determine the regions where one charge state of a defect is more favorable than the other. Although the Fermi energy remains unknown in the experiment, such diagrams allow one to identify some critical cases and help in the analysis of the experimental data. The same approach is used to determine the dependence of the defect formation energies on the position of the Fermi energy.

Conclusion

Our understanding of point defects in insulators has progressed enormously since the pioneering works of Frenkel and Schottky. Advances in experimental defect characterization combined with increasing accuracy of theoretical calculations of defect properties and reactions provide defect models of increasingly complex processes in the bulk and at surfaces of insulators. Transitioning from understanding fundamental materials behavior to development of quantitative approaches to explain and predict experimental observations requires further advances in the computational methods that take advantage of the increasingly powerful computing hardware. Material function is, however, multi-scale and is intimately linked not only to point defects considered here but also to microstructural processes (diffusion, electron transfer, chemical reactions) at the internal grain boundaries and interfaces to electrodes or contacts between insulators and other materials. The roles of microstructure of materials (particularly texture) are well established in metallurgy, but much less understood in insulators, e.g. functional ceramics, particularly when it comes to linking the atomic structure of polycrystalline materials to their function. The challenge is to merge this information at various length scales and to develop a fundamental understanding of the evolution of the microstructure and its effect on properties, such as thermal-mechanical response, electrical response, degradation, and failure. A step-change will be achieved when it is possible to predict the effect of changing the microstructure on system function and so guide the materials synthesis and processing.

References

Anderson PW (1975) Model for the electronic structure of amorphous semiconductors. *Physical Review Letters* 34: 953–955.

Bassani F and Pastori Parravicini G (1975) *Electronic States and Optical Transitions in Solids*. New York: Pergamon Press.

Carter CB and Williams DB (eds.) (2016) *Transmission Electron Microscopy*. Berlin: Springer.

Catlow CRA (ed.) (1994) *Defects and Disorder in Crystalline and Amorphous Solids*. Berlin: Springer NATO series.

Crawford JH and Slifkin LM (1972) *Point Defects in Solids: General and Ionic Crystals*. New York: Plenum Press.

Dexter D, Klick CC, and Russell GA (1956) Configuration coordinate curves for F-centers in alkali halide crystals. *Physics Review* 101: 1473–1479.

Fleetwood DM, Pantelides ST, and Schrimpf RD (eds.) (2009) *Defects in Microelectronic Materials and Devices*. New York: CRC Press.

Freysoldt C, Grabowski B, Hickel T, Neugebauer J, Kresse G, Janotti A, and Van de Walle CG (2014) First-principles calculations for point defects in solids. *Reviews of Modern Physics* 86: 253–305.

Golze D, Dvorak M, and Rinke P (2019) The GW Compendium: A practical guide to theoretical photoemission spectroscopy. *Frontiers in Chemistry* 7(paper 377): 1–66.

Grimes RW, Catlow CRA, and Shluger AL (eds.) (1992) *Quantum Mechanical Cluster Calculations in Solid State Studies*. Singapore: World Scientific Publishing.

Hayes W and Stoneham AM (1985) *Defects and Defect Processes in Non-Metallic Solids*. New York: Wiley.

Hofer WA, Foster AS, and Shluger AL (2003) Theories of scanning probe microscopes at the atomic scale. *Reviews of Modern Physics* 75: 1287–1331.

Huang K and Rhys A (1950) Theory of light absorption and non-radiative transitions in F-centres. *Proceedings of the Royal Society of London A* 204: 406–423.

Itoh N and Stoneham AM (2001) *Materials Modification by Electronic Excitation*. Cambridge: Cambridge University Press.

Kantorovich L (2004) *Quantum Theory of the Solid State: The Introduction*. London: Kluver.

Kittel C (2004) *Introduction to Solid State Physics*, 8th edition New Jersey: Wiley.

Lannoo M and Bourgoin J (1981) *Point Defects in Semiconductors, I Theoretical Aspects*. Berlin: Springer Verlag.

Maier J (2004) *Physical Chemistry of Ionic Materials: Ions And Electrons in Solids*. New Jersey: Wiley.
Martin RM (2004) *Electronic Structure: Basic theory and Practical Methods*. Cambridge: Cambridge University Press.
Mott NF and Davis EA (1979) *Non-Crystalline Solids*. Oxford: Oxford University Press.
Pacchioni G, Skuja L, and Griscom DL (eds.) (2000) *Defects in* SiO_2 *and Related Dielectrics: Science and Technology*. Berlin: Springer NATO series.
Schirmer OF (2006) O^- bound small polarons in oxide materials. *Journal of Physics: Condensed Matter* 18: R667–R704.
Song KS and Williams RT (1993) *Self-Trapped Excitons*. Berlin: Springer Verlag.
Spaeth J-M and Overhof H (2003) *Point Defects in Semiconductors and Insulators*. Berlin: Springer Verlag.
Stoneham AM (1975) *Theory of Defects in Solids*. Oxford: Oxford University Press.
Toyozawa Y (2003) *Optical Processes in Solids*. Cambridge: Cambridge University Press.
Weil JA and Bolton JR (2007) *Electron Paramagnetic Resonance: Elementary Theory and Practical Applications*. New Jersey: Wiley.

Density functional theory[☆]

Yusuke Nomura[a] **and Ryosuke Akashi**[b], [a]Department of Applied Physics and Physico-Informatics, Keio University, Yokohama, Japan; [b]Department of Physics, University of Tokyo, Bunkyo, Japan

© 2024 Elsevier Ltd. All rights reserved.

This is an update of S. Kurth, M.A.L. Marques, E.K.U. Gross, Density-Functional Theory, Editor(s): Franco Bassani, Gerald L. Liedl, Peter Wyder, Encyclopedia of Condensed Matter Physics, Elsevier, 2005, Pages 395–402, ISBN 9780123694010, https://doi.org/10.1016/B0-12-369401-9/00445-9.

Introduction 867
Basic formalism 868
Born-Oppenheimer approximation 868
Hohenberg-Kohn theorem and Kohn-Sham equation 868
Extensions 870
Approximate exchange-correlation functionals 870
LDA, GGA, and orbital dependent functionals 870
Notes on constructing approximate exchange-correlation functionals 871
Electronic structure 872
Single-particle spectrum 872
Response function 873
Kohn-Sham states in practice 873
Nuclear dynamics 875
Forces acting on nuclei 875
Interatomic force constants 875
Recent topics 876
Practical guide 877
Program packages 877
Reproducibility 877
Conclusion 877
Acknowledgments 877
References 877

Abstract

Density functional theory (DFT) is an essential building block for modern theoretical physics, chemistry, and engineering, especially those concerning electronic properties. Through decades of development, various program packages for first-principles electronic structure calculation are now available. Their sophisticated interfaces allow users to apply DFT to actual systems, even without knowing the theory. It is hence becoming more and more important to recall the fundamentals of how DFT enables accurate calculations. This article attempts to provide such knowledge with a minimal overview of DFT—its basic foundation, relations to observable electronic and nuclear dynamical properties, and some of its cutting-edge applications.

Key points

- Theoretical foundation of density functional theory is reviewed.
- Relations to experimentally observable quantities are highlighted.
- Modern applications of density functional theory are introduced.

Introduction

The motion of the electrons in atoms, molecules, and solids is described by the Schrödinger (or Dirac) equation. The computational complexity to obtain the exact solution grows exponentially with the number of electrons N. Calculating exact ground-state wave function is prohibitively expensive when N is more than a few dozen. Therefore, it has been a great challenge to develop a powerful and accurate numerical method to calculate electronic structures.

[☆] *Change History:* November 2022. Y Nomura and R Akashi updated Sections: "Introduction" "Born-Oppenheimer Approximation" "Hohenberg-Kohn theorem and Kohn-Sham equation" "Extensions" "LDA, GGA, and orbital dependent functionals" "Single-particle spectrum" "Kohn-Sham states in practice" "Nuclear dynamics".

https://doi.org/10.1016/B978-0-323-90800-9.00148-7

There are mainly two numerical approaches. One is the wave function theory. It directly deals with the many-body wave function itself and attempts to find good approximations to the exact wave function. The other is the density functional theory (DFT), for which we will give a brief review. By employing the electron density $\rho(\mathbf{r})$ (a function of three coordinate variables) as the fundamental variable instead of the many-body wave function (a function of $3N$ coordinate variables), DFT has drastically reduced the computational cost. Therefore, DFT is the most widely used method for electronic structure calculations of solids.

Here, we briefly review the fundamental and practical aspects of DFT. Section "Basic formalism" reviews the Hohenberg-Kohn theorem and the Kohn-Sham equation, which gives a foundation of DFT. We also describe several extensions of DFT. In DFT, as described below, the exchange-correlation functional is one of the most fundamental quantities. Section "Approximate exchange-correlation functionals" is devoted to a discussion of approximations to the exchange-correlation functional. Section "Electronic structure" presents several topics related to electronic structure calculations. In Section "Nuclear dynamics," we show that DFT can also be used to calculate the properties of atomic vibrations. Section "Practical guide" provides a practical guide of DFT. Finally, we give a summary in Section "Summary."

Basic formalism

We start from the full non-relativistic Hamiltonian, in which electrons and atomic nuclei interact with each other. Because the masses of nuclei are much heavier than that of electrons, the kinetic energies of nuclei are usually much smaller than that of electrons. Then, to a good approximation, we can treat electron and nuclear dynamics separately. DFT is a theory for dealing with the electronic part under this approximation. In this section, we first briefly discuss the Born-Oppenheimer approximation (Born and Oppenheimer, 1927), which is the most widely used framework to derive separate equations for the electron and nuclear dynamics. Then, we discuss the Hohenberg-Kohn theorem (Hohenberg and Kohn, 1964) and the Kohn-Sham equation (Kohn and Sham, 1965), which form the basis of DFT.

Born-Oppenheimer approximation

The Hamiltonian for interacting electrons and nuclei reads

$$\widehat{\mathcal{H}} = -\sum_I \frac{\hbar^2}{2M_I}\frac{\partial^2}{\partial \mathbf{R}_I^2} - \sum_i \frac{\hbar^2}{2m}\frac{\partial^2}{\partial \mathbf{r}_i^2} + V(\{\mathbf{r}\}, \{\mathbf{R}\}), \tag{1}$$

where

$$V(\{\mathbf{r}\}, \{\mathbf{R}\}) = \sum_{i<j}\frac{e^2}{|\mathbf{r}_i - \mathbf{r}_j|} - \sum_{i,I}\frac{Z_I e^2}{|\mathbf{r}_i - \mathbf{R}_I|} + \sum_{I<J}\frac{Z_I Z_J e^2}{|\mathbf{R}_I - \mathbf{R}_J|}$$

with $\{\mathbf{r}\}$ and $\{\mathbf{R}\}$ being the set of electron and nucleus coordinates, respectively, and i and I labeling electrons and nuclei. The Born-Oppenheimer approximation makes use of the large difference in the mass between the nuclei and electrons. Within this approximation, the electron and nuclear motions are treated separately, and the wave function of electrons and nuclei is given by a product of the electron part Ψ_e and the nuclear part Φ_n. In the following, we briefly describe the equations obtained from the Born-Oppenheimer approximation.

If we neglect the nuclear kinetic energy, which is much smaller than that of electrons, from the Hamiltonian, we obtain the electron Schrödinger equation:

$$\left[-\sum_i \frac{\hbar^2}{2m}\frac{\partial^2}{\partial \mathbf{r}_i^2} + V(\{\mathbf{r}\}, \{\mathbf{R}\})\right]\Psi_e(\{\mathbf{r}\}|\{\mathbf{R}\}) = E(\{\mathbf{R}\})\Psi_e(\{\mathbf{r}\}|\{\mathbf{R}\}). \tag{2}$$

Here, the equation is solved for fixed nuclear positions. The nuclear dynamics with a smaller energy scale are treated separately from the electron dynamics. The Schrödinger equation for the nuclear part is given by

$$\left[-\sum_i \frac{\hbar^2}{2M_I}\frac{\partial^2}{\partial \mathbf{R}_I^2} + E(\{\mathbf{R}\})\right]\Phi_n(\{\mathbf{R}\}) = \varepsilon\Phi_n(\{\mathbf{R}\}), \tag{3}$$

where the total energy of the electron part $E(\{\mathbf{R}\})$ serves as a potential for the nuclear dynamics (Born-Oppenheimer energy surface). ε is the total energy of the electron-nucleus coupled system. In the following, we explain the idea of DFT for solving the electronic part (Eq. 2). We also discuss the nuclear dynamics in Section "Nuclear dynamics."

Hohenberg-Kohn theorem and Kohn-Sham equation

The electronic part of the Hamiltonian is given by

$$\widehat{\mathcal{H}}_e = \sum_i\left(-\frac{\hbar^2}{2m}\frac{\partial^2}{\partial \mathbf{r}_i^2} - \sum_I\frac{Z_I e^2}{|\mathbf{r}_i - \mathbf{R}_I|}\right) + \sum_{i<j}\frac{e^2}{|\mathbf{r}_i - \mathbf{r}_j|}. \tag{4}$$

As is mentioned in Section "Introduction," when the number of electrons is more than a few dozen, it is prohibitively demanding to obtain the exact ground-state wave function.

In DFT, the electron density $\rho(\mathbf{r})$ is used as the fundamental variable instead of the many-body wave function. The electron density is much more tractable than the many-body wave function because it depends on only three coordinate variables, regardless of the number of electrons. This approach has been justified by the Hohenberg-Kohn theorem.

The theorem first states one-to-one correspondence between the ground-state electron density and the external potential. Therefore, once the ground-state electron density is known, the external potential is determined uniquely. Then, in principle, physical properties associated with the ground-state wave function are unambiguously determined by the electron density. In particular, the kinetic and electron-electron interaction energies of the ground state can be expressed as universal functionals of the electron density ($E_{\mathrm{kin}}[\rho]$ and $E_{\mathrm{ee}}[\rho]$, respectively). The term "universal" indicates that the forms of the functionals do not depend explicitly on the nuclear positions.

The theorem also gives a variational principle. When we define the energy functional

$$E_{\upsilon}[\rho] = E_{\mathrm{kin}}[\rho] + \int \rho(\mathbf{r})\upsilon(\mathbf{r})d\mathbf{r} + E_{\mathrm{ee}}[\rho] \tag{5}$$

for some external potential $\upsilon(\mathbf{r})$, the functional satisfies the inequality

$$E_{\upsilon}[\rho] \geq E_{\upsilon}[\rho_0] = E_0, \tag{6}$$

where ρ_0 (E_0) is the ground-state electron density (energy) under the potential $\upsilon(\mathbf{r})$, respectively. Therefore, the ground-state electron density can be obtained by searching for the electron density that minimizes the energy functional $E_{\upsilon}[\rho]$.

Although the variational principle in Eq. (6) looks simple, the major problem is that the exact forms of the functionals, $E_{\mathrm{kin}}[\rho]$ and $E_{\mathrm{ee}}[\rho]$, are unknown. For this problem, Kohn and Sham have proposed an idea of introducing "orbitals" to approximate the kinetic energy functional $E_{\mathrm{kin}}[\rho]$. This has opened up a way to perform DFT calculations with sufficient accuracy for practical use. Therefore, most of the modern DFT implementations employ the Kohn-Sham scheme; thus, we discuss this scheme in more detail below. As for the direct variational approach (orbital-free DFT), which is less accurate than the Kohn-Sham approach but has the advantage of being much faster, the current research focus is to construct accurate kinetic energy functionals. One strategy is to reproduce the Kohn-Sham kinetic energy as accurately as possible.

The Kohn-Sham scheme introduces an auxiliary non-interacting system that is designed to give the same electron density as that of the interacting system. The non-interacting system is described by single-particle Schrödinger equation (so called Kohn-Sham equation):

$$\left[-\frac{\hbar^2}{2m}\frac{\partial^2}{\partial\mathbf{r}^2} + \upsilon_{\mathrm{eff}}(\mathbf{r})\right]\phi_i(\mathbf{r}) = \varepsilon_i\phi_i(\mathbf{r}), \tag{7}$$

where $\upsilon_{\mathrm{eff}}(\mathbf{r})$ is an effective potential which is determined by Eq. (12), ϕ_i is the Kohn-Sham state, and ε_i is the Kohn-Sham energy eigenvalue. The electron density is given by

$$\rho(\mathbf{r}) = \sum_{i=1}^{\mathrm{occ}} |\phi_i(\mathbf{r})|^2, \tag{8}$$

where the summation runs over occupied Khon-Sham states.

In the Kohn-Sham scheme, to reproduce the true electron density with Eq. (8), the effective potential $\upsilon_{\mathrm{eff}}(\mathbf{r})$ is determined as follows: We first introduce the kinetic energy functional

$$E_{\mathrm{kin}}^{\mathrm{KS}}[\rho] = \sum_{i=1}^{\mathrm{occ}} \int \phi_i^*(\mathbf{r})\left(-\frac{\hbar^2}{2m}\frac{\partial^2}{\partial\mathbf{r}^2}\right)\phi_i(\mathbf{r})d\mathbf{r} \tag{9}$$

and the Hartree energy functional

$$E_H[\rho] = \frac{e^2}{2}\iint \frac{\rho(\mathbf{r})\rho(\mathbf{r}')}{|\mathbf{r}-\mathbf{r}'|}d\mathbf{r}d\mathbf{r}'. \tag{10}$$

of the Kohn-Sham system. Next, we introduce so called exchange-correlation functional, whose definition is given by the sum of corrections to the exact kinetic and electron-electron interaction energies of the original interacting system:

$$E_{\mathrm{XC}}[\rho] = \left(E_{\mathrm{kin}}[\rho] - E_{\mathrm{kin}}^{\mathrm{KS}}[\rho]\right) + \left(E_{\mathrm{ee}}[\rho] - E_{\mathrm{H}}[\rho]\right). \tag{11}$$

Then, one can show that $\upsilon_{\mathrm{eff}}(\mathbf{r})$ should be given by

$$\upsilon_{\mathrm{eff}}(\mathbf{r}) = \upsilon(\mathbf{r}) + e^2\int \frac{\rho(\mathbf{r}')}{|\mathbf{r}-\mathbf{r}'|}d\mathbf{r}' + \upsilon_{\mathrm{XC}}(\mathbf{r}), \tag{12}$$

$$\upsilon_{\mathrm{XC}}(\mathbf{r}) = \frac{\delta E_{\mathrm{XC}}[\rho]}{\delta\rho(\mathbf{r})}. \tag{13}$$

One can see that Eqs. (7), (8), and (12) form self-consistent equations. Therefore, in practical DFT calculations based on the Kohn-Sham scheme, the self-consistent equations are solved iteratively with some approximate form of the exchange-correlation functional (see Section "Approximate exchange-correlation functionals" for the detail).

Extensions

The ground states are sometimes not sufficiently characterized only by the charge density distribution. This occurs when any quantities, generally represented by the 1-reduced density matrix, are involved

$$\rho^{(1)}_{\sigma\sigma'}(\mathbf{r},\,\mathbf{r}') = \left\langle \widehat{\psi}^{\dagger}_{\sigma}(\mathbf{r})\widehat{\psi}_{\sigma'}(\mathbf{r}')\right\rangle. \tag{14}$$

$\left\langle \widehat{\mathcal{O}} \right\rangle$ denotes the expectation value of the operator $\widehat{\mathcal{O}}$. $\widehat{\psi}^{\dagger}_{\sigma}(\mathbf{r})$ and $\widehat{\psi}_{\sigma}(\mathbf{r})$ are the electron creation and annihilation operators in the Fock space, respectively. When the system is subjected to external fields or exhibits spontaneous symmetry breaking, its non-trivial components, such as spin density $\mathbf{m}(\mathbf{r}) = \sum_{\sigma\sigma'}\boldsymbol{\sigma}_{\sigma\sigma'}\rho_{\sigma\sigma'}^{(1)}(\mathbf{r},\mathbf{r})$ $[\boldsymbol{\sigma} = (\sigma_x, \sigma_y, \sigma_z)]$, may become nonzero. The framework of DFT can be extended for such situations. Namely, we can introduce $\rho_{\sigma\sigma'}^{(1)}(\mathbf{r})$ as fundamental variables in addition to the charge density distribution $\rho(\mathbf{r})$. A parallelism to the Hohenberg-Kohn theorem holds: The ground state is unambiguously characterized by $\rho(\mathbf{r})$ and combination of $\rho_{\sigma\sigma'}^{(1)}(\mathbf{r})$ The Kohn-Sham equation, which reproduces the identical ρ and $\rho^{(1)}$ in the interacting system, can be constructed with complementary exchange-correlation potentials $\upsilon^{\sigma\sigma'}_{\mathrm{XC}}(\mathbf{r},\mathbf{r}') = \delta E_{\mathrm{XC}}[\rho,\rho^{(1)}]/\delta\rho_{\sigma\sigma'}^{(1)}(\mathbf{r},\mathbf{r}')$. Such an extension has been first accomplished for the spin density (von Barth and Hedin, 1972). Calculations based on the spin DFT is now widely in practice for describing the electron spin distribution of materials. More generally, the 1-reduced density matrix functional theory has also been developed, which treats all the $\rho_{\sigma\sigma'}^{(1)}(\mathbf{r})$ components as additional variables.

The DFT framework is further extended for degrees of freedom other than the electronic charge and spin. Here we list some representative examples. In the current density functional theory, the current density $\boldsymbol{j}(\mathbf{r}) = \frac{-e\hbar}{2mi}\sum_{\sigma}$ $\left\langle \left[\widehat{\psi}^{\dagger}_{\sigma}(\mathbf{r})\nabla\widehat{\psi}_{\sigma}(\mathbf{r}) - \left[\nabla\widehat{\psi}^{\dagger}_{\sigma}(\mathbf{r})\right]\widehat{\psi}_{\sigma}(\mathbf{r})\right]\right\rangle$ is treated as a variable. Inclusion of the off-diagonal order variable $\chi_{\sigma\sigma'}(\mathbf{r},\,\mathbf{r}') = \left\langle \widehat{\psi}_{\sigma}(\mathbf{r})\widehat{\psi}_{\sigma'}(\mathbf{r}')\right\rangle$ has been addressed to deal with superconductivity. It is even possible to invent a DFT with a distribution of nuclear sites $\Gamma(\mathbf{R}_1,\mathbf{R}_2,\,\ldots)$ (treated as points in the Born-Oppenheimer approximation) as an additional variable, which is named multi-component DFT. Interestingly, by combined use of $\chi_{\sigma\sigma'}(\mathbf{r},\mathbf{r}')$ and $\Gamma(\mathbf{R}_1,\,\mathbf{R}_2,\,\ldots)$ and extension to nonzero temperature, the phonon-mediated superconductivity is consistently described within the DFT framework, which is called DFT for superconductors.

The concept of introducing a non-interacting reference system that reproduces the charge density of the interacting system can also be extended to the time dependent problem. Suppose the system is described by the time-dependent Schrodinger equation

$$i\hbar\frac{\partial}{\partial t}|\Psi_{\mathrm{e}}(\mathrm{t})\rangle = \widehat{\mathcal{H}}_{\mathrm{e}}(t)|\Psi_{\mathrm{e}}(t)\rangle \tag{15}$$

with $\widehat{\mathcal{H}}_e(t)$ including a time-dependent external field $\upsilon(\mathbf{r}, t)$. The Runge-Gross theorem states that, with a given initial state$|\Psi_{\mathrm{e}}(t_0)\rangle$, a one-to-one correspondence between the time dependent charge density $\rho(\mathbf{r}, t)$ and external potential $\upsilon(\mathbf{r}, t)$ holds (Runge and Gross, 1984). With this theorem, the time-dependent density functional theory has been established. Here, one can recast the original system to a non-interacting system

$$i\hbar\frac{\partial}{\partial t}\phi_i(\mathbf{r},\,t) = \left[-\frac{\hbar^2}{2m}\frac{\partial^2}{\partial\mathbf{r}^2} + \upsilon_{\mathrm{eff}}(\mathbf{r},\;t)\right]\phi_i(\mathbf{r},\,t). \tag{16}$$

This time-dependent Kohn-Sham equation has been used to simulate ionization and excitation dynamics of atoms, molecules, and solids.

For further reading of the present topics, see, e.g., Parr and Yang (1995), Engel and Dreizler (2010), Lüders et al. (2005), and Marques et al. (2005).

Approximate exchange-correlation functionals

Several exact formulas of the exchange-correlation energy E_{XC} are actually known. But such formulas are not useful because they involve the exact solution of the many-body Schrödinger equation. Practically, we design calculable approximate forms as explicit functionals of ρ so that they comply with correct asymptotes, and apply them to general systems. Here we look over standard approximations in use.

LDA, GGA, and orbital dependent functionals

The concept of gradient expansion gives us a useful strategy for developing the approximate functional forms. In extended systems like periodic solids, nearly uniform itinerant electrons are expected to dominate the electronic properties, and its spatial variation would be treated as a perturbation. Along this line, the accuracy of the approximate forms may be improved systematically.

The exchange-correlation energy density $\varepsilon_{\mathrm{xc}}$ is introduced by the following decomposition

$$E_{\mathrm{XC}} = \int d\mathbf{r}\rho(\mathbf{r})\varepsilon_{\mathrm{XC}}(\mathbf{r}). \tag{17}$$

Here, $\varepsilon_{\mathrm{xc}}$ is in principle a functional of the entire distribution of $\rho(\mathbf{r})$. A systematic approximation is implemented by expressing the spatial dependence of ρ in terms of the local values (semilocal approximation)

$$\varepsilon_{\mathrm{XC}}[\rho](\mathbf{r}) = \varepsilon_{\mathrm{XC}}(\rho(\mathbf{r}), \nabla\rho(\mathbf{r}), \ldots). \tag{18}$$

The first approximate form is the local density approximation (LDA)

$$\varepsilon_{\mathrm{XC}}[\rho](\mathbf{r}) \simeq \varepsilon_{\mathrm{XC}}(\rho(\mathbf{r})). \tag{19}$$

This form becomes exact in the uniform electron gas, where $\rho(\mathbf{r})$ is constant in space. Useful approximate models within the LDA can be derived from accurate calculations for uniform electron gas by sophisticated wavefunction methods such as the diffusion Monte Carlo method. The parameters in the models are determined by fitting the reference numerical data of $\varepsilon_{\mathrm{xc}}(\rho_{\mathrm{uni}})$ as functions of the uniform density ρ_{uni}. Such models, being accurate for the uniform systems, are applied to non-uniform systems with Eq. (19).

The approximation can be improved by taking into account the higher order derivatives. The generalized gradient approximation (GGA) incorporates the first-order derivative of ρ

$$\varepsilon_{\mathrm{XC}}[\rho](\mathbf{r}) \simeq \varepsilon_{\mathrm{XC}}(\rho(\mathbf{r})\nabla\rho(\mathbf{r})). \tag{20}$$

The meta-GGA incorporates the Laplacian of ρ, as well as kinetic energy density $\tau(\mathbf{r}) = \sum_i |\nabla\phi_i(\mathbf{r})|^2$

$$\varepsilon_{\mathrm{XC}}[\rho](\mathbf{r}) \simeq \varepsilon_{\mathrm{XC}}(\rho(\mathbf{r}), \nabla\rho(\mathbf{r}), \Delta\rho(\mathbf{r}), \tau(\mathbf{r})). \tag{21}$$

A common strategy for implementing the practical forms for those approximations is as follows: (i) derive asymptotic behavior of the exact functional in extreme cases, (ii) design an analytic model so that those asymptotes are reproduced, and (iii) determine the remaining model parameters, referring to some "norm" systems or any principle like maximal smoothness.

Adding the higher-order gradients may not be efficient for incorporating quantum effects such as the Pauli exclusion and dynamical/static correlations. To describe such effects, the Kohn-Sham orbitals, which are also implicit functionals of ρ, are explicitly included as variables.

For the former, the exact exchange term (EXX)

$$E^{\mathrm{EXX}} = -\frac{e^2}{2}\sum_{ij}^{\mathrm{occ.}} \iint d\mathbf{r}d\mathbf{r}'\phi_i^*(\mathbf{r})\phi_j^*(\mathbf{r}')\frac{1}{|\mathbf{r}-\mathbf{r}'|}\phi_i(\mathbf{r}')\phi_j(\mathbf{r})$$

is added to E_{xc} instead of the exchange part of the functional. The magnitude of the E^{EXX} term is tuned by a prefactor and/or cutoff for the Coulomb potential, considering its partial cancelation with the correlation effects. Functionals in this form are called hybrid functionals.

For including the dynamical and static correlation effects, a formally exact adiabatic continuation formula (Langreth and Perdew, 1975) provides a useful basis

$$E_{\mathrm{c}} = -\frac{e^2}{2}\int_0^1 d\lambda \int \frac{d\omega}{2\pi} \iint d\mathbf{r}d\mathbf{r}'\,\frac{\chi_\lambda(r', r, i\omega) - \chi_0(r', r, i\omega)}{|r-r'|} \tag{22}$$

Here, χ_λ denotes the density-density response function of the ground state with the electron-electron Coulomb interaction scaled by a factor λ. χ_0 is the Kohn-Sham response function (see also Eq. (32) below). The λ integral is taken with the density ρ fixed. Applying approximations to $\chi_\lambda(\mathbf{r}', \mathbf{r}, i\omega)$, we can obtain approximate E_{c} formulas. For example, the random phase approximation is widely used to approximate χ_λ, and the corresponding E_c successfully describes the van der Waals effect, a representative correlation effect involving unoccupied orbitals.

For a more thorough review on the LDA, GGA, and orbital-dependent functionals, see, e.g., Engel and Dreizler (2010) and Kümmel and Kronik (2008).

Notes on constructing approximate exchange-correlation functionals

As explained above, analytically derived or exactly calculated asymptotic behavior of $E_{\mathrm{xc}}[\rho]$ in the ρ space is utilized to specify the form of the approximate functionals. Still, there remains an ambiguity for general non-uniform ρ, where the exact references are unavailable. Full implementation of the approximate forms finally requires heuristic modeling with tunable parameters.

One approach is to make the model for $E_{\mathrm{xc}}[\rho]$ as simple as possible. For example, in constructing the GGA-PBE (Perdew-Burke-Ernzerhof) functional (Perdew et al., 1996), a simple smooth form has been conceived, where the parameters have been unambiguously determined so that it converges to the asymptotic formulas in the limits. A more empirical approach is to refer to data of specific systems for determining the model parameters. Experimentally observed physical quantities or those calculated with accurate wave function methods are often used for this. For example, the prefactor for E^{EXX} is tuned so that accurately calculated cohesive energies of several molecules are optimally reproduced. See, e.g., Mardirossian and Head-Gordon (2017) for a thorough review on a variety of functionals.

An attempt has been recently made to remove the ambiguity stemming from the human construction of the model form. Namely, one adopts an extremely flexible model with a huge number of parameters. The model is by design capable of representing *any* functionals in the infinite parameter limit, so that it can mimic the ideal energy functional $E[\rho]$ as a mapping from ρ to a scalar E. Parameters are tuned with a large amount of reference data. Modern machine learning models and parameter tuning methods are used to implement this scheme (see, e.g., Schmidt et al., 2019 for a review).

Electronic structure

DFT unambiguously defines the quantities related to the charge and spin densities and total energy; magnetic moment, lattice constants, bulk modulus, etc. Relating DFT to electronic single-particle properties is a more complicated issue. This is mainly due to the fact that the occupation number and Kohn-Sham orbital are auxiliary concepts (see Section "Hohenberg-Kohn theorem and Kohn-Sham equation") and not directly related to real single particle excitations. Nevertheless, the DFT calculations are widely in practical use for quantitative comparison with experimentally observed excitation spectra. The DFT results (Kohn-Sham wave functions, Kohn-Sham energies, etc.) can also be utilized as a basis for other methods such as the Green's function theory. In this section, we review those aspects.

Single-particle spectrum

Single-particle excitation can be observed with spectroscopy experiments. Among the single-particle quantities, the fundamental gap, which is the minimum energy required for manipulating one electron within the system at zero temperature, is a key quantity that distinguishes insulators from metals in solids. Here we discuss the discrepancy between the apparent gap in the Kohn-Sham spectra and experimentally observed optical gap (fundamental gap), to recall attention to the interpretation of the band structures obtained within the Kohn-Sham scheme.

Within DFT, the level difference between ground states with different numbers of electrons is well defined. Then, the fundamental gap for an N electron system is given by

$$\begin{aligned} E_{\mathrm{gap}}(N) &= (E(N-1) - E(N)) - (E(N) - E(N+1)) \\ &= I(N) - A(N). \end{aligned} \tag{23}$$

Here, I and A are the ionization energy and the electron affinity, respectively. In this section, we indicate the dependence on the total number of electrons explicitly for clarity, e.g., $E(N)$ is the total energy of the N electron system. The expression of Eq. (23) is, however, inefficient because we cannot always perform calculations with $N \pm 1$ electrons: For example, in bulk systems, the total N is taken to infinity.

To accommodate DFT to such cases, the extension to systems with fractional electron number $N + \delta$ $(0 < \delta < 1)$ has been beneficial. There, the chemical potential μ is introduced, and the occupation number $\{n_i\}$ is extended to allow fractional values. The state can be a mixed state with fractional weights, formed by the pure states of integer electron numbers. The infinitesimal variation of electron numbers can be defined with this formalism. From this Janak's theorem (Janak, 1978) is derived, which relates the change in total energy and the occupation numbers as

$$\delta E = \sum_i \delta n_i \varepsilon_i. \tag{24}$$

This theorem is sometimes referred to as it gives the Kohn-Sham orbitals physical meaning. However, one has to recall that n_i and ε_i are artificial variables. Thus, the operation "changing the number of electrons in state i" is not directly related to adding/subtracting actual electrons. Yet the frontier orbital has physical significance. Within the extended DFT, in the $N + \delta$ electron ground state, only one orbital ϕ_{f}, which is called the frontier orbital, can have a fractional occupation number $(n_i = 1\ \forall\ \varepsilon_i < \varepsilon_{\mathrm{f}};\ n_i = 0\ \forall\ \varepsilon_i > \varepsilon_{\mathrm{f}})$. Integrating Eq. (24) for $i = \mathrm{f}$ from the N to $N \pm 1$ electron states, we obtain:

$$I = \int_N^{N-1} dN \varepsilon_{\mathrm{f}}(N), \tag{25}$$

$$-A = \int_N^{N+1} dN \varepsilon_{\mathrm{f}}(N). \tag{26}$$

Another important consequence of the extended DFT is that the exact N dependence of the total energy is linear between integer N's. The fact $I = E(N-1) - E(N) \neq E(N) - E(N+1) = A$ then requires that the derivative of the total energy is discontinuous at the integer points. Therefore, the curve of $E(N)$ appears as a polygonal line with nodes at the integer points (Perdew et al., 1982). With this fact, the derivative gap

$$E_{\mathrm{gap}}^{\mathrm{deriv}} = \frac{\partial E(N)}{\partial N}\Big|_{N+\delta} - \frac{\partial E(N)}{\partial N}\Big|_{N-\delta} \tag{27}$$

is equated to the fundamental gap. Furthermore, $E_{\mathrm{gap}}^{\mathrm{deriv}}$ satisfies the following equation

$$E_{\mathrm{gap}}^{\mathrm{deriv}} = E_{\mathrm{gap}}^{\mathrm{KS}} + \Delta_{\mathrm{xc}}, \tag{28}$$

where $E_{\mathrm{gap}}^{\mathrm{KS}}$ is the gap between the lowest unoccupied and highest occupied Kohn-Sham states (Kohn-Sham gap) and Δ_{xc} is a spatially constant term so called derivative discontinuity $\frac{\partial E_{\mathrm{xc}}(N)}{\partial N}\big|_{N+\delta} - \frac{\partial E_{\mathrm{xc}}(N)}{\partial N}\big|_{N-\delta}$ (Perdew and Levy, 1983). This equality enables us to relate the observed gap to the quantities defined in the N-electron system.

When we use approximate exchange-correlation functionals, $E_{\mathrm{gap}}^{\mathrm{deriv}}$ in Eq. (28) calculated with DFT deviates from the true fundamental gap E_{gap}. Then, the fundamental gap is expressed as

$$E_{\mathrm{gap}} = E_{\mathrm{gap}}^{\mathrm{KS}} + \Delta_{\mathrm{XC}} + \Delta^{\mathrm{straight}}. \tag{29}$$

The final term $\Delta^{\mathrm{straight}}$ represents a correction term, corresponding to the deviation of the behavior of the approximate $E(N)$ from the ideal segmented straight lines.

The formula Eq. (29) implies some interesting facts of the Kohn-Sham gap $E_{\mathrm{gap}}^{\mathrm{KS}}$. First, even with the exact functional, it does not correspond to the fundamental gap because of the nonzero Δ_{xc}. Second, using the standard functionals such as those within the LDA and GGA, it departs from the fundamental gap by incorrect zero Δ_{xc} and nonzero $\Delta^{\mathrm{straight}}$. Recently, functionals design that also takes into account Eq. (29) has been broadly conducted. For example, minimization of $\Delta^{\mathrm{straight}}$ has been referred to as a criterion for tuning some modern functionals, which improves accuracy for electronic properties. The generalized Kohn-Sham scheme, which includes the orbital-dependent functionals like EXX, helps us to incorporate a major fraction of Δ_{xc} into $E_{\mathrm{gap}}^{\mathrm{KS}}$, so that the Kohn-Sham gap better agrees with the experimental fundamental gap.

See, e.g., Parr and Yang (1995), Mori-Sánchez et al. (2008), and Burke and Kozlowski (2021) for further reading of the topic in this section.

Response function

The general fluctuation-dissipation relationship says that the electronic response to external perturbations is equated to a property in the ground state. In fact, the response function is formulated exactly within the framework of DFT (Hybertsen and Louie, 1987). Suppose the system is perturbed by a change of the external potential $\delta v(\mathbf{r})$ and the charge density distribution changes by $\delta\rho(\mathbf{r})$. The density-density response function $\chi(\mathbf{r}, \mathbf{r}')$ is defined as the linear coefficient relating them:

$$\delta\rho(\mathbf{r}) = \int d\mathbf{r}'\chi(\mathbf{r}, \mathbf{r}')\delta v(\mathbf{r}') \tag{30}$$

The response function χ is given by

$$\chi = \left[1 - \chi_0\left(\frac{e^2}{|\mathbf{r} - \mathbf{r}'|} + K_{\mathrm{XC}}\right)\right]^{-1}\chi_0 \tag{31}$$

with $K_{\mathrm{xc}}(\mathbf{r}, \mathbf{r}') \equiv \delta^2 E_{\mathrm{xc}}/[\delta\rho(\mathbf{r})\delta\rho(\mathbf{r}')]$. Here, the quantities are matrices with indices $\mathbf{r}$ and $\mathbf{r}'$. The Kohn-Sham response function χ_0 is defined by

$$\delta\rho(\mathbf{r}) = \int d\mathbf{r}'\chi_0(\mathbf{r}, \mathbf{r}')\delta v_{\mathrm{eff}}(\mathbf{r}'). \tag{32}$$

Applying the perturbation theory to the Kohn-Sham equation, we can write χ_0 in terms of the Kohn-Sham eigenpairs (ε_i, ϕ_i). Note that those expressions are rigorous and well-defined within DFT, though all the ambiguities are condensed in E_{xc}. Using the time-dependent DFT (Section "Extensions"), the time-dependent response function can also be formulated.

Kohn-Sham states in practice

DFT is in principle independent from the Green's function theory since the former does not define the electron one-particle creation/annihilation operator. Nevertheless, practices are found in the literature where the Kohn-Sham eigenstates are utilized as a basis for calculating quantities formulated in the Green's function theory, showing remarkable successes in comparing with experiments. Calculations of this kind may be justified by the fact that the Green's function theory can be made basis-free when the perturbation effects are incorporated up to the infinite order (Hedin, 1965). The Kohn-Sham states, which are introduced as auxiliary quantities (see Section "Hohenberg-Kohn theorem and Kohn-Sham equation"), are then presumed as a good zeroth-order basis, which enables us relatively fast convergence with respect to the order of perturbation.

The combination of DFT and the Green's function theory has yielded tremendous success in describing the single-particle excitation of materials. The spectral function defined in the Green's function theory is directly measured by, e.g., angle-resolved photoemission spectroscopy (ARPES). Although the agreement between the Kohn-Sham and experimental spectra is not theoretically guaranteed, a number of studies have conducted comparisons between them. A classic application to copper is displayed in Fig. 1 (Courths and Hüfner, 1984). Recently, the comparison serves more and more essential roles in analyzing the detailed electronic structure of materials, with the improvement in the experimental precision: Here, we also append an example of monolayer MoS_2 in Fig. 2 (Jin et al., 2013). These theoretical spectra would need to be interpreted as results of the Green's function theory using the Kohn-Sham states as the zeroth-order basis.

The Kohn-Sham calculation is known to yield reasonable spectra in weakly correlated systems such as dense metals. However, the agreement with experiments becomes worse for insulators (especially their band gap) and dilute metals, where the exchange-correlation effects are stronger. Even in such cases, accuracy can be efficiently cured by introducing the partially screened

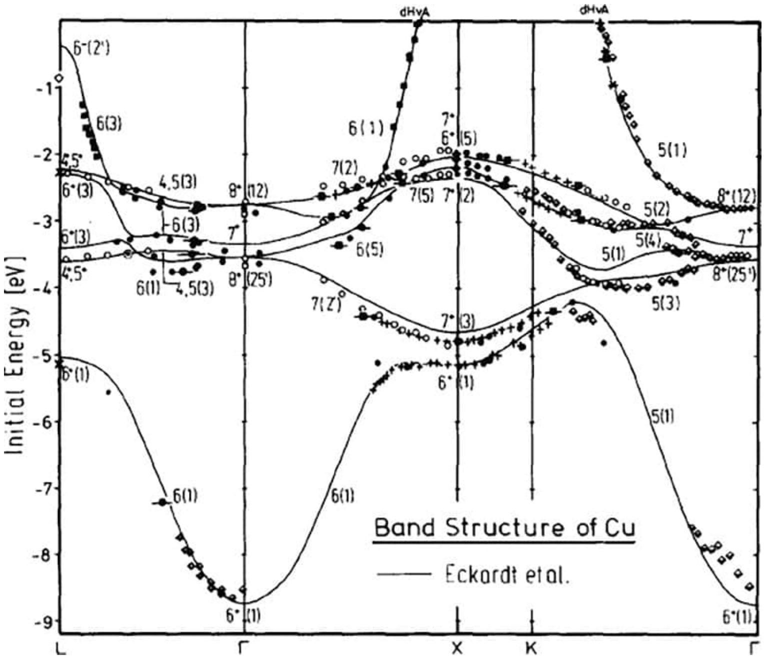

Fig. 1 Electronic band structure of copper calculated by the Kohn-Sham equation with a primary LDA functional. The points are from photoemission experiments. Reproduced from Courths R, and Hüfner S (1984) Photoemission experiments on copper. *Physics Reports* 112: 53–171, with permission from Elsevier.

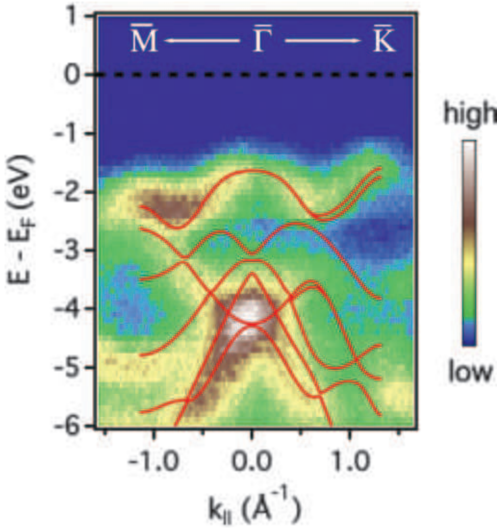

Fig. 2 Intensity map of the photoemission spectrum of exfoliated monolayer MoS_2 measured with micrometer-scale ARPES. The GGA-PBE Kohn-Sham band structure including spin-orbit interaction (Zhu et al., 2011) is indicated by the red curves. Reproduced with permission from Jin W, Yeh PC, Zaki N, Zhang D, Sadowski JT, Al-Mahboob A, van der Zande AM, Chenet DA, Dadap JI, Herman IP, Sutter P, Hone J, and Osgood RM (2013) Direct measurement of the thickness-dependent electronic band structure of MoS2 using angle-resolved photoemission spectroscopy. *Physical Review Letters* 111: 106801, Copyright (2013) by the American Physical Society.

exchange term to the functional or calculating the self-energy by perturbation theory with the Kohn-Sham eigenbasis. The GW approximation (see, e.g., Aryasetiawan and Gunnarsson, 1998 for a review) serves as a standard method for calculating the self-energy: It treats the long-range exchange-correlation effects efficiently under weak to strong Coulomb interaction.

When the correlation effects become even stronger, the one-electron description may break down. Such a situation occurs in so-called strongly-correlated materials, where energy scales of the Coulomb interaction and kinetic energies compete. Typical strongly-correlated materials are, for example, transition-metal oxides with partially-filled *d*-electron shells and heavy-fermion materials with partially-filled *f*-electron shells. The bandwidth W of partially-filled orbitals in these materials is typically narrow, and becomes comparable or even smaller than the onsite Coulomb interaction U. For such systems, the band theory based on the KS states becomes inaccurate, and it often fails to describe the spectral property around the Fermi level. For example, when we regard the Kohn-Sham energy eigenvalues as the poles of the spectral function, DFT cannot reproduce the charge gap opening in Mott insulators, where electrons are localized due to the strong Coulomb repulsion. To incorporate such many-body effects, a combination of DFT and many-body methods, such as the dynamical mean-field theory and the variational Monte Carlo method, has been developed. For more details of the conceptual and practical aspects of the combination, see, e.g., Kotliar et al. (2006) and Imada and Miyake (2010).

Nuclear dynamics

DFT is also useful in investigating nuclear dynamics. This is because the total energy of the electronic system plays a role as the potential for the atomic vibration (Eq. 3). Here, we discuss the expressions for the forces acting on nuclei and the interatomic force constants, which are used in structure optimization and phonon dispersion calculations, respectively.

Forces acting on nuclei

The force acting on Ith nucleus $\mathbf{F}_I$ is given by the derivative of the energy surface

$$F_I = -\frac{\partial E(\{\mathbf{R}\})}{\partial \mathbf{R}_I}. \tag{33}$$

The forces on nuclei vanish ($\mathbf{F}_I = \mathbf{0}$) at equilibrium geometry. Therefore, one can perform structure optimization by minimizing the forces on the nuclei. In practice, the forces (first derivative of the energy surface) can be estimated efficiently using the Hellmann-Feynman theorem (Hellmann, 1937; Feynman, 1939).

Interatomic force constants

Here, we show how the normal vibrational modes are derived. We consider the displacement of Ith nucleus $\mathbf{u}_I$ from the equilibrium position $\mathbf{R}_I^{(0)}$. The position of the Ith nucleus reads

$$\mathbf{R}_I = \mathbf{R}_I^{(0)} + \mathbf{u}_I, \tag{34}$$

Then, the kinetic energy T for the atomic vibration is given by

$$T = \frac{1}{2}\sum_I M_I |\dot{\mathbf{u}}_I|^2 = \frac{1}{2}\sum_{I\alpha} M_I \left(\dot{u}_I^\alpha\right)^2. \tag{35}$$

Here, α is the cartesian component of the displacement ($\alpha = x, y, z$). For the potential energy U, we apply the harmonic approximation:

$$U = E\left(\left\{\mathbf{R}^{(0)} + \mathbf{u}\right\}\right) - E\left(\left\{\mathbf{R}^{(0)}\right\}\right) \tag{36}$$

$$\simeq \frac{1}{2}\sum_{I\alpha}\sum_{I'\alpha'} \frac{\partial^2 E(\{\mathbf{R}\})}{\partial R_I^\alpha \partial R_{I'}^{\alpha'}} u_I^\alpha u_{I'}^{\alpha'}. \tag{37}$$

Note that the first-order terms with respect to the displacement vanish at the equilibrium geometry.

From the expression of U and T, one can derive the secular equation, which determines the frequency and displacement pattern of the normal vibrational modes:

$$\sum_{I'\alpha'} \left(C_{I,I'}^{\alpha,\alpha'} - M_I \omega^2 \delta_{II'} \delta_{\alpha\alpha'}\right) u_{I'}^{\alpha'} = 0, \tag{38}$$

where C is the matrix of so called interatomic force constants

$$C_{I,I'}^{\alpha\alpha'} = \frac{\partial^2 E(\{\mathbf{R}\})}{\partial R_I^{\alpha} \partial R_{I'}^{\alpha'}}. \tag{39}$$

The interatomic force constants play a role as "spring constants" of the "springs" between nuclei. In crystals, Eq. (38) becomes block diagonal in momentum space, and the normal modes are labeled by wave vectors. Then, the frequencies of the normal modes give the phonon dispersion in solids.

In practical calculations, there exist mainly two approaches to estimate the interatomic force constants. One is a direct method, called frozen phonon, in which forces are computed under finite amplitudes of displacements and the interatomic force constants are estimated from finite differences of the forces. The other method relies on the density-functional perturbation theory (DFPT) (Baroni et al., 2001), which shows that the interatomic force constants can be computed from the ground-state electron density and its linear response to the atomic displacements. Therefore, the frozen phonon method performs supercell calculations with finite atomic displacements, whereas the DFPT performs linear response calculations to the displacements.

As an example of phonon calculations, we show, in Fig. 3, the phonon dispersions of elemental semiconductors, Si and Ge, calculated using the DFPT (Giannozzi et al., 1991). The DFPT results show a good agreement with experiments.

Recent topics

Here, among many recent topics, we introduce two advances related to phonon properties: anharmonicity and structure prediction.

Anharmonicity is a deviation of the atomic vibrations from a harmonic oscillator, which arises from higher-order terms of the expansion of energy difference with respect to atomic displacements (Eq. 36). The anharmonic terms are crucial in describing thermal properties of atomic vibrations, such as thermal expansion, thermal conductivity, and thermodynamic stability. Optimizing these properties leads to functional materials. For example, controlling the phonon lifetime and achieving low thermal conductivity in the phonon-contributing part is essential in designing good thermoelectric materials. For more details of the recent advancements in the computation of anharmonicity, see, e.g., Tadano and Tsuneyuki (2018); McGaughey et al. (2019).

One of the dreams of materials scientists would be a theoretical prediction of functional materials. Structure prediction of materials is a very challenging task because the energy landscape $E(\{\mathbf{R}\})$ is a complicated object with a huge number of local minima. Recently, there has been a tremendous advance in numerical tools to explore the complex potential energy surface (see, e.g., Andreoni and Yip, 2020). A remarkable success of the crystal-structure search algorithm so far is, for example, a prediction of high-temperature superconductors under extremely high pressure (see, e.g., Flores-Livas et al. (2020) for details).

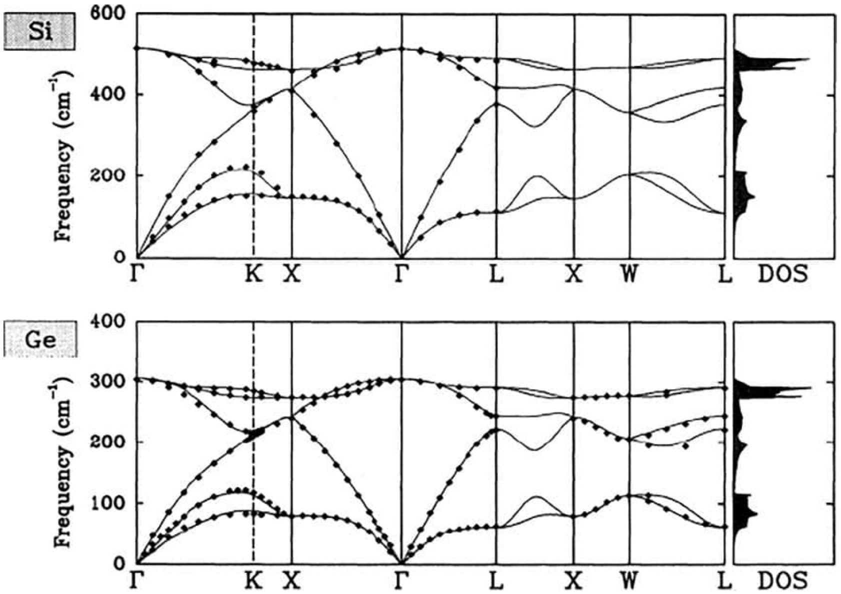

Fig. 3 Phonon dispersions and densities of states of silicon and germanium solids. The diamonds are experimental data. Reproduced with permission from Giannozzi P, de Gironcoli S, Pavone P, Baroni S (1991) Ab initio calculation of phonon dispersions in semiconductors. *Physical Review B* 43: 7231–7242, Copyright (1991) by the American Physical Society.

Practical guide

Program packages

Nowadays, there are a variety of DFT open source packages. Some of them are introduced in Talirz et al. (2021). See also, e.g., https://en.wikipedia.org/wiki/List_of_quantum_chemistry_and_solid-state_physics_software for a list.

Reproducibility

In the practical calculations of DFT, most of the open-source programs employ the Kohn-Sham formalism (see Section "Hohenberg-Kohn theorem and Kohn-Sham equation"). When the same exchange-correlation functional is employed, different programs solve the same Kohn-Sham equations. Ideally, all codes should give the same solution. However, depending on, for example, the type of the basis set [plane-wave, (linearized) augmented plane wave (L)APW, linear muffintin orbital (LMTO), and so on] and approximate ionic potentials [norm-conserving and ultrasoft pseudopotentials, projector augmented wave (PAW) method, and so on], the accuracy may differ among available packages. Therefore, it is an important task for the community to check the reproducibility of the DFT calculations. Recently, such a systematic benchmark has started to be performed. For example, Lejaeghere et al. (2016) compared various DFT packages for solids and confirmed that widely-used codes and methods give essentially identical solutions.

Conclusion

DFT is currently one of the most standard and established methods for electronic structure calculations. Many DFT open sources have been developed in recent years, allowing a wide range of researchers to enjoy DFT calculations. Nowadays, DFT is widely used to calculate the properties of solids. In addition to the ground-state electronic structure calculations, DFT is also useful for calculating excitation spectra (both single- and two-particle) and nuclear dynamics. Care must be taken then in interpreting the eigenvalues of the Kohn-Sham equation.

Although it is impossible to cover all of the vast DFT-related topics, we have provided an introductory explanation of some of them in this chapter. Please refer to the references for more details of advanced topics. We hope this chapter will be of some help to understand what can be done with DFT.

Acknowledgments

We are grateful for valuable comments from Hideo Aoki, Ryotaro Arita, Silke Biermann, Kieron Burke, Kenta Kuroda, Yasushi Shinohara, Terumasa Tadano, and Shinji Tsuneyuki.

References

Andreoni W and Yip S (eds.) (2020) *Handbook of Materials Modeling: Applications: Current and Emerging Materials*. Springer International Publishing.
Aryasetiawan F and Gunnarsson O (1998) The GW method. *Reports on Progress in Physics* 61: 237–312.
Baroni S, de Gironcoli S, Dal Corso A, and Giannozzi P (2001) Phonons and related crystal properties from density-functional perturbation theory. *Reviews of Modern Physics* 73: 515–562.
Born M and Oppenheimer R (1927) Zur Quantentheorie der Molekeln. *Annals of Physics* 389: 457–484.
Burke K and Kozlowski J (2021) Lies my teacher told me about density functional theory: Seeing through them with the hubbard dimer. In: Pavarini E and Koch E (eds.) *Simulating Correlations With Computers*. Forschungszentrum Jülich GmbH.
Courths R and Hüfner S (1984) Photoemission experiments on copper. *Physics Reports* 112: 53–171.
Engel E and Dreizler RM (2010) *Density-Functional Theory*. Springer.
Feynman RP (1939) Forces in molecules. *Physics Review* 56: 340–343.
Flores-Livas JA, Boeri L, Sanna A, Profeta G, Arita R, and Eremets M (2020) A perspective on conventional high-temperature superconductors at high pressure: Methods and materials. *Physics Reports* 856: 1–78.
Giannozzi P, de Gironcoli S, Pavone P, and Baroni S (1991) Ab initio calculation of phonon dispersions in semiconductors. *Physical Review B* 43: 7231–7242.
Hedin L (1965) New method for calculating the one-particle Green's function with application to the electron-gas problem. *Physical Review* 139.
Hellmann H (1937) *Einführung in die quantenchemie*. Franz Deuticke.
Hohenberg P and Kohn W (1964) Inhomogeneous electron gas. *Physics Review* 136: B864–B871.
Hybertsen MS and Louie SG (1987) Ab initio static dielectric matrices from the density-functional approach. I. Formulation and application to semiconductors and insulators. *Physical Review B* 35: 5585–5601.
Imada M and Miyake T (2010) Electronic structure calculation by first principles for strongly correlated electron systems. *Journal of the Physical Society of Japan* 79: 112001.
Janak JF (1978) Proof that $\frac{\partial E}{\partial n_i} = \varepsilon$ in density-functional theory. *Physical Review B* 18: 7165–7168.
Jin W, Yeh PC, Zaki N, Zhang D, Sadowski JT, Al-Mahboob A, van der Zande AM, Chenet DA, Dadap JI, Herman IP, Sutter P, Hone J, and Osgood RM (2013) Direct measurement of the thickness-dependent electronic band structure of MoS2 using angle-resolved photoemission spectroscopy. *Physical Review Letters* 111: 106801.
Kohn W and Sham LJ (1965) Self-consistent equations including exchange and correlation effects. *Physics Review* 140: A1133–A1138.

Kotliar G, Savrasov SY, Haule K, Oudovenko VS, Parcollet O, and Marianetti CA (2006) Electronic structure calculations with dynamical mean-field theory. *Reviews of Modern Physics* 78: 865–951.

Kümmel S and Kronik L (2008) Orbital-dependent density functionals: Theory and applications. *Reviews of Modern Physics* 80: 3–60.

Langreth D and Perdew J (1975) The exchange-correlation energy of a metallic surface. *Solid State Communications* 17: 1425–1429.

Lejaeghere K, Bihlmayer G, Björkman T, Blaha P, Blügel S, Blum V, Caliste D, Castelli IE, Clark SJ, Corso AD, de Gironcoli S, Deutsch T, Dewhurst JK, Marco ID, Draxl C, Dułak M, Eriksson O, Flores-Livas JA, Garrity KF, Genovese L, Giannozzi P, Giantomassi M, Goedecker S, Gonze X, Grånäs O, Gross EKU, Gulans A, Gygi F, Hamann DR, Hasnip PJ, Holzwarth NAW, Iusan D, Jochym DB, Jollet F, Jones D, Kresse G, Koepernik K, Küçükbenli E, Kvashnin YO, Locht ILM, Lubeck S, Marsman M, Marzari N, Nitzsche U, Nordström L, Ozaki T, Paulatto L, Pickard CJ, Poelmans W, Probert MIJ, Refson K, Richter M, Rignanese GM, Saha S, Scheffer M, Schlipf M, Schwarz K, Sharma S, Tavazza F, Thunström P, Tkatchenko A, Torrent M, Vanderbilt D, van Setten MJ, Speybroeck VV, Wills JM, Yates JR, Zhang GX, and Cottenier S (2016) Reproducibility in density functional theory calculations of solids. *Science* 351: aad3000.

Lüders M, Marques MAL, Lathiotakis NN, Floris A, Profeta G, Fast L, Continenza A, Massidda S, and Gross EKU (2005) Ab initio theory of superconductivity. I. Density functional formalism and approximate functionals. *Physical Review B* 72: 024545.

Mardirossian N and Head-Gordon M (2017) Thirty years of density functional theory in computational chemistry: An overview and extensive assessment of 200 density functionals. *Molecular Physics* 115: 2315–2372.

Marques MAL, Lüders M, Lathiotakis NN, Profeta G, Floris A, Fast L, Continenza A, Gross EKU, and Massidda S (2005) Ab initio theory of superconductivity. II. Application to elemental metals. *Physical Review B* 72: 024546.

McGaughey AJH, Jain A, Kim HY, and Fu B (2019) Phonon properties and thermal conductivity from first principles, lattice dynamics, and the Boltzmann transport equation. *Journal of Applied Physics* 125: 011101.

Mori-Sánchez P, Cohen AJ, and Yang W (2008) Localization and delocalization errors in density functional theory and implications for band-gap prediction. *Physical Review Letters* 100: 146401.

Parr RG and Yang W (1995) *Density-Functional Theory of Atoms and Molecules*. Oxford University Press.

Perdew JP and Levy M (1983) Physical content of the exact kohn-sham orbital energies: Band gaps and derivative discontinuities. *Physical Review Letters* 51: 1884–1887.

Perdew JP, Parr RG, Levy M, and Balduz JL (1982) Density-functional theory for fractional particle number: Derivative discontinuities of the energy. *Physical Review Letters* 49: 1691–1694.

Perdew JP, Burke K, and Ernzerhof M (1996) Generalized gradient approximation made simple. *Physical Review Letters* 77: 3865–3868.

Runge E and Gross EKU (1984) Density-functional theory for time-dependent systems. *Physical Review Letters* 52: 997–1000.

Schmidt J, Marques MRG, Botti S, and Marques MAL (2019) Recent advances and applications of machine learning in solid-state materials science. *npj Computational Materials* 5: 83.

Tadano T and Tsuneyuki S (2018) First-principles lattice dynamics method for strongly anharmonic crystals. *Journal of the Physical Society of Japan* 87: 041015.

Talirz L, Ghiringhelli LM, and Smit B (2021) Trends in atomistic simulation software usage. *Living Journal of Computational Molecular Science* 3: 1483.

von Barth U and Hedin L (1972) A local exchange-correlation potential for the spin polarized case. i. *Journal of Physics C: Solid State Physics* 5: 1629–1642.

Zhu ZY, Cheng YC, and Schwingenschlögl U (2011) Giant spin-orbit-induced spin splitting in two-dimensional transition-metal dichalcogenide semiconductors. *Physical Review B* 84: 153402.

The sign problem in quantum Monte Carlo simulations

Gaopei Pan[a,b] **and Zi Yang Meng**[c], [a]Beijing National Laboratory for Condensed Matter Physics and Institute of Physics, Chinese Academy of Sciences, Beijing, China; [b]School of Physical Sciences, University of Chinese Academy of Sciences, Beijing, China; [c]Department of Physics and HKU-UCAS Joint Institute of Theoretical and Computational Physics, The University of Hong Kong, Pok Fu Lam, Hong Kong, China

© 2024 Elsevier Ltd. All rights reserved.

Introduction **879**
Configurational weight in classical Monte Carlo simulation **880**
Configurational weight in quantum Monte Carlo simulation **881**
World-line Monte Carlo 882
Stochastic series expansion 883
Determinant Quantum Monte Carlo 883
What is the sign problem? **884**
Sign problem is basis-dependent 885
Sign problem is related to Pauli exclusion principle 886
Sign problem is related to geometric frustration 886
Sign problem is related to Aharonov-Anandan phase 886
How to cure, ease and make use of the sign problem **887**
Symmetry 887
Split orthogonal group, Majorana representation and Majorana positivity 887
Sign bound theory 888
Case 1 889
Case 2 889
Lefschetz thimble 890
Conclusion **891**
Acknowledgments **891**
References **891**

Abstract

The sign problem in quantum Monte Carlo (QMC) simulations appears to be an extremely hard yet interesting problem. In this article, we present a pedagogical overview of the origin of the sign problem in various quantum Monte Carlo simulation techniques, ranging from the world-line and stochastic series expansion Monte Carlo for boson and spin systems to the determinant and momentum-space quantum Monte Carlo for interacting fermions. We point out the basis dependency of the sign problem and summarize the progresses to cure, ease and even make use of the sign problem over the years, such as symmetry analysis of the underlying Hamiltonian, basis optimization in writing down the partition functions and many others. Moreover, we state that although traditional lore says that in the case of sign problem, the average sign in QMC simulation approaches zero exponentially fast with the space-time volume of the configurational space, there are recent breakthroughs showing this is not always the case. Based on the properties of the partition function for finite size systems, one could distinguish when the average sign has the usual exponential scaling and when it is bestowed with an algebraic scaling at the low-temperature limit. Fermionic QMC simulations with such algebraic sign problems have been successfully carried out for extended Hubbard-type and quantum Moiré lattice models.

Introduction

The quantum Monte Carlo (QMC) method is an extremely powerful and unbiased method for studying strongly correlated systems, especially in condensed matter, high energy and quantum material research (Foulkes et al., 2001; Carlson et al., 2015; Assaad and Evertz, 2008; Sandvik, 2010; Xu et al., 2019a), where the quantum many-body lattice models are in general analytically intractable. In QMC simulation, the partition function of the interacting problem is cast into a sum (or integral) over configurations in a chosen basis, and the important sampling scheme could in principle cover the exponentially large configurational space in polynomial time.

However, such practice is often hindered by the infamous "Sign Problem" (Loh et al., 1990). Sign problem means the weights of configurations in the QMC simulation become negative or even complex, and therefore the configurational weights in the Monte Carlo process cannot be further interpreted as classical probabilities, and the minus or even complex sign will render the QMC simulation with exponential complexity for obtaining the data with the same quality compared with the simulations without sign problem. It has been proven that if we could find a method to solve a nondeterministic polynomial (NP) hard problem efficiently, the method can be used to solve the QMC simulations with the sign problem (Troyer and Wiese, 2005). It's important to note that this doesn't mean the sign problem is considered to be NP-hard (Kaul et al., 2013), nor is it inconsistent with performing polynomial-time QMC simulation of specific cases that have a negative or complex sign.

https://doi.org/10.1016/B978-0-323-90800-9.00095-0

The origin of the sign problem has no universal explanation, but it is believed to come from the quantum mechanic properties of the constituent particles in the many-body systems, i.e., fermions, bosons or spins. Frustrated spin systems often have a sign problem because the off-diagonal operators in the Hamiltonian usually bring a negative amplitude (Takasu et al., 1986; Hatano and Suzuki, 1992) and the number of off-diagonal operators can be odd for a particular configuration. While in fermionic systems, negative weights usually arise from the Pauli exclusion principle (Troyer and Wiese, 2005) or different Hubbard-Stratonovich decoupling (Hirsch, 1985) schemes (which means decoupling the quartic fermion interaction term into a certain quadratic basis). At the same time, there are also proposals that the negative sign of a configuration is a topological invariant, which is an imaginary time counterpart of the Aharonov-Anandan phase and can be reduced to a Berry phase in the adiabatic limit (Iazzi et al., 2016). And the sign problem has even been linked to quantum phase transitions (Mondaini et al., 2022; Tarat et al., 2022). Moreover, it was shown recently that some interacting models may have an intrinsic sign problem, which cannot be cured (Hastings, 2016; Ringel and Kovrizhin, 2017; Smith et al., 2020; Golan et al., 2020). In general, a unified description of the sign problem is still missing. These different situations where the sign problem occurs in QMC simulations will be discussed in a case based manner in sections "Configurational weight in classical Monte Carlo simulation" and "Configurational weight in quantum Monte Carlo simulation" of this article.

Fortunately, there are many cases of quantum lattice models where there are no or weak (polynomial instead of exponential scaling) sign problems and Monte Carlo calculations can be carried out with polynomial complexity. In frustrated magnet lattice models, there is no sign problem for some bilayer models (Alet et al., 2016; Ng and Yang, 2017; Honecker et al., 2016; Stapmanns et al., 2018; StefanWessel et al., 2017) within certain parameters. Inspired by the absence of sign problems in the above models, one can choose those models as sign-problem-free reference systems and extend the simulation basis from spin to singlet-triplet or even plaquette bases, and it has been shown that QMC simulations can be carried out to the parameter space for few important 2D frustrated lattice models (such as the Shastry-Sutherland antiferromagnetic spin model) where there were sign problems in the original spin basis (Wessel et al., 2018; D'Emidio et al., 2020). Interacting fermion models (mainly Hubbard-type) at a certain basis with certain symmetries, such as anti-unitary symmetry, have been proven to be sign problem free (Congjun and Zhang, 2005; Lang et al., 1993; Koonin et al., 1997; Hands et al., 2000). Flat band quantum Morié lattice models with $C_2T + C_2P$ symmetries can also ensure that there are no sign problems (Xu et al., 2021a; Johannes et al., 2021; Ouyang and Xu, 2021; Zhang et al., 2021). There also exist cases where one can use Majorana representation to avoid the sign problem, split the fermionic operator into Majorana fermions and reuse the anti-unitary symmetry (Li et al., 2015, 2016; Li and Yao, 2019; Wei et al., 2016; Wang et al., 2015). In addition, basis transformation (D'Emidio et al., 2020; Shinaoka et al., 2015; Levy and Clark, 2021; Torlai et al., 2020; Hangleiter et al., 2020; Klassen et al., 2020; Marvian et al., 2019; Kim et al., 2020; Rossi, 2017; Rossi et al., 2017), Lefschetz thimbles (Ulybyshev et al., 2020; Alexandru et al., 2020), meron cluster (Chandrasekharan and Wiese, 1999), Fermi bags (Huffman and Chandrasekharan, 2014), split-orthogonal group (Wang et al., 2015), Majorana positivity (Wei et al., 2016), semigroup approach (Wei, 2017) and pseudo-unitary group (Xu et al., 2019b), automatic differentiation (Wan et al., 2020), machine learning techniques (Broecker et al., 2017; Wynen et al., 2021) and adiabatic method (Vaezi et al., 2021), or through some systematic expansion (Lawrence, 2020) can also solve or ease some sign problems. These cases will be discussed in sections "What is the sign problem?" and "How to cure, ease and make use of the sign problem" of this article.

If there is sign problem in the QMC simulation, the usual simulation approach is to reweight: one can take the magnitude of the original weight (or magnitude of the real part) as the new weight, and add the sign into the sampling process of physical observables and divide the average sign $\langle s\rangle$. This approach does not solve the sign problem, but only casts it into a different form. The average sign over the Monte Carlo sampling will appear in the denominator, so the average sign will affect how long it will take to obtain meaningful expectation values with controlled errorbars in the simulation. Usually $\langle s\rangle \propto e^{-N\beta\Delta f}$, where Δf is the free energy difference of the two systems before and after reweighting. This means sign often decays exponentially. And there is a lot of research that support the viewpoint. No matter what lattice (hypercubic, ladder, depleted square, Lieb, honeycomb, kagome, and triangular lattices) or parameter (temperature, interaction strength, and density), the sign usually decays exponentially. There is a good summary (Iglovikov et al., 2015) of the sign data for different geometry and parameters.

But recent developments have changed this viewpoint, there are cases in the Hubbard model at certain fillings where the average sign does not decay exponentially (Tarat et al., 2022; Ibarra-García-Padilla et al., 2021) and we have found that it is possible to prove that the average sign of quantum many-body lattice models acquire algebraic sign structure (Ouyang and Xu, 2021; Zhang et al., 2021), if their finite size partition functions satisfy the *Sign bound theory*. The details on the theory and its application on the systems with extended or long-range interaction such as the extended Hubbard (Ouyang and Xu, 2021; Da Liao et al., 2022) and quantum Moiré lattice models (Xu et al., 2018, 2021a,b; Zhang et al., 2021; Liao et al., 2021; Da Liao et al., 2021; Pan et al., 2022), are given in section "Sign bound theory" of this article.

Configurational weight in classical Monte Carlo simulation

Before presenting the details of the sign problem, we first discuss classical Monte Carlo simulation briefly such that the origin of the sign problem manifests naturally. In classical Monte Carlo, the partition function at temperature T is written as follows

$$Z = \mathrm{Tr}\left[e^{-\beta H}\right] = \sum_{C\in\Omega} e^{-\beta E(C)} = \sum_{C\in\Omega} W(C), \tag{1}$$

where $\beta = \frac{1}{k_B T}, k_B$ is the Boltzmann constant, and C stands for the configurations in the configurational space Ω, which is exponentially large in system size, such as 2^{L^d} and 4^{L^d} for d dimensional spin or fermion systems with linear dimension L. Once the partition function is written as a sum of Boltzmann weights $e^{-\beta E(C)}$, it's clear that in the classical Monte Carlo the W(C) corresponding to different configurations are always positive and real numbers. So one can easily carry Monte Carlo updates in a Markov chain by calculating the ratio of weights of different configurations.

For example, as shown in Fig. 1, the Hamiltonian of the classical 2d Ising model is: $H = \sum_{i,j} J_{i,j} s_i s_j$, where s_i denotes the state of the i-th spin which takes the value of ±1 (up or down), $J_{i,\,j}$ is the interaction strength. For the configuration in Fig. 1, the corresponding weight is $e^{-\beta\sum_{i,j}E_{i,j}(C)}$.

We know the expectation value of observable O is

$$\langle O\rangle = \frac{1}{Z}\mathrm{Tr}\left[Oe^{-\beta H}\right] = \frac{1}{Z}\sum_{C\in\Omega} O(C)W(C). \tag{2}$$

For the classical case, since $W(C)$ is a real number and $W(C) \geq 0$, one can carry out the Monte Carlo steps and obtain N_b configurations $\{\mathrm{C}_i\}$ from Ω, according to the distribution $p\ (\mathrm{C}_i) = W\ (\mathrm{C}_i)/Z$. Here N_b is number of sampling bins, and then the average value of the samples is the expectation value of the physical quantity O

$$\langle O\rangle \approx \bar{O} = \frac{1}{N_b}\sum_{i=1}^{N_b} O(C_i). \tag{3}$$

The statistical error corresponding to such an estimate of the mean value is (Geyer, 2011)

$$\varDelta O = \sqrt{\frac{\mathrm{Var}(O)2\tau_O^{\mathrm{int}}}{N_b}}, \tag{4}$$

where Var(O) is the variance of O and the integrated autocorrelation time τ_O^{int} is a measure of the autocorrelations of the sequence $\{O(C_i)\}$

$$\tau_O^{\mathrm{int}} = \frac{1}{2} + \sum_{t=1}^{\infty} A_O(t), \tag{5}$$

and the autocorrelation function $A_O(t)$ for a quantity O is defined as

$$A_O(t) = \frac{\langle O(C_{i+t})O(C_i)\rangle - \langle O\rangle^2}{\langle O\rangle^2 - \langle O\rangle^2}. \tag{6}$$

In principle, since in classical Monte Carlo weights are always real and positive and the statistical errors are inversely proportional to the number of bins $\Delta O \propto \frac{1}{\sqrt{N_b}}$, one can carry out Monte Carlo sampling in polynomial time to achieve controlled expectation values (critical slowing down is not taken into account).

Configurational weight in quantum Monte Carlo simulation

However, when we consider quantum Monte Carlo (QMC) simulation, the weight may become a negative or even a complex number and cause the sign problem in the sampling. In QMC, quantum many-body problems in d dimension are usually mapped onto a classical system in d + z dimension, where z is the dynamic exponent of the problem and usually taken to be 1 in practically simulations (Suzuki, 1976). Depending on the quantum lattice models, there are many different QMC algorithms, such as world-line Monte Carlo (Suzuki, 1976; Evertz et al., 1993; Prokof'Ev et al., 1998; Hirsch et al., 1982), stochastic series expansion (SSE) (Sandvik and Kurkijärvi, 1991; Sandvik, 1992), determinant quantum Monte Carlo (DQMC) (Hirsch, 1985; White et al., 1989), momentum space quantum Monte Carlo (Xu et al., 2021a; Pan et al., 2022; Dai, 2022) and so on. The form of the weights in these methods and the origin of the sign problem are not the same and we will discuss them one by one.

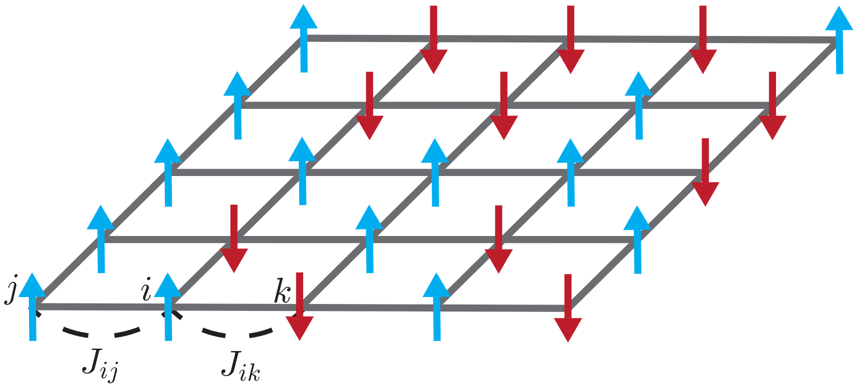

Fig. 1 Classical Ising configuration of the example $E(C) = \sum_{i,\,j} E_{i,\,j}$ and $E_{i,\,j} = J_{i,\,j}$ and $E_{i,k} = -J_{i,k}$.

World-line Monte Carlo

The usual world-line approach (Suzuki, 1976; Evertz et al., 1993; Prokof'Ev et al., 1998; Hirsch et al., 1982; De Raedt and Lagendijk, 1985; Batrouni and Scalettar, 1992) starts with discretizing the inverse temperature β, and employing the Suzuki-Trotter approximation (Trotter, 1959; Suzuki, 1985; Fye, 1986; Fye and Scalettar, 1987) to decompose the exponential of the Hamiltonian. A common world-line expansion of the partition function is

$$\begin{aligned} Z &= \mathrm{Tr}\left[e^{-\beta\hat{H}}\right] = \mathrm{Tr}\left[e^{-M\Delta\tau\hat{H}}\right] = \mathrm{Tr}\left[\left(e^{-\Delta\tau\hat{H}_1}e^{-\Delta\tau\hat{H}_2}\right)^M\right] + \mathcal{O}(\Delta\tau^2) \\ &= \sum_{i_1,\dots,i_{2M}} \left\langle i_1\left|e^{-\Delta\tau\hat{H}_1}\right|i_{2M}\right\rangle\left\langle i_{2M}\left|e^{-\Delta\tau\hat{H}_2}\right|i_{2M-1}\right\rangle\cdots \\ &\quad \left\langle i_3\left|e^{-\Delta\tau\hat{H}_1}\right|i_2\right\rangle\left\langle i_2\left|e^{-\Delta\tau\hat{H}_2}\right|i_1\right\rangle, \end{aligned} \tag{7}$$

where $|i_l\rangle\langle i_l|$, $l \in [1, 2M]$ is the complete basis of the quantum many-body problem and they are inserted between the imaginary time evolution operators. Separating $\hat{H} = \sum_i \hat{H}_i$ in such a way to facilitate the calculation of matrix elements makes it easy to consider the sign problem. We can see that the matrix elements $\left\langle i\left|e^{-\Delta\tau\hat{H}_k}\right|j\right\rangle$ in the weights of a worldline configuration are not obviously positive or negative, therefore, we in general don't know whether the product of these matrix elements is a positive real number.

For example, for spin-1/2 XXZ model in a chain, with Hamiltonian

$$\hat{H} = J_x\sum_i\left(\hat{S}_i^x\hat{S}_{i+1}^x + \hat{S}_i^y\hat{S}_{i+1}^y\right)J_z\sum_i\hat{S}_i^z\hat{S}_{i+1}^z. \tag{8}$$

We can split it in such a way

$$\hat{H} = \underbrace{\sum_n \hat{H}^{(2n+1)}}_{\hat{H}_1} + \underbrace{\sum_n \hat{H}^{(2n+2)}}_{\hat{H}_2}, \tag{9}$$

where $\hat{H}^{(i)} = J_x\left(\hat{S}_i^x\hat{S}_{i+1}^x + \hat{S}_i^y\hat{S}_{i+1}^y\right) + J_z\hat{S}_i^z\hat{S}_{i+1}^z$. By introducing spin flip operators $\hat{S}_j^{\pm} = \hat{S}_j^x \pm i\hat{S}_j^y$, we can write configurations in the spin representation. An example of QMC configuration and values of matrix elements can be seen in Fig. 2. In this case, although the corresponding weight of spin flip is negative, the periodic boundary condition guarantees that the number of spin flips must be even, so the total weight must be positive. But for other cases, there may not be similar conditions to ensure that the weight is positive.

For continuous-time world-lines, the expansion may vary, but the form of the weights is broadly similar. If $\hat{H} = \hat{H}_0 + \hat{V}$, and $\hat{V}$ is a perturbation (Prokof'Ev et al., 1998). We define $e^{-\tau\hat{\mathcal{H}}_0}\hat{U}(\tau) = e^{-\tau\left(\hat{\mathcal{H}}_0+\hat{V}\right)}$ and $\hat{V}(\tau) = e^{\tau\hat{\mathcal{H}}_0}\hat{V}e^{-\tau\hat{\mathcal{H}}_0}$. Then

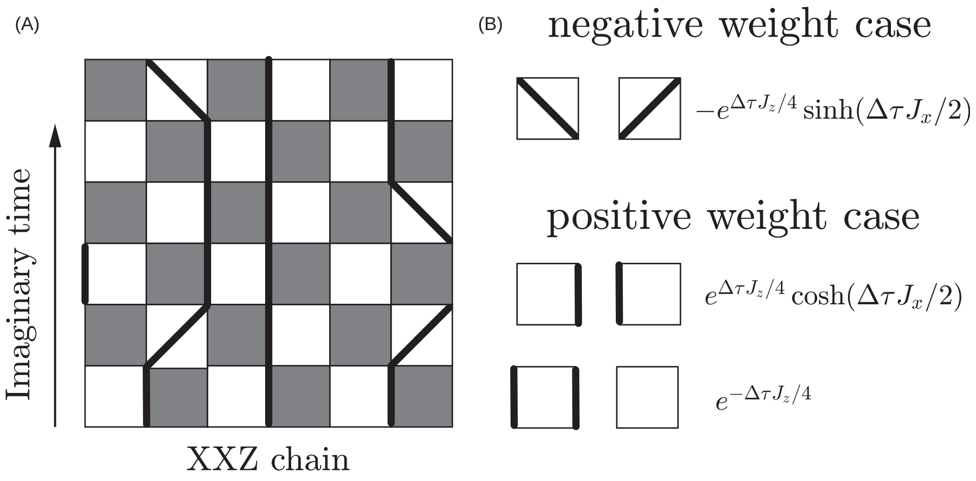

Fig. 2 World line configuration for the XXZ model. (a) The bold lines correspond to the imaginary time evolution of spin up states, and the unpassed points correspond to states with spin down. (b) Corresponding weights of matrix elements in different cases. We see that the negative weight case corresponds to the spin flip operation.

$$
\begin{aligned}
Z &= \mathrm{Tr}\left[e^{-\beta\hat{\mathscr{H}}_0}\hat{U}(\beta)\right] \\
&= \mathrm{Tr}\left[e^{-\beta\hat{\mathscr{H}}_0}\left(1-\int_0^{\beta}d\tau_1\hat{V}(\tau_1)+\int_0^{\beta}d\tau_2\int_0^{\tau_2}d\tau_1\hat{V}(\tau_2)\hat{V}(\tau_1)-\cdots\right)\right] \\
&= \mathrm{Tr}\left[\sum_{n=0}^{\infty}(-1)^n\int_0^{\beta}d\tau_n\int_0^{\tau_n}d\tau_{n-1}\cdots\int_0^{\tau_2}d\tau_1 e^{-(\beta-\tau_n)\hat{\mathscr{H}}_0}\hat{V}e^{-(\tau_n-\tau_{n-1})\hat{\mathscr{H}}_0}\times\hat{V}\cdots\hat{V}e^{-\tau_1\hat{\mathscr{H}}_0}\right] \\
&= \sum_{n=0}^{\infty}(-1)^n\sum_{\phi_n,\cdots\phi_1}^{\beta}\int_0^{\tau_2}d\tau_n\int_0^{\tau_n}d\tau_{n-1}\cdots\int_0^{\tau_2}d\tau_1\left\langle\phi_1\middle|e^{-(\beta-\tau_n)\hat{\mathscr{H}}_0}\middle|\phi_1\right\rangle\langle\phi_1|\hat{V}|\phi_n\rangle \\
&\times\left\langle\phi_n\middle|e^{-(\tau_n-\tau_{n-1})\hat{\mathscr{H}}_0}\middle|\phi_n\right\rangle\langle\phi_n|\hat{V}|\phi_{n-1}\rangle\cdots\langle\phi_2|\hat{V}|\phi_1\rangle\left\langle\phi_1\middle|e^{-\tau_1\hat{\mathscr{H}}_0}\middle|\phi_1\right\rangle.
\end{aligned}
\tag{10}
$$

where $\hat{U}(\tau)=1-\int_0^{\tau}d\tau'\hat{V}(\tau')\hat{U}(\tau')$.

Stochastic series expansion

The stochastic series expansion (SSE) method (Sandvik and Kurkijärvi, 1991; Sandvik, 1992) Taylor expands the partition function, and it can be shown that the expansion of finite size systems can be safely truncated,

$$
\begin{aligned}
Z = \mathrm{Tr}\left[\exp^{-\beta\hat{H}}\right] &= \sum_{n=0}^{\infty}\frac{(-\beta)^n}{n!}\mathrm{Tr}\left[\hat{H}^n\right] \\
&= \sum_{n=0}^{\infty}\sum_{i_1,\ldots,i_n}\frac{(-\beta)^n}{n!}\langle i_1|\hat{H}|i_2\rangle\langle i_2|\hat{H}|i_3\rangle\ldots\langle i_n|\hat{H}|i_1\rangle \\
&\equiv \sum_{n=0}^{\infty}\sum_{i_1,\ldots,i_n}p(i_1,\ldots,i_n)\equiv\sum_{C\in\Omega}W(C),
\end{aligned}
\tag{11}
$$

which is similar to the case of the world-line, the final sign of the weight is also determined by the number of negative matrix elements multiplied, i.e., usually by the number of off-diagonal elements (on the spin $\hat{S}_i^z$ basis, the spin-flip term $\hat{S}_j^+\hat{S}_{j+1}^- + \hat{S}_j^-\hat{S}_{j+1}^+$ is off-diagonal). For bipartite lattices such as square or honeycomb with the periodic boundary condition in space-time, it can be shown that the number of the off-diagonal operator is always even such that their product in the configurational weight will be positive, however, for non-bipartite lattices, such as triangle and kagome, the number of the off-diagonal operators can be odd such that the SSE simulation will have a sign problem. We note that there are recent developments in frustrated magnet lattice models, and some bilayer models (Alet et al., 2016; Ng and Yang, 2017; Honecker et al., 2016; Stapmanns et al., 2018; StefanWessel et al., 2017) within certain parameters with cluster basis are sign-problem-free. Inspired by these works and considering the model that has the same ground state as the above model, one can extend the simulation basis from spin to singlet-triplet or even plaquette bases, and it has been shown that SSE-QMC simulations for few important 2D frustrated lattice models, such as the Shastry-Sutherland antiferromagnetic spin model, can be carried out to the parameter space where there was a sign problem in the original spin basis (Wessel et al., 2018; D'Emidio et al., 2020).

Determinant Quantum Monte Carlo

For interacting fermion models, one uses different ways to write down the partition functions. In determinant quantum Monte Carlo (DQMC) (Hirsch, 1985; White et al., 1989), auxiliary fields are introduced to decouple interactions through the Hubbard-Stratonovich transformation. Taking the Hubbard model as an example, Suzuki-Trotter decomposition is still necessary

$$
Z=\mathrm{Tr}\left[e^{-\Delta\tau\hat{H}_1}e^{-\Delta\tau\hat{H}_0}e^{-\Delta\tau\hat{H}_1}e^{-\Delta\tau\hat{H}_0}\cdots e^{-\Delta\tau\hat{H}_1}e^{-\Delta\tau\hat{H}_0}\right],
\tag{12}
$$

where $\hat{H}_0=-t\sum_{\langle i,j\rangle}\left(\hat{c}_i^{\dagger}\hat{c}_j+h.c.\right)$ and $\hat{H}_I=U\sum_i\left(\hat{n}_{i\uparrow}-\frac{1}{2}\right)\left(\hat{n}_{i\downarrow}-\frac{1}{2}\right)$. $\langle i,j\rangle$ means nearest-neighbor hopping. Then Hubbard-Stratonovich transformation gives

$$
\begin{aligned}
e^{-\Delta\tau\hat{H}_I} &= \prod_i e^{-\Delta\tau U\left(\hat{n}_{i\uparrow}-\frac{1}{2}\right)\left(\hat{n}_{i\downarrow}-\frac{1}{2}\right)} \\
&= \prod_i\gamma\sum_{s_{i,l}=\pm1}e^{\alpha s_{i,l}\left(\hat{n}_{i\uparrow}-\hat{n}_{i\downarrow}\right)} \\
&= \gamma^N\sum_{s_{i,l}=\pm1}\left(\prod_i e^{\alpha s_{i,l}\hat{n}_{i\uparrow}}\prod_i e^{-\alpha s_{i,l}\hat{n}_{i\downarrow}}\right),
\end{aligned}
\tag{13}
$$

where $\gamma=\frac{1}{2}e^{-\Delta\tau U/4}$, $\cosh(\alpha)=e^{\Delta\tau U/2}$. Since we have $\mathrm{Tr}\left[e^{-\sum_{i,j}\hat{c}_i^{\dagger}A_{i,j}\hat{c}_j}e^{-\sum_{i,j}\hat{c}_i^{\dagger}B_{i,j}\hat{c}_j}\right]=\mathrm{Det}(1+e^{-\mathbf{A}}e^{-\mathbf{B}})$, then the partition function is

$$
\begin{aligned}
Z &= \sum_{s_{i,l}=\pm 1} \gamma^{NL_\tau} \mathrm{Tr}_F \left\{ \prod_{l=1}^{L_\tau} \left[\left(\prod_i e^{\alpha s_{i,l} \hat{n}_\uparrow} \right) \left(e^{-\Delta\tau c_\uparrow^\dagger T c_\uparrow} \right) \left(\prod_i e^{-\alpha s_{i,l} \hat{n}_{i,\downarrow}} \right) \left(e^{-\Delta\tau c_\downarrow^\dagger T c_\downarrow} \right) \right] \right\} \\
&= \gamma^{NL_\tau} \sum_{\{s_{i,l}\}} \prod_{\sigma=\uparrow\downarrow} \mathrm{Det}[\mathbf{I} + \mathbf{B}^\sigma(L_\tau \Delta\tau,\ (L_\tau - 1)\Delta\tau) \cdots \mathbf{B}^\sigma(\Delta,\ \tau,\ 0)],
\end{aligned}
\tag{14}
$$

where

$$
\begin{aligned}
\mathbf{B}^\uparrow(l_2\Delta\tau, l_1\Delta\tau) &= \prod_{l=l_1+1}^{l_2} e^{\alpha\,\mathrm{Diag}\left(\vec{S}_l\right)} e^{-\Delta\tau T} \\
\mathbf{B}^\downarrow(l_2\Delta\tau, l_1\Delta\tau) &= \prod_{l=l_1+1}^{l_2} e^{-\alpha\,\mathrm{Diag}\left(\vec{S}_l\right)} e^{-\Delta\tau T}.
\end{aligned}
\tag{15}
$$

and $\mathrm{Diag}\left(\vec{S}_l\right)$ is a diagonal matrix with diagonal elements $s_{i,l}$. For the space-time configuration $\{s_{i,l}\}$, the calculation of weight is converted to the calculation of the determinant of matrices. Without prior knowledge such as symmetry analysis or energy spectrum (Zhang et al., 2021), the determinant of a matrix doesn't have to be a positive real number. It is worth noting that the Hubbard-Stratonovich transformation which introduces auxiliary fields is also one of the causes of the sign problem. For example, using the world-line method, the one-dimensional Hubbard model has no sign problem (Assaad and Evertz, 2008; Hirsch et al., 1982), but for DQMC, usually there is a sign problem (Iglovikov et al., 2015). A Markov chain for the DQMC simulation for the 2d Hubbard model, with $L \times L \times \beta$ and the auxiliary fields for three consecutive configurations is given in Fig. 3.

What is the sign problem?

With the above preparation, we now discuss the real content of the sign problem. As the name implies, the simplest and most straightforward definition of the sign problem is that, the weights (probabilities) in the Monte Carlo simulation $p\ (C_i) = W\ (C_i)/Z$ are negative or become a complex number.

For the real time evolution of a quantum mechanic state, this is obviously going to happen, because the time evolution operator is e^{-itH} and the corresponding configurational weight $W(C) \sim \exp.(iS\ (C))$, here $S\ (C)$ is the action function of configuration C, which is time integral of Lagrangian $L : S = \int dt\ L(x, \dot{x})$. It's not surprising that now the weight might be a complex number. While if we consider the ensemble average at the thermal equilibrium state for classical statistical problems such as the Ising model in section "Configurational weight in classical Monte Carlo simulation," configurational weight $W(C) \sim \exp.(-\beta H(C))$, is real and positive.

When we discuss algorithms that do not suffer from the sign problem (Troyer and Wiese, 2005), it usually means that the algorithm needs polynomial complexity to evaluate the thermal average $\langle O \rangle$, i.e., with the system size $N = L^d$ and inverse temperature $\beta = \frac{1}{k_B T}$, the computational time required to make the relative error $\Delta O / \langle O \rangle$ less than ε is called $t(\varepsilon, N, \beta)$. If $t(\varepsilon, N, \beta)$ grows polynomially with N and β, then there exist integers n and m and a constant $\kappa < \infty$ such that

$$
t(\varepsilon, N, \beta) < \kappa \varepsilon^{-2} N^n \beta^m. \tag{16}
$$

Such complexity is tractable with realistic Monte Carlo simulation in both human and machine time.

One thing that needs to be clarified is that sign problem doesn't mean one cannot carry out Monte Carlo simulation on finite-size system. If there is sign problem, the usual expedient (Loh et al., 1990) is to introduce a reference system which is sign-problem-free, by reweighting

$$
\langle O \rangle = \frac{\sum_C O(C_i) W(C_i)}{\sum_C W(C_i)} = \frac{\sum_C O(C_i) s(C_i) |W(C_i)| / \sum_C |W(C_i)|}{\sum_C s(C_i) |W(C_i)| / \sum_C |W(C_i)|} \equiv \frac{\langle Os \rangle'}{\langle s \rangle'}, \tag{17}
$$

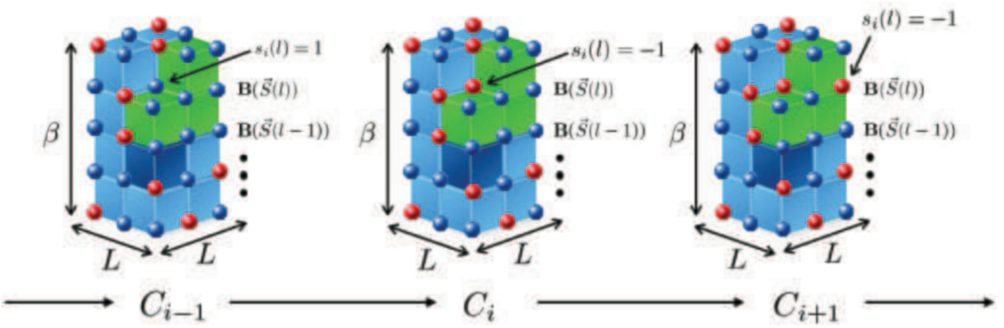

Fig. 3 The space-time auxiliary field $\{s_{i,l}\}$ introduced by Hubbard-Stratonovich transformation lives on the lattice of $d + 1$ dimension (here $d = 2$ with linear system size L), and we perform the calculation of Markov chain Monte Carlo by flipping the auxiliary field on the space-time lattice with the corresponding probability. Here the notation $\mathbf{B}\left(\vec{s}\,(l)\right)$ corresponds to the matrix containing the auxiliary field of imaginary time layer l, shown in Eq. (15).

where $s(C_i) = \frac{W(C_i)}{|W(C_i)|}$ and $\langle O\rangle' = \frac{\sum_C O(C_i)|W(C_i)|}{\sum_C |W(C_i)|}$. The average of sign, $\langle s\rangle = Z/Z'$, which is just the ratio of the partition function of the system $Z = \sum_C W(C_i)$ with weights $W(C_i)$ and the reference system used for sampling with another partition function $Z' = \sum_C |W(C_i)|$.

As the partition function is usually an exponential form of the free energy, then $\langle s\rangle = Z/Z' = \exp(-\beta N \Delta f)$, where Δf is the free energy densities differences of Z and Z'. When there is a sign problem, the term $\langle s\rangle'$ in the denominator needs to be taken into account when calculating the mean value of quantity, so the relative error $\Delta s/\langle s\rangle$ of the sign is very important, and it usually increases exponentially with inverse temperature β and system size N

$$\frac{\Delta s}{\langle s\rangle} = \frac{\sqrt{(\langle s^2\rangle - \langle s^2\rangle)/N_b}}{\langle s\rangle} = \frac{\sqrt{1 - \langle s\rangle^2}}{\sqrt{N_b}\langle s\rangle} \sim \frac{e^{\beta N \Delta f}}{\sqrt{N_b}} + O(\langle s\rangle), \tag{18}$$

where N_b is the number of bins. In most cases, Δf is a quantity that doesn't change very much in the simulation, so when there a sign problem, the QMC simulation usually takes exponential time to have a reasonable estimation of the errorbars for physical observables.

The exponential computation time seems to imply that the sign problem may be an nondeterministic polynomial (NP) problem, but is it an NP-hard problem? Here NP problems are the set of decision problems solvable in polynomial time by an nondeterministic Turing machine, and an NP-hard problem means every problem in NP can be reduced in polynomial time to it. At present, the answer still seems unclear, but explicit examples can deepen our understanding.

People try to construct a simulation with sign problem, and the calculation of its physical quantity can be transformed into a solution of an NP-complete problem. Here a problem is NP-complete means it is both NP and NP-hard. It is suggested that if the polynomial-time solution corresponding to the sign problem is found, the polynomial-time solution of the NP-complete problem can also be found, that is, the sign problem is an NP-hard problem. In Troyer and Wiese (2005), people consider a well-known special case of the classical Ising spin glass model. One can map it to a NP-hard graph problem, such as "finding ground energy" to another problem "finding a cocycle of minimum weight while a two-level grid $G = (V, E)$, and a weighting function $J : E \to \{-1, 0, 1\}$ are given" (Barahona, 1982). Here a graph $G = (V, E)$ consists of a set of vertices V, and a set E of unordered pairs of different vertices, called edges. Then it is possible to introduce a corresponding NP-complete problem (Troyer and Wiese, 2005): for given constant C, does the ground state have energy $E_0 \leq C$? And then one can map the classical Ising spin glass model to quantum Ising spin glass model with $\sigma_i^x \sigma_j^x$ term, which has a sign problem. Mathematically, because this problem is NP-complete, there exists a polynomial-time mapping to any other NP-complete problem.

However, the special spin glass example is equivalent to saying quantum spin glass problem is no easier to solve than the corresponding classical spin glass problem. The example is very special and the proof does not address QMC solutions of systems, such as Hubbard model without particle-hole symmetry and SU(2) frustrated quantum spin models, which are not directly associated with the difficulties of simulating classical frustrated glassy systems with complicated energy landscapes. So we cannot conclude that all sign problems are NP-hard. But from this example, at least we know that if we find a method to solve an NP-hard problem, this scheme can be used to solve QMC simulation with sign problem.

In addition, the definition $\langle s\rangle = Z/Z'$ can give us some other information. Just write it in zero-temperature limit

$$\langle s\rangle_R = \frac{Z}{Z^R} = \frac{g e^{-\beta E_0}}{g^R e^{-\beta E_0^R}}, \tag{19}$$

where g and g^R are the ground state degeneracy of system Z and reference system Z^R, while E_0 and E_0^R are the ground energy of systems Z and Z^R. This means the expectation value $\langle s\rangle_R$ can be used to read g, E_0 for finite size systems, if we engineer the reference system with known g_R and E_0^R.

For spin system case, if the systems Z and reference system Z^R have the same ground state, and the ground is in the set of QMC computational basis, one can see the reduction of the sign problem at low-temperature, as shown in Wessel et al. (2018) and D'Emidio et al. (2020). For the fermion case, we can also choose a good reference system Z^R, or choose a well-known $Z' \geqslant Z^R$ to get the lower bound of the sign, this will be explained in section "Sign bound theory."

Now we know the definition of sign problem, then what is the sign problem related to? The collective efforts over the years have pointed out that the sign problem has multiple origins. And we will discuss the major ones below.

Sign problem is basis-dependent

First of all, the sign problem is basis-dependent. For example, if one can diagonalize the Hamiltonian matrix and calculate the eigenstates $\{|i\rangle\}$ then $H|i\rangle = \varepsilon_i|i\rangle$ and

$$\begin{aligned}\langle O\rangle &= \mathrm{Tr}[O \exp(-\beta H)]/\mathrm{Tr}[\exp(-\beta H)] \\ &= \sum_i \langle i|O_i|i\rangle \exp(-\beta\varepsilon_i)/\sum_i \exp(-\beta\varepsilon_i).\end{aligned} \tag{20}$$

There's obviously no sign problem here. Unfortunately, it is often difficult to obtain eigenstates of a quantum many-body system in the first place. Moreover, if one already has the methods to obtain all eigenstates of the system, there is then no need to perform Monte Carlo simulations.

In addition, for interacting fermion systems, different bases will bring different effects during decoupling. In a recent paper on automatic differentiation to mitigating the sign problem (Wan et al., 2020), the authors performed different decoupling at different sites $e^{-\Delta\tau U\left(\hat{n}_{i\uparrow}-\frac{1}{2}\right)\left(\hat{n}_{i\downarrow}-\frac{1}{2}\right)} = \frac{1}{2}e^{-U\Delta\tau/4}\sum_{s_i=\pm1}e^{\lambda s_i \hat{c}_i^\dagger \sigma\cdot \boldsymbol{n}_i \hat{c}_i}$, where $\boldsymbol{n}_i = (\sin\theta_i \sin\phi_i, \sin\theta_i\cos\phi_i, \cos\theta_i)$. The choice of basis for decoupling at different sites can affect the severity of the sign problem. While for spin systems, as discussed in Eq. (19), if the ground state is a member of the computational basis, and sign-problem-free reference system have the same ground state, reduction of the sign problem at low-temperature (Wessel et al., 2018; D'Emidio et al., 2020) will be seen.

We note there exist many research works that mitigate the sign problem by basis transformation (D'Emidio et al., 2020; Shinaoka et al., 2015; Levy and Clark, 2021; Torlai et al., 2020; Hangleiter et al., 2020; Klassen et al., 2020; Marvian et al., 2019; Kim et al., 2020; Rossi, 2017; Rossi et al., 2017). However, it has also been pointed out that some sign problems turn out to be intrinsic (Hastings, 2016; Ringel and Kovrizhin, 2017; Smith et al., 2020; Golan et al., 2020) and cannot be eliminated by local unitary basis transformations.

Sign problem is related to Pauli exclusion principle

From the point of view of world-line Monte Carlo, the exchange of fermions in the world-line will bring a minus sign, which arises from the Pauli exclusion principle. A simple such process is shown in Fig. 4 and can be derived as

$$\begin{aligned}\left\langle\psi_1\middle|\hat{c}_1^\dagger\hat{c}_4\hat{c}_3^\dagger\hat{c}_2\hat{c}_4^\dagger\hat{c}_3\hat{c}_2^\dagger\hat{c}_1\middle|\psi_1\right\rangle &= \left\langle\psi_1\middle|\hat{c}_4\hat{c}_3^\dagger\hat{c}_2\hat{c}_4^\dagger\hat{c}_3\hat{c}_2^\dagger\hat{n}_1\middle|\psi_1\right\rangle \\ &= \left\langle\psi_1\middle|\hat{c}_4\hat{c}_3^\dagger\hat{c}_4^\dagger\hat{c}_3(1-\hat{n}_2)\hat{n}_1\middle|\psi_1\right\rangle \\ &= -\langle\psi_1|(1-\hat{n}_4)\hat{n}_3(1-\hat{n}_2)\hat{n}_1|\psi_1\rangle \\ &= -\langle\psi_1|\psi_1\rangle.\end{aligned} \tag{21}$$

Sign problem is related to geometric frustration

Similarly, frustrated spin or boson systems often have sign problem. For example, if we consider a boson (spin) system of three sites

$$\hat{H} = \left(\hat{b}_2^\dagger\hat{b}_2 + \hat{b}_2^\dagger\hat{b}_3 + \hat{b}_3^\dagger\hat{b}_1\right) + \text{h.c.or } \hat{H}\left(\hat{S}_1^+\hat{S}_2^- + \hat{S}_2^+\hat{S}_3^- + \hat{S}_3^+\right) + \text{h.c.} \tag{22}$$

The weight is negative for the following configuration (where $|i\rangle$ means i-th site occupied state)

$$\left\langle 1\middle|e^{-d\beta\hat{H}}\middle|2\right\rangle\left\langle 2\middle|e^{-d\beta\hat{H}}\middle|3\right\rangle\left\langle 3\middle|e^{-d\beta\hat{H}}\middle|1\right\rangle, \text{ contribution} = (-1)^3 d\beta^3. \tag{23}$$

However, frustration does not necessarily mean there must be a sign problem. A clever choice of basis can make the QMC simulation sign-problem free. As discussed in section "Stochastic series expansion," there is no sign problem for some bilayer frustrated models (Alet et al., 2016; Ng and Yang, 2017; Honecker et al., 2016; Stapmanns et al., 2018; StefanWessel et al., 2017). Inspired by these works and considering the model that has the same ground state as the above model, one can extend the simulation basis from spin to singlet-triplet or even plaquette bases, and recently there is progress in such cases by means of changing the simulation basis from spin to bond or even plaquette (Wessel et al., 2018; D'Emidio et al., 2020) to reduce the sign problem in the QMC simulation for 2D antiferromagnetic Shastry-Sutherland spin model.

Sign problem is related to Aharonov-Anandan phase

For DQMC, the sign problem is thought to be related to the topological properties of the configurations (Iazzi et al., 2016). One can define the weight as

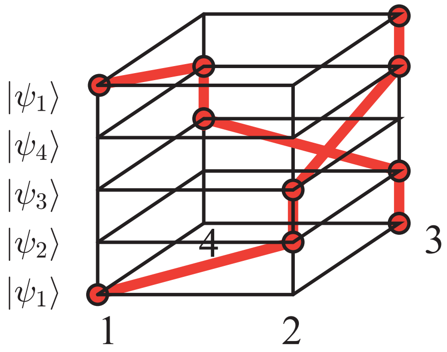

Fig. 4 An example of a configuration where particle exchange leads to negative weights. The dots represent particle occupation, and bold lines are world lines.

$$W(C_i) = \det\left[1 + e^{\beta\mu}\mathcal{T}\exp\int_0^{\beta} \mathrm{d}\tau H^{\mathrm{aux}}[C_i(\tau)]\right], \tag{24}$$

then define

$$G(\tau;\beta) = \mathcal{T}\exp\int_{\tau}^{\tau+\beta} \mathrm{d}\tau' H^{\mathrm{aux}}[C_i(\tau')] \tag{25}$$

the corresponding eigenvalue and eigenstate are:$G(\tau;\beta)|\phi_n(\tau)\rangle = \lambda_n|\phi_n(\tau)\rangle$. Now one finds the weight is

$$W(C_i) = \prod_n \left(1 + \lambda_n e^{\beta\mu}\right), \tag{26}$$

by defining $\lambda_n = e^{i\theta_n}\omega_n$ and $e^{i\theta_n} = \prod_{\tau=0}^{\beta}\langle\phi_n(\tau + d\tau)|\phi_n(\tau)\rangle$. These phases $e^{i\theta_n}$ are imaginary time versions of the Aharonov-Anandan (AA) phase. If we take $\beta \to \infty$, which means the adiabatic limit, then the eigenstate $|\psi_n(\tau)\rangle = \lim_{\beta\to\infty}|\phi_n(\tau)\rangle$ and the weights is $\exp[-\int_0^{\beta}\varepsilon_n(\tau)d\tau]$, where $\varepsilon_n(\tau)$ is eigenvalue of $H^{\mathrm{aux}}(\tau)$. Now $e^{i\theta_n}$ becomes a Berry phase of the instantaneous eigenstates $|\phi n(\tau)\rangle$.

This analogy gives us a new perspective on the sign problem, but it doesn't help to mitigate it. In the next section, we will discuss an understanding and practical implementation scheme to cure, ease and make use of the sign problem.

How to cure, ease and make use of the sign problem

There are no general methods how to reduce the exponential computation complexity introduced by the sign problem. There are, nevertheless, different solutions for different physical systems. We note only the recent *Sign bound theory* has pointed out a generic direction (Zhang et al., 2021). Below, we select a few important cases and explain their usages.

Symmetry

In DQMC for interacting fermion models, where $H = H_K + H_I$, H_K is the kinetic energy part and H_I is the part of the interaction after decoupling (Congjun and Zhang, 2005), if there exists an anti-unitary operator T, such that

$$TH_KT^{-1} = H_K, TH_IT^{-1} = H_I, T^2 = -1. \tag{27}$$

then for the eigenvalues λ_i of matrix $I + B(\beta, 0)$, where $B(\beta, 0)$ is defined in Eq. (15), we know $\prod\lambda_i$ is real and positive number. The proof is simple. If $(I + B)\ |\Psi_i\rangle = \lambda_i\ |\Psi_i\rangle$ then $T\ |\Psi_i\rangle$ is also an eigenstate of matrix $(I + B)$ with eigenvalue λ_i^*. That is, the eigenvalues λ_i and λ_i^* come in pairs, and the weight $\det(I + B) = \prod|\lambda_i|^2 \geq 0$. The orthogonality of the two eigenstates is trivial: $\langle\Psi_i|T\Psi_i\rangle = \langle\Psi_i|T^{\dagger}TT|\Psi_i\rangle^* = -\langle\Psi_i|T^{\dagger}|\Psi_i\rangle^* = -\langle T\Psi_i|\Psi_i\rangle^* = -\langle\Psi_i|T\Psi_i\rangle = 0$. The overlap of the two states is zero.

In practice, one usually divides the configurational weight of the original problem into two parts according to the degrees of freedom, such as the spin up and down, then performs a unitary transformation to show the two parts of the weights are either the same real number or complex conjugate with each other, such that their product is positive definite. For example, the Hubbard model at half-filling, if $U > 0, e^{-\Delta\tau\hat{H}_U} = \gamma\sum_{s=\pm1}e^{\alpha s\left(\hat{n}_{\uparrow}+\hat{n}_{\downarrow}-1\right)}$ where $\gamma = \frac{1}{2}e^{\Delta\tau U/4}$, $\cosh(\alpha) = e^{-\Delta\tau U/2}$, and α is an imaginary number. Now, the unitary transformation is the particle-hole transformation,

$$\begin{cases} \hat{c}_{i\downarrow}^{\dagger} \to (-1)^i\hat{c}_{i\downarrow} \\ \hat{c}_{i\downarrow} \to (-1)^i\hat{c}_{i\downarrow}^{\dagger}. \end{cases} \tag{28}$$

and

$$\alpha \text{ is an imaginary number} \to \begin{cases} \alpha\left(\hat{n}_{i\uparrow} + \hat{n}_{i\downarrow} - 1\right) \overset{PH\text{ for spin-down}}{\longrightarrow} \alpha s_i\left(\hat{n}_{i\uparrow} - \hat{n}_{i\downarrow}\right) \\ e^{\alpha s_i\left(\hat{n}_{i\uparrow}+\hat{n}_{i\downarrow}-1\right)} \overset{PH\text{ for spin-down}}{\longrightarrow} e^{\alpha s_i\left(\hat{n}_{i\uparrow}-\hat{n}_{i\downarrow}\right)}. \end{cases} \tag{29}$$

Since α is an imaginary number, it's clear to see that after such a particle-hole transformation, spin up and down parts are complex conjugated to each other.

In addition to particle-hole symmetry, other symmetries such as $C_2T + C_2P$ symmetries (Xu et al., 2021a; Johannes et al., 2021) may also make the system sign-free. In short, we want to find an anti-unitary transformation that makes the system invariant, or to apply a unitary transformation, then the weights are divided into two parts that are obviously complex conjugate to each other. Such a scheme has been widely used in the DQMC solution of interaction driven topological phase transitions, such as in the Kane-Mele Hubbard model (Hohenadler et al., 2012; Meng et al., 2014).

Split orthogonal group, Majorana representation and Majorana positivity

Subsequently, people have made more in-depth studies on sign of determinants of matrices. For example, there is a theorem (Wang et al., 2015):

If M belongs to the split orthogonal group $O(n,n)$, then

$$\det(I+M)\begin{cases}\geq 0, & \text{if}\, M\in O^{++}(n,\ n),\\ \leq 0, & \text{if}\, M\in O^{--}(n,\ n),\\ 0, & \text{otherwise},\end{cases} \tag{30}$$

where the split orthogonal group $O(n,\ n)$ is formed by all $2n\times 2n$ real matrices that preserve the metric $\eta=\operatorname{diag}\left(\underbrace{1,\ \ldots,}_{n},\ \underbrace{-1,\ \ldots,\ -1}_{n}\right), M^T\eta M=\eta$. Split orthogonal group $O(n,\ n)$ means that if we write the matrix M in the block form like: $M=\begin{pmatrix}M_{11} & M_{12}\\ M_{21} & M_{22}\end{pmatrix}$, then we have $|\det(M_{11})|\geq 1$ and $|\det(M_{22})|\geq 1$. And we use the notation $O^{\pm\pm}(n,n)$ to classify the four components of $O(n,\ n)$ by considering the signs of det (M_{11}) and det (M_{22}).

Since the fermion sign problem is related to the basis of decoupling, it can be found that some models translated to Majorana representation are sign-problem free (Li et al., 2015, 2016; Li and Yao, 2019). Majorana representation is turning fermions into Majorana fermions

$$\hat{c}_i=\frac{1}{2}\left(\gamma_i^1+i\gamma_i^2\right),\ \hat{c}_i^\dagger=\frac{1}{2}\left(\gamma_i^1+i\gamma_i^2\right). \tag{31}$$

These findings inspired research on Majorana reflection positivity or the Majorana Kramers positivity (Wei et al., 2016). One can write the H_0 and decoupled Hamiltonian under the Majorana representation: $H_{bl}=\gamma^T V\gamma$. Then.

(a) if V is a Majorana reflection positive kernel, it can be represented as

$$V=\begin{pmatrix}A & iB\\ -iB^T & A^*\end{pmatrix}, \tag{32}$$

where A and B are $N\times N$ matrices. A is complex antisymmetric matrix and B is a Hermitian matrix. Or,

(b) if there exist two transformation operators S and P such that

$$\begin{aligned}S^TVS&=V^*,\\ PVP^{-1}&=V,\end{aligned} \tag{33}$$

where S is a real antisymmetric matrix and P is a symmetric or antisymmetric Hermitian matrix, and we need P anticommutes with S. There is no sign problem in the DQMC simulation.

In Xu et al. (2019b), there is a similar discussion on the sign problem related to the structure of the fermion determinant. It is proven that if $D\in \mathrm{SU}(n,m)$, then det $(I_{n+m}+D)\in\mathbb{R}$, where $\mathrm{SU}(n,m)$ is a pseudo-unitary group. Such condition is used to guarantee the DQMC simulation for U(1) gauge field coupled to Dirac fermions in (2 + 1)d, a fundamental problem for both high-energy physics and condensed matter physics related to quantum electrodynamics and deconfined quantum criticalities, is sign-problem free (Xu et al., 2019b; Wang et al., 2019; Janssen et al., 2020).

Sign bound theory

As discussed in section "What is the sign problem?," for systems with sign problems, we can usually sample them by reweighting and the average sign is usually $\langle s\rangle=Z/Z'\sim e^{-\beta N\Delta f}$. However, the difference of free energy Δf between the reference system Z' and the system Z is not necessarily a constant with little change, but may be a quantity depending on the system size $N=L^d$ and inverse temperature $\beta=\frac{1}{k_BT}$.

In some systems, we find that in the zero-temperature limit, the sign does not decay exponentially with respect to size L but rather decays algebraically (Ouyang and Xu, 2021; Zhang et al., 2021), implying that Δf could be a logarithmic function of L. In fact, in the zero-temperature limit, the mean of the signs is $\langle s\rangle_R=\frac{Z}{Z_R}=\frac{ge^{-\beta E_0}}{g^Re^{-\beta E_0^R}}$, as given in Eq. (19). We can choose a good reference system Z^R, which has the same ground state energy $E_0^R=E_0$ with Z. Then the mean of the signs is $\langle s\rangle_R=g/g^R$, which is only related to the ratio of ground state degeneracy. And as shown in the cases below, in a few common situations, such as the lattice model for quantum Moiré materials in momentum space (Xu et al., 2021a,b; Zhang et al., 2021; Pan et al., 2022) and extended Hubbard model in real space (Ouyang and Xu, 2021; Da Liao et al., 2022, 2021; Liao et al., 2021), the ground state degeneracy is a polynomial function of the size of the system.

Even if most of the time we cannot find such a perfect Z^R, we can still consider the upper bound on the value of Z^R, which means if we know $Z^R\leq C$, then in the zero temperature limit we can get a lower bound of the sign: $\langle s\rangle_R=\frac{Z}{Z^R}\geq\frac{ge^{-\beta E_0}}{C}$. This is the *Sign bound theory* (Zhang et al., 2021). Two cases of the theory will be shown below. In case 1: $Z^R=g^Re^{-\beta E_0^R}\leq\sqrt{g'e^{-\beta E_0'}}$ and $E_0'/2=E_0$ such that $\langle s\rangle_R=\frac{Z}{Z^R}\geq\frac{ge^{-\beta E_0}}{\sqrt{g'e^{-\beta E_0'}}}=g/\sqrt{g'}e^{-\beta\left(E_0-E_0'/2\right)}=g/\sqrt{g'}$, and in case 2: $Z^R=g^Re^{-\beta E_0^R}\leq g'e^{-\beta E_0'}$ and $E_0'=E_0$ such that $\langle s\rangle_R=\frac{Z}{Z^R}\geq\frac{ge^{-\beta E_0}}{g'e^{-\beta E_0'}}=g/g'e^{-\beta\left(E_0-E_0'\right)}=g/g'$. If we succeed in finding such an upper bound on Z^R which can cancel out the $e^{-\beta E_0}$

term in the denominator, then the lower bound of the sign is just a function of the ground state degeneracy. If the ground state degeneracy is a polynomial function of the size of the system, then we can obtain a lower bound of the average sign decay with the system size algebraically.

Case 1

For example, we choose $Z^R = \sum_{\{l\}} P(\{l\})|\mathcal{R}(D(\{l\}))| \equiv \langle|\mathcal{R}(D)|\rangle$ and $Z' = \sum_{\{l\}} P(\{l\})|D|^2(\{l\}) \equiv \langle|D|^2\rangle$, where $Z = \sum_{\{l\}} P(\{l\}) D(\{l\}) \equiv \langle D\rangle = \langle\mathcal{R}(D)\rangle$. Here $D(\{l\})$ is the determinant term in weight, and $P(\{l\})$ is a normalized probability distribution. Because $\langle|\mathcal{R}(D)|\rangle \le \sqrt{\langle|D|^2\rangle}$ then $\langle s\rangle = \frac{Z}{Z^R} \ge \frac{ge^{-\beta E_0}}{\sqrt{g'e^{-\beta E_0'}}} = g/\sqrt{g'}e^{-\beta\left(E_0 - E_0'/2\right)} = g/\sqrt{g'}$, if $E_0'/2 = E_0$.

The twisted-bilayer-graphene (TBG) models, projected to the flat bands, belong to such a case (Xu et al., 2021a; Pan et al., 2022). In the chiral limit, the Hamiltonian only has density-density interaction in momentum space

$$H = \sum_{q\neq 0} V(q)\rho_{-q}\rho_q = \sum_{q\neq 0} V(q)\rho_q^\dagger \rho_q, \tag{34}$$

where $\rho_q = \sum_{i,j}\left(\lambda_{i,j}(q)\hat{c}_i^\dagger c_j - \frac{1}{2}\mu_q\right)$.

If we set λ as random number and $\mu_q = 0$, and there is no other symmetry, then $E_0 = E_0'/2$. For ground state degeneracy, it's easy to know $g = 2$ and $g' = N + 3$, by introducing a raising operator $\Delta^\dagger = \sum_{i'} c_{i',+}^\dagger c_{i',-}$. Then at low temperature, $\langle s\rangle \ge 2/\sqrt{N+3}$ (as shown in Fig. 5(a)).

We consider single valley/spin two band ($m,\ n \in \{1,-1\}$) TBG model at hall-fing and chiral limit, which means $\lambda_{i,\ j,m,n}(q) = m\cdot n\cdot\lambda_{i,\ j,m,n}(q)$ and $\mu_q \neq 0$. Similarly, we still have $E_0 = E_0'$ and $g = 2$, and now $g' = (N+1)^2 + 2$. Then at low temperature, $\langle s\rangle \ge 2/\sqrt{(N+1)^2 + 2}$ (as shown in Fig. 5(b)).

Case 2

If we consider the real space extended Hubbard model (Ouyang and Xu, 2021; Liao et al., 2021; Da Liao et al., 2021), which also offers the description of the TBG systems once the interactions are projected to the flat bands with truncation

$$\hat{H} = U\sum_{\hexagon}\left(\hat{Q}_{\hexagon} + \alpha\hat{T}_{\hexagon} - \nu\right)^2, \tag{35}$$

where $\hat{Q}_{\hexagon} = \frac{1}{3}\sum_{\sigma,\tau}\sum_{l=1}^{6}\hat{c}_{R+\delta_l,\sigma,\tau}^\dagger\hat{c}_{R+\delta_l,\sigma,\tau} - 4$, $\hat{T}_{\hexagon} = \sum_{\sigma,\tau}\sum_{l=1}^{6}\left[(-1)^l\hat{c}_{R+\delta_{l+1},\sigma,\tau}^\dagger\hat{c}_{R+\delta_l,\sigma,\tau} + \text{h.c.}\ \right]$, ν is used to control filling, σ, τ are spin and valley indexes, $R + \delta_l$ represents site l in a single R hexagon and U, α is real number coming from the overlap of Wannier functions on the Moiré scale.

Here, we choose $Z' = \sum_{\{l\}} P(\{l\})\,|D|\,(\{l\}) \equiv \langle|D|\rangle$, still $Z^R = \sum_{\{l\}} P(\{l\})\,|\mathcal{R}(D(\{l\}))|\ \equiv \langle|\mathcal{R}(D)|\rangle$ and $Z = \sum_{\{l\}} P(\{l\}) D(\{l\}) \equiv \langle D\rangle = \langle\mathcal{R}(D)\rangle$. Because $\langle|\mathcal{R}(D)|\rangle \le \langle|D|\rangle$ then $\langle s\rangle = \frac{Z}{Z^R} \ge \frac{ge^{-\beta E_0}}{g'e^{-\beta E_0'}} = g/g'e^{-\beta\left(E_0 - E_0'\right)} = g/g'$. Similarly, we still have $E_0' = E_0$. It can be computed from tensor Young tableau method that, at $\nu = \pm 2$, $g = (N+3)(N+2)(N+1)/6$, and at $\nu = 0$, $g' = (N+3)(N+2)^2(N+1)/12$ (Zhang et al., 2021). Then at low temperature, $\langle s\rangle \geqslant g/g' = 2/(N+2)$ (as shown in Fig. 5(c)).

For the model we mentioned above and its reference system, the exponential decay part cancels out, and we can easily calculate the ground state degeneracy. As shown in Fig. 5, numerically we also see that at very low temperatures the average sign decays polynomially.

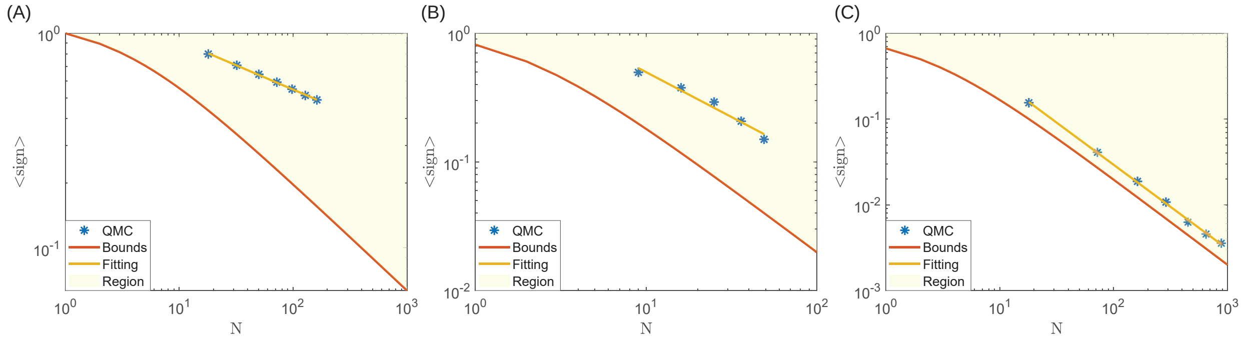

Fig. 5 The average sign for three different cases according to the *sign bound theory*. All measurement are carried out at a average sign converged temperature. The errorbars in QMC data are smaller than the symbol size. (a) momentum space case, now λ is randomly set, and the red line gives us the lower bound $\langle s\rangle \ge 2/\sqrt{N+3}$. Here $N = 18, 32, 50, 72, 98, 128, 162$. Fitting line $\propto N^{-0.23}$. (b) momentum space case, we consider $\nu = 0$ single valley/spin TBG model in chiral limit, and the red line gives us the lower bound $\langle s\rangle \ge 2/\sqrt{(N+1)^2 + 2}$. $N = 9, 16, 25, 36, 49$ and $T = 0.91$ meV. Fitting line $\propto N^{-0.70}$. (c) For real space TBG model, the red line lower bound is $\langle s\rangle \geqslant 2/(N+2)$ and $N = 18, 72, 162, 288, 450, 648, 882$. The parameters of QMC are detailed in (Ouyang and Xu, 2021). Fitting line $\propto N^{-0.98}$.

Lefschetz thimble

This is also a method that can be used to cure or reduce the sign problem in lattice fermion QMC simulations (Ulybyshev et al., 2020; Alexandru et al., 2020; Cristoforetti et al., 2013; Fukuma et al., 2019; Mukherjee and Cristoforetti, 2014; Mukherjee et al., 2013; Mooney et al., 2021; Mishchenko et al., 2021; Körner et al., 2020), here we only briefly outline its main idea.

For computing the expectation value $\langle O[x]\rangle$ in Monte Carlo sampling on the configuration space $[x]$, we have

$$\begin{aligned}\langle \mathcal{O}[x]\rangle &= \frac{1}{Z}\int dxe^{-S[x]}\mathcal{O}[x]\\ &= \frac{\int dxe^{-S_R[x]}e^{-iS_I[x]}\mathcal{O}[x]}{\int dxe^{-S_R[x]}e^{-iS_I[x]}}\\ &= \frac{\int dxe^{-S_R[x]}e^{-iS_I[x]}\mathcal{O}[x]}{\int dxe^{-S_R[x]}}\Big/\frac{\int dxe^{-S_R[x]}e^{-iS_I[x]}}{\int dxe^{-S_R[x]}}\\ &= \frac{\langle e^{-iS_I}\mathcal{O}\rangle_R}{\langle e^{-iS_I}\rangle_R},\end{aligned} \tag{36}$$

where R and I means real and imaginary parts of action $S\,[x]$. And $\langle\ \rangle_R$ is defined as $\langle O\rangle_R = \frac{\int dxe^{-S_R[x]}O}{\int dxe^{-S_R[x]}}$.

If the action $S\,[x]$ is analytic for all $x \in \mathbb{C}^n$, its saddle points are nondegenerate and Eq. (36) is convergent, then Morse theory (Banyaga and Hurtubise, 2004; Witten, 2010, 2011) told us these integrals can be evaluated using the steepest descent cycles $\mathcal{J}_\sigma$. They are called Lefschetz thimbles, which means we can replace the integration over the real domain R^n with that over curved complex n-dimensional manifolds $\mathcal{J}_\sigma$

$$\int_{\mathbb{R}^n} \mathrm{d}^n x e^{-S(x)} = \sum_\sigma n_\sigma \int_{\mathcal{J}_\sigma} \mathrm{d}^n z e^{-S(z)}, \tag{37}$$

where the Lefschetz thimbles $\mathcal{J}_\sigma$ are the union of all solutions of the gradient flow equations

$$\frac{dz(\tau)}{d\tau} = -\frac{\partial\bar{S}}{\partial z}, \tag{38}$$

and it starts from the corresponding saddle point z_σ, which means $\lim_{\tau\to\infty} z(\tau) = z_\sigma$. Here σ is the index for different saddle point/Lefschetz thimbles, τ is a parameter and the overline represents complex conjugation, and saddle point is the point on the surface of S where the derivatives in orthogonal directions are all zero, but is not a local extremum. While the thimbles always end inside regions of stability, duals thimbles (anti-thimbles) $\mathcal{K}_\sigma$ are also such solutions at a given saddle point $\lim_{\tau\to-\infty} z(\tau) = z_\sigma$ and end inside regions of instability. We can make an analogy between the dual thimble and the contour of the steepest ascent, as we did with the thimble and the contour of the steepest descent. And n_σ are intersection numbers (which decide the contribution of a particular saddle point z_σ to the partition function) of hypersurface generated by the paths of steepest ascent duals $\mathcal{K}_\sigma$ and the original region of integration $\mathbb{R}^n$

$$n_\sigma = \langle \mathcal{K}_\sigma, \mathbb{R}^n\rangle. \tag{39}$$

The important point of such construction is: Im[S] is constant on Lefschetz thimbles (mod 2π), which means there is no sign problem on each thimble. The ratio of weights in the same thimble must be a positive real number, since the phase of the weight is the same.

Let's take a trivial 1d case for the purpose of illustration (Kanazawa and Tanizaki, 2015; Bharathkumar and Joseph, 2020)

$$\int_{\mathbb{R}+i\varepsilon} \mathrm{d}x \frac{1}{x} e^{-x^2/2} = \sum_\sigma n_\sigma \int_{\mathcal{J}_\sigma} \mathrm{d}z e^{-S(z)}, \tag{40}$$

which corresponds to the case $S\,[z] = \log z + z^2/2$. The two critical points of this action are: $z_1 = i$, $z_2 = -i$. Since we know that the imaginary parts Im[S] are constant on Lefschetz thimbles, then we have: $\mathrm{Im}(S\,[z])|_{\text{along }\mathbb{R}+i\varepsilon} = \mathrm{Im}\ S\,[z_\sigma] = i\pi/2$. Following the procedure described above we can obtain the corresponding thimbles and dual thimbles (as shown in Fig. 6), and then $\int_{\mathbb{R}+i\varepsilon}\mathrm{d}x\frac{1}{x}\,\mathrm{e}^{-x^2/2} = \int_{\mathcal{J}_1}\mathrm{d}z e^{-S(z)}$.

The Lefschetz thimbles method is commonly used to calculate the value of certain integrals and in high-energy physics and real time calculations. Recently, with the application of hybrid Monte Carlo in condensed matter, there has been a lot of work using the Lefschetz thimbles method to study common condensed matter problems which have sign problems. For example, Hubbard model on the hexagonal (honeycomb) lattice at finite chemical potential with linear system size $L = 6$ and inverse temperature $\beta = 20$, has been successfully simulated with Lefschetz thimbles method in DQMC (Ulybyshev et al., 2020; Körner et al., 2020).

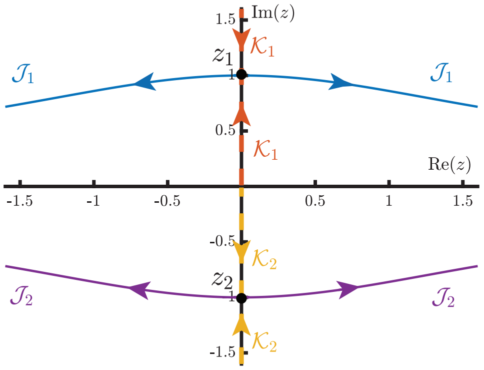

Fig. 6 A schematic plot of thimbles and dual thimbles. Here the black dots are saddle points $z_{1,2}$, while the solid blue/purple lines correspond to thimbles and the dotted red/yellow lines correspond to dual thimbles. And the arrows show the directions of the flows. See intersection numbers of dual thimbles and $\mathbb{R} + i\varepsilon$, we know $n_1 = 1$, $n_2 = 0$.

Conclusion

In this article, we give a pedagogical overview on the origin of the sign problem in various quantum Monte Carlo simulation techniques, ranging from the world-line and stochastic series expansion Monte Carlo for boson and spin systems to the determinant and momentum space quantum Monte Carlo for interacting fermions. We have elaborated on the definition of the sign problem and its possible origins, including the Pauli exclusion principle, geometric frustration and the lack of symmetry requirements, etc. In addition, we also point out the sign problem is actually basis-dependent and summarize established ways to ensure that some models are free of sign problems such as checking symmetry and Majorana positivity. We explain what to do when there is a sign problem in general: reweighting, and how to reduce the severity of sign problems, in particular that based on the properties of the finite size partition functions, the recent *sign bound theory* could distinguish when the bounds have the usual exponential scaling, and when they are bestowed with an algebraic scaling at the low temperature limit. Fermionic QMC simulations with such algebraic sign problems have been successfully carried out for extended Hubbard-type and quantum Moiré lattice models.

Acknowledgments

We thank Xu Zhang, Weilun Jiang, Yuan Da Liao and Xiao Yan Xu for insightful discussions and fruitful collaborations on related topics over the years. GPP and ZYM acknowledge the support from the Research Grants Council of Hong Kong SAR of China (Grant Nos. 17303019, 17301420, 17301721 and AoE/P-701/20), the Strategic Priority Research Program of the Chinese Academy of Sciences (Grant No. XDB33000000), the K. C. Wong Education Foundation (Grant No. GJTD-2020-01) and the Seed Funding "QuantumInspired explainable-AI" at the HKU-TCL Joint Research Centre for Artificial Intelligence. We thank the Information Technology Services at the University of Hong Kong and the Tianhe platforms at the National Supercomputer Centers for their technical support and generous allocation of CPU time.

References

Alet F, Damle K, and Pujari S (2016) Sign-problem-free monte carlo simulation of certain frustrated quantum magnets. *Physical Review Letters* 117: 197203.
Alexandru A, Basar G, Bedaque PF, and Warrington NC (2020) Complex paths around the sign problem. *arXiv*. preprint arXiv:2007.05436.
Assaad FF and Evertz HG (2008) *World-Line and Determinantal Quantum Monte Carlo Methods for Spins, Phonons and Electrons*. Berlin, Heidelberg: Springer Berlin Heidelberg 277–356.
Banyaga A and Hurtubise D (2004) *Lectures on Morse Homology*. vol. 29. Springer Science & Business Media.
Barahona F (1982) On the computational complexity of ising spin glass models. *Journal of Physics A: Mathematical and General* 15(10): 3241–3253.
Batrouni GG and Scalettar RT (1992) World-line quantum monte carlo algorithm for a one-dimensional bose model. *Physical Review B* 46: 9051–9062.
Bharathkumar R and Joseph A (2020) Lefschetz thimbles and quantum phases in zero-dimensional bosonic models. *The European Physical Journal C* 80(10): 1–20.
Broecker P, Carrasquilla J, Melko RG, and Trebst S (2017) Machine learning quantum phases of matter beyond the fermion sign problem. *Scientific Reports* 7(1): 1–10.
Carlson J, Gandolfi S, Pederiva F, Pieper SC, Schiavilla R, Schmidt KE, and Wiringa RB (2015) Quantum monte carlo methods for nuclear physics. *Reviews of Modern Physics* 87: 1067–1118.
Chandrasekharan S and Wiese UJ (1999) Meron-cluster solution of fermion sign problems. *Physical Review Letters* 83(16): 3116–3119.
Congjun W and Zhang S-C (2005) Sufficient condition for absence of the sign problem in the fermionic quantum monte carlo algorithm. *Physical Review B* 71: 155115.
Cristoforetti M, Di Renzo F, Mukherjee A, and Scorzato L (2013) Monte carlo simulations on the lefschetz thimble: Taming the sign problem. *Physical Review D* 88(5), 051501.
D'Emidio J, Wessel S, and Mila F (2020) Reduction of the sign problem near $t = 0$ in quantum monte carlo simulations. *Physical Review B* 102: 064420.
Da Liao Y, Kang J, Breiø CN, Xu XY, Wu H-Q, Andersen BM, Fernandes RM, and Meng ZY (2021) Correlation-induced insulating topological phases at charge neutrality in twisted bilayer graphene. *Physical Review X* 11: 011014.
Da Liao Y, Xu XY, Meng ZY, and Qi Y (2022) Gross-neveu and deconfined quantum criticalities in an extended hubbard model on the square lattice. *arXiv* . preprint arXiv:2204.04884.
Dai X (2022) Quantum monte carlo simulations in momentum space. *Chinese Physics Letters* 39(5): 050101.

De Raedt H and Lagendijk A (1985) Monte carlo simulation of quantum statistical lattice models. *Physics Reports* 127(4): 233–307.
Evertz HG, Lana G, and Marcu M (1993) Cluster algorithm for vertex models. *Physical Review Letters* 70: 875–879.
Foulkes WMC, Mitas L, Needs RJ, and Rajagopal G (2001) Quantum monte carlo simulations of solids. *Reviews of Modern Physics* 73: 33–83.
Fukuma M, Matsumoto N, and Umeda N (2019) Applying the tempered lefschetz thimble method to the hubbard model away from half filling. *Physical Review D* 100(11), 114510.
Fye RM (1986) New results on trotter-like approximations. *Physical Review B* 33(9): 6271.
Fye RM and Scalettar RT (1987) Calculation of specific heat and susceptibilities with the use of the trotter approximation. *Physical Review B* 36(7): 3833.
Geyer CJ (2011) Introduction to markov chain monte carlo. In: *Handbook of Markov Chain Monte Carlo, 20116022*, 45.
Golan O, Smith A, and Ringel Z (2020) Intrinsic sign problem in fermionic and bosonic chiral topological matter. *Physical Review Research* 2: 043032.
Hands S, Montvay I, Morrison S, Oevers M, Scorzato L, and Skullerud J (2000) Numerical study of dense adjoint matter in two color qcd. *The European Physical Journal C—Particles and Fields* 17(2): 285–302.
Hangleiter D, Roth I, Nagaj D, and Eisert J (2020) Easing the monte carlo sign problem. *Science Advances* 6(33): eabb8341.
Hastings MB (2016) How quantum are non-negative wavefunctions? *Journal of Mathematical Physics* 57(1), 015210.
Hatano N and Suzuki M (1992) Representation basis in quantum monte carlo calculations and the negative-sign problem. *Physics Letters A* 163(4): 246–249.
Hirsch JE (1985) Two-dimensional hubbard model: Numerical simulation study. *Physical Review B* 31: 4403–4419.
Hirsch JE, Sugar RL, Scalapino DJ, and Blankenbecler R (1982) Monte carlo simulations of one-dimensional fermion systems. *Physical Review B* 26: 5033–5055.
Hohenadler M, Meng ZY, Lang TC, Wessel S, Muramatsu A, and Assaad FF (2012) Quantum phase transitions in the kane-mele-hubbard model. *Physical Review B* 85: 115132.
Honecker A, Wessel S, Kerkdyk R, Pruschke T, Mila F, and Normand B (2016) Thermodynamic properties of highly frustrated quantum spin ladders: Influence of many-particle bound states. *Physical Review B* 93: 054408.
Huffman EF and Chandrasekharan S (2014) Solution to sign problems in half-filled spin-polarized electronic systems. *Physical Review B* 89: 111101.
Iazzi M, Soluyanov AA, and Troyer M (2016) Topological origin of the fermion sign problem. *Physical Review B* 93: 115102.
Ibarra-García-Padilla E, Dasgupta S, Wei H-T, Taie S, Takahashi Y, Scalettar RT, and Hazzard KRA (2021) Universal thermodynamics of an SU(*n*) fermi-hubbard model. *Physical Review A* 104: 043316.
Iglovikov VI, Khatami E, and Scalettar RT (2015) Geometry dependence of the sign problem in quantum monte carlo simulations. *Physical Review B* 92: 045110.
Janssen L, Wang W, Scherer MM, Meng ZY, and Xu XY (2020) Confinement transition in the qed3-gross-neveu-xy universality class. *Physical Review B* 101: 235118.
Johannes S, Hofmann EK, Vishwanath A, Berg E, and Lee JY (2021) Fermionic monte carlo study of a realistic model of twisted bilayer graphene. *arXiv* . preprint arXiv:2105.12112.
Kanazawa T and Tanizaki Y (2015) Structure of lefschetz thimbles in simple fermionic systems. *Journal of High Energy Physics* 2015(3): 1–36.
Kaul RK, Melko RG, and Sandvik AW (2013) Bridging lattice-scale physics and continuum field theory with quantum monte carlo simulations. *Annual Review of Condensed Matter Physics* 4(1): 179–215.
Kim AJ, Werner P, and Valentí R (2020) Alleviating the sign problem in quantum monte carlo simulations of spin-orbit-coupled multiorbital hubbard models. *Physical Review B* 101: 045108.
Klassen J, Marvian M, Piddock S, Ioannou M, Hen I, and Terhal BM (2020) Hardness and ease of curing the sign problem for two-local qubit hamiltonians. *SIAM Journal on Computing* 49(6): 1332–1362.
Koonin SE, Dean DJ, and Langanke K (1997) Shell model monte carlo methods. *Physics Reports* 278(1): 1–77.
Körner M, Langfeld K, Smith D, and von Smekal L (2020) Density of states approach to the hexagonal hubbard model at finite density. *Physical Review D* 102: 054502.
Lang GH, Johnson CW, Koonin SE, and Ormand WE (1993) Monte carlo evaluation of path integrals for the nuclear shell model. *Physical Review C* 48: 1518–1545.
Lawrence S (2020) Perturbative removal of a sign problem. *Physical Review D* 102: 094504.
Levy R and Clark BK (2021) Mitigating the sign problem through basis rotations. *Physical Review Letters* 126: 216401.
Li Z-X and Yao H (2019) Sign-problem-free fermionic quantum monte carlo: Developments and applications. *Annual Review of Condensed Matter Physics* 10(1): 337–356.
Li Z-X, Jiang Y-F, and Yao H (2015) Solving the fermion sign problem in quantum monte carlo simulations by majorana representation. *Physical Review B* 91: 241117.
Li Z-X, Jiang Y-F, and Yao H (2016) Majorana-time-reversal symmetries: A fundamental principle for sign-problem-free quantum monte carlo simulations. *Physical Review Letters* 117: 267002.
Liao Y-D, Xiao-Yan X, Meng Z-Y, and Kang J (2021) Correlated insulating phases in the twisted bilayer graphene. *Chinese Physics B* 30(1), 017305.
Loh EY, Gubernatis JE, Scalettar RT, White SR, Scalapino DJ, and Sugar RL (1990) Sign problem in the numerical simulation of many-electron systems. *Physical Review B* 41: 9301–9307.
Marvian M, Lidar DA, and Hen I (2019) On the computational complexity of curing non-stoquastic hamiltonians. *Nature Communications* 10(1): 1–9.
Meng ZY, Hung H-H, and Lang TC (2014) The characterization of topological properties in quantum monte carlo simulations of the kane–mele–hubbard model. *Modern Physics Letters B* 28(01): 1430001.
Mishchenko PA, Kato Y, and Motome Y (2021) Quantum monte carlo method on asymptotic lefschetz thimbles for quantum spin systems: An application to the kitaev model in a magnetic field. *Physical Review D* 104: 074517.
Mondaini R, Tarat S, and Scalettar RT (2022) Quantum critical points and the sign problem. *Science* 375(6579): 418–424.
Mooney TC, Bringewatt J, and Brady LT (2021) Lefschetz thimble quantum monte carlo for spin systems. *arXiv*. preprint arXiv:2110.10699.
Mukherjee A and Cristoforetti M (2014) Lefschetz thimble monte carlo for many-body theories: A hubbard model study. *Physical Review B* 90(3), 035134.
Mukherjee A, Cristoforetti M, and Scorzato L (2013) Metropolis monte carlo integration on the lefschetz thimble: Application to a one-plaquette model. *Physical Review D* 88(5), 051502.
Ng K-K and Yang M-F (2017) Field-induced quantum phases in a frustrated spin-dimer model: A sign-problem-free quantum monte carlo study. *Physical Review B* 95: 064431.
Ouyang Y and Xu XY (2021) Projection of infinite-*u* hubbard model and algebraic sign structure. *Physical Review B* 104: L241104.
Pan G, Zhang X, Li H, Sun K, and Meng ZY (2022) Dynamical properties of collective excitations in twisted bilayer graphene. *Physical Review B* 105: L121110.
Prokof'Ev NV, Svistunov BV, and Tupitsyn IS (1998) Exact, complete, and universal continuous-time worldline monte carlo approach to the statistics of discrete quantum systems. *Journal of Experimental and Theoretical Physics* 87(2): 310–321.
Ringel Z and Kovrizhin DL (2017) Quantized gravitational responses, the sign problem, and quantum complexity. *Science Advances* 3(9), e1701758.
Rossi R (2017) Determinant diagrammatic monte carlo algorithm in the thermodynamic limit. *Physical Review Letters* 119: 045701.
Rossi R, Prokof'ev N, Svistunov B, Van Houcke K, and Werner F (2017) Polynomial complexity despite the fermionic sign. *EPL (Europhysics Letters)* 118(1): 10004.
Sandvik AW (1992) A generalization of handscomb's quantum monte carlo scheme-application to the 1d hubbard model. *Journal of Physics A: Mathematical and General* 25(13): 3667.
Sandvik AW (2010) Computational studies of quantum spin systems. *AIP Conference Proceedings* 1297(1): 135–338.
Sandvik AW and Kurkijärvi J (1991) Quantum monte carlo simulation method for spin systems. *Physical Review B* 43(7): 5950.
Shinaoka H, Nomura Y, Biermann S, Troyer M, and Werner P (2015) Negative sign problem in continuous-time quantum monte carlo: Optimal choice of single-particle basis for impurity problems. *Physical Review B* 92: 195126.
Smith A, Golan O, and Ringel Z (2020) Intrinsic sign problems in topological quantum field theories. *Physical Review Research* 2: 033515.
Stapmanns J, Corboz P, Mila F, Honecker A, Normand B, and Wessel S (2018) Thermal critical points and quantum critical end point in the frustrated bilayer heisenberg antiferromagnet. *Physical Review Letters* 121: 127201.
StefanWessel BN, Mila F, and Honecker A (2017) Efficient Quantum Monte Carlo simulations of highly frustrated magnets: the frustrated spin-1/2 ladder. *SciPost Physics* 3: 005.

Suzuki M (1985) General correction theorems on decomposition formulae of exponential operators and extrapolation methods for quantum monte carlo simulations. *Physics Letters A* 113(6): 299–300.

Suzuki M (1976) Relationship between d-dimensional quantal spin systems and (d+1)-dimensional ising systems: equivalence, critical exponents and systematic approximants of the partition function and spin correlations. *Progress of Theoretical Physics* 56(5): 1454–1469. 11.

Takasu M, Miyashita S, and Suzuki M (1986) Monte Carlo simulation of quantum Heisenberg magnets on the triangular lattice. *Progress of Theoretical Physics* 75(5): 1254–1257.

Tarat S, Xiao B, Mondaini R, and Scalettar RT (2022) Deconvolving the components of the sign problem. *Physical Review B* 105: 045107.

Torlai G, Carrasquilla J, Fishman MT, Melko RG, and Fisher MPA (2020) Wave-function positivization via automatic differentiation. *Physical Review Research* 2: 032060.

Trotter HF (1959) On the product of semi-groups of operators. *Proceedings of the American Mathematical Society* 10(4): 545–551.

Troyer M and Wiese U-J (2005) Computational complexity and fundamental limitations to fermionic quantum monte carlo simulations. *Physical Review Letters* 94: 170201.

Ulybyshev M, Winterowd C, and Zafeiropoulos S (2020) Lefschetz thimbles decomposition for the hubbard model on the hexagonal lattice. *Physical Review D* 101: 014508.

Vaezi M-S, Negari A-R, Moharramipour A, and Vaezi A (2021) Amelioration for the sign problem: An adiabatic quantum monte carlo algorithm. *Physical Review Letters* 127: 217003.

Wan Z-Q, Zhang S-X, and Yao H (2020) Mitigating sign problem by automatic differentiation. *arXiv.* preprint arXiv:2010.01141.

Wang L, Liu Y-H, Iazzi M, Troyer M, and Harcos G (2015) Split orthogonal group: A guiding principle for sign-problem-free fermionic simulations. *Physical Review Letters* 115: 250601.

Wang W, Lu D-C, Xu XY, You Y-Z, and Meng ZY (2019) Dynamics of compact quantum electrodynamics at large fermion flavor. *Physical Review B* 100: 085123.

Wei Z-C (2017) Semigroup approach to the sign problem in quantum monte carlo simulations. *arXiv.* preprint arXiv:1712.09412.

Wei ZC, Wu C, Li Y, Zhang S, and Xiang T (2016) Majorana positivity and the fermion sign problem of quantum monte carlo simulations. *Physical Review Letters* 116: 250601.

Wessel S, Niesen I, Stapmanns J, Normand B, Mila F, Corboz P, and Honecker A (2018) Thermodynamic properties of the shastry-sutherland model from quantum monte carlo simulations. *Physical Review B* 98: 174432.

White SR, Scalapino DJ, Sugar RL, Loh EY, Gubernatis JE, and Scalettar RT (1989) Numerical study of the two-dimensional hubbard model. *Physical Review B* 40: 506–516.

Witten E (2010) A new look at the path integral of quantum mechanics. *arXiv.* preprint arXiv:1009.6032.

Witten E (2011) Analytic continuation of chern-simons theory. *AMS/IP Studies in Advanced Mathematics* 50: 347.

Wynen J-L, Berkowitz E, Krieg S, Luu T, and Ostmeyer J (2021) Machine learning to alleviate hubbard-model sign problems. *Physical Review B* 103: 125153.

Xu XY, Law KT, and Lee PA (2018) Kekulé valence bond order in an extended hubbard model on the honeycomb lattice with possible applications to twisted bilayer graphene. *Physical Review B* 98: 121406.

Xu XY, Liu ZH, Pan G, Qi Y, Sun K, and Meng ZY (2019a) Revealing fermionic quantum criticality from new monte carlo techniques. *Journal of Physics: Condensed Matter* 31(46): 463001.

Xu XY, Qi Y, Zhang L, Assaad FF, Xu C, and Meng ZY (2019b) Monte carlo study of lattice compact quantum electrodynamics with fermionic matter: The parent state of quantum phases. *Physical Review X* 9: 021022.

Xu Z, Pan G, Zhang Y, Kang J, and Meng ZY (2021a) Momentum space quantum monte carlo on twisted bilayer graphene. *Chinese Physics Letters* 38(7): 077305.

Xu Z, Sun K, Li H, Pan G, and Meng ZY (2021b) Superconductivity and bosonic fluid emerging from moir\'e flat bands. *arXiv.* preprint arXiv:2111.10018.

Zhang X, Pan G, Xu XY, and Meng ZY (2021) Sign problem finds its bounds. *arXiv.* preprint arXiv:2112.06139.

Quantum transport and electron-electron interactions in one dimension

Pedro Vianez and Christopher Ford, Cavendish Laboratory, University of Cambridge, Cambridge, United Kingdom

© 2024 Elsevier Ltd. All rights reserved.

Introduction 894
The mesoscopic regime 895
Experimental realization of a (quasi-)1D system and quantization of conductance 896
Interaction effects in 1D 899
Conclusion 903
Further reading 903
References 903

Abstract

When confined to lower dimensions, electrons often start behaving in new and unexpected ways. This is particularly striking in one dimension (1D), for here, both individual, as well as collective, properties can start to emerge, making these systems a very rich playground on which single- and many-body physics can be studied. In this chapter, we introduce the field of one-dimensional electronic systems by discussing a series of results in fundamental physics obtained over the past few decades using semiconductor devices at low temperatures. We start by reviewing the transport properties of these systems and, specifically, the observation of conductance quantization in 1D. We then focus on a series of interaction effects that have been observed in more recent years, from the well-known "0.7 structure" to the Tomonaga-Luttinger liquid and its more recent nonlinear counterparts.

Key points

This chapter describes the one-dimensional electronic system with particular emphasis on its experimental realization using semiconducting devices. It aims to provide a first introduction to the subject by highlighting some of the early work, as well as more recent developments in the field. The topics covered are:

- the experimental realization of a quasi-1D system;
- its subbands, eigenstates and conductance quantization in units of $2e^2/h$;
- the "0.7 structure," which is a feature below the lowest conductance plateau and requires an explanation in terms of many-body physics;
- the Tomonaga-Luttinger liquid, which is the exact many-body description of a true 1D system at low energies, with particular emphasis on the observation of spin-charge separation and zero-bias anomaly;
- the nonlinear Luttinger liquid, which tries to describe interacting 1D systems beyond the low-energy limit, including recent developments on 1D "replica" modes and separate Fermi seas for spin and charge.

Introduction

How do electrons move inside solids? Do they flow, like a stream down a hill, or instead remain static, close to their atomic hosts? Furthermore, when in the presence of other electrons, do they behave collectively or are they instead, for the most part, unaware of the presence of each other? The challenge posed by these questions is the bedrock of modern-day condensed-matter physics, and to answer them we must first understand how and where electrons are moving in the first place.

The world is three-dimensional, but we mainly live on a two-dimensional flat surface, and sometimes a flow is confined to a single dimension, a line, for example, in rivers and roads. In a conducting solid, electrons flow to carry a current. But a wire is huge on the scale of the distance an electron can move before being scattered, so it is not usually 1D.

With the advent of nanoelectronics, we can grow and pattern materials that are so pure that scattering can almost be ignored on the length scales of the microscopic wires in which we can channel electrons. We then start to see extraordinary new phenomena, where electrons act as waves and form standing waves across the wire, showing beautiful, equally spaced steps in the inverse of the resistance, which is called the conductance.

However, electrons are charged particles and repel each other, so interactions should be important. Remarkably, these interactions are usually hidden because excitations of a collection of interacting electrons actually behave like single electrons. In 1D, on the other hand, this is not the case—as on a single-track road, cars (or electrons) cannot get past each other. So, instead, waves of charge and spin travel along the queues of electrons, more like sound waves, and these can be detected in special experiments, as we will now discuss.

https://doi.org/10.1016/B978-0-323-90800-9.00157-8

The mesoscopic regime

The first attempt at describing charge transport inside solids (and specifically, metals) led to what came to be known as the Drude model (Drude, 1900; Ashcroft and Mermin, 1976). The goal was to explain what was empirically already established as Ohm's law, that is, that the current through a conductor is directly proportional to the voltage applied along it, with the proportionality constant defining the resistance, R, of a given material. Drude managed to explain this observation in terms of scattering of electrons against a static background of ions which, macroscopically, gave rise to an electrical resistance.

Drude's model was essentially an application of the kinetic theory of gases, whereby the electrons inside a conductor were seen as bouncing about like billiard balls and following the laws of classical Newtonian mechanics. However, once the theory of Quantum Mechanics was developed in the 1920s, it became clear that subatomic particles such as electrons should be treated as waves (or wave functions), rather than simple point-like particles. Bloch showed that the periodic potential from the crystal lattice in a solid had the effect of combining all the quantum-mechanical states on each atom into a set of waves that modulate the wave functions on each atom and broaden their quantized energy levels into "bands" (Bloch, 1929). We generally say that these plane "Bloch" waves have wavelength $2\pi/k$, where k is called the wavenumber (or, including the direction, $\mathbf{k}$, the wavevector).

Having established the existence of electronic bands, however, one must now question how to populate the available states. For simplicity, let us assume that no interactions are present, that is, everything can be described in terms of plane waves Because electrons are spin-1/2 particles, they are fermions, meaning that they follow Fermi-Dirac statistics. A well-known consequence of this is the Pauli exclusion principle. Put simply, this prevents any two fermions from occupying the same state, unless they differ in spin direction ("up" or "down"). This has profound consequences in the way electrons are distributed energetically inside a crystal, and leads us to the concept of a Fermi surface, see Fig. 1. At zero temperature, all the states are filled with electrons, starting with the lowest energy until all the available electrons have been accommodated. The Fermi energy E_F lies between the energy of this highest occupied state and the next, empty, state.

In three dimensions (3D), the Fermi surface for a system of free electrons is a simple sphere or, in two dimensions (2D), a circle. Here, the most energetic state defines the Fermi energy, $E_F = \hbar^2 k_F^2 / 2m_e$, where k_F is the Fermi wavevector and m_e the free-electron mass. In one dimension (1D), however, things start to change, as the Fermi "surface" now is simply two degenerate points at $\pm k_F$! As we will see later, this drastically affects the dynamics of electrons when confined to 1D. The principal effect of the presence of band structure is to change m_e to the "effective" mass m^*, which is a constant near the extremities of each band. Generally speaking, however, m^* tends to be a little less than m_e in semiconductors (e.g., $0.067\,m_e$ in GaAs).

The implicit assumption behind all these pictures is that the electrons can be treated as occupying single-particle states, each with a different wavevector $\mathbf{k}$, in other words neglecting the possibility of many-body effects. Similarly, by treating the electrons as purely classical point-like particles, or quantum-mechanical "wave packets" with well-defined momentum and some idea of their position, collisions are taken to be instantaneous or, at least, much shorter than the average time it takes for them to occur. This means that, when in the presence of some sort of physical gradient, (e.g., temperature, electric or magnetic fields, stress, etc.), transport across a system of characteristic length $L \gg \ell$ is typically *diffusive*, with electrons behaving as if undergoing a random walk of typical step size ℓ. Alternatively, if $L \ll \ell$, then we enter into the *ballistic* regime, meaning that electron motion can only be altered by collision with a boundary. In the middle between these two limits, we enter the *mesoscopic* regime, where one cannot average over scattering sites, such as impurities, and each "device" may behave slightly differently.

In order for mesoscopic or ballistic effects to be observed, electrons must be confined to sufficiently small structures and/or cooled to sufficiently low temperatures. The field of quantum transport concerns, generally speaking, the study of electron flow inside materials and devices confined in at least one of the dimensions to a nanometer length-scale (<100 nm) where an electron wave function comes back on itself and interferes constructively, forming one of a set of standing waves with particular allowed energies, or increasing or decreasing the transmission through the device as interference between different paths the wave can take changes from constructive to destructive.

Technological improvements have allowed for the fabrication of structures where the number of dimensions to which the electron gas is confined is two (e.g., semiconductor quantum wells, ultra-thin films, graphene), one (e.g., quantum wires, carbon

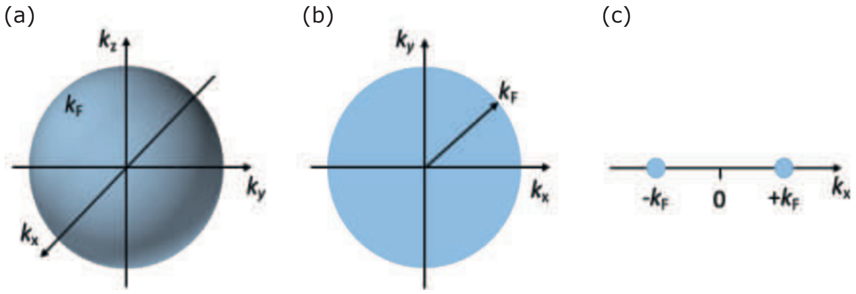

Fig. 1 Free electrons in different dimensions. The Fermi surface of a system of free electrons is a sphere in three dimensions (a), a circle in two dimensions (b), and merely two degenerate points in one dimension (c). Here, k_F is the Fermi wavevector, defined through $E_F = \hbar^2 k_F^2 / 2m_e$, where E_F is the Fermi energy and m_e the free-electron mass. Made by Pedro Vianez.

nanotubes, edge states), or even zero (e.g., quantum dots). In all these systems the key requirement is for each of the confining dimensions to be of the order, if not smaller, of the de Broglie wavelength of the electrons, given by $\lambda = h/p$, where h is Planck's constant and p the electron's momentum.

In this chapter we focus on a type of system where electrons are confined in all but one dimension. As we will see, such 1D constrictions not only give rise to quantized conductance $G(=1/R)$ but also strongly-correlated states which break away from the single-particle picture and the traditional Fermi-liquid-like behavior typically observed at higher dimensions (Giuliani and Vignale, 2005).

Experimental realization of a (quasi-)1D system and quantization of conductance

Historically, the first materials to be investigated were naturally bulk (i.e., three-dimensional, 3D) crystals, for these were already readily accessible. These were followed by two-dimensional (2D) semiconducting quantum wells in the second half of the 20th century, mostly notably GaAs/AlGaAs heterostructures, which led to Nobel-Prize-winning discoveries like the integer (Klitzing et al., 1980) and fractional (Tsui et al., 1982) quantum Hall effects. The ability to trap and manipulate individual electrons was also achieved via quantum dots, that is, zero-dimensional (0D) structures, with Coulomb blockade leading to clear demonstrations of quantization of the electrical current (Kouwenhoven et al., 1991; Blumenthal et al., 2007). One-dimensional (1D) systems, on the other hand, have always remained elusive, for these are not only difficult to probe experimentally, but also more prone to disorder effects.

A popular way of realizing a 1D system uses a pair of split gates (Thornton et al., 1986), see Fig. 2. Here, two gates with a narrow gap in between are patterned on the surface of a material containing a two-dimensional electron gas (2DEG), for instance a high-purity semiconducting GaAs/AlGaAs heterostructure grown by molecular-beam epitaxy (MBE). As a progressively more negative voltage is applied to both gates, the electron gas beneath becomes fully depleted and the depletion region spreads sideways into the gap, reducing the width of the remaining narrow strip of electrons below the ungated region until this channel pinches off completely. If there is no scattering within the width of the channel, a standing wave forms as the component of the wave across the channel interferes constructively with itself after being reflected at each edge. This gives rise to modes, like the harmonics on a violin string, each with a fixed energy E_0^n for mode n. The motion along the channel is still unconstrained, so the total energy is the sum of the corresponding kinetic energy and E_0^n, and the set of such states is called a "subband." As the channel is squeezed, the modes become spaced out in energy enough that a certain integer number N of subbands is occupied (below the Fermi energy E_F), without thermal excitation into the next subband, so $E_0^N < E_F < E_0^{N+1}$.

If we now consider the current dI traveling along this channel at energy E in a small energy range dE, we can calculate this current very simply, using the well-known formula $\mathrm{d}I = \mathrm{d}nAv(E)e$, where d$n$ is the density of electrons in this energy range dE, A the cross-sectional area, $v(E)$ the electron velocity at energy E and e the electronic charge. In 1D, dnA is just the number of charge carriers per unit length between energies E and $E + \mathrm{d}E$, which is half the product of dE, the density of states in energy $g(E)$, and the probability that a state is occupied, which is the Fermi-Dirac function $f(E_F)$, a step function broadened by temperature T. The half comes from the fact that half the states are coming from the other end of the channel and so will be considered separately. In 1D,

$$g(E) = \frac{2}{\pi}\frac{\mathrm{d}k}{\mathrm{d}E}$$

and the electron wave's "group" velocity

$$v(E) = \frac{1}{\hbar}\frac{\mathrm{d}E}{\mathrm{d}k}.$$

So, using $h = 2\pi\hbar$,

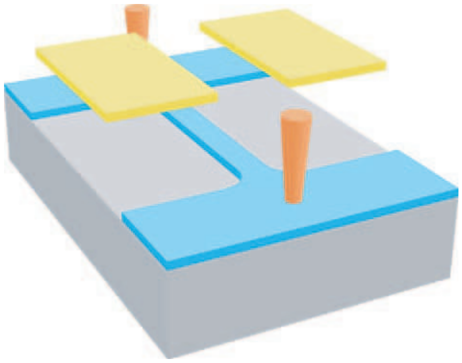

Fig. 2 The split-gate device. Schematic representation of a split-gate device patterned on the surface of a semiconductor heterostructure (e.g., GaAs/AlGaAs) for creating a (quasi-)1D system. Surface Ti/Au gates (yellow) deplete the 2DEG underneath (blue) leaving a narrow channel in between the source and drain contacts (orange). From Chapter 4, Lecture Notes from the Physics of Nanoelectronic Systems Course (Internal Cambridge course).

$$\begin{aligned} \mathrm{d}I &= \frac{1}{2}\left(\frac{2}{\pi}\frac{\mathrm{d}k}{\mathrm{d}E}\right)\left(\frac{1}{\hbar}\frac{\mathrm{d}E}{\mathrm{d}k}\right)f(E-E_\mathrm{F})e\mathrm{d}E \\ &= f(E-E_\mathrm{F})\frac{2e}{h}\,\mathrm{d}E. \end{aligned}$$

$f(E - E_\mathrm{F})$ gives the distribution of occupied energy levels around the Fermi energy. At a finite temperature, even far below E_F, all the states are occupied, and far above, they are all empty. At one end of the channel, the bias V applied there (relative to the voltage at the other end) changes the energy of all the states coming from that end by $-eV$, so for current coming from that direction, the distribution function becomes $f(E - (E_\mathrm{F} - eV))$.

The total current I is given by the integral over all energies of the current elements traveling one way along the channel minus those traveling in the opposite direction, i.e.,

$$I = \frac{2e}{h}\int_{-\infty}^{\infty}(f(E-E_\mathrm{F}) - f(E-E_\mathrm{F}+eV))\mathrm{d}E.$$

The trick for calculating this integral is to shift one distribution by eV, to line up with the other, as they are identical in shape apart from this offset in energy. That adds an amount of height 1 and width eV at the low-energy end of one function in the integrand, making the integral just equal to eV (see Fig. 3). Hence, the total current is

$$I = \frac{2e^2}{h}V.$$

Therefore, the current per unit voltage (the conductance) carried by a 1D subband does not depend on how fast electrons are traveling at E_F, nor even on how E varies with k, and is just $G_0 \equiv 2e^2/h$. When there are N subbands, the conductance is simply

$$G = I/V = Ne^2/h.$$

No theorist had dared to predict anyone would observe such a simple result before the beautiful experiments in 1988 (van Wees et al., 1988; Wharam et al., 1988)! These showed a series of steps in conductance at these values, as explained (though not predicted!) by the above calculation (Wharam et al., 1988).

A few years later, Thomas et al., using a particularly high-quality GaAs/AlGaAs heterostructure showed a very large number of quantized plateaux, see Fig. 4 (Thomas et al., 1995). The split-gate device was measured at a temperature below 100 mK. Once the 2DEG underneath the gates was depleted at around −0.6 V, a series of over 20 quantized plateaux were observed in the conductance at integer values of $2e^2/h$. One has to account for a small, constant series resistance, and the plateau accuracy is not good enough to be used as a resistance standard (unlike the plateaux in the quantum Hall effect). By briefly illuminating the sample with an LED, the carrier density is increased, moving the curve to the left and changing the series resistance, but not altering the heights of the steps, highlighting their dependence only on the fundamental constants h and e.

To understand the 1D subbands better, we can write down Schrödinger's equation for a quasi-1D system as

$$\left(\frac{p^2}{2m^*} + V(y)\right)\psi = E\psi, \tag{1}$$

where $V(y)$ is the transverse confining potential created by the gates, taking the channel to be infinitely long on the assumption that end effects can be neglected. Because there is translational invariance along the channel (i.e., the x-direction), the solutions will take the form $\psi_{k_x,\mathrm{n}} = \exp(ik_x x)\phi_\mathrm{n}(y)$, namely plane Bloch waves along the channel and a confined wavefunction $\phi_\mathrm{n}(y)$ across it.

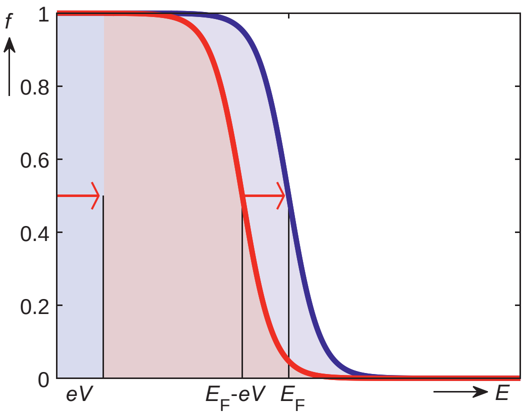

Fig. 3 The Fermi-Dirac distribution. Two Fermi-Dirac functions $f(E - E_\mathrm{F})$ (blue) and $f(E - (E_\mathrm{F} - eV))$ (red), showing how they are identical apart from the offset in energy eV. The area between the two curves is the same as the area on the left created by shifting one function to line up with the other. Made by Christopher Ford.

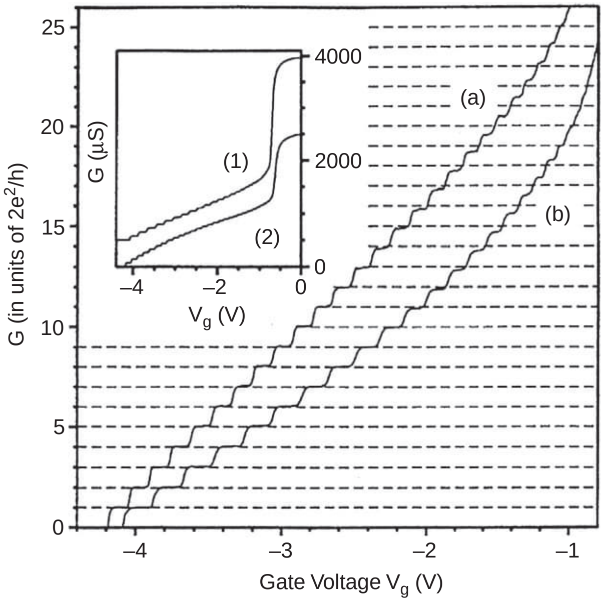

Fig. 4 Conductance quantization in 1D ballistic channels. Here, the differential conductance G can be seen to rise in steps of $2e^2/h$ (after a series resistance has been subtracted) as the gate voltage V_g, which defines the 1D constriction, is made progressively less negative. The two curves were measured before and after the sample was illuminated briefly, which changed the carrier concentration but clearly left the step heights unchanged. Over 20 steps can be observed, implying a very clean, ballistic channel. Inset: Full conductance sweep in gate voltage, for both samples, showing both the definition and pinch-off points. Reproduced from Thomas KJ, Simmons MY, et al. (1995) Ballistic transport in one-dimensional constrictions formed in deep two-dimensional electron gases. *Applied Physics Letters* 67: 109–111, with the permission of AIP Publishing.

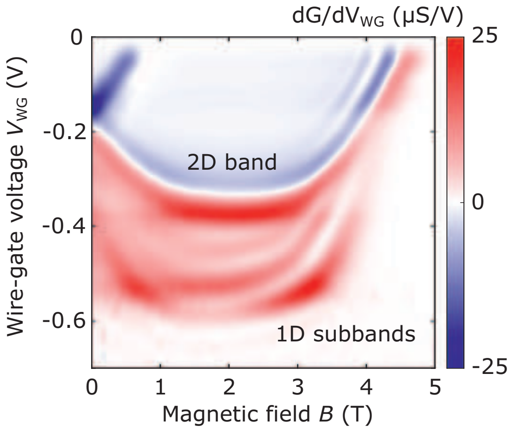

Fig. 5 Characterization of an electrostatically-defined 1D system. As the gate voltage V_G, which selectively depletes a 2DEG into forming an array of 1D wires, is made progressively more negative, the transition from a 2D band to multiple 1D subbands can be observed. The full dispersion is mapped by tracking the tunneling conductance to and from this system to another nearby 2DEG as a function of in-plane magnetic field B($\propto$ momentum). From Vianez P (2022) *Semiconductor Nanodevices as a Probe of Strong Electron Correlations.* PhD thesis. University of Cambridge, reprinted with permission.

The simplest realistic example of a confinement potential is given by the well-known quantum harmonic oscillator, that is, $V(y) = 1/2m^\star\omega_0^2 y^2$. In this case, the solutions are given by the Hermite polynomials, with the corresponding eigenvalues being

$$E_{k_x,n} = \left(n + \frac{1}{2}\right)\hbar\omega_0 + \frac{\hbar^2 k_x^2}{2m^\star}. \tag{2}$$

This is an example of the fact that, in a 1D system, the values of the kinetic energy due to motion across the channel, E_0^n, which is $\left(n + \frac{1}{2}\right)\hbar\omega_0$ for a harmonic oscillator, are quantized (the first term on the right in the above equation), with the momentum along the channel remaining unconstrained, leading to bands of energies (the second term), called 1D subbands as discussed earlier, see Fig. 5 (Vianez, 2022) As mentioned above, only subbands with E_0^n below E_F are occupied. In general, the potential changes from fairly parabolic (harmonic) for the lowest subband to more like a square well with rounded edges for much higher subbands (Laux et al., 1988).

In order to observe quantized conductance, electrons must pass along the entire narrow part of the channel without being scattered backwards, that is to say, along a "ballistic" channel. Split gates patterned using electron-beam lithography must usually therefore be less than a micron long, even when using high-quality material with the fewest background impurities and a large spacer layer between the 2DEG and the donor impurities. These short channels are also often referred to as quantum point contacts (QPCs), as some were originally made narrower at one end to minimize their length (van Wees et al., 1988). Instead of doping the material to provide the conduction electrons, one can use a central gate between the split pair, positively biased to induce electrons at an interface below this middle gate. Induced channels up to 2 μm long showed good conductance plateaux (Pyshkin et al., 2000).

One also requires low-enough temperature that the lowest energy in each subband is fully occupied or not occupied at all (otherwise the quantized conductance plateaux become shorter and less flat). At low magnetic field *B*, the system is largely unpolarized, and the factor of 2 in G_0 arises from this spin degeneracy. At high fields, the number of plateaux should double as Zeeman spin splitting breaks the degeneracy, and this is indeed observed (Wharam et al., 1988; Graham et al., 2003).

It can also be seen in Fig. 4 that the flatness and accuracy of the plateaux decrease as the number *N* of occupied subbands increases with less-negative gate voltage. The subband spacing decreases as the gates confine the channel less, increasing thermal excitation and impurity scattering between subbands. But also, the first unoccupied subband does become occupied near the ends of the channel as the confinement decreases, and tunneling between these two ends can occur along the channel, so that this subband starts being transmitted before the previous one has ceased to be partially reflected. These effects all reduce the quality of the plateaux. The potential in the channel looks like a saddle, dropping at the ends but rising at the sides, and if these two dependencies are approximated as parabolae, the ratio of their curvatures turns out to determine the quality of the plateaux, as subband spacing competes with end-to-end tunneling (Büttiker, 1990). For a precise treatment of the two-terminal conductance across a system such as the split-gate device shown in Fig. 2, we refer the reader to (Stone and Szafer, 1988), which introduces the Landauer and Landauer-Büttiker formalisms in great detail. These enable calculation of the conductances of two-terminal and multiterminal systems, respectively.

Fundamentally, the importance of observing quantized conductance along 1D channels was that it established the idea that quantization could be achieved solely by the application of an electric field and not just a magnetic field, the latter having already been established through the quantum Hall effect. Following the discovery of the fractional quantum Hall effect, similar attempts were also made at achieving fractional conductance in the absence of a magnetic field, though experimental evidence has remained lacking.

Interaction effects in 1D

The remarkable quantized conductance steps described above can be explained without considering interactions between the vast numbers of electrons carrying the current. In 2D and 3D, Landau Fermi-liquid theory shows that such interactions can be hidden by considering low-energy excitations of the system of interacting particles away from equilibrium, which behave like particles ("quasiparticles") with energies just above or below the Fermi energy. However, in a truly 1D system (infinitely long, with just one subband), such excitations are unstable and, instead, the system can be treated as having bosonic excitations (like sound waves) in the Tomonaga-Luttinger model (see below).

Experimentalists therefore searched for many-body effects in their 1D wires long after the discovery of quantized conductance, with specific focus being allocated to the possible emergence of fractional charge and conductance in low dimensions. In 1996, Thomas and collaborators reported on the observation of an anomalous new plateau-like feature around $0.7\,(2e^2/h)$, see Fig. 6, nowadays commonly known as the "0.7 structure" (Thomas et al., 1996). Interestingly, on application of an in-plane field, this feature was observed to move down to e^2/h, suggesting that the transmitted states were becoming fully spin-polarized, despite the absence of a magnetic field to define a polarization direction. Similar decrease of the plateau height was also observed upon *increase* of temperature. Proposed theoretical explanations for this phenomenon have included spontaneous spin polarization (Reilly, 2005) as initially suggested by Thomas et al., possible Wigner crystallization (Matveev, 2004; Güçlü et al., 2009), the Kondo effect (Meir et al., 2002; Rejec and Meir, 2006), ferromagnetic spin coupling (Aryanpour and Han, 2009) and, more recently and convincingly, a van Hove singularity in the local 1D density of states at either end of the pinched-off channel which enhances interactions and hence tunneling along the channel (Bauer et al., 2013).

As mentioned above, in 1D there should theoretically be a complete breakdown of the single-particle picture and Fermi-liquid theory. The Tomonaga-Luttinger liquid (TLL) model predicts, instead, a highly-correlated state of matter that forms when electrons are confined to a 1D geometry, where there are so few degrees of freedom that interactions cannot be hidden (effectively because electrons cannot get past each other along the wire). While originally proposed by Tomonaga and Luttinger in the 1950s and 60s (Tomonaga, 1950; Luttinger, 1963), the current version of the theory is credited to Haldane, who finalized it in 1981 (Haldane, 1981). Its key predictions include the emergence of new types of collective mode for spin and charge excitations (commonly dubbed spinons and holons, respectively), the appearance of power-law behavior at and around the Fermi points $\pm k_F$, and charge fractionalization. This theory is exact, but only applicable at low excitation energies, (i.e., close to the Fermi energy), as one of its key assumptions is that energy varies linearly with wavenumber *k* near E_F, whereas this dispersion relation is really parabolic and only resembles a straight line for a small range of energies around E_F.

Experimentally, work on TLLs has been carried out using a variety of systems, from transport measurements in carbon nanotubes (Bockrath et al., 1999; Ishii et al., 2003), edge states (Chang, 2003; Grayson et al., 1998) and quantum point contacts (Anthore

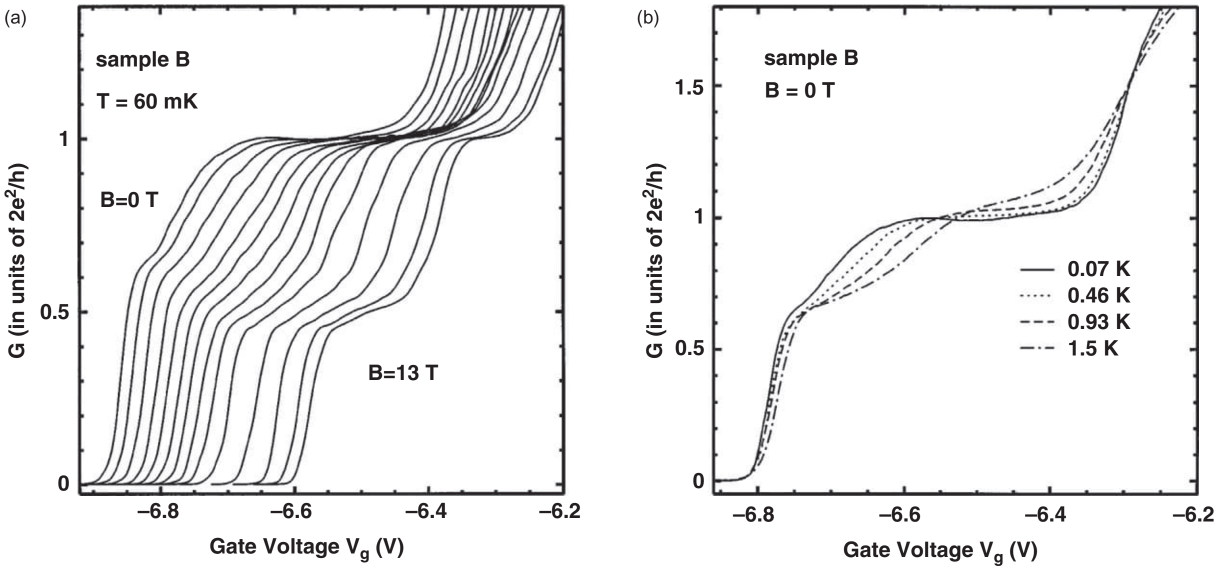

Fig. 6 The “0.7 structure.” (a) Evolution of a feature starting at $0.7(2e^2/h)$ to e^2/h when in the presence of a magnetic field B parallel to the wire. (b) Temperature dependence of the same feature shown in (a) for $B = 0$. From Thomas KJ, Nicholls JT, et al. (1996) Possible spin polarization in a one-dimensional electron gas. *Physical Review Letters* 77: 135–138, *reprinted with permission*.

et al., 2018), to ARPES measurements in high-T_c superconductors (Kim et al., 1996) and organic compounds (Zwick et al., 1998; Pouget et al., 1976) and, more recently, time-resolved measurements in cold-atom chains (Vijayan et al., 2020). All these systems have, to different extents, validated the predictions of the TLL model. A different approach, however, considered tunneling measurements done in semiconductor quantum wires (Auslaender et al., 2005; Jompol et al., 2009).

Jompol et al. showed, by conducting a series of detailed energy- and momentum-resolved tunneling measurements between an array of 1D wires and a nearby 2DEG, that the spectral function of a 1D system is indeed double-peaked near the Fermi points (Jompol et al., 2009). This allowed for a clean observation of what is now known as spin-charge separation, that is, the separation of spin and charge degrees of freedom at low energy near the Fermi points, see Fig. 7. Power-law suppression of the tunneling near zero

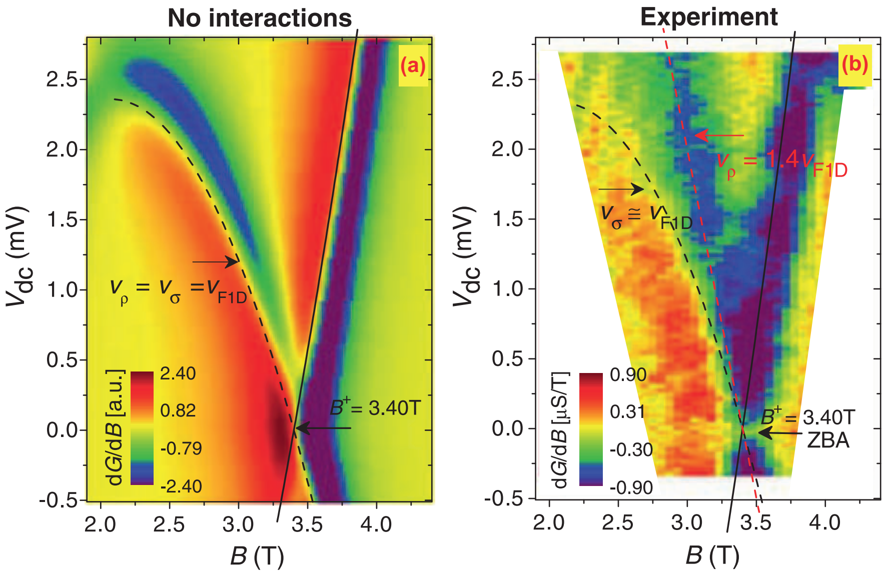

Fig. 7 Spin-charge separation—theory and experiment. (a) Simulated dispersion of non-interacting electrons in 1D close to the Fermi point ($B^+ = 3.40$ T). Here $B \propto$ momentum and $V_{dc} \propto$ energy. Note how all features track the non-interacting parabolae (black full and dashed). (b) Measured dispersion. In addition to the parabolae shown in (a), an additional feature not predicted by the non-interacting model (red dashed) is also observed. This is seen to branch away from the spin parabola (black dash) at the Fermi point, consistent with the behavior predicted by the Luttinger model for the charge mode. Note that the Fermi energy in this system is ~2.5 meV. From Jompol Y, et al. (2009) Probing spin-charge separation in a Tomonaga-Luttinger liquid. *Science* 325: 597–601, *reprinted with permission*.

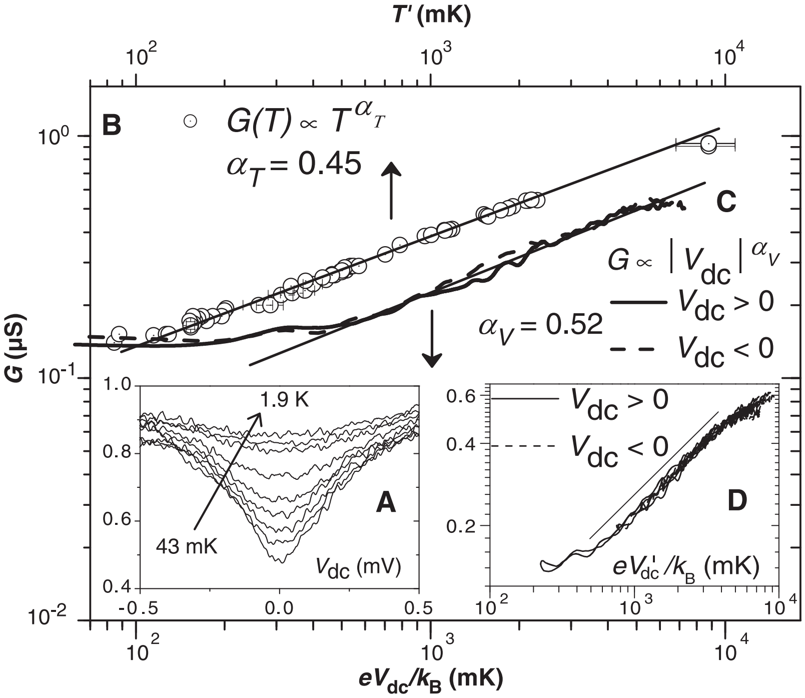

Fig. 8 The zero-bias anomaly. (a) Temperature T dependence of the ZBA at $B = 2.33$ T for bias V_{dc}. (b) Power-law dependence of the minima $G(V_{dc} = 0)$ vs T over two orders of magnitude. (c) Same as in (b) but now for $G(|V_{dc}|)$ at constant $T < 100$ mK. (d) Curves in (a) collapsed on to one curve by plotting vs $V'_{dc} = \sqrt{|V_{dc}|^2 + (3k_B T/e)^2 + V_{ac}^2}$ where V_{ac} is the AC measurement voltage. From Jompol Y, et al. (2009) Probing spin-charge separation in a Tomonaga-Luttinger liquid. *Science* 325: 597–601, *reprinted with permission.*

source-drain bias V_{dc}, known as the zero-bias anomaly, was also observed in the same system at low temperatures T, see Fig. 8. Note that neither of these results can be explained by the Fermi-liquid model, but they are predicted by the TLL model.

Given the constraints of the theory from its initial assumptions of linearity, attempts at extending it to the nonlinear regime have also been carried out theoretically, particularly by Imambekov, Glazman and Schmidt, initially ignoring spin (Imambekov and Glazman, 2009) and then including it (Schmidt et al., 2010a). Here, by taking into account explicitly the curvature of the dispersion, momentum-dependent power laws and finite lifetime for the plasmonic excitations (i.e., when spinons and holons cannot be separately resolved) were also predicted, both recently observed experimentally (Jin et al., 2019; Wang et al., 2020).

The question of what happens to spin-charge separation at high energies and, therefore, away from the linear regime remained, however, unanswered: theoretically, the TLL model is no longer valid, with the general understanding being that all collective modes would eventually become unstable far from the Fermi points, $\pm k_F$. Experimentally, on the other hand, they had long been observed to remain stable up to, at least, the Fermi energy, already significantly away from $\pm k_F$, see Fig. 7B. Recent work has proposed a novel phenomenological picture to explain this apparent contradiction, by invoking the emergence of two Fermi seas, rather than the usual single Fermi sea (Vianez et al., 2022).

By measuring the spectra of a 1D system in a similar fashion to the work done by Jompol et al., but now also carefully accounting for the "parasitic" background signal from the 2D leads, it was observed that the measured resonances gave rise to two parabolic dispersions, or "Fermi seas," see Fig. 9. These were seen to evolve separately from the already observed spin-charge feature at low energy, prompting the conclusion that the collective charge mode was still remaining stable even when at energies far above or below the Fermi points, as predicted theoretically by (Schmidt et al., 2010b; Tsyplyatyev, 2022). This work also observed a number of emerging higher-order 1D "replica" modes, in addition to the main 1D mode, as expected from the microscopic nonlinear model first developed by Tsyplyatyev (Tsyplyatyev et al., 2015, 2016; Moreno et al., 2016), see Fig. 10. Ongoing efforts, both theoretical and experimental, are currently attempting to explore these nonlinear signatures further.

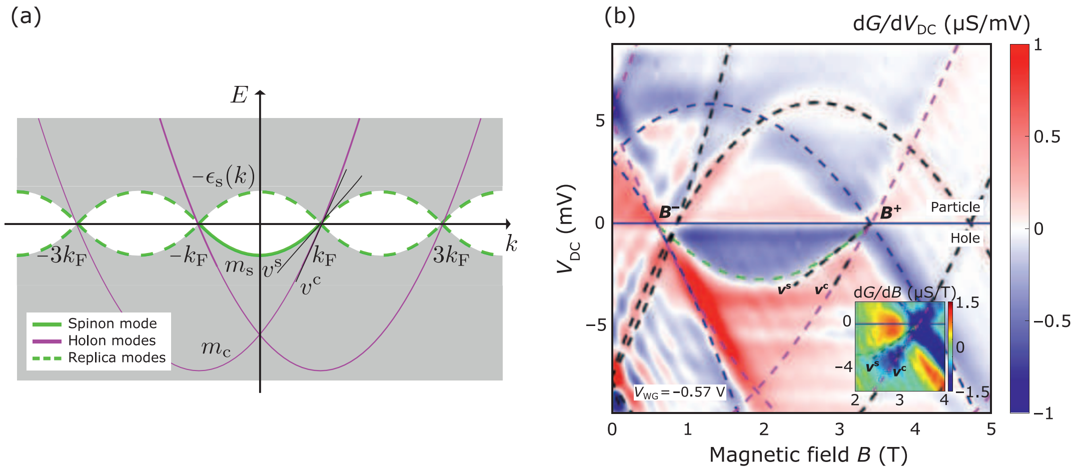

Fig. 9 Two Fermi seas for spin and charge. (a) Proposed many-body spectra for an interacting 1D systems. Here, gray marks the many-body continuum while white the forbidden regions. (b) Map of the tunneling conductance differential d*G*/dV_{DC} as a function of DC bias V_{DC}($\propto$ energy) and in-plane magnetic field *B*($\propto$ momentum), showing the dispersion of a 1D system when in the single-subband regime. Superimposed curves mark all possible single-electron tunneling processes in this system, with the resonant dispersions of the spin and charge modes being marked by green and magenta dashed lines, respectively. Inset: d*G*/d*B* differential around the $+k_F$ point showing the spin-charge separation feature from which the velocities v^s and v^c can be extracted. From Vianez PMT, et al. (2022) Observing separate spin and charge Fermi seas in a strongly correlated one-dimensional conductor. *Science Advances* 8: eabm2781, *reprinted with permission*.

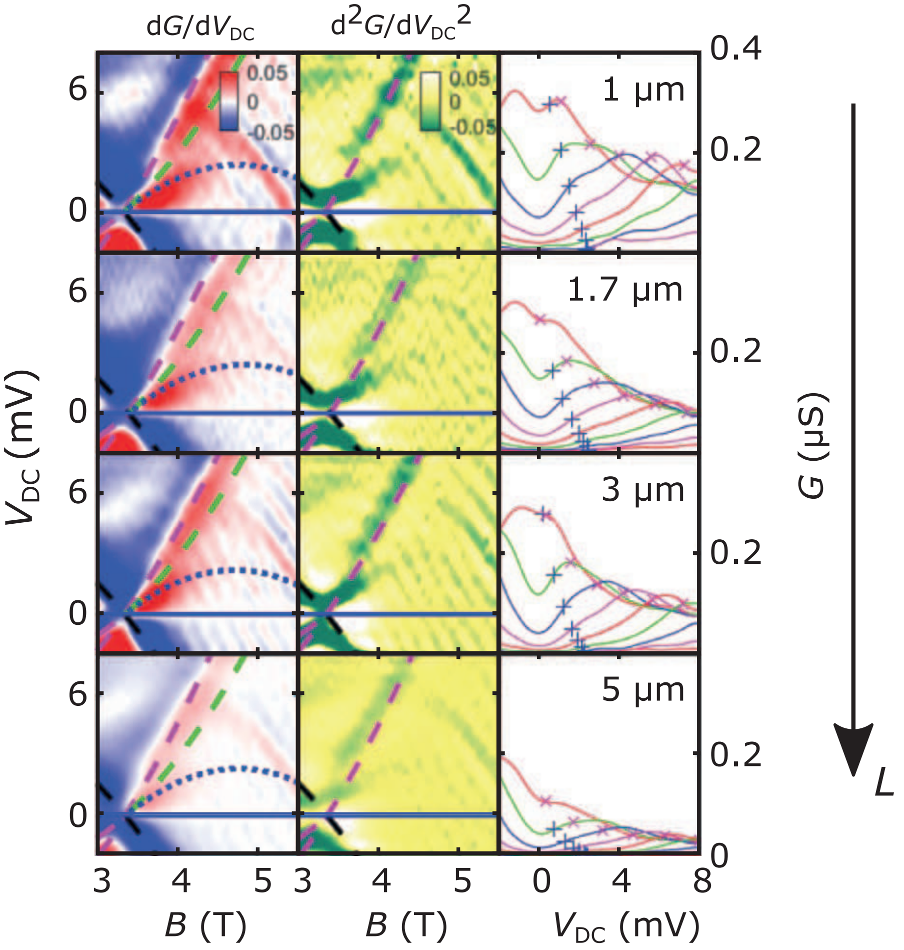

Fig. 10 Higher-order 1D "replica" modes. In addition to the main 1D dispersion, higher-order 1D features are also expected (dashed lines in Fig. 9a). Here, the first and second columns show, respectively, the d*G*/dV_{DC} and d^2*G*/dV_{DC}^2 tunneling conductance differentials, while the third columns shows line cuts of the raw data, just above the $+k_F$ point. As can be seen, a feature compatible with a 1D "replica" mode is observed experimentally to become more pronounced as the length of the system *L* is decreased, as predicted by Tsyplyatyev et al. (Tsyplyatyev et al., 2015, 2016). From Vianez PMT, et al. (2022) Observing separate spin and charge Fermi seas in a strongly correlated one-dimensional conductor. *Science Advances* 8: eabm2781, *reprinted with permission*.

Conclusion

While the experimental study of transport and interaction effects in one-dimensional semiconducting devices first started in 1988 with the simultaneous discovery of conductance quantization by two different groups (van Wees et al., 1988; Wharam et al., 1988), the field is still producing new and unexpected results, from fractional quantization (Thomas et al., 1996; Bauer et al., 2013), to spin-charge separation (Auslaender et al., 2005; Jompol et al., 2009), possible helical order in the nuclear spins (Scheller et al., 2014; Braunecker et al., 2009) and, more recently, nonlinear effects (Wang et al., 2020; Jin et al., 2019; Vianez et al., 2022). The influence of spin-orbit interaction (SOI) on transport in 1D has been studied carefully experimentally (for holes in GaAs) and theoretically very recently (Hudson et al., 2021), and SOI has been shown to separate spins leaving a 1D channel (Lo et al., 2017) and to allow control of the Kondo effect (Smith et al., 2022). Outside the solid state, recent technological improvements have also, very recently, allowed for perfect, disorder-free 1D systems to be created using a lattice of optical traps rather than a semiconductor crystal (Vijayan et al., 2020), showing good promise for future results not just in 1D but perhaps, in higher dimensions.

Further reading

For a brief, graduate-level introduction to the TLL model, see chapter 9 of Giuliani and Vignale (2005). A similar, yet much more complete, pedagogical approach can also be found in Giamarchi (2003). For an in-depth review of the theory beyond the Luttinger-liquid paradigm, see Imambekov et al. (2012). For a review on the experimental progress in the field of strongly-correlated 1D electronic systems, see Deshpande et al. (2010) and Vianez et al. (2021).

References

Anthore A, et al. (2018) Circuit quantum simulation of a Tomonaga-Luttinger liquid with an impurity. *Physical Review X* 8: 031075.

Aryanpour K and Han JE (2009) Ferro-magnetic spin coupling as the origin of 0.7 anomaly in quantum point contacts. *Physical Review Letters* 102.

Ashcroft NW and Mermin ND (1976) *Solid State Physics*. New York: Holt, Rinehart and Winston.

Auslaender OM, et al. (2005) Spin-charge separation and localization in one dimension. *Science* 308: 88–92.

Bauer F, et al. (2013) Microscopic origin of the ‘0.7-anomaly’ in quantum point contacts. *Nature* 501: 73–78.

Bloch F (1929) Über die Quantenmechanik der Elektronen in Kristallgittern. *Zeitschrift für Physik* 52: 555–600.

Blumenthal MD, et al. (2007) Gigahertz quantized charge pumping. *Nature Physics* 3: 343–347.

Bockrath M, et al. (1999) Luttinger-liquid behaviour in carbon nanotubes. *Nature* 397: 598–601.

Braunecker B, Simon P, and Loss D (2009) Nuclear magnetism and electron order in interacting one-dimensional conductors. *Physical Review B* 80: 165119.

Büttiker M (1990) Quantized transmission of a saddle-point constriction. *Physical Review B* 41: 7906–7909.

Chang AM (2003) Chiral Luttinger liquids at the fractional quantum Hall edge. *Reviews of Modern Physics* 75: 1449–1505.

Deshpande VV, et al. (2010) Electron liquids and solids in one dimension. *Nature* 464: 209–216.

Drude P (1900) Zur Elektronentheorie der Metalle. *Annalen der Physik* 306: 566–613.

Giamarchi T (2003) *Quantum Physics in One Dimension. International Series of Monographs on Physics*. Oxford, New York: Oxford University Press.

Giuliani G and Vignale G (2005) *Quantum Theory of the Electron Liquid*. Cambridge: CUP.

Graham AC, et al. (2003) Interaction effects at crossings of spin-polarized one-dimensional subbands. *Physical Review Letters* 91: 136404.

Grayson M, et al. (1998) Continuum of chiral Luttinger liquids at the fractional quantum Hall edge. *Physical Review Letters* 80: 1062–1065.

Güçlü AD, et al. (2009) Localization in an inhomogeneous quantum wire. *Physical Review B* 80: 201302.

Haldane FDM (1981) ‘Luttinger liquid theory’ of one-dimensional quantum fluids. I. Properties of the Luttinger model and their extension to the general 1D interacting spin-less Fermi gas. *Journal of Physics C: Solid State Physics* 14: 2585–2609.

Hudson KL, et al. (2021) New signatures of the spin gap in quantum point contacts. *Nature Communications* 12: 5.

Imambekov A and Glazman LI (2009) Universal theory of nonlinear Luttinger liquids. *Science* 323: 228–231.

Imambekov A, Schmidt TL, and Glazman LI (2012) One-dimensional quantum liquids: Beyond the Luttinger liquid paradigm. *Reviews of Modern Physics* 84: 1253–1306.

Ishii H, et al. (2003) Direct observation of Tomonaga–Luttinger-liquid state in carbon nanotubes at low temperatures. *Nature* 426: 540–544.

Jin Y, et al. (2019) Momentum-dependent power law measured in an interacting quantum wire beyond the Luttinger limit. *Nature Communications* 10: 2821.

Jompol Y, et al. (2009) Probing spin-charge separation in a Tomonaga-Luttinger liquid. *Science* 325: 597–601.

Kim C (1996) Observation of spin-charge separation in one-dimensional $SrCuO_2$. *Physical Review Letters* 77: 4054–4057.

Klitzing Kv, Dorda G, and Pepper M (1980) New method for high-accuracy determination of the fine-structure constant based on quantized Hall resistance. *Physical Review Letters* 45: 494–497.

Kouwenhoven LP, et al. (1991) Quantized current in a quantum-dot turnstile using oscillating tunnel barriers. *Physical Review Letters* 67: 1626–1629.

Laux SE, Frank DJ, and Stern F (1988) Quasi-one-dimensional electron states in a split-gate GaAs/AlGaAs heterostructure. *Surface Science* 196: 101–106.

Lo S-T, et al. (2017) Controlled spatial separation of spins and coherent dynamics in spin-orbit-coupled nanostructures. *Nature Communications* 8: 15997.

Luttinger JM (1963) An exactly soluble model of a many-fermion system. *Journal of Mathematical Physics* 4: 1154–1162.

Matveev KA (2004) Conductance of a quantum wire at low electron density. *Physical Review B* 70: 245319.

Meir Y, Hirose K, and Wingreen NS (2002) Kondo model for the “0.7 anomaly” in transport through a quantum point contact. *Physical Review Letters* 89: 196802.

Moreno M, et al. (2016) Nonlinear spectra of spinons and holons in short GaAs quantum wires. *Nature Communications* 7: 12784.

Pouget JP, et al. (1976) X ray observation of $2k_F$ and $4k_F$ scatterings in tetrathiafulvalene-tetracyanoquinodimethane (TTF-TCNQ). *Physical Review Letters* 37: 437–440.

Pyshkin KS, et al. (2000) Spin splitting of one-dimensional subbands in high quality quantum wires at zero magnetic field. *Physical Review B* 62: 15842–15850.

Reilly DJ (2005) Phenomenological model for the 0.7 conductance feature in quantum wires. *Physical Review B* 72.

Rejec T and Meir Y (2006) Magnetic impurity formation in quantum point contacts. *Nature* 442: 900–903.

Scheller CP, et al. (2014) Possible evidence for helical nuclear spin order in GaAs quantum wires. *Physical Review Letters* 112, 066801.

Schmidt TL, Imambekov A, and Glazman LI (2010a) Fate of 1D spin-charge separation away from fermi points. *Physical Review Letters* 104: 116403.

Schmidt TL, Imambekov A, and Glazman LI (2010b) Spin-charge separation in one-dimensional fermion systems beyond Luttinger liquid theory. *Physical Review B* 82: 245104.

Smith LW, et al. (2022) Electrically controllable Kondo correlation in spin-orbit-coupled quantum point contacts. *Physical Review Letters* 128: 027701.

Stone SD and Szafer A (1988) What is measured when you measure a resistance? The Landauer formula revisited. *IBM Journal of Research and Development* 32: 384–413.

Thomas KJ, Simmons MY, et al. (1995) Ballistic transport in one-dimensional constrictions formed in deep two-dimensional electron gases. *Applied Physics Letters* 67: 109–111.

Thomas KJ, Nicholls JT, et al. (1996) Possible spin polarization in a one-dimensional electron gas. *Physical Review Letters* 77: 135–138.

Thornton TJ, et al. (1986) One-dimensional conduction in the 2D electron gas of a GaAs-AlGaAs heterojunction. *Physical Review Letters* 56: 1198–1201.

Tomonaga S (1950) Remarks on bloch’s method of sound waves applied to many-fermion problems. *Progress of Theoretical Physics* 5: 544–569.

Tsui DC, Stormer HL, and Gossard AC (1982) Two-dimensional magneto-transport in the extreme quantum limit. *Physical Review Letters* 48: 1559–1562.

Tsyplyatyev O (2022) Splitting of the Fermi point of strongly interacting electrons in one dimension: A nonlinear effect of spin-charge separation. *Physical Review B* 105: L121112.

Tsyplyatyev O, Schofield AJ, Jin Y, Moreno M, Tan WK, Ford CJB, et al. (2015) Hierarchy of modes in an interacting one-dimensional system. *Physical Review Letters* 114: 196401.

Tsyplyatyev O, Schofield AJ, Jin Y, Moreno M, Tan WK, Anirban AS, et al. (2016) Nature of the many-body excitations in a quantum wire: Theory and experiment. *Physical Review B* 93: 075147.

van Wees BJ, et al. (1988) Quantized conductance of point contacts in a two-dimensional electron gas. *Physical Review Letters* 60(9): 848–850.

Vianez P (2022) *Semiconductor Nanodevices as a Probe of Strong Electron Correlations*. (PhD thesis) University of Cambridge.

Vianez P, Tsyplyatyev O, and Ford C (2021) Chapter Three—Semiconductor nanodevices as a probe of strong electron correlations. In: Ritchie DA (ed.) *Frontiers of Nanoscience. Semiconductor Nanodevices*, vol. 20, pp. 31–66. Elsevier.

Vianez PMT, et al. (2022) Observing separate spin and charge Fermi seas in a strongly correlated one-dimensional conductor. *Science Advances* 8: eabm2781.

Vijayan J, et al. (2020) Time-resolved observation of spin-charge deconfinement in fermionic Hubbard chains. *Science* 367: 186–189.

Wang S, et al. (2020) Nonlinear Luttinger liquid plasmons in semiconducting single-walled carbon nanotubes. *Nature Materials* 19: 986–991.

Wharam DA, et al. (1988) One-dimensional transport and the quantisation of the ballistic resistance. *Journal of Physics C: Solid State Physics* 21: L209–L214.

Zwick F, et al. (1998) Band mapping and quasiparticle suppression in the one-dimensional organic conductor TTF-TCNQ. *Physical Review Letters* 81: 2974–2977.

Quantum physics in one dimension

T Giamarchi, Department of Quantum Matter Physics, University of Geneva, Geneva, Switzerland

© 2024 Elsevier Ltd. All rights reserved.

Introduction **905**
Fundamental concepts for 1D systems **906**
1D or not 1D 906
Collective excitations and 1D physics 907
Methods 909
Complications **910**
Mott transition 910
Effect of disorder or quasiperiodic potentials 911
Coupled chains 911
Key issues and future directions **912**
Conclusion **913**
References **913**
Further reading **913**

Abstract

This chapter is an introduction to the physics of one-dimensional quantum interacting systems. It presents the basic concepts and properties of such systems as well as their differences compared to higher dimensional ones. It introduces the concept of the Tomonaga–Luttinger liquid, the cornerstone of our description of 1D quantum systems. It discusses the main theoretical methods to attack such problems, the main experimental realizations and the main challenges in the field, both current and future.

Key points

- Main ingredients in a one-dimensional quantum system
- Peculiar physics consequences of the collective character of a 1D system
- Presentation of the concept of Tomonaga–Luttinger liquid
- Main experimental realizations of 1D quantum systems
- Successes and current and future directions.

Introduction

Correlated quantum systems are one of the main outstanding problems in modern quantum physics, with far-reaching consequences ranging from solid state physics and material science to information theory. In such systems a large number of particles (anything from a few hundred in cold atomic gases to 10^{23} in solids) interact together. In addition, due to the indiscernibility of the particles (whether bosons or fermions), the wavefunction has to be totally symmetrized or antisymmetrized, leading to very complicated entanglement properties and making this problem extremely challenging to solve on classical computers. Of course the complexity of the problem is also the warrant of the richness of the physics it can lead to and such systems have led to remarkable physical phenomena, such as superconductivity or quantized Hall response, to name a few.

One could naively imagine that for such problems the spatial dimension is only marginally relevant. This is indeed the case for many properties when the dimension is two or above (there are notable exceptions, in particular for dimension two). However, one dimension stands apart. Indeed, in such a case particles cannot avoid each other, contrarily to what can happen in larger dimensions, and thus even an *infinitesimal* interaction can drastically modify the physical properties compared to the noninteracting case. In addition, edges in one dimension are reduced to two points, making it easier to classify solutions by the behavior at the edge of the system. Topological properties are thus the rule rather than the exception. Finally, the lower the dimension the stronger the thermal and quantum fluctuations, rendering typical "mean field" methods useless; one finds oneself in a realm of physics where not only the physics is radically different, but the set of methods that one must use to solve is also unusual.

Such one-dimensional quantum systems were once considered pure theoretical exercises or "toy models" that one attacks before trying the real high-dimensional challenge. Fortunately, this is not the case anymore. On the pure theory side, they have shown remarkable physics properties that are studied in their own right. They have also led to the development of analytical and numerical techniques that have changed the way we are now looking at correlated systems. Even more importantly, the number of

https://doi.org/10.1016/B978-0-323-90800-9.00233-X

experimental realizations of such systems has literally exploded in the 21st century, as well as the ways to probe such systems, in both equilibrium and out of equilibrium situations.

The goal of this chapter is thus to give a brief digest of this unusual one-dimensional quantum physics and an idea of the methods used to tackle it. Because of the structure of this chapter, most of the references will not be in the text but can be found in the various textbooks and reviews that are listed in the "Further reading" section. Some exceptional references are listed in the text as well.

Fundamental concepts for 1D systems

Let us first give a very brief digest of some of the essential properties of one-dimensional systems.

1D or not 1D

One-dimensional systems can be realized, in our three-dimensional world, essentially with three different incarnations as illustrated in Fig. 1.

The most common one comes from materials that have a three-dimensional structure but for which there is a large anisotropy in the energy scales for kinetic energies (fermions or bosons) or magnetic exchanges (localized spin systems). Let us generically denote $t_{\|}$ the energy along the "chain" direction and $t_{\perp}$ the one in the transverse direction. In that case, if either the energy at which the system is probed or more simply the temperature T satisfies $t_{\perp} \ll T \ll t_{\|}$, the system is quantum mechanically coherent along the "chain" direction but motion along the perpendicular direction is essentially incoherent, or does not have time to occur before the system is probed. In that case, one can consider that the system can be described by a one-dimensional Hamiltonian and ignore the couplings in the transverse direction. This is the most common case and is realized, for example, in spin chains and ladders,

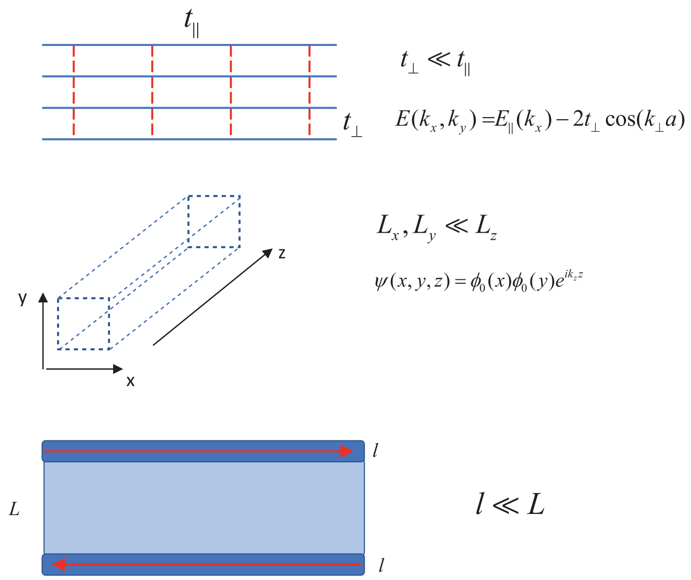
$t_{\|}$
$t_{\perp} \ll t_{\|}$
$t_{\perp}$
$E(k_x, k_y) = E_{\|}(k_x) - 2t_{\perp}\cos(k_{\perp}a)$
$L_x, L_y \ll L_z$
z
y
x
$\psi(x,y,z) = \phi_0(x)\phi_0(y)e^{ik_z z}$
l
L
$l \ll L$
l

Fig. 1 Various types of one-dimensional structures. Top: a system with many chains (here represented in two dimensions, but in general three dimensional) but with a very strong anisotropy in the kinetic energy, or as shown here, tight binding hoppings. When the temperature is much larger than the transverse hopping $T \gg t_{\perp}$ the system is incoherent in the transverse direction but perfectly coherent along the chains if $T \ll t_{\|}$. In that case the system is effectively behaving as decoupled 1D chains. When the temperature is lowered the system undergoes a dimensional crossover toward a two- (or three-) dimensional situation. This applies to three-dimensional crystals such as organic conductors and superconductors, or quantum spin chains and ladders and some cold atomic gas realizations. Middle: a structure confined enough in two directions with size small enough compared to the quantization of energy levels in the transverse direction would lead to large energy changes, much larger than the temperature or the interaction energy. In that case the transverse part of the wavefunction is blocked in the fundamental of the system $\phi_0(x)$ and these quantum numbers cannot change. The only quantum number that can change is the one along the z direction. Thus the system behaves as a perfect one-dimensional system even if its physical dimensions are not zero in the transverse directions. This system will stop being one dimensional when the temperature or the interaction becomes large enough to be able to excite the transverse degrees of freedom. In that case several transverse quantum numbers are involved and the system becomes somewhat similar to the one on the top but with a *finite* number of chains (so-called ladders). Bottom: In some systems such as fractional quantum Hall effect or topological insulators, the bulk of the system is gapped but the edges are gapless. In that case we have a special case of one-dimensional system that is chiral since the particles moving on the right direction are physically separated from the particles moving on the left.

organic conductors and superconductors, and cold atomic systems. It is important to note that in such systems when the temperature is lowered below $t_\perp$ the system will not be one-dimensional any more. This paves the way to studying the very important dimensional crossover that can occur in these systems and that we will discuss more in the Section "Key issues and future directions."

The second possibility is to confine the two transverse dimensions to small enough distances such that the quantization of transverse quantum numbers ensures large enough energy differences. Let us illustrate it by a system in which the directions x and y would be put in a harmonic confinement potential while the direction z is essentially a continuum. In that case, the wavefunction of the system is of the form

$$\psi(x, y, z) = \phi_n(x)\phi_m(y)e^{ikz} \tag{1}$$

where ϕ_n are the eigenstates of the harmonic oscillator with quantum number n and thus of energy $E_n = \hbar\omega_0(n + 1/2)$. Changing the transverse quantum numbers from, for example, $n = 0$ to $n = 1$ thus costs a finite amount of energy $\hbar\omega_0$. Similar results would be obtained by other confining potentials such as a box. Thus, provided that temperature and interactions are lower than this discrete difference in energy, the transverse quantum numbers are frozen and the system behaves quantum mechanically as a purely one-dimensional system. This realization of one-dimensional systems is directly relevant for cold atomic systems, quantum wires, and nanotubes. Note that, contrarily to the previous situation, there is not here a dimensional crossover, but if the temperature or interactions become too large it is necessary to take into account other transverse quantum numbers, as shown in Fig. 1. This is thus similar to a multiorbital or finite number of one-dimensional structures coupled together. This situation, known under the generic name of "ladders," is still one-dimensional asymptotically but in general with properties quite different than those of a single chain.

Finally, the last realization occurs when one has a system for which the bulk is gapped but edge states that are gapless can exist. This is the case, for example, in systems with fractional Hall effect or topological insulators. In that case the edge states are confined and one is for each edge state in a similar situation to the confined realization described earlier. The main difference is that now the system is chiral in the sense that right-going particles and left-going particles are separated at the edge, contrarily to the case of a normal one-dimensional structure. This has important consequences when interactions are put into play, since a right mover cannot be converted to a left mover (so called backscattering), contrary to the case of a normal one-dimensional structure.

Collective excitations and 1D physics

One-dimensional systems possess a set of characteristic features that set them apart from their higher dimensional counterparts, whether they are spins, bosons, or fermions. It is of course out of the question to be exhaustive here but we will brush the main concepts. We will see first the properties and then briefly discuss the methods that can be employed to obtain them.

Many important properties of one-dimensional systems have their origin in the fact that because of the 1D character particles cannot avoid each other. This means that it is impossible to separate the properties and even the statistics of the system from the interactions. It is relatively easy in 1D to pass from fermions to bosons to spins. Indeed, an infinite repulsion between bosons produces identical effects to the Pauli principle for fermions. A corollary of this tells us that individual particle excitations, such as those existing for free particles or those that make up the essence of Landau's Fermi liquid, the paradigmatic solution of interacting high-dimensional fermions, will not exist in general in one dimension. Any excitation will rapidly transform into *collective* excitations. A second defining property is the fact that in low dimension it is extremely difficult to break symmetries due to fluctuations. Even at $T = 0$ a continuous symmetry cannot be broken and only discrete ones can lead to true order. Thus a typical one-dimensional system has usually only quasilong range order even at $T = 0$.

Quite remarkably these properties have given rise to a unifying concept that plays a similar role to that the Fermi liquid has played for high dimensional fermionic systems, or Bogoliubov theory for bosonic and spin systems. This is known as the concept of Tomonaga–Luttinger liquid (TLL), discovered by Haldane (1980, 1981a, b), which describes the properties of many massless one-dimensional systems and serves as a stepping stone to study either more complicated situations (coupled chains, several degrees of freedom, more complicated interactions, etc.) as we will discuss in the Section "Complications." The TLL is characterized by a low-energy Hamiltonian describing excitations, that are collective excitations such as sound waves (representing density fluctuations of the system). It is fully characterized by two parameters, the velocity u of the excitations and a dimensionless parameter K. The spectrum of excitations is thus linear $\omega \sim uk$. The correlation functions are characterized by harmonics that vary in space with a wavevector multiple of $2\pi\rho_0$ where ρ_0 is the average density of the system. For fermions it is easy to see that this corresponds to $2k_F$ where k_F is the Fermi wavevector. The corresponding amplitudes of the various harmonics decay as a powerlaw of space x or imaginary time τ with exponents that are only functions of the dimensionless parameter K. Let us give an example with a one-dimensional system of interacting bosons. The single particle Green's function and the density–density correlations behave respectively as

$$\begin{aligned} \langle \psi_B(x)\psi_B^\dagger(0)\rangle &= A\left(\frac{\alpha}{x}\right)^{\frac{1}{2K}} + \cdots \\ \langle \delta\rho(x)\delta\rho(0)\rangle &= \frac{-K}{2\pi^2x^2} + B\cos(2\pi\rho_0 x)\left(\frac{\alpha}{x}\right)^{2K} + \cdots \end{aligned} \tag{2}$$

and similar decays in imaginary time. The TLL is thus a conformally invariant theory with a central charge $c = 1$. This easily allows computing of finite temperature properties. As can be expected from general grounds, the finite temperature that introduces a periodicity of period β the inverse temperature in the imaginary time direction transforms the system into essentially a classical one-dimensional system with exponentially decreasing correlation functions. The A and B are nonuniversal amplitudes that depend on the precise microscopic model and the ultraviolet cutoff α (akin to a lattice spacing and regularizing the regime that follows, for which the field theory representation is not valid any more). We will discuss in the Section "Methods" how to compute these amplitudes as well as the TLL parameters u and K.

As a consequence of having one or several correlations that decay as powerlaws, the corresponding susceptibilities can easily diverge (depending on the value of K) and the TLL is thus a system that, like a critical system, is poised at the border of ordering. It will thus be very sensitive to external perturbations such as periodic potentials or the existence of a lattice (leading to Mott transitions), disorder (leading to localized phases, with or without interactions), or coupling of several chains or degrees of freedom together.

Of course, one is not limited to a single degree of freedom and the preceding easily generalizes to several components coming, for example, from spin. This is, for example, the case for the celebrated Hubbard model of fermions with spin-1/2 and a contact interaction. This brings us to another important characteristic of one-dimensional systems: the fractionalization of excitations. Usually there is a minimal excitation that can be done in a system and all more complicated processes are multiples of this elementary process. For example, in high dimensional spin systems the minimum variation of spin in a spin 1/2 system consists of flipping one single spin with a modification of the z component of the spin by $\Delta S^z = 1$. This excitation, which is commonly referred to as a magnon, is the building brick of higher excitations. In a similar way, for a fermionic system the least one can do is to remove one electron, which removes both a charge 1 and a spin 1/2. This is the basic quantum numbers of a Landau quasiparticle. In one dimension, because the individual excitations are transformed into collective ones, they usually *decompose* into (i) nonlocal; (ii) more elementary excitations. One simple example, shown in Fig. 2, is the decomposition of the magnon (local "elementary" excitation) into two real elementary excitations, the "spinons" carrying each only a spin 1/2. These excitations are nonlocal, which is why a local probe must create these excitations in pairs. On the other hand, in the one-dimensional world nothing prevents them separating (deconfining). This leads to severe consequences such as continua of energy since the energy of an excitation with a given momentum can be spread between the two spinons in an arbitrary way. Last but not least, since the boundary in one dimension is essentially two points ($x \to -\infty$ and $x \to \infty$), it is easy to classify solutions based on the value of fields at infinity and thus to have a topological index. Thus in 1D, topological excitations are the rule rather than the exception.

This fractionalization of excitations generalizes to more complicated models such as fermions with spins. In that case the Hilbert space asymptotically separates into a sector that carries charge and no spin ("holon" excitations) and a sector that carries spin but no charge ("spinon" excitations). These two excitations deconfine, showing that individual (Landau) quasiparticles do not exist in one dimension. This phenomenon, known as spin-charge separation (see Fig. 2), has consequences in particular for the photoemission spectrum of 1D systems.

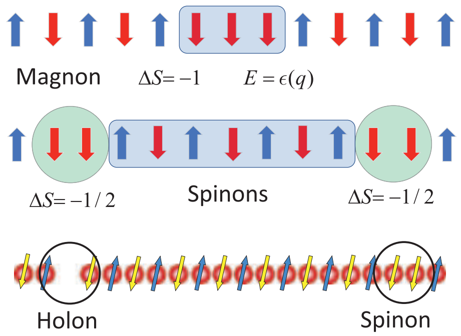

Fig. 2 Top: The most elementary excitation in a spin 1/2 chain consists of flipping a single spin. The smallest change of the spin quantum number is thus $\Delta S_z = 1$. In dimension greater than one, this is an elementary excitation (known as a magnon), with a well defined relation between the momentum of the excitation and its energy (and a finite lifetime). In real space this corresponds to the block of down spins indicated on the top figure. Middle: in one dimension this excitation can decompose in two deconfined *collective* excitations: the spinons. Each spinon carries a $\Delta S_z = 1/2$. This thus corresponds to a fractionalization of the excitations. Note that the spinon is not a local excitation since it consists both of two down spins but also of a string on the left or on the right of the two down spins of overturned spins (symbolized by the *box* in the middle figure). In a strict one-dimensional situation, this string does not cost energy and the two spinons are deconfined. In the presence of adjacent chains (thus in a higher dimensional system) the string costs an energy growing linearly with the length of the string and thus confines the spinons, leading back to the magnon as an elementary excitation. Bottom: When charge (symbolized by the *ball*) and spins (symbolized by the *arrow*) degrees of freedom are present such as in the fermionic Hubbard model, a similar fractionalization of excitations takes place. Removing a particle (thus both a charge and a spin up) leads to two deconfined excitations. The holon is missing a charge but has an otherwise undistorted spin background. The spinon has no charge missing but has a spin up missing (two close spin down).

Methods

Before going too deep into the properties of more complex 1D systems, it is important to say a word about methods. Indeed, as mentioned earlier the special nature of 1D system, invalidates many of the methods commonly used in higher dimensions such as naive mean-field theory. Methods specific to one dimension had to be developed and met with considerable success. I will examine some of them here, confining myself to the simple situations. More sophisticated cases will be mentioned together with the novel problems they refer to in the Section "Key issues and future directions."

The first type of method that comes to mind when discussing 1D systems is the Bethe ansatz (BA). Indeed, in one dimension and for very specific models it is possible to write the wavefunction of the fundamental exactly and to understand the excitations. This method, pioneered by Bethe (1931), has allowed considerable progress to be made. In particular, thanks to the works of E. Lieb, systems such as interacting bosons (Lieb and Liniger, 1963) and interacting fermions on a lattice (Hubbard model) (Lieb and Wu, 1968) could be explored in depth. The method has, however, the drawback of being limited to integrable models, and very often whether the model is integrable or not is the only information that one can extract. It is also difficult to ascertain how generic is the integrable model. Despite this limitation, this method has been extremely useful, leading to a good understanding of the excitations and the thermodynamics of several 1D models. During the last 20 years or so it has seen extremely strong progress, and now even physical correlation functions of important models such as the Lieb-Liniger model or the *XXZ* spin chain can be computed. I will also come back to this method when dealing with the more complicated case of out of equilibrium physics in the Section "Key issues and future directions." The method allows one to deal both with models in the continuum (Lieb-Liniger model of bosons) or on lattices (Fermi Hubbard model), and is of course able to deal with both finite size systems and the thermodynamic limit of an infinite size system.

The second class of method includes the numerical ones. One dimension is well adapted from the start to such methods since boundaries are quite small (on 100 sites the boundary is only 2 sites, while in two dimensions a 10 × 10 equivalent system would have a boundary of 36 sites). This makes methods such as exact diagonalization that give an essentially exact numerical answer much more efficient in one dimension (typically able to treat about 40 sites for spin 1/2 systems). Of course, all the standard numerical methods (e.g., quantum Monte-Carlo) can be used in 1D with essentially the same limitations as in higher dimensions. In addition, 1D has led to the development of specific methods that have played a major role. This is in particular the case of the so-called Density Matrix Renormalization Group (DMRG) method, invented by White (1993). This method is essentially a highly intelligent variational approach where an optimal wave function approaches the ground state in an *unbiased* way. This method has given access to static correlation functions with an unprecedented level of accuracy. It was then recast in the more general framework of matrix product states, which allowed extending it more easily to dynamical correlations and time-dependent Hamiltonians than was possible in the past. As a result, the application of this method has literally exploded in the last 20 years or so to make it an indispensable tool for the properties of 1D systems. As a result, many properties (both static and dynamics) of 1D systems (even made by a limited number of 1D legs) can be computed. Importantly, at variance with methods such as for example, quantum Monte Carlo this method does not suffer from growing errors (the so-called sign problems) and can be used generally for 1D systems. It is limited by the growth of entanglement, and thus although it works well for pure 1D systems its computational cost becomes rapidly prohibitive for coupled chains. To give some numbers, the equilibrium properties of a 1D system of typically 100 sites can be computed down to energy resolutions of $J/20$, where J is the typical energy scale of the system. This is often better than the resolution of the probe itself and, for example, structure factors of spin chains and ladders could be computed brute force with this method. It is particularly well adapted to systems on lattices, and of course is essentially exact at all energies for a given microscopic Hamiltonian.

Last but not least, 1D systems have been studied via field theory methods. The best known is called bosonization and consists of rewriting the single particle excitations of the system in terms of the collective excitations (sound waves). Given the peculiar nature of 1D, this "change of variables" is possible. The denomination is historical since it was first applied to fermionic systems for which the spectrum can be linearized near the Fermi points, allowing an analysis that becomes semicontrolled in the curvature of the dispersion relation. But this is a generic procedure, as beautifully shown by Haldane (1981a), so the important part is not so much the change of statistics as the "collectivization" of the degrees of freedom. As with any field theory, the applicability is limited to low-energy properties (long distance compared to, e.g., a lattice spacing and long times compared to an elementary time, which is the inverse of the typical energy scale). Field theory has thus the drawback of being limited to low energies and to depend on a certain number of phenomenological couplings (such as, e.g., a high energy cutoff). It has on the other hand the advantage of being quite generic and of immediately incorporating in a unified field description many different microscopic models. It is thus particularly well adapted to condensed matter problems for which we usually know poorly the real microscopic Hamiltonian (which usually contains a complicated energy-dependent screened Coulomb interaction) and for which the typical energy scales, bandwidth, or spin exchange constants are usually in the thousands of Kelvins. The phenomenological parameters are thus as good as the "original" parameters of the Hamiltonian. The field theory allows for a very simple description of the system and because it uses the right collective basis the Hamiltonian is already in a much more diagonal form than when written in terms of single particles. Thus the bosonization methods have allowed the cracking of extremely simply models or those as complicated as the Lieb-Liniger model or the fermionic Hubbard model. Much more importantly, since it is a dictionary it can be used as a stepping stone to tackle much more complicated problems (many degrees of freedom, several chains, etc.).

These three classes of methods have thus played an important role in our understanding of 1D systems. But each one of them has its own limitations, as already mentioned. BA is restricted to specific models and it is difficult to extract nonthermodynamics

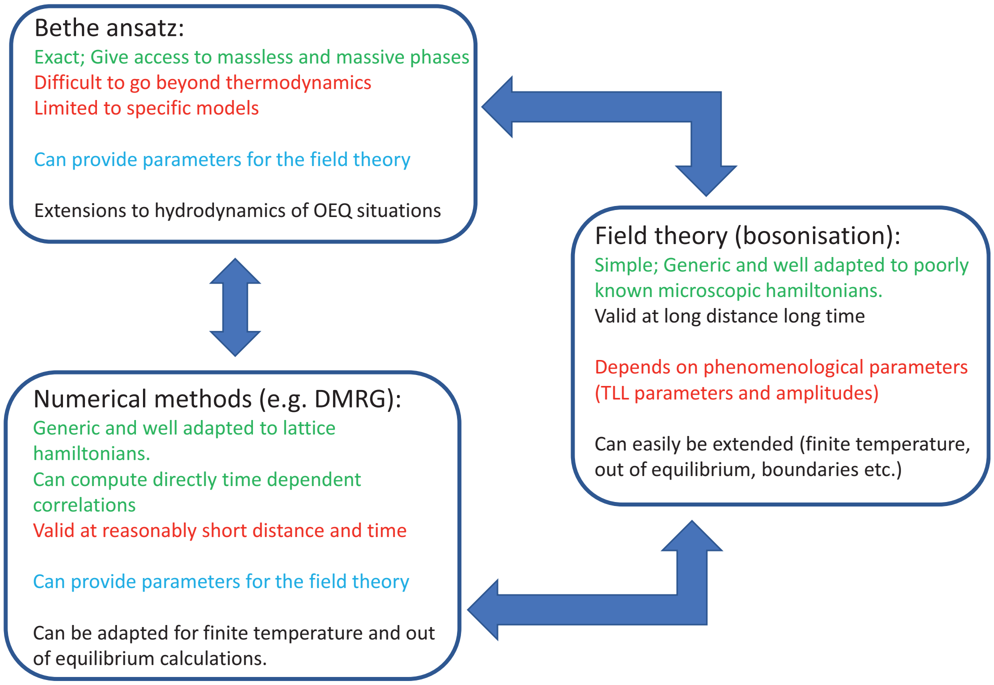

Bethe ansatz:
Exact; Give access to massless and massive phases
Difficult to go beyond thermodynamics
Limited to specific models

Can provide parameters for the field theory

Extensions to hydrodynamics of OEQ situations

Field theory (bosonisation):
Simple; Generic and well adapted to poorly known microscopic hamiltonians.
Valid at long distance long time

Depends on phenomenological parameters (TLL parameters and amplitudes)

Can easily be extended (finite temperature, out of equilibrium, boundaries etc.)

Numerical methods (e.g. DMRG):
Generic and well adapted to lattice hamiltonians.
Can compute directly time dependent correlations
Valid at reasonably short distance and time

Can provide parameters for the field theory

Can be adapted for finite temperature and out of equilibrium calculations.

Fig. 3 Symbiosis between the three main methods used in one-dimensional systems. *Green* shows the advantages of the method, *red* the main drawbacks, and *blue* some of the connections between the methods. The possibility of having these three methods working in symbiosis and used in the range of energies or parameters for which they are the most efficient has allowed solutions for most of the 1D simple problems.

quantities. Numerics is good for short times and distances and becomes inefficient at too large times and distances. Field theory rests on certain phenomenological parameters and is only efficient at large distances and times. What was remarkable in the last 20 years is that the 1D community has learned to use these methods in symbiosis and thus practically obtain a complete and semiexact description of simple 1D physics, as shown in Fig. 3. Numerics is used to obtain *directly* the correlation functions at intermediate time and distance for a given microscopic model. As mentioned, this already allows going quite far in distance and time. Moreover, using a trick developed by Haldane (1980), one can also use the numerics to obtain essentially *exactly* the phenomenological parameters, such as the TLL parameters and the amplitudes that need to be injected in the field theory. These parameters can also be extracted from the BA when available. This allows an essentially *quantitatively* exact field theory that can then be used to get the large distance and large time behavior of the correlation functions, in regimes that the numerics could simply not reach. This method has been used with great success and has allowed us to obtain essentially exact descriptions of various 1D systems, and is has put us in a unique position to use these tools to tackle more complicated situations.

Complications

Before discussing to the most active problems in the Section "Key issues and future directions", let us first examine three especially interesting complications of purely 1D systems that have been particularly fruitful and are the backbone of some of the current studies in the field.

Mott transition

As indicated earlier, 1D systems are exceptionally sensitive to perturbations, given the quasilong range order existing in several correlations. This is in particular the case for the density, and thus the effect of a lattice can be particularly important. The lattice can be either put as a weak perturbation on top of a continuum model $\int dx \cos(Qx)\rho(x)$ or can exist from the start if the model is defined on a lattice, such as, for example, Hubbard models. In both cases it is well known that the combination of lattice and interactions can lead to new insulating phases. This is the well-known Mott transition for which, at commensurate filling, the interaction can turn a metal or a superfluid into an insulator. The lattice breaks the continuous translational symmetry into a discrete one, which can be broken even in 1D at zero temperature. As a result, Mott phases exist. There are too many to be mentioned here, so some of them are pictorially shown in Fig. 4. An important difference compared to higher dimensions is that in 1D the Mott phase can be reached even for an *arbitrarily weak* lattice, provided the system is interacting enough. This has been beautifully evidenced by experiments in cold atomic gases with bosons at one particle per site. On the field theory side, the Mott transition at constant density (Mott-U transition) when the interaction is varied is described by an effective sine-Gordon theory. It is thus in the universality class

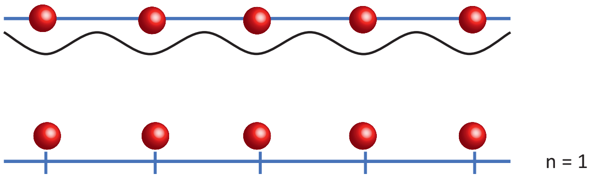

Fig. 4 Top: Particles in a continuum system to which a small periodic lattice has been added. In 1D if the repulsion between the particles is large enough, even a very small lattice much smaller than the kinetic energy of the particles can lead to a Mott insulator phase with one particle at each lattice minimum. Bottom: a tight binding model where the particles jump from site to site. Here we get only a discrete translational symmetry, and the repulsion between the particles can again lead to a Mott insulating phase, shown here with exactly one particle per site.

of the celebrated Berezinskii–Kosterlitz–Thouless (BKT) transition and indeed a mapping exists between the 1D quantum model and the two-dimensional classical XY model that is the seat of the BKT transition. This also illustrates the importance of topological excitations, as mentioned earlier. Measurements of the quantum phase transition between the Mott and the superfluid phase of bosons is in effect one of the very precise tests of the universal character of the BKT transition. The Mott transition can also occur for other commensurate fillings depending on the statistics and is always described by a modified sine-Gordon Hamiltonian. Quite interestingly, one can also study the transition when the density is varied (Mott-δ transition). The nature of the transition is very different, being now mappable on the so-called commensurate–incommensurate or Pokrovsky–Talapov transition. This transition, which corresponds to free fermions close to an empty band, has different critical exponents (for example, $z = 2$ for the dynamical exponent relating energy to momentum, contrarily to $z = 1$ for the Mott-U transition) and can also be studied and measured in great details, for example in quantum spin systems. The ability to describe such transitions is one of the clear successes of the field theory description (bosonization) of 1D systems.

Effect of disorder or quasiperiodic potentials

Another very important class of problems, somewhat connected to the case of the Mott transition, is the effect of disorder on 1D systems. Indeed, it has been known since the works of Anderson that even an infinitesimal disorder can transform a 1D interacting system from a system made of delocalized wave functions to a system where all the eigenstates are exponentially localized. This is the celebrated Anderson localization. A crucial question is, of course, how the interactions can affect this behavior, leading to the question of the localization or not of interacting particles (LIPs) For one-dimensional systems this problem can be studied in a similar way to the Mott transition by adding a term $\int dxV(x)\rho(x)$ to the Hamiltonian, where $V(x)$ is a suitable random potential. Of course, many other terms are possible, such as random hopping or quasiperiodic potentials, which have been studied both theoretically and experimentally. Field theory and numerical descriptions allow this problem to be tackled even in the case of interacting fermions and bosons and to show that the localization resists in the presence of interactions and to compute the effect of interactions on the various properties of the system. For example, for one-dimensional interacting bosons a quantum phase transition exists between a superfluid phase for moderately repulsive bosons to a Bose glass phase that is localized when the repulsion between bosons exceeds a certain threshold. This phase was also analyzed for quasiperiodic potentials and was realized experimentally in cold atomic systems. Similar results were obtained both for localized fermions and quantum spins.

One interesting question is how interactions affect the transport properties of the localized phase. This question is interesting both for the frequency dependence of the conductivity and for its temperature dependence. The frequency dependence can be computed exactly for the noninteracting system and by using the field theory and numerical approaches for the interacting one, showing a deep change of the properties both in terms of the localization length and the frequency dependence as a function of the interactions. The temperature effects are more subtle and have been the subject of intensive studies recently. In the presence of an external bath allowing exchanges of energy between the system and the bath (such as phonons), the answer was provided for the noninteracting system by Mott and is known as Mott's variable range hopping. Extensions to the case of Coulomb interaction in high dimensions were given by Efros and Schlovskii. The field theory analysis of the one-dimensional interacting system confirmed this expression and computed fully the conductivity, which becomes a function of the TLL parameters. One important question was, however, what happens in the absence of an external bath, and it was proposed that the system would stay perfectly insulating even at finite temperature. This is the so-called many-body localization (MBL) problem. Extensions of this problem allow one to ask whether even at infinite temperature the system would have a transition from a localized phase where the system is not ergodic to a phase where ergodicity is restored. Experiments in cold atoms allowed probing of these this questions.

Coupled chains

Last but not least, one important extension of 1D systems consists of coupling 1D units. This is a very natural thing to study in view of how most 1D realistic systems are constituted. In addition to looking at the coupling of an infinite number of chains as mentioned in the Section "Fundamental concepts for 1D systems" it is interesting to look at a small coupling of 1D units (ladders). This is relevant both for a certain number of experimental systems, and also from a purely theoretical point of view. Indeed, as was shown spectacularly by Haldane by looking at the dependence on the size of the spin *S* of the properties of a spin *S* chain, the properties are not smoothly evolving. There has thus been considerable activity to determine the properties of coupled chains both for a finite number of chains and for the infinite number of chains.

The question of a finite number of chains (so called ladder physics) has led to numerous studies. For spin systems this problem is deeply linked to the Haldane problem and a finite number of chains shows the same nonmonotonous dependence (two leg ladders have gapped excitations, while three legs have dominant antiferromagnetic correlations). This study is directly relevant for a certain number of experiments in quantum spin systems and such systems have even been used with success as quantum simulators. In a similar way, coupled bosonic ladders have been realized in cold atomic gases or in Josephson junction systems. A set of interesting questions comes from the competition between an insulating phase provoked by, for example, a Mott potential and the effect of interchain hopping that promotes superfluidity. Another different set of questions occurs when such ladders are subjected to an external magnetic flux. Indeed, the system becomes then a 1D variant of a superconducting film and the question of how currents at the edge and/or vortices can be observed is a nontrivial one that has been the subject of intense studies, given the realization of such systems in cold atomic gases. Fermionic ladders are the most surprising. The hopping of fermions, contrarily to the hopping of bosons or spin exchange, has no classical limit and thus cannot be treated by conventional mean-field theories. The treatment of this coupling is thus quite complicated and has succeeded thanks to the progress both in the field theories and numerics. The answers are quite surprising and two leg fermionic ladders have exhibited *d*-wave superconductivity stemming from *repulsive* local interactions. This remarkable result, which gives us one of the very few controlled paths to exotic superconductivity, is intensively studied both theoretically and more recently in cold atom experiments.

The other limit is that of coupling from the start an infinite number of chains and trying to address the question of the dimensional crossover between the 1D behavior with all the exotic excitations and the more conventional high dimensional one (in, e.g., three dimensions). For spin and bosons, a mean field treatment of the interchain coupling is usually possible in the absence of frustration, between the chains, and leads to conventional order with deeply modified critical temperatures and even order parameters due to the 1D nature of the elementary brick in the system. Such behavior could be quantitatively tested in quantum spin systems. For example, the confinement of spinons due to the presence of more than a 1D chain has been successfully observed, as well as the ordering of quantum ladder systems. Competition between 1D phases such as Mott and those provoked by the increased delocalization coming from the interchain coupling is also a deep class of problems. Although the mean-field description for spin and bosonic systems has been deeply successful in the absence of frustration the fact that we know now very well the behavior of the elementary 1D units also shows us its limitations. When frustration is present, the problem is essentially unsolved. This is also the case for fermions for which the question of the dimensional crossover between 1D and, for example, 3D is essentially open. The question of coupled chains is thus clearly one of the main challenges of 1D physics.

Key issues and future directions

The previous sections presented the success in describing 1D physics. This section discusses the main open issues in the field or those on which active research is currently being done. It also describes the trends and future directions.

One clearly exploding direction is that of studying systems that are out of equilibrium, whether because of a quench, or simply because the system is put in either a periodic (Floquet) perturbation or simply between reservoirs that impose a steady state (transport). This is clearly a novel situation for which most of the tools that were efficient in equilibrium have to be either adapted or invented anew. The field is far too broad and active to be fully described here, so I will simply give some examples. For quenches, efficient field theory descriptions had to be obtained both for massless and massive theories. But given that quenches occur on a very short timescale, the question of the possibility of a field theory description has to be raised. It is thus interesting to find more exact methods that could describe the system at all scales and at the same time take into account the nonequilibrium character. A promising development is provided by the so-called generalized hydrodynamics, a method merging the exact description of BA with the hydrodynamic nature of an out-of-equilibrium fluid. This method has already allowed the description of highly nontrivial experiments in cold atomic gases. Of course, as with any out-of-equilibrium situation the question of the asymptotic state and its thermalization, or not, is an important question that has been addressed both theoretically and experimentally. Finally, stimulated by experiments in cold atomic systems that could probe the transport through a one-dimensional structure attached through a variety of reservoirs with or without interactions, various properties of transport are currently being studied. This implies the development of new methods (for example, using the Keldysh formalism). Such situations are clearly an extremely active field at the moment.

A second direction for isolated chains involves the effects of disorder and related potentials (quasiperiodic, etc.). Although this question has been already intensively studied as discussed in the previous section, many open questions remain. This is in particular true for most of the transport quantities at finite temperature that still resist precise calculations. At infinite temperature, the very question of an MBL transition is still under debate and new methods are needed to attack this problem. Another important direction of research for isolated chains is the effect of boundaries and the presence of topological states at the edge. Most of the studies were done in the absence of interactions and of course in one dimension a very natural question comes from the very presence of interactions.

Finally, one of the most open and exciting directions is the way to go from the 1D world to the higher dimensional one. Given the reliability of field theory and numerical methods to obtain the 1D properties, it is a very natural route to explore how to couple these structures together. This can lead to novel emerging properties, as was the case for fermionic ladders, but this is certainly a way to also attack the problem of the higher dimensional strongly correlated systems – a major remaining challenge in the field. It is of course also directly relevant to a large number of experimental realizations. Quite remarkably, the studies resting on mean-field descriptions have shown the great success of such approaches for bosons and spins, but also their very strong limitations. So, new methods are being tried, such as doing mean field on larger structures such as ladders or trying to incorporate fluctuations from the start beyond the mean-field description. For fermionic systems, the challenge is considerable, and going through the quasi-one-dimensional route might be a way to avoid some of the pitfalls posed by direct numerical attack on high dimensional fermion problems. It also leads to interesting phenomena, such as confinement of 1D excitations or, on the contrary, to deconfinement of certain insulating phases, given the extra kinetic energy introduced by the higher dimensional coupling. All these questions, going using the generic name of dimensional crossover, are extremely strong challenges that are currently pursued by a combination of analytical and numerical methods.

Conclusion

This chapter gives a brief tour of the remarkable physics of interacting one-dimensional quantum systems. The very presence of interactions and the impossibility of the particles avoiding each other in 1D leads to a remarkable set of properties: all the excitations become collective excitations and thus individual excitations as such, as we know in the higher dimensional world, do not exist any more, but decompose into these collective ones. This leads to a set of remarkable features, such as the fractionalization of excitations, as well as the very natural presence of topological properties. Most of the properties of simple 1D models, whether bosons, spins, or fermions, can be summed up into a simple effective model known as the TLL model, characterized by very few constants that control the decay of all the correlations of the system. Thus 1D systems constitute remarkable laboratories in which the quantum effects, with all their quirks and remarkable features, are at their maximum. They are poised at the verge of instability, which makes them very sensitive to perturbations such as disorder, lattices, or coupling between 1D units.

The 1D field, although explored extensively since the 1960s, has known incredible developments with the coming of the 21st century. Regarding methods, novel methods have appeared or been refined, whether on the analytical front or on the numerical one. More importantly, a way to make the complementary methods of exact solutions, numerics, and field theory work together has been found, allowing each method to be used in the energy range for which it is the most efficient, thus leading to an essentially exact description at all energies. At the same time, novel questions have emerged that have pushed these new methods to their limits, such as the study of edges and topological states, novel perturbations such as strong spin–orbit coupling, and out of equilibrium physics: quenches and their consequences on the physics of the systems and its thermalization or even transport properties in clean and disordered systems. Last but not least, the experimental realizations have exploded, both with the advent of cold atomic gases that have provided an incredible laboratory in which to study 1D physics, and also with novel realizations in condensed matter providing controlled realizations to study such physics.

The 1D physics is thus a very active field at the moment, with both solid solutions and also incredibly challenging problems. It is not only interesting to study by itself, but also provides a path to tackle the questions posed by higher dimensional systems.

References

Bethe HA (1931) Zur theorie der metalle. *Zeitschrift Fur Physik* 71: 205.

Haldane FDM (1980) General relation of correlation exponents and spectral properties of one-dimensional Fermi systems: Application to the anisotropic $S = \frac{1}{2}$ Heisenberg chain. *Physical Review Letters* 45: 1358.

Haldane FDM (1981a) Effective harmonic-fluid approach to low-energy properties of one-dimensional quantum fluids. *Physical Review Letters* 47: 1840.

Haldane FDM (1981b) Luttinger liquid theory' of one-dimensional quantum fluids. I. Properties of the luttinger model and their extension to the general 1D interacting spinless Fermi gas. *Journal of Physics C* 14: 2585.

Lieb EH and Wu FY (1968) Absence of Mott transition in an exact solution of the short-range, one-band model in one dimension. *Physical Review Letters* 20: 1445.

Lieb EH and Liniger W (1963) Exact Analysis of an interacting Bose gas. I. The general solution and the ground state. *Physical Review* 130: 1605.

White SR (1993) Density-matrix algorithms for quantum renormalization groups. *Physical Review B* 48(14): 10345.

Further reading

Cazalilla MA, Citro R, Giamarchi T, Orignac E, and Rigol M (2011) One dimensional bosons: From condensed matter systems to ultracold gases. *Reviews of Modern Physics* 83: 1405.

Giamarchi T (2004) Quantum Physics in one Dimension. *International Series of Monographs on Physics.* p. 121. Oxford University Press.

Gogolin AO, Nersesyan AA, and Tsvelik AM (1999) *Bosonization and Strongly Correlated Systems*. Cambridge University Press.

The Hubbard model and the Mott–Hubbard transition

Massimo Capone, International School for Advanced Studies (SISSA) and CNR-IOM, Trieste, Italy

© 2024 Elsevier Ltd. All rights reserved.

Introduction 914
Overview 915
The Mott–Hubbard metal–insulator transition 916
Dynamical mean-field theory 918
Key issues 918
The Mott–Hubbard transition in DMFT 918
Multiorbital Hubbard model 920
Role of the Hund's coupling 921
Conclusion 921
References 922

Abstract

We introduce the Hubbard model as the paradigmatic model of materials with strongly correlated electrons. For integer filling the model undergoes a Mott–Hubbard transition as a function of the interaction strength from a metal to a Mott insulator with localized electrons. We briefly introduce Dynamical Mean-Field Theory, a powerful nonperturbative method which provides a comprehensive picture of the Mott transition. We comment about the role of multiorbital electronic structure and the Hund's coupling.

Key points

- To introduce the Hubbard model and some historical aspects
- To introduce the Mott–Hubbard transition
- To present the Dynamical Mean-Field Theory and its scenario for the Mott transition
- To provide some information about multiorbital Hubbard models and the Hund's coupling

Introduction

The Hubbard model plays a central role in modern condensed matter physics as the paradigmatic description of materials with narrow electronic bands, in which the screened Coulomb interaction leads to strong correlations between the electrons. It describes electrons hopping via quantum tunneling between the sites of a lattice and experiencing a local Coulomb repulsion which couples two electrons with opposite spin on the same lattice site, and it can be seen as a refined tight-binding model where a screened Coulomb interaction is added to the Hamiltonian describing electrons hopping between ions arranged in a periodic crystal.

The model has been first introduced independently in Hubbard (1963), Kanamori (1963), and Gutzwiller (1963) as a minimal description for narrow-band materials such as transition metals and transition metal oxides. The main motivation of these pioneering studies was the understanding of itinerant ferromagnetism, but the scope of the model turned out to be much wider. Transition metal oxides have indeed rich and complex phase diagrams, featuring different magnetic phases and metal–insulator transitions (Imada et al., 1998), as well as different fascinating phenomena including high-temperature superconductivity (Bednorz and Müller, 1986).

The Hubbard model has been shown to provide a theoretical framework to study one of the most distinctive properties of transition metal-based materials, namely, the existence of an insulating state when the electron count would imply a partially filled band (or equivalently an odd number of electrons per unit cell), in sharp qualitative contrast with the prediction of the band theory of solids. The discovery of this phenomenon dates back to de Boer and Verwey (1937), and it was shortly followed by the seminal proposal by N. Mott, who identified the interaction between electrons as the cause of the insulating state (Mott and Peierls, 1937). For this reason, these insulators have been called Mott insulators, and the transition between the Mott insulating state and a metal, which can be driven by chemical substitution, pressure, doping, and other control parameters, has been baptized as the Mott–Hubbard transition.

The field of transition metal oxides was revolutionized in 1986 after the discovery of its most influential members, a class of layered copper oxides displaying a superconducting state with large critical temperatures and many anomalies with respect to standard superconductors (Bednorz and Müller, 1986). In these materials, usually referred to as cuprates, the stoichiometric

https://doi.org/10.1016/B978-0-323-90800-9.00223-7

compound is an antiferromagnetic Mott insulator which turns into an exotic superconductor with d-wave symmetry when doped, suggesting a close and surprising relation between the physics of Mott insulators and superconductivity.

Following an incredibly influential proposal (Anderson, 1987), the vast majority of the scientific community identified a two-dimensional Hubbard model (or the related t-J and Emery models) as the main building block to describe these systems owing to their large anisotropy and the Mott insulating character of the undoped materials. The two-dimensional modeling is justified by the large anisotropy of the cuprates and by the ubiquitous presence of copper-oxygen layers in all the different compounds of the family.

The link with high-temperature superconductivity turned the Hubbard model into a cornerstone of modern condensed matter physics and led to the creation and the development of a variety of methods aiming at a solution of the model. For the reasons we mentioned above, the community largely focused on the two-dimensional case which turned out to be a formidable challenge for theoretical investigations.

It is indeed almost impossible to summarize the collective effort to solve the two-dimensional Hubbard model in a complete and unbiased way and without making oversimplifications. The holy grail of this research has obviously been the understanding of the origin of superconductivity in a system dominated by the repulsion (Maiti and Chubukov, 2013), but several other questions have been almost equally debated, including the possible deviation form a normal Fermi-liquid of the metallic state, the existence and the origin of a pseudogap region (Lee et al., 2006), and the presence and role of quantum critical points (Sachdev, 2010) and charge instabilities (Castellani et al., 1995).

Despite the huge advances in the understanding of all these phenomena, we can not consider neither of them "solved". For these reasons, in this manuscript we will not discuss the Hubbard model in relation with the properties of the cuprates and the investigations of the two-dimensional system, for which we refer to recent reviews and collaborations (LeBlanc et al., 2015; Schäfer et al., 2021; Qin et al., 2022; Arovas et al., 2022).

Even if the lack of a general consensus on some aspects of the phase diagram of the two-dimensional Hubbard model could lead to conclude that this impressive collective effort did not reach its goal, it certainly led to a huge advance of our understanding of strongly interacting quantum many-body systems both in terms of methodology and in terms of novel concepts which apply to a wide class of materials.

In particular, we have reached an unprecedented understanding of the physics of Mott transitions, of Mott insulators, and of the strongly correlated metallic phase. In this chapter we focus on this latter aspect, namely, the theoretical description of the Mott–Hubbard transition. In particular, we will introduce the dynamical mean-field theory, a powerful theoretical method which led to an important paradigm shift in the field of strongly correlated systems and a novel picture of the Mott transition, which represents a central starting point for the theoretical study of a number of strongly correlated materials. Among the many directions in which the DMFT picture of the Mott transition has been extended, in Section "The Mott–Hubbard transition in DMFT" we address the role of a multiorbital electronic structure and the Hund's coupling.

Overview

The Hubbard model describes quantum particles (here spin-1/2 fermions describing the electrons of a solid) moving in a lattice and experiencing a repulsive interaction when two of them are on the same lattice site. The Hamiltonian reads

$$\hat{H} = -t \sum_{\sigma,\, \langle i,j \rangle} \left(\hat{c}^{\dagger}_{i\sigma}\, \hat{c}_{j\sigma} + \text{h.c.} \right) + U \sum_{i} \hat{n}_{i\uparrow}\, \hat{n}_{i\downarrow}\ , \tag{1}$$

where $\hat{c}_{i\sigma}$ and $\hat{c}^{\dagger}_{i\sigma}$ are annihilation and creation operators for fermions with spin σ on the site i of a given lattice of N sites and the operator $\hat{n}_{i\sigma} = \hat{c}^{\dagger}_{i\sigma}\, \hat{c}_{i\sigma}$ is the local occupation operator for the spin species σ. The sum in the first term is restricted to pairs of nearest neighboring sites. The key control parameters are the amplitude t for a quantum tunneling (hopping) between nearest neighbor sites of a lattice and the on-site interaction between different spin species U. The other control parameter is the total filling $n = \frac{1}{N}\sum_{i\sigma}\langle \hat{n}_{i\sigma}\rangle$. The model can be seen as extremely simplified, even if absolutely nontrivial, description of materials in which narrow bands arise from orbitals which are localized around the ionic positions and the electron–electron interaction in the valence band is strongly screened by the valence electrons. As a general trend, these conditions are realized in compounds based on transition-metal atoms, where the 3d orbitals are partially filled, or rare-earth atoms with partially populated 4f levels.

The localized nature of the relevant 3d and 4f orbitals justifies to limit the hopping amplitude to nearest neighboring sites and to consider only the local components of the Coulomb interactions, as assumed in Eq. (1). The standard version of the Hubbard model (1) only contains hopping between nearest neighbor sites of the lattice, but the description of different materials usually requires to include also long-range hopping terms. We notice that the inclusion of more complete and realistic structure of hopping does not change significantly the properties of the model and it does not imply a relevant complication of the theoretical description. On the other hand, the inclusion of nonlocal interactions represents a more substantial change which can affect the physics of the model in a deeper way.

A further typical simplification assumed in Eq. (1) is to consider only one orbital per site. While this choice seems natural and justified for the high-temperature superconductors based on copper, where the electron count leads to nine electrons hosted in the

3d orbitals, many other strongly correlated materials and Mott insulators have indeed a multiorbital electronic structure, which may lead to remarkable novel phenomena that we briefly comment in Section "Key issues".

Despite its formal simplicity, Eq. (1) defies an exact solution except for the peculiar one-dimensional case (Lieb and Wu, 1968). As we anticipated in the introduction, the search for accurate solutions of the Hubbard model has been accelerated by the discovery of high-temperature superconductivity in the family of doped Mott insulators based on layers of copper and oxygen. The strong anisotropy of these materials prompted for an understanding of the two-dimensional Hubbard model, which became the subject of countless investigations and triggered the development of a variety of theoretical methods ranging from analytical (Arovas et al., 2022) to numerical approaches (Qin et al., 2022).

We emphasize that this collective enterprise has many facets. On one hand, a part of the community focused on fundamental aspects, among which the central role is the origin of superconductivity and the very question about how superconductivity can arise in a system dominated by the repulsive Coulomb interaction. Many other studies have instead aimed at a closer connection with the properties of superconducting cuprates, including material-dependent aspects. The immense body of work dedicated to these issues has advanced our understanding of all these phenomena, confirming to a large extent that the Hubbard model contains most of the relevant physics. Yet, the debate is still lively and open and only a few final answers have been given.

In this work we do not address these issues and we focus on a more general phenomenology which is not limited to two dimensions, namely, the interaction-driven Mott metal–insulator transition. We argue that this is the most direct and paradigmatic fingerprints of the electronic correlations driven by the large interaction, and its understanding is a fundamental step to address more specific questions, including those related to high-temperature superconductivity.

The Mott–Hubbard metal–insulator transition

The Hubbard model realizes the early proposal by N. Mott that the mutual interaction between electrons—neglected or treated approximately in the band theory of solids—is the reason for the insulating behavior of several transition-metal oxides with partially filled bands and of the transition between this Mott insulating state and a metal.

We stress that the main focus of this work is on a paramagnetic Mott transition where spatial symmetries are broken neither in the charge nor in the spin channels. In this way, we isolate the inherent effect of electron–electron interactions localizing the electrons from the gap opening associated with magnetic ordering. Even when the low-temperature region of the phase diagram features broken-symmetry solutions, the finite-temperature phase diagram will typically host a transition between a metal and a paramagnetic Mott insulator, a phenomenology which is indeed realized, for instance, in V_2O_3 (McWhan et al., 1973). In this section we discuss some basic arguments about the Mott transition and its relation with magnetism.

The very existence of the Mott insulating state, its magnetic ordering, and the metal–insulator transition can be predicted based on simple arguments even if, as we shall see, a comprehensive description and characterization of the Mott–Hubbard transition require to use advanced many-body methods able to treat the strongly correlated regime.

- In the *noninteracting limit* $U = 0$, the model (1) is solved exactly by Fourier transforming to momentum space, leading to a single band with a dispersion $\varepsilon(k)$ which depends on the chosen lattice. As a consequence, for every filling n different from zero and two, the model describes a metal with partially filled bands. This result does not change introducing long-range hopping amplitudes.
- In the *atomic limit* $t = 0$, the Hamiltonian simply counts the number of doubly occupied sites in which two electrons are present on the same site. It follows that, in the half-filling case $N = 1$, where the number of electrons is equal to the number of sites, there is an infinite number of degenerate ground states, each with one electron on each lattice site. When a small hopping $t \ll U$ is included, the degeneracy between these states is broken, but the system remains in the subspace with zero doubly occupied sites. At half-filling every hopping of an electron would imply the creation of a doubly occupied site and it is therefore forbidden, leading to a localization of the carriers which realizes nothing but the correlation-driven insulator proposed by Mott.

Thus, the half-filled Hubbard model with $N = 1$ has a metallic ground state in one extreme limit ($U \ll t$) and an insulating one in the opposite one ($U \gg t$). As a consequence, we expect a metal–insulator transition as a function of the ratio U/t to take place at zero temperature. The simple solution in the two extreme limits also provides us with a rationale of the difficulties to solve the model for arbitrary U/t. The model, in its simplicity, describes a paradigmatic competition between a hopping term, which is diagonal in momentum space and leads to delocalized electronic states, and an interaction term, which imposes constraints that favor localization in real space, where it is clearly diagonal.

This evolution of the system as U/t increases and the Mott transition can be described in terms of a progressive reduction of the quantum probability to have doubly occupied sites in the ground state D. For $U = 0$, we easily find that the total amplitude of doubly occupied states is $D = \frac{1}{4}$. As U increases, we expect less and less doubly occupied sites until for $U \to \infty$, $D = 0$. In the same process, the electron motion becomes harder and harder because every hopping that leads to a doubly occupied site is inhibited. At some critical value of U, we can expect that the coherent electronic motion is impossible and the electrons become localized as in the atomic limit. This interaction-driven localization is the essence of the Mott–Hubbard transition that we address in this work.

There is, however, a further complication, or enrichment, if we consider the possibility of broken-symmetry magnetic solutions. One can prove that, for nearest neighbor hopping and for bipartite lattices, the ground state of the Hubbard model is an antiferromagnetic insulator for every $U/t \neq 0$ (Lieb, 1989). This is measured by a finite staggered magnetization

$$m = \frac{1}{N}\sum_i (-1)^{R_i} \langle \hat{n}_{i\uparrow} - \hat{n}_{i\downarrow} \rangle. \tag{2}$$

The origin of the antiferromagnetic order can be rationalized in strong coupling $U \gg t$ through a strong coupling calculation that shows that the Hubbard model maps onto a Heisenberg model with positive exchange interaction (MacDonald et al., 1988)

$$H_{SC} = J\sum_{\langle i,j \rangle} \mathbf{S}_i \cdot \mathbf{S}_j, \tag{3}$$

where $\mathbf{S}_i$ is the vector of the local spin-1/2 operators describing localized electrons. The positive J favors configurations where spins of neighboring sites have opposite direction. In a bipartite lattice (a lattice which can be partitioned in two sublattices A and B in such a way that the hopping only connects A sites with B sites, such as the square and cubic lattices) one can then build a full antiferromagnetic solution on the whole lattice in which every nearest neighbor bond has the energetically favored configuration.

An antiferromagnetic insulating ground state can also be derived through a Hartree–Fock mean-field approach, which is expected to be a reasonable approximation in weak coupling. For bipartite lattices, such as the square and cubic lattices with only nearest neighbor hopping, antiferromagnetism is stable for any nonzero U. If we include next-nearest neighbor hopping, the antiferromagnetic state requires a minimum critical value of the interaction to be stabilized (Lin and Hirsch, 1987).

The weak-coupling Hartree–Fock magnetism and the strong coupling theory that we described are indeed adiabatically connected. The ground state of the Hubbard model is thus an antiferromagnet for every value of U/t. Increasing this ratio we continuously evolve from the itinerant magnetism found in Hartree–Fock (Slater, 1951) to the local moment picture of strong coupling (Sangiovanni et al., 2006).

The antiferromagnetic order is limited to $T = 0$ in two dimensions according to the Mermin–Wagner theorem (Mermin and Wagner, 1966), but it extends to finite temperature in three dimensions. Based on simple arguments, confirmed by many-body calculations (Kozik et al., 2013), the magnetic ordering temperature has the qualitative behavior reported in Fig. 1A as a *dashed line*, where a maximum is obtained for intermediate coupling, when neither of the two limiting approaches can be applied.

Therefore, if we focus on the ground state of the Hubbard model, the metal–insulator transition that we expected is replaced by an insulating magnetic state for any $U \neq 0$ and the only evolution happening from weak to strong coupling is a crossover between different kinds of antiferromagnetism. Nonetheless, the physics of the Mott transition that we discussed is expected to be relevant at finite temperature and in systems where the lattice frustrates magnetic ordering.

Precisely for these reasons, in the following we will mainly focus on the investigation of the Mott transition in a paramagnetic state where we discard the possibility of magnetic ordering, in order to disentangle the intrinsic Mott localization with the tendency toward magnetism. At the end of the discussion we will briefly comment about the relation between the paramagnetic Mott transition and magnetic ordering.

The history of the understanding and the theoretical description of the Mott–Hubbard transition are indeed deeply rooted with the introduction of the model. Among the most influential early attempts to study a Mott–Hubbard transition central roles are played by the methods introduced respectively by Hubbard and Gutzwiller. The former family of methods are based on truncation of the hierarchy of equations of motions for the Green's functions, while the latter is based on the variational principle and a wave function which includes real space constraints introducing a different weight for configurations with different numbers of doubly occupied sites starting from a noninteracting wave function. The two approaches turn out to be adequate for the two opposite limits

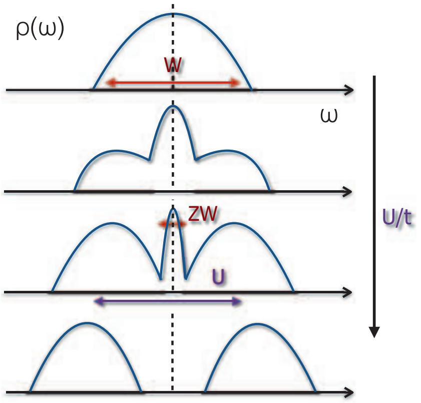

Fig. 1 Schematic representation of the evolution of the spectral function $\rho(\omega)$ within DMFT when the ratio U/t is increased from top ($U = 0$) to bottom ($U > U_c$, in the Mott insulating phase). The *vertical dotted line* marks the Fermi energy. W is the noninteracting bandwidth, ZW the width of the renormalized quasiparticle peak.

of weak coupling (Gutzwiller) and strong coupling (Hubbard), but neither of them provides a unified picture which is sufficiently accurate in both limits.

Dynamical mean-field theory

A turning point in the modern understanding of the Mott–Hubbard transition has been the development of Dynamical Mean-Field Theory (DMFT) (Georges et al., 1996), a powerful approach which treats accurately both limits of weak and strong interactions. While the origin of the method lies in pioneering investigations of the limit of infinite dimensions (Metzner and Vollhardt, 1989), the best way to understand the method is a quantum (or dynamical) version of a mean-field theory, where the effect of the rest of the lattice on a single site—representative of any other site—is described by a frequency (or time)-dependent effective field which is determined self-consistently. The self-consistency is enforced by assuming a local self-energy and that the Green's function of the effective local theory coincides with the local component of the lattice Green's function. The dynamical nature of the effective field substantially extends the scope of the method with respect to static mean field, allowing to study intrinsically many-body phenomena, among which the Mott–Hubbard transition has been the epitome.

Starting from the Hubbard model Eq. (1), DMFT defines an effective local theory for an arbitrary site "0" associated with the effective action

$$S_{eff} = \int d\tau \int d\tau' c^{\dagger}_{0\sigma}(\tau)\mathcal{G}_0^{-1}(\tau - \tau')c_{0\sigma}(\tau') + U \int d\tau n_{0\uparrow}(\tau)n_{0\downarrow}(\tau), \tag{4}$$

where τ and τ' are imaginary time variables, $c^{\dagger}_{0\sigma}$ and $c_{0\sigma}$ are Grassman fields associated with creation and annihilation of fermions with spin σ on site 0, $n_{0\sigma} = c^{\dagger}_{0\sigma}c_{0\sigma}$. The effective action describes the (imaginary) time evolution of site 0 in the presence of the local repulsion, which is controlled by the dynamical Weiss field $\mathcal{G}_0^{-1}(\tau - \tau')$, which contains the effect of the rest of the lattice on site 0. Similarly to a classical mean-field theory, the dynamical mean field is determined by a self-consistency condition which requires that the Green's function of the effective theory

$$G(\tau) = -\langle T c_{0\sigma}(\tau)c^{\dagger}_{0\sigma}(0)\rangle_{S_{eff}} \tag{5}$$

coincides with the local component of the lattice Green's function. Namely, in Matsubara frequencies

$$G(i\omega_n) = \frac{1}{N}\sum_k \frac{1}{i\omega_n + \mu - \varepsilon_k - \Sigma(i\omega_n)} \equiv \int d\varepsilon D(\varepsilon)\frac{1}{i\omega_n + \mu - \varepsilon - \Sigma(i\omega_n)}, \tag{6}$$

where $\Sigma(i\omega_n)$ is the Green's function of the effective theory, connected to the Weiss field and the Green's function by

$$\Sigma(i\omega_n) = \mathcal{G}_0^{-1}(i\omega_n) - G^{-1}(i\omega_n). \tag{7}$$

The three Eqs. (5), (6), and (7) are a closed set of equations that allow to find a self-consistent set of $\Sigma(i\omega_n)$, $\mathcal{G}_0^{-1}(i\omega_n)$, and $G^{-1}(i\omega_n)$. The lattice enters only via the self-consistency condition which depends on the noninteracting density of states. A practical implementation of DMFT amounts to a recursive solution of the effective theory (4) computing the Green's function (5) starting from a guess for $\mathcal{G}_0^{-1}(i\omega_n)$. Then the self-consistency is used to compute a new $\mathcal{G}_0^{-1}(i\omega_n)$ and the procedure is iterated until convergence is achieved. The solution of the effective theory usually exploits a mapping onto an impurity Hamiltonian which, for the Hubbard model, is an Anderson impurity model. Different "impurity solvers" can be used to obtain the Green's function, each with specific advantages and disadvantages. The combined use of different solvers led the community to a complete understanding of the Mott transition in the single-band Hubbard model which represents the basis for extensions including more orbitals or partially relaxing the DMFT approximation.

As we mentioned above, DMFT is exact not only in the limit of infinite coordination (or dimensionality) but also in finite dimensionality in the opposite limits of $U = 0$ (noninteracting limit) and $t = 0$ (atomic limit). This makes the theory ideally suited to study the Mott transition, as it correctly reproduces both the opposite limits and, being exact in one well-defined limit, it is a conserving approximation. We notice in passing that DMFT remains exact in the same limit also including other local interaction terms, like exchange terms in multiorbital systems (Georges et al., 2013) or electron–phonon coupling (Capone et al., 2010).

Key issues

The Mott–Hubbard transition in DMFT

The picture of the Mott transition in DMFT is summarized in Figs. 1 and 2. In Fig. 1, we report a schematic sketch of the evolution of the local many-body one-particle spectral function

$$\rho(\omega) = -\frac{1}{\pi} ImG(\omega) \tag{8}$$

as the ratio U/t is increased. $\rho(\omega)$ can be seen as an interacting local density of states or the integral over momentum of the spectral density $A(k, \omega)$.

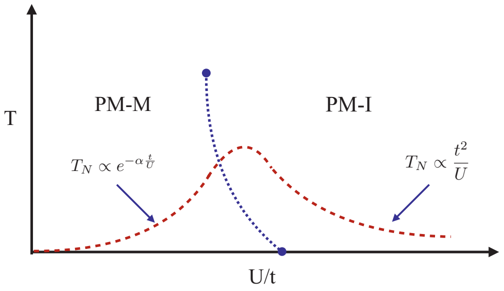

Fig. 2 Schematic phase diagram of the Mott transition for the half-filled single-band Hubbard model in the *U/t-T* plane. The *dashed red line* is the Néel temperature for anriferromagnetic order. The *blue dotted line* is the first-order Mott transition. The endpoints marked with a *blue dot* are second-order transitions. PM-M and PM-I label the paramagnetic metallic and paramagnetic insulating solutions.

For $U = 0$, the system is a metal with a half-filled band of total width W. When we increase the strength of the interaction, a part of the spectral weight shifts toward higher energy. At first this effect is essentially a broadening of the spectrum, but further increasing the interaction reveals a three-feature spectrum where a low-energy quasiparticle peak is flanked by two high-energy features centered around $\omega \simeq \pm U/2$. As the interaction grows this feature becomes clearly separated from the quasiparticle peak, which in turn shrinks. The shrinking of the low-energy feature is measured by the quasiparticle weight Z, which is obtained from the self-energy from $Z^{-1} = 1 - \frac{\partial\Sigma(\omega)}{\partial\omega}$. For $U = 0$ we have $Z = 1$, while at a critical value of the interaction U_c, Z vanishes, which means that the quasiparticle feature completely disappears, leaving behind two high-energy features which are usually referred to as Hubbard bands in connection with the original work by Hubbard. The continuous disappearance of the quasiparticle peak is the hallmark of the Mott–Hubbard transition at U_c. For a model with a semicircular density of states with half-bandwidth D (proportional to the hopping t), $U_c \simeq 2.94D$ (Bulla et al., 2001). We notice that U_c is also the largest value for which a metallic solution exists, while the insulating solution exists also for $U_{c1} < U < U_c$, with $U_{c1} \simeq 2D$, leading to a wide region of parameters where two solutions exist (Georges et al., 1996).

In Fig. 2, we show the resulting phase diagram in the plane of interaction (U/t) and temperature (T). The coexistence of solutions extends to finite temperature so that the second-order transition at zero temperature becomes at finite temperature a first-order line that ends in a finite-temperature critical point at $T \simeq 0.04D$ (Zhang et al., 1993; Georges and Krauth, 1992; Georges et al., 1996). At temperatures above the critical point, a continuous crossover connects solution with metallic and insulating character. In Fig. 2, we have also reported a sketch of the Néel temperature for a three-dimensional system. We have to stress that this curve strongly depends on the chosen lattice and on the existence of long-range hopping. For nearest-neighbor hopping the Néel temperature is indeed larger than the critical point of the Mott transition and the whole first-order line is hidden by the region of stability of the antiferromagnetic state. Yet, already for moderate values of next-neighbor hoppings, the magnetic ordering temperature is reduced and we obtain a phase diagram which resembles that of Fig. 1A, where the first-order paramagnetic Mott line emerges from the magnetic dome (Georges et al., 1996). Crucially, this phase diagram mirrors the celebrated pressure-temperature diagram of V_2O_3 (McWhan et al., 1973), which is often considered the paradigm of Mott transitions.

We summarize here some of the main new results of DMFT for which the consensus is general and many experimental confirmations have been obtained

- The Mott–Hubbard transition is of first-order at finite temperature except for the second-order endpoint without invoking the coupling with the phonons or any structural transition.
- In the strongly correlated metallic solution, metallic features and insulating features are simultaneously present at different energy scales.
- The competition with ordered phases depends on the details of the lattice, but realistic parameters provide a phase diagram close to those experimentally observed in transition-metal oxides.

The DMFT scenario for the Mott transition has been extremely influential in the field of strongly correlated systems providing the community with a solid, even if approximate, picture which is easy to visualize and compare with experiments. In particular, combining DMFT with density-functional theory (DFT) (Hohenberg and Kohn, 1964) has been extremely successful in providing a method to compute ab initio the properties of strongly correlated materials which are not accessible by standard implementations of DFT (Kotliar et al., 2006).

Another fundamental extension of DMFT is given by methods that include nonlocal dynamical correlations besides the local frequency-dependent self-energy. Several approaches have been devised and developed that can be grouped in two main categories: (i) cluster extensions of DMFT, where the single-site theory is generalized into a cluster theory and a similar self-consistent scheme is derived (Maier et al., 2005); (ii) diagrammatic extensions generalizing the DMFT construction in different directions (Rohringer et al., 2018). These approaches have a somewhat complementary character and they allowed to apply the DMFT ideas to the two-dimensional Hubbard model. As we already mentioned, this field is however still competitive and we prefer to defer the interested reader to previous review work (Maier et al., 2005; Rohringer et al., 2018).

Finally, a realistic description of most strongly correlated materials requires to go beyond the single-band Hubbard model including more than one correlated orbital in the theoretical modeling. In the next section we discuss some aspects of this physics in order to emphasize some novel phenomena characteristic of multiorbital (or multiband) Hubbard models that are simply absent in the single-band system.

Multiorbital Hubbard model

The most straightforward multiorbital extension of the Hubbard model to include M atomic orbitals (each hosting spin-1/2 fermions) is an SU(2M) invariant model of the form

$$H = \sum_{i,j,m,n,\sigma} t_{ij}^{mn} \hat{c}^{\dagger}_{im\sigma}\hat{c}_{jn\sigma} + \frac{U}{2}\sum_{i}\hat{n}_i^2, \tag{9}$$

where i and j are site indices, m and n are orbital indices ranging from 1 to M, and σ is a spin label. Hence $\hat{c}^{\dagger}_{im\sigma}$ creates a fermion with spin σ on site i and orbital m. The Coulomb term involves the total charge on site i $\hat{n}_i = \sum_{m\sigma}\hat{c}^{\dagger}_{im\sigma}\hat{c}_{im\sigma}$. This term generalizes the Hubbard repulsion to the multiorbital case, simply assuming a density–density repulsion between fermions with different quantum numbers with the same strength for any pair of indices.

The first novelty of a multiorbital model is that the Mott transition is no longer limited to the case of half-filling, which here would correspond to M electrons per site, but it can take place for any integer filling $N = 1, \ldots 2M - 1$. The physical picture is quite obvious. If U is the largest energy scale, the ground state has N electrons on any site, while any charge excitation has an energy cost U. Thus, for large U, any charge excitation is forbidden and N electrons remain localized on each site.

Solving this model with DMFT does not change qualitatively the picture we described in the previous section. The metal is strongly affected by an increased U until the quasiparticle low-energy feature is destroyed and a Mott insulator is realized. There is only a quantitative dependence of the results on the number of orbitals and the filling (Florens et al., 2002).

While these result would suggest that increasing the number of orbitals has only a quantitative effect on Mott physics, it must be noted that Eq. (9) is only an approximation of the correct Hamiltonian that one obtains expanding the Coulomb interaction on a basis of localized orbitals. The generic Coulomb integral for a given site is

$$U_{mnm'n'} = \int drdr' \phi^{*}_{m}(r)\phi^{*}_{n}(r')W(r-r')\phi_{n'}(r')\phi_{m'}(r) \tag{10}$$

where $\phi_m(r)$ is a localized wave function for an electron in the orbital m (the site index is the same for every function and it is omitted), while $W(r-r')$ is the Coulomb interaction screened by the other electronic bands.

In rather general terms we can define an intra-orbital repulsion

$$U_m = \int drdr' |\phi_m(r)|^2 W(r-r')|\phi_m(r')|^2, \tag{11}$$

an interorbital density–density repulsion

$$U'_{mn} = \int drdr' |\phi_m(r)|^2 W(r-r')|\phi_n(r')|^2, \tag{12}$$

an exchange term

$$J_{mn} = \int drdr' \phi^{*}_{m}(r)\phi^{*}_{n}(r')V_c(r-r')\phi_m(r')\phi_n(r) \tag{13}$$

and a pair integral

$$J'_{mn} = \int drdr' \phi^{*}_{m}(r)\phi^{*}_{m}(r')V_c(r-r')\phi_n(r')\phi_n(r). \tag{14}$$

If we assume that the various orbitals are equivalent $U_m \equiv U$, $U'_m \equiv U'$, $J_m \equiv J$, and $J'_m \equiv J'$. For real wave functions we also obtain $J' = J$. It follows from the definitions that $U > U' > J$. Thus the interaction Hamiltonian becomes

$$\begin{aligned} H_{int} = {} & U\sum_{im}\hat{n}_{im\uparrow}\hat{n}_{im\downarrow} + U'\sum_{i,m\neq n}\hat{n}_{im\uparrow}\hat{n}_{in\downarrow} + (U'-J)\sum_{i,m>n,\sigma}\hat{n}_{im\sigma}\hat{n}_{in\sigma} + \\ & -J\sum_{i}\sum_{m\neq n}\hat{c}^{\dagger}_{im\uparrow}\hat{c}_{im\downarrow}\hat{c}^{\dagger}_{in\downarrow}\hat{c}_{in\uparrow} + J\sum_{i}\sum_{m\neq n}\hat{c}^{\dagger}_{im\uparrow} hatc^{\dagger}_{im\downarrow}\hat{c}_{in\downarrow}\hat{c}_{in\uparrow} \end{aligned} \tag{15}$$

If we finally assume $U' = U - 2J$, the interaction becomes invariant under orbital and spin rotations and it can be written in the form

$$H_{int} = \sum_{i}\left[(U-3J)\frac{\hat{n}_i(\hat{n}_i-1)}{2} - 2J\hat{S}_i^{\,2} - \frac{J}{2}\hat{L}_i^{\,2} + \frac{5}{2}J\hat{n}_i\right], \tag{16}$$

where $\hat{L}_i$ and $\hat{S}_i$ are the orbital and spin angular momentum of the electrons on site I. The final form of the interaction conveys a clear physical meaning. The first term is a Hubbard-like interaction where the repulsion U becomes $U - 3J$, while the second and third terms, both proportional to J, give rise to the first two Hund's rules. For this reason, J is called the Hund's coupling. The fourth term can be reabsorbed in a redefinition of the chemical potential.

Role of the Hund's coupling

The inclusion of the Hund's coupling J and the corresponding terms turns out to have remarkable effects on the Mott–Hubbard transition and on the correlation properties of the metallic phase which the object of current research, both in terms of model investigations and of applications to materials, including iron-based superconductors (Haule and Kotliar, 2009; de' Medici and Capone, 2017) and ruthenates (Kim et al., 2018). In this work we do not attempt a full review of this very active field of research, for which we refer to Georges et al. (2013).

We provide however some arguments to provide some intuition about the role of the Hund's coupling. In order to estimate the effect of J on the Mott transition, we can easily estimate the critical U for the Mott transition via the atomic value of the Mott gap. For a system with a filling of n electrons per site, we can compute the atomic Mott gap as the cost of exciting one electron from one site to another as $\Delta(U, J, N) = E(N + 1) + E(N - 1) - 2E(N)$, where $E(N)$ is the atomic ground state for a system of N electrons. From this quantity we can estimate U_c from the condition $\Delta(U, J, N) = W$, where W is the bandwidth.

For a single-band model, or for $J = 0$, it is easy to see that $\Delta = U$. When we include J, we obtain two radically different results for $N = M$, that is, when the system is globally half filled, and for other integer filling $N \neq M$ (de' Medici et al., 2011; Georges et al., 2013). For $N = M$, we obtain $\Delta = U + (M - 1)J$, that is, the Mott gap is increased by J. Using the above criterion, one finds that $U_c(J) = U_c(0) - (M - 1)J$. This means that the Hund's coupling reduces the critical U for the Mott transition. On the other hand, for $N \neq M$, $\Delta = U - 3J$, that is, a reduction of the Mott gap. The critical U is increased by J according to $U_c(J) = U_c(0) + 3J$.

These estimates are indeed qualitatively confirmed by DMFT calculations for that unveiled a richer scenario with respect to the single-band model. The key point is that for small values of U and J, the latter parameter cooperates with U in localizing the electrons. This is reflected by a quasiparticle weight Z that drops faster as a function of U than in the $J = 0$ case. For $N = M$, this trend is compatible with the reduction of the critical U: As a result the Mott transition occurs in a similar way as in the absence of J (or in the single-band model), only for smaller values of U. On the other hand, for $N \neq M$ we have a dichotomy in the effect of J it first favors Mott localization but, for values of the interactions, it leads shifts he critical U to larger values. We have thus a two-step localization where a first rapid reduction of the electronic mobility is followed by a large region where Z is almost flat before a Mott transition takes place (de' Medici et al., 2011). This interaction-resistant metal has been called a Hund's metal (Haule and Kotliar, 2009). The investigation of the properties of Hund's metals is currently a very active field of research encompassing fundamental research and applications to different materials, including iron-based superconductors (de' Medici et al., 2014; de' Medici and Capone, 2017), ruthenates (Kim et al., 2018). We notice in passing that the anomalous phonondriven superconductivity of alkali-doped fullerides is understood in the terms of a model of the form (16) with a negative Hund's coupling $J = -|J|$ arising from electron–phonon coupling (Capone et al., 2009; Nomura et al., 2015).

Another quite general phenomenon which is realized in multiorbital correlated systems, especially when the Hund's coupling is sizable, is orbital-selective Mott physics. An orbital-selective Mott insulator is defined as a system in which the electrons is some orbitals are Mott localized, while those of other orbitals remain itinerant (Vojta, 2010). The metallic region close to an orbital-selective Mott transition is characterized by orbital-selective correlations, that is, the coexistence of carriers with remarkably different correlation properties. A large body of experimental data on iron-based superconductors can indeed be understood within this framework, both in the metallic normal state (de' Medici et al., 2014; Capone, 2018; Kostin et al., 2018) and in the superconducting state, in which orbital-selective pairing has been observed (Sprau et al., 2017).

Conclusion

In this work we have outlined the scenario of the Mott–Hubbard transition obtained within DMFT (Georges et al., 1996). Regardless of the accuracy of the method, the DMFT description of the Mott transition can be considered as a paradigm of "pure" Mott physics because the method treats accurately the competition between the delocalizing effect of the hopping term and the blocking effect of the Hubbard local repulsion and it allows to disentangle this intrinsic Mott localization with the tendency to form spatially ordered phases, like the antiferromagnetic phase of the single-band Hubbard model. In this sense, we consider the DMFT scenario as a paradigm to be used as the basic backbone of calculations including nonlocal dynamical correlations and/or more realistic descriptions of materials.

The picture that emerges within DMFT is richer than previously expected. The evolution from a standard metal to a paramagnetic Mott insulator is characterized by the development of a strongly correlated metallic state in which the low-energy properties of the system are those of a strongly renormalized Fermi liquid, while the high-energy behavior is similar to a precursor of an insulator. The Mott–Hubbard transition is associated with the disappearance of the low-energy quasiparticle features, leaving behind a preformed gap (Georges et al., 1996).

At finite temperature, the transition becomes a first-order line which ends in a critical point (Zhang et al., 1993; Georges and Krauth, 1992; Georges et al., 1996). The first-order character of the Mott transition is a remarkable prediction of DMFT which is actually in agreement with the phenomenology of transition-metal oxides, where a first-order line emerges from a magnetic low-temperature state. This demonstrates that the first-order character of the transition is of electronic origin, in contrast with previous expectations that the coupling with the lattice was a necessary condition to make the transition discontinuous.

The DMFT scenario of the Mott transition and its prediction on several observables have been verified in three-dimensional strongly correlated materials (McWhan et al., 1973; Furukawa et al., 2015), leading to a substantial advance both in our understanding and in our ability to accurately compute the properties of this class of materials.

However, a full account of the properties of many materials requires to relax some of the approximations behind the single-band Hubbard model and/or to address the role of low dimensionality. In particular, a realistic description of most correlated materials requires to include multiple low-energy orbitals. This extension is far from trivial, in particular when the Hund's exchange is not small (Georges et al., 2013). In this case, novel phenomena like a two-step Mott localization and orbital-selective Mott physics have been identified in the recent years.

Finally, several methods have been proposed to extend DMFT including nonlocal correlation effects. Different approaches, ranging from cluster extensions (Maier et al., 2005) to diagrammatic methods focusing on two-particle correlations (Rohringer et al., 2018) are currently being developed in order to close the gap that separates us from a complete theory of the Mott transition in two dimensions.

References

Anderson PW (1987) The resonating valence bond state in La_2CuO_4 and superconductivity. *Science* 235(4793): 1196–1198. https://doi.org/10.1126/science.235.4793.1196.

Arovas DP, Berg E, Kivelson SA, and Raghu S (2022) The Hubbard model. *Annual Review of Condensed Matter Physics* 13(1): 239–274. https://doi.org/10.1146/annurev-conmatphys-031620-102024.

Bednorz JG and Müller KA (1986) Possible high T_c superconductivity in the Ba-La-Cu-O system. *Zeitschrift fur Physik B Condensed Matter* 64: 189–193. https://doi.org/10.1007/BF01303701.

Bulla R, Costi TA, and Vollhardt D (2001) Finite-temperature numerical renormalization group study of the Mott transition. *Physical Review B* 64: 045103. https://doi.org/10.1103/PhysRevB.64.045103.

Capone M (2018) Orbital-selective metals. *Nature materials* 17(10): 855–856.

Capone M, Fabrizio M, Castellani C, and Tosatti E (2009) Colloquium: Modeling the unconventional superconducting properties of expanded A_3C_{60} fullerides. *Reviews of Modern Physics* 81: 943–958. https://doi.org/10.1103/RevModPhys.81.943.

Capone M, Castellani C, and Grilli M (2010) Electron-phonon interaction in strongly correlated systems. *Advances in Condensed Matter Physics* 2010: 920860. ISSN: 1687-8108. https://doi.org/10.1155/2010/920860.

Castellani C, Di Castro C, and Grilli M (1995) Singular quasiparticle scattering in the proximity of charge instabilities. *Physical Review Letters* 75: 4650–4653. https://doi.org/10.1103/PhysRevLett.75.4650.

de Boer JH and Verwey EJW (1937) Semi-conductors with partially and with completely filled 3d-lattice bands. *Proceedings of the Physical Society* 49(4S): 59. https://doi.org/10.1088/0959-5309/49/4S/307.

de' Medici L and Capone M (2017) Modeling many-body physics with slave-spin mean-field: Mott and Hund's physics in Fe-superconductors. In: Mancini F and Citro R (eds.) *The Iron Pnictide Superconductors: An Introduction and Overview*, pp. 115–185. Cham: Springer International.

de' Medici L, Mravlje J, and Georges A (2011) Janus-faced influence of Hund's rule coupling in strongly correlated materials. *Physical Review Letters* 107: 256401. https://doi.org/10.1103/PhysRevLett.107.256401.

de' Medici L, Giovannetti G, and Capone M (2014) Selective Mott physics as a key to iron superconductors. *Physical Review Letters* 112: 177001. https://doi.org/10.1103/PhysRevLett.112.177001.

Florens S, Georges A, Kotliar G, and Parcollet O (2002) Mott transition at large orbital degeneracy: Dynamical mean-field theory. *Physical Review B* 66: 205102. https://doi.org/10.1103/PhysRevB.66.205102.

Furukawa T, Miyagawa K, Taniguchi H, Kato R, and Kanoda K (2015) Quantum criticality of Mott transition in organic materials. *Nature Physics* 11(3): 221–224. ISSN: 1745-2481. https://doi.org/10.1038/nphys3235.

Georges A and Krauth W (1992) Numerical solution of the $d = \infty$ Hubbard model: Evidence for a Mott transition. *Physical Review Letters* 69: 1240–1243. https://doi.org/10.1103/PhysRevLett.69.1240.

Georges A, Kotliar G, Krauth W, and Rozenberg MJ (1996) Dynamical mean-field theory of strongly correlated fermion systems and the limit of infinite dimensions. *Reviews of Modern Physics* 68: 13–125. https://doi.org/10.1103/RevModPhys.68.13.

Georges A, de' Medici L, and Mravlje J (2013) Strong correlations from hund's coupling. *Annual Review of Condensed Matter Physics* 4(1): 137–178. https://doi.org/10.1146/annurev-conmatphys-020911-125045.

Gutzwiller MC (1963) Effect of correlation on the ferromagnetism of transition metals. *Physical Review Letters* 10: 159–162. https://doi.org/10.1103/PhysRevLett.10.159.

Haule K and Kotliar G (2009) Coherence-incoherence crossover in the normal state of iron oxypnictides and importance of hund's rule coupling. *New Journal of Physics* 11(2): 025021. https://doi.org/10.1088/1367-2630/11/2/025021.

Hohenberg P and Kohn W (1964) Inhomogeneous electron gas. *Physical Review* 136: B864–B871. https://doi.org/10.1103/PhysRev.136.B864.

Hubbard J (1963) Electron correlations in narrow energy bands. *Proceedings of the Royal Society of London, Series A* 276: 238–257. https://doi.org/10.1098/rspa.1963.0204. https://www.osti.gov/biblio/4151988.

Imada M, Fujimori A, and Tokura Y (1998) Metal-insulator transitions. *Reviews of Modern Physics* 70: 1039–1263. https://doi.org/10.1103/RevModPhys.70.1039.

Kanamori J (1963) Electron correlation and ferromagnetism of transition metals. *Progress of Theoretical Physics* 30(3): 275–289. ISSN: 0033-068X. https://doi.org/10.1143/PTP.30.275. https://academic.oup.com/ptp/article-pdf/30/3/275/5278869/30-3-275.pdf.

Kim M, Mravlje J, Ferrero M, Parcollet O, and Georges A (2018) Spin-orbit coupling and electronic correlations in Sr_2RuO_4. *Physical Review Letters* 120: 126401. https://doi.org/10.1103/PhysRevLett.120.126401.

Kostin A, Sprau PO, Kreisel A, Chong YX, Böhmer AE, Canfield PC, Hirschfeld PJ, Andersen BM, and Davis JCS (2018) Imaging orbital-selective quasiparticles in the Hund's metal state of FeSe. *Nature Materials* 17(10): 869–874. ISSN: 1476-4660. https://doi.org/10.1038/s41563-018-0151-0.

Kotliar G, Savrasov SY, Haule K, Oudovenko VS, Parcollet O, and Marianetti CA (2006) Electronic structure calculations with dynamical mean-field theory. *Reviews of Modern Physics* 78: 865–951. https://doi.org/10.1103/RevModPhys.78.865.

Kozik E, Burovski E, Scarola VW, and Troyer M (2013) Néel temperature and thermodynamics of the half-filled three-dimensional Hubbard model by diagrammatic determinant Monte Carlo. *Physical Review B* 87: 205102. https://doi.org/10.1103/PhysRevB.87.205102.

LeBlanc JPF, Antipov AE, Becca F, Bulik IW, Chan GK-L, Chung C-M, Deng Y, Ferrero M, Henderson TM, Jiménez-Hoyos CA, Kozik E, Liu X-W, Millis AJ, Prokof'ev NV, Qin M, Scuseria GE, Shi H, Svistunov BV, Tocchio LF, Tupitsyn IS, White SR, Zhang S, Zheng B-X, Zhu Z, and Gull E (2015) Simons Collaboration on the Many-Electron Problem. *Solutions of the two-dimensional Hubbard model: Benchmarks and results from a wide range of numerical algorithms. Physical Review X 5* 5: 041041. https://doi.org/10.1103/PhysRevX.5.041041.

Lee PA, Nagaosa N, and Wen X-G (2006) Doping a Mott insulator: Physics of high-temperature superconductivity. *Reviews of Modern Physics* 78: 17–85. https://doi.org/10.1103/RevModPhys.78.17.

Lieb EH (1989) Two theorems on the Hubbard model. *Physical Review Letters* 62: 1201–1204. https://doi.org/10.1103/PhysRevLett.62.1201.

Lieb EH and Wu FY (1968) Absence of Mott transition in an exact solution of the short-range, one-band model in one dimension. *Physical Review Letters* 20: 1445–1448. https://doi.org/10.1103/PhysRevLett.20.1445.

Lin HQ and Hirsch JE (1987) Two-dimensional Hubbard model with nearest- and next-nearest-neighbor hopping. *Physical Review B* 35: 3359–3368. https://doi.org/10.1103/PhysRevB.35.3359.

MacDonald AH, Girvin SM, and Yoshioka D (1988) $\frac{t}{U}$ expansion for the Hubbard model. *Physical Review B* 37: 9753–9756. https://doi.org/10.1103/PhysRevB.37.9753.

Maier T, Jarrell M, Pruschke T, and Hettler MH (2005) Quantum cluster theories. *Reviews of Modern Physics* 77: 1027–1080. https://doi.org/10.1103/RevModPhys.77.1027.

Maiti S and Chubukov AV (2013) Superconductivity from repulsive interaction. *AIP Conference Proceedings* 1550(1): 3–73. https://doi.org/10.1063/1.4818400.

McWhan DB, Menth A, Remeika JP, Brinkman WF, and Rice TM (1973) Metal-insulator transitions in pure and doped V_2O_3. *Physical Review B* 7: 1920–1931. https://doi.org/10.1103/PhysRevB.7.1920.

Mermin ND and Wagner H (1966) Absence of ferromagnetism or antiferromagnetism in one- or two-dimensional isotropic Heisenberg models. *Physical Review Letters* 17: 1133–1136. https://doi.org/10.1103/PhysRevLett.17.1133.

Metzner W and Vollhardt D (1989) Correlated lattice fermions in $d = \infty$ dimensions. *Physical Review Letters* 62: 324–327. https://doi.org/10.1103/PhysRevLett.62.324.

Mott NF and Peierls R (1937) Discussion of the paper by de Boer and Verwey. *Proceedings of the Physical Society* 49(4S): 72. https://doi.org/10.1088/0959-5309/49/4S/308.

Nomura Y, Sakai S, Capone M, and Arita R (2015) Unified understanding of superconductivity and Mott transition in alkali-doped fullerides from first principles. *Science Advances* 1(7): e1500568. https://doi.org/10.1126/sciadv.1500568.

Qin M, Schäfer T, Andergassen S, Corboz P, and Gull E (2022) The hubbard model: A computational perspective. *Annual Review of Condensed Matter Physics* 13(1): 275–302. https://doi.org/10.1146/annurev-conmatphys-090921-033948.

Rohringer G, Hafermann H, Toschi A, Katanin AA, Antipov AE, Katsnelson MI, Lichtenstein AI, Rubtsov AN, and Held K (2018) Diagrammatic routes to nonlocal correlations beyond dynamical mean field theory. *Reviews of Modern Physics* 90: 025003. https://doi.org/10.1103/RevModPhys.90.025003.

Sachdev S (2010) Where is the quantum critical point in the cuprate superconductors? *Physica Status Solidi (B)* 247(3): 537–543. https://doi.org/10.1002/pssb.200983037.

Sangiovanni G, Toschi A, Koch E, Held K, Capone M, Castellani C, Gunnarsson O, Mo S-K, Allen JW, Kim H-D, Sekiyama A, Yamasaki A, Suga S, and Metcalf P (2006) Static versus dynamical mean-field theory of Mott antiferromagnets. *Physical Review B* 73: 205121. https://doi.org/10.1103/PhysRevB.73.205121.

Schäfer T, Wentzell N, Šimkovic F, He Y-Y, Hille C, Klett M, Eckhardt CJ, Arzhang B, Harkov V, Le Régent F-M, Kirsch A, Wang Y, Kim AJ, Kozik E, Stepanov EA, Kauch A, Andergassen S, Hansmann P, Rohe D, Vilk YM, LeBlanc JPF, Zhang S, Tremblay A-MS, Ferrero M, Parcollet O, and Georges A (2021) Tracking the footprints of spin fluctuations: A multimethod, multimessenger study of the two-dimensional Hubbard model. *Physical Review X* 11: 011058. https://doi.org/10.1103/PhysRevX.11.011058.

Slater JC (1951) Magnetic effects and the Hartree-Fock equation. *Physical Review* 82: 538–541. https://doi.org/10.1103/PhysRev.82.538.

Sprau PO, Kostin A, Kreisel A, Böhmer AE, Taufour V, Canfield PC, Mukherjee S, Hirschfeld PJ, Andersen BM, and Davis JCS (2017) Discovery of orbital-selective Cooper pairing in FeSe. *Science* 357(6346): 75–80. https://doi.org/10.1126/science.aal1575.

Vojta M (2010) Orbital-selective Mott transitions: Heavy fermions and beyond. *Journal of Low Temperature Physics* 161(1): 203–232. ISSN: 1573-7357. https://doi.org/10.1007/s10909-010-0206-3.

Zhang XY, Rozenberg MJ, and Kotliar G (1993) Mott transition in the $d = \infty$ Hubbard model at zero temperature. *Physical Review Letters* 70: 1666–1669. https://doi.org/10.1103/PhysRevLett.70.1666.

Electron quantum optics: A testbed for the Luttinger paradigma

Dario Ferraro and Maura Sassetti, Dipartimento di Fisica dell'Università degli Studi di Genova & CNR-SPIN, Genova, Italy

© 2024 Elsevier Ltd. All rights reserved.

Introduction 924
Wave-guides, beam-splitters and on-demand single-electron sources 925
Hanbury-Brown-Twiss and Hong-Ou-Mandel interferometry with electrons 926
Luttinger liquid description of interacting quantum Hall edge channels 928
Effects of interaction in the Hong-Ou-Mandel profile: The Leviton case 930
Crystallization of Levitons in the fractional quantum Hall regime 930
Conclusion 932
Acknowledgments 933
References 933

Abstract

Electron quantum optics recently emerged as a new branch of condensed matter physics aimed at creating, manipulating and detecting electronic wave-packets ballistically propagating along one-dimensional mesoscopic channels. Here, theoretical tools elaborated in the framework of the conventional quantum optics based on photons have been reconsidered in order to properly describe interferometric experiments showing an interplay between the fermionic nature of the electrons and the ubiquitous many-body interaction among them. This allowed a direct comparison between the predictions derived within the Luttinger liquid picture for interacting electrons in one-dimension and the experimental observations. This Chapter will provide an overview on this subject, with main focus on the case of wave-packets generated by means of time-dependent voltage pulses.

Key points

- From quantum optics to electron quantum optics: the dictionary.
- Experimental milestones: electron partitioning and collisional interferometry.
- Effects of interaction: the Luttinger paradigma in action.
- Strongly correlated systems: crystallization in the time domain.

Introduction

The technological advancement in the generation, control and measurement of individual electronic degrees of freedom in solid-state devices opened the way to the development of Electron Quantum Optics (EQO) (Bocquillon et al., 2013). This branch of condensed matter physics aims at realizing quantum optics-like experiments with electrons ballistically propagating along mesoscopic channels and has been characterized since the beginning by a remarkable synergy between experimental investigations and theoretical analysis.

In this direction, the edge channels of an Hall bar in the quantum regime represent the ideal candidate for the realization of one-dimensional chiral wave-guides (Das Sarma and Pinczuk, 2004). Moreover, thank to the applications of electrostatic gates, these states can be put in contact realizing a Quantum Point Contact (QPC), which mimics the functioning of a beam-splitter. The last ingredient to complete this translation from the photonic to the electronic domain is provided by on-demand single-electron sources. Even if various techniques have been proposed to implement this essential building block, two of them emerged as more promising. The first is based on a quantum dot coupled to the Hall bar whose Fermi level is periodically driven above and below the one of the outer channel of the Hall bar in such a way to trigger the controlled injection of electrons and holes (Fève et al., 2007). The second requires the application of a periodic drive directly on the one-dimensional channels. Despite apparently simpler, this approach needs an extremely high level of control on the form of the applied voltage. Indeed, only a properly quantized train of voltage pulses with Lorentzian profile in time is able to guarantee the injection of purely electronic states, with no additional spurious particle-hole pairs, usually called Levitons (Levitov et al., 1996; Glattli and Roulleau, 2017).

Thank to the tools discussed above, two seminal electron interferometers have been realized within a condensed matter setting (Bocquillon et al., 2013). When only one train of excitations reaches the QPC, the measurement of the outgoing current fluctuations allows to access a particle partitioning reminiscent of what observed in the Hanbury-Brown-Twiss (HBT) intensity interferometer. Moreover, when two trains are injected on the opposite sides of the QPC, the electronic analogous of the Hong-Ou-Mandel (HOM) collisional interferometer is achieved. It is characterized by the presence of a dip in the current fluctuations for synchronized

https://doi.org/10.1016/B978-0-323-90800-9.00073-1

injections, signature of the fact that identical fermionic excitations cannot emerge on the same outgoing channel due to the Pauli principle. A similar feature, involving the number of coincidences instead of the fluctuations, represents the footprint of its photonic counterpart.

Despite this simple free-electron picture provides important hints of the physics at work in these devices, for technical reasons experiments in this domain are usually carried out with edge states at filling factor $\nu = 2$ or even higher, where the Coulomb interaction among the edge channels cannot be neglected. This represents a further major difference between the photonic and the electronic cases and needs to be carefully taken into account. The conventional way to do this is based on the Luttinger liquid description, which properly describes interacting one-dimensional systems, replacing the standard Fermi liquid picture valid at higher dimensions (Giamarchi, 2003). While this interaction only marginally affects the functioning of the HBT interferometer, its role dramatically emerges in HOM interferometers as we will see in the next Sections.

Even more interesting are the effects of electron-electron interaction in strongly correlated systems such as the fractional quantum Hall edge states (Das Sarma and Pinczuk, 2004). Here, the HOM noise generated by the collision of Levitons carrying a charge multiple of the electron one shows the emergence of various side dips (Ronetti et al., 2018). These can be interpreted in terms of an interaction-induced crystallization of the injected wave-packets, real-time analog of what observed in Luttinger liquids confined in a potential well.

The present Chapter aims at providing a review of the role of interaction in electron quantum optics addressing in detail the points sketched above.

Wave-guides, beam-splitters and on-demand single-electron sources

In quantum optics experiments individual photonic degrees of freedom are injected into wave-guides, such as optical fibers, and manipulated using beam-splitters, realized for example by means of half-silvered mirrors. Starting from these elementary building blocks various interferometers have been realized and used to investigate the coherence property of light, the wave/particle nature of the photons and the consequences of their bosonic statistics.

The possibility to realize analogous experiments using electrons ballistically propagating along one-dimensional mesoscopic channels in solid-state devices has been investigated since the nineties. A particularly suitable platform to implement this translation from the photonic to the electronic domain is represented by the edge states of the quantum Hall effect (Das Sarma and Pinczuk, 2004). Here, a very clean two-dimensional electron gas realized in GaAs/AlGaAs heterostructures, placed in an intense magnetic field ($\sim$10 T) and at low temperature (below $\sim$1 K), is characterized by a chiral current flowing only along one-dimensional channels localized at the edge of the Hall bar. Under these conditions, the electron propagation is unaffected by impurity-induced random backscattering, leading to impressive coherence lengths ($\sim 20\,\mu$m) at cryogenic temperatures ($\sim 20\,$mK). Moreover, thanks to a properly designed electrostatic confinement induced by gates, the electron gas can be locally pinched off. This allows to approach the opposite edge of the Hall bar creating a QPC, characterized by a controllable probability of backscattering for the electrons. The experimental set-up described so far offers the ideal conditions for the realization of the electronic counter-part of both wave-guides and beam-splitters (see Fig. 1 below).

However, the realization of on-demand sources of controlled electronic wave-packets required additional experimental effort. In this direction, two main technologies emerged during the years. The first, developed by the experimental group of the Laboratoire Pierre Aigrain in Paris (Fève et al., 2007), is based on a quantum dot capacitively coupled to the outer channels of an Hall bar. By periodically driving the Fermi level of this confined system and properly tuning the coupling, it is possible to inject into the edge channel one electron and one hole per period T. The wave-packets generated in this way are characterized by a Lorentzian profile in the energy domain (Bocquillon et al., 2013).

A conceptually easier, but experimentally more challenging, way to realize an on-demand electron source has been implemented by the experimental Nanoelectronics group in Saclay (Glattli and Roulleau, 2017). It consists in the direct application of a periodic drive to a mesoscopic channel. According to theoretical analysis (Levitov et al., 1996), the form of this voltage need to be chosen carefully. In particular, a train of Lorentzian voltage pulses in time of the form (from now on we assume $\hbar = 1$)

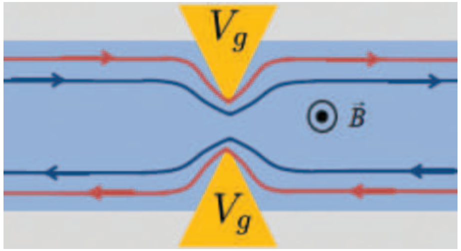

Fig. 1 Cartoon view of a two-dimensional electron gas (light blue) subject to a perpendicular magnetic field $\vec{B}$. In the quantum regime, two edge channels (outer in red and inner in blue) propagate along the boundary of the sample and can be approached by means of a gate voltage (V_g).

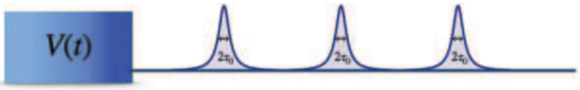

Fig. 2 Injection in a mesoscopic channel of electronic wave-packets with typical width 2 τ_0, through the application of a periodic train of Lorentzian voltage pulses in time $V(t)$.

$$V(t) = \frac{q}{e} \sum_{m=-\infty}^{+\infty} \frac{2\tau_0}{(t - mT)^2 + \tau_0^2} \tag{1}$$

with e charge of the electron and q a real parameter, leads to the periodic injection (again with period T) of purely electronic Lorentzian wave-packets of width τ_0 in the time domain in the case of integer values q (see Fig. 2 below).

This is a direct consequence of the quantization of edge conductance, given by $G = e^2/(2\pi)$, as can be seen by the simple chain of relations involving the current $I(t)$ flowing along the edge, namely

$$Q = \frac{1}{T}\int_{-\frac{T}{2}}^{+\frac{T}{2}} dtI(t) = \frac{1}{T}\int_{-\frac{T}{2}}^{+\frac{T}{2}} dt \frac{e^2}{2\pi} V(t) = qe. \tag{2}$$

In addition, if one chooses and integer value of q the created excitations, called Levitons, are characterized by the absence of spurious additional particle-hole contributions and less affected by the interaction with respect to other injected pulses. This kind of source is therefore able to generate clean and robust electronic wave-packets.

The two on-demand single-electron sources discussed above are complementary, showing a Lorentzian behavior in the energy and time domain respectively, and opened the way to the first seminal interferometric experiments in the field of EQO.

Hanbury-Brown-Twiss and Hong-Ou-Mandel interferometry with electrons

We start this discussion with a description of the electronic version of the HBT interferometer. In ideal conditions, a controlled train of electrons (and eventually holes) is generated by means of one of the two sources discussed above and injected into a quantum Hall edge channel. Once arrived at a QPC they have a probability $\mathcal{T}$ to be transmitted along the same edge and a probability $\mathcal{R} = 1 - \mathcal{T}$ to be reflected on the opposite edge, the constraint being imposed by particle number conservation (see Fig. 3 below).

To be more precise, the action of the QPC on free electrons is encoded by the unitary scattering matrix

$$s = \begin{pmatrix} \sqrt{\mathcal{R}} & i\sqrt{\mathcal{T}} \\ i\sqrt{\mathcal{T}} & \sqrt{\mathcal{R}} \end{pmatrix} \tag{3}$$

in such a way that the outgoing annihilation fermionic operators (in channels 3 and 4) are connected to the incoming ones (in channels 1 and 2) through the simple relation

$$\begin{pmatrix} c_3 \\ c_4 \end{pmatrix} = s \begin{pmatrix} c_1 \\ c_2 \end{pmatrix}. \tag{4}$$

Notice that great care is devoted by experimentalists to find a proper working point of the QPC where $\mathcal{T}$ and $\mathcal{R}$ are energy independent. This guarantees that wave-packets with a finite spread in energy are not improperly distorted at this level. According to this we have suppressed all the energy dependence in (3) and (4).

The excitations emerging from the QPC are then detected in one of the outgoing edge channels in such a way to investigate the partitioning associated with their corpuscular nature. Assuming, for sake of clarity, a unique excitation injected in the incoming

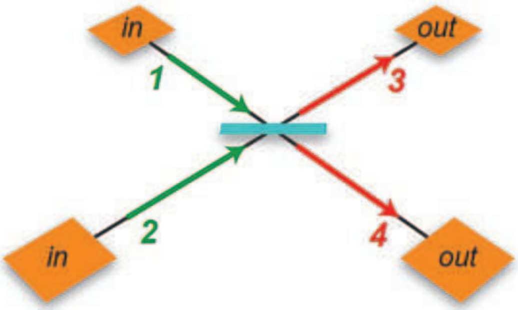

Fig. 3 Cartoon view of a set-up for partitioning and collisional experiments. Excitations flowing along the incoming channels 1 and 2 (green arrows) reach the central QPC (cyan) and emerge in the outgoing channels 3 and 4 (red arrows).

channel 1 one has obviously an average number of excitations $\langle N_1\rangle = \langle {c_1}^\dagger c_1\rangle = 1$ and $\langle N_2\rangle = \langle {c_2}^\dagger c_2\rangle = 0$ in the incoming channels with no fluctuations: $\langle(\Delta N_1)^2\rangle = \langle(\Delta N_2)^2\rangle = 0$, with $\Delta N_{1,2} = N_{1,2} - \langle N_{1,2}\rangle$. Due to the action of the QPC, in the outgoing channels one has $\langle N_3\rangle = \mathcal{R}, \langle N_4\rangle = \mathcal{T}$ with fluctuations

$$\left\langle(\Delta N_3)^2\right\rangle = \left\langle(\Delta N_4)^2\right\rangle = -\langle\Delta N_3 \Delta N_4\rangle = \mathcal{R}\mathcal{T}. \tag{5}$$

The above expression characterizes the random partitioning of corpuscular excitations at the level of the QPC and is usually indicated as partition noise.

Even more interesting is the situation for what it concerns the electronic translation of the HOM interferometer. This consists in a collisional experiment in which two identical trains of excitations are injected, with a tunable delay t_D, on the opposite sides of a QPC (channels 1 and 2) and detected in the outgoing channels. For a time delay longer than the typical width of the wave-packets in time the partitioning of the two trains of excitations at the QPC is independent and one recovers the HBT phenomenology discussed above. However, for synchronized injections ($t_D = 0$) the colliding fermionic excitations are forced to always emerge on the opposite sides of the QPC. Also in this case we can understand this phenomenology considering the action of the QPC scattering matrix (3). In this case one has $\langle N_1\rangle = \langle N_2\rangle = 1$ in the incoming channels, again with no fluctuations: $\langle(\Delta N_1)^2\rangle = \langle(\Delta N_2)^2\rangle = 0$. In the outgoing channels one has $\langle N_3\rangle = \langle N_4\rangle = 1$ with

$$\left\langle(\Delta N_3)^2\right\rangle = \left\langle(\Delta N_4)^2\right\rangle = -\langle\Delta N_3 \Delta N_4\rangle = 0. \tag{6}$$

This is a direct consequence of the Pauli principle which prevents two identical electrons to emerge in the same outgoing channel, leading to an anti-bunching effect. In order to further strengthen this statement, we observe that in a photonic HOM experiments the excitations always bounch with the emergence of pairs of photons on one of the two outgoing branch of the interferometer, namely (Bocquillon et al., 2013)

$$\left\langle\left(\Delta N_3^{(ph)}\right)^2\right\rangle = \left\langle\left(\Delta N_4^{(ph)}\right)^2\right\rangle = -\left\langle\Delta N_3^{(ph)} \Delta N_4^{(ph)}\right\rangle = 4\mathcal{R}\mathcal{T}. \tag{7}$$

In order to go beyond this simplified picture and to better understand the relevant physics at work in actual experiments, we need to properly theoretically address what can be directly measured in electronic interferometers. Indeed, while in quantum optics experiments the measurement of photo-counting and coincidences as a function of time is possible thanks to detectors placed in the outgoing branches of the interferometer, the sensitivity of their solid-state counterparts is not enough to achieve a real-time counting of outgoing excitations. To overcome this issue, experimentalists in the field investigate the current correlations, in particular the cross-correlated zero frequency noise averaged over the period T of the injection, which is defined as

$$S = \int_{-\frac{T}{2}}^{+\frac{T}{2}} \frac{dt}{T} \int_{-\infty}^{+\infty} d\tau \left[\left\langle I_3\left(t + \frac{\tau}{2}\right) I_4\left(t - \frac{\tau}{2}\right)\right\rangle_\varrho - \left\langle I_3\left(t + \frac{\tau}{2}\right)\right\rangle_\varrho \left\langle I_4\left(t - \frac{\tau}{2}\right)\right\rangle_\varrho\right]. \tag{8}$$

In the above equation I_α is the operator associated to the current flowing along the outgoing channel $\alpha = 3, 4$ and the expectations values are taken with respect to the initial density matrix ϱ, which takes into account the injection of additional excitations with respect to the Fermi level of the edge channel.

The noise discussed above is directly related to the fluctuations of the charge outgoing form the QPC in a given period. According to what discussed in (3) and (4) it is possible to connect the fluctuations of the outgoing currents with the incoming ones. This leads to the decomposition

$$S = S^{\mathrm{FS}} + \sum_{\alpha=1,2} S_\alpha^{\mathrm{HBT}} + S^{\mathrm{HOM}}(t_D). \tag{9}$$

The first terms (S^{FS}) only depends on the properties of the many-body Fermi sea of the edge channels when the electron source are switched-off, namely temperature and dc bias, and is typically subtracted in experiments. The second term is the sum of two contributions of the form

$$S_\alpha^{\mathrm{HTB}} = \mathcal{R}\mathcal{T} \frac{e^2}{2\pi} \int_{-\frac{T}{2}}^{+\frac{T}{2}} \frac{dt}{T} \int_{-\infty}^{+\infty} d\omega \Delta W_\alpha(t, \omega)\left[1 - 2f_\mu(\omega)\right]. \tag{10}$$

Here, we have introduced the Fermi distribution f_μ at fixed temperature and chemical potential μ, supposed the same for both edges of the Hall bar for sake of simplicity, and the excess Wigner function (Ferraro et al., 2013) defined as

$$\begin{aligned} \Delta W_\alpha(t, \omega) = v \int_{-\infty}^{+\infty} d\tau e^{i\omega\tau} \Big[& \left\langle \Psi_\alpha^\dagger\left(t - \frac{\tau}{2}\right) \Psi_\alpha\left(t + \frac{\tau}{2}\right)\right\rangle_\varrho \\ & - \left\langle \Psi_\alpha^\dagger\left(t - \frac{\tau}{2}\right) \Psi_\alpha\left(t + \frac{\tau}{2}\right)\right\rangle_{\mathrm{F}} \Big]. \end{aligned} \tag{11}$$

This latter quantity completely characterizes the time-energy profile of the excitations injected into the channel $\alpha = 1, 2$. In the above expression, v is the propagation velocity of the excitations along the edge channels,

$$\Psi_\alpha(t) = \frac{1}{\sqrt{v}}\int_{-\infty}^{+\infty} d\omega c_\alpha(\omega) e^{-i\omega t} \tag{12}$$

is the time representation of the annihilation operator for an electron in the incoming channel α and with F we indicate the average taken with respect to the Fermi sea in absence of injected excitations.

Finally, the last term in (9) reads

$$\begin{aligned} S^{\mathrm{HOM}}(t_D) = & -\mathcal{R}\mathcal{T}\frac{e^2}{\pi}\int_{-\frac{T}{2}}^{+\frac{T}{2}}\frac{dt}{T}\int_{-\infty}^{+\infty} d\omega \Delta W_1(t,\omega) \\ & \times \Delta W_2(t+t_D,\omega) \end{aligned} \tag{13}$$

and characterizes the overlap between excitations injected in the two incoming channels with a controlled delay t_D. Notice that this contribution goes to zero when the delay exceeds the typical time width of the injected wave-packets.

According to the above considerations, an HBT experiment is properly described by a noise contribution of the form (10). It characterizes the partition of the excitations at the QPC discussed in (5) and described here by the excess Wigner function, but takes into account also a suppression of the noise due to the unavoidable Pauli repulsion between the incoming excitations and the ones already present in the edge channels described by a Fermi sea at a cryogenic but finite temperature.

For what it concerns HOM measurements, the ratio

$$\mathcal{Q}(t_D) = \frac{S_1^{\mathrm{HTB}} + S_2^{\mathrm{HTB}} + S^{\mathrm{HOM}}(t_D)}{S_1^{\mathrm{HTB}} + S_2^{\mathrm{HTB}}} \tag{14}$$

is typically reported (Bocquillon et al., 2013; Glattli and Roulleau, 2017). As an example, in the case of a Leviton carrying a charge $q = 1$ one can find the analytical expression for the above ratio

$$\mathcal{Q}(t_D) = \frac{\sin^2\left(\pi\frac{t_D}{T}\right)}{\sinh^2\left(2\pi\frac{\tau_0}{T}\right) + \sin^2\left(\pi\frac{t_D}{T}\right)}. \tag{15}$$

It shows a dip reaching zero at $t_D = 0$, which is consistent with the previously discussed idea of total suppression of the current fluctuations in case of synchronized collisions associated to the certainty of finding exactly one excitation in each outgoing channel as a consequence of the Pauli repulsion. Moreover, it asymptotically approaches one, in the limit $\tau_0 \ll T$, recovering the HBT physics. Notice that, differently from the HBT signal, the HOM one is only marginally affected by thermal effects that will be neglected in the following.

The simple analysis given so far, inherently based on a free fermion picture, is only able to provide a qualitative description of the observations. Indeed, despite the HBT behavior is typically well depicted, discrepancies in the form of the HOM dip with respect to the reported theoretical results are observed (Bocquillon et al., 2013). This is related to the fact that measurement are typically carried out at filling factors $v = 2$, where two channels co-propagates at edge of the Hall bar. Electron-electron interaction between them need to be carefully taken into account in order to accord theory and experiments. In the following, we will discuss how to handle inter-channel interaction in the framework of the chiral Luttinger liquid picture.

Luttinger liquid description of interacting quantum Hall edge channels

Non-interacting electrons form a Fermi gas characterized by infinity long-lived electron and hole excitations. In two and three dimensions this picture can be extended to include interacting cases, leading to the notion of Fermi liquid elaborated by L. D. Landau during the fifties. Here, virtual particle-hole pairs dress the excitations with the consequent renormalization of the physical parameters, such as the effective mass, and the emergence of a finite lifetime for the excitations. Despite this, these quasi-particles maintain their individual nature. Radically different is the situations for interacting one-dimensional electrons. Here, due to the geometrical constraint, every individual degree of freedom immediately turns into density fluctuations of the overall system, leading a failure of the Fermi liquid description. These collective excitations, corresponding to electron-hole pairs close to the Fermi energy, are properly described in term of a bosonic theory known as the Luttinger liquid model (Haldane, 1981; Giamarchi, 2003). In the following, we will investigate the dynamics of the edge states of a quantum Hall bar at filling factor $v = 2$ in this framework.

On each edge of the Hall bar, the two co-propagating channels (indicated in the following with a and b respectively) interact capacitively along a region of finite length L via screened Coulomb interaction (see Fig. 4 below).

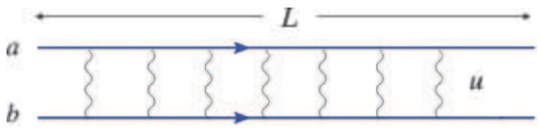

Fig. 4 Scheme of a quantum Hall edge state at filling factor $v = 2$. Here, the two channels a and b interact with a short range capacitive coupling u over a finite length L.

Consistently to experimental observations no electron tunneling occurs between the two channels. Due to the presence of the magnetic field, this situation is well represented by a chiral version of the Luttinger liquid theory in which the interacting one-dimensional edge channels are described in terms of bosonic modes usually called edge-magnetoplasmons (Wen, 1995). The Hamiltonian density of the systems can be written as

$$\mathcal{H} = \frac{1}{4\pi} \sum_{i,k=a,b} \mathcal{V}_{i,k}[\partial_x \phi_i(x) \partial_x \phi_k(x)] \tag{16}$$

with

$$\mathcal{V} = \begin{pmatrix} v & u \\ u & v \end{pmatrix} \tag{17}$$

and where the bosonic modes ϕ_i are related to the electron particle density operator of each channel through

$$\rho_i(x) = \frac{1}{2\pi} \partial_x \phi_i(x) \quad i = a,b. \tag{18}$$

The annihilation operator for an electron at point x of one of the two channels can be written in this picture in the form

$$\Psi_i(x) = \frac{\mathcal{F}_i}{\sqrt{2\pi\xi}} e^{-i\phi_i(x)} \quad i = a,b \tag{19}$$

with ξ a finite length cut-off and $\mathcal{F}_i$ playing the role of Klein factors.

In (16), for sake of simplicity, we have assumed identical propagation velocity v for both the excitations along the two edge channels and we have indicated with u the intensity of their capacitive coupling. Under these conditions the full interacting problem can be easily diagonalized through a rotation in the field space. The full Hamiltonian density then becomes

$$\mathcal{H} = \frac{1}{4\pi} \sum_{\beta=\rho,\sigma} v_\beta \left[\partial_x \phi_\beta(x)\right]^2 \tag{20}$$

in terms of the rotated fields

$$\begin{aligned} \phi_\rho(x) &= \frac{1}{\sqrt{2}} [\phi_a(x) + \phi_b(x)] \\ \phi_\sigma(x) &= -\frac{1}{\sqrt{2}} [\phi_a(x) - \phi_b(x)]. \end{aligned} \tag{21}$$

These fields are associated with a fast charged mode ($\phi_\rho(x)$) and a slow dipole mode ($\phi_\sigma(x)$) propagating with velocities $v_{\rho,\,\sigma} = v \pm u$, respectively.

Focusing, for pedagogical reasons, on the case of Levitons injection one can model the electron source as an ohmic contact which couples the outer channel a with a time-dependent voltage source $V(t)$. This leads to an additional term in the Hamiltonian density of the form

$$\mathcal{H}_V = eV(t)\rho_a(x)\Theta(-x), \tag{22}$$

where we have assumed a macroscopic contact from $-\infty$ to $x = 0$ in correspondence of the starting of the interacting region. This allows to fix the proper initial conditions for the quantum fields at the beginning of the interacting region. Taking into account the transformation in (21) and solving the complete dynamics of the system, the voltages outgoing form the interacting region and reaching the QPC in the channels a and b respectively are related to the incoming one through

$$\begin{aligned} V'_a(t) &= \frac{1}{2}\left[V\left(t - \tau_\rho\right) + V(t - \tau_\sigma)\right] \\ V'_b(t) &= \frac{1}{2}\left[V\left(t - \tau_\rho\right) - V(t - \tau_\sigma)\right], \end{aligned} \tag{23}$$

with $\tau_{\rho,\sigma} = v_{\rho,\sigma}/L$ times of flight required by the charged and dipole mode to cross the interacting region. This leads to the fractionalization of the voltage pulse illustrated in Fig. 5 below.

The consequences of this phenomenology on the form of the HOM dip will be discussed in the following.

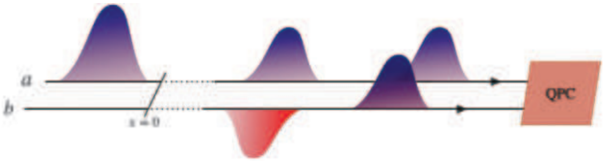

Fig. 5 Cartoon view of the fractionalization of a peaked voltage profile injected into the *a* channel, crossing an interacting region and reaching a QPC.

Effects of interaction in the Hong-Ou-Mandel profile: The Leviton case

According to what reported in (23) it is possible to Fourier expand both the HBT and the HOM contributions to the noise. The ratio in (14) can then be written, at zero temperature, as

$$\mathcal{Q}(t_D) = \frac{\sum_{l=-\infty}^{+\infty}\left|\sum_m \bar{p}_{l+m}(q)\bar{p}_m^*(q)e^{im\Omega t_D}\right|^2|l|}{2\sum_{l=-\infty}^{+\infty}\left[|\bar{p}_l(q)|^2|l+q|\right]} \tag{24}$$

where we have made explicit the dependence with respect to the number of the injected excitations q. In the above expression we have introduced $\Omega = 2\pi/T$ and the quantity

$$\bar{p}_l(q) = \sum_{n=-\infty}^{+\infty} p_{l-n}\left(\frac{q}{2}\right)p_n\left(\frac{q}{2}\right)e^{i\Omega\tau_\rho(l-n)}e^{i\Omega\tau_\sigma n} \tag{25}$$

with

$$p_l(z) = z\sum_{s=0}^{+\infty}\frac{(-1)^s\Gamma(z+l+s)e^{-2\pi\tau_0(2s+l)/T}}{\Gamma(z+1-s)\Gamma(1+s)\Gamma(1+l+s)} \tag{26}$$

giving the probability amplitude for an electron to absorb ($l > 0$) or emit ($l < 0$) l photons in the case of Lorentzian voltage pulse in time (Glattli and Roulleau, 2017).

We consider now, for sake of simplicity, the ratio $\mathcal{Q}$ evaluated in a symmetrical set-up with respect to the QPC, namely a configuration where the lengths of the two interacting regions in the incoming channels are identical. When interaction is present, by changing the time delay t_D between the right and the left moving trains of excitations, we find three characteristic signatures in the noise profile (see Fig. 6 below).

At $t_D = 0$ a central dip appears for both the free electron case described by (15) and the interacting case, while two previously absent side-dips emerge at a position $t_D = \pm|\tau_\rho - \tau_\sigma|$. The shape of these three dips is reminiscent of the Lorentzian profile in time of the wave-packet of the injected excitations while their width depends on its typical timescale (Rebora et al., 2020).

This interference pattern can be easily understood in terms of the Luttinger liquid picture discussed in the previous Section. After injection, the electrons are fractionalized into two modes: a slow dipole mode and a fast charged mode (see Fig. 5). The central dip, which corresponds to the symmetric situation of simultaneous injection of electrons, start from zero because these identical excitations reach the QPC at the same time. The destructive interference is responsible for the appearance of side-dip structures. Indeed, when $t_D = \pm|\tau_\rho - \tau_\sigma|$ the fast right moving mode and the slow dipole mode reach the QPC at the same time.

Even more dramatic features are predicted to appear in strongly interacting systems like fractional quantum Hall edge channels. These will be discussed in the following Section.

Crystallization of Levitons in the fractional quantum Hall regime

A prototypical example of strongly correlated electron systems is represented by fractional quantum Hall states with filling factor belonging to the so called Laughlin sequence, namely with $\nu = 1/(2n+1)$ with $n \in \mathbb{N}$ (Das Sarma and Pinczuk, 2004). According to the chiral Luttinger liquid picture discussed above (Wen, 1995), the up u and down d edge states of the Hall bar in

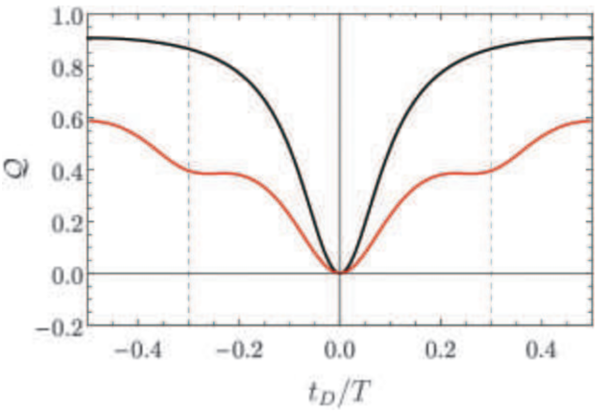

Fig. 6 Ratio $\mathcal{Q}$ for Lorentzian voltage pulses, carrying unitary charge $q = 1$, as a function of t_D/T for a symmetric setup shown for the non-interacting (black curve) and the interacting case (red curve). Other parameters are: $\tau_0/T = 0.05$, $v_\rho = 4 \times 10^5$ m/s, $v_\sigma = 1.8 \times 10^5$ m/s and $L = 2$ μm.

this regime can be both described in terms of a single chiral bosonic mode for each edge. The low energy effective Hamiltonian density for the system reads

$$\mathcal{H} = \frac{v}{4\pi}\sum_{j=u,d}\left[\partial_x\phi_j(x)\right]^2 \tag{27}$$

with particle density operators given by

$$\rho_{u,d}(x) = \pm\frac{\sqrt{v}}{2\pi}\partial_x\phi_{u,d}(x). \tag{28}$$

We assume again that a Lorentzian train of voltage pulses $V(t)$ is applied to one (HBT configuration) or both (HOM configuration) the channels by means of a capacitive coupling between the channel and an ohmic contact.

Differently from what done before, in this case it is no more possible to assume a non-interacting picture for tunneling of excitations at the level of the QPC and the scattering matrix derived from it. Therefore, a more convenient way to handle the problem requires a perturbative approach. As an additional, despite very interesting, complication in the present case the more relevant tunneling process is represented by emergent fractionally charged excitation with charge $e^* = ve$ whose annihilation is described in terms of the operator $\tilde{\Psi}_{u,d}(x)$. Their tunneling from u to d and vice versa is taken into account by the Hamiltonian contribution (Wen, 1995)

$$\mathcal{H}_\Lambda = \Lambda\tilde{\Psi}_u^\dagger(x)\tilde{\Psi}_d(x)\delta(x) + \text{H.c.} \tag{29}$$

$$= \frac{\Lambda}{2\pi\xi}e^{-i\sqrt{v}\phi_u(x)}e^{i\sqrt{v}\phi_d(x)}\delta(x) + \text{H.c.} \tag{30}$$

Here, we have introduced the tunneling amplitude Λ. Taking into account the chiral propagation of the modes along the edge, which relates the space coordinate x with the time t, the backscattering current operator due to the quasiparticles is given by

$$I_B(t) = ie^*\frac{\Lambda}{2\pi\xi}e^{-i\sqrt{v}\phi_u(t)}e^{i\sqrt{v}\phi_d(t)} + \text{H.c.} \tag{31}$$

Starting from this, it is possible to evaluate the noise perturbatively in Λ. In the following we will stop at the leading order in this expansion.

In case of identical injection on the two incoming channels, the two identical HBT contributions to the noise can be given again in terms of a Fourier series, namely

$$\begin{aligned} S_\alpha^{\text{HBT}}(q) = -2\left(e^*\right)^2\frac{|\Lambda|^2}{(2\pi\xi)^2}\sum_{l=-\infty}^{+\infty}|p_l(q)|^2\times \\ \times[P_{2v}((q+l)\Omega) + P_{2v}(-(q+l)\Omega)] \end{aligned} \tag{32}$$

where we have introduced the function

$$P_g(\omega) = \frac{2\pi}{\Gamma(g)\omega_c^g}x^{g-1}\Theta(\omega) \tag{33}$$

with $\Gamma(g)$ the Euler's Gamma function of argument g and $\omega_c = v/\xi$

In the case of a train of Lorentzian voltage pulses, the HBT noise shows a Poissonian behavior each time q is an integer (Rech et al., 2017). This is another signature of the fact that integer charged Levitons are robust excitations also in presence of strong interaction.

In the HOM case, considering the injection of two identical train of excitations carrying the same charge q on the two side of the Hall bar and following the same procedure we have used for the HBT noise, we get

$$\begin{aligned} S^{\text{HOM}}(t_D) = -2\left(e^*\right)^2\frac{|\Lambda|^2}{(2\pi\xi)^2}\sum_{l=-\infty}^{+\infty}\left|\sum_m p_{l+m}(q)p_m^*(q)e^{im\Omega t_D}\right|^2 \\ \times[P_{2v}(l\omega) + P_{2v}(-l\omega)]. \end{aligned} \tag{34}$$

The profile of the corresponding ratio $\mathcal{Q}$ as a function of the injection delay and for different values of injected charge q is shown in Fig. 7 below. It is strongly different with respect to what shown in both the free fermion case and the interacting case at filling factor $v = 2$. Indeed, one still has a central dip reaching zero at $t_D = 0$. However, by increasing the delay one observes the emergence of subdips for $q > 1$. It is worth noticing that the number of these sub-dips is equal to $2q$-2. Due to the presence of a unique edge channel, one cannot interpret this emerging structure in terms of the fractionalization discussed in the previous Sections. In contrast, this phenomenology can be explained in terms of a different process, namely a crystallization of Levitons carrying an integer charge q occurring in the time domain. This is a consequence of the fact that the injected wave-packet reorganizes into several sub-peaks at the output of the QPC due to the strong repulsion between the electrons composing it as show by the excess of particle density at the output of the QPC reported in Fig. 8 below.

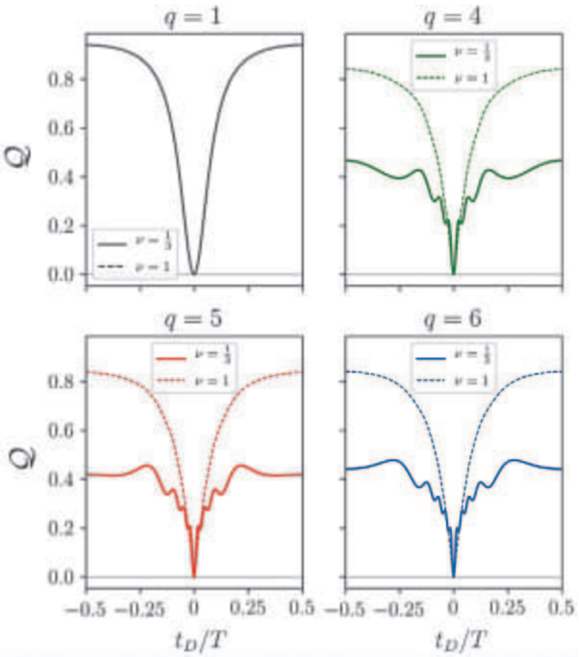

Fig. 7 Ratio $\mathcal{Q}$ as a function of t_D/T for equal injected charge $q = 1$ (black curve), $q = 4$ (green curve), $q = 5$ (red curve) and $q = 6$ (blue curve). The free fermion case at $\nu = 1$ (dashed lines) is compared to the fractional case at $\nu = 1/3$ (solid lines). The other parameters are $\tau_0/T = 0.04$ and $\omega_c = 100\Omega$. Reprinted figure with permission from Ronetti F, Vannucci L, Ferraro D, Jonckheere T, Rech J, Martin T, and Sassetti M (2018) Crystallization of levitons in the fractional quantum Hall regime. *Physical Review B* 98: 075401. Copyright 2018 by the American Physical Society.

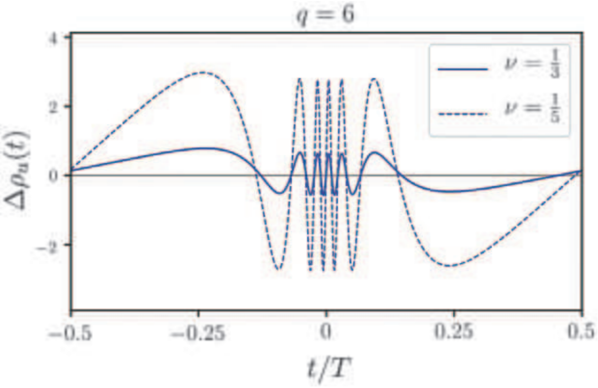

Fig. 8 Variation of the charge density $\Delta\rho_u(t)$ due to the injection of a train of Levitons carrying $q = 6$ electrons, evaluated in correspondence of a detector placed at after the QPC. Two different filling factors showing crystallization are considered: $\nu = 1/3$ (solid line) and $\nu = 1/5$ (dashed line). The other parameters are $\tau_0/T = 0.04$, $\omega_c = 100\Omega$. Reprinted figure with permission from Ronetti F, Vannucci L, Ferraro D, Jonckheere T, Rech J, Martin T, and Sassetti M (2018) Crystallization of levitons in the fractional quantum Hall regime. *Physical Review B* 98: 075401. Copyright 2018 by the American Physical Society.

Conclusion

This Chapter represents an overview of the subject of Electron Quantum Optics, with particular focus on the role played by electron-electron interaction in collisional interferometric experiments.

The analogies between conventional quantum optics experiments, based on the manipulation of individual photonic degrees of freedom, and their fermionic counterparts, involving electronic wave-packets ballistically propagating along mesoscopic channels realized in solid-state devices such as the edge states of the quantum Hall effect have been addressed.

The behavior of the electronic versions of Hanbury-Brown-Twiss and Hong-Ou-Mandel interferometers has been discussed in detail, underlying the fact that while the first provide information about the corpuscular nature of the excitations, the second can shed light on the interplay between Fermionic statistics and interaction effects. In particular, the role of statistics is encoded in the so called Pauli dip, a suppression of the current fluctuations associated to the anti-bunching of electrons that reach a quantum point contact at the same time.

To describe the effects of interaction, we have introduced the Luttinger liquid picture, universally accepted as the proper way to treat interacting systems confined in one spatial dimension, where the conventional Fermi liquid paradigma fails. To better address experimentally relevant situations, we have focused on the case of a quantum Hall state at filling factor $\nu = 2$, where two capacitively coupled edge channels co-propagate at the edge of the Hall bar. Here, a fractionalization of the injected voltage pulses occurs. At the level of collisional Hong-Ou-Mandel experiments this phenomenology leads to a deformation of the Pauli dip with the emerge of side dips.

Even more dramatic departures form the single Pauli dip profile, typical of the free fermion picture, can be observed in strongly interacting electron systems such as the fractional quantum Hall edge channels. Here, collisional experiments are characterized by the emergence of a number of side dips which grows with the charge carried by the injected pulses. This can be interpreted as a crystallization in the time domain, namely a rearrangement of the profile of a wave-packet carrying multiple electrons, as a consequence of the intense Coulomb interaction.

Acknowledgments

Authors acknowledge the support of the “Dipartimento di Eccellenza MIUR 2018-22.” We would like also to thank G. Rebora, F. Ronetti and L. Vannucci for useful discussions.

References

Bocquillon E, Freulon V, Parmentier FD, Berroir J-M, Plaçais B, Wahl C, Rech J, Jonckheere T, Martin T, Grenier C, Ferraro F, Degiovanni P, and Gwendal F (2013) Electron quantum optics in ballistic chiral conductors. *Annalen der Physik* 526: 1.

Das Sarma S and Pinczuk A (2004) *Perspectives in Quantum Hall Effects.* Wiley-VCH.

Ferraro D, Feller A, Ghibaudo A, Thibierge E, Bocquillon E, Fève G, Grenier C, and Degiovanni P (2013) Wigner function approach to single electron coherence in quantum Hall edge channels. *Physical Review B* 88: 205303.

Fève G, Mahé A, Berroir J-M, Kontos T, Plaçais B, Glattli DC, Cavanna A, Etienne B, and Jin Y (2007) An on-demand coherent single-electron source. *Science* 316: 1169.

Giamarchi T (2003) *Quantum Physics in One Dimensions.* Oxford University Press.

Glattli DC and Roulleau P (2017) Levitons for electron quantum optics. *Physica Status Solidi B: Basic Solid State Physics* 254: 1600650.

Haldane FDM (1981) Luttinger liquid theory of one-dimensional quantum fluids. I. Properties of the Luttinger model and their extension to the general 1D interacting spinless Fermi gas. *Journal of Physics C: Solid State Physics* 14: 2585.

Levitov LS, Lee H, and Lesovik GB (1996) Electron counting statistics and coherent states of electric current. *Journal of Mathematical Physics* 37: 4845.

Rebora G, Acciai M, Ferraro D, and Sassetti M (2020) Collisional interferometry of levitons in quantum Hall edge channels at $\nu = 2$. *Physical Review B* 101: 245310.

Rech J, Ferraro D, Jonckheere T, Vannucci L, Sassetti M, and Martin T (2017) Minimal excitations in the fractional quantum Hall regime. *Physical Review Letters* 118: 076801.

Ronetti F, Vannucci L, Ferraro D, Jonckheere T, Rech J, Martin T, and Sassetti M (2018) Crystallization of levitons in the fractional quantum Hall regime. *Physical Review B* 98: 075401.

Wen X-G (1995) Topological orders and edge excitations in fractional quantum Hall states. *Advances in Physics* 44: 405.

Theoretical approaches to liquid helium

Jordi Boronat, Department of Physics, Technical University of Catalonia, Barcelona, Spain

© 2024 Elsevier Ltd. All rights reserved.

Introduction 934
Early approaches 934
Microscopic theories 935
Quantum Monte Carlo methods 940
Conclusion 943
Acknowledgments 944
References 944

Abstract

In this article, we review the main theoretical methods applied to the study of liquid Helium adopting a microscopic approach, that is, starting from the many-particle Hamiltonian of the system. Following an introduction on the first early approaches, we discuss two main issues. In the first one, we report the main ingredients of a theoretical approach based on the variational method, with the discussion of the high accuracy obtained with them and the related progress in the design of highly accurate trial wave functions. In the second part, the main stochastic methods used in this study are briefly discussed. Altogether reflects the strong links between the study of liquid Helium and the progress in the development of new and extremely powerful approaches to deal with one of the most strongly quantum many-body systems in Nature.

Key points

- Main physical properties of liquid Helium, both in its superfluid and normal states
- Early phenomenological theoretical approaches to account for the main experimental data
- Development of theoretical approaches from a microscopic view: variational and correlated basis function theories
- Theoretical study based on stochastic methods: quantum Monte Carlo

Introduction

Liquid Helium was first liquefied by Kammerlingh Onnes in 1908 (Kamerlingh Onnes, 1908) and, since then, it has been one of the most studied quantum systems. Two of its isotopes are stable, ^{4}He and ^{3}He. In naturally produced Helium, the fraction of ^{3}He is extremely small, 1 part in 10^6, and is produced from radioactive decay of tritium. Both isotopes remain in liquid state even in the limit of zero temperature, manifesting in this way their intrinsic quantum nature. Contrarily to classical theory, that predicts that any material becomes solid in that limit, quantum mechanics explain this fail of the classical approach by considering the zero-point kinetic energy. The combination of the light mass of Helium atoms and their weak attraction produces the unique opportunity of observing the most paradigmatic quantum liquid. ^{4}He and ^{3}He have different masses but the most crucial difference between both isotopes affects their behavior as quantum many-body systems: ^{4}He is composed by an even number of spin 1/2 particles and thus, it is a boson, whereas ^{3}He has an odd number of constituents and behaves as a fermion. As we will discuss in this article, the different quantum statistics of the two Helium isotopes produces dramatic differences between them.

In ^{4}He, the specific heat shows a large excess at a temperature of 2.17 K, signaling the emergence of a phase transition, first observed by Keesom and Clusius (1932). The specific heat shows a shape similar to the λ Greek letter and is now universally known as the λ phase transition, with a critical temperature $T_c = 2.17$ K. This second-order transition separates two liquids with different properties and were termed liquid He I and liquid He II for $T > T_c$ and $T < T_c$, respectively. In 1938, P. Kapitza (Kapitza, 1938), from one side, and Allen and Misener (1938), on the other, published back-to-back papers announcing the discovery of superfluid ^{4}He in the Helium II phase. For an insightful historical analysis of the role played by the two independent teams on that discovery, we recommend the paper by Balibar (2007). Below T_λ, ^{4}He flows with vanishingly small viscosity producing a set of surprising effects such as the fountain effect, absence of boiling due to the large thermal conductivity, and second sound (Wilks, 1967).

Early approaches

In the early theoretical approaches to understand the extraordinary behavior of liquid Helium around the λ point, four names appear above many others: Laszlo Tisza, Lev Landau, Fritz London, and Nikolai Bogoliubov. Tisza and Landau worked in a

https://doi.org/10.1016/B978-0-323-90800-9.00180-3

quantum hydrodynamic approach with the main idea of Helium as a liquid composed by two independent liquids (velocity fields). This is the basis of the two-fluid model first introduced by Tisza (1938) and then completed by Landau (1941). The two-fluid model assumes that the total density is the sum of two partial densities: the normal and the superfluid. Below T_λ, the superfluid component dominates, thus explaining the superfluid properties of Helium II. Increasing the temperature, at $T \geq T_\lambda$, the superfluid density turns to be zero and the total density equals the normal one.

Landau (1941) introduced the concept of quasiparticle to postulate the shape of the excitation spectrum. Instead of single-particle excitations, the system presents collective modes that at low momenta are termed phonons, in resemblance with the excitation spectrum of a crystal. At low momenta, the excitations are linear with the momenta, the slope being the speed of sound. At larger momenta, Landau defined another type of collective excitations which were named rotons, since where initially related to the presence of quantized vortices. Landau predicted that below a certain velocity, termed critical velocity, the system cannot be excited and thus liquid Helium flows without friction. Combining phonons and rotons, Landau (1947) was able to draw the excitation spectrum of Helium before any measure of it was made.

The hydrodynamic theory by Tisza and Landau did not take into account the quantum statistics of ^{4}He because they believed that this feature was not relevant to understand the superfluidity and the λ phase transition. On the contrary, London (1938) argued that a Bose gas experiences a second-order phase transition that can explain, at least qualitatively, the λ transition in ^{4}He. Applying the critical temperature derived in the Bose-Einstein statistics,

$$k_B T_{\mathrm{BEC}} = \frac{2\pi\hbar^2}{m}\left(\frac{n}{g_{3/2}(1)}\right)^{2/3}, \tag{1}$$

with $g_{3/2}(1) \simeq 2.612$ and n the density, to the case of Helium London obtained 3.1 K, not so far from T_λ. Landau always ignored London approach to the problem (Balibar, 2007) because with his hydrodynamic theory he was able to account for many experimental facts. However, we know now that the quantum statistics of ^{4}He is crucial to understand superfluid ^{4}He. When samples of ^{3}He were produced, we learned that ^{3}He, which is a fermion, do not show the λ phase transition.

Bogoliubov, in 1947 (Bogoliubov, 1947), was the first to connect the elementary excitation spectrum with a Bose–Einstein gas with repulsive but small interatomic interaction. He proved that the lowest energy excitations are collective modes (phonons) that at low momenta are proportional to the speed of the sound, in agreement with Landau theory. The Bogoliubov excitation spectrum (Pitaevskii and Stringari, 2016)

$$\varepsilon(p) = \left[\frac{gn}{m}p^2 + \left(\frac{p^2}{2m}\right)^2\right]^{1/2}, \tag{2}$$

with g as the interaction strength predicts a critical velocity which is always equal to the speed of sound. Bogoliubov theory was again qualitatively correct but Helium is not a rarefied gas but a liquid with strong interparticle interactions.

Microscopic theories

We discuss first liquid ^{4}He. ^{3}He was obtained later in time due to its complex experimental production. As we commented in the previous section, Bogoliubov (1947) introduced field theoretical models in the theoretical description of liquid ^{4}He, but his approach was only applicable to dilute Bose gases, and this is far form the real properties of Helium. This is specially evident from the explicit assumption in Bogoliubov analysis that all the particles of the system are in the Bose–Einstein condensate, whereas in ^{4}He only 7% of them are really in this state due to the unavoidable role played by atomic correlations. In subsequent work, Beliaev (1958) introduced Green functions $G_{\alpha,\beta}(q,\omega)$ in the formalism, deriving a general equation for them at zero temperature. The quantum field theory for a Bose fluid was reanalyzed by Hugenholtz and Pines (1959) by the introduction of the chemical potential μ to guarantee the number conservation of the theory. Importantly, they removed the constraint of a full condensate, approaching better the characteristics of liquid Helium. An important result of this approach was the calculation of the energy of a Bose gas incorporating the first corrections to the Hartree–Fock energy

$$\frac{E}{N} = 4\pi na^3\left[1 + \frac{128}{15\sqrt{\pi}}\sqrt{na^3} + \frac{8(4\pi - 3\sqrt{3})}{3}na^3\ln(na^3) + \ \ldots\right], \tag{3}$$

the energy per particle E/N being in units of $\hbar^2/(2ma^2)$. Hugenholtz and Pines (1959) proved that, beyond the expansion terms in Eq. (3), additional contributions will depend on the specific shape of the interatomic potential and not only on the s-wave scattering length a. The coefficient of the $(na^3)^{3/2}$ term was first calculated by Lee et al. (1957), while the coefficient of the last term was first obtained by Wu (1959). Both of them were originally derived for hard spheres, but it was shown that the same expansion is valid for any repulsive potential with scattering length a (Hugenholtz and Pines, 1959). Eq. (3) has been very useful in the study of dilute Bose gases, composed by alkali atoms, due to their extreme diluteness (Pitaevskii and Stringari, 2016). However, liquid Helium is a strongly interacting quantum many-body system in which any expansion in terms of the gas parameter na^3 is completely useless.

The first theoretical approach based on the wave function of the N-body quantum system was made by Feynman (1953). This work opened a new way to deal with the properties of Helium based on a microscopic approach. Starting from general arguments, that included the symmetry of the ^{4}He atoms and their hard-core interactions at short distances, Feynman argued that the lowest energy excitations have a collective behavior since single-particle ones have always higher energy. Based on these considerations, he wrote the wave function of the excited state of the N-body fluid as

$$\Psi(\boldsymbol{r}_1, \ldots, \boldsymbol{r}_N) = \prod_{i=1}^{N} f(\boldsymbol{r}_i)\, \Phi(\boldsymbol{r}_1, \ldots, \boldsymbol{r}_N), \tag{4}$$

where $\Phi(\boldsymbol{r}_1, \ldots, \boldsymbol{r}_N)$ is the ground-state wave function. Eq. (4) is a variational approach to the problem and thus the energy of the excitation is an upper bound to the exact energy. He obtained the lowest excitation energy

$$\hbar\omega_{\mathrm{F}}(q) = \frac{\hbar^2 q^2/2m}{S(q)}, \tag{5}$$

where $S(\boldsymbol{q}) = 1/N\langle\rho^\dagger(\boldsymbol{q})\rho(\boldsymbol{q})\rangle$ is the static structure factor, and $\rho(\boldsymbol{q}) = \sum_i \exp(-i\boldsymbol{q}\cdot\boldsymbol{r}_i)$ is the density fluctuation operator. When $\boldsymbol{q} \to 0$, $S(q) = \hbar q/(2mc)$, where c is the speed of sound. In this way, Feynman recovers the phonon relation previously found by Landau and Bogoliubov, $\hbar\omega = cq$, that is, a linear behavior. At large momenta, the static structure factor tends to 1 and so one recovers the excitation energy of a free particle $\hbar^2 q^2/2m$, quadratic with q. At intermediate q values, $S(q)$ shows a peak related to the mean interparticle distance and thus the excitation energy (5) shows a local minimum that we can identify with the roton. Qualitatively, the Feynman spectrum is correct up to momenta not much larger than the one of the roton but the roton energy is nearly two times larger than the experimental one. The minimum energy (5) is obtained with a function $f(r) = \exp(i\boldsymbol{q}\cdot\boldsymbol{r})$, so the total wave function (4) is given by

$$\Psi(\boldsymbol{r}_1, \ldots, \boldsymbol{r}_N) = \prod_{i=1}^{N} e^{i\boldsymbol{q}\cdot\boldsymbol{r}_i}\, \Phi(\boldsymbol{r}_1, \ldots, \boldsymbol{r}_N) = \rho^\dagger(\boldsymbol{q})\Phi(\boldsymbol{r}_1, \ldots, \boldsymbol{r}_N), \tag{6}$$

that emerges as the creation of a collective mode of momentum $\boldsymbol{q}$ acting on the ground-state, that is not changed by the excitation.

Feynman and Cohen (1956) improved the initial theory by introducing in the wave function two-body correlations. Their idea is that when one particle moves in the fluid its neighbors *feel* the movement or, in other words, the movement of each particle depends on its local environment. They termed these correlations as backflow correlations. Explicitly, the wave function of the collective excitation turns to

$$\Psi(\boldsymbol{r}_1, \ldots, \boldsymbol{r}_N) = \prod_{i=1}^{N} \left[e^{i\boldsymbol{q}\cdot\boldsymbol{r}_i} \sum_{j\neq i} e^{ig(\boldsymbol{r}_i - \boldsymbol{r}_j)} \right] \Phi(\boldsymbol{r}_1, \ldots, \boldsymbol{r}_N). \tag{7}$$

The function $g(r)$ in Eq. (7) couples the movement of the excited particle i with the neighboring ones. In Feynman and Cohen (1956), it is taken as a dipolar term, $g(r) = \alpha\boldsymbol{q}\cdot\boldsymbol{r}/r^3$ and the imaginary exponential containing $g(r)$ is linearized to make the calculation of the energy simpler. With this correction, the difference between the Feynman roton energy (5) and the experimental one is reduced to a factor of ~ 2 but still there is a significant difference.

To reproduce as better as possible the elementary excitation spectrum of liquid ^{4}He is not the only goal of a microscopic theory. It is fundamental to have an accurate description of the ground state of the system. The most fruitful approach to account for the equation of state of liquid ^{4}He has been the variational theory since standard perturbative approaches are not applicable due to the hard core of the He–He interaction at short distances. The Hamiltonian of the N-particle system is

$$H = -\frac{\hbar^2}{2m}\sum_{i=1}^{N} \nabla_i^2 + \sum_{i<j}^{N} V(r_{ij}), \tag{8}$$

where $V(r)$ is the pair interatomic potential. One can add to Eq. (8) three-body potentials, whose analytic form is not well known. However, its contribution to the energy seems to be not relevant and the results can even worsen (Boronat and Casulleras, 1994). In the description of the bulk phases, one always assumes the thermodynamic limit: $N \to \infty$, $\Omega \to \infty$, and the density $\rho = N/\Omega$ is finite. For a trial wave function Ψ, not orthogonal to the ground state, the Ritz's variational principle of quantum mechanics states that

$$E = \frac{\langle\Psi|H|\Psi\rangle}{\langle\Psi|\Psi\rangle} \geq E_0, \tag{9}$$

where E_0 is the ground-state energy of the system. The wave function Ψ must be symmetric under the interchange of particles and approaches zero when $r_{ij} \to 0$. Also, when a set of particles is significantly far way from the rest of the system, the total wave function factorizes, that is, the cluster property is fulfilled. The first model wave function that comes to mind is a symmetrized product of single-particle wave functions which, for a bulk phase, are plane waves. However, this model clearly violates both crucial properties. Bijl (1940) and Jastrow (1955) proposed a model to account with the restrictions imposed by a strongly correlated fluid,

$$\Psi(\boldsymbol{r}_1, \ldots, \boldsymbol{r}_N) = \prod_{i=1}^{N} g(r_i) \prod_{i<j}^{N} f(r_{ij}), \tag{10}$$

where $f(r)$ is a two-body correlation factor and $g(r)$ is a one-body function that, in the bulk phase, is simply 1 (ground state). The function $f(r)$ plays an essential role in the study of Helium and satisfies two main properties: it becomes zero, approaching the hard core of the potential, and one at large distance, according to the cluster property. In Fig. 1, we show the characteristic shape of the potential and the two-body correlation factor.

The energy per particle for a Bijl–Jastrow wave function is readily obtained as

$$\frac{E}{N} = \frac{1}{2}\rho \int d\boldsymbol{r}\left[V(r) - \frac{\hbar^2}{2m}\nabla^2 \ln f(r)\right], \tag{11}$$

with $g(r)$ the two-body radial distribution function

$$g(r_{12}) = \frac{N(N-1)}{\rho^2} \frac{\int d\boldsymbol{r}_3 \ldots d\boldsymbol{r}_N |\Psi(\boldsymbol{r}_1, \ldots, \boldsymbol{r}_N)|^2}{\int d\boldsymbol{r}_1 \ldots d\boldsymbol{r}_N |\Psi(\boldsymbol{r}_1, \ldots, \boldsymbol{r}_N)|^2}, \tag{12}$$

which is proportional to the probability of finding two particles at distance $\boldsymbol{r}$. Accessing to the function $g(r)$ allows for the calculation of the energy of the system and further properties. However, as Eq. (12) shows, its estimation is very difficult due to the multidimensional integrals that need to be carried out. A fruitful approach in the study of liquid Helium has been the hypernetted chain theory (HNC) based on the summation of the series in terms of the function $h(r) = f^2(r) - 1$ in which $g(r)$ can be expressed. This function $h(r)$ is different from zero only at short distances and allows for a cluster expansion. $g(r)$ is given exactly by

$$g(r) = f^2(r)\ \exp(N(r) + E(r)), \tag{13}$$

where $N(r)$ and $E(r)$ are functions summing up specific terms of the series, known as nodal and elementary diagrams, respectively. Nodal diagrams can be calculated by solving the HNC integral equation

$$N(r_{12}) = \rho \int d\boldsymbol{r}_3 [g(r_{13}) - 1][g(r_{32}) - N(r_{32}) - 1]. \tag{14}$$

On the contrary, elementary diagrams cannot be summed up and, thus, only approximated in some way (Usmani et al., 1982b; Fabrocini and Rosati, 1982; Clements et al., 1993). Therefore, Eq. (13) cannot be evaluated in an exact and closed form using this theory.

The variational upper bound to the exact energy depends on the trial wave function. One can guess an analytic model for it, with a set of variational parameters to be optimized. Otherwise, one can approach the optimization via a functional derivative, normally written in terms of the two-body distribution function $g(r)$,

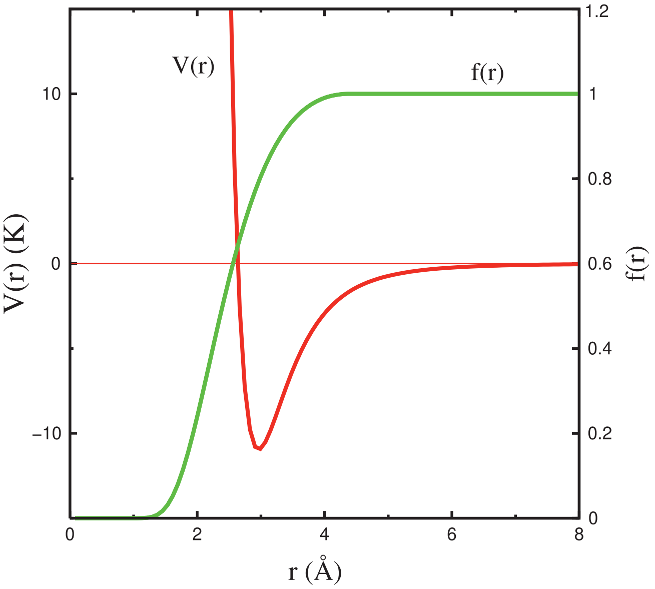

Fig. 1 He–He interatomic potential $V(r)$ and the two-body correlation factor $f(r)$.

$$\frac{\delta E[g(r)]}{\delta g(r)} = 0, \tag{15}$$

where $E[g(r)]$ is the energy of the system. This can be written only in terms of $g(r)$ by using Eq. (13),

$$E[g(r)] = \frac{\rho}{2}\int d\mathbf{r} g(r)V(r) + \frac{\hbar^2\rho}{2m}\int d\mathbf{r}\left[\left(\nabla\sqrt{g(r)}\right)^2 + \frac{1}{4}g(r)\nabla^2 E(r)\right] - \frac{\hbar^2}{8m}\frac{1}{2\pi^3\rho}\int d\mathbf{k}k^2\frac{(S(k)-1)^3}{S(k)}. \tag{16}$$

Imposing the minimization condition (15), one arrives to the Euler–Lagrange differential equation for the optimal correlation (Lantto et al., 1977; Kallio and Smith, 1977)

$$-\frac{\hbar^2}{m}\nabla^2\sqrt{g(r)} + (V(r) + W(r))\sqrt{g(r)} = 0. \tag{17}$$

This equation needs to be solved iteratively (Jackson et al., 1979) because the potential $W(r)$ depends on the correlation function. Neglecting the contribution of the elementary diagrams, this induced potential is better written in reciprocal space as

$$\tilde{W}(q) = -\frac{\hbar^2 q^2}{4m}\frac{(S(q)-1)(2S(q)+1)}{S(q)^2}, \tag{18}$$

where $S(q)$ is the static structure factor,

$$S(q) = \frac{1}{N}\langle\rho_q\rho_{-q}\rangle = 1 + \rho\int d\mathbf{r}e^{i\mathbf{q}\cdot\mathbf{r}}(g(r)-1). \tag{19}$$

At zero temperature, the function $S(q)$ satisfies $S(0) = 0$ and shows the phononic behavior at small q

$$\lim_{q\to 0} S(q) = \frac{\hbar q}{2mc}, \tag{20}$$

where c is the speed of the sound. This behavior at small q produces a long-range behavior of the two-body correlation factor (Feenberg, 1969)

$$\lim_{r\to\infty} f(r) = 1 - \frac{mc}{2\pi^2\hbar\rho r^2}. \tag{21}$$

Remarkably, the optimal $f(r)$ obtained from the Euler–Lagrange Eq. (17) satisfies the phonon behavior (21) (Castillejo et al., 1979), even if the speed of sound that derives form that differs from the experimental one.

At zero temperature, the superfluid fraction of ^{4}He is one but the occupation of the zero-momentum state, that is the Bose–Einstein condensate, is significantly smaller than one due to the relevance of correlations. Microscopically, the condensate fraction n_0, and the momentum distribution in general, can be calculated through the one-body density matrix

$$\rho(r_{11'}) = \Omega\,\frac{\int d\mathbf{r}_2\ldots d\mathbf{r}_N\Psi(\mathbf{r}_1,\ldots,\mathbf{r}_N)\Psi(\mathbf{r}_{1'},\ldots,\mathbf{r}_N)}{\int d\mathbf{r}_1\ldots d\mathbf{r}_N|\Psi(\mathbf{r}_1,\ldots,\mathbf{r}_N)|^2}, \tag{22}$$

normalized as $\rho(0) = 1$. Fourier transforming $\rho(r)$ one gets the momentum distribution

$$n(q) = n_0\delta(q) + \rho\int d\mathbf{r}(\rho(r) - n_0)e^{i\mathbf{q}\cdot\mathbf{r}}, \tag{23}$$

where $n_0 = \lim_{r\to\infty}\rho(r)$ is the condensate fraction. The momentum distribution (23) can be measured using deep inelastic neutron scattering at large momentum transfer. The condensate fraction is quite small $n_0 \sim 0.07$ and its estimation, from the dynamic structure factor $S(\mathbf{q},\omega)$, requires from an accurate analysis of final state effects (Glyde, 1994). A variational estimation of the one-body density matrix and the condensate fraction can be made using a HNC cluster expansion similar to the one developed for $g(r)$ (Fantoni, 1978).

With the best Jastrow factor, the upper bound to the energy provided by the variational calculation is still 15% above the exact quantum Monte Carlo results (see next section) for the same interatomic potential and at densities close to the equilibrium point. An important advance on the improvement of the variational energy was the introduction of three-body correlations in the trial wave function,

$$\Psi_{\mathrm{JT}}(\mathbf{r}_1,\ldots,\mathbf{r}_N) = \prod_{i<j}^{N} f(r_{ij})\prod_{i<j<k}^{N} f_3(r_{ij}, r_{ik}, r_{jk}), \tag{24}$$

which corrects the description of correlation effects at short and medium interparticle distances. The relevance of these correlations in the study of liquid Helium derives from its relatively large density, which drives this liquid into the realm of one of the most correlated quantum systems in Nature. The origin of the function f_3, and its specific functional form, can be derived in different ways: introducing a momentum dependence in the two-body correlation factor (Pandharipande, 1978) or by searching the first correction to the Jastrow factor by linearizing the imaginary-time Schrödinger equation (Boronat, 2002). It adopts the form

$$f_3(r_{ij}, r_{ik}, r_{jk}) = \exp\left(-\frac{1}{2}\, q(r_{ij}, r_{ik}, r_{jk})\right), \tag{25}$$

where

$$q(r_{ij}, r_{ik}, r_{jk}) = \sum_l \sum_{\text{cyc}} \xi_l(r_{ij})\xi_l(r_{ik})P_l(\widehat{r_{ij}}\cdot\widehat{r_{ik}}), \tag{26}$$

where l is the angular momentum and P_l the Legendre polynomial. The most important, and most used contribution, corresponds to $l = 1$. The pair function $\xi(r)$ in Eq. (26) is assumed to be a short-range correlation factor

$$\xi(r) = \sqrt{\lambda}\, \exp\left[-\left(\frac{r - r_t}{r_\omega}\right)^2 \right], \tag{27}$$

where λ, r_t, and r_ω variational parameters to be optimized. The HNC equations can be generalized to allow for the inclusion of three-body correlations in the diagrammatic expansions (Usmani et al., 1982a). The energies obtained so far reduce in a $\sim 70\%$ the difference between the Jastrow upper bound and the exact values, pointing to its importance for a right microscopic description of liquid ^{4}He.

The theoretical description of liquid Helium is not complete without understanding the dynamics of the system (Godfrin and Krotscheck, 2022). The dynamic structure function $S(\boldsymbol{q}, \hbar\omega)$ contains the maximum information about it and is experimentally accessible by inelastic scattering through

$$\frac{\partial^2 \sigma}{\partial\Omega\, \partial\hbar\omega} = b^2 \left(\frac{q_1}{q_0}\right) S(\boldsymbol{q}, \hbar\omega), \tag{28}$$

with the left part being the double differential cross section. In Eq. (28), b is the scattering length of the nucleus, and $\boldsymbol{q}_0$ and $\boldsymbol{q}_1$ are the initial and final momentum of the neutron. The momentum and energy transferred to the liquid are $\boldsymbol{q} = \boldsymbol{q}_1 - \boldsymbol{q}_0$ and $\hbar\omega$, respectively. At zero temperature, and for a N particle system,

$$S(\boldsymbol{q}, \hbar\omega) = \frac{1}{N}\sum_n |\langle \Psi_n | \rho(\boldsymbol{q}) | \Psi_0 \rangle|^2 \delta(\hbar\omega - (E_n - E_0)), \tag{29}$$

where the sum is extended to all the excited states and $\rho(\boldsymbol{q})$ is the density fluctuation operator. To calculate the dynamic response one invokes linear response theory, where the change in the density under the action of an external tiny time-dependent potential is

$$\delta\rho(\mathbf{r}, t) = \int d\mathbf{r}' dt' \chi(\mathbf{r}, \mathbf{r}', t - t')\, \delta V_{\text{ext}}(\mathbf{r}', t'), \tag{30}$$

where χ is the density–density response function. The dynamic response can be obtained from the imaginary part of the Fourier transform of χ,

$$S(\boldsymbol{q}, \hbar\omega) = -\frac{1}{N\pi} \Im\left[\int d\mathbf{r} d\mathbf{r}' e^{i\boldsymbol{q}\cdot(\mathbf{r} - \mathbf{r}')} \chi(\mathbf{r}, \mathbf{r}', \hbar\omega) \right], \tag{31}$$

and the evolution in time of $\delta\rho(\mathbf{r}, t)$ from the least-action principle $\delta S = 0$. The calculation of the dynamic response of liquid Helium has been the object of intense work for many years. Regular perturbation theory does not work because of the hard core of the He–He interaction and then it is necessary to work out the theory using correlated basis functions (CBFs). From pioneering work by Jackson and Feenberg (1962) and Lee and Lee (1975), the major progress has been achieved by dynamic many-body theory developed by Campbell and Krotscheck (2009) and Campbell et al. (2015). Recently, a comparison between very accurate experimental data, on the dynamic response and the excitation spectrum, and theoretical results obtained with dynamic many-body theory has shown an impressive agreement (Beauvois et al., 2018).

Until here, we have focused our discussion on the studies of bosonic liquid ^{4}He. But, Helium offers another stable isotope, ^{3}He, which is a fermion. At very low temperatures, it remains in a liquid state that becomes superfluid at ~ 2 mK. In the following, we refer to normal nonsuperfluid ^{3}He since superfluid ^{3}He is a very different subject which would require a completely different scope. The variational wave function incorporates the Fermi statistics in the well-known Jastrow–Slater form

$$\Psi(\boldsymbol{r}_1, \ldots, \boldsymbol{r}_N) = \prod_{i<j}^{N} f(r_{ij})\, \Phi(\boldsymbol{r}_1, \ldots, \boldsymbol{r}_N), \tag{32}$$

where Φ is an antisymmetric wave function, usually taken as the product of Slater determinants $\Phi = D_\uparrow D_\downarrow$ since the interaction is spin independent. Variational theory, based on cluster expansion and summation of proper diagrams, to calculate the pair distribution function $g(r)$ is now more involved than in Bose fluids. The extension of HNC theory is known as Fermi-hyperneted chain (FHNC), and the convergence of the series summation was proved in the seventies of the past century (Fantoni and Rosati, 1975;

Krotscheck and Ristig, 1975). This theory was reviewed in depth by Rosati (1981) and a modern update was carried out by Krotscheck (2000). As in the case of ^{4}He, the inclusion in the trial wave function (32) of triplet correlations reduces significantly the difference with quantum Monte Carlo estimations. Even with the introduction of three body factors into the variational model, the Jastrow–Slater model uses Slater determinants with free single-particle orbitals. A relevant improvement of the variational model is achieved by modifying these orbitals to include, in an approximate way, the effect of correlations on them. This is usually made with backflow correlations, where the orbitals are $\exp(i\boldsymbol{k}\cdot\tilde{\boldsymbol{r}}_i)$, with

$$\tilde{\boldsymbol{r}}_i = \boldsymbol{r}_i + \lambda \sum_{j \neq i} \eta(r_{ij}) \boldsymbol{r}_{ij}, \tag{33}$$

where $\eta(r)$ is a short-ranged function as a Gaussian (Manousakis et al., 1983). The calculation of excited states of ^{3}He has also been possible by using CBF theory with increasing complexity due to Fermi statistics (Fabrocini and Rosati, 1988). The high accuracy of CBF theory has been recently proved in a comparison between its predictions and very accurate experimental data on films of ^{3}He (Godfrin et al., 2012).

Working with the two isotopes of Helium, it is also possible to have stable mixtures of ^{3}He and ^{4}He, that is a Fermi–Bose mixture. In the limit of zero temperature, the mixture is stable up to a maximum ^{3}He concentration of 6.5% (Ebner and Edwards, 1970). This isotopic mixture was first studied neglecting the Fermi character of ^{3}He atoms showing that the isotopic Bose–Bose mixture is not stable at any finite concentration (Chakraborty, 1982). To get realistic results and finite solubilities, it is mandatory to consider ^{3}He atoms as fermions. The HNC/FHNC equations were generalized to the mixture by Fabrocini and Polls (1982) and then extended to study the momentum distribution of the mixture (Boronat et al., 1997). The limiting case of a single impurity, known also as polaron, was also studied using HNC/CBF formalism both for the ^{3}He impurity in bulk ^{4}He (Boronat et al., 1989) (Bose polaron) and for the ^{4}He impurity in ^{3}He (Arias de Saavedra et al., 1994) (Fermi polaron).

Quantum Monte Carlo methods

Variational methods discussed in the previous section have been tremendously effective in the description of liquid Helium, with special significance on the accuracy achieved in the calculations of the dynamic response. However, the application of the variational principle guarantees upper bounds to the ground-state energies and it is difficult to know what remains between the bounds and exact values. Quantum Monte Carlo methods exploit the power of stochastic simulations to go beyond the bounds of the variational theories and obtain exact estimations within some statistical noise.

We first discuss the $T=0$ ground state with projection methods. The two methods that have been used in the study of liquid ^{4}He are Green's function Monte Carlo (GFMC) and diffusion Monte Carlo (DMC). GFMC is the most accurate method because it has not any time-step dependence but its implementation is involved. Instead, DMC is a simpler method but with time-step dependence. Nowadays, DMC has become the most used tool.

The DMC method solves the Schrödinger equation, written in imaginary time,

$$-\frac{\partial \Psi(\boldsymbol{R},t)}{\partial t} = (H - E)\ \Psi(\boldsymbol{R},t), \tag{34}$$

where $\boldsymbol{R} \equiv (\boldsymbol{r}_1, \ldots, \boldsymbol{r}_N)$ is a 3N-dimensional vector (*w*alker) and t is the imaginary time. As it is usual in quantum mechanics, the time-dependent wave function of the system $\Psi(\boldsymbol{R}, t)$ can be expanded in terms of a complete set of eigenfunctions $\phi_i(\boldsymbol{R})$ of the Hamiltonian

$$\Psi(\boldsymbol{R},t) = \sum_n c_n \exp[\,-(E_i - E)t]\ \phi_i(\boldsymbol{R}), \tag{35}$$

where E_i is the eigenvalue associated to $\phi_i(\boldsymbol{R})$. The asymptotic solution of Eq. (34) for any value E close to the energy of the ground state, and for long times ($t \to \infty$), gives $\phi_0(\boldsymbol{R})$, provided that there is a nonzero overlap between $\Psi(\boldsymbol{R}, t=0)$ and the ground-state wave function $\phi_0(\boldsymbol{R})$.

A direct Monte Carlo implementation of Eq. (34) is hardly able to work efficiently, especially in liquid Helium where the interatomic potential contains a hard core. To reduce the variance, one uses importance sampling, consisting in rewriting the Schrödinger equation in terms of the wave function

$$f(\boldsymbol{R},t) \equiv \psi(\boldsymbol{R})\ \Psi(\boldsymbol{R},t), \tag{36}$$

where $\psi(\boldsymbol{R})$ is a time-independent trial wave function that describes approximately the ground state of the system at the variational level. Then, Eq. (34) turns out to be

$$-\frac{\partial f(\boldsymbol{R},t)}{\partial t} = -D\ \nabla^2_{\boldsymbol{R}} f(\boldsymbol{R},t)\ + D\ \nabla_{\boldsymbol{R}}(\boldsymbol{F}(\boldsymbol{R})\, f(\boldsymbol{R},t)\ ) + (E_L(\boldsymbol{R}) - E)\, f(\boldsymbol{R},t), \tag{37}$$

where $D = \hbar^2/(2m)$, $E_L(\boldsymbol{R}) = \psi(\boldsymbol{R})^{-1} H \psi(\boldsymbol{R})$ is the local energy, and

$$F(\boldsymbol{R}) = 2\,\psi(\boldsymbol{R})^{-1}\nabla_{\boldsymbol{R}}\psi(\boldsymbol{R}) \tag{38}$$

is called drift or quantum force. $F(\boldsymbol{R})$ acts as an external force which guides the diffusion process, involved by the first term in Eq. (37), to regions where $\psi(\boldsymbol{R})$ is large.

The r.h.s. of Eq. (37) may be written as the action of three operators A_i acting on the wave function $f(\mathbf{R}, t)$

$$-\frac{\partial f(\boldsymbol{R},t)}{\partial t} = (A_1 + A_2 + A_3)\,f(\boldsymbol{R},t) \equiv A\,f(\boldsymbol{R},t). \tag{39}$$

The Schrödinger Eq. (39) is written in an integral form by introducing the Green function $G(\boldsymbol{R}', \boldsymbol{R}, t)$, which gives the transition probability from an initial state $\boldsymbol{R}$ to a final one $\boldsymbol{R}'$ during a time t

$$f(\boldsymbol{R}', t + \Delta t) = \int G(\boldsymbol{R}', \boldsymbol{R}, \Delta t)\,f(\boldsymbol{R}, t)\,d\boldsymbol{R}. \tag{40}$$

The DMC method relies on reasonable approximations of $G(\boldsymbol{R}', \boldsymbol{R}, \Delta t)$ for small values of the time-step Δt. Considering such a short-time approximation, Eq. (40) is then iterated repeatedly until to reach the asymptotic regime $f(\boldsymbol{R}, t \to \infty)$, a limit in which one is effectively sampling the ground state.

As it is shown in Fig. 2, the accuracy achieved by the DMC method to reproduce the experimental equation of state is impressive (Boronat and Casulleras, 1994). The dependence of the energy with the density is well reproduced, in spite of a nearly constant shift that it is related to the interatomic potential used in the simulations. We observe that the shift is practically constant looking at the dependence of the pressure with the density, as shown in Fig. 2.

Quantum Monte Carlo methods are able to estimate other properties than the energy. However, direct estimations of operators which do not commute with the Hamiltonian are biased by the trial wave function used for importance sampling. To eliminate this bias, it is necessary to work with pure estimators (Casulleras and Boronat, 1995), based on the forward-walking method (Liu et al., 1974). In Fig. 3, we show DMC results for the static structure factor $S(q)$, calculated with pure estimators, in comparison with experimental data obtained from X-rays (Wirth and Hallock, 1987) and neutron scattering (Svensson et al., 1980). As one can see, the agreement between theory and experiment is excellent.

The study of the Fermi isotope ^{3}He using Monte Carlo is much more involved due to the famous sign problem. In fact, the Monte Carlo interpretation of the imaginary-time Schrödinger equation requires that $f(\mathbf{R}, t) = \psi(\mathbf{R})\Psi(\mathbf{R}, t)$ be a density, that is, $\psi\,\Psi \geq 0$ in all the domain. This boundary condition can be satisfied if ψ and Ψ change sign together and thus share the same nodes. This approximation, known as fixed-node (FN) method, (Reynolds et al., 1982) has been extensively used in the ground-state calculations of Fermi quantum liquids. It can be proved that, due to that nodal constraint, the FN energies are variational upper bounds to the exact eigenvalues for a given symmetry (Reynolds et al., 1982). Therefore, the FN results depend significantly on the quality of the trial wave function. The best upper bounds have been achieved by introducing backflow correlations, which move the nodal surface according to the interparticle interactions. Recently, an iterative backflow scheme has shown accurate results for the ^{3}He equation of state (Taddei et al., 2015), in spite of being not so good as the ones obtained in ^{4}He, where the calculation is not affected by the sign problem.

The thermal properties of liquid ^{4}He have also been deeply studied using the path integral Monte Carlo (PIMC) method. As it is well known, the knowledge of the quantum partition function at finite temperature

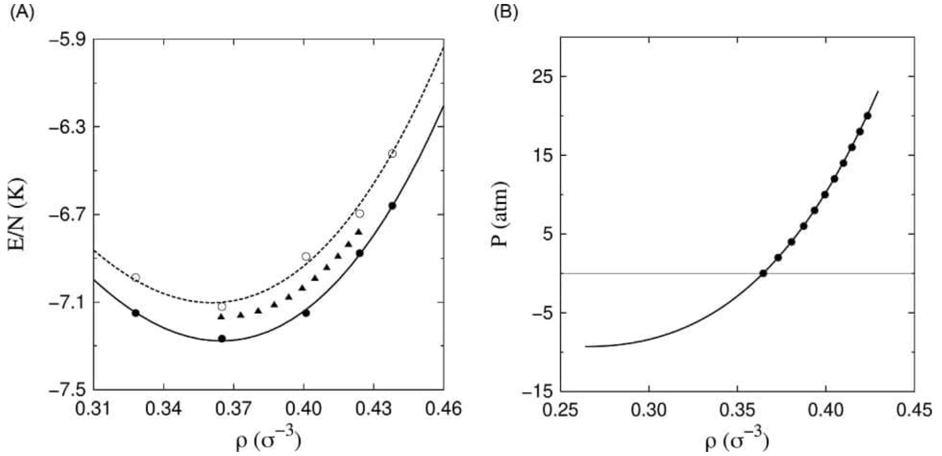

Fig. 2 *Left*: Equation of state of liquid ^{4}He (Boronat and Casulleras, 1994): open and full circles are DMC results with the Aziz (Aziz et al., 1979) and Aziz II (Aziz et al., 1987) potentials, respectively; experimental values, solid triangles, from De Bruyn Ouboter and Yang (1987). *Right*: Pressure as a function of density of liquid ^{4}He: points, experimental results (De Bruyn Ouboter and Yang, 1987), and solid line, DMC results.

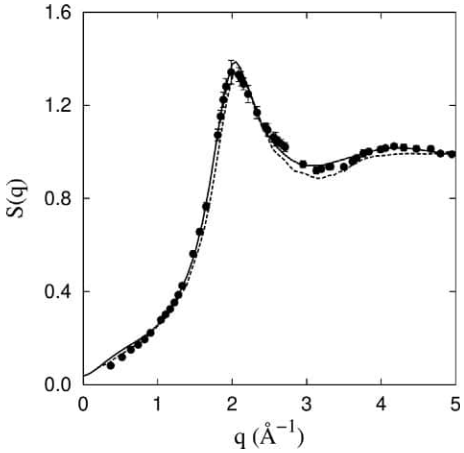

Fig. 3 DMC static structure function (points) for liquid ^{4}He at ρ_0^{expt}, in comparison with experimental determinations from Svensson et al. (1980) (*solid line*) and Wirth and Hallock (1987) (*dashed line*). The error bars of the theoretical points are only shown where larger than the size of the symbols.

$$Z = \mathrm{Tr}\, e^{-\beta\hat{H}} \tag{41}$$

allows for a full microscopic description of the properties of a given system, where $\beta = 1/T$ and $\hat{H} = \hat{K} + \hat{V}$ is the Hamiltonian. The noncommutativity of the quantum operators, kinetic $\hat{K}$ and potential $\hat{V}$ energies, makes impractical a direct calculation of the partition function Z (41). Instead, all practical implementations intended for Monte Carlo estimations of Z rely on approximations that use as a starting point the convolution property

$$e^{-\beta(\hat{K}+\hat{V})} = \left(e^{-\varepsilon(\hat{K}+\hat{V})}\right)^M, \tag{42}$$

with $\varepsilon = \beta/M$, where each one of the terms in the r.h.s. corresponds to a higher temperature MT. In the most simple approximation, known as primitive action (PA), the kinetic and potential contributions factorize

$$e^{-\varepsilon(\hat{K}+\hat{V})} \simeq e^{-\varepsilon\hat{K}}\, e^{-\varepsilon\hat{V}}, \tag{43}$$

the convergence to the exact result being warranted by the Trotter formula (Trotter, 1959)

$$e^{-\beta(\hat{K}+\hat{V})} = \lim_{M\to\infty}\left(e^{-\varepsilon\hat{K}}\, e^{-\varepsilon\hat{V}}\right)^M. \tag{44}$$

The PA is a particular case of a more general expansion in which one can decompose the action, that is

$$e^{-\varepsilon(\hat{K}+\hat{V})} \simeq \prod_{i=1}^{n} e^{-t_i\varepsilon\hat{K}}\, e^{-v_i\varepsilon\hat{V}}, \tag{45}$$

where $\{t_i, v_i\}$ are parameters to be determined. A particular implementation of this expansion put forward by Chin (2004) has proved to be a full fourth-order approximation that even can behave as sixth order by tuning properly its free parameters (Sakkos et al., 2009). Alternatively, one can use the pair-action approximation, in which the total action is built as product of pair actions that are obtained either exactly or with some approximations (Ceperley, 1995). Considering distinguishable particles, the quantum partition function Z (41) can be obtained through a multidimensional integral of the M terms (beads) in which it is decomposed,

$$Z = \int d\boldsymbol{R}_1 \ldots d\boldsymbol{R}_M \prod_{\alpha=1}^{M} \rho(\boldsymbol{R}_\alpha, \boldsymbol{R}_{\alpha+1}), \tag{46}$$

with $\boldsymbol{R} \equiv \{\boldsymbol{r}_1, \ldots, \boldsymbol{r}_N\}$ and $\boldsymbol{R}_{M+1} = \boldsymbol{R}_1$. The PIMC method is then mapped to classical closed polymers composed by beads harmonically coupled by the kinetic action (Fig. 4).

To ensure the Bose symmetry of ^{4}He, it is necessary to symmetrize the quantum partition function (41). This requires an additional sampling in the permutation space. The first applications of PIMC to liquid ^{4}He were made by proposing permutations between pairs, triplets, and more particles (Ceperley, 1995). However, this method becomes inefficient when the total number of particles in the simulation increases. A significant better performance has been achieved with the introduction of the worm algorithm, first proposed in lattice systems (Prokof'ev et al., 1998), and then extended to continuum fluids (Boninsegni et al., 2006).

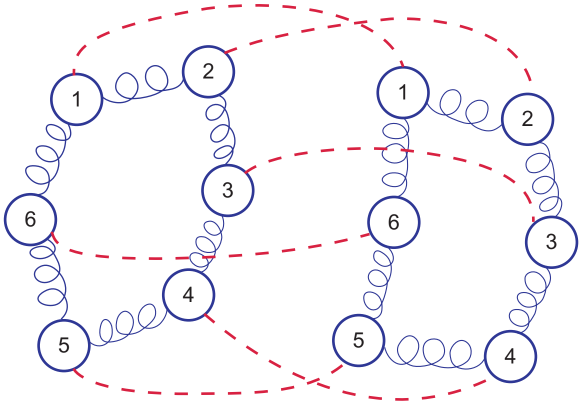

Fig. 4 Schematic representation of two particles in the PIMC formalism. The springs stand for the harmonic coupling between beads of every single atom (kinetic action) and the *dashed lines* for the interatomic potential between beads of different atoms.

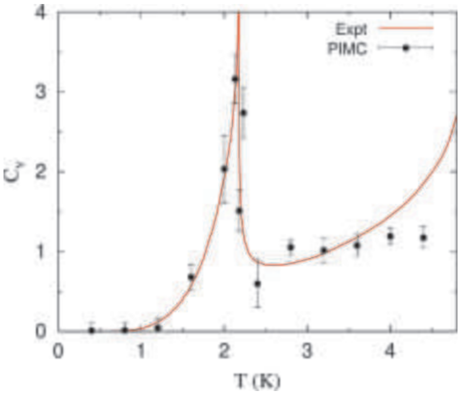

Fig. 5 Specific heat of liquid ^{4}He obtained with the PIMC method around the normal-to-superfluid λ phase transition. The line corresponds to experimental results (Wilks, 1967).

One of the more impressive successes of PIMC was the characterization of the normal-to-superfluid λ phase transition at a critical temperature $T_\lambda = 2.17$ K. In Fig. 5, we compare PIMC results of the specific heat as a function of T with experimental data. The estimation of the specific heat is numerically involved but its singularity at T_λ is well reproduced.

Conclusion

We have reported in this article some of the main theoretical approaches used in the study of liquid Helium. After an introduction on the physical properties of liquid Helium, we have discussed the early theoretical approaches used in its study. In Section "Microscopic theories," we have discussed on the application of the variational theory and CBF as a best approach for its microscopic understanding. In Section "Quantum Monte Carlo methods," we have introduced the main quantum Monte Carlo methods used in the study of liquid Helium.

This subject has been running for many years and it is impossible in practice to include all the immense work developed. Liquid Helium has been a continuous benchmark for quantum many-body theories and has been the workhorse for improving theories at all levels. This continued effort has produced a set of very accurate theoretical tools which have dramatically reproduced many experimental data. Liquid Helium is a really very strongly correlated quantum fluid where any simple perturbative scheme cannot be used. Remarkably, variational theory has proved to be the most efficient tool to deal with its microscopic description. Finally, it is also noticeable how progress in the development of quantum Monte Carlo methods has grown stimulated for the incredible amount of experimental data that we have at hands.

Acknowledgments

We acknowledge financial support from Ministerio de Ciencia e Innovación MCIN/AEI/10.13039/501100011033 (Spain) under Grant PID2020-113565GB-C21.

References

Allen JF and Misener AD (1938) Flow of liquid helium II. *Nature* 141: 75.

Arias de Saavedra F., Boronat J, Polls A, and Fabrocini A (1994) Effective mass of one 4He atom in liquid 3He. *Physical Review B* 50: 4248.

Aziz RA, Nain VPS, Carley JS, Taylor WL, and McConville GT (1979) An accurate intermolecular potential for helium. *The Journal of Chemical Physics* 70: 4330.

Aziz RA, McCourt FRW, and Wong CCK (1987) A new determination of the ground state interatomic potential for He2. *Molecular Physics* 61: 1487.

Balibar S (2007) The discovery of superfluidity. *Journal of Low Temperature Physics* 146: 441.

Beauvois K, Dawidowski J, Fåk B, Godfrin H, Krotscheck E, Ollivier J, and Sultan A (2018) Microscopic dynamics of superfluid 4He: A comprehensive study by inelastic neutron scattering. *Physical Review B* 97: 184520.

Beliaev ST (1958) Energy-spectrum of a non-ideal Bose gas. *Soviet Physics JETP* 7: 289.

Bijl A (1940) The lowest wave function of the symmetrical many particles system. *Physica* 7: 869.

Bogoliubov NN (1947) *The Journal of Physics, USSR* 11: 23.

Boninsegni M, Prokof'ev NV, and Svistunov BV (2006) Worm algorithm and diagrammatic Monte Carlo: A new approach to continuous-space path integral Monte Carlo simulations. *Physical Review E* 74: 036701.

Boronat J (2002) Monte Carlo simulations at zero temperature: Helium in one, two, and three dimensions. In: Eckhard K and Jesús N (eds.) *Microscopic Approaches to Quantum Liquids in Confined Geometries*, pp. 21–90. Singapore: World Scientific.

Boronat J and Casulleras J (1994) Monte Carlo analysis of an interatomic potential for He. *Physical Review B* 49: 8920.

Boronat J, Fabrocini A, and Polls A (1989) Variational calculation of the binding energy of one 3He impurity in liquid 4He. *Journal of Low Temperature Physics* 74: 347.

Boronat J, Polls A, and Fabrocini A (1997) Momentum distributions in 3He-4He mixtures. *Physical Review B* 56: 11854.

Campbell CE and Krotscheck E (2009) Dynamic many-body theory: Pair fluctuations in bulk 4He. *Physical Review B* 80: 174501.

Campbell CE, Krotscheck E, and Lichtenegger T (2015) Dynamic many-body theory: Multiparticle fluctuations and the dynamic structure of 4He. *Physical Review B* 91: 184510.

Castillejo L, Jackson AD, Jennings BK, and Smith RA (1979) Optimal and nearly optimal distribution functions for 4He. *Physical Review B* 20: 3631.

Casulleras J and Boronat J (1995) Unbiased estimators in quantum Monte Carlo methods: Application to liquid 4He. *Physical Review B* 52: 3654.

Ceperley DM (1995) Path integrals in the theory of condensed helium. *Reviews of Modern Physics* 67: 279.

Chakraborty T (1982) Variational theory of binary boson mixture at $t = 0$ k. *Physical Review B* 25: 3177.

Chin SA (2004) Quantum statistical calculations and symplectic corrector algorithms. *Physical Review E* 69: 046118.

Clements BE, Epstein JL, Krotscheck E, and Saarela M (1993) Structure of boson quantum films. *Physical Review B* 48: 7450.

De Bruyn Ouboter R and Yang CN (1987) The thermodynamic properties of liquid 3He-4He mixtures between 0 and 20 atm in the limit of absolute zero temperature. *Physica B* 44: 127.

Ebner C and Edwards DO (1970) The low temperature thermodynamic properties of superfluid solutions of 3He in 4He. *Physics Reports* 2: 77.

Fabrocini A and Polls A (1982) Variational study of 3He-4He mixture. *Physical Review B* 25: 4533.

Fabrocini A and Rosati S (1982) The method of interpolating integral equations for quantum fluids.—II. *Nuovo Cimento D* 1: 615.

Fabrocini A and Rosati S (1988) Correlated basis function theory for fermion systems. In: Prosperi D (ed.) *First International Course on Condensed Matter*, pp. 89–150. Singapore: World Scientific.

Fantoni S (1978) Momentum distribution of boson and fermion systems in Jastrow theory. *Nuovo Cimento A* 44: 191.

Fantoni S and Rosati S (1975) The hypernetted-chain approximation for a fermion system. *Nuovo Cimento A* 25: 593.

Feenberg E (1969) *Theory of Quantum Fluids*. New York: Academic Press.

Feynman RP (1953) Atomic theory of the λ transition in helium. *Physics Review* 91: 1291.

Feynman RP and Cohen M (1956) Energy spectrum of the excitations in liquid helium. *Physics Review* 102: 1189.

Glyde HR (1994) *Excitations in Liquid and Solid Helium.* Oxford: Clarendon Press.

Godfrin H and Krotscheck E (2023) The dynamics of quantum fluids. In: *Encyclopedia of Condensed Matter Physics*, 2e. Elsevier. ISBN 9780128035818. https://doi.org/10.1016/B978-0-323-90800-9.00029-9.

Godfrin H, Meschke M, Lauter HJ, Sultan A, Böhm H, Krotscheck E, and Panholzer M (2012) Observation of a roton collective mode in a two-dimensional fermi liquid. *Nature* 483: 576.

Hugenholtz N and Pines D (1959) Ground-state energy and excitation spectrum of a system of interacting bosons. *Physics Review* 116: 489.

Jackson HW and Feenberg E (1962) Energy spectrum of elementary excitations in helium II. *Reviews of Modern Physics* 34: 686.

Jackson AD, Lande A, and Lantto LJ (1979) Euler-lagrange equations and hypernetted chain calculations of boson matter. *Nuclear Physics A* 317: 70.

Jastrow R (1955) Many-body problem with strong forces. *Physics Review* 98: 1479.

Kallio A and Smith RA (1977) How simple can HNC be–And still be right? *Physics Letters B* 68: 315.

Kamerlingh Onnes H (1908) The liquefaction of helium. *Proceedings of the Section of Sciences, Koninklijke Nederlandse Akademie van Wetenschappen*, vol. 11, p. 168.

Kapitza P (1938) Viscosity of liquid helium below the lambda point. *Nature* 141: 74.

Keesom WH and Clusius K (1932) Ueber die spezifische Wärme des flüssigen Heliums. *Proceedings of the Section of Sciences, Koninklijke Nederlandse Akademie van Wetenschappen*, vol. 35, p. 307.

Krotscheck E (2000) Fermi-hypernetted chain theory for liquid 3He: A reassessment. *Journal of Low Temperature Physics* 119: 103.

Krotscheck E and Ristig ML (1975) Long-range Jastrow correlations. *Nuclear Physics A* 242: 389.

Landau LD (1941) Theory of the superfluidity of helium II. *Physics Review* 60: 356.

Landau LD (1947) *The Journal of Physics, USSR* 11: 91.

Lantto LJ, Jackson AD, and Siemens PJ (1977) HNC variational calculations of boson matter. *Physics Letters B* 68: 311.

Lee DK and Lee FJ (1975) Brillouin-Wigner perturbation procedure for elementary excitations in liquid 4He. *Physical Review B* 11: 4318.

Lee TD, Huang K, and Yang CN (1957) Eigenvalues and eigenfunctions of a Bose system of hard spheres and its low-temperature properties. *Physics Review* 106: 1135.

Liu KS, Kalos MH, and Chester GV (1974) Quantum hard spheres in a channel. *Physical Review A* 10: 303.

London F (1938) The λ-phenomenon of liquid helium and the Bose-Einstein degeneracy. *Nature* 141: 643.

Manousakis E, Fantoni S, Pandharipande VR, and Usmani QN (1983) Microscopic calculations for normal and polarized liquid 3He. *Physical Review B* 28: 3770.

Pandharipande VR (1978) Three-body correlations in the variational wave function of liquid 4He. *Physical Review B* 18: 218.

Pitaevskii L and Stringari S (2016) *Bose-Einstein Condensation and Superfluidity.* Oxford: Oxford University Press.

Prokof'ev NV, Svistunov BV, and Tupitsyn IS (1998) Worm algorithm in quantum Monte Carlo simulations. *Physics Letters A* 238: 253.

Reynolds PJ, Ceperley DM, Alder BJ, and Lester WA Jr (1982) Fixed node quantum Monte Carlo for molecules. *The Journal of Chemical Physics* 77: 5593.

Rosati S (1981) FHNC variational theory for strongly interacting Fermi systems. In: Molinari A (ed.). *From Nuclei to Particles, Proceedings of the International School of Physics Enrico Fermi, Course LXXIX*, pp. 73–112. Amsterdam: North Holland.

Sakkos K, Casulleras J, and Boronat J (2009) High order Chin actions in path integral Monte Carlo. *The Journal of Chemical Physics* 130: 204109.

Svensson EC, Sears VF, Woods ADB, and Martel P (1980) Neutron-diffraction study of the static structure factor and pair correlations in liquid 4He. *Physical Review B* 21: 3638.

Taddei M, Ruggeri M, Moroni S, and Holzmann M (2015) Iterative backflow renormalization procedure for many-body ground-state wave functions of strongly interacting normal fermi liquids. *Physical Review B* 91: 115106.

Tisza L (1938) Transport phenomena in helium II. *Nature* 141: 913.

Trotter HF (1959) On the product of semi-groups of operators. *Proceedings of American Mathematical Society* 10: 545.

Usmani QN, Fantoni S, and Pandharipande VR (1982) Three-body correlations in liquid 4He. *Physical Review B* 26: 6123.

Usmani QN, Friedman B, and Pandharipande VR (1982) Scaling approximation for the elementary diagrams in hypernetted-chain calculations. *Physical Review B* 25: 4502.

Wilks J (1967) *Liquid and Solid Helium*. Oxford: Clarendon Press.

Wirth FH and Hallock RB (1987) X-ray determinations of the liquid-structure factor and pair-correlation function of 4He. *Physical Review B* 35: 89.

Wu TT (1959) Ground state of a Bose system of hard spheres. *Physics Review* 115: 1390.

The dynamics of quantum fluids

Henri Godfrin[a] **and Eckhard Krotscheck**[b], [a]Univ. Grenoble Alpes, CNRS, Grenoble INP, Institut Néel, Grenoble, France; [b]Department of Physics, The State University of New York at Buffalo, Buffalo, NY, United States

© 2024 Elsevier Ltd. All rights reserved.

The helium liquids 946
^{4}He in 3D 947
^{3}He in 3D 951
^{4}He in reduced dimensions 953
^{3}He in reduced dimensions 955
Conclusion 955
References 957

Abstract

We review experimental and theoretical progress in the physical description of the dynamics of the quantum fluids ^{4}He and ^{3}He. Historically, the elementary excitations in these systems have been identified as phonons and rotons and, in^{3}He, collective zerosound and spin-fluctuations. Both recent high-precision measurements and theoretical methods have shown that the dynamics of these systems is actually very rich as will be discussed in detail in the body of this contribution.

The helium liquids

Helium (^{4}He and the less common isotope ^{3}He) and hydrogen are simple condensed matter systems, amenable to fundamental quantum mechanical descriptions. Helium remains liquid even at the absolute zero of temperature, an effect explained by Heisenberg's uncertainty principle, which has the consequence that light atoms confined in a small volume have a large kinetic energy, as is the case in a liquid or a solid, where each atom is confined by several surrounding atoms. For this reason, in helium, kinetic energies are larger than the weak interatomic potential energy. Even at the lowest temperatures, substantial atomic motion is present, and the system remains liquid, unless pressures on the order of 25 MPa are applied, and solidification is achieved. Another quantum effect plays an important role in the behavior of liquid helium: as the temperature is reduced below a few degrees Kelvin, the thermal de Broglie wave-length of the atoms becomes larger than the interatomic distance. The waves describing the helium atoms overlap significantly, and a description in terms of individual wave-packets of distinguishable particles becomes inappropriate, it must be replaced by a quantum many-body description in terms of indistinguishable particles, governed by quantum statistics.

Quantum Mechanics and Statistical Physics (Fetter and Walecka, 1971; Thouless, 1972) explain well the properties of Quantum Gases, i.e., ensembles of non-interacting particles, which necessarily belong to one of the two possible classes: Bosons having an integer spin quantum number s, or fermions with half-integer spin. ^{4}He atoms ($s = 0$) are bosons, and ^{3}He atoms $\left(s = \frac{1}{2}\right)$ are fermions.

The wave-functions of particles confined in a volume V are quantized plane waves characterized by their wave-vector $\mathbf{k}$. As shown by A. Einstein, the ground state of a Bose gas is the BEC (Bose Einstein condensate), where all particles occupy the same microscopic state with $\mathbf{k} = 0$. The ground state of a Fermi gas is very different, because Pauli's principle forbids double occupancy for Fermions: the particles form a Fermi sphere in wave-vector space, by completing successive energy levels of increasing wave-vector, up to the Fermi wave-vector k_F. The energy E_F of the last one, called the Fermi level, can be considerable.

The excitation spectrum $\varepsilon(k)$ of these quantum gases is simply given by the kinetic energies of the individual particles, $\varepsilon(k) = \hbar^2 k^2/2m$, where m is the particle mass and k the wave number. For bosons, at low temperatures, particles are excited from the common ground state. The energy spectrum is the usual parabolic spectrum of free particles described above. This behavior, however, is profoundly modified by interparticle interactions, i.e., as is the case in Quantum Fluids (Fetter and Walecka, 1971; Pines and Nozieres, 1966; Thouless, 1972; Wilks, 1967).

The Helium quantum *fluids* are unique in the sense that they are *very dense* and *very quantum*, making them a very challenging problem for theory. The issue is made quantitative by looking at the simple Lennard-Jones model of the helium fluids. In this model, the helium atoms interact via the interaction (Fig. 1)

$$V(r) = 4\varepsilon\left[\left(\frac{\sigma}{r}\right)^{12} - \left(\frac{\sigma}{r}\right)^{6}\right] \equiv \varepsilon v\left(\frac{r}{\sigma}\right)$$

where $\varepsilon = 10.22$K is the well depth of the potential and $\sigma = 2.556$Å is the core size (de Boer and Michels, 1938).

The interaction is not the very best (quantitative calculations are in fact made using the Aziz potential (Aziz et al., 1992), but it reproduces the ground state properties of the liquids within a few percent. Measuring all energies in units of the well depth, and all lengths in units of the core size, $x \equiv r/\sigma$, the Hamiltonian of the system is

https://doi.org/10.1016/B978-0-323-90800-9.00029-9

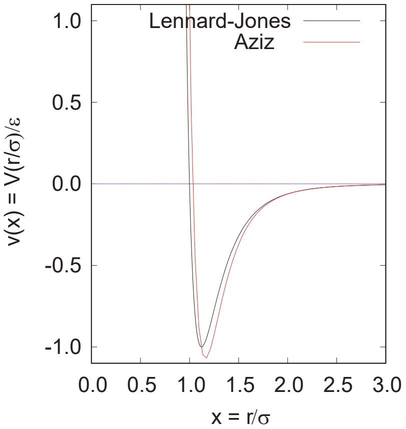

Fig. 1 Normalized Lennard-Jones "6–12" interatomic potential, as a function of the normalized interatomic distance. The normalization factors for distances (σ) and potential energies (ε) are given in the text. We also show, for comparison, the Aziz potential (Aziz et al., 1992) which is the currently accepted most accurate static 2-body interaction.

$$\frac{1}{\varepsilon} H(\mathbf{x}_1 \ldots, \mathbf{x}_N) = -\frac{\Lambda^2}{8\pi^2} \sum_i \nabla^2_{\mathbf{x}_i} + \sum_{i<j} v\left(|\mathbf{x}_i - \mathbf{x}_j|\right) \tag{1}$$

where

$$\Lambda = \frac{h}{\sigma(m\varepsilon)^{\frac{1}{2}}}$$

is de Boer's "quantum parameter" (de Boer, 1948) Λ, giving the ratio between the de Broglie wavelength and a typical diameter of the molecule. $\Lambda \approx 2.67$ for ^{4}He, $\Lambda \approx 3.09$ for ^{3}He, but $\Lambda \approx 1.3 - 1.7$ for H_2, HD, D_2, and $\Lambda < 0.1$ for heavy rare gases.

Moreover, the density of ^{4}He at zero pressure is $\rho_0 = 0.02185\text{Å}^{-3} = 0.365/\sigma^{-3}$ and for $^3\text{He}\rho_0 = 0.0163\text{Å}^{-3} = 0.273/\sigma^{-3}$, in other words the average particle distance is of the order of the core size.

^{4}He in 3D

Liquid helium (^{4}He) is the archetype of a Bose Liquid. Immediately after the discovery of the superfluidity of helium (Kapitza, 1938; Misener, 1938) by Kapitza (Moscow) and Allen and Misener (Toronto), London (1938) understood that the system was undergoing Bose-Einstein condensation, and L. Tisza proposed a "two-fluids model" featuring a coexistence of a normal fluid and a superfluid (Wilks, 1967). A Bose-Einstein condensed gas is not superfluid, however, and therefore the superfluidity observed in helium is an additional effect, associated to the interactions. A major step in the understanding of the physics of helium was made by L.D. Landau, who found a deeper interpretation of Tisza's two-fluids model. Landau postulated that the "normal fraction," which carries the entropy, is in fact the ensemble of thermal excitations of the superfluid ground state. This interpretation removed the unphysical consideration of two categories within a set of indistinguishable atoms. Landau considered elementary excitations of the fluid, in the form of quantized density fluctuations (phonons), similar to the Debye phonon modes of a crystalline solid. In order to calculate the thermodynamic properties by a Debye-like approach, where the energy is obtained by a sum over all modes, weighted by the Bose factor, Landau postulated that the dispersion relation $\varepsilon(k)$ had a linear part $\varepsilon = \hbar ck$, where c is the speed of sound, and another part displaying a minimum, the "roton gap" of energy $\triangle$. Landau's intuition was guided by specific heat measurements, showing a cubic temperature dependence at low temperatures (below 0.5 K), as expected from the linear part of the dispersion relation, as well as an exponential contribution at higher temperatures (on the order of 1 K), characteristic of an energy gap.

In a first article (Landau, 1941), Landau proposed a spectrum with two branches, with a parabolic branch centered at $k = 0$ in addition to the linear branch. This spectrum was not found satisfactory by Landau himself, the presence of two branches being reminiscent of Tisza's "two kinds of atoms."

In a second publication (Landau, 1947), he presented his celebrated "Landau dispersion relation," where a single branch of excitations characterizes the full spectrum (Fig. 2). With two parameters, the sound velocity c and the roton gap $\triangle$, both obtained from the temperature dependence of the specific heat, Landau's theory provides an excellent account of the experimental properties of superfluid helium at low temperatures. The existence of a "second sound" collective mode, where the superfluid and normal components oscillate with opposite phases while keeping the total density constant, as proposed by Tisza, corresponds in Landau's model to propagating entropy (and hence temperature) waves.

Another fundamental observation due to Landau, is that the particular shape of the dispersion relation leads to the superfluid behavior. A simple argument of energy and momentum conservation shows that the creation of excitations by the displacement of

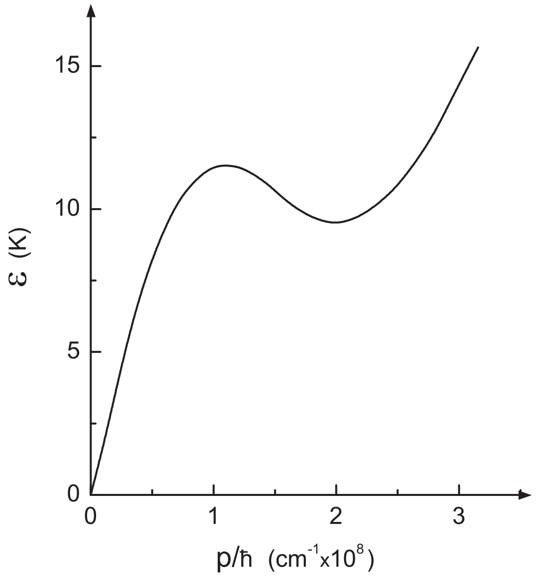

Fig. 2 The dispersion relation proposed by L. D. Landau in 1947 to describe the elementary excitations in superfluid ^{4}He at zero pressure.

an object immersed in the fluid is not possible, unless the object's velocity exceeds a critical value. The linearity of the dispersion relation at low wave vectors is essential for this to happen: in a Bose gas, where the dispersion relations is parabolic, the critical velocity is zero, the system remains normal even at the absolute zero of temperature. The evolution of the dispersion relation from the parabolic shape characteristic of a gas, to the linear behavior observed as the interaction is switched on, has been explained by Bogoliubov (1947) in the weak interaction limit. The dispersion relation of the elementary excitations plays therefore a major role in the determination of the thermal properties, and also in the superfluid nature of the liquid's ground state.

Landau's phenomenological theory introduced the fruitful concept of "quasi-particles," describing in a simple way the elementary excitations of complex many-body systems. The concept was of course already present in the Debye theory of solids, but the generalization to helium, a non-periodic system of strongly interacting particles, opened a new field of physics.

There were however two serious interrogations after Landau's theory was released. The first was obviously related to the necessity of an experimental observation of the proposed dispersion curve. And the second, to the need of a microscopic theory providing some insight in the superfluid helium behavior, and able to test the validity of Landau's model.

The first microscopic theory of superfluid helium, due to Feynman (1954), is a wonderful example of physical intuition. He found a general form for a variational wave-function which successfully explained the general shape of the dispersion relation, including the roton minimum. It was soon completed by Feynman and Cohen (1956), who introduced, improving the variational wave-functions, the concept of "backflow": the flow of helium atoms around a moving helium atom.

Dealing with many-body correlations, including dynamic effects, has been central to the development of microscopic theories, which have been considerably refined in the last decades, reaching now a quantitative power of prediction, as shown below.

Experimentally, the evidence for a Landau-like dispersion relation was missing: only indirect evidence obtained from thermodynamic measurement (specific heat, thermal conductivity, viscosity, fountain pressure, etc.) was available. Feynman and Cohen suggested the use of inelastic neutron scattering, a technique already used to measure phonon dispersion curves in crystals, to try to observe the excitation dispersion curve of superfluid helium. The first proof of the existence of a roton minimum was reported by Palevsky et al. (1957), Palevsky et al. (1958), clearly showing that the elementary excitations in superfluid helium are extremely sharp, compared to those of normal helium. These exciting results motivated extensive investigations of the dynamics of helium, covering the low energy region, i.e., the Landau-like dispersion relation, the multi-excitations region at higher energies, as well as the very high energy region of the spectrum, where BEC can be investigated (Glyde, 2018).

The principle of the inelastic neutron scattering is simple, but measurements are demanding, and high flux neutron sources (reactors, spallation sources) are needed. The helium sample is placed in an incident beam of "monochromatic" (of a given energy) neutrons, which are scattered by the helium sample, and then detected at some distance from the sample, as a function of angle and time of arrival, in the so-called time-of-flight technique (Fig. 3). Other methods (triple-axis, backscattering, spin-echo, etc.) have also been used, offering a different coverage of the momentum-energy plane, and also different resolutions in energy and momentum.

Energy and momentum conservation allow the determination of the energy transfer and the momentum transfer from the neutron to the helium sample, which correspond to the energy $\varepsilon = \hbar\omega$ and momentum $\hbar\vec{k} = \hbar\vec{Q}$ of the density fluctuations created in the helium. The incident neutron has an energy E_i and a wave-vector $\vec{k}_i$, and, after scattering, a final energy E_f and a wave-vector $\overrightarrow{k_f}$; the wave-vector transfer is $\vec{Q} = \overrightarrow{k_i} - \overrightarrow{k_f}$, and the energy transfer $\hbar\omega = E_i - E_f$ (Fig. 4).

The theory of neutron scattering (Lovesey, 1984; Glyde, 1994; Glyde, 2018) relates the double differential scattering cross section per target atom, which is the parameter measured by a scattering experiment, to the dynamic structure factor $S(Q,\omega)$ and the

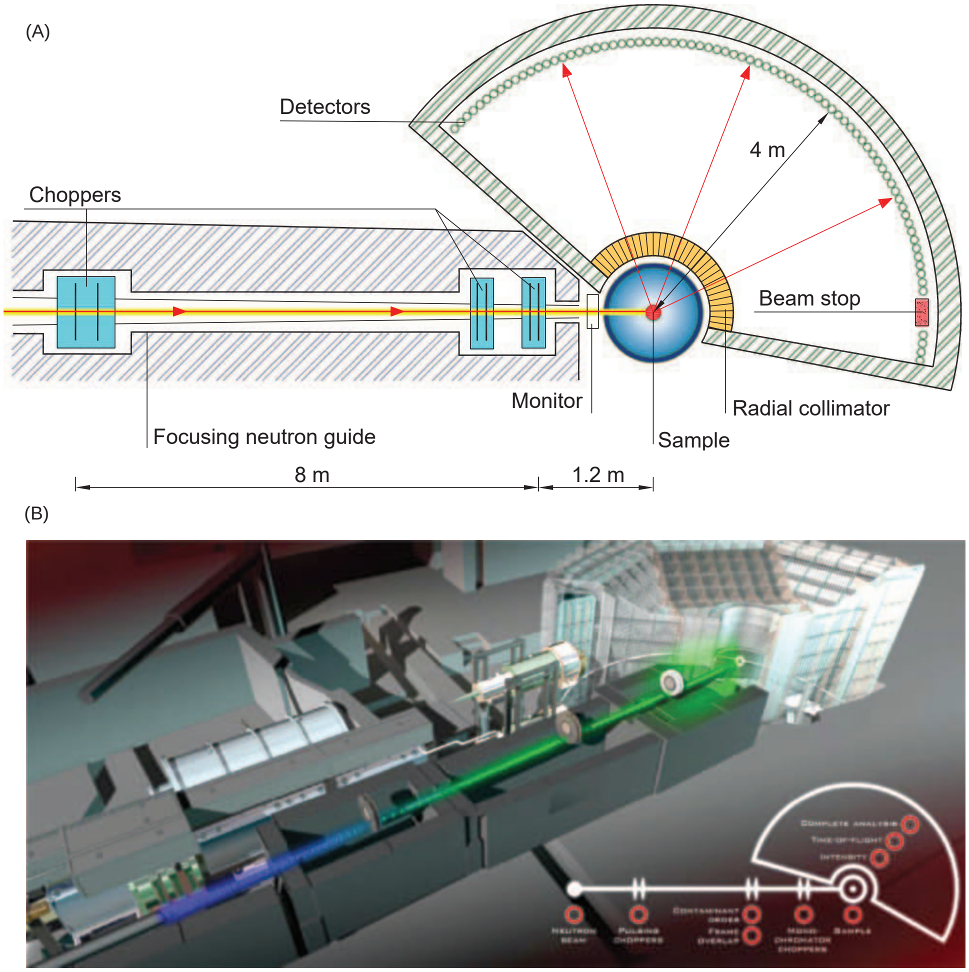
(A)
Detectors
4 m
Choppers
Beam stop
Monitor
Radial collimator
Focusing neutron guide
Sample
8 m
1.2 m
(B)
Complete analysis
Time-of-flight
Intensity
Neutron beam
Pulsing choppers
Contaminant order
Frame overlap
Mono-chromator choppers
Sample

Fig. 3 The time-of-flight neutron scattering spectrometer IN5 at the Institut Laue-Langevin.

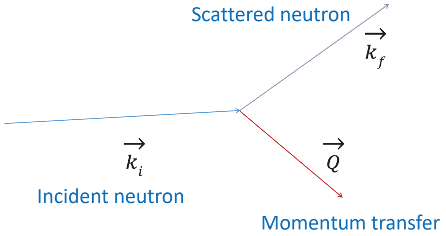
Scattered neutron
$\vec{k}_f$
$\vec{k}_i$
Incident neutron
$\vec{Q}$
Momentum transfer

Fig. 4 Neutron scattering: an incident neutron of wavevector $\vec{k}_i$ creates an excitation of momentum $\hbar\vec{k} = \hbar\vec{Q}$ in the superfluid. Q is the wavevector transfer (see text).

dynamic susceptibility $\chi(Q, \omega)$, the latter being the functions calculated by microscopic theories. They are given by the following expression, where b_c is the coherent scattering length of helium:

$$\frac{\partial^2 \sigma}{\partial \Omega \partial E_f} = \frac{b_c^2}{\hbar} \frac{k_f}{k_i} S(Q, \omega) \tag{2}$$

Results are generally presented in terms of $S(Q, \omega)$, where sharp peaks of high intensity are observed, as expected from the creation of Landau "single-excitations," as well as a more complex, broad landscape of multi-excitations. A vast literature on the subject exists, as described in the review articles by Woods and Cowley, Stirling, Glyde (see (Glyde, 2018)), the book by Glyde (Glyde, 1994), and recent works (Beauvois et al., 2018; Godfrin et al., 2021), which benefited from the substantial progress of neutron scattering facilities and instruments.

The dispersion relation $\varepsilon(k)$ of the sharp single-excitations, as measured in recent inelastic neutron scattering experiments, is shown in Fig. 5. It closely resembles the curve predicted by Landau, with a linear part at low wave-vectors (phonons), and a deep gap

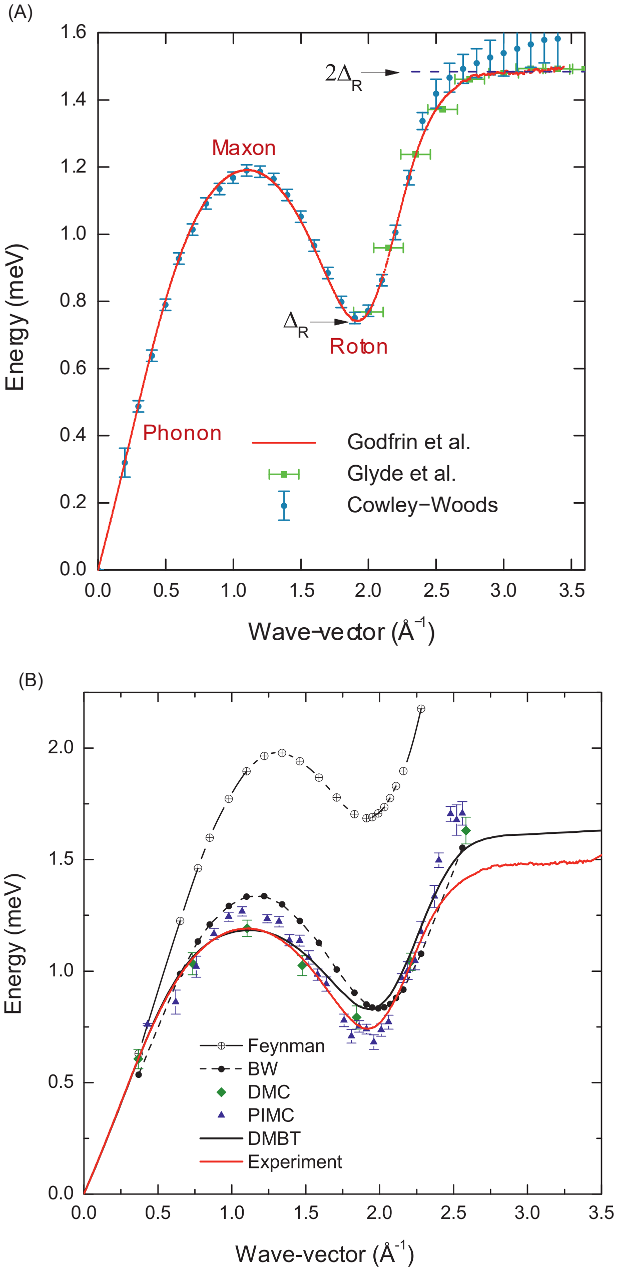

Fig. 5 The dispersion relation $\varepsilon(k)$ of excitations in superfluid ^{4}He at zero pressure. (A) Experimental data, displaying the phonon, roton, maxon, and plateau regions of the spectrum. The red dots are recent high-accuracy, highly pixelized data (seen at this scale as a continuous line, the dispersion is only visible at the highest wave-vectors) from Godfrin et al. (2021), the blue dots with error bars are from the original work by Cowley and Woods (1971) and the green dots from the high-momentum measurements by Glyde et al. (1998). (B) theoretical results, from Feynman's model (Feynman, 1954) to modern calculations such as Brillouin-Wigner perturbation theory with correlated wave function (BW; Jackson and Feenberg, 1962; Lee and Lee, 1975), diffusion (DMC; Boronat and Casulleras, 1997; Boronat and Casulleras, 1998) and path-integral (PIMC; Ferré and Boronat, 2016) Monte Carlo calculations and dynamic many-body theory (DMBT) (Campbell et al., 2015; Beauvois et al., 2018), compared to the experimental curve (Godfrin et al., 2021).

("roton" minimum) at a wave-vector $k \sim 2\text{Å}^{-1}$. The name roton is historical, no special rotation takes place; the minimum in energy reflects an incipient localization (short-range order), which eventually will lead to a liquid-solid transition under a pressure $P \sim 2.5\text{MPa}$. The dispersion curve becomes flat for $k \geq 2.8\text{Å}^{-1}$ as the energy reaches twice the roton gap, forming "Pitaevskii's plateau."

The calculation of the low temperature ($T < 1.3$ K) thermodynamic properties of helium at low temperatures only involves the statistical physics of phonons and rotons of low energy. That is, the properties of the strongly interacting bosonic system are simply given by those of a collection of non-interacting bosonic "quasi-particles" described by the phonon-roton curve (Godfrin et al., 2021). At high temperatures, where the number of rotons becomes very large, roton-roton interactions start playing a role. At the "lambda point" ($T = 2.17$ K), ^{4}He becomes a normal fluid.

Theoretical studies of the dynamic structure function in ^{4}He began with the work of Feynman (1954) and Feynman and Cohen (1956), the Feynman theory of elementary excitations was developed in a systematic Brillouin-Wigner perturbation theory by Jackson and Feenberg (Jackson and Feenberg, 1961; Jackson and Feenberg, 1962; Jackson, 1969; Jackson, 1973) in terms of a basis of Feynman excitation states

$$\{|\mathbf{k}\rangle\} = \left\{S^{-1}(k)\widehat{\rho}_{\mathbf{k}}|\Psi_0\right\} \tag{3}$$

where $\widehat{\rho}_{\mathbf{k}}$ is the density operator and $|\Psi_0\rangle$ is the ground state. An important contribution was the identification of classes of theories for the dynamic structure function (Jackson, 1974) that satisfy the ω^0 and ω^1 sum rules exactly. The most complete evaluation of the phonon–roton dispersion relation in terms of Brillouin–Wigner perturbation theory was carried out by Lee and Lee (1975) who obtained an impressive agreement with the experimental phonon–roton spectrum up the wave number of $Q = 2.5\text{Å}^{-1}$. The major drawback with these old calculations was that the required input—pair- and three-body distribution functions—were poorly known. Manousakis and Pandharipande (1986) tried to generalize the input states of the Brillouin-Wigner perturbation theory to include "backflow" correlations in the spirit of Feynman and Cohen (1956). Through the gradient operator acting on the wave function, in principle dynamic correlations are introduced to all orders. The "backflow–function" is, however, chosen per physical intuition rather than by fundamental principles, and the evaluation of the perturbative series becomes very complicated. Topologically, diagrams similar to those of Lee and Lee (1975) were included. While the accuracy of the theoretical roton energy is comparable to that of Lee and Lee, one can clearly see an inconsistency since the energy of the Pitaevskii-plateau (Pitaevskii, 1959) lies below twice the energy of the roton gap. More recent progress (Campbell and Krotscheck, 2009; Campbell et al., 2015) used a hybrid approach of Brillouin–Wigner perturbation theory and equations of motion for time-dependent multiparticle correlation functions to derive a self- consistent theory of the dynamic density–density response of ^{4}He.

In a nutshell, the Feynman theory of excitations is generalized by writing the dynamic wave function as

$$\Psi(\mathbf{r}_1, \ldots, \mathbf{r}_N; t) = \exp(U(t))\Psi_0(\mathbf{r}_1, \ldots, \mathbf{r}_N) \tag{4a}$$

$$U(t) = \sum_i \delta u_1(\mathbf{r}_i; t) + \sum_{i<j} \delta u_2(\mathbf{r}_i, \mathbf{r}_j; t) + \ldots \tag{4b}$$

The Feynman form of the wave function is obtained by omitting all n-body fluctuations $\delta u_n(\mathbf{r}_1, \ldots \mathbf{r}_n; t)$ for $n \geq 2$. The different theoretical descriptions basically differ by the way the n-body fluctuations are determined.

Recent novel numerical methods (Boronat and Casulleras, 1998; Boronat and Casulleras, 1997; Vitali et al., 2010; Roggero et al., 2013; Nava et al., 2013) give access to dynamic properties of quantum fluids. These are important algorithmic developments that may ultimately aid in the demanding elimination of background and multiple-scattering events from the raw data. Of course, it is generally agreed upon that the model of static pair potentials like the Aziz interaction (Aziz et al., 1992) describes the helium liquids accurately. Hence, given sufficiently elaborate algorithms and sufficient computing power, such calculations must reproduce the experimental data. The aim of the works cited above is different: The identification of physical effects like phonon-phonon, phonon-roton, roton-roton, maxon-roton… couplings that lead to observable features in the dynamic structure function is, from simulation data, only possible a-posteriori whereas the semi-analytic methods permit a direct identification of these effects, their physical mechanisms, their relationship to the ground state structure, and their consequences on the analytic properties of the dynamic structure function, directly from the theory.

The dynamic structure of ^{4}He is actually quite rich as seen in Fig. 6 (Campbell et al., 2015; Beauvois et al., 2018): "multi-excitations" are observed at energies above the single-excitation dispersion curve discussed above. They can be related to combinations of single-excitations, some of them are indicated in Fig. 6 by colored ellipses: in blue, an extension of the linear phonon region (ghost phonon) deep into the continuum; in red, an extension of the Pitaevskii-Plateau to small wave-vectors; in green, above the roton minimum, a broadening of the dispersion relation due to a Cherenkov effect; a red dashed ellipse at high energies indicates a region of maxon-roton couplings. Multi-excitations are well reproduced by recent theories. The mechanisms behind these are mostly the same: It is kinematically possible that a perturbation of energy/momentum (E, $\mathbf{k}$) can decay into two sharp quasiparticle excitations. For example, the "ghost phonon" is caused by the effect that a perturbation can decay into two almost collinear phonons, hence the effect disappears at about twice the energy and wave number at which the dispersion relation $\varepsilon(k)$ ceases to be linear. Similarly, the "Pitaevskii-Plateau" is caused by the effect that a perturbation of energy 2Δ can decay into two rotons of energy $\triangle$ and wave number k_Δ. Hence, energy and momentum conservation dictate that the plateau ends at a wave number of $2k_\Delta$, in this case the two roton wave vectors are parallel. Perturbations with the same energy and smaller wave numbers can decay into two rotons that are not collinear. That means that the plateau can in principle extend to zero wave number; in that case the perturbation decays into two anti-parallel rotons.

The Cherenkov effect is particularly interesting; it is caused by the fact that the group velocity of a quasiparticle excitation beyond the roton (R_+ roton) is larger than the sound velocity. The effect is observed only at low pressures.

^{3}He in 3D

The investigation of the dynamics of the ^{3}He Fermi Liquid has naturally followed that of the ^{4}He Bose fluid (Dobbs, 2001; Glyde, 1994). From the theoretical point of view, the problem is notoriously difficult, due to the antisymmetry requirement for the

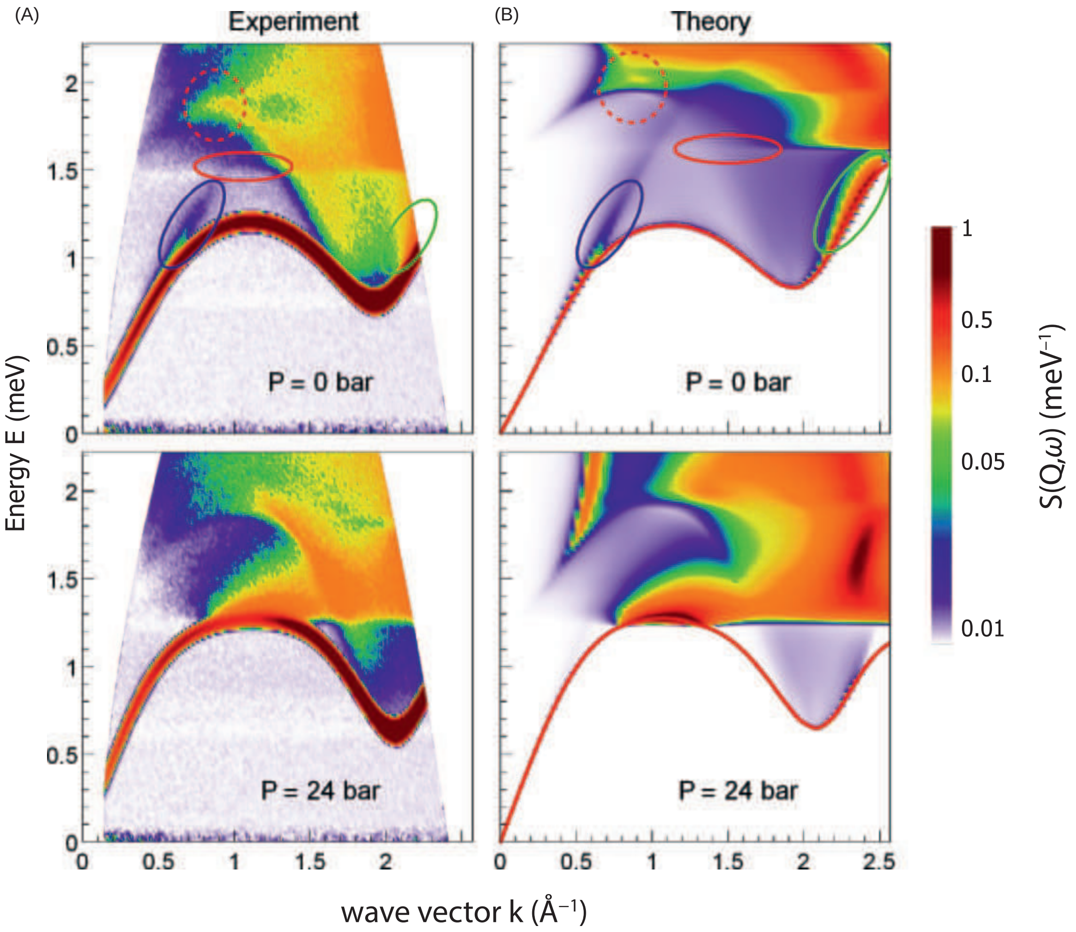

Fig. 6 Experimental (A) and theoretical (B) determinations of the dynamic structure factor of superfluid ^{4}He at zero pressure (upper graphs) and near-solidification pressure (lower graphs). In addition to the intense single-excitations dispersion seen in Fig. 5 (red lower curves), much lower intensity multi-excitations (see color scale) can be observed here. Colored ellipses indicate excitation couplings described in the text.

wave-functions of many-body fermionic systems (Fetter and Walecka, 1971; Thouless, 1972; Pines and Nozieres, 1966). Obtaining accurate results for the ground state is a challenge, even using very sophisticated variational wave functions.

The dynamics is treated analogously to the boson case (4b); the local excitation functions $\delta u_n(\mathbf{r}_1, \ldots, \mathbf{r}_n; t)$ are replaced by particle-hole operators

$$\sum_{\substack{p_1,\ldots,p_n \\ h_1\ldots h_n}} u_{p_1,\ldots,p_n;h_1\ldots h_n}(t) a^\dagger_{p_1} \ldots a^\dagger_{p_n} a_{h_n} \ldots a^\dagger_{h_1}$$

where the p_i are the quantum numbers of unoccupied (particle) states and the h_i those of occupied (hole) states. Restricting the excitation amplitudes to one-particle-one-hole components leads to a correlated version of the random phase approximation (RPA) (Krotscheck, 1982), the quantitative understanding of the experiments requires at least 2-particle-2-hole amplitudes, see Böhm et al. (2010), Krotscheck and Lichtenegger (2022).

From the experimental point of view, even though the same inelastic neutron techniques successfully applied to superfluid ^{4}He can be used to investigate liquid ^{3}He, in practice the experiments are extremely difficult due to the huge neutron absorption cross-section of the ^{3}He nucleus (Glyde, 1994). In typical ^{4}He experiments, sample thicknesses are larger than 1 cm, while absorption limits the maximum thickness in a liquid ^{3}He measurement, to about 0.1 mm. In addition, due to the lower excitation energies, experiments in ^{3}He must be performed at much lower temperatures ($\approx$0.1K) than in ^{4}He ($\approx$1K), to remain in the low temperature limit, where few excitations are present. For these reasons, in spite of the considerable interest in strongly interacting fermions, accurate theoretical and experimental results have been available only recently (Glyde et al., 2000).

In order to understand the dynamics of a Fermi *liquid*, we begin by considering the excitations of a Fermi *gas*. In the latter, excitations are created by removing a particle from an occupied state inside the Fermi sphere, and placing it outside the sphere, in a higher energy free state. The resulting states are confined to a region of the energy *vs* wave-vector space called the “particle-hole band.” The interacting fermionic system, i.e., the Fermi Liquid, behaves in a similar way. A particle-hole band can be observed in

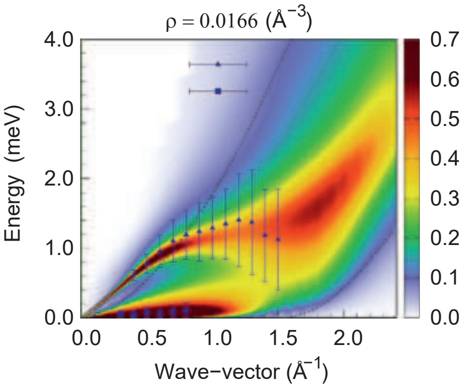

Fig. 7 Dynamic structure factor of bulk liquid ^{3}He. Measured density excitations (Fåk et al., 1990) (triangles, upper branch) and spin-density excitations (Glyde et al., 2000) (squares, lower branch) are clearly visible (bars on the data points indicate the observed width of the branch). Color intensity map, from light blue to dark red: DMBT microscopic theory including exchange (Krotscheck and Lichtenegger, 2022). The solid lines indicate the boundaries of the particle-hole band.

bulk ^{3}He (see Fig. 7), but in addition, collective modes are present. A density mode, named "zero-sound" or "collision-less sound," is observed. Its physical origin, as noted by Pines (1981), resides in the strong interactions, and hence this mode is analogous to the phonon-roton mode described above for bosons; statistics play here a minor role. Its substantial energy width results from the possibility to decay into particle-hole excitations as it enters the particle-hole band (Landau-damping mechanism).

The thermodynamic properties of bulk liquid ^{3}He are often described, at very low temperatures, by the phenomenological Landau Fermi Liquid model, where the properties of the interacting system are related to those of the Fermi gas by the introduction of an interaction function (quasiparticle interaction), leading to a renormalization of parameters (effective mass, susceptibility enhancement, etc.). Landau theory predicts, among other physical effects, the existence of collective modes, the zero-sound and paramagnon modes.

Landau's Fermi Liquid Theory is only applicable at very low temperatures. In liquid ^{3}He, where the Fermi energy, expressed in temperature units, is of the order of several kelvins, the theory is valid below 0.1 K.

The reason becomes clear if one observes the actual excitation spectrum shown in Fig. 7. The low energy mode, observed below the zero-sound excitation, is a spin-density mode, completely immersed in the particle-hole band, and hence severely Landau-damped. The origin of this mode, analogous to a dampened spin-wave and often called "paramagnon," can be traced back directly to the antisymmetry of the many-body wave function.

There are also some interesting X-ray studies of the dynamic structure function at high momentum transfers (Albergamo et al., 2007) that have led to a discussion about the location of the particle-hole band (Schmets and Montfrooij, 2008; Albergamo et al., 2008). The authors of Albergamo et al. (2007) state that *The obtained results show no evidence of such a decay: the zero-sound mode remains well defined in the whole explored wave number range*. According to that, the particle-hole continuum should be much lower than the continuum of the non-interacting Fermi system. An analysis of both the data and the theoretical predictions within DMBT (Krotscheck and Panholzer, 2011) shows that there is, when the theoretical data are convoluted with the experimental resolution, actually no contradiction to the conventional interpretation of the scenario.

Details are shown in Fig. 8. To facilitate the comparison with experiments, the theoretical spectra were convoluted with the experimental resolution. Also, the results were scaled by $1/S(k)$ such that the integrated strength is 1 for all momentum transfers. The same scaling was applied to the experimental data.

^{4}He in reduced dimensions

The dynamics of quantum fluids has also been investigated in reduced dimensions. Two-dimensional (2D) systems are obtained experimentally by adsorption of gases onto solid substrates, usually graphite. One-dimensional (1D) systems can also be created, they are obtained by confining the gases inside silica or graphite nano-tubes (Yano et al., 1998; Kato et al., 1987; Del Maestro et al., 2022). There is also theoretical interest (Stan and Cole, 1998; Stan et al., 1998; Bertaina et al., 2016; Krotscheck and Miller, 1999; Gordillo et al., 2000) in the properties of ^{4}He in *one-dimension*.

Extensive theoretical studies have clarified the nature of the excitations in such systems. Superfluid ^{4}He films of atomic thicknesses, for instance, display in-plane density modes, as well as capillary waves.

Let us first discuss the dynamics of rigorously 2D ^{4}He. Basically we see the same effects as in 3D: a linear "phonon" branch as well as, at high momentum transfers, a "roton minimum."

One can also see the somewhat finer details discussed above: At low densities, the "ghost-phonon," and at high densities the plateau coming down and extending to long wave lengths. A second striking feature is the appearance of a sharp mode below the plateau. We stress the difference: normally, the plateau is a threshold above which a wave of energy/momentum $(\hbar\omega, k)$ can decay into two rotons. This has the consequence that the imaginary part of the self-energy $\Sigma(k, \hbar\omega)$ is a step function and the real part has a

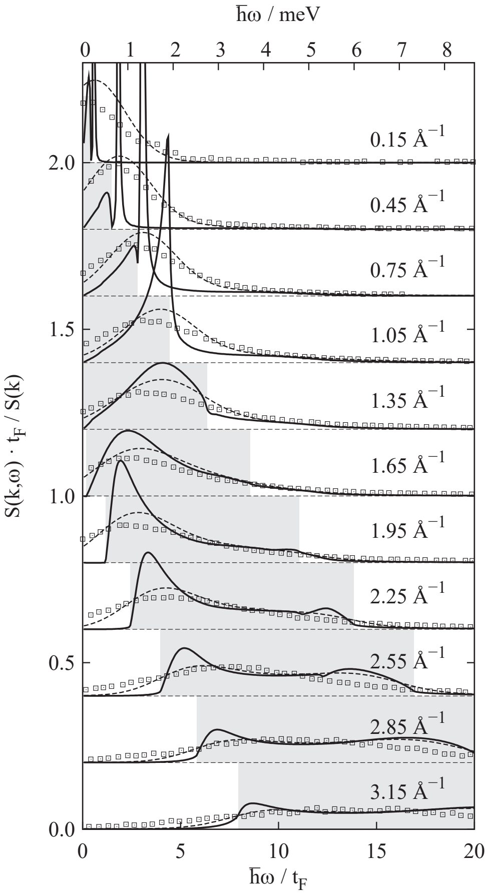

Fig. 8 The figure shows the normalized dynamic structure function $S(k;\omega)/S(k)$ of ^{3}He at a density of $\rho = 0.0166$Å^{-3}, for a sequence of wave numbers. The theoretical results obtained by DMBT (Krotscheck and Panholzer, 2011) are compared with the X-ray scattering data (Albergamo et al., 2007) (squares) at saturated vapor pressure. Also shown are the theoretical results convoluted with the experimental resolution (dashed lines). The gray-shaded area shows the particle-hole continuum of a non-interacting Fermi fluid. $t_F = \hbar^2 k_F^2/2m$ is the Fermi energy of the non-interacting system.

logarithmic singularity (Pitaevskii, 1959). A collective mode is, on the other hand, characterized by a singularity of the $S(k,\hbar\omega)$. Fig. 9 shows, for the two highest densities, the appearance of a sharp discrete mode *below* the plateau. At a wave number of $k \approx 2.6$Å^{-1}, the collective mode is still merged into the continuum. With increasing wave number, we see, however, a clearly distinguishable but rather weak ($Z(k) \approx 0.02$) mode about 0.3 K below the plateau. We have mentioned already above that the roton should be seen as an emergence of short–ranged order, the "ghost of a Bragg Spot" (Nozières, 2004; Nozières, 2006). If this is the case, then one might see a second Bragg spot. Such a thing is not seen, but location of the secondary minimum in 2D corresponds indeed to the position of a second Bragg spot of a triangular lattice.

Density modes (Krotscheck and Lichtenegger, 2015) are analogous to the phonons and rotons already mentioned in the case of bulk helium, but due to the adsorption potential of the substrate, the fluid is inhomogeneous, and solidification of the first two or three atomic layers is observed in thick films. Layered-excitations are observed in this regime.

Capillary waves, also called "ripplons," have a different nature: these are surface waves, which do not (in first approximation) correspond to compression/expansion of the fluid, but to a change of height in the external potential (gravitational in the case of a bulk helium surface, or substrate potential in adsorbed films).

A typical example is shown in Fig. 10. It corresponds to a multilayer film of about 6 atomic layers, where both density excitations and ripplons are visible with comparable intensity (Lauter et al., 1992). The experimental curve is broader than the theoretical one, an effect largely due to the mosaic spread (angular distribution) of the graphite substrate, a powder made of microscopic flat crystals.

Finally, in the sub-monolayer coverage regime, one can observe gaseous, fluid and solid phases, as well as "commensurate phases" where the atoms adopt a periodic arrangement commensurate with the substrate atomic lattice.

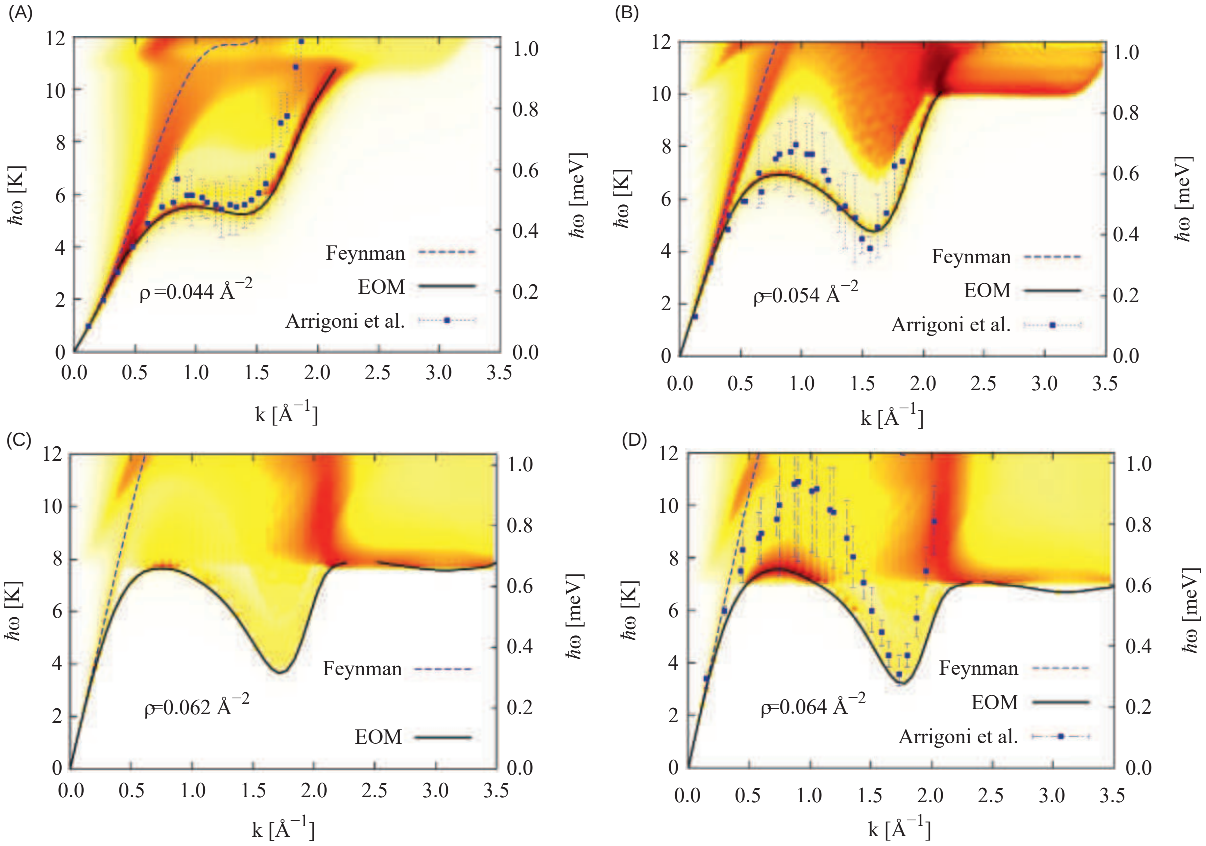

Fig. 9 The figure shows contour plots of the dynamic structure function of two-dimensional liquid ^{4}He for a sequence of areal densities as shown in the legends. The colors have been chosen to highlight the prominent features, darker colors correspond to higher values of $S(k, \hbar\omega)$. We also show the Feynman spectrum, and the simulation data of Arrigoni et al. (2013). From Krotscheck E and Lichtenegger T (2015) *Journal of Low Temperature Physics* 178: 61.

^{3}He in reduced dimensions

The excitations in ^{3}He films are shown in Fig. 11. They are very similar to those discussed above for bulk liquid, with the remarkable exception (Godfrin et al., 2012) that the roton-like excitations are at the edge of the particle-hole band and hence not strongly affected by Landau damping. These excitations can therefore propagate, suggesting interesting physical effects specific to 2D Fermi liquids.

Conclusion

The investigation of the dynamics of quantum fluids has been performed experimentally at very low temperatures using various techniques, mainly specific heat, compressibility, neutron and X-ray scattering and, for ^{3}He, nuclear magnetic susceptibility. Theoretical calculations are based on semi-phenomenological approaches (Aldrich and Pines, 1976; Aldrich III and Pines, 1978; Hsu and Pines, 1985), dynamic many body theory (DMBT) (Böhm et al., 2010; Campbell et al., 2015; Krotscheck and Lichtenegger, 2022) as well as different versions of Quantum Monte Carlo numerical calculations (PIMC, DMC) (Boronat and Casulleras, 1997; Ferré and Boronat, 2016; Arrigoni et al., 2013; Bertaina et al., 2016) to cite only a few. These have brought a very detailed understanding of these systems. It is sometimes very difficult to perform experimental measurements on some particular systems (for instance in reduced dimensionality), or even impossible to create quite arbitrary systems ("mathematical models" of interaction or external potentials, etc.). In this case the combination of numerical and microscopic techniques is essential.

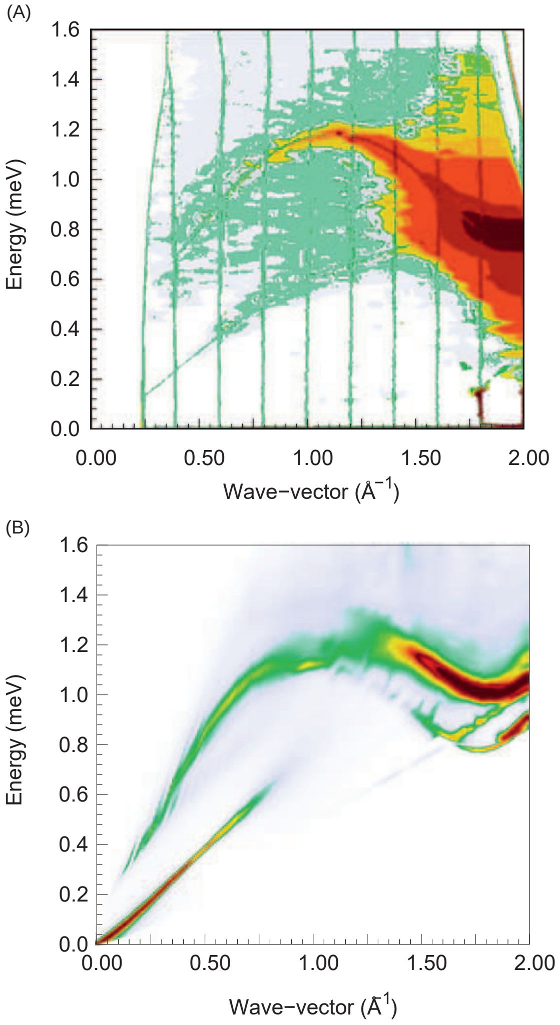

Fig. 10 Experimental (Lauter et al., 1992) (A) and theoretical (B) (Clements et al., 1996) determinations of the dynamic structure factor of a multilayer film of ^{4}He, displaying density and ripplon excitations.

The results find a natural application to many different physical systems, like nuclear matter, neutron stars, particle physics and cosmology, where strongly interacting particles are investigated. Particles themselves, in fact, can be interpreted as quantized excitations of an underlying field. The helium liquids have been, in some sense, the Ariadne thread in these investigations: Their interactions are well established (Aziz et al., 1979; Aziz et al., 1987) and, compared to nucleon interactions, quite simple. The density of these systems is very high and they are very "quantum," hence they do not permit the simple treatments that have become popular by the experimental success to generate and investigate cold quantum gases. The experimental challenge is equally high and only the very best of the experimental equipment and the experimental techniques can stand up to the challenge. Nevertheless, these challenges have been met on both the theoretical and experimental side.

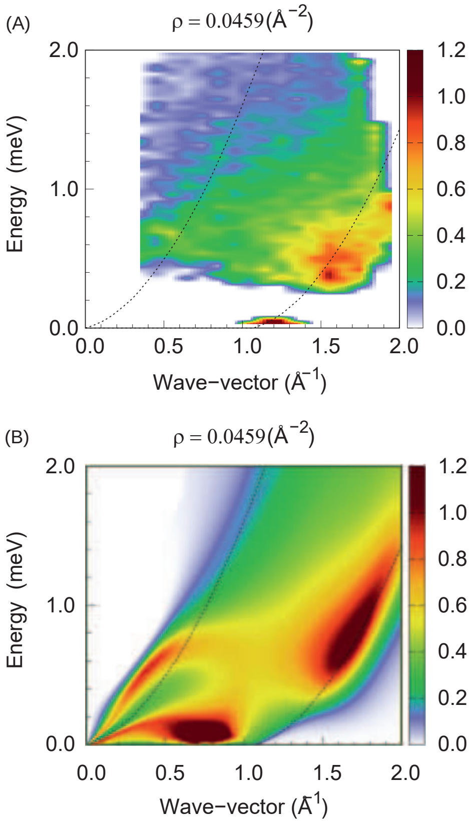

Fig. 11 Experimental (A) and theoretical (B) determinations of the dynamic structure factor of two-dimensional liquid ^{3}He (Godfrin et al., 2012). The theoretical calculation shows the density and spin-density modes; the latter is not visible experimentally, it is masked by a strong elastic signal due to the substrate. A comparison with Fig. 7 shows that the roton-like excitation in the 2D system is found outside the particle-hole band (the region limited by the blue solid lines), thus avoiding Landau damping.

References

Albergamo F, Verbeni R, Huotari S, Vankó G, and Monaco G (2007) *Physical Review Letters* 99: 205301/1.
Albergamo F, Verbeni R, Huotari S, Vankó G, and Monaco G (2008) *Physical Review Letters* 100: 239602/1.
Aldrich CH III and Pines D (1978) *Journal of Low Temperature Physics* 31: 689.
Aldrich CH and Pines D (1976) *Journal of Low Temperature Physics* 25: 677.
Arrigoni F, Vitali E, Galli DE, and Reatto L (2013) *Fizika Nizkikh Temperatur* 39: 1021.
Aziz RA, Nain VPS, Carley JC, Taylor WJ, and McConville GT (1979) *The Journal of Chemical Physics* 70: 4330.
Aziz RA, McCourt FRW, and Wong CCK (1987) *Molecular Physics* 61: 1487.
Aziz RA, Slaman MJ, Koide A, Allnatt AR, and Meath WJ (1992) *Molecular Physics* 77: 321337.
Beauvois K, et al. (2018) *Physical Review B* 97: 184520.
Bertaina G, Motta M, Rossi M, Vitali E, and Galli DE (2016) *Physical Review Letters* 116: 135302.
Bogoliubov NN (1947) *Journal of Physics* 11: 23.
Böhm HM, Holler R, Krotscheck E, and Panholzer M (2010) *Physical Review B* 82: 224505.
Boronat J and Casulleras J (1997) *Europhysics Letters* 38: 291.
Boronat J and Casulleras J (1998) *Journal of Low Temperature Physics* 110: 443.
Campbell CE and Krotscheck E (2009) *Physical Review B* 80: 174501.
Campbell CE, Krotscheck E, and Lichtenegger T (2015) *Physical Review B* 91: 184510/1.
Clements BE, Krotscheck E, and Tymczak CJ (1996) *Physical Review B* 53: 12253.
Cowley RA and Woods ADB (1971) *Canadian Journal of Physics* 49: 177.
de Boer J (1948) *Physica* 14: 139.
de Boer J and Michels A (1938) *Physica* 6: 945.
Del Maestro A, Nichols NS, Prisk TR, Warren G, and Sokol PE (2022) Experimental realization of one dimensional helium. *Nature Communications* 13: 3168. https://doi.org/10.1038/s41467-022-30752-3.
Dobbs ER (2001) *Helium Three*. Oxford: Oxford University Press.
Fåk B, Guckelsberger K, Körfer M, Scherm R, and Dianoux AJ (1990) *Physical Review B* 41: 8732.
Ferré G and Boronat J (2016) *Physical Review B* 93: 104510.
Fetter AL and Walecka JD (1971) *Quantum Theory of Many-Particle Systems*. New York: McGraw-Hill.
Feynman RP (1954) *Physics Review* 94: 262.
Feynman RP and Cohen M (1956) *Physics Review* 102: 1189.

Glyde HR (1994) *Excitations in Liquid and Solid Helium*. Oxford: Oxford University Press.
Glyde HR (2018) *Reports on Progress in Physics* 81: 014501.
Glyde HR, Gibbs MR, Stirling WG, and Adams MA (1998) *Europhysics Letters* 43: 422.
Glyde HR, et al. (2000) *Physical Review B* 61: 1421.
Godfrin H, et al. (2012) *Nature* 483: 576.
Godfrin H, et al. (2021) *Physical Review B* 103: 104516.
Gordillo MC, Boronat J, and Casulleras J (2000) *Physical Review B* 61: R878.
Hsu W and Pines D (1985) *Journal of Statistical Physics* 38: 273.
Jackson HW (1969) *Physics Review* 185: 186.
Jackson HW (1973) *Physical Review A* 8: 1529.
Jackson HW (1974) *Physical Review A* 9: 964.
Jackson HW and Feenberg E (1961) *Annals of Physics* 15: 266.
Jackson HW and Feenberg E (1962) *Reviews of Modern Physics* 34: 686.
Kapitza P (1938) *Nature* 141: 74.
Kato H, Ishioh K, Wada N, Ito T, and Watanabe T (1987) *Journal of Low Temperature Physics* 68: 321.
Krotscheck E (1982) *Physical Review A* 26: 3536.
Krotscheck E and Lichtenegger T (2015) *Journal of Low Temperature Physics* 178: 61.
Krotscheck E and Lichtenegger T (2022) *Dynamic Many Body Theory IV: (Spin-)density Fluctuations and Exchange in Normal-Liquid* ^{3}*He*. in preparation.
Krotscheck E and Miller MD (1999) *Physical Review B* 60: 13038.
Krotscheck E and Panholzer M (2011) *Journal of Low Temperature Physics* 163: 1.
Landau L (1941) *Journal of Physics* 5: 71.
Landau L (1947) *Journal of Physics* 11: 91.
Lauter HJ, Godfrin H, Frank VLP, and Leiderer P (1992) *Physical Review Letters* 68: 2484.
Lee DK and Lee FJ (1975) *Physical Review B* 11: 4318.
London F (1938) *Nature* 141: 643.
Lovesey SW (1984) *Theory of Neutron Scattering From Condensed Matter*. Oxford: Clarendon Press.
Manousakis E and Pandharipande VR (1986) *Physical Review B* 33: 150.
Misener JFAAD (1938) *Nature* 141: 75.
Nava M, Galli DE, Moroni S, and Vitali E (2013) *Physical Review B* 87: 144506/1.
Nozières P (2004) *Journal of Low Temperature Physics* 137: 45.
Nozières P (2006) *Journal of Low Temperature Physics* 142: 83.
Palevsky H, Otnes K, Larsson KE, Pauli R, and Stedman R (1957) *Physics Review* 108: 1346.
Palevsky H, Otnes K, and Larsson KE (1958) *Physics Review* 112: 11.
Pines D (1981) *Physics Today* 34: 106.
Pines D and Nozieres P (1966) *The Theory of Quantum Liquids*. vol. I. New York: Benjamin.
Pitaevskii LP (1959) *Zhurnal Éksperimental'noĭ i Teoreticheskoĭ Fiziki* 36: 1168. [Sov. Phys. JETP 9, 830 (1959)].
Roggero A, Pederiva F, and Orlandini G (2013) *Physical Review B* 88: 094302.
Schmets AJM and Montfrooij W (2008) *Physical Review Letters* 100: 239601/1.
Stan G and Cole MW (1998) *Surface Science* 395: 280.
Stan G, Crespi VH, Cole MW, and Boninsegni M (1998) *Journal of Low Temperature Physics* 113: 447–452.
Thouless DJ (1972) *The Quantum Mechanics of Many-Body Systems*, 2nd ed. New York: Academic Press.
Vitali E, Rossi M, Reatto L, and Galli DE (2010) *Physical Review B* 82: 174510/1.
Wilks J (1967) *The Properties of Liquid and Solid Helium*. New York, Oxford: Clarendon.
Yano H, Yoshizaki S, Inagaki S, Fukushima Y, and Wada N (1998) *Journal of Low Temperature Physics* 110: 573–578.

Quantum fluids of light

Iacopo Carusotto, Pitaevskii BEC Center, CNR-INO and Dipartimento di Fisica, Università di Trento, Trento, Italy

© 2024 Elsevier Ltd. All rights reserved.

Introduction 959
Microcavity devices: Non-equilibrium physics 962
Propagating geometries: Conservative dynamics 963
Strongly correlated fluids and topological states of photonic matter 964
Conclusion 965
References 965

Abstract

In this Chapter, we give a brief review of the state of the art of theoretical and experimental studies of quantum fluids of light. Such systems consist of ensembles of photons that acquire a finite mass from spatial confinement or diffraction and finite binary interactions from the optical nonlinearity of the optical medium. The peculiar properties of these fluids are highlighted in comparison with standard condensed matter systems, with a special emphasis on the novel possibilities that they offer for the generation, the manipulation and the diagnostics of the fluid, as well as on their intrinsically non-equilibrium and/or dynamical nature. Perspectives toward a new generation of experiments on strongly correlated fluids of light and toward opto-electronic applications are finally sketched.

Key points

This chapter aims to

- Illustrate the general concept of quantum fluid of light and the necessary ingredients
- Highlight the role of non-equilibrium physics under the effect of driving and dissipation in quantum fluids of light in cavity set-ups
- Introduce the $t \leftrightarrow z$ mapping underlying quantum fluids of light in propagating geometries
- Highlight the exciting perspectives in the direction of realizing strongly correlated fluids of light
- Briefly summarize how quantum fluids of light can be useful for opto-electronic and quantum applications

Introduction

Traditionally, our pictures of matter and light are very different.

Matter consists of material objects, that can be touched with our fingers and mechanically react to our manipulation in very different ways. For instance, solid matter is rigid; one can take advantage of the weight of liquid matter to float and of its internal friction to swim; complex fluidodynamic phenomena are exploited by birds and aircrafts to fly through gaseous media. At a more sophisticated level, quantum fluids combine hydrodynamics with quantum mechanical features and display a variety of exotic behaviors, from superfluidity in liquid Helium and ultracold atomic clouds (Pitaevskiĭ and Stringari, 2016), to superconductivity in electron gases (Tinkham, 2004), to quantized conductance of incompressible quantum Hall fluids in the presence of strong magnetic fields (Tong, 2016). At completely different scales of energy, exciting properties has been unveiled in the nuclear matter that forms atomic nuclei or neutron stars (Ring and Schuck, 2004).

On the contrary, light is associated to a flow of electromagnetic waves or, in a quantum description, of corpuscular photons that fly through space at the universal speed c from the emitter to the absorber (Walls and Milburn, 2006). The interesting physics occurs in between, and, in standard configurations, it consists of some in-fly modification of the properties of the beam. Of course this can be extremely rich and diverse, and may involve the interplay of reflection and refraction effects with wave interference phenomena, nonlinear optical processes due to the coupling to electronic transitions in material media, and even quantum effects due to the discrete nature of the photon. Still, all these phenomena are associated to the idea of light has to necessarily keep propagating all the time and cannot be stored in some container so to be manipulated as one normally does with matter.

The concept of *Quantum Fluid of Light (QFL)* defies this duality and merges concepts from condensed matter physics and optics to investigate the new collective physics that light displays when it is confined and, then, manipulated as a standard fluid of many interacting photons. This exotic behavior of course requires very specific conditions to happen: in particular one needs photons to acquire some finite mass and display significant inter-particle interactions (Carusotto and Ciuti, 2013).

https://doi.org/10.1016/B978-0-323-90800-9.00172-4

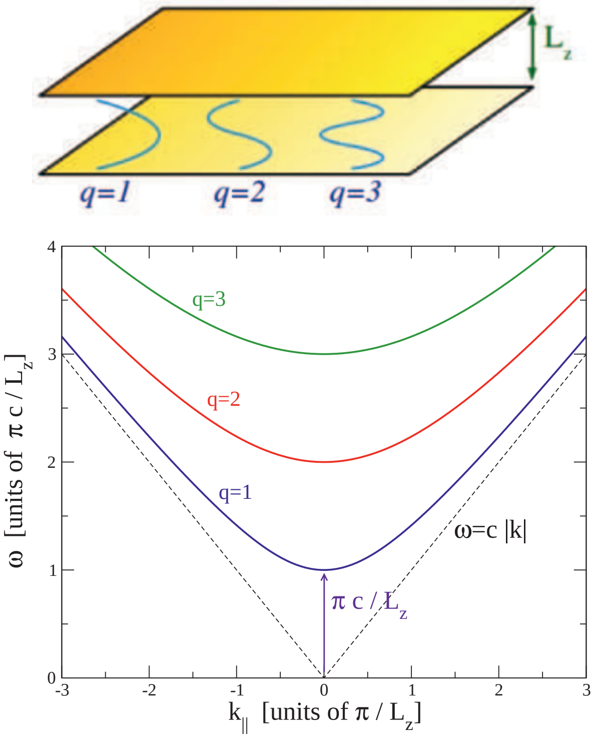

Fig. 1 Effective mass for photons confined in planar microcavities. (Upper panel) Scheme of the device and of the field configuration. (Lower panel) Relativistic in-plane dispersion of photons in the planar cavity.

From special relativity, we know that massless particles propagate at a fixed speed c and a finite *mass* is needed to put particles at rest. Photons are naturally massless particles, but may acquire a finite effective mass when they are confined in space, e.g., in between a pair of plane-parallel metallic mirrors as it is sketched in the top panel of Fig. 1. In this simplest configuration, the wavevector along the normal z direction is quantized as $k_z^{(q)} = \pi N/L_z$ in terms of the positive integer number q while the in-plane motion remains free and acquires a massive relativistic-like dispersion,

$$\omega^{(q)}\left(\mathbf{k}_\parallel\right) = ck_z^{(q)} + \frac{1}{2k_z^{(q)}}\mathbf{k}_\parallel^2 \tag{1}$$

that is plotted in the lower pane of the same Figure. The finite effective mass $m^{(q)}$ arising from the zero-point confinement along z is such that

$$m^{(q)}c^2 = \hbar ck_z^{(q)} \tag{2}$$

and grows with the quantum number q, i.e., the number of nodes of the field in the z direction. As usual, its role is twofold: as a *rest mass*, it gives the forbidden energy gap below the dispersion; as the *kinetic mass*, it gives the curvature of the dispersion around $\mathbf{k}_\parallel = 0$. A most celebrated family of experiments works with the lowest $q = 1$ band of planar semiconductor microcavities enclosed by dielectric mirrors (Carusotto and Ciuti, 2013), but a number of other exciting configurations have also been explored with peculiar properties (Schine et al., 2016).

In contrast to the linearity of Maxwell equations which guarantees a superposition principle for light fields (Jackson, 1999), photon-photon interactions naturally arise in QED from the coupling of light with the electron-positron quantum field (Heisenberg and Euler, 1936). The simplest Feynman diagram describing photon-photon interactions is sketched in the left panel of Fig. 2, and corresponds to an effective two-photon collision mediated by the creation of virtual electron-positron pairs. In any table-top experiment, the scattering cross-section corresponding to these Heisenberg-Euler processes.

$$\sigma \propto \alpha^4 \left(\frac{h}{m_{el}c}\right)^2 \left(\frac{\hbar\omega}{m_{el}c^2}\right)^6 \tag{3}$$

is however suppressed not only by the four fine-structure $\alpha = e^2/\hbar c \sim 1/137$ factors stemming from the four interaction vertices and by the small value $h/(m_{el}c) \simeq 2.4$pm of the electron Compton wavelength, but also, and much more dramatically, by the energy denominators corresponding, within perturbation theory, to the virtual intermediate states. For visible or infrared light for which

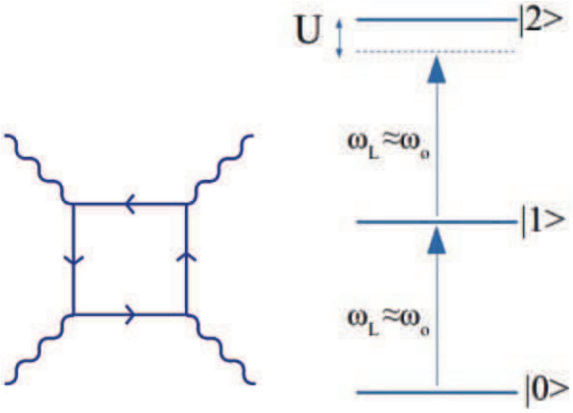

Fig. 2 Basics of photon-photon interactions: (left) Feynman diagram describing interactions mediated by virtual electronpositron pairs in QED; (right) scheme of the energy levels involved in the photon blockade effect in a nonlinear optical cavity.

photons have an energy at most in the few eV range, these are dominated by the rest mass of the virtual electronpositron pair which lies in the MeV range and, via the last factor in (3) give a huge 10^{-36} suppression factor. As a result, the direct observation of photon-photon scattering in vacuo appears extremely challenging and some experimental evidence was only reported for special configurations based on gamma-rays hitting the ultraintense quasi-bound electric field of a heavy-ion (ATLAS Collaboration, 2017).

The mathematical form of (3) also suggests possible way-outs to this difficulty: at a simplest level of description, the elementary excitations of solid-state insulating materials consist of electrons and holes, i.e., missing electrons in an otherwise filled valence band, which play a very similar role to positrons in vacuo (Ashcroft and Mermin, 2022). On the basis of this analogy, it is therefore immediate to expect an enormous reinforcement of the photon-photon scattering cross-section as, in a typical solid-state material, the energy detuning denominator in (3) involves the width of the energy gap in the eV range, and the last factor is thus of order one. This intuitive expectation is fully confirmed by all those nonlinear optical effects that are commonly observed using standard laser sources and can be reinterpreted in terms of photon-photon interaction vertices (Boyd, 2008; Butcher and Cotter, 2008). Even though this is very oversimplified view and cutting-edge experiments are based on more sophisticated media, still it offers a useful intuition of the underlying physics. A most efficient strategy to reinforce the optical nonlinearity is to mix the cavity photon mode with some electronic excitation, e.g., an excitonic transition in a quantum well embedded in the cavity layer, and work with the resulting mixed quasi-particles, the so-called exciton-polaritons (Kavokin et al., 2011).

Further enhancements can be obtained using more sophisticated optical set-ups or engineered meta-materials, so to bring the system into a regime completely at odd with the linear Maxwell equations, where photons behave as impenetrable particles (Chang et al., 2014). After a number of pioneering demonstrations (Birnbaum et al., 2005), the most celebrated and promising advances in the direction of strongly interacting fluids of light have been obtained using dressed optical photons in atomic gases in the so-called Rydberg-EIT (Electromagnetically Induced Transparency) regime (Peyronel et al., 2012) or microwave photons confined in superconductor-based circuits in the so-called circuit-QED devices (Blais et al., 2021; Carusotto et al., 2020). In both cases, the idea is that the refractive index change induced by the optical nonlinearity in the field of a single photon is already sufficient to significantly affect the propagation of the following photons that attempt to penetrate the same spatial region.

The simplest example of such phenomenon is the socalled *photon blockade* effect (Imamoglu et al., 1997): when a single-mode cavity is filled by a $\chi^{(3)}$ nonlinear medium, the dynamics of the e.m. field can be described as a nonlinear oscillator of Hamiltonian

$$H = \hbar\omega_o \hat{a}^\dagger \hat{a} + \hbar\omega_{\mathrm{nl}} \hat{a}^\dagger \hat{a}^\dagger \hat{a}\hat{a} \tag{4}$$

whose quantum eigenstates are labeled by the number of photons and have an energy $E_n = n\hbar\omega_o + \frac{n(n-1)}{2}\hbar\omega_{\mathrm{nl}}$ as sketched in the right panel of Fig. 2. Since the separation $E_{n+1} - E_n = \hbar\omega_o + (n+1)\hbar\omega_{\mathrm{nl}}$ grows with n, an incident field tuned to resonance with the $0 \to 1$ transition is detuned from the $1 \to 2$ transition by an effective interaction energy $U = \hbar\omega_{\mathrm{nl}}$. As a result, if the nonlinearity exceeds the cavity linewidth $\omega_{\mathrm{nl}} \gg \gamma$, the second transition is effectively suppressed and the cavity behaves as an effective two-level system which can only host one photon at a time as if photons were impenetrable objects.

In the following Sections we are going to review some among the most exciting advances that the concept of Quantum Fluid of Light has given in the last decades and, in particular, of the new fundamental insight that it has given to the physics of fluids in novel non-equilibrium regimes. Section “Microcavity devices: Non-equilibrium physics” and “Propagating geometries: Conservative dynamics” will be devoted to a brief presentation of the two main conceptual classes of platforms for quantum fluids of light, namely microcavity and propagating geometries. Then, in Section “Strongly correlated fluids and topological states of photonic matter” we will review the on-going research in the direction of strongly correlated fluids of light and topological states of photonic matter. Finally, in Section “Conclusion” we will draw some conclusions and we will sketch future perspectives for the field.

Microcavity devices: Non-equilibrium physics

Combining the elements presented in the previous Section, the in-plane dynamics of quantum fluids of light in microcavity configurations turns out to be well captured by a bosonic Hamiltonian of the usual form,

$$H = \int d\mathbf{r} \left[\hbar\omega_o \hat{\Psi}^\dagger(\mathbf{r})\hat{\Psi}(\mathbf{r}) + \frac{\hbar^2}{2m^*}\nabla\hat{\Psi}^\dagger(\mathbf{r})\nabla\hat{\Psi}(\mathbf{r}) + \frac{\hbar g_{\mathrm{nl}}}{2}\hat{\Psi}^\dagger(\mathbf{r})\hat{\Psi}^\dagger(\mathbf{r})\hat{\Psi}(\mathbf{r})\hat{\Psi}(\mathbf{r}) \right] \tag{5}$$

whose terms describe, in order, the effective rest energy of the photons, their kinetic energy associated to the kinetic mass, and their (contact) interactions mediated by the optical nonlinearity. This Hamiltonian clearly shows the microscopic processes at play in the quantum fluid of light and their direct equivalence to an ordinary gas of material particles. As such, it is the cornerstone of most theoretical descriptions of the quantum fluid of light (Carusotto and Ciuti, 2013).

In addition to the conservative evolution described by the Hamiltonian (5), in any realistic configuration one needs to take into account the different loss channels to which photons are naturally subject, in particular radiative losses through the cavity mirrors. In any experiment, the unavoidable radiative losses must therefore be compensated by some continuous pump mechanism to replenish the fluid. This is perhaps the most relevant peculiarity of quantum fluids of light in cavity geometries as compared to standard fluids of material particles and is sketched in Fig. 3.

Combining the conservative and the driven-dissipative parts of the evolution, the overall dynamics of a weakly interacting fluid of light can be summarized by a generalized driven-dissipative form of Gross-Pitaevskii equation for the expectation value of the Bose field operator $\psi = \langle\hat{\Psi}\rangle$ describing the in-cavity electromagnetic field,

$$i\frac{\partial\psi}{\partial t} = \left[\omega_o - \frac{\hbar\nabla^2}{2m^*}\right]\psi + g_{\mathrm{nl}}|\psi|^2\psi + \frac{i}{2}\left[\frac{P}{1+|\psi|^2/n_s} - \gamma\right]\psi + E_{\mathrm{inc}}(\mathbf{r},t) \tag{6}$$

where the first and second lines respectively include the conservative evolution and the driven-dissipative terms describing saturable incoherent pumping, losses, and coherent pumping by an external laser field.

In contrast to early belief, the presence of losses is however not just a hindrance and the ensuing driven dissipative nature of the fluid provides additional experimental knobs. On the one hand, suitably designed incident light fields can in fact be used to inject the photon fluid with the desired spatio-temporal profile and then probe its properties. On the other hand, since all properties of the in-cavity field directly transfer to the radiated field, the state of the fluid of light can be experimentally reconstructed up to its most subtle quantum correlations just by performing quantum optical measurement on the emitted light Walls and Milburn (2006).

From a wider perspective, these features constitute important assets that enlarge the possibilities of quantum fluids of light well beyond what is normally possible with standard material fluids. Even when the pump and the dissipation establish a dynamical

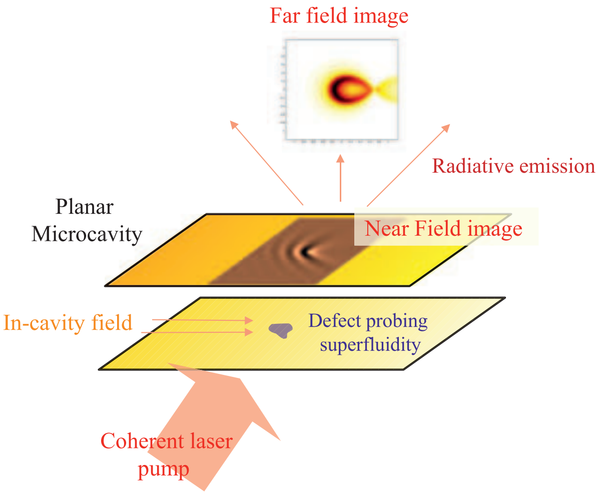

Fig. 3 Sketch of a superfluidity experiment with a fluid of light in a planar microcavity geometry. Figure inspired to the theory and experiments in Amo et al. (2009) and Carusotto and Ciuti (2004). For the parameters in the figure, the photon fluid flows faster than the critical speed for superfluidity: a significant intensity modulation appears in the near-field intensity profile (i.e., the spatial density distribution of photons) and a deformed-ring-shaped pattern appears in the far-field one (i.e., the in-plane momentum distribution).

equilibrium, the resulting Non-Equilibrium Steady-State (NESS) is not necessarily thermalized and may display novel features stemming from the non-equilibrium nature. Such a feature was first highlighted in the early '70s when a connection was drawn (Graham and Haken, 1970) between laser operation and non-equilibrium phase transitions and turned out to play a central role in the numerous studies of non-equilibrium Bose-Einstein condensation effects in fluids of light (Bloch et al., 2022). Dramatic observable consequences of the non-equilibrium condition have also been observed in different properties of the fluid, from the possibility of condensing into excited states (Richard et al., 2005; Wertz et al., 2010), to the onset of diffusive rather than sonic collective Goldstone modes (Szymańska et al., 2006; Wouters and Carusotto, 2007), to subtle features in the definition of superfluid critical velocities (Wouters and Carusotto, 2010), to peculiar spatio-temporal correlations in the Kardar-ParisiZhang universality class (Fontaine et al., 2022), just to quote a few examples.

Propagating geometries: Conservative dynamics

A conceptually different class of fluids of light originates from the formal analogy between the paraxial propagation equation for the complex-valued amplitude of monochromatic light in nonlinear bulk media

$$i\frac{\partial \mathcal{E}}{\partial z} = -\frac{1}{2\beta_0}\nabla_\perp^2 \mathcal{E} + V(\mathbf{r})\mathcal{E} + G_{\mathrm{nl}}|\mathcal{E}|^2\mathcal{E} \tag{7}$$

and the Gross-Pitaevskii equation of the dynamics of dilute two-dimensional superfluids: diffraction in the transverse xy plane provides the effective mass term, the transverse refractive index profile induces an external potential $V(\mathbf{r}) = -\beta_0\delta\varepsilon(\mathbf{r})/(2\varepsilon_0)$, and the intensity-dependent dielectric constant provides photon-photon interactions of strength

$$G_{\mathrm{nl}} = -\frac{\beta_0\chi^{(3)}}{2\varepsilon_0}. \tag{8}$$

Here, $\beta_0 = \varepsilon_0^{1/2}\omega_0/c$ is the propagation constant of light at frequency ω_0 in the medium and $\varepsilon = \varepsilon_0 + \chi^{(3)}|\mathcal{E}|^2$ is the nonlinear, intensity-dependent dielectric constant. In this formalism, the slowly-varying complex amplitude $\mathcal{E}$ is related to the real-valued physical electric field E by

$$E(\mathbf{r}, t) = \mathcal{E}(\mathbf{r})e^{i\beta_0 z}e^{-i\omega_0 t} + \text{c.c.}. \tag{9}$$

In the last decades, this configuration has been long used to observe a variety of hydrodynamic phenomena, from optical vortices (Coullet et al., 1989) to superfluid features (Fontaine et al., 2018), to condensation of classical light (Baudin et al., 2020; Krupa et al., 2017). As a most important conceptual difference from the cavity geometries considered in the previous Section, the role of time is played in these experiments by the propagation coordinate z. On the other hand, the use of monochromatic light imposes a rigid $e^{-i\omega t}$ form to the time-dependence of the field.

While this has not been a major concern as long as people were interested in hydrodynamics effects at the mean-field level of (7), a more sophisticated theoretical model is required to describe quantum phenomena related to the corpuscular nature of the photons. In particular, one needs to develop a theory that is not restricted to monochromatic beams and is able to include a fullfledged temporal dynamics of the field amplitude $\mathcal{E}(\mathbf{r}, t)$.

A most convenient way to do this is to start from the full classical propagation equation for the spatio-temporal electric field amplitude $\mathcal{E}(\mathbf{r}, t)$ (Agrawal, 2001; Rosanov, 2002). Seen from a comoving frame where $\bar{t} = t - z/v_g$, such an equation has again a GrossPitaevskii form.

$$i\frac{\partial \mathcal{E}}{\partial z} = -\frac{1}{2\beta_0}\nabla_\perp^2 \mathcal{E} + \frac{D_0}{2}\frac{\partial^2 \mathcal{E}}{\partial \bar{t}^2} + V\mathcal{E} + G_{\mathrm{nl}}|\mathcal{E}|^2\mathcal{E}, \tag{10}$$

yet in three-dimensions: the propagation distance z plays the role of a temporal coordinate, and the physical time $\bar{t}$ becomes a third spatial coordinate together with the transverse $\mathbf{r}_\parallel = (x, y)$ ones. Here, we have assumed to work with a relatively narrowband signal centered around a frequency ω_0 that propagates at a group velocity $v_g = (\partial k_z/\partial\omega)^{-1}$. The effective mass in the temporal direction is determined by the group velocity dispersion $D_0 = \partial^2 k_z/\partial\omega^2$. In addition to a spatial dependence, the potential due to the dielectric constant modulation may also display a temporal dependence, $V(\mathbf{r}, t)$.

This classical field equation can be promoted to a quantum model by means of a non-standard quantization procedure based on the so-called $t \leftrightarrow z$ *mapping* (Lai and Haus, 1989a, 1989b; Larré and Carusotto, 2015b). In contrast to the usual canonical quantization where commutation rules are imposed between operators at the same time t and different spatial position $\mathbf{r}$, $\mathbf{r}'$, here the commutation rules are to be imposed between conjugate field operators at the same z position but different rescaled times $\zeta = v_g\bar{t}$ and different positions $\mathbf{r}_\parallel$ along the transverse plane,

$$\left[\hat{\mathcal{E}}(\mathbf{r}_\parallel, \zeta; z), \hat{\mathcal{E}}^\dagger\left(\mathbf{r}'_\parallel, \zeta'; z\right)\right] = \frac{2\pi\hbar\omega_0^2 v_g}{\beta_0 c^2}\delta^{(2)}\left(\mathbf{r}_\parallel - \mathbf{r}'_\parallel\right)\delta(\zeta - \zeta'). \tag{11}$$

To complete the $t \leftrightarrow z$ mapping, we replace the propagation coordinate z with the temporal variable $\tau = z/v_g$ and write a bosonic Hamiltonian in the usual form, where spatial integration is now taken over the three dimensional space $R = (\mathbf{r}_\parallel, \zeta)$,

$$H = \frac{\beta_0 c^2}{2\pi\omega_0^2} \int d^3R \left[\frac{1}{2\beta_0} \nabla_{\parallel} \hat{\mathcal{E}}^{\dagger} \nabla_{\parallel} \hat{\mathcal{E}} - \frac{D_0 v_g^2}{2} \frac{\partial \hat{\mathcal{E}}^{\dagger}}{\partial \zeta} \frac{\partial \hat{\mathcal{E}}}{\partial \zeta} + V \hat{\mathcal{E}}^{\dagger} \hat{\mathcal{E}} + \frac{\hbar G_{\mathrm{nl}}}{2} \hat{\mathcal{E}}^{\dagger} \hat{\mathcal{E}}^{\dagger} \hat{\mathcal{E}} \hat{\mathcal{E}} \right]. \tag{12}$$

A quantum version of the paraxial propagation equation (10) then naturally arises from the Heisenberg motion equation stemming from this Hamiltonian,

$$i \frac{d\hat{\mathcal{E}}}{d\tau} = \frac{1}{\hbar} \left[\hat{\mathcal{E}}, H \right] = v_g \left[-\frac{1}{2\beta_0} \nabla_{\perp}^2 \hat{\mathcal{E}} + \frac{D_0 v_g^2}{2} \frac{\partial^2 \hat{\mathcal{E}}}{\partial \zeta^2} + V \hat{\mathcal{E}} + G_{\mathrm{nl}} \hat{\mathcal{E}}^{\dagger} \hat{\mathcal{E}} \hat{\mathcal{E}} \right] \tag{13}$$

where the v_g factor on the right-hand-side accounts for the $z = v_g \tau$ relation of the $t \leftrightarrow z$ mapping.

From the physical point of view, the main difference with respect to the cavity configurations considered in the previous Section is that the field dynamics in propagating geometries is not intrinsically subject to dissipation. Provided the nonlinear medium is transparent on the length scale of the experiment, the light field follows in fact a conservative Hamiltonian evolution similar to the one of cold atomic gases. In contrast to atomic gases, however, the fluid of light is typically found in conditions far from thermal equilibrium condition: as it is sketched in Fig. 4 rather than starting from a thermal equilibrium state, the initial condition of the quantum dynamics is imposed by the quantum state of the light field incident on the front face of the optical medium. Also in this case, all properties of the final state can be experimentally accessed by means of quantum optical measurements on the transmitted light.

From a theoretical point of view, this quantum theory of propagating light still relies on heuristic arguments and the $t \leftrightarrow z$ mapping procedure is still awaiting a formal mathematical proof. Yet, first experimental evidence of quantum effects has been reported for a fluid of light subject to a sudden quench of the interaction constant (Steinhauer et al., 2022). This suggests that propagating light is as another promising platform where to study the quantum dynamics of interacting many-body systems.

Strongly correlated fluids and topological states of photonic matter

In the previous Sections, we have highlighted a number of exciting hydrodynamic phenomena that take place in weakly interacting fluids of light. Most of these effects are accurately described via classical field equations that generalize the well-known Gross-Pitaevskii equation of dilute Bose-Einstein condensates to the novel context. The new frontier is now to explore regimes where the optical nonlinearities are so important that photons are strongly interacting particles and the fluid develops strong quantum correlations. In this case, a full quantum many-body description is typically required and, in analogy to related work in cold atomic gases (Bloch et al., 2008), a variety of exotic physical phenomena are expected to arise.

Interesting steps in this direction have been carried out in both microcavity and propagating geometries and closely connect to the on-going research on single-photon nonlinear optics (Chang et al., 2014). A basic building block in view direction is the photon blockade phenomenon already discussed in the introductory section. Beyond the single-mode cavity set-ups in which photon blockade was originally studied (Birnbaum et al., 2005; Imamoglu et al., 1997), strongly interacting fluids of light are now starting be investigated both in multi-mode cavity geometries as well as in propagating geometries.

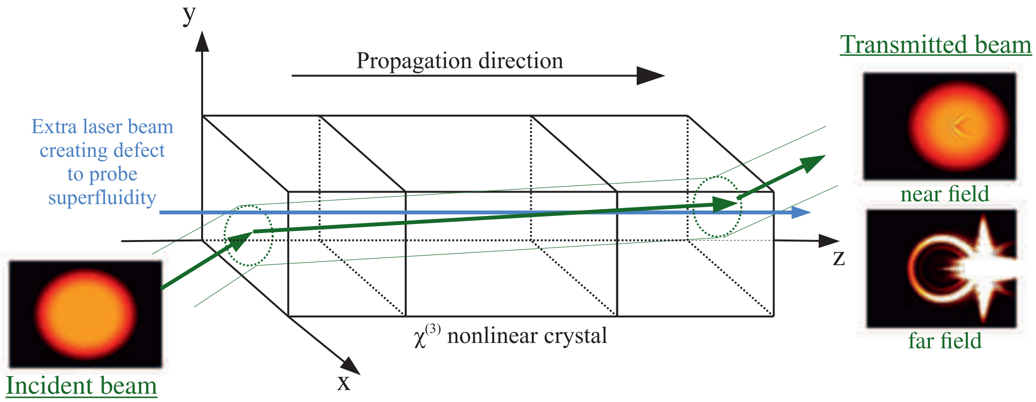
y
Propagation direction
Transmitted beam
Extra laser beam creating defect to probe superfluidity
near field
z
far field
$\chi^{(3)}$ nonlinear crystal
Incident beam
x

Fig. 4 Sketch of a superfluidity experiment with a fluid of light in a propagating geometry. Figure inspired to the theory and experiments in Larré and Carusotto (2015a) and Michel et al. (2018). Also in this figure, the parameters are chosen to have a flow speed faster than the critical speed for superfluidity and clear patterns appear in both the near- and the far-field profiles of the transmitted beam.

On the former side, a most remarkable accomplishment has been the experimental realization of a Mott insulator state of impenetrable photons in an array of nonlinear superconductor-based cavities for microwave photons (Ma et al., 2019). On the latter side, a marked antibunching has been observed in the transmitted light after propagation through a strongly nonlinear medium formed by dressed atoms in the Rydberg-EIT configuration (Peyronel et al., 2012). For a different level configuration providing attractive rather than repulsive photon-photon interactions, experimental evidence of two-photon bound states was also reported (Firstenberg et al., 2013).

An even richer variety of strongly correlated phases of matter has been anticipated to arise in fluids of light in the presence of synthetic magnetic fields and/or in topological photonic structures (Ozawa et al., 2019): in spite of the electric neutrality of the photon, photonic configurations have been in fact explored where light propagation is subject to analogs of the Lorentz force acting on charged particles in magnetic fields. As a most celebrated experimental observation, unidirectional light propagation on chiral edge states has been demonstrated for photonic lattices with topologically non-trivial band structures (Hafezi et al., 2013; Rechtsman et al., 2013; Wang et al., 2009). More recently, *topological laser* devices have been demonstrated in topological lattices endowed with gain (Bahari et al., 2017; Bandres et al., 2018; St-Jean et al., 2017): in addition to being a promising device for opto-electronic applications, such systems can be seen as a novel example of quantum fluid of light living in a chirally moving one-dimensional geometry and with peculiar statistical properties (Amelio and Carusotto, 2020). Further exciting perspectives are offered by the so-called *synthetic dimensions*, which allow to realize quantum fluids of light living in high-dimensional geometries beyond the usual three spatial dimensions (Ozawa and Price, 2019).

In combination with strong photon-photon interactions, topological photonic systems have been anticipated to lead to optical analogs of fractional quantum Hall physics (Kapit et al., 2014; Umucalılar and Carusotto, 2012). Among the most remarkable pioneering experimental results in this direction, we can mention the chiral currents observed in a few-site plaquette for strongly interacting microwave photons (Roushan et al., 2017) and the realization of baby Laughlin liquids in twisted cavities for visible photons (Clark et al., 2020). Motivated by these early achievements, a strong activity is presently in progress in the international community toward the realization of macroscopic samples of topological states of photonic matter (Kurilovich et al., 2021).

Conclusion

The exciting advances that we have summarized in this Chapter provide an overview of the intriguing physics of quantum fluids of light and suggest the promising developments that one may anticipate for this field of research in the next future. After decades where hydrodynamic descriptions of optical systems have been considered as just a mathematical analogy and an intellectual curiosity, the recent advances have demonstrated how the physical picture of light as an ensemble of interacting photons provides a novel example of condensed matter system where to explore, in particular, uncharted lands of nonequilibrium quantum many-body physics.

A further interest for these systems comes from the straightforward inclusion of quantum fluids of light in devices for opto-electronic applications: the close relationship between lasing and Bose-Einstein condensation has been known for decades (Graham and Haken, 1970), but has received a renewed interest in the last years with the development of novel concepts of coherent light sources (Bloch et al., 2022). On a longer run, an even more ambitious application could be to realize a topological quantum computing architecture (Nayak et al., 2008) based on topological states of photonic matter.

References

Agrawal GP (2001) *Applications of Nonlinear Fiber Optics*. Elsevier.

Amelio I and Carusotto I (2020) Theory of the coherence of topological lasers. *Physical Review X* 10(4): 041060.

Amo A, Lefrere J, Pigeon S, Adrados C, Ciuti C, Carusotto I, Houdre R, Giacobino E, and Bramati A (2009) Superfluidity of polaritons in semiconductor microcavities. *Nature Physics* 5(11): 805–810.

Ashcroft NW and Mermin ND (2022) *Solid State Physics*. Cengage Learning.

ATLAS Collaboration (2017) Evidence for light-by-light scattering in heavy-ion collisions with the atlas detector at the lhc. *Nature Physics* 13(9): 852–858.

Bahari B, Ndao A, Vallini F, El Amili A, Fainman Y, and Kanté B (2017) Nonreciprocal lasing in topological cavities of arbitrary geometries. *Science* 358(6363): 636–640.

Bandres MA, Wittek S, Harari G, Parto M, Ren J, Segev M, Christodoulides DN, and Khajavikhan M (2018) Topological insulator laser: Experiments. *Science* 359(6381): eaar4005.

Baudin K, Fusaro A, Krupa K, Garnier J, Rica S, Millot G, and Picozzi A (2020) Classical rayleigh-jeans condensation of light waves: Observation and thermodynamic characterization. *Physical Review Letters* 125: 244101. https://link.aps.org/doi/10.1103/PhysRevLett.125.244101.

Birnbaum K, Boca A, Miller R, Boozer A, Northup T, and Kimble H (2005) Photon blockade in an optical cavity with one trapped atom. *Nature* 436(7047): 87–90.

Blais A, Grimsmo AL, Girvin SM, and Wallraff A (2021) Circuit quantum electrodynamics. *Reviews of Modern Physics* 93: 025005. https://link.aps.org/doi/10.1103/RevModPhys.93.025005.

Bloch I, Dalibard J, and Zwerger W (2008) Many-body physics with ultracold gases. *Reviews of Modern Physics* 80(3): 885.

Bloch J, Carusotto I, and Wouters M (2022) Non-equilibrium bose–einstein condensation in photonic systems. *Nature Reviews Physics* 4(7): 470–488.

Boyd RW (2008) *Nonlinear Optics*. Academic Press.

Butcher PN and Cotter D (2008) *The Elements of Nonlinear Optics, Cambridge Studies in Modern Optics*. Cambridge University Press.

Carusotto I and Ciuti C (2004) Probing microcavity polariton superfluidity through resonant rayleigh scattering. *Physical Review Letters* 93: 166401. http://link.aps.org/doi/10.1103/PhysRevLett.93.166401.

Carusotto I and Ciuti C (2013) Quantum fluids of light. *Reviews of Modern Physics* 85(1): 299.

Carusotto I, Houck AA, Kollár AJ, Roushan P, Schuster DI, and Simon J (2020) Photonic materials in circuit quantum electrodynamics. *Nature Physics* 16(3): 268–279.

Chang DE, Vuletić V, and Lukin MD (2014) Quantum nonlinear optics—Photon by photon. *Nature Photonics* 8(9): 685–694.

Clark LW, Schine N, Baum C, Jia N, and Simon J (2020) Observation of laughlin states made of light. *Nature* 582(7810): 41–45.

Coullet P, Gil L, and Rocca F (1989) Optical vortices. *Optics Communications* 73(5): 403–408.

Firstenberg O, Peyronel T, Liang Q-Y, Gorshkov AV, Lukin MD, and Vuletić V (2013) Attractive photons in a quantum nonlinear medium. *Nature* 502(7469): 71–75.

Fontaine Q, Bienaimé T, Pigeon S, Giacobino E, Bramati A, and Glorieux Q (2018) Observation of the bogoliubov dispersion in a fluid of light. *Physical Review Letters* 121(18), 183604.

Fontaine Q, Squizzato D, Baboux F, Amelio I, Lemaître A, Morassi M, Sagnes I, Le Gratiet L, Harouri A, Wouters M, et al. (2022) Kardar–Parisi–Zhang Universality in a one-dimensional polariton condensate. *Nature* 608(7924): 687–691.

Graham R and Haken H (1970) Laserlight–first example of a second-order phase transition far away from thermal equilibrium. *Zeitschrift fur Physik A: Hadrons and Nuclei* 237: 31–46. https://doi.org/10.1007/BF01400474.

Hafezi M, Mittal S, Fan J, Migdall A, and Taylor J (2013) Imaging topological edge states in silicon photonics. *Nature Photonics* 7(12): 1001–1005.

Heisenberg W and Euler H (1936) Folgerungen aus der diracschen theorie des positrons. *Zeitschrift für Physik* 98(11): 714–732.

Imamoglu A, Schmidt H, Woods G, and Deutsch M (1997) Strongly interacting photons in a nonlinear cavity. *Physical Review Letters* 79(8): 1467–1470.

Jackson JD (1999) *Classical Electrodynamics*. Wiley.

Kapit E, Hafezi M, and Simon SH (2014) Induced self-stabilization in fractional quantum hall states of light. *Physical Review X* 4: 031039. http://link.aps.org/doi/10.1103/PhysRevX.4.031039.

Kavokin A, Baumberg J, Malpuech G, and Laussy F (2011) *Microcavities*. OUP Oxford: Oxford Science Publications. https://books.google.it/books?id=2g7wHcMcaJ0C.

Krupa K, Tonello A, Shalaby BM, Fabert M, Barthélémy A, Millot G, Wabnitz S, and Couderc V (2017) Spatial beam self-cleaning in multimode fibres. *Nature Photonics* 11(4): 237–241.

Kurilovich PD, Kurilovich VD, Lebreuilly J, and Girvin S (2022) Stabilizing the Laughlin state of light: Dynamics of hole fractionalization. *SciPost Physics* 13: 107.

Lai Y and Haus HA (1989a) Quantum theory of solitons in optical fibers. I. Time-dependent hartree approximation. *Physical Review A* 40: 844–853. http://link.aps.org/doi/10.1103/PhysRevA.40.844.

Lai Y and Haus HA (1989b) Quantum theory of solitons in optical fibers. II. Exact solution. *Physical Review A* 40: 854–866. http://link.aps.org/doi/10.1103/PhysRevA.40.854.

Larré P-É and Carusotto I (2015a) Optomechanical signature of a frictionless flow of superfluid light. *Physical Review A* 91(5), 053809.

Larré P-É and Carusotto I (2015b) Propagation of a quantum fluid of light in a cavityless nonlinear optical medium: General theory and response to quantum quenches. *Physical Review A* 92(4), 043802.

Ma R, Saxberg B, Owens C, Leung N, Lu Y, Simon J, and Schuster DI (2019) A dissipatively stabilized mott insulator of photons. *Nature* 566(7742): 51–57.

Michel C, Boughdad O, Albert M, Larré P-É, and Bellec M (2018) Superfluid motion and drag-force cancellation in a fluid of light. *Nature Communications* 9(1): 1–6.

Nayak C, Simon SH, Stern A, Freedman M, and Das Sarma S (2008) Non-abelian anyons and topological quantum computation. *Reviews of Modern Physics* 80: 1083–1159. https://link.aps.org/doi/10.1103/RevModPhys.80.1083.

Ozawa T and Price HM (2019) Topological quantum matter in synthetic dimensions. *Nature Reviews Physics* 1(5): 349–357.

Ozawa T, Price HM, Amo A, Goldman N, Hafezi M, Lu L, Rechtsman MC, Schuster D, Simon J, Zilberberg O, et al. (2019) Topological photonics. *Reviews of Modern Physics* 91(1), 015006.

Peyronel T, Firstenberg O, Liang Q-Y, Hofferberth S, Gorshkov AV, Pohl T, Lukin MD, and Vuletić V (2012) Quantum nonlinear optics with single photons enabled by strongly interacting atoms. *Nature* 488(7409): 57–60.

Pitaevskiĭ L and Stringari S (2016) *Bose-Einstein Condensation and Superfluidity. International Series of Monographs on Physics*Oxford University Press. https://books.google.it/books?id=kZGCwAAQBAJ.

Rechtsman MC, Zeuner JM, Plotnik Y, Lumer Y, Podolsky D, Dreisow F, Nolte S, Segev M, and Szameit A (2013) Photonic floquet topological insulators. *Nature* 496(7444): 196–200.

Richard M, Kasprzak J, Romestain R, Andre R, and Dang L (2005) Spontaneous coherent phase transition of polaritons in cdte microcavities. *Physical Review Letters* 94(18).

Ring P and Schuck P (2004) *The Nuclear Many-Body Problem*. Springer.

Rosanov NN (2002) *Spatial Hysteresis and Optical Patterns*. Springer Science & Business Media.

Roushan P, Neill C, Megrant A, Chen Y, Babbush R, Barends R, Campbell B, Chen Z, Chiaro B, Dunsworth A, et al. (2017) Chiral ground-state currents of interacting photons in a synthetic magnetic field. *Nature Physics* 13(2): 146. https://www.nature.com/articles/nphys3930.

Schine N, Ryou A, Gromov A, Sommer A, and Simon J (2016) Synthetic landau levels for photons. *Nature* 534(7609): 671–675.

Steinhauer J, Abuzarli M, Aladjidi T, Bienaimé T, Piekarski C, Liu W, Giacobino E, Bramati A, and Glorieux Q (2022) Analogue cosmological particle creation in an ultracold quantum fluid of light. *Nature Communications* 13(1): 1–7.

St-Jean P, Goblot V, Galopin E, Lemaître A, Ozawa T, Le Gratiet L, Sagnes I, Bloch J, and Amo A (2017) Lasing in topological edge states of a one-dimensional lattice. *Nature Photonics* 11(10): 651–656.

Szymańska MH, Keeling J, and Littlewood PB (2006) Nonequilibrium quantum condensation in an incoherently pumped dissipative system. *Physical Review Letters* 96: 230602. http://link.aps.org/doi/10.1103/PhysRevLett.96.230602.

Tinkham M (2004) *Introduction to Superconductivity*. Dover.

Tong D (2016) *Lectures on the Quantum Hall Effect*. arXiv:1606.06687.

Umucalılar RO and Carusotto I (2012) Fractional quantum hall states of photons in an array of dissipative coupled cavities. *Physical Review Letters* 108: 206809. http://link.aps.org/doi/10.1103/PhysRevLett.108.206809.

Walls DF and Milburn G (2006) *Quantum Optics*. Berlin: Springer Verlag.

Wang Z, Chong Y, Joannopoulos JD, and Soljačić M (2009) Observation of unidirectional backscattering-immune topological electromagnetic states. *Nature* 461(7265): 772–775.

Wertz E, Ferrier L, Solnyshkov DD, Johne R, Sanvitto D, Lemaitre A, Sagnes I, Grousson R, Kavokin AV, Senellart P, Malpuech G, and Bloch J (2010) Spontaneous formation and optical manipulation of extended polariton condensates. *Nature Physics* 6(11): 860–864.

Wouters M and Carusotto I (2007) Goldstone mode of optical parametric oscillators in planar semiconductor microcavities in the strong-coupling regime. *Physical Review A* 76: 043807. http://link.aps.org/doi/10.1103/PhysRevA.76.043807.

Wouters M and Carusotto I (2010) Superfluidity and critical velocities in nonequilibrium bose-einstein condensates. *Physical Review Letters* 105(2).

Floquet states

Naoto Tsuji[a,b], [a]Department of Physics, University of Tokyo, Hongo, Tokyo, Japan; [b]RIKEN Center for Emergent Matter Science (CEMS), Wako, Saitama, Japan

© 2024 Elsevier Ltd. All rights reserved.

Introduction	967
Floquet theory	968
Examples	970
High-frequency expansion	972
Periodically driven open quantum systems	973
Experimental observations	975
Conclusion	977
References	977

Abstract

Quantum systems driven by a time-periodic field are a platform of condensed matter physics where effective (quasi) stationary states, termed "Floquet states," can emerge with external-field-dressed quasiparticles during driving. They appear, for example, as a prethermal intermediate state in isolated driven quantum systems or as a nonequilibrium steady state in driven open quantum systems coupled to environment. Floquet states may have various intriguing physical properties, some of which can be drastically different from those of the original undriven systems in equilibrium. In this article, we review fundamental aspects of Floquet states, and discuss recent topics and applications of Floquet states in condensed matter physics.

Key points

- Introduce Floquet states in periodically driven quantum systems.
- Describe the basic aspects of the Floquet theory for isolated and open quantum systems.
- Discuss several examples of Floquet states, including ac Wannier–Stark effects and Floquet topological phases.
- Review experimental observations of Floquet states in solids and cold-atom systems.

Introduction

Driving quantum systems far from equilibrium provides various possibilities to control quantum states and realize new phases of matter that are otherwise inaccessible within thermal equilibrium. The interest on nonequilibrium states in condensed matter physics has grown rapidly due to recent progress both in theories and experiments, the latter of which allow for real-time observation of driven quantum states in a fast time scale in solids as well as in artificial quantum systems. There are many ways to drive quantum systems, among which time-periodic driving generates characteristic (quasi)stationary states called Floquet states, which are often accompanied by quasiparticles dressed by external driving fields. Their physical properties, such as band mass, lifetime, topological nature, etc., deviate from those of equilibrium states, depending on the driving protocol. This opens up a new avenue to control macroscopic phases dynamically.

The term, "Floquet states," originates from the Floquet theory for a set of ordinary differential equations of the type, $\dot{x}_m(t) = \sum_n C_{mn}(t)x_n(t)$, with $C_{mn}(t) = C_{mn}(t+T)$ being a periodic function with a period T, which dates back to the work of a mathematician, G. Floquet in 1883 (Floquet, 1883; Hill, 1886; Magnus and Winkler, 1966). According to the Floquet theory, there exists a solution in a form of $x_m(t) = e^{\lambda t}u_m(t)$ with a complex number λ (characteristic exponent) and a periodic function $u_m(t) = u_m(t+T)$. The application of the theory to the time-dependent Schrödinger equation in quantum mechanics laid down the foundation for the theory of Floquet states in periodically driven quantum systems (Shirley, 1965; Sambe, 1973; Grifoni and Hänggi, 1998). The Floquet theory can be viewed as a temporal analog of the Bloch theory in solid state physics, which serves as a fundamental framework to treat electronic states in a spatially periodic crystal structure.

Periodically driven quantum systems are typically classified into two types: one is the case of isolated quantum systems driven by time-periodic fields, whose time evolution is purely determined by the unitary dynamics. The other is the case of open quantum systems, that is, systems coupled to environment with dissipation. The dynamics are quite different between them (see Fig. 1). The former eventually reaches an infinite-temperature state in the long-time limit (Lazarides et al., 2014; D'Alessio and Rigol, 2014; Ponte et al., 2015a), since the energy is continuously supplied to the system by the periodic driving, which turns into heat in general (nonintegrable) systems. Before approaching the infinite-temperature state, the system may stay at an intermediate quasistationary

https://doi.org/10.1016/B978-0-323-90800-9.00241-9

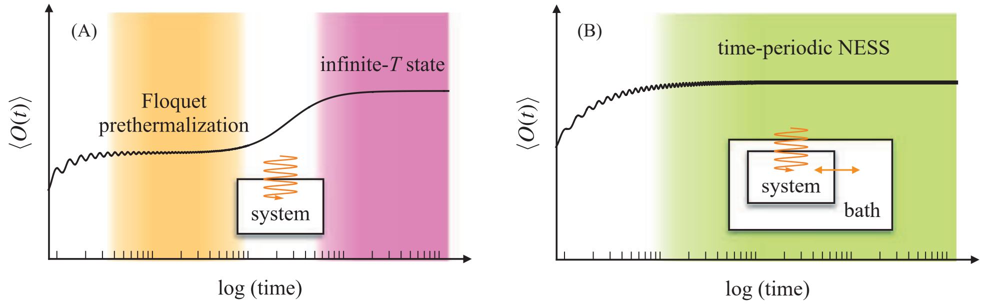

Fig. 1 Typical time evolution of an observable $\langle O(t)\rangle$ in (A) periodically driven isolated quantum systems and (B) periodically driven open quantum systems. The former reaches an infinite-temperature steady state through an intermediated quasistationary Floquet prethermal state, while the latter reaches a time-periodic nonequilibrium steady state (NESS).

state (called Floquet prethermalization) for a certain time scale, which becomes exponentially long when the driving frequency is relatively high as compared to the system's energy scale (Mori et al., 2016; Kuwahara et al., 2016; Abanin et al., 2017; Mori et al., 2018). The latter, on the other hand, may arrive at a time-periodic nonequilibrium steady state (NESS), in which the energy absorbed from the external field is balanced with that dissipating into environment (Tsuji et al., 2009; Oka and Aoki, 2009; Dehghani et al., 2014; Mikami et al., 2016; Shirai et al., 2016; Murakami et al., 2017; Ikeda and Sato, 2020).

In addition to these typical cases, nontrivial time-periodic stationary states are known to emerge in driven many-body localized systems, where heating is avoided without coupling to environment due to the effect of strong disorder (Ponte et al., 2015b; Lazarides et al., 2015; Abanin et al., 2016) and the emergence of approximately conserved charges (Das, 2010; Haldar et al., 2018; Haldar and Das, 2022). Recent studies (Sacha, 2015; Khemani et al., 2016; Else et al., 2016; Yao et al., 2017; Moessner and Sondhi, 2017) have unveiled another possibility that time-periodic steady states in periodically driven quantum systems can possess a different periodicity than that of the driving field, which is referred to as a (discrete) time crystal in the sense that the discrete time translation symmetry is spontaneously broken (as in the space translation symmetry broken in a crystal). In this way, the landscape of stationary states in periodically driven quantum systems is widely broadened, and many different types of quasiparticles can be found there.

Floquet theory

In quantum mechanics, the Floquet theory plays a fundamental role in describing Floquet states that emerge under an application of time-periodic driving fields. In the case of isolated quantum systems, the time evolution is determined by the time-dependent Schrödinger equation,

$$i\frac{d}{dt}|\psi(t)\rangle = H(t)|\psi(t)\rangle, \tag{1}$$

where $|\psi(t)\rangle$ and $H(t)$ are the system's wavefunction and hermitian Hamiltonian, respectively, and we set $\hbar = 1$ throughout the article. The Hamiltonian is assumed to have time periodicity, $H(t+T) = H(t)$, with a period T (and frequency $\omega = 2\pi/T$). The formal solution to the Schrödinger equation (1) is written as $|\psi(t)\rangle = U(t, t_0)|\psi(t_0)\rangle$ $(t \geq t_0)$, where $U(t, t_0)$ is the unitary evolution operator defined by

$$U(t, t_0) := \mathcal{T}\exp\left(-i\int_{t_0}^{t} d\bar{t}\, H(\bar{t})\right) \tag{2}$$

with $\mathcal{T}$ representing the time-ordered product.

The spirit of the Floquet theory lies in the idea of decomposing the overall dynamics into stroboscopic evolution (i.e., a sequence of snapshots at times $s \to s+T \to s+2T \to \cdots$) and micromotion (i.e., $s \to s+t$ $(0 \leq t < T)$). The former contains information about long-time and time-averaged dynamics, while the latter includes information on fast dynamics in a short-time scale. To describe stroboscopic dynamics, it is convenient to consider time evolution by one cycle, starting from time s,

$$U(s+T, s) =: e^{-iH_F(s)T}, \tag{3}$$

where we define a hermitian operator $H_F(s)$ as an effective 'static' Hamiltonian that describes time evolution over one period. Alternatively, one can write $H_F(s) = iT^{-1}\log U(s+T, s)$. The eigenvalues of $H_F(s)$ are determined only up to modulo $\omega = 2\pi/T$. Once $H_F(s)$ is known, stroboscopic dynamics from s to $s+nT$ $(n = 1, 2, 3, \ldots)$ is given by $U(s+nT, s) = e^{-inH_F(s)T}$. In general, however, $H_F(s)$ is a highly nonlocal and complicated many-body operator.

For general time evolution, one can rewrite the unitary operator $U(t, t_0)$ (2) as

$$U(t, t_0) = U(t, s)e^{i(t-s)H_F(s)}e^{-i(t-t_0)H_F(s)}e^{-i(t_0-s)H_F(s)}U(s, t_0) \tag{4}$$

with a free parameter s. The above equation indicates how $U(t, t_0)$ differs from $e^{-i(t-t_0)H_F(s)}$. If $t_0 = s$ and $t = s + T$, the two are identical, while in other cases they are not in general. The discrepancy between $U(t, t_0)$ and $e^{-i(t-t_0)H_F(s)}$ is characterized by a unitary operator

$$P_s(t) := U(t, s)e^{i(t-s)H_F(s)}, \tag{5}$$

which is time periodic ($P_s(t + T) = P_s(t)$) by construction. Using $P_s(t)$ (5), one can express the time-evolution operator as

$$U(t, t_0) = P_s(t)e^{-i(t-t_0)H_F(s)}P_s(t_0)^{-1}. \tag{6}$$

Now we are in a position to state Floquet's theorem in the present context.

Floquet's theorem—*Given a time-periodic Hamiltonian $H(t) = H(t + T)$ and the corresponding unitary evolution operator $U(t, t_0)$* (2), *there exist a time-independent hermitian operator H_F and a time-periodic unitary operator $P(t) = P(t + T)$ such that*

$$U(t, t_0) = P(t)e^{-i(t-t_0)H_F}P(t_0)^{-1}. \tag{7}$$

Since we have already given an example of explicit constructions of the operators H_F and $P(t)$ in the above (Eqs. 3 and 5), the proof of the theorem has been completed. The operator H_F and its eigenvalues are often referred to as Floquet Hamiltonian and quasienergies, respectively. If one substitutes Eq. (7) in the equation of motion, $i\partial_t U(t, t_0) = H(t)U(t, t_0)$, one obtains a relation between H_F and $P(t)$,

$$H_F = P(t)^{-1}(H(t) - i\partial_t)P(t). \tag{8}$$

The choice of the combination $\{H_F, P(t)\}$ is not unique. This can be seen in the previous example, where $H_F(s)$ (3) and $P_s(t)$ (5) depend on the free parameter s. On the other hand, $\{H_F, P(t)\}$ does not necessarily correspond to $\{H_F(s), P_s(t)\}$ for certain s.

Although the combination $\{H_F, P(t)\}$ is not unique, the eigenvalues of H_F are unique (up to mod ω). Suppose that there exist two pairs, $\{H_F, P(t)\}$ and $\{\widetilde{H}_F, \widetilde{P}(t)\}$, that satisfy Eq. (7). By defining a unitary operator $V(t_0) := P(t_0)^{-1}\widetilde{P}(t_0)$, one can see that they are related through

$$e^{-i\widetilde{H}_F T} = V(t_0)^{-1}e^{-iH_F T}V(t_0), \tag{9}$$

$$\widetilde{P}(t) = P(t)e^{-i(t-t_0)H_F}V(t_0)e^{i(t-t_0)\widetilde{H}_F}. \tag{10}$$

These are a kind of "gauge transformations" that characterize nonuniqueness of $\{H_F, P(t)\}$. Note that $e^{-i\widetilde{H}_F T}$ is related to $e^{-iH_F T}$ through the unitary transformation; hence, the eigenvalues of H_F and $\widetilde{H}_F$ are identical up to mod ω (except for the difference in order). It is always possible to choose a gauge in such a way that $P(t_0) = I$ (the identity operator). If $P(t_0) \neq I$, one can perform a gauge transformation with $V(t_0) = P(t_0)^{-1}$, which gives $\widetilde{P}(t_0) = I$. In this particular gauge, the unitary operator is simplified to $U(t, t_0) = P(t)e^{-i(t-t_0)H_F}$.

The wavefunction evolves, according to Floquet's theorem (7), as $|\psi(t)\rangle = P(t)e^{-i(t-t_0)H_F}P(t_0)^{-1}|\psi(t_0)\rangle$. If $P(t_0)^{-1}|\psi(t_0)\rangle$ is an eigenstate (say $|\psi_\alpha\rangle$) of H_F (with an eigenvalue ε_α), the wavefunction takes a form of

$$|\psi(t)\rangle = e^{-i\varepsilon_\alpha(t-t_0)}|u_\alpha(t)\rangle \tag{11}$$

with $|u_\alpha(t)\rangle := P(t)|\psi_\alpha\rangle$, which is time periodic, $|u_\alpha(t + T)\rangle = |u_\alpha(t)\rangle$. Thus, the wavefunction is decomposed into the phase factor and the time-periodic part in Eq. (11). This is analogous to the well-known Bloch's theorem for spatially periodic systems in solid-state physics, in which the Bloch wavefunction has a form of the product of a plane wave and a spatially periodic function (see Table 1 for comparison).

If $P(t_0)^{-1}|\psi(t_0)\rangle$ is not an eigenstate of H_F, one can still expand it in the complete eigenbasis of the hermitian operator H_F, $\{|\psi_\alpha\rangle\}_\alpha$, as

$$P(t_0)^{-1}|\psi(t_0)\rangle = \sum_\alpha c_\alpha|\psi_\alpha\rangle. \tag{12}$$

Then the wavefunction at time t is given by

Table 1 Comparison between Bloch's theorem for spatially periodic systems and Floquet's theorem for time-periodic systems.

	Bloch	*Floquet*
Hamiltonian	$H(\boldsymbol{r} + \boldsymbol{R}) = H(\boldsymbol{r})$	$H(t + T) = H(t)$
wavefunction	$\lvert\psi_{\boldsymbol{k}}(\boldsymbol{r})\rangle = e^{i\boldsymbol{k}\cdot\boldsymbol{r}}\lvert u_{\boldsymbol{k}}(\boldsymbol{r})\rangle$, $\lvert u_{\boldsymbol{k}}(\boldsymbol{r} + \boldsymbol{R})\rangle = \lvert u_{\boldsymbol{k}}(\boldsymbol{r})\rangle$ (crystal momentum $\boldsymbol{k}$)	$\lvert\psi_\alpha(t)\rangle = e^{-i\varepsilon_\alpha t}\lvert u_\alpha(t)\rangle$, $\lvert u_\alpha(t + T)\rangle = \lvert u_\alpha(t)\rangle$ (quasienergy ε_α)
Brillouin zone	$-\frac{\pi}{a} \leq \boldsymbol{k}_i < \frac{\pi}{a}$	$-\frac{\omega}{2} \leq \varepsilon_\alpha < \frac{\omega}{2}$

The Brillouin zone in momentum space is shown for a simple cubic lattice with a lattice constant a as an example.

$$|\psi(t)\rangle = \sum_{\alpha} c_\alpha e^{-i\varepsilon_\alpha(t-t_0)}|u_\alpha(t)\rangle, \tag{13}$$

where c_α is a time-independent coefficient. Again, the wavefunction is expressed as a combination of the phase factors and the time-periodic functions $|u_\alpha(t)\rangle$.

An observable $\langle O(t)\rangle = \langle\psi(t)|O|\psi(t)\rangle$ is not necessarily time periodic due to the presence of off-diagonal terms in the Floquet eigenbasis, $e^{i(\varepsilon_\alpha-\varepsilon_\beta)(t-t_0)}\langle u_\alpha(t)|O|u_\beta(t)\rangle$ $(\alpha \neq \beta)$. However, there are various situations where the contributions of the off-diagonal terms are suppressed, such as Floquet prethermalized states in an isolated system and NESS in open systems (Fig. 1). In those cases, time evolution of observables becomes periodic with the same periodicity as the driving field. An important exception is a discrete time crystal (Khemani et al., 2016; Sacha, 2015; Else et al., 2016; Yao et al., 2017; Moessner and Sondhi, 2017), where observables become time periodic but its periodicity is integer multiples of that of the driving field.

One can look at Floquet's theorem from another point of view, which is even closer to that of solid-state physics, that is, the band picture. By substituting the Floquet wavefunction (11) into the time-dependent Schrödinger equation (1), one obtains $i\frac{d}{dt}|u_\alpha(t)\rangle + \varepsilon_\alpha|u_\alpha(t)\rangle = H(t)|u_\alpha(t)\rangle$. Since $|u_\alpha(t)\rangle$ and $H(t)$ are both periodic in time, one can Fourier transform them into Fourier modes,

$$H_{mn} := T^{-1}\int_0^T dt\, e^{i(m-n)\omega t}H(t), \tag{14}$$

$$|u_\alpha^n\rangle := T^{-1}\int_0^T dt\, e^{in\omega t}|u_\alpha(t)\rangle. \tag{15}$$

Since H_{mn} only depends on $m - n$, one can also use a shorthand notation of $H_{m-n} := H_{mn}$. After that, the time-dependent Schrödinger equation turns into a seemingly time-independent equation,

$$\sum_n (\mathcal{H}_F)_{mn}|u_\alpha^n\rangle = \varepsilon_\alpha|u_\alpha^m\rangle, \tag{16}$$

$$(\mathcal{H}_F)_{mn} := H_{mn} - m\omega\delta_{mn}. \tag{17}$$

Here comes an idea of extending the Hilbert space in order to interpret Eq. (16) as an eigenvalue problem. Let $\mathbb{H}$ be the Hilbert space of the system, and let $\mathbb{T}$ be a vector space spanned by Fourier modes of time-periodic functions with the period T. For example, a periodic function $f(t) = f(t+T)$ is Fourier transformed as $f(t) = \sum_n f_n e^{-in\omega t}$. Then a vector $(\cdots, f_{-2}, f_{-1}, f_0, f_1, f_2, \cdots)$, whose elements are composed of Fourier coefficients, belongs to $\mathbb{T}$. Eq. (16) can be viewed as an eigenvalue equation in the extended Hilbert space $\mathbb{H}\otimes\mathbb{T}$ (Sambe space (Sambe, 1973)).

The set $\{\varepsilon_\alpha\}_\alpha$ has been defined as the eigenvalues of H_F acting on $\mathbb{H}$, while in Eq. (16) they appear as the eigenvalues of $\mathcal{H}_F$ acting on $\mathbb{H}\otimes\mathbb{T}$. Since the dimensions of $\mathbb{H}$ and $\mathbb{H}\otimes\mathbb{T}$ are different, there must be missing eigenvalues of $\mathcal{H}_F$, which can be found if one notices the fact that a vector $|u_\alpha^{n-l}\rangle$ shifted from $|u_\alpha^n\rangle$ by l components $(l = 0, \pm 1, \pm 2, \ldots)$ is also an eigenstate of $\mathcal{H}_F$ with an eigenvalue $\varepsilon_\alpha - l\omega$. This means that $\{|u_\alpha^{n-l}\rangle\}_{\alpha,l}$ consists of a complete set of the eigenstates in $\mathbb{H}\otimes\mathbb{T}$. The spectrum of the corresponding eigenvalues $\{\varepsilon_\alpha - l\omega\}_{\alpha,l}$ shows a periodic structure in energy space, in much the same way as the band structure shows a periodic pattern in momentum space for spatially periodic systems. In particular, one can restrict the energy space within $-\frac{\omega}{2} \leq \varepsilon_\alpha < \frac{\omega}{2}$ (the Floquet Brillouin zone) by shifting quasienergies by integer multiples of ω in order to represent quasienergies without mod ω redundancies.

Thus, H_F and $\mathcal{H}_F$ share the same eigenvalues up to mod ω. As we have mentioned, H_F is a complicated nonlocal many-body operator that is expected to be difficult to evaluate directly, while $\mathcal{H}_F$ is usually a well-behaved local few-body operator. On the other hand, the latter is acting on the extended space $\mathbb{H}\otimes\mathbb{T}$, whose dimension is infinitely larger than $\mathbb{H}$. In practice, one can truncate the Fourier space $\mathbb{T}$ to finite dimensions as an approximation; Off-diagonal elements, $(\mathcal{H}_F)_{mn}$, physically correspond to $m - n$ photon absorption/emission processes, which would be suppressed when $|m - n| \gg 1$ if the drive strength is not too strong.

Examples

As an example, let us consider a single-band system of noninteracting electrons driven by a time-periodic field described by the Hamiltonian

$$H(t) = \sum_{\boldsymbol{k}} \varepsilon_{\boldsymbol{k}}(t) c_{\boldsymbol{k}}^\dagger c_{\boldsymbol{k}}, \tag{18}$$

where $c_{\boldsymbol{k}}^\dagger$ is a creation operator of electrons with momentum $\boldsymbol{k}$, and $\varepsilon_{\boldsymbol{k}}(t) = \varepsilon_{\boldsymbol{k}}(t+T)$ is a band dispersion including the coupling to a time-periodic field. The eigenvalues (quasienergies) of the corresponding $\mathcal{H}_F$ (17) are given by $T^{-1}\int_0^T dt\, \varepsilon_{\boldsymbol{k}}(t) + n\omega$ $(n = 0, \pm 1, \pm 2, \ldots)$ (Tsuji et al., 2008), that is, the time-averaged dispersion shifted by integer multiples of the drive frequency ω. One can confirm that these are also eigenvalues of H_F (7) since the time evolution operator is given by $U(t, t_0) = e^{-i\int_{t_0}^{t} ds\, \sum_k \varepsilon_k(s) c_k^\dagger c_k}$ which is free from the time-ordering operator due to $[H(t), H(t')] = 0$.

If the system is a one-dimensional lattice with a nearest-neighbor hopping with a dispersion $\varepsilon_k = -2J\cos k$ driven by an ac electric field with amplitude E (represented by a vector potential $A(t) = -E\sin\omega t/\omega$), the time average of the dispersion is given by $T^{-1}\int_0^T dt\,(-2J)\cos(k - A(t)) = -2J\mathcal{J}_0(E/\omega)\cos k$, where the hopping amplitude J is multiplied by $\mathcal{J}_0(E/\omega)$, the zeroth-order Bessel-function factor. In Fig. 2, we show the corresponding quasienergy spectrum. Due to the presence of the periodic drive, the hopping amplitude is effectively reduced ($|\mathcal{J}_0(E/\omega)| \leq 1$), and electrons become heavier. When the Bessel factor exactly vanishes ($\mathcal{J}_0(E/\omega) = 0$), electrons cannot hop to neighboring sites completely, resulting in dynamical localization (Dunlap and Kenkre, 1986; Holthaus, 1992). In the spectrum (Fig. 2), there are side-band structures (labeled by the Fourier mode index n) separated by ω from the neighboring bands, which is referred to as the dynamic Wannier–Stark ladder. These arise due to the consequence of virtual n-photon absorption/emission processes.

Another example is a model of Dirac electrons in two spatial dimensions driven by circularly polarized light (Oka and Aoki, 2009; Mikami et al., 2016). The Hamiltonian reads

$$H(t) = \sum_{\boldsymbol{k}\alpha\beta} c^\dagger_{\boldsymbol{k}\alpha} h_{\boldsymbol{k}\alpha\beta}(t) c_{\boldsymbol{k}\beta}, \tag{19}$$

$$h_{\boldsymbol{k}\alpha\beta}(t) = (k_x - A_x(t))(\sigma_x)_{\alpha\beta} + (k_y - A_y(t))(\sigma_y)_{\alpha\beta}, \tag{20}$$

where $c^\dagger_{\boldsymbol{k}\alpha}$ is a creation operator of electrons with two components (corresponding to two bands near the Fermi energy), $(A_x, A_y) = (A\cos\omega t, A\sin\omega t)$ is the vector potential for circularly polarized light, and σ_x and σ_y are Pauli matrices. In this system, circularly polarized light explicitly breaks time reversal symmetry.

In Fig. 3, a typical quasienergy spectrum is shown. When the driving field is absent, the spectrum consists of a Dirac cone (linear dispersion) without energy gap near $E = 0$. As one increases the amplitude of the electric field, there emerge energy gaps at the band crossing points, accompanied by sideband structures with energy spacing ω. Especially, at $\boldsymbol{k} = 0$, the gap is given by $\Delta = \sqrt{\omega^2 + 4A^2} - \omega$ (Oka and Aoki, 2009). This phenomenon, light-induced gap opening in the quasienergy spectrum (accompanied by chiral edge modes), can be interpreted as a topological phase transition, since quasienergy bands are characterized by nonzero topological (Chern) numbers, similar to quantum Hall states in static systems. In this sense, the system is classified to a Floquet topological insulator (Oka and Aoki, 2009; Kitagawa et al., 2010, 2011; Lindner et al., 2011; Roy and Harper, 2017; Rudner and Lindner, 2020), a class of topological phases in periodically driven systems.

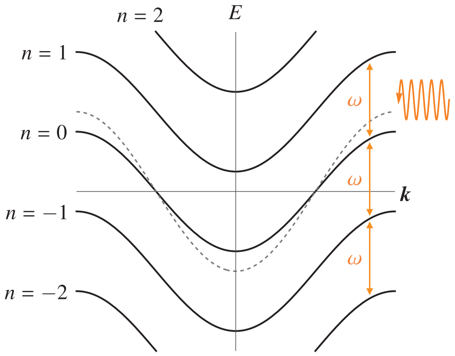

Fig. 2 The quasienergy spectrum of noninteracting electrons on a one-dimensional lattice driven by an ac electric field (*solid curves*). The *dashed curve* shows the original energy dispersion without the driving field.

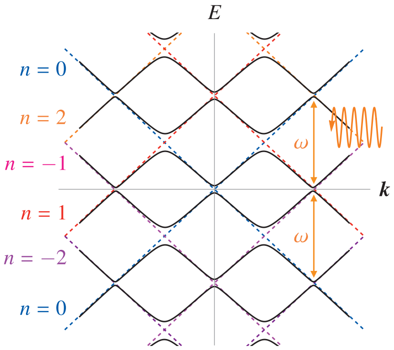

Fig. 3 The quasienergy spectrum (*solid curves*) of Dirac electrons driven by circularly polarized light ($A = 1$, $\omega = 5$). The *dashed lines* with Fourier mode labels n show the spectrum without driving.

While the above example can be understood by mapping to the corresponding static model, there are several examples that show nontrivial topological phases that do not have equilibrium counterparts (Kitagawa et al., 2010, 2012; Rudner et al., 2013; Harper et al., 2020; Nakagawa et al., 2020a; Jangjan et al., 2022): Topologically protected chiral edge modes can appear even though all the bulk Floquet bands have vanishing Chern numbers. This is possible since in Floquet systems edge modes can go across the quasienergy $\varepsilon = \pm\pi/T$ ("anomalous π modes") and wind around the Floquet Brillouin zone in the frequency domain. In this case, the system is called an anomalous Floquet topological insulator.

High-frequency expansion

The approach of the Floquet theory becomes particularly effective when the drive frequency is higher than typical energy scales included in the original (undriven) Hamiltonian. Intuitively, when the frequency is sufficiently large, physical degrees of freedom in the system cannot follow rapid oscillations of the drive field. As a result, the effect of the drive is rounded in the time average, implying that the Floquet Hamiltonian H_F defined in Floquet's theorem (7) is approximated to be the time average of the original Hamiltonian, $H_F \approx H_0 = T^{-1}\int_0^T dt\, H(t)$. This intuition is actually justified in the form of high-frequency expansions (or $1/\omega$ expansion), a typical one of which reads

$$H_F = H_0 + \sum_{n=1}^{\infty} \frac{[H_{-n}, H_n]}{n\omega} + \cdots , \tag{21}$$

where "$\cdots$" contains higher order terms in $1/\omega$. The second term on the right-hand side of Eq. (21) can be understood as a sum of second-order perturbation corrections for n-photon absorption/emission processes.

There are several ways to carry out such an expansion (e.g., Floquet-Magnus expansion (Fel'dman, 1984; Casas et al., 2001; Blanes et al., 2009; Mananga and Charpentier, 2011; Goldman and Dalibard, 2014), van Vleck perturbation theory (Eckardt and Anisimovas, 2015; Bukov et al., 2015), and Brillouin-Wigner perturbation theory (Mikami et al., 2016)), all of which are known to be equivalent to each other in the sense that they all give the same high-frequency expansion for the eigenvalues of H_F (up to mod ω). One can derive some of them, for example, by starting from Eq. (8), $H_F = e^{i\Lambda(t)}(H(t) - i\partial_t)e^{-i\Lambda(t)}$, where $\Lambda(t)$ is a hermitian operator defined by $P(t) =: e^{-i\Lambda(t)}$. This relation can be rewritten with an adjoint operator $\mathrm{ad}_{\Lambda(t)}X := [\Lambda(t), X]$ as

$$\frac{d}{dt}\Lambda(t) = \sum_{n=0}^{\infty} \frac{B_n}{n!}(-i)^n (\mathrm{ad}_{\Lambda(t)})^n [H(t) + (-1)^{n+1} H_F], \tag{22}$$

where B_n is the Bernoulli number. One can solve Eq. (22) order-by-order by expanding

$$\Lambda(t) = \sum_{k=1}^{\infty} \Lambda^{(k)}(t), \quad H_F = \sum_{k=0}^{\infty} H_F^{(k)}, \tag{23}$$

where one assigns an order 1 for $H(t)$, the order k for $\Lambda^{(k)}$, and the order $k+1$ for $H^{(k)}$. In this rule, the superscript (k) of $\Lambda^{(k)}$ and $H^{(k)}$ represents the order in $1/\omega$.

To determine the expansion, one needs to fix the gauge. For example, one can set $\Lambda(t_0) = 0$ at certain time t_0, which generates the so-called Floquet-Magnus expansion. While the expansion can be uniquely determined, there remains a spurious dependence on t_0 that appears as a phase factor in the expansion. Another choice that is often employed is $\int_0^T dt\, \Lambda(t) = 0$, which corresponds to the van Vleck perturbation expansion (Eq. 21 that does not have explicit t_0 dependence. These two expansions are related through unitary transformation.

The high-frequency expansions are usually asymptotic expansions. That is, they do not converge in the ordinary sense but give good approximation if the infinite series are truncated at a certain finite order. In fact, there is a rigorous estimate for the error induced by such a truncation, which suggests that the truncated Floquet-Magnus expansion accurately describes time evolution of periodically driven quantum systems up to a time scale which is exponentially long as a function of drive frequency. As a result, there emerges an exponentially long-lived prethermal regime (Fig. 1A) at an early stage of periodic driving, where the system shows thermal behavior with respect to the effective Hamiltonian given by the truncated expansion.

As an example, let us apply the high-frequency expansion to a model of noninteracting electrons on a honeycomb lattice driven by circularly polarized light. The Hamiltonian is given by

$$H(t) = J\sum_{\langle jk\rangle}\left[\exp\left(-i\int_{\boldsymbol{R}_k}^{\boldsymbol{R}_j} \boldsymbol{A}(t)\cdot d\boldsymbol{r}\right) c_j^\dagger c_k + \text{h.c.}\right], \tag{24}$$

where $\langle jk\rangle$ denotes nearest-neighbor sites at positions $\boldsymbol{R}_j$ and $\boldsymbol{R}_k$ on the honeycomb lattice, and $\boldsymbol{A}(t)$ represents a vector potential for circularly polarized light, which is included as a Peierls phase. In the high-frequency expansion (21), the corresponding effective Hamiltonian is given by (Mikami et al., 2016)

$$H_F = J_{\text{eff}}\sum_{\langle jk\rangle}(c_j^\dagger c_k + \text{h.c.}) + K_{\text{eff}}\sum_{\langle\langle jk\rangle\rangle}(i\tau_{j,k}c_j^\dagger c_k + \text{h.c.}) + O\left(\frac{1}{\omega^2}\right), \tag{25}$$

where $\langle\langle jk\rangle\rangle$ represents next-nearest-neighbor sites, $J_{\text{eff}} = J\mathcal{J}_0(A)$, $K_{\text{eff}} = -J^2/\omega\sum_{n\neq 0}\mathcal{J}_n(A)^2 \sin(2\pi n/3)/n$ ($\mathcal{J}_n(A)$ is the nth-order Bessel function), and $\tau_{j,k} = \pm 1$ represents the chirality of the hopping from k to j (+(−) is assigned to the clockwise (counterclockwise) path on a hexagon).

In addition to the modulated nearest-neighbor hopping, there appear next-nearest-neighbor hoppings that are purely imaginary. The resulting Hamiltonian is equivalent to the Haldane model (Haldane, 1988), a tight-binding model on a honeycomb lattice with complex next-nearest-neighbor hoppings, which is known to be a model of quantum anomalous Hall states (Chern insulators). Thus, one can understand that the system undergoes a topological phase transition induced by circularly polarized light. This is consistent with the result of the model of Dirac electrons treated in the previous section. As one reduces the drive frequency, higher order terms in the high-frequency expansion become relevant, and more complicated topological phases can be found with high Chern numbers (Mikami et al., 2016).

Periodically driven open quantum systems

In open quantum systems, the time evolution of the system is not simply given by the time-dependent Schrödinger equation (1) due to the effect of environment. Let the total Hamiltonian be given as $H = H_S + H_I + H_B$, where H_S is the system's Hamiltonian, H_I represents the interaction between the system and environment, and H_B is the Hamiltonian of environment (bath). The density matrix of the total system ρ evolves according to the von Neumann equation, $\frac{d}{dt}\rho = -i[H, \rho]$. What one is interested in here is the time evolution of the system's density matrix defined by $\rho_S = \text{tr}_B\rho$ (tr_B denotes the partial trace over environment's degrees of freedom).

One approach to describe the system's dynamics is to use a quantum Master equation, which is a quantum analog of Master equations in classical stochastic processes (Breuer and Petruccione, 2007). To derive the quantum Master equation, there are two basic assumptions: (i) Markovianity of system's time evolution (i.e., $\rho_S(t + \Delta t)$ is solely determined from $\rho_S(t)$) and (ii) absence of initial correlations between the system and environment (i.e., $\rho(0) = \rho_S(0) \otimes \rho_B(0)$). In this situation, if a map from arbitrary $\rho_S(0)$ to $\rho_S(t)$ is completely positive and trace preserving, $\rho_S(t)$ obeys the following form of the quantum Master equation (Gorini-Kossakowski-Sudarshan-Lindblad equation (Gorini et al., 1976; Lindblad, 1976)),

$$\frac{d}{dt}\rho_S = -i[H_S, \rho_S] + \sum_j \left(L_j\rho_S L_j^\dagger - \frac{1}{2}\{L_j^\dagger L_j, \rho_S\}\right), \tag{26}$$

with a certain set of operators $\{L_j\}$ called Lindblad operators (or jump operators). The second term on the right-hand side of Eq. (26) represents the effect of environment, giving nonunitary dynamics. If one defined a nonhermitian effective Hamiltonian, $H_{\text{eff}} := H_S - \frac{i}{2}\sum_j L_j^\dagger L_j$, Eq. (26) is rewritten as

$$\frac{d}{dt}\rho_S = -i(H_{\text{eff}}\rho_S - \rho_S H_{\text{eff}}^\dagger) + \sum_j L_j\rho_S L_j^\dagger. \tag{27}$$

The second term on the right-hand side of Eq. (27) represents quantum jump processes, in which the system's state discontinuously changes in a stochastic manner.

A microscopic justification of the quantum Master equation (26) often requires additional approximations. The conventional approach employs (i) the Born approximation which is valid for the weak coupling between the system and environment and (ii) the secular approximation (or the rotating-wave approximation) that can be justified when the inverse of the level spacing between the eigenvalues of H_S is much smaller than the relaxation time of the system. The latter condition does not usually hold for many-body systems since the level spacing becomes exponentially small as the system size increases. Nevertheless, the quantum Master equation has been used from a phenomenological point of view to describe the dynamics of open quantum many-body systems (Diehl et al., 2010; Prosen, 2011; Tindall et al., 2019; Nakagawa et al., 2020b; Yamamoto et al., 2021).

In the presence of periodic driving, the use of the quantum Master equation needs more careful derivation (Mori, 2023). Especially, if one is interested in nontrivial NESS, heating due to the periodic drive should be balanced with dissipation. The relaxation time then becomes comparable to the system's intrinsic time scale, which may invalidate the secular approximation. There has recently been a proposal for the derivation of quantum Master equations without relying on the secular approximation (or the rotating-wave approximation) (Nathan and Rudner, 2020, 2022). The underlying notion is that Markovianity is a property of the bath and the system-bath coupling solely, and should not depend on details of the energy level structure of the system. In fact, one can derive a Markovian quantum Master equation (called the 'universal Lindblad equation') when the correlation time of the bath is much shorter than the characteristic time scale of the system-bath interaction.

Another approach to driven open quantum systems is to use nonequilibrium Green's functions (Kadanoff and Baym, 1962; Keldysh, 1965). The advantage of this approach is that it does not necessarily rely on the Markov and secular approximations. On the other hand, since the approach is based on the Green's function formalism, one has to adopt certain diagrammatic techniques to treat many-body interactions.

One of the simplest models of environment for electrons is a free-fermion heat bath (Tsuji et al., 2009; Aoki et al., 2014), whose Hamiltonians are given by

$$H_B = \sum_{j,k} \varepsilon_k b_{j,k}^\dagger b_{j,k}, \tag{28}$$

$$H_I = \sum_{j,k} V_k (c_j^\dagger b_{j,k} + \text{h.c.}), \tag{29}$$

where $c_j^\dagger$ and $b_{j,k}^\dagger$ are creation operators of system's and bath's electrons at site j and mode k, respectively, ε_k is the energy of bath's electrons, and V_k is a coupling between system's and bath's electrons. The system's retarded, advanced, and Keldysh Green's functions are defined as

$$G_{ij}^R(t,t') = -i\theta(t-t')\langle\{c_i(t), c_j^\dagger(t')\}\rangle, \tag{30}$$

$$G_{ij}^A(t,t') = i\theta(t'-t)\langle\{c_i(t), c_j^\dagger(t')\}\rangle, \tag{31}$$

$$G_{ij}^K(t,t') = -i\langle[c_i(t), c_j^\dagger(t')]\rangle, \tag{32}$$

respectively ($\theta(t)$ is the step function). The retarded (and advanced) Green's function contains information about the single-particle spectrum of the system while the Keldysh one carries information about the occupation distribution of the spectrum.

Since the total Hamiltonian $H = H_S + H_I + H_B$ is quadratic in $b_{j,k}^\dagger$ and $b_{j,k}$, one can integrate out the bath's degrees of freedom analytically. As a result, the system's Green's function satisfies the following Dyson equation

$$\begin{pmatrix} G^R & G^K \\ 0 & G^A \end{pmatrix} = \left[\begin{pmatrix} G_0^R & G_0^K \\ 0 & G_0^A \end{pmatrix}^{-1} - \begin{pmatrix} \Sigma_b^R & \Sigma_b^K \\ 0 & \Sigma_b^A \end{pmatrix} - \begin{pmatrix} \Sigma^R & \Sigma^K \\ 0 & \Sigma^A \end{pmatrix}\right]^{-1}, \tag{33}$$

where G_0 is the system's noninteracting Green's function, Σ_b is the self-energy due to the coupling to the heat bath, and Σ is the system's self-energy. For the free-fermion bath, the retarded component of Σ_b is explicitly given in the frequency domain as

$$\Sigma_b^R(\nu) = \sum_k \frac{V_k^2}{\nu - \varepsilon_k + i\eta}, \tag{34}$$

where η is an infinitesimal positive constant. By using $1/(\nu + i\eta) = \mathcal{P}(1/\nu) - i\pi\delta(\nu)$ (with $\mathcal{P}$ being the principal value), one obtains the imaginary part of $\Sigma_b^R(\nu)$,

$$\Gamma(\nu) = \sum_k \pi V_k^2 \delta(\nu - \varepsilon_k), \tag{35}$$

which corresponds to the bath's spectral function. One often assumes a flat density of states for the bath, $\Gamma(\nu) = \Gamma$, as the simplest choice. The real part of $\Sigma_b^R(\nu)$ gives a potential shift, which can be renormalized into the chemical potential. The advanced component is simply the complex conjugate, $\Sigma_b^A(\nu) = \Sigma_b^R(\nu)^\dagger$. The Keldysh part of Σ_b is determined from the fluctuation–dissipation relation for the bath's Green's function, giving $\Sigma_b^K(\nu) = F(\nu)[\Sigma_b^R(\nu) - \Sigma_b^A(\nu)]$ with $F(\nu) = \tanh(\beta\nu/2)$ (β is the inverse temperature of the heat bath).

To summarize, the self-energy due to the coupling to the free-fermion bath takes a simple form

$$\begin{pmatrix} \Sigma_b^R(\nu) & \Sigma_b^K(\nu) \\ 0 & \Sigma_b^A(\nu) \end{pmatrix} = \begin{pmatrix} -i\Gamma & -2i\Gamma F(\nu) \\ 0 & i\Gamma \end{pmatrix}. \tag{36}$$

Although the free-fermion bath model looks somewhat artificial, it correctly reproduces the semiclassical result of Boltzmann's transport theory (Han, 2013; Aoki et al., 2014). In this context, the model can be viewed as a two-parameter phenomenology (the relaxation rate Γ and heat bath's temperature β^{-1}) to describe dissipation. One can also employ other models for a heat bath such as a model of phonons, but then the bath's degrees of freedom cannot be integrated out analytically, and one has to use certain approximations.

One can incorporate the effect of periodic driving in this approach. To this end, one assumes the existence of time-periodic NESS. Once the steady state is reached, the Green's function should satisfy the periodicity in two-time arguments, $G^\alpha(t,t') = G^\alpha(t+T, t'+T)$ ($\alpha = R, A, K$). This allows one to define the Floquet Green's function (Faisal, 1989; Martinez, 2003, 2005; Tsuji et al., 2008; Aoki et al., 2014; Liu et al., 2017),

$$G_{mn}^\alpha(\nu) := \frac{1}{T}\int_0^T ds \int_{-\infty}^{\infty} dt\, e^{i(m-n)\omega s + i\nu t} G^\alpha\left(s + \frac{t}{2}, s - \frac{t}{2}\right), \tag{37}$$

which takes a matrix form with indices m and n being the labels of Fourier modes as used in Eq. (14). The Dyson equation maintains the form of Eq. (33) with all the Green's functions and self-energies written in the above matrix form with the inverse interpreted as the matrix inverse. The Floquet matrix form of Σ_b reads $\Sigma_{b,mn}^R(\nu) = -i\Gamma\delta_{mn}$ and $\Sigma_{b,mn}^K(\nu) = -2i\Gamma F(\beta(\nu + n\omega)/2)\delta_{mn}$.

Provided that the self-energy from the system's interaction is given, the Green's function in the time-periodic NESS is determined from the Dyson equation (33). This part requires a (diagrammatic) solver for quantum many-body problems. One such approach is

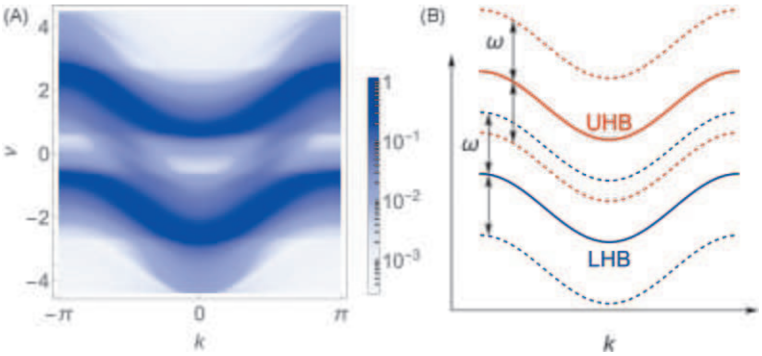

Fig. 4 (A) The single-particle spectrum $A(\nu, k)$ of the ac-field-driven Falicov–Kimball model calculated from the Floquet DMFT. (B) The corresponding schematic band structure of the ac-field-driven Mott insulator with the drive frequency ω. The upper and lower Hubbard bands (UHB and LHB) are shown by *solid curves*, and the accompanied Floquet sidebands are shown by *dashed curves*. (Adapted from Aoki et al. (2014) Nonequilibrium dynamical mean-field theory and its applications. *Reviews of Modern Physics* 86: 779.)

the so-called Floquet dynamical mean-field theory (DMFT) (Tsuji et al., 2008, 2009; Aoki et al., 2014; Joura et al., 2008; Lubatsch and Kroha, 2009), which is a combined formulation of the Floquet theory and nonequilibrium DMFT (Freericks et al., 2006; Aoki et al., 2014). The latter solves nonequilibrium quantum many-body problems under the local approximation of the self-energy (Georges et al., 1996).

In Fig. 4, an example of the result of the Floquet DMFT is shown for the ac-field-driven Falicov–Kimball model (Tsuji et al., 2008, 2009; Aoki et al., 2014), which is a simple model of correlated electrons that shows a Mott insulator-to-metal transition in equilibrium (Freericks and Zlatić, 2003). There emerges an ac-field-induced midgap state between the upper and lower Hubbard bands as Floquet sidebands with an energy spacing ω. Due to this, the system turns from a Mott-insulating state to an ac-field-induced metallic state. This exemplifies a quantum many-body Floquet state.

The nonequilibrium Green's function approach not only describes the single-particle properties but also characterizes two-particle ones such as response functions and transport coefficients. To obtain those quantities, one has to evaluate two-particle Green's functions on top of the single-particle Green's function. For example, the transport property of the ac-field-driven Falicov–Kimball model can be identified from the optical conductivity spectrum, which shows a Drude-like peak structure at low energy instead of a Mott gap, indicating that the system indeed becomes metallic due to the effect of the ac field (Tsuji et al., 2009).

Experimental observations

Floquet states have been experimentally observed in various systems. In solid-state materials, occupied single-particle spectra can be measured by angle-resolved photoemission spectroscopy (ARPES), which can map out the band structure of correlated electrons in energy and momentum spaces below the Fermi level. The technique can also be applied to study nonequilibrium states of electrons in solids, in which case pump and probe pulses are applied with a certain time delay in between (time-resolved ARPES). The former pulse is used to drive electrons out of equilibrium while the latter is used to generate photoelectrons. During irradiation of a pump pulse, the system can be approximately considered to be driven periodically in time if the pump pulse contains sufficiently large number of oscillation cycles. Thus, the time-resolved ARPES offers an opportunity to observe Floquet states for electron systems.

In Fig. 5, an example of time-resolved ARPES spectra is shown for a topological insulator Bi_2Se_3 driven by a circularly polarized laser (Wang et al., 2013). In topological insulators, there are topologically protected gapless surface states, which support an energy dispersion of Dirac cones. This is precisely the same situation as we see in Section "Examples": Dirac electrons driven by circularly polarized light undergoes a transition to a Floquet topological insulator with a gap opening at the Dirac point. In the time-resolved ARPES experiment, the energy gap is observed to appear under the excitation of a circularly polarized laser. On top of that, Floquet sideband structures are observed with the energy spacing of the drive frequency in the ARPES spectra. These are consistent with the results of the Floquet theory (Oka and Aoki, 2009) (see, e.g., Fig. 3). The subsequent experiment has also demonstrated the transition from the Floquet states to Volkov states, that is, photon-dressed states of free electrons, by time-resolved ARPES (Mahmood et al., 2016).

When Dirac electrons are driven by circularly polarized light and turn to a Floquet topological insulator, the bands around the Dirac point can acquire nonzero Chern numbers. As a result, the system shows the anomalous Hall effect, that is, current flows perpendicular to the direction of an applied dc electric field without a magnetic field. If the distribution of the occupied states is not far from that of zero-temperature equilibrium states, the Hall conductance approaches the quantized value. The Hall conductance of Dirac electrons in a monolayer graphene induced by a circularly polarized laser has been measured experimentally, using an on-chip photoconductive switch device (McIver et al., 2020). The result shows that Floquet topological bands indeed generate the anomalous Hall effect, demonstrating characteristic features of Floquet topological states.

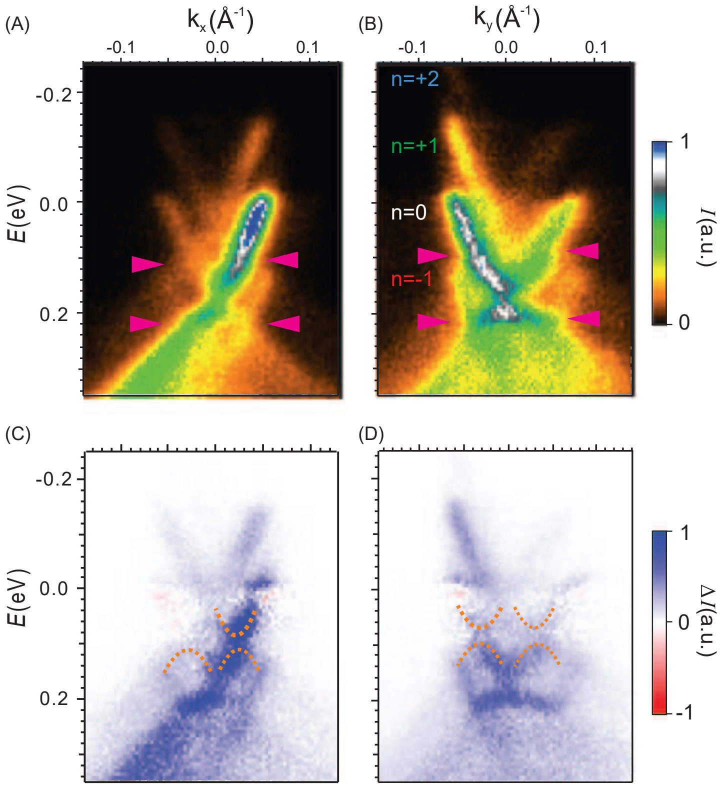

Fig. 5 Time-resolved ARPES spectra of surface states of a topological insulator Bi_2Se_3 under circularly polarized laser excitation along (A) k_x and (B) k_y directions. (C) and (D) are the corresponding spectra after subtracting the spectra at $t = -500$ fs. (Adapted from Wang et al. (2013) Observation of Floquet-Bloch States on the Surface of a Topological Insulator. *Science* 342: 453–457.)

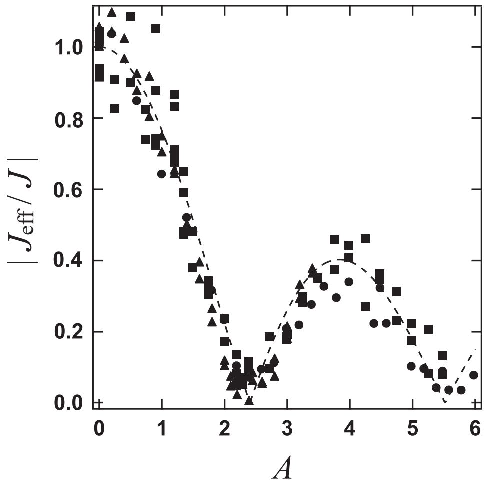

Fig. 6 Effective hopping amplitude of Bose-Einstein condensed cold atoms in a periodically shaken optical lattice as a function of the amplitude of the periodic drive. The *dashed curve* represents the Bessel function $J_0(A)$. (Adapted from Lignier et al. (2007) Dynamical Control of Matter-Wave Tunneling in Periodic Potentials. *Physical Review Letters* 99: 220403.)

In contrast to solid-state systems, artificial quantum systems provide high controllability and ideal clean situations to realize Floquet states. For example, cold atomic gases trapped in an optical lattice are well described by a lattice model of isolated quantum many-body systems. One can then drive the system by periodically shaking the optical lattice potential in real space (Eckardt, 2017), mimicking the effect of ac electric fields for electrons.

In Fig. 6, the experimentally measured effective hopping amplitude of Bose-Einstein condensates in a periodically shaken optical lattice is shown as a function of the amplitude A of the periodic drive (Lignier et al., 2007). As we see in Sections "Examples" and "High-frequency expansion," the Floquet theory predicts that the hopping amplitude is renormalized by the Bessel factor as

$J_{\mathrm{eff}} = J\mathcal{J}_0(A)$, which perfectly agrees with the experimental observation. Using this effect, one can effectively control the interaction strength with ac fields, inducing, for instance, a superfluid-to-Mott insulator transition in the Bose–Hubbard model (Eckardt et al., 2005). One can even reverse the sign of the hopping if $\mathcal{J}_0(A) < 0$, which can be used to realize frustrated classical spin systems (Struck et al., 2011) or to effectively convert the interaction from repulsive to attractive in the ac-field-driven Fermi–Hubbard model (Tsuji et al., 2011).

Periodic shaking of optical lattices has also been used to realize the Haldane model in fermionic cold-atom systems (Jotzu et al., 2014), where periodic circular shaking induces the Floquet topological insulator with complex hopping parameters on a honeycomb lattice as discussed above. The generated band gap is probed by momentum-resolved measurement of interband transitions. The effect of Berry curvature has been demonstrated by applying a constant force to atoms and finding an orthogonal drift, in the similar manner as the anomalous Hall effect. The induced Berry curvature has been reconstructed in the entire Brillouin zone experimentally (Fläschner et al., 2016).

Other physical systems that allow experimental observations of Floquet states include photonic systems (Kitagawa et al., 2012; Rechtsman et al., 2013; Maczewsky et al., 2017; Mukherjee et al., 2017; Ozawa et al., 2019), trapped ions (Kiefer et al., 2019), and superconducting qubits (Deng et al., 2015; Roushan et al., 2017).

Conclusion

Here we have reviewed basic aspects of Floquet states and their applications to various periodically driven quantum systems. It allows one to control phases of matter dynamically ("Floquet engineering" Bukov et al., 2015; Oka and Kitamura, 2019; Weitenberg and Simonet, 2021) that may not be realized in equilibrium. While our understanding of Floquet states has been deepened, the inherent potential of Floquet states has not been fully elaborated experimentally, especially in solid-state systems. This may be partly because (i) the required amplitude of electric fields is often large, (ii) one needs ultrafast time resolution to capture driven states during irradiation of a pump pulse, (iii) transitions to higher bands and modulation of the distribution may occur in real materials, (iv) heating will suppress quantum fluctuations, and (v) energy dissipation takes place in complicated ways.

While these will make it a great challenge to realize Floquet states in solids, they can also offer opportunities: The development of new materials and new devices will pave a way to explore the frontier of Floquet states. For example, a recent experiment has shown an ideal behavior of driven two-level systems with the scaling of the Bessel factor up to extremely high orders in a diamond nitrogen-vacancy center (Nishimura et al., 2022). If the interaction between the two-level systems can be implemented in those systems, it will provide an interesting playground of Floquet many-body states. Another opportunity is the effect of dissipation in open quantum systems, which can work in a favorable direction to realize (rather than suppress) new orders and new states of matter in quantum systems. For example, a two-body loss due to inelastic collisions in the Fermi–Hubbard model can effectively change the antiferromagnetic interaction to the ferromagnetic one (Nakagawa et al., 2020b), which has been recently observed in cold-atom systems (Honda et al., 2023). Finally, there has been an experimental progress in probing highly oscillating electronic states through high harmonic generation in solids (Ghimire et al., 2011; Schubert et al., 2014; Luu et al., 2015; Vampa et al., 2015; Hohenleutner et al., 2015), which will be a useful key tool to study Floquet states in the future.

References

Abanin DA, De Roeck W, and Huveneers F (2016) Theory of many-body localization in periodically driven systems. *Annals of Physics* ISSN: 0003-4916. 372: 1. https://doi.org/10.1016/j.aop.2016.03.010.

Abanin D, De Roeck W, Ho WW, and Huveneers F (2017) A rigorous theory of many-body prethermalization for periodically driven and closed quantum systems. *Communications in Mathematical Physics* 354(3): 809–827. https://doi.org/10.1007/s00220-017-2930-x.

Aoki H, Tsuji N, Eckstein M, Kollar M, Oka T, and Werner P (2014) Nonequilibrium dynamical mean-field theory and its applications. *Reviews of Modern Physics* 86(2): 779. https://doi.org/10.1103/RevModPhys.86.779.

Blanes S, Casas F, Oteo JA, and Ros J (2009) The Magnus expansion and some of its applications. *Physics Reports* ISSN: 0370-1573. 470(5): 151. https://doi.org/10.1016/j.physrep.2008.11.001.

Breuer H-P and Petruccione F (2007) *The Theory of Open Quantum Systems*. New York: Oxford University Press.

Bukov M, D'Alessio L, and Polkovnikov A (2015) Universal high-frequency behavior of periodically driven systems: From dynamical stabilization to Floquet engineering. *Advanced Physics* 64(2): 139. https://doi.org/10.1080/00018732.2015.1055918.

Casas F, Oteo JA, and Ros J (2001) Floquet theory: Exponential perturbative treatment. *Journal of Physics A: Mathematical and General* 34(16): 3379. https://doi.org/10.1088/0305-4470/34/16/305.

D'Alessio L and Rigol M (2014) Long-time behavior of isolated periodically driven interacting lattice systems. *Physical Review X* 4(4): 041048. https://doi.org/10.1103/PhysRevX.4.041048.

Das A (2010) Exotic freezing of response in a quantum many-body system. *Physical Review B* 82(17): 172402. https://doi.org/10.1103/PhysRevB.82.172402.

Dehghani H, Oka T, and Mitra A (2014) Dissipative Floquet topological systems. *Physical Review B* 90(19): 195429. https://doi.org/10.1103/PhysRevB.90.195429.

Deng C, Orgiazzi J-L, Shen F, Ashhab S, and Lupascu A (2015) Observation of Floquet states in a strongly driven artificial atom. *Physical Review Letters* 115(13): 133601. https://doi.org/10.1103/PhysRevLett.115.133601.

Diehl S, Tomadin A, Micheli A, Fazio R, and Zoller P (2010) Dynamical phase transitions and instabilities in open atomic many-body systems. *Physical Review Letters* 105(1): 015702. https://doi.org/10.1103/PhysRevLett.105.015702.

Dunlap DH and Kenkre VM (1986) Dynamic localization of a charged particle moving under the influence of an electric field. *Physical Review B* 34(6): 3625. https://doi.org/10.1103/PhysRevB.34.3625.

Eckardt A (2017) Colloquium: Atomic quantum gases in periodically driven optical lattices. *Reviews of Modern Physics* 89(1): 011004. https://doi.org/10.1103/RevModPhys.89.011004.

Eckardt A and Anisimovas E (2015) High-frequency approximation for periodically driven quantum systems from a Floquet-space perspective. *New Journal of Physics* 17(9): 093039. https://doi.org/10.1088/1367-2630/17/9/093039.

Eckardt A, Weiss C, and Holthaus M (2005) Superfluid-insulator transition in a periodically driven optical lattice. *Physical Review Letters* 95(26): 260404. https://doi.org/10.1103/PhysRevLett.95.260404.

Else DV, Bauer B, and Nayak C (2016) Floquet time crystals. *Physical Review Letters* 117(9): 090402. https://doi.org/10.1103/PhysRevLett.117.090402.

Faisal FHM (1989) Floquet Green’s function method for radiative electron scattering and multiphoton ionization in a strong laser field. *Computer Physics Reports* ISSN: 0167-7977. 9(2): 57. https://doi.org/10.1016/S0167-7977(89)80001-2.

Fel’dman EB (1984) On the convergence of the magnus expansion for spin systems in periodic magnetic fields. *Physics Letters A* ISSN: 0375-9601. 104(9): 479. https://doi.org/10.1016/0375-9601(84)90027-6.

Fläschner N, Rem BS, Tarnowski M, Vogel D, Lühmann D-S, Sengstock K, and Weitenberg C (2016) Experimental reconstruction of the Berry curvature in a Floquet Bloch band. *Science* 352(6289): 1091. https://doi.org/10.1126/science.aad4568.

Floquet G (1883) Sur les équations différentielles linéaires à coefficients périodiques. *Annales Scientifiques de l’cole Normale Suprieure* 12: 47.

Freericks JK and Zlatić V (2003) Exact dynamical mean-field theory of the Falicov-Kimball model. *Reviews of Modern Physics* 75(4): 1333. https://doi.org/10.1103/RevModPhys.75.1333.

Freericks JK, Turkowski VM, and Zlatić V (2006) Nonequilibrium dynamical mean-field theory. *Physical Review Letters* 97(26): 266408. https://doi.org/10.1103/PhysRevLett.97.266408.

Georges A, Kotliar G, Krauth W, and Rozenberg MJ (1996) Dynamical mean-field theory of strongly correlated fermion systems and the limit of infinite dimensions. *Reviews of Modern Physics* 68(1): 13. https://doi.org/10.1103/RevModPhys.68.13.

Ghimire S, DiChiara AD, Sistrunk E, Agostini P, DiMauro LF, and Reis DA (2011) Observation of high-order harmonic generation in a bulk crystal. *Nature Physics* 7(2): 138. https://doi.org/10.1038/nphys1847.

Goldman N and Dalibard J (2014) Periodically driven quantum systems: Effective Hamiltonians and engineered gauge fields. *Physical Review X* 4(3): 031027. https://doi.org/10.1103/PhysRevX.4.031027.

Gorini V, Kossakowski A, and Sudarshan ECG (1976) Completely positive dynamical semigroups of *N*-level systems. *Journal of Mathematical Physics* 17(5): 821. https://doi.org/10.1063/1.522979.

Grifoni M and Hänggi P (1998) Driven quantum tunneling. *Physics Reports* ISSN: 0370-1573. 304(5): 229. https://doi.org/10.1016/S0370-1573(98)00022-2.

Haldane FDM (1988) Model for a quantum Hall effect without Landau levels: Condensed-matter realization of the “parity anomaly”. *Physical Review Letters* 61(18): 2015. https://doi.org/10.1103/PhysRevLett.61.2015.

Haldar A and Das A (2022) Statistical mechanics of Floquet quantum matter: Exact and emergent conservation laws. *Journal of Physics. Condensed Matter* 34(23): 234001. https://doi.org/10.1088/1361-648X/ac03d2.

Haldar A, Moessner R, and Das A (2018) Onset of Floquet thermalization. *Physical Review B* 97(24): 245122. https://doi.org/10.1103/PhysRevB.97.245122.

Han JE (2013) Solution of electric-field-driven tight-binding lattice coupled to fermion reservoirs. *Physical Review B* 87(8): 085119. https://doi.org/10.1103/PhysRevB.87.085119.

Harper F, Roy R, Rudner MS, and Sondhi SL (2020) Topology and broken symmetry in Floquet systems. *Annual Review of Condensed Matter Physics* 11(1): 345. https://doi.org/10.1146/annurev-conmatphys-031218-013721.

Hill GW (1886) On the part of the motion of the lunar perigee which is a function of the mean motions of the sun and moon. *Acta Mathematica* 8: 1.

Hohenleutner M, Langer F, Schubert O, Knorr M, Huttner U, Koch SW, Kira M, and Huber R (2015) Real-time observation of interfering crystal electrons in high-harmonic generation. *Nature* 523(7562): 572. https://doi.org/10.1038/nature14652.

Holthaus M (1992) Collapse of minibands in far-infrared irradiated superlattices. *Physical Review Letters* 69(2): 351. https://doi.org/10.1103/PhysRevLett.69.351.

Honda K, Taie S, Takasu Y, Nishizawa N, Nakagawa M, and Takahashi Y (2023) Observation of the sign reversal of the magnetic correlation in a driven-dissipative fermi gas in double wells. *Physical Review Letters* 130(6): 063001. https://doi.org/10.1103/PhysRevLett.130.063001.

Ikeda TN and Sato M (2020) General description for nonequilibrium steady states in periodically driven dissipative quantum systems. *Science Advances* 6(27): eabb4019. https://doi.org/10.1126/sciadv.abb4019.

Jangjan M, Foa Torres LEF, and Hosseini MV (2022) Floquet topological phase transitions in a periodically quenched dimer. *Physical Review B* 106(22): 224306. https://doi.org/10.1103/PhysRevB.106.224306.

Jotzu G, Messer M, Desbuquois R, Lebrat M, Uehlinger T, Greif D, and Esslinger T (2014) Experimental realization of the topological Haldane model with ultracold fermions. *Nature* 515(7526): 237. https://doi.org/10.1038/nature13915.

Joura AV, Freericks JK, and Pruschke T (2008) Steady-state nonequilibrium density of states of driven strongly correlated lattice models in infinite dimensions. *Physical Review Letters* 101: 196401.

Kadanoff LP and Baym G (1962) *Quantum Statistical Mechanics*. New York: W. A. Benjamin.

Keldysh LV (1965) Diagrammatic technique for nonequilibrium processes. *Soviet Physics - JETP* 20: 1018.

Khemani V, Lazarides A, Moessner R, and Sondhi SL (2016) Phase structure of driven quantum systems. *Physical Review Letters* 116(25): 250401. https://doi.org/10.1103/PhysRevLett.116.250401.

Kiefer P, Hakelberg F, Wittemer M, Bermúdez A, Porras D, Warring U, and Schaetz T (2019) Floquet-engineered vibrational dynamics in a two-dimensional array of trapped ions. *Physical Review Letters* 123(21): 213605. https://doi.org/10.1103/PhysRevLett.123.213605.

Kitagawa T, Berg E, Rudner M, and Demler E (2010) Topological characterization of periodically driven quantum systems. *Physical Review B* 82(23): 235114. https://doi.org/10.1103/PhysRevB.82.235114.

Kitagawa T, Oka T, Brataas A, Fu L, and Demler E (2011) Transport properties of nonequilibrium systems under the application of light: Photoinduced quantum Hall insulators without Landau levels. *Physical Review B* 84(23): 235108. https://doi.org/10.1103/PhysRevB.84.235108.

Kitagawa T, Broome MA, Fedrizzi A, Rudner MS, Berg E, Kassal I, Aspuru-Guzik A, Demler E, and White AG (2012) Observation of topologically protected bound states in photonic quantum walks. *Nature Communications* 3(1): 882. https://doi.org/10.1038/ncomms1872.

Kuwahara T, Mori T, and Saito K (2016) Floquet-Magnus theory and generic transient dynamics in periodically driven many-body quantum systems. *Annals of Physics* ISSN: 0003-4916. 367: 96. https://doi.org/10.1016/j.aop.2016.01.012.

Lazarides A, Das A, and Moessner R (2014) Equilibrium states of generic quantum systems subject to periodic driving. *Physical Review E* 90(1): 012110. https://doi.org/10.1103/PhysRevE.90.012110.

Lazarides A, Das A, and Moessner R (2015) Fate of many-body localization under periodic driving. *Physical Review Letters* 115(3): 030402. https://doi.org/10.1103/PhysRevLett.115.030402.

Lignier H, Sias C, Ciampini D, Singh Y, Zenesini A, Morsch O, and Arimondo E (2007) Dynamical control of matter-wave tunneling in periodic potentials. *Physical Review Letters* 99(22): 220403. https://doi.org/10.1103/PhysRevLett.99.220403.

Lindblad G (1976) On the generators of quantum dynamical semigroups. *Communications in Mathematical Physics* 48(2): 119. https://doi.org/10.1007/BF01608499.

Lindner NH, Refael G, and Galitski V (2011) Floquet topological insulator in semiconductor quantum wells. *Nature Physics* 7(6): 490. https://doi.org/10.1038/nphys1926.

Liu DE, Levchenko A, and Lutchyn RM (2017) Keldysh approach to periodically driven systems with a fermionic bath: Nonequilibrium steady state, proximity effect, and dissipation. *Physical Review B* 95(11): 115303. https://doi.org/10.1103/PhysRevB.95.115303.

Lubatsch A and Kroha J (2009) Optically driven Mott-Hubbard systems out of thermodynamic equilibrium. *Annals of Physics (Berlin)* 18: 863.

Luu TT, Garg M, Kruchinin SY, Moulet A, Hassan MT, and Goulielmakis E (2015) Extreme ultraviolet high-harmonic spectroscopy of solids. *Nature* 521(7553): 498. https://doi.org/10.1038/nature14456.

Maczewsky LJ, Zeuner JM, Nolte S, and Szameit A (2017) Observation of photonic anomalous Floquet topological insulators. *Nature Communications* 8(1): 13756. https://doi.org/10.1038/ncomms13756.

Magnus W and Winkler S (1966) *Hill's Equation*. New York: John Wiley and Sons.

Mahmood F, Chan C-K, Alpichshev Z, Gardner D, Lee Y, Lee PA, and Gedik N (2016) Selective scattering between Floquet-Bloch and Volkov states in a topological insulator. *Nature Physics* 12(4): 306. https://doi.org/10.1038/nphys3609.

Mananga ES and Charpentier T (2011) Introduction of the Floquet-Magnus expansion in solid-state nuclear magnetic resonance spectroscopy. *The Journal of Chemical Physics* 135(4): 044109. https://doi.org/10.1063/1.3610943.

Martinez DF (2003) Floquet-Green function formalism for harmonically driven Hamiltonians. *Journal of Physics A: Mathematical and General* 36(38): 9827. https://doi.org/10.1088/0305-4470/36/38/302.

Martinez DF (2005) High-order harmonic generation and dynamic localization in a driven two-level system, a non-perturbative solution using the Floquet-Green formalism. *Journal of Physics A: Mathematical and General* 38(46): 9979. https://doi.org/10.1088/0305-4470/38/46/006.

McIver JW, Schulte B, Stein FU, Matsuyama T, Jotzu G, Meier G, and Cavalleri A (2020) Light-induced anomalous Hall effect in graphene. *Nature Physics* 16(1): 38. https://doi.org/10.1038/s41567-019-0698-y.

Mikami T, Kitamura S, Yasuda K, Tsuji N, Oka T, and Aoki H (2016) Brillouin-Wigner theory for high-frequency expansion in periodically driven systems: Application to Floquet topological insulators. *Physical Review B* 93(14): 144307. https://doi.org/10.1103/PhysRevB.93.144307.

Moessner R and Sondhi SL (2017) Equilibration and order in quantum Floquet matter. *Nature Physics* 13(5): 424. https://doi.org/10.1038/nphys4106.

Mori T (2023) Floquet states in open quantum systems. *Annual Review of Condensed Matter Physics* 14(1): 35. https://doi.org/10.1146/annurev-conmatphys-040721-015537.

Mori T, Kuwahara T, and Saito K (2016) Rigorous bound on energy absorption and generic relaxation in periodically driven quantum systems. *Physical Review Letters* 116(12): 120401. https://doi.org/10.1103/PhysRevLett.116.120401.

Mori T, Ikeda TN, Kaminishi E, and Ueda M (2018) Thermalization and prethermalization in isolated quantum systems: A theoretical overview. *Journal of Physics B: Atomic, Molecular and Optical Physics* 51(11): 112001. https://doi.org/10.1088/1361-6455/aabcdf.

Mukherjee S, Spracklen A, Valiente M, Andersson E, Öhberg P, Goldman N, and Thomson RR (2017) Experimental observation of anomalous topological edge modes in a slowly driven photonic lattice. *Nature Communications* 8(1): 13918. https://doi.org/10.1038/ncomms13918.

Murakami Y, Tsuji N, Eckstein M, and Werner P (2017) Nonequilibrium steady states and transient dynamics of conventional superconductors under phonon driving. *Physical Review B* 96(4): 045125. https://doi.org/10.1103/PhysRevB.96.045125.

Nakagawa M, Slager R-J, Higashikawa S, and Oka T (2020a) Wannier representation of Floquet topological states. *Physical Review B* 101(7): 075108. https://doi.org/10.1103/PhysRevB.101.075108.

Nakagawa M, Tsuji N, Kawakami N, and Ueda M (2020b) Dynamical sign reversal of magnetic correlations in dissipative Hubbard Models. *Physical Review Letters* 124(14): 147203. https://doi.org/10.1103/PhysRevLett.124.147203.

Nathan F and Rudner MS (2020) Universal Lindblad equation for open quantum systems. *Physical Review B* 102(11): 115109. https://doi.org/10.1103/PhysRevB.102.115109.

Nathan F and Rudner MS (2022) High accuracy steady states obtained from the Universal Lindblad Equation. *arXiv:2206.02917*. https://arxiv.org/abs/2206.02917.

Nishimura S, Itoh KM, Ishi-Hayase J, Sasaki K, and Kobayashi K (2022) Floquet engineering using pulse driving in a diamond two-level system under large-amplitude modulation. *Physical Review Applied* 18(6): 064023. https://doi.org/10.1103/PhysRevApplied.18.064023.

Oka T and Aoki H (2009) Photovoltaic Hall effect in graphene. *Physical Review B* 79(8): 081406(R). https://doi.org/10.1103/PhysRevB.79.081406.

Oka T and Kitamura S (2019) Floquet engineering of quantum materials. *Annual Review of Condensed Matter Physics* 10(1): 387. https://doi.org/10.1146/annurev-conmatphys-031218-013423.

Ozawa T, Price HM, Amo A, Goldman N, Hafezi M, Lu L, Rechtsman MC, Schuster D, Simon J, Zilberberg O, and Carusotto I (2019) Topological photonics. *Reviews of Modern Physics* 91(1): 015006. https://doi.org/10.1103/RevModPhys.91.015006.

Ponte P, Chandran A, Papić Z, and Abanin DA (2015a) Periodically driven ergodic and many-body localized quantum systems. *Annals of Physics* ISSN: 0003-4916. 353: 196. https://doi.org/10.1016/j.aop.2014.11.008.

Ponte P, Papić Z, Huveneers F, and Abanin DA (2015b) Many-body localization in periodically driven systems. *Physical Review Letters* 114(14): 140401. https://doi.org/10.1103/PhysRevLett.114.140401.

Prosen T (2011) Open *XXZ* spin chain: Nonequilibrium steady state and a strict bound on ballistic transport. *Physical Review Letters* 106(21): 217206. https://doi.org/10.1103/PhysRevLett.106.217206.

Rechtsman MC, Zeuner JM, Plotnik Y, Lumer Y, Podolsky D, Dreisow F, Nolte S, Segev M, and Szameit A (2013) Photonic Floquet topological insulators. *Nature* 496(7444): 196. https://doi.org/10.1038/nature12066.

Roushan P, Neill C, Megrant A, Chen Y, Babbush R, Barends R, Campbell B, Chen Z, Chiaro B, Dunsworth A, Fowler A, Jeffrey E, Kelly J, Lucero E, Mutus J, O'Malley PJJ, Neeley M, Quintana C, Sank D, Vainsencher A, Wenner J, White T, Kapit E, Neven H, and Martinis J (2017) Chiral ground-state currents of interacting photons in a synthetic magnetic field. *Nature Physics* 13(2): 146. https://doi.org/10.1038/nphys3930.

Roy R and Harper F (2017) Periodic table for Floquet topological insulators. *Physical Review B* 96(15): 155118. https://doi.org/10.1103/PhysRevB.96.155118.

Rudner MS and Lindner NH (2020) Band structure engineering and non-equilibrium dynamics in Floquet topological insulators. *Nature Reviews Physics* 2(5): 229. https://doi.org/10.1038/s42254-020-0170-z.

Rudner MS, Lindner NH, Berg E, and Levin M (2013) Anomalous edge states and the bulk-edge correspondence for periodically driven two-dimensional systems. *Physical Review X* 3(3): 031005. https://doi.org/10.1103/PhysRevX.3.031005.

Sacha K (2015) Modeling spontaneous breaking of time-translation symmetry. *Physical Review A* 91(3): 033617. https://doi.org/10.1103/PhysRevA.91.033617.

Sambe H (1973) Steady states and quasienergies of a quantum-mechanical system in an oscillating field. *Physical Review A* 7(6): 2203. https://doi.org/10.1103/PhysRevA.7.2203.

Schubert O, Hohenleutner M, Langer F, Urbanek B, Lange C, Huttner U, Golde D, Meier T, Kira M, Koch SW, and Huber R (2014) Sub-cycle control of terahertz high-harmonic generation by dynamical Bloch oscillations. *Nature Photonics* 8(2): 119. https://doi.org/10.1038/nphoton.2013.349.

Shirai T, Thingna J, Mori T, Denisov S, Hänggi P, and Miyashita S (2016) Effective Floquet-Gibbs states for dissipative quantum systems. *New Journal of Physics* 18(5): 053008. https://doi.org/10.1088/1367-2630/18/5/053008.

Shirley JH (1965) Solution of the Schrödinger equation with a Hamiltonian periodic in time. *Physics Review* 138(4B): B979. https://doi.org/10.1103/PhysRev.138.B979.

Struck J, Ölschläger C, Targat RL, Soltan-Panahi P, Eckardt A, Lewenstein M, Windpassinger P, and Sengstock K (2011) Quantum simulation of frustrated classical magnetism in triangular optical lattices. *Science* 333(6045): 996. https://doi.org/10.1126/science.1207239.

Tindall J, Buča B, Coulthard JR, and Jaksch D (2019) Heating-induced long-range η pairing in the Hubbard model. *Physical Review Letters* 123(3): 030603. https://doi.org/10.1103/PhysRevLett.123.030603.

Tsuji N, Oka T, and Aoki H (2008) Correlated electron systems periodically driven out of equilibrium: Floquet + DMFT formalism. *Physical Review B* 78(23): 235124. https://doi.org/10.1103/PhysRevB.78.235124.

Tsuji N, Oka T, and Aoki H (2009) Nonequilibrium steady state of photoexcited correlated electrons in the presence of dissipation. *Physical Review Letters* 103(4): 047403. https://doi.org/10.1103/PhysRevLett.103.047403.

Tsuji N, Oka T, Werner P, and Aoki H (2011) Dynamical band flipping in fermionic lattice systems: An ac-field-driven change of the interaction from repulsive to attractive. *Physical Review Letters* 106(23): 236401. https://doi.org/10.1103/PhysRevLett.106.236401.

Vampa G, Hammond TJ, Thiré N, Schmidt BE, Légaré F, McDonald CR, Brabec T, and Corkum PB (2015) Linking high harmonics from gases and solids. *Nature* 522(7557): 462. https://doi.org/10.1038/nature14517.

Wang YH, Steinberg H, Jarillo-Herrero P, and Gedik N (2013) Observation of floquet-bloch states on the surface of a topological insulator. *Science* 342(6157): 453. https://doi.org/10.1126/science.1239834.

Weitenberg C and Simonet J (2021) Tailoring quantum gases by Floquet engineering. *Nature Physics* 17(12): 1342. https://doi.org/10.1038/s41567-021-01316-x.

Yamamoto K, Nakagawa M, Tsuji N, Ueda M, and Kawakami N (2021) Collective excitations and nonequilibrium phase transition in dissipative fermionic superfluids. *Physical Review Letters* 127(5): 055301. https://doi.org/10.1103/PhysRevLett.127.055301.

Yao NY, Potter AC, Potirniche I-D, and Vishwanath A (2017) Discrete time crystals: Rigidity, criticality, and realizations. *Physical Review Letters* 118(3): 030401. https://doi.org/10.1103/PhysRevLett.118.030401.

Pump-probe spectroscopy for non-equilibrium condensed matter

Ryusuke Matsunaga[a,b] **and Kozo Okazaki**[a], [a]The Institute for Solid State Physics, The University of Tokyo, Kashiwa, Japan; [b]JST-PRESTO, Saitama, Japan

© 2024 Elsevier Ltd. All rights reserved.

Introduction 981
Time-resolved THz-TDS 982
Time-resolved ARPES 985
Intense THz pulse-induced non-equilibrium phenomena 986
Conclusion 987
Acknowledgments 987
References 989

Abstract

Pump-probe spectroscopy based on femtosecond pulsed laser technology has been utilized to study the dynamic properties of materials out of equilibrium and to unveil the hidden properties in equilibrium. In particular, recent progress in terahertz time-domain spectroscopy and angle-resolved photoemission spectroscopy has enabled the time-resolved detection of low-energy electromagnetic responses and electron dispersion relations of the order of meV, at which many-body interactions associated with phase transitions and topologically non-trivial electron dynamics emerge. We describe the basics of pump-probe spectroscopy studies, which have contributed to the understanding of non-equilibrium properties in condensed matter physics.

Key points

- Importance of terahertz spectroscopy and angle-resolved photoemission spectroscopy for condensed matter physics.
- Time-resolved spectroscopy for ultrafast phenomena.
- Nonequilibrium physics induced by intense terahertz pulse.
- Combination of terahertz pulse and angle-resolved photoemission spectroscopy.

Introduction

The states of matter far away from thermal equilibrium, which vary rapidly over time, have been attracting growing interest in the field of modern condensed matter physics. Ultrafast time-resolved spectroscopy, also called pump-probe spectroscopy, is arguably the most important experimental technique for resolving the dynamical properties of nonequilibrium materials. In this technique, a strong light pulse drives a material into a non-equilibrium state (pump). A weaker light pulse is subsequently irradiated to measure the transient change in the properties of the material (probe). The time resolution is essentially determined by the duration of the pulses. For such applications, laser light has a great advantage because ultrashort pulses as short as or even shorter than 100 fs ($=10^{-13}$ s) can be easily generated by using mode-locked pulsed lasers and amplification systems.

Most of the existing laser light sources emit light in the near-infrared (NIR) or visible range. Accordingly, ultrafast time-resolved spectroscopy has been applied mainly in the study of semiconductors or molecules, in which the excitation of electrons occurs at the photon energy scale of 1 eV. However, the development of pulsed laser techniques has also realized efficient wavelength conversion via nonlinear light-matter interaction. Second-order nonlinear responses such as optical rectification or differential frequency generation enable the generation of terahertz (THz) pulses (0.1–10 THz in frequency, 30–3000 μm in wavelength). The THz frequency range corresponds to the intermediate region between electronics and photonics. The photon energy of THz pulses is on the order of meV, at which a variety of electromagnetic responses appear in condensed matter, as shown in Fig. 1. These responses include lattice vibrations (phonons), plasmons, cyclotron resonances, antiferromagnetic magnons, exciton inner transitions, superconducting gaps, and pseudogaps in high-T_c superconductors. In particular, the low-energy response of electrons at low temperatures is highly intriguing because it is sensitive to the physics near the Fermi surfaces, which reflects the many-body interactions associated with phase transitions and/or the topological nature of solid-state materials with relativistic fermions. Pump-probe spectroscopy using THz pulses is an important experimental tool for probing the low-energy responses in non-equilibrium materials.

Another important approach in pump-probe spectroscopy for the low-energy physics is the wavelength conversion through nonlinear optics into ultraviolet (10–400 nm) or soft X-ray (<10 nm) pulses by higher-order harmonic generation. Light with photon energies larger than the work function of solids can induce the photoelectric effect, in which excited electrons are ejected into the

https://doi.org/10.1016/B978-0-323-90800-9.00109-8

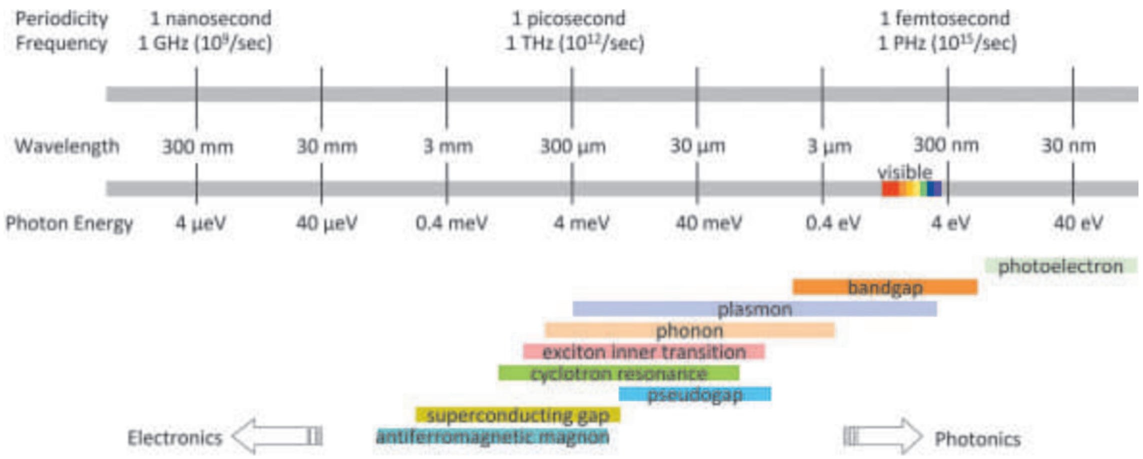

Fig. 1 Varieties of electromagnetic responses in condensed matter.

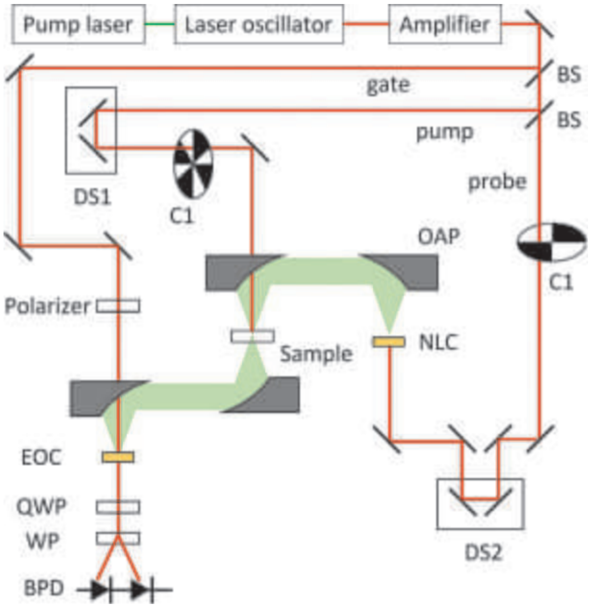

Fig. 2 A typical setup of optical pump-THz probe spectroscopy. BS: Beam splitter, DS: Delay stage, C: Chopper, NLC: nonlinear crystal, OAP: Off-axis parabolic mirror, EOC: Electro-optic crystal, QWP: Quarter-half waveplate, WP: Wollaston Prism, BPD: Balanced photodiode.

vacuum while retaining the information of their energies, momenta, and spins. By directly capturing these electrons and resolving their energies and momenta, the dispersion relations of the electrons can be mapped with excellent energy and momentum resolutions. This technique is called angle-resolved photoemission spectroscopy (ARPES). By using a short-pulsed laser, time-resolved ARPES can also be realized and utilized to elucidate the electron dynamics in non-equilibrium condensed matters.

Here, we introduce pump-probe spectroscopy using THz pulses and ARPES as a probe and show how they have contributed to the recent progresses in non-equilibrium condensed matter physics. In addition, the remarkable progress in the techniques for generating intense THz pulses has enabled the utilization of THz pulses as a pump. The low-frequency intense driving fields have opened a new avenue for the study of nonequilibrium physics that was previously inaccessible with visible or near-infrared light.

Time-resolved THz-TDS

Fig. 2 shows a typical setup for optical pump and THz probe spectroscopy. The output of the pulsed laser is separated into the (i) pump pulse, (ii) generation of THz probe pulse, and (iii) gate pulse by beam samplers or splitters. The gate pulse is used to detect the THz electric field. A representative light source is the Ti:sapphire laser, in which a Ti-doped sapphire crystal excited by green light (approximately 500 nm) emits red light centered at 800 nm (1.55 eV photon energy). Depending on the crystal thickness, broadband light from 690 to 900 nm with a typical repetition rate of 80 MHz can be emitted to realize ultrashort laser pulses with a duration of 15–100 fs. The pulsed output can be further amplified with the chirped pulse amplification scheme to obtain strong pulses >1 mJ with a typical repetition rate of 1 kHz. Recently, there is increasing demand for much higher repetition rates on the order of 100 kHz or 1 MHz for more efficient data accumulation. From this perspective, Yb-doped crystals are another candidate for lasing media. The crystals are excited by near-infrared laser diodes at approximately 980 nm and emit photons at approximately 1030 nm (1.2 eV photon energy). Because of the small Stokes shift, that is, small dissipation to the lattice, Yb-based crystals are robust for high-repetition lasing, while their pulse duration of 150–300 fs tends to be longer than that of Ti:sapphire lasers. The pump-probe spectroscopy system in Fig. 2 can be further extended into a variety of setups according to the required research purpose; for example, the pump pulse wavelength can be converted to a desired wavelength using an optical parametric amplifier.

Several techniques have been developed for efficient THz pulse generation. A well-known example is the photoconductive switch, or Auston switch, which comprises a semiconductor biased by gapped electrodes on its surface and a pulsed laser with photon energy larger than the band gap energy. When the gap between the electrodes is irradiated by a pulsed laser, photoexcited carriers are accelerated by the bias field to generate a transient current $j(t)$, which emits electromagnetic waves into free space. In the far-field, the field $E(t)$ is proportional to $dj(t)/dt$. The frequency of the electromagnetic field can reach the THz region when the carriers have short lifetimes of <1 ps. In addition to the external bias, the built-in electric field in heterostructures can also be a driving force of a transient current with laser pulse excitation. Another example is the photo-Dember effect in low-gap semiconductors such as InAs and InSb. Because of their large difference between the mobilities of photoexcited electrons and holes, photoexcitation induces a transient current perpendicularly to the surface, which acts as an efficient source of THz pulse emission.

Another approach for generating THz pulses is second-order nonlinear responses such as optical rectification or differential frequency generation in insulating nonlinear crystals. When a non-centrosymmetric crystal is irradiated by a short laser pulse with a photon energy smaller than the band gap energy, second-order polarization $P^{(2)} \propto \chi^{(2)} E_1 e^{i\omega_1 t} (E_2 e^{i\omega_2 t})^*$ can occur, where $E_j e^{i\omega_j t}$ is a component of the field that has frequency ω_j. This is called differential frequency generation. When $\omega_1 \sim \omega_2$, the generated polarization frequency $\omega_1 - \omega_2$ is very small and in the THz frequency range, and THz electromagnetic waves are emitted. In the far-field, the field $E(t)$ is proportional to $d^2P(t)/dt^2$. Note that the second-order susceptibility $\chi^{(2)}$ can be nonzero only in the crystals without inversion symmetry. To generate THz pulses efficiently in thick crystals, the phase-matching condition between the laser and THz pulses must be satisfied in the crystals so that the THz waves generated during laser pulse propagation in the crystals can interfere constructively. ZnTe and GaP are typically used as nonlinear crystals in this regard. Nonlinear organic crystals such as DAST, DSTMS, and OH1 are also efficient THz emitters, although the absorptions in THz frequency somewhat distort the waveform.

The inverse processes to the photoconductive switch and the second-order nonlinear response are known as the photoconductive antenna and the electro-optic sampling, respectively, and can be utilized to detect THz pulses. The photoconductive antenna consists of a pair of gapped electrodes on a semiconductor surface to which THz and gate pulses are applied simultaneously. The carriers photoexcited by the gate pulse at the gap are accelerated in the direction of the THz field and can be detected as a current. In the electro-optic sampling, a THz pulse and a gate pulse are applied simultaneously to a nonlinear crystal that is transparent for the gate pulse. The THz electric field changes the refractive index of the nonlinear crystal, which is known as the Pockels effect. The induced birefringence can be detected as a change in the polarization of the gating pulses using the balanced detection. In both methods, the detected signals are proportional to the THz field including its sign. By changing the optical path lengths between the THz and gate pulses, the THz field waveform $E(t)$ can be obtained as a function of time.

The THz field waveform $E(t)$ can be transformed into $\sim E(\omega)$, the field in the frequency domain, using the Fourier analysis. This is called THz time-domain spectroscopy (THz-TDS). Importantly, because $\sim E(\omega)$ is a complex quantity, the amplitude and phase of the incident light at each frequency can be determined. By detecting light after transmission of or reflection from a sample, the amplitude and phase infromation of light can give the real and imaginary parts of refractive index of the sample $\sim n(\omega) = n(\omega) + i\kappa(\omega)$. The refractive index can be further converted to the dielectric function $\varepsilon(\omega) = \sqrt{\sim n(\omega)}$ in nonmagnetic media or the optical conductivity $\sigma(\omega) = i\varepsilon_0\omega(\varepsilon(\omega) - 1)$. By using THz-TDS, the response functions can be obtained directly as complex quantities without the Kramers-Kronig conversion. This is in a stark contrast to the conventional light detection by photodetectors, in which only the intensity of light is detected without the information of phase. Furthermore, because the THz pulse duration is as short as 1 ps, THz-TDS can be used as an ultrafast probe in the pump-probe spectroscopy shown in Fig. 2, in contrast to the Fourier-transform infrared spectroscopy.

As an example of optical pump-THz probe spectroscopy, we introduce a study of the *s*-wave superconductor NbN in Fig. 3a (Beck et al., 2011). Below T_c, a superconducting gap appears in the low-frequency absorption spectrum described by $\mathrm{Re}[\sigma(\omega)]$. In contrast, $\mathrm{Im}[\sigma(\omega)]$ shows a large inductive current proportional to n_s/ω, where n_s is the superfluid density. The full information of the complex response functions can be determined directly by THz-TDS, which can be used to track ultrafast change after the optical pump. The right panel in Fig. 2a shows a two-dimensional plot of the transient THz transmission spectra after optical excitation, indicating the suppression and recovery dynamics of the superconducting gap and the order parameter. After irradiation with 50- fs optical pump pulses at 1.55 eV, the superconducting gap energy denoted by the blue circles gradually decreased over a timescale of 10 ps. The 1.55-eV photons excite hot electrons with large excess energy, which emit a large number of phonons. Subsequently, the emitted phonons break Cooper pairs and excite high-density quasiparticles, which suppresses the gaps at the slower timescale. In the recovery dynamics, two quasiparticles recombine to form a Cooper pair, and they emit a phonon, but the phonon can excite quasiparticles again. Therefore, the recovery time of the superconducting gap is determined not only by the bare quasiparticle recombination time, but also by the decay time of phonons. These dynamics can be phenomenologically described using the Rothwarf-Taylor model.

Another example of optical pump-THz probe spectroscopy is the study for photoexcited carriers in semiconductors. Fig. 3b shows the transient THz conductivity and dielectric function spectra in photoexcited GaAs (Kaindl et al., 2009). The upper panels

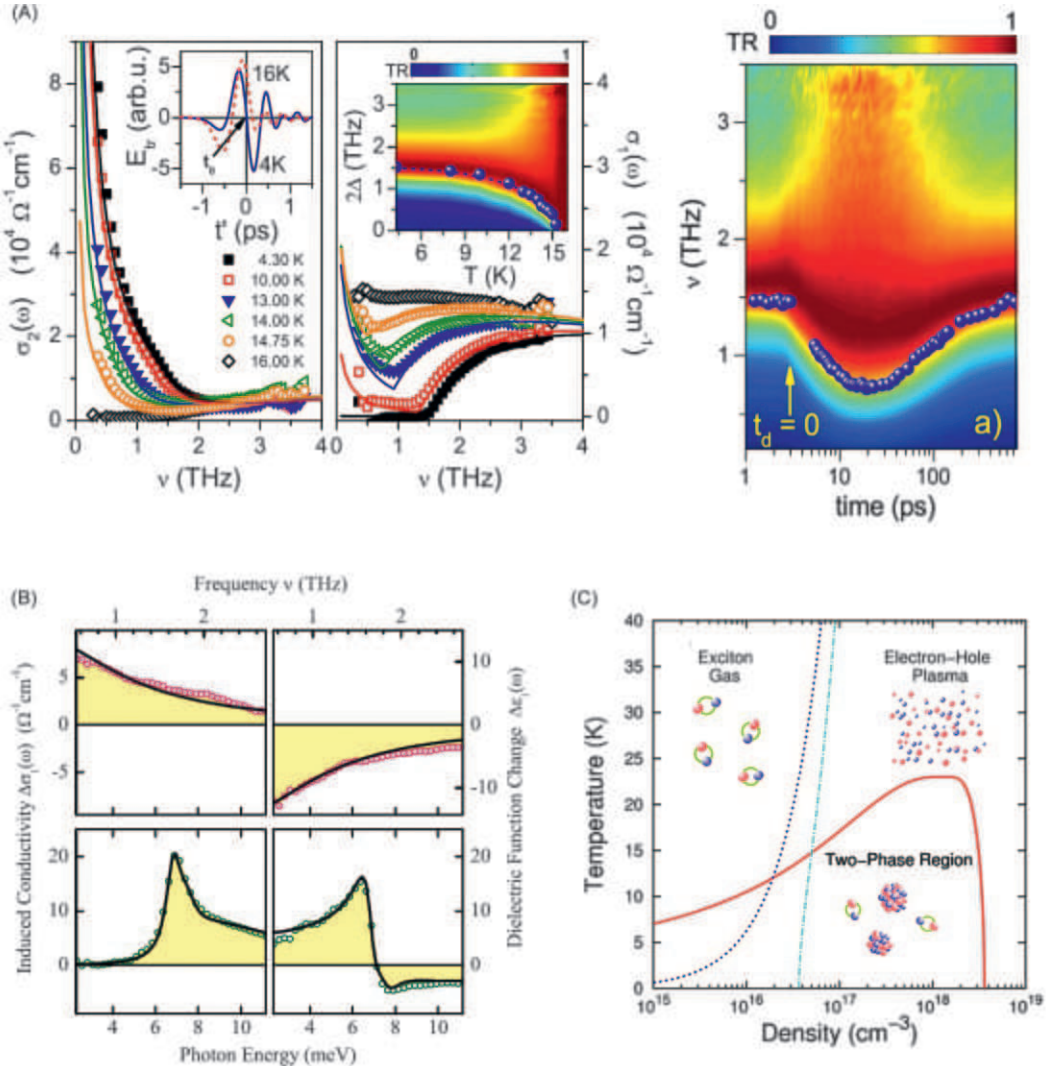

Fig. 3 (a) Time-resolved THz conductivity spectra in a photoexcited superconductor NbN (left) and dynamics of the superconducting gap (right). Reprinted with permission from Beck M et al. (2011) Energy-Gap Dynamics of Superconducting NbN Thin Films Studied by Time-Resolved Terahertz Spectroscopy. *Physical Review Letters* **107**: 177007, Copyright by the American Physical Society. (b) Time-resolved THz conductivity and dielectric function in a photoexcited GaAs with non-resonant (upper) and resonant (lower) excitations. Reprinted with permission from Kaindl RA et al. (2009) Transient terahertz spectroscopy of excitons and unbound carriers in quasi-two-dimensional electron-hole gases. *Physical Review B* **79**: 045320, 177007, Copyright by the American Physical Society. (c) A phase diagram of electron-hole systems. Reprinted with permission from Suzuki T and Shimano R (2009) Time-resolved formation of excitons and Electron-Hole droplets in si studied using terahertz spectroscopy. *Physical Review Letters* **103**: 057401, Copyright by the American Physical Society.

are the results of the excitation at 100 meV above the band gap, showing the Drude response of free electron and holes. The lower panels are the resonant excitation of 1*s* excitons, showing the Lorentzian absorption of 1*s*-2*p* inner transition. Electron-hole systems with negative and positive charges can exhibit a variety of phases such as ionized neutral plasmas, electron-hole bound states called excitons, electron-hole liquids/droplets, or quantum condensation into electron-hole BCS or exciton BECs depending on the temperature and carrier density as shown in Fig. 3c (Suzuki et al., 2009). The densities of the fermionic electron-hole gas and bosonic exciton pairs can be determined in the time-resolved THz spectroscopy, which unveils rich physics in the many-body system related with quantum condensations and the Mott transition/crossover.

The time-resolved THz spectroscopy has also been used to study a possible light-induced superconductivity in high-T_c cuprate superconductors (Fausti et al., 2011). Cuprate superconductors consist of two-dimensional metallic planes stacked along the *c*-axis with an intermediate insulating atomic layer. Below T_c, three-dimensional superconducting transport is developed across the insulating layer through Josephson tunnelling, which manifests as a Josephson plasma resonance in the reflectivity spectra. Some cuprates show a transient Josephson plasma-like response after photoexcitation, suggesting the possibility of light-induced superconductivity far above T_c even at room temperature (Kaiser et al., 2014). Such light-induced superconductivity study was further extended to fullerene superconductors recently through strong excitation of optical phonons (Mitrano et al., 2016).

Time-resolved ARPES

Several kinds of light sources have been used as probe lights for time-resolved ARPES so far. These sources are, namely, vacuum ultraviolet (VUV) light (approximately 6 eV) generated by wavelength conversion using a solid-state nonlinear optical crystal (Ishida et al., 2014), extreme ultraviolet (EUV) light of approximately 20–60 eV generated by high harmonic generation (HHG) from a noble gas (Suzuki et al., 2021a, 2021b), synchrotron radiation (Yamamoto et al., 2013), and light from a free electron laser (Hellmann et al., 2012). Hereafter, we refer to EUV light generated by HHG as a HHG laser. Among the various types of light sources for time-resolved ARPES, the HHG laser has several advantages. The higher photon energy of the HHG laser compared to that of the VUV laser enables a wider energy and momentum space range to be probed. The pulse duration of the HHG laser generated from the fundamental laser of a regenerative amplifier system with a typical pulse duration of 30–100 fs is much shorter than that of synchrotron radiation, which is at best approximately 70 ps. The higher repetition rate (>1 kHz) compared to a free electron laser (typically several tens of hertz) prevents the occurrence of the space-charge effect, which induces energy broadening of photoelectrons due to Coulomb repulsion.

Fig. 4 shows the typical setup of an HHG laser-based time-resolved ARPES system (Suzuki et al., 2021a, 2021b). The output of the Ti:sapphire amplifier system, which has a central wavelength of 800 nm, average power of 6–7 W, pulse duration of 35 fs, and repetition rate of 1 kHz or 10 kHz, is first injected into a β-BaB_2O_4 (BBO) nonlinear optical crystal. The second harmonic is generated and the photon energy is doubled to 3.1 eV to improve the conversion efficiency of the HHG. The second harmonic is then focused on a gas cell filled with Ar to generate high harmonics. One of the harmonics, typically the seventh (21.7 eV) or nineth (27.9 eV) harmonic, is selected using a pair of SiC/Mg multilayer mirrors. The resulting photoelectrons are collected using a hemispherical electron analyzer. The typical time and energy resolutions are several tens of femtoseconds and one or two hundred meV, respectively.

The greatest advantage of utilizing time-resolved ARPES over other time-resolved techniques is the ability to observe electronic band structures. This advantage allows the insulating and metallic states to be clearly distinguished during photoinduced insulator-to-metal transitions and the Floquet states generated by the temporally periodic electric field of the laser to be observed. Here, we introduce a time-resolved ARPES study of Ta_2NiSe_5 as an example of the observation of photo-induced insulator-to-metal transition (Okazaki et al., 2018a, 2018b). Ta_2NiSe_5 is a unique candidate for excitonic insulators. An exciton is a bound state of electrons and holes caused by weakly screened Coulomb interaction. Excitonic insulators are insulators in which excitons are spontaneously condensed owing to the binding energy of the excitons exceeding the band gap of an insulator or the band overlap energy of a semimetal. A photoinduced insulator-to-metal transition was recently observed using HHG laser-based time-resolved ARPES. Fig. 5a and b show the energy-momentum (E-k) maps taken using time-resolved ARPES before and after the pump, respectively. The map before pumping shows the typical behavior of an excitonic insulator with a flat band below the Fermi level (E_F). In contrast, it can be recognized that the electron and hole bands indicated by red and blue lines cross E_F after the pump, suggesting that the system was transformed to a semimetallic state.

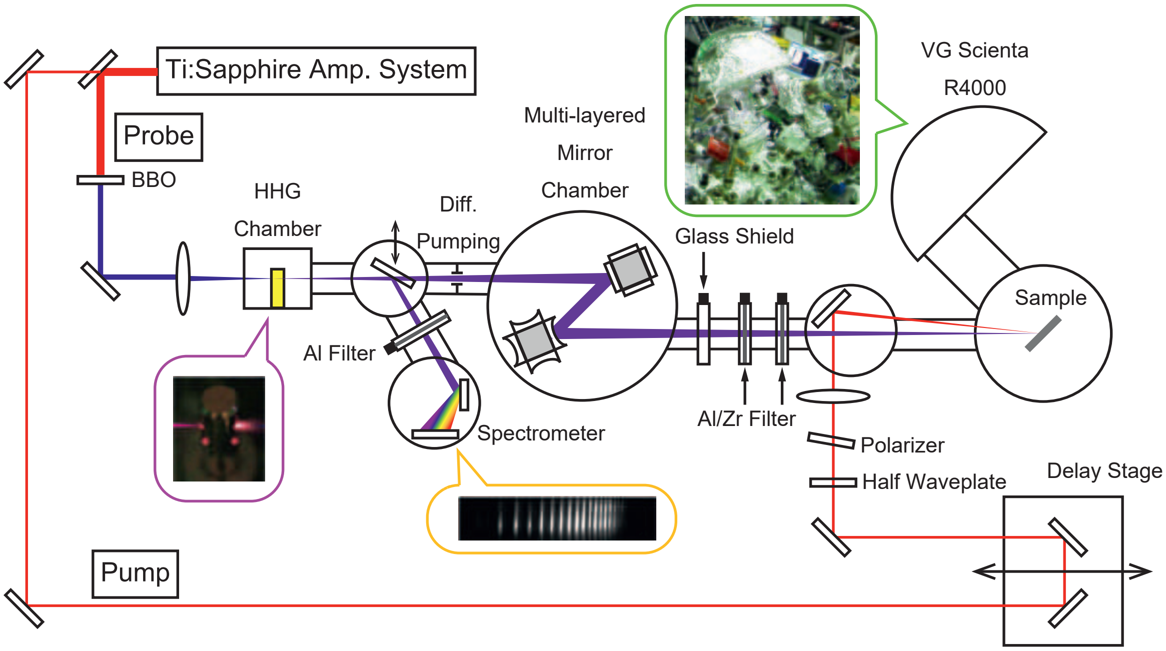

Fig. 4 Schematic illustration of the HHG-laser-based time-resolved ARPES system composed of a Ti:sapphire amplification system, HHG chamber, spectrometer, multi-layered mirror chamber, and hemispherical electron analyzer (Suzuki et al., 2021a, 2021b). BBO: β-BaB_2O_4, HHG: high harmonic generation.

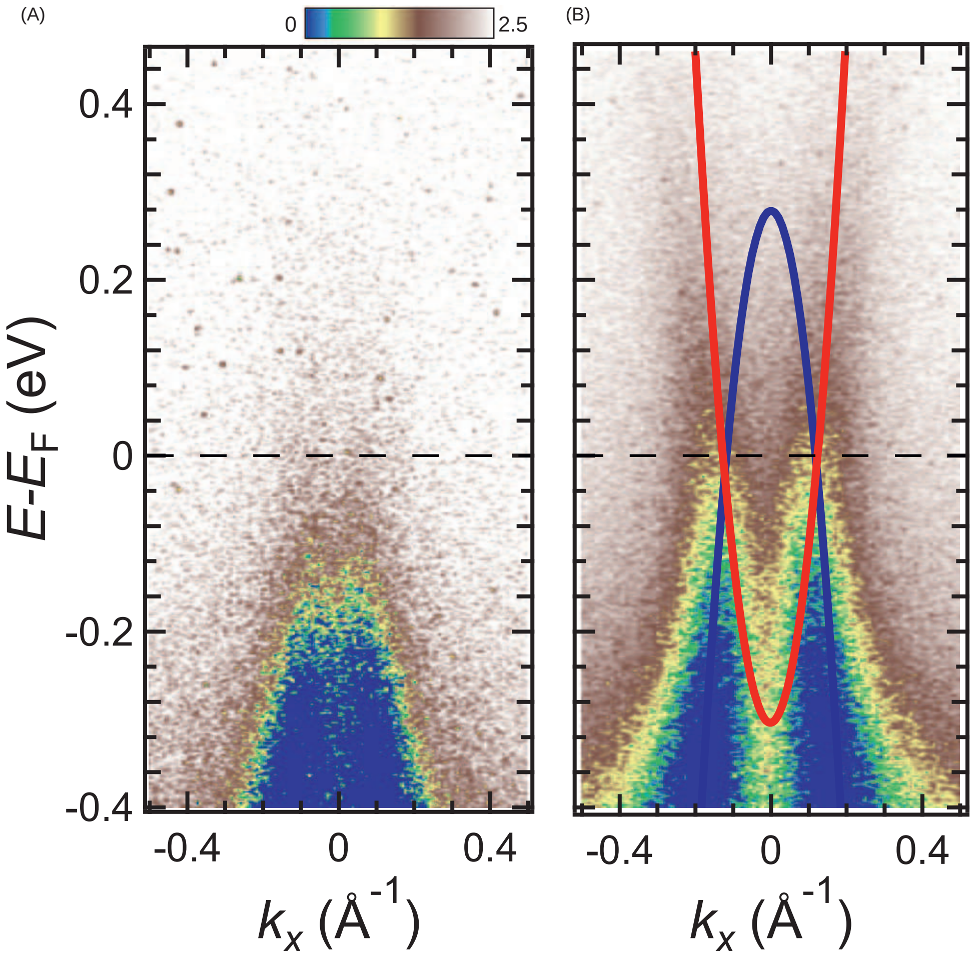

Fig. 5 Time-resolved ARPES spectra of Ta_2NiSe_5 before and after pumping (Okazaki et al., 2018a, 2018b). (a) Energy-momentum($E - k$)map before pumping, integrated in the time interval [−0.29, 0] ps. (b) Corresponding map of the transient states, integrated in [0, 1.2] ps. Red and blue parabolas indicate, respectively, the electron and hole bands crossing E_F in the non-equilibrium metallic state. These spectra were acquired with a pump fluence of 1.56 mJ/cm^2.

We introduce the observation of Floquet states and the development of frequency-domain ARPES as further examples of recent progress in time-resolved ARPES. Floquet states are states that are evenly spaced in energy generated by the temporally periodic electric field of a laser and can be regarded as the time analogue of Bloch states, which are periodic states in momentum space induced by a spatially periodic electric potential. Wang et al. first observed such states in the topological surface band of Bi_2Se_3 using a mid-infrared pulse with a lower energy than the band gap as the pump, which prevented the interband transitions of electrons (Wang et al., 2013). Another intriguing phenomenon observed by time-resolved ARPES is the excitation of coherent phonons (Okazaki et al., 2018a, 2018b; Suzuki et al., 2019; Suzuki et al., 2021a, 2021b). Coherent phonon excitations can also be observed by pump-probe optical spectroscopy, typically as temporally periodic reflectivity oscillations. By using time-resolved ARPES, the response of the electrons to excited coherent phonons through electron-phonon coupling can be observed as shifts in the band dispersions and/or modulations of the photoemission intensities. This enables deep insights into the electron-phonon coupling in the material to be obtained. Recently, a novel analysis method called frequency-domain angle-resolved photoemission spectroscopy (FDARPES) was developed and applied to the observation of the photo-induced excitonic insulator-to-semimetal transition in Ta_2NiSe_5 (Suzuki et al., 2021a, 2021b). An FDARPES image is a mapping of the coherent-phonon amplitude with respect to the energy and momentum of each frequency of coherent phonons. It can reveal the electron-phonon couplings of coherent phonons and their intriguing properties during the photo-induced phase transition.

Intense THz pulse-induced non-equilibrium phenomena

Recent remarkable progresses in intense THz pulse generation methods have allowed the low-frequency degrees of freedom in condensed matter to be resonantly or non-resonantly accessed by the strong driving forces. A well-known method for generating intense THz pulses is the optical rectification in stoichiometric $LiNbO_3$ crystals (Hebling et al., 2008), which possess a high effective nonlinear coefficient as well as a high damage threshold with doping. To satisfy the phase-matching condition, the tilted-pulse front scheme was developed to compensate the large difference between the optical group velocity and THz phase velocity in the crystal. A strong electric field exceeding 1 MV/cm is available at the low frequency of 1 THz (Hirori et al., 2011). Organic nonlinear crystals with extremely large nonlinear coefficients, such as DAST or DSTMS, are also available for generating THz pulses with frequencies of a few THz through optical rectification (Hauri et al., 2011). The use of an infrared pulsed light source is desirable to avoid damage and to satisfy the phase-matching condition. Another representative example of intense THz pulse generation is emission from a two-color laser-induced air plasma (Cook and Hochstrasser, 2000). An extremely broadband frequency from 1 THz to mid- or near-infrared at 100 or 200 THz can be emitted depending on the laser pulse energy, focusing length, and pulse duration.

Here, we introduce some examples of pump-probe experiments that revealed intriguing nonequilibrium dynamics in condensed matter through the intense THz pulse excitation. Fig. 5a shows the results of THz pump-THz probe spectroscopy performed on the *s*-wave superconductor NbN (Matsunaga et al., 2013). The signal corresponds to a decrease in the superconducting gap and order parameter by the THz pump. In contrast to the optical pump in Fig. 2a, the superconducting gap suddenly decreases because the THz pump directly excites quasiparticles at the bottom of the superconducting gap without providing excess energy, which prevents the heating of the lattice and lead to a nonadiabatic perturbation to the superconducting phase. After the sudden quenching, the order parameter oscillates, as shown in Fig. 5a. This is the collective oscillation mode of the order parameter amplitude, which is associated with spontaneous symmetry breaking and recently called the Higgs mode because of its close analogy with the Higgs boson in elementary particle physics. Fig. 5b shows another example of the observation of the Higgs mode in THz pump-THz probe spectroscopy during THz pump irradiation with a frequency below the superconducting gap (Matsunaga et al., 2014). Although the Higgs mode is not directly coupled to light in the linear response regime, it can be resonantly excited by intense THz waves in the nonlinear response regime. The order parameter oscillation induced during the pump pulse irradiation can also be observed through efficient third-order harmonic generation.

The intense THz electromagnetic fields can also be used to drive the spin system. Because spin precession motion occurs in the THz frequency range in antiferromagnets, ultrafast control of the spin order is highly demanded for applications in next-generation fast spintronics. Fig. 6c shows the magnetization dynamics of spins in the antiferromagnetic dielectric $HoFeO_3$ (Mukai et al., 2016). The magnetic field in the intense THz pulse can nonlinearly drive antiferromagnetic spin motion and induces a large change of 40% in the spontaneous magnetization. In a specific material, spin motion can also be induced by the electric field component. The intense THz electric field abruptly changes the magnetic anisotropy in the antiferromagnet $TmFeO_3$ and induces large-amplitude spin motion at 83 K, leading to all-optical spin switching (Schlauderer et al., 2019).

The combination of an intense THz pump pulse and ARPES is also a recent intriguing subject in non-equilibrium physics. Fig. 6d shows the results of time-resolved ARPES on the surface Dirac state of the topological insulator Bi_2Te_3 under irradiation by a strong THz field with sub-cycle time resolution (Reimann et al., 2018). The acceleration of the Dirac fermions into ballistic transport by the THz field was directly visualized as a significant asymmetric redistribution of electrons in the momentum space. The acceleration of electrons across the Dirac node was accompanied by a sudden flip in the sign of the electron group velocity that led to extremely efficient THz harmonic generation, which was also demonstrated recently (Cheng et al., 2020).

Conclusion

In this article, we focused on pump-probe spectroscopy studies using THz pulses and ARPES, which are important for the study of low-energy physics in nonequilibrium condensed matter. The disadvantage of detecting only the low-energy response may become evident when the spot size of the far-field focusing is too large for a tiny sample and the time resolution is limited. However, by using on-chip generation and detection of sub-THz currents, the observation of light-induced anomalous THz Hall conductivity was recently realized in a tiny flake of exfoliated graphene under circularly polarised light, which revealed a phase transition to a Floquet topological insulator (McIver et al., 2020). Other approaches using mid-infrared, near-infrared, visible, ultraviolet, or X-ray/attosecond pulses are also very important for tracking ultrafast dynamics with a better time resolution. Phase-stable light sources are now available at mid-infrared, near-infrared, and visible frequencies. Pump-probe spectroscopy using light waves with sub-cycle resolution is attracting growing interest and opening up the new research field of petahertz electronics.

Acknowledgments

This work was supported by JST PRESTO (Grant No. JPMJPR20LA), by JSPS KAKENHI (Grants No. JP19H01817), and in part by Attosecond lasers for next frontiers in science and technology (ATTO) in Quantum Leap Flagship Program (MEXT Q-LEAP).

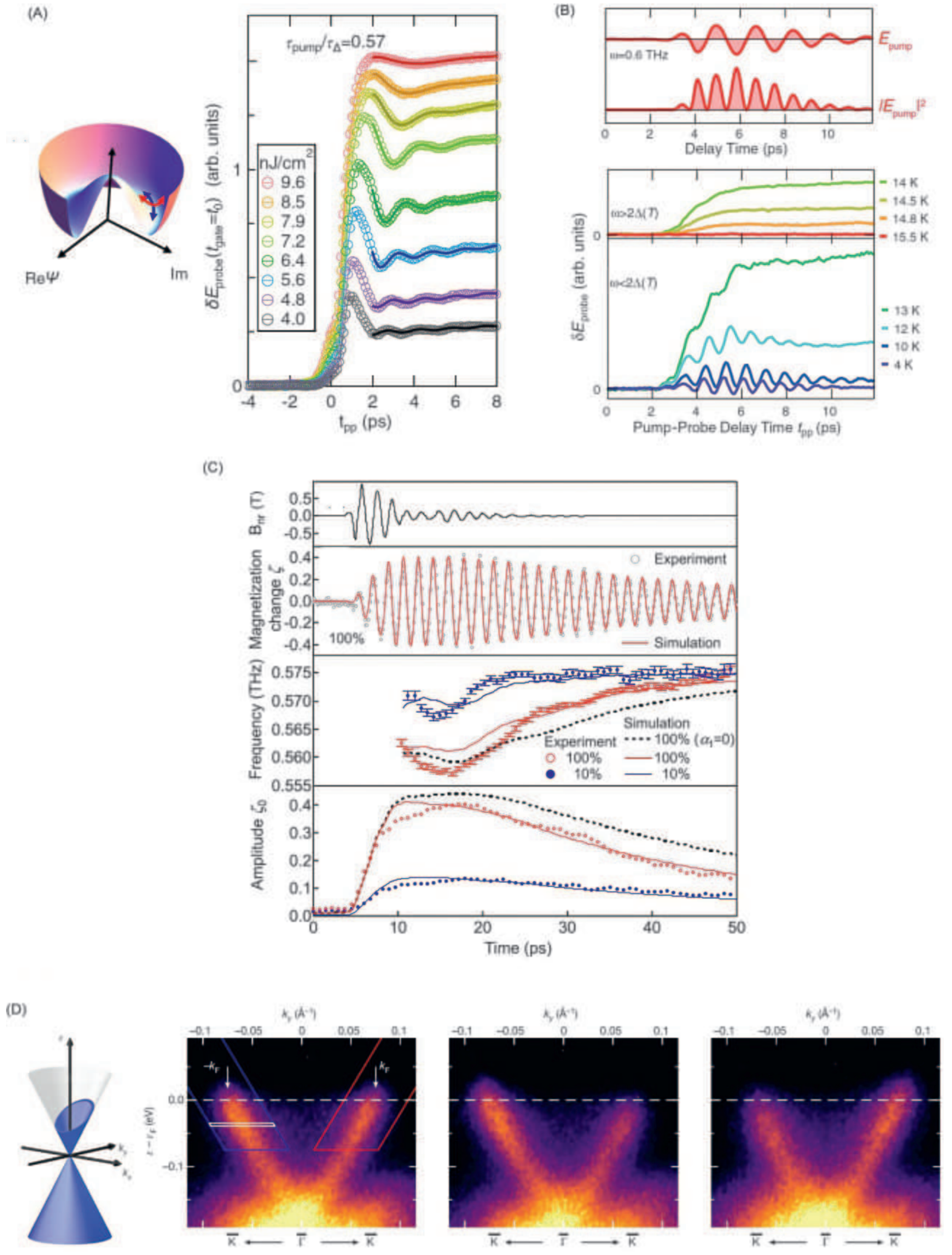

Fig. 6 (a) Oscillation of a superconducting order parameter in NbN after nonadiabatic excitation by a short THz pulse (left). Reprinted with permission from Matsunaga R et al. (2013) Higgs amplitude mode in the BCS superconductors Nb$_{1-x}$Ti$_x$N induced by terahertz pulse excitation. *Physical Review Letters* **111**: 057002, Copyright by the American Physical Society. (b) Dynamics of the order parameter during the excitation by a multicycle THz pulse (right). From Matsunaga R et al. (2014) Light-induced collective pseudospin precession resonating with Higgs mode in a superconductor. *Science* **354**: 1145. Reprinted with permission from AAAS. (c) Nonlinear magnetization dynamics of antiferromagnetic spins in HoFeO$_3$ excited by intense THz pulse (Mukai et al., 2016). (d) Dynamical change of the electron distribution in a surface state of a topological insulator excited by THz pulse. The three ARPES data panels from left to right correspond to the results in equilibrium, under positive THz field, and negative THz field, respectively. Reprinted by permission from Springer Nature Customer Service Centre GmbH: Springer, Nature, Subcycle observation of lightwave-driven Dirac currents in a topological surface band, Reimann J et al. (2018) *Nature* **562**: 396, Copyright (2018).

References

Beck M, et al. (2011) Energy-gap dynamics of superconducting NbN thin films studied by time-resolved terahertz spectroscopy. *Physical Review Letters* 107: 177007.

Cheng B, et al. (2020) Efficient terahertz harmonic generation with coherent acceleration of electrons in the dirac semimetal Cd_3As_2. *Physical Review Letters* 124: 117402.

Cook DJ and Hochstrasser RM (2000) Intense terahertz pulses by four-wave rectification in air. *Optics Letters* 25: 1210.

Fausti D, et al. (2011) Light-Induced superconductivity in a stripe-ordered cuprate. *Science* 331: 189–191.

Hauri CP, et al. (2011) Strong-field single-cycle THz pulses generated in an organic crystal. *Applied Physics Letters* 99: 161116.

Hebling J, et al. (2008) Generation of high-power terahertz pulses by tilted-pulse-front excitation and their application possibilities. *Journal of the Optical Society of America B: Optical Physics* 25: B6–B19.

Hellmann S, et al. (2012) Time-resolved x-ray photoelectron spectroscopy at FLASH. *New Journal of Physics* 14: 013062.

Hirori H, et al. (2011) Single-cycle terahertz pulses with amplitudes exceeding 1 MV/cm generated by optical rectification in $LiNbO_3$. *Applied Physics Letters* 98: 091106.

Ishida Y, et al. (2014) Time-resolved photoemission apparatus achieving sub-20-meV energy resolution and high stability. *The Review of Scientific Instruments* 85: 123904.

Kaindl RA, et al. (2009) Transient terahertz spectroscopy of excitons and unbound carriers in quasi-two-dimensional electron-hole gases. *Physical Review B* 79: 045320.

Kaiser S, et al. (2014) Optically induced coherent transport far above T_c in underdoped $YBa_2Cu_3O6+\delta$. *Physical Review B* 89(184516).

Matsunaga R, et al. (2013) Higgs amplitude mode in the BCS superconductors $Nb_{1-x}Ti_xN$ induced by terahertz pulse excitation. *Physical Review Letters* 111: 057002.

Matsunaga R, et al. (2014) Light-induced collective pseudospin precession resonating with Higgs mode in a superconductor. *Science* 345: 1145–1149.

McIver JW, et al. (2020) Light-induced anomalous Hall effect in graphene. *Nature Physics* 16: 38–41.

Mitrano M, et al. (2016) Possible light-induced superconductivity in K_3C_{60} at high temperature. *Nature* 530: 461–464.

Mukai Y, et al. (2016) Nonlinear magnetization dynamics of antiferromagnetic spin resonance induced by intense terahertz magnetic field. *New Journal of Physics* 18: 013045.

Okazaki K, et al. (2018a) Antiphase Fermi-surface modulations accompanying displacement excitation in a parent compound of iron-based superconductors. *Physical Review B* 97: 121107(R).

Okazaki K, et al. (2018b) Photo-induced semimetallic states realised in electron-hole coupled insulators. *Nature Communications* 9: 4322.

Reimann J, et al. (2018) Subcycle observation of lightwave-driven Dirac currents in a topological surface band. *Nature* 562: 396–400.

Schlauderer S, et al. (2019) Temporal and spectral fingerprints of ultrafast all-coherent spin switching. *Nature* 569: 383–387.

Suzuki T, et al. (2009) Time-resolved formation of excitons and electron-hole droplets in si studied using terahertz spectroscopy. *Physical Review Letters* 103: 057401.

Suzuki T, et al. (2019) Photoinduced possible superconducting state with long-lived disproportionate band filling in FeSe. *Communications on Physics* 2: 115.

Suzuki T, et al. (2021a) Detecting electron-phonon coupling during photoinduced phase transition. *Physical Review B* 103: L121105.

Suzuki T, et al. (2021b) HHG-laser-based time- and angle-resolved photoemission spectroscopy of quantum materials. *Journal of Electron Spectroscopy and Related Phenomena* 251: 147105.

Wang YH, et al. (2013) Observation of Floquet-Bloch states on the surface of a topological insulator. *Science* 342: 453–457.

Yamamoto S, et al. (2013) Time-resolved photoelectron spectroscopies using synchrotron radiation: Past, present, and future. *Journal of the Physical Society of Japan* 82: 021003.

Nonequilibirum physics, numerical methods

Philipp Werner, Department of Physics, University of Fribourg, Fribourg, Switzerland

© 2024 Elsevier Ltd. All rights reserved.

Introduction **990**
Wave-function based methods **991**
Exact diagonalization 991
Time-dependent DMRG and iTEBD 991
Density-functional based methods **992**
Time-dependent density functional theory 992
Functionals derived from DFT+U 992
Functionals derived from DMFT 993
Green's function based methods **993**
Lattice simulations 993
Nonequilibrium Green's function method 993
Observables 994
Self-energy approximations 994
Hartree approximation 995
Generalized Kadanoff-Baym ansatz 996
Equation of motion 996
Linear-scaling algorithm 996
Nonequilibrium dynamical mean field theory 997
Formalism 997
Impurity solvers 998
Variants of nonequilibrium DMFT 999
Floquet DMFT 999
Cluster DMFT 1000
Extended DMFT 1000
GW+EDMFT 1001
References **1001**

Abstract

Numerical simulations play an important role in theoretical investigations of nonequilibrium phenomena in correlated many-body systems. This overview focuses on lattice problems, such as the Hubbard model and its extensions. These models are relevant in the context of pump-probe experiments on solids, and for nonequilibrium studies of cold atoms in an optical lattice. The numerical approaches will be classified into (i) wave-function based methods, which may be used, for example, to obtain exact solutions for the dynamics of small systems, (ii) density-functional based methods, whose extension to strongly correlated systems is still under development, and (iii) nonequilibrium Green's function based methods, which include perturbative approaches for moderately correlated lattice problems, and dynamical mean field theory (DMFT) based methods which also provide access to the nonequilibrium properties of strongly correlated systems.

Introduction

Numerical simulations play an important role in theoretical investigations of nonequilibrium phenomena in correlated many-body systems. This overview focuses on lattice problems, such as the Hubbard model and its extensions. These models are relevant in the context of pump-probe experiments on solids (Giannetti et al., 2016), and for nonequilibrium studies of cold atoms in an optical lattice (Aoki et al., 2014). The numerical approaches will be classified into (i) wave-function based methods, which may be used, for example, to obtain exact solutions for the dynamics of small systems, (ii) density-functional based methods, whose extension to strongly correlated systems is still under development, and (iii) nonequilibrium Green's function based methods, which include perturbative approaches for moderately correlated lattice problems, and dynamical mean field theory (DMFT) based methods which also provide access to the nonequilibrium properties of strongly correlated systems.

Although the methods are applicable to a broad range of systems, most of the following discussions consider a Hubbard model with local interaction U (Gutzwiller, 1963), or a U-V Hubbard model with an additional nonlocal density-density interaction V. The Hamiltonian of the latter model is

$$H(t) = -t_{\mathrm{hop}}(t) \sum_{\langle i,j\rangle\sigma} \left(c^\dagger_{i\sigma} c_{j\sigma} + \mathrm{h.c.} \right) + U(t) \sum_i n_{i\uparrow} n_{i\downarrow} + V(t) \sum_{\langle i,j\rangle} n_i n_j - \mu \sum_i n_i, \tag{1}$$

https://doi.org/10.1016/B978-0-323-90800-9.00132-3

where $c_{i\sigma}^{\dagger}$ is the creation operator for an electron with spin σ on site $i, n_{i\sigma} = c_{i\sigma}^{\dagger} c_{i\sigma}$ measures the spin-density on site i, $n_i = n_{i\uparrow} + n_{i\downarrow}$ is the total electron density on site i, t_{hop} represents the nearest-neighbor hopping amplitude and μ is the chemical potential. In a general nonequilibrium set-up, the parameters of the model can depend on time t. A time-dependent (complex) hopping term appears for example if an electric field acts on the system in a gauge with pure vector potential (Aoki et al., 2014). In the following, $\hbar$ and the electron charge are set to unity.

Wave-function based methods

Exact diagonalization

The time evolution of small systems, e.g., Hubbard clusters or chains with up to 20 sites, can be calculated using the time-dependent Lanczos method (Park and Light, 1986). Starting from an initial state described by $|\psi(0)\rangle$, the solution of the time-dependent Schrödinger equation $\mathrm{i}\partial_t|\psi(t)\rangle = H(t)|\psi(t)\rangle$ yields the state at some later time t. In practice, the time propagation is split into small steps δt, such that $|\psi(t+\delta t)\rangle \approx e^{-\mathrm{i}H(t)\delta t}|\psi(t)\rangle$. Expansion of the time-evolution operator into a power series,

$$e^{-\mathrm{i}H(t)\delta t}|\psi(t)\rangle \approx \sum_{n=0}^{p-1} \frac{(-\mathrm{i}\delta t H(t))^n}{n!}|\psi(t)\rangle, \tag{2}$$

yields p independent vectors $\{H(t)^n|\psi(t)\rangle, n = 0, \ldots, p-1\}$, which define the so-called Krylov space. The Lanczos algorithm (Lanczos, 1950), starting from $|\phi_0\rangle = |\psi(t)\rangle$, generates an orthogonal basis of p vectors $|\phi_n\rangle$, which spans the same Krylov space, and in which the Hamiltonian $H(t)$ becomes a tridiagonal matrix. This tridiagonal matrix is small (p is typically of $\mathcal{O}(10)$) and easily diagonalized using standard numerical techniques, which yields the eigenvectors $|\psi_l\rangle$ and corresponding energy eigenvalues ε_l. In terms of these, the state vector at time $t + \delta t$ can be expressed as

$$|\psi(t+\delta t)\rangle \approx \sum_{l=0}^{p-1} e^{-\mathrm{i}\varepsilon_l \delta t}|\psi_l\rangle\langle\psi_l|\psi(t)\rangle. \tag{3}$$

While this approximation preserves the normalization of $|\psi(t+\delta t)\rangle$ for arbitrary δt, the time step needs to be chosen small enough that $H(t)$ does not vary significantly within a given time step, and the Taylor expansion up to a given order $p-1$ provides a good approximation of the time evolution operator for a single time step.

Larger systems can in some cases be treated by defining a suitable "limited functional space" (Edwards and Miyazaki, 1987; Trugman, 1988). For a single hole in the antiferromagnetic *t-J* model, the procedure works as follows (Bonca et al., 2007). Starting from a Néel state with a single hole, $|\phi_k^{(0)}\rangle = c_k|\text{Néel}\rangle$, new states are constructed by the iterative application of hopping terms. Since each hopping flips a spin against the antiferromagnetic background, this procedure will create string states in dimension $d > 1$. To reduce the number of states thus generated, and to increase the number of spin-flips in the vicinity of the hole, one imposes a constraint on the maximum distance between spin-flips. The time-dependent Lanczos procedure described above can then be applied to the Hamiltonian restricted to the limited functional space. This approach is variational in the sense that increasing the limited functional space systematically improves the description of the single-hole states.

Given the state vector $|\psi(t)\rangle$, expectation values of observables such as the current $j_\alpha = \mathrm{i}t_{\text{hop}}\sum_{\langle i,j\rangle\sigma} R_{ij}^{\alpha}(c_{i\sigma}^{\dagger}c_{j\sigma} - \text{h.c.})$, with R_{ij}^{α} the α-component of the lattice vector $R_{ij} = R_i - R_j$, can be calculated directly. To measure the time-dependent optical conductivity, one has to apply a weak probe pulse. Assuming that the probe pulse is short and of Gaussian form, the optical conductivity $\text{Re}\,\sigma_{\alpha\alpha}(\omega, t) = \frac{1}{L\omega}\,\text{Re}\int_0^{\infty} e^{\mathrm{i}(\omega+\mathrm{i}\eta)s}\langle\psi(t)|[j_\alpha(s), j_\alpha]|\psi(t)\rangle ds$ (with L the number of lattice sites and $\omega > 0$) can be measured using the formula (Shinjo and Tohyama, 2017)

$$Re\,\sigma_{\alpha\alpha}(\omega, t) = \frac{1}{L\omega}\sum_{m,n}\frac{\eta}{(\omega + \varepsilon_m - \varepsilon_n)^2 + \eta^2} \times [\langle\psi(t)|m\rangle\langle m|j_\alpha|n\rangle\langle n|j_\alpha|\psi(t)\rangle - \langle\psi(t)|j_\alpha|m\rangle\langle m|j_\alpha|n\rangle\langle n|\psi(t)\rangle], \tag{4}$$

with $|m\rangle$ and $|n\rangle$ denoting the eigenstates of the Hamiltonian with energies $\varepsilon_n, \varepsilon_m$ and η a small positive number.

While the numerical effort in exact diagonalization calculations scales linearly with time, and long times are thus in principle accessible, the simulations of small systems are affected by finite-size effects such as artificial recurrences. Correlations spread with a characteristic light-cone velocity v_{lc}, so that artifacts due to finite-size effects can be expected for times $\gtrsim L/(2v_{\text{lc}})$, where L is the linear size of the system.

Time-dependent DMRG and iTEBD

In the density-matrix renormalization group (DMRG) method (White, 1992), the state-vector $|\psi\rangle$ is approximated by a matrix-product state (MPS) with finite bond dimension m:

$$|\psi\rangle \approx \sum_{\sigma_1\ldots\sigma_L} \text{Tr}\left[\mathcal{A}_1^{\sigma_1}\ldots\mathcal{A}_L^{\sigma_L}\right]|\sigma_1\ldots\sigma_L\rangle, \tag{5}$$

where σ_i represents the local degrees of freedom at site i and $\mathcal{A}_i^{\sigma_i}$ is a $m \times m$ matrix (Cirac et al., 2021). Without any constraints on the bond dimension, the representation (5) becomes exact, but the required bond dimension in general scales exponentially with system size. Compact representations are however possible for one dimensional systems with short-range interactions, which is why DMRG is mainly used to study such systems (Schollwöck, 2011).

Given a one-dimensional lattice problem, the truncation is implemented by decomposing the system into subsystems A and B, performing a Schmidt decomposition $|\psi\rangle = \sum_{\alpha=1}^{s} s_\alpha |\alpha\rangle_A |\alpha\rangle_B$ into a new product basis with a single index α, and keeping only the m largest Schmidt coefficients $|s_\alpha|$ in the sum: $|\psi\rangle \approx \sum_{\alpha=1}^{m} s_\alpha |\alpha\rangle_A |\alpha\rangle_B$, assuming the ordering $|s_1| \geq |s_2| \geq \ldots \geq |s_s|$. Details of the implementation can be found in Schollwöck, 2011. The efficiency of the method depends on how fast the Schmidt coefficients decay, and the discarded weight $\delta = \sum_{\alpha=m+1}^{s} s_\alpha^2$ is a useful measure for the error incurred by the truncation.

Some intuitive understanding can be gained from the connection to the entanglement entropy, $S_{\mathrm{vN}} = -\sum_\alpha s_\alpha^2 \log s_\alpha^2$, and the scaling of S_{vN} with system size. If an area law holds, $S_{\mathrm{vN}} \propto L_A^{D-1}$, with L_A the linear size of subsystem A and D the dimension. In this case, for $D = 1$, one finds $S_{\mathrm{vN}}(L_A) = \text{const}$ for large enough L_A and $m \lesssim \exp\left(S_{\mathrm{vN}}(L_A)\right)$ does not increase with system size. In $D = 2$, however, the bond dimension grows exponentially with the width of the system, even if an area law holds.

In the calculation of the real-time evolution (Daley et al., 2004; Vidal, 2004; White and Feiguin, 2004), $|\psi(t)\rangle = e^{-\mathrm{i}Ht}|\psi(t=0)\rangle$, one employs a time discretization into small time steps δt and a Suzuki Trotter decomposition of the Hamiltonian $H = \sum_i h_{i,i+1}$ to end up with a product of operators $e^{-\mathrm{i}h_{i,i+1}\delta t}$, which act on just two neighboring $\mathcal{A}$ matrices in Eq. (5). Grouping the sites into sublattices A and B, the time evolution operator for a given time-step is factorized into a product of operators acting on AB bonds and BA bonds. For global quenches or electric field perturbations, $S_{\mathrm{vN}} \propto t$, which means that the bond dimension m needed to keep the same accuracy grows exponentially with time. This typically limits the time-dependent DMRG calculations to $\mathcal{O}(10)$ inverse hopping times. The parameter δt is the second parameter affecting the accuracy of the simulation, but the effect of the time-discretization can be reduced by implementing higher-order Suzuki-Trotter decompositions (Schollwöck, 2011).

Like DMRG, the infinite time-evolving block decimation (iTEBD) method (Kjäll et al., 2013; Vidal, 2007) is based on a MPS representation of the wave function and is suitable for the simulation of one-dimensional lattice problems. iTEBD assumes a state with translational symmetry (the same $\mathcal{A}$ matrix for each site) and treats the system in the thermodynamic limit. The initial ground state of the system is prepared by an imaginary time evolution, i.e., by the application of the operator $\lim_{\beta\to\infty} e^{-\beta H}$, so that iTEBD should be regarded as a power method, in contrast to DMRG, which employs a variational ground state search.

Within iTEBD, response functions $-\mathrm{i}\langle[C(t), D(0)]\rangle$ with bosonic operators C and D, such as the optical conductivity, can be computed by applying a small perturbation proportional to D at time zero. The single particle Green's function can be evaluated by introducing an auxiliary band and measuring the excitations from the system to this auxiliary band (Murakami et al., 2021; Zawadzki and Feiguin, 2019).

Density-functional based methods

Time-dependent density functional theory

Density functional theory (DFT) in combination with the local density approximation (LDA) or generalized gradient approximation (GGA) is based on a nearly homogeneous electron gas treatment of correlations (Kohn and Sham, 1965). This approach is highly successful for weakly correlated materials, but fails do describe strongly correlated systems. Time-dependent DFT (TDDFT) computes the nonequilibrium dynamics of the electron density $n(r, t)$ by solving the time-dependent Kohn-Sham equations (Runge and Gross, 1984)

$$\mathrm{i}\partial_t|\psi_j(t)\rangle = H[n](t)|\psi_j(t)\rangle, \tag{6}$$

$$n(r,t) = \sum_j \rho_j \left|\left\langle r|\psi_j(t)\right\rangle\right|^2, \tag{7}$$

where $|\psi_j\rangle$ denotes the Kohn-Sham orbitals and ρ_j the corresponding occupations. The Hamiltonian in Eq. (6) contains the kinetic term T, the external potential $V_{\mathrm{ext}}(t)$ describing the effects of the nuclei and possible external fields, the Hartree potential $V_H[n(r,t)]$ and the exchange correlation potential $V_{\mathrm{xc}}[n(r,t)]$. Depending on the gauge choice, an electric field perturbation may enter in the kinetic term or in the external potential. In a gauge with pure vector potential A, where a uniform electric field E is related to A by $E(t) = -\partial_t A(t)$, the kinetic term becomes $T = \frac{1}{2}(-i\nabla - A(t))^2$. In finite-size systems, it can instead be convenient to add a scalar potential $E(t)\cdot r$ to $V_{\mathrm{ext}}(t)$.

Functionals derived from DFT+*U*

By adding a local Hubbard U to the most strongly correlated orbitals (DFT+U method (Liechtenstein et al., 1995)) a better description of the electronic structure of correlated systems can be obtained, although DFT+U, lacking the imaginary part of the self-energy, cannot properly describe Mott physics. Comparing the Hartree-Fock expression for the on-site energy to the energy correction in terms of an effective Hubbard U and Hund coupling J used in DFT+U, Agapito et al., 2015 derived a functional of the electron density, called ACBN0 functional, which incorporates ab-initio derived U and J parameters. The functional representing the "+U" operator has the form

$$V_U^\sigma\left[n, \left\{\rho_{mm'}^\sigma\right\}\right] = (U-J)\sum_{m,m'}\left(\frac{1}{2}\delta_{mm'} - \rho_{mm'}^\sigma\right)P_{mm'}^\sigma, \tag{8}$$

where $P^\sigma_{mm'} = |\phi^\sigma_m\rangle\langle\phi^\sigma_{m'}|$ is the projector to the subspace defined by the localized orbitals $\{\phi^\sigma_m\}$ and ρ^σ is the density matrix of this subspace. The explicit formulas defining U and J in terms of the occupations can be found in (Agapito et al., 2015).

With the above potential, the time-dependent Kohn Sham equation (6) reads (Tancogne-Dejean et al., 2017)

$$\mathrm{i}\partial_t\left|\psi^\sigma_{v,k}\right\rangle = \left(-\frac{1}{2}\nabla^2 + V_{\mathrm{ext}}(t) + V_H[n(r,t)] + V_{\mathrm{xc}}\left[n(r,t)\right] + V^\sigma_U\left[n(r,t),\left\{\rho^\sigma_{mm'}\right\}\right]\right)|\psi^\sigma_{v,k}(t)\rangle, \tag{9}$$

where $|\psi^\sigma_{v,k}\rangle$ represents a Bloch state with band index v, momentum k, and spin index σ and we assume that a possible electric field excitation enters through $V_{\mathrm{ext}}(t)$.

Functionals derived from DMFT

An alternative and potentially more accurate strategy for incorporating strong correlation effects into (TD)DFT calculations is to compute an exchange-correlation functional from density-dependent energy estimates based on dynamical mean field theory (DMFT), see Section "Nonequilibrium dynamical mean field theory." For the Hubbard model, this approach was explored by Karlsson et al., 2011. In a spin-independent formulation, the total energy of the Hubbard model can be expressed as $E[n] = E_{\mathrm{kin}}[n] + E_H[n] + E_{\mathrm{xc}}[n] + \sum_i V_{\mathrm{ext},i} n_i$, where $V_{\mathrm{ext},i}$ denotes the external potential at site i, $n_i = \sum_\sigma n_{i\sigma}$, $E_H[n] = \frac{1}{4}\sum_i U_i n_i^2$ the Hartree energy for a possibly site dependent interaction U_i, and $E_{\mathrm{kin}}[n]$ the kinetic energy. The exchange-correlation potential V_{xc} can be calculated within the local density approximation as $V_{\mathrm{xc},i} = V_{\mathrm{xc}}(n_i)$, with V_{xc} derived from the exchange-correlation energy E_{xc} of the homogeneous Hubbard model. If this homogeneous reference system is treated within DMFT, one obtains $E_{\mathrm{xc}} = E_{\mathrm{DMFT}} - E_{\mathrm{kin}} - E_H$, with E_{DMFT} the DMFT estimate of the ground state energy. Computing the derivative of $E_{\mathrm{xc}}[n]$ with respect to n numerically, one obtains the exchange-correlation potential. This potential exhibits a discontinuity at $n = 1$ in the strongly correlated regime (Karlsson et al., 2011), which is a manifestation of the Mott transition in this DFT description.

Green's function based methods

Lattice simulations

Nonequilibrium Green's function method

The nonequilibrium Green's function (NEGF) method is a general and versatile approach for studying the nonequilibrium properties of lattice systems (Stefanucci and van Leeuwen, 2013). This approach is based on the numerical solution of the Kadanoff-Baym equations (KBEs) for the single-particle Green's function

$$G_k(t,t') = -\mathrm{i}\left\langle \mathcal{T}_{\mathcal{C}} c_k(t) c_k^\dagger(t')\right\rangle, \tag{10}$$

which is expressed here in momentum space. The time arguments lie on an L-shaped contour $\mathcal{C}$ in the complex plane, which runs from time 0 to some maximum time $t_{\max}$ along the real-time axis, back to time zero along the real-time axis, and finally to $-\mathrm{i}\beta$ along the imaginary time axis, where β is the inverse temperature of the initial equilibrium state (Aoki et al., 2014). $\mathcal{T}_{\mathcal{C}}$ is the contour ordering operator, which orders creation and annihilation operators along $\mathcal{C}$, and the expectation value is defined as $\langle \mathcal{T}_{\mathcal{C}} \ldots\rangle = \mathrm{Tr}\,[\mathcal{T}_{\mathcal{C}} e^{-\mathrm{i}\int_{\mathcal{C}} \mathrm{d}\bar{t} H(\bar{t})} \ldots]/Z$ with H the Hamiltonian and $Z = \mathrm{Tr}\,[\mathcal{T}_{\mathcal{C}} e^{-\mathrm{i}\int_{\mathcal{C}} \mathrm{d}\bar{t} H(\bar{t})}]$ the partition function. Denoting the quadratic part of the lattice Hamiltonian by h_k and the self-energy by Σ_k, the single-particle Green's function satisfies

$$(\mathrm{i}\partial_t - h_k(t))G_k(t,t') - \int_{\mathcal{C}} \mathrm{d}\bar{t}\,\Sigma_k(t,\bar{t})G_k(\bar{t},t') = \delta_{\mathcal{C}}(t,t'), \tag{11}$$

where $\delta_{\mathcal{C}}$ denotes the delta-function on the L-shaped contour. For the numerical solution, Eq. (11) is converted into coupled integro-differential equations for the different components, e.g., the Matsubara (M), greater (>), lesser (<) and left-mixing (⌉) components of the two-time correlators (Aoki et al., 2014). The resulting KBEs for the real-time propagation are

$$\mathrm{i}\partial_t G_k^>(tt') = h_k(t)G_k^>(tt') + [\Sigma_k * G_k]^>(tt'), \tag{12}$$

$$-\mathrm{i}\partial_t G_k^<(t't) = G_k^>(t't)h_k(t) + [G_k * \Sigma_k]^<(t't), \tag{13}$$

$$i\partial_i G_k^{\rceil}(t,\tau) = h_k(t)G_k^{\rceil}(t,\tau) + [\Sigma_k * \mathrm{G_k}]^{\rceil}(t,\tau). \tag{14}$$

The convolutions are defined by the Langreth rules (Stefanucci and Leeuwen, 2013)

$$[A_k * B_k]^{\gtrless}(t,t') = \int_0^t \mathrm{d}\bar{t} A_k^{\mathrm{R}}(t,\bar{t})B_k^{\gtrless}(\bar{t},t') + \int_0^{t'} \mathrm{d}\bar{t} A_k^{\gtrless}(t,\bar{t})B_k^{\mathrm{A}}(\bar{t},t') - \mathrm{i}\int_0^\beta \mathrm{d}\tau A_k^{\rceil}(t,\tau)B_k^{\lceil}(\tau,t')$$

and

$$[A_k * B_k]^{\rceil}(t,\tau) = \int_0^t \mathrm{d}\bar{t} A_k^{\mathrm{R}}(t,\bar{t})B_k^{\rceil}(\bar{t},\tau) + \int_0^\beta \mathrm{d}\tau' A_k^{\rceil}(t,\tau')B_k^{\mathrm{M}}(\tau'-\tau),$$

which also involve the retarded (R), advanced (A) and right-mixing ($\lceil$) components. Given the self-energy Σ_k, one first computes the Matsubara component $G_k^{\mathrm{M}}(\tau)$, which captures the initial correlations, and provides the initial conditions for the solution of Eqs. (12)–(14).

Observables

The nonequilibrium Green's functions $G_{k\sigma}(t,t')$ and corresponding spin-densities $n_{k\sigma}(t) = -\mathrm{i}G_{k\sigma}^{<}(t,t)$ allow to compute the relevant observables. The kinetic energy per lattice site is

$$E_{\mathrm{kin}}(t) = \frac{1}{N_k}\sum_{k\sigma}\varepsilon_k(t)n_{k\sigma}(t), \tag{15}$$

with ε_k the noninteracting dispersion and N_k the number of k points in the discretized Brillouin zone. The potential energy per lattice site of the Hubbard model can be evaluated as (Eckstein et al., 2010)

$$E_{\mathrm{pot}}(t) = -\frac{\mathrm{i}}{2N_k}\sum_{k}\mathrm{Tr}[\Sigma_k * G_k]^{<}(t,t), \tag{16}$$

where the star symbol represents a convolution on the contour $\mathcal{C}$ and the trace is over the spin degree of freedom. The Fourier transforms of the retarded and lesser Green's functions yield the time-dependent spectral function A_k and occupation function $A_k^{<}$,

$$A_k(\omega,t) = -\frac{1}{\pi}\mathrm{Im}\int_t^{\infty}\mathrm{d}t' e^{\mathrm{i}\omega(t'-t)}G_k^{\mathrm{R}}(t,t'), \tag{17}$$

$$A_k^{<}(\omega,t) = \frac{1}{2\pi}\mathrm{Im}\int_t^{\infty}\mathrm{d}t' e^{\mathrm{i}\omega(t'-t)}G_k^{<}(t,t'). \tag{18}$$

While in a nonequilibium situation, $A_k(\omega,t)$ and $A_k^{<}(\omega,t)$ are not guaranteed to be positive, this is the case for the time-resolved photo-emission spectrum (Freericks et al., 2009). This spectrum can be evaluated from the Fourier integral $I_k(\omega,t_p)$, which involves convolutions with the envelope function $S(t)$ of the probe pulse, centered at probe time t_p,

$$I_k(\omega,t_p) = -\mathrm{i}\int \mathrm{d}t\mathrm{d}t' S(t)S(t')e^{\mathrm{i}\omega(t'-t)}G_k^{<}\left(t+t_p, t'+t_p\right). \tag{19}$$

For physically meaningful (gauge invariant) results, one should use gauge invariant Green's functions (Aoki et al., 2014).

A time-dependent electric field can be incorporated into a single-band model like Eq. (1) via the Peierls substitution (Peierls, 1933), which in a gauge with pure vector potential adds a complex phase to the hopping terms: $t_{\mathrm{hop},ij}(t) = t_{\mathrm{hop},ij}\exp\left[-\mathrm{i}\int_{R_i}^{R_j}\mathrm{d}r r\cdot A(r,t)\right]$. For optical frequencies, the electric field varies little on the atomic scale, so that the vector potential $A(r,t)$ can be approximated as r-independent. In this case, the Peierls substitution corresponds to a time-dependent dispersion $\varepsilon_k(t) = \varepsilon_{k-A(t)}$. The current density can be evaluated as (Aoki et al., 2014)

$$j(t) = \frac{1}{L^D}\sum_{k\sigma}v_k(t)n_{k\sigma}(t), \tag{20}$$

with $v_k(t) = \frac{\partial\varepsilon_k(t)}{\partial k} = v_{k-A(t)}$ the shifted band velocity and L^D the volume. A possible strategy for computing the time- and frequency dependent optical conductivity is to apply a half-cycle electric field pulse $E_{t_p}(t)$ centered at probe time t_p, using $E(t) = -\partial_t A(t)$. From the Fourier transformations of $E_{t_p}(t)$ and the induced current $j_{t_p}(t)$, one obtains $\sigma(\omega,t_p) = j_{t_p}(\omega)/E_{t_p}(\omega)$.

Self-energy approximations

Given the exact self-energy and initial state, Eqs. (12)–(14) yield the exact nonequilibrium dynamics. In practice, however, NEGF based lattice simulations often involve approximations of the self-energy, which restrict the validity of the simulations to the weak-to-moderate correlation regime. The simplest treatment is the Hartree or Hartree-Fock approximation, which only considers the corresponding time-local self-energy diagrams (first two diagrams in Fig. 1). At the next level one may consider self-energy contributions up to the second order in the interaction. This yields the second-Born (2B) approximation, whose diagrammatic representation for a model with local and nonlocal interactions is shown in Fig. 1. Using the Feynmann rules, these diagrams can be expressed on the L-shaped contour $\mathcal{C}$, and the resulting self-energy components inserted into Eqs. (12)–(14).

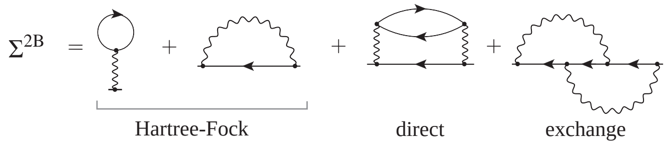

Fig. 1 Feynmann diagrams representing the second-Born approximation for the U-V Hubbard model. The first two diagrams represent the Hartree and Fock contributions, the third diagram the direct term, and the fourth diagram the exchange term. The Fock and exchange diagrams are nonzero in the presence of a nonlocal interaction V.

Other commonly used schemes are the GW approximation, which corresponds to the lowest-order self-energy correction in an expansion in terms of the dynamically screened interaction W, and the T-matrix approximation, which sums up ladder-type diagrams (Stefanucci and van Leeuwen, 2013).

Hartree approximation

A simple, but relevant problem is the Hartree dynamics in the antiferromagnetic phase of the Hubbard model (Tsuji et al., 2013), which is equivalent to the time-dependent BCS dynamics (Barankov and Levitov, 2006; Yuzbashyan and Dzero, 2006). The computational scheme can be formulated in terms of the momentum distribution functions

$$\rho^{ab}_{k\sigma}(t) = -\mathrm{i}G^{ab<}_{k\sigma}(t,t) \tag{21}$$

with a, $b = A$, B denoting sublattice indices. The nonequilibrium Green's function satisfies the 2×2 Dyson equation

$$\begin{pmatrix} \mathrm{i}\partial_t + \mu - \Sigma^A_\sigma & -\varepsilon_k \\ -\varepsilon_k & \mathrm{i}\partial_t + \mu - \Sigma^B_\sigma \end{pmatrix} * \begin{pmatrix} G^{AA}_{k\sigma} & G^{AB}_{k\sigma} \\ G^{BA}_{k\sigma} & G^{BB}_{k\sigma} \end{pmatrix} = \begin{pmatrix} \delta_{\mathcal{C}} & 0 \\ 0 & \delta_{\mathcal{C}} \end{pmatrix}, \tag{22}$$

and the corresponding conjugate equation (Tsuji et al., 2013), where Σ^a_σ is the Hartree self-energy for sublattice a and * denotes a convolution on the time arguments. The explicit expressions for the Hartree self-energies are

$$\Sigma^A_\sigma(t,t') = U(t)n^A_{\bar{\sigma}}(t)\delta_{\mathcal{C}}(t,t'), \tag{23}$$

$$\Sigma^B_\sigma(t,t') = U(t)n^B_{\bar{\sigma}}(t)\delta_{\mathcal{C}}(t,t'), \tag{24}$$

with $n^a_\sigma(t)$ the local density on sublattice a. In a system with antiferromagnetic order, the local densities can be expressed as

$$n^A_\sigma(t) = \bar{n} + \frac{1}{2}\sigma m(t), \quad n^B_\sigma(t) = \bar{n} - \frac{1}{2}\sigma m(t), \tag{25}$$

where $\bar{n}$ is the average spin-density per site and $m(t)$ is the staggered magnetization. Using the Dyson equation (22) and its conjugate together with Eqs. (23) and (24), one obtains a closed set of equations for the equal-time lesser Green's functions. One may then replace these equal-time functions by the corresponding momentum distribution functions (Eq. (21)), to obtain the following set of equations,

$$\partial_t\left[\rho^{AA}_{k\sigma}(t) + \rho^{BB}_{k\sigma}(t)\right] = 0, \tag{26}$$

$$\partial_t\left[\rho^{BA}_{k\sigma}(t) + \rho^{AB}_{k\sigma}(t)\right] = -\mathrm{i}U(t)m(t)\sigma\left[\rho^{BA}_{k\sigma}(t) - \rho^{AB}_{k\sigma}(t)\right], \tag{27}$$

$$\mathrm{i}\partial_t\left[\rho^{BA}_{k\sigma}(t) - \rho^{AB}_{k\sigma}(t)\right] = 2\varepsilon_k\left[\rho^{AA}_{k\sigma}(t) - \rho^{BB}_{k\sigma}(t)\right] + U(t)m(t)\sigma\left[\rho^{BA}_{k\sigma}(t) + \rho^{AB}_{k\sigma}(t)\right], \tag{28}$$

$$\partial_t\left[\rho^{AA}_{k\sigma}(t) - \rho^{BB}_{k\sigma}(t)\right] = -2\mathrm{i}\varepsilon_k\left[\rho^{BA}_{k\sigma}(t) - \rho^{AB}_{k\sigma}(t)\right]. \tag{29}$$

These equations can be rewritten in a more transparent form by adopting a pseudospin representation (Anderson, 1958)

$$f^x_k(t) = \frac{1}{2}\sum_\sigma \left[\rho^{BA}_{k\sigma}(t) + \rho^{AB}_{k\sigma}(t)\right], \tag{30}$$

$$f^y_k(t) = \frac{1}{2}\sum_\sigma \sigma\left[\rho^{BA}_{k\sigma}(t) - \rho^{AB}_{k\sigma}(t)\right], \tag{31}$$

$$f^z_k(t) = \frac{1}{2}\sum_\sigma \sigma\left[\rho^{AA}_{k\sigma}(t) - \rho^{BB}_{k\sigma}(t)\right]. \tag{32}$$

With the pseudospins $f_k = (f^x_k, f^y_k, f^z_k)$, the Hartree equations can be expressed as "Bloch equations,"

$$\partial_t f_k(t) = b_k(t) \times f_k(t), \tag{33}$$

where the effective magnetic field is defined as $b_k(t) = (-2\varepsilon_k, 0, U(t)m(t))$. The order parameter is selfconsistently determined by

$$m(t) = \sum_k f^z_k(t). \tag{34}$$

Equation (33) is equivalent to the time-dependent BCS equation (Barankov and Levitov, 2006; Yuzbashyan and Dzero, 2006). It is integrable and has infinitely many conserved quantities. For example, $\rho^{AA}_{k\sigma} + \rho^{BB}_{k\sigma}$ (Eq. 26) and the length of the pseudospin $|f_k| \equiv \sqrt{\left(f^x_k\right)^2 + \left(f^y_k\right)^2 + \left(f^z_k\right)^2}$ are conserved for each k.

As an illustration, the left panel of Fig. 2 shows the Hartree solution for the time evolution of the staggered magnetization $m(t)$ in a Hubbard model on a Bethe lattice with a semi-circular density of states of bandwidth 4. The interaction $U(t)$ is ramped linearly from the initial value $U_i = U(t = 0) = 2$ to the indicated final values $U_f = U(t \geq t_f)$ in a time $t_f = 8$. This ramp to lower interactions

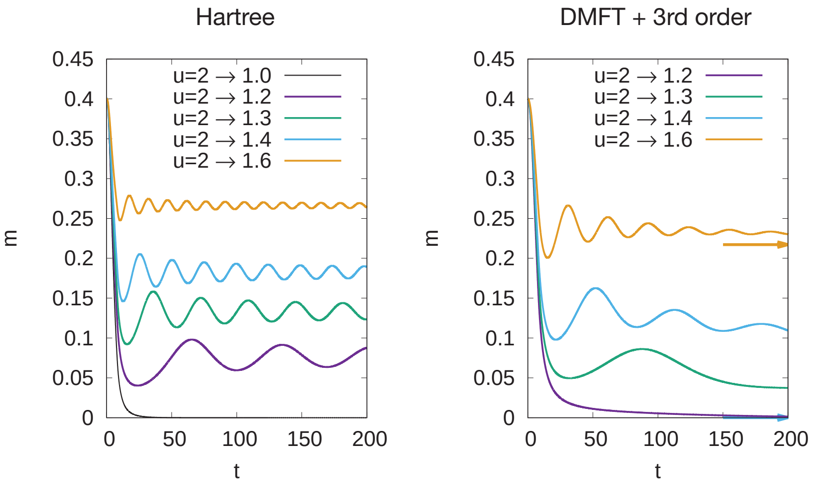

Fig. 2 Time evolution of the staggered magnetization *m* after an interaction ramp in the Hubbard model on a Bethe lattice with bandwidth 4. The left panel shows the result of the Hartree approximation and the right panel the DMFT result obtained with the third order weak-coupling expansion as impurity solver. Here, the arrows indicate the thermalized value of *m*, calculated from the total energy after the ramp.

results in two qualitatively different time evolutions. For $U_f \geq 1.2$ the solution oscillates around a nonzero m, which implies that within the Hartree approximation, the magnetic order survives, while for $U_f = 1.0$, the order parameter decays monotonically to zero (Tsuji et al., 2013). Analogous results are obtained for the BCS dynamics in the case of an attractive U (Barankov and Levitov, 2006; Yuzbashyan and Dzero, 2006).

Generalized Kadanoff-Baym ansatz

Equation of motion

A more sophisticated formalism, which also reduces the KBEs (12)–(14) to an equation of motion for the density matrix, is the generalized Kadanoff-Baym ansatz (GKBA) (Lipavsky et al., 1986). For the following discussion, we define $\rho_k^{\gtrless}(t) = -\mathrm{i}G_k^{\gtrless}(t,t)$. The equation of motion for $\rho_k^<(t)$ is

$$\frac{\mathrm{d}}{\mathrm{d}t}\rho_k^<(t) = -\mathrm{i}\left[h^{\mathrm{MF}}(t), \rho_k^<(t)\right] - [\mathcal{I}_k(t) + \mathrm{h.c.}], \tag{35}$$

with h^{MF} denoting the mean-field Hamiltonian, while the collision term $\mathcal{I}_k(t)$ is defined by

$$\mathcal{I}_k(t) = [\Sigma_k * G_k]^<(t,t). \tag{36}$$

The time off-diagonal components of the lesser and greater Green's function, which are needed for the collision integral (36), are reconstructed by the GKBA from the diagonal $\rho_k^{\gtrless}(t)$ as

$$G_k^{\gtrless}(t,t') = -G_k^{\mathrm{R}}(t,t')\rho_k^{\gtrless}(t') + \rho_k^{\gtrless}(t)G_k^{\mathrm{A}}(t,t'). \tag{37}$$

Typically, the Hartree-Fock (HF) Hamiltonian h^{HF}, which is a functional of $\rho_k^<$, is used to compute an approximate retarded Green's function,

$$G_k^{\mathrm{R}}(t,t') = -\mathrm{i}\theta(t-t')\mathcal{T}\exp\left(-\mathrm{i}\int_{t'}^{t} \mathrm{d}\bar{t}\, h_k^{\mathrm{HF}}(\bar{t})\right) \equiv -\mathrm{i}\theta(t-t')U_k(t,t'), \tag{38}$$

while $G_k^{\mathrm{A}}(t,t') = [G_k^{\mathrm{R}}(t',t)]^\dagger$. Here, $\mathcal{T}$ is the usual time ordering symbol. The time-evolution operator $U_k(t,t')$ defined by Eq. (38) can be evaluated on a uniform mesh of time points $t_n = n\delta t$ using $U_k(t_n + \delta t, t_j) = U_k(t_n + \delta t, t_n)U_k(t_n, t_j)$, where $U_k(t_n + \delta t, t_n)$ is computed, for example, with the commutator-free matrix-exponential method (Alvermann and Fehske, 2011).

In the full NEGF calculation, the initial equilibrium state is calculated on the imaginary branch of the L shaped contour. For the GKBA, however, the corresponding equilibrium approximation is not known. Thus, the many-body effects are switched on adiabatically, in a time propagation within the GKBA which starts from a noninteracting or a mean-field initial state. In this calculation, the self-energy corrections are slowly built in using a ramp function, while the system evolves to the correlated equilibrium state.

Linear-scaling algorithm

Because of the convolution in the collision term (36) the solution of the equation of motion (35) scales at least quadratically in the maximum number N_t of time steps. This scaling can for example be achieved with the second Born approximation.

Schlünzen et al., 2020 showed that it is possible to reduce the computational effort to $\mathcal{O}(N_t)$ by rewriting the problem in the form of coupled equations for the time-diagonal parts of the single-particle and two-particle Green's functions. In the following, the equations are presented for the Hubbard model, using real space Green's functions. A more general and detailed discussion can be found in (Joost et al., 2020).

Expressed in real space, the equation of motion for the time-diagonal part of the single-particle Green's function $G_{ij} = -\mathrm{i}\left\langle \mathcal{T}_{\mathcal{C}} c_i(t) c_j^\dagger(t') \right\rangle$ or density matrix $\rho^<_{ij\sigma}(t) = -\mathrm{i}G^<_{ij\sigma}(t,t)$ takes the form

$$\frac{\mathrm{d}}{\mathrm{d}t}\rho^<_{ij\sigma}(t) = -\mathrm{i}\left[h^{\mathrm{HF}}(t), \rho^<(t)\right]_{ij\sigma} - \left[\mathcal{I}_{ij\sigma}(t) + \mathrm{h.c.}\right], \tag{39}$$

where the Hartree-Fock Hamiltonian reads $h^{\mathrm{HF}}_{ij\sigma}(t) = h^{(0)}_{ij} + \delta_{ij}U(t)\rho^<_{ii\overline{\sigma}}(t)$ and the collision term $\mathcal{I}_{ij\sigma}(t) = -\mathrm{i}U(t)\mathcal{G}^{\sigma\overline{\sigma}\sigma\overline{\sigma}}_{iiji}(t)$ is related to the two-particle Green's function

$$\mathrm{G}^{(2)}_{ijkl}(t_1, t_2, t_3, t_4) = (-i)^2\left\langle \mathcal{T}_{\mathcal{C}} c_i(t_1) c_j(t_2) c_l^\dagger(t_4) c_k^\dagger(t_3) \right\rangle, \tag{40}$$

which can be decomposed into a Hartree, a Fock and a correlation contribution: $\mathrm{G}^{(2)}_{ijkl} = \mathrm{G}^{(2),\mathrm{H}}_{ijkl} - \mathrm{G}^{(2),\mathrm{F}}_{ijkl} + \mathrm{G}^{(2),\mathrm{corr}}_{ijkl}$. The time-diagonal two-particle Green's function $\mathcal{G}_{ijkl}(t)$ appearing in the collision term is defined as

$$\mathcal{G}_{ijkl}(t) = \left[\mathcal{G}^{(2),\mathrm{corr}}_{ijkl}\right]^<(t,t). \tag{41}$$

The equation of motion for this time-diagonal function reads

$$-\mathrm{i}\frac{\mathrm{d}}{\mathrm{d}t}\mathcal{G}^{\sigma\overline{\sigma}\overline{\sigma}\sigma\overline{\sigma}}_{ijkl}(t) = -\left[h^{(2),\mathrm{HF}}_{\sigma\overline{\sigma}}, \mathcal{G}^{\sigma\overline{\sigma}\sigma\overline{\sigma}}\right]_{ijkl}(t) + U(t)\Phi^{\sigma\overline{\sigma}\sigma\overline{\sigma}}_{ijkl}(t), \tag{42}$$

where $h^{(2),\mathrm{HF}}_{ijkl,\sigma\overline{\sigma}}(t) = \delta_{jl}h^{\mathrm{HF},\sigma}_{ik}(t) + \delta_{ik}h^{\mathrm{HF},\overline{\sigma}}_{jl}(t)$ and

$$\Phi^{\sigma\overline{\sigma}\sigma\overline{\sigma}}_{ijkl}(t) = \sum_p\left[\rho^>_{ip\sigma}(t)\rho^>_{jp\overline{\sigma}}(t)\rho^<_{pk\sigma}(t)\rho^<_{pl\overline{\sigma}}(t) - \rho^<_{ip\sigma}(t)\rho^<_{jp\overline{\sigma}}(t)\rho^>_{pk\sigma}(t)\rho^>_{pl\overline{\sigma}}(t)\right]. \tag{43}$$

Since $\Phi^{\sigma\overline{\sigma}\sigma\overline{\sigma}}_{ijkl}(t)$, and hence the right-hand side of Eq. (42), involves no memory term, the solution of the coupled equations (39) and (42) is linear in N_t.

Nonequilibrium dynamical mean field theory

Formalism

Nonequilibrium dynamical mean field theory (Aoki et al., 2014; Freericks et al., 2006) is a Green's function based formalism which becomes exact in the limit of infinite dimension or infinite coordination number. If applied to finite-coordination systems, DMFT becomes an approximate description, which however works directly in the thermodynamic limit. DMFT neglects the nonlocal self-energy components, but captures strong local correlation effects.

DMFT maps a correlated lattice model onto a self-consistently determined effective quantum impurity model (Georges et al., 1996). As illustrated in Fig. 3, this mapping is performed by identifying the self-energy of the lattice model, Σ^{latt}_k, with the local impurity self-energy Σ_{imp} (DMFT approximation), while the bath properties of the impurity model are fixed by a self-consistency condition which demands that the local lattice Green's function is identical to the impurity Green's function, $\mathrm{G}^{\mathrm{latt}}_{\mathrm{loc}} = \frac{1}{N_k}\sum_k \mathrm{G}^{\mathrm{latt}}_k \equiv \mathrm{G}_{\mathrm{imp}}$ (DMFT self-consistency condition). Often it is convenient to work in an action formalism, where the bath of the impurity model is represented by a hybridization function Δ. This function encodes how electrons hop in and out of the impurity site and thus plays the role of a dynamical mean field.

The self-consistent mapping from a lattice model to an impurity model can be implemented also for nonequilibrium systems (Freericks et al., 2006). The only difference in nonequilibrium DMFT, compared to equilibrium DMFT, is that the functions $G(t,t')$, $\Sigma(t,t')$ and $\Delta(t,t')$ are functions defined on the L-shaped contour $\mathcal{C}$ in the complex time-plane instead of the imaginary-time axis (Aoki et al., 2014). Since a general nonequilibrium state has no time-translation invariance, these functions depend on the two times t and t' separately, rather than on the time difference as in equilibrium. This implies a higher memory cost for storing these functions, and it also means that Dyson's equation cannot be simply solved by Fourier transformation. Instead, it has to be solved on the real-time branches of the contour $\mathcal{C}$ as an integro-differential equation, in which the self-energy plays the role of a memory kernel (Eckstein et al., 2010), see Eq. (11). If the full memory is retained, the solution of Dyson's equation scales like the third power in the maximum number N_t of time steps on the real-time branches. In many situations, however, this scaling can be reduced to linear in N_t by the use of memory truncations (Stahl et al., 2022).

In the case of the Hubbard model the effective impurity problem is an Anderson impurity model with action

$$S_{\mathrm{imp}} = \int_{\mathcal{C}} \mathrm{d}t\mathrm{d}t' \sum_\sigma c^\dagger_\sigma(t)\Delta_\sigma(t,t')c_\sigma(t') - \mu\int_{\mathcal{C}}\mathrm{d}t\sum_\sigma n_\sigma(t) + \int_{\mathcal{C}}\mathrm{d}t U(t) n_\uparrow(t) n_\downarrow(t). \tag{44}$$

The local self-energy yields, via the Dyson equation, the momentum-dependent lattice Green's functions $G_k(t,t')$ which may then be used to compute the observables (15)–(20). The impurity model also gives access to the time-dependent double occupation

$$d(t) = \langle n_\uparrow(t) n_\downarrow(t)\rangle, \tag{45}$$

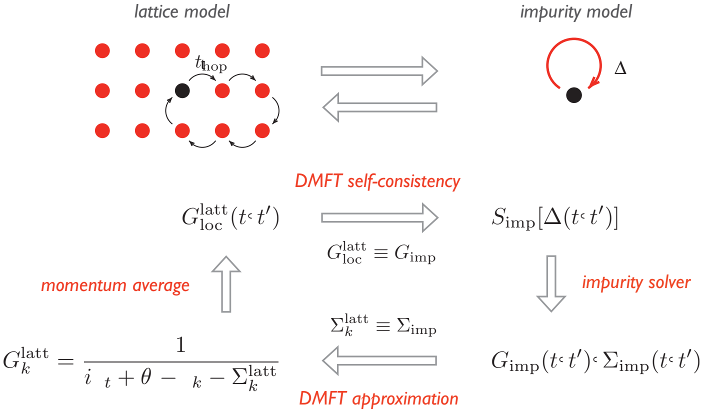
lattice model
impurity model
$t_{\rm hop}$
Δ
DMFT self-consistency
$G^{\rm latt}_{\rm loc}(t, t')$
$S_{\rm imp}[\Delta(t, t')]$
$G^{\rm latt}_{\rm loc} \equiv G_{\rm imp}$
momentum average
impurity solver
$\Sigma^{\rm latt}_k \equiv \Sigma_{\rm imp}$
$G^{\rm latt}_k = \frac{1}{i \;\; t + \theta - \;\; k - \Sigma^{\rm latt}_k}$
$G_{\rm imp}(t, t'), \Sigma_{\rm imp}(t, t')$
DMFT approximation

Fig. 3 Top panel: Self-consistent mapping of a lattice model to an effective impurity model in DMFT. Bottom panel: Selfconsistency loop, where $S_{\rm imp}$ is the impurity action with hybridization function Δ, $G_{\rm imp}$ is the impurity Green's function and $\Sigma_{\rm imp}$ the self-energy of the impurity model. By approximating the self-energy of the lattice $\Sigma^{\rm latt}_{\rm k}$ by the impurity selfenergy, one obtains an approximation for the lattice Green's function $G^{\rm latt}_k$.

and hence the potential energy per site $E_{\rm pot}(t) = Ud(t)$ of the Hubbard model. The kinetic energy can be evaluated directly from the impurity model (Aoki et al., 2014), via a convolution of the impurity Green's function and the hybridization function,

$$E_{\rm kin}(t) = -\mathrm{i}\mathrm{Tr}\left[\mathrm{G}_{\rm imp}{}^{*}\Delta\right]^{<}(tt), \tag{46}$$

where the trace is the sum over the two spin contributions.

Impurity solvers

A numerically challenging task in nonequilibrium DMFT simulations is the solution of the impurity problem, i.e., the calculation of the impurity Green's function or impurity self-energy from the action (44). This subsection presents nonequilibrium impurity solvers which have proven useful in the DMFT context.

Weak-coupling solvers. In weakly correlated systems, perturbative approaches such as the iterated perturbation theory (IPT) (Georges et al., 1996), which corresponds to a second order expansion of the impurity selfenergy, may be adequate. The IPT self-energy of the Hubbard model is given by the first and third diagram in Fig. 1, but evaluated here with bath Green's functions $\mathcal{G}_\sigma(t,t') = [\delta_{\mathcal{C}}(t,t')(i\partial_t + \mu) - \Delta_\sigma(t,t')]^{-1}$ (bare IPT) or with correlated impurity Green's functions $\mathrm{G}_{{\rm imp},\sigma}(t,t')$ (boldified IPT). The boldified version is conserving, but the short-time dynamics is more accurately described by the bare IPT (Eckstein et al., 2010).

The explicit form of the second-order bare IPT selfenergy is

$$\Sigma^{(2)}_\sigma(t,t') = U(t)U(t')\mathcal{G}_\sigma(t,t')\mathcal{G}_{\bar\sigma}(t',t)\mathcal{G}_{\bar\sigma}(t,t'). \tag{47}$$

Weak coupling solvers up to fourth order in U, and with different treatments of the Hartree term, have been discussed and benchmarked in Tsuji and Werner, 2013. As an example of an application of the third-order solver, the right panel of Fig. 2 shows the time evolution of the staggered magnetization m in the moderately correlated Hubbard model after interaction ramps. The setup is the same as for the Hartree calculation illustrated in the left panel. One finds that at early times, the dynamics in DMFT + 3rd order is qualitatively similar to the Hartree solution, in the sense that below a critical final interaction, the order parameter decays monotonically to zero, whereas for interactions above this critical value, there are oscillations around a nonzero value of m. However, in contrast to the Hartree solution, the DMFT result exhibits strongly damped oscillations, and for final interactions $U_f \leq 1.4$ the solution relaxes at long times to a paramagnetic state. Also for larger interactions, like $U_f = 1.4$, the solution eventually approaches a thermalized value with a reduced m, as indicated by the arrow. Hence, DMFT does not only capture the transient trapping in a prethermalized state with a nonthermal value of the order parameter, but also the thermalization dynamics.

QMC solvers. Independent of the interaction strength, an exact solution can in principle be obtained by the weak-coupling continuous-time Monte Carlo method (Rubtsov et al., 2005; Werner et al., 2010). Here, one first re-expresses the local terms of the Anderson impurity model using a spin-dependent chemical potential shift,

$$H_{\rm loc}(t) = U(t)\left(n_\uparrow - \alpha_\uparrow\right)\left(n_\downarrow - \alpha_\downarrow\right) - \sum_\sigma [\mu - U(t)\alpha_{\bar\sigma}]n_\sigma. \tag{48}$$

With a suitable choice of α_σ, this avoids a trivial sign problem in the repulsively interacting case (Rubtsov et al., 2005). The first term proportional to $U(t)$ corresponds to the modified interaction $H_{\rm int}$. Expanding the partition function $Z = \mathrm{Tr}\left[\mathcal{T}_{\mathcal{C}} e^{-\mathrm{i}S_{\rm imp}}\right]$ in powers of $H_{\rm int}$ and separating the trace into spin-up and spin-down factors leads to

$$\frac{Z}{Z_0} = \sum_n \frac{(-\mathrm{i})^n}{n!}\int_{\mathcal{C}} \mathrm{d}t_1 \ldots \int_{\mathcal{C}} \mathrm{d}t_n U(t_1)\ldots U(t_n) \times \prod_\sigma \langle (n_\sigma(t_1) - \alpha_\sigma)\ldots(n_\sigma(t_n) - \alpha_\sigma)\rangle_{S_0}, \tag{49}$$

with $Z_0 = \mathrm{Tr}\left[\mathcal{T}_{\mathcal{C}} e^{-\mathrm{i}S_0}\right]$ and S_0 the noninteracting part of the shifted impurity action. Wick's theorem allows to express the expectation values in Eq. (49) as the determinant of an $n \times n$ matrix M_σ^{-1}, with elements

$$\left(M_\sigma^{-1}\right)_{ij} = -\mathrm{i}\mathcal{G}_{0,\sigma}\left(t_i, t_j\right) - \alpha_\sigma \delta_{ij}, \tag{50}$$

$$\mathcal{G}_{0\sigma}(t,t') = -\mathrm{i}\left\langle \mathcal{T}_{\mathcal{C}} c_\sigma(t) c_\sigma^\dagger(t') \right\rangle_{S_0}, \tag{51}$$

and the convention $\mathcal{G}_{0\sigma}(t,t) \equiv \mathcal{G}_{0\sigma}^<(t,t)$. Eq. (49) therefore expresses $Z/Z_0 = \sum_c w(c)$ as a sum over configurations $c = \{t_1 \prec t_2 \prec \cdots \prec t_n\}$ consisting of collections of (cyclically ordered) time-points on the contour $\mathcal{C}$. The weight of the configuration c is

$$w(c) = (-\mathrm{i})^n (U(t_1)\mathrm{d}t_1) \ldots (U(t_n)\mathrm{d}t_n) \prod_\sigma \det M_\sigma^{-1}. \tag{52}$$

Here, $\mathrm{d}t_i = \mathrm{d}t$ for t_i on the forward branch, $-\mathrm{d}t$ for t_i on the backward branch, and $-\mathrm{i}\mathrm{d}\tau$ for t_i on the imaginary time branch.

A Monte Carlo sampling over all configurations c can be implemented on the basis of these weights (Werner et al., 2009). The determinants in Eq. (52) sum up all the $n!$ connected and disconnected bare diagrams for a given set of n interaction vertices. While this summation (for a proper choice of the α_σ) absorbs the sign cancelations originating from Fermi statistics, the weights $w(c)$ are in general complex. The Monte Carlo sampling thus suffers from a dynamical sign problem. This problem grows exponentially with the length of the real-time contour, and restricts the calculations to relatively short times (Eckstein et al., 2010).

Strong-coupling solvers. A numerically more efficient approximate method for strongly correlated systems sums up a subset of hybridization expansion diagrams. This approach starts from the atomic limit and is thus suitable for the description of Mott insulating states. The lowest order implementation of this scheme is known as the non-crossing approximation (NCA) (Keiter and Kimball, 1971) and the second order implementation as the one-crossing approximation (OCA) (Pruschke and Grewe, 1989). The formulation of these methods and their performance in the nonequilibrium context have been discussed in detail in Eckstein and Werner, 2010. The following discussion presents the main ideas, and the formulas for the NCA.

The partition function of the impurity problem (44), $Z = \mathrm{Tr}\left[\mathcal{T}_{\mathcal{C}} e^{-\mathrm{i}S_{\mathrm{imp}}}\right]$, can be expressed as an infinite sum over strong-coupling diagrams by performing a power series expansion in $\Delta(t,t')$ (Mühlbacher and Rabani, 2008; Werner et al., 2009). The weight of a given diagram is (up to prefactors) given by the product of hybridization functions and a product of atomic propagators, which represent the time evolution between the hybridization events. The subset of diagrams without crossing hybridization lines can be obtained by introducing pseudoparticles (Aoki et al., 2014). The bare pseudo-particle Green's function $\tilde{g}$ is defined as the matrix of atomic propagators in some basis $\{|n\rangle\}$ of the local Hilbert space. Its elements are $\tilde{g}_{mn}(t,t') = -\mathrm{i}\langle m|\mathcal{T}_{\mathcal{C}} e^{-\mathrm{i}\int_{t'}^{t} \mathrm{d}\bar{t} H_{\mathrm{loc}}(\bar{t})}|n\rangle$, where the time arguments on $\mathcal{C}$ need to satisfy the contour ordering $t \succ t'$. $\tilde{G}$ denotes the corresponding boldified pseudo-particle Green's function, which includes the effect of hybridizations. In the lowest order (NCA) approximation, the pseudo-particle self-energy is defined as

$$\tilde{\Sigma}^{\mathrm{NCA}}(t,t') = \mathrm{i}\sum_\sigma \left[\tilde{c}_\sigma^\dagger(t)\tilde{G}(t,t')\tilde{c}_\sigma(t')\Delta_\sigma(t,t') - \tilde{c}_\sigma(t)\tilde{G}(t,t')\tilde{c}_\sigma^\dagger(t')\Delta_\sigma(t',t)\right], \tag{53}$$

where the tildes on the creation and annihilation operators indicate that these are to be understood as matrices in the chosen basis (e.g., $(\tilde{c}_\sigma)_{mn} = \langle m|c_\sigma|n\rangle$). The sum of all noncrossing diagrams can then be expressed in terms of the elements of $\tilde{G}$, which are the solution of the pseudoparticle Dyson equation $\tilde{G} = \tilde{g} + \tilde{g} * \tilde{\Sigma}^{\mathrm{NCA}} * \tilde{G}$, with a cyclic constraint on the time arguments in the convolutions $\left(\text{for } t \succ t', [A * B](t,t') = \int_{\mathcal{C}, t\succ\bar{t}\succ t'} \mathrm{d}\bar{t} A(t,\bar{t}) B(\bar{t},t')\right)$. The time-propagation of the pseudo-particle Green's functions is always in a clockwise direction around the $\mathcal{C}$ contour, such that for $t \prec t'$, the lesser component of $\tilde{G}$ is defined as $\mathrm{i}\xi\tilde{G}(t,0_+)\tilde{G}(-\mathrm{i}\beta,t')$, with ξ a diagonal matrix with elements $+1(-1)$ for pseudo-particles with an even (odd) number of electrons.

The diagonal elements $\mathrm{i}\tilde{G}_{nn}(-\mathrm{i}\beta, 0_+)$ represent the contribution of the basis state $|n\rangle$ to the partition function, so that $Z_{\mathrm{NCA}} = \mathrm{i}\mathrm{Tr}\left[\tilde{G}(-\mathrm{i}\beta, 0_+)\right]$. For the measurement of the impurity Green's function, one inserts a creation operator at t' and an annihilation operator at t and evaluates

$$G_\sigma(t,t') = \frac{\mathrm{i}}{Z_{\mathrm{NCA}}} \mathrm{Tr}\left[\xi\tilde{G}(t',t)\tilde{c}_\sigma(t)\tilde{G}(t,t')\tilde{c}_\sigma^\dagger(t')\right].$$

While NCA produces qualitatively correct results only for strongly correlated systems, where the hybridization can be regarded as a small perturbation, the above procedure can be generalized to higher-order-in-Δ approximations of the self-energy, which systematically converge to the exact result and provide an adequate description in a wide range of parameters (Eckstein and Werner, 2010). A useful property of this approach in nonequilibrium simulations is that it is conserving.

Variants of nonequilibrium DMFT

Floquet DMFT

If a correlated lattice system such as the Hubbard model is driven by a time-periodic electric field or an interaction modulation with frequency Ω, and the injected energy is balanced by dissipation to some heat bath, the system reaches a time-periodic nonequilibrium steady state. Floquet DMFT (Tsuji et al., 2008) allows to describe this steady state directly, without a simulation of the transient evolution starting from some equilibrium state. The Floquet DMFT formalism is implemented on the two-branch Keldysh contour using a so called Floquet matrix representation of $G(t,t')$, $\Sigma(t,t')$ and $\Delta(t,t')$. To define the Floquet representation, one introduces the average time $t_{\mathrm{av}}=(t+t')/2$ and the relative time $t_{\mathrm{rel}}=(t-t')$ and assumes that all the relevant two-time quantities are periodic with respect to t_{av}, with period $\mathcal{T}=\frac{2\pi}{\Omega}$. For example

$$G(t_{\mathrm{rel}},t_{\mathrm{av}}+\mathcal{T})=G(t_{\mathrm{rel}},t_{\mathrm{av}}), \tag{54}$$

and similarly for the self-energy. The Floquet matrix representation of the Green's function is then defined by

$$\underline{G}_{nm}(\omega)=\frac{1}{\mathcal{T}}\int_0^{\mathcal{T}}\mathrm{d}t_{\mathrm{av}}e^{\mathrm{i}(m-n)\Omega t_{\mathrm{av}}}G\Big(\omega+\frac{m+n}{2}\Omega,t_{\mathrm{av}}\Big), \tag{55}$$

where ω is restricted to the "reduced Brillouin zone" $\left[-\frac{\Omega}{2},\frac{\Omega}{2}\right)$. An advantage of this matrix representation is that convolutions of functions satisfying the periodic relation (54) can be expressed as matrix products. The fermionic Dyson equation thus becomes the matrix equation

$$\left[\underline{G}_0^{-1}(\omega)-\underline{\Sigma}(\omega)\right]\underline{G}(\omega)=\underline{I}. \tag{56}$$

For the heat bath, one typically considers a bath of noninteracting fermions with finite bandwidth, or a boson bath. The total self-energy of the system is then defined as $\Sigma_{\mathrm{tot}}=\Sigma_{\mathrm{int}}+\Sigma_{\mathrm{bath}}$, where Σ_{int} is the self-energy obtained from the impurity Dyson equation and Σ_{bath} the self-energy originating from the coupling to the heat bath. The Floquet representation of Σ_{tot} enters as $\underline{\Sigma}$ into the lattice Dyson equation and defines the updated lattice Green's function.

Cluster DMFT

To capture the effect of short-range correlations, cluster extensions of DMFT have been developed. This formalism allows to describe the correlations within a small cluster explicitly, while longer-range correlations are treated at the mean-field level. In the dynamical cluster approximation (DCA) approach (Hettler et al., 1998), which has been applied to non-equilibrium problems (Bittner et al., 2020; Eckstein and Werner, 2016; Tsuji et al., 2014), the self-energy Σ_k^{latt} is approximated as constant within certain regions ("patches") of the first Brillouin zone, and identified with the corresponding momentum components of the cluster (impurity) self-energy: $\Sigma_k^{\mathrm{latt}}(t,t')\approx\sum_K\Sigma_K^{\mathrm{imp}}(t,t')\phi_K(k)$, where $\phi_K(k)=1$ for k inside momentum patch K and zero otherwise. The DCA self-consistency loop for each patch is analogous to Fig. 3, except that the momentum averaging on the lattice side is performed over the corresponding patch, instead of the full Brillouin zone, and that the self-consistency condition identifies this patch-averaged lattice Green's function $G_K^{\mathrm{latt,av}}$ with the cluster impurity Green's function G_K^{imp} for momentum K. The only step in the self-consistency loop where the different momenta are coupled is the solution of the impurity problem, which yields G_K^{imp} and the cluster self-energy Σ_K^{imp}.

For nonequilibrium simulations, the DCA approach is preferred over the cluster DMFT (CDMFT) (Lichtenstein and Katsnelson, 2000) variant, because the diagonal representation in momentum space avoids the memory demanding solution of matrix-valued Dyson equations (Tsuji et al., 2014).

Extended DMFT

The extended DMFT (EDMFT) formalism (Ayral et al., 2013; Si and Smith, 1996; Sun and Kotliar, 2002) allows to treat models with nonlocal interactions, such as the U-V Hubbard model (1) with $V\neq 0$, and the associated dynamical screening effects. Like conventional DMFT, EDMFT maps the lattice system to a single site impurity model, but this model now contains two dynamical mean fields, a fermionic dynamical mean field (hybridization function $\Delta(t,t')$) and a bosonic dynamical mean field, which in the case of the U-V Hubbard model is a self-consistently computed, dynamically screened impurity interaction $\mathcal{U}(t,t')$. These dynamical mean fields are determined by two coupled self-consistency loops, (i) the usual fermionic self-consistency loop which connects the self-energy Σ and (local) Green's function G of the lattice and impurity systems, and fixes Δ, and (ii) a bosonic loop which connects the local polarization Π and local screened interaction W of the lattice and impurity systems, and fixes $\mathcal{U}$. The impurity interaction $\mathcal{U}$ incorporates the effect of nonlocal screening on the local interaction.

A possible nonequilibrium solver for the EDMFT impurity problem is the combined strong/weak-coupling expansion (Golez et al., 2015), where the partition function is expanded in both the hybridization Δ and the retarded part of the interaction, $\mathcal{D}$. In the case of a model with onsite repulsion U the latter is related to the impurity interaction by $\mathcal{U}(t,t')=U\delta_{\mathcal{C}}(t,t')+\mathcal{D}(t,t')$. Within NCA, all the diagrams without crossing Δ and $\mathcal{D}$ lines are summed up, which can be accomplished by defining the pseudoparticle self-energy

$$\tilde{\Sigma}^{\mathrm{NCA}}_{\mathrm{strong/weak}}(t,t')=\tilde{\Sigma}^{\mathrm{NCA}}(t,t')-\mathrm{i}\tilde{n}(t)\tilde{G}(t,t')\tilde{n}(t')\mathcal{D}(t',t), \tag{57}$$

with $\tilde{\Sigma}^{\mathrm{NCA}}$ defined in Eq. (53) and $\tilde{n}$ the representation of the density operator in the chosen basis.

W_{imp} and $\mathcal{U}$ are related through the connected impurity charge-charge correlator $\chi_{\mathrm{imp}}=\langle\mathcal{T}_{\mathcal{C}}\bar{n}(t)\bar{n}(t')\rangle$ (with $\bar{n}=n-\langle n\rangle$) through

$$W_{\mathrm{imp}} = \mathcal{U} - \mathcal{U}^{*}\chi_{\mathrm{imp}}{}^{*}\mathcal{U} \tag{58}$$

while the bosonic self-energy Π is obtained by solving the impurity Dyson equation

$$W_{\mathrm{imp}} = \mathcal{U} + \mathcal{U}^{*}\Pi^{*}W_{\mathrm{imp}}, \tag{59}$$

where * denotes a convolution on the contour $\mathcal{C}$. The bosonic lattice Dyson equation of the EDMFT scheme reads

$$W_k = V_k + V_k{}^{*}\Pi^{*}W_k, \tag{60}$$

with V_k the Fourier transform of the local and nonlocal interaction. For example, for model (1) with nearest neighbor interactions on the square lattice with lattice spacing a, $V_k = U + 2V(\cos(k_x a) + \cos(k_y a))$.

GW+EDMFT

To incorporate nonlocal correlation and screening effects into the single-site EDMFT formalism for the U-V Hubbard model, a possible strategy is to add nonlocal Σ and Π components taken from the GW approximation (Hedin, 1965) and feed the resulting fermionic and bosonic self-energies back into the self-consistency loop (Ayral et al., 2013; Biermann et al., 2003). In this socalled GW+EDMFT formalism, the lattice self-energy and polarization is approximated as

$$\Sigma_{ij}^{\mathrm{latt}} = \Sigma^{\mathrm{EDMFT}}\delta_{ij} + \Sigma_{ij}^{GW,\mathrm{nonloc}}, \tag{61}$$

$$\Pi_{ij}^{\mathrm{latt}} = \Pi^{\mathrm{EDMFT}}\delta_{ij} + \Pi_{ij}^{GW,\mathrm{nonloc}}, \tag{62}$$

with $\Sigma_{ij}^{GW,\mathrm{nonloc}}(t,t') = \mathrm{i}G_{ij}(t,t')W_{ij}(t,t')(1-\delta_{ij})$ and $\Pi_{ij}^{GW,\mathrm{nonloc}}(t,t') = -\mathrm{i}G_{ij}(t,t')G_{ji}(t',t)(1-\delta_{ij})$ computed from the lattice Green's function and screened interaction. Nonequilibrium applications of this scheme (Golez et al., 2017) have shown that the nonlocal polarization significantly enhances the screening in photo-excited systems, compared to EDMFT.

References

Agapito LA, Curtarolo S, and Buongiorno Nardelli M (2015) *Physical Review X* 5: 011006. https://link.aps.org/doi/10.1103/PhysRevX.5.011006.
Alvermann A and Fehske H (2011) *Journal of Computational Physics* 230(15): 5930.
Anderson PW (1958) *Physics Review* 112: 1900. https://link.aps.org/doi/10.1103/PhysRev.112.1900.
Aoki H, Tsuji N, Eckstein M, Kollar M, Oka T, and Werner P (2014) *Reviews of Modern Physics* 86: 779. https://link.aps.org/doi/10.1103/RevModPhys.86.779.
Ayral T, Biermann S, and Werner P (2013) *Physical Review B* 87: 125149. https://link.aps.org/doi/10.1103/PhysRevB.87.125149.
Barankov RA and Levitov LS (2006) *Physical Review Letters* 96: 230403. https://link.aps.org/doi/10.1103/PhysRevLett.96.230403.
Biermann S, Aryasetiawan F, and Georges A (2003) *Physical Review Letters* 90: 086402. https://link.aps.org/doi/https://doi.org/10.1103/PhysRevLett.90.086402.
Bittner N, Golež D, Eckstein M, and Werner P (2020) *Physical Review B* 102: 235169. https://link.aps.org/doi/10.1103/PhysRevB.102.235169.
Bonca J, Maekawa S, and Tohyama T (2007) *Physical Review B* 76: 035121. https://link.aps.org/doi/10.1103/PhysRevB.76.035121.
Cirac JI, Pérez-García D, Schuch N, and Verstraete F (2021) *Reviews of Modern Physics* 93: 045003. https://link.aps.org/doi/10.1103/RevModPhys.93.045003.
Daley A, Kollath C, Schollwock U, and Vidal G (2004) *Journal of Statistical Mechanics: Theory and Experiment* P04005.
Eckstein M and Werner P (2010) *Physical Review B* 82: 115115.
Eckstein M and Werner P (2016) *Scientific Reports* 6: 21235. http://www.nature.com/articles/srep21235.
Eckstein M, Kollar M, and Werner P (2010) *Physical Review B* 81: 115131.
Edwards DM and Miyazaki M (1987) *Journal of Physics F: Metal Physics* 17(12), L311. http://stacks.iop.org/0305-4608/17/i=12/a=002.
Freericks JK, Turkowski VM, and Zlatić V (2006) *Physical Review Letters* 97: 266408.
Freericks JK, Krishnamurthy HR, and Pruschke T (2009) *Physical Review Letters* 102: 136401.
Georges A, Kotliar G, Krauth W, and Rozenberg MJ (1996) *Reviews of Modern Physics* 68: 13.
Giannetti C, Capone M, Fausti D, Fabrizio M, Parmigiani F, and Mihailovic D (2016) *Advances in Physics* 65(2): 58. https://doi.org/10.1080/00018732. 2016.1194044.
Golez D, Eckstein M, and Werner P (2015) *Physical Review B* 92: 195123. https://link.aps.org/doi/10.1103/PhysRevB.92.195123.
Golez D, Boehnke L, Strand HUR, Eckstein M, and Werner P (2017) *Physical Review Letters* 118: 246402. https://link.aps.org/doi/10.1103/PhysRevLett.118.246402.
Gutzwiller MC (1963) *Physical Review Letters* 10: 159. https://link.aps.org/doi/10.1103/PhysRevLett.10.159.
Hedin L (1965) *Physical Review* 139: A796. https://linkaps.org/doi/10.1103/PhysRev.139.A796.
Hettler MH, Tahvildar-Zadeh AN, Jarrell M, Pruschke T, and Krishnamurthy HR (1998) *Physical Review B* 58: R7475.
Joost J-P, Schlünzen N, and Bonitz M (2020) *Physical Review B* 101: 245101. https://link.aps.org/doi/10.1103/PhysRevB.101.245101.
Karlsson D, Privitera A, and Verdozzi C (2011) *Physical Review Letters* 106: 116401. https://link.aps.org/doi/10.1103/PhysRevLett.106.116401.
Keiter H and Kimball JC (1971) *International Journal of Magnetism* 1: 233.
Kjäll JA, Zaletel MP, Mong RSK, Bardarson JH, and Pollmann F (2013) *Physical Review B* 87: 235106.
Kohn W and Sham LJ (1965) *Physical Review* 140: A1133. https://link.aps.org/doi/10.1103/PhysRev.140.A1133.
Lanczos C (1950) *Journal of Research of the National Bureau of Standards* 45: 255.
Lichtenstein AI and Katsnelson MI (2000) *Physical Review B* 62: R9283. https://link.aps.org/doi/10.1103/PhysRevB.62.R9283.
Liechtenstein AI, Anisimov VI, and Zaanen J (1995) *Physical Review B* 52: R5467. https://link.aps.org/doi/10.1103/PhysRevB.52.R5467.
Lipavsky P, Spicka V, and Velicky B (1986) *Physical Review B* 34: 6933.
Mühlbacher L and Rabani E (2008) *Physical Review Letters* 100: 176403. https://link.aps.org/doi/10.1103/PhysRevLett.100.176403.
Murakami Y, Takayoshi S, Koga A, and Werner P (2021) *Physical Review B* 103: 035110.
Park TJ and Light JC (1986) *The Journal of Chemical Physics* 85: 5870.
Peierls R (1933) *Zeitschrift für Physik* 80: 763.
Pruschke T and Grewe N (1989) *Zeitschrift fuer Physik B* 74: 439.
Rubtsov AN, Savkin VV, and Lichtenstein AI (2005) *Physical Review B* 72: 035122.
Runge E and Gross EKU (1984) *Physical Review Letters* 52: 997. https://link.aps.org/doi/10.1103/PhysRevLett.52.997.

Schlünzen N, Joost J-P, and Bonitz M (2020) *Physical Review Letters* 124: 076601. https://link.aps.org/doi/10.1103/PhysRevLett.124.076601.
Schollwöck U (2011) *Annals of Physics* 0003-4916326(1): 96. January 2011 Special Issue https://www.sciencedirect.com/science/article/pii/S0003491610001752.
Shinjo K and Tohyama T (2017) *Physical Review B* 96: 195141. https://link.aps.org/doi/10.1103/PhysRevB.96.195141.
Si Q and Smith JL (1996) *Physical Review Letters* 77: 3391. https://link.aps.org/doi/10.1103/PhysRevLett.77.3391.
Stahl C, Dasari N, Li J, Picano A, Werner P, and Eckstein M (2022) *Physical Review B* 105: 115146. https://link.aps.org/doi/10.1103/PhysRevB.105.115146.
Stefanucci G and van Leeuwen R (2013) *Nonequilibrium Many-Body Theory of Quantum Systems: A Modern Introduction*. Cambridge University Press.
Sun P and Kotliar G (2002) *Physical Review B* 66: 085120. https://link.aps.org/doi/10.1103/PhysRevB.66.085120.
Tancogne-Dejean N, Oliveira MJT, and Rubio A (2017) *Physical Review B* 96: 245133. https://link.aps.org/doi/10.1103/PhysRevB.96.245133.
Trugman SA (1988) *Physical Review B* 37: 1597. https://link.aps.org/doi/10.1103/PhysRevB.37.1597.
Tsuji N and Werner P (2013) *Physical Review B* 88: 165115. https://link.aps.org/doi/10.1103/PhysRevB.88.165115.
Tsuji N, Oka T, and Aoki H (2008) *Physical Review B* 78: 235124. https://link.aps.org/doi/10.1103/PhysRevB.78.235124.
Tsuji N, Eckstein M, and Werner P (2013) *Physical Review Letters* 110: 136404. https://link.aps.org/doi/10.1103/PhysRevLett.110.136404.
Tsuji N, Barmettler P, Aoki H, and Werner P (2014) *Physical Review B* 90: 075117. https://link.aps.org/doi/10.1103/PhysRevB.90.075117.
Vidal G (2004) *Physical Review Letters* 93: 040502. https://link.aps.org/doi/10.1103/PhysRevLett.93.040502.
Vidal G (2007) *Physical Review Letters* 98: 070201.
Werner P, Oka T, and Millis AJ (2009) *Physical Review B* 79: 035320.
Werner P, Oka T, Eckstein M, and Millis AJ (2010) *Physical Review B* 81: 035108.
White SR (1992) *Physical Review Letters* 69: 2863. https://link.aps.org/doi/10.1103/PhysRevLett.69.2863.
White SR and Feiguin AE (2004) *Physical Review Letters* 93: 076401. https://link.aps.org/doi/10.1103/PhysRevLett.93.076401.
Yuzbashyan EA and Dzero M (2006) *Physical Review Letters* 96: 230404.
Zawadzki K and Feiguin AE (2019) *Physical Review B* 100: 195124. https://link.aps.org/doi/10.1103/PhysRevB.100.195124.

1/f noise in quantum nanoscience

Giuseppe Falci[a,b,c], **Pertti J Hakonen**[d,e], **and Elisabetta Paladino**[a,b,c], [a]Physics and Astronomy Department "Ettore Majorana", University of Catania, Catania, Italy; [b]INFN Catania Section, Catania, Italy; [c]CNR-IMM, Catania (University) Unit, Catania, Italy; [d]Low Temperature Laboratory, Department of Applied Physics, Aalto University, Otaniemi, Finland; [e]InstituteQ—The Finnish Quantum Institute, Espoo, Finland

© 2024 Elsevier Ltd. All rights reserved.

Introduction **1003**
Theoretical overview **1005**
1/f noise in nanoscience **1006**
Noise in quantum circuits 1008
Superconducting quantum interference devices 1008
Single electron tunneling devices 1009
1/*f* Noise in quantum-coherent nanodevices **1009**
Artificial atoms 1009
Quantum sensing 1011
Noise spectroscopy 1013
Conclusion **1013**
References **1014**

Abstract

Fundamental issues of $1/f$ noise in quantum nanoscience are reviewed starting from basic statistical noise processes. Fundamental noise models based on two-level systems (TLSs) are described. We emphasize the importance of TLSs in materials parameter fluctuations, such as dielectric constant. The present understanding of $1/f$ noise in superconducting quantum interferometers and in single electron devices is summarized. For coherent quantum nanoscience, we introduce superconducting qubits and the relation between decoherence and $1/f$ noise using the filter function formulation. We also clarify the qubit noise spectroscopy and emphasize the importance of materials with reduced $1/f$ noise for future quantum coherent nanodevices.

Key points

- Basic characteristics of $1/f$ noise in condensed matter systems
- Theoretical issues concerning stationarity, ergodicity, and TLS with uniform distribution for tunneling parameter
- Specific features of $1/f$ noise in nanoscale systems and quantum materials
- Significance of TLS for dissipation in superconducting materials for low-loss quantum circuits
- $1/f$ noise in quantum circuits and devices, both in the flux and charge fluctuation regimes
- Influence of $1/f$ noise on coherence properties of qubits
- Role of low-frequency fluctuations in quantum sensing

Introduction

Fluctuations with power spectral density $S(f)$ increasing with decreasing frequency have been observed in a great variety of systems from physics, electronic engineering, and biology to music, economic, and social sciences, even medicine. Solid-state materials and devices have formed the supreme arena where the command of the physics of low-frequency fluctuations has been deeply exploited. Strong motivation comes from both the fundamental research and the quest for electronic devices with improved performance. The advent of modern nanoscience has opened a new era in which this subject has entered the realm of quantum coherence.

Measurements of fluctuations in a vast number of physical systems yield a noise spectral density of the form

$$S(f) = C\, f^{-\alpha} \tag{1}$$

with α ranging from 0 to 2, down to the lowest measured frequencies $\sim \mu$Hz. Since values of $\alpha \approx 1$ are typically observed, the phenomenon is called $1/f$ noise. The alternative terms "flicker noise" or "excess noise" are less frequently used.

In solid-state materials and devices, fluctuations of transport and dielectric properties exhibit a $\sim 1/f$ spectrum in addition to intrinsic thermal noise and quantum (shot) noise (see Fig. 1). They share the same distinctive features such as the frequency dependence of the noise, the time dependence of correlations, weak stationarity, and other statistical properties.

https://doi.org/10.1016/B978-0-323-90800-9.00250-X

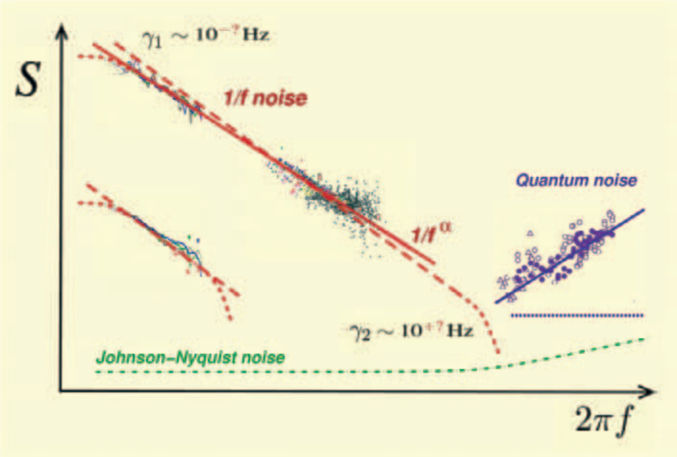

Fig. 1 Qualitative representation of noise spectrum in coherent nanodevices on a log–log scale. *Lines* describe the expected behavior in different frequency ranges. *Dots* represent typical observations in frequency windows depending on the noise detection method (*different symbols* and *dots*), see discussion in section "1/f noise in quantum-coherent nanodevices." *Long-dashed lines* indicate the 1/*f* dependence between the intrinsic low- and high-frequency cutoffs γ_1 and γ_2, which in general are not known. *Thick lines* indicate the $1/f^{\alpha}$ dependence, with $\alpha \approx 0.9$. Ω denotes the typical qubit splitting, of the order of 10^{10} Hz in superconducting qubits. In this range, quantum noise is commonly white or Ohmic (*dotted* and *thin lines*). The *dash-dotted line* indicates the linearly increasing Johnson–Nyquist noise.

With the advent of nanofabrication technologies, the number of devices and electronic components showing excess low-frequency noise have increased, and they all share the features of the ubiquitous 1/*f* noise. Charge fluctuations with 1/*f* spectrum in substrate materials have been found to influence devices operating in the Coulomb blockade regime where quantized charge in a small, weakly coupled conducting island is acting as the quantum mechanical observable. In the regime of superconducting coherence, flux noise generates unwanted currents with 1/*f* character, which is detrimental in many magnetic field sensors and superconducting qubits. Also, various heterostructures (including e.g., field effect (FET) and high-electron-mobility transistor (HEMT) structures), either based on materials deposition, modulation doping, or stacking of atomically layered two-dimensional (2D) materials, display 1/*f* noise in the number of charge carriers owing to charge traps in the vicinity of the active device channel. Beyond electronic and physical systems, 1/*f* noise is found even in healthy human heartbeat rates.

The appearance of 1/*f*-like behavior in many phenomena of diverse nature and its scale invariance, that is, the fact that each decade of frequencies contains the same integrated power, suggested that a common, deeper level description may exist, such as for the universality of the exponents in critical phenomena, that is, that 1/*f*-like behavior is an inherent property of all systems and that a universal minimum frequency exists. However, the large amount of experimental data in solid-state systems indicates that there is no universal spectrum of low-frequency noise.

In modern electronic devices, small active volume bistable switching of the resistance called random telegraph noise (RTN) is observed. The phenomenon is attributed to capture and emission processes from defects suggesting a possible microscopic mechanism of 1/*f* noise. In fact, in many solid-state systems, experiments are satisfactorily explained by the combined action of many bistable defects or traps. The distribution of the observed physical characteristics accounts for the rather large range of time constants generating 1/*f* noise.

Besides universality, other fundamental problems have been posed as the necessary existence of low-frequency cutoff to avoid unphysical divergencies and the related questions of stationarity. On the experimental side, it is often difficult to give an unambiguous interpretation of data as the ensemble-averaged power spectra provide incomplete information on individual fluctuators.

While for metals and spin glasses, some understanding of the mechanism of 1/*f* noise has been developed, the problem is still unsolved for the majority of physical systems. Advances in the study of the microscopic nature are of practical importance since 1/*f* noise limits the performance of high-end electronic devices and sensors at low frequencies. Devices for metrological applications are also affected since their high operating frequencies show fluctuations with 1/*f* spectrum.

This chapter focuses on 1/*f* noise in *quantum nanoscience*. Quantum nanoscience comprises natural or engineered nanoscale systems whose functionality and structure can only be explained through quantum mechanisms such as discretization, superposition, and entanglement (definition from Milburn and Woolley, 2008). These quantum properties facilitate, among other things, the enormous power of quantum information processing as well as novel quantum sensors. However, superposition states are fragile and quickly destroyed by 1/*f* noise, which needs to be considered for their functional applications. Our scope here is to discuss first the influence of 1/*f* noise on "traditionally-behaving" nanodevices and sensors, and then describe specific features encountered in the quantum coherent case.

New fundamental problems related to 1/*f* noise arise in quantum nanoscience and quantum information since the flicker noise may be the main source of decoherence present. For coherent quantum devices such as qubits, this has led to original ways for quantifying the impact of 1/*f* noise on the qubit, and to strategies for recovering the coherence using well-chosen pulse sequences.

Progress in quantum nanoscience has also provided new tools for the characterization of 1/*f* noise sources. Nanoelectronic devices can be employed for example to detect charge noise at the micro electron charge level, thereby allowing to chart substrate characteristics in terms of trap states or fluctuators modeled by two-level systems (TLSs). Coherent TLSs, qubits, on the other hand, can be employed as spectrometers detecting electromagnetic noise over a large span of frequencies. Qubits as spectrometers provide an excellent means to address the dynamics of impurity spins, which often form the culprit for coherence in quantum nanosystems.

Theoretical overview

For a stochastic process $x(t)$ gated in a time window T, $x(t) \neq 0$ for $|t| < T/2$, the power spectrum $S_x(f)$, representing the spectral resolved ensemble-averaged power of the signal, is independent on T if and only if the stochastic process is stationary. For $1/f$-like noise the statistical properties change slightly over time scales typically slow relative to the observation times. Thus it is considered a wide-sense (or weakly) stationary process, that is, the correlation functions up to second order are (nearly) invariant for time translation. Then Wiener–Khintchine theorem applies, stating that $S_x(f)$ is given by the unilateral Fourier transform of the autocorrelation function

$$\phi_x(\tau) := \langle \delta x(t+\tau)\, \delta x(t) \rangle = \int_0^\infty \frac{d\omega}{2\pi}\, S_x(\omega)\, \cos(\omega\tau). \tag{2}$$

The integrated power in the spectrum between two frequencies $[f_1, f_2]$ is given by

$$P_x(f_1, f_2) = \int_{f_1}^{f_2} \frac{d\omega}{2\pi}\, S_x(\omega) = C_x \, \ln\left(\frac{f_2}{f_1}\right) \tag{3}$$

implying that the integrated power per decade of frequencies is constant, a property known as scale invariance. The autocorrelation function for $\tau = 0$ yields the variance $\langle (\delta x)^2 \rangle$ of the stochastic process which according to Eq. (3) diverges logarithmically both at low and at high-frequencies. This divergence is known as a "paradox" of $1/f$ noise. Of course, the experimentally observed variance is finite since the frequency band for measurements is limited. Indeed it is bounded from below due to the finite duration of the realization of $x(t)$ being measured whose maximum value is set by the overall measurement time t_m. On the other hand, at large frequencies $1/f$ noise becomes much smaller than other contributions to fluctuations and it is not measurable; thus high frequencies are also cut off. This may happen at frequencies ranging from $\sim 10^2$ to $\sim 10^7$ Hz in different systems.

It is worth stressing that there is no experimental evidence for the existence of a low-frequency cutoff f_c. Therefore, strictly speaking the stationarity of the process is still an open question. Difficulties are due to the fact that measuring the low-frequency part of the spectrum, say down to the sub-μHz range, would require a duration $t_m \sim 1/f_c$ of weeks. Therefore experimental statistical quantities depend on t_m. In particular this applies to the variance, $\langle (\delta x)^2 \rangle = C_x \, \ln(f_2 t_m)$, which increases logarithmically with t_m. This is another peculiar property of $1/f$ noise of experimental relevance. In particular, it may have a large impact on applications in coherent nanodevices where large fluctuations produce strong dephasing. From the mathematical point of view, this behavior of statistical quantities implies that $1/f$-like noise is not strictly stationary; thus it is also nonergodic. On the other hand, the logarithmic dependence on t_m is weak enough to determine weak stationarity allowing the use of the Wiener–Khintchine theorem which relates the power spectra to correlation functions accessed experimentally. These latter show strongly nonexponential behavior decaying logarithmically with time in the important range $f_2^{-1} < t < t_m < f_c^{-1}$, another feature observed in several experiments.

Understanding the microscopic nature of $1/f$ noise is a key problem both from the fundamental point of view and for applications aiming at fabricating improved electronic and coherent devices for modern nanoscience. Typically, models for $1/f$ noise in the solid state are based on a collection of TLSs describing bistable defects or trap states with a wide distribution of tunneling rates (Dutta and Horn, 1981; Kogan, 1996; Weissman, 1988; Koelle et al., 1999; Grasser, 2020). A large collection of such states with broadly distributed parameters generates wide band $1/f$ noise and in what follows we will draw this connection.

Fluctuations of a bistable defect are described by a stochastic process $x_i(t) = \pm 1$ characterized by a single relaxation rate γ_i. Its kinetics leads to RTN where correlations decay exponentially, $\phi_i(\tau) = \exp(-\gamma_i \tau)$, yielding the Lorentzian spectral density

$$S_i(f) = 4\int_0^\infty d\tau\, \phi_i(\tau)\, \cos(2\pi f \tau) = \frac{4\gamma_i}{(2\pi f)^2 + \gamma_i^2}$$

as given by the Wiener–Khintchine theorem. The overall noise is constructed as a linear superposition of these relaxation processes, $x(t) = \sum_i p_i x_i(t)$, and its power spectrum is given by

$$S_x(f) = \sum_i p_i \, S_i(f) \; \rightarrow \; \int_0^\infty d\gamma \, p(\gamma) \, \frac{4\gamma}{(2\pi f)^2 + \gamma^2}$$

where we have allowed for a continuous distribution of relaxation rates. Since $\langle (\delta x)^2 \rangle = \int_0^\infty df \, S_x(f) = \int_0^\infty d\gamma \, p(\gamma)$, the quantity $p(\gamma)\, d\gamma$ is the contribution to the variance of processes with rates in the interval $[\gamma, \gamma + d\gamma]$. For a weighting function $p(\gamma) = C_x/\gamma$ in the interval $[\gamma_1, \gamma_2]$ and vanishing elsewhere we obtain

$$S_x(f) = \int_{\gamma_1}^{\gamma_2} \frac{4C_x \, d\gamma}{(2\pi f)^2 + \gamma^2} = \begin{cases} \text{const} & f \ll \dfrac{\gamma_1}{2\pi} \\ C_x/f & \dfrac{\gamma_1}{2\pi} \ll f \ll \dfrac{\gamma_2}{2\pi} \\ \dfrac{C_x(\gamma_2 - \gamma_1)}{(\pi f)^2} & \dfrac{\gamma_2}{2\pi} \ll f \end{cases} \tag{4}$$

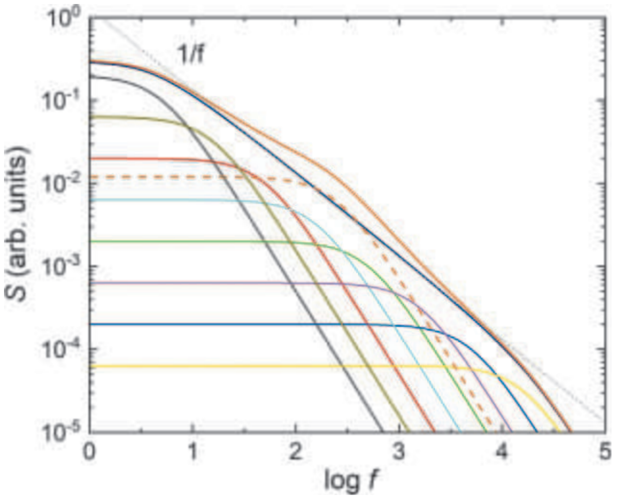

Fig. 2 Power spectral density of individual bistable fluctuators (*colored solid curves*) whose combined effect (*black solid curve*) yields close to $1/f$ spectrum (indicated by *dashed black line*). If one of the fluctuators is more strongly coupled (*dashed orange*) a bump appears in the whole power spectrum (*solid orange curve*).

reproducing the $1/f$ behavior for intermediate frequencies, $\gamma_1 \ll 2\pi f \ll \gamma_2$ (see Fig. 2). Notice that the extremal rates γ_1 and γ_2 provide soft frequency cutoffs to $S_x(f)$, avoiding the divergence of $\langle(\delta x)^2\rangle$. They are easily identified for a finite system of discrete fluctuators. We have still to justify the form of $p(\gamma)$ which is the other key assumption determining the $1/f$ behavior of the power spectrum. In the Mc Worther model (McWhorter, 1957) for semiconductors, the kinetics is modeled as tunneling processes. The rates have the form $\gamma(z) = \gamma_0 \exp(-z/C)$ depending on the parameter z summarizing the exponential dependence on the width and on the height of the tunnel barriers. Now, if z is distributed uniformly in the interval $[z_2, z_1]$, then $p(\gamma) = C/\gamma$ in $[\gamma(z_1), \gamma(z_2)]$. The same result is obtained if the kinetics stems from thermal activation, $\gamma(E) = \gamma_0 \exp(-E/k_B T)$, assuming that the activation energies E are uniformly distributed as originally proposed by Du Pré and by Van der Ziel (Du Pré, 1950; Van Der Ziel, 1950). Notice that this picture naturally accounts for the weak stationarity (implying nonergodicity) of $1/f$ noise since during the measurement, the TLSs with relaxation rates $\gamma < 1/t_m$ are frozen in some nonequilibrium configuration.

Specific models for $1/f$ noise based on quantum TLSs interacting with phonons (in insulating solids) or electrons (in metals) yielding physically motivated distributions of parameters have been used to explain observed properties of $1/f$ noise. These models apply in rater simple situations of noninteracting impurities while in general, the physical properties of disordered systems depend on their many-body nature. Still, the $1/f$ behavior in the solid-state appears to be a consequence of the universal properties of the kinetics rather than the universality of low-frequency fluctuations (Kogan, 1996).

Finally, we remark that noise from a collection of TLSs is not Gaussian. The Gaussian limit is approached when the noise is generated by a sufficiently large number of independent fluctuators each of which contributes negligibly to the variance. Non-Gaussianity in $1/f$ noise has been observed in different nanosystems, although it poses experimental challenges since it requires finite-bandwidth measurement with large observation times t_m (Weissman, 1988). On the other hand, resolving the contribution of individual fluctuators is needed in view of miniaturization and of the study of the impact of $1/f$ fluctuators on the reliability of quantum architectures. Non-Gaussian features of $1/f$ noise and their impact on phase-coherent quantum systems are discussed in depth in Paladino et al. (2014).

1/f noise in nanoscience

The relative $1/f$ resistance fluctuations $\delta R/R$ have been found to decrease as 1/Volume in bulk materials. Similarly, the relative $1/f$ current noise in FETs has been observed to scale as $\propto$ 1/Area of the gate electrode. So inevitably, the role of $1/f$ noise will grow when going to nanoscale quantum devices. Lately, nano-scale FETs have been fabricated using heterostructures of atomically thin 2D materials. In such components, the surface-to-volume ratio becomes the largest, which may lead to major issues with the quality of surfaces or interfaces in such nanodevices. As Wolfgang Pauli said “God made the bulk; surfaces were invented by the devil,” this statement becomes more and more relevant when entering the nanoscale regime.

Quantized conductance in nanoscience (mostly 1D or 2D transport) is typically described using the Landauer–Büttiker formalism (Datta, 1997), in which current is given as a sum over transmission channels with transmission τ_{ik}: $I = \Sigma \tau_{ik} G_0$, where $G_0 = 2e^2/h$ and the indices k and i refer to subbands and quantized states within them, respectively. If we take only one channel with transmission τ, the conductance can be written as $G^{-1} = (1-\tau)/\tau + G_0^{-1}$, where the first term is the four-terminal resistance and the second term describes the contact resistance for perfect contacts. Since contact resistance is constant, fluctuations in τ yield $\delta R/R = -\delta\tau/\tau$ both for the two- and four-lead resistance R. If the fluctuations in transmission channels are independent, we may add fluctuations of the channels incoherently, which yields $\delta G^2 = \Sigma\, \delta\tau_{ik}^2\, G_0^2$. Each fluctuating channel can have its own frequency dependence, which in the simplest case is Lorentzian with a cut-off given by a characteristic two-level fluctuator frequency f_{ik}^c (see below). If the cut-off frequencies f_{ik}^c are distributed uniformly on log-scale, summation over all $\delta\tau_{ik}(f)$ yields a $1/f$ noise spectrum in transmission. In practice, contacts are not ideal and may also have fluctuations. In the nearly ballistic limit, the nonidealities of contacts can be integrated into the transmission values τ_{ik}, and no distinction between scattering in the contact vs. the channel needs to be made.

The conductance in diffusive electrical transport can be written as $G = eN\mu$ where N is the total number of charge carriers and μ is their mobility; e is the electron charge. Therefore, the conductance variation is due to either mobility or carrier number fluctuations:

$$\delta G = eN\delta\mu + e\mu\delta N \tag{5}$$

In bulk metallic conductors, N can be made very large, and the relative fluctuations coming from carrier number can be made to vanish as $1/\sqrt{N}$. However, when the sample size is brought toward the nano regime, the dominance of mobility fluctuations is suppressed and both contributions have to be taken into account. Carrier number is varied by tunneling into trap states that reside in the nearby dielectric, for example in the gate dielectric of a MOSFET transistor. In a small quantum device, such as a quantum point contact (QPC), the trap state may result in distinct RTN signature in the resistance (see Section "Theoretical overview"). The RTN noise in a QPC can be described using Machlup's formula for a single two-level fluctuator (Machlup, 1954):

$$S_G(f) = [G_{\tau_1} - G_{\tau_2}]^2 \frac{w_1 w_2 \tau}{1 + (2\pi f \tau)^2} \tag{6}$$

where w_1 and $w_2 = 1 - w_1$ denote the probabilities for finding the QPC in conductance states G_{τ_1} and G_{τ_2}, respectively while $1/\tau$ denotes the total transition rate between the conductance states (sum of back and forth rates).

Even though nanoscience devices are small, more than one fluctuator is typically acting on them. The McWhorter model is obtained by considering a collection of single fluctuators which have an equal strength and a uniform distribution of corner frequencies $f_c = 1/(2\pi\tau)$ on logarithmic scale. The resulting $1/f$ spectrum is given in Eq. (4), where $1/\tau$ corresponds to γ.

This $1/f$ spectrum will cover a large frequency span provided that the trap lifetimes $[\tau_1 \ldots \tau_2]$ are distributed over a wide range. In the standard McWhorter model, the trapped charge is set to one electron charge e, but with separate TLSs, the charge change in the device induced by the fluctuators may be a fraction of e, which reduces the prefactor C_x in Eq. (4). The McWhorter model has been successfully applied to semiconductor devices and, indeed, good agreement is obtained between experimental results in MOSFETs and the model (Burstein et al., 1957; Grasser, 2020).

Typically, the noise is given as relative fluctuations $\left(\frac{\delta G}{G}\right)^2 = \left(\frac{\delta R}{R}\right)^2 = \left(\frac{\delta N}{N}\right)^2 + \left(\frac{\delta\mu}{\mu}\right)^2$, that is, scaled by the total conductance of the system. Ideally, the scaling conductance should be ruled by those processes which are governing the fluctuations. Unfortunately, this is not always the case and then the relevant scattering processes should be separated from the data before scaling. Theories can also incorporate correlations between carrier number and mobility fluctuations. The fluctuations are correlated because an electron in the trap state can also modify the scattering governing the mobility of the sample. This is common in 2D material FETs, for example, fabricated using graphene (Balandin, 2013).

Good electrical contacting is difficult to achieve in nanosamples. Consequently, the low-frequency noise formula in Eq. (5) has to be supplemented by the contact noise term, which adds incoherently with the noise arising from the nanodevice. For the relative fluctuations in the total conductance G_T, one obtains then $\left(\frac{\delta G_T}{G_T}\right)^2 = \frac{R_c^2}{(R+R_c)^2}\left(\frac{\delta R_c}{R_c}\right)^2 + \frac{R^2}{(R+R_c)^2}\left(\frac{\delta R}{R}\right)^2$ in which $R = 1/G$ and R_c denote the sample and contact resistance, respectively, and the weighting factor of the relative contact noise $\frac{\delta R_c}{R_c}$ grows with the ratio $\frac{R_c}{(R+R_c)}$.

Both $\delta\mu$ and δN in Eq. (5) may depend on temperature, which can lead to low-frequency conductance fluctuations owing to temperature fluctuations δT (Kogan, 1996). The influence of δT fluctuations is expected to increase in small nanodevices, because $\langle \delta T^2 \rangle \propto k_B T^2/C$ where C is the heat capacity of the system. These temperature fluctuations can, for example, limit the ultimate energy resolution in nanosized calorimeters, as discussed in Karimi et al. (2020).

TLSs discussed in Section "Theoretical overview" lead to noise and dissipation both in acoustic and electric systems. The acoustic coupling is due to strain fields (elastic dipole moment) that every TLS possesses when embedded into elastic material (Müller et al., 2019). Some of the TLSs possess also an electric dipole moment, which makes them a source of $1/f$ noise in electrical circuits, both for the conductance noise and for fluctuations in dielectric properties of materials (Zmuidzinas, 2012; Müller et al., 2019). Therefore, TLSs make a contribution to the real and imaginary parts of the dielectric constant $\varepsilon_{TLS}(f, T)$. In weak electric fields, the loss tangent $\delta_{TLS}(f, T)$ of the dielectric constant is dominated by TLS energies close to hf:

$$\delta_{TLS}(f, T) = \frac{\Im\varepsilon_{TLS}(f, T)}{\Re\varepsilon} = \delta_0 \tanh\left(\frac{hf}{2k_B T}\right) \tag{7}$$

where the hyperbolic tangent describes the equilibrium population difference of the two levels and δ_0 is the intrinsic loss parameter proportional to the density of TLS per unit volume and energy. If the asymmetry and tunneling parameters of two-level states are uniformly distributed in energy as assumed in the standard tunneling model (Müller et al., 2019), the low-temperature loss tangent becomes independent of frequency. In the limit $k_B T \gg hf$, the upper state will become populated, leading to $\delta_{TLS}(f, T) \propto hf/k_B T$. Clearly, the role of TLSs in dissipation vanishes when $f \to 0$. According to Kramers–Kronig relations, Eq. (7) can be utilized to obtain the reactive part of $\varepsilon_{TLS}(f, T)$, and the equations for fluctuations of reactance (capacitance) can be derived (Zmuidzinas, 2012).

The capacitance modulation due to TLSs provides an efficient means to investigate two-level fluctuators and the ensuing $1/f$ noise using superconducting microwave cavities (Zmuidzinas, 2012; Müller et al., 2019; Wang et al., 2020). Furthermore, understanding the performance limits of such cavities is vital because high-quality superconducting microwave cavities are critical elements for efficient qubit readout (Blais et al., 2021) and kinetic inductance detectors for sensitive bolometry or single photon detection (Ulbricht et al., 2021). A summary of recent results obtained for the loss tangent is given in Wang et al. (2020) for several dielectric and superconducting materials that are relevant for coherent quantum nanoscience. Most recently, promising results have been obtained for superconducting tantalum (Place et al., 2021); in comparison to Nb, this is assigned to more kinetically limited and chemically robust oxides in Ta (de Leon et al., 2021).

Measurement power is known to modify the influence of TLSs (Wang et al., 2020). Dissipation in a superconducting material is first governed by TLSs, but increasing power leads to the creation of quasiparticles that dominate losses at high rf power. On the other hand, when there are spatial variations in the superconducting order parameter, that is, the superconducting gap, it is possible to have quasiparticles trapped into local minima of this gap variation. In fact, TLSs due to trapped quasiparticles on the surface of Al superconductor have been observed to produce low-energy TLSs up to energies of h × 20 GHz (de Graaf et al., 2020). The observed-level separation agrees with theoretical values obtained using estimates of the second derivative of the spatial variation of the gap (de Graaf et al., 2020).

In standard TLS models, the number of two-level states N is evenly distributed in energy, that is, the density of states $\mathfrak{N}(E) = dN/dE = \text{const}$. Plenty of experiments have been performed to test this hypothesis (Dutta and Horn, 1981). In quantum nanodevices, there are recent experiments that indicate an energy-dependent density of states $\mathfrak{N}(E)$ (Müller et al., 2019). Energy dependence can arise for example from interactions between TLSs, which yields an Efros–Shklovskii type of pseudogap at small energies. There are indications that $\mathfrak{N}(E) \propto E^{\alpha/2}$ with $\alpha \sim 0.2$–0.7; the same exponent appears also in the temperature dependence of $1/f$ noise $S_V \propto 1/T^{\alpha}$ (Burnett et al., 2014; Müller et al., 2019), which leads to increase of $1/f$ noise with decreasing T.

Surface spins, such as physisorbed atomic hydrogen, have been found to behave as TLSs that cause significant dielectric and flux noise. Removal of surface adsorbants by suitable physical or chemical treatment has led to a factor of 10 reduction in frequency fluctuations of a microwave cavity at ~ 5 GHz frequency (de Graaf et al., 2018). The scaling of $1/f$ as $\propto$ Area is quite conspicuous in superconducting quantum nanoscience, for example in the superconducting loops SQUIDs (Superconducting Quantum Interference Devices, see Section "Noise in quantum circuits"). It is also becoming apparent that surfaces and interfaces impose large noise contributions in superconducting microwave circuits, which may even dominate the defect/impurity contributions scaling with volume.

Besides TLSs, nonequilibrium quasiparticles may cause excess noise and losses in superconductors. In general, the number of quasiparticles observed in superconducting films at $T \lesssim 150$ mK amounts to $10^{-8} \dots 10^{-6}$ per Cooper pair, which is clearly larger than predicted from the BCS theory for a superconductor in equilibrium with the environment at $T = 10$ mK. The reason for excess quasiparticles is not fully resolved yet, but recent experiments have indicated that nonequilibrium phonons, created by, for example, cosmic rays, do play an essential role in the process (McEwen et al., 2022).

Noise in quantum circuits

Quantum circuits are based on two canonically conjugate variables, charge Q and flux Φ (see Section "Artificial atoms"). The strength of quantum fluctuations in these variables depends on the impedance of the quantum circuit Z_0. If Z_0 is large (fluctuations for the impedance $Z_0 = \sqrt{L/C}$ are derived from corresponding LC oscillator, Devoret, 1995), the fluctuations of charge are given at the quantum limit by $\langle \delta Q^2 \rangle = \frac{\hbar}{2Z_0}$ while the fluctuations for flux amount to $\langle \delta \Phi^2 \rangle = \frac{\hbar Z_0}{2}$. Hence, quantum circuits at large Z_0 are susceptible to external charge noise while external flux noise is detrimental in the case of small Z_0.

Flux noise is produced by resistance fluctuations when current is passed through a normal conductor. In metallic conductors, the commonly accepted view is that $1/f$ noise is determined entirely by fluctuations in charge carrier mobility (Hooge et al., 1981). In addition to models based on localized states and fluctuating scattering cross sections (Hooge, 1994), there are more refined models based on a modification of electronic wave interference induced by a defect displacement by a hopping event. These models, the universal conductance fluctuation noise and local interference noise model, have been quite successful in accounting for many experimental observations in metals with defects as summarized in Giordano (1989).

Superconducting quantum interference devices

Classical SQUIDs are inherently low impedance devices, which is highlighted by the small shunt resistance inserted in them for stabilization of their phase dynamics. Hence, their ultimate sensitivity is limited by the low-frequency flux noise, or alternatively by internal fluctuations of the Josephson energy of the tunnel barriers. Low-frequency noise in SQUIDs displays distinct $1/f^{\alpha}$ behavior (Wellstood et al., 1987; Cantor and Koelle, 2004). In spite of 50 years of investigations, the origin of flux noise in SQUIDs is still poorly understood. It has been found that its power law exponent α varies substantially around $\alpha = 1$, and the exponent displays strong temperature dependence (Anton et al., 2013). An increase of noise linear with the area of the superconductor in the SQUID loop has been found (Anton et al., 2013), but no clear correlations have been observed neither on the selection of materials nor on the details of the device geometry. Even though the fundamental mechanism for flux noise in SQUIDs remains unclear, there are plenty of experiments indicating that impurity atoms with a spin magnetic moment are involved in the noise phenomena.

Flux noise in a SQUID may originate from paramagnetic impurities residing on the superconducting material of the SQUID loop. Paramagnetic impurities produce flux according to paramagnetic susceptibility $\chi(T) \propto 1/T$, the fluctuation of which produces flux noise. Such fluctuating paramagnetic impurities have been observed in Al, Nb, Au, Re, and Ag among others (Sendelbach et al., 2008; Bluhm et al., 2009). The fluctuating spins are believed to reside on the metal surface as the flux noise scales with the surface area of the SQUID loop (Anton et al., 2013). In order to obtain a correct order of magnitude of flux noise, one has to assume a magnetic impurity concentration of $\sim 1 \times 10^{18}/\text{m}^2$ with an impurity moment of one Bohr magneton, given by electron rest mass m_e and electron charge e as $\mu_B = \frac{e\hbar}{2m_e} = 9.274 \times 10^{-24}$ J/T, that is, a distance of 1 nm between the impurities (Sendelbach et al., 2008).

There is also experimental evidence for adsorbed oxygen molecules producing a magnetic signature and flux noise (Kumar et al., 2016). With its paramagnetism, oxygen can meet the above-stated requirement for strength and density of impurity moments.

Hydrogen atoms provide an alternate source for flux noise (De Graaf et al., 2017; Quintana et al., 2017). Electron spin resonance measurements on sapphire have revealed a resonance with a 1.42 GHz line splitting which matches free H atoms. In addition, flux noise measurements using the qubit relaxation rate indicate a peak at 1.4 GHz. Further support for the presence of H is provided by DFT calculations of interstitial hydrogen atoms embedded in bulk sapphire, which yield an ESR splitting of 1.28–1.36 GHz (Wang et al., 2018). Recently, complex radicals have also been found to contribute to the noise and decoherence phenomena (Un et al., 2022).

Single electron tunneling devices

The most sensitive charge detectors in the solid state are single electron transistors (SETs) and charge qubits. Both devices suffer strongly from background charge fluctuations which often have $1/f$ character with some overlying Lorentzian spectra due to strongly coupled TLSs (Paladino et al., 2014). Using Al/AlO$_x$/Al tunnel barriers on top of common dielectric such as Si, SiO$_2$, and Si$_3$N$_4$, the charge noise amounts to 10^{-4} – $10^{-3}\mathrm{e}/\sqrt{\mathrm{Hz}}$ at 10 Hz, both in superconducting and normal metal regimes. The best Al/AlO$_x$/Al devices using stacked design have reached $8 \times 10^{-6}\mathrm{e}/\sqrt{\mathrm{Hz}}$ at 10 Hz (Krupenin et al., 2000). Charge noise in SETs arises typically from charged two level states capacitively coupled to the island (Paladino et al., 2014). Such TLSs are present in all back-gated devices at the interface of the gate dielectric and the conducting materials. The best charge sensitivities in Al-based devices have been obtained in structures where the contact area to dielectric substrate material has been eliminated with a stacked design (Krupenin et al., 2000). The achieved levels of charge noise have not been adequate for fabricating well-functioning charge qubits, that is, Cooper pair boxes, using Al technology (Astafiev et al., 2006; Paladino et al., 2014).

$1/f$ charge noise is a very important characteristic for industrially fabricated silicon quantum dot MOSFET devices which are being developed for spin qubits (Harvey, 2022). Typical noise values in multielectron quantum dots at 1 Hz are in the range 1 – 10 μV referred to the gate electrode (Petit et al., 2018; Zwerver et al., 2022) (corresponding to 80 – 800 $\mu\mathrm{e}/\sqrt{\mathrm{Hz}}$ using a gate capacitance 10^{-17} F). Small charge noise in these quantum dots is important both for the coherence and read-out of spin qubits (Stano and Loss, 2022).

In 1D and 2D nanodevices, the density of states can be strongly energy dependent. This causes fluctuations in the chemical potential μ_F to generate carrier number fluctuations, which leads to a one-to-one correspondence between the conductance noise spectrum and the frequency spectrum of μ_F fluctuations. The fluctuations in μ_F may be induced, for example, by chemical doping or background charge fluctuations (Pellegrino et al., 2019). Such fluctuations in 1D and 2D conductors are similar to Coulomb effects, where the shift of chemical potential is given in terms of variation in the island charge $Q = Q_\mathrm{i}$. The influence of Q_i on the current I can be described using transconductance $g_m = \partial I/\partial V_g = C_{eff}\, \partial I/\partial Q_\mathrm{i}$ where C_{eff} specifies the connection of the island charge to the shift of electrochemical potential. Typical charge noise values for carbon nanotube (Roschier et al., 2001; Vitusevich et al., 2011) and 2D material devices (Karnatak et al., 2017) with good transconductance are in the range $4 \times 10^{-5} \ldots 10^{-3}\mathrm{e}/\sqrt{\mathrm{Hz}}$ at 10 Hz.

Besides charged TLSs, background fluctuations can arise from charge localized at interfaces where it can be transported by impurities or defects easier than within the bulk. This calls for extreme care when stacking 2D heterostructures in order to keep their $1/f$ noise as small (Balandin, 2013; Karnatak et al., 2017). In addition, there has been a substantial effort in studies on suspended 2D materials, in particular, graphene, which has been employed as a low-noise platform for investigations of noise induced by diffusion of mobile scattering centers on the membrane (Kamada et al., 2021). As an interpretation of the observed noise results, intrinsic long-term correlations due to clustering and declustering of adsorbed atoms have been proposed (Kamada et al., 2021). Interactions between TLSs and non-Gaussian fluctuations can also be investigated by the second spectrum (Pellegrino et al., 2023; Zeng et al. (2023) and references therein).

1/*f* Noise in quantum-coherent nanodevices

Nanoscale-based quantum technologies build on harnessing fundamental properties of quantum states, such as superposition, quantum coherence, and entanglement to enable novel functionalities (Heinrich et al., 2021). The extraordinary impetus in quantum technology research, from academia to spin-offs and industries, since the last few years of the 20th century has led to a number of breakthroughs. At the same time, it has been pointed out that fluctuations characterized by power spectral density $1/f^\alpha$ with $\alpha \approx 1$ in a setup-dependent low-frequency range are paramount in most of the coherent nanodevices. On one side, they limit the ability to control the quantum-coherent behavior of engineered nanostructures, leading to a gradual loss of phase coherent evolution or *decoherence*. On the other side, the systematic analysis of decoherence under different control sequences allows for reconstructing the frequency spectrum of stochastic signals, a task commonly referred to as *noise spectroscopy*. Here we present an overview on how fluctuations with $1/f$ spectrum influence the phase coherent evolution of artificial atoms playing the twofold roles of elementary quantum bits and of quantum sensors, in particular of noise spectrometers. We will refer to selected paradigmatic examples of coherent nanodevices.

Artificial atoms

Nowadays micro and nano solid-state devices can be fabricated. They are called *artificial atoms* (AAs) (Buluta et al., 2011) since they show functional analogies with natural atomic or molecular systems.

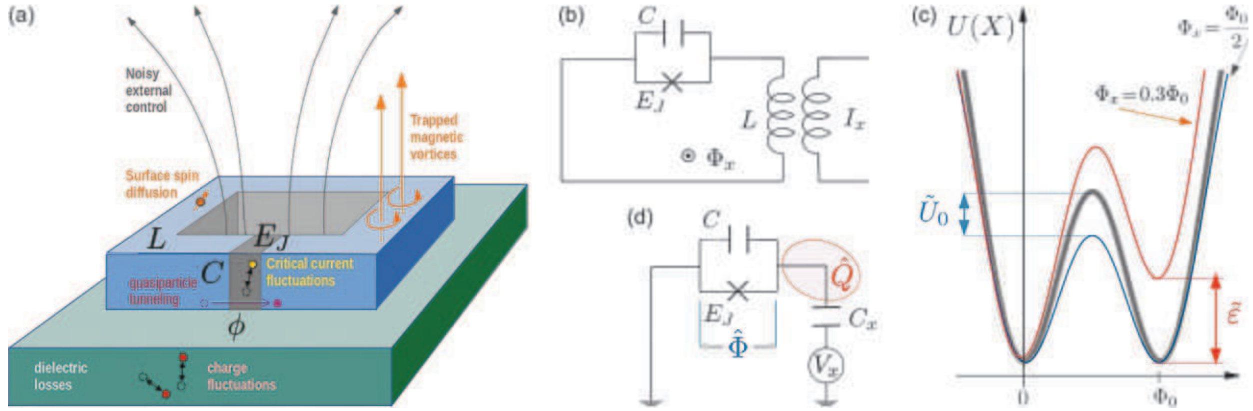

Fig. 3 (A) The rf-SQUID is a superconducting ring with inductance *L*, and associated energy $E_L = \Phi_0^2/L$, interrupted by a Josephson junction with critical current I_c, Josephson energy $E_J = 2e\, I_c/\hbar$ and capacitance *C*; several noise sources may affect its dynamics, many of them displaying a 1/*f* low-frequency behavior. (B) The equivalent circuit of the rf-SQUID, the flux Φ_x being induced by a current I_x flowing in a nearby circuit. (C) The rf-SQUID potential *U*(*X*) Eq. (8): the device is analogous to a particle of "mass" *C* moving in this potential, modulable by varying Φ_x. (D) Equivalent circuit of the Cooper-pair box, where a discrete-valued charge $\hat{Q}$ is stored in a superconducting island (*red*) connected to the circuit by a Josephson junction and modulated by the external voltage V_x via a gate capacitance C_x.

Electrons in semiconductors can be confined in a "box" called *quantum dot*, small enough that they do not behave as in bulk solids but rather as electrons in individual atoms. Indeed they have a discrete spectrum of energy and at low temperatures, electrons can occupy only the lowest energy levels. A qubit can be encoded in the charge or the spin of electronic configurations. Spin qubits couple weakly to their environment and leveraging on the available fabrication technologies they are interesting candidates for building large-scale quantum computers.

Superconducting artificial atoms are devices made of tunnel junctions displaying the Josephson effect. In a superconductor, the many-body condensate is described by a single-particle wavefunction, and in coherent devices, its phase behaves as a quantum degree of freedom analogous to the coordinate of a fictitious particle in a confining potential. Superconducting AAs may encode a qubit in the eigenstates of the potential (phase qubits), in the flux enclosed in a superconducting quantum interference device (SQUID) ring (flux qubit), in the extra charge stored in a superconducting "box" (charge qubits) to mention the simplest instances (see Fig. 3).

As an example, the rf-SQUID illustrated in Fig. 3A is modeled by an equivalent circuit with concentrated elements (Fig. 3B). The circuit's dynamics emulates a particle moving in the potential

$$U(X) = -E_J \cos\left(\frac{2\pi X}{\Phi_0}\right) + \frac{E_L}{2}\left(\frac{X - \Phi_x}{\Phi_0}\right)^2 \tag{8}$$

where the "coordinate" X is the total magnetic flux concatenated with the ring Φ_T and the "momentum" P is the charge Q accumulated at the surface of the junction's electrodes. The Hamiltonian describing the quantum-coherent regime is obtained by quantizing the canonical coordinates, which become noncommuting operators, $[\hat{Q}, \hat{\Phi}_T] = i\hbar$. Here Φ_x is the flux of an external bias field concatenated to the ring, $\Phi_0 = h/(2e) \approx 2.068833 \times 10^{-15}$ Wb is a universal constant named *flux quantum* and other circuit parameters are defined in Fig. 3.

In principle, an rf-SQUID biased by an external flux $\Phi_x \approx \Phi_0/2$ may function as a qubit. In this case $U(X)$ is a nearly symmetric double-well potential (see Fig. 3C) with a low-energy spectrum consisting of a doublet. The qubit Hamiltonian is obtained by truncating the system to these two levels. In the spin language, it is written as

$$\hat{H} = -\frac{\varepsilon(\Phi_x)}{2}\,\sigma_z - \frac{\Delta}{2}\,\sigma_x \tag{9}$$

where ε is the asymmetry of the potential, modulable by Φ_x and Δ is a tunneling matrix element between its minima. The two eigenvalues of σ_z correspond to states localized in one of the minima of the potential, the total concatenated flux being $\Phi_T = 0, \Phi_0$. These are the basic principles of the so-called flux-qubit whose actual design is a multijunction version of the rf-SQUID (Krantz et al., 2019).

Classical noise induces fluctuation of the parameters. For instance, flux noise is described by adding a stochastic external flux, $\Phi_x \to \Phi_x + \tilde{\Phi}_x(t)$, which induces fluctuations $\tilde{\varepsilon}(t)$ of the potential asymmetry, as illustrated in Fig. 3C. Instead, fluctuations of E_J due for instance to the impurities in the Josephson junction induce fluctuations of the barrier height $\tilde{U}_0$ of the potential and in turn fluctuations $\tilde{\Delta}(t)$ of the tunnel splitting. In general, the Hamiltonian acquires a fluctuating term $\delta\hat{H}(t) = -\frac{1}{2}[\tilde{\varepsilon}(t)\,\sigma_z + \tilde{\Delta}(t)\,\sigma_x]$, where $\tilde{\varepsilon}(t)$ and $\tilde{\Delta}(t)$ are classical stochastic processes. Experiments show that all of them exhibit $\sim 1/f$ behavior at low frequencies (Paladino et al., 2014; Bylander et al., 2011). The approach outlined for classical noise may be extended to describe phenomenologically quantum noise. In this case, the stochastic processes are substituted by operators describing physical fields exerted by the microscopic quantum degrees of freedom of one or more physical environments (Paladino et al., 2014).

The other prominent family of superconducting qubits, including the transmon (Koch et al., 2007), which provides the forefront device for present superconducting quantum processors (Arute et al., 2019; Jurcevic et al., 2021; Wu et al., 2021), may be introduced following the same roadmap. The simplest instance is the so-called charge qubit, Fig. 3D (Nakamura et al., 1999), where the conjugate variables are the discrete charge $\hat{Q}$ into the superconducting island and the cyclic coordinate $\hat{\Phi} = \hbar\hat{\phi}/(2e)$ related to the quantized phase difference ϕ between the macroscopic wave functions of the electrodes of the Josephson junction. Again the Hamiltonian can be written in Eq. (9) where now fluctuations $\tilde{\varepsilon}$ are related to charge noise, whereas $\tilde{\Delta}(t)$ originates from fluctuations of E_J or from flux noise.

The main effect of low-frequency noise on the dynamics of the qubit is dephasing. For instance, the populations of the eigenstates of an isolated qubit with Hamiltonian Eq. (9) undergo coherent oscillations with the angular frequency given by the qubit energy splitting (we take $\hbar = 1$) $\Omega = \sqrt{\varepsilon^2 + \Delta^2}$. Due to the coupling to the environment, which induces fluctuations of Ω, the amplitude of coherent oscillations decays as $A(t) = e^{-\Gamma(t)}$. Dephasing strongly depends on how the qubit is biased or manipulated. This extreme sensitivity is exploited to mitigate dephasing or, on the contrary, for quantum sensing of environmental noise. For instance, let's set the flux bias such that $\varepsilon(\Phi_x) = 0$ and consider the effect of fluctuations $\tilde{\Delta}$ (called "longitudinal"). Then the decay of oscillations is given by

$$\Gamma(t) = \frac{t^2}{2}\int_{t_m^{-1}}^{\infty} df\ \mathcal{F}_0(ft)\ S_\Delta(f) \tag{10}$$

being determined by the power spectrum of the fluctuations of $\tilde{\Delta}(t)$ "filtered" by the function $\mathcal{F}_0(x) = \sin^2(\pi x)/(\pi x)^2$. Longitudinal $1/f$ noise may determine a very strong decay $\Gamma(t) \approx \frac{1}{2}\langle(\delta\tilde{\Delta})^2\rangle t^2$, where $\langle(\delta\tilde{\Delta})^2\rangle \sim \int_{1/t_m}^{f_2} df\ C_\Delta/f \approx C_\Delta\ \log(f_2 t_m)$. This strong decay of coherences determines the complete phase randomization in a generic solid-state system at equilibrium. Instead, $\tilde{\varepsilon}$ noise (called "transverse") contributes at second order on the fluctuations of the qubit splitting Δ, thus their impact is more limited resulting in a power-law decay

$$\Gamma(t) = \frac{1}{4}\ \ln\left[1 + \left(\frac{\langle(\delta\tilde{\varepsilon})^2\rangle\ t}{\Delta}\right)^2\right] \tag{11}$$

Therefore, to reduce the impact of low-frequency noise, an optimal bias strategy has been used, where the qubit is biased in such a way that the main source of noise is transverse. This way, the impact of flux (charge) noise in flux (Cooper-pair box-based) qubits is minimized.

In the last generation of qubits, significant coherence times are achieved by designing the device in a way that protection from noise is stronger for a larger range of parameters. For instance, dynamical sweet spots based on the application of periodic drives have been identified (Huang et al., 2021), demonstrating reduced susceptibility to low-frequency noise and predicting an enhancement of pure dephasing by 3 orders of magnitude in the fluxonium (Nguyen et al., 2019). For a recent review on noise-protected superconducting quantum circuits, we refer the reader to Gyenis et al. (2021). Here we mention that, in addition to design strategies, considerable advances in materials science and engineering materials provided significant noise protection, as discussed in de Leon et al. (2021).

In general, amorphous or glassy materials with plenty of TLSs may be disadvantageous in coherent quantum devices. Besides residing in the tunnel barrier material, TLSs may influence the dielectric constant of substrates as well as insulating coatings between wiring layers. The inverse time constants of the two-level states have been found to range from mHz to GHz frequencies. Hence, in addition to limiting the quality factors of qubits, TLSs can influence readout resonators for qubits at GHz frequencies as well as low-frequency SQUID magnetometers, as discussed in the next paragraph.

Defects in oxides and interfaces also represent the main limitation of gate fidelities in semiconductor-based quantum dot charge qubits, where they cause voltage fluctuations on the control electrodes. Analogously to superconducting qubits, dephasing due to $1/f$-charge noise is minimized by working at sweet spots (Petersson et al., 2010; Dial et al., 2013; Thorgrimsson et al., 2017; Scarlino et al., 2019; Yang et al., 2019; Kratochwil et al., 2021). Spin-based quantum dot qubits (Loss and DiVincenzo, 1998) in semiconductors are sensitive to magnetic field noise due to the surrounding nuclear spin bath and to charge noise. Recent progress in this field has been discussed in Harvey (2022) and Laucht et al. (2021).

Quantum sensing

Coherent nanosystems are at the core of investigation also in the recent field of quantum sensing. For a recent review, we refer the reader to Degen et al. (2017) and references therein. The idea behind is to turn into an exploitable property the sensitivity to external disturbances representing an intrinsic weakness for quantum computing purposes. Quantized energy levels, quantum coherent evolution, or quantum entanglement are used to measure a physical quantity or to improve sensitivity beyond classical measurements. To function as quantum sensors, physical systems need to satisfy the DiVincenzo criteria of efficient initialization and coherent manipulation (DiVincenzo, 2000). In addition, they have to interact with the physical quantity to be detected $V(t)$, which leads to shifts of the quantized energy levels or splitting, $E(V)$. The relevant quantity is the transduction parameter $\gamma = \partial^q E/\partial V^q$, where usually $q = 1$ or $q = 2$. In any physical implementation, the sensitivity to external signals carries also coupling with unwanted external noise sources. The trade-off between strong coupling to the quantity to be detected and weak disruptive noise effects is quantified by the sensitivity which scales as $\propto 1/(\gamma\sqrt{T})$, where T is the relevant decoherence or relaxation time (Degen et al., 2017).

Quantum sensors require maximal transduction and long decoherence time. In general, the role of $1/f$ noise in these schemes is that of limiting the coherence time which governs the measurement time available for quantum sensing. Thus, lowering the amount of $1/f$ noise will increase the sensitivity and consequently also the dynamic range of quantum sensing (the largest signal is set by the smallest measurement time).

The effect of low-frequency fluctuations can be illustrated in nitrogen-vacancy (NV) centers in diamond (Doherty et al., 2013), one of the most advanced platforms for quantum sensing. The use of electron spin states of NV centers in diamond for highly sensitive magnetometry is an established fact with relevant applications. For an in-depth description of this topic, we refer to Rondin et al. (2014), Schirhagl et al. (2014), and Rembold et al. (2020). Key properties of these color centers are the possibility to optically initialize, read out, and coherently manipulate at ambient conditions. The sensing protocol is essentially the measurement of the Zeeman splitting induced by an external magnetic field. For advanced sensing applications, the transition frequency is detected via interferometric techniques. The basis of these techniques is Ramsey interference, the spin equivalent of an optical Mach–Zehnder interferometer. The qubit is prepared in the superposition $|0\rangle + e^{i\phi_0}|1\rangle$, and Ramsey interference is based on the phase accumulated by the Larmor precession during the interrogation time, This phase is related to the addressed transition frequency, which depends on the external field to be measured. This allows the detection of static, slowly varying, or broadband near-DC signals. The main limitation of DC magnetometry with NV centers is dephasing due to slowly varying inhomogeneities of the dipolar fields due to unpolarized spin impurities in the diamond crystal, mostly ^{13}C and ^{14}N.

Dynamical decoupling (DD) schemes inspired by NMR (Becker, 2000) have been used to reduce the effect of low-frequency noise components (Paladino et al., 2014). These techniques are by now routinely employed as active control tools for increasing the quality factors of quantum gates and in quantum sensors. The simplest instance is Hanh's echo, consisting of a π-pulse applied halfway of the detection in such a way as to reverse the qubit evolution so that the phases accumulated in the two-time intervals cancel out.

DD refers to sequences of multiple π-pulses which allow shaping of the frequency response of the quantum sensor, in particular attaining higher sensitivity when measuring AC magnetic fields and longer coherence times for quantum bits and gates.

The DD control protocol is conveniently formulated in terms of filter functions entering the qubit coherent oscillations, analogously to Eqs. (10) and (11). For Gaussian noise coupled longitudinally, the filter function takes the form (Uhrig, 2007)

$$\mathcal{F}_N(f,t) = \frac{1}{(2\pi f t)^2}\left|1 + (-1)^{N+1}e^{i2\pi f t} + 2\sum_{j=1}^{N}(-1)^j e^{i2\pi t_j}\right|^2 . \tag{12}$$

N is the number of pulses applied at time t_j within the measurement time, t, perpendicularly with respect to the qubit quantization axis. A variety of pulse sequences have been investigated, differentiated by pulse directions and timings. The resulting filters effectively eliminate from the qubit evolution spectral noise components to different degrees (see Fig. 4C). For instance, the Carr–Purcell sequence (Carr and Purcell, 1954), which consists of n equidistant π pulses, acts as a narrow quasi-monochromatic and tunable filter. The first pulse time, t_1 selects the pass-band frequency while n determines the filter width. The CP sequences allow the detection of monochromatic AC fields with periodicity commensurate with the $2t_1$, the interpulse timing. In NV sensor settings, periodic protocols have been exploited to detect and characterize individual ^{13}C nuclear spins placed a few nanometers apart from the NV center (Zhao et al., 2012; Taminiau et al., 2012).

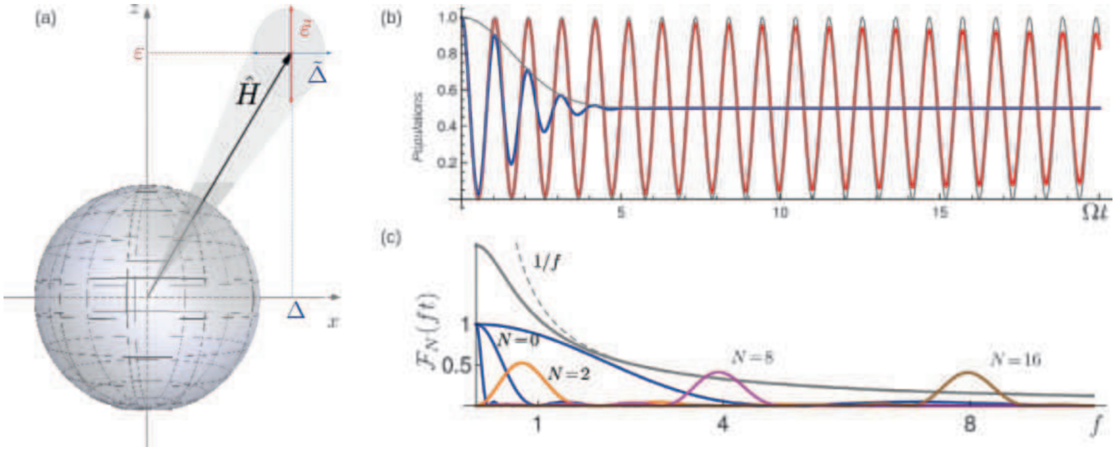

Fig. 4 (A) In the spin language, a pure state of a qubit is a unit vector of the Bloch sphere and the qubit Hamiltonian Eq. (9) is represented by a vector $\vec{H}$. Coherent oscillations correspond to a precession of the state vector about $\vec{H}$, whose direction and modulus fluctuate due to noise, affecting the qubit dynamics.
(B) Coherent oscillations of the qubit populations in an isolated system (*gray line*) are strongly suppressed by longitudinal low-frequency noise (*blue line*), while the effect of transverse noise (*red line*) is much weaker. (C) Frequencies of the $1/f$ spectrum (*gray lines*, the thick one for a finite low-frequency cutoff) entering dephasing are filtered by the qubit dynamics: the *blue curves* represent $F_0(f)$ entering Eq. (10) at different times, larger t yielding smaller bandwidths. The *orange*, *magenta*, and *green curves* represent the action of the filter Eq. (12) for periodic dynamical decoupling (DD) operated by $N\pi$-pulses, $N = 2$ representing spin echo; the bandwidth migrates to larger frequencies suppressing the effect of low-frequency noise.

Despite the extraordinary progress, the sensitivities currently achieved are lower than the theoretical limits established by the qubits' lifetimes. Material synthesis techniques have been developed to reduce paramagnetic impurities and strain effects in the host crystal. In addition, quantum optimal control (QOC) methods have been applied to quantum sensors (Giovannetti et al., 2011; Rembold et al., 2020; Hernández-Gómez and Fabbri, 2021). These techniques represent an alternative route to enhance the coherence time when noise at high-frequencies dominates.

Noise spectroscopy

Noise spectroscopy is an important tool in quantum sensing. The term refers to methods for reconstructing the frequency spectrum of stochastic signals. The most common tools are based on Ramsey interferometry or more involved rf pulse sequences (Degen et al., 2017). Noise spectroscopy can provide relevant information both on the signal to be detected and on the intrinsic noise of the sensor. It can be formulated again in terms of filter functions. In fact, in addition to the decoupling regime, there exist spectral regions of the filters of positive gain. The effect of the corresponding spectral components of noise is amplified (Paladino et al., 2014).

Noise spectroscopy is routinely used as a powerful tool to characterize $1/f$ charge and magnetic flux noise in superconducting qubits. Here we only mention some recent results in this platform. Exploiting the narrow-band filtering properties of the Carr Purcell Meibum Gill (CPMG) sequence (Meiboom and Gill, 1958), Bylander et al. (2011) measured flux noise in a persistent current qubit away from the optimal point in the spectral region 0.2–20 MHz, where $1/f^{0.9}$ noise was detected. The decay of Rabi oscillations provided an independent measurement of the noise spectrum at frequencies of the order of $\Omega_{Rabi} \approx$ MHz. Remarkably, the same power law behavior has been detected by Ramsey interferometry in the much lower frequency range 0.01–100 Hz in Yan et al. (2012). By studying the decay of Rabi oscillations under strong driving conditions, Yoshihara et al. (2014) inferred flux noise up to 1.7 GHz. Around 300 MHz, a spectrum close to $1/f$ was detected where evidence of a Lorentzian component, possibly due to a more strongly coupled fluctuator was pointed out, see Fig. 2. The result of these types of measurements is sketched in Fig. 1. Most noise spectroscopy protocols have been developed tailored to Gaussian noise models. Norris and Viola (Norris et al., 2016) introduced a noise spectroscopy protocol allowing for higher order spectral estimation of non-Gaussian noise, as demonstrated in a flux-tunable superconducting qubit sensor (Sung et al., 2019). This represents a valuable tool for characterizing discrete microscopic sources with a $1/f$ spectrum. More recently, multilevel noise spectroscopy has been realized via a spin-locking-based protocol (Sung et al., 2021). The additional information gained from probing the higher excited levels enabled the identification of contributions from different underlying noise mechanisms in a flux-tunable transmon qubit. Noise spectroscopy tracking multilevel fluctuations represents also an efficient tool for materials characterization, as it has been demonstrated in a transmon fabricated with tantalum metal (Tennant et al., 2022).

Silicon quantum dot spin qubits have also been employed as metrological devices to study the noise environment experienced by the qubit. Noise spectroscopy has been done for an implanted phosphorus donor qubit in silicon (Si:P) (Muhonen et al., 2014) and a SiGe quantum dot spin qubit (Yoneda et al., 2017). Charge noise spectroscopy in an isotopically purified electron spin qubit in a ^{28}Si/SiGe quantum dot has been realized by an independent estimate of $S(f)$ around 0.01–1 Hz by Ramsey interferometry, and around tens of kilohertz by CPMG sequence. Remarkably, the two estimates are consistent with $1/f^{1.01}$ spectrum extending over seven decades of frequencies (Yoneda et al., 2017). In this experiment, rapid spin rotations are applied by using a proximal micromagnet, which induces spin-electric coupling fields. In Chan et al. (2018), the environment of a silicon metal–oxide–semiconductor (SiMOS) quantum dot spin qubit has been characterized via CPMG DD pulse sequences. The detected charge noise is $1/f^{\alpha}$ with $\alpha \approx 0.8$–1 for frequencies between 2 and 20 kHz. Noise in the energy splitting of an electron spin qubit in a highly isotopically purified ^{28}Si/SiGe device has been detected via Ramsey spectroscopy down to 10^{-5} Hz and by Hanh-echo at higher frequencies in Struck et al. (2020). Measurements revealed a $1/f^2$ behavior below 5×10^{-3} Hz followed by $1/f$ trend. These dependencies have been found to be consistent over 8 decades with charge noise independently detected in the same setup via measurement the current noise of a nearby SET sensor.

Conclusion

It is widely recognized that the road to avoiding $1/f$ noise in nanodevices is to improve the characteristics of the employed materials. Silicon crystal growth technology has been perfected in the past, and nowadays extremely pure silicon single crystals are available. Similar quality of materials would be required for various substances that are employed in quantum technology (de Leon et al., 2021). One possible route for achieving high-quality materials is to tailor devices atom by atom (Khajetoorians et al., 2019). The era of such a "designer matter" approach has recently begun, but plenty of work lies ahead before the quality and throughput of these materials will become relevant for alleviating $1/f$ noise in mainstream quantum science and technology.

Progress in the more regular "engineered matter" is being made using composite, hybrid materials, for example, encapsulated graphene with superconducting contacts (Wang et al., 2019). Such hybrid junctions have been employed in superconducting qubits, but it appears that there is still substantial $1/f$ noise present at the interfaces (Haque et al., 2021). In addition, different mechanisms may originate critical current fluctuations, for instance, charge carrier density fluctuations might also play a role (Pellegrino et al., 2020). The resistance noise properties of regular AlO_x tunnel junctions are still superior, and the influence of their E_J (or critical current, I_c) noise on qubit coherence time is small. It will become essential when the coherence time will be in the ms range (Siddiqi, 2021).

One of the emerging, striking fields of 2D materials is the magic angle twisted bilayer graphene (MATBG), in which superconductivity (Cao et al., 2018) is assigned to flat energy bands (Kerelsky et al., 2019; Xie et al., 2019; Törmä et al., 2022). The MATBG samples can be tuned between superconductivity and Mott insulating states with a rather small change in the charge carrier density. However, owing to variations in local charge doping or in twist angle, the superconducting properties of these samples may fluctuate in space or time, and thus display $1/f$ noise in critical current. A study of such noise will establish the quality of this material for certain sensitive detector applications, for example, their use in kinetic inductance detectors for radiation.

2D materials offer a platform for the miniaturization of components for coherent quantum circuits (Antony et al., 2021; Wang et al., 2022). Large, low-loss capacitance per unit area can be achieved using a few layer hBN as an insulating layer. Furthermore, by utilizing h-BN as a gate dielectric, strong gate coupling for FETs can be obtained. Compared with amorphous hafnium oxide, the TLS density of h-BN dielectric is definitely smaller, which promises smaller $1/f$ noise for components in such 2D material technology.

With the increasing miniaturization of electronic quantum components, the relative magnitude of $1/f$ noise has been constantly growing over the years as the active part of the component is influenced strongly by one single impurity. Similar extreme purity as for single silicon crystals would be needed for other technologically relevant materials in the future (de Leon et al., 2021). An alternative solution to the $1/f$ noise dilemma is to harness independent single atoms or molecules (Yu et al., 2021) as building blocks for quantum components and sensors. This has already been achieved quite well in quantum sensors based on NV centers in diamond or in optically read magnetometers based on rubidium gas for example (Aslam et al., 2023).

Besides DD schemes, the use of limited quantum resources can be bolstered by using phase estimation algorithms (Kitaev, 1995). These algorithms provide a sensitivity improvement directly proportional to the measurement time, that is, they allow to achieve the Heisenberg limit in measurement accuracy. Combined with Bayesian learning algorithms, phase estimation schemes may provide ultimate speed for high-sensitivity sensing, for example, magnetometry (Bonato et al., 2016), in spite of the influence of $1/f$ noise embedded in the coherence time of the sensing qubit.

QOC is another promising methodology both for sensing applications and for quantum computation applications which require high-fidelity gate operation. One instance where QOC can provide a solution is in reducing the cumulative errors due to hard pulses (i.e., rectangular pulses) employed with DD sequences.

Fluctuations can provide important additional information in sensing, for example, in gas recognition. Low-frequency noise due to adsorbent molecules and atoms on graphene has been demonstrated to yield distinct $1/f$ spectra (Rumyantsev et al., 2012). In combination with supervised-learning algorithms, based on statistical learning theory, fluctuation-enhanced gas recognition has already been investigated (Lentka et al., 2015). Such an approach may provide a significant boost in gas recognition resolution for e-nose applications (Chen et al., 2022).

For future superconducting quantum technology, clean materials are essential as they increase coherence time, which improves qubit operation, and along with it, increases the sensitivity of all schemes for quantum sensing. One of the central issues in this quest for better superconducting junctions and conductors is to understand the microscopic origin of $1/f$ noise on interfaces, surfaces, and tunneling barrier dielectrics. This will call for the systematic development of materials growth, cleaning, and fabrication techniques, as well as systematic benchmarking of the realized quantum components.

References

Anton SM, Birenbaum JS, O'Kelley SR, Bolkhovsky V, Braje DA, Fitch G, Neeley M, Hilton GC, Cho HM, Irwin KD, Wellstood FC, Oliver WD, Shnirman A, and Clarke J (2013) Magnetic flux noise in dc SQUIDs: Temperature and geometry dependence. *Physical Review Letters* 110(14): 147002. ISSN: 00319007. https://doi.org/10.1103/PhysRevLett.110.147002.

Antony A, Gustafsson MV, Ribeill GJ, Ware M, Rajendran A, Govia LCG, Ohki TA, Taniguchi T, Watanabe K, Hone J, and Fong KC (2021) Miniaturizing transmon qubits using van der Waals materials. *Nano Letters* 21(23): 10122–10126. ISSN: 1530-6984. https://doi.org/10.1021/acs.nanolett.1c04160.

Arute F, Arya K, Babbush R, et al. (2019) Quantum supremacy using a programmable superconducting processor. *Nature* 574: 505–510. https://www.nature.com/articles/s41586-019-1666-5.

Aslam N, Zhou H, Urbach EK, Turner MJ, Walsworth RL, Lukin MD, and Park H (2023) Quantum sensors for biomedical applications. *Nature Reviews Physics* 1–13. ISSN: 2522-5820. https://doi.org/10.1038/s42254-023-00558-3.

Astafiev O, Pashkin YA, Nakamura Y, Yamamoto T, and Tsai JS (2006) Temperature square dependence of the low frequency 1/f charge noise in the Josephson junction qubits. *Physical Review Letters* 96(13): 137001. ISSN: 00319007. https://doi.org/10.1103/PhysRevLett.96.137001.

Balandin AA (2013) Low-frequency 1/*f* noise in graphene devices. *Nature Nanotechnology* 8(8): 549–555. ISSN: 1748-3395. http://www.nature.com/nnano/journal/v8/n8/nnano.2013.144/metrics/blogs.

Becker ED (2000) *High Resolution NMR*. San Diego: Academic Press.

Blais A, Grimsmo AL, Girvin S, and Wallraff A (2021) Circuit quantum electrodynamics. *Reviews of Modern Physics* 93(2): 025005. ISSN: 0034-6861. https://doi.org/10.1103/RevModPhys.93.025005.

Bluhm H, Bert JA, Koshnick NC, Huber ME, and Moler KA (2009) Spinlike susceptibility of metallic and insulating thin films at low temperature. *Physical Review Letters* 103(2): 026805. ISSN: 00319007. https://doi.org/10.1103/PhysRevLett.103.026805.

Bonato C, Blok MS, Dinani HT, Berry DW, Markham ML, Twitchen DJ, and Hanson R (2016) Optimized quantum sensing with a single electron spin using real-time adaptive measurements. *Nature Nanotechnology* 11(3): 247–252. ISSN: 1748-3387. https://doi.org/10.1038/nnano.2015.261.

Buluta I, Sahel Ashhab S, and Nori F (2011) Natural and artificial atoms for quantum computation. *Reports on Progress in Physics* 74: 104401. https://doi.org/10.1088/0034-4885/74/10/104401.

Burnett J, Faoro L, Wisby I, Gurtovoi VL, Chernykh AV, Mikhailov GM, Tulin VA, Shaikhaidarov R, Antonov V, Meeson PJ, Tzalenchuk AY, and Lindström T (2014) Evidence for interacting two-level systems from the 1/f noise of a superconducting resonator. *Nature Communications* 5(May): 1–6. ISSN: 20411723. https://doi.org/10.1038/ncomms5119.

Burstein E, Kingston RH, and McWhorter AL (1957) *Semiconductor Surface Physics*. Philadelphia (PA): University of Pennsylvania Press. http://lib.ugent.be/catalog/rug01:001421208.

Bylander J, et al. (2011) *Nature Physics* 7: 565.

Cantor R and Koelle D (2004) Practical DC SQUIDS: Configuration and performance. In: *The SQUID Handbook*, pp. 171–217. John Wiley & Sons, Ltd, ISBN: 9783527603640. https://doi.org/10.1002/3527603646.ch5 (Chapter 5).

Cao Y, Fatemi V, Fang S, Watanabe K, Taniguchi T, Kaxiras E, and Jarillo-Herrero P (2018) Unconventional superconductivity in magic-angle graphene superlattices. *Nature* 556 (7699): 43–50. ISSN: 0028-0836. https://doi.org/10.1038/nature26160.

Carr HY and Purcell EM (1954) *Physics Review* 94: 630. https://doi.org/10.1103/PhysRev.94.630.

Chan KW, Huang W, Yang CH, Hwang JCC, Hensen B, Tanttu T, Hudson FE, Itoh KM, Laucht A, Morello A, and Dzurak AS (2018) Assessment of a silicon quantum dot spin qubit environment via noise spectroscopy. *Physical Review Applied* 10(4): 044017. https://doi.org/10.1103/PhysRevApplied.10.044017.

Chen H, Huo D, and Zhang J (2022) Gas Recognition in E-Nose System: A Review. *IEEE Transactions on Biomedical Circuits and Systems* 16(2): 169–184. ISSN: 1932-4545. https://doi.org/10.1109/TBCAS.2022.3166530.

Datta S (1997) Electronic Transport in Mesoscopic Systems. *Cambridge Studies in Semiconductor Physics and Microelectronic Engineering.* Cambridge University Press, ISBN: 0521599431.

De Graaf SE, Adamyan AA, Lindström T, Erts D, Kubatkin SE, Tzalenchuk AY, and Danilov AV (2017) Direct identification of dilute surface spins on Al2 O3: Origin of flux noise in quantum circuits. *Physical Review Letters* 118(5): 057703. ISSN: 10797114. https://doi.org/10.1103/PhysRevLett.118.057703.

de Graaf SE, Faoro L, Burnett J, Adamyan AA, Tzalenchuk AY, Kubatkin SE, Lindström T, and Danilov AV (2018) Suppression of low-frequency charge noise in superconducting resonators by surface spin desorption. *Nature Communications* 9(1): 1143. ISSN: 2041-1723. https://doi.org/10.1038/s41467-018-03577-2.

de Graaf SE, Faoro L, Ioffe LB, Mahashabde S, Burnett JJ, Lindström T, Kubatkin SE, Danilov AV, and Tzalenchuk AY (2020) Two-level systems in superconducting quantum devices due to trapped quasiparticles. *Science Advances* 6(51): 1–9. ISSN: 2375-2548. https://doi.org/10.1126/sciadv.abc5055.

de Leon NP, et al. (2021) Materials challenges and opportunities for quantum computing hardware. *Science* 372(6539). https://doi.org/10.1126/science.abb2823.

Degen CL, Reinhard F, and Cappellaro P (2017) Quantum sensing. *Reviews of Modern Physics* 89(3): 035002. https://doi.org/10.1103/RevModPhys.89.035002.

Devoret MH (1995) Quantum fluctuations in electrical circuits. In: Reynaud S, Giacobino E, and Zinn-Justin J (eds.) *Proceedings of Les Houches Summer School.* Elsevier.

Dial OE, Shulman MD, Harvey SP, Bluhm H, Umansky V, and Yacoby A (2013) Charge noise spectroscopy using coherent exchange oscillations in a singlet-triplet qubit. *Physical Review Letters* 110(14): 146804. https://doi.org/10.1103/PhysRevLett.110.146804.

DiVincenzo DP (2000) The physical implementation of quantum computation. *Fortschritte der Physik* 48(9–11): 771–783. https://doi.org/10.1002/1521-3978(200009)48:9/11<771::AID-PROP771>3.0.CO;2-E.

Doherty MW, Manson NB, Delaney P, Jelezko F, Wrachtrup J, and Hollenberg LC (2013) The nitrogen-vacancy colour centre in diamond. *Physics Reports* 528(1): 1–45. ISSN: 0370-1573. https://doi.org/10.1016/j.physrep.2013.02.001.

Du Pré FK (1950) A suggestion regarding the spectral density of flicker noise. *Physics Review* 78(5): 615. https://doi.org/10.1103/PhysRev.78.615.

Dutta P and Horn PM (1981) Low-frequency fluctuations in solids: 1/f noise. *Reviews of Modern Physics* 53: 497. https://doi.org/10.1103/RevModPhys.53.497.

Giordano N (1989) Defect motion and low frequency noise in disordered metals. *Reviews in Solid-State Science* 3: 27–69.

Giovannetti V, Lloyd S, and Maccone L (2011) Advances in quantum metrology. *Nature Photonics* 5. https://doi.org/10.1038/nphoton.2011.35.

Grasser T (2020) *Noise in Nanoscale Semiconductor Devices*, pp. 1–729. Cham: Springer International Publishing, ISBN: 978-3-030-37499-0. https://doi.org/10.1007/978-3-030-37500-3.

Gyenis A, Di Paolo A, Koch J, Blais A, Houck AA, and Schuster DI (2021) Moving beyond the transmon: Noise-protected superconducting quantum circuits. *PRX Quantum* 2(3): 030101. https://doi.org/10.1103/PRXQuantum.2.030101.

Haque MT, Will M, Tomi M, Pandey P, Kumar M, Schmidt F, Watanabe K, Taniguchi T, Danneau R, Steele G, and Hakonen P (2021) Critical current fluctuations in graphene Josephson junctions. *Scientific Reports* 11(1): 19900. ISSN: 2045-2322. https://doi.org/10.1038/s41598-021-99398-3.

Harvey SP (2022) *Quantum Dots/Spin Qubits.* Oxford University Press. https://doi.org/10.1093/acrefore/9780190871994.013.83. https://oxfordre.com/physics/view/10.1093/acrefore/9780190871994.001.0001/acrefore-9780190871994-e-83.

Heinrich AJ, et al. (2021) Quantum-coherent nanoscience. *Nature Nanotechnology* 16: 1318–1329. https://doi.org/10.1038/s41565-021-00994-1.

Hernández-Gómez S and Fabbri N (2021) Quantum control for nanoscale spectroscopy with diamond nitrogen-vacancy centers: A short review. *Frontiers in Physics* 8. ISSN: 2296-424X. https://www.frontiersin.org/articles/10.3389/fphy.2020.610868.

Hooge FN (1994) 1/f Noise sources. *IEEE Transactions on Electron Devices* 41(11): 1926–1935. https://doi.org/10.1109/16.333808.

Hooge FN, Kleinpenning TGM, and Vandamme LKJ (1981) Experimental studies on 1/f noise. *Reports on Progress in Physics* 44: 479–532. https://doi.org/10.1088/0034-4885/44/5/001.

Huang Z, Mundada PS, Gyenis A, Schuster DI, Houck AA, and Koch J (2021) Engineering dynamical sweet spots to protect qubits from $1/f$ noise. *Physical Review Applied* 15(3): 034065. https://doi.org/10.1103/PhysRevApplied.15.034065.

Jurcevic P, Javadi-Abhari A, Bishop LS, et al. (2021) Demonstration of quantum volume 64 on a superconducting quantum computing system. *Quantum Science and Technology* 6: 025020. https://doi.org/10.1088/2058-9565/abe519.

Kamada M, Laitinen A, Zeng W, Will M, Sarkar J, Tappura K, Seppä H, and Hakonen P (2021) Electrical low-frequency $1/f^{\gamma}$ noise due to surface diffusion of scatterers on an ultra-low-noise graphene platform. *Nano Letters* 21(18): 7637–7643. https://doi.org/10.1021/acs.nanolett.1c02325.

Karimi B, Brange F, Samuelsson P, and Pekola JP (2020) Reaching the ultimate energy resolution of a quantum detector. *Nature Communications* 11(1): 367. ISSN: 2041-1723. https://doi.org/10.1038/s41467-019-14247-2.

Karnatak P, Paul T, Islam S, and Ghosh A (2017) 1/f Noise in van der Waals materials and hybrids. *Advances in Physics: X* 2(2): 428–449. ISSN: 23746149. https://doi.org/10.1080/23746149.2017.1314192.

Kerelsky A, McGilly LJ, Kennes DM, Xian L, Yankowitz M, Chen S, Watanabe K, Taniguchi T, Hone J, Dean C, Rubio A, and Pasupathy AN (2019) Maximized electron interactions at the magic angle in twisted bilayer graphene. *Nature* 572(7767): 95–100. ISSN: 0028-0836. https://doi.org/10.1038/s41586-019-1431-9.

Khajetoorians AA, Wegner D, Otte AF, and Swart I (2019) Creating designer quantum states of matter atom-by-atom. *Nature Reviews Physics* 1(12): 703–715. ISSN: 2522-5820. https://doi.org/10.1038/s42254-019-0108-5.

Kitaev AY (1995) *Quantum measurements and the Abelian stabilizer problem.* quant-ph/9511026.

Koch J, Yu TM, Gambetta J, Houck AA, Schuster DI, Majer J, Blais A, Devoret MH, Girvin SM, and Schoelkopf RJ (2007) Charge-insensitive qubit design derived from the cooper pair box. *Physical Review A* 76(4): 042319. https://doi.org/10.1103/PhysRevA.76.042319.

Koelle D, Kleiner R, Ludwig F, Dantsker E, and Clarke J (1999) High-transition-temperature superconducting quantum interference devices. *Reviews of Modern Physics* 71(3): 631–686. https://doi.org/10.1103/RevModPhys.71.631.

Kogan SM (1996) *Electronic Noise and Fluctuations in Solids.* Cambridge, England: Cambridge University Press.

Krantz P, Kjaergaard M, Yan F, Orlando TP, Gustavsson S, and Oliver WD (2019) A quantum engineer's guide to superconducting qubits. *Applied Physics Reviews* 6(2): 021318. https://doi.org/10.1063/1.5089550.

Kratochwil B, Koski JV, Landig AJ, Scarlino P, Abadillo-Uriel JC, Reichl C, Coppersmith SN, Wegscheider W, Friesen M, Wallraff A, Ihn T, and Ensslin K (2021) Charge qubit in a triple quantum dot with tunable coherence. *Physical Review Research* 3(1): 013171. https://doi.org/10.1103/PhysRevResearch.3.013171.

Krupenin VA, Presnov DE, Zorin AB, and Niemeyer J (2000) Aluminium single electron transistors with islands isolated from the substrate. *Journal of Low Temperature Physics* 118(5/6): 287–296. ISSN: 00222291. https://doi.org/10.1023/A:1004625530034.

Kumar P, Sendelbach S, Beck MA, Freeland JW, Wang Z, Wang H, Yu CC, Wu RQ, Pappas DP, and McDermott R (2016) Origin and reduction of 1/f magnetic flux noise in superconducting devices. *Physical Review Applied* 6(4): 41001. ISSN: 23317019. https://doi.org/10.1103/PhysRevApplied.6.041001.

Laucht A, et al. (2021) Roadmap on quantum nanotechnologies nanotechnology. *IOP Publishing* 32: 162003. https://doi.org/10.1088/1361-6528/abb333.

Lentka Ł, Smulko JM, Ionescu R, Granqvist CG, and Kish LB (2015) Determination of gas mixture components using fluctuation enhanced sensing and the LS-SVM regression algorithm. *Metrology and Measurement Systems* 22(3): 341–350. ISSN: 2300-1941. https://doi.org/10.1515/mms-2015-0039. http://journals.pan.pl/dlibra/publication/104348/edition/90351/content.

Loss D and DiVincenzo DP (1998) Quantum computation with quantum dots. *Physical Review A* 57(1): 120–126. https://doi.org/10.1103/PhysRevA.57.120.

Machlup S (1954) Noise in semiconductors: Spectrum of a two-parameter random signal. *Journal of Applied Physics* 25(3): 341–343. https://doi.org/10.1063/1.1721637.

McEwen M, Faoro L, Arya K, Dunsworth A, Huang T, Kim S, Burkett B, Fowler A, Arute F, Bardin JC, Bengtsson A, Bilmes A, Buckley BB, Bushnell N, Chen Z, Collins R, Demura S, Derk AR, Erickson C, Giustina M, Harrington SD, Hong S, Jeffrey E, Kelly J, Klimov PV, Kostritsa F, Laptev P, Locharla A, Mi X, Miao KC, Montazeri S, Mutus J, Naaman O, Neeley M, Neill C, Opremcak A, Quintana C, Redd N, Roushan P, Sank D, Satzinger KJ, Shvarts V, White T, Yao ZJ, Yeh P, Yoo J, Chen Y, Smelyanskiy V, Martinis JM, Neven H, Megrant A, Ioffe L, and Barends R (2022) Resolving catastrophic error bursts from cosmic rays in large arrays of superconducting qubits. *Nature Physics* 18(1): 107–111. ISSN: 17452481. https://doi.org/10.1038/s41567-021-01432-8.

McWhorter AL (1957) 1/f Noise and germanium surface properties. In: Kingston RH (ed.) *Semiconductor Surface Physics*, pp. 207–228. University of Pennsylvania Press.

Meiboom S and Gill D (1958) *The Review of Scientific Instruments* 29: 668.

Milburn GJ and Woolley MJ (2008) Quantum nanoscience. *Contemporary Physics* 49(6): 413–433. https://doi.org/10.1080/00107510802601724.

Muhonen JT, et al. (2014) Storing quantum information for 30 seconds in a nanoelectronic device. *Nature Nanotechnology* 9: 986–991. https://doi.org/10.1038/nnano.2014.211.

Müller C, Cole JH, and Lisenfeld J (2019) Towards understanding two-level-systems in amorphous solids: Insights from quantum circuits. *Reports on Progress in Physics* 82: 124501. https://doi.org/10.1088/1361-6633/ab3a7e.

Nakamura Y, Pashkin YA, and Tsai JS (1999) Coherent control of macroscopic quantum states in a single-Cooper-pair box. *Nature* 398: 786–788. https://doi.org/10.1038/19718.

Nguyen LB, Lin Y-H, Somoroff A, Mencia R, Grabon N, and Manucharyan VE (2019) High-coherence fluxonium qubit. *Physical Review X* 9(4): 041041. https://doi.org/10.1103/PhysRevX.9.041041.

Norris LM, Paz-Silva GA, and Viola L (2016) Qubit noise spectroscopy for non-Gaussian dephasing environments. *Physical Review Letters* 116(15): 150503. https://doi.org/10.1103/PhysRevLett.116.150503.

Paladino E, Galperin YM, Falci G, and Altshuler BL (2014) 1/f Noise: Implications for solid-state quantum information. *Reviews of Modern Physics* 86(2): 361–418. https://doi.org/10.1103/RevModPhys.86.361.

Pellegrino FMD, Falci G, and Paladino E (2019) Charge carrier density noise in graphene: Effect of localized/delocalized traps. *Journal of Statistical Mechanics: Theory and Experiment*: 094015. https://doi.org/10.1088/1742-5468/ab3a26. https://iopscience.iop.org/article/10.1088/1742-5468/ab3a26.

Pellegrino FMD, Falci G, and Paladino E (2020) 1/f Critical current noise in short ballistic graphene Josephson junctions. *Communications Physics* 3(1): 6. ISSN: 2399-3650. https://doi.org/10.1038/s42005-019-0275-9.

Pellegrino FMD, Falci G, and Paladino E (2023) Second spectrum of charge carrier density fluctuations in graphene due to trapping/ detrapping processes. *Applied Physics Letters* 122: 253102. https://doi.org/10.1063/5.0157327. https://pubs.aip.org/aip/apl/article-abstract/122/25/253102/2897709/Second-spectrum-of-charge-carrier-density?redirectedFrom=fulltext.

Petersson KD, Petta JR, Lu H, and Gossard AC (2010) Quantum coherence in a one-electron charge qubit. *Physical Review Letters* 105: 246804.

Petit L, Boter J, Eenink H, Droulers G, Tagliaferri M, Li R, Franke D, Singh K, Clarke J, Schouten R, Dobrovitski V, Vandersypen L, and Veldhorst M (2018) Spin lifetime and charge noise in hot silicon quantum dot qubits. *Physical Review Letters* 121(7): 076801. ISSN: 0031-9007. https://doi.org/10.1103/PhysRevLett.121.076801.

Place APM, Rodgers LVH, Mundada P, Smitham BM, Fitzpatrick M, Leng Z, Premkumar A, Bryon J, Vrajitoarea A, Sussman S, Cheng G, Madhavan T, Babla HK, Le XH, Gang Y, Jäck B, Gyenis A, Yao N, Cava RJ, de Leon NP, and Houck AA (2021) New material platform for superconducting transmon qubits with coherence times exceeding 0.3 milliseconds. *Nature Communications* 12(1): 1779. ISSN: 20411723. https://doi.org/10.1038/s41467-021-22030-5.

Quintana CM, Chen Y, Sank D, Petukhov AG, White TC, Kafri D, Chiaro B, Megrant A, Barends R, Campbell B, Chen Z, Dunsworth A, Fowler AG, Graff R, Jeffrey E, Kelly J, Lucero E, Mutus JY, Neeley M, Neill C, O'Malley PJJ, Roushan P, Shabani A, Smelyanskiy VN, Vainsencher A, Wenner J, Neven H, and Martinis JM (2017) Observation of classical-quantum crossover of 1/f flux noise and its paramagnetic temperature dependence. *Physical Review Letters* 118(5): 057702. ISSN: 10797114. https://doi.org/10.1103/PhysRevLett.118.057702.

Rembold P, Oshnik N, Müller Matthias M, M.M., Montangero S, Calarco T, and Neu E (2020) Introduction to quantum optimal control for quantum sensing with nitrogen-vacancy centers in diamond. *AVS Quantum Science* 2: 024701. ISSN: 2639-0213. https://doi.org/10.1116/5.0006785.

Rondin L, et al. (2014) Magnetometry with nitrogen-vacancy defects in diamond. *Reports on Progress in Physics* 77: 056503. https://doi.org/10.1088/0034-4885/77/5/056503.

Roschier L, Tarkiainen R, Ahlskog M, Paalanen M, and Hakonen P (2001) Multiwalled carbon nanotubes as ultrasensitive electrometers. *Applied Physics Letters* 78(21): 3295–3297. ISSN: 0003-6951. https://doi.org/10.1063/1.1362281.

Rumyantsev S, Liu G, Shur MS, Potyrailo RA, and Balandin AA (2012) Selective gas sensing with a single pristine graphene transistor. *Nano Letters* 12(5): 2294–2298. ISSN: 15306984. https://doi.org/10.1021/nl3001293.

Scarlino P, van Woerkom DJ, Stockklauser A, Koski JV, Collodo MC, Gasparinetti S, Reichl C, Wegscheider W, Ihn T, Ensslin K, and Wallraff A (2019) All-microwave control and dispersive readout of gate-defined quantum dot qubits in circuit quantum electrodynamics. *Physical Review Letters* 122(20): 206802. https://doi.org/10.1103/PhysRevLett.122.206802.

Schirhagl R, et al. (2014) Nitrogen-vacancy centers in diamond: Nanoscale sensors for physics and biology. *Annual Review of Physical Chemistry* 65: 83. https://doi.org/10.1146/annurev-physchem-040513-103659.

Sendelbach S, Hover D, Kittel A, Mück M, Martinis JM, and McDermott R (2008) Magnetism in SQUIDs at millikelvin temperatures. *Physical Review Letters* 100(22): 227006. ISSN: 00319007. https://link.aps.org/doi/10.1103/PhysRevLett.100.227006.

Siddiqi I (2021) Engineering high-coherence superconducting qubits. *Nature Reviews Materials* 6(10): 875–891. ISSN: 2058-8437. https://doi.org/10.1038/s41578-021-00370-4.

Stano P and Loss D (2022) Review of performance metrics of spin qubits in gated semiconducting nanostructures. *Nature Reviews Physics* 4(10): 672–688. ISSN: 2522-5820. https://doi.org/10.1038/s42254-022-00484-w.

Struck T, et al. (2020) Low-frequency spin qubit energy splitting noise in highly purified 28Si/SiGe. *npj Quantum Information* 6: 40. https://doi.org/10.1038/s41534-020-0276-2.

Sung Y, et al. (2019) Non-Gaussian noise spectroscopy with a superconducting qubit sensor. *Nature Communications* 10: 3715. https://doi.org/10.1038/s41467-019-11699-4.

Sung Y, et al. (2021) Multi-level quantum noise spectroscopy. *Nature Communications* 12: 967. https://doi.org/10.1038/s41467-021-21098-3.

Taminiau TH, Wagenaar JJT, van der Sar T, Jelezko F, Dobrovitski VV, and Hanson R (2012) Detection and control of individual nuclear spins using a weakly coupled electron spin. *Physical Review Letters* 109(13): 137602. https://doi.org/10.1103/PhysRevLett.109.137602.

Tennant DM, Martinez LA, Beck KM, Kelley SRO, Wilen CD, Mcdermott R, Dubois JL, and Rosen YJ (2022) Low-frequency correlated charge-noise measurements across multiple energy transitions in a tantalum transmon. *PRX Quantum* 3: 030307. https://doi.org/10.1103/PRXQuantum.3.030307.

Thorgrimsson B, et al. (2017) Extending the coherence of a quantum dot hybrid qubit. *npj Quantum Information* 3: 32. https://doi.org/10.1038/s41534-017-0034-2.

Törmä P, Peotta S, and Bernevig BA (2022) Superconductivity, superfluidity and quantum geometry in twisted multilayer systems. *Nature Reviews Physics* 4(8): 528–542. ISSN: 2522-5820. https://doi.org/10.1038/s42254-022-00466-y.

Uhrig GS (2007) *Physical Review Letters* 98: 100504. https://doi.org/10.1103/PhysRevLett.98.100504.

Ulbricht G, De Lucia M, and Baldwin E (2021) Applications for microwave kinetic induction detectors in advanced instrumentation. *Applied Sciences* 11(6): 2671. ISSN: 2076-3417. https://doi.org/10.3390/app11062671.

Un S, de Graaf S, Bertet P, Kubatkin S, and Danilov A (2022) On the nature of decoherence in quantum circuits: Revealing the structural motif of the surface radicals in α-Al2O3. *Science Advances* 8(14). ISSN: 23752548. https://doi.org/10.1126/sciadv.abm6169.

Van Der Ziel A (1950) On the noise spectra of semi-conductor noise and of flicker effect. *Physica* 16(4): 359–372. ISSN: 00318914. https://doi.org/10.1016/0031-8914(50)90078-4.

Vitusevich S, Gaspary F, Vitusevich S, and Gasparyan F (2011) Low-frequency noise spectroscopy at nanoscale: Carbon nanotube materials and devices. In: *Carbon Nanotubes Applications on Electron Devices*. InTech, ISBN: 978-953-307-496-2. https://doi.org/10.5772/20026. http://www.intechopen.com/books/carbon-nanotubes-applications-on-electron-devices/low-frequency-noise-spectroscopy-at-nanoscale-carbon-nanotube-materials-and-devices.

Wang Z, Wang H, Yu CC, and Wu RQ (2018) Hydrogen as a source of flux noise in SQUIDs. *Physical Review B* 98(2): 020403. ISSN: 24699969. https://doi.org/10.1103/PhysRevB.98.020403.

Wang JI-J, Rodan-Legrain D, Bretheau L, Campbell DL, Kannan B, Kim D, Kjaergaard M, Krantz P, Samach GO, Yan F, Yoder JL, Watanabe K, Taniguchi T, Orlando TP, Gustavsson S, Jarillo-Herrero P, and Oliver WD (2019) Coherent control of a hybrid superconducting circuit made with graphene-based van der Waals heterostructures. *Nature Nanotechnology* 14(2): 120. https://doi.org/10.1038/s41565-018-0329-2.

Wang H, McRae CRH, Gao J, Vissers MR, Brecht T, Dunsworth A, Pappas DP, and Mutus J (2020) Materials loss measurements using superconducting microwave resonators. *Review of Scientific Instruments* 91(9). ISSN: 10897623. https://doi.org/10.1063/5.0017378.

Wang C, et al. (2022) Towards practical quantum computers: Transmon qubit with a lifetime approaching 0.5 milliseconds. *npj Quantum Information* 8: 3. https://doi.org/10.1038/s41534-021-00510-2.

Weissman MB (1988) *Reviews of Modern Physics* 60: 537. https://doi.org/10.1103/RevModPhys.60.537.

Wellstood FC, Urbina C, and Clarke J (1987) Low-frequency noise in dc superconducting quantum interference devices below 1 K. *Applied Physics Letters* 50(12): 772–774. ISSN: 00036951. https://doi.org/10.1063/1.98041.

Wu Y, et al. (2021) Strong quantum computational advantage using a superconducting quantum processor. *Physical Review Letters* 127: 180501.

Xie Y, Lian B, Jäck B, Liu X, Chiu C-L, Watanabe K, Taniguchi T, Bernevig BA, and Yazdani A (2019) Spectroscopic signatures of many-body correlations in magic-angle twisted bilayer graphene. *Nature* 572(7767): 101–105. ISSN: 0028-0836. https://doi.org/10.1038/s41586-019-1422-x.

Yan F, et al. (2012) *Physical Review B* 85: 174521. https://journals.aps.org/prb/abstract/10.1103/PhysRevB.85.174521.

Yang Y, Coppersmith S, and Friesen M (2019) Achieving high-fidelity single-qubit gates in a strongly driven charge qubit with 1/f charge noise. *npj Quantum Information* 5: 12. https://www.nature.com/articles/s41534-019-0127-1.

Yoneda J, Takeda K, Otsuka T, et al. (2017) A quantum-dot spin qubit with coherence limited by charge noise and fidelity higher than 99.9%. *Nature Nanotechnology* 13: 102–106. https://doi.org/10.1038/s41565-017-0014-x.

Yoshihara F, Nakamura Y, Yan F, Gustavsson S, Bylander J, Oliver WD, and Tsai J-S (2014) Flux qubit noise spectroscopy using rabi oscillations under strong driving conditions. *Physical Review B* 89(2): 020503. https://doi.org/10.1103/PhysRevB.89.020503.

Yu C-J, von Kugelgen S, Laorenza DW, and Freedman DE (2021) A molecular approach to quantum sensing. *ACS Central Science* 7(5): 712–723. ISSN: 2374-7943. https://doi.org/10.1021/acscentsci.0c00737.

Zeng W, Tappura K, Kamada M, Seppa H, and Hakonen P (2023) Second spectrum of 1=f noise due to mobility fluctuations: Simulations vs experiments in suspended graphene. *Applied Physics Letters* 123: 013509. https://doi.org/10.1063/5.0153467. https://pubs.aip.org/aip/apl/article/123/1/013509/2901372/Second-spectrum-of-1-f-noise-due-to-mobility.

Zhao N, et al. (2012) Sensing single remote nuclear spins. *Nature Nanotechnology* 7: 657–662. https://doi.org/10.1038/nnano.2012.152.

Zmuidzinas J (2012) Superconducting microresonators: Physics and applications. *Annual Review of Condensed Matter Physics* 3(1): 169–214. ISSN: 19475454. https://doi.org/10.1146/annurev-conmatphys-020911-125022.

Zwerver AMJ, Krähenmann T, Watson TF, Lampert L, George HC, Pillarisetty R, Bojarski SA, Amin P, Amitonov SV, Boter JM, Caudillo R, Correas-Serrano D, Dehollain JP, Droulers G, Henry EM, Kotlyar R, Lodari M, Lüthi F, Michalak DJ, Mueller BK, Neyens S, Roberts J, Samkharadze N, Zheng G, Zietz OK, Scappucci G, Veldhorst M, Vandersypen LMK, and Clarke JS (2022) Qubits made by advanced semiconductor manufacturing. *Nature Electronics* 5(3): 184–190. ISSN: 2520-1131. https://doi.org/10.1038/s41928-022-00727-9.

This page intentionally left blank

Encyclopedia of
Condensed Matter Physics

Second Edition

EDITOR-IN-CHIEF:

Tapash Chakraborty
University of Manitoba, Winnipeg, Manitoba, Canada

SECTION EDITORS:

Ana M. Sanchez
Department of Physics, University of Warwick, Coventry, United Kingdom

Hideo Aoki
Department of Physics, University of Tokyo, Tokyo, Japan

Robert H. Blick
Center for Hybrid Nanostructures, University of Hamburg & DESY, Hamburg, Germany

Roberto Raimondi
Mathematics and Physics Department, Roma Tre University, Rome, Italy

Rudolf A. Roemer
Department of Physics, University of Warwick, Coventry, United Kingdom

Vladimir Mihajlovic Fomin
Leibniz Institute for Solid State and Materials Research (IFW), Dresden, Germany

ELSEVIER

ACADEMIC PRESS
An imprint of Elsevier
elsevier.com/books-and-journals

Volume ISBN
ISBN 978-0-443-21823-1
9 780443 218231

Set ISBN
ISBN 978-0-323-90800-9
9 780323 908009

ENCYCLOPEDIA OF CONDENSED MATTER PHYSICS

SECOND EDITION

ENCYCLOPEDIA OF CONDENSED MATTER PHYSICS

SECOND EDITION

EDITOR-IN-CHIEF

Tapash Chakraborty[*]

Professor, Tier-I Canada Research Chair, University of Manitoba, Winnipeg, MB, Canada

VOLUME 2

ELSEVIER

---

[*] Retired.

Elsevier
Radarweg 29, PO Box 211, 1000 AE Amsterdam, Netherlands
The Boulevard, Langford Lane, Kidlington, Oxford OX5 1GB, United Kingdom
50 Hampshire Street, 5th Floor, Cambridge MA 02139, United States

Copyright © 2024 Elsevier Ltd. All rights reserved

No part of this publication may be reproduced or transmitted in any form or by any means, electronic or mechanical, including photocopying, recording, or any information storage and retrieval system, without permission in writing from the publisher. Details on how to seek permission, further information about the Publisher's permissions policies and our arrangements with organizations such as the Copyright Clearance Center and the Copyright Licensing Agency, can be found at our website: www.elsevier.com/permissions.

This book and the individual contributions contained in it are protected under copyright by the Publisher (other than as may be noted herein).

Notices
Knowledge and best practice in this field are constantly changing. As new research and experience broaden our understanding, changes in research methods, professional practices, or medical treatment may become necessary.

Practitioners and researchers may always rely on their own experience and knowledge in evaluating and using any information, methods, compounds, or experiments described herein. In using such information or methods they should be mindful of their own safety and the safety of others, including parties for whom they have a professional responsibility.

To the fullest extent of the law, neither the Publisher nor the authors, contributors, or editors, assume any liability for any injury and/or damage to persons or property as a matter of products liability, negligence or otherwise, or from any use or operation of any methods, products, instructions, or ideas contained in the material herein.

Library of Congress Cataloging-in-Publication Data
A catalog record for this book is available from the Library of Congress

British Library Cataloguing-in-Publication Data
A catalogue record for this book is available from the British Library

ISBN 978-0-32-390800-9

For information on all publications visit our website at http://store.elsevier.com

ELSEVIER Book Aid International Working together to grow libraries in developing countries
www.elsevier.com • www.bookaid.org

Publisher: Oliver Walter
Acquisitions Editor: Oliver Walter
Content Project Manager: Naman Negi
Associate Content Project Manager: Nandhini Mahendran
Designer: Mark Rogers

EDITOR-IN-CHIEF BIOGRAPHY

Tapash Chakraborty is a retired professor of physics from the University of Manitoba, Canada, where he was also the Canada Research Chair in Nanoscale Physics (2003–17). His research focus has been on many-body theories of various quantum materials, such as nuclear matter, helium liquids, and electron-hole liquids, that he studied under the tutelage of late Professor Manfred Ristig, at the University of Köln (1979–81). Just a year after the discovery of the fractional quantum Hall effect, he (working with his coworkers) demonstrated that electron–electron interactions could actually lead to quantum Hall states with nontrivial spin configurations, and that the low-lying excitations could be described as "spin-reversed quasiparticles." This prediction motivated much experimental work from laboratories around the world, as a result of which the concept of spin-reversed quasi-particles was established.

Similarly, his work on the quantum Hall states in double layer systems has received much attention from the community. Furthermore, Dr. Chakraborty (working with Dr. P. Maksym and others) made pioneering contributions to the many-electron theory of quantum dots. Dr. Chakraborty has also contributed to the theory of electronic properties of various nanoscale systems, such as spin-orbit coupled quantum dots, quantum rings, and single- and double-layer graphene (primarily with Dr. V. Apalkov). He has authored many books and reviews: the book with Dr. Pietiläinen on the quantum Hall effect and the single-authored book on quantum dots have become standard references in their respective fields.

This page intentionally left blank

EDITORIAL ADVISORY BOARD

Ana M. Sanchez
Department of Physics, University of Warwick, Coventry, United Kingdom

Hideo Aoki
Department of Physics, University of Tokyo, Tokyo, Japan

Robert H. Blick
Center for Hybrid Nanostructures, University of Hamburg & DESY, Hamburg, Germany

Roberto Raimondi
Mathematics and Physics Department, Roma Tre University, Rome, Italy

Rudolf A. Roemer
Department of Physics, University of Warwick, Coventry, United Kingdom

Vladimir Mihajlovic Fomin
Leibniz Institute for Solid State and Materials Research (IFW), Dresden, Germany

INTRODUCTION

> Electrons in orbits contained by the quantum,
> And atoms conjoined by the dipolar force,
> Gravity balanced by pressure
> And flap of a wing.
> Here, I remember the angles and curves,
> Calculus, I learned it all –
> Each bird bit and moon fracture
> Fixed by the symmetries,
> Airborne and airless, aloft.
>
> – Alan Lightman: *Song of Two Worlds*

Condensed matter physics (CMP) is the largest discipline in physics, involving a wide variety of interesting concepts and challenges. To quote Leggett (1992), CMP embraces topics "as diverse as traditional solid-state physics, neutron stars and the physics of biological matter." He further added that, by a liberal definition "just about all of physics outside atomic, nuclear and particle physics and cosmology" fall in this vast enterprise[1]. One of the primary goals of CMP is to explore the fundamental properties of matter—solids, liquids or gasses—comprising a large number of *interacting* constituent particles (Laughlin and Pines, 2000). The quantum-mechanical nature of these many-body systems makes condensed-matter highly nontrivial, sometimes counterintuitive and even astonishing. Superconductivity and the fractional quantum Hall effect (FQHE) naturally fall within that category. In fact, for the past four decades, the quantum Hall effects (QHEs) have been the epitome of elegant CMP (von Klitzing et al., 2020). Our fundamental system of units has been redefined following the discovery of the QHE when the "von Klitzing constant" $R_K = 25,\ 812.8074593045\ \Omega$ came into being (von Klitzing, 2019; Nawrocki, 2019). Observation of the QHE in graphene[2] was crucial in determining the Dirac nature of charge carriers there (see for example, Jiang et al., 2007).

Another effect that outwardly resembles the QHE but is conceptually quite different is the FQHE, which is a quintessential manifestation of electron correlations governed by the Coulomb interaction (Störmer, 1992; Eisenstein and Stormer, 1990). To explain this fascinating effect, Laughlin (1983) introduced his eponymous wave function that not only provided the foundation for understanding the effect but also triggered a new wave of ideas with impact far beyond the realm of CMP[3]. Who would have imagined that a large collection of interacting electrons confined on a plane in a perpendicular magnetic field would result in elementary excitations (quasiholes and quasiparticles) (Chakraborty and Pietiläinen, 1988, 1995; Halperin, 1983; Clark and Maksym, 1989) carrying fractional electron charge and obeying the exotic exchange statistics of anyons (Halperin, 1984; Arovas et al., 1984)? These quasiparticles and quasiholes of the Laughlin state still remain an enigma (Laughlin, 1984; Chakraborty, 1985; Morf and Halperin, 1986). Fractional statistics is a truly path-breaking concept in CMP that was introduced by Leinaas and Myrheim (1977), and has been recently confirmed experimentally (Bartolomei et al., 2020; Nakamura et al., 2020).

Much of the history of CMP can be viewed as a series of paradigm shifts[4]. The field evolved rapidly through frequent ground-breaking discoveries that challenged existing paradigms and opened up new applications, and this evolution is expected to continue (Leggett, 2018; Cohen, 2008). For example, our current understanding of

the FQHE required deep mathematical analysis and a wide range of experimental exploration, which revealed a treasure trove of unique phenomena that are yet to be fully understood or explained. Other studies of electron correlations in low spatial dimensions have ushered in many groundbreaking notions, such as Pfaffian states, Majorana fermions in condensed matter, Chern insulators, and topological quantum materials that promise a fault tolerant means to perform quantum computation. The presence of incompressible FQHE states in monolayer graphene (Apalkov and Chakraborty, 2006), bilayer graphene (Apalkov and Chakraborty, 2010, 2011), and double-layer graphene (Liu et al., 2019) has demonstrated the robustness of the effect, and provides invaluable insight into the nature of this effect.

---

[1] Interestingly, some similarities do exist between the mathematical frameworks that describe low-temperature CMP and early-universe cosmology. See Kibble and Srivastava (2013).

[2] An isolated single layer of graphite consisting of carbon atoms bonded together in a hexagonal structure. See, e.g., Abergel et al. (2010).

[3] For example, an important aspect of Laughlin's theory is its seamless concinnity of classical plasma physics and the planar electron gas that has inspired others to use a similar approach to quark-gluon plasma (Lu, 2022).

[4] A detailed exposition of the meaning and examples of "paradigm shifts" (Kuhn-type) can be found in Leggett (2018).

The dynamics of an electron in a periodic potential subjected to a perpendicular magnetic field has been an intriguing problem for more than half a century (Obermair and Wannier, 1976; Osadchy and Avron, 2001)[5]. Within the nearest neighbor tight-binding description of the periodic potential the electron energy spectrum is described by the Harper equation (Harper, 1955). Numerical solution of this equation (Hofstadter, 1976) has revealed that the applied field splits the Bloch bands into subbands and gaps. As the field is varied, the splitting of band continues indefinitely, leading to bands within bands within bands. When plotted as a function of the magnetic flux per lattice cell, the energy spectrum depicts a *fractal* pattern (a self-similar pattern that repeats at every scale) and is known in the literature as Hofstadter's butterfly because of the resemblance of the pattern to butterflies[6]. Observation of the butterfly spectra in real systems is an arduous task. For example, in ordinary crystalline lattices, the required magnetic field to see the butterflies exceeds 1000 Tesla, which is far beyond the reach of present-day technology. Graphene seems to be the ideal system in the quest of those fractal butterflies (Weiss, 2013). It is interesting to note that a mathematical solution of the Harper equation, in contrast to the numerical solution mentioned above, remained a challenging problem (the so-called Ten Martini Problem) for mathematicians until it was solved (Avila and Jitomirskaya, 2006) in 2006.

Magnetism has been known to mankind since ancient times, and it remains a major topic in CMP. The road to understanding magnetism has been long and tortuous. At various times in history, magnets were claimed to have the healing power to cure a myriad of ailments that included epilepsy, arthritis, gout, and baldness. Magnets were the prime ingredients for the "elixir of life" by Paracelsus (1493–1541). Then there was the healing process of "animal magnetism" proposed by Franz Anton Mesmer (1734–1815) (mesmerism)[7], which was famously mocked in Mozart's *Così fan tutte* (Steptoe, 1986). Our current understanding of magnetism is deeply rooted in quantum mechanics as Van Vleck explained (Van Vleck, 1978): "Quantum mechanics is the key to understand magnetism. When one enters the first room with this key there are unexpected rooms beyond, but it is always the master key that unlocks each door." For centuries, the magnetism of certain rocks and metallic iron was only used for the practical purposes of direction finding, particularly navigation with a compass. Motors, generators, and electrical distribution networks appeared only in the 19th century after the discovery of the deep connection between electricity and magnetism. Magnetic order is a collective phenomenon akin to superconductivity and superfluidity that involves a very large number of particles. The rich variety of magnetically ordered states in solids, not only ferromagnetism but also antiferromagnetism, ferrimagnetism, and a range of noncollinear structures, was confirmed only in the middle of the 20th century, with the availability of neutron beams in research reactors. A range of new magnetic materials are taking their place as active layers in thin film sensors and memory devices (Baltz et al., 2018). Besides information storage (Blundell, 2001), important technical applications include magnetic resonance imaging (MRI) and the use of magnetic nanoparticles in medicine.

Many outstanding discoveries in magnetism and magnetic materials have resulted in rapid advances in information storage technology. Over the last two decades spintronics has emerged as an important field of research both from the point of view of fundamental science and advanced technological applications (Yamaguchi et al., 2021; Pinarbasi and Kent, 2022). The giant magnetoresistance (GMR) effect, the spin Hall effect, and the spin galvanic effects are typical examples of developments in the field. Spintronics aims at understanding how the spin degree of freedom of the electrical carriers can be controlled in order to obtain devices with new functionalities and better performance. This endeavor often combines concepts from different aspects of condensed matter systems, giving the topic a fascinating interdisciplinary flavor. Spintronic phenomena are now being studied in an impressive range of different materials ranging from metals to half-metals to semiconductors, graphene and other two-dimensional systems such as transition metal dichalcogenides.

---

[5] For a recent review on butterflies in graphene, see for example Chakraborty and Apalkov (2015).

[6] However, as one of the authors of this Encyclopedia has (somewhat humorously) pointed out, this butterfly has Lebesgue measure zero, that is, it cannot fly!.

[7] A wonderful account of the use of magnetism in medicine since ancient times can be found in Mourino (1991).

The GMR effect and the related tunnel magnetoresistance effect (TMR) found their first commercial use in magnetic field sensors for hard-disk read-heads, before broadening their field of application to include magnetic sensors for the automobile industry, solid-state compasses, biosensors, and nonvolatile magnetic memory (Hartmann, 2000). The ability to manipulate the magnetic state of ferromagnetic structures led to initial developments in spintronics, where the spin direction was controlled by externally applied magnetic fields. However, the push for downscaling and faster timescales has prompted research advances in the past decade where the manipulation of magnetic configurations is achieved by local electric currents (the spin torque effect) (Brataas et al., 2012; Locatelli et al., 2014). In recent years, various novel concepts, such as chiral spintronics, skyrmionic spin textures, and magnetic domain walls in spintronics, have been actively pursued. The rate of progress in spintronics is truly astounding (Editorial, 2022).

In the past century, superconductivity has raised many theoretical challenges and triggered numerous technical developments. Discovered in mercury in 1911, this unique phenomenon occurs when the electrical resistance of many metals and alloys drops to zero when cooled below about 4 K, the temperature of liquid helium. More significantly, the material expels magnetic flux and becomes perfectly diamagnetic. Superconductivity has been adopted or evaluated for a wide range of technical applications (Rogalla and Kes, 2012). These include electric power generation, electric power transmission, high-speed maglev transportation, and ultra-strong magnetic field generation in high-resolution MRI and other nuclear magnetic resonance (NMR) systems. Interestingly, it took almost 50 years after the original discovery for the phenomena to be explained by the BCS theory (Tinkham, 2004) of reciprocal-space electron pairing, via the electron–phonon interaction. This electron–phonon mediated superconductivity became known as "conventional superconductivity" after the discovery of "high-temperature superconductivity" (Müller and Bednorz, 1987) at liquid nitrogen temperatures in tetragonal copper oxides in 1986. This threw open a new challenge to explain the properties of strongly correlated *anisotropic* electronic systems. Further new classes of superconductors that remain to be properly understood include the iron-based pnictides discovered in 2008 (Hosono et al., 2018). Recently, a two-dimensional superlattice made from a twisted bilayer of "magic angle" graphene was found to exhibit unconventional superconductivity (Cao et al., 2018), driven by electron–electron interactions.

The phenomenon of spontaneous symmetry breaking (SSB) is ubiquitous in physics, and plays a fundamental role in CMP, particle physics, and even in cosmology. A classic illustration of SSB being Heisenberg's 1928 paper on ferromagnetism (Heisenberg, 1928). It is responsible for various collective modes, such as the famous Nambu-Goldstone (NG) and Higgs modes. Named by Baker and Glashow (Baker and Glashow, 1962), SSB corresponds to the case where the ground or lowest-energy state does not have the symmetry of the underlying dynamics. Instead, multiple degenerate ground states are available and the symmetry breaking is *spontaneous* because it is not clear, a priori, which one of those ground states will be chosen. In this well-trodden territory a simple analogy of this abstruse concept given by A. Salam is illuminating (CERN, 1977): "Imagine a banquet where guests sit at round tables. A bird's eye view of the scene presents total symmetry, with serviettes alternating with people around each table. A person could equally well take a serviette from his right or from his left. The symmetry is spontaneously broken when one guest decides to pick up from his left and everyone else follows suit." Over the years, development of the concept of SSB has taken a circuitous route (Gaudenzi, 2022): "from the land of particle physics to the physics of many bodies (solids and nuclei), from there to the province of superconductivity, and from the latter back to particle physics ... ." SSB's significance extends beyond the physics of the Higgs boson to the study of low-energy phenomena such as superconductivity, superfluidity, magnetism, and others. Historically, the particle physics community has been guided by this exploration in their quest to understand and discover particles like the Higgs boson. More to the point, when a continuous symmetry is spontaneously broken, a gapless mode, the NG mode, appears which governs the low-energy behavior of the system. As an example, in a solid, the acoustic phonon is the NG mode associated with translational symmetry breaking and determines the behavior of the specific heat at low temperature (the Debye T^3 law). Recently, signatures of Higgs and Goldstone modes have been proposed to exist in a perovskite oxide (Marthinsen et al., 2018), in other crystalline structures (Vallone, 2019), and also in various other quantum systems (Léonard et al., 2017). On a lighter note, it is the symmetry breaking that is claimed to have prevented the fabled donkey (Weintraub, 2012) in the parable by Jean Buridan (1300–50) from dying of starvation (Fubini, 1974).

Common to the theoretical descriptions of these phenomena across CMP and high-energy physics is Quantum field theory (QFT). QFT was originally developed to describe the fundamental processes in high-energy physics, but has now become a valuable tool to address problems across physics, in particular, in CMP (Fradkin, 2013; see also, Mustafa, 2023), statistical physics, modern quantum chemistry, and even in

pure mathematics (Folland, 2008). Advances in our understanding of strongly correlated electron systems in CMP such as high-temperature superconductivity and the FQHE have been aided by the QFT. It has facilitated the treatment of spontaneous symmetry broken states, such as superfluids. Interestingly, many of the conceptual developments in CMP have, in return, had a reciprocal impact in QFT. A spectacular example being Nambu's work in dynamical symmetry breaking (Weinberg, 1986; Nambu, 2009) in particle physics, based on the BCS theory of superconductivity.

A glass is a noncrystalline solid obtained by quenching a liquid. It has a liquid-like structure, but a transition from liquid to solid behavior occurs on cooling. It may have one of a continuum of possible ground states that exhibit frozen-in liquid-like disorder. The term "spin glass" was coined by B.R. Coles (Mydosh, 1993) in 1970 for a diluted magnetic material with frozen-in paramagnetic-like spin disorder where the magnetic moments interact with randomly varying positive or negative exchange interactions leading to a multitude of possible ground states with different, random orientations of the spins. As in a normal glass, the energy barriers between the continuum of metastable states prevent it from ever reaching equilibrium. This phase of condensed matter has been an important and productive area of research. Spin-glass models are conceptually simple, but embody sophisticated physics. These models have become a paradigm for the solution of complex optimization problems (Mézard, 2022): much like the undulating flight patterns of starlings around the skies over Rome (Parisi, 2023). After cooling from the paramagnetic phase, the spin glass remains out of equilibrium, and it slowly evolves. This aging phenomenon corresponds to the growth of a "spin-glass order" parameter, whose correlation length can be measured (Joh et al., 1999). A cooling temperature step during aging causes a partial "rejuvenation," while the "memory" of previous aging is stored and can be retrieved (Refregier et al., 1987; Bouchaud et al., 2001). Many glassy materials present aging, and rejuvenation and memory effects can be found in other cases, but they are usually less pronounced. Numerical simulations of these phenomena are under active investigation using custom-built computers (Baity-Jesi et al., 2023; Vincent, 2023). A general understanding of glassy systems, to which spin glasses bring some special insight, is being pursued. It was realized decades ago that the physics of spin glasses has deep connections with the behavior of complex biological systems. In fact, spin-glass type states in neural network models offer interesting insights into states of high and low brain activity, as observed in mammals (Recio and Torres, 2016). These analogies are potentially useful for applications in fields such as robotics and artificial intelligence (AI) (Andriuschenko et al., 2022).

One of the most spectacular phenomena in CMP, discovered in the last century, was Bose-Einstein condensation (BEC). This macroscopic quantum phenomenon had its genesis in the work of Satyendra Nath Bose (Bose, 1924; Blanpied, 1972; Tomczyk, 2022) (whose name is forever associated with bosons), and has fascinated physicists for decades, ever since the first observation of this exotic state of matter in an ultracold gas of rubidium atoms (Georgescu, 2020). Among the advances made in this field, we highlight only a few: simulation of correlated electron states, such as the FQHE state and a bosonic analog of the Laughlin state, and the famous BEC-BCS crossover from a BEC to a BCS superfluid of weakly bound Cooper pairs, as the interparticle interaction strength is varied. Noteworthy is the recent measurement of the dynamic structure factor in an ultracold Fermi gas of lithium-6 atoms in the "unitary" limit, where a linear phonon mode for low momentum transfer can be clearly discerned (Biss et al., 2022). Perhaps such a method might one day shed light on the Laughlin quasiparticle gap and the collective modes that are still largely unresolved (Chakraborty and Pietiläinen, 1988, 1995; Halperin, 1983; Clark and Maksym, 1989).

Liquid helium, ^{4}He, and the less common isotope ^{3}He are unique quantum systems (Volovik, 2009). They remain liquid even at absolute zero temperature, a direct manifestation of Heisenberg's uncertainty principle and zero-point energy. The light mass of helium atoms and their weak interatomic attraction leads to a substantial zero-point kinetic energy and the system remains in the liquid state at ambient pressure. Solidification occurs when a pressure of about 25 MPa is applied. The different quantum statistics of the two helium isotopes (^{4}He is a boson while ^{3}He is a fermion) are responsible for the different physical characteristics of the two systems. Microscopic approaches to understand the ground state and low-energy excitations of the liquid state have occupied researchers for many decades (see for example, Ristig and Clark, 1976; Lam et al., 1977). These highly correlated quantum fluids have been established as systems where the efficacies of different many-body theories can be tested (Kallio and Smith, 1977; Lantto et al., 1977). These systems have been described as Ariadne's thread in this Encyclopedia, where the strongly interacting constituent particles are treated by a variety of ingenious theoretical and experimental approaches. Interestingly, liquid helium has been proposed to be a medium to design multiexcitation detectors to probe *dark matter* (Schutz and Zurek, 2016) in the keV mass limit. Although this looks far afield from CMP, the interface between CMP and high-energy particle physics could inspire new horizons in CMP, as discussed earlier.

CMP also has an enormous impact on our daily lives with unceasing technological innovation stemming directly from the advances in CMP research. It is also closely associated with the progress of our understanding of materials science and mechanical, chemical, and electrical engineering that deals with properties of novel materials and devices. As some authors have very aptly pointed out (Chaikin and Lubensky, 1995): The use and understanding of matter in its condensed (liquid or solid) state have gone hand in hand with the advances of civilization and technology since the first use of primitive tools. So important has the control of condensed matter been to man that prehistoric ages—the Stone Age, the Bronze Age, the Iron Age—are named after the material dominating the technology of the time. In fact, modern civilization is entirely dependent on our deep understanding and practical use of materials, old and new: Steel, glass, and concrete have shaped our modern living with comfort, health, longevity, and material wealth. All around us, from a tiny paper clip to giant skyscrapers, from jet planes to modern medicines, and the ubiquitous plastics that are integrated into nearly all aspects of human life, are testaments to our control over the myriad behavior of materials (Miodownik, 2014). Today, a large number of materials are designed by using principles of quantum mechanics (Freeman, 2002).

The Silicon chip that launched the information age is a great example of the effect of CMP on our daily lives. The scaling of transistors down to the nanometer range has enabled them to be embedded in greater numbers in the all-pervasive electronic devices that have transformed every facet of life all around the world. The transition from room-size to pocket-size computers with ever increasing computational power and memory, that occurred in only a few decades, epitomizes the unrelenting progress made in this direction. Advances in nanoscale research have opened the door to exploration of the natural world at the ultra-small scale (Chakraborty, 2022), with the potential to shape our future world.

Quantum dots (QDs), the quasi-zero-dimensional electron systems, are one of the most extensively studied nanostructures in the past three decades. They represent the ultimate reduction in dimensionality of a semiconductor device. Here the electrons are confined (either electrostatically or structurally) in all three directions and occupy spectrally sharp energy levels similar to those found in atoms (Chakraborty, 1999), hence the popular moniker *artificial atoms* (Maksym and Chakraborty, 1990). QDs and other similar nanostructures (Chakraborty, 2003) offer a rich variety of fundamental phenomena that result from manipulation of single electrons (single electronics) or single spins at the nanoscale. The study of interacting electrons in a QD requires large-scale numerical computations involving matrices of dimensions in the millions ("monster matrices") (Chakraborty and Pietiläinen, 2005; Pietiläinen and Chakraborty, 2006). QDs are also thought to have vast potential for future technological applications. One prominent example being quantum cryptography where the QDs are used in single photon emitters (Nowak et al., 2014), and in single photon detectors (Shields et al., 2000). Quantum cryptography, in turn, forms the basis of the *quantum Internet* (Liao et al., 2018). Other applications include lasers, and spintronics in quantum computing, entertainment industry (Bourzac, 2013), and even in biology (Bruchez and Holz, 2007).

Research in recent years has increasingly revealed that quantum phenomena are also ubiquitous in the natural world (Ball, 2011). They govern how birds are able to navigate around the globe using Earth's magnetic field or how plants use photosynthesis to harvest sunlight for conversion to chemical energy. All depend on subtle quantum effects that are now coming to light, thereby ushering the topic of quantum biology into CMP. Deoxyribonucleic acid (DNA), the molecule responsible for storage of genetic information in the cells of all living organism, is entrusted with the task of preserving, copying, and transmitting information that are necessary for living beings to grow and function. It is often referred to as the body's hereditary material as DNA is replicated and transmitted from parents to their offspring. This "molecule of life" was discovered in 1869 by Friedrich Miescher in Tübingen, Germany, who called it "nuclein," as it was isolated from the nucleus of white blood cells (Dahm, 2005; Thess et al., 2021). It took more than eighty years from that momentous event, to discover that DNA has a right-handed double-helix structure with appropriate base pairing (Watson and Crick, 1953; Klug, 2004). That discovery was so important that it has been compared with the discovery of the atomic nucleus in physics (Frank-Khamenetskii, 1997). Understanding the structure of the atom heralded quantum physics, while understanding of the structure of DNA brought forth the field of molecular biology.

DNA has several remarkable properties that make this molecule a prime candidate for nano-electronic materials (Chakraborty, 2007). These include molecular recognition and the ability to self-assemble via the complementarity of the base sequences on the two strands, which means that DNA can be integrated error-free in current semiconductor technology. DNA can also detect information about its own integrity that can trigger its eventual repair mechanism. All these properties are perfectly suitable for developing nanoscale electronics involving DNA

(Taniguchi and Kawai, 2006). Despite the promise of harnessing biology to realize integrated molecular electronics remains fascinating, much work remains to be done to make it a reality (Braun and Keren, 2004).

Protein molecules play a vital role in all living organisms. They are described as Nature's robots (Tanford and Reynolds, 2001) because for every imaginable task required in a living organism, and for every step of that task, there is a protein designed to carry it out. These proteins are even programmed to know when to turn on or off. Just as the twenty-six letters in the alphabet can spell out hundreds of thousands of words, there are twenty different naturally occurring amino acids that can be combined into many more different proteins than there are atoms in the known universe! Protein's biological function is determined by its unique and native three-dimensional structures that are characteristic of individual proteins (Gomes and Faísca, 2019; Echenique, 2007). The question of how proteins fold to their unique, compact, and highly organized functional states has remained an enduring challenge ("The protein-folding problem") (Chan and Dill, 1993; Dill and MacCallum, 2012; Wolynes and Eaton, 1999). Recently, there has been a tremendous development in this area of research. In November 2020, an AI program called AlphaFold, designed to tackle the problem of protein folding, predicted the three-dimensional structures of almost every protein known to science—about 200 millions in all (Jumper et al., 2021). AlphaFold uses a machine learning methodology to bring together information from preexisting knowledge of protein structures, and other geometric and physical constraints to predict protein structures. While this has been heralded a watershed moment in structural biology (Perrakis and Sixma, 2021), there are many key questions that AlphaFold cannot address yet. These include aspects of protein behavior that cannot be understood from a static structure, such as how proteins respond to their environment or how intrinsically disordered proteins actually are organized. Some authors (Nasser et al., 2021) have likened it to solving a crime story: while AlphaFold presents a snapshot in time, the question about how we get there remains unanswered. Biological systems have developed elaborate mechanisms to ensure that proteins fold correctly, or otherwise, they are detected and degraded before any serious harm can result to the host organism. However, protein misfolding does happen and that misfolding in the cell is linked to an array of diseases, including cancers, cardiovascular disease, type II diabetes, and numerous neurodegenerative diseases, such as Alzheimer's, Parkinson's, and Huntington's disease. NMR spectroscopy has been an important technique to study protein folding where valuable insights are gained into many aspects of the folding process (Jane Dyson and Wright, 1996).

In this Encyclopedia, we strive to present a taste of all the developments in CMP described above (and much more), written by experts in the field. We are keenly aware that many important and interesting topics are not covered here. However, that is not for want of trying. As some authors had rightly pointed out (Hoddeson, 1992): The field is huge and varied and lacks the unifying features beloved of historians, neither a single hypothesis or set of basic equations underpin the field, as in quantum mechanics or relativity theory, nor a single spectacular and fundamental discovery such as uranium fission for nuclear technology or the structure of DNA for molecular biology. CMP owes what unity it has simply to a common concern with solid and liquid materials. This encompasses such a large range of theories and methods that the field resembles a confederation of interest groups rather than a single entity. Clearly, the task of collecting everything in one place is a monumental endeavor, but we do hope that our compilation of a large number of chapters in this five-volume work, covering a broad range of in-depth descriptions of varied phenomena in CMP will be a treasured source of facts and ideas for the community.

It is undeniably true that there would have been no Encyclopedia without the extraordinary contributions of the large number of authors whose valuable time and efforts brought this project to fruition. My sincere thanks to all of them. I also wish to extend my deep appreciation to the staff at Elsevier for their skillful handling of this huge project. The cover image was created by Hong-Yi Chen from National Taiwan Normal University. The image below was created by Elisabetta Collini, one of the authors. My deepest appreciation to them for taking the time to do this work. Finally, my sincere thanks to the Section editors, Vladimir Fomin, Ana Sanchez, Roberto Raimondi, Hideo Aoki, Rudolf Römer, and Robert Blick for the effort they all expended, that has contributed to the success of this venture. Special thanks go to Vladimir Fomin and Ana Sanchez for securing a large share of the chapters and for their enduring help in providing valuable advice and support to bring the project to fruition. Thanks are also due to many of my friends and colleagues, in particular, Michael Coey, Jürg Fröhlich, Sinéad Griffin, Peter Maksym, Eric Vincent, and Jakob Yngvason for their careful and critical reading of the introduction.

Tapash Chakraborty
St. Catharines
Ontario, Canada

References

Abergel DSL, Apalkov V, Berashevich J, Ziegler K, and Chakraborty T (2010) Properties of graphene: A theoretical perspective. *Advances in Physics* 59: 261. https://doi.org/10.1080/00018732.2010.487978.

Andriuschenko P, Kapitan D, and Kapitan V (2022) A new look at the spin glass problem from a deep learning perspective. *Entropy* 24: 697. https://doi.org/10.3390/e24050697.

Apalkov VM and Chakraborty T (2006) Fractional quantum Hall states of Dirac electrons in graphene. *Physical Review Letters* 97: 126801. https://doi.org/10.1103/PhysRevLett.97.126801.

Apalkov VM and Chakraborty T (2010) Controllable driven phase transitions in fractional quantum Hall states in bilayer graphene. *Physical Review Letters* 105: 036801. https://doi.org/10.1103/PhysRevLett.105.036801.

Apalkov VM and Chakraborty T (2011) Stable pfaffian state in bilayer graphene. *Physical Review Letters* 107: 186803. https://doi.org/10.1103/PhysRevLett.107.186803.

Arovas D, Schrieffer JR, and Wilczek F (1984) Fractional statistics and the quantum Hall effect. *Physical Review Letters* 53: 722. https://doi.org/10.1103/PhysRevLett.53.722.

Avila A and Jitomirskaya S (2006) Solving the ten martini problem. *Lecture Notes in Physics* 690: 5. https://doi.org/10.1007/3-540-34273-7_2.

Baity-Jesi M, et al. (2023) Memory and rejuvenation effects in spin glasses are governed by more than one length scale. *Nature Physics* 19: 978–985. https://doi.org/10.1038/s41567-023-02014-6.

Baker M and Glashow SL (1962) Spontaneous breakdown of elementary particle symmetries. *Physics Review* 128: 2462. https://doi.org/10.1103/PhysRev.128.2462.

Ball P (2011) Physics of life: The dawn of quantum biology. *Nature* 474: 272. https://doi.org/10.1038/474272a.

Baltz V, et al. (2018) Antiferromagnetic spintronics. *Reviews of Modern Physics* 90: 015005. https://doi.org/10.1103/RevModPhys.90.015005.

Bartolomei H, et al. (2020) Fractional statistics in anyon collisions. *Science* 368: 173. https://doi.org/10.1126/science.aaz5601.

Biss H, et al. (2022) Excitation spectrum and superfluid gap of an ultracold Fermi gas. *Physical Review Letters* 128: 100401. https://doi.org/10.1103/PhysRevLett.128.100401.

Blanpied WA (1972) Satyendranath Bose: Co-founder of quantum statistics. *American Journal of Physics* 40: 1212. https://doi.org/10.1119/1.1986805.

Blundell S (2001) *Magnetism in Condensed Matter*. New York: Oxford U.P.

Bose SN (1924) Plancks gesetz und lichtquantenhypothese. *Zeitschrift für Physik* 26: 178. https://doi.org/10.1007/BF01327326.

Bouchaud J-P, Dupuis V, Hammann J, and Vincent E (2001) Separation of time and length scales in spin glasses: Temperature as a microscope. *Physical Review B* 65: 024439. https://doi.org/10.1103/PhysRevB.65.024439.

Bourzac K (2013) Quantum dots go on display. *Nature* 493: 283. https://doi.org/10.1038/493283a.

Brataas A, Kent AD, and Ono H (2012) Current-induced torques in magnetic materials. *Nature Materials* 11: 372. https://doi.org/10.1038/nmat3311.

Braun E and Keren K (2004) From DNA to transistors. *Advances in Physics* 53: 441. https://doi.org/10.1080/00018730412331294688.

Bruchez MP and Holz CZ (2007) *Quantum Dots: Applications in Biology*. New Jersey: Humana Press. https://doi.org/10.1385/1597453692.

Cao Y, et al. (2018) Unconventional superconductivity in magic-angle graphene superlattices. *Nature* 556: 43. https://doi.org/10.1038/nature26160.

CERN. (1977) Gauge theories with the lid, partially, off. *CERN Courier* 17: 271. https://cds.cern.ch/record/1730245/files/vol17-issue9-p271-e.pdf.

Chaikin PM and Lubensky TC (1995) *Principles of Condensed Matter Physics*. Cambridge University Press. https://doi.org/10.1017/CBO9780511813467.

Chakraborty T (1985) Elementary excitations in the fractional quantum Hall effect. *Physical Review B* 31: 4026. https://doi.org/10.1103/PhysRevB.31.4026.

Chakraborty T (1999) *Quantum Dots: A Survey of the Properties of Artificial Atoms*. Amsterdam: North-Holland. https://doi.org/10.1016/B978-0-444-50258-2.X5000-7.

Chakraborty T (2003) Nanoscopic quantum rings: A new perspective. *Advances in Solid State Physics* 43: 79. https://doi.org/10.1007/978-3-540-44838-9_6.

Chakraborty T (ed.) (2007) *Charge Migration in DNA*. Springer. https://doi.org/10.1007/978-3-540-72494-0.

Chakraborty T (2022) *Nanoscale Quantum Materials: Musings on the Ultra-Small World*. CRC Press. https://doi.org/10.1201/9781003090908.

Chakraborty T and Apalkov VM (2015) Fractal butterflies of Dirac fermions in monolayer and bilayer graphene. *IET Circuits, Devices and Systems* 9: 19. https://doi.org/10.1049/iet-cds.2014.0275.

Chakraborty T and Pietiläinen P (1988) *The Fractional Quantum Hall Effect*. Springer Verlag. https://doi.org/10.1007/978-3-642-97101-3.

Chakraborty T and Pietiläinen P (1995) *The Quantum Hall Effects*, 2nd. Springer. https://doi.org/10.1007/978-3-642-79319-6.

Chakraborty T and Pietiläinen P (2005) Optical signatures of spin-orbit interaction effects in a parabolic quantum dot. *Physical Review Letters* 95: 136603. https://doi.org/10.1103/PhysRevLett.95.136603.

Chan HS and Dill KA (1993) The protein folding problem. *Physics Today* 46: 24. https://doi.org/10.1063/1.881371.

Clark R and Maksym P (1989) Fractional quantum Hall effect in a spin. *Physics World* 2: 39. https://doi.org/10.1088/2058-7058/2/9/23.

Cohen ML (2008) Fifty years of condensed matter physics. *Physical Review Letters* 101: 250001. https://doi.org/10.1103/PhysRevLett.101.250001.

Dahm R (2005) Friedrich miescher and the discovery of DNA. *Developmental Biology* 278: 274. https://doi.org/10.1016/j.ydbio.2004.11.028.

Dill KA and MacCallum JL (2012) The protein-folding problem, 50 years on. *Science* 338: 1042. https://doi.org/10.1126/science.1219021.

Echenique P (2007) Introduction to protein folding for physicists. *Contemporary Physics* 48: 81. https://doi.org/10.1080/00107510701520843.

Editorial (2022) New horizons in spintronics. Nature Materials 21: 1. https://doi.org/10.1038/s41563-021-01184-z.

Eisenstein JP and Stormer HL (1990) The fractional quantum Hall effect. *Science* 248: 1510. https://doi.org/10.1126/science.248.4962.1510.

Folland GB (2008) *Quantum Field Theory: A tourist guide for Mathematicians*. American Mathematical Society. https://doi.org/10.1090/surv/149.

Fradkin E (2013) *Field Theories of Condensed Matter Physics*. Cambridge University Press. https://doi.org/10.1017/CBO9781139015509.

Frank-Khamenetskii MD (1997) *Unraveling DNA: The Most Important Molecule of life*. Basic Books.

Freeman AJ (2002) Materials by design and the exciting role of quantum computation/simulation. *Journal of Computational and Applied Mathematics* 149: 27. https://doi.org/10.1016/S0377-0427(02)00519-8.

Fubini S (1974) Present trends in particle physics. In: *Proc. Intl. Conf. on High Energy Physics*. Didcot, England: Rutherford Laboratory. https://cds.cern.ch/record/417271/files/CM-P00060491.pdf.

Gaudenzi R (2022) *Historical Roots of Spontaneous Symmetry Breaking: Steps Towards an Analogy*. Springer. https://doi.org/10.1007/978-3-030-99895-0.

Georgescu I (2020) 25 Years of BEC. *Nature Reviews Physics* 2: 396. https://doi.org/10.1038/s42254-020-0211-7.

Gomes CM and Faísca PFN (2019) *Protein Folding: An Introduction*. Springer. https://doi.org/10.1007/978-3-319-00882-0_1.

Halperin BI (1983) Theory of the quantized Hall conductance. *Helvetica Physica Acta* 56: 75. https://doi.org/10.5169/seals-115362.

Halperin BI (1984) Statistics of quasiparticles and the hierarchy of fractional quantized Hall states. *Physical Review Letters* 52: 1583. https://doi.org/10.1103/PhysRevLett.52.1583.

Harper PG (1955) Single band motion of conduction electrons in a uniform magnetic field. *Proceedings of the Physical Society. Section A* 68: 874. https://doi.org/10.1088/0370-1298/68/10/304.

Hartmann U (2000) *Magnetic Multilayers and Giant Magnetoresistance: Fundamentals and Industrial Applications*. Berlin: Springer Verlag. https://doi.org/10.1007/978-3-662-04121-5.

Heisenberg W (1928) Zur theorie des ferromagnetismus. *Zeitschrift für Physik* 49: 619. https://doi.org/10.1007/BF01328601.

Hoddeson L (1992) *Out of the Crystal Maze: Chapters From the History of Solid-State Physics*. N.Y.: Oxford University Press.

Hofstadter D (1976) Energy levels and wave functions of Bloch electrons in rational and irrational magnetic fields. *Physical Review B* 14: 2239. https://doi.org/10.1103/PhysRevB.14.2239.

Hosono H, et al. (2018) Recent advances in iron-based superconductors toward applications. *Materials Today* 21: 278. https://doi.org/10.1016/j.mattod.2017.09.006.

Jane Dyson H and Wright PE (1996) Insights into protein folding from NMR. *Annual Review of Physical Chemistry* 47: 369. https://doi.org/10.1146/annurev.physchem.47.1.369.

Jiang Z, et al. (2007) Quantum Hall effect in graphene. *Solid State Communications* 143: 14. https://doi.org/10.1016/j.ssc.2007.02.046.

Joh YG, Orbach R, Wood JJ, Hammann J, and Vincent E (1999) Extraction of the spin glass correlation length. *Physical Review Letters* 82: 438. https://doi.org/10.1103/PhysRevLett.82.438.

Jumper J, et al. (2021) Highly accurate protein structure prediction with alphafold. *Nature* 596: 583. https://doi.org/10.1038/s41586-021-03819-2.

Kallio A and Smith RA (1977) How simple can HNC be and still be right? *Physics Letters B* 68: 315. https://doi.org/10.1016/0370-2693(77)90483-X.

Kibble T and Srivastava A (2013) Condensed matter analogues of cosmology. *Journal of Physics. Condensed Matter* 25: 400301. https://doi.org/10.1088/0953-8984/25/40/400301.

Klug A (2004) The discovery of the DNA double helix. *Journal of Molecular Biology* 335: 3. https://doi.org/10.1016/j.jmb.2003.11.015.

Lam PM, Clark JW, and Ristig ML (1977) Density matrix and momentum distribution of helium liquids and nuclear matter. *Physical Review B* 16: 222. https://doi.org/10.1103/PhysRevB.16.222.

Lantto LJ, Jackson AD, and Siemens PJ (1977) HNC variational calculations of boson matter. *Physics Letters B* 68: 311. https://doi.org/10.1016/0370-2693(77)90482-8.

Laughlin RB (1983) Anomalous quantum Hall effect: An incompressible quantum fluid with fractionally charged excitations. *Physical Review Letters* 50: 1395. https://doi.org/10.1103/PhysRevLett.50.1395.

Laughlin RB (1984) Primitive and composite ground states in the fractional quantum Hall effect. *Surface Science* 142: 163. https://doi.org/10.1016/0039-6028(84)90301-7.

Laughlin RB and Pines D (2000) The theory of everything. *Proceedings of the National Academy of Sciences of the United States of America* 97: 28. https://doi.org/10.1073/pnas.97.1.28.

Leggett A (1992) On the nature of research in condensed-state physics. *Foundations of Physics* 22: 221. https://doi.org/10.1007/BF01893613.

Leggett A (2018) Reflections on the past, present and future of condensed matter physics. *Science Bulletin* 63: 1019. https://doi.org/10.1016/j.scib.2018.07.004.

Leinaas JM and Myrheim J (1977) On the theory of identical particles. *Il Nuovo Cimento B* 37: 1. https://doi.org/10.1007/BF02727953.

Léonard J, et al. (2017) Monitoring and manipulating higgs and goldstone modes in a supersolid quantum gas. *Science* 358: 1415. https://doi.org/10.1126/science.aan2608.

Liao S-K, et al. (2018) Satellite-relayed intercontinental quantum network. *Physical Review Letters* 120: 030501. https://doi.org/10.1103/PhysRevLett.120.030501.

Liu X, Hao Z, Watanabe K, Taniguchi T, Halperin BI, and Kim P (2019) Interlayer fractional quantum Hall effect in a coupled graphene double layer. *Nature Physics* 15: 893. https://doi.org/10.1038/s41567-019-0546-0.

Locatelli N, Cros V, and Grollier J (2014) Spin-torque building blocks. *Nature Materials* 13: 11. https://doi.org/10.1038/nmat3823.

Lu W (2022) Quark-gluon plasma and nucleons à la Laughlin. *International Journal of Geometric Methods in Modern Physics* 19: 2250061. https://doi.org/10.1142/S021988782250061X.

Maksym P and Chakraborty T (1990) Quantum dots in a magnetic field: Role of electron-electron interactions. *Physical Review Letters* 65: 108. https://doi.org/10.1103/PhysRevLett.65.108.

Marthinsen A, et al. (2018) Goldstone-like phonon modes in a (111)-strained perovskite. *Physical Review Materials* 2: 014404. https://doi.org/10.1103/PhysRevMaterials.2.014404.

Mézard M (2022) Spin glasses and optimization in complex systems. *Europhysics News* 53: 15. https://doi.org/10.1051/epn/2022105.

Miodownik M (2014) *Stuff Matters: Exploring the Marvelous Materials That Shape Our Man-Made World*. N.Y.: Houghton Mifflin Harcourt.

Morf R and Halperin BI (1986) Monte Carlo evaluation of trial wave functions for the fractional quantized Hall effect: Disk geometry. *Physical Review B* 33: 2221. https://doi.org/10.1103/PhysRevB.33.2221.

Mourino MR (1991) From thales to lauterbur, or from the loadstone to MR imaging: Magnetism and medicine. *Radiology* 180: 593. https://doi.org/10.1148/radiology.180.3.1871268.

Müller KA and Bednorz JG (1987) The discovery of a class of high-temperature superconductors. *Science* 237: 1133. https://doi.org/10.1126/science.237.4819.1133

Mustafa MG (2023) An introduction to thermal field theory and some of its application. *The European Physical Journal Special Topics* 232: 1369–1457. https://doi.org/10.1140/epjs/s11734-023-00868-8.

Mydosh JA (1993) *Spin Glasses: An Experimental Introduction*. CRC Press.

Nakamura J, et al. (2020) Direct observation of anyonic braiding statistics. *Nature Physics* 16: 931. https://doi.org/10.1038/s41567-020-1019-1.

Nambu Y (2009) Nobel lecture: Spontaneous symmetry breaking in particle physics: A case of cross fertilization. *Reviews of Modern Physics* 81: 1015. https://doi.org/10.1103/RevModPhys.81.1015.

Nasser R, Dignon GL, Razban RM, and Dill KA (2021) The protein folding problem: The role of theory. *Journal of Molecular Biology* 433: 167126. https://doi.org/10.1016/j.jmb.2021.167126.

Nawrocki W (2019) *Introduction to Quantum Metrology*, 2nd. Springer. https://doi.org/10.1007/978-3-030-19677-6.

Nowak AL, et al. (2014) Deterministic and electrically tunable bright single-photon source. *Nature Communications* 5: 3240. https://doi.org/10.1038/ncomms4240.

Obermair GM and Wannier GH (1976) Bloch electrons in magnetic fields: Rationality, irrationality, degeneracy. *Physica Status Solidi (B)* 76: 217. https://doi.org/10.1002/pssb.2220760122.

Osadchy D and Avron JE (2001) Hofstadter butterfly as quantum phase diagram. *Journal of Mathematical Physics* 42: 5665. https://doi.org/10.1063/1.1412464.

Parisi G (2023) *In a Flight of Starlings: The Wonders of Complex Systems*. Penguin Press.

Perrakis A and Sixma TK (2021) Ai revolutions in biology. *EMBO Reports* 22: e54046. https://doi.org/10.15252/embr.202154046.

Pietiläinen P and Chakraborty T (2006) Energy levels and magneto-optical transitions in parabolic quantum dots with spin-orbit coupling. *Physical Review B* 73: 155315. https://doi.org/10.1103/PhysRevB.73.155315.

Pinarbasi M and Kent AD (2022) Perspectives on spintronics technology: Giant magnetoresistance to spin transfer torque magnetic random access memory. *APL Materials* 10: 020901. https://doi.org/10.1063/5.0075945.

Recio I and Torres JJ (2016) Emergence of low noise frustrated states in E/I balanced neural networks. *Neural Networks* 84: 91. https://doi.org/10.1016/j.neunet.2016.08.010.

Refregier P, Vincent E, Hammann J, and Ocio M (1987) Ageing phenomena in a spin-glass: Effect of temperature changes below Tg. *Journal of Physics (France)* 48: 1533. https://doi.org/10.1051/jphys:019870048090153300.

Ristig ML and Clark JW (1976) Density matrix of quantum fluids. *Physical Review B* 14: 2875. https://doi.org/10.1103/PhysRevB.14.2875.

Rogalla H and Kes PH (2012) *100 Years of Superconductivity*. Boca Raton: Taylor & Francis Group. https://doi.org/10.1201/b11312.

Schutz K and Zurek KM (2016) Detectability of light dark matter with superfluid helium. *Physical Review Letters* 117: 121302. https://doi.org/10.1103/PhysRevLett.117.121302.

Shields AJ, et al. (2000) Detection of single photons using a field-effect transistor gated by a layer of quantum dots. *Applied Physics Letters* 103: 3673. https://doi.org/10.1063/1.126745.

Steptoe A (1986) Mozart, mesmer and ‘cosi fan tutte’. *Musics and Letters* 67: 248. https://doi.org/10.1093/ml/67.3.248.

Störmer HL (1992) Two-dimensional electron correlation in high magnetic fields. *Physica B: Condensed Matter* 177: 401. https://doi.org/10.1016/0921-4526(92)90138-I.

Tanford C and Reynolds J (2001) *Nature’s Robots: A History of Proteins*. Oxford University Press.

Taniguchi M and Kawai T (2006) Dna electronics. *Physica E: Low-dimensional Systems and Nanostructures* 33: 1. https://doi.org/10.1016/j.physe.2006.01.005.

Thess A, et al. (2021) Historic nucleic acids isolated by Friedrich Miescher contain RNA beside DNA. *Biological Chemistry* 402: 1179. https://doi.org/10.1515/hsz-2021-0226.

Tinkham M (2004) *Introduction to Superconductivity*. N.Y.: Dover.

Tomczyk H (2022) Did Einstein predict Bose-Einstein condensation? *Studies in History and Philosophy of Science* 93: 30. https://doi.org/10.1016/j.shpsa.2022.02.014.

Vallone M (2019) Higgs and goldstone modes in crystalline solids. *Physica Status Solidi* 257: 1900443. https://doi.org/10.1002/pssb.201900443.

Van Vleck JH (1978) Quantum mechanics—The key to understanding magnetism. *Reviews of Modern Physics* 50: 181. https://doi.org/10.1103/RevModPhys.50.181.

Vincent E (2023) Rejuvenated but remembering. *Nature Physics* 19: 926–927. https://doi.org/10.1038/s41567-023-02097-1.

Volovik GE (2009) *The Universe in a Helium Droplet*. Oxford University Press. https://doi.org/10.1093/acprof:oso/9780199564842.001.0001.

von Klitzing K (2019) Essay: Quantum Hall effect and the new international system of units. *Physical Review Letters* 122: 200001. https://doi.org/10.1103/PhysRevLett.122.200001.

von Klitzing K, Chakraborty T, Kim P, Madhavan V, Dai X, McIver J, Tokura Y, Savary L, Smirnova D, Rey AM, Felser C, Gooth J, and Qi X (2020) 40 years of the quantum Hall effect. *Nature Reviews Physics* 2: 397. https://doi.org/10.1038/s42254-020-0209-1.

Watson JD and Crick FHC (1953) Molecular structure of nucleic acids. *Nature* 171: 737. https://doi.org/10.1038/171737a0.

Weinberg S (1986) Superconductivity for particular theorists. *Progress of Theoretical Physics Supplement* 86: 43. https://doi.org/10.1143/PTPS.86.43.

Weintraub R (2012) What can we learn from Buridan’s ass? *Canadian Journal of Philosophy* 42: 281. https://doi.org/10.1353/cjp.2012.0013.

Weiss D (2013) The butterfly emerges. *Nature Physics* 9: 395. https://doi.org/10.1038/nphys2680.

Wolynes PG and Eaton WA (1999) The physics of protein folding. *Physics World* 12: 39. https://doi.org/10.1088/2058-7058/12/9/24.

Yamaguchi A, Hirohata A, and Stadler BJH (2021) *Nanomagnetic Materials: Fabrication, Characterization and Application*. Elsevier. (Chapter 5). https://doi.org/10.1016/C2018-0-05445-6.

This page intentionally left blank

LIST OF CONTRIBUTORS FOR VOLUME 2

Joel W Ager III
Materials Sciences Division, Lawrence Berkeley National Laboratory, Berkeley, CA, United States; Materials Science and Engineering Department, University of California Berkeley, Berkeley, CA, United States

Hiroki Ago
Global Innovation Center (GIC), Kyushu University, Fukuoka, Japan; Interdisciplinary Graduate School of Engineering Science, Kyushu University, Fukuoka, Japan

Ada Altieri
Laboratoire Matière et Systèmes Complexes (MSC), Université Paris Cité CNRS, Paris, France

Marco Baity-Jesi
Eawag (ETH), Swiss Federal Institute of Aquatic Science and Technology, Dübendorf, Switzerland

KH Bennemann
Physics Department, FU-Berlin, Berlin, Germany

EH Brandt[†]

CA Downing
Department of Physics and Astronomy, University of Exeter, Exeter, United Kingdom

G Chiarotti
Physics Department, Università di Roma "Tor Vergata", Rome, Italy

Andrey V Chubukov
School of Physics and Astronomy and William I. Fine Theoretical Physics Institute, University of Minnesota, Minneapolis, MN, United States

JMD Coey
School of Physics, Trinity College, Dublin, Ireland

PF de Châtel
New Mexico State University, Las Cruces, NM, USA

Paola De Padova
Consiglio Nazionale delle Ricerche-ISM, Roma, Italy; Instituto Nazionale di Fisica Nucleare-Laboratori Nazionali di Frascati—INFN-LNF, Frascati, Italy

MC Diamantini
NiPS Laboratory, INFN and Department of Physics and Geology, University of Perugia, Perugia, Italy

Oleksandr V Dobrovolskiy
Faculty of Physics, Nanomagnetism and Magnonics, Superconductivity and Spintronics Laboratory, University of Vienna, Vienna, Austria

Shi Xue Dou
Institute of Energy Materials Science (IEMS), University of Shanghai For Science and Technology, Shanghai, China

Rembert A Duine
Institute for Theoretical Physics, Utrecht University, Utrecht, The Netherlands; Department of Applied Physics, Eindhoven University of Technology, Eindhoven, The Netherlands; Department of Physics, Center for Quantum Spintronics, Norwegian University of Science and Technology, Trondheim, Norway

Mikhail I Dyakonov
Laboratoire Charles Coulomb, Université Montpellier, Montpellier, France; Ioffe Physical-Technical Institute, Saint Petersburg, Russia

David Emin
Department of Physics and Astronomy, University of New Mexico, Albuquerque, NM, United States

Klaus Ensslin
Physics Department, ETH Zurich, Zürich, Switzerland

MI Faley
ER-C-1 (Physics of Nanoscale Systems) Forschungszentrum Jülich, Jülich, Germany

J Fernández-Rossier
International Iberian Nanotechnology Laboratory, Braga, Portugal

---

[†] Deceased. The present version has been redrafted by Grigorii Mikitik, B. Verkin Institute for Low Temperature Physics and Engineering of the NAS of Ukraine.

Andrea C Ferrari
Cambridge Graphene Centre, University of Cambridge, Cambridge, United Kingdom

Aires Ferreira
School of Physics, Engineering and Technology and York Centre for Quantum Technologies, University of York, York, United Kingdom

Pietro Gambardella
Department of Materials, ETH Zurich, Zurich, Switzerland

SD Ganichev
University of Regensburg, Regensburg, Germany

Jinghui Gao
Frontier Institute of Science and Technology, and State Key Laboratory for Mechanical Behaviour of Materials, Xi'an Jiaotong University, Xi'an, China

Kevin Garello
Universite Grenoble Alpes, CEA, CNRS, Grenoble INP, SPINTEC, Grenoble, France

D Givord
CNRS, Grenoble, France

C Goletti
Physics Department, Università di Roma "Tor Vergata", Rome, Italy

Cosimo Gorini
Université Paris-Saclay, CEA, CNRS, SPEC, Gif-sur-Yvette, France

T Goto
University of Tokyo, Kashiwa, Japan

KA Gschneidner Jr.
Iowa State University, Ames, IA, USA

A Gurevich
Old Dominion University, Norfolk, VA, United States

N Harrison
Los Alamos National Laboratory, Los Alamos, NM, United States

Christian Heyn
Center for Hybrid Nanostructures (CHyN), University of Hamburg, Hamburg, Germany

G Hilscher
Vienna Institute of Technology, Vienna, Austria

H Ikoma
Tokyo University of Science, Tokyo, Japan

Stefan Ilić
Centro de Física de Materiales (CFM-MPC), Centro Mixto CSIC-UPV/EHU, Donostia-San Sebastián, Spain

EL Ivchenko
Ioffe Institute, Russian Academy of Sciences, St. Petersburg, Russia

Yuanchao Ji
Frontier Institute of Science and Technology, and State Key Laboratory for Mechanical Behaviour of Materials, Xi'an Jiaotong University, Xi'an, China

Daniel I Khomskii
University of Cologne, Cologne, Germany

Olivier Klein
Universite Grenoble Alpes, CEA, CNRS, Grenoble INP, SPINTEC, Grenoble, France

Mikito Koshino
Department of Physics, Osaka University, Osaka, Japan

Vladimir Kozhevnikov
Tulsa Community College, Tulsa, Oklahoma, United States; KU Leuven, Leuven, Belgium

Mariusz Krawiec
Institute of Physics, Maria Curie-Sklodowska University, Lublin, Poland

VZ Kresin
University of California at Berkeley, Berkeley, CA, USA

GC La Rocca
NEST, Scuola Normale Superiore, Pisa, Italy

JL Lado
Department of Applied Physics, Aalto University, Espoo, Finland

M Litinskaya
University of British Columbia, Vancouver, BC, Canada

PB Littlewood
University of Chicago, Chicago, IL, United States

Tianyu Ma
Frontier Institute of Science and Technology, and State Key Laboratory for Mechanical Behaviour of Materials, Xi'an Jiaotong University, Xi'an, China

N Magnani
Università di Parma, Parma, Italy

Denys Makarov
Helmholtz-Zentrum Dresden-Rossendorf e.V., Institute of Ion Beam Physics and Materials Research, Dresden, Germany

G Margaritondo
Ecole Polytechnique Fédérale de Lausanne, (EPFL), Lausanne, Switzerland

D Maryenko
RIKEN Center for Emergent Matter Science(CEMS), Wako, Japan

Yusuke Masaki
Department of Physics, Tohoku University, Sendai, Miyagi, Japan; Research and Education Center for Natural Sciences, Keio University, Yokohama, Kanagawa, Japan

Davide Massarotti
Department of Electrical Engineering and Information Technologies, University Federico II of Naples, Napoli, Italy

F Mazaleyrat
Universite Paris-Saclay, Ecole Normale Supérieure, Gif-Sur-Yvette, France

Igor I Mazin
Department of Physics & Astronomy, George Mason University, Fairfax, VA, United States

H Michor
Vienna Institute of Technology, Vienna, Austria

Takeshi Mizushima
Department of Materials Engineering Science, Osaka University, Toyonaka, Osaka, Japan

Junsaku Nitta
Department of Materials Science, Tohoku University, Sendai, Japan; NTT Basic Research Laboratories, Atsugi, Japan

Muneto Nitta
Research and Education Center for Natural Sciences, Keio University, Yokohama, Kanagawa, Japan; Department of Physics, Keio University, Hiyoshi, Japan; International Institute for Sustainability with Knotted Chiral Meta Matter (SKCM^2), Hiroshima University, Higashi-Hiroshima, Hiroshima, Japan

Per Nordblad
Department of Materials Science and Engineering, Uppsala University, Uppsala, Sweden

Anna K Ott
NS3E Laboratory, UMR 3208 ISL/CNRS/UNISTRA, French-German Research Institute of Saint-Louis, Saint Louis, France

VK Pecharsky
Iowa State University, Ames, IA, USA

M Peressi
University of Trieste, Trieste, Italy

David TS Perkins
School of Physics, Engineering and Technology and York Centre for Quantum Technologies, University of York, York, United Kingdom

D Pescia
Laboratorium für Festkörperphysik der ETH Zürich, Zürich, Switzerland

Nicola Poccia
Leibniz Institute for Solid State and Materials Science Dresden, Dresden, Germany

O Portmann
Laboratorium für Festkörperphysik der ETH Zürich, Zürich, Switzerland

ME Portnoi
Department of Physics and Astronomy, University of Exeter, Exeter, United Kingdom

Oleksandr V Pylypovskyi
Helmholtz-Zentrum Dresden-Rossendorf e.V., Institute of Ion Beam Physics and Materials Research, Dresden, Germany; Kyiv Academic University, Kyiv, Ukraine

MJ Qin
Institute of Materials Engineering, Australian Nuclear Science and Technology Organisation, Menai, NSW, Australia

Xiaobing Ren
Frontier Institute of Science and Technology, and State Key Laboratory for Mechanical Behaviour of Materials, Xi'an Jiaotong University, Xi'an, China; Center for Functional Materials, National Institute for Materials Science, Tsukuba, Ibaraki, Japan

Shinsei Ryu
Department of Physics, Princeton University, Princeton, NJ, United States

F Sebastian
Centro de Física de Materiales (CFM-MPC), Centro Mixto CSIC-UPV/EHU, Donostia-San Sebastián, Spain; Donostia International Physics Center (DIPC), Donostia-San Sebastián, Spain

Giuseppe Serpico
Department of Physics, University of Naples Federico II, Naples, Italy; Leibniz Institute for Solid State and Materials Science Dresden, Dresden, Germany

Katsuya Shimizu
KYOKUGEN, Center for Science and Technology under Extreme Conditions, Graduate School of Engineering Science, Osaka University, Toyonaka, Osaka, Japan

Juan F Sierra
Catalan Institute of Nanoscience and Nanotechnology (ICN2), CSIC and the Barcelona Institute of Science and Technology (BIST), Bellaterra, Barcelona, Spain

Jairo Sinova
Institut für Physik, Johannes Gutenberg Universität Mainz, Mainz, Germany; Institute of Physics, Academy of Sciences of the Czech Republic, Staré Město, Czech Republic

Thibault Sohier
Laboratoire Charles Coulomb (L2C), Université de Montpellier, CNRS, Montpellier, France

Pablo Solís-Fernández
Global Innovation Center (GIC), Kyushu University, Fukuoka, Japan

C Stamm
Laboratorium für Festkörperphysik der ETH Zürich, Zürich, Switzerland

Sergey V Streltsov
M.N. Mikheev Institute of Metal Physics, Ekaterinburg, Russia

Hermann Suderow
Laboratory of Low Temperatures and High Magnetic Fields, Condensed Matter Physics Department, Nicolás Cabrera Institute and Condensed Matter Physics Center (IFIMAC), Associated Unit UAM-CSIC, Autonomous University of Madrid, Madrid, Spain

H Szymczak
Polish Academy of Sciences, Warsaw, Poland

Francesco Tafuri
Dipartimento di Fisica "E.Pancini", Università di Napoli Federico II, Napoli, Italy

T Takabatake
Hiroshima University, Higashi- Hiroshima, Japan

IE Tamm
Department of Theoretical Physics, P.N. Lebedev Physical Institute, Moscow, Russia; National Research University Higher School of Economics, Moscow, Russia

Gen Tatara
RIKEN Center for Emergent Matter Science (CEMS), and RIKEN Cluster for Pioneering Research (CPR), Wako, Saitama, Japan

CA Trugenberger
SwissScientific Technologies SA, Geneva, Switzerland

Shin-ichi Uchida
Department of Physics, University of Tokyo, Tokyo, Japan; Institute of Advanced Industrial Science & Technology, Tsukuba, Japan

Sergio O Valenzuela
Institució Catalana de Recerca i Estudis Avançats (ICREA), Barcelona, Spain; Catalan Institute of Nanoscience and Nanotechnology (ICN2), CSIC and the Barcelona Institute of Science and Technology (BIST), Bellaterra, Barcelona, Spain

A Vaterlaus
Laboratorium für Festkörperphysik der ETH Zürich, Zürich, Switzerland

Matthieu J Verstraete
Department of Physics, University of Liege, Liege, Belgium; European Theoretical Spectroscopy Facility, Liege, Belgium

Eric Vincent
SPEC, CEA, CNRS, Université Paris-Saclay, Gif-sur-Yvette, France

VM Vinokur
Terra Quantum AG, Terra Quantum AG, St. Gallen, Switzerland

B Voigtländer
Forschungszentrun Jülich GmbH, Jülich, Germany

Katsunori Wakabayashi
Department of Nanotechnology for Sustainable Energy, School of Science and Technology, Kwansei Gakuin University, Sanda, Japan

Dong Wang
Frontier Institute of Science and Technology, and State Key Laboratory for Mechanical Behaviour of Materials, Xi'an Jiaotong University, Xi'an, China

Yu Wang
Frontier Institute of Science and Technology, and State Key Laboratory for Mechanical Behaviour of Materials, Xi'an Jiaotong University, Xi'an, China

Yunzhi Wang
Department of Materials Science and Engineering, The Ohio State University, Columbus, OH, United States

R Winkler
Department of Physics, Northern Illinois University, DeKalb, IL, United States

Xun Xu
Institute for Superconducting & Electronic Materials, University of Wollongong, Wollongong, NSW, Australia

H Yamada
Shinshu University, Matsumoto, Japan

Michihisa Yamamoto
RIKEN Center for Emergent Matter Science, Saitama, Japan

Yang Yang
Frontier Institute of Science and Technology, and State Key Laboratory for Mechanical Behaviour of Materials, Xi'an Jiaotong University, Xi'an, China

HY Yuan
Institute for Theoretical Physics, Utrecht University, Utrecht, The Netherlands

Andrei D Zaikin
Institute for Quantum Materials and Technologies, Karlsruhe Institute of Nanotechnology (KIT), Karlsruhe, Germany

This page intentionally left blank

CONTENTS OF VOLUME 2

History of magnetism 1
JMD Coey and F Mazaleyrat

Disordered magnetic systems 18
Per Nordblad

Magnetic Order 25
D Givord and T Takabatake

Paramagnetism 35
PF de Châtel

Diamagnetism 39
PF de Châtel

Ferromagnetism 43
N Magnani

Localized and Itinerant Magnetism 55
H Yamada and T Goto

Magnetic Domains 64
O Portmann, A Vaterlaus, C Stamm, and D Pescia

Magnetic Interactions 71
G Hilscher and H Michor

Magnetic Materials and Applications 78
H Szymczak

Magnetocaloric Effect 85
VK Pecharsky and KA Gschneidner Jr.

Manganites 93
VZ Kresin

Magnetic oxides 98
Daniel I Khomskii and Sergey V Streltsov

Magnetic nanostructures 112
Denys Makarov and Oleksandr V Pylypovskyi

The spin Hall effect 132
Cosimo Gorini

The spin-transfer torque effect 143
Gen Tatara

Quantum magnonics 147
HY Yuan and Rembert A Duine

Spintronic materials 159
Sergio O Valenzuela, Pietro Gambardella, Kevin Garello, Olivier Klein, Juan F Sierra, and Jairo Sinova

The spin galvanic effect 177
SD Ganichev and EL Ivchenko

Spin–orbit coupling in solids 186
R Winkler

Spin-orbit interaction based spintronics 193
Junsaku Nitta

Spintronics in 2D graphene-based van der Waals heterostructures 205
David TS Perkins and Aires Ferreira

Optical orientation of spins in semiconductors 223
Mikhail I Dyakonov

Raman spectroscopy of graphene and related materials 233
Anna K Ott and Andrea C Ferrari

Quantum devices in graphene 248
Klaus Ensslin

Surfaces and Interfaces, Electronic Structure of 257
G Chiarotti and C Goletti

Graphene, electronic properties and topological properties 273
Katsunori Wakabayashi

Twisted bilayer graphene 288
Mikito Koshino

Graphene, transport 295
Michihisa Yamamoto

van der Waals heterostructures 310
Pablo Solís-Fernández and Hiroki Ago

Dirac materials beyond graphene 329
Paola De Padova and Mariusz Krawiec

Quantum confinement in Dirac-like nanostructures 344
CA Downing and ME Portnoi

Theory of edge states in graphene-like systems 350
JL Lado and J Fernández-Rossier

An introduction to the theory of spin glasses 361
Ada Altieri and Marco Baity-Jesi

Spin glass experiments 371
Eric Vincent

Ferroic glasses 388
Yuanchao Ji, Dong Wang, Yang Yang, Jinghui Gao, Tianyu Ma, Yu Wang, Yunzhi Wang, and Xiaobing Ren

Semiconductors, general properties 404
G Margaritondo

Semiconductors: Exciton theory 418
PB Littlewood

Polarons in condensed matter 427
David Emin

Semiconductors: Spin-density waves 446
N Harrison

Electrons and holes 456
GC La Rocca

Electron–phonon coupling and polarons in low-dimensional structures 465
Matthieu J Verstraete and Thibault Sohier

Electronic states of elemental semiconductors 475
GC La Rocca

Semiconductors: Isotope effects in solids 485
Joel W Ager III

Polaritons 497
M Litinskaya

Semiconductor Heterojunctions, Electronic Properties of 507
M Peressi

Semiconductors, Impurity and Defect States in 516
H Ikoma

Semiconductor Nanostructures 520
B Voigtländer

Epitaxy 528
D Maryenko

Epitaxy (classical MBE) 544
Christian Heyn

Superconductivity: Critical currents 554
A Gurevich

High-temperature superconductors 565
MJ Qin, Xun Xu, and Shi Xue Dou

Phase diagrams of high-temperature superconductors 580
Shin-ichi Uchida

Superconductors, hydrogen-based 592
Katsuya Shimizu

Unconventional superconductivity 598
Igor I Mazin

Superconducting density of states from scanning tunneling microscopy 600
Hermann Suderow

Josephson junctions 616
Francesco Tafuri

Superconductivity: Electronic mechanisms 632
Andrey V Chubukov

Electrodynamics of superconductors 644
Vladimir Kozhevnikov

Superconductivity: BCS theory 657
KH Bennemann

Quantum fluctuations in superconducting nanowires 670
Andrei D Zaikin and IE Tamm

Superconductor-ferromagnet hybrid structures 682
F Sebastian and Stefan Ilić

Superconductivity: Ginzburg-Landau theory and vortex lattice 693
EH Brandt

Nanodimensional superconducting quantum interference devices 702
MI Faley

Perspective in the twistronics of high-temperature superconductors 712
Giuseppe Serpico and Nicola Poccia

Critical current fluctuations in Josephson junctions 725
Davide Massarotti

Fast dynamics of vortices in superconductors 735
Oleksandr V Dobrovolskiy

Non-Abelian anyons and non-Abelian vortices in topological superconductors 755
Yusuke Masaki, Takeshi Mizushima, and Muneto Nitta

Topological superconductors 795
Shinsei Ryu

Superinsulation 804
MC Diamantini, CA Trugenberger, and VM Vinokur

History of magnetism[☆]

JMD Coey[a] **and F Mazaleyrat**[b], [a]School of Physics, Trinity College, Dublin, Ireland; [b]Universite Paris-Saclay, Ecole Normale Supérieure, Gif-Sur-Yvette, France

© 2024 Elsevier Ltd. All rights reserved.

This is an update of J.M.D. Coey, T.R. Nı Mhıocháin, Magnetism, History of, Editor(s): Franco Bassani, Gerald L. Liedl, Peter Wyder, Encyclopedia of Condensed Matter Physics, Elsevier, 2005, Pages 227–236, ISBN 9780123694010, https://doi.org/10.1016/B0-12-369401-9/00514-3.

Early history 2
From navigation to industry 4
Units 7
Fundamental understanding 8
Magnetic phenomenology and materials 10
Modern developments 12
Theory 12
Numerical simulations 13
Experimental methods 13
Materials and technology 14
Conclusion 16
References 17

Abstract

Magnetism is a science with more than two millennia of recorded history. The attraction of ferrous objects to a permanent magnet across a distance has been a source of curiosity since the iron age. Investigations of magnetic phenomena led to the invention of steel magnets—needles and horseshoes—and the compass that enabled the exploration of the planet. A host of discoveries following Oersted's 1821 demonstration of the relation between electric current and magnetic field led to the electromagnetic revolution that by the end of the 19th century had resulting in global communications and electrification. The discovery of the electron, together with the emergence of quantum theory and relativity in the early 20th century established the modern theoretical understanding of magnetism. A panoply of hard and soft magnetic materials has been developed to underpin the modern magnetics industry and a marriage of magnetism and electronics in thin film devices has eased the birth of the information revolution. Aside from the revolutionary technological advances, magnetism played a key role in clarifying basic concepts in condensed matter physics throughout the 20th century.

Key points

- Magnetic attraction was first investigated more than 2000 years ago with pieces of naturally-magnetized rocks rich in magnetite, Fe_3O_4.
- Compasses using floating or pivoted steel magnets appeared in the 12th century. They led to the great voyages of discovery and mapping of the planet.
- Gilbert identified the Earth as the source of the directional magnetic attraction in 1600, and pioneered the modern experimental method of scientific investigation.
- Oersted's 1820 discovery that electric currents create magnetic fields triggered a series of advances that culminated in Maxwell's theory of electricity, magnetism and light, and practical electromagnetic energy conversion that revolutionized energy distribution and communication by the end of the 19th century.
- Then, with the discovery of the electron, and the demonstration that magnetism is associated with angular momentum, it became possible in 1928 to use relativity and quantum mechanics to explain magnetism as a consequence of the orbital and intrinsic spin angular momenta of electrons.
- The key practical achievement of the 20th century was the mastery of hysteresis, and the achievement of a wide variety of metallic or insulating hard and soft magnetic materials. Important outcomes were analog and digital magnetic recording and high-frequency electromagnetic devices.

[☆] *Change History:* February 2023. JMD Coey and F Mazaleyrat updated the chapter. Figs. 5, 6, 7, 10, 12, 13 are new or updated. Much of the text is revised or rewritten.

- Development of technology to produce uniform magnetic films just a few nanometers thick in the1960s opened the prospect of using the spin of the electron to be used as well as its change in electronic devices. Semiconductor electronics and magnetic memory are parents of the information revolution.
- Modern theory of condensed matter in areas such as phase transitions and topology has benefitted from magnetic model systems.

Nomenclature

$\boldsymbol{\hbar}$	Planck's constant, 1.055×10^{-34} Js
B	Magnetic induction (T)
$\mathbf{c}$	Speed of light, 2.99792458×10^{8} ms^{-1}
$\mathbf{e}$	Charge on an electron, 1.602×10^{-19}C
H	Magnetic field strength (Am^{-1})
$\mathbf{J}$	Exchange integral (J)
M	Magnetization (Am^{-1})
$\mathbf{m_e}$	Mass of an electron, 9.109×10^{-31} kg
$\boldsymbol{n_W}$	Weiss molecular field coefficient
S	Spin vector
$\boldsymbol{T_c}$	Curie temperature (K)
$\boldsymbol{\epsilon_0}$	Electric permittivity of free space, 8.854×10^{-12} C^{2}N^{-1} m^{-2}
$\boldsymbol{\mu_0}$	Magnetic permeability of free space, $4\pi \times 10^{-7}$ TA^{-1} m
$\boldsymbol{\mu_B}$	Bohr magneton, 9.274×10^{-24} JT^{-1}

Early history

Feeble permanent magnets are widespread in Nature in the form of lodestones, pieces of rock that are mainly composed of the iron oxide mineral magnetite (Fe_3O_4). Outcrops can be magnetized by the huge currents in lightning strikes and such natural magnets were known and studied in ancient Greece, Egypt, China and Mesoamerica. Aristotle attributed early thoughts on the nature of magnetic attraction to Thales, who was born in Milet in Asia Minor in 624 BCE. He was an animist who credited the magnet with a soul on account of its ability to create movement. This strange idea was to persist in Europe until the 17th century. The magnet itself is thought to be named after Magnesia, a city in Asia Minor that was a source of lodestone. In the 5th century BCE, when Empedokles postulated the existence of four elements, Earth, Water, Air and Fire; magnetism was related to Air with special effluvia somehow passing through pores in magnetic material, a theory echoed much later by Descartes. The Roman poet Lucretius writing in the 1st century BCE mentions the ability of a magnet to induce magnetism in iron and the ability of two magnets to either attract or repel; repulsion had been missed earlier. However, the Greek approach of developing a philosophy into which natural observations were supposed to fit was not conducive to open-minded exploration of the natural world.

A more productive approach was followed in China (Needham, 1962), where magnetism was linked to geomancy. The art of adapting the residences of the living and the tombs of the dead to harmonize with local currents of the cosmic breath demanded a knowledge of its direction. A South-pointer consisting of a carved lodestone spoon free to rotate upon a polished baseplate (Fig. 1) was in use in the 1st century BCE, and may have been known hundreds of years earlier. An important discovery, attributed to Zheng Gongliang in 1064, was that iron could acquire a thermoremanent magnetization when rapidly cooled from red heat in the ambient magnetic field. A short step led to the suspended magnetic needle, which was described by Shen Kua around 1088 and seen to deviate, like the South-pointer, from a strictly North-South axis.

The compass made its appearance in Europe about a hundred years later, being referred to by Alexander Neckham in 1190. Floating compasses were also developed around this time. The compass (Fig. 2) was the enabling technology for the great voyages of discovery of the 15th century, leading the Ming admiral Zheng He to the coasts of East Africa in 1420, and Christopher Columbus, who rediscovered declination, to America in 1492. Columbus's landfall was on the continent of the Olmecs, who seem to have had a knowledge of magnetism in their massive stone carvings of human figures and sea turtles dating from the second millennium BCE. Not long after these heroic voyages, the land masses and oceans of our planet were mapped and explored. According to Francis Bacon, writing in *Novum Organum* in 1620, the magnetic compass was one of the three things, along with printing and gunpowder, that had "changed the whole face and state of things throughout the world". All were Chinese inventions. It was the first occasion when magnetism changed the world. Two more were to follow.

The first authentic magnetic experimentalist in Europe was the French crusader monk Petrus Peregrinus. His paper *Epistola de Magnete* recounts experiments with floating pieces of lodestone and carved lodestone sphere that he called 'terellae,' performed

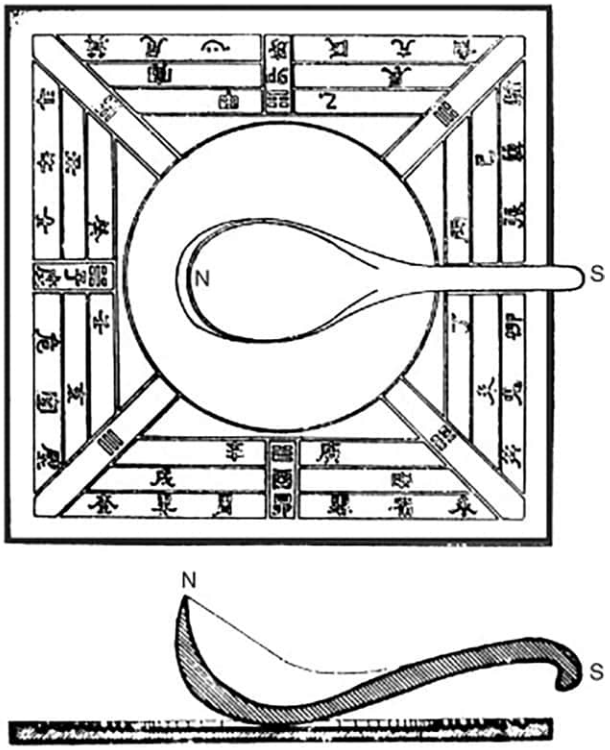

Fig. 1 Baseplate and lodestone spoon of the South-pointer used in China from the first century BC (Needham, 1962). Courtesy of Cambridge University Press.

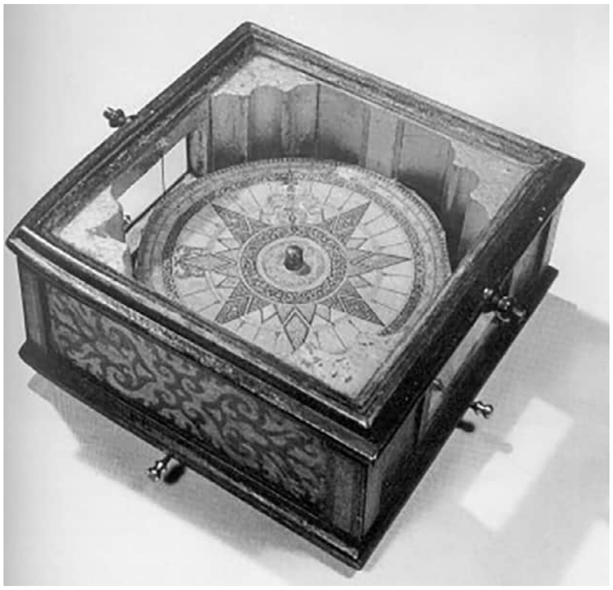

Fig. 2 18th century Portuguese mariner's compass (Boorstin, 1992). Courtesy of Editions Robert Laffont.

during the 1269 siege of Lucera, a Muslim settlement in Southern Italy. He discovered the poles of a magnet, related magnetic attraction to the celestial sphere, and included a proposal for a magnetic perpetual motion device—which has become an obsession of charlatans up to the present day. However, credit for the inauguration of the experimental method in a recognizably modern form belongs to William Gilbert. Physician to the English queen Elizabeth I, Gilbert conducted a series of experiments on terellae and concluded that the Earth itself was a great magnet. Magnets aligned themselves not with the celestial sphere, but with the Earth's poles. He induced magnetism by cooling iron in the Earth's field and destroyed it by heating or hammering. Gilbert was at pains to dispel the accretion of superstition that clung to the magnet, preferring to rely on his own experimental evidence. His investigations are described in his masterwork *De Magnete* published in 1600 (Gilbert, 1958), which is arguably the first modern scientific text.

From navigation to industry

Gilbert's theories held sway in the 17th century until the appearance of Edmond Halley's 1692 shell model of the Earth's magnetic structure, which greatly influenced compass technology and navigation. Magnetic research at the time was driven principally by naval interests. An early observation of a connection between electricity and magnetism was made in 1681, when a ship bound for Boston was struck by lightning. It was evident from the stars that "the compasses were changed; the North point was turn'd clear South"; with the compass so reversed, the ship sailed on to its destination.

The 18th century was marked by professionalization of the scientist or 'natural philosopher' as they were then called (Fara, 1966). Developments in magnetism were associated with improvements in navigation and the prestige of the great voyages of discovery. Accordingly, the natural philosopher with his mantle of theory was afforded social status, access to public funding and credibility beyond that extended to artisans on the one hand, and quacks such as the colorful Anton Mesmer with his theories of 'animal magnetism' or James Graham with his 'royal Patagonian magnetic bed' for nightly rent in a fashionable London townhouse on the other. Halley conducted magnetic surveys, producing charts of inclination and declination for seafarers (Fig. 3). The English entrepreneur Gowin Knight, representative of this new breed of natural philosopher, later improved the quality of magnetic materials and compasses for sale to the Navy, coupling scientific endeavor with commercial acumen.

A major technical breakthrough of the 18th century was the 1755 discovery by Johann Dietrich that the horseshoe was an ideal magnet shape. His invention, an ingenious practical solution to the problem of self-demagnetization in steel bar magnets, was enthusiastically promoted by his patron Daniel Bernouilli.

This period also saw rapid developments in the harnessing of electricity, from the 1660 invention of the Leyden jar, culminating in Volta's 1800 invention of the Voltaic cell. There were compelling analogies between electrostatics and magnetism and some cogent speculation relating magnetism and rotational motion such as that of Richard Kirwan (1797), but a formal link between electricity and magnetism was not established experimentally until 1820. During a public demonstration by the Danish scientist Hans Christian Oersted, a suspended compass needle was found to be deflected when an electric current was switched on in a copper wire. His report launched an experimental frenzy. François Arago (who briefly became President of France in 1848) immediately performed an experiment in Paris establishing that a current-carrying conductor behaved like a magnet. A week after Arago's report, André-Marie Ampère presented a paper to the French Academy suggesting that ferromagnetism in a body was caused by internal currents flowing perpendicular to the magnetic axis and, by analogy, that steel needles magnetized in a solenoid would show stronger magnetization. Together with Arago, he successfully demonstrated his theory in November 1820. Ten days later, the British scientist Humphrey Davy reported similar results. A practical horseshoe electromagnet was constructed by William Sturgeon in 1825, and five years later Joseph Henry in the USA built a powerful electromagnet with layers of closely-spaced copper windings; he discovered self-induction and built an electric relay and an electric bell.

In the ensuing ferment in Europe and North America, it is often difficult to attribute credit for any particular advance, distinguishing between who had the idea, who devised a convincing experimental demonstration, and who created the first practical, working machine. Scientists and engineers belonged to different communities, with different preoccupations.

19th century electromagnetic science was driven, however, by Michael Faraday. Working entirely by observation and experimentation, with no dependence on formal theory, he developed the concept of 'magnetic field'. Faraday initially classified materials as magnetic (substances which are attracted by the field, either strongly like iron, nickel and cobalt or weekly like oxyen) or diamagnetic (materials which were pushed away by the field). The distinction between ferromagnets and paramagnets came later. Working with an electromagnet, he discovered the phenomenon of 'electromagnetic induction'— that a flow of electricity can be induced by a changing magnetic field. He demonstrated electrical ↔ mechanical energy conversion in a model motor and a dynamo with steel permanent magnets, which were used in most of the early demonstrations, but electromagnets proved indispensable for later, practical electromagnetic machines. His conviction that a magnetic field should have an influence on light led to his 1845 discovery of the magneto-optic Faraday effect— the rotation of the plane of polarization of light passing through a magnetic medium in a direction parallel to its magnetization. Fig. 4 illustrates a collection of magnets from the 18th, 19th and late 20th centuries, when permanent magnets finally became indispensable for many practical applications.

A classical theory emerged to account simultaneously for magnetism and its relationship with electricity. Around 1824 Siméon Denis Poisson developed a mathematical theory of magnetostatics. Letters from Ampère to Fresnel and Faraday found after his death show that by 1822 he had considered the possibility that the currents causing ferromagnetism were 'molecular' rather than macroscopic in form. Wilhelm Weber formally presented the idea that 'molecules' of iron were capable of movement around their centers, suggesting that they lay in different directions in unmagnetized material, but aligned in a common direction in the presence of an applied magnetic field. This was the beginning of an explanation of hysteresis, the central phenomenon of technical magnetism, demonstrated experimentally by James Ewing using a board with an array of small, pivoting magnets. He then built an ingenious instrument based on the bending of a ferromagnetic current-carrying wire in the gap of an electromagnet to measure B and H under AC and DC excitation, with which he discovered and measured hysteresis loops in 1889 (Fig. 5). Ewing's activities as a young professor at the University of Tokyo in the 1890s established the strong Japanese tradition of research on magnetic materials that continues to thrive to this day.

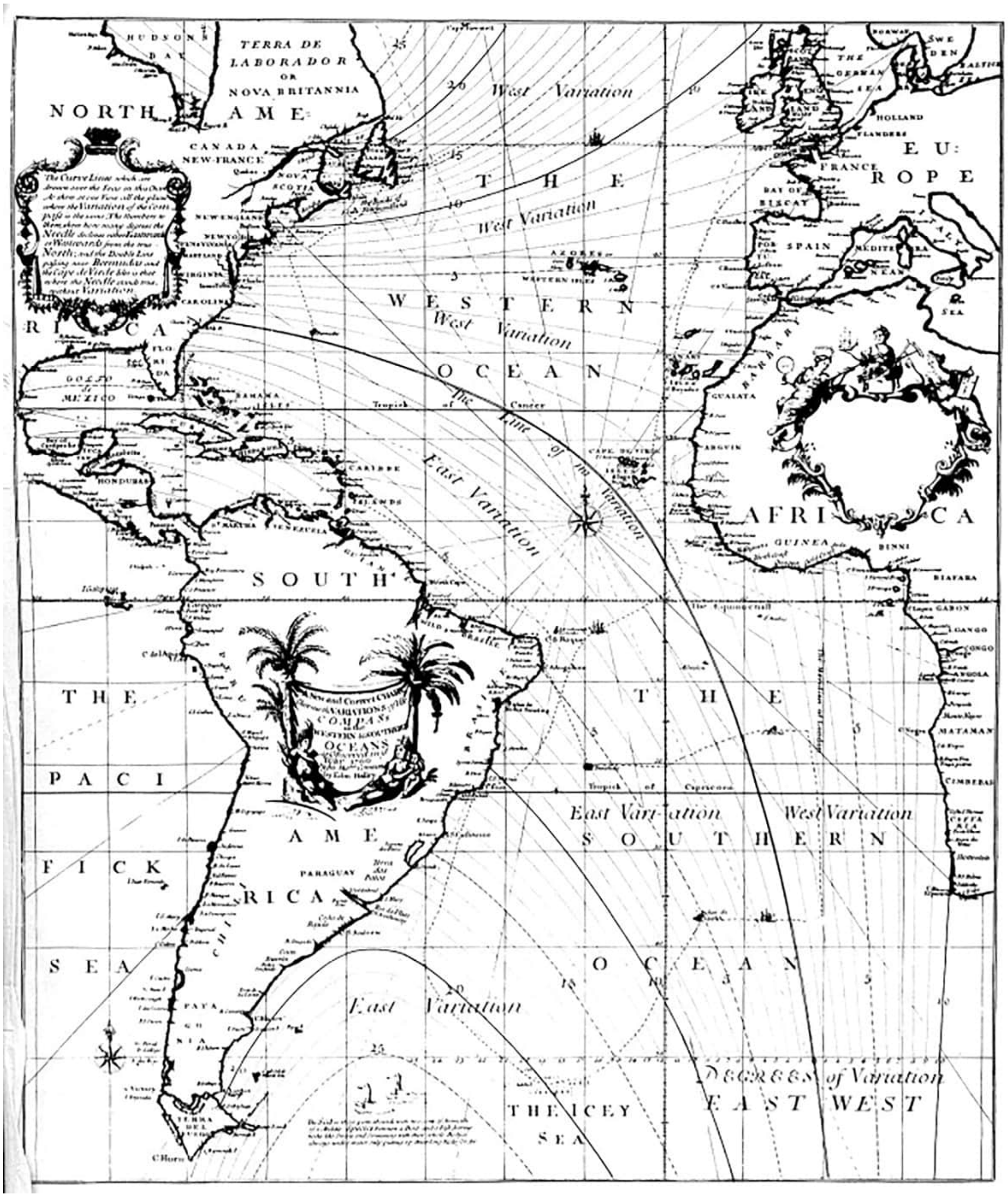
HUDSONS BAY
TERRA DE LABORADOR OR NOVA BRITANNIA
NORTH AME RICA
CANADA NEW FRANCE
NOVA SCOTIA
NEW ENGLAND
NEW YORK
VIRGINIA
CAROLINA
FLORIDA
GOLFO de MEXICO
HONDURAS
CARIBBE ISLANDS
The Curve Lines which are drawn over the Seas in this Chart do shew at one View all the places where the Variation of the Compass is the same. The Numbers to them shew how many degrees the Needle declines either Eastwards or Westwards from the true North; and the Double Line passing near Bermudas and the Cape de Virde Isles is that where the Needle stands true, without Variation.
West Variation
THE WESTERN OCEAN
AZORES
West Variation
Tropick of Cancer
The Line of no Variation
East Variation
CAPE DE VERDE
SWEDEN
THE GERMAN SEA
HOLLAND
FLANDERS
EU: ROPE
FRANCE
BAY OF BISCAY
SPAIN
MEDITERRANEAN SEA
BARBARY
GUALATA
ARGUIN
AFRICA
GUINEA
BINNI
BIAFARA
GABON
LOANGO
CONGO
ANGOLA
MATAMAN
CIMBEBAS
CAFFRARIA
SOUTH AMERICA
THE PACIFICK SEA
COMPASS
OCEANS
PARAGUAY
CHILI
PATAGONIA
TERRA DEL FUEGO
C. Horn
THE SOUTHERN OCEAN
Tropick of Capricorn
East Variation
West Variation
East Variation
THE ICEY SEA
DEGREES of Variation
EAST WEST
25
20
15
10
5

Fig. 3 A section of Halley's world chart of magnetic variation published in 1700.

James Clerk Maxwell, the Scottish theoretician, "resolved to read no mathematics on the subject till he had first read through Faraday's '*Experimental Researches in Electricity*'". Maxwell's unprecedented equations formally defined the relationship between electricity and magnetism and bridged the gap, between oscillating electric charge and magnetic field. His theory considered electromagnetic waves traveling through an all-pervading aether at speeds close to that of light, measured with 5% accuracy by Hyppolite Fizeau in 1849.—In 1888 Heinrich Hertz showed that Maxwell's electromagnetic waves were, in fact, identical with radio waves and light.

The subsequent technological developments of all these discoveries would have been impossible without a stable and powerful source of electric energy that batteries were unable to provide. Starting from Faraday's rotation, Arago's rotary magnetism and his own understanding of electrodynamics, Ampère and the young instrument maker Hypolyte Pixii demonstrated the principle of a

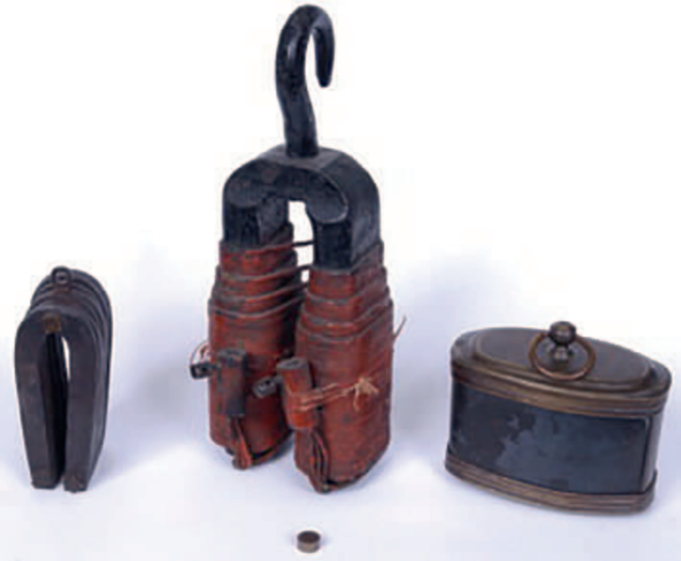

Fig. 4 Magnets of four centuries shown clockwise from the left; 18th century horseshoe magnet; 19th century electromagnet; 17th century lodestone; and 20th century $Nd_2Fe_{14}B$.

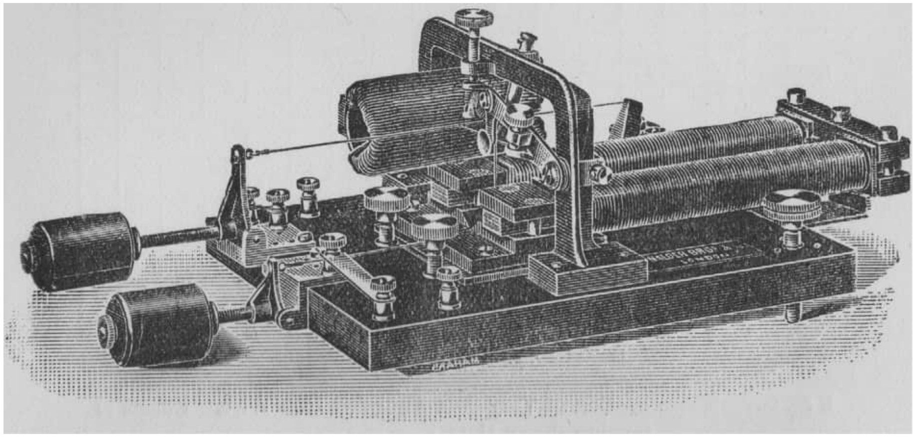

Fig. 5 James Ewing's automatic hysteresis loop tracer. The sample is in the form of two long steel bars contained within the two horizontal solenoids (Ewing, 1982).

DC generator in 1832. The first DC motor with a commutator came two years later (credit has been claimed for Moritz von Jacobi in Russia, Anyos Jedlic in Hungary and Thomas and Emily Davenport in Vermont), but the first industrial machine issued from Siemens brothers' workshop only in 1854. However, these energy converters needed very big steel magnets to work effectively. The English engineer Henry Wilde dared in 1864 to replace permanent magnets with a series of multi-turn electromagnets in a dynamo thereby reduced the mass while greatly improving the performance. A similar machine was built independently by Werner von Siemens shortly afterwards. A new design of DC generator came in 1859 from Antonio Pacinotti in Italy. His innovation, published only in 1865, was in the design of the rotor (Pacinotti's ring) that improved the efficiency. With further improvements, the design was launched commercially in 1870 by Zénobe Gramme in France. In addition to Pacinotti's ring, Gramme fed the electromagnet directly from the rotor (Fig. 6). Then with further modifications to reduce the mass and increase the efficiency, notably by Siemens, the design was stabilized. Surprisingly, the reversibility of the DC generator was observed by Hyppolite Fontaine only in 1873; he found that by applying a DC current to Gramme's machine he could make it spin.

The first electric streetlights were bright high-voltage DC arc discharge lamps with short-lived elements that replaced the gas lights of Paris in 1879, but they were deemed too dangerous for domestic use. In 1882, Thomas Edison built the first system of electric distribution for 59 customers in New York and developed a working light bulb operating at 110 V DC. However, the expansion of the electric power grid was only made possible by Nikola Tesla's AC system, which enabled efficient long-range distribution at high voltages with minimal electrical losses together with a safe local voltage achieved by means of step-down transformers. Based on Elihu Thomson's AC generator (1879), the transformer of Lucien Gaulard and John Gibbs (1881) and

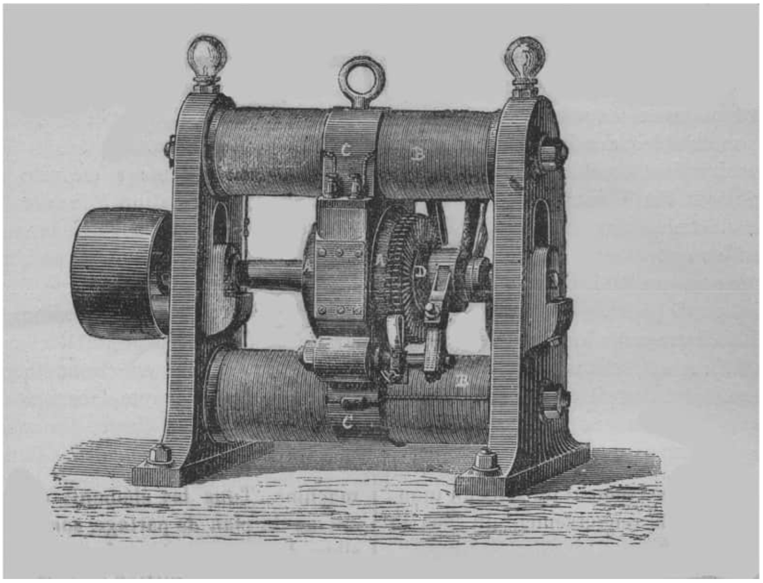

Fig. 6 Zénobe Gramme's dynamo (1870).

Tesla's induction motor (1886), this system was taken on by the Westinghouse company, and it has remained almost unchanged up to the present day.

Siemens exhibited a miniature electric locomotive pulling a little train around a 300 m track to amuse visitors at a Berlin exhibition in 1879. His company installed the first electric trams in Berlin two years later and by 1900 they had an electric train capable of 200 kmh^{-1}. Horses and their droppings soon vanished from city streets.

One of the problems besetting the development of efficient magnetic material in the 19th century was the difficulty to measure magnetization and field precisely. Coulomb adapted the principle of the electrostatic torsion balance in 1784 to measure electric charge, but it could only work approximately with the inseparable 'poles' of permanent magnets; the magnetic moment couldn't be fitted into the existing system of units. By 1880, it was possible to estimate the permeability by AC voltage and current measurements. John Hopkinson, in 1885, observed the enhancement of permeability just before reaching the temperature at which ferromagnetism disappears. After the invention of the first ballistic galvanometer or fluxmeter (actually an electromechanical voltage integrator) by Arsène d'Arsonval around 1881, it became possible to measure time- or space-varying fields. It was by using this instrument that Pierre Curie could measure a magnetic field and its gradient. With the very sensitive torsion balance illustrated in Fig. 7 that could operate in large fields and at high temperature, he determined his law of paramagnetism, showing that ferromagnets behave like paramagnets above their magnetic transition temperature—known ever since as the Curie point.

The astonishing transformation of science and society that began in 1820 is known as the *electromagnetic revolution*. By the end of the century the revolution was heralding the electrification of the planet and changing forever human communications, transportation and conditions of life and leisure. This was the second time that magnetic technology changed the world.

Finally, the century closed with the all-important discovery of the electron, the elusive carrier of electricity. A new age was born.

For further information, the reader may refer to one-volume histories of magnetism (Kloss, 1994), and of electricity and magnetism (Meyer, 1972; Mottelay, 1975), and a short accounts of in magnetism textbooks (Matthis, 1965; Coey, 2010).

Units

By the middle of the 19th century, it was becoming urgent to devise a standard set of units for electrical and magnetic quantities. The burgeoning telegraph industry, for example, needed a standard of electrical resistance to control the quality of electrical cables. Separate electrostatic and electromagnetic cgs unit systems based on the gram, centimeter and second had come into existence. Maxwell and Jenkin proposed combining them in a coherent set of units in 1863. Their Gaussian cgs system was internationally adopted in 1881. Written according to this system, Maxwell's equations relating electric and magnetic fields contain factors of c, the velocity of light. Maxwell also introduced the idea of dimensional analysis, based on three basic quantities of mass, length and time. The magnetic field $\boldsymbol{H}$ and the induction $\boldsymbol{B}$ were measured in units of Oersted and Gauss, respectively in the cgs system, but there is no numerical distinction between them in free space.

Another basic unit, that of electric current, was adopted in the Système International d'Unités (SI) in 1948. The number of basic units and dimensions in any system is an arbitrary choice; SI uses the meter, kilogram, second and ampere. It has been adopted

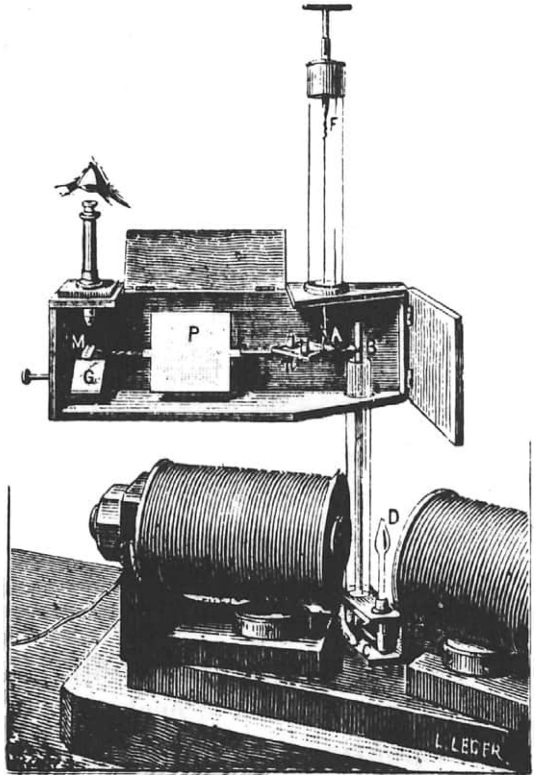

Fig. 7 Pierre Curie's torsion balance used for quantitative measurements of magnetic susceptibility at high temperature in a horizontal magnetic field gradient (Curie, 1895).

worldwide for the teaching of science and engineering, employing the familiar electrical units of volt, ampere and ohm. Maxwell's equations written in terms of two electric and two magnetic fields contain no factors of c or 4π in the SI system. The magnetic field $\boldsymbol{H}$, like the magnetization $\boldsymbol{M}$, has units of Am^{-1}. The induction $\boldsymbol{B}$ is measured in tesla ($1\ \mathrm{T} \equiv 1\ \mathrm{kgs}^2\ \mathrm{A}^{-2}$). Magnetic moments are measured in units of Am^2, clearly indicating the origin of magnetism in electric currents, and the consequent absence of magnetic 'poles' as real physical entities. The velocity of light is defined as exactly $299{,}792{,}458\ \mathrm{ms}^{-1}$. Two constants μ_0 and ε_0, the permeability and permittivity of free space respectively, are related by $\mu_0\varepsilon_0 = c^{-2}$. μ_0 was defined to be $4\pi\ 10^{-7}\ \mathrm{kgs}^2\mathrm{A}^{-2}$ until 20 May 2019, but with the new definition of the ampere and the retirement of the Pt—Ir standard kilogram, it is now defined as $1.25663706212(19) \times 10^{-6}\ \mathrm{kgs}^2\ \mathrm{A}^{-1}$ which differs only in the tenth digit from $4\pi\ 10^{-7}$.

Gaussian cgs units remain in widespread use in magnetism in some parts of the world, despite the manifest practical advantages of SI.

Fundamental understanding

The discovery of the electron in the closing years of the 19th century was a giant step towards a fundamental understanding of magnetism. The elementary charged particle with mass $m_e = 9.109 \times 10^{-31}$ kg and charge $e = -1.602 \times 10^{-19}$C had been named by the Irish scientist George Johnstone Stoney in 1891, several years before Jean Perrin identified negatively charged particles in a cathode ray tube and Joseph John Thompson measured their charge to mass ratio e/m_e by deflecting them in a magnetic field. George Francis Fitzgerald suggested in 1900 that magnetism might be due to rotation of these electrons. Electrons turned out to be the essential magnetic constituent of atoms and solids, as well as the carriers of electric current.

Based on measurements of the low-temperature saturation magnetization of iron and nickel, and the paramagnetic properties of transition metals salts, Weiss proposed in 1911 an experimental unit of atomic magnetism $\mu_W = 1.853 \times 10^{-24}\ \mathrm{JT}^{-1}$. Known as the Weiss magneton, it remained in use for about 30 years, notably by Blas Cabrera in Spain who used it to interpret very precise measurements of susceptibility above the Curie point. It was abandoned in favor of the Bohr magneton $\mu_B = e\hbar/2m_e = 9.274 \times 10^{-24}\ \mathrm{JT}^{-1}$, which involves the quantum of angular momentum $\hbar$ (Quédec, 1988). The Einstein-de Haas experiment established a relation between magnetization and angular momentum experimentally, in 1915. The intrinsic spin angular momentum of the electron was unknown at that time (Tomonaga, 1974).

Thirty years were to elapse before contradictions at the heart of early 20th century magnetism could be resolved. In these tumultuous years, classical physics and the lingering wisps of aether were blown away, and new principles of quantum mechanics and relativity were established. If, following Ampère, we believe that all magnetism is traceable to circulating electric currents, why does iron not melt? Its magnetization M is equivalent to a surface current of 1.76×10^6 Am^{-1}, how could such a current be sustained indefinitely? Weiss had postulated in 1907 the existence of an internal 'molecular field' proportional to the magnetization, $\boldsymbol{H}_i = n_W \boldsymbol{M}$, to account for the abrupt disappearance of ferromagnetism at the Curie point T_C and paramagnetism at higher temperatures. He was at a loss, however, to explain why no trace of his enormous field—a thousand tesla ($n_W \approx 1000$)—was detectable in the vicinity of a piece of fully-magnetized ferromagnetic material, as predicted by the continuity of $\boldsymbol{B}$ in Maxwell's equation. He concluded that the origin of this field must be electrostatic (Weiss and Foëx, 1926). In the unmagnetized state Weiss had accepted the existence of domains magnetized in different directions to give no resultant moment, but there are no domains in the saturated state. The 'anomalous' Zeeman splitting of spectral lines in a magnetic field was a mystery. Niels Bohr in 1911 and Hendrika van Leeuwen in 1919 had proved that at any finite temperature and in any magnetic or electric field, the net magnetization of any collection of classical electrons vanishes identically. Classical electron physics was incompatible with any kind of magnetism whatsoever!

By 1930, quantum mechanics and relativity had come to the rescue, and a new understanding of magnetism emerged in terms of the physics of Einstein, Bohr, Pauli, Dirac, Schrödinger and Heisenberg. The source of magnetism in condensed matter was identified with the *angular momentum* of elementary particles such as the electron. The perpetual currents in atoms were quantized in stationary states that did not decay, with angular momentum that was a multiple of Planck's constant $\hbar = 1.055 \times 10^{-34}$ Js. Weiss's 'molecular field' was not a magnetic field at all, but a manifestation of electrostatic Coulomb interactions constrained by Pauli's exclusion principle, which forbade the occupancy of a quantum state by two electrons with the same spin. The intrinsic spin angular momentum of an electron was found by Samuel Goudsmit and George Uhlenbeck in 1925 to have the value ½ħ. The corresponding electronic magnetic moment, however, was one Bohr magneton, twice as large as anticipated for orbital angular momentum. The problem of the electron's magnetism was finally resolved by Paul Dirac in 1928 when he succeeded in writing Erwin Schrödinger's equation in a relativistically invariant form, obtaining the electron spin in terms of the 2×2 spinor matrices previously proposed by Wolfgang Pauli. Together with Werner Heisenberg, Dirac formulated the Hamiltonian $-2J\boldsymbol{S}_i.\boldsymbol{S}_j$ to describe the coupling between the vector spins $\boldsymbol{S}_i$ and $\boldsymbol{S}_j$ of to many-electron atoms i and j. The value of the exchange integral J was directly proportional to Weiss's molecular field coefficient n_W.

The theory was almost complete after the description of spin waves by Felix Bloch in 1930 as the elementary excitations of an array of atoms coupled by Heisenberg exchange interactions, and the band theory of ferromagnetic metals developed by Edmund Stoner and John Slater in the 1930s, which accounted for the non-integral spin moments found in Fe, Co and Ni, and their alloys.

The sixth Solvay conference, held in Brussels in October 1930, (Fig. 8) was devoted to magnetism (Marage and Wallenborn, 1995). It followed 4 years of brilliant discovery in theoretical physics, which set out the modern electronic theory of matter. Yet the

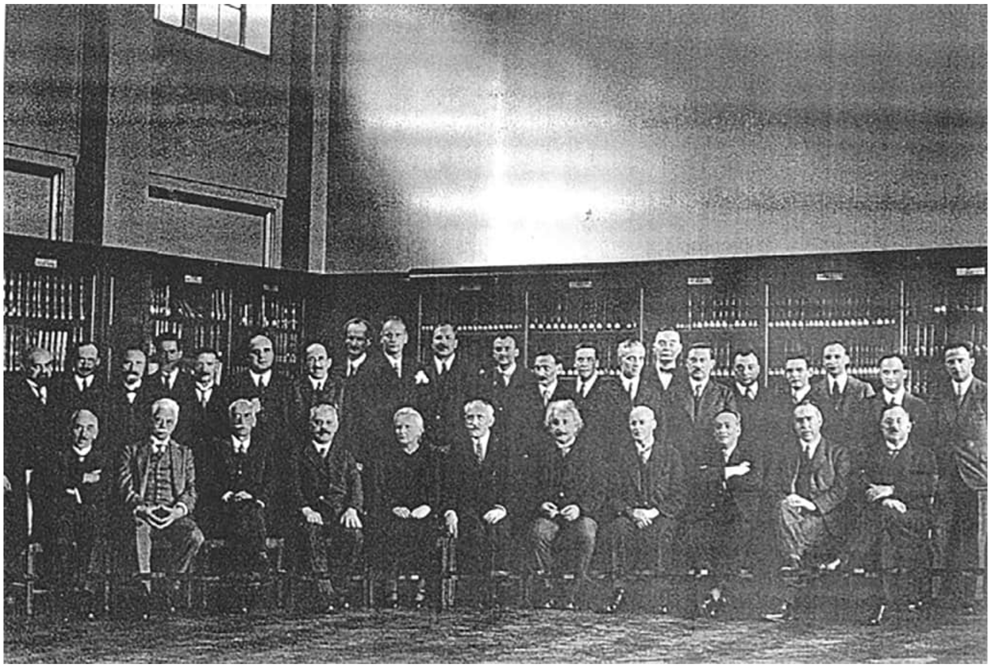

Fig. 8 The 1930 Solvay Conference on Magnetism (Marage and Wallenborn, 1995) courtesy of Université Libre de Bruxelles. Back row: Herzen, Henriot, Verschaffelt, Manneback, Cotton, Errera, Stern, Piccard, Gerlach, Darwin, Dirac, Bauer, Kapitza, Brioullin, Kramers, Debye, Pauli, Dorfman, van Vleck, Fermi, Heisenberg. Front Row: de Donder, Zeeman, Weiss, Sommerfeld, Curie, Langevin, Einstein, Richardson, Cabrera, Bohr, de Haas.

immediate effect on the practical development of magnetism was surprisingly slight. Dirac there made the perceptive remark "The underlying physical laws necessary for the mathematical theory of a large part of physics and the whole of chemistry are completely known, and the difficulty is only that the exact application of these laws leads to equations much too complicated to be soluble".

Magnetic phenomenology and materials

A less fundamental theoretical approach was needed. Louis Néel, a student of Weiss, pursued a phenomenological approach to magnetism, oblivious to the triumphs of quantum mechanics. His extension of Weiss theory to two oppositely-aligned sublattices led to the idea of anti-ferromagnetism in 1932. This hidden magnetic order awaited the development of neutron scattering in the 1950s before it could be revealed directly. Néel later explained the ferrimagnetism of oxides such as magnetite (Fe_3O_4)—the main constituent of lodestone—in terms of two unequal, antiferromagnetically-coupled sublattices. The spinel structure of magnetite has an 'A' sublattice of iron sites in tetrahedral oxygen coordination, and twice as many sites in octahedral coordination forming a 'B' sublattice. The 'B' sites are occupied by a mixture of Fe^{2+} and Fe^{3+}, and the 'A' sites by oppositely-aligned Fe^{3+}. This yields a net spin moment of $4\mu_B$ per formula—a quantitative explanation of the magnetism of the archetypical magnet in terms of lattice geometry and atomic moments associated with electron spin.

An important family of spinel ferrites derived from magnetite was developed by Jacobus Snoek at the Philips Research Laboratory, beginning in the 30's and more intensively following Néel's theory of ferrimagnetism. The expansion of radio communications has been possible, thanks to Ni—Zn ferrites and power electronics for phone or car chargers; choppers and inverters for DC and AC motors and rectifiers could not have advanced without Mn—Zn ferrites. Mg ferrite was used for television tubes and the countless thousands of 2 mm ferrite rings threaded on a lattice of copper wires that served as non-volatile computer memories in the 1970s. Another family of ferrimagnetic iron oxides, the rare-earth iron garnets, included $Y_3Fe_5O_{12}$, the ideal material for low-loss microwave components. For some time, Co ferrite was used for hard magnets, but a decisive breakthrough was the discovery at Philips in 1953 of a family of hexagonal ferrite permanent magnets based on $BaFe_{12}O_{19}$, which were the first magnets to break the shape barrier. They were endowed with sufficient coercivity to be fabricated into any desired shape without self-demagnetization. Electromagnetic machine design was freed at last from the shackles of the horseshoe. As a result, a million tons of hard ferrite is being produced every year to make billions of small DC motors and actuators.

For many practical purposes, it is possible to ignore the atomic and electronic basis of magnetism, and simply regard the magnetization of a solid as a continuous vector. The hysteresis loop $\boldsymbol{M}(\boldsymbol{H})$ (Fig. 9) is a record of the resultant of a metastable structure of domains and domain walls arising from the thermal and magnetic history of a particular sample. Evidence for discontinuous jumps in the Weiss domains as the magnetization was saturated was picked up with headphones by Heinrich Barkhausen in 1919, and in 1931 the domains were visualized in a microscope by Francis Bitter using a colloidal suspension of magnetite particles.

Bloch introduced the idea of a domain wall in 1932 as a region where the magnetization rotates continuously from one direction to another. The exchange energy cost, written in the continuum approximation as $A(\nabla M)^2$ where $A \propto J$, is balanced by the gain in magnetostatic energy $\frac{1}{2}\mu_0 H^2 dV$ associated with the magnetic field created by the ferromagnet throughout its own and the surrounding space, where V is volume. Another term, the anisotropy energy, is needed to restrict the wall width, which can arise from the sample shape, or intrinsically from spin-orbit coupling, a relativistic effect. The sum of these free energy terms, together with the Zeeman energy in an external field, is minimized to yield the domain structure. Based on these concepts, Lev Landau in 1935 explained the formation of domains such as closure domains in iron single-crystals. The complete theory of 'micromagnetism' was formulated by William Fuller Brown in 1940. However, describing the macroscopic magnetic properties from microscopic equations remains an formidable challenge. So far, hysteresis has been modelled using the approach proposed by the Hungarian engineer Ferenc Preisach, a student of Barkhausen, in 1935 (Vajda and Della Torre, 1995).

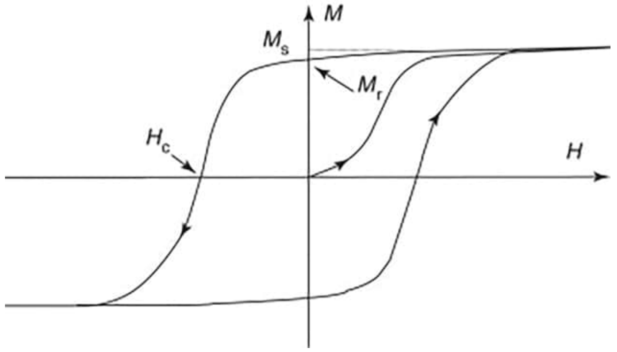

Fig. 9 The hysteresis loop of $\boldsymbol{M}$ against $\boldsymbol{H}$ for a typical permanent magnet. M_s is the saturation magnetization, M_r the remanent magnetization at zero applied field, and H_c the coercive field required to reduce the magnetization to zero.

Domain walls in solids tend to be pinned by local crystal imperfections or microstructures, leading to the metastable states represented on a hysteresis loop. The control of hysteresis was the main challenge for magnetic materials design in the 20th century, and the challenge was met more by metallurgical art than by recourse to fundamental physical theory. Back the 19th century, practical ferromagnetic magnetic materials were limited to soft low-carbon and hard high-carbon steels with additives such as Co, Cr or W. Progress with soft magnets was rapid after Robert Hadfield, working in Sheffield in 1900, discovered the improved mechanical behavior and higher resistivity of silicon steel. Mass production of Fe—Si sheets began in Germany the same year. A lower magnetization was offset by much lower AC losses, and improved efficiency of generators, motors and especially transformers after the development of textured grain-oriented silicon steels by Norman Goss in 1937.

A significant improvement of hard magnets beginning in 1932 was due to the Japanese metallurgist Tokushichi Mishima, who found that adding Al to Ni—Fe alloys improved their hard magnetic properties. Addition of Co with traces of other elements, and development of a series of complex heat treatments gave us the family of 'Alnico' alloys over the following 50 years. All have elongated nanoparticles of soft ferromagnetic Fe—Co in a paramagnetic Ni—Al matrix. The magnetic hardness and coercivity is due to the shape anisotropy of the separated nanoparticles.

The mastery of coercivity gained over the course of the 20th century (Fig. 10) was spectacular. Burgeoning applications of magnetism were the direct consequence. Microscopic quantum theory only began to contribute to this process in the 1970s after the advent of rare earth permanent magnets such as $SmCo_5$ and $Nd_2Fe_{14}B$ in particular, where an understanding of the quantum mechanics of intrinsic, magnetocrystalline anisotropy helped in the design of new permanent magnet materials.

A fertile approach to the problem of hysteresis was to focus on magnetization reversal in the simplest case of single-domain particles. Edmund Stoner and Peter Wolhfarth proposed an influential model for this in 1948. Néel had envisaged magnets made from elongated iron particles in 1942 and published some results in one the short notes he wrote for *Comptes Rendus* in 1947. Seeking to understand the remanent magnetism of baked clay, Néel proposed a model of thermally-driven 'superparamagnetic' fluctuations of the magnetization of micron-sized ferrimagnetic particles the following year. The fluctuation time depended exponentially on the ratio of the magnetization reversal energy barrier to the thermal energy. As a result, a component of magnetization became blocked on cooling in the Earth's magnetic field. Application of this idea of thermoremanent magnetization to cooling igneous rocks delivered a direct and convincing argument for continental drift, as rocks cooling at different times experienced fields of different polarity (Fig. 11). This all led to the subfield of palaeomagnetism, and establishment of the theory of global plate tectonics, which had far-reaching consequences for Earth science (McElhinney, 1973).

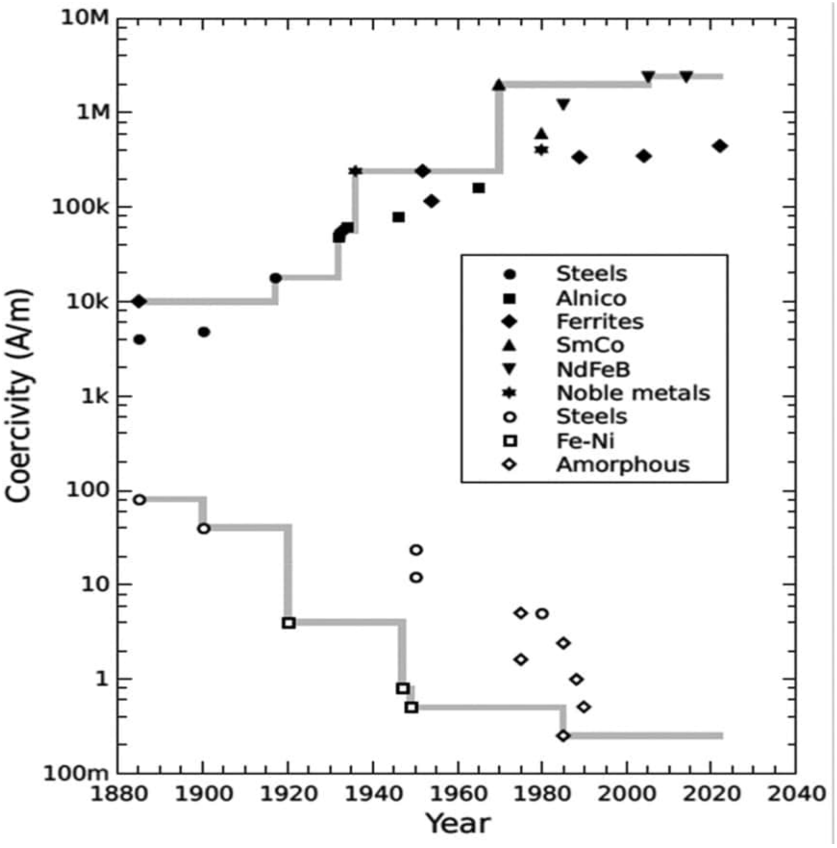

Fig. 10 The development of coercivity in the 20th century.

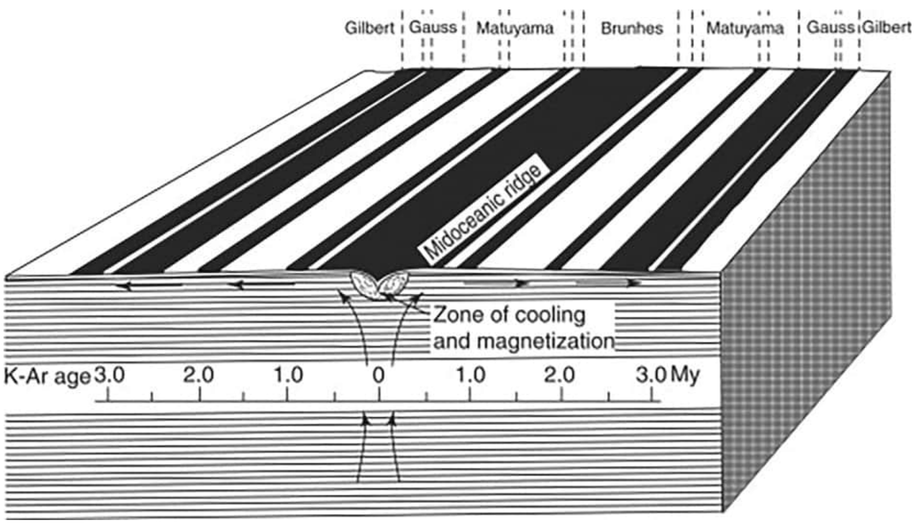
Gilbert
Gauss
Matuyama
Brunhes
Matuyama
Gauss
Gilbert
Midoceanic ridge
Zone of cooling and magnetization
K-Ar age 3.0 2.0 1.0 0 1.0 2.0 3.0 My

Fig. 11 Sign of the thermoremanent magnetization measured across the floor of the Atlantic ocean. Random reversals of the Earth's field, which are dated from other igneous lava flows, follow a chronological pattern which determines the rate of continental drift (McElhinney, 1973). Courtesy of Cambridge University Press.

The Earth's magnetism had been a perennial topic of interest since the seminal work of Gilbert. Alexander von Humboldt, who became interested in 'magnetic storms' in the course of his travels in South America where he made numerous measurements of the Earth's field, organized a group of laboratories in Paris, Freiburg, Berlin and Kazan to make synchronous measurements of the field in the course of a single day in March 1829.

Remarkably, all of them revealed the same pattern of short-term fluctuations. Humboldt's embryonic *Magnetische Verein* was soon entrusted to Wilhelm Weber and Carl Friedrich Gauss in Göttingen, who expanded the collaboration to include dozens of magnetic observatories across Europe, Asia and North America, spanning the globe from Dublin to Alaska. They collated worldwide measurements made on a daily schedule of Göttingen time in an unprecedented international scientific collaboration aimed at understanding the behavior of the Earth's magnetic field. It lasted until 1841 and continued in another guise for a further decade. Gauss developed spherical harmonic analysis to reduce the data and concluded that the greater part of the field was of internal origin. The external component was associated with an 11-year cycle of sunspot activity by Edward Sabine, but no amount of data, however scrupulously acquired, was capable of predicting the variations of system that was essentially chaotic.

Modern developments

Magnetism since 1945 has been an area of rich and productive discovery, not least because of the enormous increase in numbers of scientists and engineers working in the field. Magnet ownership for citizens of the developed world has skyrocketed from one or two magnets in 1945 to a few hundred 75 years later, or something of order a trillion if we count the individual magnetic bits on a hard disc in a personal computer! Magnetic recording dates from the final years of the 19th century, when the Danish engineer Valdemar Poulsen recorded his voice on steel wire (Daniel et al., 1999). It developed into analog recording on tape covered with ferrimagnetic microparticles in Germany in the 1930s but in the modern era, digital recording has come to overshadow all else. Hard discs, introduced by IBM in 1957 offer large amounts of nonvolatile computer memory. Initially using inductive read-write heads and particulate media, they developed to provide the bulk of the mass storage in data centers, where all the readily-accessible information of the internet is stored. Much non-volatile personal data is now recorded in semiconductor flash memory, but archival back-up storage of mountains of digital data generated daily uses magnetic tape. Magnets and semiconductors were the mainstays of the first decades of the information revolution—semiconductors to process the data and magnets to store it. The success of magnetic recording lay in its ability to keep pace with the relentless exponential doubling of the areal density of transistors on silicon chips every one or two years. This is due to the scale-invariance of the dipole field of a pattern of permanent magnetism, and the ability of spin electronics to develop magnetic field sensors based on thin film stacks that can operate on ever-smaller length scales. Magnetic recording is a pillar of the information society.

Modern achievements can be classified as those contributing to a basic understanding of condensed matter, those associated with new experimental probes, and those leading to new materials, preparation methods and industrial technologies.

Theory

From a fundamental viewpoint, magnetism has been a fertile field for cultivating condensed-matter theory. After Weiss's original mean-field theory, magnetism has inspired more sophisticated theories of phase transitions, and provided the data to support them. A milestone was Onsager's 1944 solution of the two-dimensional Ising model, where spins are regarded as scalars which take values ±1. The behavior of more complex and realistic systems such as the three-dimensional Heisenberg model were solved numerically using the renormalization group technique in the 1970s. The ability to tailor magnetic model systems having an effective spatial dimension of 1 or 2 with structures of isolated chains or planes of magnetic ions and an effective spin dimension similarly limited by anisotropy to 1, 2 or 3 in the Ising, xy or Heisenberg models, laid the foundation of the modern theory of phase transitions.

Coulomb correlations among the electrons in a metal, and their coupling to the crystal lattice, generate a wealth of ground states and unexpected phenomena in solids. Experimental studies of dilute magnetic alloys such as **Au**Fe or **Cu**Mn raised two questions that preoccupied theorists in the last decades of the 20th century. One was whether a single atomic impurity in a nonmagnetic metal can retain its magnetic moment. The question focused attention on the relation between magnetism and electronic transport in metals, a nexus that has been immensely productive. The other concerned the nature of the transition to the 'spin glass' state when the magnetic moments of the impurities freeze in random directions at sufficiently low temperatures. The single impurity problem was related to a shallow resistivity minimum at low temperature where the atom appears to lose its magnetic moment. The effect was explained by Jun Kondo using perturbation theory for spin-flip scattering, where the impurity enters a singlet state due to Coulomb interaction with the conduction electrons. The Kondo problem was eventually solved exactly in 1983 by Natan Andrei. In spin glasses, multiple dilute impurities interact with each other via indirect 'RKKY' exchange through spin polarization of the conduction electrons, which produces a symmetric Gaussian distribution of positive and negative exchange interactions J. Spin glasses show a frequency-dependent peak of the magnetic susceptibility at the spin freezing temperature T_f, which it is thought would be a thermodynamic phase transition for Heisenberg spins in four spatial dimensions. The wider problem of spin freezing in amorphous solids resulting from topologically-frustrated antiferromagnetic interactions in odd-membered rings or random single-ion anisotropy, especially for rare-earth atoms, was investigated in the context of amorphous magnetism in the 1970s, as discussed further in the following section on Materials.

Theoretical studies of the ground states of chains, ladders, triangular lattices and the two-dimensional electron gas catalyzed a wider understanding of the role of topology in condensed matter, where magnetism has provided model systems that help to clarify the concepts. Topological properties of matter are invariant under small changes of external variables—pressure, temperature, or magnetic field—unlike the usual linear response. An early example of topological quantum matter was the one dimensional, S = 1 antiferromagnetic chain that Duncan Haldane discovered in 1981 exhibited a spin gap and behaved as a quantum spin liquid. At about the same time, Klaus von Klitzig at the Grenoble High Magnetic Field Laboratory discovered that the Hall effect in the two-dimensional electron gas of a silicon MOSFET exhibited a series of steps in applied field, where the Hall conductance was a precise integral multiple of e^2/h, to within one part in a billion. This provided a new standard of resistance $h/e^2 = 25.81280745$ kΩ. A corresponding quantum anomalous Hall effect was observed in magnetic materials in the absence of an applied field. The anomalous Hall effect, itself a puzzle for over a 100 years after its discovery by Edwin Hall in 1879, was interpreted as an intrinsic feature of a ferromagnetic metal related to the topology of the band structure, characterized by its Berry curvature.

Numerical simulations

With the arrival of cheap, powerful computers in the 1990s, numerical simulations of the electronic structure and properties of ideal crystals based on spin-dependent density-functional theory became widespread. They opened the prospect of discovering potentially-interesting new magnetic materials without the bother of entering a laboratory. Simulations were successfully applied to calculate the magnetic ground state properties of correlated electrons in metallic systems, and obtain magnetization, anisotropy and Curie temperature. Phase stability may depend on stoichiometry, disorder or a variety of crystallographic defects, and a single phase may be unstable with respect to disproportionation into a lower-energy combination of two or more phases. While no new magnetic materials have yet been discovered that are worthy to join the handful that can be profitably commercialized, the method provides insight into trends in the electronic structure and properties of large numbers of ideal compounds but fall short of handling the complexity of real materials. Numerical simulations began to accompany experimental reports on properties of magnetic materials. Machine learning from large databases of known phases can improve the accuracy of predicted magnetic properties such as Curie temperature.

On a different scale, simulations based on the Landau-Lifschitz-Gilbert equation are appropriate for simulating the short-term dynamics and micromagnetism of microscopic systems. The mesoscopic scale is computationally the most demanding.

Experimental methods

Force magnetometers remained in use for most of the 20th century for static measurements of magnetization and susceptibility. DC magnetometers based on the ballistic galvanometer were replaced by electronic integrators based on John Ragazzini's valve-based operational amplifiers (1947) and their solid-state successors (1968), and then usually by digital integration. The vibrating sample magnetometer (VSM), a laboratory workhorse, was invented by Simon Foner in 1959 to measure the voltage induced in a quadrupole pickup coil by the oscillatory movement of a magnetized sample using a phase-sensitive lock-in detector, thereby converting a one-shot measurement to the continuous detection of a steady voltage. The principle is similar to that of the electric guitar microphone invented by Adolf Rickenbacker in 1931. Due to its versatility and sensitivity of order 10^{-8} Am^2 or 10^{15} μ_B, the VSM became the standard laboratory method for measuring magnetic moment, either equipped with an electromagnet or a superconducting coil. A trend in laboratory experiments has been to generate and process ever-growing quantities of data, thanks due to the ability of computers to accumulate and store digital information on ever-shorter timescales. The precision and detail of the measurement is thereby enhanced.

The discovery of magnetic resonance, the sharp absorption of microwave or radio-frequency radiation by Zeeman-split levels of an atom or nucleus in a magnetic field, was a landmark in modern magnetism. Significant mainly for the insight provided into solids and liquids at an atomic scale, electron paramagnetic resonance (EPR) and nuclear magnetic resonance (NMR) spectroscopies were later complemented by that provided by the Mössbauer effect in 1958. Hyperfine interactions of nuclei and electrons provided a point probe of electric and magnetic fields at the center of the atom. In a magnetically-ordered state, precession of the magnetic sublattices in a field leads to ferromagnetic resonance (FMR) at the Larmor precession frequency of 28 GHzT^{-1}. The ability to measure the response of materials short timescales when they are out of equilibrium has been enhanced by pump/probe methods involving short intense, sub-ns pulses of energy from lasers or particle beams. Some of the methods involve special large-scale facilities, to which many users have access to supplement the facilities in their home laboratories. Communications among academic researchers intensified in the modern period—electronic communications have replaced postal reprint requests, and the scientific literature has become increasingly accessible. Collaboration between laboratories to address a particular problem as effectively as possible is increasingly common.

Of the new experimental probes of magnetism, neutron scattering was initially the most influential and generally useful. A beam of thermal neutrons from a nuclear reactor was first exploited for neutron diffraction by Clifford Shull and Ernest Wohlan in 1951, who used the magnetic scattering to reveal the antiferromagnetic order in MnO. Countless magnetic structures have been measured since, using specially-constructed research reactors at Chalk River, Harwell, Brookhaven, Grenoble and elsewhere. Excitations could be characterized by inelastic scattering of thermal neutrons, with the help of the three-axis spectrometer developed by Bertram Brockhouse in Canada to measure the change of energy and momentum. Complete spin-wave dispersion relations were used to provide a wealth of information on anisotropy and exchange. Spallation sources at Oak Ridge and elsewhere, which provide intense pulses of neutrons by collision of highly energetic protons with a target of a heavy metal such as tungsten, are most useful for studying magnetization dynamics.

Other beams produced at large-scale facilities that proved useful for probing magnetism were muons and especially synchrotron radiation. The intense, tunable ultraviolet and X-ray radiation from the circulating electrons in a synchrotron allows the measurement of magnetic dichroism from deep atomic levels, permitting the separate determination of spin and orbital contributions to the magnetic moment by X-ray circular dichroism. The intensity of the radiation from synchrotrons and free-electron lasers is greatly enhanced by arrays of permanent magnets around the beam known as undulators or wigglers, that generate intense coherent or incoherent radiation, respectively. Bending electromagnets are used to direct and focus the charged particle beams.

Direct imaging of domain structures at surfaces or in thin films with light, electron microscopy or scanning probe, magnetic-force microscopy have all contributed to an improved understanding of micromagnetics. Bulk domain structures can be accessed, with difficulty, by neutron tomography. X-ray photo-electron microscopy offers fast time-resolved imaging of domains in thin films.

Increasing availability of commercial superconducting magnets from the late 1960s has led to a boom in diagnostic imaging of tissue based on pulsed proton NMR in magnetic fields of 1–3 T. Tens of thousands of these scanners in hospitals across the world provide images of hearts, brains and every sort of tumor. Superconducting magnets can now provide fields of over 20 T for NMR and general laboratory use. Coupled with SQUID sensors, ultrasensitive magnetometers capable of measuring magnetic moments of 10^{-11} Am^2 are widely available. Larger fields of up to 30 T require expensive special installations with water-cooled Bitter magnets consuming many megawatts of electrical power. Resistive/superconducting hybrids in Tallahassee, Grenoble and Tokyo can generate steady fields in excess of 40 T. Still higher fields above 50 T demand millisecond pulses; the higher the field, the shorter the pulse; 200 T can be reached in small volumes with a single turn sacrificial coil. Even greater transient fields can be attained by explosive flux compression.

Materials and technology

For many physical studies, magnetic materials are needed in special forms, such as single crystals or thin films. Skilled crystal-growers are assiduously cultivated by neutron scatterers and other condensed matter physicists. With large crystals, tensor properties such as susceptibility, magnetostriction and magnetotransport can be measured in any direction.

A far-reaching advance after 1970 was the appearance of multi-target thin-film growth facilities (sputtering, pulsed-lased deposition, molecular-beam epitaxy) in magnetism research laboratories. Ultra-high vacuum facilitated the study of surface magnetism at an atomic level, but much of the motivation was to investigate magnetoresistance or magneto-optics or of thin, high-quality metal films, and especially the thin film multilayer structures that have contributed massively to the development of spintronics and magnetic data storage. An example of a fairly complex stack that, after suitable heat treatment, exhibits perpendicular magnetic anisotropy and 200% tunnelling magnetoresistance (TMR) is illustrated in Fig. 12.

Conventional electronics ignored the spin of the electron because unlike electron charge, electron spin is not necessarily conserved in scattering events. A conduction electron in a metal may undergo 100 scattering events before a spin flip. If the mean free path is 2 nm it will only have travelled about 12 nm before losing its spin memory. Unpolarized electrons acquire a spin polarization on traversing a couple of nanometers of cobalt, but the spin-polarized current does not go far in an insulator or nonmagnetic metal before losing its spin memory. Hence the choice of materials in a stack and their thickness is critical. Layers of an antiferromagnet such as IrMn_3 are used for exchange bias to pin the magnetization of an adjacent ferromagnetic layer in spin valves

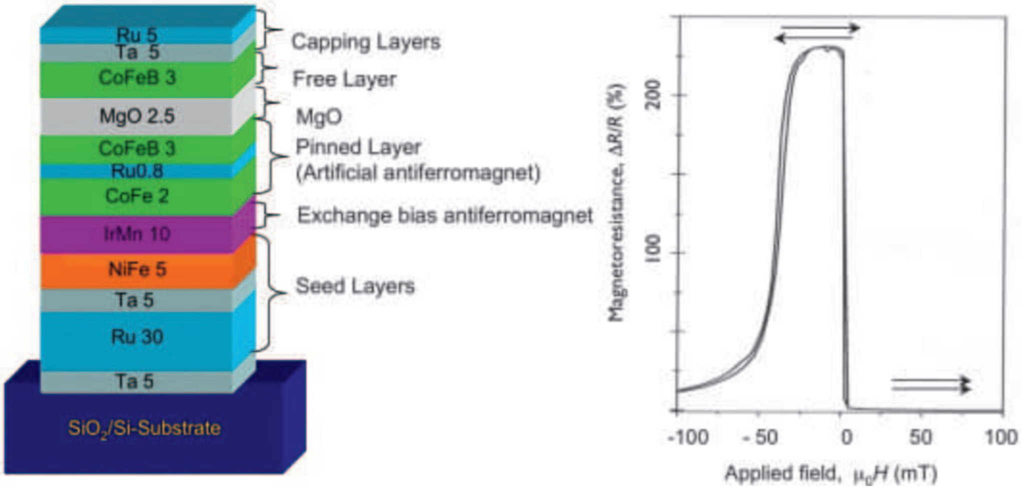

Fig. 12 A thin film stack with a magnetic tunnel junction (left). The magnetic layer below the MgO tunnel barrier is pinned by coupling to the antiferromagnetic $IrMn_3$ layer to produce the magnetoresistance characteristic (right).

from the mid-1990s. The anisotropic magnetoresistance ≈1% (AMR) of single a layer of permalloy was used for the first sensors or memory elements in the 1980s. A sandwich spin-valve structure with a nonmagnetic metal spacer layer that exhibited giant magnetoresistance ≈10% (GMR) was more versatile, with fixed and pinned layers oriented parallel for a switchable memory element and perpendicular for a linear field sensor. The moments were oriented in-plane in the first devices and perpendicular to the plane in later ones. Greater sensitivity was achieved in spin valves with an insulating tunnel barrier of amorphous AlO_s or crystalline MgO where greater tunnel magnetoresistance ≈200% could be achieved. The timeline for the adoptions of these sensors in read heads for magnetic recording where they have to read the stray fields just above the disc surface is illustrated in Fig. 13. The writer has always been a miniature electromagnet. The sensors, originally designed for magnetic recording, found important applications in partnership with magnetic nanoparticles in bio-assay.

The development of non-volatile thin film memory underwent a similar evolution beginning with thin film permalloy memory with a lattice of current carrying wires to create local magnetic fields sufficient to switch the bits, analogous to ferrite cores, in the 1960s. Then, after the discovery of giant magnetoresistance by Albert Fert, Peter Grunberg and others in 1988, spin valve memories based on half-select magnetic field toggle switching appeared in the 1990s. The field switching was not scalable, so a new generation of spin-transfer torque magnetic random-access memory developed around 2010 used the angular momentum of a spin-polarized current passing perpendicular to the stack to switch the free layer. In suitable conditions, the switch becomes an oscillator.

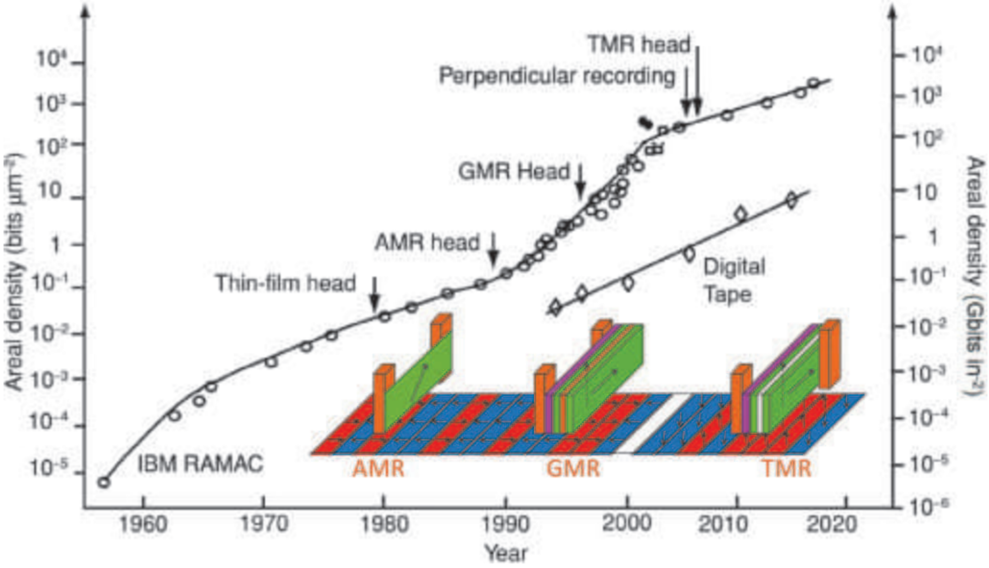

Fig. 13 Exponential growth of magnetic recording density over 60 years, with an illustration of the read/write technology.

The spin Hall effect, rediscovered in 1999 by Jaime Hirsch, is the creation of a transverse spin current flowing perpendicular to a charge current in a heavy metal, due to spin-orbit scattering. It is harnessed in heavy metal/ferromagnetic bilayers to inject angular momentum into the ferromagnet and switch its magnetization by 'spin-orbit torque', another potential scheme for magnetic memory. Magnetic recording and spin electronics became major research preoccupations in the magnetic research community after about 1990. A cognate growing discipline is magnonics, where spin waves rather than electrons are used to transmit and process data.

A quite different, earlier preoccupation arose from studies of phase transitions in model magnetic systems in the 1970s, namely the effect of atomic disorder and the absence of a crystalline lattice on magnetic order. A seed was sown by Pol Duwez in 1960 who first produced small samples of amorphous metal by splat cooling, but applications became feasible only after the invention in 1976 of continuous melt spinning, where a jet of molten metal impinges on a copper wheel rotating with a surface velocity of about 50 ms^{-1} to give a quench rate of up to 10^6 Ks^{-1}, sufficient to freeze eutectic metallic melts into amorphous solids. Other melts such as Nd—Fe—B became nanocrystalline. The first soft magnetic amorphous materials Fe_{80} $(P,B,C)_{20}$ were spun in 1976 by Robert O'Handley and Ryusuke Hazegawa and a range of Fe- Co- and FeNi-based alloys were subsequently commercialized the 1980s by Allied Chemical as *Metglas*. The amorphous alloys found niche markets in network transformers, components for power electronics and many kinds of magnetic sensors due to their exceptional magnetic softness. A parallel discovery made at Hitachi Metals by Yoshihito Yoshisawa in 1988 while trying to lower high frequency losses by pinning domain walls with micro-size crystallites was *Finemet*, a Fe—Si—B—Nb alloy with 1% of copper. This material is a composite of nanocrystals of Fe—Si in an amorphous matrix. It combines polarization of 1.25 T, larger than permalloy, and is as soft as cobalt based amorphous alloys, yet uses no cobalt. The astonishing softness of nanocrystalline materials was explained a year later by Giselher Herzer at Vacuumschmelze, where similar alloys were developed.

Perhaps the most far-reaching advances in bulk magnetic materials for electromagnetic applications in the modern period was the invention and development of rare earth permanent magnets. They are more expensive to make than hard ferrites, but they offer stored energy densities that are an order of magnitude greater. First were magnets based on the binary intermetallic phases $SmCo_5$ or Sm_2Co_{17} that were pioneered by Karl Strnat in the 1960s. A global cobalt supply crisis brought about by war in Zaire in 1979, led to a renewed effort to find an Fe-based substitute, which bore fruit in 1983 in two different ways. First was the discovery by Masato Sagawa at Sumitomo Special Metals of $Nd_2Fe_{14}B$, a tetragonal iron-rich interstitial phase with boron, using the methods of classic powder metallurgy. Favorable phase relations included a low-melting nonmagnetic Nd-rich phase that surrounded the $Nd_2Fe_{14}B$ grains and facilitated the development of coercivity. The properties were continuously improved over the following years with additives of Co or heavy rare earths (Dy, Tb) and optimized crystallite orientation and milling to increase the volume fraction and reduce the size of the hard magnetic crystallites. Many grades became available with a trade-off between remanence and coercivity, which determines the maximum operating temperature.

A different approach was adopted by John Croat at General Motors, who used melt spinning to produce isotropic nanocrystalline material that was useful for making polymer bonded material by injection or compression molding. These have lower energy products than sintered magnet, but great flexibility for manufacture of components in complex shapes.

Nd—Fe—B magnets have grown to dominate the permanent magnet market. They radically changed the design of motors for many applications. They were indispensable for the voice-coil motors in slim hard-disc drives and enhanced considerably the power density of small motors—a quadcopter could not take off without NdFeB magnets. They improve the efficiency of high-power electrical machines and applications are burgeoning in new areas of motors for electric vehicles and robotics, and in large direct-drive wind turbines now seen in landscapes everywhere.

In summary, the consequences of near-instantaneous access to virtually unlimited stores of magnetically recorded data in centers distributed across the world, and the ability to acquire and copy it electronically at practically no cost to the user is the basis of the 'big data' revolution that we are in the midst of. However, the quantities of data are so enormous that energy costs are exploding and may become prohibitive. The implications for human life and society are unpredictable but are likely to be as profound as on the previous two occasions when magnetism changed the World.

Conclusion

Past record is no guarantee of future performance, so one must be wary of extrapolating the history of any science or technology very far into the future. Magnetism, like much of physics itself, has often been dismissed as 'finished' in the past, only to confound the doomsayers with some new twist or unexpected development. The current focus on spin electronics and nanoscale magnetism in artificially-structured thin film devices will surely be sustained for some time to come.

The behavior of magnetism on increasingly short timescales, the influence of topology in normal and reciprocal space, and information transfer and processing using magnons rather than spin directly are topics that seem likely to attract continued research interest.

Industrial applications of magnetism are largely based on the properties of about a dozen commercially-produced magnetic materials. The discovery of just one more could animate the subject for a decade. It seems unlikely, though, that much advance will be achieved on the magnetic values on the hysteresis loop. There has been no advance in saturation magnetization in a century over that of $Fe_{35}Co_{65}$, and coercivity can already be controlled, albeit with much care and effort, to almost any desired value. No Curie temperature has ever exceeded that of cobalt, which has been known since 1912. The new material will probably commend itself by a useful combination of magnetic and nonmagnetic (electrical, optical, mechanical, thermal) properties.

Magnetism has served the miniaturization of information technology and electromagnetic drives well and may continue to do so in future. New frontiers in cell biology have to be explored. Applications of magnetic nanoparticles in medicine are burgeoning. There have been half a dozen paradigm shifts—completely new ways of seeing the magnet and its field—during the 3000 years encounter of magnetism with human curiosity. Magnetism has effectively transformed the world on three occasions; who can say there will not be another?

References

Boorstin D (1992) *Les Découvreurs*. Paris: Editions Robert Laffont.
Coey JMD (2010) *Magnetism and Magnetic Materials*. Cambridge University Press.
Curie P (1895) Lois expérimentales du magnétisme. *Propriétés magnétiques des corps à diverses températures Annalea de Chimie et de Physique*. vol. 5, pp. 289–415. Paris: Gauthier-Villars.
Daniel ED, Mee CD, and Clark MH (1999) *Magnetic Recording, the First Hundred Years*. New York: IEEE Press.
Ewing JA (1982) *Magnetic Induction in Iron and Other Metals*. London: The Electrician Printing and Publishing Company.
Fara P (1966) *Sympathetic Attractions: Magnetic Practices, Beliefs and Symbolism in Eighteenth-Century England*. New Jersey: Princeton University Press.
Gilbert W (1958) *De Magnete*. English translation by P F Mottelay. New York: Dover Publications.
Kirwan R (1797) *Thoughts on Magnetism*. vol. 6, Transactions of the Royal Irish Academy, pp. 177–191.
Kloss A (1994) *Geschichte des Magnetismus*. Berlin: VDE-Verlag.
Marage, P and G. Wallenborn, G. editors (1995) Les Conseils Solvay et Les Débuts de la Physique Moderne, Université Libre de Bruxelles.
Matthis DC (1965) *Theory of Magnetism*. New York: Harper and Row. ch. 1.
McElhinney MW (1973) *Palaeomagnetism and Plate Tectonics*. Cambridge University Press. (1972).
Meyer HW (1972) *A History of Electricity and Magnetism*. Norwalk, Connecticut: Bundry Library.
Mottelay PF (1975) *Bibliographical History of Electricity and Magnetism*. New York: Arno Press.
Needham J (1962) *Science and Civilization in China*. Vol. 4, Part 1. Cambridge University Press.
Quédec P (1988) Weiss' Magneton: The Sin of Pride or a Venial Mistake? *Historical Studies in the Physical and Biological Sciences* 18: 349–375.
Tomonaga S (1974) *The Story of Spin*. Chicago: University of Chicago Press.
Vajda F and Della Torre E (1995) *Ferenc Preisach, In Memoriam*. IEEE Transactions on Magnetics 31, i–ii.
Weiss P and Foëx G (1926) *Le Magnétisme*. Paris: Armand Colin.

Disordered magnetic systems[☆]

Per Nordblad, Department of Materials Science and Engineering, Uppsala University, Uppsala, Sweden

© 2024 Elsevier Ltd. All rights reserved.

This is an update of P. Nordblad, Disordered Magnetic Systems, Editor(s): Franco Bassani, Gerald L. Liedl, Peter Wyder, Encyclopedia of Condensed Matter Physics, Elsevier, 2005, Pages 452–457, ISBN 9780123694010, https://doi.org/10.1016/B0-12-369401-9/00527-1.

Introduction 19
Models 19
Spin glasses 19
Re-entrant spin glasses 22
The random field Ising model 22
Amorphous magnetic systems 23
Magnetic materials 23
Conclusion 23
References 24

Abstract

Amorphous metallic magnets, spin glasses and dense magnetic nanoparticle systems are systems where interaction between magnetic moments cause collective magnetic ordering in spite of disordered atomic or particle structure. Disordered spin-structures provide model systems, such as spin glasses and random field systems, of large interest for fundamental research. Disorder of the atomic structures of ferromagnets govern their coercivity and determine the quality of both soft and hard magnetic materials in applications.

Key points

- Models and magnetic properties of spin glasses and superspin glasses
- Descriptions of properties and models of random field Ising systems.
- Models and phase diagrams of reentrant spin glasses.
- Properties of amorphous magnetic systems.
- Effects of disorder on soft and hard ferromagnets.

Nomenclature

T	Temperature [K]
T_g	Spin glass temperature [K]
T_f	Freezing temperature [K]
t	Reduced temperature
t	Time [s]
t_w	Wait time [s]
τ	Relaxation time [s]
f	Frequency [Hz]
H	Magnetic field [Am^{-1}]
h	Magnetic field [Am^{-1}]
M	Magnetisation [Am^{-1}] alt. [a.u.]
χ	Magnetic susceptibility [SI] alt. [a.u.]
S	Spin
J	Exchange interaction
FC	Field cooled
ZFC	Zero field cooled

[☆] *Change History*: February 2023. P Nordblad has been involved in the update. The section on Re-entrant spin glasses has been revised and Fig. 3 added. Recent references have been added: Kawamura and Taniguchi (2015), Mydosh (2015), Parisi (2021), Peddis et al. (2021).

Introduction

The subject disordered magnetic systems comprise, when defined widely, the whole field of applied magnetic materials, ranging from extremely soft Permalloy to the hardest permanent magnet; as well as the physics of model systems of strongly disordered magnetic materials: Spin glasses and random field Ising systems (Young, 1998).

Magnetic ordering requires that the electron system forms local or itinerant magnetic moments and that there is interaction between these moments. Such interacting magnetic moments will eventually, as the temperature is lowered, become correlated and in certain cases form a long ranged ordered phase at a critical temperature. The simplest magnetic order in crystalline systems arises when the leading interaction is ferromagnetic and there is only one type of magnetic ions in the material. The low temperature phase then shows a regular pattern with the magnetic moments all aligned in parallel. Magnetic disorder in an ideal system of this type is enforced by thermal energy and above the critical ordering temperature, a random paramagnetic phase forms. However, intrinsic quenched disorder, due to lattice dislocations, impurities, and other defects, always appear in a real magnetic system, also in the magnetically ordered phase. This kind of disorder is the key to the macroscopic magnetic properties of an ordered ferromagnet. The disorder and the microstructure of the system then determine if a weakly anisotropic magnet becomes a good soft ferromagnet or if a strongly anisotropic system attains applicable permanent magnet properties. It is thus disorder, on nano- and micrometer length scales, that governs the quality of applied magnetic materials, whether soft or hard.

Models

A random distribution of the atomic magnetic elements in alloys and compounds introduces strong disorder and deviations from a regular interaction pattern. The interaction in-between the magnetic constituents become random in size and in cases also in sign. This causes the appearance of new magnetic phases and phenomena. An interacting magnetic Ising system can be described by its spin Hamiltonian:

$$H = -\sum_{i,j} J_{i,j} S_i S_j \tag{1}$$

where $J_{i,j}$ is the exchange interaction strength between spin S_i and spin S_j; spins that in an Ising system point either up or down. A random exchange ferromagnet is described if all $J_{i,j}$ are positive but of different magnitude and a spin glass is described if the sign of $J_{i,j}$ varies but the mean value is zero (Fisher and Hertz, 1991; Mydosh, 2015). Eq. (1) can be used to describe systems of any dimensionality and any range of interaction. Another important class of disordered magnetic Ising systems is the random field system:

$$H = -\sum_{i,j} J_{i,j} S_i S_j + \sum_i h_i S_i \tag{2}$$

where $J_{i,j}$ are positive interaction constants and h_i is a local field of random size and sign with zero mean that acts on spin number S_i. This system does not have an experimental realization, but a dilute Ising antiferromagnet in an applied homogeneous magnetic field has been shown to describe an equivalent problem:

$$H = -\sum_{i,j} J_{\varepsilon i \varepsilon j} S_i S_j + Ha \sum_i \varepsilon_i S_i \tag{3}$$

where J is a negative exchange interaction constant and ε_i is 1 if site i is occupied by a magnetic ion and 0 if the site contains a nonmagnetic element. H_a represents a homogeneous applied magnetic field, and the equation shows that the random field is proportional to this field and thus arbitrarily tunable (Belanger and Young, 1991).

Spin glasses

An alloy with magnetic ions randomly dispersed in a nonmagnetic host metal forms at low magnetic ion concentrations an archetypical spin glass material. The interaction in the system is random in size and sign due to the Ruderman-Kittel-Kasuya-Yosida (RKKY) nature of the interaction in a metal. The RKKY-interaction is mediated by the conduction electrons and is oscillatory in size and decays with the cube of the distance in-between the magnetic constituents. The signature and the initial cause of interest in this type of dilute magnetic alloys was the observation of a cusp in the in-phase component of the ac-susceptibility by Cannella and Mydosh (1972). This finding was a clear indication of a phase transition to a new kind of magnetic order and this phase, later named the spin glass phase, has been found to own surprising magnetic properties and has created a theoretical problem of much greater complexity than only a cusp in the ac-susceptibility gave promise to Mezard et al. (1987), Mydosh (2015), Nordblad (2013), Kawamura and Taniguchi (2015) and Stein and Newman (2013). Spin glasses provide a useful introduction to the physics of strongly disorder magnetic systems in general and are therefore described in some detail below.

A spin glass problem can be defined using Eq. (1) and setting the spatial dimension of the system as well as the distribution and range of the interaction $J_{i,j}$. In the Sherrington-Kirkpatrick (SK) model (Sherrington and Kirkpatrick, 1975), the sum is taken over all pairs (i,j) of N spins and a Gaussian distribution of $J_{i,j}$ with zero mean is used. The famous Parisi solution of this problem using replica symmetry breaking (RSB) forms one school of models describing spin glasses: The RSB or mean field picture (Mezard et al., 1984). An alternative model to describe finite dimensional systems is the droplet picture, which is based on the scaling hypothesis and yields a spin glass with, in parts, remarkably different properties than the mean field predictions. A main difference concerns the nature of the spin glass in a magnetic field, where the droplet picture prescribes that there is no equilibrium spin glass phase, whereas the RSB model yields a phase line in the field-temperature (H-T) plane (the Almeida-Thouless line) that separates the paramagnetic from the spin glass phase. On the other hand, in zero magnetic fields, both models anticipate a low temperature phase with relaxation processes that lasts over exceedingly wide time scales and a non-stationary nature of a system that has been quenched to a temperature below its spin glass temperature (T_g).

There is an extensive literature on the static and dynamic magnetic properties of three-dimensional spin glass materials as observed in experiments and Monte Carlo (MC) simulations on three dimensional Ising spin glass models. A quite clear empirical picture as to the magnetic properties of spin glasses can be extracted from this literature. The behavior is however complex and has allowed interpretations in terms of both the RSB and the droplet scaling model or combinations of the two pictures.

It is firmly established that there is a second order phase transition to a low temperature spin glass phase in zero field. This transition is evidenced from the dynamics through analyses of the critical slowing down on approaching the phase transition temperature (spin glass temperature) and from the static susceptibility through a divergence of the non-linear susceptibility on approaching T_g. In Fig. 1, ac-susceptibility data at different frequencies measured on the Ising spin glass $Fe_{0.5}Mn_{0.5}TiO_3$ are shown; the original spin glass signature: A (frequency dependent) cusp in the ac-susceptibility is clearly seen. The temperature dependence of the relaxation time,τ, that can be derived from the frequency dependence of the cusp (or freezing) temperature, T_f, obeys critical slowing down and implies a phase transition with a relaxation time that diverges according to critical slowing down: $\tau = \tau_0 t^{-z\nu}$, where τ_0 is an atomic relaxation time of order 10^{-13} s, $z\nu \approx 10$ is the dynamic critical exponent and t is the reduced temperature, $t = T/T_g$-1. Critical slowing down and the existence of a low temperature spin glass phase has convincingly been established from experiments and simulations on three dimensional Ising spin glasses. This is one side of the phase transition problem; a key question, which distinguishes the RSB- and droplet model predictions, is whether the phase transition persists in an applied magnetic field or not. This seemingly simple question has not been easy to answer from either experiments or simulations. However, analyses of the in-field dynamics of the Ising spin glass $Fe_{0.5}Mn_{0.5}TiO_3$ show that the slowing down of the relaxation time is significantly altered in an applied field compared to zero field and suggest that there is no phase transition in a magnetic field in a three-dimensional Ising spin glass.

The response of a spin glass to the application of a weak magnetic field in the spin glass phase extends from the atomic relaxation time (τ_0) to exceedingly long times well beyond the time scale of any experimental probe., i.e., in common with other glassy systems, the relaxation times are exceedingly long in the low temperature phase. Also, in common with other glasses, the low temperature spin glass falls out of equilibrium as the system is cooled through the spin glass transition temperature. Once the system is kept at constant temperature in the low temperature phase, it spontaneously and continuously reorganizes the spin structure—the system ages! Aging has a very characteristic influence on the response function of spin glasses. The relaxation of the magnetization $M(t)$ attains an inflection point at an observation time (t) of the order of the wait time (t_w) at constant temperature before the weak magnetic field was applied in a plot of $M(t)$ vs. log(t). Fig. 2a shows the relaxation of the magnetization $M(t)$ of a Ag(11 at.% Mn) spin glass measured after the different wait times indicated in the figure; also plotted in the figure is the relaxation

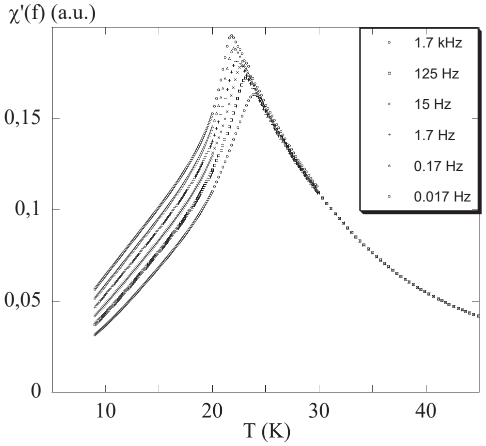

Fig. 1 The ac-susceptibility, $\chi'(f,T)$, measured along the c-axis of the Ising spin glass, $Fe_{0.5}Mn_{0.5}TiO_3$. The frequency (f) of the weak ac-field is indicated in the figure. Data from Mattsson J (1994) Dynamics of random magnets. *Comprehensive summaries of Uppsala dissertations from the Faculty of Science and Technology 48, Acta Universitatis Uppsaliensis* and Jonsson T (1998) Collective behavior of disordered magnetic systems. *Comprehensive summaries of Uppsala dissertations from the Faculty of Science and Technology 395, Acta Universitatis Uppsaliensis.*

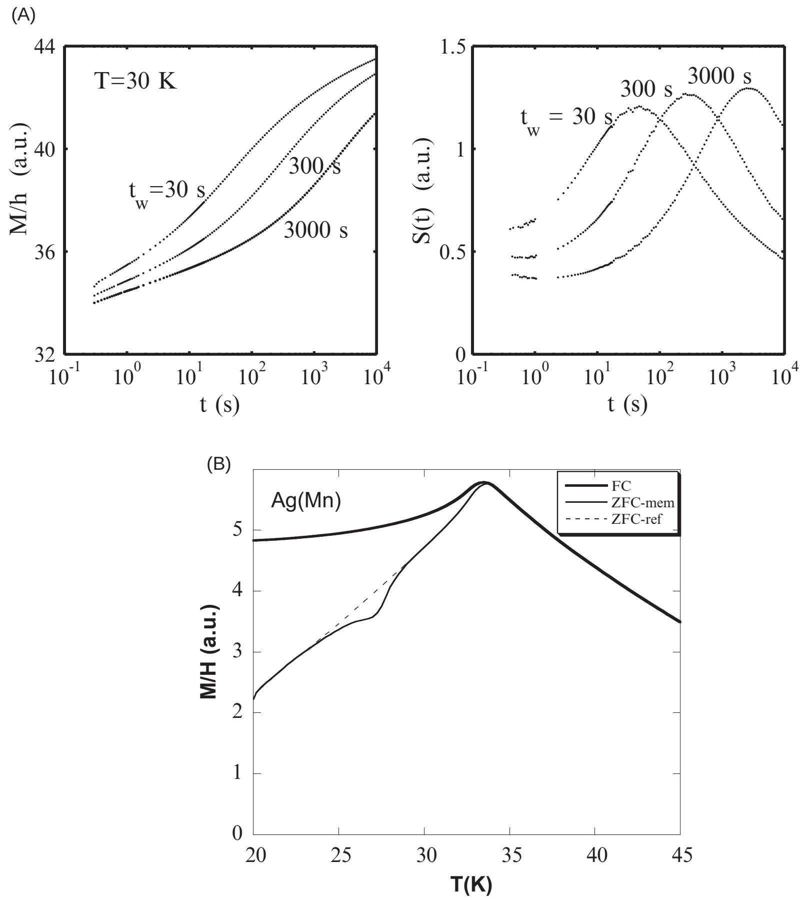

Fig. 2 (a) The left figure shows the relaxation of the zero field cooled magnetization $M(t)$ of the spin glass Ag(11 at.% Mn) at $T = 30$ K. The magnetization has been measured after different wait times at the measurement temperature as indicated in the figure. The right figure shows the relaxation rate $S(t) = \partial M(t)/h\partial \log(t)$ of the magnetization relaxation curves. $T_g \approx 32$ K, $h = 40$ Am^{-1}. (b) ZFC and FC magnetization vs. temperature ($M(T)/H$) for the spin glass Ag(11 at.% Mn). The curve labeled ZFC-ref shows the ZFC-magnetization measured after continuous cooling to low temperature, whereas the curve labeled ZFC-mem shows the corresponding curve measured after the sample has been kept at 27 K for 10^4 s during otherwise continuous cooling. $H = 8$ Am^{-1}. Panel (a): Data from Jönsson P (2002) Anisotropy, disorder and frustration in magnetic nanoparticle systems and spin glasses. *Comprehensive summaries of Uppsala dissertations from the Faculty of Science and Technology 727, Acta Universitatis Uppsaliensis*, panel (b): Data from Mathieu R (2002) Magnetism of manganites, semiconductors and spin glasses. *Uppsala dissertations from the Faculty of Science and Technology 38, Acta Universitatis Upsaliensis.*

rate, $S(t) = \partial M(t)/h\partial \log(t)$, i.e., the local slope of the relaxation curves; this quantity exhibits a pronounced maximum at an observation time equal to the wait time. Results from Monte Carlo (MC) simulations of the dynamics of three-dimensional Ising spin glass models yield similar results and confirm the existence of an aging phenomenon. A main conclusion from the aging (non-equilibrium) behavior is that the spin glass continuously evolves toward an equilibrium state at constant temperature in the spin glass phase and that this equilibrium state is different at different temperatures (the system appears chaotic).

An additional and remarkable feature of the non-equilibrium spin glass phase is that it incorporates a memory phenomenon. This phenomenon is most simply revealed by measurements according to a standard protocol to investigate the temperature dependence and irreversibility of the magnetization through the phase transition temperature of a magnetic system. The zero-field-cooled (ZFC) and field-cooled (FC) magnetization, which are measured by cooling the sample in zero field, apply a weak field at a low temperature and record the magnetization (ZFC) while continuously heating the system to a temperature above T_g and then re-cool the magnetization in the applied field while recording the magnetization (FC). Such magnetization curves are shown for the archetypical spin glass Ag(11 at.% Mn) in Fig. 2b. In addition, the figure shows a magnetization curve where the cooling of the sample has been interrupted for some hours at 27 K, and after reaching the low temperature, the magnetization was recorded on continuous heating in the same way as the ZFC-reference curve. This ZFC-mem curve shows a pronounced dip at the temperature for the stop. The system keeps a memory of the cooling history—and the memory is recalled when recording the ZFC magnetization on re-heating the spin glass. The observed dip in the ZFC-mem curve is reminiscent of the aging that occurs in the system when it is kept at constant temperature, which results in a slower relaxation with increasing age of the system as was illustrated in Fig. 2a. The memory-aging behavior are manifestations of some crucial concepts—aging, rejuvenation and chaos—that characterize the spin glass phase and are of key importance for the modeling spin glasses.

Spin glass behavior is not only confined to the model systems, with atomic magnetic moments, described above; there are several other disordered magnetic systems that have been found to show spin glass like magnetic behavior, e.g.: Interacting magnetic nanoparticle systems (superspin glasses) (Peddis et al., 2021), granular magnetic systems, some manganites and cobaltite's and certain high temperature superconductors.

Re-entrant spin glasses

A spin glass is formed when there is disorder and frustration due to an equal amount of positive and negative interactions in the system, i.e., the mean value of the interactions is close to zero. Such systems can simply be modeled by using an equal amount of interactions of the same magnitude ±J in the system or by using a Gaussian distribution of the interactions with zero mean. If the random interactions have a non-zero mean value, ferro (+) or antiferromagnetic (−), the system can show re-entrant behavior. The system first orders according to the dominant interaction at a high temperature and forms a long ranged ordered random ferromagnetic or antiferromagnetic phase, cf. the phase diagram in Fig. 3, where in the concentration range 15–24%, the system on cooling first enters a ferromagnetic phase and at a lower temperature reaches a re-entrant spin glass phase (RSG). However, on further lowering the temperature, the system seems to re-enter into a disordered phase, a spin glass phase. *Re*-entrant systems are quite common; they appear, e.g., at higher concentration of magnetic atoms in dilute magnetic alloys and amorphous metals. Re-entrant ferromagnets show some remarkable properties: Both the re-entrant spin glass phase and the long range ordered phase show an aging phenomenon and on cooling into the low temperature spin glass phase the ferromagnetic long range order seem to persist although macroscopic ac-susceptibility data indicate critical slowing down and a true re-entrance into a spin glass phase. Many unanswered questions remain as to the physics of re-entrant magnetic systems.

The random field Ising model

A random field Ising system is described by Eq. (2). The properties of that Hamiltonian has been extensively studied theoretically and by simulations and has been found to show a behavior that is very different from a random exchange or pure ferromagnetic system with respect to critical exponents, critical dimensions, and magnetic properties. Experimentally, there is no real material that provides local random fields as prescribed by the random field Ising model. However, the random field Hamiltonian is mapped by a dilute antiferromagnet in a homogeneous magnetic field: Eq. (3) above—and such materials are readily fabricated in single crystalline form and provide systems that allow a continuously tunable strength of the random field only by varying the strength of an applied homogeneous magnetic field. A major part of the experimental work on three-dimensional random field magnetic systems has been performed on the model Ising antiferromagnetic system FeF_2 diluted with non-magnetic zinc atoms: $Fe_{1-x}Zn_xF_2$ (Belanger, 2000). The study of random field systems is made more complicated by nonequilibrium effects that appear when the system is cooled to low temperatures and hinder the system to reach thermodynamic equilibrium. A quite consistent

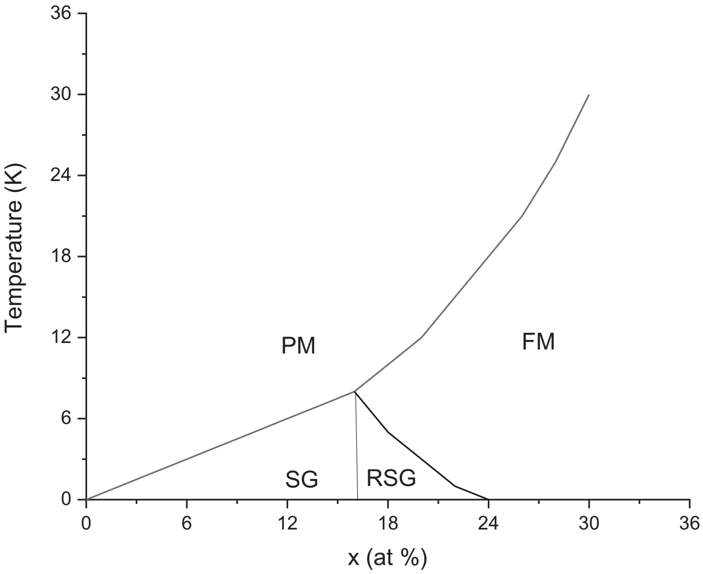

Fig. 3 A schematic phase diagram of a dilute metallic alloy where the concentration (x (at.%)) of magnetic ions increases from 0 to 36%. The alloy is paramagnetic (PM) at high temperatures, a spin glass (SG) at low temperatures and low concentration (<16%) of magnetic ions, ferromagnetic (FM) at low temperatures and high concentration of magnetic ions and finally a re-entrant spin glass (RSG) at low temperatures and concentration 16 < x < 24.

picture as to some thermodynamic equilibrium properties of random field systems of different spatial dimensionality has however been empirically attained.

The two-dimensional Ising system forms a low temperature ordered phase via a second order phase transition, the only second order phase transition that has been given an exact solution (Onsager, 1944). This transition is, both in theory and experiments, found to be destroyed by finite random fields, i.e., the lower critical dimension of the random field Ising system is two or larger. In 3d random field Ising systems, it has, after many years of experimental and theoretical controversies, been confirmed that the second order phase transition survives in random fields and both theory and experiments agree that the lower critical dimension is equal to two. The critical exponents describing the asymptotic behavior at the phase transition are significantly different from those of the pure three-dimensional Ising and also different from the random exchange Ising model values.

Nonequilibrium effects appear as the random field system is cooled into the ordered phase and cause the occurrence of domain states and relaxation phenomena that are not yet fully satisfactory described by theory and experiments. However, a quite high level of empirical understanding of the physics of random field Ising model systems has been realized by combining results from macroscopic (susceptibility, magnetization, and specific heat) measurements with results from microscopic probes (neutron scattering and X-ray scattering experiments).

Amorphous magnetic systems

Crystallographically disordered materials with an exchange interaction strength that is dependent on the distance between the magnetic entities would naturally form disordered magnetic systems that mimic a random exchange or more complicated model system. A realization of such systems is amorphous metals fabricated by rapid quenching methods and stabilized by introducing glass forming elements in the melt. Magnetic metallic glasses were first fabricated in the late 1960s and early 1970s and have provided excellent model systems for disordered magnetic systems and the influence of random exchange on the magnetic properties. There are outstanding possibilities to tailor materials using the rapid quench method, since almost any composition of different metals can be mixed without a need to consider phase segregation or consult complicated phase diagrams. It was early found that amorphous magnetic metals can form a variety of magnetic structures: Ranging from simple ferromagnets to complex ferrimagnetic spiral structures and spin glasses. However, a huge challenge and obstacle for the theoretical description of these metals is of course the lack of a periodic lattice as a backbone for the description of the electronic structure (Burton, 2013; Hansen, 1991; Hasegawa, 1991; Luborsky, 1980).

Amorphous metals are trapped in a metastable state and the structure has to be stabilized against crystallization, which severely limits the possible production processes. However, an important part of the interest in amorphous magnetic metals is due to their potential as magnetic materials in many applications. The possibility to fabricate materials with marginal magnetocrystalline anisotropy, very low magnetostriction and high resistivity compared to their crystalline counterparts promises materials with excellent soft magnetic properties for medium and high frequency applications and soft amorphous magnetic metal systems have also found important applications in, e.g., small-scale transformers, motors, and generators. The rapid quenching method does not only allow amorphous metals to form—it also yields possibilities to fabricate nano crystalline systems. Systems, which at certain microstructure sizes, form extremely hard magnetic materials with exceedingly high coercivity (which are useful building blocks for good permanent magnets) whereas they at other compositions and nano crystalline sizes provide materials with excellent soft magnetic properties (Herzer, 1997).

Magnetic materials

Disorder is the physical parameter that governs extrinsic magnetic properties, such as coercivity, remanence and energy product, of an intrinsically ferromagnetic or ferrimagnetic material. The producer of magnetic materials is thus forced to understand disorder to be able to effectively design and fabricate both soft and hard magnetic materials. It is in fact the ability to master disorder and find new material combinations that underlies the fast improvement of the technical performance that magnetic materials have been subject to during the last few decades. Maybe the prime example of such progress is found in the rapidly increasing areal storage density that magnetic information storage media has undergone and continuously is experiencing.

Conclusion

Theoretical and experimental studies of disordered magnetic model systems such as the Ising spin glass and the random field Ising model have provided new insights and understanding of the influence of disorder on the properties of not only magnetic but also other physical systems. In addition, the models and methods that have been developed in this research have found applications in many different fields of science that deal with complex and disordered systems: Examples are found in the physics of ordinary glasses and in optimization problems as well as in studies of stock markets and descriptions of social systems. The pioneering work of Prof. Giorgio Parisi in this field of science was awarded the Nobel Prize in Physics in 2021 (Parisi, 2021).

References

Belanger DP (2000) Experimental characterization of the ising model in disordered antiferromagnets. *Brazilian Journal of Physics* 30: 682–692.

Belanger DP and Young AP (1991) The random field ising model. *Journal of Magnetism and Magnetic Materials* 100: 272–291.

Burton SM (2013) *Amorphous Metallic Alloys*. Elsevier.

Cannella V and Mydosh JA (1972) Magnetic ordering in gold-iron alloys. *Physical Review B* 6: 4220–4237.

Fisher KH and Hertz JA (1991) *Spin Glasses*. Cambridge: Cambridge Univ. Press.

Hansen P (1991) Magnetic amorphous alloys. In: Buschow KHJ (ed.) *Handbook of Magnetic Materials*. vol. 6, pp. 292–452. Amsterdam: Elsevier Science Publishers B.V. Amsterdam.

Hasegawa R (1991) Amorphous magnetic materials—A history. *Journal of Magnetism and Magnetic Materials* 100: 1–12.

Herzer G (1997) Nanocrystalline soft magnetic alloys. In: Buschow KHJ (ed.) *Handbook of Magnetic Materials*. vol. 10, pp. 415–462. Elsevier Science Publishers B.V. Amsterdam.

Kawamura H and Taniguchi T (2015) Spin glasses. *Handbook of Magnetic Materials*. vol. 24, pp. 1–137. Elsevier Science Publishers B.V. Amsterdam.

Luborsky FE (1980) Amorphous Ferromagnets. In: Wohlfarth EP (ed.) *Ferromagnetic Materials*. vol. 1, pp. 451–530. Amsterdam: Elsevier Science Publishers B.V.

Mezard M, Parisi G, Sourlas N, Toulouse G, and Virasoro M (1984) Replica symmetry breaking and the nature of the spin glass phase. *Journal de Physique* 45: 843–854.

Mezard M, Parisi G, and Virasoro MA (1987) *Spin Glass Theory and Beyond*. *World Scientific Lecture Note in Physics, Singapore.* World Scientific.

Mydosh JA (2015) Spin Glasses: Redux: An updated experimental/materials survey. *Reports on Progress in Physics* 78: 052501.

Nordblad P (2013) Competing interaction in magnets: The root of ordered disorder or only frustration? *Physica Scripta* 88: 058301.

Onsager L (1944) Crystal statistics. I. A two-dimensional model with an order-disorder transition. *Physics Review* 65: 117–149.

Parisi G (2021) https://www.nobelprize.org/prizes/physics/2021/parisi/facts/.

Peddis D, Laureti S, and Fiorani D (eds.) (2021) *New Trends in Nanoparticle Magnetism*. Springer.

Sherrington D and Kirkpatrick S (1975) Solvable model of a spin glass. *Physical Review Letters* 35: 1792–1796.

Stein DL and Newman CM (2013) *Spin Glasses and Complexity*. Princeton University Press.

Young AP (ed.) (1998) *Spin Glasses and Random Fields*, In: *World Scientific Series on Directions in Condensed Matter Physics, Singapore*.

Magnetic Order[☆]

D Givord, CNRS, Grenoble, France
T Takabatake, Hiroshima University, Higashi- Hiroshima, Japan

© 2016 Elsevier Ltd. All rights reserved.

This is an update of D. Givord, T. Takabatake, Magnetic Order, Reference Module in Materials Science and Materials Engineering, Elsevier, 2016, ISBN 9780128035818, https://doi.org/10.1016/B978-0-12-803581-8.01109-7.

Introduction **26**
Magnetic Moment and Magnetic Field 26
Magnetic Moment 26
Magnetic Moments in a Magnetic Field – Paramagnetism 27
Ferromagnetic Order 27
The Molecular Field Model 27
Beyond the Molecular Field Model: Evidence for Short-Range Order 28
Exchange Interactions 29
On the Connection between Exchange Interactions and Molecular Field 30
Magnetic Anisotropy 30
Mechanisms of Magnetic Coupling 30
Nonferromagnetic Types of Magnetic Orders 31
Antiferromagnetism 31
Ferrimagnetism 31
Helimagnetism and Modulated Structures 31
Spin Glasses and Other Frustrated Systems 32
Experimental Studies of Magnetic Structures 33
Further Reading **34**

Nomenclature

$\mathscr{B}$	Brillouin function
C	Curie constant
g_J	Landé factor
H_{app}	applied magnetic field (vector)
H_{app}	applied magnetic field (magnitude)
H_{m}	molecular field
J	exchange integral
J	total angular momentum
$\boldsymbol{k}_0$	propagation vector
l	orbital quantum number
l	orbital momentum
$\mathscr{L}$	Langevin function
L	orbital momentum
m	magnetic quantum number
m_0	measured magnetic moment at 0 – K
m	magnetic moment
m_l	orbital moment
m_{s}	spin moment
m_z	projection of m along H_{app}
M	magnetization
M_{s}	spontaneous magnetization
$M_{\mathrm{s},0}$	magnetization at absolute saturation
n	molecular field coefficient
N	number of moments per unit volume
N_{D}	demagnetizing field coefficient
N_{T}	total number of moments

[☆] *Change History*: May 2015. T. Takabatake revised the last paragraph 'Experimental Studies of Magnetic Structures' and 'Further Readings'.

S	spin or spin angular momentum
T	temperature
T_{c}	critical temperature
T_{C}	Curie temperature
T_{N}	Néel temperature
v_{at}	atom volume
x	argument of the Langevin or Brillouin function
z	number of first neighbors
χ	magnetic susceptibility
μ_{B}	Bohr magneton
μ_{eff}	effective moment
μ_0	permittivity of vacuum

Introduction

Magnetism is a property of electrons within matter. Strong interactions exist between the atomic magnetic moments; they are of electrostatic origin, and are termed exchange interactions.

In the simplest case, the exchange interactions favor parallelism of all magnetic moments; this leads to ferromagnetic order. The properties of ferromagnetic materials can be described within the molecular field model. However, the experiment provides evidence for the local character of the interactions which cannot be explained within this model.

More generally, the exchange interactions may favor different types of coupling, and a large variety of different magnetic structures may exist. In the antiferromagnetic structures, the moments are arranged in two groups, termed sublattices. Within each sublattice, the moments are parallel, but they are antiparallel to the moments in the other sublattice. In many instances, the magnetic structure results from a competition between different interactions which cannot be satisfied simultaneously. This is, in particular, the case of the helimagnetic and modulated structures. When the arrangement of the magnetic atoms themselves is not periodic, spin-glass arrangements are found.

The most powerful technique for the study of magnetic structures is neutron diffraction, in which the neutron magnetic moment is used to probe the arrangement of the atomic moments.

Magnetic Moment and Magnetic Field

Magnetic Moment

Within matter, magnetism is due to electron motion around the nuclei. There are two contributions to the magnetic moment of an electron:

- The orbital moment, $\boldsymbol{m}_l$, is linked to the motion of the electrons in their orbits. It may be expressed as $\boldsymbol{m}_l = -\mu_{\mathrm{B}}\boldsymbol{l}$, where $\boldsymbol{l}$ is the orbital momentum and μ_{B}, the Bohr magneton, is the fundamental unit of magnetic moments ($1\mu_{\mathrm{B}} = 0.927 \times 10^{-23}$ A m^2). The quantum mechanical eigenvalues of $\langle \boldsymbol{l}^2 \rangle$ are equal to $l(l+1)$ where l is an integer, called the orbital quantum number. The values $l = 0,1,2$, and 3 are associated to electrons of the s, p, d, and f shells respectively. The eigenvalues of $\langle \boldsymbol{l}_z \rangle$ are integers, denoted m, where m is the magnetic quantum number; m is restricted between two limits, $+l$ and $-l$.
- The spin moment, $\boldsymbol{m}_{\mathrm{s}} = -\mu_{\mathrm{B}}\boldsymbol{s}$ is related to the electron spin momentum, $\boldsymbol{s}$, most often referred to as the 'spin.' The spin is an entity of purely quantum mechanical nature. The eigenvalues of $\langle \boldsymbol{s}^2 \rangle$ are equal to $s(s+1)$, where s, the spin quantum number, equal to 1/2. The eigenvalue of $\langle \boldsymbol{s}_z \rangle$ are +1/2 and −1/2.

Due to the electrostatic interactions existing between electrons located on the same electronic shell of a given atom, the spin and orbital momentum of individual electrons are coupled together, according to the so-called Hund's rules. The resulting orbital momentum of the considered shell is noted as L, and the resulting spin, S. L and S are strongly coupled together by the spin–orbit coupling. For a full electronic shell, $L = 0$ and $S = 0$; magnetism is a property of partly filled electronic shells.

In the solid state, only two series of stable elements may show spontaneous magnetism (the actinides may be magnetic as well).

1. In the 3d transition series, to which Fe, Co, and Ni belong, magnetism is due to the progressive filling of the 3d shell. The orbital momentum is almost quenched. In the case where the 3d electrons are localized, the maximum value of the magnetic moment is approximately equal to $-2\mu_{\mathrm{B}}S$. In 3d metallic systems, the magnetic 3d electrons have a certain itinerant character. The magnetic moments, expressed in μ_{B}, take a fractional value, which cannot be derived by the present simple considerations.
2. In the rare-earth series, from cerium to lutetium, magnetism results from the progressive filling of the 4f shells. The 4f electrons are fully localized. The maximum value of the moment is equal to $-g_J\mu_{\mathrm{B}}J$, where J is equal to $L+S$ or $L-S$, depending on the considered element and g_J is the Landé factor.

Another magnetic moment may exist within matter, associated to the constitutive elements of the nucleus. The proton moment, μ_{P}, and the neutron moment, μ_{n}, amount to $\mu_{\mathrm{B}}/657$ and $\mu_{\mathrm{B}}/959$ respectively.

Magnetic Moments in a Magnetic Field – Paramagnetism

When submitted to an applied magnetic field, $\boldsymbol{H}_{\mathrm{app}}$, a magnetic moment, $\boldsymbol{m}$, tends to align along the field direction. The corresponding energy, called Zeeman energy, e_Z, is

$$e_{\mathrm{Z}} = -\mu_0 \boldsymbol{m} \cdot \boldsymbol{H}_{\mathrm{app}} \qquad [1]$$

An assembly of moments, $\boldsymbol{m}$, may be characterized by the magnetization, M, which is the moment per unit volume measured along the field direction, z:

$$M = N\langle m_z \rangle_T \qquad [2]$$

where N is the number of moments per unit volume and $\langle m_z \rangle_T$ is the thermal averaged value of m_z, the projection of $\boldsymbol{m}$ along $\boldsymbol{H}_{\mathrm{app}}$.

At finite temperature, moment alignment is in competition with thermal activation which tends to create disorder; this characterizes paramagnetism. For a system of classical noninteracting moments, the magnetization, M, is given by

$$M = Nm_0 \mathscr{L}(x) \qquad [3]$$

In expression [3], m_0 is the value of the moment at 0 K and $\mathcal{L}(x) = \cot h(\chi) - 1/\chi$ is the Langevin function. The parameter x which enters into the Langevin function is the ratio between Zeeman energy and thermal energy:

$$x = \frac{\mu_0 \boldsymbol{m} \cdot \boldsymbol{H}_{\mathrm{app}}}{k_{\mathrm{B}}\mathrm{T}} \qquad [4]$$

where μ_0 is the permittivity of vacuum ($=4\pi \times 10^{-7}$SI) and k_{B} is the Boltzmann constant.

For small x, the Langevin function may be expanded as $\boldsymbol{\mathcal{L}}(x) \approx x/3 - x^3/45 + \ldots$ The high-temperature development of [3] is

$$M = C\frac{H_{\mathrm{app}}}{T} \qquad [5]$$

where C is the Curie constant, given by

$$C = \frac{\mu_0 N m_0^2}{3k_{\mathrm{B}}} \qquad [6]$$

A useful experimental parameter is the susceptibility, $\chi = M/H_{\mathrm{app}}$. The reciprocal susceptibility $1/\chi$ varies linearly with T, with a slope $1/C$ (**Figure 1(a)**). This constitutes the Curie law.

For systems of quantum moments, the Langevin function must be replaced by a Brillouin function, $\mathcal{B}(x)$. The moment m_0 in expression [3] is equal to $-2\mu_{\mathrm{B}}S$ (systems in which 3d localized electrons are involved) or $-g\mu_{\mathrm{B}}J$ (rare-earth-based systems), the maximum values of the projection of $\boldsymbol{m}$ along the field, whereas m_0 in expression [6] is replaced by μ_{eff}, the effective moment which is proportional to $\sqrt{S(S+1)}$ or to $\sqrt{J(J+1)}$

Ferromagnetic Order

The Molecular Field Model

There is a category of magnetic materials, where the high-temperature susceptibility does not follow the Curie law, but is given by the expression

$$\chi = \frac{C}{T - T_{\mathrm{C}}} \qquad [7]$$

where T_{C} is the Curie temperature (**Figure 1(a)**). Expression [7] constitutes the Curie–Weiss law. It may be ascribed to interactions existing between the magnetic moments. To first approximation, these interactions are equivalent to a field, termed H_{m} created by the magnetic moments themselves. Within the molecular field theory of ferromagnetism, H_{m} is assumed to be proportional to the magnetization, M:

$$H_{\mathrm{m}} = n\mathrm{M} \qquad [8]$$

where n is the molecular field coefficient, such that

$$T_{\mathrm{C}} = nC \qquad [9]$$

The value of the magnetization M may be obtained by replacing the applied field H_{app} in expression [4] by $H_{\mathrm{app}} + H_{\mathrm{m}}$ and by expressing that relations [3] and [8] must be satisfied simultaneously. Consider the special case where $H_{\mathrm{app}} = 0$. At temperatures

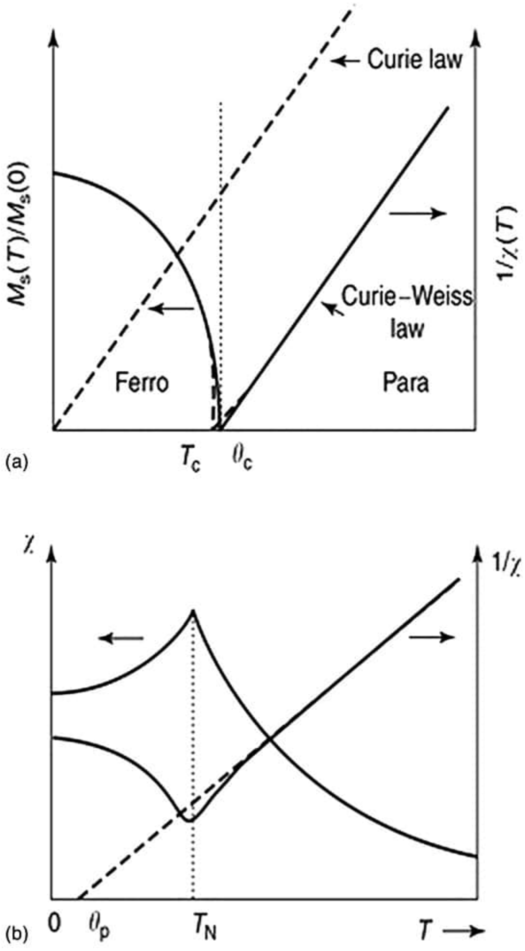

Figure 1 (a) In a system of noninteracting moments, the reciprocal susceptibility, $1/\chi(T)$, varies linearly with temperature with a slope $1/C$, where C is the Curie constant. In the presence of interactions, the molecular field model predicts a similar variation, but the representative curve is shifted towards higher temperatures. At $T = T_C$, the susceptibility becomes infinite. At $T < T_C$, a spontaneous magnetization, M_s, exists. This is ferromagnetism. The molecular field model does not properly give account for the existence of local fluctuations. These are responsible for the fact that the Curie temperature is lower than predicted and that the variation of $1/\chi(T)$ is not linear in the vicinity of T_C. (b) In an antiferromagnetic system, the susceptibility presents a maximum at the ordering temperature, T_N. In the paramagnetic state, the variation of $1/\chi(T)$ vs. T well above T_N is again linear.

$T > T_C$, the only possible solution is $M = 0$; the moments are oriented at random and the system is paramagnetic, as it is in the absence of interactions. In this temperature range, the slope of the reciprocal susceptibility versus temperature is equal to $1/C$, as it is in noninteracting systems (**Figure 1(a)**). At $T = T_C$, the susceptibility diverges (it becomes infinite) and below T_C, a 'spontaneous magnetization,' M_s, exists within matter, indicating a certain degree of common alignment of all the moments. Such behavior characterizes ferromagnetic order (**Figure 2(a)**). The spontaneous magnetization, $M_s(T)$, progressively increases as temperature is decreased; at 0 K, it reaches the value $M_S = M_{S,0} (\equiv Nm_0)$ of the magnetization at absolute saturation (**Figure 1(a)**).

Note that the magnetic energy density, associated with the formation of ferromagnetism, may be expressed as

$$E_{FM} = -\frac{1}{2}\mu_0 M_s H_m = -\frac{1}{2}\mu_0 n M_s^2 \qquad [10]$$

Beyond the Molecular Field Model: Evidence for Short-Range Order

The transition from a low-temperature ordered phase to a high-temperature disordered phase is a feature found in many physical systems. In the present case, the disordered phase is the paramagnetic phase and the ordered phase is the ferromagnetic one. First-order phase transitions are characterized by a discontinuity of thermodynamic variables such as the density or the entropy. In general, no such discontinuity exists at a paramagnetic–ferromagnetic transition. Landau has shown that second-order phase transitions are characterized by an abrupt symmetry change. In the paramagnetic phase, the system is invariant upon reversal of the magnetization; in the ferromagnetic phase, it is not invariant upon this reversal. In the vicinity of T_C, the magnetization is predicted to vary as

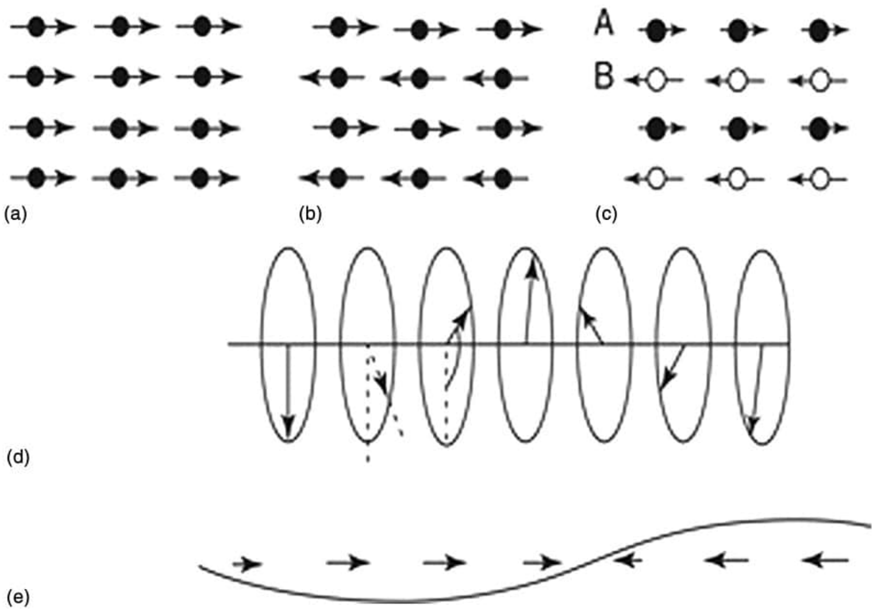

Figure 2 Schematic representations of various types of magnetic structures: (a) ferromagnetism, (b) antiferromagnetism, (c) ferrimagnetism, (d) helimagnetism, and (e) modulated structure.

$$M_s = \sqrt{\frac{a}{2b}}(T_C - T)^{1/2} \quad [11]$$

Here 1/2 is the critical exponent of the magnetization within the molecular field model. Experimentally, this critical exponent, denoted β, is found to be less than 0.5 (i.e., ~0.3–0.4). This departure from the molecular-field-predicted value is due to the existence of local fluctuations of the magnetic state. Proper values of the critical exponents are obtained within the renormalization group theory.

Fluctuations cannot be explained within the molecular field model because H_m is proportional to M_s, a macroscopic quantity. Actually, the existence of magnetic fluctuations indicates that the magnetic interactions are short-ranged. The modification of the state for a given moment influences the state of the neighboring moments, but not that of moments which are at large distances. Magnetic disorder may proceed by keeping a certain degree of local order, while allowing the system to become disordered at the macroscopic level. The magnetic energy is reduced whereas the entropy is the same as for the case of homogeneous disorder. Due to short-range order, the experimental value of the Curie temperature is always lower than that predicted by the molecular field model. Close to T_C, the local correlations existing between moments lead to nonlinearity in the temperature dependence of the reciprocal susceptibility. At temperatures far above T_C, the influence of local fluctuations become negligible and the molecular-field-temperature dependence of the reciprocal susceptibility is recovered. The extrapolated intercept with the temperature axis gives the value of the so-called paramagnetic Curie temperature, θ_C, which is higher than T_C (**Figure 1**).

The local character of the magnetic interactions manifests itself as well in the ordered magnetic state, at low temperatures. The spontaneous magnetization decreases as $T^{3/2}$, more rapidly than predicted by the molecular field model. Specific excitations such as the spinwaves occur, which allow the local alignment of neighboring moments to be better preserved than in the case of random disorder, while allowing global disorder to develop.

Exchange Interactions

In a given ferromagnetic material, the strength of the molecular field may be derived from the value of the Curie temperature, T_C (see relation [9]). In Fe metal, the Curie temperature amounts to 1043 K, and in Co metal, it amounts to 1380 K; $H_m \approx 10^9$ A m^{-1} is deduced.

From magnetostatics, it is known that a magnetic moment, $\boldsymbol{m}$, is the source of a dipolar magnetic field, H, which, at point P, is expressed as

$$H = \frac{1}{4\pi}\left[3\frac{(\boldsymbol{m}\cdot\boldsymbol{r})\boldsymbol{r}}{r^5} - \frac{\boldsymbol{m}}{r^3}\right] \quad [12]$$

where $\boldsymbol{r}$ is the vector linking point O to point P. For $m \approx 2\mu_B$, which is the order of magnitude of the Fe or Co moment in metals, the corresponding magnetic field is of the order of 10^6 A m^{-1}. This value is ~1000 times smaller than the value derived from T_C. Except in rare cases, magnetic order cannot be attributed to dipolar interactions.

As shown by Heisenberg, the interactions at the origin of magnetic order are not magnetic in origin, but result from the repulsive electrostatic interactions existing between electrons. The Hamiltonian describing an ensemble of interacting electrons contains a term, called the exchange term, which results from electron indiscernibility. Magnetism emerges when account is taken of the Pauli exclusion principle. This stipulates that two electrons cannot occupy the same quantum state, defined by both space and spin variables. It imposes full antisymmetry of the wave function representative of the electron ensemble and, as a result, the interaction energy between electrons depends on their respective spin states.

It is often convenient to distinguish two terms in the exchange interactions. The intra-atomic interactions give rise to Hund's rules which govern the formation of atom magnetic moments; the inter-atomic exchange interactions are the source of the coupling between atom moments which allows magnetic order to be understood.

On the Connection between Exchange Interactions and Molecular Field

Within the Heisenberg theory, the exchange interaction between two spins i and j is generally expressed as

$$e_{ij} = -2J_{ij}S_iS_j \qquad [13]$$

where J_{ij} is the exchange integral which represents the strength of the coupling between spins i and j. For an ensemble of N_T spins, the energy density is obtained by summing over all spins:

$$E_{ech} = -\frac{N_\mathrm{T}}{V}\sum_{i,j\neq i} J_{ij}S_iS_j \qquad [14]$$

where V is the sample volume. Assuming that all atoms are identical, S_i and S_j may be replaced by S. Thus, the magnetic energy density can be written as

$$E_{ech} = -\frac{N_\mathrm{T}S}{V}\left(\sum_{j\neq i} J_{ij}\right)S \qquad [15]$$

The first part of the right-hand expression in eqn [15] is proportional to the magnetization whereas the second part is proportional to the molecular field. Thus, this expression is equivalent to the molecular field expression of energy (eqn [10]); it also manifests the local character of magnetic interactions.

Magnetic Anisotropy

In ferromagnetic materials, the magnetic moments are aligned along well-defined crystallographic directions. This is the phenomenon of magnetic anisotropy. It is explained by considering that the electrons belonging to the magnetic shells interact with other charges in the environment, which constitute the so-called crystalline electric field (CEF). Due to the orbit asymmetry, the coupling energy depends on the orientation of the orbit within the CEF. A favored orientation of the orbital magnetic moment is intrinsically linked to the favored orientation of the orbit. Since the spin and orbital moments are linked, the total moment aligns along a preferred direction. This is the phenomenon of magnetic anisotropy. The anisotropy is high in rare-earth systems where a large orbital moment exists.

In uniaxial systems, there exists a unique easy direction of magnetization and a hard plane, perpendicular to the unique axis. The anisotropy field is the amplitude of the field applied in the plane and required to force the moments into this plane. In systems of higher symmetry, such as the cubic systems, there exist several easy directions and the anisotropy is weaker in general than in uniaxial systems.

Mechanisms of Magnetic Coupling

Exchange interactions constitute the general source of moment coupling. However, the details of the coupling mechanism may differ strongly from one system to another. In this section, this is illustrated by some representative examples.

Consider 3d electrons in iron, cobalt, nickel, or one of their alloys. The exchange-coupling existing between all electrons sitting on the same site favors a parallel coupling between their spins (Hund's rules). However, the 3d electrons have a certain degree of itinerant character, that is, they have a finite occupancy probability on the atom sites of the environment. An electron, arriving on another site, becomes exchange coupled to the electrons present on this site and again a parallel coupling between spins is favored. Thus, a parallel coupling between the two associated moments is favored. This mechanism explains high-temperature ferromagnetism observed in these systems.

In transition metal oxides, such as MnO, Fe_2O_3, CoO, or NiO, the fully localized 3d electrons are hybridized with the 2p electrons of oxygen. The d electrons, sitting on two different transition metal atoms but coupled to p electrons on the same oxygen atom, become indirectly coupled together. This mechanism constitutes super exchange. Often, it favors an antiparallel coupling between transition metal spins, that is, the exchange integral J is negative. Nonferromagnetic structures may result.

The 4f electrons of the rare-earth elements occupy an internal electronic shell, which is protected from the environment by more external shells, such as the 5d and 6s ones. The 4f electrons are strongly localized and bear well-defined magnetic moments. No interaction exists with 4f electrons on other sites. However, the 4f electrons are exchange coupled to the 5d and 6s electrons which become polarized. In metallic systems, the 5d, 6s electrons are itinerant. When they travel from one atom to the next, their polarization oscillates with a period which is characteristic of the band structure. Indirect interactions between the localized moments result in the RKKY type. They are the source of an indirect coupling between the 4f moments which is long-ranged and oscillatory.

Nonferromagnetic Types of Magnetic Orders

The possible existence of negative J values explains that diverse types of magnetic orders may exist, in addition to ferromagnetism.

Antiferromagnetism

Consider a system which contains one type of magnetic atoms, all bearing the same magnetic moment, but which may be separated into two groups, A and B, called sublattices. Within the same sublattice, the exchange integrals J_{AA} and J_{BB} (coupling moments) are positive, whereas J_{AB} (the coupling moments belonging to different sublattices) are negative. The magnetic structure is such that all moments within a given sublattice are parallel to each other and antiparallel to the moments within the other sublattice. The resulting global magnetization is zero. Such a moment arrangement characterizes antiferromagnetism (**Figure 2(b)**). Amongst many other systems, it is found in the transition metal oxides MnO, CoO, or NiO.

Antiferromagnetism may be described within the molecular field model, by decomposing the molecular field into two separate contributions, one from each sublattice. Assuming that the two sublattices are identical, the molecular field may be expressed as

$$\boldsymbol{H}_m = nM_s^{s1} - n'M_s^{s1} \tag{16}$$

where M_s^{s1} is the spontaneous magnetization within each sublattice, n (>0) is the molecular field coefficient representative of the interactions within a given sublattice, and n' (<0) is the molecular field coefficient representative of the interactions between sublattices. The coefficients n and n' are related to the J's through expressions which are similar to expression [19]. The magnetization of each sublattice is given by expression [3], but with

$$x = \frac{\mu_0 m \left(nM_s^{s1} - n'M_s^{s1}\right)}{k_B T} \tag{17}$$

One looks for solutions of expressions [3] and [16] simultaneously. Above a critical temperature, T_N, called the Néel temperature, which is the equivalent of the Curie temperature for ferromagnetism, the sublattice magnetization is equal to zero; the slope of the reciprocal susceptibility versus T is the same as found in noninteracting and ferromagnetic systems, equal to $1/C$ (**Figure 1b**). At $T = T_N$, magnetic order sets in. Below T_N, a nonzero magnetization exists within each sublattice.

In the ordered magnetic state, an applied magnetic field tends to align all moments along itself; it works against inter-sublattice exchange-coupling. As temperature decreases, the ratio of exchange-coupling energy to Zeeman energy increases. Thus, the magnetic susceptibility decreases. Combining this with the usual temperature decrease of the susceptibility in the paramagnetic state, it results that the magnetic susceptibility presents a maximum at T_N. This constitutes a common feature of antiferromagnetic-like structures, in which the global magnetization is zero.

From the point of view of quantum mechanics, Landau noted that the antiferromagnetic configuration described above, termed a Néel state, is not an eigenstate of the corresponding Hamiltonian. The actual ground state is a mixture of the two equivalent Néel states which are obtained by reversing the magnetization in the two sublattices; it is not magnetic. Due to the macroscopic nature of the antiferromagnetic domains, the Néel state is almost indistinguishable from the real ground state. Although not yet experimentally demonstrated, this is not the case in nanosystems.

Ferrimagnetism

Many transition metal oxides incorporate two different magnetic elements. The magnitude of the associated moments differs and a certain magnetization remains even when the moments are coupled antiparallel. Such ferrimagnetic structures (**Figure 2(c)**) are found in Fe oxides, such as γ-Fe_2O_3 and Fe_3O_4, where Fe moments in different ionic states coexist.

Ferrimagnetism is also found in rare-earth compounds with Fe, Co, or Ni, where an antiparallel coupling between the 3d moments and the rare-earth moments occur.

Helimagnetism and Modulated Structures

In the molecular field description of ferromagnetism, the molecular field is assumed to be a macroscopic entity. However, the local character of the magnetic interactions is established by experimental results which were mentioned above, and it emerges naturally in the Heisenberg description of the exchange interactions.

In the version of the molecular field model developed for the description of antiferromagnetism, the distinction between two different contributions gives to the molecular field a certain local character. In the spirit of a local description, the molecular field on a certain site, i, may be expressed in terms of the sum of the interactions of the moment, m_i, with all other j moments:

$$\boldsymbol{H}_i = \sum_i n_{ij}\langle m_j\rangle T \qquad [18]$$

where the n_{ij}'s are molecular field coefficients. By analogy with the analyses described above, the magnetic moment, at temperature T, is given by

$$\langle m_i\rangle_{\mathrm{T}} = m_0\mathscr{L}\left(\frac{\mu_0 m_0(H_i)}{k_{\mathrm{B}}T}\right) \qquad [19]$$

The high-temperature expansion of this expression is

$$T\langle m_i\rangle_T = \mathrm{C}\sum_j n_{ij}\langle m_j\rangle_T \qquad [20]$$

with solutions of the type

$$\langle m_i\rangle_T = A\exp(i\boldsymbol{kR}_i) \qquad [21]$$

where $\boldsymbol{R}_i$ describes the atom positions and $\boldsymbol{k}$ is a vector. One defines the quantity $\mathscr{J}(k)$ which is the Fourier transform of the exchange interactions:

$$\mathscr{J}(k) = \mathrm{C}\sum_j n_{ij}\exp\left(i\boldsymbol{k}\left(\boldsymbol{R}_i - \boldsymbol{R}_j\right)\right) \qquad [22]$$

The critical temperature is given by

$$T_{\mathrm{c}} = \mathscr{J}(\boldsymbol{k}_0) \qquad [23]$$

where T_{c} is the highest temperature for which the set of eqn [20] admits a nonzero solution, and the associated vector $\mathbf{k}_0$ which characterizes the magnetic structure is termed the propagation vector of the structure.

This approach may be illustrated by considering a linear chain of atoms, distant by a, such that the exchange interactions are positive between first neighbors (n_1), negative between second neighbors (n_2), and equal to zero for larger distances. For $n_1 \gg n_2$, the ferromagnetic solution is obtained (for n_1 large and negative, the structure is antiferromagnetic), but this is no more the case for $|n_2| > n_1/4$. When the magnetic moments are confined in the plane perpendicular to the chain by the magnetic anisotropy, a helimagnetic structure is found in which the moments rotate progressively from one to the next, along the chain (Figure 2**d**). This structure is found in some rare-earth metals, such as terbium or dysprosium. Reciprocally, when the moments are forced to align along the chain axis, a modulated structure occurs in which the amplitude of the moments oscillates periodically (Figure 2**e**). This occurs in thulium.

Helimagnetic and modulated structures belong to the large class of antiferromagnetic structures, which are characterized by the zero value of the spontaneous magnetization. However, in these two cases, the stable magnetic structure is the result of a compromise between the various interactions involved, and is said to be frustrated. The analysis of frustrated structures has recently been the topic of intense research, both theoretically and experimentally.

Spin Glasses and Other Frustrated Systems

When the magnetic atoms do not form a periodic arrangement, another type of frustrated magnetic arrangement may exist. This is the case in substitutional alloys in which two or more types of atoms are randomly distributed on a given periodic lattice, or in amorphous alloys, obtained by very fast quenching from the melt. Since the magnitude and sign of interactions depend on the distance, it may be expected that the random distribution of atoms leads to a distribution of J values which is centered at 0 such that there are as many positive and negative interactions.

As long as the interactions n_{ij} are evenly distributed from positive to negative, with zero mean value, no stable magnetic order may exist. However, if eqn [20] is squared, one obtains

$$T^2\langle m_i\rangle^2 = \mathrm{C}^2\left(\sum_j n_{ij}\langle m_j\rangle\right)^2 \qquad [24]$$

For a fully disordered system of infinite dimensions, the sum over the terms $n_{ij}n_{ij}\langle m_j\rangle\langle m_j{}'\rangle$ is zero and eqn [24] can be expressed as

$$T^2\langle m_i\rangle^2 = C^2\left(\sum_j n_{ij}^2\langle m_i\rangle^2\right) \tag{25}$$

This expression has a critical temperature given by

$$T_c = C\left(\sum_j n_{ij}^2\right)^{1/2} \tag{26}$$

Below T_c, the system is in a spin-glass state where the moments are randomly oriented. Equation [25] does not apply rigorously to finite-size systems. It has been a long debate to decide whether or not a real phase transition occurs in spin glasses. Experimentally, a peak is observed in the thermal variation of the magnetic susceptibility, but the temperature at which it occurs is found to depend on the time taken for the measurement (**Figure 3**). Initially, this type of measurement suggested that the spin-glass transition is not a real phase transition. Actually, it is now accepted that the spin-glass transition constitutes a new class of phase transitions in which the first derivative of the magnetic susceptibility versus temperature does not show any anomaly, but derivatives of higher orders do. The frequency dependence of the temperature at which the peak occurs in $\chi(T)$ is related to the fact that the critical slowing down of the magnetic fluctuations extends in spin glasses much farther from the value of the critical temperature than it does in other ordered magnetic systems.

Experimental Studies of Magnetic Structures

The macroscopic magnetic properties of magnetic materials may be derived from the magnitude of the stray field generated by the material magnetization, whether it is spontaneous or induced by the applied field. However, such measurements do not allow the moments of the various constitutive elements to be determined individually. Additionally, in the absence of applied field, antiferromagnetic-like materials do not generate any stray field. For this type of characterization, local probes such as Mössbauer spectroscopy, nuclear magnetic resonance (NMR), or muon-spin rotation (μSR) may be used. These methods measure the local magnetic field at a particular crystallographic site. Uning these methods, the magnetization of individual sublattices in an antiferromagnet can be measured. The μSR spectroscopy is ideal to investigate a material having small ordered state moment $\sim 0.1\mu_B$ or a material having a heterogenous structure, such as 'magnetic' and 'nonmagnetic' regions.

Neutron diffraction constitutes an invaluable tool for the study of magnetic arrangements. The neutron bears a small magnetic moment which probes the magnetism existing within matter. Neutron diffraction is the strict analog for the analysis of magnetic structures as X-ray diffraction is for the studies of crystallographic structures. Neutron diffractograms obtained with MnO are shown in **Figure 4**. In (a), the peak observed at 12° is due to the (1 1 1) reflection; it is characteristic of the face-centered cubic crystallographic structure of this compound. In (b), an additional peak is observed at around 6°. This peak can be indexed as 1/2, 1/2, 1/2. It is the signature of periodicity doubling. In an antiferromagnetic structure, the alternation of moment orientations leads to periodicity doubling (see scheme in the inset to **Figure 4**). The diffractograms shown in **Figure 4** have a special historical meaning. They constituted, when they were published, the first experimental proof of the existence of antiferromagnetism.

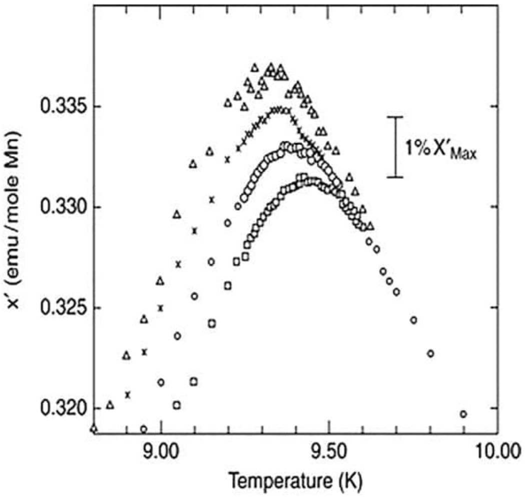

Figure 3 Thermal variation of the susceptibility in a spin glass: a Cu–Mn alloy containing 0.95% of Cu. The measurements of the susceptibility were realized under AC field of different frequencies (□1330 Hz, ○234 Hz, X 10.4 Hz, Δ 2.6 Hz). The frequency dependence of the temperature at which the peak occurs in $\chi(T)$ is related to the fact that the critical slowing down of the magnetic fluctuations extends in spin glasses much farther from the value of the critical temperature than it does in other ordered magnetic systems.

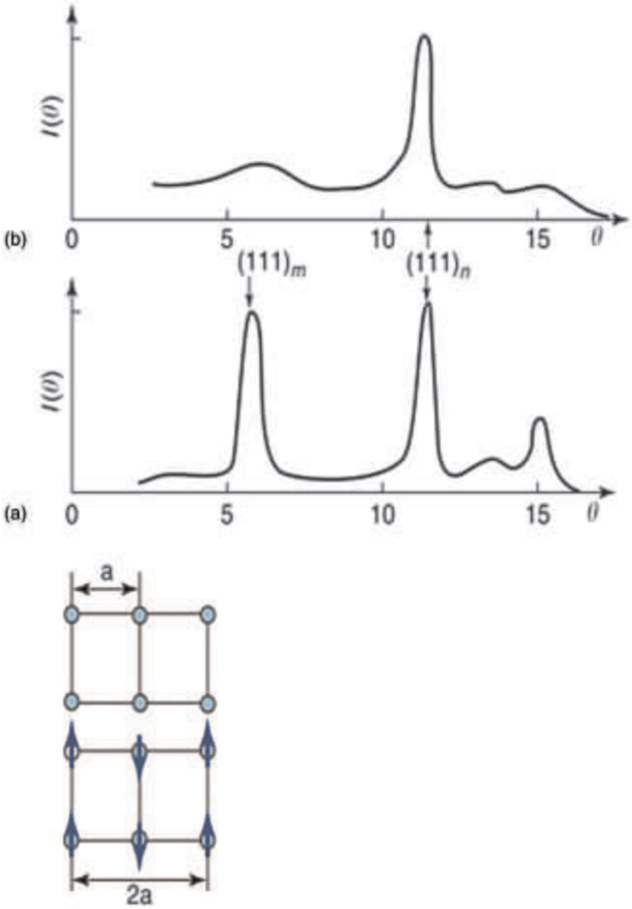

Figure 4 Neutron diffractograms obtained with MnO. (a) At 300 K, the material is paramagnetic. The observed (1 1 1) peak near $\theta = 12^\circ$ is characteristic of the cubic crystallographic structure. (b) The additional peak near $\theta = 6^\circ$ observed at 120 K reveal a doubling of the unit cell. It may be associated with the existence of an antiferromagnetic arrangement of the moments (inset).

Today, neutron diffraction has developed to a very sophisticated level; it allows very complex magnetic arrangements, including those found in spin glasses and other disordered systems, to be examined.

X-rays interact with the electrons within matter. Since spin–orbit coupling makes the bridge between electron distribution and magnetism, they probe magnetism as well. Although the magnetic interaction term is very small, magnetic studies using X-rays (X-ray magnetic circular dichroism and X-ray diffraction) have recently developed, thanks to the availability of very intense X-ray sources at synchrotron radiation facilities. A specific feature of X-ray studies is element selectivity, which occurs when the wavelength of the incident radiation corresponds to the characteristic energy of a given absorption edge for some element contained in the material examined. Using magnetic X-ray circular dichroism, the spin and orbital contributions to the magnetization density can be measured separately.

Further Reading

Bacon GE (1997) *Fifty Years of Neutron Diffraction, The Advent of Neutron Scattering*. Boca Raton, FL: CRC Press.
Chikazumi S (2009) *Physics of Ferromagnetism*. Oxford: Oxford Science Publisher.
Coey JMD (2010) *Magnetism and Magnetic Materials*. Cambridge: Cambridge University Press.
de Lacheisserie E, Gignoux D, and Schlenker M (2002) *Magnetism*. vol. 1 and 2. Boston: Kluwer Academic.
Levitt MH (2008) *Spin Dynamics: Basics of Nuclear Magnetic Resonance*. Chichester: Wiley.
Mydosh JA (1993) *Spin Glasses: An Experimental Introduction*. London: Taylor and Francis.
Schenck A and Gygax FN (1995) Magnetic Materials Studied by Muon Spin Rotation Spectroscopy. *Handbook of Magnetic Materials*. vol. 9, p. 57. Amsterdam: Elsevier.
Slichter CP (1996) *Principles of Magnetic Resonance*. Berlin: Springer.
Stein DL and Newman CM (2013) *Spin Glasses and Complexity (Primers in Complex Systems)*. Princeton, NJ: Princeton University Press.
Willis BTM and Carlile CJ (2013) *Experimental Neutron Scattering*. Oxford, NY: Oxford University Press.

Paramagnetism[☆]

PF de Châtel, New Mexico State University, Las Cruces, NM, USA

© 2016 Elsevier Ltd. All rights reserved.

This is an update of P.F. de Châtel, Paramagnetism, Reference Module in Materials Science and Materials Engineering, Elsevier, 2016, ISBN 9780128035818, https://doi.org/10.1016/B978-0-12-803581-8.01113-9.

Nomenclature

B	magnetic field (T)
H_m	molecular field (A m^{-1})
L	orbital angular momentum (kg m^2 s^{-1})
m_{at}	atomic magnetic momentum (kg m^2 s^{-1})
M	magnetization (A m^{-1})
S	Stoner enhancement factor (dimensionless)
$\rho(\varepsilon)$	density of states (J^{-1} m^{-3})

Paramagnetic materials do not order magnetically and have a positive magnetic susceptibility, which means the magnetization is pointing in the same direction as the magnetic field. Inevitably, there is also a diamagnetic susceptibility. The material is classified as paramagnetic if the sum of the two contributions is positive. Nevertheless, the paramagnetic susceptibility can be determined in both kinds of materials. In addition, the paramagnetic susceptibility of magnetically ordered materials (ferro-, ferri-, and anti-ferromagnets) above the transition temperature can be a subject of study.

In the most common paramagnetic materials, the response to an external magnetic field is due to the alignment of atomic magnetic moments under the torque exerted by the field. The potential energy of the moment $\boldsymbol{m}_{at}$ in a field $\boldsymbol{B}$ is

$$V = -m_{at} \cdot B \qquad [1]$$

The magnitude of the atomic moment is of the order of the Bohr magneton, $\mu_B = e\hbar/2m_e = 9.27 \times 10^{-24}\,\mathrm{JT}^{-1}$, where e is the electron charge, $\hbar = b/2\pi$ the Planck constant, and $\boldsymbol{m}_e$ the electron mass. Eqn [1] shows that $\boldsymbol{m}_{at}$ tends to align parallel to the magnetic field and the energy gained by alignment in a field of $1T$ is $\sim 10^{-23}$ J, less than 1% of the thermal energy per degree of freedom, $1/2\ k_B T$, at room temperature (k_B is the Boltzmann constant). At ambient temperature, in a regular electromagnet, one should not expect a substantial paramagnetic magnetization. On the other hand, if the moments are free, that is, no interaction hampers their rotation, lowering the temperature can reduce the thermal fluctuations, whereupon the paramagnetic susceptibility will increase. If none of the constituent atoms of a material has a magnetic moment, there can still be a paramagnetic moment, due to moments induced by the magnetic field. The resulting Van Vleck susceptibility is independent of temperature (see below).

The value of the atomic moment depends on the number of electrons and on their angular momentum. The filled shells of the ion cores and of fully ionized species, like O^{2-} or Cu^+, have zero angular momentum and hence no magnetic moment. The outermost electron shells are often but partially occupied and can carry a magnetic moment. However, in crystalline solids, these shells provide the delocalized Bloch states and contribute to the cohesive energy of the crystal. This requires a considerable overlap of the atomic wave functions on neighboring sites. The corresponding states are severely perturbed and cannot be labeled by the angular momentum quantum numbers ℓ and m_ℓ. In the case of transition metals, lanthanides, and actinides, under certain circumstances, there is a distinction between the outermost s and p states and the more localized states in the d and f shells, which are not fully occupied either. The former are responsible for the cohesion and determine the interatomic distances, while the latter remain localized and can form localized moments. This subtle division of electronic states makes transition and rare-earth metals and their compounds the most important ordered magnetic materials and also the strongest paramagnets.

A given number of d or f electrons will form a total angular momentum in accordance with Hund's rules, which require that (1) the total spin angular momentum S be as large as possible without violating the Pauli principle; (2) the total orbital angular momentum L be as large as possible without violating the Pauli principle and requirement (1); and (3) S and L be aligned antiparallel and form the total angular momentum, $J = |L - S|$, if the shell is less than half filled, and parallel, $J = L + S$, if it is more than half filled.

The hierarchy of the three rules of Hund reflects a hierarchy among the interactions involved. Of these, the exchange interaction, which favors the parallel-spin arrangement, rule (1), is the strongest. The preference for the alignment of orbital moments, rule (2), is dictated by the less important correlation energy, while the spin–orbit coupling, responsible for rule (3), is ineffective in transition metals and quite important in the rare earths. Table 1 shows the ground states following from the three rules for transition-metal ions in the conventional notation $(2S+1)X_J$, where $X = S, P, D$, and F stand for $L = 0,1,2$, and 3, respectively. Also shown are the

---

[☆] *Change History*: March 2015. P.F. de Châtel made minor changes to the text and added one reference to the Further Reading section.

Table 1 The ground states and effective moments of transition-metal ions

Ion	Configuration	Ground state	$\mu_{\mathrm{eff}} = g\sqrt{J(J+1)}$	$\mu_{\mathrm{eff}} = 2\sqrt{S(S+1)}$
Ti^{3+}, V^{4+}	$3d^1$	$2D_{3/2}$	1.55	1.73
V^{3+}	$3d^2$	$3F_2$	1.63	2.83
Cr^{3+}, V^{2+}	$3d^3$	$4F_{3/2}$	0.77	3.87
Mn^{3+}, Cr^{2+}	$3d^4$	$5D_0$	0	4.90
Fe^{3+}, Mn^{2+}	$3d^5$	$6S_{5/2}$	5.92	5.92
Co^{3+}, Fe^{2+}	$3d^6$	$5D_4$	6.70	4.90
Co^{2+}	$3d^7$	$4F_{9/2}$	6.63	3.87
Ni^{2+}	$3d^8$	$3F_4$	5.59	2.83
Cu^{2+}	$3d^9$	$2D_{5/2}$	3.55	1.73

Table 2 The ground states and effective moments of tripositive rare-earth ions

Ion	Configuration	Ground state	$\mu_{\mathrm{eff}} = g\sqrt{J(J+1)}$	μ_{eff} (measured)
Ce^{3+}	$4f^1$	$2F_{5/2}$	2.54	2.4
Pr^{3+}	$4f^2$	$3H_4$	3.58	3.5
Nd^{3+}	$4f^3$	$4I_{9/2}$	3.62	3.5
Pm^{3+}	$4f^4$	$5I_4$	2.68	–
Sm^{3+}	$4f^5$	$6H_{5/2}$	0.84	1.5
Eu^{3+}	$4f^6$	$7F_0$	0	3.4
Gd^{3+}	$4f^7$	$8S_{7/2}$	7.94	8.0
Tb^{3+}	$4f^8$	$7F_6$	9.72	9.5
Dy^{3+}	$4f^9$	$6H_{15/2}$	10.63	10.6
Ho^{3+}	$4f^{10}$	$5I_8$	10.60	10.4
Er^{3+}	$4f^{11}$	$4I_{15/2}$	9.59	9.5
Tm^{3+}	$4f^{12}$	$3H_6$	7.57	7.3
Yb^{3+}	$4f^{13}$	$2F_{7/2}$	4.54	4.5

effective moments, calculated for the $L-S$ coupled as well as spin-only states, which will be discussed below. Table 2 gives the corresponding data for the tripositive rare-earth ions (H and I stand for $L=5$ and 6, respectively).

If the quantum numbers of the ground state are known, the atomic magnetic moment can be calculated as $m_{\mathrm{at}}=g_J\mu_{\mathrm{B}}J$, where

$$g_J = 1 + \frac{J(J+1) + S(S+1) - L(L+1)}{2J(J+1)}$$

is the Landé g factor.

There is no classical analogy of the above procedure of determining the magnitude of the atomic moments as there should not be one, considering that the Bohr–van Leeuwen theorem precludes orbital magnetism in a classical system. What is often referred to as the classical derivation of the paramagnetic magnetization is the application of classical statistics to the quantum mechanical objects $\boldsymbol{m}_{\mathrm{at}}$. In the context of classical statistics, the partition function involves the potential energy (eqn [1]), where $m_{at}\cdot B = m_{at}B\cos\vartheta$, where ϑ is a continuous variable and integration is to be performed over φ and ϑ, the angular coordinates of the vector $\boldsymbol{m}_{\mathrm{at}}$. In the proper quantum mechanical description, a summation over the possible values of the z component of $\boldsymbol{m}_{\mathrm{at}}$ is required and the partition function takes the form

$$Z = \left(\sum_{M_J=-J}^{J} \exp\left(g_J\mu_{\mathrm{B}}BM_J/k_{\mathrm{B}}T\right) \right)^{N_{\mathrm{at}}} \qquad [2]$$

where N_{at} is the number of atoms or ions. Summation of the geometrical series leads to

$$z = \left(\frac{\sinh\left(g_J\mu_{\mathrm{B}}B(J+1/2)/k_{\mathrm{B}}T\right)}{\sinh\left(g_J\mu_{\mathrm{B}}B/2k_{\mathrm{B}}T\right)} \right)^{N_{\mathrm{at}}}$$

Deriving the free energy as $F = (-1/k_{\mathrm{B}}T)$ and using $M=(-1\,\partial F/V\partial B)$, the magnetization is found in the form

$$M = \frac{N_{\mathrm{at}}}{V} g_J\mu_{\mathrm{B}}B_J\left(g_J\mu_{\mathrm{B}}B\right)$$

where

$$B_J(x) = \frac{2J+1}{2J}\coth\frac{2J+1}{2J}x - \frac{1}{2J}\coth\frac{1}{2J}x$$

is the Brillouin function. For large values of J, $B_J(x)$ approaches the Langevin function, $L(x) = \coth x - 1/x$ which is the result of the classical treatment outlined above. The susceptibility is found to obey Curie's law,

$$\chi_c = \left(\frac{\partial M}{\partial H}\right)_{H=0} = \frac{N_{\mathrm{at}}}{V}\mu_0\frac{(g_J\mu_B)^2 J(J+1)}{3K_{\mathrm{B}}T} = \frac{C}{T} \qquad [3]$$

where $\mu_0 = 4\pi 10^{-7}\mathrm{TmA}^{-1}$ is the permeability of free space and the Curie constant, C, is implicitly defined by this equation. The Curie law is well obeyed by various salts and other compounds, where the atoms or ions carrying magnetic moments are far enough from each other, so that their interaction, the exchange interaction, is negligible. In these cases the effective magnetic moment, $\mu_{\mathrm{eff}} = g_J\mu_B\sqrt{J(J+1)}$, can be determined from the slope of χ^{-1} versus T plots. In paramagnetic rare-earth materials, the measured μ_{eff} values agree with the Hund's rule values listed in **Table 2**. In most transition-metal oxides and salts, however, the μ_{eff} values calculated from the Hund's rule spin quantum numbers alone are closer to the measured values than the ones involving J, indicating that crystal fields are strong enough to suppress ('quench') the orbital angular moment. If the exchange interaction between magnetic moments is not negligible, the Curie–Weiss law, $\chi_{\mathrm{CW}}\alpha(T-\theta)^{-1}$, often holds. To account for the interaction, whose source was unknown at that time (1907), Weiss has introduced the molecular field H_{m}, which acts, in addition to the external field H, on each atomic magnetic moment. As H_{m} is supposed to describe the tendency of atomic moments to point in the same direction, it is assumed to be proportional with the magnetization, $H_m = \lambda M$. Substituting this expression in the expression for the magnetization in the total field,

$$M = \chi_c(H + H_m) = \frac{C}{T}(H + \lambda M)$$

the magnetization can be expressed as $M = \chi_{\mathrm{cw}}H$ with

$$\chi_{\mathrm{cw}} = \frac{\chi_c}{1-\lambda\chi_c} = \frac{C}{T-\theta} \qquad [4]$$

where $\theta = C\lambda$ is the paramagnetic Curie temperature. It is seen that the slope of χ_{cw}^{-1} versus T plots are determined by the effective moment the same way as in the case of the Curie law, but the straight lines representing the measured data do not go through the origin. Deviations from the straight-line behavior may be due to crystal fields.

In most metals, the effect of the crystalline environment is so strong that all couplings imposed by Hund's rules are broken and all but the ion-core electrons are delocalized. In rare-earth materials, the f electrons are localized and form magnetic moments conforming to Hund's rules. In insulators, the d electrons of transition-metal cations remain localized, but the spin–orbit coupling is broken and the orbital angular momentum itself is destroyed. The latter process is called the quenching of angular momentum, not a particularly enlightening term. What it stands for is that, the spherical symmetry around a particular ion being broken by its neighbors in the crystal, the stationary states are no more eigenstates of the angular momentum. Due to the symmetry of the crystalline environment, some degeneracy of the eigenstates may remain. However, if all matrix elements of the three components of the angular momentum, $\hat{L}_x, \hat{L}_y$, and $\hat{L}_z$, between the degenerate wave functions vanish, its expectation value vanishes for any linear combination of these functions; the angular momentum is 'quenched.' If that is not the case, the angular momentum may be partially quenched and can be described by an effective angular momentum operator working within the multiplet of the lowest-lying crystal-field level.

Partial or complete quenching of the orbital angular momentum influences the temperature dependence of the paramagnetic susceptibility if the temperature is high enough for the thermal energy $k_{\mathrm{B}}T$ to be comparable to the splitting between the lowest and next-to-lowest crystal-field levels. At temperatures exceeding Δ/k_{B}, Δ being the total splitting of the ground-state multiplet, the Curie or Curie–Weiss susceptibility is recovered with the effective moment appropriate to that multiplet.

Higher-lying crystal-field states can influence the paramagnetic susceptibility also at very low temperatures, $T \ll \Delta/k_{\mathrm{B}}$. Even though the thermal occupancy of such states is negligible in this limit, the magnetic field will mix them into the ground state via the perturbing Hamiltonian (eqn [1]). Taking account of this perturbation to second order, the corresponding contribution to the susceptibility, the Van Vleck paramagnetic susceptibility, is found to be

$$\chi_{\mathrm{VV}} = \frac{N_{\mathrm{at}}}{V}\mu_0 2\sum_i \frac{|\int\psi_0^*(\hat{m}_{\mathrm{at}})_z\psi_i\mathrm{d}\tau^2|}{\varepsilon_i - \varepsilon_0} \qquad [5]$$

independent of temperature. Here ψ_0, ψ_1 are the wave functions and ε_0, ε_{i} the energies of the ground state and higher-lying crystal-field states, respectively. The operator representing the atomic magnetic moment is

$$m_{\mathrm{at}} = \mu_{\mathrm{B}}(\hat{L} + 2\hat{S})$$

evidently not proportional to $\hat{J}$. Therefore, $(\hat{m}_{\mathrm{at}})_z$ has nonvanishing matrix elements between the Hund's rule ground state and higher-lying eigenstates of different J values as well. In fact, Van Vleck derived for that case, with ions having small spin–orbit splitting in mind. However, the term 'Van Vleck susceptibility' is used with reference to any temperature-independent contribution to the paramagnetic susceptibility due to the quantum mechanical admixture of higher-lying states.

As mentioned above, crystal fields in insulators constitute a subtle effect, compared to the full delocalization of conduction electrons in metals. The consequence of the latter for the paramagnetic response is indeed drastic. The conduction electrons, instead of following the Curie law (eqn [3]) with $g=2$ and $S=1/2$, contribute only the Pauli paramagnetism, a small, temperature-independent susceptibility,

$$\chi_P = \mu_0 \mu_{\mathrm{B}}^2 \rho(\varepsilon_{\mathrm{F}}) \qquad [6]$$

where $\rho(\varepsilon_{\mathrm{F}})$ is the density of states per unit volume at the Fermi energy. It is indeed the Pauli principle that suppresses the $1/T$ divergence of χ: most of the electrons are unable to flip their spin, because the opposite-spin state of the same energy is occupied. Only the electrons in states with energies within $k_{\mathrm{B}}T$ from the Fermi energy are given the choice of m_{s} values implied by eqn [2]. As the density of such electrons is about $K_{\mathrm{B}}T\rho(\varepsilon_{\mathrm{F}})$, the temperature in the denominator of the Curie susceptibility is canceled out and eqn [6] can be seen to follow from eqn [3].

In the alkali metals, $\rho(\varepsilon_{\mathrm{F}}) \approx 10^{47}\ \mathrm{J}^{-1}\ \mathrm{m}^{-3}$ whence from eqn [6] $\chi_P \approx 10^{-5}$, in good agreement with the paramagnetic susceptibility derived from experiment. In transition metals, the density of states is about one order of magnitude larger, but even so, eqn [6] underestimates the paramagnetic susceptibility, which is enhanced by the exchange interaction between the d electrons. Like in the derivation of the Curie–Weiss law, here too the effect of this interaction can be described by the molecular field. The result,

$$x = \frac{\chi_P}{1 - \lambda \chi_P} \qquad [7]$$

is formally similar to eqn [4], but it should be noted that it is independent of temperature in this case. Equation [7] gives the exchange-enhanced paramagnetic susceptibility, $S = (1 - \lambda\chi_P)^{-1}$ is the Stoner enhancement factor. Among the transition metals, the largest value of S is observed in palladium, where $S = 10$.

Further Reading

Ashcroft NW and Mermin ND (1976) *Solid State Physics.* New York: Holt, Reinhart and Winston.
Blundell S (2001) *Magnetism in Condensed Matter.* Oxford University Press.
Chikazumi S (1965) *Physics of Magnetism.* New York: Wiley.
Kittel C (1986) *Introduction to Solid State Physics*, sixth edn New York: Wiley.
O'Handley RC (2000) *Modern Magnetic Materials Principles and Applications.* New York: Wiley.
Van Vleck JH (1932) *The Theory of Electric and Magnetic Susceptibilities.* Oxford: Clarendon Press.

Diamagnetism

PF de Châtel, New Mexico State University, Las Cruces, NM, USA

© 2005 Elsevier Ltd. All rights reserved.

This is an update of P.F. de Châtel, Diamagnetism, Editor(s): Franco Bassani, Gerald L. Liedl, Peter Wyder, Encyclopedia of Condensed Matter Physics, Elsevier, 2005, Pages 414–417, ISBN 9780123694010, https://doi.org/10.1016/B0-12-369401-9/00518-0.

Nomenclature

$\boldsymbol{A}$	vector potential (A)
$\boldsymbol{B}$	magnetic field (T)
$\boldsymbol{L}$	canonical angular momentum ($\mathrm{kg\,m^2\,s^{-1}}$)
$\boldsymbol{M}$	magnetization ($\mathrm{A\,m^{-1}}$)
$\boldsymbol{m_e} r\times v$	kinetic angular momentum (of electron) ($\mathrm{kg\,m^2\,s^{-1}}$)
$\boldsymbol{m_c}\mathbf{v}$	kinetic momentum (of electron) ($\mathrm{kg\,m\,s^{-1}}$)
$\boldsymbol{p}$	canonical momentum ($\mathrm{kg\,m\,s^{-1}}$)

Diamagnetic materials do not order magnetically and have a negative susceptibility, which means the magnetization is pointing opposite to the magnetic field. Possibly, there is also a paramagnetic susceptibility. The material is classified as diamagnetic if the sum of the two contributions is negative. Nevertheless, the diamagnetic susceptibility can be determined in both kinds of materials.

Diamagnetism is a very small effect, but all the more puzzling. It entails a response of all known materials to an external magnetic field, which manifests itself in a magnetization opposing that field. It appears thus that the magnetic field generates a magnetic dipole, whose orientation is most unfavorable, being at a maximum of the potential energy as a function of the angle between the magnetic field and the magnetization,

$$E = -\boldsymbol{B}\cdot\boldsymbol{M} = BM > 0$$

There is no simple, intuitive explanation for this paradox. This is not surprising though, considering that our intuition is mostly based on classical physics. The celebrated Bohr–van Leeuwen theorem states that the classical free energy of a system of charged particles moving in a magnetic field is independent of the field. Since the magnetization is proportional to the derivative of the free energy with respect to the field,

$$\boldsymbol{M} = -\frac{1}{V}\frac{\partial F}{\partial \boldsymbol{B}} \qquad [1]$$

this theorem implies that classical physics, in this case classical mechanics combined with classical statistics, cannot account for any field-induced magnetization, be it paramagnetic (aligned along the field) or diamagnetic (opposing). In the case of diamagnetic metals, whose charge carriers behave like free electrons, this conclusion contradicts what one would expect from electrodynamics. Charged classical free particles exposed to a magnetic field move in circles. Lenz's law of induction requires that the current loops represented by the orbiting electrons produce a magnetization opposed to the field which induces the currents; this should result in a diamagnetic response. It is no wonder that Niels Bohr was fascinated by this paradox. His main interest was the stability of atomic orbitals, which also contradicts classical expectation. He has formulated the rule of angular-momentum quantization, which, imposed on the classical treatment, accounted for the observed stable orbitals. As it will be shown below, the same rule, applied in the presence of a magnetic field, gives the correct answer for the diamagnetism of free atoms. The diamagnetism of free electrons cannot be understood in this semiclassical way, here a fully quantum mechanical treatment is needed.

The formal proof of the Bohr–van Leeuwen theorem is rather simple, but conceals the clue to its counterintuitive implication. Indeed, if one writes the free energy, $F = -k_B T \ln Z$, of a system of N identical particles (taking electrons of mass m_e and charge $-e$), the partition function has the form

$$Z = \prod_{i=1}^{N} \int \cdots \int \mathrm{d}\boldsymbol{r}_i\, \mathrm{d}\boldsymbol{p}_i \times \exp(-H(\{\boldsymbol{r}_i\},\{\boldsymbol{p}_i\})/k_B T) \qquad [2]$$

where H is the Hamiltonian, a function of all position vectors $\boldsymbol{r}_i$ and canonical momenta $\boldsymbol{p}_i$. The latter are written as

$$\boldsymbol{p}_i = m_e \boldsymbol{v}_i - e\boldsymbol{A}(\boldsymbol{r}_i)$$

where $\boldsymbol{A}$ is the vector potential describing the magnetic field, which enters the Hamiltonian via the kinetic energy,

$$E_{\mathrm{kin}} = \frac{1}{2} m_e v_i^2 = \frac{1}{2m_e}[\boldsymbol{p}_i + e\boldsymbol{A}(\boldsymbol{r}_i)]^2$$

To prove the independence of Z from $\boldsymbol{A}$, one changes the integration variables $\boldsymbol{p}_i$ to $\boldsymbol{p}_i' = \boldsymbol{p}_i + \boldsymbol{A}(\boldsymbol{r}_i)$ and realizes that this will not change the result of integration, because the shift of the limits of integration, $\pm\infty$, has no effect. The vector potential thus being eliminated from eqn [2], the partition function must be independent of the magnetic field.

To understand the implications of this freedom to shift parameters, it is instructive to carry out the differentiation in eqn [1] for the simple case of a system of N_a identical atoms. If the electron–electron interaction is treated in the mean-field approximation, the N electrons localized on the same atom are described by the Hamiltonian

$$H = \sum_{i=1}^{N} H^{(1)}(\boldsymbol{r}_i, \boldsymbol{p}_i)$$

with

$$H^{(1)}(\boldsymbol{r}, \boldsymbol{p}) = V(r) + [\boldsymbol{p} + e\boldsymbol{A}(\boldsymbol{r})]^2/2m_\mathrm{e} \qquad [3]$$

where $V(r)$ is the potential consisting of the potential of the nucleus and of the "other" $N-1$ electrons, the latter contribution being spherically averaged (central-field approximation). The partition function (eqn [2]) becomes then the product of N identical integrals,

$$Z = \left\{\int\int \mathrm{d}\boldsymbol{r}\,\mathrm{d}\boldsymbol{p}\exp(-H^{(1)}(\boldsymbol{r}, \boldsymbol{p})/k_\mathrm{B}T\right\}^N = \{Z^{(1)}\}^N$$

and, consequently, the free energy is a sum of N identical terms, $F = -k_\mathrm{B}TN \ln Z^{(1)}$. Choosing the gauge

$$\boldsymbol{A} = -\frac{1}{2}(\boldsymbol{r} \times \boldsymbol{B}) \qquad [4]$$

one obtains

$$\boldsymbol{M} = -\frac{N_\mathrm{a}}{V}\frac{\partial F}{\partial \boldsymbol{B}} = -\frac{N_\mathrm{a}}{V}\frac{eN}{2m_\mathrm{e}}\int\int \mathrm{d}\boldsymbol{r}\,\mathrm{d}\boldsymbol{p}\,\boldsymbol{r} \times \left[p - \frac{e}{2}(\boldsymbol{r} \times \boldsymbol{B})\right] \times \frac{\exp(-H^{(1)}(\boldsymbol{r}, \boldsymbol{p})/k_\mathrm{B}T)}{Z^{(1)}} \qquad [5]$$

where N_a is the number of atoms. The result is seen to be proportional to the thermal average of the kinetic angular momentum, $\boldsymbol{r} \times m_\mathrm{e}\boldsymbol{v}$. This is not unexpected, because currents, the sources of magnetization, are related to the velocity, not the canonical momentum $\boldsymbol{p}$, of the charge carriers. The same holds for the kinetic energy in the Hamiltonian [3], which appears in the statistical weight factor $\exp(-H^{(1)}/k_\mathrm{B}T)$.

Consider now two points in the phase space of a single electron, which are given by the same position vector $\boldsymbol{r}$ and opposite velocities,

$$\boldsymbol{r}_1 = \boldsymbol{r}_2 = \boldsymbol{r}$$
$$\boldsymbol{p}_1 - \frac{e}{2}(\boldsymbol{r}_1 \times \boldsymbol{B}(\boldsymbol{r}_1)) = -\left(\boldsymbol{p}_2 - \frac{e}{2}(\boldsymbol{r}_2 \times \boldsymbol{B}(\boldsymbol{r}_2))\right)$$

The statistical weight factors associated with these two points are identical, whereas the kinetic angular momenta have opposite signs and the same magnitude. Therefore, the sum of their contributions to the integral will vanish. The cancelation would have been more obvious, if $\boldsymbol{p}$ was shifted to $\boldsymbol{p}' = \boldsymbol{p} + (e/2)(\boldsymbol{r} \times \boldsymbol{B}(\boldsymbol{r}))$. In that case, the integrand would have become an odd function of $\boldsymbol{p}'$ resulting obviously in a vanishing $\boldsymbol{M}$. Again, the freedom to shift the canonical momentum at a given value of $\boldsymbol{r}$, which amounts to shifting the canonical angular momentum $\boldsymbol{L} = (\boldsymbol{r} \times \boldsymbol{p})$, turns out to be important in the derivation. As classical mechanics puts no constraints on $\boldsymbol{L}$ and, according to the ergodic theorem underlying classical statistics, a system will visit all possible states of different values of $\boldsymbol{L}$, it is understandable that $\boldsymbol{M}$ has to vanish on average.

These considerations suggest that the classical realm need not be left altogether. It may suffice to impose some constrains on the angular momentum, in the spirit of the Bohr model of atoms, to get sensible results for the magnetization. As a uniform magnetic field along the z-axis, $\boldsymbol{B} = (0,0,B)$, leaves all rotations around the z-axis as symmetry operations, it is postulated that L_z be limited to the values $m\hbar$, $m = \pm 1, \pm 2, \pm 3, \ldots$. To impose this condition, each integral over the entire six-dimensional $(\boldsymbol{r},\boldsymbol{p})$ phase space must be replaced by a sum of integrals, each over a subspace P_m containing only $(\boldsymbol{r},\boldsymbol{p})$ points, for which $(\boldsymbol{r} \times \boldsymbol{p})_z = m\hbar$. In particular,

$$Z^{(1)} = \sum_m \int\int_{P_m} \mathrm{d}\boldsymbol{r}\,\mathrm{d}\boldsymbol{p}\exp(-H^{(1)}(\boldsymbol{r}, \boldsymbol{p})/k_\mathrm{B}T) = \sum_m Z_m^{(1)}$$

By the definition of the subspace P_m

$$\int\int_{P_m} \mathrm{d}\boldsymbol{r}\,\mathrm{d}\boldsymbol{p}(\boldsymbol{r} \times \boldsymbol{p})_z \exp(-H^{(1)}(\boldsymbol{r}, \boldsymbol{p})/k_\mathrm{B}T) = m\hbar Z_m^{(1)}$$

so that eqn [5] can be written as

$$M_z = -\frac{N_a}{V} \sum_m \{\frac{eN}{2m_e} \frac{Z_m^{(1)}}{Z^{(1)}} \hbar m + \frac{e^2 N}{4m_e} \langle \rho^2 \rangle_m^{\mathrm{th}} B\}$$

where $NZ_m^{(1)}/Z^{(1)} = p_m$ is the thermal occupation probability of the $L_z = m\hbar$ orbit. Introducing the Bohr magneton, $\mu_B = e\hbar/2m_e$, the first term takes the form $p_m m \mu_B$, which can be recognized as the paramagnetic contribution to the magnetization. In the second term, which makes evidently a negative, diamagnetic contribution to the magnetization, $\langle \rho^2 \rangle_m^{\mathrm{th}} = \int \int_{P_m} \mathrm{d}\boldsymbol{r}\, \mathrm{d}\boldsymbol{p}\, \rho^2 \exp(-H^{(1)}(\boldsymbol{r}, \boldsymbol{p})/k_B T)/Z^{(1)}$ is the thermal average of ρ_2 for the same orbit m. Here, it is assumed that the $\boldsymbol{r}$ vector is in the $z = 0$ plane and $|\boldsymbol{r}| = \rho$, constant. It then follows that

$$M_{\mathrm{dia}} = -\frac{N_a}{V} \frac{e^2}{4m_e} \sum_m \langle \rho^2 \rangle_m^{\mathrm{th}} B$$

In practice, no thermal excitation out of the ground state will occur and $N\langle \rho^2 \rangle_m^{\mathrm{th}}$ can be replaced by the average of the squared radii of occupied orbits. Clearly, at this stage the simple Bohr model fails. It would be a tortuous extension to introduce the principal quantum number n on the basis of the Bohr–Sommerfeld model and the angular momentum quantum number ℓ on an *ad hoc* basis. Even so, only for $T = 0$ would the introduction of the Pauli principle suffice to give the correct result. For $T > 0$, Fermi–Dirac statistics should be applied, which is a further step away from classical physics. In a proper quantum mechanical treatment, (2/3) $\langle r_2 \rangle$ enters, instead of $\langle \rho^2 \rangle^{\mathrm{th}}$ where $\langle \ldots \rangle$ stands for the expectation value and the factor 2/3 accounts for the difference between the expectation values of $r^2 = x^2 + y^2 + z^2$ and $\rho^2 = x^2 + y^2$. The diamagnetic susceptibility is thus

$$\chi_{\mathrm{dia}}^{(\mathrm{Langevin})} = \frac{M_{\mathrm{dia}}}{H} = -\frac{N_a}{V} \frac{\mu_0 e^2}{6m_e} \sum_j \langle r_j^2 \rangle \qquad [6]$$

where the summation is over the occupied orbits j on each atom. Langevin's result for atomic diamagnetism was brought to this form by Pauli.

It is remarkable that Planck's constant does not appear in the expression for the diamagnetic susceptibility, whereas the importance of angular-momentum quantization in its derivation is obvious. Also, eqn [6] is an appealing result, as it enables a seemingly classical interpretation in terms of currents i_j, induced on each orbit j. Such currents will generate magnetic moments $m_j = i_j \alpha_j \propto \langle r_j^2 \rangle$, where α_j is the area enclosed by the orbit j. The sign of the moments (opposite to $\boldsymbol{B}$) can be understood in terms of Lenz's law and their magnitudes can be derived from Faraday's law of induction. This derivation, however, invokes well-defined orbits, which are modeled by tiny current loops. Bohr has grafted such orbits onto the classical treatment of particles moving in a potential proportional to r^{-1} and postulated the quantization of angular momentum. Remarkably, this supplement to the classical description was sufficient to understand quantized energy levels and line spectra, as well as diamagnetism.

The validity of eqn [6] turns out to extend beyond the case of atomic orbits. Most notably, it is applicable to ring-shaped molecules, whose structure offers extended orbits. The diamagnetic susceptibility of substances containing such molecules is known to be anisotropic, being larger in magnitude if the magnetic field is applied perpendicular to the plane of the ring-shaped molecules,

$$|\chi_{\mathrm{dia}}^{\perp}| > |\chi_{\mathrm{dia}}^{\parallel}|$$

The interpretation of this phenomenon in terms of "ring currents" goes beyond the qualitative argument that the induced magnetic moments are maximized in the perpendicular configuration. For benzene, C_6H_6, the anisotropic susceptibility

$$\chi^{\mathrm{an}} = \chi_{\mathrm{dia}}^{\perp} - \chi_{\mathrm{dia}}^{\parallel}$$

is found to be close to what eqn [6] gives. The summation in eqn [6] is to be taken over the six carbon p electrons, which, not being localized in sp^2 hybrid states, are free to move around the molecule:

$$\chi_{\mathrm{benzene}}^{\mathrm{an}} = -6 \frac{A}{V_m} \frac{\mu_0 e^2}{4m_e} \rho^2 = -\frac{A}{V_m} \frac{i_r}{H} \alpha_{\mathrm{hex}} \qquad [7]$$

Here, A/V_m is the density of molecules, A being Avogadro's number and $V_m = 89 \times 10^{-6}$ m^3 the molar volume of benzene, $\rho = 0.139$ nm is the distance from the axis of the molecule to the carbon nuclei and i_r is the total ring current carried by the six delocalized electrons. Pauling has shown in 1936 that the ratio of the anisotropic susceptibility of other, more complicated aromatic hydrocarbons to that of benzene is correctly given by a simple model of conducting networks, assuming that the "resistance" of a carbon–carbon bond is the same in all such molecules. The ultimate success of this model is the correct estimation of the anisotropic susceptibility of graphite. The crystal structure of graphite consists of honeycomb-like layers built of benzene-like units. Assuming that in each hexagonal unit a ring current is induced of the same magnitude as in benzene, one finds that the current of neighboring unit cells cancel and the current density inside the material vanishes. However, the outermost hexagons have two sides with uncompensated currents i_r flowing in a zigzag pattern at 30° from the orientation of the surface. The resulting surface current density is $j_S = i_r \cos 30°/d$, where $d = 0.335$ nm is the interlayer distance in graphite. The surface current density j_S generates a magnetization $M_{\mathrm{graphite}} = -j_S = -i_r\sqrt{3}/2d$ inside the sample. This is to be compared with $M_{\mathrm{benzene}} = -(A/V_m) i_r \alpha_{\mathrm{hex}}$ (cf. eqn [7]), leading to

$$\frac{\chi^{\mathrm{an}}_{\mathrm{graphite}}}{\chi^{\mathrm{an}}_{\mathrm{benzene}}} = \frac{\sqrt{3}V_{\mathrm{m}}}{2A\alpha_{\mathrm{hex}}d} = 7.6 \qquad [8]$$

which is close enough to the experimental value of 6.9, considering the simplicity of the model.

Semiclassical and empirical schemes like the ones used above for free atoms and aromatic compounds, respectively, cannot be applied to the diamagnetic response of conduction electrons in metals. Even the simplest model, the free-electron gas, has been a major challenge, until Landau gave his derivation of what has come to be called Landau diamagnetism. In fact, in most textbooks the Bohr–van Leeuwen theorem is only mentioned in this context, even though its validity is not violated by the presence of atomic or molecular potentials.

The Schrödinger equation was four years old, when Landau (who was twenty-one at the time) solved it for free electrons in the uniform magnetic field (eqn [6]). Instead of the symmetric gauge (eqn [4]), he has chosen

$$\boldsymbol{A} = (0, xB, 0) \qquad [9]$$

which enabled the separation of variables. The resulting differential equation in x was found to be identical with the Schrödinger equation of a harmonic oscillator with a force constant e^2B^2/m_{e}, while the ones in y and z were satisfied by plane-wave solutions. The latter is reasonable for the z dependence, considering that the Lorentz force is perpendicular to $\boldsymbol{B}$, so that the motion along the z axis is free. The density of the eigenstates described by $\mathrm{e}^{\mathrm{i}k_z z}$ is that of a one-dimensional electron gas,

$$\rho(\varepsilon) = \frac{2eB}{h^2}\sqrt{2m_{\mathrm{e}}\varepsilon} \qquad [10]$$

The motion in the (x,y) plane gives a discrete spectrum, with highly degenerate states at the energies

$$\varepsilon_n = (n + \frac{1}{2})\frac{\hbar e}{m_{\mathrm{e}}}B \qquad [11]$$

the Landau levels, which correspond to the stationary states of the harmonic oscillator. The resulting total density of states has a spiked structure. A singular contribution of the form [10] begins at each level [11]. These $\rho(\varepsilon - \varepsilon_n)$ contributions stand for the motion in the z direction while the motion in the (x,y) plane corresponds to the nth level of the harmonic oscillator. As to the x- and y-dependence of the wave functions, they are not suggestive of the circular motion resulting from the classical equations of motion for a charged particle subjected to a uniform magnetic field. This may seem to be due to the choice of the asymmetric gauge [9]. However, it is hardly surprising that the classical motion is not implied by the calculation of an effect, which does not occur at all in the classical theory.

The maxima in the density of states at energies separated by $\hbar eB/m_{\mathrm{e}}$ result in a total energy, which is a periodic function of $1/B$. Through eqn [1], a similar periodicity arises in the magnetization, which is the signature of the de Haas–van Alphen effect. In the low-field limit, the same B-dependent total-energy expression yields the diamagnetic susceptibility

$$\chi^{(\mathrm{Landau})}_{\mathrm{dia}} = -\frac{n\mu_{\mathrm{B}}^2}{\varepsilon_{\mathrm{F}}}$$

where n is the electron density and ε_{F} is the Fermi energy. This is seen to be −1/3 times the Pauli paramagnetic susceptibility, a relationship, which cannot be expected to be valid for metals in general, but seems to hold for the so-called "simple" metals, for which the nearly free-electron approximation works.

Further reading

Ashcroft NW and Mermin ND (1976) *Solid State Physics*. New York: Holt, Reinhart and Winston.
Chikazumi S (1965) *Physics of Magnetism*. New York: Wiley.
O'Handley RC (2000) *Modern Magnetic MaterialsPrinciples and Applications*. New York: Wiley.
Peierls RE (1955) *Quantum Theory of Solids*. Oxford: Oxford University Press.
Van Vleck JH (1932) *The Theory of Electric and Magnetic Susceptibilities*. Oxford: Clarendon Press.

Ferromagnetism

N Magnani, Università di Parma, Parma, Italy

© 2005 Elsevier Ltd. All rights reserved.

This is an update of N. Magnani, Ferromagnetism, Editor(s): Franco Bassani, Gerald L. Liedl, Peter Wyder, Encyclopedia of Condensed Matter Physics, Elsevier, 2005, Pages 201–210, ISBN 9780123694010, https://doi.org/10.1016/B0-12-369401-9/01115-3.

Introduction **43**
The Molecular Field Approach to Ferromagnetism **43**
Magnetostatic Energy and Demagnetizing Field **46**
Magnetic Anisotropy **46**
Magnetocrystalline Anisotropy 48
Shape Anisotropy 48
Stress Anisotropy 49
Anisotropy Induced by Magnetic Annealing 49
Magnetic Domains **49**
The Magnetization Curve **51**
The Hysteresis Cycle 51
Magnetization Rotation and Anisotropy 53
Further Reading **54**

Nomenclature

$\boldsymbol{B}$ magnetic induction (T)
$\boldsymbol{H}$ magnetic field ($\mathrm{A\,m^{-1}}$)
$\boldsymbol{M}$ magnetization ($\mathrm{A\,m^{-1}}$)
$\boldsymbol{T}$ temperature (K)
$\boldsymbol{\mu}$ magnetic moment (μ_B)

Introduction

As far as isolated atoms are concerned, only two different magnetic behaviors exist: diamagnetism and paramagnetism. The latter property is only present if the considered atoms possess a nonzero permanent magnetic dipole, and is responsible for the weak attractive force experienced by a paramagnetic substance in an applied magnetic field. However, the most interesting magnetic properties of condensed matter arise when the interaction between the individual elementary moments of each atom is considered. In particular, ferromagnetism concerns the situation where the moments have the tendency to align, one parallel to another, even in the absence of any external magnetic field, thus leading to the possibility of obtaining very large values of the magnetization with very little values of the applied magnetic field (spontaneous magnetization). Only a few elements in the periodic table (Fe, Co, Ni, Gd, Dy, and Tb) order ferromagnetically, but an extremely large number of compounds and alloys do. From the practical point of view, apart from their high values of the magnetic susceptibility and relative permeability, one of the most interesting properties of ferromagnetic compounds is the possibility of retaining a large amount of the induced magnetization when the external field is completely removed. This makes it possible to develop devices such as permanent magnets (i.e., magnetized bodies which produce a constant magnetic field in a given volume of space without the need to continuously supply electrical or chemical energy), memory storage devices, magnetic circuits, etc.

The Molecular Field Approach to Ferromagnetism

At the beginning of the twentieth century, Pierre Weiss interpreted the tendency of ferromagnets to spontaneous magnetization by introducing a "molecular field" responsible for the ordering of the elementary magnetic moments, and he assumed that this field is linearly proportional to the bulk magnetization (total magnetic moment per volume unit). It may be recalled that the magnetization of a set of identical noninteracting ions, each having total angular momentum J, in a magnetic field H can be expressed as

$$M = ng\mu_B J B_J\left(\frac{g\mu_B JH}{k_B T}\right) \qquad [1]$$

where g is the Landé factor and

$$B_J(x) = \frac{2J+1}{2J}\coth\left(\frac{2J+1}{2J}x\right) - \frac{1}{2J}\coth\left(\frac{x}{2J}\right) \qquad [2]$$

is the Brillouin function; the magnetization of a ferromagnet can then be obtained by substituting in eqn [1] the applied magnetic field H with $H + \lambda M$, leading to the implicit equation

$$\frac{M}{ng\mu_B J} = B_J\left(\frac{g\mu_B J}{k_B T}H + \frac{g\mu_B J}{k_B T}\lambda M\right) \qquad [3]$$

In order to investigate the possibility of spontaneous magnetization, the $H = 0$ case is considered; eqn [3] can be rewritten as

$$m = tx = B_J(x) \qquad [4]$$

with

$$x = \frac{g\mu_B J\lambda M}{k_B T}; \quad t = \frac{k_B T}{n\lambda(g\mu_B J)^2} \qquad [5]$$

A graphical solution of eqn [4] is given in Figure 1; if $t \geq t_C = (J + 1)/3J$, only the trivial solution $x = 0$ is present, while otherwise there is also a possible solution with $x \neq 0$. This means that there exists a critical temperature T_C (Curie temperature), below which a ferromagnetic compound can have a nonzero magnetization in the absence of an applied magnetic field. The Curie temperature and saturation magnetization for several ferromagnetic elements are listed in Table 1. It is worth noting that eqn [4] can be expressed in terms of J, $m = M(T)/M(0)$ and $t = (J + 1)/(3J)\ T/T_C$ only. In the classical limit ($J \to \infty$), $B_J(x)$ is substituted by the Langevin function $\coth x - 1/x$, and the function $m(t)$ is the same for all ferromagnetic materials; the latter statement is often referred to as the law of corresponding states.

Figure 2 shows the temperature dependence of the magnetization measured for nickel (Ni), together with the curve derived from eqn [4] considering a pure-spin moment $J = S = 1/2$. The overall agreement is fairly good, and can be further improved by the use of more accurate models (the low-temperature decrease due to spin waves and the critical behavior near T_C are shown as dashed lines for comparison).

Above T_C, the sample is in a paramagnetic phase (disordered moments), and its magnetic susceptibility can be calculated by noting that $B_J(x) \simeq (J + 1)\ x/(3J)$ for small values of x, leading to

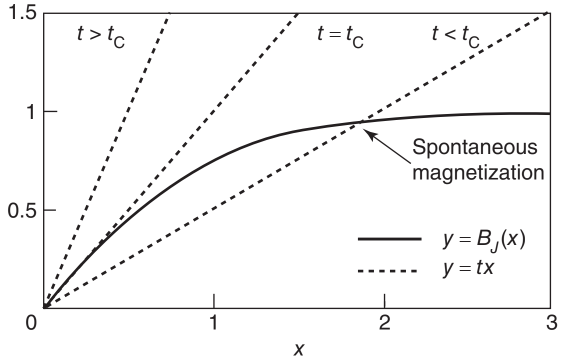

Figure 1 Graphical solution of eqn [4] (see text for details).

Table 1 Curie temperature, saturation magnetization at room-temperature, and magnetic moment per formula unit (at 0 K) of ferromagnetic elements

Element	T_C *(K)*	M_S *(10^6 A m^{-1}*	*μ_B/formula unit*
Cobalt	1388	1.42	1.72
Iron	1043	1.71	2.22
Nickel	627	0.48	0.61
Gadolinium	293		7.10
Terbium	221		9.34
Dysprosium	85		10.0

Data from: (1) Kittel C (1962) *Introduction to Solid State Physics*, 7th edn. London: Wiley; (2) Jiles D (1991) *Introduction to Magnetism and Magnetic Materials*. London: Chapman and Hall; (3) Elliott JF, Legvold S, and Spedding FH (1954) Some magnetic properties of dy metal. *Physical Review* 94: 1143; (4) Hegland DE, Legvold S, and Spedding FH (1963) Magnetization and electrical resistivity of terbium single crystals. *Physical Review* 131: 158; (5) Heller P (1967) Experimental investigations of critical phenomena. *Reports on Progress in Physics* 30: 731.

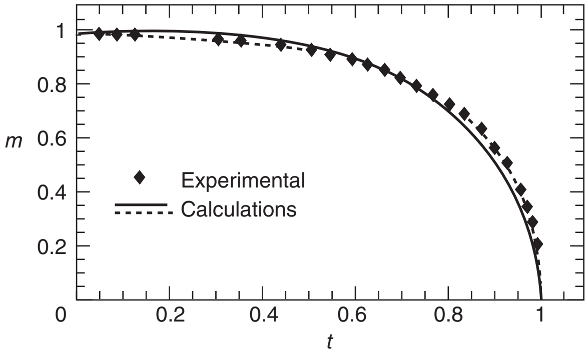

Figure 2 Experimental (diamonds) and calculated (lines) value of $m = M(T)/M(0)$ vs. $t = T/T_C$ for nickel ($J = S = 1/2$). Experimental data are taken from Weiss P and Forrer R (1926) Aimantation et phenomene magnetocalorique du nickel. *Ann. Phys.* 5: 153. The full black line is calculated by means of eqn [4]; dashed lines take into account the spin-wave excitations at low T and the critical behavior near the Curie point.

$$\chi \equiv \frac{M}{H} = \frac{C}{T-\lambda C} \qquad [6]$$

where C can be identified with the paramagnetic Curie constant ($\chi = C/T$ if no ferromagnetic order exists, i.e., $\lambda = 0$) and $T_C = \lambda C$. This very simple model gives a fairly accurate description of the experimental magnetic susceptibilities of ferromagnetic compounds at high temperatures.

It must be noted that λM can be as large as several times the maximum magnetic field which can be produced in a standard laboratory, and is about four orders of magnitude larger than the dipolar interaction due to the other magnetic ions in the crystal. The physical origin of this huge molecular field was not clear until the development of quantum mechanics made it possible to point out the role of the exchange interaction (a purely quantum effect and a direct consequence of Pauli's principle) in determining the magnetic spin alignment. The exchange interactions between a collection of N spins can be described by the Heisenberg–Dirac Hamiltonian, which has the form

$$H_{\text{H-D}} = -\sum_{i,j} J_{ij} \boldsymbol{S}_i \cdot \boldsymbol{S}_j \qquad [7]$$

where the sign of the exchange constants J_{ij} depends on whether the two spins labeled i and j are coupled ferromagnetically (positive) or antiferromagnetically (negative), and the sum usually involves only the z nearest neighbors since the interaction strength drops very rapidly as the distance increases. In the presence of an applied magnetic field $\boldsymbol{H}$, the Zeeman term

$$H_Z = -2\mu_B \sum_i \boldsymbol{H} \cdot \boldsymbol{S}_i \qquad [8]$$

must also be considered (a gyromagnetic factor of 2 was taken, in the hypothesis that pure spin moments are being dealt with). The molecular field approximation consists in reducing the N-body Hamiltonian $H_{\text{H-D}}+H_Z$ to N one-body Hamiltonians H_i, by replacing all the spin operators except S_i with their average values:

$$H_i = -\boldsymbol{S}_i \cdot \left[\sum_j J_{ij} \langle \boldsymbol{S}_j \rangle + 2\mu_B \boldsymbol{H} \right] \qquad [9]$$

The case now considered is that of a ferromagnetic body, with all the relevant exchange constants $J_{ij} = J > 0$ for simplicity. Since

$$\boldsymbol{M} = 2\mu_B \sum_l \langle \boldsymbol{S}_l \rangle \qquad [10]$$

is the total magnetization of the sample, eqn [9] can be rewritten as

$$H_i = -2\mu_B \boldsymbol{S}_i \cdot [\boldsymbol{H} + \lambda \boldsymbol{M}] \qquad [11]$$

with

$$\lambda = \frac{zJ}{4\mu_B^2 N} \qquad [12]$$

Equation [11] immediately shows that the mean-field analysis based on the Heisenberg–Dirac exchange Hamiltonian provides an *a posteriori* justification to Weiss' molecular-field hypothesis; as one might expect, the accuracy of this approximation is higher when z and J are larger, since in this case the role of the fluctuations $S_i - \langle S_i \rangle$ is practically negligible and the substitutions made in eqns [7] and [8] are well-grounded.

One word of caution is required before the end of this section. The existing theories of magnetism may roughly be divided into two groups, dealing respectively with localized and itinerant magnetic moments. The Heisenberg approach which was mentioned before belongs to the former; to give a meaning to eqn [7], it must be explicitly assumed that each ion in the crystal carries on it a well-defined magnetic moment $\boldsymbol{S}_i$ due to the electrons which are bound to it. Although this approach is very useful when dealing with certain substances and alloys and for studying critical magnetic behaviors, its validity for metals is questionable due to the presence of conduction electrons, not tied to a specific ion but belonging to the whole crystal. On the other hand, band models considering the role of itinerant electrons have managed to solve several flaws of localized theories, such as the noninteger values of the magnetic moment per atom experimentally measured in most ferromagnets (Table 1), which could not be explained within a localized-moment framework.

Magnetostatic Energy and Demagnetizing Field

One may consider a sample of a magnetic substance, composed of n magnetic atoms per unit volume, each carrying an elementary moment $\boldsymbol{\mu}$, and imagine applying a magnetic field which is strong enough to align all these dipoles along the same directions. As a result of this process, the sample will display a saturation magnetization

$$M_\mathrm{S} = n|\boldsymbol{\mu}| \qquad [13]$$

(it may be recalled that the magnetization is defined as the total magnetic moment per volume unit).

The energy required to obtain this configuration is

$$E = -\mu_0 \int \boldsymbol{H} \cdot \mathrm{d}\boldsymbol{M} \qquad [14]$$

where $\boldsymbol{H}$ indicates the magnetic field and $\boldsymbol{M}$ is the magnetization vector. In the absence of dissipative processes, an equivalent amount of magnetic potential energy is stored within the sample.

In turn, any magnetized body produces a magnetic field in its surrounding space, as one can immediately witness by means of a compass needle. In close analogy with the charge polarization of a dielectric material, one can describe this field as being generated by “free” magnetic poles (i.e., positive poles not neutralized by the presence of a negative pole in their immediate neighborhood and vice versa) on the surface; in addition to this, the presence of a magnetic field generated by an external source is usually considered. Outside the sample, the magnetic induction $\boldsymbol{B}$ and the magnetic field $\boldsymbol{H}$ are always proportional (as $\boldsymbol{B} = \mu_0[\boldsymbol{H} + \boldsymbol{M}]$ and $\boldsymbol{M} = 0$) and their flux lines are oriented from the north (N) to the south (S) poles. On the other hand, the total magnetic field $\boldsymbol{H}_\mathrm{int}$ inside the sample is found by summing the external field, which is parallel to the magnetization, and the contribution from the free poles, which is antiparallel to it (in fact, the flux lines of $\boldsymbol{H}$ always begin on N poles and end on S poles except when the magnetic field is due to electric currents, in which case they are closed and continuous). The free-poles contribution is also called demagnetizing field, and can be represented as

$$\boldsymbol{H}_\mathrm{d} = -\underline{\boldsymbol{N}}_\mathrm{d} \cdot \boldsymbol{M} \qquad [15]$$

where $\underline{N}_\mathrm{d}$ is, in general, a second-order tensor whose components depend on the geometry of the studied system; in some particular cases and/or for special directions of the magnetic field, $\boldsymbol{M}$ and $\boldsymbol{H}$ are collinear, and one can write a simpler relation where N_d is a dimensionless number called demagnetizing factor. For example, a homogeneous spherical sample (Figure 3) has $N_\mathrm{d} = 4\pi/3$, hence

$$\boldsymbol{H}_\mathrm{d} = -\frac{4\pi}{3}\boldsymbol{M} \qquad [16]$$

Demagnetizing factors for samples of various geometries and for different field directions can be found in specialized textbooks.

Magnetic Anisotropy

Another contribution to the energy balance, that is, magnetic anisotropy, will be dealt with now. While the meaning of such a locution is quite simple (the magnetic behavior of a material depends on the direction), it is not easy to understand the physical reasons behind its very existence. In fact, magnetic anisotropy may be produced by several different mechanisms, which include (but are not limited to) magnetocrystalline (or crystal-field) anisotropy, shape anisotropy, stress anisotropy, annealing in a magnetic field, etc. For the sake of simplicity, the considerations made in the following will be referred to a uniformly magnetized single-crystal sample.

From a phenomenological point of view, the effect of magnetic anisotropy may be taken into account by adding to the energy balance an extra term E_A (anisotropy energy), which depends on the relative orientation of the magnetization vector with respect to the crystallographic axes. As shown by the Russian physicist Akulov, the free anisotropy energy per unit volume can always be expressed by an infinite series

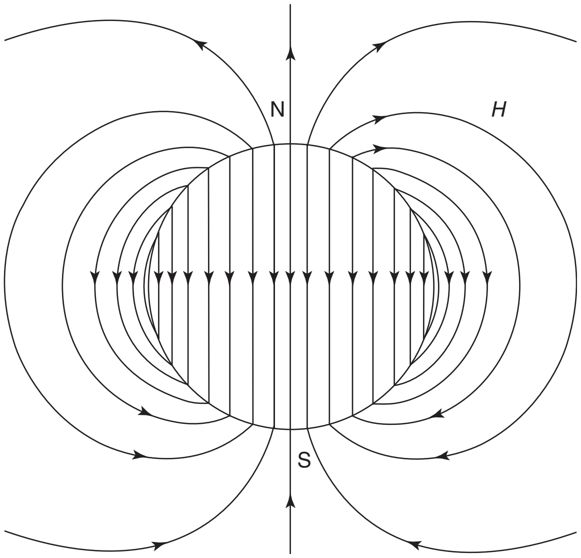

Figure 3 Magnetic field generated inside and outside a uniformly magnetized sphere. The magnetization vector ***M*** is directed from the S to the N pole; the resulting demagnetizing field (inside the sphere) is antiparallel to ***M***.

$$\begin{aligned} E_{\mathrm{A}} &= \sum_{n=1}^{+\infty}\left(\sum_{i_1=1}^{3}\sum_{i_2=1}^{3}\cdots\sum_{i_n=1}^{3} c_{i_1,i_2,\ldots,i_n}\alpha_{i_1}\alpha_{i_2}\ldots\alpha_{i_n}\right) \\ &= \sum_{i=1}^{3} c_i\alpha_i + \sum_{i=1}^{3}\sum_{j=1}^{3} c_{i,j}\alpha_i\alpha_j + \sum_{i=1}^{3}\sum_{j=1}^{3}\sum_{k=1}^{3} c_{i,j,k}\alpha_i\alpha_j\alpha_k + \sum_{i=1}^{3}\sum_{j=1}^{3}\sum_{k=1}^{3}\sum_{l=1}^{3} c_{i,j,k,l}\alpha_i\alpha_j\alpha_k\alpha_l + \cdots \end{aligned} \qquad [17]$$

where α_1, α_2, and α_3 are the direction cosines of the magnetization vector with respect to the Cartesian axes x, y, and z, and several coefficients may equal zero for symmetry reasons; for example, all the terms of the sum with odd n vanish if eqn [17] is invariant under inversion of the magnetization. In most relevant cases, eqn [17] can be rewritten as

$$E_{\mathrm{A}}\sum_{n=1}^{+\infty} K_n A_n(\alpha_1,\alpha_2,\alpha_3) \qquad [18]$$

for example, a ferromagnetic crystal with cubic lattice symmetry has $A_0(\alpha_1,\alpha_2,\alpha_3)=1$; $A_1(\alpha_1,\alpha_2,\alpha_3)=\alpha_1^2\alpha_2^2+\alpha_1^2\alpha_3^2+\alpha_2^2\alpha_3^2$; $A_2(\alpha_1,\alpha_2,\alpha_3)=\alpha_1^2\alpha_2^2\alpha_3^2$; etc. The coefficients K_n, named anisotropy constants, can be determined by magnetization measurements; a knowledge of a reliable set of anisotropy constants for a given sample can lead to a direct phenomenological interpretation of the magnetic processes and is useful to make comparisons between different systems.

For lattices with uniaxial symmetry (e.g., cylindrical, hexagonal, and tetragonal), compact expressions for the anisotropy energy can be derived as a function of the polar and azimuthal angles θ and φ, which define, respectively, the angle between the magnetization vector M and the z-axis (coincident with the symmetry axis), and the angle between the projection of M on the xy-plane and the x-axis. In this case,

$$E_{\mathrm{A}} = \sum_{n=0}^{+\infty}\sin^{2n}\theta \sum_{0\leq l<n/m} K_n^{(l)}\cos(lm\phi) \qquad [19]$$

As for the cubic phase, the K_0 term is an isotropic energy shift, and will therefore be dropped in the following. The value of m depends on the particular symmetry, leading to

$$E_{\mathrm{A}} = K_1\sin^2\theta + K_2\sin^4\theta + K_3\sin^6\theta + K_3'\sin^6\theta\cos 6\phi + \cdots \qquad [20]$$

$(m=6)$ for a hexagonal lattice and

$$E_{\mathrm{A}} = K_1\sin^2\theta + K_2\sin^4\theta + K_2'\sin^4\theta\cos 4\phi + K_3\sin^6\theta + K_3'\sin^6\theta\cos 4\phi + \cdots \qquad [21]$$

$(m=4)$ for a tetragonal system. For a perfectly cylindrical system $(m\to\infty)$, the anisotropy on the xy-plane vanishes and one is left with

$$E_{\mathrm{A}} = \sum_{n=0}^{+\infty} K_n\sin^{2n}\theta \qquad [22]$$

If no applied field is present, the sample magnetization will have the tendency to stay along a direction where the anisotropy energy is lowest; this is called in brief "easy magnetization direction" (EMD). This feature will be discussed in detail later, but it may be immediately inferred that the larger the anisotropy, the larger the magnetic field required to rotate the magnetization direction. Therefore, anisotropy is a key property to take into account when designing or choosing suitable magnetic compounds for particular applications.

In the following section, the most important physical mechanisms giving rise to magnetic anisotropy are discussed in brief.

Magnetocrystalline Anisotropy

Exchange interaction in a ferromagnet can be seen as a spin–spin coupling which aligns the spin moments along the same direction. On the other hand, the orbital moments of any magnetic ion in the lattice preferably align along given crystallographic directions due to the crystal-field potential, which reflects the local crystal symmetry. Magnetocrystalline anisotropy is generated by the spin–orbit interaction, which favors mutual alignment between the spin and orbital moments; if this coupling is relatively strong, as for rare-earths and actinides, moment directions which are farther from the crystallographic easy-axis will have a higher cost in energy. Although several types of anisotropy exist, only magnetocrystalline anisotropy is intrinsic to the material.

In terms of anisotropy constants, subsequent terms of eqn [18] will contain increasing powers of the ratio of the spin–orbit energy to that of the crystal field. As the spin–orbit interaction is weak for $3d$ metals, the series is generally truncated after the second or fourth order, and only terms in K_1 and K_2 are included. In principle, this is not possible for $4f$ elements; however, in the case of intermetallic rare-earth–transition-metal alloys, approximate expressions can be found as linear combinations of generalized Brillouin functions, with appropriate coefficients related to the decomposition in terms of spherical harmonics of the crystal-field potential at the rare-earth site. On these grounds, it is usually possible to consider $K_n = 0$ for $n \geq 4$. The typical temperature dependence of anisotropy constants is shown in Figure 4. On changing the temperature, the anisotropy constants of different order can have different relative variations; as a result of this, the EMD of a sample may spontaneously change, giving rise to a spin reorientation transition (SRT) induced by temperature even in the absence of a magnetic field.

Shape Anisotropy

The free poles on the surface of a perfectly spherical and homogeneous sample give rise to a demagnetizing field which is collinear and linearly proportional to the magnetization vector, as described by eqn [16]. In more general terms, however, one must refer to eqn [15] to find the correct value and direction of the demagnetizing field corresponding to a given magnetization vector. The relatively simple case of an elongated rotation ellipsoid with two axes of equal length is considered; for symmetry reasons, one has

$$\begin{aligned} \underline{N}_{\mathrm{d}} &= \begin{pmatrix} N_\perp & 0 & 0 \\ 0 & N_\perp & 0 \\ 0 & 0 & N_\parallel \end{pmatrix} \\ &= \begin{pmatrix} N_\perp & 0 & 0 \\ 0 & N_\perp & 0 \\ 0 & 0 & N_\perp + \Delta N \end{pmatrix} \end{aligned} \qquad [23]$$

where $\Delta N = N_\parallel - N_\perp$ According to eqn [15] and knowing that all homogeneous bodies delimited by second-order surfaces magnetize uniformly, one can write

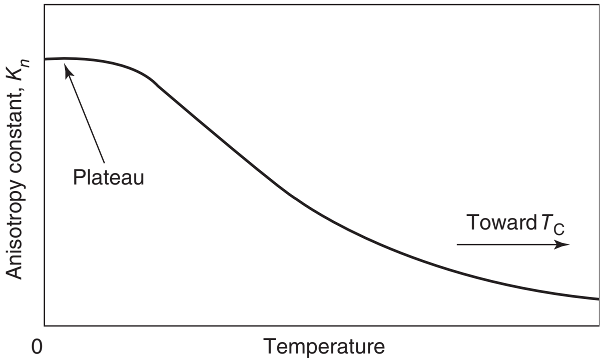

Figure 4 Typical temperature behavior of anisotropy constants (arbitrary units are used).

$$\boldsymbol{H}_\mathrm{d} = -\underline{N}_\mathrm{d}\boldsymbol{M} = -N_\perp \boldsymbol{M} - \Delta N(\boldsymbol{M}\cdot\hat{\boldsymbol{z}})\hat{\boldsymbol{z}} \qquad [24]$$

where $\hat{\boldsymbol{z}}$ is the unit vector along the direction of the elongated axis of the ellipsoid. The associated energy can be calculated as

$$E = -\mu_0 \int \boldsymbol{H}_\mathrm{d} \cdot \mathrm{d}\boldsymbol{M} = \mu_0 M^2 \left(\frac{N_\perp}{2} + \frac{\Delta N}{2}\cos^2\theta\right) = \mu_0 M^2 \left(\frac{N_\parallel}{2} - \frac{\Delta N}{2}\sin^2\theta\right) \qquad [25]$$

which corresponds to eqn [22], the only nonzero anisotropy constants being $K_0 = \mu_0 M^2 N_\parallel/2$ and $K_1 = -\mu_0 M^2 \Delta N/2$. The extrinsic character of shape anisotropy can be immediately noticed, as the calculated K_1 strongly depends on the shape and bulk magnetization of the sample. While shape anisotropy is usually smaller than crystal-field anisotropy for ferromagnetic rare-earth elements and alloys, they may be of the same order of magnitude for transition metals such as iron and cobalt.

Stress Anisotropy

Applying mechanical stress treatments such as lamination, rolling, or extrusion to a magnetic sample can lead to significant crystal deformations. Stress anisotropy may then be generated due to the magnetoelastic coupling between the lattice and the magnetic moments present in the system (magnetostriction).

Anisotropy Induced by Magnetic Annealing

Heat treatments performed under the Curie temperature of the sample in the presence of an applied magnetic field ("magnetic annealing") may result in the generation of uniaxial anisotropy with respect to the field direction. The induced anisotropy is, in general, rather small, although larger effects may be obtained when a structural transition takes place during the annealing.

Magnetic Domains

As has been mentioned in the introduction, the situation of complete alignment of the elementary magnetic dipoles present in a ferromagnetic substance is energetically favorable due to the exchange interaction. However, it is easy to verify that a piece of iron, taken off the shelves and kept below its Curie temperature, is basically unmagnetized and does not produce any magnetic field. Thermal disorder should obviously not be expected to affect the net magnetization significantly, since the exchange interaction responsible for the alignment of the moments is several orders of magnitude larger than the dipole–dipole interaction in a paramagnet. On the other hand, if one sticks to the molecular-field approach, one must be aware that the solution $M = 0$, $H = 0$ satisfies eqn [3] both above and below T_C.

In order to gain some physical insight on this point, the energy of a magnetized body, under the effect of an external magnetic field $\boldsymbol{H}$, is considered:

$$E = -\mu_0 \int (\boldsymbol{H} + \boldsymbol{H}_\mathrm{d}) \cdot \mathrm{d}\boldsymbol{M} \qquad [26]$$

In the simple case that the magnetization is uniform all over the sample and that the demagnetizing field can be expressed as $\boldsymbol{H}_\mathrm{d} = -N_\mathrm{d}\boldsymbol{M}$, eqn [26] becomes

$$E = -\mu_0 \boldsymbol{H}\cdot \int \mathrm{d}\boldsymbol{M} + \mu_0 N_\mathrm{d} \int \boldsymbol{M}\cdot\mathrm{d}\boldsymbol{M} = -\mu_0 \boldsymbol{H}\cdot\boldsymbol{M} + \mu_0 N_\mathrm{d}\frac{M^2}{2} \qquad [27]$$

The first term on the right-hand side is the familiar expression for the Zeeman energy, and can be minimized by aligning the magnetization vector with the external field and maximizing its modulus. The second term is the self-energy of the magnetized body due to the free poles, and can be minimized by minimizing the net magnetization. On the other hand, this term also represents the amount of energy which is stored in the external magnetic field generated by the sample; therefore, if the applied field $\boldsymbol{H}$ equals zero, it can be inferred that in the lowest energy state, the magnetic field generated by the sample must be as small as possible. From the microscopic point of view, the energy balance results from a competition between exchange coupling (which lowers the total energy if two spins are parallel) and the dipole–dipole interaction (which raises the total energy if two spins are parallel). As a result, the sample is divided in several macroscopic regions, each one having uniform magnetization, called domains. Within a single domain, the spins are parallel to one another; in turn, spins belonging to two different domains can have very different directions (Figure 5) in order to minimize the bulk magnetization.

One may naively expect that the subdivision in domains occurs as in Figure 6a (i.e., all the spins belonging to domains A and B are arranged along the easy-axis direction), and that spins belonging to different neighboring domains are antiparallel to one another. This configuration certainly minimizes the anisotropy energy, but at a large cost of exchange energy for the two antiparallel spins situated at the interface. In general, it is less expensive to have the spins arranged as in Figure 6b; the 180° spin rotation is performed in several different steps within a region between domains A and B, known as "Bloch wall." For the sake of clarity, consider the case of a simple cubic crystal with lattice constant a, with a nearest-neighbor exchange constant J and EMD along [1 0 0].

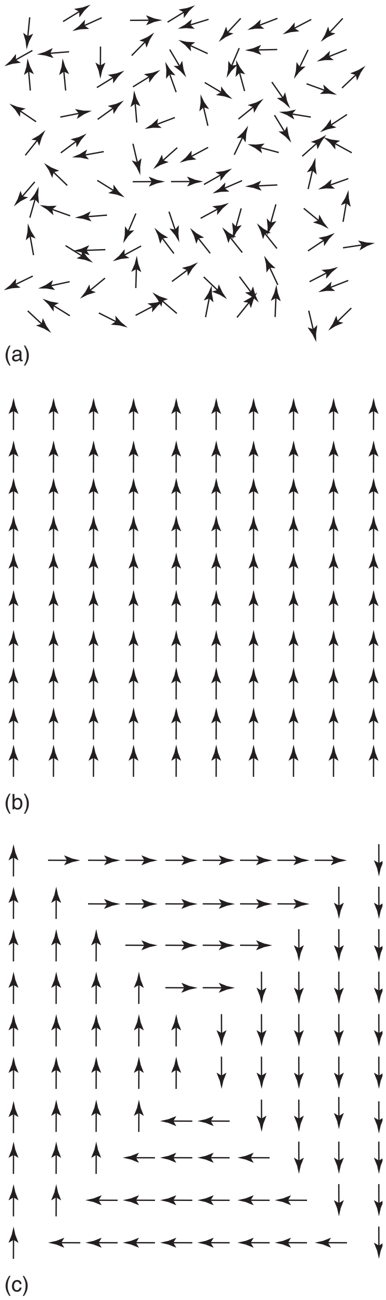

Figure 5 Schematic view of the dipole arrangements in (a) a paramagnet (or ferromagnet above T_C), (b) a magnetized (saturated) ferromagnet, and (c) an unmagnetized ferromagnet (divided into domains). While the moments in the paramagnetic phase are disordered at the atomic level, the domain size is macroscopic (even several hundred micrometers).

The energy balance may be estimated by assuming that the rotation is performed within the *xz*-plane in N equal steps, each of an angle π/N; then the total exchange energy per unit area of the Bloch wall is

$$E_{\mathrm{ex}} = -J\sum_{l=0}^{N} S_l \cdot S_{l+1} = -J\sum_{l=0}^{N} S^2 \cos\frac{\pi}{N} = -JS^2\frac{(N+1)}{a^2}\cos\frac{\pi}{N} \qquad [28]$$

while, according to eqn [18] with $\alpha_y = 1$, $\alpha_z = \cos\theta$, and $\alpha_x = \cos(\pi/2-\theta) = \sin\theta$, the anisotropy energy per area unit is

$$E_{\mathrm{A}} = a\sum_{l=0}^{N} K_1 \sin^2\frac{l\pi}{N}\cos^2\frac{l\pi}{N} = \frac{aK_1}{8}N \qquad [29]$$

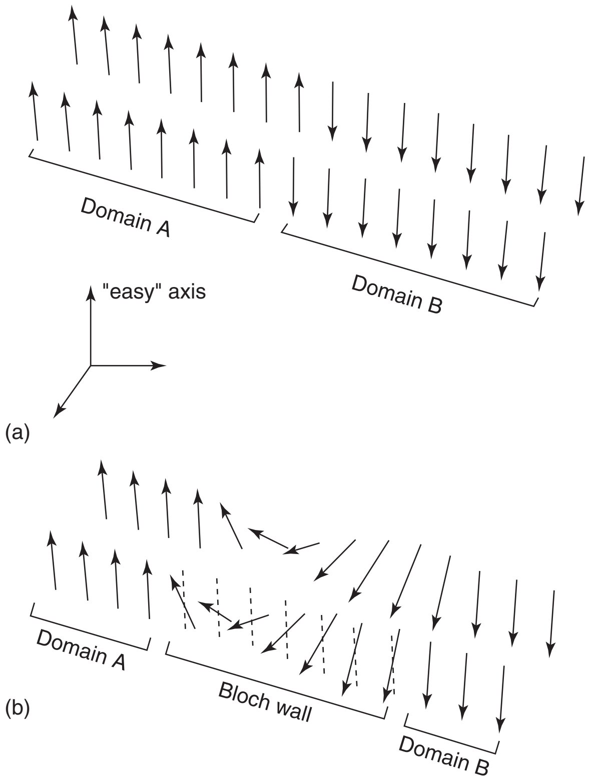

Figure 6 Schematic view of the dipole arrangements at the boundary between two domains (Bloch wall).

(strictly valid for $N > k$). E_{ex} and E_A are opposite in sign, and the absolute value of both grows with N; the actual size of the Bloch wall then results from a competition of the two, being smaller when the anisotropy dominates and larger when the exchange interaction dominates. In the large-N limit $E_{ex} \simeq JS^2\pi^2/(Na^2)$, and minimizing the total energy gives an approximate domain wall width of

$$\ell = Na \simeq 2\pi S\sqrt{\frac{2J}{aK_1}} \qquad [30]$$

typically a few hundred lattice constants for iron.

The Magnetization Curve

From the macroscopic point of view, ferromagnets may be considered at a first glance as magnetic materials with extremely large susceptibility and permeability. In practice, as both of them are strongly dependent not only on the temperature, but also on the applied field and on the past history of the sample, they are not very useful parameters and it is quite simple to describe the physical properties of a ferromagnet by means of $\boldsymbol{M}$ versus $\boldsymbol{H}$ (or $\boldsymbol{B}$ versus $\boldsymbol{H}$, being $\boldsymbol{B} = \mu_0(\boldsymbol{H} + \boldsymbol{M})$) plots, whose main characteristics will be discussed in the following sections.

The Hysteresis Cycle

When an external magnetic field is applied to a ferromagnetic sample in a demagnetized state in order to bring its resulting magnetization to saturation, one obtains the magnetization curve shown in Figure 7. Two distinct and coexistent processes must be considered in order to understand this (Figure 8): boundary motion and domain rotation. In the former case, those domains which are favorably oriented with respect to the applied field grow in size at the expense of the others, without changing their overall magnetization direction; this process is dominant at low fields. At intermediate fields, the process of sudden rotation of the magnetization of unfavorably oriented domains to the easy-axis direction(s) nearest to that of the applied field also becomes significant. At a given value of the magnetic field (labeled H_S), saturation is finally achieved ($M = M_S$, defined in eqn [13]), mainly by coherent rotation of the domain magnetization toward the applied field direction. For $H > H_S$, the $M(H)$ curve is flat since the applied field is already strong enough to align all the elementary dipoles in the sample along its direction.

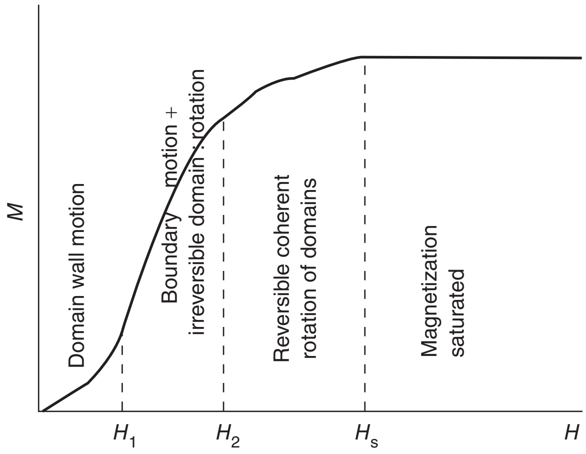

Figure 7 "Virgin" magnetization curve of a ferromagnet. The main mechanisms by which the magnetization process advances for several applied field values are indicated.

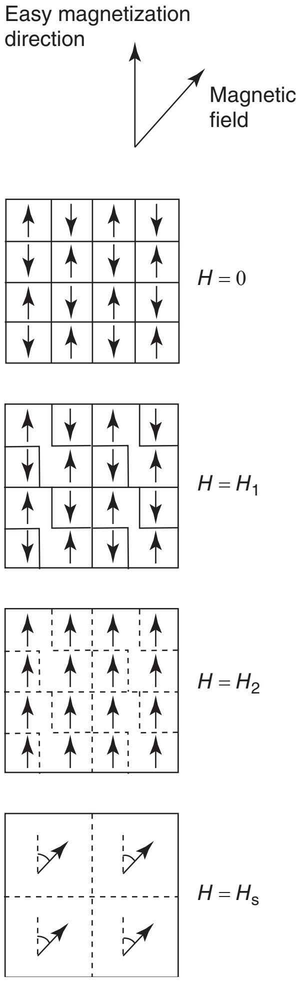

Figure 8 Schematic view of the main mechanisms by which the magnetization process advances for several applied field values.

If the value of the applied field is now reduced to zero, it is noticed that the obtained $M(H)$ curve does not coincide with the previous one apart from a small region near H_S. In particular, the magnetization at zero applied field does not go back to zero (retentivity), and its value M_R is called remanence or remanent magnetization. In order to force the magnetization to zero, it is necessary to apply a magnetic field H_C in the opposite direction; this value is called coercivity or coercive field. (Some authors make use of a distinction between remanence/coercivity (indicating the sample behavior after it has reached saturation) and remanent magnetization/coercive field (relative to a magnetization curve reaching an arbitrary value $M < M_S$).) Raising the reverse field strength to H_S leads to the saturation of the magnetization in the opposite direction as before. Reversing the field once again, one obtains the so-called hysteresis loop (Figure 9).

While "hard" magnetic materials (i.e., those displaying a large coercivity) are generally useful as permanent magnets or for memory-storage purposes (in order to avoid demagnetization due to stray magnetic fields), "soft" ones may be good candidates for the realization of power transformers or electromagnets. In the former case, apart from retentivity, coercivity, and Curie temperature, another figure of merit which is often used in practice is the maximum energy product $BH_{\max}$, which is the maximum value of the product $\boldsymbol{B} \cdot \boldsymbol{H}$ in the demagnetizing quadrant ($M > 0$, $H < 0$) of the hysteresis curve. This corresponds to the energy stored in the considered material within a magnetic circuit operating at an optimized workpoint, and should not be confused with the energy lost due to the irreversible processes during one hysteresis loop, that is,

$$\oint \boldsymbol{B} \cdot \mathrm{d}\boldsymbol{H} \tag{31}$$

Magnetization Rotation and Anisotropy

Most of the energy loss during the hysteresis cycle occurs at low fields as a result of irreversible domain boundary motion, due to inhomogeneous microstrains (dislocations) which obstructs the rotation of the magnetic moments. On the other hand, processes involving domain rotation are governed by a competition between the anisotropy and the Zeeman energy $E_Z = -\mu_0 \boldsymbol{H} \cdot \boldsymbol{M}$. To study the role of anisotropy in determining the shape of the magnetization curve, assume that the boundary motion of domain walls can be achieved with a negligibly small magnetic field. In the case of a uniaxial sample, $M(H)$ can be found by minimizing

$$E_A + E_Z = \sum_n K_n \sin^{2n}\theta - \mu_0 \boldsymbol{H} \cdot \boldsymbol{M} \tag{32}$$

Let θ be the angle between the magnetization vector and the c-axis, which will be considered also as the EMD, for simplicity. If $\boldsymbol{H}$ is applied along the c-axis, both E_A and E_Z are minimized $\boldsymbol{M} \parallel \boldsymbol{H}$ and saturation is reached immediately when the external applied field is equal to the demagnetizing field. If $\boldsymbol{H}$ is applied perpendicularly to the easy-axis, differentiating eqn [32] and knowing that $M = M_S \sin\theta$ leads to

$$HM_S = \sum_n 2nK_n \left(\frac{M}{M_S}\right)^{2n-1} \tag{33}$$

an implicit expression for the magnetization curve. By putting $M = M_S$, one can immediately find

$$H_S = \frac{2}{M_S} \sum_n nK_n \tag{34}$$

and

$$\left.\frac{\mathrm{d}M}{\mathrm{d}H}\right|_{H=0} = \frac{M_S^2}{2K_1} \tag{35}$$

Similar calculations can be made for any other orientations of the field and of the EMD, leading to the remarkable result that, in principle, complete saturation cannot be achieved if $\boldsymbol{H}$ is not parallel to an "extremal" direction (i.e., one which minimizes or maximizes the anisotropy energy).

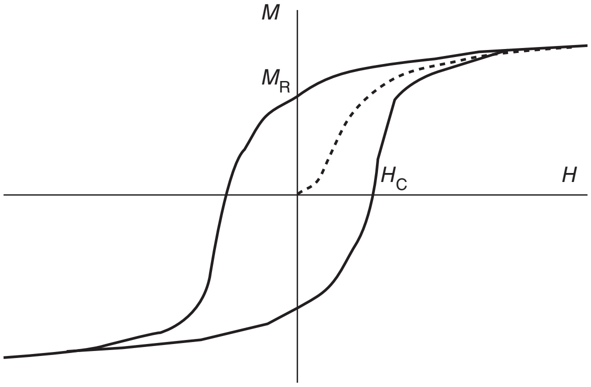

Figure 9 Hysteresis cycle of a ferromagnet. Remanence (M_R) and coercivity (H_C) are indicated on the graph axes.

Further Reading

Ashcroft NW and Mermin ND (1976) *Solid State Physics*. Philadelphia: Saunders College.
Bozorth RM (1951) *Ferromagnetism*. Princeton, NJ: Van Nostrand.
Brailsford F (1966) *Physical Principles of Magnetism*. London: Van Nostrand.
Cullity BD (1972) *Introduction to Magnetic Materials*. Reading, MA: Addison-Wesley.
Hubert A and Schaefer R (1998) *Magnetic Domains*. Berlin: Springer.
Mattis DC (1965) *The Theory of Magnetism*. New York: Harper and Row.

Localized and Itinerant Magnetism

H Yamada[a] **and T Goto**[b], [a]Shinshu University, Matsumoto, Japan; [b]University of Tokyo, Kashiwa, Japan

© 2005 Elsevier Ltd. All rights reserved.

This is an update of H. Yamada, T. Goto, Localized and Itinerant Magnetism, Editor(s): Franco Bassani, Gerald L. Liedl, Peter Wyder, Encyclopedia of Condensed Matter Physics, Elsevier, 2005, Pages 152–160, ISBN 9780123694010, https://doi.org/10.1016/B0-12-369401-9/00517-9.

Introduction **55**
Localized-Electron Model **55**
Ferromagnetism 55
Antiferromagnetism 56
Magnetizing Process of Antiferromagnets 57
Spin Waves 58
Itinerant-Electron Model **59**
Band Theory of Ferromagnetism 60
Description of Ferromagnetism by the Landau Theory 60
Band Theory of Antiferromagnetism 61
Spin Fluctuations 62
Further Reading **63**

Introduction

The quantum theory of magnetism has been developed from two opposite starting points. One is the localized-electron model, where the electrons remain on the atoms in the crystal and contribute to magnetism. The intra-atomic interaction between these electrons is so strong that the magnetic moment is determined on each individual atom by Hund's rules. The interatomic exchange interaction is, on the other hand, much smaller than the intra-atomic one, and competes with thermal disorder to determine the long-range magnetic ordering. This model is applied to insulating crystals and rare-earth metals. The other model of magnetism is based on the band structure of electrons. These electrons move around in the crystal and contribute to the electric conduction. The ferromagnetic state may be stabilized for materials with a strong exchange interaction and a high density of states at the Fermi level. This is the band model or itinerant-electron model, which is commonly applied to 3d transition metals, alloys, and compounds.

In this section, magnetic properties as well as magnetic ordering are discussed for both localized-electron and itinerant-electron models. A molecular field theory is extremely useful in describing the ground state and finite temperature properties. In this approximation, the focus is on how various magnetic properties can be explained, and then, how spin wave excitations and spin fluctuations at finite temperature can be studied. SI units are used in this article. The magnetic induction, $\boldsymbol{B}$, is given by $\mu_0(\boldsymbol{H}+\boldsymbol{M})$, where $\boldsymbol{H}$, $\boldsymbol{M}$, and μ_0 are the magnetic field, magnetization, and permeability in vacuum, respectively. The Bohr magneton is denoted by $\mu_B = e\text{h}/2m$ in this unit system, where e and m are the charge and mass of an electron, respectively, and where h is the Planck constant divided by 2π. To avoid confusion, μ_B is taken to be positive, so that the direction of magnetization is the same as that of the spin.

Localized-Electron Model

The concept of exchange coupling between the spins of two or more nonsinglet atoms arose with the Heitler–London theory of chemical bonding and was applied in 1928 to the theory of ferromagnetism by Heisenberg. The spin Hamiltonian is given by $\mathscr{H} = -\sum_{i\neq j} J_{ij}\mathbf{S}_i \cdot \mathbf{S}_j$, where J_{ij} is the interatomic exchange integral between the electrons on atoms at $\boldsymbol{R}_i$ and $\boldsymbol{R}_j$. $\boldsymbol{S}_i$ and $\boldsymbol{S}_j$ are spin operators on these atoms. The exchange integral J_{ij} comes from the antisymmetric nature of wave functions with respect to the spatial and spin coordinates, and is given by

$$J_{ij} = \frac{e^2}{4\pi\varepsilon_0}\int\int \frac{\psi_j^*(\mathbf{r})\psi_*^i(\mathbf{r}')\psi_i(\mathbf{r})\psi_j(\mathbf{r}')}{|\mathbf{r}-\mathbf{r}'-\mathbf{R}_i+\mathbf{R}_j|} d\mathbf{r}d\mathbf{r}'$$

where $\psi_i(\mathbf{r})$ is the wave function on the atomic site $\boldsymbol{R}_i$. The value of J_{ij} becomes small obviously when $|\mathbf{R}_i-\mathbf{R}_j|$ is large, as $\psi_i(\mathbf{r})$ is localized on the atom at $\boldsymbol{R}_i$ in this model. Here, J_{ij} is assumed to take a constant value, J for the nearest neighbor atomic pair at $\boldsymbol{R}_i$ and $\boldsymbol{R}_j$, and to be zero for other pairs. In this case, the Hamiltonian is written by $\mathscr{H} = -2J\sum_{\langle i,j\rangle}\mathbf{S}_i \cdot \mathbf{S}_j$, where $\langle i, j\rangle$ on the summation denotes the sum over nearest neighbor pairs at $\boldsymbol{R}_i$ and $\boldsymbol{R}_j$.

Ferromagnetism

Before the concept of quantum mechanics had been established, Weiss proposed in 1907 a very successful description of ferromagnetism by introducing a molecular field acting on atomic magnetic moments, which is assumed to be proportional to the net magnetization. The origin of the molecular field is nowadays known to be a quantum mechanical exchange interaction. A material, which consists of the same type of atoms, is considered. When the magnetic field is applied to the z direction (quantized axis of spin), the average value (or expectation value) of the spin operator $\mathbf{S}_i$ has a z component $\langle S_z \rangle$ only. The magnetization is now written as $M = Ng\mu_B \langle S_z \rangle$, where N is the number of atoms in the material, $g = 2$ (g-factor for spin system), and μ_B is the Bohr magneton. The term $\mathbf{S}_i \cdot \mathbf{S}_j$ in the Hamiltonian is approximately written by $\mathbf{S}_i \cdot \mathbf{S}_j \simeq \langle S_z \rangle S_{j,z} + S_{i,z} \langle S_z \rangle - \langle S_z \rangle^2$. One gets, together with the Zeeman energy by the magnetic induction B, $\mathscr{H} \simeq -2zJ\langle S_z \rangle \sum_i S_{i,z} - g\mu_B B \sum_i S_{i,z} + NzJ\langle S_z \rangle^2 = -g\mu_B B_{\text{eff}} \sum_i S_{i,z} + NzJ\langle S_z \rangle^2$, where z is the number of the nearest neighbor atoms in the crystal. Here, J is taken to be positive as the ferromagnetic state is discussed. The effective magnetic field is given by $B_{\text{eff}} = 2zJ\langle S_z \rangle / g\mu_B + B$. The first term $2zJ\langle S_z \rangle / g\mu_B$ corresponds to the molecular field proposed by Weiss. The molecular field coefficient ω, defined by $B_{\text{eff}} = \omega M + B$, is given by $\omega = 2zJ/N(g\mu_B)^2$.

The magnetic quantum number m_S on an atom may take $S, S-1, \ldots, -S$. The average value $\langle S_z \rangle$ is evaluated by the standard statistics as $\langle S_z \rangle = SB_S(g\mu_B S B_{\text{eff}}/k_B T)$ at finite temperature T, where $B_S(x)$ is the Brillouin function defined by

$$B_S(x) = \frac{2S+1}{2S}\coth\left(\frac{2S+1}{2S}x\right) - \frac{1}{2S}\coth\left(\frac{x}{2S}\right)$$

where $x = g\mu_B S B_{\text{eff}}/k_B T$ and k_B is the Boltzmann constant. (In the limiting case of $S = \infty$, $B_S(x)$ becomes the Langevin function, which appears when $S_{i,z}$ is treated as a classical spin vector.) The average value $\langle S_z \rangle$ is obtained as a function of T and B by solving the equation for $\langle S_z \rangle$ self-consistently, as the argument in the Brillouin function contains $\langle S_z \rangle$ itself. Figure 1 shows the calculated result of the magnetization for $S = 5/2$ as a function of T and B. T_C is the Curie temperature where $\langle S_z \rangle$ becomes zero at $B = 0$. The T-dependence of M at $B = 0$ is very weak at low T in this theory, being different from the observed results. At low T, M decreases with increasing T as $T^{3/2}$ by the thermal excitations of spin waves. This is discussed in the subsection, "Spin waves."

The susceptibility $\chi_p(=\mu_0 M/B)$ above T_C is written at high T as $\chi_p = \mu_0 C/(T - T_C)$. This is called the Curie–Weiss law. Here, T_C and C are the Curie temperature and the Curie constant respectively, given by $T_C = 2zJS(S+1)/3k_B$ and $C = N(g\mu_B)^2 S(S+1)/3k_B$. This is derived by using the approximation $B_S(x) \sim x(S+1)/3S$ at small x. At $T = T_C$, M is proportional to $B^{1/3}$. Then, the susceptibility χ_p diverges as $B^{-2/3}$ when B tends to zero. The critical index δ, defined by $M \propto B^{1/\delta}$, is 3 in the molecular field theory. However, the observed result of δ for conventional ferromagnets is ~4. The molecular field theory breaks down at $T \simeq T_C$.

Antiferromagnetism

The crystal, which consists of two equivalent sublattices A and B, may have an antiferromagnetic spin structure when the exchange integral J_{AB} between the nearest neighbor spins on the different sublattices is negative. Sublattice moments are given by $M_A = Ng\mu_B \langle S_z^A \rangle /2$ and $M_B = Ng\mu_B \langle S_z^B \rangle /2$, where the number of atoms on each sublattice is $N/2$. Here, S_z^A and S_z^B are the z components of $\mathbf{S}$ on these sublattices. Magnitudes of M_A and M_B without magnetic fields are equal to M, that is, $M_A = -M_B = M$.

Effective fields acting on the A and B sublattice spins are written by $B_{\text{eff}}^A = -\omega' M_A - \omega M_B + B$ and $B_{\text{eff}}^B = -\omega M_A + \omega' M_B + B$, where ω and ω′ are the molecular field coefficients of inter- and intra-sublattice moments given by $\omega = 4z_{AB}|J_{AB}|/N(g\mu_B)^2$ and $\omega' = 4z_{AA}J_{AA}/N(g\mu_B)^2$. Here, $J_{AA}(=J_{BB})$ is the intra-sublattice exchange integral and z_{AB} and $z_{AA}(=z_{BB})$ are the numbers of the nearest neighbor atoms on the different sublattices and on the same sublattice. By the same procedure as used in the ferromagnetic

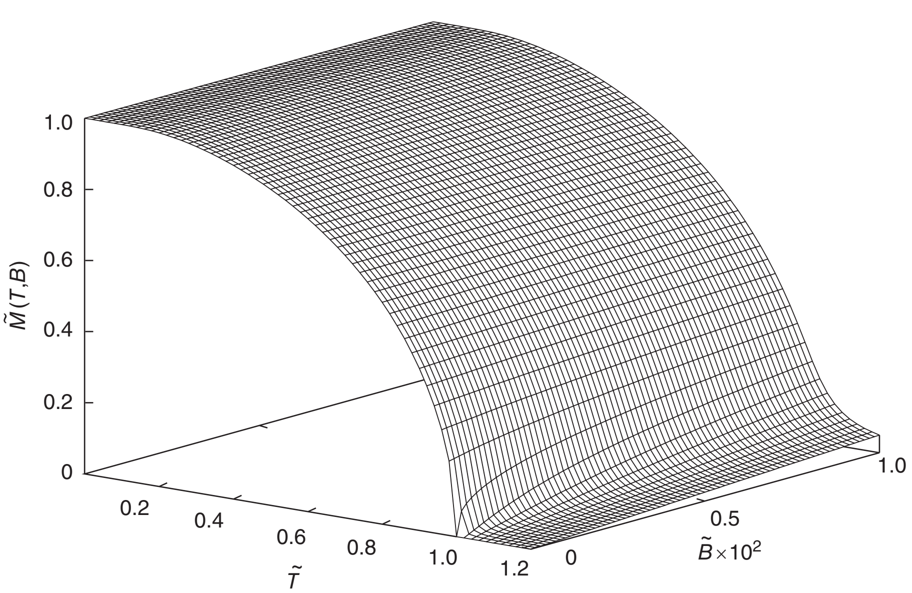

Figure 1 Temperature and field dependences of the magnetization M for $S = 5/2$. $\widetilde{M} = M/Ng\mu_B S$, $\widetilde{T} = T/T_C$ and $\widetilde{B} = g\mu_B B/2zJS$.

case, the thermal averages $\langle S_z^{\mathrm{A}}\rangle$ and $\langle S_z^{\mathrm{B}}\rangle$ are obtained by the Brillouin function as $\langle S_z^{\mathrm{A}}\rangle = SB_S(x_{\mathrm{A}})$ and $\langle S_z^{\mathrm{B}}\rangle = SB_S(x_{\mathrm{B}})$, where $x_{\mathrm{A}} = g\mu_{\mathrm{B}}SB_{\mathrm{eff}}^{\mathrm{A}}/k_{\mathrm{B}}T$ and $x_{\mathrm{B}} = g\mu_{\mathrm{B}}SB_{\mathrm{eff}}^{\mathrm{B}}/k_{\mathrm{B}}T$. The Néel temperature T_{N}, where the sublattice moment at $B = 0$ vanishes, is given by $T_{\mathrm{N}} = 2S(S+1)(z_{\mathrm{AB}}|J_{\mathrm{AB}}|+z_{\mathrm{AA}}J_{\mathrm{AA}})/3k_{\mathrm{B}}$. Solving the simultaneous equations for M_{A} and M_{B}, the susceptibility $\chi_{\mathrm{p}}(T)$ above T_{N} is obtained as $\chi_{\mathrm{p}}(T) = \mu_0C/\left(T+\Theta_{\mathrm{p}}\right)$, where $\Theta_{\mathrm{p}} = 2S(S+1)(z_{\mathrm{AB}}|J_{\mathrm{AB}}|-z_{\mathrm{AA}}J_{\mathrm{AA}})/3k_{\mathrm{B}}$ and $C = N(g\mu_{\mathrm{B}})^2S(S+1)/3k_{\mathrm{B}}$. At $T = T_{\mathrm{N}}, \chi_{\mathrm{p}}(T_{\mathrm{N}})$ is given by $\chi_{\mathrm{p}}(T_{\mathrm{N}}) = \mu_0/\omega$. When $J_{\mathrm{AA}} = 0, T_{\mathrm{N}}$ is equal to Θ_{p}. The observed value of T_{N} for conventional antiferromagnets is smaller than that of Θ_{p}.

Below T_{N}, there are two kinds of susceptibility. One is the susceptibility when the magnetic field is applied along the direction of M_{A}. In this case, M_{A} increases by $\delta M_{\parallel}/2$, and M_{B} shrinks by $\delta M_{\parallel}/2$. $\delta M_{\parallel}$ is obtained by solving simultaneous equations of M_{A} and M_{B} given by the Brillouin functions with $B_{\mathrm{eff}}^{\mathrm{A}}$ and $B_{\mathrm{eff}}^{\mathrm{B}}$. Noting that $M_{\mathrm{A}} = -M_{\mathrm{B}} = M$ at $B = 0$, one gets the susceptibility $\chi_{\parallel}(T)\left(= \mu_0\delta M_{\parallel}/B\right)$ parallel to the sublattice moment as $\chi_{\parallel}(T) = \mu_0C/\{\Theta_{\mathrm{p}}+(S+1)T/3SB_S'(x)\}$, where $x = 6MT_{\mathrm{N}}/Ng\mu_{\mathrm{B}}(S+1)T$ and $B_S'(x)$ is the derivative of $B_S(x)$ with respect to x. At $T = 0, \chi_{\parallel}(0) = 0$ as $\lim_{T\to 0}T/B_S'(x) = \infty$. At $T = T_{\mathrm{N}}, \chi_{\parallel}(T_{\mathrm{N}}) = \chi_{\mathrm{p}}(T_{\mathrm{N}}) = \mu_0/\omega$ as $B_S'(0) = (S+1)/3S$. The other is the susceptibility when the magnetic field is applied in the perpendicular direction to M_{A} and M_{B}. In this case, the induced moment $\delta M_{\perp}/2$ appears on each sublattice in the field direction. The susceptibility $\chi_{\perp}(= \mu_0\delta M_{\perp}/B)$ perpendicular to the sublattice moment is obtained by the balance of effective fields shown in Figure 2. The sublattice moments rotate by an angle θ so that $\mathbf{B}-\omega(\mathbf{M}_{\mathrm{A}}+\mathbf{M}_{\mathrm{B}}) = 0$. One gets $\chi_{\perp} = \mu_0/\omega$, which does not depend on T and also on the value of ω'. In Figure 3, $\chi_{\parallel}(T)$ and $\chi_{\perp}(T)$ below T_{N}, and $\chi_{\mathrm{p}}(T)$ above T_{N} are shown as a function of T for $S = 5/2$ and $\omega' = 0$. For polycrystalline or powder samples, the antiferromagnetic moments in domains or particles will orientate in random directions, so that $\chi(T) = \chi_{\parallel}(T)/3+2\chi_{\perp}(T)/3$ below T_{N}.

Magnetizing Process of Antiferromagnets

For the magnetizing process of antiferromagnets, magnetic anisotropy plays an important role. The magnetic moment prefers to align in a certain crystallographic direction without a magnetic field. For the sake of simplicity, consider the case of uniaxial anisotropy. Taking the easy axis of magnetization along the z-axis, the sublattice moment $\boldsymbol{M}_{\mathrm{A}}$ prefers to align in the positive (negative) z direction and $\boldsymbol{M}_{\mathrm{B}}$ in the negative (positive) z direction. The anisotropy energy is phenomenologically given by $E_{\mathrm{ani}} = -(K_{\mathrm{u}}/2)(\cos^2\theta_{\mathrm{A}}+\cos^2\theta_{\mathrm{B}})$, where θ_{A} and θ_{B} are angles between the sublattice moments and the easy axis. The coefficient K_{u} is called the uniaxial anisotropy constant. The anisotropy fields, $B_{\mathrm{ani}}^{\mathrm{A}}$ and $B_{\mathrm{ani}}^{\mathrm{B}}$ acting on the A and B sublattice moments, are defined by $B_{\mathrm{ani}}^{\mathrm{A}} = K_{\mathrm{u}}M_A^z/M^2$ and $B_{\mathrm{ani}}^{\mathrm{B}} = K_{\mathrm{u}}M_B^z/M^2$.

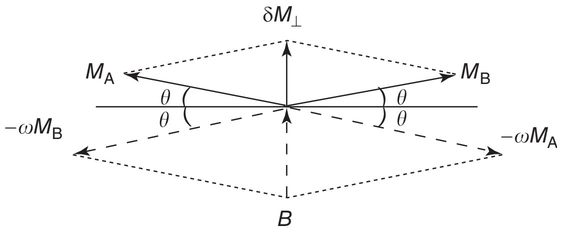

Figure 2 Magnetic induction B of the applied field and molecular fields $-\omega M_{\mathrm{A}}$ and $-\omega M_{\mathrm{B}}$ on the sublattice moments M_{A} and M_{B}, respectively. $\delta M_{\perp}$ is the induced moment.

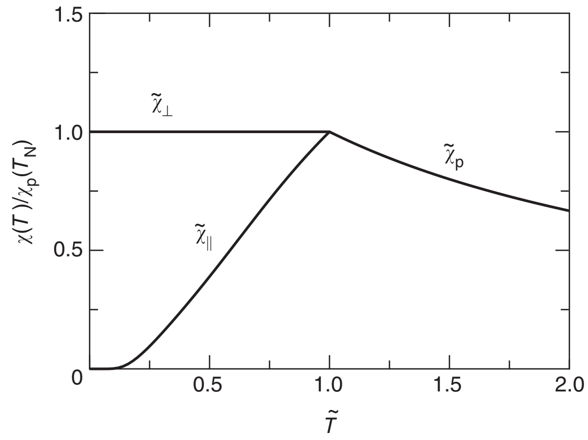

Figure 3 Parallel and perpendicular susceptibilities $\tilde{\chi}_{\parallel}(\tilde{T})$ and $\tilde{\chi}_{\perp}(T)$ below T_{N}, and of $\tilde{\chi}_p(T)$ above T_{N} for $S = 5/2$ and $\omega' = 0$. $\tilde{\chi}_{\parallel}(T) = \chi_{\parallel}(T)/\chi_{\mathrm{p}}(T_{\mathrm{N}})$, $\tilde{\chi}_{\perp}(T) = \chi_{\perp}(T)/\chi_{\mathrm{p}}(T_{\mathrm{N}})$, $\tilde{\chi}_p(T) = \chi_{\mathrm{p}}(T)/\chi_{\mathrm{p}}(T_{\mathrm{N}})$, and $\tilde{T}T/T_{\mathrm{N}}$.

The induced moment $\delta M_{\perp}$ by the field applied perpendicular to the z-axis (hard axis of magnetization) is suppressed by the anisotropy field. The susceptibility $\chi_{\perp}$ is given by $\chi_{\perp} = \mu_0/\left(\omega + K_u/2M^2\right)$. This is derived in the following way. E_{ani} is rewritten as $(K_u/2)\left(\sin^2\theta_A + \sin^2\theta_B\right) - K_u$. The anisotropy field to the hard axis of magnetization is written by $-K_u\delta M_{\perp}/2M^2$ (negative field), and then one can get the above expression of $\chi_{\perp}$. On the other hand, when the magnetic field is applied along the easy axis of magnetization and when the sublattice moments align in the hard axis, the induced moment $\delta M_{\perp}$ in the field direction is enhanced by the anisotropy field. The susceptibility, in this case, is written by $\chi'_{\perp} = \mu_0/(\omega - K_u/2M^2)$.

When the magnetic field is applied along the easy axis of magnetization, the magnetic energy together with E_{ani} is approximately given by $\Delta E_{\parallel} = -\chi_{\parallel}(T)B^2/2\mu_0 - K_u$ at low fields. On the other hand, when the magnetic field is applied along the easy axis of magnetization and when the sublattice moments align in the hard axis, the magnetic energy is given by $\Delta E_{\perp} = -\chi'_{\perp}(T)B^2/2\mu_0$. At weak magnetic fields applied along the direction of the easy axis, the sublattice moments keep to align in the easy axis by the gain of the anisotropy energy. However, under strong magnetic fields they may align in the direction perpendicular to the magnetic field, as $\chi'_{\perp}$ is larger than $\chi_{\parallel}$, and then, $\Delta E_{\perp}$ becomes lower than $\Delta E_{\parallel}$. That is, a spin flipping takes place from the parallel direction to B to the perpendicular one at a certain magnetic field. The critical value B_{sf} of the spin flipping is given by the equation $\Delta E_{\parallel} = \Delta E_{\perp}$, and one obtains $B_{\text{sf}}(T) = \left[2\mu_0 K_u/\left\{\chi'_{\perp}(T) - \chi_{\parallel}(T)\right\}\right]^{1/2}$. At $T = 0$, B_{sf} is written by $B_{\text{sf}} = \left\{B_{\text{ani}}(2B_{\text{ex}} - B_{\text{ani}})\right\}^{1/2}$, where $B_{\text{ex}} = \omega M$ and $B_{\text{ani}} = K_u/M$. When $B > 2B_{\text{ex}} - B_{\text{ani}}$, the sublattice moments become parallel to each other. The critical value is denoted by $B_c(= 2B_{\text{ex}} - B_{\text{ani}})$. The spin structures are the antiferromagnetic one at $B < B_{\text{sf}}$, the canted one at $B_{\text{sf}} < B < B_c$, and the ferromagnetic one at $B > B_c$. When T increases, B_c decreases, while B_{sf} increases slightly, as shown in Figure 4.

When B_{ani} is larger than B_{ex}, the canted spin state does not appear. The magnetization curve at $T = 0$ shows a jump from the antiferromagnetic state to the ferromagnetic one at $B = B_{\text{ex}}$. This is a field-induced metamagnetic transition. However, the transition at finite T becomes gradual at B_{ex}, as shown in Figure 5. When the magnetic field is applied to the hard axis of magnetization, the induced moment $\delta M_{\perp}$ increases as $\chi_{\perp}B/\mu_0$ up to $B'_C = 2B_{\text{ex}} + B_{\text{ani}}$ and saturates to $2M$.

Spin Waves

The low-lying energy states of spin systems coupled by exchange interactions are wave-like, as originally discussed by Bloch. This is called a spin wave or a magnon. Spin waves have been studied for all types of ordered spin arrays. In this subsection, the ferromagnetic spin wave is studied.

The energy associated with nonuniform distributions of the spin direction is given by the Heisenberg exchange energy $W = -J\sum_i\sum_\delta \mathbf{S}_i \cdot \mathbf{S}_{i+\delta}$, where $\boldsymbol{\delta}$ is the nearest neighbor vector of $\boldsymbol{R}_i$. Here, the Ss are quantum mechanical spin operators. They are treated as if they were classical vectors. $\mathbf{S}_{i+\delta}$ is expanded in a Taylor series as $\mathbf{S}_i + (\delta \cdot \nabla)\mathbf{S}_i + (1/2)(\delta \cdot \nabla)^2\mathbf{S}_i$. For lattices with inversion symmetry, the first-order term in $\boldsymbol{\delta}$ is cancelled out by the summation over δ, and one gets $W = -J\sum_i|\mathbf{S}_i|^2 - (J/2)\sum_i\sum_\delta \mathbf{S}_i \cdot \left\{(\delta \cdot \nabla)^2\mathbf{S}_i\right\}$. It is noted here that $\nabla^2(\mathbf{S}_i \cdot \mathbf{S}_i) = 0$, as $|\mathbf{S}_i|^2$ is a constant. Then, one can get the exchange energy for the local magnetization $\mathbf{M}(\mathbf{r}) = g\mu_B\sum_i \mathbf{S}_i\delta(\mathbf{r} - \mathbf{R}_i)$ as $E_{\text{ex}} = (1/2V)D\int|\nabla\mathbf{M}(\mathbf{r})|^2 d\mathbf{r}$, where $|\nabla\mathbf{M}(\mathbf{r})|^2 = \sum_\alpha\left\{(\partial M_\alpha/\partial x)^2 + (\partial M_\alpha/\partial y)^2 + (\partial M_\alpha/\partial z)^2\right\}$, $\alpha = x, y, z$, and V the volume of the sample. The coefficient D in E_{ex} is called the Landau–Lifshitz constant. The exchange field is defined by $\mathbf{B}_{\text{ex}}(\mathbf{r}) = \partial E_{\text{ex}}/\partial\mathbf{M}(\mathbf{r})$. Neglecting the boundary effects, one gets $\mathbf{B}_{\text{ex}}(\mathbf{r}) = D\nabla^2\mathbf{M}(\mathbf{r})$. Then, the torque equation is given by

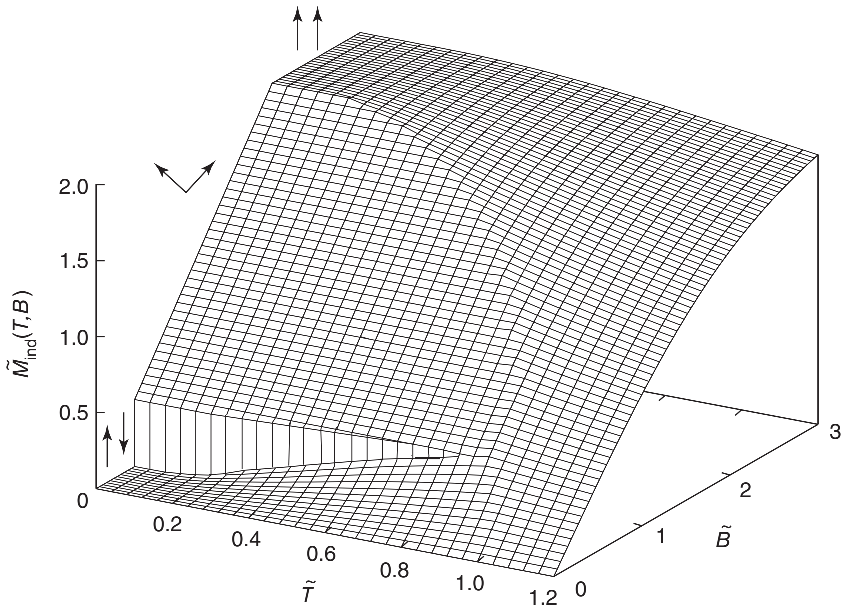

Figure 4 Temperature and field dependences of the induced moment M_{ind} for $S = 5/2$, $\omega' = 0$, and $2K_u/Nz_{AB}|J_{AB}|S^2 = 0.2$. $\widetilde{M}_{\text{ind}} = 2M_{\text{ind}}/Ng\mu_B S$, $\widetilde{T}T/T_N$, and $\widetilde{B}g\mu_B B/2z_{AB}|J_{AB}|S$.

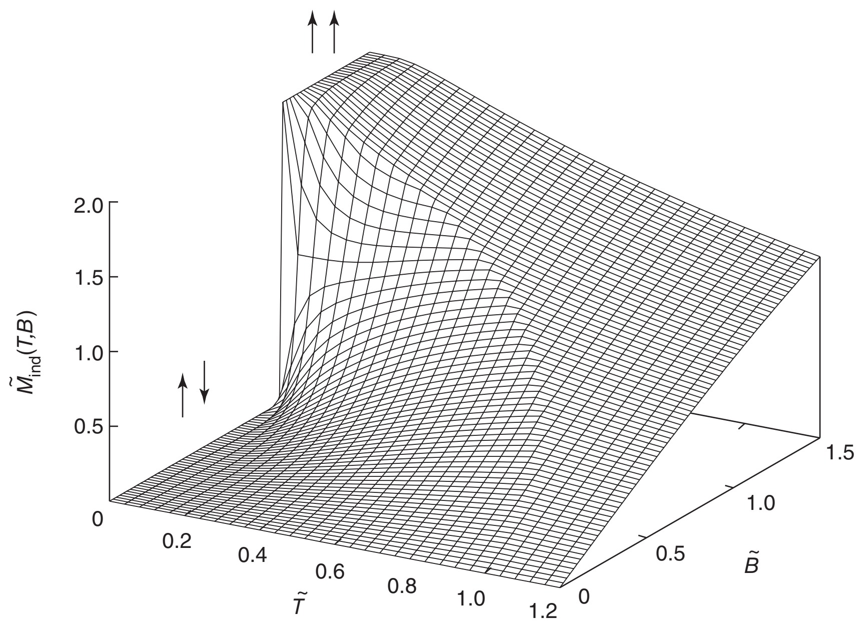

Figure 5 Temperature and field dependences of the induced moment M_{ind} for $S = 5/2$ and $\omega' = 0$ for the case of the strong anisotropic field ($B_{\mathrm{ani}} > B_{\mathrm{ex}}$). $\widetilde{M}_{\mathrm{ind}} = 2M_{\mathrm{ind}}/Ng\mu_{\mathrm{B}}S, \widetilde{T}T/T_{\mathrm{N}}$, and $\widetilde{B}g\mu_{\mathrm{B}}B/2z_{\mathrm{AB}}|J_{\mathrm{AB}}|S$.

$\partial\mathbf{M}(\mathbf{r},t)/\partial t = \gamma D\mathbf{M}(\mathbf{r},t)\nabla^2\mathbf{M}(\mathbf{r},t)$, where γ is the gyromagnetic ratio $g\mu_{\mathrm{B}}/\mathrm{h}$. One looks for travelling wave solutions of the form $M_x(\mathbf{r},t) = \delta m_x \exp\{i(\mathbf{q}\cdot\mathbf{r}-\omega t\}$, $M_y(\mathbf{r},t) = \delta m_y \exp\{i(\mathbf{q}\cdot\mathbf{r}-\omega t\}$ and $M_z \simeq M_{\mathrm{s}}$. One gets $\mathrm{h}\omega_q = g\mu_{\mathrm{B}}DM_{\mathrm{s}}q^2$ for small q. The coefficient of q^2 is called the exchange stiffness constant, which is observed by neutron scattering and spin wave resonance measurements. A schematic representation of $\mathbf{M}(\mathbf{r},t)$ at a fixed time t is shown in Figure 6.

The wave of local magnetization, that is, the spin wave is quantized. By the analogy with phonons, the Hamiltonian for the quantized spin wave (magnon) is written by $\mathscr{H} = \sum_q (n_q+1/2)\hbar\omega_q$, where n_q is the occupation quantum number of magnons with the wave-number vector $\boldsymbol{q}$. The temperature dependence of the magnetization is given by $M(T) = M_{\mathrm{s}}-2\mu_{\mathrm{B}}\sum_q\langle n_q\rangle$, where M_{s} is the spontaneous magnetization and the thermal average $\langle n_q\rangle$ is a Bose distribution function $\{\exp(\mathrm{h}\omega_q/k_{\mathrm{B}}T)-1\}^{-1}$. One obtains $\Delta M(T) = M_{\mathrm{s}}-M(T)\propto T^{3/2}$ at low temperature where $\hbar\omega_q$ is proportional to q^2. The theory of spin waves is also established in the itinerant-electron model of magnetism.

Itinerant-Electron Model

A quantum theory of ferromagnetism of conduction electrons in metals began with Bloch's paper in 1929. A free-electron gas with sufficiently low density was shown to be ferromagnetic. This means that the carriers of the magnetic moment in metals also participate in electric conductions. In 1933, Stoner pointed out that nonintegral values of the observed magnetic moment per atom

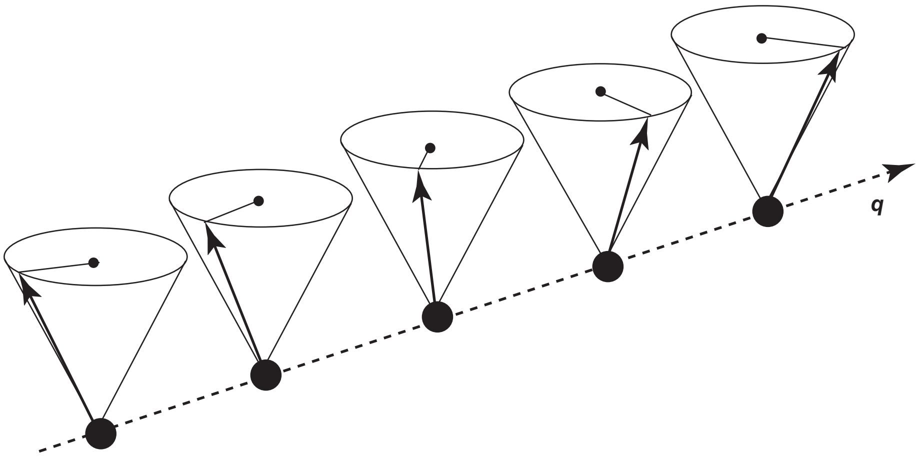

Figure 6 Schematic representation of the spin wave with wave-number vector $\boldsymbol{q}$.

in 3*d* transition metals is explained if 3*d* electrons are itinerant, having a suitable density of states (DOS) and an exchange interaction parameter. Slater discussed ferromagnetism of Ni metal, using calculated results of the electronic structure and estimating the exchange couplings between electrons from spectroscopic data.

The subsequent development of itinerant-electron magnetism has proceeded mainly along two lines. One is the study on refinements of the electronic structure. The other is the study on the interaction between electrons. For both studies, electron correlations make the problem difficult. In the former, the electron correlations are taken into account in the potential of the electrons. A local spin-density functional formalism for the band calculation is established. Ferromagnetic, antiferromagnetic, and spin-density wave states are discussed for real materials by this formalism. In the latter, the interaction between electrons is treated as a many-body problem. To discuss the electron correlations, the Hubbard Hamiltonian is often made use of.

Band Theory of Ferromagnetism

The band theory (or Stoner theory) is widely used in the study of magnetism for transition metals, alloys, and compounds. In the original paper of Stoner, the DOS of electrons is assumed to be a parabolic one with respect to the energy. However, the DOS for actual transition metals is not so simple, but has a lot of peaks, as many energy levels overlap with one another. Figure 7 denotes the calculated DOS curve for a b.c.c. Fe metal in the nonmagnetic state at the lattice constant 28.5 nm. E_F denotes the Fermi level. Electrons occupy energy levels up to E_F.

The Pauli spin susceptibility is written in terms of the DOS curve, $D(E)$, as $\chi_0(T) = 2\mu_0\mu_\mathrm{B}^2[D_0 - (\pi^2 k_\mathrm{B}^2 T^2/6)\{D_0'^2/D_0 - D_0'\}]$ at low T, where D_0, D_0' and D_0'' are the values of $D(E)$ at E_F and the first and second derivatives of $D(E)$ with respect to E at E_F, respectively. The T-dependence comes from the low temperature expansion of the integrals connected with the Fermi distribution function. One takes into account the exchange interaction by the molecular field approximation. The induced magnetic moment, M, by the external field is given by $M = \chi_0(T)(B+IM)/\mu_0$, where I is the molecular field coefficient. Then, the susceptibility $\chi(T)(=\mu_0 M/B)$ is obtained as $\chi(T) = \chi_0(T)/\{1 - I\chi_0(T)/\mu_0\}$. The factor $1/\{1 - I\chi_0(T)/\mu_0\}$ is the exchange-enhancement factor of the susceptibility. When the value of I is so large that the denominator in the enhancement factor becomes zero, the susceptibility $\chi(T)$ diverges. This is the magnetic instability in the paramagnetic state, which is called the Stoner condition for the appearance of ferromagnetism.

When $I\chi_0(0)/\mu_0 > 1$, the ferromagnetic state is stable at $T = 0$. In this case, the Curie temperature T_C is obtained by $I\chi_0(T_\mathrm{C})/\mu_0 = 1$. In the native Stoner theory, the value of I is an adjustable parameter to fit the Curie temperature. However, the value of I is nowadays obtained by the local spin-density functional formalism of the band calculation. The value of T_C estimated with the calculated value of I is much larger than the observed one, although reasonable values of the magnetic moment for 3*d* transition metals are obtained. This is because the effect of spin fluctuations at finite temperature is not taken into account in the theory.

Description of Ferromagnetism by the Landau Theory

By the fixed-spin-moment method developed recently, the magnetic energy $\Delta E(M)$ can be calculated numerically as a function of the magnetic moment M. The open circles in Figure 8 denote the calculated results of $\Delta E(M)$ for a b.c.c. Fe metal at the lattice constant 28.5 nm. The equilibrium state is achieved at $M \sim 2.2\mu_\mathrm{B}$ per Fe atom, being very close to the observed one. The calculated $\Delta E(M)$ can be fitted in the form of $\Delta E(M) = (a_0/2)M^2 + (b_0/4)M^4$, as shown by the dotted curve in the figure. This is just the Landau expansion of the magnetic energy. For some materials, the calculated $\Delta E(M)$ is expanded up to much higher order terms of M.

The Landau coefficients a_0 and b_0 are also obtained by the Stoner theory. At $T = 0$, they are written by $a_0 = [1/2D_0 - I]/\mu_0\mu_\mathrm{B}^2$, and $b_0 = [\{3D_0'^2/D_0^2 - D_0''/D_0\}/48D_0^3]/\mu_0\mu_\mathrm{B}^4$. These expressions of a_0 and b_0 are derived by a rather crude approximation of the rigid band

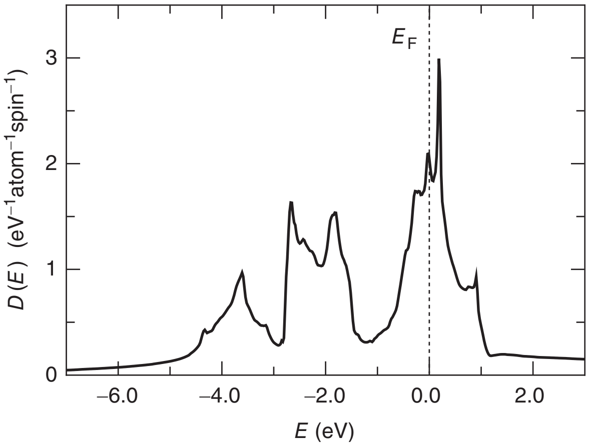

Figure 7 DOS curve for a b.c.c. Fe metal in the nonmagnetic state. E_F denotes the Fermi level. The value of D_0 is 2.05 eV^{-1} atom^{-1} spin^{-1}. The unit of energy 1 eV is 1.602×10^{-19} J.

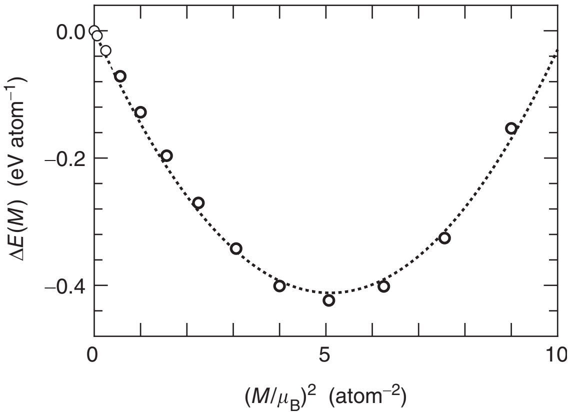

Figure 8 Magnetic energy $\Delta E(M)$ as a function of M^2 for a b.c.c. Fe metal. The unit of energy 1 eV is 1.602×10^{-19} J. The dotted curve denotes the form of $\Delta E(M) = (a_0/2)M^2+(b_0/4)M^4$ with $a_0 = -5.5910^3 \text{Tatom}\mu_B^{-1}$ and $b_0 = 1.10 \times 10^3 \text{Tatom}^3\mu_B^{-3}$.

model, where DOS curves in the up and down spin bands are assumed not to change their shapes from those in the paramagnetic state. Nevertheless, those expressions of a_0 and b_0 are still relevant. When E_F lies near a peak of the DOS, $D_0' \sim 0$, and $D_0'' < 0$, the value of b_0 is positive at 0 K. On the other hand, when E_F lies near a minimum of the DOS, $D_0' \sim 0$, and $D_0'' > 0$, b_0 is negative. Even if D_0 is so small that the Stoner condition is not satisfied, the ferromagnetic state would be stabilized when the value of b_0 is negative and large. In the case of $a_0 > 0$ and $b_0 < 0$, a magnetic field-induced metamagnetic transition from the paramagnetic state to the ferromagnetic one may take place. This is the itinerant-electron metamagnetism. Moreover, the value of I can be estimated from the calculated values of a_0 and D_0. The evaluated value of I is 0.57 eV atom for a b.c.c. Fe metal at the lattice constant 28.5 nm.

The magnetic equation of state is given by $B = a_0M+b_0M^3$, as $B = \partial\Delta E(M)/\partial M$. The spontaneous magnetic moment M_s at $B = 0$ is given by $M_s = (|a_0|/b_0|)^{1/2}$ if $a_0 < 0$ and $b_0 > 0$. It is noted that the magnetic moment in this theory increases with increasing B even at $T = 0$. The differential susceptibility $\chi_{hf}(= \mu_0 dM/dB)$ is finite $(2\mu_0|a_0|)$ at $T = 0$. This is the high-field susceptibility in the ferromagnetic state. In the localized electron model, χ_{hf} vanishes at $T = 0$. The finite value of χ_{hf} at $T = 0$ is one of the characteristics of the itinerant-electron model.

Band Theory of Antiferromagnetism

An antiferromagnetic state in the itinerant-electron model can also be described by the electronic structure. For the sake of simplicity, consider a 1D lattice, where atoms are arranged along the x direction with a lattice constant a. The wave function $\phi_k(x)$ in the nonmagnetic state is given by a Bloch function in the periodic potential by the ions. The one-electron energy $\varepsilon(k)$ is expressed with the wave number k. The wave numbers are restricted to the first Brillouin zone $(-\pi/a < k \leqslant \pi/a)$. A schematic representation of $\varepsilon(k)$ is shown by the solid curve in Figure 9a.

When the antiferromagnetic moment is given by $M_Q(x) = M_0\exp(iQx)$, where $Q = \pi/a$, the potential of electrons includes a term with the modulation of the wavelength $2a$. This modulated potential is treated by the perturbation theory of quantum mechanics. The wave function $\psi_k(x)$ in the antiferromagnetic state is given by a linear combination of the unperturbed wave functions $\varphi_k(x)$ and $\varphi_{k+Q}(x)$, as $\psi_k(x) = \alpha_k\varphi_k(x)+\beta_k\varphi_{k+Q}(x)$ with $|\alpha_k|^2+|\beta_k|^2 = 1$. One gets two energy curves $E_\pm(k) = (1/2)\left[\varepsilon(k)+\varepsilon(k+Q) \pm \left\{(\varepsilon(k)-\varepsilon(k+Q))^2+\Delta^2\right\}^{1/2}\right]$, where Δ is the off-diagonal matrix element of the perturbed potential. The broken curve in Figure 9a denotes $\varepsilon(k+Q)$. The two energy curves cross each other at $k = \pm Q/2$. A bandgap Δ appears at the crossing point, as shown in Figure 9b. The lower energy band $E_-(k)$ is that for electrons with up spin at the up-spin sites, or for

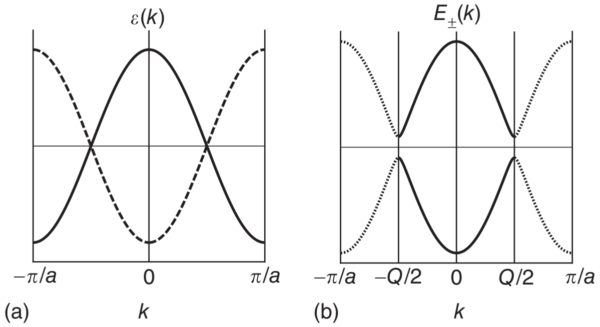

Figure 9 (a): One-electron energy $\varepsilon(k)$ in the nonmagnetic state, and (b): $E_\pm(k)$ in the antiferromagnetic state. A thin horizontal line denotes the Fermi energy.

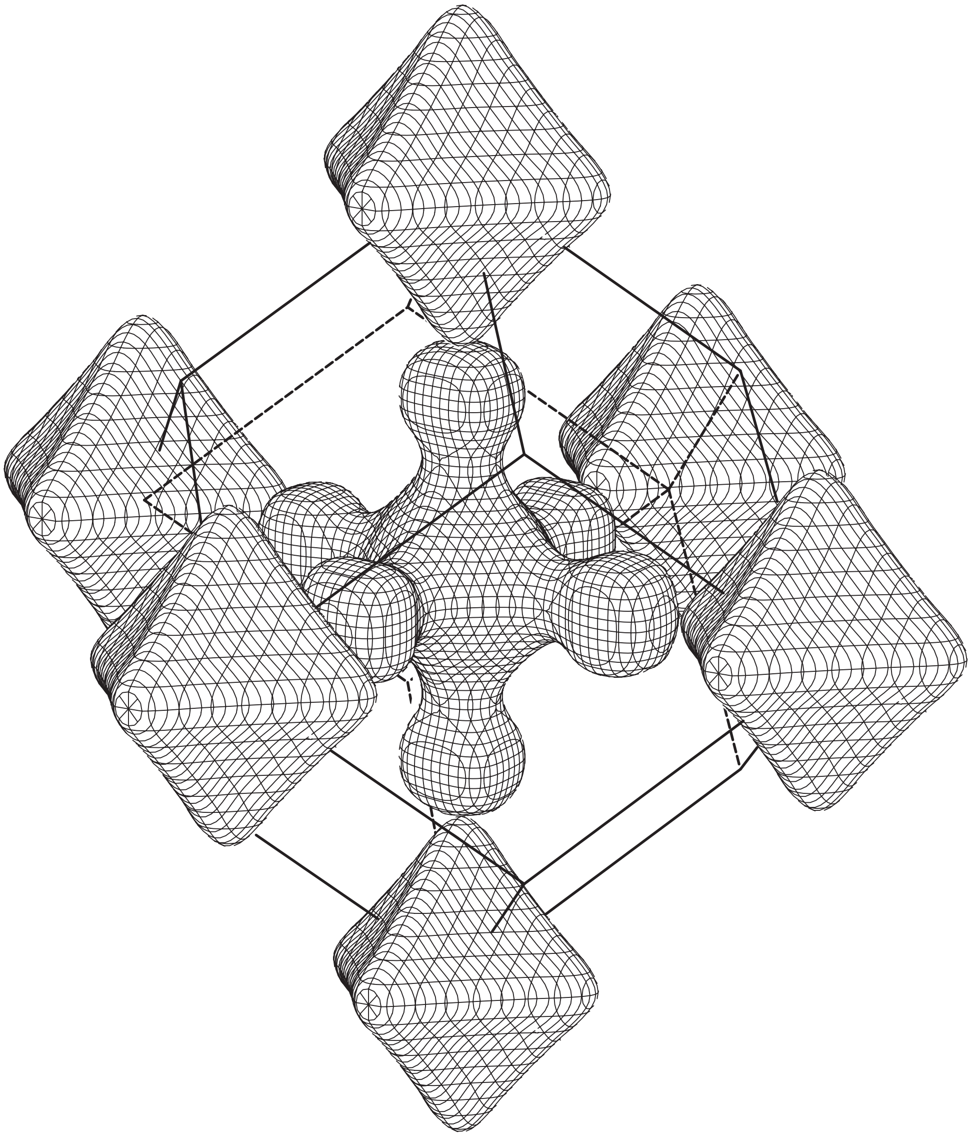

Figure 10 Main parts of the Fermi surfaces of Cr metal. The hole surface (octahedron-like) is located around H in the Brillouin zone. The surface centered at Γ (center of the Brillouin zone) is for electrons (K Nakada, unpublished work).

electrons with down spin at the down-spin sites. The higher energy band $E_+(k)$ is that for electrons with opposite spin at the up and down spin sites. This is a simple mechanism for the appearance of the antiferromagnetic state in the band theory. It is called the split band model of antiferromagnetism.

In actual materials, the situation becomes more complicated. In Figure 10, the calculated Fermi surfaces of Cr metal in the nonmagnetic state are shown. A Fermi surface denotes the equal energy surface in the reciprocal lattice space at the Fermi level. A hole surface has the octahedron-like shape centered at the H-point in the Brillouin zone and the electron surface is centered at the Γ-point (center of the Brillouin zone). Here, H and Γ are conventional symbols labeled to the symmetry points in the Brillouin zone. When the electron surface centered at Γ is shifted toward H, some portions of the electron and hole surfaces may overlap with one another. On these overlapping surfaces, the bandgap appears and the antiferromagnetic state is stabilized. Strictly speaking, the shift of the electron surface is not exactly the same as the length between the Γ- and H-points in this case. The antiferromagnetic wave-number vector $\boldsymbol{Q}$ is slightly different from that at the H-point. Then, the spin-density wave state is stabilized in the Cr metal. This is the nesting model of the Fermi surfaces.

Spin Fluctuations

As mentioned in the section, "Band theory of ferromagnetism," the value of T_C, estimated by the calculated value of I, becomes rather higher than the observed one. This is because the excitations of the collective modes of spins are not taken into account in the theory. The excitations of collective modes play an important role in the magnetic properties at finite temperature. In this subsection, it is studied within the phenomenological Ginzburg–Landau theory.

The magnetic free energy ΔF_m is written by $\Delta F_m = (1/V)\int d\mathbf{r}\Delta f_m(\mathbf{r})$, where the free energy density $\Delta f_m(\mathbf{r})$ is given by $\Delta f_m(\mathbf{r}) = (a_0/2)|\mathbf{m}(\mathbf{r})|^2+(b_0/4)|\mathbf{m}(\mathbf{r})|^4+(D/2)|\nabla\cdot\mathbf{m}(\mathbf{r})|^2$. D is the Landau–Lifshitz constant given in the section "Spin waves." ΔF_m is rewritten by using the Fourier transformation for the ith component of the magnetization density, $m_i(\mathbf{r}) = M\delta_{i,z}+(1/V)\sum_q' m_i(\mathbf{q})\exp(i\mathbf{q}\cdot\mathbf{r})$, where M is the bulk moment in the z direction. The prime on the summation denotes the sum over q except $q = 0$. The expression of ΔF_m contains terms up to the fourth power of $m_i(\mathbf{q})$. Among them, only the terms with even power of $m_i(\mathbf{q})$ are considered. In this case, ΔF_m is given by a functional of only M and $|m_i(\mathbf{q})|^2$.

The equation of state, defined by $B = \langle\partial\Delta F_m/\partial M\rangle$, is written as $B = a(T)M+b(T)M^3$, where $\langle\cdots\rangle$ denotes a thermal average. The Landau coefficients $a(T)$ and $b(T)$ are given by $a(T) = a_0+b_0\{3\langle(\delta m_\parallel)^2\rangle+2\langle(\delta m_\perp)^2\rangle\}$ and $b(T) = b_0$. $\langle(\delta m_\parallel)^2\rangle$ and $\langle(\delta m_\perp)^2\rangle$ are mean square amplitudes of the longitudinal and transverse magnetization densities given by $\langle(\delta m_i)^2\rangle = (1/V)\sum_q\langle|m_i(\mathbf{q})|^2\rangle$. The T-dependence of the Landau coefficients comes from that of the mean square amplitudes of spin fluctuations $\xi(T)^2 = \langle(\delta m_\parallel)^2\rangle+2\langle(\delta m_\perp)^2\rangle$. Isotropic spin fluctuations are assumed, that is, $\langle(\delta m_\parallel)^2\rangle = \langle(\delta m_\perp)^2\rangle$. In this case, the Landau coefficients are given by $a(T) = a_0+(5/3)b_0\xi(T)^2$ and $b(T) = b_0$. The present T-dependence of the Landau coefficients is very different from that in the Stoner theory where it comes only from the Fermi distribution function. The degeneracy temperature for electrons estimated from the Fermi level is very high, and then the T-dependence in the Stoner theory is very weak in the conventional ferromagnets. Thus, the spin fluctuations are found to play a dominant role at finite T.

In the case of $a_0 < 0$ and $b_0 > 0$, the Curie temperature is given by $\xi(T_C)^2 = 3|a_0|/5b_0$ as the inverse of the susceptibility should be zero at T_C, that is, $a(T_C) = 0$. By classical thermodynamics, the mean square amplitude of thermal fluctuations is known to increase monotonically as T increases. The susceptibility (at $\xi(T)^2 = pT$) above T_C is written in the form of the Curie–Weiss law as $\chi(T) = \mu_0 C/(T-T_C)$, where $C = 3/5b_0p$, $T_C = 3|a_0|/5b_0p$, and p a positive constant. Such a Curie–Weiss law cannot be obtained in the Stoner model. By analogy with the localized-electron model, the square of the effective magnetic moment M_p^2 in the paramagnetic state, estimated from the susceptibility, is proportional to the Curie constant C. On the other hand, the square of the spontaneous magnetization is given by $M_s^2 = |a_0|/b_0$ at $T = 0$. Then, the value of $(M_p/M_s)^2$ is shown to be proportional to $|a_0|^{-1}$, and subsequently to T_C^{-1}. This type of behavior of M_p/M_s is observed for $3d$ transition metals, alloys, and compounds (Rhodes–Wohlfarth plot). Spin fluctuations in itinerant-electron antiferromagnets have also been studied.

Further Reading

Arrott A (1966) Antiferromagnetism in metals and alloys. In: Rado GT and Shul H (eds.) *Magnetism*, vol. II B, pp. 295–416. New York: Academic Press.

Bozorth RM (1951) *Ferromagnetism*. New York: Van Nostrand.

Chikazumi S (1964) *Physics of Magnetism*. New York: Wiley.

Gautier F (1982) Itinerant magnetism. In: Cyrot M (ed.) *Magnetism of Metals and Alloys*. Amsterdam: North-Holland.

Herring C (1966) Exchange interactions among itinerant electrons. In: Rado GT and Shul H (eds.) *Magnetism*, vol. IV, pp. 1–396. New York: Academic Press.

Kittel C (1962) Magnons. In: Dewitt B, Dreyfus B, and de Gennes P (eds.) *Low Temperature Physics*, pp. 441–478. New York: Gordon and Breach.

Kübler J (2000) *Theory of Itinerant Electron Magnetism*. Oxford: Clarendon Press.

Moriya T (1985) *Spin Fluctuations in Itinerant Electron Magnetism*. Berlin: Springer.

Vonsovskii SV (1974) *Magnetism*, vols. 1 and 2. New York: Wiley.

Wohlfarth EP (ed.) (1980) In: *Iron, cobalt and nickel*, vol. 1, pp. 1–70. Amsterdam: North-Holland. *Ferromagnetic Materials*.

Magnetic Domains

O Portmann, A Vaterlaus, C Stamm, and D Pescia, Laboratorium für Festkörperphysik der ETH Zürich, Zürich, Switzerland

© 2005 Elsevier Ltd. All rights reserved.

This is an update of O. Portmann, A. Vaterlaus, C. Stamm, D. Pescia, Magnetic Domains, Editor(s): Franco Bassani, Gerald L. Liedl, Peter Wyder, Encyclopedia of Condensed Matter Physics, Elsevier, 2005, Pages 191–197, ISBN 9780123694010, https://doi.org/10.1016/B0-12-369401-9/00525-8.

Introduction 64
The Physical Basis of Magnetic Domains 64
Domain Walls 65
An Example of Magnetic Domains: Stripes 67
Acknowledgments 68
Appendix A: Magnetostatic Energy of a Localized Distribution *M*(*x*) 68
Appendix B: The Equilibrium Stripe Width 69
Further reading 70

Introduction

The Dirac equation for the relativistic quantum mechanical electron is most famous for having predicted the existence of antiparticles. One further important aspect of this equation is the explanation of the electron spin and the magnetic moment associated with it. When atoms are formed, the electron spins interact by means of the intra-atomic exchange interaction to produce atomic magnetic moments. The correct value of the atomic magnetic moments can be calculated empirically using Hund's rules and Pauli's principle. When atoms are brought together to form a body, the atomic wave functions change drastically: the atomic magnetic moments are, in general, reduced, but may remain finite in certain special cases such as Fe, Co, and Ni. Moreover, as soon as neighboring atoms are provided, the interatomic exchange interaction comes into play and may favor the parallel alignment of the neighboring magnetic moments. In this way, macroscopic regions of aligned magnetic moments are formed in the body, and the body is said to be in a ferromagnetic state.

This microscopic description of magnetism, based on the quantum mechanical exchange interaction, is not complete. Each individual magnetic moment can be viewed as an atomic current generating a magnetic field, which interacts with other magnetic moments and contributes another term to the total magnetic energy – the energy of the dipole–dipole interaction. This term is also called the magnetostatic energy, as it is described by the Maxwell equations of magnetostatics. In contrast to the exchange interaction, this term is purely classical. It is later shown that, depending for example on the shape and size of the body, this term perturbs the parallel alignment of the magnetic moments favored by the exchange interaction. Thus the parallel alignment does not extend over the whole body, but is restricted to elementary regions called magnetic domains. Within such domains, the magnetic moments are aligned, while the orientation of the magnetic moments changes upon moving to neighboring domains.

Another class of magnetic interactions arises because of the spin–orbit coupling also contained in the Dirac equation: magnetic anisotropies. A magnetic anisotropy energy determines one or more spatial directions along which the exchange-coupled magnetic moments within the domains prefer to be aligned, where "preferring" means that the total energy of the system is reduced when the moments pointf along that direction in space. Magnetic anisotropies play a crucial role in domain formation. In fact, the change of the magnetic moment direction between consecutive domains does not occur abruptly: a domain wall with finite width connects domains with different magnetic moment orientation and magnetic anisotropies stabilize this wall.

The purpose of this article is to account for the state-of-the-art knowledge on magnetic domains and the walls between them. Before going into details, it is important to estimate the energy scale of the various magnetic interactions, given by their typical strength per atom. The intra-atomic exchange interaction is of the order of eV, on a temperature scale this corresponds to 10^4 K. This energy is required to produce an excited state with no atomic magnetic moment. The interatomic exchange interaction is some 10 meV (100 K). This means that the excited state with misaligned nearest-neighbor magnetic moments is attained when the temperature exceeds some 100 K (at a temperature which is called the Curie temperature). Magnetic anisotropies range from μeV in three-dimensional solids to 0.1 meV in ultrathin films (0.01 to 1 K). The reason for this broad range is that the magnetic anisotropies are strongest when the symmetry of the system is lowered, for example, when the dimensionality is reduced. The magneto-static interaction is $\sim$0.1 meV (1 K). Clearly, the interactions relevant for domain formation are much smaller than the exchange interaction. Thus, it is not immediately evident why such small energies should have an impact in determining the total energy of the system and its ground-state magnetic moment configuration. This question is also carefully investigated in the remaining sections.

The Physical Basis of Magnetic Domains

The physical basis for the explanation of magnetic domains was laid down in a paper by Landau and Lifshitz in 1935. One can consider a body in a situation where each lattice site carries a magnetic moment vector (for simplicity, a spin vector is used, noticing that, according to Dirac's theory, the two vectors are proportional to each other). One important caveat: it will turn out that the relevant length scales intervening in domain formation are large with respect to the lattice constant. On these characteristic length scales, the number of spins is so large that one can give up the quantum description of the spin vector and consider it a classical vector. The strongest contribution to the total magnetic energy comes from the exchange interaction, which measures the energy required to turn two neighboring spins into an antiparallel configuration. If this energy is positive, the total exchange energy is minimized by a uniform spin configuration. The spin ensemble can also have a magnetic anisotropy energy contribution, which favors certain spatial directions for the spins, the so-called easy direction. In the simplest case of uniaxial anisotropy, two directions in space, say $\boldsymbol{e}$ and its negative, are energetically favored. Thus, the uniform spin configuration will be aligned either along $+\boldsymbol{e}$ or along $-\boldsymbol{e}$, as either of these directions minimizes the total energy arising from the exchange and the magnetic anisotropy. How stable is the resulting spin configuration with respect to rotations or spin nonuniformities? The magnetic anisotropy per spin is very small but it is not possible to rotate spins individually, as they are bound together by the exchange interaction. Thus, a rotation excitation would involve turning a macroscopically large amount of spins and this requires a large excitation energy which is not available at sufficiently low temperatures. If the body is divided into oppositely magnetized regions, it would not entail any lowering of the total energy; on the contrary, some energy must be introduced to form boundaries between oppositely magnetized regions, causing an increase of the total energy. A more complicated anisotropy term may have a larger symmetry, but in no case will the magnetic anisotropy lead to magnetic domains as there is no energy to be gained upon changing from one easy direction to another. The behavior is quite different when the dipolar interaction between the magnetic moments is considered. Each moment produces a magnetic field, which interacts with all the other magnetic moments by means of the Zeeman energy contribution. The most striking feature of this magnetostatic energy is that the magnetic fields arising from a magnetic moment are very long ranged, they decay only with the third power of the distance. This is in opposition to exchange and magnetic anisotropies, which are local. The energy due to the dipolar field is the most complicated (see Appendix A), but contains a distinct feature which makes it compete directly with the exchange interaction: one part of it favors an antiparallel alignment of the spins. Of course, the interaction is very weak, but its long-range character amplifies its role with respect to the competing exchange interaction. Thus, under certain circumstances, which Landau and Lifshitz showed to depend on the size and the geometry of the body, the dipolar interaction can provide enough energy gain to sustain a nonuniform spin configuration: magnetic domains arise.

The complexity of the dipolar field and the long-range character of the dipolar interaction makes it very difficult to find the spin configuration that minimizes the total energy. However, there are some rules of thumb that help in analyzing the physical situation. One of them is provided by eqn [3] in Appendix A. This equation has a simple meaning: the total magnetostatic energy of a body is the Coulomb energy of an effective magnetic charge distribution $\rho_M \doteq -\nabla \cdot \boldsymbol{M}(\boldsymbol{x})$, where $\boldsymbol{M}(x)$ is the magnetic moment per unit volume. Its length is determined by the total magnetic moment in a sufficiently small cell centered at $\boldsymbol{x}$ divided by the volume of the cell, and its direction is given by the direction of the total magnetic moments within this cell. The size of this cell has to be chosen in such a way that it is small with respect to the smallest length occurring in domain formation, that is the size of the domain wall (see next section). The effective magnetic charge is provided by the divergence of $\boldsymbol{M}(\boldsymbol{x})$, thus minimizing the magnetostatic energy means avoiding regions where $-\nabla \cdot \boldsymbol{M}(\boldsymbol{x})$ is too large. A sizeable divergence of $\boldsymbol{M}x$ exists, for instance, at the boundaries of a uniformly magnetized body. Such surface charges increase the energy of the uniform spin configuration above the value specified by the exchange interaction. To avoid such charges, the body can split into elementary regions of different magnetization. At the boundaries between such regions, the spin vectors make a finite angle so that the exchange energy is increased (at the walls) with respect to the uniform configuration. Despite this, Landau and Lifshitz have explicitly shown that by introducing domains, the total energy might effectively be lowered. In Appendix B, a simple case is worked out where the subtleties of such total-energy minimization calculations are shown.

At the end of this section, an example illustrating this "magnetic-charges" avoidance rule is discussed. One can compare a small ferromagnetic plaquette with square geometry and a uniform spin configuration (see Figure 1a) to an identical plaquette with a particular nonuniform spin configuration where the magnetization vector circulates along a closed path within the plaquette (Figure 1b). The spin configuration in Figure 1a contains some effective magnetic charges appearing at the boundaries perpendicular to the magnetization vector. The spin configuration in Figure 1b is a very peculiar one, the magnetization vectors between two consecutive domains are orthogonal and no divergence develops at the boundary between two consecutive domains. The spin configuration in Figure 1b is free of magnetic charges and has no magnetostatic energy. One can show that when the plaquette is sufficiently large, the gain in magnetostatic energy overcomes the cost of introducing domain walls: the configuration in Figure 1b is the ground state. Experimentally, this closed path configuration is indeed observed, see Figure 1c as an illustration. The butterfly shape of the plaquette in Figure 1c is more complicated than the square plaquette just considered. Correspondingly, the experimental domain distribution (indicated by arrows), is more complex. It is also evident from Figure 1c that similar triangular plaquettes – the wings in the figure – have a slightly different domain distribution, showing that unresolved differences play a crucial role in determining the actual domain configuration. However, one essential element dominates the central parts of both wings: the domains are arranged in such a way that the magnetization vector circulates within the plane of the plaquette, avoiding the formation of magnetic charges, in agreement with the rule of thumb.

Domain Walls

Although it is the magnetostatic energy contribution that drives the rearrangement of the spin configuration into domains, it is the magnetic anisotropy that stabilizes the walls between them and makes the whole rearrangement process possible. For the sake of simplicity, the creation of a domain wall in a one-dimensional spin chain is illustrated. One can consider a chain extending along

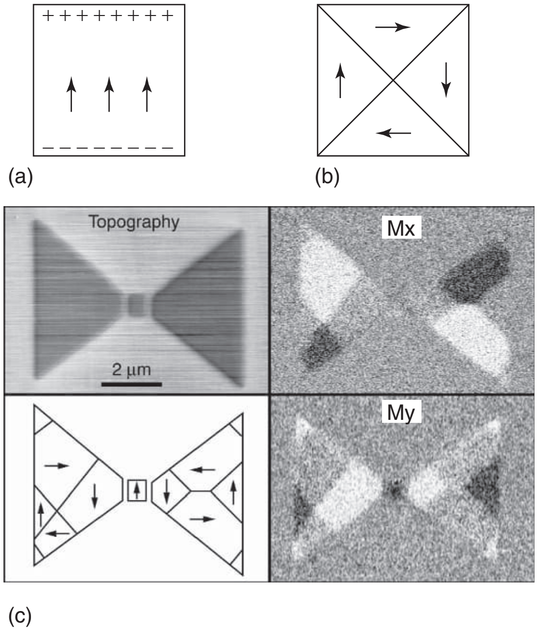

Figure 1 (a) and (b): Schematic domain distribution in a plaquette. In (a) the uniform magnetization produces magnetic surface charges, indicated in the figure. In (b) the magnetization vector follows a closed path, thus avoiding magnetic charges. (c) Image of the domain distribution in a plaquette with butterfly shape. The images were taken using scanning electron microscopy with polarization analysis (SEMPA). In SEMPA, a finely focused electron beam impinges onto the surface of a solid. Secondary electrons are ejected and used to map the topography of the surface while the beam is scanned across the surface. In the present case a ~14 nm thick Co film was deposited onto a Cu(1 0 0) surface by molecular beam epitaxy (MBE) through a mask inserted between MBE source and substrate. In this mask, a butterfly-profile was carved in by focused ion beam milling, which gives rise to the laterally patterned Co film visible in the topography image. In SEMPA, not only the secondary electron current is measured, but their spin polarization is also detected. This allows mapping the surface magnetization vector. The in-plane horizontal (M_x) and vertical (M_y) components of $\boldsymbol{M}$ are reproduced in (c) (the component perpendicular to the film plane vanishes). The black-white constrast is indicative of a strong magnetization in opposite directions. The Cu-substrate is nonmagnetic and appears gray. From the contrast maps of the two in-plane components, the domain distribution can be reconstructed as schematically summarized by the arrows.

the x direction with fixed-length spin vectors $S(x)$ being allowed to rotate in the y–z plane. Thus, $\boldsymbol{S} = S(0, \sin\theta(x), \cos\theta(x))$, S being the (dimensionless) length of the spin vector and θ the angle between the vector $\boldsymbol{S}$ and the y direction. The variable x is allowed to assume continuous values which is equivalent to say that, if any deviation from the parallel spin alignment occurs, it occurs over spatial length scales much larger than the lattice constant a. Assuming an exchange coupling between nearest neighbors of the simple form $-J \cdot \boldsymbol{S}(x) \cdot \boldsymbol{S}(x + a)$ ($J>0$ being the exchange constant), any deviation from the parallel spin alignment can be worked out to increase the exchange energy by an amount $\Delta_\Gamma = \{(\Gamma \cdot \mathrm{a})/2 \cdot \int \mathrm{d}x[\mathrm{d}\theta(x)/\mathrm{d}x]^2\}$ with the coupling constant $\Gamma = (\mathrm{J}/2)\mathrm{S}^2\mathrm{z}$ (z being the number of nearest neighbors, that is, 2 for a chain). A magnetic anisotropy term which favors the y direction for the spin is $\Delta_\lambda = (\lambda/(2\mathrm{a}))\int \mathrm{d}x\sin^2\theta(x)$ with the coupling constant λ measuring the energy required to turn the spin away from the y direction. Notice that, in accordance with the above discussion, $\Gamma > \lambda$. The equilibrium $\theta(x)$ is found by setting the functional variation of $\Delta_\Gamma + \Delta_\lambda$ to zero, which produces the Euler equation of the variational problem:

$$\Gamma \mathrm{a}\frac{\mathrm{d}^2\theta}{\mathrm{d}x^2} - \frac{\lambda}{\mathrm{a}}\sin\theta\cos\theta = 0 \qquad [1]$$

One can study the stability of a wall by solving this equation with the following boundary conditions: $\theta=\pi$ (0) for $x = -\infty(+\infty)$, and $\mathrm{d}\theta/\mathrm{d}x=0$ for $x = \pm\infty$. This establishes a spin profile with domains of opposite spins on the left- and right-hand side of $x = 0$. The solution to the Euler equation with these boundary conditions exists and was found in the work of Landau and Lifshitz:

$$\cos\theta = \tanh\frac{2x}{\mathrm{w}} \qquad [2]$$

$w = 2a\cdot\sqrt{\Gamma/\lambda}$ being the width of the region near $x=0$ over which the spin rotates from one domain to the domain of opposite magnetization, that is, the domain wall width. This solution is plotted in Figure 2b as a continuous curve. The wall energy (i.e., the energy required to establish a wall) per unit wall area can be calculated analytically by inserting the solution into the total energy expression: $\sigma_w = \left(1/\left(a^{\delta-1}\right)\right)\sqrt{\lambda\cdot\Gamma}$. The prefactor contains the dimensionality of the system δ. For the interaction strengths discussed in the introduction, w is expected to be of the order of some 100 lattice constants, which is a mesoscopic scale. A direct measurement of the spin profile inside the domain wall at the surface of an Fe single crystal indeed gives ≈200 nm. As an example, one can consider the domain image of a head-on magnetization distribution recorded in a thin epitaxial Fe film on $W(1\,1\,0)$ (Figure 2a). The spatial resolution of the image is such that the continuous in-plane rotation of the magnetization

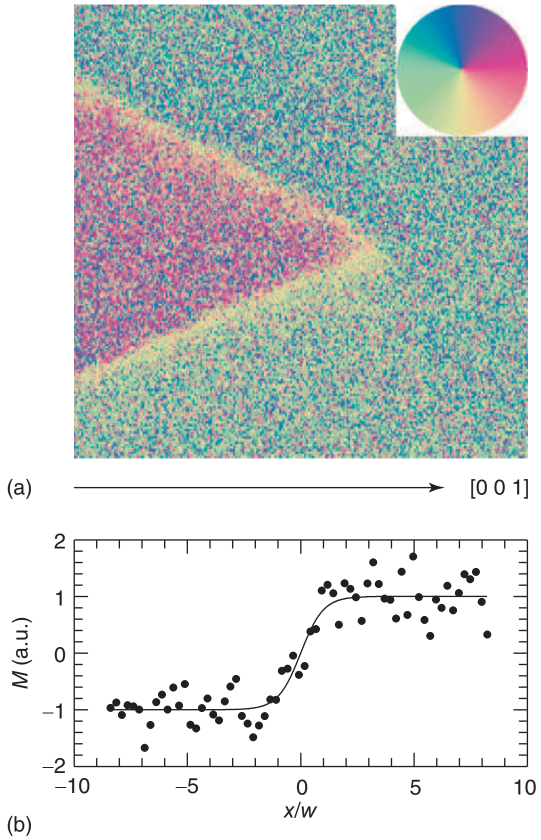

Figure 2 (a) Domain wall formation between head-on magnetized domains. The two domains, represented by different colors, are magnetized in opposite directions parallel to the horizontal axis (the [0 0 1]-direction of the cubic lattice, in this case). At the boundary between them, one recognizes that the magnetization vector rotates in the plane from one direction into the opposite one. A color code is used to represent the direction of the magnetization vector. Image size: $4.6 \times 4.6\ \mu\text{m}^2$ (b) The horizontal component of the magnetization vector (divided by its value well within the domains) is plotted along an axis x, drawn perpendicular to the domain wall (full circles). At the domain boundary, the value of the component makes a transition that can be fitted by the calculated tanh - profile (continuous curve), with a characteristic wall width $w \approx 140$ nm. To improve the statistical accuracy of the experimental profile, all experimental data points within a stripe going across the wall were averaged.

vector from one direction into the opposite direction occurring at the boundary between the two domains can be detected in detail. The rotation is illustrated with a color code explained in the caption. The experimental profile of the magnetization component that changes sign, given by the circles in Figure 2b, follows the calculated profile (continuous curve in Figure 2b), obtained by fitting the experimental data with $\tanh(2x/w)$.

An Example of Magnetic Domains: Stripes

Having established the physical basis for domain formation, the details can be worked out, which will help to achieve a deeper understanding of the energy balance which leads to domain formation. As anticipated, magnetostatic charges have to be considered, which means that the geometry and size of the body are central to the problem. For one special geometry, the appearance of domains is illustrated (for many other geometries which have been investigated so far, see the "Further reading" section). The special case of ultrathin magnetic film extending to infinity in the x_1–x_2 plane and having a finite but small thickness d in the x_3 direction (Figure 3a) is worked out in detail. The magnetization vector is taken to be perpendicular to the film plane. The perpendicular magnetization in ultrathin films is a very special configuration, requiring a strong uniaxial magnetic anisotropy to overcome the demagnetizing effect of the dipolar interaction. This demagnetizing effect is best appreciated by comparing a uniform in-plane spin configuration with a uniform perpendicular spin configuration. The in-plane configuration has no magnetostatic energy, provided the film extends to infinity. The perpendicular configuration, on the other hand, produces opposite charges at the two boundaries of the film with vacuum. This gives rise to an electrical plane condenser geometry. Using eqn [4] in Appendix A, the magnetostatic energy (per unit area) can easily be calculated to be $2\pi M_0^2 d$ and must be overcome by a strong magnetic anisotropy favoring the perpendicular configuration in order for a perpendicular magnetization to appear.

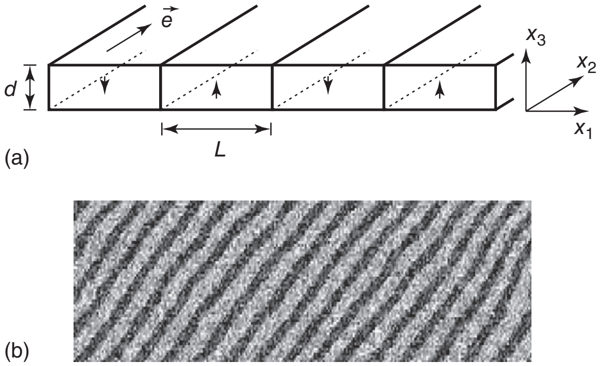

Figure 3 (a) Schematic view of an ultrathin film (thickness *d*) with a stripe configuration (stripe width: *L*) of alternating perpendicular magnetization. The geometrical elements used in Appendix B are also indicated. (b) Room temperature SEMPA image of the stripe phase in an ultrathin ($d \approx 0.3$ nm) Fe film deposited on Cu(1 0 0) by means of MBE. The image is 92.2 μm long. The component of the magnetization vector perpendicular to the film plane is shown. The black-white contrast is indicative of oppositely magnetized stripes.

The possibility of the existence of a nonuniform perpendicular spin configuration that might lower the energy of the system with respect to the uniform configuration in the given perpendicular magnetic configuration is examined. A possible nonuniform spin configuration with perpendicular magnetization is the one consisting of stripes of opposite perpendicular magnetization running parallel to say x_2 and repeating periodically along x_1, see Figure 3a. Such a configuration does certainly not introduce any extra magnetic anisotropy energy. Domain walls, however, are created and cause an increase of the exchange energy. The striped phase can only become energetically more favorable if the gain in magnetostatic energy is large enough to overcome the extra domain wall energy (this is shown to happen exactly in Appendix B). The stripes have an equilibrium width $L^* \propto w\cdot \mathrm{e}^{\pi^{L_0}/2\mathrm{d}}$. L_0 is the so-called dipolar length $L_0 \doteq \sigma_w / \left(2\pi M_0^2\right)$, and is related to the characteristic dipolar energy per atom $\left(2\pi M_0^2 \cdot a^3\right)$. Using the characteristic values as discussed in the introduction, one obtains L_0 of the order of $100a$. Thus, in the ultrathin limit $d \approx a$, the equilibrium stripe width L^* can reach astronomical values at $T = 0$: the ground state will appear to be a uniform single-domain spin configuration because the stripe width might be much larger than the size of the sample. However, when the temperature is increased, the various coupling constants renormalize and the stripe phase can penetrate the sample as its width reduces to mesoscopic lengths. This situation is indeed observed to occur in several perpendicularly magnetized ultrathin films where the stripe phase has been observed to develop. An example is given in Figure 3b for Fe films on Cu(1 0 0).

Acknowledgments

The authors thank the Swiss National Fund and ETH Zürich for financial help. They are grateful to G M Graf for making his calculation of the equilibrium stripe width (Appendix B) available for this article.

Appendix A: Magnetostatic Energy of a Localized Distribution *M*(*x*)

A useful starting point for finding the magnetostatic energy of a continuous static distribution $\boldsymbol{M}(\boldsymbol{x})$, are the Maxwell equations of magnetostatics: $\nabla\cdot\boldsymbol{B} = 0$ and $\nabla \times (\boldsymbol{B} - 4\pi\boldsymbol{M}) = 0$. The magnetic field $\boldsymbol{H}$ defined as $\boldsymbol{H} \doteq \boldsymbol{B} - 4\pi\boldsymbol{M}$ can be written in terms of a magnetic potential, $\Phi_{\mathrm{M}} : \boldsymbol{H} \doteq -\nabla\Phi_{\mathrm{M}}$. The first Maxwell equation now corresponds to the Poisson equation of an "effective magnetic charge" $\rho_M \doteq \nabla\cdot\boldsymbol{M} : \nabla^2\Phi_{\mathrm{M}} = -4\pi\rho_{\mathrm{M}}$. Thus, the magnetostatic problem has been transformed into an electrostatic problem involving charges ρ_M. Their energy amounts to (Coulomb)

$$E_M = \frac{1}{2}\int \mathrm{d}^3x\mathrm{d}^3y\,\frac{\rho_{\mathrm{M}}(\boldsymbol{x})\rho_{\mathrm{M}}(\boldsymbol{y})}{|\boldsymbol{x} - \boldsymbol{y}|} \qquad [3]$$

This expression for E_M states that a possible way to minimize the magnetostatic energy is to avoid magnetic charges, that is to minimize the magnitude of $\rho_M \doteq -\nabla\cdot\boldsymbol{M}$. A further useful expression for the energy involves the magnetic field $\boldsymbol{H}$:

$$E_M = \frac{1}{2}\int \mathrm{d}^3x\mathrm{d}^3y\,\frac{\rho_{\mathrm{M}}(\boldsymbol{x})\rho_{\mathrm{M}}(\boldsymbol{y})}{|\boldsymbol{x} - \boldsymbol{y}|} = \frac{1}{2}\int \mathrm{d}^3x\rho_{\mathrm{M}}(\boldsymbol{x})\Phi_{\mathrm{M}}(\boldsymbol{x}) = -\frac{1}{8\pi}\int \mathrm{d}^3x(\nabla^2\Phi_{\mathrm{M}}(\boldsymbol{x}))\Phi_{\mathrm{M}}(\boldsymbol{x}) = \frac{1}{8\pi}\int \mathrm{d}^3x\boldsymbol{H}^2(\boldsymbol{x}) \qquad [4]$$

where the general solution of the Poisson equation $\Phi_{\mathrm{M}}(\boldsymbol{x}) = \int \mathrm{d}^3y\rho_{\mathrm{M}}(\boldsymbol{y})/|\boldsymbol{x} - \boldsymbol{y}|$ is used. According to eqn [4], minimizing E_M means searching for a spin configuration which avoids the formation of stray fields $\boldsymbol{H}$.

From eqn [3], an often quoted expression for E_M can be derived. After a partial integration, the surface integral vanishes provided the magnetization distribution is localized. Using $\nabla^2 1/|\boldsymbol{x}-\boldsymbol{y}| = -4\pi\delta(\boldsymbol{x}-\boldsymbol{y})$, one obtains

$$\begin{aligned} E_M &= -\frac{1}{2}\int \mathrm{d}^3x\mathrm{d}^3\mathrm{y}\boldsymbol{M}(x)\cdot \nabla_x \frac{\nabla_y\cdot\boldsymbol{M}(y)}{|\boldsymbol{x}-\boldsymbol{y}|} = \frac{1}{2}\int \mathrm{d}^3x\mathrm{d}^3y\boldsymbol{M}(x)\cdot\nabla_x(\boldsymbol{M}(y)\cdot\nabla_y\frac{1}{|\boldsymbol{x}-\boldsymbol{y}|}) \\ &= \frac{1}{2}\int \mathrm{d}^3x\mathrm{d}^3y\frac{\boldsymbol{M}(\boldsymbol{x})\cdot\boldsymbol{M}(\boldsymbol{y})}{|\boldsymbol{x}-\boldsymbol{y}|^3} - 3\frac{\boldsymbol{M}(\boldsymbol{x})\cdot(\boldsymbol{x}-\boldsymbol{y})[\boldsymbol{M}(\boldsymbol{y})\cdot(\boldsymbol{x}-\boldsymbol{y})]}{|\boldsymbol{x}-\boldsymbol{y}|^5} + \frac{2\pi}{3}\int \mathrm{d}x^3\boldsymbol{M}(x)^2 \end{aligned} \qquad [5]$$

This equation states that the magnetic "dipole" $\boldsymbol{M}(\boldsymbol{x})$ interacts with a $\boldsymbol{H}$ field

$$\boldsymbol{H}(x) = \int \mathrm{d}y^3(-\frac{\boldsymbol{M}(y)}{|\boldsymbol{x}-\boldsymbol{y}|^3} + 3\frac{[\boldsymbol{M}(y)\cdot(x-y)](x-y)}{|\boldsymbol{x}-\boldsymbol{y}|^5} - \frac{4\pi}{3}\boldsymbol{M}(y)\delta(x-y)) \qquad [6]$$

produced at $\boldsymbol{x}$ by all other dipoles at $\boldsymbol{y}$ (the last term is the own field of the dipole at $\boldsymbol{x}$). This expression for E_M is often called the dipolar energy due to the dipole–dipole interaction.

A third useful equation can be derived from eqn [4] $\int \mathrm{d}^3x\boldsymbol{H}\cdot\boldsymbol{B} = 0$, holding for a localized distribution $\boldsymbol{M}(\boldsymbol{x})$:

$$E_M = 2\pi\int \mathrm{d}^3x\boldsymbol{M}^2\boldsymbol{x} - \frac{1}{8\pi}\int \mathrm{d}^3x\boldsymbol{B}^2x \qquad [7]$$

Accordingly, if the length of the magnetization vector is a constant, a spin configuration with a low magnetostatic energy requires maximizing the magnetic field $\boldsymbol{B}$.

Using the same identity, one can immediately derive

$$E_M = -\frac{1}{2}\int \mathrm{d}^3x\boldsymbol{H}\cdot\boldsymbol{M} \qquad [8]$$

Finally, one can transform eqn [7] into the interaction energy of a system of effective currents $\boldsymbol{J}_M \doteq c\nabla\times\boldsymbol{M}$. With $\boldsymbol{B} = \nabla\times\boldsymbol{A}$ and $\nabla\times(\nabla\times\boldsymbol{A}) = -\nabla^2\boldsymbol{A}$ (in the Coulomb gauge), one obtains $\nabla^2\boldsymbol{A} = -4\pi/c\boldsymbol{J}_M$. Finally, from this Poisson equation for $\boldsymbol{A}$, one can obtain

$$E_M = 2\pi\int \mathrm{d}^3x\boldsymbol{M}^2\boldsymbol{x} - \frac{1}{2c^2}\int \mathrm{d}^3x\mathrm{d}^3\mathrm{y}\frac{\boldsymbol{J}_\mathrm{M}(x)\boldsymbol{J}_M\boldsymbol{y}}{|\boldsymbol{x}-\boldsymbol{y}|} \qquad [9]$$

Thus, minimizing the magnetostatic energy means searching for a spin configuration that maximizes the curl of $\boldsymbol{M}$.

Appendix B: The Equilibrium Stripe Width

It is very instructive for the reader to follow in detail the appearance of domains for a very specific case. One can consider perpendicularly magnetized ultrathin films of thickness d extending over a large area $\Lambda_1\times\Lambda_2$ in the x_1-x_2 plane, see Figure 3a. The magnetization within each stripe points along $\pm x_3$. The stripes of width L are taken to be parallel to x_2. They are joined by walls with a finite width ω with $d < w < L$. Consecutive stripes have opposite perpendicular magnetizations. The total wall energy E_w amounts to $\sigma_w(\Lambda_1/\mathrm{L})\Lambda_2\cdot\mathrm{d}$. This is just the energy per unit wall area multiplied by the length of the wall Λ_2, the film thickness d, and the number of walls within the length Λ_1. Here, the wall energy per unit film area $\sigma_w d/L$ is the main interest.

The lowering of the magnetostatic energy upon introducing stripes can immediately be seen when one considers eqn [9]. A uniform perpendicular spin configuration is curl free, so that there is no effective current J_M anywhere in space and the total energy per unit area is simply $(2\pi M_0^2\cdot d)$. The stripe configuration, instead, develops some curl (and correspondingly some magnetic field $\boldsymbol{B}$), thus necessarily lowering the magnetostatic energy.

The following calculation shows explicitly that the energy gain is enough to overcome the wall energy introduced by the stripes. First, the effective currents are found. The stripe magnetization distribution develops a curl at the boundaries (labeled with the index n) between consecutive stripes. Along these boundaries, effective current densities $\boldsymbol{J}_n = cj_n\boldsymbol{e}$ occur where $j_n = (-1)^n 2M_0/w(n = 0, 1, \ldots, (N-1))$ and $j_N = (-1)^N M_0/w$. One contribution to the Coulomb energy, eqn [9] arises from the interaction of each current with the remaining currents. There are Λ_1/L of such interaction terms and the calculation of this part of the interaction energy reduces to the computation of the sum of elementary integrals of the type

$$\int_{-\Lambda_2/2}^{\Lambda_2/2}\int_{-\Lambda_2/2}^{\Lambda_2/2}\mathrm{d}x_2\mathrm{d}y_2\frac{1}{\sqrt{(x_2-y_2)^2+L_n^2}} \qquad [10]$$

($L_n=\pm n$, L and $n\neq 0$). Notice that the integration along (x_3, y_3) can be approximated by multiplying the remaining two-dimensional integrals with d^2. This is possible because d is considered small with respect to L, so that one can set $x_3 = y_3 = 0$ in the integrand. The integration over (x_1, y_1) can be approximated by a factor w^2, because w is considered to be much smaller than L, allowing one to set $(x_1 - y_1)^2 = L_n^2$ in the integrand. Thus, eqn [9] reduces to the elementary integral of eqn [10]. After computing these integrals, one is left with a sum that can be solved exactly because it contains in the limit $N\rightarrow\infty$ the product of Wallis. The other contribution arises from the self energy of each current. Under the integral of the self energy, $(x_1 - y_1)$ may be smaller than $|x_2 - y_2|$. Thus, the integrations over x_1, y_1 must be performed explicitly. There are again Λ_1/L such terms and their self energy per unit area contains the integral

$$\int_0^w \int_0^w \mathrm{d}x_1 \mathrm{d}y_1 \int_{-\Lambda_2/2}^{\Lambda_2/2} \int_{-\Lambda_2/2}^{\Lambda_2/2} \mathrm{d}x_2 \times \mathrm{d}y_2 \frac{1}{\sqrt{(x_2 - \mathrm{y}_2)^2 + (x_1 - \mathrm{y}_1)^2}} \qquad [11]$$

Summarizing all contributions, the total energy per unit film area is

$$2\pi M_0^2 d \cdot \{1 - \left[\left(\frac{3}{\pi} + \frac{2}{\pi}\ln\frac{2}{\pi}\right) - \frac{2}{\pi}\ln\frac{w}{d}\right]\frac{\mathrm{d}}{L} + \frac{2}{\pi}\frac{\mathrm{d}}{L}\ln\frac{\mathrm{d}}{L}\right\} + \sigma_w \frac{\mathrm{d}}{L} \qquad [12]$$

The equilibrium stripe width L^* is found by minimizing the total energy per unit area with respect to the variable $x \doteq d/L$.

$$L^* = w \cdot \mathrm{e}^{\pi(\mathrm{b}+1)/2} \cdot \mathrm{e}^{\pi \mathrm{L}_0/2\mathrm{d}} \qquad [13]$$

where the numerical factor $b = -(3/\pi + 2/\pi \ln 2/\pi)$. Notice that the equilibrium stripe width is a nonanalytic function of d for small d. It can be readily verified that the total energy of the striped phase at the equilibrium stripe width is indeed lower than the total energy of the uniform perpendicular state, by an amount $-(2/\pi)\left(2\pi M_0^2 d/L^*\right)$.

Further reading

Hubert A and Schäfer R (2000) *Magnetic Domains.* Berlin: Springer.
Jackson, J D *Classical Electrodynamics*, Third Edition, ch 5. New York: Wiley.
Kaplan B and Gehring GA (1993) *Journal of Magnetism and Magnetic Materials* 128: 111–116.
Rowlands G (1994) *Journal of Magnetism and Magnetic Materials* 136: 284–286.
Ter Haar D (ed.) (1967) *Collected Papers of L.D. Landau*, pp. 101–116. New York: Gordon and Breach.

Magnetic Interactions

G Hilscher and H Michor, Vienna Institute of Technology, Vienna, Austria

© 2005 Elsevier Ltd. All rights reserved.

This is an update of G. Hilscher, H. Michor, Magnetic Interactions, Editor(s): Franco Bassani, Gerald L. Liedl, Peter Wyder, Encyclopedia of Condensed Matter Physics, Elsevier, 2005, Pages 197–204, ISBN 9780123694010, https://doi.org/10.1016/B0-12-369401-9/00515-5.

Introduction 71
Crystalline Electric Field Interactions 71
Origin of Long-Range Magnetic Order – Exchange Interactions 73
Origin of Exchange 73
Direct Exchange 75
Indirect Exchange in Insulators – Superexchange 75
Double Exchange 75
Indirect Exchange in Metals – RKKY Interaction 75
Exchange Interactions in Free Electron Systems – Itinerant Exchange 77
Further Reading 77

Introduction

Magnetism in matter is a purely quantum mechanical phenomenon according to the Bohr–van Leeuwens theorem: van Leeuwen demonstrated in 1918 that classical Boltzmann statistics applied rigorously to any dynamical system leads neither to a susceptibility nor to a magnetic moment, which means that classical mechanics cannot account for diamagnetism, and paramagnetism or any type of collective magnetic order. However, under the assumption that a molecule or atom has a finite magnetic moment $\boldsymbol{\mu}$, the diamagnetic and paramagnetic susceptibility was derived already in 1905 by Langevin using classical statistical thermodynamics and treating these moments without interactions. The assumption of a finite magnetic moment, however, requires quantized values for the spin S and angular momentum L that is a result of quantum mechanics. The coupling of spin and angular momentum to the total angular momentum J is a relativistic interaction, which can be treated as a perturbation for not too heavy elements (Russel Sounders or L–S coupling) and the ground state is described by Hunds rules. Accordingly, magnetism arises from quantized motions of electrons giving rise to the fundamental unit of the magnetic moment, the Bohr magneton, defined by $\mu_{\mathrm{B}} = e\mathrm{h}/2m_e$ that takes the value $9.27410^{-24}\mathrm{Am}^2\mathrm{or JT}^{-1}$. Thus, the magnetic moment of an atom or a molecule is given in units of μ_{B} (e.g., the magnetic moment of pure Fe in the metallic state is $2.2\mu_{\mathrm{B}}$ per atom).

The magnetic properties of a system of electrons and nuclei are determined by the interactions of these particles with electromagnetic fields. These fields arise from two types of sources: first, there are fields due to sources external to the system such as applied electric and magnetic fields. Second, there are internal sources, which come from the charges and currents due to the particles of which the system is composed. Interactions with and between nuclear moments μ_{N} are not discussed here since μ_{N} is by a factor of $\sim$1800 smaller than μ_{B}.

A first step is to consider the magnetic moments associated with itinerant and/or localized electrons on the respective ions of a crystal to behave completely free without interacting with each other or with their surrounding. This leads to diamagnetism and paramagnetism.

In a free atom the quantum number J, the total angular momentum, is a good quantum number, which reflects the fact that a free atom has a complete rotational symmetry in the absence of external fields and its ground state is $2J+1$ fold degenerate. In a crystal, however, the surrounding ions produce an electric field to which the charge of the central atom adjusts and the $2J+1$ degeneracy is removed giving rise to a splitting of the ground multiplet. The object of the crystalline electric field (CEF) theory is to describe how the moments are affected by their local environment in a crystal. Finally, one has to consider the various interactions of magnetic moments with each other leading eventually to a long-range magnetic order.

Crystalline Electric Field Interactions

The charge distribution around a central ion produces an electric field with the local symmetry of the environment. This crystal field makes a contribution to the potential energy

$$V_{\mathrm{C}}(r) = \int \frac{e\rho(\boldsymbol{R})}{|r - \boldsymbol{R}|}\mathrm{d}\boldsymbol{R} \approx \mathrm{e}\sum_{\mathrm{i}} \frac{\mathrm{q_i}}{|r - \boldsymbol{R}_{\mathrm{i}}|}$$

where the charge distribution $\rho(\boldsymbol{R})$ in the point charge model is approximated by point charges q_i at the position $\boldsymbol{R}_i$. The denominator may be expanded in spherical harmonics. If V_{C} is small compared to the spin–orbit coupling (as in the rare-earth elements where the incomplete 4f shell is responsible for the magnetic moment), the eigenstates are adequately accounted for by the first-order perturbation theory. Provided that the ground state and the next excited states do not mix, the matrix elements of $V_{\mathrm{C}}(\boldsymbol{r})$

are proportional to those obtained with operator equivalents written in terms of $\boldsymbol{J}$, which are called the Stevens operator equivalents $O_l^m(\boldsymbol{J}_i)$ and the CEF Hamiltonian reads

$$\hat{H}_{\mathrm{CF}} = \sum_i \sum_{lm} B_l^m O_l^m(\boldsymbol{J}_i)$$

The CEF parameters B_l^m can, in principle, be calculated from the charge distribution of the environment, which yields reasonable results for insulators but is of limited success for metals.

The electrostatic interactions destroy the rotational symmetry of the ion and the electronic orbitals are linked to the symmetry of the lattice removing the $2J+1$ degeneracy of the ground multiplet of the free ion. Schematically illustrated in Figure 1 is the CEF splitting (e.g., Mn in the perovskite $\mathrm{LaMnO_3}$) resulting from the interaction between the nonspherical d-orbitals and the electrostatic field of the environment, which is also nonspherical. As an example, the d_{xy}-orbital in an octahedral surrounding (a) is energetically favored in comparison to the $d_{x^2-y^2}$ orbital (b) in the same environment. Those lobes, which point to neighboring charges, have higher overlap and correspond to higher electrostatic energy than those that point between. This gives rise to the CEF splitting displayed in Figure 1c.

An improvement on the point charge approximation for d-transition metal ions is the ligand field theory which is an extension of the molecular orbital theory that focuses on the role of the d-orbitals of the central ion and their overlap with orbitals on surrounding ions (ligands). Also for rare-earth compounds, CEF parameters can be calculated from first principles using the density-functional theory which, however, should be checked experimentally as, for example, by inelastic neutron scattering.

It is instructive to consider two rather different cases, namely the $3d$-transition metal series (Fe group) and the $4f$ series (rare earth), where the relative importance of the spin–orbit coupling and CEF splitting of the ground multiplet is inverted. The spin–orbit coupling which is proportional to Z^2 (atomic number) is much larger in the $4f$ series than in the $3d$-transition metals since rare-earth elements are significantly heavier. Furthermore, the spatial extension of the $3d$ wave functions is much more delocalized than the $4f$ wave functions that are additionally screened from CEF by the outer $6s$- and $5d$-shells. Thus, in rare-earth compounds CEF splitting is $\sim 10^2$ K and spin–orbit coupling of 10^4 K, which means that the Hunds rule ground state is usually observed both in metals and insulators and the effect of CEF interaction can be treated in terms of Stevens operators. In $3d$-compounds, V_{C} is typically of the order of 10^4 K which is larger than the spin–orbit coupling (10^2 K) and V_{C} couples mainly to the orbital part of the wave function which lifts the orbital degeneracy of the $3d$-states and Hunds rule ground state is usually not obeyed. If the CEF perturbation is strong enough and the symmetry low enough, the orbital degeneracy is completely removed. Thus, the orbital ground state is a singlet which is called the quenching of the orbital momentum (L is not anymore a good quantum number and virtually reduced to $L = 0$) and "spin-only" magnetic properties are observed. In $4d$-and $5d$-series (Pd and Pt groups),

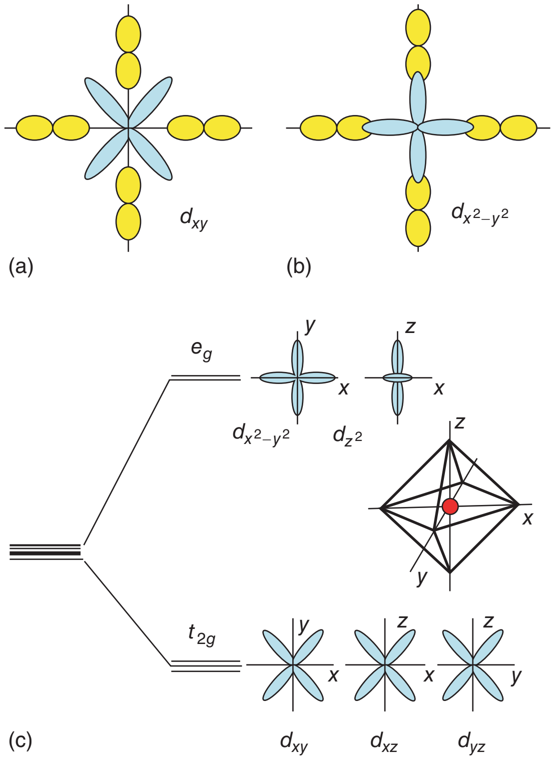

Figure 1 (a) The d_{xy}-orbital is lowered in energy with respect to the $d_{x^2-y^2}$-orbital in an octahedral environment. (b) Schematic crystal field splitting in an octahedral environment (c) The d_{z^2}-and $d_{x^2-y^2}$-orbitals are grouped together and called e_g levels (twofold degenerate). The d_{xy}, d_{xz} and d_{yz} are grouped together and called the t_{2g} levels (threefold degenerate).

the situation is less clear-cut because the heavier ions have a larger spin–orbit splitting, and the CEF and spin–orbit interaction can be of comparable magnitude.

The impact of CEF interaction on the magnetic properties is important and in combination with spin–orbit interaction it is the principal source of magnetic anisotropy, which is the dependence of magnetic properties on the direction in the compound. Further, properties influenced by CEF are magnetoelastic phenomena and transport phenomena as well as thermodynamic properties as the specific heat.

Origin of Long-Range Magnetic Order – Exchange Interactions

In the previous section, magnetic ions embedded in the CEF environment of the crystal were considered but the interaction between the magnetic moments was neglected. The classical interaction between two magnetic dipoles $\boldsymbol{\mu}_1$ and $\boldsymbol{\mu}_2$ at a distance $\boldsymbol{r}$ between each other is known as the dipole–dipole interaction. As the magnetic energy is $E_M = -\boldsymbol{\mu}\cdot\boldsymbol{H}$, the dipolar energy reads

$$E_D = \frac{\mu_0}{4\pi r^3}\left[\boldsymbol{\mu}_1\cdot\boldsymbol{\mu}_2 - \frac{3}{r^2}(\boldsymbol{\mu}_1\cdot r)(\boldsymbol{\mu}_2\cdot r)\right]$$

Thus E_D/k_B is of the order of 1 K, if one considers two moments of 1 μ_B which are separated by 1 Å. Accordingly, this interaction cannot account for Curie temperatures of 1000 K, but nevertheless can become of relevance at low and ultra-low temperatures.

Dirac and Heisenberg discovered independently that electrons are coupled by exchange interactions among which direct, indirect, itinerant exchange, and superexchange can be distinguished. Direct, indirect, and itinerant exchange occurs in metallic systems. Direct and superexchange is important in nonmetallic systems.

Origin of Exchange

In order to show how the Pauli exclusion principle together with electrostatic interactions leads to magnetic effects, consider the simplest possible case – a two-electron system – where the Hamiltonian

$$\hat{H}\sum_{i=1}^{2}\frac{p_i^2}{2m} + V(r_1, r_2)$$

does not depend on the spin. In quantum mechanics one cannot distinguish between identical particles, which means that the particle coordinates q_1 and q_2 can be permuted (exchanged) in the wave function and the system remains the same physically; the new wave function differs from the original one by a phase factor: $\psi(q_1, q_2) = e^{i\phi}\psi(q_2, q_1)$. Permuting once more gives the original wave function. Thus $e^{2i\phi} = 1$ and $\psi(q_1, q_2) = \pm\psi(q_2, q_1)$, which means the wave function must be either totally symmetric or antisymmetric under permutation. Electrons (Fermions) have totally antisymmetric wave functions; so the spin part must either be an antisymmetric singlet state $\chi_S(S = 0)$ in the case of a symmetric spatial wave function or a symmetric spin triplet state $\chi_T(S = 1)$ in the case of an antisymmetric spatial state. The overall wave function for the singlet ψ_S and the triplet state ψ_T for two electrons where both the orbital and spin part is included reads:

$$\psi_S = \frac{1}{\sqrt{2}}\chi_S[\psi_1(r_1)\psi_2(r_2) + \psi_1(r_2)\psi_2(r_1)], \text{with} \chi_S = \frac{1}{\sqrt{2}}(|\uparrow\downarrow\rangle - |\downarrow\uparrow\rangle)$$

$$\psi_T = \frac{1}{\sqrt{2}}\chi_T[\psi_1(r_1)\psi_2(r_2) - \psi_1(r_2)\psi_2(r_1)], \text{ with } \chi_T : |\uparrow\uparrow\rangle; \frac{1}{\sqrt{2}}(|\uparrow\downarrow\rangle + |\downarrow\uparrow\rangle); |\downarrow\downarrow\rangle$$

If the interaction $V = e^2/r_{12}$ is absent, then these two states would have the same energy. For $V \neq 0$, the energies of the triplet and the singlet state are different

$$E_S = \int \Psi_S^* \hat{H} \Psi_S = U + J$$
$$E_T = \int \Psi_T^* \hat{H} \Psi_T = U - J$$

with

$$U = \int\int |\psi_1(r_1)|^2 V(r_1, r_2) |\psi_1(r_2)|^2 dr_1 dr_2$$

and $\delta E = E_S - E_T = 2J$

$$J = \int\int \psi_1(r_1)\psi_1^*(r_2) V(r_1, r_2) \psi_2(r_2)\psi_2^*(r_1) dr_1 dr_2$$

where J is the exchange interaction or exchange integral, and U the Coulomb integral. The original Hamiltonian does not depend on the spin but produces an energetically favorable spin configuration for parallel spins. Thus $\hat{H}$ may now be replaced by an effective one $\hat{H}^{\text{spin}}$ acting upon the spin components only with the requirement that it should produce the same $\delta E = E_S - E_T$. What will be the form of $\hat{H}^{\text{spin}}$?

For the two-electron system, the spin operators yield the following eigenvalues:

$$\hat{S}_i^2 = \hbar^2 S_i(S_i + 1) = \hbar^2 \frac{3}{4} \text{ and}$$

$$\hat{S}^2 = \hbar^2 S(S + 1) = \hat{S}_1^2 + \hat{S}_2^2 + 2\hat{S}_1 \cdot \hat{S}_2 = \hbar^2 \frac{3}{2} + 2\hat{S}_1^2 \cdot \hat{S}_2^2$$

Accordingly, the product $\hat{S}_1^2 \cdot \hat{S}_2^2/\hbar^2 = S(S+1)/2 - 3/4$ of both operators gives −3/4 for the singlet $S = 0$ and 1/4 for triplet state $S = 0$. Hence the original spin-independent Hamiltonian can be written in the form of an effective spin Hamiltonian yielding the same eigenvalues E_S and E_T:

$$\hat{H}^{\text{spin}} = \frac{1}{4}(E_S + 3E_T) - \frac{(E_S - E_T)\hat{S}_1 \cdot \hat{S}_2}{\hbar^2}$$

$$\hat{H}^{\text{spin}} = U - J\hat{S}_1 \cdot \hat{S}_2$$

with $U = 1/4(E_S + 3E_T)$ and $J = (E_S - E_T)/\hbar^2$. If $J > 0$, $E_S - E_T > 0$ and the "parallel" coupling of the spins in the triplet state with $S=1$ is favored, while for $J<0$ the "antiparallel" coupling in the singlet state is favored.

The generalization of this simple relation for the two-electron system to a many-body system is far from trivial. The result is the Heisenberg Hamiltonian

$$\hat{H}_{\text{Heisenberg}} = -\sum_{i>j} J_{ij} \hat{S}_i \cdot \hat{S}_j$$

where J_{ij} is the exchange interaction between the ith and jth spins. Frequently, J_{ij} is taken as a constant for the nearest neighbors (and next nearest neighbors) and zero otherwise. J_{ij} is of the order of 10^2–10^3 K for direct exchange in 3*d*-compounds, 10–10^2 K for indirect exchange and superexchange. A reliable calculation of J_{ij} is a rather complex task in general.

A simple but straightforward approach to obtain a convenient expression for the exchange interaction is the mean field approximation where the exchange interaction between the ith spin and its neighbors $\sum_j J_{ij} \hat{S}_j$ is approximated by a phenomenological molecular field H_m acting upon $\mathbf{S}_i$. In the Weiss molecular field model, the molecular field is set proportional to the magnetization $H_m = \lambda M$, where the molecular field constant λ is determined by the exchange interaction yielding fields $\mu_0 H_m$ of the order of 1000 T for 3*d*-intermetallics such as Fe–Co alloys to account for their Curie temperatures of ~1000 K $(\mu H = k_B T_c)$. Nevertheless, this phenomenological molecular field is a convenient fiction but not experienced by the electrons since exchange origins from Coulomb interaction.

Some general features of exchange interactions are noteworthy. If two electrons on an isolated atom are considered, J is usually positive and favors the parallel spin configuration (triplet state) associated with an antisymmetric orbital state which reduces the Coulomb repulsion by keeping them apart. This is consistent with Hund's first rule yielding maximum total spin under the constraint of the Pauli principle.

The situation is different for electrons on neighboring ions in molecules or in a solid. In contrast to the free electron description for a simple metal, the model of tightly bound electrons is used as an approximation not only for ionic solids but also for transition metal compounds. The total wave function is a linear combination of atomic orbitals (LCAO) centered on the respective ions (which has to be in overall antisymmetric realized by a Slater determinant.) The electrons can save kinetic energy by forming bonds because their common wave function is more extended than the original atomic orbital and comprises both ions. These molecular

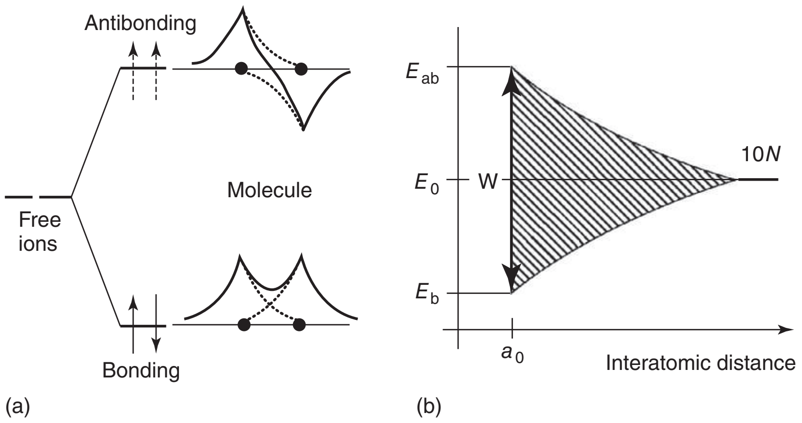

Figure 2 Schematical energy splitting of bonding (spatially symmetric) and antibonding (spatially antisymmetric) molecular orbitals in a molecule (a) yielding a singlet ground state as, e.g., in H_2 molecule. (b) Schematical formation of the bandwidth *W* in a solid by the quasicontinuous distribution of the 10*N* *d*-states between the lower and upper bonding states of the originally discrete and degenerated 5*d*-atomic states for up and down spin of *N* transition metal atoms condensed to a crystal; E_b is the energy of the bonding state and E_{ab} of the antibonding state.

orbitals can be bonding (spatially symmetric) or antibonding (spatially antisymmetric) as shown schematically in Figure 2a for the hydrogen molecule. The latter are more localized associated with higher kinetic energy. This favors the "antiparallel" singlet state as observed in H_2.

In a *d*-transition metal, the atomic 5*N* *d*-states for spin up and down give rise to a band of 10*N* levels distributed quasicontinuously between the lower bonding and the upper antibonding levels yielding together with transfer integrals and hopping integrals, the bandwidth *W* (Figure 2b). One has to distinguish between interatomic terms of the exchange and Coulomb integrals (J_{ij} and U_{ij}, $i \neq j$) and intra-atomic terms J_{ii} and U_{ii}. According to the more or less localized character of the wave function, the interatomic terms are much weaker than the intra-atomic terms. The *U* terms tend to avoid two electrons with antiparallel spins in the same orbital and the exchange terms *J* favor electrons in different orbitals with parallel spins. The latter are about one order of magnitude smaller. Thus, one may define an average exchange energy $\bar{I}$ per pair of electrons per atom, which represents the interaction favoring "ferromagnetic" alignment. On the other hand, the transfer integrals associated with the bandwidth work in the opposite direction, since the creation of parallel spins implies the occupation of higher energies in the band (i.e., with higher kinetic energy). Following this very simplified approach, the balance between kinetic and exchange energy favors the appearance of a spontaneous magnetic order for the end of the 3*d*-elements (Cr, Mn, Fe, Co, and Ni).

A proper description is performed in terms of the density-functional theory where the exchange correlation potential is added to the Coulomb correlation, which allows a straightforward determination of the exchange correlation. This treatment is called the local spin density approximation (LSDA).

To summarize, exchange can be explained in the following way: the Pauli exclusion principle keeps the electrons with parallel spins apart and so reduces their Coulomb repulsion. The difference in energy between parallel and antiparallel spin configuration is the exchange energy. This, however, is favorable for ferromagnetism if the increase in kinetic energy associated with parallel spins does not outweigh the gain in potential energy, as in the familiar examples of the H_2 molecule or the He atom. In metallic Fe, Co, and Ni, the number of parallel spins produces ferromagnetism because the cost in kinetic energy is not as great as in some other metals, where the gain in potential energy is significant yielding a paramagnetic ground state.

Direct Exchange

If there is sufficient overlap of the relevant wave functions (e.g., 3*d*-orbitals) between neighboring atoms in the lattice, the exchange interaction is called direct exchange. Although Fe, Co, and Ni are frequently referred to as typical examples for direct exchange, the situation is not that simple because of the metallic state where magnetism of itinerant electrons plays an important role. Accordingly, both the localized and band character of the electrons involved in transition metals and their intermetallics have to be taken into account as is seen in the model of covalent magnetism for transition metal intermetallics.

Indirect Exchange in Insulators – Superexchange

Superexchange is typical for insulators or materials on the border of a metal insulator transition where the ions with a magnetic moment are surrounded by ions which do not carry a moment but mediate the exchange. This type of exchange is observed in transition metal oxides. An archetypical example is MnO where two cations (Mn_{2+} in the $3d^5$ state with $S = 5/2$) are coupled via an anion (O_{2-} in the $2p^6$ state with $S = 0$); the ground state is shown schematically in Figure 3a. Because of the overlap of the wave functions, one of the *p*-electrons of the anion (O_{2-}) hops over to one of the cations Mn_{2+}. The remaining unpaired *p*-electron on the anion enters into a direct exchange with the other cation. In principle, this exchange may be ferromagnetic or antiferromagnetic. The excited state shown in Figure 3b for an antiferromagnetic coupling is in most cases energetically in favor due to the interplay of two effects: the hopping of electrons between ligands, characterized by a hopping matrix element *t* being proportional to the bandwidth, and an average Coulomb interaction *U* between electrons on the same orbital. Superexchange involves oxygen *p*-orbitals and transition metal *d*-orbitals and is therefore a second-order process. In second-order perturbation theory, the exchange interaction is given by $J \propto -t^2/U$, and normally yields antiferromagnetic coupling.

Double Exchange

Double exchange is essentially a ferromagnetic type of superexchange in mixed-valent systems. Mixed-valency means that the transition metal ion on crystallographically equivalent lattice sites exhibits different ionic states, for instance, trivalent and tetravalent Mn in perovskites (La,Sr)MnO_3 or Fe^{2+} and Fe^{3+} in magnetite (Fe_2O_3). Due to the mixed valency, holes (i.e., unoccupied states) exist in the e_g states of the transition metal ion with a higher valency with respect to a cation of the same species with a lower valency. The simultaneous hopping of an electron from $Mn^{3+} \rightarrow O^{2-}$ and concomitantly from $O^{2-} \rightarrow Mn^{4+}$ is known as double or Zehner exchange. Hopping is favored if the neighboring ion is ferromagnetically aligned since kinetic energy is saved by delocalization, while it is hindered by antiferromagnetic alignment as shown schematically in Figure 4.

Indirect Exchange in Metals – RKKY Interaction

In transition metal alloys, intermetallic compounds, and diluted magnetic alloys where magnetic ions are dissolved in a weak paramagnetic or diamagnetic host (e.g., Fe–Au or Fe–Cu alloys), the magnetic moment carrying ions are separated by other ions and a direct overlap of wave functions responsible for the magnetic moment is hardly possible. Thus, the various types of indirect

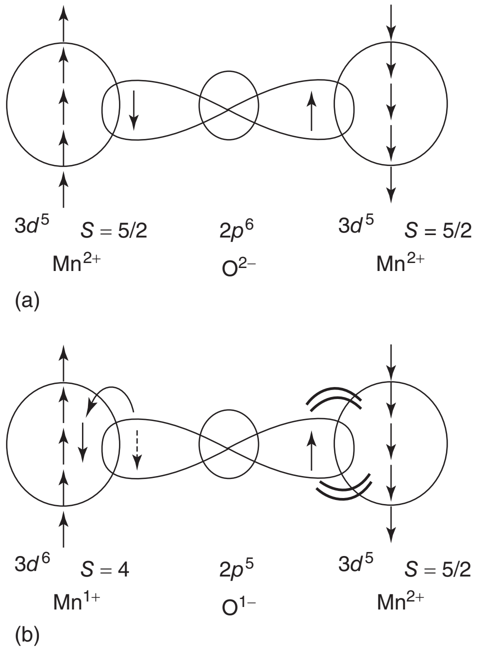

Figure 3 (a) Superexchange of a transition metal oxide as, e.g, MnO in the ground state, (b) hopping of electrons in the excited state favors antiferromagnetic coupling.

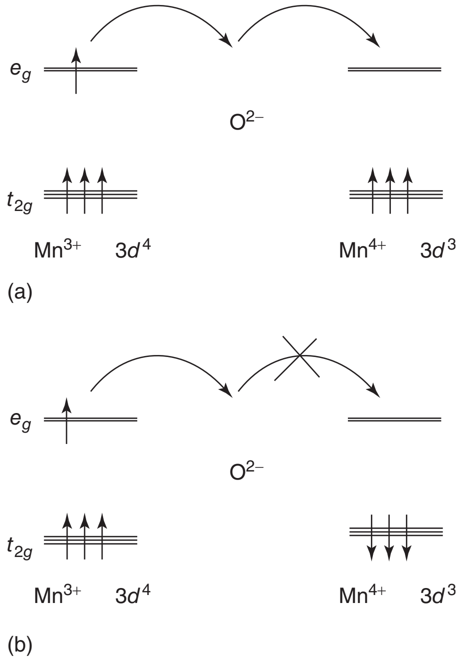

Figure 4 (a) Double exchange interaction favors hopping via an anion (O^{2-}) for ferromagnetic alignment of the transition metal ions by reducing kinetic energy, (b) while hopping is hindered by antiferromagnetic alignment.

exchange interactions between magnetic moments are mediated by conduction electrons polarized by the local moment, which is known as RKKY interaction according to Ruderman, Kittel, Kasuya, and Yoshida. Under the assumption of a spherical Fermi surface with radius k_F, the interaction is given by

$$J_{\mathrm{RKKY}} \propto \frac{\cos(2k_F r)}{r^3}$$

The RKKY interaction is long ranged and oscillates as a function of the distance r from the polarizing local moment. Hence depending on the distance, the conduction electron polarization is positive or negative, yielding ferromagnetic or antiferromagnetic

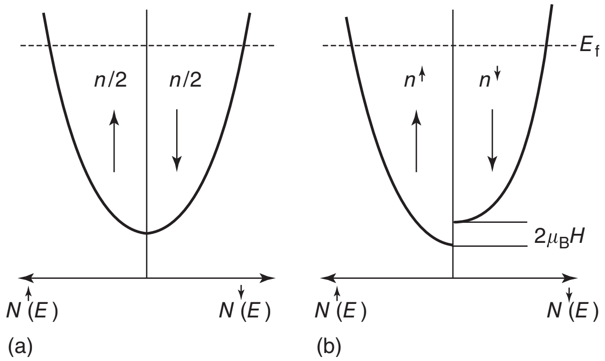

Figure 5 (a) Density of states of the free electron gas in the paramagnetic state, (b) splitting of the spin up and down bands by either an external field H_0 or by an effective exchange field H_{eff}.

coupling with the next local moment at the position *r*, and is an important mechanism to describe complex magnetic structures. Archetypical examples are rare earths (R) and their intermetallics, where the localized 4*f*-electrons are responsible for magnetism without any overlap with their nearest-neighbor 4*f* wave functions. The 4*f*-moments in these R-intermetallics compare well with those of their free ion value of R_{3+} ions according to the Hund's rules and their Curie temperature are of the order of 10 to 10^2 K. In particular for systems containing *f*-electrons, the isotropic exchange interaction has to be extended by anisotropic terms. The anisotropy of the coupling is associated with the orbital moments of the electrons involved and the general exchange operator contains, besides the bilinear term $\hat{S}_i \cdot \hat{S}_j$, higher order isotropic interactions and all types of anisotropic exchange as, for example, Dzialoshinsky–Moriya exchange $\hat{S}_i \times \hat{S}_j$, which produces magnetic components perpendicular to the principal spin axis of the ferromagnetic or antiferromagnetic alignment. The 3*d*–4*f* exchange interactions, together with CEF effects, are the origin of the large magnetic anisotropy in R-3*d*-intermetallics needed for the high coercitivity of permanent magnets such as $Nd_2Fe_{14}B$ or $SmCo_5$ and Sm_2Co_{17}.

Exchange Interactions in Free Electron Systems – Itinerant Exchange

Paramagnetism of the free noninteracting electron gas is described by the Pauli susceptibility $\chi_P = 2\mu_B^2 N(E_F)$, which relates the paramagnetic response of the system to an external field with the density of states $N(E)$ at the Fermi energy E_F. In the paramagnetic state, the number of up and down spins is equal ($n\uparrow = n\downarrow = n/2$); thus, the magnetic moment $m = \mu_B(n\uparrow - n\downarrow)$ given by the number of unpaired spins is zero; here, it is assumed that each electron carries a magnetic moment of 1 μ_B, since $S = \pm 1/2$ and gyromagnetic ratio $g = 2$ which is a good approximation for conduction electrons. If an external field H_0 is applied, the energy of an electron with spin up or down is $\pm\mu_B\mu_0 H$ depending upon the orientation of the spin with respect to the field. Thus, the external field splits the up and down spin bands with respect to each other by the energy $2\mu_B\mu_0 H$ (see Figure 5) yielding a small but finite magnetic moment $m = \mu_B(n\uparrow - n\downarrow)$ and a Pauli susceptibility $\chi_P = m/\mu_0 H_0$.

In the Stoner Wohlfahrth model, the susceptibility of the interacting electron gas, χ_S, is enhanced due to exchange interactions by a factor $S = (1 - IN(E_F))^{-1}$, known as the Stoner enhancement yielding,

$$\chi_S = \frac{2\mu_B^2 N(E_F)}{1 - IN(E_F)} = \chi_P S$$

The quantity *I* is the Stoner exchange factor describing phenomenologically, the exchange interactions of the interacting electron gas that can be interpreted as the above mentioned average exchange per pair of electrons $\bar{I}$ favoring their ferromagnetic alignment, that is, to increase $n\uparrow$ with respect to $n\downarrow$. In a more advanced treating, $\bar{I}$ corresponds to the Hubbard *U* which models the Coulomb interaction in the Hubbard Hamiltonian in combination with the hopping integrals *t*. If $IN(E_F)$ approaches 1, χ_S diverges and a second-order phase transition into a magnetically ordered state takes place. Thus $IN(E_F) \geq 1$ is the Stoner criterion for the onset of magnetism. That means for transition metals: a reasonably high density of states at E_F due to narrow enough *d*-bands together with exchange is needed for magnetic order. By analogy to the band splitting due to an external field in the paramagnetic state, the spontaneous moment in the ordered state arises from the spontaneously spin–split bands caused in a simple mean field model by an effective exchange field $H_{\text{eff}} = Im$.

Further Reading

Barbara B, Gignoux D, and Vettier C (eds.) (1988) *Lectures on Modern Magnetism*. Berlin: Spinger.
Blundells S (ed.) (2001) *Magnetism in Condensed Matter*. Oxford: Oxford University Press.
Fazekas P (1999) *Lectures on Electron Correlation and Magnetism*, Series in modern condensed matter physics, 5th edn. Singapore: World Scientific.
Jensen J and Mackintosh AR (eds.) (1991) *Rare Earth Magnetism*. Oxford: Clarendon.
Mattis DC (1981) *Theory of Magnetism I*. Solid state sciences, 17th edn. Berlin: Spinger.
Mohn P (2003) *Magnetism in the Solid State*, Solid state sciences, 134 edn. Berlin: Springer.
Richter MJ (1998) Band structure theory of magnetism in 3*d*–4*f* compounds. *Journal of Physics D: Applied Physics* 31: 1017–1048.

Magnetic Materials and Applications

H Szymczak, Polish Academy of Sciences, Warsaw, Poland

© 2005 Elsevier Ltd. All rights reserved.

This is an update of H. Szymczak, Magnetic Materials and Applications, Editor(s): Franco Bassani, Gerald L. Liedl, Peter Wyder, Encyclopedia of Condensed Matter Physics, Elsevier, 2005, Pages 204–211, ISBN 9780123694010, https://doi.org/10.1016/B0-12-369401-9/00523-4.

Introduction **78**
Soft Magnetic Materials **78**
Iron and Soft Steels 79
Nickel–Iron Alloys 80
Iron–Cobalt Alloys 80
Soft Ferrites 80
Ferrimagnetic Iron Garnets 80
Amorphous Alloys 80
Nanocrystalline Alloys 81
Hard Magnetic Materials **82**
Alnicos 82
Hexagonal Ferrites 82
Cobalt–Samarium Magnets 82
Neodymium–Iron–Boron Alloys 83
Giant Magnetostrictive Materials **83**
Manganites **84**
Further Reading **84**

Introduction

Magnetic materials play a prominent role in modern technology. They are key components of motors, generators, and transformers. In this article, various magnetic materials of technological importance are described with an emphasis on recent developments.

Magnetic materials have a long history of usage. According to Chinese data, the compass was discovered in China more than 4500 years ago. There are also claims that a natural magnet was discovered in Magnesia (Asia Minor) more than 3500 years ago. Magnetic materials have contributed vitally to the history of civilization.

Traditionally, only those materials that exhibit ferromagnetic or ferrimagnetic properties are called “magnetic.” Only nine elements are ferromagnets. All are metals, of which three (Fe, Co, Ni) are iron-group metals and the other six (Gd, Tb, Dy, Ho, Er, Tm) are rare-earth metals. The transition metals Fe and Co are the basic elements for preparation of alloys and compounds with large Curie temperature (T_C) and a large spontaneous magnetization (M_s) (see Table 1). Some of the intermetallic compounds with rare-earth metals are characterized by a very high value of magnetocrystalline anisotropy and magnetostriction.

The primary criterion allowing for classification of magnetic materials is coercivity, which is a measure of stability of the remanent state. Soft magnetic materials are characterized by low values of coercivity ($H_c < 10^3\,\mathrm{A\,m^{-1}}$), while the coercivity of hard magnetic materials (usually permanent magnets) is higher than $10^4\,\mathrm{A\,m^{-1}}$. Finally, semihard magnetic materials (mostly storage media) have coercivities in between the above two values. In addition, there exist a number of sophisticated magnetic materials with unusual properties, such as giant magnetostriction, giant magnetoresistance, and giant magnetoimpedance. All these materials are important for modern technology and will be considered here. In modern applications, magnetic properties are tailored through precision tuning of the material microstructure. Thus, a central issue in the development and application of both soft and hard magnetic materials is the connection between extrinsic magnetic properties (coercivity, remanence, hysteresis loop) and microstructure. A universal relation was established between the coercivity H_c and the anisotropy constant K_1:

$$H_c = 2\alpha K_1/\mu_o M_s - N_{\mathrm{eff}} M_s \qquad [1]$$

where the microstructural parameters α and N_{eff} describe the effects of microstructure and domain structure.

The present technology allows one to obtain a wide spectrum of microstructures ranging from amorphous, nanocrystalline to single crystals. The corresponding coercivities may vary by a factor of 10^7 to 10^8 from extremely soft to extremely hard magnetic materials.

Soft Magnetic Materials

Typical requirements for a soft magnetic material are low coercivity, high initial permeability, and low high-frequency losses. These characteristics usually go along with the following properties of the media:

- low effective magnetic anisotropy,
- high remanence,

Table 1 Magnetic properties of 3*d* and 4*f* magnetically ordered elements

Element	*Curie temperature (K)*	*Saturation moment (μ_B)*
Fe	1043	2.22
Co	1388	1.72
Ni	635	0.61
Gd	293	7.63
Tb	220	9.34
Dy	89	10.33
Ho	20	10.34
Er	20	9.1
Tm	32	7.14

- small magnetostriction (to suppress magnetoelastic contribution to the magnetic anisotropy), and
- low conductivity.

There was a remarkable progress in production and applications of soft magnetic materials in recent years. The static permeability, for example, has been increased to huge values in materials with near-zero values of magnetic anisotropy and magnetostriction. The best soft magnetic materials have permeabilities as large as $\mu > 10^5$. The permeability μ describes the response of magnetic materials to a weak magnetic field. For small fields, this response is linear and may be characterized by the initial permeability μ_i. Generally, the permeability is determined by two mechanisms: the growth of some magnetic domains at the expense of others (wall mechanism) and the rotation of magnetization within each domain (rotation mechanism). The same two mechanisms are also responsible for the hysteresis loop in soft magnetic materials. There are two classes of losses in these materials: hysteresis losses (determined by the area of hysteresis loop) and eddy current losses (related to the DC electrical resistivity). After a thermal demagnetization or after rapid changing of magnetization, almost all soft magnetic materials show a slow decrease of their permeability as a function of time (t), according to a law:

$$\delta\mu = -D \ln t \qquad [2]$$

This decay of permeability with time is called "disaccommodation." The disaccommodation is ascribed to an increase in the domain wall stiffness, which originates in the presence of mobile defects interacting with magnetization.

Iron and Soft Steels

Iron is a very good and relatively cheap soft magnetic material. It has a very high saturation magnetization at room temperature and a large Curie temperature (see Table 2). Pure iron or soft steels (low-carbon steels, silicon steels) are used in magnetic shielding, in power and distribution transformers, in small motors, in electromagnets, and in various electromechanical devices. In AC applications, low-carbon steels are used because of their high permeability and low core loss. Silicon steels are widely used in transformers, rotating power equipment, and relays. Silicon is added to pure iron to increase resistivity and permeability and to decrease magnetostriction and magnetocrystalline anisotropy. In silicon steels, the basic magnetostriction constants approach zero at a silicon level slightly greater than 6 wt.%. Such high silicon content alloys are usually produced by a fast solidification technique. This melt-spinning technique was initially developed for amorphous alloys. Silicon steels are divided into two main categories: Fe–Si sheets with nonoriented grain texture and grain-oriented Fe–Si sheets. In the latter case, a preferred crystallographic texture leads to a reduction of core loss and increase of permeability. Annealing of iron and steels removes stresses and improves the time stability of magnetic parameters. In order to avoid the $\alpha \rightarrow \gamma$ phase transition of iron the temperature of annealing should not exceed 1125 K. In the case of silicon steel, this temperature is even higher since silicon stabilizes the α-Fe phase.

Table 2 Soft magnetic materials (crystalline)

Material	*Saturation induction* B_s *(T)*	*Coercivity* H_c *(A m^{-1})*	*Initial permeability* μ_i
Iron (ingot)	2.14	80	150
Carbon steel	2.14	100	200
Silicon iron (3% Si)			
Unoriented	2.01	60	270
Oriented	2.01	7	1 400
Permalloy (79% Ni, 5% Mo)	0.80	1	40000
Permendur (49%Co, 2% V)	2.40	160	800
Supermendur (49%Co, 2% V)	2.40	16	1000
Alfenol (16%Al)	0.80	3.5	4000
MnZn ferrite	0.40	7	10000
NiZn ferrite	0.33	80	290

Nickel–Iron Alloys

Nickel–iron alloys (known as "permalloys") are used for electronic transformers and inductor applications in the 1–100 kHz range. These are characterized by high initial permeability (see Table 2) and good ductility for forming into very thin strips. Fe–Ni alloys with 80% of Ni are characterized by the almost simultaneous vanishing of anisotropy and magnetostriction. The best alloys have the composition $Fe_{15}Ni_{80}Mo_5$. Alloys with very high permeability are mainly used in safety devices and in magnetic field shielding.

Iron–Cobalt Alloys

The most important iron–cobalt soft magnetic alloys are "Permendur" (49%Fe–49%Co–2%V) and "Supermendur" (see Table 2). The technological importance of these alloys is a consequence of their high saturation magnetization and high Curie temperature. They are characterized by high permeabilities and low coercivities. Because of high cobalt content, Fe–Co alloys are relatively costly and they are used only for special purposes where cost of the magnetic material is not of great importance, for example, in airborne medium-frequency electrical engineering and in high-temperature magnetic devices.

Soft Ferrites

The term "ferrite" refers to spinel ferrites with the general formula MO Fe_2O_3, where M is a divalent cation (e.g., Mg^{2+}, Zn^{2+}, Cd^{2+}, Mn^{2+}, Fe^{2+}, Co^{2+}, Cu^{2+}). The spinel structure is cubic, with a face-centered cubic oxygen anion lattice. Metallic ions are distributed between tetrahedral (a) and octahedral (d) sites. In the "normal spinel" structure, tetrahedral sites are occupied by divalent cations and the octahedral sites by trivalent cations. In the "inverse spinel" structure, the tetrahedral sites are occupied by trivalent cations while the octahedral sites are occupied by divalent and trivalent cations. Magnetism of ferrites is usually determined by antiferromagnetic interactions between magnetic cations located at octahedral and tetrahedral sites. It leads to a relatively low value of saturation magnetization. The Curie temperature in most ferrites is lower than that in metals. The anisotropy constant K_1 of soft ferrites is usually small and negative with the $\langle 1\,1\,1 \rangle$ axis being the easy magnetization direction. Additions of Fe^{2+} or Co^{2+} ions to the lattice provide positive contribution to K_1 and a tendency to change the easy magnetization direction (to $\langle 1\,0\,0 \rangle$ axis). It also gives a possibility to achieve a near-zero value of the anisotropy constant. The resistivity of ferrites is in the insulating range and much larger than that of metallic alloys. The dominant mechanism for the conduction in soft ferrites is the transfer of electrons between Fe^{2+} and Fe^{3+} ions on the octahedral sites. It means that resistivity of ferrites is dependent on the ferrous ions content. Resistivities of Mn–Zn ferrites range from 10^{-2} to $10\,\Omega\,m$, while Ni–Zn ferrites have resistivities $\sim 10^7\,\Omega\,m$. The hopping Fe^{2+}–Fe^{3+} also determines the frequency dependence of μ_i.

Ferrites have some disadvantages: low saturation magnetization (see Table 2), relatively low Curie temperature, and inferior mechanical properties. Despite these disadvantages, ferrites are widely used in modern technology. They are used in two main fields: power electronics (mainly Mn–Zn and Ni–Zn ferrites) and low-power techniques (Ni–Zn ferrites up to 300 MHz and Mn–Zn high-permeability ferrites up to some MHz).

Ferrimagnetic Iron Garnets

The basic formula of the ferrimagnetic rare-earth iron garnets is $\{R_3^{3+}\}[Fe_2^{3+}](Fe_3^{3+})O_{12}$, where R is either a rare-earth element or yttrium. These ions occupy dodecahedral {c} sites. The iron ions are distributed between tetrahedral (d) sites and octahedral [a] sites. Garnets crystallize in the cubic system. In a ferrimagnetic garnet, the magnetic moments of the octahedral and tetrahedral sublattices are antiparallel to each other. The moments of the Gd^{3+} and heavier R^{3+} ions couple antiferromagnetically to the net moment of the Fe^{3+} sublattices. The resulting magnetization of the garnet is the sum of these three contributions:

$$M(T) = |M_a(T) - M_d(T) + M_c(T)|$$

At low temperatures the rare-earth magnetization dominates. This effect is exactly canceled out by the net magnetization of iron sublattices at the "compensation temperature" T_{comp}. Below T_{comp}, the magnetization M_c lies parallel to a saturating field, and above T_{comp} it is antiparallel. The moments of the light rare-earth ions couple ferromagnetically to the net moment of the Fe^{3+} sublattices and no compensation points exist. In the compound $Y_3Fe_5O_{12}$ (YIG) the most attractive property is the extremely narrow ferrimagnetic resonance line width, of the order of $50\,A\,m^{-1}$. Thus, YIG with various partial substitutions for Y finds wide applications in microwave devices. Garnets find major application at lower frequencies (<5 GHz). Above 5 GHz, spinel ferrites are commonly used. YIG exhibits a room temperature saturation magnetization $\mu_o M_s \approx 0.175$ T and a magnetocrystalline anisotropy $\sim 500\,J\,m^{-3}$. The saturation magnetization of light rare-earth garnets is slightly higher while it is much lower for heavy rare-earth garnets.

Amorphous Alloys

Amorphous alloys include two large classes: transition metal-metalloids with compositions near $(Fe, Co, Ni)_{80}(B, C, Si)_{20}$ and transition metals – Zr, Hf. The former type offers greater potential for technical applications. Amorphous alloys are produced mainly by rapid ($\sim 10^6\,\mathrm{K\,s^{-1}}$) quenching from the melt or by either sputtering or evaporation. The lack of long-range atomic order in amorphous magnetic alloys is responsible for: (1) high metallic resistivity ($\sim 10^{-6}\,\Omega\,\mathrm{m}$), (2) absence of macroscopic magnetocrystalline anisotropy, (3) absence of grain boundaries and dislocations playing the role of pinning centers in crystalline magnetic materials, (4) a broad range of compositions available, yielding a continuous spectrum of property values, (5) outstanding mechanical properties, and (6) excellent resistance to corrosion.

The first class of amorphous alloys is divided into three groups (see Table 3):

1. iron-based amorphous alloys with a saturation induction B_s in the 1.1–1.8 T range with excellent high-frequency (up to 100 kHz) characteristics,
2. iron–nickel based amorphous alloys with a relatively low saturation induction but at the same time a low magnetostriction, and
3. cobalt-based amorphous alloys with a near-zero magnetostriction, a very high permeability, and low losses.

In addition to the applications of Fe-based alloys in electric utility and industrial transformers, amorphous metals are increasingly used in power electronics, telecommunication equipment, sensing devices, electric power conditioning, electronic article surveillance systems, etc. Slow crystallization of materials with a high resistance to crystallization allows a decreased critical cooling and enables stable bulk metallic glass formation. In this way, Fe-based bulk amorphous alloys with good soft magnetic properties are fabricated.

In soft magnetic amorphous ribbons and wires, the "giant magnetoimpedance effect" (GMI) is observed. This effect consists of drastic changes of the complex impedance (both real and imaginary components) of amorphous alloys upon application of an external magnetic field (of a few Oe) or mechanical stresses. Sensitivity of up to 500% of relative impedance change per Oe is observed in the very low-field region. The GMI effect is strongly dependent on the frequency of the applied field and on the magnetic anisotropies present in the material. That makes GMI materials quite convenient for application in sensors of current, position, level of liquid, and pressure. The sensors are employed in technologies such as car traffic monitoring, quality control steels, detection of earthquakes, and medicine.

Nanocrystalline Alloys

Nanocrystalline alloys consist of homogeneously distributed ultrafine grains with an average size of ~5–20 nm embedded in an amorphous matrix. They are prepared from amorphous ribbons (with the addition of Cu and Nb), which are subjected to a recrystallization annealing. The volume ratio of the crystalline phase ranges from 50% to 80% and can be controlled by the annealing temperature. Nanocrystalline alloys present a lower coercivity field than the amorphous samples, higher initial permeability than the Co-based amorphous alloys (see Table 4), very low magnetostriction, and (due to the exchange softening) nearly zero effective magnetic anisotropy. The presence of Cu and Nb allows one to obtain well-differentiated microstructures. The resistivity of these materials is usually of the same order of magnitude as that of the amorphous ones, namely $1\text{–}1.5\times 10^{-6}\,\Omega\,\mathrm{m}$. The high permeability and weak energy loss of soft nanocrystalline alloys make them valuable for various sensors, safety devices, high-frequency transformers, and in many other applications.

Table 3 Soft magnetic materials (amorphous)

Material	*Curie temperature (K)*	*Saturation induction (T)*	*Coercivity (A m^{-1})*	*Magnetostriction constant (10^{-6})*
$Fe_{81}B_{13.5}Si_{3.5}C_2$	370	1.61	3.2	30
$Fe_{67}Co_{18}B_{14}Si$	415	1.80	4.0	35
$Fe_{56}Co_7Ni_7Zr_2Nb_8B_{20}$	508	0.71	1.7	10
$Fe_{72}Al_5Ga_2P_{11}C_6B_4$	605	1.07	5.1	2
$Fe_{40}Ni_{38}Mo_4B_{18}$	353	0.88	1.2	12
$Co_{67}Ni_3Fe_4Mo_2B_{12}Si_{12}$	340	0.72	0.4	0.5

Table 4 Soft magnetic materials (nanocrystalline alloys)

Material	*Curie temperature (K)*	*Saturation induction (T)*	*Coercivity (A m^{-1})*	*Magnetostriction constant (10^{-6})*
$Fe_{73.5}Cu_1Nb_3Si_{13.5}B_9$	843	1.24	0.53	2.1
$Fe_{73.5}Cu_1Nb_3Si_{16.5}B_6$	833	1.18	1.1	~0
$Fe_{56}Co_7Ni_7Zr_2Ta_8B_{20}$	538	0.85	1.5	14
$Fe_{56}Co_7Ni_7Zr_2Nb_8B_{20}$	508	0.71	1.7	10
$Fe_{90}Zr_7B_3$		1.63	5.6	−1.1
$Fe_{86}Zr_7B_6Cu_1$		1.52	3.2	1
$Fe_{78}Si_9B_{13}$	688	1.56	2.4	27

Hard Magnetic Materials

The most important hard magnetic materials suited for permanent magnets are expected to have the following intrinsic magnetic properties:

1. *High Curie temperature*. This favors the 3*d* elements which exhibit direct exchange.
2. *High saturation magnetization at room temperature*. This again favors 3*d* elements (Fe, Co). The 3*d*–4*f* intermetallics based on the light rare earth which couple parallel with the 3*d* moment, are of special interest here.
3. *High uniaxial anisotropy*. Uniaxial anisotropy is necessary for the formation of high coercivity. The main contribution to a reasonably high anisotropy comes from the 4*f* ions. This anisotropy is of the single-ion type. To combine the best features of 3*d* and 4*f* components, a strong 3*d*–4*f* coupling is required.

Permanent magnets are characterized by an extremely wide hysteresis loop. The most important extrinsic parameter is the coercivity, H_c, connected with the total anisotropy via eqn [1].

Alnicos

Alnicos are a group of heat-treated Fe–Co–Ni–Al–Cu alloys which can be divided into two main subgroups: isotropic alloys containing 0–20 wt.% Co (alnicos 1–4) and anisotropic alloys with 22–24 wt.% Co and a titanium content of 5–8 wt.% (alnicos 5–9). The anisotropy in case of alnicos 5–9 is produced by controlled cooling or isothermal heat treatment in a saturating magnetic field. The main source of anisotropy is the shape anisotropy associated with elongated Fe–Co particles in an Ni–Al matrix aligned parallel to the magnetic field during spinodal decomposition of the alloy. Alnicos are widely used as permanent magnets (see Table 5). The most important applications are loudspeakers, watt-hour meters, electric motors, generators, and alternators.

Hexagonal Ferrites

Hard ferrites have the general chemical formula $MFe_{12}O_{19}$, where M is Ba, Pb, or Sr. They have a hexagonal structure with Fe^{3+} ions located at five different crystallographic positions. The superexchange via bridging oxygen atoms leads to a collinear ferrimagnetic structure. The high magnetocrystalline anisotropy (see Table 6) has a crystal-field and dipolar origin. The intrinsic magnetic properties of hexagonal ferrites may be modified by chemical substitution. These ferrites exhibit a large coercivity ($200–300\ \mathrm{kA\,m^{-1}}$) but a relatively low remanence ($\sim$0.4 T). They are produced by ceramic techniques and are often bonded in plastic. Owing to their low price, hexagonal ferrites are widely used in electric motors in automotive and acoustic industries (electrical equipment for vehicles, starter motors, etc.).

Cobalt–Samarium Magnets

Hard magnets based on $SmCo_5$ possess the highest uniaxial anisotropies of any class of magnets ($K\sim10^7\ \mathrm{J\,m^{-3}}$, see Table 7), while magnets based on Sm_2Co_{17} exhibit higher saturation magnetization and higher Curie temperature. Each of them has a uniaxial structure ($SmCo_5$ – hexagonal; Sm_2Co_{17} – hexagonal or rhombohedral). Chemical substitution in both compounds modifies their intrinsic and extrinsic magnetic properties. A small substitution of Cu for Co leads to precipitations of a nonmagnetic phase, which increases the coercivity. In this case, the coercivity mechanism is controlled by domain wall pinning on small $SmCo_5$ particles. A similar mechanism exists in $Sm_2(Co,Cu)_{17}$. The nucleation-controlled coercive force dominates in single-phase $SmCo_5$. The defects,

Table 5 Magnetic properties of alnicos

Alloys	*Saturation induction (T)*	*Coercivity (A m^{-1})*	*Energy product $(BH)_{max}$ (kJ m^{-3})*
Alnico 3	0.5–0.6	54–40	10
Alnico 5	1.2–1.3	52–46	40–44
Alnico 7	0.74	85	24
Alnico 9	1.0–1.1	140–110	60–75

Table 6 Intrinsic magnetic properties of $MFe_{12}O_{19}$ hexagonal ferrites

M	*Curie temperature (K)*	*Saturation magnetization (T)*	*Anisotropy constant (MJ m^{-3})*	*Coercivity (T)*
Ba	742	0.48	0.33	1.7
Sr	750	0.48	0.35	1.8
Pb	725	0.40	0.25	1.5

Table 7 Magnetic properties of cobalt–samarium compounds

Compound	*Curie temperature (K)*	*Saturation magnetization (T)*	*Coercive field (kA m^{-1})*	*Anisotropy constant (MJ m^{-3})*	*Energy product (kJ m^{-3})*
$SmCo_5$	1020	1.07	1500	17.2	160
Sm_2Co_{17}	1190	1.22	1100	3.3	260

Table 8 Magnetic properties of neodymium–iron–boron

	Curie temperature (K)	*Saturation magnetization (T)*	*Coercive field (kA m^{-1})*	*Anisotropy constant (MJ m^{-3})*	*Energy product (kJ m^{-3})*
$Nd_2Fe_{14}B$	585	1.52		4.5	
Magnet (standard)			1000		260
Magnet (high remanence)			1250		400

which act as nucleation centers, are mostly associated with the surface of milled powder particles. The Curie temperature and saturation magnetization of Sm_2Co_{17} are substantially improved by partial Fe, Zr, and Cu substitution for Co. Fe is added to increase remanence, and Cu and Zr to form the required microstructure. In this case, the coercivity has a pinning-type character.

Neodymium–Iron–Boron Alloys

Permanent magnets based on $Nd_2Fe_{14}B$ have record values for the energy product $(BH)_{max}$. Except for the relatively low Curie temperature, the Nd–Fe–B magnets are superior to all other magnetic materials. The $Nd_2Fe_{14}B$ compound has a tetragonal structure. The Nd and Fe sublattices are aligned parallel to one another, giving a room temperature magnetization of 1.61 T, the largest of any rare-earth compound used for permanent magnets. The strong magnetocrystalline anisotropy of $Nd_2Fe_{14}B$ (see Table 8) results from the low symmetry of both the Nd and Fe sites. All components of $Nd_2Fe_{14}B$ can be partly substituted by metals or metalloids. Such substitution may lead to an improvement in the thermal stability of the magnetic properties above room temperature or/and to an improvement of the microstructure and performance of the magnet. For example, cobalt substitution improves the performance of $Nd_2Fe_{14}B$ by an increase of the Curie temperature, but at the same time the presence of cobalt decreases the magnetocrystalline anisotropy.

Small quantities of Dy are often substituted for Nd to improve the coercivity of Nd–Fe–B magnets. However, dysprosium reduces the magnetization of the system. Two principal fabrication routes for Nd–Fe–B magnets are: powder metallurgy (for oriented sintered magnets) and melt spinning (used mostly for bonded magnets). The optimum composition for sintered magnets was found to be $Nd_{15}Fe_{77}B_8$ which is both Nd- and B-rich with respect to the stoichiometric $Nd_2Fe_{14}B$. The ideal two-phase microstructure in Nd–Fe–B sintered magnets consists of fully aligned grains of $Nd_2Fe_{14}B$ separated by the minimum amount of a nonmagnetic intergranular phase. Coercivity of sintered magnets is dominated by the nucleation mechanism. High remanence-oriented magnets have energy product of $\sim 400\,kJ\,m^{-3}$ and a remanence approaching 1.5 T. A different microstructure and magnetization is encountered in nanocrystalline Nd–Fe–B magnets produced by melt spinning. The origin of coercivity in melt-spun Nd–Fe–B magnets is similar to that established for sintered magnets. The nanocrystalline structure of Nd–Fe–B magnets may also be developed by mechanical alloying. Milling Fe, Nd, and B to form $Nd_2Fe_{14}B$ results in formation of α-Fe (of ~ 5 nm size) and an Nd-rich amorphous phase which should be heat treated to obtain high-coercivity material. A typical composition of these magnets is $Nd_{14}Fe_{80}B_6$. In case of fully dense isotropic nanomagnets, the characteristic energy products are $\sim 100\,kJ\,m^{-3}$ while the values of remanences are ~ 0.80 T. Mechanical alloying has also been used to synthesize other nanoscale two-phase mixtures of hard and soft magnetic phases. The exchange coupling between magnetically hard and soft phases can result in significant enhancement of the remanence. These nanocomposites are known as "exchange spring magnets." For this mechanism to be effective, the size of the soft grains should not exceed a few times the domain wall width for the hard phase ($\sim$20–30 nm). In such cases, the material behaves as if it were homogeneous, with anisotropy and magnetization being equal to the mean value of the constituent phases. Some typical examples are $Nd_2Fe_{14}B/Fe_3B$, $Nd_2Fe_{14}B/Fe$, and $Sm_2Fe_{17}N_3/Fe$.

Despite their relatively low Curie temperature and their susceptibility to corrosion, Nd–Fe–B magnets have found a great number of applications where high coercivity and energy result in design advantages. The applications include voice coil motors of hard disk drives and other small compact electronic products.

Giant Magnetostrictive Materials

Rare-earth metals have intrinsically huge magnetostriction because of the strong 4*f* electrons'–crystal lattice coupling. Although this coupling is indirect, it is huge because of the large spin–orbit coupling and the highly anisotropic localized nature of the 4*f* electrons. The relatively low magnetic ordering temperatures of rare-earth metals (R) (see Table 1) make use of the high value

Table 9 Magnetostriction constants for several rare-earth materials

Material	T = *4.2 K*	*Room temperature*	
	λ_{111} (10^{-6})	*λ_{111} (10^{-6})*	*Polycrystal (10^{-6})*
$TbFe_2$	4400	2600	1750
$Tb_{0.3}Dy_{0.7}Fe_2$		1600	1200
Polymer-bonded Terfenol-D			536
$Tb_3Fe_5O_{12}$ garnet	2460		

of magnetostriction at room temperature, possible only by combining them with 3*d* metals. Such a combination was realized most effectively in the Laves phase compound RFe_2, particularly in $TbFe_2$ (see Table 9), also known as "Terfenol." However, this compound has an intrinsically large magnetocrystalline anisotropy which limits its technical application. By addition of Dy atoms with a positive magnetocrystalline anisotropy, it is possible to compensate the negative magnetocrystalline anisotropy of terbium. The compound $Tb_{0.3}Dy_{0.7}Fe_2$ known as "Terfenol-D" maintains a giant magnetostriction (at low magnetic fields) with low magnetocrystalline anisotropy and relatively high Curie temperature. In the polycrystalline state, giant magnetostriction is possible only when the grains are aligned along the easy $\langle 1\,1\,1 \rangle$ direction and the effect is measured along this direction. This is because Terfenol-D alloys exhibit enormously large anisotropy in magnetostriction $\lambda_{111} > \lambda_{100}$. These alloys are produced either by a directional solidification method, sintering, or by a polymer bonding. The last method has an advantage over the other two because including the polymer binder with a high electrical resistivity, the frequency limit of the polymer-bonded composites can be extended to hundreds of kHz. Favorable magnetostrictive properties are also observed in amorphous R–Fe alloys. The main industrial applications of "Terfenol-D" are linear actuators.

Manganites

Doped perovskite manganites $La_{1-x}A_xMnO_3$ (where A is Ba, Ca, Sr, or Pb) show a wide variety of magnetic field-induced phenomena, including the gigantic decrease of resistance under the application of a magnetic field. It is termed "colossal magnetoresistance effect (CMR)." By replacement of a trivalent rare earth by a divalent alkaline earth, the nominal valence of Mn can be continuously tuned between 3+ (for $x=0$) and 4+ (for $x=1$). The magnetic and magneto-transport properties of manganites are governed mainly by the mixed valence Mn^{3+}/Mn^{4+} ions and less affected by the oxygen ions. The *d*-electrons are subject to a variety of interactions, of which the most important are the double exchange, superexchange, and Jahn–Teller coupling. The double exchange interaction is responsible for a strong correlation between magnetization and resistivity (or magnetoresistivity). The large resistance is related to the formation of small lattice polarons in the paramagnetic state. In these interactions, an important role is played by the e_g electrons on the Mn^{3+} ions. The orbital degeneracy leads to a variety of instabilities (such as magnetic, structural, and metal–insulator transitions, collapse of charge-ordered states under a magnetic field) and is responsible for a strong magnetoelastic coupling. The e_g electrons can be itinerant and hence play the role of conduction electrons, when electron vacancies or holes are created in the e_g orbital states of the crystal. The other characteristic feature of manganites is the appearance of unusual collective state of charge order, observed mostly for $x>0.3$. This insulating state competes with two other basic phases in manganites, namely with the ferromagnetic metallic phase and the nonmetallic paramagnetic phase. A number of experiments have demonstrated that over wide ranges of compositions there can be a coexistence between the ferromagnetic metallic and charge-ordered insulating phases.

Further Reading

Baden-Fuller A (1987) *Ferrites at Microwave Frequencies*. London: Peregrinus.
Chen CW (1977) *Magnetism and Metallurgy of Soft Magnetic Materials*. Amsterdam: North-Holland Publishing Company.
Chikazumi S (1997) *Physics of Ferromagnetism*. Oxford: Clarendon.
Coey JMD, Viret M, and von Molnar S (1999) Mixed-valence manganites. *Advances in Physics* 48: 167.
Craik DJ (ed.) (1975) *Magnetic Oxides*. London: Wiley.
Cullity BD (1972) *Introduction to Magnetic Materials*. Reading Mass. *and Magnetic Materials*. Reading, MA: Addison-Wesley.
Engdahl G (2000) *Handbook of Giant Magnetostrictive Materials*. London: Academic Press.
Gibbs MRJ (ed.) (2001) *Modern Trends in Magnetostriction Study and Application*. Amsterdam: Kluwer Academic Publishers.
Kaplan TA and Mahanti SD (1999) *Physics of Manganites*. New York: Kluwer Academic Publishers.
Moorjani K and Coey JMD (1984) *Magnetic Glasses*. Amsterdam: Elsevier.
O'Handley RC (2000) *Modern Magnetic Materials: Principles and Applications*. New York: Wiley.
Skomski R and Coey JMD (1999) *Permanent Magnets*. Bristol: Institute of Physics Publishing.
Snelling EC (1988) *Soft Ferrites: Properties and Applications*. London: Butterworth.
Tokura Y (ed.) (1997) *Colossal Magnetoresistance Oxides*. Amsterdam: Gordon and Breach.
Tokura Y and Tomioka Y (1999) Colossal magnetoresistive manganites. *Journal of Magnetism and Magnetic Materials* 200: 1.
du Tremolet de Lacheisserie E, Gignoux D, and Schlenker M (2002) *Magnetism II – Materials and Application*. Dordrecht: Kluwer Academic Publishers.

Magnetocaloric Effect

VK Pecharsky and KA Gschneidner Jr., Iowa State University, Ames, IA, USA

© 2005 Elsevier Ltd. All rights reserved.

This is an update of V.K. Pecharsky, K.A. Gschneidner, Magnetocaloric Effect, Editor(s): Franco Bassani, Gerald L. Liedl, Peter Wyder, Encyclopedia of Condensed Matter Physics, Elsevier, 2005, Pages 236–244, ISBN 9780123694010, https://doi.org/10.1016/B0-12-369401-9/01127-X.

Introduction 85
Discovery and First Application of the Magnetocaloric Effect 85
Fundamentals of the Magnetocaloric Effect 86
Magnetic Order and the Magnetocaloric Effect 87
Active Magnetic Regenerator Cycle and Near-Room-Temperature Magnetic Refrigeration 90
The Future of the Magnetocaloric Effect 92
Acknowledgments 92
Further Reading 92

Introduction

The word "magnetocaloric" is derived from Greek *Magnes* (*lithos*) (literally, stone of Magnesia, ancient city in Asia Minor), that is, magnesian (stone) or "magnetite" that has been known for thousands of years to attract articles made from iron, and Latin "calor" for heat, which evolved into French "calorique" – the name of the invisible and indestructible fluid that, according to a theory prevailing in 1700s, was thought to be responsible for virtually everything related to heat. This two-part word describes one of the most fundamental physical properties of magnetic materials: that is, when a solid is exposed to a varying magnetic field, its temperature may be measurably increased or decreased with both the sign and the magnitude of the temperature difference between the final and the initial states of the material dependent on numerous intrinsic and extrinsic factors. The chemical composition, crystal structure, and magnetic state of a compound are among the most important intrinsic material parameters. The temperature, surrounding pressure, and sign of the magnetic field change are examples of extrinsic variables that affect these magnetic-field--induced temperature changes and, therefore, play a role in defining the magnetocaloric effect (MCE).

Inherent to every magnetic solid, the magnetocaloric effect has exceptional fundamental importance because it covers length, energy, and timescales spanning over many orders of magnitude: from quantum mechanics to micromagnetics, from statistical to macroscopic thermodynamics, and from spin dynamics to bulk heat flow and thermal conductivity. Mapping out this vast landscape is an enormously challenging task, yet even partial successes along the way facilitate a better understanding of how to design novel magnetic solids; in other words, they help in creating an environment in which a material could be tailored to exhibit a certain combination of magnetic and thermal properties. In addition to its basic significance, the magnetocaloric effect is the foundation of near-room-temperature magnetic refrigeration, which is poised for commercialization in the foreseeable future and may soon become an energy-efficient and environmentally friendly alternative to vapor-compression refrigeration technology. Practical applications of the magnetocaloric effect, therefore, have the potential to reduce the global energy consumption, and eliminate or minimize the need for ozone depleting, greenhouse, and hazardous chemicals.

Discovery and First Application of the Magnetocaloric Effect

MCE was originally discovered in iron by E Warburg, who reported the phenomenon in 1881. The nature of the MCE was explained and its usefulness to reach temperatures below 1 K by adiabatically demagnetizing a paramagnetic substance was suggested independently in the mid-1920s by P Debye and W F Giauque. Namely, after cooling a paramagnetic material in a large magnetic field to as low a temperature as possible by conventional means, such as pumping on liquid helium, the material was to be thermally isolated from its surroundings, the magnetic field removed, and the sample was predicted to cool well below 1 K due to the magnetocaloric effect.

Together with his student D P MacDougall, W F Giauque was the first to verify this prediction experimentally. As Giauque and MacDougall wrote in their 12 April 1933 letter to the editor of the *Physical Review*, "On March 19, starting at a temperature of about 3.4 K, the material cooled to 0.53 K. On April 8, starting at ~2 K, a temperature of 0.34 K was reached. On April 9, starting at ~1.5 K, a temperature of 0.25 K was attained." They achieved these breakthroughs by using 61 g of hydrated gadolinium sulfate, $Gd_2(SO_4)_3{\cdot}8H_2O$, and by reducing the magnetic field from 0.8 to 0 T. Giauque and MacDougal conclude their short (about 200 words) letter that was published in 1 May 1933 issue of the *Physical Review* with the following statement: "It is apparent that it will be possible to obtain much lower temperatures, especially when successive demagnetizations are utilized." This technique is known as adiabatic demagnetization refrigeration and it is successfully employed today in ultra-low-temperature research – for example, nuclear adiabatic demagnetization has been and is being used to reach micro-kelvin temperatures.

Fundamentals of the Magnetocaloric Effect

The MCE occurs due to the coupling of a magnetic sublattice with an external magnetic field, which affects the magnetic part of the total entropy of a solid. Similar to isothermal compression of a gas during which positional disorder and, therefore, the corresponding component of the entropy of a system are suppressed, isothermal magnetizing of a paramagnet near the absolute zero temperature or a ferromagnet near its spontaneous magnetic ordering temperature – the Curie temperature, T_C – greatly reduces disorder of a spin system, thus substantially lowering the magnetic part of the total entropy. In a reversible process, which resembles the expansion of a gas at constant temperature, isothermal demagnetization restores the zero field magnetic entropy of a system. The MCE, therefore, can be measured as an extensive thermodynamic quantity – the isothermal magnetic entropy change, ΔS_M, which is illustrated in Figure 1 as a difference between the two entropy functions taken at the same temperature and is marked by a vertical arrow.

When a gas is compressed adiabatically, its total entropy remains constant whereas velocities of the constituent molecules, and therefore, the temperature of the gas both increase. Likewise, the sum of the lattice and electronic entropies of a solid must be changed by $-\Delta S_M$ as a result of adiabatically magnetizing (or demagnetizing) the material, thus resulting in an increase (decrease) of the lattice vibrations and the adiabatic temperature change, ΔT_{ad}, which is an intensive thermodynamic quantity also used to measure and express the MCE. In Figure 1, ΔT_{ad} is illustrated as a difference between the two entropy functions taken at the same entropy and is indicated using a horizontal arrow. It is worth noting that in the case of a gas, it is a "change of pressure" that results either in the adiabatic temperature rise or drop, or the isothermal entropy change, while in the case of a magnetic solid it is a "change of the magnetic field" that brings about the MCE. Needless to say, no matter how strong the magnetic field around the sample, the MCE will remain zero as long as the field is kept constant.

For a given material at a constant pressure, the two quantitative characteristics of the magnetocaloric effect are functions of the absolute temperature (T) and the magnetic field change ($\Delta B = B_f - B_i$), where B_f and B_i are the final and initial magnetic fields, respectively, experienced by the material. The MCE can be easily computed provided the behavior of the total entropy (S) of a compound is known as a function of temperature in both the initial and final magnetic fields, e.g., see Figure 1:

$$\Delta S_M(T, \delta B)_{\Delta B=B_f-B_i} = S(T,B)_{B=B_f} - S(T,B)_{B=B_i} \tag{1}$$

$$\Delta T_{ad}(T, \Delta B)_{\delta B=B_f-B_i} = T(S,B)_{B=B_f} - T(S,B)_{B=B_i} \tag{2}$$

Equation [2], in which the entropy is the independent variable and the temperature is the dependent variable, is straightforwardly employed in direct measurements of ΔT_{ad}. Thus, the temperature of a sample is measured in both B_i and B_f, that is, before and after the magnetic field has been altered. The difference between the two temperatures yields the intensive MCE value, which is usually reported as a function of temperature for $B_i = 0$.

At equilibrium, both ΔS_M and ΔT_{ad} are correlated with the magnetization (M), magnetic flux density (B), heat capacity at constant pressure (C), and absolute temperature by one of the following fundamental Maxwell equations:

$$\Delta S_M(T, \Delta B)_{\Delta B=B_f-B_i} = \int_{B_i}^{B_f} \left(\frac{\partial M(T,B)}{\partial T}\right)_B \mathrm{d}B \tag{3}$$

$$\Delta T_{ad}(T, \Delta B)_{\Delta B=B_f-B_i} = -\int_{B_i}^{B_f} \left(\frac{T}{C(T,B)} \times \frac{\partial M(T,B)}{\partial T}\right)_B \mathrm{d}B \tag{4}$$

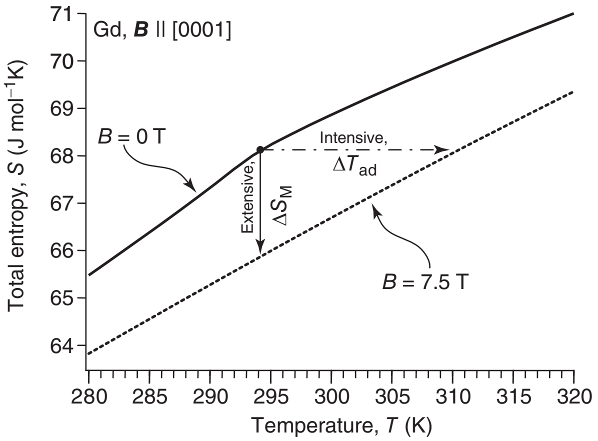

Figure 1 The total entropy of gadolinium in the vicinity of T_C=294 K in 0 and 7.5 T magnetic fields. The data are for a high-purity single crystalline Gd with the magnetic field vector parallel to the [0001] crystallographic direction of the specimen. The vertical arrow illustrates ΔS_M; the horizontal arrow represents ΔT_{ad}.

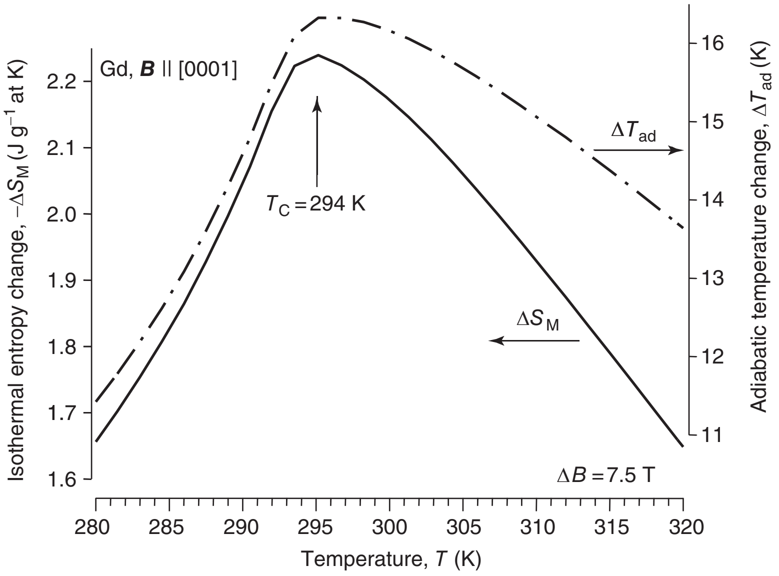

Figure 2 The extensive, ΔS_M, and intensive, ΔT_{ad}, MCE of the elemental Gd in the vicinity of its Curie temperature, T_C=294 K, for a magnetic field change from 0 to 7.5 T. The data are for a high-purity single crystalline Gd with the magnetic field vector parallel to the [0001] crystallographic direction of the specimen.

As immediately follows from eqns [1]–[4], materials whose total entropy is strongly influenced by a magnetic field and where the magnetization varies rapidly with temperature, are expected to exhibit an enhanced MCE. The latter peaks when $|(\partial M(T, B)/\partial T)_B|$ is the greatest, that is, around the T_C in a conventional ferromagnet or near the absolute zero temperature in a paramagnet. Usually, the MCE of a simple ferromagnet is gradually lowered both below and above the T_C, as is clearly seen in Figure 2.

Equations [3] and [4] are easily derived from general thermodynamics, yet both fail to describe the MCE in the vicinity of a truly discontinuous first-order phase transition when either or both $|[\partial M(T, B)/\partial T]_B|$ and $[T/C(T, B)]_B$ do not exist even if the phase volume change is negligibly small. (By definition, partial first derivatives of Gibbs free energy with respect to intensive thermodynamic variables, for example, T, P, or B, vary discontinuously at the first-order phase transition. As a result, the bulk magnetization is expected to undergo a discontinuous change at constant temperature; and the heat capacity is expected to be infinite during a first-order phase transformation. Thus, in theory, $[\partial M(T, B)/\partial T]_B$ and $[T/C(T, B)]_B$ do not exist at the temperature of the first-order transition. In reality, these changes occur over a few-kelvin-wide temperature range and both functions can be measured experimentally.) Equations [1] and [2], on the other hand, define the MCE regardless of the thermodynamic nature of the phase transformation that occurs, if any, in a material.

For a first-order phase transition, it is also possible to employ an approximation, which is based on the Clausius–Clapeyron equation:

$$\left(\frac{\mathrm{d}B}{\mathrm{d}T}\right)_{\mathrm{eq}} = \left(\frac{\Delta S}{\Delta M}\right)_T \qquad [5]$$

In eqn [5], the left-hand-side derivative is taken under equilibrium conditions, that is, when Gibbs free energies of the two phases are identical to one another. For the right-hand side, $\Delta S = S_2 - S_1$ and $\Delta M = M_2 - M_1$, where the subscripts 1 and 2 correspond to the states of the material in the initial and final magnetic fields, respectively. Obviously, eqn [5] is only applicable when B_f is strong enough to complete the transformation from a state 1 to state 2 and when the quantity $\mathrm{d}B/\mathrm{d}T$ at equilibrium is known. In other words, the B–T phase diagram for the system must be well established. By using the Clausius–Clapeyron equation, only an estimate of the extensive MCE, $\Delta S_M = \Delta S$, is possible.

Magnetic Order and the Magnetocaloric Effect

It is easy to see (Eqns [3] and [4]) that both ΔS_M and ΔT_{ad} are proportional to the derivative of bulk magnetization with respect to temperature at constant magnetic field. The ΔT_{ad} is also proportional to the absolute temperature and inversely proportional to the heat capacity at constant magnetic field. It is predictable, therefore, that any material should have the largest MCE when its magnetization is changing most rapidly with temperature. This, for example, occurs in the vicinity of a Curie temperature of a ferromagnet. (From eqn [4] it is not obvious that $\Delta T_{ad}(T)_{\Delta B}$ is at its maximum at the Curie temperature because heat capacity of a material ordering ferromagnetically also peaks around T_C. It can be shown, however, that the maximum of $\Delta T_{ad}(T)_{\Delta B}$ does indeed occur in the immediate vicinity of T_C, especially when B_i=0 and $\Delta B \to 0$. By directly measuring $\Delta T_{ad}(T)_{\Delta B}$ in low magnetic fields, it is, therefore, possible to determine the Curie temperature of a ferromagnet.) The MCE will decrease below T_C, where the magnetization approaches saturation and becomes weakly dependent on temperature, and above the Curie temperature when the magnetization shows only a paramagnetic response, that is, it is proportional to T^{-1}, while its derivative maintains a proportionality to T^{-2}.

Conventional ferromagnets, therefore, typically display "caret-like MCE." This kind of behavior is easily recognizable in Figure 2, and it is also shown in Figure 3a for a $Gd_5Si_{2.5}Ge_{1.5}$ compound. The latter orders ferromagnetically via a second-order phase transformation at 312 K. As the ΔB increases, the magnitude of the MCE of a conventional ferromagnet also increases. The rate of change of the MCE with magnetic field, that is, the instantaneous derivative of the MCE with respect to ΔB is, however, the largest at the lowest B_f. The intensive measure of the MCE can vary from a fraction of $1\ \mathrm{K T^{-1}}$ to several $\mathrm{K\,T^{-1}}$. Elemental Gd, for example, exhibits a $d[\Delta T(T, \Delta B)]/d(\Delta B)$ of $\sim 3\ \mathrm{K\,T^{-1}}$ around T_C when B_f is on the order of 1 T. The derivative falls to $\sim 1.8\mathrm{KT^{-1}}$ when B_f approaches 10 T. It is worth noting that away from absolute zero, $d[\Delta T(T, \Delta B)]/d(\Delta B)$ in conventional ferromagnetic materials is only weakly dependent on temperature (see Figure 3a).

Anomalous behaviors of the MCE are closely related to anomalous changes in the magnetic structures of solids causing unusual behaviors of the two functions, $[\partial M(T, B)/\partial T]_B$ and $[T/C(T, B)]_B$, which are carried over to both $\Delta S_M(T)_{\Delta B}$ and $\Delta T_{ad}(T)_{\Delta B}$ (see eqns [3] and [4]). One of the most commonly observed MCE anomalies is when a material undergoes two or more successive magnetic transitions in close proximity to one another. Then, instead of a conventional caret-like shape, a skewed caret, sometimes approaching a flat and an almost constant value as a function of temperature, that is, a "table-like MCE" can be observed. An example of such behavior is shown in Figure 3b for $Gd_{0.54}Er_{0.46}AlNi$. Both $\Delta S_M(T)_{\Delta B}$ (Figure 3b) and $\Delta T_{ad}(T)_{\Delta H}$ (not shown) of this material are almost constant between the two successive magnetic phase transition temperatures, which are ∼20 K apart. Anomalous MCE behaviors may also be due to low-lying crystalline electric fields and strong quadrupolar and/or

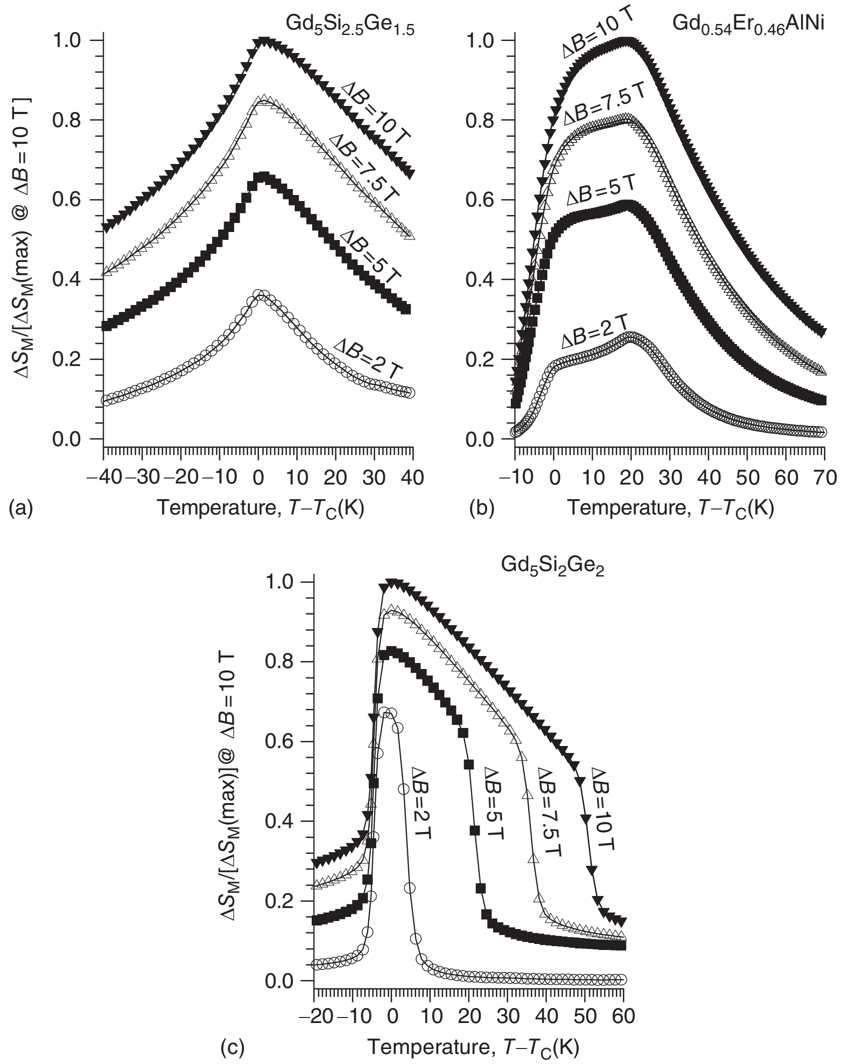

Figure 3 Normalized magnetocaloric effect of (a) $Gd_5Si_{2.5}Ge_{1.5}$ (T_C=312 K), (b) $Gd_{0.54}Er_{0.46}AlNi$ (T_C=14.5 K (the normalization temperature) and 35 K) and (c) $Gd_5Si_2Ge_2$ (T_C=273 K) shown as a function of the reduced temperature for various magnetic field changes. In all cases, B_i=0. The ΔS_M(max) values are 1.57 J g^{-1}, 0.63 J g^{-1}, and 2.61 J g^{-1} at ΔB=10 T for $Gd_5Si_{2.5}Ge_{1.5}$, $Gd_{0.54}Er_{0.46}AlNi$, and $Gd_5Si_2Ge_2$, respectively.

magnetoelastic interactions. Furthermore, the MCE can be adjusted over a broad range of behaviors by mixing two or more individual compounds or phases, each with a simple caret-like MCE, into a composite where the resulting isothermal magnetic entropy change will be a weighted sum of the corresponding values of the individual components.

Generally, a more complicated magnetic behavior results in an anomalous and a more complicated behavior of the MCE. For instance, upon cooling in a zero magnetic field, elemental Dy orders antiferromagnetically at ~180 K with a helical magnetic structure, and then transforms from the helical antiferromagnetic state to a ferromagnet at ~90 K. When the magnetic field is between 0 and ~2 T, a few additional magnetic structures emerge in pure Dy between 90 and 180 K. Thus, when the magnetic field is low, the MCE of Dy shows a sharp step-like increase at ~90 K due to a first-order ferromagnetic–antiferromagnetic transition, and then goes through a minimum immediately followed by a weak maximum at ~180 K for $\Delta B = 1\,\mathrm{T}$ (see Figure 4). The minimum exists because the application of a magnetic field to an antiferromagnet increases the magnetic entropy, thus inverting the sign of the MCE (in a ferromagnet the increasing field decreases magnetic entropy). When B_f is increased to 2 T, the magnetic field is strong enough to quench the first-order ferromagnetic–antiferromagnetic phase transition and it induces a noncollinear magnetic structure which yields a broad MCE maximum at ~127 K. Since a 2 T magnetic field is not strong enough to destroy this noncollinear structure, the slightly negative ΔT_{ad} is still observed at ~174 K. The latter is followed by a weak caret-type peak at ~181 K (Figure 4). Upon increasing the magnetic field to 5 T, it becomes strong enough to suppress all of the magnetic structures except the ferromagnetic phase and the MCE of Dy for $\Delta B = 5\,\mathrm{T}$ has a single, somewhat skewed, caret-type peak at ~181 K.

Most magnetic materials on cooling undergo a second-order phase transition from a paramagnet to a ferromagnet with a conventional MCE behavior (Figures 2 and 3a), or from a paramagnet to an antiferromagnet with a skewed caret-like MCE if the magnetic field is large enough to destroy the antiferromagnetism and cause it to change to a ferromagnetic structure (Figure 4). A few materials, however, form a ferromagnetically ordered phase through a first-order magnetic phase transition, which may also be coupled with a change of the crystal lattice. One such example is illustrated in Figure 3c. Here, since the phase transition in $Gd_5Si_2Ge_2$ is of the first order, the $|[\partial M(T, B)/\partial T]_B|$ is larger than usual (but not infinite and undefined as could happen if the transition occurs infinitely fast at constant temperature, pressure, and magnetic field), and therefore, the MCE is also larger than usual (see eqns [3] and [4]). Technically, this behavior is known as the "giant MCE." If one compares the behavior of the giant MCE in $Gd_5Si_2Ge_2$ with that of the other two materials shown in Figures 3a and 3b the most obvious difference is that at large magnetic fields the MCE versus temperature is extended considerably toward the high-temperature side of the peak, but the increase in the magnitude of the MCE with increasing field is affected to a much lesser extent than that in second-order phase transition compounds.

The MCE in first-order phase transition materials undergoing coupled magnetostructural transformations may be further enhanced by the added difference of the entropies of the two crystallographic modifications of the material, $\Delta S_{st} = \pm(S_{HF} - S_{LF})$, where HF and LF designate the high field and the low field phases, respectively:

$$\Delta S_M(T, \Delta B)_{\Delta B = B_f - B_i} = \int_{B_i}^{B_f} \left(\frac{\partial M(T, B)}{\partial T} \right)_B \mathrm{d}B + \Delta S_{st} \qquad [6]$$

It is worth noting that unlike the first factor of the right-hand side of eqn [6], which represents the conventional contribution to the isothermal magnetic entropy change (see eqn [3]), ΔS_{st} is magnetic field independent provided the change from B_i to B_f is large enough to complete the structural transformation.

Although the last factor in eqn [6] is a hidden parameter in conventional measurements of the MCE, an estimate based on comparing the MCE exhibited by the closely related materials with and without magnetic field-induced structural transformations indicates that ΔS_{st} may account for more than a half of the total magnetic entropy change in magnetic fields below 5 T. Advanced magnetocaloric materials should, therefore, exist in solid systems where extensive structural changes are coupled with ferromagnetic

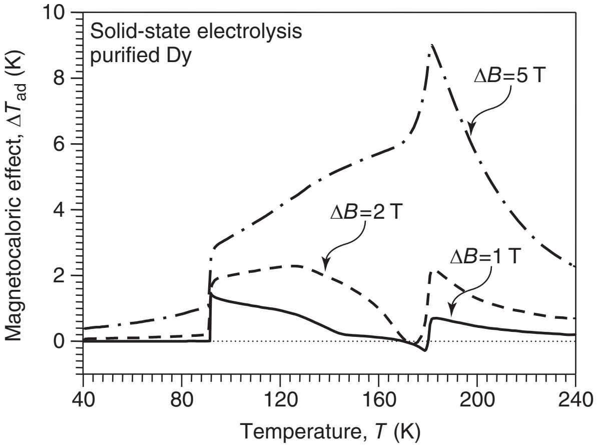

Figure 4 The magnetocaloric effect in ultrapure Dy calculated from the heat capacity data.

ordering, and therefore, can be triggered by a magnetic field. Considering eqn [6], the strongest MCE should be found in novel compounds engineered in order to maximize the entropy of a structural transformation, ΔS_{st}. An extensive listing of ΔS_M and ΔT_{ad} values can be found in the reviews by Gschneidner and Pecharsky, and Tishin and Spichkin – see the "Further reading" section.

Active Magnetic Regenerator Cycle and Near-Room-Temperature Magnetic Refrigeration

Adiabatic demagnetization refrigeration, described at the beginning of this article, is a discontinuous process for all practical reasons because it may take as much as a few hours to repeat the refrigeration cycle and reach the target temperature. The history of continuous magnetic refrigeration can be traced to the work of S C Collins and F J Zimmerman, and C V Heer, C B Barnes and J C Daunt, who in the early 1950s built and tested two magnetic refrigerators operating between ~1 and 0.2 K by periodically magnetizing and demagnetizing iron ammonium alum. The apparatus built by Heer, Barnes, and Daunt operated at 1/120 Hz frequency (2 min per cycle) and on average extracted 12.3 μJ s^{-1} from the cold reservoir at 0.2 K.

It was not, however, until 1976 when G V Brown reported a near-room-temperature continuously operating magnetic refrigerator, that it became clear that magnetic refrigeration may be successfully utilized at significantly higher temperatures and achieve much larger temperature spans than the maximum observed MCE. Brown was able to attain a 47 K no-load temperature difference between the hot end (319 K) and cold end (272 K) of his unit by regenerating a column of fluid using Gd metal and a magnetic field change from 0 to 7 T and from 7 to 0 T. The achieved temperature difference was more than three times the MCE of Gd for ΔB=7 T (see Figure 2, where for a slightly greater ΔB=7.5 T, the maximum ΔT_{ad} of Gd is around 16 K at T_C=294 K; the MCE is ~13 K and ~11 K at 319 K and 272 K, respectively).

Following the early work of Brown, the concept of active magnetic regenerator (AMR) refrigeration was introduced by W A Steyert in 1978 and developed by J A Barclay and W A Steyert in the early 1980s. It was subsequently brought to life in the later 1990s, when various magnetic refrigeration units were built in the US, Europe, and Japan. In the AMR cycle, shown schematically in Figure 5, a porous bed of a magnetic refrigerant material acts as both the refrigerant that produces refrigeration (i.e., temperature lift) and the regenerator for the heat transfer fluid. Assume that the bed is at a steady state with the hot heat exchanger at 18°C and the cold heat exchanger at 2°C. In Figure 5a, the initial temperature profile for the bed is in its demagnetized state in zero magnetic field (dashed line). When a magnetic field is applied to the refrigerant, each particle in the bed warms because of the MCE to form the final magnetized bed temperature profile (solid line). The amount each particle warms is equal to ΔT_{ad} reduced by the effect of the heat capacity of the heat transfer fluid in the pores between the particles. Next, the 2°C fluid flows through the bed from the cold end to the hot end (Figure 5b). The bed is cooled by the fluid, lowering the temperature profile across the bed (from the dashed line to the solid line), and the fluid in turn is warmed by the bed, emerging at a temperature close to the temperature of the bed at the warm end. This temperature is higher than 18°C, so heat is removed from the fluid at the hot heat sink as the fluid flows through the hot heat exchanger. After the fluid flow is stopped, the magnetic field is removed, cooling the bed by the MCE (from the dashed line to the solid line in Figure 5c). The refrigeration cycle is completed by forcing the 18°C fluid to flow from the hot to the cold end of the bed (Figure 5d). The fluid is cooled by the bed, emerging at a temperature below 2°C and removes heat from the cold sink as the fluid passes through the cold heat exchanger. After completion of this last step, the cycle is repeated beginning from step (a) (Figure 5).

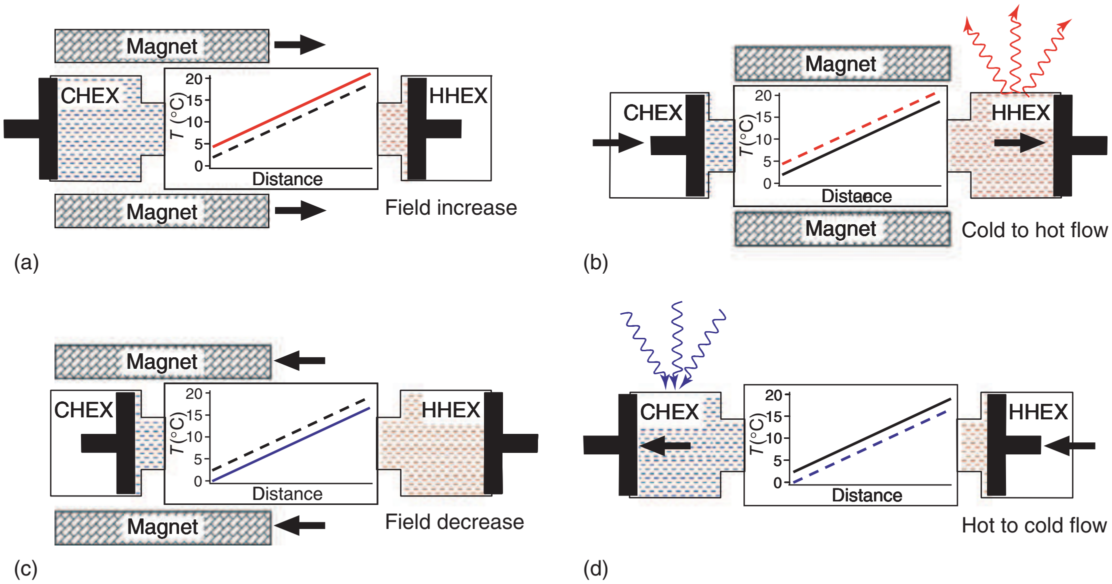

Figure 5 The four steps of the active magnetic regenerator cycle: magnetizing (a), flow from the cold heat exchanger (CHEX) to the hot heat exchanger (HHEX) (b), demagnetizing (c), and flow from HHEX to CHEX (d). This description follows that introduced by C B Zimm and A J DeGregoria in 1993.

The AMR cycle outlined above has several positive features useful for practical application in magnetic refrigeration devices. First, the temperature span of a single stage can greatly exceed that of the MCE of the magnetic refrigerant because the MCEs of the individual particles collectively change the entire temperature profile across the bed. Second, because the bed acts as its own regenerator, heat need not be transferred between two separate solid assemblies, but rather between the solid particles in a single bed via the action of a fluid. Third, the individual particles in the bed do not encounter the entire temperature span of the stage, and hence the bed may be made into layers, each containing a magnetic material with properties optimized for a particular temperature range.

The AMR refrigeration cycle has been successfully realized in a laboratory prototype magnetic refrigerator, which was recently designed and constructed by the Astronautics Corporation of America. The device is shown together with its schematic diagram in Figure 6. The refrigerator operates near room temperature in a magnetic field between 0 and ~1.5 T created by a permanent magnet. As the wheel spins, it brings one of its sections containing the magnetic refrigerant (the regenerator bed) into the high magnetic field volume, where the bed is heated due to the MCE (see Figure 6a). As long as this section of the wheel moves between the poles of the permanent magnet, it remains in the magnetized state and the heat exchange fluid (water) flows from the cold heat exchanger through the bed and into the hot heat exchanger. This corresponds to the second step of the AMR cycle shown in Figure 5b. While the wheel continues to spin, the same section exits from the high magnetic field volume. As the bed cools due to the MCE, the heat exchange fluid flow is reversed and it now flows from the hot heat exchanger through the bed toward the cold heat exchanger, thus completing steps (c) and (d) of the AMR cycle illustrated in Figure 5.

This permanent magnet-based rotating bed magnetic refrigerator was recently awarded US patent no. 6 526 759. The unit can operate at frequencies exceeding 1 Hz and it has achieved a maximum cooling power of 95 W and a maximum temperature span of 20°C. As tested by engineers at the Astronautics Corporation of America, the Carnot efficiency of this laboratory prototype system

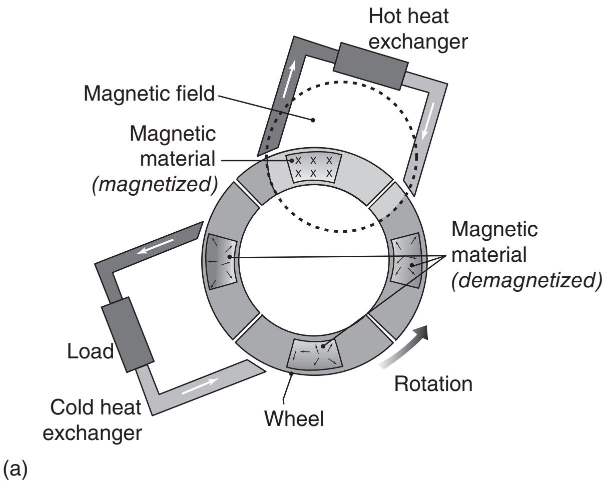

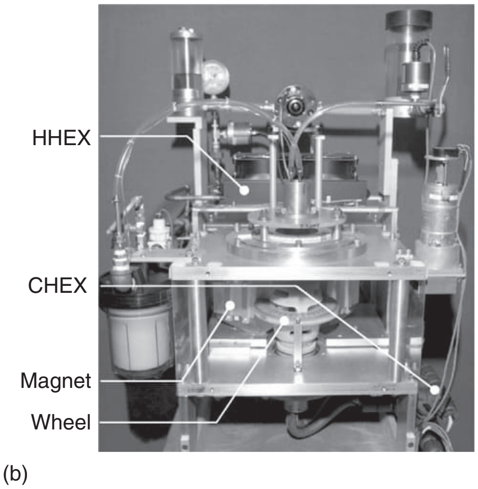

Figure 6 (a) The principal schematic diagram of the device and (b) laboratory prototype magnetic refrigerator designed and constructed by the Astronautics Corporation of America in 2001. A ~1.5 T magnetic field around the wheel filled with Gd spheres is produced by a permanent magnet. The refrigerator operates at ambient conditions with a maximum temperature span of ~20°C and maximum cooling power of 95 W. ((b) Courtesy of the Astronautics Corporation of America, 4115 N. Teutonia Avenue, Milwaukee, WI 53209.)

compares favorably with conventional vapor-cycle refrigeration devices, thus making magnetic refrigeration the first energy-efficient solid-state refrigeration technology.

The Future of the Magnetocaloric Effect

Considering practical applications of the MCE, its extent is one of the most critical parameters defining the performance of a magnetic refrigerator – the stronger the MCE the higher the efficiency of the device, all other things being equal. As is often the case with emerging technologies, numerous applications of magnetic refrigeration may stem from a reliable foundation formed by advanced magnetocaloric materials. For example, the availability of low-cost high-performance solids exhibiting enhanced MCE between $\sim$250 and $\sim$350 K is an important requirement in order to facilitate commercialization of magnetic refrigeration for a variety of consumer uses – from home appliances to climate control in motor vehicles. In another example, when suitable magnetocaloric compounds supporting continuous magnetic cooling from $\sim$300 to $\sim$20 K are developed, the energy penalty incurred during hydrogen liquefaction using the conventional gas-compression approach may no longer be a limiting factor preventing the widespread use of liquid hydrogen fuel in transportation. It is conceivable that many other areas where conventional refrigeration is inapplicable because of scaling difficulties and/or where thermoelectric refrigeration demands too much energy, magnetic refrigeration will eventually emerge as the cooling technology of choice.

To amplify the MCE, conventional wisdom calls for increasing the magnetic field change in addition to maximizing both the derivative, $|(\partial M(T, B)/\partial T)_B|$, and the region of magnetic fields and temperatures where the magnetization remains highly sensitive to temperature (see eqns [1]–[5]). Considering the current state-of-the-art of permanent magnet alloys and magnet design, it is quite unlikely that magnetic fields in excess of about 2 T at a reasonable cost will become common in the foreseeable future. That is why maximizing the MCE by manipulating chemical and phase compositions, atomic, microscopic, and magnetic structures of a material appears to be the most realistic option in order to reach the strongest possible MCEs in readily available magnetic fields. Although it remains a formidable challenge for basic science, a better understanding of the MCE, including the ability to control a variety of chemical, structural, and physical degrees of freedom that define the properties of solids will lead to improved existing materials and should eventually result in novel compounds exhibiting large MCE.

An especially promising area of research is the study of the extensive measure of the MCE, that is, the isothermal magnetic-field-induced entropy change that can be strongly enhanced by the added entropy of a structural transition (see eqn [6]). Provided the magnetic field completes the polymorphic transformation, this additional entropy is magnetic field independent, and therefore, may account for more than half of the observed MCE, especially in relatively weak magnetic fields. The design of novel materials exhibiting potent MCEs in weak magnetic fields is, therefore, possible by ensuring that (i) a structural transition can be triggered and completed (or nearly completed) by a weak magnetic field; (ii) the transformation has low thermal and magnetic field hystereses, that is, is reversible, and (iii) the difference between the entropies of different polymorphic modifications is maximized.

Acknowledgments

This work was supported by the Materials Sciences Division of the Office of Basic Energy Sciences of the US Department of Energy under a contract No. W-7405-ENG-82 with Iowa State University. The authors wish to thank Dr. Steven Russek and Dr. Carl Zimm of Astronautics Corporation of America for permission to use the photograph of their rotary magnetic refrigerator.

Further Reading

Gschneidner KA Jr. and Pecharsky VK (2000) Magnetocaloric materials. *Annual Review of Materials Science* 30: 387–429.

Gschneidner KA Jr. and Pecharsky VK (2002) Magnetic refrigeration. In: Westbrook JH and Fleischer RL (eds.) *Intermetallic Compounds. Principles and Practice*, vol. 3, pp. 519–539. New York: Wiley.

Morrish AH (1965) *The Physical Principles of Magnetism*. New York: Wiley.

Pecharsky VK and Gschneidner KA Jr. (1999) Magnetocaloric effect and magnetic refrigeration. *Journal of Magnetism and Magnetic Materials* 200: 44–56.

Tegus O, Brück E, Zhang L, Dagula, Buschow KHJ, and de Boer FR (2002) Magnetic phase transitions and magnetocaloric effects. *Physica B* 319: 174–192.

Tishin AM (1999) Magnetocaloric effect in the vicinity of phase transitions. In: Buschow KHJ (ed.) *Handbook of Magnetic Materials*, vol. 12, pp. 395–525. Amsterdam: Elsevier.

Tishin AM and Spichkin YI (2003) *The Magnetocaloric Effect and its Applications*. Bristol: Institute of Physics Publishing.

www.m-w.com

Manganites

VZ Kresin, University of California at Berkeley, Berkeley, CA, USA

© 2005 Elsevier Ltd. All rights reserved.

This is an update of V.Z. Kresin, Manganites, Editor(s): Franco Bassani, Gerald L. Liedl, Peter Wyder, Encyclopedia of Condensed Matter Physics, Elsevier, 2005, Pages 261–265, ISBN 9780123694010, https://doi.org/10.1016/B0-12-369401-9/01159-1.

Introduction 93
Structure 93
Doping: Phase Diagram 93
Main Interactions: Hamiltonian 94
Metallic Phase: CMR Phenomenon 95
Insulating State 96
Percolative Transition 96
Further Reading 97

Introduction

Manganites were discovered in 1950 (Jonner and van Santen). The materials are named after the manganese ion which is a key ingredient of the compounds due to its mixed-valence state. Unlike the usual ferromagnetics, the transition of manganites to ferromagnetic state is accompanied by a drastic increase in conductivity. Such transition from an insulating to a metallic and magnetic state is a remarkable fundamental feature of these materials. Another fundamental property is the colossal magnetoresistance effect (CMR); one can observe a thousandfold (!) change in the resistance in the presence of a moderate applied magnetic field.

The chemical composition of the manganites is A_{1-x} R_x MnO_3; usually A≡La, Pr, Nd and R≡Sr, Ca, Ba. The compound $La_{1-x}Sr_xMnO_3$ is the most studied material.

Structure

The parent (undoped) compound $LaMnO_3$ has a perovskite structure which is a distorted cubic lattice. The ideal crystal unit is shown in Figure 1. It is essential that the Mn ions are caged into oxygen octahedron, so that it is surrounded by six oxygen ions (Figure 2). Each oxygen ion is shared by neighboring octahedra. The fivefold orbital degeneracy is split by the crystal field into two well-separated terms, t_{2g} and e_{2g} (Figure 3). The t_{2g}-level contains three electrons forming the so-called "*t*-core." The last *d*-electron (e_{2g}-electron) is in a loosely bound state. The e_{2g}-electron plays a crucial role in conduction and in other properties of manganites as well as in determining its magnetic order.

Doping: Phase Diagram

The phase diagram of manganites is very rich and contains many different phases. The parent compound, $LaMnO_3$, is an insulator and its transition to the conducting state is provided by doping. The doping is realized through a chemical substitution, for example $La^{3+} \rightarrow Sr^{2+}$, that is, by placing a divalent ion into the local La^{3+} position. Such substitution leads to the change in the valence of the manganese ion valence: $Mn^{3+} \rightarrow Mn^{4+}$. That is why manganites are often called "mixed-valence magnetic oxides." The four-valent state of the Mn means that the ion loses its e_{2g}-electron. The missing electron can be described as a hole which is spread over the unit cell, being shared by eight Mn ions (see Figure 1)

As a result, one obtains a crystal $La_{1-x}Sr_xMnO_3$, where a number of La centers are randomly substituted by the Sr-ions. Even in the presence of some holes, the crystal, at first, continues to behave as an insulator. This is due to the fact that each hole is localized and the localization corresponds to the formation of local polarons. Such insulating state is preserved with an increase in doping up to some critical value $x=x_c \approx 0.16$–0.17. At $x=x_c$, the material makes a transition into the conducting (metallic) state which persists with further doping up to $x \approx 0.5$–0.6, depending on the chosen composition.

It is remarkable that the transition at $x=x_c$ is also accompanied by the appearance of the ferromagnetic state. As was noted above, the correlation between conductivity and magnetism is the most fundamental feature of manganites. The conductivity of the best samples of the Sr-doped films at low T is of order $\sigma = 10^4 - 10^5 \Omega^{-1} \text{cm}^{-1}$, and this corresponds to a typical metallic regime.

Continuous increase in doping leads to the transition from the metallic to insulating state. For many compounds one can observe a peculiar charge-ordered state. The right end of the phase diagram (e.g., $SrMnO_3$) describes the compound which does not have the e_{2g}-electrons. Naturally, this material is an insulator.

If the compound is in the metallic ferromagnetic state (e.g., it corresponds to $0.2<x<0.5$ for La_{1-x} Ca_xMnO_3), and temperature is increased (at fixed x), then at T_C (T_C is the Curie temperature) one can observe transition to the low-conducting paramagnetic state which contains local distortions. The conductivity in this state has a hopping polaronic nature.

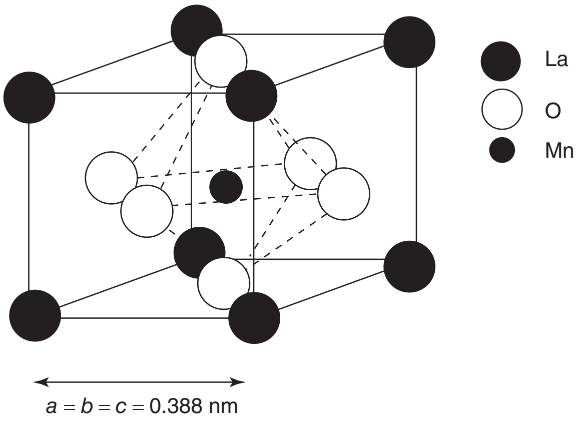

Figure 1 The ideal structure of the parent compound, La MnO_3.

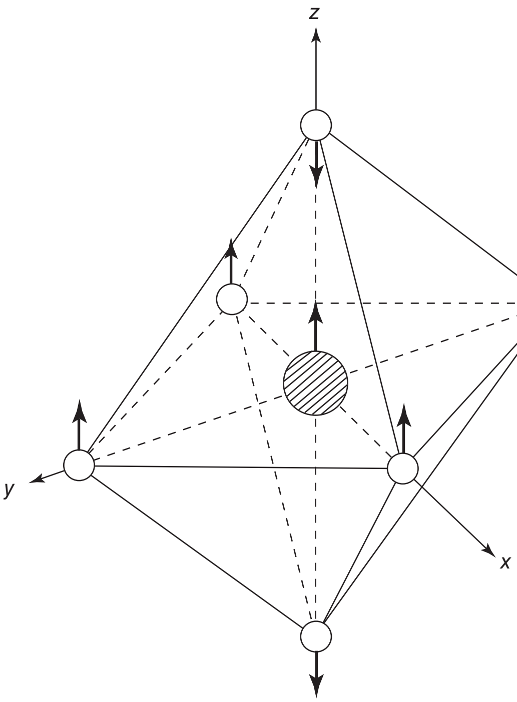

Figure 2 MnO_6 octahedron.

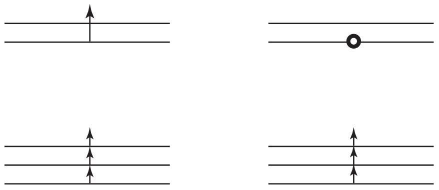

Figure 3 Electronic structures of the Mn^{3+} and Mn^{4+} ions.

Main Interactions: Hamiltonian

The loosely bound e_{2g}-electron is the key player in the physics of manganites. Its Hamiltonian can be written in the form:

$$\hat{H} = \hat{H}_t + \hat{H}_{\mathrm{H}} + \hat{H}_{\mathrm{JT}} \qquad [1]$$

where

$$\hat{H}_t = \sum_{i,\delta} \hat{t}_{i,i+\delta} \quad [2]$$

$$\hat{H}_{\mathrm{H}} = -J_H \sum_i \hat{\sigma} \cdot S_i \quad [3]$$

$$\hat{H}_{\mathrm{JT}} = \sum_i g \hat{\tau}_i Q_i \quad [4]$$

Here $\hat{t}$ is the two-by-two hopping matrix, $\hat{\sigma}$ is the Pauli spin matrix, S_i is the spin of the *t*-core, $\hat{\tau}$ is the pseudospin matrix, and Q_i is the normal mode.

The first term on the right side of eqn [1] describes the hopping of the e_{2g}-electron. The second term is the Hund's interaction which polarized the carrier's spin, and the last term corresponds to the Jahn–Teller effect which reflects the double degeneracy of the e_{2g}-term. The strength of the Hund's interaction is of the order $J_{\mathrm{H}} \approx 1$ eV; this is the largest scale of the energy. It is also essential that, because of the Hund's interaction, the conducting e_{2g}-electrons are spin-polarized. As for the hopping and the Jahn–Teller terms, they are of order $t \approx g \approx 0.1$ eV, so that $t \approx g < J_{\mathrm{H}}$.

The nature of the ferromagnetic spin alignment in manganites is different from that for usual ferromagnets. The concept, so-called "double exchange" mechanism was introduced in 1951 by Zener. Qualitatively, the nature of the mechanism is as follows. If one of the Mn^{3+} ions becomes four-valent (e.g., as a result of the $La^{3+} \rightarrow Sr^{2+}$ substitution, implying $Mn^{3+} \rightarrow Mn^{4+}$), a hole appears on this site. It allows for another e_{2g}-electron localized initially at the neighboring Mn^{3+} ions to jump on the new vacant place (this can be described as the hole moving in the opposite direction). But the e_{2g}-electron is spin-polarized because of the Hund's interaction with its *t*-core. Relative orientation of spins of the e_{2g}-electron and the "vacant" *t*-core drastically affects the hopping. For example, if the direction of the spin of the core for the Mn^{4+} ion is opposite to that one for the e_{2g}-electron of the neighboring Mg^{3+} ion, then the hopping is spin forbidden. At the same time, such hopping as any increase in a degree of delocalization is energetically favorable. As a result, the ground state of the ferromagnetically ordered system (all spins are polarized along one direction) energetically is below the state which is not ordered. That is why the *t*-cores become ferromagnetically ordered, and this, in its turn, favors "jumping" of the e_{2g}-electrons, and, therefore, conductivity. Such mechanism (it is called "double exchange") leads to ferromagnetism and to a strong correlation between ferromagnetism and conductivity.

Metallic Phase: CMR Phenomenon

Consider the sample in the metallic ferromagnetic state with a fixed carrier concentration, (e.g., $x=0.3$) and then increase the temperature. Such ferromagnetic state persists up to the Curie temperature. For example, for the $La_{0.7}Sr_{0.3}MnO_3$ to the value of $T_C \cong 170$ K. Above this temperature the compound makes the transition into paramagnetic state. In addition, resistivity drastically increases (almost insulating state).

The conductivity of the metallic manganites is provided by the delocalized e_{2g}-electrons. It is essential that these electrons are in the double-degenerate state. This leads to the two-band picture. Presence of the two energy bands allows to explain the absence of the electron–hole symmetry for the phase diagram. In addition, this feature is important for analysis of various properties of manganites. For example, optical properties are, mainly, due to the interband transitions.

The value of the Fermi energy in the metallic manganites is small relative to ordinary metals. Its value depends on the doping level and is of the order of EF≈0.2 eV. As for conductivity, its value depends strongly on the quality of the samples. As was mentioned above, for the best samples it reaches the value $\sigma \approx 10^5 \Omega^{-1} \mathrm{cm}^{-1}$.

The charge transfer in the conducting ferromagnetic manganites is provided by spin-polarized electrons. Because of such spin specifics a total number of carriers in the band of the metallic manganites is twice less than in usual metals. That is why the conducting state in manganites is called "half-metallic."

The magnetoresistance is a very important parameter of manganites. It is defined as

$$\Delta R/R_H = [R(T,H) - R(T,0)]/R(T,H) \quad [5]$$

The magnetoresistance has a sharp peak near the Curie temperature for the manganite, and the change in resistivity caused by an applied magnetic field can be huge. Such phenomenon which is dubbed as the colossal magnetoresistance effect (CMR) has been initially observed in the ferromagnetic metallic films by Jin *et al.* in 1994. It turns out that for $La_{0.67}Ca_{0.33}MnO_3$ films $\Delta R/R_H \approx -1.3x10^3$(!); $H \approx 5$ T.

The CMR phenomenon is discussed now. Below T_C the sample is characterized by usual metallic conductivity. Contrary to it, above T_C it has a large resistivity (low conducting state with hopping polaronic transport). The presence of an external magnetic field allows to establish ferromagnetic ordering at temperatures higher than T_C ($H=0$). The magnetic order provides metallic conductivity, because of the double exchange mechanism, and this leads to a large shift $\Delta R_H = R(T, H) - R(T, 0)$. The shift is negative, in accordance with the experimental observation and corresponds to the transition from a low conducting (almost insulating) to a metallic state.

Insulating State

The undoped material $LaMnO_3$ is an insulator and its magnetic ordering corresponds to the so-called A-structure. This structure is characterized by the presence of the ferromagnetically ordered layers with an opposite direction of the magnetization for the neighboring layers. In other words, ferromagnetism in layers is combined with the antiferromagnetic ordering in the direction perpendicular to the layers. The value of the Neel's temperature is relatively low ($\approx 10^2$ K).

The insulating behavior can be explained in the framework of the band picture. However, this picture should be modified in accordance with the Hamiltonian (eqn [1]). Unlike ordinary metals, the band is filled by spin-polarized electrons. Moreover, the degeneracy of the e_{2g}-state leads to the two-band situation. In addition, one should take into account the Jahn–Teller distortion. Because the O ion is shared by neighboring manganese octahedra, the cooperative Jahn–Teller effect is dealt with. If one includes all these factors, the energy bands appear to be filled, and the compound is the band insulator.

Doping leads to creation of holes, but it does not mean that the sample becomes a conductor. Initially holes are localized by Coulomb forces and form polarons. Such process is a favorable one for the layered system, because in the 2D case there is no energy barrier for the polaron formation. The transition to the metallic ferromagnetic state occurs at finite doping level $x=x_c$.

Percolative Transition

The doping leads to the situation when at some critical concentration of the dopant, x_c, one can observe the transition from insulating to metallic state. This transition can be described in terms of the percolation theory. Indeed, doping leads to the formation of the compound $A_{1-x}B_xMnO_3$. A position of atom B, which is a substitution for a parent atom, is completely random, and the statistical distribution of dopants leads to the percolation picture. As a result of initial doping metallic clusters are formed. These clusters are created inside the insulating matrix and eventually form the percolation "path." In accordance with the Zener's double-exchange mechanism, there is ferromagnetic order inside the clusters. The transition to the metallic ferromagnetic state corresponds to formation of the infinite cluster and, correspondingly, to an appearance of the macroscopic phase. The transition occurs at $x=x_c\approx 0.17$, and this value is, indeed, an invariant of the percolation theory. Therefore, the metal–insulator transition in manganites is a percolation phenomenon (Figure 4).

The percolative nature of the metal–insulator transition implies the inhomogeneity of the system, that is, one is dealing with a coexistence of two phases: metallic and insulating. This is the "phase-separation" phenomenon. This concept for the doped oxides was introduced by Gor'kov and Sokol in 1987. Manganites as well as the high-temperature superconducting cuprates are examples of such systems. Macroscopic properties at $x<x_c$ are determined by the insulating matrix, but the sample contains metallic ferromagnetic inclusions. In a similar way, the sample at $x>x_c$, being in the ferromagnetic metallic phase, contains insulating regions.

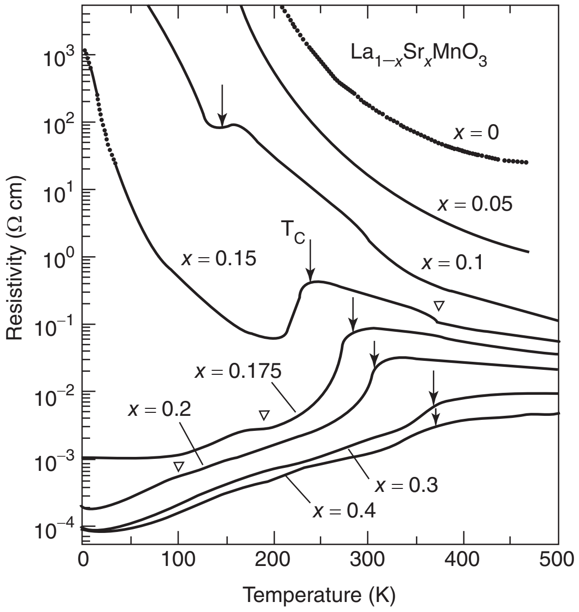

Figure 4 Temperature dependence of resistivity (for various levels of doping). The transition to the metallic state occurs at $x \approx 0.17$. (Reproduced with permission from Urishibara A, Moritomo Y, Arima T, Asamitsu A, Kido G, *et al.* (1995) Insulator–metal transition and gaint magnetoresistance in $La_{1-x}Sr_xMno_3$. *Physical Review B* 51: 14103.)

The percolative transition occurs also in the metallic sample with a fixed-level doping (e.g., $x \approx 0.3$) at $T = T_C$. The fast increase in conductivity $\sigma(T)$ at $T < T_C$ is described by the expression

$$\sigma(TT_C) \propto (T_C - T)^{\gamma} \qquad [6]$$

where γ is a critical index.

The percolative nature of the transition at $T = T_C$ also implies the intrinsic inhomogeneities of the sample, that is, the phase separation. This means that, even below T_C, the sample, being in the metallic ferromagnetic state, contains inclusions of the low-conducting paramagnetic phase.

The concept of intrinsic inhomogeneity as well as the percolation picture has a strong experimental support. Various experimental techniques, such as scanning tunneling microscopy (STM), neutron scattering, X-rays absorption fine structure spectroscopy, and heat capacity data allow us to prove the picture of phase separation. For example, one can measure electronic contribution ($\propto T$) to heat capacity at $x < x_c$. The inelastic neutron scattering as well as the X-rays spectroscopy display the presence of two different bond lengths corresponding to mixed phases. An intensive study of manganites continues. Search for new materials, synthesis of high-quality samples, and a detailed theoretical and experimental analysis of all regions of the phase diagram will lead to new insights and interesting potential applications.

Further Reading

Coey JMD, Viret M, and von Molnar S (1999) Mixed-valence manganites. *Advances in Physics* 48: 167.

Gor'Kov L and Kresin V (2004) Mixed-valence manganites: fundamentals and main properties. *Physics Reports* 400: 149.

Jin S, Tiefel TH, McCormack M, Fastnacht R, Ramesh R, and Chen LH (1994) Thousandfold change in resistivity in magnetoresistive La-Ca-Mn-O films. *Science* 264: 412.

Tokura Y (2003) Correlated-electron physics in transition-metal oxides. *Physics Today* 56: 50.

Van Tenderloo G, Lebedev O, Hervien M, and Ravean B (2004) Structure and microstructure of colossal magnetoresistant materials. *Reports on Progress in Physics* 67: 1315.

Magnetic oxides

Daniel I Khomskii[a] **and Sergey V Streltsov**[b], [a]University of Cologne, Cologne, Germany; [b]M.N. Mikheev Institute of Metal Physics, Ekaterinburg, Russia

© 2024 Elsevier Ltd. All rights reserved.

Introduction 99
Isolated magnetic ions in a crystal 99
Intersite effects 101
Exchange interaction 102
Frustrated magnetism, spin liquids, spin ice 103
Various orderings: Magnetic, charge, orbital, etc. 105
Magnetoelectrics and multiferroics 106
Insulator-metal transitions; metallic oxides 107
Superconductivity in oxides 109
Various useful properties and applications of magnetic oxides 110
Conclusion 111
Acknowledgments 111
References 111

Abstract

In this article we give a general survey of the main properties of magnetic oxides—mostly the oxides of transition metals, but sometime also containing rare earths ions. This is a very rich class of materials, among which there are insulators and metals, systems with insulator-metal transitions, and there are among them even high-temperature superconductors. One of the main features of these compounds, which attract to them special attention and which serve as a basis of many applications, are their rich magnetic properties. In this article we discuss the main physical effects determining their behavior, and describe in detail especially their magnetic properties, but not only. After shortly discussing the basic structure of isolated magnetic ions, we concentrate on the collective effects depending on the interaction between sites, especially exchange interaction, giving rise to different magnetic properties: different types of magnetic ordering in conventional systems, but also more exotic states such as spin liquid states in frustrated systems. We also cover related phenomena in magnetic oxides, such as magnetoelectric and multiferroic behavior, and discuss at the end their diverse useful properties serving as a basis of many applications.

Key points:

- There are different factors such as the spin-orbit coupling, intra-atomic Hund's exchange, crystal-field splitting and the Jahn-Teller effect controlling electronic and magnetic properties of isolated magnetic atoms.
- Intersite effects e.g., electron tunnelling between ions, strong electronic correlations or features of the Fermi surface (in metals) define exchange interaction between magnetic ions.
- Exchange coupling can be anisotropic (different between different spin components). Competition between different exchange bonds can result in very unusual magnetic structures and can lead to different anomalous magnetic states such as spin liquids and spin ice.
- There are insulating magnetic oxides (magnetoelectrics and multiferroics), in which one can influence magnetic state by electric field and, vice versa, electric polarization can be controlled by magnetic field.
- Various transitions including structural and metal-insulator transitions are possible in magnetic oxides. Moreover, some of them can be driven into a superconducting state.
- Magnetic oxides have many applications, e.g., they can be used as magnetic field sensors, for nondestructive control and in spintronics.

Abbreviations

AFM	Antiferromagnetic, antiferromagnetism
CF	Crystal-field
CT	Charge-transfer

https://doi.org/10.1016/B978-0-323-90800-9.00120-7

DM	Dzyaloshinskii-Moriya
FE	Ferroelectricity
FM	Ferromagnetic, ferromagnetism
High-Tc	High-temperature
HS	High-spin
IMT	Insulator-metal transitions
JT	Jahn-Teller
LS	Low-spin
ME	Magnetoelectric effect
MF	Multiferroic
RE	Rare-earths
RKKY	Ruderman-Kittel-Kasuya-Yosida
SOC	Spin-orbit coupling
TM	Transition metals

Introduction

Magnetism is a big and important part of fundamental and applied physics. There exist many different magnetic materials. There are among them many metals, alloys and intermetallic compounds, but also many insulators displaying rich and interesting magnetic properties. For many applications insulating magnetic materials are preferred, because they have less losses, can be used in combination with optics, etc.

Among insulating magnetic systems oxides represent probably the largest and most important group with rather diverse properties, and they already have many applications. The origin and magnetic properties are often rather different in metals and in insulators. Basic physics of magnetic oxides is quite rich, see e.g., the phase diagram of manganites shown in Fig. 1, and one can demonstrate on it many fundamental physical phenomena in solid state physics. Discussion of these the main topic of the present chapter.

When speaking of magnetic oxides, one typically has in mind oxides of transition metals (TM), most often of *3d* elements, but *4d* and *5d* and rare earths (RE) compounds become more and more popular and these systems have brought many interesting effects to the field. This chapter will be mainly focused on the most important case of TM oxides, but some comments are made also about RE compounds.

Isolated magnetic ions in a crystal

TM oxides are mostly insulating systems. The crucial role in their properties is played by electrons of partially-filled *d*-shells (or *4f*-shells for RE systems). The *d*-electrons, and even more so *f*-electrons, have relatively small radius, and they often can be treated as localized at corresponding ions. Such localized electrons have simultaneously also localized magnetic moments, and these are mainly responsible for magnetism of corresponding substances.

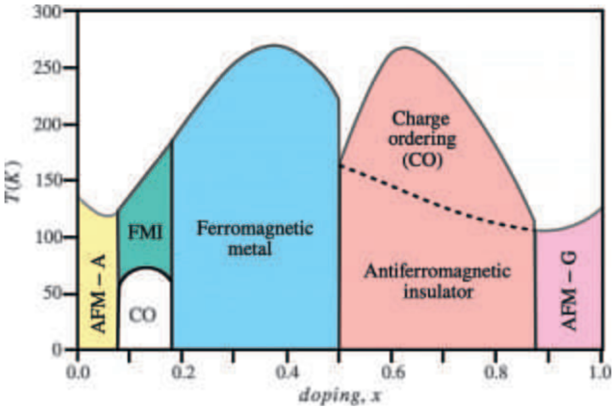

Fig. 1 Phase diagram of $La_{1-x}Ca_xMnO_3$. AFM-A and AFM-G stand for antiferromagnetic structure of the types A and G, see Fig. 10 (a); FMI stands for ferromagnetic insulator, CO: charge ordering.

The d-electrons have an orbital moment $l = 2$, i.e., for an isolated atom or ion they are $2l + 1 = 5$-fold degenerate, $l_z = -2, -1, 0, +1, +2$. In crystals such as TM oxides (NiO; Fe_2O_3, etc.) TM ions are usually located in ligand "cages" formed by anions, like O^{2-}, F^- etc., e.g., they sit in oxygen octahedra or tetrahedra. In this situation the point symmetry becomes lower: instead of spherical symmetry for isolated ions it becomes cubic or even lower due to the influence of ligands, such as oxygens. In cubic symmetry (regular octahedra or tetrahedra) the fivefold degenerate d-levels are split into a doublet e_g and triplet t_{2g}, doublet lying higher than triplet in octahedra (right part of Fig. 2a); the order of these levels being reversed in tetrahedra, left part of Fig. 2a. There exist also other co-ordinations, e.g., trigonal prisms or trigonal bipyramids, the crystal-field (CF) splitting in these cases is shown in Fig. 2a.

This CF splitting (for TM ions in octahedra or tetrahedra it is usually denoted as $\Delta_{CF} = 10\text{Dq}$) is caused by two mechanisms: (1) by the Coulomb interaction of respective electron density of corresponding orbitals. The typical shape of the five d-orbitals is shown in Fig. 2b, with the charges of surrounding ligands (here O^{2-} ions), and (2) by the covalency of d-electrons with the $2p$ orbitals of oxygens. Both mechanisms usually lead to qualitatively the same CF splitting, the second mechanism (d-p covalency) typically playing more important role.

These CF levels are filled one by one by respective d-electrons. Then one has to take into account different interactions between d-electrons, the most important being here the Hund's rule interaction which can be written as, e.g., $-J_H S_{i\alpha} S_{i\beta}$ (i is the site index, α and β—orbital indices and $\alpha \neq \beta$, S is spin, J_H is the Hund's intra-atomic exchange parameter), and also the spin-orbit coupling (SOC), which for single electron is $\zeta \vec{l}\vec{s}$, but which for the resulting many-electron terms with the total spin $\vec{S}$ and total orbital moment $\vec{L}$ per site is usually written as $\lambda \vec{L}\vec{S}$, where $\lambda = \zeta/2S$ is the spin-orbit coupling constant (Landau and Lifshitz, 1965). SOC strongly increases in going down in periodic table, $\lambda \sim Z^2$ (Landau and Lifshitz, 1965), where Z is the atomic number of the element. It is relatively weak for $3d$ ions ($\lambda \sim 20-70$ meV) (Abragam and Bleaney, 1970), but it becomes much stronger, up to $\sim$0.4 eV, for $4d$ and $5d$ ions; it often determines the properties of these compounds.

The usual filling of one-electron levels for weak SOC is determined by the interplay of CF splitting and the Hund's interaction (10Dq vs. J_H). If $J_H > 10\text{Dq}$, which is mostly the case of $3d$ oxides, electrons of TM ions with d^n configuration fill d-levels one by one from below such as to give the maximum total spin (e.g., $S = 5/2$ for d^5 configurations, Fig. 3 left part). This is the so called high-spin (HS) state, typical for $3d$ ions. But if $J_H < 10\text{Dq}$, which is usually the case for $4d$ and $5d$ ions, one would better fill the lowest CF levels, which e.g., for the d^5 configuration would give not $S = 5/2$ as for HS configuration left part of Fig. 3, but $S = 1/2$, right part of Fig. 3 (for other electron configurations the exact criterion could be modified, e.g., 10Dq vs. $2J_H$, or vs. $3J_H$). This is e.g., the situation for Ru^{3+} in $RuCl_3$ and Ir^{4+} in Na_2IrO_3—the very interesting materials with the strongly bond-dependent (so called Kitaev) exchange interaction and with nontrivial properties, see Section "Exchange interaction". This is the low-spin (LS) state, typical for $4d$ and $5d$ oxides, but also met in some $3d$ systems, e.g., those with the d^6 configuration (Fe^{2+}, Co^{3+}) in octahedra, for which six d-electrons may completely fill the lowest t_{2g} levels making the LS state of these ions nonmagnetic, $S = 0$. This is exactly the situation

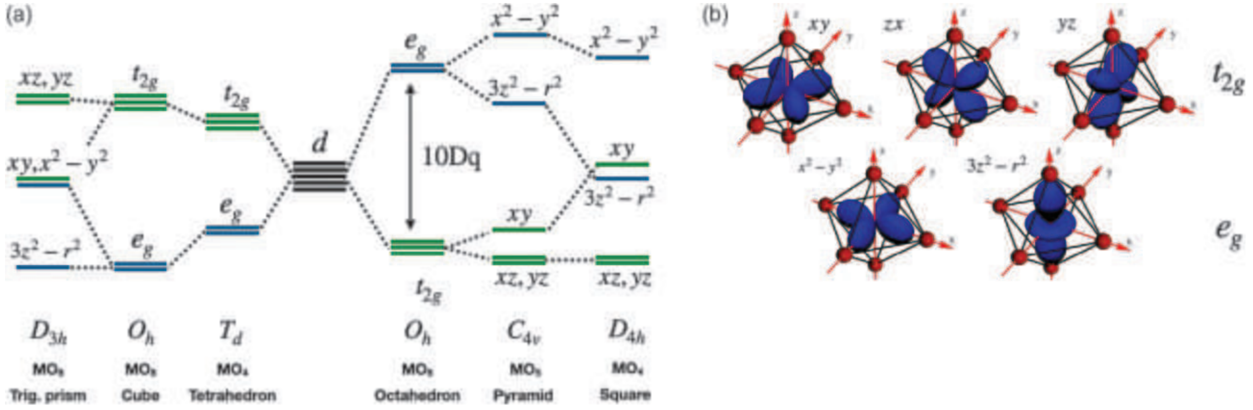

Fig. 2 (a) Crystal-field splitting of d-orbitals for different types of local surrounding of TM ions. (b) Five d-orbitals, the situation of octahedral surrounding is shown. Ligands are red balls.

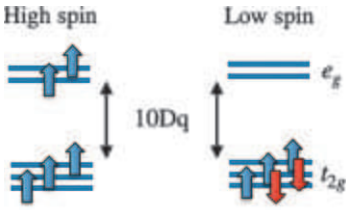

Fig. 3 Two different spin states in case of d^5 electronic configuration.

in the famous $LaCoO_3$, which is non-magnetic at low temperature, but experiences the spin-state transition to magnetic state under heating (particular scenarios are still debated), due to a thermal expansion resulting in decrease of the CF splitting.

The spin-state transitions (known also as spin crossovers in chemistry) are very important for geoscience, since under the pressure (deep in the Earth) TM-ligand distances are strongly decreased and therefore the CF splitting in contrast is increased, transforming TM ions into the LS state. Such transitions are accompanied by the change of the volume and manifests itself by variation of the density affecting seismic compressional velocities.

In certain situations the electronic filling of CF levels in symmetric situation (e.g., regular octahedra) may be such that there remains an orbital degeneracy, either double (one or three electrons on the e_g levels) or triple (partially-filled t_{2g} levels). In this case, according to the famous Jahn-Teller (JT) theorem, the symmetry of the system would spontaneously lower, leading to splitting of degenerate levels and giving a gain in electronic energy, linear in distortion, overcoming the quadratic loss of elastic energy (Kaplan and Vekhter, 1995). The spin-orbit coupling can affect the Jahn-Teller effect (Streltsov and Khomskii, 2020). The well-known ions with strong Jahn-Teller effect are e.g., Mn^{3+} and Cu^{2+}, important in manganites with colossal magnetoresistance (CMR) and in High-Tc superconductors, see below.

Intersite effects

While the ground state can be defined by the single-site physics, the intersite effects of different types are extremely important—in particular this is the intersite electron hopping. The actual hopping could lead to conductivity, eventually making the system metallic. The virtual hopping due to a quantum tunnelling in insulating situation can give rise to exchange interaction. In this case, when we allow for the change of the number of electrons at a site, the intra-atomic Coulomb interaction between electrons starts to play crucial role. In the simplest form, first ignoring orbital degrees of freedom, one can describe the situation by the Hubbard model

$$H = -\sum_{ij\sigma} t_{ij} c^{\dagger}_{i\sigma} c_{j\sigma} + U \sum_{i} n_{i\uparrow} n_{i\downarrow} \tag{1}$$

where i,j numerate lattice sites and σ is the spin index. The first term describes the intersite hopping of (here nondegenerate) electrons, and the second term is the on-site Coulomb (Hubbard) interaction. For one electron per site we can have here two situations. If $U \ll t$, the dominant role is played by the first term in (1), intersite hopping, which after Fourier transform gives the partially-filled (here half-filled) energy band and consequently a metallic state with itinerant electrons. Interaction U, assumed here to be weak, can then be treated e.g., by perturbation theory. This is the standard band theory of solids.

In the opposite case of $U \gg t$, however, the situation is very different. To avoid strong Coulomb repulsion the electrons would remain localized one per site. This is the state apparently first suggested by Peierls, the theory of which was later developed largely by Mott; this state is now called Mott insulator (Khomskii, 2014). It is this state which is the basic state of most magnetic oxides: the presence in it of localized electrons also means the presence of localized spins, or localized magnetic moments. Very schematically one can describe the general situation on a simplified diagram showing the evolution of one-electron bands with increasing Coulomb (Hubbard) repulsion U, characterizing on-site electron-electron repulsion. Here the half-filled metallic band existing for $U = 0$ transforms into two bands: the lower and upper Hubbard bands for U more than the critical value U_c (of order of the bandwidth $W = 2zt$, where z is number of nearest neighbours). These bands are divided by the energy gap $\sim U$, so that the lower band is filled and the upper one is empty. (One has only to remember that it is an effective picture, with the gap created by electron-electron repulsion, in which case the simple one-electron description is, strictly speaking, not valid. Specifically, the "volume", the number of states in each Hubbard band is not a constant but depends on the total number of electrons).

In realistic situations we have to take into account also the factors described in Section "Isolated magnetic ions in a crystal", mostly connected with orbital degrees of freedom of d-electrons. And of course, a lot depends on the type of respective crystal lattice (rock salt in monooxides like MnO, NiO; corundum structure M_2O_3, e.g., Fe_2O_3, Cr_2O_3; perovskites AMO_3, e.g., $LaMnO_3$; spinels with the general formula AM_2O_4, etc.) (Imada et al., 1998).

Very important is also to realize that usually there are anions, such as oxygen ions, between TM ions in real TM oxides. Sometimes it is sufficient to describe the situation keeping only d-electrons, as we did above, but often p-electrons of oxygen play also an important and, in some cases, crucial role. For example, in perovskites the oxygen ions are located just in between TM ions, so that the effective electron hopping between TM ions occurs via p-states of intermediate oxygens. One can describe this situation by the effective d-p model, including also p-electrons of oxygen:

$$H_{dp} = \sum_{i\sigma} \varepsilon_d d^{\dagger}_{i\sigma} d_{i\sigma} + \sum_{ij\sigma} t^{pd}_{ij} d^{\dagger}_{i\sigma} p_{j\sigma} + \text{h.c.} + U \sum_{i} n^{d}_{i\uparrow} n^{d}_{i\downarrow} \tag{2}$$

where t^{pd} is the hopping between TM d- and ligand p-orbitals ε_d and ε_p are their energies. If necessary, one should include in this description also other interactions: between d- and p-electrons, p-p interaction etc. If the oxygen p-levels are deep below d-levels of TM ions, one can exclude p-electrons and return to the description of the type of Hubbard model $\tilde{t}_{dd} \sim t^2_{pd}/(\varepsilon_d - \varepsilon_p)$, with the effective hopping $\tilde{t}_{dd}$ (more accurately one has to include here in the denominator also the effects of electron-electron interactions, which, however, may be not so important for large $\varepsilon_d - \varepsilon_p$). However if p-levels lie not far from the d-levels, the situation may change drastically. In this case the ground state may still be the same—electrons localized at TM ions, a magnetic insulator. But the lowest

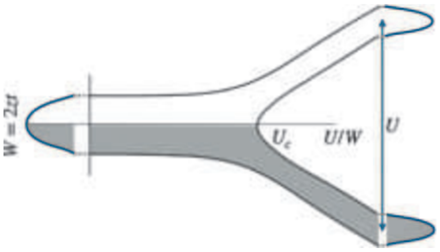

Fig. 4 Sketch illustrating formation of the lower and upper Hubbard bands due to the on-site electron-electron repulsion (characterized by the Hubbard's term U). The schematic bands and the density of states are shown.

excited states are not those following from the simple Hubbard model (1) and shown in Fig. 4, i.e., not the transfer of a *d*-electron from one TM ion to the other, the process $d^n d^n \rightarrow d^{n+1} d^{n-1}$,which costs the energy *U*, but the lowest charge-carrying excitations would be the transfer of a *p*-electron from the O^{2-} ion to the *d*-shell of TM, the process $d^n p^6 \rightarrow d^{n+1} p^5$, with the creation of an oxygen hole. The energy cost of this process is called the change transfer (CT) energy (Sawatzky and Green, 2016)

$$\Delta_{CT} = E\left(d^{n+1} p^5\right) - E\left(d^n p^6\right) \tag{3}$$

Crudely speaking, this CT energy is, according to (2), $\Delta_{CT} = \varepsilon_d - \varepsilon_p + U$, but it can also depend on the *pd* and *pp*-interactions. Correspondingly all correlated insulators can be subdivided into two big groups, see the famous Zaanen-Sawatzky-Allen diagram in Fig. 5. Thus depending on the ration between the Hubbard and CT energies we can have two types of insulators: the usual Mott insulators if $\Delta_{CT} > U$, and CT insulators for small CT energy if $\Delta_{CT} < U$. As always, the insulating states exists if both *U* and Δ_{CT} are larger than the electron hopping *t*. In the opposite case we can have metallic state for Mott part of the phase diagram, and rather nontrivial situation—possibly metallic but also sometimes insulating states, if we move on this phase diagram to the left, to the region of small or negative CT energy. We will discuss this situation below in Sections "Insulator-metal transitions; metallic oxides" and "Superconductivity in oxides".

Exchange interaction

There are various mechanisms which contribute to exchange interaction between magnetic centers in oxides. The simplest Hamiltonian to describe this interaction was proposed by Werner Heisenberg,

$$H = \sum\nolimits_{i>j} J_{ij} \vec{S}_i \vec{S}_j \tag{4}$$

who suggested that the non-local part of the Coulomb repulsion between electrons at different sites (numerated by indexes *i* and *j*) is responsible for this interaction; the strength of which is controlled by exchange constants J_{ij}. However, it was later understood that in most cases the mechanism of exchange interaction in magnetic insulators such as TM oxides is very different. In these systems electrons are mostly localized at their sites, but due to the virtual hopping, described by the first term in (1) they can tunnel between magnetic ions, which leads to decrease of total energy. However, the Fermi statistics and intra-atomic Hund's exchange interaction strongly affect this tunnelling. In elemental example sketched in Fig. 6a the hopping between FM ordered spin is forbidden by the Pauli principle and for this state we do not gain energy; therefore quantum tunnelling will stabilize AFM interaction with $J \sim 4t^2/U$ (Goodenough, 1963). If the hopping occurs directly between *d*-orbitals one speaks about the direct exchange, but often

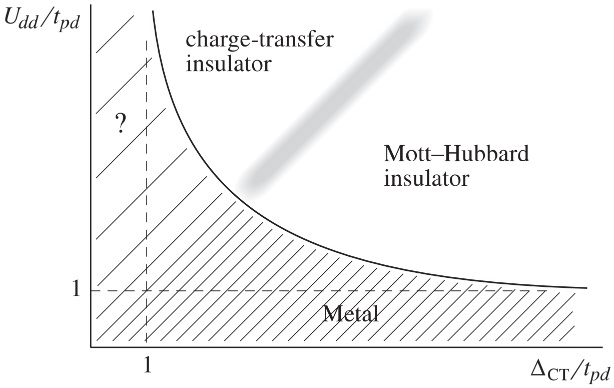

Fig. 5 Zaanen-Sawatzky-Allen diagram. It classifies insulators according to the character of the states forming valence and conduction bands. Here U_{dd} is the Hubbard on-site electron repulsion parameter, Δ_{CT}—charge-transfer energy, t_{pd}—tunnelling amplitude (hopping) from p-orbital of a ligand to d-orbital of TM ion.

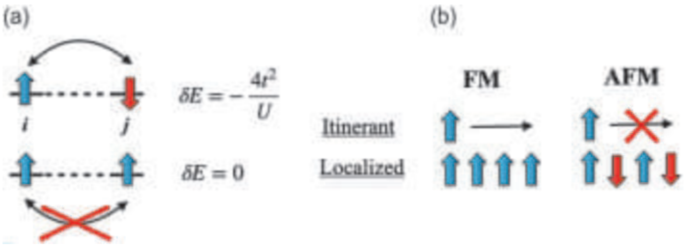

Fig. 6 (a) Sketch illustrating mechanism of the direct exchange or super exchange (for one active orbital per site): in case of FM order tunnelling processes are forbidden and cannot lower the total energy of the system, but this energy gain exist for antiparallel spins, i.e., this process leads to AFM coupling. (b) Mechanism of the double exchange leading to FM: itinerant electrons easily propagate through the lattice in case of FM order, thus gaining kinetic (band) energy, since they follow the first Hund's rule at every site.

magnetic ions are too far away from each other and *d*-electrons can hop only via ligand's *p* states. This is what is called the super exchange interaction. In real materials the situation is much more complicated, there are in fact many orbitals (five in case of TM) and there can be quite a few possible hopping paths resulting in various contributions to the total exchange, see also Section "Frustrated magnetism, spin liquids, spin ice", but still the strongest exchange (for appropriate filling of orbitals) is AFM as in Fig. 6a. This is why most of insulating TM oxides are AFM, and there are only few FM ones among them, such as, e.g., $YTiO_3$ or $NaCrGe_2O_6$, with typically low Curie temperatures (Streltsov and Khomskii, 2017).

Going to metallic magnetic oxides one needs to mention two other important exchange mechanisms. The first one is the so-called double exchange. Suppose there are two groups of electrons—localized and itinerant, as, e.g., in Sr doped $LaMnO_3$ where t_{2g} electrons are localized at Mn sites, while e_g orbitals are very different—these *d*-orbitals are directed exactly to each other in perovskite structure of $LaMnO_3$ and therefore corresponding bands are much wider. Moreover, due to not complete filling these e_g bands are metallic. Thus, there are localized t_{2g} electrons forming localized magnetic moments, and e_g ones moving on the background of these moments as illustrated in Fig. 6b. It is clear that it is much easier for them to propagate if all moments are FM, otherwise at every other Mn site e_g electrons appear in the "anti-Hund" configuration. Thus, there is a FM contribution to the exchange interaction due to the presence of such metallic electrons. Again, in real materials there will be competition between the FM double exchange and (typically) AFM super exchange, and the outcome, i.e., the resulting sign of the interaction, is not obvious. In particular, this can result in canting of the spins or in the formation of helicoidal magnetic structures.

The last exchange mechanism to mention is the Ruderman-Kittel-Kasuya-Yosida (RKKY) interaction which is characteristic for metallic systems such as metallic RE compounds. A localized moment is known to generate in metals an oscillating spin polarization of conduction electrons. Another magnetic moment interacts with these electrons and therefore feels the presence of the first moment. The resulting RKKY exchange is slowly decaying with distance and is oscillating in space, so that the sign of the RKKY exchange can be both FM or AFM (Yosida, 2010).

It has to be noted that the Eq. (3) often turns out to be oversimplified, there can appear higher order terms in spin variables, but also J is allowed to be not a scalar, but a tensor $J^{\alpha\beta}$, where $\{\alpha, \beta\} = \{x, y, z\}$. Then the diagonal part equal for all spin components gives isotropic exchange $J = J^{xx} = J^{yy} = J^{zz}$, while off-diagonal ones give anisotropic interactions, for example generate Dzyaloshinskii-Moriya (DM) interaction, which can be rewritten in a compact form as $H_{ij}^{(DM)} = \vec{D}_{ij} \cdot \left(\vec{S}_i \times \vec{S}_j\right)$, from which it becomes clear that the DM interaction favors spin canting. This is an extremely important interaction, which is responsible for appearance of various non-collinear magnetic structures, in particular skyrmions, and it can result in formation of spontaneous electric polarization in multiferroics via the so-called inverse DM effect, see Section "Magnetoelectrics and multiferroics".

The microscopic origin of DM interaction is the SOC mentioned in Section "Isolated magnetic ions in a crystal", it couples the spin space and the real space and can result in anisotropy of the exchange interaction (Abragam and Bleaney, 1970). This can not only generate off-diagonal, but can also make diagonal components of the exchange tensor very different. There can also exist a single-site anisotropy, which result in a situation, when instead of vectors in (4) one has, e.g., only *z* components of spins in effective spin Hamiltonian, i.e., $H = \sum_{i>j} J_{ij} S_i^z S_j^z$. This is the famous Ising model. Another more exotic situation is realized in Kitaev materials with a layered honeycomb structure, where due to strong SOC, specific lattice geometry and particular t_{2g}^5 electronic configuration the exchange interaction along some of the TM-TM bonds is large for *z* components of spins, while along other bonds it is large for *x* or *y* components, see Fig. 7a. In fact strong Ising-like anisotropy and bond-depended interaction were found in many oxides, e.g., Na_2IrO_3, Li_2IrO_3 (Takagi et al., 2019). These are typically systems with heavy *4d* and *5d* TM ions (since the SOC is large for them), with various orbital fillings and very different lattice geometry, such as e.g., double perovskites shown in Fig. 7b.

Frustrated magnetism, spin liquids, spin ice

The anisotropy of exchange interaction strongly restricts possible types of the ground states, and when it is combined with a lattice, which also poses its own constrains on the magnetic ordering, novel interesting physics may appear. A typical example is a triangle

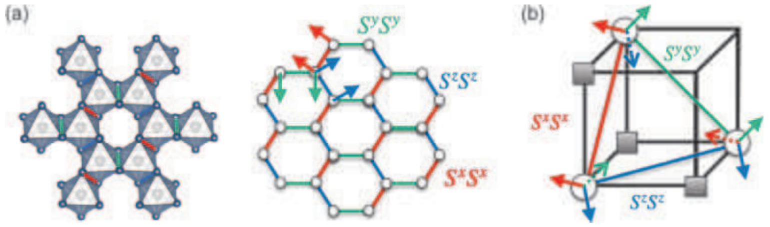

Fig. 7 Left: the crystal structure of one of the Kitaev material, Na_2IrO_3: Ir is in O_6 octahedra, which share edges shown by different colors. Right: corresponding spin lattice with the bond depended exchange interaction: for green bond the largest coupling is between S^y components, for red—S^x, and for blue—S^z.
(b) Fragment of face-centered cubic lattice, which form magnetic metals (circles) in double perovskite structure, e.g., in Ba_2CeIrO_6. In both situations strong frustration is observed.

of AFM coupled spins, described by Ising model, shown in Fig. 8. One readily realizes that it is impossible to satisfy all exchange bonds in this situation. This is what is called frustration: a system does not know how to order the spins. This results to a large degeneracy of the ground state. Already a triangular cluster has sixfold degenerate ground state, but when we have a lattice of triangles this number rapidly increases and gives finite entropy at $T = 0$. This has important implications for thermodynamics. There are many such lattices having a triangular motif: such are kagomé (e.g., $SrCr_9Ga_3O_{19}$), hyper-kagomé (e.g., $Na_4Ir_3O_8$), garnets (like $Gd_3Ca_5O_{12}$) or pyrochlore ($Pr_2Ir_2O_7$). But frustrations are also possible in other situations, e.g., AFM next-nearest neighbor exchange will frustrate AFM Ising chain, or bond-dependent anisotropic interaction in Kitaev model shown in Fig. 7a leads to the situation when each spin "does not know what to do"—exchange interactions along each bond tend to direct it in its own way (along x, y, or z direction).

Frustration suppresses a long-range magnetic order. One of its hallmarks often used in experimental physics is a large frustration parameter $f = |\theta_{CW}|/T_N$, where θ_{CW} is the Curie-Weiss temperature characterizing an average strength of exchange interaction, and T_N is the Neél temperature (or spin glass transition temperature if a system finally freezes in a disordered state), i.e., the temperature at which a long-range magnetic order sets in. Frustration suppresses such a long-range order, and the parameter f is a measure of this suppression. Typically, if $f \sim 5 - 10$, it might be taken as a signature of one might already expect to have some sort of frustration; stronger frustrations give (much) larger values of this parameter. Thus e.g., in $CuAl_2O_4$ $f \sim 65$, while in $SrCr_9Ga_3O_{19}$ it exceeds 150. (Note however that in any low-dimensional system the ordering temperature is strongly (logarithmically) suppressed by a weak interlayer of interchain exchange; this should not be mixed with the effect of frustrations).

Frustration can suppress a long-range magnetic order, while spins are still strongly coupled. By analogy with classical thermodynamics such a state with a long-range quantum mechanical entanglement of spins, but absence of a magnetic order is called a spin liquid (do not mix this state with a conventional paramagnetism, where disorder is induced by the temperature). The spin correlator can have a power-law dependence on distance $\langle \vec{S}_i \vec{S}_j \rangle \sim 1/|\vec{r_i} - \vec{r_j}|$ as in so-called algebraic spin liquids or decay exponentially $\langle \vec{S}_i \vec{S}_j \rangle \sim exp\left(-|\vec{r_i} - \vec{r_j}|/\xi\right)$ as e.g., in the Shastry-Sutherland model (physical realization of which is $SrCu_2(BO_3)_2$). Both theoretical and experimental studies of spin liquids in different models and compounds is one of the most actively developing directions in the modern condensed matter physics (Savary and Balents, 2017), each year hundreds of materials are claimed to host this mysterious state, but most of them finally reveal some sort of long-range magnetic order or appears to be atomically disordered. One of very promising system for realization of the spin-liquid is the mineral herbertsmithite $ZnCu_3(OH)_6Cl_2$ with the kagomé lattice of Cu^{2+} ions wth $S = 1/2$.

One more very interesting subject to mention in context of frustration is the spin ice systems. These are mainly pyrochlores like $Dy_2Ti_2O_7$. $Tb_2Ti_2O_7$, in which magnetic ions (Dy, Tb) form the lattice of corner-sharing tetrahedra (again with triangular motif) and are very strong Ising ions, with easy axes directed for each ion to the center of respective tetrahedron (or away from it) (Gardner et al., 2010). This leads for certain interactions (including dipole-dipole interaction) to very strong frustration and to disordered ground state. This situation reminds the crystal structure of conventional ice, where oxygens form distorted tetrahedra, and hydrogen of H_2O molecules can be attached to one or to the other oxygen, i.e., can move to the center of oxygen tetrahedra or away from it. Spins in spin ice materials are directed in the same way as the electric dipoles formed by H^+ and O^{2-} ions, see Fig. 9; that is why the very term "spin ice". Many features of spin ice systems are quite exotic, in particular excitations in these systems have properties of magnetic monopoles.

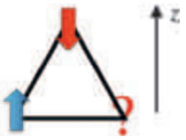

Fig. 8 Illustration of frustration. If the exchange interaction is described by the Ising model and all spins are coupled antiferromagnetically, then they cannot satisfy all exchange bonds.

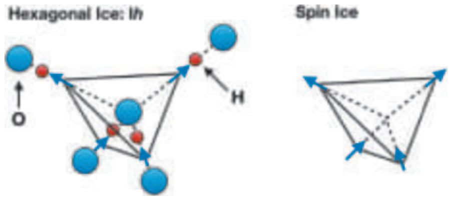

Fig. 9 Conventional and spin ices. Arrows show displacement of hydrogens (or electric dipole moments) in real ice and spin directions in spin ice.

Various orderings: Magnetic, charge, orbital, etc.

There can be very different magnetic structures in magnetic oxides. Many perovskites adopt simple two-sublattice structures as shown in Fig. 10a (e.g., $LaTiO_3$ is AFM of G-type; $CaCrO_3$ is C-type; $LaMnO_3$ is A-type), but there are also examples of very complex and seemingly counterintuitive structures, where for example spins on different sites can be nearly orthogonal to each other as in UO_2 (Fig. 10b) or $Bi_2Fe_4O_9$. Often this is the result of competition between different exchange couplings, e.g., nearest and next nearest neighbors, but various anisotropic contributions to the exchange tensor $J^{\alpha\beta}$ can also strongly change the ground state magnetic structure; this factor is especially important for *4d* and *5d* oxides.

Spin is just one of the degrees of freedom in magnetic oxides. There are also other, such as orbital and charge degrees of freedom. If metallic ions have different oxidation states, e.g., there can be Mn^{3+} and Mn^{4+} ions in the same material, they can be ordered, in which case we speak of the charge ordering or more generally about formation of the charge density wave. There are many examples of magnetic oxides with charge ordering—e.g., Fe_3O_4, AlV_2O_4, $Y_2Ni_2O_6$—and there can be very different mechanisms lying behind this effect. It can be connected with the nesting of the Fermi surface for initially metallic systems. The mechanisms of such charge ordering may be electron-phonon interaction or Coulomb interaction. There may also exist strong coupling of CO with other degrees of freedom. For example, in manganites such as $PrBaMn_2O_6$ and $NaMn_7O_{12}$ the AFM ordering, the so-called CE-type ordering (Fig. 10c) coexists (and may be caused by) the checkerboard CO of Mn^{3+} (grey circles in Fig. 10c) and Mn^{4+}. The additional electron in e_g shell of Mn^{3+} ions provide strong FM coupling with two of its neighbors by the double exchange mechanism, with this electron occupying $3x^2 - r^2$ or $3y^2 - r^2$ orbitals for horizontal or vertical legs of the zigzag. These three ferromagnetically coupled spins are the example of trimer clusters ("trimerons") also invoked to explain the details of charge ordering in magnetite Fe_3O_4.

There exit yet another very important type of ordering in oxides—orbital ordering. It usually occurs in systems with orbital degeneracy and with strong JT effect, see Section "Isolated magnetic ions in a crystal". Local distortions due to the JT effect on different centers couple to each other, leading to the cooperative effect—cooperative JT ordering, or orbital ordering. This usually occurs at a special transition, which is simultaneously a structural transition with the reduction of the symmetry of a crystal. Besides its own features such orbital ordering also very strongly influences magnetic ordering. As was explained in Section "Exchange interaction", exchange interaction between the same half-filled orbitals (ferro-orbital situation) results in AFM, see Fig. 6a, while it can be shown that if electrons occupy different orbitals (antiferro-orbital) and there is no overlap between these half-filled orbitals, then the exchange interaction can be ferromagnetic. One of the examples is $LaMnO_3$ with four *3d* electrons, one at e_g and three at t_{2g} orbitals. Antiferro-orbital ordering of one of e_g orbital results in FM in the *ab* plane, while t_{2g} states give AFM along the *c* direction, see Fig. 11.

There are many examples of magnetic oxides with orbital ordering in addition to mentioned above manganate, but the most important is that in this class of materials—magnetic oxides—spin, orbital, charge and lattice degrees of freedom are often turn out to be interrelated and may affect each other. This feature is interesting from theoretical point of view and opens up new perspectives for technological application of such systems, for example one can change electronic properties by stress or magnetic properties by external electric field or light.

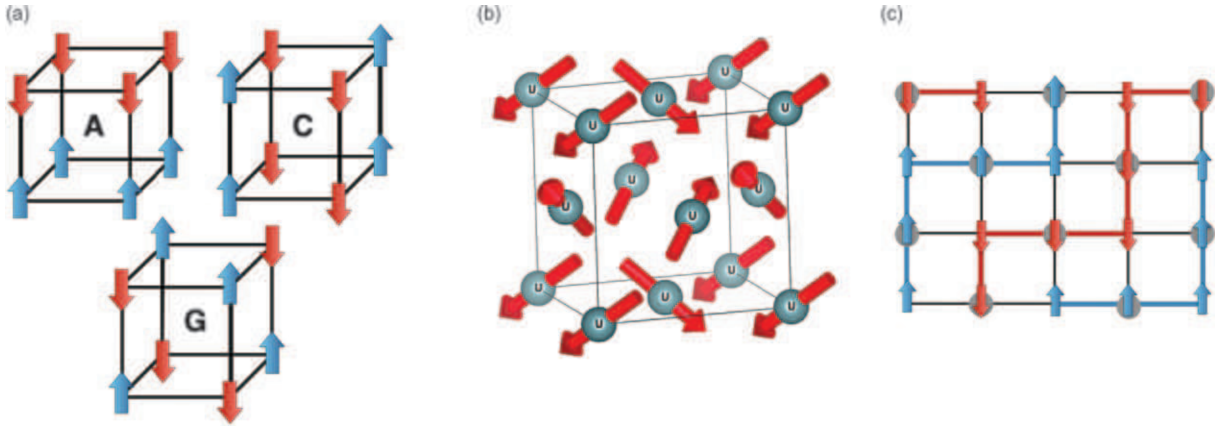

Fig. 10 (a) typical types of AFM structures for a simple cubic lattice, (b) very complicated AFM structure of UO_2, (c) CE-type of AFM with FM zigzags, realized e.g., in half-doped manganites like $La_{0.5}Ca_{0.5}MnO_3$, cf. Fig. 1.

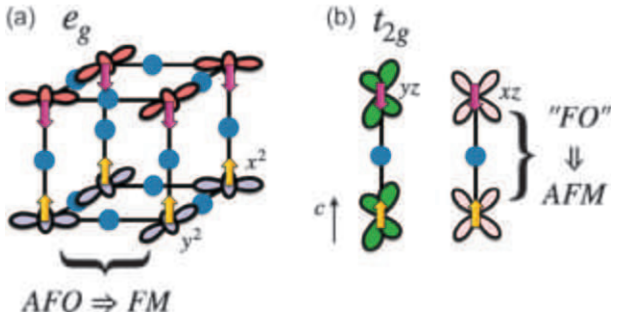

Fig. 11 Orbital ordering in $LaMnO_3$ (Mn^{3+}, $t_{2g}^3 e_g^1$). Single e_g electron occupies alternating $3x^2$-r^2 and $3y^2$-r^2 orbitals (dubbed as x^2 and y^2), which is the antiferro-orbital (AFO) ordering; it gives ferromagnetism in the ab-plane, see (a). Magnetic coupling along c is predominantly governed by the t_{2g} orbitals. There is a strong overlap between the same t_{2g} orbitals (via ligand's p-orbitals), which results in antiferromagnetism in the c-direction.

Magnetoelectrics and multiferroics

In this article we mainly concentrate on magnetic properties of oxides. However, in several specific situations there appears quite nontrivial electric behavior of these systems, closely connected with their magnetism, so that one can in principle influence magnetic state of the system by electric field. Such are the systems with (linear) magnetoelectric effect (ME), first proposed by Dzyaloshinskii in 1959 on symmetry grounds, the microscopic theory of which later on being elaborated by Moriya. This ME effect is based on the existence in systems with some special symmetries of the term in free energy of the type $\alpha_{ij}E_iH_j$ or $\tilde{\alpha}_{ij}P_iM_j$, where P is an electric polarization and M—magnetic moment, E is electric and H—magnetic field (we assume summating over repeated indices $\{i,j\} = \{x,y,z\}$). The presence of this term in the free energy leads to the possibility to induce magnetization

$$M_i = \alpha_{ij}E_j$$

by electric field or. vice versa, of electric polarization by magnetic field,

$$P_i = \alpha_{ij}H_j$$

The magnetoelectric tensor α_{ij} can have both symmetric and antisymmetric components; the symmetric one leads e.g., to the magnetic moment parallel to the applied electric field, and antisymmetric ME tensor—to the moment M perpendicular to E.

Already a year after this prediction by Dzyaloshinskii the ME effect was found by Atsrov in Cr_2O_3, and later on it was actively studied in many materials, mostly in antiferromagnetic TM oxides. But the coupling of electric and magnetic properties is not restricted to the ME systems, in which one needs external fields to observe this effect. It turned out that there also exist systems in which magnetic and electric orderings, in particular ferroelectricity (FE), coexist without external fields. Such materials were called multiferroics (MF) (besides magnetism and ferroelectricity one sometimes also includes into this class ferroelasticity, but most often nowadays by MF one means coexistence of magnetism and ferroelectricity). The study of MF materials and of related phenomena was initially started in the former Soviet Union, mainly by the groups of Smolenskii in Leningrad and by Venevtsev in Moscow, and by Schmidt in Switzerland, who coined the very term "multiferroic". After relatively slow start, this field get strong boost at the beginning of 2000-th, starting from works of Ramesh, Kimura and Cheong, and it is now a very well-developed field, with many interesting results and with the promise of important applications (Cheong and Mostovoy, 2007).

As to the physics of MF, there is now pretty good (although of course not complete) understanding of the microscopic mechanisms of MF. All MF can be divided into two big groups. In type-I MF magnetism and ferroelectricity appear independent of one another—although of course connected when both are present!—and are due to different physical mechanisms. Thus e.g., in one of the best MF, $BiFeO_3$ with perovskite structure, ferroelectricity appears first, at ~1100K, and is predominantly due to the lone pairs of Bi^{3+}. At lower temperatures, below $T_N = 643\ K$, it becomes AFM due to the ordering of spins of Fe^{3+}. Similarly, in $RMnO_3$ (R- rare earths like Y, Ho etc.) ferroelectricity and magnetism occur at different temperatures, FE at about 900 K, and AFM—at about $T_N \sim 100\ K$. Here FE is connected with the rotation and tilting of MnO_5 trigonal bipyramids, and magnetic ordering—with the usual exchange interaction of Mn ions.

Type-II multiferroics, however, are the systems in which the origin of ferroelectricity and magnetism are intrinsically connected and FE appears only in some specific magnetic structures, always in magnetically-ordered state. There are three main microscopic mechanisms of MF behavior in such systems. One is the magnetostriction: in some types of magnetically-ordered states due to magnetostriction there may appear electric polarization, see e.g., Fig. 12. Such are for example $TbMn_2O_5$ or in Ca_2CoMnO_6. The second, most widespread and probably the most interesting mechanism of MF in type-II multiferroics is realized e.g., in systems with cycloidal magnetism structures. It was shown in 2005 by Katsura, Nagaosa and Balatsky, and by Mostovoy, that for neighboring canted spins $\vec{S_i}, \vec{S_j}$ there would appear electric dipole moment, or electric polarization

$$\vec{\mathrm{P}} \sim \vec{r}_{ij} \times \left[\vec{S_i} \times \vec{S_j}\right], \tag{5}$$

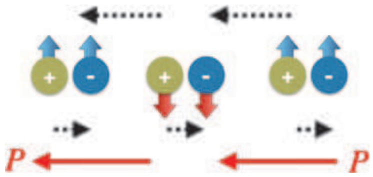

Fig. 12 The appearance of electric polarization due to magnetostriction in a system with two types of ions and with magnetic structure up-up-down-down.

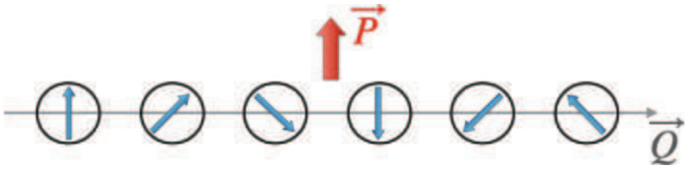

Fig. 13 Magnetic cycloid running along x, with spins rotating in the zx plane. According to (5) this results in formation of electric polarization pointing in the z direction.

where $\vec{r}_{ij}$ is the vector connecting these two sites. For cycloidal magnetic structures such dipole moments at every bond add, leading to the net polarization, i.e., to MF behaviours, see Fig. 13.

This is e.g., the mechanism of MF in $TbMnO_3$—one of the first such systems discovered. Nowadays there are many other systems, mainly TM oxides, with this property. Microscopically the mechanism of electric polarization in these systems is the inverse DM effect, requiring the presence of relativistic SOC.

There exist also one more, the third microscopic mechanism of MF, also requiring the action of SOC—the SOC-driven modification of *d-p* hybridization. This mechanism can give MF behavior for example in the helicoidal (proper screw) magnetic structures. But this situation is less common and usually less important in the field of MF.

The study of MF, besides its scientific interest, is largely driven by the possible important applications. The most important of these is the potential possibility to control magnetic memory electrically, without using electric current as in most present magnetic memory devices, but writing and reading magnetic memory just by electric field, like e.g., in gate devices, this avoiding the losses always present when one has electric currents. And one can also make very sensitive magnetic field censors using MF, with the sensitivity approaching that of SQUID but operating at room temperatures. All in all, this field of research is very active nowadays.

Insulator-metal transitions; metallic oxides

As discussed in Section "Intersite effects", systems with integer number (e.g., one) of electrons per site and with strong correlations, with the Hubbard's on-site interaction U larger than the effective electron hopping t or the respective bandwidths $W = 2zt$, are Mott insulators. When one of these conditions is violated, we can have a transition to a metallic state. One can speak of essentially three specific mechanisms of such insulator-metal transitions (IMT). The first one can be called, following Japanese literature, the bandwidths-controlled IMT (Imada et al., 1998). If, keeping the number of electrons the same, one increases the electron hopping t (or decreases the Hubbard interaction U), one can reach the situation when the bandwidths become larger than the electron repulsion, cf. Fig. 4. In this case the system may become metallic, i.e., there will occur in it an insulator-metal (or Mott) transition. This can be reached e.g., by increasing pressure, at which the atoms come closer together and the overlap or electronic functions on neighboring sites, and corresponding electron hopping, increase.[1]

Such transitions can be also driven by temperature. These are the most interesting situations. A good example is presented by the vanadium oxides, see Fig. 14. As we see, many of those have a transition from a metallic to an insulating state with change of temperature. Very often such IMT are accompanied by the change of crystal structure, and sometimes—with magnetic ordering. However, they may occur also without change of lattice symmetry. This is seen e.g., in phase diagram of V_2O_3 as a function of pressure (or chemical pressure imitating compressed samples) and temperature, Fig. 15: the transition line at higher temperatures divides paramagnetic metallic from paramagnetic insulating state, with the same corundum structure (but with the jump in volume at this I-order transition). One sees here also the effect discussed above: V_2O_3 becomes metallic at high pressures even at low temperatures. There are many examples of such Mott transitions in different TM oxides.

One can also single out the "subtype" of the same mechanism: IMT transition caused not by increase of electron hopping or a bandwidth, but by the reduction of effective Hubbard repulsion U. It seems at first glance that it is very difficult to modify it—it is a local property of an ion. But it can change for example if in a many-electron atom or an ion the intra-ionic configuration change, e.g.,

---

[1] This general tendency can be violated in certain specific cases, in particular when in an insulating state TM ions form tightly-bound small clusters, e.g. dimers. Formation of such dimers is usually accompanied by the reduction of the volume if the system, and such small-volume insulating state can be stabilized by pressured. But it is a rather rare exception; as a rule one should expect that with increasing pressure Mott insulators could be transformed into metals

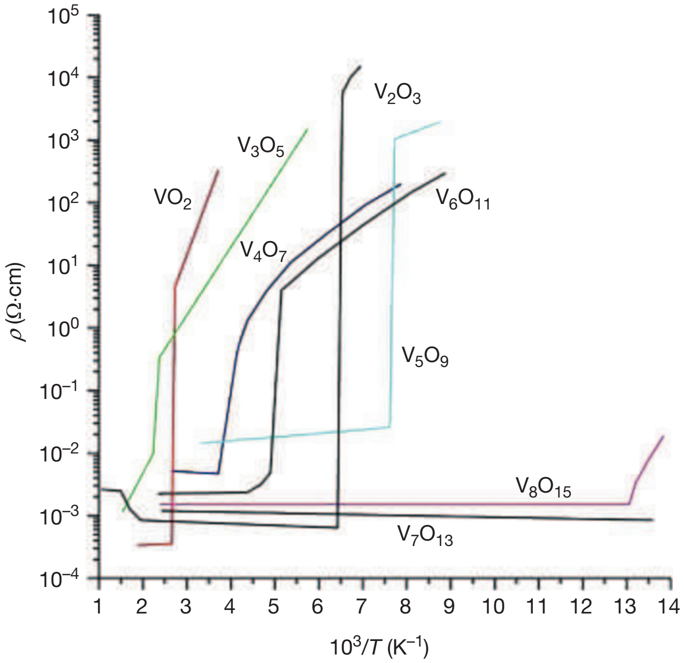

Fig. 14 Metal-insulator transitions in various V oxides as seen from temperature dependence of electrical resistance. Adapted from Pergament AL et al. (2013) *ISRN Condensed Matter Physics* 2013: 960627.

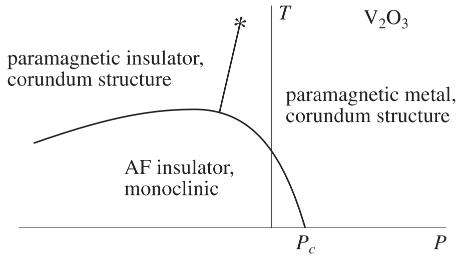
T
V_2O_3
paramagnetic insulator, corundum structure
paramagnetic metal, corundum structure
AF insulator, monoclinic
P_c
P

Fig. 15 Schematic phase diagram of V_2O_3 in pressure (P) and temperature (T) coordinates.

under pressure. Thus, for example in oxides containing the ion Fe^{3+} (configuration d^5, with the spin in the HS state $S = 5/2$) such ions transform under pressure to a LS state with the total spin $S = 1/2$ (LS state ions have smaller size than the HS ones). One can show that at this transition the effective value of the on-site Coulomb repulsion strongly decreases (U_{eff} contains not only the direct density-density repulsion, but it also depends on the intra-atomic Hund's rule exchange J_H, and its contribution strongly changes in going from the HS to LS state). One can call this mechanism the interaction-controlled IMT.

The second situation one meets when one changes the electron concentration, e.g., by doping. By that the system can also become metallic. This is the band-filling-controlled IMT. Important to realize is that the metallic state which can thus be created, still may have narrow bandwidths and strongly-interacting electrons. Therefore, such metallic state can have very different properties from those of the conventional metals like Na or Al. They may strongly deviate from the usual free-electron-like or even from Fermi-liquid behavior: the temperature dependence of many properties such as resistivity or Hall effect may be different from those of conventional metals; they may display nontrivial magnetic properties partially resembling those of localized electrons, e.g., may develop different types of magnetic ordering (FM, helicoidal, etc.); they may have different other types of orderings, including charge ordering, discussed above in Section "Various orderings: Magnetic, charge, orbital etc.". A good illustration may be provided by the rich phase diagram of colossal-magnetoresistance manganites like $La_{1-x}Ca_xMnO_3$, shown in Fig. 1. Most interesting, in some such systems one can even have a high-temperature superconductivity, discussed in more details in the next section.

Yet one more special type of IMT and the corresponding class of metallic oxides can appear in systems in which there exist strong interplay of *d*-electrons of transition metals and *p*-electrons of ligands, e.g., oxygens. As discussed in Section "Intersite effects", one has in general to include oxygen *p*-electrons in the discussion, and this can become essential if oxygen *p*-levels lie close to *d*-levels of TM. One can characterize it by the CT energy, needed to transfer an electron from O^{2-} ion to *d*-levels of TM. As mentioned in Section "Intersite effects", if Δ_{CT} is very large one can exclude *p*-electrons and go to the effective description including only *d*-electrons, with some effective parameters. But in some cases, especially in systems with high valence of TM, Δ_{CT} can be small or even negative. In such situation it may be energetically favorable to transfer some *p*-electrons from oxygens into *d*-shells of TM, thus creating oxygen holes $\underline{L}$—oxygen ions with p^5 configuration. Oxygen hole thus created can start to move in a crystal, creating metallic state. One can call this situation self-doping: one changes concentration of *d*-electrons and *p*-electrons not by external doping as in band-filling-controlled IMT, but such process occurs spontaneously due to redistribution of electrons between *p*-shells of oxygens and *d*-shells of TM. The properties of such states can be very unusual. Such states can be very important in many materials, in particular in the cuprate High-Tc superconductors discussed in the next section.

Superconductivity in oxides

Usually when speaking on superconductors one has in mind good metals like Pb or Al. Superconducting pairing in those is ascribed to electron-phonon interaction. Magnetism was always considered as the greatest enemy of superconductivity. And in most cases it is indeed true. All the more surprising was the discovery of High-Tc superconductivity by Bednorz and Mueller in 1987 in completely different class of materials: in cuprates, TM oxides usually considered good for magnetism but not for superconductivity. This discovery caused enormous activity continuing to this day and attracted common attention to the physics of correlated electron systems, to TM oxides in general and to cuprates in particular (Keimer et al., 2015).

Cuprate High-Tc superconductors, such as $La_{2\text{-}x}Sr_xCuO_4$ (LSCO) or $YBa_2Cu_3O_7$ (YBCO) contain as the main building blocks CuO_2 planes shown in Fig. 16, i.e., they can be considered as "2D perovskites".

Formally the valence of Cu in them is Cu^{2+} in undoped LSCO or in oxygen-depleted YBCO, which are actually Mott (or rather charge-transfer) insulators with magnetic ordering. Cu^{2+} is a very strong JT ion, and in these systems it is typically located either in very strongly elongated octahedra, or is fivefold or even fourfold coordinated, i.e., located in square pyramids or just in oxygen squares. The hole in d^9 configuration of Cu^{2+} is sitting on the upper x^2-y^2 orbital, rather well separated from the rest of *d*-states, cf. the right part of Fig. 2a. Superconductivity appears in these systems when they are hole-doped, so that the formal valence of Cu becomes e.g., Cu^{2+x} in $La_{2\text{-}x}Sr_xCuO_4$. But "Cu^{3+}" thus created is known to be a negative charge-transfer ions, see Section "Insulator-metal transitions; metallic oxides" above, i.e., the large fraction of thus created holes are actually in oxygens. The resulting state can be represented as $Cu^{2+}\underline{L}$, with the spins of Cu^{2+} and of the, predominantly oxygen, holes forming singlet states—the Zhang-Rice singlets. In effect one can often reduce the description of cuprates to the one-band Hubbard model, with undoped magnetic systems corresponding to the half-filled case thereof, the holes introduced by doping—Zhang-Rice singlets—playing the role of holes in such nondegenerate Hubbard model.

But in fact, besides the magnetic and superconducting states, one has found in high-Tc cuprates much more complicated behavior—the phases of "strange metals" with non-Fermi-liquid behavior, the phase with a pseudogap, with different presumed types of ordering—see the schematic phase diagram in Fig. 17.

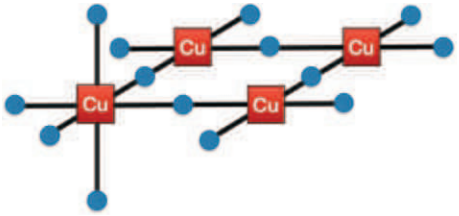

Fig. 16 Basic structure of CuO_2 layer constituting the main building block of High-Tc cuprate superconductors. Blue balls are oxygen ions (one or two apical oxygens can be missing in some members of this family).

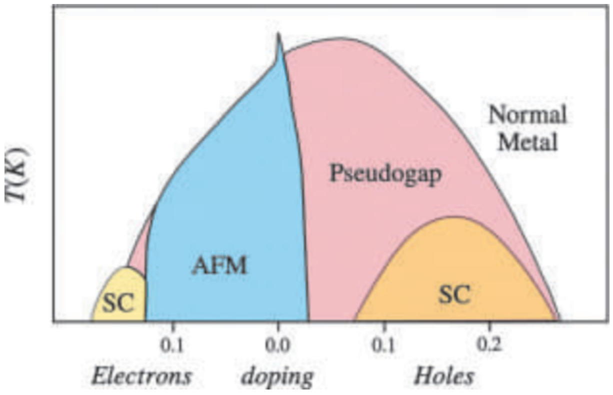

Fig. 17 Phase diagram of superconducting cuprates; superconducting region is shown in blue. SC stands for superconducting, AFM: antiferromagnetic phases.

Despite enormous progress in this field, some basic questions, such as the very mechanism of High-Tc superconductivity, and many properties of the normal state for these compositions, still remains open. It is established that in contrast to the usual superconductors the superconducting pairing in cuprates, described by the pairing wave function or the order parameter $\Delta\left(\vec{k}\right)$, is singlet but not of the *s*-wave type as in most usual superconductors, but is of the *d*-wave type, $\Delta\left(\vec{k}\right) \sim |\Delta|\left(\cos k_x - \cos k_y\right)$, i.e., it has nodes in certain directions in *k*-space. As to the mechanism of High-Tc superconductivity, it is accepted that it is predominantly not due to the usual electron-phonon interaction, but is largely due to interelectronic interactions. The proximity of High-Tc region to magnetic states is apparently not accidental, magnetic effects seems to play crucial role in establishing superconducting pairing. But the details of this process are still a matter of hot debates, 30 years after the discovery of this phenomenon.

Besides cuprates, yet one more class of high-Tc superconductors was discovered later on, also containing strongly corrected electrons—the iron-based superconductors like LaOFeAs or β – FeSe. Apparently, many properties of these have much in common with those of cuprates, although there are also important differences. As these materials do not belong to oxides, we will not discuss them further.

Various useful properties and applications of magnetic oxides

When speaking of applications of TM oxides, one can point out several specific directions. The first one is the use of their magnetic properties per se. It was in fact the first know in history application—the use in ancient China of magnetite Fe_3O_4, which is already magnetic at room temperature, for orientation of buildings under construction and for navigation: the first ever compass, on the basis of magnetite, was invented in China about 2000 years ago. Magnetic properties of oxides were used recently in such applications as magnetic memory in computers: the early memory on ferrite coils, more recently using Fe_2O_3 in older hard discs.

More elaborate applications rely on the dependence of various properties of TM oxides such as e.g., electrical resistivity on magnetic order. Thus there are attempts to use colossal magnetoresistance in manganites and some other materials as sensors. Recently there was a big activity in studying topological effects in particular in systems with strongly correlated electrons, among them in oxides. Thus for example topological Hall effect was observed in $SrRuO_3$ films.

There are the attempts to use magnetic oxides for elaborate thermopower applications. The idea is to use the extra entropy often present in these systems—magnetic, orbital entropy—for entropy transfer, which could make these systems promising candidates for new class of thermoelectric materials.

Strong magnetoelastic coupling and magnetostriction, typical for TM system with unquenched orbital moments, e.g., containing such ions as Fe^{2+}, Co^{2+}, can be used for non-destructive control of metallic products such as gas and oil pipes, etc.

For practical purposes, especially in electronics, the use of thin films is of paramount importance. Investigation of films and multilayers of different materials is going on very rapidly at the moment. TM oxides present an important playground in this direction. Three main factors can lead to the modification of the behavior of films as compared to the bulk. The first one, common for all films independent on their particular type, is spatial quantization, caused by the finite thickness of films restricting motion of electrons, magnons etc. in perpendiculars direction. Two other factors are more specific for TM oxides. First, due to strain imposed by the substrate, both magnetic and especially orbital structure of the material can change. For example, orbital occupation at the first few layers might be very different from that in the bulk. This in its turn can lead to change of exchange interaction and to different type of magnetic ordering in thin films as compared to the bulk. The third factor, important for TM films and multilayers, is the possible charge redistribution connected with the possibility to change the valence of TM ions. Thus, for example when one makes contact of $LaMnO_3$ with $LaNiO_3$, with the valence in the bulk being 3+ for both TM ions, on the interface it is favorable to transfer electrons from Mn to Ni, forming on the contact Mn^{4+} and Ni^{2+}. Indeed, the trivalent Ni is an ion with very small or even negative charge transfer gap and is not very stable: energetically Ni^{2+} is much more favorable. On the other hand, to transform Mn^{3+} to Mn^{4+} does not cost much energy. In effect this charge and valence redistribution on the contact indeed takes place in this situation, and similar phenomena should be considered also for some other combination of TM oxides in a contact.

Some TM oxides can serve as very useful substrates. The most important is $SrTiO_3$, but also many other TM oxides are used for this purpose. One can also use by that their transport and magnetic properties. Thus, $SrRuO_3$ can serve as a ferromagnetic metallic substrate, which is necessary for some applications. All in all, the behavior of TM oxides in thin films and multilayers may be quite diverse, such systems display very rich and interesting properties and can promise important applications.

One more big field in which magnetic oxides are also used widely, is spintronics—the field based on the idea to use not charge but spin of an electron for many applications, e.g., for memory and for logical elements in quantum computers, for controlling transport properties etc. This big and very active field is discussed in other articles in this volume, thus we will not dwell on this anymore; suffice is to say that it is just the diversity of the properties of TM oxides which makes them very useful in different ways in spintronics devices.

And one more important point: one should not forget that the TM oxides are quite widespread in nature and play an important role in many natural phenomena. Oxygen gives almost 50% of the total mass of Earth's crust, ocean water and atmosphere. Also, iron is quite abundant (~5%). And this iron mostly exists in Earth's crust in form of oxides which are essentially magnetic: magnetite Fe_3O_4—ferrimagnetic, hematite Fe_2O_3 (the main component of ordinary rust)—AFM with eventual spin canting.

Similarly, other TM and RE metal oxides are well represented in the Earth's crust. They are often the main ores used for metal production, especially for iron.

Most of TM oxides in the Earth's crust have some magnetic properties, although for the laymen they are not "magnetic"—they do not attract small metallic objects such as needles or nails: most of these are AFM of some kind. But their magnetic properties are widely used in geophysics for the search of novel useful mineral deposits; magnetometry is one of the most powerful tools in modern archeology, etc. And minerals are inexhaustible source of novel magnetic materials with often exotic properties. Thus, most of novel kagomé systems originate from minerals, which one sees from their names: herbertsmithite, volborthite, kapellasite, atacamite, to name just a few.

Even when a mineral itself is nonmagnetic, adding TM impurities may drastically modify its properties. Thus, the color of many precious and semi-precious stones like ruby or amethyst are due to TM impurities. And such impurities are the main ingredients in modern laser materials, starting from the ruby lasers.

And the last point: magnetic oxides are quite important for many living creatures, they were already in use by them for ages. Long before the compass with the use of magnetite was invented in ancient China, the same principle and the same material was used by birds for the orientation, and there are many other similar examples. Even bacteria may be sensitive to magnetic field, e.g., magnetotactic bacteria, mostly containing microcrystals of the same magnetite Fe_3O_4. Thus, summarizing this article, we may conclude that magnetic oxides are extremely versatile, interesting and important materials, as for their very rich and diverse properties, for their already existing and future applications, but also for many natural phenomena.

Conclusion

Thus, summarizing this article, we may conclude that magnetic oxides are extremely versatile, interesting and important materials, as for their very rich and diverse properties, for their already existing and future applications, but also for many natural phenomena. In this chapter we describe the main physical phenomena in transition metal oxides determining their properties—mostly magnetic, but also other interesting phenomena, such as insulator-metal transitions, magnetoelectricity and multiferroicity, and even High-Tc superconductivity in some of them. Basic theoretical concepts are shortly described in this chapter, and diverse properties of magnetic oxides are illustrated on many examples. We conclude by shortly mentioning several applications of magnetic oxides.

Acknowledgments

D. Kh. was supported by DFG through grant 277146847-CRC-1238, while S.S. via project Quantum 122021000038-7.

References

Abragam A and Bleaney B (1970) *Electron Paramagnetic Resonance of Transition Ions*. Clarendon Press.
Cheong SW and Mostovoy MV (2007) Multiferroics: A magnetic twist for ferroelectricity. *Nature Materials* 6: 13.
Gardner JS, Gingras MJP, and Greedan JE (2010) Magnetic pyrochlore oxides. *Reviews of Modern Physics* 82: 53.
Goodenough JB (1963) *Magnetism and the Chemical Bond*. New York: Interscience Publishers.
Imada M, Fujimori A, and Tokura Y (1998) Metal-insulator transitions. *Reviews of Modern Physics* 70: 1039.
Kaplan MD and Vekhter BG (1995) *Cooperative Phenomena in Jahn-Teller Crystals*. Plenum Press.
Keimer B, Kivelson SA, Norman MR, Uchida S, and Zaanen J (2015) From quantum matter to high-temperature superconductivity in copper oxides. *Nature* 518: 179.
Khomskii DI (2014) *Transition Metal Compounds*. Cambridge: Cambridge University Press.
Landau LD and Lifshitz EM (1965) *Quantum Mechanics*. Pergamon Press.
Savary L and Balents L (2017) Quantum spin liquids: A review. *Reports on Progress in Physics* 80: 016502.
Sawatzky G and Green R (2016) The explicit role of anion states in high-valence metal oxides. In: Pavarini E, Koch E, van den Brink J, and Sawatzky G (eds.) *Quantum Materials: Experiments and Theory Modeling and Simulation*, Vol. 6. Forschungszentrum Julich.
Streltsov SV and Khomskii DI (2017) Orbital physics in transition metal compounds: New trends. *Physics-Uspekhi* 60: 1121.
Streltsov SV and Khomskii DI (2020) The Jahn-Teller effect and spin–orbit coupling: Friends or foes? *Physical Review X* 10: 031043.
Takagi H, Takayama T, Jackeli G, Khaliullin, and Nagler SE (2019) Kitaev quantum spin liquid concept and materialization. *Nature Reviews Physics* 1: 264.
Yosida K (2010) *Theory of Magnetism*. Berlin Heidelberg: Springer.

Magnetic nanostructures

Denys Makarov[a] **and Oleksandr V Pylypovskyi**[a,b], [a]Helmholtz-Zentrum Dresden-Rossendorf e.V., Institute of Ion Beam Physics and Materials Research, Dresden, Germany; [b]Kyiv Academic University, Kyiv, Ukraine

© 2024 Elsevier Ltd. All rights reserved.

Introduction 113
Overview 113
Magnetic ordering and theoretical description 113
Atomistic models 113
Phenomenological description 114
Local magnetic interactions 115
Non-local magnetic interactions 116
Micromagnetic equations of state 116
Critical phenomena 117
Single domain particles 118
Single domain particles 118
Superparamagnetism 118
Stoner-Wohlfarth model 119
Nonuniform nontopological magnetization patterning 119
Topological magnetic textures 119
Magnetic topological solitons 119
Domain walls 120
Magnetic vortices 121
Skyrmions and magnetic bubbles 121
3D textures 121
Curvilinear nanoarchitectures 122
Energy functionals 122
Torques in the Landau-Lifshitz equation 122
Mechanically ultrasoft magnets 122
Materials and applications 122
Core-shell particles and exchange bias effect 123
Hollow particles 123
Magnetoelectric and multiferroic particles 123
Curvilinear shapes 124
2D magnetic materials 124
Heterostructures of magnetic materials and topological insulators 124
Characterization of nanoscaled magnets 124
Magnetometry studies 124
Magnetization dynamics studies 125
Tomographic imaging of nanostructures 125
Spintronic and spinorbitronic characterization 126
Conclusion 126
References 127
Further reading 131

Abstract

Magnetic nanostructures represent a reach playground for fundamental research in magnetism but also are applied in different areas including but not limited to magnetic data storage, permanent magnets, medicine, printing technologies and deep brain stimulation. This broad range of applications is enabled by the tunability of the composition of magnetic nanoscaled objects, which can consist of magnetic and non-magnetic heterostructures, possess different types of magnetic ordering and be of different geometrical shape. In this chapter, we review fundamentals of magnetic phenomena in magnetic nanostructures, address fabrication and characterization approaches as well as discuss on application scenarios. Considering the recent activities, we introduce also curvilinear nanostructures, strain coupled artificial multiferroics as well as magnetic 2D materials and heterostructures of magnetic materials and topological insulators.

https://doi.org/10.1016/B978-0-323-90800-9.00048-2

Key points

- Fundamentals of magnetic nanostructures.
- Fabrication and characterization of magnetic nanostructures.
- Applications of magnetic nanostructures.
- Introduce micromagnetic description of nanoscaled magnetic materials.
- Describe magnetization reversal, superparamagnetic transition and finite size effects in low-dimensional magnetic nanoobjects.
- Introduce framework of curvilinear magnetism.
- Describe magnetic textures in magnetic nanostructures including domain walls, vortices and skyrmions.
- Introduce determination of micromagnetic parameters based on experimental data.
- Characterization of magnetic nanostructures including 3D imaging of magnetic textures.
- Introduce application scenarios of magnetic nanostructures.

Introduction

In this chapter we discuss physics and applications of magnetic nanostructures. There are numerous definitions of the term "nanostructure", although most of them agree on when referring to an object for which there is at least one characteristic dimension in the nanometer scale. According to this definition, as nanostructures one considers not only nanoparticles (three dimensional (3D) objects of nanoscale size in all three dimensions) but also platelet-like objects (3D confined objects yet with only one nanoscale geometrical parameter, namely thickness of the platelet) as well as extended thin films (only thickness of the film is in the nanometer scale). In the following, we will follow this broader definition of the term "nanostructure" still with a bias toward 3D confined nanoobjects. In this respect, in addition to platelets and films, we will focus on regular nanoscale-sized particles. This particle can be either filled inside with the same or different magnetic materials or be nonmagnetic in its interior. In the latter case the object is either a hollow particle like a magnetic shell or a core-shell particle with a core composed of a material possessing no long range magnetic order. The differences of magnetic responses between macroscopic and nanoscale materials are usually attributed to the broken translation symmetry at the surface and enhanced surface-to-volume ratio leading to the appearance of magnetic anisotropies and frustration phenomena. For magnetic materials, a typical size of the object should be compared with the characteristic length which is linked to the exchange length or the width of the magnetic domain wall. For typical 3*d* ferromagnets like Ni, Fe, Co and their alloys, the characteristic magnetic length is about 5 nm while the domain wall can be in the range from 10 nm (for hard magnetic materials) to 100 nm (for soft magnetic materials). Therefore, magnetic nanostructures can be in either single domain or multidomain states. In this chapter, we will introduce relevant energy terms to describe magnetic interactions on the atomistic level and present their micromagnetic counterpart. As numerous applications of magnetic nanostructures rely on magnetic materials with different type of ordering, our discussion is not limited to ferromagnets but also addresses ferri- and antiferromagnetic materials. Furthermore, novel means of controlling magnetic responses explore electric field control of the magnetic order parameter (magnetization in the case of ferro- and ferrimagnets and vector of antiferromagnetism in antiferromagnets) due to promises of low-energy prospective spintronic and spin-orbitronic devices. The relevant materials (single phase like $BiFeO_3$ or heterostructures say of ferrimagnetic $CoFe_2O_4$ core and ferroelectric $BaTiO_3$ shell) can be characterized by two spontaneous order parameters, namely magnetization and electric polarization. Those materials are named multiferroics and they will be also discussed in the chapter. Another appealing material science platform for nanoscale magnetism is related to the use of magnetic 2D materials like CrI_3 or Fe_3GeTe_2. We will discuss magnetic phase transitions in magnetic 2D materials and spintronic devices, which were recently reported. Furthermore, nanoscale dimensions are relevant for magnetic topological insulators (TIs) especially for heterostructures of TIs with magnetic materials, where physics is determined by the magnetic proximity with a spatial extension in several Å only. These materials and relevant nanoscale devices for energy efficient spintronics will be briefly mentioned as well.

Overview

Magnetic ordering and theoretical description

In this section, we introduce models to describe magnetically ordered media on atomistic level (Section "Atomistic models"). Then we proceed with the phenomenological description of ordered media on macroscopic level (Section "Phenomenological description") followed by the discussion of local (Section "Local magnetic interactions") and non-local (Section "Non-local magnetic interactions") contributions to the magnetic energy. Furthermore, we discuss equations, which determine equilibrium and dynamic magnetic states (Section "Micromagnetic equations of state").

Atomistic models

Whether the given substance has a magnetically ordered state is determined by its temperature, crystallographic structure and an ability of its atoms to carry a magnetic moment. At the atomic level, ordering is developed due to the exchange interaction. In a particular case of spatially localized interacting spins of $s = 1/2$ length, the Hamiltonian can be written in the form, suggested by Heisenberg,

$$\mathcal{H}_\mathrm{x} = -J\sum_{i,j}\hat{\mathbf{s}}_i\cdot\hat{\mathbf{s}}_j \tag{1}$$

where J is the exchange integral, $\hat{\mathbf{s}}_i$ is the spin operators at i-th site and sum is taken over pairs of neighboring spins. The model of a strong spatial localization of spins assumes the integer number of electrons per ion and discrete energy levels. It works well for materials where magnetic properties are due to $4f$ electrons (rare-earth elements). Furthermore, this model is successfully applied for some materials where magnetic properties are determined by $3d$ electrons. A proper description of $3d$ materials requires taking into account delocalized electrons contributing to the formation of spin polarized energy bands. However, the Hamiltonian (1) often can address the key macroscopic properties of metallic magnets and together with its generalizations be used beyond the $s = 1/2$ assumption. Depending on the sign of J, the exchange coupling is called ferro- or antiferromagnetic. The origin of $J \neq 0$ includes direct (overlapping of wave functions of the nearest magnetic ions) and indirect (e.g., via additional ion of oxygen) exchange mechanisms. In rare-earth elements, the exchange coupling between highly-localized $4f$ electrons is mediated by conduction electrons via the Ruderman-Kittel-Kasuya-Yosida (RKKY) mechanism. We note that RKKY coupling is important to explain the microscopic origin of the antiferromagnetic coupling in magnetic field sensors relying on giant magnetoresistive (GMR) effect (Bruno and Chappert, 1992). Furthermore, interfaces in magnetic multilayer stacks provide additional contributions to the spin coupling resulting in, e.g. chiral interactions as for the case of asymmetrically sandwiched ultrathin ferromagnetic layers like Ta/Co/Pt stacks revealing interfacial Dzyaloshinskii-Moriya interaction (see Section "Local magnetic interactions") (Wiesendanger, 2016; Fert et al., 2017) and surface anisotropy, which can stabilize out-of-plane easy-axis of magnetization in Co/Pd and Co/Pt stacks (Carcia et al., 1985; Carcia, 1988) as well as giant perpendicular magnetic anisotropy in Ir/Co/Pt multilayers (Lau et al., 2019). Furthermore, the exchange bias effect is characteristic for ferromagnet-antiferromagnet interfaces, which phenomenologically acts as the unidirectional anisotropy and leads to the shift of the magnetic hysteresis loop (see Section "Core-shell particles and exchange bias effect").

In specific substances, the Hamiltonian (1) should be extended by the squares of nearest-neighbors dot products and/or next-neighbor dot products of spins. If all exchange bonds cannot be in the lowest-energy state simultaneously, the magnet is called to be frustrated. According to the criterion of Toulouse (1977), the plaquette of spins is frustrated if

$$\mathrm{F} = \prod_{\langle i,\ j\rangle} J_{i,j} < 0 \tag{2}$$

where the product is performed over all active exchange bonds with integrals $J_{i,j} \neq 0$ between i-th and j-th spins in the plaquette. A representative example of the frustrated system is a triangular lattice with the antiferromagnetic nearest-neighbor exchange and spins lying in the lattice plane.

The Hamiltonian (1) allows for a simultaneous rotation of spins on arbitrary angle. Their direction with respect to the crystal lattice is determined by weaker interactions of relativistic nature, such as spin-orbit and dipolar interactions. The simplest case of the influence of the crystal field on a single spin $\hat{s}$ is described by the Hamiltonian of the uniaxial symmetry $\mathcal{H}_\mathrm{ua} = Ds_z^2$ with D determining zero-field splitting of energy levels. The presence of an external magnetic field $\boldsymbol{H}$ makes relevant the Zeeman term $\mathcal{H}_\mathrm{Z} = \mu_\mathrm{B} g_{ij} s_i H_j$ with the Einstein summation rule being used, μ_B being Bohr magneton and g_{ij} being anisotropic $\hat{g}$-tensor. Here, and below Latin subindices for the Einstein summation rule run over x, y and z unless stated otherwise.

The interaction of magnetic dipoles represented by spins is described by the Hamiltonian

$$\mathcal{H}_\mathrm{dip} = 2\mu_\mathrm{B}^2\sum_{i\neq j}\left[\frac{\hat{\boldsymbol{s}}_i\cdot\hat{\boldsymbol{s}}_j}{r_{ij}^3} - 3\frac{\left(\hat{\boldsymbol{s}}_i\cdot\boldsymbol{r}_{ij}\right)\left(\hat{\boldsymbol{s}}_j\cdot\boldsymbol{r}_{ij}\right)}{r_{ij}^5}\right], \tag{3}$$

where $g = 2$ is assumed, the summation is carried over all spins in the lattice and $\boldsymbol{r}_{ij}$ is the radius-vector between i-th and j-th spins. The dipolar interaction is responsible for the anisotropy and magnetostatic interaction (see below). In specific nanoscaled systems, the dipolar interaction is also a source of frustration and effective exchange-like terms of higher orders in (1).

Phenomenological description

Key conclusions about the collective phenomena can be derived using symmetry considerations. The requirement to have a non-zero magnetic moment at lattice sites is assured by the broken time reversal symmetry in magnetic substances. The macroscopic properties of the substance are determined by its magnetic crystal symmetry group. In the simplest case, the magnetic moments within each unit cell are oriented parallel and such substances are referred to as ferromagnets, whose magnetization $\boldsymbol{M}$ (magnetic moment per small enough volume) is non-zero. The unit cell may contain several ions with opposite orientations of moments, but still non-zero net moment (in a wide range of temperatures), which is called as the ferrimagnetic ordering. One says, that such ions belong to the different (magnetic) sublattices. In many practical cases, ferri- and ferro- magnets can be described within the same theoretical and experimental frameworks. If the sublattices possess the same magnetic moments and the crystal symmetry group contains the operation of their exchange, such a substance is referred to as the antiferromagnet. The influence of relativistic interactions gives rise to a more detailed classification based on more complex ground states such as weak ferromagnets (canted antiferromagnets) and helimagnets to name a few.

A magnetic ordering typically appears below a critical temperature T_c (Curie and Néel temperature for ferro- and antiferromagnets, respectively). A simple (qualitative, but not quantitative) explanation of the respective phase transition is given by the Landau theory. In the vicinity of T_c, the free energy potential Φ can be written as a power series of the order parameter μ: $\Phi = \Phi_0 - a\mu^2 + b\mu^4 + \ldots$ with $a \geq 0$ and $b > 0$. Assuming that $a = a_0(T_c - T)$ and vanishes above T_c, this provides an equilibrium value of $\mu(T < T_c)$. For ferromagnets, one can choose $\mu = |\boldsymbol{M}| \equiv M_S$ with M_S being the saturation magnetization. In antiferromagnets, the length of the Néel vector $\boldsymbol{L}$ (staggered sum of different sublattices also called as the vector of antiferromagnetism) can be chosen as μ. More accurate and material-related description of phase transitions is provided by the renormalization group theory (see below). Within the classical approach, the reduction of the saturation magnetization with temperature for a Heisenberg magnet (1) is described by the Bloch law $M_S(T)/M_S(0) = 1 - (T/T_c)^{3/2}$.

Far below T_c, it is reasonable to expand the free energy into power series of components of the unit vector $\boldsymbol{n}$, which is aligned with the vector order parameter $\boldsymbol{M}$ or $\boldsymbol{L}$, and its spatial derivatives assuming that the spatial variations are small enough. The concrete form of the energy is determined by the relevant local and non-local interactions. Their classification is based on the range of spatial "sensitivity". The energy density of a local interaction is a function of the position at the given point $\boldsymbol{r}$ only. The non-local interactions make the torque, which acts on the $\boldsymbol{n}(\boldsymbol{r})$, being dependent on the state of other areas far from $\boldsymbol{r}$.

There are substances, which should be characterized by more than one order parameter at some conditions. An antiferromagnet with N sublattices in addition to $\boldsymbol{L}$ always can be characterized by the total magnetization $\boldsymbol{M}$ and N–2 additional vectors of antiferromagnetism as the secondary order parameters. However, for the macroscopic description, it is enough to use up to three vector order parameters (Andreev and Marchenko, 1980). Their relevance is determined by the crystal symmetries, spatial distribution of $\boldsymbol{L}$ and external influences. For example, weak ferromagnet Fe_2O_3 is characterized by non-zero $\boldsymbol{L}$ and $\boldsymbol{M}$, while triangular antiferromagnet Mn_3Ir has two vectors of antiferromagnetism of almost equal length in equilibrium. The crystal symmetry can allow additional terms in free energy, which are related to magnetoelectric or magnetoelastic effects, for example, $\Phi_{me} = -\alpha_{ij}H_iE_j$ (Cr_2O_3) or $\Phi_\sigma = -\beta_{ijk}\sigma_{ij}H_k$ ($FeCO_3$), respectively. Here, $\boldsymbol{E}$ is the electric field, σ_{ij} is the stress tensor, α_{ij} and β_{ijk} are magnetoelectric and magnetoelastic tensors, respectively (Glinchuk et al., 2013). In a particular case of antiferromagnet with equivalent sublattices, the presence of the center of symmetry in the crystallographic group of the given medium allows for a weak ferromagnetism and piezomagnetism and forbids the linear magnetoelectric effect, while the center of antisymmetry makes the picture to be opposite (Turov, 1994).

Local magnetic interactions

Micromagnetic framework describes the magnetic behavior at sub-micrometer scale, but far from the atomistic scale. In this respect, micromagnetism is macroscopic theory (Brown Jr, 1963). Within the micromagnetic framework, the exchange interaction for a ferromagnetic material with one magnetic sublattice has the energy density

$$w_x = (\nabla n_i)(\nabla n_i) \equiv -A\boldsymbol{n}\cdot\nabla^2\boldsymbol{n}, \tag{4}$$

where $A \propto J$ is the exchange stiffness and ∇ is the gradient operator.

In multisublattice magnets, the exchange energy density can be formulated in terms of individual sublattice magnetizations, or all relevant order parameters, with the only difference in the definition of phenomenological constants (Turov, 1965). For example, for tetragonal crystals the relevant model considers two sublattices, whose local directions characterized by the unit vectors of magnetization $\boldsymbol{m}^a(\boldsymbol{r})$ and $\boldsymbol{m}^b(\boldsymbol{r})$. In this case, the exchange energy density reads

$$\begin{aligned} w_X &= \frac{A_1}{2}\left[\left(\nabla m_i^a\right)\left(\nabla m_i^a\right) + \left(\nabla m_i^b\right)\left(\nabla m_i^b\right)\right] + A_2\left(\nabla m_i^a\right)\left(\nabla m_i^b\right) + \frac{\Lambda}{2}\boldsymbol{m}^a\cdot\boldsymbol{m}^b \\ &\equiv \Lambda\boldsymbol{m}^2 + A(\nabla n_i)(\nabla n_i), \end{aligned} \tag{5}$$

where Λ characterizes the so-called uniform exchange, $A = A_1 - A_2$ and the relations $\boldsymbol{m} = (\boldsymbol{m}^a + \boldsymbol{m}^b)/2$, $\boldsymbol{n} = (\boldsymbol{m}^a - \boldsymbol{m}^b)/2$ are used (Bogdanov et al., 2002). The terms containing gradients in the exchange energy density are referred to as the inhomogeneous exchange. For spin chains in a continuum limit, w_x should be complemented by the lifting term $w_{lif} = \lambda\boldsymbol{m}\cdot\boldsymbol{n}'$ with prime indicating the derivative along the chain, which is responsible for the ferromagnetic response of non-collinear textures (e.g., domain walls, see Section "Topological magnetic textures") (Papanicolaou, 1995), and geometry-induced weak ferromagnetism in curvilinear geometries (Pylypovskyi et al., 2021), see also Section "Curvilinear nanoarchitectures". In quantum spin chains, the presence of w_{lif} leads to the difference between systems with integer and half-integer spins.

The presence of relativistic interactions leading to the anisotropy of magnetic properties can be taken into account by the expansion of the energy density in the form

$$w_a = K_{ij}n_in_j + K_{ijkl}n_in_jn_kn_l + \ldots \tag{6}$$

The anisotropy tensors K are symmetric. Their structure is determined by the crystal symmetry. For example, for a uniaxial easy axis magnet, $w_a = K_a(n_x^2+n_y^2)$ with $K_a > 0$. This case is typical for interfacial anisotropy in Co/Pt or Co/Pd multilayers resulting in the easy axis of magnetization along z axis, which is perpendicular to the interface and is referred to as perpendicular magnetic anisotropy (PMA). Materials revealing PMA are relevant for magnetic data storage applications as media for hard disk drives (Varvaro and Casoli, 2016) and in spinorbitronics for magnetic random access memories (Cao et al., 2020). The anisotropy energy of magnets with cubic symmetry (e.g., iron) reads $w_{\rm a} = K_{\rm c}(n_x^4 + n_y^2 + n_z^2)$. In the simplest case, $K_{\rm a} \propto D$ and can incorporate, e.g., magnetostrictive effects (effects, related to the interplay between the magnetic subsystem and elastic distortions of the crystal lattice, see also Section "Phenomenological description"), interaction of neighboring dipoles and anisotropy of the exchange integral J.

The broken inversion symmetry of the environment of magnetic ions (e.g., B_{20} type alloys like MnSi or thin-film interfaces like Co/Pt multilayers) leads to the appearance of energy terms in the form of the Lifshitz invariants, $\mathcal{L}_{ij}^k = n_i\partial_k n_j - n_j\partial_k n_i$, where ∂_k represents a partial derivative over k-th spatial direction. The respective energy $w_{\rm DM}$ contribution was first considered in Dzyaloshinskii (1964) and Dzyaloshinski (1965), and the microscopic mechanism was proposed by Moriya (1960) (Dzyaloshinskii-Moriya interaction, DMI). Among the relevant DMI terms, there is the energy of interfacial type, $w_{\rm DMI}^{\rm i} = D^{\rm i}\boldsymbol{n}\cdot[[\boldsymbol{z}\times\nabla]\times\boldsymbol{n}] = D^{\rm i}[(\boldsymbol{n}\cdot\nabla)n_z - n_z(\nabla\cdot\boldsymbol{n})]$. with the interface normal along z (e.g., asymmetrically sandwiched ultrathin Co films and crystals of $C_{n\nu}$ symmetry class), and the energy of bulk-like type $w_{\rm DMI}^{\rm b} = D^{\rm b}\boldsymbol{n}\cdot[\nabla\times\boldsymbol{n}]$ (crystals of T and O symmetry classes). Note, that the sign of $D^{\rm i}$ is a matter of convention. In antiferromagnets, this type of DMI is referred to as the inhomogeneous DMI in line with the exchange interaction. DMI is responsible for the stabilization of chiral bubbles and skyrmions, see Section "Skyrmions and magnetic bubbles".

The crystal structure can allow next-neighbor exchange interactions and frustration, which are often of importance for single-layer films. Within the phenomenological approach, this is reflected in the appearance of energy density terms with higher order of spatial derivatives and their powers, e.g. $(\partial_{zz}^2 n_z)^2$ (c.f. $w_{\rm x}$), which were studied in Michelson (1977b), Michelson (1977a) and Michelson (1977c). Both, Dzyaloshinskii and Michelson terms can lead to non-collinear ground states (the order parameter is not homogeneous in space). For multisublattice substances, the free energy density can contain terms, which mix components of the order parameters. For example, the term

$$w_{\rm wf} = D_{ij}M_iL_j \tag{7}$$

with D_{ij} being the Dzyaloshinskii tensor, is responsible for the weak ferromagnetism. Weak ferromagnetism describes the appearance of the spontaneous ferromagnetic moment in antiferromagnets, which is much smaller than the sublattice magnetization, e.g. in α- $\mathrm{Fe_2O_3}$ (Dzialoshinskii, 1957; Moriya, 1960). As for the exchange, this term is referred to as the homogeneous DMI.

The competition between the exchange and other interactions introduces characteristic length scales. Depending on the dominant interactions, these length scales characterize the spatial inhomogeneity of a magnetic texture. For instance, the magnetic length $\ell = \sqrt{A/|K|}$ characterizes the spatial extension of a texture for the case of anisotropic magnetic material (the anisotropy constant can include magnetocrystalline, interfacial and shape anisotropy contributions, see Section "Non-local magnetic interactions"). The quantity $\ell_{\rm D} = 8\pi A/D$ determines the period of the Dzyaloshinskii cycloid in helimagnets.

Non-local magnetic interactions

The state of a magnetic nanostructure is significantly influenced by the magnetic fields produced by the nanostructure itself. The short-range part of the dipolar field of individual magnetic moments (3) can be accounted for as a contribution to anisotropy (Section "Local magnetic interactions"). The long-range part is described by the solution of the magnetostatic Maxwell equations giving the stray field $\boldsymbol{H}_{\rm d} = -\nabla\phi_{\rm d}$ and the respective energy

$$E_{\rm d} = -\frac{1}{2}\int \boldsymbol{M}\cdot\boldsymbol{H}_{\rm d}\mathrm{d}\boldsymbol{r}. \tag{8}$$

The magnetostatic potential $\phi_{\rm d}$ is a sum of the volume and surface integrals of the so-called volume and surface magnetostatic charges $\lambda_{\rm d} = -\nabla\cdot\boldsymbol{M}$ and $\sigma_{\rm d} = \boldsymbol{\nu}\cdot\boldsymbol{M}$, respectively, where $\boldsymbol{\nu}$ is the sample's surface normal. The magnetostatic energy $E_{\rm d}$ is responsible for the formation of domains (regions with a spatially uniform $\boldsymbol{n}(\boldsymbol{r})$) in ferromagnets (see Sections "Single domain particles" and "Topological magnetic textures") and, usually, is less relevant for the global state of antiferromagnets. There are special cases, when magnetostatics can be reduced to the effective anisotropy. In particular, a thin extended ferromagnetic film (planar or curved) with normal $\boldsymbol{\nu}$ possesses an effective anisotropy $w_{\rm a} = K_{\rm d}^{\rm shell}(\boldsymbol{n}\cdot\boldsymbol{\nu})^2$ and $K_{\rm d}^{\rm shell} = \mu_0M_{\rm s}^2/2$ with μ_0 being the vacuum magnetic permeability. The subindex "d" refers to the shape anisotropy originating from the long-range dipolar interaction. For a thin ferromagnetic wire with a circular cross-section, the easy axis of magnetization follows its tangential direction with the effective anisotropy coefficient $K_{\rm d}^{\rm wire} = \mu_0M_{\rm S}^2/4$. Depending on the relation between $K_{\rm d}$ and $K_{\rm a}$, ferromagnets are classified as soft (magnetostatics dominates) and hard (the intrinsic anisotropy is strong). The exchange length $\ell_{\rm x} = \sqrt{2A/(\mu_0M_{\rm S}^2)}$ characterizes the spatial extension of a texture for the case of magnetically soft material like Permalloy (c.f. the magnetic length in Section "Local magnetic interactions"). For materials with PMA, the relation between the shape and magnetocrystalline anisotropy is quantified by the quality factor $Q_{\rm pma} = K_{\rm a}/K_{\rm d}$, which is relevant for skyrmion- and magnetic bubble-hosting materials, see Section "Skyrmions and magnetic bubbles".

For ferro- and antiferromagnets, the magnetostriction can significantly alter the global state, being important if the deformation of different parts of the inhomogeneously magnetized body do not fit together. In particular, the minimization of the interaction energy of elastic dipoles can cause formation of domains in antiferromagnets.

Micromagnetic equations of state

Far below T_c, the temporal evolution of the order parameter $\boldsymbol{n}$ in ferromagnets is described by the Landau-Lifshitz equation (Landau and Lifshitz, 1935) supplemented by additional torques.

$$\dot{\boldsymbol{n}} = -\gamma_0 \boldsymbol{n} \times \boldsymbol{H}^{\text{eff}} + \boldsymbol{T}_{\text{rel}} + \boldsymbol{T}. \tag{9}$$

Here, overdot is the derivative with respect to time, $\gamma_0 > 0$ is the gyromagnetic ratio, $\boldsymbol{H}^{\text{eff}} = -(1/M_{\text{S}})\delta\Phi/\delta\boldsymbol{n}$ is the effective field with δ being the variational derivative, and torques $\boldsymbol{T}_{\text{rel}}$ and $\boldsymbol{T}$ describe the magnetic relaxation and other contributions, respectively. Elastic and other degrees of freedom are not taken into account. For antiferromagnets, a convenient approach is to write a system of coupled Eq. (9) for each of sublattice magnetizations, which allows to derive the equation of motion for $\boldsymbol{L}$ as well. For antiferromagnets close to T_c, the equations of motion based on the Onsager relations can be of relevance.

The equilibrium magnetic state is determined by zero net toque acting on $\boldsymbol{n}$ or, alternatively, by zero variation of the energy. In a general case, the variation of energy allows to determine the boundary conditions, which supplement the equation of motion (9). For the particular case of the DMI $w^{\text{b}}_{\text{DMI}}$ and presence of the surface anisotropy with the energy density w_{surf}, the boundary conditions read

$$\boldsymbol{n} \times \left[2A(\boldsymbol{\nu}\cdot\nabla)\boldsymbol{n} + f^{\text{bc}}_{\text{DMI}}(\boldsymbol{n}, \boldsymbol{\nu}) + \partial w_{\text{surf}}/\partial\boldsymbol{n}\right] = 0, \tag{10}$$

where $f^{\text{bc}}_{\text{DMI}}(\boldsymbol{n}, \boldsymbol{\nu}) = -D^{\text{b}}\boldsymbol{\nu} \times \boldsymbol{n}$ for the DMI of bulk type, and $f^{\text{bc}}_{\text{DMI}}(\boldsymbol{n}, \boldsymbol{\nu}) = D^{\text{i}}[\boldsymbol{z}(\boldsymbol{\nu} \cdot \boldsymbol{n}) - n_z\boldsymbol{\nu}]$ for the DMI of interfacial type with $\boldsymbol{z}$ being the normal to the interface.

The relevant relaxation mechanism expressed in $\boldsymbol{T}_{\text{rel}}$ is dependent on the temporal scales. Considering a slow enough dynamics, a common approach is to utilize the relaxation term in the Gilbert's form $\boldsymbol{T}^{\text{G}}_{\text{rel}} = \alpha_{\text{G}}\boldsymbol{n} \times \dot{\boldsymbol{n}}$, which is derived within the Lagrangian formalism and conserves $|\boldsymbol{n}| = 1$. Note, that the relaxation term introduced by Landau and Lifshitz (1935) based on symmetry reasons coincides with the Gilbert's one up to rescaling of γ_0 in (9) and α_{G}. For the case of ultrafast dynamics or finite temperatures, the longitudinal relaxation of $\boldsymbol{M}$ becomes relevant (Atxitia et al., 2017), which is taken into account in the relaxation terms of Bar'yakhtar $\boldsymbol{T}^{\text{Bar}}_{\text{rel}} = \lambda_1\boldsymbol{H}^{\text{eff}} - \lambda_2\nabla^2\boldsymbol{H}^{\text{eff}}$ and Bloch $\boldsymbol{T}^{\text{Bl}}_{\text{rel}} = \alpha_{\|}(\boldsymbol{M} \cdot \boldsymbol{H}^{\text{eff}})\boldsymbol{H}^{\text{eff}} - \alpha_{\perp}\boldsymbol{M} \times [\boldsymbol{M} \times \boldsymbol{H}^{\text{eff}}]$, respectively, where $\lambda_{1,2}$ and $\alpha_{\|,\perp}$ are some constants. Note that in this case, Eq. (9) should be written explicitly for $\boldsymbol{M}$ instead of the unit vector $\boldsymbol{n}$.

Additional torques in Eq. (9) can originate due to (i) spin-orbit coupling (Han et al., 2021; Shao et al., 2021) and (ii) - spin-transfer effects (Baraduc et al., 2010). They allow to alter magnetic textures, e.g., reorient the magnetization in a thin, soft magnetic layer lying on a hard magnet or induce its precession, an even induce spin-wave instabilities.

(i) The spin-orbit torque can be exerted due to the spin accumulation at the ferromagnet-heavy metal (Pt or Au) interface. Independently of their nature (e.g., spin Hall or Rashba effect), they can be classified by their symmetry: antidamping or field-like torques, $\boldsymbol{T}_{\text{ant}} \propto \boldsymbol{n} \times [\boldsymbol{\varsigma} \times \boldsymbol{n}]$ or $\boldsymbol{T}_{\text{f}} \propto \boldsymbol{n} \times \boldsymbol{\varsigma}$, respectively. Here, $\boldsymbol{\varsigma} = \boldsymbol{j} \times \boldsymbol{z}$ with $\boldsymbol{j}$ being the current density, which creates the electric field, and $\boldsymbol{z}$ being the normal directions to the multilayer stack.

(ii) For spin-transfer effects, the spin angular momentum is transferred from one metallic magnet to another one. The Slonczewski mechanism (Slonczewski, 1996; Berger, 1996; Slonczewski, 2002) is relevant for multilayer structures, where the electric current $\boldsymbol{j}$ flows perpendicularly to the interface (CPP, current perpendicular-to-plane geometry) leading to the torque $\boldsymbol{T}_{\text{S}} \propto \boldsymbol{n} \times [\boldsymbol{n} \times \boldsymbol{j}]$ (c.f. $\boldsymbol{T}_{\text{ant}}$). Here, the coefficient of proportionality is determined by the degree of polarization of current electrons, which flow though the polarizing magnetic layer with strong anisotropy, and alignment of the magnetization of the target magnet $\boldsymbol{n}$ with the current flow direction. If the electric current flows along the magnetic nanostructure (CIP, current-in-plane geometry), conducting electrons can be polarized as well, and their interaction with the magnetic texture is described by the torque of Zhang and Li (2004) and Bazaliy et al. (1998), $\boldsymbol{T}_{\text{ZL}} \propto \boldsymbol{n} \times [\boldsymbol{n} \times (\boldsymbol{j} \cdot \nabla)\boldsymbol{n}] + \beta_{\text{ZL}}\boldsymbol{n} \times (\boldsymbol{j} \cdot \nabla)\boldsymbol{n}$, where β_{ZL} is the nonadiabatic spin-transfer parameter.

Critical phenomena

The rigorous treatment of the behavior of $\boldsymbol{n}$ in the vicinity of the phase transition from the magnetically ordered to the paramagnetic state needs to account for thermal fluctuations, whose influence becomes decisive near T_c. This is addressed by the renormalization group theory. Within this approach, changes of physical quantities just below T_c are described in terms of power laws with the variable $t = T/T_c - 1$ with the so-called critical exponents. The main scaling laws introduce six critical exponents α, β, γ, δ, η and ν considering the specific heat $C \sim |t|^{-\alpha}$, spontaneous magnetization $M_{\text{S}} \sim |t|^{-\beta}$, susceptibility $\chi \sim |t|^{-\gamma}$, relation between the field and magnetization $H \sim M^{\delta}_{\text{S}}$, correlation function $\Gamma(x) \sim x^{2-d-\eta}$ with d being the system's dimension (e.g., $d = 1$ for a chain), and correlation length $\xi \sim |t|^{-\nu}$. In the vicinity of T_c, the exponents obey equalities (scaling laws) $\alpha + 2\beta + \gamma = 2$ (Rushbrook), $\gamma = \beta(\delta - 1)$ (Widom), $\gamma = (2 - \eta)\nu$ (Fisher) and $d\nu = 2 - \alpha$ (Josephson). The scaling laws allow to deduce all the critical exponents by knowledge of two of them. For a pure Nickel, $\beta \approx 0.42$ and $\gamma \approx 1.314$. The magnet, which is described by the Heisenberg Hamiltonian (1) only ($d = 3$), has $\beta \approx 0.313$ and $\gamma \approx 0.37$. Note, that the presence of long-range interactions alters the critical exponents.

The critical behavior is considered to be universal, in the sense that it is the same for different materials if they possess the same intrinsic symmetries independently of their electronic structure. The universality is observed far from T_c as well. For example, the sublattice magnetization $M_{\text{S}} \propto 1 - (T/T_c)^2$ for EuTe and $Y_3Fe_5O_{12}$ (cubic magnets with half-integer spin), and $M_{\text{S}} \propto 1 - (T/T_c)^3$ for Cr_2O_3 and NiO (axial magnets with integer spin) for low enough temperatures.

A central role of the symmetry (which, in addition to the unit cell structure, is determined by d and the number of free spin components N_{sp}) is revealed by the Ising model. The Ising model itself allows the only one degree of freedom of the spin vector $\boldsymbol{s}$

(e.g., along $\boldsymbol{z}$ axis, $N_{\text{sp}} = 1$) with the Hamiltonian $\mathcal{H}_{\text{I}} = -J\sum_{i,j} s_i^z s_j^z$ (c.f. (1)) with summation over neighboring spins. For a chain with $d = 1$, the Ising model is in the ordered state only at $T = 0$. The temperature driven phase transitions become possible for $d > 1$. Among extensions of the Ising model, one can mention the XY model with $N_{\text{sp}} = 2$ (the only $s^z \equiv 0$), the ANNNI model (axial next-nearest neighbor Ising), which allows competing exchange interactions and the Potts model, which introduces intrinsic states to govern the interaction between spins.

Single domain particles

The field $\boldsymbol{H}_{\text{d}}$ can be uniform within a solid sample of the ellipsoidal shape, and it's limiting cases (wires and thin films) leading to the possibility of $\boldsymbol{n} = \text{const}$ within the sample as well. This does not guarantee that this state has the minimal energy if the sample's dimensions are large enough. Uniformly magnetized particles is a convenient theoretical abstraction, which allows to understand physics of the magnetization reversal of magnetic nanostructures without involved mathematical analysis. The corresponding theory was formulated by Stoner and Wohlfarth (1948).

In the following, we consider criteria of nanoobjects to be in the single domain state (Sections "Single domain particles" and "Nonuniform nontopological magnetization patterning"), collective superparamagnetic behavior of such nanoparticles (Section "Superparamagnetism"), and their magnetization reversal in magnetic fields (section Stoner-Wohlfarth model).

Single domain particles

The critical radius of a spherical particle is defined when the energy of a domain wall spanning a spherical particle is equal the change of the magnetostatic energy for a single- and two-domain states:

$$D_{\text{s -dom}} = \frac{72\sqrt{AK_{\text{a}}}}{\mu_0 M_{\text{S}}^2} \tag{11}$$

For hard magnetic materials like FePt alloy, the critical single domain diameter of a spherically-shaped particle is 340 nm. For soft magnetic materials like Fe_3O_4, the critical size is in the range of 12 nm only.

Superparamagnetism

As in any ferroic material, long-range ordering in magnetic materials is present below a critical temperature, which is known as Curie temperature for ferro- and ferrimagnets and Néel temperature for antiferromagnets. The transition from the magnetically ordered to magnetically disordered state is the magnetic phase transition. For instance, the Curie temperature for FePt alloy is 750 K. When the size of the ferromagnetic material is decreased below a certain critical one, the magnetic moment of the particle averaged over the measurement time of the experiment can become reduced effectively to zero. As a result, at long time scales (measurement time is longer than the relaxation time of the magnetization) the particle behaves as a paramagnet although it remains magnetically ordered. Application of an external magnetic field results in a much stronger magnetic response than would be the case for a paramagnet. The relaxation time is given by the Arrhenius law $\tau = \tau_0 \exp(-E_{\text{B}}/k_{\text{B}}T)$. The energy barrier $E_{\text{B}} = K_{\text{a}}V$ is given by the anisotropy energy of the magnetic particle of volume V with the anisotropy constant K_{a}. Here, τ_0 is the natural lifetime characterizing the attempt frequency for the magnetization reversal typically taken as 10^{-9} s, which is of the order of magnitude of the frequency of the ferromagnetic resonance. The relaxation time τ should be compared to the typical measurement time, which is strongly dependent on the experimental setup. For instance, for the measurement of the magnetic moment using a conventional superconducting quantum interference devices (SQUIDs), the measurement time is in the range of 10 s. When using nuclear magnetic resonance (NMR), the characteristic time is in the range of 10^{-6} s. The superparamagnetic critical diameter for a spherical particle is given by a volume $V = \ln(\tau/\tau_0) \times k_{\text{B}}T/K_{\text{a}}$. This equation allows to determine the minimal size of magnetic nanoparticles for their stability at the given temperature for given time. This is especially useful for the determination of the stability of the written bit of information in magnetic data storage. For instance, if we request that the individual magnetic nanostructure with $K_{\text{a}} = 1\ \text{MJm}^{-3}$ should be stable over 10 years at $T = 300$ K, then the diameter of this nanostructure should be in the range of 7 nm, which can be achieved using for instance hard magnetic FePt alloys. Alternatively, it is possible to solve the relaxation equation with respect to temperature $T_{\text{B}} = \ln(\tau/\tau_0)K_{\text{a}}V/k_{\text{B}}$, which provides access to the transition temperature when the magnetic nanoparticles with the volume V and anisotropy constant K_{a} will experience transition to the superparamagnetic regime for the case when the magnetic moment is measured with a characteristic time τ. The transition temperature to the superparamagnetic regime is called blocking temperature. For a FePt nanoparticle ($K_{\text{a}} = 1\ \text{MJm}^{-3}$) with a diameter of 4 nm, the blocking temperature is about 110 K, which is substantially lower than the Curie temperature of the FePt alloy.

The magnetization of an ensemble of superparamagnetic particles measured at temperature T in a magnetic field H applied along z-axis is described via Langevin function: $M_z = M_{\text{S}}[\coth(x) - 1/x]$ with $x = \mu_0 M_{\text{S}} VH/(k_{\text{B}}T)$.

The interaction between nanoparticles embedded in a matrix can change the Langevin-like behavior of $M_z(H, T)$. For example, Fe nanoparticles embedded in Au create exchange-coupled clusters, which can be taken into account by replacing the temperature $T \rightarrow T + T^*$ with T^* being the interaction parameter (Binns et al., 2002). Beyond the so-called percolation threshold, the entire system of nanoparticles can be considered as the exchange-coupled medium with the random direction of the anisotropy axis within each particle. Its properties are determined by the correlation function of the anisotropy axes.

Stoner-Wohlfarth model

For the case of a homogeneously magnetized particle with easy axis anisotropy, it is possible to describe the magnetization reversal process analytically. This situation is applicable for an ellipsoid-shaped particles, where the magnetization switches homogeneously (all moments are parallel during the reversal process). The corresponding model, which takes into account the anisotropy energy, magnetostatic energy and Zeeman energy was solved by Stoner and Wohlfarth (1948). This model allows to calculate the coercive and nucleation fields for the magnetization reversal. For instance, when the magnetic field is applied along the easy axis of magnetization, the coercive field is $H_c = 2K_{eff}/\mu_0 M_S$, where K_{eff} includes the uniaxial magnetocrystalline and shape anisotropies. The anisotropy field is defined as the smallest field, which should be applied to switch magnetization. Without demagnetizing fields, the anisotropy field is $H_{an} = 2K_a/\mu_0 M_S$. The coercive field for the magnetization reversal decreases with the increase of temperature, $H_c = 2K_a/(\mu_0 M_S) \times \left[1 - \sqrt{\ln(\tau/\tau_0) \times k_B T/(K_a V)}\right]$. The switching field is dependent on the angle between the magnetic field and the easy axis of magnetization ψ. For a Stoner-Wohlfarth particle, the angular dependence of the switching field is given by the expression, $H_{sw} = H_{an}/(\sin^{2/3}\psi + \cos^{2/3}\psi)^{3/2}$. In contrast to the coercive field, which is usually defined as the field at which the magnetization is zero ($M = 0$), the switching field corresponds to the field of the steepest change of the magnetization with respect to field (maximum of $|\mathrm{dM/dH}|$). This angular dependence is representative for the reversal of individual nanostructures representing bits of information in magnetic bit patterned media. We note that the Stoner-Wohlfarth angular dependence is different from the one derived by Kondorsky (1937) for the case of nucleation and domain wall propagation, $H_{sw}^{K} \propto 1/\cos\psi$. For the ensemble of Stoner-Wohlfarth particles with random orientation of the easy axis of magnetization, the resulting magnetization of the ensemble is $M_S/2$ and the coercive field $H_C = 0.48 H_{an}$.

Nonuniform nontopological magnetization patterning

If the particle's lateral dimensions are of the order of the single-domain size, but the shape is not ellipsoidal, the strictly uniform state is impossible. This is reflected in a slight divergent distortion of the magnetization at the sample's ends, which is referred to as the flower state. The intermediate lateral sizes between the single- and multidomain states lead to the strongly inhomogeneous states, such as S- or C-states named according to the shape of the magnetization flow. In a general case, the magnetostatic interaction leads to the appearance of a domain structure.

Topological magnetic textures

Beyond the single-domain limit of nanoparticles (also for thin films, shells and bulk magnets), the order parameter $\boldsymbol{n}(\boldsymbol{r})$ can be characterized by the absence or presence of specific topological features, which are related to the vector nature of $\boldsymbol{n}$ only. This provides a powerful complementary approach relying on the topology to understand inhomogeneous spatial distributions of $\boldsymbol{n}$, which are referred to as magnetic textures and can be of high complexity. The introduction to the topology and its application to magnetism is given in Section "Magnetic topological solitons". For instance, relying on purely topological considerations, it is possible to predict the allowed magnetic states, e.g. in spherical geometries, where the hairy ball theorem forbids strictly tangential ordering without singularities (Kravchuk et al., 2012), or domain walls structure supported by a magnetic Möbius ring (Pylypovskyi et al., 2015). Non-trivial topological features in $\boldsymbol{n}(\boldsymbol{r})$-field are related to the stability of the respective textures, which is important for their application potential. In the following, one-dimensional (Section "Domain walls"), two-dimensional (Sections "Magnetic vortices" and "Skyrmions and magnetic bubbles"), and three-dimensional (Section "3D textures") magnetic textures with non-trivial topology are considered.

Magnetic topological solitons

A competition between the exchange and anisotropic (anisotropy itself or/and magnetostatics) or helimagnetic (next-neighbor exchange, DMI) interactions can stabilize spatially inhomogeneous magnetic textures (the distribution of the order parameter $\boldsymbol{n}(\boldsymbol{r})$). If the particular distribution connects regions in the locally ground state (e.g., along the anisotropy axis), there is no continuous transformation of $\boldsymbol{n}(\boldsymbol{r})$ into the global ground state, which is in contrast to magnetic states mentioned in Section "Nonuniform nontopological magnetization patterning". Such magnetic texture is referred to as a topological magnetic soliton (Kosevich et al., 1990; Gobel et al., 2021). Note, that there are localized solitary solutions of Eq. (9), which are stabilized by dynamics instead of topological reasons.

The topological properties of a given texture can be described by the mapping of the physical space onto the space $\mathbb{R}_{op}$ of the order parameter $\boldsymbol{n}$ (Mermin, 1979). The latter can be represented, e.g., by a unit circle $\mathbb{S}^1$ or sphere $\mathbb{S}^2$ (Bloch sphere) for the planar and three-dimensional configurations, respectively. Often, the mapping itself can be described by the first or second homotopy groups $\pi_1(\mathbb{R}_{op})$ (map of closed loops is relevant for domain walls and vortices, see Sections "Domain walls" and "Magnetic vortices", respectively) or $\pi_2(\mathbb{R}_{op})$ (map of spheres,[1] is relevant for skyrmions and vortices, see Sections "Skyrmions and magnetic bubbles" and "Magnetic vortices", respectively). Then, each topological soliton can be characterized by the degree of mapping (also referred to as topological index or charge), which reflects a number of windings made by $\boldsymbol{n} = \{\sin\theta\cos\phi, \sin\theta\sin\phi, \cos\theta\}$ between the connected ground states.

---

[1] In the sense of topology, plane and sphere are equivalent.

The $\pi_1(\mathbb{S}^1)$ charge can be introduced as $Q_1 = \int \theta' \mathrm{d}s/(2\pi) = \int \mathrm{d}\theta/(2\pi)$, where s is the coordinate along which the magnetic polar angle θ varies keeping $\phi = \text{const}$. For the case of a single domain wall (topological charge p in Section "Domain walls"), $Q_1 = \pm 1$. For merons (Section "Magnetic vortices"), Q_1 calculated for ϕ along the closed loop corresponds to the so-called vorticity.

The Pontryagin index

$$Q = \frac{1}{8\pi}\int \boldsymbol{n}\cdot\left[\partial_x \boldsymbol{n} \times \partial_y \boldsymbol{n}\right]\mathrm{d}x\mathrm{d}y \equiv \frac{1}{4\pi}\int \sin\theta \mathrm{d}\theta \mathrm{d}\phi \tag{12}$$

characterizes the mapping $\pi_2(\mathbb{S}^2)$ and, by absolute value, says how many times $\boldsymbol{n}$ covers the unit sphere. Concerning curvilinear shells, one should take into account the topology of the shell itself, which is given by the surface' genus g defining the normal Gauss map $Q_G = \mp(1 - g)$. In this way, the normally magnetized sphere can be referred to as the object in the topologically trivial state with the actual topological index $Q' = Q - Q_G = 0$ (Kravchuk et al., 2016).

The topology of 3D textures is characterized by the homotopy group $\pi_3(\mathbb{S}^2)$, i.e., mapping of a 3-sphere[2] onto a unit sphere covered by $\boldsymbol{n}(\boldsymbol{r})$. It is characterized by the Hopf index

$$\mathcal{H} = \frac{1}{16\pi^2}\int \varepsilon_{ijk}\varepsilon_{\alpha\beta\gamma\delta}\tilde{n}_\alpha \frac{\partial \tilde{n}_\beta}{\partial x_i}\frac{\partial \tilde{n}_\gamma}{\partial x_j}\frac{\partial \tilde{n}_\delta}{\partial x_k}\mathrm{d}^3x. \tag{13}$$

Here, tensors ε_{ijk} and $\varepsilon_{\alpha\beta\gamma\delta}$ are antisymmetric by all their indices, Greek indices enumerate components of the 4-dimensional vector $\tilde{\boldsymbol{n}} = \{\boldsymbol{v}\sin X,\ \cos X\}$ with the unit vector $\boldsymbol{v} \in \mathbb{R}^3$, and Latin indices run over Cartesian coordinates x, y, z. The order parameter reads $\boldsymbol{n} = \boldsymbol{z}\cos 2X + 2\boldsymbol{v}v_z\sin^2 X + [\boldsymbol{v} \times \boldsymbol{z}]\sin 2X$. Magnetic textures with different values of $\mathcal{H}$ are determined by the choice of functions $\boldsymbol{v}(\boldsymbol{r})$ and $X(\boldsymbol{r})$.

Since Eq. (9) does not allow breaks of the continuous vector field $\boldsymbol{n}$, the topological index is a conserved quantity in an infinite system, which renders the topological solitons to be perspective information carriers of high stability. Besides boundaries, the conservation of the topological index can be violated by the effects of lattice discreteness and temperature.

A frequently used analytical way to describe topological solitons is the collective variable approach, which allows to reduce a system with infinite degrees of freedom to a few variables within the Lagrangian formalism. In particular, it can be a soliton position and phase of the order parameter as in $q - \Phi$ model (Slonczewski, 1973). A particular example of this approach is the Tiele equation for dynamics of ferromagnetic solitons (Thiele, 1973).

A seminal example of the topological soliton is presented by the Belavin-Polyakov solution in 2D for an isotropic ferromagnet (Belavin and Polyakov, 1975). In the cylindrical reference frame (ρ, χ, z), the polar magnetic angle θ satisfies the relation

$$\tan\frac{\theta}{2} = \left(\frac{R}{\rho}\right)^{|Q|} \tag{14}$$

with R being the soliton radius, $Q \in \mathbb{Z}/\{0\}$ characterizing the degree of $\pi_2(\mathbb{S}^2)$ map and arbitrary in-plane phase $\phi_0 = \phi - Q\chi$. The radius R is not defined in the exchange approximation (the soliton collapses to the line defect in $\boldsymbol{n}$) and needs other interactions for stabilization of the soliton according to the Derrick-Hobart theorem in case of the absence of higher-order spatial derivatives.

Domain walls

The region between two magnetic domains is called a domain wall (DW). DWs are classified by their symmetry, which is determined by the symmetry of the energy functional. In the simplest case, the transition region can be characterized by an axis of propagation, perpendicular to this region. An achiral uniaxial magnet with the easy axis along $\boldsymbol{z}$ direction supports 180° walls with $n_z = p\tanh(x/\Delta)$, where $\boldsymbol{x}$ axis is chosen as the propagation direction for clarity, $p = \pm 1$ is the topological charge and the wall width parameter $\Delta = \sqrt{A/K_\mathrm{a}}$. The sense of rotation of $\boldsymbol{n}$ within the wall is determined by magnetostatics. In bulk samples, $\boldsymbol{n}$ rotates perpendicularly to the propagation direction to avoid volume magnetostatic charges (Bloch wall). In thin enough ferromagnetic films, the penalty due to the surface charges forces $\boldsymbol{n}$ to rotate along the propagation direction (Néel wall). The presence of DMI also favors the concrete DW type: $w_{\mathrm{DMI}}^{\mathrm{b}}$ and $w_{\mathrm{DMI}}^{\mathrm{i}}$ lead to the chiral DWs of the Bloch and Néel types, respectively, with the rotation direction of $\boldsymbol{n}$ inside them (clockwise or counter-clockwise) determined by the sign of $D^{\mathrm{b,i}}$. The head-to-head (tail-to-tail) DWs in thin nanowires, stripes and tubes, which are named accordingly to the domains' magnetization, also belong to 180° walls family. The presence of higher-order anisotropies leads to the appearance of neighboring domains, where the order parameter rotates to lower angles, e.g., 90° walls in ferroelectric-ferromagnetic heterostructures or 71° and 109° walls in cubic magnets.

Magnetic nanostripes are prototypical examples of racetracks supporting the motion of topological solitons driven by external fields or torque $\boldsymbol{T}$. Depending on the stripe thickness and width, the head-to-head DW structure can be more complex. For a thin achiral stripe, magnetostatics favors the symmetric transversal DW (magnetization rotates transversal to the stripe, in the stripe' plane). For a larger thickness, the DW becomes asymmetrically titled and for a thick enough sample the domains are separated by the vortex DW (see below). Nanotubes of large enough diameter support the formation of vortex DWs as well with a circulation of $\boldsymbol{n}$ around the tube.

---

[2] 3-sphere is an analog of a regular sphere with one more dimension and is topologically equivalent to the three-dimensional Cartesian space $\mathbb{R}^3$.

The DW dynamics is determined by the balance of the driving term and damping α. The DW velocity is proportional to the drive for a weak enough force up to the critical field (current) called the Walker limit. Above the Walker limit, the motion becomes oscillatory with the reduction of the average velocity.

Magnetic vortices

A vortex is the magnetic texture with in-plane closed circular flux of $\boldsymbol{n}$ in the vicinity of the origin. In a system with the cylindrical symmetry, its in-plane distribution reads $\phi = q\chi + \phi_0$, where $q \in \mathbb{N}$ is the vorticity $\left(\pi_1\left(\mathbb{S}^1\right)\right.$ homotopy group$\left.\right)$, χ is the polar angle and ϕ_0 is the phase. Vortices are the ground states in magnetically soft nanodisks, whose radius is sufficiently large in comparison with thickness. Their stability is supported by the magnetostatics, which provides an effective anisotropy at the disk edge to avoid $\sigma_\mathrm{d} \neq 0$ with $\phi_0 = C\pi/2$ and $C = \pm 1$ called circulation. A Gaussian-like out-of-plane magnetization in the vortex origin is referred to as the vortex core, with the polarity $p_\mathrm{vor} = \pm 1$ depending on its co- or counter-directionality with respect to $\boldsymbol{z}$-axis. The vortex core represents the Bloch line: a twist of the domain wall, which divides it onto oppositely magnetized parts (Guslienko, 2008; Gaididei et al., 2010). Vortex state is also characteristic for the ring-shaped objects, where for a sufficiently large internal radius the out-of-plane component is absent. Geometrical features as notches in magnetic rings allow to control the value of circulation C (Kläui et al., 2001).

Vortices possess half-integer topological charges $Q = p_\mathrm{vor}q/2$ and, therefore, are classified as merons in the topological sense. Values of C and p_vor can be changed by external fields (strong enough static field or resonant switching by alternating fields) or currents. The presence of DMI alters the width of the vortex core (Butenko et al., 2009).

Depending on the nanodot size and shape of the boundary, magnetostatics can stabilize other states, e.g. the Landau structure, which is similar to vortex and is formed in square-shaped soft nanodots. In astroid-shaped particles, it is possible to form antivortices with $q \in \mathbb{Z}_-$. Vortex-antivortex pairs can be dynamically created during switching of the vortex polarity, instability of the saturated state or due to thermodynamic reasons (Berezinskii-Kosterlitz-Thouless transition for the XY model (Berezinsky, 1971; Berezinsky, 1972; Kosterlitz and Thouless, 1973)). Elongated soft nanodots of large enough size host a series of vortices and antivortices (the cross-tie state).

The magnetic textures with $|q| > 1$ are unstable in the absence of the next neighbor exchange interactions. The value of Q is one of the quantities determining the gyrotropical motion of vortices. The change of the vortex polarity, mediated by the dynamical appearance of vortex-antivortex pairs (Gaididei et al., 2010), or induction of vortex-antivortex superlattices by the spin-polarized current (Volkov et al., 2011) preserves the value of Q characteristic for the ground state of the nanodot. Planar as well as curvilinear nanodots in a vortex state can be arranged in arrays can possess higher susceptibility and lower critical fields due to the magnetostatic inter-dot interaction (Guslienko, 2008; Streubel et al., 2015a, 2015b; Streubel et al., 2016).

Skyrmions and magnetic bubbles

Magnetic materials with strong uniaxial anisotropy support topologically nontrivial textures with integer Q. The magnetostatics allows to stabilize circular DWs (cylindrical domains or magnetic bubbles) of Bloch type (e.g., some garnets like YIG and amorphous films based on GdCo). The presence of DMI select the energetically preferable rotation of $\boldsymbol{n}$ within the DW (chiral bubbles or skyrmion bubbles, e.g., in Ta/CoFeB/TaO$_x$). Circular DWs can host several Bloch lines, which influence their dynamic properties.

The DMI itself can stabilize skyrmions with $Q = \pm 1$, which have smaller radii than cylindrical domains (Co/Pt and Co/Pd asymmetric stacks, MnSi, $\mathrm{Cu_2OSeO_3}$). They are characterized by a strong spatial localization and can be displaced using lower density electric current in comparison with DWs. Ferromagnetic skyrmions possess a Magnus-like force acting perpendicularly to the current direction (skyrmion Hall effect). It is canceled for two-sublattice antiferromagnetic skyrmions, leading to the straight propagation along the applied current.

Depending on the temperature and external magnetic field, applied along the anisotropy axis, skyrmions and magnetic bubbles can appear either as individual objects or in hexagonal lattices as the ground state. The specific DMI symmetry can lead to the appearance of antiskyrmions (e.g. in crystals of D_{2d} or S_4 symmetry classes).

Stable vortex-antivortex pairs in easy-plane magnets with DMI are also referred to as bimerons. They act as a skyrmion analog in the absence of a dominating easy axis. Equilibrium skyrmionic textures with $|Q| > 1$ are characteristic for frustrated magnets.

3D textures

Except cases of purely one- or two-dimensional magnets, like atom-by-atom engineered chains or van der Waals materials, and films of thickness much less than the magnetic length, magnetic textures can possess significant 3D non-uniformities. For the vortex state, this is reflected in a barrel-shaped distortion of the vortex core (narrow core at the surface and wide in a bulk). Skyrmions stabilized by the DMI of Bloch type form skyrmion lines through the magnetic medium, which can be of curved shape. Lattice defects can also stabilize curved domain walls in 3D (Donnelly et al., 2020).

Similarly to the fact, that the Bloch line can be understood as a twist of the domain wall, a twist of the Bloch line corresponds to the so-called Bloch point: a hedgehog-like 3D texture with a singularity in the center. Bloch point has properties of a magnetic monopole (an emergent electrodynamics in the solid state physics) with the singularity assured by the lattice discreteness or local reduction of M_S. In addition to the stabilization on Bloch lines, the Bloch point appears dynamically in processes of the vortex polarity switching and unwinding of skyrmion tubes. The skyrmion tube starting on the surface can be terminated by the Bloch point in equilibrium under certain conditions, forming the so-called magnetic bobbler.

Purely 3D topological solitons are represented by the Hopf solitons with non-zero Hopf index. In particular, they are characterized by magnetization distributions following torus-like configurations. As representative examples, one can consider a 3D vortex (often referred to as Hopfion) in the easy-axis magnet with the oppositely magnetized volume of toroidal shape (Kosevich et al., 1990), or vortex rings formed by the magnetization streamlines of the multiply stacked closed loop shape (Cooper, 1999). The stabilization of Hopfions in magnetic nanoparticles is possible via the next-neighbor exchange interactions with frustration and specific symmetries of DMI in finite samples.

Curvilinear nanoarchitectures

The role of the sample's shape in magnetism goes beyond shape-induced patterning such as flower states or vortices. For example, bound of the vector field $\boldsymbol{n}$ to a shell maps the topological properties of the latter onto the behavior of $\boldsymbol{n}$. For the case of a magnetically soft sample of a spherical topology, this is reflected in the inability to have $\boldsymbol{n}$ strictly tangential to the shell, hence resulting in the presence of vortices as expected according to the hairy ball theorem.

The framework of curvilinear magnetism describes how the geometric and topological properties of the sample's shape affect the behavior of magnetic textures (Makarov et al., 2022; Sheka et al., 2022). In particular, curvilinear magnetism identifies magnetic responses and effects, which manifest themselves by the curvature κ and torsion τ of nanowires and principal curvatures $\kappa_{1,2}$ of thin shells, where the respective functions are calculated with respect to the "base"[3] curve $\boldsymbol{\gamma}$ or surface $\boldsymbol{\sigma}$. In the following, we introduce the key aspects of geometry within the micromagnetic framework in the energy functional (Section "Energy functionals"), spin torques in the Landau-Lifshitz Eq. (9) (Section "Torques in the Landau-Lifshitz equation"), and interplay between magnetic and mechanical degrees of freedom in mechanically soft magnets (Section "Mechanically ultrasoft magnets").

Energy functionals

Practically relevant examples when the anisotropy axis can be spatially inhomogeneous include: (i) shape anisotropy of thin wires leading to the uni- or biaxial anisotropy with axes depending on the position along $\boldsymbol{\gamma}$ if the wire's cross-section is circular or not; (ii) interface-induced anisotropy following the shell normal $\boldsymbol{\nu}$ such as in Co/Pt multilayers; (iii) shape anisotropy of thin shells with the hard axis along $\boldsymbol{\nu}$. In comparison with a straight wire or extended film, this breaks the translational symmetry of the magnet. The symmetry can be locally restored by considering the properties of the magnet in the reference frame, which follows the anisotropy direction and, in the considered examples, the geometry of the sample. Methodologically, this means incorporation of the translationally invariant terms (including identification of the derivatives along the tangential directions) in the energy functional, while the rest terms turn out to be determined by $\kappa_{1,\ 2}$ or κ and τ. The latter includes the appearance of the geometry-driven terms with symmetries of DMI and anisotropy stemming from the exchange and intrinsic (i.e., related to the lattice unit cell) DMI. The geometry-driven weak ferromagnetism and geometry-driven effects from anisotropy are present in curvilinear antiferromagnetic spin chains (Pylypovskyi et al., 2021).

The gradient of material parameters, including the geometry-driven ones, is a source of pinning and automotion of magnetic solitons. For example, the curvature maximum and strong gradient represent the pinning potentials due to the energy gain in the exchange. Therefore, in their vicinity, the change of the energy landscape induces the geometry-driven motion of domain walls and skyrmions (Yershov et al., 2018; Korniienko et al., 2020).

Torques in the Landau-Lifshitz equation

In thin enough wires, the current flow $\boldsymbol{j}$ follows the wire's shape. This makes the torque-driven dynamics geometry-dependent via the field-like or antidamping-like torques. For the domain wall motion imposed by $\boldsymbol{T}_{\mathrm{ZL}}$, this is reflected in the reduction of the non-adiabatic parameter by $\beta^*_{\mathrm{ZL}} = p\tau\ell$ and respective modification of the Walker limit (Yershov et al., 2016).

Mechanically ultrasoft magnets

A ferromagnetic sample with small enough Young's modulus undergoes a mechanical deformation as the response on the equilibrium magnetic texture, which reflects the symmetry of the involved energy terms. For instance, the balance between the exchange and easy-axis anisotropy in rings results in the ring's shape of circular and biaxial oval symmetries. The presence of DMI supports twists and bends of ferromagnetic stripes (Gaididei et al., 2019; Yershov et al., 2019).

Materials and applications

Magnetic nanostructures can be prepared via chemical synthesis, direct writing or physical vapor deposition combined with lithographic patterning. Alternatively, nanosized particles can be prepared from powder with larger constituents upon appropriate processing. For instance, by hydrogen assisted processing, NdFeB microparticles can be processed in a powder with 300 nm large nanoparticles (Gutfleisch et al., 2002). These nanopowders of NdFeB are relevant for permanent magnet applications. The choice of the material for nanoparticles is determined by the target application. For magnetic data storage applications like bit patterned media concepts, ordered arrays of hard magnetic nanoparticles are needed. In this respect, much attention is dedicated to the realization of ordered arrays of hard magnetic monodisperse FePt nanoparticles with a size in the range of 3–10 nm (Sun, 2000).

---

[3] Under the "base" curve one means the curve, which can be extended into lateral dimension to coincide with the given wire. Similarly, the "base" surface is the surface, which can be extended into both directions along the surface normal to match the shape of the shell.

For medical applications, superparamagnetic and biocompatible particles are used like Fe_3O_4. Their synthesis is well established, for instance, based on controlled co-precipitation techniques. There is an active research on the stabilization of magnetic particles in solutions. Coatings provide the stabilization to magnetic nanoparticles against aggregation in a biological medium and in a magnetic field. Furthermore, with the decrease of the particle size, the susceptibility of nanoparticles toward oxidation increases (Lu et al., 2007). There are many stabilizers including monomeric stabilizers (e.g., phosphates, and sulfates), polymers like dextran and chitosan, dendrimers etc. For instance, dendrimers have an added advantage of not only providing stability to the magnetic nanoparticles in solution but also help in binding various biological ligands to the surface of colloids (Dietrich et al., 2012). To achieve inorganic core-shell particles, it is possible to use different sol-gel approaches. For instance, sol-gel synthesis is employed to obtain silica-coated Fe_3O_4 ferrofluids using tetraethyl orthosilicate through its hydrolysis and condensation (Narayanan et al., 2011). Furthermore, magnetic nanoparticles generated much attention in different technologies, particularly, magnetic inks for ink-jet printing (Voit et al., 2003), biosensing (Miller et al., 2002; Chen et al., 2011), targeted drug delivery (Jain et al., 2005; Chourpa et al., 2005) and contrast agent in magnetic resonance imaging (MRI) (Boutry et al., 2006; Corot et al., 2006).

Core-shell particles and exchange bias effect

Core-shell nanoparticles could be composed of two magnetic materials including two ferromagnets, say magnetically hard in the interior (core) and magnetically soft in the outer shell. Those composites are used as exchange coupled composites for high-energy permanent magnet applications (Skomski et al., 2013). At the same time, it is possible to combine magnetic materials with different ordering, like ferro- and antiferromagnetic. In these systems represented by ferromagnetic Co core and antiferromagnetic CoO shell, it is possible to observe the effect of unidirectional shift of the magnetic hysteresis loop along the magnetic field axis, which is known as exchange bias (Nogués and Schuller, 1999). This effect is the key enabler of numerous spintronic devices, including magnetic read heads in hard disk drives and magnetic random access memory devices. To observe the exchange bias effect, the sample should be cooled through its Néel temperature in a magnetic field and the magnetic hysteresis is typically measured at temperatures $T < T_c$. The most pronounced is the shift of the magnetic hysteresis loop along the field axis. However, uncompensated moments can result also in a shift of the hysteresis loop along the moment axis. The vertical shift of the loop results from the field-invariant magnetization of the antiferromagnet, and the horizontal loop shift along the field axis is a trait of the ferromagnetic film. It is widely accepted that the horizontal loop shift is influenced by the field-invariant moment of the pinning antiferromagnet (Radu and Zabel, 2008) responsible for the vertical loop shift. This field-invariant uncompensated moment is induced by cooling under exchange coupling to the ferromagnet (Salazar-Alvarez et al., 2009). Typically, exchange bias is measured relying on superconducting quantum interference device (SQUID) or vibrating sample magnetometers (VSM). However, recent improvements in the magnetotransport characterization with a precise discrimination of the components of the resistance tensor (longitudinal vs. transversal resistances) allows to access horizontal and vertical loops shifts and provides further insights in the exchange bias effect (Kosub et al., 2015).

Hollow particles

In contrast to filled magnetic particles, magnetic responses of magnetic nanoshells (hollow particles or particles with a non-magnetic core) are strongly affected by the local geometrical curvatures of the shell. As discussed in Section "Curvilinear nanoarchitectures", the presence of the geometrical curvature brings about two curvature-induced effects, namely, curvature-induced magnetic anisotropy and curvature-induced DMI. The latter interaction is chiral and allows to stabilize chiral magnetic textures including chiral domain wall and skyrmions even in an intrinsically achiral magnetic nanosized material. Those textures are in the heart of application concepts known as spin-orbitronics and antiferromagnetic spintronics. The aim here is to develop prospective energy efficient and ultra-high speed magnetic data storage devices, for instance relying on magnetic racetracks hosting magnetic solitons (domain walls and skyrmions). To synthesize metal and oxide hollow nanostructures, it is possible to explore template-assisted as well as template-free methods (He et al., 2012; An et al., 2008). The latter approaches are based on specific mechanisms, such as Ostwald ripening and Kirkendall effect. Synthesis strategies based on the Kirkendall effect are commonly used to synthesize spherical hollow nanoparticles of iron oxide (γ - Fe_2O_3, Fe_3O_4) (Cabot et al., 2007; Khurshid et al., 2010), ferrimagnetic $NiFe_2O_4$ (Jaffari et al., 2010) and antiferromagnetic (CoO (Varón et al., 2013), NiO (Chu et al., 2019)) oxides, as well as ferromagnetic metals (Co (Simeonidis et al., 2011), FeCo (Tzitzios et al., 2011)). In addition to spherical hollow particles, nano-rings and nano-tubes can be prepared by properly changing the synthesis conditions (Roca et al., 2019).

Magnetoelectric and multiferroic particles

By coupling magnetic nanoparticles with other functional nanoscaled materials revealing different spontaneous order parameter like ferroelectric, it is possible to realize heterostructures which are known as artificial multiferroic materials (Spaldin and Ramesh, 2019). In this case, the resulting nanostructure will possess two different spontaneous order parameters like magnetization (order parameter of ferro- and ferrimagnetic materials) and electric polarization (order parameter of ferroelectric materials). These two order parameters can be coupled via mechanical strain relying on the effect of magnetostriction observed in magnetic materials and effect of electrostriction in ferroelectrics. For instance, by coupling ferrimagnetic $CoFe_2O_4$ core and ferroelectric $BaTiO_3$ shell (Kim et al., 2021), it is possible to realize multiferroic nanoparticle, which can be used for medical applications for deep brain stimulation (Kozielski et al., 2021). Alternatively, single phase multiferroic nanostructures like $BiFeO_3$ are explored as prospective data storage media, where the magnetic order parameter can be manipulated by means of electric fields, promising extremely efficient information media with an energy budget required for switching individual bit of information going potentially down to 1 aJ (Prasad et al., 2020).

Curvilinear shapes

There are numerous experimental methods, which allow fabricating complex 3D shaped magnetic nanoscale objects. Those include charged aerosol particles guided with electrostatic lens (Jung et al., 2021), glancing angular deposition (GLAD) (Mark et al., 2013; Phatak et al., 2014; Eslami et al., 2014), focused electron beam induced deposition (FEBID) (De Teresa et al., 2016; Fernández-Pacheco et al., 2017; Sanz-Hernández et al., 2017; Huth et al., 2018; Winkler et al., 2019; Plank et al., 2019; Phatak et al., 2020) or a combination of two-photon lithography and electrodeposition (Burmeister et al., 2012; Williams et al., 2018). By using these methods, it is possible to fabricate complex magnetic wireframe structures (Sahoo et al., 2018; Williams et al., 2018; Askey et al., 2020; Meng et al., 2021), magnetic nanohelices (Phatak et al., 2014; Sanz-Hernández et al., 2020; Phatak et al., 2020), magnetic Möbius rings at the nanoscale (Skoric et al., 2020), magnetic knots (Pip et al., 2020), magnetic DNA-like double helices (Sanz-Hernández et al., 2020) to name just a few appealing geometries. Furthermore, magnetic nanostructures can be formed by deposition of magnetic thin films and heterostructures on non-magnetic templates prepared either lithographically (optical or electron beam lithography), using self-assembly or combination of these two methods (Kappenberger et al., 2009). The templates of different dimensions (nm to μm range) and symmetries (e.g., cylindrical or spherical) can be fabricated relying on nanosphere lithography (Albrecht et al., 2005), nanoindentations (Schulze et al., 2010) and ion-induced patterning resulting in the formation of nanoripples, nanocones and nanopyramids (Korner et al., 2014).

2D magnetic materials

2D materials offer an interesting playground for magnetism community due to peculiar criticality behavior and possibility to realize well controlled heterostructures for spintronic applications (Gibertini et al., 2019). For instance, it is known that for 3D (nano) magnets a magnetic phase transition occurs at a finite temperature (Rigamonti and Carretta, 2015), see also Section "Critical phenomena". At the same time, 1D systems can order only at $T = 0$ K (Peierls, 1936). For 2D systems, the existence of magnetic long-range order at any finite temperature crucially depends on the number N_{sp} of relevant spin components, usually called spin dimensionality, and determined by the physical parameters of the system (for example, the presence and strength of magnetic anisotropy) (Gibertini et al., 2019). If the spin dimensionality $N_{\mathrm{sp}} = 1$, the system has a strong uniaxial anisotropy and the spins point in either of the two possible orientations ("up" or "down") along a given direction. The case of spin dimensionality $N_{\mathrm{sp}} = 2$ corresponds to an easy-plane anisotropy that favors the spins to lie in a given plane, although the orientation within the plane is completely unconstrained. Isotropic systems are characterized with $N_{\mathrm{sp}} = 3$ where there is no constraint on the direction of spins. For the latter case, the Mermin-Wagner-(-Hohenberg) theorem states that thermal fluctuations destroy the long-range magnetic order in 2D systems at any finite temperature when the spin dimensionality is 3 (isotropic Heisenberg model) (Mermin and Wagner, 1966; Hohenberg, 1967). Hence, there is no isotropic 2D ferromagnet as long-wavelength excitations (spin waves) can be excited at any finite temperature as there is no gap in the spin wave spectrum (no anisotropy). 2D magnets with $N_{\mathrm{sp}} = 2$ are described by the XY model. They do not possess a conventional transition to long-range order and the susceptibility diverges below a finite temperature. Berezinskii, Kosterlitz and Thouless pointed out that this divergence is associated with the onset of topological order, characterized by an algebraic decay of spin correlations and by the presence of bound pairs of vortex and antivortex arrangements of spins (Berezinsky, 1971; Berezinsky, 1972; Kosterlitz and Thouless, 1973). Below the Kosterlitz-Thouless temperature, T_{KT}, quasi-long-range magnetic order is established, and the existence of a finite order parameter is suppressed only marginally with the system size. Currently, there is active research with magnetic 2D materials, including the semiconducting layered van der Waals material $\mathrm{CrI_3}$ (Huang et al., 2017) and a metallic 2D ferromagnet $\mathrm{Fe_3GeTe_2}$ (Liu et al., 2017). For instance, $\mathrm{Fe_3GeTe_2/hBN/Fe_3GeTe_2}$ heterostructures are integrated in 2D materials based magnetic tunnel junctions and reveal large tunneling magnetoresistance effect of more than 120% at 20 K (Wang et al., 2018). By realizing van der Waals $\mathrm{CrI_3/WSe_2}$ heterostructures it becomes possible to control the spin and valley pseudospin in $\mathrm{WSe_2}$ (Zhong et al., 2017). The change of the magnetization of the $\mathrm{CrI_3}$ layer allows to change the photoluminescence intensity of $\mathrm{WSe_2}$ relying on the ultrafast spin-dependent charge hopping across the heterostructure interface. The study of photoluminescence of valley pseudospin is suggested as a method to probe the dynamics of domains in 2D magnets.

Heterostructures of magnetic materials and topological insulators

Low-dimensional magnetic materials are also used to realize magnetic order in topological insulators (TIs) by proximity (Bhattacharyya et al., 2021). These heterostructures typically consist of a magnetic material and TI, e.g. $\mathrm{Bi_2Te_3/Cr_2Ge_2Te_6}$. There are several mechanisms for magnetic proximity effect at the interface between a magnetic material and TI including the direct exchange interaction, magnetic extension, and surface-state-assisted exchange coupling (Bhattacharyya et al., 2021). The magnetic proximity effect has a relatively short length scale (few Å). Hence, the time-reversal symmetry is broken only at the interface of the TI and magnetic material, and not in the bulk of the TI. Therefore, TI is usually sandwiched between two magnetic layers, e.g. magnetic insulators with perpendicular magnetic anisotropy (Hou et al., 2019). Magnetic TI heterostructures like $\mathrm{(Bi_{0.25}Sb_{0.75})_2Te_3/MnTe}$ and $\mathrm{Bi_2Te_3/MnTe}$ are explored as spintronic devices (Chen et al., 2020).

Characterization of nanoscaled magnets

Magnetometry studies

To understand magnetic responses of individual magnetic nanostructures and their assemblies, it is important to know their switching field at target temperature, determine superparamagnetic transition temperature, Curie temperature, magnetization, evaluate interactions between particles in an ensemble, etc. This is typically done by carrying out magnetometry measurements, for instance SQUID or VSM measurements. These devices allow to carry out magnetization vs. temperature measurements, measure magnetic hysteresis loops at different temperatures and in different geometry of the applied magnetic field. To determine relevant micromagnetic parameters, it is insightful to start with the temperature dependence of magnetization. In the vicinity of the Curie temperature, this dependence can be fitted to different criticality laws (e.g., Bloch 3/2 law for 3D materials) to get access to the exchange parameter. Furthermore, the superparamagnetic transition temperature, T_B, can be determined by performing zero field cooling (ZFC)—field cooling (FC) measurement of magnetic moment. To perform ZFC measurements, the sample is cooled down without applying magnetic field. Then it is exposed to a small magnetic field in the range of 10 Oe and the magnetic moment is measured as a function of temperature, starting at low temperatures. For the FC study, the procedure is similar, but the temperature changes from high to low temperatures in the presence of a small magnetic field. The blocking temperature can be estimated as the temperature corresponding to the maximum of the first derivative with respect to temperature of the difference between the ZFC and FC curves. This value is related to the magnetic volume, V, responsible for the magnetization reversal in magnetic nanoparticles with the anisotropy constant K_a. When the size of the particle is known, say from electron microscopy studies, the relaxation rate equation discussed in the section on superparamagnetism can be used to estimate the magnetic anisotropy constant. Alternatively, the blocking temperature can be measured by monitoring the temperature dependence of the coercive field. The temperature at which coercive field vanishes can be taken as a measure of T_B. For thin film samples or arrays of nanopatterned platelets with a well-defined easy axis of magnetization, it is possible to determine the anisotropy constant by measuring magnetic hysteresis loops along the easy and hard axis. The difference between the areas under the loops is the anisotropy energy. To assess coupling (magnetostatic vs. exchange) in the array of nanostructures, it is possible to apply the first-order-reversal-curves (FORC) analysis. FORC studies are especially useful for exchange coupled composites and exchange bias systems. For the latter, FORC analysis allows to access the switching field distribution and exchange bias (Fang et al., 2010). Furthermore, magnetometry can be used to evaluate the magnetic state of the sample (single domain, multidomain, superparamagnetic) by exploring the Day plots method (Dunlop, 2002).

Relying on the detection of magnetic stray fields, magnetic properties of individual nanostructures can be studied by the dynamic cantilever magnetometry (Degen et al., 2009; Weber et al., 2012; Mehlin et al., 2018; Braakman and Poggio, 2019), nano-SQUID magnetometry (Vasyukov et al., 2018), scanning Nitrogen vacancy (NV) magnetometry (Casola et al., 2018; Barry et al., 2020) and micro-Hall magnetometry that was applied for magnetic characterization of not only planar but also complex-shapes FEBID-fabricated nanostructures (Keller et al., 2018; Al Mamoori et al., 2018). Furthermore, the scanning reconfigurable magnetic force microscopy (MFM) (Kazakova et al., 2019; May et al., 2019; Corte-León et al., 2019) is applied to quantify 3D magnetization patterns of a magnetic nanoobject based on 2D data (Vock et al., 2014).

At the atomic scale, spin and orbital moments can be deduced by analyzing the sum rules in X-ray magnetic circular dichroism (XMCD) measurements (O'Brien and Tonner, 1994). Synchrotron-based methods can also access antiferromagnetic samples relying on the X-ray magnetic linear dichroism (XMLD). These contrast mechanisms provide the possibility to visualize magnetic states in nanostructures relying on full field and scanning X-ray microscopies like photoemission electron microscopy (PEEM) or scanning transmission X-ray microscopy (STXM). Due to their resolution down to about 10 nm, these techniques allow real space observation of magnetic states and magnetization reversal of individual nanostructures. Benefiting from the element specificity of XMCD and XMLD, it is possible to visualize magnetization processes peculiar to each layer in a heterostructure (say composed of Co and FeNi layers) or follow coupling between elements in the alloy (say FeTb alloy).

Magnetization dynamics studies

Magnetization dynamics is typically investigated using ferromagnetic resonance (FMR) methods, whose sensitivity for the study of magnetic nanoobjects could be substantially improved by utilizing microresonator loops (Lenz et al., 2019). FMR characterization can be also performed of nanostructures, which are exposed to a mechanical strain hence providing access to the magnetostrictive and magnetoelastic properties of nanoscaled objects (Challab et al., 2018; Challab et al., 2021). Linear dynamics (spin waves) can be studied relying on Brillouin light spectroscopy (BLS) (Demokritov et al., 2001), which can be also used in a highly-sensitive BLS microscopy mode (Schultheiss et al., 2019).

X-ray measurements are applied to study magnetization dynamics including real space visualization of spin waves in nanopatterned disks (Sluka et al., 2019) and motion of magnetic solitons in confined geometries (Büttner et al., 2015). For imaging of magnetic nanostructures and their dynamics, X-ray spectroholography (Eisebitt et al., 2004) is broadly applied also at free electron laser (FEL) facilities allowing to image magnetization dynamics in single shot experiments (Willems et al., 2017; Wang et al., 2012).

In addition to X-ray based imaging, magneto-optic Kerr effect (MOKE) magnetometry and microscopy is regularly applied to study magnetic hysteresis and visualize statics and dynamics of magnetic domain patterns in low-dimensional magnetic objects (McCord, 2015; Kuch et al., 2015). We note that dark-field MOKE magnetometry is applied for high-precision analysis of curvilinear structures (Sanz-Hernández et al., 2017).

Tomographic imaging of nanostructures

To visualize complex 3D geometries it is necessary to apply tomography-based approaches. Thus, XMCD-PEEM is used to image interior magnetization textures of curved magnetic nanoobjects relying on the transmission shadow contrast (Kimling et al., 2011). Furthermore, XMCD-PEEM and the magnetic transmission soft X-ray microscopy (MXTM) can be used in a tomography mode allowing to image the evolution of magnetic domain patterns of 3D mesoscale objects with a resolution in the range of 50 nm (Streubel et al., 2015a, 2015b). Even better resolution down to about 10 nm is offered by the hard X-ray magnetic tomography with ptychographic scans (Donnelly et al., 2017). Electron-based methods including Lorentz transmission electron microscopy (TEM) (Phatak et al., 2011) and off-axis electron holography (Dunin-Borkowski, 1998; Midgley and Dunin-Borkowski, 2009) enable reconstruction of magnetic textures in planar (Kläui et al., 2005; Nord et al., 2019) and 3D curved (Biziere et al., 2013; Phatak et al., 2014; Phatak et al., 2020) nanoscale structures.

Spintronic and spinorbitronic characterization

To evaluate the spintronic properties of magnetic nanostructures, they are measured in a magnetoresistance or Hall-effect configuration. Typically, temperature and magnetic field dependent changes of the electrical resistance or impedance of the sample are evaluated. Magnetoresistance can be studied not only of planar but also of curved nanoscale objects including nanotubes (Rüffer et al., 2012; Zimmermann et al., 2018), magnetic spherical nanocaps (Kimling Née Moser et al., 2010), and ferromagnetic helices (Maurenbrecher et al., 2018). If the sample layer stack supports chiral effects, magnetotransport can be used to measure spin-orbit torques (SOTs) and get access to the DMI constant. The strength of SOTs can be assessed by measuring the effective magnetic field B_{SOT}, which introduces additional harmonic components to the measured Hall voltages (Meng et al., 2017; Volkov et al., 2021). To determine the effective field B_{SOT} of the anti-damping SOT, an external magnetic field is applied in-plane (B_{IP}) perpendicular to the current flow direction and the Hall resistance is recorded. The Hall resistance reveals the presence of the first and second harmonic signals, which allow to quantitatively determine the strength of B_{SOT} based on the following relation (Meng et al., 2017):

$$B_{\mathrm{SOT}} = -2\frac{\partial R_{\mathrm{H}}^{2\omega}/\partial B_{\mathrm{IP}}}{\partial^2 R_{\mathrm{H}}^{\omega}/\partial B_{\mathrm{IP}}^2}, \tag{15}$$

where R_{H}^{ω} and $R_{\mathrm{H}}^{2\omega}$ are first and second harmonics of the Hall resistance. The obtained value of B_{SOT} is used to estimate the DMI constant accordingly to the equation (Kim et al., 2013):

$$D_0 = \frac{2A\gamma}{v_s}B_{\mathrm{SOT}}, \tag{16}$$

where $v_s = Pjg\mu_{\mathrm{B}}/(2eM_{\mathrm{S}})$ is the spin velocity, with P being the spin polarization of the current j, and e is the electron charge.

Conclusion

The chapter introduces the topic of magnetic nanostructures both theoretically and experimentally. We discuss basic theoretical concepts, which are needed to understand the ground and excited states of low dimensional samples. In this respect, not only single domain particles (and related superparamagnetism phenomenon) are introduced but also nanostructures supporting more complex textures as vortices, skyrmions, hopfions and domain walls are brought in focus. The equation of state as well as critical phenomena are introduced for ferro- and antiferromagnetic materials. Furthermore, we describe different fabrication strategies of magnetic nanoparticles ranging from chemical synthesis through preparation of nanostructures on non-magnetic templates to direct writing of complex 3D nanoarchitectures. Relevant characterization methods and techniques to study magnetization statics and dynamics of planar and 3D curved nanostructures are outlined. On the material science side, we cover not only homogeneous particles but also core-shell nanostructures. For the latter, we address ferro- and antiferromagnetic heterostructures and related phenomenon of exchange bias. Furthermore, we outline recent activities on artificial multiferroic heterostructures for low energy magnetic data storage and medical research for deep brain stimulation. Heterostructures of magnetic 2D materials and magnetic materials with topological insulators are discussed as well. Fabrication, characterization of these heterostructures and validation of their application potential is an appealing prospective research direction of nanoscale magnetism.

In addition to the discussed broad applications in magnetic data storage, biology, medicine, permanent magnets and printing technologies, magnetic nanostructures are explored for the research on artificial spin ice (Skjærvø et al., 2019). Artificial spin ice is a system with a degenerate ground state represented by arrays of nanopatterned macrospins (Ising-type nanomagnets) interacting via dipolar magnetic coupling. There are proposals and first experimental reports to use artificial spin ice for the realization of artificial spin glasses (Saccone et al., 2019; Saccone et al., 2022). These activities are appealing for future research as they offer a convenient material science platform to validate theoretical ideas for understanding of the functionality of human brain and realization of artificial neuronal networks for prospective energy efficient computing systems. Taking into account the current advances in the fabrication of 3D magnetic wireframe structures (Keller and Huth, 2018; May et al., 2019), which could act as 3D artificial spin ice systems, it is insightful to attempt the realization of 3D artificial spin glasses. For these studies, not only design and realization of an appropriately disordered 3D array of nanomagnets represent the experimental challenges but also advanced characterization methods, relying on electron-based and X-ray-based tomography and holography techniques (Wolf et al., 2021; Donnelly et al., 2015) would need to be applied.

Beside filled nanoparticles and planar nanoscale objects, we discuss geometrically curved shells (hollow particles). The theoretical approach of curvilinear magnetism is introduced to guide the analysis of complex responses of geometrically curved magnetic shells. Due to the possibility to tailor magnetic responses (chiral and anisotropic) relying on geometrical curvature, curvilinear nanoscaled objects attract strong attention both from the fundamentally and application oriented research communities. In this respect, integration of curved magnetic nanostructures in spintronic and spinorbitronic devices should be addressed in future research to confirm experimentally the appealing theoretical predictions of artificial magnetoelectric materials (Volkov et al., 2019) and high-speed racetracks based on tubular architectures (Yan et al., 2010). Until recently, the primary focus in 3D and curvilinear magnetism research lay on the impact of the geometrical curvature on magnetization textures in curved nanowires and thin films (Makarov et al., 2022). Going beyond the study of micromagnetic textures, it is insightful to address topological magnetic field nanotextures specific to 3D curved geometries (Donnelly et al., 2021). In contrast to topological magnetization textures like domain walls and skyrmions whose relevance for spintronic and spinorbitronic devices is well established, the full potential of topological magnetic field nanotextures for research and applications is yet to be understood and explored for spintronics, 3D magnonics (Barman et al., 2021) and related concepts of reservoir computing (Grollier et al., 2020). The research on 3D and curvilinear magnetism in general and topological magnetic field nanotextures in particular stimulates further development of fabrication methods to produce high quality, complex shaped magnetic objects with tunable magnetic interactions including FEBID, chemical synthesis, strain engineering origami, two photon laser lithography, or templated self-assembly.

References

Al Mamoori M, et al. (2018) Magnetic characterization of direct-write free-form building blocks for artificial magnetic 3D lattices. *Materials* 11(2): 289. https://doi.org/10.3390/ma11020289.

Albrecht M, et al. (2005) Magnetic multilayers on nanospheres. *Nature Materials* 4(3): 203–206. https://doi.org/10.1038/nmat1324.

An K, et al. (2008) Synthesis of uniform hollow oxide nanoparticles through nanoscale acid etching. *Nano Letters* 8(12): 4252–4258. https://doi.org/10.1021/nl8019467.

Andreev AF and Marchenko VI (1980) Symmetry and macroscopical dynamics of a magnet. *Soviet Physics Uspekhi* 23: 21. https://doi.org/10.1070/PU1980v023n01ABEH004859.

Askey J, et al. (2020) Use of two-photon lithography with a negative resist and processing to realise cylindrical magnetic nanowires. *Nanomaterials* 10(3): 429. https://doi.org/10.3390/nano10030429.

Atxitia U, Hinzke D, and Nowak U (2017) Fundamentals and applications of the Landau–Lifshit–Bloch equation. *Journal of Physics D: Applied Physics* 50(3), 033003. https://doi.org/10.1088/1361-6463/50/3/033003.

Baraduc C, Chshiev M, and Ebels U (Dec. 2010) Introduction to spin transfer torque. In: Nasirpouri F and Nogaret A (eds.) *Nanomagnetism and Spintronics*, pp. 173–192. World Scientific. https://doi.org/10.1142/9789814273060_0008.

Barman A, et al. (2021) The 2021 magnonics roadmap. *Journal of Physics: Condensed Matter* 33(41): 413001. https://doi.org/10.1088/1361-648x/abec1a.

Barry JF, et al. (2020) Sensitivity optimization for NV-diamond magnetometry. *Reviews of Modern Physics* 92(1), 015004. https://doi.org/10.1103/RevModPhys.92.015004.

Bazaliy YB, Jones BA, and Zhang SC (1998) Modification of the Landau–Lifshitz equation in the presence of a spin–polarized current in colossal- and giant–magnetoresistive materials. *Physical Review B* 57(6): R3213–R3216. https://doi.org/10.1103/PhysRevB.57.R3213.

Belavin AA and Polyakov AM (1975) Metastable states of a 2D isotropic ferromagnet. *JETP Letters* 22: 245.

Berezinsky VL (1971) Destruction of long range order in one-dimensional and two-dimensional systems having a continuous symmetry group. I. Classical systems. *Soviet Physics - JETP* 32: 493–500.

Berezinsky VL (1972) Destruction of long-range order in one-dimensional and two-dimensional systems possessing a continuous symmetry group. II. Quantum systems. *Soviet Physics - JETP* 34(3): 610.

Berger L (1996) Emission of spin waves by a magnetic multilayer traversed by a current. *Physical Review B* 54(13): 9353–9358.

Bhattacharyya S, et al. (2021) Recent progress in proximity coupling of magnetism to topological insulators. *Advanced Materials* 33(33): 2007795. https://doi.org/10.1002/adma.202007795.

Binns C, et al. (2002) Magnetic behavior of nanostructured films assembled from preformed Fe clusters embedded in Ag. *Physical Review B* 66(18): 184413. https://doi.org/10.1103/physrevb.66.184413.

Biziere N, et al. (2013) Imaging the fine structure of a magnetic domain wall in a Ni nanocylinder. *Nano Letters* 13(5): 2053–2057. https://doi.org/10.1021/nl400317j.

Bogdanov AN, et al. (2002) Magnetic structures and reorientation transitions in noncentrosymmetric uniaxial antiferromagnets. *Physical Review B* 66(21), 214410. https://doi.org/10.1103/physrevb.66.214410.

Boutry S, et al. (2006) Specific E-selectin targeting with a superpara-magnetic MRI contrast agent. *Contrast Media & Molecular Imaging* 1(1): 15–22. https://doi.org/10.1002/cmmi.87.

Braakman FR and Poggio M (2019) Force sensing with nanowire cantilevers. *Nanotechnology* 30(33), 332001. https://doi.org/10.1088/1361-6528/ab19cf.

Brown WF Jr. (1963) *Micromagnetics*. New York: Wiley.

Bruno P and Chappert C (1992) Ruderman-Kittel theory of oscillatory interlayer exchange coupling. *Physical Review B* 46(1): 261–270. https://doi.org/10.1103/physrevb.46.261.

Burmeister F, et al. (2012) Materials and technologies for fabrication of three-dimensional microstructures with sub-100 nm feature sizes by two-photon polymerization. *Journal of Laser Applications* 24(4), 042014. https://doi.org/10.2351/1.4730807.

Butenko AB, et al. (2009) Theory of vortex states in magnetic nanodisks with induced Dzyaloshinskii-Moriya interactions. *Physical Review B* 80(13), 134410. https://doi.org/10.1103/PhysRevB.80.134410.

Büttner F, et al. (2015) Dynamics and inertia of skyrmionic spin structures. *Nature Physics* 11(3): 225–228. https://doi.org/10.1038/nphys3234.

Cabot A, et al. (2007) Vacancy Coalescence during Oxidation of Iron Nanoparticles. *Journal of the American Chemical Society* 129(34): 10358–10360. https://doi.org/10.1021/ja072574a.

Cao Y, et al. (2020) Prospect of spin-orbitronic devices and their applications. *iScience* 23(10), 101614. https://doi.org/10.1016/j.isci.2020.101614.

Carcia PF (1988) Perpendicular magnetic anisotropy in Pd/Co and Pt/Co thin-film layered structures. *Journal of Applied Physics* 63(10): 5066–5073. https://doi.org/10.1063/1.340404.

Carcia PF, Meinhaldt AD, and Suna A (1985) Perpendicular magnetic anisotropy in Pd/Co thin film layered structures. *Applied Physics Letters* 47(2): 178–180. https://doi.org/10.1063/1.96254.

Casola F, van der Sar T, and Yacoby A (2018) Probing condensed matter physics with magnetometry based on nitrogen-vacancy centres in diamond. *Nature Reviews Materials* 3: 17088. https://doi.org/10.1038/natrevmats.2017.88.

Challab N, Zighem F, et al. (Nov. 2018) Local stiffness effect on ferromagnetic response of nanostructure arrays in stretchable systems. *Physica Status Solidi* 13(2): 1800509. https://doi.org/10.1002/pssr.201800509.

Challab N, Faurie D, et al. (2021) Differentiated strain-control of localized magnetic modes in antidot arrays. *ACS Applied Materials & Interfaces* 13(25): 29906–29915. https://doi.org/10.1021/acsami.1c05582.

Chen X, et al. (2011) Magnetochromatic polydiacetylene by incorporation of Fe_3O_4 nanoparticles. *Angewandte Chemie* 123(24): 5600–5603. https://doi.org/10.1002/ange.201100064.

Chen P, et al. (2020) Tailoring the hybrid anomalous hall response in engineered magnetic topological insulator heterostructures. *Nano Letters* 20(3): 1731–1737. https://doi.org/10.1021/acs.nanolett.9b04932.

Chourpa I, et al. (2005) Molecular composition of iron oxide nanoparticles, precursors for magnetic drug targeting, as characterized by confocal Raman microspectroscopy. *The Analyst* 130(10): 1395. https://doi.org/10.1039/b419004a.

Chu S, Yang C, and Xintai S (2019) Synthesis of NiO hollow nanospheres via Kirkendall effect and their enhanced gas sensing per- formance. *Applied Surface Science* 492: 82–88. https://doi.org/10.1016/j.apsusc.2019.06.226.

Cooper NR (1999) Propagating magnetic vortex rings in ferromagnets. *Physical Review Letters* 82: 1554–1557. https://doi.org/10.1103/PhysRevLett.82.1554.

Corot C, et al. (2006) Recent advances in iron oxide nanocrystal technology for medical imaging. *Advanced Drug Delivery Reviews* 58(14): 1471–1504. https://doi.org/10.1016/j.addr.2006.09.013.

Corte-León H, et al. (2019) Magnetic imaging using geometrically constrained nano-domain walls. *Nanoscale* 11(10): 4478–4488. https://doi.org/10.1039/c8nr07729k.

De Teresa JM, et al. (2016) Review of magnetic nanostructures grown by focused electron beam induced deposition (FEBID). *Journal of Physics D: Applied Physics* 49(24): 243003. https://doi.org/10.1088/0022- 3727/49/24/243003.

Degen CL, et al. (Jan. 2009) Nanoscale magnetic resonance imaging. *Proceedings of the National Academy of Sciences* 106(5): 1313–1317. https://doi.org/10.1073/pnas.0812068106.

Demokritov SO, Hillebrands B, and Slavin AN (2001) Brillouin light scattering studies of confined spin waves: Linear and nonlinear confinement. *Physics Reports* 348(6): 441–489. https://doi.org/10.1016/S0370-1573(00)00116-2.

Dietrich S, et al. (2012) Design, characterization and magnetic properties of Fe_3O_4-nanoparticle arrays coated with PEGylated-dendrimers. *Materials Chemistry and Physics* 132(2-3): 292–299. https://doi.org/10.1016/j.matchemphys.2011.11.015.

Donnelly C, Guizar-Sicairos M, Scagnoli V, Holler M, et al. (2015) Element-specific X-ray phase tomography of 3D structures at the nanoscale. *Physical Review Letters* 114: 115501. https://doi.org/10.1103/PhysRevLett.114.115501.

Donnelly C, Guizar-Sicairos M, Scagnoli V, Gliga S, et al. (2017) Three-dimensional magnetization structures revealed with X-ray vector nanotomography. *Nature* 547(7663): 328–331. https://doi.org/10.1038/nature23006.

Donnelly C, Metlov KL, et al. (2020) Experimental observation of vortex rings in a bulk magnet. *Nature Physics* 316–321. https://doi.org/10.1038/s41567-020-01057-3.

Donnelly C, Hierro-Rodríguez A, et al. (2021) Complex free-space magnetic field textures induced by three-dimensional magnetic nanostructures. *Nature Nanotechnology*. https://doi.org/10.1038/s41565-021-01027-7.

Dunin-Borkowski RE (1998) Magnetic microstructure of magnetotactic bacteria by electron holography. *Science* 282(5395): 1868–1870. https://doi.org/10.1126/science.282.5395.1868.

Dunlop DJ (2002) Theory and application of the Day plot (M_{rs}/M_s versus H_{cr}/H_c) 1. Theoretical curves and tests using titanomagnetite data. *Journal of Geophysical Research* 107(B3): 2056. https://doi.org/10.1029/2001jb000486.

Dzialoshinskii IE (1957) Thermodynamic theory of “weak” ferromagnetism in antiferromagnetic substances. *Soviet Physics - JETP* 5(6): 1259–1272.

Dzyaloshinski E (1965) The theory of helicoidal structures in antiferromagnets. II. Metals. *Soviet Physics - JETP* 20(1): 223.

Dzyaloshinskii IE (1964) Theory of helicoidal structures in antiferromagnets. I. Nonmetals. *Soviet Physics - JETP* 19(4): 960–971.

Eisebitt S, et al. (2004) Lensless imaging of magnetic nanostructures by X-ray spectro-holography. *Nature* 432(7019): 885–888. https://doi.org/10.1038/nature03139.

Eslami S, et al. (2014) Chiral Nanomagnets. *ACS Photonics* 1(11): 1231–1236. https://doi.org/10.1021/ph500305z.

Fang Y, et al. (2010) FORC studies of exchange biased NiFe in L1$_0$(111) FePt-based spin valve. *Journal of Physics: Conference Series* 200(7), 072002. https://doi.org/10.1088/1742-6596/200/7/072002.

Fernández-Pacheco A, et al. (2017) Three-dimensional nanomagnetism. *Nature Communications* 8: 15756. https://doi.org/10.1038/ncomms15756.

Fert A, Reyren N, and Cros V (2017) Magnetic skyrmions: Advances in physics and potential applications. *Nature Reviews Materials* 2(7): 17031. https://doi.org/10.1038/natrevmats.2017.31.

Gaididei Y, Kravchuk VP, and Sheka DD (2010) Magnetic vortex dynamics induced by an electrical current. *International Journal of Quantum Chemistry* 110(1): 83–97.

Gaididei Y, Yershov KV, et al.Jan., (2019) Magnetization-induced shape transformations in flexible ferromagnetic rings. *Physical Review B* 99: 014404. https://doi.org/10.1103/PhysRevB.99.014404.

Gibertini M, et al. (2019) Magnetic 2D materials and heterostructures. *Nature Nanotechnology* 14(5): 408–419. https://doi.org/10.1038/s41565-019-0438-6.

Glinchuk MD, Ragulya AV, and Stephanovich VA (2013) *Nanoferroics*. Netherlands: Springer. https://doi.org/10.1007/978-94-007-5992-3.

Gobel B, Mertig I, and Tretiakov OA (2021) Beyond skyrmions: Review and perspectives of alternative magnetic quasiparticles. *Physics Reports* 895: 1–28. https://doi.org/10.1016/j.physrep.2020.10.001.

Grollier J, et al. (2020) Neuromorphic spintronics. *Nature Electronics* 3(7): 360–370. https://doi.org/10.1038/s41928-019-0360-9.

Guslienko KY (2008) Magnetic vortex state stability, reversal and dynamics in restricted geometries. *Journal of Nanoscience and Nanotechnology* 8(6): 2745–2760. https://doi.org/10.1166/jnn.2008.003.

Gutfleisch O, et al. (2002) Nanocrystalline high performance permanent magnets. *Journal of Magnetism and Magnetic Materials* 242–245: 1277–1283. https://doi.org/10.1016/s0304-8853(01)00989-1.

Han X, et al. (2021) Spin-orbit torques: Materials, physics, and devices. *Applied Physics Letters* 118(12), 120502. https://doi.org/10.1063/5.0039147.

He Q, Wu Z, and Huang C (2012) Hollow magnetic nanoparticles: Synthesis and applications in biomedicine. *Journal of Nanoscience and Nanotechnology* 12(4): 2943–2954. https://doi.org/10.1166/jnn.2012.5679.

Hohenberg PC (1967) Existence of long-range order in one and two dimensions. *Physical Review* 158(2): 383–386. https://doi.org/10.1103/physrev.158.383.

Hou Y, Kim J, and Wu R (2019) Magnetizing topological surface states of Bi_2Se_3 with a CrI_3 monolayer. *Science Advances* 5(5): 5. https://doi.org/10.1126/sciadv.aaw1874.

Huang B, et al. (2017) Layer-dependent ferromagnetism in a van der Waals crystal down to the monolayer limit. *Nature* 546(7657): 270–273. https://doi.org/10.1038/nature22391.

Huth M, Porrati F, and Dobrovolskiy OV (2018) Focused electron beam induced deposition meets materials science. *Microelectronic Engineering* 185-186: 9–28. https://doi.org/10.1016/j.mee.2017.10.012.

Jaffari GH, et al. (2010) Enhancement of surface spin disorder in hollow $NiFe_2O_4$ nanoparticles. *Journal of Applied Physics* 107(1), 013910. https://doi.org/10.1063/1.3277041.

Jain TK, et al. (2005) Iron oxide nanoparticles for sustained delivery of anticancer agents. *Molecular Pharmaceutics* 2(3): 194–205. https://doi.org/10.1021/mp0500014.

Jung W, et al. (2021) Three-dimensional nanoprinting via charged aerosol jets. *Nature* 592(7852): 54–59. https://doi.org/10.1038/s41586-021-03353-1.

Kappenberger P, et al. (2009) Template-directed self-assembled magnetic nanostructures for probe recording. *Applied Physics Letters* 95(2), 023116. https://doi.org/10.1063/1.3176937.

Kazakova O, et al. (2019) Frontiers of magnetic force microscopy. *Journal of Applied Physics* 125(6), 060901. https://doi.org/10.1063/1.5050712.

Keller L and Huth M (2018) Pattern generation for direct-write three-dimensional nanoscale structures via focused electron beam induced deposition. *Beilstein Journal of Nanotechnology* 9: 2581–2598. https://doi.org/10.3762/bjnano. 9.240.

Keller L, et al. (2018) Direct-write of free-form building blocks for artificial magnetic 3D lattices. *Scientific Reports* 8(1): 6160. https://doi.org/10.1038/s41598-018-24431-x.

Khurshid H, et al. (2010) Size and composition control of core-shell structured iron/iron-oxide nanoparticles. *Journal of Applied Physics* 107(9): 09A333. https://doi.org/10.1063/1.3368720.

Kim KW, et al. (2013) Chirality from interfacial spin-orbit coupling effects in magnetic bilayers. *Physical Review Letters* 111(21), 216601. https://doi.org/10.1103/PhysRevLett.111.216601.

Kim D, et al. (2021) Magnetoelectric coupling in micropatterned $BaTiO_3/CoFe_2O_4$ epitaxial thin film structures: Augmentation and site-dependency. *Applied Physics Letters* 119(1), 012901. https://doi.org/10.1063/5.0056038.

Kimling Née Moser J, et al. (2010) Magnetoresistive effects in Co/Pd multilayers on self-assembled nanoparticles (invited). *Journal of Applied Physics* 107(9): 09C506. https://doi.org/10.1063/1.3350909.

Kimling J, et al. (2011) Photoemission electron microscopy of three- dimensional magnetization configurations in core-shell nanostructures. *Physical Review B* 84(17), 174406. https://doi.org/10.1103/physrevb.84.174406.

Kläui M, et al. (2001) Vortex circulation control in mesoscopic ring magnets. *Applied Physics Letters* 78(21): 3268–3270. https://doi.org/10.1063/1.1361282.

Kläui M, et al. (2005) Direct observation of domain-wall pinning at nanoscale constrictions. *Applied Physics Letters* 87(10), 102509. https://doi.org/10.1063/1.2042542.

Kondorsky E (1937) On the nature of coercive force and irreversible changes in magnetisation. *Physikalische Zeitschrift der Sowjetunion* 11(597): 68.

Korner M, et al. (2014) Quantitative imaging of the magnetic configuration of modulated nanostructures by electron holography. *Small*. https://doi.org/10.1002/smll.201400377.

Korniienko A, et al. (2020) Effect of curvature on the eigenstates of magnetic skyrmions. *Physical Review B* 102: 014432. https://doi.org/10.1103/PhysRevB.102.014432.

Kosevich AM, Ivanov BA, and Kovalev AS (1990) Magnetic solitons. *Physics Reports* 194(3-4): 117–238. https://doi.org/10.1016/0370-1573(90)90130-T.

Kosterlitz JM and Thouless DJ (1973) Ordering, metastability and phase transitions in two-dimensional systems. *Journal of Physics C: Solid State Physics* 6(7): 1181–1203.

Kosub T, et al. (2015) All-electric access to the magnetic-field- invariant magnetization of antiferromagnets. *Physical Review Letters* 115: 097201. https://doi.org/10.1103/PhysRevLett.115.097201.

Kozielski KL, et al. (2021) Nonresonant powering of injectable nanoelectrodes enables wireless deep brain stimulation in freely moving mice. *Science Advances* 7(3): 3. https://doi.org/10.1126/sciadv.abc4189.

Kravchuk VP, Sheka DD, et al. (2012) Out-of-surface vortices in spherical shells. *Physical Review B* 85: 144433. https://doi.org/10.1103/PhysRevB.85.144433.

Kravchuk VP, Rößler UK, et al. (2016) Topologically stable magnetization states on a spherical shell: Curvature-stabilized skyrmions. *Physical Review B* 94: 144402. https://doi.org/10.1103/PhysRevB.94.144402.

Kuch W, et al. (2015) *Magnetic Microscopy of Layered Structures*. Berlin, Heidelberg: Springer. https://doi.org/10.1007/978-3-662-44532-7.

Landau LD and Lifshitz EM (1935) On the theory of the dispersion of magnetic permeability in ferromagnetic bodies. *Physikalische Zeitschrift der Sowjetunion* 8: 153–169. [Reproduced in Ukr. J. Phys. 53 Special Issue, 14–22 (2008)].

Lau YC, et al. (2019) Giant perpendicular magnetic anisotropy in Ir/Co/Pt multilayers. *Physical Review Materials* 3(10): 104419. https://doi.org/10.1103/physrevmaterials.3.104419.

Lenz K, et al. (2019) Magnetization dynamics of an individual single-crystalline Fe-filled carbon nanotube. *Small* 15(49): 1904315. https://doi.org/10.1002/smll.201904315.

Liu S, et al. (2017) Wafer-scale two-dimensional ferromagnetic Fe_3GeTe_2 thin films grown by molecular beam epitaxy. *NPJ 2D Materials and Applications* 1(1): 30. https://doi.org/10.1038/s41699-017-0033-3.

Lu AH, Salabas EL, and Schüth F (2007) Magnetic nanoparticles: Synthesis, protection, functionalization, and application. *Angewandte Chemie International Edition* 46(8): 1222–1244. https://doi.org/10.1002/anie.200602866.

Makarov D, et al. (2022) New dimension in magnetism and superconductivity: 3D and curvilinear nanoarchitectures. *Advanced Materials* 34: 2101758. https://doi.org/10.1002/adma.202101758.

Mark AG, et al. (2013) Hybrid nanocolloids with programmed three-dimensional shape and material composition. *Nature Materials* 12(9): 802–807. https://doi.org/10.1038/nmat3685.

Maurenbrecher H, et al. (2018) Chiral anisotropic magnetoresistance of ferromagnetic helices. *Applied Physics Letters* 112(24), 242401. https://doi.org/10.1063/1.5027660.

May A, et al. (2019) Realisation of a frustrated 3D magnetic nanowire lattice. *Communications on Physics* 2(1): 13. https://doi.org/10.1038/s42005-018-0104-6.

McCord J (2015) Progress in magnetic domain observation by advanced magneto-optical microscopy. *Journal of Physics D: Applied Physics* 48(33), 333001. https://doi.org/10.1088/0022-3727/48/33/333001.

Mehlin A, et al. (2018) Observation of end-vortex nucleation in individual ferromagnetic nanotubes. *Physical Review B* 97(13), 134422. https://doi.org/10.1103/physrevb.97.134422.

Meng KK, et al. (2017) Enhanced spin-orbit torques in MnAl/Ta films with improving chemical ordering. *Applied Physics Letters* 110(14), 142401. https://doi.org/10.1063/1.4979828.

Meng F, et al. (2021) Non-planar geometrical effects on the magnetoelectrical signal in a three-dimensional nanomagnetic circuit. *ACS Nano*. https://doi.org/10.1021/acsnano.0c10272.

Mermin ND (1979) The topological theory of defects in ordered media. *Reviews of Modern Physics* 51(3): 591–648. https://doi.org/10.1103/revmodphys.51.591.

Mermin ND and Wagner H (1966) Absence of ferromagnetism or antiferromagnetism in one- or two-dimensional isotropic heisenberg models. *Physical Review Letters* 17(22): 1133–1136. https://doi.org/10.1103/PhysRevLett.17.1133.

Michelson A (1977a) Phase diagrams near the Lifshiftz point. II. Systems with cylindrical, hexagonal, and rhombohedral symmetry having an easy plane of magnetization. *Physical Review B* 16(1): 585–592. https://doi.org/10.1103/physrevb.16.585.

Michelson A (1977b) Phase diagrams near the Lifshitz point. I. Uniaxial magnetization. *Physical Review B* 16(1): 577–584. https://doi.org/10.1103/physrevb.16.577.

Michelson A (1977c) Phase diagrams near the Lifshitz point. III. Tetragonal crystals with an easy plane of magnetization. *Physical Review B* 16(11): 5121–5124. https://doi.org/10.1103/physrevb.16.5121.

Midgley PA and Dunin-Borkowski RE (2009) Electron tomography and holography in materials science. *Nature Materials* 8(4): 1476–1482. https://doi.org/10.1038/nmat2406.

Miller MM, et al. (2002) Detection of a micron-sized magnetic sphere using a ring-shaped anisotropic magnetoresistance-based sensor: A model for a magnetoresistance-based biosensor. *Applied Physics Letters* 81(12): 2211–2213. https://doi.org/10.1063/1.1507832.

Moriya T (1960) Anisotropic superexchange interaction and weak ferromagnetism. *Physical Review* 120(1): 91–98. https://doi.org/10.1103/PhysRev.120.91.

Narayanan TN, et al. (2011) Enhanced bio-compatibility of ferrofluids of self-assembled superparamagnetic iron oxide-silica core–shell nanoparticles. *Journal of Nanoscience and Nanotechnology* 11(3): 1958–1967. https://doi.org/10.1166/jnn.2011.3578.

Nogués J and Schuller IK (1999) Exchange bias. *Journal of Magnetism and Magnetic Materials* 192(2): 203–232. https://doi.org/10.1016/s0304-8853(98)00266-2.

Nord M, et al. (2019) Strain anisotropy and magnetic domains in embedded nanomagnets. *Small* 15: 1904738. https://doi.org/10.1002/smll.201904738.

O'Brien WL and Tonner BP (1994) Orbital and spin sum rules in x-ray magnetic circular dichroism. *Physical Review B* 50(17): 12672–12681. https://doi.org/10.1103/physrevb.50.12672.

Papanicolaou N (1995) Antiferromagnetic domain walls. *Physical Review B* 51(21): 15062–15073. https://doi.org/10.1103/physrevb.51.15062.

Peierls R (1936) On Ising's model of ferromagnetism. *Mathematical Proceedings of the Cambridge Philosophical Society* 32(3): 477–481. https://doi.org/10.1017/s0305004100019174.

Phatak C, et al. (2011) Nanoscale structure of the magnetic induction at monopole defects in artificial spinice lattices. *Physical Review B* 83(17), 174431. https://doi.org/10.1103/PhysRevB.83.174431.

Phatak C, Liu Y, et al. (2014) Visualization of the magnetic structure of sculpted three-dimensional cobalt nanospirals. *Nano Letters* 14(2): 759–764. https://doi.org/10.1021/nl404071u.

Phatak C, Miller CS, et al. (2020) Curved three-dimensional cobalt nanohelices for use in domain wall device applications. *ACS Applied Nano Materials* 3(6): 6009. https://doi.org/10.1021/acsanm.0c01228.

Pip P, et al. (2020) Electroless deposition of Ni–Fe alloys on scaffolds for 3D nanomagnetism. *Small* 16(24): 2004099. https://doi.org/10.1002/smll.202004099.

Plank H, et al. (2019) Focused electron beam-based 3D nanoprinting for scanning probe microscopy: A review. *Micromachines* 11(1): 48. https://doi.org/10.3390/mi11010048.

Prasad B, et al. (2020) Ultralow voltage manipulation of ferromagnetism. *Advanced Materials* 32(28): 2001943. https://doi.org/10.1002/adma.202001943.

Pylypovskyi OV, Kravchuk VP, et al. (2015) Coupling of chiralities in Spin and Physical Spaces: The Möbius ring as a case study. *Physical Review Letters* 114: 197204. https://doi.org/10.1103/PhysRevLett.114.197204.

Pylypovskyi OV, Borysenko YA, et al. (2021) Curvature-driven homogeneous Dzyaloshinskii–Moriya interaction and emergent weak ferromagnetism in anisotropic antiferromagnetic spin chains. *Applied Physics Letters* 118(18), 182405. https://doi.org/10.1063/5.0048823.

Radu F and Zabel H (2008) *Exchange Bias Effect of Ferro-/Antiferromagnetic Heterostructures. Springer Tracts in Modern Physics.* Berlin, Heidelberg: Springer. pp. 97–184. https://doi.org/10.1007/978-3-540-73462-8_3.

Rigamonti A and Carretta P (2015) Magnetic orders and magnetic phase transitions. In: *Structure of Matter*, pp. 505–538. Cham: Springer International Publishing. https://doi.org/10.1007/978-3-319-17897-4_17.

Roca AG, et al. (2019) Design strategies for shape-controlled magnetic iron oxide nanoparticles. *Advanced Drug Delivery Reviews* 138: 68–104. https://doi.org/10.1016/j.addr.2018.12.008.

Rüffer D, et al. (2012) Magnetic states of an individual Ni nanotube probed by anisotropic magnetoresistance. *Nanoscale* 4(16): 4989. https://doi.org/10.1039/c2nr31086d.

Saccone M, Scholl A, et al. (2019) Towards artificial Ising spin glasses: Thermal ordering in randomized arrays of Ising-type nanomagnets. *Physical Review B* 99(22), 224403. https://doi.org/10.1103/physrevb.99.224403.

Saccone M, Caravelli F, et al. (2022) Direct observation of a dynamical glass transition in a nanomagnetic artificial Hopfield network. *Nature Physics*. (in press).

Sahoo S, et al. (2018) Ultrafast magnetization dynamics in a nanoscale three-dimensional cobalt tetrapod structure. *Nanoscale* 10(21): 9981–9986. https://doi.org/10.1039/c7nr07843a.

Salazar-Alvarez G, et al. (2009) Direct evidence of imprinted vortex states in the antiferromagnet of exchange biased microdisks. *Applied Physics Letters* 95(1), 012510. https://doi.org/10.1063/1.3168515.

Sanz-Hernández D, Hamans RF, et al. (2017) Fabrication, detection, and operation of a three-dimensional nanomagnetic conduit. *ACS Nano* 11(11): 11066–11073. https://doi.org/10.1021/acsnano.7b05105.

Sanz-Hernández D, Hierro-Rodriguez A, et al. (2020) Artificial double-helix for geometrical control of magnetic chirality. *ACS Nano* 14(7): 8084. https://doi.org/10.1021/acsnano.0c00720.

Schultheiss K, et al. (2019) Excitation of whispering gallery magnons in a magnetic vortex. *Physical Review Letters* 122(9), 097202. https://doi.org/10.1103/physrevlett.122.097202.

Schulze C, et al. (2010) Magnetic films on nanoperforated templates: A route towards percolated perpendicular media. *Nanotechnology* 21(49), 495701. https://doi.org/10.1088/0957-4484/21/49/495701.

Shao Q, et al. (2021) Roadmap of spin–orbit torques. *IEEE Transactions on Magnetics* 57(7): 1–39. https://doi.org/10.1109/tmag.2021.3078583.

Sheka DD, et al. (2022) Fundamentals of curvilinear ferromagnetism: Statics and dynamics of geometrically curved wires and narrow ribbons. *Small* 2105219. https://doi.org/10.1002/smll.202105219.

Simeonidis K, et al. (2011) Morphology influence on nanoscale magnetism of Co nanoparticles: Experimental and theoretical aspects of exchange bias. *Physical Review B* 84(14), 144430. https://doi.org/10.1103/physrevb.84.144430.

Skjærvø SH, et al. (Nov. 2019) Advances in artificial spin ice. *Nature Reviews Physics*. https://doi.org/10.1038/s42254-019-0118-3.

Skomski R, et al. (2013) Predicting the future of permanent-magnet materials. *IEEE Transactions on Magnetics* 49(7): 3215–3220. https://doi.org/10.1109/tmag.2013.2248139.

Skoric L, et al. (2020) Layer-by-layer growth of complex-shaped three-dimensional nanostructures with focused electron beams. *Nano Letters* 20(1): 184–191. https://doi.org/10.1021/acs.nanolett.9b03565.

Slonczewski JC (1973) Theory of domain-wall motion in magnetic films and platelets. *Journal of Applied Physics* 44(4): 1759. https://doi.org/10.1063/1.1662444.

Slonczewski JC (1996) Current-driven excitation of magnetic multilayers. *Journal of Magnetism and Magnetic Materials* 159(1-2): L1–L7.

Slonczewski JC (2002) Currents and torques in metallic magnetic multilayers. *Journal of Magnetism and Magnetic Materials* 247(3): 324–338.

Sluka V, et al. (2019) Emission and propagation of 1D and 2D spin waves with nanoscale wavelengths in anisotropic spin textures. *Nature Nanotechnology* 14(4): 328–333. https://doi.org/10.1038/s41565-019-0383-4.

Spaldin NA and Ramesh R (2019) Advances in magnetoelectric multiferroics. *Nature Materials* 18(3): 203–212. https://doi.org/10.1038/s41563-018-0275-2.

Stoner E and Wohlfarth E (1948) A mechanism of magnetic hysteresis in heterogeneous alloys. *Philosophical Transactions of the Royal Society of London. Series A, Mathematical and Physical Sciences* 240(826): 599–642.

Streubel R, Kronast F, Fischer P, et al. (2015a) Retrieving spin textures on curved magnetic thin films with full-field soft X-ray microscopies. *Nature Communications* 6: 7612. https://doi.org/10.1038/ncomms8612.

Streubel R, Kronast F, Ulrich KR, et al. (2015b) Reconfigurable large-area magnetic vortex circulation patterns. *Physical Review B* 92: 104431. https://doi.org/10.1103/PhysRevB.92.104431.

Streubel R, Kronast F, Reiche CF, et al. (2016) Vortex circulation and polarity patterns in closely packed cap arrays. *Applied Physics Letters* 108(4), 042407. https://doi.org/10.1063/1.4941045.

Sun S (2000) Monodisperse FePt nanoparticles and ferromagnetic FePt nanocrystal superlattices. *Science* 287(5460): 1989–1992. https://doi.org/10.1126/science.287.5460.1989.

Thiele AA (1973) Steady–state motion of magnetic of magnetic domains. *Physical Review Letters* 30: 230–233. https://doi.org/10.1103/PhysRevLett.30.230.

Toulouse G (1977) *Communications on Physics* 2: 115.

Turov EA (1965) *Physical Properties of Magnetically Ordered Crystals*. Academic Press.

Turov EA (1994) Can the magnetoelectric effect coexist with weak piezomagnetism and ferromagnetism? *Physics-Uspekhi* 37(3): 303–310. https://doi.org/10.1070/pu1994v037n03abeh000015.

Tzitzios V, et al. (2011) Synthesis of air stable FeCo nanoparticles. *Journal of Applied Physics* 109(7): 07A313. https://doi.org/10.1063/1.3540387.

Varón M, et al. (2013) Spontaneous formation of hollow cobalt oxide nanoparticles by the Kirkendall effect at room temperature at the water-air interface. *Nanoscale* 5(6): 2429. https://doi.org/10.1039/c2nr32657d.

Varvaro G and Casoli F (eds.) (2016) *Ultra-High-Density Magnetic Recording: Storage Materials and Media Designs*. Jenny Stanford Publishing.

Vasyukov D, et al. (2018) Imaging stray magnetic field of individual ferromagnetic nanotubes. *Nano Letters* 18(2): 964–970. https://doi.org/10.1021/acs.nanolett.7b04386.

Vock S, et al. (2014) Magnetic vortex observation in FeCo nanowires by quantitative magnetic force microscopy. *Applied Physics Letters* 105(17), 172409. https://doi.org/10.1063/1.4900998.

Voit W, et al. (2003) Application of inkjet technology for the deposition of magnetic nanoparticles to form micron-scale structures. *IEE Proceedings: Science, Measurement & Technology* 150(5): 252–256. https://doi.org/10.1049/ip-smt:20030692.

Volkov OM, Kravchuk VP, et al. (2011) Spin-transfer torque and current-induced vortex superlattices in nanomagnets. *Physical Review B* 84(5), 052404. https://doi.org/10.1103/PhysRevB.84.052404.

Volkov O, et al. (2019) Concept of artificial magnetoelectric materials via geometrically controlling curvilinear helimagnets. *Journal of Physics D: Applied Physics* 52(34), 345001. https://doi.org/10.1088/1361–6463/ab2368.

Volkov OM, Kronast F, et al. (2021) Domain-wall damping in ultrathin nanostripes with dzyaloshinskii-moriya interaction. *Physical Review Applied* 15(3), 034038. https://doi.org/10.1103/physrevapplied.15.034038.

Wang T, et al. (2012) Femtosecond single-shot imaging of nanoscale ferromagnetic order in Co/Pd multilayers using resonant X-ray holography. *Physical Review Letters* 108(26), 267403. https://doi.org/10.1103/physrevlett.108.267403.

Wang Z, et al. (2018) Tunneling Spin Valves Based on Fe_3GeTe_2/hBN/Fe_3GeTe_2 van der Waals Heterostructures. *Nano Letters* 18(7): 4303–4308. https://doi.org/10.1021/acs.nanolett.8b01278.

Weber DP, et al. (2012) Cantilever magnetometry of individual Ni nanotubes. *Nano Letters* 12(12): 6139–6144. https://doi.org/10.1021/nl302950u.

Wiesendanger R (2016) Nanoscale magnetic skyrmions in metallic films and multilayers: A new twist for spintronics. *Nature Reviews Materials* 1: 16044.
Willems F, et al. (2017) Multi-color imaging of magnetic Co/Pt heterostructures. *Structural Dynamics* 4(1): 014301. https://doi.org/10.1063/1.4976004.
Williams G, et al. (2018) Two-photon lithography for 3D magnetic nanostructure fabrication. *Nano Research* 11(2): 845–854. https://doi.org/10.1007/s12274-017-1694-0.
Winkler R, et al. (2019) 3D nanoprinting via focused electron beams. *Journal of Applied Physics* 125(21), 210901. https://doi.org/10.1063/1.5092372.
Wolf D, et al. (2021) Unveiling the three-dimensional magnetic texture of skyrmion tubes. *Nature Nanotechnology*. https://doi.org/10.1038/s41565-021-01031-x.
Yan M, et al. (2010) Beating the walker limit with massless domain walls in cylindrical nanowires. *Physical Review Letters* 104(5), 057201. https://doi.org/10.1103/PhysRevLett.104.057201.
Yershov KV, Kravchuk VP, Sheka DD, and Gaididei Y (2016) Curvature and torsion effects in spin-current driven domain wall motion. *Physical Review B* 93: 094418. https://doi.org/10.1103/PhysRevB.93.094418.
Yershov KV, Kravchuk VP, Sheka DD, Pylypovskyi OV, et al. (2018) Geometry-induced motion of magnetic domain walls in curved nanostripes. *Physical Review B* 98(6). https://doi.org/10.1103/physrevb.98.060409. 060409(R).
Yershov KV, Kravchuk VP, Sheka DD, van den Brink J, et al. (2019) Spontaneous deformation of flexible ferromagnetic ribbons induced by Dzyaloshinskii-Moriya interaction. *Physical Review B* 100(14). https://doi.org/10.1103/PhysRevB.100.140407. 140407(R).
Zhang S and Li Z (2004) Roles of nonequilibrium conduction electrons on the magnetization dynamics of ferromagnets. *Physical Review Letters* 93(12), 127204. https://doi.org/10.1103/PhysRevLett.93.127204.
Zhong D, et al. (2017) Van der Waals engineering of ferromagnetic semi- conductor heterostructures for spin and valleytronics. *Science Advances* 3(5): 5. https://doi.org/10.1126/sciadv.1603113.
Zimmermann M, et al. (2018) Origin and manipulation of stable vortex ground states in permalloy nanotubes. *Nano Letters* 18(5): 2828–2834. https://doi.org/10.1021/acs.nanolett.7b05222.

Further reading

Magnetism textbooks

Coey JMD (2010) *Magnetism and Magnetic Materials*. https://doi.org/10.1017/cbo9780511845000.
Guimarães AP (2017) *Principles of Nanomagnetism*. Springer-Verlag GmbH. https://doi.org/10.1007/978-3-319-59409-5.
Lacheisserie T, Du E, Gignoux D, and Schlenker M (eds.) (2005) *Magnetism: Fundamentals*. Springer Science + Business Media, Inc.

Advanced nanomagnetism

Borovik-Romanov AS and Grimmer H (2006) Magnetic properties. In: *International Tables for Crystallography*, pp. 105–149. Chester, England: International Union of Crystallography. https://doi.org/10.1107/97809553602060000632.
Hubert A and Schäfer R (2009) *Magnetic Domains: The Analysis of Magnetic Microstructures*. Berlin: Springer.
Landau LD, Pitaevskii LP, and Lifshitz EM (1984) *Electrodynamics of Continuous Media*. Elsevier Science & Technology.
Stohr J and Siegmann HC (2006) *Magnetism: From Fundamentals to Nanoscale Dynamics*. *Springer Series in Solid-State Sciences*, vol. 152. Berlin: Springer-Verlag.

Magnonics

Gurevich AG and Melkov GA (2000) *Magnetization Oscillations and Waves*. CRC PR INC.
Rezende SM (2020) *Fundamentals of Magnonics*. Springer International Publishing. https://doi.org/10.1007/978-3-030-41317-0.

Frustrated magnets

Diep HT (ed.) (2013) *Frustrated Spin Systems*, 2nd edn World Scientific Publishing Company. https://doi.org/10.1142/8676.

Critical phenomena

Hoser A and Köbler U (2012) *Renormalization Group Theory*. Berlin Heidelberg: Springer.
Pfeuty P and Toulouse G (1977) *Introduction to the Renormalization Group and Critical Phenomena*. John Wiley & Sons Ltd.

Nanostructures

Binns C (2014) *Nanomagnetism: Fundamentals and Applications*. Elsevier Science.
Vázquez M (ed.) (2020) *Magnetic Nano- and Microwires*, 2nd edn. United Kingdom, United States: Woodhead Publishing.

The spin Hall effect

Cosimo Gorini, Université Paris-Saclay, CEA, CNRS, SPEC, Gif-sur-Yvette, France

© 2024 Elsevier Ltd. All rights reserved.

Introduction **132**
Phenomenology and basic concepts **134**
The role of spin-orbit coupling 134
Size and form of (effective) spin-orbit coupling 134
A closer look at spin currents 135
Experiments **136**
Theory **138**
An instructive example and the general framework 138
Onsager reciprocity and a non-Abelian gauge field point of view 139
Conclusion **140**
Notes on further readings **140**
Acknowledgments **140**
References **140**

Abstract

In metallic systems with spin-orbit coupling a longitudinal charge current may generate a transverse pure spin current; *vice-versa* an injected pure spin current may result in a transverse charge current. Such direct and inverse spin Hall effects share the same microscopic origin: intrinsic band/device structure properties, external factors such as impurities, or a combination of both. They allow all-electrical manipulation of the electronic spin degrees of freedom, i.e., without magnetic elements, and their transverse nature makes them potentially dissipationless. It is customary to talk of spin Hall effects in plural form, referring to a group of related phenomena typical of spin-orbit coupled systems of lowered symmetry.

Key points

- History and definition of the effect(s)
- Phenomenology and concepts: spin-orbit coupling in solids, charge *vs.* spin currents, bulk *vs.* edge effects
- Experiments: from low- to room temperature, diversity and complexity of setups
- Theory: the challenge of complexity, competition between different microscopic mechanisms, Onsager reciprocity
- The broader context: generalizations of the spin Hall effect(s) and suggested further readings

Introduction

A charge-carrying state in a metallic system is a (non-equilibrium) momentum-ordered state of an electronic ensemble: a collection of quasielectrons[1] moving preferentially in a given direction, see Fig. 1(a). However quasielectrons carry around their internal spin degrees of freedom, too. For their ensemble to be spin carrying some form of spin order is needed. There are two basic scenarios:

- Spin order is independent of momentum order. This is the situation in a ferromagnet, where the spins of charge carriers align with the magnetization via exchange coupling independently of their orbital motion.
- Spin and momentum orders are correlated. This is possible in the presence of spin-orbit coupling, which quite generally creates correlations between orbital motion (momentum) and spin.

Consider the second scenario, and to be definite the somewhat special situation sketched in Fig. 1(b), where quasiparticles with opposite spin projection along z move in opposite directions. An ensemble of such particles does not carry any overall charge—the associated charge current is zero, $\mathbf{j}^c = 0$—but it does carry angular momentum: it is a pure spin-carrying state sustaining a "pure spin current" $\mathbf{j}^s \neq 0$

$$\mathbf{j}^c \equiv q\left(\mathbf{j}^{\uparrow} + \mathbf{j}^{\downarrow}\right) = 0 \tag{1}$$

---

[1] I will restrict my discussion to systems where well-defined fermionic quasiparticles exist and make up a Fermi liquid. Words such as "quasielectron" and "electron" or "quasiparticle" and "particle" will be used interchangeably.

https://doi.org/10.1016/B978-0-323-90800-9.00101-3

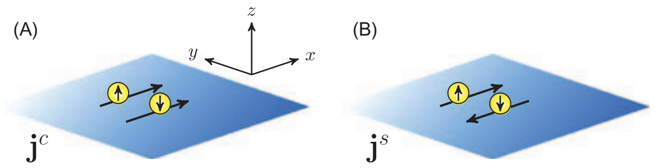

Fig. 1 Left panel: A charge current $\mathbf{j}^c$ along x, i.e., an overall spin-unpolarized ensemble of quasielectrons moving in the y direction. Right panel: A z-polarized pure spin current $\mathbf{j}^s$ flowing along x.

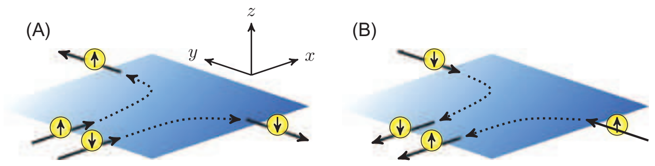

Fig. 2 Left panel: spin Hall effect. An x-flowing charge current is injected, and a z-polarized pure spin current along y is generated via spin-orbit coupling. Right panel: inverse spin Hall effect, where the role of the spin and charge currents are exchanged. Note that in the sHe/isHe the charge current, spin current and the spin quantization axis are all orthogonal to each other.

$$\mathbf{j}^s \equiv \frac{\hbar}{2}\left(\mathbf{j}^{\uparrow} - \mathbf{j}^{\downarrow}\right) \neq 0, \tag{2}$$

with q the quasiparticle charge and ħ the reduced Planck constant.

In the presence of spin-orbit coupling a transverse $\mathbf{j}^s$ can be generated from a longitudinal $\mathbf{j}^c$, or *vice-versa*, see Fig. 2. These are respectively the spin Hall effect (sHe) (Dyakonov and Perel, 1971; Hirsch, 1999) and its reciprocal version, the inverse spin Hall effect (isHe) (Dyakonov and Khaetskii, 2006; Engel et al., 2007). The sHe was first predicted by Dyakonov and Perel in 1971 (Dyakonov and Perel, 1971) but got his current name only in 1999, when Hirsch (Hirsch, 1999) sort of re-discovered it and its fortune really started. The isHe followed a similar path. In the geometry from Fig. 2 one has

$$j_y^s = (\hbar/q)\theta^{\mathrm{sHe}} j_x^c, \tag{3}$$

$$j_x^c = (q/\hbar)\theta^{\mathrm{isHe}} j_y^s \tag{4}$$

with θ^{sHe}, θ^{isHe} the spin Hall and inverse spin Hall angles. Note that from now on upper (lower) indices will denote charge/spin (real space) components. The spin Hall/inverse spin Hall angles are crucial quantities used as standard measure for the spin-charge conversion efficiency of a given setup (Valenzuela and Tinkham, 2006; Hahn et al., 2013a; Obstbaum et al., 2014; Sinova et al., 2015). In Sections "Phenomenology and basic concepts" and "Theory" we will show that their existence can be expected based on crude but general arguments, while their precise origin and values are extremely sensitive to the microscopic details of the system.

The sHe and isHe exist also in quantized form. Indeed, the "quantum spin Hall insulator" is the paradigmatic example of a time-reversal symmetric two-dimensional topologically insulating phase (Hasan and Kane, 2010). The latter is a phase of matter which is insulating in the bulk but hosts two perfectly conducting edge states which are time-reversed partners—up electrons moving in one direction, down in the opposite. In simple terms, a quantum spin Hall phase can be thought of as two time-reversed copies of a (time-reversal broken) quantum Hall state. Its existence was confirmed experimentally in HgCdTe quantum wells in 2007 (König et al., 2007). I will not discuss it further here, but refer the interested reader to the Encyclopedia Chapter "Topological Effects."

The sHe and isHe are nowadays routinely employed in metallic systems to inject and/or read out spin signals via electrical means, and their technological relevance is rapidly on the rise since the early 2000s (Dyakonov and Khaetskii, 2006; Engel et al., 2007; Sinova et al., 2015; Fert and Dau, 2019). The rest of the Chapter will focus uniquely on them. In particular I will not discuss the anomalous Hall effects, closely related phenomena which require however to break time-reversal symmetry (Dyakonov and Khaetskii, 2006; Nagaosa et al., 2010). The reader should indeed keep in mind that the spin Hall effect I will deal with in this Chapter actually belongs to a larger class of phenomena which may appear whenever quasiparticles with internal structure move in a non-trivial medium, i.e., not just in the vacuum.[2]

---

[2] In condensed matter one customarily talks of "pseudospin" internal degrees freedom, such as sublattice or valley pseudospin in graphene, which may give rise to different forms of "pseudospin Hall effect."

Phenomenology and basic concepts

The role of spin-orbit coupling

Take an electron moving with velocity **v** in presence of an electric field **E**. In its reference frame the electron sees a velocity-dependent magnetic field

$$\mathbf{B}'(\mathbf{v}) = -\gamma\frac{\mathbf{v}}{c}\times\mathbf{E}, \quad \gamma = \frac{1}{\sqrt{1-v^2/c^2}} \tag{5}$$

which couples to its spin $\mathbf{s} = (\hbar/2)\boldsymbol{\sigma}$, with $\boldsymbol{\sigma}$ the vector of Pauli matrices, as usual

$$H_{\mathrm{so}} \sim \mathbf{s}\cdot\mathbf{B}' \sim \mathbf{s}\cdot(\mathbf{v}\times\mathbf{E})\cdot \tag{6}$$

Here c is the speed of light. This is a primitive derivation of the spin-orbit interaction.

Let us assume that $\mathbf{E} = -\nabla V_{\mathrm{ext}}$ comes from an external source, e.g., the (random) electrostatic potential from an impurity, see Fig. 3(a). The quasiparticle spin thus couples to a non-homogeneous field $B'(\mathbf{v}) \to B'(\mathbf{v},\mathbf{r})$, similarly to what happens in a Stern-Gerlach apparatus. This has various consequences, e.g., it causes spin-flip (Elliot-Yafet) relaxation, but in particular it results in a spin-dependent force $\mathbf{F}\sim -\nabla[\mathbf{s}\cdot\mathbf{B}']$ orthogonal to **v**

$$F_\perp^\uparrow = -F_\perp^\downarrow \sim -\nabla_\perp B'\cdot \tag{7}$$

This sideway separation of spin-up and spin-down quasi-particles is referred to as Mott skew scattering, and can split an incoming flux of unpolarized electrons into a transverse pure spin current, i.e., it yields a finite θ^{sHe}. It is an "extrinsic" mechanism requiring the presence of scattering centers (Hirsch, 1999; Dyakonov and Khaetskii, 2006; Engel et al., 2007; Culcer et al., 2010), but a finite θ^{sHe} may also have origins which are "intrinsic" to the device and/or band structure. Consider for example $\mathrm{E} = -\nabla V_{\mathrm{int}}(z)$, with $V_{\mathrm{int}}(z)$ an internal potential which defines your structure, see Fig. 3 (b). Such a potential breaks z inversion symmetry and constrains electrons to move in the x-y plane, as in semiconductor quantum wells. One has

$$H_{\mathrm{so}} \sim \mathbf{s}\cdot\mathbf{v}\times e_z. \tag{8}$$

Now s couples to a homogeneous $\mathbf{B}'(\mathbf{v})$ which always points in plane, called a Rashba field (Bychkov and Rashba, 1984; Winkler, 2003). The eigenstates of the problem are spinors whose quantization axis depends on their direction of motion. As sketched in Fig. 3(b), under an electrical bias one expects spin-momentum correlations to arise leading to a transverse, out-of-plane-polarized spin current—that is, to a non-vanishing θ^{sHe}. Recall that in this intrinsic example inversion symmetry was explicitly broken. Some form of spatial symmetry-breaking is indeed a requirement of intrinsic scenarios beyond the present Rashba case (Engel et al., 2007; Winkler, 2003). On the other hand time-reversal symmetry is preserved by spin-orbit interaction.

Besides the canonical intrinsic and extrinsic mechanisms just described, other sources for the spin Hall effects include dynamical couplings with phonons (Gorini et al., 2015; Karnad et al., 2018) or spin fluctuations (Okamoto et al., 2019), the interplay of impurity and magnon scattering (Ohnuma et al., 2016), or fluctuations of the Rashba field (Dugaev et al., 2010). Irrespectively of the origin, and just as a normal Hall current, the spin Hall current is transverse with respect to the drift velocity and thus potentially dissipationless.

Size and form of (effective) spin-orbit coupling

Since charge carriers in a metallic system move at the Fermi velocity $v_F \ll c$, should one expect H_{so} to be only a negligible relativistic correction? The answer is "not necessarily." Electrons in solids do not move in the vacuum, but constantly get close to ionic cores from the lattice where unscreened very strong electric fields exist, compensating for their (relativistically) slow velocity. One can indeed show that s-wave Bloch electrons close to the Fermi energy feel an effective spin-orbit interaction which reads

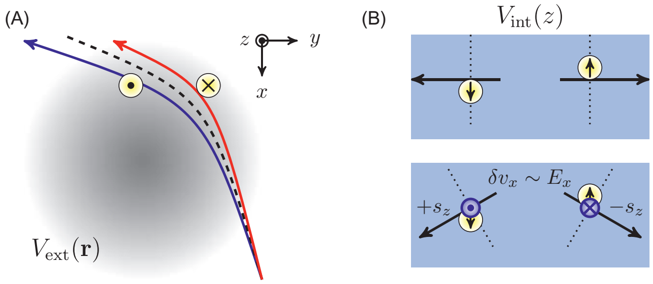

Fig. 3 Left panel: Electrons with opposite spins are deflected differently by a scattering potential V_{ext} (**r**). The dashed black line is the trajectory without spin-orbit corrections. Right panel: Electrons confined to two dimensions by $V_{\mathrm{int}}(z)$. The internal velocity-dependent field, see Eq. (8), defines the spin quantization axis, shown with dotted lines. The two electrons are time-reversed partners, and when driven by an electric field along x their spins will precess around the new (tilted) quantization axis, yielding out-of-plane components $\pm s_z$ shown in blue. The result is a z-polarized spin current in the transverse y direction.

$$H_{\mathrm{so}} = \lambda \boldsymbol{\sigma} \times \nabla \delta V \cdot \mathrm{p}, \tag{9}$$

with δV any potential other than that of the host lattice, e.g., $\delta V = V_{\mathrm{ext}}$ or $\delta V = V_{\mathrm{int}}(z)$ from our previous examples. While the form of H_{so} is the same as in the vacuum, the coupling constant λ is an effective Compton wavelength strongly renormalized by the lattice: $\lambda/\lambda_0 \sim 10^6$, with λ_0 the vacuum Compton wavelength. The standard machinery behind such renormalization is $\mathbf{k}\cdot\mathbf{p}$ theory, which, together with some auxiliary techniques (Löwding partitioning, Schrieffer-Wolff transformation, …), is just a systematic way of building low-energy models starting from the band structure (Bloch states) of a given lattice—at the simplest level it leads, e.g., to the effective mass description of electrons in solids (Engel et al., 2007; Winkler, 2003). Eq. (9) can actually be generalized to

$$H_{\mathrm{so}} = \mathbf{b}(\mathbf{p}) \cdot \boldsymbol{\sigma}, \tag{10}$$

which looks like Zeeman/exchange coupling with a momentum-dependent internal field $\mathbf{b}(\mathbf{p})$. The latter defines a momentum space spin texture—its vectorial image in reciprocal space—of central importance well beyond spin Hall physics.[3] This form of effective spin-orbit interaction is valid beyond the two example scenarios previously introduced, and is the starting point for most discussions of spin-orbit coupled transport phenomena (Engel et al., 2007; Winkler, 2003).[4]

A closer look at spin currents

The spin Hall/inverse spin Hall angles, see Eqs. (3) and (4), are crucial quantities in spin Hall physics. However to define them one needs to know exactly what a spin current is, which is not a completely trivial task. Let us see why.

Charge is a conserved quantity respecting the continuity equation

$$\partial_t n + \nabla \cdot \mathbf{j}^c = 0, \tag{11}$$

with n the charge (particle) density and $\mathbf{j}^c = \mathbf{v} n$ the current. In formal terms, this is a consequence of gauge invariance: charge (particle number) is the conserved quantity associated with the $U(1)$ gauge symmetry of the system—a case of Noether's theorem.

A purely orbital Hamiltonian H_0 without spin-orbit interaction cannot affect the dynamics of the spin degrees of freedom: not only charge, but also spin is conserved for H_0. Formally H_0 is spin-rotation invariant, which for spin 1/2 particles means that it has $SU(2)$ gauge symmetry. Spin conservation yields the continuity equation

$$\partial_t s^a + \nabla \cdot \mathbf{j}^a = 0, \quad a = x, y, z, \tag{12}$$

with s^a the density of a-polarized electrons, and $\mathbf{j}^a = \mathbf{v} s^a$ the corresponding a-spin current density.

In the presence of spin-orbit coupling, $H_0 \to H = H_0 + H_{\mathrm{so}}$, spin rotation symmetry is broken and spin is not conserved anymore. Consider first extrinsic spin-orbit due to diluted impurities. In this case spin is not conserved during scattering events, but remains so between them. The definition $\mathbf{j}^a = \mathbf{v} s^a$ is thus good during flight, but at each scattering the a-polarized flux may rotate, partially split and lose weight due to spin-flip scattering. The result is a spin relaxation rate $1/\tau_s^a$; with τ_s^a the a-spin lifetime, and some further extrinsic spin torque Γ_{ext}^a

$$\partial_t s^a + \nabla \cdot \mathbf{j}^a = -\frac{s^a}{\tau_s^a} + \Gamma_{\mathrm{ext}}^a. \tag{13}$$

The extra torque describes spin non-conservation effects beyond simple relaxation, e.g., skew-scattering physics, which may directly couple spin and charge degrees of freedom.

If intrinsic spin-orbit coupling is present things are more complicated. First, in this case the velocity $\mathbf{v} = \partial_{\mathbf{p}} H$ does not in general commute with the spin operator, which is obvious looking at Eq. (10). One can still generalize the spin current definition by symmetrization

$$\mathbf{j}^a = \frac{1}{2}\{\mathbf{v}, \ s^a\}, \tag{14}$$

with $\{A, B\} = AB + BA$ the anticommutator. However spin is now intrinsically—i.e., everywhere and always—not conserved, *ergo* the continuity equation obeyed by such a current must be modified by an intrinsic spin torque Γ_{int}^a

$$\partial_t s^a + \nabla \cdot \mathbf{j}^a = \Gamma_{\mathrm{int}}^a. \tag{15}$$

The precise form of the torque is fixed by the internal spin-orbit field (10). The intrinsic lack of a conservation law means that $\mathbf{j}^a$, and thus Γ^a are not uniquely defined now. This is no fundamental problem, in the sense that not all physically meaningful currents need be conserved. It can however be a delicate operative problem, as changing the definition of $\mathbf{j}^a$ will change the definitions of the spin Hall/inverse spin Hall angles, which is what experiments typically aim at measuring. Similarly, it will modify the estimates for the spin accumulations generated by the current, the accumulation being another popular observable. Indeed, it is not always obvious how (if) local spin currents somewhere, say in the bulk, are connected with local spin accumulations elsewhere, e.g., at the sample's edges (Dyakonov and Khaetskii, 2006; Sonin, 2007a, 2010a; Adagideli et al., 2007; Gorini et al., 2012). These issues are recurringly discussed in the specialized literature (Sonin, 2007a, 2010a,b; Adagideli et al., 2007; Gorini et al., 2012; Rashba, 2003; Nikolić et al., 2006; Shi et al., 2006; Sugimoto et al., 2006; Tokatly, 2008; Khaetskii, 2014) and can be dealt with in different ways, for example:

---

[3] In the presence of $\mathbf{b}(\mathbf{p})$ the Hilbert space of the problem is usually equipped with a non-vanishing Berry curvature, with the potential for hosting non-trivial topological phases.

[4] There are situations in which an internal field $\mathbf{b}(\mathbf{p})$ appears for microscopic reasons which have nothing to do with relativistic spin-orbit interaction. The field thus couples to some internal pseudospin degree of freedom $\boldsymbol{\tau}$ of the low-energy quasiparticles, $\mathbf{b}(\mathbf{p})\cdot\tau$. See comments in the closing of Section "Introduction".

- One can avoid referring to spin currents within the spin-orbit coupled region, and define them only in the metallic electrodes attached to sample, where H_{so} is negligible. This is the picture naturally arising in the Landauer-Büttiker approach to transport (Jacquod et al., 2012). It is often more or less implicitly assumed in phenomenological discussions of experiments.
- One can focus on spin accumulations, i.e., consider the equation of motion for the spin density without assuming a given form for the spin currents. The appropriate form of the currents may be derived from the density equations, notably in the diffusive regime (Adagideli et al., 2007; Burkov et al., 2004; Mal'shukov et al., 2005; Raimondi et al., 2006).
- One can use the non-Abelian gauge properties of the Hamiltonian H, i.e., its spin rotation $[SU(2)]$ properties, to define spin currents much as color currents are defined in high-energy physics (Tokatly, 2008; Gorini et al., 2010). This approach removes any ambiguity from the definition of $\mathbf{j}^a$, Γ^a, but cannot directly be exploited for any form of $\mathbf{b}(\mathbf{p})$. I will comment further on it in Section "Theory."
- One can try to define a conserved spin current by combining $\mathbf{j}^a$ and Γ^a (Shi et al., 2006; Sugimoto et al., 2006).

There is arguably no single "best" approach. One should decide which way to go based on the specific physical situation, and—if the physics allow—on personal tastes. It should also be kept in mind that both extrinsic and intrinsic processes are present in typical setups, and that they may yield further intrinsic-extrinsic crossed processes, i.e., the corresponding torques are not simply additive (Raimondi and Schwab, 2009; Raimondi et al., 2012). Moreover—and independently of the spin current definition—continuity equations like (12), (13), or (15) must be supplemented with appropriate boundary conditions, e.g., at interfaces between different materials or at the edges of the system, which may yield additional (local) torques (Adagideli et al., 2007; Khaetskii, 2014; Raimondi et al., 2006; Adagideli and Bauer, 2005; Tserkovnyak et al., 2007; Mal'shukov et al., 2007; Amin and Stiles, 2016; Tölle et al., 2018).

Experiments

The first spin Hall experiments were performed in the 1970s and 1980s in semiconductors (Dyakonov and Khaetskii, 2006), but relatively few got interested at the time. The business became fashionable in the early 2000s, and the spin Hall effects are nowadays not only the object of fundamental research (Zhu et al., 2019; Nakagawara et al., 2019; Li et al., 2021; Yanez et al., 2021; Boventer et al., 2021), but also established tools in more application-oriented settings (Fert and Dau, 2019; Liu et al., 2012; Safeer et al., 2020; Karube et al., 2020). In fact, while the first experiments were performed at fairly low temperatures (a few to a few tens of Kelvins) room temperature measurements are routine today, and large spin Hall angles have been reported in different materials. To give a rough idea of the progression, the spin Hall angle reported in a pioneering experiment by Valenzuela and Tinkham in 2006 was $\theta^{\mathrm{sHe}} \sim 10^{-4}$ in Al at $T = 4.2$ K, while less than 10 years later room temperature measurements in Pt, Ta or W reached $\theta^{\mathrm{sHe}} \sim 10^{-1}$ (Hahn et al., 2013a; Obstbaum et al., 2014; Liu et al., 2012; Rojas-Sánchez et al., 2014; Pai et al., 2012).

The numerous experimental schemes available can roughly be divided into three classes.

- Optical setups, historically the first to be used to detect the sHe/isHe, exploit the interaction between polarized light and the spin of charge carriers. For example, circularly polarized light can be used to generate local non-equilibrium spin accumulations which later diffuse through the system. The diffusion spin current can then be converted by the isHe into charge signals measured with standard electrodes, see Fig. 4(a). On the other hand, spin accumulations can be measured by circularly polarized

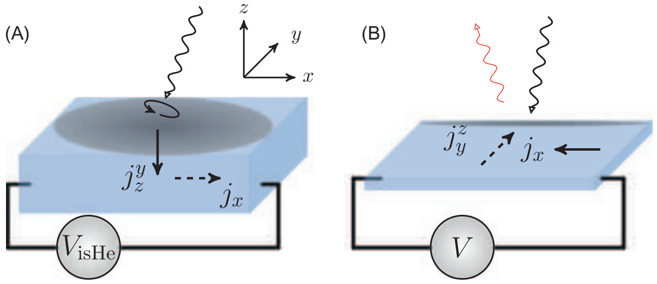

Fig. 4 Left panel: A broad spot of circularly polarized light creates a non-equilibrium spin polarization δs^y at a sample's surface (shaded region), and a diffusion spin current $j_z^y \sim \partial_z \delta s^y$ flows into the 3D bulk. Here the isHe generates a transverse charge current j_x, yielding a finite output voltage V_{isHe}. Setups of this kind were proposed already in the early days of spin Hall physics (Dyakonov and Khaetskii, 2006). Right panel: In a 2D system the charge current j_x from an applied bias V is converted into a spin Hall current j_y^z. The resulting spin accumulation at the edges (shaded region) is measured by Kerr rotation of scattered light (red). The technique was employed in the first experimental observation of the sHe in a 2D electron gas (Kato et al., 2004), and a similar one in a 2D hole gas (Wunderlich et al., 2005). The connection between bulk spin currents and edge spin accumulations can however be less direct than this cartoon suggests (Dyakonov and Khaetskii, 2006; Adagideli et al., 2007; Sonin, 2010a; Gorini et al., 2012; Nikolić et al., 2006).

electroluminescence or magneto-optical Kerr and Faraday effects. An example is shown in Fig. 4(b), where the spin accumulation at the edge of the system generated by the sHe is measured by the degree of (Kerr) rotation of light scattered off the sample. All-optical schemes are also employed (Werake et al., 2011; Seifert et al., 2016), allowing in particular time-resolved experiments on ultra-short (THz) timescales (Werake et al., 2011)—which are not accessible to electronic systems.

- Magneto-electric (spin pumping, spin torque) setups, relying on the interplay between magnetization and spin dynamics (Tserkovnyak et al., 2005). Fig. 5 shows a paradigmatic example: a spin current $\mathbf{j}^s_{\text{in}}$ is injected from an out-of-equilibrium magnetic element, e.g., a (conducting or insulating) magnet driven by microwaves, and converted into a charge current $\mathbf{j}^c_{\text{out}}$ collected at a normal metallic electrode. The latter can actually be used to run the experiment under "reverse bias": $\mathbf{j}^c_{\text{in}}$ is injected, and one measures the torque that the resulting $\mathbf{j}^s_{\text{out}}$ exerts on the adjacent magnet. The presence of magnetic elements considerably increases the degree of complexity of the overall system, and may lead to additional effects which are however beyond the scope of this short overview (Tserkovnyak et al., 2005; Manchon et al., 2019). Time-dependent experiments are also performed, e.g., to measure AC spin Hall effects (Hahn et al., 2013b; Wei et al., 2014; Weiler et al., 2014).
- All-electrical setups, conceptually probably the simplest. Fig. 6(a) shows a most basic one, without any magnetic element: A charge current $\mathbf{j}^c_{\text{in}}$ is injected by a metallic electrode, is converted into a spin signal by the sHe, and finally re-converted by the isHe into an outgoing $\mathbf{j}^c_{\text{out}}$ collected at some other electrode. A very popular scheme requiring a magnetic electrode is instead sketched in Fig. 6(b). Both are non-local—input electrodes are somewhere, output electrodes elsewhere—a common feature in spin Hall setups (Valenzuela and Tinkham, 2006; Takahashi and Maekawa, 2007).

The boundary between classes is clearly blurred, and mixed techniques are often employed. An important general observation is that experimental setups—apart perhaps from the simplest all-electrical ones—are fairly complex, consisting of multiple elements of different nature subject to various kinds of drivings. Paired with the vast number of spin-charge (or charge-spin) conversion channels available in any given system, this makes for interesting debates concerning possible microscopic interpretations of experiments.[5]

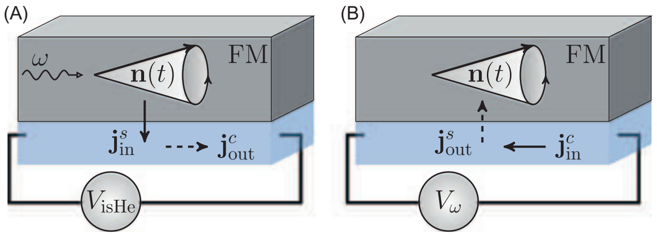
(A)
ω
$\mathbf{n}(t)$
FM
$\mathbf{j}^s_{\text{in}}$
$\mathbf{j}^c_{\text{out}}$
V_{isHe}
(B)
$\mathbf{n}(t)$
FM
$\mathbf{j}^s_{\text{out}}$
$\mathbf{j}^c_{\text{in}}$
V_ω

Fig. 5 Left panel: Sketch of a spin pumping setup. Microwaves in a ferro-/ferrimagnet FM at frequency ω drive the magnetization, $\mathbf{M} = M\mathbf{n} \to \mathbf{M}(t) = M\mathbf{n}(t)$. Its precession injects angular momentum into the underlying spin-orbit coupled normal metal, generating a spin current $\mathbf{j}^s$. The latter is converted by the isHe into a charge current $\mathbf{j}^c$ and *ergo* a measurable voltage V_{isHe}, in general with both DC and AC components (Wei et al., 2014; Weiler et al., 2014; Jiao and Bauer, 2013). Right panel: A reverse-bias scenario, in which a charge current at frequency ω is injected and converted by the sHe into an AC spin current. The latter exerts a torque on M and drives its precession. There are numerous DC and AC variations to these schemes, involving many different magneto-resistive effects modulated by spin-orbit interaction, see Sinova et al. (2015), Fert and Dau (2019) for an overview.

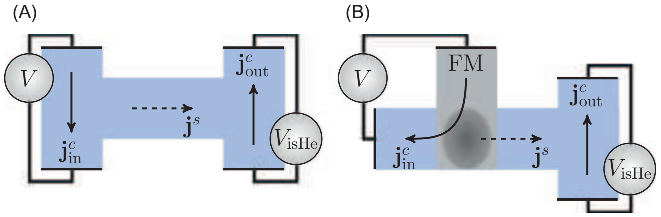
(A)
V
$\mathbf{j}^c_{\text{in}}$
$\mathbf{j}^s$
$\mathbf{j}^c_{\text{out}}$
V_{isHe}
(B)
V
FM
$\mathbf{j}^c_{\text{in}}$
$\mathbf{j}^s$
$\mathbf{j}^c_{\text{out}}$
V_{isHe}

Fig. 6 Left panel: Hall bar geometry without magnetic elements. The injected charge current $\mathbf{j}^c_{\text{in}}$ is converted into a transverse spin current $\mathbf{j}_s$ by the sHe. The latter is converted back into a charge current $\mathbf{j}^c_{\text{out}}$ by the isHe in the right arm of the setup, yielding a finite V_{isHe}. One of the earliest implementations of this setup was used to measure the ballistic sHe in a HgTe quantum well (Brüne et al., 2010). Right panel: non-local setup with a ferromagnetic (FM) electrode, shown in dark gray, deposited on top of a T-shaped metallic film. The injected current $\mathbf{j}^c_{\text{in}}$ is drained to the left contact, since the right metallic arm is at the same electrochemical potential as the FM electrode. The current $\mathbf{j}^c_{\text{in}}$ is spin polarized, therefore it creates a non-equilibrium spin accumulation underneath the FM contact, shown by the shaded area. Part of it diffuses toward the right, yielding a pure spin current $\mathbf{j}^s$ which is then converted by the isHe into a measurable transverse voltage V_{isHe}. The scheme was first employed by Valenzuela and Tinkham (2006).

---

[5] The spin galvanic and inverse spin galvanic effects are very often crucial "partners" of the spin Hall effects (Ganichev et al., 2002; Ganichev et al., 2019; Shen et al., 2014; Gorini et al., 2017). They are another common channel of spin-charge/charge-spin conversion, discussed in detail in a dedicated Encyclopedia Chapter.

Theory

An instructive example and the general framework

The spin Hall effects are non-equilibrium phenomena handled with the usual arsenal of transport theory techniques: Keldysh formalism, density matrix and semi-classical kinetics, Kubo formula, Landauer-Büttiker formalism. ... Irrespective of the techniques employed, a source of substantial theoretical challenges is complexity. In crude terms, the Hamiltonian of a spin Hall system requires numerous ingredients, recall the discussion from Section "Experiments." The resulting quasiparticle dynamics are in general quite sensitive to the presence/absence of, and competition between, each.

To see this in a concrete way it is instructive to start from the barebone model of an ideal Rashba system

$$H_{\mathrm{R}} = \frac{p^2}{2m} + \frac{\alpha}{\hbar}\left[p_y\sigma^x - p_x\sigma^y\right], \tag{16}$$

where m is the effective electron mass and $\alpha \sim \nabla V_{\mathrm{int}}(z)$ the Rashba coupling constant, proportional to the (effective) electric field confining the electrons to the x-y plane—see the heuristic discussion in Section "Phenomenology and basic concepts," Eq. (8).

Given H_R, the goal is to compute the frequency-dependent spin Hall conductivity $\sigma^{\mathrm{sHe}}(\omega)$, defined as

$$j_y^z(\omega) = \sigma^{sHe}(\omega)E_x(\omega), \tag{17}$$

with j_y^z the z-polarized spin current in the y direction. The standard choice is to take the symmetrized spin current definition (14)—other choices are possible, recall the discussion from Section "Phenomenology and basic concepts," and the consequences will be addressed below. The spin Hall conductivity can be written in terms of the spin current-charge current Kubo response function $\left\langle\left\langle j_y^z; j_x\right\rangle\right\rangle_\omega \equiv -\frac{i}{\hbar}\int_0^t \left[j_y^z(t), j_x(0)\right] e^{i\omega t}\mathrm{d}t$, with $[A,B] = AB - BA$ the commutator (Landau et al., 2008). Since the charge current couples to the vector potential as $\mathbf{j}\cdot\mathbf{A}$, and $E_x(\omega) = -i\omega A_x(\omega)$, one has

$$\sigma^{\mathrm{sHe}}(\omega) = \frac{\left\langle\left\langle j_y^z; j_x\right\rangle\right\rangle_\omega}{i\omega}. \tag{18}$$

Once the DC $\sigma^{\mathrm{sHe}} \equiv \lim_{\omega\to 0}\sigma^{\mathrm{sHe}}(\omega)$ is known the spin Hall angle follows

$$\theta^{\mathrm{sHe}} = \frac{q}{\hbar}\frac{\sigma^{\mathrm{sHe}}}{\sigma_x^c}, \tag{19}$$

with σ_x^c the longitudinal DC charge conductivity. An explicit computation yields the "universal" DC result

$$\sigma_{\mathrm{clean}}^{\mathrm{sHe}} = \frac{e}{8\pi\hbar}, \tag{20}$$

with the electron charge $q = -e < 0$. The subscript "clean" highlights that the system is without any defects. Such a beautiful result, due to the intrinsic Berry phase of electrons on the Rashba Fermi surface, is unfortunately very fragile. If one adds dirt to the model, i.e., a random impurity potential, $H_{\mathrm{R}} \to H_{\mathrm{R}} + V_{\mathrm{imp}}(\mathbf{r})$, the spin Hall conductivity exactly vanishes

$$\sigma_{\mathrm{dirty}}^{\mathrm{sHe}} = 0. \tag{21}$$

The vanishing is diagrammatically subtle: since it comes from vertex corrections, it cannot be guessed by simply introducing a disorder broadening of the momentum eigenstates in the Kubo response kernel (Schwab and Raimondi, 2002; Inoue et al., 2004; Raimondi and Schwab, 2005). Indeed, it was overlooked at first in the scientific literature (Sinova et al., 2004). On the other hand, it is easily understood with kinetic arguments (Dimitrova, 2005; Chalaev and Loss, 2005), since the homogeneous continuity equation for the y-spin component reads

$$\partial_t s^y = \underbrace{-\frac{2m\alpha}{\hbar^2} j_y^z}_{\Gamma_{\mathrm{int}}^y}. \tag{22}$$

At steady state the spin current $j_y^z = 0$.

Eq. (21) is as fragile as its clean counterpart (20). If one further adds extrinsic spin-orbit interaction, that is spin-orbit interaction with the impurity potential, $H_{\mathrm{R}} \to H_{\mathrm{R}} + V_{\mathrm{imp}}(\mathbf{r}) + \lambda\boldsymbol{\sigma} \times \nabla V_{\mathrm{imp}}(\mathbf{r}) \cdot \mathbf{p}$, the spin Hall conductivity is non-zero

$$\sigma_{\mathrm{int+ext}}^{\mathrm{sHe}} \neq 0, \tag{23}$$

and furthermore depends non-trivially on different system parameters. In particular (Raimondi and Schwab, 2009; Raimondi et al., 2012)

$$\sigma_{\mathrm{int+ext}}^{\mathrm{sHe}} \neq \sigma_{\mathrm{int}}^{\mathrm{sHe}} + \sigma_{\mathrm{ext}}^{\mathrm{sHe}}. \tag{24}$$

Equivalent results would have been reached starting from the (linear) Dresselhaus model

$$H_D = \frac{p^2}{2m} + \frac{\beta}{\hbar}\left[p_x\sigma^x - p_y\sigma^y\right], \tag{25}$$

where the coupling constant β is now due to bulk inversion asymmetry, i.e., the lack of inversion symmetry of the underlying crystal, as in zincblend compounds (Winkler, 2003).

The lesson to be learned from this example is not that low-energy effective models of Rashba or Dresselhaus type are unreliable—quite the contrary, they are pillars of spintronics, even if more complex models are often needed, e.g., for precise quantitative comparisons with experiments. It is rather that any effect crucially depending on the coupling between orbital motion and internal (spin) dynamics is subtler than standard charge-only transport phenomena, even when their description is based on the simplest models. As a corollary, attacking the problem from different angles—Kubo *vs.* kinetics in this case—can be a good idea.

The Rashba and Dresselhaus scenarios just considered are examples of a standard approach to transport widely employed throughout condensed matter. The latter starts from some low-energy ($\mathbf{k}\cdot\mathbf{p}$) effective model whose parameters can be computed with *ab-initio* methods, or left as symmetry-allowed parameters to be estimated by comparison with experiments. In our case the minimal Hamiltonian for spin 1/2 quasiparticles reads

$$H = H_0 + \mathbf{b}(\mathbf{p})\cdot\boldsymbol{\sigma} + \delta H \tag{26}$$

where H_0 describes band-bottom (top) free electrons (holes), and $\mathbf{b}(\mathbf{p})$ is the effective intrinsic spin-orbit field, see Eq. (10). Higher-dimensional models (4×4, 6×6 …) are employed whenever more than a single s-band lie close to the Fermi energy, which is the case, e.g., for graphene (Neto et al., 2009; Kochan et al., 2017; Dyrdał and Barnaś, 2012; Milletarí et al., 2017), Pt (Guo et al., 2008) or typically for holes (Engel et al., 2007; Winkler, 2003). On the other hand there are situations in which the term $\mathbf{b}(\mathbf{p})$ is negligible, e.g., in bulk Al or Cu. The last term δH contains all extra ingredients needed in the specific situation, e.g., exchange coupling with a magnetic texture, extrinsic spin-orbit coupling, disorder, phonons and so on.

The effective Hamiltonian (26) is used to study non-equilibrium dynamics with whatever analytical and/or numerical techniques one prefers. The approach is thus very general and flexible. Alternatively, it is also possible to stick to *ab-initio* methods and use an atomistic Hamiltonian throughout. In this case one typically relies on Kubo linear response formalism to compute the relevant transport coefficients, e.g., σ^{sHe} (Lowitzer et al., 2011; Ködderitzsch et al., 2015).

Onsager reciprocity and a non-Abelian gauge field point of view

The sHe and isHe connect spin currents, even under time-reversal, with charge currents, odd under time-reversal. From the general properties of Kubo response functions (Landau et al., 2008) there follows

$$\left\langle\left\langle j_y^z; j_x\right\rangle\right\rangle = -\left\langle\left\langle j_x; j_y^z\right\rangle\right\rangle, \tag{27}$$

which implies

$$\sigma^{\text{sHe}} = -\sigma^{\text{isHe}}. \tag{28}$$

This is the (linear response) Onsager relation between the sHe and isHe. It is evident that changing the definition of the spin current changes the value of σ^{sHe} and σ^{isHe}. This is critical if a direct comparison with experiments is seeked: what spin current is being excited in the experimental setup? What spin Hall angle are we talking about? As discussed in Section "Phenomenology and basic concepts" there are numerous ways to remove any ambiguity from such a comparison. In particular, if one is not interested in local quantities such as conductivities, the problem can be bypassed by considering conductances between metallic leads without spin-orbit interaction (Jacquod et al., 2012). On the other hand a change of spin current definition does not break Onsager reciprocity if done consistently, i.e., if the same definition is used to describe both the direct, say sHe, and reverse bias, say isHe, scenario.

Another source of concern in the early 2000s was that the standard definition of spin currents, Eq. (14), may yield non-vanishing equilibrium (circulating) currents (Rashba, 2003). Different authors highlighted however that there is nothing intrinsically unphysical or surprising in this (Tokatly, 2008; Sonin, 2007b): spin currents are even under time-reversal, so can exist in equilibrium, and physical systems hosting different kinds of equilibrium currents anyway exist (Tokatly, 2008; Sonin, 2010b, 2007b; Heurich et al., 2003). Indeed, adopting a non-Abelian gauge field point of view, equilibrium spin currents can be identified with the non-Abelian analogous of dissipationless Landau paramagnetic currents in solids (Tokatly, 2008).

The non-Abelian gauge field approach requires to rewrite the spin-orbit interaction in terms of a non-Abelian vector potential $\boldsymbol{\mathcal{A}}$, i.e., a tensor $\mathcal{A}_i^a$ with both spin (a) and real space (i) indices. To be definite, for the Rashba Hamiltonian (16) one has

$$H_R = \frac{(\mathbf{p} + \boldsymbol{\mathcal{A}})^2}{2m} + \text{const.} \tag{29}$$

with $\mathcal{A}_x^y = -\mathcal{A}_y^x = 2m\alpha/\hbar^2$, while $\mathcal{A}_j^a = 0$ for all other components. The spin current immediately follows from $j_i^a = \partial H_R/\partial\mathcal{A}_i^a$. It coincides with the standard definition (14) and generally consists of both transport contributions and a non-dissipative equilibrium part. Pursuing this route, e.g., in a diffusive sample, one obtains in particular a clear parallel between the standard Hall current

$\mathbf{j}_{\mathrm{Hall}}$ in presence of a magnetic field $\mathbf{B}$ and the a-polarized spin Hall current $\mathbf{j}_{\mathbf{s}\ \mathrm{He}}^{a}$ in presence of a non-Abelian pseudomagnetic field $\mathcal{B}$ generated by $\boldsymbol{\mathcal{A}}$ (Gorini et al., 2010)

$$\mathbf{j}_{\mathrm{Hall}} = \frac{q\tau}{m}\mathbf{j} \times \mathbf{B} \rightarrow \mathbf{j}_{\mathrm{sHe}}^{a} = \frac{q\tau}{4m}\mathbf{j} \times \mathcal{B}^{a}. \tag{30}$$

The non-Abelian gauge field approach is based on relatively old ideas (Mathur and Stone, 1992; Fröhlich and Studer, 1993; Brouwer et al., 2002), but was recently revived to describe spin-charge coupled transport in different settings (Gorini et al., 2010; Raimondi et al., 2012; Adagideli et al., 2012; Bergeret and Tokatly, 2013; Tokatly and Sherman, 2016; Tölle et al., 2017; Bobkova and Bobkov, 2017; Jacobsen and Linder, 2017; Mal'shukov, 2017; Aikebaier et al., 2019; König and Levchenko, 2021). While its merits are evident, one should realize that a rewriting like Eq. (29) is not always possible. I refer to the relevant literature for details.

Conclusion

The spin Hall effects are a family of transverse transport phenomena appearing in (pseudo)spin-orbit coupled systems. A good chunk of the theory and experimental background was established in the 1970s–80s, but the effects became widely known in condensed matter only starting from the early 2000s, and are nowadays cornerstones of both fundamental and applied spintronic research. Such a late blooming is probably due in good part to two roughly contemporary events. First, the widespread realization of the importance of geometry/topology-related concepts for Bloch electrons. Since the latter usually require quasiparticles to have an internal structure, this strongly increased interest for (pseudo)spin-orbit coupled dynamics. Second, technological advances which notably allowed the fabrication of high-quality semiconductor heterostructures, where spin manipulation became possible with a high level of precision, soon after followed by the discovery and functionalization of graphene and other materials with strong (pseudo)spin-orbit interaction.

In this short overview I focused on the core, standard forms of the spin Hall effects, as they exist in normal Fermi liquids. In this context they are active in a wide range of parameters, from large samples at room temperature—important for potential applications—down to mesoscopic samples at low temperatures. However they may also appear in, e.g., strongly disordered systems (Smirnov and Golub, 2017), superconductors (Takahashi and Maekawa, 2011), metallic antiferromagnets (Zhang et al., 2014; Gulbrandsen et al., 2020), as "valley Hall effects" in different materials (Gorbachev et al., 2014; Mak et al., 2014; Lensky et al., 2015) or in the propagation of magnons (Onose et al., 2010; Mook et al., 2014) and light (Hosten and Kwiat, 2008). They may also contribute to other transport effects, such as the spin Hall magnetoresistance (Chen et al., 2016, 2013; Oyanagi et al., 2021). In short, they are potentially present in any scenario where transport is due to quasiparticles with some internal structure which couples to a non-trivial background.

Notes on further readings

The literature on the spin Hall effects is vast and ramifies quickly to neighboring subfields. The bibliography given here is meant to provide barebone directions to the newcomer, but is by no means exhaustive. Numerous review articles, each with its own qualities and shortcomings, are available to the interested reader. Dyakonov and Khaetskii (2006) and Engel et al. (2007) are both must-read works. Dyakonov and Khaetskii (2006) provides in particular a thorough historical overview and excellent phenomenological discussions, while Engel et al. (2007) offers a high-quality and very compact introduction to the technical background, introducing also modern topological concepts. I also suggest Fert and Dau (2019) for a recent, short and more application-oriented discussion, and Vignale (2010) for its theory part. Finally, Sinova et al. (2015) provides an excellent experimental overview.

Acknowledgments

I am indebted to Lin Chen for a careful reading of the manuscript and to Leonid E. Golub for useful comments. I also thank all STherQO members for discussions.

References

Adagideli I and Bauer GEW (2005) *Physical Review Letters* 95: 256602.
Adagideli I, Scheid M, Wimmer M, Bauer GEW, and Richter K (2007) *New Journal of Physics* 9: 382.
Adagideli I, Lutsker V, Scheid M, Jacquod P, and Richter K (2012) *Physical Review Letters* 108: 236601.
Aikebaier F, Virtanen P, and Heikkilä T (2019) *Physical Review B* 99: 104504.
Amin VP and Stiles MD (2016) *Physical Review B* 94: 104419.
Bergeret FS and Tokatly IV (2013) *Physical Review Letters* 110: 117003.
Bobkova IV and Bobkov AM (2017) *Physical Review B* 95: 184518.
Boventer I, Simensen H, Anane A, Kläui M, Brataas A, and Lebrun R (2021) *Physical Review Letters* 126: 187201.

Brouwer PW, Cremers JNHJ, and Halperin BI (2002) *Physical Review B* 65: 081302(R).
Brüne C, Roth A, Novik EG, König M, Buhmann H, Hankiewicz EM, Hanke W, Sinova J, and Molenkamp LW (2010) *Nature Physics* 6: 448.
Burkov AA, Núnez S, and MacDonald AH (2004) *Physical Review B* 70: 155308.
Bychkov YA and Rashba EI (1984) *JETP Letters* 39: 78.
Chalaev O and Loss D (2005) *Physical Review B* 71: 245318.
Chen L, Matsukura F, and Ohno H (2013) *Nature Communications* 4: 2055.
Chen Y-T, Takahashi S, Nakayama H, Althammer M, Goennenwein SBT, Saitoh E, and Bauer GEW (2016) *Journal of Physics: Condensed Matter* 28: 103004.
Culcer D, Hankiewicz EM, Vignale G, and Winkler R (2010) *Physical Review B* 81: 125332.
Dimitrova OV (2005) *Physical Review B* 71: 245327.
Dugaev VK, Inglot M, Sherman EY, and Barnaś J (2010) *Physical Review B* 82: 121310(R).
Dyakonov MI and Khaetskii AV (2006) Spin hall effect. In: *Spin Physics in Semiconductors*, p. 211. Springer.
Dyakonov MI and Perel VI (1971) *Physics Letters A* 35: 459.
Dyrdał A and Barnaś J (2012) *Physical Review B* 86: 161401(R).
Engel H-A, Rashba EI, and Halperin BI (2007) Theory of spin hall effects in semiconductors. In: *Handbook of Magnetism and Advanced Magnetic Materials*, p. 2858. John Wiley & Sons.
Fert A and Dau FNV (2019) *Comptes Rendus Physique* 20: 817.
Fröhlich J and Studer UM (1993) *Reviews of Modern Physics* 65: 733.
Ganichev SD, Ivchenko EL, Bel'kov VV, Tarasenko SA, Sollinger M, Weiss D, Wegscheider W, and Prettl W (2002) *Nature* 417: 153.
Ganichev SD, Trushin M, and Schliemann J (2019) Spin polarisation by current. In: Tsymbal EY and Žutić I (ed.), Spintronics Handbook, 2nd edn. vol. 2, ch. 7, CRC Press Taylor & Francis Group.
Gorbachev RV, Song JCW, Yu GL, Kretinin AV, Withers F, Cao Y, Mishchenko A, Grigorieva IV, Novoselov KS, Levitov LS, and Geim AK (2014) *Science* 346: 448.
Gorini C, Schwab P, Raimondi R, and Shelankov AL (2010) *Physical Review B* 82: 195316.
Gorini C, Raimondi R, and Schwab P (2012) *Physical Review Letters* 109: 246604.
Gorini C, Eckern U, and Raimondi R (2015) *Physical Review Letters* 115: 076602.
Gorini C, Sheikhabad AM, Shen K, Tokatly IV, Vignale G, and Raimondi R (2017) *Physical Review B* 95: 205424.
Gulbrandsen SA, Espedal C, and Brataas A (2020) *Physical Review B* 101: 184411.
Guo GY, Murakami S, Chen T-W, and Nagaosa N (2008) *Physical Review Letters* 100: 096401.
Hahn C, de Loubens G, Klein O, Viret M, Naletov VV, and Ben Youssef J (2013a) *Physical Review B* 87: 174417.
Hahn C, de Loubens G, Viret M, Klein O, Naletov VV, and Youssef JB (2013b) *Physical Review Letters* 111: 217204.
Hasan MZ and Kane CL (2010) *Reviews of Modern Physics* 82: 3045.
Heurich J, König J, and MacDonald AH (2003) *Physical Review B* 68: 064406.
Hirsch JE (1999) *Physical Review Letters* 83: 1834.
Hosten O and Kwiat P (2008) *Science* 319: 787.
Inoue J-I, Bauer GEW, and Molenkamp LW (2004) *Physical Review B* 70: 041303(R).
Jacobsen SH and Linder J (2017) *Physical Review B* 96: 134513.
Jacquod P, Whitney R, Meair J, and Büttiker M (2012) *Physical Review B* 86: 155118.
Jiao H and Bauer GEW (2013) *Physical Review Letters* 110: 217602.
Karnad GV, Gorini C, Lee K, Schulz T, Conte RL, Wells AWJ, Han D-S, Shahbazi K, Kim J-S, Moore TA, Swagten HJM, Eckern U, Raimondi R, and Kläui M (2018) *Physical Review B* 97: 100405.
Karube S, Sugawara D, Tang C, Tanabe T, Oyama Y, and Nitta J (2020) *Journal of Magnetism and Magnetic Materials* 516: 167298.
Kato YK, Myers RC, Gossard AC, and Awschalom DD (2004) *Science* 306: 1910.
Khaetskii A (2014) *Physical Review B* 89: 195408.
Kochan D, Irmer S, and Fabian J (2017) *Physical Review B* 95: 165415.
Ködderitzsch D, Chadova K, and Ebert H (2015) *Physical Review B* 92: 184415.
König EJ and Levchenko A (2021) *Annals of Physics (New York)* 435: 168492.
König M, Wiedmann S, Brüne C, Roth A, Buhmann H, Molenkamp LW, Qi X-L, and Zhang S-C (2007) *Science* 318: 766.
Landau LD, Lifschitz EM, and Pitaevskii LP (2008) *Electrodynamics of Continuous Media*. Elsevier.
Lensky YD, Song JC, Samutpraphoot P, and Levitov LS (2015) *Physical Review Letters* 114: 256601.
Li P, Riddiford LJ, Bi C, Wisser JJ, Sun X-Q, Vailionis A, Veit MJ, Altman A, Li X, Mahendra DC, Wang SX, Suzuki Y, and Emori S (2021) *Physical Review Materials* 5: 064404.
Liu L, Lee OJ, Gudmundsen TJ, Ralph DC, and Buhrman RA (2012) *Physical Review Letters* 109: 096602.
Lowitzer S, Gradhand M, Ködderitzsch D, Fedorov DV, Mertig I, and Ebert H (2011) *Physical Review Letters* 106: 056601.
Mak KF, McGill KL, Parkand J, and McEuen PL (2014) *Science* 344: 1489.
Mal'shukov AG (2017) *Physical Review B* 95: 064517.
Mal'shukov AG, Wang LY, Chu CS, and Chao KA (2005) *Physical Review Letters* 95: 146601.
Mal'shukov AG, Wang LY, and Chu CS (2007) *Physical Review B* 78: 085315.
Manchon A, Zelezný J, Miron IM, Jungwirth T, Sinova J, Thiaville A, Garello K, and Gambardella P (2019) *Reviews of Modern Physics* 91: 035004.
Mathur H and Stone AD (1992) *Physical Review Letters* 68: 2964.
Milletarí M, Offidani M, Ferreira A, and Raimondi R (2017) *Physical Review Letters* 119: 246801.
Mook A, Henk J, and Mertig I (2014) *Physical Review B* 89: 134409.
Nagaosa N, Sinova J, Onoda S, MacDonald AH, and Ong NP (2010) *Reviews of Modern Physics* 82: 1539.
Nakagawara K, Kasai S, Ryu J, Mitani S, Liu L, Kohda M, and Nitta J (2019) *Applied Physics Letters* 115: 162403.
Neto AHC, Guinea F, Peres NMR, Novoselov KS, and Geim AK (2009) *Reviews of Modern Physics* 81: 109.
Nikolić BK, Zârbo LP, and Souma S (2006) *Physical Review B* 73: 075303.
Obstbaum M, Härtinger M, Bauer HG, Meier T, Swientek F, Back CH, and Woltersdorf G (2014) *Physical Review B* 89: 060407(R).
Ohnuma Y, Matsuo M, and Maekawa S (2016) *Physical Review B* 94: 184405.
Okamoto S, Egami T, and Nagaosa N (2019) *Physical Review Letters* 123: 196603.
Onose Y, Ideue T, Katsura H, Shiomi Y, Nagaosa N, and Tokura Y (2010) *Science* 329: 297.
Oyanagi K, Gomez-Perez JM, Zhang X-P, Kikkawa T, Chen Y, Sagasta E, Chuvilin A, Hueso LE, Golovach VN, Bergeret FS, Casanova F, and Saitoh E (2021) *Physical Review B* 104: 134428.
Pai C-F, Liu L, Li Y, Tseng HW, Ralph DC, and Buhrman RA (2012) *Applied Physics Letters* 101: 122404.
Raimondi R and Schwab P (2005) *Physical Review B* 71: 033311.
Raimondi R and Schwab P (2009) *EPL (Europhysics Letters)* 87: 37008.
Raimondi R, Gorini C, Schwab P, and Dzierzawa M (2006) *Physical Review B* 74: 035340.

Raimondi R, Schwab P, Gorini C, and Vignale G (2012) *Annals of Physics (Berlin)* 524: 153.

Rashba EI (2003) *Physical Review B* 68: 241315(R).

Rojas-Sánchez J-C, Reyren N, Laczkowski P, Savero W, Attané J-P, Deranlot C, Jamet M, George J-M, Vila L, and Jaffrès H (2014) *Physical Review Letters* 112: 106602.

Safeer CK, Ingla-Aynés J, Ontoso N, Herling F, Yan W, Hueso LE, and Casanova F (2020) *Nano Letters* 20: 4573.

Schwab P and Raimondi R (2002) *European Physical Journal B: Condensed Matter and Complex Systems* 25: 483.

Seifert T, Jaiswal S, Martens U, Hannegan J, Braun L, Maldonado P, Freimuth F, Kronenberg A, Henrizi J, Radu I, Beaurepaire E, Mokrousov Y, Oppeneer PM, Jourdan M, Jakob G, Turchinovich D, Hayden LM, Wolf M, Münzenberg M, Kläui M, and Kampfrath T (2016) *Nature Photonics* 10: 483.

Shen K, Raimondi R, and Vignale G (2014) *Physical Review Letters* 112: 096601.

Shi J, Zhang P, Xiao D, and Niu Q (2006) *Physical Review Letters* 96: 076604.

Sinova J, Culcer D, Niu Q, Sinitsyn NA, Jungwirth T, and MacDonald AH (2004) *Physical Review Letters* 92: 126603.

Sinova J, Valenzuela SO, Wunderlich J, Back CH, and Jungwirth T (2015) *Reviews of Modern Physics* 87: 1213.

Smirnov DS and Golub LE (2017) *Physical Review Letters* 118: 116801.

Sonin EB (2007a) *Physical Review Letters* 99: 266602.

Sonin EB (2007b) *Physical Review B* 76: 033306.

Sonin EB (2010a) *Physical Review B* 81: 113304.

Sonin EB (2010b) *Advances in Physics* 59: 181.

Sugimoto N, Onoda S, Murakami S, and Nagaosa N (2006) *Physical Review B* 73: 113305.

Takahashi S and Maekawa S (2007) *Journal of Magnetism and Magnetic Materials* 310: 2067.

Takahashi S and Maekawa S (2011) *Japanese Journal of Applied Physics* 51: 010110.

Tokatly IV (2008) *Physical Review Letters* 101: 106601.

Tokatly IV and Sherman EY (2016) *Physical Review A* 93: 063635.

Tölle S, Eckern U, and Gorini C (2017) *Physical Review B* 95: 115404.

Tölle S, Dzierzawa M, Eckern U, and Gorini C (2018) *New Journal of Physics* 20: 103024.

Tserkovnyak Y, Brataas A, Bauer GEW, and Halperin BI (2005) *Reviews of Modern Physics* 77: 1375.

Tserkovnyak Y, Halperin BI, Kovalev AA, and Brataas A (2007) *Physical Review B* 76: 085319.

Valenzuela SO and Tinkham M (2006) *Nature* 442: 176.

Vignale G (2010) *Journal of Superconductivity and Novel Magnetism* 23: 3.

Wei D, Obstbaum M, Ribow M, Back CH, and Woltersdorf G (2014) *Nature Communications* 5: 3768.

Weiler M, Shaw JM, Nembach HT, and Silva TJ (2014) *Physical Review Letters* 113: 157204.

Werake LK, Ruzicka BA, and Zhao H (2011) *Physical Review Letters* 106: 107205.

Winkler R (2003) *Spin-Orbit Coupling Effects in Two-Dimensional Electron and Hole Systems*. Springer.

Wunderlich J, Kaestner B, Sinova J, and Jungwirth T (2005) *Physical Review Letters* 94: 047204.

Yanez W, Ou Y, Xiao R, Koo J, Held JT, Ghosh S, Rable J, Pillsbury T, Delgado EG, Yang K, Chamorro J, Grutter AJ, Quarterman P, Richardella A, Sengupta A, McQueen T, Borchers JA, Mkhoyan KA, Yan B, and Samarth N (2021) *Physical Review Applied* 16: 054031.

Zhang W, Jungfleisch MB, Jiang W, Pearson JE, Hoffmann A, Freimuth F, and Mokrousov A (2014) *Physical Review Letters* 113: 196602.

Zhu L, Zhu L, Sui M, Ralph DC, and Buhrman RA (2019) *Science Advances* 5: eaav8025.

The spin-transfer torque effect

Gen Tatara, RIKEN Center for Emergent Matter Science (CEMS), and RIKEN Cluster for Pioneering Research (CPR), Wako, Saitama, Japan

© 2024 Elsevier Ltd. All rights reserved.

Introduction 143
Spin-transfer mechanism 144
Equation of motion 145
Microscopic theory 145
Spin-orbit torque 146
Antiferromagnets and other systems 146
Conclusion 146
References 146

Abstract

Torques on magnetization when an electric current is applied to magnets, called the spin torques, are overviewed.

Key points

- History, phenomenology and microscopic description of the spin-transfer torque
- Equation of motion of magnetization including the spin torques
- Touch recent topics

Introduction

The spin-transfer torque is a torque on magnetization (localized spins) induced by applying an electric current.[1] It arises from a transfer of spin angular momentum from driven electrons to the magnetization and is one of the current-induced torques of various origins.

The idea of driving magnetization structure by applying electric current was theoretically studied by Berger (1978). It was discussed theoretically that a magnetic domain wall can be driven by a current due to the counterforce of the electron scattering by the wall. The force is proportional to the resistance due to the wall, and is small in most 3d ferromagnets as domain wall is thick compared to the electron scale, the inverse Fermi wave length. The scattering force represents an exchange of linear momentum, and is different from the spin-transfer effect. In 1986, Berger discussed the effect of spin-transfer, although it was not called so, between a domain wall and electron propagating through it (Berger, 1986). The transfer occurs as a result of a strong *sd* exchange interaction between electron spin and the magnetization, which causes a flip of electron spin as it passes through the wall. The transfer is efficient for a thick wall, and the wall moves with a velocity proportional to the applied current to conserve the total spin angular momentum of the system. The term spin transfer was used by J.C. Slonczewski in the context of current-induced magnetization reversal in a magnetic multilayer (Slonczewski, 1996).

The spin-transfer torque arises from the spatial variation of magnetization (localized spin $\boldsymbol{S}(\boldsymbol{r})$), and for smooth structure, the torque at the linear-order of the spatial derivative is written as

$$\boldsymbol{\tau}_{\mathrm{st}} = -\frac{a^3}{2eS}(\boldsymbol{j}_{\mathrm{s}} \cdot \nabla)\boldsymbol{S} \tag{1}$$

where $\boldsymbol{j}_{\mathrm{s}}$ is a spin current density, $S \equiv |\boldsymbol{S}|$, a is the lattice constant. The spin-transfer torque arises when electron spin is strongly polarized along the local direction of the magnetization or the local spin, a situation called adiabatic.

The concept of spin-transfer torque was extended later. Zhang and Li (2004) and Thiaville et al. (2005) pointed out that a relaxation of electron spin leads to a torque orthogonal to the spin-transfer torque,

$$\boldsymbol{\tau}_{\beta} = -\beta\frac{a^3}{2eS}[\boldsymbol{S} \times (\boldsymbol{j}_{\mathrm{s}} \cdot \nabla)\boldsymbol{S}] \tag{2}$$

with a constant β representing the relaxation effect. In most ferromagnetic metals, the dominant origin of the parameter β is the spin-orbit interaction of the conduction electron. The relaxation induces a non adiabatic process, where electron spin deviates from

---

[1] It is sometimes called spin torque, but physical meaning becomes obscure.

https://doi.org/10.1016/B978-0-323-90800-9.00152-9

the local spin direction, and thus the relaxation-driven current-induced torque is called a non adiabatic (spin-transfer) torque or β-torque after Thiaville et al. The two orthogonal torques, $\boldsymbol{\tau}_{\mathrm{st}}$ and $\boldsymbol{\tau}_{\beta}$, are complete to describe any torque conserving the magnitude of the localized spin. Later, current-induced torques in systems with strong spin-orbit interaction, called spin-orbit torques (Manchon et al., 2019), were investigated, such as the torque arising from the Rashba interaction at interfaces and the torque due to a spin Hall effect in bilayers of a heavy metal and a ferromagnet. As the main source of electron spin relaxation represented by the parameter β is the spin-orbit interaction, the non adiabatic torque is a spin-orbit-induced torque in a broad sense. In the recent literature, spin-orbit torque often refers to the case with spin-orbit interaction having particular symmetry, such as the Rashba interaction breaking the inversion symmetry.

Spin-transfer mechanism

- Smooth magnetic structure

For electron propagation through a smooth magnetic structure, the efficiency of the spin-transfer effect is 100% in the adiabatic limit, where the electron spin has enough time to rotate during the propagation through a magnetic structure. For the case of a domain wall with thickness λ_{w}, the adiabatic condition is (Waintal and Viret, 2004)

$$\frac{\lambda_{\mathrm{w}}}{v_F} \gg \frac{\hbar}{J_{sd}}, \tag{3}$$

where $\hbar/J_{sd}$ is the time for electron spin rotation (J_{sd} being the energy for the sd exchange coupling between the localized spin and conduction electron spin), λ/v_F is the time for electron with Fermi velocity $v_F(=\hbar k_F/m)$ to pass through the wall k_F and m being the Fermi wave vector and the electron mass, respectively.[2] In the adiabatic limit, the electron spin gets rotated after passing through the wall, and the change of spin angular momentum, $2 \times \frac{\hbar}{2} = \hbar$, must be absorbed by the localized spins if dissipation is neglected. To absorb the spin change of $\hbar$, the domain wall must shift by a distance $\Delta X = [\hbar/(2\hbar S)]a$ (a is the lattice constant) (Fig. 1). When we apply a constant electric current density j with spin polarization rate P, i.e., a spin current density of $j_{\mathrm{s}} = Pj$, the rate of the angular momentum change of the conduction electron per unit time and area is $\hbar j_{\mathrm{s}}$. As the number of the localized spins in the unit area is $1/a^2$, the wall must keep moving a distance of $j_{\mathrm{s}}(a^3/2S)$ per unit time. Namely, when a spin current density is applied, the wall moves with the speed.

$$v_{\mathrm{st}} \equiv \frac{a^3}{2S} j_{\mathrm{s}}. \tag{4}$$

This is the velocity of a domain wall when spin-transfer efficiency is 100%. It is notable that the spin-transfer effect acts on any magnetic structures if smooth, and drives them at the same velocity v_{st}.

- Ferromagnetic bilayer (Fig. 2)

In the case of two ferromagnetic metallic thin films with a metallic spacer or tunneling barrier between the ferromagnetic layers, the electron spin is subject to a sudden change of the localized spin. An injected current gets spin-polarized by the first magnetic layer (fixed layer) and exerts a torque on the second magnetic layer (free layer). The nonequilibrium spin polarization of the electron injected to the second layer is written as $g_{\mathrm{st}} I_{\mathrm{e}} (S_1 \times S_2)$, where I_{e} is the injected current, S_1 and S_2 are the magnetization of the first and the second layer, respectively, and g_{st} is an efficiency constant determined by the structure. The torque acting on the second layer is thus.

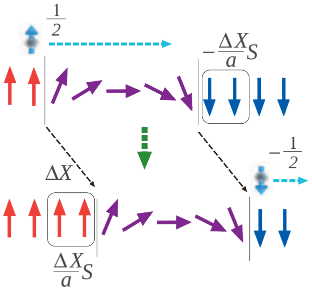

Fig. 1 Schematic figure describing the spin-transfer effect by a domain wall. Electron spin (small arrow with a sphere) is directed along the direction of localized spin (large arrows) by a strong exchange coupling. For a thick wall, the electron spin passing through the wall is therefore flipped (the adiabatic limit), resulting in the angular momentum change of $\frac{\hbar}{2} \times 2 = \hbar$. The shift of the domain wall by a distance ΔX results in a change of the spin of the localized spins $\frac{\Delta X}{a} S - \left(-\frac{\Delta X}{a} S\right) = 2S\frac{\Delta X}{a}$ (a and S are the lattice constant and magnitude of spin, respectively). The displacement needed to compensate the angular momentum of electron spin is therefore $\Delta X = \frac{a}{2S}$. Each electron passing through the wall shifts the wall by a distance ΔX.

---

[2] In dirty metals, it is modified (Stern, 1992).

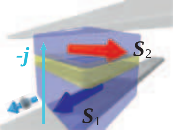

Fig. 2 The spin-transfer effect in a multilayer of two ferromagnetic films. An electron current injected from the bottom get polarized by the lower layer magnetization $\boldsymbol{S}_1$ and drives the top layer magnetization $\boldsymbol{S}_2$.

$$\boldsymbol{\tau}_{\text{bilayer}} = g_{\text{st}} I_{\text{e}} [\boldsymbol{S}_2 \times (\boldsymbol{S}_1 \times \boldsymbol{S}_2)], \tag{5}$$

which tends to align $\boldsymbol{S}_2$ along the direction $\boldsymbol{S}_1$. When $\boldsymbol{S}_1$ and $\boldsymbol{S}_2$ are close, $\boldsymbol{S}_2 \simeq \boldsymbol{S}_1 + \boldsymbol{d} \cdot \nabla \boldsymbol{S}_1$ ($\boldsymbol{d}$ is a vector representing the layer distance), and the expression reduces to the spin-transfer torque $\boldsymbol{\tau}_{\text{st}}$ for a smooth magnetization structure.

Equation of motion

The equation of motion for spin $\boldsymbol{S}$ under a magnetic field $\boldsymbol{B}$ is called the Landau-Lifshitz-Gilbert (LLG) equation, which reads

$$\dot{\boldsymbol{S}} = \gamma \boldsymbol{S} \times \boldsymbol{B} - \frac{\alpha}{S} \boldsymbol{S} \times \dot{\boldsymbol{S}} \tag{6}$$

where γ is the gyromagnetic ratio and $\alpha(\geq 0)$ is the Gilbert damping constant (usually $\alpha \ll 1$) and $S \equiv |\boldsymbol{S}|$. For localized spins with a spatial distribution, $\boldsymbol{S}(\boldsymbol{r}, t)$, the equation remains the same if the magnetic field includes the ones arising from the interactions, such as the exchange interaction and anisotropy energy. Taking account of the current-induced torques, the equation becomes

$$\dot{\boldsymbol{S}} = \gamma \boldsymbol{S} \times \boldsymbol{B} - \frac{\alpha}{S} \boldsymbol{S} \times \dot{\boldsymbol{S}} - \frac{a^3}{2eS} (\boldsymbol{j}_{\text{s}} \cdot \nabla) \boldsymbol{S} - \frac{a^3}{2eS} \beta [\boldsymbol{S} \times (\boldsymbol{j}_{\text{s}} \cdot \nabla) \boldsymbol{S}] + \boldsymbol{\tau}_{\text{na}} \tag{7}$$

Here $\boldsymbol{\tau}_{\text{na}}$ represents a nonadiabatic torque that is higher order in the spatial derivative, such as the effect of the electron reflection force.

The role of the spin-transfer torque is clearly seen in the case of a domain wall. Considering a one-dimensional domain wall structure of $\boldsymbol{S}(x, t) = S(\sin\theta \cos\phi, \sin\theta \sin\phi, \cos\theta)$ with $\cos\theta(x, t) = \tanh[(x - X(t))/\lambda]$ and a time-dependent angle of the wall plane, $\phi(t)$, the equation of motion reduces to a coupled equations for the two coordinates,

$$\dot{X} - \alpha\dot{\phi} = -v_{\text{c}} \sin 2\phi + \frac{a^3 P}{2eS} j \tag{8}$$

$$\dot{\phi} + \alpha \frac{\dot{X}}{\lambda} = \frac{\overline{\beta}}{\lambda} \frac{a^3 P}{2eS} j \tag{9}$$

where v_{c} is a constant proportional to the hard-axis magnetic anisotropy energy and $\overline{\beta} = \beta + \beta_{\text{na}}$ with β_{na} is the contribution from $\boldsymbol{\tau}_{\text{na}}$ representing the reflection force, which is proportional to the resistivity due to the wall (Tatara et al., 2008). The equations clearly indicates that the spin-transfer effect contributes to a velocity of the wall $\dot{X}$, while the non-adiabatic torques (β and $\boldsymbol{\tau}_{\text{na}}$) contribute to the equation for $\dot{\phi}$, which represents the force on the wall.

Microscopic theory

The spin-transfer effect for smooth structures is elegantly described by a microscopic theory. For spin of the injected electron having a strong exchange coupling to localized spin, a spatially-changing smooth magnetization structure acts as an effective gauge field as seen in the following argument Tatara (2019). An electron with mass m interacting with localized spin $\boldsymbol{S}$ by a strong exchange interaction J_{sd} is described by the Schrödinger equation,

$$\left(-\frac{\hbar^2}{2m} \nabla^2 - M \boldsymbol{n}(\boldsymbol{r}) \cdot \boldsymbol{\sigma} \right) |\Psi\rangle = i\hbar \frac{\partial}{\partial t} |\Psi\rangle, \tag{10}$$

where $M = J_{sd} S$ is the spin polarization, $\boldsymbol{n} \equiv \boldsymbol{S}/S$ and $|\Psi\rangle$ is a wave function with two spin components, $\boldsymbol{\sigma}$ being the vector of three Pauli matrices. The spatially-varying energy due to magnetization modulation is removed by a local unitary transformation to choose spin quantization axis along the localized spin introducing a 2×2 transformation matrix $U(\boldsymbol{r})$ satisfying $U^{-1}(\boldsymbol{n} \cdot \boldsymbol{\sigma})U = \sigma_z$. For a localized spin configuration described by a polar coordinate fields $(\theta(\boldsymbol{r}), \phi(\boldsymbol{r}))$, i.e., $\boldsymbol{n} = (\sin\theta \cos\phi, \sin\theta \sin\phi, \cos\theta)$, a choice of U is $U = e^{-\frac{i}{2}\phi\sigma_z} e^{-\frac{i}{2}\theta\sigma_y} e^{-\frac{i}{2}(\pi - \phi)\sigma_z}$. The Schrödinger equation in the rotated frame state, defined as $|\phi\rangle \equiv U^{-1} |\Psi\rangle$ is

$$\left[-\frac{\hbar^2}{2m} (\nabla - i\mathcal{A}_{\text{s}})^2 - M\sigma_z \right] |\phi\rangle = i\hbar \frac{\partial}{\partial t} |\phi\rangle, \tag{11}$$

where $\mathcal{A}_{\text{s}} \equiv -iU^{-1}\nabla U$ is a 2×2 matrix representing an effective gauge field. For large exchange coupling, the up-spin (↑) component with lower energy survives (the adiabatic limit), and the gauge field reduces to a single component (U(1)) gauge field $\boldsymbol{A}_{\rm s} \equiv (\mathcal{A}_{\rm s})_{\uparrow\uparrow}$, which explicitly reads $\boldsymbol{A}_{\rm s} = \frac{1}{2}(1-\cos\theta)\nabla\phi$. The background of localized spin configuration is thus represented by an effective gauge field coupling to a spin-polarized current $\boldsymbol{j}_{\rm s}$ by a gauge coupling $H_{A_{\rm s}} = -\boldsymbol{A}_{\rm s}\cdot\boldsymbol{j}_{\rm s}$, neglecting the second-order spatial derivative. The gauge coupling describes an interaction on the localized spin, as $\boldsymbol{A}_{\rm s}$ is a function of localized spin direction. The dynamics of localized spin with Hamiltonian H_S is described by the Landau-Lifshitz equation derived from the Lagrangian $L_S = -\hbar S(1-\cos\theta)\dot{\phi} - H_S$. When coupled to the conduction electron, the Lagrangian includes $H_{A_{\rm s}}$ to be

$$L_S - H_{A_{\rm s}} = -\hbar S(1-\cos\theta)(\partial_t - \boldsymbol{v}_{\rm st}\cdot\nabla)\phi - H_S \tag{12}$$

where $\boldsymbol{v}_{\rm st} = \frac{a^3}{2S}\boldsymbol{j}_{\rm s}$ is a velocity due to the spin-transfer torque. The Lagrangian is Galilean invariant, meaning that any magnetization structure flows with the velocity $\boldsymbol{v}_{\rm st}$, consistent with a phenomenological argument.

Spin-orbit torque

Spin-orbit torques are current-induced torques where spin-orbit interaction for the electron is essential. The torque acting on the localized spin $\boldsymbol{S}$ (or magnetization) depends strongly on the spin-orbit interaction and symmetry. Conventionally it is decomposed into two independent directions as

$$\boldsymbol{\tau}_{\rm sot} = \eta_{\rm FL}\boldsymbol{S}\times\boldsymbol{\zeta} + \eta_{\rm DL}[\boldsymbol{S}\times(\boldsymbol{S}\times\boldsymbol{\zeta})], \tag{13}$$

where $\boldsymbol{\zeta}$ is essentially a spin density induced by the spin-orbit interaction and localized spin under a current. The component with coefficient $\eta_{\rm FL}$ is called the field-like torque, as it represents an effective magnetic field proportional to $\eta_{\rm FL}\boldsymbol{\zeta}$, and the one with $\eta_{\rm DL}$ is called the damping-like torque as it points the same direction as the damping torque in the Landau-Lifshitz equation. Spin-orbit torques are often discussed for multilayers of a ferromagnet and a nonmagnetic heavy metal, where the applied current and the spin-orbit interaction in the heavy metal induces interface spin accumulation and torque. Various origins of spin-orbit torques have been argued, such as spin Hall effect, Rashba spin-orbit interaction, the inverse spin galvanic effect (Manchon et al., 2019), but what matters in any cases is the current-induced spin accumulation formed at the interface to the ferromagnetic layer.

Antiferromagnets and other systems

The concepts of spin-transfer torque and spin-orbit torque have been extended to the case of antiferromagnets, ferrimagnets, and topological insulators (Jungwirth et al., 2016; Baltz et al., 2018; Manchon et al., 2019).

Conclusion

History and phenomenological theory the spin-transfer torque was overviewed and a microscopic description was introduced. The Equation of motion of magnetization including the spin torques was argued. Recent topics were briefly touched.

References

Baltz V, Manchon A, Tsoi M, Moriyama T, Ono T, and Tserkovnyak Y (2018) Antiferromagnetic spintronics. *Reviews of Modern Physics* 90: 015005. https://link.aps.org/doi/10.1103/RevModPhys.90.015005https://doi.org/10.1103/RevModPhys.90.015005.

Berger L (1978) Low-field magnetoresistance and domain drag in ferromagnets. *Journal of Applied Physics* 49: 2156–2161. https://doi.org/10.1063/1.324716. arXiv: https://doi.org/10.1063/1.324716.

Berger L (1986) Possible existence of a josephson effect in ferromagnets. *Physical Review B* 33: 1572–1578. http://link.aps.org/abstract/PRB/v33/p1572.

Jungwirth T, Marti X, Wadley P, and Wunderlich J (2016) Antiferromagnetic spintronics. *Nature Nanotechnology* 11: 231–241. https://doi.org/10.1038/nnano.2016.18.

Manchon A, Železný J, Miron IM, Jungwirth T, Sinova J, Thiaville A, Garello K, and Gambardella P (2019) Current-induced spin-orbit torques in ferromagnetic and antiferromagnetic systems. *Reviews of Modern Physics* 91: 035004 URL: https://link.aps.org/doi/10.1103/RevModPhys.91.035004https://doi.org/10.1103/RevModPhys.91.035004.

Slonczewski J (1996) Current-driven excitation of magnetic multilayers. *Journal of Magnetism and Magnetic Materials* 159: L1–L7. https://www.sciencedirect.com/science/article/pii/0304885396000625https://doi.org/10.1016/0304-8853(96)00062-5.

Stern A (1992) Berry's phase, motive forces, and mesoscopic conductivity. *Physical Review Letters* 68: 1022–1025. https://doi.org/10.1103/PhysRevLett.68.1022.

Tatara G (2019) Effective gauge field theory of spintronics. *Physica E: Low-dimensional Systems and Nanostructures* 106: 208–238. http://www.sciencedirect.com/science/article/pii/S1386947717318398https://doi.org/10.1016/j.physe.2018.05.011.

Tatara G, Kohno H, and Shibata J (2008) Microscopic approach to current-driven domain wall dynamics. *Physics Reports* 468: 213–301. http://www.sciencedirect.com/science/article/B6TVP-4T9VP4P-1/2/1d39252a95415cb4df04a52a7c6a755fhttps://doi.org/10.1016/j.physrep.2008.07.003.

Thiaville A, Nakatani Y, Miltat J, and Suzuki Y (2005) Micromagnetic understanding of current-driven domain wall motion in patterned nanowires. *Europhysics Letters* 69: 990–996. https://doi.org/10.1209/epl/i2004-10452-6.

Waintal X and Viret M (2004) Current-induced distortion of a magnetic domain wall. *Europhysics Letters* 65: 427.

Zhang S and Li Z (2004) Roles of nonequilibrium conduction electrons on the magnetization dynamics of ferromagnets. *Physical Review Letters* 93: 127204. http://link.aps.org/abstract/PRL/v93/e127204.

Quantum magnonics

HY Yuan[a] **and Rembert A Duine**[a,b,c], [a]Institute for Theoretical Physics, Utrecht University, Utrecht, The Netherlands; [b]Department of Applied Physics, Eindhoven University of Technology, Eindhoven, The Netherlands; [c]Department of Physics, Center for Quantum Spintronics, Norwegian University of Science and Technology, Trondheim, Norway

© 2024 Elsevier Ltd. All rights reserved.

Introduction **147**
Spin waves and magnons **148**
Quantum states of magnons **150**
Magnon antibunching 150
Squeezed states 151
Magnon BEC and spin superfluidity 152
Hybrid magnonic platforms **152**
Magnon–photon system 152
Magnon-qubit system 153
Magnon–phonon system 156
Conclusion **156**
Acknowledgments **157**
References **157**

Abstract

Quantum magnonics concerns quantum states of magnons and the interplay between magnon spintronics, and quantum information science. It is a highly interdisciplinary field that combines spintronics, quantum optics, and quantum information. In this chapter, we will first introduce magnon quantum states, including magnon antibunching and squeezed states. Macroscopic quantum phenomena including spin superfluidity and Bose–Einstein condensation will also be briefly covered. Hereafter, we discuss the integration of magnonic systems with mature quantum platforms, including photonic cavities, qubits, and phononic systems, together with the applications of hybrid magnonic systems. Finally, we present an outlook on the opportunities and challenges for quantum magnonics.

Introduction

Finding efficient means to store and process big data is a central topic in modern society due to the rapid accumulation of information in science, technology, economics, and social activities. To overcome the large energy consumption and Joule heating problems of the traditional transistor technologies, spintronics, and quantum information science stand out and have been innovating the concepts of information processing over the past few decades. Spintronics emerged in the late 1980s and focuses on the manipulation of the spin of an electron, instead of its charge that is exploited in conventional electronics (Hirohata et al., 2020). Here, the information is coded in the direction of the spin as well as in the spin excitations, so-called magnons. Magnon spintronics, a subfield of spintronics, focuses on the generation, manipulation, and read-out of magnons for information processing (Chumak et al., 2015). Magnons can propagate in a magnetic insulator over long distances as a result of the low dissipation of insulating magnets, which can significantly reduce the energy consumption for information processing. On the other hand, quantum computing and quantum information science manipulate the quantum nature of spins and utilize the basic principles of quantum mechanics, such as superposition and entanglement, as a resource for computation and communication (Nielsen and Chuang, 2000). As an example, a spin-1/2 system has two degrees of freedoms and can thus represent a quantum bit. Different from a classical bit, a quantum bit or qubit is able to be in any quantum superposition of spin up and down. By integrating and manipulating many qubits coherently, the information can be processed in a more efficient and secure way (Arute et al., 2019).

Recently, the developments of magnon spintronics and quantum information have begun to overlap with each other because of the significant progress toward the understanding of the entanglement properties of quasiparticles such as photons, magnons, and phonons. Furthermore, with the advancement of material science, magnonic systems can be readily integrated with well-established quantum platforms to achieve multi-functional quantum information processing. This concerns, for example, cavity photons, superconducting qubits, and mechanical oscillators, coupled to magnonic systems. From these endeavors, the highly interdisciplinary field of quantum magnonics has emerged (Yuan et al., 2022a), which combines the concepts of magnon spintronics, quantum optics and quantum information science, and has the potential to give the development of traditional magnonics new directions.

In general, the framework of quantum magnonics includes the manipulation of quantum states of magnons and the integration of magnonic platforms with known quantum systems such as cavity photons, qubits, and phonons, as shown in Fig. 1. More broadly, macroscopic quantum phenomena including magnon Bose–Einstein condensation (BEC) and spin superfluidity also belong to the realm of quantum magnonics. In this chapter, we will first introduce the basic concepts that are involved with magnons and then follow the framework of Fig. 1 to introduce magnon quantum states as well as the hybrid quantum systems

https://doi.org/10.1016/B978-0-323-90800-9.00179-7

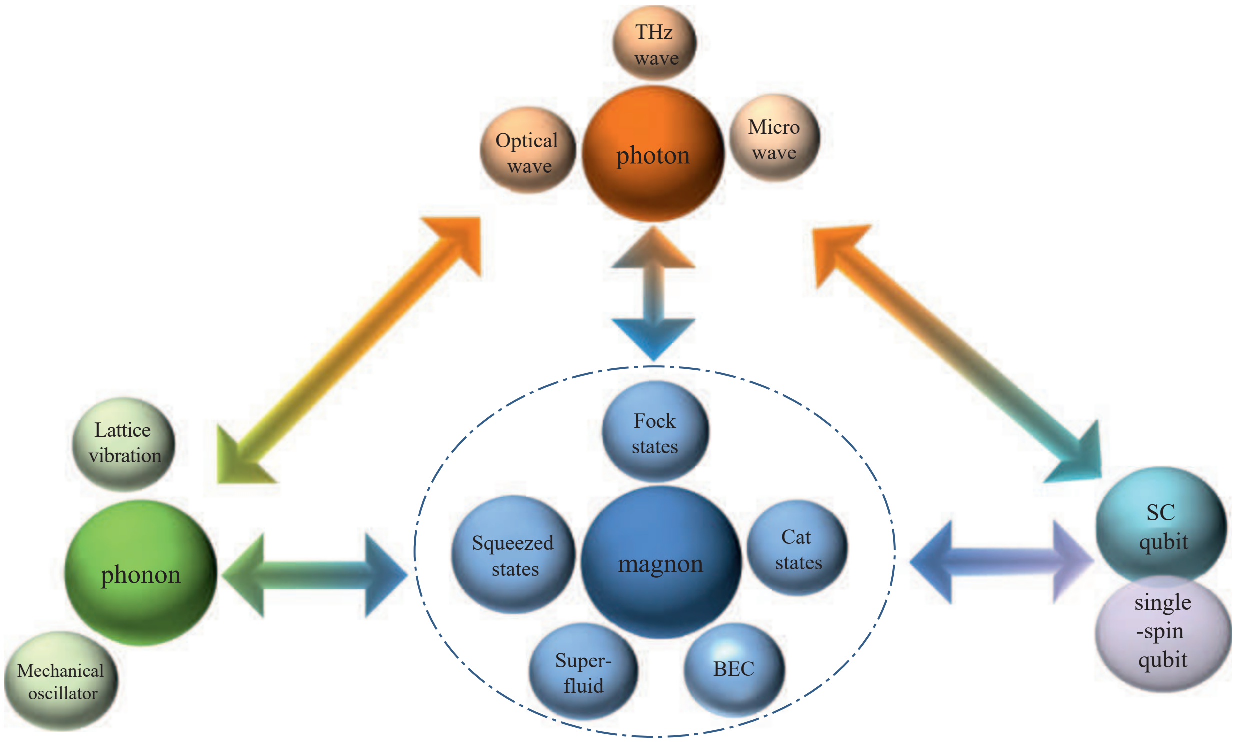

Fig. 1 Framework of quantum magnonics. The central route studies quantum states of magnons at low temperatures. The left route integrates magnons with phonons corresponding to lattice vibrations of a magnet or mechanical vibrations of external oscillators. The top route entangles magnons with photons ranging from optical down to microwave frequency. The right route couples magnons to discrete variable systems including superconducting qubits and single-spin qubit (nitrogen-vacancy centers, silicon-vacancy centers, etc.). Adapted from Yuan HY, Cao Y, Kamra A, Duine RA, and Yan P (2022a) Quantum magnonics: When magnon spintronics meets quantum information science. Physics Reports 965: 1–74. https://doi.org/10.1016/j.physrep.2022.03.002.

based on magnets. Finally, we give a summary and outlook for quantum magnonics. Unless stated otherwise, we decorate operators with a hat and set the reduced Planck constant equal to one.

Spin waves and magnons

It is known that a spin precesses around an external field and, in addition, relaxes toward this field due to its interaction with the environment. In ordered magnets, many spins are tied together through short-range exchange interactions and long-range dipolar interactions. As a result, the motion of one spin will force the motion of its neighbors and results in a wave-like pattern of spin excitation, so-called spin waves, as shown in Fig. 2A. A spin-wave mode is characterized by its frequency ω and, when the system is homogeneous, wavevector **k**. The exchange interaction usually dominates the properties of spin waves with short wavelength while dipolar interaction is important for spin waves with long wavelength, as shown in Fig. 2B. To fully quantify the spin-wave dispersion, one has to solve the Maxwell equations coupled to the equation for classical magnetization dynamics. The resulting dispersion depends on the magnetization orientation and geometry of the magnet (Kalinikos and Slavin, 1986).

In quantum mechanics, a spin state is fully represented by the spin operator $\hat{\mathbf{S}}$ and its component along the quantization axis $\hat{S}_z$ as

$$\hat{\mathbf{S}}^2|S,m\rangle = S(S+1)|S,m\rangle, \quad \hat{S}_z|S,m\rangle = m|S,m\rangle, \tag{1}$$

where the excitation of one magnon corresponds to the reduction of S_z by a quantum of angular momentum $\hbar$, as shown in Fig. 2C. Within this approach, it is not easy to treat the interaction between many spins and magnons. Holstein and Primakoff first noticed that (Holstein and Primakoff, 1940) the possible values of m can be rewritten as $m = S - n$ with $n = 0, 1, 2, \ldots, 2S$. In the new basis, we have $\hat{S}_z|S,n\rangle = (S-n)|S,n\rangle$. By comparing with the quantization of a harmonic oscillator, we readily have the second quantization form of $\hat{S}_z$ as $\hat{S}_z = S - \hat{a}^\dagger \hat{a}$, where $\hat{a}$ ($\hat{a}^\dagger$) is the annihilation (creation) operator of a spin quantum or a magnon. To show how to preserve the commutation relations for angular momentum $[\hat{S}_i, \hat{S}_j] = i\varepsilon_{ijk}\hat{S}_k$, where ε_{ijk} is the Levi-Civita symbol, we recall the spin raising and lower operators defined as $\hat{S}^\pm = \hat{S}_x \pm i\hat{S}_y$. From the properties of angular momentum, we have

$$\hat{S}^+|S,n\rangle = \sqrt{2S-(n-1)}\sqrt{n}|S,n-1\rangle = \sqrt{2S-\hat{a}^\dagger\hat{a}\hat{a}}|S,n\rangle. \tag{2}$$

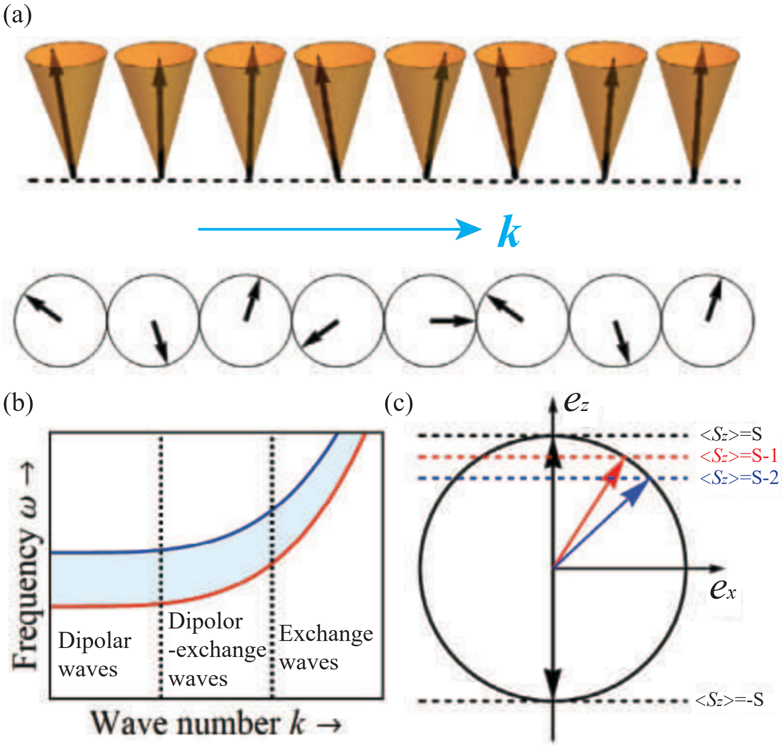

Fig. 2 (A) Schematic of magnetic-moment precession and spin-wave excitation in a classical picture. (B) Typical spin-wave dispersion of a finite ferromagnetic body. With the increase of wave number *k*, dipolar, dipolar exchange, and exchange spin waves are classified. (C) Relation between magnon excitation and a reduction of magnetic component along the quantization axis in the quantum picture. For $S = 1/2$, magnon excitation corresponds to flipping a single spin.

We therefore derive

$$\hat{S}^+ = \sqrt{2S - \hat{a}^\dagger \hat{a}}\,\hat{a},\ \hat{S}^- = \left(\hat{S}^+\right)^\dagger = \hat{a}^\dagger\sqrt{2S - \hat{a}^\dagger \hat{a}}. \tag{3}$$

The combined transformation of $\hat{S}_z$ and $\hat{S}^\pm$ allows us to express the excitation of a single spin $\hat{\mathbf{S}}$ in terms of magnon creation and annihilation operators, and is widely used to describe the interaction of magnons and the interaction between spin systems and other physical systems.

We have discussed the quantization of a single spin and how to introduce operators that describe magnons. A real magnet, however, is composed of many spins interacting with each other through exchange and dipolar interactions, and the spins themselves may have preferred orientations due to spin–orbit coupling. Depending on the competition of these interactions, the ground state of a magnet may be collinear or correspond to noncollinear magnetic textures such as domain walls, vortices, and skyrmions. To consider magnon excitations on top of a particular ground state, one can apply the Holstein–Primakoff (HP) transformation on the spin texture of the system and, in principle, derive an effective Hamiltonian including any order of magnon–magnon interaction. As an example, let us consider a biaxial magnet subject to an external field $\mathbf{H} = H\mathbf{e}_z$. The Hamiltonian reads

$$\hat{\mathcal{H}} = -J\sum_{\langle i,j\rangle}\hat{\mathbf{S}}_i\cdot\hat{\mathbf{S}}_j + K_x\sum_i\left(\hat{S}_{i,x}\right)^2 - K_z\sum_i\left(\hat{S}_{i,z}\right)^2 - \mu_0 g_e \mu_B H\sum_i \hat{S}_{i,z}, \tag{4}$$

where J is the exchange coefficient and the first sum is over the neighboring spins, the second and third terms represent the magnetic anisotropies with anisotropy coefficients K_x and K_z, and the last term is Zeeman energy. μ_0, g_e, and μ_B are vacuum susceptibility, Landé g-factor, and Bohr magneton, respectively. We consider the case $K_x > 0$, $K_z > 0$, and $H > 0$ such that the classical ground state of the system obeys $\langle\hat{\mathbf{S}}\rangle = S\mathbf{e}_z$.

By employing the HP transformation of the spin operators for this ground state, we have

$$\hat{\mathcal{H}} = -JS\sum_{\langle i,j\rangle}\left(\hat{a}_i\hat{a}_j^\dagger + h.c.\right) + \sum_i \mu_i \hat{a}_i^\dagger \hat{a}_i + \frac{K_x S}{2}\sum_i\left(\hat{a}_i\hat{a}_i + h.c.\right) + \hat{\mathcal{H}}^{(3)} + \hat{\mathcal{H}}^{(4)} + \cdots, \tag{5}$$

where $\hat{a}_i$ ($\hat{a}_i^\dagger$) is the magnon annihilation (creation) operator on the *i*th site, $\mu_i = 2ZJS + \mu_0 g_e \mu_B H + 2K_z S + K_x S$ with Z being the coordination number. $\hat{\mathcal{H}}^{(3)}$ and $\hat{\mathcal{H}}^{(4)}$ refer to three and four magnon processes, respectively. For a macroscopic magnet far below the Curie temperature, the number of magnon excitations is very small, that is $\langle\hat{a}_i^\dagger\hat{a}_i\rangle \ll S$, such that the interactions between magnons proportional to higher orders of $\langle\hat{a}_i^\dagger\hat{a}_i\rangle/S$ can be safely neglected. By switching to Fourier space and diagonalizing the Hamiltonian, we finally find the effective Hamiltonian for magnon excitations as $\hat{\mathcal{H}} = \sum_k \omega_k \hat{a}_{\mathbf{k}}^\dagger \hat{a}_{\mathbf{k}}$, where the dispersion of the magnons in the long-wavelength limit $kd \ll 1$ reads

$$\omega_k = \sqrt{[2JS(kd)^2 + \mu_0 g_e \mu_B H + 2K_x S]} \times \sqrt{[2JS(kd)^2 + \mu_0 g_e \mu_B H + 2K_z S + 2K_x S]}, \tag{6}$$

where d is the lattice constant. The ferromagnetic resonance mode with $\mathbf{k} = 0$ has the frequency

$$\omega_a = \sqrt{[\mu_0 g_e \mu_B H + 2K_x S][\mu_0 g_e \mu_B H + 2K_z S + 2K_x S]}. \tag{7}$$

For a magnetic sphere, as is widely used in cavity spintronics, $K_x = K_y = 0$, the resonance frequency is $\omega_a = \mu_0 g_e \mu_B H$. The tunability of the magnon frequency through external fields is a main advantage of hybrid magnonic systems.

Quantum states of magnons

In the traditional set-ups involving magnons, they are usually excited by strong microwaves at room temperature. The quantum aspects of the generated magnons are washed out by the thermal fluctuations. As we lower the temperature, it is expected that one can suppress the thermal effects and find quantum states of magnons, in analogy with photonic systems. Up till now, magnon antibunching, squeezed states, and Schrödinger cat states have been theoretically proposed, but remain a challenge to be experimentally verified. The exception is the single magnon excitation in a magnetic sphere, which has been detected by entangling it with a superconducting qubit (Lachance-Quirion et al., 2020), as we discuss below. In this section, we mainly introduce magnon antibunching and the magnon squeezed state.

Magnon antibunching

In the absence of driving, the excited magnons in a magnet will reach equilibrium with the environment and form a thermal magnon gas. The thermal state is well described by a super-Poissonian distribution, which is characterized by the mean magnon number being smaller than the variance of the magnon number. Under strong driving, the magnon gas will reach a coherent state, with mean magnon number equal to its variance. Coherent magnons usually behave classically. To manifest quantum effects of magnons, one can use magnon nonlinearities to generate exotic distributions of the magnon gas. One example is the magnon antibunching, which corresponds to a sub-Poissonian distribution with mean magnon number larger than the magnon number variance. A perfect antibunched magnon gas has large occupation of the first-excited state of the magnons, while the higher order excitations are zero. In general, these states are characterized by a zero-delay second-order correlation function defined as

$$g^{(2)}(0) \equiv \frac{\langle \hat{a}^\dagger \hat{a}^\dagger \hat{a} \hat{a} \rangle}{\langle \hat{a}^\dagger \hat{a} \rangle^2} = 1 + \frac{\langle (\Delta \hat{n})^2 \rangle - \langle \hat{n} \rangle}{\langle \hat{n} \rangle^2}, \tag{8}$$

where $\hat{n} = \hat{a}^\dagger \hat{a}$ is the magnon number operator, $\Delta \hat{n} = \hat{n} - \langle \hat{n} \rangle$ is the variance of the magnon number, and $\langle \hat{A} \rangle \equiv \mathrm{tr}(\hat{\rho} \hat{A})$ is the ensemble average of the observable $\hat{A}$. Three regimes are distinguished according to the value of $g^{(2)}(0)$ (Plenio and Knight, 1998): (i) When the magnon distribution is super-Poissonian, $\langle (\Delta \hat{n})^2 \rangle > \langle \hat{n} \rangle$, then $g^{(2)}(0) > 1$. For example, a thermal state has $g^{(2)}(0) = 2$. (ii) When the magnon distribution is Poissonian, for example, a coherent state, one has $(\Delta \hat{n})^2 \rangle = \langle \hat{n} \rangle$ and thus $g^{(2)}(0) = 1$. A magnonic system under strong driving falls into this class. (iii) When the magnon distribution is sub-Poissonian, $\langle (\Delta \hat{n})^2 \rangle < \langle \hat{n} \rangle$ and $g^{(2)}(0) < 1$, implying antibunched magnons. This is a purely quantum mechanical state that cannot be captured by classical statistics (Reid and Walls, 1986). The limiting case $g^{(2)}(0) = 0$ corresponds to a perfect single-magnon source. This phenomenon is also called magnon blockade because only one magnon is allowed to be excited and all the other magnon excitations are blocked.

The conventional method to generate magnon antibunching is to enhance the Kerr nonlinearity $(\hat{a}^\dagger \hat{a})^2$ of the magnonic system. To illustrate this point, let us recall the effective Hamiltonian of a biaxial magnet as shown in Fig. 3A and include the magnon–magnon interaction as

$$\hat{\mathcal{H}} = \omega_a \hat{a}^\dagger \hat{a} + w(\hat{a}^\dagger \hat{a}^\dagger + \hat{a}\hat{a}) + v(\hat{a}^\dagger \hat{a})^2 + u(\hat{a}^\dagger \hat{a}\hat{a}\hat{a} + \hat{a}^\dagger \hat{a}^\dagger \hat{a}^\dagger \hat{a}) + \xi(\hat{a} e^{i\omega_d t} + \hat{a}^\dagger e^{-i\omega_d t}), \tag{9}$$

where $\omega_a = 2K_z + K_x + \mu_0 g_e \mu_B H$, $w = K_x S/2$, $v = -K_z/N - K_x/2N$, $u = -K_x/4N$, with N being the number of spins in the magnet. Here the nonlinear terms u and v may come from either dipolar interactions or magnetocrystalline anisotropy. Since they are inversely proportional to the number of spins in the system, reducing the size of the magnet strengthens the nonlinearity, leading to anharmonic energy levels, as shown in Fig. 3B. By carefully choosing the microwave frequency $\omega_d = \omega_1 - \omega_0$, it will efficiently pump the magnons to the first energy level but cannot excite them further due to the frequency mismatch (Yuan and Duine, 2020). Therefore, magnon antibunching may be realized. A typical phase diagram of the system in the $(K_x S/2\gamma, K_z/\gamma N)$ plane is shown in Fig. 3C, with γ being the gyromagnetic ratio. Clearly, as the size of the nanomagnet is scaled down to the several nanometers, the second-order correlation function becomes smaller than one, indicating the existence of magnon antibunching.

Another way to induce anharmonicity of the magnon energy levels is to couple the magnon mode to an ancillary mode. For example, a superconducting qubit can dress the energy levels of the magnons due to their coupling (Liu et al., 2019). As a result, one

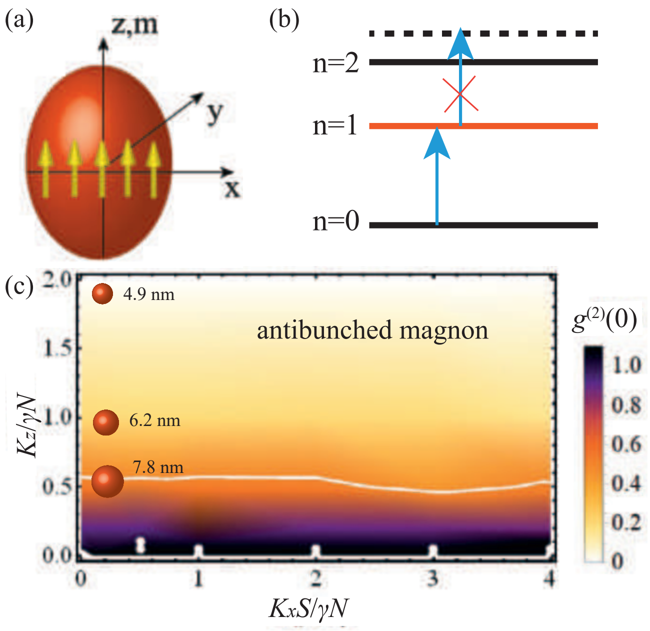

Fig. 3 (A) Schematic of a nanomagnet with spin polarized along the *z*-axis. (B) Anharmonic energy-level distribution of the magnet with strong nonlinearities. The excitation of a magnon from $n = 1$ to 2 by a microwave with frequency $\omega_1 - \omega_0$ will be suppressed due to the frequency mismatch. (C) Second-order correlation function $g^{(2)}(0)$ of magnons as a function of $K_xS/2\gamma$ and $K_z/\gamma N$. The *orange balls* sketch typical magnetic spheres with bunched and antibunched behavior. Adapted from Yuan HY and Duine RA (2020) Magnon antibunching in a nanomagnet. Physical Review B 102(10): 100402. https://doi.org/10.1103/Phys-RevB.102.100402.

can properly choose the driving field to generate antibunched magnons. Besides, one can use interference effects between different quantum channels to enhance the occupation of the single-magnon energy level (Wang et al., 2020), even in the absence of nonlinearities. To detect the antibunched magnons, one can couple the magnonic system to photons or qubits and then read the state of these ancillary modes to deduce the quantum states of the magnons.

Squeezed states

The Heisenberg uncertainty principle states that the product of quantum fluctuations of two noncommuting observables has a lower bound determined by the reduced Planck constant $\hbar$. However, it is possible to realize a state with quantum noise in one observable below the symmetric limit at the expense of increased fluctuations in the other observable. Such states are called squeezed states and have been realized in photonic systems. By denoting the photon annihilation and generation operator as $\hat{a}$ and $\hat{a}^\dagger$, the position and momentum operator of photons can be defined as $\hat{x} = (\hat{a} + \hat{a}^\dagger)/\sqrt{2}$ and $\hat{p} = -i(\hat{a} - \hat{a}^\dagger)/\sqrt{2}$. A squeezed state of a photon means that either the uncertainty of $\hat{x}$ or $\hat{p}$ is reduced below $\hbar/\sqrt{2}$. Magnons, as bosons, share similarities with photons. By comparing the definition of position and momentum of photons with the HP transformation of magnons, we immediately find that the position and momentum of magnons are equivalent to the spin components $\hat{S}_x$ and $\hat{S}_y$, respectively. Therefore a squeezed state of magnons can be interpreted as a state with the spin fluctuations in a direction perpendicular to the quantized axis (x or y here) reduced below the symmetric quantum limit $\hbar/\sqrt{2}$.

The minimum model that generates squeezed magnons is the biaxial magnet described in Eq. (4). The effective Hamiltonian of the uniform mode ($\mathbf{k} = 0$) without considering the magnon–magnon interaction reads $\hat{\mathcal{H}}_{\mathrm{FM}} = \omega_a \hat{a}^\dagger \hat{a} + w(\hat{a}^\dagger \hat{a}^\dagger + \hat{a}\hat{a})$. The ground state of the system is a single-mode squeezed state $|GS\rangle = \exp(r/2(\hat{a}\hat{a} - \hat{a}^\dagger \hat{a}^\dagger))|0\rangle$ with squeezing parameter $r = \operatorname{arctanh}(2w/\omega_a)/2 > 0$. In the magnon number basis, this state is expanded as

$$|GS\rangle = \frac{1}{\sqrt{\cosh r}} \sum_{n=0}^{\infty} (-\tanh r)^n \frac{\sqrt{(2n)!}}{2^n n!} |2n\rangle, \tag{10}$$

which only contains states with an even magnon number. The uncertainties in the total spin components $\hat{S}_x = \sum_i \hat{S}_i^x$ and $\hat{S}_y = \sum_i \hat{S}_i^y$ in this ground state are readily evaluated as $\Delta S_x \equiv \sqrt{\langle \hat{S}_x^2 \rangle - \langle \hat{S}_x \rangle^2} = e^{-r}\sqrt{NS/2}$ and $\Delta S_y \equiv \sqrt{\langle S_y^2 \rangle - \langle \hat{S}_y \rangle^2} = e^{r}\sqrt{NS/2}$. It is clear that the noise of $\hat{S}_x$ is squeezed below the symmetric limit at the sacrifice of an increase in uncertainty in the $\hat{S}_y$ component. At finite temperatures, one has to consider the relaxation and pure dephasing of magnons to recover the correct equilibrium state (Yuan et al., 2022b). In general, the uncertainty of spin components will keep increasing with temperature and finally exceed the symmetric limit at a temperature of several Kelvin. As a comparison, the elliptical precession of spins, even though it also originates from the in-plane anisotropy, is a classical phenomenon that is insensitive to the temperature.

The concept of magnon squeezing can be extended to the multimode case, which allows us to study the entanglement properties of magnons. As an example, we consider a two-sublattice antiferromagnet (AFM) described by the Hamiltonian

$$\hat{\mathcal{H}}_{\mathrm{AFM}} = J\sum_{j,\delta} \hat{\mathbf{S}}_j \cdot \hat{\mathbf{S}}_{j+\delta} - K_z \sum_j \left(\hat{S}_j^z\right)^2 - \sum_j \mathbf{H} \cdot \hat{\mathbf{S}}_j, \tag{11}$$

where $J > 0$ is the AFM exchange coupling between neighboring spins and $K_z > 0$ is the strength of easy-axis anisotropy. Again, we apply an external field along the z-axis ($\mathbf{H} = He_z$) to tune the magnon frequency. When the field is below the spin-flop transition field, the spins on the two sublattices are antiparallel to each other to guarantee the ground state is a Néel state, that is, $\langle \hat{\mathbf{S}}_{2l} \rangle = Se_z$, $\langle \hat{\mathbf{S}}_{2l+1} \rangle = -Se_z$. Employing the standard HP transformation on the two sublattices, we quantize the magnon excitation above this ground state as

$$\hat{\mathcal{H}}_{\mathrm{AFM}} = \omega_a \hat{a}^\dagger \hat{a} + \omega_b \hat{b}^\dagger \hat{b} + g_{ab}\left(\hat{a}^\dagger \hat{b}^\dagger + \hat{a}\hat{b}\right), \tag{12}$$

where $\omega_{a,b} = H_{\mathrm{ex}} + H_{\mathrm{an}} \pm H$, $H_{\mathrm{ex}} = 2ZJS^2$, $H_{\mathrm{an}} = 2K_z S$, and $g_{\mathrm{ab}} = H_{\mathrm{ex}}$ is the coupling of magnon modes excited on the two sublattices.

We diagonalize the antiferromagnetic Hamiltonian $\mathcal{H}_{\mathrm{AFM}}$ in Eq. (12) by introducing two Bogoliubov modes $\hat{\alpha} = \cosh\theta \hat{a} + \sinh\theta \hat{b}^\dagger$, $\hat{\beta} = \sinh\theta \hat{a}^\dagger + \cosh\theta \hat{b}$, where $\tanh 2\theta = -2g_{ab}/(\omega_a + \omega_b)$. In terms of the boson operators, $\hat{\alpha}$, $\hat{\beta}$, the Hamiltonian (12) is rewritten as

$$\mathcal{H}_{\mathrm{AFM}} = \omega_\alpha \hat{\alpha}^\dagger \hat{\alpha} + \omega_\beta \hat{\beta}^\dagger \hat{\beta}, \tag{13}$$

where $\omega_{\alpha,\beta} = \pm H + H_{\mathrm{sp}}$ represent the optical and acoustic magnon bands, respectively, and $H_{\mathrm{sp}} = \sqrt{H_{\mathrm{an}}(H_{\mathrm{an}} + 2H_{\mathrm{ex}})}$ is the spin-flop field of the system. We notice that, by employing the two-mode squeezing operator $S(\theta) = \exp[\theta(\hat{a}\hat{b} - \hat{a}^\dagger \hat{b}^\dagger)]$, the magnon eigenmodes are reformulated as $\hat{\alpha} = S(\theta)\hat{a}S^\dagger(\theta)$, $\hat{\beta} = S(\theta)\hat{b}S^\dagger(\theta)$, and thus the joint ground state of the $\hat{\alpha}$ and $\hat{\beta}$ modes is a two-mode squeezed state $|\theta\rangle = S(\theta)|0_a, 0_b\rangle$ (Kamra et al., 2019; Yuan et al., 2020b), where $|0_a, 0_b\rangle$ is the joint vacuum of the magnon modes a and b. Here the two-mode squeezing means that the fluctuations of the total spin component $\hat{S}_x = (\hat{a} + \hat{a}^\dagger + \hat{b} + \hat{b}^\dagger)/2\sqrt{2}$ or $\hat{S}_y = -i(\hat{a} - \hat{a}^\dagger + \hat{b} - \hat{b}^\dagger)/2\sqrt{2}$ is reduced below the symmetric limit. From the viewpoint of entanglement, the two-mode squeezed state is an entangled state of sublattice magnons. The strength of the entanglement is quantified by log negativity as $E_N = 2|\theta|$ (Yuan et al., 2020b). Note that we focus on the uniform precession mode $k = 0$. The ground-state entanglement of magnons taking into account the magnons with finite wavevectors is found in Hartmann et al. (2021) and the influence of magnon relaxation and dephasing on the entanglement of magnons can be found in Yuan et al. (2022b).

Magnon BEC and spin superfluidity

In addition to the quantum states that were discussed in the previous subsections and that involve one or a few magnons, there also exist interesting quantum many-body states of magnons. Most prominent among these is magnon BEC. A magnon BEC may exist in equilibrium or out of equilibrium (Zapf et al., 2014). In the former case, the spin system has a uniaxial symmetry which is spontaneously broken. The simplest example is that of an easy-plane magnet. For large external fields perpendicular to the easy plane, the spins are fully polarized in the direction of the field. Upon reducing the field, the magnetization tilts away from the field direction for a critical field that is of the order of the easy-plane anisotropy. As the projection of the magnetization on the easy plane is undetermined, this transition spontaneously breaks the rotation symmetry around the field direction. The transition is of second order and may be interpreted as magnon BEC for HP magnons with the quantization axis in the direction of the field. This is because in the symmetry-broken phase we have that $\langle \hat{S}_x \rangle \neq 0$ and $\langle \hat{S}_x \rangle \neq 0$, and therefore that $\langle \hat{a}_i \rangle \neq 0$. The latter order parameter signals BEC. Nonequilibrium BEC may be achieved when injecting magnons, for example, due to an increase of the temperature (Schneider et al., 2020), and if their equilibration is faster than their relaxation.

A magnon BEC, or, more generally, an easy-plane magnet in the symmetry broken phase, may exhibit spin superfluidity (Sonin, 2010). For the case of the easy-plane magnet, the spin supercurrent is expressed as the gradient of the angle that the magnetization makes in the easy plane. In-plane anisotropies that pin the magnetization within the easy plane lead to a lower critical current for superfluid spin transport. For spin currents larger than an upper critical current, the magnetization tilts out of the easy plane. Recently, the first experimental signals of spin superfluidity were reported (Yuan et al., 2018).

Hybrid magnonic platforms

Magnon–photon system

The history of coupling magnets to electromagnetic waves can be dated back to the 1960s (Auld, 1963; Chow and Hines, 1966). In the early times, one put a magnet into a microwave cavity and observed the anticrossing spectrum when the frequency of the magnetic resonance mode matched that of the cavity field. The gap of the anticrossing characterizes the coupling strength between magnon and photon, and it is determined by the overlap of the spin-wave mode and microwave mode inside the magnet. After half century of dormancy, Soykal and Flatté revisited this topic in 2010 (Soykal and Flatté, 2010) using a quantum mechanical formalism and theoretically predicted that the coupling strength can reach the strong coupling regime by putting an insulating magnetic sphere into a high-quality cavity. Three years later, Huebl et al. (2013) experimentally verified this prediction by loading gallium-doped yttrium iron garnet (YIG) into a superconducting microwave resonator. Later, Harder et al. (2018) observed energy-level attraction by delicately tuning the position of a YIG sphere in an open Fabry–Perot cavity. It has become clear that the energy-level repulsion and attraction correspond to the coherent and dissipative coupling between magnets and microwaves, respectively. In these studies, a quantum model based on the quantization of magnetic excitations and cavity electromagnetic waves provides a convenient way to understand the coupling spectrum. However, it is not sufficient to claim quantum aspects of the physics. Indeed, most of the physics can also be well understood by employing a coupled oscillator model (Yu et al., 2019; Zare Rameshti et al., 2022). How to manifest quantum correlations of magnons and photons has attracted significant attention recently.

Yuan et al. (2020a) considered the dissipative coupling between magnons and photons described by the non-Hermitian Hamiltonian

$$\hat{H} = \omega_r \hat{a}^\dagger \hat{a} + \omega_c \hat{c}^\dagger \hat{c} + g\left(\hat{c}^\dagger \hat{a} + e^{i\Phi} \hat{c} \hat{a}^\dagger\right), \tag{14}$$

where $\hat{a}$ $(\hat{a}^\dagger)$ and $\hat{c}$ $(\hat{c}^\dagger)$ are annihilation (creation) operators of magnons and photons, respectively, ω_r (ω_c) is the magnon (photon) frequency, g is the effective coupling strength between magnons and photons, and Φ is a tunable phase factor due to backaction effects. This effective Hamiltonian (14) describes the energy-level repulsion and attraction observed in experiments very well (Bhoi et al., 2019; Boventer et al., 2020; Harder et al., 2018).

Fig. 4A shows the typical spectrum of energy-level attraction with $\Phi = \pi$. By solving the quantum master equation corresponding to the Hamiltonian (14), it is found that the hybrid system evolves to a steady state with maximum entanglement $\ln 2$ in the regime of energy level attraction as illustrated in Fig. 4B. Detailed analysis shows that the steady state is a Bell state between magnon and photon, that is, $|\phi_s\rangle = (|10\rangle + |01\rangle)/\sqrt{2}$. Such entanglement is robust as along as the coupling strength is larger than the magnetic dissipation as shown in Fig. 4C. For comparison, the system keeps oscillating and no steady Bell states are generated outside the regime of level attraction.

Another way to generate entanglement between magnons and photons is to utilize the nonlinearities in magnetic systems. Li et al. (2018) studied a hybrid magnon-photon-phonon system by further including the pressure-like interaction between magnons and phonons, as $\hat{a}^\dagger \hat{a} \hat{q}$ with $\hat{q}$ being the position operator of phonons (see more details below). By driving the magnetic mode, an effective squeezing interaction between magnons and phonons is produced and contributes to both bipartite and tripartite entanglement among magnons, photons, and phonons.

Magnon-qubit system

A qubit is a quantum-mechanical two-level system that can store binary information and is the basic element for quantum computing and information processing. Quite a few types of qubits have been realized to implement quantum information tasks, such as superconducting qubits, photonic qubits, and nitrogen-vacancy (NV) centers. On the one hand, the single-spin

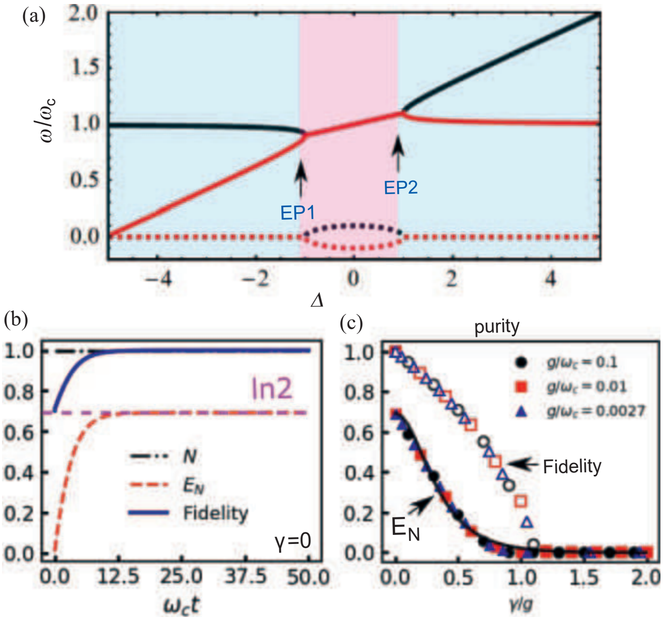

Fig. 4 (A) Level attraction of a hybrid magnet cavity described by Eq. (14) for $\Phi = \pi$. The *solid* and *dashed lines* represent the real and imaginary parts of the eigenvalues, respectively. (B) Evolution of the entanglement and the fidelity of the temporal state to the Bell state as a function of time. (C) Robustness of the steady Bell state against dissipation with different coupling strengths between magnons and photons (g). Adapted from Yuan HY, Yan P, Zheng S, He QY, Xia K, and Yung M-H (2020a) Steady bell state generation via magnon-photon coupling. Physical Review Letters 124(5): 053602. https://doi.org/10.1103/PhysRevLett.124.053602.

qubit, for example the NV center, can be used to detect magnetic states including magnetic domains, domain walls, and skyrmions, while a magnetic structure can mediate the entanglement of two and more spin qubits. On the other hand, a superconducting qubit can be coupled with the magnon mode via cavity photons and achieve mutual information transfer between magnonic system and qubit system. In this section, we will focus on these two aspects.

Trifunovic et al. (2013) first proposed to couple two spin qubits separated by a distance of several μm through magnon excitations in a ferromagnet, as shown in Fig. 5A. Here the two qubits are coupled to the ferromagnet through dipolar interactions. Therefore, the qubit has to be placed close to the magnets, that is, on the order of several tens of nanometers, to guarantee that the coupling strength is sufficiently strong. The on-and-off switching of the qubit–qubit interaction can be realized by adjusting the detuning between the qubits and the ferromagnetic resonance mode. Note that the decoherence time of the qubit T_2 depends sensitively on k_BT/Δ_F, where Δ_F is the magnon gap, which suggests that it is desirable to choose magnetic materials with a small magnon gap and to perform the quantum operations at cryogenic conditions. Neuman et al. (2020) showed that a nanomagnet can mediate the long-range coupling of two qubits as shown in Fig. 5B. By tuning the frequency of the magnon to be off-resonant with the qubit, each qubit is coupled to the magnon mode inside the nanomagnet through the transfer of virtual magnons. They found population exchange between the two qubits, which clearly demonstrates the indirect coupling between them. The effective coupling strength is three to four orders of magnitude larger than the direct coupling strength. Furthermore, the generation of two-qubit entangled states via dissipative coupling between qubit and a magnetic medium (Zou et al., 2021) and preparation of 3-qubit Greenberger–Horne–Zeilinger (GHZ) states through the emission of a squeezed magnon (Skogvoll et al., 2021) are also proposed in literature.

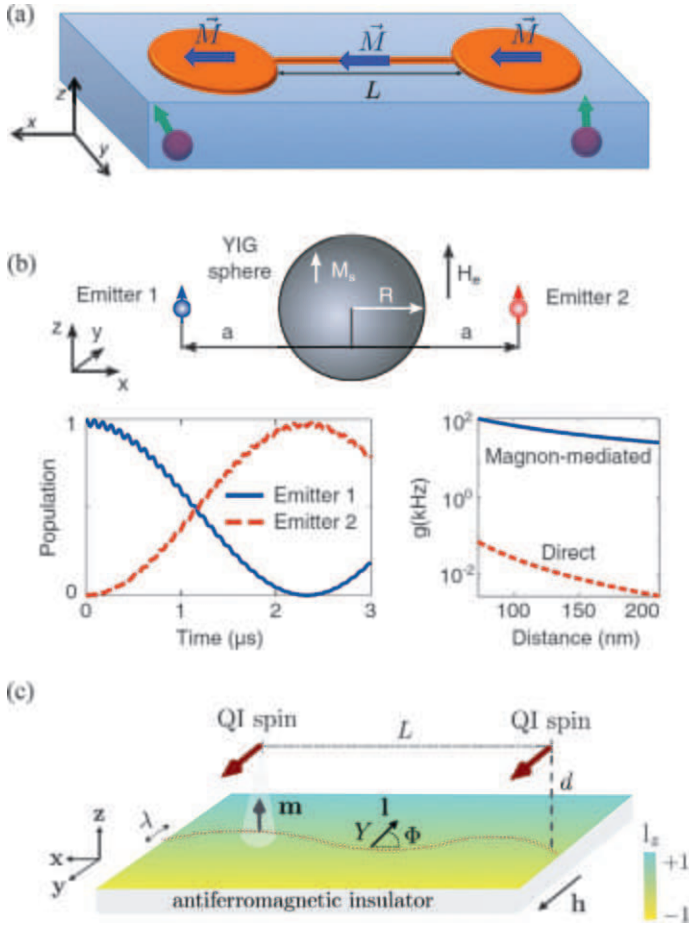

Fig. 5 (A) Schematic of a ferromagnetic coupler where the *orange dog-bone shape* denotes the ferromagnet that is coupled via dipolar interaction to spins of nearby spin qubits (*purple spheres* with *green arrows*). (B) Schematic of two qubits coupled by a magnon mode in a nanometer-sized magnetic sphere. The bottom-left panel shows the population of the two qubits as a function of time and bottom-right panel shows the effective coupling strength of two qubits mediated by magnons with and without magnets. (C) Schematic of the coupling of two qubits via the magnon mode in an AFM insulator. Here QI is the abbreviation of quantum impurity. Adapted from Flebus B and Tserkovnyak Y (2019) Entangling distant spin qubits via a magnetic domain wall. Physical Review B 99(14): 140403. https://doi.org/10.1103/PhysRevB.99.140403; Neuman T, Wang DS, and Narang P (2020) Nanomagnonic cavities for strong spin-magnon coupling and magnon-mediated spin-spin interactions. Physical Review Letters 125(24): 247702. https://doi.org/10.1103/Phys-RevLett.125.247702; Trifunovic L, Pedrocchi FL, and Loss D (2013) Long-distance entanglement of spin qubits via ferromagnet. Physical Review X 3(4): 041023. https://doi.org/10.1103/PhysRevX.3.041023.

Besides utilizing magnons excited in a collinear magnetic structure as illustrated above, Flebus and Tserkovnyak (2019) theoretically showed that an AFM domain wall is able to mediate a tunable coherent coupling between two qubits separated by a micrometer as shown in Fig. 5C. Here the planar rotation of the staggered order parameter, that is, the spin superfluid mode, is excited and simultaneously coupled to two qubits placed above the magnetic texture. We note that the experimentalists have realized the coupling between one spin qubit and a magnet (Andrich et al., 2017; Candido et al., 2020; Kikuchi et al., 2017; Wolf et al., 2016), while the demonstration of qubit–qubit entanglement through magnon modes is still lacking.

To study the coupling between magnon and superconducting qubit, Tabuchi et al. (2015) first considered a hybrid magnetic-qubit-cavity system composed of a YIG sphere and a superconducting transmon qubit, as illustrated in Fig. 6A. Here the magnons and photons are respectively coupled to the magnetic and electric components of the cavity field, and hence there is a bridge between magnons and qubits by exchanging a virtual photon, that is $\hat{\mathcal{H}}_{\text{int}} = g_{\text{mq}}\hat{\sigma}^{+}\hat{a} + g_{\text{mq}}^{*}\hat{\sigma}^{-}\hat{a}^{\dagger}$, where $\hat{\sigma}^{\pm}$ are the Pauli rising and lowering operators describing the state of a qubit. Here the effective coupling strength g_{mq} depends on the respective coupling and detuning between photons and magnons (qubits). To quantify the coupling, the authors probed the qubit state by another cavity mode and identified a typical energy-level repulsion spectrum with a gap of 10 MHz, as shown in Fig. 6B. This coupling strength is much larger than the dissipation of qubits and photons and thus it falls into the strong coupling regime. Based on the strong coupling, in a follow-up work, Lachance-Quirion *et al.* tuned the system into a strongly dispersive regime, where the detuning between magnon and qubit is much larger than their effective coupling. This generates a nonlinear interaction between magnon and

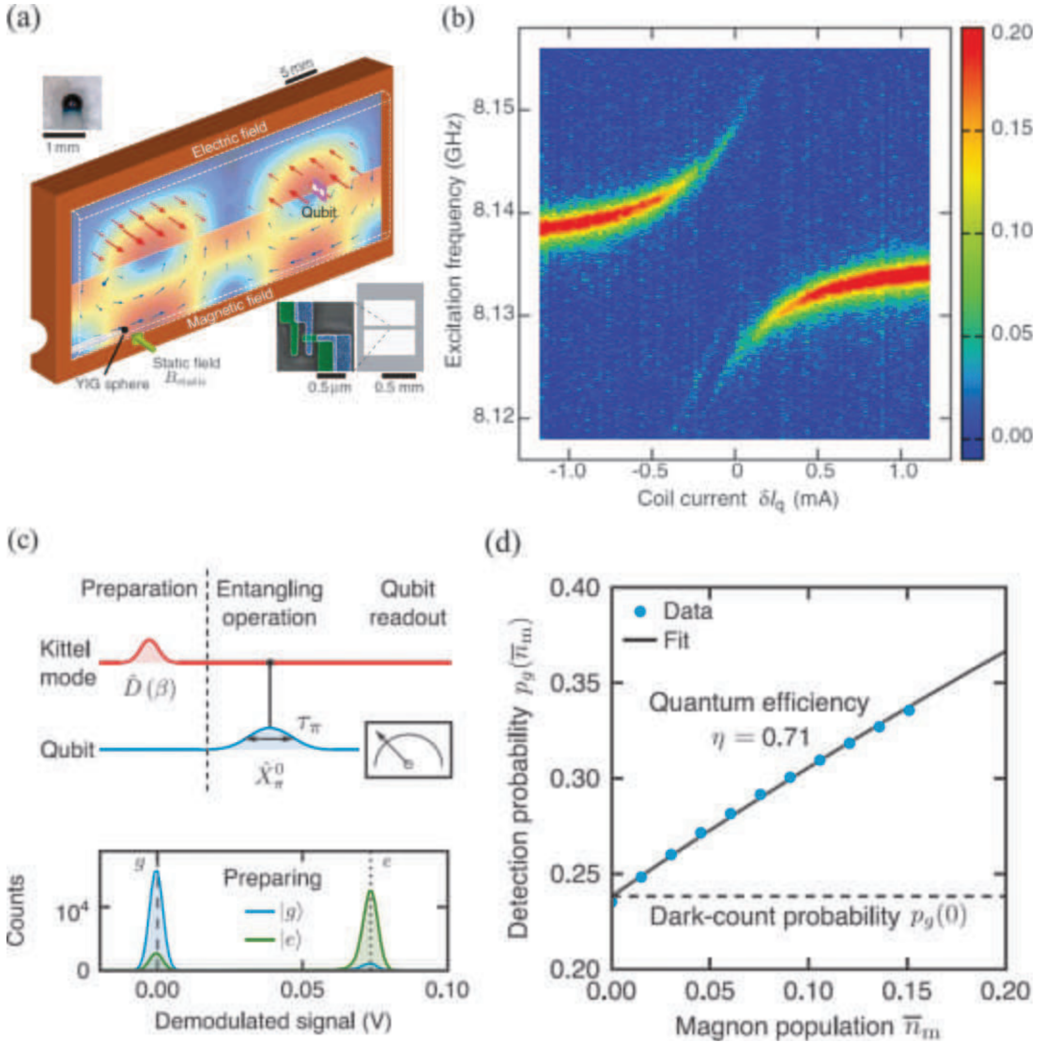

Fig. 6 (A) Schematic of a hybrid magnet-qubit-cavity system. (B) Rabi splitting due to the indirect coupling between magnons and qubits mediated by cavity photons. (C) Procedure for single-magnon detection using superconducting qubits. (D) Detection probability of magnons as a function of magnon population. Adapted from Lachance-Quirion D, Wolski SP, Tabuchi Y, Kono S, Usami K, and Nakamura Y (2020) Entanglement-based single-shot detection of a single magnon with a superconducting qubit. Science 367(6476): 425–428. https://doi.org/10.1126/science.aaz9236; Tabuchi Y, Ishino S, Noguchi A, Ishikawa T, Yamazaki R, Usami K, and Nakamura Y (2015) Coherent coupling between a ferromagnetic magnon and a superconducting qubit. Science 349(6246): 405–408. https://doi.org/10.1126/science.aaa3693. https://science.sciencemag.org/content/349/6246/405.full.pdf.

qubit in the form of $\hat{\mathcal{H}}_{\text{int}} = \chi_{\text{qm}} \hat{a}^\dagger \hat{a} \hat{\sigma}_z$ (Lachance-Quirion et al., 2017, 2020), which means that the excitation of magnons will induce a frequency shift of the qubit. Since the qubit occupation can be measured by cavity field, this provides a way to detect magnon excitations through the read-out of the qubit state. To demonstrate this idea, the authors first prepared a coherent state of magnons and then applied a conditional excitation X_π^0 pulse on the qubit to entangle the magnons and qubit, as shown in Fig. 6C. By reading the qubit through a high-power technique, the magnon excitation down to the single magnon level is detected with high precision as illustrated in Fig. 6D. This proof-of-concept experiment establishes the qubit state as single-magnon detector, which has promising applications to detect weak magnon excitations with high precision.

Magnon–phonon system

The coupling between magnons and phonons is another interesting direction. Here a phonon mode may be either the quantization of a lattice deformation of a magnet or that of a distant mechanical oscillator. While traditional spintronics mainly focuses on the excitation and transport properties of magnons mediated by phonons (Bozhko et al., 2020), quantum magnonics concerns the entanglement between magnons and phonons as well as the application of hybrid magnon-phonon systems in quantum information science.

In general, the magnetization oscillation of a magnet can induce mechanical deformations of the lattice through the magnetostrictive interaction in the form of (Rückriegel et al., 2014)

$$\hat{\mathcal{H}}_{\text{int}} = b_1 \int_V d^3r \left[\hat{m}_x^2 \varepsilon_{xx} + \hat{m}_y^2 \varepsilon_{yy} - (\hat{m}_x^2 + \hat{m}_y^2)\varepsilon_{zz}\right], \tag{15}$$

where b_1 is a magnetoelastic constant, $\varepsilon_{ij} \equiv (\partial_j u_i + \partial_i u_j)/2$ are the components of the strain tensor, $\mathbf{u}$ is the atomic displacement, and V is the volume of the magnet. By properly choosing the direction of magnetization, the interaction between magnons and phonons can be quantized as (Zhang et al., 2016)

$$\hat{\mathcal{H}}_{\text{int}} = \frac{b_1 M_s}{V} \hat{a}^\dagger \hat{a} \int d^3r (\varepsilon_{xx} + \varepsilon_{yy} - 2\varepsilon_{zz}) = g_{\text{mb}} \hat{a}^\dagger \hat{a} (\hat{b} + \hat{b}^\dagger), \tag{16}$$

where $\hat{b}$ ($\hat{b}^\dagger$) is the annihilation (creation) operator for phonons, M_s is saturation magnetization, and g_{mb} is the effective coupling strength.

Zhang et al. (2016) first studied a hybrid cavity-magnet system by taking the phonon degree of freedom into account, as shown in Fig. 7A. They tuned the magnon frequency close to the photon frequency to realize hybrid modes of the magnons and photons ($\hat{A}_\pm$) with their frequency in the gigahertz regime, as illustrated in Fig. 7B. To match the phonon frequency in the megahertz regime, a parametric driving is applied on the cavity field such that the detuning between cavity photon and the driving will be comparable to that of phonons and the phonon mode will be effectively excited. In the dressed basis, the interacting component of Hamiltonian becomes $\hat{\mathcal{H}}_{\text{int}} = g_{\text{mb}} (\hat{b} + \hat{b}^\dagger)\left(\sin^2\theta \hat{A}_+^\dagger \hat{A}_+ + \cos^2\theta \hat{A}_-^\dagger \hat{A}_-\right)$, where θ is a tunable parameter that depends on the coupling strength and detuning between magnons and photons. This interaction contains both beam-splitter-type interaction $(\hat{A}_\pm^\dagger \hat{b} + \hat{A}_\pm \hat{b}^\dagger)$ and parametric interaction $(\hat{A}_\pm^\dagger \hat{b}^\dagger + \hat{A}_\pm \hat{b})$ between the dressed mode and the phonon mode. Thanks to the tunability of magnon frequency, the relative contribution of these two types of interaction is also tunable, which enables the observation of transmission phenomena in the hybrid system, for example the magnon analog of electromagnetically induced transparency and absorption.

Based on this platform, Li et al. (2018) studied the existence of steady entanglement among magnons, photons, and phonons induced by the nonlinear interaction between magnons and phonons. Sarma et al. (2021) proposed a way to transfer the information from cavity mode to phonon mode. Due to the low damping rate of the phonon mode, the information encoded in the phononic subsystem may survive for a longer time and thus may be used as memory. Alternatively, Colombano et al. (2020) experimentally realized a hybrid magnet-mechanical system by depositing a glass of microsphere optical cavity on top of a YIG thin film. The oscillating field acting on the magnetic sphere deforms the magnetic lattice and further excites the breathing mode of the microsphere through magnetostrictive interactions. By measuring the state of the microsphere, the oscillating field can be indirectly recovered. This technique can thus be used as a magnetometer with high sensitivity in the megahertz regime.

Conclusion

In conclusion, we have briefly introduced the nascent field of quantum magnonics and discussed the recent developments concerning hybrid magnonic systems as well as their applications to quantum memories, logic gates, and high-precision sensors. Despite great success, the progress of this field is far from satisfactory. Most of the magnon quantum states including magnon antibunching, squeezed states, and cat states, are yet to be verified in experiments. There are already many proposals on how to generate these states; however, the readout as well as the applications of these quantum states have to be further developed. A key question we may have to keep asking ourselves is how magnonic systems could stand out among other quantum platforms, including superconducting qubits, single-spin qubits, and cavity photons to realize quantum information processing. The answer to this question may be crucial for the long-term development of this field.

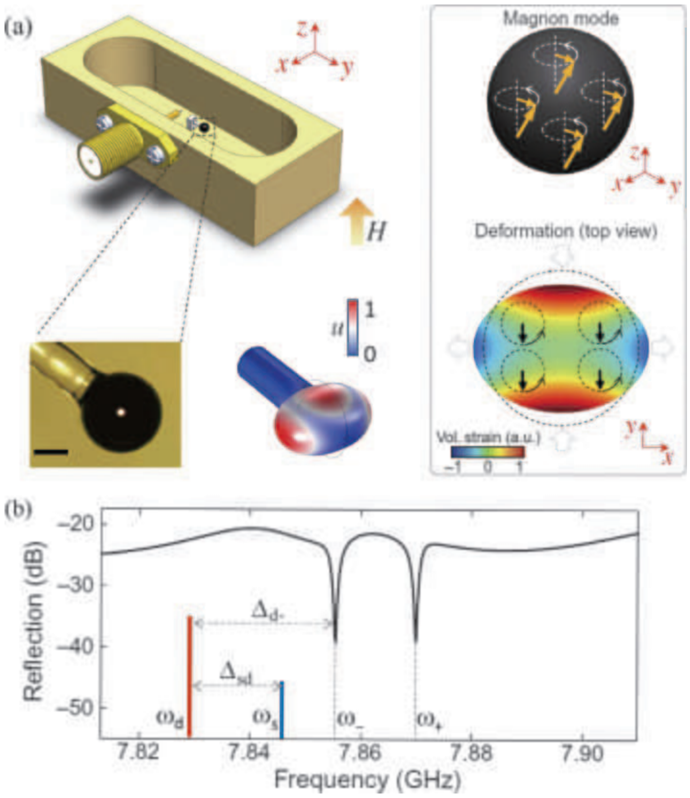

Fig. 7 (A) Schematic device containing a three-dimensional copper cavity and a YIG sphere. (B) The reflection spectrum when the magnon is on resonance with the cavity photon. The two dips represent the two hybrid modes between magnons and photons. Adapted from Zhang X, Zou C-L, Jiang L, and Tang HX (2016) Cavity magnomechanics. Science Advances 2(3). https://doi.org/10.1126/sciadv.1501286. https://advances.sciencemag.org/content/2/3/e1501286.full.pdf.

Acknowledgments

H.Y.Y acknowledges the European Union's Horizon 2020 research and innovation programme under Marie Skłodowska-Curie Grant Agreement SPINCAT No. 101018193. R.A.D. is member of the D-ITP consortium, a program of the Netherlands Organisation for Scientific Research (NWO) that is funded by the Dutch Ministry of Education, Culture and Science (OCW). R.A.D. has received funding from the European Research Council (ERC) under the European Union's Horizon 2020 research and innovation programme (Grant No. 725509).

References

Andrich P, de las Casas CF, Liu X, Bretscher HL, Berman JR, Heremans FJ, Nealey PF, and Awschalom DD (2017) Long-range spin wave mediated control of defect qubits in nanodiamonds. *npj Quantum Information* 3(1): 28. https://doi.org/10.1038/s41534-017-0029-z.

Arute F, Arya K, Babbush R, Bacon D, Bardin JC, Barends R, Biswas R, Boixo S, Brandao FGSL, Buell DA, Burkett B, Chen Y, Chen Z, Chiaro B, Collins R, Courtney W, Dunsworth A, Farhi E, Foxen B, Fowler A, Gidney C, Giustina M, Graff R, Guerin K, Habegger S, Harrigan MP, Hartmann MJ, Ho A, Hoffmann M, Huang T, Humble TS, Isakov SV, Jeffrey E, Jiang Z, Kafri D, Kechedzhi K, Kelly J, Klimov PV, Knysh S, Korotkov A, Kostritsa F, Landhuis D, Lindmark M, Lucero E, Lyakh D, Mandrà S, McClean JR, McEwen M, Megrant A, Mi X, Michielsen K, Mohseni M, Mutus J, Naaman O, Neeley M, Neill C, Niu MY, Ostby E, Petukhov A, Platt JC, Quintana C, Rieffel EG, Roushan P, Rubin NC, Sank D, Satzinger KJ, Smelyanskiy V, Sung KJ, Trevithick MD, Vainsencher A, Villalonga B, White T, Yao ZJ, Yeh P, Zalcman A, Neven H, and Martinis JM (2019) Quantum supremacy using a programmable superconducting processor. *Nature* 574(7779): 505–510. https://doi.org/10.1038/s41586-019-1666-5.

Auld BA (1963) Coupling of electromagnetic and magnetostatic modes in ferrite loaded cavity resonators. *Journal of Applied Physics* 34(6): 1629–1633. https://doi.org/10.1063/1.1702646.

Bhoi B, Kim B, Jang S-H, Kim J, Yang J, Cho Y-J, and Kim S-K (2019) Abnormal anticrossing effect in photon-magnon coupling. *Physical Review B* 99(13): 134426. https://doi.org/10.1103/PhysRevB.99.134426.

Boventer I, Dörflinger C, Wolz T, Macêdo R, Lebrun R, Kläui M, and Weides M (2020) Control of the coupling strength and linewidth of a cavity magnon-polariton. *Physical Review Research* 2(1): 013154. https://doi.org/10.1103/PhysRevResearch.2.013154.

Bozhko DA, Vasyuchka VI, Chumak AV, and Serga AA (2020) Magnon-phonon interactions in magnon spintronics (Review article). *Low Temperature Physics* 46(4): 383–399. https://doi.org/10.1063/10.0000872.

Candido DR, Fuchs GD, Johnston-Halperin E, and Flatté ME (2020) Predicted strong coupling of solid-state spins via a single magnon mode. *Materials for Quantum Technology* 1(1): 011001. https://doi.org/10.1088/2633-4356/ab9a55.

Chow KK and Hines ME (1966) Mode segregation effects in single crystal YIG. *Journal of Applied Physics* 37(13): 5000–5001. https://doi.org/10.1063/1.1708185.

Chumak AV, Vasyuchka VI, Serga AA, and Hillebrands B (2015) Magnon spintronics. *Nature Physics* 11(6): 453–461. https://doi.org/10.1038/nphys3347.

Colombano MF, Arregui G, Bonell F, Capuj NE, Chavez-Angel E, Pitanti A, Valenzuela SO, Sotomayor-Torres CM, Navarro-Urrios D, and Costache MV (2020) Ferromagnetic resonance assisted optomechanical magnetometer. *Physical Review Letters* 125(14): 147201. https://doi.org/10.1103/PhysRevLett.125.147201.

Flebus B and Tserkovnyak Y (2019) Entangling distant spin qubits via a magnetic domain wall. *Physical Review B* 99(14): 140403. https://doi.org/10.1103/PhysRevB.99.140403.

Harder M, Yang Y, Yao BM, Yu CH, Rao JW, Gui YS, Stamps RL, and Hu C-M (2018) Level attraction due to dissipative magnon-photon coupling. *Physical Review Letters* 121(13): 137203. https://doi.org/10.1103/PhysRevLett.121.137203.

Hartmann DMF, Wouters JJ, Schuricht D, Duine RA, and Kamra A (2021) Intersublattice entanglement entropy as an extensive property in antiferromagnets. *Physical Review B* 104(6): 064436. https://doi.org/10.1103/PhysRevB.104.064436.

Hirohata A, Yamada K, Nakatani Y, Prejbeanu I-L, Diény B, Pirro P, and Hillebrands B (2020) Review on spintronics: Principles and device applications. *Journal of Magnetism and Magnetic Materials* 509: 166711. https://doi.org/10.1016/j.jmmm.2020.166711.

Holstein T and Primakoff H (1940) Field dependence of the intrinsic domain magnetization of a ferromagnet. *Physics Review* 58(12): 1098–1113. https://doi.org/10.1103/PhysRev.58.1098.

Huebl H, Zollitsch CW, Lotze J, Hocke F, Greifenstein M, Marx A, Gross R, and Goennenwein STB (2013) High cooperativity in coupled microwave resonator ferrimagnetic insulator hybrids. *Physical Review Letters* 111(12): 127003. https://doi.org/10.1103/PhysRevLett.111.127003.

Kalinikos BA and Slavin AN (1986) Theory of dipole-exchange spin wave spectrum for ferromagnetic films with mixed exchange boundary conditions. *Journal of Physics C: Solid State Physics* 19(35): 7013–7033. https://doi.org/10.1088/0022-3719/19/35/014.

Kamra A, Thingstad E, Rastelli G, Duine RA, Brataas A, Belzig W, and Sudbø A (2019) Antiferromagnetic magnons as highly squeezed fock states underlying quantum correlations. *Physical Review B* 100(17): 174407. https://doi.org/10.1103/PhysRevB.100.174407.

Kikuchi D, Prananto D, Hayashi K, Laraoui A, Mizuochi N, Hatano M, Saitoh E, Kim Y, Meriles CA, and An T (2017) Long-distance excitation of nitrogen-vacancy centers in diamond via surface spin waves. *Applied Physics Express* 10(10): 103004. https://doi.org/10.7567/apex.10.103004.

Lachance-Quirion D, Tabuchi Y, Ishino S, Noguchi A, Ishikawa T, Yamazaki R, and Nakamura Y (2017) Resolving quanta of collective spin excitations in a millimeter-sized ferromagnet. *Science Advances* 3(7). https://doi.org/10.1126/sciadv.1603150. https://advances.sciencemag.org/content/3/7/e1603150.full.pdf.

Lachance-Quirion D, Wolski SP, Tabuchi Y, Kono S, Usami K, and Nakamura Y (2020) Entanglement-based single-shot detection of a single magnon with a superconducting qubit. *Science* 367(6476): 425–428. https://doi.org/10.1126/science.aaz9236.

Li J, Zhu S-Y, and Agarwal GS (2018) Magnon-photon-phonon entanglement in cavity magnomechanics. *Physical Review Letters* 121(20): 203601. https://doi.org/10.1103/PhysRevLett.121.203601.

Liu Z-X, Xiong H, and Wu Y (2019) Magnon blockade in a hybrid ferromagnet-superconductor quantum system. *Physical Review B* 100(13): 134421. https://doi.org/10.1103/PhysRevB.100.134421.

Neuman T, Wang DS, and Narang P (2020) Nanomagnonic cavities for strong spin-magnon coupling and magnon-mediated spin-spin interactions. *Physical Review Letters* 125(24): 247702. https://doi.org/10.1103/PhysRevLett.125.247702.

Nielsen MA and Chuang IL (2000) *Quantum Computation and Quantum Information*, first ed. Cambridge: Cambridge University Press.

Plenio MB and Knight PL (1998) The quantum-jump approach to dissipative dynamics in quantum optics. *Reviews of Modern Physics* 70(1): 101–144. https://doi.org/10.1103/RevModPhys.70.101.

Reid MD and Walls DF (1986) Violations of classical inequalities in quantum optics. *Physical Review A* 34(2): 1260–1276. https://doi.org/10.1103/PhysRevA.34.1260.

Rückriegel A, Kopietz P, Bozhko DA, Serga AA, and Hillebrands B (2014) Magnetoelastic modes and lifetime of magnons in thin yttrium iron garnet films. *Physical Review B* 89(18): 184413. https://doi.org/10.1103/PhysRevB.89.184413.

Sarma B, Busch T, and Twamley J (2021) Cavity magnomechanical storage and retrieval of quantum states. *New Journal of Physics* 23(4): 043041. https://doi.org/10.1088/1367-2630/abf535.

Schneider M, Brächer T, Breitbach D, Lauer V, Pirro P, Bozhko DA, Musiienko-Shmarova HY, Heinz B, Wang Q, Meyer T, Heussner F, Keller S, Papaioannou ET, Lägel B, Löber T, Dubs C, Slavin AN, Tiberkevich VS, Serga AA, Hillebrands B, and Chumak AV (2020) Bose-Einstein condensation of quasiparticles by rapid cooling. *Nature Nanotechnology* 15(6): 457–461. https://doi.org/10.1038/s41565-020-0671-z.

Skogvoll IC, Lidal J, Danon J, and Kamra A (2021) Tunable anisotropic quantum rabi model via a magnon-spin-qubit ensemble. *Physical Review Applied* 16(6): 064008. https://doi.org/10.1103/PhysRevApplied.16.064008.

Sonin EB (2010) Spin currents and spin superfluidity. *Advances in Physics* 59(3): 181–255. https://doi.org/10.1080/00018731003739943.

Soykal OO and Flatté ME (2010) Strong field interactions between a nanomagnet and a photonic cavity. *Physical Review Letters* 104(7): 077202. https://doi.org/10.1103/PhysRevLett.104.077202.

Tabuchi Y, Ishino S, Noguchi A, Ishikawa T, Yamazaki R, Usami K, and Nakamura Y (2015) Coherent coupling between a ferromagnetic magnon and a superconducting qubit. *Science* 349(6246): 405–408. https://doi.org/10.1126/science.aaa3693. https://science.sciencemag.org/content/349/6246/405.full.pdf.

Trifunovic L, Pedrocchi FL, and Loss D (2013) Long-distance entanglement of spin qubits via ferromagnet. *Physical Review X* 3(4): 041023. https://doi.org/10.1103/PhysRevX.3.041023.

Wang L, Yang Z-X, Liu Y-M, Bai C-H, Wang D-Y, Zhang S, and Wang H-F (2020) Magnon blockade in a PT-symmetric-like cavity magnomechanical system. *Annalen der Physik* 532 (7): 2000028. https://doi.org/10.1002/andp.202000028.

Wolf MS, Badea R, and Berezovsky J (2016) Fast nanoscale addressability of nitrogen-vacancy spins via coupling to a dynamic ferromagnetic vortex. *Nature Communications* 7(1): 11584. https://doi.org/10.1038/ncomms11584.

Yu W, Wang J, Yuan HY, and Xiao J (2019) Prediction of attractive level crossing via a dissipative mode. *Physical Review Letters* 123(22): 227201. https://doi.org/10.1103/PhysRevLett.123.227201.

Yuan HY and Duine RA (2020) Magnon antibunching in a nanomagnet. *Physical Review B* 102(10): 100402. https://doi.org/10.1103/PhysRevB.102.100402.

Yuan W, Zhu Q, Su T, Yao Y, Xing W, Chen Y, Ma Y, Lin X, Shi J, Shindou R, Xie XC, and Han W (2018) Experimental signatures of spin superfluid ground state in canted antiferromagnet Cr_2O_3 via nonlocal spin transport. *Science Advances* 4(4): eaat1098. https://doi.org/10.1126/sciadv.aat1098.

Yuan HY, Yan P, Zheng S, He QY, Xia K, and Yung M-H (2020a) Steady bell state generation via magnon-photon coupling. *Physical Review Letters* 124(5): 053602. https://doi.org/10.1103/PhysRevLett.124.053602.

Yuan HY, Zheng S, Ficek Z, He QY, and Yung M-H (2020b) Enhancement of magnon-magnon entanglement inside a cavity. *Physical Review B* 101(1): 014419. https://doi.org/10.1103/PhysRevB.101.014419.

Yuan HY, Cao Y, Kamra A, Duine RA, and Yan P (2022a) Quantum magnonics: When magnon spintronics meets quantum information science. *Physics Reports* 965: 1–74. https://doi.org/10.1016/j.physrep.2022.03.002.

Yuan HY, Sterk WP, Kamra A, and Duine RA (2022b) Master equation approach to magnon relaxation and dephasing. *Physical Review B* 106(22): 224422. https://doi.org/10.1103/PhysRevB.106.224422.

Zapf V, Jaime M, and Batista CD (2014) Bose-Einstein condensation in quantum magnets. *Reviews of Modern Physics* 86(2): 563–614. https://doi.org/10.1103/RevModPhys.86.563.

Zare Rameshti B, Viola Kusminskiy S, Haigh JA, Usami K, Lachance-Quirion D, Nakamura Y, Hu C-M, Tang HX, Bauer GEW, and Blanter YM (2022) Cavity magnonics. *Physics Reports* 979: 1–61. https://doi.org/10.1016/j.physrep.2022.06.001. Cavity Magnonics.

Zhang X, Zou C-L, Jiang L, and Tang HX (2016) Cavity magnomechanics. *Science Advances* 2(3). https://doi.org/10.1126/sciadv.1501286. https://advances.sciencemag.org/content/2/3/e1501286.full.pdf.

Zou J, Zhang S, and Tserkovnyak Y (2021) Bell-state generation for spin qubits via dissipative coupling. *arXiv:2108.07365*.

Spintronic materials

Sergio O Valenzuela[a,b], Pietro Gambardella[c], Kevin Garello[d], Olivier Klein[d], Juan F Sierra[b], and Jairo Sinova[e,f], [a]Institució Catalana de Recerca i Estudis Avançats (ICREA), Barcelona, Spain; [b]Catalan Institute of Nanoscience and Nanotechnology (ICN2), CSIC and the Barcelona Institute of Science and Technology (BIST), Bellaterra, Barcelona, Spain; [c]Department of Materials, ETH Zurich, Zurich, Switzerland; [d]Universite Grenoble Alpes, CEA, CNRS, Grenoble INP, SPINTEC, Grenoble, France; [e]Institut für Physik, Johannes Gutenberg Universität Mainz, Mainz, Germany; [f]Institute of Physics, Academy of Sciences of the Czech Republic, Staré Město, Czech Republic

© 2024 Elsevier Ltd. All rights reserved.

Introduction 160
Historical overview 162
Key materials: Issues and research directions 164
Conventional materials and current applications 164
  Giant magnetoresistance (GMR) 164
  Tunnel magnetoresistance (TMR) 164
  STT-MRAM 165
  SOT-MRAM 165
  Voltage-control of magnetic anisotropy (VCMA) 166
Heusler compounds (HC) 167
Two-dimensional (2D) van der Waals materials 168
Antiferromagnets and altermagnets 170
  Antiferromagnets 170
  Altermagnets 171
Magnetic insulators 172
  Magnons as carriers of information 172
  Non-linear magnonic devices 173
  Interaction of magnons with other carriers of information 173
Conclusion 173
Acknowledgments 174
References 174

Abstract

Progress in spintronics has been achieved with novel device concepts and the subsequent development of optimized materials and heterostructures to implement them. The heterostructures typically combine magnetic and nonmagnetic elements, which enable the integration of non-volatile magnetic memories and sensors in electrical circuits. This chapter provides an overview of spintronic devices that have found industrial applications with a focus on the materials and heterostructures being used. It further discusses selected material families that can potentially enhance device performance and/or create new application opportunities, including transition metals, magnetic insulators, antiferromagnets, altermagnets, Heusler compounds and van der Waals materials.

Key points

- Introduction to spintronics devices, magnetic memories and sensors
- Historical overview on spintronic concepts and material development
- Description of selected key phenomena and materials
  - Giant magnetoresistance (GMR)
  - Tunnelling magnetoresistance (TMR)
  - Magnetic random-access memory (MRAM)
    - Spin-transfer torque (STT)-MRAM
    - Spin-orbit torque (SOT)-MRAM
    - Voltage control of the magnetization (VCMA)
  - Magnonics
  - Transition metals
  - Heusler compounds
  - 2D van der Waals materials
  - Antiferromagnets and altermagnets
  - Magnetic insulators
- Future directions

https://doi.org/10.1016/B978-0-323-90800-9.00229-8

Abbreviation

AFM	antiferromagnet
AMR	anisotropic magnetoresistance
BEOL, FEOL	back-end-of-line, front-end-of-line
BP	black phosphorous
CIP	current in plane
CMOS	complementary metal-oxide semiconductor
CPP	current-perpendicular-to-plane
DW	Domain wall
FL	free layer
GMR	giant magnetoresistance
HC	Heusler compound
ISGE	inverse spin galvanic effect
IP	in-plane
MTJ	magnetic tunnel junction
MRAM	magnetoresistive random access memory
PMA	perpendicular magnetic anisotropy
OOP	out of plane
RA	resistance-area
REE	Rashba-Edelstein effect
RL	reference layer
SAF	synthetic antiferromagnet
SHE	spin Hall effect
SMR	spin Hall magnetoresistance
SOI	spin-orbit interaction
SOT	spin-orbit torque
SRAM	static random-access memory
STT	spin transfer torque
SW	spin wave
TMDC	transition metal dichalcogenide
TMR	tunnel magnetoresistance
TI	topological insulator
USMR	unidirectional spin Hall magnetoresistance
VCMA	voltage control of magnetic anisotropy
vdW	van der Waals
YIG	yttrium iron garnet

Introduction

Spintronics utilizes the electron spin degree of freedom to store and manipulate information, typically relying on material heterostructures that include magnetic and nonmagnetic elements. The interconversion of electrical and spin signals enables the seamless integration of non-volatile magnetic memories and sensors in electrical circuits, which brings substantial benefits in terms of dimensional scaling, power consumption, and data processing speed (Žutić et al., 2004). Recent advances in the understanding of charge-spin interconversion phenomena and the optimization of materials have opened new avenues to incorporate both Boolean and non-Boolean logic functions as well as high-frequency microwave devices in spintronic circuits (Sinova et al., 2015; Manchon et al., 2019; Dieny et al., 2020).

Commercial implementations of spintronic sensors and magnetic random-access memories (MRAMs) are based on the anisotropic, giant or tunnelling magnetoresistance effects (Apalkov et al., 2016; Zheng et al., 2019; Dieny et al., 2020; Khan et al., 2021). Magnetic sensors are used in automotive, consumer electronics, healthcare, and industrial applications (Zheng et al., 2019). They can detect small changes in magnetic field strength or in the orientation and position of a magnet, making them well suited for applications in hard disk drives, navigation, positioning, speed measurements and tracking. The anisotropic magnetoresistance (AMR) refers to the change in electrical resistance of a ferromagnetic material when its magnetization is rotated relative to the current direction. AMR sensors are easy to integrate, relatively small and have a low-cost compared to other magnetic sensing technologies. Giant magnetoresistance (GMR) and tunnel magnetoresistance (TMR) sensors offer higher sensitivity and resolution than AMR sensors.

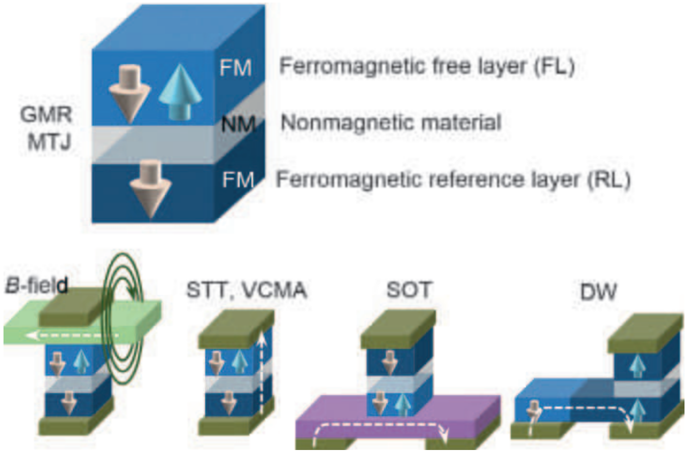
FM
Ferromagnetic free layer (FL)
GMR
MTJ
NM
Nonmagnetic material
FM
Ferromagnetic reference layer (RL)
B-field
STT, VCMA
SOT
DW

Fig. 1 (a), The basic unit of GMR and TMR devices consists of two ferromagnetic layers (FM) separated by a nonmagnetic (NM) spacer. The NM spacer can be a metal (GMR), or an insulator (TMR) to create a magnetic tunnel junction (MTJ). The magnetization of the free layer (FL) can change direction while that of the reference layer (RL) is pinned. (b), The main mechanisms to change the FL magnetization are (from left to right): the Oersted (or external magnetic) fields, spin-transfer torque (STT), the voltage control of the magnetic anisotropy (VCMA), the spin-orbit-torque (SOT) and domain-wall (DW) motion. Figure adapted from Krizakova V, Perumkunnil M, Couet S, Gambardella P, Garello K, (2022) Spin-orbit torque switching of magnetic tunnel junctions for memory applications. *Journal of Magnetism and Magnetic Materials*, 562, 169692. doi:10.1016/j.jmmm.2022.169692.

The basic unit to observe the GMR and TMR effects is a trilayer FM/NM/FM consisting of two ferromagnetic layers (FM) separated by a nonmagnetic (NM) spacer (Fig. 1). The resistance of the trilayer changes with the relative alignment of the magnetization in the two FM layers. For both sensing and memory applications, the magnetization of one of the two FM layers in the FM/NM/FM stack is pinned and serves as "reference," whereas the other is "free" to change direction under a magnetic field or a spin-polarized current. The FM layers have a preferential magnetization direction, dictated by the uniaxial magnetic anisotropy, which is induced by either crystalline, shape or interfacial effects. Additionally, a synthetic antiferromagnet (SAF) is deposited above (or below) the reference layer (RL) in order to pin its magnetization. The SAF is composed of a high-coercivity magnetic multilayer stack, which is coupled to the RL through a thin nonmagnetic spacer by the Ruderman-Yosida-Kasuya-Kittel (RKKY) interaction. Alternatively, for in-plane magnetized FM/NM/FM structures, the RL can be pinned by exchange bias to an adjacent antiferromagnetic layer (Nogués and Schuller, 1999). In magnetic memory applications, a logic bit state, 0 or 1, is encoded in the direction of the magnetization of the free layer (FL). The bit state is then read by a magnetoresistance measurement that distinguishes between the parallel (P) and antiparallel (AP) alignment between the magnetizations of the FL and RL. In sensing applications, the magnetization of the FL tilts in response to an external magnetic field, e.g., in proximity of a magnetic object, and the relative angle with the magnetization of the RL is measured by analogue variations of the GMR or TMR effects, depending on the type of device.

State-of-the-art MRAM cells rely on the TMR effect, in which the NM spacer is a thin insulator and the trilayer forms a magnetic tunnel junction (MTJ). Typical MRAM stacks are built by numerous ultrathin layers, each of them with a distinct role in determining the memory performance (Apalkov et al., 2016; Dieny et al., 2020; Yang et al., 2022). The number and purpose of the layers and the design of the MTJ have evolved over the years following several major material and technological breakthroughs aimed at increasing the TMR, lowering the power required to control the FL magnetization, and maintaining thermal stability and data retention when downscaling the MTJs. The spin-transfer torque (STT) effect has emerged as a key technology to switch the FL magnetization using electrically generated spin currents (Chappert et al., 2007; Ralph and Stiles, 2008; Stamps et al., 2014; Apalkov et al., 2016; Sander et al., 2017; Vedmedenko et al., 2020; Na et al., 2021; Brataas et al., 2012) (Fig. 1). The current through the tunnel barrier is spin-polarized, leading to the FL magnetization reversal owing to the transfer of angular momentum. STT-MRAM are commercialized as standalone memories and wearable electronics. They are also considered as the best candidates for embedded non-volatile applications, as replacement of embedded flash and static RAM (SRAM) (see Section "Conventional materials and current applications").

The figures of merit of GMR and TMR devices depend critically on the composition and thickness of all the magnetic and nonmagnetic layers in the stack, and particularly on their structural quality, including interfacial stoichiometry and roughness. For technological applications, the fact that interfacial effects dominate the GMR and TMR is an advantage, as it helps reduce the devices volume without impairing their performances and the power required to switch them. Minimizing the device size also reduces the self-demagnetizing fields produced by both the RL and the FL. For sensors, this implies a larger sensitivity of the FL to external magnetic fields, while, for memories, this implies smaller interaction between neighboring devices and therefore larger bit density. Reducing the variability of the magnetic and electrical parameters across devices patterned on the same wafer and from wafer to wafer is crucial for applications. This is important for MTJ devices, in which the TMR scales exponentially with the tunnel barrier thickness.

The growing demand for spintronic devices with high-density, high-speed and low-power consumption necessitates advances in terms of materials and device architectures (Dieny et al., 2020). This chapter starts with an historical overview of conventional and emerging materials used in spintronics. This overview is complemented by an in-depth description of the different materials, concepts and envisioned material advantages and bottlenecks. Requirements for further progress, novel materials that could meet those requirements, and the opportunities that can arise with them are also discussed. These materials include Heusler compounds, 2D van der Waals (vdW) materials, antiferromagnets, altermagnets and magnetic insulators. Fig. 2 highlights some of the main milestones for each of the selected material families.

The chapter ends with a summary of future directions. Given the intense research activity on spintronics, it is not possible to cover the vast literature available in a limited space. As a complement to this chapter, the reader is instead referred to comprehensive reviews, books, roadmaps and perspectives that have been published in recent years.

Historical overview

The development of spintronics started with the discovery of the GMR effect in 1988 (Fert and Van Dau, 2019) (Fig. 2). GMR rapidly found several applications as sensors and in 1996 as read heads in hard disk drives. The discovery of material systems with TMR exceeding 100% at room temperature led to a generational change in the early 2000s and the widespread adoption of MTJs as the basic unit of magnetic storage and sensing (Parkin et al., 2003; Miao et al., 2011; Dieny et al., 2020). Although AMR and GMR effects are still being used for low-cost sensing applications, TMR is ubiquitous in the most advanced device generations. Because the density of states of FM materials are spin-split and tunnelling is a spin conserving process, the TMR depends on the product of the effective spin polarization of the two FM electrodes. This dependence leads to a maximum room temperature TMR ratio of about 70% in amorphous Al_2O_3 barriers sandwiched between transition-metal electrodes such as CoFe, owing to the partial spin polarization of the conduction electrons near the Fermi level. A breakthrough occurred with the introduction of epitaxial junctions

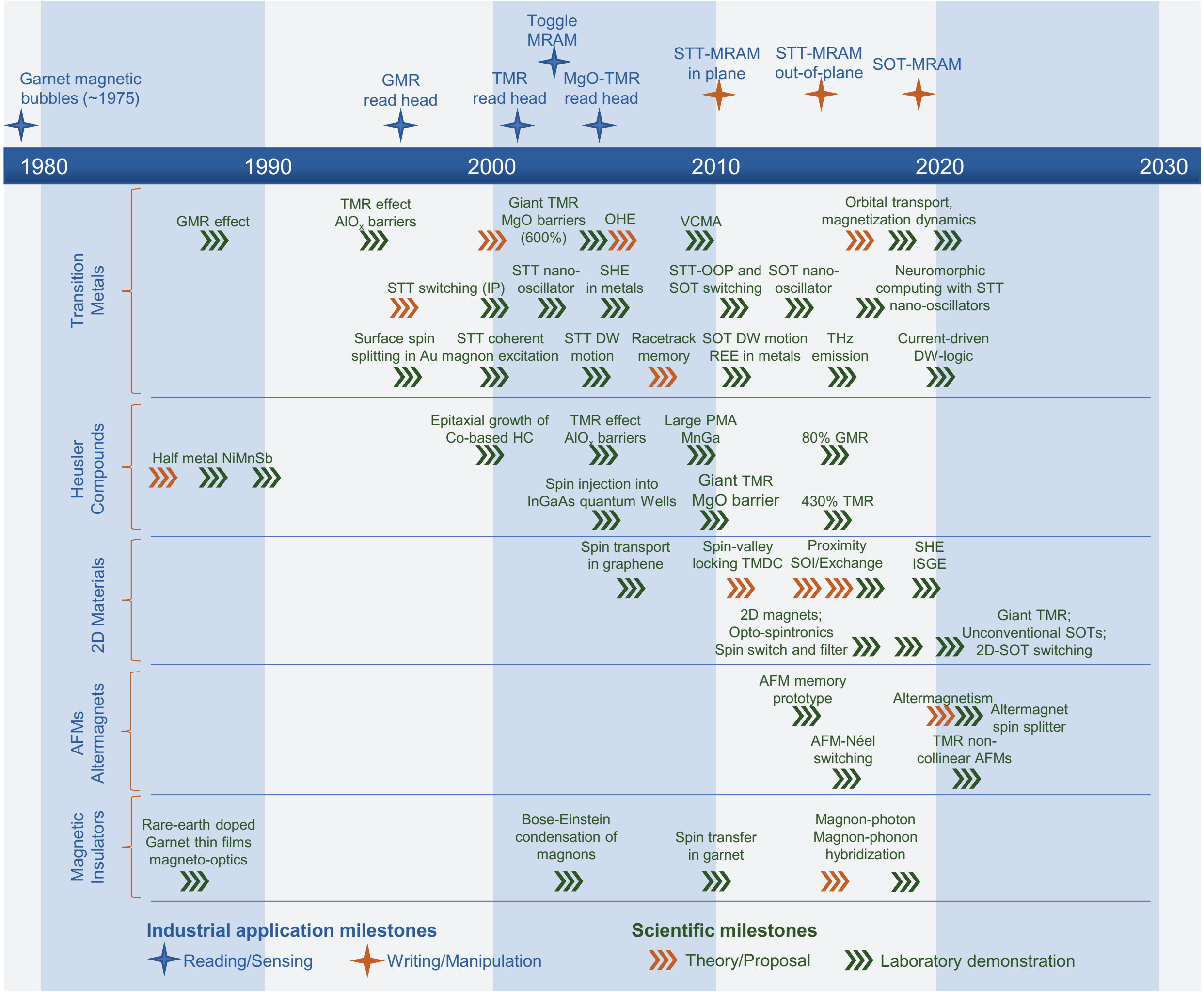
Toggle MRAM
Garnet magnetic bubbles (~1975)
GMR read head
TMR read head
MgO-TMR read head
STT-MRAM in plane
STT-MRAM out-of-plane
SOT-MRAM
1980
1990
2000
2010
2020
2030
Transition Metals
GMR effect
TMR effect AlO_x barriers
Giant TMR MgO barriers (600%)
OHE
VCMA
Orbital transport, magnetization dynamics
STT switching (IP)
STT nano-oscillator
SHE in metals
STT-OOP and SOT switching
SOT nano-oscillator
Neuromorphic computing with STT nano-oscillators
Surface spin splitting in Au
STT coherent magnon excitation
STT DW motion
Racetrack memory
SOT DW motion REE in metals
THz emission
Current-driven DW-logic
Heusler Compounds
Half metal NiMnSb
Epitaxial growth of Co-based HC
TMR effect AlO_x barriers
Large PMA MnGa
80% GMR
Spin injection into InGaAs quantum Wells
Giant TMR MgO barrier
430% TMR
2D Materials
Spin transport in graphene
Spin-valley locking TMDC
Proximity SOI/Exchange
SHE ISGE
2D magnets; Opto-spintronics Spin switch and filter
Giant TMR; Unconventional SOTs; 2D-SOT switching
AFMs Altermagnets
AFM memory prototype
Altermagnetism
Altermagnet spin splitter
AFM-Néel switching
TMR non-collinear AFMs
Magnetic Insulators
Rare-earth doped Garnet thin films magneto-optics
Bose-Einstein condensation of magnons
Spin transfer in garnet
Magnon-photon Magnon-phonon hybridization
Industrial application milestones
Reading/Sensing
Writing/Manipulation
Scientific milestones
Theory/Proposal
Laboratory demonstration

Fig. 2 Spintronic milestones for industrial developments and scientific advances associated to the material families discussed in this chapter.

and crystalline MgO barriers, in which the electron tunnelling probability additionally depends on the symmetry of the wavefunctions penetrating the barrier. Experimentally demonstrated TMR values in CoFeB/MgO/CoFeB junctions exceed 600% at room-temperature (Miao et al., 2011). The largest TMR reported so far has been obtained using $Co_xFe_{80-x}B_{20}$ electrodes with $x = 20$–40% and 1–2 nm-thick MgO barriers.

No other materials compatible with industrial process requirements have been found to improve the TMR and, in the last decade, applications have evolved around MgO-based MTJs. The crystalline properties and TMR of the structures have steadily improved and suitable SAF multilayers and interfacial perpendicular magnetic anisotropy (PMA) have been developed. However, MgO-based MTJ devices appear to be reaching their limit. As they are made smaller, and the MgO tunnel barrier thinner, several technological challenges are becoming difficult to overcome, including side wall re-deposition, the increasing aspect ratio of etched structures or the relative increase of the MgO insulator roughness.

Besides GMR and TMR, other magnetization readout mechanisms, relying on charge spin interconversion have been proposed. They include the spin Hall magnetoresistance (SMR) and unidirectional spin Hall magnetoresistance (USMR). Their sensitivity is relatively small, and their primary use has been to determine the magnetic state of insulators in fundamental research studies.

Writing in commercialized MRAM has been achieved using a magnetic field, generated by an applied current (implemented in toggle MRAM), and by the previously mentioned STT (Figs. 1 and 2). Interfacial PMA has become crucial because perpendicularly magnetized stacks downscale better than the in-plane magnetized ones (Dieny and Chshiev, 2017). This improves the trade-off between the thermal stability of the FL magnetization and the write current for the switching dynamics induced by STT. However, an enhanced PMA, required when the memory is downscaled, results in increased current densities to achieve magnetization switching, which in turn increase energy consumption and can damage the MTJ.

The voltage control of magnetic anisotropy (VCMA) has been proposed as a solution to assist or directly induce magnetization switching (Dieny and Chshiev, 2017; Miwa et al., 2018; Rana and Otani, 2019; Yamamoto et al., 2022). In addition, the spin-orbit torque (SOT) is an alternative to the STT that uses a charge current flowing in a heavy metal layer to inject a spin-polarized current into the adjacent FL through spin-orbit coupling effects such as the spin-Hall and/or Rashba–Edelstein (inverse spin galvanic) effect (Sinova et al., 2015; Manchon et al., 2019; Krizakova et al., 2022). Unlike STT technology, magnetization reversal by SOT can be achieved without passing a current through the MTJ tunnel barrier (Fig. 1). By decoupling of the write and read current paths, it circumvents write errors during read operation and reduces the risk of dielectric breakdown. Although neither VCMA nor SOT are yet sufficiently strong for implementation in commercial devices, their combination with STT is promising for improving the efficiency, reliability and speed of MRAMs (Krizakova et al., 2022).

Besides the successful magnetic sensors and MRAM, other concepts are under development such as racetrack memories and logic devices using the propagation of magnetic skyrmions or domain walls (DW), driven by either STT or SOT (Atkinson et al., 2006; Parkin and Yang, 2015; Soumyanarayanan et al., 2016; Fert et al., 2017; Hrabec et al., 2020; Dieny et al., 2020). Spintronics is also being investigated for wireless communication applications. Spin torques in nanoscale MTJs can lead not only to magnetization switching but also to self-sustained oscillations of the FL magnetization, which can be used for dc to radiofrequency (RF) conversion in microwave signal generators; the reciprocal effect can be used for microwave signal detection (Demidov et al., 2017). STT-nano-oscillators have also been investigated in neuromorphic computing architectures (Christensen et al., 2022) while THz emission has been achieved in magnetic multilayers (Vedmedenko et al., 2020). Magnonics, which has attracted significant attention in recent years, is a different approach to spin logic that encodes information in the amplitude or phase of spin waves (SW) in magnetic metals or insulators (Stamps et al., 2014; Sander et al., 2017; Brataas et al., 2020; Barman et al., 2021; Pirro et al., 2021; Chumak et al., 2022).

Regarding material processing, new protocols are required for improving the downscaling of devices (for example to avoid sidewall redeposition). Other proposals target novel families of materials while device concepts and applications are continuously put forward, which could benefit from material development. Heusler materials is one such family (Dieny et al., 2020; Hirohata and Lloyd, 2022) (Fig. 2). They comprise a vast catalogue of compounds with high degree of flexibility and physical properties, ranging from semiconductors with tuneable bandgap, superconductors, half-metallic FMs, compensated antiferromagnets, and even topological insulators. Alloys based on Heusler compounds (HC) are promising materials for spintronic applications due to their high saturation magnetization and Curie temperatures, and predicted half-metallic ferromagnetism, i.e., they exhibit metallic behavior for one spin channel and present a gap at the Fermi level for the other. Large GMR and TMR effects have been demonstrated with HCs. However, these materials tend not to perform well at high temperatures and processing with industrial compatible methods is in development.

The atomically thin nature of 2D materials offers significant opportunities (Han et al., 2014; Avsar et al., 2020; Sierra et al., 2021; Yang et al., 2022). It promotes the creation of artificial quantum materials in the form of van der Waals (vdW) heterostructures, where the 2D crystals attach to each other via weak vdW interactions. This represents a new paradigm in material design that is particularly attractive for spintronic devices, which typically harness their functionalities out of thin layers of magnetic and non-magnetic materials and the interfaces between them. Given the ever-growing number of 2D materials available, it might be plausible to replace their 3D counterparts, one by one, whenever the desired functionalities are identified (Fig. 2). VdW heterostructures have the potential advantage of atomically smooth interfaces and reduced thicknesses, eventually down to the monolayer limit, which are both required for downscaling. They would also allow engineers to seamlessly integrate multiple functionalities because the stacking of 2D materials is expected to be less restrictive regarding (crystalline) matching between the involved layers. The 2D material functionalities could go beyond applications in conventional MRAM and sensors and include opto-spintronics, antiferromagnetic spintronics and magnonics. However, the main challenges of any electronic technology based on 2D materials are upscaling and integration. 2D materials currently suffer from reproducibility and a lack of industrially compatible growth and device fabrication processes (Sander et al., 2017; Och et al., 2021; Yang et al., 2022).

Another highly influential research field in the last decade is the control and manipulation of magnetically ordered materials with zero net magnetization, such as antiferromagnets (Jungwirth et al., 2016; Baltz et al., 2018) and the recently coined altermagnets (Šmejkal et al., 2022b). The aim is to exploit the advantages that come from an absence of stray magnetic fields and a natural excitation at high frequencies, in the THz regime (Gomonay et al., 2018). The compensated magnetic order results in an insensitivity to external magnetic fields and the possibility for optimal space downscaling of memory devices due to the absence of demagnetizing fields. At the same time, the high resonant frequencies, due to the exchange enhancement effect that couples the different spin sublattices, makes these materials natural candidates for optical manipulation devices that bridge the THz communication gap (Fig. 2) The main challenges are the need to develop efficient read-out and control methods of the material magnetic state.

Conventional devices rely on the delocalized electrons present in conducting materials to carry the spin information, which induces losses by Joule heating. However, electrically insulating magnetic materials also enable the spin information to flow between localized magnetic moments via propagating SWs, which transmit information from an atomic site to the other without any Joule dissipation (Fig. 2) (Barman et al., 2021). This offers insulating materials an advantage and several research directions attempt to capitalize on it to achieve technical improvements for manipulating and transmitting information, including non-Boolean, parallel, and neuromorphic computing (Brataas et al., 2020). As in some of the other new materials discussed in this chapter, compatibility with current industrial processes and scalability are arguably the main challenges that need to be resolved.

Key materials: Issues and research directions

Conventional materials and current applications

Giant magnetoresistance (GMR)

The GMR originates from the spin-dependent conductivity of electrons in FM transition metals (Fe, Co, Ni and their alloys) and at FM/NM interfaces (Parkin, 1995). Exchange-biased GMR structures, also called spin valves, are entirely made of metals, typically several repetitions of Co/Cu/Co or Fe/Cr/Fe trilayers coupled to a metallic antiferromagnet with high Néel temperature such as IrMn or FeMn. The best NM spacers are metals with a long electron mean free path, such as Cu, Ag, and Au, and only 1–2 nm-thick in order to minimize current shunting and scattering of the spin-polarized electrons transmitted and reflected between the FM layers (Bass and Pratt, 2007). In the current-in-plane (CIP) geometry, the thickness of the FM layers must be smaller than the largest of the mean free paths of the majority and minority spin electrons in order for the current density in one FM layer to be affected by the magnetization of the next FM layer. Because interfacial spin-dependent scattering often dominates over bulk spin-dependent scattering, the optimal FM thickness is around 1–5 nm. The CIP-GMR is further decreased if the current flows in the nonmagnetic seed layers and capping layers used to promote growth and for protection, respectively. In the current-perpendicular-to-plane (CPP) geometry, in contrast, the electrons necessarily flow through the entire multilayer structure and the magnetoresistance is less affected by the mean free paths of the FM layers. In either geometry, the GMR increases when electrons propagate across many FM/NM interfaces. The largest GMR ratios, defined as $(R_{AP} - R_P)/R_P$, where $R_{AP(P)}$ is the resistance of the AP (P) state, are indeed found in structures with tens of repetitions of the thinnest possible FM and NM layers, and reach up to 65% in $[\text{Co}(0.8\text{ nm})/\text{Cu}(0.8\text{ nm})]_{60}$ multilayers at room temperature. Spin-valve devices, however, typically have lower GMR ratios of 25% or less (Parkin et al., 2003).

Tunnel magnetoresistance (TMR)

The highest TMR has been reported in Fe and CoFe grown epitaxially with body-centered cubic (bcc) structure matching the MgO crystal lattice. However, industrial MTJs are obtained by depositing amorphous CoFeB and textured MgO(001) layers using magnetron sputtering, followed by thermal annealing between 300 °C and 400 °C (Miao et al., 2011). This process minimizes the formation of defects in the barrier owing to the growth of high-quality MgO on atomically smooth CoFeB. It also leads to thermally-induced recrystallization of the electrode interfaces and diffusion of B away from the crystallized CoFe layers, which in turn provides the local epitaxial order between the bcc CoFe and MgO (001) lattices that is required for symmetry filtering of the tunnelling electrons. The deposition of B-getter layers next to the FM layers, such as Ta, W, and Hf, further improves the crystallization process and TMR, provided that the getter elements do not diffuse toward the MgO barrier upon annealing, degrading both the crystalline quality of the FM and the barrier itself. In principle, half-metal electrodes with only one spin sub-band crossing the Fermi level, such as $La_{2/3}Sr_{1/3}MnO_3$, CrO_2, and some Heusler alloys (see Section "Heusler compounds (HC)"), can achieve significantly higher TMR values than CoFeB. However, these materials do not perform well at high temperature because magnon and phonon excitations impair their half-metallic character.

Other useful properties that make the CoFeB/MgO/CoFeB system the basis of most MTJ designs are the resilience to thermal annealing required for compatibility with back-end-of-line (BEOL) complementary metal-oxide-semiconductor (CMOS) processes and the possibility to fabricate MTJs with FM layers magnetized in-plane or out-of-plane. Whereas in-plane magnetization is easily obtained using CoFeB layers with thickness above 2–3 nm owing to shape anisotropy, out-of-plane magnetized CoFeB are thinner and deposited next to a heavy metal such as Ta or W to improve the interfacial PMA. The interface between the magnetic metals and the oxide promotes PMA due to hybridization effects between the *d*-orbitals of Co and Fe and the 2*p* orbitals of oxygen (Dieny and Chshiev, 2017). The magnetic anisotropy barrier of the FL is usually expressed in terms of a uniaxial anisotropy energy constant

$K = 0.8\text{–}1.6 \times 10^6$ J/m^3 times the magnetic volume V, which determine the thermal stability factor $\Delta = KV/k_BT$. Although $\Delta \geq 40$ is required to ensure data retention over 10 years at room temperature, it is commonly assumed that $\Delta \geq 70$ is necessary to maintain information at operating temperatures, reaching up 150 °C for certain applications. MTJs based on FM layers with PMA, also called perpendicular MTJs, have better stability factors compared to in-plane MTJs of equal size, and lower stray fields, which are important properties for good readability, size reduction, and densification. On the other hand, MTJs with large Δ require larger fields or currents for switching the FL magnetization. Typical TMR reported in MTJs for MRAM applications are about 180% for perpendicular MTJs, and 250% for in-plane MTJs. This is mostly due to the thicker magnetic layers that can be used in in-plane MTJs, which improve the spin polarization of the tunnelling electrons. A further increase of Δ in perpendicular MTJs can be obtained by adopting a dual-FL/MgO structure, in which an extra MgO/CoFeB interface enhances the PMA (Dieny and Chshiev, 2017).

The RL is coupled to a hard SAF multilayer, typically $[\mathrm{Co/Pt}]_N/\mathrm{Ru}/[\mathrm{Co/Pt}]_M$, by a thin nonmagnetic metal layer such as Ru, W or Ta in order to pin its magnetization. This metal insertion is equally important to decouple the SAF layer texture, usually (111), from the (100) CoFe texture. The SAF is used also to minimize the stray field from the RL, which is crucial to ensure symmetric switching current of the FL. In general, extensive stack engineering and optimization are required to optimize the TMR and Δ while remaining compatible with the BEOL CMOS thermal budget. The device resistance is determined by the tunnel barrier thickness, which is characterized by the resistance-area-product (RA). The optimal RA is strongly dependent on the application domain and dimensions of the device. It is tuned accordingly to the reading speed requirements, i.e., impedance matching, and the minimum current that can be detected by the peripheral electronics. The RA targets are 3–5 $\Omega.\mu\mathrm{m}^2$ (5–10 kΩ) for STT-MRAMs, $\sim$0.5 $\Omega.\mu\mathrm{m}^2$ for hard drive read heads, and $\sim$1000 $\Omega.\mu\mathrm{m}^2$ for large area sensors. Decreasing the RA below 10 $\Omega.\mu\mathrm{m}^2$ is relevant for further miniaturization of the MRAM bit cells, but usually involves a decrease of the TMR.

STT-MRAM

The STT strength is proportional to the spin polarization and amplitude of the tunnelling current, which makes it naturally compatible with the materials and processes used to optimize the TMR in MTJ devices (Dieny and Prejbeanu, 2017). STT allows for using two-terminal MTJs with shared reading and writing paths (Fig. 1), leading to a compact design of the MRAM bit cells scalable to 4-6F^2, where F is the half distance between adjacent cells. The critical STT switching current is proportional to the magnetic damping parameter, magnetic volume, and magnetic anisotropy of the FL, and thus downscales favorably with the area of the MTJ. The RA product of the MgO tunnel barrier and the critical current determine the size and voltage of the transistor used to selectively switch the MTJ. Typical RA and critical currents density for STT-MRAMs are in the range of 3–5 $\Omega.\mu\mathrm{m}^2$ and 3–5 MA.cm^{-2}, respectively.

The first step of the STT-MRAM manufacturing process is the front-end-of-line (FEOL) fabrication of transistors on the semiconductor wafer followed by metallic layers (lines and via) routing their electrical contacts to a bottom electrode contact for the MTJ. The BEOL process consists of magnetic stack deposition, photolithography, etching, dielectric isolation, metal contacts and passivation (Gaidis, 2017). A chemical-mechanical polishing step is required to smooth the substrate prior to each integration module and is critical for the deposition of the magnetic stack. The root mean square substrate roughness should be of the order of 0.1 nm in order to obtain high TMR values, large breakdown voltage, and tight distribution of the electrical and magnetic parameters of the MTJs. Rough MgO interfaces should be avoided as they lead to magnetostatic coupling of the free and reference layer and pinhole formation through the barrier. The process temperature should remain below 400 °C in order to minimize interface diffusion between the different layers in the stack while remaining BEOL compatible. Subtractive patterning by ion beam etching or reactive ion etching is used to define the MTJ pillars, which requires a metallic hard mask (usually TiN) to withstand the etchants used for the magnetic materials. The hard mask also provides a self-aligned top contact to the MTJ device.

High-performance STT-MTJ cells are included in the first MRAMs that have been commercialized as replacement for embedded flash memory. Additionally, owing to their scalability, reduced write energy per bit, low leakage, high-speed and endurance, STT-MRAMs represent one of the most appealing non-volatile RAM technologies available for last-level cache memory replacement for internet of things (IoT) applications, always-on processors, and edge artificial-intelligence (AI) computing. Challenges for the further deployment of STT-MRAMs are of two types. First, the fabrication of dense STT-MRAMs arrays below the 14-nm technology node is hindered by the etching of magnetic films, which leads to by-products that cause sidewall redeposition, corrosion, and electrical short of the MTJ. Proposed solutions include combining reactive ion etching and ion beam etching as well as decreasing the thickness of the hard mask to reduce shadowing effects. Second, the shared reading/writing path increases the susceptibility to erroneous writing, read disturbance, and tunnel barrier degradation. These effects become prominent at high operation frequencies, which effectively limits the writing latency to >10–20 ns. The inherent stochastic character of STT switching also affects the writing latency for low amplitude and duration of the current pulses. The speed and endurance limits of STT-MRAMs can be significantly extended by combining STT with other writing approaches, such as SOT switching and VCMA, which promote deterministic reversal of the FL and do not require passing a strong electrical current through the MTJ barrier.

SOT-MRAM

SOT-MRAM exploits the same CoFeB/MgO/CoFeB/SAF basic structure of STT-MTJs, which makes them compatible with most of the BEOL processes developed for STT-MRAMs. The distinguishing feature is the implementation of the SOT current line as a two-terminal bottom electrode (Fig. 1). The main advantage of SOT-MRAMs is the combination of high switching speed and endurance, which allows for quasi-deterministic reversal of the FL on a 100 ps timescale with sub-ns stochastic distribution of the switching times in perpendicular MTJs. Moreover, because the switching current does not flow through the tunnel barrier, its thickness and RA can be tuned for best reading efficiency and speed without affecting the writing process.

SOTs are a manifestation of the relativistic spin-orbit interaction (SOI) that couples the orbital electron motion to the electron's spin. On the microscopic level, their origin can be explained by different mechanism (Manchon et al., 2019). When a charge current is passed through a nonmagnetic conductor, the SOI mediates its conversion into a transverse spin current that propagates toward the interfaces and where it results in spin accumulation. This mechanism is known as the spin Hall effect (SHE) and is prominent in heavy metals (Sinova et al., 2015). In the presence of broken inversion symmetry, e.g., at the conductor's interface, electrons additionally experience an electric field perpendicular to the interface plane, which acts as a magnetic field in the electron's rest frame and results in non-equilibrium spin accumulation at the interface. This mechanism is known as the Rashba-Edelstein effect (REE) or inverse spin galvanic effect (ISGE) and is prominent at the interface of metals having different electronegativity, oxide interfaces, and 2D materials (Manchon et al., 2015; Gambardella and Miron, 2011). The ISGE is also responsible for charge-spin conversion in materials with spin-momentum locked electron states, such as topological insulators and Weyl semimetals (Bihlmayer et al., 2022). A combination of these effects is also possible, in conjunction with additional phenomena due to electron scattering at the interface between magnetic and nonmagnetic conductors and the generation of spin currents within a magnetic material. Recently, orbital analogues of the SHE and ISGE have been proposed as additional mechanisms for the generation of SOT, provided that the SOI converts an orbital current into a spin current inside or outside the magnetic layer (Go et al., 2021). Overall, the multiplicity of effects that can generate the SOT allows for a wide choice of materials and optimization strategies to maximize their strength and efficiency for magnetization switching.

The most studied sources of SOT are the 5*d* heavy metals Pt, Ta, and W (Manchon et al., 2019). They exhibit torque efficiencies ξ ranging from 0.1 to 0.5, where ξ is the ratio between the spin current effectively converted into a torque and the charge current used to produce the spin current. In addition to ξ, other relevant figures of merit are the resistivity ρ, the spin Hall conductivity $\sigma_{SH} = \xi\rho^{-1}$ and the spin diffusion length λ_s. The first two parameters determine the power density dissipated in the SOT material, while the third determines its thickness. The interfacial spin accumulation decays over a distance of the order of λ_s, which is only a few nm in the 5*d* metals. This makes it possible to maximize the SOT produced by very thin nonmagnetic layers, thereby reducing the total current required to achieve, e.g., magnetic switching of an adjacent magnet. Alloys or multilayers containing 5*d* metals, such as. AuPt or $[\mathrm{Ti/Pt}]_N$, exhibit larger ξ compared to single-element systems due to enhanced electron scattering and resistivity. Owing to the combination of strong SOI and relatively small resistivity, the spin Hall conductivity in these materials is among the largest measured, reaching up to $10^5 - 10^6\ (\Omega m)^{-1}$.

Metallic antiferromagnets such as MnPt and IrMn are also strong SOT sources, which additionally provide exchange bias to the magnetic layer (Manchon et al., 2019). Interface engineering by nitrification or oxidation of the heavy metal, insertion of ultrathin spacer layers, and the use of electrically insulating antiferromagnetic layers can further improve ξ due to enhanced spin transmission and interfacial spin-orbit scattering. Among the 4*d* metals, Pd presents sizable SOT and enhances PMA. The 3*d* metals that generate strong orbital currents can also be used as SOT sources, in particular Cr, V and Ti. These materials have similar ξ and resistivity compared to the 5*d* metals, which makes them attractive for heavy-metal free applications. However, the orbital diffusion length, namely the orbital counterpart of λ_s, is of the order of 10 nm or larger, which requires relatively thick 3*d* layers to achieve a significant orbital accumulation at the interface with a ferromagnet, and the orbital current must be converted into a spin current in order to exert a torque on the magnetization. This occurs either inside the ferromagnet or in spacer layers with strong SOI, such as few nm-thick rare earth layers, for which ξ of up to 0.25 has been achieved.

Topological insulators (TIs) such as the bismuth chalcogenides Bi_2Se_3, $(Bi_{1-x}Sbx)_2Te_3$, and BiSb have also drawn significant interest as SOT sources as they exhibit giant values of ξ, typically 1–2 orders of magnitude larger than the 5*d* metals and allow for room temperature SOT-induced magnetization switching at low current densities. Other materials that can be used to generate SOTs are vdW materials, discussed later, and oxide heterostructures (Trier et al., 2022). For the time being, however, integrating nonconventional materials in devices for mass production remains a challenge.

At the threshold switching current density j_{th}, the power density is $P_{\mathrm{th}} = j_{\mathrm{th}}^2\rho \propto \xi^2\rho_p$, where ρ_p is the effective resistivity of the current channel and FL in parallel. Resistive materials typically have a high ξ. However, if the SOT electrode is too resistive, a significant portion of the current can be shunted into the FL, decreasing the SOT efficiency. Moreover, the selector transistor of each MRAM cell is not only limited in current (depending on the transistor size and associated cell footprint), but also by voltage, which scales as $j_{\mathrm{th}}\rho_p$. Therefore, the adoption of high-ξ materials such as TIs in SOT-MTJs should carefully consider the power requirements as well as BEOL-compatibility.

A drawback in SOT-MRAM based on PMA FL magnetizations is the requirement for a symmetry-breaking mechanism to unambiguously set the FL magnetic state and ensure deterministic bipolar operation. Whereas a constant in-plane magnetic field can efficiently lift the final state degeneracy, device integration requires alternative symmetry breaking mechanisms. These include effective magnetic fields produced by an embedded in-plane magnet, exchange bias from an antiferromagnet, and Dzyaloshinskii-Moriya interaction, RKKY coupling to a ferromagnetic layer, or structural symmetry breaking such as tilted anisotropy, thickness, strain and composition gradients. Additionally, the combination of SOT and STT current pulses in 3-terminal MTJs has been shown to induce field-free switching while preserving beneficial SOT characteristics in terms of speed and write error rates (Krizakova et al., 2022).

Voltage-control of magnetic anisotropy (VCMA)

The VCMA refers to the change of the interfacial magnetic anisotropy caused by an electric field applied perpendicularly to the interface of a magnetic layer. This effect is fully compatible with the MTJ structure, in which most of the voltage applied between the top and bottom electrodes falls across the tunnel barrier. Different microscopic phenomena can induce VCMA and can be roughly divided in two categories (Miwa et al., 2018). Electric-field induced charge accumulation at the interface of a magnetic layer has been shown to modify the electronic filling of *d* orbitals with different symmetry, leading to a change of the magnetocrystalline anisotropy energy that can be large enough to induce the transition from an out-of-plane to in-plane easy axis. Alternatively, electric-field induced oxygen migration from an oxide dielectric layer to the interface of the magnetic layer can induce redox reactions that also affect the symmetry and filling of the *d* orbitals in a reversible way. The efficiency of the VCMA process is measured by the coefficient η, namely the change of PMA energy per unit area divided by the applied electric field. The use of reducible oxides or high-ion-mobility gate dielectrics leads to values of η of up to 10^4 fJ/(Vm) in GdO_x/Co layers. The activation time of the redox-induced VCMA, however, is of the order of seconds, and thus too large for memory applications. The electronic VCMA occurs on timescales that are much faster than the magnetization dynamics typically $\eta \leq 10^2$ fJ/(Vm) in CoFeB/MgO layers (Miwa et al., 2018). Both effects are unipolar, i.e., the reduction of magnetic anisotropy is obtained for a given sign of the applied voltage.

The importance of VCMA is that it takes place without significant current flow across the MTJ. It is thus an energy-efficient effect to either assist or induce switching of the FL. The VCMA effect does not break time reversal symmetry and therefore does not discriminate between magnetic states with opposite magnetization. In both STT- and SOT-induced switching, the VCMA can lower the switching energy barrier, leading to a reduction of the critical switching current. In an MTJ, however, the STT and VCMA bias coincide. Because the STT switching polarity depends on the sign of the voltage, the VCMA effect inverts for parallel-to-antiparallel and antiparallel-to-parallel reversal, making it impractical to assist bipolar switching. This issue is elegantly circumvented if VCMA is used to assist SOT switching in voltage-gate-assisted SOT-MRAMs (Krizakova et al., 2022). The application of VCMA not only reduces the critical switching current, but also the switching incubation time (Krizakova et al., 2022), and allows for selectively addressing SOT-MTJs sharing a common SOT electrode. In principle, VCMA alone can also toggle the magnetization between two opposite states, provided that an external magnetic field is applied perpendicular to the easy axis and the duration of the voltage pulses is timed to half the precessional period of the free layer (Miwa et al., 2018). This toggling technique requires, pre-read and read-verify processes, or a double write process, and a careful reduction of the variability in magnetic anisotropy, damping and pulse duration in order to minimize write errors.

Applications that exploit the VCMA effect would greatly benefit from the development of material systems with higher η, higher perpendicular magnetic anisotropy, and lower damping. In order to induce VCMA-switching of a magnetic layer of area A and thermal stability Δ, a value of $\eta = \Delta k_B T/(AE)$ is required, where $E \approx 1$ V/nm is the electric field applied across the dielectric layer. Main memory applications that have thermal stability $\Delta > 70$ thus require $\eta \approx 10^3$ fJ/(Vm) of electronic origin. The most promising effort in this direction involve epitaxial Cr/ultrathin Fe/MgO junctions with in-plane anisotropy and Fe/ultrathin Ir/MgO junctions with perpendicular anisotropy, for which η of up to 370 fJ/(Vm) has been reported (Miwa et al., 2018; Yamamoto et al., 2022). The enhancement of the VCMA in the latter case is attributed to the large spin-orbit coupling and orbital moment of the Ir atoms dispersed in the Fe layer after annealing, which results also in an increase of the perpendicular magnetic anisotropy. Other approaches to improve η involve the introduction of ultrathin oxide layers with high dielectric constant in the MgO tunnelling barrier, such as TiO_x and HfO_2.

Heusler compounds (HC)

The predicted room temperature half-metallic behavior in HCs providing 100% spin polarization has promoted vast interest in this class of materials for spintronic applications, particularly as spin injector and detector in GMR and TMR devices (Palmstrøm, 2016; Graf et al., 2016; Elphick et al., 2021; Hirohata and Lloyd, 2022). Additionally, the magnetic properties of HC, *e.g.*, their saturation magnetization, can be controlled by atomic substitution of the constituent elements of the alloy, a degree of freedom that is useful for sensing and MRAM technologies, where stray magnetic fields must be minimized. However, half-metallicity, low magnetic damping, and high Curie temperatures require high crystalline order, which is challenging and depends on the lattice matching with substrates and seed layers. This is the case of the predicted half-metal MnNbSb, which has been investigated for MTJs. Although 100% spin polarization was confirmed by polarized positron annihilation and photoemission experiments in bulk MnNbSb, thin films based on co-sputtered or epitaxial growth show much lower values. Spin-polarized tunnelling experiments in epitaxially grown MnNbSb on Al_2O_3/Al yielded a spin polarization of 28%, a value that depends on atomic disorder and lattice distortion (Graf et al., 2016).

Co-based HCs are especially appealing due to their high prospects for magnetoresistive devices, PMA, spin injection into bulk semiconductors and, more recently, into 2D materials such as graphene (Hirohata and Lloyd, 2022). The list of potential candidates is long with many different compounds already tested, e.g., Co_2FeSi, Co_2MnSi, Co_2MnGe, $Co_2Fe_{0.5}Mn_{0.5}Si$, and $Co_2FeAl_{0.5}Si_{0.5}$. The first family of Heusler-based MTJs structures utilized AlO_x tunnel barrier, yielding room temperature TMR values from 15% for $Co_2Cr_{0.6}Fe_{0.4}Al$ to 70% for Co_2MnSi (Elphick et al., 2021). Besides atomic order within the HC film, the surface roughness and the interface between HCs and tunnel barriers have a strong influence on the TMR. As a result, the combination of HC magnetic electrodes with epitaxial MgO barriers have significantly improved the device performance. Room temperature TMR values of 217%, 340% and 365% were obtained for Co_2MnSi/MgO/CoFe, Co_2FeAl/MgO/CoFe and Co_2MnSi/MgO/Co_2MnSi epitaxial MTJs, respectively, suggesting a coherent tunnelling process. With partial substitution of Mn with Fe to form $Co_2Mn_{0.73}Fe_{0.27}Si$, TMR ratios increased to 430% (Elphick et al., 2021).

Co-based HCs have been also incorporated in CPP-GMR devices (Elphick et al., 2021). Room temperature GMR values of 2.5% and 36.5% using Cr and Ag metal spacers have been reported with Co_2MnSi top and bottom electrodes (Graf et al., 2016). The choice of the metal spacer becomes essential since long λ_s materials with minimal lattice mismatch with the HC electrode are required. Despite the large lattice mismatch, GMR values at room temperature of 8.5% have been obtained using Co_2MnSi layers sandwiched by a Cu metal spacer. Other approaches include full Heusler CPP-GMR devices using Ru_2CuSn spacers with GMR values of 7% at room temperature. All these considerations have led to the choice of Ag as the most optimal metal spacer. Another important aspect of Co-based HCs is the possibility to induce PMA by varying the Co concentration. Memory STT-MRAM cells based on magnetic HCs with PMA and low magnetic damping have been already developed which reflects the potential of HCs in spintronic technologies (Hirohata and Lloyd, 2022).

The approach to use Co-based HCs for spin injection would –in principle—provide highly efficient spin polarization in some spin logics or interconnect realizations (Elphick et al., 2021). Spin injection into semiconductors using HCs is promising due to their good crystal lattice matching with most semiconductors and their high Curie temperature. However, they have failed to fulfil the expectations mostly due to atomic disorder and interdiffusion of magnetic impurities at the interface with the semiconductor spin channel. Spin injection in CoMnGe/GaAs heterostructures yielded spin polarization efficiencies of 25%, which is smaller than the 40% efficiency reached in GaAs using Fe as spin injector. Lateral spin devices with Cu channels and Co_2FeSi spin injectors and detectors yielded spin injection efficiencies of 27%, the highest value reported to date in these hybrid devices. In order to enhance the spin injection efficiency, the intercalation of a MgO tunnel barrier between the semiconductor and the magnetic HC has been proposed (Farshchi and Ramsteiner, 2013).

From a practical point of view, fully ordered atomic arrangements in HCs are technically feasible but cumbersome. The growing condition of highly ordered HC requires elevated temperatures, which is an obstacle for efficient device implementation. Steady advances in thin film growth have led to improved conditions. Layer-by-layer growth has been demonstrated to reduce the crystallization energy of the materials, reducing the annealing temperatures to 225 °C, which avoids interfacial material intermixing (Dieny et al., 2020). A further reduction has been achieved when depositing HCs on a W seed layer. In this regard, the improvement in the growth conditions as well as the choice of appropriate substrates becomes essential to successfully incorporate Heusler alloy films into spintronic devices.

Two-dimensional (2D) van der Waals materials

A large variety of vdW materials are being investigated for spintronics, targeting different purposes even beyond the conventional applications described in the previous sections (Table 1). The materials that have attracted the most attention are (multilayer) graphene, transition metal dichalcogenides (TMDCs) (MX_2 with M = Mo, W, . . . and X = S, Se, Te), hexagonal boron nitride (hBN), TIs of the Bi_2Te_3 family, and several magnetic materials, which belong to the most recent class of 2D materials discovered (Han et al., 2014; Soumyanarayanan et al., 2016; Avsar et al., 2020; Gibertini et al., 2019; Sierra et al., 2021; Yang et al., 2022; Wang et al., 2022).

Graphene and bilayer graphene present excellent spin transport properties, exhibiting very long spin diffusion length (up to ~30 μm), and are considered as a keystone for spin communications and, potentially, spin logic devices (Han et al., 2014; Avsar et al., 2020; Sierra et al., 2021). The spin-current propagation has been controlled using electric drift and thermal currents (Avsar et al., 2020; Sierra et al., 2021). However, the weak-SOI enabling slow spin relaxation in graphene prevents efficient spin manipulation and charge-to-spin interconversion. Control of spin flow in graphene by means of an electric gate was achieved with MoS_2, which acted as a spin sink of variable strength. As the Schottky barrier between *n*-doped MoS_2 and graphene is suppressed with the gate, the MoS_2 shunts and absorbs the spin current, which can no longer propagate in graphene (Avsar et al., 2020; Vedmedenko et al., 2020; Sierra et al., 2021). A key element for these experiments is efficient spin injection into graphene. To circumvent the conductivity mismatch problem, resistive barriers are used (Avsar et al., 2020; Sierra et al., 2021), which are based on oxides such as AlO_x, MgO, TiO_x, YO_x and SrO or alternatives such hBN, fluorinated and hydrogenated graphene and amorphous carbon.

Table 1 Functionalities of representative van der Waals materials.

Electronic/Magnetic property	*Representative vdW materials*	*Applications*
Insulator	hBN	MTJ barrier, diffusion/intermixing barrier, encapsulation
Semiconductor	Black-Phosphorous, WS_2, WSe_2, $MoSe_2$, MoS_2, WSSe, SnS_2, $ReSe_2$, Bi_2 Te_3, etc	Spin transport (BP), SOT, optical spin injection, MTJ barrier, charge-spin conversion, SOI proximity
Semimetal	C, Si, Ge, WTe_2, $PtSe_2$, etc	MTJ barrier, spin-transport and diffusion/intermixing barrier, PMA (C), SOT, unconventional SOTs (e.g., 1 T'-WTe_2), charge-spin conversion
Metal	$MoTe_2$, $NbSe_2$, $PdTe_2$, $PtTe_2$. etc	SOT, charge-spin conversion
Ferromagnet	$Fe_{5-x}GeTe_2$ (metal), $CrTe_2$ (metal), $Cr_2Ge_2Te_6$ (semiconductor), $MnSb_2Te_4$, $CrCl_3$, $CrBr_3$, etc	Spin injector, MTJ FM layers, magnetic proximity
Antiferromagnet	CrI_3, $CrCl_3$, $MnPS_3$, $FePSe_3$, CrSBr (semiconductor), $MnBi_2Te_4$, etc	TMR: insulating AFM (e.g., CrI_3) tunnel barrier, charge-spin conversion, magnetic proximity

Proximity SOI can be imprinted in graphene with large SOI materials such as some TMDC (Žutić et al., 2019). Spin relaxation anisotropy measurements in TMDC-graphene bilayers, using oblique spin precession, demonstrated a much larger spin lifetime for out-of-plane than for in-plane spins at room temperature (Sierra et al., 2021). The anisotropy, observed even when the Fermi level lies within the TMDC energy gap, is ascribed to valley Zeeman SOI and intervalley scattering induced in graphene by the TMDC (Garcia et al., 2018; Sierra et al., 2021). Subsequent experiments, using non-local spin Hall devices, further supported this conclusion. Room-temperature tuneable SHE, related to the valley Zeeman SOI, and ISGE, associated to induced Rashba SOI, were both observed in WS_2-graphene. The strength of the SOI deduced from the SHE measurements is in good agreement with the values extracted by density functional theory. Spin relaxation anisotropy has been also found in bilayer graphene and attributed to intrinsic spin-orbit splitting (Avsar et al., 2020; Vedmedenko et al., 2020). The SOI is small (about 24 μV) but enough to induce an out-of-plane spin orbit field, which for high-quality devices reduces significantly the in-plane spin lifetime, as in the case of TMDC-graphene. The spin-relaxation anisotropy in bilayer graphene is strongly gate and temperature dependent, being maximum near the charge neutrality point and only observed at low temperatures (about 100 K).

Besides SOI, it is also possible to induce a magnetic-exchange field in graphene (Žutić et al., 2019; Vedmedenko et al., 2020; Sierra et al., 2021). Arguably, the most compelling evidence of proximity-induced exchange is reported in CrSBr-(bilayer) graphene heterostructures. CrSBr is a vdW semiconductor with a bandgap of about 1.5 eV and presents interlayer antiferromagnetic coupling with a Néel temperature of about 130 K. Within each layer, the material shows in-plane ferromagnetic order. When in contact to CrSBr, the bilayer graphene acquires a magnetization that is collinear to the magnetization of the closest CrSBr layer. By characterizing the nonlocal transport under an applied magnetic field, a large proximity exchange field of 170 T was estimated, which promoted an effective spin polarization in bilayer graphene of 14%. Additional evidence of magnetic proximity effects was found, for instance, in YIG-graphene, $Cr_2Ge_2Te_6$-graphene, $CrBr_3$-graphene, and CrSe-graphene structures.

Graphene could play a significant role in MRAM, specifically, it has been shown to act as a highly efficient diffusion barrier, able to unlock atomic layer deposition processes or to provide encapsulation or large TMR values, which can be tunable (Piquemal-Banci et al., 2017; Avsar et al., 2020; Dayen et al., 2020; Vedmedenko et al., 2020; Yang et al., 2022; Och et al., 2021). The latter are comparable to those reported in early generation AlO_x-based MTJs, but still not competitive with CoFeB/MgO based MTJs. FM junctions have successfully been fabricated with other 2D barriers such as hBN and TMDCs (Dayen et al., 2020; Och et al., 2021). In all these cases, the coupling between the 2D material and the FM plays a crucial role in determining the spin polarization and (magnetic) proximity effects. Other remarkable phenomena involving graphene, important for MRAM, include the PMA enhancement in Co-graphene and the possibility of creating artificial AFMs out of graphene-Co/graphene/Co multilayers.

Relevant TMDCs for spintronics exhibit semiconducting, metallic or semi-metallic behaviors. Among those materials belonging to the first group, WS_2 and MoS_2 have demonstrated significant spin-filtering with TMR approaching 100% and predictions orders of magnitude larger (Dayen et al., 2020). TMDCs are also potentially useful SOT materials. The reduced crystal symmetries of some TMDCs, such as semi-metallic WTe_2, can lead to unconventional torque components that are required for field-free switching in perpendicularly magnetized MRAMs (Yang et al., 2022). The SOT has been investigated using MoS_2, WSe_2, and WTe_2 as SOT materials both in hybrid 2D/3D and all-2D systems (Liu and Shao, 2020; Hidding and Guimarães, 2020; Kurebayashi et al., 2022). Magnetization switching has been observed although in a regime of domain wall motion (Yang et al., 2022).

Beyond TMDCs, efficient SOTs have been reported with vdW TIs of the $(Bi_{1-x}Sb_x)_2(Te_{1-y}Se_y)_3$ family of materials, as already discussed in Section "Conventional materials and current applications" (Yang et al., 2022). The fact that processing tools for physical vapor deposition, which are standard to deposit MTJ stacks, can be used for TI layers with high SOT efficiency, despite the polycrystalline nature and chemical disorder, is encouraging toward the realization of TI-based MRAM. Open questions remain concerning the presence of strong intermixing between conventional FMs and the TI, damage due to the 400 °C heat treatment required by CMOS processing, and topological against bulk origin of the spin current responsible for the observed SOTs (Galceran et al., 2021).

Further opportunities are present in opto-spintronics devices. In the monolayer limit, semiconducting TMDCs become direct band-gap semiconductors with the valley states at the K and K' points in reciprocal space being strongly coupled to the spin degree of freedom (Manzeli et al., 2017; Avsar et al., 2020; Vedmedenko et al., 2020). Circularly polarized light can excite a selected valley. Using time resolved Kerr rotation, spin-valley lifetimes in the microsecond scale have been observed at cryogenic temperatures. The suppression of the exciton-valley depolarization channel in WS_2-WSe_2 heterostructures has led to hole spin-valley lifetimes in WSe_2 in excess of 20 μs and propagation lengths of over 20 μm. Notably, optical generation of spin-valley polarized carriers in the TMDC can be used to inject spins into a neighboring graphene layer, providing an alternative to spin injection from FM electrodes. This has been demonstrated in MoS_2- and WSe_2-graphene heterostructures (Avsar et al., 2020; Vedmedenko et al., 2020; Sierra et al., 2021).

Magnetic proximity effects are also intensively studied in TMDCs and in TIs (Sierra et al., 2021). In TMDCs, the exchange splitting has been quantified with the reflection and photoluminescence spectra of circularly polarized light. The exchange field in WSe_2- and WS_2-EuS has been estimated in the scale of 10 and 100 T, respectively. In all-2D structures, such as WSe_2-CrI_3, the proximity effect has been found to be layered-dependent, with the largest contribution to the magnetic exchange originating from the CrI_3 interfacial layer. Some compelling signatures of magnetism in TIs have also been reported, in proximity with YIG, EuS, and other magnetic insulators, including some vdW materials. However, most of these results rely on transport experiments that are currently not fully understood.

The most recent and arguably fastest growing class of 2D materials relevant for spintronics are vdW magnets, including FMs, AFMs and, possibly, altermagnets (see Section "Antiferromagnets and altermagnets") (Gibertini et al., 2019; Och et al., 2021; Wang et al., 2022; Kurebayashi et al., 2022). Reports on monolayer materials of $CrSiTe_3$ and of the MPX_3 family (M = Fe, Mn, Ni, Cd; X = S, Se) started to appear in 2016. The following year, conclusive evidence of magnetism was observed in CrI_3 and $Cr_2Ge_2Te_6$. Their respective Curie temperatures T_C were well below 50 K in the thinnest layers investigated (monolayer CrI_3 and bilayer $Cr_2Ge_2Te_6$). Nevertheless, these results triggered intense research on 2D magnets, and a frantic search for 2D magnetism at room temperature. Possible room-temperature magnetism was reported in VSe_2 and $MnSe_2$. One advantage of thin 2D materials is their potential gate tunability and the likely maximization of VCMA (Gibertini et al., 2019). Using ion gating increased the T_C of $Cr_2Ge_2Te_6$ from 60 K to nearly 200 K. A promising material with PMA is metallic Fe_3GeTe_2, with a $T_C \sim 230$ K. Changing the Fe content x from 3 to 5 increased the T_C to just above room temperature, although results indicate a transition to in-plane anisotropy. An even larger T_C has been reported in Fe_3GaTe_2, when Fe is substituted with Co in Fe_xGeTe_2 and in Bi_2Te_3/Fe_3GeTe_2. The latter results, originally attributed to proximity effects, are not yet well understood. Another system of interest is Cr_xTe_y, which has significant complexity because of the large number of phases with different Cr and Te stoichiometry, some of them not truly vdW materials. Room temperature magnetism has also been reported in $CrTe_2$, Cr_2Te_3 and in V-doped WSe_2.

Large TMR (160%) has been observed in all-2D Fe_3GeTe_2/hBN/Fe_3GeTe_2, with even larger values predicted, including other barrier materials (Yang et al., 2022). A notable TMR exceeding 19,000% was observed in tunnel junctions with four layers of CrI_3. The coercivity in WTe_2/Fe_3GeTe_2 can be modulated with current, while SOT switching has been achieved up to 200 K in this system. Another area of intense research involves magnetic skyrmions, which have been observed in several pristine 2D magnets and 2D-magnet based heterostructures.

Antiferromagnets and altermagnets

Antiferromagnets

The recently established field of antiferromagnetic spintronics takes AFMs as the central active elements of a device-focused system (Jungwirth et al., 2016, 2018; Baltz et al., 2018). It aims at demonstrating a range of functionalities, such as memory devices based on the electrical and optical control of the Néel magnetic order, and at exploring noncollinear AFMs, hybrid AFM/FM systems, artificial realizations of AFMs in multilayer structures, and the interplay of AFMs with topological phenomena. The approach promises important advantages. The compensated magnetic order in AFMs– both collinear, noncollinear, and non-coplanar with zero magnetization—makes them insensible to external magnetic fields and is favorable for memory device densification. The high resonant frequencies of AFMs—typically of the order of THz due to the exchange enhancement effect that couples the different spin sublattices—makes them natural candidates for optical manipulation devices bridging the THz communication gap.

A challenge to integrate AFMs into present technological memory devices is the fact that their electronic structure is spin-degenerate—in the absence of SOI—and often electrically inactive, i.e., insulating. From symmetry considerations, GMR/TMR and STT effects are excluded for readout or manipulation. Therefore, in many aspects, conventional AFMs are akin to non-magnetic materials, and invisible to the macroscopic electrical or optical probes commonly used in FMs. The lack of time-reversal symmetry breaking in reciprocal space further implies that the effects associated with the direct manipulation of AFMs magnetic order must arise from SOI (relativistic) origins, which are relatively weak compared to exchange-mediated effects. An example of this manipulation is the Néel SOT where a current-induced spin accumulation couples directly to the Néel order parameter and can rotate it (Železný et al., 2018; Manchon et al., 2019). This can occur in a co-linear AFM with two sublattices possessing opposite inversion symmetry breaking. Two of the key materials fulfilling this requirement are Mn_2Au and CuMnAs.

From the symmetry perspective, any response that is proportional to the orientation of the order parameter will be observable in the electronic transport and optical regimes. For transport, this is the case for AMR, which has been observed in many AFMs. The AMR indicates up to a 90 degree rotation of the Néel vector, which can be measured either by electron tunnelling or dc-transport (Železný et al., 2018). The tunnelling AMR in AFMs was first demonstrated experimentally in a NiFe/IrMn/MgO/Pt tunnelling junction, while AMR was exploited in FeRu in one of the first AFM memory prototypes. A more direct visualization of the Néel vector can be achieved by X-ray magnetic linear dichroism (XMLD). Indeed, XMLD—photoemission electron microscopy (XMLD-PEEM) in CuMnAs confirmed the control of the Néel vector with Néel SOT (observed with AMR) when changing the polarity and direction of the applied current (Němec et al., 2018). While current-induced manipulation of the AFM order requires metallic materials, functional AFMs can be insulating. In this context, current induced switching has been demonstrated in NiO/Pt bilayer systems by exploiting the spin-Hall magnetoresistance effect in combination with XMLD-PEEM imaging.

AFMs, as many other materials, offer the possibility to generate SHEs and related spin-dependent transport, which are associated primarily with paramagnets. This is due to their spin-degenerate band structure, which is only lifted by SOI. There are many materials investigated in this context, including MnX, X = Fe, Pd, Ir and Pt. The magnitude of the SOTs generated by the spin Hall currents in these materials can compete with those in heavy metals (Manchon et al., 2019). Switching of FMs with AFMs has been demonstrated while the exchange coupling felt by the FM enables field-free switching.

Other active areas are the study of the topology in AFMs and AFM opto-spintronics (Němec et al., 2018; Šmejkal et al., 2018). Soon after the discovery of graphene, layered AFMs of the $SrMnBi_2$-type were reported to show massive Dirac quasiparticles near the Fermi level and quasi-two-dimensional quantum transport. The AFM order of Eu moments in $EuMnBi_2$ was found to change the interlayer conduction of quasi-2D Dirac carriers, tuning the transport in the quantum Hall regime. At the same time, CuMnAs was predicted to be a topological Dirac semimetal in its orthorhombic phase with the quasiparticle protection arising from non-symmorphic symmetries. A Weyl semimetal state could also emerge, which was first proposed in pyrochlore AFMs. Nontrivial surface states (the Fermi arcs connecting surface projections of the Weyl points) were predicted for the chiral non-collinear AFM

Mn_3Ge. Weyl semimetal states could also be realized in the paramagnetic and AFM phase of GdPtBi. The presence of Weyl points in the pyrochlore $Eu_2Ir_2O_7$ was inferred from optical experiments. However, despite an extensive effort, a clear material candidate for AFM Weyl semimetal remains elusive.

Light has been shown to be an efficient tool to control and detect spins and their ultrafast dynamics in AFM materials (Němec et al., 2018). As mentioned already, XMLD has proven vital in visualizing AFM domain structures. As with AMR, the quadratic dependence of the permittivity on the AFM order parameter is revealed in the magneto-refraction and magneto-absorption. The effects were observed as an intensity change of the diffracted X-rays in $La_{0.5}Sr_{1.5}MnO_4$, transmitted or reflected light in EuTe, FeRh and Cr_2O_3. A key aspect of AFM opto-spintronics is the ultrafast modification of the magnetic order. Femto-second lasers have made this field thrive. The first prediction focused on NiO, however, a key observation was the AFM to paramagnetic optically induced transition in the canted antiferromagnet iron borate $FeBO_3$, arising from an increase in magnon temperature transferred from the lattice. The ultrafast laser-induced reorientation of spins (Kirilyuk et al., 2010) in an AFM was shown in the dielectric orthoferrite $TmFeO_3$ where a temperature-dependent magnetic anisotropy is observed at 80–91 K. Related effects are reviewed extensively in Němec et al. (2018).

Altermagnets

As discussed above, the compensated magnetic order of AFMs makes them insensitive to moderate magnetic fields. At the same time, because their electronic band structure is spin degenerate—as mandated by non-relativistic symmetries—manipulation by electrical means must arise from relativistic SOI effects. This entails that, in order to control them electrically, we must circumvent the fact that their spin-responses are relatively weak, as compared to the strong spin-responses of FMs.

A direct solution to this problem comes in the discovery of a novel class of magnetic order with zero net magnetization termed altermagnetism (Šmejkal et al., 2022a,b). Altermagnets exhibit broken time-symmetry responses to an electric field akin to FMs, e.g., spin-polarized currents, and have unique properties, such as strongly asymmetric spin-polarized current response, where, for instance, a change of the current direction by 90 degrees can reverse the polarization of the current. The three collinear magnetic order classes—ferromagnetism, antiferromagnetism, and altermagnetism—are illustrated in Fig. 3. Conventional FMs are ordered in space and have principally isotropic (*s*-wave) spin-polarization order parameter in the electronic structure, Fig. 3 (left panel). AFMs are spin ordered in direct space but have no spin order, i.e., they are spin degenerate, in reciprocal space, Fig. 3 (middle). In contrast, altermagnets have an anisotropic (*d*-, *g*-. *or i*-wave) spin-polarization order, Fig. 3 (right), the naming arising from the alternating spin splitting in reciprocal space (Šmejkal et al., 2022b).

Shortly after the theoretical predictions of altermagnets, supporting evidence was shown by experiments detecting the AHE and spin-polarized currents in *d*-wave RuO_2 and Mn_5Si_3 and the anomalous Hall current in a *g*-wave MnTe. Besides these initial results, the predictions of GMR, TMR, or STT in altermagnetic multi-layer devices has opened a new avenue for spintronics, without the limiting downscaling of non-zero magnetization materials and allowing for charge-spin convertion without relying directly on SOI. This is the case for RuO_2, where its *d*-wave anisotropy of the spin-split Fermi surface allows for a pure spin currents transverse to the charge current, but without any connection to the SOI and, therefore, a potentially large λ_s. The propagation angle between spin-up and spin-down currents has been calculated to reach 34%, larger than in any known non-magnetic charge-spin conversion materials. A further unique effect is that the spin-polarized current in *d*-wave magnetic materials is the switching of the current's spin polarization when the current direction rotates by 90 degrees. There is no counterpart of this effect in the *s*-wave FMs, where polarization reversal only arises from a switching of the magnetization direction.

The basic steps to determine the altermagnetic spin group of a material are to identify: (*i*) the crystallographic group, (*ii*) the crystallographic group of the spin-sublattice (in the case of bipartite lattice the spin sublattice point group corresponds directly to Wyckoff position point group), and (*iii*) the crystallographic rotation transformation connecting the opposite-spin sublattices. For a full discussion of the symmetry considerations and classifications of altermagnets, we refer the reader to Šmejkal et al. (2022b). Material candidates for altermagnetism include both 3D and 2D crystals, in different structural or chemistry types, and can span the entire conduction spectrum from insulators, semiconductors and semimetals, to metals and superconductors. They can occur in materials with common light elements, high magnetic ordering temperatures and strong spin-coherence. They include quasi-2D oxide insulator V_2Se_2O, semimetal Cr_2O, 3D rutile fluoride or oxide insulators FeF_2, MnF_2, MnO_2 and metal RuO_2, perovskite oxide

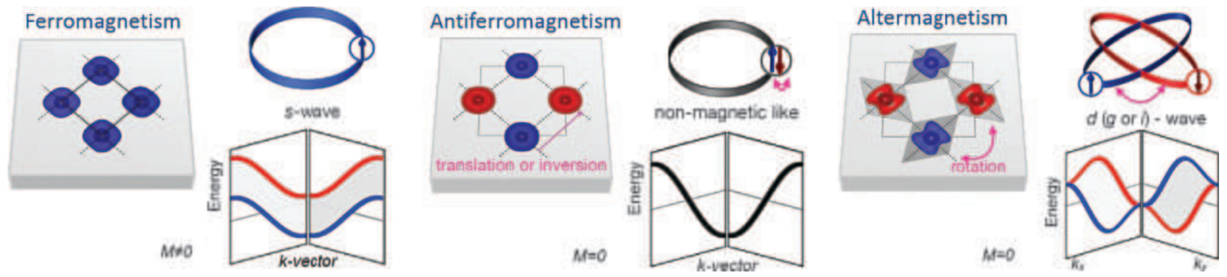

Fig. 3 Illustrative models of collinear ferromagnetism (left), antiferromagnetism (middle) and altermagnetism (right) showing the crystal-structure in direct space and non-relativistic electronic-structure in reciprocal space. *Figure adapted from Šmejkal L, Sinova J, Jungwirth T (2022) Emerging Research Landscape of Altermagnetism. Physical Review X, 12, 040501. https://doi.org/10.1103/PhysRevX.12.040501*.

insulators $LaMnO_3$, $CaCrO_3$ and parent cuprate of high-Tc superconductor La_2CuO_4, ferrite insulator Fe_2O_3, pnictide with metal-insulator transition $FeSb_2$ and metal CrSb, chalcogenide semiconductor MnTe and (semi)metal VNb_3S_6, $CoNb_3S_6$, silicide metal Mn_5Si_3, and organic insulator κ-Cl. One should also note that altermagnetism can occur in structures with inversion symmetry (e.g., rutiles), or without inversion symmetry (e.g., $VNbS_6$ or $CoNb_3S_6$).

Magnetic insulators

The spintronic applications described so far typically depend on conducting materials where the spin information is carried by delocalized electrons. However, spin information can be generated, transported and manipulated through SWs, or their quanta magnons, a field that has been coined as magnonics (Stamps et al., 2014; Sander et al., 2017; Demidov et al., 2017; Rana and Otani, 2019; Barman et al., 2021; Pirro et al., 2021; Chumak et al., 2022). In this regard, spin transport can be activated between localized electrons. When considering only magnetic insulators, the term spin insulatronics has also been used (Brataas et al., 2020). As a matter of fact, the best spin conductors are insulators. The crucial distinction in the information carrier can lead to ground-breaking changes in device designs and new applications. This necessarily introduces novel research directions with their own challenges and opportunities as described below.

Magnetic insulators are typically governed by indirect antiferromagnetic superexcharge, which results in either antiferromagnetic or ferrimagnetic order. In the former, the magnetizations of the sublattices are fully compensated, leading to overall zero magnetization, while in the latter the compensation is not complete, leading to a net magnetization. It is however possible to modify the properties of one or both sublattices of an AFM, for example by doping, to achieve a net magnetization. In addition, their characteristic SW dispersion relation can be tuned with external magnetic field; the SW frequencies and wavelengths vary from GHz to THz and from μm to nm, respectively (Gurevich and Melkov, 2020; Chumak et al., 2022). As already mentioned in Section "Antiferromagnets and altermagnets" the fast dynamics of AFMs represent an advantage for fast spintronic devices.

Among magnetic insulators, the material that has been investigated the most is yttrium iron garnet $Y_3Fe_5O_{12}$ (YIG), which is a ferrimagnetic insulator. YIG has the lowest known magnetic dissipation in nature and is characterized by an extremely small magnetic damping constant. Other materials include NiO, CoO, α-Fe_2O_3, Cro_2O_3, $BiFeO_3$ and other garnets such as $Tm_3Fe_5O_{12}$ (TmIG). Long-range spin transport has been reported in α-Fe_2O_3. Domain wall motion and the observation of skyrmions have been investigated in TmIG/Pt bilayers at room temperature, and there are reports of skyrmions in multiferroic Cu_2OSeO_3 at low temperature. In this section, several research directions are introduced that attempt to capitalize on the characteristics of magnetic insulators to achieve significant technical improvements.

Magnons as carriers of information

Spin devices with magnetic insulators capitalize on the transport properties of magnons. Here best performances are achieved in materials supporting long propagation distance for SWs. The propagation distance is here relative to their group velocity, which turns out to be slow for low-energy spin excitations (of the order of sound velocity) allowing the development of compact solutions. The concept is available in the form of (*i*) analogic devices such as filters or delay lines or (*ii*) digital devices, which exploits the ondulatory character of magnons. The later effort aims at developing Boolean functions based on wave interference to calculate the output with much smaller footprint compared to their semiconductor counterparts. More recent topics that have emerged in the field of magnonics apply to neuromorphic (Christensen et al., 2022) or bio-inspired computations, which rely on the coupling between long wavelength SWs to solve efficiently certain class of hard problems such as pattern recognition.

Among the key advantages offered by magnons are their very large energy tunability via an external magnetic field enabling a wide control range of operating frequencies spanning a spectral window from GHz to THz (Brataas et al., 2020). Another key advantage is their scalability down to the nanometer level and their wide tolerance to external settings such as the temperature of the device, which can operate from cryogenics values to hundreds of Celsius or under irradiation. The current research topics in this area are advanced computational methods such as logic or artificial intelligence (Barman et al., 2021; Chumak et al., 2022). For example, using magnonics, one can envision a neural-network implementation that is qualitatively different from all existing proposals. Instead of designing and structuring individual nonlinear elements (neurons) and their interconnections (synapses) in real space, one can propose a different paradigm in which these elements are constructed in reciprocal or *k*-space of large dimensionality. One can then imagine realizing the concept of hyper-connectivity using SWs as neurons. The key property of magnetization dynamics is its strong nonlinearity, which, when coupled with geometrical effects and external stimuli like applied fields and currents, translates into two useful features for neural networks: (*i*) nonlinear interactions through exchange and dipole-dipole interactions can potentially couple all SW modes together, thereby creating high connectivity, and (*ii*) the strength of the coupling depends on the population of each *k* mode, thereby allowing for synaptic weights to be modified dynamically. The breakthrough concept is that real-space structuration is not necessary to achieve hyper-connectivity or reconfigurable synaptic weights. One of the major roadblocks for SW computing is the difficulty to efficiently couple electrically to a magnon in an insulator. For short wavelength SWs, the inductive coupling introduces significant insertion losses that are critically detrimental to the overall energy efficiency of the device, in particular at high frequencies. The solution seems to be the exploitation of an interconversion process between the spin and charge degrees of freedom, which enables the electrical control of SWs amplitude in insulators, via the spin transfer effect from an adjacent metal electrode.

Non-linear magnonic devices

A second research direction is the exploitation of the strong propensity of magnons to behave non-linearly, which could be exploited to create spin diodes, spin amplifiers or spin rectifiers of microwave signals (Brataas et al., 2020). Reducing the magnetic damping in a magnetic material allows for a drastic decrease of the non-linear threshold for parametric instabilities. In materials with ultra-low damping, a 0.1% change in thermal occupation is usually enough to drive the magnetization dynamics into the nonlinear regime. These non-linear effects can be very useful for various nonlinear applications such as rectification, amplification, asymmetric transport (spin diode effect), mixing or generation of chaos.

Again, the spin transfer effect enables the electrical control of μ_M, the magnon chemical potential, via an electrical current in an adjacent metal electrode. The anticipated benefit is the realization of a new form of solid state spin diode obtained by shifting μ_M relative to E_g, the energy gap in the magnons' band diagram. The level-arm is set here by the magnetic damping parameter, α_{LLG}: the smaller is the damping the larger are the shifts of μ_M produced electrically.

In this respect, the ferrimagnet YIG, with the lowest known magnetic damping, is expected to lead to the highest benchmark in nonlinear transport performance. While the spin diode effect in laterally confined geometries is rather well understood, its generalization to extended thin films has so far been elusive. The corresponding difficulty is the collective dynamics that emerges inside the magnon continuum, when the level splitting between eigen-modes becomes smaller than their linewidth.

Interaction of magnons with other carriers of information

A third research direction addresses the coupling between SWs to other waveforms and carriers of information (Lachance-Quirion et al., 2019; Li et al., 2020; Zare Rameshti et al., 2022). The aim is to achieve strong coupling to preserve the coherence, which means that the phase information is preserved during the interconversion process. Such an interconversion is desirable to extend the quantum functionalities of the spin state. The figure of merit is set here by the cooperativity, which defines when the coupling strength becomes greater than the geometric mean of the coherence time of the different waveforms. In this regard, the insulating magnetic garnets are the best choice with respect to the magnon lifetime.

While optimizing the interaction by maximizing the overlap integral of two spatio-temporal patterns is primarily a design issue, diminishing the dissipation in a magnet is a complex task, which requires know-how in material research and growth technology. YIG combines extremely low magnetic damping, excellent acoustic attenuation (10× better than quartz), and optical transparency. YIG thus provides the best possible coherent interlink between magnons, phonons, and both microwave and optical photons (Lachance-Quirion et al., 2019; Li et al., 2020). The experiments performed on millimeter-size YIG single crystals have demonstrated strong coupling at microwave frequencies between magnon, photon and phonons. This encompasses the extension to the quantum regime of the magnon-photon coupling at low temperature (Lachance-Quirion et al., 2019). Devices coupling a YIG sphere to a superconducting quantum circuit have demonstrated the ability to detect a single magnon at ultra-low temperature (Zare Rameshti et al., 2022). It has been also reported that high cooperativity between two macrospins can be achieved due to magnon-phonon coupling. Acoustic phonons in garnets are likely the best waveform to couple coherently distant spins. This is because mechanical vibrations at microwave frequencies can benefit from ultralow damping in such crystals. Interestingly one can control the parity of the magnon-phonon coupling in these systems, where resonances with odd/even phonon modes correspond to out-of-phase/in-phase lattice displacements at the position of the macrospin, leading to bright/dark states in response to uniform microwave magnetic fields, respectively. While such experiments have been performed at room temperature, quantum information exchange and distant entanglement of magnons, phonons, and microwave photons could occur at low temperature. All these are crucial steps in the quest of developing integrated solutions in quantum technologies, in which long-range transport of coherent information between distant quantum gates is a key technological challenge.

These findings establish fruitful connections between the fields of magnetism and quantum information. The next step is to establish this connection with much smaller objects (ideally in the micron-size). The expected difficulties are a degradation of the damping once the size of the sample shrinks. Additional relaxation processes are expected to emerge due to the increased influence of various crystal imperfections and surface defects. In the case of elastic modes, it might be necessary to suspend the oscillating body to isolated from the substrate. However, the reasons for the deterioration of the damping in small structures are still poorly understood. Experiments with magnetic garnets of decreasing size, composition and growth/patterning methods are required to optimize magnonic devices in which large coherence times are preserved.

Conclusion

Spintronics is a very lively field, which has experienced many major advances in the last 35 years thanks to the synergy between industry and academic laboratories, where a significant proportion of novel materials and devices has been developed. Several generations of hard disk drives, sensors and non-volatile memories have adopted fundamental concepts such as GMR, TMR, spin filtering and STT in short time spans (Fig. 2). STT-MRAM products are already in the market and have proven potential for replacing various existing memories, where non-volatility, endurance and speed are required. The discovery of the SHE in metals has triggered fundamental research leading to the development of SOT-MRAM, which could be suitable for fast caches and embedded memories. VCMA, optical switching, also in combination with STT, SOT and orbital phenomena, could expand the technological opportunities for beyond-CMOS memories and devices. AFMs and altermagnets could add functionalities for dense memories and high-frequency electronics bridging the THz gap, while insulator spintronics may open the way for low-power information transport and logics.

This chapter has discussed the main device concepts and applications from a material perspective. Although, it cannot cover the entire field, it provides an overview of some of the most relevant families of practical materials including several that are being intensively investigated to overcome future technological challenges such as transition-metal alloys, Heusler compounds, 2D materials, antiferromagnets and altermagnets, and insulators. However, this list is not exhaustive, other materials such as organic magnets or semiconductors, which have been an active area of research in recent years, are not discussed. Materials for quantum information processing using single electron spins or magnetoelectric interactions for magnetic logics are also not addressed.

Research on these emerging topics and materials for spintronics will only grow in the future. Many technical challenges remain for applications, but a vast number of opportunities are envisioned. Synchronized MTJ devices can provide novel solutions for neuromorphic computing. AFM/FM bilayers present a memristor behavior like the multilevel SOT switching in bulk AFMs, which could also be relevant for neuromorphic computing. This behavior is attributed to a progressive current-induced switching of different magnetic domains in the FM, which are pinned by the exchange coupling with the AFM. Considering that magnons behave as bosons, the predicted emergence of new condensed magnon phases in insulators, such as a superfluid phase produced by a Bose-Einstein condensate, could lead to novel coherent transport phenomena.

Progress will continue to be achieved by developing novel functional materials, heterostructures and device architectures, followed by the implementation of compatible industrial processes. For example, for any technology using vdW materials to be successful, large-scale production and subsequent integration into CMOS-compatible production lines will be required. Approaches relying on chemical vapor and physical deposition are being developed for growth, which likely must be combined with reliable transfer techniques. Optimizing these processes for each material and application is crucial and must be accompanied with the development of dedicated process monitoring and metrology tools. The emergence of new material simulation methods, including machine learning and artificial intelligence, to search and identify specific functionalities could significantly accelerate the adoption of fundamental concepts into novel technologies.

Acknowledgments

SOV and JFS acknowledge support from the Spanish Ministry of Science and Innovation (MCIN) and the Spanish Research Agency (AEI/10.13039/501100011033) through grants PID2019-111773RB-I00, RYC2019-028368-I and Severo Ochoa CEX2021-001214-S. SOV and OK acknowledge support from the European Innovation Council (EIC), call HORIZON-EIC-2021-PATHFINDEROPEN-01 under GA 101046630 PALANTIRI. PG acknowledges support from ETH Zurich and the Swiss National Science Foundation through grant 200020_200465. KG acknowledges support from France 2030 government grant managed by the French National Research Agency ANR-22-PEEL-0008.

References

Apalkov D, Dieny B, and Slaughter JM (2016) Magnetoresistive random access memory. *Proceedings of the IEEE* 104: 1796–1830. https://doi.org/10.1109/JPROC.2016.2590142.

Atkinson D, Faulkner CC, Allwood DA, and Cowburn RP (2006) Domain-wall dynamicsin magnetic logic devices. In: Hillebrands B and Thiaville A (eds.) *Spin Dynamics in Confined Magnetic Structures III. Topics in Applied Physics*, pp. 207–223. Berlin, Heidelberg: Springer. https://doi.org/10.1007/10938171_6.

Avsar A, Ochoa H, Guinea F, Özyilmaz B, van Wees BJ, and Vera-Marun IJ (2020) Colloquium: Spintronics in graphene and other two-dimensional materials. *Reviews of Modern Physics* 92: 021003. https://doi.org/10.1103/RevModPhys.92.021003.

Baltz V, Manchon A, Tsoi M, Moriyama T, Ono T, and Tserkovnyak Y (2018) Antiferromagnetic spintronics. *Reviews of Modern Physics* 90: 015005. https://doi.org/10.1103/RevModPhys.90.015005.

Barman A, Gubbiotti G, Ladak S, Adeyeye AO, Krawczyk M, Gräfe J, Adelmann C, Cotofana S, Naeemi A, Vasyuchka VI, Hillebrands B, Nikitov SA, Yu H, Grundler D, Sadovnikov AV, Grachev AA, Sheshukova SE, Duquesne J-Y, Marangolo M, Csaba G, Porod W, Demidov VE, Urazhdin S, Demokritov SO, Albisetti E, Petti D, Bertacco R, Schultheiss H, Kruglyak VV, Poimanov VD, Sahoo S, Sinha J, Yang H, Münzenberg M, Moriyama T, Mizukami S, Landeros P, Gallardo RA, Carlotti G, Kim J-V, Stamps RL, Camley RE, Rana B, Otani Y, Yu W, Yu T, Bauer GEW, Back C, Uhrig GS, Dobrovolskiy OV, Budinska B, Qin H, van Dijken S, Chumak AV, Khitun A, Nikonov DE, Young IA, Zingsem BW, and Winklhofer M (2021) The 2021 magnonics roadmap. *Journal of Physics. Condensed Matter* 33: 413001. https://doi.org/10.1088/1361-648X/abec1a.

Bass J and Pratt WP (2007) Spin-diffusion lengths in metals and alloys, and spin-flipping at metal/metal interfaces: An experimentalist's critical review. *Journal of Physics. Condensed Matter* 19: 183201. https://doi.org/10.1088/0953-8984/19/18/183201.

Bihlmayer G, Noël P, Vyalikh DV, Chulkov EV, and Manchon A (2022) Rashba-like physics in condensed matter. *Nature Reviews Physics* 4: 642–659. https://doi.org/10.1038/s42254-022-00490-y.

Brataas A, Kent AD, and Ohno H (2012) Current-induced torques in magnetic materials. *Nature Materials* 11: 372–381. https://doi.org/10.1038/nmat3311.

Brataas A, van Wees B, Klein O, de Loubens G, and Viret M (2020) Spin insulatronics. *Physics Reports* 885: 1–27. https://doi.org/10.1016/j.physrep.2020.08.006.

Chappert C, Fert A, and Van Dau FN (2007) The emergence of spin electronics in data storage. *Nature Materials* 6: 813–823. https://doi.org/10.1038/nmat2024.

Christensen DV, Dittmann R, Linares-Barranco B, Sebastian A, Le Gallo M, Redaelli A, Slesazeck S, Mikolajick T, Spiga S, Menzel S, Valov I, Milano G, Ricciardi C, Liang S-J, Miao F, Lanza M, Quill TJ, Keene ST, Salleo A, Grollier J, Marković D, Mizrahi A, Yao P, Yang JJ, Indiveri G, Strachan JP, Datta S, Vianello E, Valentian A, Feldmann J, Li X, Pernice WHP, Bhaskaran H, Furber S, Neftci E, Scherr F, Maass W, Ramaswamy S, Tapson J, Panda P, Kim Y, Tanaka G, Thorpe S, Bartolozzi C, Cleland TA, Posch C, Liu S, Panuccio G, Mahmud M, Mazumder AN, Hosseini M, Mohsenin T, Donati E, Tolu S, Galeazzi R, Christensen ME, Holm S, Ielmini D, and Pryds N (2022) 2022 roadmap on neuromorphic computing and engineering. *Neuromorphic Computing and Engineering* 2: 022501. https://doi.org/10.1088/2634-4386/ac4a83.

Chumak AV, Kabos P, Wu M, Abert C, Adelmann C, Adeyeye AO, Åkerman J, Aliev FG, Anane A, Awad A, Back CH, Barman A, Bauer GEW, Becherer M, Beginin EN, Bittencourt VASV, Blanter YM, Bortolotti P, Boventer I, Bozhko DA, Bunyaev SA, Carmiggelt JJ, Cheenikundil RR, Ciubotaru F, Cotofana S, Csaba G, Dobrovolskiy OV, Dubs C, Elyasi M, Fripp KG, Fulara H, Golovchanskiy IA, Gonzalez-Ballestero C, Graczyk P, Grundler D, Gruszecki P, Gubbiotti G, Guslienko K, Haldar A, Hamdioui S, Hertel R, Hillebrands B, Hioki T, Houshang A, Hu C-M, Huebl H, Huth M, Iacocca E, Jungfleisch MB, Kakazei GN, Khitun A, Khymyn R, Kikkawa T, Kläui M, Klein O, Kłos JW, Knauer S, Koraltan S, Kostylev M, Krawczyk M, Krivorotov IN, Kruglyak VV, Lachance-Quirion D, Ladak S, Lebrun R, Li Y, Lindner M, Macêdo R, Mayr S, Melkov GA, Mieszczak S, Nakamura Y, Nembach HT, Nikitin AA, Nikitov SA, Novosad V, Otálora JA, Otani Y, Papp A, Pigeau B, Pirro P, Porod W, Porrati F, Qin H, Rana B, Reimann T, Riente F, Romero-Isart O, Ross A, Sadovnikov AV, Safin AR, Saitoh E, Schmidt G, Schultheiss H, Schultheiss K, Serga AA, Sharma S, Shaw JM, Suess D, Surzhenko O, Szulc K, Taniguchi T, Urbánek M, Usami K, Ustinov AB, van der Sar T, van Dijken S, Vasyuchka VI, Verba R, Kusminskiy SV, Wang Q, Weides M, Weiler M, Wintz S, Wolski SP, and Zhang X (2022) Advances in magnetics roadmap on spin-wave computing. *IEEE Transactions on Magnetics* 58: 1–72. https://doi.org/10.1109/TMAG.2022.3149664.

Dayen J-F, Ray SJ, Karis O, Vera-Marun IJ, and Kamalakar MV (2020) Two-dimensional van der Waals spinterfaces and magnetic-interfaces. *Applied Physics Reviews* 7: 011303. https://doi.org/10.1063/1.5112171.

Demidov VE, Urazhdin S, de Loubens G, Klein O, Cros V, Anane A, and Demokritov SO (2017) Magnetization oscillations and waves driven by pure spin currents. *Physics Reports* 673: 1–31. https://doi.org/10.1016/j.physrep.2017.01.001.

Dieny B and Chshiev M (2017) Perpendicular magnetic anisotropy at transition metal/oxide interfaces and applications. *Reviews of Modern Physics* 89: 025008. https://doi.org/10.1103/RevModPhys.89.025008.

Dieny B and Prejbeanu IL (2017) Magnetic random-access memory. In: *Introduction to Magnetic Random-Access Memory*, pp. 101–164. John Wiley & Sons, Ltd. https://doi.org/10.1002/9781119079415.ch5.

Dieny B, Prejbeanu IL, Garello K, Gambardella P, Freitas P, Lehndorff R, Raberg W, Ebels U, Demokritov SO, Akerman J, Deac A, Pirro P, Adelmann C, Anane A, Chumak AV, Hirohata A, Mangin S, Valenzuela SO, Onbaşlı MC, d'Aquino M, Prenat G, Finocchio G, Lopez-Diaz L, Chantrell R, Chubykalo-Fesenko O, and Bortolotti P (2020) Opportunities and challenges for spintronics in the microelectronics industry. *Nature Electronics* 3: 446–459. https://doi.org/10.1038/s41928-020-0461-5.

Elphick K, Frost W, Samiepour M, Kubota T, Takanashi K, Sukegawa H, Mitani S, and Hirohata A (2021) Heusler alloys for spintronic devices: Review on recent development and future perspectives. *Science and Technology of Advanced Materials* 22: 235–271. https://doi.org/10.1080/14686996.2020.1812364.

Farshchi R and Ramsteiner M (2013) Spin injection from Heusler alloys into semiconductors: A materials perspective. *Journal of Applied Physics* 113: 191101. https://doi.org/10.1063/1.4802504.

Fert A and Van Dau FN (2019) Spintronics, from giant magnetoresistance to magnetic skyrmions and topological insulators. In: *Comptes Rendus Physique, La science en mouvement 2: de 1940 aux premières années 1980—Avancées en physique 20*, pp. 817–831. https://doi.org/10.1016/j.crhy.2019.05.020.

Fert A, Reyren N, and Cros V (2017) Magnetic skyrmions: Advances in physics and potential applications. *Nature Reviews Materials* 2: 1–15. https://doi.org/10.1038/natrevmats.2017.31.

Gaidis MC (2017) Magnetic back-end technology. In: *Introduction to Magnetic Random-Access Memory*, pp. 165–198. John Wiley & Sons, Ltd. https://doi.org/10.1002/9781119079415.ch6.

Galceran R, Tian B, Li J, Bonell F, Jamet M, Vergnaud C, Marty A, García JH, Sierra JF, Costache MV, Roche S, Valenzuela SO, Manchon A, Zhang X, and Schwingenschlögl U (2021) Control of spin–charge conversion in van der Waals heterostructures. *APL Materials* 9: 100901. https://doi.org/10.1063/5.0054865.

Gambardella P and Miron IM (2011) Current-induced spin–orbit torques. *Philosophical Transactions of the Royal Society A: Mathematical, Physical and Engineering Sciences* 369: 3175–3197. https://doi.org/10.1098/rsta.2010.0336.

Garcia JH, Vila M, Cummings AW, and Roche S (2018) Spin transport in graphene/transition metal dichalcogenide heterostructures. *Chemical Society Reviews* 47: 3359–3379. https://doi.org/10.1039/C7CS00864C.

Gibertini M, Koperski M, Morpurgo AF, and Novoselov KS (2019) Magnetic 2D materials and heterostructures. *Nature Nanotechnology* 14: 408–419. https://doi.org/10.1038/s41565-019-0438-6.

Go D, Jo D, Lee H-W, Kläui M, and Mokrousov Y (2021) Orbitronics: Orbital currents in solids. *EPL* 135: 37001. https://doi.org/10.1209/0295-5075/ac2653.

Gomonay O, Baltz V, Brataas A, and Tserkovnyak Y (2018) Antiferromagnetic spin textures and dynamics. *Nature Physics* 14: 213–216. https://doi.org/10.1038/s41567-018-0049-4.

Graf T, Felser C, and Parkin SSP (2016) Heusler compounds: Applications in spintronics. In: Xu Y, Awschalom DD, and Nitta J (eds.) *Handbook of Spintronics*, pp. 335–364. Netherlands, Dordrecht: Springer. https://doi.org/10.1007/978-94-007-6892-5_17.

Gurevich AG and Melkov GA (2020) *Magnetization Oscillations and Waves*. London: CRC Press. https://doi.org/10.1201/9780138748487.

Han W, Kawakami RK, Gmitra M, and Fabian J (2014) Graphene spintronics. *Nature Nanotechnology* 9: 794–807. https://doi.org/10.1038/nnano.2014.214.

Hidding J and Guimarães MHD (2020) Spin-orbit torques in transition metal dichalcogenide/ferromagnet heterostructures. *Frontiers in Materials* 7.

Hirohata A and Lloyd DC (2022) Heusler alloys for metal spintronics. *MRS Bulletin* 47: 593–599. https://doi.org/10.1557/s43577-022-00350-1.

Hrabec A, Luo Z, Heyderman LJ, and Gambardella P (2020) Synthetic chiral magnets promoted by the Dzyaloshinskii–Moriya interaction. *Applied Physics Letters* 117: 130503. https://doi.org/10.1063/5.0021184.

Jungwirth T, Marti X, Wadley P, and Wunderlich J (2016) Antiferromagnetic spintronics. *Nature Nanotechnology* 11: 231–241. https://doi.org/10.1038/nnano.2016.18.

Jungwirth T, Sinova J, Manchon A, Marti X, Wunderlich J, and Felser C (2018) The multiple directions of antiferromagnetic spintronics. *Nature Physics* 14: 200–203. https://doi.org/10.1038/s41567-018-0063-6.

Khan MA, Sun J, Li B, Przybysz A, and Kosel J (2021) Magnetic sensors-A review and recent technologies. *Engineering Research Express* 3: 022005. https://doi.org/10.1088/2631-8695/ac0838.

Kirilyuk A, Kimel AV, and Rasing T (2010) Ultrafast optical manipulation of magnetic order. *Reviews of Modern Physics* 82: 2731–2784. https://doi.org/10.1103/RevModPhys.82.2731.

Krizakova V, Perumkunnil M, Couet S, Gambardella P, and Garello K (2022) Spin-orbit torque switching of magnetic tunnel junctions for memory applications. *Journal of Magnetism and Magnetic Materials* 562: 169692. https://doi.org/10.1016/j.jmmm.2022.169692.

Kurebayashi H, Garcia JH, Khan S, Sinova J, and Roche S (2022) Magnetism, symmetry and spin transport in van der Waals layered systems. *Nature Reviews Physics* 4: 150–166. https://doi.org/10.1038/s42254-021-00403-5.

Lachance-Quirion D, Tabuchi Y, Gloppe A, Usami K, and Nakamura Y (2019) Hybrid quantum systems based on magnonics. *Applied Physics Express* 12: 070101. https://doi.org/10.7567/1882-0786/ab248d.

Li Y, Zhang W, Tyberkevych V, Kwok W-K, Hoffmann A, and Novosad V (2020) Hybrid magnonics: Physics, circuits, and applications for coherent information processing. *Journal of Applied Physics* 128: 130902. https://doi.org/10.1063/5.0020277.

Liu Y and Shao Q (2020) Two-dimensional materials for energy-efficient spin–orbit torque devices. *ACS Nano* 14: 9389–9407. https://doi.org/10.1021/acsnano.0c04403.

Manchon A, Koo HC, Nitta J, Frolov SM, and Duine RA (2015) New perspectives for Rashba spin–orbit coupling. *Nature Materials* 14: 871–882. https://doi.org/10.1038/nmat4360.

Manchon A, Železný J, Miron IM, Jungwirth T, Sinova J, Thiaville A, Garello K, and Gambardella P (2019) Current-induced spin-orbit torques in ferromagnetic and antiferromagnetic systems. *Reviews of Modern Physics* 91: 035004. https://doi.org/10.1103/RevModPhys.91.035004.

Manzeli S, Ovchinnikov D, Pasquier D, Yazyev OV, and Kis A (2017) 2D transition metal dichalcogenides. *Nature Reviews Materials* 2: 1–15. https://doi.org/10.1038/natrevmats.2017.33.

Miao G-X, Münzenberg M, and Moodera JS (2011) Tunneling path toward spintronics. *Reports on Progress in Physics* 74: 036501. https://doi.org/10.1088/0034-4885/74/3/036501.

Miwa S, Suzuki M, Tsujikawa M, Nozaki T, Nakamura T, Shirai M, Yuasa S, and Suzuki Y (2018) Perpendicular magnetic anisotropy and its electric-field-induced change at metal-dielectric interfaces. *Journal of Physics D: Applied Physics* 52: 063001. https://doi.org/10.1088/1361-6463/aaef18.

Na T, Kang SH, and Jung S-O (2021) STT-MRAM sensing: A review. *IEEE Transactions on Circuits and Systems II: Express Briefs* 68: 12–18. https://doi.org/10.1109/TCSII.2020.3040425.

Němec P, Fiebig M, Kampfrath T, and Kimel AV (2018) Antiferromagnetic opto-spintronics. *Nature Physics* 14: 229–241. https://doi.org/10.1038/s41567-018-0051-x.

Nogués J and Schuller IK (1999) Exchange bias. *Journal of Magnetism and Magnetic Materials* 192: 203–232. https://doi.org/10.1016/S0304-8853(98)00266-2.

Och M, Martin M-B, Dlubak B, Seneor P, and Mattevi C (2021) Synthesis of emerging 2D layered magnetic materials. *Nanoscale* 13: 2157–2180. https://doi.org/10.1039/D0NR07867K.

Palmstrøm CJ (2016) Heusler compounds and spintronics. *Progress in Crystal Growth and Characterization of Materials* 62: 371–397. https://doi.org/10.1016/j.pcrysgrow.2016.04.020. Special Issue: Recent Progress on Fundamentals and Applications of Crystal Growth; Proceedings of the 16th International Summer School on Crystal Growth (ISSCG-16).

Parkin SSP (1995) Giant magnetoresistance in magnetic nanostructures. *Annual Review of Materials Science* 25: 357–388. https://doi.org/10.1146/annurev.ms.25.080195.002041.

Parkin S and Yang S-H (2015) Memory on the racetrack. *Nature Nanotechnology* 10: 195–198. https://doi.org/10.1038/nnano.2015.41.

Parkin S, Jiang X, Kaiser C, Panchula A, Roche K, and Samant M (2003) Magnetically engineered spintronic sensors and memory. *Proceedings of the IEEE* 91: 661–680. https://doi.org/10.1109/JPROC.2003.811807.

Piquemal-Banci M, Galceran R, Martin M-B, Godel F, Anane A, Petroff F, Dlubak B, and Seneor P (2017) 2D-MTJs: Introducing 2D materials in magnetic tunnel junctions. *Journal of Physics D: Applied Physics* 50: 203002. https://doi.org/10.1088/1361-6463/aa650f.

Pirro P, Vasyuchka VI, Serga AA, and Hillebrands B (2021) Advances in coherent magnonics. *Nature Reviews Materials* 6: 1114–1135. https://doi.org/10.1038/s41578-021-00332-w.

Ralph DC and Stiles MD (2008) Spin transfer torques. *Journal of Magnetism and Magnetic Materials* 320: 1190–1216. https://doi.org/10.1016/j.jmmm.2007.12.019.

Rana B and Otani Y (2019) Towards magnonic devices based on voltage-controlled magnetic anisotropy. *Communications on Physics* 2: 1–12. https://doi.org/10.1038/s42005-019-0189-6.

Sander D, Valenzuela SO, Makarov D, Marrows CH, Fullerton EE, Fischer P, McCord J, Vavassori P, Mangin S, Pirro P, Hillebrands B, Kent AD, Jungwirth T, Gutfleisch O, Kim CG, and Berger A (2017) The 2017 magnetism roadmap. *Journal of Physics D: Applied Physics* 50: 363001. https://doi.org/10.1088/1361-6463/aa81a1.

Sierra JF, Fabian J, Kawakami RK, Roche S, and Valenzuela SO (2021) Van der Waals heterostructures for spintronics and opto-spintronics. *Nature Nanotechnology* 16: 856–868. https://doi.org/10.1038/s41565-021-00936-x.

Sinova J, Valenzuela SO, Wunderlich J, Back CH, and Jungwirth T (2015) Spin Hall effects. *Reviews of Modern Physics* 87: 1213–1260. https://doi.org/10.1103/RevModPhys.87.1213.

Šmejkal L, Mokrousov Y, Yan B, and MacDonald AH (2018) Topological antiferromagnetic spintronics. *Nature Physics* 14: 242–251. https://doi.org/10.1038/s41567-018-0064-5.

Šmejkal L, Hellenes AB, González-Hernández R, Sinova J, and Jungwirth T (2022a) Giant and tunneling magnetoresistance in unconventional collinear antiferromagnets with nonrelativistic spin-momentum coupling. *Physical Review X* 12: 011028. https://doi.org/10.1103/PhysRevX.12.011028.

Šmejkal L, Sinova J, and Jungwirth T (2022b) Emerging research landscape of altermagnetism. *Physical Review X* 12: 040501. https://doi.org/10.1103/PhysRevX.12.040501.

Soumyanarayanan A, Reyren N, Fert A, and Panagopoulos C (2016) Emergent phenomena induced by spin–orbit coupling at surfaces and interfaces. *Nature* 539: 509–517. https://doi.org/10.1038/nature19820.

Stamps RL, Breitkreutz S, Åkerman J, Chumak AV, Otani Y, Bauer GEW, Thiele J-U, Bowen M, Majetich SA, Kläui M, Prejbeanu IL, Dieny B, Dempsey NM, and Hillebrands B (2014) The 2014 magnetism roadmap. *Journal of Physics D: Applied Physics* 47: 333001. https://doi.org/10.1088/0022-3727/47/33/333001.

Trier F, Noël P, Kim J-V, Attané J-P, Vila L, and Bibes M (2022) Oxide spin-orbitronics: Spin–charge interconversion and topological spin textures. *Nature Reviews Materials* 7: 258–274. https://doi.org/10.1038/s41578-021-00395-9.

Vedmedenko EY, Kawakami RK, Sheka DD, Gambardella P, Kirilyuk A, Hirohata A, Binek C, Chubykalo-Fesenko O, Sanvito S, Kirby BJ, Grollier J, Everschor-Sitte K, Kampfrath T, You C-Y, and Berger A (2020) The 2020 magnetism roadmap. *Journal of Physics D: Applied Physics* 53: 453001. https://doi.org/10.1088/1361-6463/ab9d98.

Wang QH, Bedoya-Pinto A, Blei M, Dismukes AH, Hamo A, Jenkins S, Koperski M, Liu Y, Sun Q-C, Telford EJ, Kim HH, Augustin M, Vool U, Yin J-X, Li LH, Falin A, Dean CR, Casanova F, Evans RFL, Chshiev M, Mishchenko A, Petrovic C, He R, Zhao L, Tsen AW, Gerardot BD, Brotons-Gisbert M, Guguchia Z, Roy X, Tongay S, Wang Z, Hasan MZ, Wrachtrup J, Yacoby A, Fert A, Parkin S, Novoselov KS, Dai P, Balicas L, and Santos EJG (2022) The magnetic genome of two-dimensional van der Waals materials. *ACS Nano* 16: 6960–7079. https://doi.org/10.1021/acsnano.1c09150.

Yamamoto T, Matsumoto R, Nozaki T, Imamura H, and Yuasa S (2022) Developments in voltage-controlled subnanosecond magnetization switching. *Journal of Magnetism and Magnetic Materials* 560: 169637. https://doi.org/10.1016/j.jmmm.2022.169637.

Yang H, Valenzuela SO, Chshiev M, Couet S, Dieny B, Dlubak B, Fert A, Garello K, Jamet M, Jeong D-E, Lee K, Lee T, Martin M-B, Kar GS, Sénéor P, Shin H-J, and Roche S (2022) Two-dimensional materials prospects for non-volatile spintronic memories. *Nature* 606: 663–673. https://doi.org/10.1038/s41586-022-04768-0.

Zare Rameshti B, Viola Kusminskiy S, Haigh JA, Usami K, Lachance-Quirion D, Nakamura Y, Hu C-M, Tang HX, Bauer GEW, and Blanter YM (2022) Cavity magnonics. *Physics Reports* 979: 1–61. https://doi.org/10.1016/j.physrep.2022.06.001.

Železný J, Wadley P, Olejník K, Hoffmann A, and Ohno H (2018) Spin transport and spin torque in antiferromagnetic devices. *Nature Physics* 14: 220–228. https://doi.org/10.1038/s41567-018-0062-7.

Zheng C, Zhu K, Cardoso de Freitas S, Chang J-Y, Davies JE, Eames P, Freitas PP, Kazakova O, Kim C, Leung C-W, Liou S-H, Ognev A, Piramanayagam SN, Ripka P, Samardak A, Shin K-H, Tong S-Y, Tung M-J, Wang SX, Xue S, Yin X, and Pong PWT (2019) Magnetoresistive sensor development roadmap (non-recording applications). *IEEE Transactions on Magnetics* 55: 1–30. https://doi.org/10.1109/TMAG.2019.2896036.

Žutić I, Fabian J, and Das Sarma S (2004) Spintronics: Fundamentals and applications. *Reviews of Modern Physics* 76: 323–410. https://doi.org/10.1103/RevModPhys.76.323.

Žutić I, Matos-Abiague A, Scharf B, Dery H, and Belashchenko K (2019) Proximitized materials. *Materials Today* 22: 85–107. https://doi.org/10.1016/j.mattod.2018.05.003.

Relevant websites

https://www.mram-info.com/.
IEEE Magnetic society: https://ieeemagnetics.org/.
EMA: https://magnetism.eu/.
The SpinTronic Factory: http://www.spintronicfactory.eu/.

The spin galvanic effect

SD Ganichev[a] **and EL Ivchenko**[b], [a]University of Regensburg, Regensburg, Germany; [b]Ioffe Institute, Russian Academy of Sciences, St. Petersburg, Russia

© 2024 Elsevier Ltd. All rights reserved.

Introduction 177
Phenomenological description 178
Mechanisms of the spin-galvanic effect 178
Kinetic mechanism 178
Relaxational mechanism 179
Mechanism due to the spin injection 180
Optically induced spin-galvanic effect 180
Basic experiments 180
Determination of the SIA/BIA spin splitting ratio 181
Spin-galvanic effect in transport experiments 182
Current induced spin polarization 182
Conclusion 184
Acknowledgments 184
References 184
Further reading 184

Abstract

The spin-galvanic effect is a transfer of the non-equilibrium electron spin polarization into a translational motion of free charge carriers. This spin-to-current conversion is allowed by the symmetry of the gyrotropic point groups which make no difference between some components of polar and axial vectors. We consider different mechanisms of the spin-galvanic effect, particularly, the kinetic and relaxational, that are determined by instantaneous values of the spin polarization and its time derivative, respectively. The gyrotropic symmetry allows as well the inverse spin-galvanic effect, or current-to-spin conversion. We review the basic experiments on the direct and inverse spin-galvanic effects which can be observed in various gyrotropic semiconductor systems and ferromagnet/semiconductor bilayers, at metal surfaces or interfaces and surfaces of topological insulators.

Key points

The focus of this chapter lies on the interconnection between the non-equilibrium electron spin polarization and the electric current in gyrotropic systems. The interconnection is realized in the spin-galvanic effect and its reversal. In short, the spin drives current, and the current drives spin.

- Phenomenological description of the direct and inverse spin-galvanic effects
- Kinetic and relaxational mechanisms of the spin-galvanic effect. Mechanism due to the spin injection
- Basic experiments on optically induced spin-galvanic effect
- Experimental separation of the SIA/BIA contributions to the spin-orbit coupling
- The spin-galvanic effect in transport measurements
- Current induced spin polarization in tellurium and other semiconductor systems

Introduction

Non-equilibrium spin dependent phenomena in solids and solid structures lie at the heart of the fast-growing field of spintronics, or spin electronics. Among plethora of the related concepts and ideas, the interconnection between the electron spin polarization and the electric current has attracted a lot of research interest both theoretical and experimental: in semiconductors or metals belonging to the gyrotropic point groups, a non-equilibrium homogeneous spin polarization induces an electric current and vice-versa. The former phenomenon is called the spin-galvanic effect (SGE) and the latter the inverse spin-galvanic effect (inverse SGE).

The ability of non-equilibrium spin in gyrotropic media to produce the charge current (SGE), was proposed by Ivchenko et al. (1989). Experimentally this effect has been first observed in GaAs quantum wells by spin injection under circularly polarized optical excitation by Ganichev et al. (2002). The inverse effect of current-to-spin conversion (inverse SGE) was predicted long ago

(Ivchenko and Pikus, 1978), the theory was extended by Vas'ko and Prima (1979), Aronov and Lyanda-Geller (1989), and Edelstein (1990). Further studies have shown that both the direct and inverse effects can be observed in various semiconductor systems (for review see Ivchenko and Ganichev, 2017), at metal surfaces or interfaces (Rojas Sánchez et al., 2013; Shen et al., 2014a), ferromagnet/semiconductor bilayer (Skinner et al., 2015), and surfaces of topological insulators (Shiomi et al., 2014; Mellnik et al., 2014). It should be noted that the inverse SGE is sometimes referred to as the Edelstein or Rashba–Edelstein effect and consequently the SGE to as the inverse Rashba–Edelstein effect.

Phenomenological description

In a homogeneous system of free charge carriers with a non-equilibrium spin-state occupation, but equilibrium energy distribution within each spin branch, the spin relaxation may be accompanied by generation of an electric current. Phenomenologically, the current density $\boldsymbol{j}$ and spin density $\boldsymbol{S}$ are related by a second-order tensor

$$j_\lambda = Q_{\lambda\mu} S_\mu. \tag{1}$$

More exactly, $\boldsymbol{Q}$ is a pseudotensor because it couples a conventional polar vector with a pseudovector. It is nonzero for point groups that allow optical activity or gyrotropy. The gyrotropic point-group symmetry makes no difference between at least some components of polar vectors, like current or electron momentum, and axial vectors, like a magnetic field or spin. Note that, among 21 bulk crystal classes lacking inversion symmetry, 18 groups are gyrotropic. Three nongyrotropic noncentrosymmetric classes are T_d, C_{3h} and D_{3h}. The symmetry of 2D systems is described by the layer groups, or three-dimensional groups with two-dimensional translations. There are 18 noncentrosymmetric layer point groups, among them 16 are gyrotropic and allow the SGE.

In Eq. (1), a repeated subscript is understood to imply summation over the range of this subscript. In a bulk semiconductor or superlattice the index λ runs over all three Cartesian coordinates x, y, z. In two-dimensional (2D) systems the free-carrier motion along the growth direction is quantized and the index λ enumerates two in-plane coordinates. In quantum wires or nanotubes the free movement is allowed only along one principal axis of the structure, and the coordinate λ is parallel to this axis. On the other hand, the spin polarization $\boldsymbol{S}$ can be arbitrarily oriented in space and, therefore, the index μ runs over all the three coordinates x, y and z.

In spite of the terminological resemblance, spin-to-current transfer fundamentally differs from the spin Hall effect which means the generation of a pure spin current transverse to the charge current, causes spin accumulation at the sample edges, is described by the third-rank tensor and does not require gyrotropy.

The spin-to-current conversion suggests its reciprocal phenomenon, namely, current-induced spin polarization, or the inverse SGE, described by

$$S_\mu = R_{\mu\lambda} j_\lambda. \tag{2}$$

Inversely to Eq. (1), the tensor $\boldsymbol{R}$ couples a pseudovector to a vector and also has nonzero components solely in the gyrotropic systems.

Mechanisms of the spin-galvanic effect

Microscopic mechanisms of the direct and inverse SGEs in 2D nanostructures are mostly based on the spin-orbit interaction described by the Hamiltonian

$$\mathcal{H}^{(1)} = \beta_{ij}\sigma_i k_j, \tag{3}$$

where $\boldsymbol{k}$ is the charge-carrier wave vector and σ_i are the Pauli spin matrices. Sometimes it is convenient to introduce the effective Larmor frequency with the components $\Omega_{\mathrm{k},i} = 2\beta_{ij}k_j/\hbar$ and rewrite the Hamiltonian (3) as $\hbar\boldsymbol{\Omega}_{\mathrm{k}}\boldsymbol{\sigma}/2$. The coefficients β_{ij} form a pseudotensor subjected to the same symmetry restriction as the spin-galvanic tensors $\boldsymbol{Q}$ and $\boldsymbol{R}$. Moreover, one can expect the following proportional relationship between the photocurrent and the components of tensor $\boldsymbol{\beta}$

$$j_i \propto \beta_{li} S_l, \tag{4}$$

which can be confirmed by microscopic considerations.

Kinetic mechanism

The non-equilibrium spin polarization $\boldsymbol{S}$ in Eq. (1) induces an electric current due to the following mechanism. The spin-orbit interaction (3) splits the electron energy band into spin subbands in the $\boldsymbol{k}$ space. Taking into consideration the interaction, for example, in the form $\beta_{yx}\sigma_y k_x$, we obtain two subbands shifted along k_x by $\pm k_0$ with k_0 being $\beta_{yx}m^*/\hbar^2$, where m^* is the electron effective mass. A nonzero value of S_y means that one of the subbands is more populated than the other. The Elliot–Yafet spin

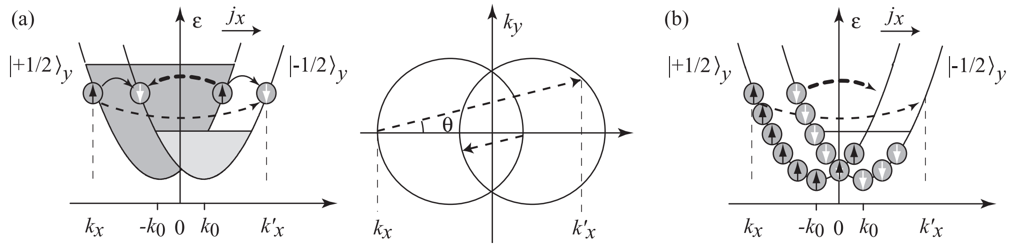

Fig. 1 (A) Microscopic origin of the kinetic spin-galvanic current. ε is the electron energy taking into account spin-orbit splitting, k_x is the x-component of the electron wave vector. Left panel: One-dimensional sketch. The spin branch $|+1/2\rangle_y$ is preferentially occupied, $S_y > 0$. Bent arrows show the spin-flip scattering processes. Two transitions denoted by solid arrows have the same rates and do not yield a current. The transitions sketched by dashed arrows yield an asymmetric filling of the subbands and, hence, a current flow. Right panel: The spin-flip transitions in the two dimensions at scattering angle θ different from 0.
(B) Current-induced spin polarization due to spin-flip scattering. Due to the drift in the electric field $\boldsymbol{E}$ applied in the positive direction of the x axis, the electron distribution within each spin branch is shifted along k_x in the same way so that the energy subbands still are equally populated. The spin-flips $-1/2 \rightarrow 1/2$ and $1/2 \rightarrow -1/2$ shown by broken bent arrows have different transition rates and, as a result, a nonzero spin polarization S_y is built up. After Ganichev SD and Prettl W (2003) Spin photocurrents in quantum wells. *Journal of Physics: Condensed Matter* 15: 935.

relaxation causes an intersubband flow of electrons. Because of the spin splitting the spin relaxation quantum transitions are asymmetric in the $\boldsymbol{k}$-space and give rise to an antisymmetric correction to the electron distribution function $f_{\boldsymbol{k}}$ which is nothing more than a flow of the electron charges, i.e. an electric current. This mechanism is termed kinetic.

Fig. 1A illustrates the generation of a spin-galvanic current in a 2D structure presented by Ganichev and Prettl, (2003). The spin-orbit interaction $\sigma_y k_x$ splits the conduction band into two parabolas with the spin $s_y = \pm 1/2$. Moreover, we take into account spin-dependent electron scattering by static defects (or acoustic phonons) in the form (Averkiev et al., 2002)

$$V_{\boldsymbol{k}'\boldsymbol{k}} = V_0 + V_{ij}\sigma_i\left(k'_j + k_j\right), \tag{5}$$

where $\boldsymbol{k}$ and $\boldsymbol{k}'$ are the initial and scattered wave vectors, V_0 and V_{ij} are scalar functions of $\boldsymbol{q} = \boldsymbol{k}' - \boldsymbol{k}$. Let the spin branch $|1/2\rangle_y$ be more populated (dark-gray) as compared with the spin $|-1/2\rangle_y$ (light-gray). As long as the carrier distribution in each subband is symmetric around the subband minimum point no current flows. The electrons are scattered from the more populated subband, e.g., the subband $|+1/2\rangle_y$, to the less populated subband $|-1/2\rangle_y$. Note that the scattering changes both k_x and k_y components of the electron wave vector as shown in the right part of Fig. 1A by dashed arrows. However, the one-dimensional sketch conveys the interpretation in a simpler and clearer way. Four different spin-flip scattering events are depicted in the left part of Fig. 1A by bent arrows. According to Eq. (5) the spin-flip scattering rate depends on values of the involved wave vectors. One can show that the spin-flip transitions shown by solid arrows in Fig. 1A have the same rates. However, two other scattering processes shown by broken arrows are inequivalent and generate an asymmetric carrier distribution around the subband minima in both subbands. This asymmetric population results in a current flow along the x-direction.

A microscopic model of the current-induced spin polarization is sketched in Fig. 1B. In equilibrium, the electron distribution in each spin branch is symmetric with respect to the corresponding point $k_x = \pm k_0$. If an external electric field $\boldsymbol{E} \parallel x$ is applied, the electrons drift in the direction of the resulting force, the distribution within each spin branch becomes asymmetric but the net spin polarization S_y does not appear. Now let us switch in the spin relaxation. As in Fig. 1A the processes indicated by broken lines have different scattering rates. Due to the asymmetric distribution along k_x and the dependence of the matrix elements (5) on wave vectors, the spin-flip relaxation processes $\pm 1/2 \rightarrow \mp 1/2$ result in an appearance of the mean spin polarization.

Relaxational mechanism

A different contribution to the current $\boldsymbol{j}$ arises in the so-called relaxational mechanism for time dependent spin polarization $\boldsymbol{S}(t)$. In this case it is enough to take into account the spin-orbit interaction (3) and the electron momentum relaxation the current to get

$$j_\lambda = 2e\tau_p \frac{\beta_{\mu\lambda}}{\hbar}\frac{dS_\mu}{dt}, \tag{6}$$

where e is the electron charge and τ_p is the momentum relaxation time. This means that, in the frequency domain representation of $\boldsymbol{j}$ and $\boldsymbol{S}$, the relaxational spin-galvanic tensor $Q^r_{\lambda\mu}(\omega)$ is proportional to $-i\omega$ and given by $-2i\omega e\tau_p\beta_{\mu\lambda}/\hbar$.The relaxational mechanism can also be understood in terms of the coherent trembling motion (Zitterbewegung) of spin-polarized electrons in an external magnetic field, $\boldsymbol{B}$. We take $\boldsymbol{B}$ parallel to the x axis in which case the Zeeman Hamiltonian has the form $(\hbar/2)\omega_L\sigma_x$ where $\omega_L = g\mu_B B/\hbar$ is the Larmor frequency, g is the electron Landé factor (or g factor) and μ_B is the Bohr magneton. The trembling motion originates from the fact that, in quantum mechanics, the electron velocity is not a conserved quantity in the presence of spin-orbit interaction. Taking into account the linear-$\boldsymbol{k}$ term (3) and the Zeeman Hamiltonian we have for the electron velocity $v_x = \hbar k_x/m^* + (\beta_{yx}/\hbar)\sigma_y$ and then obtain for the acceleration operator $\dot{v}_x = -\left(\beta_{yx}/\hbar\right)\omega_L\sigma_z$. Including the electron momentum scattering as a "friction force" we arrive at the following equation for the average electron velocity (Tarasenko et al., 2018)

$$\frac{d\overline{v}_x}{dt} + \frac{\overline{v}_x}{\tau_p} = -\frac{2\beta_{yx}}{\hbar}\omega_L s_z(t),$$

where $s_z = S_z/n_e$ is the spin polarization per particle and n_e is the electron density. In the fast scattering limit, $\omega_L\tau_p \ll 1$, the time derivative $d\overline{v}_x/dt$ is negligible and the oscillating current is given by Eq. (6) because $-\omega_L s_z = ds_y/dt$..The relaxational mechanism can be related to the time-dependent electric current induced by an ac magnetic field $\boldsymbol{B}$ and described by $j_\lambda(\omega) = -\mathrm{i}\omega\alpha_{\lambda\mu}B_\mu(\omega)$. Indeed, in the Fourier transform of Eq. (6), one can substitute $-\mathrm{i}\omega(1-\mathrm{i}\omega\tau_s)^{-1}S_\mu^{(0)}(\omega)$ instead of dS_μ/dt, where τ_s is the spin relaxation time, $\boldsymbol{S}^{(0)} = -(g\mu_B\boldsymbol{B}/4\overline{\varepsilon})n_e$, and $\overline{\varepsilon}$ is the characteristic electron energy equal to the Fermi energy at low temperature and the thermal energy k_BT at high temperature T (k_B is the Boltzmann constant). It follows then that $\alpha_{\lambda\mu}$ is proportional to the constant $\beta_{\mu\lambda}$ of the spin-orbit interaction. The principle of symmetry of the kinetic coefficients allows one to relate the tensor of the inverse SGE with the tensor $\boldsymbol{\alpha}$ as follows $R_{\lambda\mu} = \alpha_{\mu\lambda}(\sigma/g\mu_B)$, where $\sigma = e^2 n_e\tau_p/m^*$ is the electron conductivity. It is worth to note that, due to the Maxwell equation, curl $\boldsymbol{E} = -\partial\boldsymbol{B}/\partial t$, an allowance for the magnetization current, in fact, doubles the current induced by the magnetic field (Levitov et al., 1985).

Mechanism due to the spin injection

An additional contribution to the relaxational and kinetic spin-to-current conversions also comes from a continuous spin injection source. The spin generation rate $\boldsymbol{G}^{(s)}$ induces an electric current described by Eq. (6) where the time derivative of spin polarization is replaced by $-\boldsymbol{G}^{(s)}$, i.e.,

$$j_\lambda = -2e\tau_p\frac{\beta_{\mu\lambda}}{\hbar}G_\mu^{(s)}. \tag{7}$$

It follows then that, under pulsed spin generation, one should use Eq. (6) whereas, in the steady-state regime, the current is given by Eq. (7). In case of a prolonged time-dependent generation, the both currents (6) and (7) should be combined.

Burkov et al. (2004), have derived a microscopic linear response theory and proposed an electrical spin injection experiment where a voltage will develop between two ferromagnetic contacts if a spin-polarized current is injected into a 2D electron gas.

Optically induced spin-galvanic effect

Basic experiments

The uniform non-equilibrium spin $\boldsymbol{S}$ can be achieved by both optical and non-optical methods, e.g., by the spin pumping, see the next section. Optical orientation of electron spins is obtained in both bulk and low-dimensional semiconductor systems applying circularly polarized light of the wide spectral range from visible to far-infrared. It is caused by a transfer of the photon helicity to the spin of free carriers and has been demonstrated for interband absorption, resonant optical transition between size-quantized subbands and free carrier absorption. Usually, the optically excited SGE is observed simultaneously with the circular photogalvanic effect (CPGE) which is phenomenologically described by (Ivchenko and Pikus, 1978)

$$j_\lambda = IP_c\gamma_{\lambda\mu}n_\mu, \tag{8}$$

where I, P_c and $\boldsymbol{n}$ are the light intensity, degree of circular polarization and unit vector pointing in the direction of the exciting beam. Since the spin-galvanic and photogalvanic pseudotensors, $Q_{\lambda\mu}$ and $\gamma_{\lambda\mu}$, are subjected to the same symmetry restrictions they do not allow an easy experimental separation and an indivisible mixture of both effects may be observed. Nevertheless, microscopically these two effects are definitely inequivalent. Indeed, the steady-state SGE is caused by asymmetric spin-flip scattering of spin polarized carriers and determined by the spin relaxation processes. If spin relaxation is absent the spin-galvanic current vanishes. In contrast, the CPGE is a result of selective photoexcitation of carriers in the $\boldsymbol{k}$-space with circularly polarized light due to optical selection rules, it is independent of the spin relaxation if $\tau_s \gg \tau_p$.

Evidently, these two effects can behave differently upon variation of the microscopic material properties which allows their experimental separation. For instance, a dominating contribution of the SGE has been demonstrated for intersubband optical transitions excited under the oblique light incidence in n-type zinc-blende-lattice quantum wells of the C_{2v} symmetry applying qualitatively different spectral dependence of the spin-galvanic and circular photogalvanic effects (Ganichev et al., 2003). Two other methods are more general and can be applied in most cases. In one of them the effects can be separated in time-resolved measurements. Indeed, after removal of light or under pulsed photoexcitation the circular photogalvanic current decays within the momentum relaxation time τ_p whereas the spin-galvanic current decays with the spin relaxation time. Another method provides, on the one hand, a uniform distribution in spin subbands and excludes, on the other hand, the CPGE. It is based on the use of optical excitation under normal incidence and the assistance of an external magnetic field to achieve an in-plane polarization in (001)-grown low-dimensional structures (Ganichev et al., 2002).

The geometry of experiment depicted in Fig. 2 allows one to observe the SGE under steady-state photoexcitation and exclude the CPGE. The circularly polarized light is incident normally to the interface plane (001) of the quantum well, the light absorption yields a steady-state spin polarization S_{0z} in the z direction proportional to the light intensity. The symmetry of (001)-grown quantum wells forbids generation of a current proportional to the normal component of $\boldsymbol{S}$. To obtain an in-plane component of the

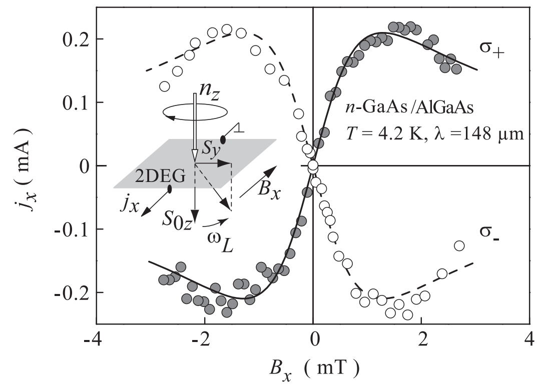

Fig. 2 Spin-galvanic current j_x as a function of magnetic field $\boldsymbol{B} \parallel x$ for normally incident right-handed (open circles) and left-handed (solid circles) circularly polarized radiation. Solid and dashed curves are fitted after Eq. (9). Inset shows optical scheme of generating a uniform in-plane spin polarization which causes a spin-galvanic current. Electron spins are oriented normal to the quantum well plane by circularly polarized radiation and rotated into the plane by the Larmor precession in the in-plane magnetic field. After Ganichev SD, Ivchenko EL, Bel'kov VV, Tarasenko SA, Sollinger M, Weiss D, Wegscheider W, Prettl W (2002) Spin-galvanic effect. *Nature* 417: 153–156.

spins, necessary for the SGE, a magnetic field $\boldsymbol{B} \parallel x$ is applied. Due to Larmor precession a non-equilibrium spin polarization S_y is induced,

$$S_y = -\frac{\omega_L \tau_{s\perp}}{1 + (\omega_L \tau_s)^2} S_{0z}, \tag{9}$$

where $\tau_s = \sqrt{\tau_{s\|}\tau_{s\perp}\perp}$ and $\tau_{s\|}$, $\tau_{s\perp}$ are the longitudinal and transverse electron spin relaxation times, ω_L is the Larmor frequency. The spin-galvanic current $\boldsymbol{j}$ appears in the x direction. In accordance with Eq. (9) the current j_x is an odd function of both the magnetic field and the light circular polarization and exhibits nonmonotonous variation with the magnetic field.

Determination of the SIA/BIA spin splitting ratio

An important application of the spin-galvanics was addressed by Ganichev et al. (2004b). It was demonstrated that angular dependent measurements of spin photocurrents allow one to separate the different contributions to the spin-orbit Hamiltonian (3). To be specific we show this method on example of (001)-oriented GaAs quantum wells for which the Hamiltonian (3) for the first subband reduces to

$$\mathcal{H}^{(1)} = \alpha\left(\sigma_x k_y - \sigma_y k_x\right) + \beta\left(\sigma_x k_x - \sigma_y k_y\right). \tag{10}$$

Here x, y are the crystallographic axes [100] and [010], the parameters α and β result from the structure-inversion and bulk-inversion asymmetries, abbreviated SIA and BIA, respectively. The first and second contributions to the Hamiltonian (10) are often called the Rashba and Dresselhaus terms. Note that, in the coordinate system $x' \| [1\bar{1}0]$, $y' \| [110]$, the matrix $\mathcal{H}^{(1)}$ gets the form

$$\beta_{x'y'}\sigma_{x'}k_{y'} + \beta_{y'x'}\sigma_{y'}k_{x'}$$

with $\beta_{x'y'} = \alpha + \beta$, $\beta_{y'x'} = -\alpha + \beta$. In Fig. 3, we show the direction of eigen spins at constant energy lines for different (A) and equal (B) strengths of BIA and SIA spin-orbit interactions presented by Ganichev and Golub, (2014). If the strengths of BIA and SIA coincide, then the 2D band structure consists of two revolution paraboloids with revolution axes symmetrically shifted in opposite directions with respect to $\boldsymbol{k} = 0$, see Fig. 3C. The case of only Rashba or Dresselhaus spin-orbit coupling is illustrated in Fig. 3D.

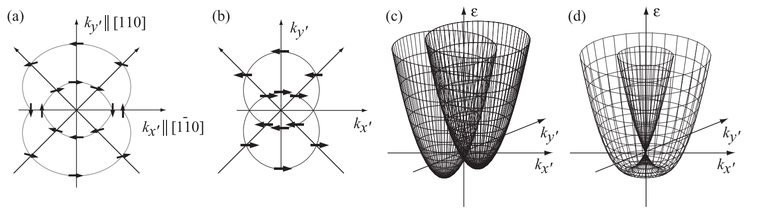

Fig. 3 The distribution of electron spin orientations at the constant energy lines calculated after Eq.(10): (A) for the general case of different strengths of the BIA and SIA terms, $\alpha \neq \beta$, and (B) for $\alpha = \beta$. Panels (C) and (D) show schematic 2D band structure for equal strength of the BIA and SIA terms in the Hamiltonian and for zero SIA/BIA, respectively. Note, that whereas the spin splitting in the latter case looks identical for pure SIA and BIA, the relative directions of the spin and electron momentum are different. After Ganichev SD and Golub LE (2014) Interplay of Rashba/Dresselhaus spin splittings probed by photogalvanic spectroscopy – A review. *Physica Status Solidi B* 251: 1801–1823.

According to Eq. (4) the current components j_x, j_y are proportional, respectively, to β_{yx} and β_{xy} and, therefore, angular dependent measurements of spin-galvanic current allow one to separate the SIA and BIA linear-$\boldsymbol{k}$ terms. By mapping the magnitude of the photocurrent in the quantum well plane the ratio of both terms can directly be determined from experiment and does not rely on theoretically obtained quantities. For the particular Hamiltonian (10) the relation between the photocurrent and spin directions can be conveniently expressed in the following matrix form.

$$\begin{pmatrix} j_x \\ j_y \end{pmatrix} \propto \begin{bmatrix} \beta & -\alpha \\ \alpha & -\beta \end{bmatrix} \begin{pmatrix} S_x \\ S_y \end{pmatrix}. \tag{11}$$

Experimentally the above method has been applied to study BIA/SIA terms in GaAs, InAs, SiGe and a number of other semiconductor low-dimensional materials. These experiments also demonstrate that growth of structures with various delta-doping layer position accompanied by experiments on SGE makes possible a controllable variation of the structure inversion asymmetry and preparation of samples with equal SIA and BIA constants or with a zero SIA constant.

Spin-galvanic effect in transport experiments

In transport measurements the SGE has been first observed by Rojas Sánchez et al. (2013), in Bi/Ag Rashba interface. The non-equilibrium spin polarization at the interface has been obtained using spin pumping. Fig. 4 shows the experimental arrangement. A vertical pure spin current J_{SH}, with opposite dc spin-up and spin-down flows and the spin polarization along the x axis, is injected from the NiFe layer into the Ag layer using a spin pumping effect operated by the ferromagnetic resonance (FMR).

The SGE converts the non-equilibrium spin at the interface into a dc electric current carried along y by the interfacial electron system subject to the Rashba spin-orbit interaction. In the situation of an open circuit shown in Fig. 4 this process gives rise to a dc voltage V. The electric current J and the voltage V are related by

$$J = \frac{aV}{R_S l},$$

where a, l and R_S are, respectively, the width, length and sheet resistance of the sample. Fig. 4B shows the derivative of the ferromagnetic absorption and the corresponding magnetic field dependence of J at the FMR for a sample with a Bi/Ag layer below NiFe.

The drift-diffusion theory derived by Shen et al. (2014a, b), is applicable to a broad variety of spin-charge transport phenomena, it describes well the experimental findings including the interpretation of the experiment by Rojas Sánchez et al. (2013).

Current induced spin polarization

Current induced spin polarization, or inverse SGE, was first observed on a chiral tellurium single crystal by Vorob'ev et al. (1979). Above we considered the case of small spin-orbit splitting, $|\beta_{ij}k_j| \ll \hbar/\tau_p$ (the collision-dominated regime). In Te crystals the

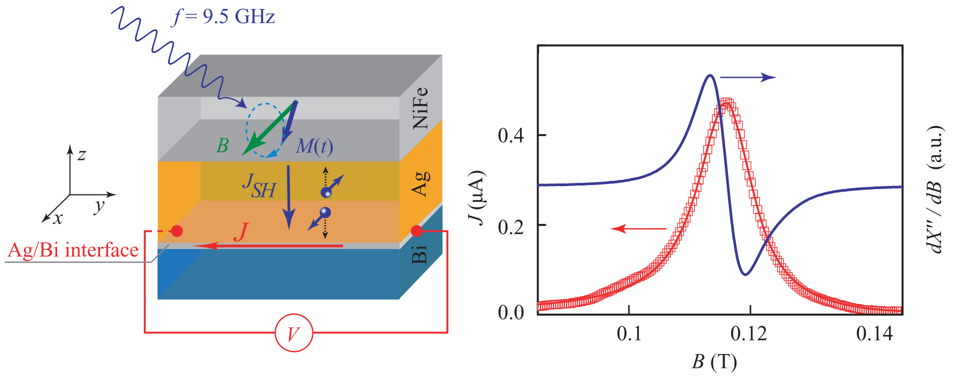

Fig. 4 (A) Scheme of the NiFe/Ag/Bi samples under ferromagnetic resonance (FMR). The radio frequency field is applied along y, and the dc magnetic field $\boldsymbol{B}$ along x. J_{SH} is the vertical dc spin current injected into the Ag/Bi interface states (back flow included), and converted into a horizontal dc charge current J by the SGE. In an open circuit situation J is balanced by the current associated to the dc voltage V. (B) FMR spectrum dX''/dB (derivative of the ferromagnetic absorption) and corresponding field dependence of the current J derived from the dc voltage V for NiFe(15)/Ag(5)/Bi(8) sample where numbers in brackets indicate layer thicknesses in nanometers. From Rojas Sánchez JC, Viva L, Desfonds G, Gambarelli S, Attané JP, De Teresa JM, Magén C, and Fert C (2013) Spin-to-charge conversion using Rashba coupling at the interface between non-magnetic materials. *Nature Communications* 4: 2944.

spin-orbit splitting $2\sqrt{\Delta_2^2 + (\beta k_z)^2}$ between the nondegenerate hole subbands H_4 and H_5 exceeds by far the uncertainty $\hbar/\tau_p$. Here Δ_2 and β are the band parameters, z is the trigonal axis. Moreover, the holes occupy only the lowest valence subband with the energy dispersion

$$\varepsilon_{\boldsymbol{k}} = Ak_z^2 + B\left(k_x^2 + k_y^2\right) - \sqrt{\Delta_2^2 + \beta^2 k_z^2} + \Delta_2.$$

The hole magnetization along z in the state $\boldsymbol{k}$ is given by

$$m_{\boldsymbol{k},z} = -\frac{1}{2}\frac{g\mu_B \beta k_z}{\sqrt{\Delta_2^2 + \beta^2 k_z^2}},$$

where g is the hole longitudinal g factor. Because of the lifted degeneracy the hole group velocity and angular momentum are strongly coupled as follows

$$v_{\boldsymbol{k},z} = \frac{2}{\hbar}\left(Ak_z + \frac{\beta m_{\boldsymbol{k},z}}{g\mu_B}\right).$$

This equation allows one, in the simplest way, to conceive the spin-to-current and current-to-spin conversions: a shift of the distribution function in the $\boldsymbol{k}$ space directly causes a change in the average angular momentum of holes and vice versa. Similarly to the Faraday effect, the current-induced magnetization can be probed by linearly polarized light via rotation of its polarization plane during propagation through the sample.

Fig. 5 shows the experimental arrangement and spectral dependence of the inverse SGE presented by Shalygin et al. (2012). In the inset θ is the angle of rotation due to the natural optical activity, and φ is an additional angle of rotation induced by the electric current j_z. It has been shown that the experimentally observed spectral dependence of the current-induced optical activity is adequately described in the framework of the existing theoretical model of Te band structure.

In bulk tellurium current-induced spin polarization is a consequence of the "camel back" valence band structure characterized by a strong spin-orbit splitting between the two upper subbands and by hybridized spin-up and spin-down states. In zinc-blende-lattice based quantum wells this effect arises in the opposite case of the collision-dominated regime as was shown theoretically by Vas'ko and Prima (1979), Aronov and Lyanda-Geller (1989), and Edelstein (1990). The inverse SGE in 2D semiconductor systems was almost simultaneously and independently observed by Ganichev et al. (2004a), Kato et al. (2004), and Silov et al. (2004). The experiments include the range of optical methods such as the Faraday rotation and linear-circular dichroism in transmission of terahertz radiation, time resolved Kerr rotation and polarized luminescence. We emphasize that current-induced spin polarization as well as the SGE were observed even at room temperature.

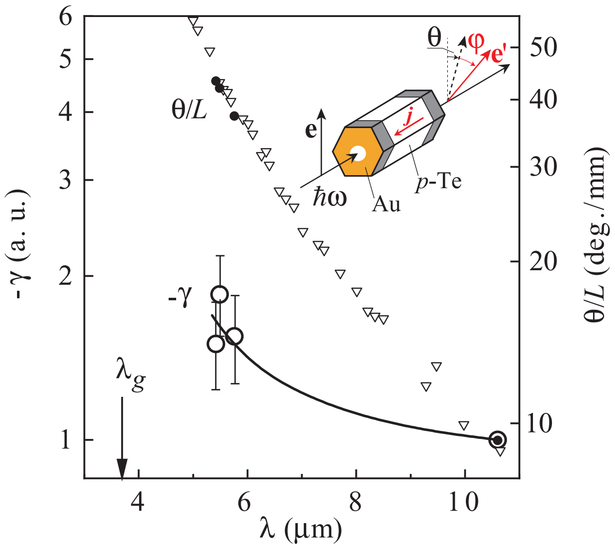

Fig. 5 Spectral dependencies of the current induced optical activity ($-\gamma$, open circles) and the natural optical activity (θ/L, closed circles) in tellurium at $T = 77$ K (experiment), the solid line corresponds to the theoretical calculation. Dots are experimental data by Shalygin et al. (2012), and triangles by Fukuda et al. (1975). Inset shows the configuration of the sample and the experimental set-up. $\boldsymbol{e}$ and $\boldsymbol{e}'$ are the unit polarization vectors of the incident and transmitted rays. From Shalygin VA, Sofronov AN, Vorob'ev LE, Farbshtein II (2012) Current-induced spin polarization of holes in tellurium. *Physics of the Solid State* 54: 2362–2373.

Conclusion

The non-equilibrium spin polarization in a homogeneous electron gas can drive an electric current due to the SGE as soon as the certain requirement is met, namely the medium belongs to the class of gyrotropic materials. The inverse SGE has also been demonstrated showing that the electric current in non-magnetic but gyrotropic materials results in a steady non-equilibrium spin orientation. It was first observed on a chiral tellurium crystal. The microscopic origin of both direct and inverse SGEs is an inherent asymmetry of electron spin-orbit coupling in gyrotropic systems with removed spin band degeneracy in the $\boldsymbol{k}$-space. The conversion between the charge current and non-equilibrium spin opens a promising way for the generation, manipulation and detection of spin polarization in spintronic devices. The SGE and its reversal allow one to separate the Dresselhaus and Rashba contributions to the spin-orbit coupling and determine spin relaxation times of resident charge carriers. It also makes it possible to probe the spin-orbit coupling at the Rashba interfaces.

Acknowledgments

The work of S.D.G was supported by the Deutsche Forschungsgemeinschaft (DFG, German Research Foundation) – Project-ID 314695032 – SFB 1277. E.L.I. acknowledges the financial support of the Russian Science Foundation (Project 22-12-00211).

References

Aronov AG and Lyanda-Geller YB (1989) Nuclear electric resonance and orientation of carrier spins by an electric field. *JETP Letters* 50: 431–434.
Averkiev NS, Golub LE, and Willander M (2002) Spin relaxation anisotropy in two-dimensional semiconductor systems. *Journal of Physics: Condensed Matter* 14: 271–283.
Burkov AA, Núñez AS, and MacDonald AH (2004) Theory of spin-charge-coupled transport in a two-dimensional electron gas with Rashba spin-orbit interactions. *Physical Review B* 70: 155308.
Edelstein VM (1990) Spin polarization of conduction electrons induced by electric current in two-dimensional asymmetric electron systems. *Solid State Communications* 73: 233–235.
Fukuda S, Shiosaki T, and Kawabata A (1975) Infrared optical activity in tellurium. *Physica Status Solidi B: Basic Solid State Physics* 68: 107–110.
Ganichev SD and Golub LE (2014) Interplay of Rashba/Dresselhaus spin splittings probed by photogalvanic spectroscopy – A review. *Physica Status Solidi B* 251: 1801–1823.
Ganichev SD and Prettl W (2003) Spin photocurrents in quantum wells. *Journal of Physics: Condensed Matter* 15: 935.
Ganichev SD, Ivchenko EL, Bel'kov VV, Tarasenko SA, Sollinger M, Weiss D, Wegscheider W, and Prettl W (2002) Spin-galvanic effect. *Nature* 417: 153–156.
Ganichev SD, Schneider P, Bel'kov VV, Ivchenko EL, Tarasenko SA, Wegscheider W, Weiss D, Schuh D, Murdin BN, Phillips PJ, Pidgeon CR, Clarke DG, Merrick M, Murzyn P, Beregulin EV, and Prettl W (2003) Spin galvanic effect due to optical spin orientation. *Physical Review B* 68: 081302.
Ganichev SD, Bel'kov VV, Golub LE, Ivchenko EL, Schneider P, Giglberger S, Eroms J, De Boeck J, Borghs G, Wegscheider W, Weiss D, and Prettl W (2004a) Experimental separation of Rashba and Dresselhaus spin-splittings in semiconductor quantum wells. *Physical Review Letters* 92: 256601.
Ganichev SD, Danilov SN, Schneider P, Bel'kov VV, Golub LE, Wegscheider W, Weiss D, and Prettl W (2004b) *Can electric current orient spins in quantum wells?* arXiv:condmat/0403641, 25 March 2004.
Ivchenko EL and Ganichev SD (2017) Spin-photogalvanics. In: Dyakonov MI (ed.) *Spin Physics in Semiconductors, Springer Series in Solid-State Sciences*, 2nd ed, Vol. 157, pp. 281–328. Springer.
Ivchenko EL and Pikus GE (1978) New photogalvanic effect in gyrotropic crystals. *JETP Letters* 27: 604–608.
Ivchenko EL, Lyanda-Geller YB, and Pikus GE (1989) Photocurrent in structures with quantum wells with an optical orientation of free carriers. *JETP Letters* 50: 175–177.
Kato YK, Myers RC, Gossard AC, and Awschalom DD (2004) Current-induced spin polarization in strained semiconductors. *Physical Review Letters* 93: 176601.
Levitov LS, Nazarov YV, and Eliashberg GM (1985) Magnetoelectric effects in conductors with mirror isomer symmetry. *Soviet Physics - JETP* 61: 133–137.
Mellnik AR, Lee JS, Richardella A, Grab JL, Mintun PJ, Fischer MH, Vaezi A, Manchon A, Kim E-A, Samarth N, and Ralph DC (2014) Spin-transfer torque generated by a topological insulator. *Nature* 511: 449.
Rojas Sánchez JC, Viva L, Desfonds G, Gambarelli S, Attané JP, De Teresa JM, Magén C, and Fert C (2013) Spin-to-charge conversion using Rashba coupling at the interface between non-magnetic materials. *Nature Communications* 4: 2944.
Shalygin VA, Sofronov AN, Vorob'ev LE, and Farbshtein II (2012) Current-induced spin polarization of holes in tellurium. *Physics of the Solid State* 54: 2362–2373.
Shen K, Vignale G, and Raimondi R (2014a) Microscopic theory of the inverse Edelstein effect. *Physical Review Letters* 112: 096601.
Shen K, Raimondi R, and Vignale G (2014b) Theory of coupled spin-charge transport due to spin-orbit interaction in inhomogeneous two-dimensional electron liquids. *Physical Review B* 90: 245302.
Shiomi Y, Nomura K, Kajiwara Y, Eto K, Novak M, Segawa K, Ando Y, and Saitoh E (2014) Spin-electricity conversion induced by spin injection into topological insulators. *Physical Review Letters* 113: 196601.
Silov AY, Blajnov PA, Wolter JH, Hey R, Ploog KH, and Averkiev NS (2004) Currentinduced spin polarization at a single heterojunction. *Applied Physics Letters* 85: 5929–5931.
Skinner TD, Olejní-k K, Cunningham LK, Kurebayashi H, Campion RP, Gallagher BL, Jungwirth T, and Ferguson AJ (2015) Complementary spin-Hall and inverse spin-galvanic effect torques in a ferromagnet/semiconductor bilayer. *Nature Communications* 6: 6730.
Tarasenko SA, Poshakinskiy AV, Ivchenko EL, Stepanov I, Ersfeld M, Lepsa M, and Beschoten B (2018) Zitterbewegung of spin split electrons. *JETP Letters* 108: 326–328.
Vas'ko FT and Prima NA (1979) Spin splitting of the spectrum of two-dimensional electrons. *Soviet Physics - Solid State* 21: 994–996.
Vorob'ev LE, Ivchenko EL, Pikus GE, Farbstein II, Shalygin VA, and Sturbin AV (1979) Optical activity in tellurium induced by a current. *JETP Letters* 29: 441–445.

Further reading

Books and reviews

Baltz V, Manchon A, Tsoi M, Moriyama T, Ono T, and Tserkovnyak Y (2018) Antiferro- magnetic spintronics. *Reviews of Modern Physics* 90: 015005.
Dyakonov MI and Khaetskii AV (2017) Spin hall effect. In: Dyakonov MI (ed.) *Spin Physics in Semiconductors*, 2nd edn., pp. 241–280. Springer.
Engel H-A, Rashba EI, and Halperin BI (2007) Theory of spin hall effects in semiconductors. In: Kronmuller H and Parkin S (eds.) *Handbook of Magnetism and Advanced Magnetic Materials*, vol. 5, pp. 2858–2877. John Wiley & Sons, NY.

Fabian J, Matos-Abiague A, Ertler C, Stano P, and Žutić I (2007) Semiconductor spintronics. *Acta Physica Slovaca* 57: 565.

Ganichev SD and Prettl W (2006) *Intense Terahertz Excitation of Semiconductors*. Oxford: Oxford University Press.

Ganichev SD, Trushin M, and Schliemann J (2019) Spin polarisation by current. In: Tsymbal EY and Žutić I (eds.) *Spintronics Handbook: Spin Transport and Magnetism*, pp. 317–337. CRC Press.

Ivchenko EL (2005) *Optical Spectroscopy of Semiconductor Nanostructures*. Harrow, UK: Alpha Science International.

Litvinov V (2019) *Magnetism in Topological Insulators*. Springer International Publishing.

Liu W and Xu Y (eds.) (2019) *Spintronics 2D Materials: Fundamentals and Applications*, p. 259. Elsevier.

Manchon A, Koo HC, Nitta J, Frolov SM, and Duine RA (2015) New perspectives for Rashba spin-orbit coupling. *Nature Materials* 14: 871–882.

Rashba EI (2007) Semiconductor spintronics: Progress and challenges. In: Luryi S, Xu JM, and Zaslavsky A (eds.) *Future Trends in Microelectronics: Up the Nano Creek*, pp. 28–40. Hoboken: Wiley InterScience.

Schliemann J (2017) Persistent spin textures in semiconductor nanostructures. *Reviews of Modern Physics* 89: 011001.

Sinova J and MacDonald A (2008) Theory of spin-orbit effects in semiconductors. In: Dietl T, Awschalom DD, Kaminska M, and Ohno H (eds.) *Semiconductors and Semimetals. Spintronics*, Vol. 82, pp. 45–89. Amsterdam: Elsevier.

Sinova J, Valenzuela SO, Wunderlich J, Back CH, and Jungwirth T (2015) Spin Hall effects. *Reviews of Modern Physics* 87: 1213–1260.

Winkler R (2007) Spin-dependent transport of carriers in semiconductors. In: Kronmuller H and Parkin S (eds.) *Handbook of Magnetism and Advanced Magnetic Materials*, vol. 5, pp. 2830–2844. John Wiley & Sons, NY.

Žutić I, Fabian J, and Das Sarma S (2004) Spintronics: Fundamentals and applications. *Reviews of Modern Physics* 76: 323.

Original papers

Adagideli I, Scheid M, Wimmer M, Bauer GEW, and Richter K (2007) Extracting current-induced spins: spin boundary conditions at narrow Hall contacts. *New Journal of Physics* 9: 382.

Bel'kov VV, Olbrich P, Tarasenko SA, Schuh D, Wegscheider W, Korn T, Schüller C, Weiss D, Prettl W, and Ganichev SD (2008) Symmetry and spin dephasing in (110)-grown quantum wells. *Physical Review Letters* 100: 176806.

Bleibaum O (2006) Spin diffusion equations for systems with Rashba spin-orbit interaction in an electric field. *Physical Review B* 73: 035322.

Chen L, Decker M, Kronseder M, Islinger R, Gmitra M, Schuh D, Bougeard D, Fabian J, Weiss D, and Back CH (2016) Robust spin-orbit torque and spin-galvanic effect at the Fe/GaAs (001) interface at room temperature. *Nature Communications* 7: 13802.

Furukawa T, Watanabe Y, Ogasawara N, Kobayashi K, and Itou T (2021) Current-induced magnetization caused by crystal chirality in nonmagnetic elemental tellurium. *Physical Review Research* 3: 023111.

Ivchenko EL, Lyanda-Geller YB, and Pikus GE (1990) Current of thermalized spin-oriented photocarriers. *Soviet Physics - JETP* 71: 550–557.

Khokhriakov D, Hoque AM, Karpiak B, and Dash SP (2020) Gate-tunable spin-galvanic effect in graphene topological insulator van der Waals heterostructures at room temperature. *Nature Communications* 11: 3657.

Kohda M, Lechner V, Kunihashi Y, Dollinger T, Olbrich P, Schönhuber C, Caspers I, Bel'kov VV, Golub LE, Weiss D, Richter K, Nittaand J, and Ganichev SD (2012) Gate-controlled persistent spin helix state in InGaAs quantum wells. *Physical Review B* 86: 081306.

Konschelle K, Tokatly IV, and Bergeret FS (2015) Theory of the spin-galvanic effect and the anomalous phase shift φ_0 in superconductors and Josephson junctions with intrinsic spin-orbit coupling. *Physical Review B* 92: 125443.

Sheikhabadi M, Miatka I, Sherman EY, and Raimondi R (2018) Theory of the inverse spin galvanic effect in quantum wells. *Physical Review B* 97: 235412.

Sih V, Myers RC, Kato YK, Lau WH, Gossard AC, and Awschalom DD (2005) Spatial imaging of the spin Hall effect and current-induced polarization in two-dimensional electron gases. *Nature Physics* 1: 31–35.

Yang CL, He HT, Ding L, Cui LJ, Zeng YP, Wang JN, and Ge WK (2006) Spectral dependence of spin photocurrent and current-induced spin polarization in an InGaAs/InAlAs two-dimensional electron gas. *Physical Review Letters* 96: 186605.

Zhang W, Wang Q, Peng B, Zeng H, Soh WT, Ong CK, and Zhang W (2016) Spin galvanic effect at the conducting $SrTiO_3$ surfaces. *Applied Physics Letters* 109: 262402.

Spin–orbit coupling in solids

R Winkler, Department of Physics, Northern Illinois University, DeKalb, IL, United States

© 2024 Elsevier Ltd. All rights reserved.

Introduction: Pauli SO coupling 186
Group theory of SO-coupled systems 187
Mechanisms of SO coupling in solids 188
Optical spin orientation 189
Spin precession and spin relaxation 189
SO coupling and band structure of solids 190
Conclusion 191
References 191

Abstract

Spin–orbit (SO) coupling is the microscopic mechanism that couples the electron's spin degree of freedom to the electron's orbital motion. It emerges from relativistic quantum mechanics described by the Dirac equation. Space and time inversion symmetry enforce characteristic degeneracies in the electronic band structure. A broken space inversion symmetry gives rise to a spin splitting of the bands, the magnitude of which is a measure of the strength of SO coupling. Important SO coupling mechanisms in solids include Rashba and Dresselhaus coupling. SO coupling provides means to address the electrons' spin degree of freedom in solids using, for example, optical orientation and spin precession.

Key points

- Origin of Pauli SO coupling
- Group theory of SO-coupled systems
- Mechanisms of SO coupling in solids
- Optical spin orientation
- Spin precession and spin relaxation
- SO coupling and band structure of solids

Introduction: Pauli SO coupling

A major justification for the relativistic Dirac equation in quantum mechanics has been its ability to reconcile the apparent contradiction observed in atomic physics, where the interaction of the electron's spin magnetic moment with a magnetic field $\boldsymbol{\mathcal{B}}$ was measured to be twice as large as what one would expect based on the interaction observed for the electron's spin magnetic moment when the electron is orbiting around a nucleus in the electric field due to the steep Coulomb potential V_0 of the atomic core. In the nonrelativistic limit of the Dirac equation, the interaction of the electron spin with a magnetic field is given by the spin Zeeman term (Sakurai, 1967)

$$H_Z = \frac{g}{2}\, \mu_B\, \boldsymbol{\sigma}\cdot\boldsymbol{\mathcal{B}}, \tag{1}$$

where $g = 2$ is the g-factor, μ_B is the Bohr magneton, and $\boldsymbol{\sigma} = (\sigma_x, \sigma_y, \sigma_z)$ is the vector of Pauli spin matrices while in the weakly relativistic limit of the Dirac equation [one order beyond Eq. (1)], the interaction of an electron spin that is moving in an electric field is given by the *Pauli spin–orbit (SO) interaction* (Sakurai, 1967)

$$H_{SO} = -\frac{\hbar}{4m^2c^2}\, (\nabla V_0)\cdot(\boldsymbol{\sigma} \times \mathbf{p}), \tag{2}$$

where $\hbar$ is Planck's constant, m is the mass of the electron, c is the velocity of light, $\mathbf{p}$ is the momentum operator, and V_0 is the potential that gives rise to the electric field seen by the electron. In Eq. (2), V_0 is typically the Coulomb potential of the atomic core. For the angular motion in a central potential $V_0(r)$ that arises for atomic cores, the Pauli SO interaction can be rephrased as an interaction between the electron's orbital angular momentum $\mathbf{L}$ and spin angular momentum $\mathbf{S} = (\hbar/2)\boldsymbol{\sigma}$.

The Dirac Hamiltonian H_D corresponding to the Dirac equation is a 4×4 matrix (Sakurai, 1967)

$$H_D = c\, \boldsymbol{\alpha}\cdot\mathbf{p} + \beta\, mc^2 + V_0 \tag{3}$$

https://doi.org/10.1016/B978-0-323-90800-9.00251-1

where

$$\boldsymbol{\alpha} = \begin{pmatrix} 0 & \boldsymbol{\sigma} \\ \boldsymbol{\sigma} & 0 \end{pmatrix}, \tag{4a}$$

$$\beta = \begin{pmatrix} \mathbb{1}_{2\times 2} & 0 \\ 0 & -\mathbb{1}_{2\times 2} \end{pmatrix}. \tag{4b}$$

The eigenfunctions of the Dirac equation are four-component spinors. Their first and second components represent spin up and down in the subspace of positive energies, whereas the third and fourth components represent spin up and down in the subspace of negative energies. The two subspaces are separated by an "energy gap" $2mc^2$. The subspaces are coupled off-diagonally proportional to the momentum $\mathbf{p}$ of the particle. In a nonrelativistic or weakly relativistic limit, the off-diagonal coupling is small. The Schrödinger equation including the spin Zeeman term (1) and Pauli SO coupling (2) is often called *Pauli equation*. It can be derived from the Dirac equation by perturbatively decoupling the "interesting" subspace of positive energies from the "uninteresting" subspace of negative energies (Sakurai, 1967). In lowest order, this yields a term $p^2/(2m)$ representing the nonrelativistic kinetic energy. This term is complemented by the Zeeman term (1). The next order yields Pauli SO coupling (2). If needed, yet higher orders can be derived in a systematic way. However, then it may become advantageous to work directly with the Dirac equation.

It is well known that the Pauli SO coupling (2) affects the energy levels of electrons in atoms. But it also affects the dynamics of electrons in solids, most importantly the band structure $E_n(\mathbf{k})$. The microscopic origin of SO coupling in solids is the steep Coulomb potential of the atomic cores. Therefore, manifestations of Pauli SO coupling (2) generally scale with the atomic number of the constituting atoms in a crystal. Large SO coupling effects generally require constituting atoms from the bottom of the periodic table.

A direct consequence of Pauli SO coupling (2) in the band structure $E_n(\mathbf{k})$ are level splittings that can be parameterized by matrix elements of the SO interaction (2). In effective theories, such matrix elements often provide a convenient parameterization for the effects of SO coupling.

Group theory of SO-coupled systems

Group theory provides a general and rigorous definition for the quantum numbers of a physical system and how these numbers describe physical properties such as matrix elements and selection rules. In the absence of SO coupling, we can discuss separately the symmetry group G of the orbital motion and the symmetry group of the decoupled spin degree of freedom. The latter group is the rotation group $SU(2)$, which reflects the fact that the spin degree of freedom is detached from the orbital motion. The symmetry group of the entire system is then the product group $G \times SU(2)$. It yields separate quantum numbers for the orbital and spin dynamics.

In the presence of SO coupling, the product group $G \times SU(2)$ must be replaced by the double group corresponding to G, and neither the quantum numbers for the orbital motion nor spin are good quantum numbers anymore. In such systems, we get new conserved quantum numbers for the coupled dynamics. In spherically symmetric atoms, the quantum numbers for orbital and spin angular momentum are replaced by total angular momentum. In crystals with band dispersion $E_n(\mathbf{k})$, the band index n becomes a common index for the orbital motion and the spin degree of freedom that classifies the bands according to the irreducible representations of the double group.

For a given wave vector $\mathbf{k}$, we can always find a spin orientation axis $\mathbf{S}(\mathbf{k})$, *local in* $\mathbf{k}$ *space*, such that we have spin-up and spin-down eigenstates with respect to the axis $\mathbf{S}(\mathbf{k})$. We may indicate the local spin orientation with an additional label $\sigma = \pm$ (unless the branches $E_n(\mathbf{k})$ are anyway spin-degenerate, see below). But we do not call the entire branches $E_{n\sigma}(\mathbf{k})$ with $\sigma = \pm$ spin-up and spin-down, because, in nonmagnetic materials, the direction of $\mathbf{S}$ varies as a function of $\mathbf{k}$ such that, when projecting $\mathbf{S}(\mathbf{k})$ on a fixed direction in spin space and averaging over all occupied states (at thermal equilibrium), the branches contain equal contributions of up and down spinor components. This reflects the fact that, in nonmagnetic materials, we have a vanishing magnetization at $\mathcal{B} = 0$. The pattern of the spin orientation $\mathbf{S}(\mathbf{k})$ as a function of $\mathbf{k}$ defines the *spin texture* that is a distinctive feature of different SO coupling mechanisms for Bloch electrons. Below we discuss examples for $\mathbf{S}(\mathbf{k})$ realized by common SO coupling mechanisms. The spin orientation $\mathbf{S}(\mathbf{k})$ can be attributed to a Zeeman term with a $\mathbf{k}$-dependent effective magnetic field $\boldsymbol{\mathcal{B}}(\mathbf{k})$, where the magnitude of $\boldsymbol{\mathcal{B}}(\mathbf{k})$ parameterizes magnitude of spin splitting.

An important consequence of symmetries are degeneracies in the energy spectrum of a Hamiltonian that result in constraints for the spin textures $\mathbf{S}(\mathbf{k})$. Here space inversion symmetry (denoted i) and time inversion symmetry (denoted θ, more accurately called reversal of motion) take a special role for the band dynamics of Bloch electrons. The wave vector $\mathbf{k}$ of Bloch electrons is a polar vector (i-odd, that is, i changes $\mathbf{k}$ into $-\mathbf{k}$), and it is also θ-odd. Spin is an axial vector (i-even) while it is θ-odd. Therefore, space inversion symmetry implies that a spinful dispersion is symmetric about $\mathbf{k} = 0$, that is, $E_{n\sigma}(\mathbf{k}) = E_{n\sigma}(-\mathbf{k})$ (even when time inversion symmetry is broken, e.g., by a magnetic field). Time inversion symmetry implies *Kramers degeneracy*, $E_{n\sigma}(\mathbf{k}) = E_{n\overline{\sigma}}(-\mathbf{k})$, where $\overline{\sigma}$ denotes the inverse of a spin orientation σ. Finally, space inversion and time inversion symmetry jointly imply *spin degeneracy* $E_{n\sigma}(\mathbf{k}) = E_{n\overline{\sigma}}(\mathbf{k})$, that is, we have (at least) a twofold degeneracy for every wave vector $\mathbf{k}$ throughout the Brillouin zone (even if i and θ happen to be broken individually). This is summarized in Table 1. If θ is a good symmetry, but a broken space inversion symmetry lifts the spin

Table 1 Band degeneracies due to inversion symmetries.

	$\mathbf{k}$	$\boldsymbol{\sigma}$	*Degeneracy*	
i	−	+	$E_{n\sigma}(\mathbf{k}) = E_{n\sigma}(-\mathbf{k})$	
θ	−	−	$E_{n\sigma}(\mathbf{k}) = E_{n\bar{\sigma}}(-\mathbf{k})$	Kramers degeneracy
$i\theta$	+	−	$E_{n\sigma}(\mathbf{k}) = E_{n\bar{\sigma}}(\mathbf{k})$	Spin degeneracy

degeneracy so that $E_{n\sigma}(\mathbf{k}) \neq E_{n\bar{\sigma}}(\mathbf{k})$, this is often called a $\mathcal{B} = 0$ *spin splitting*, as it arises in nonmagnetic structures independent of an external magnetic field $\boldsymbol{\mathcal{B}}$. The microscopic mechanism for $\mathcal{B} = 0$ spin splitting is SO coupling.

Band degeneracies enforced by symmetry for SO-coupled bands lay the foundations for more advanced topics exploiting, for example, topology (Chiu et al., 2016).

Mechanisms of SO coupling in solids

In nonmagnetic materials that preserve space and time inversion symmetry, we have an, at least, twofold spin degeneracy of the electronic band structure in the entire Brillouin zone, as discussed in the Section "Group theory of SO-coupled systems." In these systems, Pauli SO coupling (2) gives rise to gaps in the band structure (Kane, 1966) similar to the familiar SO-induced level splittings in atomic physics.

A broken space inversion symmetry manifests itself as a lifting of the twofold spin degeneracy (Section "Group theory of SO-coupled systems"). This spin splitting can be the consequence of a bulk inversion asymmetry (BIA) of the crystal structure. In confined geometries like quantum wells and heterostructures, a spin splitting may also arise due to a structure inversion asymmetry (SIA) of the confinement potential.

The different SO coupling mechanisms due to BIA can be classified according to the effective magnetic fields $\boldsymbol{\mathcal{B}}(\mathbf{k})$ they give rise to. In general, their functional form follows from the symmetry of the underlying crystal structure. *Rashba SO coupling* (Rashba and Sheka, 1959)

$$H_{\mathrm{R}} = \boldsymbol{\alpha}\cdot(\boldsymbol{\sigma} \times \mathbf{k}) \tag{5}$$

has the same functional dependence on spin $\boldsymbol{\sigma}$ and crystal momentum $\hbar\mathbf{k}$ as Pauli SO coupling (2). It is proportional to a polar vector $\boldsymbol{\alpha}$ that parameterizes the magnitude and orientation of the Rashba effect. Such a vector $\boldsymbol{\alpha}$ is allowed as a bulk property in crystal structures that belong to one of the polar crystal classes that permit a spontaneous electric polarization. Originally, the Rashba effect was first proposed for the polar wurtzite structure (Rashba and Sheka, 1959) that is realized by several III-V and II-VI semiconductors including ZnS, CdSe, GaN, and AlN. The effective magnetic field $\boldsymbol{\mathcal{B}}(\mathbf{k}) = \mathbf{k} \times \boldsymbol{\alpha}$ representing Rashba SO coupling is depicted in Fig. 1A.

Dresselhaus SO coupling (Dresselhaus, 1955)

$$H_{\mathrm{Dr}} = \beta\left[\sigma_x k_x(k_y^2 - k_z^2)+\mathrm{cp}\right], \tag{6}$$

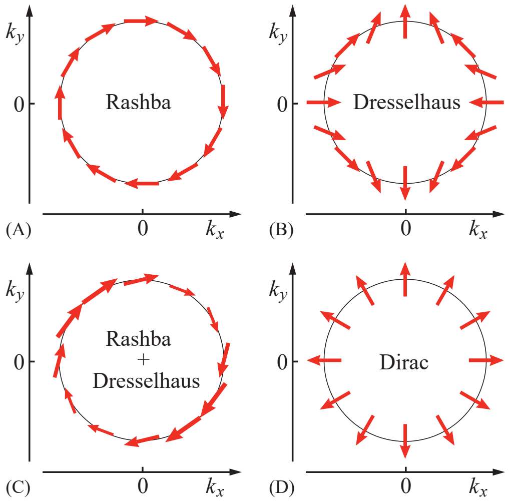

Fig. 1 Effective magnetic field $\boldsymbol{\mathcal{B}}(\mathbf{k})$ due to (A) Rashba SO coupling (5), (B) Dresselhaus SO coupling (7), (C) both Rashba and Dresselhaus SO coupling, and (D) a Dirac-like SO coupling (8). In thermal equilibrium, the resulting spin textures imply a vanishing net magnetization.

where cp denotes cyclic permutation of the preceding term, is realized in bulk zincblende structures including GaAs and InSb. It is cubic in the wave vector **k**. In quasi-2D quantum wells and heterostructures on a (001) surface, the wave vector component k_z is quantized, so that Dresselhaus SO coupling is linear in the in-plane wave vector $\mathbf{k}_\| = (k_x, k_y)$

$$H_{\mathrm{Dr}}^{2\mathrm{D}} = \beta \langle k_z^2 \rangle (\sigma_y k_y - \sigma_x k_x). \tag{7}$$

The effective magnetic field $\boldsymbol{\mathcal{B}}(\mathbf{k})$ for Dresselhaus SO coupling (7) is depicted in Fig. 1B.

A *Dirac-like SO coupling*

$$H_{\mathrm{Di}} = \gamma\, \boldsymbol{\sigma} \cdot \mathbf{k} \tag{8}$$

is realized in chiral crystal structures, that is, structures for which the crystallographic point group contains only proper rotations but no improper rotations as symmetry elements. Examples of chiral structures include α- and β-quartz, and elemental tellurium. The effective magnetic field $\boldsymbol{\mathcal{B}}(\mathbf{k})$ for Dirac-like SO coupling is depicted in Fig. 1D.

Crystal structures of sufficiently low symmetry (e.g., crystal classes C_s, C_2, and C_1) can support multiple SO coupling mechanisms. In these cases, the effective magnetic field $\boldsymbol{\mathcal{B}}(\mathbf{k})$ is the sum of the fields due to the different SO coupling mechanisms, as illustrated in Fig. 1C.

SIA spin splitting arises due to an asymmetric confinement in engineered quantum structures like quantum wells, at heterostructure interfaces, and at the surface of bulk crystals. It can generally be characterized via a macroscopic external or built-in electric field $\boldsymbol{\mathcal{E}}$ that gives rise to Rashba-type spin splitting as in Eq. (5). This effect can be understood similar to how Pauli SO coupling (2) arises in a weakly relativistic limit from the Dirac equation. This is discussed in more detail in the following Section "SO coupling and band structure of solids."

The magnitude of SO coupling can be determined experimentally using optical techniques such as optical orientation (Meier and Zakharchenya, 1984; Pikus et al., 1988, see Section "Optical spin orientation") and electric-dipole spin resonance (Rashba and Sheka, 1991). Theoretical models expand on relativistic band structure calculations (Cardona et al., 1988). Phenomenological models such as $\mathbf{k} \cdot \mathbf{p}$ theory (Kane, 1966) and empirical tight binding (Jancu et al., 1998) may use matrix elements of Pauli SO coupling (2) to parameterize SO coupling effects in the electronic band structure. These matrix elements manifest themselves not only indirectly via the SO couplings (5), (6), or (8), but also directly as energy gaps in the electronic band structure (Kane, 1966).

Electrons exposed to SO coupling H_{SO} experience a spin-dependent correction to their velocity $\mathbf{v}_{\boldsymbol{\sigma}} = \partial H_{\mathrm{SO}}/(\hbar \partial \mathbf{k})$. For Rashba SO coupling, this correction is perpendicular to the vector $\boldsymbol{\alpha}$,

$$\mathbf{v}_{\boldsymbol{\sigma}} = \frac{1}{\hbar} \boldsymbol{\alpha} \times \boldsymbol{\sigma}. \tag{9}$$

Optical spin orientation

Optical selection rules combined with SO coupling provide an efficient scheme called *optical orientation* to generate spin-polarized in nonmagnetic semiconductors (Lampel, 1968; Meier and Zakharchenya, 1984). In direct-gap semiconductors like GaAs, the electron states in the conduction band originate from *s*-like atomic orbitals (orbital angular momentum $l = 0$), whereas the hole states in the valence band originate from *p*-like orbitals ($l = 1$). Including spin, the electron states have spin $S = 1/2$, whereas the valence band splits into holes with an effective spin $S = 3/2$ and split-off holes (SH) with $S = 1/2$. The $S = 3/2$ hole states with spin z component $S_z = \pm 3/2$ are denoted heavy-hole (HH) states, whereas the light-hole (LH) states have $S_z = \pm 1/2$. Left (right) circularly polarized photons carry a z component of angular momentum of $-1(+1)$ so that conservation of angular momentum results in the selection rules for optical transitions depicted in Fig. 2. A more detailed analysis of the selection rules shows that the rates T for optical transitions from the HH states to the conduction band are three times larger than the rates for transitions originating from the LH states. In bulk semiconductors, the maximum attainable degree of spin polarization is thus $P = 50\%$, where P is defined as

$$P = \frac{N_+ - N_-}{N_+ + N_+}, \tag{10}$$

and N_+ (N_-) is the number of electrons with spin up (down), respectively. In 2D systems, the degeneracy of the HH and LH states is lifted as sketched in Fig. 2. For resonant excitation at the HH energy, the maximum attainable degree of polarization approaches $P = 100\%$, as confirmed experimentally (Pfalz et al., 2005).

Optical orientation is a direct consequence of the SO gap Δ_{SO} between the HH and LH states with $S = 3/2$ and the SH states with $S = 1/2$. It follows from the transition rates T indicated in Fig. 2 that the spin polarization P becomes zero when $\Delta_{\mathrm{SO}} \to 0$.

Spin precession and spin relaxation

When the spin **S** of an electron with wave vector **k** is not aligned with the effective magnetic field $\boldsymbol{\mathcal{B}}(\mathbf{k})$, it can precess similar to how a spin can precess in an external magnetic $\boldsymbol{\mathcal{B}}$. The equation of motion for spin precession reads

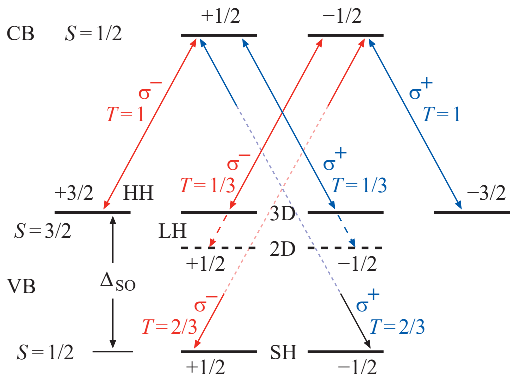

Fig. 2 Selection rules and relative transition rates T for optical transitions between valence band (VB) states having an effective spin $S = 3/2$ and $S = 1/2$ and conduction band (CB) states with $S = 1/2$ (Dyakonov and Perel, 1984). The SH states with $S = 1/2$ are separated from the topmost VB with $S = 3/2$ by a gap Δ_{SO} due to SO coupling. In bulk semiconductors the HH states ($S_z = \pm 3/2$) are degenerate with the LH states ($S_z = \pm 1/2$) whereas in quasi-2D systems the LH states (*dashed bold lines*) are lower in energy than the HH states.

$$\frac{d\mathbf{S}}{dt} = \mathbf{S} \times \boldsymbol{\mathcal{B}}. \tag{11}$$

The precession rate and the direction of the precessional motion are determined by the magnitude and the orientation of the field $\mathcal{B}$.

Random spin precession in the field $\mathcal{B}(\mathbf{k})$ is a common cause for spin relaxation known as *Dyakonov-Perel spin relaxation* (D'yakonov and Perel', 1971). Spin-polarized electrons moving diffusively in a medium with an effective magnetic field $\mathcal{B}(\mathbf{k})$ will undergo momentum scattering events that change the crystal momentum $\hbar\mathbf{k}$ of the electron and thus also the effective magnetic field $\mathcal{B}(\mathbf{k})$ in which the electron's spin precess. Frequent momentum scattering events thus stabilize the spin orientation. This mechanism is similar to motional narrowing in electron spin resonance. A second mechanism contributing to spin relaxation is the *Elliott-Yafet mechanism* that is based on the fact that electron states in the presence of SO coupling (2) are no longer spin eigenstates but a mixture of spin-up and spin-down (Elliott, 1954; Yafet, 1963). A third mechanism is the *Bir-Aronov-Pikus mechanism* that involves electron scattering off holes mediated by electron-hole exchange coupling (Bir et al., 1976). The hyperfine interaction that couples the electron and nuclear spins may also contribute to spin relaxation. Weak antilocalization observed in the magnetoconductivity of quasi-2D systems is a sensitive probe for spin precession and spin relaxation (Knap et al., 1996).

SO coupling and band structure of solids

The energy dispersion of a free Dirac particle ($V_0 = 0$) is shown in Fig. 3A. It consists of two branches representing positive and negative energies for particles and antiparticles and separated by an "energy gap" $2mc^2$. The similarity between Fig. 3A and a simple band structure in solids gives rise to remarkable analogies between relativistic quantum mechanics and the dynamics of Bloch electrons in solids (Blount, 1962; Winkler, 2003).

In the Dirac equation, wave functions are four-component spinors representing spin-up and spin-down in the subspaces of positive and negative energies. The dynamics of Dirac electrons is governed by the off-diagonal coupling between the positive- and negative-energy subspaces proportional to momentum $\mathbf{p}$, see Eq. (3). The envelope-function approximation (Luttinger and Kohn, 1955; Winkler, 2003) provides a qualitatively similar description for the dynamics of Bloch electrons based on an expansion of the electron wave function ψ at finite wave vectors $\mathbf{k}$ in terms of band edge Bloch functions at $\mathbf{k} = 0$. In the resulting effective Hamiltonian for ψ, the subspaces defined by different bands are coupled off-diagonally by terms proportional to crystal momentum $\hbar\mathbf{k}$.

Consider a generic two-band model including the topmost valence band and the lowest conduction band and taking into account the spin of the electrons (Fig. 3B). In the envelope-function approximation, this model is represented by a rescaled version of

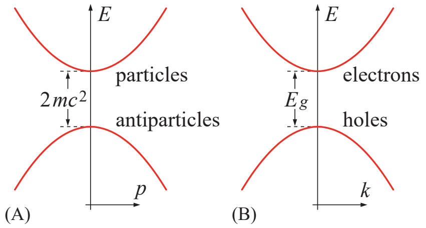

Fig. 3 Dispersion of (A) free Dirac particles and antiparticles (B) free Bloch electrons and holes according to a simple two-band model.

the Dirac Hamiltonian (3). More importantly, the perturbative decoupling procedure described in the Section "Introduction: Pauli SO coupling," that allows one to derive the Pauli equation from the Dirac equation, is likewise applicable to such a two-band model for the dynamics of Bloch electrons. It yields, in lowest order, a kinetic energy term $\hbar^2 k^2/(2m^*)$, where m^* is the effective mass of the Bloch electrons that describes the curvature of the bands. An external magnetic field $\boldsymbol{B}$ requires one to replace crystal momentum $\hbar\mathbf{k}$ by kinetic momentum $\hbar\mathbf{k} - e\boldsymbol{\mathcal{A}}$ with $\boldsymbol{\mathcal{B}} = \nabla \times \boldsymbol{\mathcal{A}}$. In this case, the decoupling procedure also yields a Zeeman term $(g^*/2)\ \mu_B\ \boldsymbol{\sigma}\cdot\boldsymbol{\mathcal{B}}$ with an effective g-factor g^*. In real materials, the effective quantities m^* and g^* may deviate substantially from the free-electron values predicted by the Dirac equation (Kane, 1966; Roth et al., 1959). Unlike the case of the effective mass m^*, the deviation of the effective g-factor g^* from its free-electron value $g = 2$ is another manifestation of Pauli SO coupling (2) (Roth et al., 1959).

In next order, in the presence of an external or built-in electric field $\boldsymbol{E}$ representing SIA, the decoupling of the two-band model yields a Rashba SO coupling term that has the same functional form as the Pauli SO coupling (2)

$$H_R = \tilde{\alpha}\ \boldsymbol{\mathcal{E}}\cdot(\boldsymbol{\sigma} \times \mathbf{p}). \tag{12}$$

The prefactor $\tilde{\alpha}$ is a material parameter that characterizes the crystal structure underlying a specific system. The electric field $\boldsymbol{\mathcal{E}}$ is tunable, for example, via external gates, so that the Rashba SO coupling (12) becomes tunable (Nitta et al., 1997).

It is a common intuitive interpretation of Rashba SO coupling (12) that, in analogy with Pauli SO coupling (2), the crystal electrons are moving with a (Fermi) velocity v in a macroscopic electric field $\mathcal{E}$ that is Lorentz transformed into a magnetic field $\mathcal{B}$ in the electron's rest frame so that the Rashba spin splitting of the moving electron becomes a Zeeman splitting in the electron's rest frame. However, this magnetic field is given by $\mathcal{B} = (v/c^2)\mathcal{E}$ (SI units) and for typical values of $\mathcal{E}$ and v, this relation predicts spin splittings that are orders of magnitude smaller than the experimentally observed values. This discrepancy is due to the fact that the idea of a Lorentz transformation neglects the contribution of the atomic cores to the SO interaction felt by a Bloch electron in a solid. In a microscopic theory, the prefactor $\tilde{\alpha}$ in Eq. (12) is proportional to matrix elements of Pauli SO coupling (2) due to the steep potential V_0 of the atomic cores. Therefore, large atomic numbers Z are generally beneficial for a large Rashba effect. The large-Z requirement generally applies also to other processes exploiting SO coupling in solid-state systems.

Pauli SO coupling (2) is inversely proportional to the gap separating the subspaces of positive and negative energies. Similarly, the Rashba SO coupling in solids is also inversely proportional to the fundamental gap E_g of the material [beyond its dependence on atomic Pauli SO coupling (2)]. However, the former gap has the fixed value $2mc^2$, whereas E_g in solids is amenable for band gap engineering. A smaller gap E_g gives rise to a larger coupling between the bands so that narrow-gap systems generally show a larger Rashba SO coupling.

For electrons in confined geometries such as quantum wells and heterostructure interfaces, the expectation value of an effective or built-in electric field $\boldsymbol{\mathcal{E}}$ vanishes according to Ehrenfest's theorem (on average, there is no force acting on a bound state). Therefore, it was argued that the Rashba effect should be negligible for such bound states (Därr et al., 1976), in contrast to many experiments confirming a large Rashba effect for such geometries. A more careful inspection of the derivation of the Rashba effect reveals that Rashba SO coupling in the conduction band results from the electric field in the valence band. In quantum-confined structures, the former and latter fields are generally different so that, indeed, Ehrenfest's theorem is not relevant for this scenario (Lassnig, 1985; Winkler, 2003).

In metals the screening length is very short so that the concept of a macroscopic electric field $\boldsymbol{\mathcal{E}}$ giving rise to a Rashba effect (12) breaks down. Nonetheless, experiments find large Rashba spin splittings on metal surfaces such as the gold (111) surface (LaShell et al., 1996). This spin splitting has also been confirmed by atomistic ab initio calculations (Bihlmayer et al., 2006). A simple tight-binding model for the Rashba spin splitting on metal surfaces was proposed by Petersen and Hedegård (2000).

Conclusion

SO coupling in solids is a relativistic effect that emerges from the Dirac equation. Specific mechanisms include Rashba and Dresselhaus SO coupling. Its functional form is a consequence of crystal symmetry. The microscopic origin of SO coupling experienced by Bloch electrons is the steep Coulomb potential of the atomic cores so that constituting atoms with large atomic numbers are generally beneficial in the quest for systems with large SO couplings.

The fundamental physics of SO coupling in solids lays the foundation for advanced topics including the spin Hall effect, the spin galvanic effect, SO interaction-based spintronics, and spin torques discussed elsewhere in this volume.

References

Bihlmayer G, Koroteev YM, Echenique PM, Chulkov EV, and Blügel S (2006) The Rashba-effect at metallic surfaces. *Surface Science* 600(18): 3888–3891.
Bir GL, Aronov AG, and Pikus GE (1976) Spin relaxation of electrons due to scattering by holes. *Soviet Physics–JETP* 42(4): 705–712.
Blount EI (1962) Formalism of band theory. In: Seitz F and Turnbull D (eds.). *Solid State Physics*, vol. 13, pp. 305–373. Academic Press.
Cardona M, Christensen NE, and Fasol G (1988) Relativistic band structure and spin-orbit splitting of zinc-blende-type semiconductors. *Physical Review B* 38(3): 1806–1827.
Chiu C-K, Teo JCY, Schnyder AP, and Ryu S (2016) Classification of topological quantum matter with symmetries. *Reviews of Modern Physics* 88(3): 035005.
Därr A, Kotthaus JP, and Ando T (1976) Electron-spin resonance in an inversion layer on InSb. In: Fumi FG (ed.) *Proceedings of the 13th International Conference on the Physics of Semiconductors*, p. 774. Amsterdam: North-Holland.
Dresselhaus G (1955) Spin-orbit coupling effects in zinc blende structures. *Physical Review* 100(2): 580–586.

D'yakonov MI and Perel' VI (1971) Spin orientation of electrons associated with the interband absorption of light in semiconductors. *Soviet Physics–JETP* 33(5): 1053–1059.

Dyakonov MI and Perel VI (1984) Theory of optical spin orientation of electrons and nuclei in semiconductors. In: Meier F and Zakharchenya BP (eds.) *Optical Orientation*, pp. 11–71. Amsterdam: Elsevier.

Elliott RJ (1954) Theory of the effect of spin-orbit coupling on magnetic resonance in some semiconductors. *Physical Review* 96(2): 266–279.

Jancu J-M, Scholz R, Beltram F, and Bassani F (1998) Empirical *spds** tight-binding calculation for cubic semiconductors: General method and material parameters. *Physical Review B* 57(11): 6493–6507.

Kane EO (1966) The k·p method. In: Willardson RK and Beer AC (eds.) *Semiconductors and Semimetals*, vol. 1, pp. 75–100. New York: Academic Press.

Knap W, Skierbiszewski C, Zduniak A, Litwin-Staszewska E, Bertho D, Kobbi F, Robert JL, Pikus GE, Pikus FG, Iordanskii SV, Mosser V, Zekentes K, and Lyanda-Geller YB (1996) Weak antilocalization and spin precession in quantum wells. *Physical Review B* 53(7): 3912–3924.

Lampel G (1968) Nuclear dynamic polarization by optical electronic saturation and optical pumping in semiconductors. *Physical Review Letters* 20(10): 491–493.

LaShell S, McDougall BA, and Jensen E (1996) Spin splitting of an Au(111) surface state band observed with angle resolved photoelectron spectroscopy. *Physical Review Letters* 77(16): 3419–3422.

Lassnig R (1985) k·p Theory, effective-mass approach, and spin splitting for two-dimensional electrons in GaAs-GaAlAs heterostructures. *Physical Review B* 31: 8076.

Luttinger JM and Kohn W (1955) Motion of electrons and holes in perturbed periodic fields. *Physical Review* 97(4): 869–883.

Meier F and Zakharchenya BP (1984) *Optical Orientation*. Amsterdam: Elsevier.

Nitta J, Akazaki T, Takayanagi H, and Enoki T (1997) Gate control of spin-orbit interaction in an inverted $In_{0.53}Ga_{0.47}As/In_{0.52}Al_{0.48}As$ heterostructure. *Physical Review Letters* 78(7): 1335–1338.

Petersen L and Hedegård P (2000) A simple tight-binding model of spin-orbit splitting of *sp*-derived surface states. *Surface Science* 459(1–2): 49–56.

Pfalz S, Winkler R, Nowitzki T, Reuter D, Wieck AD, Hägele D, and Oestreich M (2005) Optical orientation of electron spins in GaAs quantum wells. *Physical Review B* 71: 165305.

Pikus GE, Marushchak VA, and Titkov AN (1988) Spin splitting of energy bands and spin relaxation of carriers in cubic III-V crystals (review). *Soviet Physics–Semiconductors* 22(2): 115–124.

Rashba EI and Sheka VI (1959) Symmetry of energy bands in crystals of wurtzite type: II. Symmetry of bands including spin-orbit interaction. *Fizika Tverdogo Tela: Collected Papers* 2: 162–176. For an English translation, see the supplement of G. Bihlmayer, O. Rader, and R. Winkler, Focus on the Rashba effect, New J. Phys. 17 (2015) 050202.

Rashba EI and Sheka VI (1991) Electric-dipole spin resonance. In: Landwehr G and Rashba EI (eds.) *Landau Level Spectroscopy*, pp. 131–206. Amsterdam: Elsevier.

Roth LM, Lax B, and Zwerdling S (1959) Theory of optical magneto-absorption effects in semiconductors. *Physical Review* 114: 90.

Sakurai JJ (1967) *Advanced Quantum Mechanics*. Reading, MA: Addison-Wesley.

Winkler R (2003) *Spin-Orbit Coupling Effects in Two-Dimensional Electron and Hole Systems*. Berlin: Springer.

Yafet Y (1963) *g* Factors and spin-lattice relaxation of conduction electrons. In: Seitz F and Turnbull D (eds.). *Solid State Physics*, vol. 14, pp. 1–98. Academic Press.

Spin-orbit interaction based spintronics

Junsaku Nitta, Department of Materials Science, Tohoku University, Sendai, Japan; NTT Basic Research Laboratories, Atsugi, Japan

© 2024 Elsevier Ltd. All rights reserved.

Introduction 194
Origin of spin-orbit interaction in semiconductors 194
Gate controlled Rashba SOI 195
Spin relaxation and its suppression for long spin coherence 197
Spin generation and detection using SOI 198
Spin manipulation by Aharonov-Casher spin interference 200
Spin manipulations by SOI-based ESR 202
Conclusion 203
References 203

Abstract

Spin-orbit interaction (SOI) is a relativistic effect and produces a momentum dependent effective magnetic field when electron spins travel in an electric field. The spin angular momentum and orbital motion of electrons are coupled by SOI, e.g., leading to the spin Hall effect, where spin-up and -down electrons are deflected into opposite directions. By exploiting these unique features, we can create spin functionalities in SOI systems without using an external magnetic field. SOI based spintronics is often called "spin-orbitronics". This chapter focuses on Rashba and Dresselhaus SOIs and their applications for spintronics in semiconductor heterostructures. Especially Rashba SOI is rather interesting since the strength is controlled by the gate voltage on top of the semiconductor's two-dimensional electron and hole gases. By utilizing the effective magnetic field induced by the Rashba SOI, spin generation, manipulation, and detection are possible by electrostatic ways. However, the drawback of SOI is to give rise to spin relaxation because of the momentum dependent magnetic field. Long spin coherence is achieved by special spin helix state where both Rashba and Dresselhaus SOIs are equal.

Key points

- Spin-orbit interaction (SOI) is a relativistic effect and produces a momentum dependent effective magnetic field when electron spins travel in an electric field.
- Spin angular momentum and orbital motion of electrons are coupled by SOI, e.g., leading to spin Hall effect, where spin-up and -down electrons are deflected into opposite directions.
- By exploiting these unique features, we can create spin functionalities in SOI systems without using an external magnetic field.
- Rashba SOI is important since its strength is controlled by a gate voltage on top of semiconductor's two-dimensional electron and hole gases.
- By utilizing effective magnetic field induced by Rashba SOI, spin generation, manipulation, and detection are possible by electrostatic ways.
- However, drawback of SOI is to give rise to spin relaxation because of momentum dependent magnetic field.
- Long spin coherence is achieved by persistent spin helix state where both Rashba and Dresselhaus SOIs are equal.
- SOI-based electron spin resonance (ESR) techniques are developed by using ac-electric fields for spin manipulations.

Spin-orbit interaction (SOI) is a relativistic effect and produces a momentum dependent effective magnetic field when electron spins travel in an electric field. The spin angular momentum and orbital motion of electrons are coupled by SOI, e.g., leading to the spin Hall effect, where spin-up and -down electrons are deflected into opposite directions. By exploiting these unique features, we can create spin functionalities in SOI systems without using an external magnetic field. SOI based spintronics is often called "spin-orbitronics." This chapter focuses on Rashba and Dresselhaus SOIs and their applications for spintronics in semiconductor heterostructures. Especially Rashba SOI is rather interesting since the strength is controlled by the gate voltage on top of the semiconductor's two-dimensional electron and hole gases. By utilizing the effective magnetic field induced by the Rashba SOI, spin generation, manipulation, and detection are possible by electrostatic ways. However, the drawback of SOI is to give rise to spin relaxation because of the momentum dependent magnetic field. Long spin coherence is achieved by special spin helix state where both Rashba and Dresselhaus SOIs are equal.

https://doi.org/10.1016/B978-0-323-90800-9.00093-7

Introduction

Spin degeneracy in electronic bands is lifted by spin-orbit interaction (SOI) in crystals without inversion symmetry. The bulk SOI effects are established in both noncentrosymmetric zinc-blende and wurtzite semiconductors by Dresselhaus (1955) and Rashba (1960), respectively. Bychkov and Rashba extended the concept of SOI to two-dimensional electron gases (2DEG) with structure inversion asymmetry (SIA) (Bychkov and Rashba, 1984). These SOIs play important roles for many interesting spin-related phenomena in solid state physics (Manchon et al., 2015). The essence of SOI is that the moving electrons in an electric field feel an effective magnetic field even without any external magnetic field. The internal electric field of the Dresselhaus SOI originates from the microscopic Coulomb potential gradient of the atomic core region, the strength of which is generally difficult to modulate. The bulk Dresselhaus SOI coefficient γ is considered to be a material-constant parameter. It should be noted that the spin splitting energy due to the Dresselhaus SOI can be modulated by carrier density since the SOI is affected by electron velocity. On the contrary, the internal electric field of the Rashba SOI originates from both the *microscopic* Coulomb potential induced by the atomic core and the *macroscopic* potential gradient caused by hetero-interface and quantum well (QW) in semiconductor heterostructures (Winkler, 2003). Although the microscopic electric field is a material-constant parameter, as is the Dresselhaus SOI, the macroscopic electric field can be modulated by applying an external gate bias voltage of 2DEG. This enables us to electrically control Rashba SOI coefficient α (Nitta et al., 1997; Engels et al., 1997). The strength of SOI depends on both electric fields and electron momentum. It should be emphasized that the SOI effects in solids are much enhanced in contrast to that in vacuum. This is because the electric field near the atomic core is huge and the electron wave function varies rapidly in space, resulting in huge momentum.

By exploiting these unique features, we can create spin functionalities in SOI systems without using an external magnetic field. The SOI-based spintronics is often called "spin-orbitronics." The electrostatic control of spin degree of freedom can be used for generation, manipulation, and detection of spins, which are important techniques for spintronics and quantum information. This chapter focuses on Rashba and Dresselhaus SOIs and their applications in semiconductor heterostructures. However, the drawback of SOI is to give rise to spin relaxation because of the momentum dependent magnetic field. Long spin coherence is achieved by special spin helix state where both Rashba and Dresselhaus SOIs are equal.

Origin of spin-orbit interaction in semiconductors

The SOI in vacuum is described by the Thomas term in the Pauli equation,

$$H_{SO} = -\frac{1}{2m_0c^2}\mu_B\sigma\cdot\left(\vec{p}\times\nabla V_0\right) = -\mu_B\sigma\cdot\left(\frac{\vec{p}\times\vec{E}}{2m_0c^2}\right) \tag{1}$$

Here m_0, c, μ_B, σ and V_0 are the free electron mass, the light velocity, the Bohr magneton, the Pauli spin matrix, and the scalar potential, respectively. The electron momentum is given by $\vec{p} = \hbar\vec{k}$ with Planck constant $\hbar$ and wavenumber $\vec{k}$. In analogy to the Zeeman Hamiltonian, $H_Z = -\mu_B\sigma\cdot\vec{B}$, the effective magnetic field $\vec{B}_{eff}$ of SOI is given by

$$\vec{B}_{eff} = \frac{\vec{p}\times\vec{E}}{2m_0c^2} \tag{2}$$

It is clear that the effective magnetic field $\vec{B}_{eff}$ is induced perpendicular to both the electron momentum $\vec{p}$ and the electric field $\vec{E}$. In the relativistic quantum theory, $2m_0c^2$ is the energy gap between an electron and a positron, which is a negative energy particle with the negative mass predicted by Dirac. The energy scale of $2m_0c^2$ is $\sim$1 MeV; thus, SOI effects are negligible for a particle with non-relativistic momentum in vacuum. On the other hand, in crystalline solids, the energy-band gap is reduced to $\sim$1 eV in typical semiconductors. Since the Dirac gap is replaced by the energy-band gap according to the $k\cdot p$ perturbation theory (Winkler, 2003), it results in huge enhancement of the SOI in semiconductors.

The electron wave function in semiconductors is characterized by both a Bloch function and an envelope function. In the Bloch part, the electron wave is rapidly modulated by the atomic core potential, while the electron wave in the envelope part is gradually modulated by the periodic crystalline structure. The origin of the enhancement of the SOI in semiconductors is due to the Bloch part, where both the electron momentum and the electric field are enlarged by the fast oscillation of the electron wave and the strong confinement near the atomic core, respectively (Winkler, 2003).

In noncentrosymmetric zinc-blende semiconductors such as GaAs or InSb, the electric field due to the ionized atoms in the crystal can be an origin of SOI in Eq. (1). This is the so called Dresselhaus SOI. The derivation of Dresselhaus SOI is obtained from the $k\cdot p$ perturbation theory based on 14×14 matrix Hamiltonian for the extended Kane model. The bulk Dresselhaus SOI is given by the following equation.

$$H_D^{bulk} = \gamma\left[\sigma_xk_x\left(k_y^2-k_z^2\right)+\sigma_yk_y\left(k_z^2-k_x^2\right)+\sigma_zk_z\left(k_x^2-k_y^2\right)\right] \tag{3}$$

Here, γ is bulk Dresselhaus SOI coefficient which is a material constant, σ_x, σ_y, σ_z are the Pauli spin matrix and, k_x, k_y, k_z are electron wavenumber. In a zinc-blende semiconductor 2DEG QW grown along [001] direction such as GaAs and InAs, the linear Dresselhaus SOI is expressed by

$$H_{D1} = \beta_1 \left(k_x\sigma_x - k_y\sigma_y\right) \tag{4}$$

Here, we use $k_z = 0$ and $k_z^2 \rightarrow \langle k_z^2 \rangle$ for a [001] QW, and introduce a linear Dresselhaus coefficient $\beta_1 = -\gamma\langle k_z^2 \rangle$. When the QW confinement wavenumber $k_z^2 \sim (\pi/d_{QW})^2$ with the QW thickness d_{QW} is much larger than the Fermi wavenumber k_F, the Dresselhaus k-cubic term is negligible. Although the bulk Dresselhaus SOI γ is not controllable, the linear Dresselhaus SOI β_1 can be tuned by the QW thickness d_{QW}.

In addition to the Dresselhaus SOI in zinc-blende semiconductors, the spin degeneracy is lifted due to the SIA of the confining potential of 2DEG QW. When the confinement potential of QW is symmetric, the Rashba SOI caused by macroscopic electric field in the QW is zero. By applying an external gate bias on top of 2DEG, the potential profile can be modulated, and the asymmetric QW potential causes a finite Rashba SOI strength that lifts the spin degeneracy. The advantage of the Rashba SOI is that the strength of SOI can be controlled by the gate voltage (Nitta et al., 1997; Engels et al., 1997; Schäpers et al., 1998). The electric field direction is perpendicular to the 2DEG hetero-structure. By considering the z-component electric field in Eq. (1), the form of Rashba SOI is expressed by

$$H_R = \frac{\alpha}{\hbar}\left(\vec{z} \times \vec{p}\right) \cdot \sigma = \alpha\left(k_x\sigma_y - k_y\sigma_x\right) \tag{5}$$

where α is the Rashba SOI coefficient, which depends on the band parameters and the electric field in the QW.

According to the $k \cdot p$ perturbation theory (Winkler, 2003), the Rashba SOI coefficient α is given by the following equation

$$\alpha = \frac{\hbar^2 E_P}{6m_0}\left\langle \Psi(z) \middle| \frac{d}{dz}\left(\frac{1}{E_F - E_{\Gamma_7}(z)} - \frac{1}{E_F - E_{\Gamma_8}(z)}\right) \middle| \Psi(z) \right\rangle \tag{6}$$

where $\Psi(z)$ is the envelope wave function for the confined electron, E_P is the inter-band matrix element, E_F is the Fermi energy in the conduction band, and $E_{\Gamma_7}(z)$ and $E_{\Gamma_8}(z)$ are positions of the band edge energies for Γ_7 (spin split off band) and Γ_8 (the highest valence band) bands, respectively. Contribution to Eq. (6) can be split into two parts: (i) the field part, which is related the electric field in the QW and (ii) interface part, which is related to band discontinuities at the heterointerface (Schäpers et al., 1998).

For many years, there has been an intense discussion about the Rashba SOI. It had been considered that the Rashba SOI should be very small because the average electric field for the bound state in QWs should be zero, i.e., $\langle E \rangle = 0$ in order to satisfy the condition that there is no force acting on an electron bound state. In fact, this controversy is resolved by Eq. (6). It is clear that the Rashba spin splitting in conduction band originates from the electric field in the valence band.

Both Dresselhaus and Rashba SOIs induce spin split subbands in energy dispersion relation and spin-orbit (SO) effective magnetic field B_{eff}. The SO fields at the Fermi surface are illustrated in Fig. 1 for the case of (a) Rashba SOI and (b) linear Dresselhaus SOI. The arrow directions also correspond to the SO induced effective field. These momentum dependent SO fields are an origin of spin relaxation. It is important to note that the spin relaxation is suppressed when both are present with equal magnitude. As is shown in Fig. 1(c), the total SO fields are unidirectional along [110] directions, resulting in the so-called persistent spin helix state (PSH) (Schliemann et al., 2003; Bernevig et al., 2006a). We will discuss it in the following section "Spin relaxation and its suppression for long spin coherence."

Gate controlled Rashba SOI

The spin field effect transistor (spin-FET) (Datta and Das, 1990) was proposed with two assumptions (i) the gate controlled Rashba SOI and (ii) spin injection and detection using ferromagnetic contacts. The schematic spin-FET structure is illustrated in Fig. 2. The injected spin direction from the ferromagnetic contact should be perpendicular to the Rashba SOI field for effective spin precession

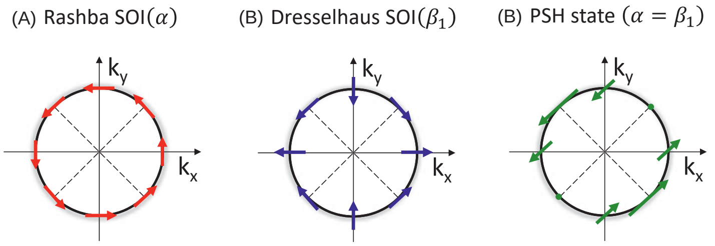
(A) Rashba SOI(α)
(B) Dresselhaus SOI(β_1)
(B) PSH state ($\alpha = \beta_1$)
k_y
k_x
k_y
k_x
k_y
k_x

Fig. 1 Spin-orbit induced effective magnetic fields at Fermi energy. (a) Rashba SOI, (b) Dresselhaus SOI, (c) Persistent spin Helix state ($\alpha = \beta_1$). The arrows correspond to the effective field directions. A. Manchon, HC Koo, J. Nitta, S. M. Froloc, RA. Duine (2015) New perspectives for Rashba spin-orbit coupling. *Nature Materials* 14: 871.

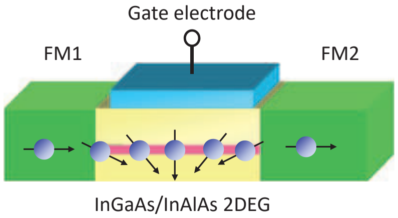

Fig. 2 Schematic for spin field effect transistor. FM1 and FM2 correspond to ferromagnetic electrodes. InGaAs/InAlAs 2DEG is used for spin precession controlled by gate voltage via SOI. S Datta and B Das (1990) Electronic analog of the electro-optic modulatir. *Applied Physics Letters* 56: 665.

control. Fundamental obstacle for spin injection from a ferromagnetic electrode to a semiconductor channel is pointed out because of conductivity mismatch (Schmidt et al., 2000). The momentum difference between spin up and down at the Fermi energy is described by $k_{F\uparrow} - k_{F\downarrow} = 2\alpha m^*/\hbar^2$, where m^* is an effective mass of electron. The spin precession angle φ is given by

$$\varphi = \frac{2\alpha m^*}{\hbar^2} L \tag{7}$$

when an electron spin travels in a channel length L of the spin-FET. It should be emphasized that spin precession angle φ does not depend on k_F and spin splitting energy $\Delta_R = 2\alpha k_F$, so that all the modes in a narrow channel can provide the same precession angle. This unique feature is important to make spintronics devices. The gate control of Rashba SOI parameter α itself instead of Δ_R is crucial to realize spintronics devices.

One of the ways to obtain the Rashba SOI parameter α is to measure the beating pattern in the Shubnikov de-Haas (SdH) oscillations (Nitta et al., 1997; Engels et al., 1997; Schäpers et al., 1998). The origin of the beating in the SdH oscillations comes from the spin-split two subband at the Fermi energy. Note that one should be careful about the origin of the beating when we have a second subband in a QW since the magneto inter-subband scattering (MIS) also makes a beating pattern in the SdH oscillations (Rowe et al., 2001).

In InGaAs- based 2DEGs, Rashba SOI strength is larger than that of Dresselhaus SOI. An InGaAs/InAlAs heterostructure used to evaluate the Rashba SOI is shown in Fig. 3(a) (Nitta et al., 1997). A Si-doped InAlAs carrier supplied layer is placed underneath an InGaAs 2DEG channel to make asymmetric QW potential profile as shown in Fig. 3(b). By application of negative gate voltage V_g, the potential profile in the QW becomes more asymmetric, leading to a reduction of $k_F = \sqrt{2\pi N_s}$ and an enhancement of α. Here, k_F is the Fermi momentum and N_s is the carrier density of the 2DEG. Beating patterns appeared in SdH oscillations are shown in Fig. 4(a), which are analyzed to evaluate α. As is expected, the obtained α is enhanced by negative voltage V_g (by reducing N_s as shown in Fig. 4(b)).

An alternative way to evaluate SOI parameter is to perform weak anti-localization (WAL) analysis. This is because the spin splitting energy Δ_R can be related to spin relaxation time τ_s if the spin relaxation is governed by the D'yakonov-Perel (DP) mechanism as is discussed in Chapter 3. It has been demonstrated that the Rashba SOI can be controlled by the design of asymmetry in QWs from the WAL analysis (Koga et al., 2002; Lin et al., 2005). Optical measurements are useful to evaluate both Rashba and Dresselhaus SOI parameters (Meier et al., 2007), however, they are not easy to apply gate-fitted samples.

The SdH oscillation and WAL analyses are not always accurate to evaluate the SOI parameter when the Rashba and Dresselhaus SOI strengths are close to each other. Recently, the theoretical model for WAL in the vicinity of PSH state was developed and Rashba and Dresselhaus SOI strengths were experimentally obtained in a GaAs/AlGaAs heterostructure (Weigele et al., 2020). A novel concept to determine the Rashba and Dresselhaus SOI ratio without any fittings was proposed (Scheid et al., 2008) and experimentally demonstrated in InGaAs wires by utilizing in-plane Zeeman field (Sasaki et al., 2014). By using this method, the gate-controlled persistent spin helix (PSH) was confirmed.

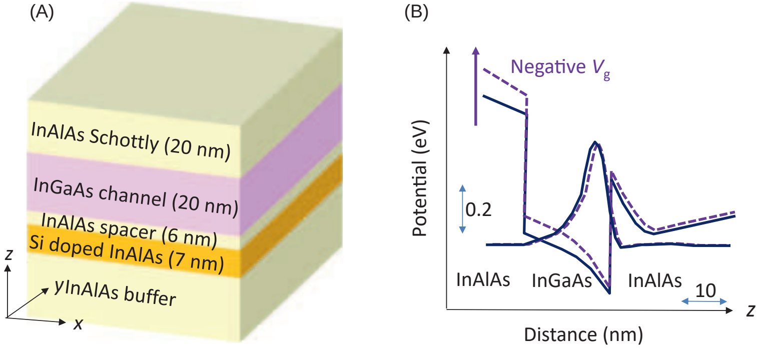

Fig. 3 (a) An InGaAs/InAlAs heterostructure used to evaluate Rashba SOI. (b) Potential profile of the heterostructure. By applying negative gate voltage the potential profile is more asymmetric, resulting in enhancement of Rashba SOI. J. Nitta, T. Akazaki, H. Takayanagi, T. Enoki, (1997) Gate control of spin-orbit interaction in an inverted InGaAs heterostructure. *Physical Review Letters* 78: 1335.

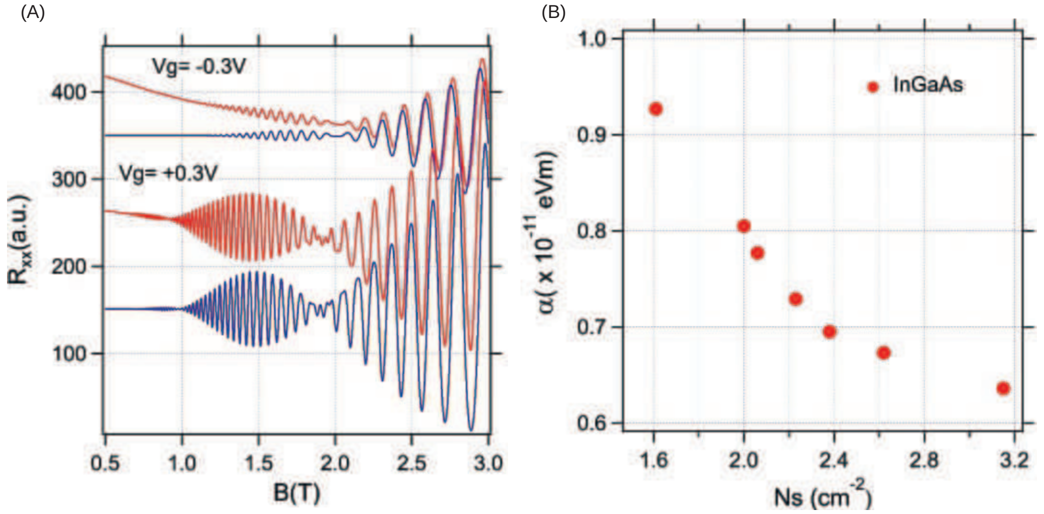

Fig. 4 (a) Red curves: Beating patterns appeared in SdH oscillations of InGaAs/InAlAs heterostructure shown in Fig. 3. Blue curves: Analyses to evaluate Rashba SOI. (b) Obtained Rashba SOI α from the SdH analyses. J. Nitta, T. Akazaki, H. Takayanagi, T. Enoki, (1997) Gate control of spin-orbit interaction in an inverted InGaAs heterostructure. *Physical Review Letters* 78: 1335.

Spin relaxation and its suppression for long spin coherence

Spins of electrons in solids are not conserved quantity in contrast to charges of electrons. The information of spins is lost and leads to the so-called spin relaxation by several reasons. In the epitaxially grown III-V compound QWs with the Rashba and Dresselhaus SOIs, the D'yakonov-Perel (DP) mechanism is generally dominant for spin relaxation (Dyakonov and Perel, 1971). The Rashba SOI causes an effective magnetic field B_{eff}which is pointing perpendicular to the momentum direction in the 2DEG plane. The spin of electrons is precessing around the effective field. In a diffusive 2DEG, the momentum direction of electron changes frequently, and hence so does the direction of B_{eff}. Due to the random change in B_{eff}, the spin orientation is randomized and the spin loses the memory of its initial spin direction. The DP spin relaxation is caused not only by the Rashba SOI but also by the Dresselhaus SOI. Generally speaking, the DP spin relaxation is expected if the system has momentum dependent effective field B_{eff} due to SOI spin splitting energy Δ_R.

From the above DP spin relaxation picture, we can estimate the spin relaxation time. The spin is initially precessing around a certain effective magnetic field direction with a typical frequency of $\omega = \Delta_R/\hbar$ and during a typical scattering time τ. After a scattering event, the direction of B_{eff} is randomly changed, and the spin starts to precess around the new B_{eff} direction. Hence, after a certain number of scattering events there is no correlataion anymore between the initial and final spin states. The precise time scale on which the spin loses its memory depends on the typical spin precession angle between scattering events $\delta\phi = \omega\tau = \Delta_R\tau/\hbar$. For $\delta\phi \ll 1$, the precession angle is small between succeeding scattering events, so that the spin vector experiences a slow angle diffusion. During a time interval t, the number of random steps is t/τ. For uncorrelated steps in the precession angle we have to sum the squared precession angles $\delta\phi^2 = (\Delta_R\tau/\hbar)^2$, and the total squared precession angle after time t is $(\Delta_R\tau/\hbar)^2 t/\tau$. The spin relaxation time τ_s can be defined as the time at which the total precession angle becomes of the order of unity. Hence the spin relaxation time is given by $\tau_s \approx \hbar^2/(\Delta_R^2\tau)$. The spin relaxation time τ_s can be derived from WAL analysis, which can be related to spin splitting energy $\Delta_R = 2\alpha k_F$ (therefore α).

It is very crucial to suppress the spin relaxation while keeping the strength and the controllability of SOI. One of the ways to suppress spin relaxation is to confine electrons to one-dimensional narrow wire structures whose width is of same scale of spin precession length $L_{so} = \hbar^2/\alpha m^*$ due to the Rashba SOI. This suppression of spin relaxation due to lateral confinement effect have been theoretically investigated (Mal'shukov and Chao, 2000; Kettemann, 2007) and have been experimentally demonstrated with optical way (Holleitner et al., 2006) and WAL analysis (Schäpers et al., 2006; Kunihashi et al., 2009).

Most effective way to suppress the DP spin relaxation is to utilize the so-call persistent spin helix (PSH) condition (Schliemann et al., 2003; Bernevig et al., 2006a,b), where Rashba SOI strength α is equal to linear Dresselhaus SOI β_1. Schematic images of spin relaxation and PSH are shown in Fig. 5(a) and (b), respectively. In the PSH condition ($\alpha = \beta_1$), conservation of spin polarization is preserved even after scattering events. This conservation is predicted to be robust against all forms of spin-independent scattering, including electron-electron interaction, but is broken by spin-dependent scattering and a cubic Dresselhaus term. The PSH in semiconductor QWs was confirmed by optical transient spin-grating spectroscopy by Koralek et al. (2009). They found enhancement of spin life time by two orders magnitude near the exact PSH point.

Under the PSH state ($\alpha = \beta_1$), the effective magnetic field is unidirectional as is shown in Fig. 1(c), resulting in coherent spin propagation with helical spin texture. This helical spin texture pattern has been observed by optical measurements (Walser et al., 2012; Ishihara et al., 2014). Furthermore, it has been demonstrated that the helical spin coherence is enhanced by introducing drift

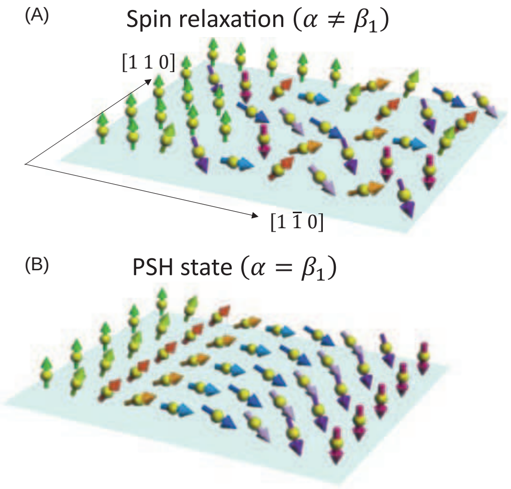
(A)
Spin relaxation $(\alpha \neq \beta_1)$
[1 1 0]
$[1\ \bar{1}\ 0]$
(B)
PSH state $(\alpha = \beta_1)$

Fig. 5 Schematic images for (a) spin relaxation and (b) persistent spin helix state. J. D. Koralek, C. P. Weber, J. Orenstein, B. A. Bernevig, Shou-Cheng Zhang, S. Mack & D. D. Awschalom (2009) Emergence of the persistent spin helix in semiconductor quantum wells. *Nature* 458: 610–613.

motion of spins by in-plane electric field (Kumihashi et al., 2016). The gate-controlled PSH state (Kohda et al., 2012a) and gate-controlled switching between PSH and inverse PSH ($-\alpha = \beta_1$) (Yoshizumi et al., 2016) have been confirmed by transport measurement. These experimental demonstrations are breakthroughs toward minimizing and controlling spin relaxation. Spin complementary field effect transistor design is proposed on the basis of gate-tunable spin helix states (Kunihashi et al., 2012).

Spin generation and detection using SOI

SOI can generate spin current and spin accumulation due to the spin and momentum coupling nature. Charge currents are converted to transverse spin currents by the spin Hall effect as shown in Fig. 6(a). The spin polarization direction is out-of-plane. SOI induced effective field B_{eff} gives rise to the Edelstein-Rashba effect (spin accumulation) as shown in Fig. 6(b). In this case, the spin polarization direction is parallel to B_{eff}, namely in-plane. In contrast to metal systems, a band structure affected by the SOI in semiconductor systems lead to an intrinsic spin Hall effect even in the absence of scattering events. The intrinsic spin Hall effect in valence-band holes was first predicted by Murakami et al. (2003). A universal intrinsic spin Hall effect in a ballistic Rashba 2DEG system was calculated by Sinova et al. (2004). The universal spin Hall conductivity is given by $e/8\pi$. It is important to note that the spin Hall conductivity vanishes in a diffusive Rashba 2DEG system (Inoue et al., 2004). The spin Hall effect in heavy-holes in confined QW was studied by Schiemann and Loss (2005). In contrast to the Rashba 2DEG systems, the intrinsic spin Hall effect in a hole system does not vanish even in a diffusive case. Quantized spin Hall conductance has been theoretically predicted (Bernevig et al., 2006a,b) and experimentally demonstrated in HgTe/CdTe QWs (Koenig et al., 2007).

Intuitive picture of the spin Hall effect in the Rashba 2DEG systems is provided by the spin transverse force (Li et al., 2005). Using the Heisenberg equation of motion and the commutation relation of the Pauli spin matrix, the second derivative of the position operator gives the following spin transverse force on a moving electron (Li et al., 2005).

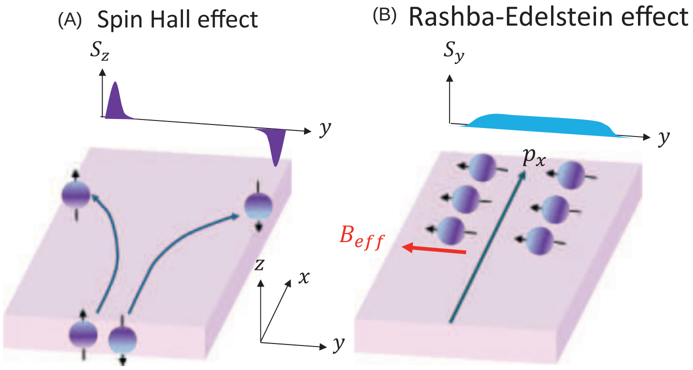

Fig. 6 Schematic illustrations for (a) spin Hall effect and (b) Rashba-Edelstein effect. G. Bauer (2004) Mesmerizing semiconductors. *Science* 306: 1898.

$$\vec{F} = -\frac{2m^*\alpha^2\sigma_z}{\hbar^3}\vec{p} \times \hat{z} \tag{8}$$

This spin transverse force tends to form a σ_z spin current perpendicular to the momentum direction $\vec{p}$. When the charge currents are flowing toward x-direction with momentum p_x, σ_z spin currents are generated along y-directions because of the spin transverse force.

Experimental observation of the spin Hall effect in bulk GaAs and strained InGaAs was demonstrated with the use of Kerr rotation microscopy. Without applying any external magnetic field, the out-of-plane spin polarized carriers with opposite sign were detected at the two edges of the sample. The amplitude of the spin polarization was so weak, and the mechanism was originated by the extrinsic spin Hall effect such as the skew scattering (Engel et al., 2005). The spin Hall effect in a GaAs 2D hole system was observed by Wunderlich et al. (2005). The out-of-plane spin polarized carriers were detected by light emitting diodes, and sign of the spin polarization was switched by the electric field direction. The authors claimed that the intrinsic spin Hall effect is responsible for their system.

SOI induced effective field B_{eff} gives rise to the spin-momentum locking effects; the Edelstein-Rashba effect (inverse spin galvanic effect) and the spin galvanic effect. These two effects are also useful to generate and to detect spin polarized carrier in non-magnetic materials. Because of the Hamilton's equation $\vec{v} = \partial H_R/\partial\vec{p}$, the spin galvanic effect is given by $\vec{j}_c = -e\alpha\left(\vec{z} \times \vec{S}\right)/\hbar$, where $\vec{S}$ is the non-equilibrium spin density created by either electrically and optically and $\vec{j}_c$ is the induced charge density (Wunderlich et al., 2009). This concept was originally developed in the context of optical manipulation of spin in semiconductors (Ivchenko and Pikus, 1978) and observed in quantum wells (Ganichev, 2008). The Onsager reciprocal of spin galvanic effect, the inverse spin galvanic effect (sometimes called the Edelstein-Rashba effect (Edelstein, 1990)) has been observed in strained semiconductor InGaAs (Kato et al., 2004a,b) and QWs (Ganichev et al., 2006). Following the Rashba symmetry the spin density generated by the current is $\vec{S} = \alpha m^*\left(\vec{z} \times \vec{j}_c\right)/e\hbar$. The spin Hall effect and the Edelstein-Rashba effect are of particular significance in ferromagnet/heavy metal bilayer systems for manipulating the magnetization of ferromagnets electrically.

An electrical detection of the spin Hall effect is difficult since the same amounts of charges are accumulated in the Hall probes. However, the inverse spin Hall effect can be used for the electrical detection of spin polarized carriers. Spin currents are converted to transverse charge currents by the inverse spin Hall effect, and the accumulated charge can be detected by the Hall probe. Wunderlich et al. (2010) have combined the concept of the spin Hall effect with the spin FET, and have successfully demonstrated the so-called spin Hall transistor operation. Spin polarized carriers are generated by circularly polarized optical light, and then the direction of spins is controlled by the gate voltage through the Rashba SOI in a GaAs 2DEG channel, and finally the modulated spins are electrically detected by the inverse spin Hall effect.

The experimentally observed spin polarization due to the spin Hall effect and the Edelstein-Rashba effect is very tiny (much less than 1%) in semiconductor channels. So the Stern-Gerlach spin filter has been proposed (Fig. 7) by using the spatial gradient of the Rashba SOI (Ohe et al., 2005). A spatial gradient of the effective magnetic field due to the Rashba SOI causes spatial spin separation similar to the Stern-Gerlach effect. Almost 100% spin polarization can be realized even without applying any external magnetic fields and without attaching ferromagnetic contacts. In this case, the spin polarized orientation is not out-of-plane σ_z but in-plane

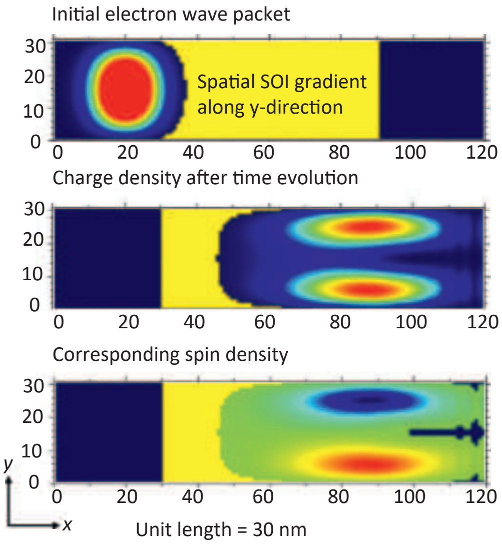

Fig. 7 Stern-Gerlach spin filter operation based on Rashba SOI. Yellow region indicates spatial gradient of Rashba SOI, resulting in spatial gradient of effective magnetic field. J Ohe, M Yamamoto, T Ohtsuki, J Nitta(2005) Mesoscopic Stern-Gerlach spin filter by nonuniform spin-orbit interaction. *Physical Review B* 72: 041308 R.

σ_y. The spin polarization persists even in the presence of randomness. This Stern-Gerlach spin filter based on inhomogeneous Rashba SOI was demonstrated in semiconductor quantum point contacts (Kohda et al., 2012a,b). In this experiment, the spin polarization of 70% was confirmed by shot noise measurements. Such a spin-filter device can be also used for electrical spin detection (Kohda et al., 2019).

Topological insulators have an insulating gap in the bulk, but have topologically protected edge states due to the time reversal symmetry. This type of insulator is realized by an inversion between conduction and valence bands due to strong SOI and the edge states have a distinct helical property: two states with opposite spin-polarization counterpropagate at a given edge; for this reason, they are also called helical edge states. In two dimensions the helical edge states give rise to the quantum spin Hall (QSH) effect, in the absence of any external magnetic field. A theoretical prediction of the QSH has been proposed and experimentally demonstrated in HgTe/CdTe semiconductor QWs (Bernevig et al., 2006a,b; Koenig et al., 2007). By varying the thickness of the QW, the band structure changes from a normal to an "inverted" type at a critical thickness d_c. For thin QWs with well width $d_{QW} < 6.3$ nm, the insulating regime shows the conventional behavior of vanishingly small conductance at low temperature. However, for thicker QWs ($d_{QW} > 6.3$ nm), the nominally insulating regime shows a plateau of residual conductance close to $2e^2/h$. The residual conductance is independent of the sample width, indicating that it is caused by edge states. Furthermore, the residual conductance is destroyed by a small external magnetic field.

Spin manipulation by Aharonov-Casher spin interference

An electron acquires a phase around magnetic flux due to the vector potential leading to the Aharonov-Bohm (AB) effect in an interference loop (Aharonov and Bohm, 1959; Tonomura et al., 1986). From the view point of inherent symmetries between magnetic field and electric field in the Maxwell equations, Aharonov and Casher have predicted that a magnetic moment acquires a phase around a charge flux line (Aharonov and Casher, 1984). It is pointed out that the AC phase shift can be derived from SOI (Balatsky and Al'tshuler, 1993). A. G. Aronov and Y. B. Lyanda-Geller have derived a spin-orbit Berry phase in conducting rings with SOI (Aronov and Lyanda-Geller, 1993). T. Qian and Z. Su have obtained the AC phase, which is the sum of spin-orbit Berry phase and spin dynamical phase in a one-dimensional ring with SOI (Qian and Su, 1994).

Mathur and Stone have theoretically shown (Mathur and Stone, 1992) that the effects of SOI in disordered conductors are manifestations of the AC effect in the same sense as the effects of weak magnetic fields are manifestations of AB effect. They have proposed the electronic AC effect in a mesoscopic interference loop made of GaAs 2DEG with the Dresselhaus SOI. The AC spin interference based on this proposal was not reported since the Dresselhaus SOI strength is not controlled by an electrostatic way.

Electrostatic manipulation of spins is of crucial for spintronics. An AC spin-interference device has been proposed on the basis of the gate controlled Rashba SOI (Nitta et al., 1999; Meijer et al., 2002). The schematic structure of the spin interference device is shown in Fig. 8. The spin interference can be expected in a ring-shaped loop with the Rashba SOI because the spins of electrons precess in opposite directions between clockwise and counter clockwise traveling directions in the ring. The relative difference in spin precession angle at the interference point causes the phase difference in the spin wave functions. The gate electrode, which covers the whole area of the ring, controls the Rashba SOI, and therefore, the interference. The advantage of this proposed spin-interference device is that conductance modulation is not washed out even in the presence of multiple modes since the spin precession angle does not depend on the wavenumber as shown in Eq. (5). Furthermore, this Rashba spin interferometer works without ferromagnetic electrodes in contrast to spin-FET.

The conductance of a one-dimensional ring with the Rashba SOI α and its radius r when electrons travel *halfway around the ring* is given by Nitta et al. (1999), Frustaglia and Richter (2004), Wang and Vasilopoulos (2005)

$$G_R = \frac{e^2}{h}\left[1 - \cos\left\{\pi\sqrt{1 + \left(\frac{2m^*\alpha r}{\hbar^2}\right)^2}\right\}\right] = \frac{e^2}{h}\left[1 - \cos\left\{\frac{2\pi r m^*\alpha}{\hbar^2}\sin\theta - \pi(1 - \cos\theta)\right\}\right] \tag{9}$$

The acquired AC spin phase can be written as the sum of two phases; $2\pi r m^*\alpha/\hbar^2$ and $\pi(1 - \cos\theta)$, as is shown in the last expression in Eq. (9). Here, θ is defined by $\tan\theta = 2m^*\alpha r/\hbar^2$, and corresponds to the effective magnetic field direction in the rotational frame of

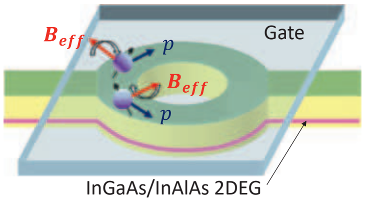

Fig. 8 Schematic illustration of spin interference device based on Rashba SOI. J. Nitta, F. Meijer, H. Takayanagi (1999) Spin-interference device. *Applied Physics Letters* 75: 695.

reference. The former term is sometimes called the dynamical part of the AC spin phase, because of its dependence on the distance traveled by the electrons and its relation to spin precession angle. The latter term is a geometrical phase since it only depends on the solid angle θ, and not on spatial parameters. Such geometric phases were discovered by Berry from the basic laws of quantum mechanics (Berry, 1984), and received considerable attention. Berry shows that the wavefunction obtains a non-trivial phase when a parameter in the Hamiltonian is changed in a cyclic and adiabatic way.

The conductance of a mesoscopic ring is affected by several quantum interference effects. The well-known AB effect results in a resistance oscillation with a magnetic flux period of h/e. The AB effect is sample specific and very sensitive to the Fermi wave length, therefore, the interference pattern is rapidly changed by the gate voltage. Complex gate voltage dependence has been reported in an AC experiment in a single ring fabricated from HgTe/HgCdTe QWs (König et al., 2006). Therefore, a detailed analysis is necessary to compare with the AC theory. In order to detect the AC effect clearly, it is better to focus another quantum interference phenomenon, the Al'tshuler-Aronov-Spivak (AAS) effect (Al'tshuler et al., 1981). The AAS effect is the AB effect of *time reversal symmetric* paths, where the two wave function parts go all around back to the origin on identical paths, but in opposite directions. If there is magnetic flux inside the paths the resistance will oscillate with the period of h/2e. In this time reversal symmetric paths, any other phases which are acquired by path geometry and/or the Fermi wave length (carrier density) differences will be identical and will be canceled out. However, the time reversal AAS effect depends on the spin phase modulated by the Rashba SOI. The time reversal symmetric AC spin interference can be picked up by using an array of rings instead of a single ring.

The experiments to detect the AC spin interference have been performed by using gate fitted 40 × 40 rings array made of an InAlAs/InGaAs 2DEG as shown in inset of Fig. 9. Magnetoresistance curves were measured for various gate voltages to tune the Rashba SOI strengths. The AAS oscillations at the gate voltage of −2.4 V are shown in Fig. 9(a). 2D plot for the gate voltage dependence of AAS oscillations is displayed in Fig. 9(b). At zero magnetic field, a phase contribution from the orbital part of the wave-function is canceled out in the time-reversal paths, therefore, the spin part of the wave-function controls the AAS amplitude through the Rashba SOI modulation by V_g. Fig. 9(c) shows the AAS amplitude plotted against the gate voltage at zero magnetic field. The result shown in Fig. 9(c) is consistent with gate voltage dependence of the Rashba SOI parameters obtained by analysis of SdH oscillations using the same InAlAs/InGaAs 2DEG. Therefore, the AAS amplitude modulation is ascribed to the spin interference in the time-reversal paths, i.e., the time-reversal AC effect (Bergsten et al., 2006; Nagasawa et al., 2012).

A geometric phase of the most fundamental spin-1/2 system, the electron spin, had not been observed directly and controlled independently from dynamical phases. The geometrical phase shift and its topological transition by in-plane Zeeman field was theoretically investigated in the AC spin interference device (Saarikoski et al., 2015). Control of the geometric phase appeared in Eq. (9) was demonstrated by gate voltage (Nagasawa et al., 2012) and Zeeman in-plane field (Nagasawa et al., 2013). It was also shown that the Aharonov-Casher oscillations in various radius arrays collapse onto a universal curve if the radius and the strength of Rashba SOI are taken into account. The result is interpreted as the observation of the effective spin dependent flux through a ring.

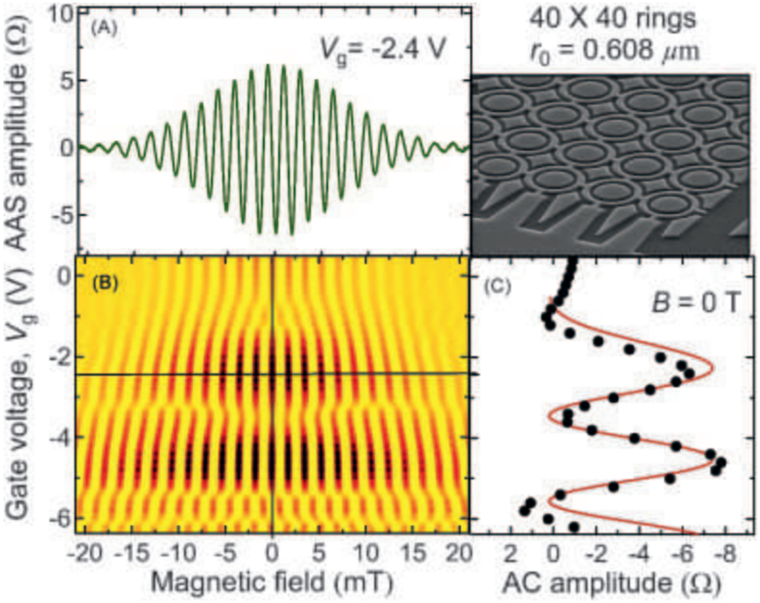

Fig. 9 (a) AAS oscillation of 40 × 40 rings array as shown inset SEM picture. Horizontal axis represents magnetic field. (b) Gate voltage dependence of the AAS oscillations. (c) AAS amplitude at B = 0 mT as a function of gate voltage (time-reversal AC effect). Vertical axis represents gate voltage. Red solid line is calculated by theory. F Nagasawa, J Takagi, Y Kunihashi, M Kohda, J Nitta (2012) Experimental demonstration of spin geometric phase: Radius dependence of time-reversal aharonov-casher oscillations. *Physical Review Letters* 108: 086801.

Spin manipulations by SOI-based ESR

Electron spin resonance (ESR) is of importance for the manipulation of individual electron spins in quantum information technologies. In general, ESR requires two external magnetic fields: a static field (B^0) to split the spin states in energy and an oscillating field (B^1) with the frequency resonant to the splitting energy. However, spin manipulation methods relying on real magnetic fields—much broader than the size of individual electrons—are energetically inefficient and unsuitable for future device applications. One of SOI-based ESR set-ups for spin manipulation is shown in Fig. 10(a). Quantum dot is formed in an InAs wire between two gate electrodes. In addition to static magnetic field B^0_{ext}, SOI induces an oscillating B^1_{eff} when an electron continuously moves back and forth by using time-dependent gate voltages V_{g1} and V_{g2}. Spin manipulations based on SOI-induced ESR have been realized by using semiconductor narrow wires, quantum dots and winding channels.

A ballistic spin resonance (BSR) was realized by utilizing oscillating field induced by the Rashba and Dresselhaus SOIs driven by the free motion of electrons that bounce at frequencies of tens of GHz in high mobility GaAs narrow channels (Frolov et al., 2009). BSR is manifested as a strong suppression of spin relaxation length when the motion of electrons is in resonance with spin precession.

Manipulation of single spins is essential for spin-based quantum information processing. Electrical control instead of magnetic control is particularly important for this purpose, because electric fields are easy to generate locally on-chip. Novak et al. experimentally realized coherent control of a single-electron spin in a GaAs/AlGaAs gate-defined quantum dot using an oscillating electric field generated by a local gate (Nowack et al., 2007).

Nadj-Perge et al. (2010) implemented a SO quantum bit (qubit) in an InAs nanowire, and realized fast qubit rotations and universal single-qubit control using electric fields; the qubits are hosted in single-electron quantum dots that are individually addressable. The authors claim that nanowires offer various advantages for quantum computing: they can serve as one-dimensional templates for scalable qubit registers, and it is possible to vary the material even during wire growth. Rabi frequencies exceeding 100 MHz were demonstrated in InSb nanowires (Van den Berg et al., 2013).

The demonstration of SO qubits coupled to superconducting resonators paves the way for a scalable quantum computing architecture. Circuit quantum electrodynamics (cQED) allows spatially separated superconducting qubits to interact via a superconducting microwave cavity that acts as a "quantum bus," making possible two-qubit entanglement and the implementation of simple quantum algorithms. Petersson et al. (2012) combine the cQED architecture with spin qubits by coupling an InAs nanowire double quantum dot to a superconducting cavity. The demonstration of SO qubits coupled to superconducting resonators paves the way for a scalable quantum computing architecture.

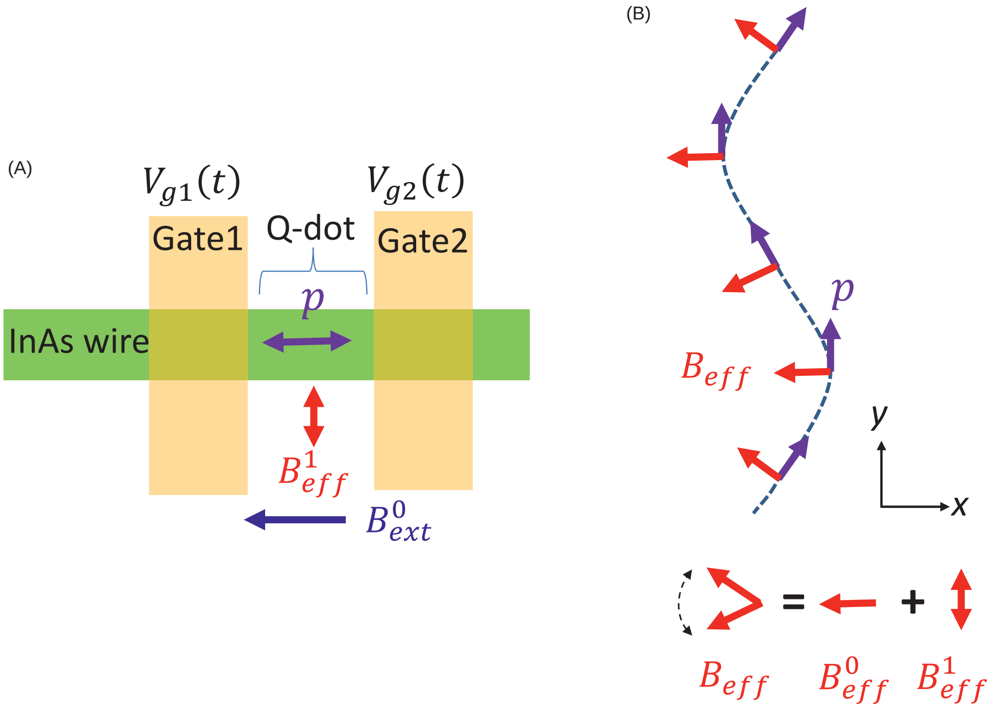

Fig. 10 (a) An SOI-based ESR example. An electron confined in quantum dot(Q-dot) is moving back and forth by time dependent gate voltages Vg1 and Vg2, leading to oscillating effective magnetic field B^1_{eff}. Frequency of the oscillation field should be resonant with spin splitting energy induced by static external magnetic field B^0_{ext} to manipulate the spin in Q-dot. (b) SOI in a winding channel induces effective static field B^0_{eff} and oscillating field B^1_{eff}. These fields are created when electron spins are carried by surface acoustic waves along the winding channel. H. Sanada, Y. Kunihashi, H. Gotoh, K. Onomitsu, M. Kohda, J. Nitta, P. V. Santos and T. Sogawa (2013) Manipulation of mobile spin coherence using magnetic-field-free electron spin resonance. *Nature Physics* 9: 280.

For ESR experiments using the SOIs so far, the spin splitting energies are induced by an external Zeeman field (or local ferromagnet) and oscillating resonant SOI fields driven by ac electric fields. Sanada et al. (2013) have demonstrated an alternative approach where the SOI of trajectory-controlled electrons induces effective static field B^0_{eff} and oscillating field B^1_{eff}. These fields are created when electron spins are carried by surface acoustic waves along winding semiconductor channels as shown in Fig. 10(b). The resultant spin dynamics—mobile spin resonance—is equivalent to the usual ESR but requires neither static nor time-dependent real magnetic fields to manipulate electron spin coherence.

Conclusion

Rashba SOI in semiconductor heterostructures is not materials constant but its strengths can be tuned by the design of QWs and an external gate voltage. Electrical spin generation, manipulation, and detection are prerequisite for future spintronics, and these spin functionalities can be realized solely by utilizing SOI. Spin polarized carriers have been generated by spin Hall effect and Stern-Gerlach spin filter. Both inverse spin Hall effect and spin filter can be also utilized for electrical spin detection. The electrical control of the magnetization direction of small magnets is currently among the most active areas in spintronics due to its interest for memory, logic and data storage applications. Spin-orbit torque (SOT) was first observed in (Ga,Mn)As (Chernyshov et al., 2009) where strained zinc-blende structure is responsible for the emergence of linear Dresselhaus SOI. SOT induced by spin Hall effect and Rashba-Edelstein effect are of importance for magnetization reversal of ferromagnets placed adjacent to SOI materials. Quantum spin Hall effect is discovered in HgTe/CdTe QWs by band inversion due to strong SOI. The quantized conductance is caused by the edge states where opposite spin-polarized currents are counter-propagating.

Gate controlled spin precession is confirmed in AC spin interference devices. This electrical control of spin precession is a basis of spintronics devices such as spin-FET. SOI-based ESR techniques are developed by using ac-electric fields for spin manipulations. Furthermore, magnetic-field-free ESR techniques based on SOI are demonstrated and can be applicable for quantum information process. Generation of both static and oscillating SOI effective fields is possible in an optimized winding channel since the SOI induced field is momentum dependent. Although SOI is an origin of spin relaxation, long spin coherence in the PSH state has been realized by making Rashba and Dresselhaus SOI equal strength. It should be emphasized that the concept of SOI demonstrated in semiconductors has inspired metal spintronics devices such as magnetization reversal using SOT, discoveries of new topological materials and innovative concepts such as Majorana fermions (Manchon et al., 2015).

References

Aharonov Y and Bohm D (1959) *Physics Review* 115: 485.
Aharonov Y and Casher A (1984) *Physical Review Letters* 53: 2964.
Al'tshuler BL, Aronov AG, and Spivak BZ (1981) *JETP Letters* 33: 94.
Aronov AG and Lyanda-Geller YB (1993) *Physical Review Letters* 70: 343.
Balatsky A and Al'tshuler B (1993) *Physical Review Letters* 70: 1678.
Bergsten T, Kobayashi T, Sekine Y, and Nitta J (2006) *Physical Review Letters* 97: 196803.
Bernevig BA, Orenstein J, and Zhang S-C (2006a) *Physical Review Letters* 97: 236601.
Bernevig BA, Hughes TL, and Zhang SC (2006b) *Science* 314: 1757.
Berry MV (1984) *Proceedings of the Royal Society of London A* 392: 45.
Bychkov YA and Rashba EI (1984) *Journal of Physics C: Solid State Physics* 17: 6039.
Chernyshov A, et al. (2009) Evidence for reversible control of magnetization in a ferromagnetic material by means of spin–orbit magnetic field. *Nature Physics* 5: 656–659.
Datta S and Das B (1990) *Applied Physics Letters* 56: 665.
Dresselhaus G (1955) *Physics Review* 100: 580.
Dyakonov MI and Perel VI (1971) *Soviet Physics - JETP* 33: 1053.
Edelstein VM (1990) Spin Polarization of conduction electrons induced by electric current in two-dimensional asymmetric electron systems. *Solid State Communications* 73: 233–235.
Engel H-A, Halperin BI, and Rashba EI (2005) Theory of spin hall conductivity in n-doped GaAs. *Physical Review Letters* 95: 166605.
Engels G, Lange J, Schäpers T, and Lüth H (1997) *Physical Review B* 55: R1958.
Frolov SM, et al. (2009) Ballistic spin resonance. *Nature* 458: 868–871.
Frustaglia D and Richter K (2004) *Physical Review B* 69: 235310.
Ganichev SD (2008) *International Journal of Modern Physics B* 22: 1–26.
Ganichev SD, Danilov SN, Schneider P, Bel'kov VV, Golub LE, Wegscheider W, Weiss D, and Prettl W (2006) Electric current-induced spin orientation in quantum well structures. *Journal of Magnetism and Magnetic Materials* 300: 127–131.
Holleitner AW, Sih V, Myers RC, Gossard AC, and Awschalom DD (2006) *Physical Review Letters* 97: 036805.
Inoue J, Bauer GE, and Molenkamp LW (2004) *Physical Review B* 70: 041303(R).
Ishihara J, Ohno Y, and Ohno H (2014) *Applied Physics Express* 7: 013001.
Ivchenko EL and Pikus GE (1978) New photogalvanic effect in gyrotropic crystals. *JETP Letters* 27: 604.
Kato YK, Myers RC, Gossard AC, and Awschalom DD (2004a) *Science* 306: 1910.
Kato YK, Myers R, Gossard A, and Awschalom DD (2004b) Current-induced spin polarization in strained semiconductors. *Physical Review Letters* 93: 176601.
Kettemann S (2007) *Physical Review Letters* 98: 176808.
Koenig M, et al. (2007) *Science* 318: 766.
Koga T, Nitta J, Akazaki T, and Takayanagi H (2002) *Physical Review Letters* 89: 046801.
Kohda M, Lechner V, Kunihashi Y, Dollinger T, Olbrich P, Schönhuber C, Caspers I, Bel'kov VV, Golub LE, Weiss D, Richter K, Nitta J, and Ganichev SD (2012a) *Physical Review B* 86: 081306(R).
Kohda M, Nakamura S, Nishihara Y, Kobayashi K, Ono T, Ohe J, Tokura Y, Mineno T, and Nitta J (2012b) *Nature Communications* 3: 1038.

Kohda M, Okayasu T, and Nitta J (2019) Spin-momentum locked spin manipulation in a two-dimensional Rashba system. *Scientific Reports* 9: 1909.
König M, Tschetschetkin A, Hankiewiccz EM, Sinova J, Hock V, Daumer V, Schaefer M, Becker CR, Buhmann H, and Molenkamp LW (2006) *Physical Review Letters* 96: 076804.
Koralek JD, Weber CP, Orenstein J, Bernevig BA, Zhang S-C, Mack S, and Awschalom DD (2009) *Nature* 458: 610.
Kumihashi Y, Sanada H, Gotoh H, Onomitsu K, Kohda M, Nitta J, and Sogawa T (2016) *Nature Communications* 7: 10722.
Kunihashi Y, Kohda M, and Nitta J (2009) *Physical Review Letters* 102: 226601.
Kunihashi Y, Kohda M, Sanada H, Gotoh H, Sogawa T, and Nitta J (2012) *Applied Physics Letters* 100: 113502.
Li J, Hu L, and Shen S-Q (2005) *Physical Review B* 71: 241305 (R).
Lin Y, Koga T, and Nitta J (2005) *Physical Review B* 71: 045328-1.
Mal'shukov AG and Chao KA (2000) *Physical Review B* 61: R2413.
Manchon A, Koo HC, Nitta J, Frolov SM, and Duine RA (2015) *Nature Materials* 14: 871–882.
Mathur H and Stone AD (1992) *Physical Review Letters* 68: 2964.
Meier L, Salis G, Shorubalko I, Gini E, Schoen S, and Ensslin K (2007) *Nature Physics* 3: 650.
Meijer FE, Morpurgo AF, and Klapwijk TM (2002) *Physical Review B* 66: 033107.
Murakami S, Nagaosa N, and Zhang SC (2003) *Science* 301: 1348.
Nadj-Perge S, Frolov SM, Bakkers EPAM, and Kouwenhoven LP (2010) Spin-orbit qubit in a semiconductor nanowire. *Nature* 468: 1084–1087.
Nagasawa F, Takagi J, Kunihashi Y, Kohda M, and Nitta J (2012) *Physical Review Letters* 108: 086801.
Nagasawa F, Frustaglia D, Saarikoski H, Richter K, and Nitta J (2013) *Nature Communications* 4: 2526.
Nitta J, Akazaki T, Takayanagi H, and Enoki T (1997) *Physical Review Letters* 78: 1335.
Nitta J, Meijer FE, and Takayanagi H (1999) *Applied Physics Letters* 75: 695.
Nowack KC, Koppens FHL, Nazarov YV, and Vandersypen LMK (2007) Coherent control of a single electron spin with electric fields. *Science* 318: 1430–1433.
Ohe J, Yamamoto M, Ohtsuki T, and Nitta J (2005) *Physical Review B* 72: 041308(R).
Petersson KD, et al. (2012) Circuit quantum electrodynamics with a spin qubit. *Nature* 490: 380–383.
Qian T-Z and Su Z-B (1994) *Physical Review Letters* 72: 2311.
Rashba EI (1960) *Soviet Physics - Solid State* 2: 1109.
Rowe ACH, Nehls J, and Stradling RA (2001) *Physical Review B* 63: 201307.
Saarikoski H, Vazquez-Lozano JE, Baltanas JP, Nagasawa F, Nitta J, and Frustaglia D (2015) *Physical Review B* 91: 241406(R).
Sanada H, Kunihashi Y, Gotoh H, Onomitsu K, Kohda M, Nitta J, Santos P, and Sogawa T (2013) *Nature Physics* 9: 280.
Sasaki A, Nonaka S, Kunihashi Y, Kohda M, Bauernfeind T, Dollinger T, Richter K, and Nitta J (2014) *Nature Nanotechnology* 9: 703–709.
Schäpers T, Engels G, Lamge J, Klocke T, Hollfelder M, and Lüth H (1998) *Journal of Applied Physics* 83: 4324.
Schäpers T, Guzenko VA, Pala MG, Zülich U, Governale M, Knobbe J, and Hardtdegen H (2006) *Physical Review B* 74: 081301(R).
Scheid M, Kohda M, Kunihashi Y, Richter K, and Nitta J (2008) *Physical Review Letters* 101: 266401.
Schiemann J and Loss D (2005) *Physical Review B* 71: 085308.
Schliemann J, Carlos Egues J, and Loss D (2003) *Physical Review Letters* 90: 146801.
Schmidt G, Ferrand D, Molenkamp LW, Filip AT, and van Wees BJ (2000) *Physical Review B* 62: R4790.
Sinova J, Culcer D, Niu Q, Sinitsyn NA, Jungwirth T, and MacDonald AH (2004) *Physical Review Letters* 92: 126603.
Tonomura A, Osakabe N, Matsuda T, Kawasaki T, and Endo J (1986) *Physical Review Letters* 56: 792.
Van den Berg J, et al. (2013) Fast spin-orbit qubit in an indium antimonide nanowire. *Physical Review Letters* 110: 066806.
Walser MP, Reichl C, Wegscheider W, and Salis G (2012) *Nature Physics* 8: 757–762.
Wang XF and Vasilopoulos P (2005) *Physical Review B* 72: 165336.
Weigele OJ, Marinescu DC, Dettwiler F, Fu J, Mack S, Egues JC, Awschalom DD, and Zumbühl DM (2020) *Physical Review B* 101: 035414.
Winkler R (2003) *Spin-Orbit Coupling Effects in Two-Dimensional Electron and Hole Systems*, p. 191. Berlin: Springer-Verlag.
Wunderlich J, Kaestner B, Sinova J, and Jungwirth T (2005) *Physical Review Letters* 94: 047204.
Wunderlich J, Irvine AC, Sinova J, Park BG, Zârbo LP, Xu XL, Kaestner B, Novák V, and Jungwirth T (2009) Spin-injection Hall effect in a planar photovoltaic cell. *Nature Physics* 5: 675–681.
Wunderlich J, Park B-G, Irvine AC, Zârbo LP, Rozkotová E, Nemec P, Novák V, Sinova J, and Jungwirth T (2010) *Science* 330: 1801.
Yoshizumi K, Sasaki A, Kohda M, and Nitta J (2016) *Applied Physics Letters* 108: 132402.

Spintronics in 2D graphene-based van der Waals heterostructures

David TS Perkins and Aires Ferreira, School of Physics, Engineering and Technology and York Centre for Quantum Technologies, University of York, York, United Kingdom

© 2024 Elsevier Ltd. All rights reserved.

Introduction **206**
Graphene and van der Waals heterostructures **207**
Honeycomb monolayers: *A tight-binding description* 209
Honeycomb monolayers: *SOC interactions* 210
Honeycomb monolayers with proximity-induced SOC: Continuum theory 211
Relativistic spin–orbit coupled transport phenomena **213**
Electronic signatures 213
Spin Hall effect 214
Inverse spin galvanic effect 216
Observing spin–charge interconversion 218
Conclusion **219**
Acknowledgments **219**
References **219**

Abstract

Spintronics has become a broad and important research field that intersects with magnetism, nano-electronics, and materials science. Its overarching aim is to provide a fundamental understanding of spin-dependent phenomena in solid-state systems that can enable a new generation of spin-based logic devices. Over the past decade, graphene and related 2D van der Waals crystals have taken center stage in expanding the scope and potential of spintronic materials. Their distinctive electronic properties and atomically thin nature have opened new opportunities to probe and manipulate internal electronic degrees of freedom. Purely electrical control over conduction-electron spins can be attained in graphene-transition metal dichalcogenide heterostructures, due to proximity effects combined with graphene's high electronic mobility. Specifically, graphene experiences a proximity-induced spin–orbit coupling that enables efficient spin-charge interconversion processes; the two most well-known and at the forefront of current research are the spin Hall and inverse spin galvanic effects, wherein an electrical current yields a spin current and nonequilibrium spin polarization, respectively. This article provides an overview of the basic principles, theory, and experimental methods underpinning the nascent field of 2D material-based spintronics.

Key points

This chapter aims to achieve the following:

- Provide a brief historic overview of how spintronics developed before and after the discovery of graphene,
- Discuss the various properties of the 2D honeycomb materials at the heart of spintronics in van der Waals heterostructures,
- Outline how the electronic structure of 2D monolayers, such as graphene, is altered by proximity-induced spin–orbit coupling using a tight-binding formalism informed by a symmetry analysis,
- Construct a low-energy theory representative of the van der Waals heterostructures used in realistic spintronic devices,
- Introduce the idea of spin–charge interconversion: how an electrical current can generate a macroscopic spin current or spin polarization, and vice versa,
- Present the framework of linear response theory used in the mathematical description of the spin Hall and inverse spin galvanic effects,
- Explain how spin–charge interconversion processes can be detected via electrical means.

Abbreviations

2DEG	Two-dimensional electron gas
BR	Bychkov–Rashba
CEE	Collinear Edelstein effect
DOF	Degree of freedom
FM	Ferromagnet or ferromagnetic

https://doi.org/10.1016/B978-0-323-90800-9.00203-1

hBN	Hexagonal boron nitride
ISGE	Inverse spin galvanic effect
ISHE	Inverse spin Hall effect
KM	Kane–Mele
SdH	Shubnikov–de Haas
SGE	Spin galvanic effect
SHE	Spin Hall effect
SOC	Spin–orbit coupling
SOT	Spin–orbit torque
SV	Spin-valley
TB	Tight binding
TMD	Transition metal dichalcogenide
vdW	van der Waals
WAL	Weak localization
WL	Weak antilocalization

Introduction

Spintronics can be considered the magnetic counterpart to electronics whereby the transfer and processing of information can be conducted through the electron's spin degree of freedom (DOF), rather than or in addition to its electronic property of charge. Specifically, spintronics concerns itself with the electrical manipulation of the electron's spin and one of its first milestones was the observation of a spin-polarized current by Tedrow and Meservey (1973). Despite this and the first controlled injection of a spin-polarized current into a nonmagnetic material being achieved in 1985 (Johnson and Silsbee, 1985), it was only in 1988 that spintronics began to bloom and flourish into the field we know today. What sparked this scientific boom was the independent observation of a giant magnetoresistance attributed to the relative orientation of the ferromagnetic (FM) layers in Fe-Cr-based systems by Baibich et al. (1988) and Binasch et al. (1989).

Since the Nobel prize winning discovery of giant magnetoresistance, initial efforts in the field focused on spin valve setups to study how the electron's spin would diffuse and relax through a normal metal when injected via a spin-polarized current using an FM contact. However, a more exotic method of spin current generation had already been proposed in 1971 by Dyakonov and Perel (Dyakonov and Perel, 1971a,b; Sinova et al., 2015), the *spin Hall effect* (SHE), where the application of an electrical current would yield a perpendicular pure spin current without the need for magnetic materials. The origin of this effect can be found in the asymmetric scattering of electrons based upon their spin due to the presence of spin–orbit coupling (SOC). Initially observed in 2004 via optical methods (Kato et al., 2004), the SHE and its inverse (ISHE) have become paradigmatic phenomena in spintronics due to their lack of reliance upon magnetic components. A major focus for the application of the SHE is in low-power magnetic memory devices, where the manifestation of a spin current results in a spin accumulation, and hence a net spin polarization, which can exert a torque on the magnetization of a nearby FM. With a large enough spin accumulation, dramatic effects like magnetization switching can be induced. Clearly, with the use of a simple electrical current, we can manipulate the spin of charge carriers in a material and induce interesting nonequilibrium phenomena at interfaces between materials, thus yielding important applications in modern information technology.

In addition to spin current, another major concept in spintronics is *spin texture*: the momentum dependence of the transport electrons' spin within a solid. In many low-dimensional systems and at heterostructure interfaces, the enhancement of the relativistic spin–orbit interaction is key to generating nontrivial spin textures that give rise to a plethora of phenomena, ranging from the spin-momentum-locked surface states in topological insulators to the topologically protected real-space spin textures seen in chiral magnets, such as skyrmions and spin spirals. Of particular interest is the emergence of a spin polarization, as in the SHE, but without a resulting spin current. This effect, the sole spontaneous generation of a spin polarization via application of an electric current, is known as the *inverse spin galvanic effect* (ISGE), though in some literature it may also be referred to as the Rashba–Edelstein or Edelstein effect. Based upon Bychkov–Rashba-type SOC (Bychkov and Rashba, 1984), arising when the mirror symmetry about a given plane is broken, this effect was initially predicted in two-dimensional electron gases (2DEGs) in semiconductor heterostructures in 1989 (Aronov and Lyanda-Geller, 1989; Edelstein, 1990; Aronov et al., 1991) but remained unobserved in experiment until 2002, when its reciprocal effect (i.e., spin-to-charge conversion) was observed (Ganichev et al., 2002). Combining both the SHE and ISGE, we find ourselves in a position with great control over the motion and net orientation of the electron spins in materials. However, to truly construct realistic devices using a spin-focused infrastructure, we must understand what makes an ideal material for providing such intricate control over spin. The two most important factors governing the effectiveness of spintronic devices are disorder and SOC: both mechanisms yield significant consequences on the transport range of electron spins and our control over them. While a larger SOC might ensure more efficient generation of spin currents and polarizations, it comes at the cost of faster spin dephasing and hence spin information is lost over a much shorter distance. In contrast, a weak SOC might allow for long range transport, but results in less efficient charge-to-spin conversion. Similarly, disorder can also change the efficiency of spin–charge interconversion. In a pristine system, the only processes present will be those intrinsic to the system. However, upon the inclusion of disorder, some intrinsic mechanisms are completely suppressed in favor of extrinsic mechanisms. Furthermore, spin–orbit active impurities can have similar effects to including a SOC into the system, due to their ability to change an electron's spin orientation. Clearly, there is a balancing act to be handled in constructing ideal spintronic devices with both disorder and SOC acting as the tuning knobs.

Prior to 2004, experiments studying spin transport focused primarily on 2DEGs realized in a multitude of systems including thin metallic films (Jedema et al., 2001), permalloys (Steenwyk et al., 1997; Dubois et al., 1999), and semiconductor heterostructures (Yang et al., 1994; Kikkawa and Awschalom, 1999; Ohno et al., 1999; Malajovich et al., 2000). In most cases, spin information was passed into the system by either a spin-polarized charge current, or via optical excitation of a semiconductor resulting in a spin imbalance of the conduction band. Despite these initial endeavors, the electrical processing of spin-encoded information was hindered by the difficulty of combining effective spin control with large enough spin lifetimes. However, with the discovery of graphene in 2004 as the first truly 2D, that is, atomically thin, solid state system, a new epoch dawned in spintronics. It was quickly established that bare graphene offered the largest spin diffusion lengths of any material to date, with many reports finding $l_s \sim 1-20$ μm, courtesy of the weak intrinsic spin–orbit and hyperfine interactions of sp^2 hybridized carbon.

Naturally, graphene's extremely small intrinsic SOC makes it difficult to have precise electrical control over the net spin orientation, but does allow for long-distance spin-information transfer. However, with the many advances in nanofabrication over the past two decades and the isolation of other 2D materials, such as transition metal dichalcogenides (TMDs), layer-by-layer assemblies of 2D materials have been imagined and constructed with the ability to alter the net behavior of the composite system based purely on the individual layers used. Thus the concept of bespoke devices combining the desirable properties of different materials has become possible in the form of van der Waals (vdW) heterostructures.

What single 2D crystals lack, vdW heterostructures may offer a way to access by enhancing certain properties by matching an appropriate set of materials. Through simple proximity effects, the properties absent or deemed too weak in the original isolated crystal can be enhanced. Semiconducting TMDs, such as MoS_2 and WTe_2, are a classic example of this; due to their composition involving transition metal atoms, they naturally possess a large SOC. By stacking this with a graphene monolayer, the electrons of the graphene sheet will experience a *proximity-induced SOC effect* due to their ability to now hop between the two layers. Furthermore, graphene's transport nature is not jeopardized by the proximity of the TMD since the low-energy states of graphene lie well within the TMD band gap. Consequently, transport is still dominated by the more conductive graphene layer, though the electronic states are now endowed with a substantial SOC. The typical size of these induced SOCs is up to order 10 meV (Wang et al., 2019), which is three orders of magnitude larger than the intrinsic SOC present in regular graphene (Kane–Mele type of order 10 μeV (Sichau et al., 2019)). The specific values of the SOCs depend on the choice of TMD partner and can be further tuned by means of external pressure (Fulop et al., 2021). This dramatic change from an isolated crystal's properties with the introduction of material partners is what makes vdW heterostructures the modern candidates par excellence for many condensed matter experiments.

Graphene and van der Waals heterostructures

Formed by stacking atomically thin layers of hexagonally packed atoms with weak vdW forces binding neighboring layers together, Fig. 1a (Geim and Grigorieva, 2013), vdW heterostructures constitute a specific class of 2D materials. Given the breadth of materials with 2D behavior—encompassing semiconductors, insulators, and semimetals—which can be exfoliated down to a monolayer, it is no surprise that the variety of vdW heterostructures is equally diverse. Furthermore, the electronic properties of such 2D compounds are sensitive to the number of layers, stacking sequence, and atomic coordination, while also being tunable "on-demand" through the controlled application of strain and electric fields (Castro Neto et al., 2009; Wang et al., 2012; Yun et al., 2012).

Monolayer graphene presents itself as a zero-gap semiconductor with a linear dispersion relation for both electrons and holes, whose unit cell consists of two distinct lattice sites that are individually referred to as A and B sublattices (Fig. 1b). The band structure of graphene is characteristic of *massless chiral Dirac fermions*, which derives from the sp^2 network of carbon atoms forming a honeycomb lattice with preserved inversion symmetry (Fig. 1b), whose presence gives rise to graphene's notable electronic properties (Castro Neto et al., 2009). Other 2D materials relevant to vdW heterostructures include (i) hexagonal boron nitride "hBN," an insulator (ii) bilayer graphene, a zero-gap semiconductor with parabolic band dispersion; and (iii) group-VI dichalcogenides, direct band-gap semiconductors with strong SOC.

What makes a material useful in vdW heterostructures varies from material to material. The band gap opening in polyatomic compounds (e.g., hBN) is a direct consequence of broken inversion symmetry. The electronic band gap in monolayer hBN is about 7 eV, making it an insulating analog of graphene. The small lattice mismatch between hBN and graphene (about 1.8%) allows for easy integration in graphene-based devices using dry transfer techniques. hBN encapsulation yields major improvements in the electronic mobility of graphene-based devices and is currently the gold standard for the fabrication of high-performance vdW heterostructures. In lateral spin transport experiments, the hBN encapsulation of graphene has enabled a 10-fold increase in room-temperature spin lifetimes compared to devices using the now obsolete silicon oxide substrates (Drögeler et al., 2014). The hBN induces an orbital gap in graphene (Fig. 2a), which results from virtual interlayer hopping processes between carbon sites in graphene and the distinct chemical species occupying the A and B sublattices of the partnered hBN layer.

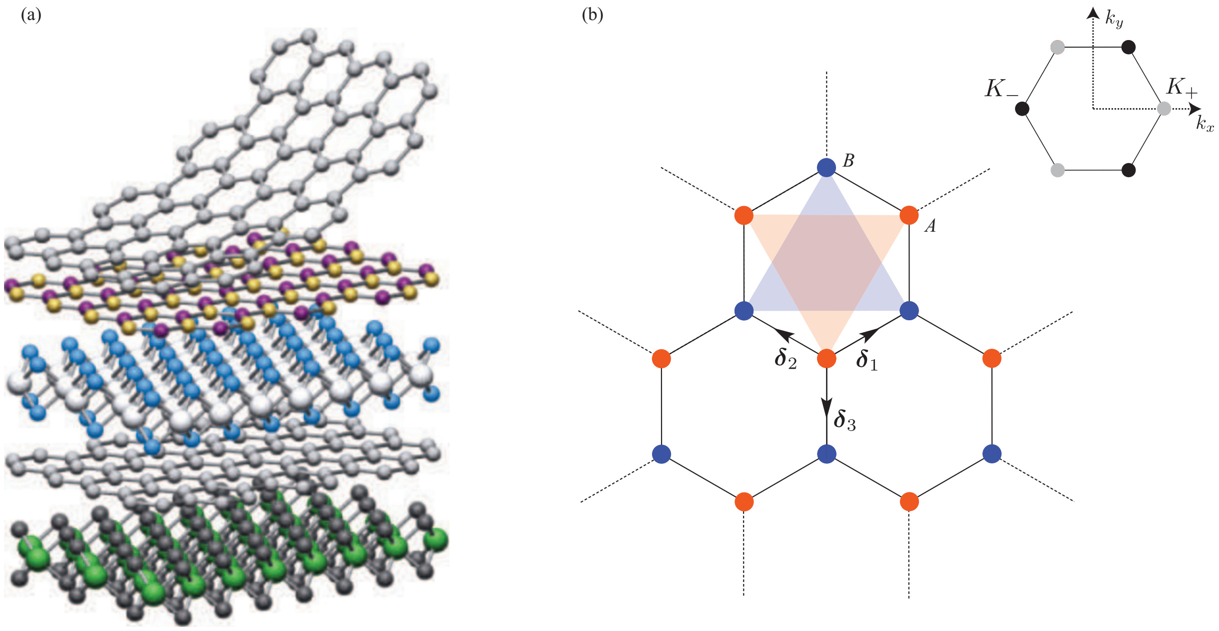

Fig. 1 (a) Vertical heterostructure built from 2D crystals. (b) The honeycomb lattice composed of two triangular Bravais lattices (top right corner shows the first Brillouin zone with two inequivalent Dirac points, $K_\pm$). The nearest-neighbor vectors read as $\boldsymbol{\delta}_i = a\,(\sin\alpha_i, -\cos\alpha_i)^{\mathrm{T}}$, where a is the bond length and $\alpha_i = \frac{2\pi}{3}(i-3)$ and $i = 1, 2, 3$. (a) Reprinted with permission from Geim AK and Grigorieva IV (2013) Van der Waals heterostructures. Nature 499(7459): 419–425. https://doi.org/10.1038/nature12385.

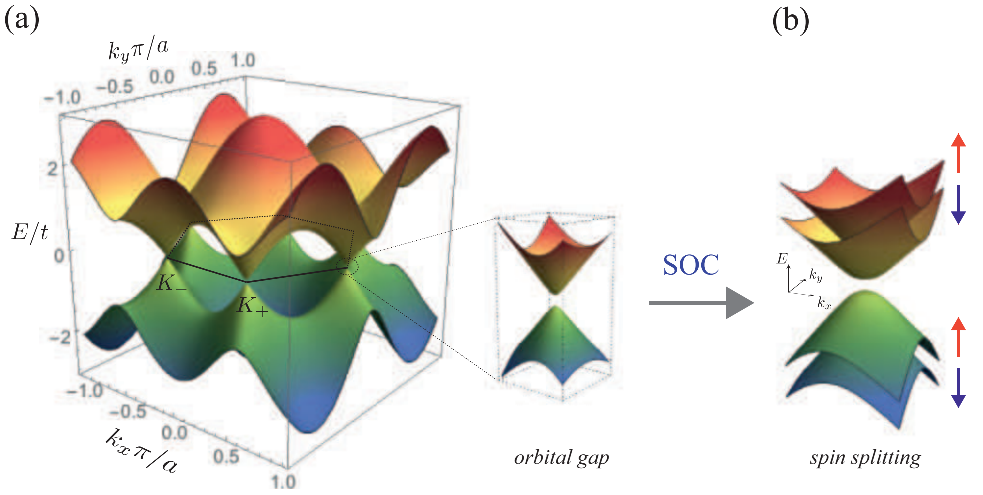

Fig. 2 (a) Low-energy dispersion of a honeycomb monolayer with a small orbital gap ($m \neq 0$). (b) Lifting of spin degeneracy due to symmetry breaking SOC (arrows indicate different spin states).

Bilayer graphene can exist in Bernal-stacked "AB" form, with atoms on opposite layers stacked on top of each other in a staggered configuration, or, less frequently, in the "AA" form, with sublattices in adjacent layers perfectly aligned (Liu et al., 2009). Similar to monolayer graphene, its conduction and valence bands touch at the Brillouin zone corners (Fig. 2a); however, low-energy excitations around the Fermi points are associated with quadratic energy dispersion (McCann and Fal'ko, 2006; Guinea et al., 2006). The finite density of states near the Fermi level exacerbate the effect of interactions leading to rich broken symmetry states even in the absence of external fields (Zhang et al., 2010; Vafek and Yang, 2010; Nandkishore and Levitov, 2010; Weitz et al., 2010). Individual layers in AB bilayer graphene can be addressed separately allowing important device functionalities, including band gap opening through gating (McCann, 2006; Castro et al., 2007). Of particular interest for spintronics is the ability to fine-tune both the SOC (proximity with a TMD) and exchange interaction (proximity with an FM) experienced by the electrons. Only the layer that is the immediate neighbor to a partner material will experience significant proximity effects. Therefore, by applying an electric field perpendicular to the graphene bilayer, the electron density of each layer can be adjusted, which in turn changes the proximity-induced SOC and exchange interaction experienced by the electrons by shifting them toward or away from the partner material (Zollner et al., 2020).

Group-VI dichalcogenides [MX_2 (M = Mo, W; X = S, Se,Te)] can be either trigonal-prismatically or octahedrally coordinated (so-called 2H and 1T phases, respectively). These polytypic structures have vastly different electronic properties: while TMDs of the 2H-MX_2 type are large-gap semiconductors, 1T-MX_2 are predominantly metals (Mattheiss, 1973; Eda et al., 2012; Voiry et al., 2015). 2H-TMD monolayers have direct band gaps in the near-infrared to the visible region, which make them well suited for a broad range of applications in optoelectronics and photonics (Mak and Shan, 2016). Owing to ultimate (2D) quantum confinement, electrons and holes are tightly held together which is responsible for enhanced light–matter interactions. Excitons have typical binding energies of 0.5 eV, which strongly impact the spin and optoelectronic properties of semiconducting TMDs (Wang et al., 2018). Moreover, the spin–valley locking of energy states in the vicinity of $K_\pm$ points, stemming from lack of inversion symmetry, lead to spin–valley-dependent optical transition rules (Wang et al., 2012), which enable the addressing of individual valleys with circularly polarized light. The spin–valley coupling in TMDs has been explored to convert optically driven valley currents into charge currents via the inverse valley Hall effect (Mak et al., 2014). In free-standing conditions, the 1T phase undergoes a spontaneous lattice distortion to a semiconducting phase dubbed 1T′, which supports robust nontrivial topological behavior (quantum spin Hall effect) (Qian et al., 2014; Tang et al., 2017; Wu et al., 2018; Shi et al., 2019).

The weak vdW forces between planes of 2D crystals offer a practical route for band structure design. A remarkable example is "twisted" bilayer graphene, where the two graphene monolayers forming bilayer graphene are offset from one another by a simple rotation about the out-of-plane axis (Lopes dos Santos et al., 2007), in addition to their stacking arrangement. For "magic angle" twisted bilayer graphene, the superlattice created by the two graphene sheets leads to strong renormalization of the band structure, which can exhibit flat bands at the Fermi level, leading to possible strongly correlated insulating states in the ultimate 2D (atomically thin) limit (Cao et al., 2018).

With the above discussion of different 2D systems and their various combinations, it is clear that vdW heterostructures offer a route toward 2D designer materials. The exact combination of the individual layers is dictated by the purpose of the device being constructed. This is particularly relevant when trying to study and apply the SHE and ISGE from a technological perspective. The specifics behind these phenomena are discussed toward the end of this article while the effect of proximity-induced SOC shall be covered shortly.

Honeycomb monolayers: *A tight-binding description*

The distinctive electronic properties of 2D layered materials and the special role played by the sublattice DOF can be best appreciated within a tight-binding (TB) model of electrons hopping on a honeycomb lattice (Fig. 1b). The minimal Hamiltonian (without SOC) reads as

$$H_{2D} = -t\sum_{\langle i,j\rangle}\left(a_i^\dagger b_j + \text{H.c.}\right) + m\sum_i\left(a_i^\dagger a_i - b_i^\dagger b_i\right) \tag{1}$$

where the fermionic operator a_i (b_i) annihilates a quasiparticle on site i belonging to sublattice $A(B)$, t is the nearest neighbor hopping energy ($t \approx 2.8$ eV in graphene Castro Neto et al., 2009), and $\langle i, j\rangle$ denotes the sum over nearest neighbors. The second term describes a staggered on-site energy with amplitude $m = (\varepsilon_A - \varepsilon_B)/2$ and is relevant for noncentrosymmetric 2D crystals (e.g., $m \approx 3.5$ eV in hBN (Román et al., 2021) and $m \approx 0.7 - 0.9$ eV in semiconducting TMDs (Xiao et al., 2012)), as well as graphene-based heterostructures displaying Moiré superlattice effects (Dean et al., 2010; Jung et al., 2015; Wallbank et al., 2015).

This tight-binding Hamiltonian provides a starting point for understanding the low-energy properties of prototypical 2D materials. The energy bands are obtained by means of the Fourier transform $a_i\ (b_i) = N^{-1}\sum_{\boldsymbol{k}} e^{-i\boldsymbol{k}\cdot\boldsymbol{x}_i} a_{\boldsymbol{k}}\ (b_{\boldsymbol{k}})$, where $\boldsymbol{k} = (k_x, k_y)^{\mathrm{T}}$ is the 2D wavevector and N is the number of sites in each sublattice ($N = N_A = N_B$). After straightforward algebra, one finds

$$H_{2D} = \sum_{\boldsymbol{k}}\begin{pmatrix} a_{\boldsymbol{k}}^\dagger & b_{\boldsymbol{k}}^\dagger \end{pmatrix}\begin{pmatrix} m & \phi^*(\boldsymbol{k}) \\ \phi(\boldsymbol{k}) & -m \end{pmatrix}\begin{pmatrix} a_{\boldsymbol{k}} \\ b_{\boldsymbol{k}} \end{pmatrix}, \tag{2}$$

with the geometric form factor

$$\phi(\boldsymbol{k}) = -t\sum_{a=1,2,3} e^{i\boldsymbol{k}\cdot\boldsymbol{\delta}_a}, \tag{3}$$

where the bond vectors, $\boldsymbol{\delta}_a$, are defined in the caption of Fig. 1. The energy dispersion is readily obtained as

$$E(\boldsymbol{k}) = \pm\sqrt{t^2|\phi(\boldsymbol{k})|^2 + m^2}, \tag{4}$$

where the sign ± selects positive (negative) energy branch of the spectrum. A band structure representative of graphene with a sublattice staggered potential is shown in Fig. 2a. Of particular note is the appearance of local extrema in the spectrum at the corners of the Brillouin zone, $K_\pm$, where $E = \pm m$, known as Dirac points. In this example, the small orbital gap ($m \ll t$) could be due to use of a lattice-matching substrate (e.g., hBN). At half-filling, the negative energy states are completely filled, and hence the low-energy physics is controlled by excitations about the Dirac points (the region around a Dirac point is known as a valley). For semiconducting TMDs and hBN, the staggered on-site energy is comparable to (or larger than) t, resulting in sizable orbital gaps at the Dirac points. The generalization of this Hamiltonian to describe the strong intrinsic SOCs inherent in semiconducting TMDs, as well as symmetry breaking SOCs in vdW heterostructures, is presented in the next section. While the extension of the effective TB model to multilayers (e.g., bilayer graphene) is straightforward, the complete details are beyond the scope of this article, though the interested readers can find details in Peres (2010) and McCann and Koshino (2013).

Honeycomb monolayers: *SOC interactions*

The electronic structure of 2D materials containing heavy elements is strongly modified by spin–orbit effects generated by the periodic crystal potential. In the nonrelativistic approximation to the Dirac equation, the intrinsic spin–orbit interaction reads as

$$H_{\mathrm{SO}} = -\frac{\hbar}{4m_e^2c^2}\,\boldsymbol{s}\cdot(\boldsymbol{p}\times\nabla V), \tag{5}$$

where $V(\boldsymbol{x})$ is the periodic crystal potential, $\boldsymbol{p}$ is the momentum operator, m_e is the electron mass, and $\mathbf{s}$ is the vector of Pauli matrices describing spin-1/2 particles (i.e., acting on the spin DOF). The (spin-dependent) hopping generated by Eq. (5) can be obtained by exploring time-reversal symmetry ($\mathcal{T}$) and the crystal symmetries. The most general H_{SO} for honeycomb lattices may therefore be written as

$$H_{\mathrm{SO}}^{\mathcal{T}} = \sum_{\langle i,j\rangle}\left(\hat{a}_i^\dagger T_{ij}^{ab}\hat{b}_j + \hat{b}_i^\dagger T_{ij}^{ba}\hat{a}_j\right) + \sum_{\langle\langle i,j\rangle\rangle}\left(\hat{a}_i^\dagger T_{ij}^{aa}\hat{a}_j + \hat{b}_i^\dagger T_{ij}^{bb}\hat{b}_j\right), \tag{6}$$

where $\hat{a}_i^\dagger/\hat{a}_i$ ($\hat{b}_j^\dagger/\hat{b}_j$) are creation/annihilation operators for the $A(B)$ sublattice with a 2-component spinor structure acting on spin space, $T_{ij}^{(\varsigma)}$ (with $\varsigma = aa, ab, bb$) are spin-dependent hopping coefficients with a 2×2 complex matrix structure satisfying $T_{ij}^{\varsigma} = [T_{ji}^{\varsigma}]^\dagger$, and $\langle\langle i,j\rangle\rangle$ denotes the sum over next-nearest neighbors. The neglect of hoppings beyond next-nearest neighbors in Eq. (6) is justified given the exponential decay of matrix elements with the distance. Note that on-site spin-dependent terms, such as $\hat{a}_i^\dagger s_z\hat{a}_i$, change sign under $\mathcal{T}$ and thus are not allowed.

The symmetries of the system are contained within the $T_{ij}^{(\varsigma)}$. Expansion of the spin hopping matrices into elements of the SU(2) spin-algebra yields

$$T_{ij} = \omega_{ij}^x\,s_x + \omega_{ij}^y\,s_y + \omega_{ij}^z\,s_z, \tag{7}$$

where sublattice superscripts have been omitted. The antiunitary operator enacting $\mathcal{T}$ is given by $\Theta = is_yK$, where K denotes complex conjugation. The requirement, $T_{ij} = \Theta\ T_{ij}\ \Theta^{-1}$, leads to the following constraint: $\omega_{ij}^\alpha = -(\omega_{ij}^\alpha)^*$ (with $\alpha = x, y, z$). As such, the coefficients of spin-dependent hopping mediated by H_{SO} are purely imaginary. The full set of spin–orbit interactions up to next-nearest neighbors are shown in Fig. 3, where the allowed hoppings are dictated by the point group symmetry. For example, D_{6h}-invariant Hamiltonians (e.g., flat pristine graphene) only permit spin-conserving next-nearest neighbor hoppings. This is the result of three symmetries. First, mirror inversion about the plane, Σ_{xy}^h, which reverses the sign of x- and y- components in Eq. (7), forbids all spin flip processes, $\omega_{ij}^{(x,y)} = 0$. Second, the mirror symmetry Σ_{yz}^d, which sets $y \rightarrow -y$ and consequently reverses the sign of s_z in Eq. (7), ensures that $\omega_{ij}^z = 0$ for all in-plane vertical hoppings, which are naturally nearest neighbor processes. Finally, combining the Σ_{yz}^d mirror symmetry with 6-fold rotational symmetry about the z-axis, we see that the vertical hoppings must map onto the other nearest neighbor hoppings and hence they too must vanish.

More generally, when space inversion or horizontal reflection symmetries are broken, other terms are allowed. Of particular relevance is the C_{3v} point group, given that it is a common subgroup of D_{3h} (e.g., hBN and TMD monolayers), D_{3d} (e.g., rippled graphene and Si- and Ge-based graphene analogs), and C_{6v} (e.g., graphene on a nonlattice-matched substrate) and hence defines the most general class of Hamiltonians compatible with the honeycomb lattice symmetries (Saito et al., 2016; Kochan et al., 2017). Altogether, C_{3v}-invariant models allow for 3 types of SOC

$$\begin{aligned} H_{\mathrm{SO}}^{C_{3v}} = {} & \frac{i}{3\sqrt{3}}\sum_{\langle\langle i,j\rangle\rangle}v_{ij}\left(\lambda_A\ \hat{a}_i^\dagger s_z\hat{a}_j + \lambda_B\ \hat{b}_i^\dagger s_z\hat{b}_j\right) + \frac{2i}{3}\sum_{\langle i,j\rangle}\left[\lambda\ \hat{a}_i^\dagger\left(\boldsymbol{s}\times\boldsymbol{d}_{ij}\right)_z\hat{b}_j + (b\leftrightarrow a)\right] \\ & + \frac{2i}{3}\sum_{\langle\langle i,j\rangle\rangle}\left[\lambda_{nn}^A\ \hat{a}_i^\dagger\left(\boldsymbol{s}\times\boldsymbol{d}_{ij}\right)_z\hat{a}_j + \lambda_{nn}^B\ \hat{b}_i^\dagger\left(\boldsymbol{s}\times\boldsymbol{d}_{ij}\right)_z\hat{b}_j\ \right], \end{aligned} \tag{8}$$

namely, spin-conserving sublattice-resolved SOC, $\lambda_{A(B)}$, Bychkov–Rashba (BR) interaction, λ, and spin-flipping sublattice-resolved SOC, $\lambda_{nn}^{A(B)}$. Here, $\boldsymbol{d}_{ij}$ is the unit vector along the line segment connecting site i and j while $v_{ij} = \pm 1$ distinguishes between clockwise and anticlockwise electron hopping, respectively.

The spin-conserving SOC (first term in Eq. 8) is a fingerprint of pseudospin-spin coupling in 2D layered materials. Two cases are of noteworthy interest: (i) centrosymmmetric crystals, where only a spin conserving SOC is permitted with $\lambda_A = \lambda_B$, as is the case in pristine graphene (D_{6h}) discussed above, and graphene-like materials with D_{3d} point group, and (ii) systems with broken inversion symmetry leading to sublattice-resolved SOC ($\lambda_A \neq \lambda_B$), as seen, for example, in 2H-TMD monolayers (D_{3h}) and graphene-TMD

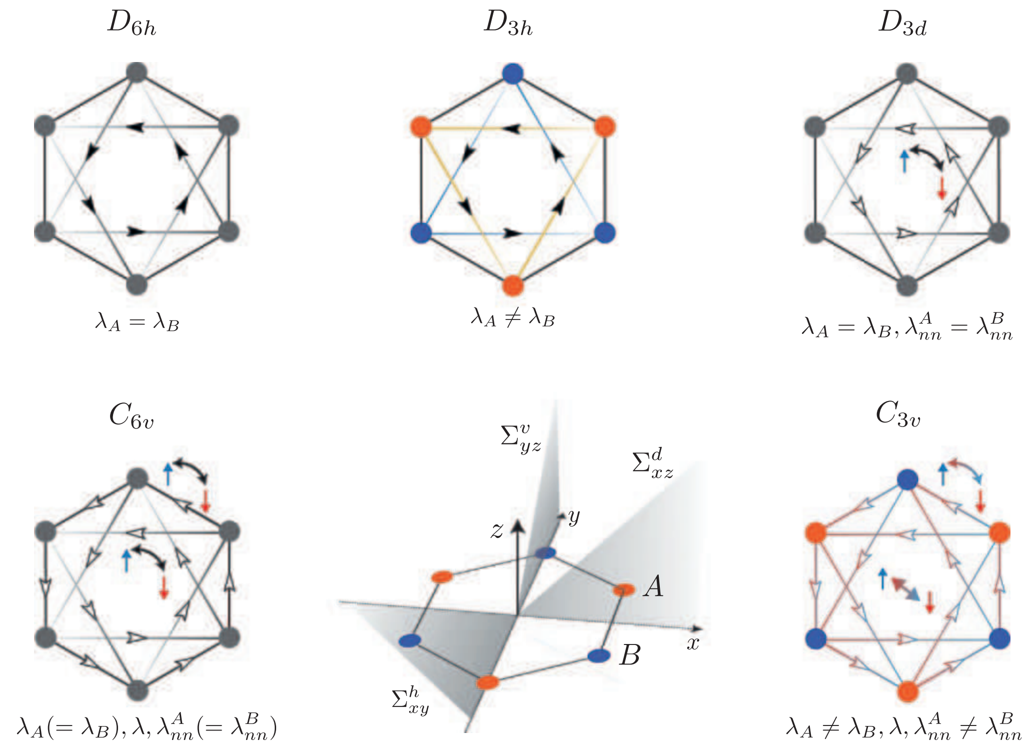
D_{6h}
D_{3h}
D_{3d}
$\lambda_A = \lambda_B$
$\lambda_A \neq \lambda_B$
$\lambda_A = \lambda_B, \lambda^A_{nn} = \lambda^B_{nn}$
C_{6v}
Σ^v_{yz}
Σ^d_{xz}
C_{3v}
z
y
A
B
x
Σ^h_{xy}
$\lambda_A(= \lambda_B), \lambda, \lambda^A_{nn}(= \lambda^B_{nn})$
$\lambda_A \neq \lambda_B, \lambda, \lambda^A_{nn} \neq \lambda^B_{nn}$

Fig. 3 Spin–orbit hopping terms compatible with subgroups of D_{6h}. Horizontal (h), vertical (v), and dihedral (d) reflections are shown (bottom, middle). Black (white) arrows indicate spin-conserving (spin-flip) hoppings. D_{6h}-, D_{3h}-, and D_{3d}-invariant systems (top panel) admit next-nearest hoppings. C_{6v}- and C_{3v}-invariant systems (bottom panel, right and left) allow for nearest neighbor spin-flip hopping.

heterostructures (C_{3v}). The BR interaction generated by the nearest-neighbor spin-flip hoppings (second term in Eq. 8) signals the lack of mirror inversion symmetry, Σ^h_{xy}, associated with reduction of the point group from D_{6h} to C_{6v}, which may occur through interfacial effects in heterostructures or via application of an electric field perpendicular to the 2D plane. Finally, next-nearest-neighbor spin-flip processes, parameterized by the couplings $\lambda^{A(B)}_{nn}$ (third term in Eq. 8) are also allowed in systems lacking out-of-plane reflection symmetry, Σ^h_{xy}, such as graphene-based vdW heterostructures or graphene placed on a generic substrate. Note that when the in-plane inversion symmetry is also broken, these processes become sublattice-resolved ($\lambda^A_{nn} \neq \lambda^B_{nn}$). This occurs, for example, in graphene-TMD heterostructures.

Honeycomb monolayers with proximity-induced SOC: Continuum theory

The low-energy electronic structure of 2D materials can be conveniently modeled using a (long-wavelength) continuum description. Expanding the geometric form factor (Eq. 3) to first order around each Dirac point, $\boldsymbol{K}_{\pm} = 4\pi/(3\sqrt{3}a)(\pm 1, 0)^{\mathrm{T}}$, that is $\phi_{\pm}(\boldsymbol{k}) \simeq (3ta/2)(\pm k_x + ik_y)$, yields the effective single-particle Hamiltonian $\mathcal{H}_{0\boldsymbol{k}} = \hbar v(\tau_z \otimes \sigma_x k_x + \tau_0 \otimes \sigma_y k_y) \otimes s_0 + m\tau_0 \otimes \sigma_z \otimes s_0$ when written in the conventional basis, $|\psi\rangle = (K_+, K_-)^{\mathrm{T}} \otimes (A, B)^{\mathrm{T}} \otimes (\uparrow, \downarrow)^{\mathrm{T}}$. Here $\boldsymbol{k}$ is the 2D wavevector measured with respect to a Dirac point, $v = 3at/2\hbar$ is the Fermi velocity of massless Dirac fermions, s_0 is the identity matrix acting on the spin DOF, and σ_i and τ_i are the Pauli matrices supplemented with identity acting on sublattice and valley DOFs, respectively. This low-energy Hamiltonian admits an even simpler and more elegant form when written using the *valley basis*, $|\psi\rangle = (K_+A, K_+B, -K_-B, K_-A)^{\mathrm{T}} \otimes (\uparrow, \downarrow)^{\mathrm{T}}$, that is, $\mathcal{H}_{0\boldsymbol{k}} = \tau_0 \otimes H_{0\boldsymbol{k}} \otimes s_0$, with

$$H_{0\boldsymbol{k}} = -i\hbar v\, \boldsymbol{\sigma} \cdot \boldsymbol{k} + m\sigma_z. \tag{9}$$

The Dirac–Weyl equation (Eq. 9) governs the low-energy properties of honeycomb monolayers with low SOC and has been extensively used in investigations of opto-electronic and transport phenomena in single-layer graphene (Peres, 2010; McCann and Koshino, 2013). For ease of notation, the writing of the tensor product between matrices acting on different DOFs is omitted from here onward.

The spin–orbit interactions in the continuum can be derived by expanding the Fourier transformed TB Hamiltonian (Eq. 8) around the K points. Here, as in the previous section for the full TB Hamiltonian, $\mathcal{T}$ and unitary (spatial) symmetries are exploited so as to constrain the allowed spin–orbit terms in the continuum theory. The time-reversal operation reverses spins $\boldsymbol{s} \to -\boldsymbol{s}$ and swaps valleys (as momentum reversal sends $\boldsymbol{K}_+ \leftrightarrow \boldsymbol{K}_-$). Since the time reversal operator is antiunitary, the σ_y pseudospin operator is also affected, $\mathcal{T}: \quad \sigma_x \rightarrow \sigma_x\ , \quad \sigma_y \rightarrow -\sigma_y\ , \quad \sigma_z \rightarrow \sigma_z$. Exploiting the $\mathcal{T}$-symmetry transformations, one finds that there are $4 \times 3 = 12$ possible terms

$$\mathcal{H}_{\mathrm{SO}}^{\mathcal{T}} = \sum_{i=x,y,z} \left(\Delta^{(i)} \tau_0\ \sigma_z + \lambda_x^{(i)} \tau_0\ \sigma_x + \lambda_y^{(i)} \tau_0\ \sigma_y + \omega^{(i)} \tau_z\ \sigma_0 \right) s_i\ . \tag{10}$$

Direct inspection of Eq. (10) shows that the majority of SOC terms lead to anisotropic energy dispersion, and hence are incompatible with the C_{3v} point group symmetry. To preserve the continuous rotational symmetry of the low-energy theory about each Dirac point, the Hamiltonian within each valley should commute with the generator of rotations within the 2D plane for that valley (the total angular momentum operator). In the valley basis, the total angular momentum is independent of the valley index and takes the form

$$J_z = -i\ \hbar \partial_\phi \tau_0\ \sigma_0\ s_0 + \frac{\hbar}{2} (\tau_0\ \sigma_z\ s_0 + \tau_0\ \sigma_0\ s_z), \tag{11}$$

where ϕ is the azimuthal angle. The first term of J_z is simply the orbital angular momentum while the s_z piece is the usual spin contribution. The σ_z term arises from spin-like sublattice DOF and is therefore characteristic of vdW materials. The requirement of J_z's commutation with the Hamiltonian yields $\Delta^{(x,y)} = \omega^{(x,y)} = \lambda^z_{x(y)} = 0\ ,\ \lambda_x^{(y)} = -\lambda_y^{(x)}$ and $\lambda_x^{(x)} = \lambda_y^{(y)}$. One of such terms, a Dresselhaus-type SOC, $\lambda_x^{(x)} \tau_0 (\sigma_x\ s_x - \sigma_y\ s_y)$, breaks the mirror reflection symmetry about the yz plane, rendering atomic sites within the same sublattice inequivalent, and is thus forbidden in C_{3v} invariant systems.

The full C_{3v}-invariant low-energy Hamiltonian in momentum space is therefore

$$H_{\boldsymbol{k}}^{C_{3v}} = \hbar v \tau_0\ \boldsymbol{\sigma} \cdot \boldsymbol{k}\ s_0 + m \sigma_z + \Delta_{\mathrm{KM}} \tau_0\ \sigma_z\ s_z + \lambda_{\mathrm{BR}} \tau_0\ \left(\sigma_x\ s_y - \sigma_y\ s_x \right) + \lambda_{\mathrm{sv}} \tau_z\ \sigma_0\ s_z, \tag{12}$$

where the above couplings have a simple correspondence to the spin-hoppings of the TB model (Eq. 8)

$$\Delta_{\mathrm{KM}} = \frac{\lambda_A + \lambda_B}{2}, \qquad \lambda_{\mathrm{sv}} = \frac{\lambda_A - \lambda_B}{2}, \qquad \lambda_{\mathrm{BR}} = \lambda\ . \tag{13}$$

The competition between the different spin–orbit energy scales in Eq. (12) influences the energy dispersion while also dictating the topological properties and the spin structure of the eigenstates. Kane–Mele SOC ($\Delta_{\mathrm{KM}} \tau_0 \sigma_z s_z$) leads to spin-degenerate bands due to its spin-conserving nature, with the ability to drive the system into a topologically nontrivial phase when it dominates (Qian et al., 2014; Wu et al., 2018; Shi et al., 2019). However, in the honeycomb monolayer systems of interest here, including TMDs and graphene-based vdW heterostructures, the Kane–Mele SOC is negligible. In contrast, the spin–valley coupling ($\lambda_{\mathrm{sv}} \tau_z \sigma_0 s_z$), also known as valley–Zeeman interaction, emerging from sublattice-resolved SOC, is generally significant and yields spin-split bands within each valley. Typically, λ_{sv} is of order 100 meV for semiconducting TMDs (intrinsic SOC) (Xiao et al., 2012) and 1 meV for graphene-TMD heterostructures (proximity-induced SOC) (Tiwari et al., 2022). The Bychkov–Rashba term, $\lambda_{\mathrm{BR}} \tau_0 \left(\sigma_x\ s_y - \sigma_y\ s_x \right)$, arising at heterostructure interfaces, leads to spin admixture in the spin states, characterized by in-plane spin-momentum locking of the Bloch eigenstates. Similar to spin–valley SOC, this term results in spin-split bands distinguished by *spin helicity* rather than simple spin. The magnitude of this coupling is typically on the order of 1–10 meV, depending on the TMD used (Tiwari et al., 2022; Wang et al., 2019). The presence of significant Rashba coupling explains the recently observed large charge-to-spin conversion via the ISGE at room temperature (Offidani et al., 2017), as discussed later on in this article. Finally, it is worth noting that the sublattice-resolved spin-flip terms ($\lambda_{nn}^{A(B)}$) (see Eq. 8) are absent in the low-energy Hamiltonian (i.e., they appear at the next order in the small-$\boldsymbol{k}$ expansion), and as such have little impact on the transport physics of 2D honeycomb layers.

The dispersion relation associated with Eq. (12) consists of two pairs of spin-split Dirac bands. A typical energy dispersion relation for a graphene-TMD heterostructure with competing Rashba and spin–valley couplings is shown in Fig. 4a. The general electronic dispersion of C_{3v} invariant systems can be readily seen as

$$\varepsilon_\zeta(k) = \pm \sqrt{\hbar^2 v^2 k^2 + \Delta_\zeta^2(k)}, \tag{14}$$

where Δ_{KM} has been neglected due to its inherently small nature compared to other SOC energy scales, $k \equiv |\boldsymbol{k}|$, $\zeta = \pm 1$ is the *spin-helicity* index, and $\Delta_\zeta^2(k)$ is the SOC-dependent mass term,

$$\Delta_\zeta^2(k) = m^2 + \lambda_{\mathrm{sv}}^2 + 2\lambda_{\mathrm{BR}}^2 + 2\zeta \sqrt{\left(\lambda_{\mathrm{BR}}^2 - m \lambda_{\mathrm{sv}} \right)^2 + \hbar^2 v^2 k^2 \left(\lambda_{\mathrm{BR}}^2 + \lambda_{\mathrm{sv}}^2 \right)}\ . \tag{15}$$

The spin texture of the eigenstates (see Fig. 4b) can be cast in the following compact form

$$\langle \boldsymbol{s} \rangle_{\zeta \tau \boldsymbol{k}} = -\zeta\ \varrho(k)\ (\hat{k} \times \hat{z}) + m_{\zeta\tau}^z(k)\ \hat{z}, \tag{16}$$

where $\tau = \pm 1$ is the $K_\pm$ valley quantum number. The first term describes the spin winding of the electronic states generated by the BR effect (Rashba, 2009). The second term is due to breaking of sublattice symmetry ($\lambda_{\mathrm{sv}} \neq 0$ or $m \neq 0$) and tilts the spins in the $\hat{z}$ direction. Because of the Dirac nature of the charge carriers, the spin texture has a strong dependence upon the Fermi energy. In fact, the spins point fully out of the plane at the Dirac point, but acquire an in-plane component as k is increased. For $\hbar v k \gg \Delta_\zeta$, one finds $\rho(k) \simeq \cos\theta$ and $m_{\zeta\tau}^z(k) \simeq \sin\theta$, with $\theta = -\tau\ \arctan(\lambda_{\mathrm{sv}}/\lambda_{\mathrm{BR}})$. The tilting angle, θ, has opposite signs in different valleys by virtue of time-reversal symmetry. Furthermore, one observes two distinct electronic regimes. For energies within the spin gap (regimes Ia and Ib in Fig. 4), the Fermi surface has a *well-defined spin helicity*, a feature reminiscent of spin–momentum locking in

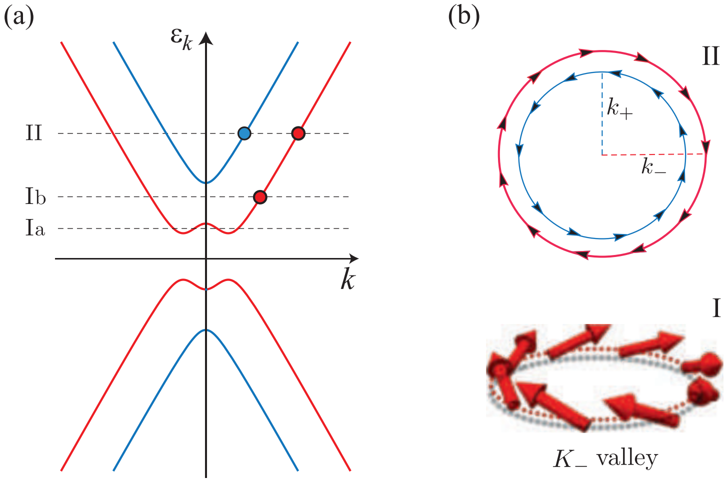

Fig. 4 (a) Energy dispersion near the Fermi level. Symmetry breaking SOC opens a spin gap. A small Mexican hat develops in the regime I due to the interplay of spin–valley coupling and Rashba SOC. (b) Tangential winding of the spin texture in regimes I (3D view) and II (top view).

topologically protected surface states (Schwab et al., 2011). Consequently, near-optimal charge-to-spin conversion is observed inside the spin gap via a large ISGE. In contrast, for energies outside the spin gap (regime II in Fig. 4), the spin helicity is no longer a well-defined concept, but the larger Fermi radius of the spin-majority band ($\zeta = -1$) nevertheless allows for a detectable ISGE (i.e., while the current-induced spin polarization arising from the two subbands have opposite signs, they do not cancel each other). These special features of the electronic and spin structure of proximitized 2D materials are ultimately responsible for the efficient current-driven spin polarization supported by graphene-TMD heterostructures (Offidani et al., 2017).

Relativistic spin–orbit coupled transport phenomena

Electronic signatures

As alluded to above, the presence of SOC in a material can drastically alter the transport properties of materials due to spin-charge inter–conversion effects. One of the earliest signatures of SOC-affected transport was measured in magnesium films (i.e., 2DEGs) (Bergman, 1982; Sharvin and Sharvin, 1981), where the electrical conductivity was seen to decrease upon the application of a magnetic field (i.e., a negative magneto-conductivity). This behavior can be traced back to the quantum interference between the many paths an electron can take when traveling through a disordered system. In the case of a material where SOC is absent, quantum interference leads to the coherent backscattering of electrons, thus yielding more localized states, and hence reduces the electrical conductivity in a phenomenon known as *weak localization* (WL). The application of a magnetic field here destroys the coherence of the backscattered electrons and hence inhibits WL. Therefore, a positive magneto-conductivity is a clear signature of WL.

In contrast, materials that are SOC-active may exhibit the complete opposite of WL, *weak antilocalization* (WAL). In this case, the paths of backscattered electrons interfere destructively to yield more delocalized states. This reversal in behavior can be understood to result from the spin DOF becoming an active participant in the Hamiltonian and scattering events. Here, the application of a magnetic field changes the interference of backscattered electrons from destructive to constructive, therefore decreasing the conductivity of a material. The natural signature of SOC-active materials is therefore a negative magneto-conductivity.

The role of localization in graphene, however, is more involved due to the presence of other spin-like DOFs, namely, the sublattice and valley DOFs. In the absence of both SOC and inter-valley scattering (i.e., disorder is smooth on the lattice scale), graphene exhibits a WAL phase, the complete opposite of what is seen in 2DEGs. The manifestation of WAL in this system is a result of graphene's π Berry phase, which precludes electrons from backscattering and thus prevents WL. Another interpretation can be found in considering the pseudospin (sublattice) DOF as an active participant in the Hamiltonian and scattering events, much in a similar manner to how spin becomes an active participant in SOC-active 2DEGs. Upon increasing the concentration of point defects and other short-range scatterers, such that inter-valley scattering no longer remains negligible, the disordered graphene system's localization phase reverses to exhibit a WL phase instead. Likewise, keeping intervalley scattering weak (i.e., intravalley scattering dominates) and instead introducing a strong SOC also pushes graphene from a WAL to a WL phase. Finally, when both disorder and SOC are strong, graphene moves back to WAL behavior (Sousa et al., 2022). Several experiments on graphene-TMD and bilayer graphene-TMD have revealed WAL phases in these systems (Wang et al., 2016; Völkl et al., 2017; Yang et al., 2017; Wakamura et al., 2018; Amann et al., 2022), indicating the presence of strong symmetry-breaking SOC. However, such observations do not provide a direct spectroscopic probe for the size of the various SOCs present. Only recently has the SOC of these systems been accessed directly (Tiwari et al., 2022; Wang et al., 2019).

Spin Hall effect

While SOC might affect the electrical conductivity of graphene-based vdW heterostructures through quantum interference, more profound and exotic behavior can be observed when considering other forms of transport. The SHE is one such example of this, whereby the generation of a pure spin current driven solely by electric fields can be achieved without the need for magnetic fields. In pristine graphene—owing to its negligible intrinsic SOC (Sichau et al., 2019)—the SHE is absent. However, this scenario changes drastically in the presence of disorder-induced SOC (Ferreira et al., 2014; Balakrishnan et al., 2014; Milletarì and Ferreira, 2016). Here, the scattering of charge carriers from spin–orbit hot spots aligns spin and orbital angular momentum in opposite directions, resulting in the formation of transverse spin currents; the magnitude of the effect is characterized by the spin Hall angle, γ.

A direct consequence of the SHE in low-dimensional systems is the accumulation of spin at the system's boundaries. Specifically, thin films (2D materials) will accrue a collection of oppositely aligned spins at opposite edges, see Fig. 5, due to the resulting spin current pumping up spins toward one boundary and down spins toward the opposite boundary. In thin wires (1D materials), the spin accumulation can be seen to wind around the wire's surface, much in a similar manner to how a magnetic field appears around a wire carrying an electrical current. Reversing the direction of the applied electrical current reverses the spin accumulation in both cases mentioned here; the up and down spins now accumulate at the opposite boundary to which they had originally found themselves in thin films, and the direction of winding is reversed in thin wires.

Broadly speaking, the SHE arises in two forms: intrinsically and extrinsically. The former of these two is a direct result of the material's band structure, as opposed to being reliant upon external perturbations or extrinsic factors, such as disorder. This manifestation of the SHE can be understood in terms of an internal force experienced by the electrons traveling through the material due to the application of a charge current. This internal force is generated by the SOC experienced by the electrons, and hence is an effect embedded within the band structure of the system. An analogy can be drawn between this spin–orbit force driving the SHE and the Lorentz force responsible for the regular Hall effect. In contrast to the intrinsic SHE is the extrinsic contribution. Here, the generation of a spin current is driven by external mechanisms such as scattering from impurities. In this case, the SHE is the result of asymmetric scattering of electrons based upon their spin; up spins are scattered with a certain directional preference while down spins are scattered with the opposite preference. This type of asymmetric scattering, known as *skew scattering*, plays a central role in graphene-based vdW heterostructures (Milletarì et al., 2017).

To illustrate the importance of disorder-induced corrections to transport for these materials, consider the Hamiltonian for graphene with just Rashba coupling (i.e., $\lambda_{\rm sv} = 0$ and neglecting $\Delta_{\rm KM}$, given its small nature in most realistic scenarios). The carrier concentration is typically large enough to place the Fermi energy well above the Rashba pseudogap (i.e., in regime II of the band structure). Assuming only nonmagnetic disorder is present, the system clearly lacks a well-defined quantization axis due to the lack of spin-valley coupling. Therefore, the SHE should not be observable simply because some form of SOC is present. With the inclusion of a spin–valley coupling, it would then be natural to expect the possible occurrence an SHE as a quantization axis will now be well-defined. However, if a theoretical analysis of the SHE for the minimal model without including disorder self-consistently is performed, it would lead one to believe that a finite SHE would exist in the absence of spin–valley coupling. This clearly emphasizes the importance of including disorder in a fully self-consistent manner (Milletarì et al., 2017; Milletarì and Ferreira, 2016).

Within the Kubo-Streda formalism of linear response (Streda, 1982; Crépieux and Bruno, 2001), the spin Hall conductivity may be written as $\sigma_{yx}^{\rm sH} = \sigma_{yx}^{\rm sH,I} + \sigma_{yx}^{\rm sH,II}$, with (Milletarì and Ferreira, 2016; Milletarì et al., 2017)

$$\sigma_{yx}^{\rm sH,I} = -\frac{1}{2\pi}\int_{-\infty}^{+\infty} d\omega \frac{df}{d\omega}\left\{{\rm Tr}\left[\mathcal{J}_y^z G_\omega^+ \tilde{j}_x G_\omega^-\right] - \frac{1}{2}{\rm Tr}\left[\mathcal{J}_y^z G_\omega^+ \tilde{j}_x G_\omega^+ + \mathcal{J}_y^z G_\omega^- \tilde{j}_x G_\omega^-\right]\right\}, \tag{17a}$$

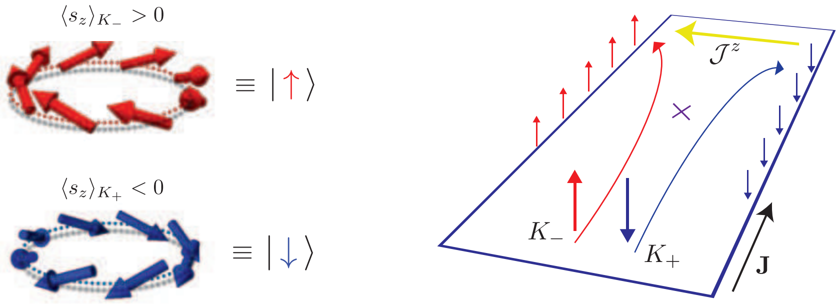
$\langle s_z \rangle_{K_-} > 0$
$\equiv |\uparrow\rangle$
$\langle s_z \rangle_{K_+} < 0$
$\equiv |\downarrow\rangle$
$\mathcal{J}^z$
×
K_-
K_+
J

Fig. 5 Left: Spin textures of spin-majority bands in each valley. The net out-of-plane spin polarization at each valley defines a quantization axis. Right: Spin accumulation at the edges of a thin film due to the SHE. Black arrow: electrical current, orange arrow: spin current, red/blue arrows: up/down spins. The electrons driven by the electrical current are scattered asymmetrically based upon their spin (skew scattering). Here, up spin electrons are scattered preferentially to the left while down spins experience the opposite.

$$\sigma_{yx}^{\mathrm{sH,II}} = \frac{1}{2\pi}\int_{-\infty}^{+\infty} d\omega f(\omega)\mathrm{Re}\left\{\mathrm{Tr}\left[\mathcal{J}_y^z \mathrm{G}_\omega^+ \tilde{j}_x \frac{\partial \mathrm{G}_\omega^+}{\partial\omega} - \mathcal{J}_y^z \frac{\partial \mathrm{G}_\omega^+}{\partial\omega}\tilde{j}_x \mathrm{G}_\omega^+\right]\right\}, \tag{17b}$$

where $\mathcal{J}_y^z$ is the z-polarized spin current operator in the y-direction, $\tilde{j}_x$ is the x component of the disorder-renormalized electric current operator, $\mathrm{G}_\omega^\pm$ are the retarded or advanced disorder-averaged Green's functions for electrons with energy ω, $f(\omega)$ is the Fermi-Dirac distribution, and the trace is over momentum and all internal DOFs (spin, sublattice, and valley). Given the applied electric field, $\boldsymbol{E}$, generating an electrical current (assumed to be along the x-axis), the resulting spin Hall current can then be determined using $\mathcal{J}_y^{\mathrm{sH}} = \sigma_{yx}^{\mathrm{sH}} E_x$.

The first term, $\sigma_{yx}^{\mathrm{sH,I}}$, is sometimes referred to as the Fermi surface contribution while the second term, $\sigma_{yx}^{\mathrm{sH,II}}$, is similarly called the Fermi sea contribution. In weakly disordered systems, the type II contribution is higher order in the impurity density and hence may be neglected. Similar reasoning applies to the G^+G^+ and G^-G^- terms in the type I contribution. Hence, it turns out that the leading order behavior is dictated solely by the cross term of $\sigma_{yx}^{\mathrm{sH,I}}$. Clearly, the SHE in the metallic regime of disordered materials is essentially a Fermi surface property.

A common representation that helps to visualize how disorder is included into linear response is that of Feynman diagrams. Fig. 6 shows the dominant cross term in diagrammatic form, alongside the Dyson series describing the disorder-averaged Green's functions and the Bethe–Salpeter equation satisfied by the disorder-renormalized vertex. Note, the discussions and analysis here assume that only nonmagnetic (spin-independent) scalar disorder is present. The *dashed lines* represent an electron (*solid line*) scattering from an impurity located at the cross. If $\sigma_{yx}^{\mathrm{sH,I}}$ is evaluated without vertex corrections for the $\lambda_{\mathrm{sv}} = 0$ case, one finds a nonvanishing result in complete contradiction to what is expected. However, including vertex corrections to any order in the number of scattering events, $\sigma_{yx}^{\mathrm{sH,I}}$ can be seen to vanish, thus recovering the expected result for zero spin–valley coupling.

Interestingly, if one were to consider a Fermi energy located within the Rashba pseudogap (regime I of the band structure, $|\varepsilon| < 2|\lambda_{\mathrm{BR}}|$), they would also find a vanishing SHE in the absence of λ_{sv}. However, in this case, the type II contribution would no longer be subleading order and hence also needs accounting for (the cross term of the type I contribution remains the dominant part of $\sigma_{yx}^{\mathrm{sH,I}}$). With this in mind, the computation of Eq. (17) yields (Milletarì et al., 2017)

$$\sigma_{yx}^{\mathrm{sH,I}} = \frac{e}{16\pi}\frac{|\varepsilon|}{\lambda_{\mathrm{BR}}} = -\sigma_{yx}^{\mathrm{sH,II}}. \tag{18}$$

Hence, $\sigma_{yx}^{\mathrm{sH}} = 0$ and so the SHE remains absent even in regime I due to the Fermi surface contribution being counteracted by off-surface processes.

Shifting focus to the experimentally relevant situation in which $\lambda_{\mathrm{BR}} \neq 0$ and $\lambda_{\mathrm{sv}} \neq 0$ while the SHE is expected to be observable (due to emergence of an effective spin quantization axis around each valley, see Fig. 5), the role played by disorder changes drastically. If disorder is only accounted for within the Born approximation, where all processes involving three or more scatterings from a single impurity are neglected, then one finds that Eq. (17a) yields a vanishing result. Only upon the inclusion of at least third-order scattering events (at least three scatterings from a single impurity) into the vertex correction does one find a nonzero value for $\sigma_{yx}^{\mathrm{sH,I}}$. By accounting for these higher order processes, a scattering event can now distinguish between left and right based upon the electron's spin along the well-defined quantization axis courtesy of the spin–valley coupling, that is, skew scattering has been included. Therefore, not only are vertex corrections key to understanding the SHE completely, but so too are the higher order scattering mechanisms allowing for the manifestation of the SHE. In other words, the extrinsic SHE due to scalar disorder effects in graphene-based vdW heterostructures is controlled entirely by skew scattering, which is always active provided the existence of a tilted BR-type spin texture at the Fermi level.

As a final note on intrinsic effects, couplings such as electron–phonon and electron–electron interactions, as well as structural defects such as ripples and shears in the individual layers of the heterostructure, are also considered as being intrinsic to the system.

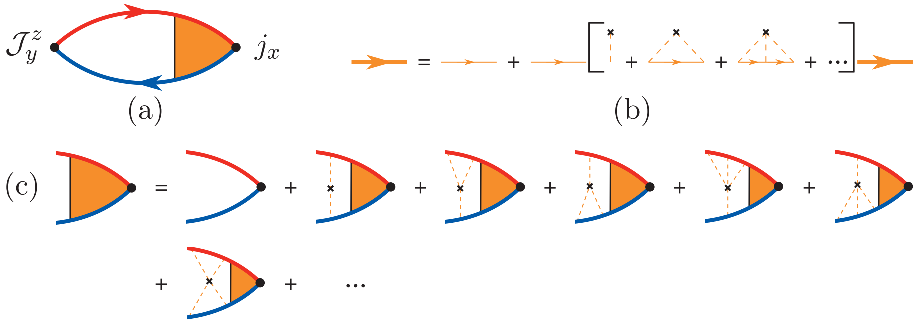

Fig. 6 Diagrammatic representation of the cross term in $\sigma_{yx}^{\mathrm{sH,I}}$ (a), the disorder-average Green's function (b), and vertex correction due to disorder (c). The thick red/blue lines denote retarded/advanced disorder-averaged Green's functions describing electron propagation, thick orange lines can be either retarded/advanced disorder-averaged electron Green's functions but must all be of the same type, thin orange lines indicate the free electron Green's functions, the black circles represent the current and spin current operators (vertices), black crosses represent an impurity, and the orange dashed lines denote an electron scattering from the impurity.

Consequently, the intrinsic SHE can potentially play an important role in clean systems, where electron–phonon coupling dominates at room temperature, or in materials with sharp boundaries between structural domains. Just how major these effects are is still a current area of study; hence they shall not be covered in this article.

Inverse spin galvanic effect

A natural partner to the SHE is the ISGE: the accumulation of spin upon application of an electric field without an associated spin current. Unlike the SHE, this spin accumulation manifests throughout the whole system. Rather, a nontrivial spin texture, facilitated by the interfacial breaking of inversion symmetry, is enough to allow for a nonzero spin polarization when an electrical current is passed through the system. To demonstrate this, consider, once again, the minimal Dirac–Rashba Hamiltonian (only $\lambda_{\mathrm{BR}} \neq 0$). It was shown above that the electron spins are locked in-plane and perpendicular to the electron momentum. In the absence of an electric field (i.e., in equilibrium), the Fermi rings forming the Fermi surface (two in regime II and Ia and one in regime Ib) are perfect circles around each Dirac point. Consequently, the electrons forming these rings yield a net spin polarization of zero (as expected of the nonmagnetic materials discussed here). However, when an electric field is introduced, these Fermi rings are shifted such that they are no longer rotationally symmetric about their respective Dirac points, see Fig. 7. Therefore, the sum of the electron spins from each Fermi ring yields a nonzero spin polarization.

The direction of the resulting spin polarization is entirely dependent upon the system's spin texture. In the case of the Dirac–Rashba model above, the ISGE yields a spin polarization that is perpendicular to the applied electric field. The inclusion of a spin–valley coupling does not change the resulting spin polarization compared to the Dirac–Rashba model (the Onsager-reciprocal phenomena, namely, the SHE and ISGE, were measured in Camosi et al., 2022). This is due to the out-of-plane component gained by the electron spins being opposite in sign between valleys (i.e., ± in the $K_\pm$ valleys). Hence, summing over the contribution from both valleys, one finds a vanishing z component of spin accumulation. The role of the Kane–Mele-type SOC in these systems is negligible and hence does not contribute any meaningful changes to the spin texture either.

An alternative method to manipulating the spin texture of these materials has been found through the introduction of a twist between a graphene monolayer and a TMD monolayer (Li and Koshino, 2019; David et al., 2019; Péterfalvi et al., 2022; Veneri et al., 2022). By introducing a rotational off-set between the two layers, both the Rashba and spin–valley couplings are affected and acquire a twist-angle, θ, dependence. Not only are the magnitudes of these SOCs changed by twisting, but so too is the form of the Rashba term in the Hamiltonian. Upon the introduction of twisting, the spin–valley term maintains the same form as in Eq. (12) but with λ_{sv} replaced by $\tilde{\lambda}_{\mathrm{sv}}(\theta)$ ($\tilde{\lambda}_{\mathrm{sv}}(0) = \lambda_{\mathrm{sv}}$), and the Rashba term becomes

$$H_{\mathrm{R}}(\theta) = \tilde{\lambda}_{\mathrm{BR}}(\theta) e^{is_z\alpha_{\mathrm{R}}(\theta)/2}(\sigma_x s_y - \sigma_y s_x) e^{-is_z\alpha_{\mathrm{R}}(\theta)/2}, \tag{19}$$

where $\tilde{\lambda}_{\mathrm{BR}}(0) = \lambda_{\mathrm{BR}}$, and $\alpha_{\mathrm{R}}(\theta)$ is known as the *Rashba phase*. The exact way in which the Rashba coupling, spin–valley coupling, and Rashba phase vary with twist-angle depends heavily upon the material that graphene is paired with. A guaranteed property, however, is that $\alpha_{\mathrm{R}}(\theta) = c_1\pi$ for $\theta = c_2\pi/6$ for $c_1, c_2 \in \mathbb{Z}$. In any case, the spin texture will clearly be affected by the change in the Rashba coupling term's form. In fact, as the layers are twisted relative to one another, the electron spins can be seen to also rotate away from being locked perpendicular to their momenta. This rotation of the spin texture can be seen in Fig. 8, where the out-of-plane component due to spin–valley coupling has been neglected for ease of illustration. It turns out that, for some materials, there exists a critical angle, θ_c, where the spin texture is entirely radial (Fig. 8c), sometimes referred to as a *Weyl-type* or *hedgehog* spin texture. Clearly, by being the perpendicular analog of the untwisted case, the resulting spin polarization will be perfectly collinear to the applied electric field. For any twist-angles away from $\theta = 0, \pm \theta_c, \pi/6$, the net spin polarization will be in-plane but neither perpendicular nor collinear to an applied electrical current. The value of θ_c is sensitive to the partner TMD used, atomic registry, strain distribution, and external perturbations (e.g., perpendicular electric field, Naimer et al., 2021), and hence will vary significantly between materials. Consequently, meaningful predictions for θ_c are challenging to make. For example, graphene-WSe$_2$

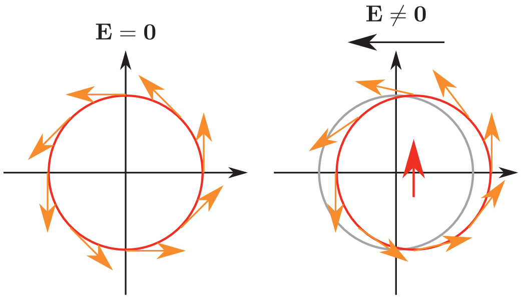

Fig. 7 The manifestation of a nonequilibrium spin polarization with the application of an electric field is pictured above for a system with only Rashba SOC. Focus is placed on a single Fermi ring for ease of illustration. Left: Fermi ring for a system with zero current. The sum of electron spins (orange arrows) yields zero by symmetry. Right: an applied electric field shifts the Fermi ring from its original position (gray), with the electron spins on the Fermi surface rotating to maintain the spin–momentum locking typical of Rashba SOC, resulting in a nonzero spin polarization (red arrow). By inspection, all spins, except those on the x-axis, can be seen to rotate toward alignment with the y-axis. As a result, the net spin polarization is parallel to the y-axis in this case.

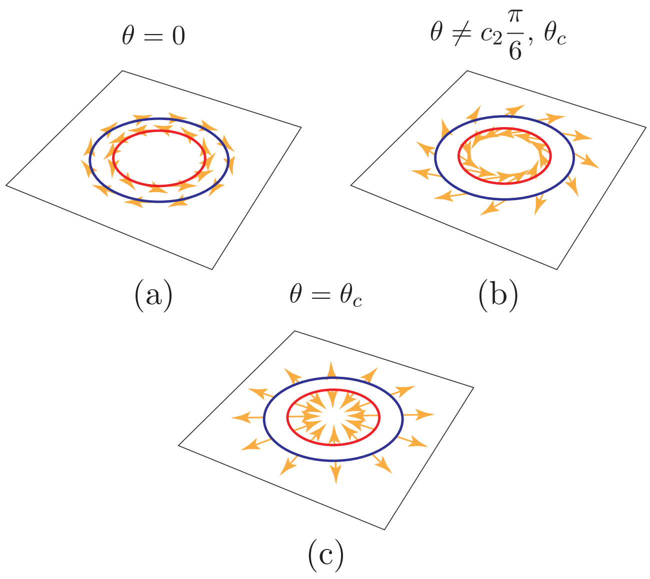
$\theta = 0$

$\theta \neq c_2 \dfrac{\pi}{6}, \theta_c$

$\theta = \theta_c$

Fig. 8 Introduction of a twist between the layers of a graphene-TMD vdW heterostructure can be seen to rotate the spin texture of the Fermi rings. (a) $\theta = 0$, all spin are locked in-plane and perpendicular to the momentum. (b) At arbitrary twist angles, $\theta \neq c_2\pi/6$, θ_c, the electron spin are still fixed in-plane but not perpendicular of (anti-)parallel to the electron momentum. (c) At critical twist angles, $\theta = \theta_c$, the electron spins (anti-)align with their momentum.

has been predicted to host a $\theta_c \approx 14°$ (this prediction is based on an 11-band tight-binding model of the twisted heterostructures informed by both density functional theory calculations (Fang et al., 2015; Gmitra et al., 2016) and available angle-resolved photoemission data (Pierucci et al., 2016; Nakamura et al., 2020). In contrast, even the existence of a critical twist angle for graphene-MoS$_2$ is difficult to ascertain given the variation in the reported material parameters of theory and experiment (Péterfalvi et al., 2022).

Defects and structural disorder are also expected to play a significant role. Of particular relevance is *twist-angle disorder*, a type of spatial inhomogeneity that is ubiquitous in realistic systems (Uri et al., 2020). Its impact on transport properties is expected to depend crucially on the comparative sizes of the spin diffusion length, l_s, and the twist-puddle size, ξ (i.e., typical size of regions with a similar twist-angle). When $l_s \ll \xi$, the twist-angle disorder can be considered smooth and hence can be incorporated into linear-response calculations through an appropriate averaging procedure (e.g., a Gaussian or box weighting could be applied, Veneri et al., 2022). Though it is challenging to make first-principles predictions about the twist-angle behavior of the Rashba phase for realistic systems, the dependence of coupled spin-charge transport phenomena on the Rashba phase can be reliably studied by replacing the standard Rashba SOC in the low-energy Hamiltonian of Eq. (12) with Eq. (19). In this case, the point group symmetry of the system, and therefore Hamiltonian, is once more reduced, going from C_{3v} to C_3 for nontrivial twist angles.

To understand this from a quantitative perspective, one notes that the ISGE can be written mathematically as $S_\alpha = K_{\alpha\beta}E_\beta$ (assuming Einstein summation), where $K_{\alpha\beta}$ are the elements of the *spin susceptibility* tensor. As in the SHE, the spin susceptibility tensor can be determined using linear response theory (Milletarì and Ferreira, 2016; Milletarì et al., 2017), $K_{\alpha\beta} = K^{\mathrm{I}}_{\alpha\beta} + K^{\mathrm{II}}_{\alpha\beta}$,

$$K^{\mathrm{I}}_{\alpha\beta} = -\frac{1}{4\pi}\int_{-\infty}^{+\infty} d\omega \frac{df}{d\omega}\left\{\mathrm{Tr}\left[s_\alpha G^+_\omega \tilde{j}_x G^-_\omega\right] - \frac{1}{2}\mathrm{Tr}\left[s_\alpha G^+_\omega \tilde{j}_x G^+_\omega + s_\alpha G^-_\omega \tilde{j}_x G^-_\omega\right]\right\}, \tag{20a}$$

$$K^{\mathrm{II}}_{\alpha\beta} = \frac{1}{4\pi}\int_{-\infty}^{+\infty} d\omega f(\omega)\mathrm{Re}\left\{\mathrm{Tr}\left[s_\alpha G^+_\omega \tilde{j}_\beta \frac{\partial G^+_\omega}{\partial\omega} - s_\alpha \frac{\partial G^+_\omega}{\partial\omega}\tilde{j}_x G^+_\omega\right]\right\}, \tag{20b}$$

where the Green's functions now contain the twisted form of the Rashba Hamiltonian. For disordered materials the G^+G^+ and G^-G^- of the type I contribution, as well as the type II contribution, can once again be neglected. Consequently, the results for the in-plane components of the twisted spin susceptibility tensor can be related back to the untwisted ISGE, albeit with modified Rashba and spin–valley couplings,

$$\begin{aligned} K_{xx}(\tilde{\lambda}_{\mathrm{BR}}(\theta), \tilde{\lambda}_{\mathrm{sv}}(\theta); \theta) &= K_{yx}(\tilde{\lambda}_{\mathrm{BR}}(\theta), \lambda_{\mathrm{sv}}(\theta); 0)\sin\alpha_{\mathrm{R}}(\theta), \\ K_{yx}(\tilde{\lambda}_{\mathrm{BR}}(\theta), \tilde{\lambda}_{\mathrm{sv}}(\theta); \theta) &= K_{yx}(\tilde{\lambda}_{\mathrm{BR}}(\theta), \lambda_{\mathrm{sv}}(\theta); 0)\cos\alpha_{\mathrm{R}}(\theta), \end{aligned} \tag{21}$$

$$K_{yx}(\tilde{\lambda}_{\mathrm{BR}}, \tilde{\lambda}_{\mathrm{sv}}; 0) = \frac{4ev\varepsilon}{\pi n u_0^2}\frac{\tilde{\lambda}^3_{\mathrm{BR}}(\varepsilon^2 + \tilde{\lambda}^2_{\mathrm{sv}})}{\varepsilon^4(\tilde{\lambda}^2_{\mathrm{BR}} + \tilde{\lambda}^2_{\mathrm{sv}}) - \varepsilon^2\tilde{\lambda}^4_{\mathrm{sv}} + 3\tilde{\lambda}^2_{\mathrm{BR}}\tilde{\lambda}^4_{\mathrm{sv}}}, \tag{22}$$

where n is the impurity concentration and u_0 is the strength of the scalar impurities. These results are strictly valid for perfectly aligned heterostructures. For systems with smooth twist-disorder landscapes ($l_s \ll \xi$), an intuitive approximate result can be obtained by taking the convolution of Eq. (21) with a suitable twist-disorder distribution function (Veneri et al., 2022). For twist angles $\theta \neq \theta_c$, $c_2\pi/6$, both in-plane components of the spin susceptibility tensor will be nonvanishing, thus yielding a nontrivial polarization (S_x, $S_y \neq 0$). At the critical twist angle, the Rashba phase must vanish ($\alpha_R(\theta_c) = 0$), and hence a *collinear Edelstein effect* (CEE) can be achieved, whereby the resulting spin polarization will be purely (anti-)parallel to the applied electrical current (c.f. Fig. 8c). What makes these twisted graphene-TMD vdW heterostructures appealing is the ease with which the SOC and spin texture can be manipulated; only a simple twist is needed to adjust them. This sets these systems apart from 2DEGs, where both Rashba-type and Dresselhaus-type SOC are required (Trushin and Schliemann, 2007). Control of these SOCs in 2DEGs is achieved via asymmetric doping and the tuning of quantum well widths (Ganichev and Golub, 2014), a set of processes far more complicated and involved than simple twisting. For further details, the reader is referred to Veneri et al. (2022) where the CEE phenomenon was predicted.

Observing spin–charge interconversion

To make use of graphene's large l_s while also studying the effects of proximity-induced SOC, spin-valve setups are typically used to measure the ISHE and SGE (the inverse SHE and spin galvanic effect, respectively). In this case, rather than trying to measure a spin current using an FM contact, an electrical current is measured instead by converting an injected spin current into an electrical current (Valenzuela, 2009). A schematic of a spin-valve experiment is shown in Fig. 9.

Spin valves operate by using a single FM contact to inject a spin current into graphene. This spin current is then able to flow along the isolated graphene channel until it reaches a T-junction, where it enters a region of high SOC. This region is no longer characterized by just monolayer graphene; instead, it now contains graphene layered on top of a TMD. As a result, the spin current entering this region undergoes the ISHE (due to any out-of-plane spin components) and generates an electrical current perpendicular to the injected spin current. Likewise, the electrons entering the high SOC region naturally also have a component of in-plane spin polarization and so are subject to the SGE, which also generates a perpendicular electrical current. Specifically, the component of the electron's spin parallel to the spin current generates an electrical current via the SGE while the component of spin in-plane and perpendicular to the spin current yields an electrical current via the collinear SGE (if the material permits this process). The ensuing nonlocal resistance measured across the T-junction is therefore characterized by the spin–charge interconversion effects at the heart of modern spintronics.

In order to distinguish between the different electrical signals arising from the ISHE, SGE, and collinear SGE, a combination of magnetic fields must be used in conjunction with various FM orientations. The effect of applying a magnetic field to this setup is to cause spin precession about the applied field. The strength of the measured resistance in the T-junction will then depend on the magnetic field strength (how quickly the spins precess), and the length of the graphene channel (how long the spins have to precess). By combining the spin-valve measurements for various magnetic fields and FM orientations, the electrical signals associated to each of the aforementioned proximity-induced ISHE, and SGE can be isolated by means of a simple symmetry analysis (Cavill et al., 2020). A set of recent spin-valve experiments have revealed graphene-TMD heterostructures to yield room-temperature nonlocal resistances of order 1–10 mΩ due to the ISHE and SGE (Safeer et al., 2019a; Ghiasi et al., 2019; Benítez et al., 2020). Alternatively, the Onsager-reciprocal phenomena, namely, the SHE and ISGE, can be discerned by measuring the spin accumulation in the direction of the spin current at opposite sides of the high SOC region, as was done in the experiment of Camosi et al. (2022). The latter approach requires a complex multiterminal architecture but has the advantage that it permits isolation of the SHE and ISGE in situations for which the TMD is conducting and thus directly influences the spin–charge conversion processes (due to its high intrinsic SOC).

Additionally, spin-valve measurements allow us to distinguish between conventional and anisotropic spin-charge conversion processes. An anisotropic SGE has been recently observed in graphene proximity-coupled to semimetallic (low-symmetry) TMDs (Safeer et al., 2019b). Likewise, an anisotropic ISGE characterized by the presence of spin polarization components parallel and orthogonal to the driving current has been reported experimentally in Camosi et al. (2022). However, an experimental demonstration exploiting twist-angle control in a graphene-semiconducting TMD heterostructures as described by Eq. (21) has yet to be achieved.

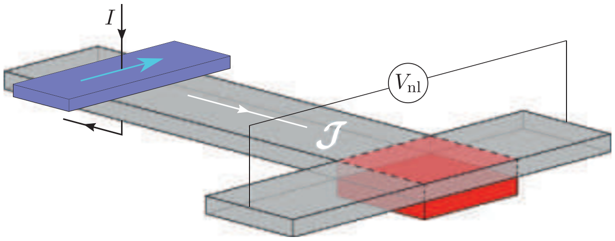

Fig. 9 Graphene-based spin valve setup. An electrical current, *I*, passed through a ferromagnetic contact (blue box) injects a spin current into a graphene sheet. This spin current then travels along a graphene channel and into a region of enhanced SOC (dashed red region), due to proximity with a TMD (red box). This generates a charge accumulation in the arms of the T-junction due to the ISHE and SGE, which yields a nonlocal voltage in the steady state, V_{nl}, across the bar under the open circuit conditions.

While spin-valve setups are ideally suited for studies of spin dynamics and spin–charge interconversion processes, they do not allow one to discern the size of the SOC present in a graphene-on-TMD heterostructure. To do this, measurement of the Shubnikov–de Haas (SdH) oscillations must be made. The reconstruction of the low-energy electronic structure from SdH data allows for the determination of the average SOC, $\overline{\lambda} = \sqrt{\lambda_{\mathrm{BR}}^2 + \lambda_{\mathrm{sv}}^2}$ (Tiwari et al., 2022). Experiments have revealed that the typical SOC present in these materials is $\overline{\lambda} \simeq 2.51$ meV. This average value is in accord to the predictions of microscopic theories for vdW heterostructures (Milletarì et al., 2017; Offidani et al., 2017) regarding the observation of significant spin–charge interconversion efficiencies at room temperature, and is indeed compatible with the spin-valve measurements (Safeer et al., 2019a; Ghiasi et al., 2019; Benítez et al., 2020; Camosi et al., 2022; Li et al., 2020; Hoque et al., 2021), thus demonstrating that proximity-induced SOC is responsible for the observed nonlocal resistances.

Conclusion

This article has presented the role of graphene in modern spintronic devices, with a specific emphasis on how its partnership with other 2D materials can allow for bespoke systems with desirable electronic and spin transport properties. By constructing a low-energy theory of graphene, it becomes clear that transport phenomena in graphene-based systems will be dominated by the behavior of electrons around the Dirac points. From a physical point of view, one of the most striking features of isolated graphene is the description of its electrons as massless chiral Dirac fermions. Furthermore, the decoherence of spins in graphene occurs over large distances, allowing for long-range spin transport, a direct result of the extremely weak intrinsic SOC (Kane–Mele) appearing naturally in graphene. However, despite its ability to host long-range spin diffusion, graphene does not have a natural mechanism allowing for distinct spin control. This can ideally be achieved by pairing it with other materials that enhance its SOC.

In particular, the use of TMDs proximity-coupled to graphene gives rise to significant SOCs, of the order of meV, which allows meaningful spin currents and nonequilibrium spin polarizations, via the SHE and ISGE, respectively, to manifest in the graphene layer. Consequently, electronic control of spin transport can be easily achieved and hence amalgamates well with current technological architectures. One major focus of spintronics is the implementation of the SHE and ISGE to generate large spin accumulations and polarizations that can be used to change the magnetization of a ferromagnet. In this case, the magnetization experiences a torque due to the SOC-related phenomena and so is referred to as a *spin-orbit torque* (SOT). The use of SOTs in technology could allow for the realization of SOT-based magnetic random access memory (SOT-MRAM), removing our reliance upon volatile memory and thus reducing energy consumption. This route away from traditional RAM appears to bear much promise and remains as a current area of interest in research with many facets and subtleties still requiring further study.

As a final note, while not covered in this article, interface-induced magnetic exchange interaction is also becoming increasingly important in the field (e.g., as means to allow the manifestation of quantum anomalous Hall phases and spin-dependent Seebeck effect in graphene (Offidani and Ferreira, 2018; Ghiasi et al., 2021)), and the reader is referred to the literature for further details. The same goes for high-temperature topologically nontrivial phases of matter—exhibiting technologically relevant phenomena like the quantum spin Hall effect (Wu et al., 2018)—and the discovery of 2D vdW magnets (Lee et al., 2016; Gong et al., 2017; Huang et al., 2017), which are likely to open up interesting avenues across many emergent fields, including topological quantum computation, spin-orbitronics, magnonics, and antiferromagnetic spintronics (Freedman et al., 2003; Dolui et al., 2020; Xing et al., 2019; Xiao and Tong, 2022).

Acknowledgments

The authors acknowledge support from the Royal Society through Grants No. URF/R/191021 (A.F.) and No. RF/ERE/210281 (A.F. and D.T.S.P.). We are indebted to Yue Wang and Robert A. Smith for helpful comments on the manuscript.

References

Amann J, Völkl T, Rockinger T, Kochan D, Watanabe K, Taniguchi T, Fabian J, Weiss D, and Eroms J (2022) Counterintuitive gate dependence of weak antilocalization in bilayer graphene/WSe$_2$ heterostructures. *Physical Review B* 105(11): 115425. https://doi.org/10.1103/PhysRevB.105.115425.

Aronov AG and Lyanda-Geller YB (1989) Nuclear electric resonance and orientation of carrier spins by an electric field. *Pis'ma v Zhurnal Eksperimental'noi i Teoreticheskoi Fiziki* 50(9): 398–400 [JETP Letters 50: 431–434 (1989)].

Aronov AG, Lyanda-Geller YB, and Pikus GE (1991) Spin polarization of electrons by an electric current. *Zhurnal Eksperimental'noi i Teoreticheskoi Fiziki* 100(3): 973–981 [Soviet Physics–JETP 73: 537–541 (1991)].

Baibich MN, Broto JM, Fert A, Van Dau FN, Petroff F, Etienne P, Creuzet G, Friederich A, and Chazelas J (1988) Giant magnetoresistance of (001)Fe/(001)Cr magnetic superlattices. *Physical Review Letters* 61(21): 2472–2475. https://doi.org/10.1103/PhysRevLett.61.2472.

Balakrishnan J, Koon GKW, Avsar A, Ho Y, Lee JH, Jaiswal M, Baeck S-J, Ahn J-H, Ferreira A, Cazalilla MA, Castro Neto AH, and Özyilmaz B (2014) Giant spin Hall effect in graphene grown by chemical vapour deposition. *Nature Communications* 5(1): 4748. https://doi.org/10.1038/ncomms5748.

Benítez LA, Torres WS, Sierra JF, Timmermans M, Garcia JH, Roche S, Costache MV, and Valenzuela SO (2020) Tunable room-temperature spin galvanic and spin Hall effects in van der Waals heterostructures. *Nature Materials* 19(2): 170–175. https://doi.org/10.1038/s41563-019-0575-1.

Bergman G (1982) Influence of spin-orbit coupling on weak localization. *Physical Review Letters* 48(15): 1046–1049. https://doi.org/10.1103/PhysRevLett.48.1046.

Binasch G, Grünberg P, Saurenbach F, and Zinn W (1989) Enhanced magnetoresistance in layered magnetic structures with antiferromagnetic interlayer exchange. *Physical Review B* 39(7): 4828–4830. https://doi.org/10.1103/PhysRevB.39.4828.

Bychkov YA and Rashba EI (1984) Properties of a 2D electron gas with lifted spectral degeneracy. *Pis'ma v Zhurnal Eksperimental'noi i Teoreticheskoi Fiziki* 39(2): 66–69 [JETP Letters 39: 78–81 (1984)].

Camosi L, Josef Světlík J, Costache MV, Torres WS, Aguirre IF, Marinova V, Dimitrov D, Gospodinov M, Sierra JF, and Valenzuela SO (2022) Resolving spin currents and spin densities generated by charge-spin interconversion in systems with reduced crystal symmetry. *2D Materials* 9(3): 035014. https://doi.org/10.1088/2053-1583/ac6fec.

Cao Y, Fatemi V, Fang S, Watanabe K, Taniguchi T, Kaxiras E, and Jarillo-Herrero P (2018) Unconventional superconductivity in magic-angle graphene superlattices. *Nature* 556 (7699): 43–50. https://doi.org/10.1038/nature26160.

Castro EV, Novoselov KS, Morozov SV, Peres NMR, Lopes dos Santos JMB, Nilsson J, Guinea F, Geim AK, and Castro Neto AH (2007) Biased bilayer graphene: Semiconductor with a gap tunable by the electric field effect. *Physical Review Letters* 99(21): 216802. https://doi.org/10.1103/PhysRevLett.99.216802.

Castro Neto AH, Guinea F, Peres NMR, Novoselov KS, and Geim AK (2009) The electronic properties of graphene. *Reviews of Modern Physics* 81(1): 109–162. https://doi.org/10.1103/RevModPhys.81.109.

Cavill SA, Huang C, Offidani M, Lin Y-H, Cazalilla MA, and Ferreira A (2020) Proposal for unambiguous electrical detection of spin-charge conversion in lateral spin valves. *Physical Review Letters* 124(23): 236803. https://doi.org/10.1103/PhysRevLett.124.236803.

Crépieux A and Bruno P (2001) Theory of the anomalous Hall effect from the kubo formula and the Dirac equation. *Physical Review B* 64(1): 014416. https://doi.org/10.1103/PhysRevB.64.014416.

David A, Rakyta P, Kormányos A, and Burkard G (2019) Induced spin-orbit coupling in twisted graphene-transition metal dichalcogenide heterobilayers: Twistronics meets spintronics. *Physical Review B* 100(8): 085412. https://doi.org/10.1103/PhysRevB.100.085412.

Dean CR, Young AF, Meric I, Lee C, Wang L, Sorgenfrei S, Watanabe K, Taniguchi T, Kim P, Shepard KL, and Hone J (2010) Boron nitride substrates for high-quality graphene electronics. *Nature Nanotechnology* 5(10): 722–726. https://doi.org/10.1038/nnano.2010.172.

Dolui K, Petrović MD, Zollner K, Plecháč P, Fabian J, and Nikolić BK (2020) Proximity spin-orbit torque on a two-dimensional magnet within van der Waals heterostructure: Current-driven antiferromagnet-to-ferromagnet reversible nonequilibrium phase transition in bilayer CrI_3. *Nano Letters* 20(4): 2288–2295. https://doi.org/10.1021/acs.nanolett.9b04556.

Drögeler M, Volmer F, Wolter M, Terrés B, Watanabe K, Taniguchi T, Güntherodt G, Stampfer C, and Beschoten B (2014) Nanosecond spin lifetimes in single- and few-layer graphene-hBN heterostructures at room temperature. *Nano Letters* 14(11): 6050–6055. https://doi.org/10.1021/nl501278c.

Dubois S, Piraux L, George JM, Ounadjela K, Duvail JL, and Fert A (1999) Evidence for a short spin diffusion length in permalloy from the giant magnetoresistance of multilayered nanowires. *Physical Review B* 60(1): 477–484. https://doi.org/10.1103/PhysRevB.60.477.

Dyakonov MI and Perel VI (1971a) Possibility of orienting electrons spins with current. *ZhETF Pis. Red.* 13(11): 657–660 [Soviet Physics Journal of Experimental and Theoretical Physics Letters 13: 467–469 (1971)].

Dyakonov MI and Perel VI (1971b) Current-induced spin orientation of electrons in semiconductors. *Physics Letters A* 35(6): 459–460. https://doi.org/10.1016/0375-9601(71)90196-4.

Eda G, Fujita T, Yamaguchi H, Voiry D, Chen M, and Chhowalla M (2012) Coherent atomic and electronic heterostructures of single-layer MoS_2. *ACS Nano* 6(8): 7311–7317. https://doi.org/10.1021/nn302422x.

Edelstein VM (1990) Spin polarization of conduction electrons induced by electric current in two-dimensional asymmetric electron systems. *Solid State Communications* 73(3): 233–235. https://doi.org/10.1016/0038-1098(90)90963-C.

Fang S, Kuate Defo R, Shirodkar SN, Lieu S, Tritsaris GA, and Kaxiras E (2015) Ab initio tight-binding hamiltonian for transition metal dichalcogenides. *Physical Review B* 92(20): 205108. https://doi.org/10.1103/PhysRevB.92.205108.

Ferreira A, Rappoport TG, Cazalilla MA, and Castro Neto AH (2014) Extrinsic spin Hall effect induced by resonant skew scattering in graphene. *Physical Review Letters* 112(6): 066601. https://doi.org/10.1103/PhysRevLett.112.066601.

Freedman MH, Kitaev A, Larsen MJ, and Wang Z (2003) Topological quantum computation. *Bulletin of the American Mathematical Society* 40: 31–38. https://doi.org/10.1090/S0273-0979-02-00964-3.

Fulop B, Marffy A, Zihlmann S, Gmitra M, Tovari E, Szentpeteri B, Kedves M, Watanabe K, Taniguchi T, Fabian J, Schonenberger C, Makk P, and Csonka S (2021) Boosting proximity spin-orbit coupling in graphene-WSe2 heterostructures via hydrostatic pressure. *npj 2D Materials and Applications* 5: 82. https://doi.org/10.1038/s41699-021-00262-9.

Ganichev SD and Golub LE (2014) Interplay of Rashba/Dresselhaus spin splittings probed by photogalvanic spectroscopy—A review. *Physica Status Solidi B* 251(9): 1801–1823. https://doi.org/10.1002/pssb.201350261.

Ganichev SD, Ivchenko EL, Bel'kov VV, Tarasenko SA, Sollinger M, Weiss D, Wegscheider W, and Prettl W (2002) Spin-galvanic effect. *Nature* 417(6885): 153–156. https://doi.org/10.1038/417153a.

Geim AK and Grigorieva IV (2013) Van der Waals heterostructures. *Nature* 499(7459): 419–425. https://doi.org/10.1038/nature12385.

Ghiasi TS, Kaverzin AA, Blah PJ, and van Wees BJ (2019) Charge-to-spin conversion by the Rashba-Edelstein effect in two-dimensional van der Waals heterostructures up to room temperature. *Nano Letters* 19(9): 5959–5966. https://doi.org/10.1021/acs.nanolett.9b01611.

Ghiasi TS, Kaverzin AA, Dismukes AH, de Wal DK, Roy X, and van Wees BJ (2021) Electrical and thermal generation of spin currents by magnetic bilayer graphene. *Nature Nanotechnology* 16(7): 788–794. https://doi.org/10.1038/s41565-021-00887-3.

Gmitra M, Kochan D, Högl P, and Fabian J (2016) Trivial and inverted Dirac bands and the emergence of quantum spin Hall states in graphene on transition-metal dichalcogenides. *Physical Review B* 93(15): 155104. https://doi.org/10.1103/PhysRevB.93.155104.

Gong C, Li L, Li Z, Ji H, Stern A, Xia Y, Cao T, Bao W, Wang C, Wang Y, Qiu ZQ, Cava RJ, Louie SG, Xia J, and Zhang X (2017) Discovery of intrinsic ferromagnetism in two-dimensional van der Waals crystals. *Nature* 546(7657): 265–269. https://doi.org/10.1038/nature22060.

Guinea F, Castro Neto AH, and Peres NMR (2006) Electronic states and Landau levels in graphene stacks. *Physical Review B* 73(24): 245426. https://doi.org/10.1103/PhysRevB.73.245426.

Hoque AM, Khokhriakov D, Zollner K, Zhao B, Karpiak B, Fabian J, and Dash SP (2021) All-electrical creation and control of spin-galvanic signal in graphene and molybdenum ditelluride heterostructures at room temperature. *Communications on Physics* 4(1): 124. https://doi.org/10.1038/s42005-021-00611-6.

Huang B, Clark G, Navarro-Moratalla E, Klein DR, Cheng R, Seyler KL, Zhong D, Schmidgall E, McGuire MA, Cobden DH, Yao W, Xiao D, Jarillo-Herrero P, and Xu X (2017) Layer-dependent ferromagnetism in a van der Waals crystal down to the monolayer limit. *Nature* 546(7657): 270–273. https://doi.org/10.1038/nature22391.

Jedema FJ, Filip AT, and van Wees BJ (2001) Electrical spin injection and accumulation at room temperature in an all-metal mesoscopic spin valve. *Nature* 410(6826): 345–348. https://doi.org/10.1038/35066533.

Johnson M and Silsbee RH (1985) Interfacial charge-spin coupling: Injection and detection of spin magnetization in metals. *Physical Review Letters* 55(17): 1790–1793. https://doi.org/10.1103/PhysRevLett.55.1790.

Jung J, DaSilva AM, MacDonald AH, and Adam S (2015) Origin of band gaps in graphene on hexagonal boron nitride. *Nature Communications* 6(1): 6308. https://doi.org/10.1038/ncomms7308.

Kato YK, Myers RC, Gossard AC, and Awschalom DD (2004) Observation of the spin Hall effect in semiconductors. *Science* 306(5703): 1910–1913. https://doi.org/10.1126/science.1105514.

Kikkawa JM and Awschalom DD (1999) Lateral drag of spin coherence in gallium arsenide. *Nature* 397(6715): 139–141. https://doi.org/10.1038/16420.

Kochan D, Irmer S, and Fabian J (2017) Model spin-orbit coupling Hamiltonians for graphene systems. *Physical Review B* 95(16): 165415. https://doi.org/10.1103/PhysRevB.95.165415.

Lee J-U, Lee S, Ryoo JH, Kang S, Kim TY, Kim P, Park C-H, Park J-G, and Cheong H (2016) Ising-type magnetic ordering in atomically thin $FePS_3$. *Nano Letters* 16(12): 7433–7438. https://doi.org/10.1021/acs.nanolett.6b03052.

Li Y and Koshino M (2019) Twist-angle dependence of the proximity spin-orbit coupling in graphene on transition-metal dichalcogenides. *Physical Review B* 99(7): 075438. https://doi.org/10.1103/PhysRevB.99.075438.

Li L, Zhang J, Myeong G, Shin W, Lim H, Kim B, Kim S, Jin T, Cavill S, Kim BS, Kim C, Lischner J, Ferreira A, and Cho S (2020) Gate-tunable reversible Rashba-Edelstein effect in a few-layer graphene/2H-TaS2 heterostructure at room temperature. *ACS Nano* 14(5): 5251–5259. https://doi.org/10.1021/acsnano.0c01037.

Liu Z, Suenaga K, Harris PJF, and Iijima S (2009) Open and closed edges of graphene layers. *Physical Review Letters* 102(1): 015501. https://doi.org/10.1103/PhysRevLett.102.015501.

Lopes dos Santos JMB, Peres NMR, and Castro Neto AH (2007) Graphene bilayer with a twist: Electronic structure. *Physical Review Letters* 99(25): 256802. https://doi.org/10.1103/PhysRevLett.99.256802.

Mak KF and Shan J (2016) Photonics and optoelectronics of 2D semiconductor transition metal dichalcogenides. *Nature Photonics* 10(4): 216–226. https://doi.org/10.1038/nphoton.2015.282.

Mak KF, McGill KL, Park J, and McEuen PL (2014) The valley Hall effect in MoS_2 transistors. *Science* 344(6191): 1489–1492. https://doi.org/10.1126/science.1250140.

Malajovich I, Kikkawa JM, Awschalom DD, Berry JJ, and Samarth N (2000) Coherent transfer of spin through a semiconductor heterointerface. *Physical Review Letters* 84(5): 1015–1018. https://doi.org/10.1103/PhysRevLett.84.1015.

Mattheiss LF (1973) Band structures of transition-metal-dichalcogenide layer compounds. *Physical Review B* 8(8): 3719–3740. https://doi.org/10.1103/PhysRevB.8.3719.

McCann E (2006) Asymmetry gap in the electronic band structure of bilayer graphene. *Physical Review B* 74(16): 161403. https://doi.org/10.1103/PhysRevB.74.161403.

McCann E and Fal'ko VI (2006) Landau-level degeneracy and quantum Hall effect in a graphite bilayer. *Physical Review Letters* 96(8): 086805. https://doi.org/10.1103/PhysRevLett.96.086805.

McCann E and Koshino M (2013) The electronic properties of bilayer graphene. *Reports on Progress in Physics* 76(5): 056503. https://doi.org/10.1088/0034-4885/76/5/056503.

Milletarì M and Ferreira A (2016) Quantum diagrammatic theory of the extrinsic spin Hall effect in graphene. *Physical Review B* 94(13): 134202. https://doi.org/10.1103/PhysRevB.94.134202.

Milletarì M, Offidani M, Ferreira A, and Raimondi R (2017) Covariant conservation laws and the spin Hall effect in Dirac-Rashba systems. *Physical Review Letters* 119(24): 246801. https://doi.org/10.1103/PhysRevLett.119.246801.

Naimer T, Zollner K, Gmitra M, and Fabian J (2021) Twist-angle dependent proximity induced spin-orbit coupling in graphene/transition metal dichalcogenide heterostructures. *Physical Review B* 104(19): 195156. https://doi.org/10.1103/PhysRevB.104.195156.

Nakamura H, Mohammed A, Rosenzweig P, Matsuda K, Nowakowski K, Küster K, Wochner P, Ibrahimkutty S, Wedig U, Hussain H, Rawle J, Nicklin C, Stuhlhofer B, Cristiani G, Logvenov G, Takagi H, and Starke U (2020) Spin splitting and strain in epitaxial monolayer WSe_2 on graphene. *Physical Review B* 101(16): 165103. https://doi.org/10.1103/PhysRevB.101.165103.

Nandkishore R and Levitov L (2010) Dynamical screening and excitonic instability in bilayer graphene. *Physical Review Letters* 104(15): 156803. https://doi.org/10.1103/PhysRevLett.104.156803.

Offidani M and Ferreira A (2018) Anomalous Hall effect in 2D Dirac materials. *Physical Review Letters* 121(12): 126802. https://doi.org/10.1103/PhysRevLett.121.126802.

Offidani M, Milletarì M, Raimondi R, and Ferreira A (2017) Optimal charge-to-spin conversion in graphene on transition-metal dichalcogenides. *Physical Review Letters* 119(19): 196801. https://doi.org/10.1103/PhysRevLett.119.196801.

Ohno Y, Young DK, Beschoten B, Matsukura F, Ohno H, and Awschalom DD (1999) Electrical spin injection in a ferromagnetic semiconductor heterostructure. *Nature* 402(6763): 790–792. https://doi.org/10.1038/45509.

Peres NMR (2010) Colloquium: The transport properties of graphene: An introduction. *Reviews of Modern Physics* 82(3): 2673–2700. https://doi.org/10.1103/RevModPhys.82.2673.

Péterfalvi CG, David A, Rakyta P, Burkard G, and Kormányos A (2022) Quantum interference tuning of spin-orbit coupling in twisted van der Waals trilayers. *Physical Review Research* 4 (2): L022049. https://doi.org/10.1103/PhysRevResearch.4.L022049.

Pierucci D, Henck H, Avila J, Balan A, Naylor CH, Patriarche G, Dappe YJ, Silly MG, Sirotti F, Johnson ATC, Asensio MC, and Ouerghi A (2016) Band alignment and minigaps in monolayer MoS_2-graphene van der Waals heterostructures. *Nano Letters* 16(7): 4054–4061. https://doi.org/10.1021/acs.nanolett.6b00609.

Qian X, Liu J, Fu L, and Li J (2014) Quantum spin Hall effect in two-dimensional transition metal dichalcogenides. *Science* 346(6215): 1344–1347. https://doi.org/10.1126/science.1256815.

Rashba EI (2009) Graphene with structure-induced spin-orbit coupling: Spin-polarized states, spin zero modes, and quantum Hall effect. *Physical Review B* 79(16): 161409(R). https://doi.org/10.1103/PhysRevB.79.161409.

Román RJP, Costa Costa FJR, Zobelli A, Elias C, Valvin P, Cassabois G, Gil B, Summerfield A, Cheng TS, Mellor CJ, Beton PH, Novikov SV, and Zagonel LF (2021) Band gap measurements of monolayer h-BN and insights into carbon-related point defects. *2D Materials* 8(4): 044001. https://doi.org/10.1088/2053-1583/ac0d9c.

Safeer CK, Ingla-Aynés J, Herling F, Garcia JH, Vila M, Ontoso N, Calvo MR, Roche S, Hueso LE, and Casanova F (2019a) Room-temperature spin Hall effect in graphene/MoS_2 van der Waals heterostructures. *Nano Letters* 19(2): 1074–1082. https://doi.org/10.1021/acs.nanolett.8b04368.

Safeer CK, Ontoso N, Ingla-Aynés J, Herling F, Pham VT, Kurzmann A, Ensslin K, Chuvilin A, Robredo I, Vergniory MG, de Juan F, Hueso LE, Calvo MR, and Casanova F (2019b) Large multidirectional spin-to-charge conversion in low-symmetry semimetal $MoTe_2$ at room temperature. *Nano Letters* 19(12): 8758–8766. https://doi.org/10.1021/acs.nanolett.9b03485.

Saito R, Tatsumi Y, Huang S, Ling X, and Dresselhaus MS (2016) Raman spectroscopy of transition metal dichalcogenides. *Journal of Physics: Condensed Matter* 28(35): 353002. https://doi.org/10.1088/0953-8984/28/35/353002.

Schwab P, Raimondi R, and Gorini C (2011) Spin-charge locking and tunneling into a helical metal. *Europhysics Letters* 93(6): 67004. https://doi.org/10.1209/0295-5075/93/67004.

Sharvin DY and Sharvin YV (1981) Magnetic-flux quantization in a cylindrical film of a normal metal. *Pis'ma v Zhurnal Eksperimental'noi i Teoreticheskoi Fiziki* 34(5): 285–288 [JETP Letters 34: 272–275 (1981)].

Shi Y, Kahn J, Niu B, Fei Z, Sun B, Cai X, Francisco BA, Wu D, Shen Z-X, Xu X, Cobden DH, and Cui Y-T (2019) Imaging quantum spin Hall edges in monolayer WTe_2. *Science Advances* 5(2): eaat8799. https://doi.org/10.1126/sciadv.aat8799.

Sichau J, Prada M, Anlauf T, Lyon TJ, Bosnjak B, Tiemann L, and Blick RH (2019) Resonance microwave measurements of an intrinsic spin-orbit coupling gap in graphene: A possible indication of a topological state. *Physical Review Letters* 122(4): 046403. https://doi.org/10.1103/PhysRevLett.122.046403.

Sinova J, Valenzuela SO, Wunderlich J, Back CH, and Jungwirth T (2015) Spin Hall effects. *Reviews of Modern Physics* 87(4): 1213–1260. https://doi.org/10.1103/RevModPhys.87.1213.

Sousa F, Perkins DTS, and Ferreira A (2022) Weak localisation driven by pseudospin-spin entanglement. *Communications on Physics* 5(1): 291. https://doi.org/10.1038/s42005-022-01066-z.

Steenwyk SD, Hsu SY, Loloee R, Bass J, and Pratt WP (1997) Perpendicular-current exchange-biased spin-valve evidence for a short spin-diffusion length in permalloy. *Journal of Magnetism and Magnetic Materials* 170(1): L1–L6. https://doi.org/10.1016/S0304-8853(97)00061-9.

Streda P (1982) Theory of quantised Hall conductivity in two dimensions. *Journal of Physics C: Solid State Physics* 15(22): L717–L721. https://doi.org/10.1088/0022-3719/15/22/005.

Tang S, Zhang C, Wong D, Pedramrazi Z, Tsai H-Z, Jia C, Moritz B, Claassen M, Ryu H, Kahn S, Jiang J, Yan H, Hashimoto M, Lu D, Moore RG, Hwang C-C, Hwang C, Hussain Z, Chen Y, Ugeda MM, Liu Z, Xie X, Devereaux TP, Crommie MF, Mo S-K, and Shen Z-X (2017) Quantum spin Hall state in monolayer 1T'-WTe_2. *Nature Physics* 13: 683–687. https://doi.org/10.1038/nphys4174.

Tedrow PM and Meservey R (1973) Spin polarization of electrons tunneling from films of Fe, Co, Ni, and Gd. *Physical Review B* 7: 318–326. https://doi.org/10.1103/PhysRevB.7.318.

Tiwari P, Jat MK, Udupa A, Narang DS, Watanabe K, Taniguchi T, Sen D, and Bid A (2022) Experimental observation of spin-split energy dispersion in high-mobility single-layer graphene/WSe_2 heterostructures. *npj 2D Materials and Applications* 6: 68. https://doi.org/10.1038/s41699-022-00348-y.

Trushin M and Schliemann J (2007) Anisotropic current-induced spin accumulation in the two-dimensional electron gas with spin-orbit coupling. *Physical Review B* 75: 155323. https://doi.org/10.1103/PhysRevB.75.155323.

Uri A, Grover S, Cao Y, Crosse JA, Bagani K, Rodan-Legrain D, Myasoedov Y, Watanabe K, Taniguchi T, Moon P, Koshino M, Jarillo-Herrero P, and Zeldov E (2020) Mapping the twist-angle disorder and Landau levels in magic-angle graphene. *Nature* 581(7806): 47–52. https://doi.org/10.1038/s41586-020-2255-3.

Vafek O and Yang K (2010) Many-body instability of coulomb interacting bilayer graphene: Renormalization group approach. *Physical Review B* 81: 041401. https://doi.org/10.1103/PhysRevB.81.041401.

Valenzuela SO (2009) Nonlocal electronic spin detection, spin accumulation and the spin Hall effect. *International Journal of Modern Physics B* 23(11): 2413–2438. https://doi.org/10.1142/S021797920905290X.

Veneri A, Perkins DTS, Péterfalvi CG, and Ferreira A (2022) Twist angle controlled collinear Edelstein effect in van der Waals heterostructures. *Physical Review B* 106: L081406. https://doi.org/10.1103/PhysRevB.106.L081406.

Voiry D, Mohite A, and Chhowalla M (2015) Phase engineering of transition metal dichalcogenides. *Chemical Society Reviews* 44: 2702–2712. https://doi.org/10.1039/C5CS00151J.

Völkl T, Rockinger T, Drienovsky M, Watanabe K, Taniguchi T, Weiss D, and Eroms J (2017) Magnetotransport in heterostructures of transition metal dichalcogenides and graphene. *Physical Review B* 96: 125405. https://doi.org/10.1103/PhysRevB.96.125405.

Wakamura T, Reale F, Palczynski P, Guéron S, Mattevi C, and Bouchiat H (2018) Strong anisotropic spin-orbit interaction induced in graphene by monolayer WS_2. *Physical Review Letters* 120: 106802. https://doi.org/10.1103/PhysRevLett.120.106802.

Wallbank JR, Mucha-Kruczyński M, Chen X, and Fal'ko VI (2015) Moiré superlattice effects in graphene/boron-nitride van der Waals heterostructures. *Annalen der Physik* 527(5-6): 359–376. https://doi.org/10.1002/andp.201400204.

Wang QH, Kalantar-Zadeh K, Kis A, Coleman JN, and Strano MS (2012) Electronics and optoelectronics of two-dimensional transition metal dichalcogenides. *Nature Nanotechnology* 7: 699–712. https://doi.org/10.1038/nnano.2012.193.

Wang Z, Ki D-K, Khoo JY, Mauro D, Berger H, Levitov LS, and Morpurgo AF (2016) Origin and magnitude of 'designer' spin-orbit interaction in graphene on semiconducting transition metal dichalcogenides. *Physical Review X* 6: 041020. https://doi.org/10.1103/PhysRevX.6.041020.

Wang D, Che S, Cao G, Lyu R, Wantanabe K, Taniguchi T, Lau CN, and Bockrath M (2019) Quantum Hall effect measurement of spin–orbit coupling strengths in ultraclean bilayer graphene/WSe_2 heterostructures. *Nano Letters* 19(10): 7028–7034. https://doi.org/10.1021/acs.nanolett.9b02445.

Wang G, Chernikov A, Glazov MM, Heinz TF, Marie X, Amand T, and Urbaszek B (2018) Colloquium: Excitons in atomically thin transition metal dichalcogenides. *Reviews of Modern Physics* 90: 021001. https://doi.org/10.1103/RevModPhys.90.021001.

Weitz RT, Allen MT, Feldman BE, Martin J, and Yacoby A (2010) Broken-symmetry states in doubly gated suspended bilayer graphene. *Science* 330(6005): 812–816. https://doi.org/10.1126/science.1194988.

Wu S, Fatemi V, Gibson QD, Watanabe K, Taniguchi T, Cava RJ, and Jarillo-Herrero P (2018) Observation of the quantum spin Hall effect up to 100 kelvin in a monolayer crystal. *Science* 359(6371): 76–79. https://doi.org/10.1126/science.aan6003.

Xiao F and Tong Q (2022) Tunable strong magnetic anisotropy in two-dimensional van der Waals antiferromagnets. *Nano Letters* 22(10): 3946–3952. https://doi.org/10.1021/acs.nanolett.2c00401.

Xiao D, Liu G-B, Feng W, Xu X, and Yao W (2012) Coupled spin and valley physics in monolayers of MoS_2 and other group-VI dichalcogenides. *Physical Review Letters* 108: 196802. https://doi.org/10.1103/PhysRevLett.108.196802.

Xing W, Qiu L, Wang X, Yao Y, Ma Y, Cai R, Jia S, Xie XC, and Han W (2019) Magnon transport in quasi-two-dimensional van der Waals antiferromagnets. *Physical Review X* 9: 011026. https://doi.org/10.1103/PhysRevX.9.011026.

Yang Q, Holody P, Lee S-F, Henry LL, Loloee R, Schroeder PA, Pratt WP, and Bass J (1994) Spin flip diffusion length and giant magnetoresistance at low temperatures. *Physical Review Letters* 72: 3274–3277. https://doi.org/10.1103/PhysRevLett.72.3274.

Yang B, Lohmann M, Barroso D, Liao I, Lin Z, Liu Y, Bartels L, Watanabe K, Taniguchi T, and Shi J (2017) Strong electron-hole symmetric Rashba spin-orbit coupling in graphene/monolayer transition metal dichalcogenide heterostructures. *Physical Review B* 96: 041409. https://doi.org/10.1103/PhysRevB.96.041409.

Yun WS, Han SW, Hong SC, Kim IG, and Lee JD (2012) Thickness and strain effects on electronic structures of transition metal dichalcogenides: 2H-mX_2 semiconductors ($M = $ Mo, W; $X = $ S, Se, Te). *Physical Review B* 85: 033305. https://doi.org/10.1103/PhysRevB.85.033305.

Zhang F, Min H, Polini M, and MacDonald AH (2010) Spontaneous inversion symmetry breaking in graphene bilayers. *Physical Review B* 81: 041402. https://doi.org/10.1103/PhysRevB.81.041402.

Zollner K, Gmitra M, and Fabian J (2020) Swapping exchange and spin-orbit coupling in 2D van der Waals heterostructures. *Physical Review Letters* 125: 196402. https://doi.org/10.1103/PhysRevLett.125.196402.

Optical orientation of spins in semiconductors

Mikhail I Dyakonov, Laboratoire Charles Coulomb, Université Montpellier, Montpellier, France; Ioffe Physical-Technical Institute, Saint Petersburg, Russia

© 2024 Elsevier Ltd. All rights reserved.

Introduction: Historical background **224**
Overview of the subject **224**
Band structure of gallium arsenide **225**
Spin interactions **225**
The Pauli principle 225
Exchange interaction 226
Spin-orbit interaction 226
Hyperfine interaction with nuclear spins 226
Magnetic interaction 227
Photo-generation of carriers and luminescence **227**
Angular momentum conservation in optical transitions 227
Optical spin orientation and detection **227**
Spin relaxation **228**
Generalities 228
$\omega\tau_c \ll 1$ (most frequent case) 228
$\omega\tau_c \gg 1$ 228
Spin relaxation mechanisms 229
Elliott-Yafet mechanism 229
Dyakonov-Perel mechanism 229
Bir-Aronov-Pikus mechanism 229
Relaxation via hyperfine interaction with nuclear spins 229
Spin relaxation of holes in the valence band 229
Influence of magnetic field on spin relaxation 230
Spin relaxation of two-dimensional electrons and holes 230
Hanle effect **230**
Interconnections between spin and charge **231**
Electric current inducing spin current (Spin Hall Effect) 231
Electric current inducing homogeneous spin polarization 231
Conclusion **231**
References **232**

Abstract

This brief review presents the historical background together with the theoretical and experimental results on optical spin orientation in semiconductors obtained during half a century of intense studies. Absorption of a circularly polarized photon results in the creation of an electron-hole pair with the total spin equal to the angular momentum of the photon. The degree of circular polarization of the recombination radiation serves as a useful and sensitive indicator of the carriers′ spin state and its changes under the influence of external factors and relaxation processes. Physical phenomena observed with spin-polarized electrons are briefly reviewed.

Key points

- Historical background: spin physics
- Description of the phenomenon of optical orientation
- Relevant spin-dependent interactions in semiconductors
- Role of the spin in optical phenomena
- Description of spin relaxation
- Role of spin in transport phenomena

https://doi.org/10.1016/B978-0-323-90800-9.00020-2

Introduction: Historical background

Maybe the first step toward today's activity was made nearly a century ago by Robert Wood when even the notion of electron spin was not yet introduced. In a charming paper, Wood and Ellett (1924) describe how the initially observed high degree of polarization of mercury vapor fluorescence (resonantly excited by polarized light) was unexpectedly found to diminish significantly in later experiments. "It was then observed that the apparatus was oriented in a different direction from that which obtained in earlier work, and on turning the table on which everything was mounted through ninety degrees, bringing the observation direction East and West, we at once obtained a much higher value of the polarization."

In this way Wood and Ellet discovered what we now know as the Hanle effect, i.e. depolarization of luminescence by transverse magnetic field (the Earth's field in their case). It was Hanle (1924) who carried out detailed studies of this phenomenon and provided the physical interpretation.

The subject did not receive much attention until 1949 when Brossel and Kastler (1949) initiated profound studies of optical pumping in atoms. (See Kastler's Nobel Prize award lecture, 1967.) The basic physical ideas and the experimental technique of today's research originate from these seminal papers: creation of a non-equilibrium distribution of atomic angular momenta by optical excitation, manipulating this distribution by applying *dc* or *ac* fields, and detecting the result by studying the luminescence polarization.

The relaxation times for the decay of atomic angular momenta can be quite long, especially when hyperfine splitting due to the nuclear spin is involved. A number of important applications have emerged from these studies, such as gyroscopes and hypersensitive magnetometers. The detailed understanding of various atomic processes and of many aspects of interaction between light and matter was pertinent to the future developments, e.g. for laser physics.

The first experiment on optical spin orientation of electrons in a *semiconductor* (Si) was done by Lampel (1968), as a direct application of the ideas of optical pumping in atomic physics. The great difference, which has important consequences, is that now those are the free conduction band electrons (or holes) that get spin-polarized, rather than electrons bound in an atom. This pioneering work was followed by experimental and theoretical studies mostly performed by small research groups at Ioffe Institute in St. Petersburg (Leningrad) and at Ecole Polytéchnique in Paris in the 1970s and early 1980s.

At the time, this research met with almost total indifference by the rest of the physics community, and the entire world population of researchers in the field never exceeded 20 persons. Now it can be counted by the hundreds and the number of publications by the thousands. The entire field is reviewed in the "Spin Physics in Semiconductors" book (Dyakonov, 2017).

Overview of the subject

In the process of interband absorption of a photon in a semiconductor, an electron in the conduction band and a hole in the valence band are generated, the total spin of the electron and the hole being equal to the angular momentum of the photon absorbed. Photons of right or left circularly polarized light have a projection of the angular momentum on the direction of the wave vector equal to +1 or −1, respectively (in units of the Planck constant $\hbar$). This angular momentum is distributed between the photoexcited electron and hole according to the selection rules determined by the band structure of the semiconductor.

The photoexcited electrons and hole live some time τ before recombination. During this time the spin orientation of carriers decreases due to various relaxation processes. If the orientation has not entirely disappeared by the time of recombination, the recombination radiation will be partially circularly polarized. Thus the process of optical orientation includes two stages: creation of spin-oriented carriers in absorption of circularly polarized light, and spin relaxation during the carriers' lifetime. The degree of circular polarization of the recombination radiation serves as a useful and sensitive indicator of the carriers' spin state and its changes under the influence of external factors and relaxation processes determining the kinetics of the nonequilibrium carriers in a semiconductor.

Along with the optical one, other methods of detection of the carriers' spin orientation are possible. Thus in the experiments of Lampel (1968) nuclear magnetic resonance was used as a detection method. The ^{29}Si nuclei in a silicon crystal were polarized due to their hyperfine interaction with optically oriented electrons.

Optical detection was first used by Parsons (1969) in his studies of optical spin orientation in GaSb, see also Parsons (1971). A typical experiment on optical orientation is schematically presented in Fig. 1. The degree of spin orientation of photoexcited carriers is determined by the details of the band structure, the type of optical transition, the relaxation processes, as well as by the influence of various external factors. This is why optical orientation is an effective method of studying a number of physical processes in semiconductors.

In the most detailed way optical orientation was studied in GaAs and (GaAl) As solid solutions. The first experiments on optical orientation in these materials were performed by Ekimov and Safarov (1970) and by Zakharchenya et al. (1971). Optical orientation reveals itself in all types of edge luminescence, in particular in recombination radiation of optically oriented excitons. Exciton orientation was discovered in hexagonal crystals of CdSe by Gross et al. (1971). Measurements of the polarization of hot luminescence allow to study the energy and momentum relaxation of hot electrons.

A quite special kind of phenomena involves optical effects due to dynamic polarization of the lattice nuclei of a semiconductor. The nuclei, polarized by optically oriented electrons, via *hyperfine interaction* create an effective magnetic field which, in turn, acts on

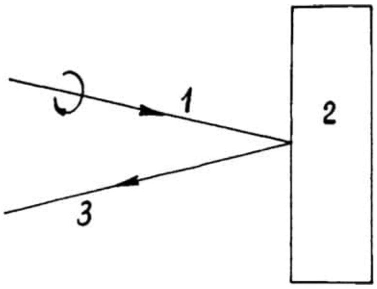

Fig. 1 Schematical drawing of a typical experiment on optical spin orientation. A circularly polarized beam of light (1) induces interband transitions in a semiconductor (2). The degree of circular polarization of the recombination radiation (3) is measured.

the electron spins and thereby on the circular polarization of the luminescence. Studies of associated phenomena began since the work of Ekimov and Safarov (1972) who detected nuclear magnetic resonance (NMR) for the lattice nuclei of a (GaAl)As solid solution by resonant changes in the degree of circular polarization of luminescence.

Below the basic theoretical ideas related to optical orientation of electrons and nuclei in semiconductors, as well as the main experimental results, are reviewed. Although most of the considerations are quite general, we shall, for definitiveness, consider semiconductors with the band structure of GaAs, for which processes accompanying optical orientation are best studied experimentally.

Band structure of gallium arsenide

Most of the experimental work on optical spin orientation was conducted with GaAs crystals and GaAlAs solid solutions. The band structure of GaAs, a typical zinc-blend semiconductor, is schematically presented in Fig. 2. Near the center of the Brillouin zone there is a simple isotropic conduction band, which is doubly degenerate in spin. The valence band, consists of the sub-bands of light (*lh*) and heavy (*hh*) holes which are anisotropic, and the isotropic split-off band (*so*), all doubly degenerate.

Spin interactions

Here we enumerate the possible types of spin interactions that can be encountered in a semiconductor. The existence of an electron spin, $s = 1/2$, and the associated magnetic moment of the electron, $\mu = e\hbar/2mc$, has many consequences, some of which are very important and define the very structure of our physical world, while others are subtler, but still quite interesting. Below is a list of these consequences in the order of decreasing importance.

The Pauli principle

Because of $s = 1/2$, the electrons are fermions, and so no more than one electron per quantum state is allowed. Together with Coulomb law and Schrödinger equation, it is this principle that is responsible for the structure of atoms, chemical properties, and the physics of condensed matter, biology included. It is interesting to speculate what would our world look like without the Pauli

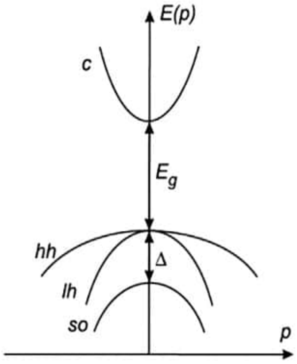

Fig. 2 Band structure of GaAs: *c* – conduction band, *hh* -heavy hole band, *lh* – light hole band, *so* – split-off band.

principle and whether any kind of life would be possible in such a world. Probably, only the properties of the high-temperature, fully ionized plasma would remain unchanged!

Note that the Pauli exclusion principle is not related to any interaction: if we could switch off the Coulomb repulsion between electrons (but leave intact their attraction to the nuclei), no serious changes in atomic physics would occur, although some revision of the Periodic Table would be needed. Other manifestations of the electronic spin are due to interactions, either electric (the Coulomb law) or magnetic (related to the electron magnetic moment μ).

Exchange interaction

It is, in fact, the result of the electrostatic Coulomb interaction between electrons, which becomes spin-dependent because of the requirement that the wavefunction of a pair of electrons be anti-symmetric with respect to the interchange of electron coordinates and spins. If the electron spins are parallel, the coordinate part of the wavefunction should be *antisymmetric*: $\psi_{\uparrow\uparrow}(\mathbf{r}_2, \mathbf{r}_1) = -\psi_{\uparrow\uparrow}(\mathbf{r}_1, \mathbf{r}_2)$, which means that the probability that two electrons are very close to each other ($\mathbf{r}_1 = \mathbf{r}_2$) is small compared to the opposite case, when the spins are antiparallel and accordingly their coordinate wavefunction is *symmetric*. Electrons with parallel spins are then better separated in space, so that their repulsion is less and consequently the energy of electrostatic interaction for parallel spins is lower. This *exchange interaction* is responsible for ferromagnetism. In semiconductors, it is normally not of major importance, except for magnetic semiconductors (like CdMnTe) and for the semiconductor-ferromagnet interfaces.

Spin-orbit interaction

If an observer moves with a velocity $\boldsymbol{v}$ in an external electric field $\boldsymbol{E}$, he will see a magnetic field $\boldsymbol{B} = (1/c)\boldsymbol{E} \times \boldsymbol{v}$, where c is the velocity of light. This magnetic field acts on the electron magnetic moment. This is the physical origin of the spin-orbit interaction, the role of which strongly increases for heavy atoms (with large Z). The reason is that there is a certain probability for the outer s-electron to approach the nucleus and thus to see the very strong electric field produced by the unscreened nuclear charge $+Ze$ at the center. Due to spin-orbit interaction, any electric field acts on the spin of a moving electron.

Being perpendicular both to $\boldsymbol{E}$ and $\boldsymbol{v}$, in an atom the vector $\boldsymbol{B}$ is normal to the plane of the orbit, thus it is parallel to the orbital angular momentum L. The energy of the electron magnetic moment in this magnetic field is $\pm \mu B$ depending on the orientation of the electron spin (and its magnetic moment) with respect to $\boldsymbol{B}$ (or to $\boldsymbol{L}$). Thus the spin-orbit interaction can be written as $A\boldsymbol{L} \cdot \boldsymbol{S}$, the constant A depending on the electron state in an atom. This interaction results in a splitting of atomic levels (the *fine structure*), which strongly increases for heavy atoms.

In semiconductors, the spin-orbit interaction depends not only on the velocity of the electron (or its quasi-momentum), but also on the structure of the Bloch functions defining the motion on the atomic scale. Like in isolated atoms, it defines the values of the electron g-factors. Spin-orbit interaction is key to our subject as it enables optical spin orientation and detection (the electrical field of the light wave does not interact directly with the electron spin). It is (in most cases) responsible for spin relaxation. And finally, it makes the transport and spin phenomena interdependent.

Hyperfine interaction with nuclear spins

This is the magnetic interaction between the electron and nuclear spins, which may be quite important if the lattice nuclei in a semiconductor have non-zero spin (like in GaAs). If the nuclei get polarized, this interaction is equivalent to the existence of an effective nuclear magnetic field acting on electron spins. The effective field of 100% polarized nuclei in GaAs would be several Tesla! Because the nuclear magnetic moment is so small ($\sim$ 2000 times less than that of the electron) the equilibrium nuclear polarization at the very high magnetic field of 100 T and a temperature of 1 K would be only about 1%. However, much higher degrees of polarization may be easily achieved through *dynamic nuclear polarization* due to hyperfine interaction with non-equilibrium electrons. Experimentally, non-equilibrium nuclear polarization of several percent is easily achieved. Similar to the spin-orbit interaction, the hyperfine interaction may be expressed in the form $A\boldsymbol{I}\cdot\boldsymbol{S}$ (the Fermi contact interaction), where $\boldsymbol{I}$ is the nuclear spin, $\boldsymbol{S}$ is the electron spin, and the hyperfine constant A is proportional to $|\psi(0)|^2$, the square of the electron wave function at the location of the nucleus.

Like spin-orbit interaction, the hyperfine interaction strongly increases in atoms with large Z, and for the same reason. An s-electron in an outer shell has a certain probability to be at the center of the atom, where the nucleus is located, and the nearer it is to the center, the less is the nucleus shielded by the inner electrons. Thus the electron wavefunction of an s-electron will have a sharp spike in the vicinity of the nucleus. For example, for the In atom the value of $|\psi(0)|^2$ is 6000 times larger than in the Hydrogen atom! For p-states (angular momentum $l = 1$), and generally for states with $l \neq 0$, the Fermi interaction does not work, since $\psi(0) = 0$, and the electron and nuclear spins are coupled by the much weaker dipole-dipole interaction.

The dynamic nuclear polarization under conditions of optical orientation of electrons is in fact a result of deep *cooling* of the nuclear spin system. Convincing experimental proof of such an interpretation was obtained by Fleisher et al. (1976) Optically oriented electrons and polarized lattice nuclei form a strongly coupled system. High sensitivity to small external magnetic fields, long relaxation times and typical nonlinear effects (hysteresis, self-sustained oscillations) are characteristic of this system.

Magnetic interaction

This is the direct dipole-dipole interaction between the magnetic moments of a pair of electrons. For two electrons located at neighboring sites in a crystal lattice this gives energy on the order of 1 K. This interaction is normally too weak to be of any importance in semiconductors.

Photo-generation of carriers and luminescence

In the process of interband absorption of a photon with energy $\hbar\omega > E_g$ in a semiconductor, an electron in the conduction band and a hole in the valence band are generated. During the process the (quasi)momentum is conserved, however the photon momentum $\hbar k = 2\pi\hbar/\lambda$, where λ is the photon wavelength, is very small (compared, to the electron thermal momentum) and normally may be neglected. In this approximation the optical transitions are *vertical*: to see what happens, we must simply apply a vertical arrow of length $\hbar\omega$ to Fig. 1, so that the arrow touches one of the valence bands and the conduction band. The ends of the arrow will give us the initial energies of the generated electrons and holes. An electron may be created in company with heavy hole, or a light hole; for $\hbar\omega > E_g + \Delta$ the electron-hole pair can also involve a hole in the split-off band.

Note, that for a given photon energy the initial electron energy will be different for those three processes. The photoexcited carriers live some time τ before recombination, which may be radiative (i.e. accompanied by photon emission, which results in luminescence), or non-radiative. In direct-band semiconductors, like GaAs, the recombination is predominantly radiative with a lifetime on the order of 1 *ns*. It is important to realize that this time is normally *very long* compared to the carriers' thermalization time. Thermalization means energy relaxation of carriers in their respective bands due to phonon emission and absorption, which results in an equilibrium Boltzmann (or Fermi, depending on temperature and concentration) distribution function of electrons and holes. Thermal equilibrium *between electrons and holes* is established by recombination, on the time scale τ.

Because the recombination time τ is so long compared to the energy relaxation time, the luminescence is produced mostly by *thermalized* carriers and the emitted photons have energies close to the value of E_g, irrespective of the energy of exciting photons.[1] It should be noted that semiconductors are normally either intentionally, or non-intentionally doped by impurities. In a *p*-type semiconductor at moderate excitation power the number of photo-generated holes is small compared to the number of equilibrium holes, so that the photo-created electron will recombine with these equilibrium holes, rather than with photo-generated ones.

Angular momentum conservation in optical transitions

Along with energy and momentum conservation, the conservation of the angular momentum is a fundamental law of Physics. Just like particles, electromagnetic waves have angular momentum. Photons of right or left polarized light have a projection of the angular momentum on the direction of their propagation (helicity) equal to +1 or −1, respectively (in units of $\hbar$). Linearly polarized photons are in a superposition of these two states.

When a circularly polarized photon is absorbed, this angular momentum is distributed between the photoexcited electron and hole according to the selection rules determined by the band structure of the semiconductor. Because of the complex nature of the valence band, this distribution depends on the value of the momentum of the created electron-hole pair ($\boldsymbol{p}$ and $-\boldsymbol{p}$). However, it can be shown that if we take the average over the directions of $\boldsymbol{p}$, the result is the same as in optical transitions between atomic states with $j = 3/2$, $m_j = -3/2, -1/2, +1/2, +3/2$ (corresponding to bands of light and heavy holes) and $j = 1/2$, $m_j = -1/2, +1/2$ (corresponding to the conduction band).

Possible transitions between these states, as well as between states in the split-off band and the conduction band, for absorption of a right circularly polarized photon with corresponding relative probabilities are presented in Fig. 3.

Note, that if we add up all transitions, which is the correct thing to do if the photon energy sufficiently exceeds $E_g + \Delta$ the two spin states in the conduction band will be populated equally. This demonstrates the role of spin-orbit interaction for optical spin pumping.

Optical spin orientation and detection

To date, the most efficient way of creating non-equilibrium spin orientation in a semiconductor is provided by interband absorption of circularly polarized light. It can be seen from Fig. 2 that for $E_g < \hbar\omega < E_g + \Delta$ this absorption produces an average electron spin along the direction of excitation equal to $(-1/2)(3/4) + (+1/2)(1/4) = -1/4$ and an average hole spin equal to $+5/4$, with a sum +1, equal to the angular momentum of the absorbed right circularly polarized photon. Thus in a *p*-type semiconductor the degree of spin polarization of the photo-excited electrons will be −50%, the minus sign indicating that the spin orientation is opposite to the direction of the angular momentum of incident photons.

---

[1] A small part of the excited electrons can emit photons before losing their energy by thermalization. The studies of the spectrum and polarization properties of this so-called *hot luminescence* reveal interesting and unusual physics, (Dymnikov, 1976; Mirlin, 1984).

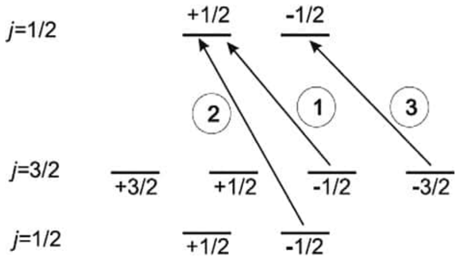

Fig. 3 Optical transitions between levels with $j = 3/2$ and $j = 1/2$ (the bands of light and heavy holes, and the split-off band) and the levels with $j = 1/2$ (the conduction band) during an absorption of a right-polarized photon. The probability ratio for the three transitions can be calculated to be 3:2:1.

If our electron immediately recombines with its partner hole, a 100% circularly polarized photon will be emitted. However in a *p*-type semiconductor electrons will predominantly recombine with the majority holes, which are not polarized. Then the same selection rules show that the circular polarization of luminescence should be $P_0 = 25\%$, if the holes are not polarized, and if no electron spin relaxation occurs during the electron lifetime τ, i.e. if $\tau_s \gg \tau$, where τ_s is the electron spin relaxation time. Generally, the degree P of circular polarization of the luminescence excited by circularly polarized light is less than P_0:

$$P = P_0\left(1 + \frac{\tau}{\tau_s}\right) \tag{1}$$

In an optical spin orientation experiment a semiconductor (usually *p*-type) is excited by circularly polarized light with $\hbar\omega > E_g$. The circular polarization of the luminescence is analyzed, which gives a direct measure of the electron spin polarization. Actually, the degree of circular polarization is simply equal to the average electron spin. Thus various spin interactions can be studied by simple experimental means. The electron spin polarization will be measured provided the spin relaxation time τ_s is not very short compared to the recombination time τ, a condition, which often can be achieved even at room temperature.

Spin relaxation

Spin relaxation, i.e. disappearance of initial non-equilibrium spin polarization, is the central issue for all spin phenomena. Spin relaxation can be generally understood as a result of the action of fluctuating in time magnetic fields. In most cases, these are not real magnetic fields, but rather “effective” magnetic fields originating from the spin-orbit, or, sometimes, exchange interactions.

Generalities

A randomly fluctuating magnetic field is characterized by two important parameters: its amplitude and its correlation time, τ_c, i.e. the time during which the field may be roughly considered as constant. Instead of the amplitude, it is convenient to use the *rms* value of the spin precession frequency in this random field, ω. Thus we have the following physical picture of spin relaxation: the spin makes a precession around the (random) direction of the effective magnetic field with a typical frequency ω and during a typical time τ_c. After a time τ_c the direction and the absolute value of the field change randomly, and the spin starts its precession around the new direction of the field. After a certain number of such steps the initial spin direction will be completely forgotten. How this happens, depends on the value of the dimensionless parameter $\omega\tau_c$, which is the typical angle of spin precession during the correlation time. Two limiting cases may be considered:

$\omega\tau_c \ll 1$ *(most frequent case)*

The precession angle is small, so that the spin vector experiences a slow angular diffusion. During a time t, the number of random steps is t/τ_c, for each step the squared precession angle is $(\omega\tau_c)^2$. These steps are not correlated, so that the total squared angle after a time t is $(\omega\tau_c)^2 \cdot (t/\tau_c)$. The spin relaxation time may be defined as the time at which this angle becomes of the order of 1. Hence: $\tau_s \sim \omega^2\tau_c$. This is essentially a *classical* formula (the Planck constant does not enter), although certainly it can be also derived quantum-mechanically. Note, that in this case $\tau_s \gg \tau_c$.

$\omega\tau_c \gg 1$

This means that during the correlation time the spin will make many rotations around the direction of the magnetic field. During the time on the order of $1/\omega$ the spin projection transverse to the random magnetic field is (on the average) completely destroyed, while its projection along the direction of the field is conserved.

At this stage the spin projection on its initial direction will diminish 3 times. [Let the random magnetic field have an angle θ with the initial spin direction. After many rotations the projection of the spin on the initial direction will diminish as $(\cos\theta)^2$. In three dimensions, the average of this value over the possible orientations of the random field yields 1/3.] After time τ_c the magnetic field changes its direction, and the initial spin polarization will finally disappear. Thus in the case $\omega\tau_c \gg 1$ the decay of spin polarization is not exponential in time, and the process has two distinct stages, the first one has a duration $1/\omega$, and the second one has a duration τ_c. The overall result is: $\tau_s \sim \tau_c$. This consideration is quite general and applies to any mechanism of spin relaxation. We have only to understand the values of the relevant parameters ω and τ_c for a given mechanism.

Spin relaxation mechanisms

There are several possible mechanisms providing the fluctuating magnetic fields responsible for spin relaxation.

Elliott-Yafet mechanism

The electrical field, accompanying lattice vibrations, or the electric field of charged impurities is transformed to an effective magnetic field through spin-orbit interaction. Thus momentum relaxation should be accompanied by spin relaxation (Elliott, 1954; Yafet, 1963). For phonons, the correlation time is on the order of the inverse frequency of a typical thermal phonon. Spin relaxation by phonons is normally rather weak, especially at low temperatures. For scattering by impurities, the direction and the value of the random magnetic field depends on the geometry of the individual collision (the impact parameter). This random field cannot be characterized by a single correlation time, since it exists only during the brief act of collision and is zero between collisions. In each act of scattering the electron spin rotates by some small angle φ. These rotations are uncorrelated for consequent collisions, so the average square of spin rotation angle during time t is on the order of $<\varphi^2> (t/\tau_p)$, where τ_p is the momentum relaxation time and $<\varphi>$ is the average of φ^2 over the scattering geometry. Thus $1/\tau_s \sim <\varphi^2>/\tau_p$. The relaxation rate is obviously proportional to the impurity concentration.

Dyakonov-Perel mechanism

The mechanism is related to the spin-orbit band splitting caused by the absence of inversion symmetry (Dyakonov and Perel, 1971a, 1972). For a given $\boldsymbol{p}$, let $\Omega(\boldsymbol{p})$ be the spin precession frequency in this field. It was shown theoretically (Dresselhaus, 1955) that for non-centrosymmetric semiconductors, like GaAs, this frequency is cubic in momentum and given by:

$$\Omega_x \sim p_x\left(p_y{}^2 - p_z{}^2\right), \Omega_y \sim p_y\left(p_z{}^2 - p_x{}^2\right), \Omega_z \sim p_z\left(p_x{}^2 - p_y{}^2\right), \tag{2}$$

The effective magnetic field changes in time because the direction of $\boldsymbol{p}$ varies due to electron collisions. Thus the correlation time is on the order of the momentum relaxation time, τ_p, and if $\Omega\tau_p \ll 1$, which is normally the case, we get: $1/\tau_s \sim \Omega^2\tau_p$.

In contrast to the Elliott-Yafet mechanism, now the spin rotates not during, but *between* the collisions. Accordingly, the relaxation rate increases when the impurity concentration decreases (i.e. when τ_p becomes longer). It happens that this mechanism is often the dominant one, both in bulk $A^{III}B^{V}$ and $A^{II}B^{VI}$ semiconductors, like GaAs, as well as in 2D structures.

Bir-Aronov-Pikus mechanism

This is a mechanism of spin relaxation of non-equilibrium electrons in p-type semiconductors due to the exchange interaction between the electron and hole spins or, expressing it otherwise, the exchange interaction between an electron in the conduction band and all the electrons in the valence band (Bir et al., 1976). This spin relaxation rate, being proportional to the number of holes, may become the dominant one in heavily p-doped semiconductors.

Relaxation via hyperfine interaction with nuclear spins

The electron spin interacts with the spins of the lattice nuclei, which are normally in a disordered state. Thus the nuclei provide a random effective magnetic field, acting on the electron spin. The corresponding relaxation rate is rather weak, but may become important for localized electrons, when other mechanisms, associated with electron motion, do not work.

Spin relaxation of holes in the valence band

The origin of this relaxation is in the splitting of the valence band into sub-bands of light and heavy holes. In this case, $\hbar\Omega(\boldsymbol{p})$ is equal to the energy difference between light and heavy holes for a given $\boldsymbol{p}$ and the correlation time is again τ_p. However, in contrast to the situation for electrons in the conduction band, we have now the opposite limiting case: $\Omega(p)\tau_p \gg 1$. So, the hole spin relaxation time is on the order of τ_p, which is very short. One can say that the hole "spin" $\boldsymbol{J}$ is rigidly fixed with respect to its momentum $\boldsymbol{p}$, and because of this, momentum relaxation leads automatically to spin relaxation. For this reason, normally it is virtually *impossible* to maintain an appreciable non-equilibrium polarization of bulk holes. However, Hilton and Tang (2002) have managed to observe the spin relaxation (on the femtosecond time scale) of both light and heavy holes in undoped bulk GaAs. The general theory of the relaxation of spin, as well as helicity and other correlations between ***J*** and ***p***, for holes in the valence band was given by Dyakonov and Khaetskii (1984).

Influence of magnetic field on spin relaxation

In the presence of an external magnetic field ***B***, the spins perform a regular precession with a frequency $\Omega = g\mu B/\hbar$, and one should distinguish between relaxation of the spin component along ***B*** and the relaxation, or dephasing, of the perpendicular components. In the magnetic resonance literature it is customary to denote the corresponding longitudinal and transverse times as T_1 and T_2 respectively.

To understand what happens, it is useful to go to a frame rotating around ***B*** with the spin precession frequency Ω. In the absence of random fields, the spin vector would remain constant in the rotating frame. Relaxation is due to random fields in the rotating frame, and obviously these fields now rotate around ***B*** with the same frequency Ω. Thus random fields directed along ***B*** are the same as in the rest frame, and cause the same relaxation of the perpendicular spin components with a characteristic time $T_2 \sim \tau_s$. However the perpendicular components of the random field, which are responsible for the relaxation of the spin component along ***B***, do rotate. The importance of this rotation is determined by the parameter $\Omega\tau_c$, the angle of rotation of the random field during the correlation time. If $\Omega\tau_c \ll 1$, then rotation is of no importance, since the random field will anyway change its direction after a time τ_c. However, for $\Omega\tau_c \gg 1$ the rotating random field will effectively average out during the correlation time, resulting in a decrease of the longitudinal spin relaxation rate. A simple calculation gives:

$$\frac{1}{T_1} = \frac{1}{\tau_s}\frac{1}{1+(\Omega\tau_c)^2} = \frac{\omega^2\tau_c}{1+(\Omega\tau_c)^2}. \tag{3}$$

Interestingly, with increasing magnetic field the longitudinal spin relaxation rate changes from being proportional to τ_c to becoming proportional to $1/\tau_c$. Again, the above classical formula can be also derived quantum-mechanically. From the quantum point of view the longitudinal relaxation is due to flips of the spin projection on ***B***, which requires an energy $g\mu B$. Since the energy spectrum of the random field has a width $\sim 1/\tau_c$, the process becomes ineffective when $g\mu B \gg \hbar/\tau_c$, or equivalently, when $\Omega\tau_c \gg 1$. Ivchenko (1973) has calculated the influence of magnetic field on the Dyakonov-Perel spin relaxation. The result coincides with Eq. (2) with $\tau_c = \tau_p$, except that the spin precession frequency Ω is replaced by the (greater) electron cyclotron frequency, ω_c. The reason is that for this case the variation of the vector $\Omega(\boldsymbol{p})$ is primarily due to the rotation of the electron momentum ***p*** in magnetic field.

Spin relaxation of two-dimensional electrons and holes

Usually the Dyakonov-Perel mechanism is the dominant one. The relaxation rate is governed by the linear momentum dependence of the effective magnetic field, or the vector $\Omega(\boldsymbol{p})$, see above. The spin relaxation is generally anisotropic and depends on the growth direction (Dyakonov and Kachorovskii, 1986). As seen from Eq. (7), for quantum wells grown in the $\langle 001\rangle$ direction the effective magnetic field lies in the 2D plane. As a consequence, the spin component perpendicular to the plane decays 2 times faster than the spin in-plane components.

More details on spin-orbit interaction in two dimensional systems can be found in Winkler's book (Winkler, 2003).

Hanle effect

Depolarization of luminescence by a transverse magnetic field, first discovered by Wood and Ellett (1924) (in their case it was the magnetic field of the Earth!) and studied in more detail by Hanle (1924), is effectively employed in experiments on spin orientation in semiconductors. The reason for this effect is the precession of electron spins around the direction of the magnetic field. Under continuous illumination, this precession leads to the decrease of the average projection of the electron spin on the direction of observation, which defines the degree of circular polarization of the luminescence. Thus the degree of polarization decreases as a function of the transverse magnetic field. Measuring this dependence under steady state conditions makes it possible to determine both the spin relaxation time and the recombination time. This effect is due to the precession of electron spins in a magnetic field ***B*** with the Larmor frequency Ω. This precession, along with spin pumping, spin relaxation, and recombination is described by the following simple equation of motion of the average spin vector ***S***:

$$\frac{d\boldsymbol{S}}{dt} = \boldsymbol{\Omega} \times \boldsymbol{S} - \frac{\boldsymbol{S}}{\tau_s} - \frac{\boldsymbol{S} - \boldsymbol{S}_0}{\tau} \tag{4}$$

where the first term on the *rhs* describes spin precession in a magnetic field ($\Omega = g\mu B/\hbar$), the second term describes spin relaxation, and the third one describes generation of spin by optical excitation ($\boldsymbol{S}_0/\tau$) and recombination ($-\boldsymbol{S}/\tau$). The vector $\boldsymbol{S}_0$ is directed along the exciting light beam, its absolute value is equal to the initial average spin of photo-created electrons. In the stationary state ($d\boldsymbol{S}/dt = 0$) and in the absence of a magnetic field, one finds:

$$S_z(B) = \frac{S_z(0)}{1 + (\Omega\tau^*)^2}, \qquad \frac{1}{\tau^*} = \frac{1}{\tau} + \frac{1}{\tau_s}. \tag{5}$$

The effective time τ^* defines the width of the depolarization curve. Thus the spin projection S_z (and hence the degree of circular polarization of the luminescence) decreases as a function of the transverse magnetic field. Combining the measurements of the zero-field value $P = S_z(0)$ and of the magnetic field dependence in the Hanle effect, we can find the two essential parameters: the electron lifetime, τ, and the spin relaxation time, τ_s, under steady-state conditions.

Interconnections between spin and charge

Because of spin-orbit interaction, charge and spin are interconnected: there is a number of phenomena where an electrical current produces spin current and/or homogeneous spin polarization and vice versa. Generally, an electric current induces a transverse spin current leading to spin accumulation at the boundaries, or a uniform spin polarization, or both effects simultaneously. Inverse effects exist too.

Phenomenologically, all these effects can be derived from pure symmetry considerations, according to the general principle: *everything that is not forbidden by symmetry or conservation laws will happen*. The microscopic theory should provide the physical mechanism of the phenomenon under consideration, as well as the values of observable quantities.

Electric current inducing spin current (Spin Hall Effect)

Spin accumulation at the lateral boundaries of a current-carrying sample (the Spin Hall Effect) was predicted in 1971 by Dyakonov and Perel (1971b, 1971c), together with the Inverse Spin Hall Effect (Dyakonov and Perel, 1971b), which was observed for the first time in 1984 by Bakun et al. (1985). The name "Spin Hall Effect" was given by Hirsch (1999) who re-predicted this phenomenon 28 years later.

The first experimental observations of the direct Spin Hall Effect were reported by Kato et al. (2004a) and by Wunderlich et al. (2005). Related phenomena that have attracted much attention are the Spin Hall Magnetoresistance (Dyakonov, 2007) and the swapping effect - a mutual transformation of spin currents, introduced by Lifshits and Dyakonov (2009).

Electric current inducing homogeneous spin polarization

In gyrotropic systems (like Te crystals, or III-V quantum wells) the electric current can also generate *homogeneous* spin polarization. This effect was predicted by Ivchenko and Pikus (1978) for bulk Te crystals and observed by Vorob'ev et al. (1979).

In two dimensions this effect was treated theoretically by Vas'ko (1979), Vas'ko and Prima (1979), by Levitov et al. (1985), by Edelstein (1990), and by Aronov et al. (1991). Experimentally it was observed in quantum wells by Silov et al. (2004), by Ganichev et al. (2006), and also, for strained bulk materials, by Kato et al. (2004b).

Inversely, spin polarization in such systems can induce electric current as it was shown theoretically by Ivchenko et al. (1989). The first experimental demonstration of this effect, named the *spin-galvanic effect*, was reported by Ganichev et al. (2002). Furthermore, the interconnection between the spin polarization, spin current, and charge current is particularly pronounced under polarized radiation giving rise to photo-galvanic phenomena. The circular photo-galvanic effect was independently predicted by Ivchenko and Pikus (1978) and by Belinicher (1978). It was first observed in Te crystals by Asnin et al. (1978) and in quantum wells by Ganichev et al. (2001).

This kind of effects has been re-discovered theoretically several times. Hence, a large variety of different names exist labelling one and the same thing: appearance of non-equilibrium spin polarization induced by dc electric current in gyrotropic media with linear in *p* spin splitting of energy bands, and vice versa.[2]

Conclusion

Optical orientation of electron (and nuclear) spins in semiconductors is a well-developed field of research with many hundreds of publications. During more than 50 years since the first experiments, an enormous progress has been made in discovering and understanding the physical mechanisms involving various interactions between electron and nuclear spins in solids with optical radiation, electric and magnetic fields, and a large number of new and sometimes unexpected effects has been discovered.

---

[2] Some of the labels used are: current-induced spin polarization (CISP), inverse spin-galvanic effect (ISGE), current-induced spin accumulation (CISA), magneto-electric effect (MEE), kinetic magneto-electric effect (KMEE), Edelstein effect (EE), inverse Edelstein effect (IEE), and Rashba-Edelstein effect (REE).

References

Aronov AG, Lyanda-Geller YB, and Pikus GE (1991) Spin polarization of electrons by an electric current. *Soviet Physics - JETP* 73: 537–541.

Asnin VM, Bakun AA, Danishevskii AM, Ivchenko EL, Pikus GE, and Rogachev AA (1978) Observation of a photo-emf that depends on the sign of the circular polarization of light. *Soviet Journal of Experimental and Theoretical Physics Letters* 28: 74–77.

Bakun AA, Zakharchenya BP, Rogachev AA, Tkachuk MN, and Fleisher VG (1985) Pis'ma Zh. Eksp. Teor. Fiz. 40, 464 (1984). *JETP Letters* 40: 1293.

Belinicher VI (1978) Space-oscillating photocurrent in crystals without symmetry center. *Physics Letters A* 66: 213–214.

Bir GI, Aronov AG, and Pikus GE (1976) Spin relaxation of electrons due to scattering by holes. *Soviet Physics - JETP* 42: 705–712.

Brossel J and Kastler A (1949) La détection de la résonance magnétique des niveaux excités : l'effet de dépolarisation des radiations de résonance optique et de fluorescence. *Comptes rendus de l'Académie des Sciences* 229: 1213–1215.

Dresselhaus G (1955) Spin-Orbit Coupling Effects in Zinc Blende Structures. *Physics Review* 100: 580–586.

Dyakonov MI (2007) Magnetoresistance due to edge spin accumulation. *Physical Review Letters* 99: 126601.

Dyakonov MI (ed.) (2017) *Spin Physics in Semiconductors*, 2nd edn Springer International Publications AG.

Dyakonov MI and Kachorovskii VY (1986) Spin relaxation of two dimensional electrons in non-centrosymetric semiconductors. *Soviet Physics – Semiconductors* 20: 110–116.

Dyakonov MI and Khaetskii AV (1984) Relaxation of nonequilibrium carrier-density matrix in semiconductors with degenerate bands. *Soviet Physics - JETP* 59: 1072–1078.

Dyakonov MI and Perel VI (1971a) Spin orientation of electrons associated with the interband absorption of light in semiconductors. *Soviet Physics - JETP* 33: 1053–1059.

Dyakonov MI and Perel VI (1971b) Possibility of orienting electron spins with current. *Soviet Journal of Experimental and Theoretical Physics Letters* 13: 467–469.

Dyakonov MI and Perel VI (1971c) Current-induced spin orientation of electrons in semi-conductors. *Physics Letters A* 35: 459–460.

Dyakonov MI and Perel VI (1972) Spin relaxation of conduction electrons in non-centrosymmetric semiconductors. *Soviet Physics - Solid State* 13: 3023–3026.

Edelstein VM (1990) Spin polarization of conduction electrons induced by electric current in two-dimensional asymmetric electron systems. *Solid State Communications* 73: 233–235.

Ekimov AI and Safarov VI (1970) Optical orientation of carriers in interband transitions in semiconductors. *JETP Letters* 12: 198–201.

Ekimov AI and Safarov VI (1972) Optical detection of dynamic polarization of nuclei in semiconductors. *Soviet Journal of Experimental and Theoretical Physics Letters* 15: 257–261.

Elliott RJ (1954) Theory of the effect of spin-orbit coupling on magnetic resonance in some semiconductors. *Physics Review* 96: 266–279.

Fleisher VG, Dzhioev RI, and Zakharchenya BP (1976) Optical cooling of a nuclear spin system of a conductor in a weak oscillating magnetic field. *JETP Letters* 23: 18–22.

Ganichev SD, Ivchenko EL, Danilov SN, Eroms J, Wegscheider W, Weiss D, and Prettl W (2001) Conversion of spin into directed electric current in quantum wells. *Physical Review Letters* 86: 4358–4361.

Ganichev SD, Ivchenko EL, Bel'kov VV, Tarasenko SA, Sollinger M, Weiss D, Wegscheider W, and Prettl W (2002) Spin-galvanic effect. *Nature* 417: 153–156.

Ganichev SD, Danilov SN, Schneider P, Bel'kov VV, Golub LE, Wegscheider W, Weiss D, and Prettl W (2006) Electric current-induced spin orientation in quantum well structures. *Journal of Magnetism and Magnetic Materials* 300: 127–131.

Gross EF, Ekimov AI, Razbirin BS, and Safarov VI (1971) Optical orientation of free and bound excitons in hexagonal crystals. *Soviet Journal of Experimental and Theoretical Physics Letters* 14: 70–73.

Hanle W (1924) Über magnetische beeinflussung der polarisation der resonanz fluoreszenz. *Zeitschrift für Physik* 30: 93–105.

Hilton DJ and Tang CL (2002) Optical Orientation and Femtosecond Relaxation of Spin-Polarized Holes in GaAs. *Physical Review Letters* 89: 146601-(1-4).

Hirsch JE (1999) Spin hall effect. *Physical Review Letters* 83: 1834–1837.

Ivchenko EL and Pikus GE (1978) New photogalvanic effect in gyrotropic crystals. *Soviet Journal of Experimental and Theoretical Physics Letters* 27: 604–608.

Ivchenko EL (1973) Fiz. Tverd. Tela (Leningrad) 15, 1566 (1973). *Soviet Physics*. *Solid State* 15: 1048.

Ivchenko EL, Lyanda-Geller YB, and Pikus GE (1989) Photocurrent in structures with quantum wells with an optical orientation of free carriers. *Soviet Journal of Experimental and Theoretical Physics Letters* 50: 175–177.

Kastler A (1967) Optical methods for studying hertzian resonances. *Science* 158: 214–221.

Kato YK, Myers RC, Gossard AC, and Awschalom DD (2004a) Observation of the spin Hall effect in semiconductors. *Science* 306: 1910–1913.

Kato YK, Myers RC, Gossard AC, and Awschalom DD (2004b) Current-induced spin polarization in strained semiconductors. *Physical Review Letters* 93: 176601-(1-4).

Lampel G (1968) Nuclear dynamic polarization by optical electronic saturation and optical pumping in semiconductors. *Physical Review Letters* 20: 491–493.

Levitov LS, Nazarov YV, and Eliashberg GM (1985) Magnetoelectric effects in conductors with mirror isomer symmetry. *Soviet Physics - JETP* 61: 133–137.

Lifshits MB and Dyakonov MI (2009) Swapping spin currents: Interchanging spin and flow directions. *Physical Review Letters* 103: 186601–186604.

Mirlin DN (1984) Optical alignment of electron momenta in GaAs-type semiconductors. In: Meier F and Zakharchenya BP (eds.) *Optical Orientation*, pp. 133–171. North Holland: Amsterdam.

Parsons RR (1969) Band-to-band optical pumping in solids and polarized photoluminescence. *Physical Review Letters* 23: 1152–1154.

Parsons RR (1971) Optical pumping and optical detection of spin-polarized electrons in a conduction band. *Canadian Journal of Physics* 49: 1850–1860.

Silov AY, Blajnov PA, Wolter JH, Hey R, Ploog KH, and Averkiev NS (2004) Current-induced spin polarization at a single heterojunction. *Applied Physics Letters* 85: 5929–5931.

Vas'ko FT (1979) Spin splitting in the spectrum of two-dimensional electrons due to the surface potential. *Soviet Journal of Experimental and Theoretical Physics Letters* 30: 541–544.

Vas'ko FT and Prima NA (1979) Spin splitting of spectrum of 2-dimensional electrons. *Soviet Physics - Solid State* 21: 994–998.

Vorob'ev LE, Ivchenko EL, Pikus GE, Farbstein II, Shalygin VA, and Sturbin AV (1979) Optical activity in tellurium induced by a current. *Soviet Journal of Experimental and Theoretical Physics Letters* 29: 441–445.

Winkler R (2003) *Spin-Orbit Coupling Effects in Two-Dimensional Electron and Hole Systems*. Berlin: Springer.

Wood RW and Ellett A (1924) Polarized resonance radiation in weak magnetic fields. *Physics Review* 24: 243–254.

Wunderlich J, Kaestner B, Inova J, and Jungwirth T (2005) Experimental observation of the spin hall effect in a two-dimensional spin-orbit coupled semiconductor system. *Physical Review Letters* 94: 047204-(1-4).

Yafet Y (1963) g-factors and spin-lattice relaxation of conduction electrons. *Solild State Physics* 14: 1–98.

Zakharchenya BI, Fleisher VG, Dzhioev RI, Veshchunov YP, and Rusanov IB (1971) Effect of optical orientation of electron spins in a GaAs crystal. *JETP Letters* 13: 137–139.

Raman spectroscopy of graphene and related materials

Anna K Ott[a] **and Andrea C Ferrari**[b], [a]NS3E Laboratory, UMR 3208 ISL/CNRS/UNISTRA, French-German Research Institute of Saint-Louis, Saint Louis, France; [b]Cambridge Graphene Centre, University of Cambridge, Cambridge, United Kingdom

© 2024 Elsevier Ltd. All rights reserved.

Introduction **233**
Brief overview of light scattering processes **233**
Raman scattering process **234**
Raman spectroscopy of graphene and graphene layers **236**
Counting graphene layers: 2D peak and ultra-low frequency modes 237
The Raman spectrum of strained graphene 238
The Raman spectrum of doped graphene 241
The Raman spectrum of defected graphene 242
Magnetic fields 244
Key issues **244**
Conclusion **245**
Acknowledgments **245**
References **246**

Abstract

Raman spectroscopy is one of the main characterization techniques for graphene and related materials. It is a non-destructive technique that can give insight in the material's quality, the number of layers, and is sensitive to any changes in electric or magnetic fields, band structure and temperature, making it ideal to probe layered materials.

Key points

- Brief introduction to Raman scattering
- Explanation of the Raman spectrum of graphene/graphene layers and how it changes as function of doping, defects, and strain
- Summary of the capabilities of Raman spectroscopy of graphene
- Overview of the current challenges and general outlook

Introduction

A single layer of graphene (SLG) (Novoselov et al., 2004) can be seen by using a microscope if placed over a Si+SiO_2 thickness ~100 nm or ~ 300 nm (Casiraghi et al., 2007a). The SiO_2 layer acts as a cavity for the light and results in either constructive or destructive interference depending on its thickness (Casiraghi et al., 2007a). Fig. 1 shows the calculated optical contrast as function of laser wavelength and SiO_2 thickness with contrast maxima at ~100 and ~ 300 nm thickness for commonly used laser wavelengths between ~450 and ~ 600 nm. While imaging by optical contrast can give an idea of its thickness, it is not enough to get more quantitative information, such as doping, disorder, strain, etc.

Raman spectroscopy is a powerful characterization technique for carbons in general, ranging from fullerenes, nanotubes, graphitic carbons to amorphous and diamond-like carbons (Ferrari and Robertson, 2000; Tuinstra and Koenig, 1970; Dresselhaus et al., 2005; Dresselhaus et al., 1996). In graphene, Raman spectroscopy can now be routinely used to extract the number of layers, N, to estimate the type and amount of doping and strain, as well as to check the quality of graphene as it this spectroscopic technique is also sensitive to defects (Ferrari and Basko, 2013).

Brief overview of light scattering processes

Light scattering can be either elastic, i.e. the incident and scattered light have the same frequency, or inelastic, where the scattered light has a different frequency with respect to the incident light. In classical electrodynamics, when light impinges on a medium, electrons within that medium start to oscillate at the same frequency as the incident electromagnetic wave. This periodic perturbation of the electron cloud results in the creation of an oscillating dipole moment leading to the emission of light with the same frequency as the incident light, i.e. elastic scattering of light. Examples are Mie scattering (Mie, 1908) and Rayleigh

https://doi.org/10.1016/B978-0-323-90800-9.00252-3

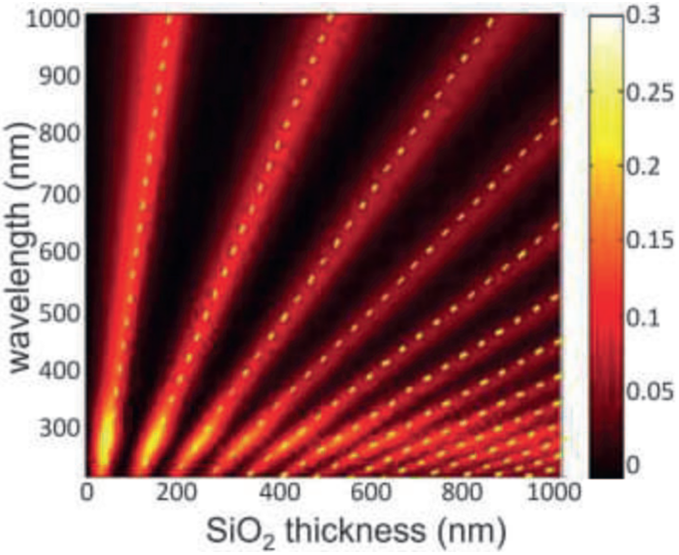

Fig. 1 Calculated optical contrast of graphene on Si/SIO$_2$ as a function of wavelength and SiO$_2$ thickness. Reprinted with permission from Casiraghi C, Hartschuh A, Lidorikis E, Qian H, Harutyunyan H, Gokus T, Novoselov KS, and Ferrari AC (2007a) Rayleigh imaging of graphene and graphene layers. *Nano Letters* 7: 2711–2717. Copyright 2007 American Chemical Society.

scattering (Strutt, 1871), depending on the particle size in the medium. Light scattering off particles larger than the wavelength and having a refractive index different from that of the continuous medium in which they are embedded is referred to as Mie scattering, which can be observed when sun light scatters from the water droplets within clouds. If the particle size is smaller than the wavelength of light, such as is the case for atoms or molecules, the process is called Rayleigh scattering. An example is the color of the sky, either blue during the day or red at sun rise or sunset, where light is scattered off the molecules in the atmosphere.

In the case of inelastic light scattering, the scattered light has a different frequency or energy with respect to the incident light. This process can be more conveniently described by quantum theory, whereas an electron absorbs a photon, leaving behind an empty space (a hole), and as a result is promoted to an energetically higher level. The electron can then either fall directly back to a lower level, while emitting a photon with energy corresponding to the energy level difference, or scatter with the lattice, i.e. create or annihilate/absorb a phonon, before recombining radiatively with a hole. Examples for inelastic light scattering are Brillouin and Raman scattering. While Brillouin scattering involves low frequency lattice vibrations, i.e. acoustic phonons, Raman scattering involves optical phonons in first order scattering processes (Brüesch, 1986).

The Raman scattering process was first theoretically predicted in 1923 by Austrian physicist Smekal (Smekal, 1923). The experimental proof was delivered in 1928 by Landsberg and Mandelstam (Landsberg and Mandelstam, 1928) in crystals and by Raman and Krishnan (Raman and Krishnan, 1928) in liquids. For his findings Raman was awarded the Nobel Prize in physics in 1930 (Nobel-Prize). Since then - and even more so after the invention of the laser in 1960 (Schawlow and Townes, 1958; Maiman, 1960) - Raman spectroscopy has become a standard materials characterization tool as it is non-destructive, fast and easy to use (Ferrari and Basko, 2013).

Raman scattering process

Raman scattering is the inelastic scattering between light, i.e. a photon, and matter. It involves the exchange of rotational or vibrational quanta of energy in molecules or the creation and annihilation of phonons with frequency Ω in solids (Cardona and Güntherodt, 1982). If light of frequency ω_L is incident on a material, most of the light is elastically scattered. This Rayleigh scattering process is shown in Fig. 2. From a classical point of view, light can be described as a propagating electromagnetic wave with $E(t) = E_0 \cos(\omega_L t)$ with amplitude E_0 and frequency ω_L. The electron cloud responds to the fast changing electric field and this will induce a dipole moment $\mu(t)$ proportional to the electric field of the incoming light (Yu and Cardona, 1996):

$$\mu(t) = \alpha E(t) = \alpha_0 E_0 \cos(\omega_L t) \quad (1)$$

where the proportionality constant α is the polarizability. This describes the ability of, e.g., molecules to be polarized, and depends on the relative position of the individual atoms. Atomic vibrations are confined to certain energetic levels and are quantized into phonons. The physical displacement of the atoms dQ about their equilibrium position associated with a phonon can be described as: $dQ = Q_0 \cos(\Omega t)$, where Ω is the phonon frequency and Q_0 is the displacement about the equilibrium position. A material's response to electromagnetic radiation depends on the atomic positions. The atomic displacements change the susceptibility, thus its polarization, depending on the phonon involved. At room temperature (RT) the atomic displacement is small

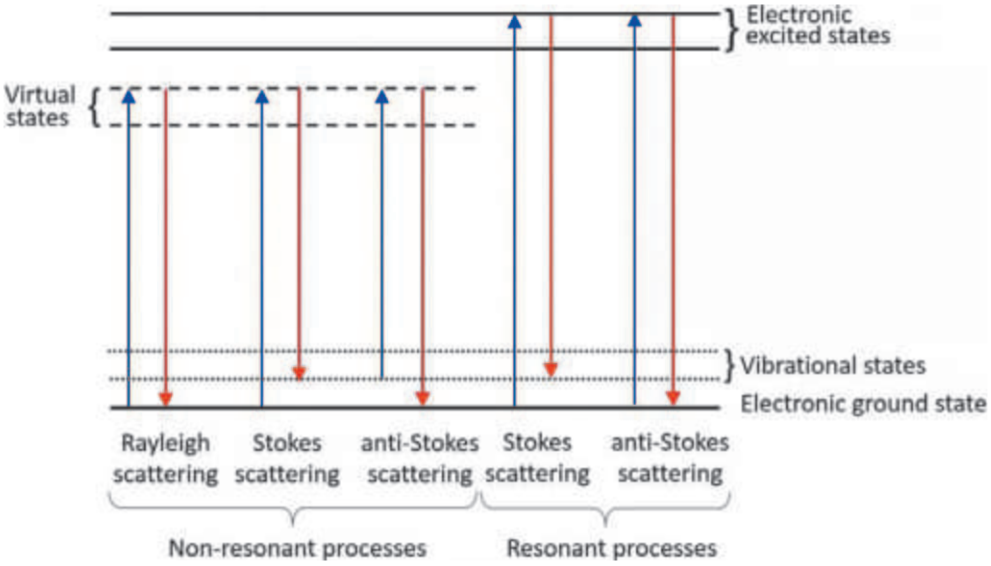

Fig. 2 Energy level diagram showing Rayleigh and Raman scattering (Stokes and anti-Stokes) processes. Blue lines depict absorption of a photon, while red lines depict emission of a photon. Non-resonant processes involve virtual states, while resonant scattering processes involve real states.

compared to the lattice constant. Therefore, the polarizability α can be approximated by a Taylor series expansion around the lattice displacement. Considering only first order terms we get:

$$\alpha = \alpha_0 + \left.\frac{\partial\alpha}{\partial Q}\right|_0 dQ + \ldots = \alpha_0 + \left.\frac{\partial\alpha}{\partial Q}\right|_0 Q_0 \cos(\Omega t) \tag{2}$$

Inserting Eq. (2) in (1) gives:

$$\mu(t) = \alpha_0 E_0 \cos(\omega_L\, t) + \left.\frac{\partial\alpha}{\partial Q}\right|_0 E_0 Q_0 \cos(\Omega t) \cos(\omega_L t)$$

Using a trigonometric identity for the product of the cosine terms leads to

$$\mu(t) = \alpha_0 E_0 \cos(\omega_L\, t) + \frac{1}{2}\left.\frac{\partial\alpha}{\partial Q}\right|_0 E_0 Q_0 \{\cos[(\Omega - \omega_L)t] + \cos[(\Omega + \omega_L)t]\} \tag{3}$$

The intensity of the scattered light I_{Sc} is proportional to $|\ddot{\mu}|$, where $\ddot{\mu}$ is the second derivative of μ with respect to time, t:

$$I_{Sc} \propto \cos^2(\omega_L) + \cos^2[(\omega_L + \Omega)t] + \cos^2[(\omega_L - \Omega)t] + \text{cross terms} \tag{4}$$

The first term corresponds to the *elastically* scattered light, i.e. Rayleigh scattering, since it only depends on ω_L,while the other two terms describe the inelastically scattered light, i.e. Raman scattering. Here we distinguish between Stokes (S) and anti-Stokes (AS) scattering, both named after Sir G. G. Stokes (Larmor, 1907). In S-scattering a phonon is created by energy transfer from the electron to the lattice resulting in the $(\omega_L - \Omega)$ term, meaning the scattered light has a lower frequency with respect to the incident light, while in AS-scattering a phonon is annihilated (or absorbed), giving the $(\omega_L + \Omega)$ term. The S and AS Raman scattering processes are depicted in Fig. 2. AS Raman scattering involves the absorption of a phonon. Consequently, the scattering process starts directly from a vibrational state as shown in Fig. 2.

At RT the AS-Raman peaks have lower intensity compared to S, but their intensity increases with rising temperature (T). This can be explained by considering the Bose-Einstein distribution, whereby the number of phonons in a certain energy state strongly depends on T, and increases with T (Kittel, 2005). If n_q is the phonon occupation number, then the S-Raman scattering intensity will be proportional to $n_q + 1$, since a phonon is created during the scattering process. For AS, we start at an excited (vibrational) state and a phonon is annihilated, giving rise to intensity proportional to n_q. Thus, the S/AS intensity ratio can be expressed as (Placzek, 1934; Krishnan and Narayanan, 1950):

$$\frac{I_{Stokes}}{I_{anti-Stokes}} = \left(\frac{\omega_L - \Omega}{\omega_L + \Omega}\right)^4 \exp\left(\frac{\hbar\Omega}{k_B T}\right), \tag{5}$$

where k_B is the Boltzmann constant, ω_L is the frequency of the laser light, Ω is the phonon frequency, $\hbar$ is the reduced Planck constant. By re-arranging Eq. (5) for T, the sample T can be determined by fitting the peak intensity of a peak on S and AS side of the Raman spectrum.

The intensity of the scattered light also strongly depends on whether we have a resonant or non-resonant process (Loudon, 1965). In a resonant process, real electronic states are involved, while in non-resonant Raman scattering virtual states are used to describe the process. The intensity of the Raman scattered light depends on the polarization of the incident and scattered light as well as on the phonon involved in the scattering process. The symmetry of the phonon mode is incorporated in the so-called Raman tensor $\mathfrak{R}$. Introducing a unit vector in direction of the lattice displacement $\widehat{Q}$ this term can be expressed as (Yu and Cardona, 1996)

$$\mathfrak{R} = \left.\frac{\partial\alpha}{\partial Q}\right|_0 \widehat{Q} \tag{6}$$

Assuming $\widehat{e}_i$ and $\widehat{e}_{Sc}$ to be unit vectors of the polarization of the incoming and scattered light, the Raman intensity is proportional to $I \propto |\widehat{e}_i\, \mathfrak{R}\, \widehat{e}_{Sc}|^2$ (Yu and Cardona, 1996). Thus, for Raman scattering to occur, the term $\left.\frac{\partial\alpha}{\partial Q}\right|_0$ has to be non-zero, meaning the polarizability has to change. By doing polarization dependent measurements, the symmetry of the Raman tensor, thus that of the corresponding phonon, can be obtained (Cardona and Güntherodt, 1982). This is very useful for correct assignment of the Raman peaks.

During the scattering process, energy and momentum conservation have to hold: $\hbar\omega_L = \hbar\omega_{Sc} \pm \hbar\Omega$ and $\boldsymbol{k}_L = \boldsymbol{k}_{Sc} \pm \boldsymbol{q}$, where $\hbar$ is the reduced Planck constant, ω_L, ω_{Sc}, Ω are the frequency of the incident light, the scattered light and the phonon, respectively, and $\boldsymbol{k}_L$, $\boldsymbol{k}_{Sc}$, $\boldsymbol{q}$ are the corresponding wave vectors and the phonon momentum. The wavevectors can be expressed in terms of wavelength λ via $k = 2\pi\lambda^{-1}$. The lattice constant of a material is of the order of a few $\AA$, thus much smaller than λ (in the order of a few hundreds of nm), giving k_L, $k_{Sc} \ll \pi a^{-1}$, which is the size of the first Brillouin zone (BZ), where a is the lattice constant. Combining this with the equations for energy and momentum conservation we can deduct that $q \ll \pi a^{-1}$ meaning $q \approx 0$. This is called the fundamental Raman selection rule, and tells us that the phonons contributing to first order Raman scattering stem from the BZ center. For higher order scattering processes, i.e. processes involving multiple phonons, the selection rule becomes $\sum \boldsymbol{q} = 0$. So, in a second order Raman process, two phonons with equal but opposite momentum are contributing since $\boldsymbol{q} + (-\boldsymbol{q}) = 0$.

Raman spectroscopy of graphene and graphene layers

In real space, single layer graphene (SLG) has a hexagonal structure resulting in a hexagonal structure in reciprocal space as well, where Γ marks the BZ center and the high symmetry points at the corner are labelled as **K** and **K**′, Fig. 3A. At these so-called Dirac points, SLG has a unique linear dispersion relation (Dirac cones).

In SLG there are two atoms per unit cell giving rise to six normal modes (two being doubly degenerate) at Γ with irreducible representation: $A_{2u} + B_{2g} + E_{1u} + E_{2g}$ (Nemanich et al., 1977). The E_{2g} and B_{2g} modes are both doubly degenerate, whereas the E_{2g} mode is Raman active and the B_{2g} is silent, i.e. neither Raman nor IR active (Nemanich et al., 1977). The A_{2u} and E_{1u} modes are both IR active modes (Ferrari and Basko, 2013).

The Raman spectrum of graphite and multilayer graphene consists of two different sets of peaks: those at higher wavenumbers, such as the D, G, 2D and 2D′ modes due to in-plane vibrations, and those at low frequency, such as the shear (C) and layer breathing modes (LBMs), due to the relative movement of the whole atomic planes, either parallel or perpendicular (Ferrari and Basko, 2013; Tan et al., 2012), Fig. 4. In SLG only the first set of peaks is visible (Ferrari et al., 2006).

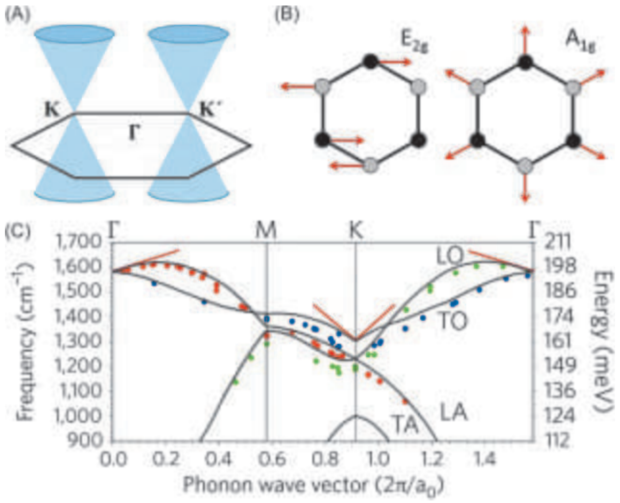

Fig. 3 (A) SLG structure in reciprocal space (BZ). The high symmetry points and a schematic of the electronic dispersion at K and K′ (Dirac cones) are indicated. (B) Doubly degenerate E_{2g} mode and A_{1g} breathing mode giving rise to the G and D peak in SLG. (C) SLG Phonon dispersion. The red lines indicate the positions of Kohn anomalies. (C) Reprinted with permission from Piscanec S, Lazzeri M, Mauri F, Ferrari AC, and Robertson J (2004) Kohn anomalies and electron-phonon interactions in graphite. *Physical Review Letters* 93: 185503. Copyright (2004) by the American Physical Society.

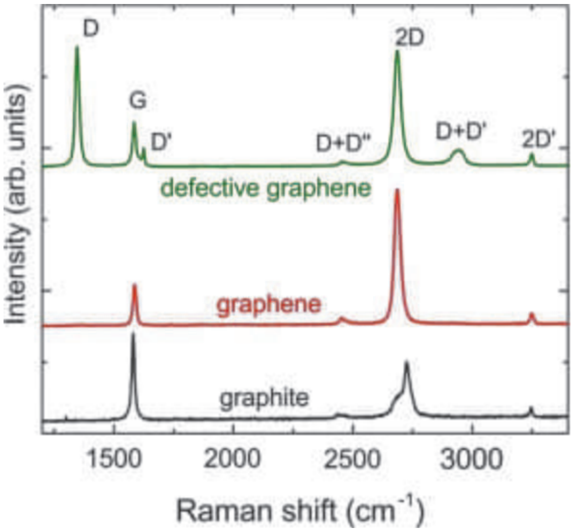

Fig. 4 Comparison of Raman spectra of pristine graphene, defective graphene and graphite.

The G peak ~1580 cm^{-1} arises from an E_{2g} phonon stemming from the Γ-point, Fig. 3B and C. The D peak, corresponding to an A_{1g} phonon (Fig. 3B), is due to the breathing mode of six-atom rings and requires a defect for its activation (Ferrari and Robertson, 2000; Thomsen and Reich, 2000; Tuinstra and Koenig, 1970) to fulfill the fundamental Raman selection rule. This peak is activated by an *inter*valley double resonance process (Thomsen and Reich, 2000), connecting **K** and **K**′, and comes from a transverse optical (TO) phonon at the **K** point, Fig. 3C. Due to the presence of a Kohn anomaly (Piscanec et al., 2004), i.e. a damping of the phonon dispersion (red lines in Fig. 3C), it is also highly dispersive with excitation energy shifting by ~50 cm^{-1} eV^{-1} (Pocsik et al., 1998). Similarly, an *intra*valley double resonance scattering process at **K** or **K**′ gives rise to another defect-activated peak, the D′ peak. In defective graphene also the combination mode D + D′ starts to appear. The 2D and 2D′ peaks are the second order modes of the D and D′ peak, where the momentum conservation is fulfilled by scattering of two phonons with opposite wave vectors. Thus, these peaks do not require defects for their activation and are always present in the Raman spectrum of graphene (Ferrari et al., 2006; Basko et al., 2009). This means that only the G peak in the Raman spectrum of graphene fulfills the fundamental Raman selection rule directly as its origin is at the center of the Brillouin zone where $\boldsymbol{q} = 0$. All scattering processes are depicted in Fig. 5.

Counting graphene layers: 2D peak and ultra-low frequency modes

The Raman peaks of graphene can be fitted with a Lorentzian line shape, which arises from a finite, homogeneous lifetime broadening. Here we use the following notation (Ferrari and Basko, 2013) to refer to the peak fitting parameters: 'I' for peak height (intensity), 'A' for peak area, 'Pos' for peak position and 'FWHM' for the full-width at half-maximum of the peak.

The Raman scattering process in SLG is always resonant due to its linear band structure. The band structure of SLG and multilayer graphene (MLG) is reflected in the shape of the 2D peak (Ferrari et al., 2006). In SLG, the 2D peak is one sharp peak that can be fitted with a single Lorentzian line, while in Bernal stacked bilayer graphene (BLG) it splits into four components following the evolution of the band structure, Fig. 6A and B. Thus, the 2D peak shape can be used to estimate N. However, beyond ~5–10 layers, the 2D peak will start looking like that of graphite, Fig. 6A, and the 2D peak shape cannot be used, alone, to estimate N correctly. Low frequency modes are far more sensitive to N, even beyond $N = 5$, Fig. 6C. For accuracy the resulting peak positions of C and/or LBMs can be calculated as the mean value of the fitted S/AS peak positions.

The C peak changes its position with N, Fig. 6D. Following a linear chain model where each layer is estimated as one mass coupled by a spring to the next mass (layer), the relation between the position of the C peak (in cm^{-1}) and N can be written as (Tan et al., 2012):

$$\mathrm{Pos}(C)_N = \frac{1}{\sqrt{2}\pi c}\sqrt{\frac{\alpha}{\mu}}\sqrt{1 + \cos\left(\frac{\pi}{N}\right)} \tag{7}$$

where the pre-factor $(1/\pi c)\sqrt{\alpha/\mu}$ corresponds to $\mathrm{Pos}(C)_\infty$ in graphite with $N \to \infty$, $\alpha \sim 12.8 \times 10^{18}$ Nm^{-3} is the interlayer coupling constant, $\mu = 7.6 \times 10^{-27}$kgÅ^{-2} is the SLG mass per unit area and c is the speed of light in cm s^{-1}.

Thus, by knowing Pos(C) in bulk graphite one can extract the interlayer coupling constant, thus get fundamental information about the interaction between the layers. This model can be applied to all layered materials (LMs), see e.g. refs. (Pizzi et al., 2021; Zhang et al., 2013).

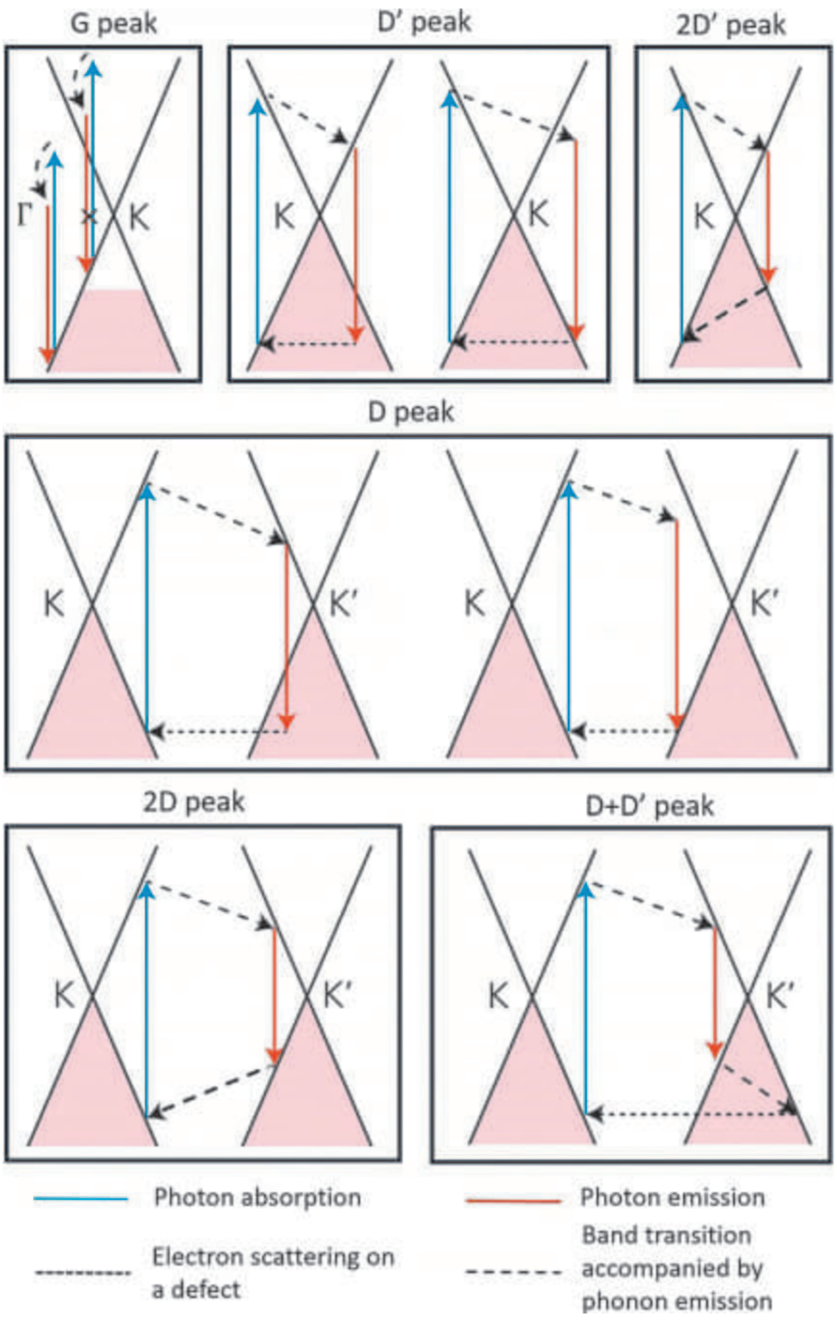
G peak
D′ peak
2D′ peak
Γ
K
K
K
K
D peak
K
K′
K
K′
2D peak
D+D′ peak
K
K′
K
K′
Photon absorption
Photon emission
Electron scattering on a defect
Band transition accompanied by phonon emission

Fig. 5 Raman scattering processes in SLG. The red shaded area within the linear dispersion relation shows the occupied states. The G peak arises from one phonon scattering. Depending on doping, some processes will no longer be allowed. The D′ (intravalley scattering), D (intervalley scattering) and D + D′ peak require defects for their activation. The two different processes for the D and D′ peak depicted here give the largest contribution. The two-phonon (second order) modes, 2D and 2D′ peak, do not require a defect. Schematics from Ref. Ferrari AC and Basko DM (2013) Raman spectroscopy as a versatile tool for studying the properties of graphene. *Nature Nanotechnology* 8: 235–246. Reprinted by permission from Springer Nature Customer Service Centre GmbH: Springer Nature, Nature Nanotechnology, COPYRIGHT (2013).

The Raman spectrum of strained graphene

SLG can be stretched up to at least ~20% without breaking (Bunch et al., 2007; Lee et al., 2008). Strain in graphene has not only a major effect on its structure but also on its Raman spectrum. Strain can occur in different forms: Uniaxial (Mohiuddin et al., 2009; Yoon et al., 2011; Mohr et al., 2010; Huang et al., 2010), i.e. strain along one direction, and biaxial strain, i.e. isotropic strain (Ding et al., 2010; Zabel et al., 2012; Metzger et al., 2010). Both types can either be applied as tensile or compressive.

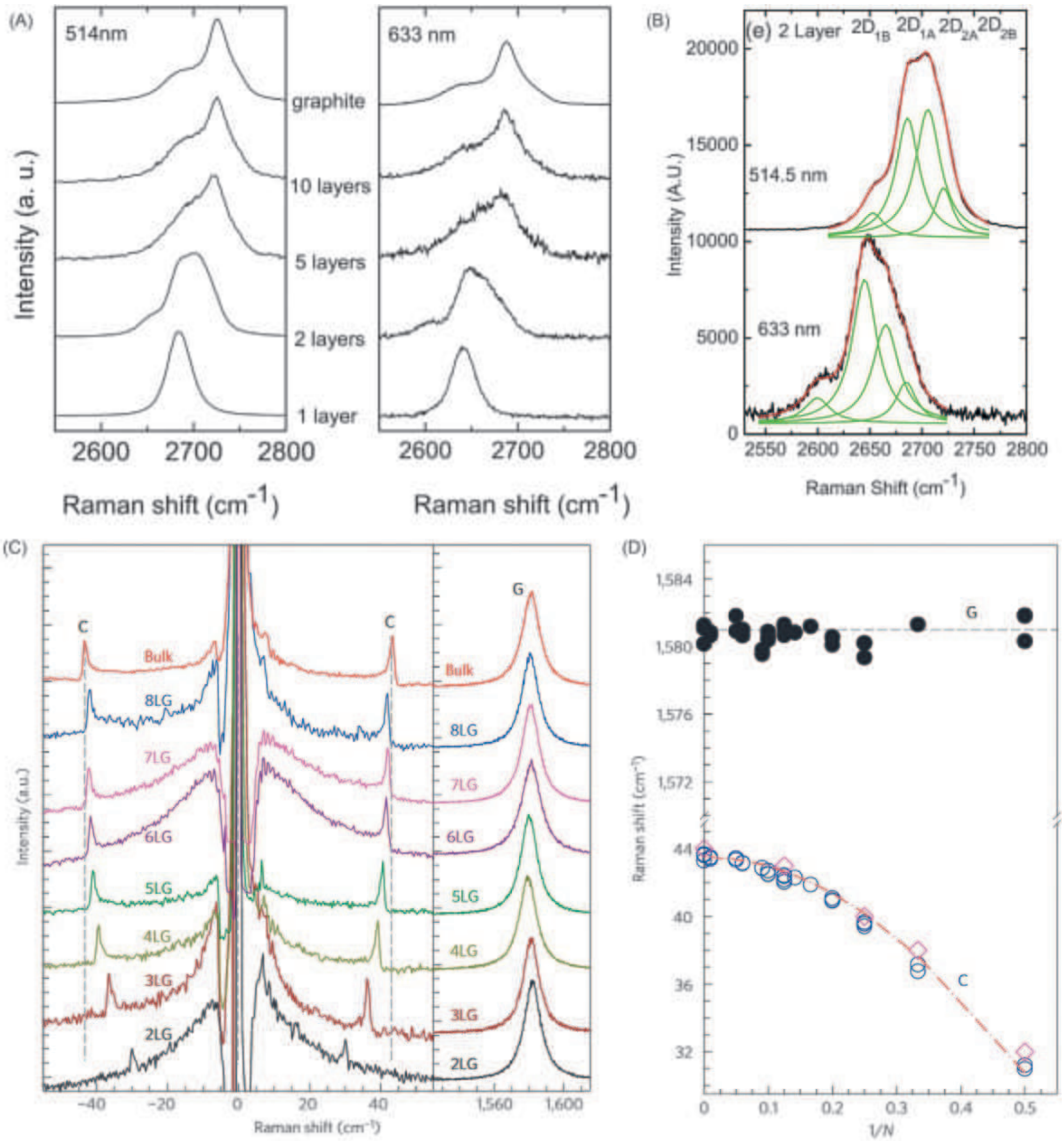

Fig. 6 (A) 2D peak as function N. (B) For BLG, the 2D peak splits into 4 components. (C) Ultra-low frequency and G peak region of graphene layers. (D) Fitted C and G peak positions. (A and B) Reprinted figure with permission from Ferrari AC, Meyer JC, Scardaci V, Casiraghi C, Lazzeri M, Mauri F, Piscanec S, Jiang D, Novoselov KS, Roth S, and Geim AK (2006) Raman spectrum of graphene and graphene layers. *Physical Review Letters* 97: 187401. Copyright (2006) by the American Physical Society. (C and D) From Springer Nature Customer Service Centre GmbH: Springer Nature, Nature Materials, Tan PH, Han WP, Zhao WJ, Wu ZH, Chang K, Wang H, Wang YF, Bonini N, Marzari N, Pugno N, Savini G, Lombardo A, and Ferrari AC (2012) The shear mode of multilayer graphene. *Nature Materials* 11: 294–300, COPYRIGHT (2012).

In general, compressive strain results in an upshift of all Raman peaks, arising from the shortening of the interatomic bond lengths, while tensile causes a downshift, due to the elongation of the bond lengths resulting in a weakening of the vibrational modes. Biaxial strain preserves the hexagonal symmetry in SLG, i.e. it only leads to an isotropic expansion or compression of the hexagonal lattice, resulting in a linear peak shift. The linear change in peak position or frequency $\partial\omega$ is $\partial\omega_G/\partial\varepsilon \approx -57\ \text{cm}^{-1}/\%$ for the G peak and $\partial\omega_{2D}/\partial\varepsilon \approx -140\ \text{cm}^{-1}/\%$ for the 2D peak (Zabel et al., 2012; Mohiuddin et al., 2009). Unless induced intentionally it is very unlikely to find biaxial strain in graphene samples. Uniaxial strain also results in linear peak shifts (Fig. 7), however it will break the hexagonal symmetry, which has an effect on the Raman peak shape. The G peak is a doubly degenerate mode and uniaxial strain makes both components visible: The peak splits into two components G^+ and G^-, one parallel and one perpendicular to the direction of applied strain (Mohiuddin et al., 2009), Fig. 7A–C. The rate of change is (Mohiuddin et al., 2009): $\partial\omega_{G^+}/\partial\varepsilon \approx -10.8\ \text{cm}^{-1}/\%$ and $\partial\omega_{G^-}/\partial\varepsilon \approx -31.7\ \text{cm}^{-1}/\%$ for the G peak and $\partial\omega_{2D}/\partial\varepsilon \approx -64\ \text{cm}^{-1}/\%$ for the 2D peak. A similar splitting of the 2D peak has been reported when the uniaxial strain exceeds ~0.5% and is applied along a high-symmetry axis

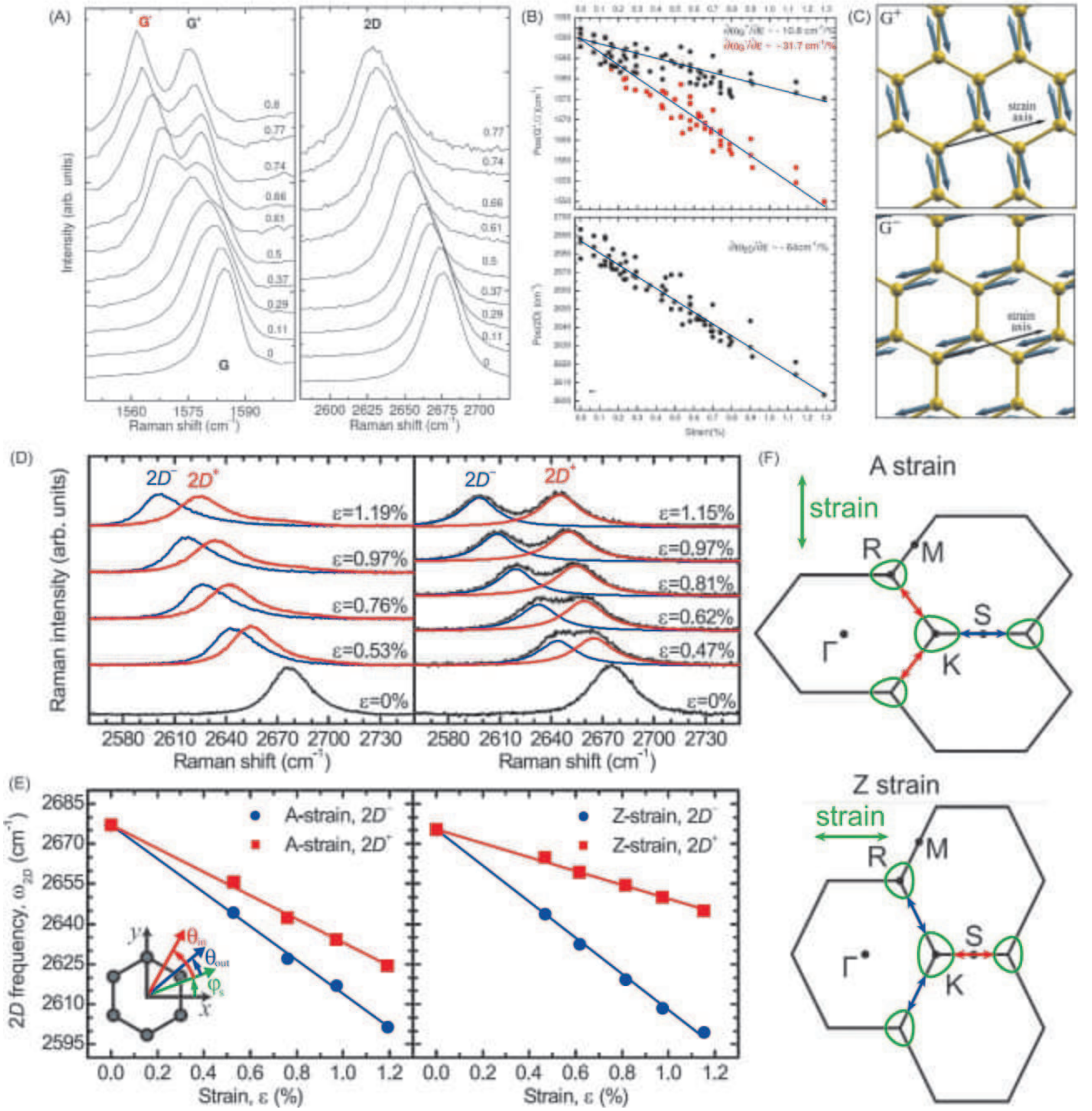

Fig. 7 Effect of uniaxial strain on the SLG Raman spectrum. (A) Splitting of the G peak and a linear peak shift for increasing uniaxial stain. (B) Fitted peak positions as function of strain. (C) Schematic showing the origin of the G peak splitting. Eigenvectors of G^+ and G^- modes, perpendicular and parallel to the strain direction. (D) Evolution of the 2D peak as function of strain. A splitting of the 2D peak can be observed. (E) Fitted peak positions as function of strain. (F) Schematics showing strain induced distortions of SLG and resulting change in distance between K and R (strained K′) points. (A, B, C) Reprinted figures with permission from Mohiuddin TMG, Lombardo A, Nair RR, Bonetti A, Savini G, Jalil R, Bonini N, Basko DM, Galiotis C, Marzari N, Novoselov KS, Geim AK, and Ferrari AC (2009) Uniaxial strain in graphene by Raman spectroscopy: G peak splitting, Gruneisen parameters, and sample orientation. *Physical Review B* 79: 205433. Copyright (2009) by the American Physical Society. (D, E, F) Reprinted figures with permission from Yoon D, Son Y-W, and Cheong H (2011) Strain-dependent splitting of the double-resonance Raman scattering band in graphene. *Physical Review Letters* 106: 155502. Copyright (2011) by the American Physical Society.

(Huang et al., 2010; Mohr et al., 2010; Yoon et al., 2011), Fig. 7D and E. The 2D peak arises from an intervalley scattering process connecting **K** and **K′** points. Considering the structure of graphene, each **K** point has three neighboring **K′** points, leading to three contributions to the scattering process. Fig.7F shows a schematic depicting the possible scattering processes for the 2D peak in strained graphene. The relative position of the Dirac points has been disturbed such that the three scattering mechanisms connecting **K** and **K′** are no longer identical (Huang et al., 2010; Yoon et al., 2011). In the example shown in Fig. 7F two of the three possible scattering mechanism lead to one 2D peak component, while the remaining one gives rise to the second 2D peak component (red and blue arrows in Fig. 7F), depending on the direction of strain either parallel or perpendicular to the armchair edge in graphene.

The Raman spectrum of doped graphene

Most graphene samples produced by either micromechanical cleavage (MC), chemical vapor deposition (CVD), liquid phase exfoliation (LPE) or carbon segregation from SiC or metal substrates are doped due to the sensitivity of graphene to adsorbates, e.g. moisture, and/or due to the interaction with the underlying substrate (Bonaccorso et al., 2012; Backes et al., 2020). Doping can also be applied on purpose either electrically or chemically and has a marked effect on the Raman spectrum of (Basko et al., 2009; Das et al., 2008; Bruna et al., 2014; Kalbac et al., 2010; Casiraghi et al., 2007b): In doped SLG Pos(G) increases, while FWHM(G) decreases for both electron (e) and hole (h) doping, see Fig. 8A and C. The increase in Pos(G) is due to a non-adiabatic removal of the Kohn anomaly at Γ, while the decrease of FWHM(G) is due to Pauli blocking of the phonon decay channel into e-h pairs when the e-h gap is higher than the phonon energy, and saturates when the Fermi energy, E_F, is bigger than half the phonon energy (Basko et al., 2009; Das et al., 2008). The 2D peak, allows distinguishing between e and h doping, as Pos(2D) increases for h doping and decreases for e doping (Das et al., 2008), Fig. 8B. This can be explained by taking the change of the equilibrium lattice parameter into account with a consequent stiffening/softening of the phonon modes, as a result of h and e doping, respectively. Both, intensity and area ratios, I(2D)/I(G) and A(2D)/A(G) depend on E_F. The ratios are maximum for $E_F = 0$, and decrease with increasing E_F (Basko et al., 2009; Das et al., 2008), Fig. 8D. Using the fitting parameters Pos(G), FWHM(G), Pos(2D), I(2D)/I(G) and A(2D)/A(G) with the corresponding graphs as function of E_F presented in refs. (Basko et al., 2009, Das et al., 2008), E_F can be extracted from the Raman spectrum.

Additional effects occur for high doping levels ∼0.9 eV. In this case an enhancement of the G peak intensity I(G) can be observed (Zhao et al., 2011). Doping changes the occupation of electronic states and since transitions from an empty state or to a filled state are impossible (Pauli exclusion principle), this can exclude some of the BZ regions from contributing to the Raman matrix element

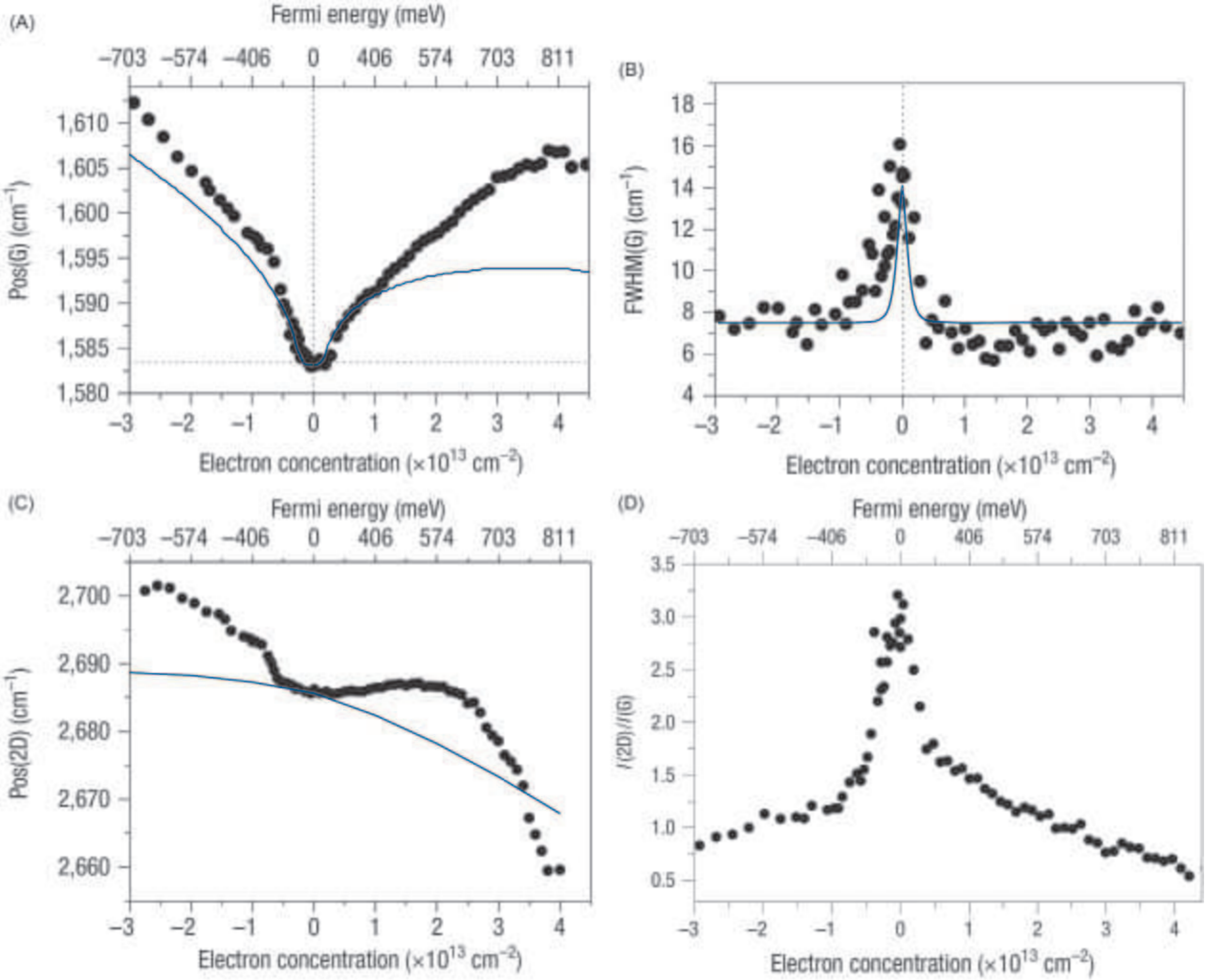

Fig. 8 (A) Pos(G), (B) Pos(2D), (C) FWHM(G) and (D) I(2D)/I(G) as function of doping. Reprinted by permission from Springer Nature Customer Service Centre GmbH: Nature/Springer, Nature Nanotechnology, Das A, Pisana S, Chakraborty B, Piscanec S, Saha SK, Waghmare UV, Novoselov KS, Krishnamurthy HR, Geim AK, Ferrari AC, and Sood AK (2008) Monitoring dopants by Raman scattering in an electrochemically top-gated graphene transistor. *Nature Nanotechnology* 3: 210–215. COPYRIGHT (2008).

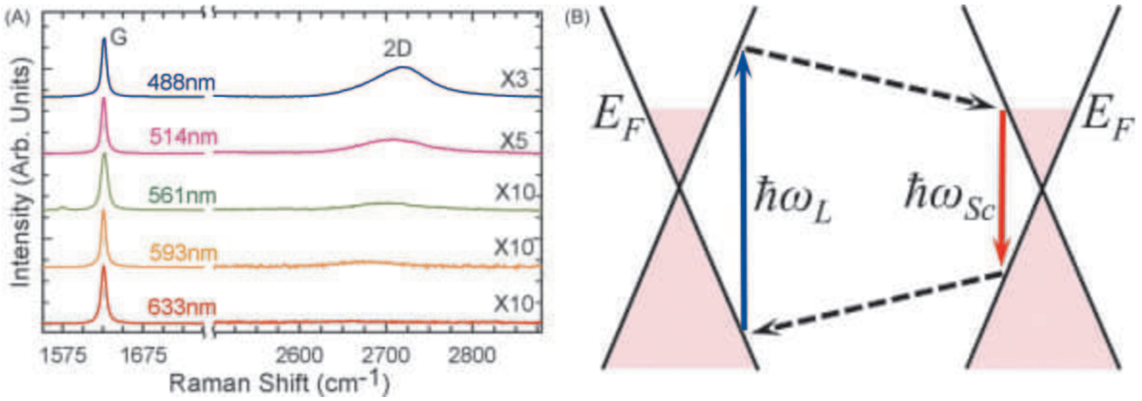

Fig. 9 Effect of high doping on the Raman spectrum of SLG. (A) The 2D peak is suppressed for certain excitation wavelengths. (B) Schematic of SLG band structure for e doped SLG, and 2D peak Raman scattering process. (A) Reprinted with permission from Zhao W, Tan PH, Liu J, and Ferrari AC (2011) Intercalation of few-layer graphite flakes with $FeCl_3$: Raman determination of fermi level, layer by layer decoupling, and stability. *Journal of the American Chemical Society* 133: 5941–5946. Copyright 2011 American Chemical Society; (B) Reprinted by permission from Springer Nature Customer Service Centre GmbH: Springer Nature, Nature Nanotechnology, Ferrari AC and Basko DM (2013) Raman spectroscopy as a versatile tool for studying the properties of graphene. Nature *Nanotechnology* 8: 235–246. COPYRIGHT (2013).

(Zhao et al., 2011). Because of suppression of destructive interference this leads to an enhancement of the G peak when $|E_F|$ matches half of the laser excitation energy $\hbar\omega_L/2$ (Zhao et al., 2011). At high doping the 2D peak is suppressed when the conduction band becomes filled at the energy probed by the laser (Zhao et al., 2011), Fig. 9A. There are 3 cases that can occur in highly doped samples (Ferrari and Basko, 2013): (i) the energy of the scattered (subscript 'Sc') and incoming photon (subscript 'L') are larger than twice E_F, i.e. $\omega_L, \omega_{Sc} > \frac{2E_F}{\hbar}$. in this case the 2D peak scattering mechanism is allowed, Fig. 9B; (ii) $\omega_{Sc} < 2|E_F|/\hbar < \omega_L$, the photon absorption is allowed but the phonon emission is excluded by Pauli blocking; (iii) ω_L, $\omega_{Sc} < 2|E_F|/\hbar$ both photon absorption and phonon emission are blocked.

The Raman spectrum of defected graphene

There are many production methods for graphene, such as MC, CVD, LPE, etc. (Bonaccorso et al., 2012; Backes et al., 2020) and the quality may vary depending on the production technique. E.g. MC SLG is still thought to give the most intrinsic, defect-free and clean samples (Purdie et al., 2018). High quality samples with RT mobility~70,000 cm^{2}V^{-1} s^{-1} in single crystal CVD and 30,000 cm^{2}V^{-1} s^{-1} in polycrystalline CVD can be achieved by using optimized transfer processes (De Fazio et al., 2019). A measure for quality is the number of defects. Anything that breaks the hexagonal symmetry in graphene can be called a defect. Defects in graphene can occur as chemical adsorbates, edges or structural defects, such as vacancies. Perfect zig-zag edges in graphene cannot produce a D peak (Casiraghi et al., 2009; Cançado et al., 2004).

Raman spectroscopy in SLG is sensitive to defects and additional peaks appear. Ref. (Ferrari and Robertson, 2000) introduced a three-stage model of amorphisation going from stage 1: perfect SLG/graphite to nanocrystalline graphene, stage 2: nanocrystalline graphene to low-sp^3 amorphous carbon and stage 3: low-sp^3 amorphous carbon to highly disordered carbon, i.e. tetrahedral amorphous carbon. Here we will focus on stage 1, where the Raman spectrum evolves as follows:

1. The D peak appears and the ratio of D to G peak intensities, I(D)/I(G), increases
2. The D′ peak appears
3. All peaks broaden
4. The D + D′ peak appears
5. At the end of stage 1 the G and D′ peak are so wide that it is sometimes more convenient to consider them as a single, upshifted, wide G peak at 1600 cm^{-1}

Fig. 10 plots the evolution of the Raman spectrum of defected SLG within stage 1. A correlation between the intensity ratio I(D)/I(G) and the average crystal size L_a was first suggested by Tuinstra and Koenig (1970):

$$\frac{\mathrm{I(D)}}{\mathrm{I(G)}} = \frac{\mathrm{C}(\lambda)}{\mathrm{L_a}} \tag{8}$$

where C is a proportionality constant depending on the laser wavelength λ, and C(514 nm) ~4.4 nm (Tuinstra and Koenig, 1970; Knight and White, 1989).

Initially this was interpreted in terms of phonon confinement: the intensity of the forbidden process would be ruled by the 'amount of lifting' of the selection rule (Tuinstra and Koenig, 1970). Now we known that the D peak is produced only in a small region of the crystal near a defect or an edge (Casiraghi et al., 2009). For a nanocrystallite, I(G) is proportional to the sample area,

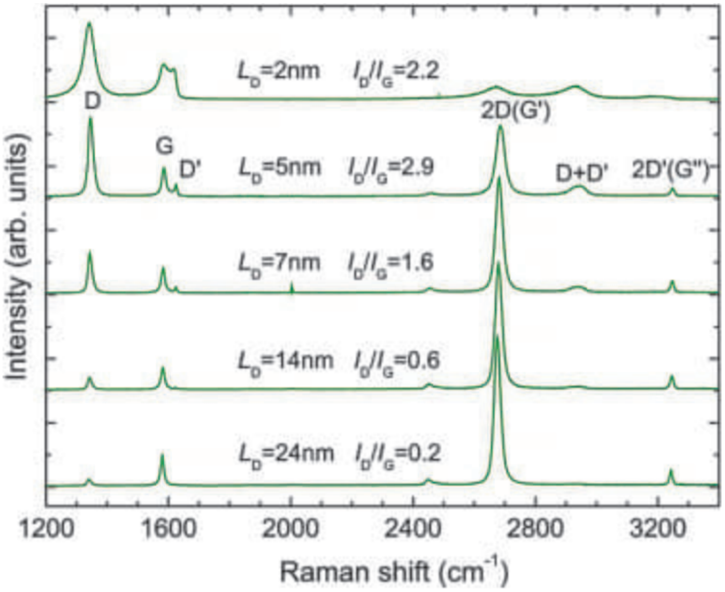

Fig. 10 Evolution of SLG Raman spectrum for increasing amount of defects (stage 1) introduced by Ar$^+$ bombardment. Reprinted with permission from Cançado LG, Jorio A, Ferreira EHM, Stavale F, Achete CA, Capaz RB, Moutinho MVO, Lombardo A, Kulmala TS, and Ferrari AC (2011) Quantifying defects in graphene via Raman spectroscopy at different excitation energies. *Nano Letters* 11: 3190–3196. Copyright 2011 American Chemical Society.

$\propto L_a^2$, while I(D) is proportional to the overall length of an edge, which scales as $\propto L_a$ (Ferrari and Basko, 2013) and thus $I(D)/I(G) \propto 1/L_a$. In stage 1, for a sample with defects, I(D) is proportional to the total number of defects probed by the laser spot. Therefore for an average interdefect distance L_D and laser spot size L_L there are on average $(L_L/L_D)^2$ defects in the area probed by the laser spot and $I(D) \propto (L_L/L_D)^2$ (Ferrari and Basko, 2013). On the other hand, I(G) is proportional to the total area probed by the laser spot $\propto L_L^2$, thus $I(D)/I(G) = C''(\lambda)/L_D^2$. This gives $C''(\lambda)/L_D^2 = I(D)/I(G) = C(\lambda)/L_a$ (Ferrari and Basko, 2013). However, for an increasing amount of defects the Tuinstra-Koenig relation will no longer hold (Ferrari and Robertson, 2000), as in this case $I(D)$ starts to decrease. The D peak is due to a breathing mode in 6-atoms rings (Ferrari and Robertson, 2000). With increasing amount of defects these rings will start to break and, as a result, I(D) will decrease, which is the onset of stage 2.

Taking the excitation energy dependence (E_L^4) of the Raman peak intensities into account, the following relation for the interdefect distance has been extracted (Cançado et al., 2011):

$$L_D^2\left[\mathrm{nm}^2\right] = \frac{(4.3 \pm 1.3) \times 10^3}{E_L^4\ \left[\mathrm{eV}^4\right]}\left(\frac{I(D)}{I(G)}\right)^{-1} \tag{9}$$

with the relation $n_D[\mathrm{cm}^{-2}] = 10^{14}/(\pi L_D^2)$, the defect concentration n_D can be related to I(D)/I(G) (Cançado et al., 2011):

$$n_D\left[\mathrm{cm}^{-2}\right] = (7.3 \pm 2.2) \times 10^9 E_L^4\left[\mathrm{eV}^4\right]\left(\frac{I(D)}{I(G)}\right) \tag{10}$$

Eqs. (9) and (10) can then be used directly to estimate the interdefect distance and corresponding defect concentration in SLG by calculating I(D)/I(G) from the fitted D and G peaks. These relations are limited to Raman active defects. Perfect zig-zag edges (Beams et al., 2011; Casiraghi et al., 2009), charged impurities (Casiraghi et al., 2007b; Das et al., 2008), intercalants (Zhao et al., 2011) and uniaxial or biaxial strain (Mohiuddin et al., 2009; Lee et al., 2008; Proctor et al., 2009; Zabel et al., 2012) do not generate a D peak. Other Raman signatures can be used for these 'silent' defects.

Eqs. (8) and (9) are valid for undoped SLG. However, most samples are not intrinsic and show $E_F \sim 200$–500 meV (Bruna et al., 2014). In the combined case of defects and doping a modified formula has to be used to correctly estimate the defect concentration and interdefect distance, due to the E_F dependence of I(D). (Bruna et al., 2014). Ref. Bruna et al. (2014) showed that I(D) decreases as E_F increases, Fig. 11, which would result in an underestimation of defects in doped SLG. By including the correction for the doping dependence of I(D), Eqs. (9) and (10) become (Bruna et al., 2014):

$$L_D^2\left[\mathrm{nm}^2\right] = \frac{(1.2 \pm 0.3) \times 10^3}{E_L^4\ \left[\mathrm{eV}^4\right]}\left(\frac{I(D)}{I(G)}\right)^{-1}\{E_F[eV]\}^{-(0.54\pm0.04)} \tag{11}$$

and

$$n_D\left[\mathrm{cm}^{-2}\right] = (2.7 \pm 0.8) \times 10^{10} E_L^4\left[\mathrm{eV}^4\right]\left(\frac{I(D)}{I(G)}\right)\{E_F[eV]\}^{(0.54\pm0.04)} \tag{12}$$

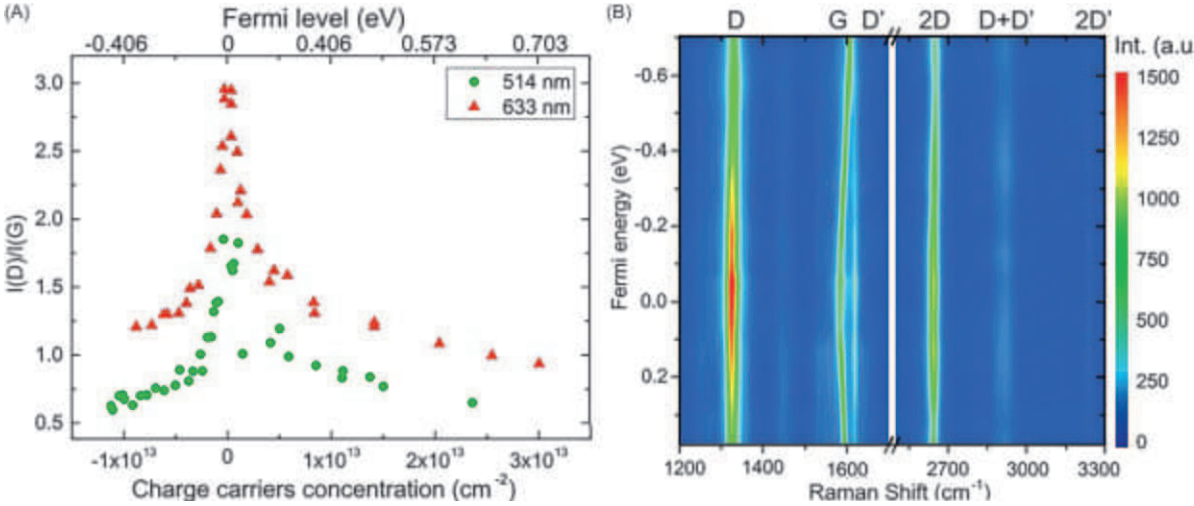

Fig. 11 (A) I(D)/I(G) as function of Fermi level E_F and charge carrier concentration. (B) Contour plot of the intensity of the Raman signal as function of E_F. Reprinted with permission from Bruna M, Ott AK, Ijäs M, Yoon D, Sassi U, and Ferrari AC (2014) Doping dependence of the Raman spectrum of defected graphene. *ACS Nano* 8: 7432–7441. Copyright 2014 American Chemical Society.

The doping dependence of the D peak intensity can be explained by taking the scattering rate or line broadening energy $\gamma = \hbar\tau^{-1}$ into account, where τ is the lifetime of an electronic state (Basko et al., 2009). In the presence of defects and doping the total scattering rate γ_{tot} is governed by electron-phonon interactions as well as scattering due to defects and e-e interactions, which in turn strongly depends on the E_F. It is given by (Bruna et al., 2014): $\gamma_{tot} = \gamma_{e-ph} + \gamma_D + \gamma_{ee}(E_F)$, where $\gamma_{ee}(E_F) = 0.06|E_F|$ (Basko et al., 2009). Thus, for increasing E_F, γ_{ee} will increase, and so will γ_{tot}. A higher scattering rate indicates a shorter lifetime, which, in turn, results in an increase in peak width and decrease in peak intensity. Eqs. (11) and (12) are valid for defects within stage 1 and for $E_F < E_L/2$ in order to avoid Pauli blocking (Bruna et al., 2014).

Magnetic fields

Magnetic fields have also an effect on the Raman spectrum of graphene. In the presence of a magnetic field, electronic trajectories will become circular, thus the backscattering condition of the Raman scattering process will be modified, such that the emitted phonons have smaller momenta (Ando, 2007; Goerbig et al., 2007). Ref. (Faugeras et al., 2010) observed a shift toward lower wavenumbers and a broadening of the 2D peak in SLG when applying a perpendicular magnetic field up to 30 T. In the presence of such a strong magnetic field the electronic states are quantized into discrete levels, called Landau levels (Kittel, 2005). Raman spectroscopy can also be used to probe those Landau levels and extract the Fermi velocity (Ferrari and Basko, 2013). Without magnetic field, electronic excitations in SLG have a continuous spectrum (Wallace, 1947). In the presence of a magnetic field, as result of this electronic quantization, inelastic scattering of photons occurs due to inter-Landau level transitions (Faugeras et al., 2011) resulting in sharp B-field dependent peaks where, instead of a phonon, an e-h pair is emitted (Kashuba and Fal'ko, 2012; Kashuba and Fal'ko, 2009; Mucha-Kruczyński et al., 2010). Applying magnetic fields can also be used to estimate the e-phonon coupling and probe the electronic Landau levels (Faugeras et al., 2011; Kim et al., 2012; Kossacki et al., 2011).

Key issues

While acquiring Raman spectra is not particularly difficult, the data analysis needs to be done considering the contribution of different influences, such as strain, doping, defects, etc. Instead of taking single point spectra, Raman measurements are often performed as mapping, where spectra are recorded in a grid pattern across areas of several $\sim\mu m^2$. Having a high spatial resolution is important for Raman mapping. The laser spot size, thus the spatial resolution, in conventional Raman spectroscopy is dictated by the diffraction limit of light, in turn proportional to the laser wavelength, thus of the order of ~1 µm (Cardona and Güntherodt, 1982).

To analyze small flakes (<1 µm) with weak Raman signals, enhanced Raman scattering techniques, such as surface enhanced Raman scattering (SERS) (Kneipp et al., 2006) or tip-enhanced Raman scattering (TERS) can be used (Stöckle et al., 2000; Cao and Sun, 2022; Hartschuh et al., 2003). Both techniques exploit surface plasmons excited in metallic nanostructures by the incident radiation field of the laser, whereas in TERS the metallic nanostructure is provided by the apex of an atomic force microscopy tip coated with a noble metal such as Au or Ag (Cao and Sun, 2022). With TERS, samples can be raster scanned with very high spatial resolution around tens of nm or less. Information can be derived combining topography with Raman at each raster point (Cao and Sun, 2022). SLG is ideal to study SERS effects of differently shaped and sized plasmonic nanostructures (Schedin et al., 2010; Lee et al., 2011). TERS has also been used to study twisted BLG (Gadelha et al., 2021), extracting the moiré wavelength and imaging different stacking regions (Gadelha et al., 2021). TERS can used for LMs in general, to identify local inhomogeneities, such as local strain, doping or defects (Malard et al., 2021; Rabelo et al., 2020).

Conclusion

We have given an overview of Raman scattering in graphene. We have discussed how Raman spectroscopy is sensitive to the number of layers and structural defects as well as external influences such as doping, strain and magnetic fields. Raman spectroscopy is a powerful technique to extract quantitative information about the quality of graphene, its doping, and type and amount of strain, crucial for further processing graphene for any kind of device (Backes et al., 2020). It is key for quality control when moving toward industrial scale production of graphene (Backes et al., 2020). Raman spectroscopy has also been employed to study device performances and to understand their working principle. E.g. it was used to shed light on the charge-discharge process of graphene-based energy storage devices (Share et al., 2016). Raman spectroscopy continues to be used for fundamental material studies (Cong et al., 2020).

Raman spectroscopy is a prime characterization techniques for all types of carbons and contributed significantly to the understanding of graphene and LMs. However, there are over 1800 exfoliable or potentially exfoliable LMs (Mounet et al., 2018), of which only a small fraction has been studied so far. Raman spectroscopy is already being used to characterize LMs beyond graphene and to study the interaction between different LMs in heterostructures in the high and low frequency range. E.g. Raman spectroscopy has been used to study magnetic ordering in magnetic LMs (Kim et al., 2019).

Other advanced Raman techniques such as coherent anti-Stokes Raman scattering (CARS) are emerging for the characterization of LMs (Virga et al., 2019). CARS is a non-linear optical process that exploits the interaction between two laser pulses and is used for imaging samples. As for conventional Raman scattering, the first laser beam 'pump', ω_{p}, will cause S-Raman scattering, ω_{S}, creating a phonon, Fig. 12. This phonon can then be used directly for an AS-Raman process under the condition that the correlated photon energies (ω_{p}) match (Virga et al., 2019), Fig. 12. During this process the interaction of laser pulses and sample results in the generation of vibrational coherences, i.e. the atoms oscillate with the same phase, which in turn can lead to a signal enhancement of several orders of magnitude (Virga et al., 2019). CARS is particularly interesting for biological research due to its marker free imaging and ability to suppress fluorescence that would otherwise overshadow the Raman signal of the sample (Begley et al., 1974).

Acknowledgments

We acknowledge funding from ERC grants GIPT, Hetero2D, GSYNCOR, EU Graphene Flagship, EU Grants Graph-X, GREENCAP, EIC grant CHARM, and EPSRC grants EP/X015742/1, EP/V000055/1, EP/N010345/1, EP/L016087/1, EP/P00119X/1.

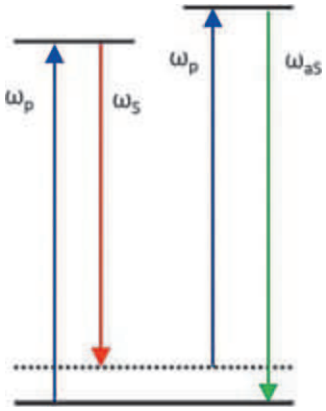

Fig. 12 Schematic of the coherent anti-Stokes Raman scattering process.

References

Ando T (2007) Magnetic oscillation of optical phonon in graphene. *Journal of the Physical Society of Japan* 76: 024712.

Backes C, Abdelkader AM, Concepción A, Andrieux-Ledier A, et al. (2020) Production and processing of graphene and related materials. *2D materials* 7: 022001.

Basko DM, Piscanec S, and Ferrari AC (2009) Electron-electron interactions and doping dependence of the two-phonon Raman intensity in graphene. *Physical Review B* 80: 165413.

Beams R, Cançado LG, and Novotny L (2011) Low temperature Raman study of the electron coherence length near graphene edges. *Nano Letters* 11: 1177–1181.

Begley RF, Harvey AB, and Byer RL (1974) Coherent anti-Stokes Raman spectroscopy. *Applied Physics Letters* 25: 387.

Bonaccorso F, Lombardo A, Hasan T, Sun Z, Colombo L, and Ferrari AC (2012) Production and processing of graphene and 2d crystals. *Materials Today* 15: 564–589.

Brüesch P (1986) *Phonons: Theory and Experiments II*. Springer.

Bruna M, Ott AK, Ijäs M, Yoon D, Sassi U, and Ferrari AC (2014) Doping dependence of the Raman spectrum of defected graphene. *ACS Nano* 8: 7432–7441.

Bunch JS, van der Zande AM, Verbridge SS, Frank IW, Tanenbaum DM, Parpia JM, Craighead HG, and McEuen PL (2007) Electromechanical resonators from graphene sheets. *Science* 315: 490–493.

Cançado LG, Jorio A, Ferreira EHM, Stavale F, Achete CA, Capaz RB, Moutinho MVO, Lombardo A, Kulmala TS, and Ferrari AC (2011) Quantifying defects in graphene via Raman spectroscopy at different excitation energies. *Nano Letters* 11: 3190–3196.

Cançado LG, Pimenta MA, Neves BRA, Dantas MSS, and Jorio A (2004) Influence of the atomic structure on the Raman spectra of graphite edges. *Physical Review Letters* 93: 247401.

Cao Y and Sun M (2022) Tip-enhanced Raman spectroscopy. *Reviews in Physics* 8: 100067.

Cardona M and Güntherodt G (1982) *Light Scattering in Solids II*. Springer.

Casiraghi C, Hartschuh A, Lidorikis E, Qian H, Harutyunyan H, Gokus T, Novoselov KS, and Ferrari AC (2007a) Rayleigh imaging of graphene and graphene layers. *Nano Letters* 7: 2711–2717.

Casiraghi C, Hartschuh A, Qian H, Piscanec S, Georgi C, Fasoli A, Novoselov KS, Basko DM, and Ferrari AC (2009) Raman spectroscopy of graphene edges. *Nano Letters* 9: 1433–1441.

Casiraghi C, Pisana S, Novoselov KS, Geim AK, and Ferrari AC (2007b) Raman fingerprint of charged impurities in graphene. *Applied Physics Letters* 91: 233108.

Cong X, Liu X-L, Lin M-L, and Tan P-H (2020) Application of Raman spectroscopy to probe fundamental properties of two-dimensional materials. *npj 2D Materials and Applications* 4: 13.

Das A, Pisana S, Chakraborty B, Piscanec S, Saha SK, Waghmare UV, Novoselov KS, Krishnamurthy HR, Geim AK, Ferrari AC, and Sood AK (2008) Monitoring dopants by Raman scattering in an electrochemically top-gated graphene transistor. *Nature Nanotechnology* 3: 210–215.

de Fazio D, Purdie DG, Ott AK, Braeuninger-Weimer P, Khodkov T, Goossens S, Taniguchi T, Watanabe K, Livreri P, Koppens FHL, Hofmann S, Goykhman I, Ferrari AC, and Lombardo A (2019) High-mobility, wet-transferred graphene grown by chemical vapor deposition. *ACS Nano* 13: 8926–8935.

Ding F, Ji H, Chen Y, Herklotz A, Dörr K, Mei Y, Rastelli A, and Schmidt OG (2010) Stretchable graphene: A close look at fundamental parameters through biaxial straining. *Nano Letters* 10: 3453–3458.

Dresselhaus MS, Dresselhaus G, and Eklund PC (1996) Raman scattering in fullerenes. *Journal of Raman Spectroscopy* 27: 351–371.

Dresselhaus MS, Dresselhaus G, Saito R, and Jorio A (2005) Raman spectroscopy of carbon nanotubes. *Physics Reports* 409: 47–99.

Faugeras C, Amado M, Kossacki P, Orlita M, Kühne M, Nicolet AAL, Latzshev YI, and Potemski M (2011) Magneto-Raman scattering of graphene on graphite: Electronic and phonon excitations. *Physical Review Letters* 107: 036807.

Faugeras C, Kossacki P, Basko DM, Amado M, Sprinkle M, Berger C, de Heer WA, and Potemski M (2010) Effect of a magnetic field on the two-phonon Raman scattering in graphene. *Physical Review B* 81: 155436.

Ferrari AC and Basko DM (2013) Raman spectroscopy as a versatile tool for studying the properties of graphene. *Nature Nanotechnology* 8: 235–246.

Ferrari AC, Meyer JC, Scardaci V, Casiraghi C, Lazzeri M, Mauri F, Piscanec S, Jiang D, Novoselov KS, Roth S, and Geim AK (2006) Raman spectrum of graphene and graphene layers. *Physical Review Letters* 97: 187401.

Ferrari AC and Robertson J (2000) Interpretation of Raman spectra of disordered and amorphous carbon. *Physical Review B* 61: 14095–14107.

Gadelha AC, Ohlberg DAA, Rabelo C, Neto EGS, Vasconcelos TL, Campos JL, Lemos JS, Ornelas V, Miranda D, Nadas R, Santana FC, Watanabe K, Taniguchi T, van Troeye B, Lamparski M, Meunier V, Nguyen V-H, Paszko D, Charlier J-C, Campos LC, Cançado LG, Medeiros-Ribeiro G, and Jorio A (2021) Localization of lattice dynamics in low-angle twisted bilayer graphene. *Nature* 590: 405–409.

Goerbig MO, Fuchs JN, Kechedzhi K, and Fal'ko VI (2007) Filling-factor-dependent magnetophonon resonance in graphene. *Physical Review Letters* 99: 087402.

Hartschuh A, Sánchez EJ, Xie XS, and Novotny L (2003) High-resolution near-field Raman microscopy of single-walled carbon nanotubes. *Physical Review Letters* 90: 095503.

Huang M, Yan H, Heinz TF, and Hone J (2010) Probing strain-induced electronic structure change in graphene by Raman spectroscopy. *Nano Letters* 10: 4074–4079.

Kalbac M, Reina-Cecco A, Farhat H, Kong J, Kavan L, and Dresselhaus MS (2010) The influence of strong electron and hole doping on the Raman intensity of chemical vapor-deposition graphene. *ACS Nano* 4: 6055–6063.

Kashuba O and Fal'ko VI (2012) Role of electronic excitations in magneto-Raman spectra of graphene. *New Journal of Physics* 14: 105016.

Kashuba O and Fal'ko VI (2009) Signature of electronic excitations in the Raman spectrum of graphene. *Physical Review B* 80: 241404.

Kim K, Lee J-U, and Cheong H (2019) Raman spectroscopy of two-dimensional magnetic van der Waals materials. *Nanotechnology* 30: 452001.

Kim Y, Ma Y, Imambekov A, Kalugin NG, Lombardo A, Ferrari AC, Kono J, and Smirnov D (2012) Magnetophonon resonance in graphite: High-field Raman measurements and electron-phonon coupling contributions. *Physical Review B* 85: 121403.

Kittel C (2005) *Introduction to Solid State Physics*. John Wiley and Sons, Inc.

Kneipp K, Moskovits M, and Kneipp H (2006) *Surface Enhanced Raman Scattering: Physics and Applications*. Springer.

Knight DS and White WB (1989) Characterization of diamond films by Raman spectroscopy. *Journal of Materials Research* 4: 385–393.

Kossacki P, Faugeras C, Kühne M, Orlita M, Nicolet AAL, Schneider JM, Basko DM, Latyshev YI, and Potemski M (2011) Electronic excitations and electron-phonon coupling in bulk graphite through Raman scattering in high magnetic fields. *Physical Review B* 84: 235138.

Krishnan RS and Narayanan PS (1950) Intensity ratio of the Raman lines in diamond. *Proceedings of the Indian Academy of Sciences - Section A* 32: 352.

Landsberg G and Mandelstam L (1928) Über die Lichtzerstreuung in Kristallen. *Zeitschrift für Physik* 50: 769–780.

Larmor J (1907) *Memoir and scientific correspondence of the late Sir George Gabriel Stokes*, 2 vols. Cambridge University Press.

Lee C, Wei X, Kysar JW, and Hone J (2008) Measurement of the elastic properties and intrinsic strength of monolayer graphene. *Science* 321: 385.

Lee J, Shim S, Kim B, and Shin HS (2011) Surface-enhanced Raman scattering of single- and few-layer graphene by the deposition of gold nanoparticles. *Chemistry – A European Journal* 17: 2381–2387.

Loudon R (1965) Theory of the resonance Raman effect in crystals. *Journal de Physique France* 26: 677–683.

Maiman TH (1960) Stimulated optical radiation in ruby. *Nature* 187: 493–494.

Malard LM, Lafeta L, Cunha RS, Nadas R, Gadelha A, Cançado LG, and Jorio A (2021) Studying 2D materials with advanced Raman spectroscopy: Cars, SRS and TERS. *Physical Chemistry Chemical Physics* 23: 23428–23444.

Metzger C, Rémi S, Liu M, Kusminskiy SV, Castro Neto AH, Swan AK, and Goldberg BB (2010) Biaxial strain in graphene adhered to shallow depressions. *Nano Letters* 10: 6–10.

Mie G (1908) On optical characteristics of turbid media, with special reference to colloid metallic solutions. *Ann. Phys.* 330: 377–445.

Mohiuddin TMG, Lombardo A, Nair RR, Bonetti A, Savini G, Jalil R, Bonini N, Basko DM, Galiotis C, Marzari N, Novoselov KS, Geim AK, and Ferrari AC (2009) Uniaxial strain in graphene by Raman spectroscopy: *G* peak splitting, Grüneisen parameters, and sample orientation. *Physical Review B* 79: 205433.

Mohr M, Maultzsch J, and Thomsen C (2010) Splitting of the Raman 2D band of graphene subjected to strain. *Physical Review B* 82: 201409.

Mounet N, Gibertini M, Schwaller P, Campi D, Merkys A, Marrazzo A, Sohier T, Castelli IE, Cepellotti A, Pizzi G, and Marzari N (2018) Two-dimensional materials from high-throughput computational exfoliation of experimentally known compounds. *Nature Nanotechnology* 13: 246–252.

Mucha-Kruczyński M, Kashuba O, and Fal'ko VI (2010) Spectral features due to inter-Landau-level transitions in the Raman spectrum of bilayer graphene. *Physical Review B* 82: 045405.

Nemanich RJ, Lucovsky G, and Solin SA (1977) Infrared active optical vibrations of graphite. *Solid State Communications* 23: 117–120.

Novoselov KS, Geim AK, Morozov SV, Jiang D, Zhang Y, Dubonos SV, Grigorieva IV, and Firsov AA (2004) Electric field effect in atomically thin carbon films. *Science* 306: 666–669.

Piscanec S, Lazzeri M, Mauri F, Ferrari AC, and Robertson J (2004) Kohn anomalies and electron-phonon interactions in graphite. *Physical Review Letters* 93: 185503.

Pizzi G, Milana S, Ferrari AC, Marzari N, and Gibertini M (2021) Shear and breathing modes of layered materials. *ACS Nano* 15: 12509–12534.

Placzek G (1934) *Rayleigh-Streuung und Raman-Effect*. Leipzig: Akademische Verlagsgesellschaft.

Pocsik I, Hundhausen M, Koos M, and Ley L (1998) Origin of the D peak in the Raman spectrum of microcrystalline graphite. *Journal of Non-Crystalline Solids* 227: 1083–1086.

Proctor JE, Gregoryanz E, Novoselov KS, Lotya M, Coleman JN, and Halsall MP (2009) High-pressure Raman spectroscopy of graphene. *Physical Review B* 80: 073408.

Purdie DG, Pugno NM, Taniguchi T, Watanabe K, Ferrari AC, and Lombardo A (2018) Cleaning interfaces in layered materials heterostructures. *Nature Communications* 9: 5387.

Rabelo C, Vasconcelos TL, Publio BC, Miranda H, Cançado LG, and Jorio A (2020) Linkage between micro- and nano-Raman spectroscopy of defects in graphene. *Physical Review Applied* 14: 024056.

Raman CV and Krishnan KS (1928) A new type of secondary radiation. *Nature* 121: 501–502.

Schawlow AL and Townes CH (1958) Infrared and optical masers. *Physical Review* 112: 1940–1949.

Schedin F, Lidorikis E, Lombardo A, Kravets VG, Geim AK, Grigorenko AN, Novoselov KS, and Ferrari AC (2010) Surface-enhanced Raman spectroscopy of graphene. *ACS Nano* 4: 5617–5626.

Share K, Cohn AP, Carter RE, and Pint CL (2016) Mechanism of potassium ion intercalation staging in few layered graphene from in situ Raman spectroscopy. *Nanoscale* 8: 16435–16439.

Smekal A (1923) Zur Quantentheorie der Dispersion. *Naturwissenschaften* 11: 873–875.

Stöckle RM, Suh YD, Deckert V, and Zenobi R (2000) Nanoscale chemical analysis by tip-enhanced Raman spectroscopy. *Chemical Physics Letters* 318: 131–136.

Strutt JW Lord Rayleigh (1871) On the light from the sky, its polarization and colour. *Philosophical Magazine* 41: 274.

Tan PH, Han WP, Zhao WJ, Wu ZH, Chang K, Wang H, Wang YF, Bonini N, Marzari N, Pugno N, Savini G, Lombardo A, and Ferrari AC (2012) The shear mode of multilayer graphene. *Nature Materials* 11: 294–300.

The Nobel Prize (2022) *The Nobel Prize in Physics 1930: Sir Chandrasekhara Venkata Raman*. https://www.nobelprize.org/prizes/physics/1930/raman/facts/. [Accessed].

Thomsen C and Reich S (2000) Double resonant Raman scattering in graphite. *Physical Review Letters* 85: 5214–5217.

Tuinstra F and Koenig JL (1970) Raman spectrum of graphite. *The Journal of Chemical Physics* 53: 1126–1130.

Virga A, Ferrante C, Batignani G, De Fazio D, Nunn ADG, Ferrari AC, Cerullo G, and Scopigno T (2019) Coherent anti-stokes Raman spectroscopy of single and multi-layer graphene. *Nature Communications* 10: 3658.

Wallace PR (1947) The band theory of graphite. *Physical Review* 71: 622–634.

Yoon D, Son Y-W, and Cheong H (2011) Strain-dependent splitting of the double-resonance Raman scattering band in graphene. *Physical Review Letters* 106: 155502.

Yu PY and Cardona M (1996) *Fundamentals of Semiconductors: Physics and Material Properties*. Springer.

Zabel J, Nair RR, Ott A, Georgiou T, Geim AK, Novoselov KS, and Casiraghi C (2012) Raman spectroscopy of graphene and bilayer under biaxial strain: Bubbles and balloons. *Nano Letters* 12: 617–621.

Zhang X, Han WP, Wu JB, Milana S, Lu Y, Li QQ, Ferrari AC, and Tan PH (2013) Raman spectroscopy of shear and layer breathing modes in multilayer MoS_2. *Physical Review B* 87: 115413.

Zhao W, Tan PH, Liu J, and Ferrari AC (2011) Intercalation of few-layer graphite flakes with $FeCl_3$: Raman determination of Fermi level, layer by layer decoupling, and stability. *Journal of the American Chemical Society* 133: 5941–5946.

Quantum devices in graphene

Klaus Ensslin, Physics Department, ETH Zurich, Zürich, Switzerland

© 2024 Elsevier Ltd. All rights reserved.

Introduction 248
One-dimensional systems in graphene 249
Quantum dots in graphene 250
Pauli blockade in graphene double quantum dots 252
Spin lifetimes in graphene quantum dots 253
Prospects of graphene qubits 254
Acknowledgments 255
References 255

Abstract

Graphene is a material with exceptional electronic properties, only comparable to the best and cleanest semiconductors. Most semiconductors have a bandgap which is of the order of 1 eV, i.e. much larger than the thermal energy at room temperature. Confining charge carriers to reduced dimensions mostly relies on this bandgap. Graphene is a promising material to host individual charge carriers and spins for qubit applications with long coherence times. However, single-layer graphene does not have a bandgap and hence similar gating schemes as they have been successful to confine carriers in materials such as Si and GaAs are not feasible. In this review we describe how quantum confinement of excellent quality can be achieved in bilayer graphene, that has an electric field-tunable bandgap. We discuss quantized conductance in one-dimensional channels, Coulomb blockade in zero-dimensional islands called quantum dot as well as controlled single hole and single electron occupation of these dots. We close by discussing how spin and valley qubits in graphene could become useful objects for physics studies as well as for quantum information applications.

Key points

- A gap can be opened in bilayer graphene by suitable back and top-gate voltages
- If the Fermi energy is positioned in the gap current is completely suppressed
- Using patterned electrodes one can define lateral confinement potentials
- Quantum point contacts display quantized conductance
- Quantum dots show high-quality Coulomb blockade
- Using transport spectroscopy in magnetic field the spin and valley degrees of freedom for each carrier number can be determined
- Charge detectors can be built using the same gating technology
- Spin coherence times exceeding 50 ms are measured using spin-to-charge conversion

Introduction

Graphene displays excellent electronic properties. For example, the experimentally detected high-quality fractional quantum Hall states (Bolotin et al., 2009) even in CVD-grown samples (Schmitz et al., 2020) compare with the best transport data in AlGaAs-GaAs heterostructures, the workhorse for high-mobility electron transport for the last 30 years. Graphene has become a versatile material to investigate novel physics in two-dimensional systems. To further confine carriers to one-dimension, so-called quantum wires, or even zero-dimensional systems, so-called quantum dots, the potential landscape in which the charge carriers reside needs to have barriers. The simplest way is to etch the material away in areas, where carriers should not be. In graphene this technological approach has worked to some extent, but in the end was limited by the charges and imperfections occurring at the sample edges (Bischoff et al., 2015). In semiconductors the Fermi level at a surface is typically pinned to some midgap energy. For a free surface this means that carriers are depleted away from the surface and occupy bulk sites where the Fermi level is above (below) the conduction (valence) band edge. Graphene being a semi-metal without a gap leads to the peculiar situation that the electronic wavefunction of the charge carriers extends all the way to an edge and side depletion does not occur. In this sense graphene combines the properties of a metal, namely no surface (side) depletion, with the low carrier density and therefore large Fermi wavelength of a semiconductor.

The best quantum devices in semiconductors are obtained by so-called split-gate techniques. This technique was introduced for quantum point contacts in AlGaAs-GaAs heterostructures (van Wees et al., 1988; Wharam et al., 1988). Split-gates were patterned

https://doi.org/10.1016/B978-0-323-90800-9.00221-3

between the source and drain electrodes. The carrier density below the split gates was depleted by suitable gate voltages such that the current had to flow through the narrow one-dimensional channel between the split gates. This led to the discovery of quantized conductance in one-dimension (van Wees et al., 1988; Wharam et al., 1988). The general use of split gates as well as more sophisticated double layer gating techniques are now routinely used to define zero-dimensional systems or quantum dots in GaAs, Si and Ge (Zwerver et al., 2022). Such an approach fundamentally fails in single layer graphene because of the absence of gap. Charge carriers can not be depleted by gate electrodes.

Bilayer graphene comes to the rescue, since a bandgap can be opened by vertical electric fields (Oostinga et al., 2008). Typical bandgaps are 50–100 meV for displacement fields of order 1 V/nm. For measurements these bandgaps are expected to be large enough to create barriers that the carriers cannot overcome by thermal excitation if the experiments are performed at temperatures of 1 K or below. While the bandgaps were detected and quantified both in transport and optical measurements, the electrical resistance across a gate-defined barrier remained low for many years as reported by many groups, see e.g. (Zhu et al., 2017).

The difference was made by using a graphite back gate rather than a metallic back gate (Overweg et al., 2018a). This way resistances across gate barriers larger than 10^{10} Ohm were measured. Using split-gate electrodes a narrow one-dimensional channel was realized. In contrast to semiconductors, where the bandgap is independent of gate voltages, an additional top gate on top of the constriction created by the split gates was used to tune the electronic width of the channel and observe quantized conductance in graphene (Overweg et al., 2018a). This technology was further developed over the years to fabricate highly tunable quantum devices, build graphene-based qubits and measure their lifetimes.

One-dimensional systems in graphene

Fig. 1 shows a schematic of a device which was used to measure quantized conductance. The bilayer graphene was produced in a usual exfoliation process using a graphite sample. In a subsequent stacking process the bilayer graphene was encapsulated by hexagonal boron nitride (hBN) layers and then placed on a graphite back gate. The whole stack was placed on an oxidized Si substrate. Source and drain edge contacts were made followed by the definition of split gates that leave a gap between them open. Finally, a layer of Al_2O_3 was deposited by atomic layer deposition followed by a channel gate that allows the tuning of the Fermi energy in the one-dimensional channel defined between the split gates.

The conductance between source and drain was measured as a function of voltages applied to split gates and back gate (Overweg et al., 2018a). The gate voltages were adjusted to maximize the gap opening in bilayer graphene and keep the Fermi energy in the gap. This way the carrier gas is depleted in the regions of bilayer graphene covered by the split-gates and the current will flow through the opening, called quantum point contact, defined by the split gates. In quantum point contacts realized on GaAs-AlGaAs heterostructures one would then tune the split gates to even more negative voltage to deplete the narrow channel as a consequence of the fringing electric fields emanating from the split gates. This is not possible in the configuration shown in Fig. 1, since tuning the split gate voltages would move the Fermi energy in the regions below the split gates out of the bilayer graphene bandgap and confinement would be lost. One therefore needs another tuning parameter, which is the additional channel gate shown in orange in Fig. 1. In the regions where it is above one of the split gates it will not affect the carrier gas in graphene because of screening. The voltage applied to the channel gate will only affect the carriers directly in the one-dimensional channel.

Fig. 2 shows the sample conductance versus channel gate voltage V_{ch} while keeping back gate and split gate voltages constant, as described above (for details see Lee et al., 2020). For this particular configuration the bulk of the sample as well as the one-dimensional channel was occupied with electrons. For negative channel voltages (here below −6.5 V) the one-dimensional channel is depleted and the entire device is pinched off. For channel voltages more positive than the pinch-off voltage of the channel the conductance starts to increase and shows plateaus separated by $\Delta G = 4\ e^2/h$.

Such quantized conductance plateaus have been observed in semiconductor one-dimensional channels more than 30 years ago (van Wees et al., 1988; Wharam et al., 1988). In that case the plateaus were quantized in units of $2\ e^2/h$, where the factor of 2 arose

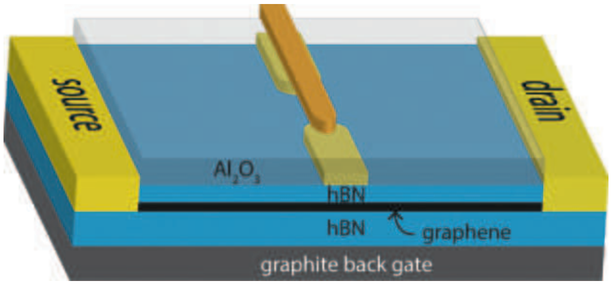

Fig. 1 Sample layout. A bilayer graphene flake is encapsulated in hexagonal boron nitride (hBN). It is contacted by a source and drain contact and has a graphite back gate (gray) below, two split gates (yellow) and a channel gate (orange) on top. The channel gate is separated from the split gates by a dielectric layer of Al_2O_3. Adapted from Ref. Overweg H, Eggimann H, Chen X, Slizovskiy S, Eich M, Pisoni R, Lee Y, Rickhaus P, Watanabe K, Taniguchi T, Fal'ko V, Ihn T, and Ensslin K (2018a) Electrostatically induced quantum point contacts in bilayer graphene. *Nano Letters* 18: 553.

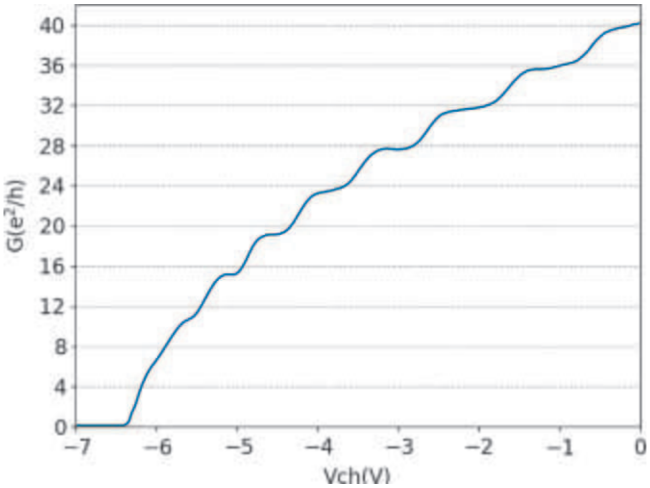

Fig. 2 Conductance G of the induced channel function of V_{CH}. The conductance shows steps of $\Delta G = 4\ e^2/h$. Adapted from Ref. Lee Y, Knothe A, Overweg H, Eich M, Kurzmann A, Taniguchi T, Wantanabe K, Fal'ko V, Ihn T, Ensslin K, and Rickhaus P (2020) Tunable valley splitting due to topological orbital magnetic moment in bilayer graphene quantum point contacts. *Physical Review Letters* 124: 126802.

from spin degeneracy. When graphene became available it seemed obvious that quantized conductance should also be observable in one-dimensional channels. Despite different technological approaches it took much longer than expected to reach this goal. The data shown in Fig. 2 shows one important aspect of graphene, which directly reflects its peculiar bandstructure. The honeycomb arrangement of the C atoms in real space means that the primitive unit cell contains two atoms. As a consequence there are two inequivalent points in reciprocal space, the so-called K and K'points, leading to an additional valley degeneracy. The factor of 4 in the conductance quantization in graphene directly reflects spin and valley degeneracy.

The bandstructure of graphene offers more surprises compared to the relatively simple parabolic band dispersion in most semiconductors. For large displacement fields in bilayer graphene, which are required to maximize the gap of the insulating regions, the band dispersion becomes Mexican hat-like and topological effects become relevant (McCann et al., 2007). This leads to peculiar magnetic field dependencies of the conductance plateaus (Overweg et al., 2018b) very different from what has been observed in semiconductors.

Quantum dots in graphene

Quantum dots in semiconductors are among the contenders for a successful qubit-based technology. High quality quantum dots in graphene that can be controlled down to the single carrier regime have become available within the last 5 years. Fig. 3 shows a schematic of the device. The vertical structure is similar to what is shown in Fig. 1 for the one-dimensional system. The main difference here is that the channel defined by the split gates is elongated and the Fermi energy along the channel can be locally controlled by various finger gates. The tuning of back gate and split gates is similar as in the one-dimensional case. The

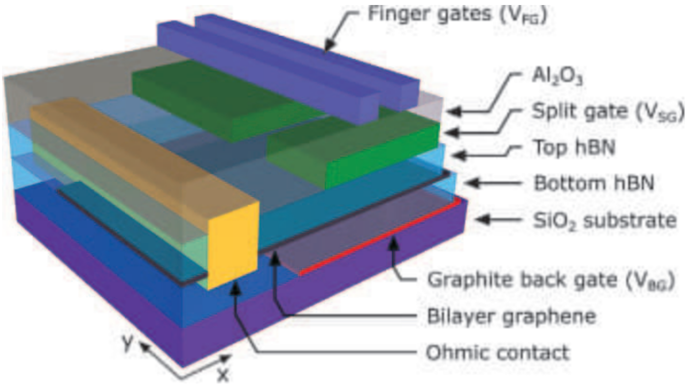

Fig. 3 3D sketch of part of the device showing the different layers of gates and dielectrics. Edge contacts to the bilayer are colored in yellow, split gates are shown in green, and the finger gates are shown in blue. Adapted from Ref. Eich M, Herman F, Pisoni R, Overweg H, Lee Y, Rickhaus P, Watanabe K, Taniguchi T, Sigrist M, Ihn T, and Ensslin K (2018a) Spin and valley states in gate-defined bilayer graphene quantum dots. *Physical Review X* 8: 031023.

corresponding voltages are adjusted such that the displacement field-induced energy gap is maximized and the Fermi energy is in the gap. This forces any current between source and drain contact to flow in the channel formed between the split gates. The sign of the charge of the carriers, i.e. electrons or holes, in the bulk of the sample as well as in the one-dimensional channel depends on the sign of the back gate voltage. Once voltages on split gates and back gate are adjusted, the Fermi energy along the one-dimensional channel can be locally controlled by the voltages applied to the finger gates, for details see Eich et al. (2018a).

Fig. 4 shows the conductance measured through the one-dimensional channel while sweeping one of the finger gates (see Ref. Garreis et al., 2021). The measurement is similar as in Fig. 2, but now the bulk of the sample as well as the channel contain holes. As the finger gate voltage (V_{QD} in Fig. 4) is made more positive, first all holes are depleted from the channel and the channel is pinched off. For further more positive voltages, the Fermi energy passes the conduction band edge below the finger gates and electrons enter this local potential minimum one-by-one. The conductance traces in Fig. 4 show resonances, each indicating the addition of one electron to the potential minimum, which we call a quantum dot.

Traces like the one in Fig. 4 have been recorded for metallic islands and quantum dots in various semiconductor environments. In very clean systems, such as GaAs and Si, single charge occupancy has been reported (Ciorga et al., 2000). The data shown in Fig. 4 for graphene is as clean as in state-of-the-art semiconductor dots. The horizontal axes, i.e. the voltage applied to the finger gate, is approximately proportional to energy. The peaks are roughly equidistant which reflects the fact that the main energy cost to add an electron to the system is the charging energy. As the dot is filled with electrons, the bare confinement potential is screened and becomes wider and consequently the charging energy becomes smaller, as the overall capacitance becomes larger. There are special situations, labelled by vertical arrows in Fig. 4, where the peak spacing is larger than the spacing between neighboring peaks. In this case a new orbital level is occupied and an additional orbital energy cost arises upon adding an electron. For a circularly symmetric potential, as it is roughly the case for the sample investigated in Fig. 4, the first orbital state is expected to be s-like. Because of spin degeneracy and valley degeneracy (see discussion for one-dimensional channels in graphene in previous section) one can fill the first four electrons into the first orbital state. The next orbital state is p-like and therefore two-fold degenerate. Considering again spin and valley degeneracies one arrives at a total degeneracy of $8 = 2^*2^*2$.

The data is Fig. 4 shows that the next degeneracy should be 12. Here another important parameter of the graphene band structure enters the considerations. Low energy approximations give rise to Dirac cones in case of monolayer graphene and a rotationally symmetric parabolic dispersion in case of bilayer graphene. For high energies the bandstructure must reflect the underlying symmetry of the lattice which is hexagonal. This leads to distortions of the circular constant energy surfaces and is called trigonal warping. In the case of large displacement fields, as they are present in these quantum dot devices, the originally high energy characteristics of the band structure also influence the low energy dispersion. As the quantum dot is filled with electrons, the potential is screened, increases in real space, and shrinks in k-space. This will ultimately lead to three equivalent potential pockets, caused by trigonal warping of the bandstructure. The orbital degeneracy in this case is 3. This explains the larger energy cost for adding electron No. 25 in Fig. 4. The addition spectrum of this graphene quantum dot is directly impacted by the underlying bandstructure of bilayer graphene.

In graphene there is a continuous transition from electron to hole occupancy because of the absence of a bandgap. Since the bandgap in the confining barriers is entirely gate-controlled, as is the quantum dot occupancy, the occupation of the quantum dots can also be tuned from electron to hole populations (Banszerus et al., 2020; Tong et al., 2021). The quantum dot shown in Fig. 4 is occupied by electrons and confined by p-n junctions that connect to the p-type leads. This is an unusual confinement potential generally not accessible in semiconductors. In graphene it is also possible to create "standard" tunneling barriers, as in semiconductor systems, where two gates control the tunneling barriers and another gate in the middle (plunger gate) tunes the dot occupancy. This large range of tunability for the dot occupancy as well as for the kind and strength of the tunneling barriers is unique in graphene and enables the realization of complex coupled quantum dot systems (Eich et al., 2018b). On the other hand it is challenging to build charge detectors (Kurzmann et al., 2019a) which rely on basically opaque to slow down electron transport to be within the detector bandwidth. The finite bandgap of bilayer graphene requires relatively wide barriers (≈100 nm) to electrically isolate various sample regions.

An interesting situation occurs when a graphene quantum dot is filled with two electrons (see spectrum in Fig. 5). For standard semiconductor quantum dots two electrons can form four spin states: one singlet with its energy lowered by the exchange energy

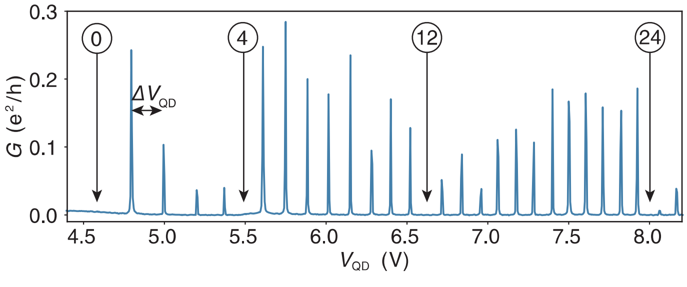

Fig. 4 Conductance trace through the dot with respect to the applied finger-gate voltage V_{QD}. Adapted from Ref. Garreis R, Knothe A, Tong C, Eich M, Gold C, Watanabe K, Taniguchi T, Fal'ko V, Ihn T, Ensslin K, Kurzmann A (2021) Shell filling and trigonal warping in graphene quantum dots. *Physical Review Letters* 126: 147703.

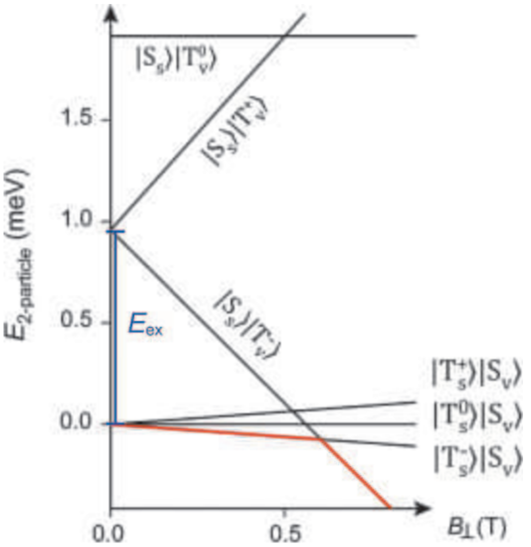

Fig. 5 Energy levels for two carriers occupying a QD. A finite exchange interaction lowers the spin-triplet states by E_{ex} in energy. A magnetic field splits the spin-triplet states by $g_S\mu_B B$, while a finite perpendicular component of the magnetic field splits mainly the valley-triplet states by $g_V\mu_B B_\perp$. Adapted from Ref. Tong C, Kurzmann A, Garreis R, Wister Huang W, Jele S, Eich M, Ginzburg L, Mittag C, Watanabe K, Taniguchi T, Ensslin K, and Ihn T (2022) Pauli blockade of tunable two-electron spin and valley states in graphene quantum dots. *Physical Review Letters* 128: 067702.

with respect to the three triplets. In graphene, the valley degree of freedom plays again an important role. The overall wavefunction has to be anti-symmetric under the exchange of particles. The wavefunction is now composed of three parts: the orbital part, the spin part and the valley part, which also has orbital character but is an additional degree of freedom. This leads to a total of 16 different states. If we assume that the orbital wavefunction is symmetric, i.e. s-like, then the product of spin and valley part of the wavefunction has to be antisymmetric. This leaves as a combination either a valley triplet T_V and spin singlet S_S, or a valley singlet S_V and spin triplet T_S. These are six states in total. The spin states can be split be the Zeeman energy $g_S\mu_B B$. The valley states can be split by the corresponding valley Zeeman effect $g_V\mu_B B_\perp$. It turns out that the valley g-factor is one to two orders of magnitude larger than the spin g-factor ($g_S = 2$ in graphene) and can actually be tuned over wide ranges by controlling the size of the dot (Tong et al., 2021). The valley splitting depends only on the perpendicular component of the magnetic field $B_\perp$ because it is ultimately an orbital effect.

Fig. 5 summarizes the energy spectrum as it is found in the experiment. By measuring the excited state spectrum using finite bias spectroscopy of the quantum dot in a magnetic field, one can distinguish spin and valley states, for details see Tong et al. (2022). It is found in many experiments that the ground state of a two-carrier quantum dot in graphene is a spin triplet T_S and a valley singlet S_V (Kurzmann et al., 2019b). This interesting finding puts graphene quantum dots aside from all other quantum dots in semiconductors, and also in carbon nanotubes. It opens challenging questions on possible qubit implementations in graphene.

Pauli blockade in graphene double quantum dots

Spin blockade (Ono et al., 2002) has become a versatile tool to investigate spin lifetimes in qubits. The idea is that two electrons occupying two quantum dots (in semiconductors) can have a singlet ground state, if both electrons are in the same dot. If each dot contains one electron then their wave function overlap is strongly reduced and the exchange splitting between singlet and triplet states vanishes. This way spin selection rules arise which lead to blocking of carrier transport even if the process was energetically allowed.

In graphene quantum dots it was shown in the previous section that the two-carrier ground state is a spin triplet T_S and a valley singlet S_V. The spin blocking process described before does not work in this case. Rather another interesting process is likely to occur which is valley blockade, also based on the Pauli exclusion principle but very different in nature and also in the possible mechanisms lifting this blockade situation.

The energy spectrum in Fig. 5 shows the evolution of the two-particle states as a function of magnetic field. Since the valley g-factor is much larger than the spin g-factor, $g_V \gg g_S$, the spin singlet-valley triplet becomes the ground state at sufficiently large perpendicular magnetic fields, here at around 600 mT. In this case one is back to the spin configuration known from semiconductor quantum dots at $B = 0$.

Fig. 6 shows finite bias triangles for both bias directions at finite magnetic field $B = 800$ mT. The horizontal/vertical axes are gate voltages tuning the left/right quantum dot occupation. The configurations (i,j) mark the carrier numbers in the various regions. The triple points, which correspond to the states in the dots being in resonance with each other and with the Fermi levels of the leads,

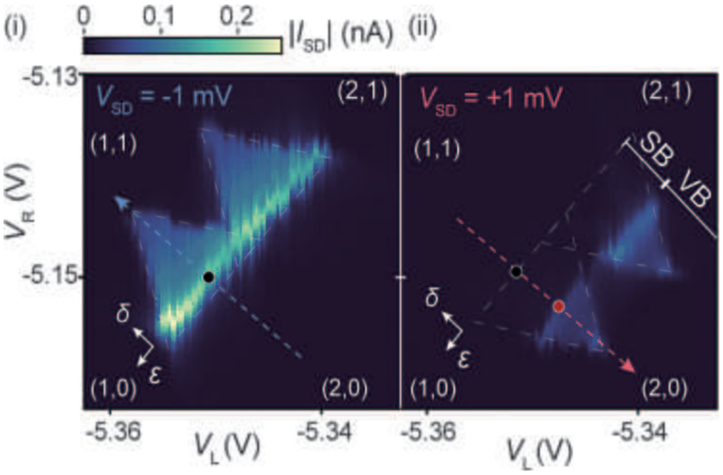

Fig. 6 Finite-bias triangles B = 800 mT with negative (left) and positive (right) source-drain bias. ε is the total energy, and detuning $\delta = \varepsilon_L - \varepsilon_R$ the interdot energy difference. Adapted from Ref. Tong C, Kurzmann A, Garreis R, Wister Huang W, Jele S, Eich M, Ginzburg L, Mittag C, Watanabe K, Taniguchi T, Ensslin K, and Ihn T (2022) Pauli blockade of tunable two-electron spin and valley states in graphene quantum dots. *Physical Review Letters* 128: 067702.

broaden into bias triangles as finite bias is applied across the dots. It is clearly visible in Fig. 6, that the current at the baseline is suppressed for positive voltage bias (right) compared to negative voltage bias (left). This is a signature of Pauli spin blockade. One can also see in the right hand side of Fig. 6, that the current recovers for larger detuning of the energy levels δ, but not to the current level seen on the left hand side of Fig. 6 at the tip of the triangles. The reason for this suppression is valley blockade.

The phase space of possible spin and valley configurations in a two-carrier double quantum dot is much richer than it was known for semiconductor dots. This leads to a more complex energy spectrum with more elaborate selection rules, but also more opportunities. It turns out that a three-electron double quantum dot offers yet more prospects of spin blockade at B = 0 but this is beyond the scope of the review.

Spin lifetimes in graphene quantum dots

Spin qubits are among the most promising contenders for a quantum information processor. The reason is that spins usually live long (longer than charges) because they couple little to the environment. The spin decay times T_1 as well as the coherence times T_2 have been measured for a large number of materials and devices, for a review see Stano and Loss (2022). The dominant decoherence mechanisms are hyperfine coupling of electron spins to nuclear spins and spin-orbit coupling. Natural carbon consists of 99% ^{12}C, which has no nuclear spin. The strength of the spin-orbit coupling roughly scales with the size of the atom. With C being element No. 6 in the periodic table, one would expect long spin decay and coherence times in C-based materials in general and for graphene in particular. While there is a lot of experimental data for semiconductor-based spin qubits (Stano and Loss, 2022), the experimental situation is scarce for graphene, mostly because high-quality graphene quantum dots have only become available recently.

The first experiment follows the so-called Elzerman read-out scheme (Elzerman et al., 2004), which has been pioneered for GaAs-based quantum dots. A charge sensor is capacitively coupled to a quantum dot to detect the charge occupation. If the tunneling barriers coupling the quantum dot to its source and drain leads are sufficiently opaque, such that carrier transport through the quantum dot is slow enough to fall into the bandwidth of the detector, then one can measure in a time-resolved way when carriers enter and leave the quantum dot.

The idea of the Elzerman read-out is sketched in the top panels of Fig. 7. Applying a pulsed voltage to the finger gate of the quantum dot (see Fig. 3), one first lowers the quantum dot states below the Fermi levels of source and drain to load one carrier into the dot (load phase). As a finite magnetic field is applied, the Zeeman splitting is larger than the thermal energy kT. During the read phase, the Zeeman-split levels are positioned with respect to Fermi levels of source and drain, such that the lower (upper) state is below (above) the Fermi levels of source and drain. If, during the load phase, a charge carrier was loaded into the higher energy spin state, see upper left panel of Fig. 7, then it may leave the dot to source/drain and is replaced by a carrier occupying the lower spin state. This event is observed by the charge detector, see lower left panel in Fig. 7. Here we assume that the time for the spin to decay from the higher to the lower spin state without leaving the dot is longer than the tunneling times.

The other situation, where the carrier is loaded into the lower spin state is sketched in the top right panel of Fig. 7. In this case the carrier just stays there during the read phase and the detector does not detect any time dependent charging of the dot, see lower right panel of Fig. 7, for details see Gächter et al. (2022).

When increasing the load time, the likelihood for the carrier loaded into the excited states to decay to the ground state is increased. By taking many such measurements as shown in Fig. 7 and changing the load time, one can extract the decay time from

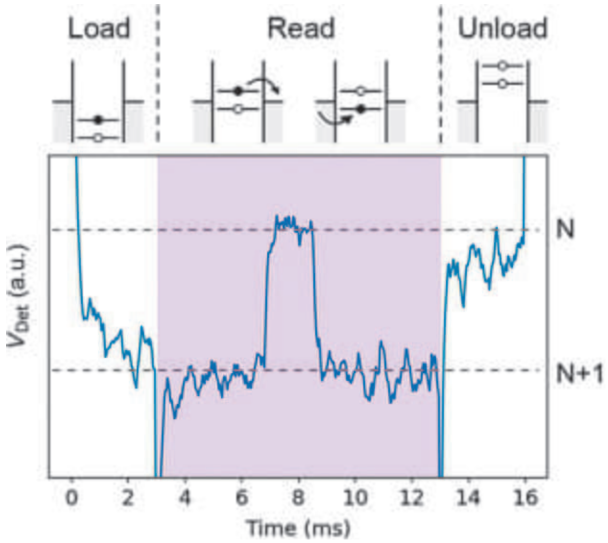

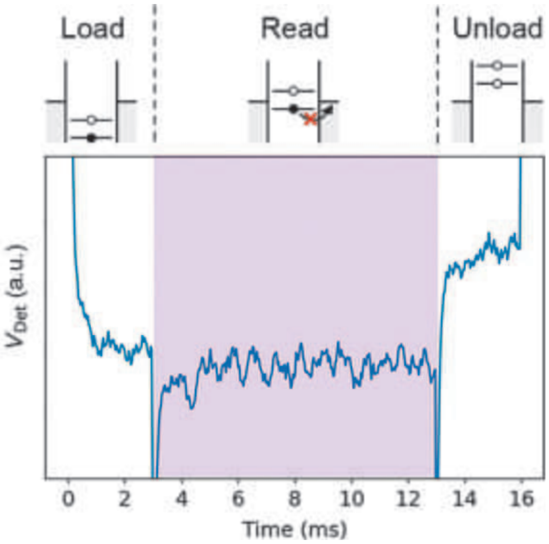

Fig. 7 Top: Three-level pulse scheme applied to the plunger gate. Read-level configuration allowing for single-shot read-out. Bottom: Exemplary traces for a carrier loaded into the spin state which is above (left) or below (right) the Fermi level in the read phase. Adapted from Ref. Gächter LM, Garreis R, Tong C, Josef Ruckriegel M, Kratochwil B, Kornelis de Vries F, Kurzmann A, Watanabe K, Taniguchi T, Ihn T, Ensslin K, Wei Huang W (2022) Single-shot readout in graphene quantum dots. *PRX Quantum* 3: 020343.

the excited to the ground state. We find values of the order $T_1 \approx 50$ ms which compares well with the best results for semiconductor devices (Stano and Loss, 2022). This result is important in view of the prospects of qubit physics and technology in graphene.

Prospects of graphene qubits

Graphene has emerged as a marvelous material with exciting electronic, mechanical and thermal properties. Only during the last 5 years it has become feasible to prepare high-quality quantum devices that are on par with what has been realized in the semiconductor world. The breakthrough occurred when it became possible to define charge carriers by electrostatically defined barriers. In bilayer graphene this is based on a significant bandgap that can be opened by appropriate gate voltages. What seems relatively straight forward today required hard work and technology development by many researchers over many years. Today many graphene quantum dot devices are operated in several research groups that reproducibly show single charge occupation and stable operation as a function of time and other parameters, which is crucial for qubit technologies. First results on long-lived spins have been demonstrated and experiments measuring spin coherence times are just around the corner.

The electronic spectrum of graphene quantum dots has been measured and understood in great detail for single, double and triple charge occupation. In this review we have mostly dealt with arguments based on a single-particle picture to keep the discussion comprehensible. It should be noted, however, that there is a significant spin-valley coupling of the order of 60–80 μeV (Kurzmann et al., 2021; Banszerus et al., 2021) lifting the four-fold degeneracy of the ground state even for one-carrier occupancy. Also the Kondo effect has been observed (Kurzmann et al., 2021) indicating a significantly richer spectrum than for comparable semiconductor systems. These effects will impact future experiments and technological developments for graphene quantum dots.

One of the most important differences between graphene and semiconductors is the valley degree of freedom. While Si also has a valley degree of freedom, it is difficult to control and mostly avoided for qubit operation. For graphene, on the other hand, this valley degree of freedom is entwined with the fact that the primitive unit cell of the honeycomb lattice has two atoms. The valley degree of freedom in graphene is well controlled, understood and its influence on the energy spectrum can be tuned by gate voltages and magnetic fields. The valley degree of freedom profoundly impacts the energy levels of a quantum point contact in a magnetic field. In quantum dots it leads to a dramatic increase of the size of the Hilbert space already for two carrier operation. It has so far unknown consequences for spin decay and coherence times and opens the door for valley qubits, a term used in the larger community for many years but not experimentally realized so far. The prospects here are amazing. In order to have intervalley coupling one requires a scattering event on the scale of the lattice constant, which is very unlikely in smoothly defined confinement potentials. At the same time one has to think about manipulation mechanisms for valley qubits. If valley qubits will really be as long-lived as these arguments suggest, one may consider coupled charge-spin-valley qubit system, where manipulation and coupling is done in one part of parameter space and storage of quantum information in another one.

Two-dimensional materials such as graphene are one atomic layer thin by definition, i.e. much thinner than corresponding semiconductor environments. Given the fact that all nanotechnology to pattern these materials is top-down, involving lithography, etching and gating, the pattern size that can be realized for lateral dimensions is ultimately limited by the vertical dimension.

With hBN an almost perfect insulator exists. One could presumably build an hBN/bilayer graphene/hBN stack with the thickness of a few nm, i.e. much thinner than anything possible with semiconductors. Assuming further, that our lithographic capabilities will improve to prepare for example split-gate geometries on the sub 10 nm scale, one may be able to build quantum devices which are much smaller than today, have much larger confinement energies, can maybe be operated at higher temperatures and may display much stronger coupling between neighboring devices.

The big advantage of semiconductor quantum devices is the availability of wafer-scale processing and compatibility with industrial classical technology. The best graphene devices today, on the other hand, are all build by exfoliation techniques using sticky tape, the same way graphene was originally prepared by Geim and Novoselov. It has been demonstrated that single-layer graphene can be grown by MOCVD (Schmitz et al., 2020) with an electronic quality leading to the observation of the fractional quantum Hall effect. This catalytic self-limiting process typically does not work well to grow bilayer material, a process still to be developed. The high-quality insulator hBN prepared by K. Watanabe and T. Taniguchi and used by most graphene groups also exists only in flakes. Efforts are underway to prepare large area hBN, which might have consequences way beyond graphene, including other two-dimensional materials such as TMDs, and maybe even standard semiconductors. It is clear that from the material side there are many obstacles to be overcome in order to have large area/wafer scale and high quality heterostructures of two-dimensional materials.

The connection to other two-dimensional materials offers new opportunities. Transition-metal dichalcogenides (TMDs) are electronically of not as high quality presently as graphene. This might change, however, and then two-dimensional materials with a bandgap comparable to standard semiconductors will be available. Heterostructures of TMDs with graphene can be used to induce spin-orbit coupling, which is very strong in TMDs, into graphene (Wang et al., 2016). This valuable experimental approach has not yet been used to design quantum device in graphene. The bandstructure in graphene can also be modified by twisting the graphene layers, culminating in the discovery of superconductivity (Cao et al., 2018). First devices have been built on this platform (de Vries et al., 2021; Rodan-Legrain et al., 2021; Portolés et al., 2022). Overall, the world of two-dimensional materials offers unique opportunities to build hybrid quantum devices of all facets, mostly in view of new physical discoveries, but also with the prospect to impact qubit technologies in the future.

Acknowledgments

This article is based on collaborations with Marius Eich, Jonas Gerber, Lisa Gächter, Rebekka Garreis, Lev Ginzburg, Carolin Gold, Thomas Ihn, Wister Huang, Benedikt Kratochwil, Annika Kurzmann, Yongjin Lee, Michele Masseroni, Hiske Overweg, Elías Portoles, Riccardo Pisoni, Peter Rickhaus, Max Ruckriegel, Chuyao Tong, Fokko De Vries, and Giulia Zheng.

References

Banszerus L, Rothstein A, Fabian T, Möller S, Icking E, Trellenkamp S, Lentz F, Neumaier D, Watanabe K, Taniguchi T, Libisch F, Volk C, and Stampfer C (2020) Electron–hole crossover in gate-controlled bilayer graphene quantum dots. *Nano Letters* 20: 7709.

Banszerus L, Möller S, Steiner C, Icking E, Trellenkamp S, Lentz F, Watanabe K, Taniguchi T, Volk C, and Stampfer C (2021) Spin-valley coupling in single-electron bilayer graphene quantum dots. *Nature Communications* 12: 5250.

Bischoff D, Varlet A, Simonet P, Eich M, Overweg HC, Ihn T, and Ensslin K (2015) Localized charge carriers in graphene nanodevices. *Applied Physics Reviews* 2: 031301.

Bolotin KI, Ghahari F, Shulman MD, Stormer HL, and Kim P (2009) Observation of the fractional quantum Hall effect in graphene. *Nature* 462: 196.

Cao Y, Fatemi V, Fang S, Watanabe K, Taniguchi T, Kaxiras E, and Jarillo-Herrero P (2018) Unconventional superconductivity in magic-angle graphene superlattices. *Nature* 556: 43.

Ciorga M, Sachrajda AS, Hawrylak P, Gould C, Zawadzki P, Jullian S, Feng Y, and Wasilewski Z (2000) Addition spectrum of a lateral dot from Coulomb and spin-blockade spectroscopy. *Physical Review B* 61: R16315.

de Vries FK, Portoles E, Zheng G, Taniguchi T, Watanabe K, Ihn T, Ensslin K, and Rickhaus P (2021) Gate-defined Josephson junctions in magic-angle twisted bilayer graphene. *Nature Nanotechnology* 16: 760.

Eich M, Herman F, Pisoni R, Overweg H, Lee Y, Rickhaus P, Watanabe K, Taniguchi T, Sigrist M, Ihn T, and Ensslin K (2018a) Spin and valley states in gate-defined bilayer graphene quantum dots. *Physical Review X* 8: 031023.

Eich M, Pisoni R, Pally A, Overweg H, Kurzmann A, Lee Y, Rickhaus P, Watanabe K, Taniguchi T, Ensslin K, and Ihn T (2018b) Coupled quantum dots in bilayer graphene. *Nano Letters* 18: 5042.

Elzerman JM, Hanson R, Willems van Beveren LH, Witkamp B, Vandersypen LMK, and Kouwenhoven LP (2004) Single-shot read-out of an individual electron spin in a quantum dot. *Nature* 430: 431.

Gächter LM, Garreis R, Tong C, Ruckriegel MJ, Kratochwil B, de Vries FK, Kurzmann A, Watanabe K, Taniguchi T, Ihn T, Ensslin K, and Huang WW (2022) Single-shot readout in graphene quantum dots. *PRX Quantum* 3. 020343.

Garreis R, Knothe A, Tong C, Eich M, Gold C, Watanabe K, Taniguchi T, Fal'ko V, Ihn T, Ensslin K, and Kurzmann A (2021) Shell filling and trigonal warping in graphene quantum dots. *Physical Review Letters* 126. 147703.

Kurzmann A, Eich M, Overweg H, Mangold M, Herman F, Rickhaus P, Pisoni R, Lee Y, Garreis R, Tong C, Watanabe K, Taniguchi T, Ensslin K, and Ihn T (2019a) Excited states in bilayer graphene quantum dots. *Physical Review Letters* 123: 026803.

Kurzmann A, Overweg H, Eich M, Pally A, Rickhaus P, Pisoni R, Lee Y, Watanabe K, Taniguchi T, Ihn T, and Ensslin K (2019b) Charge detection in gate-defined bilayer graphene quantum dots. *Nano Letters* 19: 5216.

Kurzmann A, Kleeorin Y, Tong C, Garreis R, Knothe A, Eich M, Mittag C, Gold C, de Vries FK, Watanabe K, Taniguchi T, Fal'ko V, Meir Y, Ihn T, and Ensslin K (2021) Kondo effect and spin–orbit coupling in graphene quantum dots. *Nature Communications* 12: 6004.

Lee Y, Knothe A, Overweg H, Eich M, Kurzmann A, Taniguchi T, Wantanabe K, Fal'ko V, Ihn T, Ensslin K, and Rickhaus P (2020) Tunable valley splitting due to topological orbital magnetic moment in bilayer graphene quantum point contacts. *Physical Review Letters* 124: 126802.

McCann E, Abergel DSL, and Falko V (2007) The low energy electronic band structure of bilayer graphene. *The European Physical Journal Special Topics* 148: 91.

Ono K, Austing D, Tokura Y, and Tarucha S (2002) Current rectification by Pauli exclusion in a weakly coupled double quantum dot system. *Science* 297: 1313.

Oostinga JB, Heersche HB, Liu X, Morpurgo AF, and Vandersypen LMK (2008) Gate-induced insulating state in bilayer graphene devices. *Nature Materials* 7: 151–157.

Overweg H, Eggimann H, Chen X, Slizovskiy S, Eich M, Pisoni R, Lee Y, Rickhaus P, Watanabe K, Taniguchi T, Fal'ko V, Ihn T, and Ensslin K (2018a) Electrostatically induced quantum point contacts in bilayer graphene. *Nano Letters* 18: 553.

Overweg H, Knothe A, Fabian T, Linhart L, Rickhaus P, Wernli L, Watanabe K, Taniguchi T, Sanchez D, Burgdörfer J, Libisch F, Fal'ko VI, Ensslin K, and Ihn T (2018b) Topologically non-trivial valley states in bilayer graphene quantum point contacts. *Physical Review Letters* 121: 257702.

Portolés E, Iwakiri S, Zheng G, Rickhaus P, Taniguchi T, Watanabe K, Ihn T, Ensslin K, and de Vries FK (2022) A tunable monolithic SQUID in twisted bilayer graphene. *Nature Nanotechnology* 17: 1159.

Rodan-Legrain D, Cao Y, Park JM, de la Barrera SC, Randeria MT, Watanabe K, Taniguchi T, and Jarillo-Herrero P (2021) Highly tunable junctions and non-local Josephson effect in magic-angle graphene tunnelling devices. *Nature Nanotechnology* 16: 769.

Schmitz M, Ouaj T, Winter Z, Rubi K, Watanabe K, Taniguchi T, Zeitler U, Beschoten B, and Stampfer C (2020) Fractional quantum Hall effect in CVD-grown graphene. *2D Materials* 7: 041007.

Stano P and Loss D (2022) Review of performance metrics of spin qubits in gated semiconducting nanostructures. *Nature Reviews Physics* 4: 672–688.

Tong C, Garreis R, Knothe A, Eich M, Sacchi A, Watanabe K, Taniguchi T, Fal'ko V, Ihn T, Ensslin K, and Kurzmann A (2021) Tunable valley splitting and bipolar operation in graphene quantum dots. *Nano Letters* 21: 1068.

Tong C, Kurzmann A, Garreis R, Huang WW, Jele S, Eich M, Ginzburg L, Mittag C, Watanabe K, Taniguchi T, Ensslin K, and Ihn T (2022) Pauli blockade of tunable two-electron spin and valley states in graphene quantum dots. *Physical Review Letters* 128: 067702.

van Wees BJ, van Houten H, Beenakker CWJ, Williamson JG, Kouwenhoven LP, van der Marel D, and Foxon CT (1988) Quantized conductance of point contacts in a two-dimensional electron gas. *Physical Review Letters* 60: 848.

Wang Z, Ki D-K, Khoo JY, Mauro D, Berger H, Levitov LS, and Morpurgo AF (2016) Origin and magnitude of 'designer' spin-orbit interaction in graphene on semiconducting transition metal dichalcogenides. *Physical Review X* 6: 041020.

Wharam DA, Thornton TJ, Newbury R, Pepper M, Ahmed H, Frost JEF, Hasko DG, Peacock DC, Ritchie DA, and Jones GAC (1988) One-dimensional transport and the quantisation of the ballistic resistance. *Journal of Physics C* 21: L209.

Zhu MJ, Kretinin AV, Thompson MD, Bandurin DA, Hu S, Yu GL, Birkbeck J, Mishchenko A, Vera-Marun IJ, Watanabe K, Taniguchi T, Polini M, Prance JR, Novoselov KS, Geim AK, and Ben Shalom M (2017) Edge currents shunt the insulating bulk in gapped graphene. *Nature Communications* 8: 14552.

Zwerver AMJ, Krähenmann T, Watson TF, Lampert L, George HC, Pillarisetty R, Bojarski SA, Amin P, Amitonov SV, Boter JM, Caudillo R, Correas-Serrano D, Dehollain JP, Droulers G, Henry EM, Kotlyar R, Lodari M, Lüthi F, Michalak DJ, Mueller BK, Neyens S, Roberts J, Samkharadze N, Zheng G, Zietz OK, Scappucci G, Veldhorst M, Vandersypen LMK, and Clarke JS (2022) Qubits made by advanced semiconductor manufacturing. *Nature Electronics* 5: 184.

Surfaces and Interfaces, Electronic Structure of☆

G Chiarotti and C Goletti, Physics Department, Università di Roma "Tor Vergata", Rome, Italy

© 2024 Elsevier Ltd. All rights reserved.

This is an update of G. Chiarotti, C. Goletti, Surfaces and Interfaces, Electronic Structure of, Editor(s): Franco Bassani, Gerald L. Liedl, Peter Wyder, Encyclopedia of Condensed Matter Physics, Elsevier, 2005, Pages 133–144, ISBN 9780123694010, https://doi.org/10.1016/B0-12-369401-9/00476-9.

Introduction **258**
Surface reconstruction and relaxation **258**
Electronic surface states **260**
Examples of reconstruction of relevant semiconductor surfaces **263**
Si(100)2 × 1 264
Si(1 1 1)2 × 1 264
Si(1 1 1)7 × 7 266
Interfaces **267**
Surfaces in real-world environment 269
Conclusion **270**
References **271**
Further reading **271**

Abstract

The effect of a plane terminating the crystal is presented through the modifications introduced in the atomic and electronic structure of the solid. Reconstruction and relaxation of the surface layer, and the subsequent appearance of new electronic states are discussed, reporting significant examples from semiconductors. The formation of an interface is then introduced, with a spotlight on the solid-liquid interface. In this case, under definite experimental conditions surface structures like those observed in ultra-high vacuum are obtained, thus moving the investigation from clean surfaces towards real-world environment.

Key points

- Clean surfaces are obtained in Ultra High Vacuum (UHV) conditions, by several preparation methods (cleavage, ion bombardment and annealing, high-temperature annealing, molecular beam epitaxy, etc.).
- When the surface is prepared, two deviations from the ideal case are possible: relaxation and reconstruction.
- The structural variations associated with reconstruction have important consequences on the electric properties of the surface.
- New electronic states appear, localized at the surface layer with energies in the forbidden gap: these are "surface states".
- In semiconductors, the presence of surface states—especially when localized in the bulk gap- modify many of the sample properties significantly.
- The position of the Fermi level at the surface is altered by accumulation of charge into surface states, introducing a "band bending".
- Interfaces are the regions connecting two different physical systems.
- When the interface forms and thermal equilibrium is reached, the Fermi levels of the two sides line up. This alignment produces a charge redistribution to preserve the overall neutrality of the system, changing the electrical properties of the contact zone.
- The presence of surface states at the interface (interface states) has important consequences on the electrical behavior of the system.
- A heterojunction is a particular interface, created between two different semiconductors.
- Beyond clean surfaces in UHV, also surfaces immersed in a liquid reconstruct.

Nomenclature

k	Wave vector (cm^{-1})
L_D	Debye length (cm)

☆*Change History:* November 2022. C Goletti has been involved in preparing the update. Only main text and references have been updated.

ΔEc	Conduction band discontinuity (eV)
ΔEv	Valence band discontinuity (eV)
$\boldsymbol{\rho}^{\mathbf{local}}$	Local density of states (states atom^{-1} eV^{-1})
$\boldsymbol{\rho}^{\mathbf{tot}}$	Total density of states (states atom^{-1} eV^{-1})
$\boldsymbol{\Phi}$	Work function (eV)
$\boldsymbol{\Phi}_{\mathbf{SB}}$	Schottky barrier (eV)
$\boldsymbol{\chi}$	Electron affinity (eV)
$\boldsymbol{\psi}$	Wave function

Introduction

The presence of the surface modifies significantly the atomic and electronic structure of the first few layers of the solid. Since some of the properties of the solid are to some extent properties of its surface (e.g., the work function, the photoelectric threshold, chemisorption and physisorption, conductivity in the surface channel(s), optical reflectance, and the scattering of electrons, ions, and atoms by the solid), a detailed knowledge of the surface is important for solid-state physics and chemistry as well as for materials science and technical applications.

In this article, the discussion is limited to the so-called "clean surfaces," or surfaces that are atomically clean (i.e., with a controlled chemical composition) and crystallographically well defined. "Real surfaces" (i.e., surfaces with unspecified chemical impurities, crystallographic defects, macroscopic faults, etc.) are considered only occasionally.

Clean surfaces are obtained in ultrahigh vacuum (UHV) conditions (10^{-10} Torr or better) by cleavage, ion bombardment and annealing (IBA), high-temperature annealing, molecular beam epitaxy (MBE), etc. Conversely, real surfaces are obtained and handled at ordinary pressures, mechanically ground, chemically etched, etc., and their properties often depend upon the way of preparation.

This article discusses the surface reconstruction and relaxation, electronic surface states, examples of reconstruction of relevant semiconductor surfaces and interfaces.

Surface reconstruction and relaxation

The structure of an "ideal surface" is that of a half crystal obtained by dividing the crystal in two halves with a lattice plane as a boundary, removing all atoms on one side and leaving the other atoms in their original positions. An ideal surface is then characterized by the Miller indices of the boundary plane.

It should be considered, however, that the atoms in the ideal surface plane experience a force different from that of their partners in the bulk. Moreover, they have a larger freedom of movement so that some rearrangement takes place due to the reduction of the free energy of the surface. Two deviations from the ideal surface are possible: relaxation and reconstruction. Relaxation consists of a rigid displacement of all the atoms of the surface plane (in general, perpendicularly to it) that leaves unaltered the translational symmetry of the surface. On the contrary, reconstruction is a displacement of individual atoms that changes the translational symmetry in the surface plane.

The two situations are schematically shown in Fig. 1 (where it is assumed that the planes are stacked on top of each other to obtain the three-dimensional (3D) crystal). It is seen that in case (b), which represents relaxation, the surface unit cell is still a square of side a, while in cases (c), (d) and (e), which represent reconstruction, the surface unit cell is a rectangle of sides a and 2a. In Wood's notations, these last reconstructions are called 2 × 1. It is seen that Wood notations do not univocally characterize the

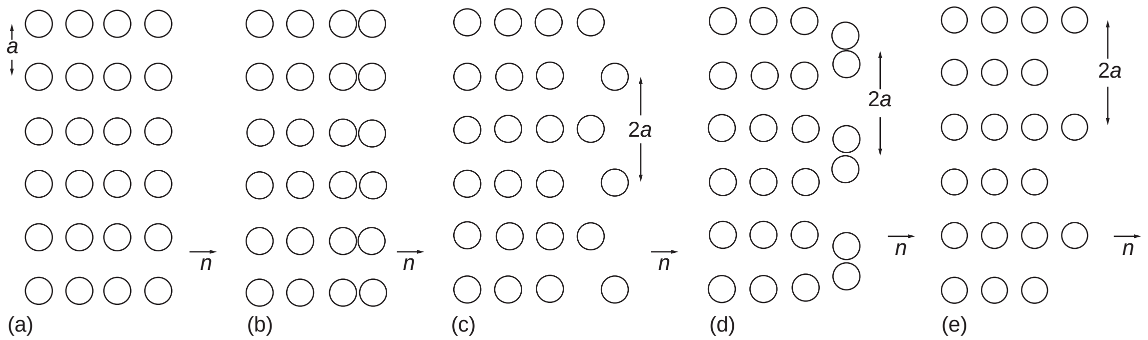

Fig. 1 Schematic representation of a surface: (a) ideal surface, (b) relaxed surface, (c), (d), and (e) reconstructed surfaces (simplified examples of buckling, dimerization, and missing row models).

surface: they only give the symmetry of the reconstruction. As such, they are directly obtained from the LEED (low energy electron diffraction) patterns. The experimental determination of the actual coordinates of the atoms of the first few layers (that would completely characterize the reconstructed surface) is a very complex problem that may require the use of various techniques and the comparison with theoretical models. Among the most common techniques used for this purpose are: dynamical LEED, STM (scanning tunneling microscopy), ARUPS (angle-resolved ultraviolet photoemission), inverse photoemission, optical reflectance with polarized light, high-energy electron diffraction, elastic and inelastic scattering of atoms, ions, and electrons, etc. Energies associated with reconstruction are $\sim 10^{-2}$ eVatom^{-1} for metals and $\sim 10^{-1}$ eVatom^{-1} for semiconductors. Metals are then seldom reconstructed, while semiconductors are very often so. In metals, in fact, electrons are delocalized so that the free energy does not depend much on the position of the single atoms. The opposite is true in semiconductors where directional bonding is significant. Tables 1 and 2 list a few examples of reconstruction of metals and semiconductors. It is seen that, for a given surface, various reconstructions are possible, depending upon the method by which the surface is obtained (shown in the last column). In a few instances, reversible transformations between two phases of reconstruction have been observed as a function of temperature. On the other hand, impurities and defects may stabilize some phases. The tables show clearly that reconstruction is a problem of extreme variety and complexity, as well as of the greatest interest. Up to now, a theory that explains the occurrence of the various types of reconstruction is not available from first principles. Guidelines and heuristic models are discussed in the section "Examples of reconstruction of relevant semiconductor surfaces."

Table 1 Surface structure of (some) metals.

Metal	*Face*	*Reconstruction*	*Model*	*Preparation and remarks*
Ag	(1 0 0)	1×1	Relaxation	Epitaxial film on MgO. 1×1 stable for $T < 773$ K
	(1 1 0)	1×1	Relaxation (7–10%)	Roughening transition at $T \cong 700$ K
	(1 1 1)	1×1	Relaxation	$30 < T < 140$ K
Au	(1 0 0)	5×20	One layer with hexagonal symmetry	IBA + ann. at $T > 373$ K. Equilibrium configuration
		1×5	Slightly distorted hexagonal structure with buckling	Epitaxial film on MgO
	(1 1 0)	1×2	Missing row	$T < 670$ K
	(1 1 1)	23×1	Three domains rotated by 120°; Compression along [1 1 0]	22×1, 21×1 Structures also observed
Cu	(1 0 0)	1×1	Relaxation—1%	$300 < T < 1300$ K
	(1 1 0)	1×1	Relaxation $\cong$ 8%	$300 < T < 1000$ K
	(1 1 1)	1×1	Relaxation $\cong$ 2%	
Pt	(1 0 0)	1×1	Unrelaxed	Metastable, $T < 400$ K
	(1 1 0)	1×2	Missing row	
	(1 1 1)	1×1	Relaxation 2.3%	
W	(1 0 0)	$c(2 \times 2)$	In-plane zig-zag displacements	$T < 200$ K
	(1 1 0)	1×1	Unrelaxed	

Table 2 Surface structure of (some) semiconductors.

Semiconductor	*Face*	*Reconstruction*	*Model*	*Preparation and remarks*
Diamond	(1 0 0)	2×1	Dimers	Polishing + ann. $T > 1300$ K
	(1 1 0)	1×1		Polishing + ann.
	(1 1 1)	2×1	π-Bonded chains	Cleavage; Polishing + ann. $T > 1200$ K
Si	(1 0 0)	2×1	Buckled dimers	IBA/MBE
		$p(2 \times 2)$	Ordered arrangement of buckled dimers	MBE; IBA. Present locally depending on the temperature
		$c(4 \times 2)$	Ordered arrangement of buckled dimers	MBE; IBA. Present locally depending on the temperature
	(1 1 0)	16×2	Dimers + adatoms (?)	Ann. $T > 1300$ K 32×2 structures also observed
		4×5	Uncertain	IBA+ ann. Impurity stabilized (Ni?)
		5×1	Uncertain	IBA+ ann. Impurity stabilized (Ni?)
	(1 1 1)	2×1	π-Bonded chains	Cleavage. Transforms into 7×7 at $T > 550$ K
		7×7	DAS (dimers-adatoms-stacking faults)	MBE; IBA+ ann.; cleavage + ann. $T > 550$ K
		5×5	DAS	MBE. Present locally near steps
Ge	(1 0 0)	2×1	Dimers	IBA; MBE
		$p(2 \times 2)$	Ordered structure of dimers	MBE. Present locally
		$c(4 \times 2)$	Ordered structure of dimers	MBE. Present locally
	(1 1 1)	2×1	π-Bonded chains	Cleavage. Transforms into $c(2 \times 8)$ at $T > 400$ K
		$c(2 \times 8)$	Adatoms	MBE; cleavage + ann. at $T > 400$ K

(*Continued*)

Table 2 (Continued)

Semiconductor	*Face*	*Reconstruction*	*Model*	*Preparation and remarks*
GaAs	(1 0 0)Ga	(4 × 2), *c*(8 × 2)	Complex structure with dimers in the second layer	MBE; IBA
	(1 0 0)As	2 × 4	Dimers	MBE
	(1 1 0)	1 × 1	Rotation-relaxation	Cleavage; IBA
	(1 1 1)Ga	2 × 2	Ga vacancies	MBE
	(1 1 1)As	2 × 2	As trimers	MBE
InSb	(1 1 0)	1 × 1	Rotation-relaxation	Cleavage
	(1 1 1)In	2 × 2		IBA; MBE
	(1 1 1)Sb	3 × 3		IBA; MBE
ZnO	(0001)Zn	1 × 1		Cleavage; IBA. Faceting present
	(0 0 0 1)O	1 × 1		Cleavage. Faceting present

ann. = annealing; IBA = ion bombardment + annealing; MBE = molecular tom epitaxy.

Electronic surface states

The structural variations associated with reconstruction have important consequences on the electronic properties of the surface. Regardless of this, however, the reduction of the translational invariance caused by the surface is enough to introduce additional levels in the electronic structure of the solid. This was shown, for a Kronig-Penney potential, by I. Tamm in 1932 and extended to a more realistic case by W. Shockley in 1939. A 1D potential with a surface at $z = 0$ is shown schematically in Fig. 2a. Inside the solid ($z < 0$) the wave function is given, according to the Bloch theorem, by

$$\Psi(z, t) = u_k(z)\exp[\mathrm{i}(kz - \omega t)] \tag{1}$$

where $u_k(z)$ is a function with the same periodicity of the lattice, $k = 2\pi/\lambda$ is the wave number, and $E = \hbar\omega$ is the energy of the electron. For an unbound lattice ($-\infty < z < +\infty$), k must be a real number so that Eq. (1) represents a wave propagating along z. Imaginary values of k are discarded because the wave function cannot be normalized. Since the energy is a function of k, real (imaginary) values of k correspond to allowed (forbidden) bands. In the presence of a surface, however, imaginary values of k cannot be discarded since now, the wave function can be normalized and states localized at the surface, with energies in the forbidden gaps, become possible. If it is assumed that $k = i\mu$ (with μ real), the spatial part of the wave function can be written (for $z < 0$) as

$$\psi_\mu(z) = u_\mu(z)e^{-\mu z} \tag{2}$$

When $\mu < 0$, the wave function can be matched, at the surface, to that appropriate for $z < 0$ (a decaying exponential if the potential is given by a step function). This is shown in Fig. 2b that represents schematically a state localized at the surface with energy in the forbidden gap. Such a state is called a "surface state." The matching, however, can also be done when k is real, giving rise to the state shown in Fig. 2c that represents a bulk electron scattered at the surface. In three dimensions, the translational symmetry is preserved on the surface plane so that the surface state is now represented by a Bloch wave propagating along the surface with wave vector $k_\parallel$; damped on both sides of the surface as in the 1D example. In this case, however, the energy of the surface state does not necessarily fall into the forbidden gaps because of the energy (kinetic and potential) associated to the motion along the surface.

When the degeneracy of the surface state with the bulk bands is not limited to energy but extends to k-values, the state is called a "resonant state." A 1D example is shown schematically in Fig. 2d. In a naïve picture, such a resonant state corresponds to a bulk electron that is scattered at the surface, though dwelling there for some time. In order to present the correlation between surface and bulk states, it is customary to project the bulk bands on the surface Brillouin zone and plot the surface bands there. This is done for unreconstructed Si(111) in Fig. 3. Surface states are represented by dotted lines, surface resonances by full lines, while projected bulk bands are shown as hatched regions.

When the surface is reconstructed, the calculation of the bands is more difficult and can be done only on the basis of a model. A common procedure is to pile up a number of crystallographic planes where atoms are displaced from their ideal positions according to a given model of reconstruction. The slab should be large enough (10–20 layers) so that in the interior, the structure of the bulk is resumed. Each slab exposes two surfaces. The slabs are then arranged periodically with spacing (between each two) large enough to avoid a sizable perturbation. This fictitious periodic structure allows the use of the theorems of the 3D band theory. The results are usually presented in terms of the so called "local density of states." As it is known, the "total density of states" $\rho^{\mathrm{tot}}(E)$ gives the number of states present in a unit energy range around E:

$$\rho^{\mathrm{tot}}(E) = \sum_i \delta(E - E_i) \tag{3}$$

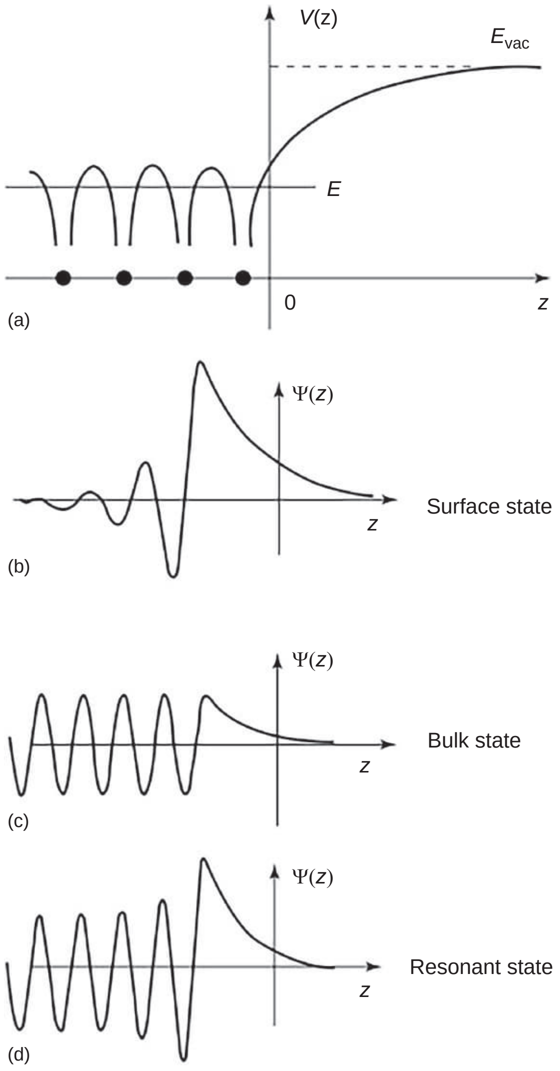

Fig. 2 Schematic representation of a surface in a 1D model: (a) potential energy of an electron, (b) wave function for a surface state with energy in the gap, (c) bulk electron scattered at the surface, and (d) surface resonant state.

where δ is the Dirac function and the sum runs over the energy states E_i.

In turn, the local density of states is defined as:

$$\rho^{\mathrm{local}}(x, y, z; E) = \sum_i |\Psi_i(x, y, z)|^2 \delta(E - E_i) \tag{4}$$

that is, each state is weighed with the probability of finding an electron at *x*, *y*, *z*. Fig. 4 shows the local density of states for the ideal surface Si(1 1 1)1 × 1. The figure clearly shows the presence of unsaturated bonds (dangling bonds, DB) on atoms of the first layer.

An important development for calculating the structural and electronic properties of a surface came from the application of the so-called Car-Parrinello method that consists of simulating the dynamical evolution of a reduced set of atoms (~100), starting from an initial configuration that can as well be the ideal surface (Car and Parrinello, 1985). For each configuration, the electronic energy is calculated and, through the Hellman-Feynman theorem of quantum mechanics, the force on the single atoms is determined and so is the dynamical evolution of the system.

Eventually, a stable configuration is reached that corresponds to the reconstructed surface. This "ab initio" calculation requires, however, a high computational power and some "educated guesses," especially if the reconstruction is not that of thermodynamical equilibrium.

In metals, one-electron theories are generally inadequate, and calculations must be done on the basis of the many-body theory. A model that has given reliable results for the work function of several metals is the so-called "jellium" (Lang and Kohn, 1970), which assumes that the electrons form a gas of negatively charged particles neutralized by a continuous distribution of fixed positive charge that goes abruptly to zero at the surface. Fig. 5 shows the electron density distribution near the surface for two cases representative of

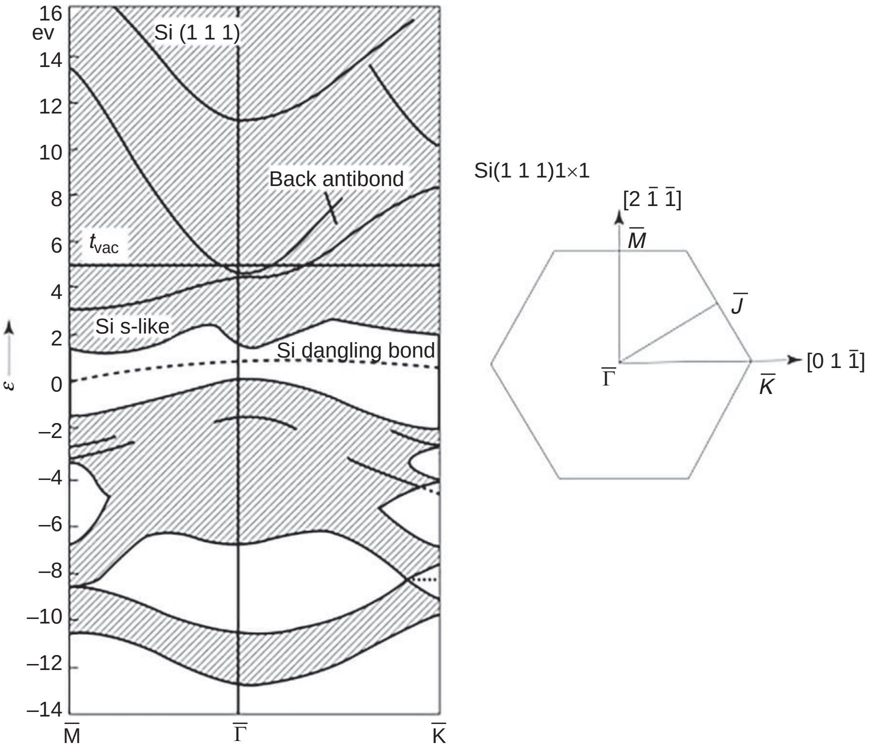

Fig. 3 Bulk bands projected into the surface Brillouin zone for the ideal (un-reconstructed) surface of Si(1 1 1). Bulk bands are hatched: surface states are shown with dotted lines: surface resonances with full lines. The surface Brillouin zone is shown on the right. After Schlüter M and Cohen ML (1978) *Physical Review B* 17: 716.

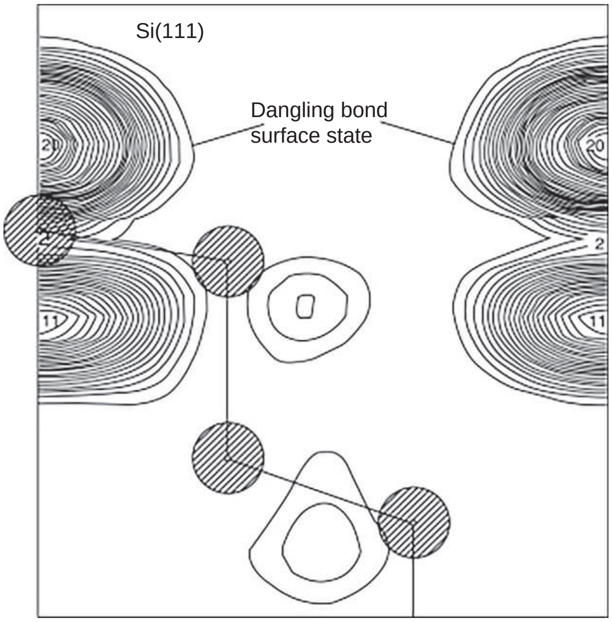

Fig. 4 Charge density contours in the (110) plane (perpendicular to the (1 1 1) surface) for the un-reconstructed (ideal) surface of Si(1 1 1). The dangling bonds protruding into vacuum are clearly visible on the atoms of the surface layer. After Schlüter M, Chelikowsky JR, Louie GS and Cohen ML (1975) *Physical Review B* 12: 4200.

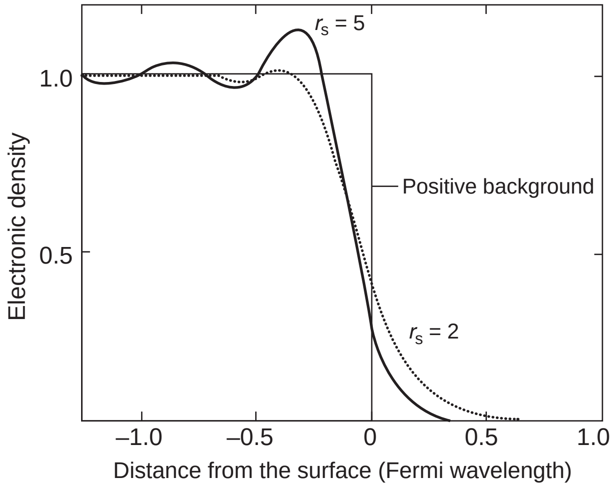

Fig. 5 Surface charge density for the jellium model of a metal, plotted for two values of the electron densities. The radius r_s (in atomic units) is that of the sphere that contains one electron. $r_s = 2, 5$ correspond approximately to the cases of Al and Cs, respectively. After Lang ND and Kohn W (1970) Theory of metal surfaces: Charge density and surface energy. *Physical Review B* **1**: 4555.

Al (dashed line) and of K (continuous line). Electrons protrude from the surface giving rise to an electric dipole directed inwards, which reduces the work function. Characteristic oscillations of the electron density (Friedel oscillations) should be noticed.

A further peculiarity of metals is that the major contribution to the surface barrier comes from the image force of electrostatics. The potential energy is then, at a large distance from the surface, Coulomb-like. If the electron energy corresponds to a gap, the electron cannot penetrate the solid and remains confined in a sort of a well that extends from $z = 0$ to the Coulomb barrier. In such a well, quantized levels called "image states" exist (Echenique et al., 1985). Each state is characterized by an integer quantum number, $n \geq 1$. In this scheme, the Shockley (or Tamm) states are those with $n = 0$.

The states discussed so far are called "intrinsic surface states" and can be observed only on clean surfaces. On real surfaces, electronic states associated with mesoscopic defects such as steps, kinks, islands, terraces, and pits, or with surface impurities are also present. Such states are called "extrinsic surface states" and may modify the properties of technical surfaces.

In semiconductors, the presence of surface states (both intrinsic and extrinsic), especially when localized in the gap, modifies many of the properties of the sample significantly. The accumulation of charge into surface states creates a macroscopic potential that alters the position of the Fermi level at the surface and introduces a "band bending" that extends for a length of the order of the Debye length defined as L_D

$$L_D = \sqrt{\frac{\varepsilon_b \varepsilon_0 kT}{e^2(n_b + p_b)}} \tag{5}$$

where ε_b (ε_0) is the dielectric constant and n_b, p_b the densities of negative and positive carriers in the bulk. L_D spans from a fraction of an Å at metal densities to a fraction of a mm in large gap semiconductors. Such a band bending bears a great importance on many functions of the metal oxide semiconductor (MOS), Schottky barrier, and heterostructure devices.

Examples of reconstruction of relevant semiconductor surfaces

A few examples of reconstruction of relevant surfaces of semiconductors and some of their associated electronic properties are given below. An outline of the basic experimental evidence is also presented for each surface.

Covalent or partially ionic semiconductors such as C (diamond), Si, Ge, GaAs, GaP, GaSb, InAs, InP, and InSb, crystallize in the diamond, zinc blende (or wurtzite) structures in which each atom is tetrahedrally coordinated with four neighbors. The chemical bond is essentially of the directional sp^3 type. The presence of the surface introduces a number of unsaturated bonds called dangling bonds (DBs) that play a great role in reconstruction.

Since the energy associated with sp^3 bonds is rather high, the atoms on the surface tend to rearrange in order to reduce the number of DBs. This can be done in a number of ways: dimerization, formation of adatoms (i.e., atoms that have left their ordinary position to sit in the interstice on top of three atoms), p-bonding, etc. It should be observed in this respect that the sp^3 bond is easily deformable, in the sense that little energy is required to change the angles among the bonds. Reconstruction takes advantage of this flexibility, allowing several different structures to be present even on the same surface.

Si(100)2 × 1

The ideal (1 0 0) face exposes two DBs per surface atom and is then highly unstable. Dimerization is a process that produces the 2 × 1 reconstruction usually observed. The 2 × 1 reconstructed surface is shown schematically in Fig. 6: (a) in top view and (b), (c) in side view. The dimers are symmetric in (b) and asymmetric (buckled) in (c). A small buckling is believed to stabilize the surface. The saturation of the DB cannot be complete so that other types of reconstruction are observed, namely p(2 × 2) and c(4 × 2) that occur on ≈5% of the surface. Two STM pictures that show the three types of reconstruction on the same surface are presented in Fig. 7: in the upper picture dimers are seen most distinctly in rows 7, 1, 13 while the p(2 × 2) reconstruction is seen in rows 14–15. On the other hand, the c(4 × 2) reconstruction is seen in rows 2–3 of the lower picture (Tromp et al., 1985).

Si(1 1 1)2 × 1

The (1 1 1) face is the cleavage plane of Si and exposes one DB per surface atom. The 2 × 1 reconstruction is observed after cleavage at $T < 550$ K at which temperature it transforms irreversibly into the more stable 7 × 7 structure. The electronic structure consists of two bands (one full and one empty) separated by a gap of ~0.5 eV, from which optical transitions are observed (Chiarotti et al., 1971; Chiaradia et al., 1984). The opening of the gap is probably the process that stabilizes the surface.

Several models have been proposed for this surface. The only one that satisfies the various experimental findings is that proposed in 1981 by K C Pandey, which consists of π-bonded chains along [110] directions (Pandey, 1981). The model is shown in Fig. 8 in top and side views. It is seen that in order to create the chains some bonds should be broken. This, however, can be done almost adiabatically (with negligible activation energy) as can be seen from Fig. 9, where the local density of states is plotted for various configurations starting from a slightly buckled (almost ideal) surface.

The chain model explains, among others, the following experimental results: (1) the great anisotropy of optical transitions that occur only if the electric vector lies on one of the [1 1 0] directions (Chiaradia et al., 1984) and (2) the strong dispersion of the occupied states observed in photoemission (Himpsel et al., 1981). The model has been subsequently verified directly by STM (Feenstra et al., 1986). A small buckling along the chain (Fig. 8c) is necessary to explain the relatively large optical gap.

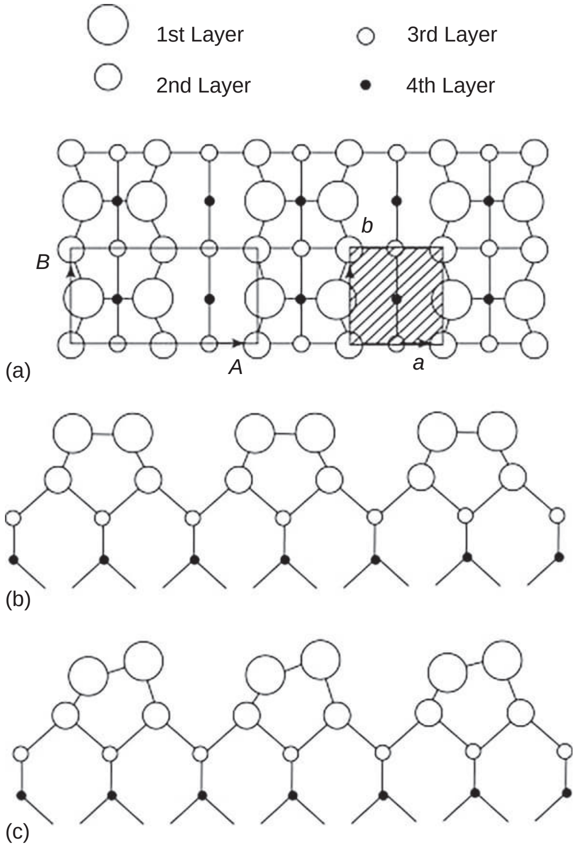

Fig. 6 Stick and ball model of the surface of Si(1 0 0) reconstructed 2 × 1 through dimerization: (a) top view. The 1 × 1 unit cell (hatched, basis vectors a, *b*) and the 2 × 1 ceil (basis vectors *A*, *B*) are shown: (b) side view; (c) side view with buckled dimers.

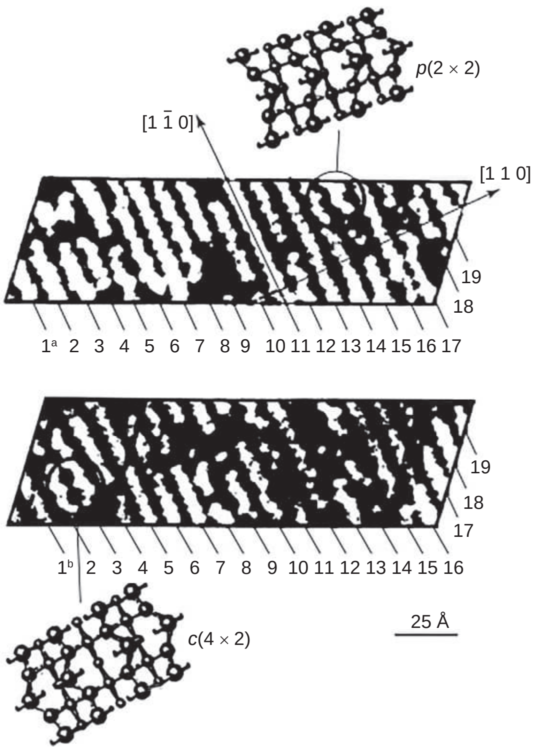
p(2 × 2)
[1 1̄ 0]
[1 1 0]
19
18
1a 2 3 4 5 6 7 8 9 10 11 12 13 14 15 16 17
19
18
17
1b 2 3 4 5 6 7 8 9 10 11 12 13 14 15 16
c(4 × 2)
25 Å

Fig. 7 STM pictures of the Si(1 0 0)2 × 1 surface. The photographs show locally *p*(2 × 2) reconstruction (rows 14, 15 in the upper picture) and *c*(4 × 2) reconstruction (rows 2, 3 in the lower picture). From Tromp RM, Hamers RJ and Demuth JE (1985) Si(001) dimer structure observed with scanning tunneling microscopy. *Physical Review Letters* **55**: 1303.

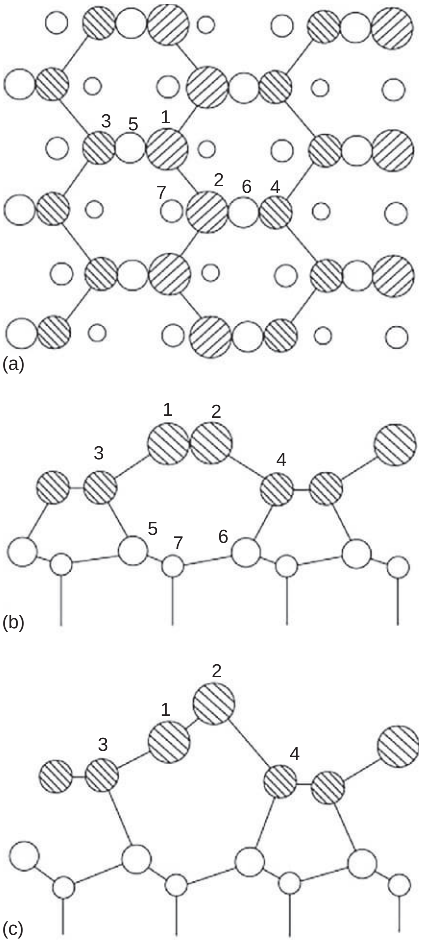
3
5
1
7
2
6
4
(a)
1
2
3
4
5
7
6
(b)
2
1
3
4
(c)

Fig. 8 Stick and ball model of the Si(1 1 1)2 × 1 surface, according to the π-bonded chain reconstruction: (a) top view; (b) side view; and (c) side view for a buckled chain.

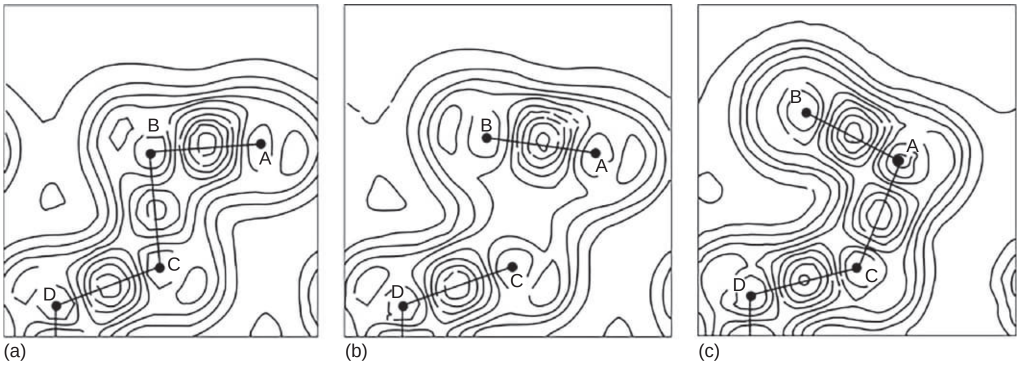

Fig. 9 Theoretical contour plots of charge density in the (1 1 0) plane of Si(1 1 1)2 × 1: (a) for a slightly buckled (nearly ideal) surface; (b) for an intermediate geometry; and (c) for the chain model of Fig. 8. After Northrup JE and Cohen ML (1982) *Physical Review Letters* **49**: 1349.

Si(1 1 1)7 × 7

As already mentioned, this is the equilibrium reconstruction of the (1 1 1) face. The elementary cell contains 49 atoms in the uppermost plane. It has then a complex structure that resisted, for at least two decades, all attempts at theoretical explanation.

By combining accurate electron diffraction at high energies (to avoid multiple scattering), STM pictures (Binnig et al., 1983), and theoretical considerations, K. Takayanagi and collaborators proposed in 1985 the reconstruction model shown in Fig. 10 (Takayanaji et al., 1985). The elementary cell is a rhomb with two nonequivalent halves and four vacancies at the corners. Dimers can be seen along the sides and the shorter diagonal. 12 adatoms and 6 so-called "rest atoms" (i.e., atoms that have maintained their original positions) are also visible. A stacking fault is present in the left half of the elementary cell. The model is then called DAS (dimers-adatom-stacking fault) and is universally accepted. The number of DB (which were 49 in the unreconstructed cell) has now been reduced to 19 (12 on the adatoms, 6 on the rest atoms, 1 in the vacancy). A similar 5 × 5 structure (with 6 adatoms, 2 rest atoms, and 4 corner vacancies) is seen in surfaces prepared by MBE and is often associated with the more common 7 × 7.

From the electronic point of view, the 7 × 7 structure has a metallic character as shown by photoemission and by the absence of optical transitions in the gap.

The distribution of surface states is shown in Fig. 11 where data of photoemission spectroscopy (left curve) and inverse photoemission spectroscopy (right curve) are plotted as a function of energy. The figure shows clearly that there is a continuous distribution of states across the gap, giving rise to the metallic conductivity of the surface.

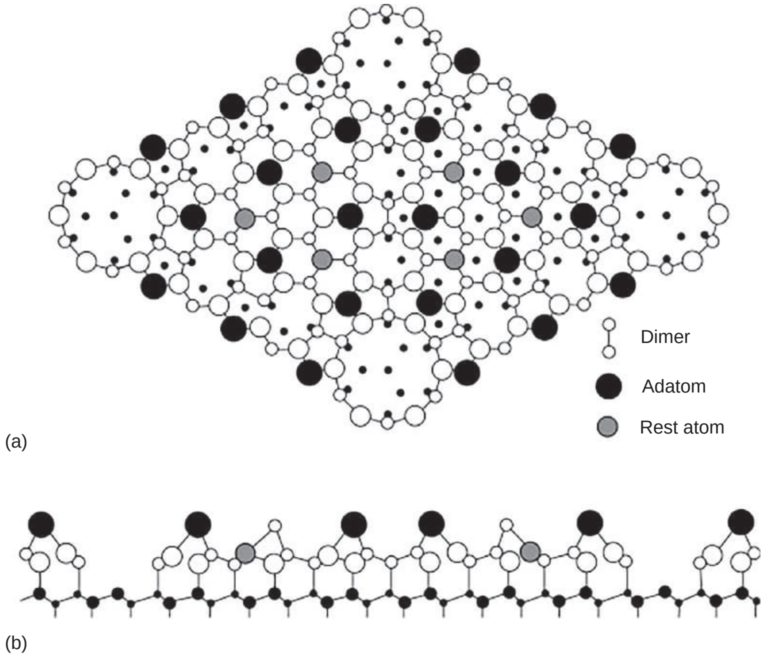

Fig. 10 Structure of the Si(1 1 1)7 × 7 surface according to the DAS model: (a) top view; (b) side view. Notice the different positions of the lower neighbors of the rest atoms in the left and right half of the elementary cell, caused by the presence of the stacking fault.

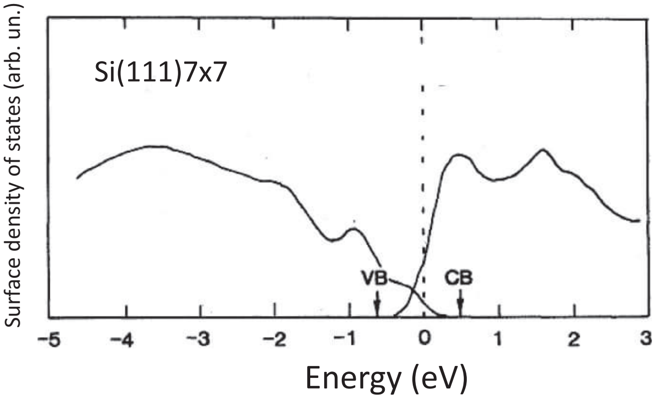

Fig. 11 Schematic distribution of occupied and empty surface states as obtained by photoemission spectroscopy that detects occupied states (left curve) and inverse photoemission that detects empty states (right curve). The energy scale has been referred to the Fermi level (E_F) position.

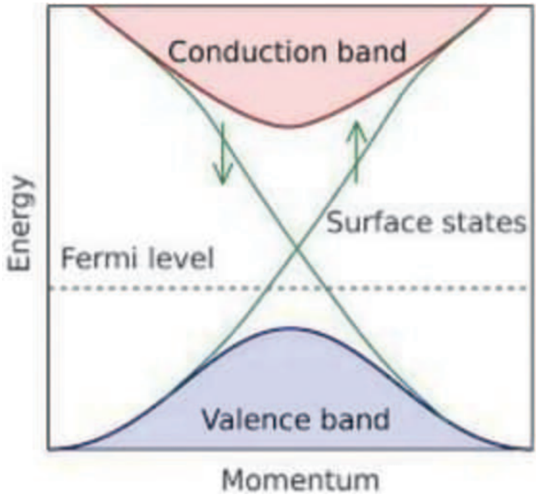

Fig. 12 Idealized band structure for a topological insulator. The Fermi level falls within the bulk band gap which is traversed by topologically-protected surface states, brought down from the conduction band and raised from the valence band. By A13ean - Own work, CC BY-SA 3.0, https://commons.wikimedia.org/w/index.php?curid=11101461.

A completely different example are the so called Topological Insulators (as for example alpha-Sn(001), or bismuth and antimony chalcogenide based materials (Bi_2Se_3, Bi_2Te_3, Sb_2Te_3, $Bi_{1-x}Sb_x$, $Bi_{1.1}$ $Sb_{0.9}Te_2S$)) in which there are no broken bonds at the surface and the metallic conductivity arises from a shearing deformation that maintains the local topology at the surface (Hasan and Kane, 2010).

From the theoretical point of view, the conductivity is due to a crossed or inverted gap states. In the simplified model shown in Fig. 12, states of the conduction band and valence band coexist at the Fermi level thus giving rise to conductivity.

Interfaces

The interface is the region that connects two different physical systems, for example, a metal and a semiconductor (Schottky barrier), two different semiconductors (heterojunction) and, in an extended sense, the surface itself, which defines the boundary between the solid and the vacuum (or a different environment, as a liquid).

When the interface forms and thermal equilibrium is reached, the Fermi levels of the two sides line up. This alignment produces a charge redistribution to preserve the overall neutrality of the system, changing the electrical properties of the contact zone.

If two metals come into contact, the difference between the respective work functions results in a flow of electrons from the metal with lower work function Φ_1 into the metal with higher work function Φ_2. A contact potential difference $\Delta = (\Phi_2 - \Phi_1)/e$ develops between the metals (Volta effect), and a dipole layer appears at the interface. Due to the high charge density in metals, the thickness of the interface region is only a fraction of an angstrom.

If the junction connects a metal and a semiconductor, the Fermi level alignment in both materials results in the band scheme of Fig. 13 where the band structures are shown in equilibrium: (a) before and (b) after the contact. An electron moving from the metal to the semiconductor (or vice versa) experiences a barrier (Schottky barrier, Φ_{SB}) given by

$$\Phi_{SB} = \Phi - \chi \tag{6}$$

where χ is the electron affinity of the semiconductor.

The space charge layer in the semiconductor has a much larger width than in the metal because of the difference of carrier densities and screening lengths (for the definition of Debye screening length see the section "Examples of reconstruction of relevant semiconductor surfaces", Eq. (5)).

In Fig. 14, the experimental values of the Schottky barrier for different metals deposited onto the Si(1 1 1)2 × 1 surface are shown. Though the general trend of Eq. (6) is maintained, it is apparent that the simple theory outlined above (dotted line) is inadequate to fit the experiments. The qualitative explanation is that in deriving Eq. (6), the presence of electronic surface states at the interface (interface states) has been neglected. If their density is sufficiently large, they pin the Fermi level at the surface of the semiconductor, making the Schottky barrier independent of the work function of the metal (dashdotted line in Fig. 14). The experimental situation is intermediate between the two hypotheses (i.e., absence of interface states and complete pinning of the Fermi level).

The nature of the interface states has been the subject of extended research. An important advancement came from the introduction of the so-called metal-induced gap states (MIGS) (Heine, 1965). Consider again Fig. 2c of the section "Electronic surface states," where the scattering of a bulk electron at the surface is outlined. If the electron at the metal side of the junction has an energy corresponding to the semiconductor gap, it cannot propagate for $z > 0$. A situation similar to that of Fig. 2c is then a reasonable approximation for the interface wave function: the electronic charge spills into the semiconductor giving rise to a density of states localized at the interface in the semiconductor side (MIGS).

On the other hand, extrinsic states due to defects, mismatching, impurities, and structural changes induced by interface chemical reactions have the same general effect as MIGS. A comprehensive theory of the electronic structure of interfaces is at present not available.

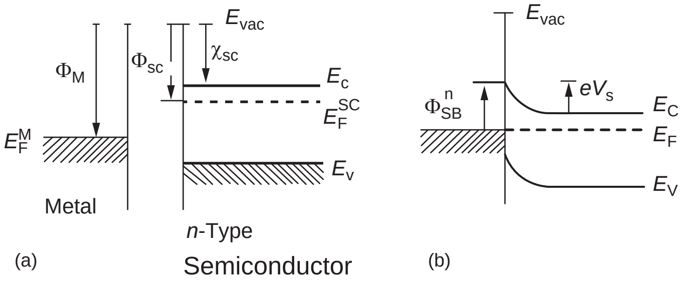

Fig. 13 Band scheme of a metal-semiconductor (*n*-type) system: (a) before the contact is established; (b) in equilibrium after the contact. $\Phi_M \cdot (\Phi_{SC})$ are the work functions of the metal (semiconductor), χ_{SC} the electron affinity of the semiconductor. Φ_{SB} the Schottky barrier height, and eV_S the band bending at the surface.

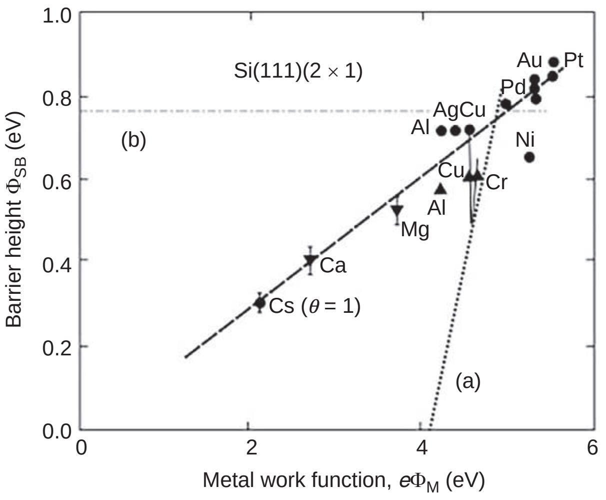

Fig. 14 Experimental values of Schottky barriers for several metals on top of Si(1 1 1)2 × 1. The lines represent (a) the Schottky behavior given by Eq. (6) (dotted) and (b) the case of complete pinning of Fermi level at the surface (Bardeen behavior, dash-dotted). After Mönch W (1986) Festkörperprobleme. In: *Advances in Solid State Physics*, vol. 26. Braunschweig: Vieweg.

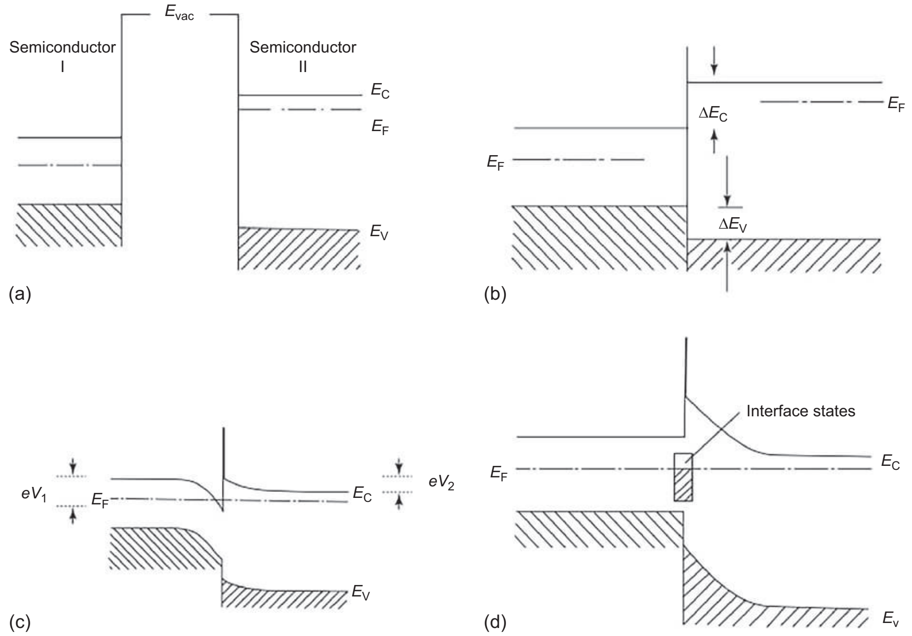

Fig. 15 Band scheme of a heterojunction: (a) when the materials are not in contact, (b) after the contact is established, but before equilibrium (Fermi levels not aligned), (c) in equilibrium, (d) in equilibrium, when interface states are present.

If the interface is created between two different semiconductors, it is called a heterojunction. The alignment of the Fermi levels on both sides determines the band scheme shown in Fig. 15. The difference between the forbidden gaps of the two semiconductors is distributed between the valence-band discontinuity (ΔE_v) and the conduction-band discontinuity (ΔE_c). Moreover, band bending (eV_1 and eV_2) occurs at the two sides of the interface. Given their great influence on carrier transport, they are the important parameters determining the performance of the interface and play a central role in the behavior of real heterojunction devices (diodes, solar cells, photodetectors, lasers, quantum devices, etc.).

The presence of electronic states at the interface modifies the distribution of charge producing the situation schematically presented in Fig. 15d. Such states originate, in analogy to MIGS, from the tailing of the semiconductor wave function in the forbidden gaps.

In the ideal heterojunction, the two materials have the same (or slightly different) lattice parameters so that there is little strain at the interface, and the materials maintain their original properties up to the abrupt junction. If the lattice parameters are different, strain results at the junction, with the formation of dislocations, defects, and disorder. Sizable interdiffusion and chemical reactions may also occur. Such defects give rise to extrinsic electron states.

Three significant examples are given below:

1. The interface resulting after growth of GaAs (lattice parameter $a = 5.6531$ Å) onto AlAs ($a = 5.6622$ Å) is a representative example of a nearly ideal heterojunction between materials with a very small lattice mismatch ($\Delta a/a = 0.5\%$). The resulting interface is atomically abrupt, with a very low number of defect states.
2. The interface between Ge ($a = 5.6578$ Å) and Si ($a = 5.4307$ Å) presents a lattice mismatch of 4%, too large to be simply accommodated by a strained layer. The interface is then characterized by intermixing, with the formation of a Ge—Si alloy.
3. In the junction between Ge ($a = 5.6578$ Å) and GaAs ($a = 5.6531$ Å), the mismatch is extremely favorable (about 8×10^{-4}). Nevertheless, the chemistry of materials, that is, the high chemical affinity of Ge, Ga, and As produces a great complexity of the interface composition, with possible effects on doping. Ge acts as a donor or an acceptor in bulk GaAs, while Ga and As are, respectively, an acceptor or a donor when the Ge atom is substituted.

Heterojunctions and heterostructures (i.e., the sequence of a high number of heterojunctions, as in a superlattice) are usually grown by MBE or metalorganic chemical vapor deposition (MOCVD). These epitaxial techniques allow the production of graded junctions that are important in many semiconductor devices.

Surfaces in real-world environment

The investigation of surfaces immersed in liquids is remarkably less common with respect to the case of surfaces in UHV. However, important technologies are based on processes that occur at the solid/liquid interface, like electro-catalysis, grafting, biofunctionalization of surfaces, electrodeposition and electro etching of metals down to the nanometer scale. Also biophysical and biochemical systems are commonly prepared and studied in aqueous solutions, and processes of high scientific relevance take place at the contact with the liquid ambient. These facts urge to bridge the gap between the research on surfaces under ideal conditions (as in UHV) and on surfaces under realistic conditions.

Although the cleanliness conditions (under preparation protocols for both the surface and the liquid) allow the maintenance of the clean phase for a surface in solution during the time necessary for experiments, only a few spectroscopies and methods can penetrate a thin layer of liquid and reach the solid/liquid interface for in situ study. Photon-based probes [as optical techniques -e.g. Reflectance Anisotropy spectroscopy (RAS)- or X-ray diffraction methods] do not suffer this limitation, provided that the liquid is not absorbing in the selected photon energy range, as already demonstrated in pristine electroreflectance measurements. Also scanning probes (AFM and STM, the latter after the metal tip has been insulated by an appropriate coating) allow the investigation of immersed surfaces, and real space images of their structure can be acquired with atomic resolution.

It has thus been shown that single crystalline surfaces of metals in liquid exhibit clean phases as in UHV (Fig. 16a) (Wilms et al., 1999). Furthermore, in electrolytes the adsorption/desorption of ions -effectively assisted by appropriate voltage values applied to the surface with respect to solution- can induce the reconstruction of the surface, determining differently ordered layers (Fig. 16b). Similarly, if different species (ions and/or molecules) coexist within the solution, competing for adsorption sites on the surface, the choice of the potential applied to the sample can tune processes otherwise not possible in UHV (as the electro-compression/--decompression of iodide layers on Cu(100) and Cu(111)). Electrochemical reactions at the solid-liquid interface can be monitored in real time, as shown in Fig. 17, where the interaction of chloride ions with a (110) copper surface in hydrochloric acid solution is followed in situ by RAS and STM (Goletti et al., 2015).

Conclusion

The termination of a crystal with a cutting plane, producing what we call *the surface*, is not merely the introduction of a geometrical boundary, but creates a new fascinating world having peculiar structural and electronic properties with respect to the underlying bulk. Any surface is then an *interface*, that is a region separating (with a quite abrupt discontinuity) the solid and a different phase in contact (solid, liquid, gaseous), associated to important physical and chemical processes in sensors, piezoelectric and optoelectronic devices, fuel cells, catalysts, solar cells, nanotechnology, etc.. Surfaces are the *skin* of the materials, the interface with the external world, and consequently the place where fundamental phenomena happen. Clean surfaces in UHV have represented the playground where nearly all the computational methods and the experimental techniques developed for about 50 years in solid state physics have been applied. In the last years new (sometimes revolutionary) topics have appeared, confirming that the physico-chemical properties of surfaces and interfaces govern the interfacial transport of light, excitons, electrons, ions, energy as well as the transduction of electrons into the molecular language of cells. To mention some important examples: (i) topological materials, with surfaces that are robust against any perturbations as long as respecting symmetry of the system (Moore, 2010); (ii) graphene and 2D van der Waals (vdW) layered semiconductors, truly surface materials providing applications in numerous quantum mechanical devices (Duong et al., 2017); (iii) surfaces of wide bandgap and metal oxide materials (SiC, GaN, Ga_2O_3, ZnO, diamond, TiO_2), with an overwhelming range of physical and chemical applications (Diebold et al., 2010); (iv) biological and organic interfaces, leading to the new challenges of the organic bioelectronics emerging field (Fahlman et al., 2019); (v) superhydrophobic surfaces, whose investigation has become a hot topic for its outstanding properties and wide application values in recent years (Jiaqiang et al., 2018).

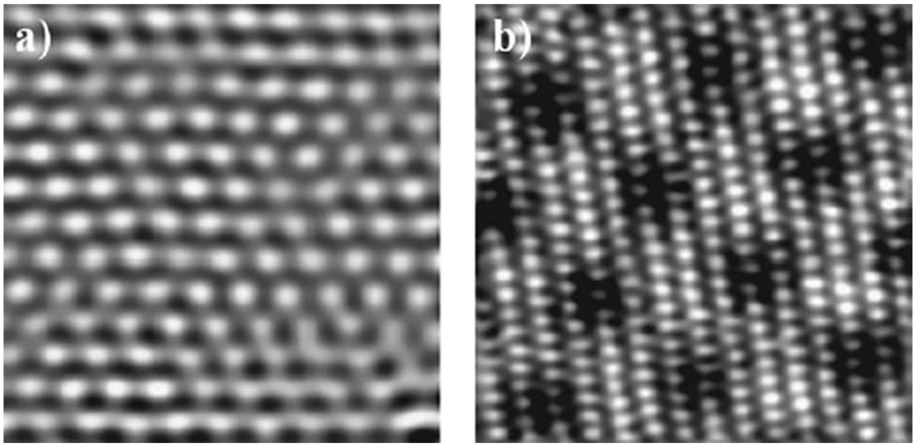

Fig. 16 Panel (a) Atomic structure of clean Cu(111) in 5 mM H_2S04 (2.7 nm × 2.7 nm, $I_t = 51$ nA, $U_{bias} = 286$ mV). The potential applied to the surface is −800 mV vs. Hg/Hg_2S04. Panel (b) Adsorbate structure on Cu(111) in the same solution, when the applied voltage is −440 mV vs. Hg/Hg_2S04 (9.6 nm × 9.6 nm, $I_t = 51$ nA, $U_{bias} = 195$ mV). The small bright dots in panel b represent individual sulfate or bisulfate anions; the long range intensity modulation indicates a Moire superstructure. From Wilms M, Kruft M, Bermes G and Wandelt K (1999) A new and sophisticated electrochemical scanning tunneling microscope design for the investigation of potentiodynamic processes. *Review of Scientific Instruments* 70: 3641.

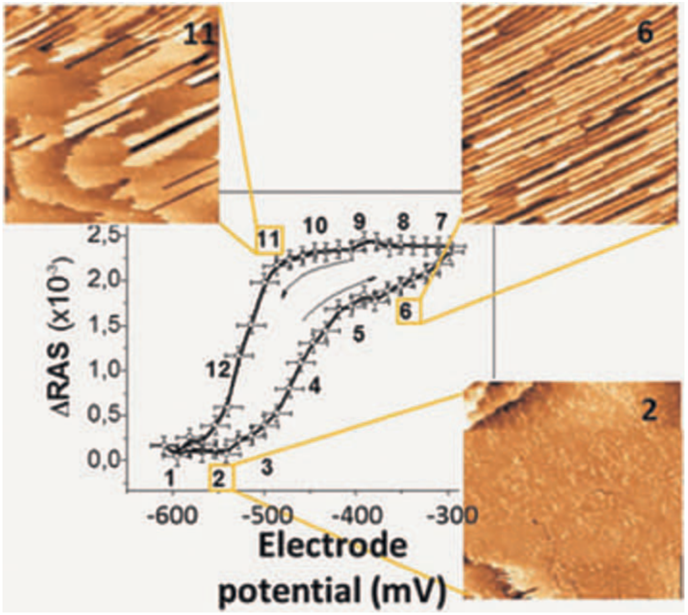

Fig. 17 Evolution of the optical anisotropy signal of a Cu(110) surface immersed in hydrochloric acid solution (0.1×10^{-3} M) as a function of the potential applied to the surface with respect to a reference electrode. The signal is acquired at fixed photon energy (2.5 eV), corresponding to the maximum of the RAS spectrum due to the adsorption of chloride ions on the copper surface. ΔRAS measures the variation of the RAS signal with respect to the clean copper surface (occurring at −600 mV). The arrows inside the curve indicate the scan direction of the potential (positive and negative direction). Reported STM images (81×81 nm^2, V_{BIAS} 30 mV, I_t 1.4 nm) have been acquired in liquid in the same conditions: (2) clean copper surface; (6) stripes of adsorbed chlorine running along the [001] direction of the surface; (11) copper terraces reappearing after partial desorption of chlorine. From Goletti C, Bussetti G, Violante A, Bonanni B, Di Giovannantonio M, Serrano G, Breuer S, Gentz K and Wandelt K (2015) Cu(110) surface in hydrochloric acid solution: Potential dependent chloride adsorption and surface restructuring. *The Journal of Physical Chemistry C* **119**: 1782.

References

Binnig G, Rohrer H, Gerber C, and Weikel E (1983) 7x7 reconstruction on Si(111) resolved in real space. *Physical Review Letters* 50: 120.
Car R and Parrinello M (1985) Unified approach for molecular dynamics and density-functional theory. *Physical Review Letters* 55: 2471.
Chiaradia P, Cricenti A, Selci S, and Chiarotti G (1984) Differential reflectivity of Si(111)2x1 surface with polarized light: A test for surface structure. *Physical Review Letters* 52: 1145.
Chiarotti G, Nannarone S, Pastore R, and Chiaradia P (1971) Optical absorption of surface states in ultrahigh vacuum cleaved (111) surfaces of Ge and Si. *Physical Review B* 4: 3398.
Diebold U, Li SC, and Schmid M (2010) Oxide Surface Science. *Annual Review of Physical Chemistry* 61: 129.
Duong DL, Yun SY, and Lee YH (2017) van der Waals Layered Materials: Opportunities and Challenges. *ACS Nano* 11: 11803.
Echenique PM, Flores F, and Sols F (1985) Lifetime of image surface states. *Physical Review Letters* 55: 2348.
Fahlman M, Fabiano S, Gueskine V, Simon D, Berggren M, and Crispin X (2019) Interfaces in organic electronics. *Nature Reviews Materials* 4: 627.
Feenstra RM, Thompson WA, and Fein AP (1986) Real-space observation of π-bonded chains and surface disorder on Si(111)2 1. *Physical Review Letters* 56: 608.
Goletti C, Bussetti G, Violante A, Bonanni B, Di Giovannantonio M, Serrano G, Breuer S, Gentz K, and Wandelt K (2015) Cu(110) surface in hydrochloric acid solution: Potential dependent chloride adsorption and surface restructuring. *The Journal of Physical Chemistry C* 119: 1782.
Hasan MZ and Kane CL (2010) Colloquium: Topological insulators. *Reviews of Modern Physics* 82: 3045.
Heine V (1965) Theory of surface states. *Physical Review* 138: A1689.
Himpsel FJ, Heimann P, and Eastman DE (1981) Surface states on Si(111)-(2x1). *Physical Review B* 24: 2003.
Jiaqiang E, Jin Y, Deng Y, Zuo W, Zhao X, Han D, Peng Q, and Zhang Z (2018) Wetting models and working mechanisms of typical surfaces existing in nature and their application on superhydrophobic surfaces: A review. *Advanced Materials Interfaces* 5: 1701052.
Lang ND and Kohn W (1970) Theory of metal surfaces: Charge density and surface energy. *Physical Review B* 1: 4555.
Moore JE (2010) The birth of topological insulators. *Nature* 464: 194.
Pandey KC (1981) New π-bonded chain model for Si(111)-(2x1) surface. *Physical Review Letters* 47: 1913.
Takayanaji K, Tanishiro Y, Takahashi M, and Takashi S (1985) Structural analysis of Si(111)-7×7 by UHV-transmission electron diffraction and microscopy. *Journal of Vacuum Science and Technology A* 3: 1502.
Tromp RM, Hamers RJ, and Demuth JE (1985) Si(001) dimer structure observed with scanning tunneling microscopy. *Physical Review Letters* 55: 1303.
Wilms M, Kruft M, Bermes G, and Wandelt K (1999) A new and sophisticated electrochemical scanning tunneling microscope design for the investigation of potentiodynamic processes. *Review of Scientific Instruments* 70: 3641.

Further reading

Bechstedt F (2003) *Principles of Surface Physics.* Berlin: Springer.
Bechstedt F and Enderlein R (1988) *Semiconductor Surfaces and Interfaces.* Berlin: Akademie-Verlag.
Chiarotti G (ed.) (1993-1996) *Physics of Solid Surfaces: Landolt-Börnstein New Series, Group III/24.* In: *Physics of Solid Surfaces*, vol. 4. Berlin: Springer.

Heine V (1965) Theory of surface states. *Physical Review* 138: A1689.
Lannoo M and Friedel P (1991) *Atomic and Electronic Structure of Surfaces*. Berlin: Springer.
Lüth H (2001) *Solid Surfaces, Interfaces and Thin Films*, 4th edn Berlin: Springer.
Lüth H (1993) *Surfaces and Interfaces of Solid Materials*. Berlin: Springer Verlag.
Mönch W (1995) *Semiconductor Surfaces and Interfaces*, 2nd edn Berlin: Springer.
Mönch W (1986) Festkörperprobleme. *Advances in Solid State Physics*. 26: Braunschweig: Vieweg.
Wandelt K and Thurgate S (eds.) (2003) *Solid–Liquid Interfaces: Macroscopic Phenomena-Microscopic Understanding*. In: *Solid-Liquid Interfaces*Berlin: Springer Verlag.
Wandelt K (ed.) (2016) *Surface and Interface Science: Solid/liquid and Biological Interfaces.* In: *Solid-Liquid Interfaces*, vol. 7. Wiley VCH.
Zangwill A (1988) *Physics at Surfaces*. Cambridge: Cambridge University Press.

Graphene, electronic properties and topological properties

Katsunori Wakabayashi, Department of Nanotechnology for Sustainable Energy, School of Science and Technology, Kwansei Gakuin University, Sanda, Japan

© 2024 Elsevier Ltd. All rights reserved.

Introduction 273
Electronic state of graphene 274
Topological properties of graphene 277
Graphene nanoribbons and edge states 278
Charge polarization and Zak phase 280
Energy spectrum and wave functions: Graphene nanoribbons 281
Armchair nanoribbons 281
Zigzag nanoribbons 282
Electronic states of carbon nanotubes 284
Conclusion 286
References 286

Abstract

Graphene is a one-atomic thickness carbon sheet with a hexagonal lattice structure. The low-energy electronic states of graphene near the Fermi energy are well-described by massless Dirac equation, which gives conical energy dispersion and nontrivial Berry phase. The analysis of Zak phase (known also as $\mathcal{Z}_2$ Berry phase or one-dimensional version of Berry phase) clarifies the existence of topological edge states at graphene zigzag edges. In this chapter, we provide an overview of electronic and topological properties of graphene. The analytic properties of energy spectrum for graphene nanoribbons and carbon nanotubes are also presented.

Key points

- Electronic and topological properties of graphene are presented.
- Low-energy electronic states of graphene are well-described by massless Dirac equation, resulting in the linear energy dispersion with Berry phase π.
- Analysis of Zak phase on electronic wave functions of graphene predicts the existence of graphene edge states.
- Analytic properties of energy spectrum for graphene nanoribbons are presented.
- Analytic properties of energy spectrum for carbon nanotubes are presented.

Introduction

Graphene is a one-atomic thickness monoatomic carbon sheet, which has the hexagonal lattice structure (Geim and Novoselov, 2007; Novoselov et al., 2004, 2005; Zhang et al., 2005). Since carbon atoms in graphene form sp^2 hybridization, each carbon atom provides one π-electron which itinerates over the graphene. The π-electron of sp^2 carbon atoms governs the electronic properties of graphene near the Fermi energy (Aoki and Dresselhaus, 2014; Foa Torres et al., 2014; Katsnelson, 2012; Neto et al., 2009; Saito et al., 1998; Wallace, 1947). Owing to the honeycomb crystal structure of graphene, there are two inequivalent sublattices (two geometrically nonequivalent carbon atoms) in the unit cell, which work as the internal degree of freedom for electron wave functions. In particular, the motion of electrons in graphene near the Fermi energy is well described by the massless Dirac equation (Weyl equation), which can be obtained from tight-binding model for π-electrons by expanding the wave function at the Fermi points (Ajiki and Ando, 1993; Ando, 2005; Ando et al., 1998). At these points, graphene has the conical energy dispersion, i.e., Dirac cone, where the valence and conduction bands conically touch with each other. Since the wave function at Dirac cone has the same form with the eigenfunction of a spin in magnetic monopole field, it accompanies with the nontrivial topological phase, i.e., Berry phase (Berry, 1984).

Further topological aspect can also be observed by inspecting the edge effect on electronic properties of graphene. The presence of edges in graphene has strong implications for the low-energy spectrum of the π-electrons (Fujita et al., 1996; Nakada et al., 1996; Wakabayashi et al., 1999). There are two basic edge shapes, *armchair* and *zigzag*, which determine the properties of graphene nanoribbons (GNRs). It has been shown that nanoribbons with zigzag edges (zigzag graphene nanoribbons, ZGNRs) possess localized edge states with energies close to the Fermi level (Fujita et al., 1996; Nakada et al., 1996; Wakabayashi et al., 1999). In contrast, edge states are absent for nanoribbons with armchair edges (armchair graphene nanoribbons, AGNRs). The origin of

https://doi.org/10.1016/B978-0-323-90800-9.00139-6

edge states can be understood by the consequences of finite Zak phase of bulk wave function of graphene. Zak phase is one-dimensional version of Berry phase (Zak, 1989).

In this chapter, we give an overview of topological aspects on electronic properties of graphene. We start with the basics of π-electronic states of graphene using tight-binding model, and derive the massless Dirac equation to show the singular topological properties at Fermi points. Further, we give the overview of edge effect on π-electronic states of graphene on the basis of GNRs, where it is shown that zigzag edges provide robust topological edge states. Finally, we give analytic properties of energy spectrum for GNRs and carbon nanotubes.

Electronic state of graphene

We employ a single-orbital nearest-neighbor tight-binding model for the π-electron network to describe the electronic states of graphene (Neto et al., 2009; Wallace, 1947). Fig. 1A and B show the lattice structure and the first Brillouin zone (BZ) of graphene, respectively. The corners of the first BZ are called K_+ or K_- points, which are also referred to as Dirac points because the energy spectrum at these corners can be described by the massless Dirac equation (Weyl equation).

Let us define the wave functions at $\boldsymbol{R_A}$ of a lattice site A and $\boldsymbol{R_B}$ of a lattice site B as $\psi_A(\boldsymbol{R_A})$ and $\psi_B(\boldsymbol{R_B})$, respectively. These wave functions can be related by the following Schrödinger equations of the tight-binding model;

$$E\psi_A(\boldsymbol{R_A}) = -\gamma_0 \sum_{l=1}^{3} \psi_B(\boldsymbol{R_A} - \boldsymbol{\tau}_l), \tag{1}$$

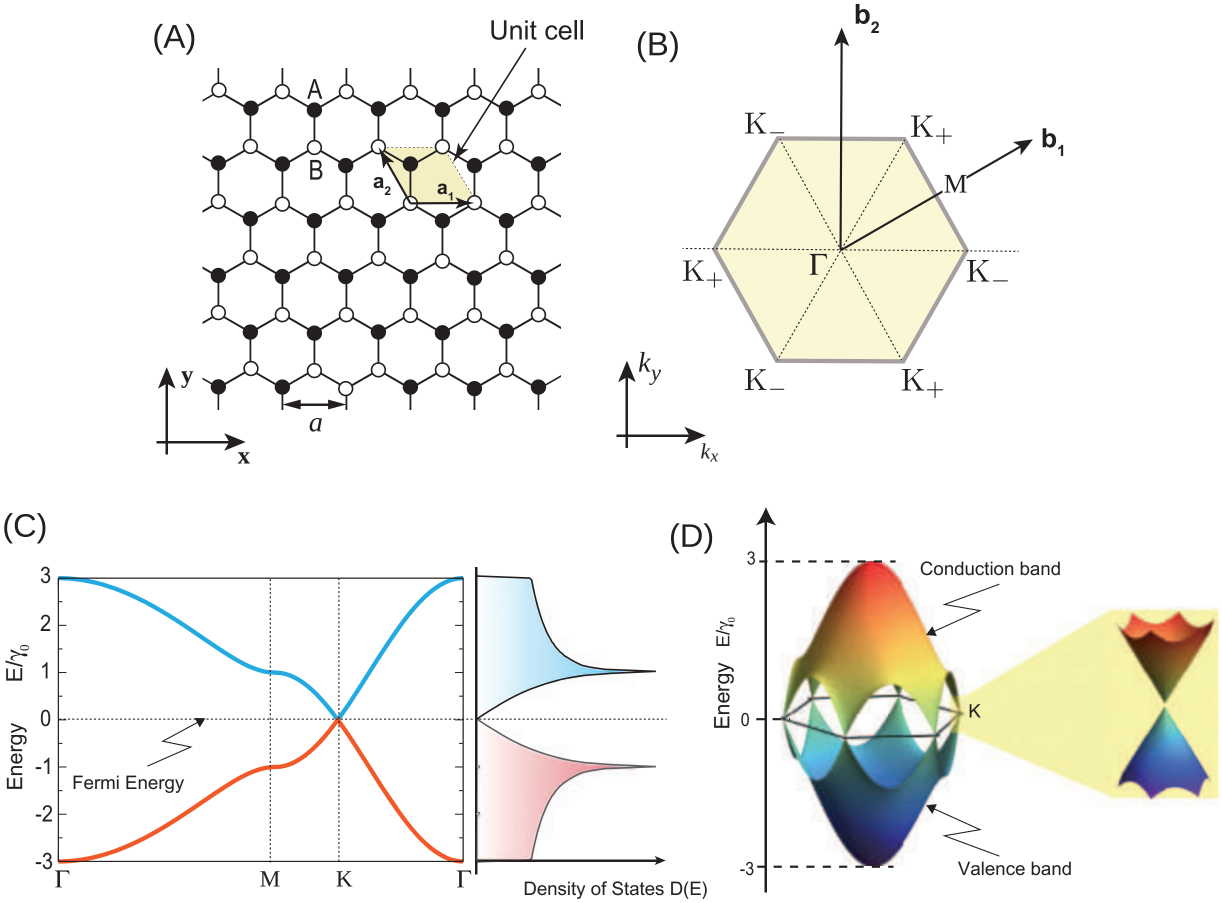

Fig. 1 (A) Graphene sheet in real space, where the black (white) circles denote A(B)-sublattice sites; a is the lattice constant and $\boldsymbol{a_1} = (a, 0)$ and $\boldsymbol{a_2} = \left(-a/2, \sqrt{3}a/2\right)$ are the primitive vectors. (B) First BZ of graphene. $\boldsymbol{K_+} = \frac{2\pi}{a}\left(\frac{1}{3}, \frac{1}{\sqrt{3}}\right), \boldsymbol{K_-} = \frac{2\pi}{a}\left(\frac{2}{3}, 0\right), \boldsymbol{\Gamma} = (0, 0)$. Note that there are three $\boldsymbol{K_+}$ and $\boldsymbol{K_-}$ points, which can be connected by the reciprocal lattice vectors. The valence and conduction bands are in contact at the degeneracy points, $\boldsymbol{K}$ and $\boldsymbol{K'}$. (C) Energy band structure of graphene within the irreducible BZ, together with DOS of a graphene sheet. (D) (left) 3D plot of the energy band structure for π-electrons. (right) Zoom of energy band structure around K-points, where the energy dispersion has conical shape, i.e., Dirac cone.

$$E\psi_B(\boldsymbol{R_B}) = -\gamma_0 \sum_{l=1}^{3} \psi_A(\boldsymbol{R_B} + \boldsymbol{\tau}_l). \tag{2}$$

Here E is the eigenenergy. $\boldsymbol{R_A} = n_1\boldsymbol{a}_1 + n_2\boldsymbol{a}_2 + \boldsymbol{\tau}_3$ and $\boldsymbol{R_B} = n_1\boldsymbol{a}_1 + n_2\boldsymbol{a}_2$, where integers n_1 and n_2 represent the locations of sites A and B, respectively. $\tau_3 = \left(a/2, -a/2\sqrt{3}\right)$ is the relative vector between A and B atoms. $a = 2.46$ Å is the lattice constant of graphene. γ_0 is the transfer integral between nearest-neighbor carbon sites, which has been estimated to be about 2.75 eV in a graphene system.

Here we assume a plane wave form of the wave function, i.e., $\psi_A(\boldsymbol{R_A}) \propto f_A(\boldsymbol{k}) \exp\left(i\boldsymbol{k}\cdot\boldsymbol{R_A}\right)$ and $\psi_B(\boldsymbol{R_B}) \propto f_B(\boldsymbol{k}) \exp\left(i\boldsymbol{k}\cdot\boldsymbol{R_B}\right)$, where $\boldsymbol{k} = (k_x, k_y)$ is the wavenumber vector. Thus, we obtain the eigenvalue equation

$$H(\boldsymbol{k})\begin{pmatrix} f_A(\boldsymbol{k}) \\ f_B(\boldsymbol{k}) \end{pmatrix} = E\begin{pmatrix} f_A(\boldsymbol{k}) \\ f_B(\boldsymbol{k}) \end{pmatrix}, \tag{3}$$

with the Hamiltonian

$$H(\boldsymbol{k}) = \begin{pmatrix} 0 & h^*(\boldsymbol{k}) \\ h(\boldsymbol{k}) & 0 \end{pmatrix}. \tag{4}$$

Here

$$h(\boldsymbol{k}) = -\gamma_0\left(1 + \mathrm{e}^{-i\boldsymbol{k}\cdot\boldsymbol{a}_1} + \mathrm{e}^{-i\boldsymbol{k}\cdot\boldsymbol{a}_2}\right) = -\gamma_0|h(\boldsymbol{k})|\mathrm{e}^{i\phi_{\boldsymbol{k}}}, \tag{5}$$

and $\phi_{\boldsymbol{k}}$ is the phase measured from k_x axis. Thus, the energy bands are given by $E_S = s\,|f(\boldsymbol{k})|$, namely,

$$E_s(\boldsymbol{k}) = s\gamma_0\sqrt{1 + 4\cos\frac{k_x a}{2}\cos\frac{\sqrt{3}k_y a}{2} + 4\cos^2\frac{k_x a}{2}} \tag{6}$$

with $s = \pm 1$. Because one carbon site has one π-electron on average, only the $E_-(\mathbf{k})$ band is completely occupied. Thus, $s = +1$ and $s = -1$ correspond to the conduction and valence bands, respectively. The wave function can be written as

$$\begin{pmatrix} f_A(\boldsymbol{k}) \\ f_B(\boldsymbol{k}) \end{pmatrix} = \frac{1}{\sqrt{2}}\begin{pmatrix} 1 \\ s\mathrm{e}^{i\phi_{\boldsymbol{k}}} \end{pmatrix}. \tag{7}$$

Thus, the Bloch wave function of graphene has a relative phase between A and B sublattice sites. The density of states (DOS) is calculated as

$$D(E) = -\frac{1}{\pi}\mathrm{Im}\sum_{s=\pm}\int_{1\mathrm{stBZ}} \mathrm{d}k\,\frac{1}{E - E_s(\boldsymbol{k}) + i\eta}, \tag{8}$$

where the $\boldsymbol{k}$-integration is over the first BZ and η is an infinitesimally small real number.

Fig. 1C shows the energy band structure of graphene for π-electrons and corresponding DOS. Fig. 1D shows 3D plot of the energy band structure. Near the Γ point, both valence and conduction bands can be expressed as quadratic functions of k_x and k_y, i.e., $E(\boldsymbol{k}) = \pm\gamma_0(3 - 3|\boldsymbol{k}|^2/4)$. At the M points, which are the midpoints of the sides of the hexagonal first BZ, a saddle point appears in the energy dispersion in the vicinity of $E = \pm\gamma_0$, resulting in logarithmic divergence of the DOS as can be seen in Fig. 1C. Near the K point at the corner of the hexagonal first BZ, the energy dispersion is a linear function of the magnitude of the wave vector, $E(\boldsymbol{k}) = \pm\sqrt{3}\gamma_0 a|\boldsymbol{k}|/2$, where the DOS linearly depends on energy. Here $a(=|\boldsymbol{a}_i|(i = 1, 2))$ is the lattice constant. The Fermi energy is located at the K points, and there is no energy gap at these points because $E(\boldsymbol{k})$ vanishes there owing to the hexagonal symmetry. Owing to the linear dispersion at K points, graphene has the conical dispersion as shown in the zoom of Fig. 1D. The slope of the conical dispersion gives the Fermi velocity v_F of graphene, i.e.,

$$v_F = \frac{1}{\hbar}\nabla_{\boldsymbol{k}}E(\boldsymbol{k}) = \frac{\sqrt{3}}{2}\frac{\gamma_0 a}{\hbar}, \tag{9}$$

which is approximately $v_F \sim 10^6$ m/s. Hence, the Fermi velocity of graphene is about 1/300 of the speed of light.

The electronic state in the vicinity of a K point can be described by the massless Dirac equation, i.e., Weyl equation (Ajiki and Ando, 1993; Ando et al., 1998). In the continuum limit of lattice coordination, the wave function around $\boldsymbol{K}_+$ point can be written as

$$\begin{cases} \psi_A(\boldsymbol{r}) = \mathrm{e}^{i\boldsymbol{K}_+\cdot\boldsymbol{r}}\phi_A^{\boldsymbol{K}_+}(\boldsymbol{r}) \\ \psi_B(\boldsymbol{r}) = \mathrm{e}^{i\boldsymbol{K}_+\cdot\boldsymbol{r}}\phi_B^{\boldsymbol{K}_+}(\boldsymbol{r}) \end{cases} \tag{10}$$

Here $\phi_A^{K_+}(\boldsymbol{r})$ and $\phi_B^{K_+}(\boldsymbol{r})$ are the envelope functions for A and B sublattice at the electron coordinate $\boldsymbol{r} = (x, y)$. Applying the Taylor expansion after we substitute these form into the tight-binding equations, we obtain the following equation,

$$\gamma\begin{pmatrix} 0 & \hat{k}_x - i\hat{k}_y \\ \hat{k}_x + i\hat{k}_y & 0 \end{pmatrix}\boldsymbol{\Phi}^{K_+}(\boldsymbol{r}) = E\boldsymbol{\Phi}^{K_+}(\boldsymbol{r}), \tag{11}$$

where $\boldsymbol{\Phi}^{K_+}(\boldsymbol{r})$ is two-component envelope functions

$$\boldsymbol{\Phi}^{K_+}(\boldsymbol{r}) = \begin{pmatrix} \phi_A^{K_+}(\boldsymbol{r}) \\ \phi_B^{K_+}(\boldsymbol{r}) \end{pmatrix}. \tag{12}$$

$\hat{k}_x$ and $\hat{k}_y$ are wave number operators and are replaced with the differential operators of the coordinates $\hat{k}_x \rightarrow -i\frac{\partial}{\partial x}$ and $\hat{k}_y \rightarrow -i\frac{\partial}{\partial y}$. The band parameter γ is given by

$$\gamma = \frac{\sqrt{3}a}{2}\gamma_0. \tag{13}$$

Similarly, for $\boldsymbol{K}_-$ point, we have

$$\gamma \begin{pmatrix} 0 & \hat{k}_x + i\hat{k}_y \\ \hat{k}_x - i\hat{k}_y & 0 \end{pmatrix} \boldsymbol{\Phi}^{K_-}(\boldsymbol{r}) = E\boldsymbol{\Phi}^{K_-}(\boldsymbol{r}). \tag{14}$$

Eq. (11) is mathematically equivalent to the two-dimensional version of Weyl equation, which describes the motion of massless relativistic particle, and also refereed as massless Dirac equation. The discussion can be also extended to multi-layer graphene and twisted bilayer graphene (Bistritzer and MacDonald, 2011; Guinea et al., 2006; Koshino and Ando, 2007; Koshino et al., 2018; McCann and Fal'ko, 2006; Nilsson et al., 2006).

In terms of the Pauli spin matrices

$$\sigma_x = \begin{pmatrix} 0 & 1 \\ 1 & 0 \end{pmatrix}, \sigma_y = \begin{pmatrix} 0 & -i \\ i & 0 \end{pmatrix}, \sigma_z = \begin{pmatrix} 1 & 0 \\ 0 & -1 \end{pmatrix}, \tag{15}$$

Eq. (11) can be written as

$$\gamma\boldsymbol{\sigma}\cdot\hat{\boldsymbol{k}}\Phi^{K_+}(\boldsymbol{r}) = E\Phi^{K_+}(\boldsymbol{r}), \tag{16}$$

where $\boldsymbol{\sigma} = (\boldsymbol{\sigma}_x, \boldsymbol{\sigma}_y)$ and $\hat{\boldsymbol{k}} = \left(\hat{k}_x, \hat{k}_y\right)$. Similarly, Eq. (14) can be rewritten as

$$\gamma\boldsymbol{\sigma}^*\cdot\hat{\boldsymbol{k}}\Phi^{K_-}(\boldsymbol{r}) = E\Phi^{K_-}(\boldsymbol{r}), \tag{17}$$

where $\boldsymbol{\sigma}^* = (\boldsymbol{\sigma}_x, -\boldsymbol{\sigma}_y)$.

The energy spectrum and eigenfunction of massless Dirac equation can be obtained by assuming the plane wave form as a solution of the envelope function, namely,

$$\boldsymbol{\Phi}^{K_\pm}(\boldsymbol{r}) \propto \begin{pmatrix} f_A \\ f_B \end{pmatrix} \exp\,(i\boldsymbol{k}\cdot\boldsymbol{r}). \tag{18}$$

Here it should be noted that the wave number $\boldsymbol{k}$ is measured from either $\boldsymbol{K}_+$ or $\boldsymbol{K}_-$ point. From this, we can immediately obtain the linear spectrum of energy as

$$E_S(\boldsymbol{k}) = s\gamma|\boldsymbol{k}|, \quad \text{with} \quad s = \pm 1. \tag{19}$$

The wave function can be written as

$$\boldsymbol{\Phi}_{s\boldsymbol{k}}^{K}(\boldsymbol{r}) = \frac{1}{\sqrt{L_x L_y}}\exp(i\boldsymbol{k}\cdot\boldsymbol{r})\boldsymbol{\Phi}_{s\boldsymbol{k}}^{K}, \tag{20}$$

with the *spin* sector

$$\Phi_{s\boldsymbol{k}}^{K_\pm} = \frac{1}{\sqrt{2}}\begin{pmatrix} 1 \\ se^{\mp i\theta_k} \end{pmatrix}. \tag{21}$$

Here $\boldsymbol{\theta}_{\boldsymbol{k}}$ is defined as the angle between wave vector $\boldsymbol{k}$ and the k_x-axis, i.e., $k_x + ik_y = |\,\boldsymbol{k}\,|\,e^{i\boldsymbol{\theta}_k}$. Note that the term "spin" appearing here does not mean the real spin of the electron, since the eigenfunction for the *spin sector* describes the amplitude of the wave function on A and B sublattices. Thus, it is normally called *pseudo-spin* to distinguish it from the real electron spin. It should be noted that $\boldsymbol{K}_+$ and $\boldsymbol{K}_-$ points have opposite phase $\boldsymbol{\theta}_{\boldsymbol{k}}$. Using Eq. (19), Eq. (16) can be rewritten as

$$\frac{\boldsymbol{\sigma}\cdot\hat{\boldsymbol{k}}}{|\boldsymbol{k}|}\Phi^{K_+}(\boldsymbol{r}) = s\Phi^{K_+}(\boldsymbol{r}). \tag{22}$$

It should be noted that $\frac{\boldsymbol{\sigma}\cdot\hat{\boldsymbol{k}}}{|\boldsymbol{k}|}$ represents the helicity operator. Thus, the helicity of electrons in graphene depends on the band index s. Similarly, the expectation value of pseudo-spin around $\boldsymbol{K}_+$point is given as

$$\langle\boldsymbol{\sigma}\rangle = \left(\langle\boldsymbol{\sigma}_x\rangle, \langle\boldsymbol{\sigma}_y\rangle\right) = s(\cos\boldsymbol{\theta}_k, \sin\boldsymbol{\theta}_k). \tag{23}$$

These results indicate that the electron (hole) near $\boldsymbol{K}_+$ point has a definite pseudo-spin direction, which is parallel (antiparallel) to the direction of motion. These properties are also refereed as *chirality*. For the state near $\boldsymbol{K}_-$ point, the chirality is obtained by reversing the sign of s, i.e., $s \rightarrow -s$. Thus, $\boldsymbol{K}_+$ and $\boldsymbol{K}_-$ have opposite chirality from each other, which is the consequences of two-dimensional analog of the Fermion doubling (Aoki and Dresselhaus, 2014). In addition, the chiral property of wave function leads to the Klein tunneling effect (Katsnelson, 2012; Katsnelson et al., 2006).

Topological properties of graphene

The wave function of pseudo-spin sector contains the nontrivial Berry phase (Ando et al., 1998). To see this fact further, here we briefly summarize the key results for topological aspects (Bernevig and Hughes, 2013; Berry, 1984; Vanderbilt, 2018; Xiao et al., 2010). Now let us consider a physical system in which Hamiltonian H smoothly depends on the parameter $\boldsymbol{R}$, i.e., $H = H(\boldsymbol{R})$. This parameter slowly changes with time and moves along an arbitrary enclosed path C in $\boldsymbol{R}$ space. To be more specific, let us denote $t = 0$ as the initial time, and $t = T$ as the final time, so the $\boldsymbol{R}(t)$ satisfies $\boldsymbol{R}(0) = \boldsymbol{R}(T)$ for a closed path. Now we consider the time-evolution of wave function. The time-dependent Schrödinger equation is

$$H(\boldsymbol{R}(t))|\boldsymbol{\psi}(t)\rangle = i\hbar\frac{\partial}{\partial t}|\boldsymbol{\psi}(t)\rangle. \tag{24}$$

For each time, we assume that the wave function satisfies the orthonormal basis set $\{\phi_n(\boldsymbol{R}(t))\}$ with the eigenvalue equation

$$H(\boldsymbol{R}(t))|\phi_n(t)\rangle = E_n(\boldsymbol{R}(t))|\phi_n(t)\rangle. \tag{25}$$

By assuming that the wave function adiabatically changes, the wave function at time t can be written as

$$|\phi_n(t)\rangle = \mathrm{e}^{i\gamma_n(t)}|\phi_n(\boldsymbol{R}(t))\rangle. \tag{26}$$

In general, the phase $\gamma_n(t)$ does not need to be zero. Substituting $|\phi_n(t)\rangle$ into Eq. (24), we obtain

$$E_n(\boldsymbol{R}_n)|\phi_n(\boldsymbol{R})\rangle = \hbar\left(\frac{d}{dt}\gamma_n\right)|\phi_n(\boldsymbol{R})\rangle + i\hbar\frac{d}{dt}|\phi_n(\boldsymbol{R})\rangle.$$

Taking the inner product with $\langle\phi_n(\boldsymbol{R})|$, we obtain

$$\begin{aligned} i\frac{\partial}{\partial t}\gamma_n &= -\frac{i}{\hbar}E_n(\boldsymbol{R}) - \langle\phi_n(\boldsymbol{R})|\frac{\partial}{\partial t}|\phi_n(\boldsymbol{R})\rangle \\ &= -\frac{i}{\hbar}E_n(\boldsymbol{R}) - \langle\phi_n(\boldsymbol{R})|\nabla_{\boldsymbol{R}}|\phi_n(\boldsymbol{R})\rangle\cdot\frac{\partial\boldsymbol{R}}{\partial t}. \end{aligned}$$

Since we are considering a closed path for the parameter $\boldsymbol{R}$, the system Hamiltonian returns to the initial state after the time T. However, the phase difference between the initial and last time is as follows.

$$\begin{aligned} &\gamma_n(T) - \gamma_n(0) \\ &= \int_0^T \frac{\partial\gamma_n(t)}{\partial t}dt \\ &= -\frac{1}{\hbar}\int_0^T E_n(\boldsymbol{R}(t))dt + i\oint_C \langle\phi(\boldsymbol{R})|\nabla_{\boldsymbol{R}}|\phi(\boldsymbol{R})\rangle\cdot d\boldsymbol{R} \end{aligned} \tag{27}$$

The first term is the conventional dynamical phase. The second part is the geometric phase which depends on the path C, and called Berry phase. When we define the Berry connection $A_n(\boldsymbol{R})$ as

$$A_n(\boldsymbol{R}) = -i\langle\phi(\boldsymbol{R})|\nabla_{\boldsymbol{R}}|\phi(\boldsymbol{R})\rangle, \tag{28}$$

we can rewrite the Berry phase as

$$\gamma_n[C] = -\oint_C A_n(\boldsymbol{R})\cdot d\boldsymbol{R}. \tag{29}$$

Physically, the Berry connection can be understood as the vector potential in $\boldsymbol{R}$ space, and its rotation $\boldsymbol{F}(\boldsymbol{R}) = \nabla\times\boldsymbol{A}(\boldsymbol{R})$ can be understood as the magnetic field in $\boldsymbol{R}$ space, which is called Berry curvature. Using Stokes' theorem, the line integral can be written as surface integral

$$\gamma_n[C] = -\oint_S \nabla\times A_n(\boldsymbol{R})\cdot d\boldsymbol{S} = -\oint_S F_n(\boldsymbol{R})d\boldsymbol{S} \tag{30}$$

Thus, the Berry phase can be understood as arising from magnetic flux in $\boldsymbol{R}$ space.

Let us now consider the electronic states of graphene near $K_\pm$ points, i.e., Dirac cone. We consider the Bloch wave vector $\boldsymbol{k}$ as the parameter of Hamiltonian $H(\boldsymbol{k})$. From Eq. (21), we can immediately calculate the Berry connection as follows,

$$A_s^{K_\pm}(\boldsymbol{k}) = \langle\Phi_{s\boldsymbol{k}}^{K_\pm}|\nabla_{\boldsymbol{k}}|\Phi_{s\boldsymbol{k}}^{K_\pm}\rangle = \mp\frac{1}{2}\nabla_{\boldsymbol{k}}\theta_{\boldsymbol{k}}. \tag{31}$$

It should be noted that $\boldsymbol{K}_+$and $\boldsymbol{K}_-$ points have opposite signs for Berry connection. The Berry phase is obtained by the line integration along a closed path with anti-clockwise direction, i.e.,

$$\begin{aligned}\gamma_s^{K_\pm}[C] &= \oint_C \boldsymbol{A}_s^{K_\pm}(\boldsymbol{k})\cdot d\boldsymbol{k} \\ &= \begin{cases} \mp\pi & \text{if C encloses } \boldsymbol{k}=\boldsymbol{0}, \\ 0 & \text{if C dose not enclose } \boldsymbol{k}=\boldsymbol{0}. \end{cases}\end{aligned} \tag{32}$$

If we recall that the Berry connection $A(\boldsymbol{k})$ is the vector potential in $\boldsymbol{k}$ space, the Berry phase indicates the magnetic flux through the area enclosed by the path C. Thus, there is a magnetic flux at $\boldsymbol{k}=\boldsymbol{0}$ with the magnitude of π, i.e.,

$$F_s^{K_\pm}(\boldsymbol{k}) = \pm\pi\boldsymbol{\delta}(\boldsymbol{k}). \tag{33}$$

We should note that the Berry curvature only exists at Dirac point.

In general, if the system has time-reversal symmetry, Berry curvature satisfies $\boldsymbol{F}(\boldsymbol{k}) = -\boldsymbol{F}(-\boldsymbol{k})$. If the system has the crystal inversion symmetry, Berry curvature satisfies $\boldsymbol{F}(\boldsymbol{k}) = \boldsymbol{F}(-\boldsymbol{k})$. Hence, if the system has both time-reversal and crystal inversion symmetries, Berry curvature becomes $\boldsymbol{F}(\boldsymbol{k}) = 0$. Since $\boldsymbol{K}_+$and $\boldsymbol{K}_-$ points are connected with the time-reversal symmetry, they have opposite Berry curvature. However, as can be seen below, at Dirac $\boldsymbol{K}_+$ and $\boldsymbol{K}_-$ points, graphene acquires non-zero Berry curvature but opposite sign. Owing to this topological singularity, the Boltzmann conductivity of graphene at $E=0$ gives the universal value $e^2/\pi\hbar$ even in the vanishing of density of states (Ando, 2005).

In later section, we will inspect Zak phase (also known as $\mathcal{Z}_2$ Berry phase or one-dimensional version of Berry phase) of graphene. Zak phase illustrates the topological origin of graphene edge states.

Graphene nanoribbons and edge states

The presence of a graphene edge has a strong impact on the electronic states of Dirac electrons. In this section, we briefly summarize the electronic structures of GNRs using the tight-binding model to see the edge effect on the electronic states of graphene.

There are two types of graphene edges: *armchair* and *zigzag* edges. These two edges have a 30° difference in their orientation within the graphene sheet. A large difference in the π-electronic structures is induced by the two types of graphene edges (Fujita et al., 1996). In particular, a zigzag edge exhibits localized states, whereas an armchair edge does not exhibit such localized states. The origin of edge state is the topological properties of bulk wave function, which will be explained in the next section.

The lattice structures of GNRs are shown in Fig. 2A and B. Fig. 2A shows a schematic of AGNR. The primitive vector for AGNR is $\boldsymbol{a} = (0, a_T)$, where $a_T = \sqrt{3}a$ with a being the lattice constant of graphene. Fig. 2B shows a schematic of ZGNR. Similarly, the primitive vector for this system is given by $\boldsymbol{a} = (a, 0)$. We define the width of GNRs as N, where N is the number of dimer (two carbon sites) lines for AGNRs and the number of zigzag lines for ZGNRs.

It is assumed that all dangling bonds at graphene edges are terminated by hydrogen atoms and thus do not contribute to the electronic states near the Fermi level. We employ a single-orbital tight-binding model for the π-electron network. Details of the calculation of the eigenenergy spectrum and eigenfunctions are described in the last section. Here we briefly overview the electronic

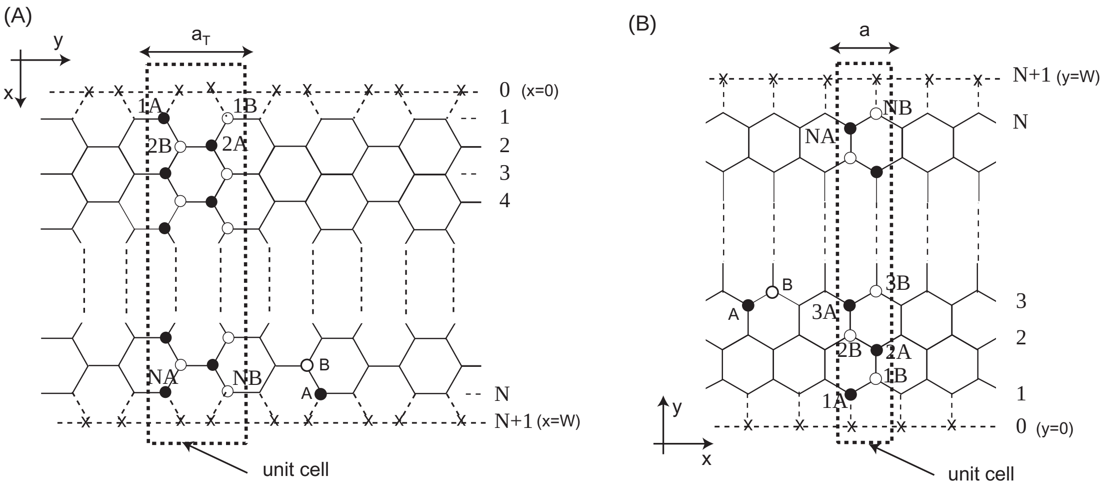

Fig. 2 Structure of graphene nanoribbons with (A) armchair edges (armchair ribbon) and (B) zigzag edges (zigzag ribbon). The dashed rectangles define the unit cells; a_T and a are the respective unit cell widths for armchair and zigzag nanoribbons; N defines the ribbon width. The × marks indicate the missing carbon atoms for the edge boundary condition. The nanoribbon width is defined as $W = \frac{1}{2}(N+1)a$ for armchair nanoribbons and $W = \frac{\sqrt{3}}{2}Na + \frac{a}{\sqrt{3}}$ for zigzag nanoribbons.

states of GNRs. Experimentally, GNRs can be fabricated by using either bottom-up (Cai et al., 2010) or top-down technology (Baringhaus et al., 2014; Han et al., 2007; Kosynkin et al., 2009).

Fig. 3A–C show the DOS and energy band structures of AGNRs for three different ribbon widths. The top of the valence band and the bottom of the conduction band are located at $ka = 0$. Note that the ribbon width determines whether the system is metallic or semiconducting. As shown in Fig. 3B, the system is metallic when $N = 3m - 1$, where $m = 1,2,3,\cdots$. For semiconducting ribbons, the direct band gap decreases with increasing ribbon width and approaches zero in the limit of very large N. For narrow undoped metallic AGNR, an energy gap can be formed by Peierls instabilities at low temperatures (Fujita et al., 1996), which is consistent with density functional theory (DFT) calculations (Son et al., 2006a).

For ZGNRs, however, a remarkable feature arises in the band structure, as shown in Fig. 4A–C. The top of the valence band and the bottom of the conduction band are always degenerate at $k = \pi/a$, and the degeneracy of the center bands at $k = \pi/a$ does not originate from the intrinsic band structure of graphene. These two special center bands flatten with increasing ribbon width. A pair of partial flat bands appears within the region $2\pi/3a \leq |k| \leq \pi/a$, where the bands are located in the vicinity of the Fermi level.

The electronic states in the partial flat bands of ZGNRs can be understood as localized states near the zigzag edge by examining the charge density distribution (Fujita et al., 1996; Nakada et al., 1996; Wakabayashi et al., 1999). The emergence of the edge states can be explained by considering a semi-infinite graphene sheet with a zigzag edge. First, we show the distribution of charge density in flat band states for different wave numbers in Fig. 5A–D, where the amplitude is proportional to the circle radius. The wave function has a non-bonding character, i.e., it only has a finite amplitude on one of the two sublattices that include the edge sites. It is completely localized at the edge site when $ka = \pi$ and starts to gradually penetrate into the inner sites when ka deviates from π, reaching an extended state at $k = 2\pi/3a$.

Considering the translational symmetry, we can start constructing the analytical solution for the edge state by letting the Bloch components of the linear combination of atomic orbitals (LCAO) wave function be $\ldots, e^{ika(n-1)}, e^{ikan}, e^{ika(n+1)}, \ldots$ on successive edge sites, where n denotes a site located on the edge. Then, the mathematical condition necessary for the wave function to be exact for $E = 0$ is that the sum of the components of the complex wave function over the nearestneighbor sites becomes zero. In Fig. 5E, the above condition implies that $e^{ika(n+1)} + e^{ikan} + x = 0$, $e^{ikan} + e^{ika(n-1)} + y = 0$ and $x + y + z = 0$. Therefore, the wave function components x, y and z are found to be $D_k e^{ika(n+1/2)}$, $D_k e^{ika(n-1/2)}$ and $D_k^2 e^{ikan}$, respectively. Here, $D_k = -2\cos(ka/2)$. Thus, the charge density is proportional to $D_k^{2(m-1)}$ at each non-nodal site of the m-th zigzag chain from the edge. Then the convergence condition $|D_k| \leq 1$ is required, for otherwise the wave function would diverge in a semi-infinite graphene sheet. This convergence condition defines the region $2\pi/3a \leq |k| \leq \pi/a$, where the flat bands appear.

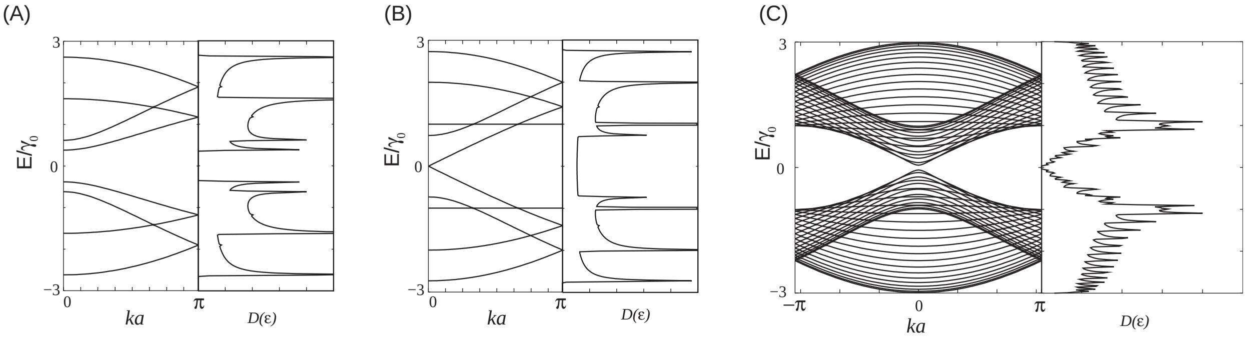

Fig. 3 Energy band structure $E(k)$ and DOS $D(E)$ of armchair ribbons of various widths: (A) $N = 4$, (B) $N = 5$ and (C) $N = 30$.

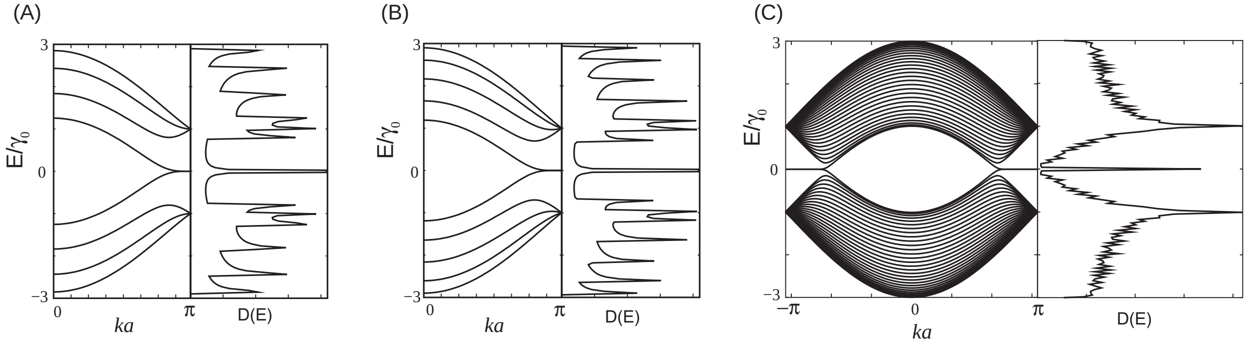

Fig. 4 Energy band structure E(k) and DOS $D(E)$ of zigzag ribbons of various widths: (A) $N = 4$, (B) $N = 5$ and (C) $N = 30$.

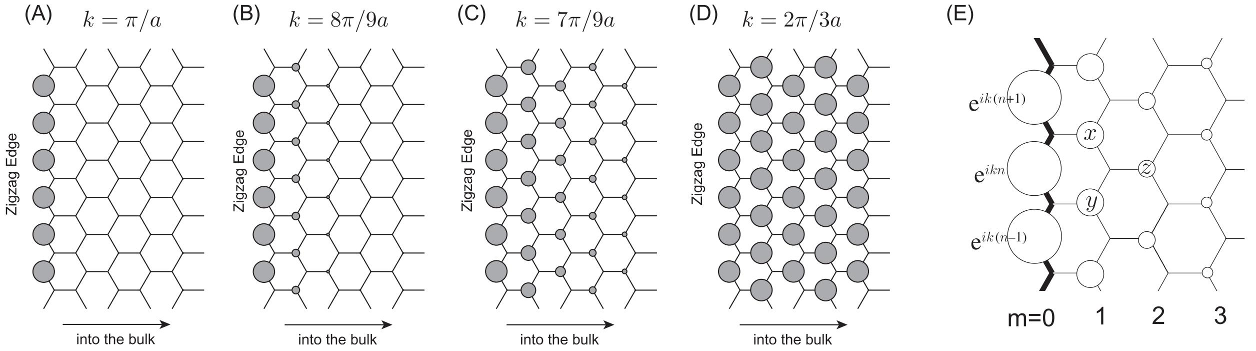

Fig. 5 Charge density plot for analytical solution of the edge states in a semi-infinite graphene sheet for several wave numbers: (A) $k = \pi/a$, (B) $k = 8\pi/9a$, (C) $k = 7\pi/9a$ and (D) $k = 2\pi/3a$. (E) Analytical form of the edge state for a semi-infinite graphene sheet with a zigzag edge, shown by the bold lines. Each carbon site is specified by a location index n on the zigzag chain and by a chain order index m, which increases from the edge. The magnitude of the charge density at each site, such as x, y and z, is obtained analytically (see text). The radius of each circle is proportional to the charge density on each site, and the drawing corresponds to $k = 7\pi/9a$.

The graphene edge states give rise to large contribution to DOS at the Fermi energy when the system size has a nanometer scale. Even a weak electron-electron interaction gives the spin polarized states with ferrimagnetic correlation along the zigzag edge (Fujita et al., 1996; Son et al., 2006a). Such magnetic states involve particular interests for the application of spintronics devices (Son et al., 2006b).

Charge polarization and Zak phase

Charge polarization can be expressed in terms of geometric center of electronic wave functions (King-Smith and Vanderbilt, 1993; Marzari et al., 2012; Resta, 1994; Vanderbilt and King-Smith, 1993; Zak, 1989). For one-dimensional (1D) crystalline system, the charge polarization of n-th energy band is given as a Wannier center, i.e., $P_n = \langle w_n(x)|x|w_n(x)\rangle$, where $w_n(x)$ is a Wannier function of n-th energy band (Marzari et al., 2012). Owing to gauge freedom of Wannier functions, P_n is well-defined up to a lattice constant. The edge states of zigzag edge can be understood as a charge polarization owing to the nontrivial topological phase of bulk wave function (Delplace et al., 2011; Hatsugai, 2009; Ryu and Hatsugai, 2002). In this section, we relate the appearance of edge states at graphene zigzag edges to the finite Zak phase of bulk wave function of graphene.

To relate P_n to Berry connection, one can apply Fourier transformation to w_n and x, which results in (Marzari et al., 2012)

$$P_n = \frac{1}{2\pi}\int_0^{2\pi} \langle \psi_n | i\partial k | \psi_n \rangle dk, \tag{34}$$

where ψ_n is the periodic part of Bloch function of n-th energy band, and $A_n = \langle \psi_n | i\partial k | \psi_n \rangle$ is Berry connection. We refer to the integration part of Eq. (34) as Zak phase (Zak, 1989).

In a finite chain, fractional charges $P = \pm \sum_n^{n_{occ}} P_n$ accumulate at the ends of the chain, where the summation is taken over all the occupied energy bands. When inversion symmetry is present, P_n is quantized to 0 or 1/2. In following discussions, we interchangeably use *Zak phase* and *charge polarization* to mean the same quantity.

In 2D crystalline system, Eq. (34) has the dependence of wavenumber. Charge polarization is given as

$$P_n(k) = \frac{1}{|\mathscr{P}|}\oint_{\mathscr{P}} \mathbf{A}_n(k, k_\perp) dk_\perp, \tag{35}$$

where $\mathbf{A}_n(k,k_\perp) = \langle \boldsymbol{\psi}_n(\boldsymbol{k}) \mid i\partial_{k_\perp} \mid \boldsymbol{\psi}_n(\boldsymbol{k})\rangle$ is Berry connection of n-th energy band in 2D momentum space. Here, k is the wavenumber along longitudinal translational invariant direction of GNR. $k_\perp$ is perpendicular to k, i.e., transverse direction of GNRs. $\mathscr{P}$ is a straight path connecting two equivalent $\mathbf{k}$ points in momentum space along $k_\perp$ direction. Similar to 1D systems, fractional charge $\sum_n^{n_{occ}} \mathbf{P}_n \cdot \mathbf{n}_i$ accumulates on the edge if a material possesses finite charge polarization.

To calculate Zak phase, we use the periodic part of bulk wave function given as Eq. (7), i.e.,

$$|\boldsymbol{\psi}_k\rangle = \frac{1}{\sqrt{2}}\begin{pmatrix} 1 \\ se^{i\boldsymbol{\phi}_k} \end{pmatrix}. \tag{36}$$

Thus, the Berry connection along $k_\perp$ for the valence band is

$$\mathbf{A}(k, k_\perp) = -\frac{1}{2}\partial_{k_\perp}\boldsymbol{\phi}_k. \tag{37}$$

The Zak phase is

$$\mathcal{Z}(k) = \oint_{\mathscr{P}} \mathbf{A}(k, k_\perp)dk_\perp = -\frac{1}{2}\oint_{\mathscr{P}} \partial_{k_\perp}\boldsymbol{\phi}_{\boldsymbol{k}}. \tag{38}$$

Thus, the Zak phase is given as the integration of phase $\phi_{\boldsymbol{k}}$ along the path $\mathscr{P}$. Zak phase becomes zero if the integration path is taken in a simply connected region, otherwise Zak phase becomes finite. Fig. 6A shows reciprocal space of graphene and the integration path for Zak phase calculation. $\mathscr{P}_A(k)$ and $\mathscr{P}_Z(k)$ are the integration path for AGNR and ZGNR, respectively. Since the zigzag edge is parallel to a_1, k is parallel to k_x. Thus, the integration path $\mathscr{P}_Z(k)$ should be taken along k_y for ZGNR. Similarly, armchair edges are parallel to γ, i.e., $(-\boldsymbol{a}_1 + \boldsymbol{a}_2)/2$, k is parallel to $\boldsymbol{b}_1 - \boldsymbol{b}_2$. Hence, the integration path $\mathscr{P}_A(k)$ should be taken along $\boldsymbol{b}_1 + \boldsymbol{b}_2$ for AGNR.

Fig. 6B shows the phase mapping of ϕ_k in the momentum space. The phase jumps of 2π periodically appear along the direction of $\boldsymbol{b}_1 + \boldsymbol{b}_2$. Hence, the integration path $\mathscr{P}_Z(k)$ crosses the phase jump if $2\pi/3a < |k| < \pi/a$, resulting in finite Zak phase. However, no such phase jump appear for the path $\mathscr{P}_A(k)$ for arbitrary k.

For AGNR, the Zak phase is identically zero, i.e.

$$\mathcal{Z}(k) = 0. \tag{39}$$

However, for ZGNR, the Zak phase is

$$\mathcal{Z}(k) = \begin{cases} \pi, & 2\pi/3a < |k| < \pi/a, \\ 0, & |k| < 2\pi/3a. \end{cases} \tag{40}$$

The k-region of finite Zak phase coincides with the region of zigzag edge states. Hence, the edge states are attributed to the Zak phase of bulk wave function. The finite Zak phase tells us the existence of edge states. This discussion can be applied to bearded edges (Delplace et al., 2011) and corner states of graphene (Liu and Wakabayashi, 2021). The reason why the edge states appear at $E = 0$ is supported by the particle-hole (chiral) symmetry of graphene (Ryu and Hatsugai, 2002).

Energy spectrum and wave functions: Graphene nanoribbons

In this section, we briefly summarize the analytic solutions of energy spectrum and wave functions for GNRs on the basis of tight-binding model (Wakabayashi et al., 2010).

Armchair nanoribbons

The set of equations of motion for AGNRs based on the nearest-neighbor tight-binding model is described by

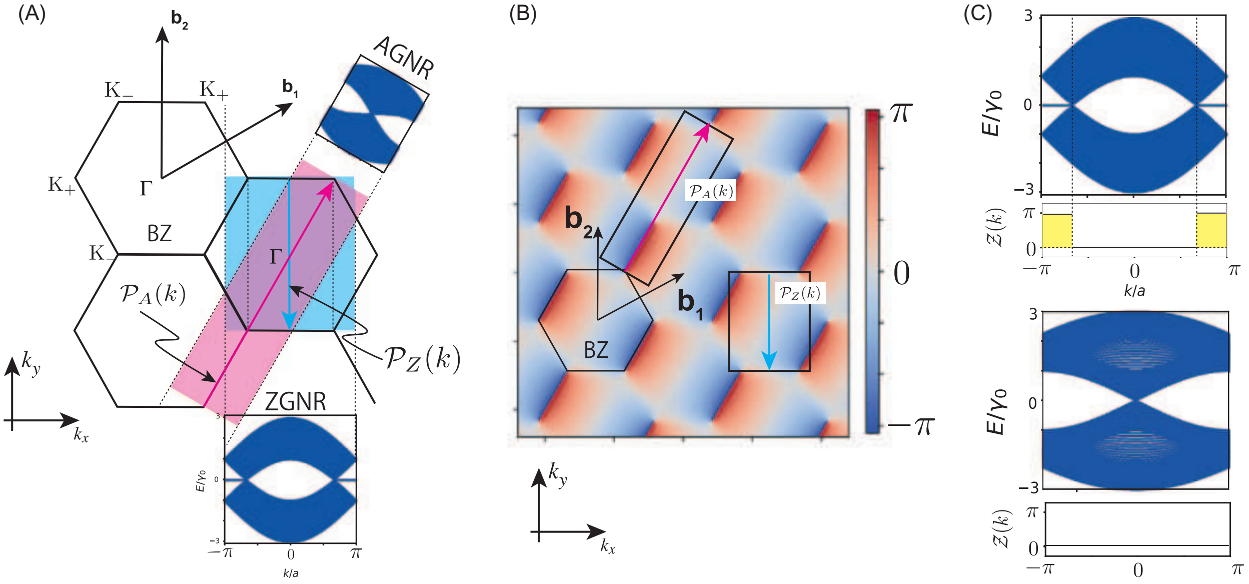

Fig. 6 (A) Reciprocal space of graphene sheet. $\boldsymbol{b}_1 = \frac{2\pi}{a}\left(1, 1/\sqrt{3}\right)$, $\boldsymbol{b}_2 = \frac{2\pi}{a}\left(0, 2/\sqrt{3}\right)$ are primitive reciprocal vectors. The magenta (cyan) rectangle zone represents the translational invariance of armchair (zigzag) edges. $\mathscr{P}_A(k)$ and $\mathscr{P}_Z(k)$ are the integration path for calculation of Zak phase of armchair and zigzag edges, respectively. (B) Phase mapping of $\phi_{\boldsymbol{k}}$ which is the phase of bulk wave function. The phase jumps of 2π periodically appears along the direction of $\boldsymbol{b}_1 + \boldsymbol{b}_2$. When the integration path for Zak phase crosses the phase jump line, finite Zak phase is obtained. (C) Energy band structure and corresponding Zak phase $Z(k)$ for (top panel) ZGNR and (bottom) AGNR. ZGNR has finite Zak phase π for $2\pi/3 < |k| \leq \pi$ (indicated by yellow rectangles).

$$(E/\gamma_0)\boldsymbol{\psi}_{m,A} = -e^{-ik/2}\boldsymbol{\psi}_{m,B} - \boldsymbol{\psi}_{m-1,B} - \boldsymbol{\psi}_{m+1,B}, \tag{41}$$

$$(E/\gamma_0)\boldsymbol{\psi}_{m,B} = -e^{+ik/2}\boldsymbol{\psi}_{m,A} - \boldsymbol{\psi}_{m-1,A} - \boldsymbol{\psi}_{m+1,A}, \tag{42}$$

where $m = 1,2,3, \cdots N$. $\boldsymbol{\psi}_{m,\ A}$ and $\boldsymbol{\psi}_{m,\ B}$ are the wave functions at the mA and mB-sites, respectively. The site indices are given in Fig. 2A. The boundary condition for AGNRs is

$$\boldsymbol{\psi}_{0,A} = \boldsymbol{\psi}_{0,B} = \boldsymbol{\psi}_{N+1,A} = \boldsymbol{\psi}_{N+1,B} = 0. \tag{43}$$

The energy spectrum for AGNRs is given as

$$E_s = s\gamma_0\sqrt{1 + 2\varepsilon_p\cos\left(\frac{k}{2}\right) + \varepsilon_p^2}, \tag{44}$$

where p is the wave number in the transverse direction. Here, $\varepsilon_p = 2\cos(p)$ and $s = \pm 1$; $s = +1$ $(s = -1)$ corresponds to the conduction (valence) energy band. Note that E_s becomes zero at $k = 0$ and $p = 2\pi/3$, which corresponds to a Dirac point. The transverse wave number p is quantized owing to the ribbon boundary condition as

$$p = \frac{r}{N+1}\pi, \quad r = 1,2,3, \cdots, N. \tag{45}$$

Note that $E_S = 0$ at $k = 0$ whenever $N = 3\ m - 1$ $(m = 1,2,3,\cdots)$, which is simply the condition for metallic AGNRs.

Fig. 7A shows the relation between the BZ of graphene and that of AGNRs. The hexagonal BZ of graphene is mapped onto the bold black line on the k_y - axis$(-\pi \le k_y \le \pi)$ as the BZ of AGNRs. The shaded rectangle corresponds to the phase space of variables k and p of Eq. (44). Note the range of p is $0 \le p \le \pi$. The five red lines parallel to the k_y - axis correspond to the cutting lines of the case for AGNR of $N = 5$ (metallic). The cutting line of $r = 4$ clearly passes through the Dirac point, i.e., the nanoribbon is metallic. Fig. 7B shows the energy band structure of AGNR $(N = 5)$ with subband indices. In this case, since the cutting line of $r = 4$ gives $p = 2\pi/3$, the corresponding subband passes through the Dirac point, i.e., the nanoribbon has a metallic band structure with linear dispersion. Thus, the energy band structures of AGNRs can be obtained by slicing the band structure of graphene, as in the case of carbon nanotubes (Saito et al., 1991).

The wave function is written as

$$\begin{pmatrix}\boldsymbol{\psi}_{m,A}\\ \boldsymbol{\psi}_{m,B}\end{pmatrix} = N_c\begin{pmatrix}-s\\ \sqrt{\dfrac{\varepsilon_p + e^{+ik/2}}{\varepsilon_p + e^{-ik/2}}}\end{pmatrix}\sin(mp). \tag{46}$$

Here N_c is the normalization constant.

Zigzag nanoribbons

The set of equations of motion for ZGNRs is given by

$$(E/\gamma_0)\boldsymbol{\psi}_{m,A} = -\boldsymbol{\psi}_{m-1,B} - g_k\boldsymbol{\psi}_{m,B}, \tag{47}$$

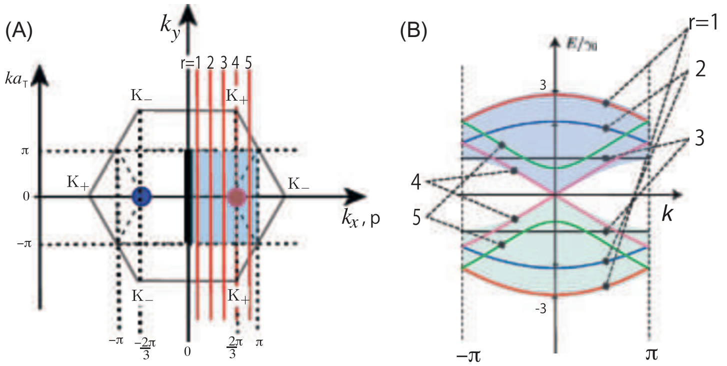

Fig. 7 (A) Relation between the BZ of graphene and that of AGNRs. The hexagonal BZ of graphene is mapped onto the bold black line on the k_y - axis $(-\pi \le k_y \le \pi)$ as the BZ of AGNRs. The shaded rectangle corresponds to the phase space of variables k and p of Eq. (44). Note the range of p is $0 \le p \le \pi$. The K and K' points of graphene BZ are mapped on to the red and blue circles on k_x-axis in the reduced BZ, respectively. The five red lines parallel to the k_y - axis correspond to the cutting lines of the case for the AGNR of $N = 5$ (metallic). The cutting line of $r = 4$ clearly passes through the Dirac point, i.e., the nanoribbon is metallic. (B) Energy band structure of AGNR $(N = 5)$ with subband indices. The shaded area indicates the energy spectrum of bulk graphene.

$$(E/\gamma_0)\boldsymbol{\psi}_{m,B} = -\boldsymbol{\psi}_{m+1,A} - g_k\boldsymbol{\psi}_{m,A}. \tag{48}$$

Here $g_k = 2\cos(k/2)$ is originated from the Bloch phase, and the site index is $m = 0,1,2,\cdots,N+1$. $\boldsymbol{\psi}_{m,A}$ and $\boldsymbol{\psi}_{m,B}$ describe the wave functions at the mA- and mB-sites, respectively. The site indices are given in Fig. 2B. The boundary condition for ZGNRs is given by $\boldsymbol{\psi}_{0,B} = \boldsymbol{\psi}_{N+1,A} = 0$.

The energy spectrum of ZGNRs is given as

$$E_s = s\gamma_0\sqrt{1 + g_k^2 + 2g_k\cos(p)}, \tag{49}$$

where $s = \pm 1$, and $s = +1$ ($s = -1$) corresponds to the conduction (valence) energy band. The transverse wave number p is related with longitudinal wave number k as

$$F(p,N) \equiv \sin[pN] + g_k\sin[p(N+1)] = 0. \tag{50}$$

Fig. 8A shows the relation between the BZ of graphene and that of ZGNRs. The shaded rectangle corresponds to the phase space of variables k and p, i.e., $|k| < \pi$ and $0 \le p \le \pi$. The numerically obtained solutions of Eq. (50) are shown in Fig. 8B for the case of ZGNR with $N = 5$. Let us call the solutions $F(p,N) = 0$ for fixed N as $p_r(r = 1,2,\cdots,p_n)$ within $0 < p < \pi$, i.e., excluding $p = 0$ and π. All these p_i solutions give the extended states. The number of p_r, i.e., p_n, depends on the region of k,

$$p_n = \begin{cases} N, & |k| \le k_c, \\ N-1, & k_c < |k| \le \pi, \end{cases} \tag{51}$$

where k_c is given as

$$k_c = 2\arccos\left(\frac{1}{2}\cdot\frac{1}{1+1/N}\right) \sim \frac{2}{3}\pi + \frac{2}{\sqrt{3}}\cdot\frac{1}{N}. \tag{52}$$

In the limit of large N, k_c converges to $2\pi/3$ which corresponds to the Dirac K point. In other words, the cutting lines never go through the Dirac points in ZGNRs.

One missing solution of Eq. (50) for the range of $k_c < |k| \le \pi$ can be obtained by analytic continuation as

$$p \to \pi + i\eta. \tag{53}$$

Then, Eq. (50) is rewritten as

$$\sinh(\eta N) - g_k\sinh(\eta(N+1)) = 0, \tag{54}$$

which gives two solutions of η as shown in the Fig. 8B. The energy spectrum can be obtained by using

$$E_s = s\gamma_0\sqrt{1 + g_k^2 - 2g_k\cosh\eta}, \tag{55}$$

which give the central partial flat bands in the region of $k_c < |k| \le \pi$.

The wave function for extended states is written as

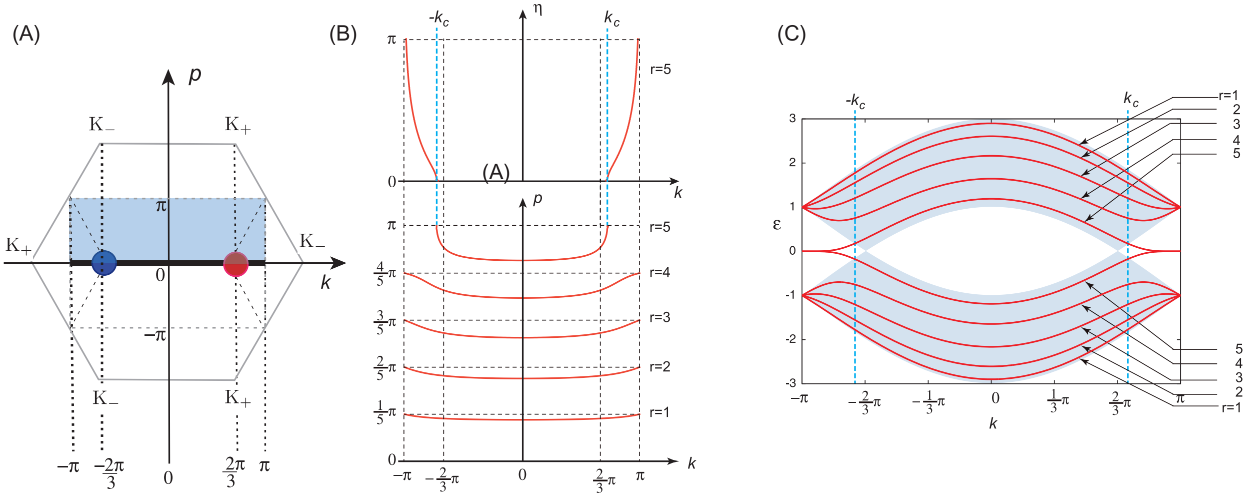

Fig. 8 (A) Relation between the BZ of graphene and that of ZGNRs. The shaded rectangle corresponds to the phase space of variables k and p of Eq. (50). The K and K' points of graphene BZ are mapped on to the red and blue circles on k-axis in the reduced BZ, respectively. (B) The cutting lines of the case for ZGNR of $N = 5$ in the k–p space. The cutting line of $r = 5$ has the imaginary component η for $|k| \ge |k_c|$, which corresponds to the mode of the partial flat bands due to the edge states. (C) Energy band structure of ZGNR ($N = 5$) with subband indices. The shaded area indicates the energy spectrum of bulk graphene.

$$\begin{pmatrix} \boldsymbol{\psi}_{m,A} \\ \boldsymbol{\psi}_{m,B} \end{pmatrix} = N_c \begin{pmatrix} (-1)^r s \sin(p(N+1-m)) \\ \sin(pm) \end{pmatrix} \tag{56}$$

with the normalization constant N_c. Thus, the wave function for the subband with odd (even) r has the even (odd) parity. Similarly the wave function for the edge states can be written as

$$\begin{pmatrix} \boldsymbol{\psi}_{m,A} \\ \boldsymbol{\psi}_{m,B} \end{pmatrix} = N_c' e^{i\pi m} \begin{pmatrix} (-1)^r s \sinh(\eta(N+1-m)) \\ \sinh(\eta m) \end{pmatrix}, \tag{57}$$

with a normalization constant N_c'.

Note that the wave function for AGNRs given by Eq. (46) has a phase difference between sublattice sites A and B due to the chiral nature of graphene. On the other hand, the wave function for ZGNRs is always real and thus has no phase, irrespective of whether the state is extended or localized. This difference in wave functions between AGRNs and ZGRNs is related to the nature of pseudospin in graphene. Although ZGNRs conserve the total time-reversal symmetry, pseudo-time-reversal symmetry (time-reversal symmetry in each valley) is broken owing to the edge states. This nature gives rise to the perfectly conducting channel of ZGNRs (Wakabayashi et al., 2007). It is also possible to derive the analytic wave function of GNRs from the massless Dirac equation (Brey and Fertig, 2006; Wakabayashi, 2000).

Electronic states of carbon nanotubes

The electronic states of GNRs are obtained by imposing the open boundary condition in one direction for the electronic states of graphene, and are characterized by the edge structures. In this section, we shall consider imposing the periodic boundary condition in one direction of graphene, which derives the electronic states of carbon nanotubes (CNTs).

CNT is a one-dimensional carbon nanomaterial which can be constructed by rolling a graphene into a cylinder form. It was discovered by S. Iijima in 1991 (Iijima, 1991). The structure of CNT is uniquely determined by the chiral vector $\boldsymbol{C_h}$, which is defined as

$$\boldsymbol{C_h} = n\boldsymbol{a}_1 + m\boldsymbol{a}_2 \equiv (n, m). \tag{58}$$

Here m, n are integers and $0 \leq m \leq n$. In order to conform to commonly used notation in the research field of CNT, we have redefined the primitive vectors of graphene as $\boldsymbol{a}_1 = \left(\frac{\sqrt{3}}{2}a, \frac{a}{2}\right), \boldsymbol{a}_2 = \left(\frac{\sqrt{3}}{2}a, -\frac{a}{2}\right)$, as shown in Fig. 9A. It should be noted that lattice structure is also rotated by 90 degree compared with Fig. 1A. The shortened notation (n,m) is widely used to characterized the geometry of CNT. In general, CNTs are classified as chiral $(0 < m < n)$ and achiral $(m = 0$ or $m = n \neq 0)$. Especially, $m = 0$ CNTs are known as zigzag nanotube, and $m = n$ CNTs are known as armchair nanotubes.

Fig. 9B shows the atomic structures of CNTs with several different chiral indices. Figs. 9C–F show the energy band structures and corresponding DOS for several different CNTs based on the nearest-neighbor tight-binding model. In general, CNTs are known to be metallic with linear dispersion when $m - n$ is multiple of 3, otherwise semiconducting with energy band gap (Hamada et al., 1992; Mintmire et al., 1992; Saito et al., 1991). Please also see the reviews for further details (Charlier et al., 2007; Laird et al., 2015; Saito et al., 1998). In the rest of this section, we shall explain the relation between the energy spectrum of CNTs and the energy band structure of graphene.

The structure of CNT can be characterized by its diameter d_t and chiral angle θ_t from a zigzag axis. Since the length of CNT circumference is $|\boldsymbol{C_h}|$, the diameter d_t of CNT is given by

$$d_t = a\sqrt{n^2 + nm + m^2}/\pi. \tag{59}$$

The unit cell of a CNT is a rectangle bounded by the vector $\boldsymbol{C_h}$ and translational vector $\boldsymbol{T}$ as shown in the rectangle of Fig. 9A. The translational vector is given as

$$\boldsymbol{T} = t_1\boldsymbol{a}_1 + t_2\boldsymbol{a}_2. \tag{60}$$

t_1 and t_2 are integers, which are determined by $C_h \cdot \boldsymbol{T} = 0$ and $\mathrm{gcm}(t_1, t_2) = 1$. Here, $\mathrm{gcm}(m, n)$ means the great common measure of the two integers m and n. The area of CNT unit cell is calculated as $|\boldsymbol{C_h} \times \boldsymbol{T}| = \sqrt{3}a^2(n^2 + nm + m^2)/d_R$, where $d_R = \mathrm{gcm}(2n + m, 2m + n)$. Using d_R, t_1 and t_2 can be written as $t_1 = (2m + n)/d_R$, $t_2 = -(2n + m)/d_R$. Dividing $|\boldsymbol{C_h} \times \boldsymbol{T}|$ by the area of the unit cell of graphene $|\boldsymbol{a}_1 \times \boldsymbol{a}_2| = \sqrt{3}a^2/2$, the number N of hexagons in unit cell of CNT can be obtained, i.e., $N = 2(n^2 + nm + m^2)/d_R$.

The unit vectors in the reciprocal lattice of graphene can be given as $\boldsymbol{b}_1 = \frac{2\pi}{a}\left(1/\sqrt{3}, 1\right), \boldsymbol{b}_2 = \frac{2\pi}{a}\left(1/\sqrt{3}, -1\right)$. These vectors are derived by the relation $\boldsymbol{a}_i \cdot \boldsymbol{b}_j = 2\pi\delta_{ij}$, where δ_{ij} is the Kronecker delta. In similar manner, the reciprocal vectors of CNT can be derived by using the following relations

$$C_{\boldsymbol{h}} \cdot \boldsymbol{K}_1 = \boldsymbol{T} \cdot \boldsymbol{K}_2 = 2\pi, \tag{61}$$

$$C_{\boldsymbol{h}} \cdot \boldsymbol{K}_2 = \boldsymbol{T} \cdot \boldsymbol{K}_1 = 0, \tag{62}$$

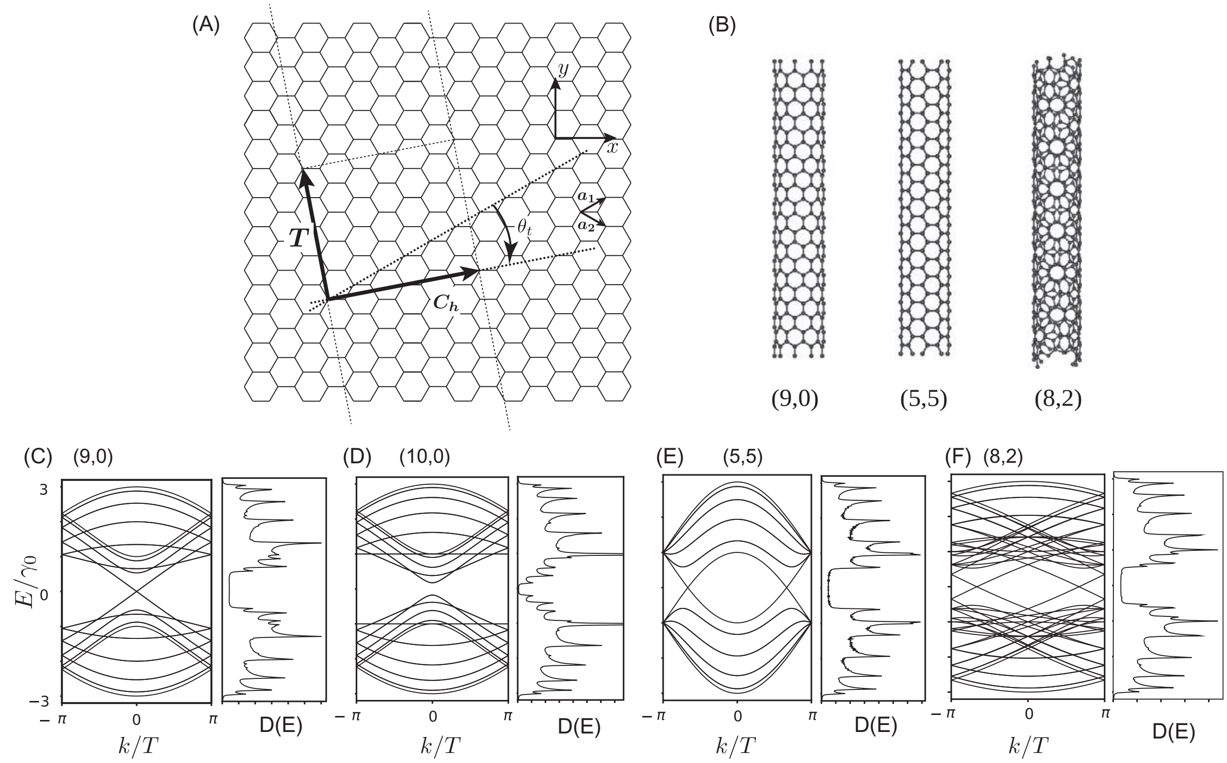

Fig. 9 (A) An unrolled CNT projected onto the graphene lattice. When the CNT is rolled up in a cylinder form, the chiral vector $\boldsymbol{C_h}$ gives the circumference of cylinder and the translation vector $\boldsymbol{T}$ aligns along the cylinder axis. θ_t is chiral angle measured from the zigzag axis. In this section, we have redefine the primitive vector of graphene as $\boldsymbol{a_1} = \left(\frac{\sqrt{3}}{2}a, \frac{a}{2}\right)$ and $\boldsymbol{a_2} = \left(\frac{\sqrt{3}}{2}a, -\frac{a}{2}\right)$. (B) Atomic structures of (9,0) zigzag CNT (left), (5,5) armchair CNT (middle) and (8,2) chiral CNT (right). Energy band structure and corresponding DOS for (C) (9,0) zigzag CNT, (D) (10,0) zigzag CNT, (E) (5,5) armchair CNT and (F) (8,2) chiral CNT.

where the vector $\boldsymbol{K_1}$ is the wavevector along the circumferential direction and $\boldsymbol{K_2}$ is along the CNT axis. Explicitly, one can write as

$$\boldsymbol{K}_1 = \frac{1}{N}(-t_2\boldsymbol{b}_1 + t_1\boldsymbol{b}_2), \tag{63}$$

$$\boldsymbol{K}_2 = \frac{1}{N}(m\boldsymbol{b}_1 - n\boldsymbol{b}_2). \tag{64}$$

1st BZ of CNT is given as $-\frac{\pi}{T} < k \leq \frac{\pi}{T}$ along the $\boldsymbol{K_2}$ direction.

Since $N\boldsymbol{K_1} = -t_2\boldsymbol{b_1} + t_1\boldsymbol{b_2}$ corresponds to a reciprocal lattice vectors of graphene, two wave vectors which differ by $N\boldsymbol{K}_1$ are equivalent. In addition, since t_1 and t_2 lack a common divisor other than unity, none of the $N-1$ vectors $\mu\boldsymbol{K}_1(\mu = 1, 2, \cdots, N-1)$ are reciprocal lattice vectors of graphene. Thus, the N wave vectors $\mu\boldsymbol{K}_1$ give rise to N discrete k vectors. These arise from the quantized wave vectors associated with the periodic boundary condition due to $\boldsymbol{C_h}$.

Therefore, the energy spectrum of CNT can be obtained by

$$E_\mu(k) = E_{2D}\left(k\frac{\boldsymbol{K_2}}{|\boldsymbol{K_2}|} + \mu\boldsymbol{K_1}\right), \tag{65}$$

where

$$\mu = 0, 1, \cdots, N-1, -\frac{\pi}{T} < k \leq \frac{\pi}{T}. \tag{66}$$

Here $E_{2D}(k_x, k_y)$ is the energy spectrum of graphene, i.e.,

$$E_{2D}\left(k_x, k_y\right) = \pm\gamma_0\sqrt{1 + 4\cos\frac{k_y a}{2}\cos\frac{\sqrt{3}k_x a}{2} + 4\cos^2\frac{k_y a}{2}}. \tag{67}$$

Note that k_x and k_y are exchanged compared with Eq. (6), because graphene lattice is rotated by 90 degree.

The N pairs of energy dispersion curves given by Eq. (65) correspond to cross-section of the two-dimensional energy dispersion surface of Eq. (67), where cuts are made along the lines of $k\frac{\boldsymbol{K_2}}{|\boldsymbol{K_2}|} + \mu\boldsymbol{K_1}$. If such cutting line of (n, m) CNT passes through the Dirac

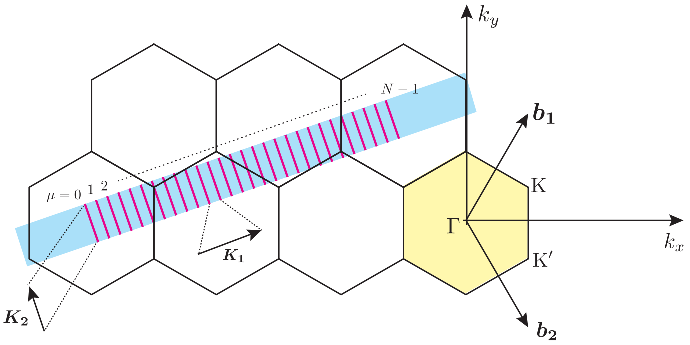

Fig. 10 Reciprocal space of graphene lattice. Magenta lines in the cyan rectangle represent the cutting lines for the (8,2) chiral CNT to produce the 1D energy band structure from the energy band of 2D graphene. The cutting lines are labeled by $\mu = 0, 1, 2, \cdots, N-1$. $\boldsymbol{K_1}$ is the wavevector along the circumference of CNT and $\boldsymbol{K_2}$ is the wavevector along the CNT axis. The cyan rectangle is a eye guide which represents the zone having the translational invance of the CNT. The length of $\boldsymbol{K_2}$ exactly corresponds to the length of 1st BZ of the CNT. $\boldsymbol{b_1}$ and $\boldsymbol{b_2}$ are the reciprocal lattice unit vectors of graphene lattice. For (8,2) chiral nanotube, $N = 28$. The cutting lines with $\mu = 6$, 22 pass through K or K' point, i.e. metallic.

K points, the energy gap between valence and conduction bands vanishes with linear dispersion. In this case, (n, m) CNT become metallic. On the other hand, if the cutting line does not pass through a *K* point, CNT becomes semiconducting with finite energy gap between valence and conduction bands. In Fig. 10, the cutting lines for the (8, 2) chiral CNT are shown. By collecting the *N* pairs of energy dispersion curves on the magenta lines, the energy band structure of the (8, 2) chiral CNT is obtained, which is shown in Fig. 9F.

In short, (n,n) armchair nanotubes are always metallic and $(n,0)$ zigzag nanotube are metallic when n is a multiple of 3. In general, (n, m) CNT becomes metallic if n - m is a multiple of 3.

Conclusion

In this chapter, we provide an overview of electronic and topological properties of graphene. The low-energy electronic states of graphene near the Fermi energy are well-described by massless Dirac equation, which gives conical energy dispersion and nontrivial Berry phase. Since graphene has both time-reversal and crystal inversion symmetries, total Berry phase is zero. However, the analysis of Zak phase clarifies the existence of topological edge state at graphene zigzag edges. Also, we have presented the relation of energy spectrum between graphene and carbon nanotubes.

References

Ajiki H and Ando T (1993) *Journal of the Physical Society of Japan* 62(4): 1255.
Ando T (2005) *Journal of the Physical Society of Japan* 74.
Ando T, Nakanishi T, and Saito R (1998) *Journal of the Physical Society of Japan* 67(8): 2857.
Aoki H and Dresselhaus M (2014) *Physics of Graphene*. Springer.
Baringhaus J, Ruan M, Edler F, Tejeda A, Sicot M, Taleblbrahimi A, Li A-P, Jiang Z, Conrad ED, Berger C, Tegenkamp C, and de Heer WA (2014) *Nature* 506: 349–354.
Bernevig BA and Hughes T (2013) *Topological Insulators and Topological Superconductors*. Princeton University Press.
Berry MV (1984) *Proceedings of The Royal Society A Mathematical Physical and Engineering Sciences* 392(1802): 45.
Bistritzer R and MacDonald AH (2011) *Proceedings of the National Academy of Sciences* 108(30): 12233. 1009.4203.
Brey L and Fertig HA (2006) *Physical Review B* 73(23): 235411.
Cai J, Ruffieux P, Jaafar R, Bieri M, Braun T, Blankenburg S, Muoth M, Seitsonen AP, Saleh M, Feng X, Müllen K, and Fasel R (2010) *Nature* 466(7305): 470.
Charlier J-C, Blase X, and Roche S (2007) *Reviews of Modern Physics* 79: 677.
Delplace P, Ullmo D, and Montambaux G (2011) *Physical Review B* 84(19): 195452.
Foa Torres LEF, Roche S, and Charlier J-C (2014) *Introduction to Graphene-Based Nanomaterials*. Cambridge University Press.
Fujita M, Wakabayashi K, Nakada K, and Kusakabe K (1996) *Journal of the Physical Society of Japan* 65(7): 1920.
Geim AK and Novoselov KS (2007) *Nature Materials* 6(3): 183.
Guinea F, Castro Neto AH, and Peres NMR (2006) *Physical Review B* 73: 245426.
Hamada N, Sawada S-I, and Oshiyama A (1992) *Physical Review Letters* 68: 1579.
Han MY, Özyilmaz B, Zhang Y, and Kim P (2007) *Physical Review Letters* 98: 206805.
Hatsugai Y (2009) *Solid State Communications* 149(27): 1061. recent Progress in Graphene Studies.
Iijima S (1991) *Nature* 354(6348): 56.
Katsnelson MI (2012) *The Physics of Graphene*. Cambridge University Press.
Katsnelson MI, Novoselov KS, and Geim AK (2006) *Nature Physics* 2(9): 620.
King-Smith RD and Vanderbilt D (1993) *Physical Review B* 47: 1651.
Koshino M and Ando T (2007) *Physical Review B* 76: 085425.
Koshino M, Yuan NFQ, Koretsune T, Ochi M, Kuroki K, and Fu L (2018) *Physical Review X* 8: 031087.
Kosynkin D, Higginbotham A, Sinitskii A, Lomeda JR, Dimiev A, Price BK, and Tour JM (2009) *Nature* 458: 872–876.

Laird EA, Kuemmeth F, Steele GA, Grove-Rasmussen K, Nygård J, Flensberg K, and Kouwenhoven LP (2015) *Reviews of Modern Physics* 87: 703.
Liu F and Wakabayashi K (2021) *Physical Review Research* 3: 023121.
Marzari N, Mostofi AA, Yates JR, Souza I, and Vanderbilt D (2012) *Reviews of Modern Physics* 84(4): 1419.
McCann E and Fal'ko VI (2006) *Physical Review Letters* 96: 086805.
Mintmire JW, Dunlap BI, and White CT (1992) *Physical Review Letters* 68: 631.
Nakada K, Fujita M, Dresselhaus G, and Dresselhaus MS (1996) *Physical Review B* 54(24): 17954.
Neto AHC, Guinea F, Peres NMR, Novoselov KS, and Geim AK (2009) *Reviews of Modern Physics* 81(1): 109.
Nilsson J, Neto AHC, Guinea F, and Peres NMR (2006) *Physical Review Letters* 97: 266801.
Novoselov KS, Geim AK, Morozov SV, Jiang D, Zhang Y, Dubonos SV, Grigorieva IV, and Firsov AA (2004) *Science* 306(5696): 666.
Novoselov KS, Geim AK, Morozov SV, Jiang D, Katsnelson MI, Grigorieva IV, Dubonos SV, and Firsov AA (2005) *Nature* 438(7065): 197.
Resta R (1994) *Reviews of Modern Physics* 66: 899.
Ryu S and Hatsugai Y (2002) *Physical Review Letters* 89: 077002.
Saito R, Fujita M, Dresselhaus G, and Dresselhaus MS (1991) *Physical Review B* 46(3): 1804.
Saito R, Dresselhaus G, and Dresselhaus M (1998) *Physical Properties of Carbon Nanotubes*. Imperial College Press.
Son Y-W, Cohen ML, and Louie SG (2006a) *Physical Review Letters* 97: 216803.
Son Y-W, Cohen ML, and Louie SG (2006b) *Nature* 444(7117): 347.
Vanderbilt D (2018) *Berry Phases in Electronic Structure Theory*. Cambridge University Press.
Vanderbilt D and King-Smith RD (1993) *Physical Review B* 48: 4442.
Wakabayashi K (2000) *Low-Energy Physical Properties of Edge States in Nano-Graphites*. Ph.D. thesis University of Tsukuba.
Wakabayashi K, Fujita M, Ajiki H, and Sigrist M (1999) *Physical Review B* 59: 8271.
Wakabayashi K, Takane Y, and Sigrist M (2007) *Physical Review Letters* 99: 036601.
Wakabayashi K, Sasaki K-I, Nakanishi T, and Enoki T (2010) *Science and Technology of Advanced Materials* 11(5): 054504.
Wallace PR (1947) *Physics Review* 71(9): 622.
Xiao D, Chang M-C, and Niu Q (2010) *Reviews of Modern Physics* 82: 1959.
Zak J (1989) *Physical Review Letters* 62.
Zhang Y, Tan Y-W, Stormer HL, and Kim P (2005) *Nature* 438(7065): 201.

Twisted bilayer graphene

Mikito Koshino, Department of Physics, Osaka University, Osaka, Japan

© 2024 Elsevier Ltd. All rights reserved.

Introduction 288
Moiré pattern and moiré Brillouin zone 288
Effective continuum model 289
Band structure 290
Superconductivity and correlated phenomena 292
Magneto spectra and quantum hall effect 292
Conclusion 293
References 293

Abstract

Twisted bilayer graphene is a pair of graphene layers rotationally stacked with an arbitrary twist angle. The moiré interference pattern with a nanometer-scale period significantly modifies the original band structure of graphene, giving rise to a number of unusual phenomena not observed in a regular monolayer graphene. At the so-called magic angle, in particular, the energy band becomes completely flat, and superconducting phases and correlated insulating phases emerge due to the enhanced electron-electron interaction. In magnetic fields, the spectrum exhibits a fractal Hofstadter's structure due to the interference of the magnetic field and the long-range moiré periodicity. This article gives a brief overview on the electronic properties of twisted bilayer graphene mainly from the theoretical point of view.

Key points

- Twisted bilayer graphene is a pair of graphene layers stacked with a relative rotation.
- The moiré interference pattern creates a flat band in the electronic band structure.
- Superconducting phases and correlated insulating phases emerge in the flat band due to the enhanced electron-electron interaction.

Introduction

Twisted bilayer graphene (TBG) is a pair of graphene layers rotationally stacked with an arbitrary orientation. The physical property of TBG sensitively depends on the twist angle θ, which is the relative angle between lattice vectors of the individual graphene layers. When θ is small, in particular, the interference of the lattice periods gives rise to a long-period moiré beating pattern (Fig. 1a), which hybridizes the Dirac cones of single-layer graphenes into a series of moiré subbands. At the so-called magic angle, $\theta \sim 1^\circ$, the lowest subbands become almost completely flat, where unusual correlated phenomena such as superconductivity and correlated insulating states take place due to a strong enhancement of the electron-electron interaction. The discovery of TBG is followed by extensive research and development of moiré systems composed of various kind of two-dimensional materials.

Moiré pattern and moiré Brillouin zone

A TBG is composed of a pair of hexagonal lattices stacked with a relative rotation angle θ. One can define the primitive lattice vectors of layer 1 as $\mathbf{a}_1 = a(1,0)$ and $\mathbf{a}_2 = a\left(1/2, \sqrt{3}/2\right)$ with the lattice constant $a \approx 0.246$ nm, and those of the layer 2 as $\mathbf{a}'_i = R\,\mathbf{a}_i$ with the rotation matrix $R = R(\theta)$, as shown in Fig. 1b. Accordingly, the reciprocal lattice vectors of layer 1 are given by $\mathbf{b}_1 = (2\pi/a)\left(1,\ -1/\sqrt{3}\right)$ and $\mathbf{b}_2 = (2\pi/a)\left(0, 2/\sqrt{3}\right)$, layer 2 by $\mathbf{b}'_i = R\,\mathbf{b}_i$..

In small $\theta \ll 1$, the interference of the lattice periods in the two layers gives rise to a moiré pattern with a period much greater than the atomic scale (Fig. 1a). The reciprocal lattice vectors for the moiré pattern are given by

$$\mathbf{G}_i^M = \mathbf{b}_i - \mathbf{b}'_i = (1 - R)\mathbf{b}_i \qquad (i = 1, 2). \tag{1}$$

The corresponding lattice vectors in the real space, $\mathbf{L}_i^M$, are defined by $\mathbf{L}_i^M \cdot \mathbf{G}_j^M = 2\pi\delta_{ij}$. As a result, the moiré period $L_M \equiv |\mathbf{L}_i^M|$ becomes

$$L_M = \frac{a}{2\,\sin(\theta/2)} \approx a/\theta. \tag{2}$$

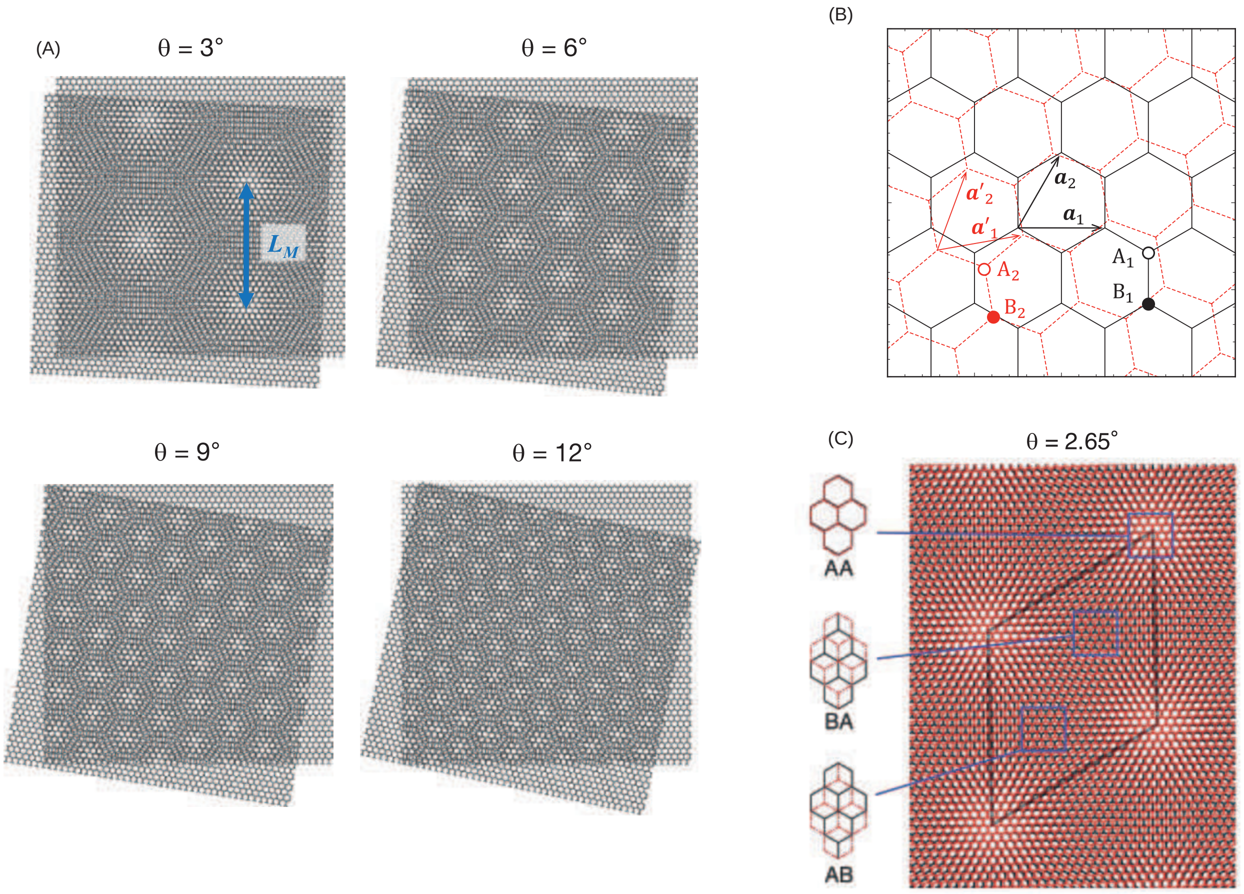

Fig. 1 (a) Atomic structures of TBG with different twist angles. (b) The lattice vectors and sublattices in TBG. (c) The detailed atomic structure at $\theta = 2.65°$. The local structure resembles a non-rotated bilayer such as AA, AB, BA-stacking (see the text).

In decreasing θ, the moiré period L_M increases in inversely proportional to θ. At the magic angle ($\theta \sim 1°$), L_M is about 14 nm, where the unit cell includes more than 10,000 atoms. Fig. 1c shows a detailed atomic structure at $\theta = 2.65°$. The local structure resembles a non-rotated bilayer such as AA, AB, BA-stacking, and it slowly varies as a function of position. Here AA-stacking refers to a configuration where A-site of layer 1 is located just above A-site of layer 2, and therefore the honey-comb lattices completely overlap. The AB-stacking is the graphite's structure, where A is just above B. The BA-stacking is just a 180° rotation of the AB-stacking.

The Dirac points (the band touching points) of each graphene layer are located at the Brillouin zone corners K_+ and K_- (referred to as valleys), where $\mathbf{K}_\xi = -\xi(2\mathbf{b}_1 + \mathbf{b}_2)/3$ for layer 1 and $\mathbf{K}_\xi' = R\mathbf{K}_\xi$ for layer 2. In TBG, K_ξ ($\xi = \pm$) of layer 1 and 2 are displaced by

$$\Delta K = 2K \sin(\theta/2) \approx K\theta, \tag{3}$$

where $K = 4\pi/(3a)$ is the distance from the origin to $K\pm$. The moiré-Brillouin zone (superlattice Brillouin zone spanned by $\mathbf{G}_i^M$) becomes a small hexagon with side length of ΔK as shown in Fig. 2. The zone tiling pattern near K_+ and that near K_- are not generally consistent with each other, and this corresponds to the fact that the moiré pattern is not generally commensurate with the atomic period of graphene, i.e., the system does not have an exact translational symmetry as a whole. The electronic states of K_+ and those of K_- are hardly hybridized when the moiré period is sufficiently larger than the atomic period (equivalent with $K \gg \Delta K$), so one can treat these distant valleys as independent subsystems.

Effective continuum model

When the twist angle θ is small, the electronic band structure of TBG is well described by a long-range effective theory. The effective Hamiltonian for valley $\xi = \pm$ is obtained by extracting the matrix elements near K_ξ with small wave-number shift (Bistritzer and MacDonald, 2011a; Lopes dos Santos et al., 2007). It is given by a 4×4 matrix,

$$\mathscr{H} = \begin{pmatrix} H_0 & U^\dagger(\mathbf{r}) \\ U(\mathbf{r}) & H_0 \end{pmatrix}, \tag{4}$$

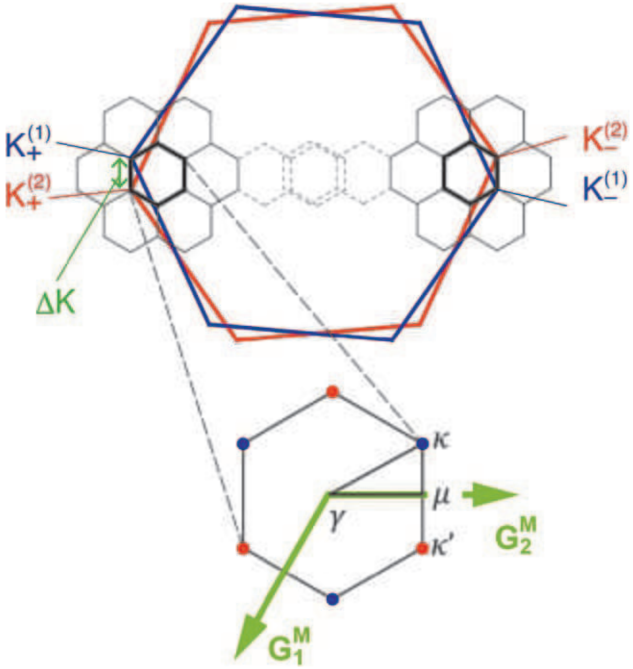

Fig. 2 Brillouin zone (BZ) folding in TBG. Large hexagons represent the BZ of graphene layer 1 and 2, and small ones are the moiré BZ.

where

$$H_0 = -\hbar v \begin{pmatrix} 0 & \xi k_x - ik_y \\ \xi k_x + ik_y & 0 \end{pmatrix}, \tag{5}$$

$$U(\mathbf{r}) = \sum_{j=0,1,2} e^{i\xi \Delta \mathbf{K}_j \cdot \mathbf{r}} \begin{pmatrix} t & t' e^{-i\frac{2\pi}{3}j} \\ t' e^{i\frac{2\pi}{3}j} & t \end{pmatrix}. \tag{6}$$

The Hamiltonian works on a four-component wave-function $(\psi_{A_1}, \psi_{B_1}, \psi_{A_2}, \psi_{B_2})$ where ψ_{A_1} stands for the wavefunction on sublattice A of layer 1, etc. H_0 is the Dirac Hamiltonian of the monolayer graphene. $U(\mathbf{r})$ is the moiré interlayer coupling, where

$$\Delta \mathbf{K}_j = \Delta K(-\sin(2\pi j/3), \cos(2\pi j/3)) \tag{7}$$

for $j = 0, 1, 2$ is a triplet of 120° rotated vectors, which connect the Dirac points of layer 1 and 2. Here t, t' represent the coupling strength of AA-stacking and AB-stacking regions, respectively. In the rigid graphene model assuming perfect honeycomb lattices for graphene layers, one has $t = t' \sim 0.1$ eV. In real systems, the honeycomb lattices are relaxed to optimize the interlayer stacking energy, and the effect can be incorporated as a difference between t and t' $(t < t')$ (Koshino et al., 2018).

The physical meaning of $U(\mathbf{r})$ is clearly seen when one considers the matrix U at a specific $\mathbf{r}$ point. At $\mathbf{r} = 0$, for instance, the diagonal components of U become 3 t while the off-diagonal ones are zero. This corresponds to the AA stacking region (Fig. 1c), where the A_1 and A_2 (also B_1 and B_2) are vertically aligned and strongly coupled. At AB-stacking position, on the other hand, A_1 and B_2 are vertically aligned giving an off-diagonal element 3 t', while other three elements vanish.

The biggest advantage of the effective continuum model is that one can obtain band structure in any small twist angles regardless of the commensurability of the exact lattice structure. When the rotation angle is relatively large (>20°) and the moiré period becomes the atomic scale, however, the long-range effective theory is not applicable anymore, and the system becomes essentially quasiperiodic in that incommensurate periodicities coexist. In particular, the 30-degree rotated TBG has a feature of 12-fold rotational symmetric quasicrystal, which is intimately related to a quasiperiodic tiling in mathematics. The 30-degree TBG was experimentally fabricated by an epitaxial growth on silicon-carbide surface (Ahn et al., 2018; Moon et al., 2019).

Band structure

Fig. 3 shows an example of the band calculation for TBGs with some twist angles (Nam and Koshino, 2017), where κ, γ, μ and κ' in the horizontal axis represent the symmetric points in the moiré Brillouin zone in Fig. 2. The black solid curve and the red dashed curve represent the energy bands with and without the lattice relaxation, which is important in the small angle regime $\theta < 2°$. In $\theta = 2.65$ (Fig. 3a), the linear band at κ, κ' are remnants of the Dirac cones of monolayer graphene. In decreasing the twist angle, the band velocity of the Dirac cone is significantly reduced, and nearly flat bands emerge at ~1°, which is called the magic

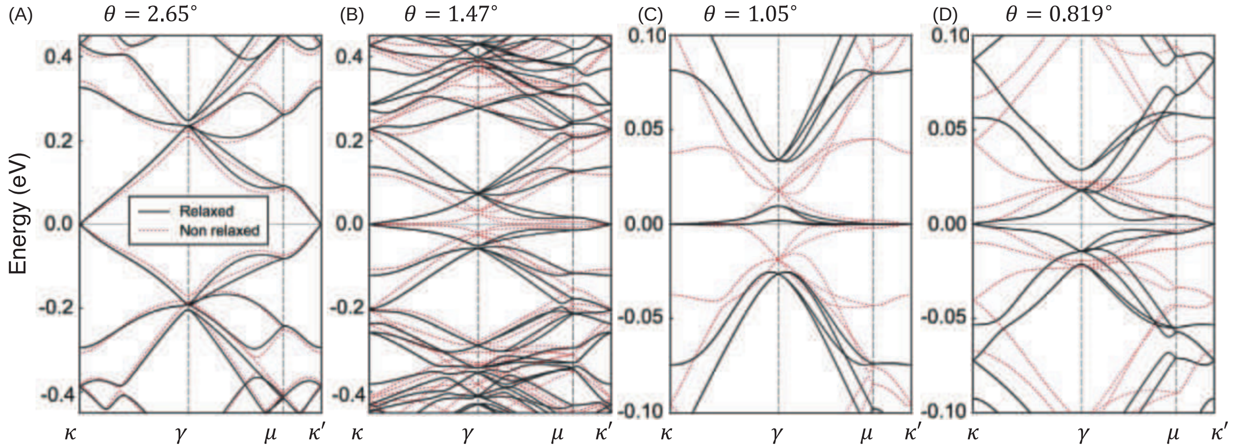

Fig. 3 Band calculation for TBGs with different twist angles. The label κ, γ, μ and κ' represent the symmetric points in the moiré Brillouin zone (Fig. 2). The black solid curves and the red dashed curves, respectively, are the energy bands with and without the lattice relaxation. From Ref. Nam NNT and Koshino M (2017) Lattice relaxation and energy band modulation in twisted bilayer graphene. *Physical Review B* 96(7): 075311. Errata: *Phys. Rev. B* 101: 099901 (2020).

angle (Bistritzer and MacDonald, 2011a). There are two flat bands in each spin/valley sector, and hence eight flat bands in total. The number of electrons accommodated in a single flat band (i.e., per spin and valley) is given by $n_0 = 1/S_M$, where $S_M = (\sqrt{3}/2)L_M^2$ is the area of the moiré unit cell. The lattice relaxation effect opens energy gaps between the flat bands and excited bands. When θ is further decreased beyond the magic angle, the band width is broadened again, and the band structure changes in a complex manner.

The reduction of the band velocity and the formation of the moiré subband can be understood by the following argument. Fig. 4a shows the hybridization of the Dirac cones of monolayers. The layer 1's cone at the center is hybridized with layer 2's cones shifted by $\Delta\mathbf{K}_j$'s in Eq. (7). A band anti-crossing occurs at intersections of the cones, as schematically illustrated in Fig. 4b. The system has two characteristic energy scales: the interlayer hopping energy t (or t') ~ 0.1 meV, which determines the gap width in the anti-crossing, and $\hbar v \Delta K \propto \theta$, which is the energy distance between the Dirac point and the band crossing point. The structure of the moiré subband is determined by the relative magnitude of t to $\hbar v \Delta K$. When $\theta > 5^\circ$, one has $t \ll \hbar v \Delta K$ so that the interlayer hopping can be treated as a perturbation for the Dirac cone, giving a small gap at the intersection. In decreasing θ, the ratio $t/(\hbar v \Delta K)$ increases in inversely proportional to θ, and it exceeds 1 at $\theta < 1^\circ$. This is a strong coupling regime, where the interlayer coupling completely reconstructs the Dirac cone into a series of the moiré subbands.

An extreme model with $t \to 0$ is called the chiral limit, as the Hamiltonian becomes chiral symmetric (Tarnopolsky et al., 2019). There the lowest energy bands are shown to be exactly flat at a series of angles and the magic angle argued above ($\theta \sim 1^\circ$) corresponds to the greatest one in the series.

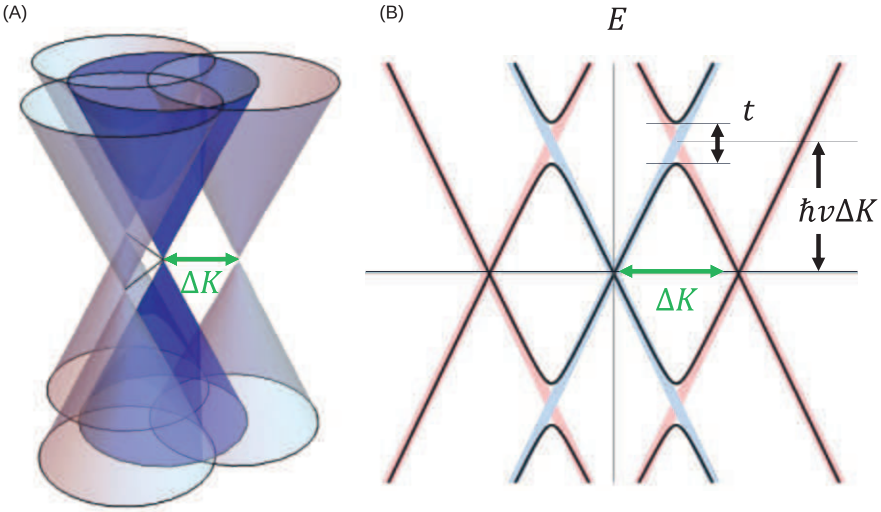

Fig. 4 (a) Hybridization of graphene's Dirac cones in TBG. The central Dirac cone of layer 1 (blue) is coupled with the surrounding Dirac cones of layer 2 displaced by ΔK. (b) Schematic cross-sectional picture of the Dirac cone hybridization.

Superconductivity and correlated phenomena

The flat band in the magic angle TBG is expected to be a strongly correlated system governed by the electron-electron interaction, since the kinetic energy (band energy) is quenched. Indeed, it was found that TBG samples near 1° exhibit the superconductivity in the low temperature around 1 K (Cao et al., 2018a, 2018b). The superconducting state is highly sensitive to the twist angle, suggesting that the phenomena is related to the band flatness.

Fig. 5 is the schematic phase diagram of the magic angle TBG, where the horizontal axis represents the electron density in units of n_0 (the number of electrons per a moiré band) and the vertical axis is temperature. The flat band region corresponds to $-4 \leq n/n_0 \leq 4$, where the $n = 0$ is the charge neutral point. In Fig. 5, thick strips at $n/n_0 = \pm 4$ represent the band insulator phases, where the Fermi energy is located in the band gap above / below the flat bands. In decreasing the temperature, one sees extra insulating phases at $n/n_0 = \pm 2$ due to the electron-electron interaction, which are called the correlated insulating (CI) phases. The superconducting phase emerges by slightly doping carriers to the CI phases. Experimentally, the phase diagram is obtained just from a single TBG sample by controlling the charge density by the gate electric field effect. This is in contrast to 3D materials, where changing carrier density requires chemical doping.

It was reported that some TBG samples exhibit insulating phases also at the odd fillings $n/n_0 = \pm 1, \pm 3$ (Yankowitz et al., 2019), and superconducting phases nearby (Lu et al., 2019). The ferromagnetism and anomalous Hall effect were also reported at $n/n_0 = 3$ (Serlin et al., 2020; Sharpe et al., 2019). The detailed structure of the phase diagram, particularly at the odd filling, is highly dependent on samples, presumably due to the non-uniformity of the moiré stacking structure and also the effect of the substrate under the TBG.

The mechanism of the superconductivity and correlated insulating states in TBG is still under debate. The insulating behavior at the integer filling suggests an analogy to the quantum Hall ferromagnetism where the spin/valley degenerate Landau levels spontaneously split under electron-electron interaction. Various many-body states, such as the inter valley coherent states, were also proposed as possible candidates of the ground states in the magic angle TBG (Bultinck et al., 2020).

The superconductivity and correlated phases were also found in other moiré graphene systems, such as twisted double bilayer graphene (i.e., twisted pair of Bernal bilayer graphenes) (Cao et al., 2019; Liu et al., 2019; Shen et al., 2020) and twisted trilayer graphene (Hao et al., 2021; Lin et al., 2020; Park et al., 2021; Zhu et al., 2020), where the band flatness is supposed to be essential as in TBG.

Magneto spectra and quantum hall effect

In strong magnetic fields, the energy spectrum of TBG exhibits a fractal gap structure called Hofstadter's butterfly (Bistritzer and MacDonald, 2011b; Moon and Koshino, 2012). The Hofstadter spectrum generally occurs in two dimensional systems subject to both magnetic field and periodic electrostatic potential (Hofstadter, 1976), where the fractal gap structure is observed when the magnetic length $\sqrt{\hbar/(eB)}$ and the potential period are comparable. While conventional atomic lattices with periodicities of less than 1 nm require unfeasibly large magnetic fields ($B > 10,000$ Tesla) to reach this condition, the TBG with a periodic modulation of the order of 10 nm enables experimental access to the fractal spectrum at a few 10 Tesla.

Fig. 6 shows an example of Hofstadter's spectrum calculated for TBG of $\theta = 2.65°$ (Moon and Koshino, 2012). The left panel, Fig. 6a presents the energy spectrum plotted against the magnetic field amplitude, where the black part indicates the energy regions where electron states exist, and the white part is energy gap. The middle panel (b) shows the same spectrum, but with color and number inside each gap indicating the quantized Hall conductivity when the Fermi energy lies in the gap. The right-most panel (c) is the zero-field band structure in the same energy range. In Fig. 6a, the spectrum is characterized by the number of magnetic field

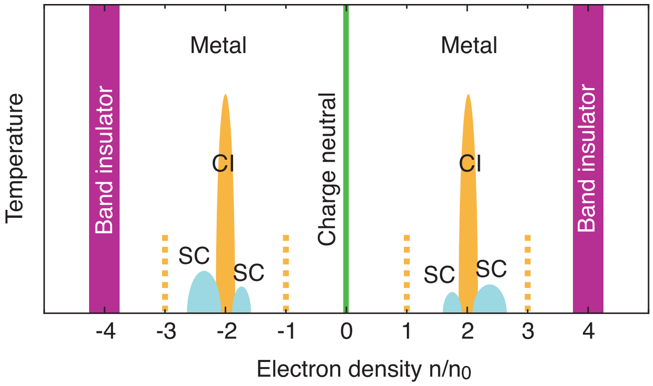

Fig. 5 Schematic phase diagram of the magic angle TBG, against the electron density and temperature. CI stands for correlated insulating phase, and SC stands for superconducting phase. Vertical dashed lines indicate correlated insulating phases at the odd fillings observed in some experiments.

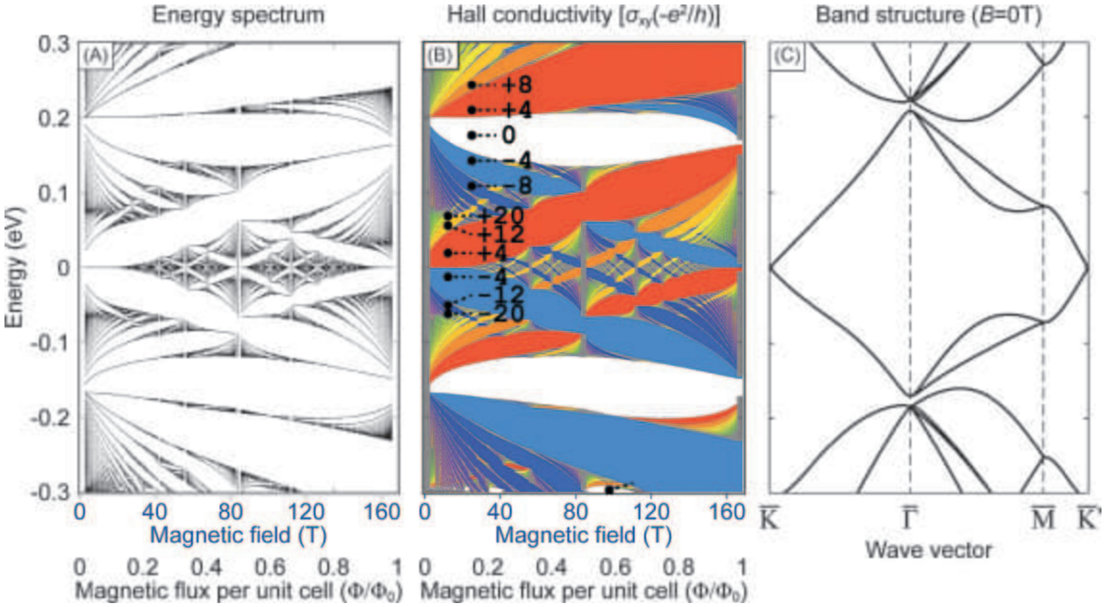

Fig. 6 (a) Energy spectrum plotted against the magnetic field calculated for TBG of $\theta = 2.65°$. The black and white regions indicate energy bands and energy gaps, respectively. (b) The same spectrum, but with color and number inside each gap indicating the quantized Hall conductivity. (c) Corresponding band structure at zero magnetic field. $\overline{K}, \overline{\Gamma}, \overline{M}, \overline{K}'$ correspond to κ, γ, μ, κ' in Fig. 2, respectively. From Ref. Moon P and Koshino M (2012) Energy spectrum and quantum hall effect in twisted bilayer graphene. *Physical Review B* 85: 195458.

quanta per a moiré unit cell, Φ/Φ_0, where $\Phi = BS_M$ is the magnetic flux penetrating the moiré unit area S_M, and $\Phi_0 = h/e$ is the magnetic flux quantum. The quantized Hall conductivity in the mini-gaps behaves non-monotonically as a function of Fermi energy, as usually expected in the Hofstadter butterfly. The recursive gap structure was first observed experimentally in the moiré superlattice of graphene on hexagonal-boron-nitride (hBN) (Dean et al., 2013; Hunt et al., 2013; Ponomarenko et al., 2013).

Conclusion

The electronic properties of TBG were briefly reviewed. It was shown that the moiré period, of typically a few to tens of nanometer, significantly modifies the original band structure of graphene, giving rise to a number of unusual phenomena not observed without the moiré stacking. The energy width of the moiré subbands decreases as the twist angle is reduced, and dispersionless flat bands appear at the magic angle near 1°, where superconducting phases and correlated insulating phases emerge due to the electron-electron interaction. In magnetic fields, the spectrum exhibits a fractal Hofstadter's structure due to the interference of the magnetic field and the long-range moiré periodicity.

The discovery of TBG is followed by extensive research of various moiré superlattices other than graphenes. For instance, a twisted stack of transition metal dichalcogenide (e.g., MoS_2, WS_2, WSe_2, etc.) is a moiré superlattice with unusual optical properties, where an optical excitation gives rise to localized excitons trapped to the moiré pattern (Jin et al., 2019; Seyler et al., 2019; Tran et al., 2019). The search for novel physics in twisted systems is extended to a wide variety of two-dimensional systems, including magnetic and superconducting 2D materials and topological insulators.

References

Ahn SJ, Moon P, Kim T-H, Kim H-W, Shin H-C, Kim EH, Cha HW, Kahng S-J, Kim P, Koshino M, et al. (2018) Dirac electrons in a dodecagonal graphene quasicrystal. *Science* 361(6404): 782–786.

Bistritzer R and MacDonald A (2011a) Moiré bands in twisted double-layer graphene. *Proceedings of the National Academy of Sciences* 108(30): 12233.

Bistritzer R and MacDonald A (2011b) Moiré butterflies in twisted bilayer graphene. *Physical Review B* 84(3): 035440.

Bultinck N, Khalaf E, Liu S, Chatterjee S, Vishwanath A, and Zaletel MP (2020) Ground state and hidden symmetry of magic-angle graphene at even integer filling. *Physical Review X* 10(3): 031034.

Cao Y, Fatemi V, Demir A, Fang S, Tomarken SL, Luo JY, Sanchez-Yamagishi JD, Watanabe K, Taniguchi T, Kaxiras E, et al. (2018a) Correlated insulator behaviour at half-filling in magic-angle graphene super-lattices. *Nature* 556(7699): 80.

Cao Y, Fatemi V, Fang S, Watanabe K, Taniguchi T, Kaxiras E, and Jarillo-Herrero P (2018b) Unconventional superconductivity in magic-angle graphene superlattices. *Nature* 556(7699): 43.

Cao Y, Rodan-Legrain D, Rubies-Bigorda O, Park JM, Watanabe K, Taniguchi T, and Jarillo-Herrero P (2019) Electric field tunable correlated states and magnetic phase transitions in twisted bilayer-bilayer graphene. *arXiv preprint arXiv.1903.08596*.

Dean C, Wang L, Maher P, Forsythe C, Ghahari F, Gao Y, Katoch J, Ishigami M, Moon P, Koshino M, Taniguchi T, Watanabe K, Shepard K, Hone J, and Kim P (2013) Hofstadter/'s butterfly and the fractal quantum hall effect in moire superlattices. *Nature* 497(7451): 598–602.

Hao Z, Zimmerman A, Ledwith P, Khalaf E, Najafabadi DH, Watanabe K, Taniguchi T, Vishwanath A, and Kim P (2021) Electric field–tunable superconductivity in alternating-twist magic-angle trilayer graphene. *Science* 371(6534): 1133–1138.

Hofstadter D (1976) Energy levels and wave functions of bloch electrons in rational and irrational magnetic fields. *Physical Review B* 14(6): 2239.

Hunt B, Sanchez-Yamagishi J, Young A, Yankowitz M, LeRoy B, Watanabe K, Taniguchi T, Moon P, Koshino M, Jarillo-Herrero P, and Ashoori R (2013) Massive dirac fermions and hofstadter butterfly in a van der waals heterostructure. *Science* 340(6139): 1427–1430.

Jin C, Regan EC, Yan A, Utama MIB, Wang D, Zhao S, Qin Y, Yang S, Zheng Z, Shi S, et al. (2019) Observation of moiré excitons in wse 2/ws 2 heterostructure superlattices. *Nature* 567(7746): 76–80.

Koshino M, Yuan NF, Koretsune T, Ochi M, Kuroki K, and Fu L (2018) Maximally localized wannier orbitals and the extended hubbard model for twisted bilayer graphene. *Physical Review X* 8(3): 031087.

Lin F, Qiao J, Huang J, Liu J, Fu D, Mayorov AS, Chen H, Mukherjee P, Qu T, Sow C-H, et al. (2020) Hetero-moiré engineering on magnetic bloch transport in twisted graphene superlattices. *Nano Letters* 20(10): 7572–7579.

Liu X, Hao Z, Khalaf E, Lee JY, Watanabe K, Taniguchi T, Vishwanath A, and Kim P (2019) Spin-polarized correlated insulator and superconductor in twisted double bilayer graphene. *arXiv preprint arXiv.1903.08130*.

Lopes dos Santos J, Peres N, and Castro Neto A (2007) Graphene bilayer with a twist: Electronic structure. *Physical Review Letters* 99(25): 256802.

Lu X, Stepanov P, Yang W, Xie M, Aamir MA, Das I, Urgell C, Watanabe K, Taniguchi T, Zhang G, Bachtold A, MacDonald AH, and Efetov DK (2019) Su-perconductors, orbital magnets and correlated states in magic-angle bilayer graphene. *Nature* 574(7780): 653–657.

Moon P and Koshino M (2012) Energy spectrum and quantum hall effect in twisted bilayer graphene. *Physical Review B* 85: 195458.

Moon P, Koshino M, and Son Y-W (2019) Quasicrystalline electronic states in 30° rotated twisted bilayer graphene. *Physical Review B* 99(16): 165430.

Nam NNT and Koshino M (2017) Lattice relaxation and energy band modulation in twisted bilayer graphene. *Physical Review B* 96(7): 075311. Errata: *Phys. Rev. B* 101: 099901 (2020).

Park JM, Cao Y, Watanabe K, Taniguchi T, and Jarillo-Herrero P (2021) Tunable strongly coupled superconductivity in magic-angle twisted trilayer graphene. *Nature* 590(7845): 249–255.

Ponomarenko LA, Gorbachev RV, Yu GL, Elias DC, Jalil R, Patel AA, Mishchenko A, Mayorov AS, Woods CR, Wallbank JR, Mucha-Kruczynski M, Piot BA, Potemski M, Grigorieva IV, Novoselov KS, Guinea F, Fal'ko VI, and Geim AK (2013) Cloning of dirac fermions in graphene superlattices. *Nature* 497(7451): 594–597.

Serlin M, Tschirhart C, Polshyn H, Zhang Y, Zhu J, Watanabe K, Taniguchi T, Balents L, and Young A (2020) Intrinsic quantized anomalous hall effect in a moiré heterostructure. *Science* 367(6480): 900–903.

Seyler KL, Rivera P, Yu H, Wilson NP, Ray EL, Mandrus DG, Yan J, Yao W, and Xu X (2019) Signatures of moiré-trapped valley excitons in mose 2/wse 2 heter-obilayers. *Nature* 567(7746): 66–70.

Sharpe AL, Fox EJ, Barnard AW, Finney J, Watanabe K, Taniguchi T, Kastner M, and Goldhaber-Gordon D (2019) Emergent ferromagnetism near three-quarters filling in twisted bilayer graphene. *Science* 365(6453): 605–608.

Shen C, Chu Y, Wu Q, Li N, Wang S, Zhao Y, Tang J, Liu J, Tian J, Watanabe K, et al. (2020) Correlated states in twisted double bilayer graphene. *Nature Physics* 16(5): 520–525.

Tarnopolsky G, Kruchkov AJ, and Vishwanath A (2019) Origin of magic angles in twisted bilayer graphene. *Physical Review Letters* 122(10): 106405.

Tran K, Moody G, Wu F, Lu X, Choi J, Kim K, Rai A, Sanchez DA, Quan J, Singh A, et al. (2019) Evidence for moiré excitons in van der waals heterostructures. *Nature* 567(7746): 71–75.

Yankowitz M, Chen S, Polshyn H, Zhang Y, Watanabe K, Taniguchi T, Graf D, Young AF, and Dean CR (2019) Tuning superconductivity in twisted bilayer graphene. *Science* 363(6431): 1059–1064.

Zhu Z, Carr S, Massatt D, Luskin M, and Kaxiras E (2020) Twisted trilayer graphene: A precisely tunable platform for correlated electrons. *Physical Review Letters* 125(11): 116404.

Graphene, transport

Michihisa Yamamoto, RIKEN Center for Emergent Matter Science, Saitama, Japan

© 2024 Elsevier Ltd. All rights reserved.

Introduction 295
Overview 296
Electronic structures of graphene 296
Topological properties 297
Carrier scattering in graphene devices 298
Ballistic transport and electron optics 301
Valley Hall transport in the presence of charged impurities 302
Nonlocal transport and edge transport 304
Hydrodynamic transport 307
Conclusion 308
References 308
Further reading 309

Abstract

We describe transport properties of graphene and related experiments. The main source of carrier scattering in graphene is charged impurities at low temperatures. This leads to the linear relationship between the conductivity and the carrier density. High-mobility graphene devices also exhibit unique ballistic transport such as the Klein tunneling. At high temperatures, electron-electron scattering becomes significant in clean graphene devices, and carriers behave as fluids. Topological valley transport also occurs in graphene when the inversion symmetry is broken. The topological valley current has been detected in nonlocal transport experiments.

Key points

- Charged impurity scattering, ballistic transport, topological transport, nonlocal transport, hydrodynamic transport.

Introduction

Graphene is a monolayer of carbon atoms in a honeycomb lattice. Its properties had been theoretically investigated already before its discovery, but monolayer had been thought to be too unstable to exist. In 2004, it was shown by Novoselov, Geim, and coworkers that it is possible to exfoliate a monolayer graphene flake from graphite by a scotch tape and transfer it onto a SiO_2 substrate (Novoselov et al., 2004). It also became possible to measure the electrical conductivity of graphene by depositing contact metal electrodes on exfoliated graphene flakes. Owing to the unique combination of physical properties of graphene such as high mobility, high transparency, relativistic natures, great mechanical strength, large thermal conductivity, etc., intense studies have been conducted for revealing the electronic properties of graphene by electrical transport experiments.

Graphene on SiO_2 has high carrier mobility exceeding 10,000 cm^2/Vs. The main source of scattering for carriers in graphene is the charged impurities attached during the fabrication process. By annealing the graphene devices, influence of the charged impurities can be suppressed to some extent. Temperature dependence of the conductivity also revealed influence of scattering by phonons. Graphene devices display ballistic transport properties when the device dimension becomes submicron scale at relatively low temperatures. The quantum Hall effect is also observed for graphene on SiO_2 owing to its high mobility (Novoselov et al., 2005; Zhang et al., 2005). The high quality of graphene layers also enabled identification of the band structure of few-layer graphene (Craciun et al., 2011).

Several years after the discovery of graphene, even higher-quality graphene devices suffering less from charge disorder than those on SiO_2 became available by using a suspended graphene and current annealing (Du et al., 2008; Bolotin et al., 2008). The development of layer-by-layer transfer technique has also allowed for stacking different layered materials while precisely tuning their relative angles. When graphene is encapsulated by an atomically flat insulator, hexagonal boron nitride (h-BN) flakes, prepared high-quality graphene devices become stable (Dean et al., 2010). Once graphene is encapsulated, further contamination is avoided. Electrical contacts to graphene are taken by the "edge contacts." The transport properties of graphene became able to be measured more reproducibly and intrinsic properties of graphene that can be found only in high-quality devices have been investigated. The mobility of suspended or encapsulated graphene exceeds 100,000 cm^2/Vs.

https://doi.org/10.1016/B978-0-323-90800-9.00104-9

Even in high-quality graphene, charge disorder is still one of the main sources of carrier scattering at low temperatures. In a clean graphene device at high temperatures, the electron-electron scattering length can become smaller than the mean free path and electron-phonon scattering length. The carrier transport then obeys hydrodynamics. The viscosity of graphene induced by strong electron-electron interaction is indeed larger than those of standard semiconductors such as the high electron mobility transistor (HEMT) of a GaAs/AlGaAs heterostructure.

When the symmetry of graphene is broken, topological transport associated with the valley contrasting intrinsic Hall conductivity occurs. The symmetry breaking is induced by aligning relative angle between graphene and h-BN such that graphene is affected by the potential from boron and nitrogen atoms, or by applying a perpendicular electric field to a few-layer graphene. For an encapsulated few-layer graphene, one can independently control the carrier density and perpendicular electric field by the top gate and back gate through h-BN layers.

Owing to above-mentioned unique properties, graphene attracts considerable attention. In addition, because graphene appears on the surface and can constitute a "van der Waals heterostructure" (Geim and Grigorieva, 2013), it can be combined with various materials in novel functional devices.

Overview

In this article, we mainly focus on transport properties of pristine monolayer and bilayer graphene observed in real graphene devices. While graphene can be combined with other various materials in van der Waals heterostructures and be used for spintronics and superconducting device applications, externally induced properties are out of scope in this article. The quantum Hall effect in graphene is also discussed in the other articles of this encyclopedia (Zhang, 2023; McCann, 2006, 2023).

We start with description of the intrinsic electronic structure of graphene and discuss corresponding transport properties. We then discuss carrier scatterings in graphene mostly dominated by charged impurities. We also discuss ballistic transport, where device dimension is smaller than or comparable with the mean free path. We then move to the nonlocal transport that is used to detect the topological transport in real graphene devices. Finally, we describe experimental observations of hydrodynamic transport dominated by the electron-electron scattering in graphene devices.

Electronic structures of graphene

Monolayer graphene is a zero-gap semiconductor. Energy band of graphene can be calculated using a tight banding model for the honeycomb lattice (Wallace, 1947; Castro Neto et al., 2009). The unit cell consists of two carbon atoms A and B, forming two sublattices. We only consider the nearest neighbor hopping in the first approximation. It is straightforward to derive effective Hamiltonians for the two energetically degenerate but nonequivalent valleys K and K′

$$H_K = \hbar v_F \begin{pmatrix} 0 & k_x - ik_y \\ k_x + ik_y & 0 \end{pmatrix}$$

$$H_{K'} = -\hbar v_F \begin{pmatrix} 0 & k_x + ik_y \\ k_x - ik_y & 0 \end{pmatrix}$$

operating on $(|A\rangle, |B\rangle)^T$, where $|A\rangle$ and $|B\rangle$ are, respectively, Bloch wave function components on the A and B sublattices, $\boldsymbol{k} = (k_x, k_y)$ is the wave vector measured from the valley center, $\hbar$ is Planck constant divided by 2π, and $v_F \sim 1 \times 10^6$ m^2/s is the velocity of carriers. Using Pauli matrices, we can rewrite it as

$$H^{\mathrm{MLG}} = \hbar v_F \left(\tau_z k_x \sigma_x + k_y \sigma_y\right), \tag{1}$$

where τ_z is the valley index, i.e., $\tau_z = 1$ for valley K and $\tau_z = -1$ for valley K′.

This Hamiltonian leads to the linear dispersion

$$\varepsilon(\boldsymbol{k}) = \pm \hbar v_F k \tag{2}$$

implying that carriers in graphene are massless with the energy independent velocity v_F. Here the + and – denotes those of electrons and holes. The $\varepsilon(\boldsymbol{k}) = 0$ point is termed the Dirac point or the charge neutrality point because the carrier density $n = n_e - n_h$ defined by the density n_e and n_h of electrons and holes becomes zero. Eq. (4) also indicates that the pseudospin defined by the presence of an electron in either of the sublattices and the wave vector $\boldsymbol{k}$ are coupled. In the absence of atomic-scale short-range scattering, pseudospin should be conserved. This prohibits backscattering of electrons because flip of $\boldsymbol{k}$ direction should accompany flip of the pseudospin. This suggests that the backscattering is suppressed near zero energy in the absence of short-range scattering induced by lattice defects. When $\boldsymbol{k}$ rotates once in the xy-plane, the pseudospin also rotates once. This leads to the Berry phase of π at K valley and $-\pi$ at K′ valley.

In AB-staked bilayer graphene, there are four atoms in the unit cell labeled as A1, B1, A2, and B2. A1 and B1 are on the bottom layer and A2 and B2 are on the top layer. There is a vertical hopping γ between A2 and B1. The effective Hamiltonian is expressed as a 4×4 matrix

$$H = \begin{pmatrix} \begin{matrix} & \\ H^{\mathrm{MLG}} & \\ & \end{matrix} & \begin{matrix} 0 & 0 \\ -\gamma & 0 \end{matrix} \\ \begin{matrix} 0 & -\gamma \\ 0 & 0 \end{matrix} & \begin{matrix} & \\ H^{\mathrm{MLG}} & \\ & \end{matrix} \end{pmatrix}$$

where H^{MLG} is the effective Hamiltonian for monolayer graphene (Eq. 1). For the small energy $|\varepsilon(\boldsymbol{k})| \ll \gamma$, this Hamiltonian can be reduced into the two-band Hamiltonian for the $(|A1\rangle, |B2\rangle)^T$ basis as

$$H_K = \frac{\hbar^2}{2m_{\mathrm{BL}}} \begin{pmatrix} 0 & \left(k_x - ik_y\right)^2 \\ \left(k_x + ik_y\right)^2 & 0 \end{pmatrix}$$

$$H_{K'} = -\frac{\hbar^2}{2m_{\mathrm{BL}}} \begin{pmatrix} 0 & \left(k_x + ik_y\right)^2 \\ \left(k_x - ik_y\right)^2 & 0 \end{pmatrix}$$

where $m_{\mathrm{BL}} = \gamma/(2v_F^2)$ is the effective mass of the bilayer graphene (McCann, 2006, 2023). The low energy bands are parabolic that touch each other at zero energy. Using the azimuthal angle ϕ of $\boldsymbol{k}$ and $k^2 = k_x^2 + k_y^2$, the effective Hamiltonian is rewritten as

$$H^{\mathrm{BLG}} = \frac{\hbar^2 k^2}{2m_{\mathrm{BL}}} \left(\cos(2\phi)\sigma_x + \tau_v \sin(2\phi)\sigma_y\right). \tag{3}$$

This Hamiltonian indicates the Berry phase 2π at K valley and -2π at K′ valley.

The band structure of thicker N-layer graphene ($N > 2$) depends on the stacking. ABC-stacked N-layer graphene has k^N dispersion and Berry phase $N\pi$. ABA-stacked multilayer graphene consists of monolayer-like (linear) band and bilayer-like (parabolic) bands. The monolayer-like band exists only for odd N. These bands as well as the Berry phase can be experimentally identified by the measurement of the quantum Hall effect (Zhang, 2023; McCann, 2006, 2023).

While both monolayer and bilayer graphene are zero-gap semiconductors, the band gap can be induced by breaking the inversion symmetry. When there is a potential difference 2Δ between A and B sites of monolayer graphene, the mass term $\Delta\sigma_z$ is added to the effective Hamiltonian. The effective Hamiltonian becomes

$$H^{\mathrm{MLG}} = \hbar v_F \left(\tau_z k_x \sigma_x + k_y \sigma_y\right) + \Delta\sigma_z. \tag{4}$$

This results in nonlinear bands

$$\varepsilon(\boldsymbol{k}) = \pm\sqrt{\left(\hbar v_F k\right)^2 + \Delta^2}$$

and the effective mass $m^* = \Delta/v_F^2$ at the band bottom.

For bilayer graphene, when there is a potential difference 2Δ between A1 and B2 sites, the effective Hamiltonian becomes

$$H^{\mathrm{BLG}} = \frac{\hbar^2 k^2}{2m_{\mathrm{BL}}} \left(\cos(2\phi)\sigma_x + \tau_v \sin(2\phi)\sigma_y\right) + \Delta\sigma_z. \tag{5}$$

This results in the non-parabolic bands $\varepsilon(\boldsymbol{k}) = \pm\sqrt{\left(\frac{\hbar^2 k^2}{2m_{\mathrm{BL}}}\right)^2 + \Delta^2}$ with the gap opening by 2Δ. The advantage of bilayer graphene is that this gap can be induced by the application of a perpendicular electric field D that introduces the potential difference between the two layers. We readily expect insulating behavior at the charge neutrality $n = 0$ in the presence of D for bilayer graphene. This also applies to ABC-stacked multilayer graphene.

Topological properties

The effective Hamiltonian of massive graphene in Eqs. (4) and (5) leads to non-zero Berry curvature for $\Delta \neq 0$ (Xiao et al., 2007). The Berry curvature is defined as

$$\boldsymbol{\Omega}(\boldsymbol{k}) = i\nabla_{\boldsymbol{k}} \times \langle u(\boldsymbol{k})|\nabla_{\mathbf{k}} u(\boldsymbol{k})\rangle, \tag{6}$$

using the Fourier transformation $u(\boldsymbol{k})$ of the periodic part of the Bloch function. Since the Berry phase is given by the integral of $i\langle u(\boldsymbol{k})|\nabla_{k} u(\boldsymbol{k})\rangle$ along a closed loop in the momentum space, $\boldsymbol{\Omega}(\boldsymbol{k})$ corresponds to the magnetic flux density in the momentum space. This is in analogy with the Aharonov-Bohm phase given by the integral of the vector potential $\boldsymbol{A}$ along a closed loop in the real space, and the magnetic flux density defined by $\boldsymbol{B}(\boldsymbol{r}) = \nabla_{\boldsymbol{r}} \times \boldsymbol{A}(\boldsymbol{r})$. Indeed, the role of $\boldsymbol{\Omega}(\boldsymbol{k})$ in the semi-classical dynamics in the Bloch bands is understood as a correction to the group velocity $\boldsymbol{v} = \dot{\boldsymbol{r}} = \frac{\partial\varepsilon(\boldsymbol{k})}{\hbar\partial\boldsymbol{k}}$ in the presence of an in-plane electric field $\boldsymbol{E}$:

$$\dot{\boldsymbol{r}} = \frac{\partial \varepsilon(\boldsymbol{k})}{\hbar \partial \boldsymbol{k}} + \dot{\boldsymbol{k}} \times \boldsymbol{\Omega}(\boldsymbol{k}). \tag{7}$$

We see that $\boldsymbol{\Omega}(\boldsymbol{k})$ works as a magnetic flux density in the momentum space by comparing Eq. (7) with $\hbar\dot{\boldsymbol{k}} = -e\boldsymbol{E} - e\dot{\boldsymbol{r}} \times \boldsymbol{B}$. The second term in Eq. (7) driven by $\boldsymbol{E} = -\frac{\hbar}{e}\dot{\boldsymbol{k}}$ is called anomalous velocity:

$$\boldsymbol{v}_{\mathrm{A}} = -\frac{e}{\hbar}\boldsymbol{E} \times \boldsymbol{\Omega}(\boldsymbol{k}). \tag{8}$$

This term leads to the intrinsic Hall conductivity:

$$\sigma_{\mathrm{H}}^{\mathrm{int}} = g_S \frac{e^2}{\hbar} \int \frac{d^2k}{(2\pi)^2} f(\boldsymbol{k}) \Omega(\boldsymbol{k}), \tag{9}$$

where g_S is the spin degeneracy (usually $g_S = 2$), $\Omega(\boldsymbol{k})$ is the z-component of the Berry curvature, and $f(\boldsymbol{k})$ is the Fermi-Dirac distribution function. It is straightforward to derive the Berry curvature for the two-level system represented in Eqs. (4) and (5).

For massive monolayer graphene, the Berry curvature is

$$\Omega(\boldsymbol{k}) = \tau_z \frac{\gamma^2 \Delta}{2\varepsilon(\boldsymbol{k})^3}, \tag{10}$$

which becomes maximum or minimum at K and K′ point. This leads to the valley-dependent intrinsic Hall effect for low energy carriers. Energy dependence of the intrinsic valley Hall conductivity defined as $\sigma_{xy}^{\mathrm{v}} \equiv \sigma_{\mathrm{H}}^{\mathrm{int},K} - \sigma_{\mathrm{H}}^{\mathrm{int},K'}$ becomes

$$\sigma_{xy}^{\mathrm{v}}(\varepsilon) \equiv \sigma_{\mathrm{H}}^{\mathrm{int},K} - \sigma_{\mathrm{H}}^{\mathrm{int},K'} = \begin{cases} \dfrac{2e^2}{h}\dfrac{\Delta}{|\varepsilon|} & (|\varepsilon| > \Delta) \\ \dfrac{2e^2}{h} & (|\varepsilon| < \Delta) \end{cases} \tag{11}$$

at zero temperature. In analogy with the spin Hall effect, where spin current is induced in the transverse direction to the injected charge current, valley current is induced by an applied in-plane electric field $\boldsymbol{E}$ to the transverse direction. This phenomenon is called valley Hall effect. σ_{xy}^{v} corresponds to the conversion ratio between the induced valley current density and $\boldsymbol{E}$.

For bilayer graphene, the Berry curvature and the zero-temperature valley Hall conductivity become

$$\Omega(\boldsymbol{k}) = \tau_z \frac{\hbar^2}{m^*} \frac{\Delta\sqrt{\varepsilon(\boldsymbol{k})^2 - \Delta^2}}{\varepsilon(\boldsymbol{k})^3} \tag{12}$$

$$\sigma_{xy}^{\mathrm{v}}(\varepsilon) = \begin{cases} \dfrac{4e^2}{h}\dfrac{\Delta}{|\varepsilon|} & (|\varepsilon| > \Delta) \\ \dfrac{4e^2}{h} & (|\varepsilon| < \Delta) \end{cases} \tag{13}$$

with Δ tuned by the perpendicular electric field.

Carrier scattering in graphene devices

A typical graphene device is supported by a substrate. Graphene is capacitively coupled with a gate electrode (usually a back gate) that can be used to tune the carrier density n. In some devices, graphene is sandwiched by the back gate and top gate through insulating layers. In such a dual-gated device, the carrier density n and the perpendicular electric field D can be independently controlled. This dual-gated structure is useful to control the electronic state of bilayer graphene. By depositing metal electrodes on graphene, one can measure the electrical transport through graphene. The electrical contact is realized with various metals such as Cu, Ag, Au, Ni, and Pd (Giubileo and Di Bartolomeo, 2017). The deposited metal dopes carriers in the region beneath the metal, allowing the electron transport between the metal and graphene. Transfer length or the effective length of the contact region is of the order of micron. The contact resistance usually depends on the length of the deposited metal contact rather than its area. Electrical contacts can also be taken to the edges of graphene. Even though the improvement of the electrical contact is still an important issue, the contact resistance (typically order of 100 Ωμm) is usually smaller than the resistance of graphene itself in a wide range of temperature. Therefore, the electrical conductance of graphene can be measured precisely as a function of n using a graphene field effect transistor like device and sweeping the gate voltage.

Because monolayer graphene has the linear dispersion, the carrier density is proportional to the energy squared $n = \frac{g_s g_v \varepsilon^2}{4\pi\hbar^2 v_F^2}$, where $g_S = 2$ and $g_v = 2$ are the spin degeneracy and valley degeneracy, respectively. The density of states $D(\varepsilon) = dn/d\varepsilon$ is proportional to ε. If the scattering probability $\hbar/\tau_m(\varepsilon)$ is proportional to $D(\varepsilon) \propto \varepsilon$ of the final state, the momentum relaxation time $\tau_m(\varepsilon)$ is proportional to ε^{-1}. Therefore, the electrical conductivity $\sigma = e^2 D(\varepsilon_F)\left(\frac{v_F^2 \tau_m(\varepsilon_F)}{2}\right) \propto D(\varepsilon_F)\tau_m(\varepsilon_F)$ should be energy and density

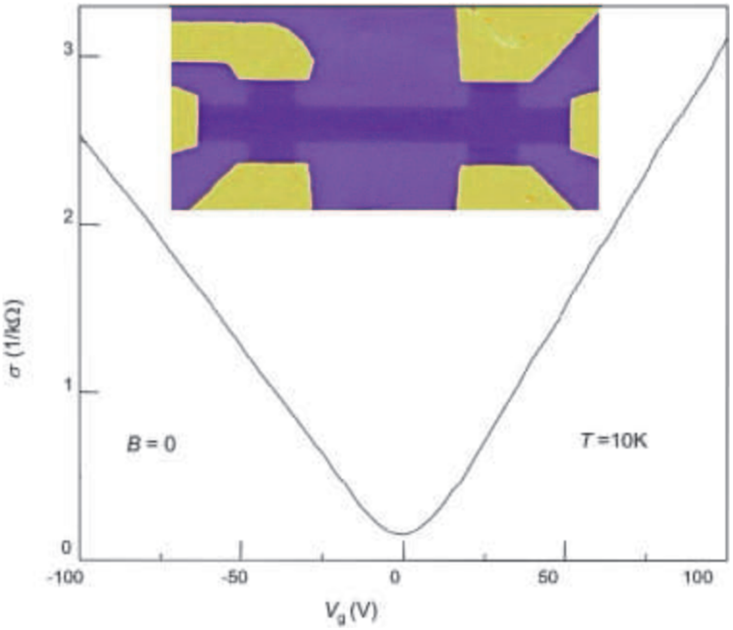

Fig. 1 Typical conductivity of graphene as a function of the back gate voltage. Inset shows a typical device on a SiO_2 substrate. Adopted from Castro Neto AH, et al. (2009) The electronic properties of graphene. *Reviews of Modern Physics* 81: 109.

independent (Shon and Ando, 1998). Despite this initial expectation, σ is proportional to n at relatively low temperatures in experiments (see Fig. 1) (Novoselov et al., 2005; Das Sarma et al., 2011; Castro Neto et al., 2009).

This n-linear dependence of σ is assigned to the scattering by charged impurities. For the δ-function-like scattering with the potential extension smaller than the wavelength $\lambda = 2\pi/k$, the scattering probability is proportional to ε. However, it is proportional to ε^{-1} for long-range scattering, leading to $\sigma \propto \varepsilon^2 \propto n$, as we will discuss in the following.

We consider carrier transport in the Boltzmann formalism by linear response of the distribution function $f_{\boldsymbol{k}} = f_0 + \delta f_{\boldsymbol{k}}$ to the in-plane electric field $\boldsymbol{E}$, where f_0 is the Fermi distribution function and $\delta f_{\boldsymbol{k}}$ is the $\boldsymbol{E}$ linear term. The scattering probability

$$W(\boldsymbol{k}', \boldsymbol{k}) = \frac{2\pi}{\hbar}\left\langle |V_{\boldsymbol{k}',\boldsymbol{k}}|^2 \right\rangle \delta(\varepsilon(\boldsymbol{k}) - \varepsilon(\boldsymbol{k}')) \tag{14}$$

between the initial and final wave vectors $\boldsymbol{k}$ and $\boldsymbol{k}'$ is determined by the matrix element $V_{\boldsymbol{k}',\boldsymbol{k}}$ of the scattering potential and its squared average $\langle |V_{\boldsymbol{k}',\boldsymbol{k}}|^2 \rangle$ over the scatterers' configurations. The solution becomes

$$\delta f_{\boldsymbol{k}} = e\tau_m(\varepsilon_{\boldsymbol{k}}) \frac{\partial f_0}{\partial \varepsilon_{\boldsymbol{k}}} \boldsymbol{v} \cdot \boldsymbol{E} \tag{15}$$

with the relaxation time given by

$$\frac{1}{\tau_m(\varepsilon_{\boldsymbol{k}})} = \int \frac{d\boldsymbol{k}'}{(2\pi)^2}(1 - \cos\theta_{\boldsymbol{k},\boldsymbol{k}'}) W(\boldsymbol{k}'\boldsymbol{k}), \tag{16}$$

where $\theta_{\boldsymbol{k},\boldsymbol{k}'}$ is the scattering angle. For randomly distributed scatters with identical potential shape $V(\boldsymbol{r} - \boldsymbol{r}_i)$ and density n_i, the matrix element term becomes

$$\left\langle |V_{\boldsymbol{k}',\boldsymbol{k}}|^2 \right\rangle = n_i |V(\boldsymbol{k}' - \boldsymbol{k})|^2 F(\boldsymbol{k}' - \boldsymbol{k}), \tag{17}$$

where $V(\boldsymbol{q})$ is the Fourier transform of $V(\boldsymbol{r})$ and $F(\boldsymbol{k}' - \boldsymbol{k}) = (1 + \cos\theta_{\boldsymbol{k},\boldsymbol{k}'})/2$ is the form factor associated with the inner product of the wave functions of the initial and final states. From Eqs. (14) and (16), we obtain the relaxation time as

$$\frac{1}{\tau_m(\varepsilon_{\boldsymbol{k}})} = \frac{n_i}{\hbar}\frac{|\varepsilon|}{(\hbar v_F)^2}\int_0^\pi \frac{d\theta}{2\pi}(1 - \cos^2\theta)\langle |V(\boldsymbol{q})|^2 \rangle \tag{18}$$

with $\boldsymbol{q} = \boldsymbol{k}' - \boldsymbol{k}$. Here, $\langle |V(\boldsymbol{q})|^2 \rangle = |V(q)|^2$ with $q = 2k\sin(\theta/2)$. In Eq. (18), $(1 - \cos^2\theta)$ term originating from $F(\boldsymbol{k}' - \boldsymbol{k})$ indicates suppression of the backscattering or large-angle scattering near $\theta = \pi$. This is unique in graphene and related with the coupling of $\boldsymbol{k}$ and pseudospin (sublattice degree of freedom) as we have discussed for Eq. (1).

For the short-range (δ-function-like) scattering, $V(q)$ becomes q-independent and is replaced with a constant. Eq. (18) leads to $\frac{1}{\tau_m(\varepsilon)} \propto |\varepsilon|$ and σ being independent of n. For real devices, however, we need to consider the screening effect to discuss the Coulomb scattering. Following the representation in Ando et al. (1982), the screened potential of the charged impurity is given by

$$V(q) = \frac{2\pi e^2}{\kappa q \varepsilon(q)}, \tag{19}$$

where κ is the effective dielectric constant determined by the system environment and $\varepsilon(q)$ is determined by the screening by electrons in graphene. The screening effect is represented by the polarization function $\Pi(q)$ defined as

$$\varepsilon(q) = 1 + \frac{2\pi e^2}{\kappa q}\Pi(q). \tag{20}$$

$\Pi(q)$ at zero temperature becomes constant for $q < 2k_F$ and is simply replaced with the density of states $D(\varepsilon_F)$ (Ando, 2006; Hwang and Das Sarma, 2007). Therefore, at low enough temperature, the Thomas-Fermi approximation holds with the constant screening constant q_s as

$$V(q) = \frac{2\pi e^2}{\kappa(q + q_s)}, \tag{21}$$

where q_s is given by

$$q_s = \frac{2\pi e^2}{\kappa}\int\left(-\frac{\partial f_0}{\partial \varepsilon}\right)D(\varepsilon)d\varepsilon. \tag{22}$$

This q dependence of $V(q)$ in Eq. (18) leads to the $n\varepsilon^{-1} \propto \varepsilon$ dependence of the momentum relaxation time. The relaxation time $\tau_m(\varepsilon_{\boldsymbol{k}})$ and the resulting conductivity calculated by integral of Eq. (15) becomes

$$\tau_m(\varepsilon) = \frac{n}{\pi g_S g_v n_i}\frac{\hbar}{|\varepsilon|}H \tag{23}$$

$$\sigma = \frac{e^2}{4\pi^2\hbar}\frac{|n|}{n_i}H, \tag{24}$$

where H is the dimensionless constant determined by κ (Ando, 2006; Adam et al., 2007). This result accounts for the experimental observation $\sigma \propto n$. The mobility is independent of n and depends on the concentration of charged impurities:

$$\mu = \frac{e}{4\pi^2\hbar}\frac{1}{n_i}H. \tag{25}$$

The mobility is experimentally evaluated from the carrier density or gate voltage dependence of the conductivity.

At the charge neutrality $n = 0$, the conductivity becomes minimum. The minimum conductivity is predicted to be

$$\sigma_{min} = \frac{g_s g_v e^2}{2\pi^2\hbar}, \tag{26}$$

for the short-range scattering irrespective of the value of the scattering probability W (Shon and Ando, 1998). However, in the presence of the long-range scattering, $\sigma_{\min}$ increases with W (Noro et al., 2010). Experimentally, $\sigma_{\min}$ differs sample by sample (Tan et al., 2007), which is consistent with the charged impurity scattering. Around $n = 0$, electron-hole puddles are locally present owing to inhomogeneity of graphene devices. Using the induced local carrier density n_p at the conductivity minimum, $\sigma \propto n$ is modified to $\sigma \sim \sigma_{min}\sqrt{1 + \frac{n^2}{n_p^2}}$ around $n = 0$.

For bilayer graphene, the parabolic dispersion leads to $n \propto \varepsilon$ and $D(\varepsilon) \propto \varepsilon^0$. The form factor in Eq. (17) becomes $F(\boldsymbol{k}' - \boldsymbol{k}) = (1 + \cos 2\theta_{\boldsymbol{k},\boldsymbol{k}'})/2$, allowing large-angle scattering (no suppression at $\theta_{\boldsymbol{k},\boldsymbol{k}'} = \pi$). In a similar argument, we find $\sigma \propto n$ for the short-range scattering and $\sigma \propto n^2$ for the long-range scattering. Experimentally, $\sigma \propto n$ is observed in a wide range of n (Morozov et al., 2008). Therefore, it has been pointed out there is a scattering by a short-range disorder in addition to the screened charged impurities in bilayer graphene. $\sigma \propto n$ for both monolayer and bilayer graphene indicates that screening is much stronger in bilayer graphene than in monolayer graphene. Indeed, we find $q_s \propto n^{-1/2}$ in bilayer graphene (as in standard two-dimensional electron gas) while $q_s \propto n^0$ in monolayer graphene. The ratio of the screening constant between the bilayer and monolayer graphene $q_s^{\mathrm{BLG}}/q_s^{\mathrm{MLG}} \approx 16/\sqrt{n/10^{10}\mathrm{cm}^{-2}}$ becomes significantly small (screening becomes significantly stronger in bilayer) as n increases (Das Sarma et al., 2011).

In the presence of a perpendicular electric field for bilayer graphene, the gap 2Δ opens (McCann, 2006, 2023; Oostinga et al., 2008). When the Fermi energy is tuned into the gap, the conductivity is suppressed. Such a gapped state can be prepared in a dual-gated device by tuning the carrier density n and the perpendicular electric field D independently. However, the conductivity in the gap is not so suppressed as in conventional semiconductors, where the conductivity is scaled to $\exp(-\Delta/k_BT)$ owing to the thermal activation across the gap. The low temperature transport in this regime is described by the variable range hopping through impurity-induced states. The conductivity is proportional to $\exp(-(T_0/T)^{1/3})$, where T_0 depends on the disorder in the device.

In general, the conductivity becomes approximately the sum of contributions from the variable range hopping and thermal activation across the gap:$G \approx G_1 \exp\left(-\Delta/k_B T\right) + G_2 \exp\left(-(T_0/T)^{1/3}\right)$ (Miyazaki et al., 2010). The first term becomes more dominant for higher temperatures.

At high temperatures, carriers in graphene also suffer from scattering by phonons. Electrons are scattered by longitudinal acoustic (LA) phonons, optical phonons on the substrate, and ripples of graphene lattice. The resistivity ρ_{LA} induced by LA phonons (major contribution) is proportional to the temperature T, except at low temperature below Bloch-Grüneisen temperature $T_{\mathrm{BG}} \approx 54\sqrt{n(\times 10^{12}\mathrm{cm}^2)}$ K, where the phonon is degenerate and ρ_{LA} is suppressed as $\rho_{\mathrm{LA}} \propto T^4$ (Stauber et al., 2007; Hwang and Das Sarma, 2008). Contributions of other phonons are nonlinear with T.

The contribution of phonon scattering in carrier transport is usually (in present devices) minor compared to the charge impurity scattering even close to the room temperature. For $T < T_{\mathrm{BG}}$, intrinsic phonon-limited mobility is high and exceeds 10^6 cm^2 V^{-1} s^{-1} (Hwang and Das Sarma, 2008).

Ballistic transport and electron optics

In typical clean graphene devices, the mean free path $l_m = \tau_m v_F$ is of the order of several microns when n is sufficiently large. This long mean free path allows for realization of ballistic transport by making the device dimension comparable with or smaller than l_m. Ballistic transport has already been observed and investigated in conventional semiconductors that have similar properties. However, unlike conventional two-dimensional electron gas systems, it is possible in graphene to tune the Fermi energy locally between the conduction and valence bands by means of local gates. This allows us to prepare in-plane p-n junctions in the ballistic regime. In this section, we discuss unique ballistic transport in bipolar graphene junctions. We focus on the Klein tunneling and electron optics in monolayer graphene. Unique properties in bipolar graphene devices originate from the pseudospin-momentum coupling as we have discussed.

It was predicted that a relativistic particle incident on an infinite potential barrier transforms into an anti-particle inside the barrier and moves freely in this otherwise forbidden region, resulting in perfect transmission through the barrier. This phenomenon is known as the Klein tunneling. In graphene, which has relativistic charge carriers, it is possible to demonstrate this Klein paradox on a chip (Katsnelson et al., 2006). We consider a normal incident charge carrier to a graphene n-p interface with a smooth potential which does not introduce inter-valley scattering by an atomic-scale short-range scattering. According to the pseudospin-momentum coupling in Eq. (1), the pseudospin of an incoming electron in the K point is parallel to the momentum. Since we assume the smooth n-p interface potential, the pseudospin is conserved in the tunneling process. Therefore, the electron impinging perpendicular onto the n-p junction cannot be backscattered into a counter propagating electron state which would be in the K′ point. Instead, it is scattered into a hole state which has opposite momentum direction but with the same pseudospin as the impinging electron. This leads to the perfect transmission through the n-p junction.

In general, while normally incident particles perfectly transmit through the n-p interface, obliquely incident particles have a transmission probability which depends on the angle of incidence. There is also an analogy between the transmission of the carriers at the graphene n-p interface and optical refraction at the surface of metamaterials with negative refraction index. Using such refraction, incident particles can be focused by graphene n-p junctions. This is the principle of the electric current lenses in n-p-n or p-n-p structures, known as Veselago lenses in optics, in the ballistic transport regime (Cheianov et al., 2007).

The Klein tunneling has been demonstrated in dual-gated graphene p-n-p (n-p-n) junction devices. The junction is ballistic when the mean free path l_m is larger than the distance between the two n-p interfaces. The electrical resistance is larger in the ballistic transport regime than in the diffusive regime. This is because the tunneling probability for obliquely impinging electrons to each p-n junction is lower in the ballistic regime than in the diffusive regime due to the Klein tunneling process.

In a ballistic n-p-n or p-n-p graphene junction, quantum interference also occurs due to a resonant cavity between the two n-p interfaces (Shytov et al., 2008). The conductivity oscillates as a function of the carrier density of the cavity region. But this interference is suppressed for the normal incidence owing to the perfect transmission at both interfaces. The interference is dominated by modes at incident angles, where neither the transmission nor reflection probabilities are too large. The magnitude and phase of the transmission and reflection coefficients can be evaluated by this quantum interference in a perpendicular magnetic field B. The magnetic field B bends the trajectories of the carriers and modifies the incident angles of the carriers at the n-p interfaces. It also modifies the transmission and reflection coefficients at the interfaces. In a certain B range, contributions of zero transverse (y-direction) momentum modes become dominant, where the incident angles at the two interfaces have the same sign (see Fig. 2(b)). The trajectory of a particle in a round trip between the two interfaces encloses the origin $k_x = k_y = 0$ in the momentum space and the particle thus acquires the Berry phase π. This π phase shift is the hallmark of the Klein tunneling that should lead to the perfect transmission (zero reflection) in the normal incidence. The π phase shift of the conductivity oscillation was first observed by Young and Kim as shown in Fig. 2(d) (Young and Kim, 2009).

There are also other experimental works on electron optics in ballistic bipolar graphene junction devices. Chen et al. demonstrated Snell's law at the n-p interface by a magnetic focusing experiment (Chen et al., 2016). It was experimentally confirmed that refraction is negative at a n-p interface while it is positive at a n-n′ or p-p′ (the same polarity with different carrier densities) interface.

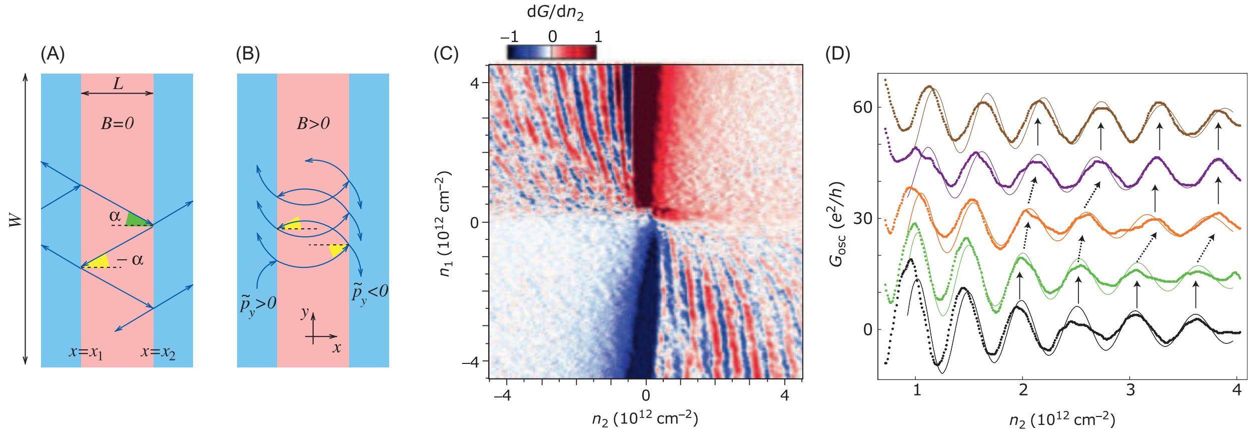

Fig. 2 Demonstration of the Klein tunneling in graphene. (a) schematic of interference in a n-p-n or p-n-p junction at $B = 0$. (b) schematic of interference for $B > 0$. (c) a color-coded plot of the derivative of the conductance with respect to the charge density induced by the top gate (n_2) as a function of top (n_2) and back (n_1) gate-induced charge densities. The top gated region is between the two n-p interfaces. The oscillations in conductance are apparent when the densities n_1 and n_2 have opposite signs. (d) Conductance G vs n_2 for fixed n_1 at different external magnetic field values applied perpendicular to the sample (from the bottom to the top conductance curve $B = 0$, 200, 400, 600 and 800 mT); the dots represent data, the smooth lines are the result of the simulations. The sudden phase shift of π that signals the presence of perfect transmission is indicated by dotted arrows. We find by tracing the arrows that the phase of oscillation changes by π between the green and purple curves. It corresponds to the change of the incident angle from the one depicted in (a) to that in (b). Curves are offset for clarity. Panels (a) and (b): From Shytov AV, Rudner MS, and Levitov LS (2008) Klein backscattering and Fabry–Perot interference in graphene heterojunctions. *Physical Review Letters* 101: 156804. Panels (c) and (d): From Young A and Kim P (2009) Quantum interference and Klein tunnelling in graphene heterojunctions. *Nature Physics* 5: 222–226; Craciun MF, et al. (2011) Tuneable electronic properties in graphene. *Nano Today* 6: 42–60.

Valley Hall transport in the presence of charged impurities

Berry curvature that we discussed in a previous section characterizes the intrinsic valley Hall effect. However, there are always extrinsic effects, i.e., influence of scatterers. It is more convenient to consider velocity operator to investigate influence of the scattering by charged impurities. Furthermore, discussion of the valley Hall effect in terms of the Berry curvature in Eq. (10) is semi-classical. Using the velocity operator and standard Kubo formula in the linear regime, we can investigate valley related quantum transport. The following argument was developed by Ando (2015a).

The velocity operator is defined as

$$\boldsymbol{v} = (v_x, v_y) = v_F\boldsymbol{\sigma} = v_F(\sigma_x, \sigma_y).$$

We consider massive monolayer graphene in Eq. (4). We perform a unitary transformation $U = \begin{pmatrix} 0 & 1 \\ -1 & 0 \end{pmatrix}$ on the Hamiltonian for K′ valley ($\tau_z = -1$), which interchanges the sublattices. The Hamiltonian becomes

$$H = \hbar v_F(k_x\sigma_x + k_y\sigma_y) + \tau_z\Delta\sigma_z. \tag{27}$$

The equation of motion of the velocity operator becomes

$$\dot{\boldsymbol{v}} = \frac{1}{i\hbar}[\boldsymbol{v}, H] = 2v_F^2(\boldsymbol{k}\times\boldsymbol{\sigma}) - 2\tau_z\frac{\Delta}{\hbar}\boldsymbol{v}\times\boldsymbol{e}_z \tag{28}$$

using the commutation relation of the Pauli matrices. The first term is the Zitterbewehgung term. The second term corresponds to the anomalous Hall conductivity. It can be viewed as the Lorentz force due to the valley dependent effective magnetic field in the z-direction

$$\boldsymbol{B}_{\text{eff}} = \tau_z\left(\frac{\Delta}{\mu_B^*}\right)\boldsymbol{e}_z. \tag{29}$$

Here $\mu_B^* \equiv e\hbar/2m^*$ is the effective Bohr magneton for the orbital magnetic moment of the valley. The role of the mass term is the valley Zeeman energy induced by the effective magnetic field in the real space.

The valley Hall conductivity for zero inter-valley scattering is calculated using the Kubo formula

$$\sigma_{xy}^K = \frac{4\hbar}{\pi i L^2}\int d\varepsilon f(\varepsilon)\left\langle \mathrm{Tr}\left[j_x\left(\frac{\partial}{\partial\varepsilon}\mathrm{Re}\,G(\varepsilon + i0)\right)j_y\mathrm{Im}G(\varepsilon + i0) - (x \leftrightarrow y)\right]\right\rangle, \tag{30}$$

where L^2 is the system size, $\boldsymbol{j} = -e\boldsymbol{v}$ is the current operator, $G(\varepsilon) = (\varepsilon - H)^{-1}$ is the Green's function, and $\langle\ldots\rangle$ denotes average over configurations of scatterers. This also leads to Eq. (11). Note that the Berry curvature characterizes the response of the system to the shift in momentum space, while the effective magnetic field discussed here characterizes that to the charge diffusion. Similarly to that the drift charge current driven by the shift in momentum space and the diffusion current driven by the charge density gradient are carried by the same conductivity, the Berry curvature and the effective magnetic field in Eq. (29) lead to the same Hall conductivity.

The work of Ando analyzes the influence of charged impurity scattering on the valley Hall effect. It is shown that even the slightest degree of scattering in the "clean limit" significantly modifies the valley Hall conductivity. The analytical result for zero temperature by the self-consistent Born approximation is given as

$$\sigma_{xy}^{\mathrm{v}}(\varepsilon) = \begin{cases} \dfrac{2e^2}{h} \dfrac{8|\delta|(\Gamma_0 - \Gamma_1)\left[\left(1+\delta^2\right)\Gamma_0 - 2\delta^2\Gamma_1 - \left(1-\delta^2\right)\Gamma_2\right]}{\left[\left(1+3\delta^2\right)\Gamma_0 - 4\delta^2\Gamma_1 - \left(1-\delta^2\right)\Gamma_2\right]^2} & (|\varepsilon| > \Delta) \\ \dfrac{2e^2}{h} \quad (|\varepsilon| < \Delta) \end{cases} \tag{31}$$

with $\delta = \Delta/\varepsilon$, and Γ_n are the broadening parameters that go to zero in the clean limit and are defined by the impurity density and potential profile. We find that the scattering does not modify $\sigma_{xy}^{\mathrm{v}}(\varepsilon)$ in the band gap. Close to the gap but within the band continuum, we have

$$\sigma_{xy}^{\mathrm{v}}(\varepsilon) \approx \frac{2e^2}{h} \frac{|\varepsilon|}{\Delta}. \tag{32}$$

Far away from the gap ($|\delta| \ll 1$), we have

$$\sigma_{xy}^{\mathrm{v}}(\varepsilon) \approx \frac{2e^2}{h} \frac{\Delta}{|\varepsilon|} \frac{8(\Gamma_0 - \Gamma_1)}{\Gamma_0 - \Gamma_2}. \tag{33}$$

These show enhancement of $\sigma_{xy}^{\mathrm{v}}(\varepsilon)$ in the band continuum. In particular, for the limit of short-range scattering, only Γ_0 remains nonzero. We therefore have

$$\sigma_{xy}^{\mathrm{v}}(\varepsilon) \approx \frac{2e^2}{h} \frac{\Delta}{|\varepsilon|} \frac{8\left(1+\delta^2\right)}{\left(1+3\delta^2\right)^2}, \tag{34}$$

showing 8 times enhancement of $\sigma_{xy}^{\mathrm{v}}(\varepsilon)$ for $|\delta| \ll 1$ from that in Eq. (11). The results for different potential profiles are shown in Fig. 3. We see double-peak structure in $\sigma_{xy}^{\mathrm{v}}(\varepsilon)$, plotted as a function of the energy, which persists unless the band gap is too small. In general, enhancement of $\sigma_{xy}^{\mathrm{v}}(\varepsilon)$ in the band continuum is larger for the shorter-range scattering. This enhancement is also predicted for bilayer graphene (Ando, 2015b).

Enhancement of $\sigma_{xy}^{\mathrm{v}}(\varepsilon)$ in the clean limit may be somewhat surprising. It already indicates that the intrinsic picture based on the Berry curvature cannot fully capture the valley Hall physics. It may have an analogy with the anomalous Hall effect driven by spin-orbit interaction. It is known there that the ultra-clean samples fall into the extrinsic regime, where the influence of external scatterers is dominant. The intrinsic regime is achieved in the moderately dirty regime. Similarly, the valley Hall effect in the clean limit is significantly affected by the profile of scatterers.

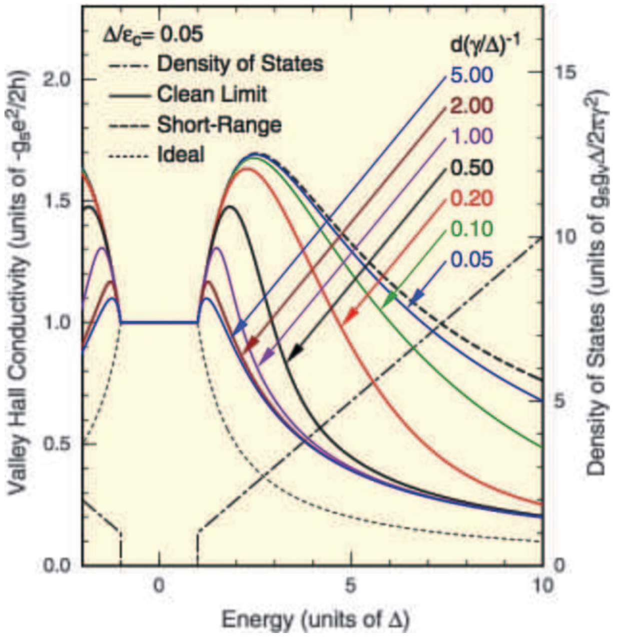

Fig. 3 Valley Hall conductivity and the density of states in the clean limit for scatters with Gaussian potential with varying potential range *d*. $\varepsilon_C \approx \hbar v_F$ is the cutoff energy. From Ando T (2015) Theory of valley hall conductivity in graphene with gap. *Journal of the Physical Society of Japan* 84: 114705.

Nonlocal transport and edge transport

The measurement of the nonlocal transport is widely used to detect the Hall conductivity. Once we have both the electrical conductivity σ_{xx} and valley Hall conductivity σ_{xy}^{v}, we can formulate the charge current and valley current in the presence of in-plane electric field semi-classically. The following conductance matrix form allows us to examine the conversion between the electric field $\boldsymbol{E}$ (in the x direction) and the electric current density j_{c}, and that between $\boldsymbol{E}$ and the valley current density j_{v} (in the y direction) on a homogenous sheet:

$$\begin{pmatrix} j_{\mathrm{c}} \\ j_{\mathrm{v}} \end{pmatrix} = \begin{pmatrix} \sigma_{xx} & -\sigma_{xy}^{\mathrm{v}} \\ \sigma_{xy}^{\mathrm{v}} & \sigma_{xx} \end{pmatrix} \begin{pmatrix} E \\ E_{\mathrm{v}} \end{pmatrix}, \tag{35}$$

where

$$E_{\mathrm{v}} \equiv \frac{1}{2e}\frac{\partial}{\partial x}\delta\mu_{\mathrm{v}} \tag{36}$$

is defined as the "valley field" induced by the chemical potential difference $\delta\mu_{\mathrm{v}} = \mu_K - \mu_{K'}$ between the two valleys referred to as the "valley voltage." Taking $E_{\mathrm{v}} = 0$, the valley Hall effect is described by

$$j_{\mathrm{v}} = \sigma_{xy}^{\mathrm{v}} E. \tag{37}$$

as the conversion of the electric field into the valley current. Taking $j_{\mathrm{c}} = 0$ and the inverse of the conductance matrix in Eq. (35), we find

$$E = \frac{\sigma_{xy}^{\mathrm{v}}}{(\sigma_{xx})^2 + \left(\sigma_{xy}^{\mathrm{v}}\right)^2} j_{\mathrm{v}}. \tag{38}$$

This describes conversion of the valley current into the electric field.

The main source of valley relaxation is the scattering at armchair edges and atomic defects. To take into account inter-valley scattering, we employ a valley diffusion equation:

$$\frac{\partial^2}{\partial x^2}\delta\mu_{\mathrm{v}} = \frac{1}{(l_{\mathrm{v}})^2}\delta\mu_{\mathrm{v}} \tag{39}$$

This equation assumes homogeneous inter-valley scattering length l_{v}. Combining Eqs. (35) and (38) under an appropriate boundary condition, one can characterize the valley-related transport in a device.

Three groups have reported valley-mediated transport in a nonlocal measurement setup as shown in Fig. 4 (Yamamoto et al., 2015). Similar Hall bar devices have also been used for measurements of the spin Hall effect. In this setup, charge current I_{C} is injected into the left side of the device (between the contacts A and D), and voltage V induced in the right side of the device (between the contacts B and C) is measured. Nonlocal resistance is defined as $R_{\mathrm{NL}} = V/I_{\mathrm{C}}$. For $\sigma_{xy}^{\mathrm{v}} \ll \sigma_{xx}$, the valley-mediated transport can be

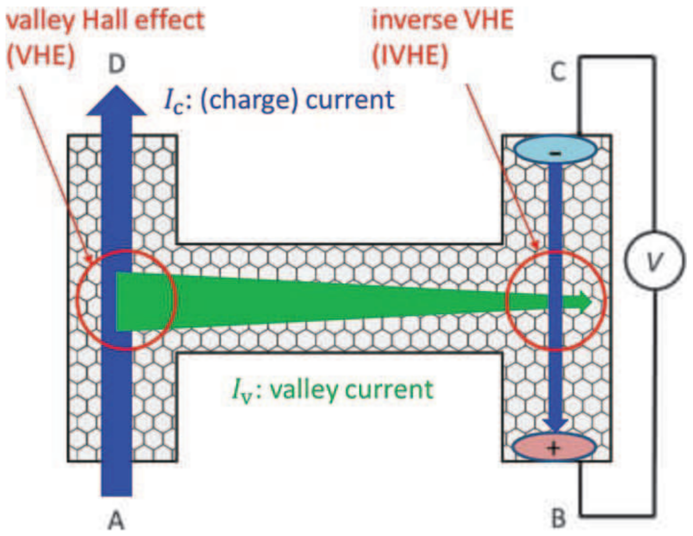
valley Hall effect
(VHE)
D
I_{C}: (charge) current
inverse VHE
(IVHE)
C
−
V
I_{v}: valley current
+
A
B

Fig. 4 Hall bar geometry and nonlocal resistance measurement setup for generation and detection of the pure valley current. The charge current I_{c} between contacts A and D generates a pure valley current in its transverse direction via the valley Hall effect. This valley current is converted into a voltage between contacts B and C via the inverse valley Hall effect.

understood by a sequential conversion picture; the charge current I_c on the left is first converted into the transverse valley current with the conversion ratio given by the valley Hall angle $\alpha = \sigma_{xy}^{v}/\sigma_{xx}$ (valley Hall effect). This valley current is then converted back to the transverse charge current on the right with the conversion ratio again given by $\alpha = \sigma_{xy}^{v}/\sigma_{xx}$ (inverse valley Hall effect). This charge current is finally converted to the voltage V. Taking the conversion ratio of each process, we find that

$$R_{\mathrm{NL}} \propto \alpha^2 \cdot \frac{1}{\sigma_{xx}} = \left(\sigma_{xy}^{v}\right)^2 \rho^3, \tag{40}$$

where $\rho = 1/\sigma_{xx}$ is the resistivity of the device. Using the horizontal width W of the Hall bar and the lateral distance L between contacts A and C, R_{NL} is given by

$$R_{\mathrm{NL}} = \frac{W}{2l_v} \frac{\left(\sigma_{xy}^{v}\right)^2}{\left(\sigma_{xx}\right)^3} \exp\left(-\frac{L}{l_v}\right). \tag{41}$$

For $\sigma_{xy}^{v} \gg \sigma_{xx}$, on the other hand, we obtain

$$R_{\mathrm{NL}} = \frac{W}{2l_v} \frac{1}{\sigma_{xx}} \exp\left(-\frac{L}{l_v}\right) \propto \left(\sigma_{xy}^{v}\right)^0 \rho^1. \tag{42}$$

The behaviors expressed by Eqs. (41) and (42) should be compared with the van der Pauw formula describing the contribution to R_{NL} of classical diffusive transport. Since graphene has high crystal quality, inter-valley scattering mainly occurs at the edges and therefore $l_v \sim W$.

The first experimental demonstration of the generation of pure valley current was reported for monolayer graphene aligned on hexagonal Boron Nitride (h-BN) crystal (Gorbachev et al., 2014). Since h-BN also has a hexagonal lattice with its lattice constant close to that of graphene, graphene aligned on h-BN is subjected to the periodic potential fluctuation of the boron and nitrogen atoms with its period observed as a moiré pattern. For appropriate angular alignment, this periodic potential produces mini-bands and associated band gap in the energy bands of graphene. Since the spatial inversion symmetry is broken owing to this periodic potential modulation, the valley Hall effect should occur. In the experiment performed by Gorbachev et al. (2014), such a high-quality monolayer graphene shaped into a Hall bar geometry aligned on single-crystal h-BN was employed to measure nonlocal resistance as discussed in the previous section.

Gorbachev et al. found that the nonlocal resistance R_{NL} is orders of magnitude larger than that estimated for the current diffusion. It was also confirmed that nonaligned graphene on h-BN, which is not subjected to the periodic potential modulation from the h-BN, does not show such a large R_{NL}. Observation of large R_{NL} was therefore attributed to valley-mediated transport. In addition, R_{NL} has a much sharper response to the gate voltage (which modulates the carrier density) than the resistivity ρ. It was interpreted as the consequence of nonlinearity of R_{NL} vs ρ in Eq. (40).

This experiment called forth debate concerning the microscopic picture of the nonlocal transport. In the experiment, the valley Hall effect was analyzed for metallic samples while the gap opening is supposed to be a necessary condition to confirm inversion symmetry breaking. It is now known that commensurate graphene/h-BN regions and incommensurate strained regions can form a domain-like structure (Woods et al., 2014) and thus the gap can be locally present even if the sample is metallic. Then the next question is whether the valley transport is mediated by the edge or bulk. Lensky et al. showed that bulk currents just beneath the gap may have dominant contribution to the valley current (Lensky et al., 2015). However, criticism was made that Eq. (40) is inapplicable for metallic samples because it is based on semi-classical theory. Indeed, theory by Ando indicates that the scattering by charged impurities should modify the theoretical curve of σ_{xy}^{v} used in the analysis. Based on the quantum transport model, completely different scenario for the experimental observation, where transport at the trivial edges make the dominant contribution to the observed R_{NL}, was suggested (Kirczenow, 2015; Marmolejo-Tejada et al., 2018). Recent observation of the non-topological edge current in charge-neutral graphene by a scanning SQUID (Aharon-Steinberg et al., 2021) also seems to support this scenario. Note, however, that existence of the trivial edge state was only observed at low (liquid helium) temperature and that the edge state is disordered.

Sui et al. (2015) and Shimazaki et al. (2015) employed a dual-gated structure, where a bilayer graphene flake is sandwiched by top and back gates through insulating h-BN layer. Independent control of n and D enabled them to investigate the valley Hall effect in the "insulating" regime.

Fig. 5 shows the gate voltage dependence of R_{L} and R_{NL} (data presented by Shimazaki et al., 2015). At the charge neutrality point (CNP), R_{L} is enhanced when D is increased due to the increase of band gap. R_{NL} also increases with D around the CNP. This is because σ_{xx} is reduced while σ_{xy}^{v} is enhanced with increasing D at the CNP. The measured R_{NL} is more than three orders of magnitude larger than the calculated ohmic contribution, excluding the ohmic contribution as the origin of the observed large R_{NL}.

Fig. 5(c) shows the scaling at the CNP for $T = 70$ K obtained by Shimazaki et al. (2015). At 70 K, the crossover between the band conduction (thermally activated transport across the band gap) and hopping conduction regimes occurs upon changing D. A cubic scaling (Eq. 40) is obtained in the band conduction regime of small D (green line) whereas saturation of R_{NL} is observed in the hopping conduction regime of large D by sweeping D at a fixed T. Sui et al. also observed similar nonlinear scaling between ρ and R_{NL} by sweeping T at a fixed D (Sui et al. 2015).

Since the device is highly resistive in this case, R_{NL} should be proportional to ρ if the edge transport is dominant. Sui et al. further excluded the edge contribution by employing a sample with a long edge (Sui et al., 2015). The nonlocal signal was comparable as

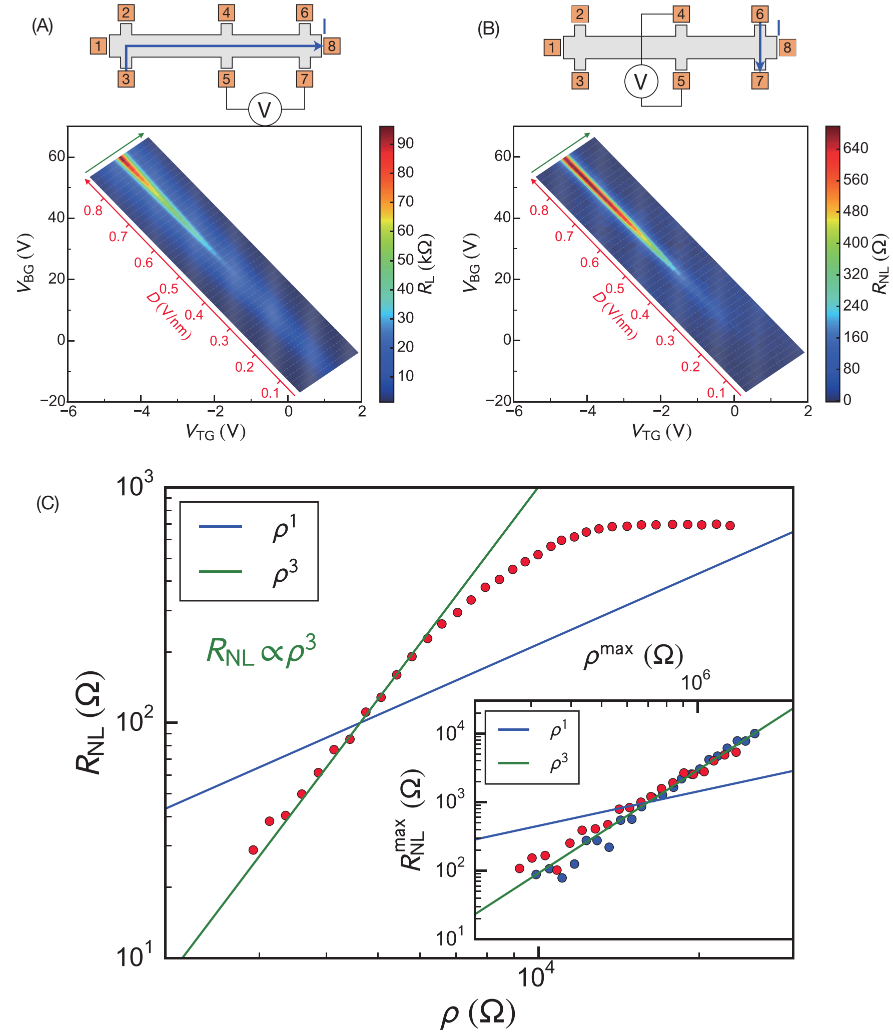

Fig. 5 Valley Hall effect demonstrated by the nonlocal transport measurement. A dual-gated bilayer graphene Hall bar device was employed, where bilayer graphene is sandwiched by the top gate and the back gate though h-BN flakes. (a) Gate voltage dependence of the local resistance R_L. It was measured as a function of the top gate voltage V_{TG} and the back gate voltage V_{BG}. The perpendicular electric field D is modulated along the red axis while the carrier density n is modulated along the green axis. The inset is a schematic description of the measurement configuration. The blue arrow stands for the charge flow. (b) Gate voltage dependence of the nonlocal resistance R_{NL}. (c) Scaling relation between the resistivity ρ and R_{NL} at the charge neutrality point (CNP). Each data point is extracted from the data in (a) and (b) for D ranging from 0.22–0.85 V/nm at the CNP. The inset shows the scaling relation in the band conduction regime observed with a different sample. Details are presented by Shimazaki et al. (2015).

long as the active sample length and width were the same, irrespective of the length of the sample edge. This result supports occurrence of the valley transport in the bulk.

The cubic scaling is the expected scaling for the intrinsic valley Hall effect (constant σ_{xy}^{v}) for $\sigma_{xy}^{v} \ll \sigma_{xx}$ near the CNP. For $\sigma_{xy}^{v} \gg \sigma_{xx}$, R_{NL} for the intrinsic regime is described by $R_{NL} \propto \rho$. The observed saturation of R_{NL} for large D and ρ may imply deviation from the intrinsic regime in the hopping conduction regime influenced by charged impurities. Microscopic picture of the observed valley-mediated transport is, however, not yet well understood.

Recently, similar nonlocal transport was reported for the charge neutral encapsulated bilayer graphene at $D = 0$ in the presence of a perpendicular magnetic field B, i.e., for the hall-filled 0th Landau level (Tanaka et al., 2021). Here, the electronic correlation leads to gap opening and the ground state becomes the interlayer antiferromagnetic state, where the spins align ferromagnetically in the in-plane direction within each layer but become opposite between the layers (Kharitonov, 2012). Such a state appears even at $B = 0$ for suspended bilayer graphene (Weitz et al., 2010), where the screening effect is weaker than encapsulated graphene. Each spin state is polarized in one of the layers, which is equivalent to the presence of a spin-dependent spontaneous perpendicular electric field that induces the spin-dependent valley Hall effect. This charge-neutral spin-dependent valley current mediates the nonlocal transport. It was shown that the large nonlocal transport in this state is observed even for a long-edge device and that it only appears when there is a quasi-long-range spin order in the bulk, i.e., below the Kosterlitz-Thouless transition temperature (Tanaka et al., 2022). This observation implies that this nonlocal transport is also mediated by the bulk region despite the criticism made for a different regime (Aharon-Steinberg et al., 2021).

Hydrodynamic transport

We have discussed carrier transport mostly in a single particle picture. However, at high temperatures where the electron-electron scattering time becomes shorter than that of scattering by charged impurities or phonons, carriers behave as fluids rather than independent particles or quasi-particles (Levitov and Falkovich, 2016).

Electron-electron scattering time in graphene is given by $\tau_{ee} \sim \hbar\varepsilon_F/(k_BT)^2$ in the degenerate case (far from the charge neutrality point). In a clean graphene device, the mean free path, or more precisely, the momentum relaxation length l_m can exceed the electron-electron scattering length $l_{ee} = v_F\tau_{ee}$ at high temperatures. The system then enters the "viscous" regime. Note that both the momentum relaxation time τ_m by the charged impurities and τ_{ee} are proportional to $\varepsilon_F \propto \sqrt{n}$. Therefore, l_m/l_{ee} has a weak dependence on n, and the viscous regime appears in a wide range of n. On the other hand, the temperature dependence is different between l_m and l_{ee}. While l_m decays slowly (slower than T^{-1}) with increasing temperature, l_{ee} decays quickly as T^{-2}. The viscous regime $l_{ee} < l_m$ appears at high temperatures typically above 100 K in a clean graphene device. Electron-phonon scattering length l_{e-p} induced by LA phonons is proportional to T^{-1}, decaying slower than l_{ee} for increasing temperature. Therefore, scattering by phonons does not become dominant over the electron-electron scattering and the viscous regime persists even close to the room temperature. This is in contrast with conventional semiconductors, where the viscous transport can be observed only at low temperatures ($<\sim$30 K for HEMT).

The viscous flow can lead to local reversal of the current direction (Levitov and Falkovich, 2016; Bandurin et al., 2016). When an electric current is injected from a narrow constriction, current vortices appear near the constriction (see Fig. 6). The size of the vortices is characterized by $D_\nu = \sqrt{\nu\tau_m}$, which is determined by the viscosity $\nu \approx (1/2)v_F^2\tau_{ee}$. Such a vortex induces a voltage drop at the position near the constriction, which is also interpreted as a hydrodynamic electron pump (Govorov and Heremans, 2004). D_ν reaches submicron scale around the room temperature. Generally, electron transport for $l_{ee} \ll l_m$ is described by the following hydrodynamic equations:

$$\nabla \cdot \boldsymbol{j}(\boldsymbol{r}) = 0$$

$$\frac{\sigma_0}{e}\nabla\phi(\mathbf{r}) + D_\nu^2\nabla^2\boldsymbol{j}(\boldsymbol{r}) - \boldsymbol{j}(\boldsymbol{r}) = 0, \tag{43}$$

where $\boldsymbol{j}(\boldsymbol{r})$ is the current density, $\phi(\mathbf{r})$ is the electrostatic potential, and σ_0 is the Drude-like bare conductivity. The vorticity defined as

$$\boldsymbol{\omega}(\boldsymbol{r}) \equiv n^{-1}\nabla \times \boldsymbol{j}(\mathbf{r})$$

can be used to rewrite the hydrodynamic equation

$$\boldsymbol{j}(\boldsymbol{r}) = \frac{\sigma_0}{e}\nabla\phi(\mathbf{r}) - nD_\nu^2\nabla \times \boldsymbol{\omega}(\boldsymbol{r}), \tag{44}$$

which leads to $\omega_z(\boldsymbol{r}) = D_\nu^2\nabla^2\omega_z(\boldsymbol{r})$, i.e., exponential decay of the vorticity over the length scale of D_ν.

The hydrodynamic electron pump had been observed for a two-dimensional electron gas on a GaAs/AlGaAs heterostructure by injecting a current jet through a quantum point contact at low temperatures (Taubert et al., 2010). However, it appears more

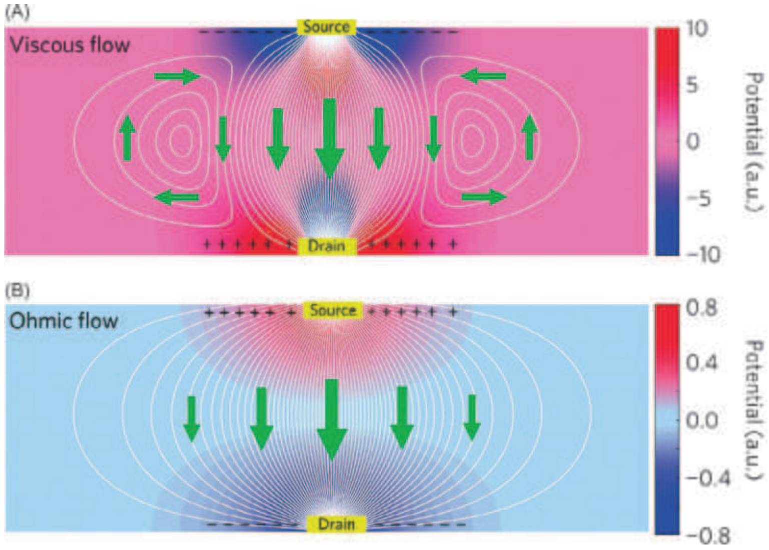

Fig. 6 Current flow in the viscous (fluid transport) regime (a) and ohmic (particle transport) regime (b). White lines show current streamlines, colors show electrical potential, and arrows show the direction of current. Vorticities are generated for the viscous flow, which leads to the negative nonlocal voltage. From Levitov L and Falkovich G (2016) Electron viscosity, current vortices and negative nonlocal resistance in graphene. *Nature Physics* 12: 672–676.

robustly in graphene in a much wider range of the temperature. The voltage drop near the current jet is observed in the nonlocal transport when the distance L between the voltage probe contact and the current injection contact is less than or comparable with D_ν. Bandurin et al. observed this voltage drop using a Hall bar device with $L = 1$ μm for the temperature between $\sim$100 K and $\sim$250 K (Bandurin et al., 2016). The result agrees with the behavior expected from Eq. (43).

An even more remarkable phenomenon in the viscous regime is the "superballistic" flow (Guo et al., 2017) through a short constriction observed by Krishna Kumar and coworkers (Krishna Kumar et al., 2017). The conductance $G = G_{\rm sh} + G_\nu$ in the viscous regime is enhanced from the Sharvin formula $G_{\rm sh} = 4e^2 w\sqrt{\pi|n|}/(h\pi)$ for non-interacting electrons by $G_\nu = e^2 w^2 v_F\sqrt{\pi|n|}/(32\hbar\nu)$, if the width w of the constriction is larger than l_{ee}. This enhancement of the conductance is attributed to the additional contribution of slow-moving fluid near the edges of the constriction. The unusual w^2 scaling of the viscous conductance G_ν was observed at high temperatures around 100 K (Krishna Kumar et al., 2017).

At the charge neutrality, carriers in clean graphene become the electron-hole plasma known as the Dirac fluid (Müller and Sachdev, 2008; Müller et al., 2009; Crossno et al., 2016; Gallagher et al., 2019). The Dirac fluid of graphene serves as the experimental model for high energy physics such as the black hole and quark-gluon plasma. The particle scattering time is given by $\tau_{ee} \sim \hbar/(k_B T)$, known as the Planckian time, the shortest possible timescale for particles to relax. Note that the Planck time in the Planck units is defined as $t_p = \sqrt{\hbar G/c^5}$ using the gravitational constant G and the speed of light c. Using the Planck temperature $T_p = \sqrt{\hbar c^5/\left(G k_B^2\right)}$, the Planck time can be rewritten as $t_p = \hbar/(k_B T_p)$.

The residual carrier density at the charge neutral point should be made smaller than the density of thermally excited carriers to realize the Dirac fluid. The viscous flow of the graphene Dirac fluid was observed recently by imaging the current flow through graphene channels using the scanning quantum spin magnetometer of nitrogen vacancy centers in diamond at room temperature (Ku et al., 2020). When the width w of the channel is smaller than l_m, the current density concentrates more around the center of the channel than close to the edges. From its profile, it was confirmed that the scattering rate is close to that of the ideal Planckian limit.

Conclusion

Fundamental transport properties of graphene have been revealed both experimentally and theoretically. High-mobility graphene devices exhibit unique ballistic transport while the main source of carrier scattering in graphene is charged impurities at low temperatures. At high temperatures, electron-electron scattering becomes significant in clean graphene devices, and carriers behave as fluids. Topological valley transport also occurs in graphene when the inversion symmetry is broken. All these properties have been experimentally confirmed. Based on the obtained fundamental transport properties, novel functional devices are being developed. Graphene can also be used in combination with other materials in van der Waals heterostructures.

While most of the properties are now understood, there are still some ongoing controversies. These include topological transport in the gapped states in the presence of disorder. Recent experimental and theoretical works have pointed out contribution of unwanted edge transport in the nonlocal transport experiment. Further study should address microscopic picture of the topological transport in future.

References

Adam S, Hwang EH, Galitski VM, and Das Sarma S (2007) A self-consistent theory for graphene transport. *Proceedings. National Academy of Sciences. United States of America* 104(18): 392.

Aharon-Steinberg A, et al. (2021) Long-range nontopological edge currents in charge-neutral graphene. *Nature* 593: 528–534.

Ando T (2006) Screening effect and impurity scattering in monolayer graphene. *Journal of the Physical Society of Japan* 75: 074716.

Ando T (2015a) Theory of valley hall conductivity in graphene with gap. *Journal of the Physical Society of Japan* 84: 114705.

Ando T (2015b) Theory of valley hall conductivity in bilayer graphene. *Journal of the Physical Society of Japan* 84: 114704.

Ando T, Fowler AB, and Stern F (1982) Electronic properties of two-dimensional systems. *Reviews of Modern Physics* 54: 437.

Bandurin DA, et al. (2016) Negative local resistance caused by viscous electron backflow in graphene. *Science* 351: 1055–1058.

Bolotin KI, et al. (2008) Temperature-dependent transport in suspended graphene. *Physical Review Letters* 101: 096802.

Castro Neto AH, et al. (2009) The electronic properties of graphene. *Reviews of Modern Physics* 81: 109.

Cheianov VV, Falko V, and Altshuler BL (2007) The focusing of electron flow and a veselago lens in graphene p-n junctions. *Science* 315: 1252.

Chen S, et al. (2016) Electron optics with p-n junctions in ballistic graphene. *Science* 353: 1522.

Craciun MF, et al. (2011) Tuneable electronic properties in graphene. *Nano Today* 6: 42–60.

Crossno J, et al. (2016) Observation of the Dirac fluid and the breakdown of the Wiedemann–Franz law in graphene. *Science* 351: 1058–1061.

Das Sarma S, et al. (2011) Electronic transport in two-dimensional graphene. *Reviews of Modern Physics* 83: 407.

Dean C, et al. (2010) Boron nitride substrates for high-quality graphene electronics. *Nature Nanotechnology* 5: 722–726.

Du X, et al. (2008) Approaching ballistic transport in suspended graphene. *Nature Nanotechnology* 3: 491–495.

Gallagher P, et al. (2019) Quantum-critical conductivity of the Dirac fluid in graphene. *Science* 364: 158–162.

Geim A and Grigorieva I (2013) Van der Waals heterostructures. *Nature* 499: 419–425.

Giubileo F and Di Bartolomeo A (2017) The role of contact resistance in graphene field-effect devices. *Progress in Surface Science* 92: 143–175.

Gorbachev RV, et al. (2014) Detecting topological currents in graphene superlattices. *Science* 346: 448–451.

Govorov AO and Heremans JJ (2004) Hydrodynamic effects in interacting fermi electron jets. *Physical Review Letters* 92: 026803.

Guo H, et al. (2017) Higher-than-ballistic conduction of viscous electron flows. *Proceedings of the National Academy of Sciences of the United States of America* 114: 3068–3073.

Hwang EH and Das Sarma S (2007) Dielectric function, screening and plasmons in 2D graphene. *Physical Review B* 75: 205418.

Hwang EH and Das Sarma S (2008) Acoustic phonon scattering limited carrier mobility in two-dimensional extrinsic graphene. *Physical Review B* 77: 115449.

Katsnelson M, Novoselov K, and Geim A (2006) Chiral tunnelling and the Klein paradox in graphene. *Nature Physics* 2: 620–625.

Kharitonov M (2012) Canted antiferromagnetic phase of the $\nu = 0$ quantum hall state in bilayer graphene. *Physical Review Letters* 109: 046803.

Kirczenow G (2015) Valley currents and nonlocal resistances of graphene nanostructures with broken inversion symmetry from the perspective of scattering theory. *Physical Review B* 92: 125425.

Krishna Kumar R, et al. (2017) Superballistic flow of viscous electron fluid through graphene constrictions. *Nature Physics* 13: 1182–1185.

Ku MJH, et al. (2020) Imaging viscous flow of the Dirac fluid in graphene. *Nature* 583: 537–541.

Lensky YD, et al. (2015) Topological valley currents in gapped dirac materials. *Physical Review Letters* 114: 256601.

Levitov L and Falkovich G (2016) Electron viscosity, current vortices and negative nonlocal resistance in graphene. *Nature Physics* 12: 672–676.

Marmolejo-Tejada JM, et al. (2018) Deciphering the origin of nonlocal resistance in multiterminal graphene on hexagonal-boron-nitride with ab initio quantum transport: Fermi surface edge currents rather than Fermi sea topological valley currents. *Journal of Physics: Materials* 1: 015006.

McCann E (2006) Asymmetry gap in the electronic band structure of bilayer graphene. *Physical Review B* 74: 161403(R).

McCann E (2023) Monolayer and bilayer graphene. In: Aoki H (ed.) *Encyclopedia of Condensed Matter Physics*, 2nd ed. Amsterdam: Elsevier Inc.

Miyazaki H, et al. (2010) Influence of disorder on conductance in bilayer graphene under perpendicular electric field. *Nano Letters* 10: 3888–3892.

Morozov SV, et al. (2008) Giant intrinsic carrier mobilities in graphene and its bilayer. *Physical Review Letters* 100: 016602.

Müller M and Sachdev S (2008) Collective cyclotron motion of the relativistic plasma in graphene. *Physical Review B* 78: 115419.

Müller M, Schmalian J, and Fritz L (2009) Graphene: A nearly perfect fluid. *Physical Review Letters* 103: 025301.

Noro M, Koshino M, and Ando T (2010) Theory of transport in graphene with long-range scatterers. *Journal of the Physical Society of Japan* 79: 094713.

Novoselov KS, et al. (2004) Electric field effect in atomically thin carbon films. *Science* 306: 666–669.

Novoselov K, Geim A, Morozov S, et al. (2005) Two-dimensional gas of massless Dirac fermions in graphene. *Nature* 438: 197–200.

Oostinga J, et al. (2008) Gate-induced insulating state in bilayer graphene devices. *Nature Materials* 7: 151–157.

Shimazaki Y, et al. (2015) Generation and detection of pure valley current by electrically induced Berry curvature in bilayer graphene. *Nature Physics* 11: 1032–1036.

Shon NH and Ando T (1998) Quantum transport in two-dimensional graphite system. *Journal of the Physical Society of Japan* 67: 2421–2429.

Shytov AV, Rudner MS, and Levitov LS (2008) Klein backscattering and Fabry–Perot interference in graphene heterojunctions. *Physical Review Letters* 101: 156804.

Stauber T, Peres NMR, and Guinea F (2007) Electronic transport in graphene: A semiclassical approach including midgap states. *Physical Review B* 76: 205423.

Sui M, et al. (2015) Gate-tunable topological valley transport in bilayer graphene. *Nature Physics* 11: 1027–1031.

Tan Y-W, et al. (2007) Measurement of scattering rate and minimum conductivity in graphene. *Physical Review Letters* 99: 246803.

Tanaka M, et al. (2021) Charge neutral current generation in a spontaneous quantum hall antiferromagnet. *Physical Review Letters* 126: 016801.

Tanaka M, et al. (2022) Temperature-induced phase transitions in the correlated quantum Hall state of bilayer graphene. *Physical Review B* 105: 075427.

Taubert D, et al. (2010) Electron-avalanche amplifier based on the electronic Venturi effect. *Physical Review B* 82: 161416(R).

Wallace PR (1947) The band theory of graphite. *Physics Review* 71: 622.

Weitz RT, et al. (2010) Broken-symmetry states in doubly gated suspended bilayer graphene. *Science* 330: 812.

Woods CR, et al. (2014) Commensurate-incommensurate transition in graphene on hexagonal boron nitride. *Nature Physics* 10: 451–456.

Xiao D, Yao W, and Niu Q (2007) Valley-contrasting physics in graphene: Magnetic moment and topological transport. *Physical Review Letters* 99: 236809. (2007).

Yamamoto M, et al. (2015) Valley hall effect in two-dimensional hexagonal lattices. *Journal of the Physical Society of Japan* 84: 121006.

Young A and Kim P (2009) Quantum interference and Klein tunnelling in graphene heterojunctions. *Nature Physics* 5: 222–226.

Zhang Y (2023) Experimental aspects of graphene. In: Aoki H (ed.) *Encyclopedia of Condensed Matter Physics*, 2nd ed. Amsterdam: Elsevier Inc.

Zhang Y, Tan YW, Stormer H, et al. (2005) Experimental observation of the quantum Hall effect and Berry's phase in graphene. *Nature* 438: 201–204.

Further reading

Aoki H and Dresselhaus M (eds.) (2014) *Physics of Graphene*. Springer.

Das Sarma S, Geim AK, Kim P, and MacDonald AH (eds.) (2007) *Exploring Graphene: Recent Research Advances, A Special Issue of Solid State Communications*. In: vol. 143. New York: Elsevier.

Enoki T and Ando T (eds.) (2019) *Physics and Chemistry of Graphene: Graphene to Nanographene*, 2nd ed. Pan Stanford Publishing.

Geim AK and Novoselov KS (2007) The rise of graphene. *Nature Materials* 6: 183.

Peres NMR (2010) Colloquium: The transport properties of graphene: An introduction. *Reviews of Modern Physics* 82: 2673.

van der Waals heterostructures

Pablo Solís-Fernández[a] **and Hiroki Ago**[a,b], [a]Global Innovation Center (GIC), Kyushu University, Fukuoka, Japan; [b]Interdisciplinary Graduate School of Engineering Science, Kyushu University, Fukuoka, Japan

© 2024 Elsevier Ltd. All rights reserved.

Introduction 310
Overview 311
van der Waals layered materials and their heterostructures 311
Assembly and growth of vdW heterostructures 312
Clean interlayer interfaces 313
Moiré patterns and twistronics 314
Superlubricity and self-rotation of layers 315
Atomic reconstruction 316
Twisted bilayer graphene and superconductivity 317
Graphene/hBN heterostructures 319
TMD heterostructures 319
2D Heterostructures by intercalation 322
Characterization 323
Conclusion 327
Acknowledgments 327
References 327

Abstract

van der Waals (vdW) materials are composed of weakly bonded two-dimensional (2D) layers that can be easily isolated and re-stacked into heterostructures composed of different 2D materials. The vdW heterostructures add an increased range of functionalities to the variety of existing 2D materials, owing to the large variety of heterostructures that can be engineered. The properties of heterostructures can be further tuned by controlling the twist angle, the stacking order, or the contents of the interlayer spacing, among other things. All these make of the vdW heterostructures potential candidates for a plethora of applications for novel electronic and optoelectronic devices.

Key points

- van der Waals heterostructures are made of weakly-bonded 2D layers.
- Heterostructures can be assembled layer by layer.
- The weak interlayer interaction and the absence of dangling bonds allow a high flexibility for the stacks, without the usual restrictions for non-layered materials.
- But albeit weak, the interaction between adjacent layers can have an strong impact in their atomic structures and band structures.
- Overall, the physical properties of the heterostructures arise from the interaction between the different layers, giving rise to more complex behaviors than in isolated 2D materials.
- Among the different parameters that control the properties of the heterostructures are the relative orientation of the layers, their specific sequence and thickness, and the interlayer distance.
- The well-defined interlayer space can also be used to control the properties of the heterostructures by the intercalation of different species.
- The emergence of unconventional superconductivity and strong electron correlations, topological conducting channels, and moiré interlayer excitons are a few of the interesting phenomena observed in heterostructures so far.

Introduction

van der Waals (vdW) materials are composed of stacked atomically thin layers bonded together by weak vdW interactions, but with strong covalent bonding within each layer. The weak bonding between adjacent layers allows to isolate individual layers, having thicknesses that range from single- to a few-atoms depending on the specific material. The quantum confinement due to the decreased thickness in these layers has a profound impact on their electronic, optical, and magnetic properties, which can largely differ from that of their bulk counterpart and are hence considered as two-dimensional (2D) materials. In 2004 graphene was

https://doi.org/10.1016/B978-0-323-90800-9.00115-3

obtained from graphite, becoming the first 2D material isolated from its corresponding bulk crystal and leading to the development of the 2D materials research field (Novoselov et al., 2004). Since then, the increased interest in these ultimately thin materials has allowed to continuously expand the library of available 2D vdW materials. The 2D materials discovered so far encompass a broad range of optical and electronic properties, making them interesting candidates for several applications.

The nature of the vdW forces and the absence of dangling bonds in the surface of the 2D materials allow to stack layers of different materials into heterostructures, without the constraints existing for non-layered materials (Koma, 1992). It is thus possible to produce heterostacks with arbitrary kinds of layers and with any relative orientations between them. Ultimately, the properties of the heterostructures depend on both the specific layers that compose them, as well as on their relative orientation and on the interlayer distance. This provides unprecedented ways to finely tune the properties of the heterostructures that are not available for bulk materials. It was thus soon realized that the range of options provided by the 2D materials could be vastly expanded by their combination into different kinds of vdW heterostructures. But although weakly bonded, the adjacent layers conforming the heterostructure can strongly affect each other, experiencing structural changes and modifications in their band structures that must be considered and that originate many of the observed properties.

The first examples of vdW heterostructures involved the use of hexagonal boron nitride (hBN), with a structure similar to that of graphene, as a high-quality dielectric to improve the performance of graphene devices (Dean et al., 2010; Haigh et al., 2012). The amount of heterostructures studied since then has grown remarkably, including layers of 2D materials as graphene, hBN, different transition metal dichalcogenides (TMD), among others, and spanning a wide variety of mechanical, electrical, optical and chemical properties. The assembly methods have continuously improved, allowing to produce high quality heterostructures with virtually clean interlayer spaces. All these has led to the discovery of novel and unexpected phenomena, such as the superconductivity in certain heterostructures, along with the realization of functional devices that exploit the advantages of the vdW heterostructures. But despite all the progress, improvements in the fabrication and handling of heterostructures toward industrial scalability are still required.

Overview

van der Waals layered materials and their heterostructures

The vdW layered materials are composed by stacks of planar crystalline layers. Each of the layers is composed of covalently bonded atoms in the in-plane direction, while their surface is free of dangling bonds. Hence, the stacked layers are held together to each other only by the weak vdW interactions between adjacent layers. This structure of weak bonded layers makes vdW materials different from other 3D materials, and allows for the easy exfoliation of individual layers without causing them any structural damage. These isolated layers, known as 2D materials, are crystalline structures with either single- (e.g., in the case of graphene), or few-atom thickness (e.g., any TMD or bismuth strontium calcium copper oxide (BSCCO)). The currently existing 2D materials encompass the whole range of electronic properties, from superconductors (e.g., $NbSe_2$, BSCCO), metals (e.g., borophene, VS_2), semimetals (e.g., graphene, 1T-$TiSe_2$), half metals (e.g., 1 T-CrO_2), semiconductors with different sized gaps and band alignments (e.g., MoS_2, WS_2, InSe, black phosphorus), topological insulators (e.g., Bi_2Te_3) and insulators (e.g., hBN), ferromagnetic and antiferromagnetic 2D materials (e.g., CrI_3, $FePS_3$), and ferroelectric (e.g., SnSe). The most famous member of the 2D family is graphene, consisting of a honeycomb of sp^2-bonded C atoms. Graphene is a semimetallic material, with conical valence and conduction bands for low energies that cross at the corners of the Brillouin zone (Dirac points). The linear dependence between the energy and the momentum results in the charge being carried by massless Dirac quasiparticles, described by the relativistic Dirac equation and moving at the Fermi velocity in graphene ($\sim 10^6$ m/s). This results in graphene having exceptional electronic properties, including the highest mobilities reported so far for any known material.

High quality flakes of the different 2D materials can be easily obtained by mechanical exfoliation from their corresponding bulk crystal, which in general produces flakes with very high qualities. However, this is a low yield method that only provides flakes with limited lateral sizes. Synthesis for the direct growth of 2D materials, such as by chemical vapor deposition (CVD), molecular beam epitaxy (MBE) or vapor-phase epitaxy based methods, are being continuously developed and improved (Cai et al., 2018). The advances realized in the growth of vdW materials have made possible the obtention of several of the known 2D materials at wafer-scale sizes, and with qualities that in certain cases can match those of their mechanically exfoliated counterparts. The methods for the growth of graphene and of some transition dichalcogenides (TMD) are specially developed, allowing to synthesize them with a good control of the quality and uniformity. Existing methods can in certain cases also provide some control in the thickness of the 2D materials, ranging from single to few layers, although the uniformity usually decreases for crystals thicker than one layer. But despite the considerable advances mentioned, improvements in the synthesis and the processing of 2D materials are still necessary to meet the requirements for large-scale practical implementations.

The absence of dangling bonds in the surface of the 2D materials, together with the universality of the vdW forces, ensures the opportunity to stack layers of 2D materials into heterostructures without the usual restrictions for other materials. It is thus possible to stack layers of completely different vdW materials without restrictions in their structure, lattice constant or relative orientation, and with well-defined interfaces (Koma, 1992; Liu et al., 2021). This, along with the variety of existing 2D materials, provides a great flexibility to realize vdW heterostructures with completely different characteristics and properties. When layers are assembled into heterostructures, the coupling between them induces complex interlayer interactions, enhancing the hopping of carriers and the charge redistribution between layers, and causing lattice reconstructions. Hence, the properties of the heterostructure cannot be explained by a simple superposition of the properties of each layer. As will be seen below, the properties of the heterostructures depend on the specific sequence of the stacked layers, their thickness, and their relative orientation.

To highlight the large impact that stacking of 2D materials can have in their properties, the special case of vdW heterostructures comprised of layers from the same material can be considered. In the case of bilayer graphene (BLG), the band structure differs from that of the single layer graphene (SLG). The energy dispersion of AB-stacked BLG is parabolic, with the charge carriers being massive Dirac fermions, and the possibility to open a bandgap by applying a vertical electrical field. And as will be shown below the band structure of BLG is very sensitive to the twist angle between the layers, with the most spectacular effect being the emergence of unconventional superconductivity for low twist angles. It is also worth mentioning the case of stacks of black phosphorus (phosphorene) layers. Phosphorene is a semiconducting allotrope of P with a direct bandgap that decreases with the thickness, from ~1.5 eV for one layer to ~0.3 eV for bulk black phosphorous. This tunable bandgap and the relatively large mobilities that possess ($\sim 1000\ cm^2 V^{-1} s^{-1}$) make of phosphorene an interesting material with properties bridging those of graphene and TMDs. However, phosphorene is easily degraded by oxygen, water, and light, thus requiring handling in controlled environments, and a proper encapsulation and/or surface passivation of the final devices.

Assembly and growth of vdW heterostructures

The most extended way to fabricate vdW heterostructures consist in assembling them by stacking thin flakes exfoliated from bulk materials (Frisenda et al., 2018). The technique has improved through the years, with the current preferred methods relying on the vdW layer-by-layer pick up (Fig. 1). In these, a 2D flake (generally hBN) is mounted on a polypropylene carbonate (PPC)/polymeric stamp and then used to assemble the heterostructure by the successive pick-up of flakes that were previously exfoliated onto SiO_2 substrates. The strong adhesion between the layers of the different vdW materials is key here for the success of the transfer. The main advantage of this layer-by-layer pick up is that the trapped interlayer contamination is significantly reduced, as the layers of the heterostructure are never in direct contact with any polymer during the whole assembly process. Another benefit is the possibility to perform the assembly in an inert ambient in order to produce heterostacks of air-sensitive 2D materials, such as phosphorene, encapsulated by hBN that eventually protect them from damage from air exposure. The *layer-by-layer* assembly methods also provide a way to produce heterostacks with controlled relative twisting of adjacent layers, provided that the orientation of each flake has been previously determined. Control of the twist is especially precise in the assembly variant known as *tear-and-stack* (Fig. 2), in which a part of a single crystal flake is picked by the hBN/stamp (*tear*), rotated the desired angle, and then transferred onto the rest of the flake (*stack*) (Kim et al., 2016). This method allows to assemble vdW stacks with sub-degree accuracies in the twist angle and without the need to determine the crystal orientation of the original flake.

The downside of the existing assembly methods is the low yield and the limitation to small areas, which is unsuitable for large-scale processing. The obtention of 2D crystals by mechanical exfoliation results in very sparse flakes located at random positions and of small areas, making the task to identify and process them into heterostructures extremely difficult. To improve this, progress is being made in automating the assembly with the aid of robotic systems (Masubuchi et al., 2018). These systems can autonomously find exfoliated flakes with the required thickness and assemble them into the specified heterostructures. The use of such systems substantially increases the assembly speeds compared to manual methods. But although suitable for small-scale research studies, the problem of the small size of the exfoliated flakes persists. To achieve the large-scale assembly of vdW

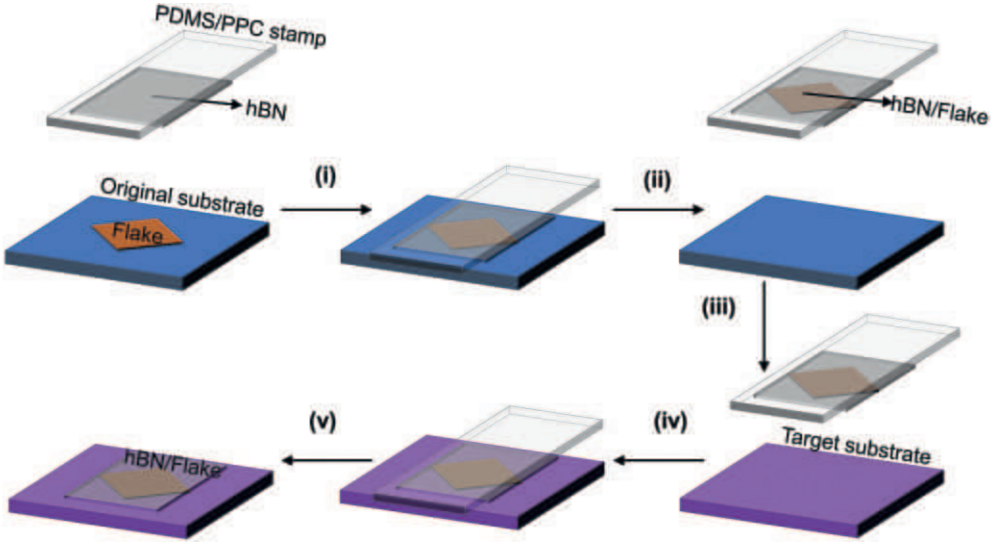

Fig. 1 Schematics of the vdW *layer-by-layer pick up* technique to fabricate heterostructures. An hBN mounted in a PPC/polymer stamp (i) is used to pick up a flake previously exfoliated on a SiO_2 substrate (ii). The process can be repeated, and eventually the heterostructure is brought to contact with the target substrate (iii, iv) and the stamp is removed, leaving the heterostructure on the new substrate (v).

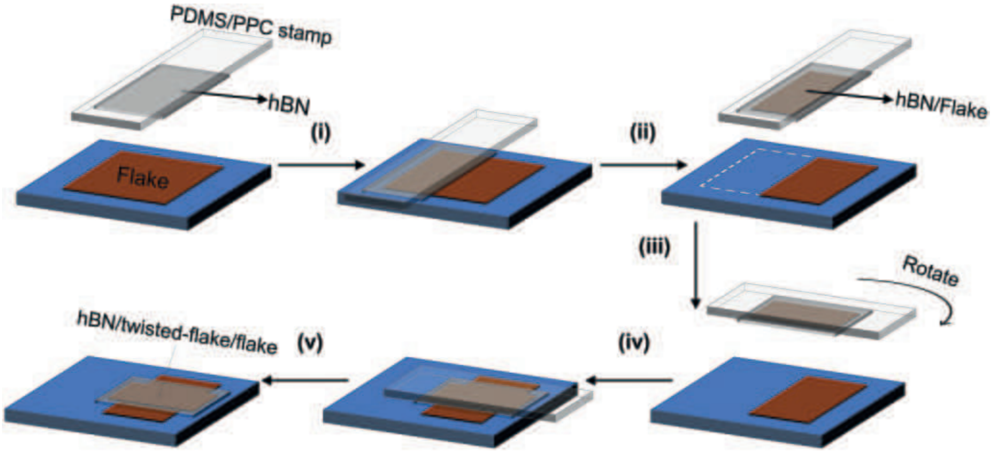

Fig. 2 Schematics of the *tear-and-stack* technique to fabricate heterostructures with controlled twist angles. In this case, the hBN only picks part of the flake (i, ii), while the rest remains on the substrate. The hBN is then rotated to the desired twist angle (iii), and brought to contact with the remaining part of the flake (iv, v).

heterostructures, alternatives to the mechanically exfoliation are required. As mentioned in the previous section, scalable methods to produce and process most of 2D materials are being continuously developed. This is crucial for the practical implementation of heterostructures at industrial-scale processes. Other than the availability of large areas, the use of bottom-up synthesized 2D materials possesses other advantages, such as the possibility to control the crystal orientation during the growth (e.g., for CVD and MBE growths on certain substrates). On the other hand, the crystal quality does not always match that achieved by mechanical exfoliation yet. Also, the assembly techniques for large areas are still not as developed as those for small crystals, although methods specialized in wafer-scale sizes and rigid substrates are being actively developed (Quellmalz et al., 2021).

The next step to improve the scalability is the direct growth of the vdW heterostructures, which can avoid the difficulties arising during the assembly by artificial stacking. The epitaxial growth of heterostructures of van der Waals layered materials, with thickness down to a single layer, was already reported in pioneering works in the last decades of the past century (Koma et al., 1984; Ueno et al., 1990; Koma, 1992). The direct growth methods can also potentially result in cleaner layer interfaces by avoiding the trapped contamination originated during the assembly. However, the progress here is not as developed as for the growth of 2D materials, as processes involved in the direct synthesis of heterostructures are usually more complex. This is caused in part by the different growth conditions required for each of the different materials conforming the heterostructure. These different growth conditions and the instability of some 2D materials can also result in damage of one of the materials during the synthesis of the rest. Moreover, the uniformity of the heterostructures that have been grown so far are usually low and limited to small sizes. The control of the stacking angle is also more difficult when directly growing heterostructures. Whereas the assembly methods easily allow to produce heterostructures with arbitrary stacking orders, the relative orientation of the layers in direct growths tends to correspond to the most stable stackings. Thus, as-grown TMD/TMD heterostructures commonly form 0° and 60° twist angles, for BLG the most stable configurations are 0° (or AB) and 30°, while graphene/hBN heterostructures tend to be aligned. But although still limited, methods already exist for the direct growth of vdW heterostructures. The most paradigmatic case is the growth of TMD heterostructures in which the layers differ only by a chemical element, i.e., when they share the same chalcogen ($MX_2/M'X_2$) or the same metal (MX_2/MX'_2). The vapor phase growth of such TMD heterostructures, e.g. of WS_2/MoS_2, is made possible by carefully selecting the precursors and the temperatures (Gong et al., 2014). Transition metal oxides (TMO), such as WO_3 or MoO_3, are commonly used as precursors for the vapor phase growth of TMDs. This enables the growth of TMO/TMD heterostacks by controlling the synthesis process (Zheng et al., 2019). The growth of heterostructures can sometimes involve two-step approaches in which one of the layers is grown first. This first layer usually serves as a template for the growth of the next layers, by either slightly adjusting the growth conditions (e.g., the precursors or the temperature reaction) or by a completely different growth procedure (Solís-Fernández et al., 2017). Among the most used template layers are graphene and hBN, for which the growth of several heterostructures have been documented, such as hBN/graphene (or graphene/hBN) and of hBN or graphene with different TMDs. The template layer can also be engineered to promote the growth of the subsequent layers, for example by the controlled introduction of defects. Other than to facilitate the growth of the heterostructure, this also provides a way to selectively nucleate the second layer at the desired positions and obtain arbitrary arrangements (Li et al., 2020). Finally, it is worth mentioning that besides from the vertical heterostructures covered here, there are also direct growth methods for growing in-plane heterostructures with 1D interfaces (Solís-Fernández et al., 2017). This kind of heterostructures, which are interesting to produce in-plane devices, cannot be accomplished by artificial assembly methods.

Clean interlayer interfaces

One important factor in the fabrication of high-quality vdW heterostructures is the obtention of well-defined and free of contamination interfaces between adjacent layers. As an example, the mobility of hBN/SLG/hBN devices can increase up to an order of magnitude when the interfaces between the layers are clean. As previously mentioned, the *layer-by-layer pick up* assembly

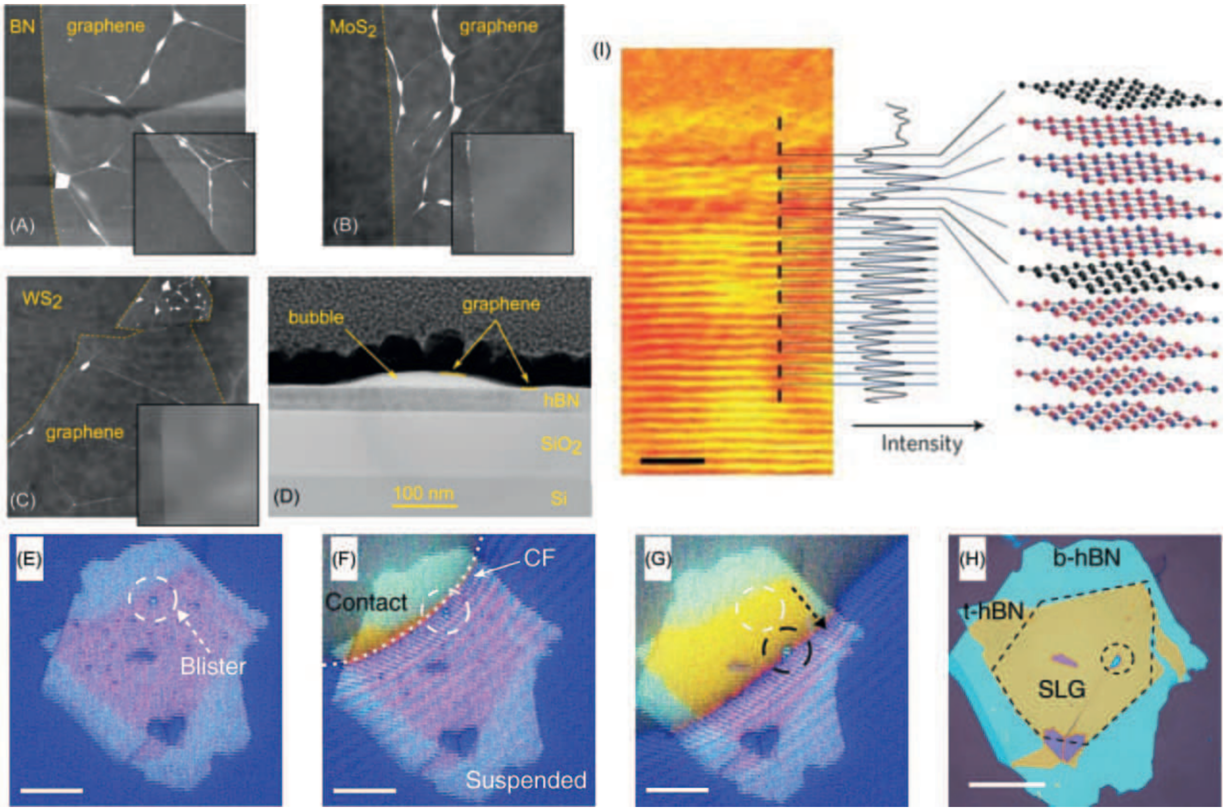

Fig. 3 (A–C) AFM images of graphene on hBN (A), MoS$_2$ (B) and WS$_2$ (C), showing the presence of bubbles and wrinkles resulting from the aggregation of the interlayer contamination due to the self-cleaning mechanism. (D) Cross-sectional TEM image of a graphene/hBN heterostacks along one of the contamination bubbles. (E–H) Mechanically pushing the contamination bubbles in a hBN/graphene/hBN heterostacks during the transfer to produce cleaner interfaces.
(i) Cross-sectional STEM image and the corresponding schematics of a clean SLG/hBN/SLG/hBN heterostructure. The graphene layers are evidenced in the averaged intensity profile along the dashed line. The lack of contamination is evidenced by the interlayer spacing between the SLG and hBN regions being indistinguishable from the interlayer distance of bulk hBN within the experimental accuracy. (A–D) Adapted with permission Kretinin AV et al. (2014) Electronic properties of graphene encapsulated with different two-dimensional atomic crystals. *Nano Letters*, 14: 3270–3276. Copyright 2014 American Chemical Society. (E–H) Reproduced with permission Purdie DG et al. (2018). Cleaning interfaces in layered materials heterostructures. *Nature Communications* 9: 5387. Copyright 2018, The Authors.
(I) Reproduced with permission Haigh SJ et al. (2012) Cross-sectional imaging of individual layers and buried interfaces of graphene-based heterostructures and superlattices. *Nature Materials* 11: 764–767. Copyright © 2012, Nature Publishing Group.

methods significantly decrease the amount of contamination as compared with other transfer techniques, even when the assembly is performed in air at ambient conditions. Interestingly, the atomically flat surface of the layers and their mutual interactions produces a *self-cleansing* of the interface (Haigh et al., 2012; Kretinin et al., 2014; Novoselov et al., 2016). The contaminants existing in the interlayer space, mainly composed of hydrocarbons, water and air, aggregate into bubbles due to the larger inter-layer affinity as compared with that of the layer-contaminant (Fig. 3A–D). The cleansing mechanism ensures that most of the interlayer area remains clean, allowing to obtain interlayer distances of the artificial stacks almost indistinguishable from those observed in natural crystals. Additional cleaning can be achieved by annealing the heterostructure, which increases the mobility of the contamination bubbles and allows them to further aggregate into larger ones or to escape from the edge of the heterostructure. Heating is especially effective during the last step of the *layer-by-layer* assembly when the assembled heterostack/stamp is brought into contact with the target substrate. The increased bubble mobility at high temperatures can be combined with a mechanical pushing of the bubbles, as seen in Fig. 3E–H, in which the bubbles in the heterostack (Fig. 3E) are being pushed away as the sample is carefully brought into contact with the substrate (Fig. 3F and G), leaving a nearly clean interface in most of the heterostack (Fig. 3H) (Purdie et al., 2018). The contamination bubbles can thus be pushed out of the active areas of devices during the transfer procedure, leading to virtually clean device stacks (Fig. 3I).

Moiré patterns and twistronics

The possibility to stack layers of 2D materials with arbitrary twist angles provides an additional degree of freedom to tune the band structure of the vdW heterostructures. A moiré pattern with a periodicity larger than the original lattice constants is formed when there is a lattice mismatch and/or a misalignment between adjacent layers in a vdW heterostructure. In most cases, the wavelength of the moiré superlattice can be expressed as

$$\lambda = (1+\delta)a/\sqrt{2(1+\delta)(1-\cos\theta)+\delta^2} \qquad (1)$$

for a twist angle θ and a lattice mismatch $\delta = a/b - 1$, where a, b are the lattice constants of the crystal layers. The expression can be approximated as $\lambda \approx a/\sqrt{\theta^2+\delta^2}$ for crystals with similar lattice constants ($\delta \ll 1$) and small twist angles, evidencing that long period superlattices are formed for small twist angles and crystals with similar lattice constants. For the case of no lattice mismatch (e.g., when stacking layers of the same material), the expression simplifies to $\lambda = a/\sqrt{2(1-\cos\theta)}$ ($\approx a/\theta^2$ for small twist angles). Fig. 4 shows scanning tunneling microscope (STM) and scanning transmission electron microscope (STEM) images of moiré patterns on twisted bilayer graphene (TBG) with different twist angles, evidencing the wavelength decrease with the twist angle (Lin et al., 2021b). The orientation of the moiré superlattice relative to the crystal lattices (ϕ) is given by $\tan\phi = -\sin\theta/((1+\delta)-\cos\theta)$.

The physical properties of vdW heterostructures are strongly dependent on the moiré superlattice. The interlayer separation and the band structure vary with the moiré superlattice. This allows to modify the optical and electrical properties of the heterostructure in novel ways, giving rise to a nascent research field known as twistronics. The occurrence of the moiré pattern causes a modulation of the interlayer coupling that results in a superlattice potential. This eventually induces the emergence of different properties in vdW heterostacks, including ferromagnetism, the occurrence of topological conducting channels, moiré excitons, and of unconventional superconductivity and strong electron correlations. Given their importance, the cases of low angle TBG and of twisted graphene/hBN heterostructures will be described in subsequent sections. The effects of the twist in interlayer excitons will also be explored in the section devoted to TMD heterostructures.

Superlubricity and self-rotation of layers

As discussed in the previous section, one of the factors defining the properties of vdW heterostructures is the relative orientation of the adjacent layers, or the twist angle. It is thus of paramount importance to control the twist angles with a great accuracy when assembling the heterostructures. However, the nature of vdW interlayer interactions resulting in clean interfaces and weakly bonded layers, allows the layers to both slide and self-rotate up to some extent when displaced from their equilibrium configuration, in order to attain a favorable stacking that minimizes the interlayer vdW energy.

States of ultra-low friction have been measured and predicted between layers of graphite, in a phenomenon coined as superlubricity Dienwiebel et al. (2004). In general, superlubricity can happen when two weakly bonded crystal surfaces are stacked in an

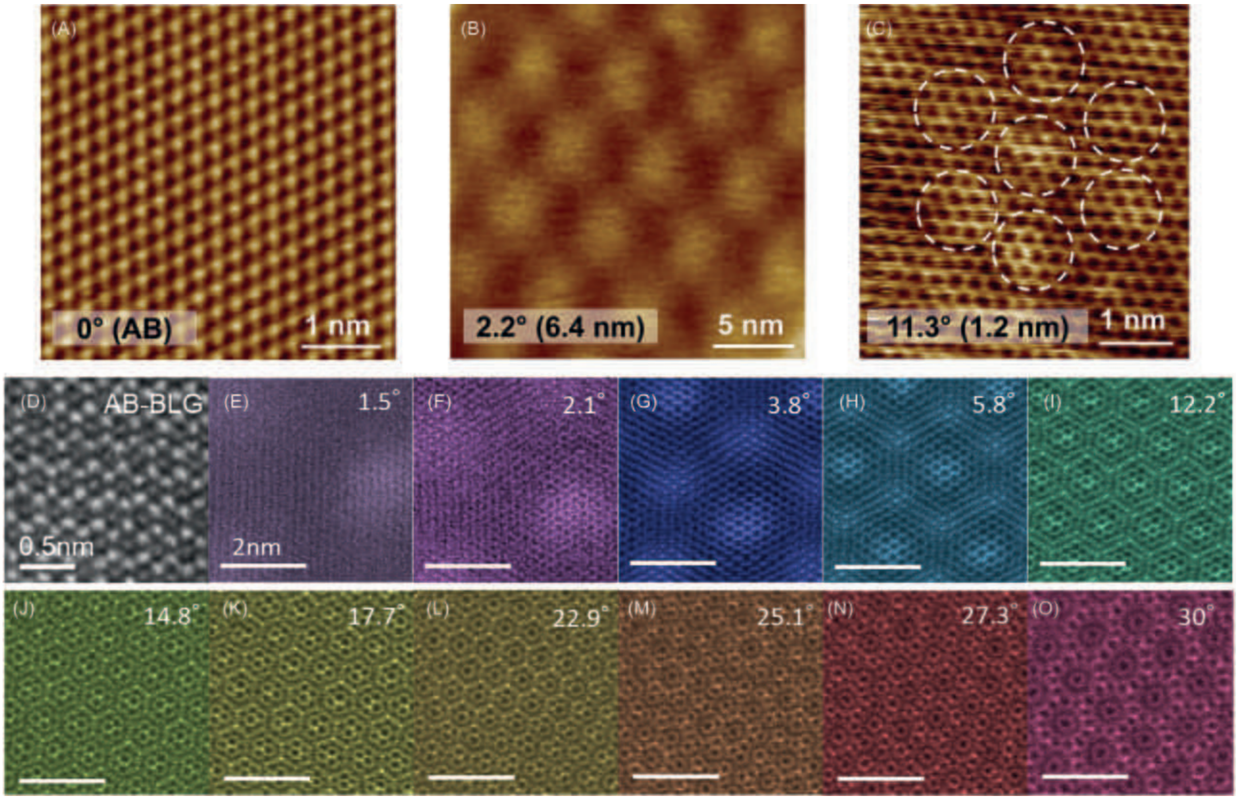

Fig. 4 Moiré patterns on TBG with different twist angles seen by STM (A–C) and STEM (D–O). The insets show both the twist angle and the moiré wavelength (in parenthesis) of each of the images. (D–O) Adapted with permission Lin Y-C, Motoyama A, Solís-Fernández P et al. (2021b) Coupling and decoupling of bilayer graphene monitored by electron energy loss spectroscopy. *Nano Letters* 21: 10386–10391. Copyright 2021 American Chemical Society.

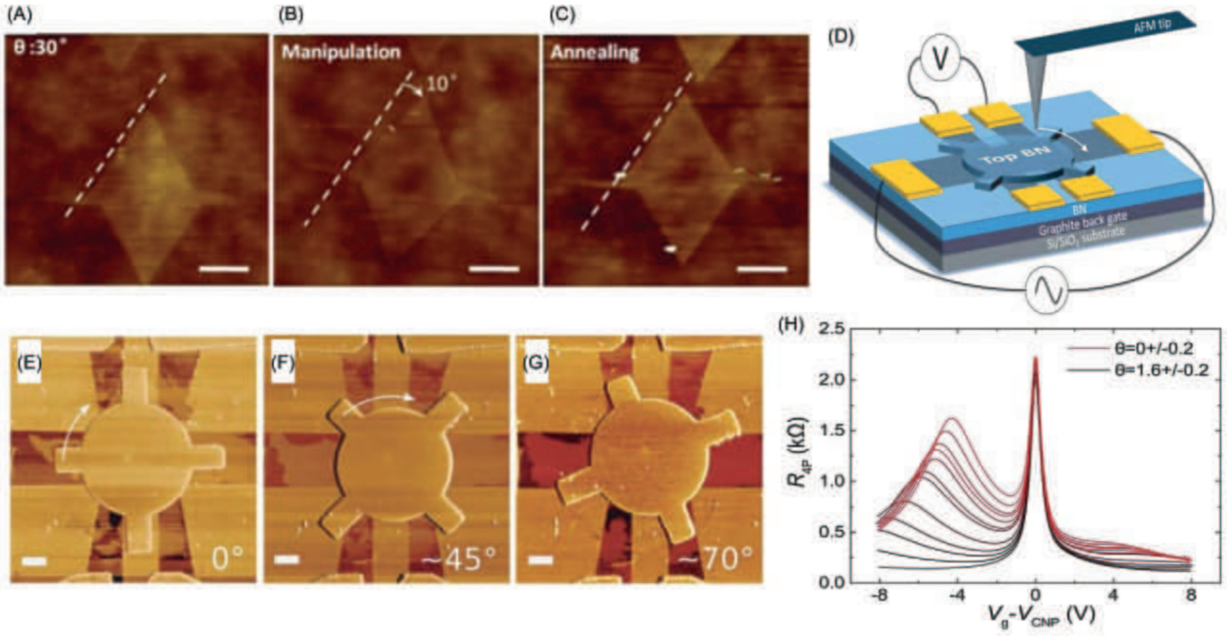

Fig. 5 (A–C) AFM images of a graphene flake on hBN. (A) The graphene is initially stacked at a stable configuration (30°) with respect to the hBN. (B) The low lubricity allows the manipulation of the flake with the AFM tip, inducing a rotation of ~10° that leaves the stack in an unstable configuration. (C) After annealing, the stack tends to relax to the stable configuration. (D) Schematic of a graphene device with an hBN cover that allows manipulating the relative twist angle using an AFM tip. (E–F) AFM images showing the hBN cover after controlled rotations. (H) Transfer curve of the graphene/hBN device for twist angles in the range 0° – 1.6°, with R_{4P}, V_g and V_{CNP} being the four probe resistance, the applied gate-voltage and the voltage of the charge neutrality point, respectively. Additional resistance peaks can be observed at low twist angles, ascribed to the emergence of superlattice Dirac points. (A–C) Reprinted with permission Wang D et al. (2016) Thermally induced graphene rotation on hexagonal boron nitride. *Physical Review Letters* 116: 126101. Copyright 2016 by the American Physical Society. (D–H) Reproduced from Ribeiro-Palau R et al. (2018) Twistable electronics with dynamically rotatable heterostructures. *Science* 361: 690–693.

incommensurable state, either due a relative rotation or to a displacement. This low friction allows for easy rotations and/or sliding between commensurate states (Fig. 5A–C). Such low friction regimes have for example been observed in the case of TBG stacks, of graphene/h-BN heterostacks, and of heterostacks of a TMD and graphene or h-BN. In the case of graphene/h-BN, rotations of over 10° and for crystals with sizes of up to few tens of microns can be observed upon annealing at temperatures over 100 °C, tending to produce the most stable stackings of 0° and 30° (Fig. 5A–C) (Wang et al., 2016; Woods et al., 2016). All this must be accounted when stacking layers, and attention must be paid to achieve the required twist angles. As an example, producing TBG with low stacking angles (which will be covered later) requires working at low temperatures and assembling the stack with a slightly larger angle than the final target angle. This is done to account for some relaxation to the preferred Bernal stacking even at room temperature. But although detrimental in most cases, the low friction between layers can be exploited to construct rotatable vdW heterostructures in which the characteristics can be finely tuned at demand by precise rotations (Fig. 5D–H) (Ribeiro-Palau et al., 2018).

Atomic reconstruction

Other than by self-rotation, the interlayer energy in vdW heterostructures can decrease by local atomic rearrangements. Atomic reconstruction in adjacent layers of vdW heterostructures can happen when either the layers have similar lattice constants, or when the twist angle is low for two similar layers. The moiré superlattice gradually varies across the surface in the absence of reconstruction (Fig. 6A). Although the vdW interactions between the layers are usually considered to be weak (generally a few meV per atom), they cannot be neglected for small twist angles. When the interlayer coupling is strong enough, the atoms of each layer can relocate to a new configuration that equilibrates the inter and intralayer forces (Fig. 6B), thus minimizing the stacking potential energy. This results in a commensurate-incommensurate transition and the formation of commensurate regions, either by small local shifts of the layers or by strain to adjust the different periodicities of the lattices. The commensurate regions are limited by sharp soliton boundaries that concentrate most of the deformation. Reconstructions have been experimentally observed in several kinds of heterostructures, including TBG, graphene/hBN, or in different TMDs heterostructures. The process of the reconstruction can be exemplified by the case of TBG represented in Fig. 6C–F (Carr et al., 2018; Yoo et al., 2019). For small twist angles a series of triangles can be seen in images from different experimental techniques (e.g., TEM and AFM), corresponding to alternating domains of almost perfect AB- and BA-stacking limited by sharp soliton boundaries. The contrast between the regions decreases as the twist angle increases, and for angles larger than ~1° the lattice commences to appear like a non-reconstructed rigid moiré

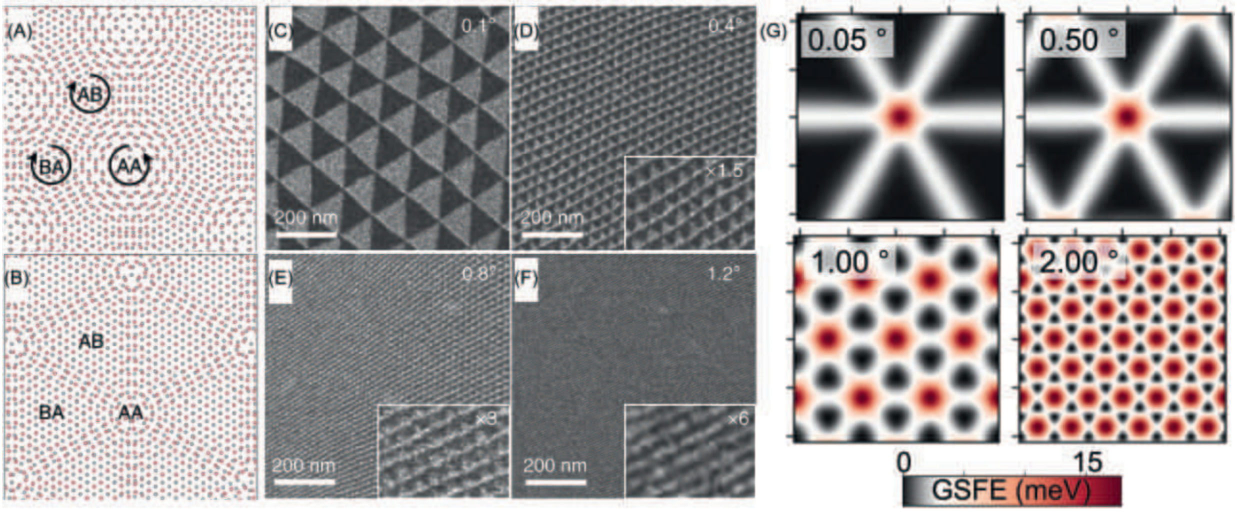

Fig. 6 (A, B) Schematic of TBG before (A) and after (B) the atomic reconstruction. (C–F) Dark-field TEM images of TBG with different twist angles. The triangles seen at lower angles correspond to the reconstructed AB and BA areas. The contrast between those regions weakens as the angle increases, and eventually linear fringes emerge, commonly observed in the absence of reconstruction. (g) Real space map of the calculated interlayer energy per unit cell of relaxed TBG for different incommensurate twist angles (the size of each area is 40×40 nm^2). (A–F) Reproduced with permission Yoo H et al. (2019) Atomic and electronic reconstruction at the van der Waals interface in twisted bilayer graphene. *Nature Materials* 18: 448. Copyright © 2019, Nature Publishing Group. (G) Reprinted with permission Carr S et al. (2018) Relaxation and domain formation in incommensurate two-dimensional heterostructures. *Physical Review B* 98: 224102. Copyright 2018 by the American Physical Society.

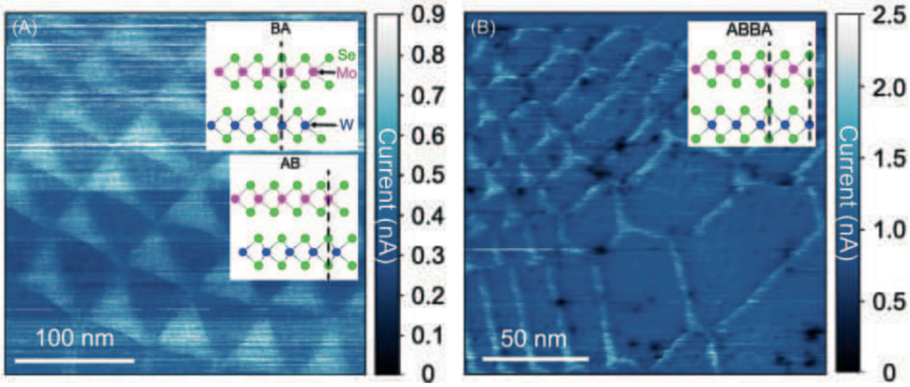

Fig. 7 (A–B) Conductive AFM images showing the atomic reconstruction in a $MoSe_2/WSe_2$ for a twist angle close to 0° (A) and to 60° (B). Triangular regions with different conductivities corresponding to reconstructed AB and BA regions can be seen in (A). In (B) hexagonal-shaped domains are visible, corresponding to reconstructed energetically favorable ABBA regions, separated by sharp domain walls. (A–B) Adapted with permission Rosenberger MR et al. (2020) Twist angle-dependent atomic reconstruction and moiré patterns in transition metal dichalcogenide heterostructures. *ACS Nano* 14: 4550–4558. Copyright © 2020, American Chemical Society.

superlattice. The transition from the relaxed to the rigid regime when increasing the twist angle has been observed for other heterostructures, although the critical angles vary depending on the specific material. Such trend in the relaxation has also been described by theoretical models (Fig. 6G). Stacks of other 2D materials can result in more complex atomic reconstructions, as exemplified by the case of TMD heterostacks, such as the $WSe_2/MoSe_2$ shown in Fig. 7 (Rosenberger et al., 2020). In this case, for twist angles close to 0° the reconstruction includes AB and BA triangular domains similar to those occurring in TBG. However, the symmetry of the TMDs results in a reconstruction into hexagonal shaped domains of a single arrangement (ABBA) for twist angles close to 60°.

Twisted bilayer graphene and superconductivity

One of the most paradigmatic and studied cases of the moiré influence on the band structure is that of the emergence of *unconventional* superconductivity in low-angle TBG. The occurrence of large AA- and AB-stacked regions for such low angles introduces small variations of the interlayer distance for the different regions, which result in fluctuations of the interlayer coupling

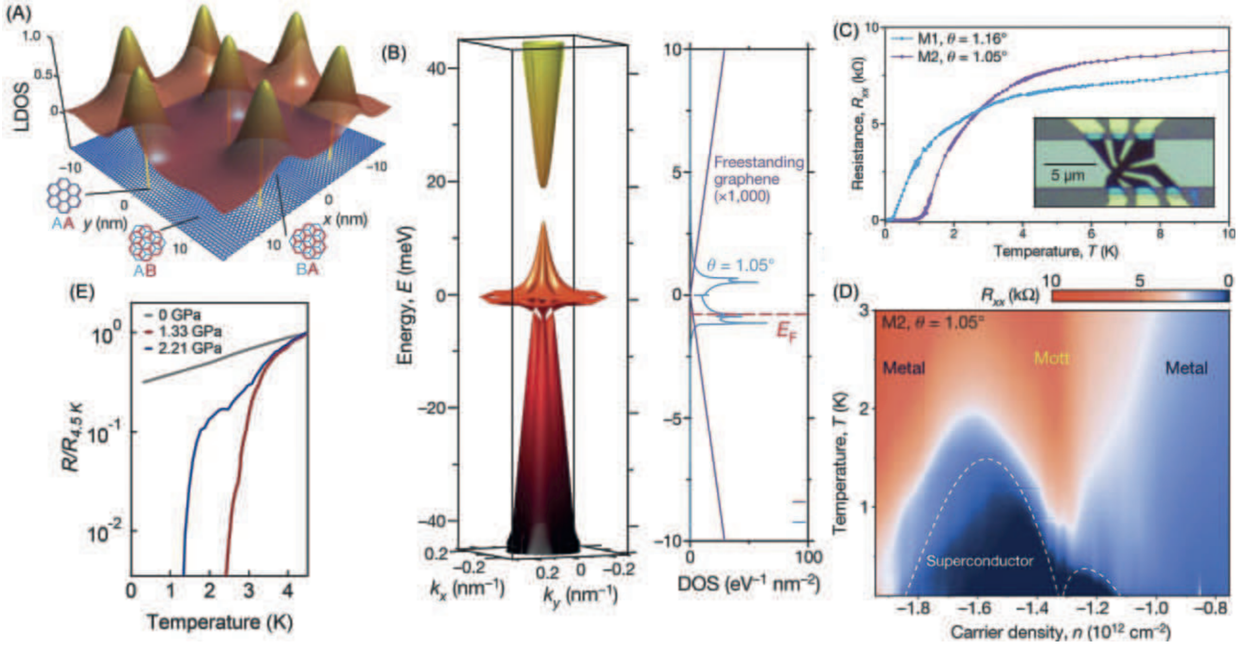

Fig. 8 (A) Calculated normalized local density of states of the flat bands with $E > 0$ of TBG with a twist angle of 1.08°. The wavefunctions are concentrated on the AA regions, having a much smaller amplitude in the AB and BA regions. (B) Band energy in the first mini-Brillouin zone of the superlattice of TBG with a twist angle of 1.05°, and the corresponding density of states with the Fermi energy located at the half-filled state of the flat band with $E < 0$ in which the superconductivity is observed. For comparison, the density of states of two layers of single-layer graphene without interlayer interaction is also included. (C) Four-probe resistance curves of TBG devices with twist angles of 1.05° and 1.16° (an optical image of the latter is shown in the inset), with critical temperatures of 1.7 K and 0.5 K, respectively. Each measurement is performed for the Fermi energy near the half-filled state of the $E < 0$ energy flat band. (D) Four-probe resistance plotted as a function of the carrier density and temperatures for a TBG device with a twist angle of 1.05° and a critical temperature of up to 1.7 K. The two superconductive domes (in blue) near the half-filled state are located at a carrier density of around $n \approx -1.3 \times 10^{12}$ cm^{-2}. (E) Temperature dependence of the four-probe resistance curves of a TBG device with a twist angle of 1.27° at different applied pressures. The high-pressure measurements in (E) were done at the optimal doping of the superconductor. (A) Reproduced with permission Cao Y, Fatemi, V, Demir A et al. (2018a) Correlated insulator behaviour at half-filling in magic-angle graphene superlattices. *Nature* 556: 80–84. Copyright © 2018, Nature Publishing Group. (B–D) Reproduced with permission Cao Y, Fatemi V, Fang S et al. (2018b) Unconventional superconductivity in magic-angle graphene superlattices. *Nature* 556, 43–50. Copyright © 2018, Nature Publishing Group. (E) Reproduced from Yankowitz M, Chen S et al (2019a) Tuning superconductivity in twisted bilayer graphene. *Science* 363: 1059–1064.

strength. These fluctuations were used to predict the vanishing of the Fermi velocity in TBG and the occurrence of flat bands near the charge neutrality for certain low twist angles, known as *magic angles*, with the first one occurring at ~1.1° (Cao et al., 2018b; Andrei and MacDonald, 2020). The flat bands are mainly localized in the AA-stacked regions, as evidenced in Fig. 8A, and correspond to levels with energies that are mostly independent of the electron momentum (Cao et al., 2018a). The flat band energy and the corresponding density of states are depicted in Fig. 8B. Interaction between the electrons increases for twists near the *magic angles*, and a strongly correlated system is formed with Mott-like insulating states at half-filling of the flat bands, i.e., for two charge carriers per moiré unit cell. However, the complete implications of these strong correlations were not clear until experimental results could be obtained a few years later, in 2018. The low carrier densities at which the flat bands occur, slightly over 10^{12} cm^{-2}, are easily attained by electrostatic doping in conventional gated devices. The main difficulty arises from the complexity to fabricate the devices with the exact required twist angles, while avoiding the tendency of the TBG to relax to AB-stacking. The experimental results revealed the emergence of *unconventional* superconductive states for TBG with a twist angle of ~1.1° (Fig. 8C) (Cao et al., 2018b). The term *unconventional* refers to the fact that these states are not originated by the weak electron-phonon interactions of conventional superconductors, but are instead supposed to arise from the aforementioned strong correlations between electrons in the flat bands. The *magic angle* TBG have a low critical temperature (T_C) of up to ~1.7 K that depends on the twist angle. Although this T_C is low for any practical application, the simplicity of TBG is expected to help understanding the mechanism underlying unconventional superconductivity and lead to the development of superconductors with higher T_C. The superconductive states were originally observed near the correlated-insulating states at half-filling of the flat bands of the valence band ($E_F < 0$), displayed as the two low-resistance domes at both sides of the insulating states in Fig. 8D. Conversely, no superconductivity was observed near the flat bands of the conduction band. Since then, superconductive states have been found at lower temperatures in a wider range of fillings in both the conduction and valence bands (Lu et al., 2019). It is also worth mentioning the emergence of ferromagnetic states near three-quarters filling of the conduction band, for which the magnetization can be controlled by applying a small current (Sharpe et al., 2019).

Superconductivity can also be induced in TBG with angles larger than the *magic angle* and at higher critical temperatures by tuning the interlayer distance, for example by the application pressure (Fig. 8E) (Yankowitz et al., 2019a). This highlights the importance of the interlayer coupling in the properties of the heterostructures and provides an additional parameter to tune the properties of vdW heterostructures.

Other than for TBG, the emergence of correlated insulated states and of superconductivity has also been predicted in other twisted bilayer vdW heterostructures, including bilayers of hBN and of TMDs, and for some trilayer or thicker heterostructures. The most recent experimental results show signatures of superconductivity in certain heterostructures, such as in twisted trilayer graphene (TLG) superlattices, in superlattices between ABC-stacked TLG and hBN, and in twisted WSe_2. However, the complexity of experimentally realizing such heterostructures is slowing down the confirmation of predictions.

Graphene/hBN heterostructures

The case of graphene/hBN heterostructures will be described here in some detail, as it is one of the most studied vdW heterostructures given its technological importance. For a more exhaustive review on the topic, the reader is referred to Yankowitz et al. (2019b). The 2D materials are very susceptible to their immediate environment, given that most of their atoms are in their surface. Hence, some 2D materials can be unstable and damaged when exposed to oxygen, moisture or to light. The environment can also significantly alter the properties of stable 2D materials, as can be seen in the p-doping of graphene exposed to air. It is thus important to properly isolate them by selecting adequate substrates and encapsulating them. One of the most employed substrates for devices based on 2D materials is SiO_2, as it allows to easily find isolated layers of certain 2D materials by their optical contrast. However, the surface roughness of the SiO_2 and the existence of charged surface states limit the performance of the devices due to the scattering of charge carriers. Historically, this has had a negative impact on the mobility of graphene devices, with measured mobilities being much lower than the predicted values. hBN is a vdW material with a similar structure as that of graphene, but with the two C atoms of the unit cell being replaced by B and N atoms. The distinct B and N sublattices cause a lack of inversion symmetry that results in hBN having properties very different from those of graphene, being a dielectric vdW material with a large bandgap of $\sim$6 eV. Moreover, hBN has a flat and inert surface free of charge traps, and with a small lattice mismatch with graphene ($\sim$ 1.8%). All this makes hBN an ideal candidate as a substrate for other 2D materials (Fig. 9A and B) (Decker et al., 2011). In particular, the mobility of graphene devices on hBN increases by almost an order of magnitude compared with devices on SiO_2 substrates (Fig. 9C). The performance of the devices can still be improved when the graphene is completely encapsulated by hBN, providing ballistic transport for distances of tens of microns and with record mobilities of $\sim$1.000,000 cm^2/Vs attained at low temperatures (<40 K). The mobilities obtained at room temperature for hBN-encapsulated graphene approach the theoretical predicted limits (Fig. 9D) (Wang et al., 2013). Slightly modest increases in mobility can also be observed when the graphene is encapsulated in certain vdW layered materials, such as TMDs. These increases in mobility are in part ascribed to the self-cleansing mechanism discussed above, and which is absent between the surface of the graphene and the SiO_2. Hence, similar improvements can be obtained when hBN is used to isolate other 2D materials (Fig. 9E) (Knobloch et al., 2021).

But although hBN can be considered as an excellent substrate for graphene, the interaction between both materials can significantly alter the electronic band structure of graphene. When the lattices of the graphene and the hBN are aligned or misaligned by just a small twist angle, the mismatch of their lattices causes an atomic reconstruction and the occurrence of moiré patterns with periods larger than those of the original lattices. The wavelength of the moiré superlattice can be obtained for any given twist angle according to Eq (1), with values $a = 2.46\ \AA$ and $\delta = 1.8\%$ for the lattice constant of graphene and the lattice mismatch between graphene and hBN, respectively. The effect of the periodic moiré potential in the band structure involves the appearance of additional Dirac points at low energies, and can even give rise to flat bands and correlated states similar to those described in the section about twisted bilayer graphene (Sun et al., 2021). This has led to the observation of phenomena like the Hofstadter butterfly spectrum (Fig. 10A) (Hunt et al., 2013), due to the 2D-confined electrons being subjected to the periodic moiré potential and to a high magnetic field, and of valley currents in the graphene at zero magnetic field (Fig. 10B) (Gorbachev et al., 2014). Additionally, the atomic reconstruction results in a breakage of the sublattice symmetry of graphene, inducing the opening of finite bandgaps of up to a few tens of meV at both the primary and secondary Dirac points. The discussed effects on the band structure of graphene can be further enhanced when the graphene is encapsulated in aligned hBN/graphene/hBN stacks. Similar to the case of TBG, the interaction between graphene and hBN can also be tuned by applying pressure to the heterostacks. This effectively decreases the interlayer distance and increases the interlayer coupling strength. When the graphene is aligned with one of the hBN layers the application of pressure can result in a two-fold increase of the moiré-induced bandgaps (Yankowitz et al., 2018).

TMD heterostructures

Of special importance is the case of vdW stacks of TMDs. The structure of TMDs, with the general formula MX_2, consist of two layers of a chalcogen element X (e.g., S or Se) with a transition metal layer M sandwiched in between (commonly Mo or W). Due to the broken inversion symmetry, most single layer TMDs are semiconductors with direct bandgaps ranging between 1 and 2 eV. However, the bandgap changes from direct for single layers to indirect for bi- or thicker homostacks, which have strong implications for the optoelectronic properties of the TMDs (Fig. 11A) (Ajayan et al., 2016). TMDs have strong optical absorptions of up to $\sim$10% of the visible light for monolayer thickness, and up to $\sim$40% for thicker flakes. For all these, TMDs are interesting candidates for ultrathin flexible optoelectronic devices.

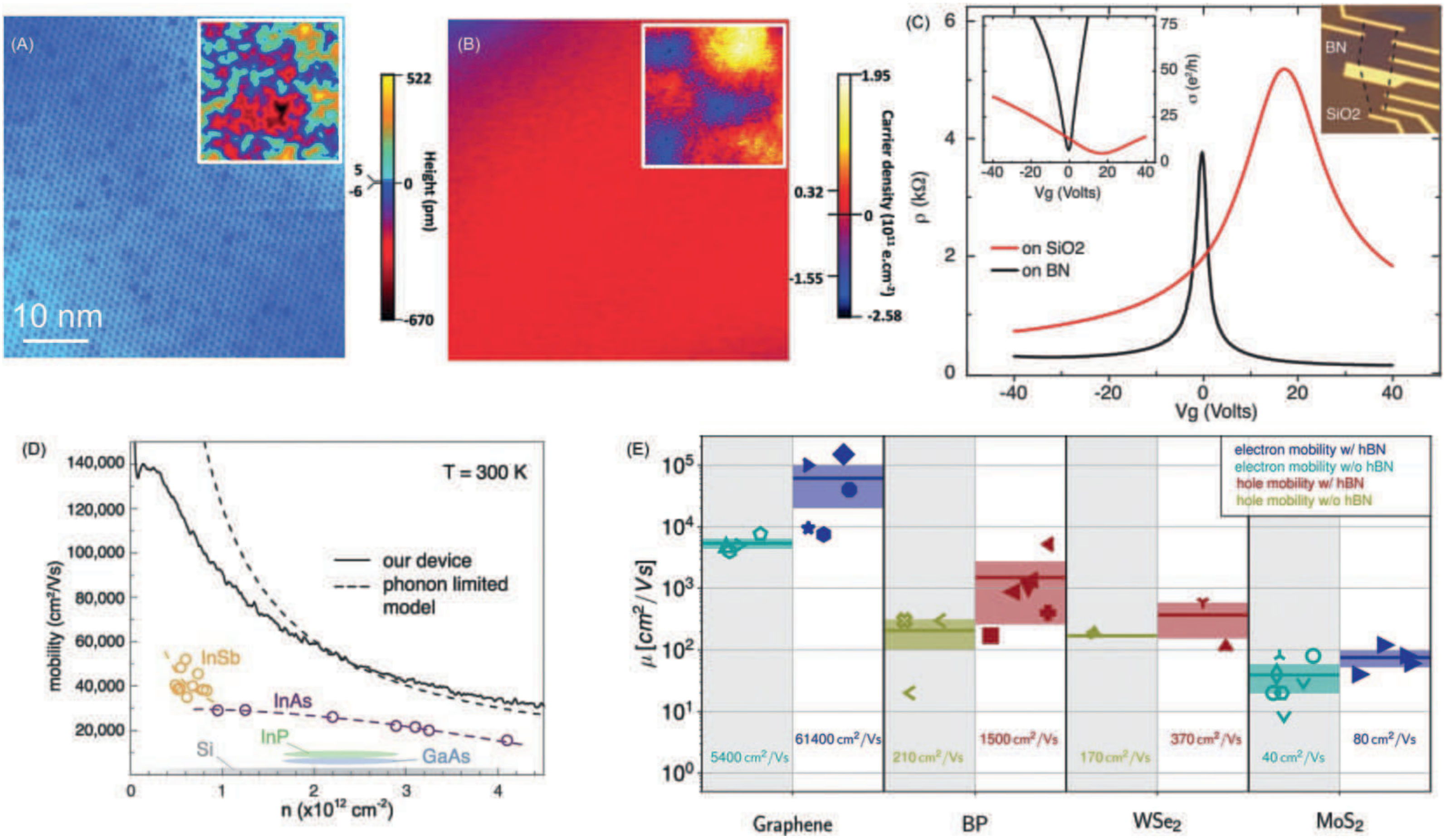

Fig. 9 (A, B) STM images of an area of graphene on top of hBN, showing the topography (A) and the calculated charge density (B). The insets show the images of a graphene area of the same size but supported on SiO_2. (C) Resistivity and conductivity (left inset) of a graphene flake for areas supported on SiO_2 (red) and on hBN (black), for which the extracted carrier mobilities are 2000 cm^2/Vs and 20,000 cm^2/Vs, respectively. (D) Room temperature mobility of graphene encapsulated by hBN. The theoretical acoustic-phonon-limited mobility is included (dotted line), along with experimental mobility values of other 2D materials. (E) Effect of hBN in the mobility of different 2D materials (values collected from existing literature). (A–B) Adapted with permission Decker R et al. (2011) Local electronic properties of graphene on a BN substrate via scanning tunneling microscopy. *Nano Letters* 11: 2291–2295. Copyright 2011 American Chemical Society. (C) Reproduced with permission Dean CR et al. (2010) Boron nitride substrates for high-quality graphene electronics. *Nature Nanotechnology* 5: 722–726. Copyright © 2010, Nature Publishing Group. (D) Reproduced from Wang L et al. (2013) One-dimensional electrical contact to a two-dimensional material. *Science* 342: 614–617. (E) Reproduced with permission Knobloch T et al. (2021) The performance limits of hexagonal boron nitride as an insulator for scaled CMOS devices based on two-dimensional materials. *Nature Electronics* 4: 98–108. Copyright © 2021, Nature Publishing Group.

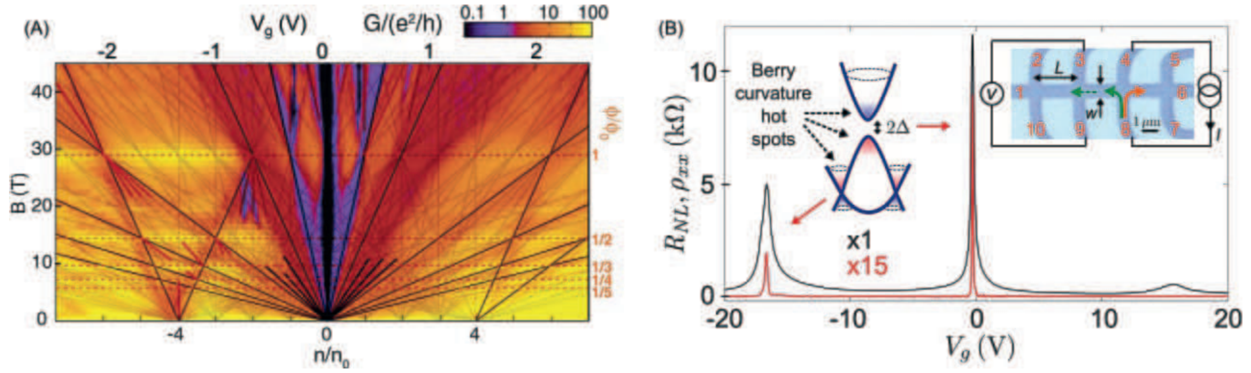

Fig. 10 (A) Landau fan showing the magnetoresistance of a two-terminal device with a graphene channel supported by hBN. The alignment between the graphene and the hBN is below 2°. The superimposed lines are the computed gaps in the Hofstadter spectrum, with n/n_0 and ϕ/ϕ_0 being the normalized carrier density and magnetic flux, respectively. The gaps follow linear trajectories given by the Diophantine equation $\phi/\phi_0 = (n/n_0 - s)/t$, with s and t being integers.
(B) Longitudinal resistance (black curve), and topological currents observed in non-local resistance measurements (red curve) in the absence of an external magnetic field, for an aligned graphene/hBN device. The non-local measurements are performed according to the schematic of the top right inset. The topological current peaks can be observed for carrier densities corresponding to the primary and secondary (hole) Dirac points, in the spots with finite Berry curvature (left inset), and are much narrower than those of the longitudinal resistance. (A) Adapted from Hunt B et al. (2013). Massive Dirac fermions and Hofstadter butterfly in a van der Waals heterostructure. *Science* 340: 1427–1430. (B) Reproduced from Gorbachev RV et al. (2014) Detecting topological currents in graphene superlattices. *Science* 346: 448–451.

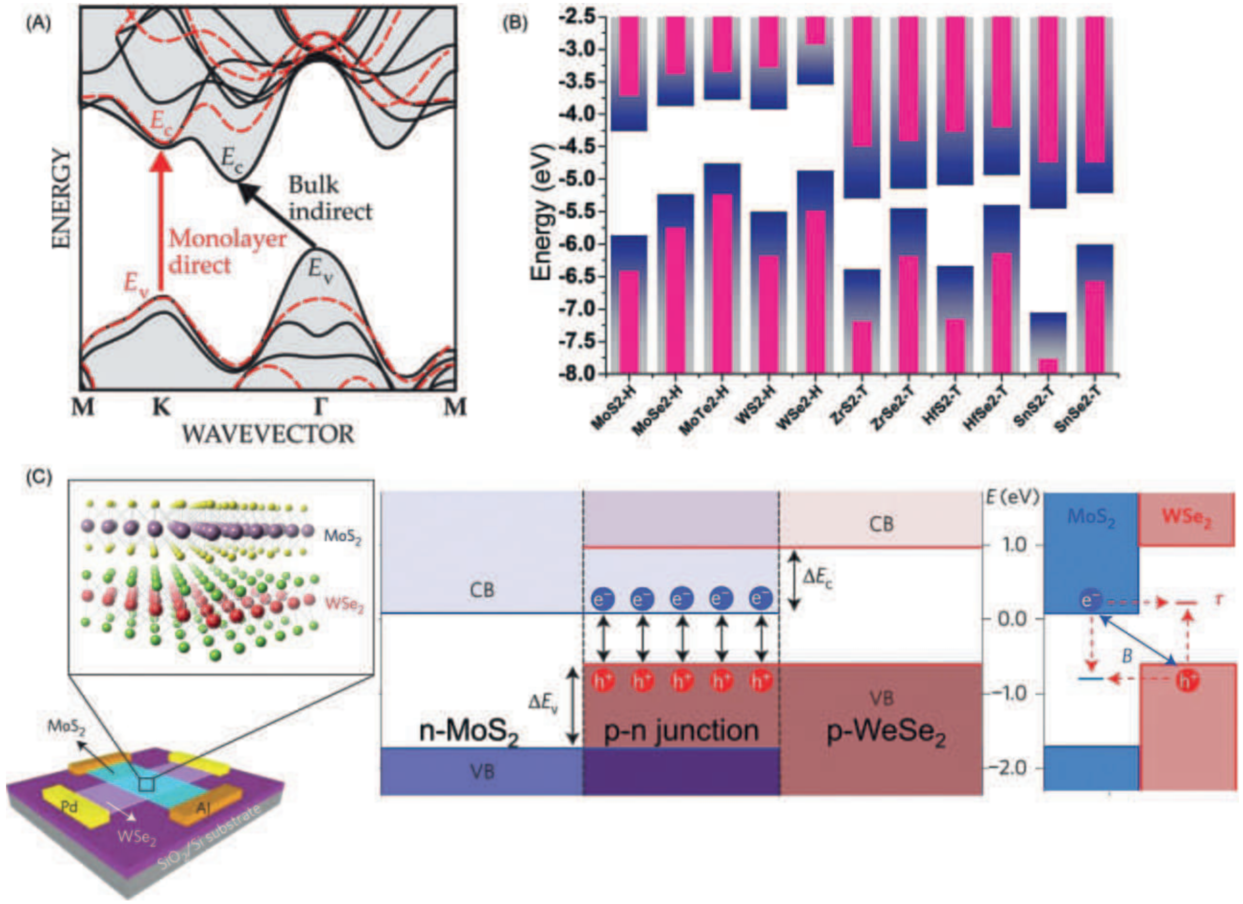

Fig. 11 (A) Band structure of single (red) and bulk (black) MoS_2, showing the change of the bandgap from indirect to direct when decreasing the thickness to 1 layer. (B) Energy levels showing edges of the conduction and valence bands of some single layer semiconducting TMDs. Values are obtained by density functional theory calculation with generalized gradient approximation of Perdew-Burke-Ernzerhof functionals (DFT-PBE) and G0W0, colored as blue and pink, respectively. (C) Schematics of a MoS_2/WSe_2 p-n junction device, and of the band edges in the lateral (middle) and vertical (right) directions at a forward bias of 0.6 V. The lack of band bending at forward biases results in the current being governed by the interlayer recombination of the majority carrier of each layer. (A) Reproduced from Ajayan P, Kim P, and Banerjee K (2016) Two-dimensional van der Waals materials. *Physics Today* 69: 38–44. (B) Reproduced with permission Zhang C et al. (2017). Systematic study of electronic structure and band alignment of monolayer transition metal dichalcogenides in Van der Waals heterostructures. *2D Materials* 4: 015026. Copyright © 2016, IOP Publishing. (C) Adapted with permission Lee C-H et al. (2014) Atomically thin p–n junctions with van der Waals heterointerfaces. *Nature Nanotechnology* 9: 676–681. Copyright © 2014, Nature Publishing Group.

The band alignment of most of TMDs heterostacks is of type II, with the maximum of the valence band and the minimum of the conduction band lying in different layers (Fig. 11B) (Rivera et al., 2018; Zhang et al., 2017). Holes and electrons can be produced in the heterostacks by photoexcitation, forming excitons (Coulomb-bounded electron-hole pairs) that then relax to their lowest energy states. As these states lie in different layers for each kind of carrier, there is a charge transfer across the junction with the carriers occupying different layers. The interlayer excitons have large binding energies owing to the small interlayer separation, while the separation is large enough for their lifetimes to be much larger than those of intralayer excitons. The high orbital velocities in the outer d-orbitals of the *M* heavy atoms induce a strong spin-orbit coupling. This results in splitting of the valence and conduction bands by a few hundred of meV and a few tens meV, respectively. These values depend on the specific TMD, with e.g., the band splitting being larger in WS_2 than in MoS_2. The conduction and valence band edges (valleys) of TMDs at the K points are energetically degenerate (+K, −K), and hence electrons have an additional degree of freedom. Optically generated interlayer excitons have valley polarization, retaining the circular polarization of the excitation light. This makes these heterostructures interesting for the future development of spintronic and valleytronic devices.

Photovoltaic devices can be realized in TMD heterostacks with the appropriate band alignments, as in the case of MoS_2 and WSe_2 to accumulate the electrons and the holes, respectively (Fig. 11C). Open circuit voltages of $\sim$0.5 V can be obtained in such heterostacks. In conventional devices each layer is contacted in one side by an electrode, and hence carrier collection is done by the lateral diffusion of the carriers along their corresponding layers. The low mobility of TMDs results in the carriers remaining in the junction area for times of the order of the recombination lifetimes, hence decreasing the efficiency of photovoltaic cells with lateral electrodes. The efficiency can be improved by using graphene as vertical transparent electrodes (graphene/MoS_2/WSe_2/graphene). This allows for a faster collection of the carriers in the vertical direction and hence recombination is decreased (Lee et al., 2014). The efficiency can also be increased by increasing the thickness of the TDM layers. This leads to higher optical absorptions, although the photocurrent is in this case limited by lower charge collection and higher recombination rates.

The interlayer excitons in TMD heterostructures are also affected by the presence of the moiré superlattice. It is worth mentioning the occurrence of excitons trapped by the moiré superlattice in twisted heterostacks of TMDs (Seyler et al., 2019). The moiré pattern act as an array of quantum dot-like zero dimensional traps for the excitons. In the momentum space, the twist results in a separation of K valleys of the layers. This causes the optical transitions to change from direct to indirect with the introduction of a twist, resulting in increased interlayer exciton lifetimes with the twist angle (Choi et al., 2021). The control of the lifetime is interesting to further tune the properties of different optoelectronic devices, with light-emitting devices benefiting from the short lifetimes of the small twist angles.

Strain can also play an important role in the optoelectronic properties of the TMD heterostacks, specially for stacks in the regime of large moiré periodicities (Shabani et al., 2021). As the moiré wavelength increases for twist angles close to 0° or 60°, strain induced 1D soliton patterns can be observed in TMD stacks (Bai et al., 2020). At low energies, the excitons are confined within the 1D lines. Their broad, intense, and linearly polarized photoluminescence emission significantly differs from that of excitons trapped in hexagonal moiré lattices.

2D Heterostructures by intercalation

One of the current trends of vdW heterostructures consists in leveraging the interlayer space existing between the adjacent layers by the intercalation of different atoms or molecules (Ago et al., 2022). Given the nature of the interlayer interactions of vdW materials, there exists a clearly defined 2D nanospace between adjacent layers, typically ranging from 3 to 7 Å depending on the specific material. This space can be intercalated by foreign species that affect the physical properties of the host, allowing to further tune the properties of the heterostructure. The study of graphite intercalated compounds (GIC) has been conducted since 1841 (Dresselhaus and Dresselhaus, 2002), with the intercalation being a key role in the development of technologies such as anodes for Li-ion batteries. Only recently the concept of intercalation has begun to be studied for thin 2D materials.

Different metal chlorides have been intercalated in bilayer and in thin flakes of graphene, including $FeCl_3$, $MoCl_5$ and $AlCl_3$ among others. The charge transfer of these intercalants induces a doping that decreases the sheet resistance of BLG while keeping a high transparency (Fig. 12A). This makes intercalated BLG an interesting candidate for the fabrication of flexible transparent electrodes, competing in efficiency with conventional indium titanium oxide (ITO) based optoelectronic devices (Kinoshita et al., 2017). The degree of intercalation is affected by the twist angle of the BLG, providing a way to control the intercalation. The strong interlayer coupling at low twist angles makes intercalation difficult, while the intercalation is easier for large twist angles when the layers decouple. For polycrystalline samples in which the twist angle can vary across the surface, this allows to produce regions with differenced degrees of doping.

Alkali and alkaline-earth metals have also been intercalated in BLG. The emergence of superconductive states in bi- and few-layer graphene have been reported upon the intercalation of K, Ca and Li alkali or alkali earth atoms (Fig. 12B) (Ichinokura et al., 2016). Moreover, the reported densities can exceed those normally obtained in GIC. As an example, reversible superdense Li intercalation has been observed in BLG, with densities exceeding the LiC_6 expected for GIC (Fig. 12C–E) (Kühne et al., 2018). This opens the possibility to develop more efficient batteries with larger capacities.

The small thickness of the van der Waals heterostructures allows to study these intercalates with techniques that are not available for thicker intercalate compounds. This opens the possibility to get a more profound understanding of the mechanisms that govern the intercalation. The use of TEM has allowed to study the in-situ intercalation/deintercalation of alkali metals from solid

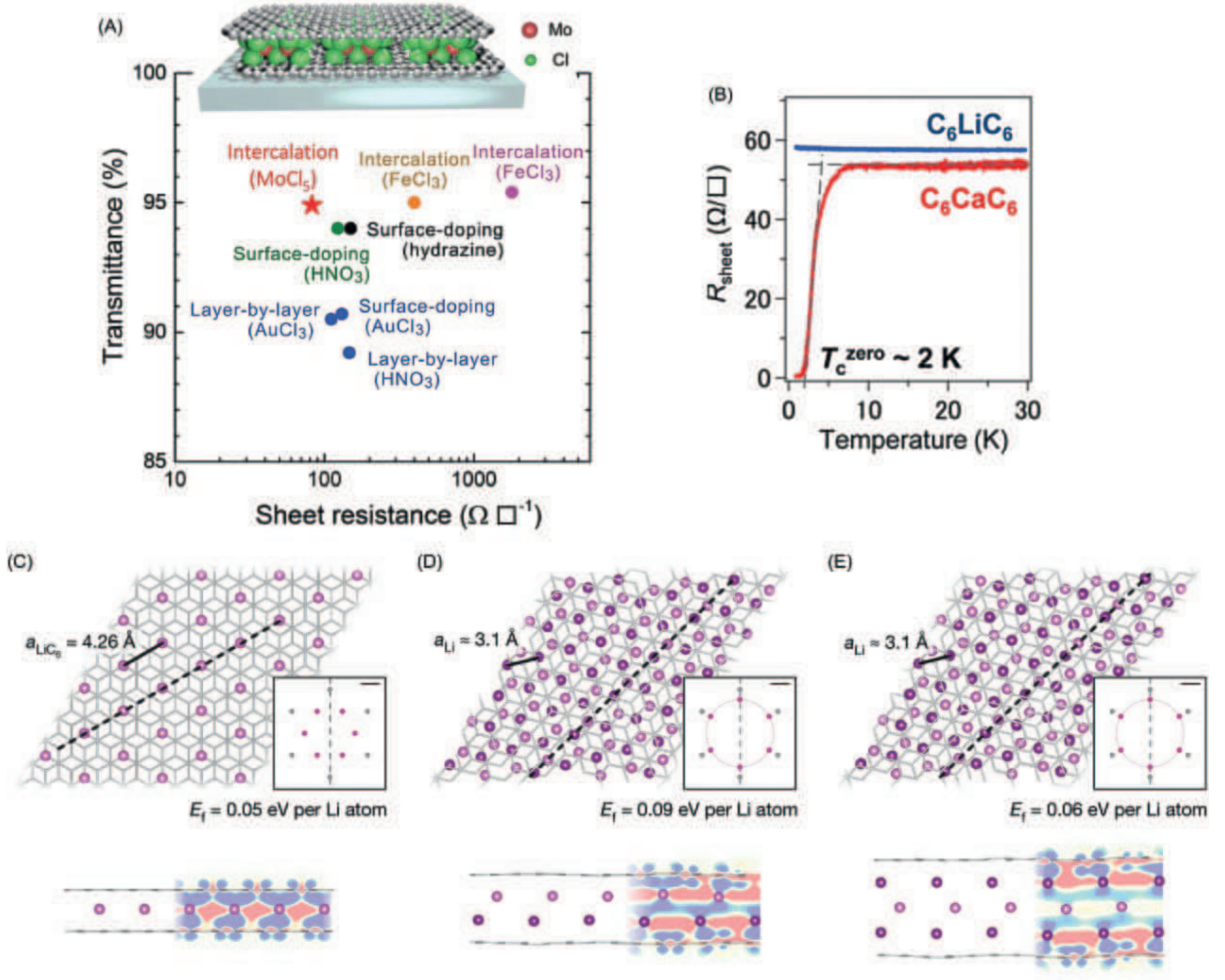

Fig. 12 (A) Schematics of BLG intercalated by MoCl$_5$, and the corresponding values for the transmittance and sheet resistance (red star). Values for other intercalants and of surface doping obtained from the literature are included for comparison. (B) Superconductive transition of Ca intercalated BLG (red curve), evidenced by a drop of the sheet resistance at temperatures below $\sim$4 K. The sheet resistance of Li intercalated BLG is shown for comparison (blue curve). (C–E) Top and section views of the atomic models of Li intercalation into BLG. The insets to the top views represent the expected diffraction patterns for each of the structures. The contour plots in the section views represent the charge transfer between graphene and Li, with the blue and red representing increased and decreased electron densities, respectively. (C) The C$_6$LiC$_6$ usually reported in GIC, and the dense configurations with (D) two and (E) three Li layers. (A) Reproduced with permission Kinoshita H et al. (2017) Highly conductive and transparent large-area bilayer graphene realized by MoCl5 intercalation. *Advanced Materials* 29: 1702141. Copyright 2017, Wiley-VCH. (B) Reproduced from Ichinokura S et al. (2016) Superconducting calcium-intercalated bilayer graphene. *ACS Nano* 10: 2761–2765. Copyright 2016, American Chemical Society. (C–E) Reproduced with permission Kühne M. et al. (2018) Reversible superdense ordering of lithium between two graphene sheets. *Nature* 564: 234. Copyright © 2018, Nature Publishing Group.

electrolytes into e.g., BLG and some TMDs (Fig. 13A). In the case of TMDs, the intercalation of alkali metals induces structural phase transitions that can depend on the twist angle (Fig. 13B–D) (Ji et al., 2021). By STEM, novel polymorphic phases have been described after intercalation of metal chlorides in BLG (Fig. 13E–G) (Lin et al., 2021c). Along with the higher densities of intercalant reported, these results point to the possibility to obtain new materials with exotic properties by the intercalation of 2D materials.

Characterization

Among the most prevalent methods of characterization of 2D materials and of vdW heterostructures are those based on their optical properties, including optical microscopy, and Raman and photoluminescence (PL) spectroscopy. These are usually fast, reliable, and non-destructive techniques that can provide information about the constituent layers, their thickness and stacking order, the presence of defects, contamination, and the degrees of doping and strain.

Optical microscopy is a direct method to identify the thickness of 2D materials. It is based on the increase of the optical absorption with the thickness, combined with interference effects arising from the thickness of the 2D material and the substrate

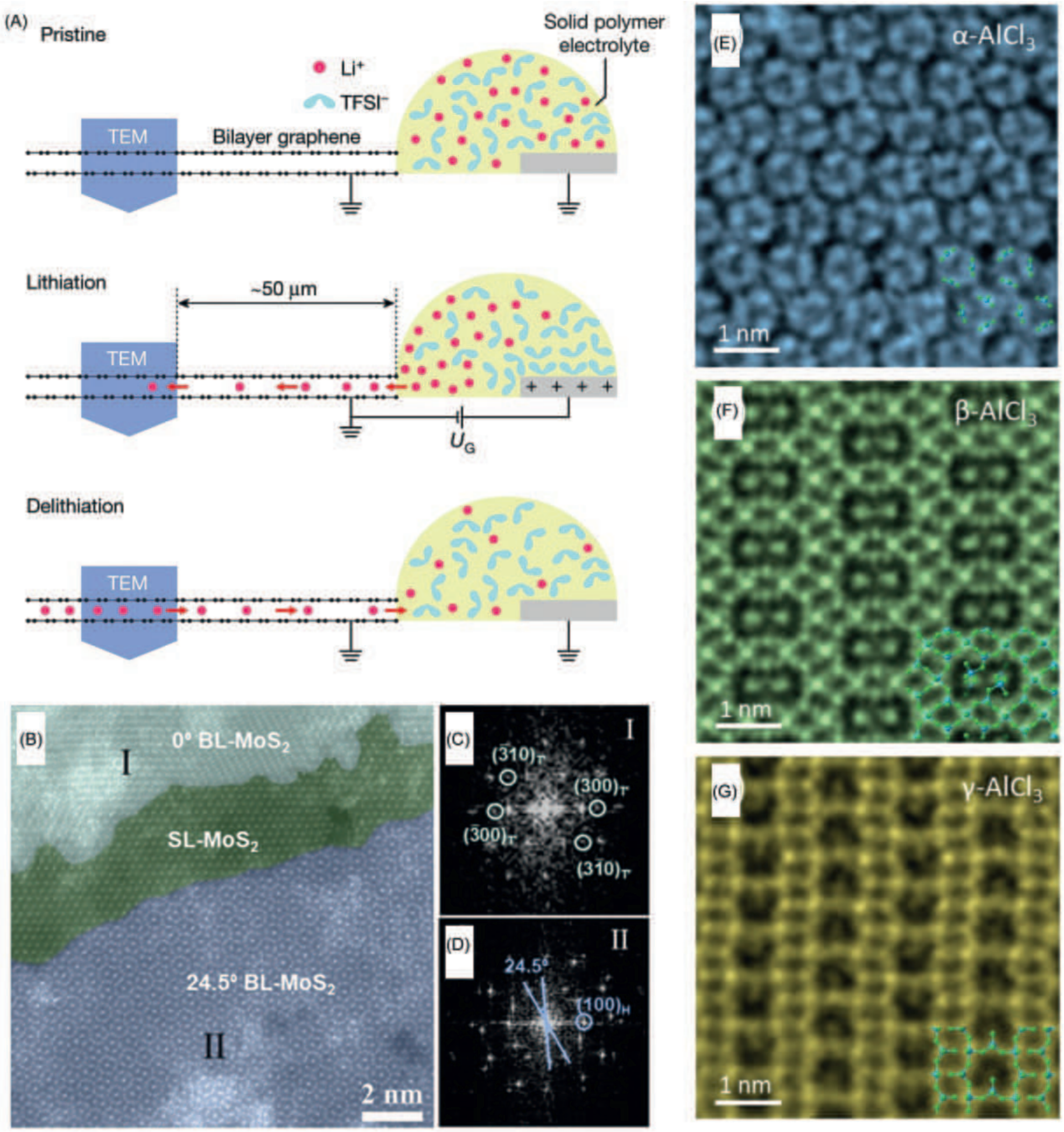

Fig. 13 (A) Schematics of the process for the in-situ TEM observation of the intercalation of Li into BLG. By applying differences of voltage between the electrolyte and the graphene, the Li can be reversibly intercalated (lithiation) and deintercalated (delithiation). (B–D) False colored ADF-STEM image of Li intercalated in non-twisted (area I) and twisted (area II) bilayer MoS$_2$. As evidenced by the superlattice spots of each region (C, D), the region I underwent an H to T' phase transition upon intercalation whereas region II remained in the phase H. (E–G) Artificially colored STEM images of three different phases AlCl$_3$ phases that can be found when intercalated into BLG. (A) Reproduced with permission Kühne M. et al. (2018) Reversible superdense ordering of lithium between two graphene sheets. *Nature* 564: 234. Copyright © 2018, Nature Publishing Group. (B–D) Adapted with permission Ji X et al. (2021) Interlayer coupling dependent discrete H ⟶ T′ phase transition in lithium intercalated bilayer molybdenum disulfide. *ACS Nano* 15: 15039–15046. Copyright © 2021, American Chemical Society. (E–G) Reproduced with permission Lin Y-C, Motoyama A, Kretschmer S et al. (2021c) Polymorphic phases of metal chlorides in the confined 2D space of bilayer graphene. *Advanced Materials* 33: 2105898. Copyright 2021, Wiley-VCH.

(usually a thin SiO$_2$ layer on a Si substrate) and from their different refractive indexes (Li et al., 2013; Puebla et al., 2022) (Fig. 14). The small light absorption of the ultrathin 2D materials requires optimized substrates to provide high optical contrasts. In general, the contrast between a given 2D material and the substrate can be improved by choosing a suitable combination of the substrate (e.g., by altering the thickness of the SiO$_2$) and the wavelength of the incident light. As the contrast highly depends on the specific 2D material, there is no universal substrate that provides high optical contrast for all 2D materials. Thus, the widely used 300 nm thick SiO$_2$ provides reasonably good contrast for graphene, several TMDs and some other materials, but a very low contrast for hBN. The twist angle can also have a small effect on the optical absorption, and hence the optical contrast of vdW heterostructures can

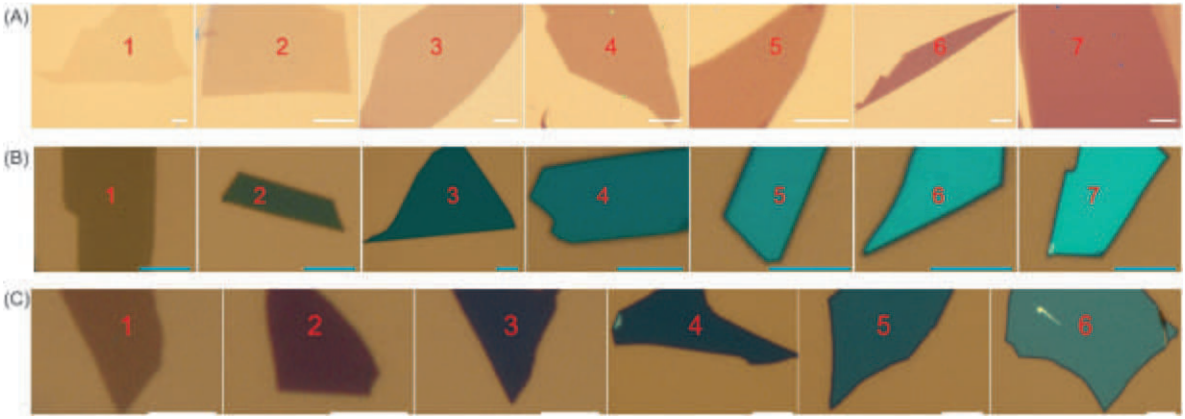

Fig. 14 (A–C) Optical images of graphene (A), MoS_2 (B) and WSe_2 (C) flakes with different number of layers (indicated by red numbers), supported on 90 nm SiO_2/Si. The scale bars are 10 μm (A) and 5 μm (B, C). (A–C) Reproduced with permission Li H. et al. (2013) Rapid and reliable thickness identification of two-dimensional nanosheets using optical microscopy. *ACS Nano*, 7: 10344–10353. Copyright 2013, American Chemical Society.

slightly vary with it. As an example, optical differences are apparent for TBG with twist angles of ~10–12° under white light illumination. This method is however quite limited and cannot be used for the optical determination of the twist angle. In the case of 2D crystals with well-defined regular shapes, it is still possible to determine the twist angle from the alignment of the edges with an accuracy of ~1°. But despite being a fast and simple method, optical microscopy offers limited information about the components of 2D heterostructures. It is thus commonly employed as a fast way to locate and estimate the thickness of the 2D materials for further characterization with other techniques.

Raman spectroscopy is a useful and common technique for the study of 2D materials, being fast, non-destructive, and providing a wide array of information. As an in-depth study of the technique and its application to 2D materials is out the scope of this book chapter, the reader is referred to Ferrari and Basko (2013) and Zhang et al. (2016) for more detailed information on the topic. Most 2D materials possess characteristic Raman spectra arising from their specific crystal structure, providing a way to determine the specific material and differentiate it from others. This makes Raman spectroscopy a useful tool to provide information about the specific components of vdW heterostructures. Variations in the shift, linewidth and relative intensity of the Raman bands can also provide information about the condition of the crystal, as the presence of defects, strain, or doping can alter the Raman spectrum in identifiable ways. Moreover, the Raman spectrum is also influenced by the interaction between the different layers. It is thus possible to determine additional information such as the thickness of each component, along with the twist angle or stacking order of the heterostructure, although the kind of information depends on the nature of the actual heterostructure. In the case TBG the evolution of the shape of the main Raman bands (named G and 2D), and of additional bands at low Raman frequencies arising from the coupling of the layers, can be used to determine the twist angle with even sub-degree accuracies for certain ranges of the twist angle (Barbosa et al., 2022) (Fig. 15A). For heterostructures of SLG and hBN the changes are more subtle but it is still possible to follow the twist angle by using Raman spectroscopy (Ribeiro-Palau et al., 2018). The Raman spectrum of TMDs stacks is also sensitive to the twist angle especially in the low-frequency regions corresponding to the breathing and shear interlayer modes (Lin et al., 2018, 2021a) (Fig. 15B and C).

For heterostructures including semiconducting layers, PL spectroscopy is another useful characterization technique. In the general case, the PL spectra of the heterostructure contain peaks corresponding to those of the layer that conform it. However, the interlayer charge transfer that can exist between layers tends to decrease the PL intensity. As pointed out in a previous section, the interaction between layers can also lead to the formation of interlayer excitons. These appear at lower energies than the original peaks, and for twist angles in which the layers are strongly coupled (Fig. 15D) (Nayak et al., 2017).

Concerning the atomic structure, several scanning probe (SPM) techniques including STM and different atomic force microscopy (AFM) modes are readily available. They can provide information about the atomic structure of the heterostructure, including the direct visualization of moiré patterns and of atomic reconstruction (Fig. 4A–C). The versatility of these techniques also allows to obtain sub-nanometer information about different physical properties of the heterostructures, including the electrical conductivity, the magnetic fields and the friction, as exemplified in Fig. 7 for the conductivity of an atomically reconstructed heterostructure and in Fig. 9A and B for the charge distribution. TEM-based techniques are also very extended, given the small thickness of the specimens. Similar to the case of SPM, the atomic structure of the heterostructures can be realized (Figs. 4D–O, and 6C–F). It is also possible to directly study the interface of the layers in cross-sectional TEM, as in Fig. 3D and I, allowing to obtain information about the number of layers, the stacking order and of the presence of foreign species in the interlayer spaces.

Traditional characterization techniques can be assisted by the use of robotic and machine-learning based methods, increasing the productivity and efficiency. Machine learning-based methods have been proposed to increase the efficiency and speed in the recognition and characterization of 2D materials and heterostructures by different methods. An example of this is the optical identification of exfoliated flakes mentioned in a previous section, which combined with the use of robotic systems can hugely

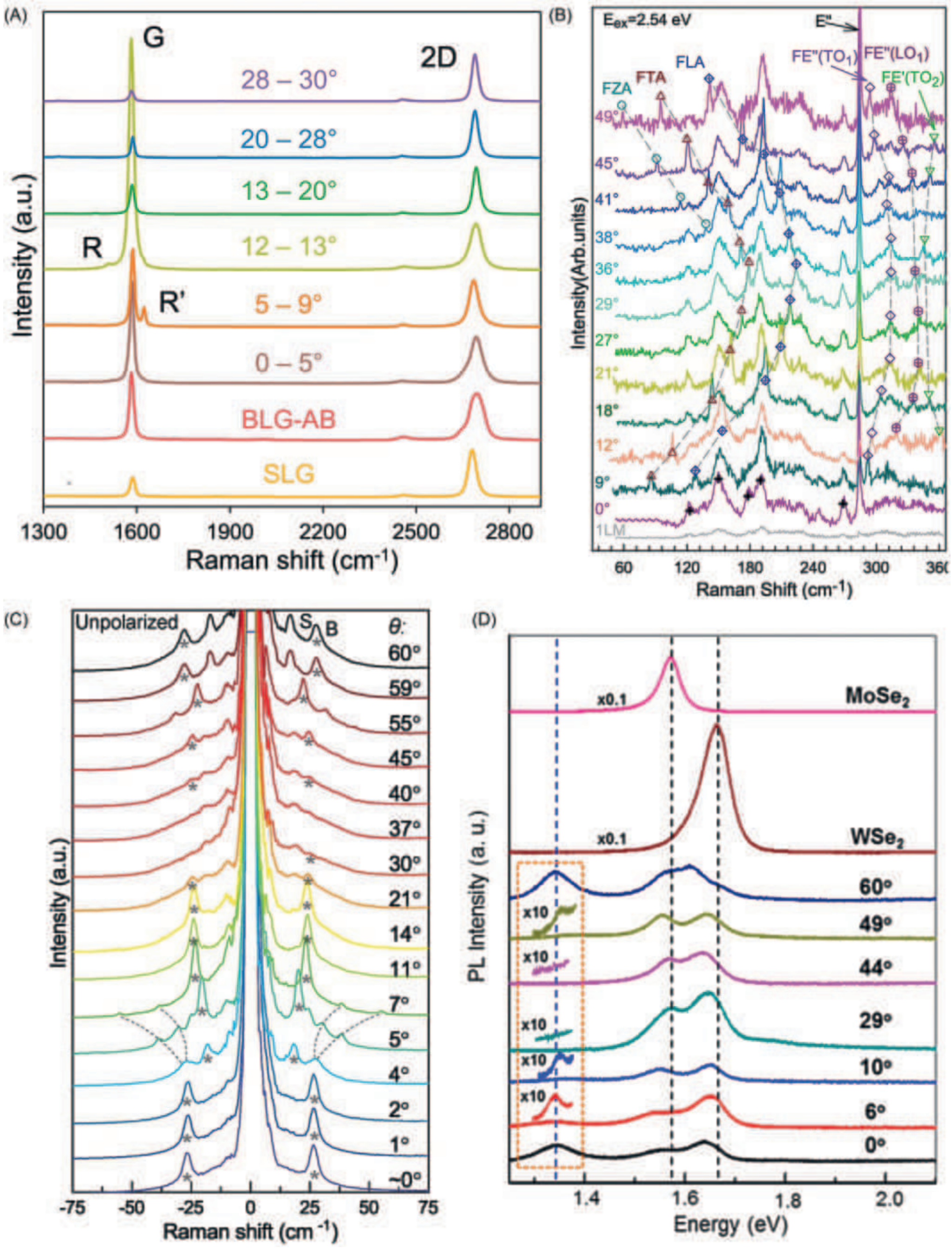

Fig. 15 (A) Average Raman spectra (532 nm excitation) of SLG and of TBG with different twist angles. The most characteristic Raman bands are labelled. (B, C) Low-frequency Raman spectra of bilayer MoS_2 (488 nm excitation) (B) and of bilayer WSe_2 (532 nm excitation) (C) with different twist angles. (D) Room-temperature PL spectra of $MoSe_2/WSe_2$ heterostacks with different twist angles. The exciton peak positions of each layer are marked by vertical black dashed lines (the spectra of the individual layers are added for comparison). The interlayer exciton peak appears at lower energies ($\sim$1.35 eV, blue dashed line) for twist angles close to 0° and 60°. (A) Adapted with permission Solís-Fernández P and Ago H (2022) Machine learning determination of the twist angle of bilayer graphene by Raman spectroscopy: Implications for van der Waals heterostructures. *ACS Applied Nano Materials* 5: 1356–1366. Copyright © 2022, American Chemical Society. (B) Reproduced with permission Lin M-L et al. (2018) Moiré phonons in twisted bilayer MoS2. *ACS Nano* 12: 8770–8780. Copyright © 2018, American Chemical Society. (C) Reproduced from Lin K-Q et al. (2021a) Large-scale mapping of moiré superlattices by hyperspectral Raman imaging. *Advanced Materials* 33: 2008333. © 2021 The Authors. Advanced Materials published by Wiley-VCH GmbH. (D) Reproduced with permission Nayak PK et al. (2017) Probing evolution of twist-angle-dependent interlayer excitons in MoSe2/WSe2 van der Waals heterostructures. *ACS Nano* 11: 4041–4050. Copyright © 2017, American Chemical Society.

increase the throughput for the assembly of heterostructures. Machine-learning can also be used for fast and reliable identification and classification of different spectral signals, such as it can be the case of the Raman spectra for TBG (Solís-Fernández and Ago, 2022). On their side, the use of deep learning is relatively widespread in the case of TEM and STEM, helped by the maturity of image processing techniques based in convolutional neural networks (CNN) (Madsen et al., 2018). These are helpful to unravel the atomic structures, the presence of defects, and of strain, among other things, from collected experimental images.

Conclusion

Continuing with the trend of the 2D materials, the 2D van der Waals heterostructures is an emerging and relatively recent field. The integration of 2D materials into heterostructures opens new possibilities, and a plethora of novel physical phenomena has already been observed. But despite all the progress in recent years, a lot of effort is still needed to make it a technology that can be considered mature. Some of the current difficulties in developing vdW heterostructures are inherited from the still immature parent field of 2D materials, although they are compounded by the increased complexity of both handling heterostructures and understanding interlayer interactions. Theories that can predict and understand new physical phenomena brought about by 2D integration are still needed. This is evidenced by the lack of a completely satisfactory explanation for the superconducting states found in some twisted two-dimensional materials.

There are currently a few practical impediments for the industrial scaling and adoption of vdW heterostructures. The first is the obtention and processing of van der Waals heterostructures at larger scales. Existing dry-transfer methods for stacking 2D materials are suitable for scientific research and have led to major advances in the understanding of heterostructures at a fundamental level. However, these are mainly based on time consuming artisanal processes that are quite laborious and produce heterostructures with very limited areas. The integration of vdW heterostructures into industrial processes require a substantial increase in process automation, accompanied by the possibility to assemble wafer-scale homogeneous heterostructures. A first step toward this goal is the development of wafer-scale transfer techniques for as-grown 2D materials, along with efficient methods to arrange them into heterostructures, while maintaining qualities and homogeneities similar to those achieved by mechanical exfoliation at small scales. Eventually, the direct growth of large-scale heterostructures is a desirable achievement for industrial applications, potentially simplifying the processes involved in the assembly of heterostructures and alleviating many of the resulting problems. Although direct growth of heterostructures is currently mainly limited to heterostructures of hBN, graphene and some TMDs, low-temperature growth methods, such as by plasma assisted CVD, are promising for obtaining high-quality heterostructures with high qualities of diverse materials. The second challenge to overcome is the development of techniques for the fabrication and integration of vdW heterostructures into existing CMOS processing techniques. In this sense, the development of techniques for growing 2D materials at lower temperatures while maintaining their quality is especially crucial. Although a diverse selection of isolated electronic and optoelectronic devices with vdW heterostructures has been made, only limited effort has been made to produce integrated circuits consisting entirely of 2D materials and on wafer scales. Another current limitation for the industrial scaling is the lack of characterization techniques at wafer scales. Current existing methods are relatively slow and only allow the inspection of areas of limited sizes. As in the case of wafer defect inspection systems adopted by the industry, there is a need to develop wafer-scale characterization methods for 2D and related materials that enable rapid quality assessment with high sensitivity and spatial resolution.

Acknowledgments

This work was supported by the JSPS Grant-in-Aid for Scientific Research on Innovative Areas “Science of 2.5 Dimensional Materials: Paradigm Shift of Materials Science Toward Future Social Innovation” (KAKENHI grant numbers 21H05232, 21H05233), and JSPS KAKENHI grant number 21K18878, JST CREST grant numbers JPMJCR18I1, JPMJCR20B1 and the JSPS A3 Foresight Program.

References

Ago H, et al. (2022) Science of 2.5 dimensional materials: Paradigm shift of materials science toward future social innovation. *Science and Technology of Advanced Materials* 23: 275–299.
Ajayan P, Kim P, and Banerjee K (2016) Two-dimensional van der Waals materials. *Physics Today* 69: 38–44.
Andrei EY and MacDonald AH (2020) Graphene bilayers with a twist. *Nature Materials* 19: 1265–1275.
Bai Y, et al. (2020) Excitons in strain-induced one-dimensional moiré potentials at transition metal dichalcogenide heterojunctions. *Nature Materials* 19: 1068–1073.
Barbosa TC, et al. (2022) Raman spectra of twisted bilayer graphene close to the magic angle. *2D Materials* 9: 025007.
Cai Z, et al. (2018) Chemical vapor deposition growth and applications of two-dimensional materials and their heterostructures. *Chemical Reviews* 118: 6091–6133.
Cao Y, Fatemi V, Demir A, et al. (2018a) Correlated insulator behaviour at half-filling in magic-angle graphene superlattices. *Nature* 556: 80–84.
Cao Y, Fatemi V, Fang S, et al. (2018b) Unconventional superconductivity in magic-angle graphene superlattices. *Nature* 556: 43–50.
Carr S, et al. (2018) Relaxation and domain formation in incommensurate two-dimensional heterostructures. *Physical Review B* 98: 224102.
Choi J, et al. (2021) Twist angle-dependent interlayer exciton lifetimes in van der Waals heterostructures. *Physical Review Letters* 126: 047401.
Dean CR, et al. (2010) Boron nitride substrates for high-quality graphene electronics. *Nature Nanotechnology* 5: 722–726.
Decker R, et al. (2011) Local electronic properties of graphene on a BN substrate via scanning tunneling microscopy. *Nano Letters* 11: 2291–2295.

Dienwiebel M, et al. (2004) Superlubricity of graphite. *Physical Review Letters* 92: 126101.

Dresselhaus MS and Dresselhaus G (2002) Intercalation compounds of graphite. *Advances in Physics* 51: 1–186.

Ferrari AC and Basko DM (2013) Raman spectroscopy as a versatile tool for studying the properties of graphene. *Nature Nanotechnology* 8: 235–246.

Frisenda R, et al. (2018) Recent progress in the assembly of nanodevices and van der Waals heterostructures by deterministic placement of 2D materials. *Chemical Society Reviews* 47: 53–68.

Gong Y, et al. (2014) Vertical and in-plane heterostructures from WS_2/MoS_2 monolayers. *Nature Materials* 13: 1135–1142.

Gorbachev RV, et al. (2014) Detecting topological currents in graphene superlattices. *Science* 346: 448–451.

Haigh SJ, et al. (2012) Cross-sectional imaging of individual layers and buried interfaces of graphene-based heterostructures and superlattices. *Nature Materials* 11: 764–767.

Hunt B, et al. (2013) Massive Dirac fermions and Hofstadter butterfly in a van der Waals heterostructure. *Science* 340: 1427–1430.

Ichinokura S, et al. (2016) Superconducting calcium-intercalated bilayer graphene. *ACS Nano* 10: 2761–2765.

Ji X, et al. (2021) Interlayer coupling dependent discrete $H \longrightarrow T'$ phase transition in lithium intercalated bilayer molybdenum disulfide. *ACS Nano* 15: 15039–15046.

Kim K, et al. (2016) van der Waals heterostructures with high accuracy rotational alignment. *Nano Letters* 16: 1989–1995.

Kinoshita H, et al. (2017) Highly conductive and transparent large-area bilayer graphene realized by $MoCl_5$ intercalation. *Advanced Materials* 29: 1702141.

Knobloch T, et al. (2021) The performance limits of hexagonal boron nitride as an insulator for scaled CMOS devices based on two-dimensional materials. *Nature Electronics* 4: 98–108.

Koma A (1992) Van der Waals epitaxy––a new epitaxial growth method for a highly lattice-mismatched system. *Thin Solid Films* 216: 72–76.

Koma A, Sunouchi K, and Miyajima T (1984) Fabrication and characterization of heterostructures with subnanometer thickness. *Microelectronic Engineering* 2: 129–136.

Kretinin AV, et al. (2014) Electronic properties of graphene encapsulated with different two-dimensional atomic crystals. *Nano Letters* 14: 3270–3276.

Kühne M, et al. (2018) Reversible superdense ordering of lithium between two graphene sheets. *Nature* 564: 234.

Lee C-H, et al. (2014) Atomically thin p–n junctions with van der Waals heterointerfaces. *Nature Nanotechnology* 9: 676–681.

Li H, et al. (2013) Rapid and reliable thickness identification of two-dimensional nanosheets using optical microscopy. *ACS Nano* 7: 10344–10353.

Li J, et al. (2020) General synthesis of two-dimensional van der Waals heterostructure arrays. *Nature* 579: 368–374.

Lin M-L, et al. (2018) Moiré phonons in twisted bilayer MoS_2. *ACS Nano* 12: 8770–8780.

Lin K-Q, et al. (2021a) Large-scale mapping of moiré superlattices by hyperspectral Raman imaging. *Advanced Materials* 33: 2008333.

Lin Y-C, Motoyama A, Solís-Fernández P, et al. (2021b) Coupling and decoupling of bilayer graphene monitored by electron energy loss spectroscopy. *Nano Letters* 21: 10386–10391.

Lin Y-C, Motoyama A, Kretschmer S, et al. (2021c) Polymorphic phases of metal chlorides in the confined 2D space of bilayer graphene. *Advanced Materials* 33: 2105898.

Liu Y, et al. (2021) Moiré superlattices and related moiré excitons in twisted van der Waals heterostructures. *Chemical Society Reviews* 50: 6401–6422.

Lu X, et al. (2019) Superconductors, orbital magnets and correlated states in magic-angle bilayer graphene. *Nature* 574: 653–657.

Madsen J, et al. (2018) A deep learning approach to identify local structures in atomic-resolution transmission electron microscopy images. *Advanced Theory and Simulations* 1: 1800037.

Masubuchi S, et al. (2018) Autonomous robotic searching and assembly of two-dimensional crystals to build van der Waals superlattices. *Nature Communications* 9: 1413.

Nayak PK, et al. (2017) Probing evolution of twist-angle-dependent interlayer excitons in $MoSe_2/WSe_2$ van der Waals heterostructures. *ACS Nano* 11: 4041–4050.

Novoselov KS, et al. (2004) Electric field effect in atomically thin carbon films. *Science* 306: 666–669.

Novoselov KS, et al. (2016) 2D materials and van der Waals heterostructures. *Science* 353: aac9439.

Puebla S, et al. (2022) Apparent colors of 2D materials. *Advanced Photonics Research* 3: 2100221.

Purdie DG, et al. (2018) Cleaning interfaces in layered materials heterostructures. *Nature Communications* 9: 5387.

Quellmalz A, et al. (2021) Large-area integration of two-dimensional materials and their heterostructures by wafer bonding. *Nature Communications* 12: 917.

Ribeiro-Palau R, et al. (2018) Twistable electronics with dynamically rotatable heterostructures. *Science* 361: 690–693.

Rivera P, et al. (2018) Interlayer valley excitons in heterobilayers of transition metal dichalcogenides. *Nature Nanotechnology* 13: 1004–1015.

Rosenberger MR, et al. (2020) Twist angle-dependent atomic reconstruction and moiré patterns in transition metal dichalcogenide heterostructures. *ACS Nano* 14: 4550–4558.

Seyler KL, et al. (2019) Signatures of moiré-trapped valley excitons in $MoSe_2/WSe_2$ heterobilayers. *Nature* 567: 66–70.

Shabani S, et al. (2021) Deep moiré potentials in twisted transition metal dichalcogenide bilayers. *Nature Physics* 17: 720–725.

Sharpe AL, et al. (2019) Emergent ferromagnetism near three-quarters filling in twisted bilayer graphene. *Science* 365: 605–608.

Solís-Fernández P and Ago H (2022) Machine learning determination of the twist angle of bilayer graphene by Raman spectroscopy: Implications for van der Waals heterostructures. *ACS Applied Nano Materials* 5: 1356–1366.

Solís-Fernández P, Bissett M, and Ago H (2017) Synthesis, structure and applications of graphene-based 2D heterostructures. *Chemical Society Reviews* 46: 4572–4613.

Sun X, et al. (2021) Correlated states in doubly-aligned hBN/graphene/hBN heterostructures. *Nature Communications* 12: 7196.

Ueno K, et al. (1990) Heteroepitaxial growth of layered transition metal dichalcogenides on sulfur-terminated GaAs{111} surfaces. *Applied Physics Letters* 56: 327–329.

Wang L, et al. (2013) One-dimensional electrical contact to a two-dimensional material. *Science* 342: 614–617.

Wang D, et al. (2016) Thermally induced graphene rotation on hexagonal boron nitride. *Physical Review Letters* 116: 126101.

Woods CR, et al. (2016) Macroscopic self-reorientation of interacting two-dimensional crystals. *Nature Communications* 7: 10800.

Yankowitz M, et al. (2018) Dynamic band-structure tuning of graphene moiré superlattices with pressure. *Nature* 557: 404.

Yankowitz M, Chen S, et al. (2019a) Tuning superconductivity in twisted bilayer graphene. *Science* 363: 1059–1064.

Yankowitz M, Ma Q, et al. (2019b) van der Waals heterostructures combining graphene and hexagonal boron nitride. *Nature Reviews Physics* 1: 112.

Yoo H, et al. (2019) Atomic and electronic reconstruction at the van der Waals interface in twisted bilayer graphene. *Nature Materials* 18: 448.

Zhang X, et al. (2016) Review on the Raman spectroscopy of different types of layered materials. *Nanoscale* 8: 6435–6450.

Zhang C, et al. (2017) Systematic study of electronic structure and band alignment of monolayer transition metal dichalcogenides in Van der Waals heterostructures. *2D Materials* 4: 015026.

Zheng B, et al. (2019) WO_3–WS_2 vertical bilayer heterostructures with high photoluminescence quantum yield. *Journal of the American Chemical Society* 141: 11754–11758.

Dirac materials beyond graphene

Paola De Padova[a,b] **and Mariusz Krawiec**[c], [a]Consiglio Nazionale delle Ricerche-ISM, Roma, Italy; [b]Instituto Nazionale di Fisica Nucleare-Laboratori Nazionali di Frascati—INFN-LNF, Frascati, Italy; [c]Institute of Physics, Maria Curie-Sklodowska University, Lublin, Poland

© 2024 Elsevier Ltd. All rights reserved.

Introduction 329
Overview on Dirac materials beyond graphene 330
Key issues on elemental 2D Dirac materials beyond graphene 331
(3 × 3)/(4 × 4) silicene on Ag(111), planar silicene on Au(111)/Si(111), and (√3 × √3)R30° multilayer silicene 331
(3 × 3)/(4 × 4) silicene on Ag(111) 331
Planar silicene on Au(111)/Si(111) 333
(√3 × √3)R30° multilayer silicene/Ag(111) 333
The case of Stanene on supported substrates: Buckled Stanene/InSb(111) and flat Stanene/Cu(111) 334
Buckled Stanene grown on InSb(111) 335
Flat Stanene grown on Cu(111) substrate 336
The case of bismuthene 337
Ultra-flat bismuthene on SiC(0001) 338
Brief summary on 2D-TMDs 339
The case of 1T′-WS2 on bilayer graphene/SiC(0001) 339
Conclusion 339
References 340

Abstract

The meaning of Dirac's materials, in its most common sense, has been explored by taking a quick look at the Dirac equation, as originally formulated, and subsequently applied to the structure of condensed matter, of two-dimensional (2D) materials beyond graphene.

What makes 2D materials exceptional, as well as the discovery of new allotropic forms, is the possibility of having extraordinary physical properties, such as energy dispersion, which immediately can correlate electrons to their being Dirac fermions.

Through experimental and theoretical examples, we report structural and electronic properties of 2D materials beyond graphene, which today represent the frontier of condensed matter physics.

Key points

- Overview on Dirac materials
- Illustrative examples
- Conclusions

Introduction

The Dirac equation is the wave equation that describes the motion of fermions in a relativistically invariant way (Dirac, 1928). Born to describe massless particles with relativistic behavior, in 1928, it waited for several decades to be dusted off in the framework of the structure of matter, helping to award a Nobel Prize in physics (2010) to the two-dimensional (2D) atomic crystal (Novoselov et al., 2005a), currently the most famous in the world, graphene, a single layer of carbon (C) atoms arranged in a honeycomb lattice. 2D transition metal dichalcogenides (TMDs), such as MoS_2, $MoSe_2$, WS_2, $MoTe_2$, WSe_2, are naturally exfoliated, and today, largely artificially synthesized (Li et al., 2020, Lv et al., 2015, Samadi et al., 2018).

What made the difference and represented a significant increasing forward in the research of 2D synthetic materials, constituting a breakthrough in the field of condensed matter, was, first, the artificial synthesis of silicon in the graphene-like allotropic form (Vogt et al., 2012), experimentally realized, for the first time, on the oriented face of the single crystal Ag (111) (Vogt et al., 2012), paving the way for the search for other 2D elemental materials (Krawiec, 2018). This silicon allotrope, with Si atom arranged in a buckled honeycomb structure, not present in Nature, was already predicted in 1994, as a corrugated layer of Si, analogous to graphite (Takeda and Shiraishi, 1994). It was called silicene, by analogy to graphene in 2007 (Guzmán-Verri and Lew Yan Voon, 2007). Its electronic properties have been investigated, predicting electronic structure with Dirac cone, similar to graphene (Lebègue and Eriksson, 2009; Cahangirov et al., 2009).

https://doi.org/10.1016/B978-0-323-90800-9.00169-4

Actually, as in the case of graphene, silicene, has remarkable physical properties, hosting Dirac fermions, as well as providing new template for a stacked growth of multilayer silicene (De Padova et al., 2013a,b, 2017), and opening the door to the family of synthetic 2D elemental materials (De Padova et al., 2022).

In the popular work "*Two-dimensional gas of massless Dirac fermions in graphene,*" the electron transport is basically described by the Dirac relativistic equation, where the charge carriers, both electrons and holes in their ambipolar behavior, in graphene, simulate the relativistic particles having *quasi* zero rest mass with an effective "*speed of light*" $c^* \approx 10^6\ \mathrm{ms}^{-1}$, exhibiting the anomalous room-temperature quantum Hall effect, characteristic of two-dimensional Dirac fermions (Novoselov et al., 2004, 2005b).

Thus, a large family of materials, which include graphene and more generally the 2D materials, and *d*-wave superconductors, have in common the particularity that their fermions at low energy, near the Fermi level (FL), behave as massless Dirac particles that do not follow the Schrödinger classical Hamiltonian, but rather that of Dirac (Dirac, 1928). This new emergent class of materials identified with particular physical properties of condensed matter structure, is today called "*Dirac materials.*"

As it may concerns, it is necessary to consider the special features in the density of states (DOS) connected to the Van Hove singularities (Van Hove, 1953), whose wave vectors at which they occur are referred as critical points in the Brillouin zone (BZ). The so-called Dirac points in graphene, in the k-space, reciprocal space, to which Dirac cones are associated, are Van-Hove singularity, as well as in twisted graphene layers, showing pronounced Van-Hove singularities in the DOS due to the interlayer coupling (Bostwick et al., 2007; Brihuega et al., 2012; Ohta et al., 2006).

This expression, Dirac cone, derives directly from the energy bands of organized solids, where angular resolved photoemission spectroscopy (ARPES) (Kevan, 1992; Hüfner, 2010) is a very important spectroscopic technique for studying Dirac materials.

In graphene, and bilayer graphene (Bostwick et al., 2007; Ohta et al., 2006), the two special, inequivalent points, K and K′, representing the apexes of the hexagon, in the k-space, where the filled, π, and empty, π^* bands, meet at the FL, in the Dirac points, with zero gap, causing energy bands dispersions cone-shaped. It is here that the structural form of atomic arrangement comes into play in close conjunction with the dispersion of the bands, and the realm of direct space, atomic structure, and electronic properties, energy band structure, takes on all its extreme importance. Scanning tunneling microscopy (STM), scanning tunneling spectroscopy (STS) and ARPES represent, in the direct and reciprocal space, respectively, the main characteristics, both of the surface crystal structure, atomic positions arrangement, and of the local- and long-range electronic properties, giving, these techniques, an immediate amazing ability in the study and classification of Dirac's materials.

The electrons, as well as holes, behave, neglecting all scattering phenomena as massless particles, travel undisturbed toward the FL, or toward a separating gap of the two Dirac cones associated with the filled and empty bands, respectively.

This inverse relationship between the direct and reciprocal space of matter has established an intimate relationship between the honeycomb-like atomic arrangement and Dirac's fermions, quasiparticles that follow the behavior dictated by Dirac equation and their precise position in 3D, 2D and 1D of k-space.

Thus, the search for artificial or natural 2D honeycomb-like materials constitutes a real extraordinary opportunity for the discovery of new physical properties of condensed matter that lead to intense research with the ultimate dual purpose both in the field of fundamental and applied physics. Monolayer topological insulators, giving rise to modern terms such as *spintronics* and *walleytronics*, new terms that refer to Dirac's innovative 2D materials, which could exploit novel electronic devices, based on these emergent physical properties of electronic structures (Ezawa et al., 2018).

Of a great importance, it is the spin orbit interactions, named also spin orbit coupling (SOC), which leads to quantum spin Hall effect (QSHE) in graphene, converting it to a quantum spin Hall insulator, from an ideal two-dimensional semi-metallic state (Kane and Mele, 2005a,b). This gives rise to a novel electronic state of matter, with time-reversal invariance, typically of the so-called topological insulator (TI) materials, gapped in the bulk and able to undisturbed transport the spin and charge in the gapless edge states propagating at the sheet boundaries (Kane and Mele, 2005a,b). These electronic states, close to the Fermi edge, are very important for their transport behavior. Due to their spin directionality, these states are protected, that is, imperturbable against the effect of exposure to foreign adatoms, as well as to intrinsic or extrinsic disorder and/or scattering processes (Kane and Mele, 2005a). In a strict sense, the QSHE occurs at the time-invariant points of the Brillouin zone, which is not the case in 2D honeycomb materials, like graphene. Nevertheless, similar state can still exist, and the edge states are robust against weak disorder and still contribute to the spin-Hall conductance (Kane and Mele, 2005a). Unfortunately in graphene the spin-orbit induced gap at the Dirac point, is extremely weak as 0.8×10^{-3} meV, it is a second order process, occurring only at unrealistically low temperature (Yao et al., 2007).

In this work we will report on some impressive examples of the so-called systems, *par excellence,* Dirac materials, 2D materials beyond graphene. The most relevant experimental measurements and theoretical calculations of the current scientific research specific to this wonderful field of surface physics and, in general, condensed matter will be related. 2D elemental materials beyond graphene and TMD exfoliated and/or supported on template investigated through the main techniques, the heart of the investigation of the structure of matter, STM, STS, and ARPES, will be discussed.

Overview on Dirac materials beyond graphene

In addition to the QSHE in graphene, it was also proposed to obtain the QSH state, a state of matter with topological properties distinct from those of conventional insulators, in HgTe/CdTe quantum well, tuning the thickness of the HgTe layer, demonstrating, thus, that when the thickness of the quantum well is varied, at a critical value, the electronic bands at the time-invariant k-points become inverted, thus exhibiting the QSH effect with a single pair of helical edge states (Bernevig et al., 2006). Just few time later, the QSH insulator state in HgTe quantum wells was experimentally observed, below liquid helium temperature (König et al., 2007).

Two-dimensional elemental topological insulators of group-IVA beyond graphene, including silicene, germanene (Liu et al., 2011a; Salomon et al., 2020), stanene (Liu et al., 2011b; Xu et al., 2013), and plumbene (Yu et al., 2017) are a new class of Dirac materials characterized by a predicted QSHE, exhibiting band gap generated from spin-orbit coupling with much larger SOC gap values, of 1.55 meV, for silicene, which makes it a robust TI up to ~15 K (Liu et al., 2011a); 23.9 meV for germanene and functionalized germanene (much higher than the liquid nitrogen temperature) (Liu et al., 2011a; Si et al., 2014), and ~100 meV for stanene (Xu et al., 2013), and ~200 meV for plumbene (Yu et al., 2017).

Very frequently, this gap makes these topological materials, electrically insulating in the atomic sheets (or bulk) and conductive with the edge of the sheets (or surface), which support the one dimensional (1D) topological edge states, possess quasiparticles obeying the Dirac equation, and having honeycomb-like atomic arrangement.

So far, to the 2D elemental materials beyond graphene of group-IVA, already presented, those belonging to group-IIIA-VA-VIA, IVB [for exhaustive literature see Ref. (De Padova et al., 2022)] such as: borophene (Mannix et al., 2015), gallenene (Tao et al., 2018) blue phosphorene (Zhang et al., 2016a; Gu et al., 2017), thallene (Gruznev et al., 2020), arsenene (Shah et al., 2020), antimonene (Lei et al., 2016; Jałochowski and Krawiec, 2019), bismuthene (Reis et al., 2017), selenene (Qin et al., 2017a), tellurene (Zhu et al., 2017), and hafnene (Li et al., 2013) have been recently synthesized, as well as theoretically predicted (Huang et al., 2014; Jin and Jhi, 2015).

To be more complete, a short mention to other emerging metal-enes, less realized but extremely interesting, such as Rh nanosheets (Duan et al., 2014; Zhao et al., 2015), monolayer goldene intercalated in graphene layers (Yuan et al., 2020), freestanding monatomic thick 2D Gold (Wang et al., 2019), iron membranes suspended in graphene pores (Zhao et al., 2014), which promise to exhibit remarkable physical properties.

Silicene is the oldest member of the graphene followers family. It was first synthesized on Ag(111) substrate (Vogt et al., 2012), and later also on surfaces of other crystals, $ZrB_2(0001)$ (Fleurence et al., 2012), Ir(111) (Meng et al., 2013), ZrC(111) (Aizawa et al., 2014), Ru(0001) (Huang et al., 2017), and, as predicted in (Podsiadły-Paszkowska and Krawiec, 2015), on ultrathin Pb(111) (Stępniak-Dybala and Krawiec, 2019). Furthermore, we have to remark that supported germanene was successful synthesized on oriented (111) substrates such as: platinum (Li et al., 2014), gold (Dávila et al., 2014), aluminum (Derivaz et al., 2015), molibdemun disulfide (Zhang et al., 2016b), cupper (Qin et al., 2017b) and silver (Lin et al., 2018).

Continuing further with Dirac's 2D elementary materials of group-IVA, recently discovered, the case of plumbene, a single atomic layer of Pb arranged in a honeycomb lattice, is also of great interest. As a strong analog of graphene, plumbene is expected to be a two-dimensional material with strong spin-orbit coupling effects.

From theoretical point of view, monolayer and bilayer plumbene were predicted (Huang et al., 2014; Rivero et al., 2014; Zhang et al., 2018), as well as a class of new QSH insulators, PbX (PbX; X = H, F, Cl, Br, and I), obtained decorating plumbene monolayers, exhibiting extraordinarily nontrivial giant-gap in the range of 1.03 to 1.34 eV (Zhao et al., 2016). Indeed, plumbene, as mentioned, was found to be a topological insulator with a large bulk gap (~200 meV) through electron doping (Yu et al., 2017), possible, for instance, using gate-tunable method (Yu et al., 2015), maintaining, thus, a robust nontrivial state with respect to external strain. Experimentally, a large area of plumbene was obtained, with success, by segregation process by depositing Pb thin films on Pd(111) (Yuhara et al., 2019), and a flat honeycomb Pb was synthesized on a Fe monolayer on Ir(111) interface (Bihlmayer et al., 2020).

Key issues on elemental 2D Dirac materials beyond graphene

As the family of Dirac materials discovered nowadays is very rich, including as mentioned, for instance, many groups- of the periodic table, -IIIA, IVA, VA-VIA, and IVB, such as borophene, gallenene, thallenene, silicene, germanene, phosphorene, stanene, arsenene, antimonene, bismuthene, selenene, tellurene, hafnene, and TMDs, both in the form of elementary 2D materials and under that of composite compounds, we provide the essential crucial discoveries by separating them, in various paragraphs in the next section. The suffix-ene, in analogy to graphene, for the particular atom considered, represents its corresponding honeycomb-like lattice.

From each group of the periodic table of elements we take the significant works that highlight both theoretical calculations and experimental results underlining the importance of the ARPES, STM, and STS to study the electronic properties in conjunction with their relevant atomic honeycomb structures.

(3 × 3)/(4 × 4) silicene on Ag(111), planar silicene on Au(111)/Si(111), and (√3 × √3)R30° multilayer silicene

The following three paragraphs summarize the main results obtained on silicene and multilayer silicene grown on different substrates.

(3 × 3)/(4 × 4) silicene on Ag(111)

From theoretical point of view silicene and germanene were predicted to assume honeycomb-like arrangement, although, unlike in graphene, with two sublattices displaced vertically, making the structures not completely planar, as illustrated in Fig. 1 However, planar forms have also been predicted (Cahangirov et al., 2009). In spite of the buckled geometry, the electronic properties

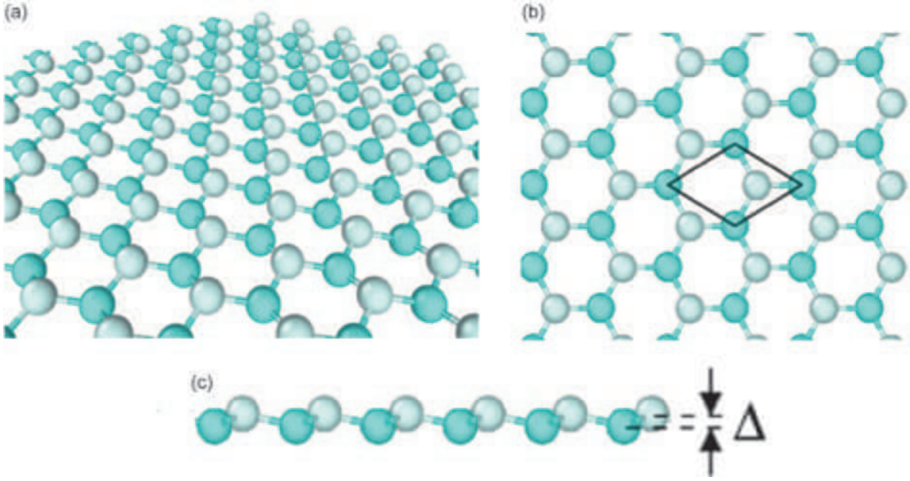

Fig. 1 Structural model of a freestanding 2D honeycomb-lattice material in its low-buckled form. Panels (a)-(c) show perspective, top and side views. Two sublattices separated vertically by Δ (c) are marked by different colors. The unit cell is indicated in (b). Adapted from Fig. 1 of Krawiec M (2018) Functionalization of group-14 two-dimensional materials. *Journal of Physics: Condensed Matter* 30: 233003–29.

characteristic of graphene are preserved and express electronic structures with Dirac cones at K and K′ points, of hexagon in the reciprocal space, hosting the π-π^* Dirac bands with linear behavior (Takeda and Shiraishi, 1994; Guzmán-Verri and Lew Yan Voon, 2007; Lebègue and Eriksson, 2009; Cahangirov et al., 2009).

Furthermore, owing to the buckling and mixed sp^2/sp^3 bonding, silicene is more chemically active than graphene. This feature can be recognized as an advantage, as it allows for quite easy functionalization by different means (Krawiec, 2018). For example, the energy gap in the energy spectrum can be open and tuned by external electric field (Ni et al., 2012; Drummond et al., 2012), which has led to the fabrication of the first field-effect transistor based on silicene (Tao et al., 2015).

Experimentally, the fascinating proof for the first graphene-like 2D silicene was successful achieved in its prototypical (3 × 3)/(4 × 4) reconstruction, on Ag(111) single crystal, by depositing Si in UHV, at a temperature of about 490 K (Vogt et al., 2012). Subsequently, numerous authors synthesized silicene on Ag(111) and others on different substrates (Aizawa et al., 2014; Du et al., 2014; Feng et al., 2012; Fleurence et al., 2012; Huang et al., 2017; Lin et al., 2012; Meng et al., 2013; Stępniak-Dybala and Krawiec, 2019; Stępniak-Dybala et al., 2019).

The salient electronic and structural characteristics of (3 × 3)/(4 × 4) silicene epitaxially grown on Ag (111) [the (3 × 3) silicene unit cells coincide with a (4 × 4) Ag(111)] (Vogt et al., 2012), are described in the following.

Fig. 2(a) shows the ARPES dispersions from the (3 × 3)/(4 × 4) silicene on Ag(111) measured along the Ag $\overline{\Gamma} \rightarrow \overline{K}$ direction through the $\overline{K}$ silicene point. The BZ scheme, where the red arrow indicates the ARPES measurement direction, is reported in Fig. 2 (b). Panels (c)–(e) display the filled-states STM images of clean Ag(111) (1 × 1) and the flower-like (3 × 3)/(4 × 4) silicene, while the model of silicene on Ag(111), obtained from DFT calculations, is depicted in (e). The larger orange balls denote the Si atoms directly sit on top of Ag atoms; the smaller ones those located between the Ag atoms, and the gray balls the substrate Ag atoms. In addition, the ball-and-stick model for the freestanding silicene is displayed in the bottom right panel (e) corner.

Very interestingly, the ARPES energy dispersions vs. the parallel momentum, collected at the special point $\overline{K}^{\mathrm{Si}}$ (a) of the smaller (1 × 1) silicene hexagon scheme of the first BZ (b), that of Ag(111) (1 × 1) in the reciprocal space is also shown, along the Ag $\overline{\Gamma} \rightarrow \overline{K}$ direction, displays a linear dispersion (Vogt et al., 2012). This linear dispersion, showing a velocity of $\sim 1.3 \cdot 10^6\ m\,s^{-1}$ similar to that of graphene (Novoselov et al., 2005b), was attributed to the π branch of a silicene Dirac cone, pointing to massless Dirac fermions in silicene (Vogt et al., 2012). The band seems to disappear at ~0.3 eV below the Fermi level EF, so that an energy gap of approximately 0.6 eV, between the π and π^* silicene bands was deduced (Vogt et al., 2012). The (3 × 3) reconstruction of silicene induced band folding, leading to cone-like structures at $\overline{\Gamma}_{00}$, as well as at Ag $\overline{\mathrm{M}}$, which is the $\overline{\Gamma}_{02}$ point along $\overline{\mathrm{M}}$–$\overline{\Gamma}$–$\overline{\mathrm{M}}$ direction of the (3 × 3) reconstructed silicene BZ (Avila et al., 2013).

Although this assignment of the silicene π structure was debated, trying to not assigning any Dirac fermion character caused by the supposed hybridization between the Si and Ag bands (Guo et al., 2013), other groups affirmed, by first-principles calculations and taking into account the influence of the Ag substrate, the presence of Dirac fermions with a finite band gap (Huang et al., 2013), and nevertheless the hybridization with the silver bands, related to the specific (3 × 3)/(4 × 4) silicene reconstruction (Cahangirov et al., 2013).

Furthermore, the presence of the silicene linear band at $\overline{K}^{\mathrm{Si}}$ (Vogt et al., 2012), crossing indeed the FL, probably related to a different silicene/Ag coverage ratio leading to silicene doping, and the Dirac cone at Ag $\overline{\mathrm{M}}$ point, with interesting characteristic of saddle point, given to a possible anisotropic electron delocalization, were confirmed as belonging to the (3 × 3)/(4 × 4) silicene (Tsoutsou et al., 2013). Notably, six pairs of Dirac cones, located at the $\overline{K}^{\mathrm{Si}}$ of the (3 × 3) reconstructed silicene BZ have been measured by ARPES (Feng et al., 2016). We note that the substrate temperature is an important issue for the growth of (3 × 3)/(4 × 4)

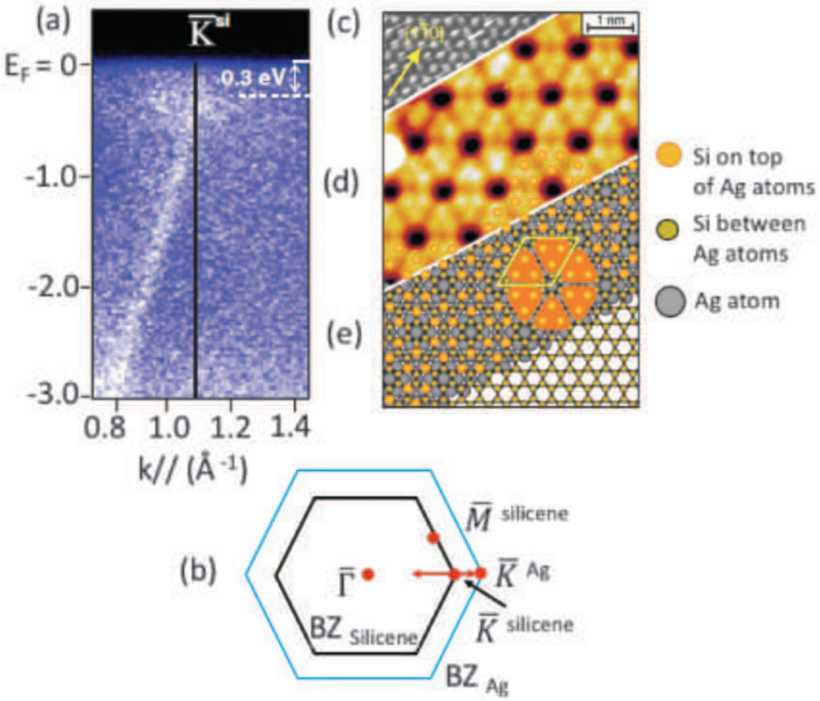

Fig. 2 ARPES dispersions at hν = 126 eV from the (3 × 3)/(4 × 4) silicene on Ag(111) measured along the Ag $\overline{\Gamma} \rightarrow \overline{K}$ direction through the $\overline{K}$ silicene point (a); BZ scheme where the red arrow indicates the ARPES measurement direction (b); filled-states STM images of clean Ag(111) (1 × 1) (c); STM of the 4 × 4 silicene (d); model of silicene on Ag(111): the larger orange balls denote the Si atoms sitting on top of Ag atoms; the smaller balls those located between the Ag atoms, and the gray balls the Ag atoms (e). The ball-and-stick model for the freestanding silicene layer is displayed in the bottom right corner of (e). Adapted from Fig. 3 and Fig. 4 of Vogt P, De Padova P, Quaresima C, Avila J, Frantzeskakis E, Asensio MC, Resta A, Ealet B, and Le Lay G (2012) Silicene: Compelling experimental evidence for graphenelike two-dimensional silicon. *Physical Review Letters* 108: 155501–5.

silicene, exhibiting Dirac fermion features (Liu et al., 2014b; Fukaya et al., 2013). They used linear dichroism ARPES, in addition to tight-binding model, and first-principles calculations, to attest that these six pairs of Dirac cones mainly derived from the original cones at the $\overline{K}$ ($\overline{K'}$) points of free-standing silicene (Feng et al., 2019), splitted by the external periodic potentials originated from the substrate-overlayer interaction (Feng et al., 2019), confirming the origin of the Dirac cones in the (3 × 3) silicene/Ag(111) (Vogt et al., 2012).

From proposed structural model, the Si atoms located directly on top of Ag atoms are displaced in z direction with respect to those at the bottom. The distance between the top (bottom) Si atoms and the first silver layer is of 0.292 and 0.217 nm (Vogt et al., 2012), giving, interestingly, to the silicene sheet, a buckling of 0.075 nm between the orange and yellow Si atoms as marked in Fig. 2(e).

Planar silicene on Au(111)/Si(111)

While the planar form of the isolated silicene was predicted to be dynamically unstable (Cahangirov et al., 2009), it can exist when placed on a substrate, as demonstrated in the case of thin Au slab on the Si(111) (Stępniak-Dybala et al., 2019). It has been shown that ultimately flat layer of Si atoms arranged in a honeycomb lattice, as evidenced in Fig. 3, can be synthesized in the process of the surface segregation. The exceptionally low buckling, an order of magnitude lower than in the free-standing form, is a consequence of significant interaction between Si and underlying Au atoms.

This is also responsible for deformation of hexagons, making the silicene lattice substantially strained (Nazzari et al., 2021). In addition to that, the continuous layer of the planar silicene undergoes long-range structural deformations, similar to graphene.

In the case of Au/Si(111) substrate the planar silicene is a part of a more complex heterostructure containing also twisted buckled phase of silicene (Jaroch et al., 2021), and may serve as a platform for developing 2D magnetism (Krawiec et al., 2021).

(√3 × √3)R30° multilayer silicene/Ag(111)

Multilayer silicene, showing the evidence of Dirac fermions, was predicted beyond silicene monolayer both in bilayer and different stacking configurations (Hoffmann, 2013; Kamal et al., 2013; Cahangirov et al., 2014), and realized (De Padova et al., 2013a) in the √3 ×√3R30° reconstruction on top of the (3 × 3)/(4 × 4) monolayer silicene (Vogt et al., 2012), with a growth that proceeds by successive flat terraces separated by ~3 nm and a unit cell of ~0.64 nm (De Padova et al., 2013a; Vogt et al., 2014).

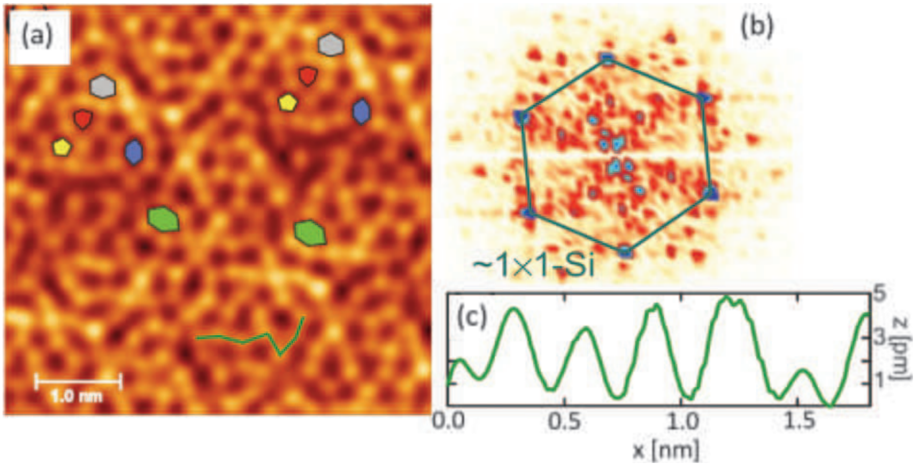

Fig. 3 (a) Atomically resolved STM image of planar silicene on Au(111) thin films on Si(111) substrate. (b) 2D Fourier transform of the STM image shown in (a). (c) Topography profile along the line marked in (a). Adapted from Fig. 2 of Stępniak-Dybala A, Dyniec P, Kopciuszyński M, Zdyb R, Jałochowski M, Krawiec M (2019) Planar silicene: A new silicon allotrope epitaxially grown by segregation. *Advanced Functional Materials* 29: 1906053–5.

Numerous other experimental evidences have been reported on synthesis of multilayer silicene (De Padova et al., 2013a,b, 2014, 2016; Du et al., 2016; Grazianetti et al., 2017; Li et al., 2016; Salomon et al., 2014; Vogt et al., 2014), although a debate existed if this $\sqrt{3} \times \sqrt{3}$ R30° reconstruction was, indeed, induced by Ag atoms on Si(111) (Shirai et al., 2014).

Clear evidence of the synthesis of multilayer silicene was provided by a study done using x-rays, where the characteristics of ordinary silicon and multilayer silicene are clearly distinguished (De Padova et al., 2016). The discrepancy of the conflicting results, reported in the literature, is most likely attributable to the preparation of the samples, being the temperature applied to the substrate and the flow of the silicon cell for evaporation, the fundamental ingredients for the formation of the silicene multilayer or ordinary silicon.

Moreover, recently the multilayer silicene has been realized on other templates such as Si covered with Ag or Bi atoms (De Padova et al., 2017, 2019; Garagnani et al., 2022). Very interestingly a model performed with DFT calculations for three layer silicene grown on Ag-Si(111) template with AA′B stacking was successfully proposed (De Padova et al., 2017).

It should also not be forgotten that in addition to the transistor made using a silicene monolayer (Tao et al., 2015), one based on silicene multilayer was also designed and produced (Grazianetti et al., 2017).

Thus, It is extremely interesting to report the case of multilayer silicene on Ag(111), where the presence of the Dirac cones excellently assign to this new allotrope of silicon a good example of Dirac material. In fact, the following Fig. 4 shows some characteristics that highlight the electronic properties of the silicene multilayer (4.5 MLs silicene layers) epitaxially grown on top of first $(3 \times 3)/(4 \times 4)$ monolayer on Ag(111) (De Padova et al., 2013a).

ARPES pattern in Fig. 4(a) was collected by using a synchrotron radiation photon energy of 126 eV, along the $\overline{\Gamma} \rightarrow \overline{K}^{\text{silicene}}$ on the $\sqrt{3} \times \sqrt{3}$ R30° multilayer silicene, its waterfall line profiles is displayed in Fig. 4(b), as a guide for the eyes (De Padova et al., 2013a).

The energy band dispersion clearly shows the linear $\wedge$ and $\vee$ shape at $\overline{\Gamma}_0$, where the $\overline{K}_{(1\times1)\text{ silicene}}$ and $\overline{K}'_{(1\times1)\text{ silicene}}$ bands fold, as drown in the BZs scheme of Fig. 4(c) giving rise to the Dirac cones (De Padova et al., 2013a). These linear bands were assigned to the π and π^* of the $\sqrt{3} \times \sqrt{3}$ R30° multilayer silicene, with the π^* state are partially filled by the charge transfer from Ag substrate, no gap between the π and π^* bands and their crossing at Dirac point—0.25 eV (De Padova et al., 2013a). This electronic features exhibit at RT a Fermi velocity of $\sim 0.3 \cdot 10^6\ m \cdot s^{-1}$ (De Padova et al., 2013a) only a bit smaller to that found by STM quantum interference pattern at low temperature (Chen et al., 2012). In addition, the inner structure inside the more external π cone is related to the presence of the (1×1) silicene layer in its successive terraces growth. Moreover, to show the Dirac features along the other six $\overline{\Gamma}$ points (from $\overline{\Gamma}_1$ to $\overline{\Gamma}_6$) of the $\sqrt{3} \times \sqrt{3}$ R30° multilayer silicene, the Fig. 4(d) displays the dispersion pattern vs. the azimuthal angle, very well evidencing all the linear bands belonging to multilayer silicene, in addition to the *sp* silver bands (De Padova et al., 2013b). Here, the constant energy contour obtained on the $\sqrt{3} \times \sqrt{3}$ R30° multilayer silicene, evidencing the characteristics of the Dirac cones, have been amply studied. In Fig. 4(e) there is the scheme of the Dirac cone cut, along with the dispersion measured (De Padova et al., 2013b).

The case of Stanene on supported substrates: Buckled Stanene/InSb(111) and flat Stanene/Cu(111)

The following two paragraphs summarize the main results obtained on buckled and flat stanene grown on InSb(111) and Cu(111) substrates.

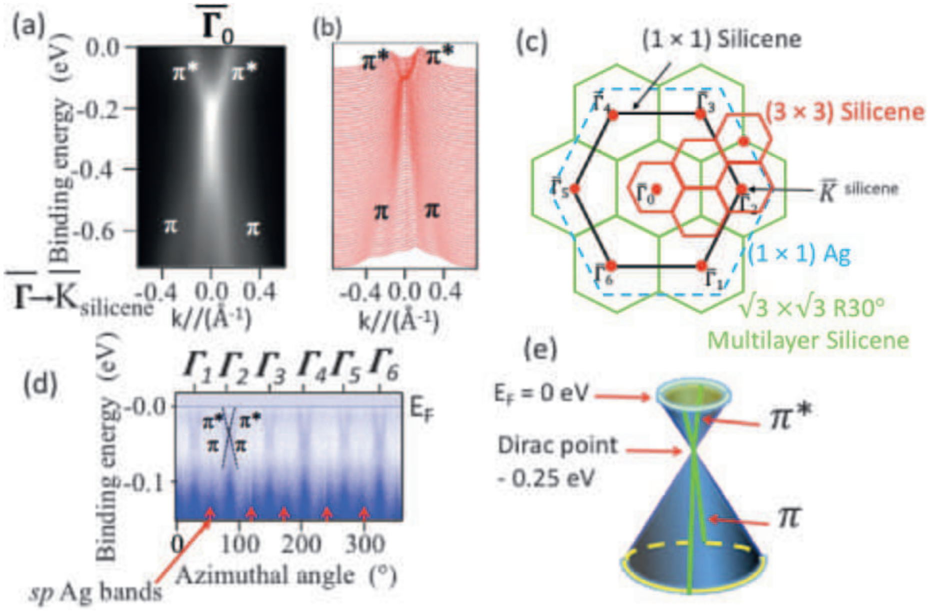

Fig. 4 ARPES Dirac cones of √3 ×√3 R30°multilayer silicene and (1 × 1) silicene layer measured at $\overline{\Gamma}_0$ along the $\overline{\Gamma} \rightarrow \overline{K}^{\text{silicene}}$ direction (hν = 126 eV) showing linear π and π * bands (a), scheme of the surface Brillouin zones (b), and the waterfall line profiles of (a), as a guide for the eyes (c); the Dirac dispersion pattern vs. the azimuthal angle along the six $\overline{\Gamma}$ (from $\overline{\Gamma}_1$ to $\overline{\Gamma}_6$) points of the √3 ×√3 R30* multilayer silicene is reported in (d), and scheme of the Dirac cone cut, along with the dispersion was measured is in (e). Adapted from Fig. 1 of De Padova P, Vogt P, Resta A, Avila J, Razado-Colambo I, Quaresima C, Ottaviani C, Olivieri B, Bruhn T, Hirahara T, Shirai T, Hasegawa S, Asensio MC, and Le Lay G (2013a) Evidence of Dirac fermions in multilayer silicene. *Applied Physics Letters* 102: 163106–4, and Fig. 4 of De Padova P, Avila J, Resta A, Razado-Colambo I, Quaresima C, Ottaviani C, Olivieri B, Bruhn T, Vogt P, Asensio M-C, and Le Lay G (2013b) The quasiparticles band dispersion in epitaxial multilayer silicene. *Journal of Physics: Condensed Matter* 25: 382202–7.

Buckled Stanene grown on InSb(111)

Within the topological insulator materials, the new state of quantum matter, we must mention a monolayer of tin film called stanene, in analogy with graphene, germanene and silicene. It was proposed as a large-gap quantum spin Hall insulator, supporting QSH and quantum anomalous Hall (QAH) states predicted at near room temperature (RT) in honeycomb materials (Xu et al., 2013).

Based on first-principles calculations, stanene performed its entry into 2D materials, exhibiting, in freestanding stanene, a gap value of ~100 meV, sufficiently large for any practical applications at RT (Liu et al., 2011b; Wu et al., 2014; Xu et al., 2013). In addition, their QSH states were found tunable up to an extraordinary gap of ~300 meV, through chemical functionalization by halogen atoms adsorption and/or applying an external strain (Xu et al., 2013).

The optimal geometries for freestanding stanene and freestanding decorated stanene present a low-buckled configuration found more stable, at variance of planar geometry of graphene. This is due to the relatively weak Sn-Sn π-π bonding, thus the buckling stabilizes the system, enhancing the overlap between the σ and π tin orbitals (Xu et al., 2013).

In 2015, the breakthrough experiment, verified, for the first time, as the growth of a single-layer of buckled stanene, material previously largely theoretically predicted, on $Bi_2Te_3(111)$ by molecular beam epitaxy (MBE) (Zhu et al., 2015), opening the way to the search of other suitable templates.

Honeycomb stanene in buckled and/or planar structure was, thus, deposited by MBE on several substrates such as semi-metallic Sb(111) (Gou et al., 2017), PbTe(111) (Zhang et al., 2018), InSb(111) (Xu et al., 2018), Ag(111) (Yuhara et al., 2018), Cu(111) (Deng et al., 2018), Au(111) (Liu et al., 2019), and Sb_2Te_3 (Li et al., 2020b), demonstrating its successful synthesis.

Stanene grown on the surface of InSb(111) is a classic case in which the Sn honeycomb lattice exhibits a buckling (Xu et al., 2018). Single Stanene layer was epitaxially grown by MBE on the surface of InSb(111)B face (Sb terminated) at RT (Xu et al., 2018). Following the intensity of the reflection high energy electron diffraction (RHEED) pattern, during the Sn atoms deposition, stanene was grown on the typical 3 × 3 RHEED pattern of InSb substrate. This substrate reconstruction was completely modified to a 1 × 1 pattern, belonging to stanene, upon the deposition of one layer of tin. At variance of graphene and/or graphite, which exhibit planar sp^2 bonding, the gray tin, often called α-tin, is characterized by sp^3 bonding, attributing to its honeycomb structure a lattice buckling.

As shown in Fig. 5(a), which reports top and side views of the schematic atomic structure of the honeycomb stanene, and Fig. 5 (b), showing the side view of its buckled atomic structure, including in addition four layers of the InSb substrate Sb terminated, stanene, here, is not flat like graphene. The optimized structure obtained by first principle calculations determined a vertical spacing of 2.85 Å to the down-buckled Sn atoms that lied on top of the surface Sb sites of InSb, as indicated in Fig. 5(b). The buckling found

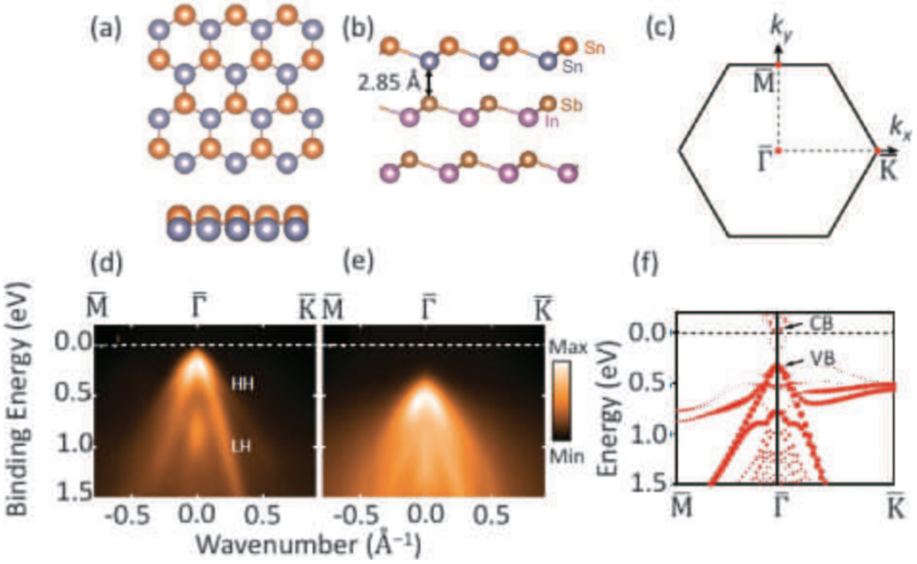

Fig. 5 Schematic atomic structure of the buckled honeycomb stanene, top and side views (a); atomic structure of stanene on InSb(111), side view (b); BZ of stanene (c); ARPES from InSb(111) substrate (d) and from Sn/InSb(111) (e) along the high-symmetry $\overline{\Gamma}\,\overline{K}$ and $\overline{\Gamma}\,\overline{M}$ directions, respectively. The bands of the heavy hole (HH) and light hole (LH) are indicated. Calculated stanene band structures considering six InSb(111) layers are shown in (f). The top and the bottom of the valence (VB) and conduction bands (CB) are also marked, whereas, the Fermi level was set at the conduction band bottom. Adapted from Fig. 1 and 2 of Xu CZ, Chan YH, Chen P, Wang XX, Flötotto D, Hlevyack JA, Bian G, Mo SK, Chou MY, and Chiang TC (2018). Gapped electronic structure of epitaxial stanene on InSb(111). *Physical Review B* 97: 035122–5.

on this honeycomb lattice of stanene leads unaffected the BZ displayed in Fig. 5(c), where the high-symmetry $\overline{\Gamma}\,\overline{K}$ and $\overline{\Gamma}\,\overline{M}$ directions are indicated.

As we can easily observe from Fig. 5(d), the ARPES structures of InSb(111) surface, show the characteristic heavy hole (HH) and light hole (LH) features along the two high-symmetry $\overline{\Gamma}\,\overline{K}$ and $\overline{\Gamma}\,\overline{M}$ directions, reaching at $\overline{\Gamma}$ point the Fermi level, set at the conduction band bottom, corresponding to a lightly n-doped substrate (Xu et al., 2018).

Interestingly enough, after the stanene formation on InSb(111) surface, the ARPES dispersions, displayed in Fig. 5(e), drastically modified, pushing down the top of valence band, opening, therefore, a large gap of about 0.44 eV (Xu et al., 2018). Fig. 5(f) reports the calculated band structures of the honeycomb stanene, including the two top layers of the InSb substrate. These band structures were found, in good agreement with the experiment, confirming that stanene on InSb(111) is an insulator exhibiting a large gap value of 0.44 eV (Xu et al., 2018). Compared to the calculated band gap for freestanding stanene, which was of only ~0.1 eV (Xu et al., 2013), this enhanced band gap was interpreted due to the interaction established between stanene and substrate atoms, similarly to what occurs when halogens are adsorbed on freestanding stanene, then, inducing gap widening (Xu et al., 2013).

This gap for stanene results much larger than the RT thermal energy $k_BT = 25$ meV, attesting that the stanene film grown on InSb could be a promising candidate for QSH applications at RT and/or higher (Xu et al., 2018).

Flat Stanene grown on Cu(111) substrate

In Fig. 6 the results obtained in stanene grown on Cu(111) substrate by low-temperature molecular beam epitaxy are reported, where, interestingly, an ultra-flat honeycomb stanene, graphene-like, exhibiting topological features was discovered (Deng et al., 2018).

The Sn atoms (0.9 ML) were deposited in UHV by Knudsen effusion cell on Cu(111) substrate kept at about 200 K. For STM and STS measurements the Sn/Cu(111) was, successively, cooled to 5 K. After Sn deposition, the Cu(111) substrate resulted mainly covered by an uniform and continuous Sn film, except for a small part of substrate, giving the possibility to trace a profile, which shows an apparent height of the Sn film of 0.18 nm, pointing to a single Sn atomic layer (Deng et al., 2018). The high-resolution STM image from Sn on Cu(111), see Fig. 6(a), shows an impressive stanene honeycomb lattice, whose schematic atomic model is presented in Fig. 6(b). The line profile reported in Fig. 6(c), obtained along the blue line traced in the STM image in Fig. 6(a), evidenced clearly that adjacent Sn atoms have an identical apparent height, with a Sn-Sn distance of 2.94 Å. From the STM image a lattice constant of 0.51 nm is derived, which is exactly twice that of the Cu(111) surface ($a_{Cu}/\sqrt{2} = 0.361/1.414$ nm $= 0.255$ nm), pointing to a formation of a 2 × 2 stanene superstructure. The marked unit cell of this ultra-flat honeycomb stanene includes the two inequivalent Sn atoms, with Sn-Sn bond length very similar to that of bulk α-Sn of 2.81 Å and/or 2.83 Å attributed to freestanding stanene (Xu et al., 2013).

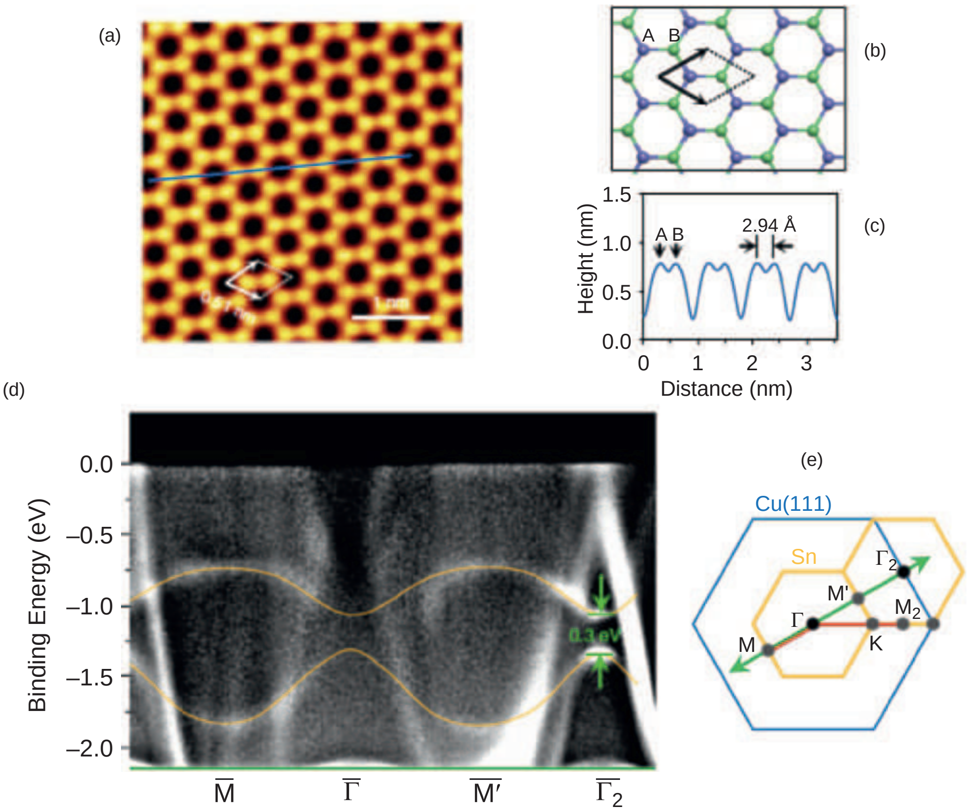

Fig. 6 Atomic resolution STM image of the stanene film on Cu(111) (Vs = 1 V, *I* = 0.4 nA) (a), a lattice constant of 0.51 nm is marked; schematic atomic model of the honeycomb stanene (b); profile along the blue line traced in (a), evidencing that the adjacent Sn atoms have an identical apparent height, with a Sn-Sn distance of 2.94 Å. ARPES map of 0.9 ML stanene on Cu(111) along the $\overline{M}\overline{\Gamma}\overline{M'}\overline{\Gamma}_2$ paths (d), following the green line in (e) is displayed. In (e) is outlined the BZ of Cu(111) (blue), and the 2 ×2 superstructure hexagons of stanene. The orange lines in the ARPES map are the energy bands of Sn orbitals, whereas at $\overline{\Gamma}_2$ point new Sn bands with a gap of 0.3 eV are clearly present. Adapted from Fig. 1 of Deng J, Xia B, Ma X, Chen H, Shan H, Zhai X, Li B, Zhao A, Xu Y, Duan W, Zhang S-C, Wang B, and Hou JG (2018) Epitaxial growth of ultraflat stanene with topological band inversion. *Nature Materials* 17: 1081–1086.

ARPES map of 0.9 ML stanene on Cu(111) (Deng et al., 2018) along the $\overline{M}\overline{\Gamma}\overline{M'}\overline{\Gamma}_2$ paths is displayed in Fig. 6(d), following the green line marked in panel (e), where is outlined the BZ of Cu(111) (blue), and the 2 ×2 hexagons of stanene. The orange lines in the ARPES data are attributed to the energy bands of Sn orbitals. At $\overline{\Gamma}_2$, in the second BZ, a significant gap opening in the Sn bands, centered at around −1.25 eV, with a value of 0.3 eV is clearly evident, more than in $\overline{\Gamma}$, presenting analogies to the p_{xy} orbitals and large SOC gap predicted for fluorine atoms adsorbed on stanene (Xu et al., 2013). Interestingly, first-principles calculations revealed the delicate role played by the stanene lattice stretching, in conjunction to the strong substrate interactions that are important to stabilize the amazing zero-buckling geometry in stanene/Cu(111), creating this honeycomb lattice p_{xy} orbitals mediated by orbital filtering effect of Cu substrate. The discovered in-plane *s-p* band inversion mechanism in communion to the large SOC justified this topological gap here found, at the Γ point (Deng et al., 2018).

It is also extremely important to note that the topologically derived edges states, as predicted by the theory (Xu et al., 2013), have been observed (Deng et al., 2018), making this ultra-flat honeycomb stanene the seed-platform for the observation of physical phenomena typical of Dirac's 2D materials.

Remarkably, remaining in the frame of planar honeycomb stanene, we also mention the results obtained on epitaxially grown stanene/Ag (111), where the electronic structures exhibited the characteristic surface 2D parabolic dispersion, and any evident presence of spin-orbit -coupling effect, fact that attributed to the strong interaction with substrate, hosting, before stanene honeycomb condensation, an underlying 2D Ag_2Sn surface alloy (Yuhara et al., 2018).

The case of bismuthene

As a representative of 2D material of the group-VA, we report the supported √3 ×√3 R30° bismuthene, synthesized on the SiC(0001) substrate in a planar configuration.

Ultra-flat bismuthene on SiC(0001)

The scheme of planar √3 ×√3 R30° bismuthene layer placed on the threefold-symmetric SiC(0001) substrate is illustrated in Fig. 7(a). Combining theory and experiment, the bismuthene on SiC(0001) system was found to represent a *quasi*-2D topological insulator, with large QSH gap, determined by strong SOC (Reis et al., 2017).

The high resolution filled-states STM image of Fig. 7(b), shows the bismuthene characteristic honeycomb pattern (Reis et al., 2017), whereas the DFT band-structure calculations, performed with the hybrid exchange-correlation functional including SOC (Liu et al., 2014a) are displayed in Fig. 7(c), showing at the $\overline{\Gamma}$ point a direct energy gap of 1.06 eV, much larger than in graphene, which was calculated to be about 10^{-3} meV (Yao et al., 2007). The conduction band at $\overline{\Gamma}$ has a wide indirect band gap $E_{gap} = 0.67$ eV, marked by the dashed lines in DFT bands. In conjunction ARPES measurements are displayed in Fig. 7(d) and the surface BZ scheme in Fig. 7(e). ARPES band dispersion, the zero of energy (E_F) was aligned to the Fermi level of the spectrometer, was probed along the critical points $\overline{\Gamma}$, $\overline{K}$ $\overline{M}$ of the SBZ of Fig. 7(e). Clearly the maximum of the valence band and the large band splitting of about 0.43 eV at $\overline{K}$ point, identified as the Rashba fingerprint of the system (Reis et al., 2017), are in very good agreement with the theoretical calculations reported in Fig. 7(c) (Reis et al., 2017). By STS measurements conductive edge states were stimulatingly probed (Reis et al., 2017), constituting together to the results reported on stanene/Cu(111) (Deng et al., 2018) an excellent platform for the conductive topologically derived boundary states (TDSs) (Reis et al., 2017).

Very interesting, this archetype work demonstrated the importance of the substrate in controlling the orbitals in 2D QSH insulator (Reis et al., 2017). Actually, in the bismuthene on SiC(0001), the physical mechanism for rising the QSH gap and controlling the not trivial topological invariant, is different from graphene (Kane and Mele, 2005a), where the gap emerges from the SOC between next-nearest neighbors, and it is, as mentioned, a second order process, and/or other 2D material of group-IVA, such as silicene, although with larger gap, where the SOC is still next-nearest–neighbor type, having as relevant orbital the p_z character. At variance, in bismuthene on SiC, their low-energy electronic properties are piloted by an huge on-site SOC p_x and p_y orbitals (Reis et al., 2017; Liu et al., 2014a). In addition, to the large atomic (on-site) SOC related to heavy Bi atom, there is also the interaction with substrate, due to the large lattice parameter assumed by planar, without buckling, strain-free bismuthene in the epitaxial growth on SiC(0001) (Reis et al., 2017). Further evidence of the importance of the occurrence of strain, external induced or due to the epitaxial growth, is given by the case of functionalized stanene, where QSH states can be effectively tuned by chemical functionalization and by external strain (Xu et al., 2013); and/or compressed germanene synthesized on MoS_2 (Zhang et al., 2016b).

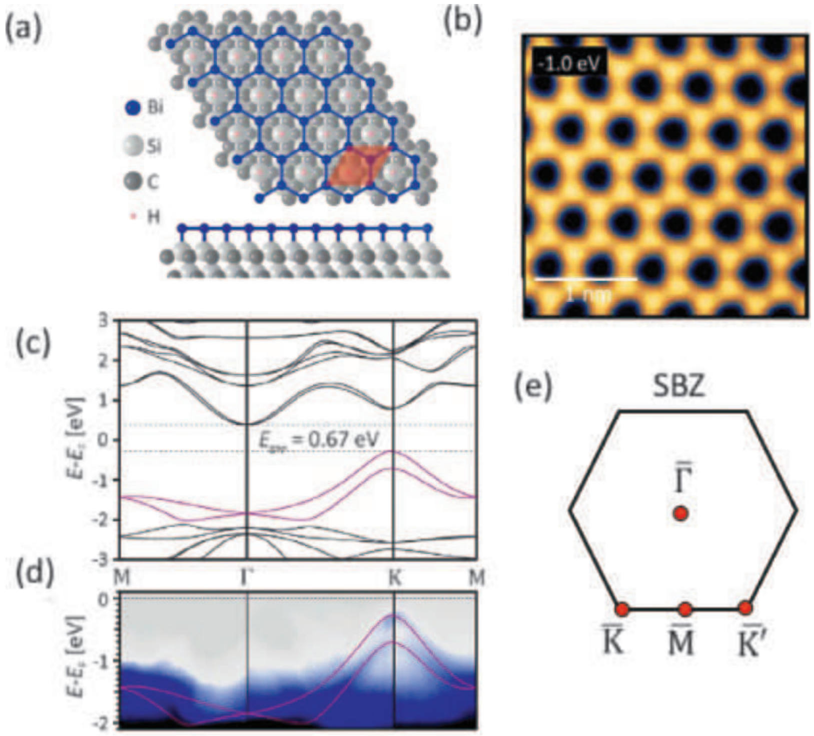

Fig. 7 Scheme of planar √3 ×√3 R30° a bismuthene layer placed on the threefold-symmetric SiC(0001) substrate (a); high-resolution STM filled-states image, providing the bismuthene honeycomb structure (b); DFT band-structure calculations for monolayer bismuthene on SiC(0001) (c) compared to ARPES data (d); surface BZ of the Bi hexagonal lattice (e). Adapted from Fig. 1 and Fig. 2 of Reis F, Li G, Dudy L, Bauernfeind M, Glass S, Hanke W, Thomale R, Schäfer J, Claessen R (2017) Bismuthene on a SiC substrate: A candidate for a high-temperature quantum spin Hall material. *Science* 357: 287–290.

Brief summary on 2D-TMDs

Nowadays, others two-dimensional materials likewise transition metal dichalcogenides have pushed the research toward a new conception of nanoelectronics and optoelectronics owing to their amazing physical properties (Wang et al., 2012). At variance of graphene, the TMDs can be considered as consisting of a sandwiched structure of a transition metal layer (such as Mo, W, Nb) between two chalcogen layers (such as S, Se, Te).

These are, layered materials with strong in-plane σ and very weak out-of-plane π bondings, exhibiting van der Waals interactions, facilitating their exfoliation in single- and multi-2D layers and/or their atomic condensation, trough evaporation methods, generally irrespective of any rigorous substrate epitaxy matching.

Thus, although the TMDs have been explored for long time, recent advances in nanoscale materials control, characterization and device assembly have opened to these stacked van der Waals 2D materials new opportunities to investigate features related to charge transfer and photon–exciton interactions (Butler et al., 2013), and to exhibit chemical properties very versatile (Chhowalla et al., 2013).

Molybdenum disulfide (MoS_2) (Splendiani et al., 2010) and tungsten disulfide (WS_2) (Cong et al., 2014) are, for instance, very fascinating among the 2D TMDs, exhibiting sizable band gaps that change from indirect to direct in single layers (Cong et al., 2014; Mak et al., 2010) opening the door to their applications in photoelectronics (Choi et al., 2013; Lee et al., 2012).

A new class of large-gap QSH insulators in 2D TMDs with 1T′ structure, i.e., 1T′-MX2 with M = W or Mo and X = Te, Se, or S, was predicted, by using first-principles calculations (Qian et al., 2014).

The monolayer TMDs–MX_2 keep polytypic structures type 1H, 1T, and 1T′ (Eda et al., 2012; Heising and Kanatzidis, 1999; Qian et al., 2014; Wilson and Yoffe, 1969), where the 1H sandwich structure have the three planes of 2D hexagonally packed atoms (X–M–X) ABA Bernal stacking; the 1T has the three atomic planes that form the ABC rhombohedral stacking, where the metal atoms are in octahedral coordination with the chalcogen atoms. This structure in free-standing form is unstable and devoted to go to a spontaneous lattice distortion (Qian et al., 2014). This lattice distortion in the x direction forms a periodic 2 × 1 distorted structure, the so called 1T′, consisting of 1D zigzag W atoms chains, upset from the original octahedral positions, along the perpendicular y direction (Eda et al., 2012; Qian et al., 2014; Tang et al., 2017).

The 1T′ structure was the issue of the work reported in Ref. (Qian et al., 2014), where it was found that an intrinsic band inversion between chalcogenide-*p* and metal-*d* bands is originated by this structural distortion, and, in addition, the SOC opens a tunable gap, both upon a vertical electric field and strain.

The case of 1T′ -WS2 on bilayer graphene/SiC(0001)

As a witness to the richness of the electronic properties of this class of Dirac 2D materials among the TMDs, we report one of the most significant example in quantum spin Hall state observed in monolayer 1T′-WTe_2 (Tang et al., 2017).

A monolayer 1T′-WTe_2 was epitaxially grown on bilayer graphene/ SiC(0001) and studied by ARPES and first-principles calculations, providing the signature of the topological band inversion and band gap opening, trademarks of the QSH state in this material (Tang et al., 2017).

Fig. 8(a) reports the 1T′-WTe_2 crystal structure with the 2 × 1 periodicity induced by the spontaneous lattice distortion from 1T phase; the unit cell is indicated by the red rectangle.

The schematic panel that details the mechanism of the transition from a topologically trivial phase, ($Z_2 = 0$), to a non-trivial phase and then to a bulk band opening due to SOC ($Z_2 = 1$) for a bulk band is displayed in Fig. 8(b), whereas the calculated band structures for WTe_2, which evidence the evolution from 1T-WTe_2 to 1T′-WTe_2 without SOC, and 1T′-WTe_2 with SOC, along the $\overline{\Gamma} - \overline{Y}$ direction are shown in Fig. 8(c–e). Here, the red and blue dotted bands feature the two bands involved in band inversion, and the + and – signs denote the parity of the Bloch states at the $\overline{\Gamma}$ point (Tang et al., 2017).

The measured ARPES pattern, along the $\overline{Y} - \overline{\Gamma} - \overline{Y}$ direction, from 1T′-WTe_2, its second derivative spectrum, the band structure calculations (including the $\overline{\Gamma} - \overline{Y}$—P/P′) and the rectangular BZ are displayed in (f–i), respectively. A very nice agreement between the ARPES measurements and calculation, points to a clearly band inversion, and a large bulk band gap opening of 55 meV.

Furthermore, in addition, the STS showed the evidence of the insulating bulk and conductive edge nature of 1T′-WTe_2, giving the compelling experimental evidence of a QSH insulator phase in monolayer 1T′-WTe_2 (Tang et al., 2017).

Conclusion

This chapter has been conceived to offer an overview of the most significant works of Dirac's 2D systems, carried out in the last few years after the graphene discovery.

The richness of the specific characteristics of 2D Dirac materials beyond graphene, belonging to group-IIIA, IVA, VA, VIA, IVB, as well as the TMDs, have been considered both from a theoretical and an experimental point of view, showing their hidden features seen through the eyes of modern research.

Examples of these elemental 2D Dirac materials following a timeline for their discovery, such as silicene and multilayer silicene, showing the Dirac cone; stanene, bismuthene, as well as the 1T′-WS_2 TMD, exhibiting large QSH effect have been largely mentioned.

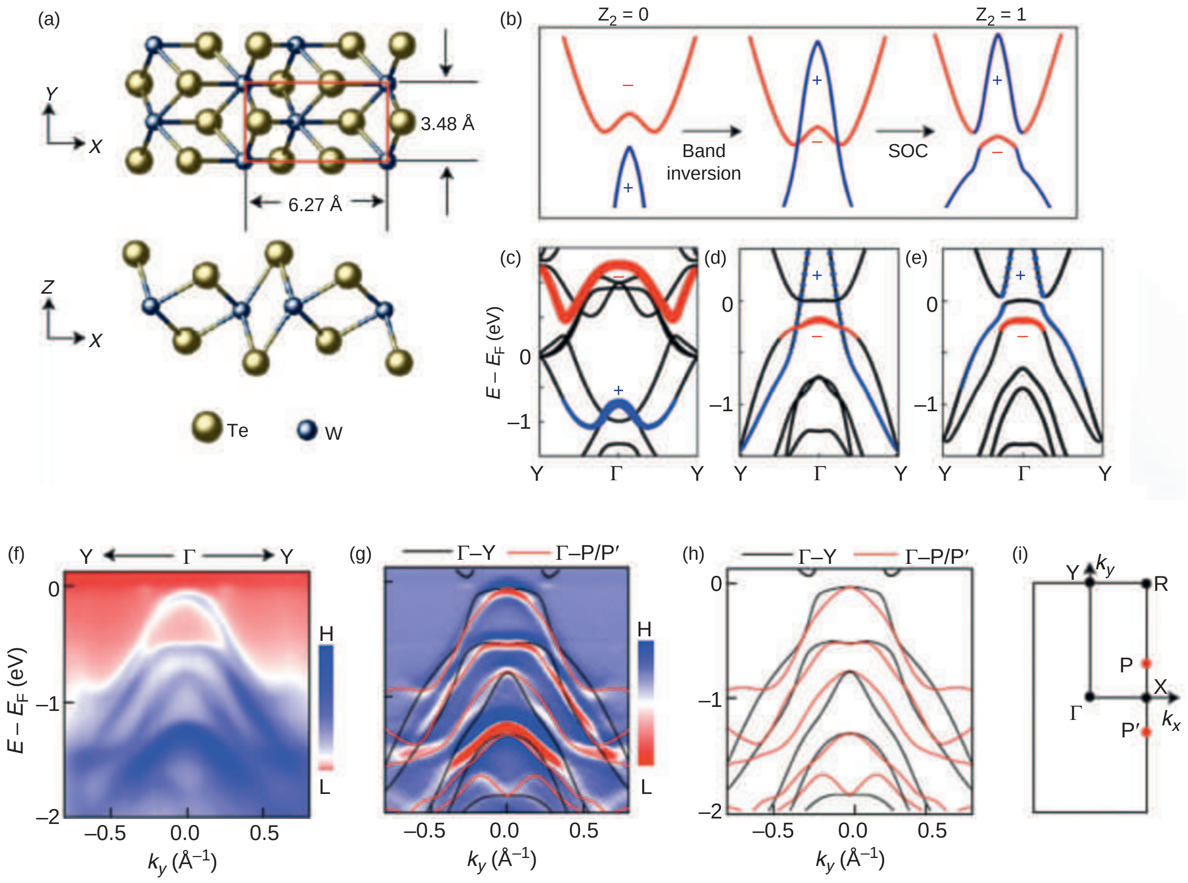

Fig. 8 1T′-WTe$_2$ crystal structure with the 2 × 1 periodicity; the units cell is indicated by the red rectangle (a); schematic panel which describes a bulk band changing from a topologically trivial phase, ($Z_2 = 0$), to a non-trivial phase and then to a bulk band opening due to SOC ($Z_2 = 1$) (b). The calculated band structures for WTe$_2$, which evidences the evolution from 1T-WTe$_2$ (c) to 1T′-WTe$_2$ without SOC (d), and 1T′-WTe$_2$ with SOC (e), along the $\overline{\Gamma}-\overline{Y}$ direction. The measured ARPES on 1T′-WTe$_2$, its second derivative spectrum, the band structure calculations, and the rectangular BZ are displayed in (f–i), respectively. Adapted from Fig. 1 and Fig. 2 of Tang S, Zhang C, Wong D, Pedramrazi Z, Tsai H-Z, Jia C, Moritz B, Claassen M, Ryu H, Kahn S, Jiang J, Yan H, Hashimoto M, Lu D, Moore RG, Hwang C-C, Hwang C, Hussain Z, Chen Y, Ugeda MM, Liu Z, Xie X, Devereaux TP, Crommie MF, Mo S-K, and Shen Z-X (2017). Quantum spin Hall state in monolayer 1T'-WTe2. *Nature Physics* 13: 683–687.

All these excellent reported cases have marked a paradigm, capable to stimulate a remarkable way to design new Dirac 2D monolayer and/or monolayer-substrate composites with large QSH gap and conductive spin-protected TDBSs, as well as unexpected physical properties, under appropriate materials engineering, which could be applied in a near future.

Definitely, quantum spin Hall Dirac materials could hold the promise of having revolutionary devices with dissipationless spin current, with opportune large gap, operating at high temperature. Strain engineering, surface epitaxy, both flat and buckled 2D system, in conjunction with outstanding insights and physical apparatus, can highlight the importance of the elemental adlayer-substrate in obtaining artificial 2D Dirac materials, for exploring new condensed matter physical properties.

In addition, the TMDs QSH insulator should provide new opportunities for both fundamental studies and novel device applications.

In conclusion, the 2D artificial elemental materials with the suffix-ene that came after the progenitor graphene first, and successively silicene, known as Xenes, have been enormously attracted the attention of the scientific research world both from experimental and theoretical point of view. Furthermore, the hint for new 2D silicon/stanene/plumbene systems for superconductivity purpose, will pushes the research toward the epitaxial growth through the formation of a substrate-metal-silicon interface.

References

Aizawa T, Suehara S, and Otani S (2014) Silicene on zirconium carbide (111). *Journal of Physical Chemistry C* 118: 23049–23057.

Avila J, De Padova P, Cho S, Colambo I, Lorcy S, Quaresima C, Vogt P, Resta A, Le Lay G, and Asensio MC (2013) Presence of gapped silicene-derived band in the prototypical (3 × 3) silicene phase on silver (111) surfaces. *Journal of Physics: Condensed Matter* 25: 262001–262008.

Bernevig BA, Hughes TL, and Zhang S-C (2006) Quantum spin Hall effect and topological phase transition in HgTe quantum wells. *Science* 314: 1757–1761.

Bihlmayer G, Sassmannshausen J, Kubetzka A, and Blügel S (2020) Plumbene on a magnetic substrate: A combined scanning tunneling microscopy and density functional theory study. *Physical Review Letters* 124: 126401–126405.

Bostwick A, Ohta T, Seyller T, Horn K, and Rotenberg E (2007) Quasiparticle dynamics in graphene. *Nature Physics* 3: 37–40.

Brihuega I, Mallet P, González-Herrero H, Trambly de Laissardière G, Ugeda MM, Magaud L, Gômez-Rodríguez JM, Ynduráin F, and Veuillen J-Y (2012) Unraveling the intrinsic and robust nature of van hove singularities in twisted bilayer graphene by scanning tunneling microscopy and theoretical analysis. *Physical Review Letters* 109: 196802–5.

Butler SZ, Hollen SM, Cao L, Cui Y, Gupta JA, Gutiérrez HR, Heinz TF, Hong SS, Huang J, Ismach AF, Johnston-Halperin E, Kuno M, Plashnitsa VV, Robinson RD, Ruoff RS, Salahuddin S, Shan J, Shi L, Spencer MG, Terrones M, Windl W, and Goldberger JE (2013) Progress, challenges, and opportunities in two-dimensional materials beyond graphene. *ACS Nano* 7: 2898.

Cahangirov S, Topsakal M, Aktürk E, Sahin H, and Ciraci S (2009) Two- and one-dimensional honeycomb structures of silicon and germanium. *Physical Review Letters* 102: 236804–4.

Cahangirov S, Audiffred M, Tang P, Iacomino A, Duan W, Merino G, and Rubio A (2013) Electronic structure of silicene on Ag(111): Strong hybridization effects. *Physical Review B* 88: 035432–6.

Cahangirov S, Özçelik VO, Rubio A, and Ciraci S (2014) Silicite: The layered allotrope of silicon. *Physical Review B* 90: 085426–5.

Chen L, Liu C-C, Feng B, He X, Cheng P, Ding Z, Meng S, Yao Y, and Wu K (2012) Evidence for Dirac fermions in a honeycomb lattice based on silicon. *Physical Review Letters* 109: 056804–5.

Chhowalla M, Shin HS, Eda G, Li L-J, Loh KP, and Zhang H (2013) The chemistry of two-dimensional layered transition metal dichalcogenide nanosheets. *Nature Chemistry* 5: 263–275.

Choi MS, Qu D, Lee D, Liu X, Watanabe K, Taniguchi T, and Yoo WJ (2013) Lateral MoS$_2$ p-n junction formed by chemical doping for use in high-performance optoelectronics. *ACS Nano* 8: 9332.

Cong C, Shang J, Wu X, Cao B, Peimyoo N, Qiu C, Sun L, and Yu T (2014) Synthesis and optical properties of large-area single-crystalline 2D semiconductor WS$_2$ monolayer from chemical vapor deposition. *Advanced Optical Materials* 2: 131.

Dávila ME, Xian L, Cahangirov S, Rubio A, and Le Lay G (2014) Germanene: A novel two-dimensional germanium allotrope akin to graphene and silicene. *New Journal of Physics* 16: 095002–10.

De Padova P, Vogt P, Resta A, Avila J, Razado-Colambo I, Quaresima C, Ottaviani C, Olivieri B, Bruhn T, Hirahara T, Shirai T, Hasegawa S, Asensio MC, and Le Lay G (2013a) Evidence of Dirac fermions in multilayer silicene. *Applied Physics Letters* 102: 163106–4.

De Padova P, Avila J, Resta A, Razado-Colambo I, Quaresima C, Ottaviani C, Olivieri B, Bruhn T, Vogt P, Asensio MC, and Le Lay G (2013b) The quasiparticle band dispersion in epitaxial multilayer silicene. *Journal of Physics: Condensed Matter* 25: 382202–382207.

De Padova P, Ottaviani C, Quaresima C, Olivieri B, Imperatori P, Salomon E, Angot T, Quagliano L, Romano C, Vona A, Muniz-Miranda M, Generosi A, Paci B, and Le Lay G (2014) 24 h stability of thick multilayer silicene in air. *2D Materials* 1: 021003–11.

De Padova P, Generosi A, Paci B, Ottaviani C, Quaresima C, Olivieri B, Salomon E, Angot T, and Le Lay G (2016) Multilayer silicene: Clear evidence. *2D Materials* 3: 031011–7.

De Padova P, Feng H, Zhuang J, Li Z, Generosi A, Paci B, Ottaviani C, Quaresima C, Olivieri B, Krawiec M, and Du Y (2017) Synthesis of Multilayer Silicene on Si(111)$\sqrt{3} \times \sqrt{3}$-Ag. *Journal of Physical Chemistry C* 121: 27182–27190.

De Padova P, Generosi A, Paci B, Ottaviani C, Quaresima C, Olivieri B, Kopciuszynski M, Zurawek L, Zdyb R, and Krawiec M (2019) New findings on multilayer silicene on Si(111)$\sqrt{3}\times\sqrt{3}$R30°–Ag template. *Materials* 12. https://doi.org/10.3390/ma12142258. 2258–13.

De Padova P, Olivieri B, Ottaviani C, Quaresima C, Du Y, Jalochoski M, and Krawiec M (2022) Defects in two-dimensional elemental materials beyond graphene. In: Addou R and Colombo L (eds.) *Defects in Two-Dimensional Materials*, pp. 73–88. Amsterdam, United Kingdom, Cambridge, MA: Elsevier.

Deng J, Xia B, Ma X, Chen H, Shan H, Zhai X, Li B, Zhao A, Xu Y, Duan W, Zhang S-C, Wang B, and Hou JG (2018) Epitaxial growth of ultraflat stanene with topological band inversion. *Nature Materials* 17: 1081–1086.

Derivaz M, Dentel D, Stephan R, Hanf M-C, Mehdaoui A, Sonnet P, and Pirri C (2015) Continuous germanene layer on Al(111). *Nano Letters* 15: 2510–2516.

Dirac PAM (1928) The quantum theory of the electron. *Proceedings of the Royal Society of London. Series A, Containing Papers of a Mathematical and Physical Character* 117: 610–624.

Drummond ND, Zolyomi V, and Falko VI (2012) Electrically tunable band gap in silicene. *Physical Review B* 85: 075423–7.

Du Y, Zhuang J, Liu H, Xu X, Eilers S, Wu K, Cheng P, Zhao J, Pi X, See KW, Peleckis G, Wang X, and Dou SX (2014) Tuning the band gap in silicene by oxidation. *ACS Nano* 8: 10019–7.

Du Y, Zhuang J, Wang J, Li Z, Liu H, Zhao J, Xu X, Feng H, Chen L, Wu K, Wang X, and Dou SX (2016) Quasi-freestanding epitaxial silicene on Ag(111) by oxygen intercalation. *Science Advances* 2: , e1600067.

Duan H, Yan N, Yu R, Chang C-R, Zhou G, Hu H-S, Rong H, Niu Z, Mao J, Asakura H, Tanaka T, Dyson PJ, Li J, and Li Y (2014) Ultrathin rhodium nanosheets. *Nature Communications* 5: 1–8. https://doi.org/10.1038/ncomms4093.

Eda G, Fujita T, Yamaguchi H, Voiry D, Chen M, and Chhowalla M (2012) Coherent atomic and electronic heterostructures of single-layer MoS$_2$. *ACS Nano* 6: 7311–7317.

Ezawa M, Salomon E, De Padova P, Solonenko D, Vogt P, D'avila ME, Molle A, Angot T, and Le Lay G (2018) Fundamentals and functionalities of silicene, germanene, and stanene. *La Rivista del Nuovo Cimento* 41: 175–224.

Feng B, Ding Z, Meng S, Yao Y, He X, Cheng P, Chen L, and Wu K (2012) Evidence of silicene in honeycomb structures of silicon on Ag(111). *Nano Letters* 12: 3507–3511.

Feng Y, Liu D, Feng B, Liu X, Zhao L, Xie Z, Liu Y, Liang A, Hu C, Hu Y, He S, Liu G, Zhang J, Chen C, Xu Z, Chen L, Wu K, Liu Y-T, Lin H, Huang Z-Q, Hsu C-H, Chuang F-C, Bansil A, and Zhou XJ (2016) Direct evidence of interaction-induced Dirac cones in a monolayer silicene/Ag(111) system. *Proceedings. National Academy of Sciences. United States of America* 113: 14656–14661.

Feng B, Zhou H, Feng Y, Liu H, He S, Matsuda I, Chen L, Schwier EF, Shimada K, Meng S, and Wu K (2019) Superstructure-induced splitting of dirac cones in silicene. *Physical Review Letters* 122: 196801–196806.

Fleurence A, Friedlein R, Osaki T, Kawai H, Wang T, and Yamada-Takamura Y (2012) Experimental evidence for epitaxial silicene on diboride thin films. *Physical Review Letters* 108: 245501–245505.

Fukaya Y, Mochizuki I, Maekawa M, Wada K, Hyodo T, Matsuda Y, and Kawasuso A (2013) Structure of silicene on a Ag(111) surface studied by reflection high energy positron diffraction. *Physical Review B* 88: 205413–205414.

Garagnani D, De Padova P, Ottaviani C, Quaresima C, Generosi A, Paci B, Olivieri B, Jałochowski M, and Krawiec M (2022) Evidence of sp2-like hybridization of silicon valence orbitals in thin and thick Si grown on α-phase Si(111) $\sqrt{3} \times \sqrt{3}$R30°-Bi. *Materials* 15: 1730–19.

Gou J, Kong L, Li H, Zhong Q, Li W, Cheng P, Chen L, and Wu K (2017) Strain-induced band engineering in monolayer stanene on Sb(111). *Physical Review Materials* 1: 054004-6.

Grazianetti C, Cinquanta E, Tao L, De Padova P, Quaresima C, Ottaviani C, Akinwande D, and Molle A (2017) Crossover between multilayer silicene and diamond-like growth regime. *ACS Nano* 11: 3376–3382.

Gruznev DV, Bondarenko LV, Tupchaya AY, Mihalyuk AN, Eremeev SV, Zotov AV, and Saranin AA (2020) Thallene: Graphene-like honeycomb lattice of Tl atoms frozen onsingle-layer NiSi$_2$. *2D Materials* 7: 045026–7.

Gu C, Zhao S, Zhang JL, Sun S, Yuan K, Hu Z, Han C, Ma Z, Wang L, Huo F, Huang W, Li Z, and Chen W (2017) Growth of quasi-free-standing single-layer blue phosphorus on tellurium monolayer functionalized Au(111). *ACS Nano* 11: 4943–4949.

Guo Z, Furuya S, Iwata J-I, and Oshiyama A (2013) Absence and presence of Dirac electrons in silicene on substrates. *Physical Review B* 87: 235435–10.

Guzmán-Verri GG and Lew Yan Voon LC (2007) Electronic structure of silicon-based nanostructures. *Physical Review B* 76: 075131–10.

Heising J and Kanatzidis MG (1999) Exfoliated and restacked MoS_2 and WS_2: Ionic or neutral species? Encapsulation and ordering of hard electropositive cations. *Journal of the American Chemical Society* 121: 11720–11732.

Hoffmann R (2013) Small but strong lessons from chemistry for nanoscience. *Angewandte Chemie, International Edition* 52: 93–103.

Huang S, Kang W, and Yang L (2013) Electronic structure and quasiparticle bandgap of silicene structures. *Applied Physics Letters* 102: 133106–5.

Huang Z-Q, Hsu C-H, Chuang F-C, Liu Y-T, Lin H, Su W-S, Ozolins V, and Bansil A (2014) Strain driven topological phase transitions in atomically thin films of group IV and V elements in the honeycomb structures. *New Journal of Physics* 16: 105018–10.

Huang L, Zhang Y-F, Zhang Y-Y, Xu W, Que Y, Li E, Pan J-B, Wang Y-L, Liu Y, Du S-X, Pantelides ST, and Gao H-J (2017) Sequence of silicon monolayer structures grown on a Ru surface: From a herringbone structure to silicene. *Nano Letters* 17: 1161–1166.

Hüfner S (2010) *Photoelectron Spectroscopy: Principles and Applications*, 3rd edn. Berlin: Springer.

Jałochowski M and Krawiec M (2019) Antimonene on Pb quantum wells. *2D Materials* 6: 045028–7.

Jaroch T, Krawiec M, and Zdyb R (2021) Layered heterostructure of planar and buckled phases of silicene. *2D Materials* 8: 035038–8.

Jin KH and Jhi SH (2015) Quantum anomalous hall and quantum spin-hall phases in flattened Bi and Sb bilayers. *Scientific Reports* 5: 8426–8432.

Kamal C, Chakrabarti A, Banerjee A, and Deb SK (2013) Silicene beyond mono-layers: Different stacking configurations and their properties. *Journal of Physics. Condensed Matter* 25: 085508–10.

Kane CL and Mele EJ (2005a) Quantum spin hall effect in graphene. *Physical Review Letters* 95: 226801–226804.

Kane CL and Mele EJ (2005b) Z_2 topological order and the quantum spin hall effect. *Physical Review Letters* 95: 146802–146804.

Kevan SD (ed.) (1992) *Angle Resolved Photoemission: Theory and Current Applications*. Amsterdam, London, NY, Tokyo: Elsevier.

König M, Wiedmann S, Brüne C, Roth A, Buhmann H, Molenkamp LW, Qi X-L, and Zhang S-C (2007) Quantum spin hall insulator state in HgTe quantum wells. *Science* 318: 766–770.

Krawiec M (2018) Functionalization of group-14 two-dimensional materials. *Journal of Physics: Condensed Matter* 30: 233003–233029.

Krawiec M, Stępniak-Dybala A, Bobyk A, and Zdyb R (2021) Magnetism in Au-supported planar silicene. *Nanomaterials* 11: 2568–2569.

Lebègue S and Eriksson O (2009) Electronic structure of two-dimensional crystals from ab initio theory. *Physical Review B* 79: 115409–4.

Lee HS, Min SW, Chang YG, Park MK, Nam T, Kim H, Kim JH, Ryu S, and Im S (2012) MoS_2 nanosheet phototransistors with thickness-modulated optical energy gap. *Nano Letters* 12: 3695.

Lei T, Liu C, Zhao J-L, Li J-M, Li Y-P, Wang J-O, Wu R, Qian H-J, Wang H-Q, and Ibrahim K (2016) Electronic structure of antimonene grown on Sb_2Te_3 (111) and Bi_2Te_3 substrates. *Journal of Applied Physics* 119: 015302–5.

Li L, Wang Y, Xie S, Li X-B, Wang Y-Q, Wu R, Sun H, Zhang S, and Gao H-J (2013) Two-dimensional transition metal honeycomb realized: Hf on Ir(111). *Nano Letters* 3: 4671–4674.

Li L, Lu S-Z, Pan J, Qin Z, Wang Y-Q, Wang Y, Cao G-Y, Du S, and Gao H-J (2014) Buckled germanene formation on Pt(111). *Advanced Materials* 26: 4820–4824.

Li Z, Zhuang J, Chen L, Ni Z, Liu C, Wang L, Xu X, Wang J, Pi X, Wang X, Du Y, Wu K, and Dou SX (2016) Observation of van Hove singularities in twisted silicene multilayers. *ACS Central Science* 2: 517–521.

Li Z, Song Y, and Tang S (2020a) Quantum spin Hall state in monolayer 1T′-TMDCs. *Journal of Physics: Condensed Matter* 32: 333001–333014.

Li J, Lei T, Wang J, Wu R, Qian H, and Ibrahim K (2020b) In-plane crystal field constrained electronic structure of stanene. *Applied Physics Letters* 116: 101601–101604.

Lin CL, Arafune R, Kawahara K, Tsukahara N, Minamitani E, Kim Y, Takagi N, and Kawai M (2012) Structure of silicene grown on Ag(111). *Applied Physics Express* 5: 045802–3.

Lin CH, Huang A, Pai WW, Chen WC, Chen TY, Chang TR, Yukawa R, Cheng CM, Mou CY, Matsuda I, Chiang TC, Jeng HT, and Tang SJ (2018) Single-layer dual germanene phases on Ag(111). *Physical Review Materials* 2: 024003–8.

Liu CC, Feng WX, and Yao YG (2011a) Quantum spin hall effect in silicene and two-dimensional germanium. *Physical Review Letters* 107: 076802–4.

Liu C-C, Jiang H, and Yao Y (2011b) Low-energy effective Hamiltonian involving spin-orbit coupling in silicene and two-dimensional germanium and tin. *Physical Review B* 84: 195430–11.

Liu C-C, Guan S, Song Z, Yang SA, Yang J, and Yao Y (2014a) Low-energy effective Hamiltonian for giant-gap quantum spin Hall insulators in honeycomb X-hydride/halide (X=N–Bi) monolayers. *Physical Review B* 90: 085431–10.

Liu ZL, Wang M-X, Liu C, Jia JF, Vogt P, Quaresima C, Ottaviani C, Olivieri B, De Padova P, and Le Lay G (2014b) The fate of the $2\sqrt{3}\times 2\sqrt{3}R(30^{\circ})$ silicene phase on Ag(111). *APL Materials* 2: 092513–5.

Liu YN, Gao N, Zhuang JC, Liu C, Wang JO, Hao WC, Dou SX, Zhao JJ, and Du Y (2019) Realization of strained stanene by interface engineering. *Journal of Physical Chemistry Letters* 10: 1558–1565.

Lv R, Robinson JA, Schaak RE, Sun D, Sun Y, Mallouk TE, and Terrones M (2015) Transition metal dichalcogenides and beyond: Synthesis, properties, and applications of single- and few-layer nanosheets. *Accounts of Chemical Research* 48: 56–64.

Mak F, Lee C, Hone J, Shan J, and Heinz TF (2010) Atomically thin MoS_2: A new direct-gap semiconductor. *Physical Review Letters* 105: 136805.

Mannix AJ, Zhou X-F, Kiraly B, Wood JD, Alducin D, Myers BD, Liu X, Fisher B, Santiago U, Guest JR, Yacaman MJ, Ponce A, Oganov AR, Hersam MC, and Guisinger NP (2015) Synthesis of borophenes: Anisotropic, two-dimensional boron polymorphs. *Science* 350: 1513–1516.

Meng L, Wang Y, Zhang L, Du S, Wu R, Li L, Zhang Y, Li G, Zhou H, Hofer WA, and Gao H-J (2013) Buckled silicene formation on Ir(111). *Nano Letters* 13: 685–690.

Nazzari D, Genser J, Ritter V, Bethge O, Bertagnolli E, Ramer G, Lendl B, Watanabe K, Taniguchi T, Rurali R, Kolibal M, and Lungstein A (2021) Highly biaxially strained silicene on Au(111). *Journal of Physical Chemistry C* 125: 9973–9980.

Ni Z, Liu Q, Tang K, Zheng J, Zhou J, Qin R, Gao Z, Yu D, and Lu J (2012) Tunable bandgap in silicene and germanene. *Nano Letters* 12: 113–118.

Novoselov KS, Geim AK, Morozov SV, Jiang D, Zhang Y, Dubonos SV, Grigorieva IV, and Firsov AA (2004) Electric field effect in atomically thin carbon films. *Science* 306: 666–669.

Novoselov KS, Jiang D, Schedin F, Boot TJ, Khotkevich VV, Morozov SV, and Geim AK (2005a) Two-dimensional atomic crystals. *PNAS* 102: 10451–10453.

Novoselov KS, Geim AK, Morozov SV, Jiang D, Katsnelson MI, Grigorieva IV, Dubonos SV, and Firsov AA (2005b) Two-dimensional gas of massless Dirac fermions in graphene. *Nature* 438: 197–200.

Ohta T, Bostwick A, Seyller T, Horn K, and Rotenberg E (2006) Controlling the electronic structure of bilayer graphene. *Science* 313: 951–954.

Podsiadły-Paszkowska A and Krawiec M (2015) Dirac fermions in silicene on Pb(111) surface. *Physical Chemistry Chemical Physics* 17: 2246–2251.

Qian X, Liu J, Fu L, and Li J (2014) Quantum spin Hall effect in two-dimensional transition metal dichalcogenides. *Science* 346: 1344–1347.

Qin J, Qiu G, Jian J, Zhou H, Yang L, Charnas A, Zemlyanov DY, Xu C-Y, Xu X, Wu W, Wang H, and Ye PD (2017a) Controlled growth of a large-size 2D selenium nanosheet and its electronic and optoelectronic applications. *ACS Nano* 11: 10222–10229.

Qin ZH, Pan JB, Lu SZ, Yan S, Wang Y, Du S, Gao HJ, and Cao GY (2017b) Direct evidence of Dirac signature in bilayer germanene islands on Cu(111). *Advanced Materials* 29: 1606046–5.

Reis F, Li G, Dudy L, Bauernfeind M, Glass S, Hanke W, Thomale R, Schäfer J, and Claessen R (2017) Bismuthene on a SiC substrate: A candidate for a high-temperature quantum spin Hall material. *Science* 357: 287–290.

Rivero P, Yan J-A, García-Suárez V, Ferrer J, and Barraza-Lopez S (2014) Stability and properties of high-buckled two-dimensional tin and lead. *Physical Review B* 90: 241408(R)–5.

Salomon E, Ajjouri RE, Le Lay G, and Angot T (2014) Growth and structural properties of silicene at multilayer coverage. *Journal of Physics: Condensed Matter* 25: 185003–185004.

Salomon E, Beato-Medina D, De Padova P, Angot T, and Le Lay G (2020) Silicene. In: Rocca M, Rahman TS, and Vattuone L (eds.) *Springer Handbook of Surface Science*, pp. 1199–1215. Switzerland: Springer.

Samadi M, Sarikhani N, Zirak M, Zhang H, Zhang H-L, and Moshfegh AZ (2018) Group 6 transition metal dichalcogenide nanomaterials: synthesis, applications and future perspectives. *Nanoscale Horizons* 3: 90–204.

Shah J, Wang W, Sohail HM, and Uhrberg RIG (2020) Experimental evidence of monolayer arsenene: An exotic 2D semiconducting material. *2D Materials* 7: 025013–025017.

Shirai T, Shirasawa T, Hirahara T, Fukui N, Takahashi T, and Hasegawa S (2014) Structure determination of multilayer silicene grown on Ag(111) films by electron diffraction: Evidence for Ag segregation at the surface. *Physical Review B* 89: 241403(R)–5.

Si C, Liu J, Xu Y, Wu J, Gu B-L, and Duan W (2014) Functionalized germanene as a prototype of large-gap two-dimensional topological insulators. *Physical Review B* 89: 115429–5.

Splendiani A, Sun L, Zhang Y, Li T, Kim J, Chim C-Y, Galli G, and Wang F (2010) Emerging photoluminescence in monolayer MoS_2. *Nano Letters* 10: 1271.

Stępniak-Dybala A and Krawiec M (2019) Formation of silicene on ultrathin Pb(111) Films. *Journal of Physical Chemistry C* 123: 17019–17025.

Stępniak-Dybala A, Dyniec P, Kopciuszyński M, Zdyb R, Jałochowski M, and Krawiec M (2019) Planar silicene: A new silicon allotrope epitaxially grown by segregation. *Advanced Functional Materials* 29: 1906053–1906055.

Takeda K and Shiraishi K (1994) Theoretical possibility of stage corrugation in Si and Ge analogs of graphite. *Physical Review B* 50: 14916–14922.

Tang S, Zhang C, Wong D, Pedramrazi Z, Tsai H-Z, Jia C, Moritz B, Claassen M, Ryu H, Kahn S, Jiang J, Yan H, Hashimoto M, Lu D, Moore RG, Hwang C-C, Hwang C, Hussain Z, Chen Y, Ugeda MM, Liu Z, Xie X, Devereaux TP, Crommie MF, Mo S-K, and Shen Z-X (2017) Quantum spin Hall state in monolayer 1T'-WTe_2. *Nature Physics* 13: 683–687.

Tao L, Cinquanta E, Chiappe D, Grazianetti C, Fanciulli M, Dubey M, Molle A, and Akinwande D (2015) Silicene field-effect transistors operating at room temperature. *Nature Nanotechnology* 10: 227–231.

Tao M-L, Tu Y-B, Sun K, Wang Y-L, Xie Z-B, Liu L, Shi M-X, and Wang J-Z (2018) Gallenene epitaxially grown on Si(111). *2D Materials* 5: 035009–5.

Tsoutsou D, Xenogiannopoulou E, Golias E, Tsipas P, and Dimoulas A (2013) Evidence for hybrid surface metallic band in (4 × 4) silicene on Ag(111). *Applied Physics Letters* 103: 231604–231605.

Van Hove L (1953) The occurrence of singularities in the elastic frequency distribution of a crystal. *Physics Review* 89: 1189–1193.

Vogt P, De Padova P, Quaresima C, Avila J, Frantzeskakis E, Asensio MC, Resta A, Ealet B, and Le Lay G (2012) Silicene: Compelling experimental evidence for graphenelike two-dimensional silicon. *Physical Review Letters* 108: 155501–155505.

Vogt P, Berthe M, Resta A, De Padova P, Bruhn T, Le Lay G, and Grandidier B (2014) Synthesis and electrical conductivity of multilayer silicene. *Applied Physics Letters* 104: 021602–5.

Wang QH, Kalamtar-Zadeh K, Kis A, Coleman JN, and Strano MS (2012) Electronics and optoelectronics of two-dimensional transition metal dichalcogenides. *Nature Nanotechnology* 7: 699–712.

Wang X, Wang C, Chen C, Duan H, and Du K (2019) Free-standing monatomic thick two-dimensional gold. *Nano Letters* 19: 4560–4566.

Wilson JA and Yoffe AD (1969) The transition metal dichalcogenides discussion and interpretation of the observed optical, electrical and structural properties. *Advances in Physics* 18: 193–335.

Wu S-C, Shan G, and Yan B (2014) Prediction of near-room-temperature quantum anomalous hall effect on honeycomb materials. *Physical Review Letters* 113: 256401–256405.

Xu Y, Yan B, Zhang H-J, Wang J, Xu G, Tang P, Duan W, and Zhang S-C (2013) Large-gap quantum spin hall insulators in tin films. *Physical Review Letters* 111: 136804–136805.

Xu CZ, Chan YH, Chen P, Wang XX, Flötotto D, Hlevyack JA, Bian G, Mo SK, Chou MY, and Chiang TC (2018) Gapped electronic structure of epitaxial stanene on InSb(111). *Physical Review B* 97: 035122–5.

Yao Y, Ye F, Qi X-L, Zhang S-C, and Fang Z (2007) Spin-orbit gap of graphene: First-principles calculations. *Physical Review B* 5: 041401R-4.

Yu Y, Yang F, Lu XF, Yan YJ, Cho Y-H, Ma L, Niu X, Kim S, Son Y-W, Feng D, Li S, Cheong S-W, Chen XH, and Zhang Y (2015) Gate-tunable phase transitions in thin flakes of 1T-TaS_2. *Nature Nanotechnology* 10: 270–276.

Yu X-L, Huang L, and Wu J (2017) From a normal insulator to a topological insulator in plumbene. *Physical Review B* 95: 125113–125118.

Yuan W, Deng Z, Ren Z, Shen Y, Xi W, and Luo J (2020) Monolayer goldene intercalated in graphene layers. *Applied Physics Letters* 117: 233102–233104.

Yuhara J, Fujii Y, Nishino K, Isobe N, Nakatake M, Xian L, Rubio A, and Le Lay G (2018) Large area planar stanene epitaxially grown on Ag(111). *2D Materials* 5: 025002–8.

Yuhara J, He B, Matsunami N, Nakatake M, and Le Lay G (2019) Graphene's latest cousin: Plumbene epitaxial growth on a "nano water cube" *Advanced Materials* 31: 1901017–6.

Zang YY, Jiang T, Gong Y, Guan ZY, Liu C, Liao MH, Zhu KJ, Li Z, Wang LL, Li W, Song CL, Zhang D, Xu Y, He K, Ma XC, Zhang SC, and Xue QK (2018) Realizing an epitaxial decorated stanene with an insulating bandgap. *Advanced Functional Materials* 28: 1802723.

Zhang JL, Zhao S, Han C, Wang Z, Zhong S, Sun S, Guo R, Zhou X, Gu CD, Yuan KD, Li Z, and Chen W (2016a) Epitaxial growth of single layer blue phosphorus: A new phase of two- dimensional phosphorus. *Nano Letters* 16: 4903–4908.

Zhang L, Bampoulis P, Rudenko AN, Yao Q, van Houselt A, Poelsema B, Katsnelson MI, and Zandvliet HJW (2016b) Structural and electronic properties of germanene on MoS_2. *Physical Review Letters* 116: 256804–256806.

Zhang L, Zhao H, Ji W-X, Zhang C-W, Li P, and Wang P-J (2018) Discovery of a new quantum spin Hall phase in bilayer plumbene. *Chemical Physics Letters* 712: 78–82.

Zhao J, Deng Q, Bachmatiuk A, Sandeep G, Popov A, Eckert J, and Rümmeli MH (2014) Free-standing single-atom-thick iron membranes suspended in graphene pores. *Science* 343: 1228–1232.

Zhao L, Xu C, Su H, Lian J, Lin S, Gu L, Wang X, Chen M, and Zheng N (2015) Single-crystalline rhodium nanosheets with atomic thickness. *Advancement of Science* 2: 1500100–1500105.

Zhao H, Zhang C, Ji W, Zhang R, Li S, Yan S, Zhang B, Li P, and Wang P (2016) Unexpected giant-gap quantum spin hall insulator in chemically decorated plumbene monolayer. *Scientific Reports* 6: 20152.

Zhu F-F, Chen W-J, Xu Y, Gao C-L, Guan D-D, Liu C-H, Qian D, Zhang S-C, and Jia J-F (2015) Epitaxial growth of two-dimensional stanene. *Nature Materials* 14: 1020–1024.

Zhu Z, Cai X, Yi S, Chen J, Dai Y, Niu C, Guo Z, Xie M, Liu F, Cho J-H, Jia Y, and Zhang Z (2017) Multivalency-driven formation of Te-based monolayer materials: A combined first-principles and experimental study. *Physical Review Letters* 119: 106101–106105.

Quantum confinement in Dirac-like nanostructures

CA Downing and ME Portnoi, Department of Physics and Astronomy, University of Exeter, Exeter, United Kingdom

© 2024 Elsevier Ltd. All rights reserved.

Introduction 344
Klein tunneling 345
Confinement in two-dimensions 345
Maxwell's fish-eye lens and bound states 346
Experiments 347
Conclusion 349
Acknowledgments 349
References 349

Abstract

In Westminster Abbey, in a nave near to Newton's monument, lies a memorial stone to Paul Dirac. The inscription on the stone includes the relativistic wave equation for an electron: the Dirac equation. At the turn of the 21st century, it was discovered that this eponymous equation was not simply the preserve of particle physics. The isolation of graphene by Andre Geim and Konstantin Novoselov in Manchester led to the exploration of a novel class of materials—Dirac materials—whose electrons behave like Dirac particles. While the mobility of these quasi-relativistic electrons is attractive from the perspective of potential ultrafast devices, it also presents a distinct challenge: how to confine Dirac particles so as to avoid making inherently leaky devices? Here we discuss the unconventional quantum tunneling of Dirac particles, we explain a strategy to create bound states electrostatically, and we briefly review some pioneering experiments seeking to trap Dirac electrons.

Key points

- The Dirac equation has utility in condensed matter physics, where it can describe the electrons in materials such as graphene.
- Confinement in Dirac materials is notoriously difficult due to the Klein paradox (which arises during quantum tunneling of quasi-relativistic particles).
- Unexpectedly, bound states may form at the Dirac point (that is, at the apex of the cone formed in the electron energy-momentum relation of quasi-relativistic particles).
- Recent experiments have measured the signatures of confinement in electrostatically defined graphene quantum dots.

Introduction

Friday nights in the laboratory of Andre Geim and Konstantin Novoselov at the University of Manchester were routinely set aside for more playful work. One such speculative idea was to rip layers of carbon from a lump of graphite using sticky tape (Novoselov, 2011; Geim, 2011). Remarkably, they were able to isolate a single atomic layer of graphite: graphene. Just a few years later in 2010, they were jointly awarded the Nobel Prize in physics for their discovery of (and groundbreaking experiments with) graphene, whose atoms are arranged in a purely two-dimensional honeycomb array resembling chicken wire (Castro Neto et al., 2009; Abergel et al., 2010; Peres et al., 2010; Das Sarma et al., 2011).

Of all of the many wonderful properties of the 2-D material graphene, perhaps the most interesting stem from its link to particle physics (Katsnelson, 2012). Near to the Fermi level the electron band structure in graphene is linear,

$$E_{\pm} = \pm v_{\mathrm{F}}|p|, \tag{1}$$

suggesting its electrons and holes, of momentum p, are massless particles which travel with some constant speed v_{F} (in some sense, an effective speed-of-light for the material). Furthermore, the Hamiltonian describing these charge carries formally maps onto a massless, two-dimensional Dirac equation such that a treasure trove of quasi-relativistic phenomena arise in a humble pencil trace of graphite (Shen, 2012; Thaller, 2013). Some examples of such phenomena include Klein tunneling, atomic collapse, and Lorentz boosts (Chen et al., 2007; Shytov et al., 2007; Shytov et al., 2009).

Explicitly, the single electron Hamiltonian $\widehat{H}$ describing massless Dirac fermions in two-dimensions $r = (x, y)$ reads

$$\widehat{H} = v_{\mathrm{F}}\boldsymbol{\sigma}\cdot\widehat{p} + V(r), \tag{2}$$

https://doi.org/10.1016/B978-0-323-90800-9.00074-3

where v_F is the Fermi velocity of the Dirac material, the two-dimensional momentum operators are $\hat{p} = \left(\hat{p}_x, \hat{p}_y\right)$, $\sigma = (\sigma_x, \sigma_y, \sigma_z)$ are Pauli's spin matrices and $V(r)$ is a scalar confinement potential. Importantly, the 2×2 matrix Hamiltonian $\hat{H}$ of Eq. (2) must act on a two-component spinor wavefunction Ψ, where

$$\Psi(r) = \begin{pmatrix} \psi_A(r) \\ \psi_B(r) \end{pmatrix}, \tag{3}$$

which in the case of graphene has arisen from the two interlocking triangular sublattices A and B, together creating the overall honeycomb lattice.

Klein tunneling

The spinor wavefunction of graphene gives rise to the concept of pseudospin (Beenakker, 2008), which is encapsulated by the relation $\sigma \cdot \hat{p}/|p| = \pm 1$. This neat equations shows that the direction of the charge carrier motion is pinned: for electrons $\sigma \cdot \hat{p}/|p| = \pm 1$ and for holes $\sigma \cdot \hat{p}/|p| = -1$. As such, it is difficult to backscatter massless Dirac particles, which makes them highly desirable for electronic devices requiring significant mobilities.

In nonrelativistic quantum mechanics, a particle impinging upon a one-dimensional potential barrier can tunnel pass through the obstacle despite classical physics suggesting it would be reflected. Nevertheless, the transmission probability decreases exponentially with increasing barrier height. However, in relativistic quantum mechanics an even more counter initiative phenomena can occur. When a relativistic particle meets a large potential barrier it may pass through perfectly, that is with a transmission probability of one (Allain and Fuchs, 2011). This effect is known as Klein tunneling, and it can be understood as arising due to the conservation of pseudospin (Katsnelson et al., 2006). An electron moving to the right becomes a right-moving hole under the high potential barrier and an electron again outside of the barrier, always ensuring $\sigma \cdot \hat{p}/|p| = 1$ throughout the propagation, such that the particle continues its rightwards journey. Clearly, confining massless Dirac particles electro-statically in one dimension presents a nontrivial task due to this tunneling phenomenon.

Confinement in two-dimensions

The Hamiltonian $\hat{H}$ of Eq. (2) acts upon a spinor wavefunction Ψ, which has two-components as shown in Eq. (3). When considering radially symmetric problems, such that the scalar potential $V(r) = V(r)$, the wavefunction Ψ in radial coordinates (r,θ) has the separable form

$$\Psi(r, \theta) = \frac{e^{im\theta}}{\sqrt{2\pi}} \begin{pmatrix} \chi_A(r) \\ ie^{i\theta}\chi_B(r) \end{pmatrix}, \tag{4}$$

where the two radial functions $\chi_A(r)$ and $\chi_B(r)$ are to be found, and the prefactor $1/\sqrt{2\pi}$ normalizes the angular part of the wavefunction. The integer quantum number $m = 0, \pm 1, \pm 2, \ldots$ arises from a consideration of the total angular momentum quantum number j_z, where

$$\mathrm{j_z = m + 1/2}. \tag{5}$$

Explicitly, the spinor wavefunction of Eq. (4) satisfies the eigenvalue equation $\hat{J}_z\Psi = j_z\Psi$, where the angular momentum operator $\hat{J}_z$ reads

$$\hat{J}_z = -i\partial_\theta + \sigma_z/2. \tag{6}$$

The wavefunction Ψ given by Eq. (4) can then be seen to separate the two spatial variables in the Schrödinger equation

$$\hat{H}\Psi(r, \theta) = E\Psi(r, \theta), \tag{7}$$

so that, after using the momentum component relations $\hat{p}_x = -i\hbar\partial_x$ and $\hat{p}_y = -i\hbar\partial_y$, as well as the Cartesian to polar coordinate partial derivatives

$$\partial_x = \cos\theta\,\partial_r - \frac{\sin\theta}{r}\partial_\theta, \quad \partial_y = \sin\theta\,\partial_r + \frac{\cos\theta}{r}\partial_\theta, \tag{8}$$

one arrives at a pair of coupled first-order differential equations for the two radial components $\chi_A(r)$ and $\chi_B(r)$,

$$\left(\partial_r + \frac{m+1}{r}\right)\chi_B = [\varepsilon - U(r)]\chi_A, \tag{9a}$$

$$\left(-\partial_r + \frac{m}{r}\right)\chi_A = [\varepsilon - U(r)]\chi_B. \tag{9b}$$

Here the scaled eigenvalue $\varepsilon = E/\hbar v_F$, and the scaled potential function $U(r) = V(r)/\hbar v_F$, absorb the dependence on the Fermi velocity v_F.

A second-order differential equation for the upper component of the radial wavefunction $\chi_A(r)$ only can be computed by disentangling the system of two equations given by Eqs. (9a) and (9b) resulting in

$$\chi_A'' + \left(\frac{1}{r} + \frac{U'}{\varepsilon - U}\right)\chi_A' + \left([\varepsilon - U]^2 - \frac{m^2}{r^2} - \frac{m}{r}\frac{U'}{\varepsilon - U}\right)\chi_A = 0. \tag{10}$$

Here the notation $'$ and $''$ denotes taking one or two derivatives of the function with respect to r. A corresponding equation for the lower radial wavefunction component $\chi_B(r)$ may be obtained upon making the replacements $A \rightarrow B$ and $m \rightarrow -(m+1)$ in Eq. (10), as follows from Eqs. (9a) and (9b).

Importantly, a consideration of any fast-decaying function $U(r)$ allows one to neglect all terms involving both U and U' in Eq. (10), such that the equation essentially becomes Bessel's differential equation. The two linearly independent solutions, being Bessel functions of the first and second kinds, are standard scattering solutions and so one is lead to conclude bound states are seemingly not possible, as was pointed out by Tudorovskiy and Chap-lik (Tudorovskiy and Chaplik, 2007). However, this argument implicitly assumes the states considered have a nonzero energy, such that $\varepsilon \neq 0$ always in Eq. (10). If one allows for zero energy states ($\varepsilon = 0$) then Eq. (10) no longer maps onto Bessel's differential equation, opening up an opportunity for bound states with electrostatic confining potentials to plausibly emerge (Bardarson et al., 2009).

Maxwell's fish-eye lens and bound states

Let us try to construct zero energy ($\varepsilon = 0$) solutions of the massless Dirac equation, associated with the Hamiltonian of Eq. (2). Inspired by the Lorentzian function exploited by Maxwell for his fish-eye lens (Niven, 1890), we shall choose the smooth confining potential (Downing et al., 2011; Downing and Portnoi, 2017)

$$V(r) = \frac{-V_0}{1 + r^2/d^2}, \tag{11}$$

where the potential strength is V_0, while d measures the spatial extent of the potential. Remarkably, this bell-shaped function allows for an exact solution of Eq. (7).

One may solve the coupled Eqs. (9a) and (9b) by initially finding just the upper radial wavefunction component $\chi_A(r)$. A short-range analysis of Eq. (10) suggests that at $r \rightarrow 0$ the solution should be of the form

$$\chi_A \sim r^{|m|}, \tag{12}$$

where the alternative solution $\chi_A \sim r^{-|m|}$ is discarded due to its divergence at the origin, as is familiar from non-relativistic central potential problems. A similar long-range analysis as $r \rightarrow \infty$ suggests the proper solution should decay like

$$\chi_A \sim \frac{1}{r^{2p_m - |m|}}. \tag{13}$$

In the above equation, we have introduced the m-dependent parameter p_m, defined as

$$p_m = \frac{1}{2}(1 + |m| + |1 + m|). \tag{14}$$

For later convenience, if we switch to a new variable ξ, where

$$\xi = (r/d)^2, \tag{15}$$

an appropriate ansatz solution of Eq. (10), which accounts for both the short-range and long-range behaviors as encapsulated by Eqs. (12) and (13) respectively, is

$$\chi_A = \frac{C}{d}\frac{\xi^{\frac{|m|}{2}}}{(1 + \xi)^{p_m}} w(\xi), \tag{16}$$

where we have introduced the dimensionless number C as a normalization constant for the radial part of the wavefunction, which ensures that

$$\int_0^\infty \left(|\chi_A|^2 + |\chi_B|^2\right) r dr = 1. \tag{17}$$

In Eq. (16), $w(\xi)$ is an unknown function which has no influence on the small or large asymptotics of the overall upper radial wavefunction component χ_A. Upon substituting Eq. (16) into Eq. (10), we find the following second-order differential equation determining the as yet unspecified function $w(\xi)$

$$\begin{aligned}&\xi(1+\xi)^2 w''(\xi)\\&+(1+\xi)[1+|m|+(2+|m|-2p_m)\xi]w'(\xi)\\&+\left[\left(\frac{V_0 d}{2\hbar v_F}\right)^2-p_m^2\right]w(\xi)=0.\end{aligned} \tag{18}$$

The solution of Eq. (18) can be given in terms of the Gauss hypergeometric function ${}_2F_1(a,b;c;z)$, which has the power series definition

$${}_2F_1(a,b;c;z)=1+\frac{ab}{c}\frac{z}{1!}+\frac{a(a+1)b(b+1)}{c(c+1)}\frac{z^2}{2!}+\ldots \tag{19}$$

One finds the explicit form of the solution of Eq. (18) as

$$w(\xi)={}_2F_1\left(p_m+\frac{V_0 d}{2\hbar v_F},p_m-\frac{V_0 d}{2\hbar v_F};1+|m|;\frac{\xi}{1+\xi}\right), \tag{20}$$

while the precise structure of χ_B is now readily obtained from Eq. (9b) since χ_A has been found.

It is implicit that the infinite power series inside Eq. (20) must be terminated, so that χ_A satisfies the required conditions on its limiting behavior, as determined at the outset by Eq. (12) and Eq. (13). Given this termination, the radial asymptotics of the radial component wavefunctions are

$$\lim_{r\to\infty}\begin{pmatrix}\chi_A\\ \chi_B\end{pmatrix}\propto\begin{pmatrix}1/r^{1+|1+m|}\\ 1/r^{1+|m|}\end{pmatrix}, \tag{21}$$

which suggests that the presence of algebraically decaying, but marginally non-square-integrable, extended states with quantum numbers $m=\{0,-1\}$, and otherwise genuine, fully square-integrable bound states with $m\neq\{0,-1\}$. Some typical bound states are plotted in Fig. 1.

The quantization condition for zero energy ($\varepsilon=0$ or equivalently $E=0$) bound states arises by assigning the second argument in the hypergeometric function of Eq. (20) to be a non-positive integer n, thus terminating the power series and leading to the bound state conditions

$$\frac{V_0 d}{\hbar v_F}=2(n+p_m),\quad E=0, \tag{22}$$

where $n=0, 1, 2\ldots$, and the m-dependent parameter p_m is defined in Eq. (14). All of the modes of Eq. (22) appear at even integer values of the dimensionless quantity $V_0 d/\hbar v_F$, which are associated with increasingly large degeneracies. For example, at the bound state condition $V_0 d/\hbar v_F=4$ there is a two-fold degeneracy, due to the states $(n,m)=(0,1)$ and $(0,-2)$, and there is a four-fold degeneracy when $V_0 d/\hbar v_F=6$, due to the states $(n,m)=(0,2)$, $(0,-3)$, $(1,1)$ and $(1,-2)$.

The features of this fish-eye lens model suggest some general conclusions about bound states of massless Dirac particles may be drawn. Firstly, bound states may only arise at the apex of the energy-momentum cone (the so-called Dirac point) so they are zero-energy bound states ($E=0$). Secondly, they are only supported at critical values of the dimensionless parameter arising from the potential strength and shape (in this case, $V_0 d/\hbar v_F$). Thirdly, there is a threshold value at which the first bound state appears (in our example, $V_0 d/\hbar v_F=4$). Finally, the angular momentum quantum number m is required to be $m\geq 1$ or $m\leq -2$ for the state to be normalizable. States with $m=0$ and $m=-1$, or equivalently from Eq. (6) with total angular momentum number $j_z=|1/2|$, are a marginal kind of extended state.

Experiments

The quest to observe bound states of massless Dirac particles in graphene and related materials started soon after the isolation of graphene by Geim and Novoselov in Manchester in 2004. Early work used methods like applying high magnetic fields or chemical engineering (Goerbig, 2011), but such techniques are arguably undesirable for future technological applications. Therefore, electrostatic confinement remained a holy grail in the early years of massless Dirac fermion research.

A breakthrough was reported in 2015 by Yue Zhao and co-workers, who were influenced by the so-called whispering gallery modes known from the closed acoustics of cathedrals (Zhao et al., 2015). The team used a scanning tunneling probe to create a circular p-n junction, and exploited the tunability of the charge carriers of graphene to engineer controllable whispering gallery mode resonators. They observed various degrees of confinement via resonances in the tunneling spectrum, where particularly strong confinement was found by carefully tuning the cavity radius using gate potentials. Therefore, this pioneering work provided a clear perspective for the creation of zero-energy bound states electrostatically.

Soon afterwards, Juwon Lee and colleagues observed bound states in graphene quantum dots in a landmark paper from 2016 (Lee et al., 2016). They fabricated circular quantum dots by careful manipulations of defect charges in the insulator substrate sitting below the monolayer of graphene. The team was able to map spatially the electronic structure inside and outside the quantum dot, providing insight into the quantum interference patterns associated with longer living states.

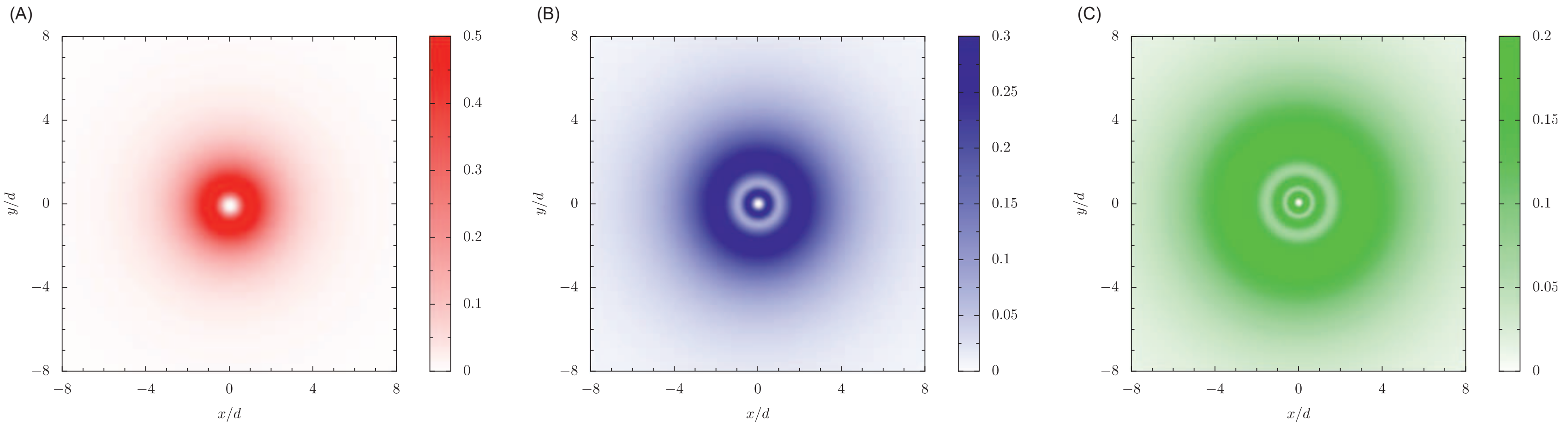

Fig. 1 Probability densities of bound states in a Lorentzian confining potential [cf. Eq. (22)]. Panels (a, b, c): the quantum number $n = 0, 1, 2$ respectively. In the figure, the quantum number angular momentum $m = 1$.

In the same year, Christopher Gutierrez and co-workers similarly used substrate engineering to create a circular graphene quantum dot (Gutierrez et al., 2016). They revealed long-lived states locally pinned within a larger monolayer sheet of graphene. In particular, they observed essentially bound states, at particular energies and of a certain angular momentum, which were achieved by carefully tuning the geometry of the barrier.

Taken together, these three aforementioned experimental works suggest that the creation and mastery of electrostatic confinement with massless Dirac particles, with a view toward future exploitation in nanoscopic devices, remains an important area of condensed matter physics research.

Conclusion

We have discussed how Dirac materials, such as the Nobel Prize winning wonder material graphene, allow one to explore some aspects of quantum electrodynamics in condensed matter physics thanks to their shared reliance on various forms of Dirac equation. One such example is Klein tunneling, or the perfect tunneling of massless particles normally incident on high potential barriers. This effect suggests that the creation of electrostatic quantum dots in Dirac materials is a highly nontrivial task.

We have considered theoretically a possible route to create trapping of massless particles, by considering zero energy states in electrostatic confining potentials. Via a beautiful, exactly-solvable model, inspired by Maxwell's fish-eye lens, we have described some key properties of such novel bound states arising at the Dirac point.

Finally, we have briefly reviewed some exciting experimental work on graphene quantum dots. As it stands, the complete mastery of the confinement of massless particles, a key blockage preventing the development of ultrafast, ultracompact electronics based on Dirac materials, remains fertile ground for modern condensed matter physics studies.

Acknowledgments

CAD is supported by the Royal Society via a University Research Fellowship (URF/R1/201158). MEP is supported by the EU H2020-MSCA RISE projects TERASSE (Project No. 823878) and DiSeTCom (Project No.823728).

References

Abergel DSL, et al. (2010) Properties of graphene: A theoretical perspective. *Advances in Physics* 59: 261.
Allain PE and Fuchs JN (2011) Klein tunneling in graphene: Optics with massless electrons. *The European Physical Journal B* 83: 301.
Bardarson JH, et al. (2009) Electrostatic confinement of electrons in an integrable graphene quantum dot. *Physical Review Letters* 102: 226803.
Beenakker CWJ (2008) Colloquium: Andreev reflection and Klein tunneling in graphene. *Review of Modern Physics* 80: 1337.
Castro Neto AH, et al. (2009) The electronic properties of graphene. *Review of Modern Physics* 81: 109.
Chen H-Y, et al. (2007) Fock-Darwin states of Dirac electrons in graphene-based artificial atoms. *Physical Review Letters* 98: 186803.
Das Sarma S, et al. (2011) Electronic transport in two-dimensional graphene. *Review of Modern Physics* 83: 407.
Downing CA and Portnoi ME (2017) Bielectron vortices in two-dimensional Dirac semimetals. *Nature Communications* 8: 897.
Downing CA, et al. (2011) Zero-energy states in graphene quantum dots and rings. *Physical Review B* 84: 155437.
Geim AK (2011) Nobel lecture: Random walk to graphene. *Review of Modern Physics* 83: 851.
Goerbig MO (2011) Electronic properties of graphene in a strong magnetic field. *Review of Modern Physics* 83: 1193.
Gutierrez C, et al. (2016) Klein tunnelling and electron trapping in nanometre-scale graphene quantum dots. *Nature Physics* 12: 1069.
Katsnelson M, et al. (2006) Chiral tunnelling and the Klein paradox in graphene. *Nature Physics* 2: 620.
Katsnelson MI (2012) *Graphene: Carbon in Two Dimensions*. Cambridge University Press.
Lee J, et al. (2016) Imaging electrostatically confined Dirac fermions in graphene quantum dots. *Nature Physics* 12: 1032.
Niven WD (1890) In: Niven WD (ed.) *The Scientific Papers of James Clerk Maxwell*. Dover Publications.
Novoselov KS (2011) Nobel lecture: Graphene: Materials in the flatland. *Review of Modern Physics* 83: 837.
Peres NMR, et al. (2010) Colloquium: The transport properties of graphene: An introduction. *Reviews of Modern Physics* 82: 2673.
Shen S-Q (2012) *Topological Insulators: Dirac Equation in Condensed Matters*. Berlin Heidelberg: Springer.
Shytov AV, et al. (2007) Atomic collapse and quasi-Rydberg states in graphene. *Physical Review Letters* 99: 246802.
Shytov AV, et al. (2009) Atomic collapse, Lorentz boosts, Klein scattering, and other quantum-relativistic phenomena in graphene. *Solid State Communications* 149: 1087.
Thaller B (2013) *The Dirac Equation*. Berlin Heidelberg: Springer.
Tudorovskiy TY and Chaplik AV (2007) Spatially inhomogeneous states of charge carriers in graphene. *JETP Letters* 84: 619.
Zhao Y, et al. (2015) Creating and probing electron whispering-gallery modes in graphene. *Science* 348: 672.

Theory of edge states in graphene-like systems

JL Lado[a] **and J Fernández-Rossier**[b,*], [a]Department of Applied Physics, Aalto University, Espoo, Finland; [b]International Iberian Nanotechnology Laboratory, Braga, Portugal

© 2024 Elsevier Ltd. All rights reserved.

Introduction **350**
Main properties of graphene band structure 350
Graphene-like systems 351
Edges and edge states 351
Theory of quantum states in 2D honeycomb lattices **351**
Graphene-like states in two dimensions 351
Band-gap opening 353
Calculation methods for edge states in graphene-like systems **354**
Energy bands of 1D stripes 354
Green's function 354
Analytical results 355
Edge states in gapless graphene **355**
Edge states in topological graphene **355**
Quantum Hall phase 356
Edge states in the Chern insulator and QSH phases 357
Importance of edge states **359**
Conclusion **359**
Acknowledgments **360**
References **360**

Abstract

Systems that can be described with the same mathematical models that account for the properties of electrons in graphene are known as graphene-like systems. These include magnons, photons, polaritons, acoustic waves, and electrons in honeycomb lattices, either natural or artificial. All of them feature an outstanding property, the existence of states localized at the edges. We distinguish two classes of edge states depending on whether or not a topological band gap is present in the two-dimensional energy bands. We introduce the theory of edge states in terms of tight-binding models and discuss their properties, with an emphasis on the interplay between their one-way character and the topological nature of the bulk phase.

Key points

- Graphene-like systems can be modeled with a tight-binding model that describes a honeycomb lattice with one state per site, resulting in peculiar energy dispersions, both in bulk, with Dirac cones, and at the edges.
- States localized at the boundaries are known as edge states.
- The properties of the edge states are intimately related to the topological properties of the bulk. When a topological gap opens in bulk, in-gap edge states exist in all boundaries. Otherwise, zero-energy edge states exist only along certain crystallographic directions.

Introduction

Main properties of graphene band structure

Graphene is a two-dimensional material made of carbons forming a honeycomb lattice. Its electronic properties are often described (Castro Neto et al., 2009) with a tight-binding model with only one atomic orbital per carbon and first-neighbor hopping. This model has three outstanding properties:

1. It has two energy bands, on the account of the two sites in the unit cell of the honeycomb lattice.
2. The two energy bands become degenerate at two points in the six corners of the hexagonal Brillouin zone.
3. In the neighborhood of these degenerate points, the energy bands form two Dirac cones with electron-hole symmetry.

---

[*] On permanent leave from Departamento de Física Aplicada, Universidad de Alicante, Spain.

https://doi.org/10.1016/B978-0-323-90800-9.00207-9

In the rest of this chapter, we choose our energy origin, $E = 0$, at the degeneracy points and we refer to them as the Dirac points. The lattice shows C_3 symmetry, that remains invariant under rotations of 120 degrees. Only two groups of three equivalent corners or Dirac points are actually different states of the crystal. We refer to these groups as *valleys*, and we label them as K and K'.

Importantly, there are several physically relevant perturbations to the first-neighbor hopping tight-binding model that lead to the opening of a *gap* between the two bands. In some cases, these perturbations make graphene enter a topological phase, different from conventional insulators, having an important impact on the edge states. We shall distinguish two broad types of topological states in graphene, Chern insulators (Haldane, 1988) and Quantum Spin Hall insulators (Kane and Mele, 2005). The Quantum Hall phase promoted in graphene by the application of an external magnetic field perpendicular to the honeycomb plane (Castro Neto et al., 2009) belongs to the Chern-insulator type.

Graphene-like systems

Many of these properties, including the Dirac cones in the bulk dispersion, the topological-gap openings, are shared by a class of systems that can be described with the same mathematical models than graphene and its topological variants (Polini et al., 2013; Lado et al., 2015). The relevant degrees of freedom in these graphene-like systems are not only electrons but also magnons, photons of various wavelengths, polaritons, and sound waves. Some of these graphene-like systems are artificial arrays of various different types and length-scales: atomically-precise lattices crafted with a scanning tunneling microscope on a surface, arrays of quantum dots in silicon, millimeter size dielectric resonators arranged in a honeycomb lattice, and cm-scale acoustic resonators. The list of graphene-like systems, either topological or not, includes:

- Electrons in other 2D materials with honeycomb lattices and sp^2, such as silicene and germanene, in and nanofabricated honeycomb lattices (Singha et al., 2011), surfaces with arrays of CO molecules (Gomes et al., 2012) and molecular crystals
- Magnons in ferromagnetic crystals where the magnetic atoms are disposed in a honeycomb lattice (Owerre, 2016) such as $\mathrm{CrI_3}$ (Huang et al., 2017)
- Cold atoms trapped in tunable optical lattices with honeycomb geometry (Tarruell et al., 2012)
- Exciton polaritons in honeycomb arrays of micropillars (Jacqmin et al., 2014)
- Photons in honeycomb photonic lattices (Plotnik et al., 2013)
- Acoustic waves in honeycomb lattices of millimeter scale cylinders (Torrent and Sánchez-Dehesa, 2012; Khanikaev et al., 2015)

This list illustrates the diversity of physical systems, length-scales and degrees of freedom that can be described in terms of the same mathematical models.

Edges and edge states

Edge states can occur at the boundaries of graphene, where carbon atoms have only two carbon first neighbors, instead of three. They are localized in the direction perpendicular to the boundary and can be extended along the boundary. The boundaries of semi-infinite graphene are one-dimensional (1D) and they can host one-dimensional extended edge states. Very often, the energy of edge states is in the neighborhood of the Dirac points.

Edges in graphene-like systems are characterized by their orientation relative to the two high-symmetry directions in the honeycomb lattice, armchair, and zigzag (see Fig. 1A, C, and D). The most studied edges are parallel to one of these two directions. However, edges along arbitrary directions, known as chiral edges, can be considered (see Fig. 1F)

We distinguish two types of edge states, depending on whether or not graphene has a topological gap. For gapless graphene, edge states only occur for edges in a range of orientations. For instance, zigzag edges host edge states, whereas armchair do not. In gapless graphene, edge states have strictly $E = 0$ energy forming flat 1D bands (Nakada et al., 1996).

In the presence of a topological gap in the bands of 2D crystal, all boundaries of graphene do host edge states, and they have dispersive energy bands $E(k)$. For Quantum Spin Hall insulators, edge states have spin-momentum locking: at a given edge electrons with opposite spin projection along the off-plane direction propagate in opposite directions (Kane and Mele, 2005). Thus, back-scattering entails a spin-flip. In the case of Quantum Hall and Chern insulators, all edge states are chiral: propagation only occurs in one direction, regardless of the spin, making back-scattering strictly forbidden (Haldane, 1988; Lado et al., 2015).

Theory of quantum states in 2D honeycomb lattices

Graphene-like states in two dimensions

The honeycomb lattice of 2D graphene can be treated as two interpenetrating triangular lattices that we label as A and B in Fig. 1A. Thus, the honeycomb lattice is a triangular lattice with two atoms per unit cell that naturally leads, within the simple TB model, to this 2 × 2 Bloch Hamiltonian (Castro Neto et al., 2009):

$$\mathcal{H}_0(\vec{k}) = t\begin{pmatrix} 0 & f(\vec{k}) \\ f^*(\vec{k}) & 0 \end{pmatrix} \tag{1}$$

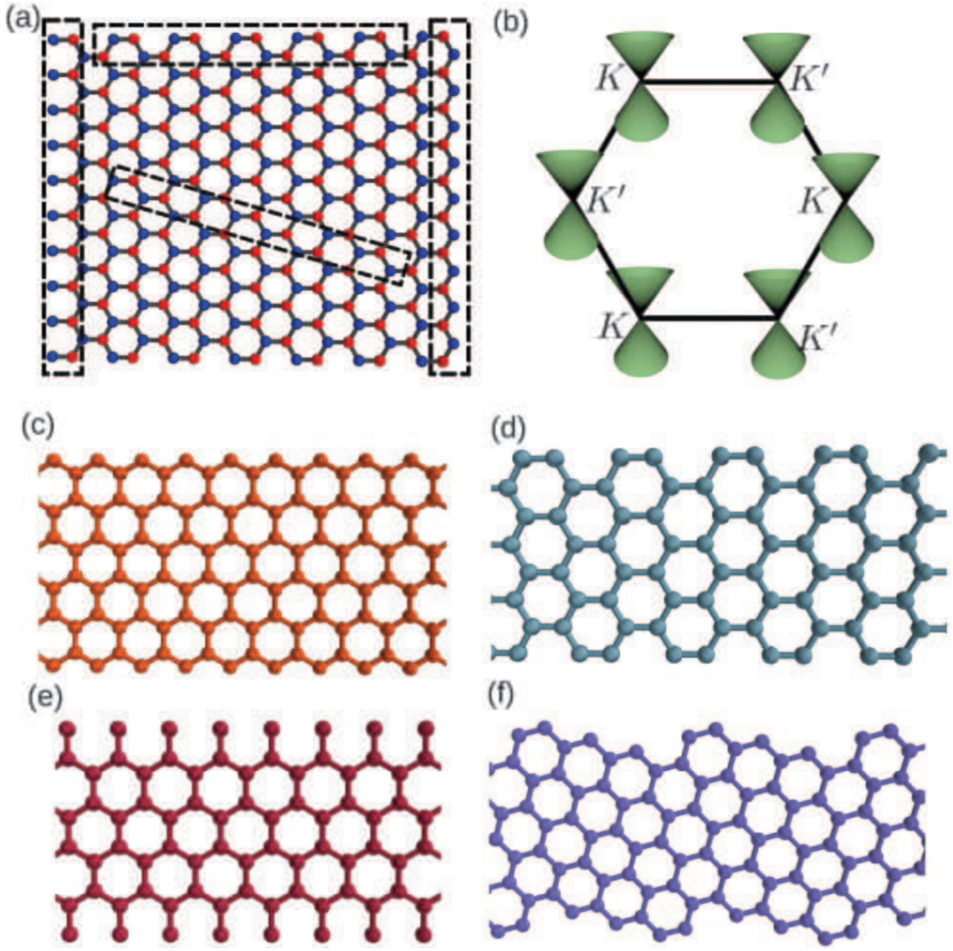

Fig. 1 (A) Honeycomb lattice, with the two triangular sublattices, *A* and *B*, are displayed with fake color, *red* and *blue*. (B) Brillouin zone associated to the honeycomb lattice, including the plot of the two energy bands forming Dirac cones in the neighborhood of *K* and *K*′ points (see text). Four types of edges, zigzag (C), armchair (D), bearded (E), and chiral (F).

where t is the first neighbor hopping and $f(\vec{k}) = 1 + e^{i\vec{k}\cdot\vec{a}_1} + e^{i\vec{k}\cdot\vec{a}_2}$ is the Bloch hopping associated to first neighbor hopping in the honeycomb lattice, and

$$\begin{aligned} \vec{a}_1 &= \frac{a}{2}\left(\sqrt{3}, 1\right) = a\left(\cos 30^\circ,\ \sin 30^\circ\right) \\ \vec{a}_2 &= \frac{a}{2}\left(\sqrt{3},\ -1\right) = a\left(\cos 30^\circ,\ -\sin 30^\circ\right) \end{aligned} \tag{2}$$

where a is the unit cell spacing, which coincides with the second neighbor distance and it satisfies the relation $a = \sqrt{3}a_{CC}$ with the first neighbor distance. The resulting energy bands, $\varepsilon_\pm(\vec{k}) = \pm|t|\sqrt{|f(\vec{k})|^2}$, are shown at low energies in Fig. 1B. The function $f(\vec{k})$ vanishes at the K and K' points so that the two bands meet at those points, with energy $\varepsilon = 0$. Due to the bipartite character of the honeycomb lattice, the energy bands have the so called *electron-hole* symmetry, that is, for every state with energy $+E$, there is another with energy $-E$.

At this point, we introduce the concept of sublattice as a pseudo spin degree of freedom, with Pauli matrices σ_a, $a = x, y, z$, such that σ_z is the sublattice operator. By so doing, we can write down the Bloch Hamiltonian in terms of the Pauli matrices σ_x, σ_y:

$$\mathcal{H}_0(\vec{k}) = t\left[Re(f(\vec{k}))\sigma_x + Im(f(\vec{k}))\sigma_y\right] \tag{3}$$

The resulting Bloch states can be found to be:

$$\psi_{\vec{k},\nu=\pm1} = e^{i\vec{k}\cdot\vec{r}}\begin{pmatrix} 1 \\ \nu e^{i\phi(\vec{k})} \end{pmatrix} \tag{4}$$

where $\phi(\vec{k})$ is the phase of the complex number $f(\vec{k})$. Importantly, all finite-energy eigenstates of $\mathcal{H}_0$, and any other bipartite model, have an equal weight on both sublattices.

In order to describe the low-energy physics of graphene, it is enough to expand the Bloch Hamiltonian of Eq. (1) the neighborhood of the K and K' points, denoted by the label $\tau_z = \pm 1$. By so doing we obtain:

$$\mathcal{H}_0(\vec{q}) = \hbar v_F \left(q_x \sigma_x + \tau_z q_y \sigma_y \right) \tag{5}$$

where $\vec{q} \equiv \vec{k} - \vec{K}_\tau$ and $\hbar v_F = \frac{3}{2} t a_{CC}$, where a_{CC} is the first-neighbor distance in the honeycomb lattice. We thus see that, in the neighborhood of the K and K' point, the graphene tight-binding Hamiltonian of Eq. (1) can be mapped into two copies, one per valley, of a Dirac Hamiltonian. Many of the low energy properties of graphene-like systems can be understood in terms of the Dirac Hamiltonian.

Band-gap opening

We now discuss different extra perturbations in the model of Eq. (1) that, while preserving the overall structure of the graphene bands, lead to band-gap openings that may or may not be topological. We start with the simplest case of a nontopological band-gap opening induced by a sublattice symmetry breaking term, as it would happen for instance in 2D boron nitride:

$$\mathcal{H}_{BN} = \begin{pmatrix} \frac{\Delta}{2} & t f(\vec{k}) \\ t f^*(\vec{k}) & -\frac{\Delta}{2} \end{pmatrix} \tag{6}$$

It is apparent that, at the Dirac points, the off-diagonal terms vanish and the eigenvalues are $E = \pm \frac{\Delta}{2}$ so that a band gap of dimension Δ opens up at the Dirac points. Importantly, Δ is momentum independent so that it has the same sign at both valleys.

We now consider the Haldane model (Haldane, 1988) that also leads to a gap opening at the valleys, but with opposite sign. This turns out to be essential to make this gap topological. The Haldane model amounts to add to Eq. (1) a term that accounts for local magnetic fields with a vanishing total flux. These magnetic fields give rise to an imaginary second-neighbor hopping:

$$\mathcal{H}_{\text{Haldane}} = \begin{pmatrix} t_H g(\vec{k}) & t f(\vec{k}) \\ t f^*(\vec{k}) & -t_H g(\vec{k}) \end{pmatrix} \tag{7}$$

where $g(\vec{k}) = 2(\sin\phi_2 - \sin\phi_1 + \sin(\phi_1 - \phi_2))$, where $\phi_{1,2} \equiv \vec{k} \cdot \vec{a}_{1,2}$. In graphene, the magnetic field required to realize the Haldane term cannot be directly created externally on account of their very rapid space modulation. In contrast, in some graphene-like systems, the second-neighbor Haldane hopping can be engineered in the lab. For instance, in the case of magnons, second-neighbor Dzyaloshinskii–Moriya interactions give rise to Haldane-type terms in the magnon Hamiltonian (Owerre, 2016).

A *kp* expansion of the Haldane term around the Dirac point would yield the following extra term in the Dirac Hamiltonian:

$$\delta\mathcal{H} = \frac{3}{2}\sqrt{3} t_H \tau_z \sigma_z = \frac{\Delta}{2} \tau_z \sigma_z \tag{8}$$

so that a gap of magnitude $\Delta = 3\sqrt{3} t_H$ opens up at the Dirac point. If we define the *sign* of the gap, encoded in τ_z, the gap in the two valleys of the Haldane model has opposite signs.

This gap turns out to be topological. To see that, we define the Chern number associated to a band n as the integral over the Brillouin zone

$$\mathcal{C}_n = \frac{1}{2\pi} \int_{BZ} \Omega_n d^2k \tag{9}$$

where Ω_n is the Berry curvature

$$\Omega_n = i\left(\partial_{k_x} \langle \Psi_n | \partial_{k_y} | \Psi_n \rangle - \partial_{k_y} \langle \Psi_n | \partial_{k_x} | \Psi_n \rangle \right) \tag{10}$$

These expressions, valid for nondegenerate bands, can be easily generalized to the multiband case.

The Chern number can only take integer values when the integral encompasses the whole Brillouin zone. Parametric deformations of a Hamiltonian that preserve the symmetry and do not close the gap do not change the Chern number. This robustness is the key property of topological insulators. Importantly, the value of the Chern number determines the Hall conductance via the TKNN formula, $\sigma_{xy} = \frac{e^2}{\hbar} \sum_n \mathcal{C}_n f_n$, where $f_n = 0, 1$ marks the occupation of the band n at zero temperature. For trivial two-dimensional insulators, the Chern number vanishes, and so it does the Hall conductance. For a class of two-dimensional topological insulators, including graphene and other 2D systems in the Quantum Hall regime, the Chern number is finite and the Hall conductance is quantized. The Haldane model was the first example of a band insulator with nonvanishing Chern number and no Landau Levels. The existence of edge states in topological insulators is essential for the quantized Hall conductance.

The Chern number for the two bands of the Haldane model is (Haldane, 1988; Lado et al., 2015):

$$\mathcal{C}_{\pm} = \pm \mathrm{sign}(t_H) \tag{11}$$

For the Haldane model, the dominant contribution to the Chern number in Eq. (9) comes from the neighborhood of the K and K' points. We can actually compute the Berry curvature of a massive Dirac model $\mathcal{H}_0 + \delta\mathcal{H} = \hbar v_F \left(q_x\sigma_x + \tau_z q_y \sigma_y \right) + \frac{\Delta}{2}\sigma_z$ as

$$\mathcal{C}(\Delta, \tau_z) = \frac{1}{2}\tau_z \frac{\Delta}{|\Delta|} \tag{12}$$

For the sake of the discussion we can think of the Berry curvature as a magnetic field and the Chern number as a flux. From Eq. (12) we see that in the Haldane, model the sum over the two valleys leads to a $\mathcal{C} = 1$. In contrast, when the gap is opened by the breaking of sublattice symmetry, as in Eq. (6) the total Chern number vanishes.

So far, the discussion has ignored the spin degree of freedom and all our statements hold true for each spin channel separately. Therefore, if we define a Haldane model for spinful fermions, the Chern number would be 2. In 2004, Kane and Mele (Kane and Mele, 2005) found out that the model Hamiltonian that describes graphene with intrinsic spin orbit coupling is mathematically equivalent to a *spin-dependent second-neighbor Haldane coupling*:

$$\mathcal{H}_{\mathrm{KM}} = \begin{pmatrix} s t_{KM} g(\vec{k}) & t f(\vec{k}) \\ t f^{*}(\vec{k}) & -s t_{KM} g(\vec{k}) \end{pmatrix} \tag{13}$$

where $s = \pm 1$ labels the spin. Thus, graphene was predicted to have a gap at the Dirac point, given by $3\sqrt{3}t_{KM}$. Unlike the Haldane model, the Kane–Mele model preserves time reversal symmetry and, consequently, the total Chern number, once we sum over the spins, is zero. Therefore, the Kane–Mele model does not describe a Chern insulator. Yet, the model defines a topological insulator, different from vacuum, that is characterized by a Z_2 topological index and the emergence of spin-chiral edge states (see next section). The magnitude of the gap is predicted to be smaller than a fraction of meV, on account of the very small spin–orbit coupling of carbon. Therefore, for most practical purposes, graphene can be considered gapless. Yet, the conceptual importance of this prediction was very important, as it triggered the quest of artificial graphene realizations with this type of topological gap (Jotzu et al., 2014; Marrazzo et al., 2019, 2018).

Once spin degree of freedom is considered, there are at least two other mechanisms to turn graphene into a Chern insulator. The first mechanism, proposed by Qiao et al. (2010), combines an off-plane Zeeman splitting, induced for instance by spin proximity with a ferromagnet with off-plane easy axis, and a second type of spin–orbit interaction that arises in graphene when mirror symmetry is broken, the so called Rashba spin–orbit coupling. The Zeeman splitting of the Dirac cones leads to crossing of the electron-like band of one spin channel with the hole-like band of the other, exactly at $E = 0$, with coincides with the Fermi energy at half-filling. Rashba spin–orbit coupling mixes the two spin channels, leading to a band-gap opening at the Dirac energy, that turns out to have a finite Chern number. An alternative mechanism not relying on spin–orbit coupling consists on using exchange interaction to a magnetic skyrmion lattice placed underneath graphene (Lado and Fernández-Rossier, 2015).

Calculation methods for edge states in graphene-like systems

The calculation of edge states in graphene is not as straightforward as the calculation of bulk states on account of the reduced crystal symmetry of the problem. The are two widespread methods: (1) Computation of energy bands of 1D stripes or ribbons. (2) Green's function methods.

Energy bands of 1D stripes

We choose a crystal direction and a given width W and define a 1D crystal or ribbon with two edges. When the width of the ribbon is sufficiently large, compared to the penetration length of the edge states, the interactions between the edges are negligible, allowing to study the properties of the edge states as if they were decoupled. This method is very versatile as it permits one to include all types of terms in the Hamiltonian, including a magnetic field.

Green's function

In this approach (Lado et al., 2015), we calculate the Green's function of a semi-infinite two-dimensional crystal using the recursion method. Using the translation invariance along the direction parallel to the edge, it is possible to write the Hamiltonian of the semi-infinite crystal as a one-dimensional semi-infinite crystal whose effective Hamiltonian depends on the transverse wave vector $k_{\|}$. By so doing, the Green's function of the unit cell in the semi-infinite crystal reads:

$$G(k_{\|}, E) = \left(E - h_0(k_{\|}) - \Sigma(k_{\|}, E) + i\varepsilon \right)^{-1} \tag{14}$$

where $\Sigma(k_{\|})$ is the self-energy induced by the coupling to the rest of the crystal:

$$\Sigma(k_{\parallel}, E) = t(k_{\parallel})G(k_{\parallel}, E)t^{\dagger}(k_{\parallel}) \tag{15}$$

where $h_0(k_{\parallel})$ and $t(k_{\parallel})$ are the intracell and intercell matrices of the Block Hamiltonian. Eqs. (14) and (15) define a set of nonlinear coupled matrix equations that is solved by numerical iteration. Once the surface Green's function is derived, the density of states can be obtained through $A(k_{\parallel}, E) = -\frac{1}{\pi}\mathrm{Im}\big(G(k_{\parallel}, E)\big)$. Contour plots in the $k_{\parallel}$, E plane can reveal the existence of in-gap edge states. This method avoids the inter-edge coupling issues that may arise in the method of graphene ribbons when W is not sufficiently large.

Analytical results

We can derive edge states in the case of gapless graphene by looking for Bloch states that have imaginary momentum in the armchair direction, $\vec{k} = (i\kappa, k_y)$, and requesting they have $E = 0$. Those states would be thus evanescent in half of the plane, and itinerant along the zigzag direction. There are two ways in which we can have a state with $E = 0$: either $f(i\kappa, k_y) = 0$ and the wave function localized in sublattice A or $f^{*}((i\kappa, k_y)) = 0$ and the wave function localized in sublattice B. These two situations lead to the following equation that relates κ and k_y is:

$$e^{\pm\frac{\sqrt{3}}{2}\kappa a} = \frac{-1}{2\cos\left(\frac{k_y a}{2}\right)} \tag{16}$$

Since the left-hand side of this equation is positive, for real κ, we need to have $cos\left(\frac{k_y a}{2}\right) < 1$. In addition, depending on the sign of the exponent of the left-hand side, this entails $|cos\left(\frac{k_y a}{2}\right)|$ to be either smaller or larger than $\frac{1}{2}$. Altogether, these two conditions impose limits to the values that the transverse momentum of the edge state, k_y, can take: either in region $\frac{2\pi}{3} < |k_y a| < \pi$ or outside of this region. As we shall show right now, these two types of edge state correspond to two types of edge termination: zigzag, or the so called "bearded," both of them along the zigzag direction. In the zigzag (bearded) case, with edge states in (out of) the $\frac{2\pi}{3} < |k_y a| < \pi$ region, the density of edge states per edge atom is 1/3 (2/3)

Edge states in gapless graphene

We now consider edge states in gapless graphene for zigzag edges. The prediction of Eq. (16) is confirmed by inspection of the energy bands of two very wide graphene ribbons with zigzag boundary conditions (see Fig. 2A). Most of the bands in these figures correspond to confined *bulk* (2D) states. Since the ribbons have two edges, there are two flat bands with energy $E \simeq 0$. In the case of zigzag (bearded) in the region, $\frac{2\pi}{3} < |k_y a| < \pi$. Since the extinction factor κ goes to zero for $k_y a = \frac{\pm 2\pi}{3}$, there is a small hybridization of the two edge states in that region, due to the finite width of the simulation ribbon. For a given edge, inspection of the wave functions shows that wave functions are sublattice polarized at opposite sublattices for the two terminations, as expected from the analytical argument. An analogous calculation with a ribbon with armchair termination does not show edge states.

Zigzag edge states can also exist in finite size graphene systems, provided the edges are long enough. For zigzag termination, edge states occupy one-third of the Brillouin zone. Thus, there is an average of 1/3 of edge state per edge atom. Accordingly, graphene fragments host edge states when they have zigzag edges with at least 3 edge sites. For a structure with N_A and N_B sites in the A and B sublattices, respectively, the first-neighbor TB model predicts the existence of at least $|N_A - N_B|$ zero energy states. These zero energy states, or zero modes, are sublattice polarized and very often these are localized at the edges.

Whereas the zigzag edge states occur in the absence of a topological gap in the band structure of 2D graphene, the existence of an edge state with momentum k can still be understood in terms of bulk-edge correspondence between the quantized value of the Zak phase $Z(k)$, which is a Berry phase across an appropriately chosen one-dimensional Brillouin zone (Delplace et al., 2011).

As a result of the large density of edge states at $E = 0$, which is the Fermi energy of charge-neutral graphene, zigzag edges are prone to magnetic instabilities, on account of electron–electron interactions (Yazyev, 2010). As a result, local moments are expected to exist at zigzag edges. The small magnetic anisotropy and their one-dimensional character prevent the formation of long-range magnetic order and promote quantum-disordered states instead.

Edge states in topological graphene

We now consider edge states associated to the various topological phases of graphene. There are two main differences with the edge states of gapless graphene. First, edge states occur for all edges. Second, they are dispersive. Third, for a given edge, the group velocity of edge states takes one sign only: they are *one-way states*.

We discuss three different topological phases in graphene: the Quantum Hall phase, the Chern insulator phases, and the Quantum Spin Hall phase.

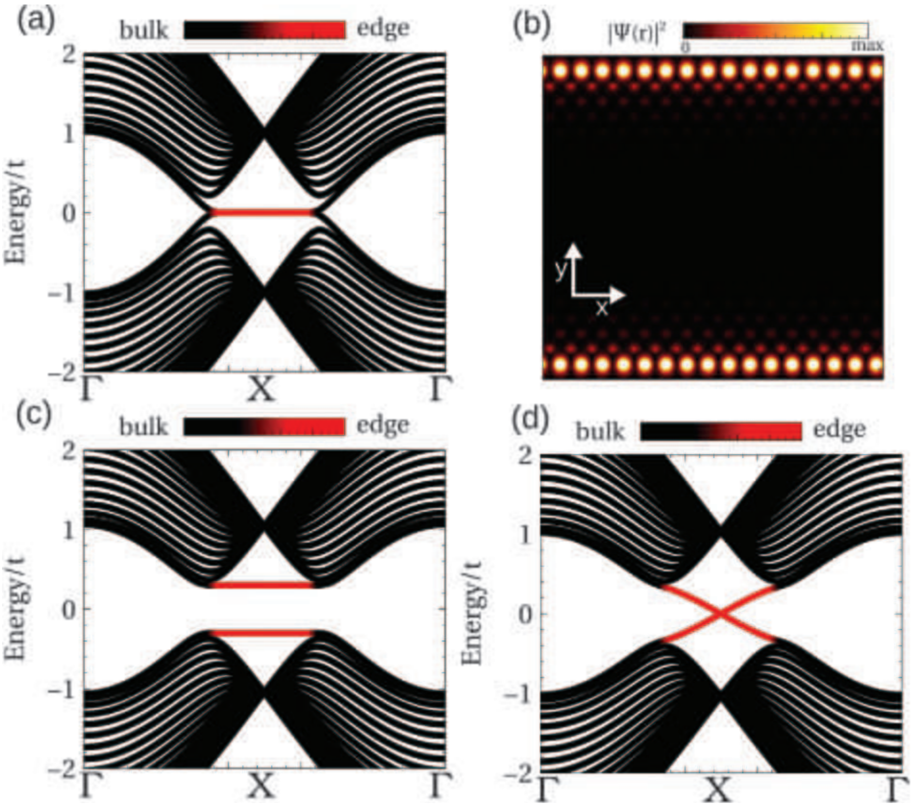

Fig. 2 (A) Energy bands for zigzag ribbon in the gapless regime ($t_{KM} = t_H = \Delta = 0$). The states localized at the edges are plotted in red. (B) Wave function of the one of the $E = 0$ modes at the X point showing a strong localization in one of the edges. (C) Bands for the same system adding a sublattice imbalance term Δ in the Hamiltonian: a band gap opens in the edge states. (D) Bands for the same system with a finite value of t_H: the edge states, in *red color*, acquire now a dispersion. The positive and negative velocity edge states are localized at opposite edges.

Quantum Hall phase

Application of a magnetic field perpendicular to a two-dimensional electron gas (2DEG) results in the Landau quantization of the energy spectrum. Classically, electrons follow closed orbits. Quantum mechanically, electrons occupy finite size states, with a discrete energy spectrum $\varepsilon_n = \hbar\omega_0\left(n + \frac{1}{2}\right)$, where $\omega_c = \frac{eB}{m}$ is the cyclotron frequency and n are integer numbers greater than 0. These are so-called Landau levels. Landau levels have a macroscopic degeneracy, associated to the location of the classical orbits across the plane. The density of such orbits, and thereby the degeneracy of the Landau levels, is determined by the magnetic field. When the density of electrons matches the density of states per Landau Level, the occupation of Landau levels at zero temperature is either complete or null: this is a Quantum Hall insulator, with the Fermi energy lying in the gap between Landau levels. Unlike normal insulator, Quantum Hall insulators have in-gap edge states and their Hall conductance is finite and quantized (Klitzing et al., 1980) in units of e^2/h. Edge states are often interpreted in terms of semiclassical skipping orbits: scattering of electrons with the edge prevents them from completing closed loops (Halperin, 1982). However, the robustness of edge states and their contribution to Quantum Hall conductance quantization lies ultimately in the topological nature of bulk states (Thouless et al., 1982), and not on the specifics of the edges.

The Quantum Hall phase picture just described holds for graphene with several differences. For Dirac electrons, instead of just one, there are two sets of Landau levels with electron-hole symmetry, one for electrons and one for holes (Castro Neto et al., 2009). Thus, for the valley $\tau = \pm 1$, there are two sets of Landau Levels $E_n = \pm\frac{\hbar\omega_{0g}}{2}\sqrt{n + \frac{1-\tau}{2}}$ where $\omega_0 = \frac{2v_F}{\ell_B}$, $\ell_B = \sqrt{\frac{\hbar}{eB}}$, and v_F is the velocity of the Dirac electrons. In addition to these four sets of finite energy Landau levels (two per valley), there are two $E = 0$ Landau levels, one per valley.

These Landau levels, and the edge states, can be described with the same tight-binding model that describes a finite width graphene ribbon, including the effect of the magnetic field on the orbital motion of the electrons by using the Peierls substitution, where the hopping between sites α and β is replaced by:

$$t_{\alpha\beta} \to t_{\alpha\beta} e^{i\Phi_{\alpha,\beta}} \tag{17}$$

where $\Phi_{\alpha,\beta} = \int_{\vec{r}_\alpha}^{\vec{r}_\beta} \vec{A} \cdot d\vec{r}$ is the Peierls phase of the vector potential $\vec{A}$ associated to the magnetic field $\vec{B} = \vec{\nabla} \times \vec{A}$. For a constant magnetic field, we can choose the vector potential as $\vec{A} = B(-y, 0, 0)$ so that translational invariance is broken along the y direction, taken to be perpendicular to the boundaries of the ribbon. Therefore, the energy states can be classified in one-dimensional energy bands.

In Fig. 4 we show the bands of graphene ribbons with armchair, zigzag, bearded, and chiral terminations. All bands have two regions, a dispersionless region that corresponds to Landau Levels, localized away from the edges, and a dispersive region associated to edge states. The calculation shows that finite energy levels have a twofold degeneracy, broken a the edges, associated to the valley degree of freedom. In contrast, the $E = 0$ LL is formed of a duet of nondegenerate electron-type and a hole-type Landau level. In the figure we also show the how that dispersive states correspond to edge states and their velocity is opposite for opposite edges.

Both for the 2DEG and for graphene, the Quantum Hall conductance is given by the TKNN formula (Thouless et al., 1982) so that it is apparent the ultimate origin of its quantization is the topological nature of the band gap.

Edge states in the Chern insulator and QSH phases

We now discuss the properties of the edge states of the Chern insulating phase, as described by the Haldane model, and the Quantum Spin Hall (QSH) phase, as described by the Kane and Mele model. In both cases, there are dispersive in-gap edge states, regardless of their crystal orientation (see Figs. 2D, 3, and 5C for the Haldane model, and Fig. 5D, all of them for armchair edges). In the case of Fig. 5 we show the local-density of states, computed with the Green's function method, resolved in transverse-momentum, at the armchair boundary of a semi-infinite honeycomb lattice for three models: gapless graphene (panel 5B), Haldane model (panel 5C), and Kane–Mele model (panel 5D). At a given edge, the sign of the slope of the in-gap edge state in the Haldane model is given by the sign of t_H. Since the Kane–Mele model is equivalent to two copies of the Haldane model where the sign of the coupling is given by the spin projection along the off-plane direction, it is immediately apparent that each edge host two edge states, one per spin channel, with opposite velocities. This is clearly seen in Fig. 5D, obtained for a single edge using the Green's function method.

A graphical summary of the different types of edge states is shown in Fig. 6. For the topologically equivalent Quantum Hall and Chern insulating phases, the edge states circulate around the sample with sense of rotation dictated by the term in the Hamiltonian

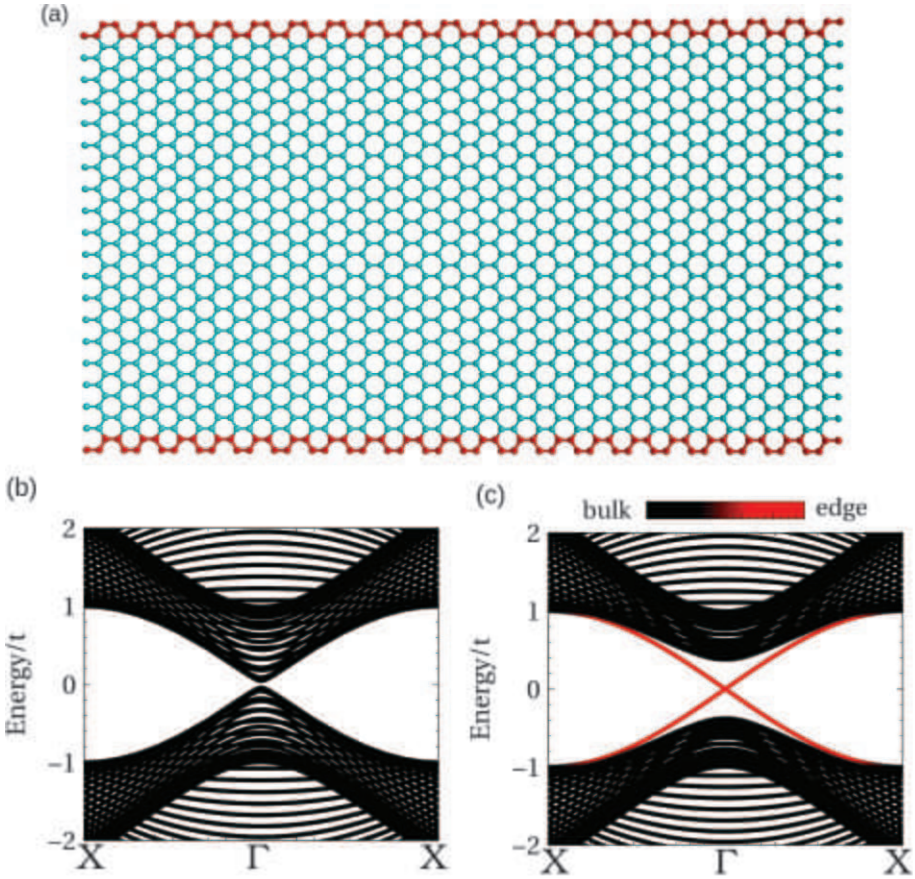

Fig. 3 (A) Snapshot of the unit cell to generate the graphene ribbon, with the edge atoms marked in *red*. (B) Energy bands for armchair ribbon in the gapless regime ($t_{KM} = t_H = \Delta = 0$). The ribbon has a gaped spectrum and no edge states. (C) Bands for the same system, with a finite value of t_H: two dispersive edge states, in *red color*, appear in the gap. This supports the statement that topological edge states appear in all boundaries regardless of their geometry.

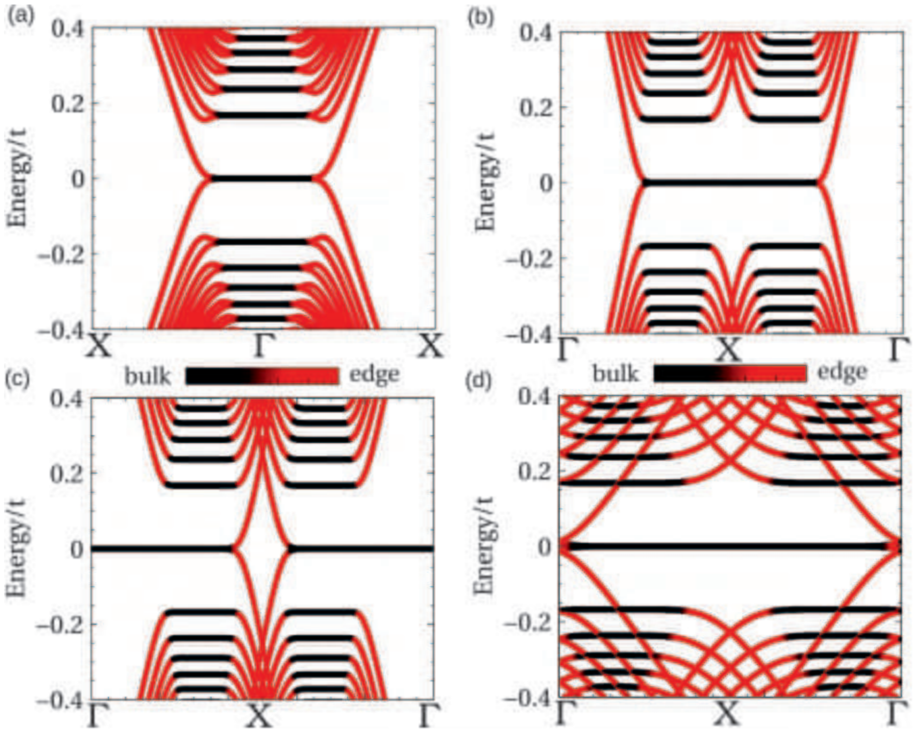

Fig. 4 Energy levels for armchair (A) zigzag (B) bearded (C) and chiral (D) graphene ribbons under the influence of a magnetic field B applied perpendicular to the ribbon. For the sake of clarity, spin effects are not included in the calculation. Two types of states are shown. Dispersive edge states in *red* and dispersionless states in *black*, corresponding to Landau levels localized away from the edges. In addition, for the zigzag case, there are $E = 0$ flat edge states that were already present for $B = 0$. In the zigzag, bearded, and chiral geometry, the presence of two sets of Landau levels, corresponding to the two valleys, is apparent. In the armchair geometry, the valley degeneracy manifested as a twofold degeneracy of the Landau Levels.

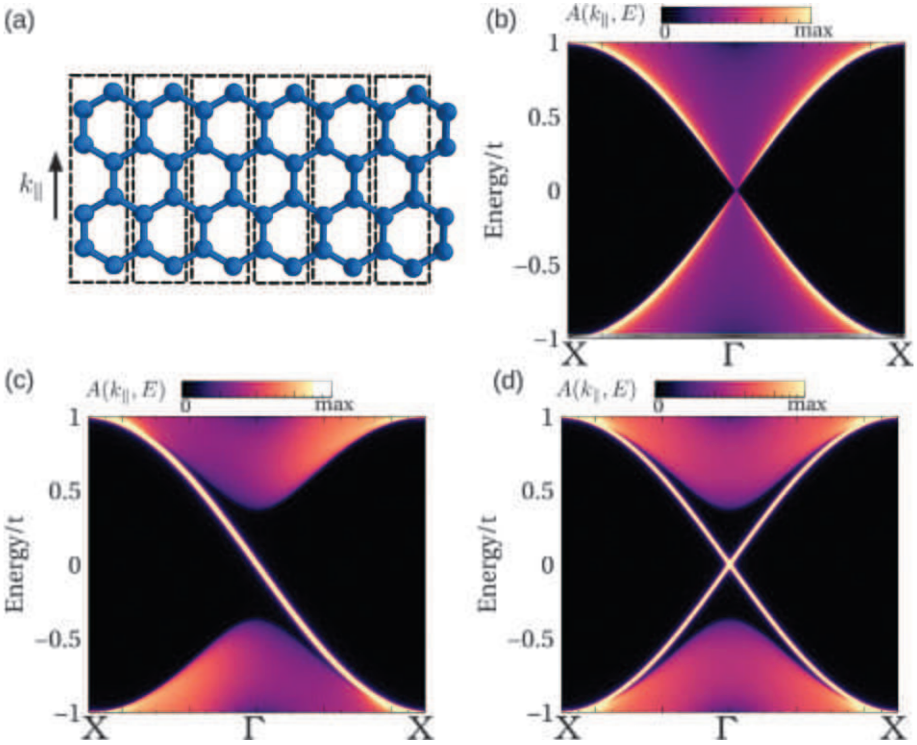

Fig. 5 Schematic of the Green's function method for an armchair edge (A), and edge spectral function for a gapless armchair edge (B), with Haldane coupling (C), and with Kane–Mele coupling (D).

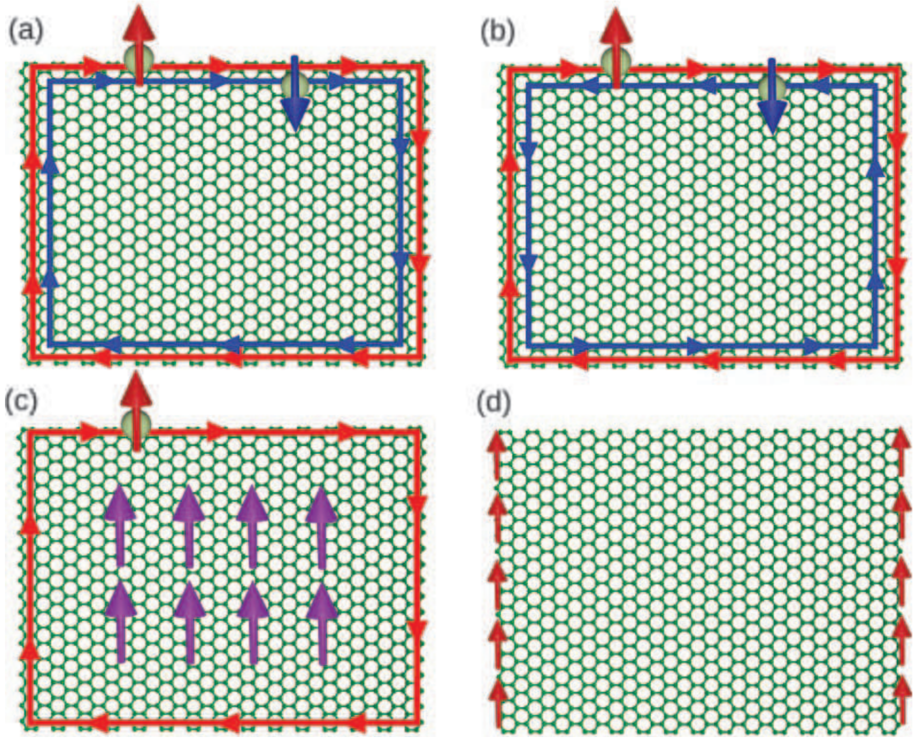

Fig. 6 Schematic of quantum Hall edge states (A), quantum spin Hall edge states (B), quantum anomalous Hall edge states (C) and zigzag edge states (D).

that breaks time reversal symmetry, either the external magnetic field in the Quantum Hall case or the Haldane term in the Haldane model. Edge states for these two phases cannot undergo intra-edge elastic backscattering as there are no states with opposite momentum and the same energy available. This can be connected both with the perfect quantization of their Hall conductance and their longitudinal conductance. In the case of the Kane–Mele model the edge states feature counter-propagating states with opposite spin projections. Therefore, elastic backscattering is permitted in the presence of spin-flip perturbations and not permitted if time-reversal symmetry is preserved.

Importance of edge states

Edge states have attracted interest for several reasons. In the case of nondispersive edge states, it is expected that Coulomb repulsion will promote the emergence of local moments, on account of the flat bands at the Fermi energy. There is a large body of research papers, mostly theoretical, devoted to the study of magnetism in zigzag edge states in graphene. Intra-edge interactions are expected to be ferromagnetic, at least when interactions are short-ranged (Hubbard type). However, long-range ferromagnetic order in spin-isotropic systems is not stable in 1D, on account of quantum and thermal fluctuations. Therefore, zigzag edges are expected to host fluctuating local moments, and behave as paramagnets with an enhanced spin suceptibility.

Dispersive edge states feature by the topological phases attract also enormous interest. The notion of *one way* states is of course very appealing, not only for electrons but also for other excitations. For instance, the prediction of topological magnons in 2D ferromagnetic materials with honeycomb lattices implies the existence of in-gap *one way* magnon states that may find some application in magnonbased spintronics. The perfect quantization of Hall conductance of the Quantum Hall phase is used to define the standard of the Von Klitzing constant (Klitzing et al., 1980), h/e^2. A holy grail in quantum materials is the quest of a Chern insulator that features quantized Hall conductance without an external magnetic field.

Conclusion

We have presented the concept of graphene-like systems and we have discussed their edge states. We have stressed the interplay between the existence, or else, of a topological gap in the energy bands of the two-dimensional honeycomb system and the properties of the edge states. Specifically, for the nontopological gapless graphene phase, edge states exist only along some crystallographic directions, most notably the zigzag direction and they form flat bands, prone to magnetic instabilities. In contrast, for topological phases, edge states exist in all edges, regardless of crystallographic orientation, and they have a finite velocity and topological protection against back-scattering.

Acknowledgments

J.F.R. acknowledges financial support from FCT (Grant No. PTDC/FIS-MAC/2045/2021), SNF Sinergia (Grant Pimag), FEDER /Junta de Andalucía — Consejería de Transformación Económica, Industria, Conocimiento y Universidades, (Grant No. P18-FR-4834), Generalitat Valenciana funding Prometeo2021/017. and MFA/2022/045 and funding from MICIIN-Spain (Grant No. PID2019-109539GB-C41). J.L.L. acknowledges the computational resources provided by the Aalto Science-IT project, and the financial support from the Academy of Finland Projects No. 331342 and No. 336243 and the Jane and Aatos Erkko Foundation.

References

Castro Neto AH, Guinea F, Peres NMR, Novoselov KS, and Geim AK (2009) The electronic properties of graphene. *Reviews of Modern Physics* 81(1): 109–162. https://doi.org/10.1103/RevModPhys.81.109.

Delplace P, Ullmo D, and Montambaux G (2011) Zak phase and the existence of edge states in graphene. *Physical Review B* 84(19): 195452. https://doi.org/10.1103/PhysRevB.84.195452.

Gomes KK, Mar W, Ko W, Guinea F, and Manoharan HC (2012) Designer Dirac fermions and topological phases in molecular graphene. *Nature* 483(7389): 306–310. https://doi.org/10.1038/nature10941.

Haldane FDM (1988) Model for a quantum Hall effect without Landau levels: Condensed-matter realization of the “Parity Anomaly”. *Physical Review Letters* 61(18): 2015–2018. https://doi.org/10.1103/PhysRevLett.61.2015.

Halperin BI (1982) Quantized hall conductance, current-carrying edge states, and the existence of extended states in a two-dimensional disordered potential. *Physical Review B* 25(4): 2185–2190. https://doi.org/10.1103/PhysRevB.25.2185.

Huang B, Clark G, Navarro-Moratalla E, Klein DR, Cheng R, Seyler KL, Zhong D, Schmidgall E, McGuire MA, Cobden DH, Yao W, Xiao D, Jarillo-Herrero P, and Xu X (2017) Layer-dependent ferromagnetism in a van der Waals crystal down to the monolayer limit. *Nature* 546(7657): 270–273. https://doi.org/10.1038/nature22391.

Jacqmin T, Carusotto I, Sagnes I, Abbarchi M, Solnyshkov DD, Malpuech G, Galopin E, Lemaître A, Bloch J, and Amo A (2014) Direct observation of Dirac cones and a flatband in a honeycomb lattice for polaritons. *Physical Review Letters* 112(11): 116402. https://doi.org/10.1103/PhysRevLett.112.116402.

Jotzu G, Messer M, Desbuquois R, Lebrat M, Uehlinger T, Greif D, and Esslinger T (2014) Experimental realization of the topological Haldane model with ultracold fermions. *Nature* 515 (7526): 237–240. https://doi.org/10.1038/nature13915.

Kane CL and Mele EJ (2005) Z_2 Topological order and the quantum spin Hall effect. *Physical Review Letters* 95(14): 146802. https://doi.org/10.1103/PhysRevLett.95.146802.

Khanikaev AB, Fleury R, Mousavi SH, and Alù A (2015) Topologically robust sound propagation in an angular-momentum-biased graphene-like resonator lattice. *Nature Communications* 6(1): 8260. https://doi.org/10.1038/ncomms9260.

Klitzing Kv, Dorda G, and Pepper M (1980) New method for high-accuracy determination of the fine-structure constant based on quantized Hall resistance. *Physical Review Letters* 45(6): 494–497. https://doi.org/10.1103/PhysRevLett.45.494.

Lado JL and Fernández-Rossier J (2015) Quantum anomalous Hall effect in graphene coupled to skyrmions. *Physical Review B* 92(11): 115433. https://doi.org/10.1103/PhysRevB.92.115433.

Lado JL, García-Martínez N, and Fernández-Rossier J (2015) Edge states in graphene-like systems. *Synthetic Metals* 210: 56–67. https://doi.org/10.1016/j.synthmet.2015.06.026.

Marrazzo A, Gibertini M, Campi D, Mounet N, and Marzari N (2018) Prediction of a large-gap and switchable Kane-Mele quantum spin Hall insulator. *Physical Review Letters* 120(11): 117701. https://doi.org/10.1103/PhysRevLett.120.117701.

Marrazzo A, Gibertini M, Campi D, Mounet N, and Marzari N (2019) Relative abundance of Z2 topological order in exfoliable two-dimensional insulators. *Nano Letters* 19(12): 8431–8440. https://doi.org/10.1021/acs.nanolett.9b02689.

Nakada K, Fujita M, Dresselhaus G, and Dresselhaus MS (1996) Edge state in graphene ribbons: Nanometer size effect and edge shape dependence. *Physical Review B* 54(24): 17954–17961. https://doi.org/10.1103/PhysRevB.54.17954.

Owerre SA (2016) A first theoretical realization of honeycomb topological magnon insulator. *Journal of Physics: Condensed Matter* 28(38): 386001. https://doi.org/10.1088/0953-8984/28/38/386001.

Plotnik Y, Rechtsman MC, Song D, Heinrich M, Zeuner JM, Nolte S, Lumer Y, Malkova N, Xu J, Szameit A, Chen Z, and Segev M (2013) Observation of unconventional edge states in ‘photonic graphene’. *Nature Materials* 13(1): 57–62. https://doi.org/10.1038/nmat3783.

Polini M, Guinea F, Lewenstein M, Manoharan HC, and Pellegrini V (2013) Artificial honeycomb lattices for electrons, atoms and photons. *Nature Nanotechnology* 8(9): 625–633. https://doi.org/10.1038/nnano.2013.161.

Qiao Z, Yang SA, Feng W, Tse W-K, Ding J, Yao Y, Wang J, and Niu Q (2010) Quantum anomalous Hall effect in graphene from Rashba and exchange effects. *Physical Review B* 82(16): 161414. https://doi.org/10.1103/PhysRevB.82.161414.

Singha A, Gibertini M, Karmakar B, Yuan S, Polini M, Vignale G, Katsnelson MI, Pinczuk A, Pfeiffer LN, West KW, and Pellegrini V (2011) Two-dimensional Mott-Hubbard electrons in an artificial honeycomb lattice. *Science* 332(6034): 1176–1179. https://doi.org/10.1126/science.1204333.

Tarruell L, Greif D, Uehlinger T, Jotzu G, and Esslinger T (2012) Creating, moving and merging Dirac points with a Fermi gas in a tunable honeycomb lattice. *Nature* 483(7389): 302–305. https://doi.org/10.1038/nature10871.

Thouless DJ, Kohmoto M, Nightingale MP, and den Nijs M (1982) Quantized Hall conductance in a two-dimensional periodic potential. *Physical Review Letters* 49(6): 405–408. https://doi.org/10.1103/PhysRevLett.49.405.

Torrent D and Sánchez-Dehesa J (2012) Acoustic analogue of graphene: Observation of Dirac cones in acoustic surface waves. *Physical Review Letters* 108(17): 174301.

Yazyev OV (2010) Emergence of magnetism in graphene materials and nanostructures. *Reports on Progress in Physics* 73(5): 056501. https://doi.org/10.1088/0034-4885/73/5/056501.

An introduction to the theory of spin glasses

Ada Altieri[a] **and Marco Baity-Jesi**[b], [a]Laboratoire Matière et Systèmes Complexes (MSC), Université Paris Cité CNRS, Paris, France; [b]Eawag (ETH), Swiss Federal Institute of Aquatic Science and Technology, Dübendorf, Switzerland

© 2024 Elsevier Ltd. All rights reserved.

Introduction **361**
Experimental SGs 362
Self-averaging 362
Order parameter 363
Analytical methods for spin glasses **363**
The replica method 363
The replica structure of two common MF spin glass models 364
The Thouless–Anderson–Palmer (TAP) approach 365
The cavity method 366
Beyond mean-field: Multilayer construction and loop corrections 366
Dynamical mean-field theory (DMFT) 367
Spin glasses in three dimensions **368**
Numerical methods 368
Spatial correlations 368
The spin-glass phase in low dimensions 368
Pictures for the nature of the low-temperature phase in three dimensions 368
Evidence on the nature of the spin glass phase in 3*d* 369
Outlook on the nature of the spin glass phase 369
Conclusion **369**
Universality classes 369
Open problems 369
Acknowledgments **370**
Further reading **370**

Abstract

We review the main methods used to study spin glasses. In the first part, we focus on methods for fully connected models and systems defined on a tree. These include the replica method, the Thouless-Anderson-Palmer formalism, the cavity method, and the dynamical mean-field theory. In the second part, we deal with the description of low-dimensional systems, mostly in three spatial dimensions, which are mostly studied through numerical simulations. We conclude by mentioning some of the main open problems in the field.

Key points

- An introduction to spin glasses and how they are modeled
- Analytical methods for the study of spin glasses
- Numerical results on the nature of the spin glass phase in low dimensions
- Perspectives and interdisciplinary applications.

Introduction

Spin glasses (SGs) are paradigmatic complex systems, for which disorder plays a central role. Although the term was originally coined to describe certain magnetic materials that exhibit an exotic phase behavior, associated models and theory have since found applications in a wide variety of fields, thus making the study of SGs an intrinsically interdisciplinary endeavor.

Here, we provide an overview of SGs, from their experimental context to their common theoretical models. We notably present several theoretical methods developed within the context of their study, describe the differences between mean-field and three-dimensional SGs, discuss various interdisciplinary applications, and introduce some open questions in the field.

https://doi.org/10.1016/B978-0-323-90800-9.00249-3

Experimental SGs

As materials, SGs are disordered magnetic alloys containing strongly interacting ions immersed in a weakly interacting substrate. They are prepared by rapidly cooling the liquid alloy, thus fixing the strongly interacting particles at random positions within the resulting solid. The pairwise exchange interaction between ions is then positive or negative, depending on the distance vector **r** between ions, such as they are for Ruderman–Kittel–Kazuya–Yosida (RKKY) interactions,

$$J(\mathbf{r}) \sim \frac{1}{|\mathbf{r}|^3}\cos(\mathbf{k}\cdot\mathbf{r}), \tag{1}$$

where the modulus of the frequency **k** is of the order of the Fermi vector. SGs also arise in systems with interactions different from RKKY. The general idea is that because ion positions depend on the specific realization of the alloy, distances between them are randomly distributed (and a priori unknown), and therefore values of $J(\mathbf{r})$ are randomly positive and negative.

To make these systems more physically tractable, we can define SG models assuming that the distances between ions are fixed (e.g., on a lattice), and that the coupling between two ions—commonly called spins—is a quenched random variable. *Quenched* variables here refer to random quantities that appear in the Hamiltonian as parameters that do not change during the evolution of the system so as to capture that ions' positions are fixed over the relevant experimental time scales. This formulation leads to the generic SG Hamiltonian

$$\mathcal{H} = -\sum_{i<j}^{N} s_i \cdot J_{ij} s_j, \tag{2}$$

where the N dynamical variables are spins s_i coupled through pairwise interactions of quenched magnitude J_{ij}. Spins can be formulated in different ways, but in this section we restrict our consideration to Ising spins, $s_i = \pm 1$, both because of their simplicity and because experimental systems are typically spatially anisotropic, thus rendering effective interactions Ising-like. The quenched random variables are extracted from a distribution $P(J_{ij})$, which has support on both positive and negative values. In fully connected models, all couplings are extracted from $P(J_{ij})$ while in other models, some of the couplings are set to zero. For example, the Edwards–Anderson model (EAM) is defined by Hamiltonian (2) on a d-dimensional square lattice, so if s_i and s_j are not nearest neighbors, then J_{ij} is suppressed.

Although Eq. (2) is not the only way to model SGs (e.g., interactions can be more than pairwise), two of its features are nevertheless generic: quenched disorder and frustration. Frustration here refers to the impossibility to satisfy simultaneously all local constraints, which follows from the couplings being independent identically distributed (i.i.d.) variables that can be both positive and negative. As illustrated in Fig. 1, along a loop local coupling cannot all be minimized.

Self-averaging

Because of the quenched disorder, every SG Hamiltonian is different from all others. In other words, every *sample* corresponds to a different set of couplings J_{ij}. Interestingly, even though samples are microscopically different, experimental SG realizations display the same macroscopic behavior. SG descriptions thus work under the assumption, which holds in most relevant cases, that large SG

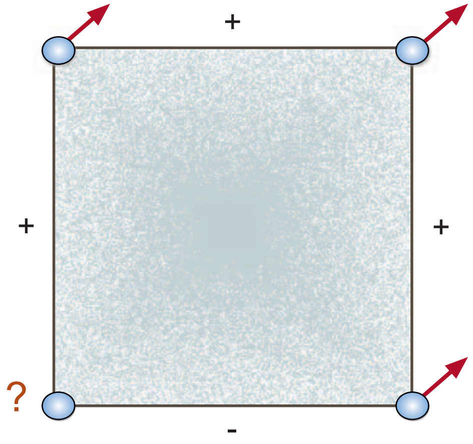

Fig. 1 Disordered interactions result in frustration. The signs along the edges indicate whether two neighboring spins prefer to point in the same (+) or opposite (–) directions. It is therefore impossible to satisfy all the couplings simultaneously on the square plaquette.

samples display equivalent average behavior. Therefore, although a *quenched partition function*, Z_J, can be computed for each sample, the quantity of physical interest is the *quenched free energy* averaged $\overline{(\ldots)}$ over the couplings distribution,

$$\mathcal{F} = \overline{F_J} = -T\,\overline{\log Z_J}, \tag{3}$$

for Boltzmann constant set to unity $k_{\mathrm{B}} = 1$, temperature T.

Order parameter

The SG order parameter is also an important matter. In a ferromagnetic system, magnetization, $M = \frac{1}{N}\langle \sum_i s_i \rangle$, distinguishes between the ferromagnetic and the paramagnetic phases. However, for the Hamiltonian in Eq. (2)—if $P(J_{ij})$ is symmetric around zero—the magnetization is zero for all temperatures.

If a low-temperature SG phase exists, there must nevertheless be some configurations that are preferred over others. One way of identifying these preferred configurations is through the *Edwards–Anderson overlap*,

$$q_{\mathrm{EA}} = \frac{1}{N} \lim_{t\to\infty} \sum_{i=1}^{N} \langle s_i(0) s_i(t) \rangle_t, \tag{4}$$

where $\langle (\ldots) \rangle_t \equiv \frac{1}{t}\int_0^t (\ldots) dt$ marks a time average. If spins s_i have no preferred value, as in the paramagnetic phase, then the products in Eq. (4) vanish on average, and $q_{\mathrm{EA}} = 0$; but if some configurations are preferred, each spin has a preferential value, and $q_{\mathrm{EA}} > 0$.

As further discussed in Section "The replica method," the overlap can also be expressed without resorting to time averages, through the concept of replicas. Replicas of a system have exactly the same couplings J_{ij} but evolve independently. For $s_i^{(a)}$ and $s_i^{(b)}$ denoting spins that belong to replicas a and b of the same sample, we can then write the overlap as

$$q_{ab} = \frac{1}{N} \sum_{i=1}^{N} \left\langle s_i^{(a)} \cdot s_i^{(b)} \right\rangle. \tag{5}$$

As above, the overlap will be zero if there is no preferred configuration, and positive otherwise.

Analytical methods for spin glasses

Some of the most successful methods for studying SG Hamiltonians were developed to describe fully connected models as well as models defined on tree-like graphs. The first geometry corresponds to the mean-field (MF) approximation, which becomes exact in the limit of $d \to \infty$ spatial dimensions while the second goes beyond the MF description but neglects contributions from feedback loops.

The replica method

At variance with the partition function, which is typically nonself-averaging, the free energy is key to probing the low-temperature behavior of SGs (as shown in Eq. 3). However, calculating the average of the logarithm in Eq. (3) can be challenging. The *replica method* overcomes this difficulty by replacing the calculation of $\overline{\ln(Z)}$ with that of $\overline{Z^n}$ through the identity

$$\overline{\ln Z} = \lim_{n\to 0} \frac{\overline{Z^n} - 1}{n}, \tag{6}$$

and by treating Z^n as the partition function for n replicas of the same sample. Treating the index n as an integer, however, hinges on the assumption that the analytical continuation $n \to 0$ exists. Assuming it does, the replicated partition function can then be rewritten as a function of the overlap matrix Q_{ab} describing the overlap between two replicas a and b:

$$\overline{Z^n} = \int \prod_{(ab)} \frac{dQ_{ab}}{2\pi} e^{N\mathcal{A}[Q_{ab}]}. \tag{7}$$

Taking advantage of the thermodynamic limit $N \to \infty$, the above expression can be evaluated by the Laplace method of saddle-point approximation, which extremizes the action $\mathcal{A}$ with respect to the reference order parameter. The final result, therefore, depends on the structure of Q_{ab}.

The simplest and most intuitive ansatz for that structure is the replica symmetric (RS) one. In this case, the overlap among different replicas is the same for any pair of replicas, with the exception of the overlap between a replica and itself. In the RS scenario, the matrix Q_{ab} therefore admits only two values: a diagonal contribution q_d (for $a = b$) and an off-diagonal one q_0 (for $a \neq b$).

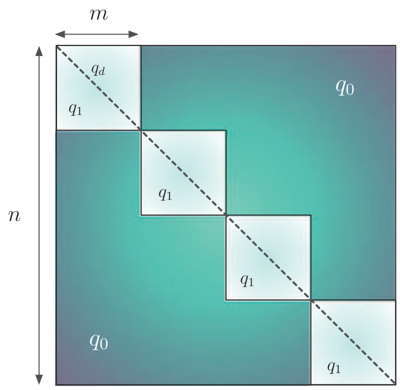

Fig. 2 1-RSB parametrization of the Parisi overlap matrix. q_1 represents the degree of similarity between two replicas inside the innermost block of size $m \times m$, whereas q_0 is the outermost block value.

As expected, the RS ansatz correctly describes the high temperature and large external magnetic field regimes. But as these control parameters are lowered, some models reach a critical de Almeida-Thouless (dAT) line, below which the RS solution becomes unstable. Physically, a *spin glass* phase emerges when the RS solution is no longer stable.

More technically, below the dAT line, the correct solution requires a matrix Q_{ab} with an iterative block structure, which breaks the symmetry between different pairs of replicas. For the first iteration of replica symmetry breaking (noted 1-RSB), the $n \times n$ matrix is parametrized by a diagonal value q_d and two off-diagonal values that can be either q_1, if the two replicas belong to the same block of size $m \times m$, or q_0, if the replicas fall outside the innermost block (see Fig. 2). If the low-temperature phase remains unstable after 1-RSB, this procedure can be iterated within each of these blocks, leading to a k-step RSB (or k-RSB). Depending on the specifics of the Hamiltonian, SG phases can have different levels of RSB. The limit $k \to \infty$ corresponds to the full-RSB scenario, according to which the overlap matrix is parametrized by a continuous function $q(x)$, with $x \in [0, 1]$. The overlap density distribution, $P(q)$, being nonzero over a continuous range of q, is a signature of the presence of an infinite number of symmetry-breaking points.

In the replica formalism, all the mutual information about pairs of equilibrium configurations is encoded in the overlap, which is a measure of their mutual distance. Given the hierarchical way in which the full-RSB construction is obtained, in systems with a full-RSB phase, the states have an *ultrametric* structure, meaning that their mutual distance can be described through a taxonomic or genealogical tree.

The replica structure of two common MF spin glass models

For the sake of concreteness, let's consider two paradigmatic MF spin glass models. Both have a low-temperature SG phase, but with different levels of RSB, and therefore present different free energy minima structures.

- The **spherical *p*-spin** model has Hamiltonian

$$\mathcal{H} = -\sum_{i_1,\ldots,i_p=1}^{N} J_{i_1,i_2,\ldots,i_p} s_{i_1} \ldots s_{i_p}, \tag{8}$$

  where p indicates p-wise interactions to which each spin participates. Spins are continuous variables subject to the global constraint $\sum_{i=1}^{N} s_i^2 = N$, and the random couplings are extracted from a Gaussian distribution $P(J) = \exp\left(-J^2 \frac{N^{p-1}}{p!}\right)$, where the factor N^{p-1} guarantees the extensivity of the free energy in the thermodynamic limit. For $p \geq 3$, this class of mean-field systems is characterized by a 1-RSB low-temperature phase, with an emergent number of minima that grows exponentially with N, and those are separated by extensive barriers.

  Small variations to this model result in significantly different physical behaviors. In particular, setting $p = 2$ results in only one single free-energy minimum (so there is no SG phase), whereas replacing the spherical with Ising spins results in the 1-RSB phase becoming unstable toward a full-RSB phase at low temperatures.
- The **Sherrington–Kirkpatrick** model (SK) has a Hamiltonian with an external uniform field h

$$\mathcal{H} = -\sum_{(ij)} J_{ij} s_i s_j - h \sum_i s_i, \tag{9}$$

  where the sum runs over distinct pairs. The spins are Ising variables, $s_i = \pm 1$, and the random couplings are extracted from a Gaussian distribution $\mathcal{P} \simeq e^{-NJ_{ij}^2/(2J^2)}$ with zero mean and variance J^2/N. The low-temperature phase of this model is characterized by a hierarchical organization of energy minima, as given by the Parisi solution. The emergent number of minima is subexponential in system size, and those are separated by subextensive barriers. The transition from single equilibrium (RS) to multiple equilibria (full-RSB) is second-order-like, with diverging correlation lengths and power-law singularities.

The solution of the SK model obtained by the replica method was rigorously proven 30 years later. Even though there is no rigorous demonstration that the replica method is generally correct, it has since been proven to provide the correct result in several specific cases, and no counter-example is known.

The Thouless–Anderson–Palmer (TAP) approach

The TAP approach aims to probe complex energy and free-energy landscape properties through a perturbative high-temperature expansion (also known as *Plefka* or *Georges–Yedidia expansion*) by defining a Legendre transform $\mathcal{F}[\mathbf{m}]$ of the free energy as a function of the average magnetization $\mathbf{m}$. Such an expansion can detect the metastable states of the system, which correspond to the local minima of an appropriately defined nonconvex functional.

The underlying idea is to enforce the system to have single-site magnetization m_i by means of Lagrange multipliers $\lambda_i^{(\beta)}$ that depend on the inverse temperature β. Then, from the Legendre transform, one obtains

$$\mathcal{F}^{(\beta)}[\boldsymbol{m}] = \log \sum_{\boldsymbol{s}} e^{-\beta\mathcal{H}[\boldsymbol{s}]+\sum_i \lambda_i^{(\beta)}(s_i - m_i)} \tag{10}$$

given the stationarity condition $\lambda_i^{(\beta)} = -\frac{\partial\mathcal{F}^{(\beta)}[\boldsymbol{m}]}{\partial m_i}$. In the $\beta \to 0$ limit, spins are uncorrelated, making the computation of the first derivatives[1] of the free-energy functional with respect to β very straightforward:

$$\left.\frac{d\mathcal{F}^{(\beta)}[\boldsymbol{m}]}{d\beta}\right|_{\beta=0} = -\langle\mathcal{H}\rangle, \tag{11}$$

$$\left.\frac{d^2\mathcal{F}^{(\beta)}[\boldsymbol{m}]}{d\beta^2}\right|_{\beta=0} = \left\langle \left[\mathcal{H}[\boldsymbol{s}] - \langle\mathcal{H}\rangle - \sum_i \frac{\partial\lambda_i^{(\beta)}}{\partial\beta}(s_i - m_i)\right]^2 \right\rangle. \tag{12}$$

The second derivative involves both the connected part of the Hamiltonian and the partial derivatives of the Lagrange multipliers. The TAP free energy can then be written as a second-order expansion around the $\beta = 0$ limit. For the SK model, it reads

$$\mathcal{F}_{\mathrm{TAP}}^{\mathrm{SK}}[\boldsymbol{m}] = -\frac{1}{\beta}\sum_i s_0(m_i) - \frac{1}{2}\sum_{i\neq j} J_{ij} m_i m_j - \frac{N\beta}{4}(1-q)^2, \tag{13}$$

where the first term on the right-hand side accounts for entropic effects, the second term is average energy contribution, and the last one, the *Onsager reaction term*, represents a first correction to the MF approximation. It is also worth noting that since the couplings in the SK model are of order $1/\sqrt{N}$, $O(\beta^2)$ terms do matter in the final TAP expression. This contrasts with the purely ferromagnetic case (the fully connected Ising model), for which the couplings are of order $1/N$.

In the case of the spherical p-spin model, the TAP free energy reads

$$\mathcal{F}_{\mathrm{TAP}}^{\mathrm{pspin}}[\mathbf{m}] = -\frac{1}{\beta}\sum_i s_0(m_i) - \frac{1}{p!}\sum_{i_1,\ldots,i_p} J_{i_1,\ldots,i_p} m_1 \ldots\ m_p - \frac{\beta N}{4}\left[1 - pq^{p-1} + q^p(p-1)\right], \tag{14}$$

where, again, the last term represents the Onsager reaction term. By setting $m_i = 0$, one can immediately check that the TAP free energy is equal to $-\beta/4$, which is the free energy of the paramagnetic state.

In principle, the equilibrium probability distribution—hence the partition function—can always be decomposed into a combination of *pure states* α, with a free-energy density f_α. These pure states are entirely determined by a set of local observables, such as local magnetizations. The partition function can therefore be expressed as a sum over such states

$$Z = e^{-\beta NF} \simeq \sum_\alpha e^{-\beta N f_\alpha} = \int df \sum_\alpha \delta(f - f_\alpha) e^{-\beta N f} = \int df\ e^{N[\Sigma(f,\beta)-\beta f]} \simeq e^{N[\Sigma(f^*,\beta)-\beta f^*]}, \tag{15}$$

where in the last step we applied the saddle-point method. The configurational entropy Σ represents the logarithm of the total number of states. Evaluated at the states with f^*, which contribute maximally to Z, it leads to a simple temperature dependence of the TAP free energy with the identification $\partial\Sigma(f,\beta)/\partial f|_{f^*(\beta)} = \beta$.

In the p-spin model, this decomposition in pure states discloses a rich behavior in terms of the number of pure states that, at a given temperature, participate in the thermodynamic behavior of the system. At high temperatures, the free-energy density is ruled by a single state, the paramagnetic (Boltzmann-Gibbs) state. Upon lowering the temperature, one reaches a *dynamical transition* at temperature T_d, at which the emergence of an exponentially large number of clusters of pure states is accompanied by a dramatic slowing down of the dynamics. Surprisingly, the transition is not associated with any thermodynamic transition because the free

---

[1] In the thermodynamic limit, all higher order terms but the first two can be neglected in a fully connected system.

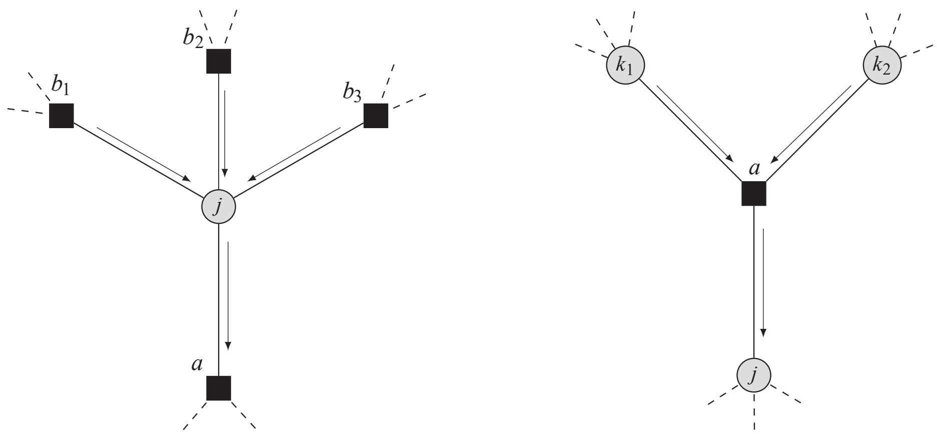

Fig. 3 Left: Graph representation for the message $\hat{v}_{b\to j}(s_j)$, from the function node (*square*) to the variable node (*circle*). Right: corresponding part of the graph for the computation of the message $\hat{v}_{a\to j}(s_j)$, function of $v_{k\to a}(\sigma_k)$ from the variable node to the function node.

energy preserves its analyticity. The thermodynamic transition occurs at a lower temperature, T_s, known as *static* or *condensation transition*, where all different clusters of states collapse to the same state as a clear signature of vanishing configurational entropy.

Although the TAP approach was conceived as a high-temperature expansion, it can also be developed in terms of other perturbative quantities, such as a fictitious coupling associated with an effective energy cost. In this case, the Plefka-like expansion offers a playground for the definition of suitable effective high-dimensional potentials in situations where the energy is either ill-defined or trivially zero, such as in nonconvex constraint satisfiability problems.

The cavity method

The cavity method[2] was originally devised as a way to solve the SK model without resorting to the replica formalism, but can also be used to go beyond the MF approximation. It can notably consider correlations between spins, thanks to the fact that it is exact in systems with a loopless interaction graph—or with divergingly wide loops—such as in trees and some random graphs. In the following, we will focus on finite-connectivity graphs, $\mathcal{G} = (V, E)$, defined by V nodes and E edges. The Hamiltonian in Eq. (2) can be then rewritten as $E(\mathbf{s}) = -\sum_{(i,\ j)\in E} J_{ij} s_i s_j$, where i and j belong to the same edge E. The graph $\mathcal{G}$ together with the set of random couplings J_{ij} then defines a sample.

The main goal of the cavity method is to calculate the probability distribution of each spin, $P(s_j)$. The idea behind the approach is that $P(s_j)$ is determined by the local fields induced by all the neighbors of s_j, which are in turn determined by their own neighbors, and so on (Fig. 3). Because of the tree-like structure of the graph, the neighbors of s_j are mutually independent, and hence $P(s_j)$ can be factorized and determined through the incoming local fields, $\hat{v}_{a\to j}(s_j)$ (where a indicates a neighboring interaction): $P(s_j) \simeq \prod_{a\in\partial j} \hat{v}_{a\to j}(s_j)$. At the same time, the interaction a influencing s_j is defined by the marginal distribution of all the spins k in the neighborhood of a, once s_j is removed, $v_{k\to a}(s_j)$. Therefore, the cavity formalism results in a set of coupled equations for the marginal probability laws

$$\begin{cases} v_{j\to a}(s_i) \propto \prod\limits_{b\in\partial j\setminus a} \hat{v}_{b\to j}(s_j), \\ \hat{v}_{a\to j}(s_j) \propto \sum\limits_{\mathbf{s}\in\partial a\setminus j} \psi_a(\mathbf{s}_{\partial a}) \prod\limits_{k\in\partial a\setminus j} v_{k\to a}(s_k), \end{cases} \tag{16}$$

where ψ_a is called *compatibility function*, which is analogous to the Boltzmann weight, and $\partial a\setminus j$ indicates the spins near a excluding j.

The resulting free energy as a function of fixed-point messages turns out to be a combination of three contributions coming from all function nodes, all variable nodes, and the edges connecting i to any possible function node (see Fig. 3). When the size of the loops is larger than the correlation length, the signals entering j are independent. In this case, if there is a unique solution for the state in j, the cavity method can recover it exactly. For instance, at the RS level, where there is only one pure state, the cavity approach is formally equivalent to the replica method. If the system is not RS, or if the loops are short, the approach needs to be refined. For example, 1-RSB cavity protocols have been developed to extract properties of the pure state decomposition and satisfiability conditions in generic optimization problems. Such 1-RSB message passing equations go by the name of *survey propagation* and have been generalized as *population dynamics algorithms*.

Beyond mean-field: Multilayer construction and loop corrections

The cavity method stops being exact in a non-tree-like topology and is indeed hindered by the presence of loops. Furthermore, because of its nonperturbative nature, any small parameter expansion used to compute corrections to mean-field theory appears to be unfeasible. One can nevertheless build an M-layer model, where M copies of the original lattice are stacked on top of each other assuming the same distribution of random couplings. The idea—originally proposed in computer science by Vontobel—has been reworked recently in disordered systems based on a rewiring procedure. By inducing random permutations of the links, interlayer connections, and hence spatial loops, are automatically generated by a generalized transfer matrix formalism on uncorrelated one-dimensional chains. The perturbative computation of finite-size corrections in powers of $1/M$ notably offers a reliable formal method to study critical phenomena in finite-dimensional systems. The advantage of this tree-based approach is that it can recover phase transitions that deviate from the behavior of fully connected models and are instead more similar to the finite-dimension phenomenology. This situation arises, for instance, in the Random Field Ising Model, which is strongly affected by nonperturbative effects in low dimensions, and in the Anderson localization in the quantum realm.

---

[2] In computer science and artificial intelligence, the cavity method is also known as *Belief Propagation*, whereas in statistical physics, it is referred to as *Bethe-Peierls*.

Dynamical mean-field theory (DMFT)

Understanding the dynamics of SGs is one of the oldest and most challenging problems in the theory of matter. One characteristic feature of the SG dynamics is that its relaxation depends on the history of the system itself, that is, it ages. In other words, the autocorrelation between a time t and $t' > t$ does depend not only on $(t' - t)$ but also on the *age* of the system, t. An aging system relaxes extremely slowly without ever reaching an equilibrium state. During its exploration, the system wanders across states that are not the relevant ones from a thermodynamic viewpoint and whose static properties cannot be defined rigorously.

An MF solution for the dynamics in glassy systems was first suggested by Sompolinsky and Zippelius for equilibrium properties. Intriguing off-equilibrium features came emerged from a deeper investigation of specific models, for which a closed set of integro-differential equations could be solved.

For the sake of simplicity, in the following, we shall consider the overdamped Langevin dynamics of a system in contact with a thermal bath,

$$\frac{ds_i}{dt} = -\frac{\partial \mathcal{H}}{\partial s_i} + \eta_i(t) \tag{17}$$

whose behavior is captured by Gaussian white noise with zero mean and variance $\langle \eta_i(t)\eta_j(t')\rangle = 2T\delta_{ij}\delta(t-t')$. The index $i = 1, \ldots, N$ runs over the total number of spins in the system. The Hamiltonian $\mathcal{H}$ typically incorporates a single-spin potential $V(s)$ plus a disordered part, which explicitly depends on the quenched disordered couplings (see e.g., Eq. 9), which need to be averaged out. The dynamical MF procedure allows to average over the couplings and coarsen the time dependence of the system as that of a single average spin $s(t)$. For the p-spin model, the resulting DMFT equation reads:

$$\dot{s}(t) = -\frac{\partial V(s(t))}{\partial s} + \frac{p(p-1)}{2}\int_0^t dt'\, R(t,t')C^{p-2}(t,t')s(t') + \xi(t) \tag{18}$$

where the noise $\xi(t)$ accounts for the interaction with the rest of the system and has an extra colored term, that is, $\langle \xi(t)\xi(t')\rangle = 2T\delta(t-t') + C(t,t')$.

The dynamical equation above is expressed in terms of the two-time correlation function

$$C(t,t') = \frac{1}{N}\sum_i s_i(t)s_i(t'), \tag{19}$$

and of the response function to an external pulse perturbation

$$R(t,t') = \frac{1}{N}\sum_i \left.\frac{\delta s_i(t)}{\delta h_i(t')}\right|_{h_i=0}. \tag{20}$$

In the thermodynamic limit, the above equations converge to a unique nonfluctuating solution, which is the only one allowed by causality. At equilibrium, $C(t-t')$ and $R(t-t')$ are related by the fluctuation-dissipation theorem, $R(t-t') = -\frac{1}{T}\Theta(t-t')\frac{d}{dt}C(t-t')$. While, for finite N, the correlation and response functions are expected to decay exponentially in time, this property is no longer generically true in the thermodynamic limit, as the relaxation time might diverge, thus signaling a dynamical transition (Section "The Thouless–Anderson–Palmer (TAP) approach").

Based on the long-time limit analysis first performed in the spherical p-spin model, one can separately analyze the fast regime, in which relevant degrees of freedom rapidly equilibrate preserving time translation invariant (TTI) properties, and the slow regime, in which violations of fluctuation–dissipation relations and nonequilibrium phenomena emerge. In the large-time limit, for $t, t' \to \infty$, the correlation function can be split as $C(t,t') = C_{\mathrm{TTI}}(t-t') + C_{\mathrm{Aging}}(t,t')$. Depending on the appearance of either a single diverging timescale or a multiplicity of progressively slower timescales, the slow part of the correlator, $C_{\mathrm{Aging}}(t,t')$, can be captured by a combination of involved functions each associated with a slow timescale.

Notably, by assuming the MF picture of aging as a starting point (such as Eq. 18), it is possible to investigate the properties of asymptotic regimes without explicitly solving the integro-differential equations for the correlation and response functions (e.g., Eqs. 19 and 20). The outcome is different depending on whether the low-T phase is 1-RSB or full-RSB. For the latter, a dynamical effective stochastic process for the slow-evolving effective part of Eq. (18) has been worked out, which exactly maps into the ultrametricity condition associated with the Parisi solution in the replica formalism. Hence, DMFT both in the presence of a single slow timescale and in the ultrametric scenario explicitly links the aging dynamics with the replica-based description.

Spin glasses in three dimensions

Numerical methods

Although MF treatments provide elegant exact solutions for SGs defined on a fully connected or tree-like graph, extending those findings to three dimensions is quite challenging. For instance, even the existence of an SG phase in the $3d$ EAM has yet to be proven analytically. Most progress, therefore, arise from numerical simulations. In particular, there is convincing numerical evidence that, as their experimental counterparts, SG models in three dimensions exhibit a continuous phase transition at a temperature T_c.

The low-temperature dynamics of SGs is, however, very slow, due to the competition between short- and long-range interactions, and the presence of temperature chaos. In the SG phase, the free energy profile indeed changes drastically even for infinitesimal changes in temperature. The numerical study of SGs at low T is therefore highly challenging. Numerical strategies advanced for studying SGs notably include: the construction and use of special-purpose computers, GPUs, the formulation parallelization techniques, such as multi-spin coding, which, by encoding every spin on a single bit and restricting to bit-to-bit operations, allows one to simulate 64 replicas (the number of bits in a long integer) in the time of one; and the development of algorithms, such as *parallel tempering*, which consists of simultaneously simulating several replicas at different temperatures, and proposing Monte-Carlo updates, which exchange the temperatures among replicas.

Spatial correlations

A key feature of low-dimensional systems is the characteristic extent of spatial correlations, ξ. Its typical experimental determination is through the magnetic response to an external magnetic field h, which provides the coherence length ξ_{Zeeman}. In numerical simulations, the size of the correlated domains is instead calculated through correlation functions of the form

$$C(\mathbf{r}) = \frac{1}{N} \sum_{\mathbf{x}}^{N} q_{\mathbf{x}} q_{\mathbf{x}+\mathbf{r}}, \tag{21}$$

where $\mathbf{x}$ indicates a position in the lattice, $\mathbf{r}$ is a displacement vector, and $q_{\mathbf{x}}$ is usually the overlap at site $\mathbf{x}$, $q_{\mathbf{x}} = q_{\mathbf{x}}^{(ab)} = s_{\mathbf{x}}^{(a)} s_{\mathbf{x}}^{(b)}$, or the link overlap, $q_{\mathbf{x}} = q_{\mathrm{link},\mathbf{x}}^{(ab)} = q_{\mathbf{x}}^{(ab)} q_{\mathbf{x}+\hat{e}}^{(ab)}$ ($\hat{e}$ is a unit vector) since these quantities are equivalent in the limit $d \to \infty$. There are several ways to extract a correlation length ξ_{micro} from $C(\mathbf{r})$. For example, $\xi_{\mathrm{micro}} = \sqrt{\frac{\int r^2 C(r) dr}{\int C(r)}}$. While, out of equilibrium, ξ_{Zeeman} and ξ_{micro} have different behaviors, and at equilibrium they match. These length scales can be used to identify phase transitions through finite-size scaling, by comparing simulations performed in systems of different linear sizes L. Because quantities such as $\frac{\langle \xi(T) \rangle}{L}$ are scale-invariant at T_c, one can identify critical points by investigating where the curves $\frac{\langle \xi(T) \rangle}{L}$ cross for different L. For the study of SGs, it has also proven useful to consider other quantities, such as ratios of susceptibilities, possibly conditioned to given values of the overlap.

The spin-glass phase in low dimensions

Pictures for the nature of the low-temperature phase in three dimensions

Just like there is no rigorous proof of the existence of T_c in three dimensions, there is no first-principles theory on the nature of the spin-glass phase in this case either[3]. Two main phenomenological scenarios have been proposed: the Droplet and the RSB pictures. The former is based on a renormalization group approach on the EAM, which is exact in one dimension, and depicts the SG phase as having only two pure states, with $q = \pm q_{\mathrm{EA}}$, reminiscently of the behavior of the ferromagnetic Ising model. One consequence of this proposal is that the size of the surface separating different magnetic domains scales as L^{d_s}, with $d_s < d$ (for the Ising ferromagnet $d_s = d - 1$), and the energy of the smallest excitation grows with L. Another consequence is that the low-temperature phase disappears as soon as an external magnetic field is applied to the system.

The RSB picture is based on the opposite limit, $d = \infty$. It assumes that the SG phase of the EAM is qualitatively similar to that of the SK model, with an overlap distribution $P(q)$, which is nonzero over a wide interval of q. This picture prescribes that the domain surfaces are space-filling ($d_s = d$) and the smallest excitation remains $\mathcal{O}(1)$ when $L \to \infty$. In addition, the SG phase survives when a finite magnetic field is applied, with a dAT line $h_c(T)$ separating the paramagnetic from the SG phase (as described in Section "The replica method"). Whether either of the two theories holds remains, however, a matter of debate.

---

[3] The results in this section refer to the $3d$ EAM, which is the most studied model.

Evidence on the nature of the spin glass phase in 3d

Evidence to falsify or support the Droplet and RSB scenarios has principally been sought through numerical simulations. For example, equilibrium runs of the $3d$ EAM with linear size $L \leq 32$ deep in the SG phase show that $P(q)$ has wide support, and $P(0)$ is stable as L increases. This observation is in contradiction with the Droplet prediction, $P(q) \propto [\delta(q - q_{\mathrm{EA}}) + \delta(q + q_{\mathrm{EA}})]$, which assumes $P(0) = 0$.

When an external magnetic field is applied to the system, equilibrium simulations appear perturbed by finite-size effects, and there is disagreement on the existence of a dAT line. Arguments stemming from numerical simulations on the $3d$ EAM state that a phase transition could be present at temperatures that are 40% lower than those accessible. Those are opposed by arguments from simulations on SG chains with long-ranged interactions, which mimic $3d$ systems, claiming that no transition exists. We note, however, that the upper critical dimension is $d_{\mathrm{up}} \geq 6$, and that there is strong evidence for a dAT transition in $d = 4$. Perturbative renormalization group analysis in $d = 6 - \varepsilon$ is consistent with the presence of a dAT line, with a nontrivial fixed point appearing at second order in ε.

Outlook on the nature of the spin glass phase

The current numerical evidence does not confirm the Droplet picture, but it has been argued that the observations might change if larger system sizes were simulated. It is to be noted, however, that times and system sizes of numerical simulations nowadays closely approach those of experiments. Therefore, if even there is a limit of very large L in which the Droplet theory applies, this might not be experimentally relevant. Evidence in favor of the RSB picture is, however, not decisive, and relevant beyond-MF mechanisms might arise in low dimensions. Alternative or intermediate scenarios could also be valid, such as the trivial-nontrivial picture, according to which the domain surfaces are not space-filling (as in the Droplet picture) but there are large-scale excitations whose energy does not increase with size (as prescribed by the RSB scenario).

Conclusion

Universality classes

While our discussion thus far focused on few specific SG models, changing details of the Hamiltonian can change general features of the energy landscape such that new physics emerges. As discussed above, dimensionality plays a crucial role, with the $d = 1, \infty$ limits having dissimilar behaviors that might both differ from $d = 3$. Altering the distribution of the couplings, $P(J_{ij})$, does not seem to influence the universality class of the models as long as they are not fat-tailed. Changing the interaction *range* is also a relevant perturbation, in that a system with longer ranged interactions is more MF like. This effect has notably led to the search for a correspondence between short-ranged high-dimensional models and long-ranged SGs in $d = 1$.

Another important is the nature of the spins. As described in Section "The replica method," one can soften spins, passing from Ising to spherical spins. For pairwise interactions in $d = \infty$, this completely changes the landscape, which passes from complex to simple. (The dynamics nevertheless remains slow due to a large number of flat directions.) Alternatively, one can use spins that are normalized vectors with m components. For high m, the landscape becomes trivial, both in high- and low-dimensional systems, which points toward using the limit $m \to \infty$ for studies of the $1/m$ expansions. Because the $m \to \infty$ behavior seems radically different from any finite m, however, this approach has not been extensively pursued.

One can also consider Hamiltonians that mix interactions with different numbers of bodies, such as *mixed p-spin models*. These models display several crossover temperatures at which the dynamical behavior changes qualitatively, apparently without any thermodynamic transitions. This behavior is reminiscent of that of supercooled liquids.

An important aspect, which goes beyond the description of the specific model, is that over the years SGs have become a theoretical paradigm for modeling many different complex systems across disciplines, with an extremely broad spectrum of equilibrium and out-of-equilibrium properties. In fact, theories based on disordered systems often reveal to be beneficial for the treatment of problems outside the domain of SGs. Heterogeneous systems, either with quenched or self-generated disorder, are much more general than it might be believed at first glance, ranging from neural networks and optimization problems, signal reconstruction, random lasers, financial markets, topological superfluids, supercooled liquids, and jammed packings and theoretical ecology, and thermodynamic and dynamic formalisms rooted in spin-glass theory can still be used to solve them.

Open problems

SGs can be defined simply, but many questions remain open. We note: the nature of the SG phase *[does replica symmetry breaking occur in finite-dimensional systems?]*; their out-of-equilibrium behavior *[how and which length scales describe their evolution? how are equilibrium states related to the closest local minima?]*; or activated dynamics *[how does the dynamics take place at times $t \gg N$?]*; temperature chaos *[how and why does the landscape change drastically even with small temperature changes and how can we harness it to obtain low-temperature configurations?]*; the identification of metastates *[can we explicitly measure the pure states of the SG phase?]*; connection to other kinds of systems *[can we map the SG behavior onto other systems such as supercooled liquids or deep neural networks?]*.

These questions are not mere academic curiosities about a disordered magnetic alloy because—as it has happened several times in the past already—spin-glass theory can significantly impact other fields. We take theoretical ecology as a final example.

It is well known that the kind of sparsity of the interaction matrix of couplings between species has a crucial influence on the behavior of the ecosystem and that these couplings are typically sparse in nature. Therefore, if we could harness low-dimensional SGs, which, for example, have spatial fluctuations, our understanding of ecological and biological communities would significantly advance.

Acknowledgments

We thank Patrick Charbonneau, Silvio Franz, Victor Martín-Mayor, Michael A. Moore, and Francesco Zamponi for careful reading and suggestions on the manuscript.

Further reading

Binder K and Young AP (1986) Spin glasses: Experimental facts, theoretical concepts, and open questions. *Reviews of Modern Physics* 58(4): 801–976. https://doi.org/10.1103/RevModPhys.58.801.

Castellani T and Cavagna A (2005) Spin-glass theory for pedestrians. *Journal of Statistical Mechanics: Theory and Experiment* 2005: P05012. https://doi.org/10.1088/1742-5468/2005/05/P05012.

Charbonneau P (2022) From the replica trick to the replica symmetry breaking technique. *arXiv:2211.01802*.

Martin-Mayor V, Ruiz-Lorenzo JJ, Seoane B, and Young AP (2022) Numerical simulations and replica symmetry breaking. In: *Spin Glass Theory & Far Beyond—Replica Symmetry Breaking After 40 Years*. World Scientific.

Mézard M, Parisi G, and Virasoro M (1987) *Spin-Glass Theory and Beyond*. Singapore: World Scientific.

Mydosh JA (1993) *Spin Glasses: An Experimental Introduction*. London: Taylor and Francis.

Nishimori H (2001) *Statistical Physics of Spin Glasses and Information Processing: An Introduction*. Clarendon Press. 111.

Nordblad P (2005) Disordered magnetic systems. In: *Encyclopedia of Condensed Matter Physics*, pp. 452–457. Elsevier.

Vincent E (2022) Spin glass experiments. *arXiv:2208.00981*.

Spin glass experiments

Eric Vincent, SPEC, CEA, CNRS, Université Paris-Saclay, Gif-sur-Yvette, France

© 2024 Elsevier Ltd. All rights reserved.

Introduction **372**
The spin-glass phase **372**
A frozen state 372
Critical dynamics of freezing 373
A genuine thermodynamic phase transition 374
The spin-glass transition: Open questions 375
Slow dynamics and aging in spin glasses **375**
Relaxation of the magnetization 375
Magnetic noise 376
Aging, rejuvenation and memory effects **379**
Temperature step experiments 379
Multiple memories 380
Domain growth and hierarchy of states 380
An experiment gathering the various aspects of aging 382
A correlation length for spin-glass order **383**
The spin-glass order made measurable 383
A bridge between experiments and simulations 384
Conclusion **385**
Acknowledgments **385**
References **386**

Abstract

A spin glass is a diluted magnetic material in which the magnetic moments are randomly interacting, with a huge number of metastable states which prevent reaching equilibrium. Spin-glass models are conceptually simple, but require very sophisticated treatments. These models have become a paradigm for the understanding of glassy materials and also for the solution of complex optimization problems. After cooling from the paramagnetic phase, the spin glass remains out of equilibrium, and slowly evolves. This aging phenomenon corresponds to the growth of a mysterious "spin-glass order," whose correlation length can be measured. A cooling temperature step during aging causes a partial "rejuvenation," while the "memory" of previous aging is stored and can be retrieved. Many glassy materials present aging, and rejuvenation and memory effects can be found in some cases, but they are usually less pronounced. Numerical simulations of these phenomena are presently under active development using custom-built supercomputers. A general understanding of the glassy systems, for which spin glasses bring a prominent insight, is still under construction.

Key points

- Introduction to what is a spin glass
- Critical features of the spin-glass transition
- Out-of-equilibrium properties of the spin-glass phase, aging
- Investigation of the slow dynamics of the spin-glass phase by means of dc, ac and noise measurements
- Fluctuation-Dissipation Theorem modification in the spin-glass phase
- Effect on aging of temperature changes
- Rejuvenation and memory phenomena
- Multiple memories in the spin-glass phase
- Mean-field versus droplet theoretical models and experimental results
- Comparison with other glassy systems
- A correlation length for spin-glass order
- A bridge between experiments and numerical simulations

https://doi.org/10.1016/B978-0-323-90800-9.00070-6

Introduction

A spin glass is a set of interacting magnetic moments, originating from spins, in which the magnetic interactions are randomly distributed in sign. In the well-known case of ferromagnets, the interactions are positive, tending to align the moments along the same direction, and producing a net macroscopic magnetization. In antiferromagnets, the interactions are negative, driving the moments to anti-alignment, and establishing a set of two interpenetrating ferromagnetic sublattices, oriented in opposite directions.

We can simply describe the case of spin glasses as a mixture of both ferro- and antiferromagnetic situations. The theoretical definition of the spin glass is that of an ensemble of randomly interacting magnetic moments. The total energy H is the sum over interacting neighbors (S_i, S_j) of the coupling energies $J_{i,j}S_iS_j$, where the $\{J_{i,j}\}$ are random variables, usually gaussian or $\pm J$ distributed (Edwards and Anderson, 1975):

$$H = -\sum_{i,j} J_{i,j} S_i S_j \tag{1}$$

The magnetic moments (or spins) are in random sign interactions, that is, each moment experiences contradicting constraints from its neighbors. This situation of contradicting influences has been termed *frustration*. No simple symmetric configuration of the set of spins corresponds to an equilibrium state. Conversely, the abundance of different spin configurations which have similar energy values produces a huge number of metastable states. The states are separated by free-energy barriers of all heights, which generate a very wide spectrum of response times, from paramagnetic times ($\approx 10^{-12}$ s) up to astronomical scales. Finding the absolute minimum is thus extremely difficult and, from a practical point of view, a spin glass is virtually always out of equilibrium. At low temperature, the spin glass is in a (partially) frozen phase, but this state slowly evolves, with no apparent time limit (for a comprehensive presentation of spin glasses and other disordered magnetic systems, see Nordblad, 2023).

In a spin glass, the disorder lies in the magnetic interactions, which are fixed. Contrary to this situation of a so-called *frozen* disorder, the disorder in usual (structural) glasses lies in the random positions of the molecules. A structural glass is a frozen liquid, in which the molecules are slowly moving, thereby changing the disorder configuration. The spin glass problem, with frozen disorder, is conceptually simpler. It has allowed rich, far-reaching theoretical developments: mean-field treatment by Sherrington and Kirkpatrick (1975), with a solution by Parisi in a model with "continuous RSB," standing for *continuous replica symmetry breaking*, a sophisticated mathematical method (Parisi, 1979; Mezard et al., 1987; Altieri and Baity-Jesi, 2023). The numerical simulations have brought many results, up to spectacular recent progresses by the Janus collaboration with special-purpose supercomputers (Baity-Jesi et al., 2018; Zhai et al., 2020; Baity-Jesi et al., 2022). Although involving different natures of disorder, both spin glasses and structural glasses share a lot of similitudes, and the spin glass is usually considered a powerful model for the description and understanding of various glassy materials, among which "ferroic" materials have recently received a particular interest (Lookman and Ren, 2018; Ji et al., 2023).

The first studied spin-glass materials were non-magnetic metals (Au, Ag, Pt…) in which a few percent of magnetic atoms (Fe, Mn…) were dispersed at random (Cannella and Mydosh, 1972). The magnetic atoms are separated by random distances, and the oscillating character of the Ruderman-Kittel-Kasuya-Yosida (RKKY) interaction with respect to distance makes their coupling energies take a random sign. As explained in Mydosh (1993), the term "spin glass" was first suggested by B.R. Coles in 1970 to be applied to the strange magnetic behavior of an Au:Co alloy, and appeared again at Coles' instigation in Anderson (1970). Examples of spin glasses have also been found within diluted magnetic insulators with shorter-ranged interactions (Alba et al., 1982). Although chemically very different, these various compounds have been found to show a common general behavior that is now understood as generic for spin glasses. A fairly comprehensive review of the theoretical and experimental aspects of spin glasses can be found in Kawamura and Taniguchi (2015). Another interesting review has been given by Mydosh (2015), with emphasis on new spin glass materials and related topical problems in condensed matter physics.

The spin-glass phase

The spin-glass phase forms below a characteristic glass temperature T_g, whose magnitude is governed by the strength of the interactions. At temperatures T much higher than T_g, thermal magnetic fluctuations dominate against interactions, and the spins are fluctuating paramagnetically (Fig. 1A). The magnetization M obtained under a low field H follows a Curie-Weiss law.

$$M/H \propto C/(T-\theta) \tag{2}$$

which is characteristic of a paramagnetic phase (C is proportional to the square of the individual magnetic moments, and θ is a temperature proportional to the energy of the interactions).

A frozen state

Below T_g, the magnetic behavior as a function of temperature becomes history-dependent, the spins are in a frozen phase. In the "FC" (field-cooled) procedure, a magnetic field is applied above T_g, and $M(T)$ is measured upon slowly cooling in the field. The same $M(T)$ curve is obtained upon re-heating, the FC curve is usually stable within 1%, and is mostly flat.

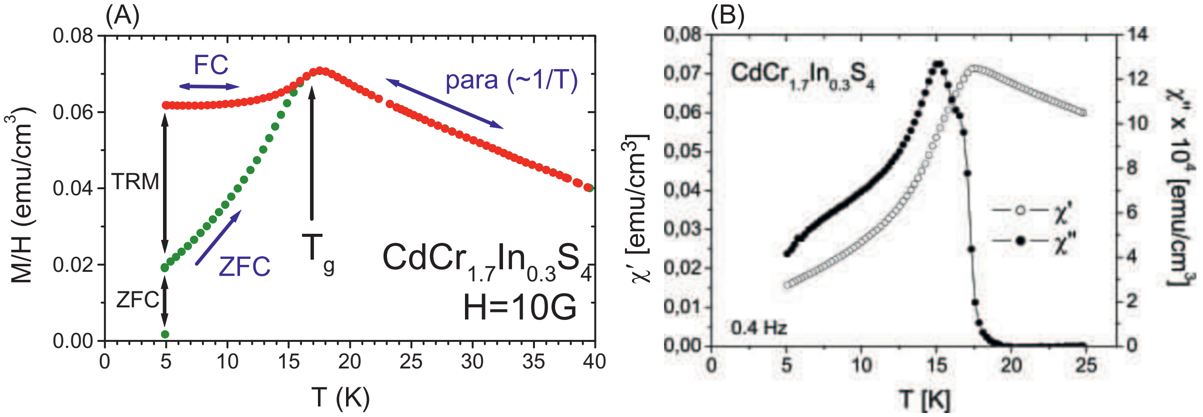

Fig. 1 Typical magnetic characterization of a spin glass (Dupuis, 2002). The sample is an insulating spin glass prepared by M. Noguès (Alba et al., 1982). Left (A): *dc* measurements. Above the glass temperature $T_g = 16.7$ K, the magnetization has a paramagnetic shape. In the spin-glass phase, below T_g, the field-cooled (FC) and zero-field cooled (ZFC) curves are split, showing a history-dependent behavior. Right (B): *ac* measurements. The in-phase component χ' of the *ac* susceptibility has a peak at a frequency-dependent freezing temperature. The out-of-phase (dissipative) component χ'' is null in the paramagnetic phase, and rises up when entering the spin-glass phase.

On the other hand, in the "ZFC" (zero-field cooled) procedure, the sample is cooled in zero field, and the field is applied at the lowest temperature. Since the spins are in a frozen state, the magnetization cannot reach an equilibrium value (which we consider to be the FC value). It slowly increases with time. Then, as we increase the temperature, the magnetization curve $M(T)$ progressively rises up, finally merging with the FC curve in the vicinity of T_g.

Fig. 1A shows typical FC-ZFC measurements (Dupuis, 2002). When cooling from the paramagnetic phase, the magnetization rises up, until reaching T_g, below which the FC curve is essentially flat. This apparent "solidification" of the spin system at T_g, with no further significant evolution of the magnetization, suggests a collective behavior of the spins, with a sudden freezing into a long-range correlated state. We show below that the process of freezing at T_g presents a critical character, and we describe how this amazing *glassy ordered* state of matter can be characterized.

We can also explore the spin-glass phase by means of *ac* field measurements, which usefully complete the *dc* procedures described above. When a weak *ac* magnetic field is applied, the observed *ac* susceptibility χ is usually decomposed into two components: χ' (in-phase component), and χ'' (out-of-phase, or dissipative, component). Fig. 1B shows the *ac* susceptibility of a spin glass at frequency $\omega/2\pi = 0.4$ Hz, as a function of temperature (Dupuis, 2002). χ' has the same shape as the ZFC (*dc*) magnetization in Fig. 1A, which can be thought as an *ac* measurement at a frequency that is the inverse of the time spent at each heating temperature step in the ZFC curve.

The out-of-phase response χ'' is null above T_g, in the paramagnetic phase the spins are oscillating in phase with the excitation field. Upon cooling down, the approach of T_g is signalled by a sharp increase of χ'': the magnetic response is delayed, the spin system is freezing.

Critical dynamics of freezing

The χ' peak coincides with the inflection point of the χ'' rise. It takes place at a freezing temperature $T_f(\omega)$ which depends on the frequency $\omega/2\pi$: for higher frequencies, higher freezing temperatures are observed, in the same way as, on a photo taken with a shorter aperture time, faster events can be seen being still. We consider that T_g is the zero-frequency limit of $T_f(\omega)$. Studying the frequency dependence of $T_f(\omega)$ allows checking whether the freezing transition at T_g is a dynamical process (like for independent superparamagnetic particles), or presents the collective character of a thermodynamic phase transition (Tholence, 1981).

If the freezing process at T_g is a collective process, then there should be a divergence of a correlation length ξ at the approach of the transition at T_g, according to:

$$\xi = \xi_0 \left[\left(T_f(\omega) - T_g \right) / T_g \right]^{-\nu} \tag{3}$$

(ν being the usual critical exponent for the correlation length at a phase transition). The dynamic scaling hypothesis states that the response time τ of a spin ensemble of size ξ goes like

$$\tau \propto \xi^z, \tag{4}$$

where z is defined as a dynamical exponent. In this way we obtain the critical dynamics scaling relation (Binder and Young, 1984):

$$\tau = \tau_0 \left[\left(T_f(\omega) - T_g \right) / T_g \right]^{-z\nu} \tag{5}$$

The precise frequency dependence of $T_f(\omega)$ has been studied in many spin-glass examples. It clearly shows a divergence of the response times as ω goes to zero, attesting the critical character of the freezing process at T_g. The value of the exponent $z\nu$ ranges from

5 to 11 in the various samples (Bontemps et al., 1984; Vincent and Hammann, 1986; Kawamura and Taniguchi, 2015). This collective behavior of the interacting spins at the spin-glass transition marks an important difference with other classes of freezing processes. As an example, for non-interacting superparamagnetic nanoparticles, the freezing process involves response times τ which follow an Arrhenius law.

$$\tau = \tau_0 \ exp\,(U/k_BT) \tag{6}$$

The superparamagnetic fluctuations of the nanoparticles are freezing because of thermal slowing down due to their individual anisotropy barriers U. On the contrary, if the nanoparticles are concentrated enough to have significant magnetic interactions, they form a *superspin* glass that has also been well characterized (Dormann et al., 1996; Nakamae et al., 2012).

A genuine thermodynamic phase transition

In order to complete the characterization of a critical behavior in the dynamics, it is interesting to check whether the spin-glass transition also presents a critical character for static quantities. In a ferromagnet, the order parameter is the spontaneous magnetization, and the order parameter susceptibility is the usual magnetic susceptibility. In a spin glass, defining an order parameter of the "glassy order" is not straightforward. A theoretical definition has been proposed by Edwards and Anderson (1975), in which the order parameter is the average over the sample of the squared moduli of the spins. The corresponding order parameter susceptibility has been shown to be the non-linear part of the magnetic susceptibility (Suzuki, 1977; Chalupa, 1977; Suzuki and Miyashita, 1981). The *dc* magnetic susceptibility χ can be expanded in even powers of the magnetic field H:

$$\chi = \chi_0 - a_3H^2 + a_5H^4 \ldots, \tag{7}$$

χ_0 being the linear susceptibility. The coefficients of the non-linear terms are expected to diverge at T_g, with the critical exponents β,γ corresponding to the spin glass order parameter:

$$a_3 \propto \left(T - T_g\right)^{-\gamma}, a_5 \propto \left(T - T_g\right)^{-(\beta+\gamma)}, \text{etc.} \tag{8}$$

Their determination implies extensive measurements of the magnetic susceptibility as a function of the field, at various temperatures close to T_g, and careful extrapolation to zero field. Fig. 2 shows the example of Ag:Mn$_{0.5\%}$ (Bouchiat, 1986). The non-linear part of the susceptibility is plotted as a function of the field. As the temperature T decreases toward T_g, a significant increase of the initial slope of the curves is clearly visible. Below $1.1T_g = 2.97$ K, the low-field behavior of the non-linear susceptibility goes from

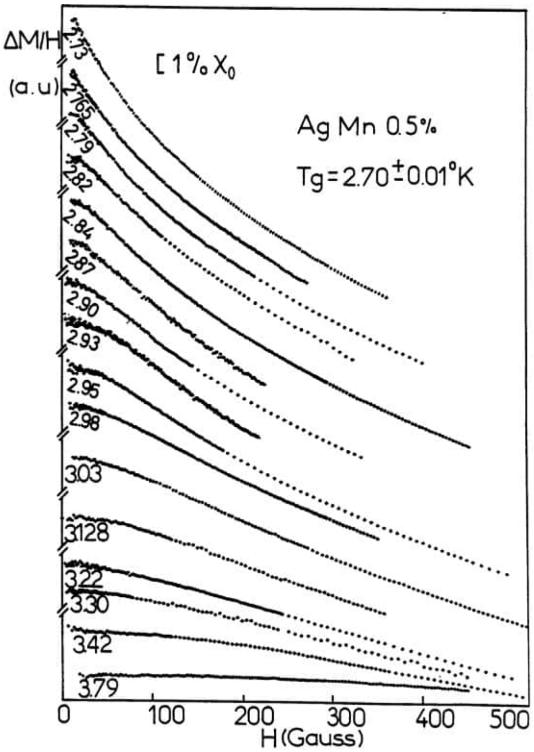

Fig. 2 Non-linear susceptibility (obtained as the difference ΔM between the total magnetization and its field-linear part, divided by the applied magnetic field H), as a function of field H, at different temperatures approaching the critical temperature $T_g = 2.70$ K. The relative origins on the Y-axis are arbitrary. 1% of the linear susceptibility χ_0 is indicated. As $T \rightarrow T_g$, a sharp increase of the slope at the origin is clearly visible, pointing to a divergence of the coefficients in the non-linear susceptibility (Eqs. 7–8). From Bouchiat H (1986) Determination of the critical exponents in the Ag Mn spin glass. *Journal de Physique* 47: 71–88.

quadratic to singular. This increase (together with the analysis of other data) allows the characterization of the diverging character of a_3,a_5 (Eqs. 7-8), and a coherent determination of the critical exponents β, γ, δ. Similar results have been obtained in numerous different spin glass samples (see references in Kawamura and Taniguchi, 2015). Thus, the transition to the spin-glass phase has the same characteristics as a genuine thermodynamic transition to an ordered state.

The non-linear susceptibility can also be accessed through the study of the harmonics in the response to an *ac* field. Pioneering measurements of the 3rd harmonics have been performed by Miyako et al. as early as in 1979. Lévy (1988) determined the whole set of critical exponents of AgMn samples by carefully measuring the 3rd, 5th and even 7th harmonics of the *ac* susceptibility.

The spin-glass transition: Open questions

The critical character of the spin-glass transition, which takes place in a fully disordered system, raises a number of issues. From the critical dimensions obtained in the mean-field theory of spin glasses, in $d = 3$ a phase transition is expected for Ising (scalar) spins, but not for Heisenberg (vector) spins (Mezard et al., 1987, and references therein). However, a phase transition is found in real $d = 3$ spin glasses, and it has been observed as well with Ising as with Heisenberg-like spins. A way to an explanation can be found in the scenario proposed by Kawamura of a chirality driven phase transition of spins (1-step-like RSB class model). This mechanism has been detailed and argued both analytically and numerically. A remarkable agreement of the predicted critical exponents with the experiments has been found (Kawamura, 1992; Kawamura and Taniguchi, 2015). A direct experimental access to chirality freezing is difficult, but some pioneering measurements of the anomalous Hall effect in spin glasses have already given very interesting results (Pureur et al., 2004; Taniguchi, 2007).

In the Parisi solution of the mean-field Ising spin glass (Parisi, 1979), an infinite number of different pure states is obtained, yielding a complex structure of the spin glass phase (this class of models corresponds to a continuous RSB, also called full-RSB, see in Mezard et al., 1987, Altieri and Baity-Jesi, 2023). It suggests that, after cooling from the paramagnetic phase, many domains with different types of spin-glass order should coexist and compete. A phase diagram with a transition line is obtained as a function of the magnetic field. On the other hand, with a very different point of view, scaling theories of the spin-glass behavior have been developed for Ising spins (droplet model by Fisher and Huse, 1988a, b; domain model by Koper and Hilhorst, 1988). In these models, there are simply two (spin reversal symmetric) pure states, and the phase transition is expected to be destroyed by any magnetic field. Let us briefly comment on these questions at the light of the experimental results.

(i) The question of a multiple or single nature of the ground state in the spin glass is very difficult to address directly in experiments, in which no ground state is ever reached. Some arguments are given in the discussion on the temperature dependence of aging effects (Section "Domain growth and hierarchy of states"). A more direct way can be searched from the theoretical suggestion by Carpentier and Orignac (2008), stating that the correlation of the conductance fluctuations in two spin states should be a direct function of their overlap. A new experimental approach using transport measurements on mesoscopic samples has started (Capron et al., 2013). Measurements of the universal conductance fluctuations in mesoscopic spin glasses are challenging, but they can be a promising way to obtain information on the nature of the pure states. Resistivity measurements on mesoscopic wires are now on the way (Forestier et al., 2020).

(ii) The vanishing of the phase transition in presence of a magnetic field has been reported in a study of critical dynamics on a $Fe_{0.5}Mn_{0.5}TiO_3$ single crystal, which is a good example of a short-range Ising spin glass (Mattsson et al., 1995). Interestingly, recent experiments on $Dy_xY_{1-x}Ru_2Si_2$ show that the phase transition persists in a field in this example of an Ising but long-range (RKKY) system (Tabata et al., 2017). For Heisenberg-like spin glasses, data from torque measurements bring robust evidence for a true spin glass ordered state that survives under high applied magnetic fields (Petit et al., 2002).

The nature of the glass transition is also a hot topic for structural glasses. We now understand that the non-linear dielectric susceptibility plays a similar role as in spin glasses (Bouchaud and Biroli, 2005). It has been recognized for a long time that the drastic dynamical slowing down at the glass transition of the most "fragile" glasses can be compared with the critical slowing down observed in spin glasses (Souletie and Bertrand, 1991). Non-linear dielectric susceptibility measurements in glycerol and other viscous liquids have now allowed determining the growth of correlations at the approach of the transition and in the glassy phase during aging (Brun et al., 2012; Albert et al., 2019).

In experiments on spin glasses, what we see is essentially an out-of-equilibrium behavior, with many interesting properties. We now describe some of them.

Slow dynamics and aging in spin glasses

Relaxation of the magnetization

After cooling the spin glass from above to below T_g in a field, we reach a state in which the magnetization is approximately constant (FC state, Fig. 1A). There are some signs that this frozen state is not at equilibrium. If we now turn the magnetic field to zero, the magnetization does not go to zero value, which for symmetry reasons should be the equilibrium value. The non-zero remanent magnetization obtained in this procedure, called *thermo-remanent magnetization* (TRM), slowly relaxes as a function of time. Such TRM curves are shown in Fig. 3 on a logarithm time scale.

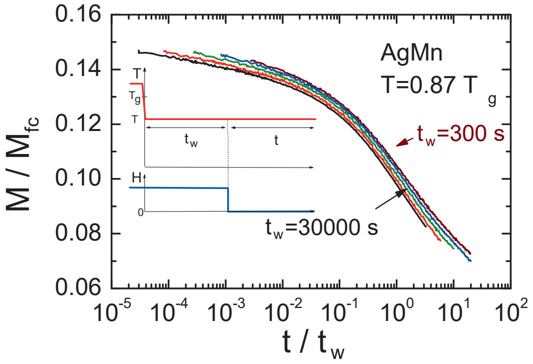

Fig. 3 Relaxation of the thermo-remanent magnetization (TRM) of the Ag:Mn$_{2.7\%}$ spin glass. The procedure is sketched in the inset. The magnetization decay curves obtained for 5 t_w values ranging from 300 s to 30,000 s are presented on a logarithmic scale, as a function of t/t_w to emphasize their t_w-dependence (called "aging"). Data from the Saclay group, figure from Vincent E, Hammann J, Ocio M, Bouchaud J-P, and Cugliandolo LF (1997) Slow dynamics and aging in spin glasses, in: *Complex Behaviour of Glassy Systems*, Rubi M (ed.), Berlin: Springer-Verlag Lecture Notes in Physics, 492: 184.

These experiments involve a second time parameter called the *waiting time* t_w (inset of Fig. 3). The sample is rapidly cooled in a weak field $H = 0.1\ Oe$ from above T_g to $T = 0.87T_g$ (quench), and is kept at temperature T during a given t_w (5 values from 300 to 30,000 s in Fig. 6). After waiting t_w, the field is cut, and the relaxation is measured as a function of the observation time t elapsed since the field cut-off. The inflection point of curves (maximum of the relaxation rate) shifts toward longer times as t_w increases, always taking place around $t \approx t_w$. Presented as a function of the ratio t/t_w, they are almost superimposed. So, after a longer waiting time t_w, the response to the field change becomes slower, with characteristic times of the order of t_w itself. The spin-glass phase has been evolving during the time spent below T_g (it has become "more frozen"), although the FC-magnetization remains roughly constant. This phenomenon is called *aging* (from similar effects observed in polymer mechanics, Struik, 1978).

When studied in more details, the t_w effect can be accurately taken into account. The shift between the curves obtained for different t_w's is not exactly *log* t_w, but rather μ.*log* t_w, μ being a sample-dependent coefficient of order 0.8–0.9. Hence, the relevant variable is $t_w^{\ \mu}$, and when it is properly accounted the relaxation curves can all be superimposed very precisely (Ocio et al., 1985a; Vincent et al., 1997; see an example in the inset of Fig. 5 below).

We want to emphasize that the magnetic field applied in these experiments is weak (0.1–10 Oe), that is, not larger than a few percent of the value that, at low temperature, would bring the spin glass back to the paramagnetic phase. Such a weak field has a negligible effect on the properties that we describe here, linear response is obeyed, the field can be considered as a non-disturbing probe field. This will not hold for higher values of the field (see Fig. 2.8 in Vincent, 2007). Interestingly, some differences in the dynamics of the spin-glass phase with and without a field have recently been characterized very close to T_g, both in experiments and numerical simulations (Paga et al., 2022). In the field and temperature range of the measurements presented here, no difference was visible within the experimental accuracy.

It can also be useful to clarify that aging during t_w is not related to the presence of the field. The mirror procedure of the TRM experiment can be performed with the same conclusions. Cooling the sample in zero field from above T_g, waiting t_w at low temperature, and applying a field in the ZFC state yields a *ZFC(t)* relaxation which is the mirror image of the *TRM(t)* curve, and presents the same t_w-dependence. It has been demonstrated that $ZFC(t_w,t) + TRM(t_w,t) = FC$ (this relation even holds when a slight relaxation of the FC magnetization can be seen, $FC \equiv FC(t)$) (Djurberg et al., 1995).

The phenomenon of aging has been known for a long time in the mechanical properties of a wide class of materials called "glassy polymers". When a piece of e.g. PVC is submitted to a mechanical stress, its response (elongation, torsion ...) is logarithmically slow. And the response depends on the time elapsed since the polymer has been quenched below its freezing temperature. Like in spin glasses, for increasing aging time the response becomes slower. The t_w^{μ}-dependence of the dynamics of glassy polymers has been expressed as a scaling law (Struik, 1978) that could be applied successfully to the case of spin glasses (Ocio et al., 1985a). Numerous glassy materials show similar aging phenomena. Numerical simulations of packed hard spheres provide us with very powerful toy models of simple glasses (Jin and Yoshino, 2017).

Magnetic noise

We have shown above how aging in spin glasses can be studied by measuring the waiting time dependence of the magnetic response to cutting a magnetic field at low temperature (TRM relaxation). In statistical mechanics, the response to a field change is related to the spontaneous fluctuations by the Fluctuation-Dissipation theorem (FDT), established for ergodic systems at equilibrium (see references in Hérisson and Ocio, 2002, 2004). Applying FDT to the situation of TRM experiments, we can relate the relaxation function $\sigma(t',t)$ ($\sigma = M/H$, magnetic response at t after cutting off a field H at t') to the autocorrelation C of the fluctuations of the magnetization m, namely $= <M(t').M(t)>$:

$$\sigma = C/k_BT, \tag{9}$$

with k_B being the Boltzmann constant.

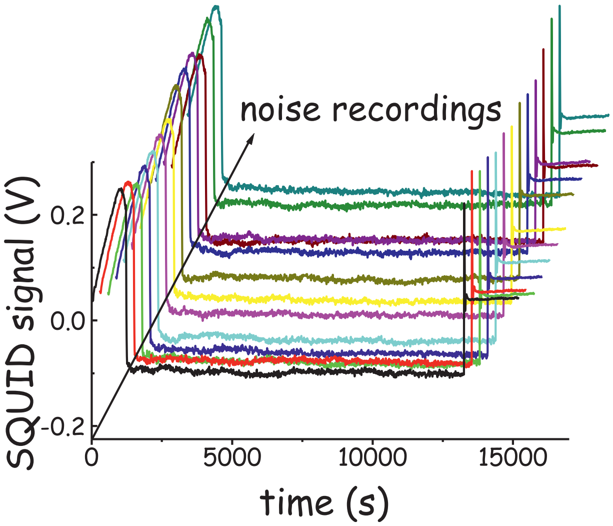

Fig. 4 The signal from the SQUID detector, proportional to the magnetization with an arbitrary offset, is shown as a function of time in a series of successive noise recording experiments. The spontaneous fluctuations of the magnetization (magnetic noise) are observed here in the absence of any excitation. Data from Hérisson D. and Ocio M. (2004) Off-equilibrium fluctuation-dissipation relation in a spin glass. *European Physical Journal B* 40: 283.

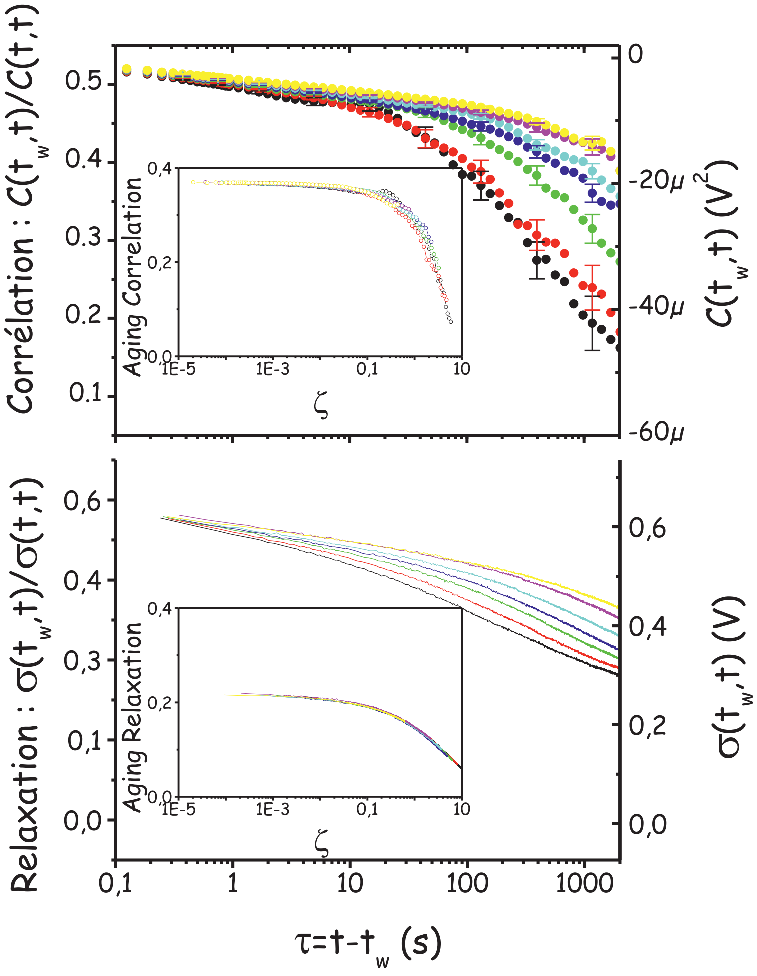

Fig. 5 TRM-relaxation (bottom), and noise autocorrelations functions presented in the same fashion as the TRM curves (top). The different curves correspond, in ascending order, to 5 values of the waiting time t_w, increasing from 100 to 10,000 s. The insets show a superposition of the aging part of the curves using the scaling procedure of Ocio et al., 1985a (see also Vincent et al., 1997). This double figure allows an overall comparison of the response and autocorrelation functions, which are related by the Fluctuation-Dissipation Theorem (FDT). The experiment aims at testing FDT in the non-equilibrium conditions of aging. Data from Hérisson D and Ocio M (2004) Off-equilibrium fluctuation-dissipation relation in a spin glass. *European Physical Journal B* 40: 283.

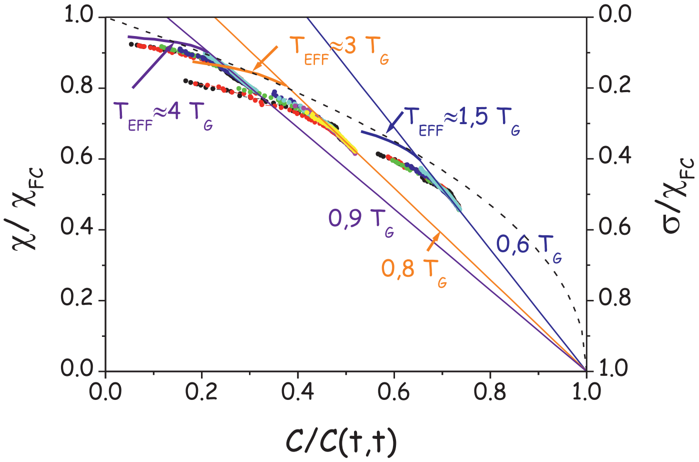

Fig. 6 Response function versus autocorrelation (so-called "FDT plot"), for 3 different temperatures *T*. The straight lines show the *1/T* equilibrium regime of FDT. The points are the raw results. The solid curves are a long time extrapolation of the data, which is necessary for a comparison with the mean-field theory. The dashed line is a fit to $\chi = (1\text{-}C)^{0.47}$, in reference to the continuous RSB model (Marinari et al., 1998). From Hérisson D and Ocio M (2004) Off-equilibrium fluctuation-dissipation relation in a spin glass. *European Physical Journal B* 40: 283.

The measurement of the spontaneous fluctuations of the magnetization ("magnetic noise") in spin glasses is very difficult because of a very weak signal. Yet, it has been a strong motivation for the experimentalists to check how far FDT can be obeyed in the out-of-equilibrium situation of the spin glass, for which the aging regime is considered archetypal. Pioneering measurements started early (Ocio et al., 1985b). Later on, important theoretical efforts have been devoted to extensions of FDT to non-equilibrium situations (see for example Franz et al., 1998). A prominent result by Cugliandolo and Kurchan (1994) and Cugliandolo et al. (1997) is a modified FDT relation which reads

$$\sigma = C \cdot F(C)/k_B T \tag{10}$$

where $T/F(C)$ takes the meaning of an *effective temperature* T_{eff}, different from the sample temperature T. In this approach, for large t', the obtained correction factor $F(C)$ is a function of the autocorrelation C only, i.e. it does not explicitly depend on t and t', but has a time dependence through the value of $C(t',t)$ only. Hérisson and Ocio (2002, 2004) have built a special purpose SQUID magnetometer in which response and fluctuations could both be measured in the same geometry. Important care was taken for eliminating all electromagnetic parasite sources.

An example of noise recordings is presented in Fig. 4, from the $CdCr_{1.7}In_{0.3}S_4$ thiospinel sample. Each trace shows the SQUID output (proportional to the sample magnetization, with an arbitrary offset) during one experiment, starting from above T_g and cooling. Due to a slight residual field, the trace shows the magnetization peak observed when crossing T_g. After cooling, the temperature is stabilized at $T = 0.7T_g$, and the magnetization fluctuations are recorded as a function of time during $\sim 10^4$ s. After that the sample is re-heated above T_g. The experiment is repeated $\sim$300 times. On each of the recorded traces, for any choice of times (t_w,t) the correlation $M(t_w).M(t_w+t)$ can be computed. This value is strongly fluctuating from one experiment to the other, but the average over $\sim$300 measurements is taken and after properly subtracting offsets the noise autocorrelation $C(t_w,t) = <M(t_w).M(t_w+t)>$ is obtained.

Fig. 5 (bottom part) shows TRM experiments performed in the same setup, with a very small excitation field of $\sim 10^{-3}$ Oe. Fig. 5 (top part) shows the noise autocorrelation, presented in the same way as the TRM results, as a function of t for various fixed values of t_w.

Both sets of results present the same overall shape, but a precise comparison is best illustrated in the plot of Fig. 6 (sometimes called "FDT plot"), in which the response function $\sigma(t_w,t)$ (or the susceptibility $\chi = 1\text{-}\sigma$) is plotted as a function of $C(t_w,t)$ for 3 different temperatures $T = 0.6$, 0.8 and $0.9T_g$. For each of the 3 temperatures, the point cloud is the set of "raw" results obtained for various values of (t_w,t). The straight lines with $1/T$ slope show the prediction for classical FDT with no correction. There is a clear $1/T$ regime for the higher values of C, and a crossover toward a weaker slope $1/T_{eff}$ with $T_{eff} > T$ as C decreases. These deviations show the first experimental observation in a spin glass of deviations from the normal FDT in the aging regime (Hérisson and Ocio, 2004).

The results in Fig. 6 strongly suggest that the correction factor $F(C)$ to FDT is only a function of C, as predicted by Cugliandolo and Kurchan (1994) and Cugliandolo et al. (1997). They allow a comparison with different models of the spin-glass phase, provided that a long-time extrapolation of the data can be made (see more details in Hérisson and Ocio, 2004). The observed mean slopes correspond to $T_{eff}(0.6T_g) \sim 1.5T_g$, $T_{eff}(0.8T_g) \sim 3T_g$, and $T_{eff}(0.9T_g) \sim 4T_g$. An infinite T_{eff} value (horizontal slope of the data), as expected in domain growth type models (Barrat, 1998) like the droplet model (Fisher and Huse, 1988a, b), seems to be very unlikely. In models like the mean-field spin glass with continuous RSB (Mezard et al., 1987), a $\chi = (1\text{-}C)^{1/2}$ behavior is predicted. The dashed line in Fig. 6 shows a $\chi = (1\text{-}C)^{0.47}$ fit (Marinari et al., 1998) which gives at least a rough account of the results. However, in their 2004 paper, Hérisson and Ocio comment on the possibility of also analyzing the results on the basis of a 1-step RSB model, confirming a possible relevance of the chiral scenario proposed by Kawamura (1992).

Aging, rejuvenation and memory effects

Temperature step experiments

The cooling rate has a strong influence on the state of a structural glass: slower cooling yields smaller values of the enthalpy and specific volume, which are closer to equilibrium values (Struik, 1978; Simon and McKenna, 1997; Ediger and Harrowell, 2012). In the case of spin glasses, can we play with the cooling rate, or design clever temperature procedures, in order to bring the spin glass closer to equilibrium? This question was the starting point of a class of experiments (Refregier et al., 1987), which have led to the observation of the astonishing phenomena of rejuvenation and memory (see a review in Vincent, 2007; Vincent and Dupuis, 2018).

Aging can also be observed in *ac* susceptibility measurements (like in Fig. 1B). After cooling from the paramagnetic phase to some fixed temperature in the spin-glass phase, both components χ' and χ'' are seen to slowly relax downwards due to aging. The variation in relative value is more important for the out-of-phase susceptibility χ'' (Dupuis, 2002; Vincent and Dupuis, 2018), therefore most experiments have focused on the measurement of χ''. Fig. 7 presents an *ac* experiment in which temperature steps have been applied during aging (Lefloch et al., 1992).

After a normal cooling (~ 100 s) from 1.3 T_g to 0.7 $T_g = 12$ K ($T_g = 16.7$ K), the sample is kept at the constant temperature of 12 K for $t_1 = 300$ min. During this time, χ'' shows a strong downwards relaxation (aging). After 300 min, the temperature is lowered one step further from $T = 12$ K to $T\text{-}\triangle T = 10$ K. What is then observed is a χ'' jump and a renewed relaxation. This behavior upon further cooling was termed *rejuvenation*, because the restart of the relaxation suggests that aging is starting anew at $T\text{-}\triangle T$. Apparently, there is no influence of former aging at T. The rejuvenation effect is at variance with the common expectation that a slower cooling rate should help approaching equilibrium. Waiting t_1 at T did not help approaching equilibrium at $T\text{-}\triangle T$.

One may naturally ask whether this renewed relaxation corresponds to a full rejuvenation of the sample. The answer is no. Two remarks should be made at this point:

(i) Clearly, for continuity reasons, the amount of rejuvenation must be modulated by the value of $\triangle T$. A restart cannot be expected after a tiny temperature variation. The temperature interval must be sufficiently large, here we need $\triangle T \geq 2$ K.

(ii) We should keep in mind that the time window explored in an experiment is limited, whereas the aging state of the spin glass involves relaxation processes on a very wide time range. Hence, from this sole experiment we do not have the knowledge of the overall state at all time scales.

The final part of the measurement completes the answer to the question of the occurrence of a full rejuvenation. After observing the renewed relaxation during $t_2 = 300$ min at $T\text{-}\triangle T = 10$ K, the temperature is turned back to $T = 12$ K. Then, what we see is that χ'' goes up to the point that was attained at the end of the stay at the original temperature T. And the relaxation continues in precise continuity of the former one, as if nothing of relevance for the state at T had happened at $T\text{-}\triangle T$. This can be checked by shifting the third relaxation to the end of the first one (inset of Fig. 7): they are in continuity, and can be superposed on the reference curve which has been separately measured in simple aging at constant $T = 12$ K.

Hence, during aging at $T\text{-}\triangle T$ and despite the strong associated χ''-relaxation, the spin glass has kept a *memory* of previous aging at T. This memory is retrieved when heating back to T. This experiment made with $\triangle T = 2$ K illustrates in a spectacular manner the phenomenon of rejuvenation and memory in a spin glass. For smaller $\triangle T$ values, the situation is obviously more complex: one finds a weaker rejuvenation, and some mutual influence of aging at both temperatures ("cumulative" aging at both temperatures, similar to a cooling rate effect). Details on the results in this regime of small temperature variations, together with their discussion in terms of a random energy model, can be found in Sasaki et al. (2002). A wide set of experiments have been performed by the Saclay group

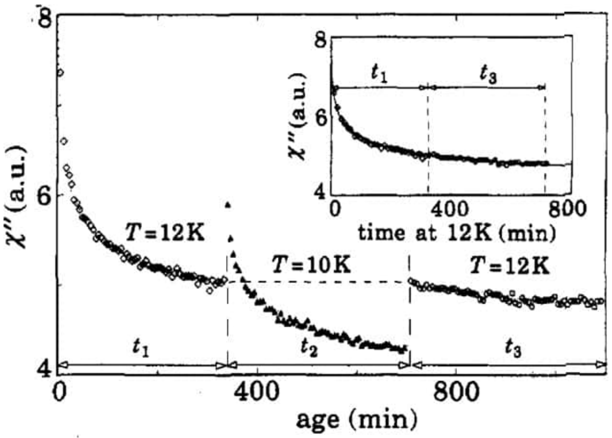

Fig. 7 AC experiment at 0.01 Hz, relaxation of the out-of-phase susceptibility χ'' during a negative temperature cycle following a temperature quench. The points show aging at 12 K, rejuvenation at 10 K, and memory at 12 K. The inset shows that, despite rejuvenation at 10 K, both relaxations at 12 K are in continuation of each other (memory). The sample is the $CdCr_{1.7}In_{0.3}S_4$ thiospinel spin glass ($T_g = 16.7$ K). From Lefloch F, Hammann J, Ocio M, and Vincent E (1992) Can aging phenomena discriminate between the droplet model and a hierarchical description in spin glasses? *Europhysics Letters* 18: 647–652.

(see references in Vincent, 2007) and by the Uppsala group (see, for example, Jönsson et al., 2002), with similar results, although sometimes discussed in slightly different terms regarding the comparison with the droplet model (Fisher and Huse, 1988a, b).

Very recently, Zhai et al. (2022) could accurately measure the effect of temperature variations on the tiny relaxation ($\approx$0.5%) of the FC magnetization in a CuMn spin glass. They can precisely distinguish a regime of cumulative aging for small temperature variations, and another one obtained for larger temperature variations, which shows some rejuvenation of the relaxation and is discussed in terms of "temperature chaos," a theoretical notion which corresponds to an extreme sensitivity of the glass to temperature changes (Bray and Moore, 1987).

Multiple memories

The ability of the spin glass to keep a memory despite rejuvenation has been further explored in experiments with multiple temperature steps. The first *memory dip* experiments, suggested by P. Nordblad, were developed in a collaboration between the Uppsala and Saclay groups (Jonason et al., 1998, 2000). An example of a "multiple dip" experiment is shown in Fig. 8 (Bouchaud et al., 2001; Dupuis, 2002). This is a χ'' measurement in which the sample is cooled from above T_g to 4 K by steps of 2 K, with a stop at each step. Then, the sample is reheated continuously (inset of Fig. 8). Starting from $T > T_g$ where $\chi'' = 0$ (paramagnetic phase), χ'' rises up when crossing $T_g = 16.7\ K$, and when the cooling is stopped at 16 K, 14 K, etc., the relaxation of χ'' due to aging is recorded during 30 min.

After waiting 30 min at constant temperature, upon further cooling by another 2 K step, a χ'' jump of rejuvenation is found, and the relaxation due to aging again takes place. At each new cooling step, rejuvenation and aging are seen, and this happens ~6 times in the experiment of Fig. 8.

In the second part of the experiment, the sample is re-heated continuously at a slow rate (0.001 *K/s*, equal to the average cooling rate). Amazingly, apart from the rather noisy low-*T* region, the memory of each of the aging stages performed during cooling is revealed in shape of "memory dips" in $\chi''(T)$, tracing back the lower value of χ'' which was attained at each of the aging temperatures. Thus, the spin glass is able to keep the simultaneous memory of 5 or 6 aging stops in a row, performed at lower and lower temperatures. The curve obtained while increasing the temperature after that reveals the memories (and meanwhile erases them).

Domain growth and hierarchy of states

In the droplet model (Fisher and Huse, 1988a, b), the spin glass is thought in the same terms as a ferromagnet, having two symmetric equilibrium states of opposed spin directions (with no trivial ordered alignment of the spins). Aging is described as the slow growth of domains of this "spin-glass order" of hidden symmetry, starting from the random configuration created by the quench from the paramagnetic phase. In a naive interpretation, domain growth processes should progress continuously during temperature variations, with some influence of temperature on the growth rate, similar to cooling rate effects. But, in that case, it is difficult to imagine how rejuvenation and memory effects may arise. In the droplet model, they are related to "temperature chaos" effects (Bray and Moore, 1987). Discussions on the relevance of this scenario to experiments can be found in Yoshino et al. (2001)

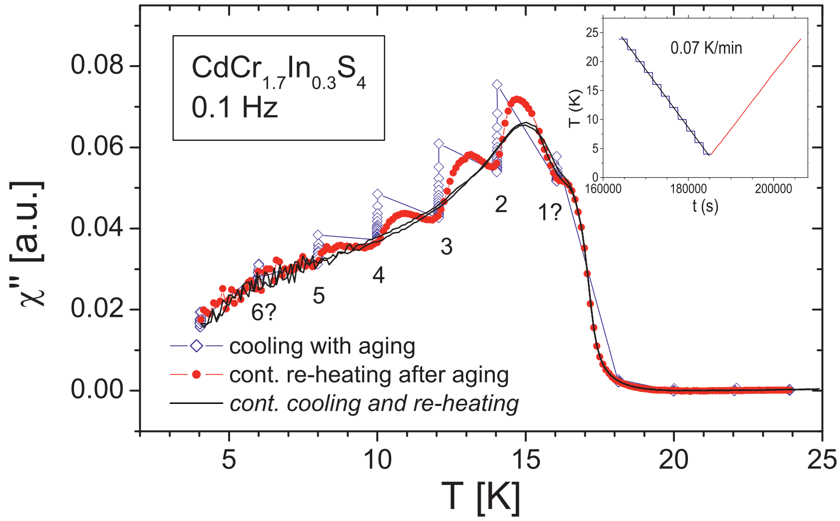

Fig. 8 An example of multiple rejuvenation and memory steps. The inset is a sketch of the procedure. The sample was cooled by 2 K steps, with an aging of time of 30 min at each step, after which rejuvenation can be seen (open blue diamonds). Continuous reheating at 0.001 K/s (full red circles) shows memory dips at each temperature of aging. The solid black line shows a reference measurement with continuous cooling/heating and no steps. From Dupuis V (2002) *Dynamique lente des systèmes magnétiques désordonnés*, PhD Thesis, Orsay University (France), https://tel.archives-ouvertes.fr/tel-00002623/document.; Bouchaud J-P, Dupuis V, Hammann J, and Vincent E (2001) Separation of time and length scales in spin glasses: Temperature as a microscope. *Physical Review B* 65: 024439.

and Jönsson et al. (2004). The notion of a growing size of cooperative regions, encountered in many glassy systems, as well in experiments as in theoretical models, may well be at the heart of aging phenomena, as detailed by Corberi et al. (2011).

The theoretical ingredients that are necessary for rejuvenation and memory effects to arise are not yet well determined. Early studies of frustrated magnetic systems have shown that average effective interactions can be defined, which may present a strong temperature dependence (Miyashita, 1983). The temperature variation of the effective interactions can cause rejuvenation effects (Miyashita and Vincent, 2001). Still, the preservation of memory despite rejuvenation requires considering other processes in addition (Tanaka and Miyashita, 2005).

On the other hand, a different point of view has been proposed by the Saclay group to account for the rejuvenation and memory effects. The guideline is to consider a hierarchical organization of the metastable states as a function of temperature, inspired by the hierarchical organization of the pure states in the Parisi solution of the mean-field spin glass (Mezard et al., 1987;). Indeed, it could be shown that rejuvenation and memory effects can be expected in the dynamics of this model (Cugliandolo and Kurchan, 1999).

In this scheme, pictured in Fig. 9 (Dotsenko et al., 1990; Refregier et al., 1987), the effect of temperature changes is represented by a modification of the free-energy landscape of the metastable states (not only a change in the transition rates between them). At fixed temperature T, aging corresponds to the slow exploration of the numerous metastable states (at level T in Fig. 9). When going from T to T-ΔT, the free-energy valleys subdivide into smaller ones, separated by new barriers (level T-ΔT in Fig. 9). Rejuvenation arises from the transitions that are now needed to equilibrate the population rates of the new sub-valleys: this is a new aging stage. For large enough ΔT (and in the limited experimental time window), the transitions can only take place between the sub-valleys inside the main valleys, in such a way that the population rates of the main valleys are untouched, keeping the memory of previous aging at T. Hence the memory can be retrieved when re-heating and going back to the T-landscape.

This tree picture allows a qualitative description of the rejuvenation and memory effects, but it is also able to reproduce quantitatively many features of the experiments (see discussions of the effect on aging of small temperature changes in Sasaki et al., 2002; Vincent, 2007). Tree models, starting with Derrida's generalized random energy model (GREM, Derrida and Gardner, 1986) and Bouchaud's trap model (Bouchaud and Dean, 1995), offer a fruitful framework for modelling out-of-equilibrium systems (Hoffmann and Sibani, 1989; Sasaki and Nemoto, 2001). Samarakoon et al. (2017) have investigated memory effects in various magnetic glassy materials (high-temperature superconductors, spin-orbit Mott insulators, frustrated magnets, and a metallic spin glass). They observed memory effects, sharper in the spin glass, less pronounced and closer to a cooling rate effect in other systems. By comparing with a model of random walk on a tree structure, the authors show that the memory effect depends on the hierarchical character of the tree. Recently, Zhang et al. (2021) characterized a disappearance of the glassy behavior and the memory effect above a critical value of tree branching ratio.

The hierarchical scheme in Fig. 9 shows free-energy barriers that are growing as the temperature decreases. The slowing down observed in the dynamics is indeed more drastic than expected from thermally activated dynamics in a fixed landscape. In a series of experiments, the growth of the free-energy barriers upon lowering temperature has been measured (Hammann et al., 1992). The results suggest that some barriers are diverging at all temperatures below T_g, making a link between the hierarchical organization of the metastable states as a function of temperature and that of the pure states in the mean-field spin glass model (a slightly different barrier analysis is presented in Bouchaud et al., 2001).

Let us try to merge into a common framework both views of aging phenomena that we have considered in this discussion:

- a domain growth picture (suggested by the slowing down of the dynamical response during aging), and
- a hierarchical organization of some entities to be defined (suggested by rejuvenation and memory effects).

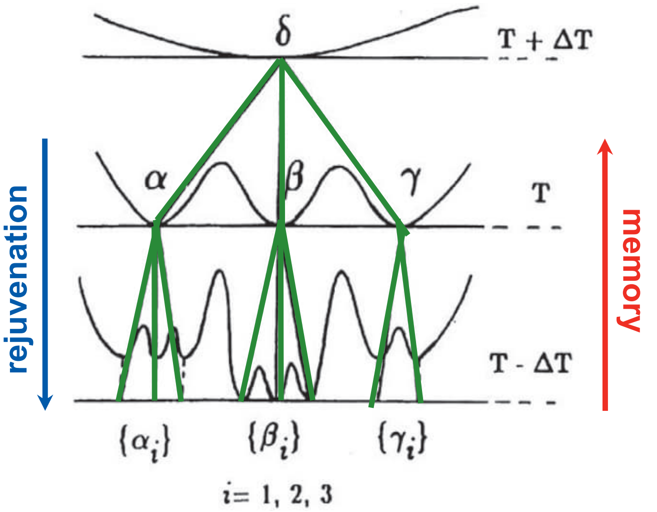

Fig. 9 Schematic picture of the hierarchical structure of the metastable states as a function of temperature. From Dotsenko VS, Feigel'man MV, and Ioffe LB (1990) Spin glasses and related problems. *Soviet Scientific Reviews Section A Physics Reviews* 15: 1–250; Refregier P, Vincent E, Hammann J, and Ocio M (1987). Ageing phenomena in a spin-glass: Effect of temperature changes below Tg. *Journal de Physique* 48: 1533–1539.

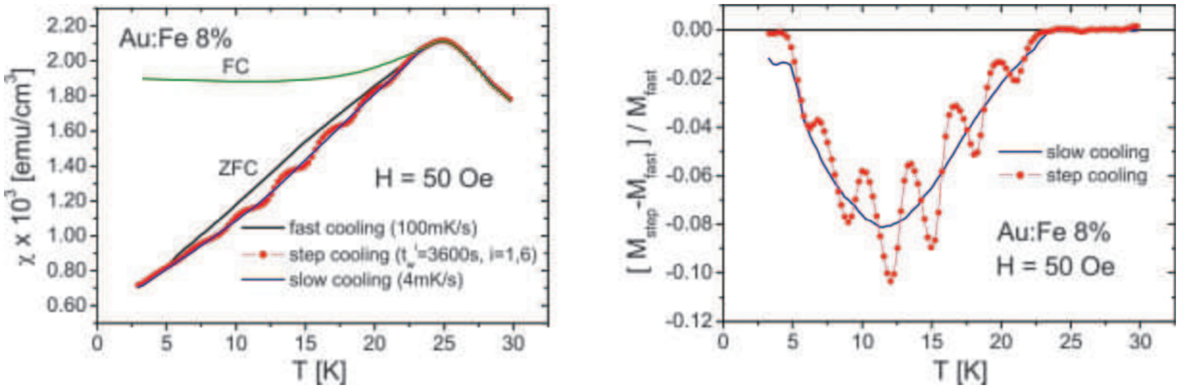

Fig. 10 Left: Effect of various cooling procedures on the ZFC susceptibility (magnetization divided by field) of the Au: Fe8% spin-glass. Comparison of the effect of fast and slow cooling, with and without stops. Right: difference with the magnetization obtained after fast cooling, emphasizing the memory dips on top of a cooling rate effect.

When large domains have been established during aging at temperature T, with size L_T, rejuvenation at $T\text{-}\Delta T$ implies that new processes take place at $L_{T\text{-}\Delta T} < L_T$. In order to ensure the preservation of memory at T, we need $L_{T\text{-}\Delta T} << L_T$, together with a freezing of the L_T processes at $T\text{-}\Delta T$. This is the "temperature-microscope effect" proposed by (Bouchaud et al., 2001). In experiments like those from Figs. 7, 8 and 10, at each temperature stop aging should take place at well-separated length scales $L_n < \ldots < L_2 < L_1$, as if the magnification of the microscope were strongly varied at each temperature step.

This "hierarchy of embedded length scales" as a function of temperature is a real space equivalent of the hierarchy of metastable states in the configuration space (Fig. 9). In such a scheme, the domains are not compact, they are embedded cooperative entities in which the spins are correlated up to a characteristic length, which varies quickly with temperature (the crucial point for memory is that the characteristic times increase quickly with decreasing temperature). Later below, in Section "A correlation length for spin-glass order," we describe experiments in which the correlation length of the spin-glass order can be measured, which bring more information about these embedded length scales.

An experiment gathering the various aspects of aging

We now show an experiment in which cooling rate effects, illustrative of domain-growth processes, can be observed together with memory phenomena.

This is a ZFC-type procedure (*dc*, like in Fig. 1A), proposed by the Uppsala group (Mathieu et al., 2001). The sample is cooled in zero-field with several different thermal procedures, and after applying the field at low temperature the ZFC magnetization is measured while increasing the temperature continuously at fixed speed (small steps of 0.1 K/min).

The results are shown in Fig. 10. Firstly, we can observe the effect of a slow cooling in comparison with that of a fast cooling: the ZFC-curve obtained after a slow cooling lies below the one obtained after a fast cooling. That is, after a slower cooling, the response to the application of the field at low temperature is weaker, the spin-glass state has been more robustly established: the growth of spin-glass ordered domains has been favored by the slower cooling.

Secondly, memory effects can also be observed in this experiment, using now a procedure in which the cooling is interrupted at several temperatures during a one hour waiting time (like in the χ'' experiment in Fig. 8). The magnetization measured during re-heating after this step-cooling procedure shows clear dips at all temperatures at which the sample has been aging. These effects are emphasized in the right part of Fig. 10 where we have plotted the difference between the curves obtained after a specific cooling history and the reference one obtained after a fast cooling. Sharp oscillations (memory dips) show up on top of a wide bump (cooling rate effect).

We may wonder whether the structural glasses, usually considered to be dominated by cooling rate effects, also present rejuvenation and memory phenomena. Experiments have been designed to search for such effects in various glassy systems (including polymers, gels…). They have indeed identified comparable phenomena, although usually less marked than in spin glasses (e.g. Bellon et al., 2002; see references in Vincent and Dupuis, 2018). In simulations of polydisperse repulsive particles, Scalliet and Berthier (2019) have shown that rejuvenation and memory effects are found for packing fractions corresponding to soft colloids and granular materials, whereas such effects are not seen in the regime describing dense supercooled liquids like structural glasses.

An interesting example concerns the mechanical properties of gelatine (Parker and Normand, 2010). Gelatine is a complex protein made of folded helices, and it has many degrees of freedom related to helix unfolding in the vicinity of room temperature. The experiment that we show in Fig. 11 is an *ac* measurement of the elastic modulus G', it can be compared with the *ac* experiment on a spin glass in Fig. 8. G' has first been measured during simple cooling and re-heating (dashed line, reference). Another measurement has been performed with two stops at two different temperatures during cooling (solid line). During each stop, G' relaxes upwards (the gelatine stiffens, this is aging), and upon further cooling some rejuvenation can be seen. When re-heating, G' shows a dip at each of both stop temperature, the two memory dips are overlapping, but they can be clearly distinguished.

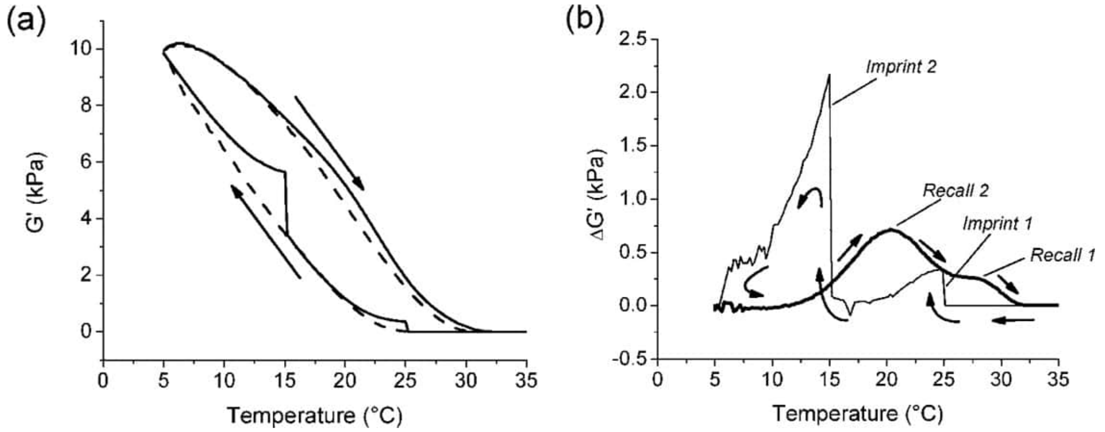

Fig. 11 Measurement of the elastic modulus *G'* of a gelatine gel, showing aging and memory effects during temperature cycles. Two stops of 2 h were made at 25 and 15 °C during cooling. The left part (A) shows *G'* as a function of temperature, in solid line for the cycle with stops, and in dashed line for a cycle without stops. During the stops, *G'* increases slowly (aging). Upon re-heating, a widespread excess of *G'* is seen when compared with the curve obtained without stops. In the right part (B) of the figure, which shows the difference plot, the memory of both stops shows up clearly. From Parker A and Normand V (2010) Glassy dynamics of gelatin gels. *Soft Matter* 6: 4916–4919.

A correlation length for spin-glass order

The spin-glass order made measurable

It is not obvious to observe the spin-glass ordered domains, since these correlated entities do not present any macroscopic symmetry. Still, the existence of correlated domains separated by frustrated regions has already been mentioned ("clusters") in early studies of the $\pm J$ spin-glass model (Miyashita and Suzuki, 1981), and small scale simulations allowed the visualization of some long-living domains by studying the spin autocorrelation function (Takano and Miyashita, 1995). Also, in their simulations of the Heisenberg spin glass, Berthier and Young (2004) studied the relative orientations of the spins in two copies ("replicas") of the system which, starting from different random states, evolve independently by a Monte-Carlo algorithm. Regions of the sample where the spins have a constant angle between both replicas can be rather clearly distinguished. These replica-correlated regions are in a sense equivalent to spin-glass ordered domains, and their growth as a function of time is visible (Fig. 5 in Berthier and Young, 2004).

Yet, it is a challenge to observe these domains in real spin-glass materials. Starting from an idea of R. Orbach, experiments could be developed which allow the measurement of the correlation length of growing domains during aging (Joh et al., 1999). Until this point, we presented experiments which were performed at very low magnetic field, i.e. in which the field is probing but not influencing the spin-glass state (as explained in Section "Slow dynamics and aging in spin glasses"). When using higher amplitudes of the field, we observed that the magnetization relaxation following a field change becomes faster (this can be seen as well in TRM as in ZFC procedures).

The TRM-relaxation curves can be characterized by their inflection point, t_i, which at low field takes place at $t_i \approx t_w$ (TRM curves in Fig. 3). According to thermally activated dynamics, the time t_i defines a typical free-energy barrier U that can be overcome at temperature T after a time t_i (with an attempt time $\tau_0 \approx 10^{-12}$ s defined by the paramagnetic fluctuations):

$$U(t_i) = k_B T \, Ln(t_i/\tau_0). \tag{11}$$

For a low field TRM relaxation as in Fig. 3, $t_i \approx t_w$, but for higher field amplitudes the relaxation is accelerated and the inflection point t_i shifts toward shorter times (Joh et al., 1999, 2000). Hence, as the field increases, the characteristic barrier $U(t_i)$ decreases (t_i becomes smaller than t_w). We ascribe this energy decrease $U(t_w)$-$U(t_i)$ to the increase with the field of the Zeeman energy E_Z which couples the magnetic field to the spins. In terms of spin-glass ordered domains involving a typical number of correlated spins N_s with total magnetization M, $E_Z = \mathrm{M}.\mu_0.H$ (here, M is an extensive quantity, not per unit volume as is M in the rest of the paper; μ_0 is the magnetic permeability of vacuum). A natural hypothesis is $\mathrm{M} \propto N_s$, but for small numbers $\mathrm{M} \propto N_s^{1/2}$ (typical fluctuation for N_s randomly aligned spins) has also been considered (Bert et al., 2004). The recent comparisons of experiments and simulations now offer a better understanding of this question (Zhai et al., 2020; Paga et al., 2021). Let us simply consider here $\mathrm{M} \propto N_s$.

For TRM experiments at a given t_w, measuring the field dependence of the inflection point of the curves allows the determination of $N_s(t_w)$. Repeating the measurements for various t_w values yields the time variation of N_s. Fig. 12 shows results obtained from different spin-glass samples (Joh et al., 1999, 2000; Bert et al., 2004).

In this plot, the results from 3 samples do all fall on the same line. The number of correlated spins is, as expected, an increasing function of t_w, reaching during the experiments 10^4–10^6, which means a range of 10–100 lattice units for the correlation length (considering crudely that the size L goes like $N^{1/3}$). The 3 samples have a common behavior which is well fitted by a unique straight line, the solid line in the graph is a power law dependence $N_S = (t_w/\tau_0)^{0.45T/Tg}$.

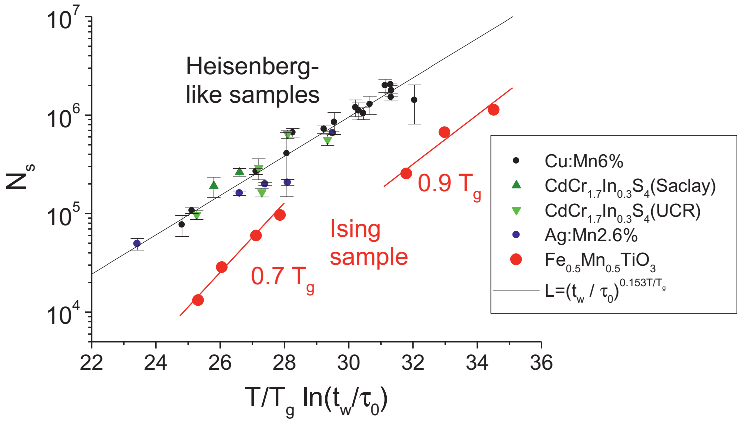

Fig. 12 Number of correlated spins extracted from field change experiments, as a function of the reduced variable $T/T_g \ln(t_w/\tau_0)$. The points with error bars correspond to Heisenberg-like spin-glasses, they are well fitted by the straight line $N_S \sim (t_w/\tau_0)^{0.45T/T_g}$. The full circles lying below the others are from the $Fe_{0.5}Mn_{0.5}TiO_3$ Ising sample and call for a more detailed discussion (Bert et al., 2004; Paga et al., 2021). From Joh YG, Orbach R, Wood JJ, Hammann J, and Vincent E (1999) Extraction of the spin glass correlation length. *Physical Review Letters* 82: 438–441; Joh YG, Orbach R, Wood GG, Hammann J, and Vincent E (2000) Finite size effects on spin glass dynamics. *Journal of the Physical Society of Japan* 69 Suppl. A: 215–222; Bert F, Dupuis V, Vincent E, Hammann J, and Bouchaud J-P (2004) Spin anisotropy and slow dynamics in spin glasses. *Physical Review Letters* 92: 167203.

Extrapolating this dependence to $T = T_g$ allows a connection with the dynamic scaling hypothesis $\tau \propto \xi^z$ (Eq. 4). Taking $N_S \propto \xi^3$ yields $z = 1/0.15 = 6.7$, in fair agreement with the dynamic scaling fits to the results of *ac* measurements. Recent experiments on a single crystal of the CuMn spin glass very close to T_g ($T/T_g = 0.9$) have allowed reaching still larger values of the correlation length, up to 240 lattice units (≈150 nm), almost at the macroscopic scale (Zhai et al., 2019).

Also, experiments on spin-glass thin films have further investigated the relevance of the spin-glass correlation length. When the correlation length reaches the thickness of the sample, modifications of the rejuvenation and memory effects are seen (Ge:Mn layers of 15.5 nm, Guchhait and Orbach, 2015), and a crossover from 3d to 2d behavior is observed (CuMn layers of 5–20 nm, Zhai et al., 2017).

Let us mention that, in experiments exploring the glassy state formed by interacting magnetic nanoparticles, other data in the intermediate time range have been obtained (Nakamae et al., 2012, and references therein). The microscopic flip time of the *superspins* born by the nanoparticles (10^4–10^6 ferromagnetically coupled spins in each nanoparticle) is much longer than 10^{-12} s, ranging up to milliseconds, in such a way that in τ_0 units the explored times are closer to those in simulations. The data from superspins are in continuity with those from spins in both experiments and simulations.

A bridge between experiments and simulations

The numerical simulations of the Edwards-Anderson model (Eq. 1) allow the exploration of the microscopic organization of the spins, which remains inaccessible to the experiments. But an important difficulty is that, due to frustration, the evolution toward equilibrium is very slow, implying time consuming computations. The experiments on real spin glasses are typically exploring the 10^0–10^5 s time range, which in units of the paramagnetic spin flip time $\tau_0 \approx 10^{-12}$ s corresponds to 10^{12}–10^{17} τ_0. Taking $\tau_0 = 1$ Monte-Carlo (MC) step for comparison, the first numerical simulations were exploring up to $\approx 10^7$ MC steps, a rather short-time regime compared with the experiments (Berthier and Young, 2005). In the Janus and Janus II projects, dedicated supercomputers have been built, which allow computation up to $\approx 10^{11}$ MC steps and more.

In simulations, the correlation length has first been determined from a 4-point correlation function (Marinari et al., 1996), which is not directly related to that measured in the above experiments. In a later stage, it has become possible to fully simulate the experimental procedure in which the correlation length is extracted from the effect of the field on the speed of the magnetization relaxation (method used in Fig. 12). Values of the correlation length up to 17 lattice units could be reached (Baity-Jesi et al., 2018). Since the same method can be used in both experiments and simulations, very interesting comparisons can now be made (Zhai et al., 2019), recently yielding to common publications by experimentalists and theoreticians (Zhai et al., 2020; Paga et al., 2021). Some discrepancies have been found for large applied fields or close to T_g, but a coherent overall description of the results could be reached by defining appropriate scaling laws. The successful modelling of important experimental features of real spin glasses is a crucial progress for a better understanding of complex systems in general.

There has already been an active search for rejuvenation and memory effects in numerical simulations of the Edwards-Anderson model. For Ising spins, they were initially found in d = 4, but not in d = 3 (Berthier and Bouchaud, 2002, and references therein). For Heisenberg spins, which imply still longer computation times, rejuvenation and memory effects have been seen, but the comparison of the correlation growth in Ising and Heisenberg systems goes at variance between simulations (Berthier and Young, 2005) and experiments (Bert et al., 2004), so the situation is not fully clear. It is likely that the correlation lengths $L_{T-\Delta T}$, L_T (Section "Domain growth and hierarchy of states") which could be reached by simulations at different temperatures were not spread enough to allow $L_{T\text{-}\Delta T} << L_T$ and a clear characterization of rejuvenation and memory effects. More space is needed for a full hierarchy of embedded lengths to be at play. Very recently, at the time when this article is being completed, the Janus collaboration could overcome this fundamental hurdle, and succeed in observing rejuvenation and memory effects in the simulated relaxation of the ZFC magnetization (Baity-Jesi et al, 2022).

Temperature chaos is an issue that deserves a new light. It has long been considered as a possible key to rejuvenation (Jönsson et al., 2004), which is a dynamical effect, whereas temperature chaos has been defined in an equilibrium context (Bray and Moore, 1987). Also, it should allow the existence of memory despite rejuvenation. In both Ising and Heisenberg early simulations, the authors indicated that they found no sign of temperature chaos. In the recent large-scale simulations ($L = 160$) by the Janus collaboration, some first signs of a dynamic temperature-chaos effect have been found (Baity-Jesi et al., 2021). In their most recent results, chaos could be clearly characterized, and related with the occurrence of rejuvenation effects (Baity-Jesi et al., 2022)

Conclusion

Within the wide class of disordered materials, spin glasses occupy a special place because of their conceptually simple definition of randomly interacting spins. Spin glasses are disordered magnetic materials which all share a number of common properties, laying down the definition of a generic spin glass behavior.

The spin glass state develops below a well-defined temperature T_g, above which the spins are in paramagnetic state. At T_g, the transition to the spin-glass state presents the same features as for a thermodynamic phase transition to an ordered state, but no macroscopic spin alignment can be seen like in ferromagnets or antiferromagnets. The spin-glass order has a mysterious hidden symmetry, corresponding to spin configurations minimizing the spin-spin interaction energies, which have randomly distributed values.

At T_g, a frozen state is established, but this state is not at equilibrium, it is not totally frozen. After cooling from the paramagnetic phase, starting from a random configuration, the spin-glass order is progressively establishing at longer and longer range, causing aging phenomena that show up in the measured magnetic properties. The characteristic size of the growing cooperative regions has been determined in specific experiments, defining a correlation length for the spin-glass order. Recent developments of numerical simulations, taking benefit of powerful custom-built supercomputers, allow very interesting comparisons of this correlation length of a hidden order in real spin glasses and in the conceptually simple (although highly non-trivial) theoretical models (Paga et al., 2021). A better understanding of these models has important consequences, because they are now part of a tool kit of statistical physics which is used for a wide variety of "complex system" problems, such as econophysics, biology, data compressing, optimization etc.

No simple way has been found to bring a real spin glass closer to an equilibrium state, whose nature is still debated (is it unique, or multiple?). A slower cooling may help partly, as can be efficiently done for structural glasses, but as the temperature is lowered new processes need to be equilibrated, and rejuvenation phenomena show up. Yet, the memory of previous aging states prepared during the cooling can be retrieved upon re-heating. The ability of a spin glass to store several memories of aging at different temperatures is astonishing. A detailed microscopic understanding of the rejuvenation and memory effects at the scale of spin configurations is still lacking. The forthcoming numerical simulations of spin-glass models will probably allow exploring the hierarchy of embedded correlation lengths that is thought to be necessary to observe rejuvenation effects while keeping memory.

In structural and polymer glasses, the dominant scenario is the continuation of aging from one temperature to another. Still, using appropriate procedures, some rejuvenation and memory processes could often be found (as we showed in the case of gelatin). Structural glasses may pertain to a slightly different class of models (spin glass with p-spin interactions, 1-step RSB model, Bouchaud et al., 1996), in which no hierarchy of pure states is found. What are the necessary features of a model in order to obtain rejuvenation and memory phenomena? This has not yet become fully clear. It is an exciting and important challenge to develop a common understanding of glassy systems, and the spin-glass models clearly have a powerful potential in this direction.

On the side of the experiments on real spin glasses, more and more accurate and refined measurements bring a lot of new information (e.g. Zhai et al., 2022). Anomalous Hall effect measurements bring in principle a direct access to spin-chirality freezing (Kawamura, 1992); if they could be pursued, they should shed some light on the nature of the spin-glass transition for Heisenberg spins (Pureur et al., 2004; Taniguchi, 2007). However, one may consider that, for making a significant breakthrough in the understanding of real spin glasses, it is necessary to find some way to access to spin configurations. The key may lie in the study of mesoscopic samples (difficult, due to weak signals), in which the growing correlation length may hit the sample size or a "chaos length" (as for the thin layers in Guchhait and Orbach, 2015, Zhai et al., 2017). Transport measurements on mesoscopic wires may offer some insight in the spin configurations by the universal conductance fluctuations (Carpentier and Orignac, 2008), and provide new perspectives on the spin-glass transition (Forestier et al., 2020).

Acknowledgments

The author deeply thanks V. Dupuis and F. Ladieu for their detailed re-reading of the manuscript and highly relevant suggestions. He also benefitted a lot from very helpful discussions with T. Chakraborty, H. Kawamura, E. Marinari, S. Miyashita and S. Nakamae. H. Bouchiat and A. Parker are warmly thanked for the permission to reuse their figures.

References

Alba M, Hammann J, and Noguès M (1982) Phase diagrams of two dilute insulating systems with competing interactions. *Journal of Physics C* 15: 5441–5454.

Albert S, Michl M, Lunkenheimer P, Loidl A, Déjardin PM, and Ladieu F (2019) Third and fifth harmonic responses in viscous liquids. *Journal of Statistical Mechanics: Theory and Experiment* 124003.

Altieri A and Baity-Jesi M (2023) *An Introduction to the Theory of Spin Glasses*. Article in the 2023 edition of this Encyclopedia.

Anderson PW (1970) Localisation theory and the Cu-Mn problem: Spin glasses. *Materials Research Bulletin* 5: 549–554.

Baity-Jesi M, Calore E, Cruz A, Fernandez LA, Gil-Narvion JM, Gordillo-Guerrero A, Iñiguez D, Maiorano A, Marinari E, Martin-Mayor V, Moreno-Gordo J, Muñoz-Sudupe A, Navarro D, Parisi G, Perez-Gaviro S, RicciTersenghi F, Ruiz-Lorenzo JJ, Schifano SF, Seoane B, Tarancon A, Tripiccione R, Yllanes D, and Janus Collaboration (2018) Aging rate of spin glasses from simulations matches experiments. *Physical Review Letters* 120: 267203.

Baity-Jesi M, Calore E, Cruz A, Fernandez LA, Gil-Narvion JM, Gonzalez-Adalid Pemartin I, Gordillo-Guerrero A, Iñiguez D, Maiorano A, Marinari E, Martin-Mayor V, Moreno-Gordo J, Muñoz-Sudupe A, Navarro D, Paga I, Parisi G, Perez-Gaviro S, Ricci Tersenghi F, Ruiz-Lorenzo JJ, Schifano SF, Seoane B, Tarancon A, and Yllanes D (2022) Memory and rejuvenation in spin glasses: Aging systems are ruled by more than one length scale. *Janus Collaboration.* https://arxiv.org/abs/2207.06207v2.

Baity-Jesi M, Calore E, Cruz A, Fernandez LA, Gil-Narvion, Gonzalez-Adalid Pemartin I, Gordillo-Guerrero A, Iñiguez D, Maiorano A, Marinari E, Martin-Mayor V, Moreno-Gordo J, Muñoz-Sudupe A, Navarro D, Paga I, Parisi G, Perez-Gaviro S, Ricci Tersenghi F, Ruiz-Lorenzo JJ, Schifano SF, Seoane B, Tarancon A, Tripiccione R, Yllanes D, and Janus Collaboration (2021) Temperature chaos is present in off-equilibrium spin-glass dynamics. *Communications on Physics* 4: 74. https://doi.org/10.1038/s42005-021-00565-9.

Barrat A (1998) Monte Carlo simulations of the violation of the fluctuation-dissipation theorem in domain growth processes. *Physical Review E* 57: 3629–3632.

Bellon L, Ciliberto S, and Laroche C (2002) Advanced memory effects in the aging of a polymer glass. *European Physical Journal B* 25: 223–231.

Bert F, Dupuis V, Vincent E, Hammann J, and Bouchaud J-P (2004) Spin anisotropy and slow dynamics in spin glasses. *Physical Review Letters* 92: 167203.

Berthier L and Bouchaud J-P (2002) Geometrical aspects of aging and rejuvenation in the Ising spin glass: A numerical study. *Physical Review B* 66: 054404.

Berthier L and Young AP (2004) Aging dynamics of the Heisenberg spin glass. *Physical Review B* 69: 184423.

Berthier L and Young AP (2005) Temperature cycles in the Heisenberg spin glass. *Physical Review B* 71: 214429.

Binder K and Young AP (1984) Logarithmic dynamic scaling in spin-glasses. *Physical Review B* 29: 2864.

Bontemps N, Rajchenbach J, Chamberlin RV, and Orbach R (1984) Dynamic scaling in the $Eu_{0.4}Sr_{0.6}S$ spin-glass. *Physical Review B* 30: 6514.

Bouchaud JP and Biroli G (2005) Nonlinear susceptibility in glassy systems: A probe for cooperative dynamical length scales. *Physical Review B* 72: 064204.

Bouchaud J-P and Dean DS (1995) Aging on Parisi's Tree. *Journal de Physique I* 5: 265.

Bouchaud J-P, Cugliandolo L, Kurchan J, and Mezard M (1996) Mode-coupling approximations, glass theory and disordered systems. *Physica A* 226: 243.

Bouchaud J-P, Dupuis V, Hammann J, and Vincent E (2001) Separation of time and length scales in spin glasses: Temperature as a microscope. *Physical Review B* 65: 024439.

Bouchiat H (1986) Determination of the critical exponents in the Ag Mn spin glass. *Journal de Physique* 47: 71–88.

Bray AJ and Moore MA (1987) Chaotic immature of the spin-glass phase. *Physical Review Letters* 58: 57–60.

Brun C, Ladieu F, L'Hôte D, Biroli G, and Bouchaud J-P (2012) Evidence of growing spatial correlations during the aging of glassy glycerol. *Physical Review Letters* 109: 175702.

Cannella V and Mydosh JA (1972) Magnetic ordering in gold-iron alloys. *Physical Review B* 6: 4220–4237.

Capron T, Forestier G, Perrat-Mabilon A, Peaucelle C, Meunier T, Baüerle C, Lévy LP, Carpentier D, and Saminadayar L (2013) Magnetic dephasing in mesoscopic spin glasses. *Physical Review Letters* 111: 187203.

Carpentier D and Orignac E (2008) Measuring overlaps in mesoscopic spin glasses via conductance fluctuations. *Physical Review Letters* 100: 057207.

Chalupa J (1977) The susceptibilities of spin glasses. *Solid State Communications* 22: 315–317.

Corberi F, Cugliandolo LF, Yoshino H, and van Saarlos W (2011) Growing length scales in aging systems. In: Berthier L, Biroli G, Bouchaud J-P, and Cipelletti L (eds.) *Dynamical Heterogeneities in Glasses, Colloids and Granular Media.* Oxford University Press.

Cugliandolo LF and Kurchan J (1994) On the out-of-equilibrium relaxation of the Sherrington-Kirkpatrick model. *Journal of Physics A* 27: 5749–5772.

Cugliandolo LF and Kurchan J (1999) Mean-field theory of temperature cycling experiments in spin glasses. *Physical Review B* 60: 922–930.

Cugliandolo LF, Kurchan J, and Peliti L (1997) Energy flow, partial equilibration, and effective temperatures in systems with slow dynamics. *Physical Review E* 55: 3898.

Derrida B and Gardner E (1986) Solution of the generalised random energy model. *Journal of Physics C* 19: 2253.

Djurberg C, Mattsson J, and Nordblad P (1995) Linear response in spin glasses. *Europhysics Letters* 29: 163–168.

Dormann JL, D'Orazio F, Lucari F, Tronc E, Prené P, Jolivet JP, Fiorani D, Cherkaoui R, and Noguès M (1996) Thermal variation of the relaxation time of the magnetic moment of g-Fe_2O_3 nanoparticles with interparticle interactions of various strengths. *Physical Review B* 53: 14291–14297.

Dotsenko VS, Feigel'man MV, and Ioffe LB (1990) Spin glasses and related problems. *Soviet Scientific Reviews Section A Physics Reviews*, vol. 15, 1–250.

Dupuis V (2002) *Dynamique lente des systèmes magnétiques désordonnés*. PhD Thesis France: Orsay University. https://tel.archives-ouvertes.fr/tel-00002623/document.

Ediger MD and Harrowell P (2012) Perspective: Supercooled liquids and glasses. *The Journal of Chemical Physics* 137: 080901.

Edwards SF and Anderson PW (1975) Theory of spin glasses. *Journal of Physics F* 5: 965.

Fisher DS and Huse DA (1988a) Nonequilibrium dynamics of spin glasses. *Physical Review B* 38: 373–385.

Fisher DS and Huse DA (1988b) Equilibrium behavior of the spin glass ordered phase. *Physical Review B* 38: 386–411.

Forestier G, Solana M, Naud C, Wieck AD, Lefloch F, Whitney R, Carpentier D, Lévy LP, and Saminadayar L (2020) Spin-glass phase transition revealed in transport measurements. *Physical Review B* 102: 024206.

Franz S, Mézard M, Parisi G, and Peliti L (1998) Measuring equilibrium properties in aging systems. *Physical Review Letters* 81: 1758.

Guchhait S and Orbach RL (2015) Temperature chaos in a Ge:Mn thin-film spin glass. *Physical Review B* 92: 214418.

Hammann J, Lederman M, Ocio M, Orbach R, and Vincent E (1992) Spin-glass dynamics, Relation between theory and experiment: A beginning. *Physica A* 185: 278–294.

Hérisson D and Ocio M (2002) Fluctuation-dissipation ratio of a spin glass in the aging regime. *Physical Review Letters* 88: 257202.

Hérisson D and Ocio M (2004) Off-equilibrium fluctuation-dissipation relation in a spin glass. *European Physical Journal B* 40: 283.

Hoffmann H and Sibani P (1989) Hierarchical models for aging and relaxation of spin glasses. *Physical Review Letters* 63: 2853.

Ji Y, Dong W, Yunzhi W, and Xiaobing R (2023) *Ferroic Glasses*. Elsevier. Article in the 2023 edition of this Encyclopedia.

Jin Y and Yoshino H (2017) Exploring the complex free-energy landscape of the simplest glass by rheology. *Nature Communications* 8: 14935.

Joh YG, Orbach R, Wood JJ, Hammann J, and Vincent E (1999) Extraction of the spin glass correlation length. *Physical Review Letters* 82: 438–441.

Joh YG, Orbach R, Wood GG, Hammann J, and Vincent E (2000) Finite size effects on spin glass dynamics. *Journal of the Physical Society of Japan* 69 Suppl. A: 215–222.

Jonason K, Vincent E, Bouchaud JP, and Nordblad P (1998) Memory and chaos effects in spin glasses. *Physical Review Letters* 81: 3243–3246.

Jonason K, Nordblad P, Vincent E, Hammann J, and Bouchaud J-P (2000) Memory interference effects in spin glasses. *European Physical Journal B* 13: 99–105.

Jönsson PE, Yoshino H, and Nordblad P (2002) Symmetrical temperature-chaos effect with positive and negative temperature shifts in a spin glass. *Physical Review Letters* 89: 097201.

Jönsson PE, Mathieu R, Nordblad P, Yoshino H, Aruga KH, and Ito A (2004) Nonequilibrium dynamics of spin glasses: Examination of the ghost domain scenario. *Physical Review B* 70: 174402.

Kawamura H (1992) Chiral ordering in Heisenberg spin glasses in two and three dimensions. *Physical Review Letters* 68: 3785.

Kawamura H and Taniguchi T (2015) In: Buschow KHJ (ed.) *Spin glasses, in Handbook of Magnetic Materials*. vol. 24. Elsevier. ch. 1.

Koper GJM and Hilhorst HJ (1988) A domain theory for linear and nonlinear aging effects in spin glasses. *Journal de Physique* 49: 429–443.

Lefloch F, Hammann J, Ocio M, and Vincent E (1992) Can aging phenomena discriminate between the droplet model and a hierarchical description in spin glasses? *Europhysics Letters* 18: 647–652.

Lévy LP (1988) Critical dynamics of metallic spin glasses. *Physical Review B* 38: 4963–4973.

Lookman T and Ren X (2018) *Frustrated Materials and Ferroic Glasses. Springer Series in Material Science 275.* Springer Nature Switzerland AG.

Marinari E, Parisi G, Ruiz-Lorenzo J, and Ritort F (1996) Numerical evidence for spontaneously broken replica symmetry in 3D spin glasses. *Physical Review Letters* 76: 843.

Marinari E, Parisi G, Ricci-Tersenghi F, and Ruiz-Lorenzo JJ (1998) Violation of the fluctuation-dissipation theorem in finite-dimensional spin glasses. *Journal of Physics A* 31: 2611–2620.

Mathieu R, Jönsson P, Nam DNH, and Nordblad P (2001) Memory and Superposition in a Spin Glass. *Physical Review B* 63: 092401.

Mattsson J, Jonsson T, Nordblad P, Aruga KH, and Ito A (1995) No phase transition in a magnetic field in the Ising spin glass $Fe_{0.5}Mn_{0.5}TiO_3$. *Physical Review Letters* 74: 4305–4308.

Mezard M, Parisi G, and Virasoro MA (1987) *Spin Glass Theory and Beyond*. Singapore: World Scientific.

Miyako Y, Chikazawa S, Saito T, and Yuochunas YG (1979) Non-linear magnetization at the spin glass phase transition temperature. *Journal of the Physical Society of Japan* 46: 1951–1952.

Miyashita S (1983) Spin correlation functions on frustrated lattices. *Progress of Theoretical and Experimental Physics* 69: 714–724.

Miyashita S and Suzuki M (1981) Frustration and clusters in spin glasses. *Journal of the Physical Society of Japan* 50: 1840.

Miyashita S and Vincent E (2001) A microscopic mechanism for rejuvenation and memory effects in spin glasses. *European Physical Journal B* 22: 203–211.

Mydosh JA (1993) *Spin Glasses, an Experimental Introduction*. Taylor & Francis Group. https://doi.org/10.1201/9781482295191.

Mydosh JA (2015) Spin glasses: Redux: An updated experimental/materials survey. *Reports on Progress in Physics* 78: 052501. 25 pp.

Nakamae S, Crauste-Thibierge C, L'Hôte D, Vincent E, Dubois E, Dupuis V, and Perzynski R (2012) Dynamic correlation length growth in superspin glass: Bridging experiments and simulations. *Applied Physics Letters* 101: 242409.

Nordblad P (2023) *Disordered Magnetic Systems*. Elsevier. Article in the 2023 edition of this Encyclopedia.

Ocio M, Alba M, and Hammann J (1985a) Time scaling of the ageing process in spin-glasses: A study in $CsNiFeF_6$. *Journal de Physique Lettres* 46: L1101–L1107.

Ocio M, Bouchiat H, and Monod P (1985b) Observation of 1/f magnetic fluctuations in a spin glass. *Journal de Physique Lettres* 46: L647–L652.

Paga I, Zhai Q, Baity-Jesi M, Calore E, Cruz A, Fernandez LA, Gil-Narvion JM, Gonzalez-Adalid PI, Gordillo-Guerrero A, Iñiguez D, Maiorano A, Marinari E, Martin-Mayor V, Moreno-Gordo J, Muñoz-Sudupe A, Navarro D, Orbach RL, Parisi G, Perez-Gaviro S, Ricci-Tersenghi F, Ruiz-Lorenzo JJ, Schifano SF, Schlagel DL, Seoane B, Tarancon A, Tripiccione R, and Yllanes D (2021) Spin-Glass Dynamics in the Presence of a Magnetic Field: Exploration of Microscopic Properties. *Journal of Statistical Mechanics: Theory and Experiment* 033301.

Paga I, Zhai Q, Baity-Jesi M, Calore E, Cruz A, Cummings C, Fernandez LA, Gil-Narvion JM, Gonzalez-Adalid Pemartin I, Gordillo-Guerrero A, Iñiguez D, Kenning GG, Maiorano A, Marinari E, Martin-Mayor V, Moreno-Gordo J, Muñoz-Sudupe A, Navarro D, Orbach RL, Parisi G, Perez-Gaviro S, Ricci-Tersenghi F, Ruiz-Lorenzo JJ, Schifano SF, Schlagel DL, Seoane B, Tarancon A, and Yllanes D (2022) Magnetic-field symmetry breaking in spin glasses. https://arxiv.org/abs/2207.10640v2.

Parisi G (1979) Toward a mean field theory for spin glasses. *Physics Letters* 73A: 203–205.

Parker A and Normand V (2010) Glassy dynamics of gelatin gels. *Soft Matter* 6: 4916–4919.

Petit D, Fruchter L, and Campbell IA (2002) Ordering in Heisenberg spin glasses. *Physical Review Letters* 88: 207206.

Pureur P, Wolff FF, Schaf J, and Campbell IA (2004) Chiral susceptibility in canonical spin glass and re-entrant alloys from Hall effect measurements. *Europhysics Letters* 67: 123–129.

Refregier P, Vincent E, Hammann J, and Ocio M (1987) Ageing phenomena in a spin-glass: Effect of temperature changes below T_g. *Journal de Physique* 48: 1533–1539.

Samarakoon AM, Takahashi M, Zhang D, Yang J, Katayama N, Sinclair R, Zhou HD, Diallo SO, Ehlers G, Tennant DA, Wakimoto S, Yamada K, Chern G-W, Sato TJ, and Lee S-H (2017) Scaling of memories and crossover in glassy magnets. *Scientific Reports* 7: 12053.

Sasaki M and Nemoto K (2001) Numerical study of aging in the generalized random energy model. *Journal of the Physical Society of Japan* 70: 1099–1104.

Sasaki M, Dupuis V, Bouchaud J-P, and Vincent E (2002) Deviations from perfect memory in spin glass temperature cycling experiments. *European Physical Journal B* 29: 469–479.

Scalliet C and Berthier L (2019) Rejuvenation and memory effects in a structural glass. *Physical Review Letters* 122: 255502.

Sherrington D and Kirkpatrick S (1975) Solvable model of a spin-glass. *Physical Review Letters* 35: 1792–1796.

Simon SL and McKenna GB (1997) Interpretation of the dynamic heat capacity observed in glass-forming liquids. *The Journal of Chemical Physics* 107: 8678.

Souletie J and Bertrand D (1991) Glasses and spin glasses: A parallel. *Journal de Physique I* 1: 1627–1637.

Struik LCE (1978) *Physical Ageing in Amorphous Polymers and Other Materials*. Houston: Elsevier.

Suzuki M (1977) Phenomenological theory of spin-glasses and some rigorous results. *Progress in Theoretical Physics* 58: 1151–1165.

Suzuki M and Miyashita S (1981) Order parameters and non linear susceptibilities in spin glasses. *Physica* 106A: 344–354.

Tabata Y, Waki T, and Nakamura H (2017) Dynamic scaling analysis of the long-range RKKY Ising spin glass $Dy_xY_{1-x}Ru_2Si_2$. *Physical Review B* 96: 184406.

Takano H and Miyashita S (1995) Relaxation of the spin autocorrelation function in the Ising spin glass. *Journal of the Physical Society of Japan* 64: 423.

Tanaka S and Miyashita S (2005) Dynamical properties of temperature chaos and memory effect. *Progress of Theoretical Physics Supplements* 157: 34–37.

Taniguchi T (2007) Chiral susceptibility of canonical spin glasses from Hall effect measurements. *Journal of Physics. Condensed Matter* 19: 145213.

Tholence JL (1981) A.C. susceptibility of CuMn and AgMn spin-glasses. *Physica* 108B: 1287–1288.

Vincent E (2007) Ageing, rejuvenation and memory: The example of spin-glasses. *Lecture Notes in Physics* 716: 7–60.

Vincent E and Dupuis V (2018) Spin glasses: Experimental signatures and salient outcomes. In: Lookman T and Ren X (eds.) *Frustrated Materials and Ferroic Glasses*, *Springer Series in Materials Science 275.* p. 31.

Vincent E and Hammann J (1986) Dynamic critical behaviour of the $CdCr_{2x0.85}In_{2x0.15}S_4$ spin-glass. *Solid State Communications* 58: 57–62.

Vincent E, Hammann J, Ocio M, Bouchaud J-P, and Cugliandolo LF (1997) Slow dynamics and aging in spin glasses. In: Rubi M (ed.) *Complex Behaviour of Glassy Systems*. vol. 492, p. 184. Berlin: Springer-Verlag Lecture Notes in Physics.

Yoshino H, Lemaître A, and Bouchaud J-P (2001) Multiple domain growth and memory in the droplet model for spin-glasses. *European Physical Journal B* 20: 367–395.

Zhai Q, Harrison DC, Tennant D, Dalhberg E, Dan KGG, and Orbach RL (2017) Glassy dynamics in CuMn thin-film multilayers. *Physical Review B* 95: 054304.

Zhai Q, Martin-Mayor V, Schlagel DL, Kenning GG, and Orbach RL (2019) Slowing down of spin glass correlation length growth: Simulations meet experiments. *Physical Review B* 100: 094202.

Zhai Q, Paga I, Baity-Jesi M, Calore E, Cruz A, Fernandez LA, Gil-Narvion JM, Gonzalez-Adalid Pemartin I, Gordillo-Guerrero A, Iñiguez D, Maiorano A, Marinari E, Martin-Mayor V, Moreno-Gordo J, Muñoz-Sudupe A, Navarro D, Orbach RL, Parisi G, Perez-Gaviro S, Ricci-Tersenghi F, Ruiz-Lorenzo JJ, Schifano SF, Schlagel DL, Seoane B, Tarancon A, Tripiccione R, and Yllanes D (2020) Scaling law describes the spin-glass response in theory, experiments, and simulations. *Physical Review Letters* 125: 237202.

Zhai Q, Orbach RL, and Schlagel DL (2022) Evidence for temperature chaos in spin glasses. *Physical Review B* 105: 014434.

Zhang D, Chen T, Vucelja M, Lee S-H, and Chern G-W (2021) Memory effect and phase transition in a hierarchical trap model for spin glasses. *Physical Review E* 104: 064105.

Ferroic glasses

Yuanchao Ji[a], Dong Wang[a], Yang Yang[a], Jinghui Gao[a], Tianyu Ma[a], Yu Wang[a], Yunzhi Wang[b], and Xiaobing Ren[a,c], [a]Frontier Institute of Science and Technology, and State Key Laboratory for Mechanical Behaviour of Materials, Xi'an Jiaotong University, Xi'an, China; [b]Department of Materials Science and Engineering, The Ohio State University, Columbus, OH, United States; [c]Center for Functional Materials, National Institute for Materials Science, Tsukuba, Ibaraki, Japan

© 2024 Elsevier Ltd. All rights reserved.

Introduction to ferroic glasses 389
Definition, classification of ferroic glasses, and their physical nature 389
History of ferroic glasses 390
Generic phase diagram of a ferroic glass system: Link between ferroic LRO and ferroic frozen SRO 391
Origin of ferroic glasses and theoretical models 391
Signatures of a ferroic glass or a ferroic glass transition 392
Novel properties and potential applications of ferroic glasses 395
Strain glasses 396
Relaxors: achieving high permittivity over a wide temperature range by coexisting relaxor nanodomains 397
Crossover relaxor: achieving high electrostrain and small hysteresis simultaneously 398
Re-entrant strain glass showing low modulus and high damping 398
Ferromagnetic strain glass: A multi-ferroic glass showing large magnetostriction at a small magnetic field 399
Isothermal "crystallization" of strain glass as the origin of isothermal martensitic transformation 400
Conclusion 402
Acknowledgments 402
References 402

Abstract

Ferroic glass, a concept coined recently, refers to a generic class of frozen disordered ferroic (=*ferro*elastic, *ferro*electric, *ferro*magnetic) materials with short-range ferroic order; the short-range ferroic order manifests itself as nano-sized ferroic domains which engender from a ferroic glass transition. Ferroic glasses include strain glass in ferroelastic/martensitic systems, relaxor in ferroelectric systems, and cluster spin glass in magnetic systems. They contrast with "ferroic crystals" (i.e., ferroelastics/martensite, ferroelectrics, and ferromagnets), which are characterized by long-range ferroic order or large ferroic domains (mostly micrometer-size) formed by a thermodynamic ferroic transition. The unique short-range order nature of ferroic glasses endows them with technologically important properties not possessed by the corresponding ferroic crystals, such as shape memory and superelasticity in non-martensitic alloys, zero linear thermal expansion (linear Invar effect) and temperature-independent elastic modulus (Elinvar effect), temperature insensitive quasi-linear superelasticity, large dielectric permittivity and electrostrain over wide temperature range, highly sensitive magnetostriction. Ferroic glasses are also found to be the key to understanding a number of longstanding puzzles in ferroic crystals, such as the origin of isothermal martensitic transformation. In this article we overview the state-of-the-arts of ferroic glass research, and present their classification, physical origin, key signatures, novel properties and potential applications in a way understandable to non-specialists. Emphasis is put on the recently-discovered strain glass and physical parallelism among three types of ferroic glasses.

Key points

- Ferroic glasses are a unique class of ferroic (=ferroelastic, ferroelectric, ferromagnetic) materials that have no long-range ferroic order but have frozen short-range ferroic order.
- Ferroic glasses include strain glass in ferroelastic/martensitic systems, relaxor in ferroelectric systems, and cluster spin glass in magnetic systems, and they are physically parallel to one another.
- The unique short-range order nature of ferroic glasses endows them with technologically important properties such as shape memory and superelasticity in non-martensitic alloys, zero linear-thermal expansion (linear Invar effect) and temperature-independent elastic modulus (Elinvar effect), temperature insensitive quasi-linear superelasticity, large dielectric permittivity and electrostrain over wide temperature range, highly sensitive magnetostriction, etc.

https://doi.org/10.1016/B978-0-323-90800-9.00219-5

Introduction to ferroic glasses

Definition, classification of ferroic glasses, and their physical nature

Ferroic glass is an emerging research area in materials science and physics. The concept was first proposed in 2007 (Wang et al., 2007) and coined recently (Ren, 2014; Ji et al., 2017; Lookman and Ren, 2018). It refers to a frozen disordered form of ferroic (=*ferro*elastic, *ferro*electric, *ferro*magnetic) materials with frozen short-range order (SRO) manifested microstructurally by nano-sized ferroic domains, as illustrated in Fig. 1a. They include strain glass, relaxor, and cluster spin glass, which exist in ferroelastic, ferroelectric, and magnetic systems, respectively (Ren, 2014). Ferroic glasses contrast with the long-range ordered (LRO) or "crystal" form of ferroic materials (i.e., ferroelastics/martensites, ferroelectrics, and ferromagnets), the latter being characterized microstructurally by large ferroic domains (usually micrometer-sized) (Fig. 1b). The relation between a ferroic glass and a ferroic crystal is analogous to that between an amorphous glass and a crystal. An amorphous glass is a frozen and structurally disordered state with frozen short-range structural order, and a crystal is a structurally long-range-ordered state with the same crystal structure spanning the whole crystalline grain (usually micrometer-size). A ferroic glass has a similar physical picture with an amorphous glass but with a difference in that a ferroic glass is structurally ordered phase (i.e., a crystal) and its frozen disorder or SRO lies in its ferroic order parameter; i.e., lattice strain, ferroelectric dipole, and magnetic moment (Ren, 2014). This is why it is called ferroic glass. As can be expected, the fundamental difference between the glass and the crystal form of ferroic materials can endow ferroic glasses with novel properties not seen in ferroic crystals.

Ferroic glasses can be classified into three subsets according to their microstructural features (Fig. 1a): (i) canonical ferroic glass which is characterized by ferroic nanodomains (SRO only) (Fig. 1a(1)), (ii) crossover ferroic glass which is a composite composed of both ferroic nanodomains and large ferroic domains (a mixture of SRO and LRO or a crossover state from SRO to LRO) (Fig. 1a(2)), and (iii) re-entrant ferroic glass which is characterized by ferroic nanodomains embedded in large ferroic domains of a different ferroic order (SRO embedded in LRO) (Fig. 1a(3)). It is noted that subset (ii) and (iii) contain LRO, and thus are not "canonical ferroic glass"; but they still exhibit glass features despite the existence of LRO. As will be shown later, these non-canonical ferroic glasses are responsible for a number of interesting properties not possessed by canonical ferroic glasses.

Table 1 lists the three subsets of ferroic glasses in ferroelastic/martensitic, ferroelectric, and ferromagnetic systems, respectively. Besides these subsets, there could also exist multi-ferroic glasses which possess two or more kinds of ferroic order with at least one

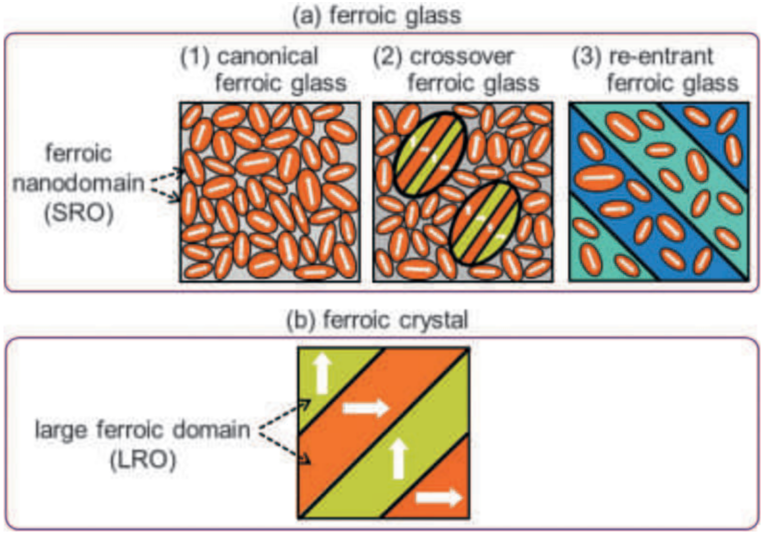
(a) ferroic glass
(1) canonical ferroic glass
(2) crossover ferroic glass
(3) re-entrant ferroic glass
ferroic nanodomain (SRO)
(b) ferroic crystal
large ferroic domain (LRO)

Fig. 1 Microstructural feature of (*a*) ferroic glasses (with frozen ferroic SRO) and (*b*) ferroic crystal (LRO only). Three types of ferroic glasses are shown in (*a*) according to the relation between SRO and LRO: (1) canonical ferroic glass (SRO only), (2) crossover ferroic glass (a mixture of SRO and LRO), and (3) re-entrant ferroic glass (SRO embedded in LRO of a different ferroic order). Nanodomains with an arrow represent a different ferroic order as those without the arrow. LRO domains of different color represent differnt domain states.

Table 1 Subsets of ferroic glasses in ferroelastic, ferroelectric, and ferromagnetic materials based on microstructural features.

	Ferroelastic order (strain)	*Ferroelectric order (polarization)*	*Ferromagnetic order (magnetic moment)*
Canonical ferroic glass	Strain glass	Relaxor	Cluster spin glass
Crossover ferroic glass	Crossover strain glass	Crossover relaxor	Crossover cluster spin glass
Re-entrant ferroic glass	Re-entrant strain glass	Re-entrant relaxor	Re-entrant cluster spin glass

ferroic order being frozen short-range. For example, ferromagnetic strain glass (to be discussed in Section "Ferromagnetic strain glass: A multi-ferroic glass showing large magnetostriction at a small magnetic field") belongs to this category, as it possesses long-range magnetic order while demonstrating nano-sized strain domains. As will be seen in Section "Novel properties and potential applications of ferroic glasses," these different types of ferroic glasses can provide a wide range of novel properties of technological importance.

Being similar with the case of an amorphous glass, ferroic glasses are non-equilibrium states because a disordered or high-entropy glass state is not favored at low temperature according to the 3rd law of thermodynamics, which stipulates that the stable state of any substance should be one possessing zero entropy at 0 K. This universal thermodynamic requirement is the origin of almost all phase transitions, such as the familiar gas-liquid-crystal transition. For ferroic systems the thermodynamically favored state at low temperature is the ferroic crystal because it has long-range order and thus lower entropy. Then an interesting question arises why and how a ferroic glass can form despite its thermodynamic disadvantage as compared with the corresponding ferroic crystal counterpart. The answer to this question will be given in Section "Origin of ferroic glasses and theoretical models."

History of ferroic glasses

Historically, glass phenomena in three kinds of ferroic systems were discovered independently in three different communities at different period of time (Fig. 2). Relaxor and spin glass have been known from 1960 to 70s in ferroelectric and magnetic communities, respectively; but their counterpart glass in ferroelastic/martensitic materials had remained missing for nearly half a century. With the discovery of the strain glass by Sarkar et al. (2005) in a ferroelastic/martensitic system Ti-Ni, perfect physical parallelism was revealed among three types of ferroic glasses and the concept "ferroic glass" was suggested by Wang et al. (2007). This terminology was coined recently with the publication of several review papers and Springer books (Ren, 2014; Ji et al., 2017; Lookman and Ren, 2018), together with the increasing research activities in international research communities (Monroe et al., 2015; Sun et al., 2020; Xu et al., 2021; Kong et al., 2022; Huang et al., 2020).

In ferroelectric community, it has been found since 1960s that the sharp and frequency-independent permittivity peak at a normal ferroelectric transition is often changed into a broad and frequency-dependent peak by heavy doping. As this phenomenon is similar with the dielectric relaxation phenomenon and it was named "relaxor" (Smolenskii and Agranovskaya, 1960). Although it was realized later that the "relaxor" is not caused by a dielectric relaxation but by a glass transition of ferroelectric order (Bokov and Ye, 2006), it was too late to change this familiar terminology and thus we shall still use it in the present article. In fact, it would be more appropriate to use "polarization glass" instead of "relaxor," as the former reflects its glass nature and matches the corresponding terminology in other two types of ferroic glasses: strain glass and cluster spin glass.

In magnetic community, it has long been known the existence of a "dirty magnetism," i.e., many magnetic systems do not show a normal Curie-Weiss peak at their magnetic transition; Instead, they show a frequency-dependent susceptibility cusp, and ferromagnetism is absent even down to 0 K. This phenomenon was named "spin glass" transition in early 1970s (Cannella and Mydosh, 1972). In the spin glass literature, spin glass is conceptually subdivided into two subsets: a "dilute spin glass" with nearly isolated and disordered spins being frozen, and a "cluster spin glass" with frozen nano-sized ferromagnetic domains or clusters (Mydosh, 1993), although a clear-cut difference in the experimental signatures does not seem to exist. In the present article, we shall confine our discussion to cluster spin glass when mentioning spin glass, as it is physically parallel to strain glass and relaxor, both being cluster glasses. For a detailed discussion of spin glass and the related experiments, readers may refer to the article by Vincent (2022) in this edition of Encyclopedia.

In ferroelastic/martensitic community, although the long-range ordered form of strain order, known as martensite or ferroelastic, has been known for more than one century and some of these materials like martensitic steels and shape memory alloys have found wide applications, the glass form of strain order, i.e., strain glass, has not been discovered until 2005 (Sarkar et al., 2005). It was

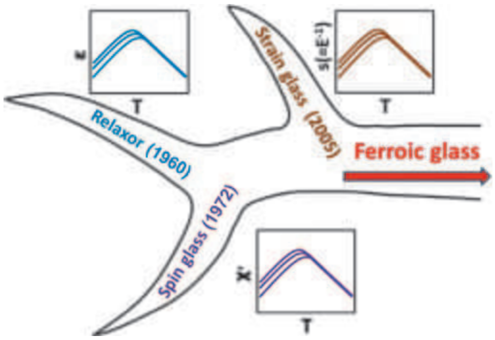

Fig. 2 Historical development of relaxor, spin glass, strain glass, and the advent of the concept "ferroic glass" (Ren, 2014). The three insets show a universal feature of ferroic glass transition, the frequency-dependence of susceptibility peak *vs.* temperature, where T is temperature, ε, χ', s are dielectric, magnetic, and mechanical susceptibility, respectively, and E is elastic modulus.

found that strain glass is characterized by a frequency-dependency peak in the elastic susceptibility (the inverse of elastic modulus), which very much resembles that of a relaxor and a cluster spin glass, as shown in the insets of Fig. 2.

It should be noted that before the experimental discovery of strain glass transition in 2005 (Sarkar et al., 2005), there had existed some theoretical effort to use "spin-glass-like models" to understand "premartensitic tweed" phenomenon that occurs prior to the onset of a martensitic transition (Kartha et al., 1991; Semenovskaya and Khachaturyan, 1997). These models predicted a glassy transition in the premartensitic state but they did not gain experimental confirmation (Ren et al., 2010). Now it becomes clear that the premartensitic state is not yet a frozen strain glass state.

The discovery of strain glass completed the physical parallelism among three types of glasses in three ferroic systems. Therefore, a generalized concept "ferroic glass" was suggested (Wang et al., 2007), which means a frozen state of certain ferroic order (Ren, 2014; Ji et al., 2017; Lookman and Ren, 2018). This concept enables a unified understanding of glass phenomena in three types of ferroic systems (see Section "Origin of ferroic glasses and theoretical models").

Generic phase diagram of a ferroic glass system: Link between ferroic LRO and ferroic frozen SRO

Fig. 3a show the generic phase diagram of a ferroic glass (Ren et al., 2010), which captures the common features of phase diagrams in strain glass (Sarkar et al., 2005), relaxor (Sun et al., 2013) and cluster spin glass systems (Wang et al., 2015) (Fig. 3b–d). Such phase diagrams are essential to understand ferroic glasses as they reveal the relationship among all possible ferroic states in a ferroic system. These states include para-phase ("ferroic liquid"), ferroic crystal (long-range ferroic order), unfrozen ferroic glass (a sticky to less-sticky ferroic liquid, or precursory tweed), and ferroic glass (frozen short-range ferroic order) as shown in Fig. 3a. A crossover from ferroic transition (at T_C) to ferroic glass transition (at T_g) occurs when defect (dopant) concentration x exceeds a critical value x_c. Note that in the crossover region, the ferroic glass can transform into the ferroic crystal upon cooling or by applying an external field, and such a transition is called spontaneous or field-induced transition from ferroic glass to ferroic crystal. It is physically analogous to the crystallization transition of an amorphous glass. This crossover region corresponds to the ferroic glass subset "crossover ferroic glass" shown in Fig. 1(a2).

The striking similarity in phase diagram among the three different types of ferroic glasses suggests a common physical nature for all ferroic glasses. The phase diagrams also suggest that a ferroic glass state is derived from a ferroic crystal state by introducing sufficient defects (dopants). This important feature of ferroic glass imposes an important constraint to possible ferroic glass theories: a correct theory must explain the crossover from a ferroic crystal state to a ferroic glass state by defects.

Origin of ferroic glasses and theoretical models

The 3nd law of thermodynamics stipulates that all substances should take an ordered form at 0 K so as to ensure zero entropy. This thermodynamic requirement is the origin of almost all phase transitions including gas-liquid-crystal transition, and ferroic transitions from a para (ferroic liquid) state into a long-range ordered ferrroic crystal state (i.e., ferroelastic/martensite, ferroelectric, and ferromagnetic state), because these transitions result in long-range ordering of ferroic order and consequently reduce entropy.

However, a ferroic glass seems at variance with the above general picture, since its frozen ferroic disordered state is a high entropy state that can persist down to 0 K; thus it is against the thermodynamic requirement of zero entropy at 0 K. Therefore, the formation of a ferroic glass, i.e., ferroic glass transition, is not a conventional thermodynamic transition and its origin needs explanation.

A cartoon illustrated in Fig. 4a and b schematically shows the origin of a normal ferroic transition (i.e., LRO) and that of a ferroic glass by using a domino array without and with "stone disturbance." It can be seen easily that a pure ferroic system (without "stones") will undergo a normal ferroic transition with long-range ferroic ordering, as required by thermodynamics. However, when a ferroic system is doped with many defects (many "stones"), it becomes impossible to form a long-range ordered ferroic phase due to the disturbance of the randomly distributed defects; instead, the system is frozen into a disordered state with short-range ferroic order only. Therefore, ferroic glass and ferroic glass transition originate from random defects that produce "random field" and thus

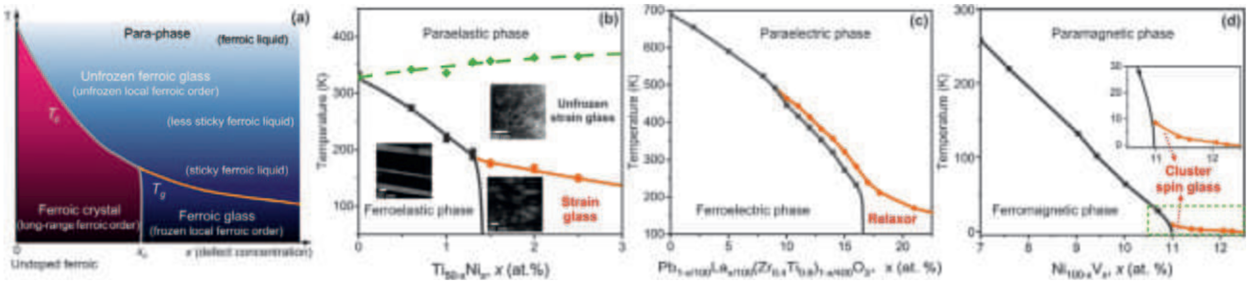

Fig. 3 (a) Generic phase diagram of a ferroic glass with all possible ferroic states shown (generalized from Ren et al., 2010). (b) Experimental phase diagram of a strain glass system $Ti_{50-x}Ni_{50+x}$, the insets being microstructural features of different strain states (Sarkar et al., 2005). (c) Experimental phase diagram of a relaxor system $Pb_{1-x/100}La_{x/100}(Zr_{0.4}Ti_{0.6})_{1-x/400}O_3$ (Sun et al., 2013). (d) Experimental phase diagram of a cluster spin glass system $Ni_{1-x}V_x$ (Wang et al., 2015).

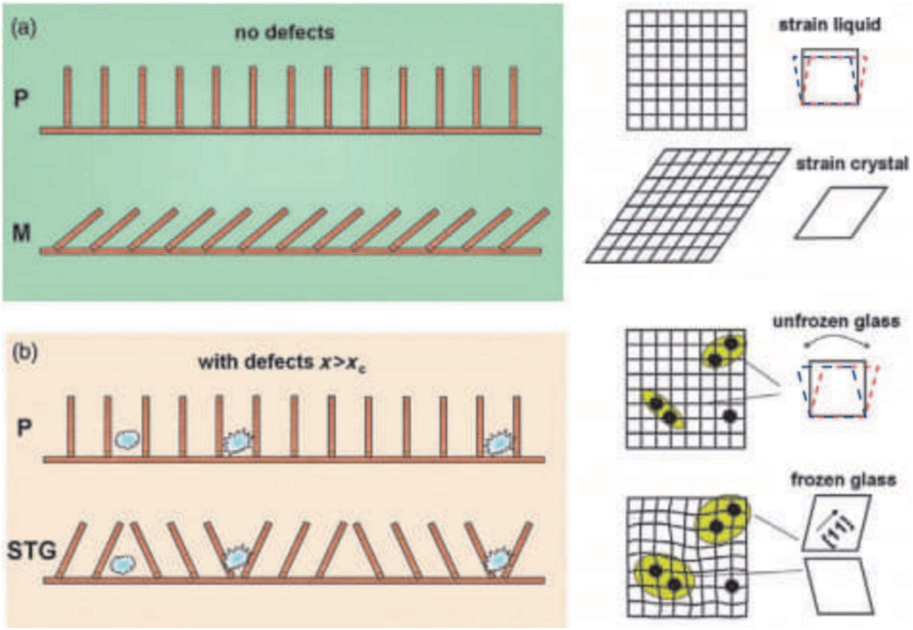

Fig. 4 A cartoon showing the origin of (a) ferroic crystal and (b) ferroic glass and its relation to random defects (represented by "stone") (Ren, 2014). Here a strain system is taken as an example but the generic picture applies to magnetic and polar systems. P denotes the parent phase or strain liquid state; M represents the martensitic phase or strain crystal; the "stones" in (b) represent defects or dopants, and STG represents strain glass state or frozen local strain state.

prohibit the formation of long-range ferroic ordering, or a ferroic crystal. Instead, a ferroic glass (a frozen short-range ordered ferroic state) is formed, and such a metastable state can persist down to 0 K.

Rigorous phase field models reflecting the above physical picture have been developed for strain glass (Wang et al., 2010) and for relaxor (Wang et al., 2012; Hong et al., 2022), and a similar phase field theory is expected for cluster spin glass but is lacking so far. The kernel of these phase-field models is a Landau-Ginzburg free energy that favors a normal ferroic crystal transition, and random field caused by defects that tend to destroy the long-range ferroic order. The competition between the two effects creates a crossover from a normal ferroic transition into ferroic glass transition when defect concentration is beyond a critical value. Therefore, these models provide a reasonable explanation for the most important fact about ferroic glasses: the existence of a crossover from ferroic crystal to ferroic glass by defect doping, as shown in Fig. 3.

Examples of the calculated phase diagrams of a strain glass and a relaxor, together with the evolution of ferroic microstructure with defect doping level and temperature, are shown in Fig. 5a–d, respectively (Wang et al., 2010, 2012). The calculated phase diagrams (Fig. 5c and d) and microstructure features (Fig. 5a and b) are in qualitative agreement with the experimental phase diagrams and microstructures shown in Fig. 3. The theories also reproduce all other signatures of ferroic glasses as shown in the next section.

It is noted that alternative theories about ferroic glasses have been proposed (Lloveras et al., 2008, 2009; Sherrington, 2008, 2014; Vasseur and Lookman, 2010), and interested readers can refer to these references for details.

Signatures of a ferroic glass or a ferroic glass transition

As ferroic glass is formed through a ferroic glass transition, the signatures of a ferroic glass are also those of a ferroic glass transition. The key experimental signatures of a ferroic glass transition or a ferroic glass are given below (Ren, 2014, 2012; Ji et al., 2017; Lookman and Ren, 2018).

(i) Absence of a ferroic crystal transformation (Fig. 6)

As a ferroic glass is formed via a freezing transition from a ferroic liquid (para-state) into a frozen disordered state (ferroic glass state), it involves no change in long-range ferroic order or average structure. Therefore, a ferrroic glass appears like a non-transforming material and shows no ferroic transition signature when average ferroic order is monitored. Fig. 6 shows an example of a strain glass alloy (Wang et al., 2006), which exhibits an invariance of average structure (=XRD peaks) with temperature, and no thermal hysteresis in resistivity curves. A strain glass also exhibits no latent heat peak in differential scanning calorimetry (DSC) curves (Sarkar et al., 2005), which contrasts the case for a normal ferroelastic transition.

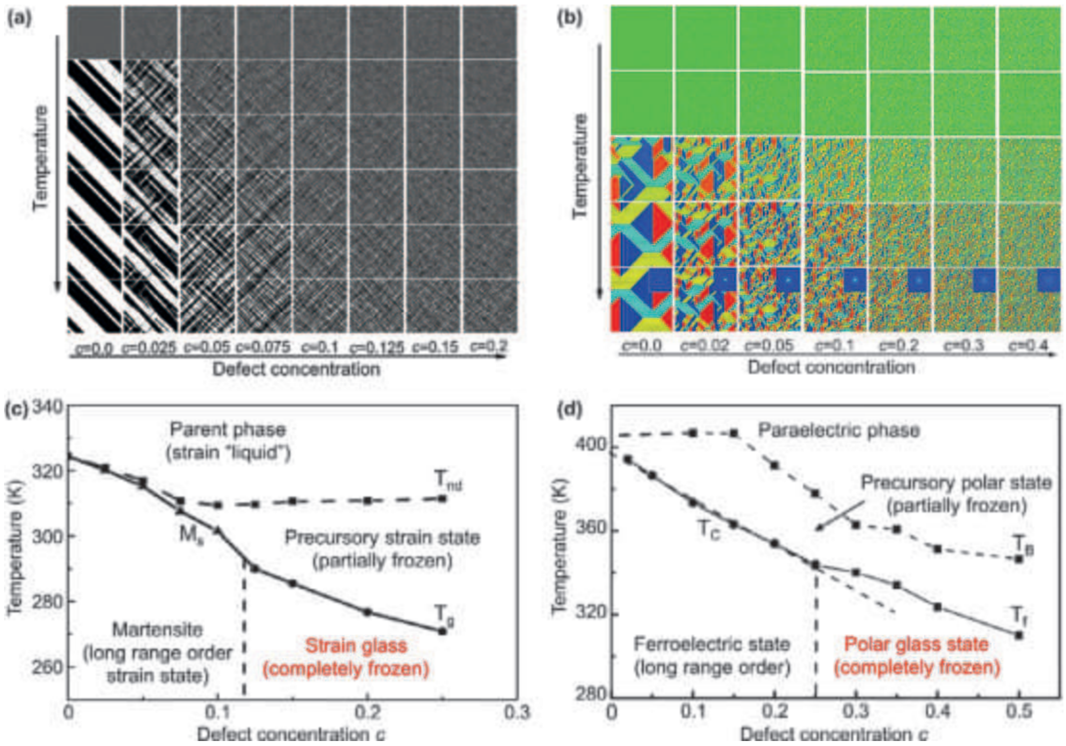

Fig. 5 Phase field simulation results for strain glass (a, c) (Wang et al., 2010), and relaxor (b, d) (Wang et al., 2012): calculated ferroic glass phase diagram and evolution of domain pattern as a function of defect concentration and temperature.

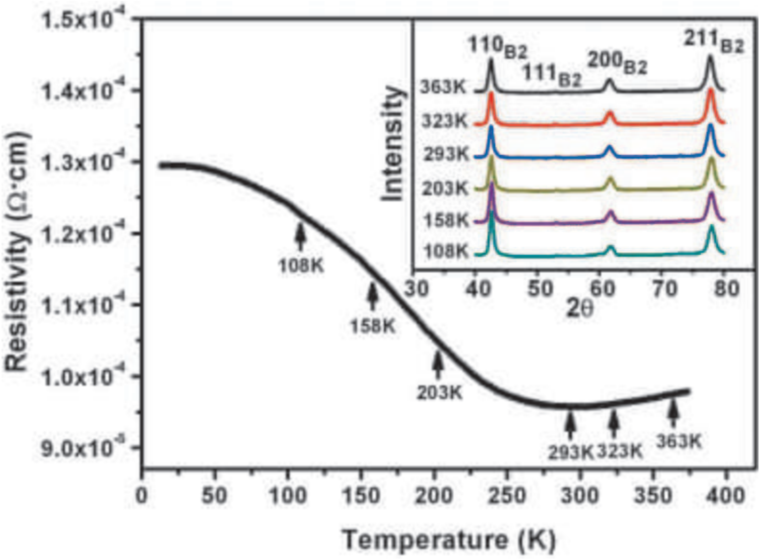

Fig. 6 Invariance of average structure in a strain glass $Ti_{48.5}Ni_{51.5}$ alloy (Wang et al., 2006), which has a strain glass transition at $T_g \sim 168$ K. The XRD pattern in the inset shows an average B2 structure over the entire temperature range of strain glass transition. The resistivity curves during cooling and heating show no thermal hysteresis.

(ii) Freezing signature as manifested by dynamic measurement (Fig. 7)

The existence of a ferroic glass transition can be easily seen by measuring its "ferroic stickiness," i.e., the appearance of a Vogel-Fulcher-type frequency-dependent anomaly in its dynamic ferroic property, which is dynamic mechanical susceptibility/modulus, dielectric permittivity, and magnetic susceptibility for strain glass, relaxor, and cluster spin glass, respectively (Ren, 2014).

Fig. 7a shows that a strain glass transition is characterized by a frequency-dependent peak/dip in the dynamic elastic modulus/loss around its freezing temperature T_g. T_g follows the Vogel-Fulcher relation $\omega = \omega_0 \exp[-E_a/k_B(T_g-T_0)]$, which is a signature of any glass, where T_g is the dip/peak temperature at frequency ω and T_0 the "ideal" freezing temperature (T_g at 0 Hz), E_a is the activation

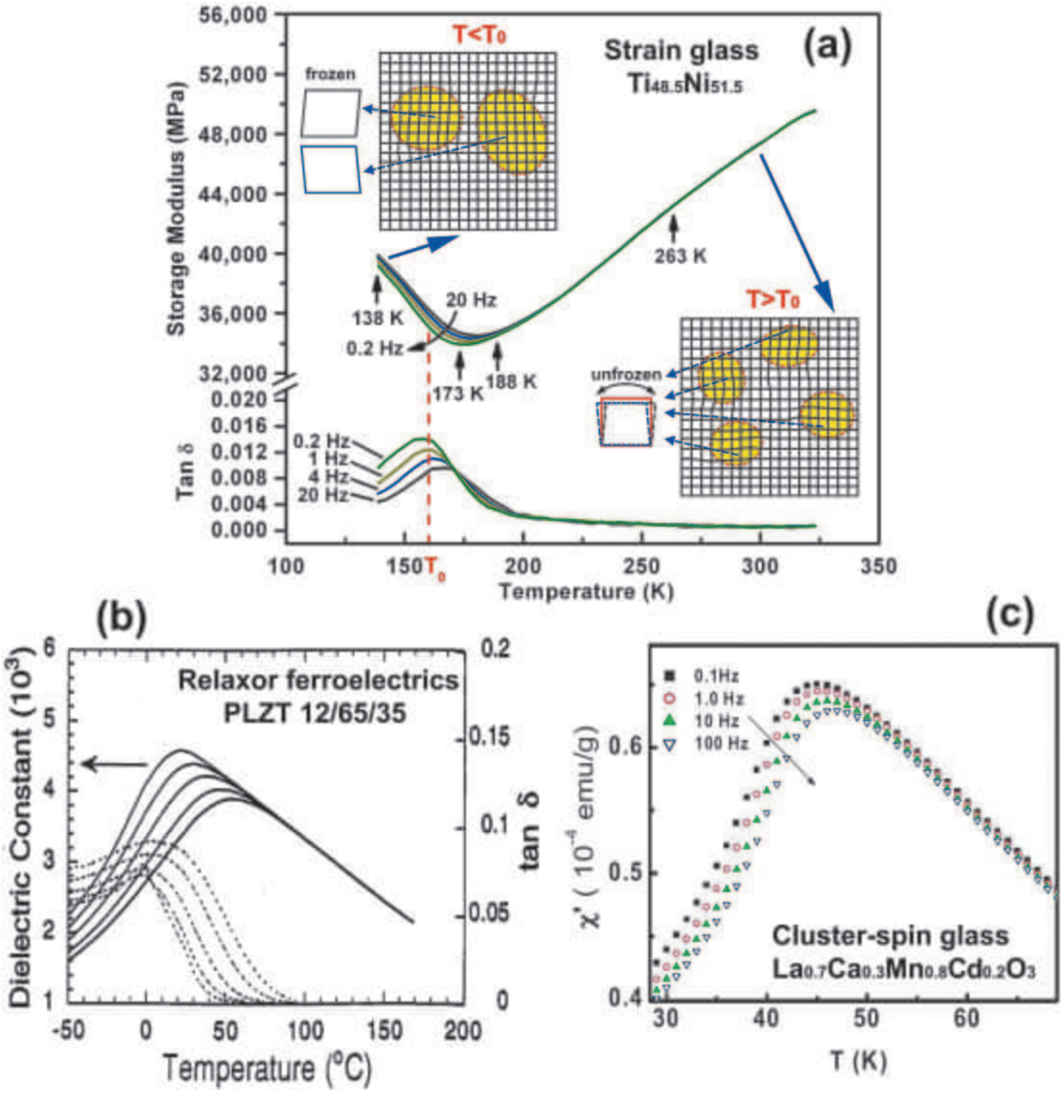

Fig. 7 Frequency-dependent anomaly associated with (a) a strain glass transition revealed by dynamic mechanical analysis (DMA) (Sarkar et al., 2005), the inset showing schematically the microscopic picture of the strain freezing process, (b) a relaxor transition revealed by dielectric permittivity measurement (Tan et al., 2000), and (c) a cluster-spin glass ($La_{0.7}Ca_{0.3}Mn_{0.8}Co_{0.2}O_3$) revealed by magnetic susceptibility measurement (Karmakar et al., 2006).

energy and k_B is the Boltzmann constant. Fig. 7b and 7c show very similar frequency dependent anomaly at T_g exists in other two types of ferroic glasses, relaxor (Tan et al., 2000) and cluster spin glass (Karmakar et al., 2006), respectively.

(iii) Broken ergodicity as signified by branching zero-field-cool/field-cool (ZFC/FC) curves (Fig. 8)

An important signature of a ferroic glass transition is ergodicity-breaking, or history dependence of sample state when entering a glass state. This is usually done with a ZFC/FC experiment, which generates two different histories to the sample. Fig. 8a shows the mechanical ZFC/FC curves of a strain glass $Ti_{48.5}Ni_{51.5}$ alloy (Wang et al., 2007). The branching ZFC and FC curves below T_g suggests a broken ergodicity in the strain glass state. Relaxor (Viehland et al., 1992) and cluster spin glass transition (Gayathri et al., 1997) also demonstrate strikingly similar ZFC/FC curves (Fig. 8b and c, respectively), although the driving field (electric and magnetic field here) is different.

(iv) Existence of nano-sized ferroic domains revealing the SRO ferroic ordering nature (Fig. 9)

Although a ferroic glass possesses no LRO (i.e., absence of large ferroic domains), it can show short-range ferroic order down to 0 K. The short-range ferroic order manifests itself as nano-sized ferroic domains, as exemplified in a strain glass (Fig. 9) revealed by *in-situ* high-resolution transmission electron microscopy (HRTEM) observation (Zhou et al., 2014). Similar nanodomains have also been reported in relaxors (Wang et al., 2021), confirming the common SRO nature of this type of ferroic glass. Unfortunately, direct microscopic imaging of magnetic nanodomains in cluster spin glass are scarce, due to the difficulty in high-resolution imaging of nano-sized magnetic domains. Effort towards this direction is much desired.

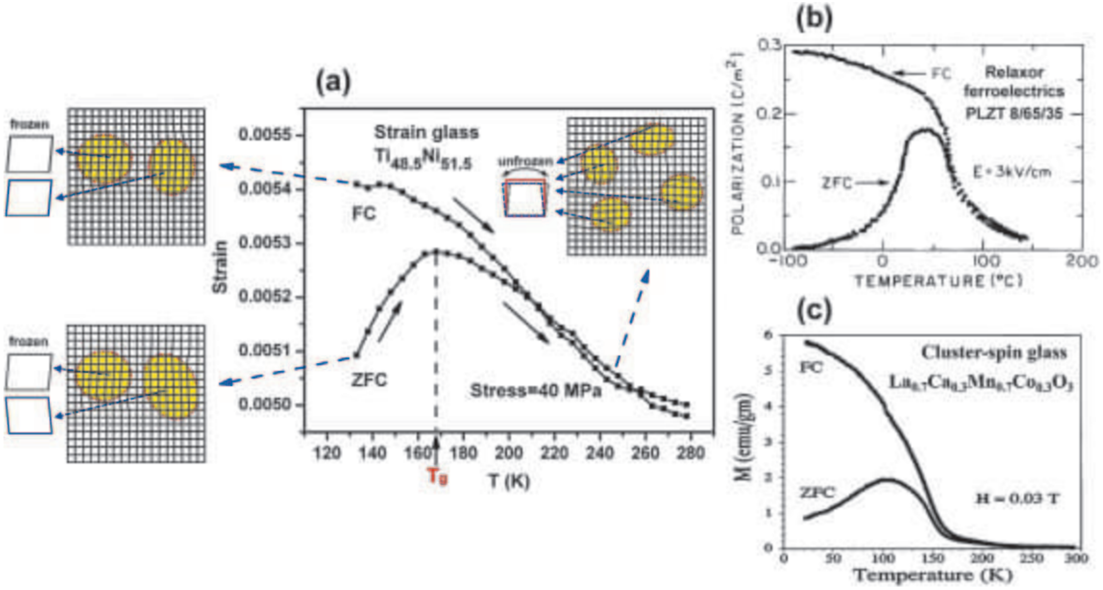

Fig. 8 ZFC/FC curves of (a) $Ti_{48.5}Ni_{51.5}$ strain glass (Wang et al., 2007), with insets showing different strain state depending on different thermal histories, (b) a ferroelectric relaxor (PLZT 8/65/35) (Viehland et al., 1992), and (c) a cluster-spin glass $La_{0.7}Ca_{0.3}Mn_{0.7}Co_{0.3}O_3$) (Gayathri et al., 1997) .

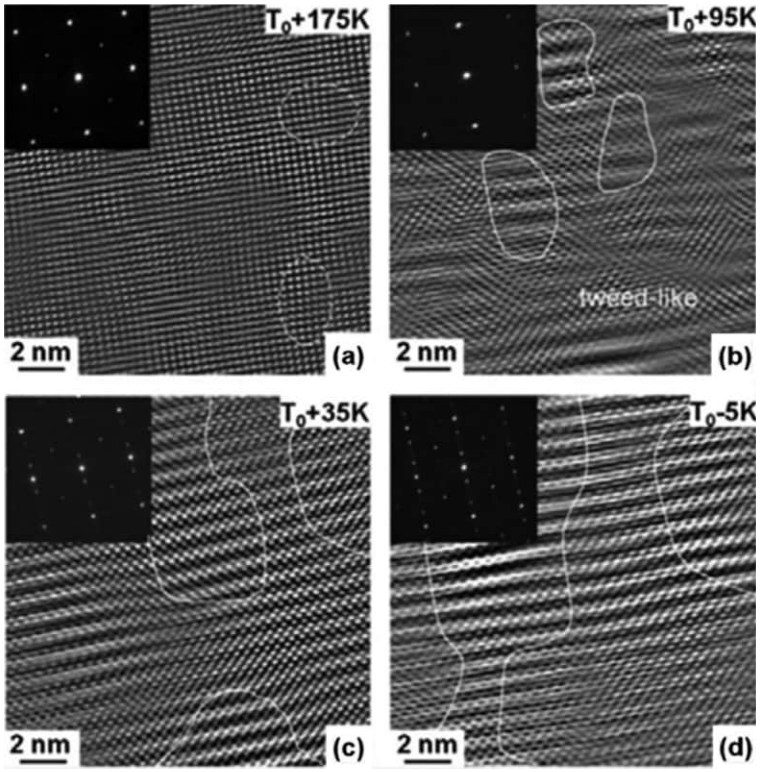

Fig. 9 High-resolution TEM observation of nano-sized strain domains in a $Ti_{50}Pd_{41}Cr_9$ strain glass and their evolution with temperature (Zhou et al., 2014). Insets show the corresponding diffraction patterns. T_0 is the ideal strain glass transition temperature.

Novel properties and potential applications of ferroic glasses

Just like amorphous glasses possess many properties unattainable in crystalline materials, ferroic glasses also demonstrate interesting novel properties not achievable in ferroic crystals. Below we give a few examples of recent findings about novel properties of ferroic glasses.

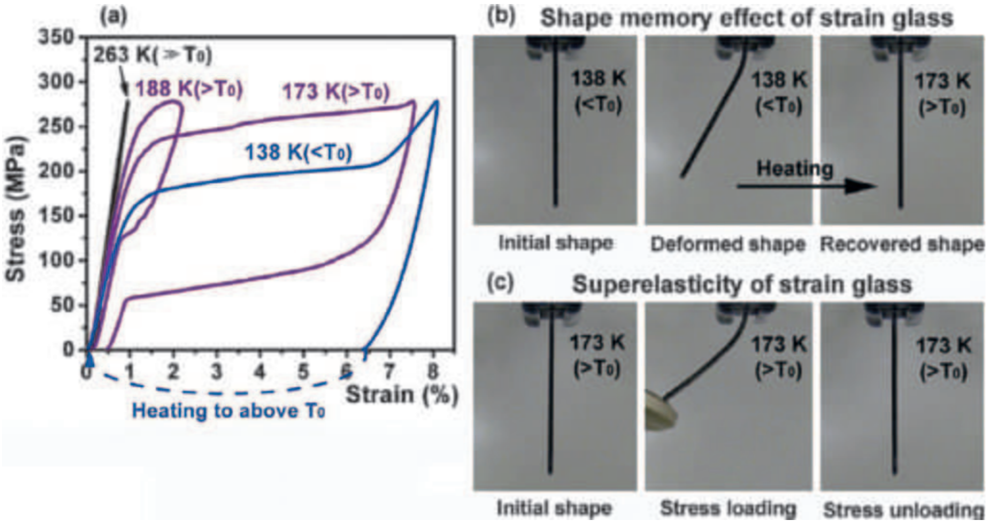

Fig. 10 (a) Shape-memory effect (deformed below T_g) and superelasticity (deformed above T_g) of a $Ti_{48.5}Ni_{51.5}$ strain glass alloy. (b, c) Visual evidence for shape-memory effect and superelasticity, respectively. (Wang et al., 2006).

Strain glasses

(i) Shape memory effect and superelasticity in strain glass alloys.

It is a striking surprise when a strain glass is found to exhibit shape memory effect and superelasticity (Fig. 10) (Wang et al., 2006), because such properties are usually associated with an alloy undergoing a spontaneous martensitic transformation but a strain glass does not undergo such martensitic transformation. These unexpected properties arise from a stress-induced strain glass to martensite transformation and its reverse transition. Shape memory effect occurs when a strain glass is deformed below its glass transition T_g (to form martensite) and subsequently warmed up to above T_g (to transform the martensite into unfrozen strain glass). Superelasticity is found when a strain glass is deformed above its glass transition T_g because the stress-induced martensite is thermodynamically unstable and thus recovers the original unfrozen strain glass state upon unloading. The existence of shape memory effect and superelasticity in non-martensitic alloys (i.e., strain glasses) is expected to open a new avenue for the applications of strain glass as a novel class of smart materials.

(ii) Linear Invar effect and Elinvar effect in Ti-based and Mg-based strain glass alloys.

Invar effect refers to dimension invariance with temperature, i.e., zero thermal expansion, and Elinvar effect refers to elastic modulus invariance with temperature. These two effects exist in few alloys and have found important applications in precision instruments but the origin has remained unclear. Over the past decade, these unusual properties were reported in a non-transforming "Gum metal," a heavily doped Ti-alloy, after severe cold-rolling (Saito et al., 2003). It is interesting to note that the Invar effect in Gum metal exists only along the rolling direction of the sample and thus it can be called "linear Invar effect." The origin of these interesting properties in the Gum metal had also remained unclear.

Wang et al. (2014) found that the Gum metal is actually a strain glass alloy, and as a consequence the linear Invar effect and Elinvar effect can be explained. The linear Invar effect occurs as a result of length compensation by oriented strain glass nanodomains which offset the ever-present thermal expansion. Elinvar effect occurs as a result of modulus compensation by the appearance of elastically harder strain glass nanodomains which offset the softening matrix.

Very recently Liu et al. (2022) reported that a lightweight Mg-Sc strain glass alloy exhibits Elinvar effect (Fig. 11), and it is the lightest Elinvar alloy reported so far. They showed that this behavior originates from its strain glass nature and the alloy may found applications in space technologies where stable elasticity is required.

(iii) Quasi-linear superelasticity associated with dislocation-induced strain glass.

Differing from the usual case that strain glass is formed by point defect doping, it has been shown by Liang et al. (2017, 2022) that strain glass can also be formed by introducing high density of dislocations into a martensitic alloy. They found that the dislocation-induced strain glass exhibits a "quasi-linear" superelasticity which is stable over a superwide temperature range (Fig. 12). This overcomes the key drawback of conventional superelasticity of shape memory alloys where superelasticity is highly temperature sensitive and vanishes below martensitic transformation temperature. Although the quasi-linear superelastic strain (~4%) is not as large as the conventional non-linear superelasticity in Ti-Ni alloys (~8%), its temperature stability, high strength, relatively low modulus make the dislocation-induced strain glass a promising elastic material.

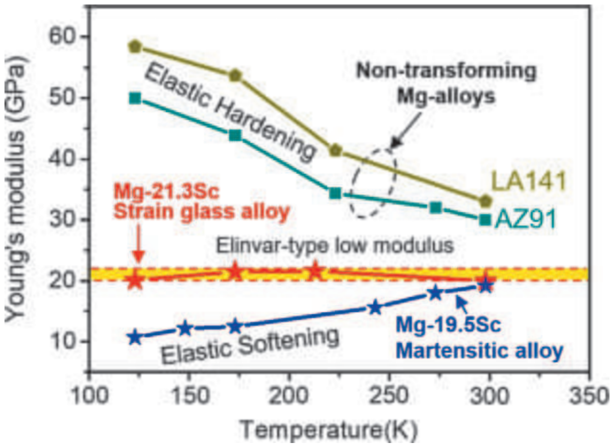

Fig. 11 Elinvar-type low modulus in a lightweight Mg-Sc strain glass alloy (Liu et al., 2022). It is noted that neither non-transforming Mg-alloys nor martensitic Mg-alloys show the Elinvar behavior.

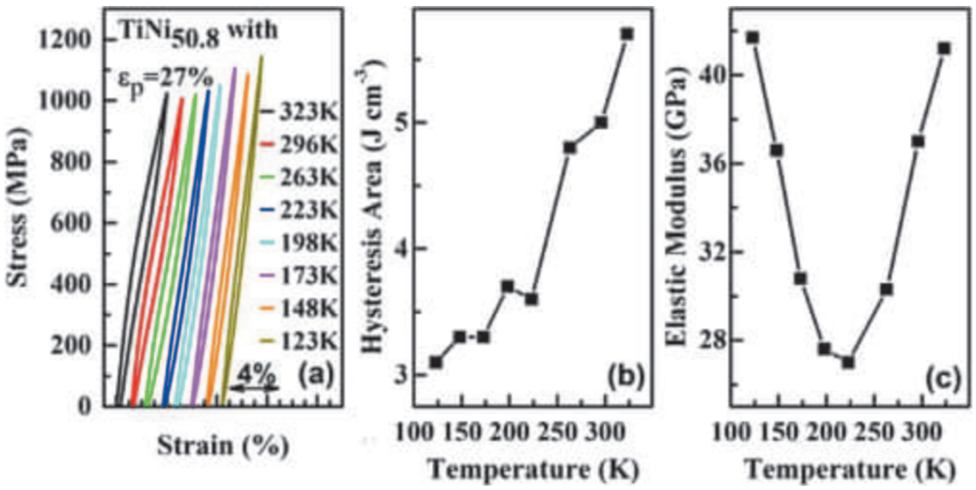

Fig. 12 (a) Temperature insensitive quasi-linear superelasticity in a dislocation-induced $Ti_{49.2}Ni_{50.8}$ strain glass alloy. The alloy experienced cold-rolling by 27% thickness reduction before testing. (b) Stress hysteresis as a function of temperature. (c) Variation of elastic modulus with temperature. (Liang et al., 2017).

In addition to dislocation-induced strain glass mentioned above, Ji et al. (2013) showed that high-density 3D defects of nano-precipitates can also change a martensitic alloy into a strain glass one. Jiang et al. (2021) further showed that high-density grain boundaries in a nanocrystalline TiNiPt alloy can also induce a strain glass transition, and the grain-boundary-induced strain glass exhibits significant superelasticity of 6%. Therefore, it seems that sufficient defects of 0D (point defects), 1D (dislocations), 2D (grain boundaries), and 3D (nano-precipitates) can destroy the long-range order of an otherwise martensitic material, and change it into a strain glass, which is characterized by frozen SRO strain.

Relaxors: achieving high permittivity over a wide temperature range by coexisting relaxor nanodomains

A desired property of ferroelectric materials is achieving high permittivity over a wide temperature range. However, this is impossible for normal ferroelectric materials and normal relaxors. This is because the former has a very high permittivity at T_C but it sharply decreases when temperature deviates from T_C; on the other hand, relaxor has a broad permittivity peak and thus less temperature sensitive but its permittivity value is much lower than a ferroelectric permittivity peak value.

By adjusting relaxor compositions Yang et al. (2019) were able to design a special relaxor composed of two kinds of different ferroic nanodomains (with rhombohedral and tetragonal local symmetry, respectively), and this special relaxor state in the phase diagram is termed "morphotropic relaxor boundary or MRB," as shown in Fig. 13. They found that the MRB relaxor can lead to a 1.5 time increase in permittivity and a 3-time increase in electrostrain. In addition, the enhancement effect can persist over a wide temperature range of over 100 K. Further studies on high-T_g MRB systems (Yang et al., 2021; Zhu et al., 2022; Pan et al., 2019; Chen et al., 2023; Xia et al., 2021) confirmed this important effect and showed that large enhancement effect can be achieved at room temperature, a result crucial for the use of this effect in room temperature devices.

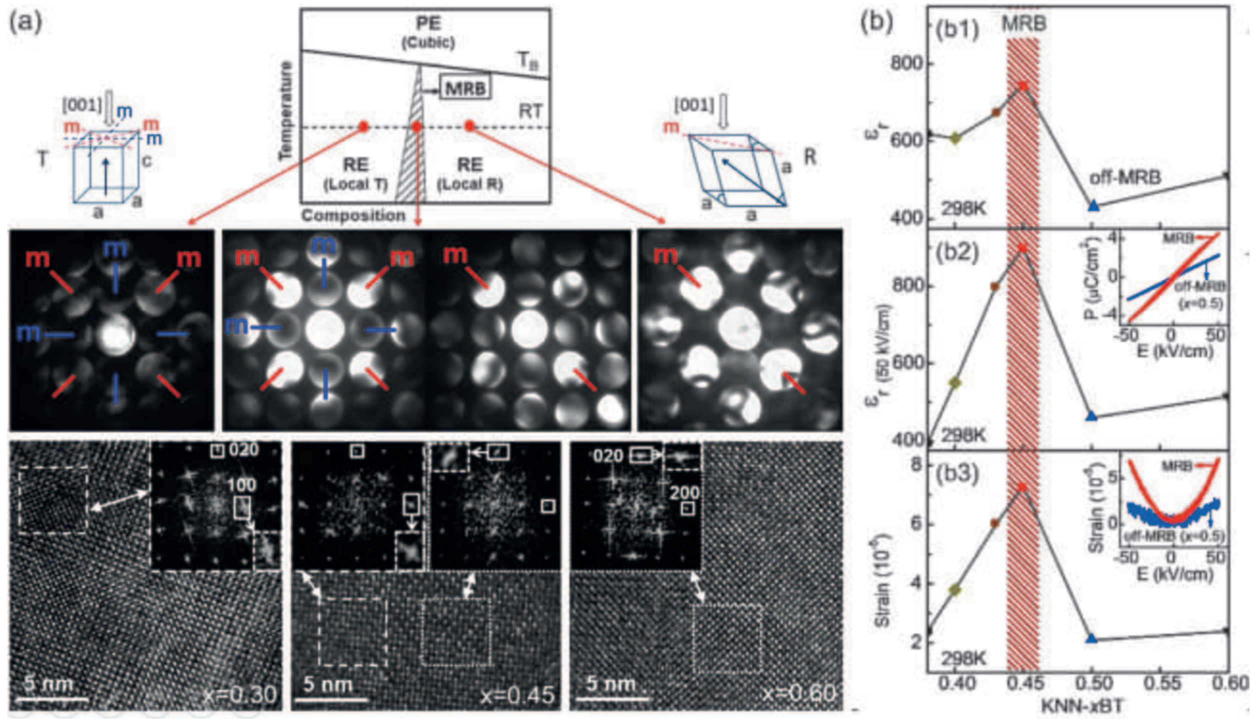

Fig. 13 (a) The existence of a morphotropic relaxor boundary (MRB) in the phase diagram of $(K_{0.5}Na_{0.5})NbO_3$-$BaTiO_3$ relaxor system (Yang et al., 2019). Local probes of convergent beam electron diffraction (CBED) and high-resolution electron microscopy (HREM) provide direct evidence for a composition-induced local symmetry boundary (i.e., MRB). (b) Property enhancement at the MRB composition in comparison with the off-MRB compositions. (b1) (b2) and (b3) are composition dependence of small-field dielectric permittivity (at 10^4 Hz), high-field dielectric permittivity, and electrostriction at room temperature (298 K). The high-field dielectric permittivity at 50 kV/cm is calculated through the slope of the P-E relation (inset).

Recently, Wang et al. (2021) succeeded in fabricating a "tri-relaxor," which is a mixture of three kinds of ferroic nanodomains (with rhombohedral, orthorhombic, tetragonal local symmetry, respectively) by engineering a tri-critical quadruple-point ferroelectric into a relaxor state through suitable doping (Fig. 14). They demonstrated that the tri-relaxor possesses an outstanding combination of high permittivity (~17,000) with a large temperature span (~34 K). Recently He et al. (2021) reported that a large electrostrain with nearly-vanished hysteresis in Bi-doped $Ba(Zr_{0.2}Ti_{0.8})O_3$-x$(Ba_{0.7}Ca_{0.3})TiO_3$ ceramics by establishing a "tri-relaxor." Therefore, both MRB relaxor and tri-relaxor can become important strategies in improving dielectric and electrostrain properties of relaxor materials.

Crossover relaxor: achieving high electrostrain and small hysteresis simultaneously

Fang et al. (2018) designed a unique crossover relaxor in a ferroelectric BT-5Bi-xSn system, as shown in Fig. 15. It is a crossover state between a relaxor and ferroelectric. As microstructually the crossover relaxor appears as a composite composed of relaxor and ferroelectric, it is called "re-entrant relaxor-ferroelectric composite (RRFC)." The RRFC is found to exhibit an excellent combination of low hysteresis and large electrostrain—usually such a technologically-desired property is difficult to achieve due to the trade-off relation between large strain and small hysteresis. The unique property of RRFC can be understood based on the ferroelectric and relaxor coexisting microstructure.

Dai *et al.* showed in several ferroelectric/relaxor systems (Dai et al., 2020a,b; Dai et al., 2021; Dai et al., 2022) that by engineering the materials into a ferroelectric/relaxor crossover state, an excellent combination of both high storage density of electric energy (i.e., high permittivity) and good energy storage efficiency (i.e., small hysteresis) is achieved. Such a property has been difficult to obtain for either ferroelectric materials (LRO materials) or relaxor materials (SRO materials), but is essential for electric energy storage by using dielectric materials. Therefore, a ferroelectric/relaxor mixture state may be an effective solution to this demand.

Re-entrant strain glass showing low modulus and high damping

Very recently Wang et al. (2022) discovered a re-entrant strain glass transition in a well-known shape memory alloy $Ti_{50}Ni_{34}Cu_{16}$. The re-entrant strain glass transition is characterized by the gradual formation and freezing of 4H strain glass domains in a B19 martensite matrix (Fig. 16). It differs from a conventional strain glass in that the strain glass nanodomains do not form from a disorder phase (parent phase) but from an ordered matrix (i.e., martensite). The re-entrant strain glass transition stems from Cu

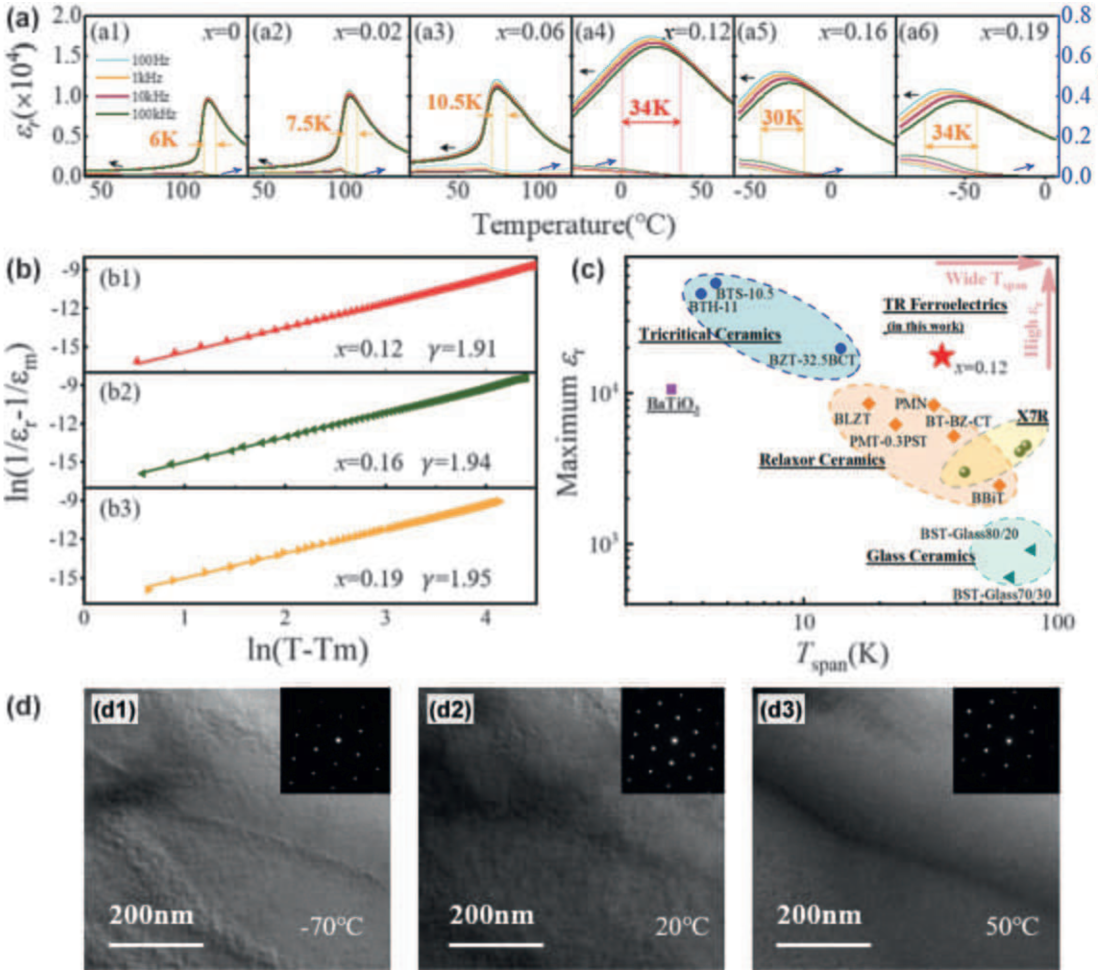

Fig. 14 (a) Large and temperature-insensitive dielectric permittivity of a tri-relaxor as compared with off-tri-relaxor compositions (Wang et al., 2021). (b) Modified Curie-Weiss fitting for $x = 0.12$, 0.16, and 0.19 compositions showing slope parameter $\gamma \rightarrow 2$, which suggests the characteristic of a relaxor. (c) Outstanding permittivity *vs.* temperature-span benchmark of tri-relaxor as compared with various ferroelectric and relaxor materials. (d1–d3) Temperature-insensitive nanodomain structure of the tri-relaxor.

dopants which stabilize the B19 phase but hinders the formation of long-range 4H martensite phase at low temperature through their random field. As a result, a short-range ordered 4H nanodomains are formed out of the B19 matrix without the formation of 4H martensite.

Interestingly, the re-entrant strain glass transition was found to lead to very low modulus (~24 GPa) and high damping (tan δ >0.075) over a wide temperature range (>100 K). This suggests that re-entrant strain glass alloy may be used as low-modulus high-damping alloy.

Very recently, Fang et al. (2023) reported that a re-entrant strain glass transition in a La-doped $CaTiO_3$ ceramic, which can toughen the brittle ceramic down to cryogenic temperatures, and thus may become a promising strategy to toughen brittle materials.

Ferromagnetic strain glass: A multi-ferroic glass showing large magnetostriction at a small magnetic field

As mentioned at the beginning of this article, a multi-ferroic glass is expected to exist in a system with more than one type of ferroic order. Ren et al. (2017) showed such a multi-ferroic glass does exist in a $Fe_{67.7}Pd_{32.3}$ alloy, which is ferromagnetic but undergoes a strain glass transition in the ferromagnetic state. Therefore, the alloy is a ferromagnetic strain glass, a subclass of multi-ferroic glass.

The $Fe_{67.7}Pd_{32.3}$ ferromagnetic strain glass overcomes the trade-off relation between large magnetostriction and small hysteresis, which is known for existing ferromagnetic materials (Fig. 17a). It shows a large magnetostriction of 800 ppm at a low critical field of 0.8 kOe (Ren et al., 2017). This desired highly sensitive magnetostriction effect originates from the ferromagnetic strain glass nanodomains being switchable at small magnetic field (Fig. 17b). This discovery suggests that ferromagnetic strain glass could be an effective approach to design extraordinary magnetostrictive materials.

Ferromagnetic strain glasses have also been reported in many other ferromagnetic martensite systems and interesting magnetostrictive properties are also demonstrated (Ma et al., 2015; Khan et al., 2020; Wang et al., 2018).

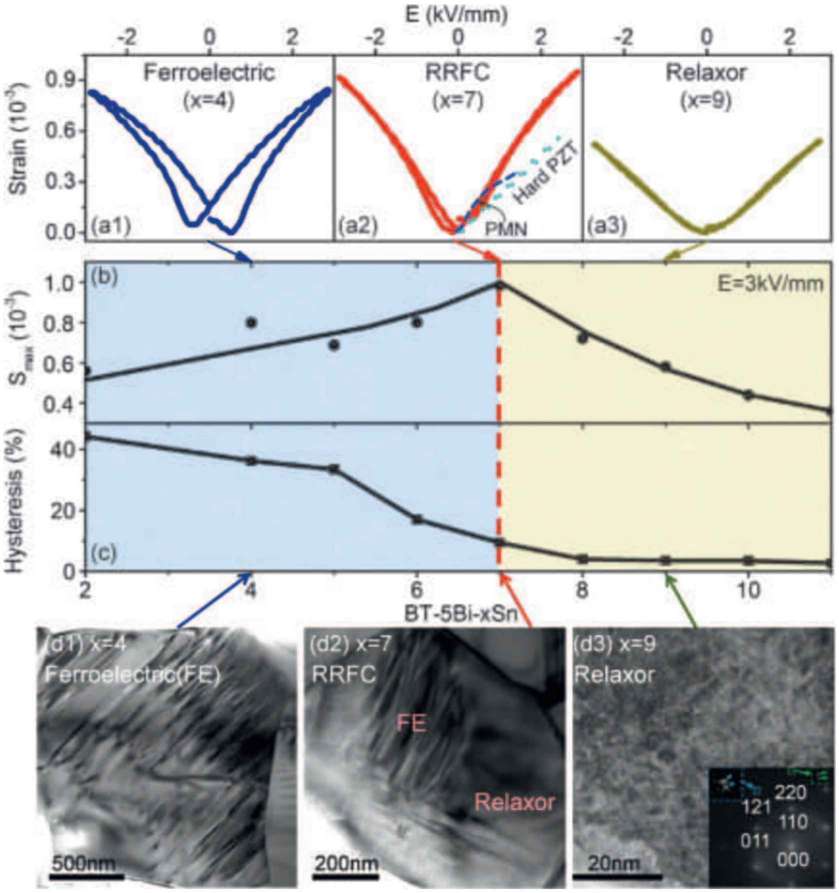

Fig. 15 Combination of low hysteresis and large strain of the *RRFC* at room temperature (Fang et al., 2018). (a) Electrostrain of ferroelectric (x = 4), *RRFC* (x = 7) and relaxor (x = 9), with hard PZT piezoelectric and electrostrictive PMN relaxor being a reference. (b,c) Composition dependence of maximus strain S_{max} and hysteresis under the electric field of 3 kV/mm. (d) TEM images show the corresponding microstructure of typical ferroelectric (x = 4), *RRFC* (x = 7), and relaxor (x = 9), respectively. The inset is a fast Fourier transform of the image which shows the spot splitting and suggests local ferroelectric order.

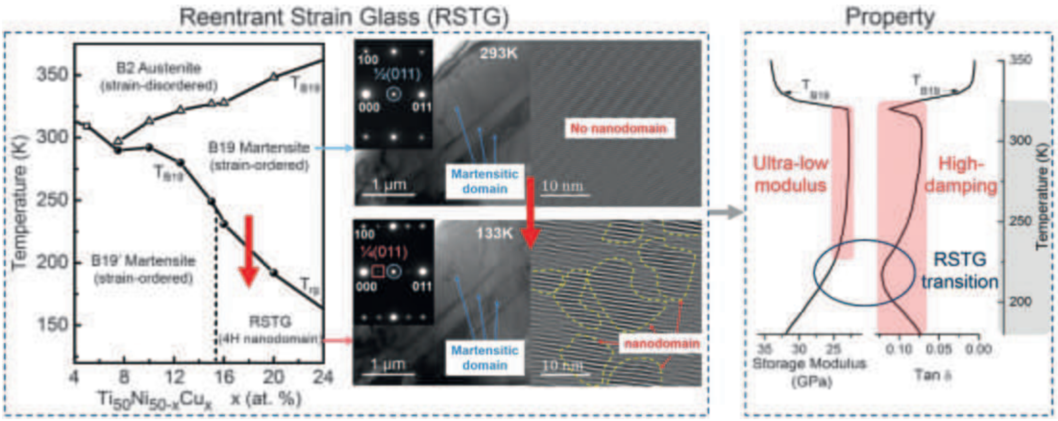

Fig. 16 (a) Phase diagram of a re-entrant strain glass (RSTG) alloy system (Wang et al., 2022). (b) Microstructure feature of a re-entrant strain glass above and below its glass transition temperature. (c) Ultralow elastic modulus and high damping over a wide temperature range associated with a re-entrant strain glass transition.

Isothermal "crystallization" of strain glass as the origin of isothermal martensitic transformation

A long-standing puzzle in martensite community since 1930s is the origin of isothermal martensitic transformation—a gradual formation of martensite over a time scale as long as hours and days. For a diffusional transition like water freezing, the time-dependence of the transition is natural because atomic diffusion takes time and it is impossible to complete instantaneously.

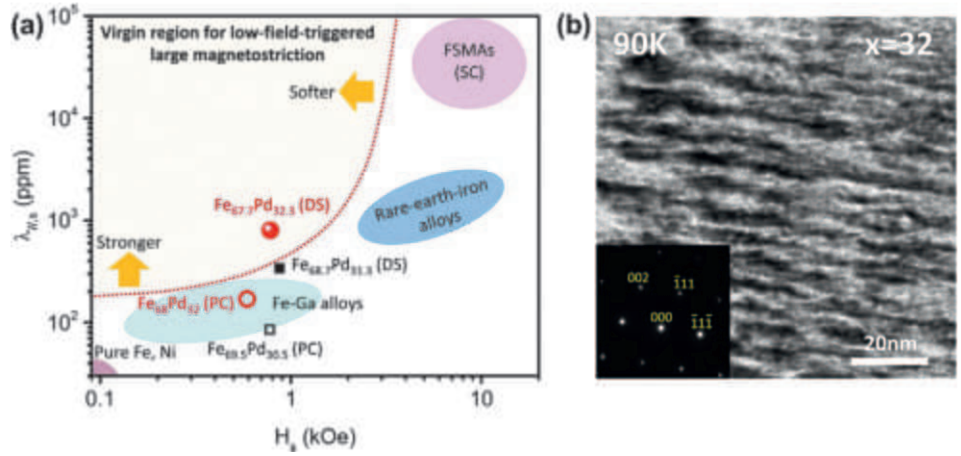

Fig. 17 (a) Benchmark of magnetostriction *vs.* saturation magnetic field H_S for Fe-Pd ferromagnetic strain glass and other typical magnetostrictive materials, "DS" represents directionally solidified alloys, and "PC" strands for polycrystalline alloys. (b) TEM picture of this ferromagnetic strain glass. (Ren et al., 2017).

However, for a diffusionless transition like martensitic transition (as well as other ferroic transitions), the transition can complete at a speed of sound because it involves with a collective displacement/shift of the atoms without needing a time-consuming diffusion process. Therefore, martensitic transformation is usually found to be time-independent but temperature dependent, and thus it is called "athermal" transition, meaning "caused by temperature change." However, exceptions to this general picture have been reported in a number of martensitic alloys since 1930, but its origin had remained unclear.

By studying a martensitic alloy $Ti_{48.7}Ni_{51.3}$ which locates at the strain-glass/martensite crossover composition, Ji et al. (2015) discovered an important clue that can resolve this longstanding puzzle. They found that the "isothermal martensitic transformation" is not a transform from parent phase (a strain disordered phase) into a martensite, as commonly assumed; rather it is a transition from a frozen strain glass (a SRO phase) into a martensite (a LRO phase) (Fig. 18). Therefore, it is a spontaneous

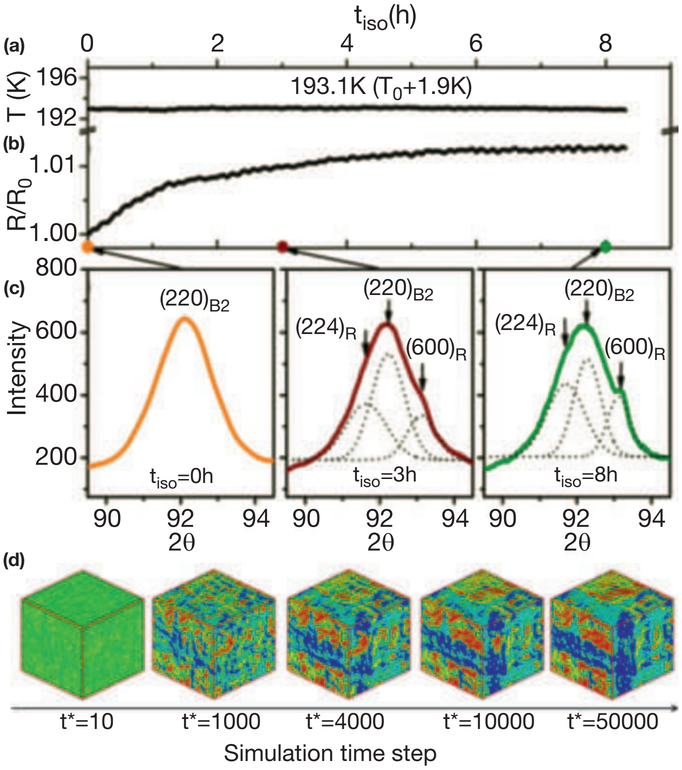

Fig. 18 Spontaneous "crystallization" of a strain glass as the origin of isothermal martensitic transformation (Ji et al., 2015). (a) Temperature monitor of the isothermal aging experiment. (b) Resistivity increase during isothermal aging, which reveals the formation of R-martensite. (c) Time dependence of in situ X-ray diffraction patterns. Additional peaks gradually appear close to $(220)_{B2}$ peak and are determined to be the $(224)_R$ and $(600)_R$, respectively. (d) Simulated microstructure evolution with time through phase field modeling.

"crystallization" of strain glass into a strain crystal—the martensite. Because the growth of nano-sized strain glass domains into large martensite domains takes time, this spontaneous crystallization process is time-dependent. This provides a transparent explanation for the existence of isothermal martensitic transformation and for why such transformation exists only in defect-containing alloys.

A similar study on a relaxor/ferroelectric crossover composition in a PZT-La system shows that an isothermal ferroelectric transition occurs under such a condition (Sun et al., 2013). Therefore, the puzzling isothermal transition in certain ferroic materials originates from the time-dependent crystallization of ferroic glasses into ferroic crystals when composition is located around the glass/crystal crossover of the phase diagram.

Conclusion

In this article we have presented a concise introduction to ferroic glasses, their classifications, physical origin, and experimental signatures, together with their physical properties and potential applications. Ferroic glasses are a unique class of ferroic materials characterized by nano-sized ferroic domains (or frozen SRO) formed through a ferroic glass transition. Just like amorphous glasses being contrasted with crystalline materials with their unique properties, ferroic glasses also exhibit many unique properties not possessed by their ferroic crystal counterparts. Some of these properties have been revealed recently and discussed in this article but more are to be discovered in the future. These novel properties are expected to lead to promising applications. Therefore, ferroic glass is an emerging research field that not only provides a new playground for materials scientists and physicists but also will lead to novel materials for exciting applications.

Acknowledgments

This work is supported by National Key R&D Program of China (2022YFB3808700, 2021YFB3803003, 2021YFB3501401), National Natural Science Foundation of China (9196311, 51831006, 52071255, 52071257, 12204368 and U2241242), 111 Project 2.0 (BP0618008), China Postdoctoral Science Foundation (2021M692513), and Shaanxi Provincial Natural Science Basic Research Program (2021JQ-001). Xiaobing Ren acknowledges the support by JSPS Kakenhi (No.20H02471). Yunzhi Wang acknowledges the support from the US National Science Foundation under Grant DMR-1923929, which has facilitated this international collaboration.

References

Bokov AA and Ye ZG (2006) Recent progress in relaxor ferroelectrics with perovskite structure. *Journal of Materials Science* 41: 31–52.

Cannella V and Mydosh JA (1972) Magnetic ordering in gold-iron alloys. *Physical Review B* 6(11): 4220–4237.

Chen L, Li F, Gao B, Zhou C, Wu J, Deng S, Liu H, Qi H, and Chen J (2023) Excellent energy storage and mechanical performance in hetero-structure $BaTiO_3$-based relaxors. *Chemical Engineering Journal* 452: 139222.

Dai Z, Xie J, Fan X, Ding X, Liu W, Zhou S, and Ren X (2020a) Enhanced energy storage properties and stability of $Sr(Sc_{0.5}Nb_{0.5})O_3$ modified $0.65BaTiO_3$-$0.35Bi_{0.5}Na_{0.5}TiO_3$ ceramics. *Chemical Engineering Journal* 397: 125520.

Dai Z, Xie J, Liu W, Wang X, Zhang L, Zhou Z, Li J, and Ren X (2020b) Effective strategy to achieve excellent energy storage properties in lead-free BaTiO3-based bulk ceramics. *ACS Applied Materials & Interfaces* 12(27): 30289–30296.

Dai Z, Xie J, Chen Z, Zhou S, Liu J, Liu W, Xi Z, and Ren X (2021) Improved energy storage density and efficiency of $(1\text{-}x)Ba_{0.85}Ca_{0.15}Zr_{0.1}Ti_{0.9}O_3$-$xBiMg_{2/3}Nb_{1/3}O_3$ lead-free ceramics. *Chemical Engineering Journal* 410: 128341.

Dai Z, Zhang F, Wang S, Lei Y, Liu Y, Chen H, Pan Y, and Ding X (2022) High energy storage properties for $BiMg_{0.5}Ti_{0.5}O_3$-modified KNN ceramics under low electric fields. *Journal of Materials Science* 57(33): 15919–15928.

Fang M, Ji Y, Zhang Z, Yang Y, Liu C, Wang D, Zhang L, Gao J, and Ren X (2018) Re-entrant relaxor–ferroelectric composite showing exceptional electromechanical properties. *NPG Asia Materials* 10(11): 1029–1036.

Fang M, Ji Y, Ni Y, Wang W, Zhang H, Wang X, Xiao A, Ma T, Yang S, and Ren X (2023) Toughening ceramics down to cryogenic temperatures by reentrant strain-glass transition. *Physical Review Letters* 130(11): 116102.

Gayathri N, Raychaudhuri AK, Tiwary SK, Gundakaram R, Arulraj A, and Rao N (1997) Electrical transport, magnetism, and magnetoresistance in ferromagnetic oxides with mixed exchange interactions: A study of the $La_{0.7}Ca_{0.3}Mn_{1\text{-}x}Co_xO_3$ system. *Physical Review B* 56(3): 1345.

He L, Wang D, Xu M, Zhang L, Ye F, Wu M, Zhang L, Wang DY, Pan X, and Ren X (2021) Large electrostrain with nearly-vanished hysteresis in eco-friendly perovskites by building coexistent glasses near quadruple point. *Nano Energy* 90: 106519.

Hong Z, Ke X, Wang D, Yang S, Ren X, and Wang Y (2022) Role of point defects in the formation of relaxor ferroelectrics. *Acta Materialia* 225: 117558.

Huang Y, Tsao C, and Wu S (2020) Structural evolution and mechanism of strain glass transition in $Ti_{48.7}Ni_{51.3}$ shape memory alloy studied by anomalous small-angle X-ray scattering. *Scientific Reports* 10: 9402.

Ji Y, Ding X, Lookman T, Otsuka K, and Ren X (2013) Heterogeneities and strain glass behavior: Role of nanoscale precipitates in low-temperature-aged $Ti_{48.7}Ni_{51.3}$ alloys. *Physical Review B* 87(10): 104110.

Ji Y, Wang D, Ding X, Otsuka K, and Ren X (2015) Origin of an isothermal R-martensite formation in Ni-rich Ti-Ni solid solution: Crystallization of strain glass. *Physical Review Letters* 114(5): 055701.

Ji Y, Wang D, Wang Y, Zhou Y, Xue D, Otsuka K, Wang Y, and Ren X (2017) Ferroic glasses. *npj Computational Materials* 3: 43.

Jiang D, An J, Liu Y, Ma Z, Liu F, Yang H, Ren X, Yu K, Zhang J, Jiang X, Ren Y, and Cui L (2021) Nanocrystalline strain glass TiNiPt and its superelastic behavior. *Physical Review B* 104(2): 024102.

Karmakar S, Taran S, Chaudhuri BK, Sakata H, Sun C, Huang C, and Yang H (2006) Disorder-induced short-range ferromagnetism and cluster spin-glass state in sol-gel derived $La_{0.7}Ca_{0.3}Mn_{1\text{-}x}Cd_xO_3(0 \leq x \leq 0.2)$. *Physical Review B* 74(10): 104407.

Kartha S, Castan T, Krumhansl JA, and Sethna JP (1991) Spin-glass nature of tweed precursors in martensitic transformations. *Physical Review Letters* 67(25): 3630.

Khan PY, Ren S, Ma T, and Ren X (2020) Magnetostriction enhancement in ferromagnetic strain glass by approaching the crossover of martensite. *Applied Physics Letters* 116(7): 072402.

Kong L, Wang B, Sun S, Gao Z, and Meng X (2022) Elastocaloric effect induced by the strain glass behavior of Ti-18Zr-11Nb-3Sn alloy covering a wide temperature range. *Materials Letters* 308: 131083.

Liang Q, Wang D, Zhang J, Ji Y, Ding X, Wang Y, Ren X, and Wang Y (2017) Novel B19′ strain glass with large recoverable strain. *Physical Review Materials* 1(3): 033608.

Liang Q, Zhao S, Liang C, Zhao T, Wang D, Ding X, Li S, Wang Y, Zheng Y, Ren X, Mills M, and Wang Y (2022) Strain states and unique properties in cold-rolled TiNi shape memory alloys. *Acta Materialia* 231: 117890.

Liu C, Ji Y, Tang J, Otsuka K, Wang Y, Hou M, Hao Y, Ren S, Luo P, Ma T, Wang D, and Ren X (2022) A lightweight strain glass alloy showing nearly temperature-independent low modulus and high strength. *Nature Materials* 21(9): 1003–1007.

Lloveras P, Castán T, Porta M, Planes A, and Saxena A (2008) Influence of elastic anisotropy on structural nanoscale textures. *Physical Review Letters* 100(16): 165707.

Lloveras P, Castán T, Porta M, Planes A, and Saxena A (2009) Glassy behavior in martensites: Interplay between elastic anisotropy and disorder in zero-field-cooling/field-cooling simulation experiments. *Physical Review B* 80(5): 054107.

Lookman T and Ren X (eds.) (2018) *Frustrated Materials and Ferroic Glasses*. Cham, Switzerland: Springer.

Ma T, Liu X, Yan M, Wu C, Ren S, Li H, Fang M, Qiu Z, and Ren X (2015) Suppression of martensitic transformation in $Fe_{50}Mn_{23}Ga_{27}$ by local symmetry breaking. *Applied Physics Letters* 106(21): 211903.

Monroe JA, Raymond JE, Xu X, Nagasako M, Kainuma R, Chumlyakov YI, Arroyave R, and Karaman I (2015) Multiple ferroic glasses via ordering. *Acta Materialia* 101: 107–115.

Mydosh JA (1993) *Spin Glasses: An Experimental Introduction*. London, UK: Taylor & Francis.

Pan H, Li F, Liu Y, Zhang Q, Wang M, Lan S, Zheng Y, Ma J, Gu L, Shen Y, Yu P, Zhang S, Chen L, Lin Y, and Nan C (2019) Ultrahigh-nergy density lead-free dielectric films via polymorphic nanodomain design. *Science* 365(6453): 578–582.

Ren X (2012) Strain glass and strain glass transition. In: Kakeshita T, Fukuda T, Saxena A, and Planes A (eds.) *Disorder and Strain-induced Complexity in Functional Materials*, pp. 201–225. Cham, Switzerland: Springer.

Ren X (2014) Strain glass and ferroic glass—Unusual properties from glassy nano-domains. *Physica Status Solidi B* 251: 1982–1992.

Ren X, Wang Y, Zhou Y, Zhang Z, Wang D, Fan G, Otsuka K, Suzuki T, Ji Y, Zhang J, Tian Y, Hou S, and Ding X (2010) Strain glass in ferroelastic systems: Premartensitic tweed versus strain glass. *Philosophical Magazine* 90(1–4): 141–157.

Ren S, Xue D, Ji Y, Liu X, Yang S, and Ren X (2017) Low-field-triggered large magnetostriction in iron-palladium strain glass alloys. *Physical Review Letters* 119(12): 125701.

Saito T, Furuta T, Hwang JH, Kuramoto S, Nishino K, Suzuki N, Chen R, Yamada A, Ito K, Seno Y, Nonaka T, Ikehata H, Nagasako N, Iwamoto C, Ikuhara Y, and Sakuma T (2003) Multifunctional alloys obtained via a dislocation-free plastic deformation mechanism. *Science* 300(5618): 464–467.

Sarkar S, Ren X, and Otsuka K (2005) Evidence for strain glass in the ferroelastic-martensitic system $Ti_{50-x}Ni_{50+x}$. *Physical Review Letters* 95(20): 205702.

Semenovskaya S and Khachaturyan AG (1997) Coherent structural transformations in random crystalline systems. *Acta Materialia* 45(10): 4367–4384.

Sherrington D (2008) A simple spin glass perspective on martensitic shape-memory alloys. *Journal of Physics: Condensed Matter* 20: 304213.

Sherrington D (2014) A spin glass perspective on ferroic glasses. *Physica Status Solidi B* 251(10): 1967–1981.

Smolenskii GA and Agranovskaya AI (1960) Dielectric polarization and losses of a number of complex compounds. *Soviet Physics-Solid State (English Translation)* 1: 1429–1437.

Sun X, Cong D, Ren Y, Liss K, Brown DE, Ma Z, Hao S, Xia W, Chen Z, Ma L, Zhao X, He Z, Liu J, Li R, and Wang Y (2020) Magnetic-field-induced strain-glass-to-martensite transition in a Fe-Mn-Ga alloy. *Acta Materialia* 183: 11–23.

Sun Z, Xue D, Wu H, Ji Y, Ding X, Wang D, Yang Y, and Ren X (2013) Time-dependent ferroelectric transition in $Pb_{(1-x)}(Zr_{0.4}Ti_{0.6})_{(1-x/4)}O_3$–xLa system. *Applied Physics Letters* 102(22): 222907.

Tan Q, Li J, and Viehland D (2000) Role of potassium comodification on domain evolution and electrically induced strains in La modified lead zirconate titanate ferroelectric ceramics. *Journal of Applied Physics* 88(6): 3433–3438.

Vasseur R and Lookman T (2010) Effects of disorder in ferroelastics: A spin model for strain glass. *Physical Review B* 81(9): 094107.

Viehland D, Li J, Jang S, Cross LE, and Wuttig M (1992) Glassy polarization behavior of relaxor ferroelectrics. *Physical Review B* 46(13): 8013.

Vincent E (2022) Spin glass experiments. In: *Reference Module in Materials Science and Materials Engineering*. Elsevier, ISBN: 9780128035818. https://doi.org/10.1016/B978-0-323-90800-9.00070-6.

Wang Y, Ren X, and Otsuka K (2006) Shape memory effect and superelasticity in a strain glass alloy. *Physical Review Letters* 97(22): 225703.

Wang Y, Ren X, Otsuka K, and Saxena A (2007) Evidence for broken ergodicity in strain glass. *Physical Review B* 76: 132201.

Wang D, Wang Y, Zhang Z, and Ren X (2010) Modeling abnormal strain states in ferroelastic systems: The role of point defects. *Physical Review Letters* 105(20): 205702.

Wang D, Ke X, Wang Y, Gao J, Wang Y, Zhang L, Yang S, and Ren X (2012) Phase diagram of polar states in doped ferroelectric systems. *Physical Review B* 86(5): 054120.

Wang Y, Gao J, Wu H, Yang S, Ding X, Wang D, Ren X, Wang Y, Song X, and Gao J (2014) Strain glass transition in a multifunctional β-type Ti alloy. *Scientific Reports* 4(1): 3995.

Wang R, Ubaid-Kassis S, Schroeder A, Baker PJ, Pratt FL, Blundell SJ, Lancaster T, Franke I, Möller JS, and Vojta T (2015) Evidence for magnetic clusters in $Ni_{1-x}V_x$ close to the quantum critical concentration. *Journal of Physics: Conference Series* 592(1): 012089.

Wang Y, Huang C, Wu H, Gao J, Yang S, Song X, and Ren X (2018) Premartensite serving as an intermediary state between strain glass and martensite in ferromagnetic Ni-Fe-Mn-Ga. *Materials & Design* 152: 102–109.

Wang Y, Wang D, Xu J, Zhong L, Gao J, Xiao A, Wu M, He Z, Yao R, and Li S (2021) Trirelaxor ferroelectric material with giant dielectric permittivity over a wide temperature range. *ACS Applied Materials & Interfaces* 13(28): 33272–33281.

Wang W, Ji Y, Fang M, Wang D, Ren S, Otsuka K, Wang Y, and Ren X (2022) Reentrant strain glass transition in Ti-Ni-Cu shape memory alloy. *Acta Materialia* 226: 117618.

Xia X, Jiang X, Zeng J, Zheng L, Man Z, Zeng H, and Li G (2021) Critical state to achieve a giant electric field-induced strain with a low hysteresis in relaxor piezoelectric ceramics. *Journal of Materiomics* 7(5): 1143–1152.

Xu S, Pons J, Santamarta R, Karaman I, Benafan O, and Noebe RD (2021) Strain glass state in Ni-rich Ni-Ti-Zr shape memory alloys. *Acta Materialia* 218: 117232.

Yang Y, Ji Y, Fang M, Zhou Z, Zhang L, and Ren X (2019) Morphotropic relaxor boundary in a relaxor system showing enhancement of electrostrain and dielectric permittivity. *Physical Review Letters* 123(13): 137601.

Yang Y, Liu C, Ji Y, He L, and Ren X (2021) Designed morphotropic relaxor boundary ceramic exhibiting large electrostrain and negligible hysteresis. *Acta Materialia* 208: 116720.

Zhou Y, Xue D, Tian Y, Ding X, Guo S, Otsuka K, Sun J, and Ren X (2014) Evidence for local symmetry breaking during a strain glass transition. *Physical Review Letters* 112(2): 025701.

Zhu K, Ge G, Yan F, Lin J, Bai H, Li G, Jiang H, Shen B, Zhai J, and Chou X (2022) Morphotropic relaxor boundary construction highly boosts the piezoelectric properties of Bi-based lead-free thin films. *ACS Applied Materials & Interfaces* 14(6): 8115–8125.

Semiconductors, general properties[☆]

G Margaritondo, Ecole Polytechnique Fédérale de Lausanne, (EPFL), Lausanne, Switzerland

© 2024 Elsevier Ltd. All rights reserved.

This is an update of G. Margaritondo, Semiconductors, General Properties, Editor(s): Franco Bassani, Gerald L. Liedl, Peter Wyder, Encyclopedia of Condensed Matter Physics, Elsevier, 2005, Pages 311–321, ISBN 9780123694010, https://doi.org/10.1016/B0-12-369401-9/00656-2.

Introduction: Insulators and semiconductors 404
Effective mass, electrons, and holes 405
Electrons in a crystal 405
Mobilities 408
Doping 408
Current rectification by Schottky diodes and *p*–*n* junctions 410
Heterojunctions and field-effect transistors 412
Important semiconducting materials 413
Silicon and germanium 413
III–V compounds and organic semiconductors 414
Optical properties and their applications 414
LED mechanism 416
Conclusion 417
Further reading 417

Abstract

This presentation starts with a general description of the electronic energy structure of insulators. This is the background of basic semiconductor features including the bands and the forbidden gap, the effective mass, the mobility and doping with donors or acceptors. Then, the rectification mechanisms of Schottky barriers and *p-n* junctions are outlined. The next part is a short presentation of some important semiconducting materials. Finally, optical properties are discussed together with their use for devices.

Key points

- Semiconductors: electronic energy structure
- Bands and gaps
- Effective masses, mobility
- Doping
- Diodes
- Important semiconductors
- Optical devices

Introduction: Insulators and semiconductors

When atoms are connected together by chemical bonds to form solids, their electronic states and energy levels are modified. For insulating materials, the valence electrons occupy "bonding" states whose energies form the "valence band." Above the valence band there is a "forbidden gap" with no states and then the "conduction band" corresponding to "antibonding" states (Fig. 1a).

At absolute zero temperature, $T = 0$ K, the valence band is completely full and the conduction band completely empty. The electronic states of the valence band are globally symmetric and produce no net electric current.

This situation changes if the temperature is higher than absolute zero (Fig. 1b). Some electrons are thermally promoted above the gap and into the conduction band. An applied voltage can shift them to nearby empty states, breaking the global symmetry and producing a current. This effect is stronger for smaller gaps that allow more electrons to be promoted to the conduction band. In addition, the states left empty in the valence band allow breaking its global symmetry, also contributing to the current when a bias voltage is applied.

[☆] *Change History:* November 2022. G Margaritondo updated all sections and figures.

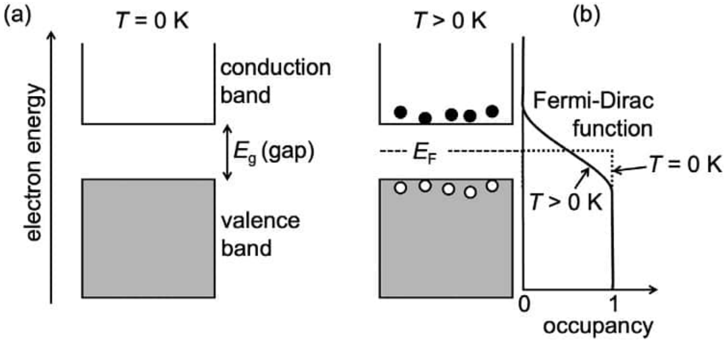

Fig. 1 (a) The electronic states in an insulator or a semiconductor correspond to a valence band of energies and to a conduction band, separated by a forbidden gap of width E_g. At absolute zero temperature, all valence-band states are occupied and all conduction-band states are empty. (b) At finite temperatures, some electrons are present in the conduction band leaving empty states in the valence band. The state occupation is ruled by the Fermi-Dirac function (plotted here for $T = 0$ K and $T > 0$ K) and in particular by its Fermi level E_F.

The gap width E_g marks the difference between "insulators" and "semiconductors." Indeed, a semiconductor is an insulator with a sufficiently small gap to allow a significant number of electrons in the conduction band at room temperature. In practice, for most semiconductors E_g does not exceed 2.5–3 eV.

The densities of electrons in the conduction band and of empty states in the valence band are determined by thermodynamic statistics. The electrons are particles with spin 1/2, thus they are ruled by the Fermi-Dirac quantum statistics function—which is a consequence of the Pauli exclusion principle. The function, with occupancy ranging from 0 to 1, is plotted in Fig. 1b.

At absolute zero temperature, the Fermi-Dirac function is a sharp step: the occupation probability is 100% up to the Fermi level E_F and zero above it. Thus, E_F for an insulator or a semiconductor falls within the forbidden gap. At finite temperatures, the Fermi-Dirac function allows some empty states below E_F and some electrons above it.

In a metal, E_F falls in the conduction band rather than in a gap. An applied voltage creates a current by changing the states of electrons close to E_F, with no need to thermally excite them above a forbidden gap. Thus, many more electrons contribute to the electrical conduction in a metal than in a semiconductor. However, a semiconductor has a marked advantage: as we shall see, its properties can be modified and controlled by exploiting mechanisms not active in metals, opening the door to many applications.

As a consequence, semiconductors have become the protagonists of modern electronics. In practice, this is mainly due to three facts: (1) the possibility to control their conduction mechanisms by "doping" them with suitable impurities; (2) the possibility of electrically and chemically passivating their surfaces with high-quality, ultrathin insulating layers, as required to integrate a huge number of microdevices into a single semiconductor slice (the "planar technology" of integrated circuits); (3) properties other than electrical conduction, such as the optical ones, that are controlled and exploited for special devices like visible-light emitters and solar cells.

In order to understand how semiconductor devices work, we must first analyze the basic conduction mechanisms of the materials. We must specifically discover the role of the electrons in the conduction band and of the empty electronic states in the valence-band, described by the so-called "holes."

Effective mass, electrons, and holes

We shall begin by analyzing an electron not subject to forces, free to move along a straight line, i.e., in one dimension. Its momentum is:

$$mv = p = \hbar k, \tag{1}$$

where m is the mass, v the velocity and k the wave number of the electron wave (which in three-dimensions becomes the $\boldsymbol{k}$-vector). And its (kinetic) energy is:

$$E = mv^2/2 = p^2/(2\,m) = \left[\hbar^2/(2\,m)\right]k^2. \tag{2}$$

Therefore, the "dispersion curve" $E(k)$ is a parabola—see Fig. 2a. Note that:

$$m = \hbar^2/\left(\mathrm{d}^2E/\mathrm{d}k^2\right), \tag{3}$$

and

$$(1/\hbar)(\mathrm{d}E/\mathrm{d}k) = (\hbar/m)k = p/m = v \tag{4}$$

Electrons in a crystal

Assume now that the electron is no longer free but subject to a periodic potential caused by the positively charged nuclei in a crystal. We shall perform our analysis again in one dimension, for a potential with period a as shown in Fig. 2b.

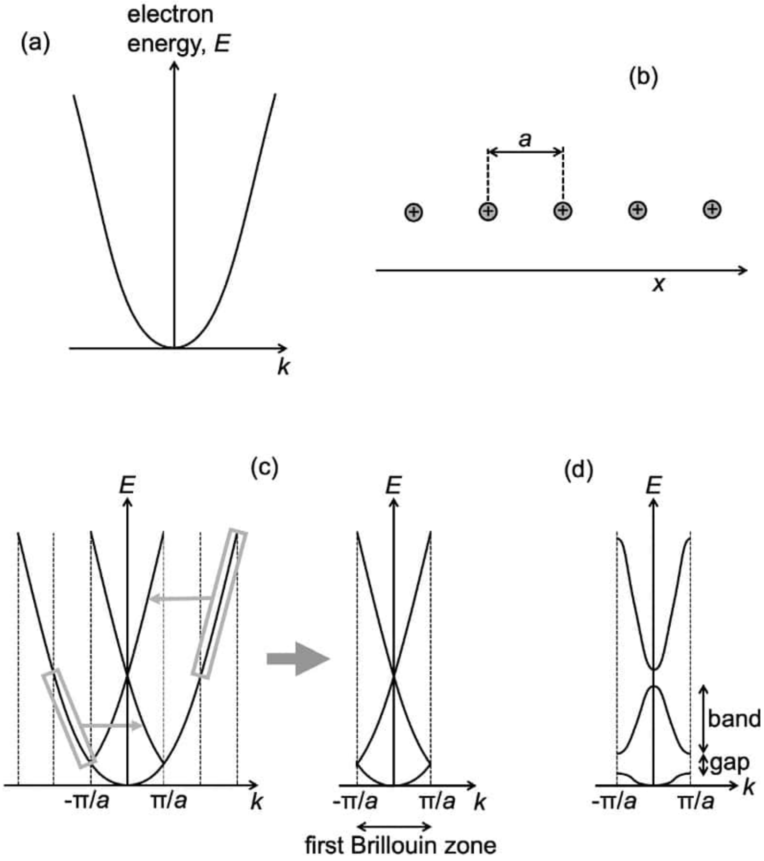

Fig. 2 (a) $E(k)$ curve for a free electron. (b) Periodic potential created by the nuclei in a one-dimensional crystal. (c) "Folding" of the $E(k)$ curves into the first Brillouin zone. (d) Deformations of the E(k) curves by the "Bragg reflections," which create bands and gaps.

The electron behaves as a wave interacting with the nuclei. In turn, the array of nuclei can be seen as a standing wave of positive electric charge with period a. Mathematics show that this standing wave can be expressed as a sum of "propagating waves" moving in opposite directions, with wave number $k = \pm\xi 2\pi/a$ and momentum $\hbar k = \pm\xi 2\pi\hbar/a$, where ξ is an integer number.

In any phenomenon involving an electron wave, the interaction with the "propagating waves" of the nuclei can change its momentum by $\pm\xi 2\pi\hbar/a$ and its k-value by an integer multiple of $2\pi/a$. To automatically take into account all these possible changes, when treating phenomena affecting the electrons we can first "fold" them into the so-called "first Brillouin zone" of k-values—centered at the origin and of width $2\pi/a$ as shown in Fig. 2c. We specifically see in the figure branches of the free-electron $E(k)$ curve "folded" into the first zone.

In addition to folding, the periodic potential of the nuclei has a second relevant effect. The electron waves reflected by the nuclei can interact between them. Particularly important is the case of waves with wavenumbers given by:

$$k = n\pi/a, \tag{5}$$

with $n =$ integer—the corresponding wavelengths being $2\pi/k = 2a/n$. Such wavelengths allow the waves reflected by different nuclei to interfere constructively between them. This is the equivalent for electron waves of the "Bragg reflections" for X-ray photons.

In practice, the waves obeying Eq. (5) are Bragg-reflected back and forth and cannot propagate. This means that their (group) velocity v_g is zero. From the equivalent of Eq. (4) we get:

$$v_g = (1/\hbar)(dE/dk), \tag{6}$$

thus v_g is zero if the $E(k)$ curve has zero derivative, e.g., it is at a maximum or a minimum. This implies that the periodic potential of the nuclei deforms the $E(k)$ curves as shown in Fig. 2d.

From this figure, we derive once again the existence of energy bands separated by forbidden gaps. This new derivation, however, is limited to periodic crystals—whereas the previous one, based on bonding and antibonding states, is more general.

Consider now the $E(k)$ curves folded in the first Brillouin zone—the so-called "band structure"—for energies close to the gap (Fig. 3a). We see at $T = 0$ K the completely filled valence band and the empty conduction band as in Fig. 1a. For each filled valence-band electronic state in the positive direction there is a symmetric state in the negative direction. We thus confirm what we already mentioned: the valence-band states are globally symmetric, so a completely filled valence band produces no overall electric current.

At $T > 0$ K, some electrons are thermally promoted to the conduction band becoming "free electrons." Fig. 3b shows one free electron and the corresponding empty state in the valence band.

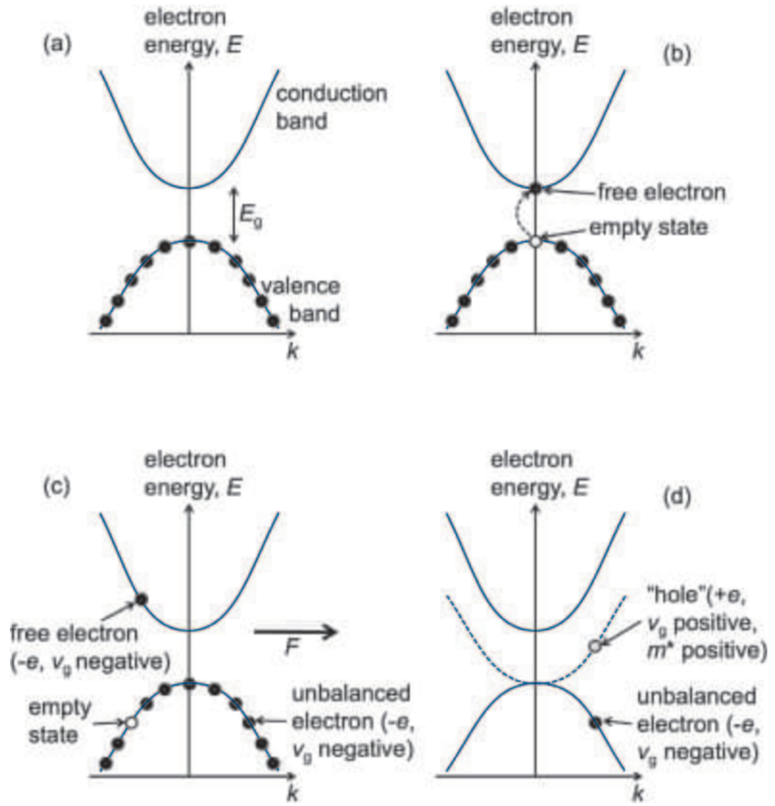

Fig. 3 (a) $E(k)$ plots for the valence and conduction bands of a one-dimensional semiconductor. At $T = 0$ K, the valence band is completely filled and the conduction band is empty. The valence-band electronic states are symmetric and there is no conduction. (b) Thermal excitation of an electron to the conduction band leaving an empty state in the valence band. (c) An external electric field F is applied in the positive direction: the conduction-band electron is subject to a negative force $-eF$ and shifts toward the negative side of the k-axis. This electron has negative charge $-e$ and negative group velocity $v_g = (1/\hbar)(dE/dk)$; therefore, its contribution $(-e)v_g$ to the current density is in the positive direction as the field F. The electrons in the valence band are also subject to the negative force $-eF$. But their "effective" mass $m^* = \hbar^2/(d^2E/dk^2)$ is negative, so the acceleration = force/mass is positive. Thus, they shift in the positive k-direction forcing the empty state to shift in the negative direction. The empty state now corresponds to an "unbalanced" electron whose contribution to the current is not offset by a symmetric electronic state. This unbalanced electron has negative charge and negative v_g, thus its contribution to the current is again in the positive direction. (d) The effects of the empty valence-band state can be described in terms of a pseudo-particle called "hole," with positive charge +e and positive group velocity: the dashed line shows its dispersion curve.

Suppose now that an external electric field F is applied in the positive direction (Fig. 3c). The conduction-band electron is subject to the force $-eF$ and moves to a negative value of k. The symmetry is broken allowing a current.

To describe the different contributions to this current, we must analyze in detail the effect of the applied electric field F. Its force can be treated with Newton's equation:

$$\text{force} = -eF = \mathrm{d}p/\mathrm{d}t = \hbar \mathrm{d}k/\mathrm{d}t. \tag{7}$$

From the expression of the "group velocity," Eq. (6), we get:

$$\mathrm{d}v_g/\mathrm{d}t = (1/\hbar)\left[\mathrm{d}^2E/(\mathrm{d}k\mathrm{d}t)\right] = (1/\hbar)\left(\mathrm{d}^2E/\mathrm{d}k^2\right)(\mathrm{d}k/\mathrm{d}t),$$

which, combined with Eq. (7), becomes:

$$-eF = m^*\left(\mathrm{d}v_g/\mathrm{d}t\right), \tag{8}$$

that is, an equation of Newtonian form except that the free-electron mass m is replaced by an "effective mass":

$$m^* = \hbar^2/\left(\mathrm{d}^2E/\mathrm{d}k^2\right). \tag{9}$$

In first approximation, the $E(k)$ curve near the minimum of the conduction band has a parabolic form whose second derivative is positive and does not change with k. So, m^* as defined by Eq. (9) is nearly constant as the real electron mass, although different in value.

Eq. (8) confirms our previous conclusion: the negative force $-eF$ on an electron at the bottom of the conduction band decreases v_g, causing the shift toward the negative side of the k-axis (Fig. 3c). The shift, however, does not continue indefinitely. Indeed, the effects of the external electric field are eventually countered by the scattering mechanisms responsible for resistivity.

The contribution to the current density of the conduction-band electron of Fig. 3c equals $-ev_g$, its negative charge multiplied by the group velocity of Eq. (6). Since v_g is negative, this contribution is in the positive direction—the direction of the electric field F.

But this is not the only contribution to the current caused by F. We must also consider the empty valence-band state in Fig. 3b. When the external electric field F is applied (Fig. 3c), all electrons in the valence band are subject to the negative force $-eF$. The effects are again described by Eq. (8). But now the effective masses of Eq. (9) are negative, so the acceleration is positive, shifting all valence-band electronic states in the positive k-direction. This pushes the empty state in the negative direction, as shown in Fig. 3c.

The valence-band electron opposite to the empty state is no longer balanced and produces a net current. This "unbalanced" electron has negative charge and negative group velocity. Thus, it produces a positive current—in the same direction as the electric field and as the current of the conduction-band electron. Summarizing, the total current is given by the combination of two contributions in the same direction, from electrons in the conduction band and from empty states in the valence band.

The effects of the empty valence-band states can also be treated in terms of the so-called "holes." This notion is suggested by the fact that the "unbalanced electron" in Fig. 3c—with negative charge $-e$, negative m^* and negative v_g—gives the same contribution to the current as an imaginary pseudo-particle ("hole") with positive charge $+e$, positive effective mass and positive group velocity $|v_g|$. The dispersion curve for this "hole" is shown by the dashed line in Fig. 3d.

The behavior of holes in semiconductor devices is easier to analyze than that of unbalanced electrons. The "holes" are, therefore, universally adopted when treating semiconductor electronics.

Our description was so far confined to one dimension. For a three-dimensional material, the wave number k is replaced by the k-vector $\boldsymbol{k}$. And the band structure does not consist only of $E(k)$ dispersion curves but of $E(\boldsymbol{k})$ surfaces. The top of the valence band and the bottom of the conduction band correspond to a maximum and to a minimum of such surfaces.

In three-dimensions, the effective mass is no longer a scalar quantity but a directional tensor. And several $E(\boldsymbol{k})$ surfaces can be found near the valence-band top and near the conduction-band bottom, corresponding to different effective masses for electrons and for holes.

Mobilities

The previous discussion justifies the following equation for the total current density created in a semiconductor by an external electric field F:

$$j = -nev_e + pev_h \tag{10}$$

where n and p are the free-electron density and the hole density. Here, v_e is the average group velocity for electrons in the conduction band. This average is determined by the balance between the effects of the applied field F and of the scattering mechanisms responsible for the resistivity (i.e., by impurities or defects or lattice vibrations). And v_h is the average group velocity for holes. Note (Fig. 3d) that the group velocities for electrons and holes are in opposite directions. Thus, the two terms on the right-hand side of Eq. (10) are both in the same direction, as expected.

In first approximation, $\mathrm{v_e}$ and $\mathrm{v_h}$ are proportional to the applied electric field F:

$$v_e = \mu_e F; \qquad v_h = \mu_h F, \tag{11}$$

where the parameters μ_e and μ_h are called "electron mobility" and "hole mobility." These are scalar quantities for a one-dimensional semiconductor. However, in a three-dimensional case they have directional character.

The combination of Eqs. (10) and (11) gives.

$$j = (-ne\mu_e + pe\mu_h)F, \tag{12}$$

where $(-ne\mu_e + pe\mu_h) = \sigma$ is the "conductivity."

Eq. (12) implies a basic difference between the conduction in a semiconductor and that in a simple metal: the opposite effects of the temperature. In a metal, the temperature primarily affects the electron mobility. Indeed, as the temperature increases, the scatterings by lattice vibrations increase, and the mobility decreases as well as the conductivity. In a semiconductor, the temperature affects not only the mobilities but also the carrier densities n and p—which increase as the temperature increases. This last effect dominates, so the conductivity of a semiconductor increases with the temperature—whereas in a metal it decreases.

Doping

What, besides the Fermi-Dirac function, can influence the free-electron concentration n and the hole concentration p in a semiconductor? We can easily understand that they can be modified by impurities: let us see how.

So far, we have assumed that the forbidden gap contains no electronic states. Therefore, each hole corresponds to an empty state in the valence-band and to a free electron in the conduction band. Thus, $n = p$.

We can realize from Fig. 1b that n and p are determined by the Fermi–Dirac function, and specifically by the position of E_F with respect to the valence and conduction bands. And we can intuitively understand that the $n = p$ condition requires E_F to be close to the middle of the gap (Fig. 4a).

Another important implication of the $n = p$ condition can be discovered with the so-called "law of mass action." The mathematical form of the Fermi-Dirac function is $1/\{\exp.[(E - E_F)/(kT)] + 1\}$, where k is the Boltzmann constant. Assume

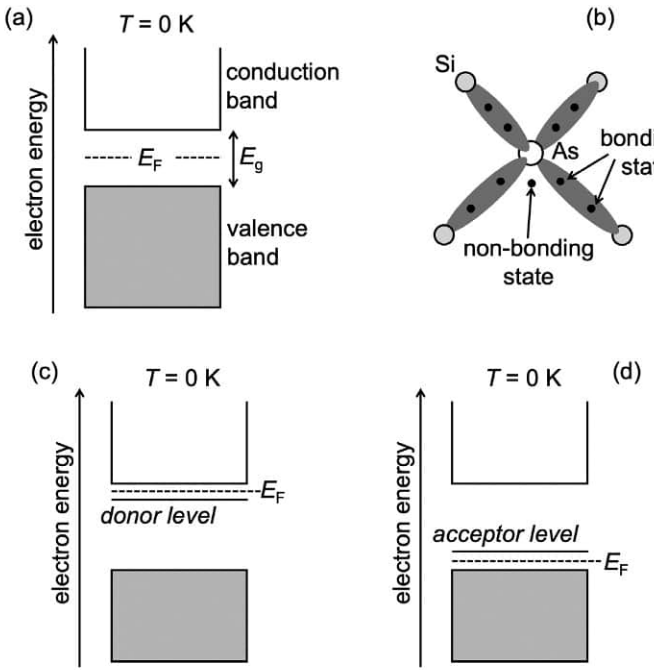

Fig. 4 (a) In an ideal semiconductor completely free from impurities, the condition $n = p$ implies that the Fermi level E_F is close to the middle of the gap. (b) An arsenic impurity in a silicon crystal: four of its electrons are engaged in sp^3 chemical bonds with neighboring silicon atoms. The fifth one is in a "nonbonding" (impurity) state. (c) The corresponding impurity energy level is inside the gap and near the bottom of the conduction band. At finite temperatures, the impurity levels can "donate" electrons to the conduction band by thermal excitation. (d) Symmetrically, an impurity with three valence electrons per atom such as gallium can inject holes in the valence band acting as an "acceptor".

(Fig. 1b) that all the free electrons are close to the bottom of the conduction band E_c, and all the holes are close to the top of the valence band E_v. Further assume that E_F is far from both E_c and E_v, i.e.,. near the middle of the gap.

Then, the free-electron density n is proportional to the Fermi-Dirac function at E_c, $1/\{\exp.[(E_c – E_F)/(kT)] + 1\} \approx \exp.[(E_F – E_c)/(kT)]$. Symmetrically, p is proportional to $\approx\exp.[(E_v – E_F)/(kT)]$. And the product np is approximately proportional to $\exp.[(E_v – E_c)/(kT)] = \exp.[–E_g/(kT)]$. Thus, np is only a function of the temperature, independent of the position of E_F. For a fixed temperature, it is a constant: this is the aforementioned "law of mass action."

It can be easily shown that if np is constant the condition $n = p$ gives the minimum value of the total carrier density $n + p$. One cannot increase the carrier density above this minimum if each free electron corresponds to a hole.

To break this condition, however, one can "dope" the semiconductor by adding impurities in a controlled way. How do the impurities work?

Consider, for example (Fig. 4b), arsenic impurities in a silicon crystal. The chemical bonds in pure silicon are formed by the sp^3 hybridization of four 3*s* and 3*p* valence electrons for each atom. An atom forms chemical bonds with four nearest neighbors; thus, each bond involves two electrons, one per atom. The "bonding" sp^3 hybridized states correspond to the valence band, whereas the "antibonding" ones correspond to the conduction band.

Suppose now that one silicon atom is replaced by an arsenic atom with five rather than four valence electrons (Fig. 4b). Four of them form chemical bonds with neighboring silicon atoms, and the corresponding sp^3 states contribute to the conduction and valence bands. The fifth arsenic electron is not engaged in chemical bonding: its state is "nonbonding." And its energy is intermediate between those of the "bonding" and "antibonding" states. Thus, it falls within the forbidden gap (Fig. 4c).

Not being engaged in a chemical bond, this electron can be easily freed from the impurity and promoted to the conduction band. This means that the impurity energy level is close to the bottom of the conduction band, as seen in Fig. 4c. Thermal excitation easily allows the impurity to "donate" electrons to the conduction band: this is why arsenic in silicon is called a "donor" impurity.

At $T = 0$ K, however, there is no thermal excitation at all: the donor electronic states are all full and the conduction band states are empty. Thus (Fig. 4c), the Fermi level falls between the donor energy level and the bottom of the conduction band—and is no longer close to the middle of the gap.

At $T > 0$ K, electrons are thermally promoted from the impurity level to the conduction band. The corresponding energy distance is smaller than E_g, so there is a large concentration n of impurity-donated free electrons. The $n = p$ rule is broken and the total carrier density $n + p$ is larger than the minimum value. The material is an "*n*-type" semiconductor, whereas an impurity-free sample with $n = p$ is an "intrinsic" semiconductor.

A symmetric mechanism enables impurities with three valence electrons per atom ("acceptors")—such as gallium—to inject a large number of holes in the silicon valence band—producing a "*p*-type" material. In this case (Fig. 4d), the impurity has an empty level near the top of the valence band that can easily capture thermally excited electrons from the valence band. This creates empty states in the valence band and increases the hole density p.

At $T = 0$ K, however, all acceptor levels are empty and all valence band states are filled. Thus, the Fermi for a p-type material level falls between the top of the valence band and the acceptor impurity level—see Fig. 4d.

Impurities are normally present in a semiconductor, so that the samples are naturally doped n-type or p-type. But chemical processes can change the character from p to n and vice versa.

Quite difficult, however, is to produce samples with low impurity concentrations, so that $n = p$, the total carrier concentration $n + p$ is low, and the material has low conduction. The $n = p$ condition is more easily achieved with high but equal concentrations of donors and acceptors. An intrinsic material of this kind is said to be "compensated."

Current rectification by Schottky diodes and *p–n* junctions

Controlling the transport properties by doping is a key factor in the realization of semiconductor devices. Two simple examples are qualitatively discussed here: the Schottky barrier and the p–n junction, both of which are building blocks of many complex devices.

A Schottky barrier (Fig. 5a) is formed by joining a semiconductor and a metal. The semiconductor can be either n-type or p-type. We shall consider here (Fig. 5b and c) the n-type case—the analysis for the p-type case being symmetrical and based on holes.

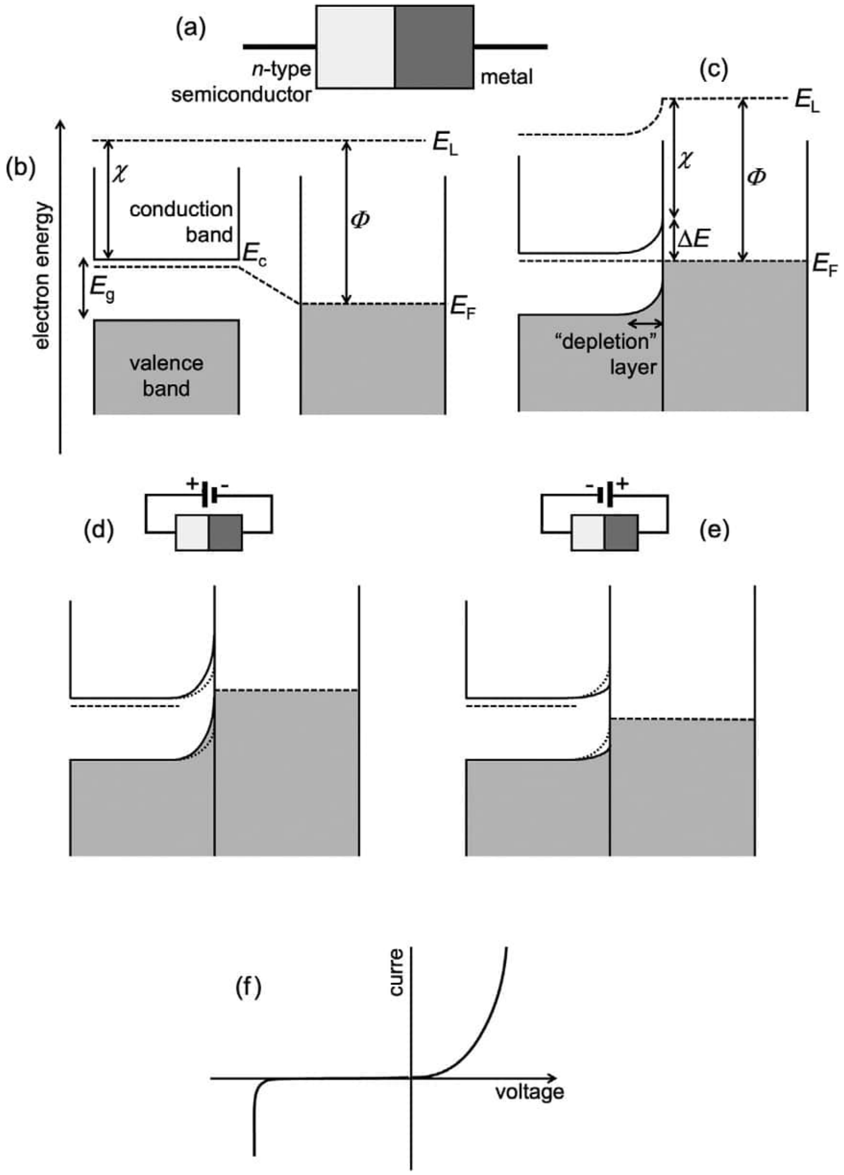

Fig. 5 (a) Structure of a metal-semiconductor Schottky diode. (b) Band structure before the two sides are joined together. (c) Band structure after the junction is formed, producing the band bending in the "depletion layer" and creating a barrier ΔE. (d) The barrier is increased by a "reverse" bias, whereas (e) it is decreased by a "forward" bias. (f) Current-voltage curve showing the rectification.

Imagine (Fig. 5b) the semiconductor still separated from the metal: the Fermi level is not the same for the two materials. Consider now the "vacuum level" E_L, i.e., the minimum energy for an electron to be completely free from a material. E_L is the same for the metal and for the semiconductor. We shall define the "work function" of the metal, Φ, as the difference between E_L and the metal Fermi level. And we shall define χ, the "electron affinity" of the semiconductor, as the difference between E_L and the bottom of the conduction band, E_c.

When the metal and the semiconductor are brought in direct contact, their Fermi levels cannot remain different. Otherwise, it would be possible to lower the energy of the system by moving electrons to lower-energy states, whereas equilibrium corresponds to a minimum of the total energy. To equalize E_F, electrons in the semiconductor donor levels near the interface quit them, leaving the donors positively charged. The result is an electric field at the interface preventing more electrons from leaving the semiconductor.

The new equilibrium situation is shown in Fig. 5c, with the same Fermi level everywhere and a "band bending" on the semiconductor side caused by the electric field of the positively charged donors. In the "band bending" region, E_F is below the donor levels and close to midgap. Thus, the region is an insulating "depletion layer" with no carriers.

Because of the electric field of the charged donors and of the consequent band bending, electrons at the bottom of the conduction band in the semiconductor face an energy barrier ΔE. This barrier prevents them from diffusing across the depletion layer and reaching the metal.

Assume now that an external voltage bias is applied to the junction trying to create a current (Fig. 5d). The voltage drop occurs across the insulating "depletion" layer, changing the band bending and ΔE.

If the bias is in the "reverse" direction of Fig. 5d, it acts against the passage of electrons from the semiconductor to the metal. This means that the barrier ΔE is further increased. However, the barrier was already high enough to prevent a current of free electrons. Thus, the reverse bias causes no changes and in particular no current.

On the contrary (Fig. 5e), if the voltage bias attracts electrons to the metal, then the barrier ΔE is decreased facilitating the flow of electrons. This "forward" bias thus creates a current, as shown in Fig. 5f.

Overall, therefore, the metal-semiconductor junction acts as a rectifying diode, allowing a current to be created only in one direction. However, we see in Fig. 5f that a "reverse" voltage bias eventually reaches a level that causes a large current. This is due to a so-called "avalanche" mechanism and limits the operating voltage-bias range of the rectifying diode.

The behavior of Fig. 5f finds wide applications in electronics. And it is primarily characterized by the barrier parameter ΔV. We can see from Fig. 5c that:

$$\Delta E = \Phi - \chi, \tag{13}$$

therefore, for a given semiconductor different metals should give different Schottky barriers according to their work functions.

This, however, is often not true. The reason is the creation of electronic states localized at the interface when the junction is formed. Such states can locally "pin" the Fermi level and influence the barrier. In general, both the interface states and the metal work function determine ΔE. The interplay of such mechanisms is quite complicated and changes from interface to interface.

We shall now analyze another widely used rectifying device, the p–n junction. Which consists of a semiconductor sample with two different regions, one n-type and the other p-type (Fig. 6a). In practice, the junction can be fabricated starting from a sample of one type and then changing the doping of part of it with a suitable procedure, such as gas-phase exposure.

In the band diagram of the np junction (Fig. 6b) the n-type and p-type regions are again separated by a "depletion layer"—where E_F is close to the middle of the gap. This situation is similar to an insulating (intrinsic or compensated) semiconductor with low total carrier density. As for Schottky junctions, the Fermi level must be the same everywhere. Thus, in the depletion region there is a band bending and an energy barrier ΔE.

Free electrons do not cross from the n-region to the p-region due to the energy barrier. Similarly, holes in the p-region do not cross to the n-region since they face a symmetric barrier.

Imagine now that an external voltage bias V is applied to the junction, trying to create a current. A "reverse" bias (Fig. 6c), positive on the n- side and negative on the p- side, increases the ΔE barrier, making it even more difficult for carriers to cross the junction—so that no (or very little) current is produced. On the contrary, a "forward" bias (Fig. 6d) decreases the barrier and makes it easier for electrons and holes to cross it, producing a current.

Overall, the junction exhibits a rectifying behavior similar to that shown in Fig. 5f for Schottky diodes. Under rather idealized hypotheses, the current I can be described (except for the reverse-bias breakdown) by the equation:

$$I = I_0 \left\{ \exp . [eV/(\eta kT)] - 1 \right\} \tag{14}$$

where V the applied voltage bias, k the Boltzmann constant, and η the so-called "ideality factor" ($\eta = 1$ being the limit, most ideal case).

The above descriptions of Shottky diodes and p-n junctions are oversimplified. However, they are suitable to understand the basic facts and, in particular, the crucial role of doping in the fabrication of semiconductor devices.

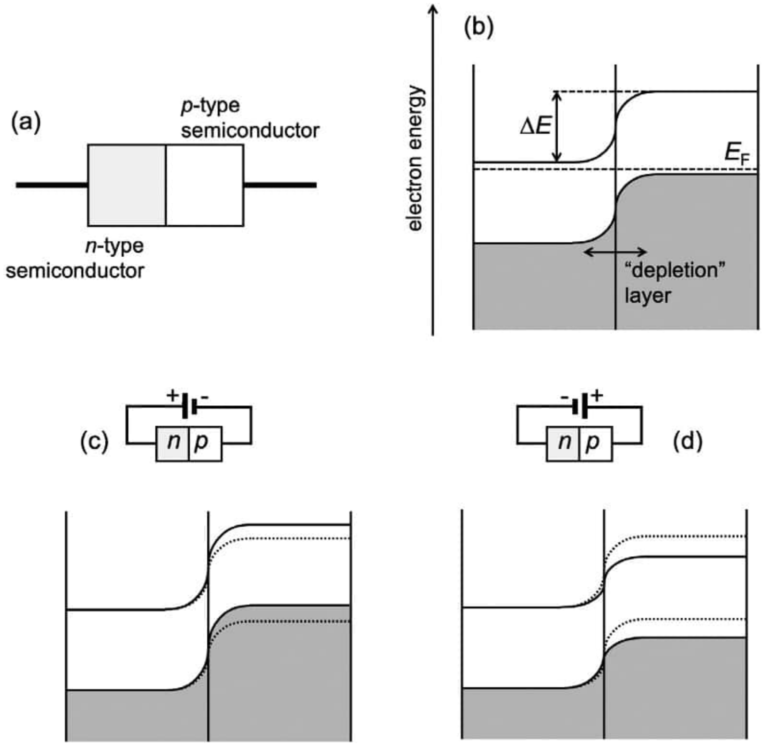

Fig. 6 (a) A *p–n* junction and (b) the corresponding energy band diagram. Free electrons from the *n*-side cannot cross the depletion region due to the energy barrier ΔE. A symmetric conclusion is valid for holes from the *p*-side. (c) An external voltage bias applied in the "reverse" direction increases the barrier ΔE and generates no current. (d) A "forward" bias decreases the barrier making it easier for electrons and holes to overcome it, producing a current.

Heterojunctions and field-effect transistors

Certain electronic devices include the so-called "heterojunctions." These are combinations of two different semiconducting materials with different gaps. One example is shown in Fig. 7, which illustrates the band diagram of the junction of a large-gap *p*-type materials and a small-gap *n*-type material.

The diagram exhibits a feature not found in *p-n* junctions nor in Schottky diodes: band discontinuities. Such discontinuities are required to accommodate the difference between the two gaps, which is partitioned between the valence and conduction band discontinuities ΔE_v and ΔE_c.

The possibility to control this partitioning adds flexibility to the design of devices. This control can be achieved with suitable fabrication procedures, in the framework of the so-called "bandgap engineering."

Semiconductors are now used in a huge variety of devices, many of them composed by a few basic "building blocks." Besides the rectifying diodes, one must note the transistors, operating as switches or as amplifiers.

Quite common are the "bipolar junction" transistors. However, the most widely used today are, by far, the field-effect transistors (FETs). And the majority of these are the "MOSFETs" (metal-oxide-semiconductor FETs).

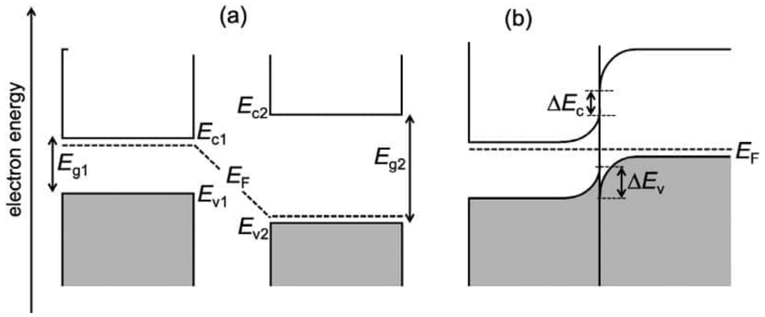

Fig. 7 (a) Band diagrams of two different semiconductors with different gap widths before forming a heterojunction. (b) The formed heterojunction with the valence and conduction band discontinuities ΔE_v and ΔE_c that accommodate the gap difference.

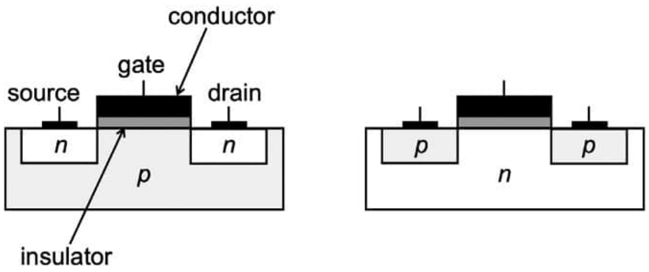

Fig. 8 Simplified cross-sectional schemes of the MOSFET structure, with the two possible doping configurations.

The present impact of the MOSFET technology on microelectronics defies the imagination. The total number included in one integrated device recently (2021) approached 60 billion. And the estimated number of MOSFETs produced every year in the world exceeds 10^{22} (ten thousand billions of billions). Which is half million times larger than the number of rice grains harvested worldwide (and the unit cost of MOSFETs is much lower).

Fig. 8 shows a simplified scheme of a MOSFET structure. In essence, the device controls the current flowing between the two electrodes "source" and "drain," connected to two *n*-type semiconductor regions separated by a *p*-type region (or to two *p*-type regions separated by a *n*-type region). The control is achieved by applying a voltage to a third electrode, the "gate," connected to a conducting (metal or polycrystalline silicon) region, which sits on a very thin insulating layer (typically silicon oxide).

The control mechanism ("field effect") is very efficient. And the MOSFET structure is suitable for extreme miniaturization, packing huge numbers in each integrated device. This explains its leading present role in microelectronics.

Important semiconducting materials

Many different elemental and compound semiconductors have a potential for applications but only a few are actually used. Among these, silicon largely dominates—in particular in the MOSFETs. This is due to the its very advanced technologies and to some specific properties. For example, the quality of its oxide as an insulating (passivating) layer and the success in growing very large high-quality crystals.

In addition to Si, also used for practical applications are germanium and some III–*V* compounds, such as GaAs, GaP, InP, and GaN. And increasingly important are the organic semiconductors.

Silicon and germanium

Both of these elemental materials have, in their crystalline forms, the cubic structure of diamond shown in Fig. 9a. In which each atom is tetrahedrally bound to its four nearest neighbors.

The band structures of the two materials are shown in Figs. 9b and c. Here, $E(k)$ curves are plotted along two high-symmetry crystallographic directions, $\langle 111 \rangle$ and $\langle 100 \rangle$.

For both materials, the bottom of the conduction band and the top of the valence band occur for two different *k*-vectors. The corresponding gaps are called "indirect," whereas when the bottom of the conduction band and the top of the valence band occur for the same *k*-vector the gap is "direct"—as seen for the GaAs band structure in Fig. 10b.

The direct or indirect character of the gap strongly influences the physical properties of the material. For example, the transitions of electrons across the gap imply no change of the *k*-vector for a direct gap, whereas the contrary is true for an indirect gap. And a

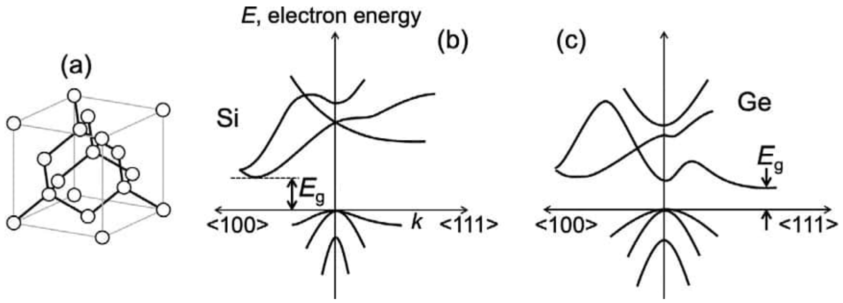

Fig. 9 (a): the characteristic tetrahedrally coordinated cubic diamond crystal structure of silicon and germanium. (b) Band structure of silicon along the $\langle 111 \rangle$ and $\langle 100 \rangle$ directions of the *k*-vector. Note that the gap is "indirect": the conduction-band minimum is at a different *k*-vector than the valence-band maximum. (c) The band structure of germanium also has an indirect gap.

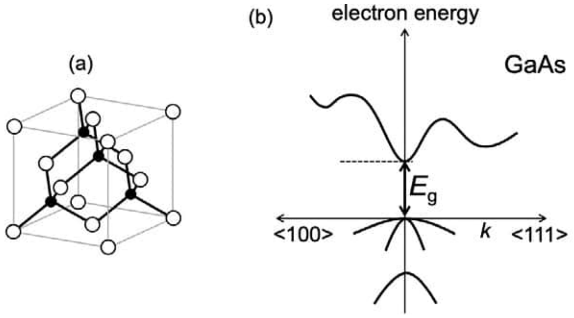

Fig. 10 (a): the zincblende crystal structure of many III–V semiconductors. (b) Band structure of GaAs with its direct gap.

change in the k-vector corresponds to a change in the momentum. This requires the intervention of another party—such as a lattice vibration—to guarantee momentum conservation.

Note that for both the Si and Ge band structures there are two $E(k)$ curves at the top of the valence band, with different curvatures d^2E/dk^2—corresponding to differences in the effective masses (Eq. (9)). Holes can belong to either one of them, so they can have different m^* values. Accordingly, the two valence-band $E(k)$ curves in Figs. 9b and c are called "heavy-hole" band and "light-hole" band.

These are the values of some important parameters of Si and Ge (the effective masses are expressed in terms of the free electron mass):

	Si	*Ge*
E_g (300 K)	1.12 eV	0.67 eV
Electron effective masses (heavy and light)	0.98, 0.19	1.6, 0.08
Hole effective masses (heavy and light)	0.49, 0.16	0.33, 0.04

III–V compounds and organic semiconductors

Binary materials in the III–V class exhibit a wide spectrum of properties of concrete or potential interest for practical applications. Fig. 10a shows the typical zincblende crystal structure of many of such compounds. This structure is related to that of diamond, but it includes two atomic species rather than one.

Fig. 10b shows the band structure of the leading III–V semiconductors, GaAs. As for Si and Ge, we see heavy-hole and light-hole bands. The gap is direct for GaAs but not for all III–V compounds: for example, it is indirect for GaP. The gap widths at 300 K for the important III–V semiconductors GaAs, GaP, InP, and GaN are 1.42, 2.26, 1.35, and 3.44 eV.

There exist many more semiconducting materials that those mentioned above. We shall limit our attention on a few additional ones because of their massive applications.

Optical properties and their applications

Quite important are the semiconductors used in devices emitting visible light—for illumination and for the displays of computers, portable telephones or television sets. As we shall see shortly, the production of visible light requires materials with large gaps. A typical example is GaN, whereas Si is not ideal because of its rather small gap.

GaN is indeed largely used at present for "light-emitting diodes" (LEDs). There is, however, a strong competition with "organic" LEDs (OLEDs), based on organic semiconductors formed by small organic molecules or by polymers.

Strictly speaking, organic semiconductors are not really semiconductors but insulators because of their large gaps. However, they share with conventional semiconductors important properties such as the possibility to inject electron and holes with biased electrodes.

Both LEDs and OLEDs offer advantages and disadvantages. For example, the efficiency and image quality of OLED displays is superior, but the lifetime is typically shorter. Technological research for both classes of materials is very active, so the relative weight of advantages and disadvantages could significantly change in the future.

The operation of LEDs is based on the interactions of semiconductors with photons. In turn, such interactions are dominated by the forbidden gaps. For example, electronic transitions between the valence band and the conduction band cannot cause the emission or absorption of photons of energy smaller than E_g (without involving impurity levels).

Note that the gaps of Si and Ge correspond to infrared photon energies, so they are not ideal for visible-light devices. This is also true for GaAs and InP, whereas for GaP E_g corresponds to visible photons and for GaN to the border between ultraviolet and visible.

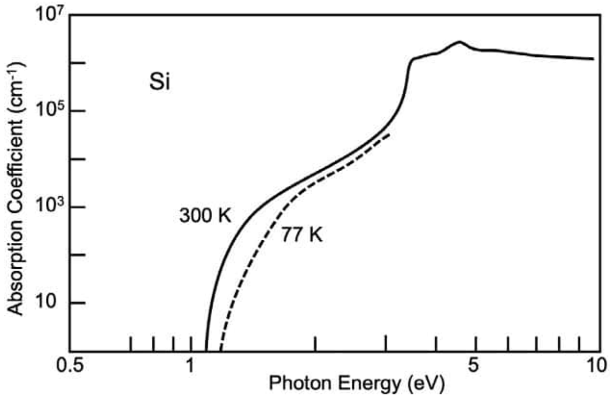

Fig. 11 Absorption coefficient of silicon measured for two temperatures in the photon energy range near the gap width value E_g. Note the steep threshold related to E_g.

Fig. 11 shows the absorption coefficient of silicon plotted in a photon energy range near E_g. There is a sharp edge: the absorption is minimal below E_g, but it rapidly increases above it due to optical transitions of valence-band electrons to empty states above the gap.

Photon emission is symmetric to photon absorption. The process takes place when electrons are injected in the conduction band and undergo optical transitions to empty states in the valence band. Such transitions can be also described as the recombination of electrons and holes.

Real optical processes are often more complicated than the above simplified descriptions. Which, for example, did not consider the interactions between electrons. In reality, the electrons do interact—in particular, the free electrons in the conduction band with the electrons in the valence band. This causes the so-called "excitonic effects."

The simplest case of such effects is the formation of "Wannier excitons." An exciton of this kind is created by the Coulomb attraction between a free electron and a hole, binding them together. The two particles form a system similar to a hydrogen atom, in which the proton is replaced by a much lighter hole and the dielectric constant is that of the semiconducting material.

A Wannier exciton has bound states corresponding to hydrogen-like energy levels, whereas its ionization states constitute the conduction band. This kind of exciton is quite delocalized, justifying the use of effective masses—whereas the so-called "Frenkel" excitons are localized.

The excitation of an electron from the valence band by absorption of a photon can take place in two different ways: by entirely freeing the electron into the conduction band or by forming an exciton. The latter corresponds to a transition to one of the exciton energy levels.

Therefore, in the plot of absorption vs. the photon energy the "continuum" above the E_g edge is preceded by excitonic absorption peaks. The first peak corresponds to the creation of an exciton in the ground 1*s* hydrogen-like level. And other discrete levels can produce other peaks.

However, the actual detection of excitonic peaks is not easy, since it requires sufficient spectral resolution and a low temperature to avoid excessive thermal broadening. Fig. 12a shows that excitonic absorption peaks are indeed seen for GaAs when the temperature is low.

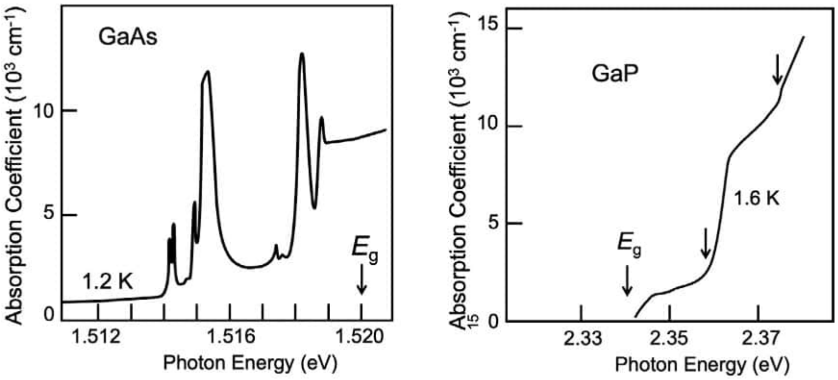

Fig. 12 On the left: excitonic peaks in the low-temperature absorption spectrum of GaAs. On the right: the absorption edge of indirect-gap GaP, also at low temperature. The arrows mark spectral features related to the gap and to specific phonons that guarantee the momentum conservation.

Photon absorption becomes more complicated when the gap is not direct as for GaAs, but indirect. As mentioned above, the optical transitions must be assisted by a suitable "third party" besides the photon and the electron (or the hole)—which guarantee the conservation of the momentum. Lattice vibrations (i.e., phonons) can play this role.

Fig. 12b illustrate this point with the absorption edge of indirect-gap GaP. We see several spectral features related to the participation of specific phonons that absorb part of the photon energy and contribute to the momentum. As for excitonic peaks, the detection of these features requires low temperature and high spectral resolution.

Excitonic effects affect not only the absorption but also the emission of photons. In that case, the important excitons are those "bound" to impurities.

In general terms, impurity levels in the forbidden gap allow the emission (and the absorption) of photons with energies smaller than E_g. Consider, for example, GaP: its room-temperature gap, 2.26 eV, corresponds to green visible photons. The corresponding light-emitting devices could be quite effective since the peak of the human eye response occurs for green light.

However, photon emission from pure GaP is rather ineffective, because its indirect gap requires the intervention of phonons as seen in Fig. 12b, limiting the electron–hole recombination rates. Doped GaP can be more effective in some cases by not requiring phonons, but its emission corresponds to excitonic impurity levels in the gap. The emitted photons are no longer green but shifted to the red—where the human eye is less efficient.

From the above discussion, we can realize that the ideal semiconducting material for visible LEDs should have a large gap and be suitable for doping with different types of impurities. Such impurities can produce optical transitions at different photon energies smaller than the gap, ideally covering the entire visible spectrum. The material can then emit different colors and be used in LEDs for variable color emission or for white light.

We have seen that an excellent solution is offered by the wide gap of GaN. Doped with suitable impurities, GaN emits blue light as well as other colors. In recent decades, excellent progress in the GaN technology led to the aforementioned fabrication of very efficient white-emitting LEDs. The rather spectacular results are now visible in everyday life.

LED mechanism

How does a semiconductor LED work? Fig. 13a schematically shows a simple type based on a forward-biased *p*–*n* junction. As we have seen, this bias lowers the barriers for electrons and holes. Electrons from the *n*-region can cross the junction into the *p*-region, where they find a large density of holes. This allows electron–hole recombination and the emission of photons.

Symmetrically, the reduced barrier enables some holes to cross from the *p*-region to the *n*-region. There, they find a large density of free electrons, and produce photons by electron–hole recombination.

The *p*–*n* junction is also the foundation of another important type of optoelectronic device: light detectors or photodiodes. Fig. 13b schematically shows how it operates.

The *p*–*n* junction is now reverse biased, so that normally very little current flows through it. When photons with energies larger than E_g reach the junction, their absorption can excite electrons into the conduction band. Suppose that the excitation occurs in the interface region. The free electrons find a voltage drop that sweeps them into the *n*-region and then to the external circuit. Symmetrically, the holes are swept into the *p*-region, also contributing to the current. The photon beam thus produces a photocurrent that reveals its arrival on the diode—which acts as a light detector.

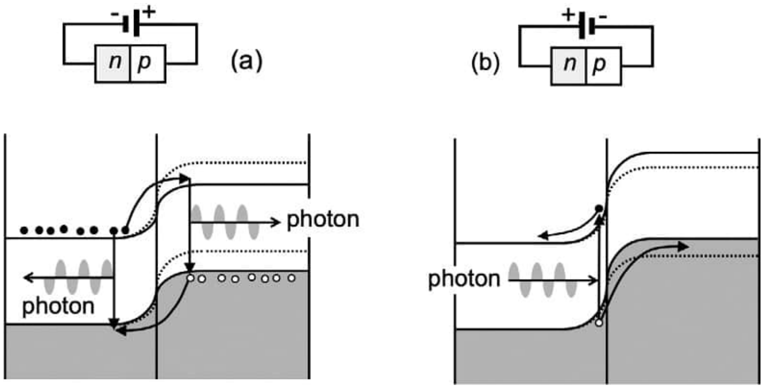

Fig. 13 Simple types of semiconductor optoelectronic devices based on the *p*–*n* junction. (a) The forward bias of an LED lowers the barriers for electrons and holes, which can cross the junction reaching the opposite region, where they recombine and emit photons. (b) With reverse bias, very little current normally flows through the junction. When photons with energy larger than the gap illuminate the device, they can excite electrons within the depletion layer into the conduction band, creating holes. The bias sweeps these electrons into the *n*-region and the holes into the *p*-region, from which they can reach the external circuit and cause a photocurrent. The junction can thus operate as a light detector or a solar cell.

Similar to the light detectors are the semiconductor solar cells—that convert the energy of photons into electric power, providing an alternate source of energy of increasing importance. In this case, the semiconductor materials must be optimized for the absorption of a large part of the solar spectrum.

The solar cell technology is currently dominated by silicon. However, alternate solutions have emerged like the “Graetzel” cells and the solar cells based on materials of the class “perovskites.” Time will identify the winning technology—or perhaps the winning combination of different approaches.

Conclusion

The transport and optical properties linked to the electron energy structure of semiconductors led to practical devices that influence every aspect of our life today. There is no question that this role will continue in the future. In fact, the expanded use of properties like the optical absorption will further expand this role, in particular in strategic areas like the production of clean energy.

Further reading

Ashcroft NW and Mermin ND (1976) *Solid State Physics*. Pacific Grove: Brooks/Cole.
Brütting W, Adachi C, and Holmes RJ (2012) *Physics of Organic Semiconductors*. Weinheim: Wiley.
Dugaev V and Litvinov V (2021) *Modern Semiconductor Physics and Device Applications*. Boca Raton: CRC Press.
Grosso G and Pastori Parravicini G (2000) *Solid State Physics*. Amsterdam: Academic Press.
Harrison WA (1980) *Electronic Structure and the Properties of Solids*. New York: Freeman.
Kittel C (1995) *Introduction to Solid State Physics*. Hoboken: Wiley.
Neamen DA (2012) *Semiconductor Physics and Devices*. New York: McGraw-Hill.
Ortion J (2004) *The Story of Semiconductors*. New York: Oxford.
Seeger K (1999) *Semiconductor Physics: An Introduction*. New York: Springer.
Sze SM (1981) *Physics of Semiconductor Devices*. Hoboken: Wiley.
Tiwari S (2020) *Semiconductor Physics*. Oxford: Oxford University Press.
Wenckebach WT (1999) *Essentials of Semiconductor Physics*. Hoboken: Wiley.
Yu PY and Cardona M (2001) *Fundamentals of Semiconductors: Physics and Materials Properties*. New York: Springer.

Semiconductors: Exciton theory

PB Littlewood, University of Chicago, Chicago, IL, United States

© 2024 Elsevier Ltd. All rights reserved.

This is an update of P.B. Littlewood, Excitons: Theory, Editor(s): Franco Bassani, Gerald L. Liedl, Peter Wyder, Encyclopedia of Condensed Matter Physics, Elsevier, 2005, Pages 179–184, ISBN 9780123694010, https://doi.org/10.1016/B0-12-369401-9/00660-4.

Introduction and basic ideas **418**
Binding of excitons **419**
Frenkel excitons 419
Hydrogenic excitons 419
Indirect excitons 421
Confined excitons: Quantum wells, wires, and dots 421
Interactions between excitons **422**
Excitonic molecules and complexes 422
Electron-hole liquid 422
Coherence and Bose-Einstein condensation 423
Optical properties **424**
Dipole coupling 424
Exciton polaritons 424
Conclusion **426**
References **426**

Abstract

Excitons are the lowest energy optical excitation in a semiconductor. Light absorbed by a semiconductor above the bandgap creates an electron-hole pair which is then bound by the Coulomb attraction to form an atomic-like bound state, that may nonetheless be mobile throughout the solid, and is a composite boson. Excitons may have excited states, may form complexes with multiple excitons, and may bind extra electrons or holes to form charged 'trions.' When there is a dipole-allowed recombination to a photon, there is a composite boson formed known as a polariton. Polaritons are bosonic quasiparticles with a very light mass, and can form a phase-coherent ground state that is a non-equilibrium Bose Einstein condensate.

Key points

- Description of an exciton as a bound excited electron-hole pair in a semiconductor
- Optical spectrum of an exciton
- Excitonic interactions and excitonic matter
- Exciton-photon coupling and the polariton

Introduction and basic ideas

The electronic band structure in a solid gives a formal accounting of the excitation energy $E_n(\mathbf{k})$ for adding to the ground state of the system a *single* carrier in the state of momentum $\mathbf{k}$. If the energy is greater than the chemical potential - i.e. an empty state - this refers to an electron; if the energy is below the chemical potential - a filled state - the excitation is a hole. In a semiconductor or insulator there is a gap between the creation of electrons and holes. Of course adding one electron and one hole in different bands or with different momenta creates an excited state of the system - and if the electrons and holes did not interact, we could of course enumerate the energies of the excited states just from the one-particle bands. However, the electron and hole are oppositely charged and therefore attract - the minimum energy required to create an electron-hole pair is therefore always less than to create either particle separately. The attraction between these two oppositely charged single particle excitations creates a bound state called an *exciton* - just as the Coulomb attraction between a proton and an electron creates the bound states of the Hydrogen atom. This is schematically described in Fig. 1.

Excitons recapitulate within a solid much of the physics of solids themselves, but with the added richness provided by the complexity of the bandstructure on which they are based. There are varieties of excitons, just as there are varieties of excited atomic states. Excitons themselves interact: there exist excitonic molecules, excitonic liquids, and possibly even coherent condensed states akin to the Bose-Einstein condensation of cold atoms - though these have not yet been unequivocably observed. In some materials, excitons are heavy and easily localized, whereas in others they are very light and readily propagate throughout the solid. Excitons are composite

https://doi.org/10.1016/B978-0-323-90800-9.00131-1

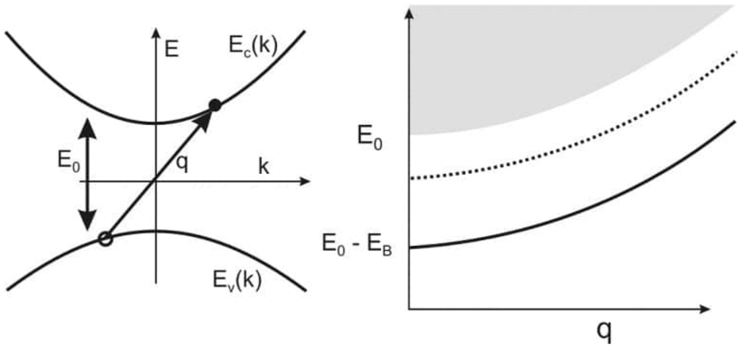

Fig. 1 On the left is a sketch of the lowest conduction $E_c(k)$ and highest valence $E_v(k)$ bands for a simple direct gap semiconductor with a quadratic dispersion and masses for electron and hole of m_e, m_h. If these bands described non-interacting particles, the lowest excitation energy of total wavevector q is then $E_o + \hbar^2 q^2/2M$, where $M = m_e + m_h$, which marks the edge of a continuum of excitations of free electrons and free holes, shown by the gray hatched region on the right. Allowing for the binding of the electron and hole, the lowest excitations are now excitons - a series of discrete states that disperse approximately parallel to the bottom of the continuum, but shifted downward by the binding energy E_B.

bosons (formed from two fermions) and have spin degrees of freedom. They may trap on defects and disorder, and may also have strong interactions with the lattice leading to the formation of excitonic polarons. And most importantly, excitons often interact strongly with light, so that they are often the dominant feature in optical spectra of solids. Excitons may be observed in such a case by their absorption profile, but more frequently by their luminescence - the recombination emission of light which is therefore at the total energy of the electron-hole pair. Even if they do not decay radiatively, excitons are of course transient phenomena - they have a finite lifetime, which can however be very long in some materials at low temperature. Good overviews of this broad topic are available in several books (Knox, 1963, Cho, 1979). Excitons and excitonic physic are important for practical applications of photonics in semiconductors, including lasers, light-emitting diodes, and solar cells (Chuang, 1995; Haug and Koch, 1993).

Binding of excitons

Frenkel excitons

Conceptually the simplest picture of an exciton emerges for crystals made of tightly bound electron states, such as rare gases or highly ionic solids. In these materials the electronic bands are narrow, and excitations within the solid are thus nearly localized. An atomic excited state, embedded within a lattice of unexcited atoms, is a cartoon for a *Frenkel exciton* - but of course since all the atoms in the solid are identical this excitation hops from atom to atom throughout the solid to form a weakly dispersing band with a large mass. While the original concept of a Frenkel exciton was based on a transition occurring in a lattice of neutral atoms, highly localized excitons may also involve charge transfer between orbitals on nearby atoms or groups of atoms. This latter is often the dominant situation in polymers, and organic materials (Davydov, 1971). Often the correct description is a mixture of Frenkel and charge transfer exciton, as one can see in Fig. 2 by the shift of absorption and the development of new structure between an isolated molecule, and a crystal.

Generally, these highly localized excitons require detailed microscopic theory to analyse their spectral structure. Being localized, they couple strongly to vibrational degrees of freedom of the molecule, often producing extra "vibronic" structure.

Hydrogenic excitons

The opposing limit of weakly bound excitons is much more straightforward to analyse, and this produces the excitons familiar in direct gap semiconductors such as GaAs. Here the band dispersion is large, so that the energy cost of occupying states of large momentum $k \approx \pi/a$ (where a is the lattice constant) is large. Hence the excitonic bound state is a wavepacket made up from electron and hole states near $k \approx 0$. The valence and conduction band states are Bloch states, of the form

$$\psi_{n\mathbf{k}}(\mathbf{r}) = u_{n\mathbf{k}}(\mathbf{r}) e^{i\mathbf{k}\cdot\mathbf{r}}, \tag{1}$$

where u is a periodic function on the crystal lattice, and $n = c, v$ will refer to the conduction and valence bands respectively. If we neglect the momentum dependence of u_{nk}, the wavefunction for an exciton becomes separable,

$$\Psi(\mathbf{r}_e, \mathbf{r}_h) = u_{c\mathbf{k}=0}(\mathbf{r}_e) \times u_{v\mathbf{k}=0}(\mathbf{r}_h) \times f(\mathbf{r}_e - \mathbf{r}_h) \times e^{i\mathbf{q}\cdot\mathbf{R}}. \tag{2}$$

Here R is the center of mass coordinate, and q the corresponding momentum (see Fig. 1). $f(\mathrm{r})$ is the exciton wavefunction in relative coordinates, and satisfies the Schrödinger equation

$$\left[\frac{-\hbar^2}{2\mu}\nabla^2 - \frac{e^2}{4\pi\epsilon\epsilon_o r}\right] f(\mathbf{r}) = (E - E_0) f(\mathbf{r}). \tag{3}$$

where $\mu = m_e m_h/(m_e + m_h)$ is the reduced mass, ϵ the relative dielectric constant, and E_0 the single particle gap.

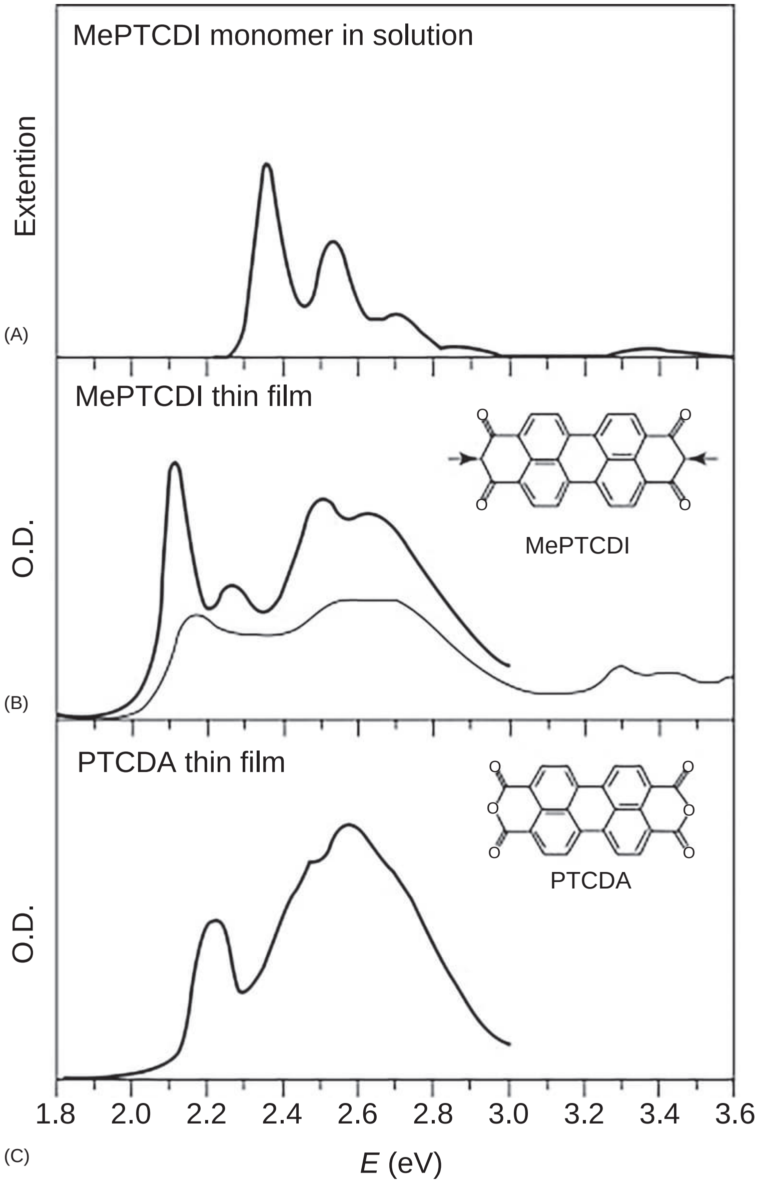

Fig. 2 A comparison of absorption spectra of monomers with crystals where the excitons are highly localized. (A) shows the absorption of isolated molecules in solution, whereas (B) shows the optical density of a polycrystalline film of the same material. The thick curve is at 5 K in p-polarization and the thin curve at 293 K in s-polarization. (C) is from a crystalline film of a similar compound at 5 K. Reproduced with permission from Hoffmann M, Schmidt K, Fritz T, Hasche T, Agranovich VM, and Leo K (2000) *Chemical Physics* 258: 73.

This *Wannier exciton* then has the spectrum of a hydrogen atom, with the difference being that in direct gap semiconductors like GaAs the effective mass is small ($\mu/m \approx 0.1$) and the dielectric constant is large ($\epsilon \approx 10$). This means that the binding energy

$$E_B = \frac{\mu e^4}{8\epsilon^2\epsilon_o^2 h^2} = \frac{\mu}{m}\frac{1}{\epsilon^2} Ryd. \tag{4}$$

may be a small fraction of the Rydberg ($Ryd. = 13.6\ eV$). The size of the exciton is given by an effective Bohr radius

$$a^* = \frac{\epsilon\epsilon_o h^2}{\pi\mu e^2} = \epsilon\frac{m}{\mu}a_o \tag{5}$$

much larger than the Hydrogen Bohr radius $a_o = 0.05\ nm$. Thus the wavefunction extends over several unit cells, which justifies the approximate expression made for the wavefunction in eq. (2). The hydrogenic-like series of lines is well seen in the higher principal quantum number states in Cu_2O, Fig. 3.

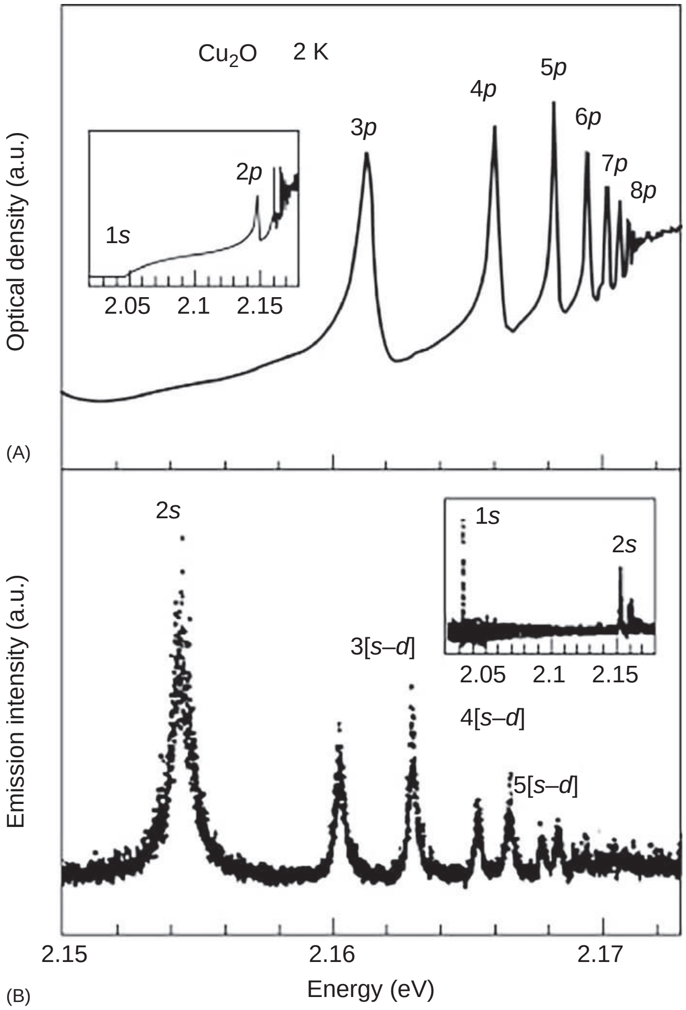

Fig. 3 Exciton spectrum in *Cu$_2$O*. The upper panel is derived from one-photon absorption (and thus begins with the 2p state) and the lower panel shows the two photon absorption, showing thus s- and d- series. The insets show the full spectrum. Reproduced with permission from Matsumoto H et al. (1996) *Solid State Communications* 97: 125.

Indirect excitons

It is not necessary for exciton states correspond to vertical band transitions (i.e. $q = 0$ in Fig. 1) because we can construct a wave packet about *any* band extremum. So for example in Ge the lowest excited state is made from wave packets of holes at $k = 0$ and electrons at the equivalent conduction band minima along the [111] direction at the Brillouin zone boundary. A similar situation pertains for Si, except that the electrons are confined to six pockets in the [100] directions (inside the Brillouin zone). These excitons are called *indirect* because they require a non-zero momentum to connect the electron and hole. Momentum conservation then does not allow the exciton to directly decay into a photon, and one requires either a process involving recombination also with emission of a phonon, or scattering from an impurity or a surface or other confinement. This is typically very inefficient, which is why Si is not used for optical devices.

Confined excitons: Quantum wells, wires, and dots

The engineering of quantum wells in semiconductors can also be used to manipulate excitonic states. In $GaAs/Ga_{1-x}Al_xAs$ quantum wells (the canonical system, though many of the III–V and II-VI series are used) one may confine both electron and hole to a narrow sheet, comparable or smaller in size than the effective Bohr radius a^*. It is also possible to create more complicated structures including quantum wires, and quantum dots. There are two principal effects. Firstly, the extra confinement brings the electron and hole closer together and increases (sometimes substantially) the binding energy producing a shift in the energy of absorption and luminescence in comparison to bulk material. The second effect arises because of the structure of the top of the valence band which in a bulk system has a degeneracy between the light and heavy hole bands at $k = 0$ (the states are p-like, which therefore have a threefold orbital degeneracy under cubic symmetry; with spin-orbit coupling the pair of bands are the fourfold-degenerate $J = 3/2$).

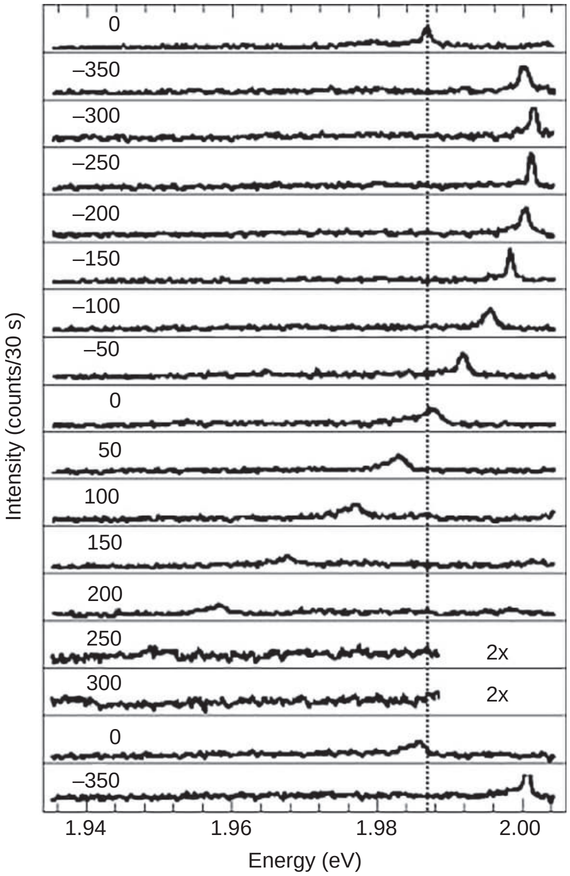

Fig. 4 Luminescence of a 7.5 nm CdSe nanocrystal shows the quantum confined Stark effect. The position of the exciton line shifts under a range of electric fields - values in kV/cm are shown for each trace. Reproduced with permission from Empedocles SA and Bawendi MG (1997) *Science* 278: 2114.

This degeneracy is broken by the quantum well, which fixes a local axis, and splits the light and heavy hole bands, leading to a further separation of the two types of exciton.

The exciton energy, and its binding, are affected by applied electric fields, since an applied field will pull the electron and hole apart from each other. In a bulk system quite small fields can ionize the exciton, but if the exciton is confined either to a well or a quantum dot (see Fig. 4) the electron and hole will be trapped and very large shifts of the exciton luminescence with electric fields can be produced. This is the *quantum-confined Stark effect*, a principle used in semiconductor laser modulators.

Interactions between excitons

Excitonic molecules and complexes

Like atoms, excitons interact and may bind to form molecules and other complexes. Atomic H binds to form H_2 in an exothermic reaction that generates about $1/3$ *Ryd*. per molecule. The analog of H_2 is the biexciton (sometimes labeled as X_2) - which is however typically less bound than H_2 because of the finite hole mass. In a bulk semiconductor with equal mass electrons and holes, the binding energy of a (hydrogenic) biexciton is about $0.03\ E_B$, proportionately one order of magnitude smaller than for H_2; but in GaAs, where the hole is proportionately heavy, the binding energy can be substantial (see Fig. 5).

Stable species can also be made when excitons bind to electrons and holes (*trions*) - a situation which can arise upon optical excitation of a low-density electron or hole gas in a semiconductor. In general, many exciton complexes have been discovered.

Electron-hole liquid

If the density of excitons is increased so that they overlap, they lose their individual character as atoms, as the electrons and holes become unbound. The high density two-component plasma so formed is then an electrical conductor - with one fermi surface each for electrons and holes - similar to an equilibrium semimetal. The transition between the excitonic insulator and the plasma state occurs at the density $n(a^*)^d \approx 1$ as for the Mott metal-insulator transition. This has for many years been a focus of study in semiconductors because the large effective Bohr radius means that this regime can be reached at moderate excitation levels. A typical semiconductor laser is in this density range, though also usually at a temperature well exceeding the exciton binding energy.

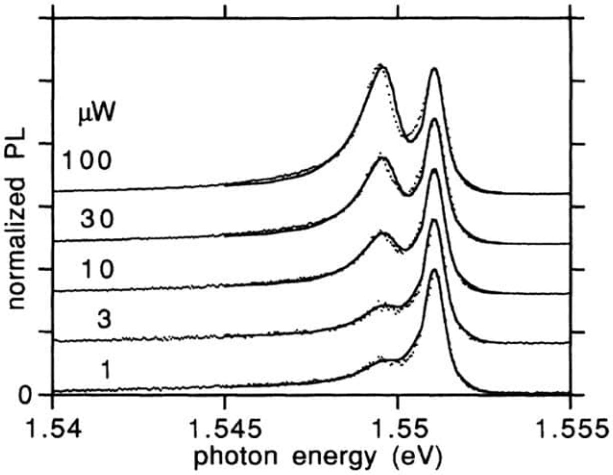

Fig. 5 Optical emission from excitons and biexcitons in GaAs, normalized to the intensity of the excitonic peak and resulting from optical pumping at an energy well above the exciton emission. At increasing intensities of illumination, the biexciton emission grows because two excitons must collide and bind within the time scale for recombination. The solid line is a fit to the data. Reproduced with permission from Phillips RT et al. (1992) *Physical Review B* 45: 4308.

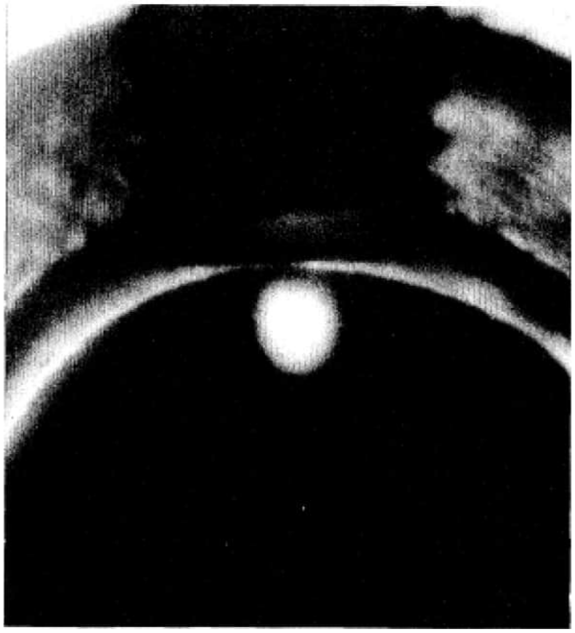

Fig. 6 Electron-hole liquid in Ge. A photograph of a droplet of electron-hole liquid at 2 K in a 4 mm diameter Ge disk, stressed by a nylon screw (top) along (110) and viewed through an (001) face. The central bright region is the e-h recombination luminescence from the liquid confined in a potential well of maximum shear stress. The bright ring around the sample is recombination luminescence scattered from the surface of the crystal. Reproduced with permission from Markiewicz RS, Wolfe JP, and Jeffries CD (1977) *Physical Review B* 15: 1988.

In Si and Ge, it turns out that the dense plasma phase is lower in energy than to distribute the electron-hole pairs as a dilute gas of excitons or biexcitons. The origin of this phenomenon is the multivalley nature of the conduction band in these materials - in the plasma phase the kinetic energy cost of the excitons is distributed over many valleys so its stability is correspondingly enhanced. In consequence, high density *electron-hole droplets* (Fig. 6) form spontaneously - and can also be manipulated by applied elastic strain (Jeffries and Keldysh, 1983).

Coherence and Bose-Einstein condensation

Because excitons are light-mass bosons (albeit composite), there has also long been interest to observe Bose-Einstein condensation of excitons. In order to explore such physics, one needs to lower the temperature below the point where the thermal de Broglie wavelength exceeds the interparticle spacing, i.e. a temperature $k_B T_o = \hbar^2 n^{2/3}/M$. Among the systems studied are Cu_2O (which has long-lived excitons that are dipole forbidden), *CuCl* (which has very stable biexcitons) and two-dimensional quantum wells (in which the electrons and holes can be physically separated). Such a state would be interesting not just for its statistical physics, but also because of the presence of spontaneous phase coherence, as in superfluid He, or cold atomic condensates (Moskalenko and Snoke, 2000).

While it has proved possible to enforce or encourage coherence through optical means, evidence for Bose-Einstein condensation of excitons in thermal equilibrium is still meager, though it is well-established for a closely-related composite particle that is a superposition of an exciton and a photon (Proukakis et al., 2017).

Optical properties

As discussed above, one of the principal reasons that excitons are so evident is because of their strong effects on the optical properties of solids. For very localized Frenkel excitons, it is largely correct to think of excitons as being atomic or molecular species, localized on specific sites in the solid. In general, it is not simple to calculate optical properties of excitons, except for the specific (and fortunately rather common) case of the hydrogenic Wannier exciton.

Dipole coupling

We consider here only the common case where the conduction and valence bands are of relative odd parity (as in zincblende II–VI and III–V semiconductors) so that the dipole matrix element

$$p_{cv} = \langle \psi_{ck} | \mathbf{e} \cdot \hat{\mathbf{p}} | \psi_{vk} \rangle_{k=0} \tag{6}$$

is non-zero and in a cubic system independent of the polarization direction e. The probability P per unit time and per unit volume that an electromagnetic wave with a vector potential $A\mathbf{e}e^{i\omega t - \mathbf{q}\cdot\mathbf{r}}$ will be absorbed to create an exciton is given by the *Elliott formula* (Elliott, 1957).

$$P = \frac{4\pi}{\hbar}\left(\frac{eA}{m}\right)^2 |p_{cv}|^2 f(0)^2 \delta(E_{ex} - E_0 - \hbar\omega). \tag{7}$$

where we have assumed that the wavelength of light is long enough so that we may set $\mathbf{q} = 0$.

The answer is a sequence of lines at the energies $\hbar\omega_n = E_0 - Ryd^*/n^2$ corresponding to the principal quantum numbers $n = 1, 2, 3, \ldots$, their intensities depending on the relative wavefunction $f(r)$ evaluated at the origin (when the electron and hole are coincident). Thus the absorption is largest if the exciton is tightly bound (since $f(0)^2 = 1/\pi(a^* n)^3$) and also if the basis states supporting the Bloch states are strongly dipole active. Eq. (7) gives only the Rydberg series below the continuum, but above and close to the edge of the continuum absorption, the excitonic effects enhance the absorption above that to be expected in free electron theory, as shown in Fig. 7.

Exciton polaritons

A peak in the absorption such as shown in Fig. 7 corresponds to a pole in the real part of the dielectric function, so below the gap,

$$\epsilon(\omega) \approx \epsilon_\infty + \frac{A_n}{\omega_n - \omega}, \tag{8}$$

where the amplitudes A_n are proportional to the coefficients in eq. (7). A pole in the dielectric response is a free mode of oscillation of the polarization; when light travels in a polarizable medium such as this the coupled modes are called *polaritons.* These modes can be made beautifully visible by confining the light between mirrors to form a planar microcavity. See Fig. 8.

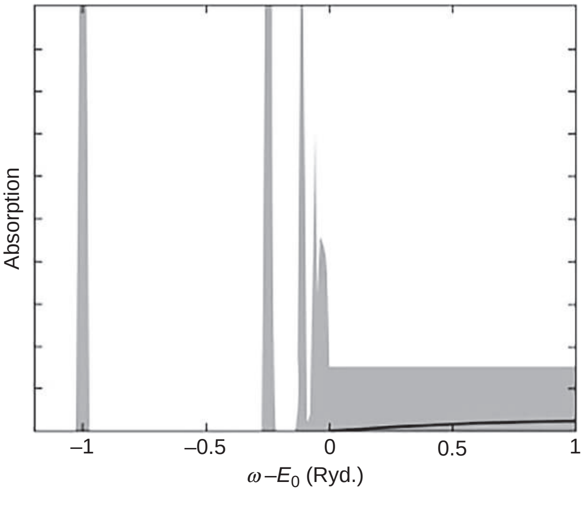

Fig. 7 Absorption predicted by the Elliott formula of eq. (7). Notice that even above the continuum edge at E_0 the absorption (gray) is enhanced over that predicted in the absence of Coulomb interactions (solid line).

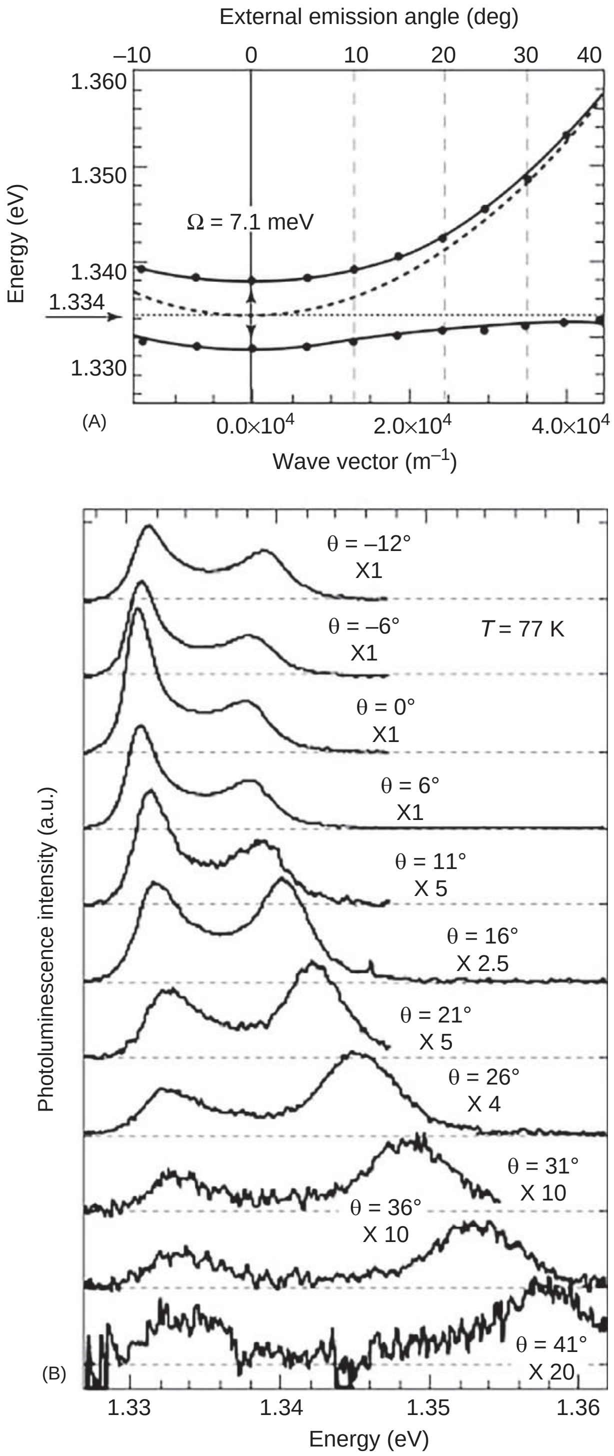

Fig. 8 Dispersion of two-dimensional microcavity polaritons. (a) Light is confined between two planar mirrors so as to fix the perpendicular momentum and to give a dispersion $\omega = \sqrt{\omega_0^2 + c^2k^2}$ where k is the momentum parallel to the plane. $\omega_o \approx c\pi/L$ where L is the separation between the mirrors, and this can be chosen to be resonant with the exciton energy as in the figure (A). On the scale of the wavelength of light, the exciton dispersion is negligible. The mixing of the two modes gives rise to level repulsion, and the dispersion marked by the solid points. (b) This dispersion is derived from the lower figure, which shows the luminescence from the microcavity as a function of angle, which can be directly converted into the parallel momentum k. Reproduced with permission from Houdre R, Weisbuch C, Stanley RP, Oesterle U, Pellandini P, and Ilegems M (1994) *Physical Review Letters* 73: 2043.

Polaritons have been seen to spontaneously condense into a phase coherent state as a Bose-Einstein Condensate (Kasprzak et al., 2006).

For excitons that are strongly localized and thus subject to disorder and incoherent fluctuations, one rarely observes fully coherent modes. But nevertheless the resonant process that transfers an exciton from one localized state to a resonant one nearby can be important, in a process called *Förster transfer*.

Conclusion

This article has provided an elementary introduction to the physics of the most elementary electronic excitation in an undoped semiconductor. The exciton controls the observed optical spectrum, and exciton recombination is the source of light emission in lasers and light-emitting diodes. Exciton physics is also important for - and usually detrimental to - the performance of solar cells. So while the basic phenomena have been long understood, there continues to be considerable research activity to optimize materials for practical function, and also to exploit the collective behavior of excitonic matter for novel electrooptical devices.

References

Cho K (1979) *Excitons*. Berlin: Springer.

Chuang SL (1995) *Physics of Optoelectronic Devices*. NY: Wiley.

Davydov AS (1971) *Theory of Molecular Exciton*. NY: Plenum.

Elliott RJ (1957) *Physics Review* 108: 1384.

Haug H and Koch SW (1993) *Quantum Theory of the Optical and Electronic Properties of Semiconductors*, 2nd edn. Singapore: World Scientific.

Jeffries CD and Keldysh LV (eds.) (1983) *Electron-hole Droplets in Semiconductors*. New York: Elsevier.

Kasprzak J, Richard M, Kundermann S, Baas A, Jeambrun P, Keeling JMJ, Marchetti FM, Szymańska MH, André R, Staehli JL, Savona V, Littlewood PB, Deveaud B, and Dang LS (2006) *Nature* 443: 409–414.

Knox RS (1963) *Theory of Excitons*. New York: Academic Press.

Moskalenko SA and Snoke DW (2000) *Bose-Einstein Condensation of Excitons and Biexcitons and Coherent Nonlinear Optics with Excitons*. Cambridge: Cambridge University Press.

Proukakis NP, Snoke DW, and Littlewood PB (eds.) (2017) *Universal Themes of Bose-Einstein Condensation*. Cambridge University Press.

Polarons in condensed matter

David Emin, Department of Physics and Astronomy, University of New Mexico, Albuquerque, NM, United States

© 2024 Elsevier Ltd. All rights reserved.

This is an update of E.I. Rashba, Polarons, Editor(s): Franco Bassani, Gerald L. Liedl, Peter Wyder, Encyclopedia of Condensed Matter Physics, Elsevier, 2005, Pages 347–355, ISBN 9780123694010, https://doi.org/10.1016/B0-12-369401-9/00662-8.

Introduction **427**
Long-range electron-phonon interactions 429
Short-range electron-phonon interactions 429
Self-trapping: Formation of a strong-coupling polaron 430
Large- and small-bipolaron formation 431
Disorder-induced small-polaron formation 433
Coherent and incoherent polaron transport 433
Large-polaron transport 434
Small-polaron transport: Elemental hops 435
Small-polaron relaxation phenomena 437
Polarons' Seebeck coefficients 438
Polarons' Hall mobilities 439
Polaron absorption 440
Interactions between polarons 441
Superconductivity of a large-bipolaron liquid 442
Conclusion **444**
References **445**
Further reading **445**

Abstract

Polarons are composite quasiparticles comprising electronic charge carriers taken together with the alterations they induce in surrounding condensed matter. Strong-coupling polarons form when electronic charge carriers become 'self-trapped:' bound within potential wells stabilized by carriers' presence. Distinctively, exciting these bound carriers generates broad absorption bands. Strong-coupling polarons are slow and massive since moving them requires atomic motion. Their transport differs qualitatively from that of conventional electronic charge carriers. Large strong-coupling polarons move coherently with mobilities that fall with rising temperature. These massive quasiparticles' very weak scatterings by phonons produce much lower room-temperature mobilities than those permitted of conventional electronic charge carriers. Moreover, the long scattering times associated with large polarons' weak scattering relegates their principal ac (Drude) transport to below phonon frequencies. Small strong-coupling polarons move incoherently with even lower thermally assisted mobilities. Strikingly, a magnetic field often deflects small polarons in the opposite sense than it does conventional charge carriers, thereby producing anomalously signed Hall Effects. In exceptional circumstances charge carriers self-trap in pairs thereby forming large and small bipolarons. Some transport features distinguish them from polarons. Interference between carrier-induced atomic displacement patterns produce attractive interactions between like-charged polarons and short-range repulsive interactions between oppositely charged polarons.

Key points

- An electronic carrier is self-trapped when it is bound in a potential well produced by atoms assuming displaced equilibrium positions stabilized by the carrier's presence.
- Displaced distant ions generate the potential well which binds a large strong-coupling polaron's multi-site self-trapped carrier. Displacements of nearby atoms create the potential well which drives the collapse of a small strong-coupling polaron's self-trapped carrier to a single site. Disorder fosters small-polaron formation.
- Unusual transport and optical properties of large and small polarons distinguish them from each other and from conventional electronic carriers.
- Polarons tend to form in unusually complex materials. Polarons' distinctive properties enable unexpected applications.

Introduction

Adding electronic charge carriers to condensed matter generally affects its atoms' motion. A polaron is defined as the composite quasiparticle composed of an electronic carrier plus the altered atomic motion its presence induces.

There are two regimes in which polaron effects have been studied. In the weak-coupling regime, the relaxation of the electronic charge carrier in response to atomic movements only alters their frequencies. An electronic carrier then lowers the ground-state energy of the interacting system by a modest amount that vanishes as atomic vibrations are suppressed. Much larger energy shifts occur in the strong-coupling regime. Then the electronic carrier is 'self-trapped:' bound within the potential well produced by carrier-induced shifts of atoms' equilibrium positions. A dynamically stable strong-coupling polaron forms when the binding energy of the self-trapped electronic carrier greatly exceeds the characteristic phonon energy. Carrier-induced reductions of the frequencies with which atoms vibrate about their displaced equilibrium positions then make subsidiary contributions to a strong-coupling polaron's energy.

Unlike weak-coupling polarons, strong-coupling polarons have electronic and optical properties which distinguish them from conventional electronic charge carriers. Henceforth, this article will only consider strong-coupling polarons.

Self-trapping, the distinctive feature of strong-coupling polarons, is a nonlinear phenomenon. The potential well within which a self-trapped electronic carrier is bound results from atoms' assuming displaced equilibrium positions. However, these displacements of atoms' equilibrium positions are driven by the presence of the bound electronic carrier. That is, the potential well which binds a strong-coupling polaron's electronic carrier depends on its wavefunction. Solution of the carrier's nonlinear wave-equation generally permits two distinct types of strong-coupling polaron. A large-polaron's self-trapped carrier extends over multiple structural units. By contrast, a small-polaron's electronic carrier collapses to its minimal volume, e.g., a single structural unit.

A polaron's formation is governed by the forces between its electronic charge carrier and surrounding displaceable atoms. These interactions are often termed electron-lattice or electron-phonon interactions. A large polaron's formation usually requires long-range Coulomb-based interactions (e.g., the Fröhlich interaction) between its electronic carrier and condensed-matter's distant displaceable ions. By contrast, a small polaron's formation is usually generated by the energy of its electronic carrier depending on separations between the atoms it contacts. Separate large-polaron and small-polaron solutions can occur in the general case in which the electron-phonon interaction is the sum of long-range and short-range components.

The ratio of the static to optical dielectric constant, $\varepsilon_0/\varepsilon_\infty$, measures the prevalence of displaceable ions within a semiconductor. In particular, a ratio comparable to 1 indicates a covalent material with its purely short-range electron-phonon interaction. By contrast, ratios greater than or comparable to 2 (the value typifying alkali halides) indicate sufficiently displaceable ions to support the long-range electron-phonon interaction required for large-polaron formation. Ratios that greatly exceed 2 open the possibility of exceptional polaron effects, such as self-trapped carriers pairing to thereby form bipolarons.

A large polaron's self-trapped electronic carrier extending over multiple sites insures that its motion between adjacent sites is also coherent. Unlike the coherent transport of a conventional electronic charge carrier, a large polaron's motion is contingent on the movement of atoms. Therefore, a large polaron's motion is orders-of-magnitude slower and its effective mass is orders-of-magnitude greater than those of conventional electronic charge carriers. As a result, coherent large-polaron transport occurs with much lower mobilities than can be ascribed to conventional electronic charge carriers. In particular, the minimum mobility possible for a carrier's coherent transport occurs when its mean-free-path falls to its diameter, its de Broglie wavelength. This value is $qh/m_c kT$, where q and m_c denote the magnitudes of a carrier's charge and effective mass, T represents the absolute temperature while h and k respectively signify the Planck and Boltzmann constants. This minimum mobility is 300 cm^2/V-s at room temperature for a carrier with a free electron's charge and mass. Thus, smaller room-temperature mobilities than this are inconsistent with the transport of conventional electronic charge carriers. However, such small mobilities are compatible with those of large polarons. For example, the mobility of a large polaron scattered by acoustic phonons is $qc_s R_{lp}/kT$ above a fraction of the Debye temperature, where c_s denotes the sound velocity and R_{lp} represents the large-polaron radius.

The distinctively extreme localization of a small-polaron's self-trapped carrier generates incoherent charge transport. Small polarons then move by successions of jumps between sites. The resulting small-polaron mobility is extremely small, $\ll 1$ cm^2/V-s, and rises with increasing temperature. This thermally assisted hopping is Arrhenius above a significant fraction of the characteristic phonon temperature. A small-polaron's mobility manifests a progressively weaker temperature dependence as the temperature is lowered below this characteristic phonon temperature.

Large and small polarons also manifest optical properties which distinguish them from one another and from conventional electronic charge carriers. Unlike conventional charge carriers, large and small polarons both generate very broad asymmetric absorption bands that peak at energies well above phonon energies. A large-polaron's broad absorption band is generated by photo-ionizing its self-trapped electronic charge carrier from the potential well within which it is bound. With increasing photon energy, a large-polaron absorption band rises toward its peak and diminishes more slowly thereafter. A small-polaron's absorption of a photon induces its self-trapped carrier to hop. Each absorbed photon produces a small-polaron jump. With rising temperature, increased atomic vibrations increase the ranges of initial and final-state electronic energies involved in these photo-induced transitions. The width of a small-polaron absorption band is thereby thermally broadened. With increasing photon energy, a typical small-polaron absorption band rises toward its peak and then diminishes relatively rapidly. Thus, the thermally broadened asymmetry of a small-polaron absorption band distinguishes it from a large-polaron absorption band.

Large-polarons' coherent motion also produces an absorption analogous to the Drude absorption of conventional electronic charge carriers. Distinctively, a large polaron's huge mass causes it to be only very weakly scattered by ambient phonons that reflect off its softened atomic vibrations. As such, a large-polaron's motion is characterized by an extremely long relaxation time (proportional to its mass) that limits its Drude-like contribution to below the characteristic phonon frequency. Thus, there is a pseudo-gap in a large-polaron's absorption spectrum between its very low-frequency Drude-like absorption and the onset of its broad high-frequency photo-ionization band. This pseudo gap opens with decreasing temperature as phonon scattering is progressively suppressed.

General features governing the formation and properties of strong-coupling polarons were succinctly described in this introductory section. However, other dramatic manifestations of the formation and transport of strong-coupling polarons rely on specific features of the condensed matter in which they form. For example, the controlled imposition of disorder can induce charge carriers' abrupt transformation between their being conventional charge carriers or large polarons and being small polarons. Unlike conventional carriers, small-polarons often form in materials whose local site arrangements generate Hall Effect sign anomalies. Small polarons are then deflected by a magnetic field in the opposite sense to that of free particles bearing the same charge. The self-trapping of holes on oxides' oxygen-related states transfers electrons to surrounding cations. As such, formation of such polarons can alter magnetic moments of surrounding magnetic cations. Special features emerge in materials containing especially displaceable ions as manifested by exceptionally large ratios of their static to high-frequency dielectric constants. These situations favor attractive interactions among large polarons inducing their pairing into bipolarons. Furthermore, a gas of large bipolarons can even condense into a large-bipolaron liquid. Short-range repulsive interactions between polarons of opposite charge suppress their recombination thereby increasing the lifetimes of optically induced polarons. These and other topics will be addressed in the following sections.

Long-range electron-phonon interactions

Polaron effects address the responses of electronic charge carriers to the comparatively slow movements of condensed-matter's relatively massive atoms. These responses are driven by electron-phonon interactions. Electron-phonon interactions arise from dependences of an electronic charge carrier's potential energy on the positions of the nuclei of the atoms within which it is immersed.

An electronic carrier's Coulomb interactions with ions that surround it generate a long-range component of its electron-phonon interactions. A simple model for the long-range component considers only ions that are outside of the electronic carrier's radius. Treating the condensed medium as a continuum, the polarizability associated with displacing nuclei is represented as the difference between the continuum's net polarizability and that due to its bound electrons. As such, the effective coupling constant considers a Coulomb interaction modified by the factor $1/\varepsilon_\infty - 1/\varepsilon_0$, the difference between the reciprocals of the high-frequency dielectric constant ε_∞ and the static dielectric constant ε_0. This model's coupling strength is the Fröhlich constant, $\alpha \equiv e^2(1/\varepsilon_\infty - 1/\varepsilon_0)(m_e/2\hbar^3\omega)^{1/2}$, where e and m_e respectively denote the electronic carrier's charge and effective mass with ω signifying an optic-mode atomic vibration frequency. This continuum theory addresses a very large-radius self-trapped state with $\alpha^2\,\hbar\omega$ essentially being its binding energy. This model has been applied to self-trapped electrons in alkali halides.

Electrons in polar liquids such as water and ammonia are self-trapped. In these instances, the liquids' polar molecules are oriented to produce the potential well which binds the self-trapped electrons. Thus, for example, water molecules' electropositive hydrogen atoms are closer to the self-trapped electron than are their electronegative oxygen atoms.

Short-range electron-phonon interactions

The electron-phonon interaction in covalent semiconductors, termed the deformational-potential, is short-range. In particular, a charge carrier's energy depends on the separations between the atoms linked by the bonding or anti-bonding state that it occupies. The dependence of an electronic carrier's energy on the inter-atomic separation is typically quite large, 2–3 eV/Å. For comparison, the Coulomb interaction between two elementary charges separated by 3 Å is less than 5 eV even when the reduction associated with the dielectric constant (12 and 16 in Si and Ge, respectively) is ignored.

The short-range electron-phonon interaction's effect on an electronic state is inversely proportional to the number of atoms or bonds it contacts. Thus, for example, the electron-phonon interaction in a covalent semiconductor has a very much smaller effect on a large-radius donor state (e.g., a P donor state in Si) than it does on a well-localized donor state. Similarly, the effect of the short-range electron-phonon interaction on an electronic carrier in a molecule tends to decrease as its size increases.

A short-range electron-phonon interaction can predominate even in ionic solids such as alkali halides. For example, a hole in the alkali halide KCl is shared between two nearest-neighbor Cl anions to produce the molecular anion $(Cl_2)^-$: hole + $2Cl^- \rightarrow (Cl_2)^-$. In other words, this self-trapped hole is severely localized in the chemical bond which forms between two displaced Cl anions.

Charge transfer between oxygen anions and surrounding cations generates a distinctive short-range electron-phonon interaction. Despite an isolated oxygen atom only having an electron affinity for one electron, oxygen anions are widely represented as having an oxidation state of −2. That is, the cations that typically surround an oxygen anion in a solid facilitates its accommodating an extra electron. This electron will leave an oxygen anion as surrounding cations are displaced away from it.

Cations in ionic solids sometimes possess magnetic moments. Without charge carriers, super-exchange between these magnetic cations usually drives these solids to form anti-ferromagnetic insulators. Dopants and defects can introduce charge carriers. Intra-atomic exchange interactions between charge-carriers' spins and the cations' magnetic moments foster their ferromagnetic alignment. A carrier-induced ferromagnetic cluster within an antiferromagnetic is termed a magnetic polaron. Although the electronic carrier bound within a prototypical magnetic polaron (e.g., an electron in EuTe) may be only mildly localized, electron-phonon interactions will increase its localization.

Self-trapping: Formation of a strong-coupling polaron

A strong-coupling polaron is defined by having its electronic charge carrier self-trapped. A self-trapped electronic carrier is bound within the potential well generated by surrounding atoms assuming equilibrium positions consistent with the electronic carrier occupying its bound state. Moving such a polaron requires displacing atoms from their carrier-induced equilibrium positions. The validity of this approach is generally taken to require that the binding energy of the self-trapped electronic carrier $-E_{st}$ exceed the phonon energy characterizing associated atoms' vibrations $\hbar\omega$.

The carrier-induced displacements of atoms' equilibrium positions are found by minimizing the Born-Oppenheimer adiabatic potential. This potential energy is the sum of (1) the potential energy associated with displacing atoms from their carrier-free equilibrium positions plus (2) the electronic energy as a function of atoms' positions. The adiabatic potential with atoms at these displaced equilibrium positions establishes the potential well within which an electronic carrier is self-trapped.

The chemistry underlying these interactions can be complex. Nonetheless, here, as is typical, electronic-carrier's energies and inter-atomic strain energies are simply modelled to respectively have linear and quadratic dependences on atoms' displacements from their carrier-free equilibrium values.

A general approach to self-trapping proceeds by treating the solid as a deformable continuum. The ground-state wave function for the self-trapped electronic carrier $\varphi(\boldsymbol{r})$ with energy E_{st} is then the solution of the non-linear wave equation:

$$\left[\frac{-\hbar^2}{2m_e}\nabla_r^2 - \frac{1}{S}\int d\boldsymbol{r}'|\varphi(\boldsymbol{r}')|^2 \int d\boldsymbol{u}\, F(\boldsymbol{r}-\boldsymbol{u})F(\boldsymbol{r}'-\boldsymbol{u})\right]\varphi(\boldsymbol{r}) = E_{st}\varphi(\boldsymbol{r}). \tag{1}$$

Here m_e denotes the electronic carrier's effective mass and S represents the continuum's stiffness constant per unit volume. The electron-phonon force per unit volume $F(\boldsymbol{r}-\boldsymbol{u})$ describes how the electronic potential energy at location $\boldsymbol{r}$ depends on a fiducial deformation of the continuum at location $\boldsymbol{u}$.

This non-linear wave equation can be utilized to express the self-trapping energy as a functional of its wavefunction. This functional is then recognized to depend simply on the dimensionless radius R of the self-trapped electron's normalized wavefunction. For a charge carrier which can move among sites with dimensionality d embedded within a three-dimensional ionic medium:

$$E_{st}(R) = \frac{T_e}{R^2} - \frac{2V_S}{R^d} - \frac{2V_L}{R}. \tag{2}$$

Here T_e, V_S and V_L are constants related to the self-trapped electronic carrier's kinetic energy and contributions to its potential energy from the short-range and long-range components of its electron-phonon interaction. Finally, the polaron energy $E_p(R)$ is obtained by combining $E_{st}(R)$ with the strain energy required to establish the potential well which binds the electronic charge carrier:

$$E_p(R) = E_{st}(R) + V_{strain}(R) \equiv \frac{T_e}{R^2} - \frac{V_S}{R^d} - \frac{V_L}{R}. \tag{3}$$

To obtain this result the strain potential energy $V_{strain}(R)$ is recognized as the sum of components from the same regions that contribute V_S and V_L. Here, for our simple model, each of these contributions is positive with half of the magnitude as that in Eq. (2).

This formula for the polaron binding energy in a continuum model is now augmented by a boundary condition. This boundary condition acknowledges that a self-trapped electronic carrier can shrink to no smaller than a minimal structural unit (e.g., ion, atom, bond or molecule). This effect is mimicked by choosing R to be the self-trapped electronic state's radius divided by its value when confined to a single structural unit. Thus our formula only applies for $R \geq 1$.

A minimum of $E_p(R)$ at a finite-radius gives the energy of the strong-coupling polaron in terms of T_e, V_S and V_L. However, essential features of polaron formation can be elucidated without knowing details. In particular, polaron formation depends critically on the range of the electron-phonon interaction and on the dimensionalities of (1) the electronic-carrier's motion and (2) the medium within which it is immersed.

Fig. 1 compares $E_p(R)$ plotted against R for a covalent material ($V_L \rightarrow 0$) with the electronic carrier being (a) unconstrained ($d = 3$), (b) constrained to a plane ($d = 2$), (c) confined to a chain ($d = 1$). For $d = 3$ the only possible finite-radius minimum is at

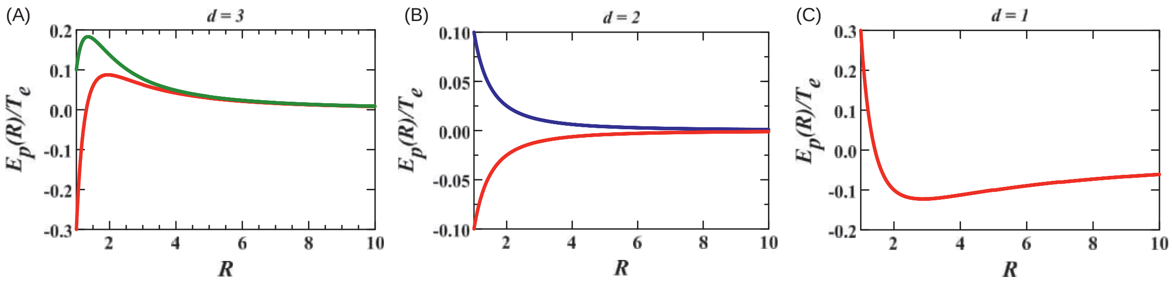

Fig. 1 (A) The effect of electronic dimensionality d on adiabatic self-trapping with a pure short-range electron-phonon interaction. Either a metastable or stable small-polaron state coexists with a free-carrier state when $d = 3$. (B) Only a stable small-polaron state or a free-carrier state is permitted when $d = 2$. (C) A stable self-trapped state, illustrated here as a large polaron, always exists when $d = 1$.

$R = 1$ indicating formation of a small polaron when $V_S > 2T_e/3$. The small polaron is either metastable ($T_e > V_S > 2T_e./3$) or stable ($V_S > T_e$) with respect to the carrier remaining free. Shrinking of a the electronic carrier from $R = \infty$ to $R = 1$ necessitates overcoming the "barrier to self-trapping," $4T_e^3/27V_S^2$. For $d = 2$ the electronic carrier will severely self-trap ($R = 1$) when $V_S > T_e$ thereby forming a small polaron. Alternatively, the carrier will remain free when $V_S < T_e$. For $d = 1$ there is a single finite-radius minimum. For $V_S < 2T_e$ this minimum is at $R = 2T_e/V_S$ corresponding to the formation of a large polaron with energy $-V_S^2/4T_e$. For $V_S > 2T_e$ the minimum is at $R = 1$ corresponding to the formation of a small polaron. Thus, the requirement for stable small-polaron formation becomes more stringent as the electronic dimensionality is decreased: $V_S > T_e$ for $d = 3$ or 2 while $V_S > 2T_e$ for $d = 1$.

Although idealized systems of diminished electronic dimensionality are studied, their realization may be difficult to achieve. In particular, investigations of quasi-one-dimensional systems find that extreme anisotropies are required to achieve the idealized $d = 1$ limit.

Short-range interactions between a carrier and the atoms it contacts are presumably ubiquitous. In this sense, models with only a long-range interaction with displaceable ions are artificial. Moreover, we have already established general features of such polarons. In particular, examination of the above equation for $E_p(\mathrm{R})$ shows that the case of a carrier within a three-dimensional ionic medium without short-range electron-phonon interactions ($V_S = 0$) is isomorphic to the $d = 1$ case with a pure short-range interaction ($V_L = 0$) that was discussed above.

Estimates of V_S obtained from experiments and computations range from over several tenths of an eV to several eV. Meanwhile, V_L is essentially the Coulomb repulsion between two elementary charges confined to a single site, ≈ 10 eV, multiplied by the factor $[(1/\varepsilon_\infty)-(1/\varepsilon_0)]/2$. Without displaceable ions this factor is near zero. By contrast, for an alkali halide, a prototypical ionic solid, this factor rises to about 0.1.

Combining short-range and long-range components of the electron-phonon interaction can produce several distinct self-trapping scenarios. Consider a three-dimensional model in which the long-range interaction generated by displaceable ions is progressively added to a modest short-range interaction which by itself is presumed to be too weak to produce even a metastable self-trapping, $V_S < 2T_e/3$. Fig. 2 plots $E_p(R)/Te$ for progressively increasing values of V_L. Curve *a*, for $V_L = 0$. shows no self-trapping. Curve *b* shows an increase of V_L introducing an energetically stable large-polaron state at $R = 2T_e/V_L$ along with a metastable small-polaron state at $R = 1$. Curve *c* shows a further increase of V_L stabilizing the small-polaron state with respect to the large-polaron state. Finally, curve *d* shows the collapse of the large-polaron state into the small-polaron state when $3V_LV_S > T_e^2$.

Atoms generally vibrate about their carrier-induced displaced equilibrium positions. The stiffness constants governing such vibrations are found from the second derivatives of the adiabatic potential with respect to atomic displacements evaluated at their carrier-induced equilibrium position. The stiffness linking positions $\boldsymbol{u}$ and $\boldsymbol{u}'$ is reduced by the polarization of a self-trapped carrier as it adjusts to alterations of its self-trapping potential well induced by atomic vibrations. Thus, a self-trapped carrier is generally associated with both (1) displacements of the equilibrium positions of surrounding atoms and (2) softening of the stiffness constants governing their vibrations. Carrier-induced softening of atoms' vibrations reduces their frequencies and thereby lowers a polaron's free energy. For simplicity, this contribution to polaron stability has heretofore been neglected in our discussion of the formation of strong-coupling polarons. Nonetheless, carrier-induced softening is central to large-polarons' transport.

Large- and small-bipolaron formation

Charges in solids often pair as singlets. A two-center covalent bond forms as an electron shifts from each of two atoms to being centered between them. Concomitantly, the two atoms move toward one another. The two electrons then overcome their mutual

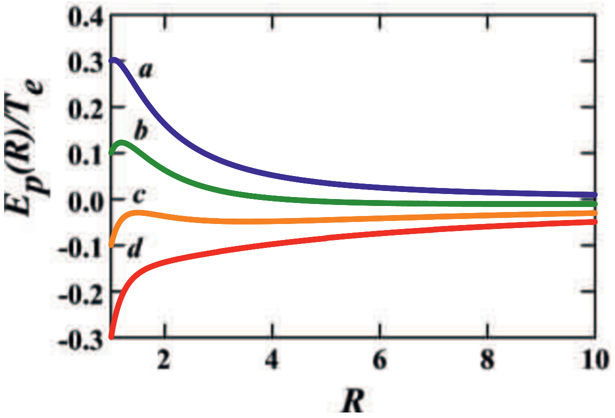

Fig. 2 Addition of the long-range component of the electron-phonon interaction facilitates self-trapping. (a) No self-trapped state with $V_L = 0$. Progressively increasing V_L introduces (b) metastable small-polaron state with stable large-polaron state and then (c) stable small-polaron state with metastable large polaron state. (d) Large-polaron state collapsing yields only a stable small-polaron state.

Coulomb repulsion as each of them benefits from its attraction to the bond's two atoms. Similarly, electronic charge carriers can doubly occupy a self-trapping potential well to form a strong-coupling singlet bipolaron.

The model developed to address formation of a strong-coupling polaron can be extended to address the formation of a singlet bipolaron. A bipolaron's two uncorrelated self-trapped electronic carriers each benefits from their doubling of their carrier-induced displacements of atoms' equilibrium positions. Thus, both short-range and long-range contributions to the polaron potential energy are augmented four-fold, $4 = 2 \times 2$. Meanwhile the Coulomb-repulsion between the two self-trapped electronic carriers is reduced by the high-frequency dielectric constant ε_∞, associated with electronic polarization of the medium. Thus, the energy of a bipolaron $E_{bp}(R)$ becomes:

$$E_{bp}(R) = \frac{2T_e}{R^2} - \frac{4V_S}{R^d} - \frac{4V_L}{R} + \frac{U}{\varepsilon_\infty R} = 2E_p(R) + \frac{U}{\varepsilon_0 R} - \frac{2V_S}{R^d}. \tag{4}$$

The bipolaron energy is then compared with that of two well-separated polarons $2E_p(R)$ where it has been noted that the long-range component of the electron-phonon interaction V_L is simply related to the bare Coulomb interaction between a pair of charges on a minimal structural unit U: $V_L = [(1/\varepsilon_\infty)-(1/\varepsilon_0)]U/2$.

The final two terms on the right-hand side of this equation describe the essential physics of bipolaron formation. Bipolaron formation is energetically favorable when the paired carriers' residual mutual Coulomb repulsion, $U/\varepsilon_0 R$ is overwhelmed by the additional binding provided by the short-range electron-phonon interaction, $2V_S/R^d$. In particular, large-bipolaron formation, $R > 1$, is fostered in systems whose electronic carriers have reduced dimensionality.

Bipolaron formation on an embedded plane, $d = 2$, is investigated by comparing the minima of $E_{bp}(R)$ and $2E_p(R)$ with respect to R. A planar large-bipolaron will form if the minimum of $E_{bp}(R)$ occurs at $R > 1$ with a lower energy than the minimum value of $2E_p(R)$. In particular, a planar large-bipolaron can form if

$$\frac{4(\varepsilon_0/2\varepsilon_\infty) - 3}{2(\varepsilon_0/2\varepsilon_\infty)^2 - 1} \le \frac{2V_S}{T_e} \le 1. \tag{5}$$

Thus, the value of V_S that drives large-bipolaron formation must be large enough to foster its energetic stability without being so large as to collapse the large bipolaron into a small bipolaron. These requirements can be met in unusual circumstances where $\varepsilon_0/2\varepsilon_\infty$ rises above 1.

Cuprates are prime candidates for large-bipolaron formation because (1) their charge carriers are confined to CuO_2 planes, $d = 2$, that are (2) embedded within media with exceptionally displaceable ions, $\varepsilon_0 \gg 2\varepsilon_\infty \gg 1$. An hypothesized microscopic model (Emin, 2017) envisions a large-bipolaron's paired holes in a CuO_2 plane of p-doped antiferromagnetic La_2CuO_4 occupying out-of-plane non-bonding oxygen orbitals. As depicted in Fig. 3, the core of such a large-bipolaron hole removes two electrons from the four contiguous O^{2-} anions thereby shifting their equilibrium positions inward while shifting the equilibrium positions of the four surrounding Cu cations outward. Concomitantly, electrons transferred from the four oxygen anions to the four copper cations convert each of them from a spin-½ Cu^{2+} to a spin-less Cu^{1+}. Such large-bipolarons thereby eliminate the doped material's magnetism. Two electrons then remain distributed over the out-of-plane orbitals of the four oxygen anions: 2 holes + $4O^{2-} + 4Cu^{2+} \rightarrow (O_4)^{2-} + 4Cu^{1+}$. The lowest-frequency largest-amplitude optic-mode type radial vibration of these ions has d-symmetry.

Boron carbides' high-density of low-mobility hopping-type charge carriers appear to pair as singlet small bipolarons since they do not contribute unpaired spins to its magnetic susceptibility (Emin, 2006). Paired carriers' small mutual Coulomb repulsion results from their being constrained to the surface of spheroidal boron-rich 12-atom icosahedra in a material with a large electronic polarizability, $\varepsilon_\infty >> 1$.

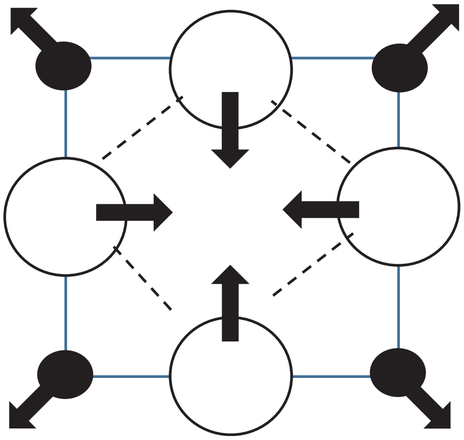

Fig. 3 Removing two electrons from four contiguous oxygen anions (large open circles) of the basic structural unit of a CuO_2 plane shifts their equilibrium positions inward and those of the copper cations (smaller filled circles) outward.

Disorder-induced small-polaron formation

There is a qualitative dichotomy between states that are only minimally affected by electron-phonon interactions and small-polaronic states. Moreover, rough estimates of the pertinent constants indicate many situations that are close to the boundaries between these two radically different situations.

Disorder, by increasing the localization or slowing of charge carriers, can trigger their collapse into small polarons. Different models (c.f., Further reading) have been employed to illustrate these effects.

One approach envisions disorder generating potential wells that confine charge carriers. In particular, disorder is presumed to introduce contributions to the adiabatic potential of the form $-V_{disorder}/R^n$. Electron-phonon interactions then synergistically enhance carriers' localization. As a carrier's disorder-induced localization is progressively increased, it ultimately abruptly collapses into a small-polaron, confining a carrier to a single structural unit. The situation is analogous to that portrayed in Fig. 2, in which a progressively stronger long-range component of the electron-phonon interaction, $-V_L/R$, ultimately drives a carrier's collapse into a small polaron.

An explicit example considers the abrupt collapse of a large-radius donor state in the ferromagnetic semiconductor EuO. The donor electron moves between Eu cations' $S = 7/2$ spins. The intra-atomic exchange I between the donor electron and each of the Eu cations it contacts fosters their alignment even as rising temperature drives misalignment of the spins of other Eu cations. As the temperature is raised toward the EuO Curie temperature, $T_C \approx 70$ K, the large-radius donor abruptly collapses to a small-radius donor. Concomitantly, the number of aligned Eu spins shrinks. The product of the temperature and the difference between the spin-misalignment entropy associated with large-radius and small-radius states is the transition's latent heat. The free-energy functional for this system is:

$$F_{bmp}(R, T) = \frac{\left[T_e - C\left(\frac{I}{kT_C}\right)kT\right]}{R^2} - \frac{V_S}{R^d} - \frac{(V_L + V_d)}{R}, \tag{6}$$

where C denotes a numerical constant which for EuO is estimated to be between 0.01 and 0.1 and V_d represents the electron's Coulomb attraction to its donor (e.g., a dopant or an oxygen vacancy). The minimum of this free-energy functional can collapse from that for a large-radius donor, $R \gg 1$, to that for a small-polaronic state, $R = 1$, as the temperature is raised above 50 K.

Strikingly, the magnetic disorder which drives this transition is controlled by the temperature and is therefore readily reversible. This collapse also can be reversed by applying a magnetic field which fosters alignment of the Eu cations' spins. In particular, the temperature of the collapse rises as the square-root of the applied magnetic field.

Disorder can also induce the self-trapping of freely moving electronic excitations. For example, excitons in crystalline TlCl or TlBr move freely while those in the mixed crystal $TlCl_xBr_{1-x}$ self-trap. Holes injected into crystalline orthorhombic sulfur appear to move with a moderate mobility which falls with increasing temperature until the crystal's softening temperature is reached. Then, once the crystal's S_8 molecules lose registry with one another, the mobility drops precipitously. As the temperature is raised further the mobility rises in an Arrhenius manner, typical of small polarons. Charge carriers in crystalline Si and Ge have large Hall mobilities that fall with increasing temperature. By contrast, the Hall mobilities of amorphous Si and Ge are very low, rise in an Arrhenius manner with increasing temperature and display the sign anomalies expected for both electron and hole small polarons.

Nearest-neighbor inter-atomic separation are nearly the same for crystalline and amorphous semiconductors. By contrast, amorphous covalent semiconductors have large ($>10°$) variations of their bond angles. The electronic transfer energies of electrons in anti-bonding states and holes in bonding states are very sensitive to bond-angle variations.

The effect of transfer-energy variations on small-polaron formation is now considered. Self-trapping was previously addressed by determining whether an electronic carrier will be bound within the potential well generated by fixing surrounding atoms at their carrier-induced displaced equilibrium positions (the adiabatic limit). With just the ubiquitous short-range component of the electron-phonon interaction, an electronic carrier in a three-dimensional deformable continuum will either self-trap as a small-polaron or remain free.

An electronic carrier remains free if its energy band extends below the small-polaron energy. Disorder-induced transfer-energy variations by themselves can then introduce sites at which small-polaron formation is stable. Moreover, transfer energies emanating from such sites are suppressed since moving a self-trapped electronic carrier requires substantial movement of the associated atoms. Sites with stable small-polaron formation are thereby extended to some adjacent sites. Ultimately, through this nonlinear feedback mechanism, modest transfer-energy disorder can trigger global small-polaron formation. All told, transfer-energy disorder significantly reduces the electron-phonon coupling strength required to stabilize small-polaron states with respect to free-carrier states.

Such a small-polaron collapse requires transfer-energy variations (non-diagonal disorder) that are comparable to the small-polaron energy and the electronic carrier's bandwidth. By contrast, severe Anderson localization requires diagonal-disorder energies that are an order of magnitude greater than the electronic carrier's bandwidth, as envisioned for impurity conduction in very lightly doped compensated semiconductors.

Coherent and incoherent polaron transport

A strong-coupling polaron's motion requires shifting surrounding atoms away from the displaced equilibrium positions they assume when generating the potential well which binds its self-trapped electronic carrier. A self-trapped electronic carrier only moves in response to these atoms' movements.

In the most extreme case, atoms may move enough to completely eliminate the self-trapping potential well thereby liberating its electronic carrier. The electronic carrier can then move away until atoms elsewhere in the material bind it within another self-trapping potential well. This transport mode corresponds to free-carrier motion limited by occasional self-trapping.

Transport of a strong-coupling polaron occurs when the centroid of its self-trapped electronic carrier moves between sites in response to atoms' movements shifting the potential well that binds it. The motion of a strong-coupling polaron is regarded as coherent when its self-trapped electronic carrier extends over multiple sites. As such, the self-trapped electronic carrier of a large polaron moves continuously in response to the classical motion of surrounding atoms. In particular, the mass for a three-dimensional large-polaron is $\approx E_p/(\omega R_p)^2$, where E_p and R_p respectively denote the polaron energy and radius while ω represents the frequency characterizing vibrations of the relevant atoms. The effective mass for a one-dimensional large-polaron interacting with acoustic phonons is $4E_p/{c_s}^2$, where c_s denotes the sound velocity. These polaron masses are generally orders of magnitude greater than the free-electron mass.

Since the huge masses of strong-coupling large polarons result from the requisite atomic motion, they can only be observed at frequencies below those characterizing atomic motion. By contrast, masses measured at high frequencies correspond to those of electronic charge carriers, e.g., an electronic carrier moving within the self-trapping potential well that binds it.

Distinctively, the transport of a small polaron is usually incoherent. Its severely localized self-trapped electronic carrier moves discontinuously between sites in response to atomic movements. Small-polaron transport is generally described as occurring via sequences of phonon-assisted hops.

It should be noted that a polaron in a crystal can equally well occupy any of its geometrically equivalent sites. Therefore, its eigenstates extend throughout the crystal. However, unlike purely electronic Bloch states, polaron eigenstates transfer the pattern of displaced atomic equilibrium positions collaterally with the self-trapped electronic carrier. Therefore, the width of such a polaron band is proportional to the product of the overlaps between each atom's vibrational wavefunction when its self-trapped electronic carrier is shifted between neighboring sites. For example, the maximum nearest-neighbor transfer energy associated with a small-polaron adiabatically shifted between adjacent sites with the electron-phonon interaction taken as purely short-range is

$$t_{sp} \cong \sqrt{\frac{E_p \hbar\omega}{\pi}} e^{-\left(\frac{E_p}{\hbar\omega}\right) coth\left(\frac{\hbar\omega}{2kT}\right)}, \tag{7}$$

where the strong-coupling condition insures that $E_p \gg \hbar\omega$. It should be observed that t_{sp} is (1) very small, $t_{sp} \ll \hbar\omega$, (2) decreases with rising temperature, and (3) vanishes in the classical limit, $\hbar \rightarrow 0$. The extreme narrowness of a small-polaron band implies that its coherent motion associated with it will be suppressed by any realistic perturbations.

Large-polaron transport

The mobility μ of a coherently moving carrier of charge q can be schematically written in terms of the average of the product of its velocity v and its mean-free-path ℓ: $\mu = \mathrm{e} < v\ell > /kT$. The minimum mobility for coherent transport corresponds to the carrier mean-free-path falling to its size, its de Broglie wavelength $\lambda = h/p = h/m_c v$, where m_c denotes the carrier's effective mass: $\mu_{\min} = (eh/m_c kT)$. The minimum coherent-transport mobility associated with a carrier mass equal to the free-electron mass is about 300 cm^2/V-*sec* at room temperature. Since this minimum mobility is inversely proportional to the carrier effective mass, room-temperature mobilities that are much lower than this minimum imply very large effective masses such as those of large polarons.

A large-polaron's transport depends critically on the phonon modes involved in constructing the potential well in which its electronic carrier is self-trapped. These modes are locally softened by relaxation of the large-polaron's self-trapped electronic carrier to their atoms' vibratory displacements. A large polaron's local softening of these vibrational modes impedes passage of the solid's indigenous phonons through it. This regional phonon softening is the origin of the scattering between a large polaron and ambient phonons.

The huge mass of a strong-coupling large polaron insures that its thermal momentum near room temperature exceeds that of the phonons with which it scatters. Thus, while conventional electronic charge carriers undergo wide-angle scattering by phonons, a large polaron primarily "reflects" incident phonons. This difference may manifest itself in a solid's carrier-induced thermal conductivity.

The dynamics of the scattering between a large polaron and a solid's phonons depends on the velocity with which vibrational energy can be transported through a solid. This feature of phonon transport is governed by their vibrational dispersion. Two examples illustrate contrasting limits. Acoustic phonons have substantial dispersion with the velocity of their longitudinal branch being just that of sound, c_s. Optic phonons are frequently represented as Einstein oscillators, which possess zero vibrational dispersion. Therefore, the huge mass of a large polaron causes it to move more slowly than the acoustic phonons which it scatters. However, a large polaron moves faster than Einstein oscillators that are static.

The scattering rate for a large polaron by acoustic phonons is

$$\frac{1}{\tau_{lp}} \cong \langle \mathrm{N}_{ac}\sigma\left(\frac{2\hbar \mathrm{q}}{\mathrm{m}_{lp}}\right)\rangle \cong \frac{kT}{m_{lp} c_s R_p}, \tag{8}$$

where N_{ac} denotes the density of thermally available acoustic phonons, σ represents the cross-section for scattering between a large polaron and acoustic phonons, and the final factor is the change of a large polaron's velocity generated by its reflection of an acoustic phonon of momentum $\hbar q$. The final expression on the right results from evaluating the average at or near room-temperature upon recognizing that the relevant phonons have wavelengths comparable to the polaron radius R_p. It is noteworthy that this scattering rate is inversely proportional to the large-polaron mass, m_{lp}. That is, a large polaron is not easily scattered by acoustic phonons which possess much smaller momenta.

A distinctive characteristic of a large polaron is its extremely long scattering time, $\tau_{lp} \approx (E_p/kT)/\omega \gg 1/\omega$. This feature manifests itself by the real part of the large-polaron conductivity as a function of applied frequency Ω, proportional to $1/(1 + \Omega^2\tau_{lp}{}^2)$, only being appreciable at frequencies well below the phonon frequency ω. Moreover, as will be discussed subsequently in the section on polaron's optical properties, a large polaron's conductivity also has a very broad peak beginning at frequencies well above that of its characteristic phonon. Thus, there is a pseudo gap between the low-frequency, $\Omega \ll \omega$, and the high frequency, $\Omega \gg \omega$, contributions to a large polaron's conductivity and related absorption. By contrast, a conventional electronic carrier's scattering time is very short, $\tau \ll 1/\omega$. Thus, the frequency dependence of the real part of a conventional electronic carriers' conductivity, its Drude conductivity, is appreciable at frequencies that are many orders of magnitude higher than that for a large polaron.

The large-polaron mobility corresponding to its long scattering time τ_{lp} and huge effective mass m_{lp} is:

$$\mu_{lp} \equiv e\frac{\tau_{lp}}{m_{lp}} = \frac{ec_sR_{lp}}{kT}. \tag{9}$$

This mobility is typically comparable to 1 cm^2/V-*sec* at room temperature, much smaller than that for conventional electronic charge carriers.

This mobility's monotonic decrease with increasing temperature distinguishes it from that for a large polaron interacting with dispersion-less phonons, Einstein oscillators. The mobility arising from the scattering of a large polaron with Einstein optic vibrations involves a competition between two factors. First, the density of optic phonons increases with rising temperature. Second, the efficacy of their scattering of a large-polaron diminishes as its de Broglie wavelength decreases with increasing temperature. Strikingly, this effect is reported to make a large-polaron's mobility rise with increasing temperature above a small fraction of the optic-phonon temperature.

Small-polaron transport: Elemental hops

A small-polaron's severe localization renders its transport incoherent. This incoherent transport is best described as proceeding via successions of thermally assisted jumps. A small-polaron's hop is governed by movements of the atoms to which its self-trapped electronic carrier is coupled. The motions of these atoms are controlled by the system's adiabatic potential.

The processes governing an elemental small-polaron hop depends on its two-site adiabatic potential. A simple model has the portion of the adiabatic potential governing a jump depending on a single relative atomic configurational coordinate. A small-polaron hop then corresponds to motion of a fictitious particle with an appropriate reduced atomic mass moving between minima of this two-site adiabatic potential.

Fig. 4 shows the two-site adiabatic potential $V_{ad,2}(x)$ as a function of the relative atomic-configuration coordinate x. An energy barrier exists between equivalent minima located at x_i and x_f. A fictitious particle's occupation of one of these two equivalent minima corresponds to the self-trapped carrier occupying one of the two equivalent sites between which this small polaron can move.

At low temperatures the charge carrier moves from initial to final sites as the associated atoms undergo quantum-mechanical tunneling between the configurations they assume when the electronic carrier occupies corresponding initial and final sites. This relatively slow atomic tunneling process is depicted in Fig. 4 by the thin blue arrow passing through the thick portion of its energy barrier.

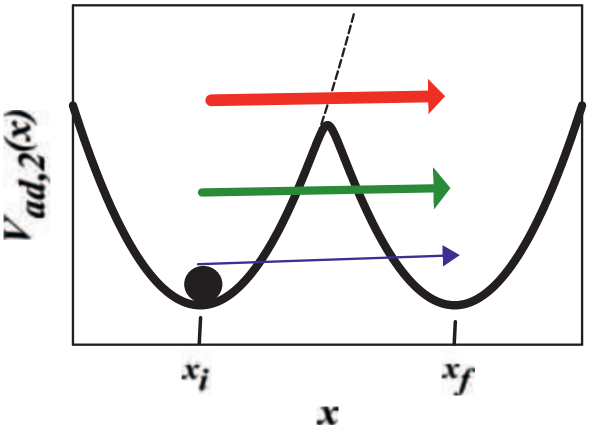

Fig. 4 The two-site adiabatic potential energy for a small-polaron hop is plotted against the relative atomic configurational coordinate *x*. The dashed line indicates the extension of the adiabatic potential for occupation of the initial site in the absence of electronic transfer to the hop's final site.

As the temperature is raised, the amplitudes of atoms' oscillations increase. The fictitious particle, the large black dot in Fig. 4, then rises higher in its potential well before tunneling through a relatively thin portion of this figure's energy barrier. The green arrow depicting this tunneling is thicker than that of the blue arrow to indicate that the tunneling rate increases as the width of the energy barrier decreases. The decrease in the energy barrier indicates reduced disparity of the positions of atoms involved in their quantum-mechanical tunneling.

At sufficiently high temperatures, the fictitious particle can move between potential wells by transcending the energy barrier rather than tunneling through it. The predominant small-polaron hopping process then does not involve atoms' tunneling. As indicated by the thickness of the red arrow the small-polaron jump rates exceeds that of processes requiring atomic tunneling.

Fig. 5 plots the elemental adiabatic small-polaron jump rate for a hop between equivalent sites. At high temperatures the jump rate is Arrhenius. Its activation energy corresponds to the energy difference between the minima of the adiabatic potential and the height of the energy barrier shown in Fig. 4. This activation energy is the minimum energy required to displace atoms from the equilibrium positions they assume when a hop's initial site is occupied so as to bring the electronic energies of the jump's initial and final sites into coincidence. As the temperature is lowered the small-polaron jump rate becomes non-Arrhenius. This behavior indicates the progressive freeze out of multi-phonon processes requiring the absorption of more energy than is the minimum consistent with the requirement of energy conservation. The details of these non-Arrhenius temperature dependences depend upon the particular phonons that are coupled to the electronic charge carrier. However, the transition between Arrhenius and non-Arrhenius behavior typically occurs at about one third of the characteristic phonon temperature.

The example presented here presumed that the sites between which hopping occurs are equivalent to one another, as they are in a perfect crystal. Nonetheless, except at very low temperatures, the adiabatic small-polaron jump rate between inequivalent sites is usually only modified by the factor exp.$(-\Delta/2kT)$, where Δ denotes the difference between final and initial sites. At extremely low temperatures the energy absorbed in a hop falls to the minimum energy consistent with energy conservation. Then the rate for a hop upward in energy is proportional to exp.$(-|\Delta|/kT)$ while that for a hop downward in energy is temperature independent.

A small-polaron's adiabatic jump rate's temperature dependence (e.g., its activation energy) implicitly measures the distances that atoms surrounding a jump's pair of sites must move to generate a hop. This effect depends on the range of an electronic charge carrier's electron-phonon interaction. Nonetheless, the temperature-dependence of a small-polaron's adiabatic jump rate generally increases as the separation between initial and final sites is increased. Thus, the activation energy for a hop increases with its distance. By itself, this effect favors short hops over longer hops.

Application of a dc electric field E alters the temperature dependences of the jump rates for hops emanating from a site. This effect is greatest for long jumps. The resulting effect usually increases the net jump rate from a site. Frenkel-Poole behavior denotes the applied electric-field E increasing the net jump rate from a site by the factor exp.$[CE^{1/2}/kT]$, where C denotes a constant.

Arrhenius small-polaron hopping is adiabatic when its self-trapped electronic carrier readily moves between sites in response to atoms' movements establishing the requisite coincidence event. The magnitude of the electronic transfer energy t_{tr} must then exceed the energy spread $\Delta E_{dur} \approx [\hbar\omega(E_A kT)^{1/2}]^{1/2}$, determined by the Heisenberg uncertainty principle, associated with the establishment of an energy coincidence. Fig. 6 displays the probability P of a hop being adiabatic plotted against the ratio $t_{tr}/\Delta E_{dur}$.

For computational simplicity, initial studies of small-polaron hopping presumed that the inter-site transfer energy of an electronic carrier is so small that it rarely moves between sites even when atomic movements enable it to do so, $P \approx 2(t_{tr}/\Delta E_{dur})^2 \ll 1$. However, estimates of $t_{tr}/\Delta E_{dur}$ often imply adiabatic hopping, $P \approx 1$. Fortunately, the value of P can often be estimated from experiments. In particular, the pre-exponential factor for Arrhenius small-polaron hopping mobility is $(ea^2\nu/kT)P$, where a denotes the separation between small-polaron sites. In addition, the corresponding pre-exponential factor of the dc conductivity for thermally generated small polarons is $(e^2\nu/akT)P$. Typical estimates of the bracketed expressions in these two pre-exponential factors are respectively about 1 cm^2/V-*sec* and 10^3 S/cm. The frequent observations of pre-exponential factors that are close to these values implies that their small-polaron hopping is adiabatic, $P \approx 1$.

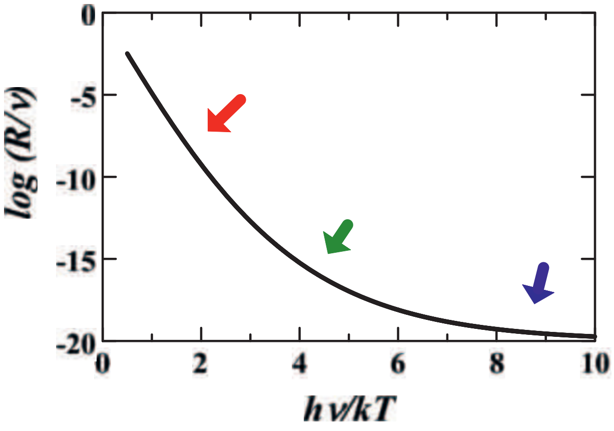

Fig. 5 The rate for an elemental adiabatic small-polaron jump between equivalent states divided by the hop's characteristic phonon frequency ν is plotted versus $h\nu/kT$. The colored arrows correspond to those in Fig. 4 which indicate the processes which predominate in each temperature regime.

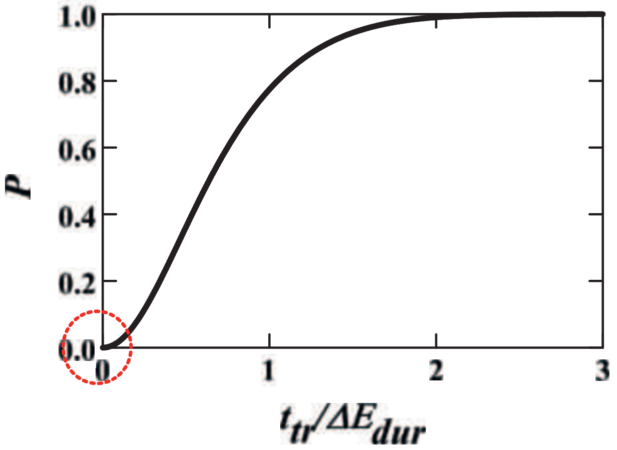

Fig. 6 The probability P of a self-trapped electronic carrier adiabatically moving between sites during a coincidence event is plotted versus $t_{tr}/\Delta E_{dur}$. The circle indicates the non-adiabatic regime where $P \propto t_{tr}^2$.

Small bipolarons also move by thermally assisted hopping. At low temperatures small-bipolarons move together as singlet pairs. However, at high temperatures pairs separate and charge transport becomes predominately that of small polarons. The activation energy for pair-breaking and subsequent small-polaron hopping is the sum of two contributions. The contribution from pair separation is half of the binding energy of the bipolaron with respect to forming two separate polarons, $(2E_p - U)/2$, where U represents a pair's on-site Coulomb repulsion. As before, the activation energy for small-polaron hopping is below $E_p/2 - t_{tr}$. Therefore the activation energy for breaking a pair and subsequent small-polaron hopping is less than $3E_p/2 - U/2 - t_{tr}$. By comparison, the activation energy for the pair jumping as a unit is $2E_p - t_{2tr}$, where t_{2tr} denotes the transfer energy for the paired electronic carriers moving as a unit in response to a coincidence event, $t_{2tr} \ll t_{tr}$. Thus, due to its smaller activation energy, high-temperature small-bipolaron transport is dominated by pair breaking. Distinctively, the paramagnetic susceptibility then garners a high-temperature Arrhenius contribution from the collateral generation of unpaired self-trapped electronic charge carriers. This phenomenon appears to occur in boron carbides, $B_{12+x}C_{3-x}$ with $0.15 < x < 1.7$, where $x/2$ denotes the fraction of unit cells with hole-like small bipolarons (Emin, 2006).

Small-polaron hopping is qualitatively different from very low temperature inter-impurity hopping conduction in lightly doped compensated crystalline semiconductors (e.g., P and B doped Si). The small doping concentrations (e.g., 10^{15} cm^{-3}) imply very long (e.g., 1000 Å) non-adiabatic jumps. The large dopant radii (e.g., 20 Å and 45 Å in Si and Ge, respectively) and small conductivity activation energies (e.g., 10^{-4}–10^{-3} eV) imply each hop involves absorption or emission of only a single very long wavelength acoustic phonon. As such, the elemental jump rates are proportional to $\exp.[-(\Delta + |\Delta|)/2kT]$ in the very low-temperature limit and proportional to T at higher temperatures. All told, inter-impurity hops are primarily non-adiabatic, proportional to t_{tr}^2, and between sites whose near-random energies are determined by their proximity to the doped-semiconductors' charged impurity centers. Rates for individual inter-impurity hops therefore involve competitions between (1) transfer energies which favor short jumps and (2) energy absorptions which favor long jumps. By itself, these effects would lead to variable-range hopping. By contrast, small-polaron hops are usually short (<10 Å), adiabatic and multi-phonon. As such, small-polaron jump rates are non-Arrhenius below a fraction of the phonon temperature and Arrhenius at higher temperatures with activation energies between 0.1 and 1 eV.

Small-polaron relaxation phenomena

Small-polaron hopping involves local accumulation and dissipation of atoms' vibrational energy. In particular, the elemental thermally assisted small-polaron hop described in Fig. 4. begins as the amplitudes of atomic vibrations increase while the self-trapped electronic carrier occupies its initial site and ends with vibrational energy being dissipated to surrounding atoms after the electronic carrier transfers to its final site. Thus, the jump process involves vibrational dispersion.

Early studies of small-polaron hopping only explicitly addressed the actual inter-site transfer of an electronic charge carrier. The processes governing local accrual and subsequent dispersal of vibrational energy were ignored. Rather, the energies of local vibrations were assumed to retain their equilibrium distribution. This procedure is justified in the non-adiabatic limit since the probability of an electronic transfer in response to atoms assuming favorable configurations is then arbitrarily small. As such, dispersion-related transfers of atoms' vibrational energies are always fast enough to establish equilibrium prior to an electronic charge carrier transferring between sites. However, as noted earlier, small-polaron hopping is typically adiabatic. In this situation, the inter-site transfer of an electronic charge carrier occurs in less than a vibrational period while the accumulation and dissipation of vibrational energy is much slower. Transport of vibrational energy then affects small-polaron hopping.

Following a hop, vibrational energy is dissipated away from the involved sites. In a three-dimensional vibrational system, the time for the sites' vibrational energy to fall to $kT/2$ following a hop with activation energy E_A is $\tau_{\text{relax}} \approx (1/\Delta\omega)(2E_A/kT)^{2/3}$, where

$\Delta\omega$ denotes the spread of frequencies characterizing the phonons involved in the jump. This relaxation time will generally exceed that governing atoms' vibrations: $\omega\tau_{\mathrm{relax}} \gg 1$, where $\omega \gg \Delta\omega$ and $E_A \gg kT$. Thus, relaxation from one hop may not be completed before vibrations establish another adiabatic jump. Hopping will then be correlated. Adiabatic small-polaron hops occur in flurries separated by dormant intervals. Within a flurry, the probability of back and forth hopping between a pair of sites is greatly enhanced while jumps to previously unvisited sites are also enhanced but to a lesser extent.

As shown in Fig. 4, a self-trapped electronic carrier's adiabatic over-the-barrier shuttling between a pair of sites is governed by the broad double-well adiabatic potential. By contrast, a carrier confined to the initial site is governed by the single harmonic potential depicted by the dashed curve. The difference in vibrational free energy between that with the carrier transferring back-and-forth and that with it confined to its initial site, $\Delta F_{vib} < 0$, augments the jump rate. The jump rate is also halved because the shuttling carrier only ends on the final site half of the time. The formula for the Arrhenius jump rate then becomes:

$$R_{M\text{-}N} = \left[\frac{\nu}{2}\, exp\left(-\frac{\Delta F_{vib}}{kT}\right)\right] exp\left(-\frac{E_A}{kT}\right) \rightarrow \left[\frac{\nu}{2}\, exp\left(\frac{E_A}{t_{tr}}\right)\right] exp\left(-\frac{E_A}{kT}\right), \tag{10}$$

where the final expression applies when $t_{tr}^{\,2} > E_A kT$ (Emin, 2013). In accord with the observed Meyer-Neldel compensation effect, this expression has its temperature-independent factor increasing exponentially with the hopping activation energy E_A. The rise of the jump rate's temperature-independent factor with increasing E_A partially compensates for the decrease of the rate's thermally activated factor.

Electronic charge carriers injected into condensed matter must dissipate a significant amount of energy in the process of their becoming self-trapped. In particular, for an injected electronic carrier to form an equilibrated small polaron an energy at least comparable to its binding energy (greater than several tenths of an eV) must be transferred into the vibrations of associated atoms. The resulting very large athermal vibrations can facilitate establishing the energetic coincidences required for small-polaron hopping. Thus, transient hopping can occur without significant additional absorption of vibrational energy. As a result, transitory adiabatic small-polaron hopping will be nearly activation-less. It will occur with a mobility of about $ea^2\nu/kT \approx 1\ \mathrm{cm}^2/\mathrm{V}\text{-}sec$. Time-of-flight measurements report such transient mobilities in materials whose steady-state thermally activated mobilities suggest small-polarons.

Polarons' Seebeck coefficients

The Seebeck coefficient S measures the open circuit e.m.f. $\Delta\phi$ developed across a material in response to the application of the temperature difference ΔT: $S \equiv \Delta\phi/\Delta T$. In physical terms the Seebeck coefficient S is the entropy transported with a carrier divided by its charge q. A charge carrier's Seebeck coefficient is related to its Peltier heat, $\Pi = qTS$, the heat transported with a charge carrier.

Analysis of Seebeck coefficient measurements aids understanding charge transport generally and polaron transport, in particular. Combined measurements of the Seebeck coefficient and the dc conductivity distinguish between small-polaron hopping and other models of hopping transport. Large and unusual polaron-based Seebeck coefficients have been exploited to produce novel thermoelectric devices.

There are several different contributions to the Seebeck coefficient. The primary contribution is often the change of the entropy-of-mixing upon adding a carrier of energy E and charge q to a system of chemical potential μ: $< E - \mu >_{\sigma}/qT$, where the brackets indicate an average of states' energies weighted by their contributions to the electrical conductivity σ.

It is sometimes useful to consider the entropy-of-mixing contributions to Seebeck coefficients as functions of c, the ratio of the number of charge carriers to the number of a material's equivalent structural units. When carriers exist in an energy band that is narrower than kT the Seebeck coefficient becomes temperature independent equal to $(k/e)\ln[(2-c)/c]$ for fermions that can doubly occupy a state, $(k/e)\ln[2(1-c)/c]$ for fermions that can singly occupy a state but with a two-fold spin degeneracy, and $(k/2e)\ln[(2-c)/c]$ for carriers that pair as $c/2$ singlet bipolarons which can only singly occupy a state.

The magnitude of the entropy-of-mixing contribution to a semiconductor's Seebeck coefficient is usually much greater than $(k/e) = 86\ \mu\mathrm{V/K}$. Nonetheless, the third law of thermodynamics requires that the entropy and hence the Seebeck coefficient vanish at absolute zero. The magnitude of a semiconductor's Seebeck coefficient drops precipitously to near zero when the ratio of kT to the carrier bandwidth becomes very small (Emin, 2016). Thus, the temperature of this dramatic fall indicates whether the carrier's energy band is consistent with conventional charge carriers, several eV, or with polarons, less than the phonon energy, 0.03–0.1 eV.

The magnetic moment of a charge carrier is found by measuring the magnetic-field dependence of the Seebeck coefficient. In particular, the magnetic field H breaks the two-fold spin degeneracy of singly occupied states. The Seebeck coefficient's spin degeneracy factor then becomes $(k/e)\{\ln[2\cosh(\mu_B H/kT)] - (\mu_B H/kT)\tanh(\mu_B H/kT)\}$, where μ_B represents the carrier's magnetic moment. A significant H-dependent fall of this factor from $(k/e)\ln(2)$ to zero is expected below 10 K at fields exceeding 10 T. The absence of this Seebeck-coefficient magnetic-field dependence implies that charge carriers have no net magnetic moment since they have paired into singlet bipolarons.

The conductivity activation energy for Arrhenius small-polaron hopping between equivalent states is the sum of that for carrier generation and that of the mobility: $(E_S - \mu) + E_A$, while the characteristic energy of the Seebeck coefficient is simply $E_S - \mu$. Therefore, the difference of the characteristic energies obtained from dc conductivity and Seebeck coefficient measurements is just that of the mobility E_A. Observing a significant value of E_A is often taken as evidence of small-polaron hopping.

As in a semiconductor's band tail, phonon-assisted hopping can be envisioned as occurring between severely localized states that are strongly coupled to phonons and weakly-localized states that are weakly coupled to phonons. The transported vibrational energy from a hop between states i and j then contributes to the Seebeck coefficient:

$$S_{i,j} = \frac{E_i\left(\frac{\Gamma_j}{\Gamma_i + \Gamma_j}\right) + E_j\left(\frac{\Gamma_i}{\Gamma_i + \Gamma_j}\right) - \mu}{qT}, \tag{11}$$

where and Γ_i and Γ_j denotes the electron-phonon coupling of these states. When one initial state is much more strongly coupled to phonons than the other state, $\Gamma_s \gg \Gamma_w$, the Seebeck coefficient between them is always related to the more weakly coupled state, $(E_w - \mu)/qT$. Thus, the Seebeck energy for thermally exciting carriers from deep within a bandgap to near a band- or mobility-edge is comparable to that of the conductivity. By contrast, the Seebeck energy for small-polaron hopping is significantly smaller than the conductivity activation energy.

Self-trapped electronic carriers adjust to displacements of surrounding atoms from their equilibrium positions. These adjustments generally reduce the frequencies of these atoms' vibrations. The associated carrier-induced increase of the net vibrational entropy contributes to the Seebeck coefficient. With increasing temperature this contribution to the Seebeck coefficient rises from zero at absolute zero to its high-temperature limit: $(k/q)\Sigma_i\ (-\Delta\omega_i/\omega_i)$ for moderate frequency shifts, $(-\Delta\omega_i/\omega_i) \ll 1$, where $\Delta\omega_i$ denotes the carrier-induced change of the frequency of the i-th vibration mode ω_i.

By itself, carrier-induced softening also fosters vibrational energy being transported with a phonon-assisted hop. For example, the contribution to the Seebeck coefficient from a high-temperature Arrhenius small-polaron hop between equivalent states is $(1/qT)\Sigma_i\ (-\Delta\omega_i/\omega_i)(E_{p,i}/2)$, where $E_{p,i}$ denotes the i-th vibrational mode's contribution to the small-polaron's binding energy. This contribution rises with decreasing temperature to a peak at a fraction of the characteristic phonon temperature and then falls to zero at absolute zero. The large Seebeck coefficients, >200 μV/K above 300 K, seen in boron carbides despite their very high bipolaron densities are attributed to bipolaron-induced vibrational softening (Emin, 2006).

Carrier-induced magnetic changes also manifest themselves in the Seebeck coefficient. In particular, the previously-suggested model of large-bipolaron formation within the CuO_2 planes of doped-La_2CuO_4 has each large-bipolaron removing a spin-1/2 from each of its four adjacent Cu cations. Distinctively, this effect lowers the Seebeck coefficient of such a large bipolaron by eliminating the entropy associated with these spins' orientations. In the high-temperature paramagnetic region the spin-related reduction of these large-bipolarons' Seebeck coefficients reaches $-(k/e)[4\ln(2)]$.

Polarons' Hall mobilities

A current produced by an electric field tends to be deflected by the application of a transverse magnetic field. This deflection angle, the Hall angle, divided by the magnetic field's strength defines the Hall mobility μ_H. By contrast, a charge carrier's drift velocity divided by the electric field driving its flow defines the usual mobility μ. Since μ_H and μ measure different phenomena, they generally differ from one another. Nonetheless, a simple treatment of coherent transport in an energy band that is much wider than the thermal energy kT yields $\mu_H = \mu$. However, significant differences between μ_H and μ emerge for coherent charge transport in energy bands that are narrower than the thermal energy kT. The dissimilarity between these two mobilities becomes profound for charge carriers that move incoherently by thermally assisted hopping. Then μ_H and μ differ from one another in magnitude, temperature dependence and often even in sign. These distinctive features facilitate identifying charge carriers as small polarons.

The Hall Effect centers on the deflection of charge carriers in a magnetic field. As such, the small-polaron Hall Effect requires considering at least a planar array of sites. Models for studying the Hall Effect envision a magnetic field applied perpendicular to a planar lattice comprising tiles of equilateral triangles and a planar lattice comprising square tiles.

A magnetic field alters transport among the sites of a planar lattice's primary structural unit, equilateral triangle or square. The magnetic field contributes a site-dependent phase factor to each site's electronic wavefunction. Electronic transfer energies therefore garner magnetic phase factors that depend on the linked sites. From this starting point two complementary approaches have been employed to calculate the small-polaron Hall Effect in the high-temperature Arrhenius regime.

The non-adiabatic limit presumes very small electronic inter-site transfer energies. Then an electronic carrier rarely moves between sites in response to opportunities presented by atoms' motions. Concomitantly, this approach's basis states are each localized on a site. The magnetic field's influence then results from interference between different transfer processes. For example, interference on a triangle occurs between a direct inter-site transfer and an indirect transfer through the third site. This interference depends on the magnetic flux through a lattice's primary structural unit.

The adiabatic limit presumes that an electronic carrier always responds to atomic movements by moving to the lowest-energy site of its molecular orbital. This behavior can be portrayed with a generalization of the one-dimensional configuration-coordinate diagram of Fig. 4. In particular, an electronic charge carrier moving among the three sites of an equilateral triangle corresponds to a fictitious particle moving among three mutually adjacent quasi-harmonic potential wells of a two-dimensional adiabatic potential surface. The magnetic field converts the real wavefunction describing the electronic carrier's non-degenerate molecular orbital into a complex wavefunction. As a result, terms proportional to atomic momenta of the adiabatic Hamiltonian survive to act like a fictitious vector potential. The magnetic field corresponding to this fictitious vector potential is proportional to the real applied magnetic field. This magnetic field affects the motion of the adiabatic potential's fictitious particle. Moreover, the fictitious magnetic field is strongest along the ridges separating adjacent quasi-harmonic potential wells. The magnetic field thereby shifts fictitious-particle trajectories corresponding to shifting the final site of an electronic carrier's hop. Analysis of these trajectories yields the adiabatic small-polaron Hall Effect.

The Hall mobility is ideally intrinsic, unaffected by trapping, since the Lorentz force only deflects a moving charge carrier. The magnitude of the small-polaron Hall mobility is at most comparable to 1 cm^2/V-s. Most importantly, the activation energy of the small-polaron Hall mobility in its high-temperature Arrhenius regime is always less than that of the conventional mobility. In particular, although the ratio of these two activation energies depends on the details of the model, the activation energy of μ_H for small-polaron hopping is often about one-third that of μ. Furthermore, the Hall mobility activation energy even can be small enough that the temperature dependence of μ_H is dominated by that of its pre-exponential factor. In these instances, the Hall mobility will decrease with increasing temperature.

The sign of the Hall coefficient in wide-band conventional semiconductors is (1) negative for electrons in states with positive effective mass near conduction-band minima and (2) positive for vacant electronic states with negative effective mass near valence-band maxima. This simple situation does not always apply for energy bands which are narrower than the thermal energy kT. Moreover, Hall-Effect sign anomalies, opposite those for charge carriers in conventional semiconductors, are common for small-polaron hopping.

The sign of the Hall coefficient for hopping conduction is given by

$$sgn\,(R_H) = sgn\left[(-q)(\delta)^{n+1}\prod_{i=1}^{n} t_{i,i+1}\right], \tag{12}$$

where q denotes the bona-fide carrier's charge (negative for electrons). In addition, δ indicates the filling of the states between which carriers hop ($\delta = -1$ for nearly empty states and $\delta = 1$ for nearly filled states). The final factor in the above equation is the product of electronic transfer energies $t_{i,i+1}$ integrals around a closed loop of n elements.

The sign of the Hall coefficient is conventional when the charge carriers are electrons ($q < 0$) moving among sites for symmetric structures in which n is even. Then the Hall coefficient sign is just that of δ: negative for nearly empty states ($\delta = -1$) and positive for nearly filled states ($\delta = 1$). Similarly, the sign of the entropy-of-mixing contribution to the Seebeck coefficient, proportional to ln $[c/2(1-c)]$ or ln$[c/(1-c)]$, is negative for a nearly empty narrow band of electrons, $c < 1/2$, and positive for a nearly full narrow electron band, $c > 2/3$.

By contrast, the sign of the Hall coefficient is often anomalous for electrons moving among sites for which n is odd, as frequently occurs for non-crystalline structures. Then the sign of the Hall coefficient is just that for the product of electronic transfer energies, independent of state filling. The sign of this product only depends on the symmetry of the orbitals between which electrons transfer.

The product of n-transfer energies between node-less electronic states (e.g., bonding, lone-pair or ground-state impurity orbitals) is simply $(-1)^n$ because of the negative potential in orbitals' overlap regions. The sign of the Hall coefficient is then negative when n is odd, even while the sign of the Seebeck coefficient is positive for transport among nearly filled bonding, lone-pair or impurity-state orbitals.

Furthermore, the product of n-transfer energies between anti-symmetric (e.g., anti-bonding) orbitals is always positive. Thus, the sign of the Hall coefficient is positive for hopping in structures dominated by odd membered loops of antibonding orbitals. This result is opposite to the negative Hall coefficient for conventional transport involving transport among anti-bonding orbitals of a covalent semiconductor's conduction band.

Very low, <1 cm^2/V-s, thermally activated Hall mobilities have been reported in many non-crystalline solids. Their Hall mobility activation energies are generally considerably smaller than the mobility activation energies inferred from comparison of the temperature dependences of these materials' dc conductivities and Seebeck coefficients. Hall-Effect sign anomalies are also widely reported in disordered structures that manifest hopping transport. Most strikingly, positive Hall coefficients are reported when doping introduces low-mobility hopping electrons to amorphous elemental Si and As. Negative Hall coefficients with Arrhenius Hall mobilities are also reported when dopants remove electrons from amorphous elemental Si and Ge. Unlike their crystalline counterparts, these elemental covalent semiconductors are thought to contain significant numbers of odd-membered rings. Negative Hall coefficients and positive Seebeck coefficients are widely reported for chalcogenide glasses where transport is thought to be between lone-pair orbitals on chalcogen atoms. Small-polaron-like transport between dopant-related states in heavily doped semiconductors also display negative Hall coefficients with positive Seebeck coefficients.

Polaron absorption

Large- and small-polarons generate broad absorption bands. Features of their absorptions distinguish between them.

A large-polaron's principal absorption arises from photo-exciting its self-trapped electronic carrier into the energy band which is its genesis. The potential well binding a large-polaron's electronic carrier is approximated as that formed with surrounding atoms fixed at their carrier-induced equilibrium positions. For a Coulomb-like self-trapping potential well, the threshold for photo-ionizing its electronic carrier occurs when the photon energy $\hbar\Omega$ exceeds three times the large-polaron binding energy $3E_p$. Since $E_p \gg \hbar\omega$ for a strong-coupling large-polaron, the threshold for its main absorption lies above the characteristic phonon energy $\hbar\omega$. Above this threshold the absorption increases as it mirrors the rise of the energy band's density-of-states beyond its edge. This large-polaron's absorption band subsequently declines gradually as the wave-lengths of the energy band's Bloch states fall below the self-trapped electronic carrier's spatial extent. Thus, a large-polaron primary absorption band tends to rise more sharply with increasing Ω below its peak than it declines subsequently. In addition, subsidiary narrow absorption bands can emerge from exciting self-trapped electronic carriers into their intra-well excited states.

Coherently moving charge carriers exhibit a Drude-type absorption corresponding to the real part of the frequency-dependent conductivity, $\mathrm{Re}[\sigma(\Omega)] = \sigma(0)/[1 + (\Omega\tau)^2]$, where τ denotes the carrier's scattering time. Large polarons are extremely slow-moving, heavy-massed and weakly scattered compared with conventional electronic charge carriers. In particular, the scattering time associated with a large-polaron's scattering by acoustic phonons is so long that the large-polaron Drude absorption is confined to well below the characteristic phonon energy $\hbar\omega$. Moreover, this scattering time increases as the temperature is reduced. Therefore, the pseudo-gap between a large-polaron's low-frequency Drude absorption, $\Omega < \omega$, and the threshold of its high-frequency broad absorption band, $\Omega > \omega$, widens as the temperature is lowered. This signature behavior is unlike that of conventional electronic carriers whose Drude absorption simply falls monotonically with increasing frequency up to very high frequencies, e.g., $\Omega \approx 10^{15}$ Hz.

A small-polaron absorption is a photo-induced transition between severely localized electronic states. It elevates a small-polaron's self-trapped electron from its adiabatic ground-state into a severely localized state centered on a nearby unoccupied site. With a short-range electron-phonon interaction the absorption's peak is at twice the small-polaron binding energy. This absorption is broadened as vibrations of atoms surrounding its initial and final sites spread their electronic energies. With increasing temperature this broadening increases from that due to atoms' zero-point vibrations to that due to their thermal vibrations. The asymmetry of a small-polaron absorption band is opposite that of a large-polaron's primary high-frequency absorption band. In particular, the small-polaron absorption rises more slowly with increasing Ω below its peak than it falls above its peak.

Interactions between polarons

Transient absorptions, recombination and possible luminescence are governed by the interactions between injected oppositely-charged carriers that form polarons. Polarons are indicated by their mobilities being well below the minimum for non-polaron carriers, $q\hbar/m_c kT$, about 300 cm^2/V-s at room temperature. Since polarons are slow moving, the energy of their mutual Coulomb interaction is reduced by their material's static dielectric constant ε_0. Well-separated polarons also each lower their energies by their polaron binding. However, as oppositely charged polarons approach close enough to one another the pair increasingly presents itself to surrounding atoms and ions as being charge neutral. As a result, their net polaron binding energy is reduced, increasing the energy of a pair of oppositely charged polarons. In other words, there is a short-range repulsion between oppositely charged polarons. Finally, when electron and hole polarons share a common site, they simply become a self-trapped exciton. Consistent with its charge neutrality, an exciton has a much smaller energy reduction from displacement of surrounding atoms than do a separated electron and hole. These features are illustrated in Fig. 7, where, the energy of oppositely charged polarons is plotted against their separation s. The short-range repulsion between oppositely charged polarons is most severe in materials with especially displaceable ions, solids with exceptionally large static dielectric constants. The suppression of recombination in such materials (e.g., perovskites) fosters their functioning as especially efficient solar cells (Emin, 2018).

Repulsive interactions occur between polarons of like-charge as their self-trapped electronic carriers compete to displace intervening atoms. Self-trapping then becomes untenable at sufficiently large charge-carrier densities. This effect is the basis of a mechanism to switch a low-conductivity small-polaron semiconductor into a higher conductivity state. Specifically, current flow drives conventional electronic charge carriers from conducting leads into a semiconductor in which they form small-polarons. Small polarons diffuse much slower than conventional carriers. As a result, increasing current flow causes small polarons to progressively accumulate in the semiconductor near its interfaces with its conducting contacts. A high enough current will augment this interfacial

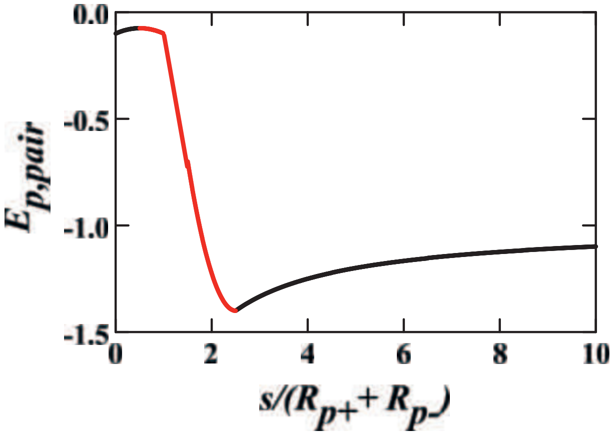

Fig. 7 The energy of a pair of oppositely charged polarons $E_{p,pair}$, in units of the net energy of the pair of well-separated polarons, is plotted against their mutual separation s in units of the sum of the radii of their self-trapped electronic carriers, R_{p+} and R_{p-}. The energy reduction from relaxation of well-separated charged polarons, $s \rightarrow \infty$, is much larger than that for a self-trapped exciton, $s \rightarrow 0$. The repulsive portion of the curve is shown in red.

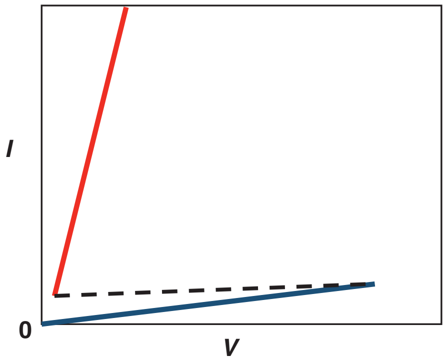

Fig. 8 The current *I* is plotted versus the voltage *V* for a threshold switch. The low-conductivity state is shown in blue and the high-conductivity state is depicted in red. The high-conductivity state is maintained provided *I* is kept above its threshold value.

concentration of small polarons enough to destabilize them, converting them into conventional carriers. The large interfacial concentration of small polarons thereby propagates into the semiconductor. If the propagated small-polaron concentration remains sufficiently large it too will be destabilized. The avalanche of converting small-polarons into conventional carriers will continue until the excessive small-polaron concentration is relieved (e.g., by recombination with oppositely charged carriers entering from the opposing contact). The resistance of the switched semiconductor is then primarily that of the residual region whose charge carriers remain as small polarons. The hallmark of such switching is that the resistance in the high-conductivity state is independent of the semiconductor's length since it mainly depends on the length of the residual region. As illustrated in Fig. 8, the higher conductivity state persists as long as the current is maintained above the threshold needed to initiate switching from the low-conductivity state. Furthermore, threshold switches can be converted into memory switches if their relatively large current flows induce ("burns in") structural changes into the semiconductor. Such switching has been reported for about a century in materials (e.g., chalcogenide glasses) whose very low thermally activated mobilities suggest that their charge carriers are small-polarons.

A large singlet bipolaron has two self-trapped electronic carriers with opposing spin alignments sharing a common multi-site ground-state orbital. The Pauli principle requires that further electronic carriers added at the bipolaron's location be placed in orbitals of higher energy. This promotion energy destabilizes such multi-carrier entities with respect to separating into bipolarons and polarons. Thus, singlet bipolarons are the only multi-carrier polarons. In other words, there is a hard-core short-range repulsion between singlet bipolarons. Bipolarons also experience a mutual Coulomb repulsion. Since a bipolaron's motion is very slow, governed by associated atoms' movements, this long-range repulsion is reduced by its material's static dielectric constant, ε_0. This suppression is severe for large singlet bipolarons since, as noted earlier, their stability with respect to both (1) separating into two large polarons and (2) collapsing into a small bipolaron requires a material with exceptionally displaceable ions, $\varepsilon_0 > 2\varepsilon_\infty \gg 1$. The polarization of a large bipolaron's self-trapped electronic carriers in response to related atoms' vibrations reduces their energies. This softening of atoms' vibrations increases with the density of large-bipolarons. In other words, there is a phonon-mediated intermediate-range attraction between large bipolarons. The combination of large-bipolarons' mutual short-range repulsion, suppressed Coulomb repulsion and intermediate-range attraction fosters a gas of large bipolarons condensing into a large-bipolaron liquid. In addition, the liquid's density is limited in order to avoid destabilizing its large bipolarons.

Superconductivity of a large-bipolaron liquid

Conventional superconductivity occurs in elemental metals such as Al, Hg, Pb, La, Nb, Sn and Ta with transition temperatures below 10 K. Unconventional superconductivity occurs in doped transition-metal-oxide insulators with especially displaceable ions, as indicated by their exceptionally large values of $\varepsilon_0/\varepsilon_\infty$. The ferroelectric insulator $SrTiO_3$ is a perovskite ferroelectric whose structure can be viewed as comprising alternating planar TiO_2 and SrO layers. It displays superconductivity below 1 K when charge carriers are introduced by Nb substitutions or oxygen vacancies. Much higher superconducting transition temperatures are found upon doping cuprate insulators which have more complicated perovskite-based structures. For example, La_2CuO_4 is comprised of CuO_2 layers alternating with two LaO layers. Holes are introduced in the CuO_2 layers when divalent cations such as Sr^{2+} or Ba^{2+} cations are substituted for La^{3+}. Cuprate superconductors have superconducting transition temperatures, between about 30 K and 130 K.

The charge carriers in the normal states of conventional superconductors are quasi-free electrons. By contrast, the charge-carriers in transition-metal oxides are widely viewed as some type of polaron. In particular, polarons related to the relatively narrow bands associated with motion between transition-metal ions usually are small. Polarons associated with the relatively wide oxygen-based electronic bands are typically large. Moreover, singlet large-bipolaron formation is strongly promoted when carriers are confined to a plane embedded within a medium for which $\varepsilon_0/\varepsilon_\infty \gg 1$.

Conventional superconductivity's genesis is a phonon-mediated attraction between quasi-free electrons that induces their condensing into singlet pairs. These Cooper pairs overlap very strongly with one another to produce a quantum liquid whose ground state has an energy gap in its excitation spectrum. An unconventional model of superconductivity envisions the phonon-mediated intermediate-range attraction between large bipolarons driving their condensation into a liquid of non-overlapping charged bosons. The ground state of this liquid remains fluid, rather than condensing into a solid, if its large bipolarons do not order in a manner commensurate with its solid's underlying lattice. Large-bipolaron superconductivity is then akin to the superfluidity of a liquid of neutral mobile bosons, liquid ^{4}He, but with mobile bosons of charge $2e$, a large-bipolaron liquid. As such, the liquid's long-wavelength excitations are just the large-bipolarons' plasma oscillations. These excitations' characteristic energy is $\hbar\Omega_p \equiv \hbar[4\pi(2e)^2 n_{lbp}/m_{lbp}\varepsilon_0]^{1/2}$, where n_{lbp} and m_{lbp} respectively denote the large-bipolaron density and effective mass. The very large values of m_{lbp} and ε_0, which characterize large bipolarons and their formation, limit $\hbar\Omega_p$ to less than that of related phonons $\hbar\omega$. The liquid's Bose condensation and the onset of large-bipolaron superconductivity occurs when kT falls below $\hbar\Omega_p$. The liquid's collective ground state is characterized by the synchronous zero-point vibrations of the atoms whose displaced-equilibrium positions generate the potential wells that self-trap the singlet pairs of its large bipolarons.

Superconductors based on doped ionic insulators display properties consistent with two-fluid large-bipolaron superconductivity. The scattering of channeled ions and the positron annihilation rate progressively fall as the homogeneous synchronous vibrating condensate grows upon lowering the temperature below the superconducting transition temperature.

Distinctive properties reported for superconductors based on doped ionic insulators are consistent with those of large bipolarons. The very high superconducting transition temperatures in cuprates may simply result from their large values of ε_0 (≥ 50) being considerably smaller than those of doped-$SrTiO_3$, a bona-fide ferroelectric, with $\varepsilon_0 \approx 20{,}000$ near its superconducting temperature, about 1 K.

As illustrated in Fig. 9, large-bipolarons' superconductivity requires their density to be (1) large enough to avoid their being bound to dopants, (2) small enough to preclude their destabilization, and (3) incommensurate with their ground-state's global solidification. For example, superconductivity in tetragonal $La_{2-x}Ba_xCuO_4$ only exists over a restricted doping range and disappears at an intermediate doping level that is commensurate with bipolarons' global solidification: a bipolaron centered on every fourth CuO_2 unit in the x and y directions of its planar square lattice, $2/(4 \times 4) = 1/8$.

The pseudo-gaps observed in cuprate superconductors' absorption spectra resemble the temperature-dependent gap between a large-(bi)polaron's low-frequency, $<\hbar\omega$, Drude absorption and the broad high-frequency, $>\hbar\omega$, absorptions generated by exciting its self-trapped electronic carriers. Normal-state carrier mobilities in cuprates, about 1 cm^2/V-s, are much less than the minimum for coherent transport, eh/kTm_c, if the carrier mass m_c is comparable to that of an electron. However, measured mobilities are compatible with large-(bi)polarons' huge effective masses.

As illustrated in Fig. 3, the core of a large-bipolaron in single-cuprate-layer superconductors is envisioned as two electrons being removed from the four O^{2-} anions circumscribed by four spin-1/2 Cu^{2+} cations residing at the corners of a CuO_2 planar square unit (Emin, 2017). Self-trapping occurs as the oxygen anions relax inward and the copper cations relax outward. Concomitantly, four electrons are transferred from the oxygen anions to the copper cations thereby converting them to spin-less Cu^{1+} cations. The carrier-induced loss of magnetism and its spin entropy generates a negative contribution to the large-bipolaron-hole's Seebeck coefficient. It falls toward $-(k/2e)[4\ln(2)]$ with rising temperature. The superconducting state's synchronous lowest-frequency and largest-amplitude radial zero-point optic-mode vibrations of carrier-induced-displaced oxygen and copper atoms have d-symmetry. The adiabatic principle insures that the symmetries of these atoms' equilibrium and zero-point vibratory displacements will be reflected in their electronic states.

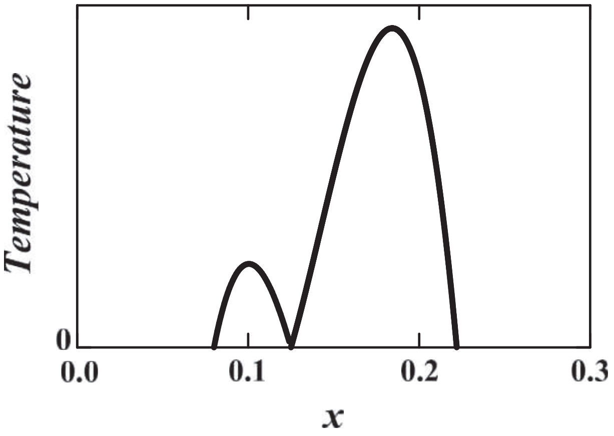

Fig. 9 The superconducting transition temperature of tetragonal $La_{2-x}Ba_xCuO_4$ is plotted versus x, the idealized concentration of doping-induced holes. Superconductivity exists between limiting dopant concentrations. Distinctively, as observed, superconductivity also vanishes at the intermediate hole concentration $x = 1/8$. This concentration corresponds to doping-induced holes ordering as bipolarons commensurate with the basal plane's CuO_2 square lattice at $x = 2/(4 \times 4) = 1/8$.

Conclusion

An electronic charge carrier is self-trapped when it is bound within the potential well generated by displacing atoms to new equilibrium positions. Self-trapping requires that the binding energy of the self-trapped carrier exceed $h\nu$, where ν denotes the characteristic frequency of associated atoms' vibrations. The electronic carrier then circulates within the potential well that binds it before the associated atoms move appreciably. Relaxation of self-trapped electronic carriers to these atoms' vibrations lowers their frequencies. A strong-coupling polaron refers to the composite quasiparticle comprising the self-trapped electronic carrier taken together with the alterations it induces in related-atoms' equilibrium positions and vibrations.

Polaron formation is driven by a charge carrier's short-range and long-range electron-phonon interactions. These interactions result from the respective dependences of an electronic charge carrier's energy on the locations of the atoms it contacts and on displacements of distant ions. A macroscopic measure of the displaceability of these ions is the difference between the reciprocals of a material's high-frequency and static dielectric constants: $\varepsilon_\infty^{-1} - \varepsilon_0^{-1}$. For ionic and polar media $\varepsilon_0 \gg \varepsilon_\infty$, but for covalent media $\varepsilon_0 \approx \varepsilon_\infty \gg 1$. Carrier-induced changes in the separations between dissimilar atoms shift charge between them.

The adiabatic limit, $\nu \to 0$, presumes that electronic charge carriers always adjust to the motions of medias' relatively massive and slow moving atoms. The adiabatic potential energy is the sum of the potential energy arising from atomic displacements plus the electronic carrier as a function of atoms' positions. Adoption of a scaling argument enable the adiabatic potential to be readily studied as a function of an electronic carrier's spatial extent, its radius. A minimum of the adiabatic potential with respect to a carrier's radius indicates its being self-trapped. There are two distinct types self-trapped state. A large-polaron minimum, corresponding to a self-trapped electronic carrier extending over multiple sites, forms when long-range electron-phonon interactions predominate. A small-polaron minimum, characterized by the self-trapped electronic carrier collapsing to the most severely localized state consistent with condensed-matter's atomicity, forms when the short-range electron-phonon interaction predominates.

Self-trapped charge carriers move very slowly since their movement is contingent on atomic movements. Strong-coupling large polarons move coherently albeit with huge effective masses. As such, the minimum mobility permitted for coherently moving charge carriers (eh/kTm_c, where m_c denotes a charge-carrier's effective mass) is much lower for large polarons than for conventional electronic charge carriers. Nonetheless, large-polaron mobilities are higher than might be expected because such heavy-massed quasi-particles tend to be difficult to scatter. Large-polaron mobilities are frequently about 1–10 cm^2/Vs at room temperature.

Small polarons generally move incoherently by thermally assisted hopping. Small-polaron mobilities are Arrhenius at high temperatures and become non-Arrhenius as the temperature is lowered below about $h\nu/3\,k$. In particular, the high-temperature adiabatic small-polaron mobility is $(ea^2\nu/kT)\exp.(-E_A/kT)$, where a denotes the jump distance and $E_A > h\nu$. By itself, the increase of E_A with increasing jump distance favors short hops over long hops. The slowness of transfers of vibrational energy between the atoms directly related to a hop and the remainder of the medium causes hopping to occur in flurries separated by quiescent periods. An injected charge carrier's relaxation as it forms a small polaron generates a region of enhanced vibrational agitation. Its transient hopping is thereby enhanced until its full equilibration is achieved.

The Seebeck coefficient, the entropy transported with a carrier divided by its charge, displays features which distinguish polarons from conventional charge carriers. Often the change of the entropy-of-mixing generated by adding a charge carrier provides the dominant contribution to the Seebeck coefficient. Then the Seebeck coefficient just depends on the carrier concentration. By contrast, the dc conductivity also depends on charge-carriers' mobility. Taken in tandem, measurements of the Seebeck coefficient and the dc conductivity permit determination of whether the carrier mobility manifest the Arrhenius high-temperature behavior characteristic of small-polaron hopping. The Seebeck coefficients of large (bi)polarons are also distinctive in that they have contributions from carrier-induced reductions of related atoms' vibration frequencies.

Distinctively, the Hall mobility, the mobility determined from a Hall-Effect measurement, for small-polaron hopping generally rises more slowly with increasing temperature than does the mobility which enters into the dc conductivity. Moreover, the sign of the small-polaron Hall Effect is often opposite that were the charge carriers conventional. These anomalous situations occur in many amorphous semiconductors, for semiconductors' impurity conduction, and for some crystalline structures.

Since large polarons are massive and relatively difficult to scatter, the declines of the real part of their conductivities with increasing applied frequency primarily occur well below those of atomic vibrations, 10^{13} Hz, rather than at the relative high frequencies, 10^{15} Hz, characterizing conventional electronic charge carriers. In addition, the large-polaron frequency-dependent conductivity associated with exciting its self-trapped electron carrier occurs above atomic vibration frequencies. Thus, unlike a conventional electronic carrier, a large-polaron's absorption spectrum has a low-energy gap which widens with decreasing temperature. Small polarons' absorption spectra are also qualitatively distinct from those of conventional electronic charge carriers. The photon-assisted inter-site transfer of a small-polaron generates a broad absorption band which peaks at an energy of about four times the hopping activation energy.

Distinctive features of (bi)polarons' mutual interactions support some device applications. In particular, as oppositely charged polarons approach one another their net interaction with distant ions progressively diminishes. The net polaron-formation energy is thereby reduced. In other words, there is a short-range repulsion between oppositely charged polarons (Emin, 2018). By suppressing recombination of oppositely charged large polarons in ionic solids this effect fosters their solar cell efficiency. This effect may account for the high efficiencies of perovskite solar cells whose (1) very large values of $\varepsilon_0/\varepsilon_\infty$, (2) moderate carrier mobilities (i.e., about 1 cm^2/V-s at 300 K), and (3) distinctive absorption spectra suggest large-polaron formation. This effect would also increase the feasibility of high-efficiency, long-lived, high-power, beta-voltaic devices (Emin, 2019). These devices are stacks of p-n junctions of doped icosahedral boride semiconductors in which a reliable, high intensity beta-particle flux from a radio-isotope (e.g., ^{90}Sr) replaces a solar-cell's intermittent moderate-intensity solar flux.

The density of stable polarons is limited by their competition to displace surrounding atoms. Thus, introducing ever higher concentrations of polarons into a semiconductor ultimately destabilizes them with respect to their forming conventional high-mobility electronic charge carriers. Thus, driving a large enough current through a semiconductor whose equilibrated carriers are small polarons cause it to switch into a low resistance state. This low-resistance state is maintained by keeping the current above the threshold value at which switching in initiated.

Charge carriers can pair as singlet large-bipolarons in materials with exceptionally displaceable ions as indicated by $\varepsilon_0/\varepsilon_\infty \gg 1$. The phonon-mediated attraction between large bipolarons, generated by their self-trapped electrons' collective response to atoms' vibrations, fosters their condensing into a liquid. Superconductivity is associated with the Bose condensation of this large-bipolaron liquid. Distinctive features distinguish this superconductivity from metals' conventional superconductivity. In particular, (1) large bipolarons and their liquid only exist for moderate carrier concentrations, (2) the normal-state large-bipolaron mobility is much less than that permitted for conventional electronic charge carriers, and (3) large-bipolarons' normal-state absorption spectra have low-energy gaps that widen with decreasing temperature.

Electronic charge carriers that self-trap, thereby forming strong-coupling (bi)polarons, display transport and optical properties which distinguish them from conventional carriers. Large polarons display exceptionally low mobilities that decrease with increasing temperature. A large-polaron's absorption spectra consist of a broad high-frequency band that is separated by a pseudo energy gap from an extremely narrow low-frequency Drude-type absorption. Small polarons manifest thermally-assisted mobilities which are usually very much lower than even large-polaron mobilities. Distinctively, small-polaron mobilities become Arrhenius at high temperatures. A small-polaron's Hall-Effect mobility increases with rising temperature more gently than that of the mobility which enters into the dc conductivity. In many materials a magnetic field deflects a small polaron in the opposite direction as it would deflect a free carrier of the same charge. A broad small-polaron absorption band is associated with photon-assisted hopping. Oppositely charged polarons experience mutual short-range repulsion which impede their recombination. Polarons of like charge can combine to form singlet bipolarons in materials with exceptionally displaceable ions. Large bipolarons may even condense into a liquid which undergoes a Bose condensation to yield unconventional superconductivity. Reports of most of these extraordinary effects already exist. Observations of the unusual properties which identify strong-coupling polarons may become more common as increasingly complex semiconductors are investigated.

References

Emin D (2006) Unusual properties of icosahedral boron-rich solids. *Journal of Solid State Chemistry* 179: 2791–2798.

Emin D (2013) Theory of Meyer-Neldel compensation for adiabatic charge transfer. *Monatshefte für Chemie – Chemical Monthly.* 144: 3–10.

Emin D (2016) Determining a hopping polaron's bandwidth from its Seebeck coefficient: Measuring the disorder energy of a non-crystalline semiconductor. *Journal of Applied Physics* 119: 045101.

Emin D (2017) Dynamic d-symmetry Bose condensate of a planar-large-bipolaron-liquid in cuprate superconductors. *Philosophical Magazine* 97: 2931–2945.

Emin D (2018) Barrier to recombination of oppositely charged large polarons. *Journal of Applied Physics* 123: 055105.

Emin D (2019) Proposed high-capacity efficient energy cells from MgAlB$_{14}$-type icosahedral-boron semiconductors. *AIP Advances* 9: 055226.

Further reading

Emin D (2013) *Polarons*. Cambridge: Cambridge University Press.

Semiconductors: Spin-density waves

N Harrison, Los Alamos National Laboratory, Los Alamos, NM, United States

© 2024 Elsevier Ltd. All rights reserved.

This is an update of N. Harrison, Spin Density Waves and Magnons, Editor(s): Franco Bassani, Gerald L. Liedl, Peter Wyder, Encyclopedia of Condensed Matter Physics, Elsevier, 2005, Pages 19–27, ISBN 9780123694010, https://doi.org/10.1016/B0-12-369401-9/00667-7.

Introduction	448
Fermi surface nesting and spin-density wave formation	448
Microscopic theory	449
Basic static properties	450
Collective excitations: Phasons	450
Collective excitations: Magnons	452
Field-induced spin-density waves	453
Conclusion	455
References	455

Abstract

This chapter explores extremely narrow gap semiconductors and semimetals resulting from microscopic interactions between itinerant electrons. It focuses on spin-density waves, which emerge from Coulomb interactions, transforming metals into antiferromagnetic systems. The chapter discusses their perturbations of electronic bands, thermodynamic coupling, and stability under magnetic fields. It examines the instability at the Fermi surface, static and dynamic properties, and transitions between field-induced phases. Potential applications to other density wave states are briefly discussed. This review provides a concise understanding of spin-density waves' phenomena and their significance in semiconductors.

Key points

- Focus on spin-density waves as a consequence of Coulomb interactions between electrons, leading to antiferromagnetic behavior in a metal.
- Consider spin-density waves as perturbations of electronic bands of quasiparticles in a metal, with smaller gaps and metallic carriers surviving in some cases.
- Explore the mapping of antiferromagnetism onto the case of a Heisenberg antiferromagnet, with smaller moments and spatial periodicities.
- Investigate the thermodynamic coupling between spin-density waves and charge degrees of freedom, leading to phase excitations and changes in spin orientation.
- Analyze the instability at the Fermi surface responsible for spin-density wave formation and discuss their static and dynamic properties.
- Examine field-induced spin-density waves and the role of orbital contributions in stabilizing ground states under a strong magnetic field.
- Explore transitions between different field-induced spin-density wave phases and their connection to the bulk quantum Hall effect.
- Refer to the potential application of spin-density wave formalisms to other density wave states involving pseudospins, such as quadrupole-density waves, valley-density waves, or chirality-density waves.

Nomenclature

t_b'	Transfer integral along b (second nearest neighbor) [J, eV]
$\varepsilon_\perp$	Electronic dispersion orthogonal to **x** [J, eV]
2Δ	Gap energy [J, eV]
A or B	Arbitrary integers [dimensionless]
a or b	Lattice constant along **x** or **y** [m]
A	Vector potential [Tm]
B or B	Magnetic flux density (magnetic field) [T]
B_{eff}	Heisenberg molecular field [T]

https://doi.org/10.1016/B978-0-323-90800-9.00262-6

D	Anisotropy energy [J, eV]
E	Electric field [Vm^{-1}]
e	Electron charge [C]
g	Electronic g-factor [dimensionless]
$\mathbf{H}$	Heisenberg spin Hamiltonian [J, eV]
$\mathbf{H}_{\perp}$	Anisotropy Hamiltonian [J, eV]
h	Planck constant [Js]
$\hbar$	Planck constant divided by 2π [Js]
i	Square root of -1 [dimensionless]
J	Heisenberg interaction [J, eV]
j_{SDW}	Current of collective mode [Cs^{-1}]
k	Electronic wave vector [m^{-1}]
k	Wave number [m^{-1}]
k_{F}	Fermi wave vector [m^{-1}]
k_x, k_y or k_z	Electronic wave vector along $\mathbf{x}$, $\mathbf{y}$ or $\mathbf{z}$ [m^{-1}]
l	Landau level index [dimensionless]
m or $\boldsymbol{\mu}$	Moment of spin [Am^2 or units ofμ_{B}]
m	Effective mass [kg]
n	Carrier density (3D) [m^{-3}]
N	Number of electrons per unit cell [dimensionless]
p or q	Indices of spin [dimensionless]
Q	Quasiparticle excitation wave vector [m^{-1}]
Q_0 or Q_0	Optimum nesting vector [m^{-1}]
S or S	Spin per unit cell [dimensionless]
T	Temperature [K]
t	Time [s]
t_b	Transfer integral along b (nearest neighbor) [J, eV]
T_{SDW}	Transition temperature [K]
U	Coulomb potential [J, eV]
V	Volume of unit cell [m^3]
v_{F} or v_{F}	Quasiparticle group velocity at Fermi surface [ms^{-1}]
W	Electronic bandwidth [J, eV]
x	Spatial dimension along $\mathbf{x}$ [m]
ε	Electronic dispersion [J, eV]
ε_{F}	Fermi energy [J, eV]
$\boldsymbol{\lambda}$	Effective coupling constant [dimensionless]
$\boldsymbol{\Lambda}$	Period of spin modulation [m]
ν	Landau level filling factor [dimensionless]
ρ	Charge density per unit length [Cm^{-1}]
ρ_{xy}	Hall resistivity [Ωm]
σ	Electronic spin [dimensionless]
σ_{coll}	Conductivity of collective mode [Ω^{-1} m^{-1}]
σ_{xx}	Conductivity (diagonal) [Ω^{-1} m^{-1}]
σ_{xy}	Hall conductivity [Ω^{-1} m^{-1}]
τ	Relaxation time (transport) [s]
$\boldsymbol{\Phi}$	Free energy per unit cell [J^{-1}, eV^{-1}]
ϕ	Phase [radians]
χ	Spin susceptibility [dimensionless]
ψ	Electronic wave function [dimensionless]
ω_0	Pinning frequency [s^{-1}]
ω_{A}	Amplitudon frequency [s^{-1}]
ω_b	One-dimensional Fermi surface traversal frequency [s^{-1}]
ω_{m}	Magnon frequency [s^{-1}]
ω_{ϕ}	Phason frequency [s^{-1}]
l	One-dimensional Fermi surface traversal length [m]
$n(\varepsilon)$	Electronic density of states per unit cell [J^{-1}, eV^{-1}]

Introduction

A review of semiconductors would be incomplete without the inclusion of those classes of extremely narrow gap semiconductors and semimetals, that result from microscopic interactions between itinerant (or nearly free) electrons in a correlated metal. This section of the *Encyclopedia* is devoted to spin-density waves, which are a consequence of Coulomb interactions between electrons causing a system, which would otherwise be a conventional metal, to become antiferromagnetic (Blundell, 2001; Fawcett, 1988; Fawcett et al., 1994; Gruner, 1994, 1996; Kulikov and Tugushev, 1984). Perhaps the most extreme example is that where the Coulomb interactions between electrons exceeds the total electronic bandwidth, leading to an insulator that can be very well described by the Hubbard model. Spin-density waves are subtle by comparison, being much more dependent on details of the Fermi surface topology. It is therefore more convenient to consider spin-density waves as perturbations of electronic bands of quasiparticles in a metal. The gaps are significantly smaller, enabling quasiparticles to be easily excited across the spin-density wave gap, with tiny pockets of metallic carriers surviving in many cases.

The antiferromagnetism that results can often be mapped onto the simple case of a Heisenberg antiferromagnet (Gruner, 1996). The moments are nevertheless smaller with comparatively long spatial periodicities of the spin modulation projected in preferred crystallographic directions that are predetermined by the details of the bandstructure. The existence of thermodynamic coupling between the spin-density wave and charge degrees of freedom of the electronic bands causes these systems to be subject to phase excitations (or phasons) in a similar manner to charge-density wave systems (Gruner, 1996). Changes in the orientation of the spins, in contrast, take place via spin wave excitations (or magnons), which are qualitatively similar to those that occur in Heisenberg antiferromagnets.

We begin this chapter by considering the instability at the Fermi surface responsible for spin-density wave formation, and then continue by discussing their static and dynamic properties. These include collective excitations involving both electronic (phason) and spin (magnon) degrees of freedom (Gruner, 1996). Finally, we turn to the topic of field-induced spin-density waves in which orbital contributions to the total free energy help stabilize such ground states in the presence of a strong magnetic field. Transitions between different field-induced spin-density wave phases involving different levels of orbital quantization give rise to a novel manifestation of the bulk quantum Hall effect (Chaikin, 1996; Maki, 1986).

In general, the some of the formalisms that apply to a spin-density wave may also apply to density wave states involving other degrees of freedom where these other degrees of freedom can be presented as pseudospins. Possible examples include quadrupole-density waves in rare earth and actinide systems (Hafner et al., 2022), valley-density waves systems that exhibit a valley degeneracy (Schrade and Fu, 2019), or chirality-density waves (Kung et al., 2015).

Fermi surface nesting and spin-density wave formation

The term 'spin-density wave' refers to a simple one-dimensional (1D) antiferromagnetic modulation of the local spin density $\mathbf{S} = \mathbf{S}_0 \cos(\mathbf{r} \cdot \mathbf{Q}_0 + \phi_0)$ condensed from electrons that subsequently become insulating (Blundell, 2001; Fawcett, 1988; Fawcett et al., 1994; Gruner, 1994, 1996; Kulikov and Tugushev, 1984). An essential precondition for spin-density wave formation to be energetically favorable is that a large fraction of the electron and hole quasiparticles share the same group velocity $\mathbf{v}_\mathrm{F}$ at the Fermi energy ε_F. The residual Coulomb potential between quasiparticles U must also be significant, but smaller than the total electronic bandwidth W. These requirements tend to be more easily met in systems where the calculated electronic bands (i) are very narrow and (ii) are highly anisotropic or have large flat sections of Fermi surface that can efficiently nest. The term `nesting' refers to the process by which the translational symmetry breaking of the crystalline lattice at a characteristic wavevector $\mathbf{Q}_0$ eliminates major sections of the Fermi surface upon opening a gap 2Δ. In a spin-density wave system, this gap opens up wherever spin-up and spin-down electronic bands cross. Fig. 1 shows an example of the cross-section of a Fermi surface amenable to nesting. The combined process of nesting and gap formation saves energy by greatly reducing the total electronic density of states at ε_F.

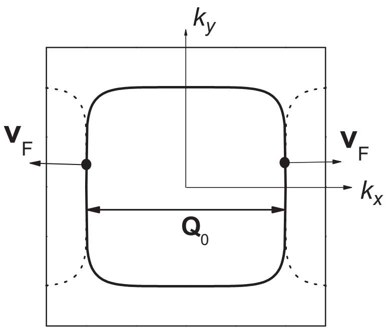

Fig. 1 An example of a fictional Fermi surface susceptible to nesting. The Fermi velocity $\mathbf{v}_\mathrm{F}$ is always perpendicular to the Fermi surface. Translation of the Fermi surface by the nesting vector $\mathbf{Q}_0$ enables sections of Fermi surface with opposing Fermi velocities to meet each other tangentially. The nested sections become dielectric if the bands anticross upon opening of a gap. The dotted lines represent shadows of the translated Fermi surface.

Spin-density wave ground states occur most commonly in molecular or organic metals, although classic examples occur in elemental chromium and its alloys. The antiferromagnetic ground states of heavy fermion systems, which have quasiparticle effective masses many times the free electron mass, can also sometimes be understood in terms of spin-density waves. While many of these materials have complicated electronic structures, spin-density wave theory is most easily applied to systems with only a single quasi-one-dimensional electronic band

$$\varepsilon_{k,\sigma} = \hbar^2 k_x^2/2m + \varepsilon_{\perp}\left(k_y, k_z\right) + \sigma g \mu_{\rm B} B \tag{1}$$

crossing $\varepsilon_{\rm F}$. The simplest case, by far, is that for a metal where this band has a significant dispersion only along chains parallel to **x**, where k_x is the x component of the momentum vector **k** and $\sigma = \pm 1/2$ represents the up and down spin branches. A purely one-dimensional dispersion is obtained by setting the limit $\varepsilon_{\perp}(k_y, k_z) \to 0$. Because spin-density wave formation only involves states that are close to $\varepsilon_{\rm F}$, it is often convenient to consider a linear approximation of the form

$$\varepsilon_{k,\sigma} = \hbar v_{\rm F} |k_x - k_{\rm F}| + \sigma g \mu_{\rm B} B, \tag{2}$$

where $v_{\rm F} = \hbar k_{\rm F}/m$ at the 1D Fermi surface where $k = \pm k_{\rm F}$. Theoretical models of spin-density waves regularly consider a dispersion of the form given by Eq. (2) in conjunction with a lattice spacing along **x** equal to $a = 2k_{\rm F}/\pi$. This situation then corresponds to a half-filled band containing one electron per unit cell. There are two reasons why theoreticians make such a choice. One is that stoichiometric metals always contain an integral number of electrons per unit cell, where 1 is then the simplest number. The other is that half-filled bands facilitate direct comparisons with the Hubbard model, which can also yield antiferromagnetic ground states. In the present *Encyclopedia*, Eq. (2) is assumed to apply to more general band fillings. Fig. 2A shows a sketch of this dispersion relation for which $\varepsilon_{\perp}(k_y, k_z) \approx 0$ and the degeneracy of the spin-up and spin-down states is lifted by a finite B in order to demonstrate the independence of $Q_0 = 2k_{\rm F}$ on magnetic field. Fig. 2B shows this same dispersion relation after undergoing translational symmetry breaking with respect to nesting vector and gap formation. The resulting multiple bands are obtained by solving

$$\left(2\varepsilon_{\Delta} - \left(\varepsilon_{k,\sigma} + \varepsilon_{nQ_0 - k,\sigma}\right)\right)^2 - \left(\varepsilon_{k,\sigma} - \varepsilon_{nQ_0 - k,\sigma}\right)^2 = 4\Delta^2 \tag{3}$$

For ε_{Δ}. The existence of a 1D Fermi surface enables perfect nesting in this case, giving rise to a fully gapped quasiparticle spectrum. Because spin-up and spin-down bands are entangled, spin is no longer a good quantum number for quasiparticle excitations across the gap.

Microscopic theory

The opening of the gap 2Δ can be formally described in terms of the Bardeen-Cooper-Schrieffer (BCS) theory that applies to superconductivity, but with the pairing occurring at a finite momentum $Q = Q_0$ between electron and hole quasiparticles of opposite spin (or electrons of like spin) (Gruner, 1994, 1996). The distinction between electrons and holes is purely a relative one, introduced to account for the fact that their group velocities oppose. In charge- and spin-density wave systems alike, the Fermi surface instability originates from a divergency in the Q-dependent charge and spin susceptibilities at $Q_0 = 2k_{\rm F}$ which becomes logarithmic $\chi_0 \propto \ln|(Q + Q_0)/(Q - Q_0)|$ when the electronic dispersion is 1D as given by Eq. (2). Spin-density wave formation becomes increasingly favorable over charge-density wave formation when the spin susceptibility is enhanced by a Q-dependent Stoner factor, such that $\chi(Q) = \chi_0(Q)/(1 - U\chi_0(Q)/2\mu_0\mu_{\rm B}^2)$. Because Q_0 is independent of magnetic field, spin-density waves are particularly robust in magnetic fields, and in some cases can even be strengthened, as will be shown to be the case for field-induced-spin-density wave systems. For the dispersion relation given by Eq. (2) and Fig. 2A, mean field theory yields

$$\Delta_{T=0} = We^{-1/\lambda} \tag{4}$$

at zero temperature, where $\lambda = Un(\varepsilon_{\rm F})$ is the effective coupling constant, and where $n(\varepsilon_{\rm F}) \cong W^{-1}$ is the density of electronic states (per unit cell) at $\varepsilon_{\rm F}$. The effective electronic bandwidth is $W = \pi\hbar v_{\rm F}/a$ for the dispersion relation given by Eq. (2). As is the case for superconductivity, the transition into a spin-density wave phase is expected to be second order in the absence of an applied magnetic field and additional interactions, with the transition temperature $T_{\rm SDW}$ given by

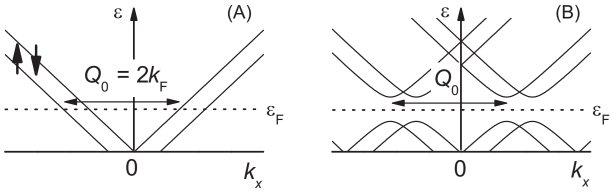

Fig. 2 (A) The electronic dispersion according to Eq. (2) with a finite magnetic B included to lift the spin degeneracy. The up and down arrows indicate the spin-up and spin-down branches respectively, while Q_0 denotes the nesting vector. (B) The same bands, according to Eq. (3) after Fermi surface nesting and gap formation. The size of the gap at $\varepsilon_{\rm F}$ is 2Δ.

$$2\Delta \cong 3.52 k_B T_{SDW} \tag{5}$$

in the weak coupling limit. The single particle electronic density of states becomes

$$n(\varepsilon) = W^{-1}\, Re \left\{ \frac{|\varepsilon - \varepsilon_F|}{\sqrt{(\varepsilon - \varepsilon_F)^2 - \Delta^2}} \right\} \tag{6}$$

upon opening a gap, which can be obtained by differentiating k_x in Eq. (3) with respect to energy ε. The spin-density wave condensation energy at zero temperature is given by

$$\Phi = -\frac{1}{2} n(\varepsilon_F)\Delta^2, \tag{7}$$

which is, again, similar to that in superconductivity. Since the present model considers only the case of a 1D dispersion, the coherence length is $\xi_0 = \hbar v_F / \pi\Delta$.

Basic static properties

In high quality samples at temperatures far below T_{SDW}, the correlation length over which the spin-density wave remains periodic greatly exceeds the coherence length (Gruner, 1994, 1996). It often follows that the low temperature, low electric field, low frequency conducting properties are those of a simple semiconductor or semimetal. In the case of the simple dispersion given by Eq. (2), perfect nesting leads to a classic semiconductor-like behavior of the conductivity.

$$\sigma_{xx} = \sigma_0 e^{-\Delta/k_B T}. \tag{8}$$

Ordinary quasiparticles must be thermally excited across the spin-density wave gap in order to contribute to the electrical conductivity, just as in a semiconductor. In metals with more complicated band structures, such as chromium, however, imperfect nesting leaves behind residual electron and hole pockets that continue to conduct in a conventional metallic fashion. In such a case, the electrical properties of the ground state are those of a semimetal, for which the conductivity contribution from quasiparticles excited across the spin-density wave gap is comparatively negligible. An important exception occurs in the case of magnetic field-induced spin-density waves, where the gap is augmented by a magnetic field as a consequence of Landau quantization.

The magnetic properties of spin-density waves are qualitatively similar to those of an antiferromagnet with a reduced moment

$$\mu = g\mu_B S = \frac{4\Delta}{U}\mu_B \tag{9}$$

and with a long period

$$\Lambda = \frac{2\pi}{Q_0} \tag{10}$$

that is matched to $2k_F$ rather that the crystalline lattice period a. The direction in which the spins preferentially align is determined by the effective coupling constants between them. The primary coupling constant for a simple 1D chain is given by

$$J = \hbar v_F \frac{(1-\lambda)^{1/2}}{\Lambda} \tag{11}$$

in the weak coupling limit. If the spins order in a preferred direction orthogonal to the chains, the magnetic susceptibility $\chi_{\parallel}$ along that preferred direction is zero at temperatures $T \ll T_{SDW}$, provided the applied magnetic field is lower than that required to flop the spin. In other directions, the spins are able to cant, giving rise to a finite spin susceptibility $\chi_{\perp} = Ng^2\mu_0\mu_B^2/2VJ$, where V is the volume per unit cell.

In a similar manner to charge-density waves, the commensurability of a spin-density wave is determined by the number of electrons per unit cell, $N = Q_0 a/\pi$, where $2\pi/a$ is the length of the 1D Brillouin zone prior to ordering. If N can be accurately reduced to a simple fraction of the form $N = A/B$, where A and B here refer to integers, the superlattice period over which both the spin-density and atomic positions repeat is aB, in which case the spin-density wave is considered to be commensurate. The spin-density wave is incommensurate if N is an irrational number.

Collective excitations: Phasons

The close correlation between the periodicity of spin-density waves and the electronic structure near the Fermi energy implies that they can undergo charge excitations like charge-density waves (Gruner, 1994, 1996; Kulikov and Tugushev, 1984). These excitations then determine the electrodynamics of spin-density waves. It serves as a useful approximation to simplify the treatment of the charge degrees of freedom by expanding the free energy in even powers of the order parameter and its spatial and temporal derivatives so as to obtain

$$\Phi = \alpha|\Delta|^2 + \beta\left(\frac{d\Delta}{dx}\right)^2 + \gamma\left(\frac{d\Delta}{dt}\right)^2. \tag{12}$$

Compatibility with the mean field theory is obtained by setting $\alpha = -n(\varepsilon_F)/2$, $\beta = n(\varepsilon_F)(\hbar v_F/2\Delta)^2$ and $\gamma = n(\varepsilon_F)(\hbar/2\Delta)^2$. The order parameter itself can be expanded as

$$\Delta = (\Delta_0 + \delta)e^{i\phi} \tag{13}$$

where δ represents a small perturbation in its amplitude and $\phi = \mathbf{Q}\cdot\mathbf{r} = Qx$ accounts for the phase of the spin modulation described in the introduction. The dispersion relations for the excitation of the spin-density wave can then be obtained by assuming independent oscillatory variations $\delta = \delta_0 e^{i(\omega_A t - kx)}$ and $\phi = \phi_0 + \delta\phi e^{i(\omega_\phi - kx)}$ of the amplitude and phase of the spin-density wave respectively. Noting that the first two terms on the right-hand-side of Eq. (12) are potential energy terms while the third is a kinetic energy term, the application of Lagrangian mechanics yields

$$(\hbar\omega_A)^2 = 2\Delta^2 + (\hbar v_F k)^2 \tag{14a}$$

and

$$\omega_\phi = v_F k \tag{14b}$$

for the amplitude and phase modes respectively, which are sketched in Fig. 3. The first mode occurs at energies comparable to the gap. Since $S \propto \Delta$, this mode is effectively a high energy magnon mode. The second mode vanishes at $k = 0$, therefore corresponding to a collective sliding mode of the spin-density wave phase, which carries a dissipationless current analogous to the Fröhlich mode in charge-density wave systems. In practice, spin-density waves become strongly coupled to impurities and defects in the crystalline lattice, resulting in the opening of a small gap at $k = 0$. This inhibits dissipationless sliding, thereby restoring the familiar semiconducting properties of the spin-density wave state at low excitation energies.

The frequency dependent conductivity can be estimated by considering an electric field $E(t) = E_0 e^{i(\omega_\phi t - kx)}$, that then couples directly to the condensate charge. The equation of motion becomes

$$\frac{d^2\phi}{dt^2} + v_F^2\frac{d^2\phi}{dx^2} = \frac{2k_F eE(\omega_\phi)}{m} \tag{15}$$

where

$$\rho = \frac{e}{\pi}\frac{d\phi}{dx} \tag{16}$$

is the accumulated electrical charge resulting from compression or tension of the spin-density wave and

$$j_{SDW} = \frac{e}{\pi}\frac{d\phi}{dt}, \tag{17}$$

is the electrical current resulting from its sliding motion. The solution of Eq. (15) yields a frequency-dependent conductivity of the collective mode of the form

$$\sigma_{coll}(\omega_\phi) = \frac{ne^2}{m}\left(\frac{\pi}{2}\delta(\omega_\phi) + \frac{i}{\omega_\phi}\right), \tag{18}$$

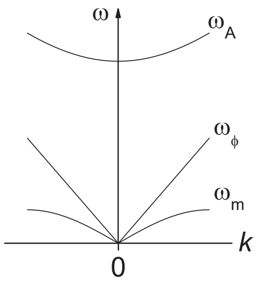

Fig. 3 Approximate dispersions relations of excitations of a simple spin-density wave ground state at low temperatures, ignoring the effects of impurities and magnetic anisotropy. ω_A is the amplitude mode, which effectively corresponds to high energy magnon excitations. ω_ϕ is the phason mode, corresponding to deformation and translational motion of the spin-density wave. ω_m is the magnon mode, corresponding to spin-waves involving purely rotational degrees of freedom of the spins.

where n is the carrier density (becoming N/a in one dimension) and $\delta(\omega_\phi)$ is a Dirac delta singularity. Since it does not include pinning interactions with impurities, which occur in real systems, this result is somewhat academic. Such interactions have two effects. The first is to bind the spin-density wave to the lattice, causing the Dirac delta singularity to be shifted to finite frequencies $\delta(\omega_\phi - \omega_0)$. The second is to resist the sliding motion of the spin-density wave causing losses that broaden the collective mode. This broadening can be phenomenologically modeled by considering an effective relaxation time τ. In spite of these complications, Eq. (18) is a useful result because an integration $(2/\pi)\int \sigma_{\mathrm{coll}} d\omega_\phi$ of the conductivity over the frequency yields the same total spectral weight ne^2/m as is obtained in the normal metallic state. The implication of this result is that the spin-density wave collective mode is then able to account for all of the spectral weight. This contrasts with the case of a charge-density wave where coupling to the ionic lattice distortion causes the collective mode to acquire a heavy effective mass, reducing its share of the spectral weight

A convenient means of modeling the effects of impurities on the frequency-dependent conductivity is to assume that the pinning forces dominate for small local perturbations of the spin-density wave position compared to the spin-density period $\Lambda = 2\pi/Q_0$, causing it to resonate about pinning sites at a characteristic frequency ω_0. This can be formally accomplished by inserting a pinning restoring force $\omega_0^2 x$ and a damping term $(1/\tau)d\phi/dt$ into Eq. (15), and by assuming rigid motion of the spin-density wave whereby $v_{\mathrm{F}}^2(d^2\phi/dx^2) = 0$. Hence,

$$\frac{d^2\phi}{dt^2} + \frac{1}{\tau}\frac{d\phi}{dt} + \omega_0^2\phi = \frac{2k_F eE(\omega_\phi)}{m}, \tag{19}$$

which facilitates a particularly trivial solution of the form

$$\sigma_{\mathrm{coll}(\omega_\phi)} = \frac{ne^2}{i\omega_\phi m}\left(\frac{\omega_\phi^2}{\omega_0^2 - \omega_\phi^2 - i\omega_\phi/\tau}\right). \tag{20}$$

Owing to the simplifications made in Eq. (19), Eq. (20) can only be considered as an approximation. As well as not taking into consideration deformations of the phase, it also does not consider any details of the mechanism by which spin-density waves interact with impurities and defects. In the case of a charge-density wave, for example, the collective mode consists of a spatial modulation of the local charge, providing a direct means of coupling to charged impurities in the lattice. A spin-density wave must undergo relative phase shifts between its spin-up and spin-down components in order to realize a qualitatively similar type of coupling. In spite of these limitations, Eq. (20) provides a surprisingly good account of the frequency-dependent conductivity observed in most spin-density wave systems. The conductivity at yet higher frequencies then includes an additional resonance corresponding to quasiparticle excitations across the gap 2Δ, which is typically two to three orders of magnitude larger than ω_0.

By taking appropriate limits, Eqs. (19) and (20) also provide us with a rough phenomenological understanding of the reaction of spin-density waves to a constant electric field. By setting $\omega_\phi = 0$ in Eq. (20), for example, we obtain zero conductivity, which is appropriate value for small values of the electric field E_0 at $T = 0$. By seeking a time-independent solution to Eq. (19), meanwhile, we can see that the spin-density wave will undergo continuous sliding motion provided the electric field exceeds a threshold value $E_0 > m\omega_0^2\phi/2ek_{\mathrm{F}}$, where pinning force should eventually reverse and oscillate with x for $\phi > {}^{\pi}\!/_{2}$. This leads to a situation for large E_0 where the force of the electric field is balanced against the damping term, yielding a Drude-like conductivity.

Collective excitations: Magnons

In Eq. (14a), the amplitude of the spin-modulation can be seen to undergo excitations, but with a rather large gap 2Δ equivalent to that for quasiparticle excitations at $T = 0$ (Blundell, 2001; Gruner, 1994, 1996). Low energy magnon modes are not obtained from the simple model of the free energy given by Eq. (12), because it does not consider the rotational degrees of freedom of the spins that are necessary to produce spin waves. These can instead be obtained by mapping the spin degrees of freedom onto a simple 1D Heisenberg antiferromagnet Hamiltonian of the form

$$H = \left(\frac{\mu}{\mu_{\mathrm{B}}}\right)^2 J\sum_p \mathbf{S}_{2p}\mathbf{S}_{2P+1} - g\mu_{\mathrm{B}}\mathbf{B}\sum\nolimits_p \mathbf{S}_{2p} + H_\perp. \tag{21}$$

Here, the prefactor accounts for the reduced moment, while the index p refers to a system with the periodicity Λ of reconstructed Brillouin zone rather than the original lattice. The magnetization is expected to be isotropic for isolated chains, in which case $H_\perp=0$, leading to gapless spin wave behavior.

The equation of motion

$$\hbar\frac{dS_{p+1}}{dt} = \mathbf{m}\times\mathbf{B}_{eff} \tag{22}$$

for spin waves is obtained by equating the rate of change of angular momentum against the torque imposed on spins rotated with respect to each other along the chain. Here, $\mathbf{m} = \mu g\mathbf{S}$ is the reduced moment expressed in vector form to account for its orientation. Since we are dealing with an antiferromagnet, the total effective molecular field

$$\mathbf{B}_{eff} = (-1)^q \frac{J}{g\mu_\mathrm{B}} \left(\mathbf{S}_{2p+q-1} + 2\mathbf{S}_{2p+q} + \mathbf{S}_{2p+q+1}\right) \tag{23}$$

felt by each moment due to its two nearest neighbors alternates between odd and even q sites. The solution to Eq. (22) is well known to have the form

$$\hbar\omega_\mathrm{m} = 2JS\left|\sin\frac{\Lambda k}{2}\right|, \tag{24}$$

where $\Lambda/2$ is the effective separation between spins along the chain. The dispersion relation given by Eq. (24) is sketched in Fig. 3, along with the other modes, and can be seen to be approximately linear at low excitation energies.

In real spin-density wave systems, the crystal extends in three dimensions, leading to the possibility of additional couplings between the chains. Should the spins then have preferred axes of orientation, the antiferromagnet becomes anisotropic. The spins may no longer be free to rotate under such circumstances, causing the linear dispersion given by Eq. (24) to become gapped. These effects are usually modeled by considering the anisotropy term $H_\perp$ in Eq. (21) to include contributions that increase or reduce the energy D associated with the alignment of spins along certain directions. The size of the gap is typically of order $2S\sqrt{JD}$.

Field-induced spin-density waves

Eq. (3), as depicted in Fig. 2A, yields a set of bands that change with magnetic field, but where the gap in the density of electronic states at ε_F remains symmetric about ε_F (Chaikin, 1996; Maki, 1986). This occurs because the spin-density waves are the consequence of pairing between electron and hole quasiparticles of opposite spin, causing simple spin-density wave systems to be independent of a magnetic field. This situation changes, however, as soon as the nesting becomes imperfect. Imperfect nesting leaves behind small pockets of Fermi surface that then undergo orbital quantization in a magnetic field. Orbital quantization has a pronounced effect on the free energy of the total system at low temperatures, providing an additional source of energy that can help make the spin-density wave ground states more stable in a magnetic field. Such effects should occur in all spin-density wave systems with imperfect nesting, including elemental chromium, but are more pronounced in systems where the transition temperature into the spin-density wave phase is low, or where the electronic bands are highly anisotropic. By far the most striking behavior occurs in systems with an incipient spin-density wave, as has been shown to be the case in certain examples of the Bechgaard salts. By "incipient" we mean that the Coulomb interactions are present to the extent that the metal is on the threshold of forming a spin-density wave phase, but where the efficiency of the nesting is insufficient to make a spin-density wave ground state stable at zero magnetic field. The system then has the potential to undergo transitions into spin-density wave phases in a magnetic field; hence the term "field-induced spin-density waves." At zero magnetic field, the ground state can be a normal metal or a superconductor. The spin-density wave phase supersedes superconductivity in a magnetic field, simply because superconductivity is inhibited by magnetic fields.

One way to understand the origin of field-induced spin-density waves is through the process of one-dimensionalization of the electron motion in a magnetic field. A simple model to consider is that where the k_y component of the electronic dispersion given by Eq. (1) has the form

$$\varepsilon_\perp\left(k_y\right) = -2t_b\cos k_y b - 2t_b'\cos 2k_y b, \tag{25}$$

where $t_b < W/4$ and $t_b' < t_b$ are the nearest neighbor and second nearest neighbor electron transfer energies along the b axis of a crystal. As shown in Fig. 4A, the Fermi surface can no longer be nested by $\mathbf{Q}_0 = (2k_\mathrm{F}, 0)$ or $\mathbf{Q}_0 = (2k_\mathrm{F}, \pi/b)$ owing to the finite values of the transfer integrals along b. A magnetic field causes electrons on the two-dimensional Fermi surface to follow a snake-like path like that in Fig. 4B, where its real space width $4bt_b/\hbar\omega_b$ and period $l = 2\pi v_\mathrm{F}/\omega_b$ decrease inversely proportionately with the frequency

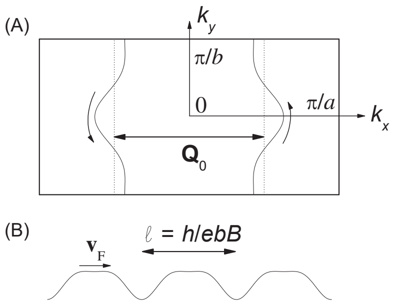

Fig. 4 (A) A sketch of a Fermi surface like that found in the Bechgaard salts, in which the nesting at vector $\mathbf{Q}_0$ is imperfect. The dotted lines show what the Fermi surface looks like when $\varepsilon_\perp(k_y) = 0$, whereupon perfect nesting is recovered. Arrows indicate the direction of motion of quasiparticles on the Fermi surface for a magnetic field pointing out of the page. (B) The trajectory of a quasiparticle in real space, obtained through the equation of motion, $\hbar d\mathbf{k}/dt = e\mathbf{v}_F \times \mathbf{B}$, where $\mathbf{v}_F = \nabla_k\varepsilon(\mathbf{k})$. The spatial dimensions of the real space trajectory are inversely proportional to the magnetic field strength. The product lb encloses a single flux quantum.

$\omega_b = eBv_F b/\hbar$, and hence the magnetic field B. One can make that qualitative argument that the motion becomes 1D as soon as $4t_b < \hbar\omega_b$, whereupon quasiparticles are mostly confined to single 1D chains.

From the quantum mechanical perspective, the one-dimensionalization can be understood by making a Landau-Peierls substitution, $\mathbf{k} \rightarrow i\nabla\ = e\mathbf{A}/\hbar$, into the dispersion relation given by Eqs. (1) and (25). This yields a 1D Schrödinger equation,

$$\frac{\hbar^2}{2m}\frac{d^2}{dx^2}\psi(x) - 2t_b\cos\left(k_y - \frac{2\pi}{l}x\right) - 2t'_b\cos\left(2k_y b - \frac{4\pi}{l}x\right) = \varepsilon\psi(x), \tag{26}$$

that is a function only of x where k_y then merely determines the shift in the coordinate of the center of the wavefunction.

Spin-density wave formation now involves the nesting of ε as determined by Eq. (26). In spite of the added complexity, the thermodynamics is shown to be surprisingly similar to that of a conventional spin-density wave ground state. Notably, Eqs. (4), (5) and (7) continue to apply, but with the effective coupling constant having a modified form

$$\lambda = Un(\varepsilon_F)J_0^2\left(\frac{2t'_b}{\omega_b}\right), \tag{27}$$

Where J_0 is a zeroth order Bessel function. The electronic density of states continues to be fully gapped, but where 2Δ also functions as a Landau gap between Landau bands dispersed with respect to k_x, in which the orbital motion of quasiparticles is quantized. The orbital angular momentum of each quasiparticle in each Landau band is given by $\hbar\left(\nu + \frac{1}{2}\right)$ where the quantum number has values $\nu = 0, 1, 2\cdots$ as for Landau levels in a simple two-dimensional electron gas. The Landau bands are each separated in energy by an effective cyclotron energy $\hbar\omega_c$ that depends on the details of the nested band structure. By making an analogy with two-dimensional electron gas systems, we gain further insight into understanding why imperfectly nested spin-density waves are stabilized by a magnetic field. The free energy of a two-dimensional electron gas experiences sharp minima as a function of B whenever ε_F is situated in a Landau gap (i.e. somewhere in the gap between two adjacent Landau levels ν and $\nu + 1$). It is by utilizing such minima between Landau bands that field-induced spin-density waves become stable. This therefore exacts a constraint by which ε_F must always be situated within a Landau gap in a field-induced spin-density wave phase.

The above constraint has two important implications for field-induced spin-density wave systems. The first is that the Landau bands are always completely filled, giving rise to a type of integer quantum Hall effect where

$$\sigma_{xy} = \pm\frac{2\nu e^2}{\hbar} \tag{28}$$

per layer, where ν is the quantum number of the highest occupied Landau level and where the sign depends on whether the one or two closed pockets contain a net number of electrons or holes. The second implication is that the nesting vector is quantized, where

$$Q_0 = \left(2k_F \pm \frac{2\pi\nu}{l}, \frac{\pi}{b} + \delta k_y\right) \tag{29}$$

in the simplest case, in order to sustain an integer filling factor ν. This type of quantum Hall effect differs from that in conventional two-dimensional electron gas systems in several ways. The first is the factor of 2 in the numerator of Eq. (28), which results from the fact that up and down-spin states are paired with no net spin quantum numbers, giving rise to completely spin-degenerate Landau bands. The second is that the net slope of the Hall resistivity $\rho_{xy} = 1/\sigma_{xy}$ throughout the field-induced spin-density wave phases, depicted in Fig. 5, does not intersect $\rho_{xy} = B = 0$. Finally, the quantum Hall effect does not depend on the existence of localized states in the tails of Landau levels as it does in conventional two-dimensional electron gas systems. The inability of ε_F to reside in a Landau band implies that a change in the value of the quantized Hall conductivity must be realized by means of a first order phase transition between phases with different optimal values of ν. An alternative possibility is that the normal metallic phase is restored between stable Hall plateaux. Orbital quantization within field-induced spin-density wave phases causes the off-diagonal components of the conductivity tensor to dominate over the diagonal ones, giving rise to a low resistivity state, $\rho_{xx}\sim\sigma_{xx}/\sigma_{xy}^2 \rightarrow 0$, as in the conventional quantum Hall effect. This contrasts with the semiconductor-like behavior seen in perfectly nested spin-density wave phases.

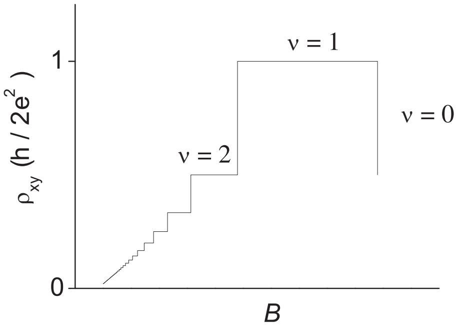

Fig. 5 A plot of the Hall resistivity (per layer) of a field-induced spin-density wave system versus magnetic field, exhibiting quantized Hall plateaux. Sharp changes are expected to occur between different states characterized by different values of ν owing to the first-order nature of the transitions.

Conclusion

Spin-density waves are a type of antiferromagnetic modulation of the local spin density in a correlated metal. They result from interactions between itinerant electrons and can cause a metal to become insulating. Spin-density waves are characterized by a one-dimensional modulation of the spin density and can be described by the Bardeen-Cooper-Schrieffer (BCS) theory. They are most commonly observed in molecular or organic metals, as well as in elemental chromium and its alloys.

The formation of spin-density waves is favored when a large fraction of electron and hole quasiparticles have the same group velocity at the Fermi energy and when the Coulomb potential between quasiparticles is significant but smaller than the electronic bandwidth. Spin-density wave formation is facilitated in systems with narrow and anisotropic electronic bands that can efficiently ″nest″ upon opening a gap in the electronic density of states. The spin-density wave gap opens wherever spin-up and spin-down electronic bands cross, and the energy gap can be described by the BCS theory.

The properties of spin-density waves include collective excitations involving both electronic (phason) and spin (magnon) degrees of freedom. The stability and behavior of spin-density waves are influenced by magnetic fields, and field-induced spin-density waves can exhibit novel phenomena such as the bulk quantum Hall effect. Spin-density waves can also be commensurate or incommensurate, depending on the number of electrons per unit cell.

In terms of static properties, spin-density waves exhibit semiconductor-like behavior in high-quality samples at low temperatures, where thermal excitation is required for quasiparticles to contribute to electrical conductivity. The magnetic properties of spin-density waves are similar to those of antiferromagnets, with a reduced magnetic moment and a long period determined by the effective coupling constants. The spin alignment is influenced by the direction of preferred coupling.

Overall, spin-density waves play a significant role in understanding the behavior of correlated metals and their magnetic properties. They offer insights into the interplay between electronic structure, magnetism, and collective excitations in condensed matter systems.

References

Blundell S (2001) *Magnetism in Condensed Matter*. Oxford: Oxford University Press.
Chaikin PM (1996) Field induced spin density waves. *Journal de Physique I* 6: 1875–1898.
Fawcett E (1988) Spin-density wave antiferromagnetism in chromium. *Reviews of Modern Physics* 60: 209–283.
Fawcett E, Alberts HL, Galkin VY, Noakes DR, and Yakhmi JV (1994) Spin-density wave antiferromagnetism in chromium alloys. *Reviews of Modern Physics* 66: 25–127.
Gruner G (1994) *Density Waves in Solids, Frontiers in Physics*, vol. 89. Addison-Wesley Publishing Company.
Gruner G (1996) The dynamics of spin density waves. *Reviews of Modern Physics* 66: 1–24.
Hafner D, et al. (2022) Possible quadrupole density wave in the superconducting kondo lattice $CeRh_2As_2$. *Physical Review X* 12: 1–10.
Kulikov NI and Tugushev VV (1984) Spin-density waves and itinerant antiferromagnetism in metals. *Uspehkhi Fizicheskikh Nauk* 144: 643–680.
Kung HH, et al. (2015) Chirality density wave of the “hidden order” phase in URu_2Si_2. *Science* 347: 1339–1342.
Maki K (1986) Thermodynamics of field-induced spin-density-waves states in Bechgaard salts. *Physical Review B* 33: 4826–4829.
Schrade C and Fu F (2019) Spin-valley density wave in moiré materials. *Physical Review B* 100: 035413.

Electrons and holes[☆]

GC La Rocca, NEST, Scuola Normale Superiore, Pisa, Italy

© 2024 Elsevier Ltd. All rights reserved.

This is an update of G.C. La Rocca, Electrons and Holes, Editor(s): Franco Bassani, Gerald L. Liedl, Peter Wyder, Encyclopedia of Condensed Matter Physics, Elsevier, 2005, Pages 110–116, ISBN 9780123694010, https://doi.org/10.1016/B0-12-369401-9/00659-8.

Introduction 456
Electron and hole pockets 457
Donors and acceptors 460
Free carrier density 460
Carrier mobility and electrical conductivity 461
Electron-hole complexes 464
Conclusion 464
References 464

Abstract

An overview of the physics of free carriers, electrons in the conduction band and holes in the valence band, is presented focusing on how they affect the electronic properties of semiconductors. Electron and hole pockets, and the corresponding effective masses, are illustrated for several key semicondutors. Doping, conductivity, mobility, Hall effect and cyclotron resonance are discussed.

Key points

- The shape of the electron and hole pockets are described for the most important semiconductors.
- The role of intentional doping via donors and acceptors is discussed.
- The behaviour of the free carrier density as a function of temperature and doping level is shown.
- The carrier mobility as due to different scattering mechanisms is described.
- The electrical conductivity and its dependence on temperature and doping level is discussed.
- Excitons and trions are briefly introduced.

Introduction

The paramount role of semiconductors in today's technology since the invention of the transistor consists mainly in their use in electronic devices, particularly very large scale integrated circuitry, in which electric currents are due to mobile electrons and holes. The possibility of growing single crystals of very high purity and to control their transport properties through intentional n-type and p-type doping has been crucial to the development of the electronic industry. Silicon is presently the material of choice for electronic devices not only because of its outstanding processing properties, but also because its native oxide forms a high quality semiconductor-insulator interface. Semiconductors have at the same time attracted a lot of attention from the viewpoint of basic science, and understanding their electronic structure, optical and transport properties has been a great success of solid state physics (Bassani and Pastori Parravicini, 1975; Yu and Cardona, 1995).

The resistivity of semiconductors is intermediate between that of metals and insulators, varying at room temperature between 10^{-4} and 10^{10} Ω cm, and is extremely sensitive to the presence of impurities. The value of the resistivity is not the best criterium defining a semiconductor, but rather the property that in pure enough samples the resistivity decreases with increasing temperature in a way that is exponential with the inverse temperature (intrinsic regime). Another property of semiconductors is that not only the electrons, but also positive charge carriers, i.e., the holes, may be responsible for electrical conductivity, as shown by the sign of the Hall coefficient. Finally, it is of crucial technological importance the possibility to control the carrier concentration by intentional doping (extrinsic regime).

Semiconductors are characterized by an energy gap of the order of the electronvolt separating the highest occupied band (the valence band) from the lowest unoccupied one (the conduction band); the former may be populated by mobile holes (corresponding to missing electrons), the latter by mobile electrons. In the following, the behavior of electrons and holes in

---

[☆] *Change History*: September 2022. GC La Rocca (original author) prepared the update. New paragraph on IV-VI semiconductors and new Table 1 are added. New section Electron-hole complexes. Very minor amendments (mostly typos) elsewhere.

homogeneous semiconductors will be described considering relevant electronic band structure properties, doping and equilibrium carrier concentration, mobility and electrical conductivity (Landolt-Börnstein, 1982; Seeger, 1991; Singh, 1994; Sze, 1985).

Electron and hole pockets

The transport properties of semiconductors are dominated by carriers (electrons and holes introduced by doping or excited across the energy gap) which occupy the bottom of the conduction band or the top of the valence band. An accurate description of the electronic energy bands near these extrema is usually obtained employing the $\vec{k}\cdot\vec{p}$ perturbative method. Then, the response of the carriers to external perturbations, such as electric and magnetic fields, slowly varying on the scale of the lattice constant can be dealt with using the effective mass approximation.

The $\vec{k}\cdot\vec{p}$ method consists of a perturbative calculation of the electronic states with a Bloch wave vector k close to a given $\vec{k}_0$ point (usually of high symmetry) in the Brillouin zone (BZ) corresponding to a maximum in the valence band (hole pocket) or a minimum in the conduction band (electron pocket). For a non-degenerate band, as typical for electrons, a single band approximation is usually employed, the interaction with all other bands being treated in perturbation theory up to second order in $\left(\vec{k} - \vec{k}_0\right)$. In this case, one gets simply:

$$E\left(\vec{k}\right) = E\left(\vec{k}_0\right) + \frac{\hbar^2}{2}\left(\vec{k} - \vec{k}_0\right)\cdot\overleftrightarrow{m}\ -1\cdot\left(\vec{k} - \vec{k}_0\right), \tag{1}$$

where the inverse effective mass tensor $\overleftrightarrow{m}\ -1$ for the extremum of interest has been introduced. Finally, measuring the energy from $E\left(\vec{k}_0\right)$ and the wavevector from $\vec{k}_0$, and choosing the $\hat{1}$,$\hat{2}$ and $\hat{3}$ directions along the principal axes of $\overleftrightarrow{m}\ -1$, the standard expression for ellipsoidal pockets is obtained:

$$E\left(\vec{k}\right) = \frac{\hbar^2}{2}\left(\frac{k_1^2}{m_1} + \frac{k_2^2}{m_2} + \frac{k_3^2}{m_3}\right). \tag{2}$$

Then, in the presence of slowly varying external perturbations, the dynamics of the electrons in a conduction band minimum can be described as that of free carriers (i.e., without considering the rapidly varying crystal potential) with a positive (anisotropic) effective mass and a negative charge e. In particular, they will give rise to a current in the same direction of the applied electric field while moving in the opposite direction. Likewise, a hole pocket is associated to a maximum in the valence band and is characterized by negative values of the effective mass parameters appearing in Eq. (2). Such states which in a pure crystal at zero temperature are completely occupied may become empty and, upon the action of an applied electric field, give rise to a current that can be thought of as due to positively charged particles with a positive (anisotropic) effective mass. This is so because instead of considering the motion of the very large number of electrons which fill almost the entire valence band, it is convenient to focus on the dynamics of the few empty states whose electrons are missing, i.e., the hole states. As the energy of a hole state increases when the energy of the corresponding missing electron decreases, in the hole picture used in the following, the sign of the effective mass parameters of a hole pocket will be taken as positive and at the same time the charge of a hole as $+e > 0$. A hole moves in the same direction of the applied electric field and contributes to a current in the same direction.

The symmetry of the dispersion relation of electron (or hole) pockets as well as the values of the corresponding effective mass parameters can be measured by cyclotron resonance, i.e., the absorption of radio-frequency radiation in the presence of an external magnetic field $\vec{B}$. The resonance frequency is $\omega_c = \left(eB/m^*\left(\hat{B}\right)c\right)$, with

$$m^*\left(\hat{B}\right) = \sqrt{\frac{m_1 m_2 m_3}{m_1\left(\hat{B}\cdot\hat{1}\right)^2 + m_2\left(\hat{B}\cdot\hat{2}\right)^2 + m_3\left(\hat{B}\cdot\hat{3}\right)^2}}. \tag{3}$$

From the dependence of the observed absorption on the magnitude and direction of the magnetic field, the symmetry of the pockets of carriers as well as their effective mass parameters can be determined. Also magnetoresistance measurements are sensitive to the mass anisotropy and other band structure features, in particular from the strong dependence on the current and magnetic field directions with respect to the cubic axes, the symmetry of the carrier pockets involved can be identified, similarly to the case of cyclotron resonance measurements.

The conduction band of Ge has four electron pockets at the L point of the BZ (see Fig. 1; the half pockets at $\vec{k}$ and $-\vec{k}$ are to be combined together); they are ellipsoids of revolution elongated along the $<111>$ directions. The values of the longitudinal mass $m_L = m_3 \simeq 1.6m$ and of the transverse mass $m_T = m_1 = m_2 \simeq 0.08\ m$ have been determined from cyclotron resonance measurements such as those shown in Fig. 2 (Dresselhaus et al., 1955): with $\vec{B}$ along $\left[\sqrt{3}/\sqrt{2},\ \sqrt{3}/\sqrt{2},\ 1\right]/2$ the four $<111>$ electron pockets split into three groups inequivalently oriented with respect to the magnetic field, each one of these giving rise to a distinct resonance according to Eq. (3). The conduction band of Si has six electron pockets along the $<100>$ directions (see Fig. 3); they are ellipsoids of revolution elongated along the same directions with a longitudinal mass $m_L = m_3 \simeq 1.0\ m$ and a transverse mass $m_T = m_1 = m_2 \simeq 0.08\ m$ (measured from cyclotron resonance, see Fig. 4 (Dresselhaus et al., 1955) where due to the choice of

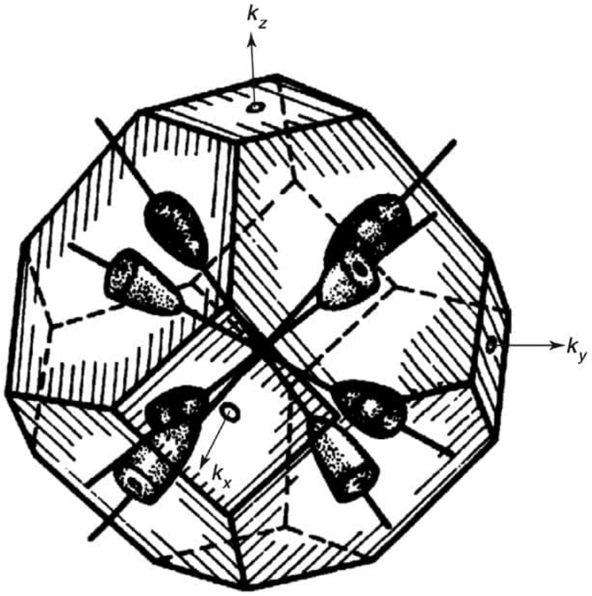

Fig. 1 Electron pockets in Ge.

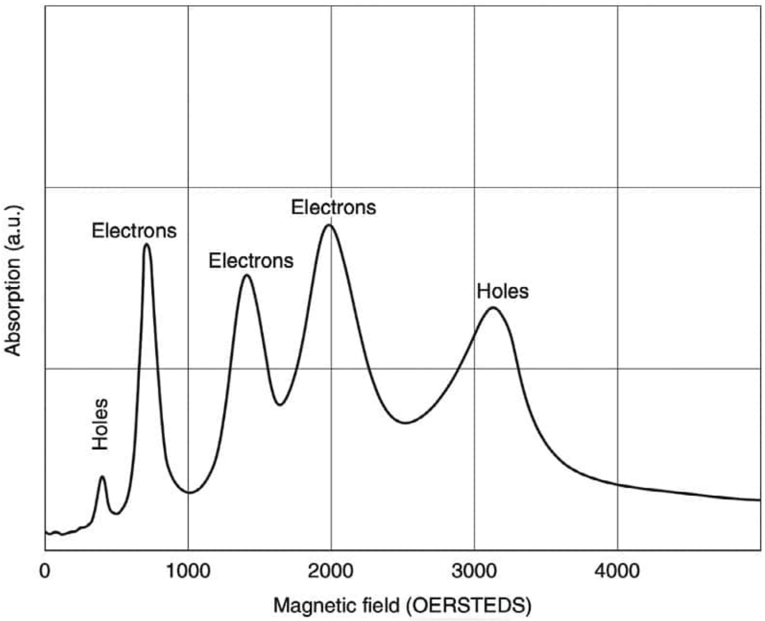

Fig. 2 Cyclotron resonance in Ge (at a frequency of 24 GHz and a temperature of 4 K) with magnetic field in the (110) plane at 60° from the [001] axis. From Dresselhaus, G, Kip, AF, Kittel, C (1955) *Physics Review* 98: 368.

magnetic field orientation two distinct electronic resonances show up). Typical zinc-blende semiconductors have a simple electron pocket at the center of the BZ (Γ point) with an isotropic effective mass; for instance, the electron effective mass of GaAs is 0.067 m.

The hole pockets in Si, Ge and typical zinc-blende semiconductors are at the center of the BZ and correspond to a three-fold p-like degenerate band (without spin) that splits due to the spin-orbit interaction into an upper fourfold degenerate ($J = 3/2$) band and a lower two-fold degenerate ($J = 1/2$) band (spin included). The former corresponds to the top of the valence band and the latter to the split-off valence band which, apart from spin, is non degenerate. The split-off hole states can be described as a simple band with an isotropic effective mass $m_{so} \simeq 0.25\ m$ in Si, $m_{so} \simeq 0.08\ m$ in Ge, $m_{so} \simeq 0.2\ m$ in GaAs. In a rough approximation, the topmost hole states can be described as belonging to two distinct spherical pockets each characterized by an isotropic mass: the heavy hole pocket (with mass $m_{hh} \simeq 0.5\ m$ for Si, $m_{hh} \simeq 0.3\ m$ for Ge, $m_{hh} \simeq 0.5\ m$ for GaAs) and the light hole pocket (with mass $m_{lh} \simeq 0.16\ m$ for Si, $m_{lh} \simeq 0.044\ m$ for Ge, $m_{lh} \simeq 0.09\ m$ for GaAs). Also the hole masses have been determined from cyclotron resonance measurements such as those shown in Fig. 2 and Fig. 4. A complete description of the hole states beyond this simple picture could only be given within a multi-band $\vec{k} \cdot \vec{p}$ approach, in which the valence band degeneracy is fully accounted for.

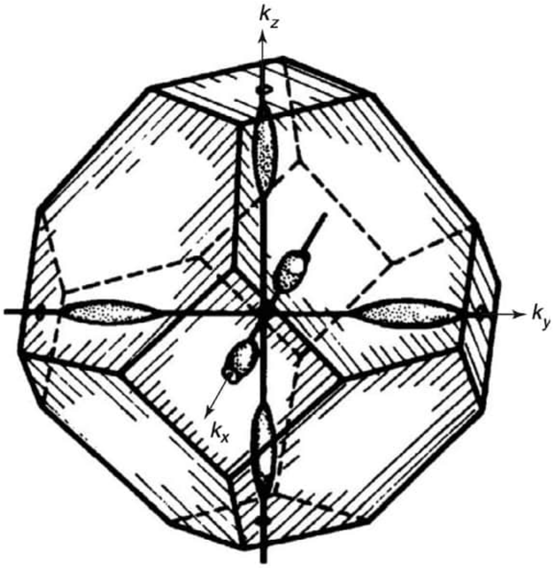

Fig. 3 Electron pockets in Si.

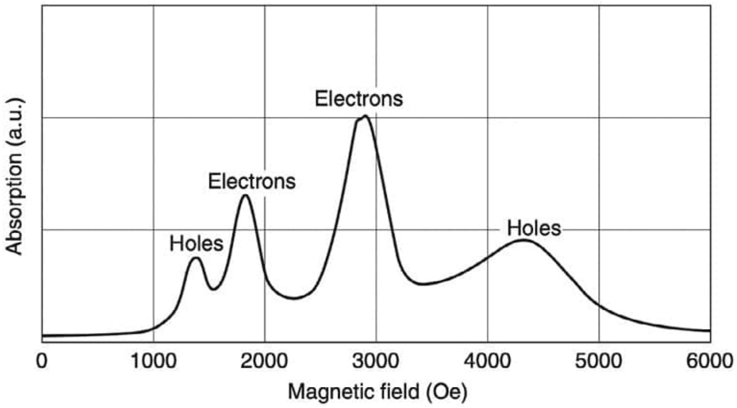

Fig. 4 Cyclotron resonance in Si (at a frequency of 24 GHz and a temperature of 4 K) with magnetic field in the (110) plane at 30° from the [001] axis. From Dresselhaus, G, Kip, AF, Kittel, C (1955) *Physics Review* 98: 368.

Table 1 Longitudinal and transverse effective masses of electrons and holes in IV-VI lead-salts.

	PbTe	*PbSe*	*PbS*
m_L^e	0.240	0.070	0.105
m_T^e	0.024	0.040	0.080
m_L^h	0.310	0.068	0.105
m_T^h	0.022	0.034	0.075

From de Andrada e Silva, EA (1999) *Physical Review B* 60: 8859.

Another important class of semiconductors are the narrow gap IV-VI lead-salts (PbTe, PbSe, PbS) which crystallize in the rocksalt cubic structure. They are characterized by a direct gap at the edge of the Brillouin zone along the [111] direction (i.e., the *L* point). The small gap (about 0.2 eV) and the symmetry of the conduction and valence bands make the four electron pockets almost identical to the four hole pockets in these semiconductors (and both similar to the Ge electron pockets shown in Fig. 1). The respective longitudinal and transverse effective masses for electrons and for holes are given in Table 1 (from de Andrada e Silva, 1999).

Donors and acceptors

The ability to control the content of impurities is a key issue in semiconductor technology: the concentration of undesired dopants in Si is typically kept below 10^{12} cm^{-3}. A foreign atom may give rise to electronic states, more or less localized around the impurity site, with energies lying in the forbidden energy gap of the host material. The impurity levels may either be close to the conduction or valence band edges (shallow donor or acceptor states) or to the middle of the gap (deep states). In the first case, they behave as dopants and dominate the transport properties providing extrinsic free carriers; in the second case, they mainly affect the recombination of free electron-hole pairs by trapping them at the same site.

Depending on their chemical valency, foreign atoms typically used as dopants may provide one extra electron or one extra hole (i.e., one missing electron) with respect to the host atoms they replace. For instance, a group V impurity, say P, substituting a group IV host atom, such as Si, provides an extra electron to the crystal (donor behavior), while a substitutional group III impurity, say B, at the same site would provide an extra hole (acceptor behavior). The extra hole or electron, with respect to the fully occupied valence band, is bound to the defect site by the long range Coulomb potential due to the charge difference between the impurity and host nuclei. Because of the low effective masses ($m^* \simeq 0.2\ m$) and the high dielectric constants ($\varepsilon \gtrsim 10$) typical of semiconductors, the corresponding localized states extend over many unit cells and may be described within the effective mass approximation as a solid state analogue of the hydrogen atom with scaled down Rydberg energy $R^* = (m^* e^4/2\hbar^2\varepsilon^2)$ and Bohr radius $a^* = (\hbar^2\varepsilon/m^* e^2)$ ($R^* \simeq 20$ meV, $a^* \simeq 50$Å). As their binding energy is small, such impurity levels are shallow, i.e., close to the bottom of the conduction band for the case of donors and close to the top of the valence band for the case of acceptors. Thus, they are easily thermally ionized providing free electrons to the conduction band (n-type doping) or free holes to the valence band (p-type doping), as discussed below.

Free carrier density

According to the Boltzmann distribution law (valid at typical carrier concentrations and temperatures, i.e., excluding the case of quantum degeneracy), the density n of electrons in the conduction band and of holes p in the valence band can be expressed as

$$n(T,\ \mu) = N_c(T)\ \exp\ ((\mu - E_c)/k_B T) \tag{4}$$

$$p(T,\ \mu) = N_v(T)\ \exp\ ((E_v - \mu)/k_B T) \tag{5}$$

with a chemical potential μ well inside the energy gap between E_v and E_c (the top of the valence band and the bottom of the conduction band, respectively), being $N_c = \left(\frac{K_B T}{\pi\hbar^2}\right)^{3/2} \frac{\left(m_c{}^{(D)}\right)^{3/2}}{\sqrt{2}}$ and $N_v = \left(\frac{k_B T}{\pi\hbar^2}\right)^{3/2} \frac{\left(m_v{}^{(D)}\right)^{3/2}}{\sqrt{2}}$, where $\mathrm{m}^{(\mathrm{D})}$ is the density of states effective mass given for a many-valley conduction band by an average over the equivalent valleys $m_c^{(D)} = g^{2/3}(m_T^2 m_L)^{1/3}$, g being the valley degeneracy (6 for Si, 4 for Ge), and for the valence band by an average over heavy and light holes $m_v^{(D)} = (m_{lh}^{3/2} + m_{hh}^{3/2})^{2/3}$. The densities of electrons and holes in thermal equilibrium at temperature T satisfy the law of mass action

$$np = N_c N_v\ e^{-E_g/k_B T}. \tag{6}$$

In a pure (intrinsic) semiconductor, the density of electrons n_i thermally excited into the conduction band equals the density of holes p_i left behind in the valence band and they are given by

$$n_i = p_i = \sqrt{N_c N_v} \exp\ \left(-E_g/2k_B T\right);$$

the intrinsic concentration of carriers is dominated by the exponential dependence on $E_g/(2\mathrm{k}_B T)$. For instance, one obtains at room temperature for Si $E_g = 1.1$ eV, $N_c \simeq 3.10^{19}\mathrm{cm}^{-3}$, $N_v \simeq 1.10^{19}\mathrm{cm}^{-3}$, $n_i = p_i \simeq\ 1.5 \cdot 10^{10}\mathrm{cm}^{-3}$; for Ge $E_g = 0.66$ eV, $E_g = 0.66$ eV, $N_c \simeq 1.10^{19}\mathrm{cm}^{-3}$, $N_v \simeq 6.10^{18}\mathrm{cm}^{-3}$, $n_i = p_i \simeq 2.3 \cdot 10^{13}\mathrm{cm}^{-3}$;for GaAs $E_g = 1.43$ eV, $N_c \simeq 4.4 \cdot 10^{17}\mathrm{cm}^{-3}$, $N_v \simeq 8 \cdot 10^{18}\mathrm{cm}^{-3}$, $n_i = p_i \simeq 2 \cdot 10^{6}\mathrm{cm}^{-3}$. For the non-degenerate regime here considered, the intrinsic Fermi level (chemical potential) is given by $\mu_i = (E_c + E_v)/2 + (3/4)\ k_B T\ \ln\left(m_v^{(D)}/m_c{}^{(D)}\right)$, and is close to the center of the gap (i.e., $(E_c + E_v)/2$).

In a doped semiconductor with a concentration of donors N_d and of acceptors N_a, if $N_d > N_a$ (n-type) the electron (majority carrier) density is approximately $n = N_d - N_a$ and the hole (minority carrier) density is correspondingly $p = (n_i p_i)/\mathrm{n}$; if $N_d < N_a$ (p-type) similar formulas hold with the role of majority and minority carriers interchanged. In n-type semiconductors the chemical potential μ is shifted a bit closer to E_c with respect to μ_i, as given by

$$\frac{N_d - N_a}{2n_i} = \sinh\left(\frac{\mu - \mu_i}{k_B T}\right); \tag{7}$$

the converse is true for p-type semiconductors. In the above, the temperature has been assumed to be high enough to ionize all the impurities, but not so high that the concentration of intrinsic carriers (i.e., those thermally excited across the energy gap) should

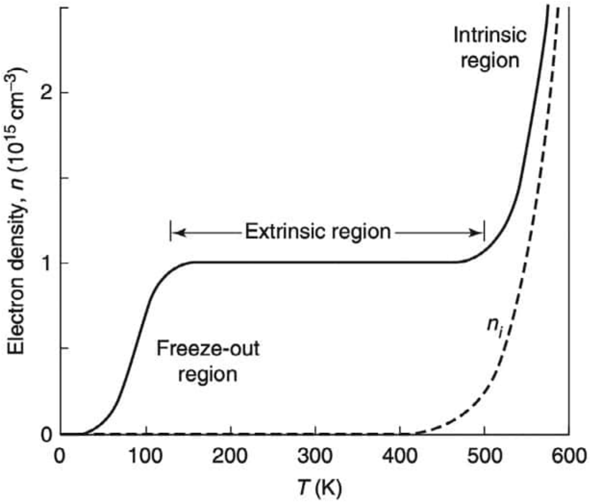

Fig. 5 Temperature dependence of majority carrier concentration in n-doped Si ($N_d = 10^{15}$ cm^{-3}). The intrinsic carrier concentration is shown by the dashed line for comparison.

be comparable to the majority carrier concentration. In this case, i.e., the extrinsic regime, the carrier concentration is independent of temperature and determined by the doping level. At lower temperatures, the concentration of ionized impurities decreases because more and more electrons fall in the impurity bound states and the concentration of free carriers drops (freeze-out regime). The typical temperature dependence of the majority carrier concentration in a doped semiconductor over a wide temperature range is depicted in Fig. 5. The wide plateau (extrinsic regime) around room temperature shows how the carrier concentration can be suitably fixed by intentional doping, a characteristic semiconductor behavior of paramount importance for electronic applications.

Carrier mobility and electrical conductivity

In a cubic semiconductor, the low field conductivity tensor relating the current density $\vec{j}$ to the electric field $\vec{E}$ is a scalar $\vec{J} = \sigma\vec{E}$ given by

$$\sigma = e\left(n\mu_n + p\mu_p\right), \tag{8}$$

where n and p are the densities of conduction band electrons and valence band holes, respectively, and μ_n and μ_p the corresponding mobilities, relating the average drift velocities of electrons or holes to the electric field, given by

$$\mu_{n,p} = \left(e/m^{(\sigma)}_{n,p}\right)\tau_{n,p}, \tag{9}$$

where $m^{(\sigma)}$ the appropriate effective mass and $\tau_{n,p}$ the appropriate momentum relaxation time as determined by the scattering mechanisms briefly discussed below. For a many-valley band extremum, such as for the electron pockets in Si and Ge, the conductivity effective mass to be used above is an average given by

$$1/m^{(\sigma)}_n = (2/m_T + 1/m_L)/3, \tag{10}$$

and n is the total density of electrons equally distributed among the equivalent valleys. From the values of the electron transverse and longitudinal masses, one obtains for Si $m^{(\sigma)}_n \simeq 0.27m$ and for Ge $m^{(\sigma)}_n \simeq 0.12\,m$. When more than one electron or hole bands are populated, e.g., light and heavy hole bands, their contributions add up in the above expression for σ. The conductivity of a semiconductor, in contrast to that of a metal, varies strongly because of the dramatic dependence of the electron and hole densities on the temperature and the doping level; only a smoother variation is brought about by mobility changes. The carrier mobilities are related to the respective diffusion coefficients by the Einstein relation $e\,D_{n,p} = \mu_{n,p}\,k_B\mathrm{T}$.

At room temperature, in pure or moderately doped elemental semiconductors, the mobility is limited mainly by phonon scattering, whereas, at lower temperatures or heavy doping levels, the ionized impurity scattering is dominant. In nonpolar semiconductors such as Si and Ge, the main electron-phonon scattering mechanism is due to longitudinal acoustic phonon deformation potential scattering with a scattering rate $1/\tau_{ac}$ depending on temperature like $T^{3/2}$. However, significant deviations from this behavior are observed, mostly due to the mixture of acoustic and optical phonon scattering. In zinc-blende semiconductors such as GaAs, at room temperature the main scattering mechanism is due to polar longitudinal optical phonon scattering with a stronger dependence on temperature. The mobility values in pure materials at room temperature are for Si $\mu_n \simeq 1500\ \mathrm{cm}^2/(\mathrm{Vsec})$, $\mu_p \simeq 500\ \mathrm{cm}^2/(\mathrm{Vsec})$; for Ge $\mu_n \simeq 3900\ \mathrm{cm}^2/(\mathrm{Vsec})$, $\mu_p \simeq 1900\ \mathrm{cm}^2/(\mathrm{Vsec})$; for GaAs $\mu_n \simeq 8500\ \mathrm{cm}^2/(\mathrm{Vsec})$, $\mu_p \simeq 400\ \mathrm{cm}^2/(\mathrm{Vsec})$. The impurity Coulomb scattering rate $1/\tau_{im}$, instead, is proportional to $T^{-3/2}\ N_{im}$, being N_{im} the density of ionized impurities. Experimentally, it is not easy to see the $T^{3/2}$ dependence of the impurity scattering limited mobility as the temperature range in which this mechanism is dominant is restricted at low temperatures by the carrier freeze-out and at high temperatures by the onset of phonon scattering. However, when more sources of scattering are competing the total resistivity is approximately given by the sum of the resistivities obtained from each single scattering mechanism at a time (Matthiessen's rule). As a result, the mobility of doped semiconductors may exhibit a maximum at the temperature corresponding to the crossover from impurity scattering to phonon scattering. Such a behavior is evident in Fig. 6 and Fig. 7 which show, respectively, the electron mobility in Si and GaAs vs. temperature for various doping levels.

The temperature dependence of the conductivity of Si at different doping levels is shown in Fig. 8 (Morin and Maita, 1954). The intrinsic regime is evident over most of the temperature range; the flattening of some of the curves at about room temperature corresponds to the extrinsic regime in which the conductivity is determined by the doping level. The temperature dependence of σ is

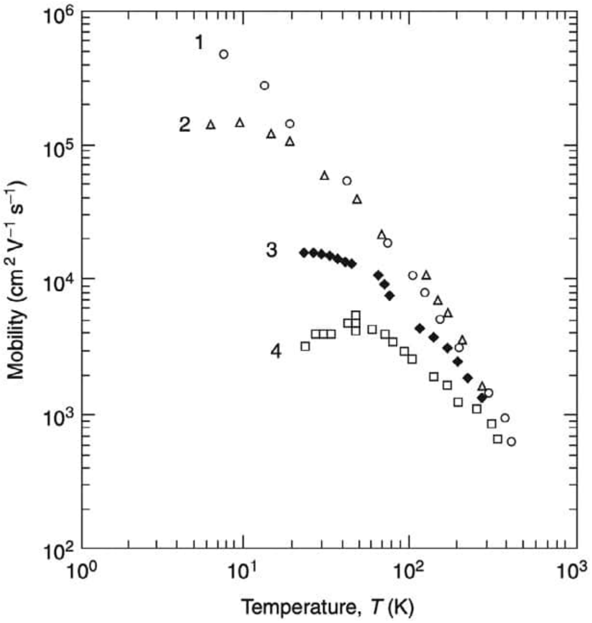

Fig. 6 Temperature dependence of mobility in n-type Si at various doping levels: (1) $N_d < 10^{12}\ \mathrm{cm}^{-3}$ (high purity), (2) $N_d < 10^{13}\ \mathrm{cm}^{-3}$ (high purity), (3) $N_d = 1.6 \cdot 10^{16}\mathrm{cm}^{-3}$, (4) $N_d = 1.3 \cdot 10^{17}\mathrm{cm}^{-3}$. From the database NSM maintained by the Ioffe Institute.

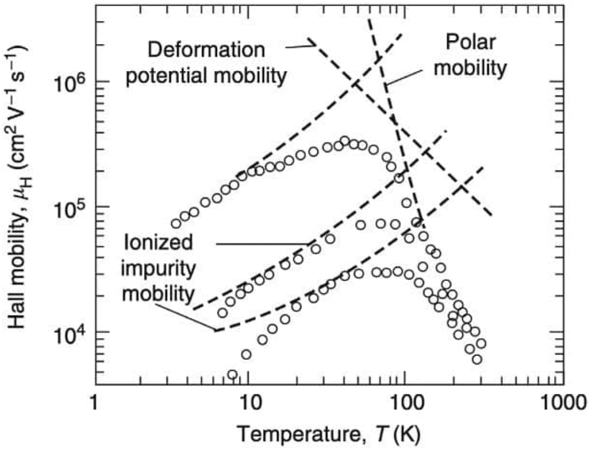

Fig. 7 Temperature dependence of mobility in n-type GaAs at various doping levels: top curve $N_d = 5 \cdot 10^{14}\mathrm{cm}^{-3}$, middle curve $N_d = 10^{15}\mathrm{cm}^{-3}$, bottom curve $N_d = 5 \cdot 10^{15}\mathrm{cm}^{-3}$. From the database NSM maintained by the Ioffe Institute.

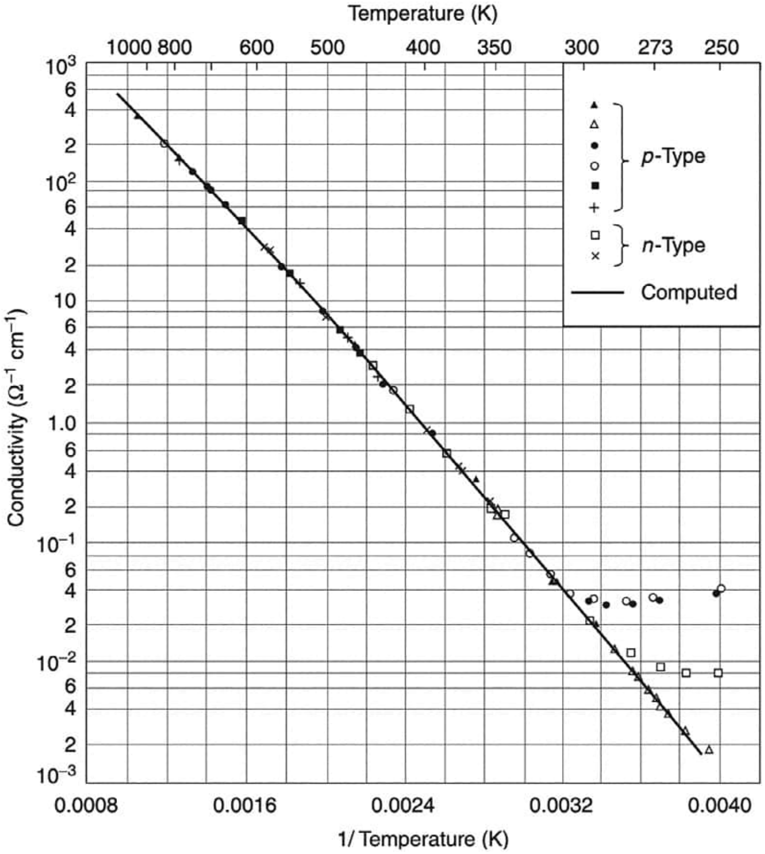

Fig. 8 Temperature dependence of conductivity in Si at various doping levels. From Morin EJ and Maita JP (1954) *Physics Review* 94: 1525.

dominated by that of the carrier concentration in the intrinsic regime, whereas its weaker variation in the extrinsic regime is due to the temperature dependence of the mobility.

Measuring the Hall coefficient is a widely used method to characterize the concentration (and type) of free carriers; the Hall coefficient R_H is given by

$$R_H = \frac{p\mu_p^2 - n\mu_n^2}{ce\left(p\mu_p + n\mu_n\right)^2}. \tag{11}$$

In weak fields, the mobilities appearing in the numerator of the above expression are in general to be multiplied by corrective factors of order unity (i.e., the ratios of Hall mobilities to drift mobilities: μ_H/μ) which depend on the scattering mechanism and the band structure details. Notice that in p-type samples the sign of R_H is positive, i.e., opposite to that of n-type samples.

So far we have considered the low field conductivity corresponding to the ohmic regime. With increasing field strength, the free carrier drift velocity approaches their thermal velocity and hot carrier effects become important. In particular, in Si and Ge, the high field mobility (limited mainly by inelastic phonon scattering) eventually decreases linearly with the electric field and the drift velocity saturates to values close to 10^7 cm/s at electric fields of the order of 10 kV/cm. In the presence of hot carriers, the equivalent valleys need not be equally populated and, as a consequence, even in a cubic material like n-type Ge, the current need not be parallel to the electric field. Moreover, also inequivalent, higher energy valleys may become populated: for instance, dramatic changes in the Hall coefficient of n-type Ge at electric fields higher than 1 kV/cm are brought about by the transfer of electrons from the $<111>$ lowest minima to the $<100>$ higher minima, the Hall coefficient is dominated by the contribution of the $<111>$ high mobility valleys and starts to increase as their population starts to decrease. In several compound semiconductors such as GaAs, such a carrier transfer to inequivalent valleys is responsible for a decrease of drift velocity leading to negative differential resistance (at a field value of about 3 kV/cm in GaAs, as shown in Fig. 9) and also to peculiar current oscillations (Gunn effect) at microwave frequencies. In the presence of hot holes, complex features of the degenerate valence band become important, such as the non-parabolicity of the hole dispersion, i.e., the variation with kinetic energy of the effective mass.

Finally, increasing the electric field strength beyond the saturation regime, a sudden "run-away" growth of the conductivity is eventually observed (breakdown). This is due to the avalanche multiplication of the number of free carriers: the field is so strong

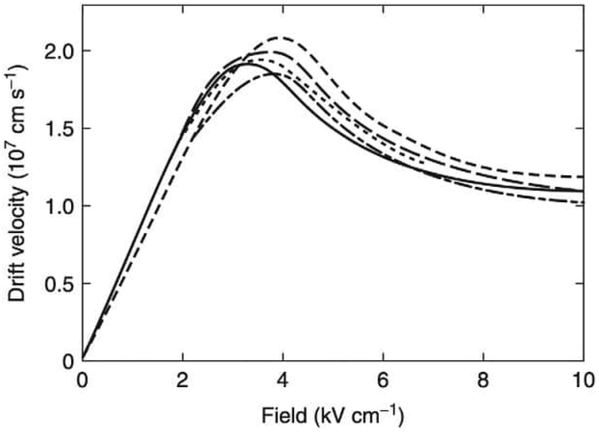

Fig. 9 Temperature dependence of conductivity in Si at various doping levels. From Morin EJ and Maita JP (1954) *Physics Review* 94: 1525.

that a carrier can gain between two collisions enough kinetic energy to knock out an electron from the valence to the conduction band. Typical breakdown electric fields are 10^5 V/cm for Ge, $3 \cdot 10^5$ V/cm for Si and $4 \cdot 10^5$ V/cm for GaAs.

Electron-hole complexes

The discussion above neglects interactions among the free carriers, electrons in the conduction band and/or holes in the valence band. However, when a semiconductor is optically excited at low temperatures it is possible to generate an electron-hole pair absorbing a photon with an energy less than the corresponding interband gap because the electron and the hole attract each other and can form bound states known as excitons. In typical inorganic semiconductors, due to large dielectric constants and small effective masses, such bound states have a large radius (much larger than the lattice constant) and small binding energies (of order 10 meV). Electron-hole complexes larger than excitons also occur, such as biexcitons corresponding to a bound pair of excitons. In the presence of an excess of free carriers, charged electron-hole complexes can also form, the simplest case being that of trions: an exciton bound to either an electron (negative trion) or a hole (positive trion). At high excitation densities, excitons unbind giving way to an electron-hole plasma.

Conclusion

The paramount role of semiconductors in the electronic industry is mainly due to the possibility of suitably controlling their electronic properties via intentional doping. The features of their electron and hole pockets, and in particular the effective masses, affect their functional behavior. We have reviewed the main aspects of the physics of free carriers in semiconductors focusing on transport properties (conductivity and mobility, cyclotron resonance, Hall effect) and their dependence on doping levels and temperature.

References

Bassani F and Pastori Parravicini G (1975) *Electronic States and Optical Transitions in Solids*. Oxford: Pergamon Press.
de Andrada e Silva EA (1999) *Physical Review B* 60: 8859.
Dresselhaus G, Kip AF, and Kittel C (1955) *Physics Review* 98: 368.
Landolt-Börnstein (ed.) (1982) *Physics of Group IV Elements and III-V Compounds*. In: vol. 3–17a. Berlin: Springer-Verlag.
Morin EJ and Maita JP (1954) *Physics Review* 94: 1525.
Seeger K (1991) *Semiconductor Physics*. Berlin: Springer-Verlag.
Singh J (1994) *Semiconductor Devices*. New York: McGraw-Hill.
Sze SM (1985) *Semiconductor Devices*. New York: Wiley.
Yu PY and Cardona M (1995) *Fundamentals of Semiconductors*. Berlin: Springer-Verlag.

Electron–phonon coupling and polarons in low-dimensional structures

Matthieu J Verstraete[a,b] **and Thibault Sohier**[c], [a]Department of Physics, University of Liege, Liege, Belgium; [b]European Theoretical Spectroscopy Facility, Liege, Belgium; [c]Laboratoire Charles Coulomb (L2C), Université de Montpellier, CNRS, Montpellier, France

© 2024 Elsevier Ltd. All rights reserved.

Introduction **465**
Overview **466**
Historical models 466
Microscopic ab initio formalism 467
Discretization of the electron and/or phonon bulk states 468
New phonons and couplings 469
Key issues (current debates regarding the topic) **470**
Conclusion **471**
Summary 471
Future directions 472
References **472**
Further reading **474**

Abstract

Electron–phonon coupling is discussed in the context of nanostructures and low-dimensional materials from a theoretical and modeling perspective. After a short review of historical models and modern first-principles techniques, we focus on the effects of nanostructuring and dimensionality. Various mechanisms are considered, from modifications of the joint density of states and energy selection rules, to the emergence of intrinsically different types of electron–phonon coupling in low-dimensional materials. Finally, key issues and perspectives for the future of the field are discussed.

Key points

- Theory of electron–phonon coupling and polarons in condensed matter
- Changes in low-dimensional systems 0D, 1D, 2D
- Polaronic effects

Introduction

The interaction between electrons and atomic vibrations is central to many phenomena in condensed matter physics. Electrons are the main active particle in matter, carrying electrical charge, creating chemical bonds, and interacting with light, magnetization, and other degrees of freedom; vibrations, quantized as phonons, are the lowest energy excitations universally present in any condensed matter systems—metallic or insulating, magnetic or not.

The combination of a charge carrier with the perturbation of the lattice it may induce is called a polaron. This hybrid quasiparticle is a bound state, as it lowers the system's energy. It is characterized by a shift of the associated electron and phonon energies, and, for sufficiently strong coupling, by a net shift of the atoms' equilibrium positions.

One of the most spectacular macroscopic consequences of the coupling between electrons and vibrations (electron–phonon coupling—EPC) is conventional superconductivity, where the vibrational interaction allows electrons to assemble in Cooper pairs, which can condense at low temperature into a quantum state with no electrical resistance (Bennemann, 2023; Chubukov, 2023). Recent progress in 2020 has even shown conventional superconductivity above ambient temperature, by applying extremely high pressures to hydrogen-rich alloys (Shimizu, 2023).

In the normal (nonsuperconducting) state, phonons interfere with the conduction of electrons, and explain the change of the electrical resistivity with temperature in metals, or of the mobility in doped semiconductors. Thermoelectric transport translates a temperature gradient into an open-circuit electrical potential difference (Seebeck effect), and is a direct combination of the electron dispersion relations (energies and group velocities) with the limitation of the electron mean free path by interaction with phonons. At low temperatures, the effect can even be enhanced by phonon drag, where a phonon heat current transfers momentum to the electrons, boosting the Seebeck coefficient.

https://doi.org/10.1016/B978-0-323-90800-9.00181-5

Structural distortions coupled to electronic reorganization also explain the closely related phenomena of charge density waves, and Peierls and Jahn–Teller instabilities. By condensing a phonon mode displacement, the system gains electronic energy at the expense of elastic deformation, with a net stabilization at low temperature, often accompanied by a metal to insulator transition.

At the nanoscale, electron transport through individual molecules is very sensitive to the energy of the electrons. Inelastic electron tunnelling spectroscopy measures a current from an atomically sharp tip into a molecule, and is sensitive not only to the discrete electronic states of the molecule but also to vibrational sidebands, where an electron hops on to or off of the molecule either emitting or absorbing a vibrational quantum. By scanning the bias voltage of the tip, current peaks are observed in resonance with the molecular electronic levels, plus additional peaks offset by the vibrational frequencies. More generally, many spectroscopic experiments present phonon-dependent features such as peak broadenings and/or the appearance of satellite peaks, offset by the energy of the corresponding phonon mode, and with an intensity governed by the electron–phonon interaction.

The EPC enters many physical observables (transport, superconductivity, etc.), but in an averaged way: summing over the interactions of all phonons with all electrons. The most interesting probes of EPC are microscopic, resolved in electron and/or phonon states. One of the most powerful is angle resolved photo-emission spectroscopy (ARPES), which measures the electron spectral function, that is, a momentum-resolved generalization of the density of states. Phonon renormalization induces a shift and broadening of the original electron bands, kinks where the electron and phonon dispersions cross, and satellite replica, as shown in Fig. 1 for a 2D bilayer of BN and graphene (Chen et al., 2018). The BN valence band presents replica images lowered by one or two vibrational quanta. In these nanostructured interfaces the vibrations are characteristic of the combined bilayer system.

Another example of rather direct and nanoscale access to the EPC is the diffusion of alpha particles off of solid surfaces, which allows to determine the dispersion of surface phonons. The diffusion probability is proportional to the electron–phonon coupling, as the He interacts mainly with the electron cloud, which then launches the phonons (Campi et al., 2015). This is shown in Fig. 2 for a surface of xenon.

In this chapter, we present the current state-of-the-art of the phenomenology and theory of electron–phonon coupling, with a specific focus on the effects of nanostructuring and dimensionality in ultrathin layers (2D), wires or tubes (1D), and nanoparticles (0D). We finish by presenting open issues of debate and future perspectives in the field.

Overview

In this section we survey the main theoretical and modeling approaches used for the coupling of electrons and phonons, their consequences for transport, spectroscopy and other observables, and how these change in lower dimensions. The interaction of an electron (or hole) with ambient phonons lowers the total energy, producing a combined bound state known as a polaron. Here we will concentrate on the electron–phonon coupling itself, and first-principles formalisms calculate EPC and derived observable quantities, and in particular on the effects of dimensionality. We will mainly treat semiconducting and insulating materials, though most expressions hold for metals as well.

Historical models

Several models have been used in the past to understand polaronic behaviors and EPC. One of the simplest is the Holstein Hamiltonian (Holstein, 1959) involving a single phonon mode, electrons on a tight binding lattice, and a linear, on-site electron

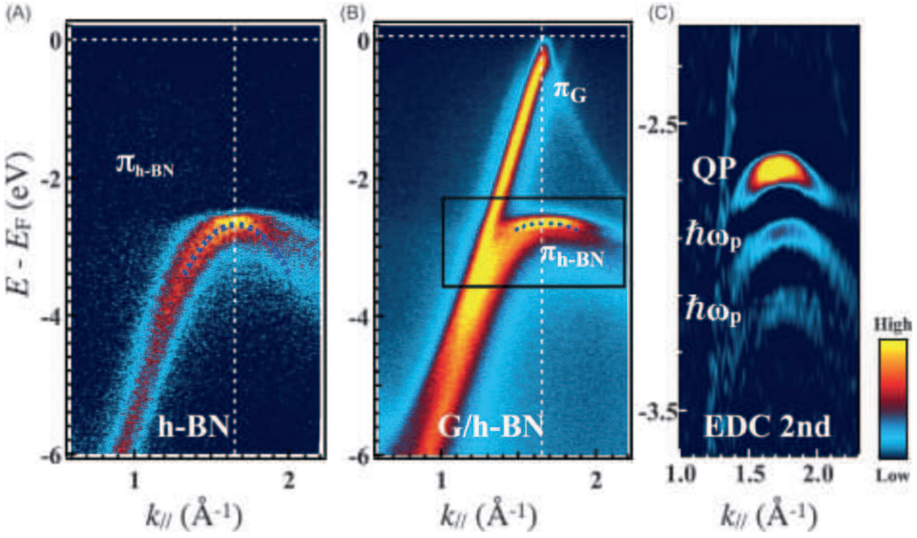

Fig. 1 ARPES bands of h-BN alone (A) and in heterostructure with graphene (B), which shows in (C) polaronic satellite replica of the main BN band, due to phonons hybridized with graphene. Adapted from Chen C, Avila J, Wang S, Wang Y, Mucha-Kruczyński M, Shen C, Yang R, Nosarzewski B, Devereaux TP, Zhang G, Asensio MC, 2018. Emergence of interfacial polarons from electron–phonon coupling in graphene/h-Bn van Der AU7 Waals heterostructures. Nano Letters 18 (2), 1082–1087. ISSN 15306992. https://doi.org/10.1021/acs.nanolett.7b04604. 1707.00184v2.

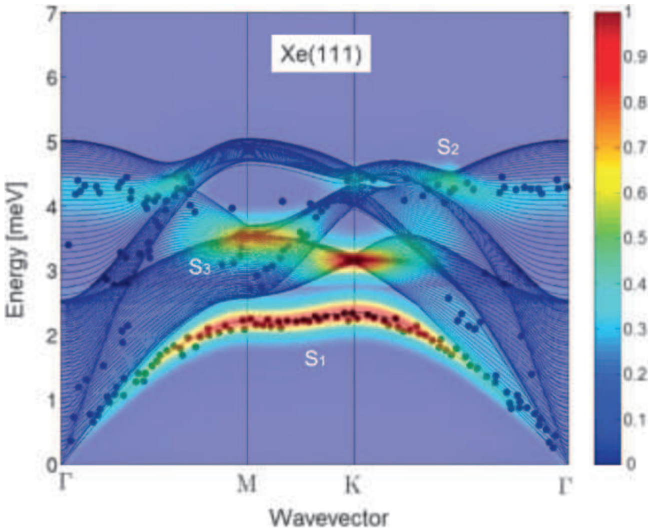

Fig. 2 Phonon dispersion relation for a xenon surface. The color intensity highlights the surface character of the modes S1, 2, 3, and the dots are helium atom scattering experiments, which is sensitive to the electron surface–phonon coupling. Adapted from Campi D, Bernasconi M, Benedek G, Toennies JP, 2015. Surface dynamics of Xe(111): An ambiguous nobility. The Journal of Physical Chemistry C 119 (26), 14579–14584. ISSN 1932-7447, 1932-7455. https://doi.org/10.1021/jp511886f.

phonon coupling term. It is useful for strongly localized carriers and phonons, as in molecular crystals, leading to small polarons and hopping transport.

In the 1D Su Schrieffer Heeger (Su et al., 1979) model the EPC is an inter-site exchange-like term, where the phonon and electron both hop from one site to another. Prototypically in an acetylene chain, alternating bond lengths can be seen as the freezing-in of an atomic vibration, with corresponding localization of an electron in a C = C bond. This gives rise to traveling charged excitations and solitons.

An omnipresent type of EPC involves acoustic phonons at small wavevector. By approximating the acoustic phonon by a homogeneous elastic dilation known as the deformation potential (Bardeen and Shockley, 1950), the resulting change in electron band energies will be linear. This yields a simple Hamiltonian in reciprocal space for a parabolic band and isotropic acoustic phonons.

In band insulators and semiconductors with more than one atomic species, the perturbation of the lattice by optical phonons generates dipoles, and the associated electric fields couple to electrons. This effect is strongest in ionic crystals, and was described by the Fröhlich model (Fröhlich, 1952), used to model large polarons with variable coupling strength. The Hamiltonian is expressed as

$$H^{\mathrm{Fr}} = \sum_{k} \frac{k^2}{2} \hat{c}_k^{\dagger} \hat{c}_k + \sum_{q} \hat{a}_q^{\dagger} \hat{a}_q + \sum_{k,q} \frac{1}{q} \left(\frac{2\sqrt{2}\pi\alpha}{V} \right)^{\frac{1}{2}} \hat{c}_{k+q}^{\dagger} \hat{c}_k \left(\hat{a}_q^{\dagger} + \hat{a}_{-q} \right) \tag{1}$$

where k and q are electron and phonon momenta, respectively. This Hamiltonian contains a single dispersionless longitudinal optical (LO) phonon frequency ω_{LO} ($\hat{a}_q$ operators), and a parabolic electron band with effective mass m^* ($\hat{c}$ operators) in a volume V. The coupling is a long-range dipolar interaction between the electron and the macroscopic electric field produced by the LO phonon. The EPC varies with q and depends on a reduced coupling parameter:

$$\alpha = \left(\frac{1}{\epsilon^{\infty}} - \frac{1}{\epsilon_0} \right) \sqrt{\frac{m^*}{2\omega_{\mathrm{LO}}}} \tag{2}$$

mixing the phonon frequency, electron mass, and electronic (ϵ^{∞}) and static (ϵ_0) dielectric constants, respectively, at large frequency (much higher than the vibrations) and zero frequency. A full solution was found using the path integral method (Feynman, 1955), and more recently using diagrammatic Monte Carlo (Mishchenko et al., 2000).

The models presented each focus on a specific type of EPC and require measurements or choices for the parameters. A more systematic and quantitatively predictive approach arises from first-principles methods (Giustino, 2017).

Microscopic ab initio formalism

The electron–phonon coupling is defined as the quantum probability of interaction between an electron and a phonon. We will mainly consider the case of ideal periodic crystalline solids, and associate a wavevector, band index, and energy for both the electron ($\vec{k}n$) and phonon ($\vec{q}j$). Most of our development is also valid for molecular crystals with more localized electron and phonon states, which then hop between molecules: the main difference is the dispersion relations, the phonon states being fully localized ($q = 0$), and the electron bands being almost dispersionless with high effective mass.

In their ground state without EPC, the electrons occupy eigenstates of the unperturbed Hamiltonian, for atoms in their equilibrium high-symmetry positions. A displacement of the atoms collectively following a vibrational normal mode will produce a change δV in the potential felt by the electrons. If this change is small, to first order the probability amplitude of scattering an electron is given by

$$g^{\vec{q}j}_{nm\vec{k}} = \langle \psi_{\overrightarrow{k+q}m} | \delta V^{\vec{q}j} | \psi_{\vec{k}n} \rangle \tag{3}$$

where the final state must conserve energy ($\epsilon_{\overrightarrow{k+q}m} = \epsilon_{\vec{k}n} + \hbar\omega_{\vec{q}j}$) and momentum (final state at $\overrightarrow{k+q}$). Within many-body perturbation theory (MBPT), the effect of the phonons on the electrons can be included via a self-energy: an effective energy-dependent potential which translates the consequences of interactions on the "bare" independent carriers. To first order in phonons (Migdal, 1958 showed that this approximation is a very good one) there are two pieces of the EPC self-energy, the so-called Fan and Debye–Waller terms. The former is energy dependent and corresponds to the emission and later re-absorption of a phonon:

$$\Sigma^{\mathrm{FAN}}_{n\mathbf{k}}(\omega) = \frac{1}{N_{\mathbf{q}}} \sum_{mj\mathbf{q}} \left| g^{j\mathbf{q}}_{nm\mathbf{k}} \right|^2 \left(\frac{n_{j\mathbf{q}}(T) + f_{m\mathbf{k}+\mathbf{q}}(T)}{\omega - \varepsilon_{m\mathbf{k}+\mathbf{q}} + \omega_{j\mathbf{q}} + i\eta} + \frac{n_{j\mathbf{q}}(T) + 1 - f_{m\mathbf{k}+\mathbf{q}}(T)}{\omega - \varepsilon_{m\mathbf{k}+\mathbf{q}} - \omega_{j\mathbf{q}} + i\eta} \right) \tag{4}$$

The latter is instantaneous and energy independent, corresponding to the phonon-induced creation of virtual electron–hole pairs. Within a rigid ion approximation, it can be rewritten in a form similar to the Fan term. The importance of retaining both terms was recognized after much debate in the 1960s and 1970s. A synthesis was realized by Allen, Heine, and Cardona (Allen and Heine, 1976), to calculate the renormalization of the optical band gap at $T = 0$ K, and its evolution with temperature.

In practice the ingredients (electron and phonon states and coupling matrix elements) are most often calculated within density functional theory (DFT, Nomura and Akashi, 2023) and the corresponding perturbation theory (DFPT). We will not go into any detail about DFT theory: the coupling matrix elements can be evaluated explicitly within DFPT, then summed with the expressions above, or included implicitly through a configuration average over thermally populated configurations in a "supercell" approach. In the latter case, specific observables (dielectric function, band structure and gap, etc.) are evaluated and averaged for many disordered configurations sampling a canonical average. However this approach is static and adiabatic, and some limitations are discussed below. The historical Fröhlich model can be advantageously leveraged to make ab initio computations more accurate and tractable. In 2015, several groups (Sjakste et al., 2015; Verdi and Giustino, 2015) combined Fröhlich with first principles calculations of EPC. In three dimensions and for polar materials, the EPC matrix elements diverge for vanishing phonon momenta at the Brillouin zone center (usually as $1/q$, but not always, see Poncé et al., 2015), which bedevils numerical convergence. This divergence is treated by subtracting an analytical Fröhlich EPC interaction, then later adding it back. This amounts to separating long-ranged (small q) dipolar interactions from the other short-ranged, better-behaved interactions. Many quantities depend on reciprocal space integrations which can be performed accurately only with this technique. Phenomena such as ferroelectricity and piezoelectricity can be addressed quantitatively. In 2020 the same principle was carried over to quadrupole effects (Brunin et al., 2020; Jhalani et al., 2020). The quadrupole EPC does not diverge, but it does present discontinuities and a nonanalytic behavior around the Brillouin zone center.

Combining recent progress on low-dimensional materials and hindsight on decades of research into nanostructured systems, one may distinguish two types of dimensionality effects on electron–phonon interactions: (i) discretization of the electron and/or phonon bulk states and (ii) new phonons and couplings. These are discussed in the following sections.

Discretization of the electron and/or phonon bulk states

By reducing the dimensions in which electrons and phonons can propagate, one affects first and foremost their density of states. Confining boundary conditions on the electron's wavefunctions or the phonon's displacement pattern impose discrete values for the momenta in the confined directions. This is reflected in the density of states (DOS) of the free electron gas, which goes from a continuous square root of the energy in 3D to a discontinuous function with repeating features in lower dimensions, coming from the discrete values of the confined momenta: steps in 2D, inverse square roots in 1D, and Dirac peaks in 0D. Because of the conservation of energy and momentum, this will immediately affect the selection rules involved in electron–phonon interactions (Ridley, 1982), and the consequences have been observed in quantum wells, wires, and dots for several decades. The joint density of states represents the statistical availability of each quasiparticle, as well as the energy and momentum selection rules involved in the transitions. When the joint density of states is large, both electrons and phonons have many options to scatter, leading to short scattering times (average time between two scattering events) and a broadening of their respective spectra, whose width goes as the inverse of the scattering time (e.g., Lazzeri et al., 2006). As dimensionality is reduced, so is the joint density of states, and the scattering time associated with each quasi particle is generally expected to increase, for example, for the phonon bottleneck effect in quantum dots (Inoshita and Sakaki, 1996). On the other hand, one may also observe hybrid quasi-particles (polarons) at specific resonance conditions between electron and phonon energies. Standard realizations are quantum wells in a magnetic field, with 0D electron states which are tunable via the cyclotron frequency (Klimin and Devreese, 2003), or quantum dots with electron energy spacings corresponding to LO phonon energies (Hameau et al., 1999).

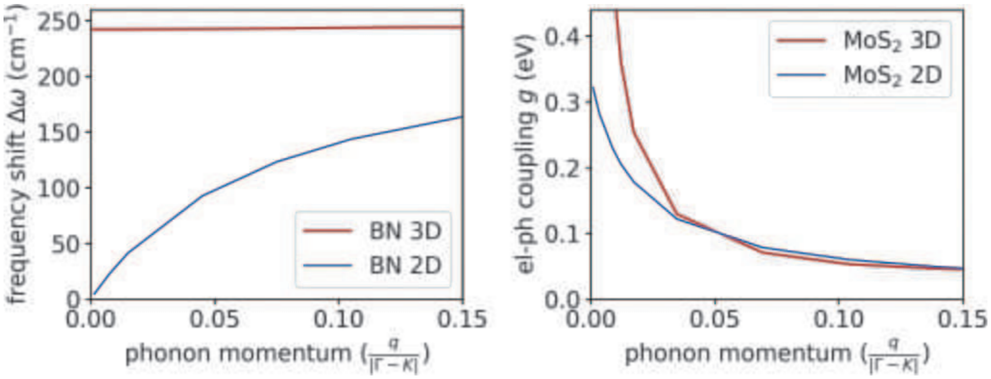

Fig. 3 DFPT simulation of polar-optical phonons in BN and MoS_2. Dimensionality affects the dispersion of polar-optical phonons, as well as their coupling to electrons. The frequency shift associated to dipolar interactions is constant in 3D, while it breaks down at zone center ($q \rightarrow 0$) in 2D, as seen on the left panel for BN. The Fröhlich electron–phonon coupling with the LO phonons diverges as the inverse of the phonon momentum in 3D (bulk MoS_2), while it stays finite in 2D (monolayer MoS_2) at zone center. Adapted from Sohier T, Calandra M, Mauri F, 2016. Two dimensional Fröhlich interaction in transition-metal dichalcogenide monolayers: theoretical modeling and first-principles calculations. Physical Review B 94 (8), 085415. ISSN 2469-9950. https://doi.org/10.1103/PhysRevB.94.085415; Sohier T, Gibertini M, Calandra M, Mauri F, Marzari N, 2017b. Breakdown of optical phonons' splitting in two-dimensional materials. Nano Letters 17 (6), 3758–3763. ISSN 15306992. https://doi.org/10.1021/acs.nanolett.7b01090. 1612.07191.

The reduction of dimensionality will change the dielectric screening, as well as the dispersion of the polar (Fröhlich-type) EPC, as shown in Fig. 3. With reduced screening and stronger interactions, the formation of bipolarons (bound states composed of two polarons) is also easier in lower dimensions. Depending on the mechanical and electrical boundary conditions, with a surface or embedding in a matrix, one can also be in mixed dimensions, for example, 2D electrons interacting with 3D phonons. Extensive work was carried out in the 1990s and 2000s linking polarons, dimensionality, and superconductivity in 2D gases and cuprates (Alexandrov and Devreese, 2010).

New phonons and couplings

We now focus on the second category of dimensionality effects: the emergence of new phonons and couplings. Relatively large nanostructures can be approximated as containing a combination of bulk and surface states. Nanostructuring a bulk 3D material creates boundaries and generates phonon and electron states that are different from the bulk. At the interface between two materials (or a material and vacuum), electronic surface states are formed as the potential transitions sharply to that of the other medium (Chiarotti and Goletti, 2005). Several types of surface phonons can emerge. Some have frequencies well separated from the bulk dispersion, clearly implying surface localization (see mode S1 in Fig. 2). Other "embedded surface modes" have frequencies within the bulk phonon bands, yet are still localized on the surface, which induces resonances in the bulk spectrum (Benedek et al., 2020). Due to their spatial localization, such surface electron and phonon states couple mostly to each other, with a limited joint density of states. The resulting states can be observed with experimental surface techniques such as ARPES (Hofmann et al., 2009).

Smaller nanostructures or low-dimensional materials, on the other hand, may lose more of their similarity with the bulk. Any phonon with atomic displacements in directions which are not periodic will necessarily differ strongly from the bulk modes.

This is clear for phonons with out-of-plane atomic displacements in 2D materials. The acoustic out-of-plane mode (ZA) follows a distinctive quadratic dispersion, leading to much smaller energy and larger occupations at small finite momenta than in 3D. The optical out-of-plane mode (ZO) is typically less energetic than its in-plane counterparts as well. Both do not couple to electrons at linear order unless mirror symmetry is broken by the material itself (Zhang et al., 2021) or by an external electric field, as suggested notably for graphene (Gunst et al., 2017; Politano et al., 2015; Sohier et al., 2017a). Similar conclusions apply to phonons with displacements perpendicular to the periodic direction in 1D systems like nanotubes, chains, or thin nanowires.

Phonons with atomic displacements in the bulk-like direction may also change with nanostructuring. This is the case of polar-optical phonons, and the contribution of dipolar interactions to the energy of longitudinal optical (LO) modes. If there exist transverse phonon modes (TO) which are degenerate in the absence of the long range electrostatic interaction, this leads to the so-called LO/TO splitting (hardening of the LO mode). The dimensionality of the sample leads to different dispersions for the phonons near the Brillouin zone center. Notably in 2D the LO/TO splitting vanishes in the very long wavelength limit (De Luca et al., 2020) and has a linear increase at small q (Sohier et al., 2017b), see Fig. 3. The dispersion is also affected by the screening of the dipolar interactions, which depends on dimension. The dielectric function of 2D materials is characterized by a crossover between screening by the environment at long wavelengths, to screening from the layer itself at shorter wavelengths (Royo and Stengel, 2021).

The LO/TO splitting is a field-mediated mechanism, and, for the same reasons, field-mediated electron–phonon coupling in general will be affected by dimensionality. This is the case of the Fröhlich coupling with LO modes, and the piezoelectric coupling with transverse and longitudinal acoustic phonons (TA/LA). The Fröhlich coupling with polar-optical phonons results from the above-mentioned dipoles (and higher multipoles) which are formed when moving atoms with different charges. Piezoelectricity denotes the capacity of certain materials to generate an electric field under strain. Long wavelength TA and LA phonons can be considered as a periodic strain, so in piezoelectric materials a periodic electric field is generated. Dimensionality affects the charge

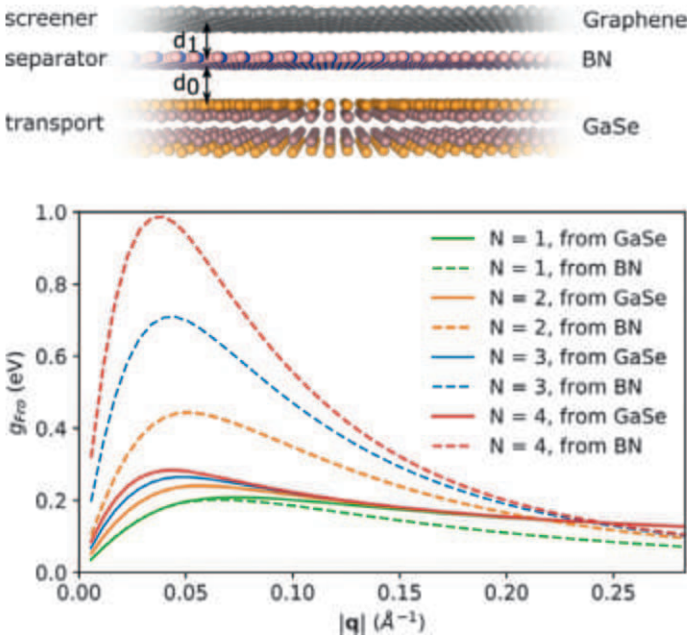

Fig. 4 Ab initio-based semi-analytical model of remote polar-optical phonon coupling in the van der Waals heterostructure depicted at the top where the number of BN layers (*N*) is increased from 1 to 4. The curves show the coupling between transport electrons in GaSe and the LO phonons of either GaSe or BN. All the couplings are screened remotely by the doped graphene, but the effect fades as *N* increases, leading to an increase of the couplings, and lower mobility. The couplings due to BN phonons increase more dramatically as the dielectric contributions from each layer add up. Adapted from Sohier T, Gibertini M, Verstraete MJ, 2021. Remote free-carrier screening to boost the mobility of Fröhlich-limited two-dimensional semiconductors. Physical Review Materials 5 (2), 024004. ISSN 2475-9953. https://doi.org/10.1103/PhysRevMaterials.5.024004 (2011.04961).

density perturbations as well as their screening. The Fröhlich coupling as a function of momentum diverges at zone center in 3D, while it stays finite in 2D (Sohier et al., 2016), as shown in Fig. 3. A similar dependency on the dimensionality is expected for the piezoelectric coupling, as seen by comparing 3D (Jhalani et al., 2020) and 2D models (Kaasbjerg et al., 2013).

Finally, the juxtaposition of low-dimensional systems along their nonperiodic directions leads to the emergence of remote interactions between electrons and phonons belonging to different nanostructures. This is particularly true for field-mediated couplings since the electric fields generated are long range. The remote couplings to different flavors of polar-optical phonons are now understood in several situations. They can in general be modeled by simple electrostatics and dielectric models. The first and now well-known instance of such a mechanism is the coupling to surface optical phonons (Wang and Mahan, 1972). These appear at the surface of supporting substrates, their energy is somewhere between the TO and LO modes of the bulk, and they will generically scatter electrons in whatever system is on the substrate (Fischetti et al., 2001). In van der Waals heterostructures, the relevant modes are the LO phonons of the different layers, which scatter electrons in surrounding layers (Sohier et al., 2021), as shown in Fig. 4. In both cases, the nature of the phonon and the coupling mechanism are very similar. The generated electric field, and thus the associated coupling, is damped as e^{-qd} where q is the phonon momentum and d is the distance between the locations of the phonon and the electrons. Other phonons may couple to electrons remotely, such as acoustic phonons via the piezoelectric coupling or ZO phonons. Ab initio methods have evolved and adapted to simulate dimensionality effects in EPCs. A central challenge is that plane wave codes (those most commonly used to access EPCs) rely on 3D periodic boundary conditions. Nanostructures or low-dimensional systems are thus repeated artificially in the nonperiodic dimension. Certain perturbations, and phonons in particular, lead to long-range interactions in the response of the system. The periodic images can then interact with each other, changing the behavior of the electron–phonon coupling. Truncation techniques have been developed to overcome those issues, and one can now perform phonon and electron–phonon calculations in 2D with the proper boundary conditions (Sohier et al., 2017a). 2D material EPCs are then readily accessible. Surface electron–phonon interaction requires other methodological efforts, using slabs or Green's functions (Hofmann et al., 2009), which have been resolved well before the periodic image interactions. Remote phonons are accessible in those frameworks, but new technical issues arise, such as the need for large supercells to accommodate the mismatch in different materials' lattices. Semi-numerical methods have been developed to tackle this issue (Sohier et al., 2021).

Key issues (current debates regarding the topic)

As shown above, electronic screening is an essential ingredient of electron–phonon interactions. It is also a complex quantity to simulate from first-principles calculations. The vast majority of calculations to date are based on DFT, with semi-local exchange-correlation functionals (local or generalized gradient approximations). A few studies have used hybrid functionals (with a fraction of exact Hartree–Fock exchange) or the GW approximation, for example, in graphene (Lazzeri et al., 2008) and diamond (Antonius et al., 2014). Both treatments tend to open the band gap, lower screening, and increase the EPC. There is not yet a clear consensus about a recipe for the use of higher order methods in the dielectric screening: many purely DFT calculations are quantitatively within experimental error bars for mobility, zero point renormalization, or superconductivity. However, given the complexity of advanced calculations and many possible missing effects (defects and dislocations, anharmonicity, boundary scattering) there will be a systematic need for better screening to push accuracy further.

Consistent treatment of EPC within many-body theory implies that the interaction vertex (essentially the EPC matrix element) should appear once screened and once "unscreened" in the self-energy (Calandra et al., 2010; Giustino, 2017), as is also the case for electron–electron interactions. Most practical calculations use matrix elements from DFPT, screened by the DFT dielectric response, in all of the self-energy insertions. This has led to an extensive and not yet fully resolved debate about the importance of the approximation involved in screening all vertices the same way, and the proper way to unscreen or rescreen DFPT results.

A crucial consideration in all perturbation theories is the separation of energy scales. Neglecting the energy of a phonon before that of an electron yields an effectively adiabatic interaction, continuously following a single potential energy surface for the electrons. In explicit expressions, such as the Fan self-energy above, the phonon frequency can be included (or not) in energy denominators, leading to a direct test of the consequences of nonadiabaticity. Techniques averaging supercell properties are always implicitly adiabatic (static) with respect to the phonon, and it has become clear recently that this is incorrect for certain quantities.

Macroscopic properties of semiconductors are often computed by plugging the neutral EPCs into models for different transport and optical quantities. However, gate doping and optical pumping are ubiquitous in experiments on nanostructures, implying that the carrier occupations are not those of the neutral material. Instead, extra electrons and/or holes are created. This changes the EPCs, the most obvious consequence being the screening of the EPCs by the added free carriers, generally corresponding to a suppression of the couplings with doping. Thus, in principle, the EPC matrix elements should be computed with the nonequilibrium, nonneutral occupations. Semi-numerical models have been developed to correct the EPCs of neutral semiconductors (Gjerding et al., 2020; Verdi et al., 2017). Those models allowed, for example, to understand the transition between polaronic and Fermi liquid states observed in the ARPES spectra of transition metal oxides (Verdi et al., 2017). A more systematic ab initio treatment of doped semiconductors has recently been proposed in 3D semiconductors (Macheda et al., 2022), and the EPCs of gate-doped 2D semiconductors have become accessible directly within DFPT (Sohier et al., 2017a).

The simplest models of EPC consider a single valley at the band edge. Multivalley band structures, however, complicate this picture. Beyond the emergence of intervalley scattering, the intravalley EPC of 2D transition metal dichalcogenides (TMDs) has been shown to be enhanced when two kinds of valleys are occupied (Sohier et al., 2019b). The coupling can be described by a "multivalley" deformation potential that has the peculiarity of perturbing the different valleys of the conduction band with opposite phase, which leads to vanishing screening and a counterintuitive enhancement of the EPC with doping.

The detailed study of transport and optical properties of TMDs has revealed the importance of the interplay between electron–phonon scattering and spin-orbit coupling. Electron–phonon interactions are mostly spin-conserving, implying that the spin texture of a band structure will dictate which electronic states can be coupled via phonons. This has clear consequences on excitonics and carrier relaxation in general, which should be systematically accounted for.

The standard flavors of EPCs were identified in the 1950s with the deformation potential (Bardeen and Shockley, 1950), and the Fröhlich interaction (Fröhlich, 1952). There are other kinds of couplings. The piezoelectric interaction coming from acoustic phonons (Jhalani et al., 2020) is generally weaker and vanishes at small momenta, and it has been studied somewhat less intensely than the (also field-mediated) Fröhlich coupling with optical phonons, in particular with respect to nanostructuring and dimensionality effects. The deformation potential formalism was initially formulated in the framework of acoustic phonons, describing an energy shift of the band edge induced by a strain (volume change). It can however be extended to describe a similar energy shift induced by any phonon perturbation, such as optical phonons. Another important type of EPC that was particularly studied in graphene is the so-called "gage-field." Intuitively, it can be understood as producing a shift in momentum of the valleys (rather than energy), as the atoms follow the phonon displacement pattern. It has the peculiarity of being insensitive to screening, and so it is robust with respect to a change in the dielectric environment or doping. Finally, intervalley EPCs, that is, large momenta phonons coupling electronic states in different valleys, can play a significant role in electron relaxation (Sohier et al., 2019a).

All the "nonstandard" flavors of EPCs are straightforwardly accessible within DFPT. EPC models limited to the deformation potential are still widely used to estimate transport properties, although with very limited accuracy in certain situations. A clear understanding of the nature of the different kinds of couplings is crucial for EPCs in nanostructures.

Conclusion

Summary

The coupling of electrons and phonons has made immense progress in the past half century. In particular the incorporation of first-principles electronic structure ingredients has made quantitative predictions possible and led to a resurgence of the field since the 2000s, with applications to polarons, mobility and transport, and phase transitions and spectroscopy. This chapter presents the current state of the art in the calculation of EPC and derived quantities, with a specific focus on the effects of dimensionality and nanostructuring. Geometric quantum confinement changes the density of states of both electrons and phonons, though not necessarily to the same extent, for example, for electrons in quantum dots embedded in the lattice vibrations of a matrix. Further, the phonons themselves and the mechanisms by which they couple to electrons are affected by dimensionality. For example, the dielectric screening is less efficient in lower dimensions, which qualitatively changes the Coulomb interaction and long wavelength phonon dispersion.

Different types of phonons lead to different couplings. Traditional focus on acoustic modes (deformation potential) and longitudinal optical modes (Fröhlich) has now broadened into a rich variety of behaviors including piezoelectric, gage field, and multivalley deformation potentials, and even "nonpolarons" (de Abreu et al., 2022; Emin and Bussac, 1994).

Future directions

The exploration of novel types of couplings as well as their myriad consequences on physical observables is a very active field of research. We list below some promising directions for future investigation. The community has begun addressing a systematic combination of different interactions within many-body perturbation theory. In this light electron–electron, electron–phonon, and phonon–phonon interactions should all be included, though they can present very different energy scales and intensities. A first step is the renormalization of the ingredients for EPC calculations, for example, using the GW approximation to improve the electronic band energies, or using self-consistent harmonic approximations to improve the temperature dependency of the phonons, and then combining these with the $T = 0$ DFPT EPC. First attempts at a fuller theory have been proposed within MBPT, as the addition of the e–e and e–ph self-energies to correct the noninteracting electron Green's function. More broadly, extensive effort is being invested in the interaction between phonons and other quasiparticle excitations such as excitons (electron–hole pairs) and polaritons (electron–photon or phonon–photon hybridization).

The explicit representation of polarons remains an active challenge: wavefunction Ansätze were usually restricted to Gaussian functions with a single variational parameter in their width. Using first-principles ingredients, more evolved polaron wavefunctions can be constructed as recently shown by Sio et al. (2019). Bridging the gap between small and large polaron scales, and weak to strong coupling with a unique formalism is still a distant perspective. Many-body approaches based on perturbation theory can manage relatively strong couplings but still break down in nonrenormalizable cases such as small localized polarons. The interplay between polaron strength, localization, and dimensionality will be a further challenge.

Ultrafast real time dynamics of electron and phonon populations have been demonstrated using the ingredients described above (Caruso, 2021; Tong and Bernardi, 2021). A fully nonequilibrium theory, where the EPC itself evolves in time, will be the next frontier, linked to the many-body considerations above.

Beyond optical properties, polaronic effects may also impact transport in materials with relatively strong electron–phonon couplings. A cumulant approach was used to renormalize the electron–phonon self-energy (Story et al., 2014), and more recently applied to model spectroscopy and transport in this regime, paving the way for further study of the electrical characterization of polaronic effects.

While EPCs in standalone 2D materials have already raised considerable interest, there is still much to understand about EPCs in twisted heterostructures of 2D systems. As found in twisted bilayer graphene, both electron and phonon states can be dramatically affected by the Moiré pattern created when aligning lattices at different angles. Significant consequences on EPCs naturally emerge as well (Choi and Choi, 2021), and their understanding will surely shed light on the many experiments conducted on this kind of 2D systems.

Finally, as the energy and momentum resolution of experimental techniques progress, various pathways to measure EPCs are now available. Over the last decade there have been spectacular improvements in neutron scattering, nonresonant inelastic X-ray scattering and Raman spectroscopy to probe EPCs via phonons, and ARPES to probe EPCs via electrons. Recent progress in the postprocessing of techniques like resonant inelastic X-ray scattering (Dashwood et al., 2021; Devereaux et al., 2016) or time-resolved ARPES (De Giovannini et al., 2020; Hein et al., 2020) have allowed a more direct, momentum- and mode-resolved access to EPCs.

This progress heralds an exciting back and forth between experiments and theory, as experiments zero in on the measurement of specific electron–phonon coupling matrix elements, rather than averaged macroscopic quantities.

References

Alexandrov AS and Devreese JT (2010) Advances in Polaron Physics. *Springer Series in Solid-State Sciences.* , vol. 159. Berlin: Springer. ISBN 978-3-642-01895-4 978-3-642-01896-1.

Allen PB and Heine V (1976) Theory of the temperature dependence of electronic band structures. *Journal of Physics C: Solid State Physics* ISSN: 0022-3719. 9(12): 2305–2312. https://doi.org/10.1088/0022-3719/9/12/013.

Antonius G, Poncé S, Boulanger P, Côté M, and Gonze X (2014) Many-body effects on the zero-point renormalization of the band structure. *Physical Review Letters* ISSN: 10797114. 112(21). https://doi.org/10.1103/PhysRevLett.112.215501.

Bardeen J and Shockley W (1950) Deformation potentials and mobilities in non-polar crystals. *Physical Review* ISSN: 0031-899X. 80(1): 72–80. https://doi.org/10.1103/PhysRev.80.72.

Benedek G, Bernasconi M, Campi D, Toennies JP, and Verstraete MJ (2020) Surface phonons: Theoretical methods and results. In: Rocca M, Rahman TS, and Vattuone L (eds.) *Springer Handbook of Surface Science*, pp. 737–782. Cham: Springer International Publishing.

Bennemann KH (2023) Superconductivity: BCs theory. *Encyclopedia of Condensed Matter Physics v2*. Oxford: Elsevier.

Brunin G, Miranda HPC, Giantomassi M, Royo M, Stengel M, Verstraete MJ, Gonze X, Rignanese G-M, and Hautier G (2020) Electron–phonon beyond Fröhlich: Dynamical quadrupoles in polar and covalent solids. *Physical Review Letters* ISSN: 0031-9007. 125(13): 136601. https://doi.org/10.1103/physrevlett.125.136601 (2002.00628).

Calandra M, Profeta G, and Mauri F (2010) Adiabatic and nonadiabatic phonon dispersion in a Wannier function approach. *Physical Review B* ISSN: 1098-0121. 82(16): 165111. https://doi.org/10.1103/PhysRevB.82.165111.

Campi D, Bernasconi M, Benedek G, and Toennies JP (2015) Surface dynamics of Xe(111): An ambiguous nobility. *The Journal of Physical Chemistry C* 119(26): 14579–14584. https://doi.org/10.1021/jp511886f. ISSN 1932-7447, 1932-7455.

Caruso F (2021) Nonequilibrium lattice dynamics in monolayer MoS^2. *The Journal of Physical Chemistry Letters* ISSN: 1948-7185, 1948-7185. 12(6): 1734–1740. https://doi.org/10.1021/acs.jpclett.0c03616.

Chen C, Avila J, Wang S, Wang Y, Mucha-Kruczyński M, Shen C, Yang R, Nosarzewski B, Devereaux TP, Zhang G, and Asensio MC (2018) Emergence of interfacial polarons from electron-phonon coupling in graphene/h-Bn van Der Waals heterostructures. *Nano Letters* ISSN: 15306992. 18(2): 1082–1087. https://doi.org/10.1021/acs.nanolett.7b04604. 1707.00184v2.

Chiarotti G and Goletti C (2005) Surfaces and interfaces, electronic structure of. *Encyclopedia of Condensed Matter Physics*, pp. 133–144. Elsevier.

Choi YW and Choi HJ (2021) Dichotomy of electron-phonon coupling in graphene Moiré Flat bands. *Physical Review Letters* 127(16): 167001. https://doi.org/10.1103/PhysRevLett.127.167001. ISSN 0031-9007, 1079-7114.

Chubukov A (2023) Modern view of superconductivity. *Encyclopedia of Condensed Matter Physics v2.* Oxford: Elsevier.

Dashwood CD, Geondzhian A, Vale JG, Pakpour-Tabrizi AC, Howard CA, Faure Q, Veiga LSI, Meyers D, Chiuzbăian SG, Nicolaou A, Jaouen N, Jackman RB, Nag A, García-Fernández M, Zhou KJ, Walters AC, Gilmore K, McMorrow DF, and Dean MPM (2021) Probing electron–phonon interactions away from the Fermi level with resonant inelastic X-ray scattering. *Physical Review X* ISSN: 2160-3308. 11(4): 041052. https://doi.org/10.1103/PhysRevX.11.041052.

de Abreu JC, Nery JP, Giantomassi M, Gonze X, and Verstraete MJ (2022) Spectroscopic signatures of nonpolarons: The case of diamond. *Physical Chemistry Chemical Physics* 24(20): 12580–12591. https://doi.org/10.1039/D2CP01012G. ISSN 1463-9076, 1463-9084.

De Giovannini U, Hübener H, Sato SA, and Rubio A (2020) Direct measurement of electron-phonon coupling with time-resolved ARPES. *Physical Review Letters* ISSN: 0031-9007. 125 (13): 136401. https://doi.org/10.1103/physrevlett.125.136401 (2004.11082).

De Luca M, Cartoixa X, Indolese DI, Martín-Sanchez J, Watanabe K, Taniguchi T, Schönenberger C, Trotta R, Rurali R, and Zardo I (2020) Experimental demonstration of the suppression of optical phonon splitting in 2D materials by Raman spectroscopy. *2D Materials* ISSN: 20531583. 7(3): 035017. https://doi.org/10.1088/2053-1583/ab81b1.

Devereaux TP, Shvaika AM, Wu K, Wohlfeld K, Jia CJ, Wang Y, Moritz B, Chaix L, Lee W-S, Shen Z-X, Ghiringhelli G, and Braicovich L (2016) Directly characterizing the relative strength and momentum dependence of electron-phonon coupling using resonant inelastic X-ray scattering. *Physical Review X* ISSN: 2160-3308. 6(4): 041019. https://doi.org/10.1103/PhysRevX.6.041019.

Emin D and Bussac M-N (1994) Disorder-induced small-polaron formation. *Physical Review B* 49(20): 14290–14300. https://doi.org/10.1103/PhysRevB.49.14290. ISSN 0163-1829, 1095-3795.

Feynman RP (1955) Slow electrons in a polar crystal. *Physical Review* ISSN: 0031-899X. 97(3): 660–665. https://doi.org/10.1103/PhysRev.97.660.

Fischetti MV, Neumayer DA, and Cartier EA (2001) Effective electron mobility in Si inversion layers in metal oxide semiconductor systems with a high-κ insulator: The role of remote phonon scattering. *Journal of Applied Physics* 90(9): 4587–4608. https://doi.org/10.1063/1.1405826. ISSN 0021-8979, 1089-7550.

Fröhlich H (1952) Interaction of electrons with lattice vibrations. *Proceedings of the Royal Society of London. Series A. Mathematical and Physical Sciences* 215(1122): 291–298. https://doi.org/10.1098/rspa.1952.0212. 0080-4630, 2053-9169.

Giustino F (2017) Electron-phonon interactions from first principles. *Reviews of Modern Physics* ISSN: 0034-6861. 89(1): 015003. https://doi.org/10.1103/RevModPhys.89.015003 (1603.06965).

Gjerding MN, Cavalcante LSR, Chaves A, and Thygesen KS (2020) Efficient ab initio modeling of dielectric screening in 2D van Der Waals materials: Including phonons, substrates, and doping. *The Journal of Physical Chemistry C* ISSN: 1932-7447. 124(21): 11609–11616. https://doi.org/10.1021/acs.jpcc.0c01635.

Gunst T, Kaasbjerg K, and Brandbyge M (2017) Flexural-phonon scattering induced by electrostatic gating in graphene. *Physical Review Letters* ISSN: 0031-9007. 118(4): 046601. https://doi.org/10.1103/PhysRevLett.118.046601.

Hameau S, Guldner Y, Verzelen O, Ferreira R, Bastard G, Zeman J, Lemaître A, and Gérard JM (1999) Strong electron-phonon coupling regime in quantum dots: Evidence for everlasting resonant polarons. *Physical Review Letters* 83(20): 4152–4155. https://doi.org/10.1103/PhysRevLett.83.4152. ISSN 0031-9007, 1079-7114.

Hein P, Jauernik S, Erk H, Yang L, Qi Y, Sun Y, Felser C, and Bauer M (2020) Mode-resolved reciprocal space mapping of electron-phonon interaction in the Weyl semimetal candidate Td-WTe2. *Nature Communications* ISSN: 2041-1723. 11(1): 2613. https://doi.org/10.1038/s41467-020-16076-0.

Hofmann P, Sklyadneva IY, Rienks EDL, and Chulkov EV (2009) Electron-phonon coupling at surfaces and interfaces. *New Journal of Physics* ISSN: 1367-2630. 11(12): 125005. https://doi.org/10.1088/1367-2630/11/12/125005.

Holstein T (1959) Studies of polaron motion. *Annals of Physics* 8(3): 325–342. ISSN: 00034916. https://doi.org/10.1016/0003-4916(59)90002-8.

Inoshita T and Sakaki H (1996) Electron-phonon interaction and the so-called phonon bottleneck effect in semiconductor quantum dots. *Physica B: Condensed Matter* 227(1-4): 373–377. ISSN: 09214526. https://doi.org/10.1016/0921-4526(96)00445-0.

Jhalani VA, Zhou J-J, Park J, Dreyer CE, and Bernardi M (2020) Piezoelectric electron-phonon interaction from ab initio dynamical quadrupoles: Impact on charge transport in wurtzite gaN. *Physical Review Letters* 125(13): 136602. ISSN: 0031-9007. https://doi.org/10.1103/physrevlett.125.136602. 2002.08351.

Kaasbjerg K, Thygesen KS, and Jauho A-P (2013) Acoustic phonon limited mobility in two-dimensional semiconductors: Deformation potential and piezoelectric scattering in monolayer MoS 2 from first principles. *Physical Review B* 87(23): 235312. ISSN: 10980121. https://doi.org/10.1103/PhysRevB.87.235312 (1206.2003v2).

Klimin SN and Devreese JT (2003) Cyclotron resonance of an interacting polaron gas in a quantum well: Magnetoplasmon-phonon mixing. *Physical Review B* 68(24): 245303. https://doi.org/10.1103/PhysRevB.68.245303. ISSN 0163-1829, 1095-3795.

Lazzeri M, Piscanec S, Mauri F, Ferrari AC, and Robertson J (2006) Phonon linewidths and electron-phonon coupling in graphite and nanotubes. *Physical Review B* 73(15): 155426. https://doi.org/10.1103/PhysRevB.73.155426. ISSN 1098-0121, 1550-235X.

Lazzeri M, Attaccalite C, Wirtz L, and Mauri F (2008) Impact of the electron–electron correlation on phonon dispersion: Failure of LDA and GGA DFT functionals in graphene and graphite. *Physical Review B* 78(8): 081406. ISSN: 1098-0121. https://doi.org/10.1103/PhysRevB.78.081406.

Macheda F, Barone P, and Mauri F (2022) Electron–phonon interaction and longitudinal-transverse phonon splitting in doped semiconductors. *Physical Review Letters* 129(18): 185902. https://doi.org/10.1103/PhysRevLett.129.185902. ISSN 0031-9007, 1079-7114.

Migdal AB (1958) Interaction between electrons and lattice vibrations in a normal metal. *Soviet Physics–JETP* 7(6): 996–1001.

Mishchenko A, Prokof'ev N, Sakamoto A, and Svistunov B (2000) Diagrammatic quantum Monte Carlo study of the Fröhlich polaron. *Physical Review B* 62(10): 6317–6336. https://doi.org/10.1103/PhysRevB.62.6317. ISSN 0163-1829, 1095-3795.

Nomura Y and Akashi R (2023) Density-functional theory. *Encyclopedia of Condensed Matter Physics v2.* Oxford: Elsevier.

Politano A, de Juan F, Chiarello G, and Fertig HA (2015) Emergence of an out-of-plane optical phonon (ZO) Kohn anomaly in quasifreestanding epitaxial graphene. *Physical Review Letters* 115(7): 075504. ISSN: 0031-9007. https://doi.org/10.1103/PhysRevLett.115.075504.

Poncé S, Gillet Y, Laflamme Janssen J, Marini A, Verstraete M, and Gonze X (2015) Temperature dependence of the electronic structure of semiconductors and insulators. *Journal of Chemical Physics* 143(10): 102813. ISSN: 00219606. https://doi.org/10.1063/1.4927081 (1504.05992).

Ridley BK (1982) The electron–phonon interaction in quasi-two-dimensional semiconductor quantum-well structures. *Journal of Physics C: Solid State Physics* 15(28): 5899–5917. ISSN: 0022-3719. https://doi.org/10.1088/0022-3719/15/28/021.

Royo M and Stengel M (2021) Exact long-range dielectric screening and interatomic force constants in quasi-two-dimensional crystals. *Physical Review X* 11(4): 041027. ISSN: 2160-3308. https://doi.org/10.1103/PhysRevX.11.041027.

Shimizu K (2023) Superconductors, hydrogen-based. *Encyclopedia of Condensed Matter Physics v2.* Oxford: Elsevier.

Sio WH, Verdi C, Poncé S, and Giustino F (2019) *Ab Initio* theory of polarons: Formalism and applications. *Physical Review B* 99(23): 235139. https://doi.org/10.1103/PhysRevB.99.235139. ISSN 2469-9950, 2469-9969.

Sjakste J, Vast N, Calandra M, and Mauri F (2015) Wannier interpolation of the electron-phonon matrix elements in polar semiconductors: Polar-optical coupling in GaAs. *Physical Review B–Condensed Matter and Materials Physics* 92(5): 054307. ISSN: 1550235X. https://doi.org/10.1103/PhysRevB.92.054307 (1508.06172).

Sohier T, Calandra M, and Mauri F (2016) Two dimensional Fröhlich interaction in transition-metal dichalcogenide monolayers: Theoretical modeling and first-principles calculations. *Physical Review B* 94(8): 085415. ISSN: 2469-9950. https://doi.org/10.1103/PhysRevB.94.085415.

Sohier T, Calandra M, and Mauri F (2017a) Density functional perturbation theory for gated two dimensional heterostructures: Theoretical developments and application to flexural phonons in graphene. *Physical Review B* 96(7): 075448. ISSN: 2469-9950. https://doi.org/10.1103/PhysRevB.96.075448 (1705.04973).

Sohier T, Gibertini M, Calandra M, Mauri F, and Marzari N (2017b) Breakdown of optical phonons' splitting in two-dimensional materials. *Nano Letters* 17(6): 3758–3763. ISSN: 15306992. https://doi.org/10.1021/acs.nanolett.7b01090 (1612.07191).

Sohier T, Gibertini M, Campi D, Pizzi G, and Marzari N (2019a) Valley-engineering mobilities in two-dimensional materials. *Nano Letters* 19(6): 3723–3729. ISSN: 1530-6984. https://doi.org/10.1021/acs.nanolett.9b00865.

Sohier T, Ponomarev E, Gibertini M, Berger H, Marzari N, Ubrig N, and Morpurgo AF (2019b) Enhanced electron-phonon interaction in multivalley materials. *Physical Review X* 9(3): 031019. ISSN: 21603308. https://doi.org/10.1103/PhysRevX.9.031019 (1901.08012).

Sohier T, Gibertini M, and Verstraete MJ (2021) Remote free-carrier screening to boost the mobility of Fröhlich-limited two-dimensional semiconductors. *Physical Review Materials* 5 (2): 024004. ISSN: 2475-9953. https://doi.org/10.1103/PhysRevMaterials.5.024004 (2011.04961).

Story SM, Kas JJ, Vila FD, Verstraete MJ, and Rehr JJ (2014) Cumulant expansion for phonon contributions to the electron spectral function. *Physical Review B* 90(19): 195135. ISSN: 1550235X. https://doi.org/10.1103/PhysRevB.90.195135.

Su WP, Schrieffer JR, and Heeger AJ (1979) Solitons in polyacetylene. *Physical Review Letters* 42(25): 1698–1701. ISSN: 0031-9007. https://doi.org/10.1103/PhysRevLett.42.1698.

Tong X and Bernardi M (2021) Toward precise simulations of the coupled ultrafast dynamics of electrons and atomic vibrations in materials. *Physical Review Research* 3(2): 023072. ISSN: 2643-1564. https://doi.org/10.1103/PhysRevResearch.3.023072.

Verdi C and Giustino F (2015) Fröhlich electron–phonon vertex from first principles. *Physical Review Letters* 115(17): 176401. ISSN: 0031-9007. https://doi.org/10.1103/PhysRevLett.115.176401.

Verdi C, Caruso F, and Giustino F (2017) Origin of the crossover from polarons to Fermi liquids in transition metal oxides. *Nature Communications* 8(1): 15769. ISSN: 2041-1723. https://doi.org/10.1038/ncomms15769.

Wang SQ and Mahan GD (1972) Electron scattering from surface excitations. *Physical Review B* 6(12): 4517–4524. ISSN: 0556-2805. https://doi.org/10.1103/PhysRevB.6.4517.

Zhang C, Cheng L, and Liu Y (2021) Role of flexural phonons in carrier mobility of two-dimensional semiconductors: Free standing vs on substrate. *Journal of Physics: Condensed Matter*. https://doi.org/10.1088/1361-648X/abe8fa. ISSN 0953-8984, 1361-648X.

Further reading

Baroni S, et al. (2001) Phonons and related crystal properties from density-functional perturbation theory. *Reviews of Modern Physics* 73: 515.

Katsnelson MI, Cowley RA, and Parlinski K (2005) *Lattice Dynamics Encyclopedia of Condensed Matter Physics*, first ed, pp. 77–102. Elsevier Academic Press.

Ponce S, et al. (2020) First-principles calculations of charge carrier mobility and conductivity in bulk semiconductors and two-dimensional materials. *Reports on Progress in Physics* 83: 036501.

Electronic states of elemental semiconductors

GC La Rocca, NEST, Scuola Normale Superiore, Pisa, Italy

© 2024 Elsevier Ltd. All rights reserved.

This is an update of G.C. La Rocca, Elemental Semiconductors, Electronic States of, Editor(s): Franco Bassani, Gerald L. Liedl, Peter Wyder, Encyclopedia of Condensed Matter Physics, Elsevier, 2005, Pages 133–140, ISBN 9780123694010, https://doi.org/10.1016/B0-12-369401-9/00459-9.

Introduction 475
Crystal structure and symmetry 476
Energy band calculations 476
Band structures of Si, Ge and α-tin 478
Comparison with experimental data 480
Direct gap elemental semiconductors 482
Conclusion 483
References 484

Abstract

An overview of the electronic band structures of elemental semiconductors is presented, emphasizing the role of symmetry in determining their qualitative aspects. Their relation to the optical spectra and photoemission data is discussed. Besides Si and Ge, which have an indirect gap, a few other examples of semiconductors with a "zero-gap" or a direct gap are illustrated.

Keypoints

- Electronic band structure
- Electronic band gaps
- Si, Ge, α -tin, black phosphorous
- Crystal symmetry
- Tight-binding, pseudopotential, DFT
- Optical transitions

Introduction

Silicon, the paradigmatic elemental semiconductor, is by far the most relevant material in the electronic industry and possibly the best known solid both from the point of view of basic science and technology. Our present understanding of virtually all the properties of a crystalline solid such as Si is based on an accurate knowledge of its electronic states, i.e., its electronic band structure. Quantum mechanics predicts the energies and wavefunctions available to the electrons in the periodic crystal potential (Bassani and Pastori Parravicini, 1975). Differently from the case of atoms or molecules, the translational symmetry of the crystal leads to extended states characterized by a Bloch wave-vector $\vec{k}$. Just like in atoms and molecules, the Pauli exclusion principle dictates how the distinct electronic states are occupied each by a single electron starting from the lowest energy levels. From such information, mechanical, transport and optical properties can be inferred (Bassani and Pastori Parravicini, 1975; Cohen and Chelikowsky, 1988; Yu and Cardona, 1995).

Semiconductors have typically an energy gap (E_g) between the highest occupied states (top of the valence band) and the lowest unoccupied ones (bottom of the conduction band) comparable to 1 eV and are characterized by the possibility to be doped. Silicon ($E_g = 1.17$ eV) and germanium ($E_g = 0.774$ eV) are the most important elemental semiconductors, belong to group IV of the periodic table, are tetrahedrally coordinated and crystallize in the diamond structure with cubic symmetry. We will focus here on Si and Ge, which have an indirect gap, and to a lesser extent on grey tin (α-Sn, a "zero-gap semiconductor"), black phosphorous and hexagonal germanium, both of which have a direct gap.

The main features of the electronic bands are determined by the symmetry of the crystal more than by the detailed shape of the crystal potential, and there are strong similarities in the band structures of Si, Ge and α-Sn, which have the diamond crystal structure. In the following, we will first describe the symmetry properties of the diamond crystal and the main ingredients to calculate the energy bands, then the electronic band structures of Si, Ge and α-Sn and their direct comparison with optical and photoemission experiments. Finally, we will consider two elemental semiconductors, hexagonal germanium and black phosphorous, which have a different crystal structure and are of interest for light-emitting applications.

Crystal structure and symmetry

The group IV elemental semiconductors, like carbon, are characterized by four electrons in the outer shell, with an electronic configuration $s^2 p^2$ which in the solid gives rise to four tetrahedrally oriented $s p^3$ hybrid orbitals. The resulting network of covalently bonded atoms corresponds to a face-centered cubic crystal in which each atom occupies an equivalent position. Such diamond crystal belongs to the $Fd3m$ $(O_h{}^7)$ crystallographic space group having the point group full cubic symmetry O_h.

Its translational symmetry is described by a Bravais FCC lattice of primitive translations: $\vec{\tau}_1 = (a/2)(0, 1, 1), \vec{\tau}_2 = (a/2)(1, 0, 1)$ and $\vec{\tau}_3 = (a/2)(1, 1, 0)$, where a is the side of the conventional unit cell, i.e., the crystal is invariant for translations by any vector $\vec{R} = n_1\vec{\tau}_1 + n_2\vec{\tau}_2 + n_3\vec{\tau}_3$, with integral values of n_1, n_2 and n_3. The lattice constants of cubic elemental semiconductors are $a = 5.43$ Å for Si, $a = 5.65$ Å for Ge, $a = 6.46$ Å for α-Sn. The corresponding reciprocal lattice is body-centered cubic (BCC) with primitive vectors: $\vec{K}_1 = (2\pi/a)(\bar{1}, 1, 1), \vec{K}_2 = (2\pi/a)(1, \bar{1}, 1)$ and $\vec{K}_3 = (2\pi/a)(1, 1, \bar{1})$; thereciprocal lattice vectors, $\vec{G}(\vec{G} = m_1\vec{K}_1 + m_2\vec{K}_2 + m_3\vec{K}_3)$, with m_1 m_2 and m_3 integers, have the property: $e^{i\vec{R}\cdot\vec{G}} = 1$, for any lattice translation $\vec{R}$. The primitive (symmetric) cell of the reciprocal lattice, i.e., the first Brillouin zone (BZ), of the diamond structure is shown in Fig. 1. The physical significance of the reciprocal lattice and of the BZ is that, as a consequence of the periodic translational symmetry, the extended electronic states in a crystal are described by wavefunctions of the form $\Psi_{\vec{k}}(\vec{r}) = e^{i\vec{k}\cdot\vec{r}}u(\vec{r})$ (Bloch's theorem), where the wavevector $\vec{k}$ belongs to the BZ and the function u is invariant under lattice translations $(u(\vec{r} + \vec{R}) = u(\vec{r}))$.

Beside the FCC lattice translations, the rotations and reflections belonging to the full cubic group (O_h) leave the diamond structure invariant. At the microscopic level, though, half of the 48 symmetry operations of O_h are accompanied by a fractional translation such that the two interpenetrating fcc lattices are exchanged (the space-group of diamond being a non-symmorphic space-group with a basis of two atoms). This is the main difference with respect to the zinc-blend symmetry of compound semiconductors such as GaAs in which the two sublattices are not equivalent. In particular, an elemental semiconductor such as Si has inversion symmetry with respect to the middle point of its homonuclear covalent bond, whereas in a compound semiconductor such as GaAs this symmetry is lacking. The point-group symmetry determines the degeneracies of the electronic levels as a function of their wavevector $\vec{k}$ in the BZ zone. In particular, the electronic wavefunctions at points and lines of high symmetry in the BZ, those marked in Fig. 1, are characterized by their transformation properties under point-group symmetry operations that leave their wavevector unchanged (i.e., they belong to the irreducible representations of the little group of their wavevector).

Beside space-group symmetry, time-reversal symmetry also affects the properties of a crystal, and it may bring about additional degeneracies of the electronic states. In particular, when the spin of the electrons is taken into account, in a crystal with inversion symmetry (such as Si) at each wavevector $\vec{k}$ the electronic states are (at least) doubly degenerate, because the state $|\vec{k},\uparrow>$ with spin up is degenerate with the state $|-\vec{k},\uparrow>$ by inversion symmetry and the latter is degenerate with the state $|\vec{k},\downarrow>$ by time-reversal symmetry. The spin degeneracy between the states $|\vec{k},\uparrow>$ and $|\vec{k},\downarrow>$ is, in general, absent in materials lacking an inversion center (such as in GaAs). Standard group theoretical methods are employed to obtain systematically all the wealth of information that symmetry alone provides.

Energy band calculations

Even though translational symmetry enormously simplifies the computation of the electronic states in a crystal, reducing the size of the problem to that of a unit cell, still a quantitative band structure calculation usually adopts a number of approximations. The electrons are considered to move in the presence of nuclei fixed at the equilibrium positions of the lattice (adiabatic

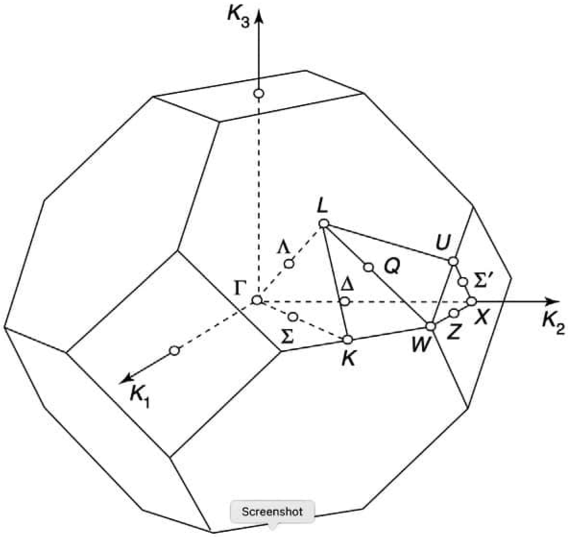

Fig. 1 Brillouin zone of the diamond crystal; lines and points of high symmetry are indicated.

approximation). The electron-electron interactions are treated at the mean field level neglecting many body correlations (one particle approximation). Finally, the interactions with the nuclei, including typically also the core of inner electronic shells, and with all other electrons in average are lumped into a local potential $V(\vec{r})$ which has the full symmetry of the crystal (band approximation). The crystal potential $V(\vec{r})$ can be either chosen empirically or determined within a self-consistent *ab initio* scheme. The solution of the corresponding Schrödinger equation for the electronic states

$$\left[\frac{p^2}{2m}+V\left(\vec{r}\right)\right]\Psi_{n,\vec{k}}\left(\vec{r}\right)=\mathrm{E}_n\left(\vec{k}\right)\Psi_{n,\vec{k}}\left(\vec{r}\right),$$

gives the (possibly degenerate) Bloch eigenfunctions Ψ with a wavevector $\vec{k}$ in the BZ and a band index n, which correspond to the electronic energy levels $E_n(\vec{k})$, i.e., the energy bands which depend continuously on $\vec{k}$. Relativistic corrections can be included in the above equation and may be important for heavy elements as discussed later on.

There are numerous and diverse methods to calculate the energy bands. In particular, some consider a crystal as a collection of atoms (localized orbital methods), while others treat it as a perturbed uniform fluid (plane-wave methods). A very popular localized orbital approach is the tight-binding method in which the wavefunctions are expanded in a basis of linear combination of atomic orbitals (LCAO); usually, only a limited number of atomic orbitals are included and only the interactions among a limited number of neighbors are considered. This method, at least in its simpler semiempirical versions, is transparent and economic; it has been very successful in calculating both electronic and structural properties of semiconductors and establishing their chemical trends. The minimal tight binding model to rationalize the electronic band structure of elemental semiconductors, at least concerning their valence band states, is sketched in Fig. 2. For each one of the two atoms in the elementary unit cell, a basis of atomic states is chosen including only one *s* and one *p* level (respectively, two and six times degenerate including spin). If we imagine to bring two atoms close together as in a diatomic molecule, each level would give rise to one bonding and one antibonding molecular orbital, the former having a lower energy. In the Ge crystal, e.g., such states give rise at the center of the BZ at $\vec{k}=0$(the Γ point) to a sequence of levels having the full cubic symmetry and corresponding, in order of increasing energies, to an s-bonding-like Γ_1 level, a p-bonding-like $\Gamma_{25}{}'$ level, an s-antibonding-like $\Gamma_2{}'$ level and a p-antibonding-like Γ_{15} level. The eight outer shell electrons (four for each atom in the unit cell) fill the Γ_1 and $\Gamma_{25}{}'$ levels completely, the latter being thus the top of the valence band, while the $\Gamma_2{}'$ and Γ_{15} levels remain empty (conduction states). State of the art tight binding calculations, of course, are based on larger basis sets, possibly including also *d* states (Jancu et al., 1998), and can describe well also the more delocalized conduction band states (see Table 1).

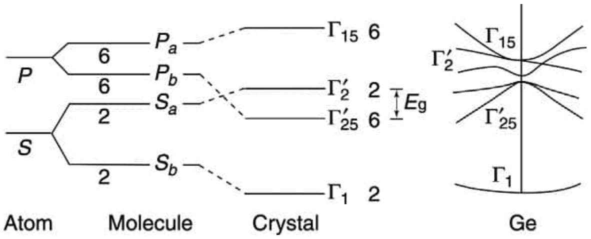

Fig. 2 Scheme showing how lower lying bonding (b) and higher lying antibonding (a) molecular levels give rise to Bloch states of specific symmetry at the Γ point in Ge.

Table 1 Energy levels in silicon and germanium in eV, from the top of the valence band; the double-group symmetry labels including parity are indicated.

	Si	*Ge*
$\Gamma_6{}^+$	−11.7	−12.7
$\Gamma_7{}^+$	−0.04	−0.29
$\Gamma_8{}^+$	0.00	0.00
$\Gamma_6{}^-$	+3.09	+3.04
$\Gamma_8{}^-$	+3.13	+3.37
$\Gamma_7{}^-$	+4.32	+0.90
X_5	−8.43	−8.84
X_5	−3.00	−3.36
X_5	+1.30	+1.12
$L_6{}^-$	−10.4	−10.7
$L_6{}^+$	−7.01	−7.63
$L_6{}^-$	−1.20	−1.37
$L_{4.5}{}^-$	−1.16	−1.12
$L_6{}^+$	+2.47	+0.74

From empirical tight-binding calculations, courtesy of Dr. J.-M. Jancu.

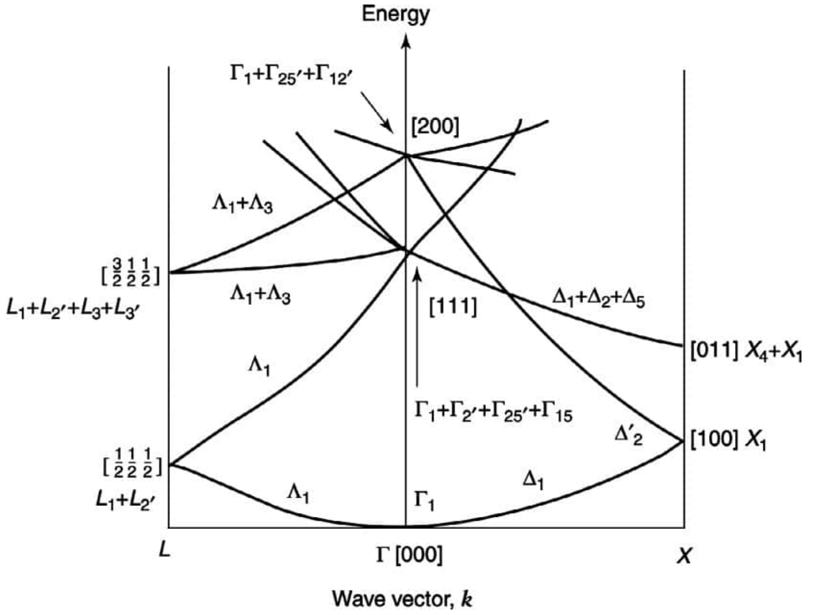

Fig. 3 Empty lattice band structure for a diamond-like crystal.

The plane-wave based methods take an opposite point of view and start considering the electronic states in the presence of a very small crystal potential: in such "empty lattice" the zeroth order eigenfunctions of nearly free electrons are just plane waves folded back in the BZ according to the translational symmetry as sketched in Fig. 3. For instance, looking again at the Γ point, the lowest energy level corresponds to a plane wave with a vanishing wave vector (Γ_1 state in the cubic crystal), while the next higher level includes the eight plane waves having a wave vector of the form $\vec{q} = (2\pi/a)(\pm 1, \pm 1, \pm 1)$, which differ from zero by one of the shortest non zero reciprocal lattice vectors. When the crystal potential is turned on, these 8 states (16 including spin) split into several levels according to the cubic symmetry as indicated. However, the actual crystal potential is not small at all; the most important plane-wave based method developed to circumvent this problem is the pseudopotential approach. In a crystal, the valence (or conduction) band wavefunctions are rapidly varying near each atomic site as they are orthogonal to those of the core states; therefore, their expansions in plane-waves are very slowly convergent. It is possible, though, to substitute them with pseudowavefunctions which are smooth (nodeless) near the atomic sites while replacing the ionic potential with a much smaller pseudopotential, in such a way that the energies $E_n(\vec{k})$ of valence and conduction band states can be computed using a limited number of plane-waves; furthermore, from the pseudowavefunctions, the electronic charge density outside the cores can also be obtained. The pseudopotential (or rather its first few Fourier components) can be empirically chosen to reproduce a set of significant data (mostly optical transition energies and effective masses). For instance, empirical calculations using only three Fourier components of the pseudopotential can already give a reasonable description of the lowest energy bands of elemental semiconductors. A significant improvement is obtained using energy dependent nonlocal pseudopotentials.

For state of the art *ab-initio* selfconsistent calculations, made possible by the great increase of computational capabilities, the pseudopotential method has also been very successful in conjunction with density functional theory in the local density approximation (LDA), i.e., using an exchange-correlation potential dependent only on the local electronic charge density. Such local density approximation is not quite satisfactory; in particular, the energy gaps of semiconductors are usually significantly underestimated (even though the shapes of both valence and conduction bands are well described). This shortcoming can be mended by going beyond the one-electron approximation and calculating quasi-particle selfenergies including (approximately) many-body effects, or adopting a time dependent version of density functional theory.

Band structures of Si, Ge and α-tin

The band structures of group IV elemental semiconductors show pronounced similarities and definite chemical trends. Strong analogies are expected in view of the identical configuration of the outermost electronic shell and of the identical crystalline symmetry. At the same time, going from Si to α-Sn, decreasing energy gaps accompany larger lattice constants due to the increasing size of the atomic cores.

The band structure of Si, qualitatively similar to that of diamond, is shown in Fig. 4 (Chelikowsky and Cohen, 1976) neglecting relativistic effects. The top of the valence band is at the Γ point and correspond to the $\Gamma_{25}{}'$ level (three times degenerate, spin excluded). The bottom of the conduction band is along the Δ line from the Γ to the X point at $\vec{k} \simeq (2\pi/a)(0.85, 0, 0)$ and has Δ_1 symmetry (non degenerate, spin excluded). Thus, the conduction electrons have six pockets centered at the six equivalent conduction band minima (multivalley structure); they are ellipsoids of revolution elongated along the $<100>$ directions with a

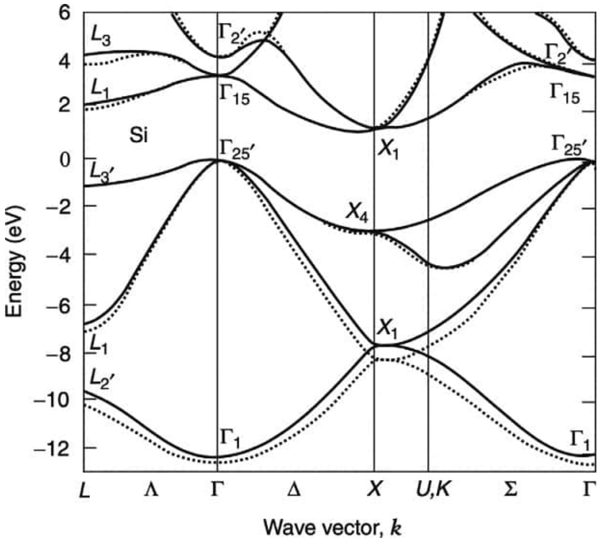

Fig. 4 Band structure of silicon from an empirical nonlocal (full line) or local (dotted line) pseudopotential calculation. From Chelikowsky JR and Cohen ML (1976). *Physical Review B* **14**: 556.

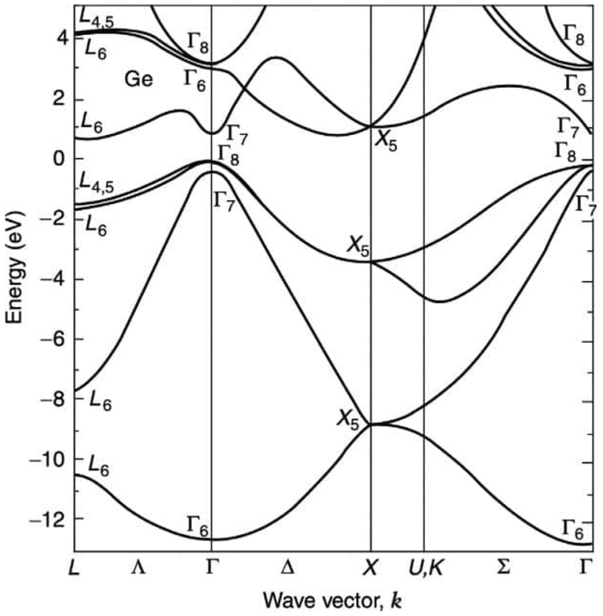

Fig. 5 Band structure of germanium from an empirical nonlocal pseudopotential calculation. From Chelikowsky JR and Cohen ML (1976). *Physical Review B* **14**: 556.

longitudinal mass $m_L \simeq 1.0\ m$ and a transverse mass $m_T \simeq 0.2\ m$, as measured from cyclotron resonance. A peculiarity of the band structure of silicon, showing up in its optical spectrum around 3.4 eV as discussed below, is the fact that along the Λ line from the Γ to the L point the higher valence band (of symmetry Λ_3) and the lowest conduction band (of symmetry Λ_1) are very nearly parallel.

The band structure of Ge is shown in Fig. 5 (Chelikowsky and Cohen, 1976) including the spin-orbit coupling interaction. This is a relativistic effect which, similarly to the atomic case, can reduce the degeneracy of the levels. For instance, without spin-orbit coupling, the top of the valence band would be, just as in Si, a p-bonding-like Γ_{25}'. In the presence of spin-orbit coupling, the sixfold degenerate states obtained from the Γ_{25}' ones by the inclusion of spin are split into a fourfold degenerate Γ_8^+ level and a twofold degenerate Γ_7^+ level, which play the role, respectively, of $J = 3/2$ and $J = 1/2$ total angular momentum states. The corresponding spin-orbit gap is $\Delta = 0.3$ eV (the corresponding value for Si is only 0.04 eV). Besides spin-orbit splitting, other relativistic effects become more important in the heavier Ge than in Si; in particular, there are corrections affecting primarily s-derived states which lower their energy. These effects and the presence in the core of Ge of *d* electrons that, together with *p* electrons, contribute to push to higher energies the Γ_{15} states (corresponding to the Γ_8^- and Γ_6^- spin-orbit split states), through orthogonalization to the core states, explain why in Ge the s-derived Γ_2' level (i.e., the Γ_7^- state, spin included) is lower than the Γ_{15} states. The interchange of the conduction band energy level sequence at the Γ point with respect to Si is accompanied by the fact that the minimum of the conduction band in Ge occurs at the L point at the BZ border (the L_6^+ level). The conduction band of Ge therefore leads to a multivalley structure with four electron pockets (half pocket for each of the eight L points at the BZ border); they are ellipsoids of revolution elongated along the $<111>$ directions. The values of the longitudinal mass $m_L \simeq 1.6\ m$ and of the transverse mass $m_T \simeq 0.08\ m$ have been determined from cyclotron resonance measurements.

The top of the valence band in both Si and Ge is at the center of the BZ: Γ_{25}' without spin, Γ_8^+ and Γ_7^+ including spin, as discussed above. The Γ_7^+split-off hole states can be described as a simple band with an effective mass $m_{so} \simeq 0.25\ m$ in Si and $m_{so} \simeq 0.08\ m$ in Ge. In a rough approximation, the Γ_8^+ hole states can be described as belonging to two distinct spherical pockets each characterized by an isotropic mass: the heavy hole pocket (with mass $m_{hh} \simeq 0.5\ m$ for Si and $m_{hh} \simeq 0.3\ m$ for Ge) and the light hole pocket (with mass $m_{lh} \simeq 0.16\ m$ for Si and $m_{lh} \simeq 0.044\ m$ for Ge). Also these hole effective masses have been determined from cyclotron resonance measurements in low magnetic fields (classical regime). However, this simple picture is not quite correct: because of the valence band degeneracy, the hole bands are not isotropic, but "warped" (particularly, the heavy hole ones). A complete description of the hole states can be given using the multi-band effective mass approach, in which the valence band degeneracy is fully accounted for.

The tendency to have a lower energy s-derived Γ_7^- level is even stronger in gray tin where this level is positioned between the spin-orbit split Γ_8^+ and Γ_7^+ levels ("inverted gap" configuration). As a consequence, the band structure of α-Sn, shown in Fig. 6 (Chelikowsky and Cohen, 1976), is characterized by the fact that the fourfold degenerate (spin included) Γ_8^+ states correspond at the same time to the topmost filled valence band and to the lowest empty conduction band which touch each other at the Γ point. Grey tin is thus a "zero-gap semiconductor" rather than a semiconductor proper.

Comparison with experimental data

Just as for atoms and molecules, even for solids the most direct and informative experimental techniques to study their electronic structure over a wide range of energies are optical spectroscopy and photoelectron spectroscopy.

In crystalline semiconductors such as Si and Ge the absorption due to direct interband transitions is very strong and reflectivity measurements are more popular than transmission ones. From reflectivity spectra taken over a large frequency range it is possible to obtain the real and imaginary part of the complex dielectric function $\varepsilon = \varepsilon_1 + i\varepsilon_2$ (via Kramers-Kronig analysis) and, thus, all the linear optical properties. From the theoretical point of view, the imaginary part $\varepsilon_2(\omega)$ can be calculated summing over all possible transitions between filled (valence) states and empty (conduction) states corresponding to the absorption of a photon of frequency ω. As the wavelength of light is much larger than the lattice constant, such optical transitions take place between electronic states having the same wavector within the first Brillouin zone (direct or "vertical" transitions) and differing in energy by $\hbar\omega$, thus:

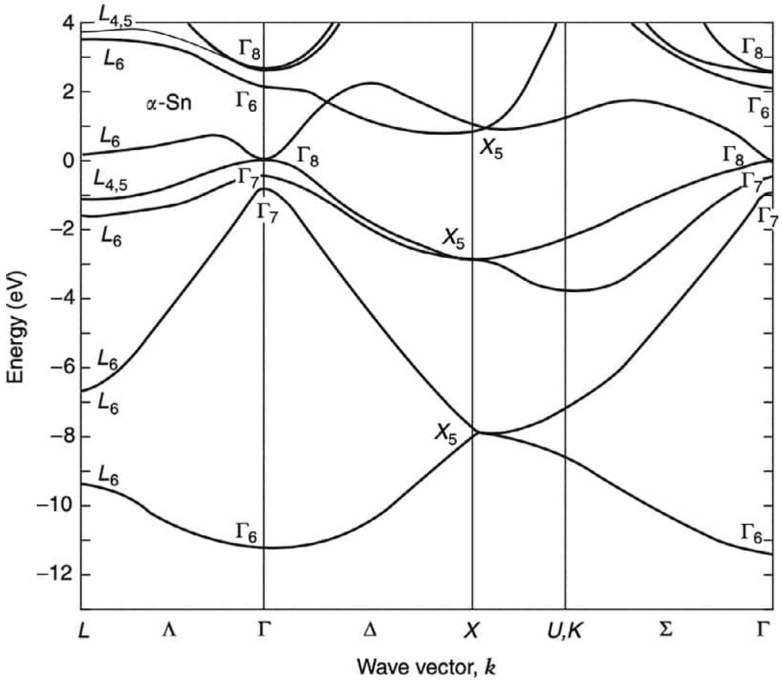

Fig. 6 Band structure of α-Sn from an empirical nonlocal pseudo-potential calculation. From Chelikowsky JR and Cohen ML (1976). *Physical Review B* **14**: 556.

$$\varepsilon_2(\omega) = \frac{1}{\pi}\sum_{v,c}\int_{BZ} d^3k|d_{cv}|^2\,\delta\left(E_c\left(\vec{k}\right) - E_v\left(\vec{k}\right) - \hbar\omega\right);$$

where d_{cv} is the transition electric dipole matrix element between the initial and final state. It is to be noticed that, because of the energy conserving delta function in the equation above, specific singularities in the frequency dependence of ε_2 are obtained when $\vec{\nabla}_k\left(E_c\left(\vec{k}\right) - \mathrm{E}_v\left(\vec{k}\right)\right) = 0$ (critical points). Such structures (many of which are dictated by symmetry alone) have been found in all elemental semiconductors, and this has allowed the identification of the critical point transition peaks and the verification of the band structure.

As a classical and pioneering example, we report in Fig. 7 (Brust et al., 1962) the optical excitation spectrum of Ge, measured as explained above and computed from the equation above on the basis of an empirical pseudopotential band structure calculation. We stress that not only have the critical points been identified, but also the full band structure has been put to test by the described analysis of the optical properties. A better resolution of the critical point behavior can be obtained by employing various kinds of modulation spectroscopy (e.g., piezoreectance, electroreectance) that amounts to measure the first (or higher) derivatives of the dielectric function. As a further example, we consider a recent calculation of the optical absorption of Si shown in Fig. 8 (Onida et al., 2002) in comparison with experimental data. The time dependent density functional theory includes electron-hole correlations (i.e., excitonic effects) which are crucial to reproduce the conspicuous peak at about 3.4 eV associated with interband transitions near the L point.

The direct optical transitions discussed so far are usually dominant when allowed by energy conservation. It is however possible, through the absorption or emission of a phonon, to have indirect transitions in which the wavector of the initial and final electronic states are different. These transitions are much weaker, but in the case of indirect gap semiconductors such as Si and Ge having the top of the valence band and the bottom of the conduction band at different points in the BZ they give rise to absorption at energies below the onset of the much stronger direct transitions. The corresponding (temperature dependent) characteristic features have been also observed and compared with theory providing additional evidence for the band structure determination.

Photoelectron spectroscopy has also proved to be a very useful experimental technique to measure the electronic structure of semiconductors. The photoemission process takes place through the following steps: first upon absorption of an incoming photon an electron is excited from a filled band to a higher empty band, then the excited electron travels toward the surface and, finally, if energetic enough, it escapes into the vacuum to be detected. Thus, low energy conduction states below the vacuum level are not involved in photoemission processes as they can be neither initial states (because empty in the ground state) nor final states (because unable to escape from the solid once excited). These levels can be investigated by inverse photoemission which is, in a sense, the time reversed process of photoemission: an incoming electron falls in an electronic level available in the solid emitting a photon which is then detected. In photoelectron spectroscopy, the energy, wavevector and polarization (spin) of the photon

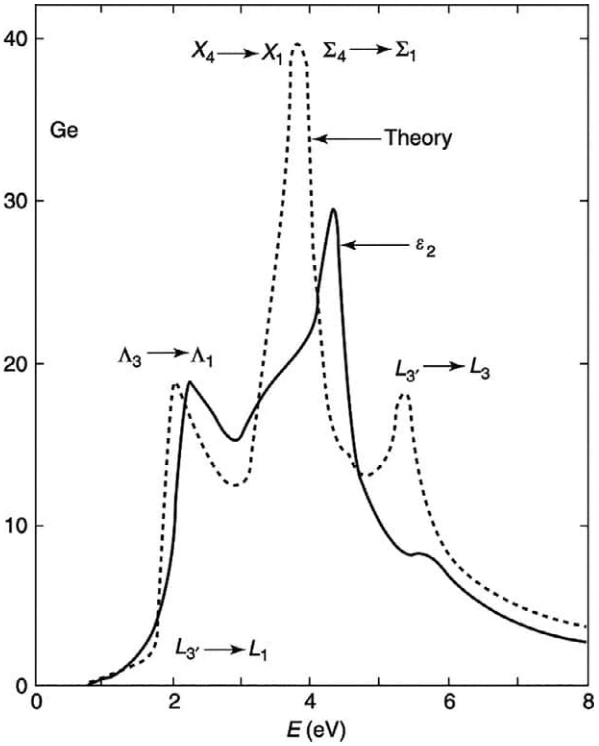

Fig. 7 Imaginary part of the dielectric function of Ge: the solid line is experimental, the dashed one theoretical; optical transitions at critical points are identified. From Brust, D., Phillips, J.C., Bassani, F., Physical Review Letters 9, 94 (1962).

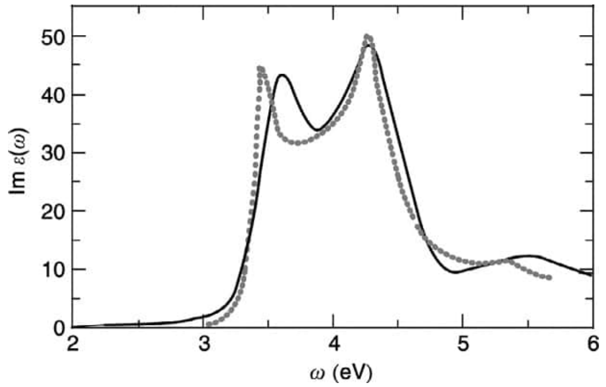

Fig. 8 Imaginary part of the dielectric function of Si: the dots are experimental data, the solid line theory. From Onida G, Reining L, and Rubio A (2002). *Reviews of Modern Physics* **74**: 601.

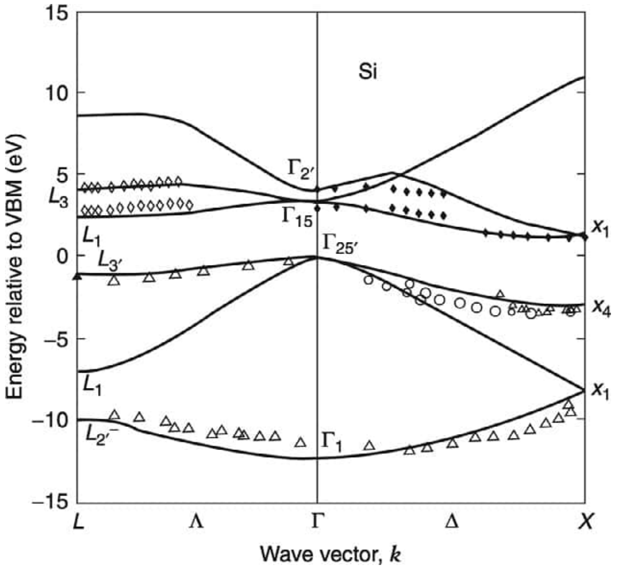

Fig. 9 Conduction and valence band dispersions of Si from angle resolved photoemission and inverse photoemission. From Ortega JE and Himpsel FJ (1993). *Physical Review B* **47**: 2130.

(electron) can be selectively chosen or averaged over. The main advantage of photoemission and inverse photoemission with respect to optical spectroscopy is the capability of providing absolute energy levels rather than energy differences between levels. Besides lower resolution and (especially for inverse photoemission) lower statistics, the main disadvantage for the study of bulk properties is that photoelectron spectroscopy is much more surface sensitive because of the short escape or penetration depths of electrons (of the order of 10 Å).

The detailed analysis of angle resolved (inverse) photoemission data allows to obtain the complete band structure of a semiconductor. In Figs. 9 and 10 (Ortega and Himpsel, 1993), the energy bands of Si and Ge obtained by first principle quasi-particle calculations are compared with photoemission and inverse photoemission data showing very good agreement.

Direct gap elemental semiconductors

While the role of Si as the semiconductor of choice for all electronics applications cannot be disputed, its indirect gap hampers its potential use in light-emitting devices. Among elemental semiconductors, phosphorous (P, from group V) has an allotropic form with a direct gap, known as black phosphorous (bP), which is a layered orthorhombic crystal. As shown in Fig. 11, its direct gap of 0.3 eV opens at the Z point of its Brillouin zone, i.e., at the zone edge along the (001) direction, and the optical transition between the corresponding valence (Z_2^+) and conduction (Z_4^-) states is allowed, albeit polarization dependent (Qiao et al., 2014). Recently, bP has also attracted much interest (Carvalho et al., 2016) as it can be exfoliated into a monolayer (i.e., phosphorene).

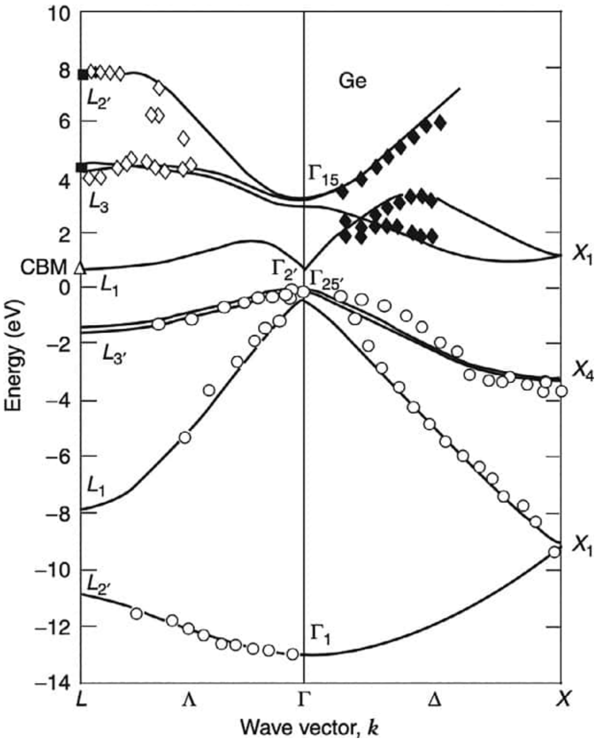

Fig. 10 Conduction and valence band dispersions of Ge from angle resolved photoemission and inverse photoemission. From Ortega JE and Himpsel FJ (1993). *Physical Review B* **47**: 2130.

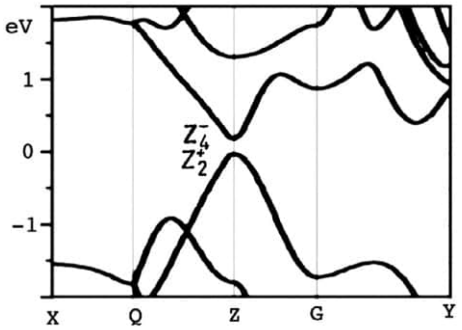

Fig. 11 Band structure of black phosphorous. From calculations reported in Qiao J, Kong X, Hu Z-X, Feng Y and Ji W (2014). *Nature Communications* **5**: 4475.

For optoelectronic applications, including lasing, it would be of paramount importance to integrate a direct gap semiconducting material on silicon chips. This long standing goal has been pursued employing, e.g., III–V semiconductors, SiGe alloys and also porous silicon (Zhou et al., 2015). Considering bulk elemental semiconductors, a promising candidate is hexagonal germanium (2H-Ge) that, differently from the common cubic crystal (c-Ge), has a direct band gap of 0.3 eV at the Γ point as shown in Fig. 12, with an allowed optical transition $\Gamma_{9v}^{+} \rightarrow \Gamma_{8c}^{-}$. With respect to the band structure of c-Ge, this can be seen as the effect of folding the conduction band minimum from the L point to the Γ point. Most importantly, Si can be alloyed into 2H-Ge to form 2H-$\text{Si}_y\,\text{Ge}_{(1-y)}$ which for $y < 0.35$ maintains a direct gap tunable within the energy 0.3–0.7 eV (Fadaly et al., 2020).

Conclusion

All the main features of the band structure of elemental semiconductors are firmly established both from the theoretical and the experimental point of view. An overview of the field has been presented with illustrative examples taken from the main semiconductor families. These results represent one of the most important achievements in solid state physics and provide a framework within which not only virtually all material properties can be understood, but also novel materials can be designed (Giannozzi et al., 2009).

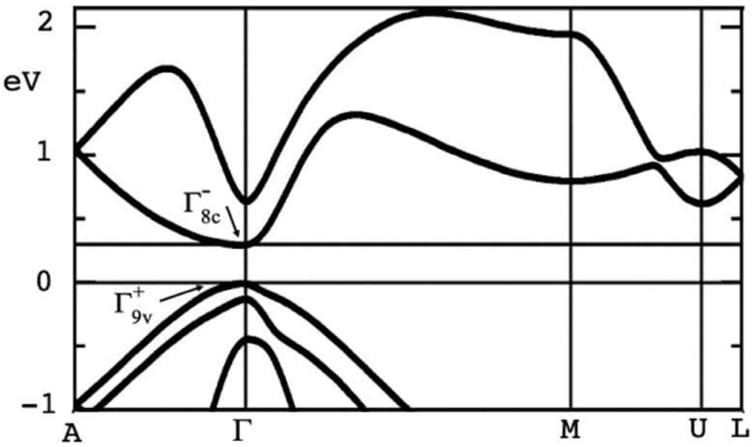

Fig. 12 Band structure of hexagonal germanium. From calculations reported in Fadaly EMT, Dijkstra A, Suckert, JR, Ziss D, van Tilburg MAJ, Mao C, Ren Y, van Lange VT, Korzun K, Kolling S, Verheijen MA, Busse D, Rodl C, Furthmuller J, Bechstedt F, Stangl J, Finley JJ, Botti S, Haverkort JEM, Bakkers EPAM (2020). *Nature* **580**: 205.

References

Bassani F and Pastori Parravicini G (1975) *Electronic States and Optical Transitions in Solids*. Oxford: Pergamon Press.
Brust D, Phillips JC, and Bassani F (1962) *Physical Review Letters* 9: 94.
Carvalho A, Wang M, Zhu X, Rodin AS, Su H, and Castro Neto AH (2016) *Nature Reviews Materials* 1: 16061.
Chelikowsky JR and Cohen ML (1976) *Physical Review B* 14: 556.
Cohen ML and Chelikowsky JR (1988) *Electronic Structure and Optical Properties of Semiconductors*. Berlin: Springer-Verlag.
Fadaly EMT, Dijkstra A, Suckert JR, Ziss D, van Tilburg MAJ, Mao C, Ren Y, van Lange VT, Korzun K, Kolling S, Verheijen MA, Busse D, Rodl C, Furthmuller J, Bechstedt F, Stangl J, Finley JJ, Botti S, Haverkort JEM, and Bakkers EPAM (2020) *Nature* 580: 205.
Giannozzi P, et al. (2009) *Journal of Physics: Condensed Matter* 21: 395502.
Jancu J-M, Scholz R, Beltram F, and Bassani F (1998) *Physical Review B* 57: 6493.
Onida G, Reining L, and Rubio A (2002) *Reviews of Modern Physics* 74: 601.
Ortega JE and Himpsel FJ (1993) *Physical Review B* 47: 2130.
Qiao J, Kong X, Hu Z-X, Feng Y, and Ji W (2014) *Nature Communications* 5: 4475.
Yu PY and Cardona M (1995) *Fundamentals of Semiconductors*. Berlin: Springer-Verlag.
Zhou Z, Yin B, and Michel J (2015) *Light Science and Applications* 4: e358.

Semiconductors: Isotope effects in solids

Joel W Ager III[a,b], [a]Materials Sciences Division, Lawrence Berkeley National Laboratory, Berkeley, CA, United States; [b]Materials Science and Engineering Department, University of California Berkeley, Berkeley, CA, United States

© 2024 Elsevier Ltd. All rights reserved.

This is an update of E.E. Haller, J.W. Ager, Isotopic Effects in Solids, Editor(s): Franco Bassani, Gerald L. Liedl, Peter Wyder, Encyclopedia of Condensed Matter Physics, Elsevier, 2005, Pages 43–52, ISBN 9780123694010, https://doi.org/10.1016/B0-12-369401-9/01140-2.

Introduction **485**
Atomic mass-related properties **485**
Structure 485
Phonon dispersion 486
Thermal conductivity 488
Electronic structure 489
Self- and dopant diffusion 490
Local vibrational modes 492
Spin-related properties **493**
Neutron transmutation doping **494**
Conclusion **495**
References **495**

Abstract

Most semiconductors contain elements which have more than one stable isotope. The ability to manipulate the isotopic composition of semiconductors has made study of isotope effects possible. Phonon scattering and thermal conductivity are affected significantly by isotope disorder scattering, whereas there is a smaller, but measurable effect on bandgap. Use of isotope superlattices have enabled fundamental studies of solid-state diffusion. Spin coherence times are significantly lengthened in isotopically enriched material, which has significance for experimental realization of quantum computing concepts. Neutron transmutation enables precise and uniform control of doping in selected cases.

Key points

- Isotope effects due to atomic mass differences
- Isotope effects due to nuclear spin differences
- Isotope effects due to differences in thermal neutron capture cross sections.

Introduction

Close to 80% of the elements in the periodic table are multi-isotopic. Most semiconductors contain at least one element that consists of more than one stable isotope with Al, As, and P being important mono-isotopic exceptions (Berglund and Wieser, 2011). For example, silicon is composed of the three isotopes $^{28}_{14}$Si, $^{29}_{14}$Si, $^{29}_{14}$Si with abundances of 92.23%, 4.67% and 3.10%, respectively. Gallium arsenide consists of mono-isotopic As and two Ga isotopes $^{69}_{31}$Ga (60.11%) and $^{70}_{31}$Ga (39.89%). Recent advances in isotope separation technology have led to the availability of semiconductors with controlled isotopic composition (Cardona and Thewalt, 2005). Very high levels of enrichment, >99.985%, have been achieved for ^{28}Si in the context of efforts to more precisely define Avogadro's constant (Becker et al., 2010).

Many physical properties of semiconductors depend on isotopic composition. Some of these are affected relatively weakly while others, thermal conductivity for example, can be influenced strongly. Here, we divide the isotope related effects into three groups: (1) those that are due to atomic mass differences between the isotopes; (2) those that are due to nuclear spin differences between isotopes; and (3) those that are due to differences in thermal neutron capture cross sections.

Atomic mass-related properties

Structure

The lattice constants of large, chemically pure and crystallographically highly perfect crystals can be measured with high precision x-ray diffraction techniques. As a consequence of zero-point motion atomic volumes are expected to change with isotopic composition. The resulting effect on the lattice constant a_0 has been carefully studied for a number of elemental semiconductors including C, Si, and Ge which have the diamond structure. A theoretical analysis of the dependence of the lattice constant on isotopic composition at temperatures low compared to the Debye temperature of the material yields the following relationship (London, 1958):

$$\frac{\Delta a}{a} = -\frac{C}{a^3}\frac{\Delta M}{M}\left(\gamma_0\hbar\omega_0 + \frac{3}{4}\gamma_0 k_B\theta\right)$$

where C is the isothermal compressibility, M is the atomic mass, γ_o and γ_a are the Grüneisen parameters for optical and acoustic phonons, respectively, ω_o is the optical phonon frequency, k_B is Boltzmann's constant, and θ is the Debye temperature (constant mode Grüneisen parameters and a Debye frequency spectrum for the phonon modes are assumed). Evidently, the effect will be the largest for semiconductors with light atomic masses, large compressibilities, and high Debye temperatures. For context, the Debye temperatures of C, Si, and Ge are 2250 K, 645 K, and 374 K, respectively. Experimental data for diamond are shown in Fig. 1 (Holloway et al., 1991). The reduction of the lattice constant for ^{13}C diamond compared to ^{12}C diamond is 150 ppm, which is in qualitative agreement with the simple theory illustrated above. A more recent analysis uses first principles calculations to predict the temperature dependence of Δa_0 for C, Si, and Ge (Pavone and Baroni, 1994).

Phonon dispersion

A number of isotope effects in semiconductors are related to changes in the properties of phonons with atomic mass. A very simple harmonic analysis within the virtual crystal approximation predicts that the frequency ω of a given phonon should vary with the inverse square of the average mass M:

$$\omega \propto M^{-1/2}$$

As shown in Fig. 2 (Fuchs et al., 1992), this dependence is indeed observed for the zone-center optical phonon for a series of isotopically enriched single crystals of germanium with average masses between 70 and 76 amu (M of natural Ge is 72.59 amu).

Modern thin-film growth techniques have made isotopically engineered structures available to the experimentalist. Very interesting phonon effects can be observed in isotope superlattices (SLs), which consist of alternating layers with different isotopic composition. In contrast to SLs consisting of different materials such as GaAs and AlGaAs, the electronic band structure in isotope SLs is not significantly affected by the mass differences and the material looks bulk-like for electrons throughout the crystal layers. However, the changes in the phonon properties are sufficiently large to observe confinement effects.

A number of detailed experimental studies have been performed with Ge isotopes in structures consisting of a series of alternating sets of atomic planes of ^{A}Ge and ^{B}Ge where A and B are different atomic masses (Spitzer et al., 1994). Experimentally observed and theoretically calculated Raman spectra are compared in Fig. 3 for zone-center optical phonons for $^{70}\text{Ge}_n/^{74}\text{Ge}_n$ [001] oriented structures with n, the number of atomic layers, varying from 2 to 32. The Raman frequencies and mode mixing calculated by a simple bond-charge model and the force constants of natural Ge and the relative peak intensities determined by a bond polarizability approach are in good agreement with the experimental data. The shortest periods studied consisted of two atomic layers each and produce a single Raman line corresponding to the zone center optical phonon in a Ge crystal with $M = 72$ amu, the linear average of the two masses. That is, the phonon behavior is the same as in a bulk crystal with $M = 72$ amu. Confinement effects are observed at higher values of n as folded optical modes become Raman-active at the zone center. For example, in the

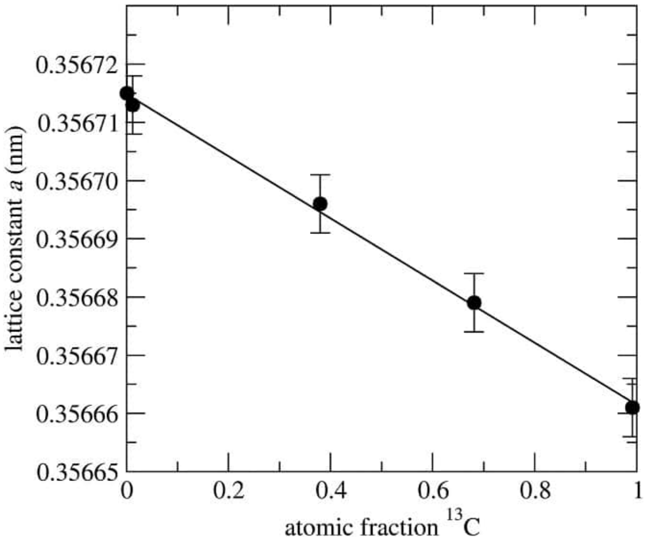

Fig. 1 Lattice constant of diamond as a function of isotopic composition at 25C; the lattice constant decreases with increasing atomic mass. Adapted from Holloway H et al. (1991) Isotopic dependence of the lattice constant of diamond. *Physical Review B*, 44(13): 7123–7126, https://doi.org/10.1103/PhysRevB.44.7123.

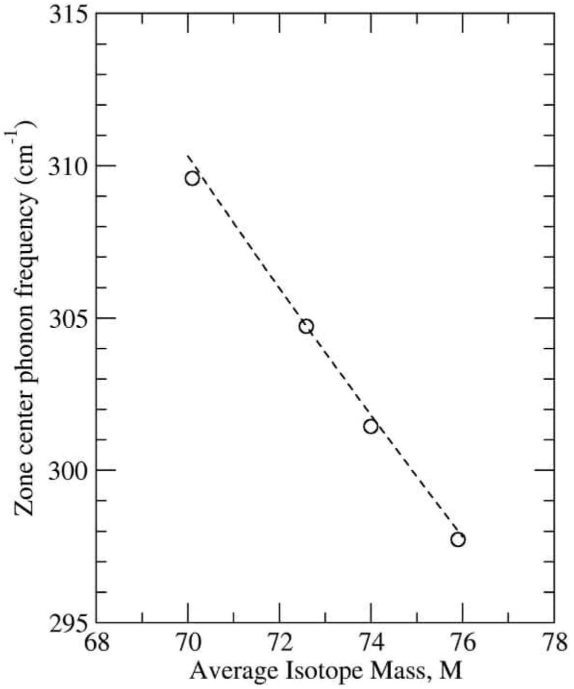

Fig. 2 Zone center phonon observed by Raman spectroscopy at 90 K for single crystal germanium of varying isotopic composition. Dotted line shows the predicted $M^{-1/2}$ dependence. Adapted from Fuchs HD et al. (1992) Isotopic disorder-effects on the phonons in germanium. *Solid State Communications* 82(4): 225–228, https://doi.org/10.1016/0038-1098(92)90631-I.

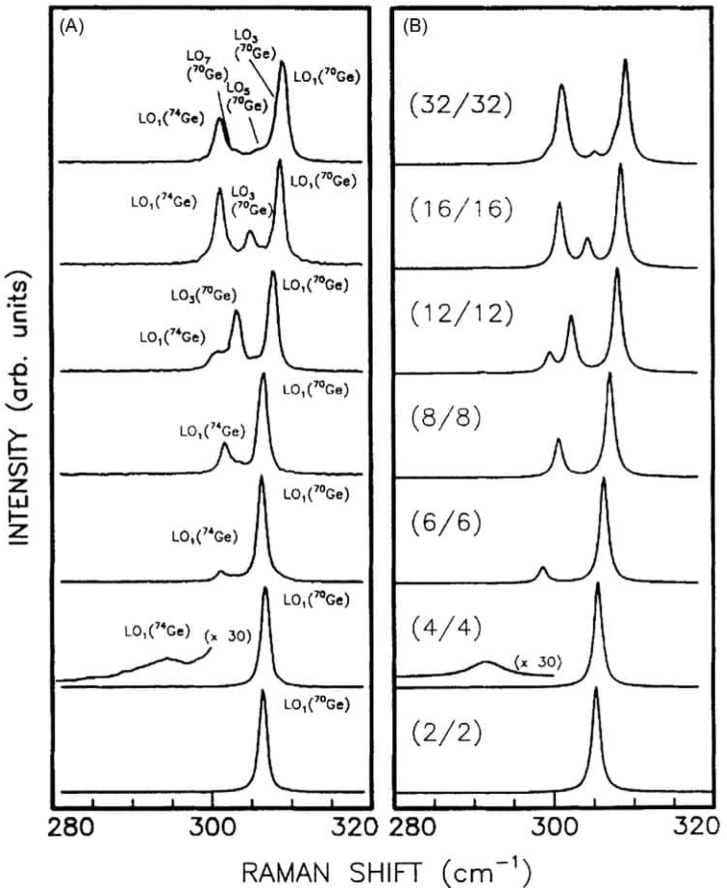

Fig. 3 (A) Measured at $T = 10$ K and (B) calculated Raman spectra for a series of isotope superlattices $^{70}Ge_n/^{74}Ge_n$ grown along [001] with $n = 2, 4, 6, 8, 12, 16$, and 32. A number of modes confined to the ^{70}Ge and ^{74}Ge layers are evident. When there are only two ^{70}Ge and ^{74}Ge layers a single mode is observed. Adapted with permission from Spitzer J et al. (1994) Raman scattering by optical phonons in isotopic 7070 (Ge)n-74(Ge)n superlattices, *Physical Review Letters* 72(10): 1565–1568, https://doi.org/10.1103/PhysRevLett.72.1565.

$n = 12$ superlattice at least three strong Raman lines are observed. For $n = 32$ the Raman spectra begin to approach the structure expected for two isotopically pure bulk crystals, one made up of ^{70}Ge, the other of ^{74}Ge.

Thermal conductivity

The most dramatic phonon-related isotope effect is found for the thermal conductivity. Pomeranchuck was the first to point out in 1942 that in a multi-isotopic material, minority isotopes must be treated as mass defects and that they will lead to scattering of acoustic phonons, reducing thermal conductivity with respect to a mono-isotopic material (Pomeranchuk, 1942). The first experimental measurements of what can be a very strong dependence of the thermal conductivity (which depends on acoustic phonons) on small degrees of isotopic disorder were performed in the late 1950s in germanium (Geballe and Hull, 1958). The most dramatic effect is found, however, in diamond. Fig. 4 illustrates the 5 fold increase in thermal conductivity found near 100 K in isotopically enriched ^{12}C (Wei et al., 1993). The measured value, 410 W cm^{-1} K^{-1}, is the highest measured for any material above liquid nitrogen temperature (77 K).

The most successful modeling of the effect of isotopic disorder on thermal conductivity splits the thermal conductivity into four terms – normal, Umklapp, boundary, and isotope processes – which are inversely proportional to the phonon lifetime τ associated with the specific effect:

$$\begin{aligned}
\tau_{\text{Normal}}^{-1} &= AvT^{3}\lambda^{-1}\\
\tau_{\text{Umklapp}}^{-1} &= BvT^{3}\lambda^{-1}\exp(-C/T)\\
\tau_{\text{Boundary}}^{-1} &= v/D\\
\tau_{\text{Isotope}}^{-1} &= 4\pi^{3}v\lambda^{-4}V_{0}x(1-x)(12+x)^{-2}
\end{aligned}$$

where v and λ are the average phonon velocity and wavelength, x is the isotope fraction of ^{13}C, V_0 is the atomic volume, and A, B, C, and D are adjustable parameters. These relations not only can be used to reproduce the observed temperature dependence but can also predict the limits of thermal conductivity for samples with very high isotopic purity. Using this method, the inset in Fig. 4 shows the prediction of a thermal conductivity above 2000 W cm^{-1} K^{-1} for very highly enriched ^{12}C at 80 K.

Similar increases of the thermal conductivity at low temperature of the enriched semiconductors Ge and Si have been measured (Asen-Palmer et al., 1997; Inyushkin et al., 2018). Extremely highly enriched Si (99.995% of ^{28}Si) has a thermal conductivity of 450 ± 10 W cm^{-1} K^{-1} at 24 K, which is the highest measured value for any bulk dielectric and is 10 times greater than that for Si with natural isotopic composition.

It is important to note that at temperatures well above the thermal conductivity maximum, the isotope-enrichment-related increases decline rapidly. For example, the increase in thermal conductivity at 300 K for highly enriched ^{28}Si compared to natural Si

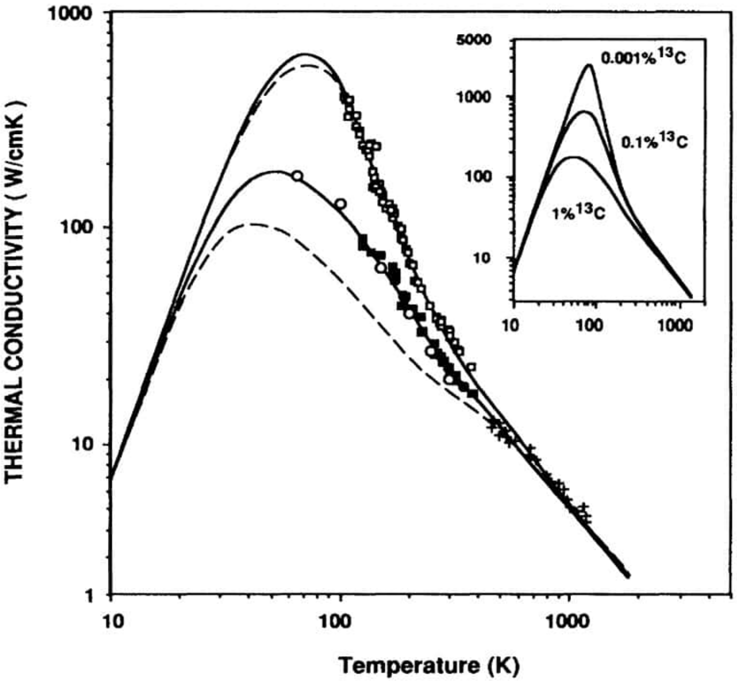

Fig. 4 Thermal conductivity of natural abundance (1.1% ^{13}C) diamond (lower squares), isotopically enriched (0.1% ^{13}C) diamond (upper squares), together with the low temperature data of (Slack, 1973), (circles) and the high temperature data (Olson et al., 1993) (crosses). The solid curves are the result of fitting the Callaway theory described in the text. The inset shows the calculated thermal conductivity corresponding to 1%, 0.1%, and 0.001% ^{13}C concentrations according to the Callaway theory. Adapted with permission from Wei L et al. (1993) Thermal conductivity of isotopically modified single crystal diamond. *Physical Review Letters* 70(24): 3764–3767, https://doi.org/10.1103/PhysRevLett.70.3764.

is in the range of 10–15%. Increases in thermal conductivity have also been reported for compound semiconductors. SiC enriched to >99.5% in ^{28}Si and ^{12}C has an 18% higher thermal conductivity compared to natural abundance material (Lundqvist et al., 2013).

Varying the isotopic composition of a semiconductor allows for control of the thermal conductivity independent of its electrical conductivity, which is relevant to applications such as thermoelectrics (Bracht et al., 2014). Isotope heterostructures are also a convenient platform for experimental investigations. Additionally, boundary scattering reduces thermal conductivity at small spatial dimensions: the thermal conductivity of 50 nm Si nanowires is 100× smaller than bulk Si at room temperature (Hochbaum et al., 2008). Interestingly, isotope effects can be very large at the nanoscale: ^{28}Si (99.92% enriched) nanowires have up to 150% higher thermal conductivity compared to natural abundance nanowires with similar diameters and surface morphology (Ci et al., 2022).

Electronic structure

Isotope composition affects the electronic structure through the electron-phonon coupling and through the change of volume with isotopic mass (see above section on lattice constants). The effect most often studied experimentally is the influence of isotopic mass on the band gap of the semiconductor. For example, using optical modulation techniques the isotope dependence of the direct and indirect bandgaps of germanium have been determined. The effect is small but satisfactorily predicted by theory (Davies et al., 1993).

Isotopically enriched Si allows for a careful comparison between theory and experiment. A sensitive way to measure the band gap dependence on M uses the very narrow no-phonon exciton photoluminescence (PL) lines found near the indirect gaps of Si and Ge. Measurements of the energies of these impurity bound excitons allow direct determination of band gap shifts because their radiative recombination does not require phonon participation. Furthermore, due to their large Bohr orbits, their energy depends only on the average isotopic mass and not on the isotopic disorder. Fig. 5A shows the change in the Si indirect bandgap measured using the phosphorus no-phonon line P_{NP} for a series of samples enriched in ^{28}Si, ^{29}Si and ^{30}Si (Karaiskaj et al., 2001).

In general, the contribution to the band gap shift from the isotopically induced volume change is the smaller of the two effects and can be addressed with the methods described above for the lattice constant effects. The analysis of the electron-phonon coupling effect is similar to that used to understand the change of band gap with temperature. The change is described by structure factors, which include electron-phonon interaction terms (Debye-Waller factors) and self-energy terms. These terms are then expanded in powers of the atomic displacements u. The leading terms are proportional to the mean-square displacements $<u^2>$. These, in turn, can be modeled as harmonic oscillators:

$$\langle u^2 \rangle = \hbar\left(\frac{1}{2}+n\right)/M\omega.$$

As temperature increases, n and thus $<u^2>$ increase, and the band gap is reduced. At low temperature, $n = 0$. Substituting the dependence of ω on M, we find

$$\langle u^2 \rangle \propto M^{-\frac{1}{2}}.$$

For increasing M, this analysis predicts decreasing $<u^2>$ and a bandgap increase, in agreement with observation.

For Si, combining photoluminescence and wavelength-modulated transmission spectra of phonon-assisted indirect excitonic transitions have enabled the most precise measurement of its fundamental bandgap. As shown by the measurements of ^{28}Si, ^{29}Si, and ^{30}Si in Fig. 5B, $E_{gx}(M = \infty) = (1213.8 \pm 1.2)$ meV, which is the purely electronic value in the absence of electron-phonon interaction and volume changes associated with anharmonicity (Tsoi et al., 2004). This value corresponds well to the best first

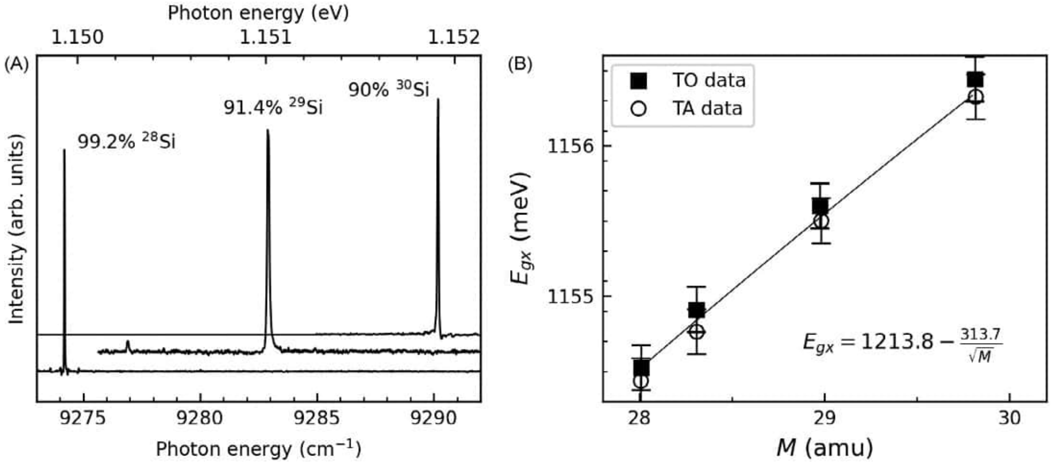

Fig. 5 (A) Effect of Si isotopic composition on the Si bandgap as observed by the shift of the P_{NP} PL line observed at 4 K as a function of isotopic enrichment. The bandgap increases with increasing atomic mass. The three curves are offset for clarity. (B) the excitonic indirect band gap of Si as a function of M. Adapted from Tsoi S et al. (2004) Electron-phonon renormalization of electronic band gaps of semiconductors: Isotopically enriched silicon. *Physical Review B. American Physical Society*, 70(19): 193201, https://doi.org/10.1103/PhysRevB.70.193201.

principles theory based on quasiparticle calculations (Zhu and Louie, 1991). A similar spectroscopic approach was used for the precise measurement of the E_0' and E_1 direct bandgaps of Si (Tsoi et al., 2005).

Self- and dopant diffusion

The study of self- and dopant diffusion in semiconductors has been advanced significantly through the use of isotopically controlled multilayer structures (Shaw, 2017). Diffusion measurements performed with radiotracer methods are limited by the half-lives of radioactive isotopes, by the damage produced during their introduction and by near surface effects. In contrast, the use of Secondary Ion Mass Spectrometry (SIMS) in isotope superlattice structures provides quantitative concentration profiles of the masses of the matrix as well as the dopant atoms.

In the simplest case two layers with different isotopes of a semiconductor are grown on a substrate of natural composition. The results of annealing such a structure are illustrated in Fig. 6 for a ^{nat}Ge/^{74}Ge/^{70}Ge/^{nat}Ge-substrate configuration (Fuchs et al., 1995). The ^{70}Ge concentration profile in the ^{74}Ge layer can be fitted with a simple complimentary error function (the solution to the 1-D

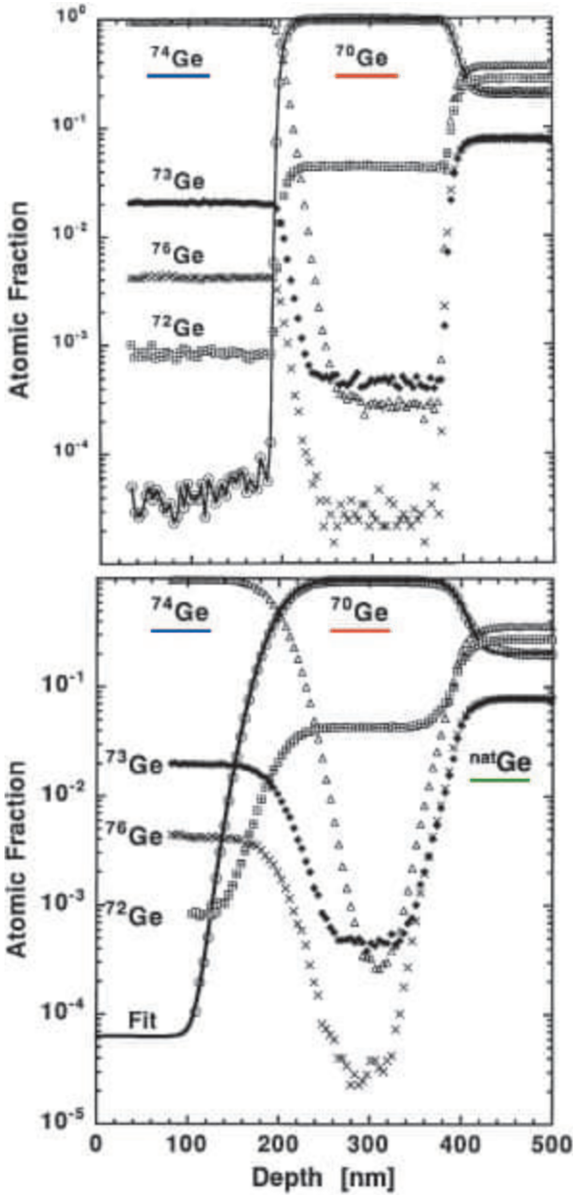

Fig. 6 Secondary Ion Mass Spectrometry (SIMS) profile of a ^{nat}Ge/^{74}Ge/^{70}Ge/^{nat}Ge-substrate structure before (top) and after annealing for 55.55 h at a temperature of 586 °C (bottom). The self-diffusion of the ^{70}Ge into the ^{74}Ge layer can be modeled with a simple complimentary error function to a very high level of precision. Adapted with permission from Fuchs, H. D. et al. (1995) Germanium 70Ge/74Ge isotope heterostructures: An approach to self-diffusion studies. *Physical Review B*, 51(23): 16817–16821, https://doi.org/10.1103/PhysRevB.51.16817.

simple Fick's law diffusion equation) over a range of four and one half orders of magnitude in concentration, yielding very precise self-diffusion data. Similar structures of silicon isotopes have been used to obtain precise measurements of the Si self-diffusion coefficient shown as a function of the absolute inverse temperature in Fig. 7 (Bracht et al., 1998).

The influence of the Fermi level (and hence of specific native defects) on self- and dopant diffusion has been studied with the aid of silicon isotope multilayers capped with an amorphous layer of natural silicon. Ion-implantation into the amorphous layer was used a source of the desired dopant and to affect Fermi level control inside the structure. Such a dopant source has been found to produce only the expected electronic effects that are due to dopant-related shifts in Fermi level position. A representative SIMS result of silicon self- and As dopant diffusion is shown in Fig. 8. The modeling of the silicon isotope and the arsenic concentration profiles yields the unambiguous result that the negatively charged vacancy is the major native defect involved in the diffusion process.

Isotopically controlled compound semiconductor structures offer the possibility of observing self-diffusion of each of the constituent atoms. Using this method, a very spectacular result of self-diffusion has been reported for the III–V semiconductor GaSb (Bracht et al., 2000). Both host elements, Ga and Sb, have two isotopes occurring at comparable concentrations; a double-labeled $^{69}Ga^{121}Sb/^{71}Ga^{123}Sb$ heterostructure was used for the study. Fig. 9 shows the concentration profiles of the four

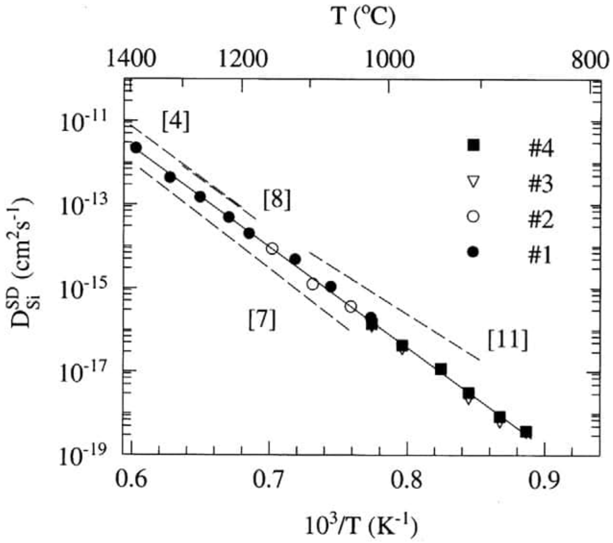

Fig. 7 Self-diffusion coefficient of Si measured using multilayer structures of the stable isotopes. Adapted with permission from Bracht H, Haller EE, and Clark-Phelps R (1998) Silicon self-diffusion in isotope heterostructures. *Physical Review Letters* 81(2): 393–396, https://doi.org/10.1103/PhysRevLett.81.393.

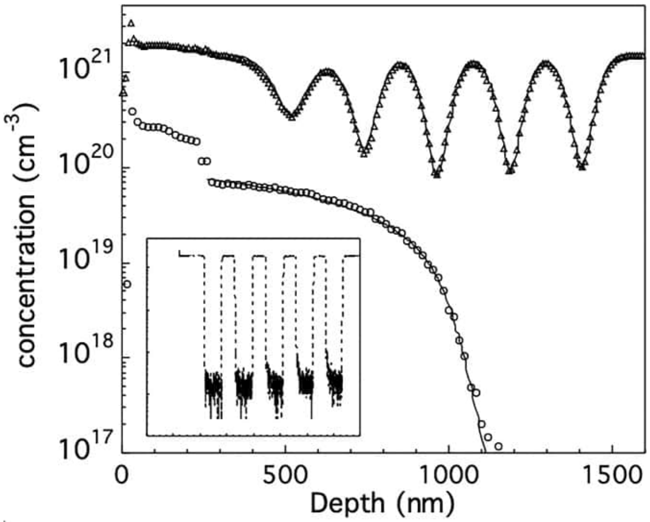

Fig. 8 Depth profiles of ^{30}Si (triangles) and As (circles) in an a-Si/($^{30}Si/^{nat.}Si$)/$^{nat.}Si$ structure with 5 $^{30}Si/^{nat.}Si$ periods, measured with Secondary Ion Mass Spectrometry (SIMS). Consistent modeling of both the dopant, As, and self-diffusion profiles (solid lines) shows that the singly negatively charged self-interstitial is the mediating native defect responsible for the diffusion of both species. Inset figure shows the SIMS depth profile of the as-grown isotope structure, with the same axis limits. Adapted with permission from Silvestri HH, PhD thesis, UC Berkeley 2004, unpublished.

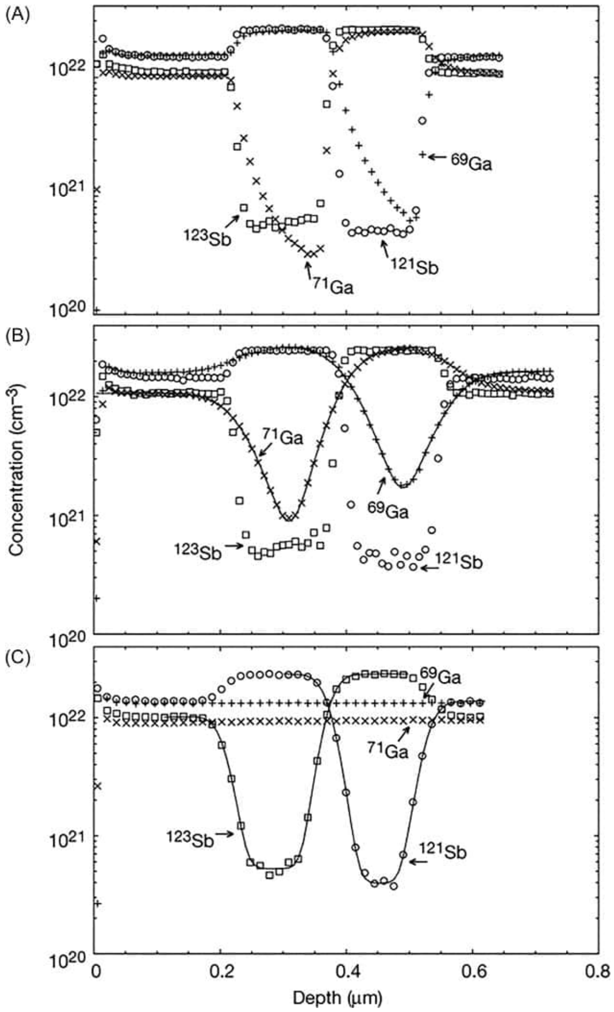

Fig. 9 Concentration–depth profiles of Ga and Sb isotopes in GaSb isotope heterostructures measured with SIMS: ^{69}Ga (plus symbols), ^{71}Ga (crosses), ^{121}Sb (circles) and ^{123}Sb (squares). (A) Ga and Sb profiles of the as-grown ^{69}Ga^{121}Sb/^{71}Ga^{123}Sb heterostructure. (B, C) Profiles after annealing the isotope structure under Sb-rich conditions at 700 °C for 105 min (B) and 18 days (C). The Ga and Sb diffusion coefficients were determined by fitting the solution of Fick's law for self-diffusion across an interface to the Ga and Sb profiles measured after annealing. Solid lines in B and C show best fits. Adapted with permission from Bracht H et al. (2000) Large disparity between gallium and antimony self-diffusion in gallium antimonide. *Nature* 408(6808): 69–72, https://doi.org/10.1038/35040526.

isotopes ^{69}Ga, ^{71}Ga, ^{121}Sb and ^{123}Sb for the as-grown structure and after thermal annealing at different times and temperatures. The Ga host atoms diffuse by a factor of ~1000 faster than the Sb atoms. Even after 4 days at a temperature just under the bulk melting point of GaSb and long after the labeled Ga atoms have diffused into the bulk, the Sb atoms have barely moved. The large difference can be explained with the formation of Ga_{Sb} antisites that suppress the formation of Sb vacancies required for the diffusion of this constituent.

Local vibrational modes

The vibrations of light impurity atoms in a semiconductor can occur at much higher frequencies than the maximum single phonon frequencies of the host lattice. In this case, the coupling to the host lattice is weak, such that this local vibrational mode (LVM) can have a long lifetime and a very narrow spectral linewidth as observed by infrared absorption, Raman scattering, or other techniques. Depending on the details of the lattice location of the impurity, particularly on symmetry and on how many bonds are formed with host lattice atoms, a number of normal vibrational modes are observed. Because of the simple dependence of vibrational frequencies on the inverse square root of the vibrating mass, isotope substitution of the impurity is used to obtain unambiguous proof for the association of an LVM feature with a certain impurity. The largest isotope shift caused by such a substitution of stable isotopes is close to 40% and is obtained for hydrogen substituted by deuterium.

In order to obtain a crude understanding of an LVM spectrum, it usually suffices to model the impurity and the nearest bound neighbors as a quasi-molecule imbedded in the host crystal. The model can be improved substantially by taking into account next

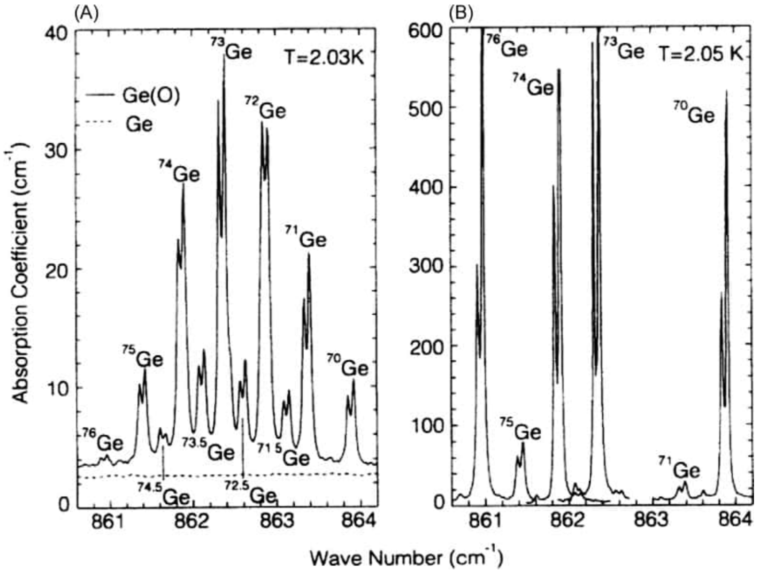

Fig. 10 (A) Spectrum of the Ge_2O quasi molecules in natural Ge at 2.05 K. Eleven lines split by $\nu_2 + \nu_3$ coupling excitations correspond to the distinct isotopic mass combinations of the two Ge atoms in the quasi molecule. An oxygen free sample produced the dashed line. (B) The spectrum of an oxygen doped, highly enriched sample of ^{70}Ge. The lines labeled ^{71}Ge are caused by traces of ^{72}Ge in ^{70}Ge. Adapted with permission from Mayur AJ et al. (1994) Fine structure of the asymmetric stretching vibration of dispersed oxygen in monoisotopic germanium. *Physical Review B* 49(23): 16293–16299, https://doi.org/10.1103/PhysRevB.49.16293.

nearest neighbor atoms in the form of an additional mass correction, the "host interaction mass" and by extending the linear force dependence on impurity displacement with higher terms (anharmonicity). When the host lattice consists of several stable isotopes with some of these present at significant atomic fractions (Ge is an example), LVM spectra can contain many closely spaced or overlapping lines because the impurity and its host lattice neighbors form quasi-molecules with a number of different reduced masses. Isotope enrichment of the host material can lead to drastic simplification of the LVM spectra in such cases. This is illustrated in Fig. 10 for the LVM of oxygen in Ge (Mayur et al., 1994). Taking into account two nearest neighbors, the ^{x}Ge-O-^{y}Ge molecule has three fundamental modes. The "wag" mode (ν_3) has the highest frequency. It leads to 11 lines resulting from the different mass combinations of ^{x}Ge and ^{y}Ge, each one split into several components whose intensities depend on temperature. Isotopic enrichment not only greatly simplifies the spectrum (one split line is observed instead of 11), it also allows a quantitative study of the linewidth and of the coupling between ν_3 and the other modes as a function of temperature. In this way, it was shown that the observed splitting is a result of the nonlinear superposition of the ν_2 and ν_3 modes and that the temperature dependence is due to the thermal population of low frequency ν_2 mode, which can be significant, even at near liquid helium temperature.

Spin-related properties

A number of elements found in typical semiconductors have half-odd nuclear spins I and hence magnetic moments. Examples are ^{73}Ge ($I = 9/2$), ^{29}Si ($I = 1/2$), ^{31}P ($I = 1/2$), and both stable isotopes of Ga: ^{69}Ga ($I = 3/2$) and: ^{71}Ga ($I = 3/2$). The magnitude of the magnetic moment and the spin-lattice (T_1) and transverse (decoherence, T_2) lifetimes of non-equilibrium nuclear spin populations are measured with nuclear magnetic resonance (NMR). In high-quality single crystal material, lifetimes can be long. For example, the spin lattice relaxation time of the ^{29}Si (4.67% natural abundance) nuclear spin can be as long as several hours at room temperature (Shulman and Wyluda, 1956); decoherence times can be as long as 25 s at cryogenic temperatures in ultrahigh purity single crystals (Ladd et al., 2005).

In the case of electron spin resonance (ESR), soon after the demonstration of the effect in the late 1950s, the effects of isotopic enrichment on the spin dynamics of donor electrons bound to ^{31}P were investigated. At that time, a doubling of T_2 from 0.2 to 0.5 ms was observed by removing the hyperfine spin orbit coupling interaction between the electron spin and the nuclear spin of the ^{29}Si (Feher et al., 1958). Modern measurements on higher purity >99% ^{28}Si enriched material have demonstrated $T_2 > 100$ s (Steger et al., 2012).

These and related effects are expected to be important in developing solid state quantum computing schemes based on electron and/or nuclear spin as qubits (Kane, 1998). Highly enriched ^{28}Si is extremely valuable for experimental work in this area, as it can be thought of as a "semiconductor vacuum," with properties almost identical to those of Si, but with almost no nuclear spins, and optical linewidths approaching their homogeneous, lifetime-limited values (Steger et al., 2012). It is also possible to use both the electron and nuclear spin on ^{31}P in experimental demonstrations of quantum information. Fig. 11 depicts the coherent transfer of a superposition state in an electron-spin "processing" qubit to a nuclear-spin "memory" qubit, using a combination of microwave

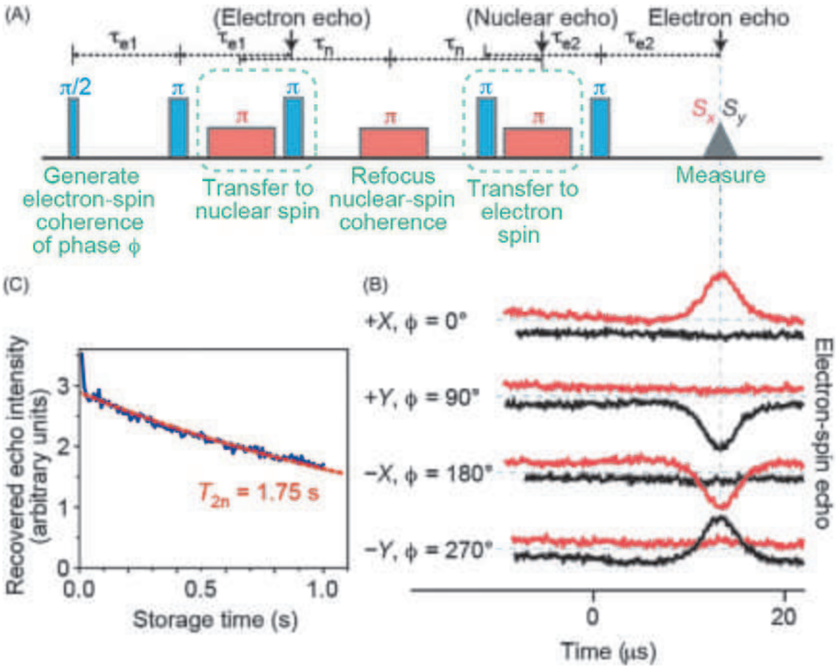

Fig. 11 Coherent storage of an electron-spin state in a nuclear-spin state, using a ^{31}P-doped ^{28}Si-enriched silicon single crystal. (A) The general sequence for the storage and revival of the electron-spin state comprises microwave and RF pulses with relative timings defined by τ_{e1}, τ_{e2} and τ_n. (B) Electron-spin coherence is stored in the nuclear spin for $2\tau_n \approx 50$ ms, at 7.2 K. Real (red) and imaginary (black) parts of the recovered electron-spin echo are shown for different initial phases ϕ. The echo is of comparable intensity to that obtained at the beginning of the sequence, even though the electron-spin coherence time, T_{2e}, is considerably shorter, about 5 ms. The lifetime of the stored state is limited instead by the considerably longer nuclear decoherence time, T_{2n}. c, Measurements of the recovered echo intensity as a function of the storage time at 5.5 K yield a T_{2n} exceeding 1 s. Adapted with permission from Morton JJL et al. (2008) Solid-state quantum memory using the 31P nuclear spin. *Nature* Macmillan Publishers Limited. All rights reserved 455(7216): 1085–1088, https://doi.org/10.1038/nature07295.

and radio-frequency pulses applied to ^{31}P donors in an isotopically pure ^{28}Si crystal (Morton et al., 2008). The state is left in the nuclear spin on a timescale that is long compared with the electron decoherence time, and is then coherently transferred back to the electron spin, thus demonstrating the ^{31}P nuclear spin as a solid-state quantum memory with a lifetime of over 1 s.

Neutron transmutation doping

The extreme versatility of semiconductors in their wide range of applications is based on our ability to dope these solids with donors and acceptors. For device fabrication dopants are introduced at or near the surface either by diffusion or by ion implantation. Bulk crystal doping is typically achieved by adding the appropriate minute quantities of dopant elements to the melt from which the crystal is pulled. An alternative doping technique is neutron transmutation doping (NTD).

The radioactive decay of an isotope of one element into an isotope of a different element forms the foundation of NTD of semiconductors. We illustrate NTD of Si here. The NTD process is typically performed in a nuclear reactor. During exposure of natural silicon to thermal neutrons (n_{th}) all three isotopes capture neutrons with well known capture cross sections, and the following reactions occur:

$$^{28}_{14}\mathrm{Si} + \mathrm{n}_{th} \rightarrow {}^{29}_{14}\mathrm{Si}$$
$$^{29}_{14}\mathrm{Si} + \mathrm{n}_{th} \rightarrow {}^{30}_{14}\mathrm{Si}$$
$$^{30}_{14}\mathrm{Si} + \mathrm{n}_{th} \rightarrow {}^{31}_{14}\mathrm{Si} \overset{\tau_{1/2} 2.62\ \mathrm{hr}}{\longrightarrow} {}^{31}_{14}\mathrm{P} + \beta^- + \nu_e^-$$

The third reaction leads to the formation of the donor P. NTD differs from other dopant technologies in that very high doping uniformity can be obtained. The unmatched doping uniformity achieved by NTD is based on three factors. First, the stable isotopes are truly randomly distributed in a semiconductor of natural composition. Second, the source of thermal neutrons is typically larger than the semiconductor crystal to be doped. This, in turn, leads to a large homogenous thermal neutron field guaranteeing identical exposure of all parts of the crystal. Third, the capture cross section for thermal neutrons is typically of the order of a few barns ($1\ \mathrm{b} = 10^{-24}\ \mathrm{cm}^2$) which means that a few centimeters of material absorb the thermal neutron flux by significantly less than 1%, maintaining the nearly uniform neutron flux throughout the depth of the sample.

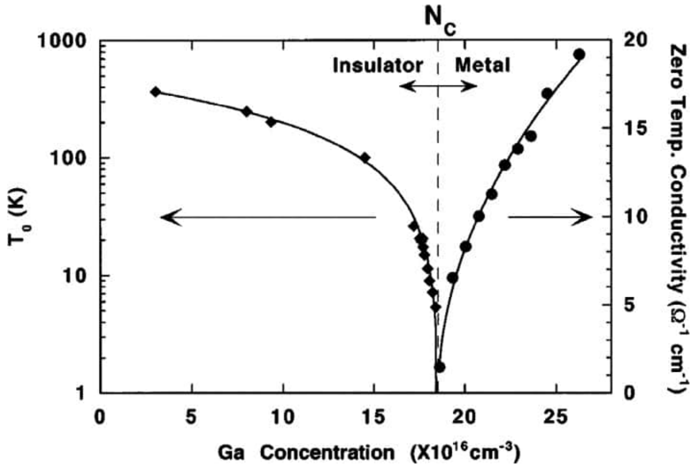

Fig. 12 Extrapolated zero temperature electrical conductivity (right axis) and characteristic temperature T_0 (left axis) for variable range hopping for 14 samples with carefully controlled concentrations of ^{71}Ga-doped ^{70}Ge made with neutron transmutation doping. The metal insulator transition (MIT) is found to occur at an acceptor concentration of 1.86×10^{17} cm^{-3}. Adapted with permission from Itoh KM et al. (1996) Hopping conduction and metal-insulator transition in isotopically enriched neutron-transmutation-doped 70Ge:Ga. *Physical Review Letters* 77(19): 4058–4061, https://doi.org/10.1103/PhysRevLett.77.4058.

For this reason, semiconductors that are used in high power, high voltage applications, such as Si rectifiers (SCRs), are manufactured using NTD Si (von Ammon, 1992). Scientifically, NTD enables researchers to more precisely control doping levels. For example, it is possible to precisely dope Ge with Ga very close to the metal-insulator transition (MIT). As shown in Fig. 12, it was found that the critical concentration was 1.86×10^{17} cm^{-3} when the MIT was approached from both above and below (Itoh et al., 1996). Also, instrumentation for far infrared and submillimeter wave astronomy and astrophysics have profited from NTD. Small temperature sensing elements of crystalline NTD germanium are assembled into large arrays in the focal planes of all modern far IR telescopes (Haller, 2006).

Conclusion

An overview of the effect of the distribution of stable isotopes has been provided. Most effects are due to differences in atomic mass. In general, the lattice constant increases with increasing mass, as can be seen in diamond whose average atomic mass can be controlled between 12 and 13 amus and in silicon where control between 28 and 30 amus is possible. Phonons are relatively strongly affected by isotopic disorder and isotopically enriched material can have significantly enhanced thermal conductivity. Electronic properties are affected but less strongly. However, use of isotopic control allows for quantification of fundamental bandgaps, which is the purely electronic value in the absence of electron-phonon interaction and volume changes associated with anharmonicity. Isotopically controlled heterostructures have been invaluable in the study of solid-state diffusion and in the spectroscopy of local vibrational modes. Linewidths of optical transitions and electron spin lifetimes are significantly enhanced in isotopically enriched Si, which has enabled a number of compelling demonstrations in quantum information science. In certain cases, neutron transmutation doping is possible, and precise control and uniformity of doping can be achieved.

References

Asen-Palmer M, et al. (1997) Thermal conductivity of germanium crystals with different isotopic compositions. *Physical Review B* 56(15): 9431–9447. https://doi.org/10.1103/PhysRevB.56.9431.

Becker P, et al. (2010) Enrichment of silicon for a better kilogram. *Physica Status Solidi* 207(1): 49–66. https://doi.org/10.1002/pssa.200925148.

Berglund M and Wieser ME (2011) Isotopic compositions of the elements 2009 (IUPAC Technical Report). *Pure and Applied Chemistry* 83(2): 397–410. https://doi.org/10.1351/PAC-REP-10-06-02.

Bracht H, Haller EE, and Clark-Phelps R (1998) Silicon self-diffusion in isotope heterostructures. *Physical Review Letters* 81(2): 393–396. https://doi.org/10.1103/PhysRevLett.81.393.

Bracht H, et al. (2000) Large disparity between gallium and antimony self-diffusion in gallium antimonide. *Nature* 408(6808): 69–72. https://doi.org/10.1038/35040526.

Bracht H, et al. (2014) Thermal conductivity of isotopically controlled silicon nanostructures. *New Journal of Physics* 16(1): 15021. https://doi.org/10.1088/1367-2630/16/1/015021.

Cardona M and Thewalt MLW (2005) Isotope effects on the optical spectra of semiconductors. *Reviews of Modern Physics* 77(4): 1173–1224. https://doi.org/10.1103/RevModPhys.77.1173.

Ci P, et al. (2022) Giant isotope effect of thermal conductivity in silicon nanowires. *Physical Review Letters* 128(8), 085901. https://doi.org/10.1103/PhysRevLett.128.085901.

Davies G, et al. (1993) Isotope dependence of the lowest direct energy gap in crystalline germanium. *Semiconductor Science and Technology* 8(12): 2201–2204. https://doi.org/10.1088/0268-1242/8/12/028.

Feher G, et al. (1958) Spontaneous emission of radiation from an electron spin system. *Physical Review* 109(1): 221–222. https://doi.org/10.1103/PhysRev.109.221.

Fuchs HD, et al. (1992) Isotopic disorder-effects on the phonons in germanium. *Solid State Communications* 82(4): 225–228. https://doi.org/10.1016/0038-1098(92)90631-I.

Fuchs HD, et al. (1995) Germanium ^{70}Ge/^{74}Ge isotope heterostructures: An approach to self-diffusion studies. *Physical Review B* 51(23): 16817–16821. https://doi.org/10.1103/PhysRevB.51.16817.

Geballe TH and Hull GW (1958) Isotopic and other types of thermal resistance in germanium. *Physical Review* 110(3): 773–775. https://doi.org/10.1103/PhysRev.110.773.

Haller EE (2006) Germanium: From its discovery to SiGe devices. *Materials Science in Semiconductor Processing* 9(4–5): 408–422. https://doi.org/10.1016/j.mssp.2006.08.063.

Hochbaum AI, et al. (2008) Enhanced thermoelectric performance of rough silicon nanowires. *Nature* 451(7175): 163–167. https://doi.org/10.1038/nature06381.

Holloway H, et al. (1991) Isotopic dependence of the lattice constant of diamond. *Physical Review B* 44(13): 7123–7126. https://doi.org/10.1103/PhysRevB.44.7123.

Inyushkin AV, et al. (2018) Ultrahigh thermal conductivity of isotopically enriched silicon. *Journal of Applied Physics* 123(9), 095112. https://doi.org/10.1063/1.5017778.

Itoh KM, et al. (1996) Hopping conduction and metal-insulator transition in isotopically enriched neutron-transmutation-doped ^{70}Ge:Ga. *Physical Review Letters* 77(19): 4058–4061. https://doi.org/10.1103/PhysRevLett.77.4058.

Kane BE (1998) A silicon-based nuclear spin quantum computer. *Nature* 393(6681): 133–137. https://doi.org/10.1038/30156.

Karaiskaj D, et al. (2001) Photoluminescence of isotopically purified silicon: How sharp are bound exciton transitions? *Physical Review Letters* 86(26): 6010–6013. https://doi.org/10.1103/PhysRevLett.86.6010.

Ladd TD, et al. (2005) Coherence time of decoupled nuclear spins in silicon. *Physical Review B* 71(1), 014401. https://doi.org/10.1103/PhysRevB.71.014401.

London H (1958) The difference in the molekular volume of isotopes. *Zeitschrift für Physikalische Chemie* 16(3_6): 302–309. https://doi.org/10.1524/zpch.1958.16.3_6.302.

Lundqvist B, et al. (2013) Thermal conductivity of isotopically enriched silicon carbide. In: *19th International Workshop on Thermal Investigations of ICs and Systems (THERMINIC)*, pp. 58–61. IEEE. https://doi.org/10.1109/THERMINIC.2013.6675243.

Mayur AJ, et al. (1994) Fine structure of the asymmetric stretching vibration of dispersed oxygen in monoisotopic germanium. *Physical Review B* 49(23): 16293–16299. https://doi.org/10.1103/PhysRevB.49.16293.

Morton JJL, et al. (2008) Solid-state quantum memory using the ^{31}P nuclear spin. *Nature* 455(7216): 1085–1088. https://doi.org/10.1038/nature07295. Macmillan Publishers Limited. All rights reserved.

Olson JR, et al. (1993) Thermal conductivity of diamond between 170 and 1200 K and the isotope effect. *Physical Review B* 47(22): 14850–14856. https://doi.org/10.1103/PhysRevB.47.14850.

Pavone P and Baroni S (1994) Dependence of the crystal lattice constant on isotopic composition: Theory and ab initio calculations for C, Si, and Ge. *Solid State Communications* 90(5): 295–297. https://doi.org/10.1016/0038-1098(94)90154-6.

Pomeranchuk I (1942) On the thermal conductivity of dielectrics at temperatures lower than that of Debye. *Journal of Physics USSR* 6: 237.

Shaw D (2017) Diffusion in semiconductors. In: Kasap S and Capper P (eds.) *Springer Handbook of Electronic and Photonic Materials*. *Springer Handbooks*, pp. 133–150. Springer. https://doi.org/10.1007/978-3-319-48933-9_6.

Shulman RG and Wyluda BJ (1956) Nuclear magnetic resonance of ^{29}Si in n- and p-type silicon. *Physical Review* 103(4): 1127–1129. https://doi.org/10.1103/PhysRev.103.1127.

Slack GA (1973) Nonmetallic crystals with high thermal conductivity. *Journal of Physics and Chemistry of Solids* 34(2): 321–335. https://doi.org/10.1016/0022-3697(73)90092-9.

Spitzer J, et al. (1994) Raman scattering by optical phonons in isotopic ^{70}70 (Ge)$_n$-^{74}(Ge)$_n$ superlattices. *Physical Review Letters* 72(10): 1565–1568. https://doi.org/10.1103/PhysRevLett.72.1565.

Steger M, et al. (2012) Quantum information storage for over 180 s using donor spins in a ^{28}Si "semiconductor vacuum" *Science* 336(6086): 1280–1283. https://doi.org/10.1126/science.1217635.

Tsoi S, et al. (2004) Electron-phonon renormalization of electronic band gaps of semiconductors: Isotopically enriched silicon. *Physical Review B* 70(19): 193201. https://doi.org/10.1103/PhysRevB.70.193201. American Physical Society.

Tsoi S, et al. (2005) Isotopic dependence of the E_0' and E_2 direct gaps in the electronic band structure of Si. *Physical Review B* 72(15): 153203. https://doi.org/10.1103/PhysRevB.72.153203. American Physical Society.

von Ammon W (1992) Neutron transmutation doped silicon — Technological and economic aspects. *Nuclear Instruments and Methods in Physics Research Section B: Beam Interactions with Materials and Atoms* 63(1–2): 95–100. https://doi.org/10.1016/0168-583X(92)95176-R.

Wei L, et al. (1993) Thermal conductivity of isotopically modified single crystal diamond. *Physical Review Letters* 70(24): 3764–3767. https://doi.org/10.1103/PhysRevLett.70.3764.

Zhu X and Louie SG (1991) Quasiparticle band structure of thirteen semiconductors and insulators. *Physical Review B* 43(17): 14142–14156. https://doi.org/10.1103/PhysRevB.43.14142.

Polaritons[☆]

M Litinskaya, University of British Columbia, Vancouver, BC, Canada

© 2024 Elsevier Ltd. All rights reserved.

This is an update of M. Litinskaya, Polaritons, Editor(s): Franco Bassani, Gerald L. Liedl, Peter Wyder, Encyclopedia of Condensed Matter Physics, Elsevier, 2005, Pages 334–341, ISBN 9780123694010, https://doi.org/10.1016/B0-12-369401-9/00663-X.

Introduction **497**
Definition 497
Theoretical approaches 498
Strong coupling, weak coupling, and ultrastrong coupling 499
Polaritons in bulk **499**
Dispersion equation 499
Anisotropic media 500
Spatial dispersion and additional waves 500
Surface polaritons **501**
Surface polaritons at the interface between two semi-infinite media 501
Surface polaritons in more complex geometry 502
Polaritons in nanostructures with reduced dimensionality **503**
Cavity polaritons **503**
Dark-state polaritons in atomic gases **505**
Conclusion **505**
References **506**
Further reading **506**

Abstract

Polaritons are elementary excitations describing light strongly coupled to material resonances ('light-matter waves'). This chapter reviews basic properties of polaritons in condensed media of various dimensions and at interfaces. It also discusses the effect of spatial dispersion, Bose–Einstein condensation of cavity polaritons and dark-state polaritons in gases.

Key points

- Electromagnetic waves in a condensed medium can strongly couple to dipole-active resonances of the medium, forming hybrid excitations known as polaritons.
- The article reviews two complementary frameworks, the semi-classical approach and the second quantization formalism, that conveniently describe polaritons.
- The number of polaritonic modes at a given frequency is determined by spatial dispersion of the resonant material excitation.
- General properties of polaritons depend more on the geometry of the solid than on the character of the material excitation that couples to light. We will discuss polaritons in a variety of geometries, including low-dimensional structures.

Introduction

Definition

Polaritons are quasiparticles (elementary excitations in a condensed medium) that form as a result of interaction and mixing of light with dipole-active transitions of the medium. The classical theory of light waves in ionic crystals near optical phonon frequencies was proposed by Tolpygo (1950) and Huang (1951) in the early 1950s. Later, the quantum theory of light waves near excitonic resonances and the concept of polaritons were developed in works by Fano (1956), Hopfield (1958), and Agranovich (1959).

Consider an electromagnetic wave propagating in a medium, and let the frequency of the wave be close to some resonance frequency of that medium. These resonances are generally associated with some elementary excitations of the medium

---

[☆] Change History: March 2022. M. Litinskaya updated figures, added 'Key points' and 'Conclusions,' corrected minor typos, revised the whole text, updated the chapter 'Cavity Polaritons' to include some of modern research directions, and revised section 'Surface polaritons'; 4 papers were added to the list of references, and 2 to further reading list. April 2015. M. Litinskaya added Keywords, Abstract, a few paragraphs into the section 'Cavity polaritons' and a section 'Dark-state polariton,' and updated the address. The list of literature was split into References and Further reading, with four additional items added. April 2019.
M. Litinskaya revised the whole text and updated the chapter 'Cavity Polaritons' to include some of modern research directions. Seven papers were added to the list of references.

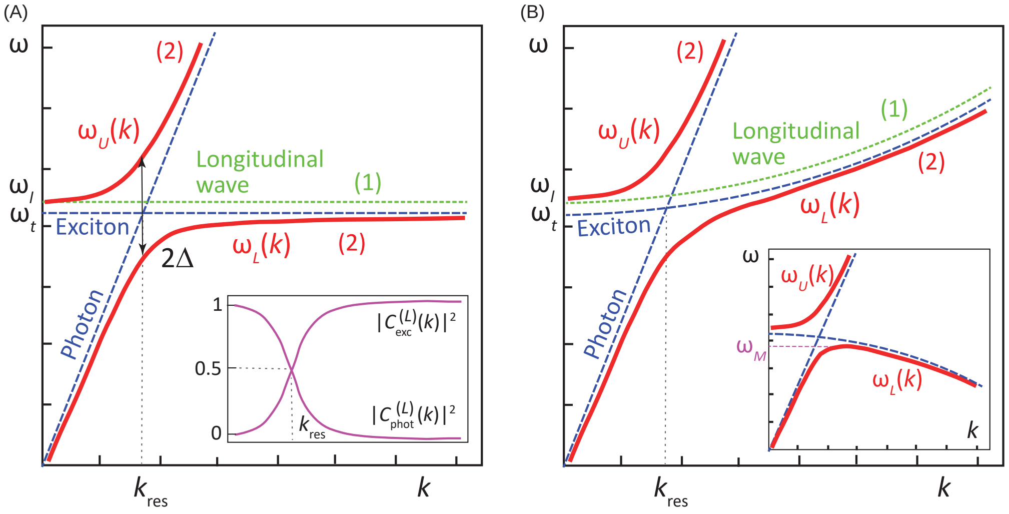

Fig. 1 Dispersion of bulk exciton-polaritons (thick red lines) and of the longitudinal wave (short-dash green lines). The polaritonic splitting, 2Δ, is shown by the black arrow in panel (A). The numbers in brackets indicate the degeneracy of each mode. Long-dash blue lines show the dispersions of 'bare' photon and 'bare' transverse exciton. (A) Spatial dispersion is neglected. The inset shows the exciton and photon weight coefficients $|C^{(L)}_{\mathrm{exc}}(k)|^2$ and $|C^{(L)}_{\mathrm{phot}}(k)|^2$for the lower polaritonic branch (they are defined in Eq. 2). (B) Spatial dispersion is taken into account, and $m_t > 0$, $m_l > 0$. Here and below the plots are not to scale. The inset shows the spectrum of transverse waves for $m_t < 0$, with ω_{M} being the maximum frequency of the lower polariton branch.

(quasiparticles). They can be of electronic nature, such as Frenkel or Wannier–Mott excitons, or lattice vibrations, such as optical phonons in ionic crystals. The electromagnetic field polarizes the medium, and the polarization, which is high near the resonance frequency, in turn influences the electromagnetic field. One can regard it as an interaction between the 'bare' photon and 'bare' medium excitation (hence the term 'light-matter interaction'). When the interaction is strong enough, the excitation spectrum of the medium essentially changes. Near the resonance between the light mode and the medium excitation, their 'bare' dispersion curves transform into two – the 'lower' and the 'upper' – split modes know as polaritonic branches. These hybrid modes show anticrossing behavior, so that a gap of the size 2Δ, where Δ is the coupling strength defined below, opens in the excitation spectrum (see Fig. 1). This situation is referred to as the 'strong-coupling regime.' Polaritons inherit the properties of both 'bare' photons and 'bare' medium excitations, and this mixed – half-light, half-matter – character of polaritons leads to many interesting physical properties.

In solids, the type of crystal excitation, which participates in the formation of polaritons, is encoded in a prefix: 'exciton–polaritons,' 'plasmon–polaritons,' and 'optical phonon–polaritons.' The quasiparticles, which appear as a result of interaction between the electromagnetic field and the resonances of magnetic permeability, are known as 'magnetic polaritons.' In gases, the term 'polariton' is widely used to describe the coupled state of electric field and atomic or molecular transitions in the gas.

Theoretical approaches

Many processes with the participation of polaritons, as well as their dispersion law, can be described within the macroscopic semiclassical approach using the system of Maxwell's equations for the electromagnetic fields in the medium. For spatially restricted systems, the problem must be supplemented by the fields outside the crystal and by proper boundary conditions. These equations are combined with the material equation, which connects the fields $\boldsymbol{D}$ and $\boldsymbol{E}$ through the tensor of dielectric permittivity $\varepsilon_{ij}(\omega, \boldsymbol{k})$. The tensor $\varepsilon_{ij}(\omega, \boldsymbol{k})$ that describes the response of the medium is obtained from the microscopic theory or from experiment. In general, in an infinite homogeneous isotropic medium with the account of spatial dispersion,

$$\varepsilon_{ij}(\omega, k) = \varepsilon_t(\omega, k)\left(\delta_{ij} - \frac{k_i k_j}{k^2}\right) + \varepsilon_l(\omega, k)\frac{k_i k_j}{k^2} \tag{1}$$

where ω is the frequency, $\boldsymbol{k}$ is the wave vector, $\varepsilon_t(\omega, \boldsymbol{k})$ and $\varepsilon_l(\omega, \boldsymbol{k})$ are transverse and longitudinal dielectric permittivities, and δ_{ij} is the Kronecker symbol. The condition $\varepsilon_l(\omega, \boldsymbol{k}) = 0$ determines the dispersion $\omega = \omega_l(k)$ of a longitudinal wave, which does not interact with transverse photons. In turn, the poles $\omega = \omega_t(k)$ of the function $\varepsilon_t(\omega, \boldsymbol{k})$ determine transverse 'bare' excitations of the medium (excitons, plasmons or optical phonons). As shown below, polaritons are the transverse normal modes (i.e., the solutions of Maxwell's equations) of the medium near these frequencies. The macroscopic description holds as long as the wavelength of light strongly exceeds the lattice constant and the excitonic Bohr radius.

In the framework of the alternative microscopic (quantum) approach, polaritons appear due to account of retardation. Excitons are collective electronic material excitations in the approximation when only the instantaneous Coulomb interaction between the molecules (or atoms) is considered (i.e., in the limit $c \to \infty$). Retardation, as known from quantum electrodynamics, is equivalent to taking into account the interaction with transverse electromagnetic field. Hence, polaritons appear as a result of interaction between excitons and transverse photons. This approach utilizes the second-quantization formalism, where polaritons are the eigenstates of the full Hamiltonian of the crystal, which is a sum of the Hamiltonians of 'bare' transverse photons, 'bare' excitons, and the Hamiltonian of their interaction. The polariton operators are linear combinations of the operators of 'bare' photons and 'bare' excitons. Near the resonance, these operators are

$$\begin{aligned} \xi_{k,\rho}^{+} &= C_{\text{phot}}^{(\rho)}(k)a_k^{+} + C_{\text{exc}}^{(\rho)}(k)B_k^{+} \\ \xi_{k,\rho} &= C_{\text{phot}}^{(\rho)*}(k)a_k + C_{\text{exc}}^{(\rho)*}(k)B_k \end{aligned} \tag{2}$$

where $a_{\boldsymbol{k}}^{+}$, $a_{\boldsymbol{k}}$ and $B_{\boldsymbol{k}}^{+}$, $B_{\boldsymbol{k}}$ are the creation and annihilation operators of photons and excitons, and $\rho = \text{U, L}$ denote the upper or the lower polaritonic branch. The coefficients $C_{\text{phot}}^{(\rho)}(k)$ and $C_{\text{exc}}^{(\rho)}(k)$ are the amplitudes of the photon and the exciton in each polaritonic state, and their squared modules are the weights of the 'bare' excitations in the polaritonic states. They vary between 0 and 1 with the change of the wave vector k, and at the resonance

$$\left|C_{\text{phot}}^{(U,L)}(k_{\text{res}})\right|^2 = \left|C_{\text{exc}}^{(U,L)}(k_{\text{res}})\right|^2 = 1/2$$

Within linear optics, these two approaches yield identical results, and the choice between them is a matter of convenience. The semiclassical (macroscopic) approach is often used to calculate the optical response, while quantum (microscopic) formalism is convenient for studies of non-linear processes. Quantum description is also used to discuss the collective properties of polaritons and their statistics, and for the description of the eigenfunctions of the crystal (in particular, the polaritonic vacuum state is not equivalent to an independent-particle vacuum). Furthermore, quantum description is valid for low-dimensional structures (such as a monolayer, or a chain of molecules), when a dielectric tensor cannot be introduced, and the macroscopic description is not valid.

Strong coupling, weak coupling, and ultrastrong coupling

The strong-coupling regime can be destroyed by various dephasing processes. Many of them (such as exciton–phonon interactions and scattering of polaritons by structural disorder) act on polaritons through their material (excitonic) component. In addition, the lifetime of polaritons is restricted by finite lifetime of the photon within the finite-size crystal. The strong-coupling regime holds as long as the exciton–photon coupling strength Δ exceeds all the involved dephasing rates. If this condition is violated, the system is in the so-called weak-coupling regime, when the gap in the spectrum of elementary excitations does not form. In the quantum language, the strong-coupling regime is described by vacuum Rabi oscillations (reversible exchange of energy quanta between light and matter 'bare' states), whereas the weak-coupling regime corresponds to irreversible spontaneous decay of the collective 'bare' material excitations of the medium. In the strong-coupling regime the polariton splitting Δ is a small fraction of the frequency of the material excitation, ω_t. Since recently, a new regime – ultrastrong coupling, with the coupling strength Δ and excitation frequency ω_t being of the same order – became experimentally available.

The impact of phonons can be diminished by decreasing the temperature. For instance, in good GaAs crystals, the strong coupling regime holds below 20 K in bulk, and below 70 K in microcavities. Disorder appears as impurities in bulk crystals, and interface roughness and/or alloy fluctuations for cavity- and surface polaritons. The main effect of disorder is that it introduces local excitonic levels, which trap polaritonic states and eventually can destroy them. In the state-of-the-art optical microcavities, the role of disorder can be brought almost to nothing.

Polaritons in bulk

Dispersion equation

In the framework of the macroscopic approach, the dispersion equation for polaritons in a bulk (3D) medium can be obtained by solving the wave equation for the fields $\boldsymbol{D}$ and $\boldsymbol{E}$:

$$\Delta E + \frac{\omega^2}{c^2} D - \text{grad}\,\text{div}\,E = 0 \tag{3}$$

combined with a material equation. In a uniform isotropic medium, where the wave vector $\boldsymbol{k}$ conserves, and neglecting the dissipation, the dielectric permittivity $\epsilon_t(\omega, k)$ near an electronic transition is

$$\varepsilon_t(\omega, k) = \varepsilon_b + \frac{A}{\omega^2(k) - \omega^2} \tag{4}$$

where ε_b is the background dielectric constant, and A is proportional to the oscillator strength f_{osc} of the transition. Dropping the resonance term would describe 'bare' photon in that medium. Furthermore, $\omega_t(k)$ is the dispersion of the crystal excitation, which, for small k, we can write in the effective-mass approximation:

$$\omega_t(k) = \omega_t + \frac{hk^2}{2m_t}, \qquad \omega_t \equiv \omega_t(k=0) \tag{5}$$

Here m_t is the effective mass of the material excitation, it determines the curvature of its dispersion. If the dependence of the dielectric permittivity on the wave vector (i.e., spatial dispersion) is neglected, then $\omega_t(k) = \omega_t$ and $\varepsilon_t(\omega,k) \equiv \varepsilon(\omega)$. This approximation works well for optical phonon–polaritons and some of Frenkel exciton–polaritons, while for Wannier–Mott exciton–polaritons the dependence of $\varepsilon_t(\omega,k)$ on k is usually important.

In an infinite isotropic medium, the wave equation, Eq. (3), has three solutions. One is a longitudinal wave, and its dispersion law $\omega=\omega_l(k)$ is determined by $\varepsilon_l(\omega,k) = 0$. In addition, there are two twice-degenerate (corresponding to two possible polarizations) transverse waves, which are polaritons. Their dispersion law can be found from the equation

$$\frac{c^2k^2}{\omega^2} = \varepsilon_t(\omega, k) = \varepsilon_b + \frac{A}{\omega_t^2(k) - \omega^2} \tag{6}$$

which for $\omega \sim \omega_t$ simplifies as

$$(\omega - \omega_{\text{phot}}(k))(\omega - \omega_t(k)) = \Delta^2 \tag{7}$$

where $\Delta = \sqrt{A/(4\varepsilon_b)} \propto \sqrt{f_{\text{osc}}}$ is the light-matter coupling strength, and $\omega_{\text{phot}}(k) = ck/\sqrt{\varepsilon_b}$ is the dispersion of the photon in the crystal. Near the resonance (i.e., for $\omega \sim \omega_t(k) \approx \omega_{\text{phot}}(k)$), the polaritonic branches anticross. The smallest separation between them is at the resonance, and is equal to 2Δ. Far from the resonance, the polaritonic effect is negligible, and polaritonic dispersion curves approach the dispersion curves of the bare photon and material excitation. The solutions of (7) $\omega = \omega_{U,L}(k)$ are

$$\omega_{U,L}(k) = \frac{1}{2}\left[\omega_{\text{phot}}(k) + \omega_t(k) \pm \sqrt{(\omega_{\text{phot}}(k) - \omega_t(k))^2 + 4\Delta^2}\right] \tag{8}$$

The dispersion curves of bulk exciton-polaritons are plotted in Fig. 1 together with 'bare' excitations and the longitudinal wave, which does not couple to light ((A) without and (B) with spatial dispersion). These modes have been seen in many semiconductors (such as CuCl, GaAs, CdS) in a variety of optical experiments (for instance, two-photon absorption measured at different angles or hyper-Raman scattering measurements).

Anisotropic media

Some of Frenkel excitons have large oscillator strength and hence interact strongly with light. Organic molecular crystals, which support Frenkel excitons, are optically anisotropic. The properties of polaritons in anisotropic crystals are determined by the structure of the dielectric tensor $\varepsilon_{ik}(\omega,\mathbf{k})$ of the crystal (see Eq. 1), which relates the fields $\boldsymbol{D}$ and $\boldsymbol{E}$ as

$$D_i(\omega, \mathbf{k}) = \varepsilon_{ik}(\omega, \mathbf{k})E_k(\omega, \mathbf{k})$$

Then the equation analogous to (6), which yields the dispersion of polaritons $\omega = \omega(k)$, can be obtained from the zeros of the following determinant:

$$\left|\frac{\omega^2}{c^2}\varepsilon_{ik}(\omega, \ k) - k^2\delta_{ik} + k_ik_k\right| = 0 \tag{9}$$

For an arbitrary direction of the wave vector $\boldsymbol{k}$, polaritons in anisotropic crystals have a mixed longitudinal–transverse character.

Spatial dispersion and additional waves

Spatial dispersion, which manifests as dependence of dielectric permittivity ε on the wave vector, reflects the ability of the material excitations to propagate in the crystal due to internal interaction forces. If spatial dispersion is neglected, then there are no bulk waves in the frequency interval $\omega_t < \omega < \omega_l = \omega_l(0)$, and for all other frequencies the dispersion equation allows for a single propagating bulk wave. In other words, all the frequencies ω and wave vectors k are in one-to-one correspondence (see Fig. 1A). The account of spatial dispersion corresponds to finite (as opposed to infinite) effective mass of the material excitation, m_t, and hence results in bending of the dispersion curves of 'bare' material excitations, so that near the resonances, at the concave side of the dispersion curve, one-to-one correspondence between the wave vectors and frequencies becomes broken (Fig. 1B). As a result, in narrow frequency intervals near the resonances, more than one wave can propagate at a given frequency. The existence of large-wave-vector waves, which appear in addition to "regular" small-wave-vector polaritons, was first pointed out by Pekar (1957). They are called 'additional waves.'

The spatial dispersion shows up as the wave vector dependence of the excitonic resonance, as in Eq. (5) (isotropic medium is assumed). The curve $\omega_t(k)$ bends up or down, depending on the sign of m_t. The curve $\omega_l(k)$ also bends up or down depending on the sign of the effective mass m_l of the longitudinal exciton, since in general $m_l \neq m_t$. According to the signs of m_l and m_t, a number of scenarios emerge. Some examples are given below. For instance, in an isotropic nongyrotropic medium with $m_t > 0$, for $\omega > \omega_l$, there always exist two propagating transverse waves, a small-wave-vector upper polariton and a large-wave-vector lower polariton (see Fig. 1B). A lower polariton state exists also in the 'forbidden' region ($\omega_t < \omega < \omega_l$). In Fig. 1B, m_l is taken to be positive, that is typical for inorganic semiconductors. Then for $\omega > \omega_l$ the longitudinal wave coexists with two transverse polaritons. As another example, consider $m_t < 0$, which holds in some molecular crystals. Now there are two propagating transverse waves (both are lower-branch polaritons) for $\omega < \omega_{\text{M}} < \omega_t$ (see the inset in Fig. 1B). Out of these two waves, the polariton with the larger wave vector has a negative

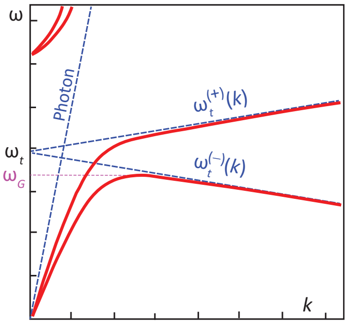

Fig. 2 Dispersion of bulk polaritons (thick red lines) in a gyrotropic cubic crystal. Dashed blue lines show the dispersion of 'bare' excitons and 'bare' photon, ω_G is the maximum frequency of the lower polariton branch.

group velocity, and therefore at interfaces it exhibits unusual refraction known as 'negative refraction.' As for the longitudinal wave (not shown in the inset), for $m_l > 0$ it exists at $\omega > \omega_l$ together with the upper polaritonic branch, while for $m_l < 0$ the longitudinal wave is the third wave at $\omega < \omega_M$, and it is the only one wave at $\omega_M < \omega < \omega_l$. Yet one more interesting case to consider is a cubic gyrotropic crystal, where the dispersion curve of the exciton splits into two branches with linear dispersions: $\omega_t^{(\pm)}(k) = \omega_t \pm \alpha k + O(k^2)$. The corresponding polaritonic spectrum with three propagating waves at $\omega < \omega_G < \omega_t$ and one propagating wave at $\omega > \omega_G$ is shown in Fig. 2. Again, the polaritonic branch, which asymptotically follows $\omega_t^{(-)}(k)$, exhibits negative refraction.

For spatially restricted media (e.g., when calculating the reflectance of a bulk crystal) at the frequencies where the one-to-one correspondence between ω and k is broken and an additional wave or waves exist, one has to introduce the so-called additional boundary conditions (ABCs), since usual Maxwell's boundary conditions are not sufficient to find the relation between the amplitudes of the waves. From a microscopic point of view, ABCs describe the behavior of the fields close to the surface. The character of ABCs essentially depends on the properties of the medium, its surface, and on the properties of the material excitations (excitons). In the most general case, in the framework of linear optics, ABCs are constructed as some linear combinations of the fields $\boldsymbol{E}$, $\boldsymbol{P}$ and their derivatives. The first ABC proposed by Pekar (1957) is $\boldsymbol{P} = 0$ at the boundary of the medium. It is good for molecular crystals, but is often suitable also for semiconductors. A widely used approach proposed by Hopfield and Thomas (1963) introduces a 'dead layer' of some thickness l near the surface, where excitons cannot penetrate. The thickness l and other phenomenological constants entering ABCs are to be determined from a microscopic theory or from comparison with experiment.

Surface polaritons

Surface polaritons are normal modes that propagate along the surface of the medium, or along an interface between two media, or along interfaces of layered structures. The electromagnetic field in these modes decays exponentially with the distance from the surface. As shown below, surface polaritons require the dielectric permittivity of the medium to be negative, which is possible near a resonance frequency of the medium. Surface polaritons can give us information about the surface of the crystal. Furthermore, they may be important as possible final states in various processes of interaction or scattering of electromagnetic waves in crystals.

Surface polaritons at the interface between two semi-infinite media

Let a semi-infinite isotropic medium with the dielectric permittivity $\varepsilon(\omega)$ (spatial dispersion is neglected) be in contact with an isotropic half-space with the dielectric constant ε_{out}. Let $\boldsymbol{k}_{||}$ be a two-dimensional wave vector parallel to the surface. The surface mode is TM-polarized (see the inset in Fig. 3) and has the following dispersion relation:

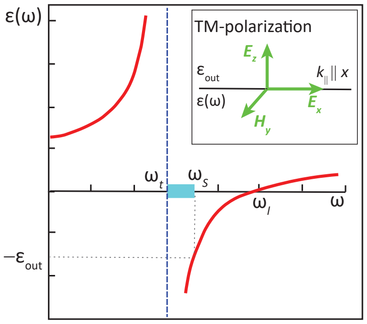

Fig. 3 Red solid line: graph of the function $\varepsilon(\omega)$. At the interface between the materials with the dielectric permittivities $\varepsilon(\omega)$ and ε_{out}, surface polaritons exist at the frequency interval $\omega_t < \omega < \omega_S$ highlighted in blue, where $-\varepsilon_{out} < \varepsilon(\omega) < 0$. The inset shows the electric and magnetic fields in a TM-polarized mode.

$$\frac{\varepsilon(\omega)}{\sqrt{k_{\|}^{2}-\omega^{2}\varepsilon(\omega)/c^{2}}}=-\frac{\varepsilon_{\text{out}}}{\sqrt{k_{\|}^{2}-\omega^{2}\varepsilon_{\text{out}}/c^{2}}} \tag{10}$$

Assuming that, as usual, $\varepsilon_{\text{out}} > 0$, the dispersion equation of surface polaritons can be satisfied only if $\varepsilon(\omega) < 0$. The dispersion equation (10) can be rewritten in a more convenient form:

$$k_{\|}^{2}=\frac{\omega^{2}}{c^{2}}\frac{\varepsilon(\omega)\varepsilon_{\text{out}}}{\varepsilon(\omega)+\varepsilon_{\text{out}}} \tag{11}$$

From here it is seen that the interval of the frequencies where surface polaritons can exist is narrower than $\omega_t < \omega < \omega_l$, since for real $k_{||}$ the negative dielectric permittivity $\varepsilon(\omega)$ must necessarily be less than $-\varepsilon_{\text{out}}$. Let ω_S denote the upper boundary of the surface polaritons frequency range: $\varepsilon(\omega_S) = -\varepsilon_{\text{out}}$. When ϵ_{out} approaches ϵ_b, $\omega_S \to \omega_l$. For a dielectric material, the function $\varepsilon(\omega)$ is given by (4); its graph is shown in Fig. 3, and the frequency interval where a surface polariton exists is highlighted. For a metal, when $\varepsilon(\omega) = 1 - \omega_p^2/\omega^2$ (ω_p is the plasma frequency), surface plasmon–polariton exists for $0 < \omega < \omega_p/\sqrt{1+\varepsilon_{\text{out}}}$. Fig. 4A shows surface polaritons neglecting the effects of spatial dispersion (thick magenta line marked as SP). The blue dashed lines $\omega = ck_{\|}/\sqrt{\varepsilon_{\text{out}}}$ and $\omega = ck_{\|}/\sqrt{\varepsilon_{\text{b}}}$ show, respectively, the photonic modes in the adjacent half-space and in the crystal (propagating parallel to the crystal surface), and the thick red lines marked as LP and UP are bulk polariton dispersion curves, shown here for reference. The photonic and bulk polaritonic dispersions do not intersect with the dispersion curve of the surface polariton, hence surface polaritons cannot be excited by an incident photon (or, once excited, cannot transform into bulk polaritons or leave the crystal as photons) – the laws of conservation of energy and wave vector cannot be simultaneously satisfied for such processes. To excite surface polaritons, one has to make use of a prism (attenuated total-reflection technique) or a grating on the crystal surface. Surface polaritons were seen as dips in the total reflection of TM-polarized light in many such experiments.

If spatial dispersion is taken into account, the spectrum becomes more complicated, since then (assuming a positive effective mass m_t) the large-wave-vector lower 'bulk' polariton becomes resonant with the small-wave-vector surface polariton (see Fig. 4B). As discussed above, it requires introduction of ABCs, which mix surface polaritons with bulk lower polaritons. The mixing leads to leakage of the energy of the surface wave into the interior of the crystal, providing a new (nonradiative and nondissipative) damping mechanism for surface polaritons.

Surface polaritons in more complex geometry

The presence of a surface transition layer can essentially alter the dispersion of surface polaritons. The transition layer may be either natural or artificial (a thin film on a substrate). As shown by Agranovich and Mal'shukov (1974), if an oscillation in the layer is resonant with the surface polariton, a gap with a magnitude Δ_S opens in the surface polariton spectrum. This is similar to what happens to bulk electromagnetic waves near the resonance frequency with the difference that both the excitation in the layer and the surface electromagnetic wave have a two-dimensional character. While usually the effects of a thin layer are of the order of $d/\lambda \ll 1$ (d is the layer thickness, λ is the wavelength of the light), here $k_{\|}^{2}=\frac{\omega^{2}}{c^{2}}\frac{\varepsilon(\omega)\varepsilon_{\text{out}}}{\varepsilon(\omega)+\varepsilon_{\text{out}}}$, and therefore the gap was observed in a number of experiments, both in the infrared spectral region and in the spectral region of electronic transitions.

Surface texture, either controllable (a grating) or natural (surface roughness), as well as imperfections of the crystal that supports surface polariton (such as polycrystalline grains) alter the dispersion of surface polaritons in significant ways. As is typical for disordered samples, the surface polariton frequency acquires a shift, which results in the change of the polariton's group velocity. Furthermore, the mode is attenuated while propagating along the surface, due to its interaction with surface imperfections (for

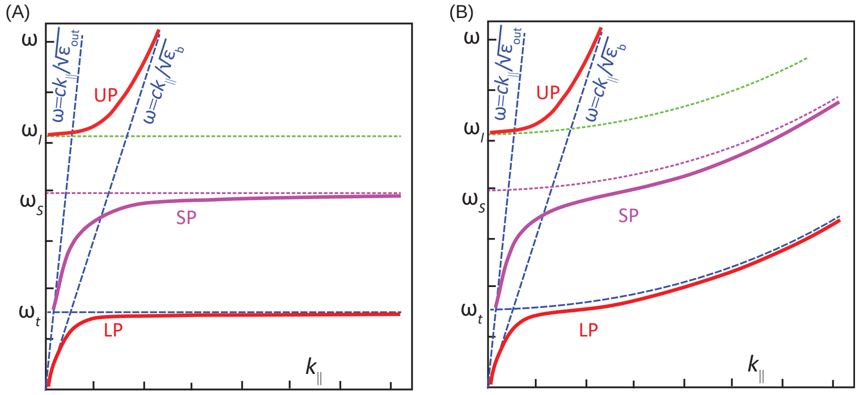

Fig. 4 Dispersion of surface polariton (magenta solid line) at an interface between a resonant isotropic crystal with dielectric function $\varepsilon(\omega)$ and an isotropic material with a dielectric constant ε_{out} (A) without and (B) with spatial dispersion. Thick red lines show the dispersions of bulk polaritons, and thin dashed lines show the dispersion of the photons outside the crystal and of the 'bare' photon in the crystal. UP, LP, and SP denote, respectively, the upper, lower, and the surface polariton branches.

rough surfaces) or scattering at the grains' boundaries (for polycrystals). Finally, while still being predominantly localized near the interface, the mode can acquire a radiative component, and hence a finite radiative lifetime. In other words, the imperfections scatter a surface polariton wave into other surface polariton modes and into vacuum radiation.

Polaritons in nanostructures with reduced dimensionality

In bulk crystals the interaction of excitons with an electromagnetic field does not give rise to radiative decay of the exciton. Instead, the energy oscillates back and forth between exciton and photon states (vacuum Rabi oscillations). This can be attributed to the conservation of total wave vector of bare excitations: An exciton with a given wave vector interacts with only one photon with the same wave vector, and there is no density of states for irreversible radiative decay.

Another situation occurs in a confined geometry, i.e. in two- (2D) and one-dimensional (1D) crystals, where an exciton has less degrees of freedom than a photon. As noted by Agranovich and Dubovsky (1966), in such crystals the radiative decay is restored, since in these cases only two (in 2D) or one (in 1D) of the components of the total wave vector are conserved.

Consider polaritonic effects in quasi-2D quantum wells and quasi-1D quantum wires. The translational symmetry is preserved (and, consequently, the wave vector $\boldsymbol{k}_{||}$ of the exciton is a good quantum number) only in the plane of the quantum well in the first case, and only along the quantum wire in the second case. The component of the total wave vector perpendicular to $\boldsymbol{k}_{||}$ is denoted by $\boldsymbol{k}_{\perp}$. Photons are 3D, as before.

It turns out that the system supports two distinct kinds of states. Consider first the states with small values of the wave vector $k_{||} < k_0 \equiv \omega\sqrt{\varepsilon_b}/c$. They are degenerate with photons and hence can decay into them. One can regard it as a coupling of an exciton with a wave vector $\boldsymbol{k}_{||}$ with a reservoir of photons with the same component $\boldsymbol{k}_{||}$ parallel to the quantum well or the quantum wire, but with all possible values of $\boldsymbol{k}_{\perp}$. These photons act as a dissipative bath, and instead of forming stable hybrid states similar to polaritons in the bulk, the exciton decays irreversibly.

The corresponding radiative lifetimes can be calculated treating exciton–light coupling as a perturbation. For Frenkel exciton–polaritons, the decay times in 1D and 2D are $\tau_{1D}^{(F)} = (2\pi a/\lambda)\tau_0$ and $\tau_{2D}^{(F)} = (2\pi a/\lambda)^2\tau_0$, where $\sim$: $\tau_0 \sim 10^{-9}$–10^{-8} s is the radiative lifetime of the excitation of an isolated molecule, and a is the lattice constant (i.e., the radiative decay is enhanced proportionally to the number of molecules within the wavelength of light, λ). The radiative lifetime of exciton–polaritons in 2D is then $\sim 10^{-12}$ s, and such a 'superradiant decay' was observed in anthracene. For Wannier–Mott exciton–polaritons, the lifetime of 2D exciton–polariton for $k_{||} = 0$ was found to be $\tau_{2D}^{(WM)} = m_1 c\sqrt{\varepsilon_b}/(2\pi e^2 f_{osc})$ and is about 10 ps for the parameter of GaAs. The account of the effects of thermalization and disorder-induced partial localization of polaritons considerably complicates the picture both in 1D and 2D cases.

For $k_{||} > k_0$, the modes are nonradiative. In quantum wells, to some extent, they are similar to surface polaritons, since the electromagnetic field in them decays exponentially outside of the quantum well plane. Similarly, the propagating modes can be excited using a prism or a surface grating. Radiative polaritons with $k_{||} < k_0$ can be excited directly by incident light and were observed in many semiconductor nanostructures in absorption, photoluminescence, and reflectivity spectra.

Cavity polaritons

In nanostructures called optical planar microcavities both excitons and photons have a 2D character. The interaction between them leads to formation of states similar to bulk polaritons known as 'cavity polaritons.' These states are stable in the sense that an exciton with a given 2D wave vector $\boldsymbol{k}_{||}$ interacts with only one cavity photon with the same $\boldsymbol{k}_{||}$, and, similarly to bulk polaritons, the energy oscillates back and forth between these states. In other words, in contrast to the low-dimensional nanostructures described in the previous section, where photons were 3D and the material excitons had a reduced dimension, in a planar microcavity there is no density of states for irreversible radiative decay of the exciton. After several oscillations, however, photons escape the cavity due to a finite transmission of the cavity mirrors. Cavity polaritons were observed for the first time by Wesbuch et al. (1992) in a GaAs planar microcavity.

An optical microcavity modifies the photonic density of states and reduces its quantization volume. As a result of confinement both the binding energy of the Wannier–Mott exciton and the exciton–light coupling are enhanced, so that Wannier–Mott exciton–polaritons are considerably more stable in the 2D geometry than in the bulk, and the polariton splitting 2Δ is much more pronounced. Furthermore, lower polaritons have a finite (rather than zero) energy at $k_{||} = 0$, and this lowest-energy state may, in principle, work as a 'trap' when polaritons undergo phonon-assisted relaxation after non-resonant excitation.

Since the mirrors of planar microcavities are often fabricated as distributed Bragg reflectors, a detailed description of cavity polaritons requires simulating a multi-layered structure. The dispersion equation of cavity polaritons can be obtained from Maxwell's equations with the help of the transfer-matrix method, which relates the transmission and reflectance at each interface of the multiple layers. Near the resonance, one obtains the dispersion equation of the type (7) with solutions similar to (8), with the energies of 'bare' exciton and photon dependent on the in-plane wave vector $k_{||}$. A significant difference arises for the cavity photon dispersion, since the perpendicular component of its total wave vector is fixed by the boundary conditions at the microcavity mirrors, leading to parabolic (for small $k_{||}$) dispersion of the cavity photon, which, in a simplifying assumption of ideal mirrors, reads:

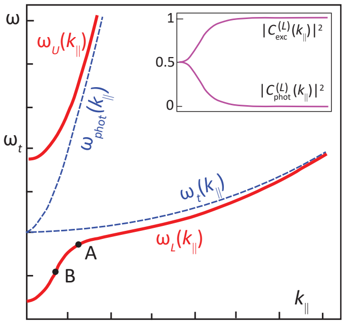

Fig. 5 Dispersion of cavity polaritons (red solid lines) for zero detuning, i.e., when $\omega_c = \omega_t$. Blue dashed lines correspond to the dispersions of 'bare' cavity photon and 'bare' exciton. The inset shows the dependence on the wave vector of the exciton and photon weight coefficients $|C_{exc}^{(L)}(k)|^2$ and $|C_{phot}^{(L)}(k)|^2$ defined in Eq. (2) for the lower branch.

$$\omega_{\text{phot}}(k) = \omega_c + \frac{hk^2}{2\mu} \tag{12}$$

where $\omega_c \equiv \omega_{\text{phot}}(0) = \pi c/\left(L_c\sqrt{\varepsilon_b}\right)$, L_c is the microcavity thickness, and $\mu = \pi\hbar\sqrt{\varepsilon_b}/(cL_c)$ is its effective mass, which is very small ($\sim 10^{-5} m_e$, m_e is the electron mass). The dispersion curves of cavity polaritons are plotted in Fig. 5.

The detuning between the cavity photon and quantum-well exciton $u = \omega_c - \omega_t$ determines the ratio between exciton and photon weights in the polaritonic states for each $k_{||}$. Since this ratio determines the properties of the polaritonic states (including their ability to interact with each other and disorder), the detuning serves as a control parameter in designing polaritonic properties. The value of detuning is determined by the cavity thickness and, due to a wedge-shaped microcavity profile, can be varied in experiments.

At moderate excitation powers, the relaxation of polaritons into the ground state $\omega_L(0)$ is impeded due to the so-called bottleneck effect observed in photoluminescence experiments. Polaritons accumulate near the 'knee' at the lower polariton dispersion curve just below the exciton energy (near the point A in Fig. 5), since there the acoustic phonon-assisted relaxation is not effective due to an abrupt decrease of the density of final states. Qualitatively, at this point lower-branch polaritons change their character from exciton-like to photon-like, which essentially impedes the phonon-assisted relaxation (Tassone et al., 1997).

Macroscopic population of excitations in $\omega_L(0)$ state can be reached exploiting the bosonic nature of cavity polaritons. Bosonic effects had first manifested themselves in the experiments on stimulated scattering of cavity polaritons in a GaAs/AlGaAs microcavity (Savvidis et al., 2000). In these experiments, lower-branch polaritons were excited resonantly near the inflection point of their dispersion curve (point B in Fig. 5). A convex–concave character of the dispersion curve at this point allows for the polariton–polariton scattering process, when one polariton is scattered into the state with $k_{||} = 0$ ('signal'), and one is scattered to a higher-energy state ('idler'). A weak stimulation of $k_{||} = 0$ state by a probe beam leads to a giant ($\sim$100-fold) amplification of the 'signal' due to the fact that the scattering rate of bosons is proportional to $n_i(1 + n_f)$, where n_i and n_f denote, respectively, the populations of the initial and final states. Several years later, Kasprzak et al. (2006) experimentally demonstrated Bose–Einstein condensation (BEC) of polaritons in a CdTe/CdMgTe microcavity. Above a threshold excitation density, the observed broad emission from a non-resonantly pumped microcavity transformed to a narrow peak centered at $k_{||} = 0$. This was accompanied by spontaneous build-up of coherent polarization of the condensed polaritons out of depolarized population below the threshold. The polariton occupancy followed Maxwell-Boltzmann distribution with the effective temperature as high as 19 K.

Since then, condensation of cavity polaritons and the polariton lasing were demonstrated by other groups in a variety of settings. The materials with larger oscillator strength, such as GaN (Christopoulos et al., 2007), ZnO (Li et al., 2013), organic materials (Kena-Cohen and Forrest, 2010) and mono-atomic layers of transition metal dichalcogenides (TMDCs; Waldherr et al., 2018) allowed for achieving room-temperature polariton lasing. For practical purposes, polaritonic laser requires not only room temperature operation, but also electrical injection of carriers. Research in this direction is underway.

The unprecedentedly high-temperature polaritonic BEC owes to small (compared to atoms) effective mass of cavity polaritons. However, polaritonic BEC differs in many ways from text-book BEC of bosonic particles. Many efforts are done to understand polaritonic BEC in presence of such factors as a finite lifetime of polaritons within the cavity, external pumping, strong polariton-polariton interactions, disorder, polarization degree of freedom, and vibronic excitations (in organic materials). Various scenarios are possible. Generally speaking, two-dimension character of polaritons implies that polaritons undergo Berezinskii-Kosterlitz-Thouless (BKT) phase transition, rather than "true" Bose–Einstein condensation. This had been confirmed experimentally by Roumpos et al. (2012), by measuring the first order spatial correlation function of polaritons, which showed typical for BKT superfluid phase power-low decay, however modified by the non-equilibrium character of the polariton condensate: Polaritons undergo decay and reappear via pumping, instead of reaching thermalization in a closed system. At the same time, structural disorder combined with driven-dissipative nature of the polariton condensate may lead to appearance of pinned vortices (Lagoudakis et al., 2008) – which are different from vortices formed spontaneously as a result of thermal fluctuations in BKT transition to a superfluid phase. This direction was further explored by Sanvitto et al. (2011), who demonstrated experimentally and modelled theoretically all-optical control of motion of vortices and formation of controllable vortex-antivortex pairs in an optical potential, which played the role of artificial disorder. Quite recently, polaritonic condensation served as a basis for realization of an exciton-polariton topological insulator (Klembt et al., 2018). Polaritonic condensate was also suggested as a candidate system for high-temperature superconductivity (Laussy et al., 2010).

Yet another direction of research under the umbrella of cavity polaritons is currently gaining momentum. It is often called 'molecular polaritons,' and it studies ensembles of molecules strongly coupled to optical cavity vacuum or to surface plasmons. These systems exploit rich level structure of the molecules, with large oscillator strength of some transitions giving rise to strong and even ultrastrong coupling (both for electronic and for dipole-active vibronic transitions), and with a multitude of dark or weakly coupled to light states that take part in the relaxation dynamics of excitations. In particular, organic molecules are responsible for the observation of room-temperature single-molecule strong coupling in plasmonic nanocavities, which are made of gold nanoparticles separated by a sub-nm spacer from a gold substrate (Chikkaraddy et al., 2016). Furthermore, a pioneering observation of a cavity-induced slowing of photoisomerization rate of a photochrome by Hutchison et al. (2012) gave rise to a rapidly evolving direction conventionally referred to as 'polariton chemistry.' The key idea is that the strong coupling modifies the level structure of molecules, and hence the energy landscapes governing reactions pathways. As a result, a cavity-embedded molecule under properly chosen resonance conditions may exhibit a different (with respect to a cavity-free scenario) chemical properties (such as isomerization and reactivity), as well as different energy transfer ability.

Dark-state polaritons in atomic gases

Nowadays many efforts are devoted to creating techniques for controllable and reversible trapping of photonic states into atomic degrees of freedom. Photons are perfect carriers of information, while the atomic subsystem may act as a storage facility and simultaneously provide interactions between stored photons. Therefore, possible applications in quantum information and optical communication.

Recent experiments demonstrated photon trapping in coherently driven atomic gases, first in an ultracold gas, and soon after in warm alkali vapors. The generic scheme involves two electric fields ('probe' and 'control') and three atomic levels (which we denote by $|g_1\rangle$, $|g_2\rangle$ and $|e\rangle$; the first two are long-lived low-energy states, the third is an excited state of the atom). Strong control field, which resonantly couples the states $|g_2\rangle$ and $|e\rangle$, dramatically modifies the propagation of a weak probe field in a narrow spectral window near the frequency of the $|g_1\rangle \rightarrow |e\rangle$ transition. The refractive index of the gas experienced by the probe has a zero imaginary part at the resonance, and hence the probe propagates without absorption, owing to which this phenomenon is known as 'electromagnetically induced transparency.' In addition, near the resonance the real part of the refractive index exhibits strong variation as a function of frequency, and hence the group velocity of the probe is strongly modified. The group velocity of the probe appears to be

$$v_g = \frac{c}{\left(1 + \Delta^2/\Omega_c^2\right)} \tag{13}$$

where $\Omega_c = E_c d_{|g_2\rangle \rightarrow |e\rangle}/\hbar$ is the Rabi frequency of the control field with the amplitude E_c driving the transition $|g_2\rangle \rightarrow |e$, and Δ is, as before, the vacuum Rabi frequency of the $|g_1\rangle \rightarrow |e >$ transition.

The expression (13) shows that the group velocity of the probe can be modified by varying the intensity of the control field. Decreasing E_c results in slowing the probe down to velocities as small as several meters per second ('slow light'), or even brings a light pulse to a full stop. When $E_c = 0$ (control beam is turned off), v_g vanishes, and the photon is trapped in the atomic gas. The trapped photon is retrieved by turning the control laser on again. The storage is completely coherent as long as the entire process is adiabatic.

These dynamics happen because inside the gas the probe light is strongly coupled to the collective excitation of the atomic ensemble driven by the control field. The result of this coupling is called 'dark-state polariton.' When E_c vanishes, the polariton is mapped onto purely atomic excitations, and the propagation stops.

Conclusion

We have discussed polaritons – excitations that form if the strength of interaction between light and a dipole-active material resonance in a solid medium exceeds existing losses and relaxation rates. Though many 'types' of polaritons can be distinguished (as determined by the physical nature of the resonance the light couples with), with some reservations it is correct to say that the properties of polaritons depend more on the geometry of the system than on the specifics of the resonance. This is not surprising, given that polaritons can be viewed simply as a doublet of states originating from coupling between two oscillators. The hybrid polaritonic states possess simultaneously some properties of light (higher tolerance of structural disorder, light-like propagation) and some features of material excitations (non-linear interactions, coupling with phonons). Exploring this duality is what makes polaritons unique, and polaritonic field of research attractive and flourishing.

References

Agranovich VM (1959) Dispersion of electromagnetic waves in crystals. *Zhurnal Eksperimental'noi i Teoreticheskoi Fiziki* 37: 430. (1960, *Soviet Physics ZhETP* **10:** 307).

Agranovich VM and Dubovsky OA (1966) Influence of retardation on spectrum of excitons in one- and two-dimensional crystals. *Pis'ma v Zhurnal Eksperimental'noi i Teoreticheskoi Fiziki* 3: 345.. (1966, *Journal of Experimental and Theoretical Physics (JETP) Letters*, 3: 223).

Agranovich VM and Mal'shukov AG (1974) Surface polariton spectra if the resonance with the transition layer vibrations exist. *Optics Communications* 11: 169.

Chikkaraddy R, de Nijs B, Benz F, Barrow SJ, Scherman OA, Rosta E, Demetriadou A, Fox P, Hess O, and Baumberg JJ (2016) Single-molecule strong coupling at room temperature in plasmonic nanocavities. *Nature Letters* 535: 127.

Christopoulos S, Höger GB, von Högersthal AJDG, Lagoudakis PG, Kavokin AV, Baumberg JJ, Christmann G, Butté R, Feltin E, Carlin J-F, and Grandjean N (2007) Room-Temperature Polariton Lasing in Semiconductor Microcavities. *Physical Review Letters* 98: 126405.

Fano U (1956) Atomic theory of electromagnetic interactions in dense materials. *Physical Review* 103: 1202.

Hopfield JJ (1958) Theory of the contribution of excitons to complex dielectric constants of crystals. *Physical Review* 122: 1555.

Hopfield JJ and Thomas DG (1963) Theoretical and experimental effects of spatial dispersion on the optical properties of crystals. *Physical Review* 132: 563.

Huang K (1951) On the interaction between the radiation field and ionic crystals. *Proceedings of the Royal Society of London Series A* 208: 352.

Hutchison JA, Schwartz T, Genet C, Devaux E, and Ebbesen TW (2012) Modifying Chemical Landscapes by Coupling to Vacuum Fields. *Angewandte Chemie, International Edition* 51: 1592.

Kasprzak J, Richard M, Kundermann S, et al. (2006) Bose–Einstein condensation of cavity poalritons. *Nature* 443: 409.

Kena-Cohen S and Forrest SR (2010) Room-temperature polariton lasing in an organic single-crystal microcavity. *Nature Photonics* 4: 371.

Klembt S, Harder TH, Egorov OA, Winkler K, Ge R, Bandres MA, Emmerling M, Worschech L, Liew TCH, Segev M, Schneider C, and Höfling S (2018) Exciton-polariton topological insulator. *Nature* 562: 552.

Lagoudakis KG, Wouters M, Richard M, Baas A, Carusotto I, Aandre R, Dang LS, and Deveaud-Pledran B (2008) Quantized vortices in an exciton—polariton condensate. *Nature Physics* 4: 706.

Laussy FP, Kavokin AV, and Shelykh IA (2010) Exciton-polariton mediated superconductivity. *Physical Review Letters* 104: 106402.

Li F, Orosz L, Kamoun O, Bouchoule S, Brimont C, Disseix P, Guillet T, Lafosse X, Leroux M, Mexis M, Mihailovic M, Patriarche G, Reveret F, Solnyshkov D, Zuniga-Perez J, and Malpeuch G (2013) From excitonic to photonic polariton condensate in z ZnO-based microcavity. *Physical Review Letters* 110: 196406.

Pekar SI (1957) The theory of electromagnetic waves in a crystal in which excitons are produced. *Zhurnal Eksperimental'noi i Teoreticheskoi Fiziki* 33: 1022.. (1958, *Sov. Phys. ZhETP* 6: 785).

Roumpos G, Lohse M, Nitsche WH, Keeling J, Szymańska MH, Littlewood PB, Löffler A, Höfling S, Worschech L, Forchel A, and Yamamoto Y (2012) Power-law decay of the spatial correlation function in exciton-polariton condensates. *PNAS* 109: 6467.

Sanvitto D, Pigeon S, Amo A, et al. (2011) All-optical control of the quantum flow of a polariton condensate. *Nature Photonics* 5: 610.

Savvidis PG, Baumberg JJ, Stevenson RM, Skolnick MS, Whittaker DM, and Roberts JS (2000) Angle-resonant stimulated polariton amplifier. *Physical Review Letters* 84: 1547.

Tassone F, Piermarocchi C, Savona V, Quattropani A, and Schwendimann P (1997) Bottleneck effects in the relaxation and photoluminescence of microcavity polaritons. *Physical Review B* 56: 7554.

Tolpygo KB (1950) Physical properties of a lattice of rock salt type composed from deformable ions. *Zhurnal Eksperimental'noi i Teoreticheskoi Fiziki* 20: 497. (in Russian).

Waldherr M, Lundt N, Klaas M, Betzold S, Wurdack M, Baumann V, Estrecho E, Nalitov A, Cherotchenko E, Cai H, Ostrovskaya EA, Kavokin AV, Tongay S, Klembt S, Höfling S, and Schneider C (2018) Observation of bosonic condensation in a hybrid monolayer $MoSe_2$-GaAs microcavity. *Nature Communications* 9: 3286.

Wesbuch C, Nishioka M, Ishikawa A, and Arakawa Y (1992) Observation of the coupled exciton–photon mode splitting in a semiconductor quantum microcavity. *Physical Review Letters* 69: 3314.

Further reading

Agranovich VM and Ginzburg VL (1984) *Crystal Optics with Spatial Dispersion, and Excitions*. Berlin: Springer.

Agranovich VM and Mills DL (1982) *Surface Polaritons*. Amsterdam, North-Holland: Modern Problems in Condensed Matter Sciences.

Agranovich VM and Bassani GF (2003) Electronic excitations in nanostructures. *Thin Films and Nanostructures*. vol. 31, pp. 129–184. Amsterdam: Elsevier.

Herrera F and Owrutsky J (2020) Molecular polaritons for controlling chemistry with quantum optics. *The Journal of Chemical Physics* 152: 100902.

Kaganov MI, Pustylnik NB, and Shalaeva TI (1997) Magnons, magnetic polaritons and magnetostatic waves. *Uspekhi Fiz. Nauk (Physics-Uspekhi)* 167: 191.

Kavokin A, Malpuech G, Agranovich VM, and Taylor D (2003) Cavity polaritons. *Thin Films and Nanostructures*. vol. 32. Amsterdam: Elsevier.

Khitrova G, Gibbs HM, Jahnke F, Kira M, and Koch SW (1999) Nonlinear optics of normal-mode-coupling semicondcutor microcavities. *Reviews of Modern Physics* 71: 1591–1639.

Lukin MD (2003) Colloquium: Trapping and manipulating photon states in atomic ensembles. *Reviews of Modern Physics* 75: 457.

Ribeiro RF, Martínez-Martínez LA, Du M, Campos-Gonzalez-Angulo J, and Yuen-Zhou J (2018) Polariton chemistry: controlling molecular dynamics with optical cavities. *Chemical Science* 9: 6325.

Yamamoto Y, Tassone F, and Cao H (2000) *Semiconductor Cavity Quantum Electrodynamics*. Berlin: Springer.

Semiconductor Heterojunctions, Electronic Properties of

M Peressi, University of Trieste, Trieste, Italy

© 2005 Elsevier Ltd. All rights reserved.

This is an update of M. Peressi, Semiconductor Heterojunctions, Electronic Properties of, Editor(s): Franco Bassani, Gerald L. Liedl, Peter Wyder, Encyclopedia of Condensed Matter Physics, Elsevier, 2005, Pages 273–281, ISBN 9780123694010, https://doi.org/10.1016/B0-12-369401-9/01136-0.

Introduction 507
Electronic Properties: Band Alignments 509
Measuring Band Offsets 509
Predicting Band Offsets 511
Band Offset Trends 512
Lattice-Matched Semiconductor Interfaces 512
Isovalent semiconductor heterojunctions 512
Heterovalent semiconductor heterojunctions 512
Lattice-Mismatched Semiconductor Interfaces 513
Band Offset Engineering 513
Localized Interface States 514
Semiconductor Heterostructures and Spintronics 514
Further Reading 514

Nomenclature

a_0	lattice parameter
e	electron charge
E_c	conduction band
E_g	fundamental bandgap
E_v	valence band
n	electron density
ΔE_c	conduction band difference (with respect to reference levels in the bulks)
ΔE_g	fundamental bandgap difference
ΔE_v	valence band difference (with respect to reference levels in the bulks)
ΔV	electrostatic potential lineup
ε	dielectric constant

Introduction

Semiconductor heterojunctions are built by joining, at a planar face, two semiconductors formed by different chemical elements but usually with similar lattice structure and chemical binding, as schematically indicated in Figure 1. From the simple heterojunction constituted by two thick slabs of different materials, which presents only one interface, different heterostructures can be formed – from the double heterojunction showing confinement properties for the charge carriers to the repeated heterojunctions (multiple quantum wells and superlattices) and new artificial structures based on sequences of alternating different semiconductors of varying thickness (10–1000 Å).

Semiconductor heterojunctions show peculiar electronic properties giving rise to physical phenomena of a quantum mechanical nature, some of them not possible even in any "natural" bulk material. These peculiar electronic features are determined by the spatial profile of the electronic bands, which is in turn controlled both by intrinsic characteristic of constituent semiconductors, such as lattice constants, energy gaps, doping, and extrinsic features such as chemical and structural details in the interface region, where the bands exhibit discontinuities (see Figure 2). The spatial profile of the electronic bands can be used to properly tailor the space-charge distribution and the behavior of the charge carriers both in the growth direction (transport properties) and in the potential wells parallel to the interface planes (confinement properties), giving the semiconductor heterojunctions a crucial role in modern electronic and optoelectronic devices.

The introduction of heterojunctions dates back to almost 50 years ago. Herbert Kroemer and Zhores I Alferov obtained the Nobel Prize in Physics in 2000 "for developing semiconductor heterostructures used in high-speed- and opto-electronics." In 1957, Herbert Kroemer published the first proposal for a heterostructure transistor. His theoretical work showed that heterostructure devices could offer superior performance compared to conventional transistors. In 1963, H Kroemer and Zhores I Alferov

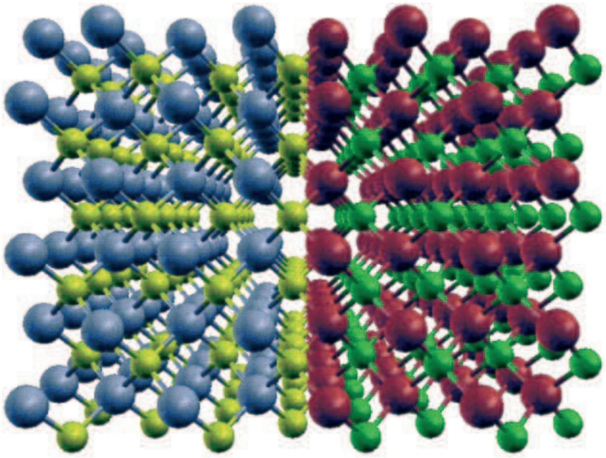

Figure 1 Stick-and-ball model of an abrupt semiconductor heterojunction between two zinc blende semiconductors with no-common ions. The interface is (0 0 1) oriented. (Adapted from Sorba L, *et al.* (1992) Structure and local dipole of Si interface layers in AlAs–GaAs heterostructures. *Physical Review B* 46: 6834.)

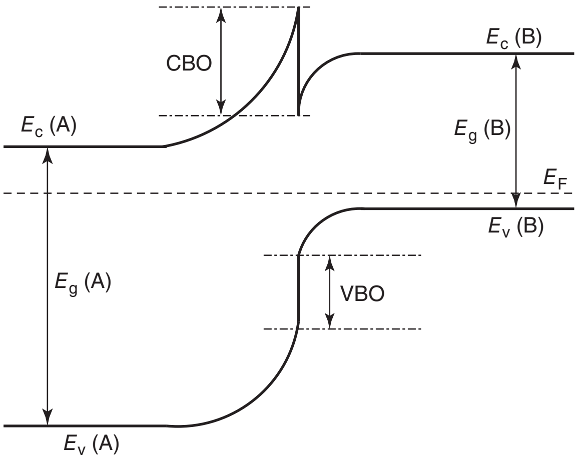

Figure 2 Schematic spatial profile of the valence and conduction bands along the growth direction for a semiconductor heterojunction, with band bending due to space-charge effects and definition of band offsets, VBO and CBO.

independently proposed ideas to build semiconductor lasers from heterostructure devices, using a double heterostructure to confine carriers. Alferov built the first semiconductor laser from gallium arsenide and aluminum arsenide in 1969.

The traditional semiconductor heterojunctions involve elements of the central portion of the periodic table, starting from Si and GaAs. Si- and GaAs-based technology is the most mature, but many other III–V and II–VI binary compounds as well as alloys are used nowadays, the choice depending on the particular application. Among alloys, perhaps the most widely studied and used is $Al_xGa_{1-x}As$, in particular, in its interface with GaAs.

High-quality semiconductor interfaces are easily built from two semiconductors which are isovalent and lattice-matched, but more generally they can be also heterovalent (involving semiconductors of different groups) and lattice-mismatched, with slightly different lattice parameters. With the addition of nitrides of II(IV)–VI compounds and of magnetic semiconductors to the most conventional ones, the range of the lattice constants and of the energy gaps which is covered by the different constituents used to form heterostructures is very large, as indicated by Figure 3, suggesting possibilities for new fundamental physics and device applications.

Thanks to the improvement of experimental techniques such as molecular beam epitaxy (MBE) and metal–organic chemical–vapor deposition (MOCVD), it is possible to grow high-quality pseudomorphic heterostructures without misfit dislocations or other defects, also with semiconductors with a rather small lattice mismatch (i.e., less than a few percent), and with different but almost commensurate structures.

A heterojunction indicated with A/B typically corresponds to a particular growth order: B is the substrate and A the epilayer. Another specific feature that is usually indicated is the crystallographic growth axis, which determines the interface plane.

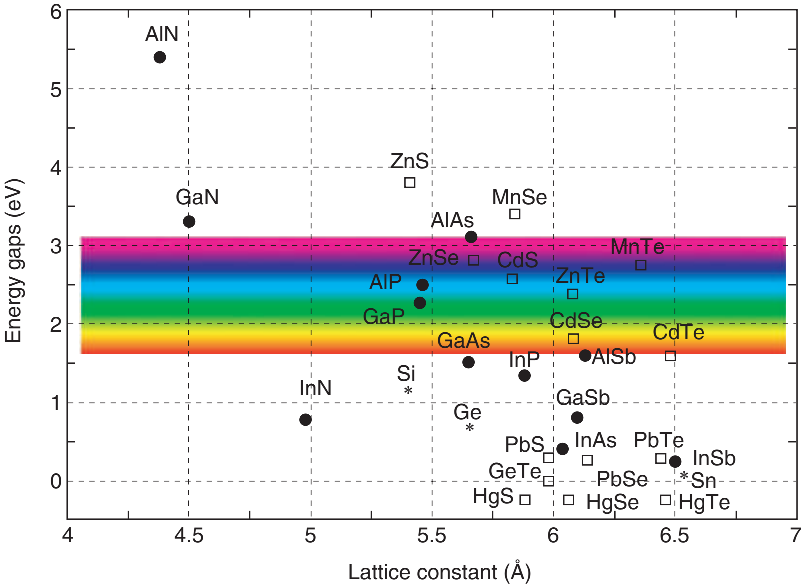

Figure 3 Energy gaps vs. lattice constants for various IV (stars), III–V (closed circles), II(IV)–VI (open squares) zinc blende semiconductors. The visible electromagnetic spectrum is also indicated.

Electronic Properties: Band Alignments

The spatial profile of the electronic bands is mostly determined by the band discontinuities at the interface. The bandgap difference ΔE_g, normally existing between the constituent materials, is shared among valence and conduction bands, thus giving rise to the valence and conduction band offsets (VBO and CBO):

$$\Delta E_g = \text{VBO} + \text{CBO} \quad [1]$$

There are different types of band lineups which are possible, schematically indicated in Figure 4. The straddling or type-I lineup characterizes, for instance, the GaAs/$Ga_xAl_{1-x}As$ interface. Modern optoelectronic devices – including quantum well lasers – are based on such a lineup, typically with a double or repeated heterojunction, where the charge carriers are both confined in the slab of material with the lowest energy gap (see Figure 5). Other types of lineups are the staggered or type-II and the broken-gap or type-II-misaligned lineups, which could be preferred for some specific applications.

Extensive theoretical and experimental work has targeted the problem of band alignments since a long time. In particular, an important and general issue widely debated is whether the band discontinuities are essentially determined by the bulk properties of the constituents, or if some interface-specific phenomena, such as crystallographic orientation and abruptness, may affect them in a significant way. A large joint experimental and theoretical/computational effort has been performed to finally clarify, quite recently, the physical mechanisms which give rise to the band alignment. Several books and review articles are available on the subject, as indicated in the "Further reading" section. Some of them are focused on the problem of band offset engineering, that is, on the possibility of controlling the interfaces thus providing a way to manipulate the band lineups and tune the transport properties across the junctions.

Measuring Band Offsets

Several experimental techniques are available for measuring energy band discontinuities, including optical and transport measurements. Since the late 1970s, spectroscopic techniques have emerged as a fundamental tool for investigating heterojunctions on a microscopic scale. In photoemission spectroscopy, for instance, a direct measurement of the band discontinuities can be done by comparing specific core-level binding energies E_{cl} with respect to valence band top edges E_v in bulk samples with those from the heterostructure:

$$\text{VBO} = [E_{cl}(\text{Ga } 3d) - E_v(\text{Ga As})] - [E_{cl}(\text{Al } 2p) - E_v(\text{Al As})] + \Delta E_{cl} \quad [2]$$

An example is schematically shown in Figure 6 for the AlAs/GaAs(0 0 1) interface.

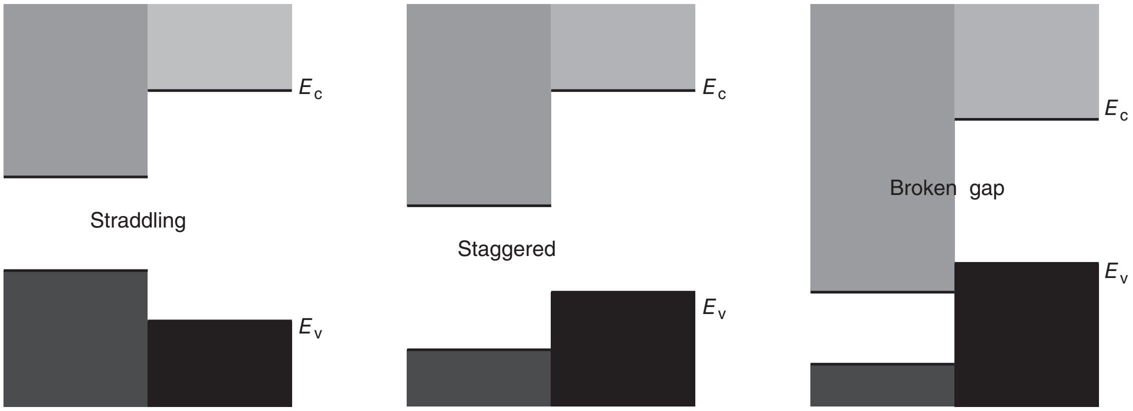

Figure 4 Schematic possible types of band alignments: (a) straddling, (b) staggered, and (c) broken gap. Flat bands are represented, as the focus is on a region which is of the order of 10 atomic units, and the band bending is negligible at this scale.

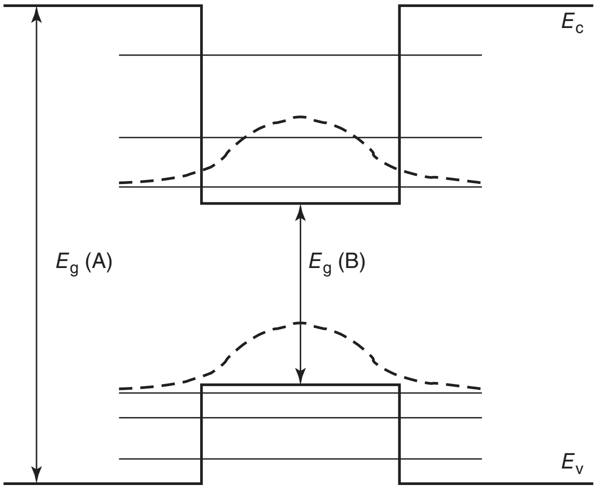

Figure 5 Confinement of electrons and holes in the slab of a material with the lower gap in a double semiconductor heterostructure with straddling-type band alignment.

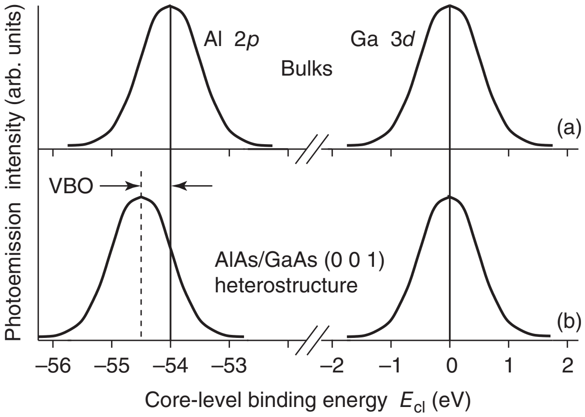

Figure 6 Example of a photoemission measurement of the band offset at the semiconductor heterojunction AlAs/GaAs(0 0 1). Core-level binding energy distribution curves for Al 2*p* and Ga 3*d* states referred to the corresponding AlAs and GaAs valence band top edges are schematically drawn. The zero of the energy scale is arbitrarily taken at the center of the Ga 3*d* emission peak. The variation of the separation ΔE_{cl} of the core level peaks from the case of the two bulks, considering the topmost valence bands of the two materials aligned (a) and the heterojunction (b) is a direct measurement of the VBO.

Predicting Band Offsets

Theoretical and numerical investigations based on different approaches have contributed toward predicting band offset values and identifying the basic mechanism responsible for band offsets. These investigations can be divided mainly into two classes: (1) models and approaches making simplifying and sometimes drastic approximations in describing the interface, but retaining important physical concepts, and (2) accurate computational predictions based on fully self-consistent *ab initio* approaches, which allow one to fully take into account the interface details, such as orientation, abruptness, and defects.

In general, no universal energy scale exists on which the band structures of the different semiconductors can be easily and uniquely referred, but simple and old models based on intrinsic reference levels have been widely used and have given successful predictions for a number of heterostructures: from the oldest models by Anderson, Frensley, and Kroemer, based on the difference between the electron affinities of the two semiconductors and the concept of charge neutrality levels, to Tersoff's model emphasizing the role of interface dipoles. More refined quantum mechanical approaches, based on the envelope function concept or using the tight-binding method have also been widely and successfully applied. They are reviewed in the books cited above.

The second class of theoretical/computational investigations, more recent, includes *ab initio* approaches, which are based on the solution of quantum mechanical equations for the system under consideration without any use of empirical parameters. This seemingly unaffordable task has been made feasible, thanks to the density-functional theory (DFT) proposed by Walter Kohn, who received the Nobel Prize in Chemistry in 1998 for the same, and for its approximations for practical applications, such as the local-density approximation. DFT has proven to yield reliable results, at an acceptable computational cost, on the electronic ground-state properties of complex crystalline systems, allowing a meaningful comparison with experiment or even accurate predictions of quantities not yet accessible experimentally, with an extremely useful predictive power.

In *ab initio* approaches, semiconductor heterostructures are normally modeled using periodically repeated supercells with a limited number of atoms. The relevant effects due to the presence of the interface are confined in a small region, and the bulk features of the charge density distribution and electrostatic potential are completely recovered within a few atomic units from the interface. This justifies the concept of abrupt discontinuities of the electronic bands across the interfaces which is used in the schematic diagrams of electronic band profiles.

The supercell self-consistent calculations provide the electronic charge density distribution and the corresponding electrostatic potential, as shown in Figure 7. Filtering out the microscopic oscillations with the bulk-like periodicity, one can unambiguously define an "interface dipole" and extract a potential difference across the interface, ΔV, which, in principle, depends on the interface structural

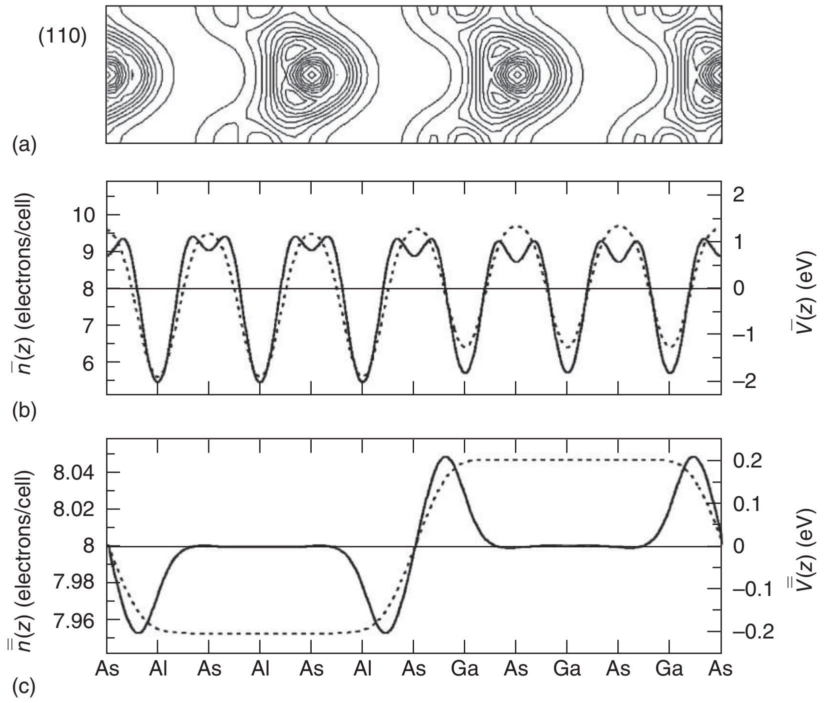

Figure 7 Contour plot of the valence electron density distribution (a) for GaAs/AlAs(0 0 1) heterojunction over a (1 1 0) plane containing the growth axis and centered on the interface anion. Profiles of the electron density and of the electrostatic potential along the growth direction averaged over planes parallel to the interface ($\bar{n}(z)$ and $\bar{V}(z)$) (b), and further averaged along the growth direction with a filter equal to the periodicity of bulks ($\bar{\bar{n}}(z)$ and $\bar{\bar{V}}(z)$) (c).

and chemical details. The final band offsets VBO and CBO are determined by the difference ΔE_v and ΔE_c between the relevant band edges in the two materials, measured with respect to the average electrostatic potential in the corresponding bulk crystals:

$$\mathrm{VBO} = \Delta V + \Delta E_v \qquad [3]$$

$$\mathrm{CBO} = \Delta V + \Delta E_c \qquad [4]$$

When the two semiconductors constituting the heterostructure are rather similar (in structure and chemical composition), their differences can be quite minute with respect to the typical bulk variations, and a low-order perturbation approach is appropriate.

The state-of-the-art theoretical approaches allow one not only to compute band discontinuities accurately but also to obtain an insight into the atomic-scale mechanisms which determine the band lineups, and interpret and predict their trends. However, the predictive capability of theoretical schemes is actually limited by the difficulty in predicting the actual atomic-scale arrangement at the interfaces, and their kinetic versus thermodynamic character.

Band Offset Trends

Some peculiar trends in band offsets at semiconductor heterojunctions have been clarified, thanks to the large joint experimental and computational effort: at lattice-matched isovalent heterojunctions, the band offsets depend only on the bulk properties of the two materials, whereas at heterovalent heterojunctions they crucially depend on the interface orientation and other microscopic details. These results are briefly reviewed and justified in the following section.

Lattice-Matched Semiconductor Interfaces

Isovalent semiconductor heterojunctions

The GaAs/AlAs heterojunction is the simplest prototype of lattice-matched common-anion heterojunctions. The different cations are isovalent; therefore, the induced potential drop across the interface is only due to the electronic charge. Measurements and accurate numerical investigations show that the VBO and CBO are independent of the interface orientation and abruptness. These results can also be generalized to isovalent no-common-ion heterojunctions such as InAs/GaSb and InP/$\mathrm{Ga_{0.47}In_{0.53}As}$, where the lattice-matching conditions result from a balance between the differences of the cationic and anionic core radii, and consequently an important microscopic and configuration-dependent interfacial strain may establish.

Consequences of the bulk-like character of the VBO and CBO are the commutativity and transitivity relationships, which are valid, at least approximately, in the whole class of isovalent semiconductor heterojunctions:

$$\mathrm{VBO}(A/B) = -\mathrm{VBO}(B/A) \qquad [5]$$

$$\mathrm{VBO}(A/B) = \mathrm{VBO}(A/C) + \mathrm{VBO}(C/B) \qquad [6]$$

Heterovalent semiconductor heterojunctions

For the sake of clarity, the reader is referred to the case of Ge/GaAs as the simplest prototype of heterovalent semiconductor heterojunctions, but similar considerations apply to other heterojunctions characterized by a valence mismatch between the constituent atoms, such as those among ZnSe, Ge, and GaAs.

In the (1 1 0) direction, each atomic plane is characterized by the same average ionic charge, so that an abrupt junction does not carry ionic charge contribution and the lineup is due only to the electrons. At variance, ideally abrupt interfaces along a polar direction such as (0 0 1) would be charged and hence thermodynamically unstable, as already emphasized first by Harrison in 1978. The simplest neutral and stable interfaces one can envision are terminated by one mixed plane of anions or cations, $\mathrm{As_{0.5}Ge_{0.5}}$ or $\mathrm{Ga_{0.5}Ge_{0.5}}$ (see Figure 8). These two interfaces are stoichiometrically inequivalent, and, because of ionic point charges contribution due to the different valence of the atoms involved (Ge vs. Ga, Ge vs. As), they also correspond to different band offsets. Elementary electrostatics together with a linear response theory predict that the screened ionic point-charge contribution to the offsets is equal in magnitude and opposite in sign for the two interfaces: $\Delta V_{\mathrm{ionic}} = \pm \pi e^2/2a_0\langle\varepsilon\rangle$, where a_0 is the lattice parameter involved and $\langle\varepsilon\rangle$ a proper average of the dielectric constants of the constituents. The maximum predicted possible variation with interface composition of the band offset at these interfaces is thus $\pi e^2/a_0\langle\varepsilon\rangle \approx 0.8\mathrm{eV}$ for Ge/GaAs. For ZnSe/Ge, where the valence difference between the constituting elements is twice, the maximum possible variation would be $2\pi e^2/a_0\langle\varepsilon\rangle \approx 1.3\mathrm{eV}$.

In general, the atomic interdiffusion which may also occur across the interface over several atomic planes, depending on the growth conditions, reduces the point-charge contribution to the offset, and the observed variations of the offsets are smaller. However, for heterovalent heterostructures deviations from the commutativity and transitivity rule definitely beyond the experimental resolution, up to ≈0.5 eV, are observed, and these are a clear fingerprint of the formation of inequivalent interfaces.

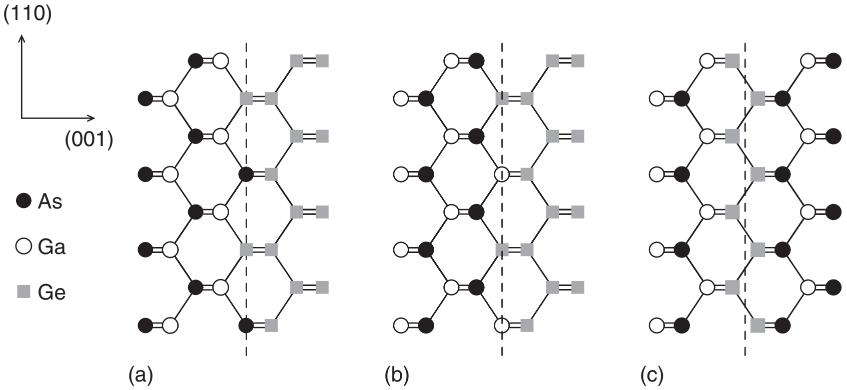

Figure 8 Atomic configurations for the two simplest neutral Ge/GaAs interfaces (a), (b), and for a Ge bilayer embedded in GaAs (c). (Adapted from Sorba L *et al.* (1992) *Physical Review B* 46: 6834.)

Lattice-Mismatched Semiconductor Interfaces

In lattice-mismatched heterojunctions, the band offsets are affected by the stress state of the two materials, depending on the substrate. In pseudomorphically grown heterostructures, the epilayer accommodates its mismatch with the substrate with an almost homogeneous strain and a lattice constant $a_{\perp}$ along the growth direction, which essentially depends on its elastic properties and on the mismatch with the substrate. The strain state of the epilayer affects the band edges with a combined effect of shift and split. The former affects the averages of the band edge manifolds, calculated with respect to the reference electrostatic potential, and depends on the hydrostatic component of the strain, that is, on the relative volume change with respect to the cubic unstrained material. Splitting effects depend on the orientation and sign of the strain (tensile or compressive). The total variation of the VBO with strain also includes the variation of the electrostatic potential lineup ΔV.

The simplest case of lattice-mismatched heterojunctions is Si/Ge, which is an example of isovalent homopolar interfaces. The predicted variation of the VBO at this heterojunction is ~0.5 eV, changing the substrate from Si to Ge. Larger effects could be, in principle, possible at heterovalent lattice-mismatched heterojunctions, such as Si/GaAs, or in presence of larger lattice mismatches. However, the difficulty of growing high-quality lattice-mismatched heterojunctions drastically limits their formation and their use in practice.

Band Offset Engineering

In bulk semiconductor technology, one of the most important and widely used features has been the possibility of intentionally varying the electronic properties by alloying and doping. For semiconductor heterojunctions, a similarly important challenge is to control and artificially modify the band offsets.

As already mentioned, the VBO and CBO at lattice-matched isovalent semiconductor heterojunctions are mostly determined by the bulk properties of the constituents, and interface details such as orientation and stoichiometry play a very minor role, whereas at heterovalent heterojunctions they are very sensitive to these extrinsic features. As a consequence, heterovalent heterojunctions seem to be ideal candidates as tunable heterojunctions, while using only isovalent materials, it seems that the only way to tune the offset is to act on their bulk properties with strain or with alloying.

Actually, the peculiarity of heterovalent interfaces leads naturally to a practical way for modifying the offset also at isovalent heterojunctions, or even for creating an offset at a homojunction. For instance, joining together the two inequivalent interfaces Ge/GaAs(0 0 1) (Ge–As and Ge–Ga terminated), one has the following sequence of atomic planes: ⋯ As–Ga–As–$Ge_{0.5}Ga_{0.5}$–$Ge_{0.5}As_{0.5}$–Ga–As–Ga⋯. Therefore, using the difference between the VBOs of these two inequivalent interfaces, a net potential drop $\Delta V = \pi e^2/a_0\langle\varepsilon\rangle$ is predicted across the mixed bilayer. This potential drop is the same that would result from a microscopic capacitor whose plates are placed at a distance $a_0/4$, and carry a surface charge $\sigma = e/a_0^2$. The above sequence of atomic planes can also be thought of as due to the transfer of a proton per atomic pair from the As to the Ga planes.

This viewpoint is easily generalized to arbitrary concentrations of Ge in a pair of consecutive compensated GaAs planes, Ge_xGa_{1-x} and Ge_xAs_{1-x}, to ensure local charge neutrality. The maximum potential drop would be, in principle, $\Delta V_{\max} = 2\pi e^2/a_0\langle\varepsilon\rangle$ for the case $x = 1$, that is, for an entire Ge bilayer embedded (see Figure 8). The above results can be further generalized to the heterojunctions, for example, doping a GaAs/AlAs interface with ultrathin layers of Si or Ge. In this case, the interlayer contribution can reduce or increase the intrinsic VBO according to the growth sequence. These predictions have been indeed experimentally confirmed for Si interlayers at GaAs/AlAs and AlAs/GaAs (0 0 1) junctions and analogous effects have also been observed in other systems.

Localized Interface States

Another important issue in the heterojunction electronic structure concerns the presence of localized interface states in heterojunctions, their origin, and their role in determining the electronic characteristics of the junctions. The existence of localized interface states is generally claimed whenever anomalous features are observed in photoemission, optical, or transport measurements. Their unambiguous identification, however, is a difficult task in experiments. Reflectance anisotropy spectroscopy has been recently applied to a few interfaces and seems to be a promising tool for more direct investigations.

The electronic states of a heterojunction can be extended everywhere, localized in one material or the other (acting as a quantum well), or localized at the interface. The true interface states are not degenerate with bulk Bloch states, decay exponentially away from the interface, and exist only in the mutual energy gaps. The comparison of the band structures of the two bulk materials with the spectrum of the heterojunction allows one to identify those states which do not belong to the bulk band structures, and are, therefore, candidates to be interface states. Localized electronic states can be successfully identified in numerical investigations also by the local density of states: far from the interface on the two sides of the junction, it yields the bulk densities of states of the two materials, whereas its deviations with respect to the constituting bulk state densities in the interface region would indicate the presence of states which are localized there.

Interface states can have different physical origins. In some cases, they are associated with defects which typically arise at junctions between two morphologically different phases (e.g., cubic and wurtzite). But localized electronic states can also occur, in principle, at semiconductor heterojunctions with constituents having the same or similar structure but different chemical properties. Simple electron-counting schemes indicate that the valence mismatch between neighboring atoms from opposite sides of the junction could result in localized interface states corresponding to donor or acceptor bonds. Therefore, heterovalent heterojunctions, which exhibit such kind of bonds in the interface region, are natural candidates for the existence of localized interface states. Localized states have been experimentally detected at diamond/zinc blende interfaces, for example, Ge/ZnSe, at zinc blende/zinc blende heterovalent interfaces, for example GaAs/ZnSe, and even at isovalent no-common-ion interfaces, for example, BeTe/ZnSe.

Accurate calculations predict that interface electronic states critically depend not only on the type of heterojunction (i.e., heterovalent rather than isovalent), but on the particular atomic-scale morphology of the interface.

Semiconductor Heterostructures and Spintronics

The word "spintronics" denotes electronic-like heterostructures where the relevant physical quantity is the spin of the carriers and its interactions with external magnetic fields, rather than the charge of holes and electrons and the associated electronic properties.

Semiconductor heterostructures using carrier spin as a new degree of freedom offer new functionality with respect to conventional junctions. A large effort is currently devoted to integrate traditional III–V and II–VI semiconductors with ferromagnetic semiconductors or, more generally, with other ferromagnetic materials including metals and half-metals. There are, however, several advantages using all-semiconducting devices: interface properties, such as lattice matching and band offsets, are more understood and controllable, and the integration with the existing conventional semiconductor technology is easier. The diluted ferromagnetic semiconductors are semiconductor compounds where a fraction of the constituent ions is replaced by magnetic ions. This is the case, for instance, of (Ga,Mn)As, which has received particular attention: Mn is a heterovalent substitutional impurity for Ga in GaAs (valence II with respect to the valence III of Ga), and therefore, it can be used as a source of spin-polarized holes. An Mn content up to 5% is sufficient to make (Ga,Mn)As ferromagnetic.

Furthermore, there is the possibility of a good integration of half-metals with conventional semiconductors: these are materials that have only one occupied band at the Fermi level, and behave as a metal in one spin channel and as a semiconductor in the other. Current effort, both experimental and theoretical, is nowadays devoted to predict those particular heterostructures where half-metallicity is also maintained in the presence of the interface.

Further Reading

Bastard G (1988) *Wave Mechanics Applied to Semiconductor Heterostructures*. Les Ulis, Cedex: Les Editions de Physique.

Brillson LJ (1992) Surfaces and interfaces: atomic-scale structure, band bending and band offsets. In: Landsberg PT (ed.) *Handbook on Semiconductors*, vol. 1, pp. 281–417. Amsterdam: North-Holland. ch. 7.

Capasso F (1987) Band-gap engineering: from physics and materials to new semiconductor devices. *Science* 235: 172–176.

Capasso F and Margaritondo G (eds.) (1987) *Heterojunction Band Discontinuities: Physics and Device Application*. Amsterdam: North-Holland.

Franciosi A and van de Walle CG (1996) Heterojunction band offset engineering. *Surface Science Reports* 25(1–4): 1–140.

Grimmeiss HG (ed.) (1996) *Heterostructures in Semiconductors*. Proceedings of the Nobel symposia in physics, Physica Scripta, vol T68, Stockholm.

Harrison WA, Kraut EA, Waldrop JR, and Grant RW (1978) Polar heterojunction interfaces. *Physical Review B* 18: 4402–4410.

http://www.nobel.se/physics/laureates/1973/esaki-lecture.html

http://www.nobel.se/physics/laureates/2000/alferov-lecture.html

http://www.nobel.se/physics/laureates/2000/kroemer-lecture.html

Margaritondo G (ed.) (1988) *Electronic Structure of Semiconductor Heterojunctions*. Dordrecht: Kluwer.

Ohno Y, Young DK, Beschoten B, Matsukura F, Ohno H, and Awschalon DD (1999) Electrical spin injection in a ferromagnetic semiconductor heterostructure. *Nature* 402(6763): 790–792.

Peressi M, Binggeli N, and Baldereschi A (1998) Band engineering at interfaces: theory and numerical experiments. *Journal of Physics D: Applied Physics* 31: 1273–1299.

Yu ET, McCaldin JO, and McGill TC (1992) Band offsets in semiconductor heterojunctions. In: Ehrenreich H and Turnbull D (eds.) *Solid State Physics*, vol. 46, pp. 1–146. Boston: Academic Press.

Vurgaftman I, Meyer JR, and Ram-Mohan LR (2001) Band parameters for III–V compound semiconductors and their alloys. *Journal of Applied Physics* 89(11): 5815–5875.

Wolf SA, Awschalom DD, Buhrman RA, Daughton JM, von Molnar S, et al. (2001) Spintronics: a spin-based electronics vision for the future. *Science* 294(5546): 1488–1495.

Semiconductors, Impurity and Defect States in

H Ikoma, Tokyo University of Science, Tokyo, Japan

© 2024 Elsevier Ltd. All rights reserved.

This is an update of H. Ikoma, Semiconductors, Impurity and Defect States in, Editor(s): Franco Bassani, Gerald L. Liedl, Peter Wyder, Encyclopedia of Condensed Matter Physics, Elsevier, 2005, Pages 330–334, ISBN 9780123694010, https://doi.org/10.1016/B0-12-369401-9/00470-8.

Introduction 516
Structural and Electrical Properties of Impurities and Crystal Defects 516
Theory of the Electronic States of the Shallow Impurities 516
Experimental Determination of the Shallow Energy Levels 518
Theory of the Electronic States of the Deep Impurities (or Defects) 518
Experimental Determination of the Deep Energy Levels 519
Further Reading 519

Introduction

The role of mobile charge carriers is a key factor in semiconductor device operations. These free carriers are supplied by doping semiconductors with certain kinds of impurities. The electrical properties of semiconductors can thus be controlled by adding a small amount of impurities. However, some other impurities and crystal defects often have detrimental effects on the performance of the device. These impurities and defects create discrete energy levels in the bandgap of the host semiconductor, and exert various influences (usefully or detrimentally) on the semiconductor characteristics. Therefore, a knowledge of the electronic structure of the impurities and defect states in semiconductors is very important.

Structural and Electrical Properties of Impurities and Crystal Defects

Impurity atoms normally substitute the atoms of the host semiconductor (substitutional impurity atom). However, some of them, especially those with small atomic radii, often enter the interstitial site in the host crystal lattice (interstitial impurity atom). On the other hand, the well-known point defects – the vacancies (lattice points where atoms are lacking) and the interstitials (atoms of the host semiconductor occupying the interstitial sites) – are examples of the intrinsic crystal defects. These point defects sometimes generate a complex center such as the Frenkel defect (the pair of vacancy and interstitial atoms in the neighboring lattice sites). There are two types of impurities and defects from the electrical point of view. One of them supplies free electrons and the other provides holes in the host crystal. The former is called donor and the latter, acceptor. For example, when V-column elements such as P and As are doped in Si (IV-element), one excess valence electron is easily liberated (the impurity atom is ionized) in the Si lattice even at room temperature because of the low binding energy between the electron and the impurity atom. Also, when a III-element such as B is introduced into Si, one valence electron is deficient so that one hole is created and easily released in the Si lattice at room temperature due to their very low binding energy. These impurities, having very low binding (ionization) energies are termed shallow impurities (shallow donor and shallow acceptor). If Si is doped with VI-elements (S, Se, and so on) or II-elements (Zn, Cd, and so on), two free electrons or two holes per impurity atom, respectively, are created (double donor and double acceptor). On the other hand, some impurity elements (and crystal defects) have very high binding energies so that electrons or holes are not easily liberated in the host crystal at room temperature. These impurities with high binding energies are called deep impurities. Heavy metals such as Fe, Ni, and Cu in Si, for example, are deep impurities. In compound semiconductors, the same impurity atom behaves both as a donor and an acceptor depending on its occupied site (amphoteric impurities). The Si atom in GaAs behaves as a donor if it occupies the Ga site and as an acceptor when it substitutes the As atom. When IV-elements (Ge, C, etc.) are doped in Si, they also behave as donors or acceptors although there are cases when they are not electrically active. These impurities are called isoelectronic impurities. With doping of the impurities in semiconductors, the discrete energy levels are normally generated in the bandgap of the host semiconductor. For shallow donors and acceptors, these energy levels are located very near the bottom of the conduction band and the top of the valence band, respectively. On the other hand, the energy levels for the deep impurities occur near the middle of the bandgap.

Theory of the Electronic States of the Shallow Impurities

Shallow impurities can be theoretically treated using the effective mass approximation and the hydrogen atom model. Consider the case of the donor (the acceptor can also be considered similarly). The excess electron moves in an orbit round the impurity ion due to the Coulomb interaction between them in the host crystal, just like the hydrogen atom. The Coulomb potential is much smaller than that in the hydrogen atom due to the screening effect of the valence electrons (the change of the valence electron distributions around the impurity ion) in the crystal lattice. The screened Coulomb potential is written as $U = Zq^2/\varepsilon_s r$, where Z is the valence number of the impurity ion, q the electronic charge, ε_s the dielectric constant of the host semiconductor and, r is the distance between the electron and impurity ion. The screening effect is effectively represented by the dielectric constant ε_s. Thus, the electron is very loosely bound by the impurity ion (very low binding energy) and its wave function extends in the wide range of the crystal lattice. Hence, the electron moves feeling both the periodic potential of the host crystal and the screened Coulomb potential. The effect of the periodic potential on the motion of electrons is well described in terms of the "effective mass" m^*, that is, electrons in the periodic potential of crystal behave as if they are free electrons with their mass m^* being different from that (m_0) in a vacuum. Therefore, the electrons in the orbital round the shallow impurity ions can be considered as electrons with an effective mass m^* moving in the screened Coulomb potential U. The fundamental Schrödinger equation for these electrons is written as follows:

$$\left[\left(\frac{\hbar}{2m_0}\right)\nabla^2 + (V - U)\right]\Psi(\mathbf{r}) = E\Psi(\mathbf{r})$$

Here, $\nabla^2 = (\partial^2/\partial x^2 + \partial^2/\partial y^2 + \partial^2/\partial z^2)$ is an operator, $\Psi(\mathbf{r})$ the wave function of the electron, $r = (x, y, z)$ the position vector of the electron, V and U the periodic potential in the perfect crystal and the screened Coulomb potential, respectively, and E is the energy of the electron. In the case of U=0 (perfect crystal), the solution of the above equation is given by the Bloch wave function $\Psi n\mathbf{k}(\mathbf{r}) = \exp(\mathrm{i}\mathbf{k}\mathbf{r})u_{nk}(\mathbf{r})$, where $\exp(ikr)$ is the wave function of the free electron (plane wave) extending to the whole crystal, and $u_{nk}(\boldsymbol{r})$ is the function having the periodicity of the crystal lattice with n and $\boldsymbol{k}$ being the quantum number specifying the energy bands and the wave number vector, respectively. For applying the effective mass approximation to the shallow impurity problem, the wave function $\Psi(\mathbf{r})$ is expanded by the Bloch functions or their Fourier transforms (the Wannier functions) and substituted in the equation. Thus, the following equation is obtained:

$$\left[\frac{\hbar}{2m^*}\nabla^2 - U\right]\mathbf{\Phi}(\mathbf{r}) = E\mathbf{\Phi}(\mathbf{r})$$

This equation is the same as that for the hydrogen atom except for the difference in the electron mass. The wave functions of the electrons are given as the product of $\mathbf{\Phi}(\mathbf{r})$ and the function which has the periodicity of the crystal lattice. The above equation is for the case of the isotropic conduction band (in which the effective mass is the same for all crystal orientations). For example, some compound semiconductors such as GaAs and InP have this type of conduction bands. On the other hand, the conduction bands are anisotropic in semiconductors such as Si, Ge, and GaP, that is, the effective mass is different in different crystal orientations. The valence bands of most semiconductors have degeneracy in which the energies of the "heavy" holes and the "light" holes coincide at the top of the band. For these cases, the above equation should be modified to take the anisotropy or degeneracy of the band structures into consideration. The details of the same are not discussed here.

The solution of the above equation is well known for the "hydrogen atom." The electronic states of the hydrogen atom are specified by the principal (Bohr) quantum number n, the angular momentum quantum number l, the magnetic quantum number m, and the spin quantum number s. The principal quantum number n is the positive integer and the angular momentum quantum number $l \leq n - 1$ for each n value. The magnetic quantum number m is given as $m = l, l - 1, l - 2, 0, \ldots, -l - 1, -l (l \geq m \geq -l)$ and the spin quantum number $s = \pm 1/2$. The electronic states corresponding to l=0, 1, and 2 are called s, p, and d states, respectively. Then the state of$n$=1 and l=0 is called as the 1s state (the ground state: the state of the lowest energy). The higher energy states (the excited states) are thus called as 2s (n=2,l=0), 2p(n=2, l=1), 3s(n=3, l=0), 3p(n=3, l=1), 3d(n=3, l=2) states and so on. The energies E_n of these states obtained from the above equation are given as

$$E_n = -E_0/n^2 \qquad (n=1, 2, 3, \ldots)$$
$$E_0 = (\varepsilon_0/\varepsilon_s)^2 (m^*/m_0) E_H$$

Here E_0 is the energy of the ground (1s) state and, ε_0 and ε_s are the dielectric constants of the vacuum and semiconductor respectively. E_H is given as $E_H = (1/\varepsilon_0)^2 (q^4 m_0/2\hbar^2) = 13.6\mathrm{eV}$ and is the ground-state energy of the real hydrogen atom (the Rydberg constant). From the above equations, it is obvious that the energy E_n is only dependent on the principal quantum number n (degenerate with respect to the other quantum numbers l, m, and s) in the case of the isotropic conduction band. For the donor and acceptor, respectively, the ionization energies (the binding energies) E_D and E_A from the ground state can be calculated as $E_D = E_C - E_0$ and $E_A = E_V - E_0$, where E_C and E_V are, respectively, the energies of the bottom of the conduction band and the top of the valence band. In Figure 1, the shallow impurity levels are schematically shown.

The wave function is $\Phi_{1s}(r)$ of the ground state is written in the following:

$$\Phi_{1s}(r) = (1/\pi)^{1/2}(1/a^*)^{3/2}\exp(-r/a^*)$$

Here, it is assumed that z=1a^* is the Bohr radius given as $a^* = (\varepsilon_0 m^*)(\mathrm{h}^2/m_0 q^2)$ and represents the extent of the electronic wave function in the real crystal space. The wave function exhibits a sharp decrease at $r > a^*$. The wave functions of some excited states are as follows:

$$\mathbf{\Phi}_{2s}(r) = (1/\boldsymbol{\pi})^{1/2}(1/2a^*)^{3/2}[2 - (r/a^*)]\exp(-r/2a^*)$$
$$\Phi_{2p}(r) = (1/\pi)^{1/2}(1/2a^*)^{3/2}(r/\sqrt{3})\exp(-r/2a^*)$$

In these excited states, the electron wave functions show a strong decay as

$$r > 2a^*$$

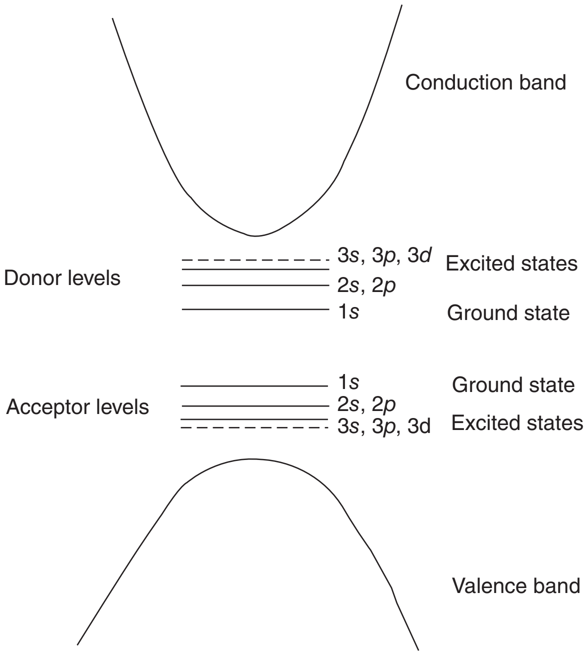

Figure 1 Shallow impurity level scheme in the wave number (*k*) space.

Experimental Determination of the Shallow Energy Levels

The energy levels of shallow impurities can be determined accurately using the infrared absorption measurements at very low temperatures. It is well known that electrons bound to a hydrogen atom can be excited to higher energy levels by the absorption of light. Similarly, electrons captured by shallow impurity levels are transferred to higher energy levels by absorbing infrared light. These optical transitions are allowed only when the difference (Δl) in the angular momentum quantum numbers (l) between two related energy levels is 1 ($\Delta l = 1$) (the selection rule). Thus the electrons can be excited from the 1*s* (ground) state to the $2p, 3p, 4p, \ldots$ (excited) states. However, the transitions $1s \rightarrow 2s$, $1s \rightarrow 3s, \ldots$ (and so on) are not allowed. The absorption peaks of the infrared light are very sharp because these energy levels are completely discrete. By measuring the infrared absorption spectrum at very low temperature (~4.2 K), one can accurately determine the energies between the ground state and many excited states. The excited levels with very large principal quantum numbers n are located very close to the conduction or valence band edge so that one can determine the ground-state (1*s*) level and any excited ($2p, 3p, \ldots$) levels measured from the band edge (ionization energies). In Table 1, some examples of the measured shallow donor and acceptor levels (ionization energies) in Si are shown together with the calculated ones. The agreement between the measured and calculated values is excellent.

Theory of the Electronic States of the Deep Impurities (or Defects)

For the deep impurities, electrons (or holes) are very tightly bound to the impurity atom nucleus due to the highly localized core potential. The motion of the bound electrons (or holes) is strongly affected by this core potential and the wave functions of these carriers are also highly localized around the impurity atoms (or defect centers). Therefore, both the effective mass approximation and the hydrogen atom model cannot be applied to the deep level cases. The tight binding approximations, such as the linear combination of atomic orbitals (LCAO) method, are suitable to treat the deep-level problem. Since the core potentials are not small, the

Table 1 Some examples of the ionization energies of the ground states of shallow donors and acceptors

Host semiconductors	*Impurities*	*Experimental value(meV)*	*Theoretical value(meV)*
Si	P (D)	45.5	44.3
	As (D)	53.7	53.1
	Sb (D)	42.7	31.7
	B (A)	45.0	31.6
GaAs	Si (D)	5.84	5.72
	Ge (D)	5.88	5.72
InP		7.14	7.14
InSb	Te (D)	0.6	0.6

D: donor; A: acceptor.

conventional perturbation theory is not applicable and the Green-function approach is useful to solve the fundamental Schrödinger equation. The Schrödinger equation describing the motion of the electron bound to the deep impurity is given as follows:

$$(H_0 + U)\Psi(r) = E\Psi(r)$$

Here, H_0 is the Hamiltonian operator for the perfect crystal and U is the localized potential due to the deep impurity atom. In order to solve the above equation, the impurity potential U needs to be determined. However, this is very difficult for the following reason. In many cases of deep impurities, the impurity atoms are slightly displaced from the lattice point of the host semiconductor, and a microstrain is induced around the impurity atoms. It is assumed that if the impurity atom occupies the lattice point (as is the case for shallow impurities), a shallow energy level of E_D is generated. When this impurity atom is somewhat displaced from the lattice point (the lattice relaxation occurs), a deep energy level E_0 is assumed to be created. Also, a lattice relaxation energy (strain energy) E_L occurs. If E_0+E_L is higher than E_D, it is energetically stable to form the deep level with a small displacement of the impurity atom from the lattice point rather than the shallow levels. If the mixed semiconductor crystal AlGaAs is doped with Si, a deep-level center (called the DX center) is created while Si atoms act as shallow donors in GaAs. This DX center is considered to be as the above stated case. In order to determine the impurity potential U, the effect of the lattice relaxation should be taken into account exactly, which, however, is a very difficult problem. Many calculations have been performed by assuming various forms of the impurity potential U. The wave function $\Psi(r)$ is expanded in terms of the sp^3 atomic orbital functions $\left(\Phi_j\right)$ as $\Psi = \sum_j a_j \boldsymbol{\Phi}_j$ (LCAO). Then the Schrödinger equation is solved using the Green-function approach under the various assumptions of the impurity potentials. However, quantitative comparisons between the calculated and observed energy levels are difficult because of the difficulty in including the lattice relaxation effect in the analysis.

There are some cases of deep levels, in which the energy level merges into the conduction or the valence band of the host semiconductor. This level is called the resonant level. The existence of this level affects the band structure of the host crystal because the density of states of the impurities are superposed to those of the conduction or the valence band. With doping of the isoelectronic impurities, this resonant level is often observed. These resonant energy levels can also be calculated using the above Green-function approach.

Experimental Determination of the Deep Energy Levels

The deep level transient spectroscopy (DLTS) is the most powerful tool to determine deep energy levels. This method is based on the measurements of the transient electrical capacitances of the metal–semiconductor (Schottky) contact as the pulsed reverse bias voltage is applied. The transient Schottky capacitance $C(t)$ is written as follows.

$$C(t) = C_\infty\left[1 - \left(\frac{N}{2}\right)\exp\left(\frac{-t}{T}\right)\right]$$

Here $N = N_T/(N_D + N_T)$, N_T and N_D are the density of the deep impurity and the shallow donor, respectively. $C_\infty = \{(\varepsilon_s\varepsilon_0/2)(V + V_D)(N_D - N_T)\}^{1/2}$, ε_s and ε_0 are the dielectric constant of the semiconductor and a vacuum, respectively, and V_D is the diffusion potential of the Schottky contact. The relaxation time τ can be written as $e_n = 1/\tau$, where e_n is the electron (or hole) emission coefficient of the deep impurity and given as $e_n \propto C_n \exp[-(E_C - E_T/kT)]$ because electrons (and holes) are emitted from the deep levels by thermal activation. Here, C_n is the capture cross section of the deep impurity, E_T and E_C are the deep impurity energy level and the bottom of the conduction band, respectively. T and k are the absolute temperature and the Boltzmann constant, respectively. If the transient capacitance $C(t)$ is measured as a function of temperature T, the temperature dependence of e_n is obtained. From the plot of $\ln e_n$ versus $1/T$ (the Arrhenius plot), the deep energy level E_T can be easily determined. The capture cross section C_n and the deep impurity density N_T are at the same time determined. The famous example of the deep level is the EL2 center observed in the semi-insulating GaAs single crystal which is the cause of the high resistivity. The ionization energy of this EL2 center was measured to be 0.7~0.8 eV (located near the middle of the bandgap of GaAs).

Further Reading

Pantelides S (1978) The electronic structure of impurity and defect states in semiconductors. *Reviews of Modern Physics* 50: 797–858.
Pantelides S (1986) *Deep Centers in Semiconductors, A State of the Art Approach.* New York: Gordon and Breach.
Yu PY and Cardona M (1996) *Fundamentals of Semiconductors.* Berlin: Springer.

Semiconductor Nanostructures

B Voigtländer, Forschungszentrun Jülich GmbH, Jülich, Germany

© 2005 Elsevier Ltd. All rights reserved.

This is an update of B. Voigtländer, Semiconductor Nanostructures, Editor(s): Franco Bassani, Gerald L. Liedl, Peter Wyder, Encyclopedia of Condensed Matter Physics, Elsevier, 2005, Pages 290–297, ISBN 9780123694010, https://doi.org/10.1016/B0-12-369401-9/00589-1.

Introduction **520**
Physical Principles of Self-Organized Growth **520**
Semiconductor Nanoislands **521**
Lateral Positioning of Nanoislands by Growth on Templates 522
Vertical Stacking of Nanoislands 523
Semiconductor Nanowires **523**
Nanowires on Facetted Surfaces 523
Monolayer Thick Wires at Step Edges 523
Free-Standing Semiconductor Nanowires Grown by Vapor Liquid Solid Growth 524
Hybrid Systems – Combination of Lithography and Self-Organized Growth **525**
Further Reading **527**

Introduction

Two conceptually different methods are used to fabricate semiconductor nanostructures. In the top–down approach, lithography is used to fabricate nanostructures. In the bottom-up approach, small nanostructures form by self-organization during epitaxial growth. The greatest advantage of the top–down approach is the large variety of different structures, which can be generated by lithographic methods. In the case of the bottom-up approach, the variety of structures is much more limited. Islands, wires, rods, and rings have been fabricated bottom-up. However, the bottom-up approach offers the unique opportunity to fabricate very small nanostructures down to the one-digit nanometer range beyond the limits of current lithography techniques. Another advantage of self-organized fabrication of semiconductor nanostructures is the inherent parallel approach, in which billions of nanostructures are generated in parallel.

The focus of this article is the self-organized growth of semiconductor structures with lateral dimensions below 100 nm. Semiconductor quantum-well structures are nanostructures in the growth directions and not lateral nanostructures, and will not be considered in this article. The actual growth techniques used to fabricate the nanostructures like molecular beam epitaxy (MBE) and chemical vapor deposition (CVD) will be considered in separate articles. The methods used to analyze the nanostructures are scanning tunneling microscopy (STM), scanning force microscopy (AFM or SFM), transmission electron microscopy (TEM), and low energy electron microscopy (LEEM). Different properties of semiconductor nanostructures, and the applications of self-organized nanostructures in devices are discussed elsewhere in this encyclopedia. As examples for the self-organized growth of nanostructures, material systems such as Si/Ge and GaAs/InAs are used predominantly.

After introducing the self-organized semiconductor nanoislands grown on planar substrates, the aligned growth on prestructured samples is discussed. Subsequently, self-organized nanowires grown on facetted surfaces and the growth of monolayer thick wires by step-flow growth are presented. Finally, the growth of nanowires by vapor liquid solid (VLS) epitaxy and hybrid systems, where nanowires aligned to lithographically defined structures are fabricated, are presented.

Physical Principles of Self-Organized Growth

Semiconductor nanostructures can be fabricated by self-organization using heteroepitaxial growth, which is the growth of a material B on a substrate of a different material A. In heteroepitaxial growth, the lattice constants of the two materials are often different. The lattice mismatch for the two most commonly used material systems Si/Ge and GaAs/InAs is 4.2% and 7%, respectively (schematically shown in Figure 1a). This lattice mismatch leads to a buildup of elastic stress in the initial two-dimensional (2D) growth in heteroepitaxy. In the case of Ge heteroepitaxy on Si, the Ge is confined to the smaller lattice constant of the Si substrate, that is, the Ge is strained to the Si lattice constant. This results in a buildup of elastic stress (Figure 1b). One way to relax this stress is the formation of 3D Ge islands. In the 3D islands, only the bottom of the islands is confined to the substrate lattice constant. In the upper part of the 3D island, the lattice constant can relax to the Ge bulk lattice constant and reduce the stress energy this way (Figure 1c). This growth mode characterized by the formation of a 2D wetting layer and the subsequent growth of (partially relaxed) 3D islands is called Stranski–Krastanov growth mode.

The driving force for the formation of self-organized semiconductor nanoislands in heteroepitaxial growth is the buildup of elastic strain energy in the stressed 2D layer. As a reaction to this, a partial stress relaxation by the formation of 3D islands can lower the free energy of the system. The process of island formation close to equilibrium is a trade-off between elastic relaxation by formation of 3D islands which lowers the energy of the system and an increase of the surface area which increases the energy. Apart

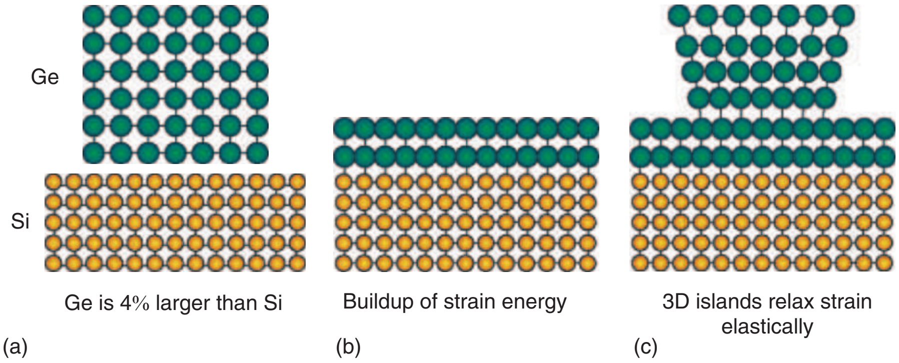

Figure 1 (a) Schematic representation of Si and Ge crystals with different lattice constants, (b) buildup of elastic strain energy during 2D growth with Ge confined to the Si lattice constant, and (c) elastic relaxation by formation of 3D islands (Stranski–Krastanov growth). In the upper part of the 3D island, the lattice constant relaxes towards the Ge bulk constant. The usual form of the 3D islands is a pyramid and not like the one shown in this schematic sketch.

from the formation of 3D islands, there is another process which can partially relax the stress of a strained 2D layer: the introduction of misfit dislocations. This corresponds to the removal of one lattice plane of a compressively strained 2D layer. If a lattice plane is removed in regular distances in the 2D layer, a misfit dislocation network forms.

Depending on the growth parameters, temperature, and growth rate, the self-organized growth can be close to equilibrium or in the kinetically limited regime. Close to equilibrium, that is, at high-growth temperatures or low-deposition rates, the occurring morphology (strained layer or 3D islands or a film with dislocations) is only determined by the energies of the particular configurations. The morphology with the lowest energy will be formed. If the growth is kinetically limited, the activation barriers are important. For instance, an initially flat strained layer can transform to a morphology with 3D islands or to a film with dislocations. What actually happens depends on the kinetics of the growth process, that is, on the activation energy for formation of 3D islands compared to the activation energy for the introduction of misfit dislocations.

Semiconductor Nanoislands

Stranski–Krastanov growth occurs in InAs/GaAs growth. An example of InAs nanoislands grown on a GaAs substrate is shown in the atomic force microscopy image in Figure 2. The InAs islands were grown by MBE at a growth temperature of 800 K. The width of the islands is 20 nm and the height 6 nm with a density of 10^{10} cm^{-2}. The challenges in the growth of these semiconductor islands are to grow islands of the desired size and density and with a high-size uniformity. In general, a higher growth temperature generally leads to the formation of larger islands; a higher growth rate leads to the formation of smaller islands. The size of the islands increases with the coverage. Often the density of the islands saturates at an early stage of the growth. These are general trends which may depend on the material system and the particular deposition technique. In some cases (self-limiting growth), the size of the islands saturates and the density increases with coverage. This kind of growth mode leads to a high-size uniformity of the islands. The size uniformity achieved in self-organized growth of semiconductor islands can be as small as ~10%. For optoelectronic applications, the nanoislands have to be capped (i.e., embedded in a semiconductor to prevent oxidation of the islands under ambient conditions where the optic measurements are performed) and care has to be taken that they change their shape and composition

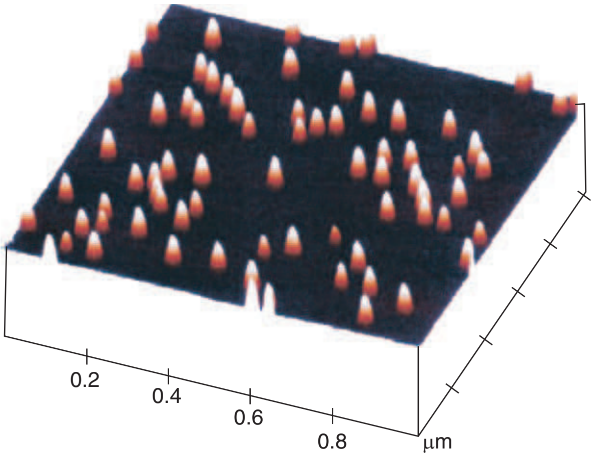

Figure 2 InAs nanoislands grown on a GaAs surface imaged by AFM. (Courtesy of A Lorke; reproduced with permission from Warburton RJ (2002) *Contemporary Physics* 44: 351; © Taylor & Francis Ltd. (http:www.tandf.co.uk).)

during the capping process. The confinement of charge carriers in all three directions gives rise to atomic-like energy levels. Quantum dot lasers operating at room temperature have now been realized. The islands grown on a flat substrate are usually not ordered laterally due to the random nature of the nucleation process. In the following sections, it is shown how nucleation at specific sites can be achieved.

Lateral Positioning of Nanoislands by Growth on Templates

On homogenous substrates, the location of the nanostructured islands formed were not predictable due to the stochastic nature of the nucleation process. It is desirable to position islands at specific (preselected) locations. This is desirable if the islands are used as functional units of nanoelectronic devices. Electric contacts can be structured easier when the location of an island is predefined. The approaches are now discussed where island nucleation occurs not randomly, but at specific locations. These predefined locations are usually specific sites on regularly prestructured substrates. Examples of such prestructured substrates are: regularly stepped substrates, facetted substrates, a regular arrangement of dislocations, or long-range surface reconstructions.

An example of ordered nucleation at a prestructured substrate is shown in Figure 3. Here Ge islands nucleate above dislocation lines. An SiGe film is grown on an Si(0 0 1) substrate. At the interface between the SiGe film and the substrate, dislocations form. The driving force for the formation of the dislocations is the relief of elastic strain, which arises due to the different lattice constants between the Si substrate and a Ge/Si film on this substrate. Due to the crystal structure of the substrate, the dislocations are aligned in straight lines along the two perpendicular high-symmetry directions of the substrate. During annealing, the dislocations form a relatively regular network, due to a repulsive elastic interaction between the dislocations. Figure 3 shows growth of Ge islands on this prestructured substrate. Rows of islands grow preferentially above the dislocation lines. The nucleation of Ge islands is more favorable at the relaxed areas above the dislocations, which have a lattice constant closer to that of Ge than the strained areas of the SiGe film, where the lattice constant is confined to that of the Si substrate. Islands have a lower energy if they grow with their natural lattice constant compared to growth at a different lattice constant (strained islands). This leads to a preferred nucleation of Ge islands above the dislocations. The nucleation does not occur randomly at the surface, but simultaneously at sites which have the same structure. This can lead to a narrower size distribution than for the growth on unstructured Si(0 0 1) substrates.

In the case of the growth on a prestructured substrate, another process of self-organization occurs (before the growth of islands) during the formation of the regular arrangement of the defect structures. Here, it is often a repulsive elastic interaction, which leads to a regular distance between steps or dislocations under equilibrium conditions. Since island nucleation occurs at the defect sites, the distances are determined by the distances of the defects. Nucleation at predefined defect sites has two advantages over the random nucleation. First, the islands are located at specific sites and second, the size distribution is narrower due to simultaneous nucleation at sites with identical environment.

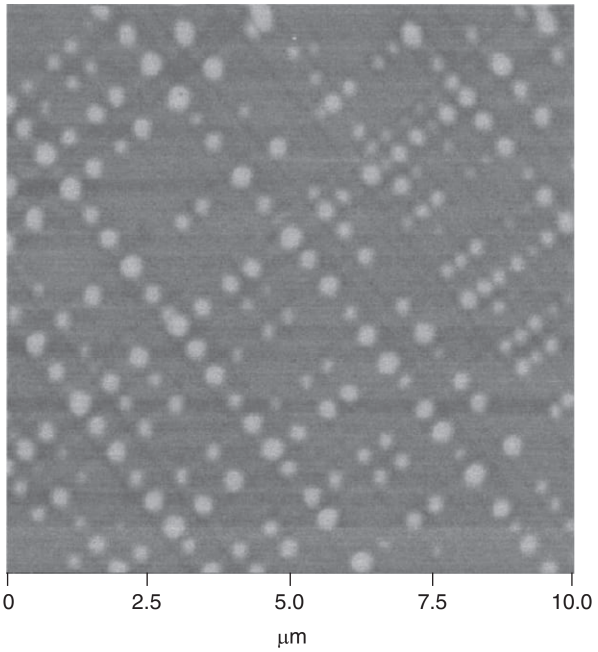

Figure 3 Ordered nucleation of Ge islands which is prestructured by an underlying network of dislocations. Image size 7 μm. (Reprinted figure with permission from Shiryaev SY, Jensen F, Lundsgaard Hansen J, Wulff Petersen J, and Nylandsted Larsen A (1997) *Physical Review Letters* 78: 503; © American Physical Society.)

Vertical Stacking of Nanoislands

A nucleation of nanoislands preferentially above existing ones can be achieved when a new layer of Ge (InAs) islands is grown on top of an Si (GaAs) spacer layer. If the spacer layer is sufficiently thin, the nucleation of islands occurs just above pre-existing islands. This vertical stacking of islands is shown in Figure 4 and can be explained as follows: the lattice constant of the top part of the Ge islands is increased close to the bulk constant. Subsequent Si deposition leads to an increased lattice constant of the Si spacer layer just above the Ge islands. Upon the nucleation of the next Ge island layer, Ge islands nucleate preferentially at locations on the Si spacer layer where the lattice constant is closest to the Ge lattice constant. This is just the case above the Ge islands. The residual strain field of the Ge islands in the lower layer seeds the nucleation in the upper layer. It was observed that the size uniformity of the 3D islands in subsequent layers is improved.

Semiconductor Nanowires

Nanowires on Facetted Surfaces

Some surfaces such as the Si(1 1 3) surface are known to facet, that is, to form alternating regions with a very high step density (step bunches) alternating with flat surface regions. Subsequent growth of Ge can result in preferential growth of nanowires in the step-bunch region. This effect is even more pronounced in Si/Ge multilayers. In Figure 5, a cross-sectional TEM image of a stack of five alternating depositions of Ge and Si is shown. Ge nanowires with a thickness of ~4.5 nm and a width of ~100 nm are formed. The formation of these nanowires is explained as a strain relaxation effect of Ge growing at the step-bunch regions where it can relax the elastic strain more effectively than on a compact 2D layer. After growth of an Si buffer layer, the next SiGe wire structure nucleates above the previous one. This is a strain-induced effect similar to the one shown for the vertical stacking of the islands.

Monolayer Thick Wires at Step Edges

Regular surface steps can be used to fabricate monolayer thick Ge wires using step-flow growth. Pre-existing step edges on the Si(1 1 1) surface are used as templates for the growth of 2D Ge wires at the step edges. When the diffusion of the deposited atoms is sufficient to reach the step edges, these deposited atoms are incorporated exclusively at the step edges and the growth proceeds by a homogenous advancement of the steps (step-flow growth mode). If small amounts of Ge are deposited, the steps advance only some nanometers, and narrow Ge wires can be grown. A key issue for the controlled fabrication of nanostructures consisting of different materials is a method of characterization, which can distinguish between the different materials on the nanoscale. In case of the important system Si/Ge, it has been difficult to differentiate between Si and Ge due to their similar electronic structure. However, if the surface is terminated with a monolayer of Bi, it is possible to distinguish between Si and Ge. Figure 6a shows an STM image after repeated alternating deposition of 0.15 atomic layers of Ge and Si, respectively. Due to the step-flow growth, Ge and Si wires are formed at the advancing step edge. Both elements can be easily distinguished by the apparent heights in the STM images. It turns out that the height measured by the STM is higher on areas consisting of Ge (red stripes) than on areas consisting of Si (orange stripes). The assignment of Ge and Si wires is evident from the order of the deposited materials (Ge, Si Ge, Si and Ge, respectively in this case). The initial step position is located right from the grown Ge wires. The step edge has advanced towards the left after the growth of the nanowires. The reason for the height difference in STM between Si and Ge is the different electronic structure of a Ge–Bi bond compared to an Si–Bi bond. The apparent height of Ge areas is ~0.1 nm higher than the apparent height of Si wires (Figure 6b). The width of the Si and Ge wires is ~3.5 nm as measured from the cross section (Figure 6b). The nanowires are 2D with a height of only one atomic layer (0.3 nm). Therefore, the cross section of a 3.3 nm wide Ge nanowire contains only 21 atoms (Figure 6c). The height difference arises due to an atomic layer of Bi which was deposited initially. The Bi floats always on top of the growing layer because it is less strongly bound to the substrate than Si or Ge. The Si/Ge wires are homogenous in width over larger distances and have a length of several thousand nanometers. Different widths of the wires can be easily achieved by different amounts of Ge and Si deposited.

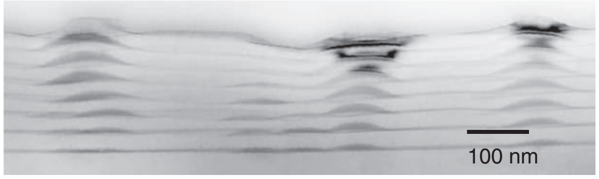

Figure 4 Cross-sectional TEM image of a stack of Ge islands in 40 nm thick Si spacer layers. The islands are aligned on top of underlying islands. (Reproduced from Vescan L (1998) *Thin Solid Films* 336: 244, with permission from Elsevier.)

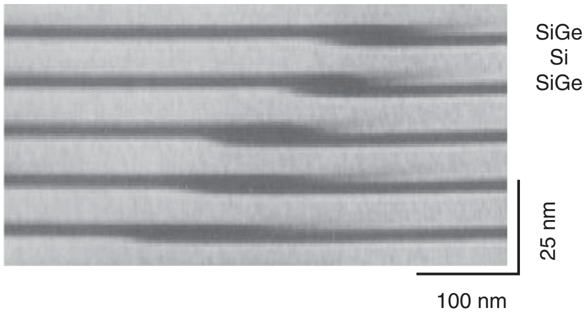

Figure 5 Cross-sectional TEM image of stacked Ge nanowires grown on a facetted Si(1 1 3) surface. (Reproduced with permission from Brunner K (2002) Si/Ge Nanostructures. *Report of Progress in Physics* 65: 27–72; © IOP Publishing.)

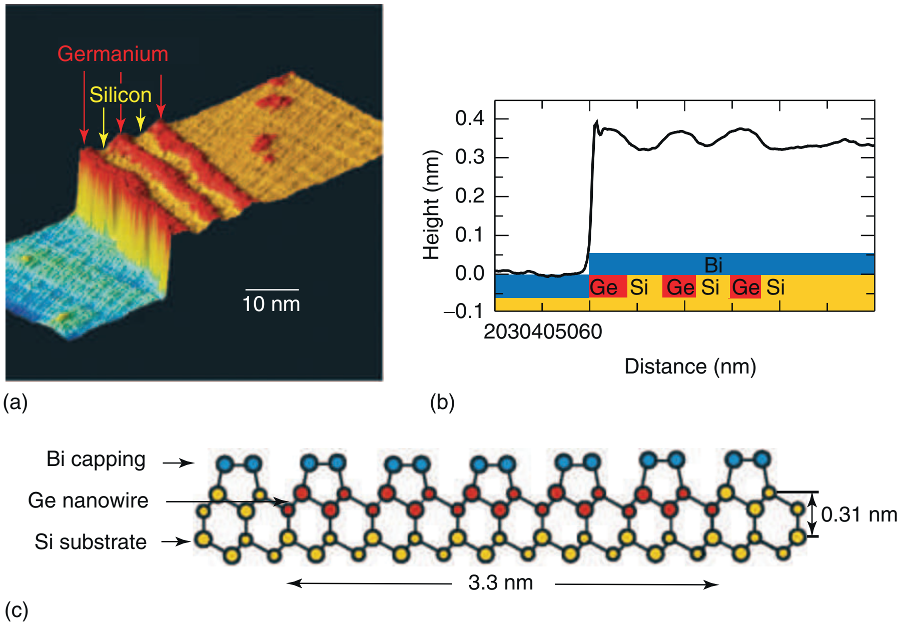

(a) (b) (c)

Figure 6 (a) STM image of 2D Ge/Si nanowires grown by step flow at a pre-existing step edge on a Si(1 1 1) substrate. Si wires (orange) and Ge wires (red) can be distinguished by different apparent heights. (b) The cross section shows the dimensions of the Si and Ge nanowires. The width of the wires is 3.5 nm and the height is only one atomic layer (0.3 nm). (c) Atomic structure of a 3.3 nm wide Ge wire on the Si substrate capped by Bi. The cross section of the Ge wire contains only 21 Ge atoms. (Reproduced with permission from Voigtländer B (2001) Fundamental processes in Si/Si and Ge/Si epitaxy studied by scanning tunneling microscopy during growth, *Surface Science Reports* 43: 127.)

Free-Standing Semiconductor Nanowires Grown by Vapor Liquid Solid Growth

In the VLS method, small catalytic nanoparticles (often gold) induce the growth of a homogenous rod of a semiconductor, with the diameter of the rod determined by the nanoparticle. The gold nanoparticles can be fabricated by heating a thin evaporated gold film, which breaks up and reshapes into nanoscale droplets. Alternatively, gold aerosol nanoparticles with sizes of a few tens of nanometers are used. The gold nanoparticles form a eutectic alloy with the substrate material (for instance, GaAs). Using MBE or metallorganic vapor phase epitaxy, nanowires can be grown. These nanowires are different from the ones discussed so far, in that they are free-standing on the substrate and grow vertically. The previously considered nanowires were epitaxially grown along their length on the substrate or even embedded into the substrate during growth.

The VLS method was used for the Si/Ge and the GaAs material system. This growth method can even be used to grow semiconductor heterostructures within the nanowires with atomically sharp interfaces. Figure 7 shows an InAs nanowire (green) with several InP barriers (red). The rapid alternation of the composition is controlled by the supply of precursor atoms to the eutectic melt supplied as molecular beams. Of particular interest is the fact, that the very small cross section allows efficient lateral relaxation of the nanowire, thereby providing freedom to combine materials with very different lattice constants to create heterostructures within the nanowire. The problem of incorporation of misfit dislocations, when a critical thickness is exceeded, does not occur due to the small lateral size of the nanowires. The VLS method is also used to grow semiconductor heterostructures, not along the wire, but radial heterostructures, the so-called core-shell structures.

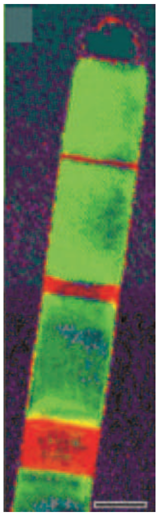

Figure 7 Composition profile of an InAs nanowire, containing several InP heterostructures, using reciprocal space analysis of lattice spacings with a TEM. InAs lattice spacings have been color-coded with green and InP spacings with red. (Reproduced with permission from Björk MT, Ohlsson BJ, Sass T, Persson AI, Thelander C, *et al.* (2002) *Nano Letters* 2: 88.)

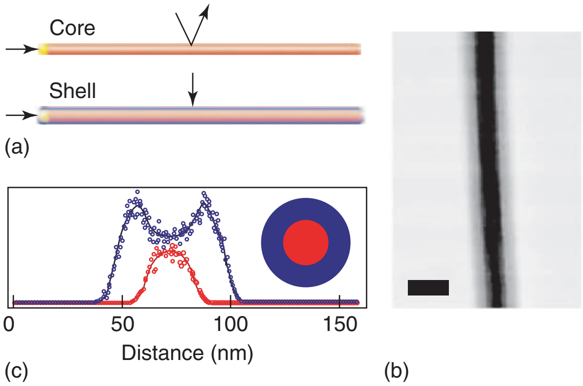

Figure 8 (a) Schematic of the core-shell growth of a radial Ge/Si structure (b) TEM image of a Ge/Si core-shell nanowire. Scale bar is 50 nm. (c) Elemental mapping along the cross section showing the Ge (red circles) and Si (blue circles) concentrations. (Reproduced with permission from Lauhon LJ, Gudiksen MS, Wang D, and Lieber CM (2002) Epitaxial core-shell and core-multishell nanowire heterostructures. *Nature* 420: 57.)

The synthesis of Si/Ge core-shell nanowires by chemical vapor deposition is achieved by the following process schematically shown in Figure 8a. Initially a Ge nanowire is grown by vapor phase epitaxy growth from a gold nanoparticle. In this case, the substrate serves only as a support and the nanowires are not epitaxially connected to the substrate. The deposition temperature is chosen so low that no germane (GeH_4) is decomposed along the wire and radial growth is suppressed. Only axial growth occurs by the VLS mechanism at the gold nanoparticle. Subsequently, a boron-doped Si shell is grown by CVD. The addition of diborane serves to lower the decomposition temperature of silane (SiH_4) and "turns on" the radial growth. Figure 8b shows a TEM image of the Ge core (imaged darker) and the Si shell (lighter gray) with a diameter of ~50 nm. The elemental TEM cross-sectional mapping shown in Figure 8c shows the radial chemical composition in a wire (core diameter 26 nm, shell thickness 15 nm). By oxidation of a shell of the radial heterostructure, it is possible to build a coaxially gated nanowire transistor.

Hybrid Systems – Combination of Lithography and Self-Organized Growth

In hybrid methods, self-organization is combined with lithographic patterning. In this approach, self-organization is used to form nanostructures on a smaller scale than the one accessible by lithography. Most importantly, the hybrid methods provide a direct contact of nanostructures formed by self-organization to lithographically patterned structures. As an example, the self-organized growth of Ge islands in oxide holes is shown in Figures 9a–9d. The staring surface is a silicon substrate with a thin oxide layer at the surface. Electron lithography is used to remove the oxide and form holes of a diameter of 0.5 μm where the bare Si surface is

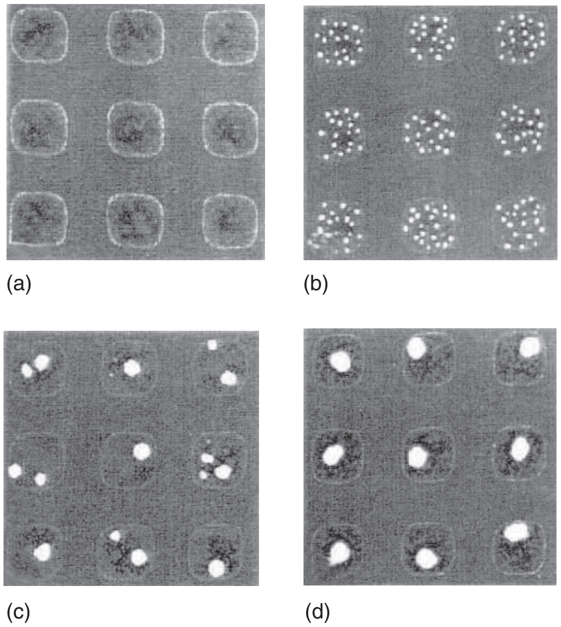

Figure 9 (a–d) Growth of Ge islands in holes on an oxidized Si substrate. (Reproduced with permission from Kim ES, Usami N, and Shiraki Y (1999) *Semiconductor Science and Technology* 14: 257; © IOP Publishing Limited.)

exposed. Self-organized growth of Ge leads to the formation of Ge islands, which can be smaller than the size scale of the electron beam lithography. The gas phase growth of Ge is selective, that is, Ge only grows inside the holes in the oxide and not on the oxide itself. Figure 9 shows the nucleation of Ge islands in the holes in the oxide for different growth temperatures. At lower temperatures, the island density is so large that several islands nucleate in one oxide hole. If the temperature is increased finally, only one Ge island nucleates in each oxide hole. The size of the Ge island is smaller than the lithographically defined oxide hole. This approach is called lithographic downscaling. However, the positioning of the islands is not perfect. As seen in Figure 9d, the position of the Ge island inside the oxide hole is not defined but is rather randomly in the center or at the corner of the oxide hole. Due to the fact that the Ge does not grow on the oxide, the edges of the oxide hole are not sinks for deposited Ge atoms. Therefore, the Ge adatom concentration is homogenous across the hole, and the nucleation of the Ge island is random within the oxide hole. If the edges of the hole were sinks for Ge atoms (for instance, if the edges of the hole consisted of Si), the adatom density would have a maximum at the center of the hole and the nucleation of the Ge islands would occur preferentially at the center of the oxide holes.

A simple structure formed by lithographic methods is a mesa (from the Spanish table), which is a flat terrace separated from the rest of the wafer by trenches. A silicon mesa structure is imaged by electron microscopy and shown in Figure 10. It has been observed that the growth of Ge on this mesa leads to preferential nucleation of Ge islands at the mesa edges. Figure 10 shows a regular alignment of Ge islands along the mesa edges. This preferred nucleation of islands at the convex part of the surface profile is quite

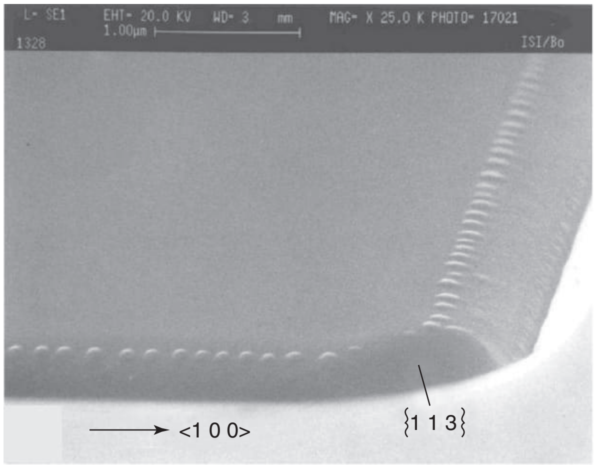

Figure 10 Regular alignment of Ge islands at the edge of a mesa which was fabricated by optical lithography. (Reproduced from Vescan L (1989) *Journal of Crystal Growth* 194: 173, with permission from Elsevier.)

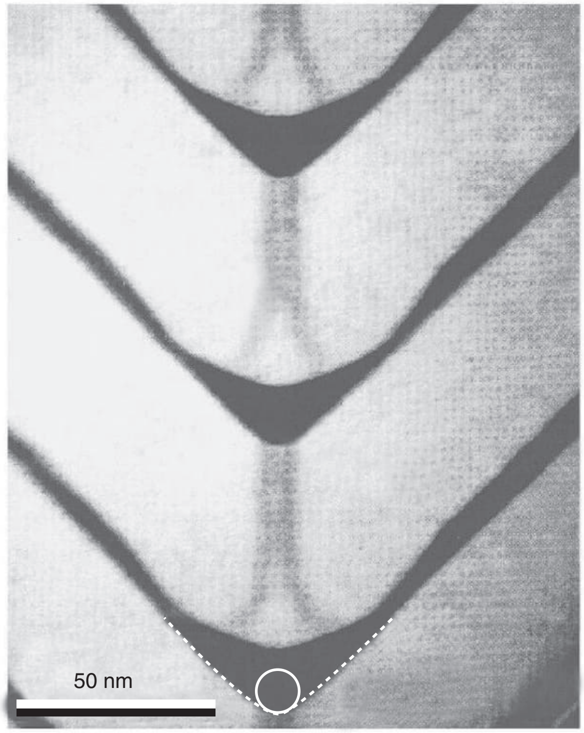

Figure 11 Cross-sectional TEM image of vertically stacked GaAs nanowires and AlGaAs barriers aligned along a lithographically defined V-groove. (Reproduced with permission from Gustafsson A, Reinhardt F, Baisiol G, and Kapon E (1995) *Applied Physics Letters* 67: 3673; © American Institute of Physics.)

unexpected. Considering the surface curvature alone, the chemical potential is lowest at locations with a concave curvature. Atoms diffuse toward the lower chemical potential, that is, to the concave parts of the surface. This reasoning is true for homoepitaxy. In heteroepitaxy, another contribution is important: the strain-dependent contribution to the chemical potential. The convex regions are most favorable for strain relaxation of the strained Ge wetting layer covering the Si substrate. Therefore, the strain contribution to the chemical potential has a minimum at convex edges. In the current case, this strain-induced contribution to the chemical potential overwhelms the curvature contribution and leads to a minimum in the total chemical potential at the convex edges. Therefore, these convex edges with a minimum in the chemical potential provide a favorable nucleation site for Ge islands.

Also, nanowires can be fabricated, aligned to lithographically defined structures. V-grooves can be defined by lithography and anisotropic wet chemical etching with a low-etch speed for the crystal plane forming the side facets of the V-groove. The formation of nanowires at the bottom of the V-groove is induced by the self-limiting nature of the growth front of AlGaAs on the grooved substrate. Vertically stacked arrays of GaAs/AlGaAs nanowires exhibiting 5–10% size uniformity have been demonstrated (Figure 11). The layer structure consists of GaAs nanowires separated by $Al_{0.42}Ga_{0.58}As$ barriers. The formation of the crescent-shaped GaAs wires is based on the formation of slow-growing side facets along the V-grooves. The migration of adatoms away from these side-walls toward the V-groove bottom produces the concave surface profiles in the corners of the V-grooves.

PACS: 68.65.–k

Further Reading

Berbezier I, Ronda A, and Portavoce A (2002) Si/Ge nanostructuresnew insights into growth processes. *Journal of Physics: Condensed Matter* 14: 8283.

Bimberg D, Grundmann M, and Ledentsov NN (1989) *Quantum Dot Heterostructures*. New York: Wiley.

Gustafsson A, Reichhardt F, Baisiol G, and Kapon E (1995) Low-pressure organometallic chemical vapor deposition of quantum wires on V-grooved substrates. *Applied Physics Letters* 67: 3673.

Moriarty P (2001) Nanostructured materials. *Reports of Progress in Physics* 64: 297.

Motta N (2002) Self-assembling of Ge/Si(1 1 1) quantum dotsscanning microscopy probe studies. *Journal of Physics: Condensed Matter* 14: 8353.

Stangl J, Holy V, and Bauer G (2004) Structural properties of self-organized semiconductor nanostructures. *Reviews of Modern Physics* 76: 725.

Teichert C (2002) Self-organization of nanostructures in semiconductor heteroepitaxy. *Physics Report* 365: 335.

Yang B, Feng Liu MG, and Lagally (2004) Local strain-mediated chemical potential control of quantum dot self-organization in heteroepitaxy. *Physics Review Letters* 92: 025502.

Epitaxy

D Maryenko, RIKEN Center for Emergent Matter Science(CEMS), Wako, Japan

© 2024 Elsevier Ltd. All rights reserved.

This is an update of L. Miglio, A. Sassella, Epitaxy, Editor(s): Franco Bassani, Gerald L. Liedl, Peter Wyder, Encyclopedia of Condensed Matter Physics, Elsevier, 2005, Pages 157–166, ISBN 9780123694010, https://doi.org/10.1016/B0-12-369401-9/00692-6.

Introduction 528
Substrate and lattice matching 529
Modes of film growth 530
Material characterization 533
Epitaxy techniques 534
Chemical vapor deposition 534
Liquid-phase epitaxy 535
Solid-phase epitaxy 535
Molecular beam epitaxy 536
Pumping system 536
Material evaporation source 537
Flux measurement and stoichiometry 537
Oxide compound 538
Pulsed laser deposition 539
Sputtering 541
Conclusion 541
References 541
Further reading 543

Abstract

Epitaxy refers to the growth of well-oriented crystalline layer on top of the other. The ability to produce such layers with high crystalline quality allows to form novel material combinations that do not exist in nature. The emerging property of artificial is important not only for fundamental studies but also for the application. Therefore various growth techniques have been developed, which are widely applied in different branches of solid state electronics. Here, we describe some aspects of epitaxial growth that appear to be important from the practical standpoint and should make the reader acquainted with epitaxy.

Introduction

In 1928, Louis Royer coined the term epitaxy to describe the crystal-oriented growth of one crystalline material on top of the other (Royer, 1928). The term is composed of two Greek words epi (επι), meaning "above", and taxies (ταξιζ), meaning "order". By that time the phenomenon of oriented crystal growth has been known to occur in nature, and many examples have been already documented (Barker, 1906). Pashley et al. refer to the work of Moritz L. Frankenheim in 1836 as the first recorded example of epitaxial growth of sodium nitrate $NaNO_3$ on a cleaved calcite crystal $CaCO_3$ (Frankenheim, 1836; Pashley, 1956). An earlier work by Wakkernagel in 1825 is mentioned to be disputed (Wakkernagel, 1825; Pashley, 1956).

Since then the epitaxial growth has evolved tremendously and became a key enabler in the development of modern technologies and synthesis of advanced materials. Epitaxial methods allow to achieve the structural quality that can even be superior to that obtained in the bulk. The ability of epitaxial methods to produce thin layers and multilayers of different materials, sharp interfaces, and spatially resolved doping allowed to obtain entirely novel physical properties. Light-emitting diodes, semiconductor lasers, high frequency transistors, and amplifiers are just few examples of how the development of epitaxial methods affected our daily life. Fundamental discoveries (such as quantum Hall effect, and Giant Magnetoresistance) were also brought by the development of high-quality structures.

In the epitaxy, we address two main questions–how the material grows and how to grow the materials. An epilayer (a layer of material formed by epitaxial growth) on a substrate forms from a metastable phase brought by deposition of amorphous compound (SPE), liquid phase (LPE), vapor and gas (vapor-phase epitaxy). The driving force for the formation of an epilayer is the chemical potential difference between metastable and stable phases of material. The crystalline phase of the epilayer material will try to minimize the total energy of the system. Therefore, the surface tensions are important for the epitaxial growth. When two materials grown on top each other are isochemical in their composition, we refer to the homoepitaxial growth process. In an ideal homoepitaxial growth the epitaxial layer is the continuation of a bulk crystal so that any evidence of substrate–film interface is absent. In such a growth, the homoepitaxial layer can have a higher crystal structure quality (e.g., less defects) or the material can be chemically doped, producing a thin conducting layer. When two materials combined together in an epitaxial way are heterochemical, we refer to heteroepitaxial growth and the synthesized structures are called heterostructures.

https://doi.org/10.1016/B978-0-323-90800-9.00208-0

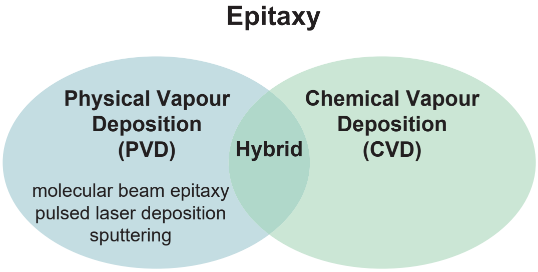

Fig. 1 **Vapor-phase epitaxy** is widespread growth method. Other epitaxial techniques include liquid-phase epitaxy (LPE) and solid-phase epitaxy (SPE).

Vapor-phase epitaxy is perhaps the mostly employed and widespread epitaxial method. Depending on the transport mechanism of gaseous species, we distinguish chemical vapor deposition (CVD) and physical vapor deposition (PVD) (Fig. 1). CVD is subclassified according to the chemistry of source gases (MOCVD = metal-organic CVD), growth conditions, etc. PVD refers to the vaporization of source materials in vacuum. The classes of PVD methods are again distinguished by the vaporization methods (thermal evaporation, sputtering). Famous PVD methods are pulsed laser deposition (PLD), where the vapor is produced by laser ablation, and molecular beam epitaxy (MBE), where the source material is vaporized by thermal heating. Metalorganic MBE (MOMBE) is a hybrid method of CVD, and PVD allows to overcome the limitation of MBE and produces high-quality semiconductor and recently even oxide structures.

This article touches some aspects of epitaxy that are important from the practical point of view and should help the reader to get acquainted with this topic. An interested reader is referred to the "Further reading" section.

Substrate and lattice matching

The growth process of epitaxial layers (also epilayers or epitaxial film) is influenced by the substrate at the very initial stage. The formation of the first epitaxial layer is pivotal for the growth of the next following layers, as its quality will dictate the subsequent growth process. Therefore, the selection of the appropriate substrate is crucial for achieving high crystalline perfection of the epitaxial layers. The substrates may require some pretreatment to obtain a clean crystalline surface with atomically flat terraces before initiating the growth. The preparation steps can include mechanical polishing, chemical treatment, degassing/oxidation, and annealing. The preparation procedure depends on the substrate material and its crystal orientation, whereas specific recipes may already be established. The choices for substrates and especially of those with good crystallinity are limited. Therefore, epitaxial growth happens between materials with not only different chemical compositions but also different structural parameters. The condition on similar crystal structure for epilayer and substrate is not strict. It should be noted that the epitaxial layers and the substrate can have different crystallographic orientation and even different crystal structures. From a pure geometrical consideration there can be such crystal orientation relationships between substrate and epilayer for which the three-dimensional film and substrate lattices coincide most closely at their two-dimensional interface (Balluffi et al., 1982; Zur and McGill, 1984). However, if the size of the common superlattice, formed by lattice coincidence, is large, the chemistry at the interface may play a major role and the epitaxial relation between the substrate and the deposit may not be obvious.

There are several ways how the difference in structural parameters (lattice mismatch) can be accommodated at the interface. If the interaction across the interface is weak, such as in van der Waals systems (graphene and other 2D layered materials), the epilayer will not be strained and will lie on the substrate. The weak forces at the interface can maintain the rotational alignment with the substrate. A more common situation occurs when the epilayer is chemically bonded to the substrate. The growth process depends strongly whether the epilayer is coherent or incoherent with the substrate. The growth is incoherent, when the epilayer assumes any in-plane lattice constant to minimize the free energy. In case of coherent growth, the epilayer adopts the in-plane lattice constant of the substrate as shown in Fig. 2A. The resulting elastic strain energy increases the free energy significantly. To quantify the degree of lattice mismatch, a parameter is defined:

$$f = \frac{a_{film} - a_{sub}}{a_{sub}} \tag{1}$$

where a_{sub} is the lattice constant of the substrate and a_{film} is the lattice constant of unstrained epilayer. Epitaxial layers with larger lattice constants than the substrate are under compressive strain, while the converse results in tensile strain. Since the strain imposed by the substrate is of a 2D character, the epilayer's lattice parameter perpendicular to the interface will change in such a way that its internal energy is minimized. The change of the lattice constant is by the three-dimensional form of Hooke's law. The resulting strain components are parallel and perpendicular to the surface. They are opposite in sign since the natural tendency of the strained structure is to preserve the volume of the unit cell. It is important to emphasize that such a crystallographic approach to match the substrate and the epilayer may not always be sufficient. One of the strongest points of epitaxy is that it can also stabilize crystal phases, which are not stable in the bulk form (Bruinsma and Zangwill, 1986). Thermodynamical consideration of the growth

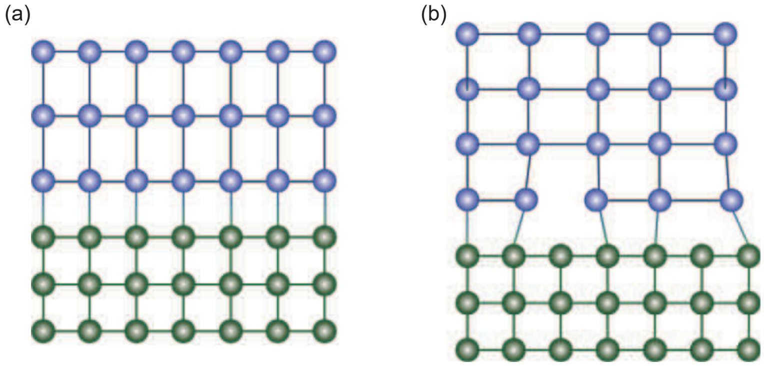

Fig. 2 **Crystal lattice accommodation:** (A) Substrate stains the epilayer by imposing the in-plane lattice constant of the epilayer. Out-of-plane lattice constant alters so that the volume of the unit cell is preserved. (B) Elastic strain of the epilayer relaxes by forming defects, when a critical layer thickness is exceeded.

dictates that the epitaxial stabilization is governed by the interplay between surface diffusion and the nucleation energy during the growth. Therefore, elemental tin assumes metastable diamond structure on the (001) surface of InSb and CdTe (Farrow et al., 1981), and anatase phase of TiO_2 is stabilized on $SrTiO_3$ (001) (Hsieh et al., 2002). Similarly such approach is demonstrated for the growth of several other oxides such as $SrMnO_3$, $BaMnO_3$, and $CaCuO_2$ (Farrow, 1983; Gorbenko et al., 2002).

In the coherent growth, it is considered that only the epilayer is strained since it is much thinner than the substrate. However, when the substrate thickness and the epilayer thickness become comparable, the stress is distributed between both of them. Such situation is realized when a free standing membrane (so-called compliant substrate) is employed in the epitaxial growth (Lo, 1991; Teng and Lo, 1993; Jesser et al., 1999; Feng and Liu, 1983). When the elastic energy reaches a certain value, it becomes more favorable for the structure to relieve the stress by breaking and reforming the bonds, such as shown in Fig. 2. These features are called misfit dislocations. The overall strain will be reduced but the dislocation energy increases. The thickness at which the misfit dislocation forms is called critical thickness (der Merve, 1962; Matthews and Blakeslee, 1974; People and Bean, 1986). Such dislocations are local inhomogeneities, which change the heterostructure properties (by acting as a trap, scattering center, etc.) and deteriorate the device performance based on this material. Besides misfit dislocations, other types of defects can form, such as point defects, dislocations, stacking faults, twins, and antiphase boundaries in alloys and compound multilayers. All of them act degrading on the physical properties of the materials. It is the aim of epitaxial growth to avoid the defect formation as much as possible by optimizing the growth parameters, the growth conditions, and improving epitaxial technique.

Modes of film growth

Epitaxial growth takes place on a surface of a material, called substrate. Chemical elements of the desired material are supplied toward the surface in a way that depends on a particular epitaxial method. Fig. 3A exemplifies evaporation of atoms of two different species reaching the substrate surface with a step-terrace structure. Upon arrival a series of surface processes are involved in the epitaxial growth, which are schematically illustrated in Fig. 3A. Among them, the following are the most important:

- immediate re-evaporation or adsorption of species impinging on the substrate surface,
- surface diffusion and in case of molecules also dissociation,
- incorporation of the constituent atoms into the crystal lattice of the substrate or the formed epilayer
- desorption of the species not incorporated into the crystal lattice.

In all thermal processes a characteristic activation energy (for adsorption, re-evaporation, etc.) has to be overcome, whose value depends on the details of the process. Respectively, the number of particle participating in the particular process is given by the Arrhenius exponential law.

On a phenomenological level, there are three distinct modes of film growth depicted in Fig. 3B–D. One of them is Frank–van der Merwe growth mode or also known as layer-by-layer growth mode (Frank and Van der Merve, 1949). It is realized when the interaction between the atoms of deposit and the substrate is stronger than the bonding between deposited atoms. Thus the first atoms condense on the substrate surface and form a complete monolayer. It is followed by the formation of a somewhat less tightly bound second layer. Given that the interaction with the substrate decreases with the number of epitaxial layers, the binding tends toward the value for a bulk crystal of the deposit. As a result, each new layer can start to form only when the last layer has been complete. Another growth mode occurs when the atoms of the deposit are stronger bound to each other than to the substrate. In such case the epitaxial material favors the formation of islands. Therefore, this growth mode is called island growth mode or Volmer–Weber growth mode (Volmer and Weber, 1926).

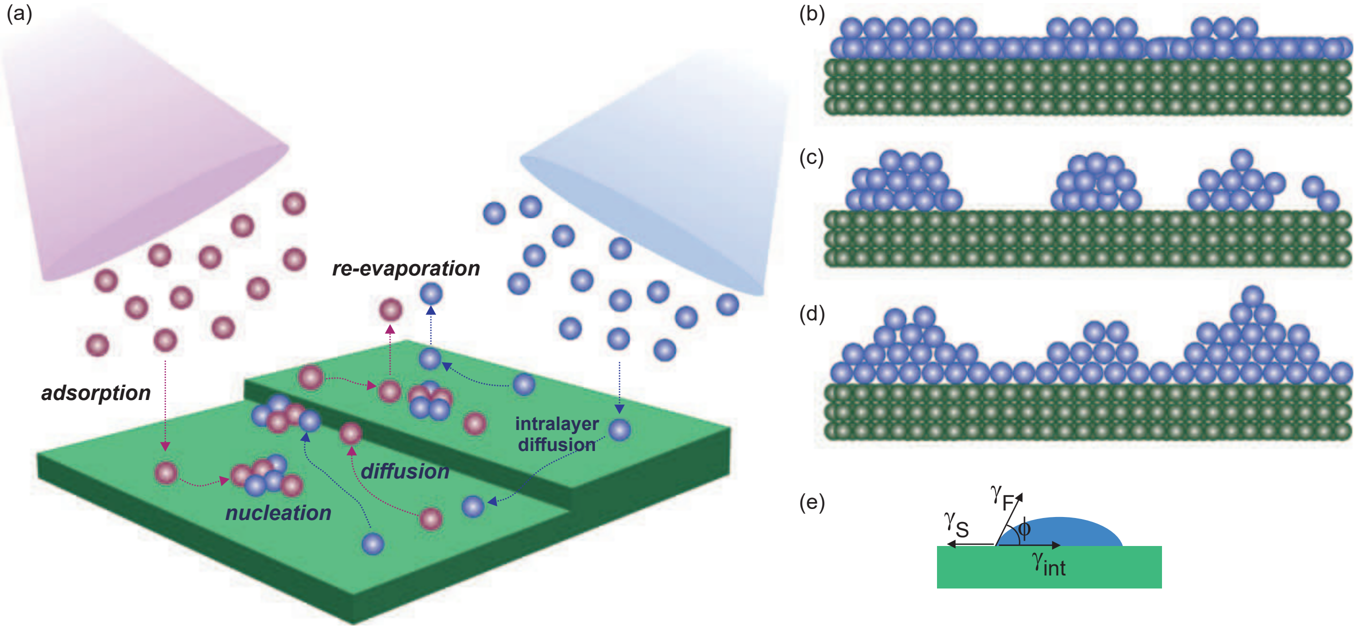
(a)
re-evaporation
adsorption
intralayer diffusion
diffusion
nucleation
(b)
(c)
(d)
(e)
γ_F
γ_S
ϕ
γ_{int}

Fig. 3 **Thin film growth.** (A) Schematic representation of film growth mechanism on the surface. Two species are supplied to the growth surface. Several processes are possible: adsorption (attaching to the surface), desorption (re-evaporation from the surface), diffusion, nucleation/incorporation. (B) Frank-Van der Merwe growth mode. (C) Volmer–Weber growth mode. (D) Stranski–Krastanov growth mode. (E) Balance of surface tension forces acting on the epitaxial layer defines the growth mode.

An intermediate growth mode is layer-plus-island growth mode also known as Stranski–Krastanov growth mode (Stranski and Krastanov, 1938). After the formation of one of few monolayers, the subsequent layer growth becomes unfavorable and islands start forming on top of the full layers. Many factors might account for this mixed growth mode. Among them are a large lattice mismatch between substrate and epitaxial film, and the symmetry or orientation of the overlayers with respect to substrate.

The occurrence of different growth modes can also be comprised in terms of the relations between surface and interface free energies γ, which describes a characteristic free energy needed to create an additional surface area (Grabow and Gilmer, 1988). Since γ can also be treated as a force per unit length of boundary, the force equilibrium between the contact point of the 3D film island and the substrate can be written as

$$\gamma_S = \gamma_{S-F} + \gamma_F \cos\phi \tag{2}$$

where γ_S is the surface free energy of the substrate surface, γ_F is the surface free energy of the film surface, and γ_{S-F} is the free energy of the substrate–film interface. Fig. 3E presents schematically the forces acting on the surface of the film formation. Respectively, the layer-by-layer growth is realized for $\phi = 0$, and the condition above becomes $\gamma_S \leq \gamma_{S-F} + \gamma_F \cos\phi$. The other limiting case is the island growth with $\phi > 0$ and thus $\gamma_S < \gamma_{S-F} + \gamma_F \cos\phi$.

This model captures also the mixed Stranski–Krastanov growth mode. At the initial stage of the growth layer-by-layer growth mode is realized. But the formation of intermediate layers alters gamma values, changing subsequently the force balance at the interface. The changes in gamma values can be understood by considering a lattice mismatch between deposited film and substrate. The lattice of the epitaxial layer tries to adjust to the substrate crystal lattice at the cost of elastic deformation energy. The transition from layer to island growth occurs when the spatial extent of the elastic strain field exceeds the range of the adhesion forces within the deposited material.

The simple relation does not consider the gas phase of material above the surface of deposited film. When the particle transfers from the vapor phase into condensed phase at some pressure p, the free enthalpy changes by:

$$\Delta G = n\Delta\mu = nkT\ln(p/p_0) \tag{3}$$

where p_0 is the equilibrium vapor pressure, n is the particle number, and $\Delta\mu$ is the change of chemical potential between solid and vapor phases. The ratio p/p_0 is associated with the degree of supersaturation. Taking the vapor phase into account, the conditions for layer-by-layer or island growth have to be supplemented. They become:

- $\gamma_S \leq \gamma_{S-F} + \gamma_F \cos\phi + CnkT\ln(p/p_0)$, layer growth
- $\gamma_S < \gamma_{S-F} + \gamma_F \cos\phi + CnkT\ln(p/p_0)$, island growth

The equations indicate that the supersaturation can be the driving force for the formation of epitaxial layers. More importantly, they indicate that the growth mode is not constant material parameter, but can be changed by varying the supersaturation condition. Layer-by-layer growth mode is favored with increasing supersaturation condition. This property is employed in the epitaxial growth of III–V compounds with MBE, where the group V component has relatively high equilibrium vapor pressure.

In case when homoepitaxial growth is realized, the balance of free energies of interface, film, and substrate surfaces predicts an epitaxial growth in layer-by-layer mode (Frank–van der Merve). However, the kinetic energy of atoms on the surface of the substrate can add variation in the thin film growth process. For a simplified consideration, interlayer and intralayer diffusion processes are of prime interest. The first process describes the atoms diffusion on a terrace, while the second diffusion process considers the atom motion across the step edge onto a lower terrace (Fig. 3A). Note that an atom traveling on a lower terrace will be incorporated at the step edge due to its higher binding energy. Depending on the relative interlayer and interlayer diffusion rates, three different nucleation process are realized:

- Step-flow mode. It takes place when the intralayer mobility is so high that all atoms reach the steps before the nucleation on the terrace occurs.
- Layer-by-layer growth. It is realized when the interlayer diffusion dominates. The diffusion length is smaller than the terrace width. The nucleation proceeds on the terraces and subsequent growth of adatom islands. This growth mode leads to a periodic change of surface morphology: the surface flatness recovers after completing the formation of an atomic layer.
- Multilayer growth. In ideal case it is realized when no atom transport takes place. Every atom stays on the level where it was deposited.

Based on this consideration, it appears reasonable that the growth mode can be tuned by adjusting the substrate temperature at a fixed deposition rate. At lowering the temperature, the step-flow growth mode goes over to layer-by-layer growth mode and reaches finally the multilayer 3D growth mode. Experimentally an ideal layer-by-layer growth is difficult to realize since the nucleation on a layer always takes place before the layer formation is fully completed. Consequently, the epitaxial surface always becomes rough after the deposition of many layers. In practice, one strives to obtain epitaxial layers with a low surface roughness. The surface atoms in the uppermost epitaxial layer differ from those in the bulk due to the absence of chemical bonding on one side. As a result, the surface atoms shift from their positions in the bulk so that a new equilibrium state is achieved. One distinguishes two main rearrangement effects. Relaxation is attributed to the shift of atoms normal to the surface. In this case the lateral periodicity is preserved with respect to the bulk. Usually few top most layers are involved in this rearrangement type. Reconstruction is another type of atom rearrangement on the surface. Here the surface energy is minimized when the atoms restore some broken bonds. This is accompanied by the shift of atoms parallel to the surface. Thus the unit cell of the reconstructed surface differs from that in the bulk. The observation of diffraction pattern, such as performed with RHEED (see section below), can detect the surface reconstruction.

Material characterization

The quality of the synthesized film can be accessed by various characterization techniques. The main goal of characterization is to help a grower to optimize the growth conditions for improving the crystal structure quality, reducing defects, achieving desirable stoichiometry, etc. Quality of crystal affects the physical properties of the synthesized material. The list of the characterization techniques presented here is by far not complete:

Atomic force microscopy (AFM). The technique allows to measure the roughness of the surface down to the atomic level. Scanning probe technique monitors the force between the sharp scanning tip and the sample surface. The change of the force is used to produce the images of surface. The method has also high lateral spatial resolution and can operate at ambient conditions.

X-ray diffraction and reflection (XRD). Diffraction of X-ray on the sample surface provides information on the crystal structure of epitaxial layers: lattice parameters (in-plane and out-of-plane), orientation relation between epitaxial layer and substrate, thickness the surface roughness (involving some modeling) can be measured.

Scanning electron microscopy (SEM). It is an electron microscope that provides images by scanning focused electron beam across the surface and detecting the signal from secondary or backscattered electrons. It images the surface topology, grain size and shape, film voids, microcracks, etc.

Energy dispersive X-ray (EDX). The signal of backscattered electrons in SEM is used to evaluate the chemical composition of the material. The signal comes from the thickness of about 1μm with lateral resolution of a comparable size. EDX's detection limit is 0.1% and it can detect elements with atomic number higher than 11. Usually EDX unit is installed together with SEM.

Secondary ion mass spectroscopy (SIMS). This technique allows to evaluate the composition, of the epilayer. It uses a focused ion beam to sputter the surface of the sample and analyze the ejected secondary ions. The technique allows to obtain the depth profile information on material composition. Own to its high sensitivity, SIMS is used to quantify the incorporated impurities.

Transmission Electron Microscope (TEM). It provides high-resolution plan-view lattice images and transverse film section. It can thus visualize lattice orientations, interface quality and defects, atom mixing at interface, superlattices, etc.

X-Ray photoelectron spectroscopy (XPS). It is a photoemission spectroscopy analyzing the energy of the electrons emitted from the surface as a result of irradiation by single-energy X-ray photons. XPS is a surface-sensitive method and provides information on surface composition as well as its chemical state. It detects all elements with the exception of hydrogen and helium.

Ellipsometry. The technique is based on the analysis of polarized light reflected from the sample. It probes the complex refractive index and allows to extract the information about layer thickness and roughness.

Almost all of these techniques characterize the material after the growth. An outstanding technique that can probe the surface of the substrate and monitor the growth processes is Reflection High-Energy Electron Diffraction. Since this technique is compatible with the vacuum environment, it is widely employed to monitor the growth process in PLD and MBE (Hasegawa, 2012; Ichimiya and Cohen, 2004; Haeni et al., 2000).

Reflection high-energy electron diffraction (RHEED). As the name implies, the technique exploits diffraction of electrons by surface atoms and thus probes the periodic arrangement of atoms at the surface. In this technique an electron gun (e-gun) generates a monochromatic electron beam with a typical energy of 10–50 keV, which strikes the surface of the sample at a grazing angle of about 1 degree. At this energy the electron wavelength is in sub-angstrom range, which is thus smaller than the thickness of an atomic layer. Furthermore, due to a small incident angle, the penetration depth is only few atomic layers below the surface, which explains the sensitivity of RHEED technique to the surface morphology. The diffracted electrons interfere constructively at specific angles given by the electron wavelength, crystal structure, crystal orientation, and atom arrangement on the surface. The resulting diffraction pattern can instantly be visualized on a photoluminescent screen. It is the subject of analysis since it carries the information on surface processes.

When the sample surface is smooth, the diffracted intensity is a maximum. However, when the epitaxial surface is partially covered, the diffracted intensity decreases due to destructive interference in the diffracted electron beam from different areas of the surface. Hence, when the layer-by-layer epitaxial growth mode is realized, the diffracted intensity reveals an oscillatory behavior. This is visualized by plotting the specular spot intensity as a function of time during the epitaxial growth. The oscillations are routinely employed to measure the thickness of the epitaxial films and superlattice layers since each period of oscillations corresponds to the completion of one monolayer. Furthermore, by counting the number of RHEED oscillations, one can calibrate the deposition flux, control alloy composition, and adjust it respectively. If the surface does not become smooth after completion of each monolayer, the amplitude of RHEED oscillations decays gradually due to destructive interference. The RHEED oscillations are characterized by their period, amplitude, phase, damping of the oscillations, their initial behavior at the beginning of growth, and their recovery after growth. These features can provide valuable information about the growth process.

Besides the diffraction spots from the surface, which are anticipated from the kinematic scattering analysis, additional intensity lines and curves appear in the diffraction pattern. They are the result of the dynamical scattering and are known as Kikuchi lines.

They emerge as a result of nonlinear effects and originate from electrons scattered incoherently from the crystal by phonons, plasmons, defects, or electron–electron interactions. The observation of sharp and clear Kikuchi lines is an indication of a flat and crystalline surface (Hasegawa, 2012).

Epitaxy techniques

Various deposition techniques can be distinct by the kinetic energy of particles impinging on the substrate surface and can be grouped in three kinetic energy regimes (Cuomo et al., 1991). Low energy process (on the order of 0.1 eV) encompasses chemical vapors deposition and thermal evaporation. Here the particle kinetic energy is on the order of the thermal energy associated with the temperature of the substrate. Atoms impinging on the substrate surface thermalize almost immediately with the substrate, get adsorbed, and diffuse on the surface until they get permanently bonded at a nucleation site. At a given temperature, the condensation rate can be increased by increasing the vapor flux. At elevated substrate temperature the enhanced kinetic energy of atoms facilitates to overcome the surface traps and to find energetically more favorable states. This results in a growth of films with fewer defects. In this kinetic energy regime, the material forms thermodynamically stable state.

Another deposition regime with energies above 1eV is realized when the material flux is created by sputtering, laser vaporization, etc. The energy of such species corresponds to the equivalent temperatures exceeding the temperature of the accommodating surface. It is rather associated with the atomic energy and bond strength. In this case the interaction with the surface becomes significant. As a result the impinging species can create defects on the surface, which can become important for the formation of interfaces between materials. In this energy regime metastable material phases can form.

In the other deposition regime, the kinetic energies are above 100 eV and the particles can even penetrate the surface and be implanted in the material.

Chemical vapor deposition

CVD is a widely used material deposition technique in which thin films are synthesized on a heated substrate via a chemical reaction of supplied precursors. In contrast to PVD, such as MBE and PLD (discussed later), CVD heavily relies on chemical reactions. Therefore, thermodynamics governs the CVD reaction and indicates the direction in which the reaction proceeds. Perhaps the first report on using the CVD technique dates back to 1946, when Teal et al. deposited silicon film on ceramic surfaces by flowing silicon tetrachloride ($SiCl_4$) and hydrogen gas (Teal et al., 1946). Due to the chemical reaction

$$SiCl_4 + 2H_2 \rightarrow Si + 4HCl \tag{4}$$

a smooth silicon film forms at 1100C. CVD process consists of several steps which are pictorially depicted in Fig. 4:

- Transport of reactants to the deposition region
- Diffusion of reactants from the main gas stream to the wafer surface. Prior to that, the reactant gases can undergo reaction and form an intermediate reactant.
- Adsorption on the wafer surface and diffusion on the surface
- Surface processes (chemical decomposition and reaction, site incorporation, nucleation) lead to the thin film synthesis and growth. Additional stimulators (light, plasma, temperature) can be introduced to promote the chemical reaction.
- Desorption of byproducts from the surface and their transport away from the deposition region

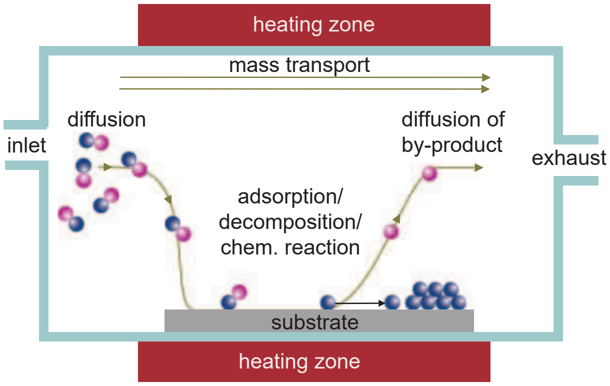

Fig. 4 Chemical vapor deposition. Schematic representation of processes during CVD. Shown are the sequence of gas transport and reaction contributing to the thin film growth. The molecules are dissociated from the growth surface and undergo a chemical reaction on it. The by products are removed from the active zone.

The main components of a CVD system are the reaction chamber and gas handling system (gas delivery and exhaust gas treatment system). In a most common configuration the reactor is a horizontal quartz tube, where the substrate is placed on a boat/susceptor made of quartz or graphite. A gas inlet injector is connected to one side of the tube, where the gas supply is regulated by the mass flow controller. In case the precursor is in a solid state form, it can be supplied to the deposition region either by sublimation or by dissolution in an appropriate solvent. The other side of the reactor is connected to the exhaust to remove the by products of thin film growth. Potentially hazardous by products should be removed by introducing suitable traps. The reactor can be connected to the vacuum system to purge the deposition chamber before the deposition and to achieve the necessary pressure for the transport of reactants. The temperature of the substrate can be raised locally by resistance heating or by raising the temperature of the entire reaction camber using an external furnace. For obtaining high quality film it is essential not only to select the proper substrate (for instance due to its catalytic ability or other chemical properties), but requires also the optimization of the growth condition such as temperature, gas flow rate, pressure etc.

There are various CVD types which differ from each other by reactor (growth chamber) configuration, operation conditions, substrate heating methods, stimulators to promote the chemical reaction, precursor type, etc. Among them are:

- Metal-organic CVD (MOCVD), also known as MOVPE (metal-organic vapor-phase epitaxy), employs metal-organic precursors to form thin films. The precursors are usually volatile and toxic so that a particular precaution has to be taken. This CVD method is widely used for the growth of III-V semiconductor structures for optoelectronic applications.
- Plasma-enhanced CVD uses plasma (partially ionized gas) to promote the chemical reactions.
- Atomic layer deposition (ALD). The precursors are introduced in a pulsed manner. They are absorbed in a self-limiting chemical reaction on the substrate surface. Between pulses the carrier gas removes the remaining precursors. Layer-by-layer growth can be achieved, whereas the film thickness can be controlled by the number of precursor cycles.

Started with the growth of silicon-based coating, CVD became an important technique for semiconductor industry to produce thin films. It also plays an important role in developing and exploring novel materials. Versatile CVD techniques are employed for the large-scale synthesis of graphene and polymeric thin films, and 2D layered materials such as transition metal dichalcogenides (Sun et al., 2021).

Liquid-phase epitaxy

LPE is the crystal growth deposition technique of a single crystalline layer from a liquid phase (a solution or melt) on a substrate acting as a seed (Dawson, 1972; Stringfellow, 1982). The idea behind the growth technique is to create a supersaturated solution of a material that has to be deposited. The substrate is then brought in contact with the melt, from which a solid-state layer precipitates as an epitaxial film on the substrate. The growth process occurs close to thermodynamic equilibrium so that the system reaches a thermodynamic state of lower free energy. This distinguishes LPE from deposition techniques such as PLD, MBE, and vapor-phase epitaxy (VPE). Although multiple layer systems can be synthesized from solutions of different compositions, the feasibility to combine them is driven by the thermodynamic processes. Therefore, materials must have, for instance, similar or controllable liquidus temperatures. The growth can also be impeded by the lattice mismatch between seeding and epitaxial layers. Furthermore, the mass transport and diffusion between the layers limit the interface sharpness and can result in unintentional compositional and doping gradings. Because of thermodynamics, LPE is sensitive to temperature changes, solution composition, surface tension, quality of seeding substrate, etc.

The great advantages of LPE growth are the high growth rate, exceptional high purity crystals with low defect density (impurities tend to segregate rather than to be incorporated into the epilayer), and high selectivity on patterns, substrates, and facetted growth, which can produce shaped crystals and selectively nucleated crystals with high aspect ratios. This made LPE to the pioneering growth method to produce the optoelectronic devices (LED, laser, solar cells) based on II-VI and III-V semiconductors (Nelson, 1963; Rupprecht et al., 1967; Woodall, 1972; Alferov et al., 1969). Other compounds, including oxides and superconductors, can also be grown with LPE (Ehrentraut et al., 2006; Klemenz and Scheel, 1993; Nagarajan et al., 2011; Yamada et al., 1993). See "Further reading" for more information on this epitaxy method.

Solid-phase epitaxy

SPE refers to the type of growth when a material undergoes a transition from amorphous phase to a crystalline phase. Usually the material is deposited in an amorphous form on a crystalline substrate, which serves as a template for crystal growth(Mayer et al., 1968; Cho, 1969a; Marks et al., 2021). When heated, atoms in the amorphous phase reorder by local bond rearrangements at the crystalline–amorphous interface. The material phase transformation can also be induced by laser, electron, or ion irradiation. An annealing step to recrystallize layers during the ion implantation or to heal defects can also be considered as a SPE (Streit et al., 1984; Norga et al., 2006). SPE is also employed for growing a buffer layer to improve heteroepitaxy of lattice-mismatched heterostructures. See "Further reading" for more information on this epitaxy method.

Molecular beam epitaxy

MBE is a physical vapor deposition technique, which is frequently used in research laboratories and industry. The technique was introduced in 1960s by A. Y. Cho and J. R. Arthur (Arthur, 1968; Cho and Arthur, 1975; Cho, 1969a, 1970). MBE is low-energy deposition technique in ultra-high vacuum. The constituent elements of the crystalline solid are supplied from the source to the substrate as a directed ray of neutral molecules and atoms, so called molecular beam. Such transport implies that the mean free path of species is larger than the distance between the source and the substrate. As a result, the atoms experience no collision before they reach the substrate. A thin epitaxial layer crystalizes via reactions between molecular beams, and a substrate surface holds at high temperature. Therefore, the composition of the epilayer depends on the relative arrival rates of the constituent elements. By controlling the evaporation rate of the source, the arrival rate of molecular beam and thus the epilayer composition can be adjusted. Such a control of epilayer stoichiometry is one of the key strengths of MBE growth. A low growth rate ($1 \mu m\ h^{-1}$) assures that the species absorbed on the substrate surface can diffuse (Fig. 3A). Therefore, MBE allows to achieve smooth epilayer surface. Each molecular beam source is equipped with a mechanical shutter, which is placed in front of it and is used to start and stop the growth fluxes by blocking the emitting flux from the substrate in a time much shorter than the time needed to grow a monolayer. This allows to establish a sharp interface between two materials. A high purity of original element source and high vacuum help to reduce the contamination of epilayer by impurities. The vacuum environment offers an excellent opportunity to monitor the growth process in situ. RHEED is frequently installed in the growth chambers. Thus MBE can produce high-quality thin film structures with layer thickness precision on the atomic level.

Fig. 5 is a schematic view of an MBE chamber that contains essential elements of MBE equipment independent of its purpose. Not shown is a load-lock chamber system that allows to introduce the wafer (or substrates) into the growth chamber without breaking the high vacuum.

Pumping system

It is one of the essential components to assure the molecular beam propagation between source and substrate. The mean free path L changes with the pressure P as $L = 5 \times 10^{-3}/P$, where the distance is given in cm and the pressure in Torr. Thus under high vacuum of 10^{-9} Torr, the mean free path is about 5×10^{6} cm. The vacuum is generated by pumps and cryoshrouds. The layout of the pumping system is crucial for an MBE setup; it must also assure an effective evacuation of residual source gases and reactant byproduct gases. Depending on the purpose, an MBE system can be equipped with various pump systems, such as turbo-molecular pump, ion pump, and cryogenic pump.

Material evaporation source is another important components of an MBE layout. Depending on the material to be evaporated, different sources for producing molecular beam are available.

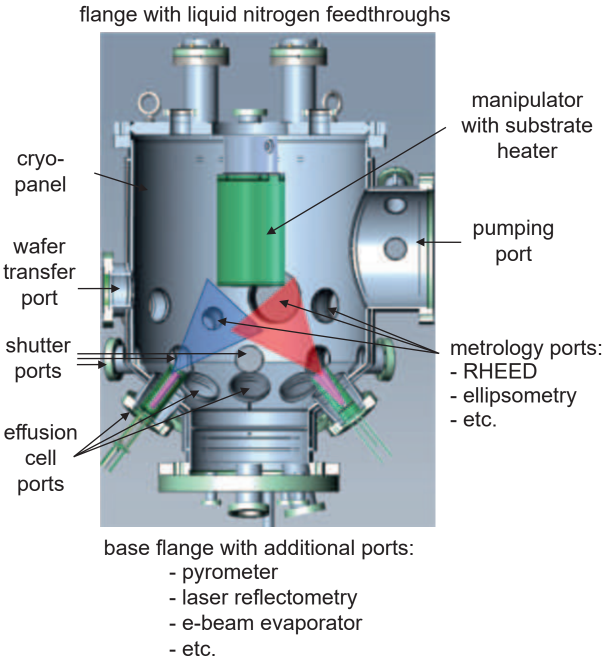

Fig. 5 **MBE** Schematic view of the growth chamber of an MBE machine. The drawing is the courtesy of VEECO.

Material evaporation source

Cells. Knudsen' cell is by far the most important type of evaporation source in a molecular beam system. It is filled with ultrahigh purity materials, which reduces incorporation of impurities in the epilayers. Basically a Knudsen cell is a tubular crucible (made of pyrolytic boron nitride, quartz, tungsten, or graphite), filled with the desired chemical element and is heated resistively up to the level of desired material flux. The Knudsen cells installed in MBE have large opening and thus they are different from the true Knudsen source (Knudsen, 1915), which should have an orifice size comparable with the mean free path of the gas molecule at the temperature of evaporation. The material flux from the cell and its angular distribution in a real MBE system depend not only on the crucible shape but also on the evaporant fill level. Owing to the large thermal mass the cell temperature and thus the evaporation rate cannot be changed quickly. The temperature is usually controlled with a thermocouple. A special type of effusion cell is a cracker cell. Some elements (such as As and P) evaporate as tetramers, although their dimers show a better sticking coefficient to the substrate surface and thus a better growth performance. Breaking of tetramers (As_4) in dimers (As_2) is accomplished in a cracker cell, which is a Knudsen cell having two zones of temperature. The low temperature zone produces the tetramer vapor and the high temperature zone cracks the tetramers to dimers. The cracking efficiency depends on the catalyst, whereas Ta and Rh are very effective.

Gaseous sources. Alternative material flux source was initially introduced by Panish due to difficulty of growth of semiconductor compounds with elemental source of phosphorus (Panish, 1980; Panish et al., 1985). AsH_3 and PH_3 gas sources were introduced to grow InGaAsP. The hydrates are injected into the chamber and are dissociated in cracker cell so that dimers of elements are formed. Also metalorganic (MO) compounds are employed as alternative material sources, which thus borrows an idea from chemical vapor deposition technique (MOVPE). Metalorganic compounds are less thermally stable and can dissociate directly on a growing substrate. The by products are removed from the environment, whereas the cryopumps can be employed to maintain a good vacuum condition. MBE system equipped with MO source is often called MOMBE. The advantage of it is that MO needs a low temperature to produce sufficient flux; it is stored outside of MBE chamber and thus can be readily replaced; a high growth rate can be achieved. MO compounds are however toxic and less pure than the elemental source material.

E-gun. The operation of Knudsen cells is limited to a temperature of about 1400C. Yet, some elements require a higher temperature to be evaporated and to obtain a sufficient material flux for the epitaxial growth. In this case, the materials such as Ti, Si, Mo, and W. can be evaporated using intense beams of high-energy electrons, so called e-beam gun (Kasper, 1982; Koenig et al., 1979; Ota, 1983). The heating energy is transferred by electrons on just an evaporating surface of target. Although such evaporation technique is more prone to flux instability, the introduction of active feedback loops between evaporation parameters and flux can minimize the fluctuations. Since this technique can evaporate a large number of elements, the e-beam evaporators are frequently employed in the epitaxy (Yamamoto et al., 2013).

Laser was also employed for heating the sources in MBE growth of II-VI compounds. With this technique, $Hg_{1-x}Cd_xTe$ epitaxial layers and superlattices were grown (Cheung and Madden, 1987; Cheung et al., 1986).

Flux measurement and stoichiometry

Accurate flux measurements and flux stability are crucial for the growth of high-quality films with well-defined stoichiometry. Fluxes from the effusion cells can be characterized by various techniques. Quartz crystal microbalance (QCM) measures the flux by relating the shift in the resonance frequency to the accumulation of mass on the probe located at the substrate position. Beam equivalent pressure (BEP) can be obtained by inserting an ion gauge in front of the substrate, so called beam flux monitor (BFM). Atomic absorption spectroscopy and cross-beam mass spectroscopy are other examples for monitoring the material flux of each effusion cell. Despite the variety of methods, an excellent control of flux and thus stoichiometry is difficult. Moreover, the flux stability will also depend on the stability of the cell temperature. All these lead to the deviation of the desired compound composition. The desired structure accumulates defects or can even form other crystalline phases. As a result, the physical properties of the desired compound are altered. Yet, the thermodynamics can enable a stoichiometric compound composition within some range of growth parameters (substrate temperature and material flux). Such thermodynamic regime is also known as an adsorption-controlled growth. One talks also about an opening of a growth window. A prerequisite for this is that one of the constituent elements has to be volatile. This requirement is fulfilled for the growth of III-V semiconductors, which has thus significantly contributed to the success of semiconductors' growth. The respective thermodynamic conditions can be estimated from the equilibrium lines in a pressure–temperature diagram (Arthur, 1968; Cho, 1971). The lower bound is given by As condensation on a Ga-rich GaAs surface, while the upper bound is given by the vapor pressure curve of As. Between two boundaries, sufficient As is supplied to saturate each Ga monolayer, and any excess As desorbs from the surface and enters the vapor phase. Thus, the growth rate is determined by the Ga flux and the self-regulated growth can be obtained. Since the equilibrium lines are separated from each other by orders of magnitude in the As gas pressure, the request on the precise control of the flux and temperature is relaxed. In principal, if the growth conditions are within the growth window, an identical crystalline compound forms. If the parameters are outside of the growth window, the compound decomposes, for instance by forming liquid Ga and solid As phases. The regime of adsorption-controlled growth is also realized for some oxide compounds with volatile elements Pb and Bi, such as $PbTiO_3$, $BiFeO_3$, $BiMnO_3$, and (Rb, Ba)BiO_3 (Theis et al., 1998; Ihlefeld et al., 2008; Lee et al., 2010; Hellman and Hartford, 1990).

Oxide compound

The growth of oxides constitutes one of the important fields in the material science, as the oxides show a diverse range of physical phenomena in bulk and thin films and therefore are considered as a promising material platform for realizing novel functionalities (Schlom et al., 2008; Hwang et al., 2012). High-quality structures are realized in an MBE chamber equipped with a suitable oxygen source, which can be molecular oxygen O_2 (suitable for easy oxidizing compounds), oxygen plasma (activated by RF plasma source), or ozone, which is the most reactive and the cleanest oxygen source (Schlom et al., 1988; Eckstein et al., 1989; Berkley et al., 1988, 1989). By using a highly reactive oxidizer a long mean free path should be guaranteed to avoid gas-phase reactions. Usually the nozzle of oxygen line is positioned about 10 cm away from the substrate surface. A complete oxidation of epilayers is always a matter of concern in oxide MBE. Yet, it is possible to achieve high-quality oxide structures. ZnO is one of the examples. The heterostructures based on ZnO feature high electron mobility, giving rise to a variety of quantum phenomena (Tsukazaki et al., 2010; Falson et al., 2011, 2016, 2015; Maryenko et al., 2018, 2021). High-quality ternary oxides, such as $SrTiO_3$ perovskite, are grown by employing metalorganic precursor (MO) as the source for Ti element, that is titanium(IV)isopropoxide (TTIP, $Ti[OCH(CH_3)_2]_4$). A high vapor pressure of TTIP enables an adsorption controlled growth and therefore offers an excellent control over the epilayer stoichiometry (Endo et al., 1991; Jalan et al., 2009a, b, c; Brahlek et al., 2018). Once TTIP molecule reaches the hot substrate surface, it decomposes in nonvolatile TiO_2 and by products consisting of volatile C_3H_6 and H_2O. TiO_2 reacts with SrO formed on the surface, leading to the formation of a stoichiometric $SrTiO_3$ layer. The structures synthesized in this way allowed to achieve high electron mobility (Son et al., 2010) and to demonstrate the quantum Hall effect for the first time in oxide perovskite structures (Matsubara et al., 2016). Oxide MBE with MO sources is referred as hybrid MBE.

The approach to synthesize oxide perovskite with MOs has been extended on the growth on vanadium perovskite, using vanadium-triisopropoxide (VTIP) as a source of vanadium (Moyer et al., 2013; Brahlek et al., 2018) and high mobility $BaSnO_3$, employing hexamethylditin (HMDT) as a precursors to supply tin (Chambers et al., 2016). The reactive environment of oxide growth requires the use of oxidation-resistive materials for components that are particularly exposed to high temperatures. Heating of substrate is also an important part of consideration for oxide MBE. The usage of laser heating system instead of resistive heaters allows not only to achieve even higher growth temperatures but also to reduce the heat load on the growth environment. As a result, the incorporation of undesired impurities collected on the chamber walls of the heating system is reduced. Due to the local heating by laser, the heat capacitance is reduced and the quick change of the growth temperature can be achieved, which can be favorable for growth protocols requiring the temperature changes. High temperature can even prepare in situ the substrate surfaces suitable for the growth (Jaeger et al., 2018; Braun et al., 2020).

Fig. 6 is the photograph of an oxide MBE machine installed at RIKEN. It is equipped with several retractable Knudsen cells, supply of metal-organic precursors, and ozone source. Laser heater system allows to achieve temperature well above 1000C. The pumping system, consisting of turbomolecular pump and cryopump, allows to remove the by products of metalorganic

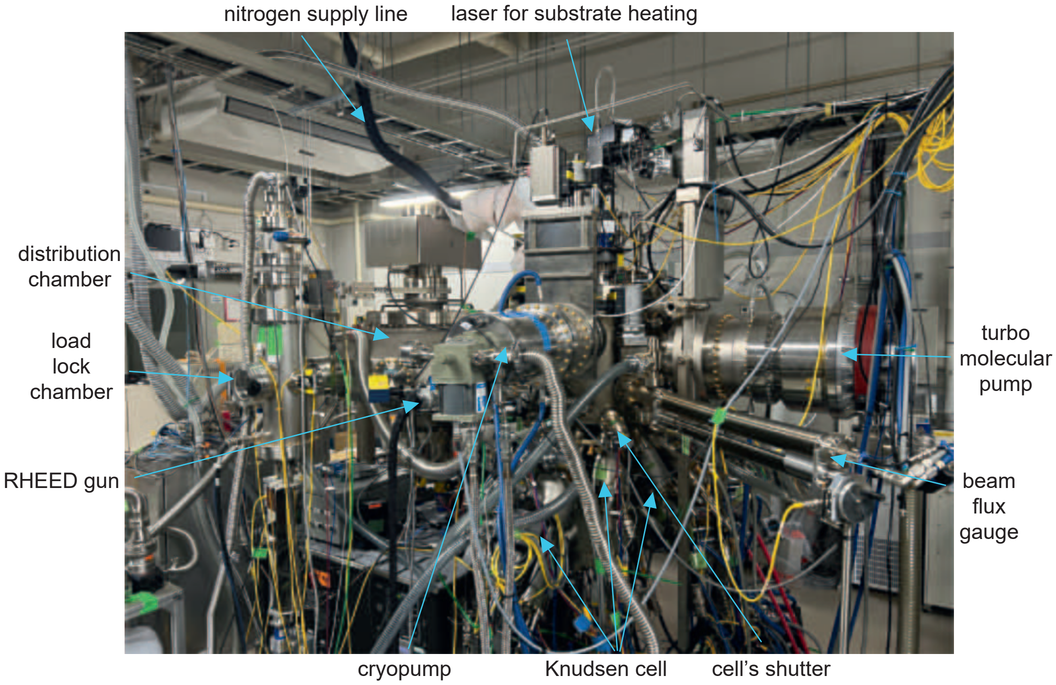

Fig. 6 Photograph of oxide MBE VEECO GEN10 installed at RIKEN. Additionally it is equipped with the ozone source and gas cell for supply of metalorganic precursor. The laser beam for substrate heating is guided by the optical fiber to the growth chamber.

precursors effectively. Cryogenic panels cooled with liquid nitrogen minimize the thermal load of the growth chamber and allow to trap impurities from the gas phase during thin film deposition.

Pulsed laser deposition

PLD is one of the PVD process techniques, where the material to be deposited is ablated (evaporated) by highly energetic laser beam focused on the starting material, so called target. This growth technique emerged due to the development of laser technology. In fact, the first demonstration of PLD growth technique was in 1965 by Smith and Turner, who used ruby laser to synthesis optical coatings (Smith and Turner, 1965). However, a broad proliferation of PLD growth method has been triggered by the work by Dijkkamp and coworkers demonstrating the thin film growth of high temperature superconductors $YBa_2Cu_3O_7$ (Dijkkamp et al., 1987). Since then PLD has been employed for synthesis of all kinds of materials, encompassing oxides, nitrides, carbides, organic materials, polymers, and metallic systems. Because of the similarity with MBE growth technique, one finds for PLD growth also the notation as laser-assisted MBE or laser MBE.

Fig. 7 shows the main concept of PLD process. A pulsed laser beam passes through an optical window of a vacuum chamber and is focused onto a target, where it is partially absorbed. A dense layer of vapor forms in front of the target, whose temperature and pressure increase during the light absorption process, resulting in a partial ionization of the ablated materials. The formed layer expands from the target surface and appears as a forward-directed luminous plume. During the expansion, internal thermal and ionization energies are converted into the kinetic energy of ablated particles. The ablation plume provides thus the material flux for the film growth. The threshold power of high energy laser needed to produce such a plume depends on the target material, its morphology, and the laser pulse wavelength and duration. A typical laser fluence amounts to 1–10 $\mathrm{Jcm^{-2}}$. Excimer laser or high harmonics of Nd:YAG solid-state laser can provide such high energy laser pulses and are frequently employed in PLD setups. For an efficient ablation, the optical absorption coefficient of the target material should be high at the laser operation wavelength. The target materials do not have to have the same phase as the desired thin film; only the cation stoichiometry needs to be preserved, assuming stoichiometric transfer between target and film. Each ablation pulse provides material amount sufficient for the deposition of a submonolayer of the desired thin film phase. Therefore, PLD deposition is very suitable for multilayer and interface formation where submonolayer control is required (Fig. 8).

The kinetic energy of species arriving at the substrate can modify the thin-film growth. Upon ablation the species in the ablated plume interact with the gas atmosphere introduced during the growth. So the particles, kinetic energy at the substrate surface depends on the gas parameter, mass, and pressure. Thus the kinetic energy can range from high initial energy (several hundred electron volts) with no gas atmosphere to low energies (few tenths of electron volts) from thermalization at sufficiently large ambient pressure. Upon arrival at the substrate surface, the diffusion time of the atoms usually exceeds the optical pulse duration, leading effectively to instantaneous deposition. During the time between subsequent optical pulses, the adatoms can rearrange on the surface by diffusion and are subsequently incorporated through nucleation and growth. Such a separation of the growth process in two steps, instantaneous deposition and nucleation, is unique for thin film synthesis with PLD. The two steps can be controlled independently from each other. While the instantaneous deposition rate can be controlled by adjusting the laser energy density

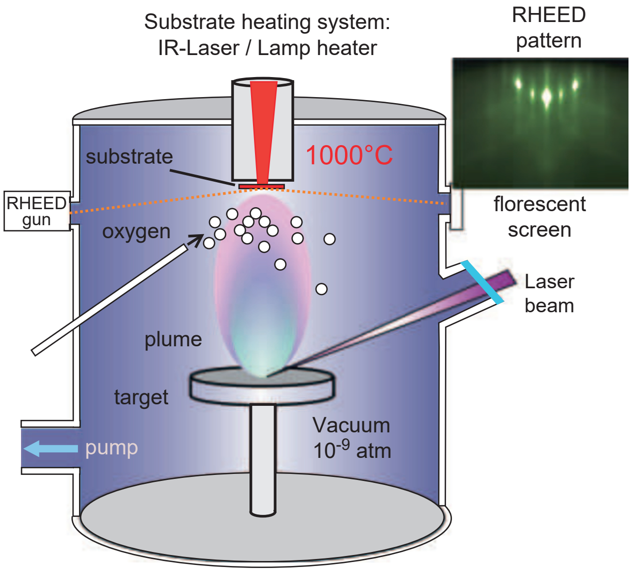

Fig. 7 Schematic view of PLD. The laser beam ablates the target and creates a plume that propagates toward the substrate kept at high temperature. RHEED is used to monitor the growth process. Inset shows the RHEED pattern as observed on the fluorescent screen. Spots of RHEED pattern and Kikuchi lines indicate a good film quality.

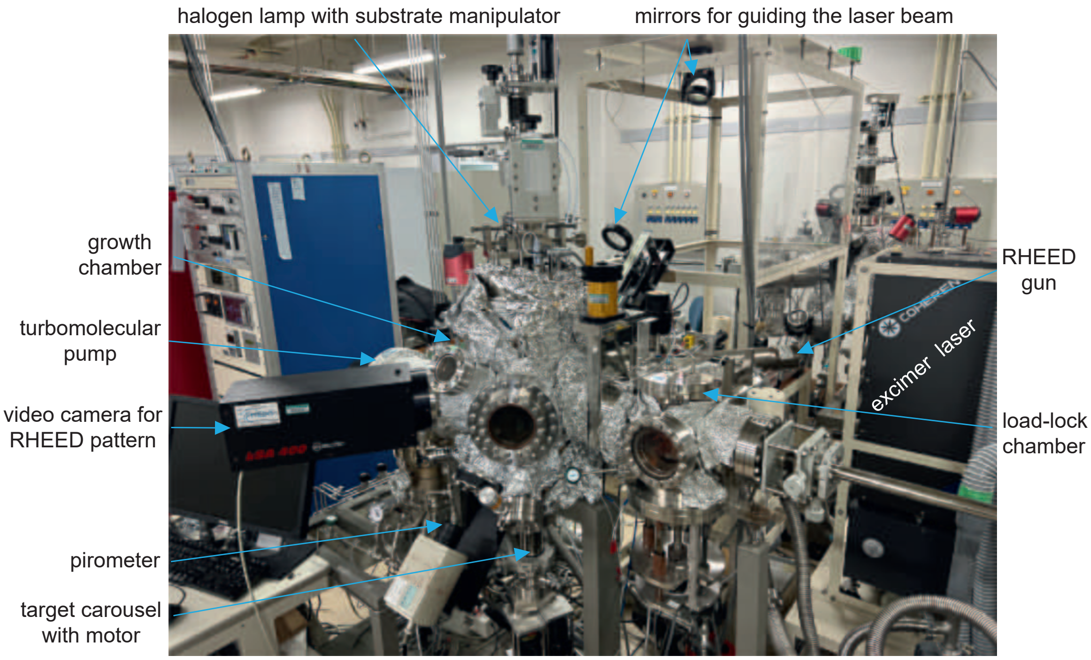
halogen lamp with substrate manipulator
mirrors for guiding the laser beam
growth chamber
turbomolecular pump
video camera for RHEED pattern
pirometer
target carousel with motor
RHEED gun
excimer laser
load-lock chamber

Fig. 8 **Photograph of a PLD** installed at RIKEN.

(pulse energy and laser focus on the target), ambient gas condition, distance between target and substrate, and the growth rate are determined by the laser pulse repetition rate. Moreover, the growth process will depend on the substrate surface preparation quality and the substrate temperature.

Besides the UHV optical view port for introducing the laser light into the growth chamber, a usual PLD chamber contains a vacuum pumping system (turbomolecular pumps) to maintain a background pressure between 10^{-6} and 10^{-11} Torr. Substrate heater, target manipulator, and gas inlet are also essential components of PLD setup. The substrate heating system can be realized in various ways; it can be a conventional SiC heater as well as halogen lamp or an infrared laser. For the deposition of oxides, halogen lamp and infrared laser are widely used, since they do not oxidize in oxygen reactive atmosphere. The substrate is usually placed about 2–10 cm away from the target. The target manipulator can be a carousel containing several targets. The targets can be in situ exchanged, facilitating the synthesis of multilayer structures consisting of different materials. Also various gases (molecular O_2, N_2, Ar, etc.) can be introduced into the chamber through the gas inlet during thin film deposition to promote the reaction of the evaporated species. To increase the reaction rate, oxygen plasma, nitrogen plasma, or even ozone can be introduced through the gas inlet. The growth process is monitored with the help of RHEED.

The PLD technique is probably one of the most versatile thin film synthesis methods as it offers a number of advantages (Willmott and Huber, 2000):

- Almost any material can be grown with PLD.
- The source of material evaporation (pulsed laser) is outside of the growth chamber, offering the flexibility in geometrical arrangement and material choice.
- Nearly there is one-to-one stoichiometry transfer from target to the film, even for chemically complex systems.
- There is synthesis of materials with a chemical composition far from equilibrium. This opens the way for attaining materials with novel electronic states, which cannot be obtained under thermal conditions.
- There is tunability of the growth rate due to laser operation in a pulse regime.

Besides numerous advantages that PLD can offer, there are several fundamental and technical drawbacks as well:

- Ablation target process can also produce ejecta, which will lead to the defect formation in the synthesized films.
- Target contains impurities either introduced during sintering of the target or from the source material. As a result, impurities can be incorporated into the epitaxial layers.
- high kinetic energy species in the plume bombard the surface of substrate as well as subsequently formed epitaxial layers. This results in the formation of crystallographic defects, which can be detrimental for the formation of sharp interfaces.
- The process of plume formation leads to an inhomogeneous distribution of flux and angular distribution within the plume. As a result, the synthesized structures can be inhomogeneous.
- Stoichiometric transfer from target to the desired materials is not always granted. The stoichiometry transfer can depend on the deposition condition, such as laser fluence or temperature (Groenendijk et al., 2016; Ohnishi et al., 2008; Tomar et al., 2019). For targets with volatile elements, the target has to be enriched with the respective element. The change of a stoichiometric

composition requires a fabrication of a new target. Moreover, the ablation of the target can modify its surface, which can lead to the variation of the target stoichiometry at the position of the laser focus. In extreme case the change of the target stoichiometry can lead to the decrease of the growth rate.

Sputtering

Sputtering is the ejection of particles from the target by its bombardment with energetic particles. Sputtering process relies on production of plasma through electrical discharge and electrostatic acceleration of ions, inert gas ions like argon, towards the source material. The impinging ions transmit energy and momentum to the source material and knock out the particles form the surface of the target. Ejected particles are the source material for films grown by sputter deposition. The particles ejected in sputtering are predominantly neutral atoms in the ground state, although ions and atomic clusters can also be present in the emitted flux. Such process of creating particle flux is similar to that of PLD, except that in PLD the target is ablated by laser light. There are different kinds of sputtering processes, depending on condition (reactive sputtering, bias sputtering) or configuration (ion beam sputtering, DC sputtering, RF sputtering, magnetron sputtering). For instance, magnetron sputtering implies that a magnetic field is created in the vicinity of target holder, which bends the ionized particles on a specific area of a target. This increases the deposition rate and the deposition area. Sputtering deposition technique is cost-effective, shows a high throughput and can produce large-area films. Such characteristics make the deposition technique attractive for industrial growth applications. See “Further reading” for more information on this epitaxy method.

Conclusion

Epitaxy is a broad research field concerning with the mechanism and methods to grow-well oriented crystalline layers. Over the last century a various practical methods have been developed that allowed the synthesis of an enormously large pallet of materials. GaAs-based structures are a striking example of the opportunities that open when structures are optimized and the growth technique is refined (Pfeiffer and West, 2003; Pfeiffer et al., 1989; Umansky et al., 2009; Gardner et al., 2016; Chung et al., 2018, 2021). In this context, the continuous improvement of material quality, the development of new materials and their multilayers including hybrid structures is an important direction, that will enable to open new horizon not only in fundamental science but also in applications. Epitaxial methods are therefore essential for traversing along this path.

References

Alferov ZI, Andreev VM, Korolkov VI, Portnoi EL, and Tretyakov DN (1969) Coherent radiation of epitaxial heterojunction structures in AlAs-GaAs system. *Soviet Phys. Semiconductors* 2: 1289.

Arthur JR (1968) Interaction of Ga and As_2 molecular beams with GaAs surfaces. *Journal of Applied Physics* 39: 4032.

Balluffi RW, Brokman A, and King AH (1982) CSL/DSC lattice model for general crystal-crystal boundaries and their line defects. *Acta Metallurgica* 30: 1453.

Barker TV (1906) *Journal of the Chemical Society, Transactions* 89: 1120.

Berkley DD, Johnson BR, Anand N, Beauchamp KM, Conroy LE, Goldman AM, Maps J, Mauersberger K, Mecartney ML, Morton J, Tuominen M, and Zhang YJ (1988) In situ formation of superconducting $yba_2cu_3o_7$ thin films using pure ozone oxidation. *Applied Physics Letters* 53: 1973–1975.

Berkley DD, Goldman AM, Johnson BR, Morton J, and Wang T (1989) Techniques for the growth of superconducting oxide thin films using pure ozone vapor. *Review of Scientific Instruments* 60: 3769–3774.

Brahlek M, Gupta AS, Lapano J, Roth J, Zhang H-T, Zhang L, Haislmaier R, and Engel-Herbert R (2018) Frontiers in the growth of complex oxide thin films: Past, present, and future of hybrid MBE. *Advanced Functional Materials* 28: 1702772.

Braun W, Jaeger M, Laskin G, Ngabonziza P, Voesch W, Wittlich P, and Mannhart J (2020) In situ thermal preparation of oxide surfaces. *APL Materials* 8: 071112.

Bruinsma R and Zangwill A (1986) Structural transitions in epitaxial overlayers. *Journal de Physique* 47: 2055.

Chambers SA, Kaspar TC, Prakash A, Haugstad G, and Jalan B (2016) Band alignment at epitaxial $BaSnO_3/SrTiO_3$ (001) and $BaSnO_3/LaAlO_3$(001) heterojunctions. *Applied Physics Letters* 108(15): 152104.

Cheung JT and Madden J (1987) Growth of HgCdTe epilayers with any predesigned compositional profile by laser molecular beam epitaxy. *Journal of Vacuum Science and Technology B* 5: 705.

Cheung JT, Niizawa G, Moyle J, Ong NP, Paine BM, and Vreeland T (1986) HgTe and CdTe epitaxial layers and HgTe-CdTe superlattices grown by laser molecular beam epitaxy. *Journal of Vacuum Science and Technology A* 4: 2086.

Cho AY (1969a) Epitaxy by periodic annealing. *Surface Science* 17: 494.

Cho AY (1970) Morphology of epitaxial growth of GaAs by a molecular beam method: The observation of surface structures. *Journal of Applied Physics* 41: 2780.

Cho AY (1971) Film deposition by molecular-beam techniques. *Journal of Vacuum Science and Technology* 8: S31.

Cho AY and Arthur JR (1975) Molecular beam epitaxy. *Progress in Solid State Chemistry* 10: 157.

Chung YJ, Baldwin KW, West KW, Shayegan M, and Pfeiffer LN (2018) Surface segregation and the Al problem in GaAs quantum wells. *Physical Review Materials* 2: 034006.

Chung YJ, Villegas Rosales KA, Baldwin KW, Madathil PT, West KW, Shayegan M, and Pfeiffer LN (2021) Ultra-high-quality two-dimensional electron systems. *Nature Materials* 20: 632–637.

Cuomo JJ, Pappas DL, Bruley J, Doyle JP, and Saenger KL (1991) Vapor deposition processes for amorphous carbon films with sp^3 fractions approaching diamond. *Journal of Applied Physics* 70: 1706–1711.

Dawson LR (1972) Liquid phase epitaxy. *Progress in Solid State Chemistry* 7: 117. 039.

der Merve JHV (1962) Crystal Interfaces. Part II. Finite Overgrowths. *Journal of Applied Physics* 34: 123.

Dijkkamp D, Venkatesan T, Wu XD, Shaheen SA, Jisrawi N, Min-Lee YH, McLean WL, and Croft M (1987) Preparation of Y-Ba-Cu oxide superconductor thin films using pulsed laser evaporation from high T_c bulk material. *Applied Physics Letters* 51: 619–621.

Eckstein JN, Schlom DG, Hellman ES, von Dessonneck KE, Chen ZJ, Webb C, Turner F, Harris JS, Beasley MR, and Geballe TH (1989) Epitaxial growth of high-temperature superconducting thin films. *Journal of Vacuum Science & Technology B: Microelectronics Processing and Phenomena* 7: 319–323.

Ehrentraut D, Sato H, Miyamoto M, Fukuda T, Nikl M, Maeda K, and Niikura I (2006) Fabrication of homoepitaxial ZnO films by low-temperature liquid-phase epitaxy. *Journal of Crystal Growth* 287: 367–371.

Endo K, Saya S, Misawa S, and Yoshida S (1991) Preparation of yttrium barium copper-oxide superconducting films by metalorganic molecular-beam epitaxy. *Thin Solid Films* 206: 143.

Falson J, Maryenko D, Kozuka Y, Tsukazaki A, and Kawasaki M (2011) Magnesium doping controlled density and mobility of two-dimensional electron gas in $Mg_xZn_{1-x}O$/ZnO heterostructures. *Applied Physics Express* 4: 091101.

Falson J, Maryenko D, Friess B, Zhang D, Kozuka Y, Tsukazaki A, Smet JH, and Kawasaki M (2015) Even-denominator fractional quantum Hall physics in ZnO. *Nature Physics* 11: 347.

Falson J, Kozuka M, Uchida Y, Smet JH, Arima T, Tsukazaki A, and Kawasaki M (2016) MgZnO/ZnO heterostructures with electron mobility exceeding 1x $10^6cm^2V^{-1}cm^{-1}$. *Scientific Reports* 6: 26598.

Farrow RFC (1983) The stabilization of metastable phases by epitaxy. *Journal of Vacuum Science & Technology B: Microelectronics Processing and Phenomena* 1: 222–228.

Farrow RFC, Robertson DS, Williams GM, Cullis AG, Jones GR, Young IM, and Dennis PNJ (1981) The growth of metastable, heteroepitaxial films of α-Sn by metal beam epitaxy. *Journal of Crystal Growth* 54: 507.

Feng ZC and Liu HD (1983) Generalized formula for curvature radius and layer stresses caused by thermal strain in semiconductor multilayer structures. *Journal of Applied Physics* 54: 83.

Frank FC and Van der Merve JH (1949) One-dimensional dislocations. I. Static theory. *Proceedings of the Royal Society of London* A198: 205–216.

Frankenheim ML (1836) *Annalen der Physik* 37: 516.

Gardner GC, Fallahi S, Watson JD, and Manfra MJ (2016) Modified MBE hardware and techniques and role of gallium purity for attainment of two dimensional electron gas mobility $> 35 \times 10^6$cm^2/Vs in AlGaAs/GaAs quantum wells grown by MBE. *Journal of Crystal Growth* 441: 71–77.

Gorbenko OY, Samoilenkov SV, Graboy IE, and Kaul AR (2002) Epitaxial stabilization of oxides in thin films. *Chemistry of Materials* 14: 4026–4043.

Grabow MH and Gilmer GH (1988) Thin film growth modes, wetting and cluster nucleation. *Surface Science* 194: 333.

Groenendijk DJ, Manca N, Mattoni G, Kootstra L, Gariglio S, Huang Y, van Heumen E, and Caviglia AD (2016) Epitaxial growth and thermodynamic stability of sriro3/srtio3 heterostructures. *Applied Physics Letters* 109: 041906.

Haeni J, Theis C, and Schlom D (2000) RHEED intensity oscillations for the stoichiometric growth of $SrTiO_3$ thin films by reactive molecular beam epitaxy. *Journal of Electroceramics* 4: 385–391.

Hasegawa S (2012) Reflection high-energy electron diffraction. In: *Characterization of Materials*, pp. 1–14. John Wiley & Sons, Ltd.

Hellman ES and Hartford EH (1990) Adsorption controlled molecular-beam epitaxy of rubidium barium bismuth oxide. *Journal of Vacuum Science and Technology B* 5: 332.

Hsieh CC, Wu KH, Juang JY, Uen TM, Lin J-Y, and Gou YS (2002) Monophasic TiO_2 films deposited on $SrTiO_3$(100) by pulsed laser ablation. *Journal of Applied Physics* 92: 2518–2523.

Hwang H, Iwasa Y, Kawasaki M, Keimer B, Nagaosa N, and Tokura Y (2012) Emergent phenomena at oxide interfaces. *Nature Materials* 11: 103.

Ichimiya A and Cohen PI (2004) *Reflection High-Energy Electron Diffraction*. Cambridge.

Ihlefeld JF, Podraza NJ, Liu ZK, Rai RC, Xu X, and Heeg T (2008) Optical band gap of $BiFeO_3$ grown by molecular-beam epitaxy. *Applied Physics Letters* 92: 142908.

Jaeger M, Teker A, Mannhart J, and Braun W (2018) Independence of surface morphology and reconstruction during the thermal preparation of perovskite oxide surfaces. *Applied Physics Letters* 112: 111601.

Jalan B, Engel-Herbert R, Cagnon J, and Stemmer S (2009a) Growth modes in metal-organic molecular beam epitaxy of TiO_2 on r-plane sapphire. *Journal of Vacuum Science and Technology A* 27: 230.

Jalan B, Engel-Herbert R, Wright NJ, and Stemmer S (2009b) Growth of high-quality $SrTiO_3$ films using a hybrid molecular beam epitaxy approach. *Journal of Vacuum Science and Technology A* 27: 461.

Jalan B, Moetakef P, and Stemmer S (2009c) Molecular beam epitaxy of $SrTiO_3$ with a growth window. *Applied Physics Letters* 95: 032906.

Jesser WA, van der Merve JH, and Stoop PM (1999) Misfit accommodation by compliant substrates. *Journal of Applied Physics* 85: 2129.

Kasper E (1982) Growth kinetics of Si-molecular beam epitaxy. *Applied Physics A: Materials Science & Processing* 28: 129.

Klemenz C and Scheel HJ (1993) Liquid phase epitaxy of high-Tc superconductors. *Journal of Crystal Growth* 129: 421–428.

Knudsen M (1915) Die maximale Verdampfungsgeschwindigkeit des Quecksilbers. *Annalen der Physik (Leipzig)* 47: 697.

Koenig U, Kibbel H, and Kasper E (1979) Si-MBE: Growth and Sb doping. *Journal of Vacuum Science and Technology B* 16: 985.

Lee JH, Ke X, Misra R, Ihlefeld JF, Xu XS, and Mei ZG (2010) Adsorption-controlled growth of $BiMnO_3$ films by molecularbeam epitaxy. *Applied Physics Letters* 96: 262905.

Lo YH (1991) New approach to grow pseudomorphic structures over the critical thickness. *Applied Physics Letters* 59: 2311.

Marks SD, Lin L, Zuo P, Strohbeen PJ, Jacobs R, Dongxue D, Waldvogel JR, Liu R, Savage DE, Booske JH, Kawasaki JK, Babcock SE, Morgan D, and Evans PG (2021) Solid-phase epitaxial growth of the correlated-electron transparent conducting oxide $SrVO_3$. *Physical Review Materials* 5: 083402.

Maryenko D, McCollam A, Falson J, Kozuka Y, Bruin J, Zeitler U, and Kawasaki M (2018) Composite fermion liquid to Wigner solid transition in the lowest Landau level of zinc oxide. *Nature Communications* 9: 4356.

Maryenko D, Kawamura M, Ernst A, Dugaev VK, Sherman EY, Kriener M, Bahramy MS, Kozuka Y, and Kawasaki M (2021) Interplay of spin-orbit coupling and Coulomb interaction in ZnO-based electron system. *Nature Communications* 12: 3180.

Matsubara Y, Takahashi K, Bahramy M, Kozuka Y, Maryenko D, Falson J, Tsukazaki A, Tokura Y, and Kawasaki M (2016) Observation of the quantum Hall effect in δ-doped $SrTiO_3$. *Nature Communications* 7: 11631.

Matthews JW and Blakeslee AE (1974) Defects in epitaxial multilayers: 1. Misfit dislocations. *Journal of Crystal Growth* 27: 118.

Mayer JW, Eriksson L, Picraux ST, and Davies JA (1968) Ion implantation of silicon and germanium at room temperature. Analysis by means of 1.0-MeV helium ion scattering. *Canadian Journal of Physics* 45: 663.

Moyer JA, Eaton C, and Engel-Herbert R (2013) Highly conductive $SrVO_3$ as a bottom electrode for functional perovskite oxides. *Advanced Materials* 25: 3578.

Nagarajan M, Sudhakar S, Lourdudoss S, and Baskar K (2011) Growth of Zn_3As_2 on GaAs by liquid phase epitaxy and their characterization. *Journal of Crystal Growth* 314(1): 119–122.

Nelson H (1963) *RCA Review* 24: 503.

Norga GJ, Marchiori C, Rossel C, Guiller A, Locquet JP, Siegwart H, Caimi D, Fompeyrine J, Seo JW, and Dieker C (2006) Solid phase epitaxy of $SrTiO_3$ on (Ba, Sr)O/Si(100): The relationship between oxygen stoichiometry and interface stability. *Journal of Applied Physics* 99: 084102.

Ohnishi T, Shibuya K, Yamamoto T, and Lippmaa M (2008) Defects and transport in complex oxide thin films. *Journal of Applied Physics* 103: 103703.

Ota Y (1983) Silicon molecular-beam epitaxy. *Thin Solid Films* 106: 3.

Panish MB (1980) Molecular beam epitaxy of GaAs and InP with gas sources for arsine and phosphine. *Journal of the Electrochemical Society* 127: 2729.

Panish MB, Temkin H, and Sumski S (1985) Gas source MBE of InP and $Ga_xIn_{1-x}P_yAs_{1-y}$ - material properties and heterostructure lasers. *Journal of Vacuum Science and Technology B* 3: 657.

Pashley DW (1956) The study of epitaxy in thin film surface films. *Advances in Physics* 5: 173–240.

People R and Bean JC (1986) Erratum: Calculation of critical layer thickness versus lattice mismatch for Ge_xSi_{1-x}/Si strained layer heterostructures. *Applied Physics Letters* 49: 229.

Pfeiffer L and West KW (2003) The role of MBE in recent quantum Hall effect physics discoveries. *Physica E: Low-dimensional Systems and Nanostructures* 20(1): 57–64.

Pfeiffer L, West KW, Stormer HL, and Baldwin KW (1989) Electron mobility exceeding 10^7cm^2/Vs in a modulation-doped GaAs. *Applied Physics Letters* 55: 1888–1890.

Royer L (1928) Recherches expérimentales sur l'épitaxie ou orientation mutuelle de cristaux d'espèces différentes. *Bulletin de la Société française de Minéralogie* 51: 7–159.

Rupprecht H, Woodall JM, and Pettit GD (1967) Efficient visible electroluminescence at 300K from $Ga_{1-x}Al_xAs$ p-n junctions grown by liquid-phase epitaxy. *Applied Physics Letters* 11: 81.

Schlom DG, Eckstein JN, Hellman ES, Streiffer SK, Harris JS, Beasley MR, Bravman JC, Geballe TH, Webb C, von Dessonneck KE, and Turner F (1988) Molecular beam epitaxy of layered Dy-Ba-Cu-O compounds. *Applied Physics Letters* 53: 1660–1662.

Schlom DG, Chen L-Q, Pan X, Schmehl A, and Zurbuchen MA (2008) A thin film approach to engineering functionality into oxides. *Journal of the American Ceramic Society* 91: 2429.

Smith HM and Turner AF (1965) Vacuum deposited thin films using a ruby laser. *Applied Optics* 4: 147–148.

Son J, Moetakef P, Jalan B, Bierwagen O, Wright NJ, Engel-Herbert R, and Stemmer S (2010) Epitaxial $SrTiO_3$ films with electron mobility exceeding 30000 $cm^2V^{-1}s^{-1}$. *Nature Materials* 9: 482.

Stranski IN and Krastanov L (1938) Zur theorie der orientierten ausscheidung von ionenkristallen aufeinander. *Ber. Akademie der Wissenschaften und der Literatur* 146: 797.

Streit D, Metzger RA, and Allen FG (1984) Doping of silicon in molecular beam epitaxy systems by solid phase epitaxy. *Applied Physics Letters* 44: 234–236.

Stringfellow GB (1982) Epitaxy. *Reports on Progress in Physics* 45: 469.

Sun L, Yuan G, Gao L, Yang J, Chhowalla M, Gharahcheshmeh MH, Gleason KK, Choi YS, Hong BH, and Liu Z (2021) Chemical vapour deposition. *Nature Reviews Methods Primers* 1: 5.

Teal GK, Fisher JR, and Treptow AW (1946) A new bridge photo-cell employing a photo-conductive effect in silicon. Some properties of high purity silicon. *Journal of Applied Physics* 17: 879–886.

Teng D and Lo YH (1993) Dynamic model for pseudomorphic structures grown on compliant substrates: An approach to extend the critical thickness. *Applied Physics Letters* 62: 43.

Theis CD, Yeh J, Schlom DG, Hawley ME, and Brown GW (1998) Adsorption-controlled growth of $PbTiO_3$ by reactive molecular beam epitaxy. *Thin Solid Films* 325: 107.

Tomar R, Varma RM, Kumar N, Sarma DD, Maryenko D, and Chakraverty S (2019) Conducting $lavo_3$/$srtio_3$ interface: Is cationic stoichiometry mandatory? *Advanced Materials Interfaces* 7: 1900941.

Tsukazaki A, Akasaka S, Nakahara K, Ohno Y, Ohno H, Maryenko D, Ohtomo A, and Kawasaki M (2010) Observation of the fractional quantum Hall effect in an oxide. *Nature Materials* 9: 889.

Umansky V, Heiblum M, Levinson Y, Smet J, Nübler J, and Dolev M (2009) MBE growth of ultra-low disorder 2DEG with mobility exceeding 35×10^6 cm^2/Vs. *Journal of Crystal Growth* 311(7): 1658–1661.

Volmer M and Weber A (1926) Keimbildung in fibersattigten Gebilden. *Zeitschrift fr Physikalische Chemie* 119: 277.

Wakkernagel F (1825) *Kastner's Archly. f. gesammte Naturlehre* 5: 293.

Willmott PR and Huber JR (2000) Pulsed laser vaporization and deposition. *Reviews of Modern Physics* 72: 315–328.

Woodall JM (1972) Solution grown $Ga_{1-x}Al_xAs$ superlattice structures. *Journal of Crystal Growth* 12: 32.

Yamada A, Tamada H, and Saitoh M (1993) Liquid phase epitaxial growth of $LiNbO_3$ thin film using Li_2O-B_2O_3 flux system. *Journal of Crystal Growth* 132(1): 48–60.

Yamamoto H, Krockenberger Y, and Naito M (2013) Multi-source mbe with high-precision rate control system as a synthesis method sui generis for multi-cation metal oxides. *Journal of Crystal Growth* 378: 184–188.

Zur A and McGill TC (1984) Lattice match: An application to heteroepitaxy. *Journal of Applied Physics* 55: 378.

Further reading

Asahi H and Horikoshi Y (2019) *Molecular Beam Epitaxy: Materials and Applications from Electronics and Optoelectronics*. Wiley.

Eason R (2007) *Pulsed Laser Deposition of Thin Films*. Wiley.

Harsha KSS (2005) *Principles of Physical Vapor Deposition of Thin Films*. Elsevier.

Henini M (2013) *Molecular Beam Epitaxy: From Research to Mass Production*. Elsevier.

Herman MA and Sitter H (1988) *Molecular Beam Epitaxy: Fundamental and Current Status*. Springer-Verlag.

Herman MA, Richter W, and Sitter H (2004) *Epitaxy: Physical principles and technical implementation*.

Ichimiya A and Cohen PI (2004) *Reflection High Energy Electron Diffraction*. Cambridge.

Koster G, Huijben M, and Rijnders G (2015) *Epitaxial Growth of Complex Metal Oxides*. Elsevier.

Lüth H (2015) *Solid Surfaces, Interfaces, and Thin Films*. Springer-Verlag.

Nishinga T (2015) *Handbook of Crystal Growth. Thin Film Epitaxy: Materials, Processes, and Technology*. Elsevier.

Panish MB and Temkin H (1993) *Gas Source Molecular Beam Epitaxy*. Springer-Verlag.

Pohl UW (2013) *Epitaxy of Semiconductors*. Springer.

Tsao JY (1993) *Materials Fundamentals of Molecular Beam Epitaxy*. Academic Press.

Epitaxy (classical MBE)

Christian Heyn, Center for Hybrid Nanostructures (CHyN), University of Hamburg, Hamburg, Germany;

© 2024 Elsevier Ltd. All rights reserved.

Introduction **544**
Epitaxy in technology **545**
Molecular beam epitaxy (MBE) 545
Nucleation and epitaxial growth modes **546**
Strain in epitaxy **548**
Self-assembly of nanostructures **549**
Strain-induced self-assembly 549
Droplet-based self-assembly 550
Vapor–liquid–solid (VLS) growth of nanowires 550
In situ growth monitoring **551**
Conclusion **552**
References **552**

Abstract

This chapter describes general aspects of epitaxy which denotes the growth of crystalline layers with order given by a crystalline substrate. A focus is on molecular beam epitaxy (MBE) representing a powerful method for epitaxy in particular of ultra-clean two-dimensional semiconductor heterostructures, where the precise control on the composition, size, and roughness of the deposited layers enables an engineering of the band gaps and doping profiles. Using self-assembled growth schemes, also one-dimensional nanowires and zero-dimensional quantum dots can be fabricated without the need for lithography. Discussed topics are technological aspects, basics of crystal growth, epitaxy of strained layers, strain-induced and droplet-based self-assembly, and in situ growth monitoring with focus on electron diffraction.

Introduction

Epitaxy denotes a kind of crystal growth where new crystalline layers are formed with order given by a crystalline substrate. The term epitaxy reflects this oriented overgrowth by referring the Greek language with *epi* meaning above and *taxis* meaning in an ordered manner. Epitaxy can form small crystalline clusters in contact with a substrate or epitaxial layers covering the substrate at a large lateral extent. Historically, first experimental studies on the oriented overgrowth of a crystalline material on a crystalline substrate are reported 1928 by L. Rover (Poppa, 1964).

Depending on the involved materials one distinguishes between homoepitaxy where substrate and new layer are composed of the same material and heteroepitaxy where substrate and new layer are made from different materials. Homoepitaxy is technologically important for example, for the fabrication of ultra-pure and low-defect single crystals, whereas heteroepitaxy is much more flexible and allows for example, the creation of so-called heterostructures, which are stacked crystalline layers of different materials. In particular heterostructures made from semiconductor materials with different band gaps are technologically very important and enable the fabrication of layered quantum structures like quantum wells (QWS) and superlattices by the so-called band-gap engineering (Arthur, 2002). A popular material combination is here GaAs/AlGaAs which allows a significant variation of the band gap whereas the lattice constants are almost equal. In addition to semiconductors, also metallic systems (Bauer, 1982) and even organic materials (Lee et al., 2014) can be grown epitaxially.

In an idealized picture, the substrate is a perfect single-crystal characterized by the symmetry of the unit cell and the lattice constant a_{sub}. For epitaxial growth, the new layer should have the same crystal symmetry and lattice constant a_{layer}. However, epitaxy is possible also for material combinations with slightly different lattice constants, which is described by the lattice mismatch

$$f = \frac{|a_{layer} - a_{sub}|}{a_{sub}} \tag{1}$$

A lattice mismatch larger than zero induces strain energy in the crystal which can be relaxed by formation of dislocations or by switching to an island growth mode (see Section "Nucleation and epitaxial growth modes").

https://doi.org/10.1016/B978-0-323-90800-9.00205-5

Epitaxy in technology

Epitaxy is widely used for instance in semiconductor technology for the fabrication of devices where layers of elementary or compound semiconductors with controlled thickness, band gap, and doping profile are requested. Several approaches to realize epitaxial growth are applied. One major difference between the methods is the state of matter in which the source material for the new layers is supplied. In solid-phase epitaxy (SPE), an amorphous film in contact with a crystalline substrate is recrystallized during a thermal annealing step. Liquid-phase epitaxy (LPE) is a method to grow crystal layers from a molten material (Fig. 1). Here the substrate is often a small seed crystal which defines the crystallographic order of the new layers. For crystallization, the temperature of the melt is reduced to a value below the melting point or the melting point is reduced by adding a further material. For example, liquid gallium droplets in contact with a GaAs substrate can be crystallized to GaAs by adding arsenic in the so-called droplet epitaxy (see Section "Droplet-based self-assembly"). Both techniques, SPE and LPE, are used for the fabrication of semiconductor crystals with a low defect density.

However, a fast change of the source materials for the new layers, which is essential for the fabrication of heterostructures, is difficult to realize using SPE or LPE. Here, methods are advantageous where the source material is supplied as a vapor in the gas phase. In physical vapor deposition (PVD), the source materials in solid or liquid phase are not in contact with the substrate. A vapor is generated from the source materials by thermal heating (evaporation) or by irradiation with light (pulsed-laser deposition), electrons (electron-beam PVD), or ions (sputter deposition). The vapor is transported through a vacuum to the substrate and condenses there (Fig. 1). It should be noted that PVD is often used for the coating of devices where an epitaxial growth is not required. A type of PVD that is optimized for the growth of epitaxial layers is the molecular beam epitaxy (MBE, see Section "Molecular beam epitaxy (MBE)"). Another vapor-based technique for epitaxy is the chemical vapor deposition (CVD) where the source materials are supplied as chemical precursors usually from a gas source. The precursor molecules are dissociated on the substrate and the desired material is incorporated into the growing layer (Fig. 1). This is in contrast to MBE where usually elementary source materials are supplied and directly incorporated.

In a rough comparison, MBE requires expensive ultra-high vacuum (UHV) equipment, typically works at a rather slow growth speed of about 1 μm/h, and the growth is directed perpendicular to the evaporation sources. CVD uses reaction chambers with less expensive vacuum requirements, the growth speed is typically higher at about 10 μm/h, and the growth can be undirected. The usage of precursor molecules in a CVD process allows a chemically selective growth that can be used for instance for an area selective deposition (ASD) or for deposition of highly conformal thin films by sequential reaction of mono-layered precursor molecules in atomic layer deposition or epitaxy (ALD, ALE). To summarize, MBE is a rather slow and expensive technique, but allows the fabrication of ultra-pure heterostructures with excellent crystal quality and is often used for projects in fundamental research on quantum systems or as a pioneering technology to evaluate new materials or device concepts. CVD systems are usually cheaper with a higher throughput which suggests this method also for industrial device fabrication.

Molecular beam epitaxy (MBE)

The foundations of molecular beam epitaxy were established in the late 1960s by J.R. Arthur and A. Y. Cho starting with focus on III/V compound semiconductors (Cho and Arthur, 1975). MBE takes place in an UHV environment in the 10^{-10} to 10^{-12} Torr range to minimize the level of unintentional background doping. This requires a thorough preparation of the vacuum chamber, powerful vacuum pumps, and large usually liquid–nitrogen cooled cryo-shrouds inside the chamber. In solid-source MBE, pure elements are evaporated in thermally heated effusion cells, the vapor travels through the vacuum as a directed beam, and finally condenses on the substrate surface. Kinetic gas theory estimates at a pressure of 1×10^{-6} Torr inside a vapor beam a rate of gas impingement on the substrate of about 1 monolayer (ML) per s, which corresponds for GaAs to a growth speed of 1 μm/h, typical for MBE. On the other side, assuming a very low background pressure of 10^{-12} Torr inside the vacuum chamber, the rate of unintentional gas impingement is about 10^{-6} ML/s. In a worst case scenario where all impinging species are incorporated, this would result in a contaminated

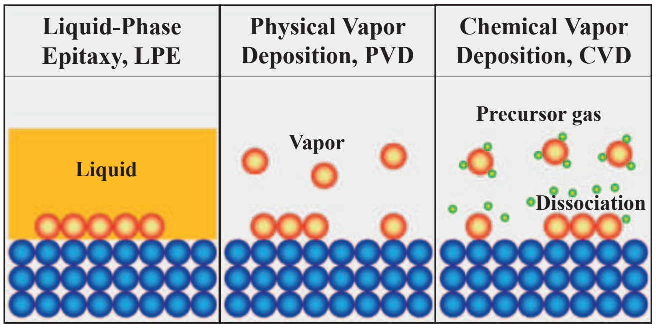
Liquid-Phase Epitaxy, LPE
Physical Vapor Deposition, PVD
Chemical Vapor Deposition, CVD
Liquid
Vapor
Precursor gas
Dissociation

Fig. 1 Illustrations of various methods used for epitaxial growth on a crystalline substrate. In liquid-phase epitaxy (LPE) a molten material in contact with a substrate is crystallized. Vapor-phase-based methods take place in a vacuum and the source material is supplied in an elementary form in physical vapor deposition (PVD) or as a precursor gas in chemical vapor deposition (CVD).

crystal. Fortunately, at usual MBE growth temperatures, only a minor part of the species contributing to the background pressure is incorporated into the growing film. Critical species during MBE of III/V-compound semiconductors are often oxygen or carbon which can significantly degrade the optoelectronic properties of the deposited layers. This indicates the total pressure as an inadequate quantity for the characterization of an MBE system. More meaningful are the partial pressures of the relevant species.

A further important point is the stoichiometry of the materials during epitaxy of compound semiconductors. As an example, for MBE of GaAs, the group III element Ga is typically evaporated at a temperature of about $T_{Ga} \simeq 900°C$ and the group V element As at about $T_{As} \simeq 200°C$. The different evaporation temperatures are given by the respective vapor pressures of the elements. This yields three regimes for the substrate temperature T_{sub}. For a substrate temperature $T_{sub} < T_{As}$ below the minimum temperature required for evaporation, all deposited material will stick on the substrate and the stoichiometry of the deposit must be maintained by adjusting perfectly equal fluxes of Ga and As. Due to technical limitations, equal fluxes are hard to realize and this regime usually results in the formation of nonstoichiometric films with a poor crystalline quality. The regime with $T_{sub} > T_{Ga}$ is also not applicable since here all deposited material will be re-evaporated. In the intermediate regime, $T_{As} < T_{sub} < T_{Ga}$, Ga will stick and As should be re-evaporated. However, due to a strong chemical bond between Ga and As, only excessive As without bond to a Ga atom re-evaporates. That means, for an As flux higher than that of Ga, this mechanism can provide perfectly stoichiometric GaAs layers. This example illustrates that epitaxy of stoichiometric compounds is possible, but requires appropriate temperatures and material combinations.

Assuming a sufficient group V element flux to maintain stoichiometry, the thickness and composition of a deposited layer are precisely controlled by the sum of the fluxes of the group III elements. The individual material fluxes toward the substrate are adjusted by the temperatures of the respective effusion cells. However, for abrupt interfaces between layers composed of different materials, a temperature change is not fast enough. This issue is solved by so-called shutters in front of each effusion cell, which allow an abrupt switching of the respective flux within typically 0.1 s. Considering a usual growth speed of 1 ML/s, the shutters enable the deposition of layers with thickness below one ML. For instance, closing and re-opening of an Al shutter can generate a GaAs QW embedded in AlGaAs with atomically sharp interfaces. Other important MBE grown structures are for instance quantum cascade lasers utilizing multiple QWs for intersubband transitions, or high-electron-mobility transistors (HEMTs), which is a special type of a field-effect transistor where the conductive channel is spatially separated from the doped region to reduce the charge-carrier scattering.

In the last years, the range of materials grown by MBE was expanded from the initial arsenides to other III/V compounds such as phosphides and nitrides, II/VI compounds, elementary semiconductors, oxides, diluted magnetic semiconductors, topological insulators, and organic semiconductors. Due to the high crystal quality of MBE grown material, the possibility to deposit layers of controlled band gap and doping with atomic precision, and its flexibility regarding the materials, MBE has contributed to several Nobel Prizes in Physics, including the fractional quantum Hall effect (1998), semiconductor heterostructures (2000), and solid state lighting (2014). Recent overviews on MBE are given for instance in Orton and Foxon (2015) and Asahi and Horikoshi (2019).

Nucleation and epitaxial growth modes

This section describes the basic mechanisms of epitaxial growth using an MBE configuration as example. Usually, MBE growth takes place far away from equilibrium since new material arriving on the growing surfaces covers already deposited material before this moves to surface positions with a minimal energy. That means energetically unfavorable configurations are possible and kinetic models are required for a description of the growth process.

Fig. 2 gives an overview about the basic processes during MBE. Growth is driven by adatoms from the vapor beam which arrive with a rate F on a crystalline substrate. The following description assumes a single-compound material, and an atomically flat substrate surface with discrete adsorption sites given by the crystal lattice. The surface coverage θ of the new material is characterized in the units of monolayers (MLs), where a coverage of one ML indicates that in average every surface site is occupied by one adatom.

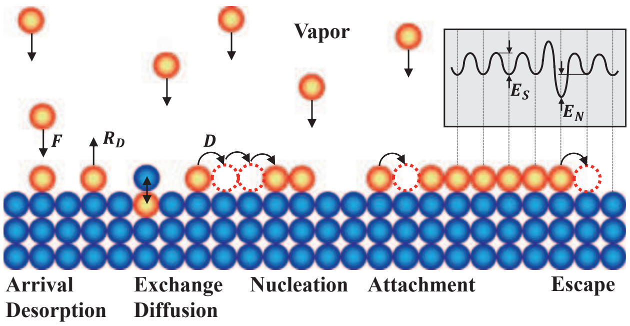

Fig. 2 Schematic illustration of the basic processes during MBE growth from a vapor beam which can be described by the rate for arrival from the beam flux F, the desorption rate R_D, and the surface diffusion rate D. The inset shows the potential landscape with the energy barrier for surface diffusion E_S, and the nearest-neighbor binding energy E_N.

After arrival, the adatoms can be incorporated into the growing film or they can be re-evaporated by desorption with a rate R_D. The probability for incorporation is described by the sticking coefficient $\alpha = (F - R_D)/F$. At usual process temperatures T, the sticking coefficient $\alpha \simeq 1$ and the adatoms migrate on the substrate surface which is called surface diffusion. Further possible processes like the exchange of new adatoms with atoms from the substrate crystal are neglected in the following: Kinetic approaches describe surface diffusion by jumps of adatoms to neighboring surface sites with a thermally activated rate $D = \nu \exp[-E_S/(k_B T)]$, where ν is a vibrational frequency, E_S is the activation energy for surface diffusion, and k_B is Boltzmann's constant. In this picture, a single adatom on the surface will not be incorporated but instead performs a permanent diffusion. A second adatom arrives after a time interval $1/F$ and now a nucleus can be formed by a collision between the migrating adatoms. The additional lateral binding energy E_N between the neighboring adatoms inside the nucleus strongly reduces the surface diffusion rate where now for the activation energy a value $E_S + nE_N$ must be considered, with the number n of neighboring atoms. For large values of E_N, the lateral bonds inside a nucleus cannot be broken which is called irreversible aggregation. Often reversible aggregation is observed, where small values of E_N allow an escape of adatoms from a nucleus. This can result in the dissolution of a nucleus and reduce the density N of nuclei on the surface. Usually the size of a nuclei increases with deposition time and is balanced by the rates of adatom attachment and escape. With larger size, the initial nuclei are often called growth islands or clusters.

Models of nucleation and island growth often use coupled rate equations to describe the time-dependent average densities of adatoms and islands (Venables et al., 1984; Zinke-Allmang et al., 1992). With some approximations, the maximum island density can be estimated from

$$N \propto (F/D)^p \tag{2}$$

where the scaling parameter is $p \simeq 1/3.5$ for 3D islands and $p \simeq 1/3$ for 2D islands. That means, the island density increases with increasing flux F and decreases with increasing temperature and, thus, increasing diffusion rate D. In a simple picture assuming one adatom and one island on the surface, a high D means a long diffusion length and a high probability that the adatom attaches to the island before a second adatom arrives for a nucleation. On the other side, at a low D or high F, the second adatom will arrive before the first atom can attach to the existing island and the probability for nucleation of a new island is high.

As an example for the influence of the substrate temperature on the nucleation, Fig. 3 shows the density of Al and Ga droplets on an AlGaAs substrate. Such droplets are relevant for the so-called droplet epitaxy of semiconductor nanostructures (see Section "Droplet-based self-assembly"). Clearly visible is the tunability of the droplet density over several orders of magnitude. Furthermore, the slope of the droplet density versus T depends on the materials, which indicates material-dependent values of E_S and E_N. The general trend of the experimental data agrees with Eq. (2), but for a detailed analysis, more elaborated models are required. In Fig. 3, the experimental droplet densities data are quantitatively reproduced by a model based on coupled rate equations (Heyn and Feddersen, 2021).

In the literature, three possible epitaxial growth modes are assumed (Venables et al., 1984), which are illustrated schematically in Fig. 4. In the layer or Frank-van der Merwe mode, the deposited material starts with the formation of a complete monolayer on the substrate surface. After its completion, a second monolayer is formed and so on. This growth mode is usually observed for material systems where the deposited adatoms are more strongly bound to the substrate than to each other ($E_S > E_N$). Since the layer mode provides very smooth two-dimensional (2D) surfaces or heterostructures with abrupt inner interfaces, it is technologically very important for instance for the semiconductor device fabrication. In the layer plus island or Stranski–Krastanov mode, growth starts similar to the layer mode with the formation of monolayers which form the so-called wetting layer (WL). However, after WL formation, subsequent layer growth is energetically unfavorable and the initial 2D growth front switches to the formation of

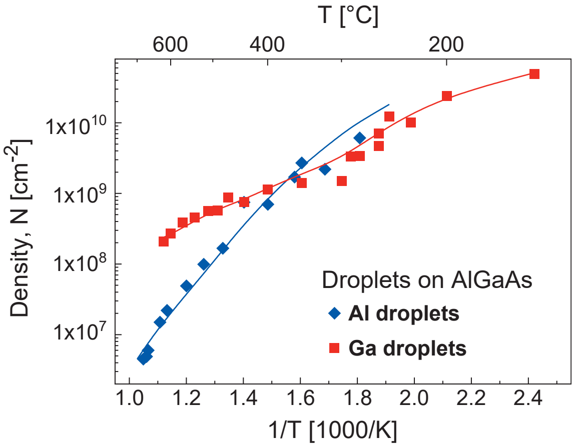

Fig. 3 Density N of Al and Ga droplets deposited by MBE on an AlGaAs substrate for droplet epitaxy as function of the deposition temperature T. The experimental data (symbols) are taken from atomic force microscopy (AFM) images. The lines are calculated using a model based on coupled rate equations with two material-dependent model parameters, the energy barrier for surface diffusion E_S, and the nearest-neighbor binding energy E_N (Heyn and Feddersen, 2021).

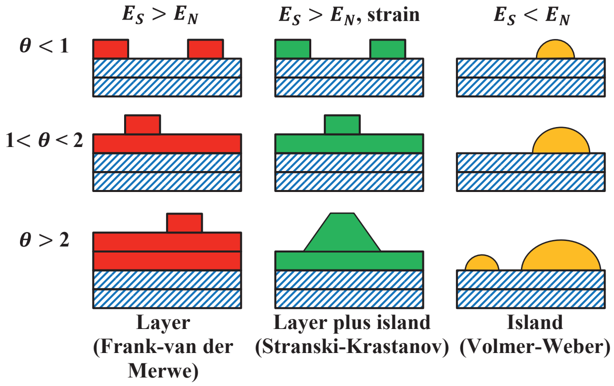

Fig. 4 Schematic representation of the three crystal growth modes: layer or Frank-van der Merwe mode, layer plus island or Stranski–Krastanov mode, and island or Volmer–Weber mode. θ represents the coverage in monolayers (MLs).

three-dimensional (3D) islands. The layer plus island mode is often observed in strained systems with a substantial lattice mismatch between the substrate and the deposit. Applications of the Stranski–Krastanov mode are for instance the self-assembled generation of semiconductor quantum structures (see Section "Strain-induced self-assembly"). In the island or Volmer–Weber mode, the deposited material forms 3D islands directly on the substrate surface. This happens when the deposited adatoms are more strongly bound to each other than to the substrate ($E_S < E_N$). Island growth can be also utilized for the self-assembled creation of semiconductor quantum structures in the so-called droplet epitaxy (see Section "Droplet-based self-assembly").

Strain in epitaxy

Often, material combinations used for heteroepitaxy have different lattice constants causing a lattice mismatch f (see Eq. (1). A prominent exception is the material combination of AlGaAs and GaAs, where f is negligible small. For most other material combinations, a lattice mismatch induces strain in the growing crystal which is energetically unfavorable. When the strain energy becomes too high, it can be relaxed by formation of dislocations or by switching to layer plus island growth.

Fig. 5A illustrates as an example the different regimes for growth of $In_xGa_{1-x}As$ on a GaAs substrate, with the indium content x. The lattice mismatch for pure InAs on GaAs is 7.3%, for $In_xGa_{1-x}As$ it becomes $f = x7.3\%$. Transitions between the three different regimes are observed at so-called critical thicknesses. In the pseudomorphic regime for rather thin layers, the strain energy is not relaxed and can be used constructively. For instance, pseudomorphic silicon layers on SiGe substrates are used in semiconductor industry for the fabrication of fast transistors, where the strained Si exhibits a reduced electron effective mass and, thus, a higher electron mobility. Another example is self-rolling semiconductor nanotubes (Prinz et al., 2000; Schmidt and Eberl, 2001). Fig. 5D

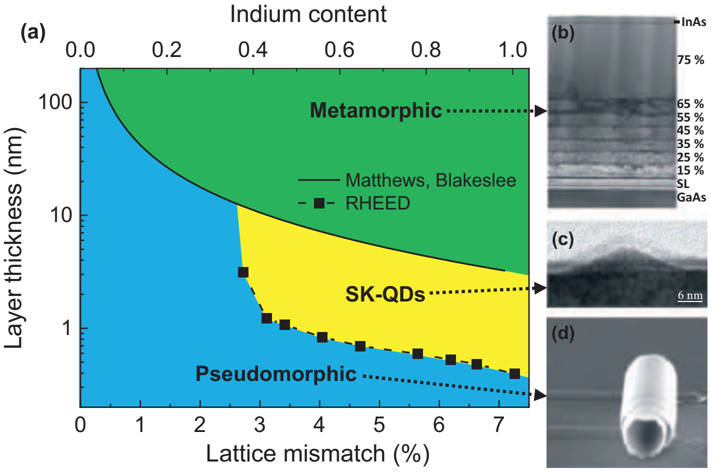

Fig. 5 (A) Regimes of strain-energy relaxation for growth of $In_xGa_{1-x}As$ on GaAs. Three regimes are separated by critical thicknesses that depend on the lattice mismatch f (which is controlled by the indium content x). (B) Cross-sectional transmission electron microscopy (TEM) image of an InAs quantum well (QW) on a GaAs wafer with a virtual substrate and a metamorphic buffer for strain relaxation (Mendach et al., 2002). (C) Cross-sectional TEM image of a strain-induced InAs quantum dot (QD) grown in Stranski–Krastanov (SK) mode. (D) Scanning electron microscopy (SEM) image of a self-rolling nanotube, where the rolling mechanism is driven by the strain energy inside of a GaAs/InGaAs bilayer.

shows such a nanotube composed of a GaAs/InGaAs bilayer. Here, the outer InGaAs layer with larger lattice constant than the inner GaAs layer causes a strong bending of the bilayer which finally leads to its self-rolling.

At a larger layer thickness, the regime changes from pseudomorphic to metamorphic where the strain is relaxed by misfit dislocations. Both regimes are separated by the critical thickness above which misfit dislocations are formed. This critical thickness can be calculated according to Matthews and Blakeslee (1974) and is plotted in Fig. 5A. Growth in the metamorphic regime can be used for the fabrication of strain-free so-called virtual substrates with an adjustable lattice constant. The example in Fig. 5B shows a pure InAs QW on a GaAs wafer with a virtual substrate and a metamorphic buffer for strain relaxation Mendach et al. (2002). Coming from the bottom, the structure is started with a GaAs/AlAs superlattice (SL) for surface smoothing and cleaning. This is followed by a sequence of layers where the In content is increased from 15% up to 75% in steps of 10% every 100 nm. According to Fig. 5A, the first 100-nm thick layer with $x = 15\%$ is in the metamorphic regime and misfit dislocations are formed at the interface to the substrate. Also visible are misfit dislocations at the other interfaces toward higher x (Fig. 5B). The last 430-nm thick layer with 75% In content has a low dislocation density and represents an unstrained virtual substrate for the InAs QW.

At an In content above 40%, growth in layer plus island mode is energetically favorable in comparison to the formation of dislocations. This regime is used for the creation of QDs in Stranski–Krastanov mode (Fig. 5C) and is addressed in more detail in Section "Strain-induced self-assembly." The critical thickness for QD formation can be measured using in situ reflection high-energy electron diffraction (RHEED), which is discussed in Section "In situ growth monitoring."

Self-assembly of nanostructures

In the context of crystal growth, the term self-assembly means a structural reorganization of the incoming material to form an ordered structure without external direction. For vapor-based growth methods like MBE, self-assembly often yields a clustering of the planarly deposited material. Regarding the three epitaxial growth modes (see Section "Nucleation and epitaxial growth modes"), obviously the layer mode is not self-assembled since here the structure of the new layers directly follows the planar deposition. On the other side, both, layer plus island and island mode, rely on a transformation of the planarly deposited material into localized clusters which is considered as a self-assembled process. The application of both modes for the generation of self-assembled nanostructures is addressed in the following sections. A more detailed overview on self-assembled nanostructures is given for instance in Henini (2008).

Strain-induced self-assembly

The strain-induced self-assembly of InAs 3D islands on GaAs substrates during MBE in the Stranski–Krastanov mode has become very popular after the first demonstration in 1994 (Leonard et al., 1994; Madhukar et al., 1994; Moison et al., 1994). Such InAs 3D islands exhibit a zero-dimensional (0D) density of states which motivates the name quantum dots (QDs). They are highly interesting for fundamental research and for applications in the quantum information technology, where single dots act as quantum emitters at the usual wavelengths for fiber-based communication. Furthermore, the 0D density of states suggests QD ensembles for efficient lasers or solar cells. Self-assembled Ge QDs on Si represent another popular material combination for strain-induced QD formation.

The driving force for self-assembly in Stranski–Krastanov mode is the lattice mismatch f between the substrate crystal and the deposited material (see Section "Strain in epitaxy"). The strain energy of a thin layer with lattice constant a_{layer} on a thick substrate with smaller lattice constant a_{sub} can be estimated using Hooke's law $E_{strain} = \varepsilon/(2\mu^2)V\,[(a_{layer} - a_{sub})/a_{layer}]^2 = \varepsilon/(2\mu^2)V\,[f/(f+1)]^2$ with Young's modulus ε, the Poisson number μ, and the volume V of the deposited layer. This identifies two possible mechanisms for a reduction of E_{strain}: First, a reduction of the strained volume and second, a reduction of f. The first mechanism is the origin for the formation of 3D QDs instead of a planar layer since atoms in higher regions of the islands are almost unstrained. The second mechanism is the driving force for intermixing of the QDs with material from the substrate.

Fig. 6 illustrates the evolution of a typical growth process in Stranski–Krastanov mode. First a strained planar layer is formed, the so-called WL. Due to a strong chemical attraction to the substrate, atoms in the WL will not form 3D islands for strain relaxation. With increasing deposited coverage θ, strained 2D islands are formed on top of the WL. So far, growth is similar to growth in the layer mode (see Section "Nucleation and epitaxial growth modes"). Above a critical coverage θ_C, the strain energy inside the 2D islands exceeds a threshold value and now growth switches abruptly to the formation of 3D QDs for a reduction of the strain energy. This abrupt transition from 2D islands to 3D QDs can be observed in situ using electron diffraction (see Section "In situ growth monitoring") and for InAs on GaAs typically values of $\theta_C = 1.5\ldots2$ ML are measured. The relevant process for the 2D to 3D transition is the upward migration of atoms from the island border toward the upper regions of the dot. A further reduction of the strain energy by intermixing with substrate material is often observed Joyce et al. (1998). This changes the composition of the QDs and with this also their optoelectronic properties. Fig. 5C shows an example of a self-assembled InAs QD grown in Stranski–Krastanov mode on GaAs. The surface density and structural properties of the dots can be tuned by the process parameters like deposition temperature, growth speed, and deposited volume.

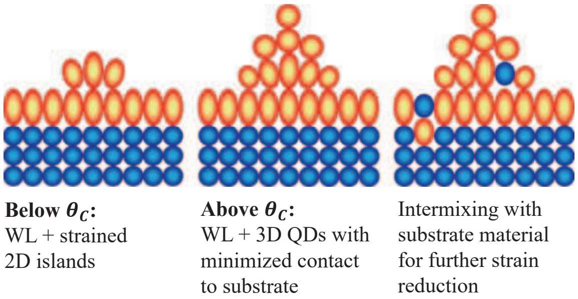

Fig. 6 Schematics of the surface morphology evolution during strain-induced formation of self-assembled 3D QDs in Stranski–Krastanov mode with the wetting layer (WL). θ_C denotes the critical thickness for the transition from growth of strained 2D islands to formation of 3D QDs.

Droplet-based self-assembly

The utilization of metal droplets during semiconductor epitaxy was initiated in 1990 for Ga droplets on ZnSe (Chikyow and Koguchi, 1990). In the following, the method was expanded for other material systems and widely used for the self-assembled fabrication of semiconductor quantum structures like QDs or rings (Mano et al., 2000; Gurioli et al., 2019). Droplet epitaxy takes place in two steps. In a first step, the droplet material is deposited and in a second step the droplets are crystallized into semiconductor quantum structures. The droplets are formed in Volmer–Weber mode (see Section "Nucleation and epitaxial growth modes"), where the deposited adatoms are more strongly bound to each other than to the substrate ($E_S < E_N$). Usually metal droplets like Ga, In, or Al are used for droplet epitaxy, which are in a liquid state and have no crystalline structure. That means the mechanism for self-assembly is fundamentally different compared to the strain-driven Stranski–Krastanov mode.

The morphology of a liquid in contact with the surface of a solid material is determined by the surface and interface tensions. In detail, there is the surface tension γ_L of the liquid, the surface tension γ_S of the solid substrate, and the interface tension γ_{SL}. The shape of a droplet is characterized by the contact angle α_C between the liquid and solid surfaces, which can be calculated using Young's Equation $\cos\alpha_C = (\gamma_S - \gamma_{SL})/\gamma_L$. For Ga droplets on AlGaAs, values of $\alpha_C = 45\ldots55°$ are observed and for Al droplets on AlGaAs $\alpha_C = 60\ldots70°$ (Heyn et al., 2015). The general mechanism for droplet formation is illustrated for Ga droplets on GaAs as an example. Here the tensions are $\gamma_L = 0.67$ J/m^2, $\gamma_S = 1.04$ J/m^2, and $\gamma_{SL} = 0.61$ J/m^2 (Heyn et al., 2015). For a planar Ga layer, the total energy would be $\gamma_L + \gamma_{SL}$. Droplet formation yields a total energy according to $(1 - A)\gamma_S + 4A\gamma_L + A\gamma_{SL}$, with the normalized contact area A between droplets and substrate. Since $\gamma_S < \gamma_L + \gamma_{SL}$, this simple estimation indicates that droplet formation reduces the total energy for a small A. Furthermore, it predicts a minimal total energy for a minimal A, that is, only one droplet on the surface. Since this is experimentally not observed, it can be concluded that the system is not in equilibrium and that kinetic processes are also important. An example for a kinetic modeling of droplet densities is given in Section "Nucleation and epitaxial growth modes," Fig. 3.

For a functionalization as semiconductor quantum structures, the liquid metal droplets can be crystallized. Using MBE, a typical process starts with the droplet deposition on a semiconductor substrate. For instance Ga droplets are deposited on AlGaAs with only the shutter of the Ga effusion cell open (see Section "Molecular beam epitaxy (MBE)"). After droplet formation, the Ga shutter is closed and the As shutter is opened for the crystallization of the Ga droplets into epitaxial GaAs quantum structures. As a huge advantage in comparison to QDs grown in Stranski–Krastanov mode, droplet epitaxy allows the generation also of unstrained structures. On the other side, the fabrication of quantum structures with high optical quality by droplet epitaxy requires thoroughly optimized process conditions.

As an alternative to droplet epitaxy, the deposited droplets can be used also to drill self-assembled nanoholes into a substrate surface (Wang et al., 2007; Heyn et al., 2015). This local droplet etching (LDE) allows the integration of self-assembled top-down strategies into the usually bottom-up MBE growth. The nanoholes are shaped similar to an inverted cone and can be filled with a material different from the substrate for functionalization. For instance, filling of nanoholes in an AlGaAs substrate with GaAs allows the fabrication of strain-free GaAs QDs.

Vapor–liquid–solid (VLS) growth of nanowires

A further droplet-based growth method is the VLS growth of semiconductor nanowires in CVD or MBE. In contrast to the droplet epitaxy (see Section "Droplet-based self-assembly"), here the droplet material is not consumed by the process but instead acts as a kind of catalyst initiating the growth of nanowires for example, for one-dimensional quantum systems (Gazibegovic et al., 2017). In a first step, the droplets (often Au) are deposited on a semiconductor surface. Here, the melting point of the droplet material can be reduced by alloying with substrate material. During the subsequent nanowire growth, the droplets adsorb atoms from the vapor beams which then crystallize at the liquid–solid interface. This provides a directed growth of the nanowires with the droplet on top. In this sense, the droplets represent a guidance for the planarly deposited source materials for a localized growth. The structural parameters of the nanowires like diameter and length can be adjusted by the process conditions. Furthermore, also core-shell nanowires can be fabricated by switching the process conditions from catalytic nanowire growth to conventional growth. Here, a semiconductor material with a large band gap surrounds a nanowire core with smaller band gap.

In situ growth monitoring

In situ growth monitoring allows the evaluation of crystalline properties during growth and, thus, is an important prerequisite for the precise control of epitaxial growth and for the optimization of the process parameters. Real-space imaging techniques like TEM or AFM are hard to realize in an environment for epitaxial growth, reciprocal space-based methods are much easier to implement. A technique often used in MBE is RHEED (Cho and Arthur, 1975). Here, an electron beam is directed to the substrate surface under a shallow incident angle of about 1 degree and the reflected electrons are detected by a phosphorous screen usually in combination with a camera for data analysis. This geometry has technical advantages since the equipment for RHEED does not conflict with the position of the evaporation sources. Furthermore, due to the shallow incidence angle, the electrons interact mainly with the topmost atoms of the growing crystal which yields a high surface sensitivity for this technique. The RHEED technique provides detailed information about the macroscopic surface morphology as well as about the local arrangement of the surface atoms (the so-called surface reconstruction). Using RHEED for an in situ monitoring allows the study also of dynamic phenomena.

Fig. 7 illustrates typical RHEED pattern for surface morphologies with a different dimensionality. Diffraction patterns can be interpreted as the intersection of the Ewald sphere with the reciprocal lattice. For a surface with 3D islands, the diffraction conditions are close to transmission diffraction through a bulk crystal and the reciprocal lattice is composed by regularly arranged lattice points. Fig. 7A shows as an example for a diffraction pattern from a rough GaAs wafer surface with 3D islands before MBE growth. GaAs crystallizes in a zinc blende lattice, which is a face-centered cubic (fcc) lattice. The reciprocal lattice of fcc is body-centered cubic (bcc), which is represented by the spots in the RHEED pattern. For a smooth 2D surface morphology, the electron beam interacts mainly with the topmost layer of the sample and the reciprocal lattice consists of so-called crystal truncation rods (CTRs). The CTRs can be broadened by surface features like 2D islands. Here, the interaction with the Ewald sphere typically yields parallel lines as diffraction pattern, the so-called streaks (Fig. 7B). For nearly atomically smooth surfaces, the CTRs are almost sharp and the interaction with the Ewald sphere yields a pattern of spots arranged on a so-called Laue circle (Fig. 7C).

A further important feature indicated by the RHEED data in Fig. 7 is the surface reconstruction (Cho and Arthur, 1975), where atoms located at a crystal surface minimize their energy by taking positions with spacing and symmetry different from the bulk lattice. The bulk lattice constant is visible in the horizontal spacing of the 3D reciprocal-lattice points in Fig. 7A. In contrast to that, for a 2D surface morphology in [110] azimuth the spacing between the reciprocal-lattice elements is 1/2 (Fig. 7B) and in [−110] azimuth it is 1/4 (Fig. 7C). This indicates a (2 × 4) surface reconstruction, where in [110] azimuth every second real-space lattice position deviates from the bulk and in [−110] azimuth every 4th position. For GaAs surfaces, the 2× periodicity is caused by the formation of As dimers on the surface and the 4× periodicity often by missing dimers. Depending on the process parameters like temperature and As pressure many different surface reconstructions are observed.

The above RHEED-features surface reconstruction and widening of the CTRs allow already an extensive evaluation of the evolution of the surface morphology during growth. For the layer growth mode, further information can be gathered from the dynamic evolution of the RHEED specular reflex (Fig. 7B). In contrast to the RHEED patterns related to diffraction, the specular reflex is originated by reflection. During growth in layer mode, the intensity of the specular reflex often shows strong oscillations (Fig. 8A), the so-called RHEED oscillations (Neave et al., 1983). RHEED oscillations are attributed to the periodic nucleation and coalescence of 2D islands (Fig. 4), where step edges at the island borders cause diffuse scattering and reduce the intensity of the specular reflex (Clarke and Vvedensky, 1987). Usually the period of one RHEED oscillation indicates the growth of one monolayer, which allows an easy and accurate calibration of the beam fluxes from the growth rate-determining effusion cells. A further analysis of the RHEED oscillations can provide insights into the dynamics of island nucleation.

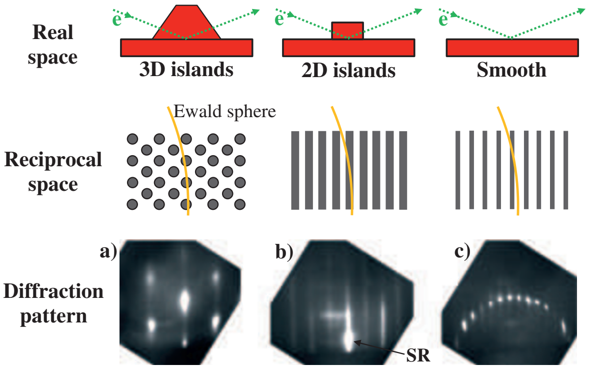

Fig. 7 Schematics of the reciprocal space for different real-space surface morphologies together with examples of corresponding reflection high-energy electron diffraction (RHEED) pattern. The *dashed green lines* denote the direction of the incident electron beam and the *orange lines* illustrate the cross sections between the Ewald sphere and the respective reciprocal lattices. The RHEED pattern is taken from (001) GaAs surfaces with (A) 3D islands in [110] azimuth, (B) small 2D islands in [110] azimuth, and (C) large 2D islands in [−110] azimuth. SR in (B) indicates the specular reflex which is used to measure RHEED oscillations.

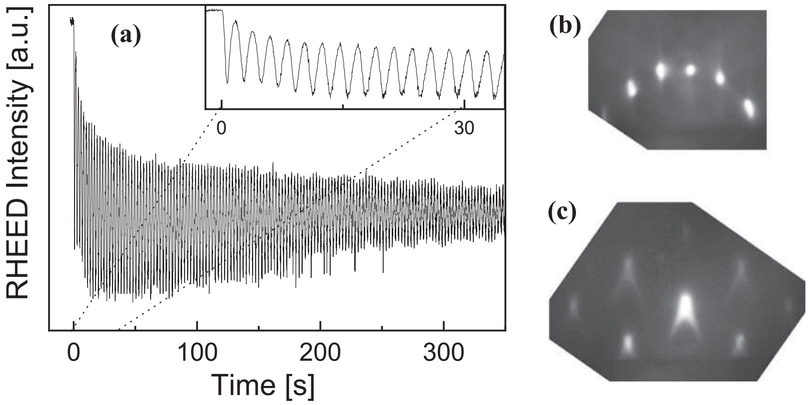

Fig. 8 (A) RHEED oscillations during layer growth of AlAs on a (001) GaAs substrate. (B) RHEED pattern from a (001) GaAs surface in [−110] azimuth showing a Laue circle. (C) RHEED pattern from a (001) GaAs surface with self-assembled InAs QDs in [−110] azimuth.

Also the transition from layer growth to the formation of 3D islands in Stranski–Krastanov mode can be detected by RHEED. Fig. 7B and C show as an example a GaAs surface before and after InAs deposition for QD generation. Clearly visible is the transition in the RHEED pattern from a smooth 2D surface featuring a Laue circle to 3D transmission diffraction. The RHEED pattern from the surface with QDs shows the InAs reciprocal lattice-related spots plus so-called chevrons linked to the bulk reflexes. The chevrons represent CTRs caused by the tilted crystalline surfaces of the QDs. In particular the presence of chevrons is a clear indication for QD formation and allows an evaluation of the QD shape. Furthermore, the critical coverage θ_C for QD formation (Fig. 5) can be determined from the instant of the 2D to 3D transition.

To summarize, RHEED provides real-time information about the growth rate, the surface reconstruction and roughness, kinetic phenomena like nucleation, and the dynamics and morphology of self-assembled QDs. Additional methods for monitoring are used to obtain further information. Reflectance anisotropy spectroscopy is sensitive to the roughness of epitaxial layers, the growth rate, and the sample temperature. Pyrometry and band-edge thermometry allow a temperature monitoring of the sample. Residual gas analysis allows a characterization of the background species; it can be used for studies of surface chemistry and kinetics, and it is important for leak tests.

Conclusion

Epitaxy is a striking type of crystal growth which is a premise for the fabrication of a large number of semiconductor devices for modern electronics and for future quantum information technologies. In particular the molecular beam epitaxy (MBE) is an established technology for the epitaxial growth of ultra-clean semiconductor heterostructures, where the precise control on composition, size, and roughness of the deposited layers enables a versatile engineering of the band gaps and doping profiles. Exceeding the possibilities of 2D heterostructures, the utilization of self-assembly mechanisms for a localized growth enables also the generation of 1D nanowires and 0D QDs without the need of any lithography. This comprehensive control on band gap energies, doping, size, and dimensionality of the created semiconductor structures suggests MBE as an essential tool for devices studied in fundamental research as well as for industrial applications.

References

Arthur JR (2002) Molecular beam epitaxy. *Surface Science* 500(1): 189–217. ISSN: 0039-6028. https://doi.org/10.1016/S0039-6028(01)01525-4.

Asahi H and Horikoshi Y (2019) *Molecular Beam Epitaxy: Materials and Applications for Electronics and Optoelectronics*. Whiley. https://www.wiley.com/en-ae/Molecular+Beam+Epitaxy%3A+Materials+and+Applications+for+Electronics+and+Optoelectronics-p-9781119355014.

Bauer E (1982) Epitaxy of metals on metals. *Applications of Surface Science* 11-12: 479–494. ISSN: 0378-5963. https://doi.org/10.1016/0378-5963(82)90094-0.

Chikyow T and Koguchi N (1990) MBE growth method for pyramid-shaped GaAs micro crystals on ZnSe(001) surface using Ga droplets. *Japanese Journal of Applied Physics* 29(Part 2, No. 11): L2093–L2095. https://doi.org/10.7567/JJAP.29.L2093. http://jjap.jsap.jp/link?JJAP/29/L2093/.

Cho AY and Arthur JR (1975) Molecular beam epitaxy. *Progress in Solid State Chemistry* 10: 157–191. ISSN: 0079-6786. https://doi.org/10.1016/0079-6786(75)90005-9.

Clarke S and Vvedensky DD (1987) Origin of reflection high-energy electron-diffraction intensity oscillations during molecular-beam epitaxy: A computational modeling approach. *Physical Review Letters* 58(21): 2235–2238. https://doi.org/10.1103/PhysRevLett.58.2235.

Gazibegovic S, Car D, Zhang H, Balk SC, Logan JA, de Moor MWA, Cassidy MC, Schmits R, Xu D, Wang G, Krogstrup P, Op het Veld RLM, Zuo K, Vos Y, Shen J, Bouman D, Shojaei B, Pennachio D, Lee JS, van Veldhoven PJ, Koelling S, Verheijen MA, Kouwenhoven LP, Palmstrøm CJ, and Bakkers EPAM (2017) Epitaxy of advanced nanowire quantum devices. *Nature* 548(7668): 434–438. ISSN: 1476-4687. https://doi.org/10.1038/nature23468. https://www.nature.com/articles/nature23468.

Gurioli M, Wang Z, Rastelli A, Kuroda T, and Sanguinetti S (2019) Droplet epitaxy of semiconductor nanostructures for quantum photonic devices. *Nature Materials* 18(8): 799–810. ISSN: 1476-4660. https://doi.org/10.1038/s41563-019-0355-y. https://www.nature.com/articles/s41563-019-0355-y.

Henini M (2008) *Handbook of Self Assembled Semiconductor Nanostructures for Novel Devices in Photonics and Electronics*, first ed. Elsevier, ISBN: 978-0-08-046325-4. https://www.elsevier.com/books/handbook-of-self-assembled-semiconductor-nanostructures-for-novel-devices-in-photonics-and-electronics/henini/978-0-08-046325-4.

Heyn C and Feddersen S (2021) Modeling of Al and Ga droplet nucleation during droplet epitaxy or droplet etching. *Nanomaterials* 11(2): 468. https://doi.org/10.3390/nano11020468. https://www.mdpi.com/2079-4991/11/2/468.

Heyn C, Bartsch T, Sanguinetti S, Jesson D, and Hansen W (2015) Dynamics of mass transport during nanohole drilling by local droplet etching. *Nanoscale Research Letters* 10(1): 67. ISSN: 1556-276X. https://doi.org/10.1186/s11671-015-0779-5. http://www.nanoscalereslett.com/content/10/1/67/abstract.

Joyce PB, Krzyzewski TJ, Bell GR, Joyce BA, and Jones TS (1998) Composition of InAs quantum dots on GaAs(001): Direct evidence for (InGa)As alloying. *Physical Review B* 58(24): R15981–R15984. https://doi.org/10.1103/PhysRevB.58.R15981.

Lee C-H, Schiros T, Santos EJG, Kim B, Yager KG, Kang SJ, Lee S, Yu J, Watanabe K, Taniguchi T, Hone J, Kaxiras E, Nuckolls C, and Kim P (2014) Epitaxial growth of molecular crystals on van der Waals substrates for high-performance organic electronics. *Advanced Materials* 26(18): 2812–2817. ISSN: 1521-4095. https://doi.org/10.1002/adma.201304973.

Leonard D, Krishnamurthy M, Fafard S, Merz JL, and Petroff PM (1994) Molecular-beam epitaxy growth of quantum dots from strained coherent uniform islands of InGaAs on GaAs. *Journal of Vacuum Science & Technology B: Microelectronics and Nanometer Structures Processing, Measurement, and Phenomena* 12(2): 1063–1066. ISSN: 1071-1023. https://doi.org/10.1116/1.587088.

Madhukar A, Xie Q, Chen P, and Konkar A (1994) Nature of strained InAs three-dimensional island formation and distribution on GaAs(100). *Applied Physics Letters* 64(20): 2727–2729. ISSN: 0003-6951. https://doi.org/10.1063/1.111456.

Mano T, Watanabe K, Tsukamoto S, Koguchi N, Fujioka H, Oshima M, Lee C-D, Leem J-Y, Lee HJ, and Noh SK (2000) Nanoscale InGaAs concave disks fabricated by heterogeneous droplet epitaxy. *Applied Physics Letters* 76(24): 3543–3545. ISSN: 0003-6951, 1077-3118. https://doi.org/10.1063/1.126701.

Matthews JW and Blakeslee AE (1974) Defects in epitaxial multilayers: I. Misfit dislocations. *Journal of Crystal Growth* 27: 118–125. ISSN: 0022-0248. https://doi.org/10.1016/S0022-0248(74)80055-2.

Mendach S, Hu CM, Heyn C, Schnull S, Oepen HP, Anton R, and Hansen W (2002) Strain relaxation in high-mobility InAs inserted-channel heterostructures with metamorphic buffer. *Physica E-Low-Dimensional Systems & Nanostructures* 13(2-4): 1204–1207. ISSN: 1386-9477. https://doi.org/10.1016/S1386-9477(02)00336-3. WOS:000176869100259.

Moison JM, Houzay F, Barthe F, Leprince L, André E, and Vatel O (1994) Self-organized growth of regular nanometer-scale InAs dots on GaAs. *Applied Physics Letters* 64(2): 196–198. ISSN: 0003-6951. https://doi.org/10.1063/1.111502.

Neave JH, Joyce BA, Dobson PJ, and Norton N (1983) Dynamics of film growth of GaAs by MBE from Rheed observations. *Applied Physics A* 31(1): 1–8. ISSN: 0947-8396, 1432-0630. https://doi.org/10.1007/BF00617180.

Orton J and Foxon T (2015) *Molecular Beam Epitaxy: A Short History.* Oxford: Oxford University Press, ISBN: 978-0-19-969582-9. https://doi.org/10.1093/acprof:oso/9780199695829.001.0001. https://oxford.universitypressscholarship.com/10.1093/acprof:oso/9780199695829.001.0001/acprof-9780199695829.

Poppa H (1964) In-situ studies of Epitaxial thin-film growth. *Zeitschrift für Naturforschung A* 19(7): 835–843. https://www.degruyter.com/document/doi/10.1515/zna-1964-7-803/html.

Prinz VY, Seleznev VA, Gutakovsky AK, Chehovskiy AV, Preobrazhenskii VV, Putyato MA, and Gavrilova TA (2000) Free-standing and overgrown InGaAs/GaAs nanotubes, nanohelices and their arrays. *Physica E: Low-dimensional Systems and Nanostructures* 6(1): 828–831. ISSN: 1386-9477. https://doi.org/10.1016/S1386-9477(99)00249-0.

Schmidt OG and Eberl K (2001) Thin solid films roll up into nanotubes. *Nature* 410(6825): 168. ISSN: 1476-4687. https://doi.org/10.1038/35065525. https://www.nature.com/articles/35065525. 168.

Venables JA, Spiller GDT, and Hanbucken M (1984) Nucleation and growth of thin films. *Reports on Progress in Physics* 47(4): 399–459. ISSN: 0034-4885. https://doi.org/10.1088/0034-4885/47/4/002.

Wang ZM, Liang BL, Sablon KA, and Salamo GJ (2007) Nanoholes fabricated by self-assembled gallium nanodrill on GaAs(100). *Applied Physics Letters* 90(11): 113120–113122. ISSN: 0003-6951, 1077-3118. https://doi.org/10.1063/1.2713745.

Zinke-Allmang M, Feldman LC, and Grabow MH (1992) Clustering on surfaces. *Surface Science Reports* 16(8): 377–463. ISSN: 0167-5729. https://doi.org/10.1016/0167-5729(92)90006-W.

Superconductivity: Critical currents

A Gurevich, Old Dominion University, Norfolk, VA, United States

© 2024 Elsevier Ltd. All rights reserved.

This is an update of A. Gurevich, Superconductivity: Critical Currents, Editor(s): Franco Bassani, Gerald L. Liedl, Peter Wyder, Encyclopedia of Condensed Matter Physics, Elsevier, 2005, Pages 82–88, ISBN 9780123694010, https://doi.org/10.1016/B0-12-369401-9/00737-3.

Introduction 555
Elementary pinning mechanisms 555
Single-vortex and collective pinning by point defects 557
Pinning and current blocking by extended defects 559
Global critical currents of superconductors 560
Conclusion 563
References 564

Abstract

This article gives a background on basic mechanisms of critical currents, which are determined by the physics of interacting vortices and their pinning by multiscale defect structures in superconducting materials.

Key points

- Single-vortex and collective pinning
- Strong-to-weak pinning crossover
- Optimum pinning configurations
- Pinning and current blocking by grain boundaries
- Thermally-activated flux creep

Nomenclature

$\mathbf{B}$	Magnetic induction
$\mathbf{E}$	Electric field
$\mathbf{E_c}$	Electric field criterion for J_c
$\mathbf{f_p}$	Elementary pinning force
$\mathbf{H}$	Magnetic field
$\mathbf{H^*}$	Irreversibility field
$\mathbf{H_{c1}}$	Lower critical field
$\mathbf{H_{c2}}$	Upper critical field
$\mathbf{J_c}$	Critical current density
$\mathbf{J_d}$	Depairing current density
$\mathbf{L_c}$	Longitudinal pinning correlation length
$\mathbf{n_p}$	Density of pinning centers
$\mathbf{R_c}$	Transverse pinning correlation length
$\mathbf{r_p}$	Pinning interaction radius
$\mathbf{T_c}$	Critical temperature
$\mathbf{U(J)}$	Flux creep activation energy
$\boldsymbol{\varepsilon}$	Line energy of the vortex
$\boldsymbol{\lambda}$	London penetration depth
$\boldsymbol{\xi}$	Coherence length
$\boldsymbol{\phi_0}$	Magnetic flux quantum

https://doi.org/10.1016/B978-0-323-90800-9.00018-4

Introduction

The superconducting state in the bulk of type-II superconductors exists at temperature T below the critical temperature T_c and magnetic fields below the upper critical field $H_{c2}(T)$. Such superconductors can carry weakly dissipative currents of density J smaller than the critical current density $J_c(T, H)$ in the region of the H–T–J phase diagram shown in Fig. 1. Both the critical current density $J_c(T, H)$ and the irreversibility field $H^*(T) < H_{c2}(T)$ at which $J_c(T, H^*)$ vanishes are the main parameters of merit for applications of superconductors in power transmission lines, magnets for medical magnetic resonance imaging systems, etc. (Larbalestier et al., 2001; Yao and Ma, 2021).

There are two types of superconductors, which exhibit very different mechanisms of current transport. For instance, in type-I superconductors represented mostly by pure metals, such as Al, Pb, and Sn, non-dissipative current along a wire can only flow in a narrow surface layer due to the magnetic flux expansion and the ideal diamagnetism of the superconducting state (the Meissner effect). Once the magnetic field generated by the transport current I at the surface exceeds the thermodynamic critical field H_c, a type-I superconductor switches into an intermediate resistive state at the critical current $I_c = 2\pi R H_c$ for a round wire of radius R (Tinkham, 1996). However, most superconducting alloys, intermetallic compounds, high-T_c cuprates or iron pnictides are type-II superconductors which can carry both the surface Meissner currents at low magnetic field $H < H_{c1}$ and bulk non-dissipative currents above the lower critical field H_{c1} but below the upper critical field H_{c2}. Bulk critical current densities in type-II superconductors in the mixed state at $H_{c1} < H < H_{c2}$ are determined by pinning of vortices by defects of the crystalline structure and by transparency of grain boundaries to current flow in polycrystals. Because the upper critical fields H_{c2} of many compounds can reach $\sim$ 20–100 T, it is the high-field type-II superconductors, which are of prime interest for power and magnet applications. The current-carrying capability of these superconductors is determined by multiple mechanisms operating on different length scales: from the nanometer scales set by the size of vortex cores to the micrometer and larger scales, which define the scales of current flow in polycrystals with macroscopic materials defects. An optimum defect structure can be produced by appropriate materials treatments. For instance, J_c of polycrystalline high-T_c cuprates can be increased greatly by reducing the current-blocking effect of grain boundaries and incorporating artificial structures of oxide nanoprecipitates (Larbalestier et al., 2001; Maiorov et al., 2009; Haugan et al., 2020).

Elementary pinning mechanisms

Under equilibrium conditions, magnetic flux penetrates into the bulk of a type-II superconductor above the lower critical field $H_{c1}(0) \simeq 10 - 100$ mT for many high-field materials. In a defect-free superconductor at $H > H_{c1}$this magnetic flux exists in the form of a hexagonal lattice of quantized vortices. Each vortex can be regarded as a tube of radius of the London magnetic penetration depth $\lambda(T)$ in which screening currents circulate around a small non-superconducting core of radius $\xi(T)$, where the coherence length $\xi(0) \simeq \hbar v_F / 2\pi k_B T_c$ at $T = 0$ quantifies the size of the Cooper pairs, and v_F is the Fermi velocity (Tinkham, 1996). Vortices become energetically favorable at $H > H_{c1}$ if the Ginzburg–Landau parameter $\kappa = \lambda/\xi$ exceeds $2^{-1/2}$, as it happens in many superconducting compounds, especially such extreme type-II superconductors as Nb_3Sn or layered high-T_c cuprates or Fe-based superconductors (FBS) with $\kappa = 20 - 100$. The magnetic flux produced by screening currents in a vortex equals the flux quantum $\phi_0 = 2 \times 10^{-15}$ Wb, so the vortex density B/ϕ_0 is proportional to the magnetic induction B. Bulk superconductivity is destroyed as the normal cores of vortices overlap at the upper critical field, $H_{c2}(T) = \phi_0 / 2\pi\mu_0\xi^2(T)$. In isotropic superconductors such as Nb—Ti and Nb_3Sn, vortex lines are continuous, but in highly anisotropic layered high-T_c compounds, such as $Bi_2Sr_2Ca_2Cu_3O_x$ and $Bi_2Sr_2CaCu_2O_x$, vortex lines break into stacks of weakly coupled "pancake" vortices whose circulating currents are mostly confined within the superconducting CuO_2 planes (Blatter et al., 1994). The current density $\mathbf{J}$ exerts the Lorentz force $f_L = \phi_0[\mathbf{J} \times \hat{\mathbf{z}}]$ per unit length of the vortex line directed along the unit vector $\hat{\mathbf{z}}$, so that f_L is perpendicular to both $\mathbf{J}$ and $\hat{\mathbf{z}}$. Vortices can also exist in thin films of type-I superconductors in a perpendicular magnetic field if the film thickness d is much smaller than λ (Pearl, 1964; Blatter et al., 1994; Brandt, 1995). Here we mostly focus on bulk $J_c(H, T)$ in type-II superconductors with large κ and transverse sizes much larger than λ at magnetic fields well above H_{c1}. In this case $J_c(T, H)$ is not affected by demagnetizing effects which make H_{c1}

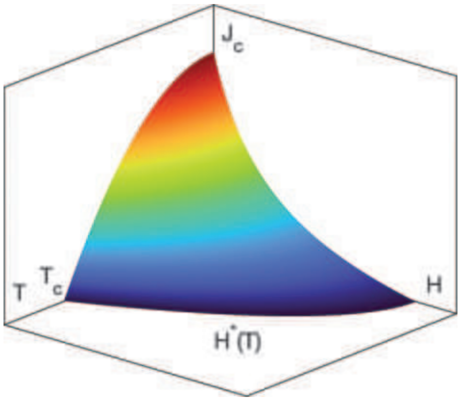

Fig. 1 A typical $J_c(T, H)$ surface which defines the region $J < J_c$ on the H–T diagram, where a type-II superconductor can carry weakly dissipative transport currents at electric fields $E < E_c$ with E_c depending on a particular application. Intersection of the $J_c(T, H)$ surface with the T-H plane defines the irreversibility field $H^*(T)$ at which a resistive transition to a flux flow state occurs.

dependent on the sample geometry, and the magnetic induction $\boldsymbol{B} = \mu_0 \boldsymbol{H}$ in a superconductor is directly proportional to the applied field $\boldsymbol{H}$ (Campbell and Evetts, 1972). In addition, the surface superconductivity can occur at $H_{c2} < H < H_{c3}$ for the field parallel to a perfect surface of a single crystal, where $H_{c3} \approx 1.7 H_{c2}$ at $T \approx T_c$ (Tinkham, 1996). Yet for realistic imperfect surfaces in high-J_c superconductors in inclined magnetic fields, the third critical field H_{c3} is very close to H_{c2} so the surface superconductivity does not play a significant role in current transport controlled by pinning of vortices in the bulk.

Superconductors carry bulk weakly-dissipative (due to thermally-activated flux creep) currents caused by a vortex density gradient (or bending of vortices in thin films) described by the Maxwell equation $\nabla \times \mathbf{B} = \mu_0 \mathbf{J}$. This magnetic flux gradient can only be sustained by pinning of vortices by microstructural defects. Flux pinning is determined by local gains in the free energy of curvilinear vortices due to interactions of their normal cores and screening currents with these microstructural imperfections. Furthermore, a macroscopic current density $\mathbf{J}$ exerts the Lorentz force $\mathbf{F}_L = \mathbf{J} \times \mathbf{B}$ per unit volume of the magnetic flux. The critical current density $J_c(T,B)$ is then determined by the balance of the pinning and Lorentz forces $J_c(T,B)B = F_p(T,B)$, where F_p is the volume pinning force produced by the materials defects (Campbell and Evetts, 1972). Ideally, a type-II superconductor can carry any non-dissipative current density J smaller than J_c but if J exceeds J_c, a superconductor switches into a dissipative flux flow state in which vortices are driven by the Lorentz force. In any case, J_c cannot exceed the depairing current density J_d at which the transport current breaks the Cooper pairs:

$$J_c = \frac{\phi_0}{3^{3/2}\pi\mu_0\lambda^2\xi} \tag{1}$$

Here J_d is of the order of the current density circulating near the normal vortex, where $J_d(T) = J_d(0)(1 - T/T_c)^{3/2}$ at $T \approx T_c$.

Pinning defects can be classified by their spatial extent and by mechanisms of the elementary pinning forces f_p between vortices and defects (Campbell and Evetts, 1972; Blatter et al., 1994; Brandt, 1995). These defects can be either small pinning centers like non-superconducting precipitates and oxygen vacancies in high-T_c superconductors, or defects extended along vortex lines (grain boundaries, dislocations, columnar radiation tracks of nanorods). In turn, elementary pinning interactions can be due to either a short-range interaction of the vortex cores with point defects or a long-range magnetic interaction with extended planar defects. The core pinning results from a gain in the superconducting condensation energy at the core trapped by a defect, the strongest pinning force corresponding to defect sizes $\sim\xi$ (see Fig. 2).

Magnetic pinning results from the deformation of vortex screening currents near a planar defect on the scale $\sim\lambda$, as shown in Fig. 3. The magnetic pinning force $f(x) = \phi_0^2/4\pi\mu_0\lambda^2 x$ can be rather strong if the distance x between the vortex and the defect is smaller than the interaction length $l = \phi_0/2\pi\mu_0\lambda^2 J_b$. Here, $l < \lambda$ is the distance from the vortex core at which the circulating current density $J(x)$ equals the maximum current density J_b which can pass through the defect.

If the distance between the normal cores of bulk vortices and the defect is smaller than $l = \phi_0/2\pi\mu_0\lambda^2 J_b$, vortices are attracted strongly to the defect. Vortices trapped by the defect may have no normal cores which turn into extended regions of length l along the defect in which the superconducting gap is not suppressed by circulating vortex currents. These elongated vortices on the defect have a highly anisotropic pinning force, which is maximum for $\mathbf{J}$ parallel to the defect and minimum for $\mathbf{J}$ perpendicular to the defect.

Identification of the most effective pinning defects in a particular material is a difficult task. Practical limits to flux pinning in high-field superconductors have been inferred from extensive studies of Nb–47%Ti, in which strong pinning by a dense $\sim$20–25 vol% lamellar structure of metallic α-Ti ribbons $\sim$1 nm (0.2ξ) thick can produce J_c that approaches 5–10% of J_d at zero field and 4.2 K (Larbalestier et al., 2001). The mechanism of flux pinning is also known for Nb_3Sn, in which J_c is determined by the magnetic interaction of vortices with Sn-deficient grain boundaries (Campbell and Evetts, 1972; Durrell et al., 2011). These materials have zero-field J_c values, which can exceed 10^{10}–10^{11} A m^{-2} at 4.2 K.

In high-T_c cuprates or Fe-based superconductors (FBS) the coherence length $\xi \simeq 1.5 - 2$ nm is so small that practically any common atomic-size defects such as vacancies or dislocations can pin vortices. The critical temperature of high-T_c superconductors is also sensitive to the carrier density, which, in turn, is determined by local non-stoichiometry, so that even a weak hole-depletion at crystalline defects may locally drive a high-T_c cuprate into an antiferromagnetic insulator. The proximity of the superconducting state in high-T_c cuprates or FBS to antiferromagnetic state, the d-wave pairing symmetry, the short in-plane coherence length $\xi(0) \simeq 1.5 - 2$ nm and the large Thomas-Fermi screening length $l_D \sim \xi(0)$, all combine to weaken superconductivity near crystal defects, such as impurities, dislocations, and grain boundaries, thus making them effective pinning centers (Gurevich, 2014). Typical parameters of some high-J_c superconductors with strong pinning are given in Table 1. These parameters can vary significantly, depending on concentrations of impurities and the materials treatments (Larbalestier et al., 2001; Hosono et al., 2018; Yao and Ma, 2021).

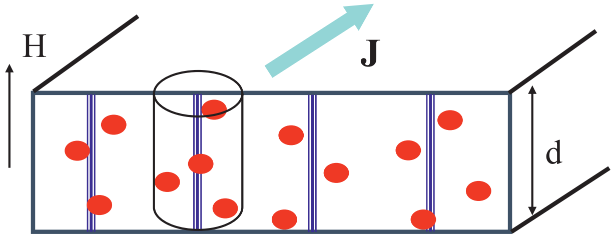

Fig. 2 Pinning of vortex cores (vertical lines) by uncorrelated defects (red dots) in a film of thickness d in a magnetic field H. The cylindrical region around the vortex cores depicts the region of circulating screening currents.

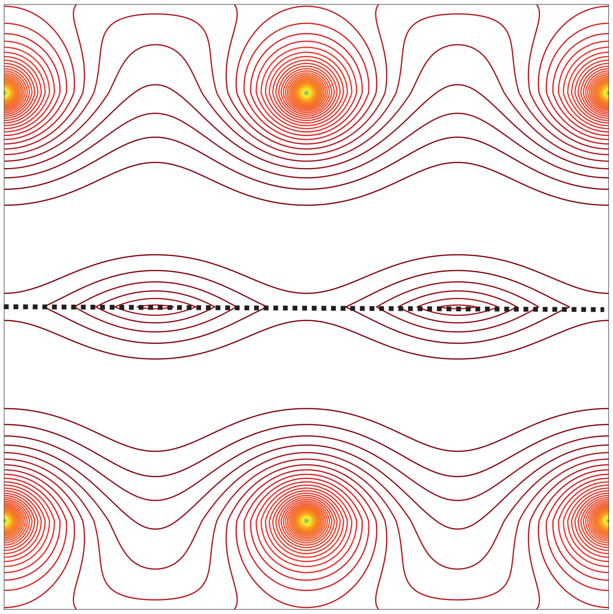

Fig. 3 Deformation of vortex current streamlines near a planar defect shown by a horizontal dashed line.

Table 1 Characteristic parameters of some high-J_c type-II superconductors.

Material	T_c, *K*	$\lambda(0)$, *nm*	$\xi(0)$, *nm*	H_{c2}, *T*	H^*, *T*	J_d, *A m*$^{-2}$	J_c, *A m*$^{-2}$
Nb–Ti	9	240	4	12 (4.2 K)	10.5 (4.2 K)	1.6×10^{11} (4.2 K)	$\sim 4 \times 10^{9}$ (5 T, 4.2 K)
Nb_3Sn	18	65	3	27 (4.2 K)	24 (4.2 K)	5.2×10^{12} (4.2 K)	$\sim 10^{10}$ (0 T, 4.2 K)
$YBa_2Cu_3O_{7-x}$	91	150 ($H\|c$)	1.7 (ab plane)	$>100H\|c$ (4.2 K)	7–11 (77 K)	1.5×10^{11} (77 K)	$\sim 4 \times 10^{10}$ (0 T, 77 K)
$Bi_2Sr_2Ca_2Cu_3O_x$	108	150 ($H\|c$)	1.5 (ab plane)	$>100H\|c$ (4.2 K)	~ 0.2 (77 K)	$\sim 3 \times 10^{12}$ (4.2 K)	$\sim 10^{10}$ (0 T, 4.2 K)
$Ba_{0.6}K_{0.4}Fe_2As_2$	38	200 ($H\|c$)	2 (ab plane)	$>100H\|c$ (4.2 K)	$>100H\|c$ (4.2 K)	$\sim 10^{12}$ (4.2 K)	$\sim 10^{10}$ (0 T, 4.2 K)

Single-vortex and collective pinning by point defects

Calculation of J_c requires summation of elementary pinning forces acting on flexible, strongly interacting vortex lines (Campbell and Evetts, 1972; Blatter et al., 1994; Brandt, 1995). The basic physics of the pinning force summation can be understood by evaluating J_c for a rigid straight vortex interacting with randomly distributed small non-superconducting precipitates in a film of thickness d (Fig. 2). If d is much greater than the mean spacing l_i between the precipitates, a vortex interacts with $N \sim r_p^2 d n_p$ pinning centers, adjusting its position so that the net force vanishes. Here r_p is the pinning interaction radius, and $n_p = l_i^{-3}$ is the density of pins. The transport current displaces the vortex from a local minimum in the pinning potential, so that elementary pinning forces do not compensate each other. The balance of the total pinning force from uncorrelated defects in the volume dr_p^2 against the Lorentz force, $f_p N^{1/2} \simeq d\phi_0 J_c$ yields

$$J_c \simeq \frac{1}{\phi_0}\sqrt{\frac{\gamma}{d}} \tag{2}$$

where $\gamma = f_p^2 r_p^2 n_p$ is the pinning parameter. As follows from Eq. (2), the critical current density $J_c(d)$ decreases as the film thickness increases. If $d \to \infty$, Eq. (2) gives $J_c = 0$ because the net pinning force of a rigid infinite straight vortex in a random pinning potential averages to zero.

Evaluation of bulk J_c must take into account bending of vortices near pinning centers. The effect of vortex elasticity can be understood using the following approach of a theory of weak collective pinning (Blatter et al., 1994; Brandt, 1995). Define a correlation length L_c along the vortex line by the relation $\langle u(L_c)u(0)\rangle = r_p^2$, where $\langle u(z)u(0)\rangle$ is a correlation function of pinning-induced transverse vortex displacements. The relative displacement of the ends of a vortex segment of length L_c exceeds the pinning interaction radius r_p, so a vortex may be regarded as an array of straight segments of length L_c pinned independently. Therefore, J_c can be evaluated from Eq. (2) with d replaced by L_c. In turn, L_c is evaluated by equating a characteristic pinning energy $\phi_0 J_c r_p$ and an elastic bending energy $\varepsilon(r_p/L_c)^2$, where $\varepsilon = \phi_0^2/4\pi\mu_0\lambda^2$ is the vortex line energy scale. The condition $\phi_0 J_c r_p \simeq \varepsilon(r_p/L_c)^2$ along with Eq. (2) at $d \simeq L_c$ yield:

$$J_c \simeq \frac{\gamma^{\frac{2}{3}}}{\phi_0 \varepsilon^{\frac{1}{3}} r_p^{\frac{1}{3}}},\ L_c \simeq \frac{\varepsilon^{2/3} r_p^{2/3}}{\gamma^{1/3}} \tag{3}$$

Due to the collective interaction of a vortex with many pins, J_c increases as the line energy ε decreases because a softer vortex bends more easily to accommodate the pinning centers. Meanwhile, the correlation length L_c increases as the pinning parameter γ decreases, resulting in a "dimensional crossover" in films, from the two-dimensional pinning of rigid straight vortices at $d < L_c$ to the three-dimensional pinning of flexible vortices for $d > L_c$ (Blatter et al., 1994; Brandt, 1995).

A theory of weak collective pinning in strong fields $H \gg H_{c1}$ involves two characteristic spatial scales: the correlation length along the vortex lines $L_c(T, B, \gamma)$ and the correlation length $R_c(T, B, \gamma)$ perpendicular to the vortex lines. These lengths define the correlation volume $V_c = R_c^2 L_c$ - a mesoscopic region in which pinned vortices approximately maintain the positional hexagonal short-range order of the ideal flux line lattice. The positional long-range order of vortices is destroyed by pinning on scales larger than the correlation lengths L_c and R_c. The critical current density is then defined by the balance of the Lorentz force applied to the correlation volume, BJ_cV_c against the pinning force from spatially uncorrelated defects, $f_p N_c^{1/2}$, where $N_c = n_p V_c$. Hence,

$$J_c \sim \frac{f_p}{BR_c}\sqrt{\frac{n_p}{L_c}} \tag{4}$$

where both $L_c(T, B, \gamma)$ and $R_c(T, B, \gamma)$ depend not only on T and B, but also on the pinning parameter γ. The lengths $L_c(T, B, \gamma)$ and $R_c(T, B, \gamma)$ are determined from the conditions $\langle u(R_c, 0)u(0, 0)\rangle = r_p^2$ and $\langle u(0, L_c)u(0, 0)\rangle = r_p^2$, where the correlation function of vortex displacements $\langle u(\mathbf{r})u(0)\rangle$ is calculated using an elasticity theory for the vortex lattice. Depending on the relations between the pinning correlation lengths, the London penetration depth and the vortex spacing $a = (\phi_0/B)^{1/2}$, the collective pinning theory predicts a variety of behaviors of $L_c(T, B, \gamma)$ and $R_c(T, B, \gamma)$ which manifest themselves in different temperature and field dependencies of $J_c(T, B)$. For layered high-T_c superconductors, the pinning theory takes into account anisotropic elastic response of the vortex lattice. A crossover from a weak collective pinning to a strong single-vortex pinning occurs at lower B for which $R_c(T, B, \gamma)$ becomes smaller than the vortex spacing.

Unlike the collective pinning of vortices by many uncorrelated weak pins, interaction of a vortex with a strong pinning center can occur in a hysteretic manner because the elastic vortex line bends toward the pin and jumps into it once the spacing between the vortex and the pin gets smaller than a trapping distance which depends on the pin strength and the flux density B/ϕ_0. The transition from the weak collective pinning to the hysteretic strong core pinning occurs if $k_L = f_p/\xi\overline{C} > 1$. Here $k_L$is the Labusch parameter which quantifies the strength of a single pin in terms of the ratio of the pinning force and bending elasticity of the vortex $\overline{C}$ (Blatter et al., 2004). At low fields $B \ll B_{c2}$, the vortex elasticity theory gives $\overline{C} \simeq 4(2\pi B/\phi_0)^{1/2}\varepsilon$ and the criterion of strong pinning $k_L > 1$ takes the form:

$$\mathrm{k_L} \sim \frac{\mathrm{f_p}\sqrt{\phi_0}}{4\xi\varepsilon\sqrt{2\pi \mathrm{B}}} > 1 \tag{5}$$

Eq. (5) shows that the strong hysteretic pinning tends to occur in the case of large pinning force, soft vortex line and low magnetic field. Increasing the density of pinning centers can push J_c toward the depairing limit, as it can indeed occur in optimized NbTi alloys or some of high-T_c cuprates. For instance, oxide nanoparticles of Y_2O_3 or $BaZrO_3$ incorporated into $YBa_2Cu_3O_{7\text{-x}}$ films can be tuned by varying the shape, size and distribution of oblate or prolate nanoprecipitates, self-assembled chains of nanoparticles or nanorods, typically spaced by 4–10 nm and being 2–4 nm in diameter to provide the strongest core pining of vortices (Maiorov et al., 2009; Haugan et al., 2020). The artificial pinning centers do enhance J_c at low field $B < 1$ tesla where $J_c(77K, 0) \approx (5-8) \times 10^{10}$ A m^{-2} in $YBa_2Cu_3O_{7\text{-x}}$ films at self-field can approach 10-20% of J_d. Such "designer" pinning nanostructures also increase J_c at intermediate fields most relevant to magnet applications. For instance, the high values of $J_c(0, 77K) \simeq 2.7 \times 10^{10}$ A m^{-2} and of $J_c(5T, 77K) \simeq 10^9$ A m^{-2} were observed on $YBa_2Cu_3O_{7\text{-x}}$ films with Y_2O_3 nanoparticles. Technological advances have resulted in high $J_c(0, 77K) \gtrsim 4 \times 10^{10}$ A m^{-2} in FBS as well (Hosono et al., 2018; Yao and Ma, 2021).

Shown in Fig. 4 are two examples of strong pinning due to a dense array of spherical dielectric pins (a) and columnar pins with suppressed T_c (b). The very high J_c values in the cuprates and FBS mentioned above imply that pinning centers subdivide vortices into segments nearly as short as the vortex core diameter $2^{3/2}\xi$. To illustrate how far could J_c be increased, let us estimate J_c for strong core pinning by insulating nanoprecipitates of radius $r_0 \approx \xi$ which chop vortices into segments of length $l \ll \lambda$, as shown in Fig. 4A.

If the ends of each vortex segments are fixed by the strong pins, J_c is determined by the pin breaking mechanism due to cutting and reconnection of vortex semi-loops in the limit of $k_L \gg 1$ (Brandt, 1995). In this case vortex segments bow out under the action of flowing current, then reconnect and escape at the critical current density (Gurevich, 2014):

$$J_c \simeq \frac{\phi_0}{2\pi\mu_0\lambda^2\Gamma l}\ln\left(\frac{\Gamma l}{2\xi}\right)\left[1 - \frac{4\pi r_0^3}{3x_c l^3}\right] \tag{6}$$

Eq. (6) describes the limit of J_c in a uniaxial superconductor, where λ and ξ are the field penetration depth and the coherence length in the isotropic ab plane, and the anisotropy parameter $\Gamma = (m_c/m)^{1/2} > 1$ depends on the ratio of electron mass m_c along the c-aixs to the mass m in the ab plane (typical values of Γ in $YBa_2Cu_3O_{7\text{-x}}$ and FBS range from 2 to 7). The factors in front of the brackets in Eq. (6) describe J_c due to pin breaking of a flexible vortex segment of length l. The factor in the brackets of Eq. (6) accounts for the reduction of the current-carrying cross section by randomly distributed dielectric pins, where the percolation threshold x_c varies

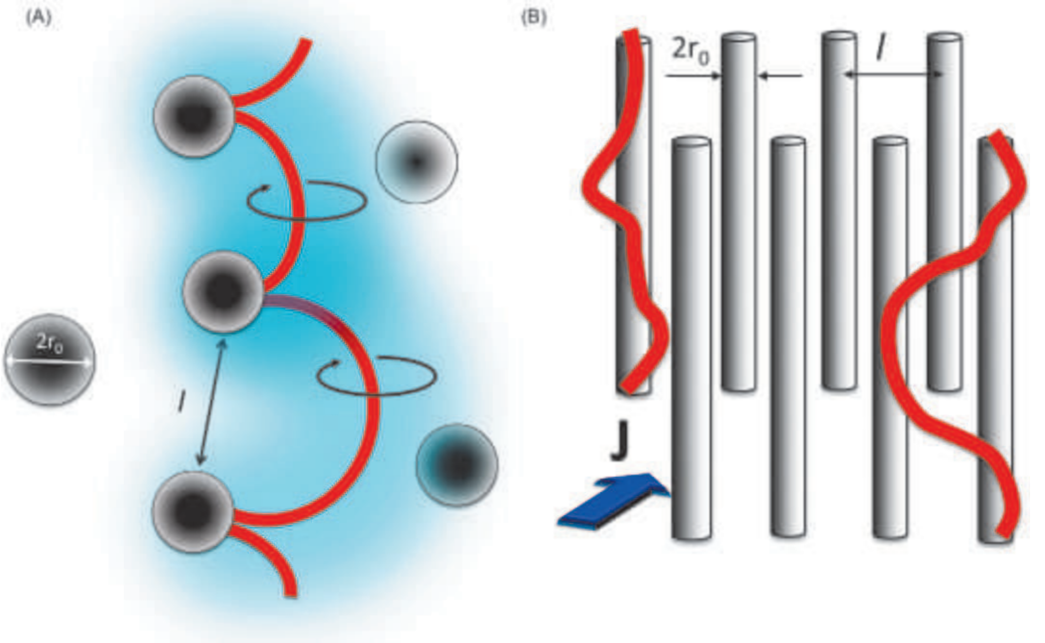

Fig. 4 Configurations of pinned curvilinear vortices (the cores of vortices of diameter $\simeq 2\xi$ are shown by red) for: (A) strong pinning by dielectric nano precipitates, where the blue region of width $\simeq \lambda$ in shows the spatial extend of superconducting currents (depicted by black arrows) circulating around the vortex cores. (B) pinning of fluctuating vortices by columnar defects with suppressed T_c.

from 1/2 in the two-dimensional limit of layered materials $\Gamma \gg 1$ to $x_c \approx 2/3$ in the isotropic 3D limit ($\Gamma = 1$). Interplay of pinning and current blocking by pins results in a maximum $J_c(l)$ at $l_m \approx (16\pi/3x_c)^{1/3} r_0$ (Gurevich, 2014). This yields the optimal volume fraction of nanoprecipitates, $x_m \approx 9 - 12\%$and the maximum $J_c \approx (0.2 - 0.3)J_d$. These numbers are close to the maximum values which have been achieved in NbTi (Larbalestier et al., 2001) or $YBa_2Cu_3O_{7-x}$ with optimized pinning nanostructure (Haugan et al., 2020; Stangl et al., 2021). The maximum in $J_c(x)$ at an optimum volume fraction of pins has also been obtained in numerical simulations of the time-dependent Ginzburg-Landau equations for vortices pinned by metallic inclusions or regions with reduced T_c (Kwok et al., 2016).

Pinning and current blocking by extended defects

Pinning by extended defects, such as grain boundaries or columnar radiation defects shown in Figs. 3 and 4B, respectively differs from pinning by uncorrelated disorder, because a single extended defect parallel to **B** can pin a long vortex segment greater than the correlation length $L_c = \xi(J_d/J_c)^{1/2}$ of the collective pinning theory. Pinning by extended defects can be rather effective and result in high J_c values if the vortex is aligned with the defect. Indeed, a single vortex trapped by a cylindrical cavity of radius $r_0 \approx \xi$, has the pinning energy U_p of the order of the condensation energy of the vortex core $\phi_0^2/4\pi\mu_0\lambda^2$, yielding a very high $J_c \simeq U_p/\xi\phi_0$ of the order of the depairing current density. This model has been used to describe experiments on irradiation of high-T_c superconductors with 1–10 GeV heavy ions (Pb, Au, Xe, etc.), which can produce 10–100 μm columnar tracks of about 5–10 nm in diameter comparable to ξ (see Fig. 4B) The areal density of columnar defects $n_\square$ is customary expressed in terms of the matching field $B_m = \phi_0 n_\square$ which typically ranges from 0.1 to 10 T for different irradiation conditions. For $B < B_m$, each vortex is trapped by a columnar defect, resulting in a significant enhancement of J_c in high-T_c superconducting films, as has been shown in many experiments. Columnar defects are most effective for vortices aligned with the defects, but J_c decreases strongly if the magnetic field is misaligned, so that J_c becomes very anisotropic with respect to the direction of **B**.

Pinning by extended planar defects such as grain boundaries (GBs) in Nb_3Sn, or by thin α-Ti metallic ribbons in Nb—Ti can also result in high $J_c \sim 10^{10} - 10^{11}$ A m^{-2} at 4.2 K in self field (see Table 1). Chemical nonstoichiometry, lattice disorder, strain, and charging effects associated with GBs cause local suppression of superconductivity in the cuprates and FBS. This can give rise to weakly linked GBs and magnetic granularity especially pronounced in high-T_c cuprates in which the critical current density through the grain boundaries J_b decreases exponentially as a function of the misorientation angle θ between the neighboring grains if $\theta > \theta_0 \approx 4 - 5^\circ$ (Hilgenkamp and Mannhart, 2002). As a result, J_b through GBs or thin α-Ti ribbons in Nb—Ti, is smaller than J_d in the bulk. It is the reduction of J_b as compared to J_d, which causes a strong magnetic and core interaction between a vortex and a planar defect, particularly, the radical change in the structure of the vortex core as it moves closer to the defect shown in Fig. 3. This results in two different types of vortices in polycrystals: vortices in the grains pinned by a long-range magnetic interaction with GBs and elongated vortices on GBs. Here J_c can be evaluated by balancing the total Lorentz force $F_p \sim BJ_cD^3$ in the grain of size $\sim D$

against the total pinning force proportional to the surface area of the grain $\sim D^2$. This yields a descending dependence of $J_c \propto D^{-1}$ on the grain size, as has been observed in Nb_3Sn with $1\mu m \lesssim D \lesssim 10\ \mu m$ (Durrell et al., 2011).

Grain boundaries can play a dual role in which they both pin vortices and block macroscopic current flow. In this case current loops can form in the grains if the critical current density due to pinning of vortices in the grains, is higher than the current density J_b, which can pass through GBs. This effect of magnetic granularity can limit global critical current density of superconducting polycrystals. In turn, it indicates that there is an optimum value of J_b, which maximizes J_c, because J_c vanishes in the two limiting cases of $J_b = J_d$ (no pinning, since GBs do not disturb currents circulating around vortices) and $J_b = 0$ (current cannot pass through grain boundaries). Calculation of the optimum J_c, in addition to the summation of vortex pinning interactions, requires taking into account the geometry of the grains and microscopic mechanisms of current transport through the GB.

Current transport through GBs is particularly important for high-T_c polycrystals, for which the weak link behavior of high-angle GBs is one of the most serious current-limiting mechanisms. This behavior is due to rapid decrease of $J_b(\theta) = J_0 \exp(-\theta/\theta_0)$ with the misorientation angle θ and the resulting increase of the vortex core size, from ξ to $l(\theta) = \xi J_d/J_b(\theta)$ at $l(\theta) \lesssim \lambda$ to the Josephson core length $l(\theta) = [\xi\lambda J_d/J_b(\theta)]^{1/2}$ for $l(\theta) \gtrsim \lambda$. The extended core of the GB vortices leads to their weaker pinning force parallel to the boundary against the Lorentz force of the transport current flowing perpendicular to the boundary. As a result, the global J_c of polycrystals may be limited by depinning of a small fraction of vortices, which can move more easily along a network of GBs. This percolative motion of vortices along GBs is impeded by structural defects along GBs (such as facets, nanoprecipitates) and by magnetic pinning shear stress as the GB vortices move past more strongly pinned vortices in the grain (see Fig. 3). The significant reduction of J_b of GBs in high-T_c superconductors is due to the sensitivity of their critical temperature to a hole depletion, which can drive the high-T_c superconducting state into an antiferromagnetic insulator. The local hole depletion near GBs can be due to local oxygen nonstoichiometry, charging and strain effects produced by the crystalline dislocations which form the GB, or more macroscopic strain fields due to faceting (Hilgenkamp and Mannhart, 2002). The values of J_b can be improved by oxygen overdoping or local doping with appropriate impurities, such as Ca in $YBa_2Cu_3O_7$ or Sn in Nb_3Sn. The current-carrying capability of $YBa_2Cu_3O_7$ or FSB polycrystals can also be improved by depositing the superconducting films onto "biaxially textured" metallic substrates to eliminate the weakest high-angle GBs.

Global critical currents of superconductors

Multiple pinning mechanisms manifest themselves in different dependencies of the critical current density on T and B, which is often described by a scaling relation (Campbell and Evetts, 1972):

$$J_c(h) = J_{c0}(T)h^{-p}(1-h)^q \tag{7}$$

where $h(T) = H/H^*(T)$ is a reduced field, and $J_{c0}(T)$, p and q are the material-dependent parameters. For instance, Eq. (7) with $p = 0$ and $q = 1$ describes $J_c(B)$ in optimized Nb–Ti alloys, while $J_c(B)$ in Nb_3Sn is usually described by Eq. (7) with $p \approx 1/2$ and $q \approx 2$, consistent with pinning of vortices by grain boundaries. In high-T_c superconductors, $J_c(T,H)$ at elevated temperatures $T > 20 - 30$ K often exhibits an exponential field dependence $J_c(H) = J_{c0} \exp(-H/H_0)$, where the field $H_0(T)$ can be much smaller than $H_{c2}(T)$, especially in layered $Bi_2Sr_2CaCu_2O_x$. The irreversibility field $H^*(T)$ in layered high-T_c superconductors can be much smaller than $H_{c2}(T)$, whereas in low-T_c superconductors, such as Nb—Ti and Nb_3Sn, or "intermediate-T_c" compound MgB_2 with $T_c = 40$ K and some of the FBS, $H^*(T) \approx (0.8 - 0.9)H_{c2}(T)$ is not that different from $H_{c2}(T)$, as shown in Fig. 5 (see also Table 1). As a result, layered high-T_c cuprates $Bi_2Sr_2CaCu_2O_x$ and $Bi_2Sr_2Ca_2Cu_3O_x$, despite their very high H_{c2}, can carry weakly dissipative currents at the liquid nitrogen temperature of 77 K only in a small part of the H–T diagram. This restriction is due to strong magnetic "flux creep" caused by thermally-activated hopping of flexible vortices between neighboring pinning positions at the current density J below J_c.

Vortex creep velocity $\mathbf{v}$ is parallel to the driving Lorentz force $[\mathbf{J} \times \mathbf{B}]$, causing the electric field $\mathbf{E} = [\mathbf{v} \times \mathbf{B}]$ directed along $\mathbf{J}$ (in isotropic materials). The E–J characteristic of a superconductor at $J < J_c$ has the form (Blatter et al., 1994):

$$\boldsymbol{E} = E_c \exp\left[-\frac{U(J,\ T,\ B)}{k_B T}\right]\frac{\boldsymbol{J}}{J}, \tag{8}$$

where the Boltzmann factor $\exp(-U/k_B T)$ accounts for a fraction of depinned thermally-activated vortices resulting in the global flux motion. The flux creep activation energy $U(J,T,B)$ depends on the current density, which makes the E-J curve highly nonlinear at $J < J_c$. It is convenient to define the activation energy $U(J)$ in such a way that it vanishes at $J = J_c$, using one of the conventional approximations: (1) $U = (1 - J/J_c)U_0$, (2) $U = U_0 \ln(J/J_c)$, (3) $U = U_0[(J_c/J)^\mu - 1]$, where $U_0(T,B)$ is an energy scale for thermally activated hopping of vortices. These models give an exponential increase of E with J at $J \approx J_c$, but different behaviors of $E(J)$ at $J \ll J_c$. Low-T_c superconductors typically have $U_0 \simeq 500 - 1000$ K, whereas high-T_c superconductors can have considerably smaller $U_0 \simeq 100 - 400$ K, since mobile pancake vortices on neighboring ab planes are weakly coupled due to the layered structures of these materials.

Because of weak dissipation at $J < J_c$, the critical current depends on the electric field E_c at which J_c is measured. Generally, J_c is defined as a crossover current density at which a resistive transition from an exponentially small $E(J)$ to a linear flux flow E–J curve occurs as shown in Fig. 6 (a conventional practical criterion of $E_c = 1\ \mu\text{V cm}^{-1}$ is often used). The relation between J_c and J_c' measured at different electric fields E_c and E_c' can be obtained from Eq. (8) by linearizing the activation energy $U(J) = U_0(1 - J/J_c)$ near J_c:

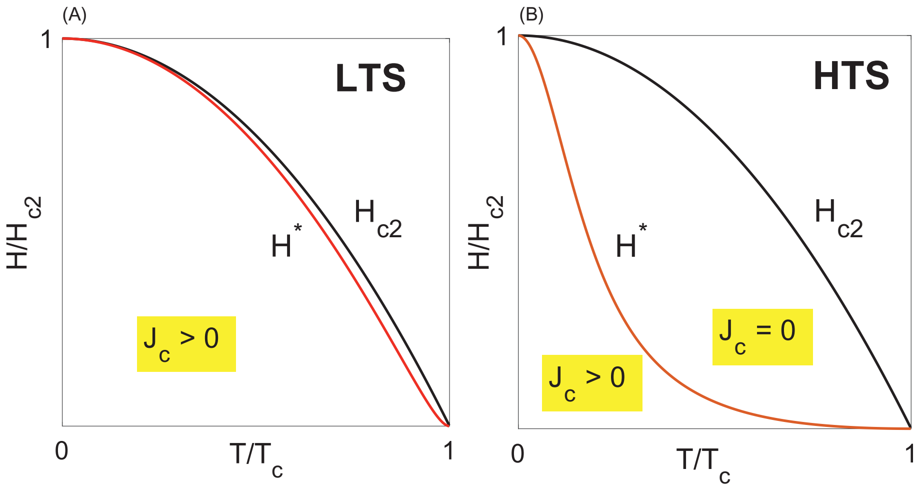

Fig. 5 (A) Magnetic phase diagram of low-T$_c$ superconductors, for which $H^*(T) \approx H_{c2}(T)$. (B) Magnetic phase diagram of high-T$_c$ superconductors which cannot carry critical currents in a wide field range $H^*(T) < H < H_{c2}(T)$. Both cases (A) and (B) correspond to extreme type-II superconductors ($\kappa \gg 1$) for which the lower critical field $H_{c1} \ll H_{c2}$ is not shown.

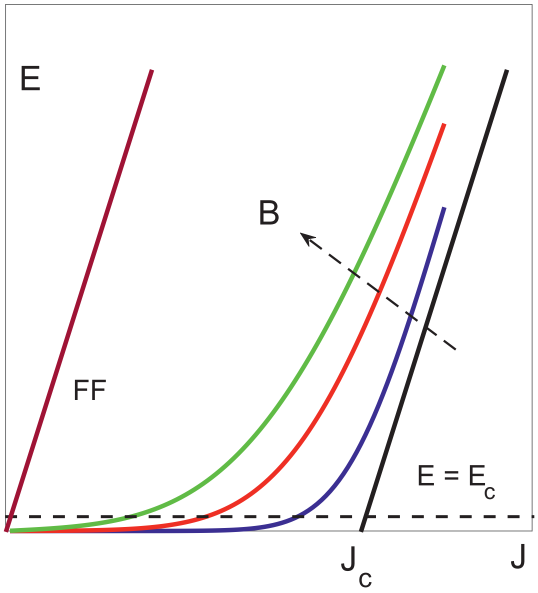

Fig. 6 Broadening of the E–J characteristics as B increases. Here the green curve corresponds to B close to but below the irreversibility field B*, while the FF line shows the Ohmic flux flow E–J characteristic at B > B*. The dashed line shows the electric field criterion E$_c$ at which J$_c$ is defined.

$$J_c' = \left(1 + \frac{k_B T}{U_0} \ln \frac{E_c'}{E_c}\right) J_c \tag{9}$$

In low-T$_c$ superconductors with $k_B T_c/U_0 \sim 10^{-2}$, the critical current density $J_c(E_c)$ varies only by a few percent in a practically accessible electric field window of 10 nV m^{-1} < E < 100 mV m^{-1}. By contrast, high-T$_c$ superconductors with $k_B T_c/U_0 \sim 10^{-1}$ have a broader resistive transition at $J \approx J_c$ and a larger difference between J_c and J_c'. The ratio $k_B T_c/U_0$ also defines the rate of slow time decay of currents in superconductors due to thermally-activated flux creep, $J(t) = J_c[1 - (k_B T/U_0) \ln (t/t_0)]$. The condition $U_0(H^*, T) \sim k_B T$ determines the irreversibility field $H^*(T)$ at which a nonlinear E-J curve turns into a nearly linear $E(J)$, as shown in Fig. 6. In layered high-T$_c$ superconductors, such as Bi$_2$Sr$_2$Ca$_2$Cu$_3$O$_x$, the activation energy of pancake vortices is only a few times greater than $k_B T_c$. In this case of $H^*(T) \ll H_{c2}(T)$ at high temperatures pinning becomes ineffective in a significant part of the H–T diagram (Fig. 5B). In low-T$_c$ superconductors, the dissipative region $H^* < H < H_{c2}$ shown in Fig. 5A is rather narrow, as discussed above (see also Table 1).

Thermal fluctuations of vortices give rise to the broadening of the resistive transition of a superconductor in a magnetic field and the region of $J_c = 0$ in Fig. 5. Such thermal depinning of vortices follows from the field and temperature dependencies of the activation energy $U_0(T, B) = U_{00}(H_0/H)^z(1 - T/T_c)^s$ at $T \approx T_c$ and $J \to 0$, where the magnitudes of U_{00} and H_0 and the exponents z and s depend on particular pinning mechanisms (Blatter et al., 1994). For weak broadening, the width of the resistive transition ΔT can be evaluated from the condition $U_0(H, \Delta T) \sim k_B T_c$, which yields

$$\frac{\Delta T}{T_c} \simeq \left(\frac{k_B T_c}{U_{00}}\right)^{\frac{1}{s}} \left(\frac{H}{H_0}\right)^{\frac{z}{s}} \tag{10}$$

Hence, the width of the resistive transition increases with the magnetic field. For instance, if $z = 1$ and $s = 3/2$, Eq. (10) gives $\Delta T \propto H^{2/3}$. Thermal wandering of vortices also results in melting of the vortex lattice at $H < H_m(T) < H_{c2}(T)$. The melting field $H_m \simeq H^*$ is controlled by the dispersive line tension of the vortex $\varepsilon(k)$ for short wavelength bending distortions with the wave number $k \ll \lambda^{-1}$ (Blatter et al., 1994; Brandt, 1995):

$$\varepsilon_k \simeq \frac{\varepsilon}{\Gamma^2} \ln \frac{1}{k\xi_c}, \varepsilon = \frac{\phi_0^2}{4\pi\mu_0\lambda^2} = \frac{\pi\hbar^2 n_s}{4m} \tag{11}$$

where m is the effective electron mass in the ab plane, ξ_c is the coherence length along the c-axis, $n_s(T)$ is the superfluid density, and $\Gamma = \lambda_c/\lambda$ is the anisotropy parameter, and λ_c is the magnetic penetration depth along the ab planes. As follows from Eq. (11), high anisotropy and low superfluid density n_s can strongly reduce the bending rigidity of a vortex. For instance, $\varepsilon_k \simeq 10^4$ K nm^{-1} in Nb with $\lambda(0) \simeq 40\ nm$, $\Gamma = 1$, while in $YBa_2Cu_3O_{7-x}$ with $\lambda(77\ K) \simeq 400\ nm$, $\Gamma \approx 5$, we have $\varepsilon_k \simeq 5$ K nm^{-1}. Most FBS have $\varepsilon_k \simeq (200 - 500)(1 - T^2/T_c^2)$ K nm^{-1}, while the layered Bi-based cuprates have much lower $\varepsilon_k < 1$ K nm^{-1} at 77 K. As a result, vortices in Nb form the rigid Abrikosov lattice, whereas in cuprates at 77 K thermal fluctuations can displace vortex segments by distances larger than the pin spacing thus smearing out the pinning potential and reducing $J_c(T, H)$. For instance, the vortex segments of length $\sim k_B T/\varepsilon \sim 10 - 100$ nm shown in Fig. 4A can hop and reconnect at neighboring pins, causing thermally-activated flux creep at $J < J_c$, no matter how strong the elementary pinning forces may be. The flux creep in arrays of columnar pins occurs via proliferation of vortex kinks between neighboring pins, as shown in Fig. 4B. In this case the flux creep rate can be reduced by splaying the columnar defects, which increases the vortex activation energy as compared to the parallel columnar pins (Maiorov et al., 2009).

In addition to the multiscale pinning mechanisms, a global critical current density $J_c = I_c/A_{eff}$ of a conductor with a critical current I_c can be limited by macroscopic defects such as large second phase precipitates or microcracks which reduce an effective current-carrying cross section A_{eff}. Here, A_{eff} is determined by current percolation through arrays of large second-phase precipitates, colonies of high-angle grain boundaries, microcracks, and other inhomogeneities much greater than the spacing between vortices. This results in nonuniform current distributions in superconductors, which have been revealed by magneto-optical imaging or micro-Hall probes (Larbalestier et al., 2001). Macroscopic current flow in superconductors can be described by a nonlinear Maxwell equation $\nabla \cdot (J(\nabla\varphi)) = 0$ for the electric potential φ, where $E(J)$ is determined by Eq. (8). The strong nonlinearity of $E(J)$ at $J < J_c$ results in extended electric field hot spots near defects on scales much greater than the defect size b. Shown in Fig. 7 is an example of the spatial distribution of electric field around a microcrack of length b calculated for $E = E_c(J/J_c)^n$. In this case the electric field hot spot has the length $L_\perp \sim nb$ perpendicular to current flow and $L_\parallel \sim b\sqrt{n}$ parallel to current flow. For typical of low-T_c superconductors values of $n \simeq 30 - 50$, planar defects blocking only a few percent of the sample cross section can cause noticeable voltage drops on the conductor and reduce its current-carrying capability (Friesen and Gurevich, 2001).

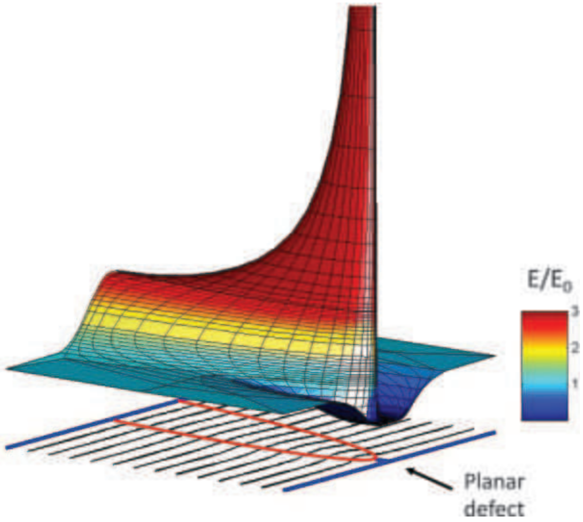

Fig. 7 Spatial distribution of the electric field magnitude in a hot spot near a planar cut of length $b = 0.05w$ in a film of width w, calculated for the power-law E–J characteristic $E = E_c(J/J_c)^n$ with $n = 30$. Here, E_0 is the uniform field far away from the defect. Shown below the surface of $E(x, y)$ are the corresponding current streamlines in the film, where the red lines depict the boundaries of a flux jet emitted from the defect perpendicular to current flow.

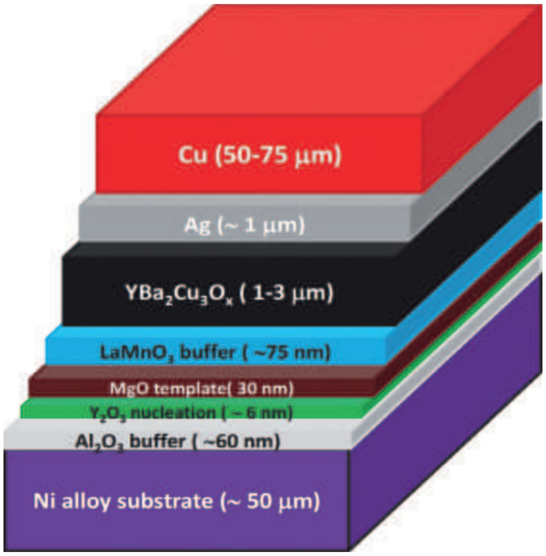
Cu (50-75 μm)
Ag (~ 1 μm)
$YBa_2Cu_3O_x$ (1-3 μm)
$LaMnO_3$ buffer (~75 nm)
MgO template(30 nm)
Y_2O_3 nucleation (~ 6 nm)
Al_2O_3 buffer (~60 nm)
Ni alloy substrate (~ 50 μm)

Fig. 8 A coated conductor in which the $YBa_2Cu_3O_{7-x}$ film is grown on a textured Ni alloyed substrate with a complex buffer layer structure, which enables replication of the low-angle grain structure of the substrate in $YBa_2Cu_3O_{7-x}$ and protects it from chemical contamination. The stabilizing layers of Ag and Cu on top of the 1–2 μm thick $YBa_2Cu_3O_{7-x}$ film provide protection of the conductor against thermal runaway. The superconducting current-carrying film takes only a few % of the conductor cross-section.

Strong pinning of vortices and high irreversibility field are not yet sufficient for applications which require long polycrystalline wires. One of the main issues for the cuprates (and to a lesser extent for FBS) is that grain boundaries between misoriented crystallites impede current flow. This is because the GB critical current density $J_b = J_0 \exp(-\theta/\theta_0)$ drops exponentially with the misorientation angle θ, as it was mentioned above. For the cuprates, $\theta_0 \approx 3 - 5^o$ so the spread of misorientation angles $\Delta\theta \approx 40^o$ in polycrystals can reduce J_b by 2–3 orders of magnitude. FBS also have weak-linked GBs but the larger values of $\theta_0 \approx 7 - 9^o$ in FBS make them less prone to the electromagnetic granularity, (Durrell et al., 2011; Hosono et al., 2018).

Discovered in 1988, the current-limiting GBs in $YBa_2Cu_3O_{7-x}$ bicrystals were immediately recognized as a serious obstacle for applications because, instead of flowing along the wire, current breaks into disconnected loops circulating in the grains. This problem has been addressed by the coated conductor technology in which a fraction of high-angle GBs with $\theta > 5 - 7^o$ is reduced by growing $YBa_2Cu_3O_{7-x}$ films on textured metallic substrates. Fig. 8 shows an example of the coated conductor, which has made the idea of $YBa_2Cu_3O_{7-x}$ "single crystal by the mile" a reality available for magnet dc applications. FBS coated conductors have also been developed (Hosono et al., 2018; Yao and Ma, 2021). While the coated conductors can carry high critical currents at 77 K, they utilize only a few % of the current-carrying cross-section, so J_c of the $YBa_2Cu_3O_{7-x}$ film must be pushed to the limit by incorporating dense arrays of dielectric nanoprecipitates (Maiorov et al., 2009; Haugan et al., 2020). However, the composite tapes shown in Fig. 8 have very high hysteretic remagnetization losses in alternating magnetic fields (Campbell and Evetts, 1972). For this reason, ac applications of superconductors in motors and generators require round composite wires in which twisted superconducting filaments are embedded in a highly conductive Cu or Ag normal matrix. This technology has been developed for multifilamentary Nb—Ti and Nb_3Sn round wires (Larbalestier et al., 2001), as well as for multifilamentary wires of the biaxially-textured $Bi_2Sr_2CaCu_2O_x$ in Ag matrix, and FBS wires (Yao and Ma, 2021).

Conclusion

Critical currents in superconductors are determined by multiscale pinning of strongly interacting curvilinear vortices by materials defects. Here non-superconducting defects can play a dual role by both pinning the vortices and blocking current flow, as it happens, for example, in Nb_3Sn in which pinning is caused by grain boundaries. As the volume fraction x of pinning centers increases, $J_c(x)$ of low-T_c superconductors can be pushed to a fundamental limit at an optimum value x_c determined by interplay of pinning and current blocking effects. The field range in which a superconductor can carry weakly-dissipative critical currents can be widened significantly by increasing H_{c2} by nonmagnetic impurities.

The physics of critical currents in anisotropic high-T_c cuprates and FBS with small Fermi energies, low superfluid densities and competing anti-ferromagnetic orders is further complicated by strong thermal fluctuations of vortices at high temperatures which can drastically reduce J_c and the irreversibility field. This manifests itself in different mechanisms of $J_c(T, H)$ at low and high temperatures. At $T \ll T_c$ the effect of vortex fluctuations is weak so J_c is determined by flux pinning in the same way as in low-T$_c$ superconductors and J_c in the cuprates can be increased greatly by incorporating strong pinning structure of oxide nanoprecipitates. However, as T increases, the effect of vortex fluctuations in layered high-T$_c$ superconductors becomes dominant and the field region $H_{c1} < H < H^*(T)$, where they can carry weakly dissipative currents shrinks much faster than the decrease of $H_{c2}(T)$ with T. It turned out that the designer pinning nanostructures that increase J_c by several orders of magnitude at low temperatures in $YBa_2Cu_3O_{7\text{-}x}$ are less effective in increasing $H^*(T)$ at 77 K, although a combination of random nanoprecipitates and splayed pinning nanorods can reduce the effect of thermally-activated flux creep (Maiorov et al., 2009; Haugan et al., 2020). Understanding the ways by which pinning can be optimized to increase the irreversibility field in anisotropic high-T$_c$ superconductors at 77 K remains an important outstanding problem.

References

Blatter G, Feigel'man MV, Geshkenbein VB, Larkin AI, and Vinokur VM (1994) Vortices in high-temperature superconductors. *Reviews of Modern Physics* 66: 1125–1388.

Blatter G, Geshkenbein VB, and Koopmann JAG (2004) Weak to strong pinning crossover. *Physical Review Letters* 92: 067009.

Brandt EH (1995) The flux-line lattice in superconductors. *Reports on Progress in Physics* 58: 1465–1594.

Campbell AM and Evetts JE (1972) *Critical currents in superconductors*. London: Taylor and Frances.

Durrell JH, Eom CB, Gurevich A, Hellstrom EE, Tarantini C, Yamamoto A, and Larbalestier DC (2011) The behavior of grain boundaries in Fe-based superconductors. *Reports on Progress in Physics* 74: 124511.

Friesen M and Gurevich A (2001) Nonlinear current flow in superconductors with restricted geometries. *Physical Review B* 63: 064521.

Gurevich A (2014) Challenges and opportunities in applications of unconventional superconductors. *Annual Reviews of Condensed Matter Physics* 5: 35–56.

Haugan T, Puig T, Matsumoto K, and Wu J (2020) Artificial pinning centers in (Y,Re)-Ba-Cu-O superconductors: Recent progress and future perspectives. *Superconductor Science and Technology* 30: 040301.

Hilgenkamp H and Mannhart J (2002) Grain boundaries in high-T$_c$ superconductors. *Reviews of Modern Physics* 74: 485–549.

Hosono H, Yamamoto A, Hiramatsu H, and Ma Y (2018) Recent advances in iron-based superconductors toward applications. *Materials Today* 21: 278–301.

Kwok WK, Welp U, Glatz A, Koshelev AE, Kihlstrom KJ, and Crabtree GW (2016) Vortices in high-performance high-temperature superconductors. *Reports on Progress in Physics* 79: 116501.

Larbalestier D, Gurevich A, Feldmann DM, and Polyanskii A (2001) High-T$_c$ superconducting materials for electric power applications. *Nature* 414: 368–377.

Maiorov B, Baily SA, Zhou H, Ugurlu O, Kennison JA, Dowden PC, Holesinger TG, Foltyn SR, and Civale L (2009) Synergetic combination of different types of defects to optimize pinning landscape using $BaZrO_3$-doped $YBa_2Cu_3O_7$. *Nature Materials* 8: 398–404.

Pearl J (1964) Current distribution in superconducting films carrying fluxons. *Applied Physics Letters* 5: 65–66.

Stangl A, Palau A, Deutscher G, Obradors X, and Puig T (2021) Ultra-high critical current densities of superconducting $YBa_2Cu_3O_{7-\delta}$ thin films in the overdoped state. *Scientific Reports* 11: 8176.

Tinkham M (1996) *Introduction to Superconductivity*, 2nd edn. New York: McGraw-Hill.

Yao C and Ma Y (2021) Superconducting materials. Challenges and opportunities for large-scale applications. *iScience* 24: 102541.

High-temperature superconductors

MJ Qin[a], **Xun Xu**[b], **and Shi Xue Dou**[c], [a]Institute of Materials Engineering, Australian Nuclear Science and Technology Organisation, Menai, NSW, Australia; [b]Institute for Superconducting & Electronic Materials, University of Wollongong, Wollongong, NSW, Australia; [c]Institute of Energy Materials Science (IEMS), University of Shanghai For Science and Technology, Shanghai, China

© 2024 Elsevier Ltd. All rights reserved.

This is an update of M.J. Qin, S.X. Dou, Superconductors, High Tc, Editor(s): Franco Bassani, Gerald L. Liedl, Peter Wyder, Encyclopedia of Condensed Matter Physics, Elsevier, 2005, Pages 112–120, ISBN 9780123694010, https://doi.org/10.1016/B0-12-369401-9/00706-3.

Introduction 566
Overview 566
Crystal structures 566
Phase diagram 567
Superconducting properties 567
Critical temperature T_c 568
Coherence length ξ 568
Penetration depth λ 568
Critical fields 569
Pairing symmetry 570
Energy gap 571
Type-II superconductivity 572
Vortex structure 572
Irreversibility field 573
Critical currents and flux pinning 573
Flux creep 574
Melting of the vortex lattice 575
Mixed-state phase diagram 575
Normal-state properties 576
Experimental methods 576
Magnesium diboride (MgB_2) 577
Iron-based superconductor 577
Thin films 577
Bulk materials 577
Tapes and wires 578
Coated conductors 578
Conclusion 578
References 579

Abstract

This chapter reviews some of the fundamentalproperties of high-temperature superconductors (HTSC), which include crystal structures, phase diagrams, superconducting properties, mechanisms, material processing and some newly developing superconductor. These would show a strong trait behavior of the high-temperature superconductivity that has been the subject of intensive study. It has received much attention due to its industrial applications.

Key points

- Crystal structures of most HTSCs can be obtained by stacking perovskite, rock salt and/or fluorite structure.
- The optimum T_c values above the liquid nitrogen temperature (77 K). Superconductivity happens when charge carriers overcome their mutual electrostatic repulsion, bind together into Cooper pairs, and condense into a single quantum state below a certain temperature.
- HTSCs are typical type-II superconductors by varying the external field H, at the lower critical field H_{c1}.
- Due to short coherence lengths and high anisotropy in cuprate superconductors, the vortex structures, and critical currents are different from those in conventional superconductors.
- Due to high-operating temperatures and reduced pinning compared to conventional superconductors, relaxation in HTSCs is very large.
- Thin films, bulk materials, tapes and wires, and coated conductors have received much attention

Introduction

In 1911, Kamerlingh Onnes discovered superconductivity in mercury with a transition temperature Tc of 4.2 K, at which the DC resistance of mercury dropped to zero. The second characteristic of a superconductor was its perfect diamagnetism, discovered by Meissner and Ochsenfeld in 1933. A theoretical understanding of superconductivity is based on the BCS microscopic theory, proposed by Bardeen, Cooper, and Schrieffer in 1957. Before 1986, the highest Tc in the now so-called low-temperature superconductors (LTSC) was found in Nb_3Ge ($23K$). In 1986, Bednorz and Muller reported superconductivity in $(LaBa)_2CuO_4$ with a Tc of 35 K, in contrast to the previous record of 23 K in LTSC. Their discovery opened up the era of high-temperature superconductivity. The discovery of high-temperature superconductors (HTS) materials marked a significant milestone in the field of superconductivity, as it revealed the potential for superconductivity at higher temperatures than had previously been thought possible. Shortly after that, $YBa_2Cu_3O_7$ (Tc = 90 K), $Bi_2Sr_2Ca_2Cu_3O_{10}$ (Tc = 110 K), and $Tl_2Ba_2Ca_2Cu_3O_{10}$ (Tc = 125 K) were discovered. Since then, high-temperature superconductivity has been the subject of intensive study. In 2001, it was discovered that magnesium diboride (MgB_2) exhibits superconductivity with a Tc value of around 40 K, which is relatively high compared to most previously known superconductors. Since 2008, the Hideo Hosono group has been actively studying iron-chalcogenide and iron-pnictide superconductors. This article reviews some of the fundamental properties of high-temperature superconductors (HTSC) (Blatter et al., 1994; Campbell and Evetts, 1972; Cohen and Jensen, 1997; de Gennes, 1966; Ginsberg, 1989; Canfield and Crabtree, 2003; Biswal and Mohanta, 2021; Nagamatsu, 2001; Bednorz and Müller, 1986).

Overview

The year 1986 was a remarkable year for superconductivity physics. It was followed by a worldwide superconductivity research boom called the gold rush by superconducting physicists, which led to the discovery of seven series of HTSC materials with T_c above 90 K. The newly discovered HTSC have many exotic properties, such as small superconducting coherence length and anisotropic nature of the coherence length; anisotropic large penetration depth; anisotropic large energy gap; superconducting carriers are all holes; the existence of pseudo-energy gap; anisotropic and nonlinear characteristics of the normal state resistivity with temperature; nonlinear characteristics of the Hall coefficient with temperature; the parent is an antiferromagnetic structure, and the structure of the material is typical of the second class of superconductors with superconducting layers interspersed between charge bank phases. The material is a typical type II superconductor with a charge reservoir layer interspersed with superconducting layers.

Since the discovery of HTSC, the BCS theory has been used to explain them, but the T_c of HTSC have far exceeded those predicted by the theory, and the BCS theory has never given results on the phase anisotropy of superconductor parameters.

Superconducting physicists have proposed various models of strongly coupled superconducting matter (Fermi liquid model, non-Fermi liquid model) in an attempt to explain the mechanism of superconductivity in HTSC, but until now, no theory has been able to explain all the properties of HTSC. Although proposed by renowned physicists, the various theories that have been proposed to explain the mechanism of high-temperature superconductivity (HTSC) in materials like cuprates have not yet been universally accepted as definitive explanations for the phenomenon.

Although the BCS theory has obvious flaws, superconducting physicists still use it as a basis for studying and measuring the results of superconductivity studies. The reason is that the carriers of both LTSC and HTSC are Cooper electron pairs, and in this respect, they are the same. This is the basic premise of most superconducting physicists to acquiesce to the correctness of BCS theory. Therefore, the study of superconducting physics is of great theoretical significance and great practical significance (Huebener, 1970; Jin, 1993; Senoussi, 1992; Silver et al., 2002; Tinkham, 1996).

Numerous reviews have been written on the topic of high-temperature superconductors (HTS) materials, covering various aspects such as their properties, theory, and applications. Some of the most well-known and highly cited reviews in the field, which helped establish the field of HTS by presenting the first examples of materials that exhibit superconductivity at temperatures higher than previously thought possible (Anderson, 1987; Bednorz and Müller, 1988; Taillefer, 2010; Armitage and Greene, 2010).

Crystal structures

Crystal structures of most HTSCs can be obtained by stacking perovskite, rock salt and/or fluorite structure along the *c*-axis. As an example, Fig. 1 shows the orthorhombic $YBa_2Cu_3O_{7-\delta}$ unit cell. Other families of HTSCs can be constructed in a similar way. The CuO chains are unique to $YBa_2Cu_3O_{7-\delta}$; however, the most important features of the crystal structures of HTSCs are the two-dimensional copper oxide CuO_2 conduction planes, which are critical for high-temperature superconductivity. Carriers are doped into the CuO_2 conduction planes by transfer of charges resulting from the introduction of foreign ions, interstitial defects, and vacancies in structural blocks between two CuO_2 planes. These blocks are called charge reservoirs. The crystal structure of $YBa_2Cu_3O_{7-\delta}$ consists of stacked layers of CuO_2 planes and CuO chains, with Y and Ba ions located between these layers. The CuO_2 planes are the main sites of superconductivity, as they contain the Cu ions in a square planar arrangement that can form strong electron pairing. The CuO chains, on the other hand, act as charge reservoirs and can affect the doping level of the CuO_2 planes. In the orthorhombic phase of $YBa_2Cu_3O_{7-\delta}$, the CuO_2 planes are perpendicular to the crystallographic c-axis, and

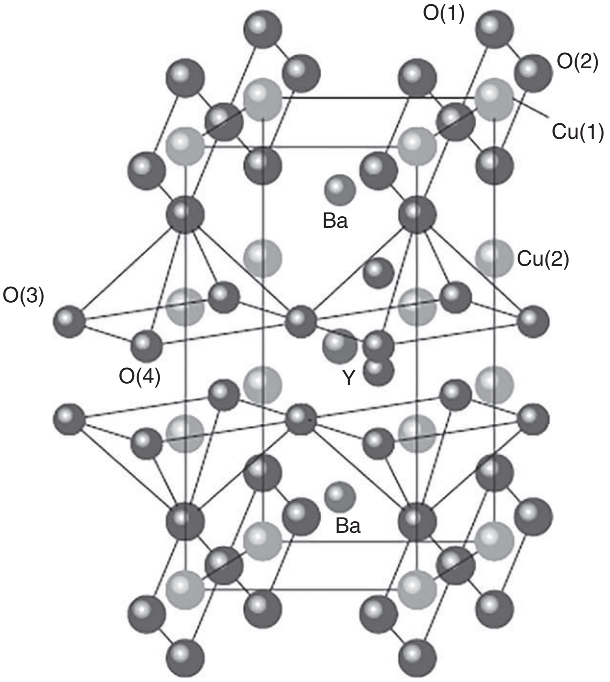

Fig. 1 Crystal structure of orthorhombic $YBa_2Cu_3O_{7-\delta}$. Reproduced from Qin MJ and Dou SX (2005) Superconductors, high Tc. *Encyclopedia of Condensed Matter Physics*, 1st edn, vol. 6, pp. 112–120. Amsterdam: Elsevier.

the unit cell is elongated along the b-axis. The CuO chains run along the a-axis, and each CuO_2 plane is separated from the adjacent planes by one CuO chain. This arrangement of CuO_2 planes and CuO chains is often referred to as a "bilayer" structure, and it is one of the distinguishing features of the high-temperature superconductors.

Phase diagram

Depending on the temperature and the doping level, HTSCs demonstrate a wide variety of behaviors (see the phase diagram for hole-doped HTSCs in Fig. 2). Undoped HTSCs are antiferromagnetic Mott insulators with nearest-neighbor Cu^{2+}–Cu^{2+} antiferromagnetic exchange interaction in the CuO_2 planes. The Néel temperature T_N for the antiferromagnetic-to-paramagnetic transition decreases with increasing doping level. At a certain doping level, the antiferromagnetism vanishes and one enters the pseudogap or underdoped region. The normal-state properties in this region are significantly different from those of a Fermi liquid. Some of the most interesting behaviors of HTSCs are observed in this region. Superconductivity arises upon further doping. The transition temperature T_c first increases with increasing doping level, reaching a maximum T_c at an optimal doping level, then decreases and finally vanishes with further increases in doping (overdoped regime). The non-Fermi liquid region above the superconducting region is well described by the so-called marginal Fermi liquid (MFL) hypothesis.

Superconducting properties

The most unusual fundamental properties of HTSCs, compared to LTSCs, are high-transition temperature, short coherence length, and high anisotropy. The high anisotropy results from the layered structure shown in Fig. 1. A phenomenological description can be achieved by means of the anisotropic Ginzburg–Landau equation. A phenomenological description of high-temperature superconductors (HTSCs) can be achieved by means of the anisotropic Ginzburg-Landau (AGL) equation, which takes into account the anisotropic nature of these materials due to their layered crystal structure (Blatter et al., 1994). The AGL equation is a generalization of the GL equation, which is a widely used phenomenological model for describing the behavior of superconductors near the critical temperature. The AGL equation has been used to explain various superconducting properties of HTSCs, such as their anisotropic magnetic response and their nonlinear transport behavior (Brandt, 1995; Zhu and Ting, 2009).

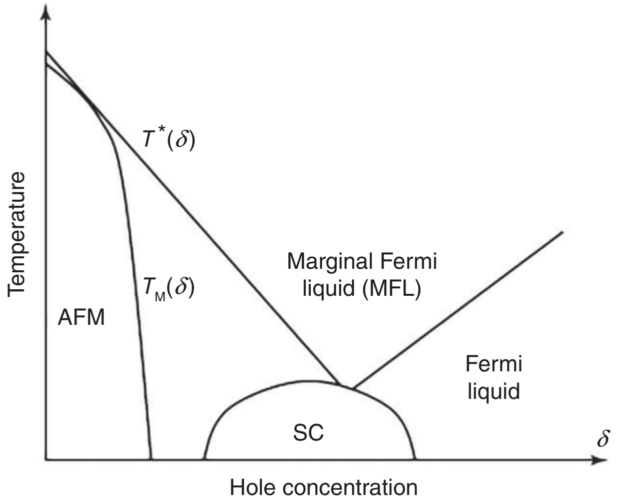

Fig. 2 Generic temperature (*T*) vs. doping level (δ) phase diagrams of cuprates in zero magnetic field. (AFM: antiferromagnetic phase; SC: superconducting phase; T_N, and T^* are the Neel and pseudogap transition temperatures, respectively). Reproduced from Qin MJ and Dou SX (2005) Superconductors, high Tc. *Encyclopedia of Condensed Matter Physics*, 1st edn, vol. 6, pp. 112–120. Amsterdam: Elsevier.

Critical temperature T_c

The critical temperature (i.e., transition temperature from normal state to superconducting state) is one of the most important parameters characterizing superconductors. The optimum T_c values for some of the HTSCs are listed in Table 1. T_c values above the liquid nitrogen temperature (77 K) open the way for many applications. However, higher operating temperatures also introduce large thermal fluctuations in HTSCs. Based on the two principal properties of superconductors (zero-resistance and perfect diamagnetism), the usual methods to obtain T_c are to measure the resistance versus temperature curve R(T) or the AC susceptibility versus temperature $\chi(T)$ curve. Other methods such as measurement of DC magnetization versus temperature $M(T)$ and heat capacity versus temperature $C(T)$ are also applied to measure T_c.

Coherence length ξ

It determines the distance over which the Cooper pairs are correlated. The short coherence lengths observed in HTSCs give rise to several unusual properties. Because the coherence length is much shorter than the penetration length, high-temperature cuprates are all type-II superconductors (see below). The short coherence length makes it very difficult to fabricate homogeneous high-temperature superconducting samples. Also associated with the short coherence length is the weak pinning of flux lines in HTSCs, compared with the pinning in LTSCs. To measure the coherence length, one usually needs to measure the upper critical fields $H_{c2}^{ab}(0)$ and $H_{c2}^{c}(0)$, then the coherence lengths can be derived according to the equations based on the anisotropic Ginzburg–Landau equation

$$\mu_0 H_{c2}^{c}(0) = \Phi_0 / 2\pi\xi_{ab}^2(0)$$
$$\mu_0 H_{c2}^{ab}(0) = \Phi_0 / 2\pi\xi_{ab}(0)\xi_c(0)$$

Here, $H_{c2}^{ab}(0)$ and $H_{c2}^{c}(0)$ indicate the upper critical fields at $T = 0$ K for fields applied parallel to the *ab*-plane and the *c*-axis, respectively. Typical values for the coherence lengths are $\xi_{\mathrm{ab}}(0) = 1.2$–$1.6$ nm, $\xi_c(0) = 0.15$–0.3 nm, for $YBa_2Cu_3O_{7-\delta}$, $\xi_{ab}(0) = 2.7$–3.9 nm, $\xi_c(0) = 0.045$–1.6 nm for $Bi_2Sr_2CaCu_2O_{8+\delta}$, and $\xi_{ab}(0) = 2.1$ nm, $\xi_c(0) = 0.03$ nm for $Tl_2Ba_2CaCu_2O_{8+\delta}$.

Penetration depth λ

It determines the distance that the applied DC magnetic field can penetrate exponentially into the superconductor. There are several methods to measure the penetration depth, such as muon spin resonance (μSR), electron paramagnetic resonance (EPR), and the polarized neutron reflection techniques. The penetration depth can also be derived from measurements of susceptibility or magnetization on samples with dimensions similar to the penetration depth. Typical values for the penetration depths are for

Table 1 Space group, crystal structure, and optimum T_c of selected cuprate superconductors.

Compound	*Space group*	*Structure*	*Optimum T_c*
La_2CuO_4	*I4/mmm*	214-T	40
	$P4_2/ncm$		
	Bmab	214-O	40
	Fmmm		
Nd_2CuO_4	*I4/mmm*	214-T	25
$(Nd,Ce,Sr)_2\ CuO_4$	*P4/mmm*	214-T	
$YBa_2Cu_3O_6$	*P4/mmm*	123-T	0
$YBa_2Cu_3O_7$	*Pmmm*	123-O	90
$YBa_2Cu_4O_8$	*Ammm*	124	80
$Y_2Ba_4Cu_7O_{15}$	*Ammm*	247	40
$(Ba,Nd)_2(Nd,Ce)_2Cu_3O_8$	*I4/mmm*	223	40
$Pr_2Ysr_2Cu_3O_8$	*P4/mmm*	2123	70
	Cmmm		
$Bi_2Sr_2CuO_6$	*Amaa*	Bi-2201	10
	A2/a		
	C2		
$Bi_2Sr_2CaCu_2O_8$	*Fmmm*	Bi-2212	95
	Amaa		
$Bi_2Sr_2Ca_2Cu_3O_{10}$	*I4/mmm*	Bi-2223	110
$Tl_2Ba_2CuO_6$	*I4/mmm*	Tl-2201	
	Fmmm		
$Tl_2Ba_2CaCu_2O_8$	*I4/mmm*	Tl-2212	115
$Tl_2Ba_2Ca_2Cu_3O_{10}$	*I4/mmm*	Tl-2223	125
$Tl_2Ba_2Ca_3Cu_4O_{12}$	*I4/mmm*	Tl-2234	
$TlBa_2CuO_5$	*P4/mmm*	Tl-1201	
$TlBa_2CaCu_2O_7$	*P4/mmm*	Tl-1212	
$TlBa_2Ca_2Cu_3O_8$	*P4/mmm*	Tl-1223	
$TlBa_2Ca_3Cu_4O_{11}$	*P4/mmm*	Tl-1234	

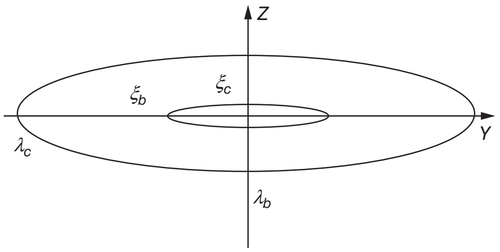

Fig. 3 Schematic diagram of a single vortex when H is parallel to the ab-plane, showing the anisotropic penetration depth and coherence length. Reproduced from Qin MJ and Dou SX (2005) Superconductors, high Tc. *Encyclopedia of Condensed Matter Physics*, 1st edn, vol. 6, pp. 112–120. Amsterdam: Elsevier.

YBCO, the in-plane penetration depth λab(0) is in the range of 130–180 nm, while the out-of-plane penetration depth λc(0) is in the range of 500–800 nm. In contrast, for BSCCO, λab(0) is greater than or equal to 3700 nm, while λc(0) is in the range of 270–300 nm. Fig. 3 shows schematically the length scales (λ and ξ) of a vortex when the applied field is parallel to the *ab*-plane.

Critical fields

High-temperature cuprates are all type-II superconductors with three characteristic critical fields: the lower critical field H_{c1}, the upper critical field H_{c2}, and the thermodynamic critical field H_c (see Fig. 4). $\mu_0H_c^2/2$ is the free-energy difference between the superconducting and normal states. When the applied field is lower than H_{c1}, the superconductor shows perfect diamagnetism (called the Meissner state); when the applied field is larger than H_{c1} but lower than H_{c2}, the applied field penetrates into the superconductor in the form of vortices (the so-called mixed state); when the applied field is larger than H_{c2}, the superconductor is forced into the normal state (see Fig. 4). As the upper critical fields at low temperatures are experimentally inaccessible, one is normally interested in H_{c2} close to T_c; then using the dirty limit equation

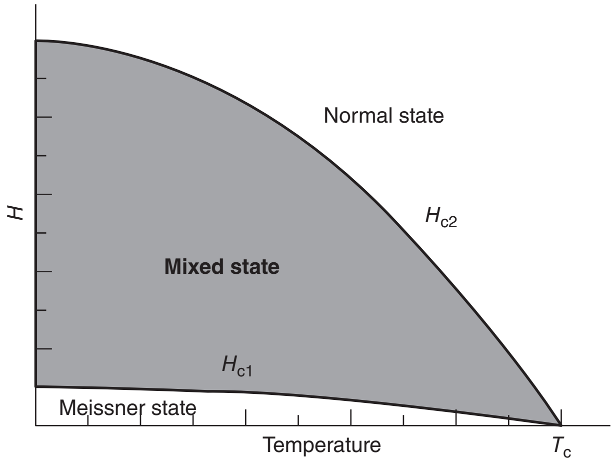

Fig. 4 Phase diagram for a type-II superconductor. Reproduced from Qin MJ and Dou SX (2005) Superconductors, high Tc. *Encyclopedia of Condensed Matter Physics*, 1st edn, vol. 6, pp. 112–120. Amsterdam: Elsevier.

$$H_{c2}(0) = -0.693 \times \left(\frac{dH_{c2}}{dT}\right)_{T_c} T_c$$

to obtain $H_{c2}(0)$. Typical values for $YBa_2Cu_3O_{7-\delta}$ are $\mu_0 H_{c2}^{ab}(0) = 200$ T and $\mu_0 H_{c2}^{c}(0) = 40$ T. The lower critical field H_{c1} can be obtained from the virgin magnetization curves; typical values for $YBa_2Cu_3O_{7-\delta}$ at 4.2 K are $\mu_0 H_{c1}^{c} = 90$ mT, and $\mu_0 H_{c1}^{ab} = 20$ mT.

Pairing symmetry

The pairing symmetry is very important for the discovery of the pairing mechanism. After the discovery of HTSCs, experiments such as those involving the observation of magnetic flux states of a polycrystalline $YBa_2Cu_3O_{7-\delta}$ ring, Andreev reflection, the Shapiro step of a Josephson junction, the high-resolution Bitter pattern technique, and Little–Parks oscillations have been performed to test whether Cooper pairing operates as in conventional superconductors. The results have confirmed electronic pairing in cuprate superconductors. In conventional superconductors, the phonon mediated electron–electron interaction gives rise to spin-singlet pairing with *s*-wave symmetry. However, the pairing symmetry in cuprate superconductors has been a controversial topic. Phase sensitive techniques (superconducting quantum interference device (SQUID)) interferometry, single Josephson junction modulation, thin film magnetometry, etc., combined with the refinement of several other symmetry-sensitive techniques (penetration depth, specific heat, thermal conductivity, angle-resolved photoemission, Raman scattering, nuclear magnetic resonance, nonlinear Meissner effect), have provided evidence in favor of *d*-wave symmetry pairing in cuprate superconductors. The energy gap, quasiparticle state, vortex state, and the surface and interfaces of *d*-wave superconductors are distinctly different from the *s*-wave case.

The pairing symmetry in high-temperature superconductors (HTSC) and low-temperature superconductors (LTSC) can be different. In conventional low-temperature superconductors, such as niobium or lead, the electron pairing is mainly due to electron-phonon interactions and the pairing symmetry is well described by the BCS theory, which predicts a s-wave pairing symmetry. This means that the electron pairs have no angular momentum and the energy gap in the electronic density of states is isotropic.

In contrast, the electron pairing mechanism in high-temperature superconductors is still a matter of debate, and several unconventional pairing symmetries have been proposed. Some high-temperature superconductors, such as cuprate superconductors, have a d-wave pairing symmetry, where the energy gap in the electronic density of states has nodes along the directions of the crystal lattice. Other high-temperature superconductors, such as iron-based superconductors, have different types of pairing symmetry, such as s±, s++, or dxy-wave symmetry.

The difference in the pairing symmetry between HTSC and LTSC arises due to the different nature of the electron pairing mechanism. In HTSC, the electron pairing is believed to arise from the interplay of different competing orders, such as antiferromagnetism and superconductivity, and the symmetry of the superconducting order parameter is strongly influenced by these competing orders. In LTSC, on the other hand, the electron-phonon interaction is the dominant pairing mechanism, and the symmetry of the superconducting order parameter is determined by the properties of the phonon modes in the crystal lattice. Detailed discussions can be found in the references (Tsuei and Kirtley, 2000; Scalapino, 2012; Norman et al., 2011; Lee et al., 2006; Mazin et al., 2008).

Energy gap

The energy gap indicates the minimum energy required to excite a quasiparticle from a phase-coherent Cooper-pair condensate. The BCS theory predicts a universal ratio between the energy gap and the thermal energy $2\Delta(0)/k_BT_c = 3.53$, here $\Delta(0)$ is the energy gap at $T = 0$ K. For HTSCs, the energy gap can be determined from experiments such as single-electron tunneling, Andreev reflection, Raman scattering, photoemission spectra. Typical values for $YBa_2Cu_3O_{7-\delta}$ are $2\Delta_{ab}(0)/k_BT_c = 6\text{–}8$, $2\Delta_c(0)/k_BT_c = 3\text{–}3.5$; and for $Bi_2Sr_2CaCu_2O_{8+\delta}$ are $2\Delta_{ab}(0)/k_BT_c = 8\text{–}11$, $2\Delta_c(0)/k_BT_c = 5\text{–}7$. For conventional superconductors, the Cooper pairs have an isotropic *s*-wave symmetry, which means that the energy gap is 2Δ everywhere in *k*-space (see Fig. 5). However, for a *d*-wave symmetry superconductor, in momentum space when $k_x = \pm k_y$, the energy gap is zero, which implies that it would change sign at $k_x = \pm k_y$ (see Fig. 5). Both properties will have important implications from both fundamental and applied points of view.

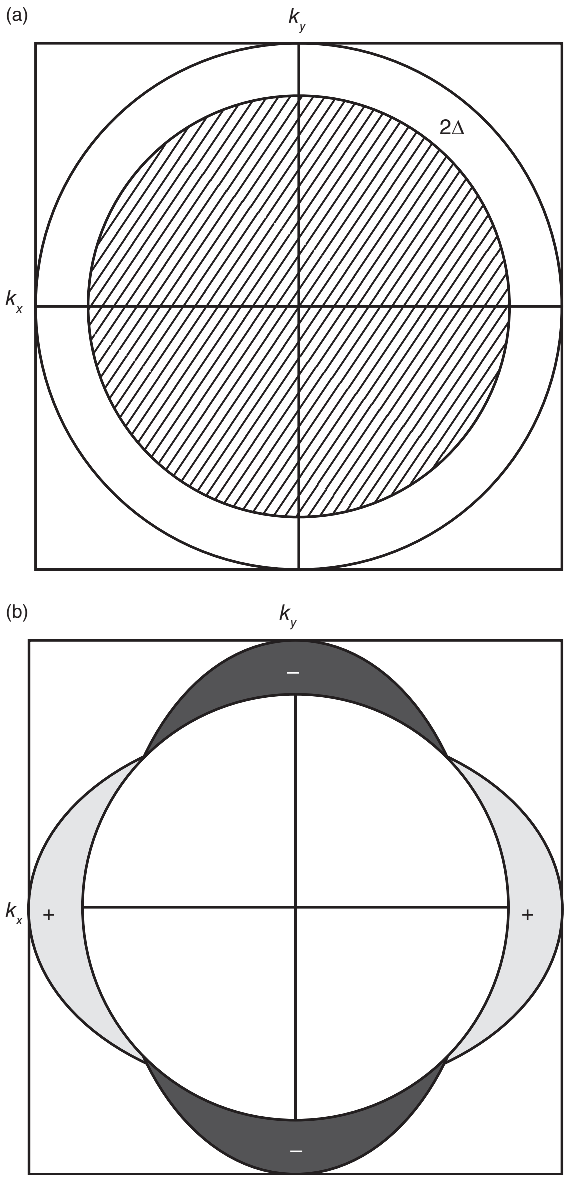

Fig. 5 The energy gap for s-wave superconductors (upper panel) and *d*-wave superconductors (lower panel). The *s*-wave symmetry has an isotropic value of 2Δ, while for a d-wave symmetry the gap vanishes and changes sign at $k_x = k_y$. Reproduced from Qin MJ and Dou SX (2005) Superconductors, high Tc. *Encyclopedia of Condensed Matter Physics*, 1st edn, vol. 6, pp. 112–120. Amsterdam: Elsevier.

Type-II superconductivity

HTSCs have very short coherence lengths ξ and large penetration depths, so the Ginzburg–Landau parameter $\kappa = \lambda/\xi \gg 1$, and HTSCs are typical type-II superconductors. In this section, some of the properties in the mixed state are discussed (Ginsberg, 1989).

In particular, The Lawrence-Doniach model is an important theoretical tool for studying the behavior of type-II superconductors, including 2D superconductors, in the presence of a magnetic field (Lawrence and Doniach, 1971).

The LD model was first proposed by Lawrence and Doniach in 1971 and has since been used extensively to study the properties of type-II superconductors, including high-temperature superconductors (HTS) and 2D superconductors. The model takes into account the anisotropy of the superconductor, as well as the effects of the magnetic field on the electronic states and the order parameter of the superconductor.

In the LD model, the superconductor is described as a stack of many 2D layers, with the magnetic field applied perpendicular to the layers. Within each layer, the superconducting order parameter is assumed to vary smoothly along the direction parallel to the layers, while it is assumed to be uniform along the perpendicular direction. The LD model also takes into account the anisotropy of the superconductor, which arises from the fact that the coherence length (the characteristic length scale over which the superconducting order parameter varies) is different along different crystallographic directions.

The LD model can be used to calculate the irreversibility line, which is the boundary between the reversible and irreversible regimes of the superconductor in the presence of a magnetic field. Below the irreversibility line, the superconductor can expel the magnetic field and maintain its superconducting state. Above the irreversibility line, the superconductor is no longer able to expel the magnetic field and enters a mixed state, where vortices start to penetrate the superconducting layer.

Using the LD model, it is possible to calculate the distribution of vortices in the superconductor as a function of the applied magnetic field and the temperature. The model can also be used to calculate the critical current, which is the maximum current that can flow without destroying the superconducting state. In addition, the LD model can be used to study the effects of defects and impurities on the behavior of the superconductor, including the pinning of vortices and the enhancement of the critical current (Brandt, 1995; Campbell and Evetts, 1972; Kim and Beasley, 1975; Dew-Hughes, 1981; Blatter et al., 1994).

Vortex structure

Due to the high anisotropy of cuprate superconductors, the vortex structures are different from those in conventional superconductors. When the applied field is along the *ab*-plane, the screening current flows both along the *ab*-plane and along the *c*-axis. There exist insulating layers alternating with conduction layers along the *c*-axis, the current is the Josephson current in the insulating layers (see Fig. 6). When the applied field is parallel to the c-axis or at an angle to the *c*-axis, the vortices can be regarded as pancake vortices stacked along the *c*-axis (see Fig. 7). Each pancake vortex is located in one of the conduction planes. The pancake vortices in the neighboring layers are coupled by means of a Josephson current, which forms a Josephson vortex. The forces between pancake vortices in the conduction plane are repulsive, while the forces between pancake vortices in the neighboring layers are attractive. Depending on the temperature and the magnetic field, the vortex system can go through a 3D to 2D transition. The magnetic properties of 2D superconductors can be described by the Lawrence–Doniach (LD) model.

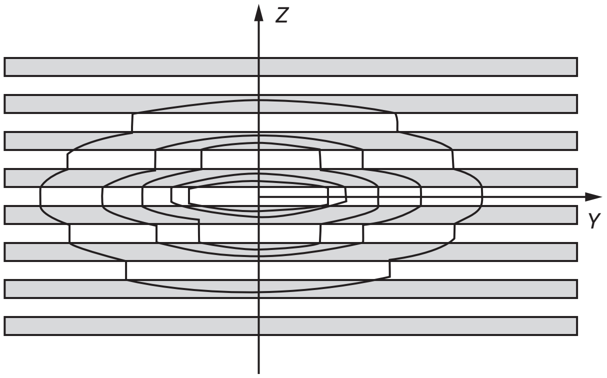

Fig. 6 Schematic diagram of a single vortex when the applied magnetic field is parallel to the *a*-axis (*x*-direction). Gray areas indicate the superconducting layers. Reproduced from Qin MJ and Dou SX (2005) Superconductors, high Tc. *Encyclopedia of Condensed Matter Physics*, 1st edn, vol. 6, pp. 112–120. Amsterdam: Elsevier.

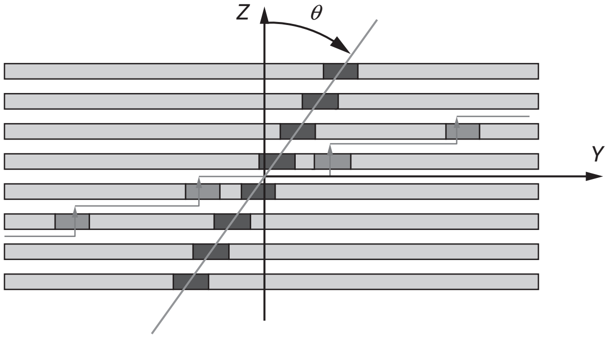

Fig. 7 Schematic diagram for pancake vortices when the applied magnetic field is at an angle to the *c*-axis (*z*-direction). Gray areas indicate the superconducting layers. Reproduced from Qin MJ and Dou SX (2005) Superconductors, high Tc. *Encyclopedia of Condensed Matter Physics*, 1st edn, vol. 6, pp. 112–120. Amsterdam: Elsevier.

Irreversibility field

After the discovery of cuprate superconductors, it was soon reported that zero-field-cooled (ZFC) and field-cooled (FC) magnetization of La–Ba–Cu–O versus temperature at a fixed applied magnetic field can be separated into two regions. Below T_{irr}, ZFC and FC magnetization are different and irreversible, above T_{irr}, ZFC and FC magnetization are the same and reversible. T_{irr} is dependent on the magnetic field. $T_{\mathrm{irr}}(H)$ or $H_{\mathrm{irr}}(T)$ is called the irreversibility line. $H_{\mathrm{irr}}(T)$ is lower than H_{c2} but larger than H_{c1} and separates the mixed state into two regions, a vortex liquid above $H_{\mathrm{irr}}(T)$ and a vortex solid below $H_{\mathrm{irr}}(T)$. The irreversibility line can also be obtained by hysteresis loop measurements and I–V characteristics measurements. Generally, the irreversibility line follows $1 - T_{\mathrm{irr}}/T_{c0} = CH_{\mathrm{irr}}^{q}$, with T_{c0} the zero-field transition temperature, and $½ < q < 3/4$, depending on different materials. The vortex system depends on three energy scales: the pinning potential Epin, the thermal energy Eth and the vortex–vortex interaction energy Evv. When the Eth ≈ Epin, the system reaches the reversible region (Ullmaier, 1975).

Critical currents and flux pinning

Due to short coherence lengths and high anisotropy in cuprate superconductors, critical currents are much more complicated than in conventional superconductors. For an anisotropic superconductor, three critical currents are defined depending on the direction of the applied magnetic field (see Fig. 8). Critical currents result from the interaction between vortices and crystal defects (pinning effect). Twin boundaries and screw dislocations in single crystal $YBa_2Cu_3O_{7-\delta}$ and Y_2BaCuO_5 phase, as well as stacking faults and dislocations in melt-textured-growth (MTG) $YBa_2Cu_3O_{7-\delta}$, have all been reported to act as pinning centers. Heavy ion and particle irradiation have also been used to enhance the critical current density in cuprate superconductors. Due to the short coherence length, point defects such as vacancies and substitution atoms may play an important role in cuprate superconductors (Huebener, 1970).

Critical current can be directly obtained from transport I–V measurements. From hysteresis loop measurements, the critical state model is used to derive the current density from the measured hysteresis loop,

$$J_{ab,c} = \frac{20\Delta M}{a(1 - a/3b)} \quad \left(H\middle\|c\right)$$

Because a larger electric field criterion is used in transport measurement, it usually provides a larger critical current density than magnetic measurements. What it means is that when critical current density is measured using transport measurements (such as resistivity measurements), a larger electric field criterion is typically used compared to when it is measured using magnetic measurements. This is because the electric field criterion is related to the resistive behavior of the material, whereas the magnetic measurements are related to the pinning of vortices.

The use of a larger electric field criterion typically results in a higher critical current density because it allows for higher current densities to flow without causing the material to become resistive. Magnetic measurements, on the other hand, typically use lower field strengths, resulting in lower critical current densities because the magnetic field has a stronger effect on vortex pinning.

In polycrystalline samples, the current density across grains, called the intergrain critical current density, is very small, and shows the properties of a Josephson current. This is due to large angle grain boundaries in polycrystalline samples, and therefore these grain boundaries are called weak links. In order to have high critical current density, weak links should be avoided, by using, for example, melt-textured-growth (MTG) for $YBa_2Cu_3O_{7-\delta}$ bulk materials. Intragrain critical current densities up to 10^6 A cm^{-2} at 77 K and 0 T has been reported for $YBa_2Cu_3O_{7-\delta}$ thin films.

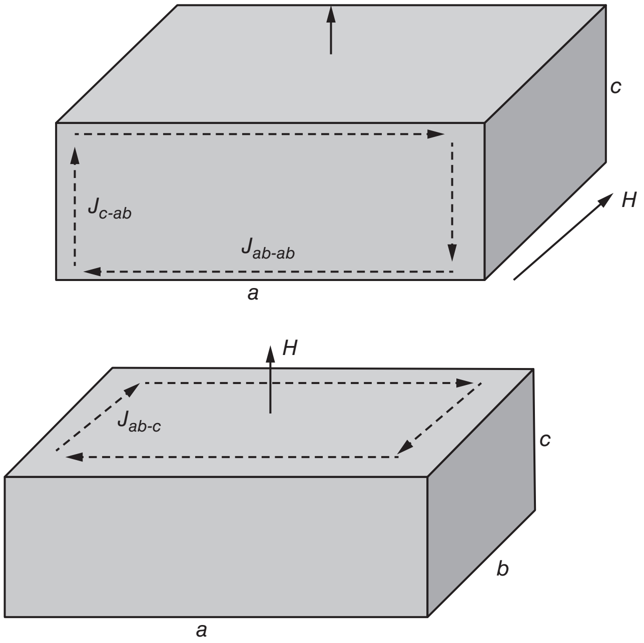

Fig. 8 Schematic diagram showing the anisotropic critical current density in cuprate superconductors, when $H \| ab$ (upper panel) and $H \| c$ (lower panel). Reproduced from Qin MJ and Dou SX (2005) Superconductors, high Tc. *Encyclopedia of Condensed Matter Physics*, 1st edn, vol. 6, pp. 112–120. Amsterdam: Elsevier.

Flux creep

In conventional superconductors, the current density was observed to decrease logarithmically with time at fixed temperature and field, an effect called magnetic relaxation. Magnetic relaxation specifically refers to the behavior of the current density in a superconductor over time under the influence of a magnetic field. In conventional superconductors, the presence of magnetic vortices can disrupt the flow of current through the material, leading to a decrease in current density over time as vortices become thermally activated and move through the material. This logarithmic decrease in current density with time is known as magnetic relaxation (Brandt, 1995). This effect was explained by vortices thermally activated out of the pinning potential (flux creep) with the hopping frequency.

$$v = v_0 \exp\left[\frac{-U(j)}{k_B T}\right]$$

where v_0 is the attempt frequency and $U(j)$ the effective activation energy depending linearly on the current density,

$$U(j) = U_0\left(\frac{1 - j}{j_{c0}}\right)$$

The current density decreases logarithmically with time as

$$j(t) = j_{c0}\left[1 - \left(\frac{k_B T}{U_0}\right)\ln\left(\frac{t}{t_0}\right)\right]$$

In cuprate superconductors, strong and nonlogarithmic relaxation has been observed (see Fig. 9). Due to high-operating temperatures and reduced pinning compared to conventional superconductors, relaxation in HTSCs is very large. Nonlogarithmic relaxation in HTSCs results from a nonlinear $U(j)$ relationship. A logarithmic $U(j)$ relationship has been proposed to account for the experimental results:

$$U(j) = U_0 \log\left(\frac{j_c}{j}\right)$$

On the other hand, according to the vortex glass theory, the $U(j)$ relationship is

$$U(j) = \left(\frac{U_0}{\mu}\right)\left[\left(\frac{j_c}{j}\right)^{\mu} - 1\right]$$

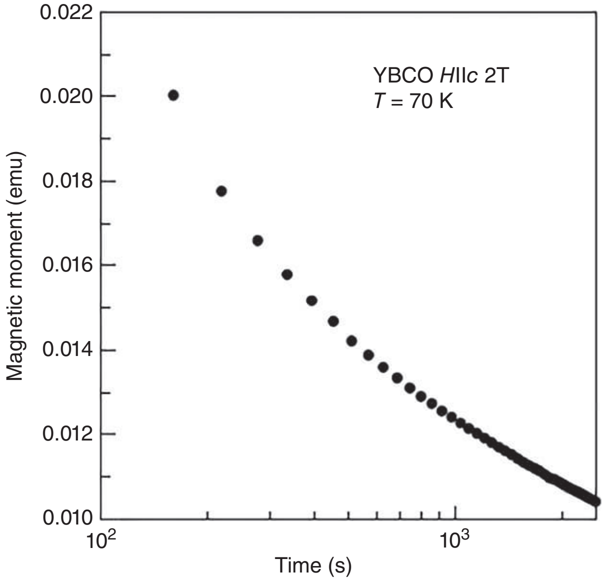

Fig. 9 Magnetic relaxation of a melt-texture-growth (MTG) YBCO sample at $H \| c = 2$ T and 70 K, showing nonlogarithmic relaxation. Reproduced from Qin MJ and Dou SX (2005) Superconductors, high Tc. *Encyclopedia of Condensed Matter Physics*, 1st edn, vol. 6, pp. 112–120. Amsterdam: Elsevier.

Here, the exponent μ depends on the dimensionality of the vortex system.

Magnetic relaxation measurements have been extensively performed on HTSCs to study the flux dynamics. The purpose is to determine the effective pinning potential U(j) and compare it with theoretical predictions. Several methods such as the Maley method, the generalized inversion scheme, and dynamic relaxation and the AC susceptibility technique have been developed for this purpose. However, because too many parameters are used in theoretical predictions, it is impossible to unambiguously determine the effective activation energy from experiments. Most results in this area are not conclusive (Clem and Coffey, 1990; Matsuda and Tsuneto, 1989; Yeshurun et al., 1996; Kes et al., 1991).

Melting of the vortex lattice

Thermal fluctuations in HTSCs are much more important than in conventional superconductors. According to the Lindemann melting criterion, as the displacement away from the ideal configuration by thermal fluctuation reaches 10–30% of the average flux-line separation, melting transition from vortex solid-to-vortex liquid (shear modulus equal to zero) might take place. The curve $T_m(H)$ in the H–T phase diagram at which the flux lattice melts is called the melting line. It has been suggested that in clean samples with negligible pinning the vortex solid-to-vortex liquid transition is expected to be of the first order, while static disorders drive the transition to the second order as in the vortex glass theory. Evidence for a first-order melting transition comes from a jump in the reversible magnetization, changes in latent heat, a frequency-independent peak in the AC susceptibility and a sharp, hysteretic, resistive transition. However, the effect of static disorders and their dimensionality on the order of transition is unclear as yet (Wördenweber, 1999).

Mixed-state phase diagram

For a type-II superconductor, by varying the external field H, at the lower critical field H_{c1}, a phase transition from the Meissner phase to the Abrikosov phase (or mixed phase) takes place. The basic unit of the mixed state is the vortex, which contains a flux quantum given by $\Phi_0 = ch/2e = 2.07 \times 10^{-7}$G cm^2, penetrating the system and forming a perfect triangular crystal (the Abrikosov lattice). At the upper critical field H_{c2}, the system is forced to undergo a second phase transition to the normal state. The simple phase diagram shown in Fig. 4 neglects disorders and thermal fluctuations, which is very serious in cuprate superconductors due to higher operating temperatures. When thermal fluctuations are taken into account, the first modification applied to the phase diagram ought to be the inclusion of the “water-like” melting phenomenon discussed above. In clean systems, the melting curve stretches from H_{c1} up to H_{c2} (see Fig. 10). In case of disordered systems, the melting line terminates at much lower fields (characterized by the first-order transition). In practice, one is often far from the critical fields, leading to the unified phase diagram in Fig. 11. Then, one has to discriminate between a sharp first-order phase transition at lower fields separating Bragg glass and vortex liquid and a more continuous second-order-like transition at higher fields separating vortex glass and vortex liquid.

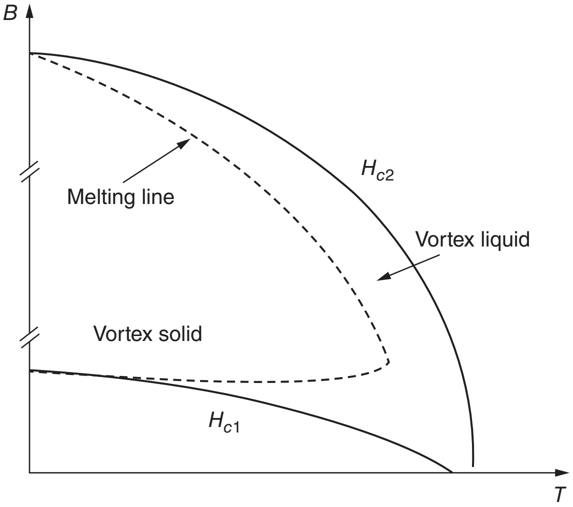

Fig. 10 Schematic vortex phase diagram for high-temperature superconductors without disorder. Reproduced from Qin MJ and Dou SX (2005) Superconductors, high Tc. *Encyclopedia of Condensed Matter Physics*, 1st edn, vol. 6, pp. 112–120. Amsterdam: Elsevier.

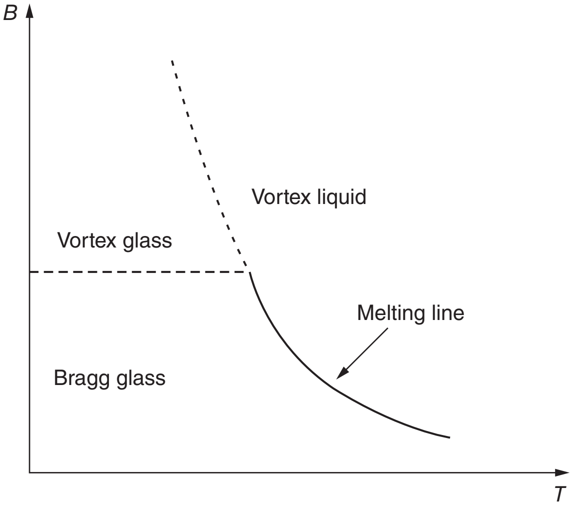

Fig. 11 Schematic vortex phase diagram for high-temperature superconductors with disorder. Reproduced from Qin MJ and Dou SX (2005) Superconductors, high Tc. *Encyclopedia of Condensed Matter Physics*, 1st edn, vol. 6, pp. 112–120. Amsterdam: Elsevier.

Normal-state properties

Properties in the normal state of cuprate superconductors have been found to be very useful for the understanding of the mechanism of high-temperature superconductivity. These properties include resistivity, Hall coefficient, thermopower, magnetism, thermal conductivity, and optical properties. Although superconducting properties of cuprate superconductors are quite similar to those of conventional superconductors, the normal-state properties are unique. As an example, some general features for normal-state resistivity are listed: (1) the resistivity is anisotropic with the *c*-axis resistivity ρ_c two orders of magnitude larger than the in-plane resistivity ρ_{ab}, (2) ρ_{ab} shows metallic behavior, but ρ_c mostly shows semiconductor behavior. (3) ρ_{ab} is close to linear in *T*, which is the most striking normal-state property of cuprate superconductors. Theoretical explanations for these behaviors and other unique behaviors observed in optical and thermal properties remain controversial.

Experimental methods

Here are some examples of experimental methods and studies that are commonly used to determine scaling lengths and energies in HTSCs, along with corresponding references: Angle-resolved photoemission spectroscopy (ARPES): This technique is used to measure the electronic structure of a material, including the superconducting gap, which can provide information about the coherence length and energy scale of the superconducting state (Damascelli et al., 2003; Norman, 1998). Scanning tunneling microscopy and spectroscopy (STM/STS): These techniques can be used to directly probe the local density of states and the superconducting gap in a material, which can provide information about the coherence length and energy scale of the superconducting state (Fisher et al., 2011; McElroy et al., 2005). Microwave surface impedance measurements: These measurements can be used to determine the superfluid density of a material, which can provide information about the penetration depth and energy scale of the superconducting state (Prozorov et al., 1998). Magnetic field dependence of critical current density (J_c): This measurement can be used to determine the magnetic field penetration depth and coherence length of a material, which are related to the energy scale and correlation length of the superconducting state (Brandt, 1995).

Magnesium diboride (MgB_2)

MgB2 has superior properties such as the thermodynamic and transport properties, the isotope effect, band structures, promising critical current density, the ability of doping effect and pressure effect. However, after the discovery of its superconducting properties in 2001 by Akimitsu's group, it has been a promising compound in superconductivity applications. MgB_2 is competitive among high-temperature superconductors (HTS) because it has fascinating advantages such as simple crystal structure, low material cost and small anisotropy. As it is, MgB_2 has opened our eyes to previously unrealized possibilities for electron–phonon superconductivity. Higher transition temperatures and other compounds now occupy our dreams and novel basic phenomena such as two-gap superconductivity drive theory and experiments in new directions. Unlike the still controversial cuprates, the physical picture and quantitative theoretical description for MgB_2 are now available. The behavior near Tc is determined by the large 2D gap, which produces a step as expected for a conventional one-gap superconductor (Canfield and Crabtree, 2003).

Iron-based superconductor

In recent years, Fe-based superconductors have found a lot of unanticipated surprises. These types of superconductors consist of different classes of iron materials, like pnictides, chalcogenides, intermetallics and oxides. Although each group has its own features, some most important properties of the materials are quite similar. In the study of superconductors of iron-chalcogenides and iron-pnictides, Hideo Hosono group is active since 2008 (Hosono et al., 2015). Distinctly HTSC copper oxide superconductors, from magnetic properties, structures and superconducting behavior, the *Tc* of Fe-based superconductors is as much as 55 K, the electron-phonon interaction is quite too weak. Fe-based superconductors can be spread into a number of types of substances consisting of 3 households of iron-based superconductors such as '1111' system RFeAsO (R: the rare earth element) consisting of LaFeAsO, SmFeAsO, PrFeAsO etc. '111' type LiFeAs, NaFeAs & LiFeP etc., '122' type $BaFe_2As_2SrFe_2As_2$ or $LaFe_2As_2$ etc. The iron-based superconductors give a wonderful likelihood of understanding unconventional superconductivity which could be useful to explain the mechanism of High-T_c superconductivity, and also the implementation of iron-based superconductors, especially in tapes and wires that can be fabricated for industry applications (Biswal and Mohanta, 2021).

Thin films

$YBa_2Cu_3O_{7-x}$(YBCO) thin films are the most studied high-temperature superconducting thin films. Critical current densities up to 10^6 A cm^{-2} have been achieved in high-quality YBCO thin films, making them very attractive for applications. There are, in general, two main methods for fabricating high-temperature superconducting thin films: in situ or ex situ film growth. In situ films are oxygen-treated before they are removed from the growth chamber, and therefore are superconducting after growth. Ex situ thin films must be annealed in an oxygen-rich environment after growth to be superconducting. Nearly every growth technique has been tried on high-temperature superconducting thin films, including evaporation, pulsed laser deposition (PLD), metal organic chemical vapor deposition (MOCVD), and on-axis and off-axis sputtering. Every technique has its merits and drawbacks, details of which can be found in the references. The search for substrate materials is an active research area. High-quality YBCO thin films have been deposited on $LaAlO_3$, $SrTiO_3$, MgO, YSZ, etc. BiSrCaCuO and TlBaCaCuO thin films have also been extensively studied. However, it is very difficult to obtain single-phase BiSrCaCuO thin films, while Tl is very toxic, creating problems in fabricating TlBaCaCuO thin films. The main application of superconducting thin films is in the area of superconducting electronics.

Bulk materials

Many large-scale applications such as flywheel energy-storage systems need HTSCs in bulk form. Sintered YBCO polycrystalline samples used to have very low critical current densities (100–1000 A cm^{-2}), which was attributed to weak links at grain boundaries, such as structural disorder at grain boundaries, chemical or structural variations at grain boundaries and non-superconducting materials along grain boundaries, as well as microcracking. Texture processing has been developed as a means to avoid or minimize the effects of weak links in polycrystalline YBCO. The initial success with bulks was due to the melt-textured-growth (MTG) process, which enhanced the critical current density two to three orders of magnitude over that of sintered materials. Several modified MTG methods were developed later in order to further enhance the critical current density. These include the quench-and-melt-growth (QMG) process, the melt-powder-melt-growth (MPMG) process, the power-melting process (PMP), the floating-zone-melt (FZM) process, the platinum-doped melt-growth (PDMG) process, and the horizontal Bridgman method.

Tapes and wires

The majority of the work on superconducting tapes and wires focuses on the $Bi_2Sr_2Ca_2Cu_3O_{10-x}$(BSCCO) system. The reasons are that the BSCCO system has a higher critical current at high magnetic fields, and that the BSCCO system does not suffer from the weak link problems of YBCO. The fabrication of BSCCO tapes and wires is usually carried out by means of the so-called oxide power-in-tube (OPIT) method. The powder is packed in a tube (typically Ag), then the Ag tube is drawn to a small diameter and rolled into a flat tape. The tape is then annealed, re-rolled and re-annealed again to obtain the best superconducting properties. Critical current densities up to 7000 A cm^{-2} for a 650 m long and 19-filament-rolled tape have been achieved. Tapes and wires are widely used in applications such as motors and generators, magnet, transformers, and transmission lines.

Coated conductors

Coated conductors are YBCO thin films deposited onto polycrystalline substrates. The films are biaxially textured, thus overcoming the phenomenon of weak links. This has been achieved by preparing a biaxially textured buffer layer, upon which the YBCO film is subsequently grown epitaxially. The two most advanced techniques are the ion beam-assisted deposition (IBAD) process, and the rolling-assisted biaxially textured substrate (RABiTS) process. In addition, inclined substrate deposition (ISD) has also emerged as a promising method for the fabrication of YBCO conductors. The coated conductors potentially have a performance superior to the first generation bismuth-based HTS compounds (BSCCO), such as high current carrying capacities, strong mechanical properties, and extraordinary magnetic field tolerances. Recently, it has been demonstrated that current densities up to 10^6 A cm^{-2} have been achieved in conductors prepared by coating thick films of YBCO onto flexible metallic substrates. One of the biggest hurdles to widespread application of YBCO-coated conductor tape is developing a manufacturing process that will produce it in long lengths and at prices competitive to copper for applications such as motors, generators, transmission cables, and other power systems.

Conclusion

In Summary, Superconductivity occurs when charge carriers form Cooper pairs and enter a single quantum state at a temperature below a threshold. In conventional superconductors, phonons are responsible for pairing, while in HTSCs, the mechanism is controversial. Several theories have been proposed, but no comprehensive theory accounts for all experimental observations. HTS materials have unique properties, such as the ability to carry large amounts of electrical current with zero resistance, operate at higher temperatures, and possess unique mechanical and thermal properties that offer potential for various applications. Continued research and development in this field will likely lead to further discoveries and new applications of these materials. The production techniques, performance, and low price are crucial in realizing practical and cheap cryogenic systems. Nanomaterials and superconducting physics are both branches of condensed matter physics, and a breakthrough in either discipline will have a chain reaction leading to rapid development.

Certainly. Here are some examples of novel and unconventional functionalities that HTS materials have brought compared to LTS materials:

1. HTS materials have very high critical current densities, allowing them to operate at much higher magnetic fields than LTS materials. This makes them attractive for applications such as magnets for MRI machines, fusion reactors, and particle accelerators.
2. HTS materials can be fabricated as thin films and coatings using techniques such as pulsed laser deposition, sputtering, and metal-organic deposition. This allows for the development of high-performance, flexible, and lightweight superconducting materials for various technological applications.
3. The unique properties of HTS materials have opened up new possibilities for developing novel superconducting devices and systems, such as superconducting microwave filters and resonators, superconducting power transmission lines, and superconducting fault current limiters.
4. HTS materials exhibit improved stability compared to LTS materials, particularly at high magnetic fields and temperatures. This makes them more suitable for practical applications where stability is critical.
5. There have been recent reports of HTS materials exhibiting superconductivity at or near room temperature, which could revolutionize the field of superconductivity and lead to a wide range of new applications.

Overall, HTS materials have brought a range of novel and unconventional functionalities that have expanded the field of superconductivity and opened up new possibilities for technological applications. However, they also present unique challenges and require continued research and development to fully realize their potential.

References

Anderson PW (1987) High-temperature superconductivity: An overview. *Science* 235(4793): 1196–1198.

Armitage NP and Greene RL (2010) High-temperature superconductivity in cuprates: The non-BCS paradigm and its implications. *Reviews of Modern Physics* 82(1): 242–268.

Bednorz JG and Müller KA (1986) Possible high Tc superconductivity in the Ba-La-Cu-O system. *Zeitschrift fur Physik B: Condensed Matter* 64(2): 189–193.

Bednorz JG and Müller KA (1988) Physics of high-temperature superconductors. *Nature* 332(6162): 283–287.

Biswal G and Mohanta KL (2021) A recent review on iron-based superconductor. *Materials Today: Proceedings* 35: 207–215.

Blatter G, Feigel'Man MV, Geshkenbein VB, Larkin AI, and Vinokur VM (1994) Vortices in high-temperature superconductors. *Reviews of Modern Physics* 66: 1125.

Brandt EH (1995) The flux-line lattice in superconductors. *Reports on Progress in Physics* 58(11): 1465–1594.

Campbell AM and Evetts JE (1972) Critical currents in superconductors. *Advances in Physics* 21(2): 199–428.

Canfield PC and Crabtree GW (2003) Magnesium diboride: Better late than never. *Physics Today* 56(3): 34.

Clem JR and Coffey WA (1990) Thermally activated flux flow in superconductors. *Physical Review B* 42: 6209–6223.

Cohen LF and Jensen HJ (1997) Open questions in the magnetic behavior of high-temperature superconductors. *Reports of Progress in Physics* 60: 1581.

Damascelli A, Hussain Z, and Shen ZX (2003) Angle-resolved photoemission studies of the cuprate superconductors. *Reviews of Modern Physics* 75(2): 473.

de Gennes PG (1966) *Superconductivity of Metals and Alloys*. New York: Benjamin.

Dew-Hughes D (1981) Flux pinning and its measurement. *Advances in Physics* 30(4): 111–159.

Fisher O, et al. (2011) Local pairing and pseudogap in the heavily overdoped superconductor $Bi_2Sr_2CaCu_2O_8+ \delta$. *Nature Physics* 7(8): 611–616.

Ginsberg DM (ed.) (1989) *Physical Properties of High Temperature Superconductors I, II, III, IV*. Singapore: World Scientific.

Huebener RP (1970) *Magnetic Flux Structures in Superconductors*. Berlin: Springer.

Hosono H, Hayashi K, Shimakawa M, and Takagi H (2015) Iron-based superconductors: An overview. *Materials Research Society Bulletin* 40(8): 646–656.

Jin SH (ed.) (1993) *Processing and Properties of High Tc Superconductors*. Singapore: World Scientific.

Kes PH, Tsuei CC, Scharnberg K, Gupta A, Kapitulnik A, Li TW, Schenstrom A, Klemm RA, and Clark WG (1991) Flux creep and magnetic relaxation in high-temperature superconductors. *Physical Review Letters* 67: 1911–1914.

Kim YB and Beasley MR (1975) Critical current measurements in thin-film superconductors. *Physical Review B* 12(9): 4158–4163.

Lawrence WE and Doniach S (1971) Nonlinear conductivity and fluctuation effects in superconductors. *Proceedings of the Royal Society of London. Series A: Mathematical and Physical Sciences* 324(1559): 301–312.

Lee PA, Nagaosa N, and Wen XG (2006) Doping a Mott insulator: Physics of high-temperature superconductivity. *Reviews of Modern Physics* 78(1): 17–85.

Mazin II, Singh DJ, Johannes MD, and Du MH (2008) Unconventional superconductivity with a sign reversal in the order parameter of LaFeAsO1-xFx. *Physical Review Letters* 101(5): 057003.

Matsuda T and Tsuneto T (1989) Flux creep in type-II superconductors. *Journal of the Physical Society of Japan* 58: 3656–3666.

McElroy K, et al. (2005) Spin-density wave suppression of superconductivity in stripe-ordered La1.875$Ba_{0.125}CuO_4$: Scanning tunneling microscopy and spectroscopy studies. *Physical Review Letters* 94(19): 197005.

Nagamatsu J (2001) Superconductivity at 39 K in magnesium diboride. *Nature* 410(6824): 63–64.

Norman MR, Pines D, and Kallin C (2011) The unconventional superconductivity in the heavy fermion compounds. *Advances in Physics* 60(5): 451–563.

Norman MR (1998) Materials science: The gap seen up close. *Nature* 392(6672): 125–126.

Prozorov R, et al. (1998) Muon spin rotation and microwave surface impedance measurements of the superconducting energy gap in $YBa_2Cu_3O_{7-\delta}$. *Physical Review B* 58(5): R292.

Scalapino DJ (2012) A common thread: The pairing interaction for unconventional superconductors. *Reviews of Modern Physics* 84(4): 1383–1417.

Senoussi S (1992) Review of the critical current densities and magnetic irreversibilities in high Tc superconductors. *Journal of Physics (III), France* 2: 1102.

Silver T, Pan AV, Ionescu M, Qin MJ, and Dou SX (2002) Developments in high temperature superconductivity. Annual Report Progress. *Chemistry* 98(C): 323.

Taillefer L (2010) The pseudogap in high-temperature superconductors: An experimental survey. *Annual Review of Condensed Matter Physics* 1: 51–70.

Tinkham M (1996) *Introduction to Superconductivity*, 2nd edn. New York: McGraw Hill.

Tsuei CC and Kirtley JR (2000) Pairing symmetry in cuprate superconductors. *Reviews of Modern Physics* 72: 969.

Ullmaier H (1975) *Irreversible Properties of Type II Superconductors*. Berlin: Springer.

Wördenweber R (1999) Mechanism of vortex motion in high temperature superconductors. *Reports of Progress in Physics* 62: 187.

Yeshurun Y, Malozemoff AP, and Shaulov A (1996) Magnetic flux structures in superconductors with strong pinning. *Reviews of Modern Physics* 68: 911–941.

Zhu JX and Ting CS (2009) Nonlinear electronic transport in high-temperature superconductors. *Reports on Progress in Physics* 72(2): 026501.

Phase diagrams of high-temperature superconductors

Shin-ichi Uchida, Department of Physics, University of Tokyo, Tokyo, Japan; Institute of Advanced Industrial Science & Technology, Tsukuba, Japan

© 2024 Elsevier Ltd. All rights reserved.

Introduction **581**
Overview **581**
Uniqueness of the cuprates 581
Temperature-doping phase diagram 582
Key issues **583**
Spin order 583
Spin fluctuations 583
Unconventional superconductivity 584
Precursor pairing 584
Charge order 585
CDW fluctuations 585
Pseudogap regime 586
Stripe order 586
Overdoped regime 588
Strange metal regime 588
Conclusion **589**
Summary 589
Outlook 590
Magnetic phase diagram 590
New spectroscopy and hidden orders 590
References **590**
Further reading **591**

Abstract

Since the discovery in 1986, enormous research efforts have remarkably advanced our understanding of the high-T_c cuprates, but some important issues remain unresolved. Primarily strong electronic correlations lead to superconductivity with unconventional *d*-wave pairing, which emerges upon doping into the Mott insulating state. The temperature-doping phase diagram of the cuprates is extremely complex with several orders or incipient orders showing up. In particular, the pseudogap and strange-metal regimes encompass a wide region and appear to be home not only to the superconducting order but also to various spin and charge orders.

Key points

- The cuprate phase diagrams are much more complex than previously anticipated as a standard one with antiferromagnetic, superconducting, Fermi liquid phases, and pseudogap regime as main players. The generic phase diagram further incorporates short-range and incipient spin, charge, and superconducting orders as well as strange metal regime.
- The short-range spin order –spin-density-wave (SDW)- in the heavily underdoped region is replaced by the short-range charge order –charge-density-wave (CDW)- as doping proceeds, and simultaneously the *d*-wave superconducting order sets in.
- The doping dependence of the superconducting transition temperature T_c shows a dome and T_c is controlled mainly by the superfluid density rather than the superconducting gap magnitude.
- Above T_c, there is a regime of precursory pairing -superconductivity without global phase coherence- in which the superconducting gap is almost unaffected. The precursory pairing state is a two-dimensional superconducting state without interlayer phase coherence and also a vortex liquid state under magnetic fields.
- The pseudogap regime is a playground for these orders and possibly other hidden orders, being intertwined and sometimes competing with one another. However, its origin remains a puzzle, and whether or not the doping, at which the pseudogap collapses, is a quantum critical point continues to be a matter of intense debate.
- Both SDW and CDW fluctuations are pervasively present over the entire superconducting doping range, extending to temperatures far above T_c with large energy scales of a few tenths of eV.
- The stripe order observed specific to the La-based cuprates is a showcase displaying how the spin-charge-pairing orders are intertwined and may thus be viewed as a pseudogap regime in a different appearance.

https://doi.org/10.1016/B978-0-323-90800-9.00216-X

- The hole overdoped regime is not a simple Fermi liquid as formerly thought. On passing through the optimal doping, the superfluid density starts to decrease despite that the normal-state carrier density continues to increase. Its reason is currently under hot debate.
- Above the pseudogap temperature in the underdoped region and above T_c in the overdoped region, the metallic state is recognized as a strange or bad metal. In this regime, the charge transport properties are difficult to reconcile with the notion of quasiparticles in the Landau-Boltzmann theory. The mechanism of the charge transport in this regime is at present difficult to be elucidated. However, apparently this regime is a home to both pseudogap and Fermi liquid, and hence is a key to resolve the high-T_c problems.

Introduction

The copper oxides (cuprates) stand out in their high T_c values, and are only family that achieved T_c well above the liquid nitrogen temperature at ambient pressure. High-T_c superconductivity (HTS) in the cuprates was discovered by Bednorz and Müller in 1986. Even after intensive research efforts over 35 years unraveling the mechanism of HTS and searching for higher T_c continue to be two grand challenges in condensed matter sciences. The understanding of the high-T_c cuprate materials and their electronic properties has substantially advanced. A consensus that has been achieved is that primarily repulsive electron-electron interactions lead to superconductivity with unprecedentedly high T_c as well as unconventional Cooper pairs. The common structural unit, CuO_2 plane, is an insulator driven by strong electron-electron repulsive interaction (a Mott insulator). Unconventional superconductivity emerges upon doping into the insulating CuO_2 plane.

Another consensus is that characterization of the "normal" state, in particular, the pseudogap regime above T_c and the 'strange metal' regime at elevated temperatures in the phase diagram, is indispensable for unraveling the mechanism. Recent progress is the discovery of a "plethora of orders" with broken-symmetry and their fluctuations that manifest in the pseudogap regime. In this chapter, starting from an overview of how the cuprates are unique in their electronic structure and what are necessary ingredients for high T_c, are described the current understanding and the key issues of the doping (p)-temperature (T) phase diagram and relationship of various emergent orders with the superconducting order.

Overview

Uniqueness of the cuprates

High-temperature superconductivity with T_c well exceeding the liquid-nitrogen temperature (77 K) is found only in a class of materials whose basic structural unit is the surprisingly simple CuO_2 plane, layers of Cu and O arranged in a square lattice (see Figs. 1A and B). The neighboring CuO_2 planes are separated by so-called "charge reservoir" layers/blocks. Roles of the charge reservoir layers are to supply carriers to the CuO_2 planes by chemical substitution and/or by adding or reducing oxygen atoms, and to stabilize the cuprate crystal structure the negatively charged CuO_2 planes, $[Cu^{2+}O^{2-}{}_2]^{2-}$, are neutralized by forming an alternating stack with positively charged layers.

The undoped CuO_2 plane is a "Mott" or charge transfer (CT) insulator due to the strong Coulomb repulsion ($U \sim 6$–8 eV) between electrons on the $3d$ orbitals of Cu atoms. As schematically depicted, the energy gap is actually created between occupied O$2p$ band and empty Cu$3d$ band (the upper Hubbard band), so it is called as a charge-transfer (CT) gap E_{CT} (Fig. 1C). A Cu^{2+} ion has 9 electrons in the $3d$ orbitals and it is four-fold coordinated in a CuO_2 square lattice. As a consequence, the uppermost $3d$ orbital is $3d_{x2\text{-}y2}$ and occupied by a single electron (hole) as depicted in Fig. 1D. This lone electron (hole) is localized on Cu due to strong Coulomb repulsion, leaving a magnetic moment associated with the $S = 1/2$ spin quantum number. The Cu spins align antiferromagnetically on the CuO_2 plane in the undoped cuprate due to superexchange interaction J between neighboring Cu spins via an intervening O atom. The singly occupied Cu 3 $d_{x2\text{-}y2}$ level form a single band by the hybridization with the O$2p_x$ and O$2p_y$ states which would be half-full, if the Coulomb repulsion were not strong. Since Cu is at the end of the $3d$ transition metal series in the periodic table, the energies of Cu$3d$ states are incidentally close to those of the O$2p$ states as schematically shown. This makes the CT energy gap small, $E_{CT} = 1.5$–2.0 eV, compared with that in other transition-metal oxide. In particular, the wavefunction of $3d_{x2\text{-}y2}$ has large overlap with that of O$2p_x$ and O$2p_y$. The overlap integral or hopping matrix element t_{pd} is large, ~ 0.3–0.4 eV, leading to strong hybridization between the two.

The unique features of the cuprates and widely anticipated necessary conditions for high T_c are thus summarized as.

(1) layer structure,
(2) strong electronic correlations,
(3) $S = 1/2$ spin state,
(4) accidental degeneracy between Cu$3d$ and O$2p$ energies.

No other materials so far known have all these features simultaneously.

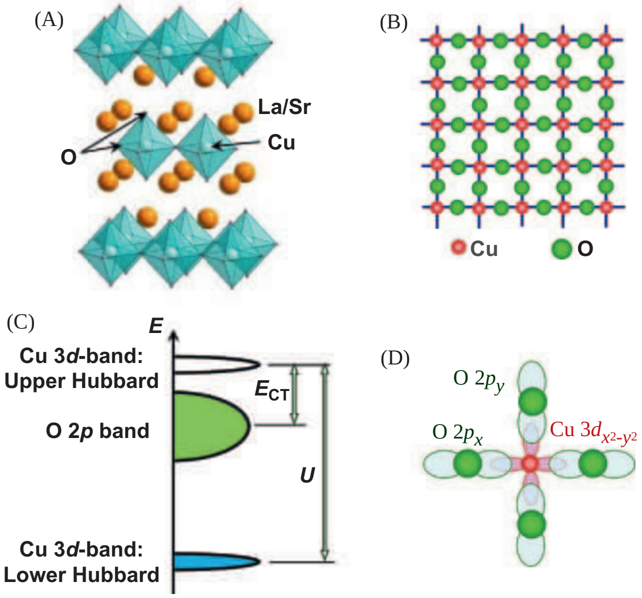

Fig. 1 (A) Crystal structures (schematic) of a representative high-T_c cuprate, $La_{2-x}Sr_xCuO_4$, and (B) the CuO_2 plane. (C) Schematic energy scheme of the insulating undoped cuprate showing a strong electronic correlation (U) on a Cu atom and a charge-transfer (CT) energy gap between O2p and Cu3d upper Hubbard band. (D) Orbital configuration of a CuO_2 unit showing relevant Cu3d_{x2-y2} and O2p_σ (σ = x or y) orbitals, both being strongly hybridized.

The large overlap integral t_{pd} and the closeness of 3d and 2p levels, i.e., small CT gap, give rise to strong covalent nature of the Cu-O bond as well as to the unusually large spin superexchange interaction $J \sim t_{\text{pd}}^4/E_{\text{CT}}^3 \sim 0.15$ eV. The strong covalent bond makes the phonon frequency corresponding to the modulations of the Cu-O bond length (or bond angle) fairly high ($\hbar\Omega_0 \sim 0.07$ eV). The large energy scales of the charge (t_{pd}), spin (J), and phonon (Ω_0) related excitations are probably sources of strong pairing interactions and hence high T_c.

The layer structure leads to their highly two-dimensional (2D) character of the electronic state, and $S = 1/2$, the minimal spin quantum number, makes the spin fluctuation maximal. Because of these two, the otherwise very stable AF order (due to large J) becomes fragile against doping and raising temperature. Finally, the strong correlations favor unconventional pairing with nodes in the superconducting (SC) gap.

Temperature-doping phase diagram

In the 'standard' phase diagram (Orenstein and Millis, 2000) sketched in Fig. 2, antiferromagnetic (AF), superconducting (SC), and overdoped 'Fermi liquid' (FL) phases evolve with increase of doping (either electrons or holes). In the case of the electron-doped

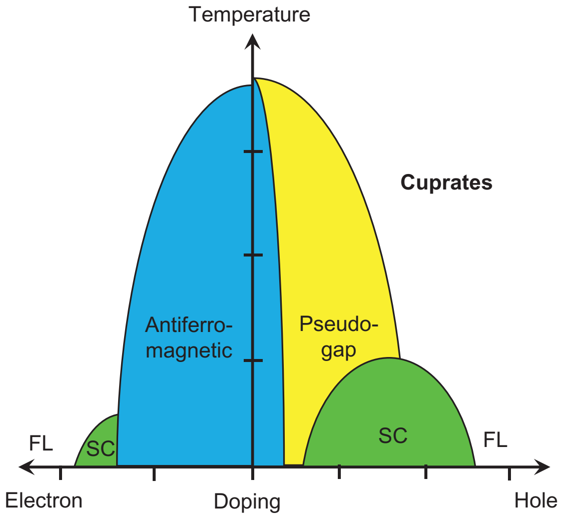

Fig. 2 'Standard' phase diagram of electron- and hole-doped cuprates. With increase of doping, the antiferromagnetic phase transforms to the superconducting (SC) and then the Fermi liquid (FL) phase. A broad antiferromagnetic phase and a wide pseudogap regime are characteristic of electron- and hole doped cuprates, respectively.

cuprates, $Nd_{2-x}Ce_xCuO_4$ ($T_c^{max} = 25$ K) and so-called infinite-layer $Sr_{1-x}La_xCuO_2$ ($T_c^{max} = 40$ K), the AF phase is robust, while the SC phase is realized in a narrow doping range. The superconducting T_c values are distinctly low, although the superconductivity is conceived to be unconventional *d*-wave. On the other hand, in the phase diagram of the hole doped cuprates pseudogap (PG) regime prevails, and at high temperatures there is a "strange" metal regime in which the in-plane (current flowing along the CuO_2 planes) resistivity continues to increase linearly with T without showing a tendency for saturation.

Key issues

This chapter focuses on the phase diagram of the hole-doped cuprates. They are genuine high-T_c superconductors, and the understanding of their phase diagram is believed to be a key to unravel the mechanism of high-T_c superconductivity. Recent progress in various advanced spectroscopies has revealed that the phase diagram, shown in Fig. 3, is much more complicated than previously anticipated, and incorporates various orders (broken symmetries). It turns out that various ordering phenomena including various types of fluctuating orders take place in the pseudogap regime.

Spin order

Local $S = 1/2$ spin magnetic moments on Cu atoms align antiferromagnetically in the CuO_2 plane (the Néel order with ordering wavevector $\boldsymbol{Q}_{AF} = (0.5,\ 0.5)$ in the unit of $2\pi/a$) by the huge superexchange interaction J between neighboring Cu spins. The long-range antiferromagnetic (AF) order sets on at $T = T_N$ ($\sim$ 300 K for the parent compound) in a second order phase transition. The ordering temperature T_N is much lower than $J \sim 1500$ K because the AF order is subject to strong thermal and quantum mechanical fluctuations. The former arises from the two-dimensionality, while the latter from the $S = 1/2$ minimal spin quantum number. This phase is essentially Mott insulating and the insulating gap is a Cu3*d*-O2*p* charge-transfer (CT) gap, $E_{CT} = 1.5$–2.0 eV, arising from the strong on-Cu site electronic repulsion.

The long-range AF order is quite fragile against hole doping. The long-range AF order collapses upon doping holes of about 0.02 per Cu atom, but spin order persists as a short-range spin-density-wave (SDW) order which is incommensurate with the underlying lattice. Different from the long-range AF order, the short-range SDW freezes gradually with lowering temperature. The onset temperature of SDW is low $T_{SDW} < 50$ K. The spin correlation length is short but finite at all temperatures showing slow dynamics with a wide distribution of the relaxation rates, characterized as a spin-glass. For further doping, typically $p = 0.05$–0.08, the short-range SDW disappears, and the superconducting order sets on.

Spin fluctuations

Even after SDW disappears, dynamical spin fluctuations remain up to very high dopings. The spin excitation spectrum or the dispersion of spin excitations is similar in all cuprate families. The undoped cuprates with commensurate AF order show spin wave (magnon) dispersion from zero at a wavevector (0.5, 0.5) in the unit of $2\pi/a$ up to a high energy of $\sim$0.3 eV reflecting extremely large superexchange coupling J (100–150 meV). With hole doping, the magnons evolve into heavily damped excitations (called paramagnons) dispersing upward from a characteristic energy ω_r (Fong et al., 2000). Below ω_r, the excitations are less damped with downward dispersion toward incommensurate spin ordering wavevectors $(0.5 \pm \delta_s)$, $\delta_s = Q_{SDW}$. This hourglass-shaped dispersion of spin excitations is in common among the cuprate families.

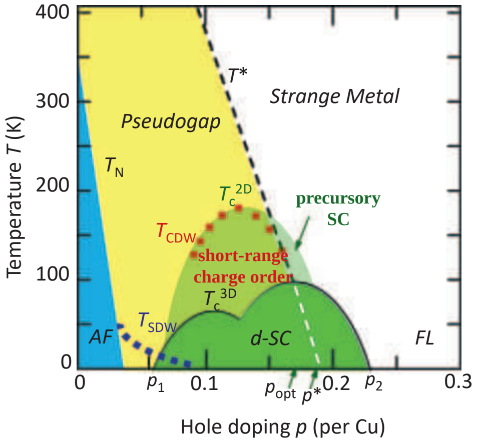

Fig. 3 Generic temperature (T) - doping (p) phase diagram of the hole-doped cuprates. Various orders emerge below the T^* line. The onset of short-range charge order is indicated by red square, and below T_{SDW} (blue dashed curve) a short-range spin order exists. Signatures of precursory superconductivity are observed within the subdome shadowed by pale green.

The low-energy spin excitations are gapless, but when p exceeds 0.08 (around the onset of SC), a gap in the spin excitations (spin gap) starts to develop and simultaneously a short-range charge order (charge-density-wave) appears. The spin fluctuations or dynamic antiferromagnetic spin correlations are still intact up to high doping region (Dean et al., 2013). These dynamic spin fluctuations in cuprates are much stronger than in conventional metals,

Unconventional superconductivity

As regards the SC phase, there are many differences from conventional superconductors:

1) T_c is unprecedentedly high.
2) The SC gap function, $\Delta(\boldsymbol{k})$, has an unconventional d-wave symmetry (Tsuei and Kirtley, 2000), strongly momentum ($\boldsymbol{k}$) dependent, $2\Delta\ (\boldsymbol{k}) = \Delta_0\ [\cos(k_x a) - \cos(k_y a)]$, a being the in-plane lattice constant. It changes sign on the Fermi surface (FS) and hence vanishing at some $\boldsymbol{k}$'s (gap nodes). The gap nodes are along the Brillouin-zone diagonal, and the gap magnitude is maximum (called as "antinodes") at the zone edges, (±0.5, 0) and (0, ±0.5) in the unit of $2\pi/a$, as schematically depicted in Fig. 4.
3) The SC transition temperature T_c as a function of hole doping p, $T_c\ (p)$, shows non-monotonic variation with p, consisting of a dome, starting to rise from p_1, showing a weak cusp (or plateau) at $p \sim 1/8$ for $La_{2\text{-}x}Sr_xCuO_4$ ($YBa_2Cu_3O_{7\text{-}y}$), reaching a maximum at so-called "optimal" doping p_{opt}, and then dropping to zero at p_2. In real cuprate samples both ends, p_1 and p_2, of the T_c dome are not sharp boundaries. Due to unavoidable inhomogeneity in the local dopant density, the superconducting state near the ends is granular in nature and hence the SC transition is percolative. On the other hand, the amplitude of $\Delta(\boldsymbol{k})$, typically 30–40 meV, is only weakly dependent on p, so there appears no direct link between T_c and Δ_0 (unlike in conventional s-wave SC $\Delta \sim 2k_B T_c$).
4) T_c appears to have a more intimate link to the superfluid density. The superfluid density or SC phase stiffness ρ_s ($\sim n_s/m^*$, n_s and m^* being Cooper pair density and carrier effective mass, respectively) in cuprates is by orders of magnitude smaller than that in conventional superconductors. T_c increases linearly with ρ_s in the underdoped region (Uemura et al., 1989), stops increasing or saturates around p_{opt}, and then starts to decrease beyond p_{opt}. ρ_s is, in principle, a very basic quantity that characterizes the SC order, but in conventional superconductors ρ_s is so high that it does not explicitly appear in the superconducting properties. By contrast, ρ_s in the high-T_c cuprates is anomalously low, and consequently shows up as a relevant parameter in various properties including T_c.

Precursor pairing

As the superfluid density or the phase stiffness ρ_s is low and the materials are effectively two-dimensional (2D), the cuprates are expected to subject to strong SC phase fluctuations (Emery and Kivelson, 1995). The best circumstantial evidence for a precursory SC (or phase-disordered SC) state comes from diamagnetism at high magnetic fields (Li et al., 2010) that is observed from T_c up to T_{pair} (about 1.5 T_c). Though weak compared to full Meissner screening, it is still large compared to that of simple metals. Compelling evidence is in the temperature evolution of the gap itself; The SC gap observed by angle-resolved photoemission spectroscopy (ARPES) does not collapse at T_c but persists up to temperature about T_{pair} (Chen et al., 2019). The large Nernst effect observed in the temperature range between T_c and T_{pair} (Xu et al., 2000) is also a signature of precursory SC. It cannot be ascribed to the motion of normal-state charge carriers, but most likely arises from moving vortices in the SC condensate which destroy the global phase coherence without affecting the SC gap. Such Nernst effect is reminiscent of genuine 2D superconductors where the pairs establish a long-range coherence through a Berezinskii-Kosterlitz-Thouless (BKT) transition. The BKT transition is driven by

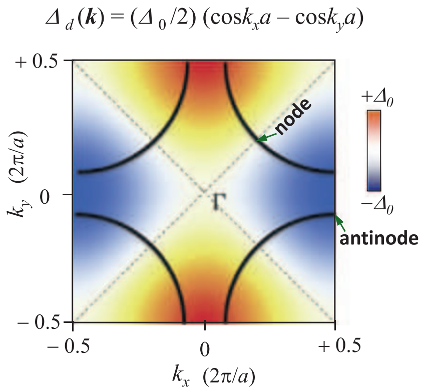

Fig. 4 Variation of the magnitude and sign of the d-wave superconducting gap in the first Brillouin zone. The Fermi surface for the optimally doped cuprate is superposed on the gap map. The gap nodes are along the zone-diagonal and the gap magnitude is maximal at the zone edges (antinodes).

proliferation of vortices. These signatures differ from superconducting fluctuations observed in classic superconductors which are fluctuations of the amplitude of the pair wavefunction and observed only in the close vicinity of T_c. In the case of cuprates, the amplitude remains finite above T_c, and the fluctuations are primarily of the phase.

Magnetic field penetrates a type-II superconductor as vortices, and the vortices form a regular array (vortex solid). For a conventional superconductor the vortex lattice is collectively pinned by impurities or defects, so that the full diamagnetic response (Meissner effect) and the zero-resistivity disappears only when the magnetic field (B) reaches the upper critical field H_{c2}. By contrast, the vortex lattice in cuprates easily melt by increasing B to a field value $H_m(T)$ much smaller than H_{c2}. The observed large Nernst signal and the diamagnetic response above T_c indicate that a vortex liquid state exists even above T_c up to the temperature T_{pair} (Li et al., 2013). The persistence of the vortex liquid is thought to be due to the small interlayer phase stiffness in conjunction with the extremely large pairing energy scale. The former makes the interlayer SC phase coherence to be destroyed at a weak field comparable to the lower critical field H_{c1}, and the latter does the pairing amplitude $|\Psi|$ robust against raising T above T_c and against increasing B. Therefore, the vortex liquid phase is regarded as a manifestation of the 2D precursory pairing phase.

Charge order

Charge order (CO) or periodic spatial modulations of charge density (charge density wave, CDW). CO was first discovered in the La-based cuprates with the K_2NiF_4 structure (La214), $La_{2-x-y}Nd_ySr_xCuO_4$ and $La_{2-x}Ba_xCuO_4$ (LBCO) at $x \sim 1/8$ as *stripe order* (Tranquada et al., 1995). The stripe charge order is a long-range order and coexists with the spin order. Recently, CDW has been discovered for almost all the cuprate families, typically $YBa_2Cu_3O_{7-y}$ (YBCO). In contrast to the stripe order, the short-range SDW order is not seen in YBCO in the doping range larger than 0.08 where the CDW order is observed. In this regime, spin excitations are gapped, while charge excitations are gapless.

The x-ray scattering experiments find a gradual onset of static and short-range CDW order at $T_{\text{CDW}} = 100\text{–}160$ K (Chang et al., 2012; Ghiringhelli et al., 2012). The incommensurate CDW has ordering vectors ($\boldsymbol{Q}_{\text{CDW}}$) always along one of the Cu-O bond directions and hence unidirectional. Q_{CDW} is typically 0.25–0.3 ($2\pi/a$), depending on material, doping as well as temperature. The CDW correlation length (ξ) estimated from the x-ray scattering peak width is about a few CDW periods, $\sim 15\text{–}25$ Å in many cuprate families. The microscopic observation of CDW in $Bi_2Sr_2CaCu_2O_{8+\delta}$ (Bi2212) by scanning-tunneling-spectroscopy (STS) has confirmed a unidirectional charge order (Kohsaka et al., 2007). In the direction perpendicular to the planes, the CDW has almost no correlation between neighboring layers, so it is confined within a CuO_2 plane, i.e., two-dimensional (2D). Experimental probes with longer time scales, such as nuclear-magnetic-resonance (NMR) (Wu et al., 2011), have confirmed that the short-range charge order is almost static, presumably due to pinning of correlated charge fluctuations by lattice disorder.

As a function of doping, the onset temperature T_{CDW} forms another dome between 0.08 and 0.18 with a maximum at $p \sim 1/8$ (Blanco-Canosa et al., 2014). Intriguingly, the onset temperature of the precursory pairing, T_{pair}, is comparable with T_{CDW}, and both show similar doping dependence. Both T_{CDW}- and T_{pair}-subdomes share nearly the same doping region within the superconducting T_c dome. T_{CDW} is highest near $p = 1/8$ where T_c shows a shallow dip or a plateau but T_{pair} is also highest. This indicates that CDW in cuprates is not a mere competitor of *d*-SC, but it is obviously "intertwined" with *d*-SC in marked contrast to the known CDW systems in which CDW and SC are competing and mutually exclusive orders.

CDW fluctuations

The recent extensive study of the resonant-inelastic-x-ray-scattering (RIXS) of $NdBa_2Cu_3O_{7-y}$ (and YBCO) has observed a broad peak, being centered near $\boldsymbol{Q}_{\text{CDW}}$, attributable to charge density fluctuations signal arising from dynamic CDW correlations. The dynamic CDW correlations are found to exist over a wide region of the $T - p$ phase diagram (Arpaia et al., 2019). They persist up to temperatures well above T_{CDW} and even above the PG temperature T^*, and are thought to be precursor to the low-temperature quasi-static CDW. The precursor CDW is also two-dimensional, and temperature independent. The in-plane CDW correlation length ξ_{CDW} is extremely short, only one CDW period or less and *T*-independent. Along the doping-axis, they are observed from the lowest end ($p \sim 0.08$) of the quasi-static CDW to even the overdoped region ($p \sim 0.2$). Notably, the integrated scattering intensity (spectral weight) of the fluctuating CDW is by about an order of magnitude larger than that of the quasi-static CDW, indicating that only a small fraction of the total CDW correlations condenses into the quasi-static low-temperature CDW order due possibly to pinning by lattice disorder.

There are two possibilities on the mechanism of the formation of charge order in cuprates: One is the real-space mechanism based on the strong electronic correlations and the other is the momentum-space mechanism such as Fermi surface nesting assisted by electron-phonon coupling for the classical CDW systems. The universal dynamic CDW correlations with high-temperature and high-energy scales point toward the strong electronic correlations as a primary driving force of the cuprate charge order.

Now that both AF (or SDW) and CDW fluctuations are pervasively present in the entire SC doping region, an important question to be answered in future is which fluctuations of either spin or charge or both orders drive the high-T_c superconductivity. The spectrum of CDW fluctuations covers a wide momentum region and extends to the energy scale of 0.2–0.3 eV, comparable to that of the hourglass-shaped spin fluctuations. It is theoretically argued that if the spin fluctuations contributed to the pair formation as a glue, the charge fluctuations would play either as an independent glue to enhance SC order or as a pair breaker for *d*-wave pairing.

Pseudogap regime

This, sometimes called as an underdoped regime, is the most mysterious regime in the phase diagram, and the understanding its origin and nature is considered to be a key to resolve the high-T_c mechanism: The pseudogap (PG) regime covers a wide T - p area of the phase diagram ($T < T^*$ and $p < \sim p_{opt}$) in which various spectroscopies indicate a suppression of low energy electronic excitations below the pseudogap temperature T^*. There remain puzzles in the origin of PG, but it is a playground for various types of ordering phenomena, SDW, CDW as well as *d*-SC. As described above, the quasistatic incommensurate spin and charge short-range orders as well as precursory pairing develop within the PG regime.

In the PG regime below the T^* line various spectroscopies show a suppression of low energy electronic excitations (Homes et al., 1993). An energy scale of the PG is typically ~0.1 eV, significantly larger than the SC gap scale (typically 30–40 meV). PG opens in the portion of the Fermi surface near antinodes (the Brillouin-zone edges, $\boldsymbol{k} = (0.5, 0)$ and $(0, 0.5)$ in the unit of $2\pi/a$), leaving behind the Fermi arc centered at nodes on which gapless and coherent quasiparticles reside (Marshall et al., 1996). This anisotropic gap gives rise to a dramatic change in various properties at T^*. For example, the *c*-axis (directed perpendicular to the CuO_2 planes) resistivity shows an upturn below T^* as T is decreased like an insulator, whereas the in-plane resistivity drops at T^* associated with a drop in the carrier scattering rate.

The structure of the pseudogap in momentum space was directly mapped by ARPES experiments. In the temperature range between T^* and T_c, the charge excitations are gapless on the Fermi arc and a gap is present near antinodes (Ding et al., 1996; Loeser et al., 1996), which crudely mimics the *d*-wave SC gap (the pseudogap is apparent only in the "antinodal" regions at which the *d*-wave gap is largest). In the SC phase, PG coexists with *d*-wave SC gap in non-trivial manner. Below T_c *d*-wave SC gap starts to open on the Fermi arc, whereas PG in the antinodal region remain almost unchanged with magnitude larger than inferred *d*-wave gap extrapolated from the Fermi arc region (Tanaka et al., 2006).

Given that there is no evidence that the SC gap energy scale is diminished by the presence of PG, it is likely that PG is also home to the SC pairing correlation. Hence, PG is not necessarily a competing order of *d*-SC, but appears to be home to various orders including SC.

It continues to be a matter of debate whether the T^* line indicates a phase transition or a crossover. T^* rapidly decreases with increasing p, and the $T^*(p)$ line appears to penetrate the T_c dome, extrapolating to a hole density $p^* \sim 0.18$. If PG is a phase associated with some broken symmetry, then p^* would be a quantum critical point (QCP) at which a continuous phase transition takes place at zero temperature. CDW with broken translational symmetry is a candidate for the PG phase, but in the phase diagram the CDW order exists in the doping region narrower than that of PG and T_{CDW} is significantly lower than T^*.

There are experimental observations that are suggestive of broken symmetries below T^* other than translational symmetry associated with SDW and CDW. Spin-flip neutron scattering experiments (Fauqué et al., 2006) indicate intra-unit cell time-reversal symmetry breaking ($\boldsymbol{q} = 0$ staggered magnetic order), supposedly arising from counter-circulating orbital current inside the unit cell (Varma, 2006). Scanning-electron-tunneling spectroscopy (STS) also suggests a rotational symmetry breaking inside the unit cell ($\boldsymbol{q} = 0$ nematic order) (Lawler et al., 2010). A signature of rotational symmetry breaking was also detected by thermodynamic probes. However, the intra-unit-cell ($\boldsymbol{q} = 0$) orders cannot open a gap by themselves, and even if a gap opens with a help of some secondary order, it is difficult to account for such a large PG energy scale.

The presence of a QCP at p^* is also challenged by the most recent experiments (Cooper et al., 2009; Chen et al., 2019). Thus, the origin of the PG has yet been identified. Apart from the presence or otherwise of QCP, the PG regime is a playground for various types of $\boldsymbol{q} \neq 0$ short-range orders including SDW, CDW and precursory pairing (or pair-density-wave) which can, in principle, create a gap. Since they are intertwined to each other, it is possible to speculate that the observed pseudogap is a spin-charge-pair entangled gap (Loret et al., 2019).

Stripe order

The stripe order in cuprates is a unique spin and charge order and a visible case of an intertwined charge, spin, and electron-pair orders. A plausible structure of the static spin-charge stripe order, illustrated in Fig. 5A, is a periodic array of charge stripes with antiferromagnetically ordered spin stripes between neighboring charge stripes (Tranquada et al., 1995). The periods of the spin and charge stripe array are typically 8*a* and 4*a*, respectively, for the doping $x = 1/8$ in LBCO. The periods change with changing doping, but the charge order wavevector $\boldsymbol{Q}_{CO}$ of the charge stripes is locked to that ($\boldsymbol{Q}_{SO}$) of the spin stripes with $\boldsymbol{Q}_{CO} = 2\boldsymbol{Q}_{SO}$. In the materials showing stripe order a structural phase transition from high-temperature-orthorhombic (HTO) to low-temperature-tetragonal (LTT) occurs before the stripe order starts to develop. The LTT lattice deformation acts as a pinning potential for the charge stripes. Matching to the LTT structure, the orientation of the stripes changes by 90° as one moves from one layer to the next, forming three-dimensional (3D) spin-charge stripe order. The magnitude of the ordering wavevector Q_{CO} of the charge stripes increases with doping as expected in a real space picture, that is, Q_{CO} is determined by a distance between charge stripes with the same hole concentration. Though special to La214 cuprates, the stripe order helps in understanding the interplay between SDW, CDW and SC orders (including precursory SC) all of which are important ingredients for shaping the 'generic' phase diagram of the cuprates, in particular, the PG regime.

The spin stripe order onsets at lower temperature, T_{SO}, than the onset of the charge stripe order, T_{CO}. Triggered by the LTT lattice deformation, segregation of doped holes starts to form charge stripes at T_{CO}. After the holes are fully segregated on the charge stripes, the AF ordered domains, or spin stripe order, are created between neighboring charge stripes at T_{SO}. Distinct from the insulating

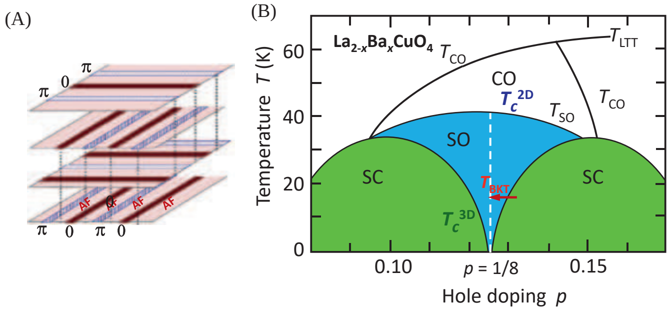

Fig. 5 (A) A schematic structure of spin-charge stripe order. (B) Phase diagram of the stripe-ordered La$_{2-x}$Ba$_x$CuO$_4$. At $x = 1/8$ the stripe order is most stable. The onset of charge (spin) stripe is indicated by T_{CO} (T_{SO}). The formation of charge stripe is triggered by the structural phase transition at T_{LTT}, and the onset of spin stripe coincides with the onset (T_c^{2D}) of two-dimensional superconductivity. The three-dimensional superconductivity is suppressed at $x = 1/8$, but soon recovers with increase or decrease of x from 1/8.

stripes in other doped Mott-insulators such as nickelates and cobaltites. The cuprate stripe ordered state stays metallic and even superconducting. While the stripe order suppresses bulk (three-dimensional, 3D) superconductivity, there is growing evidence that pairing, in a form distinct from the spatially uniform *d*-wave SC order, is taking place (Li et al., 2007). This superconducting order can be viewed as a spatially modulated SC order, pair-density-wave (PDW), Given that the stripe orientation varies 90° on moving from one layer to the next, and if SC order between one charge stripe and the next is antiphase within a layer, the Josephson coupling between layers is completely frustrated (Himeda et al., 2002; Berg et al., 2007). This interlayer decoupling isolates each superconducting CuO$_2$ plane and thus a two-dimensional superconducting state (2D-SC), likely PDW, emerges in the stripe-ordered state.

The phase diagram of LBCO is shown in Fig. 5B. For $x = 1/8$ ($T_{CO} = 55$ K) the onset of 2D pairing correlation within the CuO$_2$ plane coincides with the onset of the spin-stripe order ($T_{SO} \sim 40$ K). At T_{SO} a steep drop of the in-plane resistivity (ρ_{ab}) is observed whereas the *c*-axis resistivity (ρ_c) continues to increase. With further cooling below ~16 K, ρ_{ab} becomes vanishingly small but ρ_c is still finite, evidencing that the pairs establish a long-range coherence within a plane - 2D superconductivity order - through a Berezinskii-Kosterlitz-Thouless (BKT) transition observed at $T_{BKT} \sim 16$ K (Li et al., 2007). The pronounced nonlinear current-voltage characteristics observed below 16 K yields further support the 2D-SC.

Different from other cuprate families, the coexisting spin stripe order in the La214 family is a prerequisite for realizing the supposed PDW state with antiphase SC order between neighboring charge stripes within a layer. In an array of antiphase charge stripes the pair wavefunction can get zero where the amplitude of spin stripe is maximum which matches the empirical rule that static SC order avoids spatial overlap with static AF order. This might be the reason why the onset of 2D-SC coincides with T_{SO}.

To achieve three-dimensional superconductivity (3D-SC), it is necessary to lock together the phases of the superconducting CuO$_2$ planes via interlayer Josephson coupling. When the 2D superconducting correlations within the plane sufficiently develop, even a small interlayer Josephson coupling is enough to realize 3D-SC. The frustration of the interlayer Josephson coupling is strongest at $x = 1/8$. As a consequence, 3D bulk superconductivity does not easily occur. When the Ba content x in LBCO is changed to slightly smaller or larger values than 1/8, the stripe order and hence PDW order gets weaker. As a consequence, the 3D-SC or uniform *d*-SC order rapidly develops due to weakening of the frustration of interlayer Josephson coupling. The onset of the 3D-SC, T_c^{3D}, shows a steep and deep dip at $x = 1/8$, forming two T_c-domes. Thus, it is likely that 3D SC in $x = 1/8$ LBCO below $T_c^{3D} \sim 5$ K develops due to inhomogeneity in the local hole density, resulting from Josephson coupling between dilute patches in the neighboring layers where the hole density deviates from $p = 1/8$.

The presence of fluctuating charge stripe has been confirmed for the La214 cuprate family (Miao et al., 2017). In LBCO with $x = 1/8$, static stripe order is absent above $T_{CO} = 55$ K ($= T_{LTT}$), instead the charge-stripe fluctuations with dynamic stripe correlations are observed by RIXS at temperatures above 55 K. They show up in RIXS as a broad peak centered near Q_{CO} via the x-ray resonant scattering process. This high-*T* scattering is found to comprise spectral weight by about 7 times larger than that of the low-*T* scattering from static charge stripes, similar to the relation between the precursory CDW and the quasistatic CDW in the YBCO family.

Regardless of the stripe order in La214 and the CDW in other cuprates, they show up as dynamic CDW correlations almost ubiquitously observed at high temperatures. At low temperatures, Q_{CO} (or Q_{CDW}) in La214 would be determined by coupling between CDW and SDW that organizes well-correlated stripe order. On the other hand, in other cuprates this mechanism does not work due to the presence of a spin gap and the absence of the LTT lattice structure. In this case, other material-specific details may be relevant for determining the characteristics of the quasi-static CDW.

The PG temperature T^* is not clearly defined in the stripe ordered cuprates, but a gap distinct from the *d*-SC gap opens near antinodes below T_{SO} ($= T_c^{2D}$) (He et al., 2009). Its momentum dependence is almost the same as that for underdoped Bi2212 below T_{pair} where PG and *d*-SC coexist. Also, in common with the canonical PG state is that SDW, CDW and pairing orders and their precursors are intertwined. From these, the stripe ordered state may be regarded as a PG state with a different appearance, and the onset of precursory SC at T_{pair} in the generic phase diagram would correspond to the onset of 2D superconductivity within a

CuO_2 plane without interlayer phase coherence. In fact, with lowering T below T_{pair} a BKT-like transition is observed in strongly anisotropic Bi2212 at T slightly above T_c, preempting the onset of 3D superconductivity (Corson et al., 1999; Li et al., 2005).

The generic phase diagram suggests that short-range and possibly fluctuating charge, spin, and pairing orders might be intertwined in the PG regime. The 2D superconductivity in the stripe ordered cuprates is best explained by the presence of PDW, a typical spin-charge-pair intertwined order. Also for non-La214 cuprates, a series of the STS experiments on Bi2212 have yielded evidences for PDW with spatially modulated superfluid density and superconducting gap magnitude that coexist with the uniform *d*-wave SC order below T_c (Hamidian et al., 2016; Edkins et al., 2019; Du et al., 2020) and persists to the PG regime above T_c. PDW appears in common with all the cuprate families and hence another candidate for the origin of PG.

Overdoped regime

This regime is roughly divided into two regions at around the higher end p_2 of the T_c dome, although p_2 is not a sharp boundary and dependent on homogeneity of doped hole density in real materials. One region is lightly overdoped region covering from the doping optimal for SC (p_{opt}) or a putative end of PG (p^*) to p_2 (see Fig. 3). T_c starts to gradually decrease and then is rapidly diminished toward p_2. It appears that a Fermi liquid begins to be established with a well-developed large Fermi surface consistent in detail with the prediction of one electron band theory. This is supported by ARPES measurements where now relatively sharp peaks are observed even in the vicinity of the antinodes. In this "lightly overdoped region" CDW and other orders are not seen, but SC apparently survives maintaining fairly high T_c. The T^2 component in the in-plane resistivity in the normal state, characteristic of a Fermi liquid, gradually dominates. However, the T-linear component remains, which is characteristic of the resistivity above T^* in the PG regime and is interpreted as a sign of 'strange' metallicity.

Inelastic neutron scattering (INS) data indicate a dramatic suppression of magnetic spectral weight near the antiferromagnetic wavevectors $\boldsymbol{Q}_{AF} = (0.5, 0.5)$ (Wakimoto et al., 2007), which may be interpreted as a disappearance of the spin-fluctuation pairing glue, explaining why T_c goes down. Curiously the superfluid density $\rho_s(0)$ at $T \sim 0$ also starts to decrease for p beyond p_{opt} or p^*, although the normal-state carrier density continues to increase (Uemura et al., 1993; Bernhard et al., 2001; Bozovic et al., 2016). This is quite anomalous, since, in a clean conventional superconductor, all carriers are expected to form the SC condensate.

A typical interpretation of the reduction in $\rho_s(0)$ is a dominance of pair breaking due to disorder (high density of dopant atoms) coupled with a diminished pairing amplitude Δ_0 in the overdoped regime (Lee-Hone et al., 2017). Another is based on existence of two fluids in this region; one fluid involves incoherent quasiparticles (QPs), possibly related to SC condensate, and the other does coherent QPs originating from a non-SC Fermi liquid. In a real-space picture, the origin of the decreased superfluid density is a phase separation. With increasing p toward p_2, non-SC phase, probably the genuine FL phase well beyond p_2 is gradually mixed up with the SC phase due to a significant distribution of local hole density p. If this lightly overdoped region were not a single phase but spatially phase separated, then a single-phase uniform d-SC state might be unstable in the cuprates. It is also possible to speculate a momentum-space "phase separation". In this doping region, QPs are coherent on a large portion of the Fermi surface, contributing to the charge transport, but there remain incoherent QPs on some small portion which is responsible for the T-linear component in the resistivity and form superfluid below T_c.

For further overdoping ($p > p_2 \sim 0.25$) in the "heavily overdoped region", SC is completely suppressed, and quasiparticles are coherent throughout the large FS, which is confirmed by both ARPES and quantum oscillations measurements. Most of the properties in this region are normal except for that the spin wave, characteristic of localized spins, is robustly present without changing its dispersion in the AF ordered phase. While spin fluctuations at $\boldsymbol{Q}_{AF}$ fade out, pronounced spin fluctuations remain at smaller wavevectors (Dean et al., 2013), implying that strong electron correlations persist even in heavily overdoped cuprates. Then, it is speculated that a second high-T_c dome may appear in the doping region (e.g., $p > 0.4$) next to the heavily overdoped FL (Maier et al., 2019). This region is not accessible for the representative cuprate families such as LSCO, YBCO, Bi2212, and even overdoped Tl2201. At present, at least two cuprate materials, $Cu_{0.75}Mo_{0.25}Sr_2YCu_2O_{7.54}$ and Ba_2CuO_{4-y} synthesized under high pressures, show SC with $T_c \sim 80$ K and are supposed to have doped hole density in the range between 0.4 and 0.5.

Strange metal regime

The metallic state in the high T region above the PG T^* and that in the region from the putative critical doping p^* to near the end of the T_c dome are recognized as "bad" metal and "strange" metal, respectively. In the high-temperature "bad" metal regime, the in-plane resistivity continues to increase linearly with T without a tendency for saturation, while in the low-temperature "strange" metal regime the T-linear resistivity persists even toward $T = 0$ (Martin et al., 1990; Cooper et al., 2009) when superconductivity is suppressed by strong magnetic fields or by disorder (see Fig. 6). These two are in principle distinct - a system can be bad without being strange and vice versa. However, the cuprates are apparently both bad and strange. In a range of doping, near p_{opt}, the resistivity is linear in T all the way from $T \sim 0$ (when SC is suppressed) up to the highest temperatures as measured (typically $\sim$1000 K) (Gurvitch and Fiory, 1987). The slope of the T-linear resistivity is constant, showing no discernible crossover from "strange" to "bad" metal regime. Given that both are not distinguished in the cuprates, the high-temperature "bad metal" regime above T^* is labeled by "strange metal" in the phase diagram (Fig. 3),

The basic difference of the high-T strange metal from a conventional metal is the absence of quasiparticles. In a normal metal, the resistivity saturates at high temperatures when the mean free path (l) of charge carrier becomes of the order of its de Broglie wavelength λ_F ($\lambda_F = 2\pi/k_F$ where k_F is the Fermi wavenumber) – the Mott-Ioffe-Regel (MIR) limit. Since the magnitude of the

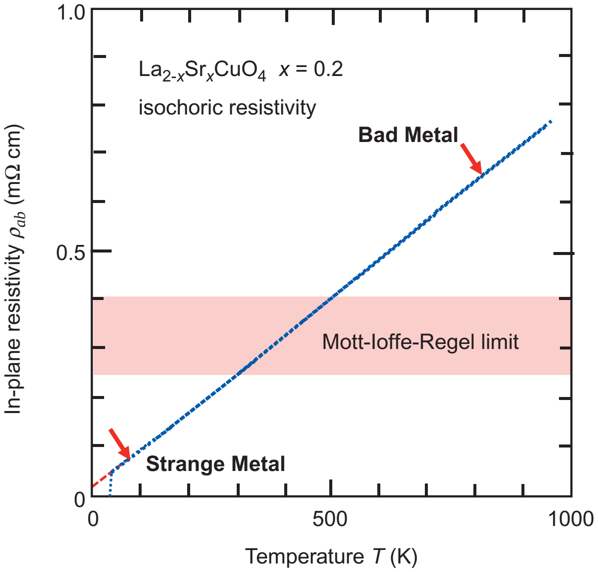

Fig. 6 Typical temperature dependent in-plane resistivity measured for $La_{2-x}Sr_xCuO_4$ with $x = 0.20$. The resistivity values measured under constant pressure are transformed to the values at constant sample volume (isochoric) using the data of the pressure dependence of resistivity and bulk modulus. The resistivity increases linearly to the highest temperatures without showing saturation at temperatures well exceeding the Mott-Ioffe-Regel limit (shaded region; its numerical value is somewhat arbitrary). The T-linear resistivity persists even toward $T = 0$ (red dashed line) when the superconducting transition is suppressed by magnetic fields.

cuprate resistivity in the high-T region is larger than that of typical metals by more than an order, the resistivity well exceeds the MIR limit in the high T region (Hussey et al., 2004). Nevertheless, the resistivity shows a "metallic" linear-in-T dependence. Therefore, well-defined quasiparticles do not exist and hence the resistivity is difficult to be interpreted in terms of propagating quasiparticles in the Boltzmann transport theory. The failure of the ordinary physics of good metals has provided strong motivation for proposing quite an exotic theory such as holographic duality (Zaanen, 2019). The origin of this behavior is, however, still a subject of much debate, but is of obvious importance since PG and/or FL appear to get born upon cooling from this regime, perhaps one of the most mysterious aspects of cuprates. PG and FL emerge from totally incoherent 'strange metal' by partial restoration of quasiparticle coherence over a range of the Fermi surface (Fermi arc) in the former and a complete restoration in the latter.

In the low-T strange metal regime, the T-linear resistivity persistent down to $T \sim 0$ indicates a scale invariance or a vanishing intrinsic energy scale which is characteristic of quantum critical metals. When subjected to infrared photons with frequency ω, the low-energy optical conductivity of scale invariant metals is set by the larger energy scale between k_BT and $\hbar\omega$, that is, the inelastic scattering rate of electrons, $\hbar/\tau \sim \max\,[k_BT, \hbar\omega]$ (van der Marel et al., 2003). In the same way, under external magnetic fields B, the magnetoresistance, $\Delta\rho/\rho_0 = [\rho(B) - \rho(0)]/\rho(0)$, is controlled by $\hbar/\tau \sim \max\,[k_BT, \mu_BB]$, μ_B being the Bohr magneton. A crossover in magnetoresistance is actually observed at low temperatures from $\Delta\rho/\rho_0 \sim B^2$ at low fields to $\Delta\rho/\rho_0 \sim B$ at high fields (Ayres et al., 2021).

The recent experimental findings challenge the view of the scale invariance in association with QCP. First, experimental effort to unambiguously identify the presence of the QCP is limited by the onset of SC at fairly high temperature. Second, the T-linear resistivity extending to $T \sim 0$ persists over a broad doping range, from p_{opt} to around the end of the T_c dome in contrast to the above QCP scenario. Third, concerning the quantum critical wedge in the higher doping side, $p > p^*$, a big question that remains unanswered is how really different the supposed Fermi liquid at lower temperatures is from the strange metal at higher temperatures. ARPES shows there is only a weak crossover line that separates these two regimes, but other experimental probes fail to identify it.

Conclusion

Summary

Recent progress in various advanced spectroscopies has revealed that the T-p phase diagram of hole-doped cuprates is much more complicated than the widely spread 'standard' phase diagram (Fig. 2). The generic phase diagram incorporates various spin, charge and electron-pair orders in addition to the unconventional d-wave SC order. It turns out that various ordering phenomena including their precursory orders predominantly take place in the PG regime. Thus, the PG regime seems a home to these orders. The PG regime appears to also accommodate some intra-unit-cell ($\boldsymbol{q} = 0$) orders such as circulating orbital current order and nematic order, which are observed exactly below the pseudogap temperature T^*, but they cannot create a gap by themselves. These recent findings pose additional questions, which are primary orders and how they are inter-related (or intertwined) to shape the generic phase diagram and finally to establish superconductivity at T_c of $\sim$100 K with global phase coherence. To this, the spin-charge stripe order realized in the La-based cuprates is an instructive example. The stripe order displays how the spin and charge orders are intertwined with the pairing correlation to form a spatially modulated SC order, PDW, and thereby 2D superconductivity.

The high-temperature metallic state above T^* is recognized as a strange or bad metal regime which cannot be described by the quasiparticle picture. The quasiparticles are totally absent or completely incoherent, but nonetheless the T-linear resistivity persists up to the highest temperature measured. The origin of this behavior is still a subject of much debate, but the understanding of this regime is of obvious importance since PG in the underdoped region and probably FL in the heavily overdoped region appear to get born upon cooling from this regime. The failure of the ordinary physics of good metals has provided strong motivation for proposing quite a exotic theory such as holographic duality.

Another important observation by the advanced spectroscopy is the persistence of spin and charge excitations with SDW (or AF) and CDW correlations up to temperatures even higher than T^* and in the entire SC doping region. Both cover a wide momentum region centered at AF and CDW wavevectors and extend to very high energies of order of a few tens of eV. They are not only possible sources of strong electron scattering that makes the electrons completely incoherent but also possible glues for the formation of Cooper pairs. The AF spin fluctuations have been widely believed as a strong candidate of the pairing glue. A question to be answered is whether the CDW fluctuations play a role of an independent or additional glue to enhance the SC T_c or conversely as a pair breaker for d-SC.

Outlook

Magnetic phase diagram

Since the various orders emerge with doping into the Mott insulating phase, the cuprate phase diagram has been investigated mainly in the temperature-doping plane. In order to better understand the known phases and to search for hidden phases, it would be helpful to explore a phase diagram using a control parameter other than doping. Pressure and magnetic field are typical control parameters for other systems. While pressure, either uniaxial or hydrostatic, is not an effective perturbation to change the completion and/or intertwining among different phases in cuprates, intense magnetic field (B) has recently been found to substantially affect the SC state as well as the competition between SC and CDW orders (Yu et al., 2016).

The B-T phase diagram of cuprates with B in the direction perpendicular to the CuO_2 planes, has not been fully investigated because of the limitation of available magnetic field strength, and continues to be a matter of debate. One of the unsettled problems is that experiments so far made have never observed the upper critical field H_{c2}, i.e. the pair-breaking field, convincingly even near T_c. The vortex lattice in cuprates easily melt at a field value $H_m(T)$ much weaker than the inferred $H_{c2}(T)$, and the vortex liquid state is found to persist above T_c up to T_{pair} (Li et al., 2013). As a consequence, the vortex liquid phase occupies a surprisingly large region of the B-T phase diagram. Extending to a temperature T_{pair} and to an experimentally inaccessible high field. Further, the spatially modulated SC state (PDW), a spin-charge-pairing intertwined order typically observed in the stripe order, appears to be stabilized in the region of a vortex halo as evidenced by the STS measurement on Bi2212 (Edkins et al., 2019). However, effects of magnetic field on CDW and SDW orders that probably coexist with the vortex liquid state remain open. Perhaps related open question is whether or not an electron Fermi surface pocket, which is supposed to emerge as a consequence of Fermi-surface-reconstruction in the presence of a static CDW, exists in the vortex liquid region suggested by the observation of quantum oscillations (Doiron-Leyraud et al., 2007).

New spectroscopy and hidden orders

Unraveling the origin of the pseudogap (PG) state of the high-T_c cuprates has been an issue of continuous challenge for almost three decades. PG turns out to be a playground of several orders. Among them, SDW order, superconducting order and CDW order are now well known and experimentally confirmed. These three orders and their precursors are found to exist in the PG regime. Nevertheless, it remains unclear how they form the PG state above T_c. This suggests that there might be a hidden order which has not been detected by the currently available experimental probes, and would be a remaining piece for finally resolving the PG puzzle.

To uncover hidden orders, a challenge for developing a new spectroscopy may be needed, such as one, for example, that allows for a detection of dipole-forbidden optical excitations or is sensitive to various forms of vortices or topological defects as well as to orders and excitations involving orbital degree of freedom. In the history of the research of high-T_c superconductivity, breakthroughs have always been made by new spectroscopy.

References

Arpaia R, et al. (2019) Dynamical charge density fluctuations pervading the phase diagram of a Cu-based high-T_c superconductor. *Science* 365: 906–910.

Ayres J, et al. (2021) Incoherent transportacross the strange metal regime of highly overdoped cprates. *Nature* 595: 661–667.

Berg E, et al. (2007) Dynamical layer decoupling in a stripe-ordered high-T_c superconductor. *Physical Review Letters* 99: 127003.

Bernhard C, et al. (2001) Anomalous peak in the superconducting condensate density of cuprate high-T_c superconductors at a unique critical doping state. *Physical Review Letters* 86: 1614–1617.

Blanco-Canosa S, et al. (2014) Resonant x-ray scattering study of charge-density wave correlations in $YBa_2Cu_3O_{6+x}$. *Physical Review B* 90: 054513.

Bozovic I, He X, Wu J, and Bollinger AT (2016) Dependence of the critical temperature in overdoped copper oxides on superfluid density. *Nature* 536: 309–311.

Chang J, et al. (2012) Direct observation of competition between superconductivity and charge density wave order in $YBa_2Cu_3O_{6.67}$. *Nature Physics* 8: 871–876.

Chen SD, et al. (2019) Incoherent strange metal sharply bounded by a critical doping in Bi2212. *Science* 366: 1099–1102.

Cooper RA, et al. (2009) Anomalous criticality in the electrical resistivity of $La_{2-x}Sr_xCuO_4$. *Science* 323: 603–607.

Corson J, Mallozzi R, Orenstein J, Eckstein JN, and Bozovic I (1999) Vanishing of phase coherence in underdoped $Bi_2Sr_2CaCu_2O_{8+\delta}$. *Nature* 398: 221–223.

Dean MPM, et al. (2013) Persistence of magnetic excitations in $La_{2-x}Sr_xCuO_4$ from the undoped insulator to the heavily overdoped non-superconducting metal. *Nature Materials* 12: 1019–1023.

Ding H, et al. (1996) Spectroscopic evidence for a pseudogap in the normal state of underdoped high-T_c superconductors. *Nature* 382: 51–54.

Doiron-Leyraud N, et al. (2007) Quantum oscillations and the Fermi surface in an underdoped high-T_c superconductor. *Nature* 447: 565–568.

Du Z, et al. (2020) Imaging the energy gap modulations of the cuprate pair-density-wave state. *Nature* 580: 65–70.

Edkins SD, et al. (2019) Magnetic field-induced pair density wave in the cuprate vortex halo. *Science* 364: 976–980.

Emery VJ and Kivelson SA (1995) Importance of phase fluctuations in superconductors with small superfluid density. *Nature* 374: 434–437.

Fauqúe B, et al. (2006) Magnetic order in the pseudogap phase of high-T_c superconductors. *Physical Review Letters* 96: 197001.

Fong HF, et al. (2000) Spin susceptibility in underdoped $YBa_2Cu_3O_{6+x}$. *Physical Review B* 61: 14773–14786.

Ghiringhelli G, et al. (2012) Long-range incommensurate charge fluctuations in $(Y,Nd)Ba_2Cu_3O_{6+x}$. *Science* 337: 821–825.

Gurvitch M and Fiory AT (1987) Resistivity of $La_{1.825}Sr_{0.175}CuO_4$ and $YBa_2Cu_3O_7$ to 1100 K: Absence of saturation and its implication. *Physical Review Letters* 59: 1337–1340.

Hamidian MH, et al. (2016) Detection of a Cooper-pair-density-wave in $Bi_2CaCu_2O_{8+x}$. *Nature* 532: 343–347.

He R-H, et al. (2009) Energy gaps in the failed high-T_c superconductor $La_{1.875}Ba_{0.125}CuO_4$. *Nature Physics* 5: 119–123.

Himeda A, Kato T, and Ogata M (2002) Stripe statewith spatially oscillating *d*-wave superconductivity in the two-dimensional t-t'-J model. *Physical Review Letters* 88: 117001.

Homes CC, et al. (1993) Optical conductivity of *c* axis oriented $YBa_2Cu_3O_{6.70}$: Evidence for a pseudogap. *Physical Review Letters* 71: 1645–1648.

Hussey NE, Takenaka K, and Takagi H (2004) Universality of the Mott-Ioffe-Regel limit of metals. *Philosophical Magazine* 84: 2847–2864.

Kohsaka Y, et al. (2007) An intrinsic bond-centered electronic glass with unidirectional domains in underdoped cuprates. *Science* 315: 1380–1385.

Lawler MJ, et al. (2010) Intra-unit-cell electronic nematicity of the high-T_c copper-oxide pseudogap states. *Nature* 466: 347–351.

Lee-Hone NR, Dodge JS, and Broun DM (2017) Disorder and superfluid density in overdoped cuprate superconductors. *Physical Review B* 96: 024501.

Li L, Wang Y, Naughton MJ, Ono S, Ando Y, and Ong NP (2005) Strongly nonlinear magnetization above T_c in $Bi_2Sr_2CaCu_2O_{8+\delta}$. *Europhysics Letters* 72: 451–457.

Li Q, Hucker M, Gu GD, Tsvelik AM, and Tranquada JM (2007) Two-dimensional superconducting fluctuations in stripe-ordered $La_{1.875}Ba_{0.125}CuO_4$. *Physical Review Letters* 99: 067001.

Li L, et al. (2010) Diamagnetism and Cooper pairing above T_c in cuprates. *Physical Review B* 81: 054510.

Li L, Yayu W, and Ong NP (2013) Reply to "Comment on 'Diamagnetism and Cooper pairing above T_c in cuprates'". *Physical Review B* 87: 056502.

Loeser AG, et al. (1996) Excitation gap in the normal state of underdoped $Bi_2Sr_2CaCu_2O_{8+\delta}$. *Science* 273: 325–329.

Loret B, et al. (2019) Intimate link between charge density wave, pseudogap and superconducting energy scales in cuprates. *Nature Physics* 15: 771–775.

Maier T, Berlijn T, and Scalapino DJ (2019) Two pairing domes as Cu^{2+} varies to Cu^{3+}. *Physical Review B* 99: 224515.

Marshall DS, et al. (1996) Unconventional electronicstructure evolution with hole doping in $Bi_2Sr_2CaCu_2O_{8+\delta}$: Angle-resolved photoemission results. *Physical Review Letters* 76: 4841–4844.

Martin S, Fiory AT, Fleming RM, Schneemeyer LF, and Waszczak JV (1990) Normal-state transport properties of $Bi_{2+x}Sr_{2-y}CuO_{6+\delta}$ crystals. *Physical Review B* 41: 846–849(R).

Miao H, et al. (2017) High-temperature charge density wave correlations in $La_{1.875}Ba_{0.125}CuO_4$ without spin-charge locking. *Proceedings of the National Academy of Sciences of the United States of America* 114: 12430–12435.

Orenstein J and Millis AJ (2000) Advances in the physics of high-temperature superconductivity. *Science* 288: 468–474.

Tanaka K, et al. (2006) Distinct Fermi-momentum-dependent energy gaps in deeply underdoped Bi2212. *Science* 314: 1910–1913.

Tranquada JM, Sternlieb BJ, Axe JD, Nakamura Y, and Uchida S (1995) Evidence for stripe correlations of spins and holes in copper oxide superconductors. *Nature* 375: 561–563.

Tsuei CC and Kirtley JR (2000) Pairing Symmetry in cuprate superconductors. *Reviews of Modern Physics* 72: 969–1016.

Uemura YJ, et al. (1989) Universal correlations between T_c and n_s/m^* in high-T_c cuprate superconductors. *Physical Review Letters* 62: 2317–2320.

Uemura YJ, et al. (1993) Magnetic-field penetration depth in $Tl_2Ba_2CuO_{6+\delta}$ in the overdoped regime. *Nature* 364: 605–607.

van der Marel D, et al. (2003) Quantum critical behavior in a high-T_c superconductor. *Nature* 425: 271–274.

Varma C (2006) Theory of the pseudogap state of the cuprates. *Physical Review B* 73. 155113.

Wakimoto S, et al. (2007) Disappearance of antiferromagnetic spin excitations in overdoped $La_{2-x}Sr_xCuO_4$. *Physical Review Letters* 98. 247003.

Wu T, et al. (2011) Magnetic-field-induced charge-stripe order in the high-temperature superconductor $YBa_2Cu_3O_y$. *Nature* 477: 191–194.

Xu ZA, et al. (2000) Vortex-like excitations and the onset of superconducting phase fluctuation in underdoped $La_{2-x}Sr_xCuO_4$. *Nature* 406: 486–488.

Yu F, et al. (2016) Magnetic phase diagram of underdoped $YBa_2Cu_3O_y$ inferred from torque magnetization and thermal conductivity. *Proceedings of the National Academy of Sciences of the United States of America* 113: 12667–12672.

Zaanen J (2019) Planckian dissipation, minimal viscosity and the transport in cuprate strange metals. *SciPost Physics* 6: 061.

Further reading

Agterberg DF, et al. (2020) The physics of of pair density waves. *Annual Review of Condensed Matter Physics* 11: 231–270.

Keimer B, Kivelson SA, Norman MR, Uchida S, and Zaanen J (2015) From quantum matter to high-temperature superconductivity in copper oxides. *Nature* 518: 179–186.

Lee PA, Nagaosa N, and Wen X-G (2006) Doping a Mott insulator: Physics of high-temperature superconductivity. *Reviews of Modern Physics* 78: 17–85.

Sachdev S (1999) *Quantum Phase Transitions*. Cambridge: Cambridge University Press.

Scalapino DJ (2012) A common thread: the pairing interaction for unconventional superconductors. *Reviews of Modern Physics* 84: 1383–1417.

Tranquada JM (2020) Cuprate superconductors as viewed through a stripe lens. *Advances in Physics* 69: 437–509.

Zaanen J, Sun Y, Liu Y, and Schalm K (2015) *Holographic duality for condensed matter physics*. Cambridge: Cambridge University Press.

Superconductors, hydrogen-based

Katsuya Shimizu, KYOKUGEN, Center for Science and Technology under Extreme Conditions, Graduate School of Engineering Science, Osaka University, Toyonaka, Osaka, Japan

© 2024 Elsevier Ltd. All rights reserved.

Introduction **592**
Superconductivity and high pressure **592**
The Holy Grail 592
Hydrogen-rich compounds 593
High pressure 593
Theoretical predictions 594
Synthesis of superconducting hydrides **594**
Pressure generation and measurement technique 594
Synthesis through molecular dissociation 595
Direct synthesis from element and hydrogen 595
Near room-temperature superconductivity in hydrides **595**
Lanthanum hydride 595
USOs (unidentified superconducting objects) 596
Future prospects **596**
Toward higher temperatures 596
Toward lower pressure 596
Control of hydrogenation 596
Conclusion **597**
References **597**

Abstract

Superconductivity, which was previously believed to occur only at low temperatures close to zero Kelvin, has recently been believed to occur even at room temperature. Experimental results of superconductivity at high temperatures close to room temperature have been reported in hydrogen-based materials, hydrides, although ultrahigh pressures in excess of 100 GPa are required.

Key points

- Explore the occurrence of superconductivity at higher temperatures, including room temperature.
- Experimental results of hydrogen-based superconductivity.
- Requirement of very high pressures for hydrogen-based high-temperature superconductivity.

Introduction

Superconductivity, which was previously believed to occur only at low temperatures close to zero Kelvin, has recently been believed to occur even at room temperature. Although it requires extreme pressure conditions of over 1 million atmospheres (about 100 GPa), the RTS (room-temperature superconductivity) is not a dream but has become a concrete possibility, raising hopes for the emergence of superconducting materials without cooling in the near future. For over a century since the discovery of the superconductivity in the early 20th century, researchers have focused on increasing the critical temperature (T_c) for reducing the cooling costs. The historical progression is illustrated in Fig. 1. Following the rapid rise in the T_c observed in the 1980s with the discovery of copper oxide superconductors, the recent surge in research on hydride superconductors (hydrogen-based superconductor) has sparked considerable interest. How did this rapid development occurred?

https://doi.org/10.1016/B978-0-323-90800-9.00270-5

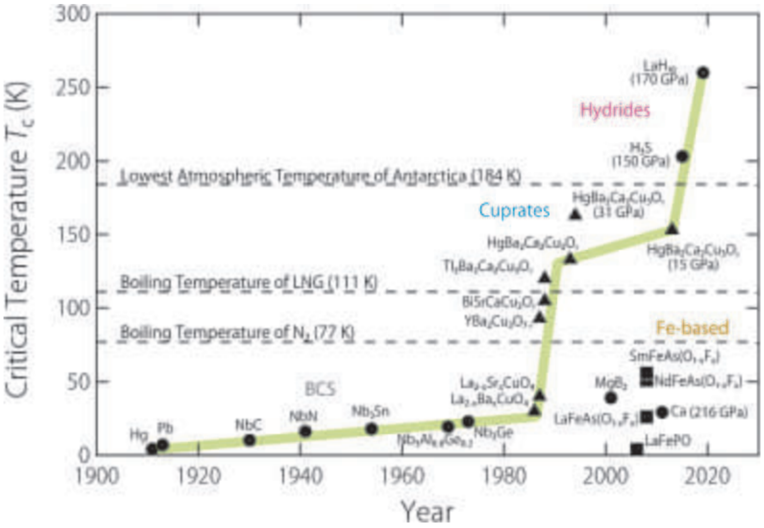

Fig. 1 History of superconducting transition temperatures (T_c). Experimentally observed superconducting transition temperatures are shown for the year of discovery. Symbols are classified according to the type of superconductivity. ●: conventional (BCS), ▲: unconventional (not explained by BCS), ■: iron-based.

Superconductivity and high pressure

The Holy Grail

There is something often referred to as the Holy Grail by researchers in the field of high-pressure science. It is solid metallic hydrogen. Hydrogen, atomic number 1, is the most fundamental element consisting of one proton and one electron. What would be the nature of hydrogen at extremely high dense condition? Hydrogen is normally a gas, forming molecules (H_2), but when compressed, it transitions through a liquid phase and become a solid. With further compression, the molecules are expected to dissociate into monatomic structure, with protons forming a crystalline lattice, resulting in solid metallic hydrogen. According to the BCS theory, which explains the mechanism of superconductivity, metallic hydrogen, with its strong electron-phonon interaction and high lattice vibration frequency, is expected to exhibit superconductivity with very high T_c, room-temperature superconductivity (Ashcroft, 1968). On the other hand, liquid metallic hydrogen exists in the interiors of gas giant planets such as Jupiter, and it is believed to be the source of their geomagnetic field. This is the same principle as the generation of geomagnetism by liquid iron in the Earth's interior. Liquid metallic hydrogen has already been produced in the laboratory (Weir et al., 1996; Ohta et al., 2015), solid metallic hydrogen has remained elusive due to the lack of sufficient pressure achieved by current high-pressure techniques. This is why it is referred to as the Holy Grail.

Hydrogen-rich compounds

As an alternative to metallic hydrogen, hydrogen-rich compounds had been proposed as candidates for room-temperature superconductors. Instead of compressing hydrogen itself, the proposal is to compress hydrogen-rich compounds, where hydrogen within the crystal can approach a state similar to metallic hydrogen at lower pressures than compressing hydrogen itself, thus creating a metallic hydrogen-like state in the hydrogen-rich compound (Ashcroft, 2004). In 2015, a German research group has conducted extensive experiments upon this concept, they discovered superconductivity with a T_c exceeding 200 K by pressurizing hydrogen sulfide (H_2S) (Drozdov et al., 2015). This breakthrough led to hydrogen-rich compounds, hydrides, becoming strong candidates for high-temperature superconductors.

High pressure

It is fair to say that the properties of matter are determined by the interaction of electrons. This is not limited to superconductivity; changing the distance between atoms with pressure can change this interaction between electrons and significantly alter the properties of matter. When higher pressure is applied, crystals not only shrink but also change their arrangement (crystal structure), leading to the emergence of new properties resulting from the new structure.

Theoretical predictions

It is generally not easy and challenging to theoretically predict the crystal structure and resulting properties of a material under high pressure, which greatly influences its characteristics. However, recent advancements in computational methods have significantly improved the accuracy of prediction of stable structures under pressure. The discovery of superconductivity in hydrogen sulfide (Drozdov et al., 2015) was initiated by theoretical predictions (Li et al., 2014) and later confirmed through experiments, which revealed that the observed crystal structure and T_c (Einaga et al., 2016) were consistent with the theoretical predictions (Duan et al., 2014). This not only proves the accuracy of the theoretical prediction, but also that this superconductivity is based on the BCS theory. The success of this theoretical prediction led to the search for the next hydride superconductor, and calculations were actively carried out. One element was selected from the periodic table to be combined with hydrogen, and the ratio of hydrogen, pressure, and structure at which the hydride would be stable were calculated. They then use these structural parameters to calculate the superconducting properties, proposing various hydrogen-rich compounds as potential candidates for high-temperature superconductivity. In other words, hydride synthesis experiments are being conducted in the computer before actual experiments in laboratory. Table 1 lists some of the candidates that have the potential to realize room temperature superconductivity (Wang et al., 2012; Feng et al., 2015; Liu et al., 2018).

Synthesis of superconducting hydrides

Pressure generation and measurement technique

Before discussing the specific details of hydride superconductors, the generation of high-pressure environments exceeding 100 GPa and the techniques for measuring superconductivity within these environments are briefly introduced in Fig. 2. See references (Shimizu et al., 2005) for details. High pressure is generated by a Diamond-Anvil Cell (DAC). A photograph of the DAC for low-temperature use is shown in Fig. 2C, and its pressure generation section is shown in Fig. 2B. The DAC is composed of two diamond anvils. The sample and pressure transmitting medium are enclosed in a space between two diamond anvils. Four electrodes are usually placed on the sample to perform a four-terminal electrical resistance measurement. These electrodes can also be deposited on the surface of the upper diamond anvil. External heating of the sample can apply to the sample by irradiating with infrared lasers.

Table 1 Candidate hydrides with potential for room temperature superconductivity.

Hydrides	T_c*(K)*	P *(GPa)*
MgH_6	260	300
CaH_6	220– 235	150
YH_6	251– 264	120
YH_{10}	305– 326	120
LaH_{10}	274	200

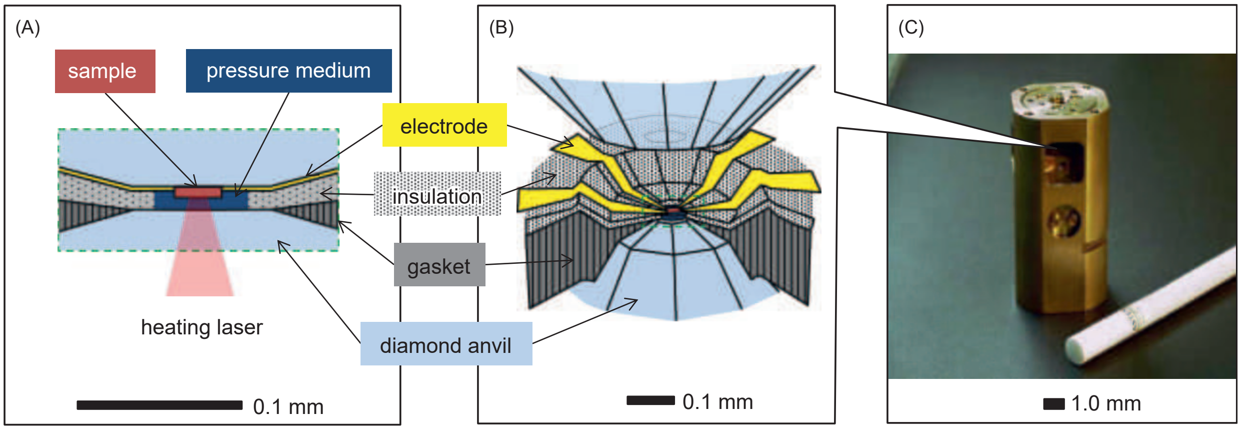

Fig. 2 Preparation of high-pressure experiments. (A) cross section of the heart of DAC (Diamond- Anvil Cell). The sample is pressurized by upper and lower diamond anvil through the pressure medium. The electrical resistance of the sample is measured by four electrodes. (B) schematic drawing of the assembly of the sample and electrodes between diamond anvils. (C) photograph of DAC.

Synthesis through molecular dissociation

Hydrogen sulfide (H_2S) is a gas molecule at ambient temperature and pressure. Its boiling point is approximately 200 K, and it can be liquefied by introducing H_2S gas into a DAC that has been cooled below its boiling point using a refrigerator. Thus, in the case of H_2S, the sample and pressure medium in Fig. 2A are combined and equal to sample. Upon pressurization, H_2S liquid immediately solidifies, and further pressurization leads to the metallization, then the superconductor with a T_c of 200 K is achieved (Drozdov et al., 2015).

Reproduction experiments and structural analysis using synchrotron X-rays (SPring-8) have revealed that hydride (H_3S: sulfur hydride SH_3), whose hydrogen content is higher than that of hydrogen sulfide (H_2S), is the true entity of the 200 K superconductor. Furthermore, X-ray structural analysis revealed that sulfur is precipitated during the synthesis process, and as shown in Eq. (1), H_3S with a higher hydrogen content is formed from parent substance, H_2S displacing sulfur under high pressure as Fig. 3.

$$3H_2S \rightarrow 2H_3S + S \tag{1}$$

This is an example of hydride synthesis through the molecular dissociation. For the candidate substances listed in Table 1, there is currently no parent substance (such as H_2S for H_3S) at this moment.

Direct synthesis from element and hydrogen

After the discovery of the superconductivity of hydrogen sulfide (Drozdov et al., 2015), a direct synthesis of hydride from sulfur and hydrogen was attempted. By substituting sulfur for the sample and hydrogen for the pressure medium in Fig. 2, this synthesis was performed. After pressurization up to 150 GPa, sulfur transformed to metal, but any reaction with hydrogen did not occur. When the metallic sulfur was heated by an infrared laser, the hydrogen in contact with the sulfur was heated together and the synthesis reaction ($2S + 3H_2 \rightarrow 2H_3S$) occurred. This was monitored by the powder X-ray diffraction analysis, which was performed simultaneously with this laser heating and electrical resistivity measurements. When the DAC was cooled afterwards, the superconducting transition was observed at about 200 K, as in Drozdov et al., 2015 reported. In comparison to the synthesis through the molecular dissociation mentioned, this direct synthesis method was expected to have an advantage in purity and crystallinity of H_3S without the excess sulfur, but the observed T_c remained the same (Nakao et al., 2019).

This direct synthesis method served as a model for the syntheses of superconducting hydrides, and most of the later synthesis experiments employed this method.

Near room-temperature superconductivity in hydrides

Lanthanum hydride

Among the candidates listed in Table 1, the synthesis of lanthanum hydride (LaH_{10}) and its superconductivity with a transition temperature exceeding 250 K were reported nearly simultaneously by research groups from the United States and Germany in 2019. In both cases, the superconductivity was discovered at pressures and temperatures that were approximately equal to the values shown in Table 1 (Somayazulu et al., 2019; Drozdov et al., 2019). LaH_{10} has a structure in which hydrogen atoms surround lanthanum atoms in a cage-like arrangement as shown in Fig. 3; although the position of the hydrogen element cannot be determined by X-ray structure analysis, the structure formed by lanthanum is consistent with what theoretical calculations predict. The synthesis methods of both groups are based on Fig. 2A, with the German group (Drozdov et al., 2019) using hydrogen and the

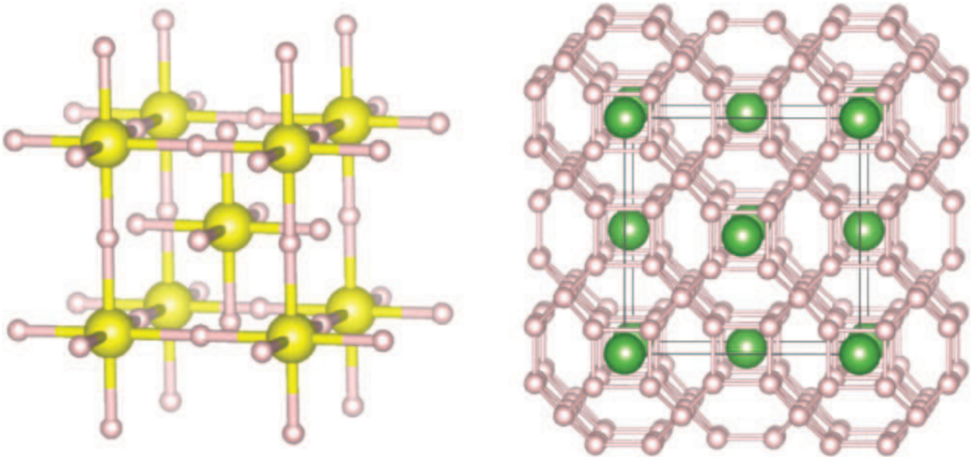

Fig. 3 Typical crystal structures of superconducting hydrides. (left) H_3S. Hydrogen atoms are arranged in a straight line between the lattices of sulfur atoms. (right) LaH_{10}. Hydrogen atoms surround lanthanum atoms.

US group (Somayazulu et al., 2019) using ammonia borane (NH_3BH_3) as a hydrogen source. After pressurizing the sample at room temperature to the theoretically predicted pressure, the sample was heated by an infrared laser and synthesized by reacting the sample with hydrogen in contact with the sample or with hydrogen generated from ammonia borane. The use of ammonia borane as a hydrogen source has become more common in recent years due to the convenience of experimental setup compared to using hydrogen directly.

USOs (unidentified superconducting objects)

Many hydride superconductors have been predicted from theoretical calculations and many demonstration experiments have been reported. It is foreseen that the day when the superconducting transition temperature exceeds room temperature is approaching. In this context, in 2020, a report emerged of observing the superconductivity with the T_c exceeding room temperature at 250 GPa in a carbon-sulfur hydride compound (CSH) (Snider et al., 2020). Furthermore, in 2023, the observation of room-temperature superconductivity in nitrogen-doped Lu hydride (NLuH) at very low pressure, ~1 GPa was announced (Dasenbrock-Gammon et al., 2023). There on the Web and in newspapers are claiming "room-temperature superconductivity has finally been achieved." However, at the time of writing this article, no research group has been able to reproduce these experiments, and the paper (Snider et al., 2020) has been retracted.

These things remind us the term of "Unidentified Superconducting Object" (USO) that defined by Prof. Kitazawa to refer to materials that failed to satisfy all of the following conditions during the fever of copper oxide superconductors in the 1980s: (1) observation of zero resistance, (2) observation of the Meissner effect, (3) determination of crystal structure, and (4) reproduction by other research groups. At the moment, (3) and (4) are missing from both CSH and NLuH, so a follow-up report will be forthcoming.

Future prospects

Toward higher temperatures

How can we achieve higher transition temperatures (T_c)? One approach is to substitute or add lighter elements as constituents. In the case of hydrogen sulfide, this would involve replacing sulfur with a lighter element in the same group, such as oxygen, or adding oxygen to the system. Such proposals based on theoretical calculations have been put forward, including the suggestion of adding phosphorus (Ge et al., 2016; Nakanishi et al., 2018). These substitutions and additions have been common strategies employed whenever a new superconductor is discovered. However, as of now, no significant increase in T_c has been observed through these methods in superconducting hydrides.

Toward lower pressure

Theoretical calculations and experiments are underway for ternary hydrides with one more parent element. The purpose of this research is to explore superconducting hydrides that can be synthesized at lower pressures, in addition to achieving higher transition temperatures (T_c). The ultimate goal is to synthesize room-temperature, ambient-pressure superconductors that do not require pressure. If the synthesis pressure can be reduced to less than 50 GPa, which can be generated by a high-pressure apparatus such as a KAWAI-type press, it will make possible to synthesize the superconductors with millimeter-sized samples. Further reduction of the pressure to a few GPa could enable the synthesis of centimeter-sized samples. This would enable the neutron diffraction experiments with sufficient intensity and reveal the nature of hydrogen, the key element in hydride superconductors. Then this would contribute to a better understanding of hydride superconductors and the development of pressure-free room-temperature superconductors will become more realistic.

Control of hydrogenation

There have been several theoretical proposals for hydrides exceeding room temperature, but experimental verification has been challenging. This is partly due to the high cost of experiments consuming diamonds, but also because successful examples that match the theoretical predictions are limited. For example, different hydrides with different amounts of hydrogen are synthesized. During the synthesis process, it is possible that more stable hydrides with a different hydrogen content exist along the temperature-pressure path, which prevents further hydrogenation. There may be an optimal temperature and pressure pathway that avoids this problem, but it is considered difficult to clarify the synthesis pathway by theoretical calculation due to the large amount of calculation.

There is no doubt that hydrogen-rich compounds are strong candidates to realize room-temperature superconductivity. Many candidate materials will be theoretically proposed, experimentally tested, and valuable results will be fed back to theory. This will lead to a more precise selection of candidate materials.

Conclusion

Although an extreme environment of ultrahigh pressure is necessary, hydrogen has been growing expectations not only as an energy source but also as a source of superconductor to conserve energy. However, it is expected to take some more time before we can fully utilize this near room-temperature superconductivity. Current efforts focus on reducing the required pressure and on considering utilizing them even at high pressures. Hydrides are a strong candidate for room-temperature superconductivity, and at the same time, a significant exercise in materials science.

References

Ashcroft NW (1968) Metallic hydrogen: A high-temperature superconductor? *Physical Review Letters* 21: 1748–1749.

Ashcroft NW (2004) Hydrogen dominant metallic alloys: High temperature superconductors? *Physical Review Letters* 92: 187002.

Dasenbrock-Gammon N, Snider E, McBride R, Pasan H, Durkee D, Khalvashi-Sutter N, Munasinghe S, Dissanayake SE, Lawler KV, Salamat A, and Dias RP (2023) Evidence of near-ambient superconductivity in a N-doped lutetium hydride. *Nature* 615: 244–250.

Drozdov AP, Eremets MI, Troyan IA, Ksenofontov V, and Shylin SI (2015) Conventional superconductivity at 203 kelvin at high pressures in the sulfur hydride system. *Nature* 525: 73–76.

Drozdov AP, Kong PP, Minkov VS, Besedin SP, Kuzovnikov MA, Mozaffari S, Balicas L, Balakirev FF, Graf DE, Prakapenka VB, Greenberg ED, Knyazev A, Tkacz M, and Eremets MI (2019) Superconductivity at 250 K in lanthanum hydride under high pressures. *Nature* 569: 528–531.

Duan D, Liu Y, Tian F, Li D, Huang X, Zhao Z, Yu H, Liu B, Tian W, and Cui T (2014) Pressure-induced metallization of dense $(H_2S)_2H_2$ with high-T_c superconductivity. *Scientific Reports* 4: 6968.

Einaga M, Sakata M, Ishikawa T, Shimizu K, Eremets MI, Drozdov AP, Troyan IA, Hirao N, and Ohishi Y (2016) Crystal structure of the superconducting phase of sulfur hydride. *Nature Physics* 12: 835–838.

Feng X, Zhang J, Gao G, Liu H, and Wang H (2015) Compressed sodalite-like MgH_6 as a potential high-temperature superconductor. *RSC Advances* 5: 59292–59296.

Ge Y, Zhang F, and Yao Y (2016) First-principles demonstration of superconductivity at 280 K in hydrogen sulfide with low phosphorus substitution. *Physical Review B* 93: 224513.

Li Y, Hao J, Liu H, Li Y, and Ma Y (2014) The metallization and superconductivity of dense hydrogen sulfide. *The Journal of Chemical Physics* 140: 174712.

Liu H, Naumov II, Hoffmann R, Ashcroft NW, and Hemley RJ (2018) Potential high-T_c superconducting lanthanum and yttrium hydrides at high pressure. *PNAS* 114: 6990–6995.

Nakanishi A, Ishikawa T, and Shimizu K (2018) First-principles study on superconductivity of P- and Cl-doped H_3S. *Journal of the Physical Society of Japan* 87: 124711.

Nakao H, Einaga M, Sakata M, Kitagaki M, Shimizu K, Kawaguchi S, Hirao N, and Ohishi Y (2019) Superconductivity of pure H_3S synthesized from elemental sulfur and hydrogen. *Journal of the Physical Society of Japan* 88: 123701.

Ohta K, Ichimaru K, Einaga M, Kawaguchi S, Shimizu K, Matsuoka T, Hirao N, and Ohishi Y (2015) Phase boundary of hot dense fluid hydrogen. *Scientific Reports* 5: 6560.

Shimizu K, Amaya K, and Suzuki N (2005) Pressure-induced superconductivity in elemental materials. *Journal of the Physical Society of Japan* 74: 1345–1357.

Snider E, Dasenbrock-Gammon N, McBride R, Debessai M, Vindana H, Vencatasamy K, Lawler KV, Salamat A, and Dias RP (2020) Room-temperature superconductivity in a carbonaceous sulfur hydride. *Nature* 586: 373–377.

Somayazulu M, Ahart M, Mishra AK, Geballe ZM, Baldini M, Meng Y, Struzhkin VV, and Hemley RJ (2019) Evidence for Superconductivity above 260 K in Lanthanum Superhydride at Megabar Pressures. *Physical Review Letters* 122: 027001.

Wang H, Tse JS, Tanaka K, Iitaka T, and Ma Y (2012) Superconductive sodalite-like clathrate calcium hydride at high pressures. *PNAS* 109: 6463–6466.

Weir ST, Mitchell AC, and Nellis WJ (1996) Metallization of fluid molecular hydrogen at 140 GPa (1.4 Mbar). *Physical Review Letters* 76: 1860–1863.

Unconventional superconductivity

Igor I Mazin, Department of Physics & Astronomy, George Mason University, Fairfax, VA, United States

© 2024 Elsevier Ltd. All rights reserved.

Abstract

The division of the broad field of superconductivity into *conventional* and *unconventional* is conditional, just as any binary division based on a subjective notion of "conventionality". It is often in the eye of the beholder. Still, it is often a useful, even if fuzzy, line between superconductivity that follows, with modifications, the traditional framework established by Bardeen, Cooper, Schrieffer, and Eliashberg, and that which deviates from that path.

Key points

- Defining unconventional superconductivity
- Higher angular momenta
- Examples of unconventional superconductors
- Odd-frequency order parameter
- Conditions conducive for unconventional superconductivity
- Some useful theorems
- Multigap superconductors
- Further reading

Unconventional superconductivity is an umbrella term that has been used by different researchers with different meaning. Common definitions refer to conventionality in three separate aspects: pairing mechanism, pairing symmetry, and transition temperature. In addition, occasionally conventional in their mechanism superconductors are considered unconventional because of their specific unusual properties. Examples of that include, for instance, Ising superconductors and topological superconductivity.

The most restrictive definition of conventional superconductors (CSC) stipulates that CSC are (a) mostly mediated by adiabatic (*e.g.*, respecting the Migdal theorem) harmonic phonons, (b) have isotropic or nearly-isotropic s-wave order parameter and (c) have critical temperature below 20–30 K. Such a limiting definition is rarely called for. Recently discovered superconducting superhydrates are believed to be phonon-mediated and isotropic s-wave, despite having critical temperatures approaching the room temperature and possibly nonadiabatic and anharmonic phonons, yet they are usually classified as CSC. In fact, these criteria are not independent. Indeed, a purely attractive interaction, such as phonon-mediated, cannot generate a superconducting state with a sign-changing order parameter, and, conversely, a pure repulsive (in the momentum space) interaction cannot generate a state that has an order parameter of the same sign everywhere.

Most scientists agree that a pairing state that involves an order parameter of lower point group symmetry than the hosting crystal (p-wave, d-wave etc.) should be classified as unconventional, regardless of the transition temperature. Obviously, such states cannot originate from pure phonon attraction, so pairing interaction is by definition unconventional in that sense. On the other hand, repulsive interactions, such as those of magnetic origin, may result in a sign-changing order parameter of the s-wave angular symmetry. Such states are often called $s_{\pm}$, and also usually classified as unconventional.

At the dawn of superconductivity it was believed that unconventional superconductors are but a theoretical Kunststück that is not supposed to occur in real materials, for the reason that nonmagnetic impurities are pair-breaking for such a state, and—as it was thought—would kill such superconductivity dead except in exceptionally clean samples.

It turned out that reality is not that bleak, and, in particular, that unconventional superconductors tend to have short coherence lengths, and therefore less prone to pair breaking (which is controlled by the ratio of the coherence length and the mean free path). In the moment, a number of well-studied superconductors have been convincingly demonstrated to have unconventional pairing symmetries. This includes high-T_c cuprates (d-wave), Fe-based superconductors ($s_{\pm}$); a number of heavy fermion systems, where the exact symmetry of the order parameter has not been established above reasonable doubt, are generally believed to host unconventional, possibly triplet, superconductivity. Same can be said about many organic (quasi-1D) superconductors. An interesting case is Sr_2RuO_4: For at least 20 years it was believed it was a triplet p-wave superconductors, but recent experiments convincingly point toward a singlet state. Yet, there is little doubt that superconductivity there, while still unresolved, is unconventional.

A separate, even more exotic case is the so-called odd-frequency superconductivity, whereby the frequency-dependent order parameter is assumed to change sign not (or not only) in the momentum space, but when the frequency argument changes its sign. No realistic candidates among real materials have been identified, albeit there were some proposals of this character, but there is some experimental evidence that such states can be generated by proximity effects near superconductor-ferromagnet interfaces.

https://doi.org/10.1016/B978-0-323-90800-9.00160-8

The number of unconventional superconductivity candidates identified in the last decades is considerable, and suggests several empirical rules that are conducive for UCSC. These tend to be low-dimensional (quasi-1D or quasi- 2D), and tend to have a phase diagram where superconductivity emerges near magnetic (usually antiferromagnetic) states. This is not unexpected, given that UCSC is likely to be mediated by some kind of spin fluctuations, and both proximity to magnetism and low dimensionality favor spin fluctuations.

Let us now discuss in more details the principal classes of UCSC.

High-T_c cuprates emerge in the vicinity of the Mott-Hubbard metal insulator transition. The Cu^{2+} ions have one hole in the rather localized d-shell, which is therefore subject to strong local Coulomb repulsion, $U \gg t$, where t is the one-electron hopping parameters for d-electrons. This generates a nearest neighbor antiferromagnetic superexchange, proportional to t^2/U. In parent compounds this results in a checkerboard antiferromagnetic ordering with the wave vector $\mathbf{Q} = (1,1,0)\ \pi/a$. Upon doping the magnetic order melts and the insulating state is being transformed into a strongly correlated metal. Instead of the static order, Cu spins now fluctuate with the same wave vector $\mathbf{Q}$.

The one-electron band structure of these cuprates is formed by a single x^2–y^2 orbital, so the corresponding Fermi surface is close to a circular cylinder. It is easy to see that if one postulates the d-wave order parameter with the same symmetry, x^2–y^2, spin fluctuations with the wave vector $\mathbf{Q}$ will be spanning two parts of the Fermi surface with the opposite signs of the order parameter and therefore be pairing. This simple argument has led to the view, shared by a majority of researchers, that superconductivity in cuprates is driven by spin-fluctuations.

Similarly, in Fe-based superconductors, the magnetic order in the parent antiferromagnets corresponds to $\mathbf{Q} = (1,0,0)\pi/a$ in the single-Fe unit cell, and the Fermi surface, in most cases, consists of two groups, one centered around $\mathbf{q} = (0,0,0)\pi/a$ and the other around $\mathbf{q} = (1,0,0)\pi/a$; so assigning different signs to the order parameters in the two sets assures that spin-fluctuations are pairing. Thus, a plurality, and may be even majority of scientists believe these materials, as well, to be fluctuations-driven.

These two example are, arguably, the best studied UCSC. Yet, there is a solid body of evidence in favor of unconventional pairing in numerous other materials, including, but not limited to organic metals, heavy fermions, or twisted bilayer graphene.

Some useful theorems regarding unconventional pairing symmetries are: (1) A fully local (*i.e.*, contact) Coulomb repulsion, such as the Hubbard interaction, cancels out if the order parameter integrates to zero over the entire Fermi surface (regardless of the nature of the pairing interaction). This can be also reformulated by applying the Fourier transform and considering the structure of a Cooper pair in coordinate space. In this case, the component of the pair are localized on different lattice sites. In case of cuprates (d-wave) these are nearest neighbors in the square lattice, and in case of Fe-based superconductors ($s_\pm$) on the second neighbors. (2) While the order parameters itself may follow a lower-symmetry representation than the full crystal symmetry (A_{1g}), its amplitude, *i.e.*, the excitation gap, usually does follow the full symmetry (some exceptions to this rule, often called "nematic" superconductivity, have been proposed theoretically). (3) Even if the order parameter does not obey the point group, it is, including the phase, subject to the Bloch theorem, so that $\Delta(\mathbf{k}) = \Delta\ (\mathbf{k} + \mathbf{G})$, where $\mathbf{G}$ is a reciprocal lattice vector. It is a powerful theorem because it forces order parameter nodes at some special high-symmetry points.

Finally, it is worth bringing up yet another class of materials, multigap superconductors, where the magnitude of the order parameter changes exceptionally strongly over the Fermi surface or between different Fermi surface pockets. These are not usually called UCSC now, but they were not appreciated (albeit theoretically discussed already in the late 50s) until the discovery of a two-gap superconductivity in MgB_2 in 2001—at that time MgB_2 was routinely referred to as an unconventional, but phonon-driven superconductor.

Further reading: (Sigrist and Ueda, 1991; Zhou et al., 2021; Norman, 2011; Moriya and Ueda, 2003) (general), (Mazin and Antropov, 2003) (MgB_2), (Lee et al., 2006) (cuprates), (Hirschfeld et al., 2011; Hosono and Kuroki, 2015) (Fe-based).

References

Hirschfeld PJ, Korshunov MM, and Mazin II (2011) Gap symmetry and structure of Fe-based superconductors. *Reports on Progress in Physics* 74: 124508.

Hosono H and Kuroki K (2015) Iron-based superconductors: Current status of materials and pairing mechanism. *Physica C: Superconductivity and Its Applications* 514: 399.

Lee PA, Nagaosa N, and Wen X-G (2006) Doping a Mott insulator: Physics of high-temperature superconductivity. *Reviews of Modern Physics* 78: 17.

Mazin II and Antropov VP (2003) Electronic structure, electron-phonon coupling, and multiband effects in MgB_2. *Physica C: Superconductivity* 385: 49.

Moriya T and Ueda K (2003) Antiferromagnetic spin fluctuation and superconductivity. *Reports on Progress in Physics* 66: 1299.

Norman MR (2011) The challenge of unconventional superconductivity. *Science* 332: 196.

Sigrist M and Ueda K (1991) Phenomenological theory of unconventional superconductivity. *Reviews of Modern Physics* 63: 239.

Zhou X, Lee W-S, Imada M, Trivedi N, Phillips P, Kee H-Y, Törmä P, and Eremets M (2021) High-temperature superconductivity. *Nature Reviews Physics* 3: 462.

Superconducting density of states from scanning tunneling microscopy

Hermann Suderow, Laboratory of Low Temperatures and High Magnetic Fields, Condensed Matter Physics Department, Nicolás Cabrera Institute and Condensed Matter Physics Center (IFIMAC), Associated Unit UAM-CSIC, Autonomous University of Madrid, Madrid, Spain

© 2024 Elsevier Ltd. All rights reserved.

Introduction **600**
Overview **601**
Tunneling conductance 601
Distribution of values of the superconducting gap 602
Behavior at defects and impurities 603
Key issues **604**
Superconductors with a small gap anisotropy 604
Two-gap superconductivity in MgB_2 604
Layered transition metal dichalcogenides 605
Nickel borocarbides 606
Summary and future directions **607**
Summary 607
Future directions 607
Cuprate superconductors 608
Pnictide- and Fe-based superconductors 608
Topological superconductors 609
Highly disordered superconductors 609
Conclusion **610**
Acknowledgments **610**
References **610**

Abstract

In Bardeen, Cooper and Schrieffer's (BCS) theory of superconductivity, the usual metallic parabolic nearly-free-electron band is modified by opening a gap at the Fermi level. The electronic density of states is zero within the gap and presents peaks at the gap edges. Many materials have superconducting properties that deviate from BCS theory and, as a consequence, the density of states is very different, too. The differently shaped density of states signals new paradigms in superconductivity, such as two-band, anisotropic, or multigap superconductivity. Here, measurements of the density of states obtained using Scanning tunneling microscopy (STM) in representative compounds are reviewed and future prospects of advances in superconductivity using STM are discussed.

Key points

- Present basic aspects of the superconducting density of states.
- Discuss the tunneling conductance in representative examples.
- Discuss methods to address new superconductors.

Introduction

The superconducting state is characterized by the condensation of pairs of electrons into Cooper pairs described by a macroscopic quantum wave function $\Psi(\boldsymbol{r})$ which has a smooth dependence on the position $\boldsymbol{r}$ (Leggett, 2005; Larkin, 2005). Consequences are the establishment of dissipationless transport and of flux quantization (Kirtley and Tsuei, 2005; Brandt, 2005), both of great importance for applications (Bishop, 2005a; Gurevich, 2005). The occurrence of superconductivity is described by Bardeen, Cooper and Schrieffer's (BCS) theory (Bennemann, 2005, 2023). BCS theory describes the condensate as well as its excitations. The latter are located at an energy E above the superconducting gap Δ. Within BCS theory, the pairing interaction energy is of the order of the Debye temperature and much larger than the superconducting gap Δ, both also much smaller than the Fermi energy E_F.

After more than 66 years of BCS theory, numerous compounds and systems have been shown to be superconducting, with critical temperatures ranging from below a mK up to near room temperature (Bishop, 2005b; Qin and Dou, 2005). The pairing

https://doi.org/10.1016/B978-0-323-90800-9.00240-7

interaction energy and Fermi temperatures vary across many orders of magnitude, too (Nozières and Schmitt-Rink, 1985; Fazio and van der Zant, 2001; Shibauchi et al., 2020; Blatter et al., 1994). The energy dependence of the excitations of the superconducting state depends on the pairing interaction and on the coexistence with other magnetic or charge ordering phenomena. As a consequence, the electronic excitations can be very different in different superconducting materials.

In Fig. 1A, the energy dispersion relation within BCS theory is schematically shown. The superconducting density of states is obtained by integrating over the wavevector (Fig. 1B). In BCS theory, superconductivity modifies the free electron parabolic electronic energy dispersion relation and opens a gap with size $\pm\Delta$ above and below the Fermi level. This provides sharp peaks in the density of states at the superconducting gap energy $\pm\Delta$ and no states for $|E| < \Delta$ (Fig. 1B).

The superconducting density of states can be probed by many measurements, such as specific heat, thermal conductivity, nuclear magnetic resonance, and penetration depth. All these probes address however the energy integral of the density of states. To obtain the energy dependence of the density of states, one has to measure directly the electronic band structure. This requires injecting or retrieving electronic excitations from the superconductor, which can be done by tunneling or by photoemission (Cleland, 2005; Margaritondo, 2005). Tunneling conductance experiments can be usually made at lower temperatures than photoemission. Furthermore, a magnetic field can be applied. Thus, tunneling conductance measurements have been more widely applied to superconductors.

Tunneling conductance can be measured between a superconductor and another electrode through an evaporated insulating barrier (Dragoman and Dragoman, 2005) or by approaching a tip to the surface of a superconductor and using vacuum as the tunneling barrier. Here the focus is on results obtained using the latter approach with a Scanning tunneling microscope (STM). Other aspects of superconductivity and tunneling, such as DC and AC Josephson effects, Andreev reflection or superconducting vortex physics are discussed by Cleland (2005), Fischer et al. (2007), Suderow et al. (2014), Tafuri (2023), and Mikitik (2023).

Overview

Tunneling conductance

Bringing two metallic electrodes at a sufficiently short distance, of the order of the nm, produces a tunneling current that flows between both electrodes. This is schematically shown in Fig. 2. The tunneling current is given by the overlap between the

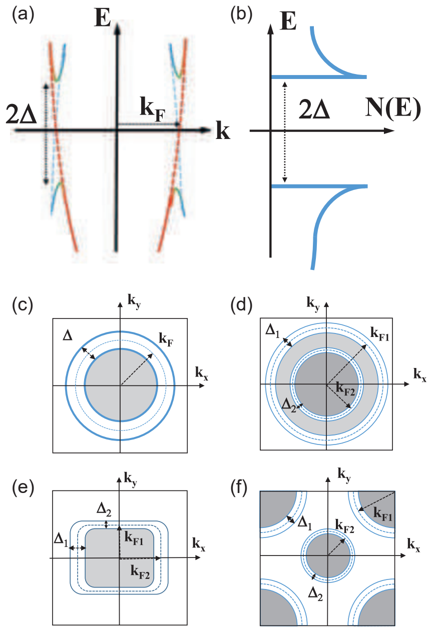

Fig. 1 (A) The dispersion relation for free electrons is shown by the *red dashed line*. In a superconductor below T_c, the dispersion relation is modified by the opening of the superconducting gap, following BCS theory. The corresponding band structure is shown by the colored *red* and *blue lines*. *Red* is for electron-like excitations and *blue* is for hole-like excitations. (B) The BCS density of states as a function of the energy (*blue line*). (C)–(F) Schematic view of different gap structures is shown as *blue lines* within a two-dimensional Brillouin zone (*black square*). *Dashed blue lines* provide the Fermi wave vector. (C) S-wave BCS single gap. The gap magnitude (Δ) is constant over all the Fermi surface. (D) Two disk-shaped Fermi surfaces (*grey circles*) having two different magnitudes of the superconducting gap. (E) A square-shaped Fermi surface, with two different values of the superconducting gap along two directions. (F) Fermi surface of a band structure that crosses the Brillouin zone. The gap magnitude is different on the central pocket as compared to the pockets at the corners of the Brillouin zone.

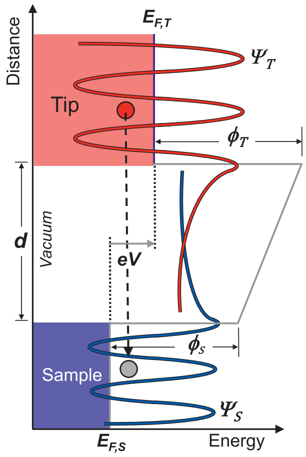

Fig. 2 Schematic view of tunneling between tip and sample in an STM. The tunneling gap of width *d* is shown by the *vertical arrow*. The electronic wave functions (Ψ_T and Ψ_S for tip and sample) are schematically represented by the *blue* and *red lines*. The bias voltage is shown by a *horizontal grey arrow*. Work functions of each electrode are shown schematically as Φ_T and Φ_S for tip and sample, respectively.

wavefunctions extending into vacuum. Bardeen's formalism, modified by Tersoff and Hamann for STM (Bardeen, 1961; Tersoff and Hamann, 1983, 1985; Agrait et al., 2003), describes the tunneling current as

$$I(V) = \frac{4\pi e}{\hbar}\int_{-\infty}^{\infty} dE|M|^2 N_s(E-eV)N_t(E)(f(E-eV-f(E)), \tag{1}$$

where e is the electron charge, $\hbar$ is the Planck's constant, E is the energy, V is the applied voltage, M is the tunneling matrix element, $N_s(E-eV)$ and $N_t(E)$ are the densities of states of tip and sample, and $f(E)$ is the Fermi function.

Here the focus is on the situation where a normal metal such as Au or Pt is used for the tip.[1] At energies approximately below ± 100 meV of the Fermi level, N_t is approximately flat and constant and can be taken out of Eq. (1). Then one can write for the bias voltage dependence of the tunneling conductance $\sigma(V) = \frac{dI}{dV}$:

$$\sigma(V) \propto \int_{-\infty}^{\infty} dE N_s(E)\frac{\partial f(E-eV)}{\partial V}. \tag{2}$$

At sufficiently low temperatures, $\frac{\partial f(E-eV)}{\partial V}$ is close to a δ function, for which one obtains that the tunneling conductance versus bias voltage V follows the superconducting density of states $\sigma(V) \simeq N_s(eV)$.

In a simple metal, with only a single band crossing the Fermi level and a fully spherical Fermi surface, BCS theory leads to an equally isotropic superconducting gap, schematically shown in Fig. 1C (in two dimensions for clarity). Then, Eq. (2) provides an excellent account of the tunneling conductance, which closely follows the BCS relation $\sigma(V) \simeq N_s(E=eV) \propto \frac{E}{\sqrt{E^2-\Delta^2}}$.

Distribution of values of the superconducting gap

Most materials are however not simple metals and can have quite an intricate set of bands crossing the Fermi level. Let us consider a hypothetical metal with two isotropic bands crossing the Fermi level (Fig. 1D). To find the superconducting density of states, one has to integrate the reciprocal wave vector dependence. The result is a sum with two contributions $N(E) = N_{s,1}(E) + N_{s,2}(E)$, each $N_{s,i=1,2}(E)$ eventually following the BCS relation for a fully opened superconducting gap with generally different values Δ_1 and Δ_2. Similarly, a superconductor with an anisotropic crystal lattice might have a single band crossing the Fermi level, but different values of the superconducting gap along different crystalline directions (Fig. 1E). Alternatively, there can be bands located at different places on the Brillouin zone, showing different values of the superconducting gap (Fig. 1F). The latter cases might again lead to $N(E) = N_{s,1}(E) + N_{s,2}(E)$ with different gap values $\Delta_{1,2}$. Generally there can be many contributions to $N(E)$ from portions of the band structure close to the Fermi level located in places in the Brillouin zone with very different values of the superconducting gap Δ_i.

---

[1] When using a superconducting tip as Al, Pb, or Nb, $N_t(E-eV)$ is strongly featured in a similar energy range as the superconducting counter electrode. In that case, Eq. (1) has to be evaluated in full to understand the tunneling conductance (Rodrigo and Vieira, 2004; Rodrigo et al., 2004a; Proslier et al., 2006; Guillamon et al., 2008; Kohen et al., 2006; Liu et al., 2021a; Pan et al., 1998; Heinrich et al., 2018), with resulting curves that can be very rich, showing, for example, ranges with a negative differential resistance (Hatter et al., 2015; Huang et al., 2020), enhanced resolution in energy (Heinrich et al., 2018; Ruby et al., 2015; Kim et al., 2020), divergent behavior at the gap edge of the tip or situations in which $I(V)$ follows quite closely the superconducting N_s (Crespo et al., 2012).

In an STM experiment, one measures the tunneling conductance at an atomically well-defined position on the surface of the superconducting sample. To discuss the actual shape of the tunneling conductance measured with an STM at atomic scale, let us go back to Eq. (1). The term $|M|^2$ depends on the wave function overlap between tip and sample, which depends of course on the actual atomic level position of the tip. But in presence of an anisotropic band structure, the different wave function overlap also produces different contributions to $N_s(E - eV)$ from different portions of the band structure close to the Fermi level. The relative weight of these contributions varies at the atomic scale. Thus, both $|M|^2$ and $N_s(E - eV)$ are different at each atomically resolved position over the surface of the sample. This provides a certain spatial dependence of the combined term $|M|^2 N_s(E - eV)$. To find the values of the superconducting gap in different portions of the band structure from the tunneling conductance, one can write

$$N_s(E) = \sum_i \gamma_i Re\left(\frac{E}{\sqrt{E^2 - \Delta_i^2}}\right) \tag{3}$$

where γ_i is the relative weight of the contribution of a certain portion of the band structure and Δ_i is the corresponding value of the superconducting gap. For the schematic gap structures shown in Fig. 1C–F, one finds $N_s(E)$ as a sum of two BCS densities of states, each peaked at Δ_1 and Δ_2.

But the actual gap distribution γ_i in a superconducting material can be smooth, with many Δ_i varying for different values and directions of the reciprocal space wave vector $\boldsymbol{k}$. Generally, this eliminates the divergent quasiparticle peaks of the BCS expression $N_{BCS}(E) = \frac{E}{\sqrt{E^2 - \Delta^2}}$ and produces instead $N_s(E)$ with rounded peaks at the values where the gap distribution Δ_i concentrates.

Note that rounded peaks are also obtained when taking into account lifetime broadening effects in the calculation of the density of states (Dynes et al., 1978). Lifetime broadening is a consequence of the pairing interaction and can considerably influence the BCS expression for the density of states. When lifetime broadening is large, it generally leads to an increased density of states at zero energy. Eq. (3) instead refers to a gap broadening due to the superconducting anisotropy and leads to a vanishing zero bias conductance as long as $\Delta_i \gg k_B T$ for all i.

Studying the γ_i and Δ_i as a function of the position on the surface, one can extract considerable information over the shape of the superconducting gap (Rodrigo and Vieira, 2004; Guillamón et al., 2008). For example, in a two-gap superconductor with Δ_i distributed around two main values centered at $\Delta_{1,avg}$ and $\Delta_{2,avg}$, tunneling into a certain surface can produce a $N_s(E)$ with a contribution from portions of the band structure highlighting $\Delta_{1,avg}$ or $\Delta_{2,avg}$, depending on the actual atomic termination at each surface (Cho et al., 2017; Fente et al., 2018).

Even when scanning with the tip over a certain surface, one can find different contributions to the tunneling conductance at different atomic positions (Guillamon et al., 2008). This does not mean that the superconducting density of states changes at atomic length scales (usually far below the superconducting coherence length). Instead, it shows that the contribution to the tunneling current at each atomic position depends on the contributions to the tunneling density of states from different places of the Brillouin zone. The overall superconducting density of states is by contrast the sum over the whole band structure and does not change as a function of the position in absence of disturbances of the superconducting condensate.

Behavior at defects and impurities

When measuring the surface of a single crystal, there are often impurities or defects. Charge screening implies an oscillatory density of states around impurities or defects, with a wave vector of the order of the Fermi wave vector $\boldsymbol{k_F}$. The usual Friedel oscillations in a metal are a consequence of the spatial dependence of the charge density summed from the bottom of the band to the Fermi energy (Ziman, 1972). STM allows measuring the density of states on the surface at different energies E. Maps of the tunneling conductance $\sigma(eV)$ at a bias voltage $eV = E_0$ provide the spatial dependence of $N_s(x, y)$ at E_0. These maps present often oscillations, at each energy E_0, created by impurities or defects. The wave vector of the oscillations is related to the value of the electronic wave vector at the energy E_0. Thus, the wave vector follows the electron dispersion relation as a function of the energy E_0.

Note that these are not really Friedel oscillations in the usual sense. One can understand the oscillatory behavior observed by STM by using scattering of electrons confined to surfaces, as opposed to Friedel oscillations which are obtained by integrating the density of states over all energies. At the end, the result is similar, except that surface states scatter electrons and lead to an oscillatory signal, whereas the bulk band structure leads to Friedel oscillations whose projection on the surface is observed, too (Crommie et al., 1993; Heller et al., 1994; Crommie et al., 1995; Fiete and Heller, 2003; Petersen et al., 1998; Hoffman et al., 2002; McElroy et al., 2003; Hoffman, 2011; Pascual et al., 2004; Ortuzar et al., 2022).

The wave vector observed in the maps of the tunneling conductance $\sigma(eV)$ is two times the wave vector of the dispersion relation. Elastic scattering joins portions of the band structure at opposite wave vectors, $\boldsymbol{k}$ and $-\boldsymbol{k}$. One can write for the Fourier transform of the spatial dependence of the superconducting density of states with a modulation:

$$g(E, \boldsymbol{q}) \propto |V(E, \boldsymbol{q})| J(E, \boldsymbol{q}), \tag{4}$$

where g is the Fourier transform of the tunneling conductance, $V\ (E, \boldsymbol{q})$ is the scattering potential, J is the joint density of states, $J(E, \boldsymbol{q}) \propto N_s(E, \boldsymbol{k_1}) N_s(E, \boldsymbol{k_2})$ and $\boldsymbol{q} = \boldsymbol{k_2} - \boldsymbol{k_1}$ the scattering wave vector joining pairs of states at the same energy E (Hoffman et al., 2002; Fente et al., 2018). One can see that the scattering intensity and pattern depend on the scattering properties of the impurity or defect (the scattering potential $V\ (E, \boldsymbol{q})$) and on the density of states. For example, an impurity with a twofold anisotropy can produce scattering along the impurity's anisotropy axis. Quasiparticle peaks located at the same gap values $E = \Delta_{i,j}$ also produce enhanced scattering. Thus, if one considers isotropic impurities or defects, one can obtain the variation of the superconducting gap in reciprocal space.

Key issues

In this section, a selection of superconductors with a density of states deviating from most simple s-wave BCS theory is presented. These systems have been widely studied during past years. One can probably safely state that there is an ample consensus about the interpretation of the observed tunneling density of states and its relation to the bulk superconducting properties.

Superconductors with a small gap anisotropy

In Fig. 3 the tunneling conductance in superconducting Al and Pb is shown (Martín-Vega et al., 2021). The density of states is zero within the superconducting gap and the quasiparticle peaks are well developed, following closely the BCS density of states $N_{BCS}(E)$. Similar results have been obtained for Nb, V, La or Re (Guillamon et al., 2008; Pan et al., 1998; Assig et al., 2013; Ruby et al., 2015; Fernández-Lomana et al., 2021; Senkpiel et al., 2020; Tonnoir et al., 2013; Senkpiel et al., 2022; Ast et al., 2016; Eltschka et al., 2015; le Sueur et al., 2008; Lo Conte et al., 2022; Kim et al., 2018; Nadj-Perge et al., 2014; Palacio-Morales et al., 2019). In spite of being elemental superconductors, some materials can have several bands crossing the Fermi level. When single crystalline samples are measured, the associated difference in the gap magnitude over the Fermi surface is well resolved. For example, Pb has two well defined values of the superconducting gap, as shown by Ruby et al. (2015). When nonsingle-crystalline samples are measured, there is often a small distribution of values of the superconducting gap Δ_i (see Eq. 3), following a Gaussian shape around the value expected from the single-gap BCS theory (Rodrigo and Vieira, 2004; Rodrigo et al., 2004a, b; Suderow et al., 2002).

A similar result is observed in many binary intermetallic superconducting compounds (Herrera et al., 2023b). Some are shown in Fig. 4. In these cases, often the distribution of Δ_i is more extended than in elemental superconductors.

Two-gap superconductivity in MgB_2

The best known example for a two-gap superconductor is MgB_2 (Nagamatsu et al., 2001; Rubio-Bollinger et al., 2001; Bud'ko et al., 2001). There are different bands crossing the Fermi level with small interband interactions and very different electron–phonon coupling. Bands derived from B σ-orbitals have a small overlap to bands from B π-orbitals. At the same time, there is a very strong electron–phonon coupling due to the in-plane B atom vibrations (Kortus et al., 2001; Choi et al., 2002). This leads to large values of the superconducting gap in the σ-derived bands, whereas the gap remains small in the π-derived bands. The tunneling conductance (Fig. 5) nicely shows the two superconducting gaps, and there is quite a wide distribution of gap values around the two main gap values ($\Delta_{1avg} = \Delta_\pi \approx 2.2$ meV and $\Delta_{2avg} = \Delta_\sigma \approx 7.1$ meV) (Martinez-Samper et al., 2003; Rubio-Bollinger et al., 2001; Giubileo et al., 2001).

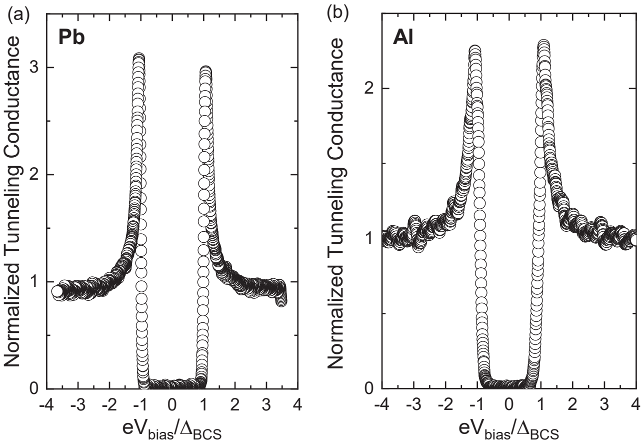

Fig. 3 Tunneling conductance obtained in Pb (A) and in Al (B). The tunneling conductance is normalized to its value at voltages well above the superconducting gap. The bias voltage is normalized to the BCS value of the superconducting gap Δ_{BCS}. (A) Adapted from Martín-Vega, F., Barrena, V., Sánchez-Barquilla, R., Fernández-Lomana M, Benito Llorens J, Wu B, Fente A, Perconte Duplain D, Horcas I, López R, Blanco J, Higuera JA, Mañas-Valero S, Jo NH, Schmidt J, Canfield PC, Rubio-Bollinger G, Rodrigo JG, Herrera E, Guillamón I, and Suderow H (2021) Simplified feedback control system for scanning tunneling microscopy. Review of Scientific Instruments 92(10): 103705. https://doi.org/10.1063/5.0064511 with the permission of AIP Publishing. (B) Adapted from Fernández-Lomana M, Wu B, Martín-Vega F, Sánchez-Barquilla R, Álvarez Montoya R, Castilla JM, Navarrete J, Marijuan JR, Herrera E, Suderow H, and Guillamón I (2021) Millikelvin scanning tunneling microscope at 20/22 T with a graphite enabled stick-slip approach and an energy resolution below 8 μev: Application to conductance quantization at 20 T in single atom point contacts of Al and Au and to the charge density wave of 2H-NbSe2. Review of Scientific Instruments 92(9): 093701. https://doi.org/10.1063/5.0059394 with the permission of AIP Publishing.

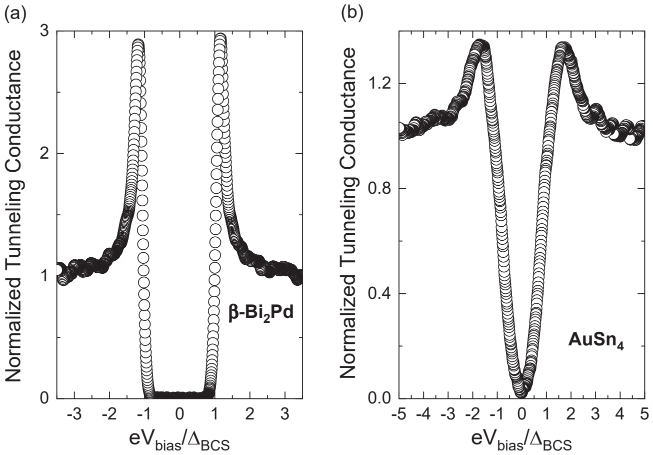

Fig. 4 Tunneling conductance obtained in β-Bi$_2$Pd (A)and in AuSn$_4$ (B). The tunneling conductance is normalized to its value at voltages well above the superconducting gap. The bias voltage is normalized to the BCS value of the superconducting gap Δ_{BCS}. (A) Adapted with permission from Herrera E, Guillamón I, Galvis JA, Correa A, Fente A, Luccas RF, Mompean FJ, García-Hernández M, Vieira S, Brison JP, and Suderow H (2015) Magnetic field dependence of the density of states in the multiband superconductor β-Bi2Pd. Physical Review B 92(5): 054507. https://doi.org/10.1103/PhysRevB.92.054507, copyrighted by the American Physical Society. (B) Adapted with permission from Herrera E, Wu B, O'Leary E, Ruiz AM, Águeda M, Talavera PG, Barrena V, Azpeitia J, Munuera C, García-Hernández M, Wang L-L, Kaminski A, Canfield PC, Baldoví JJ, Guillamón I, and Suderow H (2023b) Band structure, superconductivity, and polytypism in AuSn$_4$. Physical Review Materials 7(2): 024804. https://doi.org/10.1103/PhysRevMaterials.7.024804 copyrighted by the merican Physical Society. See also Choi D-J, Fernández CG, Herrera E, Rubio-Verdú C, Ugeda MM, Guillamón I, Suderow H, Pascual JI, and Lorente N (2018) Influence of magnetic ordering between Cr adatoms on the Yu-Shiba-Rusinov states of the β-Bi2Pd superconductor. Physical Review Letters 120(16): 167001. https://doi.org/10.1103/PhysRevLett.120.167001 and Lv Y-F, Wang W-L, Zhang Y-M, Ding H, Li W, Wang L, He K, Song C-L, Ma X-C, and Xue Q-K (2017) Experimental signature of topological superconductivity and Majorana zero modes on β-Bi$_2$Pd thin films. Science Bulletin 62(12): 852–856. ISSN 2095-9273. https://doi.org/10.1016/j.scib.2017.05.008.

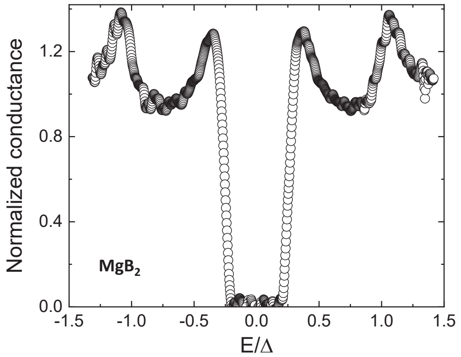

Fig. 5 Tunneling conductance obtained in MgB$_2$. The tunneling conductance is normalized to its value at voltages well above the superconducting gap. The bias voltage is normalized to the BCS value of the superconducting gap Δ_{BCS}. Adapted with permission from Elseview from Martinez-Samper P, Rodrigo JG, Rubio-Bollinger G, Suderow H, Vieira S, Lee S, and Tajima S (2003) Scanning tunneling spectroscopy in MgB$_2$. Physica C: Superconductivity 385(1): 233–243. ISSN 0921-4534. https://doi.org/10.1016/S0921-4534(02)02296-7.

Layered transition metal dichalcogenides

Transition metal dichalcogenides also have Fermi surfaces with different bands crossing the Fermi level (Inosov et al., 2008; Zhao et al., 2021). These compounds consist of blocks of a transition metal and two chalcogen atoms. They have a layered crystalline structure with weak bonding among layers. The arrangement of layers and of the blocks inside each layer is different for each polytype of the crystalline structure. The double hexagonal polytypes, marked as 2H, show superconductivity in 2H-NbSe$_2$, 2H-NbS$_2$, 2H-TaS$_2$, and 2H-TaSe$_2$. Their band structure consists mainly of two transition-metal-derived bands crossing the Fermi level, although there can be bands derived from the chalcogen (Johannes et al., 2006). In all cases except 2H-NbS$_2$, superconductivity coexists with a charge density wave (CDW). The latter leads to a large in-plane anisotropy, with opening of a gap in some portions of the normal-state band structure. The superconducting density of states, shown in Fig. 6, is compatible with a superconducting gap that is different in the two bands crossing the Fermi level in 2H-NbS$_2$ (Guillamón et al., 2008). In 2H-NbSe$_2$, there is in addition a strong gap anisotropy (middle curve of Fig. 6), with a feature in the tunneling conductance pointing out a significant

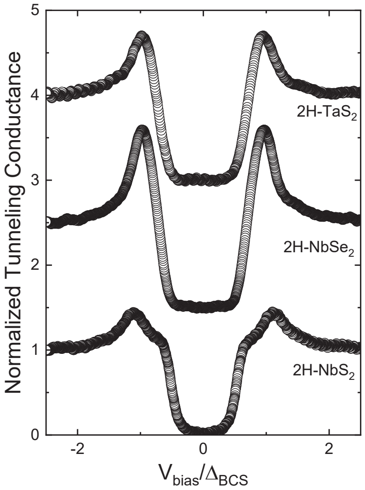

Fig. 6 Tunneling conductance obtained in 2H-NbSe$_2$, 2H-NbS$_2$, and 2H-TaS$_2$. The tunneling conductance is normalized to its value at voltages well above the superconducting gap. Curves are displaced along the *y*-axis by 1.5 units of normalized conductance. The bias voltage is normalized to the BCS value of the superconducting gap Δ_{BCS}. Adapted with permission from Guillamon I, Suderow H, Guinea F, and Vieira S (2008) Intrinsic atomic-scale modulations of the superconducting gap of 2H-NbSe$_2$. Physical Review B 77(13): 134505. https://doi.org/10.1103/PhysRevB.77.134505; Guillamón I, Suderow H, Rodrigo JG, Vieira S, Rodière P, Cario L, Navarro-Moratalla E, Martí-Gastaldo C, and Coronado E (2011) Chiral charge order in the superconductor 2H-TaS2. New Journal of Physics 13(10): 103020. https://doi.org/10.1088/1367-2630/13/10/103020; Guillamón I, Suderow H, Vieira S, Cario L, Diener P, and Rodière P (2008) Superconducting density of states and vortex cores of 2H-NbSe$_2$. Physical Review Letters 101(16): 166407. https://doi.org/10.1103/PhysRevLett.101.166407, copyrighted by the American Physical Society. See also Noat Y, Silva-Guillén JA, Cren T, Cherkez V, Brun C, Pons S, Debontridder F, Roditchev D, Sacks W, Cario L, Ordejón P, García A, and Canadell E (2015) Quasiparticle spectra of 2H-NbSe$_2$: Two-band superconductivity and the role of tunneling selectivity. Physical Review B 92(13): 134510. https://doi.org/10.1103/PhysRevB.92.134510 and Galvis JA, Chirolli L, Guillamón I, Vieira S, Navarro-Moratalla E, Coronado E, Suderow H, and Guinea F (2014) Zero-bias conductance peak in detached flakes of superconducting 2H-TaS$_2$ probed by scanning tunneling spectroscopy. Physical Review B 89(22): 224512. https://doi.org/10.1103/PhysRevB.89.224512

reduction of the gap at some portions of the Fermi surface (Guillamon et al., 2008; Noat et al., 2015). Furthermore, there is an intrinsic atomic-scale modulation of the superconducting properties through a pair density wave (Liu et al., 2021b). 2H-TaS$_2$ presents a significant correlation between the CDW and superconductivity, and an enhancement of the superconducting gap magnitude at some locations (Guillamón et al., 2011).

2H-TaSe$_2$ has the smallest T_c (below 0.15 K in the bulk) and presents the most peculiar superconducting properties, with a density of states that strongly varies as a function of the position (Galvis et al., 2013). Possibly, superconductivity is enhanced at the surface but influenced by normal underlying layers. There is a large zero-bias anomaly in single layers, which also appears in 2H-TaS$_2$ and has been associated with unconventional two-dimensional superconductivity (Galvis et al., 2014, 2013; Chen et al., 2019). Further experiments in single layers of dichalcogenides deposited or grown on different substrates show a reduction of the gap anisotropy and strong variations in the superconducting gap magnitude, which might decrease (as in 2H-NbSe$_2$) or increase (as in 2H-TaS$_2$) with the thickness (Navarro-Moratalla et al., 2016; Rubio-Verdú et al., 2020; Valencia-Ibáñez et al., 2022).

Nickel borocarbides

The rare-earth-nickel borocarbides RNi$_2$B$_2$C (with R = Gd-Lu, Y) present superconductivity up to about 16 K in nonmagnetic RNi$_2$B$_2$C (R = Lu, Y) and coexisting magnetic order for rare earths *R* with unfilled 4*f* shells RNi$_2$B$_2$C (R = Gd-Tm) (Cava et al., 1994; Bud'ko and Canfield, 2006; Canfield et al., 1998; Mazumdar et al., 1993; Müller and Narozhnyi, 2001; Cho et al., 1996, 1995).

Superconductivity in nonmagnetic RNi$_2$B$_2$C (R = Lu, Y) arises from a highly anisotropic electron–phonon interaction related to a nesting feature at the Fermi surface (Dugdale et al., 2008; Bullock et al., 1998; Dugdale et al., 1999). The superconducting gap is fully developed, although the quasiparticle peaks are very broad, pointing out a large distribution of values Δ_i (Fig. 7). There is a small feature for energies below the quasiparticle peaks, which could indicate a distribution of gaps around two values (Martínez-Samper et al., 2003; De Wilde et al., 1997; Sakata et al., 2000; Kaneko et al., 2012).

Measurements in magnetic rare-earth-nickel borocarbides RNi$_2$B$_2$C (R = Tm, Er) show a fully opened gap in the antiferromagnetic phase of TmNi$_2$B$_2$C and a closed gap in the ferromagnetic phase of ErNi$_2$B$_2$C (Fig. 7) (Crespo et al., 2006; Suderow et al., 2001). The latter points out that there is significant pair breaking related to the ferromagnetic phase.

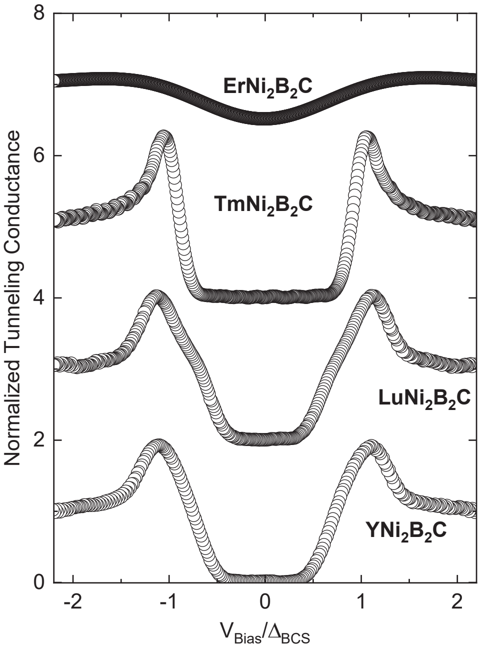

Fig. 7 Tunneling conductance obtained in $TmNi_2B_2C$, $ErNi_2B_2C$, $LuNi_2B_2C$, and YNi_2B_2C. The tunneling conductance is normalized to its value at voltages well above the superconducting gap. Curves are displaced along the *y*-axis by 1 unit of normalized conductance. The bias voltage is normalized to the BCS value of the superconducting gap Δ_{BCS}. Adapted with permission from Martínez-Samper P, Suderow H, Vieira S, Brison JP, Luchier N, Lejay P, and Canfield PC (2003) Phonon-mediated anisotropic superconductivity in the Y and Lu nickel borocarbides. Physical Review B 67(1): 014526. https://doi.org/10.1103/PhysRevB.67.014526; Crespo M, Suderow H, Vieira S, Bud'ko S, and Canfield PC (2006) Local superconducting density of states of $ErNi_2B_2C$. Physical Review Letters 96(2): 027003. https://doi.org/10.1103/PhysRevLett.96.027003; Suderow H, Martinez-Samper P, Luchier N, Brison JP, Vieira S, and Canfield PC (2001) Tunneling spectroscopy in the magnetic superconductor $TmNi_2B_2C$. Physical Review B 64(2): 020503. https://doi.org/10.1103/PhysRevB.64.020503, copyrighted by the American Physical Society

Summary and future directions

Summary

From the examples discussed above, one can see that the tunneling conductance, as measured with STM, is a powerful tool to obtain the superconducting density of states and can lead to insightful descriptions of the superconductor. The tunneling conductance provides the energy dependence of the electronic properties and vividly shows the degree of anisotropy and of the difference of properties in multiple bands.

This text mostly discusses until now simple and well-understood examples where the distribution of values of the superconducting gap can be readily associated with the band structure or to the appearance of charge or magnetic order. This can be further explored by using the capability of the STM to scan spatially the superconducting density of states, which leads to direct measurements of the superconducting properties in real space, providing vivid images of the vortex lattice or of real-space anisotropic properties (Fischer et al., 2007; Suderow et al., 2014). In addition, the structure of the superconducting gap in reciprocal space can be also obtained.

Presently, STM is widely applied to practically any superconducting material as long as the surface can be prepared with sufficient cleanliness to allow for vacuum tunneling. There are many topical compounds and systems in which STM provides new information, which is mostly under debate. The following paragraphs aim to discuss the latter, presenting a brief view of recent advances in a few topical superconductors.

Future directions

The systems discussed below can be understood as "unconventional" superconductors (Mazin, 2023). The term "unconventional superconductivity" can be defined as "superconductivity with nontrivial Cooper pairing" (Mineev and Samokhin, 1999). A possible meaning of "nontrivial" is that the symmetry of the superconducting wave function is reduced with respect to the lattice symmetry. The broken gauge symmetry of the superconducting state, analogous to the broken time-reversal symmetry in a ferromagnet, would be the "trivial" situation. The breaking of additional symmetries combined with gauge symmetry might lead to "nontrivial" behavior, in analogy to the many kinds of wavy magnetic order (antiferromagnetism, ferrimagnetism, spiral magnetism, etc.). But the variety of behaviors that do not follow the basic principle of BCS theory of a spin-singlet Cooper pair wave function which is isotropic in real and reciprocal space is very large. Thus, there are many authors who use the term "unconventional" for all those systems with an anisotropic or spatially varying Cooper pair wave function, often in materials where one can find enhanced electronic (Coulomb) interactions (Chubukov, 2023).

Cuprate superconductors

Cuprate superconductors have been intensively studied by STM (Fischer et al., 2007). The layered structure often leads to high quality surfaces where atomic features are visualized with beautiful detail and/or the superconducting density of states is measured accurately (Renner et al., 1998; Hoogenboom et al., 2001; Maggio-Aprile et al., 1997; Berthod et al., 2017). The superconducting gap anisotropy was measured by tracing the superconducting density of states as a function of the position in presence of scatterers (Hoffman et al., 2002; McElroy et al., 2003). Furthermore, studies of scattering on nonmagnetic pair breaking impurities vividly showed the sign changes of the superconducting wave function over different reciprocal space directions, demonstrating d-wave superconductivity (Pan et al., 2000).

Further work includes the observation of a pair density wave (Berg et al., 2009b, a; Agterberg et al., 2020). A uniform superconductor in which superconductivity coexists with a CDW presents oscillations of the density of states at the surface $N_s(\boldsymbol{r})$ at $\boldsymbol{q}_{CDW}$, $N_s(\boldsymbol{r}) \propto cos(\boldsymbol{q}_{CDW} \cdot \boldsymbol{r})$ eventually on top of a background N_s (Guillamon et al., 2008). A pair density wave at $\boldsymbol{q}_{PDW}$ eventually shares the same wavevector as a CDW in the same system (the latter can be actually considered as a secondary order arising from the pair density wave, Agterberg and Garaud, 2015; Dai et al., 2018; Agterberg et al., 2020).

The oscillations of the combined pair density and Cooper pair wave function lead to a combined order parameter which changes sign as a function of the position (Berg et al., 2009a, b). The expected resulting oscillatory behavior of the combined order parameter is proportional to $cos(\boldsymbol{q}_{PDW} \cdot \boldsymbol{r})$. It can be located at the same wavevector as the pair density wave although it changes sign (Liu et al., 2021b). Other sign changing modulated superconducting states, due to the interaction with magnetism, are known at ferromagnetic–superconductor interfaces and at high magnetic fields (Casalbuoni and Nardulli, 2004; Buzdin, 2005, 2012; Bergeret et al., 2001; Bergeret and Ilic, 2023). The $N_s(\boldsymbol{r})$ due to a pair density wave might eventually drop down to zero, if nothing else contributes to N_s except the combined pair density and superconducting order parameters. On the other hand, the expected oscillations of the pair density wave state in the density of states are due to the product of the pair density wave function with its complex conjugate, leading to $N_s(\boldsymbol{r}) \propto cos(2\boldsymbol{q}_{PDW} \cdot \boldsymbol{r})$ and have different spatial dependencies when oscillations are enhanced at an impurity or at a vortex (Wang et al., 2018).

Nevertheless, the CDW oscillations of the density of states are never purely harmonic, for which one can also expect higher order density of states oscillations, purely from coexisting CDW and superconducting order. Thus, both features of pair densities waves, the measurement of the sign change in the oscillatory behavior and the behavior of higher order oscillations, are quite difficult to address and require careful comparisons of tunneling conductance maps made under different conditions.

The pair density wave has been studied using density of states as well as Josephson effect measurements (Liu et al., 2021b; Choubey et al., 2020; Edkins et al., 2019). It could well be related to observations of oscillatory behavior in other superconductors that have remained unexplained or unstudied (Agterberg et al., 2020).

Pnictide- and Fe-based superconductors

Pnictide- and Fe-based superconductors have been also intensively studied with STM (Hoffman, 2011; Paglione and Greene, 2010; Fernandes et al., 2014; Song et al., 2011). In one specific case, which is FeSe and related doped compounds, the atomic lattice has been observed by many groups, allowing for in-depth investigations of the tunneling conductance and of tunneling conductance maps. One of the defining features of these superconductors, and in particular of FeSe, is the structural transition between a high temperature tetragonal phase and a low temperature orthorhombic phase. While the lattice parameters in both phases are often very similar, the electronic structure turns out to be highly anisotropic in the orthorhombic phase. This leads to very anisotropic electronic features that have been termed "electronic nematic" in analogy to the nematic state of liquid crystals (Wang et al., 2022; Fernandes and Millis, 2013; Li et al., 2017; Chuang et al., 2010; Watson et al., 2015).

The nematicity is often associated with an antiferromagnetic order, except in FeSe where it has been linked to magnetic fluctuations and frustrated magnetism (Wang et al., 2015; Glasbrenner et al., 2015; Yu and Si, 2015). The nematicity leads to highly anisotropic scattering features in tunneling conductance maps, both in normal and superconducting phases (Chuang et al., 2010; Allan et al., 2013; Kasahara et al., 2014). Nematicity is intimately related to the orbital structure (Sprau et al., 2017; Rhodes et al., 2022; Kang et al., 2018; Yu et al., 2018; Hu et al., 2018; Liu et al., 2018; Baek et al., 2015; Li et al., 2020). The orbital contribution to the electronic band structure is considerably modified in the low temperature nematic phase. But the microscopic mechanism to enter the nematic phase is still under debate and requires more in-depth investigations of the local structure of superconductivity in FeSe.

Recent developments have allowed to address superconductivity in $CaKFe_4As_4$. This is a stoichiometric compound with a large critical temperature of $T_c = 35$ K (Iyo et al., 2016; Meier et al., 2016, 2017; Liu et al., 2020). Other pnictide- and Fe-based superconductors are nonstoichiometric at their highest T_c's. $CaKFe_4As_4$ presents two-gap superconductivity from tunneling conductance measurements (Cho et al., 2017). Studying tunneling conductance maps, one can extract the opening of the superconducting gap in different bands (Fente et al., 2018). Substitution of Ca or K leads to superconductivity coexisting with new phases, such as hedgehog magnetism or ferromagnetism (Meier et al., 2018; Bao et al., 2018; Kim et al., 2021; Collomb et al., 2021). The superconducting gap and band structure in each phase are strongly modified (Llorens et al., 2021; Stolyarov et al., 2020).

Topological superconductors

Topological superconductors can be defined in analogy to topological insulators. In the latter, the usual orbital sequence of bands is inverted in the bulk. Often in light semiconductors, the *s* electrons form the conduction band while the valence band is formed by *p* and *d* electrons. When one takes a semiconducting compound having a heavy element, the shape of *s* orbitals is modified due to a stronger attraction potential and it might fall in energy sufficiently that the *s*-derived bands fall below the bands derived from *p* and *d* orbitals. Such an orbital sequence cannot be transferred into vacuum, where the influence of the heavy element is absent. Thus, bands must cross the Fermi level at the surface and lose band inversion in the vacuum. This leads to a surface state which is topologically protected and occurs forcibly in any semiconductor with band inversion.

In a superconductor with an orbitally antisymmetric superconducting order parameter (as opposed to the spin antisymmetric usual BCS state), there are also topologically protected surface states. The gap must close in some form at the surface, leading to a considerable modification of the superconducting density of states. This has been analyzed for the Landau framework of superconductivity by Sigrist and Ueda (1991) and Mineev and Samokhin (1999) and, more recently, within the topological classification by Schnyder et al. (2008) and Ryu (2023).

Many intermetallic compounds have band structure properties in the normal phase that lead to topologically nontrivial surface states. Some of them are superconducting. Efforts to observe unconventional superconducting properties have been made, for example, in the low temperature superconductor Au_2Pb (Martín-Vega et al., 2022). Indeed, a gapless state was observed. However, it is very difficult to separate a modification of the properties at the surface by changes in the band structure from modifications due to the presence of a topologically enforced surface state. The complexity arising from the surface is not yet resolved, being worsened in Au_2Pb because of the absence of an atomically flat surface. Further efforts have been carried out in $\beta-Bi_2Pd$, where the surface state is better defined, although the superconducting gap is fully open (Herrera et al., 2015; Choi et al., 2018; Li et al., 2019; Sakano et al., 2015; Lv et al., 2017; Kačmarčík et al., 2016). Important advances have been made in Te doped FeSe, where a Te *p*-electron-derived band is located near the Fermi level and can lead to band inversion and thus topological superconductivity (Zhang et al., 2018; Chen et al., 2018).

Possibly more promising are systems in which the appearance of unconventional superconducting properties is intimately related to strong electronic correlations (Kohn and Luttinger, 1965), such as heavy-fermion and ferromagnetic superconductor (Coleman, 2007; Aoki et al., 2011; Flouquet, 2005). Electronic correlations at the surface in these systems remain largely unstudied. Very recently, quantized states have been observed on the surface of a heavy fermion superconductor (Herrera et al., 2023a). This is a very promising result, which should help understanding surface features in unconventional superconductors.

One system, where topological superconductivity from electronic correlations is suspected since long, is Sr_2RuO_4 (Mackenzie and Maeno, 2003; Sigrist, 2005; Kallin, 2012). Here, atomically flat surfaces have been observed, leading to the determination of the normal-state band structure by defect scattering (Kreisel et al., 2021; Wang et al., 2017; Firmo et al., 2013). An opened superconducting gap has only been observed in absence of atomically flat surfaces (Suderow et al., 2009). This provides a clue about possible advancement routes. It is possibly important to take into account the influence of electronic correlations and surface states on the tunneling conductance at the surface.

Further work on the surface properties of potential topological superconductors might help to disentangle the expectations from theory in the surface state of topological systems, which include for instance Majorana modes presenting non-Abelian statistics.

Highly disordered superconductors

In the presence of disorder, electron screening is expected to decrease (Altshuler and Aronov, 1985). The influence of Coulomb correlations thus increases, leading to interesting behaviors in numerous thin film or layered superconducting systems where disorder is be controlled with a tuning parameter.

The superconductor-to-insulator transition is a quantum phase transition whose properties have been studied in detail using tunneling conductance (Goldman, 2010; Goldman and Marković, 1998; Lin et al., 2015; Vinokur, 2023). At both sides of the transition, there is a gap, one is the insulating gap and another one is the superconducting gap (Sacépé et al., 2010; Roy et al., 2019; Valles et al., 1989; Butko et al., 2000; Sherman et al., 2012; Sacépé et al., 2011; Feigel'man et al., 2007). There is an intimate relation among both gap features (Vinokur et al., 2008; Bouadim et al., 2011; Bielejec et al., 2001). For example, the superconducting gap is considerably enhanced with respect to BCS theory when approaching the transition (Sacépé et al., 2010; Sacépé et al., 2008). Furthermore, the electronic properties both in the normal and superconducting phase are inhomogeneous (Mondal et al., 2011; Kamlapure et al., 2013; Ganguly et al., 2017).

The inhomogeneity is not ordered, and does not provide modulations of the density of states, which lead to the peaks in the Fourier transform observed in ordered metals. Instead, it produces long wave-length fluctuations without a particular direction (Bouadim et al., 2011; Postolova et al., 2020; Feigel'man et al., 2010; Carbillet et al., 2020). The actual electronic symmetry imposed by the crystal vanishes, which leads to slowly varying normal and superconducting state properties. Then, the fluctuations induced by Coulomb interactions are seen in the part of the Fourier transform of small wave vectors as a blob. Its dependence on the bias voltage is eventually connected to the energy dependence of the density of states, presenting enhanced fluctuations when the density of states increases, for instance, at the quasiparticle peaks (Postolova et al., 2020).

Conclusion

The full extent of STM, tunneling conductance, and its spatial dependence, provide important information about the nature of the superconducting state, helping to identify systems with fundamentally new properties. Here the very basic aspects, connected to BCS theory taught in the classroom, have been reviewed. The first part mostly deals with rather conclusive insights. The second part includes a few lines of work addressing topical problems in superconductivity, which, quite often, provide new questions, sometimes about the technique itself, that point toward the next step.

This hopefully serves as an introduction to the study of tunneling spectroscopy in superconductors, with the caveat that the reader should seek for further information, as some important developments have been certainly left out of the list, for the sake of clarity and space.

Acknowledgments

The author acknowledges help with figures and intense discussions with Edwin Herrera, Beilun Wu, José Gabriel Rodrigo, and Isabel Guillamón. Discussions, help, and guidance from Prof. Sebastián Vieira are also acknowledged. Support by the Spanish Research State Agency (PID2020-114071RB-I00, TED2021-130546B-I00 and CEX2018-000805-M), by the Comunidad de Madrid through program NanomagCOST-CM (no. S2018/NMT-4321) and EU program Cost CA21144 (Superqumap) is also acknowledged. The SEGAINVEX at UAM is acknowledged for the design and construction of STM electronics and of cryogenic equipment.

References

Agrait N, Yeyati AL, and van Ruitenbeek JM (2003) Quantum properties of atomic-sized conductors. *Physics Reports* 377(2): 81–279. ISSN: 0370-1573. https://doi.org/10.1016/S0370-1573(02)00633-6.

Agterberg DF and Garaud J (2015) Checkerboard order in vortex cores from pair-density-wave superconductivity. *Physical Review B* 91(10): 104512. https://doi.org/10.1103/PhysRevB.91.104512.

Agterberg DF, Davis JCS, Edkins SD, Fradkin E, Van Harlingen DJ, Kivelson SA, Lee PA, Radzihovsky L, Tranquada JM, and Wang Y (2020) The physics of pair-density waves: Cuprate superconductors and beyond. *Annual Review of Condensed Matter Physics* 11(1): 231–270. https://doi.org/10.1146/annurev-conmatphys-031119-050711.

Allan MP, Chuang T-M, Massee F, Xie Y, Ni N, Bud'ko SL, Boebinger GS, Wang Q, Dessau DS, Canfield PC, Golden MS, and Davis JC (2013) Anisotropic impurity states, quasiparticle scattering and nematic transport in underdoped $Ca(Fe_{1-x}Co_x)_2As_2$. *Nature Physics* 9(4): 220–224. ISSN: 1745-2481. https://doi.org/10.1038/nphys2544.

Altshuler BL and Aronov AG (1985) Chapter 1—Electron–electron interaction in disordered conductors. In: Efros AL and Pollak M (eds.) *Electron-Electron Interactions in Disordered Systems, Modern Problems in Condensed Matter Sciences, vol. 10*, pp. 1–153. Elsevier. ISSN: 0167-7837. https://doi.org/10.1016/B978-0-444-86916-6.50007-7.

Aoki D, Hardy F, Miyake A, Taufour V, Matsuda TD, and Flouquet J (2011) Properties of ferromagnetic superconductors. *Comptes Rendus Physique* 12(5): 573–583. ISSN: 1631-0705. https://doi.org/10.1016/j.crhy.2011.04.007 (Superconductivity of strongly correlated systems).

Assig M, Etzkorn M, Enders A, Stiepany W, Ast CR, and Kern K (2013) A 10 mK scanning tunneling microscope operating in ultra high vacuum and high magnetic fields. *Review of Scientific Instruments* 84(3): 033903. https://doi.org/10.1063/1.4793793.

Ast CR, Jäck B, Senkpiel J, Eltschka M, Etzkorn M, Ankerhold J, and Kern K (2016) Sensing the quantum limit in scanning tunnelling spectroscopy. *Nature Communications* 7(1): 13009. ISSN: 2041-1723. https://doi.org/10.1038/ncomms13009.

Baek S-H, Efremov DV, Ok JM, Kim JS, van den Brink J, and Büchner B (2015) Orbital-driven nematicity in FeSe. *Nature Materials* 14(2): 210–214. ISSN: 1476-4660. https://doi.org/10.1038/nmat4138.

Bao J-K, Willa K, Smylie MP, Chen H, Welp U, Chung DY, and Kanatzidis MG (2018) Single crystal growth and study of the ferromagnetic superconductor $RbEuFe_4As_4$. *Crystal Growth & Design* 18(6): 3517–3523. https://doi.org/10.1021/acs.cgd.8b00315.

Bardeen J (1961) Tunnelling from a many-particle point of view. *Physical Review Letters* 6(2): 57–59. https://doi.org/10.1103/PhysRevLett.6.57.

Bennemann KH (2005) Superconductivity: BCS theory. In: Bassani F, Liedl GL, and Wyder P (eds.) *Encyclopedia of Condensed Matter Physics*, pp. 72–81. Oxford: Elsevier, ISBN: 978-0-12-369401-0. https://doi.org/10.1016/B0-12-369401-9/00701-4.

Bennemann KH (2023) Superconductivity: BCS theory. In: Tafuri F (ed.) *Encyclopedia of Condensed Matter Physics*. Oxford: Elsevier.

Berg E, Fradkin E, and Kivelson SA (2009a) Charge-4e superconductivity from pair-density-wave order in certain high-temperature superconductors. *Nature Physics* 5(11): 830–833. ISSN: 1745-2481. https://doi.org/10.1038/nphys1389.

Berg E, Fradkin E, and Kivelson SA (2009b) Theory of the striped superconductor. *Physical Review B* 79(6): 064515. https://doi.org/10.1103/PhysRevB.79.064515.

Bergeret S and Ilic S (2023) Superconductor-ferromagnet hybrid structures. In: Bergeret S and Ilic S (eds.) *Encyclopedia of Condensed Matter Physics*. Oxford: Elsevier.

Bergeret FS, Volkov AF, and Efetov KB (2001) Long-range proximity effects in superconductor-ferromagnet structures. *Physical Review Letters* 86(18): 4096–4099. https://doi.org/10.1103/PhysRevLett.86.4096.

Berthod C, Maggio-Aprile I, Bruér J, Erb A, and Renner C (2017) Observation of Caroli-de Gennes-Matricon vortex states in $YBa_2Cu_3O_{7-\delta}$. *Physical Review Letters* 119(23): 237001. https://doi.org/10.1103/PhysRevLett.119.237001.

Bielejec E, Ruan J, and Wu W (2001) Hard correlation gap observed in quench-condensed ultrathin beryllium. *Physical Review Letters* 87(3): 036801. https://doi.org/10.1103/PhysRevLett.87.036801.

Bishop DJ (2005a) Superconductivity: Applications. In: Bassani F, Liedl GL, and Wyder P (eds.) *Encyclopedia of Condensed Matter Physics*, pp. 66–72. Oxford: Elsevier, ISBN: 978-0-12-369401-0. https://doi.org/10.1016/B0-12-369401-9/00708-7.

Bishop DJ (2005b) Superconductors, metallic. In: Bassani F, Liedl GL, and Wyder P (eds.) *Encyclopedia of Condensed Matter Physics*, pp. 121–128. Oxford: Elsevier, ISBN: 978-0-12-369401-0. https://doi.org/10.1016/B0-12-369401-9/00705-1.

Blatter G, Feigel'man MV, Geshkenbein VB, Larkin AI, and Vinokur VM (1994) Vortices in high-temperature superconductors. *Reviews of Modern Physics* 66(4): 1125–1388. https://doi.org/10.1103/RevModPhys.66.1125.

Bouadim K, Loh YL, Randeria M, and Trivedi N (2011) Single- and two-particle energy gaps across the disorder-driven superconductor-insulator transition. *Nature Physics* 7(11): 884–889. ISSN: 1745-2481. https://doi.org/10.1038/nphys2037.

Brandt EH (2005) Superconductivity: Ginzburg-Landau theory and vortex lattice. In: Bassani F, Liedl GL, and Wyder P (eds.) *Encyclopedia of Condensed Matter Physics*, pp. 98–105. Oxford: Elsevier, ISBN: 978-0-12-369401-0. https://doi.org/10.1016/B0-12-369401-9/00702-6.

Bud'ko SL and Canfield PC (2006) Magnetism and superconductivity in rare earth-nickel-borocarbides. *Comptes Rendus Physique* 7(1): 56–67. ISSN: 1631-0705. https://doi.org/10.1016/j.crhy.2005.11.011. Superconductivity and magnetism.

Bud'ko SL, Lapertot G, Petrovic C, Cunningham CE, Anderson N, and Canfield PC (2001) Boron isotope effect in superconducting MgB$_2$. *Physical Review Letters* 86(9): 1877–1880. https://doi.org/10.1103/PhysRevLett.86.1877.

Bullock M, Zarestky J, Stassis C, Goldman A, Canfield P, Honda Z, Shirane G, and Shapiro SM (1998) Low-energy phonon excitations in superconducting RNi$_2$B$_2$C. *Physical Review B* 57(13): 7916–7921. https://doi.org/10.1103/PhysRevB.57.7916.

Butko VY, DiTusa JF, and Adams PW (2000) Coulomb gap: How a metal film becomes an insulator. *Physical Review Letters* 84(7): 1543–1546. https://doi.org/10.1103/PhysRevLett.84.1543.

Buzdin AI (2005) Proximity effects in superconductor-ferromagnet heterostructures. *Reviews of Modern Physics* 77(3): 935–976. https://doi.org/10.1103/RevModPhys.77.935.

Buzdin A (2012) Non-uniform Fulde-Ferrell-Larkin-Ovchinnikov (FFLO) state. *Physica B: Condensed Matter* 407(11): 1912–1914. ISSN: 0921-4526. https://doi.org/10.1016/j.physb.2012.01.062. Proceedings of the International Workshop on Electronic Crystals (ECRYS-2011).

Canfield PC, Gammel PL, and Bishop DJ (1998) New magnetic superconductors: A toy box for solid-state physicists. *Physics Today* 51(10): 40–46. https://doi.org/10.1063/1.882396.

Carbillet C, Cherkez V, Skvortsov MA, Feigel'man MV, Debontridder F, Ioffe LB, Stolyarov VS, Ilin K, Siegel M, Roditchev D, Cren T, and Brun C (2020) Spectroscopic evidence for strong correlations between local superconducting gap and local Altshuler-Aronov density of states suppression in ultrathin NbN films. *Physical Review B* 102(2): 024504. https://doi.org/10.1103/PhysRevB.102.024504.

Casalbuoni R and Nardulli G (2004) Inhomogeneous superconductivity in condensed matter and QCD. *Reviews of Modern Physics* 76(1): 263–320. https://doi.org/10.1103/RevModPhys.76.263.

Cava RJ, Takagi H, Zandbergen HW, Krajewski JJ, Peck WF, Siegrist T, Batlogg B, van Dover RB, Felder RJ, Mizuhashi K, Lee JO, Eisaki H, and Uchida S (1994) Superconductivity in the quaternary intermetallic compounds LnNi$_2$B$_2$C. *Nature* 367(6460): 252–253. ISSN: 1476-4687. https://doi.org/10.1038/367252a0.

Chen M, Chen X, Yang H, Du Z, Zhu X, Wang E, and Wen H-H (2018) Discrete energy levels of caroli-de gennes-matricon states in quantum limit in FeTe$_{0.55}$Se$_{0.45}$. *Nature Communications* 9(1): 970. ISSN: 2041-1723. https://doi.org/10.1038/s41467-018-03404-8.

Chen W, Zhu Q, Zhou Y, and An J (2019) Topological ising pairing states in monolayer and trilayer TaS$_2$. *Physical Review B* 100(5): 054503. https://doi.org/10.1103/PhysRevB.100.054503.

Cho BK, Canfield PC, and Johnston DC (1995) Onset of superconductivity in the antiferromagnetically ordered state of single-crystal DyNi$_2$B$_2$C. *Physical Review B* 52(6): R3844–R3847. https://doi.org/10.1103/PhysRevB.52.R3844.

Cho BK, Canfield PC, and Johnston DC (1996) Breakdown of de gennes scaling in r$_{1-x}$R$_x$Ni$_2$B$_2$C compounds. *Physical Review Letters* 77(1): 163–166. https://doi.org/10.1103/PhysRevLett.77.163.

Cho K, Fente A, Teknowijoyo S, Tanatar MA, Joshi KR, Nusran NM, Kong T, Meier WR, Kaluarachchi U, Guillamón I, Suderow H, Bud'ko SL, Canfield PC, and Prozorov R (2017) Nodeless multiband superconductivity in stoichiometric single-crystalline CaKFe$_4$As$_4$. *Physical Review B* 95(10): 100502. https://doi.org/10.1103/PhysRevB.95.100502.

Choi HJ, Roundy D, Sun H, Cohen ML, and Louie SG (2002) The origin of the anomalous superconducting properties of MgB$_2$. *Nature* 418(6899): 758–760. ISSN: 1476-4687. https://doi.org/10.1038/nature00898.

Choi D-J, Fernández CG, Herrera E, Rubio-Verdú C, Ugeda MM, Guillamón I, Suderow H, Pascual JI, and Lorente N (2018) Influence of magnetic ordering between Cr adatoms on the Yu-Shiba-Rusinov states of the β-Bi$_2$Pd superconductor. *Physical Review Letters* 120(16): 167001. https://doi.org/10.1103/PhysRevLett.120.167001.

Choubey P, Joo SH, Fujita K, Du Z, Edkins SD, Hamidian MH, Eisaki H, Uchida S, Mackenzie AP, Lee J, Davis JCS, and Hirschfeld PJ (2020) Atomic-scale electronic structure of the cuprate pair density wave state coexisting with superconductivity. *Proceedings of the National Academy of Sciences* 117(26): 14805–14811. https://doi.org/10.1073/pnas.2002429117.

Chuang T-M, Allan MP, Lee J, Xie Y, Ni N, Bud'ko SL, Boebinger GS, Canfield PC, and Davis JC (2010) Nematic electronic structure in the parent state of the iron-based superconductor Ca(Fe$_{1-x}$Co$_x$)$_2$As$_2$. *Science* 327(5962): 181–184. https://doi.org/10.1126/science.1181083.

Chubukov A (2023) Superconductivity: Electronic mechanisms. In: Mazin I (ed.) *Encyclopedia of Condensed Matter Physics*. Oxford: Elsevier.

Cleland AN (2005) Superconductivity: Tunneling. In: Bassani F, Liedl GL, and Wyder P (eds.) *Encyclopedia of Condensed Matter Physics*, pp. 105–112. Oxford: Elsevier, ISBN: 978-0-12-369401-0. https://doi.org/10.1016/B0-12-369401-9/00704-X.

Coleman P (2007) Heavy fermions: Electrons at the edge of magnetism. In: *Handbook of Magnetism and Advanced Magnetic Materials*. John Wiley and Sons, Ltd, ISBN: 9780470022184. https://doi.org/10.1002/9780470022184.hmm105.

Collomb D, Bending SJ, Koshelev AE, Smylie MP, Farrar L, Bao J-K, Chung DY, Kanatzidis MG, Kwok W-K, and Welp U (2021) Observing the suppression of superconductivity in RbEuFe$_4$As$_4$ by correlated magnetic fluctuations. *Physical Review Letters* 126(15): 157001. https://doi.org/10.1103/PhysRevLett.126.157001.

Crespo M, Suderow H, Vieira S, Bud'ko S, and Canfield PC (2006) Local superconducting density of states of ErNi$_2$B$_2$C. *Physical Review Letters* 96(2): 027003. https://doi.org/10.1103/PhysRevLett.96.027003.

Crespo V, Maldonado A, Galvis JA, Kulkarni P, Guillamon I, Rodrigo JG, Suderow H, Vieira S, Banerjee S, and Rodiere P (2012) Scanning microscopies of superconductors at very low temperatures. *Physica C: Superconductivity* 479: 19–23. ISSN: 0921-4534. https://doi.org/10.1016/j.physc.2012.02.014 (Proceedings of VORTEX VII Conference).

Crommie MF, Lutz CP, and Eigler DM (1993) Imaging standing waves in a two-dimensional electron gas. *Nature* 363(6429): 524–527. ISSN: 1476-4687. https://doi.org/10.1038/363524a0.

Crommie MF, Lutz CP, Eigler DM, and Heller EJ (1995) Waves on a metal surface and quantum corrals. *Surface Review and Letters* 02(01): 127–137. https://doi.org/10.1142/S0218625X95000121.

Dai Z, Zhang Y-H, Senthil T, and Lee PA (2018) Pair-density waves, charge-density waves, and vortices in high-T_c cuprates. *Physical Review B* 97(17): 174511. https://doi.org/10.1103/PhysRevB.97.174511.

De Wilde Y, Iavarone M, Welp U, Metlushko V, Koshelev AE, Aranson I, Crabtree GW, and Canfield PC (1997) Scanning tunneling microscopy observation of a square Abrikosov lattice in LuNi$_2$B$_2$C. *Physical Review Letters* 78(22): 4273–4276. https://doi.org/10.1103/PhysRevLett.78.4273.

Dragoman D and Dragoman M (2005) Tunneling devices. In: Bassani F, Liedl GL, and Wyder P (eds.) *Encyclopedia of Condensed Matter Physics*, pp. 269–277. Oxford: Elsevier, ISBN: 978-0-12-369401-0. https://doi.org/10.1016/B0-12-369401-9/01143-8.

Dugdale SB, Alam MA, Wilkinson I, Hughes RJ, Fisher IR, Canfield PC, Jarlborg T, and Santi G (1999) Nesting properties and anisotropy of the Fermi surface of LuNi$_2$B$_2$C. *Physical Review Letters* 83(23): 4824–4827. https://doi.org/10.1103/PhysRevLett.83.4824.

Dugdale SB, Utfeld C, Wilkinson I, Laverock J, Major Z, Alam MA, and Canfield PC (2008) Fermi surfaces of rare-earth nickel borocarbides. *Superconductor Science and Technology* 22(1): 014002. https://doi.org/10.1088/0953-2048/22/1/014002.

Dynes RC, Narayanamurti V, and Garno JP (1978) Direct measurement of quasiparticle-lifetime broadening in a strong-coupled superconductor. *Physical Review Letters* 41(21): 1509–1512. https://doi.org/10.1103/PhysRevLett.41.1509.

Edkins SD, Kostin A, Fujita K, Mackenzie AP, Eisaki H, Uchida S, Sachdev S, Lawler MJ, Kim E-A, Davis JCS, and Hamidian MH (2019) Magnetic field induced pair density wave state in the cuprate vortex halo. *Science* 364(6444): 976–980. https://doi.org/10.1126/science.aat1773.

Eltschka M, Jäck B, Assig M, Kondrashov OV, Skvortsov MA, Etzkorn M, Ast CR, and Kern K (2015) Superconducting scanning tunneling microscopy tips in a magnetic field: Geometry-controlled order of the phase transition. *Applied Physics Letters* 107(12): 122601. https://doi.org/10.1063/1.4931359.

Fazio R and van der Zant H (2001) Quantum phase transitions and vortex dynamics in superconducting networks. *Physics Reports* 355(4): 235–334. ISSN: 0370-1573. https://doi.org/10.1016/S0370-1573(01)00022-9.

Feigel'man MV, Ioffe LB, Kravtsov VE, and Yuzbashyan EA (2007) Eigenfunction fractality and pseudogap state near the superconductor-insulator transition. *Physical Review Letters* 98(2): 027001. https://doi.org/10.1103/PhysRevLett.98.027001.

Feigel'man MV, Ioffe LB, Kravtsov VE, and Cuevas E (2010) Fractal superconductivity near localization threshold. *Annals of Physics* 325(7): 1390–1478. ISSN: 0003-4916. https://doi.org/10.1016/j.aop.2010.04.001. July 2010 Special Issue.

Fente A, Meier WR, Kong T, Kogan VG, Bud'ko SL, Canfield PC, Guillamón I, and Suderow H (2018) Influence of multiband sign-changing superconductivity on vortex cores and vortex pinning in stoichiometric high-T_c $CaKFe_4As_4$. *Physical Review B* 97(13): 134501. https://doi.org/10.1103/PhysRevB.97.134501.

Fernandes RM and Millis AJ (2013) Nematicity as a probe of superconducting pairing in iron-based superconductors. *Physical Review Letters* 111(12): 127001. https://doi.org/10.1103/PhysRevLett.111.127001.

Fernandes RM, Chubukov AV, and Schmalian J (2014) What drives nematic order in iron-based superconductors? *Nature Physics* 10(2): 97–104. ISSN: 1745-2481. https://doi.org/10.1038/nphys2877.

Fernández-Lomana M, Wu B, Martín-Vega F, Sánchez-Barquilla R, Álvarez Montoya R, Castilla JM, Navarrete J, Marijuan JR, Herrera E, Suderow H, and Guillamón I (2021) Millikelvin scanning tunneling microscope at 20/22 T with a graphite enabled stick-slip approach and an energy resolution below 8 μev: Application to conductance quantization at 20 T in single atom point contacts of Al and Au and to the charge density wave of 2H-$NbSe_2$. *Review of Scientific Instruments* 92(9): 093701. https://doi.org/10.1063/5.0059394.

Fiete GA and Heller EJ (2003) Colloquium: Theory of quantum corrals and quantum mirages. *Reviews of Modern Physics* 75(3): 933–948. https://doi.org/10.1103/RevModPhys.75.933.

Firmo IA, Lederer S, Lupien C, Mackenzie AP, Davis JC, and Kivelson SA (2013) Evidence from tunneling spectroscopy for a quasi-one-dimensional origin of superconductivity in Sr_2RuO_4. *Physical Review B* 88(13): 134521. https://doi.org/10.1103/PhysRevB.88.134521.

Fischer O, Kugler M, Maggio-Aprile I, Berthod C, and Renner C (2007) Scanning tunneling spectroscopy of high-temperature superconductors. *Reviews of Modern Physics* 79(1): 353–419. https://doi.org/10.1103/RevModPhys.79.353.

Flouquet J (2005) On the heavy fermion road. In: Halperin WP (ed.) *Progress in Low Temperature Physics*, vol. 15, pp. 139–281. Elsevier. https://doi.org/10.1016/S0079-6417(05)15002-1.

Galvis JA, Rodière P, Guillamon I, Osorio MR, Rodrigo JG, Cario L, Navarro-Moratalla E, Coronado E, Vieira S, and Suderow H (2013) Scanning tunneling measurements of layers of superconducting 2H-$TaSe_2$: Evidence for a zero-bias anomaly in single layers. *Physical Review B* 87(9): 094502. https://doi.org/10.1103/PhysRevB.87.094502.

Galvis JA, Chirolli L, Guillamón I, Vieira S, Navarro-Moratalla E, Coronado E, Suderow H, and Guinea F (2014) Zero-bias conductance peak in detached flakes of superconducting 2H-TaS_2 probed by scanning tunneling spectroscopy. *Physical Review B* 89(22): 224512. https://doi.org/10.1103/PhysRevB.89.224512.

Ganguly R, Roy I, Banerjee A, Singh H, Ghosal A, and Raychaudhuri P (2017) Magnetic field induced emergent inhomogeneity in a superconducting film with weak and homogeneous disorder. *Physical Review B* 96(5): 054509. https://doi.org/10.1103/PhysRevB.96.054509.

Giubileo F, Roditchev D, Sacks W, Lamy R, Thanh DX, Klein J, Miraglia S, Fruchart D, Marcus J, and Monod P (2001) Two-gap state density in MgB_2: A true bulk property or a proximity effect? *Physical Review Letters* 87(17): 177008. https://doi.org/10.1103/PhysRevLett.87.177008.

Glasbrenner JK, Mazin II, Jeschke HO, Hirschfeld PJ, Fernandes RM, and Valentí R (2015) Effect of magnetic frustration on nematicity and superconductivity in iron chalcogenides. *Nature Physics* 11(11): 953–958. ISSN: 1745-2481. https://doi.org/10.1038/nphys3434.

Goldman AM (2010) Superconductor-insulator transitions of quench-condensed films. *Low Temperature Physics* 36(10): 884–892. https://doi.org/10.1063/1.3517172.

Goldman AM and Marković N (1998) Superconductor-insulator transitions in the two-dimensional limit. *Physics Today* 51(11): 39–44. https://doi.org/10.1063/1.882069.

Guillamon I, Suderow H, Guinea F, and Vieira S (2008) Intrinsic atomic-scale modulations of the superconducting gap of 2H-$NbSe_2$. *Physical Review B* 77(13): 134505. https://doi.org/10.1103/PhysRevB.77.134505.

Guillamón I, Suderow H, Vieira S, Cario L, Diener P, and Rodière P (2008) Superconducting density of states and vortex cores of 2H-$NbSe_2$. *Physical Review Letters* 101(16): 166407. https://doi.org/10.1103/PhysRevLett.101.166407.

Guillamon I, Suderow H, Vieira S, and Rodiere P (2008) Scanning tunneling spectroscopy with superconducting tips of Al. *Physica C: Superconductivity and its Applications* 468(7): 537–542. ISSN: 0921-4534. https://doi.org/10.1016/j.physc.2007.11.066. Proceedings of the Fifth International Conference on Vortex Matter in Nanostructured Superconductors.

Guillamón I, Suderow H, Rodrigo JG, Vieira S, Rodière P, Cario L, Navarro-Moratalla E, Martí-Gastaldo C, and Coronado E (2011) Chiral charge order in the superconductor 2H-TaS2. *New Journal of Physics* 13(10): 103020. https://doi.org/10.1088/1367-2630/13/10/103020.

Gurevich A (2005) Superconductivity: Critical currents. In: Bassani F, Liedl GL, and Wyder P (eds.) *Encyclopedia of Condensed Matter Physics*, pp. 82–88. Oxford: Elsevier, ISBN: 978-0-12-369401-0. https://doi.org/10.1016/B0-12-369401-9/00737-3.

Hatter N, Heinrich BW, Ruby M, Pascual JI, and Franke KJ (2015) Magnetic anisotropy in Shiba bound states across a quantum phase transition. *Nature Communications* 6(1): 8988. ISSN: 2041-1723. https://doi.org/10.1038/ncomms9988.

Heinrich BW, Pascual JI, and Franke KJ (2018) Single magnetic adsorbates on s-wave superconductors. *Progress in Surface Science* 93(1): 1–19. ISSN: 0079-6816. https://doi.org/10.1016/j.progsurf.2018.01.001.

Heller EJ, Crommie MF, Lutz CP, and Eigler DM (1994) Scattering and absorption of surface electron waves in quantum corrals. *Nature* 369(6480): 464–466. ISSN: 1476-4687. https://doi.org/10.1038/369464a0.

Herrera E, Guillamón I, Galvis JA, Correa A, Fente A, Luccas RF, Mompean FJ, García-Hernández M, Vieira S, Brison JP, and Suderow H (2015) Magnetic field dependence of the density of states in the multiband superconductor β-Bi_2Pd. *Physical Review B* 92(5): 054507. https://doi.org/10.1103/PhysRevB.92.054507.

Herrera E, Guillamón I, Barrena V, Herrera WJ, Galvis JA, Yeyati AL, Rusz J, Oppeneer PM, Knebel G, Brison JP, Flouquet J, Aoki D, and Suderow H (2023a) Quantum-well states at the surface of a heavy-fermion superconductor. *Nature* 616: 465–469. https://doi.org/10.1038/s41586-023-05830-1.

Herrera E, Wu B, O'Leary E, Ruiz AM, Águeda M, Talavera PG, Barrena V, Azpeitia J, Munuera C, García-Hernández M, Wang L-L, Kaminski A, Canfield PC, Baldoví JJ, Guillamón I, and Suderow H (2023b) Band structure, superconductivity, and polytypism in $AuSn_4$. *Physical Review Materials* 7(2): 024804. https://doi.org/10.1103/PhysRevMaterials.7.024804.

Hoffman JE (2011) Spectroscopic scanning tunneling microscopy insights into Fe-based superconductors. *Reports on Progress in Physics* 74(12): 124513. https://doi.org/10.1088/0034-4885/74/12/124513.

Hoffman JE, McElroy K, Lee D-H, Lang KM, Eisaki H, Uchida S, and Davis JC (2002) Imaging quasiparticle interference in $Bi_2Sr_2CaCu_2O_{8+\delta}$. *Science* 297(5584): 1148–1151. https://doi.org/10.1126/science.1072640.

Hoogenboom BW, Kadowaki K, Revaz B, Li M, Renner C, and Fischer Ø (2001) Linear and field-independent relation between vortex core state energy and gap in $Bi_2Sr_2CaCu_2O_{8+\delta}$. *Physical Review Letters* 87(26): 267001. https://doi.org/10.1103/PhysRevLett.87.267001.

Hu H, Yu R, Nica EM, Zhu J-X, and Si Q (2018) Orbital-selective superconductivity in the nematic phase of FeSe. *Physical Review B* 98(22): 220503. https://doi.org/10.1103/PhysRevB.98.220503.

Huang H, Padurariu C, Senkpiel J, Drost R, Yeyati AL, Cuevas JC, Kubala B, Ankerhold J, Kern K, and Ast CR (2020) Tunnelling dynamics between superconducting bound states at the atomic limit. *Nature Physics* 16(12): 1227–1231. ISSN: 1745-2481. https://doi.org/10.1038/s41567-020-0971-0.

Inosov DS, Zabolotnyy VB, Evtushinsky DV, Kordyuk AA, Büchner B, Follath R, Berger H, and Borisenko SV (2008) Fermi surface nesting in several transition metal dichalcogenides. *New Journal of Physics* 10(12): 125027. https://doi.org/10.1088/1367-2630/10/12/125027.

Iyo A, Kawashima K, Kinjo T, Nishio T, Ishida S, Fujihisa H, Gotoh Y, Kihou K, Eisaki H, and Yoshida Y (2016) New-structure-type Fe-based superconductors: $CaAFe_4As_4$ (A = K, Rb, Cs) and $SrAFe_4As_4$ (A = Rb, Cs). *Journal of the American Chemical Society* 138(10): 3410–3415. https://doi.org/10.1021/jacs.5b12571. PMID: 26943024.

Johannes MD, Mazin II, and Howells CA (2006) Fermi-surface nesting and the origin of the charge-density wave in $NbSe_2$. *Physical Review B* 73(20): 205102. https://doi.org/10.1103/PhysRevB.73.205102.

Kallin C (2012) Chiral p-wave order in Sr_2RuO_4. *Reports on Progress in Physics* 75(4): 042501. https://doi.org/10.1088/0034-4885/75/4/042501.

Kamlapure A, Das T, Ganguli SC, Parmar JB, Bhattacharyya S, and Raychaudhuri P (2013) Emergence of nanoscale inhomogeneity in the superconducting state of a homogeneously disordered conventional superconductor. *Scientific Reports* 3(1): 2979. ISSN: 2045-2322. https://doi.org/10.1038/srep02979.

Kaneko S-i, Matsuba K, Hafiz M, Yamasaki K, Kakizaki E, Nishida N, Takeya H, Hirata K, Kawakami T, Mizushima T, and Machida K (2012) Quantum limiting behaviors of a vortex core in an anisotropic gap superconductor. *Journal of the Physical Society of Japan* 81(6): 063701. https://doi.org/10.1143/JPSJ.81.063701.

Kang J, Fernandes RM, and Chubukov A (2018) Superconductivity in FeSe: The role of nematic order. *Physical Review Letters* 120(26): 267001. https://doi.org/10.1103/PhysRevLett.120.267001.

Kasahara S, Watashige T, Hanaguri T, Kohsaka Y, Yamashita T, Shimoyama Y, Mizukami Y, Endo R, Ikeda H, Aoyama K, Terashima T, Uji S, Wolf T, von Löhneysen H, Shibauchi T, and Matsuda Y (2014) Field-induced superconducting phase of FeSe in the BCS-BEC cross-over. *Proceedings of the National Academy of Sciences* 111(46): 16309–16313. https://doi.org/10.1073/pnas.1413477111.

Kačmarčík J, Pribulová Z, Samuely T, Szabó P, Cambel V, Šoltýs J, Herrera E, Suderow H, Correa-Orellana A, Prabhakaran D, and Samuely P (2016) Single-gap superconductivity in β-Bi_2Pd. *Physical Review B* 93(14): 144502. https://doi.org/10.1103/PhysRevB.93.144502.

Kim H, Palacio-Morales A, Posske T, Rózsa L, Palotás K, Szunyogh L, Thorwart M, and Wiesendanger R (2018) Toward tailoring Majorana bound states in artificially constructed magnetic atom chains on elemental superconductors. *Science Advances* 4(5): eaar5251. https://doi.org/10.1126/sciadv.aar5251.

Kim H, Rózsa L, Schreyer D, Simon E, and Wiesendanger R (2020) Long-range focusing of magnetic bound states in superconducting lanthanum. *Nature Communications* 11(1): 4573. ISSN: 2041-1723. https://doi.org/10.1038/s41467-020-18406-8.

Kim TK, Pervakov KS, Evtushinsky DV, Jung SW, Poelchen G, Kummer K, Vlasenko VA, Sadakov AV, Usoltsev AS, Pudalov VM, Roditchev D, Stolyarov VS, Vyalikh DV, Borisov V, Valentí R, Ernst A, Eremeev SV, and Chulkov EV (2021) Electronic structure and coexistence of superconductivity with magnetism in $RbEuFe_4As_4$. *Physical Review B* 103(17): 174517. https://doi.org/10.1103/PhysRevB.103.174517.

Kirtley JR and Tsuei CC (2005) Superconductivity: Flux quantization. In: Bassani F, Liedl GL, and Wyder P (eds.) *Encyclopedia of Condensed Matter Physics*, pp. 89–95. Oxford: Elsevier, ISBN: 978-0-12-369401-0. https://doi.org/10.1016/B0-12-369401-9/00703-8.

Kohen A, Proslier T, Cren T, Noat Y, Sacks W, Berger H, and Roditchev D (2006) Probing the superfluid velocity with a superconducting tip: The Doppler shift effect. *Physical Review Letters* 97(2): 027001. https://doi.org/10.1103/PhysRevLett.97.027001.

Kohn W and Luttinger JM (1965) New mechanism for superconductivity. *Physical Review Letters* 15(12): 524–526. https://doi.org/10.1103/PhysRevLett.15.524.

Kortus J, Mazin II, Belashchenko KD, Antropov VP, and Boyer LL (2001) Superconductivity of metallic boron in MgB_2. *Physical Review Letters* 86(20): 4656–4659. https://doi.org/10.1103/PhysRevLett.86.4656.

Kreisel A, Marques CA, Rhodes LC, Kong X, Berlijn T, Fittipaldi R, Granata V, Vecchione A, Wahl P, and Hirschfeld PJ (2021) Quasi-particle interference of the van hove singularity in Sr_2RuO_4. *npj Quantum Materials* 6(1): 100. ISSN: 2397-4648. https://doi.org/10.1038/s41535-021-00401-x.

Larkin AI (2005) Superconductivity: General aspects. In: Bassani F, Liedl GL, and Wyder P (eds.) *Encyclopedia of Condensed Matter Physics*, pp. 95–98. Oxford: Elsevier, ISBN: 978-0-12-369401-0. https://doi.org/10.1016/B0-12-369401-9/00700-2.

le Sueur H, Joyez P, Pothier H, Urbina C, and Esteve D (2008) Phase controlled superconducting proximity effect probed by tunneling spectroscopy. *Physical Review Letters* 100(19): 197002. https://doi.org/10.1103/PhysRevLett.100.197002.

Leggett AJ (2005) Quantum mechanics: Foundations. In: Bassani F, Liedl GL, and Wyder P (eds.) *Encyclopedia of Condensed Matter Physics*, pp. 51–56. Oxford: Elsevier, ISBN: 978-0-12-369401-0. https://doi.org/10.1016/B0-12-369401-9/00616-1.

Li J, Pereira PJ, Yuan J, Lv Y-Y, Jiang M-P, Lu D, Lin Z-Q, Liu Y-J, Wang J-F, Li L, Ke X, Van Tendeloo G, Li M-Y, Feng H-L, Hatano T, Wang H-B, Wu P-H, Yamaura K, Takayama-Muromachi E, Vanacken J, Chibotaru LF, and Moshchalkov VV (2017) Nematic superconducting state in iron pnictide superconductors. *Nature Communications* 8(1): 1880. ISSN: 2041-1723. https://doi.org/10.1038/s41467-017-02016-y.

Li Y, Xu X, Lee M-H, Chu M-W, and Chien CL (2019) Observation of half-quantum flux in the unconventional superconductor β-Bi_2Pd. *Science* 366(6462): 238–241. https://doi.org/10.1126/science.aau6539.

Li J, Lei B, Zhao D, Nie LP, Song DW, Zheng LX, Li SJ, Kang BL, Luo XG, Wu T, and Chen XH (2020) Spin-orbital-intertwined nematic state in FeSe. *Physical Review X* 10(1): 011034. https://doi.org/10.1103/PhysRevX.10.011034.

Lin Y-H, Nelson J, and Goldman AM (2015) Superconductivity of very thin films: The superconductor-insulator transition. *Physica C: Superconductivity and its Applications* 514: 130–141. ISSN: 0921-4534. https://doi.org/10.1016/j.physc.2015.01.005. Superconducting Materials: Conventional, Unconventional and Undetermined.

Liu D, Li C, Huang J, Lei B, Wang L, Wu X, Shen B, Gao Q, Zhang Y, Liu X, Hu Y, Xu Y, Liang A, Liu J, Ai P, Zhao L, He S, Yu L, Liu G, Mao Y, Dong X, Jia X, Zhang F, Zhang S, Yang F, Wang Z, Peng Q, Shi Y, Hu J, Xiang T, Chen X, Xu Z, Chen C, and Zhou XJ (2018) Orbital origin of extremely anisotropic superconducting gap in nematic phase of FeSe superconductor. *Physical Review X* 8(3): 031033. https://doi.org/10.1103/PhysRevX.8.031033.

Liu W, Cao L, Zhu S, Kong L, Wang G, Papaj M, Zhang P, Liu Y-B, Chen H, Li G, Yang F, Kondo T, Du S, Cao G-H, Shin S, Fu L, Yin Z, Gao H-J, and Ding H (2020) A new Majorana platform in an Fe-As bilayer superconductor. *Nature Communications* 11(1): 5688. ISSN: 2041-1723. https://doi.org/10.1038/s41467-020-19487-1.

Liu X, Chong YX, Sharma R, and Davis JCS (2021a) Atomic-scale visualization of electronic fluid flow. *Nature Materials* 20(11): 1480–1484. ISSN: 1476-4660. https://doi.org/10.1038/s41563-021-01077-1.

Liu X, Chong YX, Sharma R, and Davis JCS (2021b) Discovery of a Cooper-pair density wave state in a transition-metal dichalcogenide. *Science* 372(6549): 1447–1452. https://doi.org/10.1126/science.abd4607.

Llorens JB, Herrera E, Barrena V, Wu B, Heinsdorf N, Borisov V, Valentí R, Meier WR, Bud'ko S, Canfield PC, Guillamón I, and Suderow H (2021) Anisotropic superconductivity in the spin-vortex antiferromagnetic superconductor $CaK(Fe_{0.95}Ni_{0.05})_4As_4$. *Physical Review B* 103(6): L060506. https://doi.org/10.1103/PhysRevB.103.L060506.

Lo Conte R, Bazarnik M, Palotás K, Rózsa L, Szunyogh L, Kubetzka A, von Bergmann K, and Wiesendanger R (2022) Coexistence of antiferromagnetism and superconductivity in Mn/Nb(110). *Physical Review B* 105(10): L100406. https://doi.org/10.1103/PhysRevB.105.L100406.

Lv Y-F, Wang W-L, Zhang Y-M, Ding H, Li W, Wang L, He K, Song C-L, Ma X-C, and Xue Q-K (2017) Experimental signature of topological superconductivity and Majorana zero modes on β-Bi_2Pd thin films. *Science Bulletin* 62(12): 852–856. ISSN: 2095-9273. https://doi.org/10.1016/j.scib.2017.05.008.

Mackenzie AP and Maeno Y (2003) The superconductivity of Sr_2RuO_4 and the physics of spin-triplet pairing. *Reviews of Modern Physics* 75(2): 657–712. https://doi.org/10.1103/RevModPhys.75.657.

Maggio-Aprile I, Renner C, Erb A, Walker E, and Fischer Ø (1997) Critical currents approaching the depairing limit at a twin boundary in $YBa_2Cu_3O_{7-\delta}$. *Nature* 390(6659): 487–490. ISSN: 1476-4687. https://doi.org/10.1038/37312.

Margaritondo G (2005) Photoelectron spectromicroscopy. In: Bassani F, Liedl GL, and Wyder P (eds.) *Encyclopedia of Condensed Matter Physics*, pp. 272–279. Oxford: Elsevier, ISBN: 978-0-12-369401-0. https://doi.org/10.1016/B0-12-369401-9/00587-8.

Martín-Vega F, Barrena V, Sánchez-Barquilla R, Fernández-Lomana M, Benito Llorens J, Wu B, Fente A, Perconte Duplain D, Horcas I, López R, Blanco J, Higuera JA, Mañas-Valero S, Jo NH, Schmidt J, Canfield PC, Rubio-Bollinger G, Rodrigo JG, Herrera E, Guillamón I, and Suderow H (2021) Simplified feedback control system for scanning tunneling microscopy. *Review of Scientific Instruments* 92(10): 103705. https://doi.org/10.1063/5.0064511.

Martín-Vega F, Herrera E, Wu B, Barrena V, Mompeán F, García-Hernández M, Canfield PC, Black-Schaffer AM, Baldoví JJ, Guillamón I, and Suderow H (2022) Superconducting density of states and band structure at the surface of the candidate topological superconductor Au_2Pb. *Physical Review Research* 4(2): 023241. https://doi.org/10.1103/PhysRevResearch.4.023241.

Martinez-Samper P, Rodrigo JG, Rubio-Bollinger G, Suderow H, Vieira S, Lee S, and Tajima S (2003) Scanning tunneling spectroscopy in MgB_2. *Physica C: Superconductivity* 385(1): 233–243. ISSN: 0921-4534. https://doi.org/10.1016/S0921-4534(02)02296-7.

Martínez-Samper P, Suderow H, Vieira S, Brison JP, Luchier N, Lejay P, and Canfield PC (2003) Phonon-mediated anisotropic superconductivity in the Y and Lu nickel borocarbides. *Physical Review B* 67(1): 014526. https://doi.org/10.1103/PhysRevB.67.014526.

Mazin I (2023) Unconventional superconductivity. In: Mazin I (ed.) *Encyclopedia of Condensed Matter Physics*. Oxford: Elsevier.

Mazumdar C, Nagarajan R, Godart C, Gupta LC, Latroche M, Dhar SK, Levy-Clement C, Padalia BD, and Vijayaraghavan R (1993) Superconductivity at 12 K in Y-Ni-B system. *Solid State Communications* 87(5): 413–416. ISSN: 0038-1098. https://doi.org/10.1016/0038-1098(93)90788-O.

McElroy K, Simmonds RW, Hoffman JE, Lee D-H, Orenstein J, Eisaki H, Uchida S, and Davis JC (2003) Relating atomic-scale electronic phenomena to wave-like quasiparticle states in superconducting $Bi_2Sr_2CaCu_2O_{8+\delta}$. *Nature* 422(6932): 592–596. ISSN: 1476-4687. https://doi.org/10.1038/nature01496.

Meier WR, Kong T, Kaluarachchi US, Taufour V, Jo NH, Drachuck G, Böhmer AE, Saunders SM, Sapkota A, Kreyssig A, Tanatar MA, Prozorov R, Goldman AI, Balakirev FF, Gurevich A, Bud'ko SL, and Canfield PC (2016) Anisotropic thermodynamic and transport properties of single-crystalline $CaKFe_4As_4$. *Physical Review B* 94(6): 064501. https://doi.org/10.1103/PhysRevB.94.064501.

Meier WR, Kong T, Bud'ko SL, and Canfield PC (2017) Optimization of the crystal growth of the superconductor $CaKFe_4As_4$ from solution in the FeAs-$CaFe_2As_2$-KFe_2As_2 system. *Physical Review Materials* 1(1): 013401. https://doi.org/10.1103/PhysRevMaterials.1.013401.

Meier WR, Ding Q-P, Kreyssig A, Bud'ko SL, Sapkota A, Kothapalli K, Borisov V, Valentí R, Batista CD, Orth PP, Fernandes RM, Goldman AI, Furukawa Y, Böhmer AE, and Canfield PC (2018) Hedgehog spin-vortex crystal stabilized in a hole-doped iron-based superconductor. *npj Quantum Materials* 3(1): 5. ISSN: 2397-4648. https://doi.org/10.1038/s41535-017-0076-x.

Mikitik G (2023) Superconductivity: Ginzburg-Landau theory and vortex lattice. In: Mikitik G (ed.) *Encyclopedia of Condensed Matter Physics*. Oxford: Elsevier.

Mineev VP and Samokhin KV (1999) *Introduction to Unconventional Superconductivity*. Gordon and Breach Science Publishers.

Mondal M, Kamlapure A, Chand M, Saraswat G, Kumar S, Jesudasan J, Benfatto L, Tripathi V, and Raychaudhuri P (2011) Phase fluctuations in a strongly disordered *s*-wave NbN superconductor close to the metal-insulator transition. *Physical Review Letters* 106(4): 047001. https://doi.org/10.1103/PhysRevLett.106.047001.

Müller K-H and Narozhnyi VN (2001) Interaction of superconductivity and magnetism in borocarbide superconductors. *Reports on Progress in Physics* 64(8): 943. https://doi.org/10.1088/0034-4885/64/8/202.

Nadj-Perge S, Drozdov IK, Li J, Chen H, Jeon S, Seo J, MacDonald AH, Bernevig BA, and Yazdani A (2014) Observation of Majorana fermions in ferromagnetic atomic chains on a superconductor. *Science* 346(6209): 602–607. https://doi.org/10.1126/science.1259327.

Nagamatsu J, Nakagawa N, Muranaka T, Zenitani Y, and Akimitsu J (2001) Superconductivity at 39 K in magnesium diboride. *Nature* 410(6824): 63–64. ISSN: 1476-4687. https://doi.org/10.1038/35065039.

Navarro-Moratalla E, Island JO, Mañas-Valero S, Pinilla-Cienfuegos E, Castellanos-Gomez A, Quereda J, Rubio-Bollinger G, Chirolli L, Silva-Guillén JA, Agraït N, Steele GA, Guinea F, van der Zant HSJ, and Coronado E (2016) Enhanced superconductivity in atomically thin TaS_2. *Nature Communications* 7(1): 11043. ISSN: 2041-1723. https://doi.org/10.1038/ncomms11043.

Noat Y, Silva-Guillén JA, Cren T, Cherkez V, Brun C, Pons S, Debontridder F, Roditchev D, Sacks W, Cario L, Ordejón P, García A, and Canadell E (2015) Quasiparticle spectra of 2H-$NbSe_2$: Two-band superconductivity and the role of tunneling selectivity. *Physical Review B* 92(13): 134510. https://doi.org/10.1103/PhysRevB.92.134510.

Nozières P and Schmitt-Rink S (1985) Bose condensation in an attractive fermion gas: From weak to strong coupling superconductivity. *Journal of Low Temperature Physics* 59(3): 195–211. ISSN: 1573-7357. https://doi.org/10.1007/BF00683774.

Ortuzar J, Trivini S, Alvarado M, Rouco M, Zaldivar J, Yeyati AL, Pascual JI, and Bergeret FS (2022) Yu-Shiba-Rusinov states in two-dimensional superconductors with arbitrary Fermi contours. *Physical Review B* 105(24): 245403. https://doi.org/10.1103/PhysRevB.105.245403.

Paglione J and Greene RL (2010) High-temperature superconductivity in iron-based materials. *Nature Physics* 6(9): 645–658. ISSN: 1745-2481. https://doi.org/10.1038/nphys1759.

Palacio-Morales A, Mascot E, Cocklin S, Kim H, Rachel S, Morr DK, and Wiesendanger R (2019) Atomic-scale interface engineering of Majorana edge modes in a 2D magnet-superconductor hybrid system. *Science Advances* 5(7): eaav6600. https://doi.org/10.1126/sciadv.aav6600.

Pan SH, Hudson EW, and Davis JC (1998) Vacuum tunneling of superconducting quasiparticles from atomically sharp scanning tunneling microscope tips. *Applied Physics Letters* 73(20): 2992–2994. https://doi.org/10.1063/1.122654.

Pan SH, Hudson EW, Lang KM, Eisaki H, Uchida S, and Davis JC (2000) Imaging the effects of individual zinc impurity atoms on superconductivity in $Bi_2Sr_2CaCu_2O_{8+\delta}$. *Nature* 403 (6771): 746–750. ISSN: 1476-4687. https://doi.org/10.1038/35001534.

Pascual JI, Bihlmayer G, Koroteev YM, Rust H-P, Ceballos G, Hansmann M, Horn K, Chulkov EV, Blügel S, Echenique PM, and Hofmann P (2004) Role of spin in quasiparticle interference. *Physical Review Letters* 93(19): 196802. https://doi.org/10.1103/PhysRevLett.93.196802.

Petersen L, Sprunger PT, Hofmann P, Lægsgaard E, Briner BG, Doering M, Rust H-P, Bradshaw AM, Besenbacher F, and Plummer EW (1998) Direct imaging of the two-dimensional Fermi contour: Fourier-transform STM. *Physical Review B* 57(12): R6858–R6861. https://doi.org/10.1103/PhysRevB.57.R6858.

Postolova SV, Mironov AY, Barrena V, Benito-Llorens J, Rodrigo JG, Suderow H, Baklanov MR, Baturina TI, and Vinokur VM (2020) Superconductivity in a disordered metal with Coulomb interactions. *Physical Review Research* 2(3): 033307. https://doi.org/10.1103/PhysRevResearch.2.033307.

Proslier T, Kohen A, Noat Y, Cren T, Roditchev D, and Sacks W (2006) Probing the superconducting condensate on a nanometer scale. *Europhysics Letters* 73(6): 962. https://doi.org/10.1209/epl/i2005-10488-0.

Qin MJ and Dou SX (2005) Superconductors, high Tc. In: Bassani F, Liedl GL, and Wyder P (eds.) *Encyclopedia of Condensed Matter Physics*, pp. 112–120. Oxford: Elsevier, ISBN: 978-0-12-369401-0. https://doi.org/10.1016/B0-12-369401-9/00706-3.

Renner C, Revaz B, Genoud J-Y, Kadowaki K, and Fischer O (1998) Pseudogap precursor of the superconducting gap in under- and overdoped $Bi_2Sr_2CaCu_2O_{8+\delta}$. *Physical Review Letters* 80(1): 149–152. https://doi.org/10.1103/PhysRevLett.80.149.

Rhodes LC, Eschrig M, Kim TK, and Watson MD (2022) FeSe and the missing electron pocket problem. *Frontiers in Physics* 10. ISSN: 2296-424X. https://doi.org/10.3389/fphy.2022.859017.

Rodrigo JG and Vieira S (2004) STM study of multiband superconductivity in $NbSe_2$ using a superconducting tip. *Physica C: Superconductivity* 404(1): 306–310. ISSN: 0921-4534. https://doi.org/10.1016/j.physc.2003.10.030. Proceedings of the Third European Conference on Vortex Matter in Superconductors at Extreme Scales and Conditions.

Rodrigo JG, Suderow H, and Vieira S (2004a) On the use of STM superconducting tips at very low temperatures. *The European Physical Journal B–Condensed Matter and Complex Systems* 40(4): 483–488. ISSN: 1434-6036. https://doi.org/10.1140/epjb/e2004-00273-y.

Rodrigo JG, Suderow H, Vieira S, Bascones E, and Guinea F (2004b) Superconducting nanostructures fabricated with the scanning tunnelling microscope. *Journal of Physics: Condensed Matter* 16(34): R1151. https://doi.org/10.1088/0953-8984/16/34/R01.

Roy I, Ganguly R, Singh H, and Raychaudhuri P (2019) Robust pseudogap across the magnetic field driven superconductor to insulator-like transition in strongly disordered NbN films. *The European Physical Journal B* 92(3): 49. ISSN: 1434-6036. https://doi.org/10.1140/epjb/e2019-90488-0.

Rubio-Bollinger G, Suderow H, and Vieira S (2001) Tunneling spectroscopy in small grains of superconducting MgB_2. *Physical Review Letters* 86(24): 5582–5584. https://doi.org/10.1103/PhysRevLett.86.5582.

Rubio-Verdú C, García-García AM, Ryu H, Choi D-J, Zaldívar J, Tang S, Fan B, Shen Z-X, Mo S-K, Pascual JI, and Ugeda MM (2020) Visualization of multifractal superconductivity in a two-dimensional transition metal dichalcogenide in the weak-disorder regime. *Nano Letters* 20(7): 5111–5118. ISSN: 1530-6984. https://doi.org/10.1021/acs.nanolett.0c01288.

Ruby M, Heinrich BW, Pascual JI, and Franke KJ (2015) Experimental demonstration of a two-band superconducting state for lead using scanning tunneling spectroscopy. *Physical Review Letters* 114(15): 157001. https://doi.org/10.1103/PhysRevLett.114.157001.

Ryu S (2023) Superconductors, topological. In: Ryu S (ed.) *Encyclopedia of Condensed Matter Physics*. Oxford: Elsevier.

Sacépé B, Chapelier C, Baturina TI, Vinokur VM, Baklanov MR, and Sanquer M (2008) Disorder-induced inhomogeneities of the superconducting state close to the superconductor-insulator transition. *Physical Review Letters* 101(15): 157006. https://doi.org/10.1103/PhysRevLett.101.157006.

Sacépé B, Chapelier C, Baturina TI, Vinokur VM, Baklanov MR, and Sanquer M (2010) Pseudogap in a thin film of a conventional superconductor. *Nature Communications* 1(1): 140. ISSN: 2041-1723. https://doi.org/10.1038/ncomms1140.

Sacépé B, Dubouchet T, Chapelier C, Sanquer M, Ovadia M, Shahar D, Feigel'man M, and Ioffe L (2011) Localization of preformed Cooper pairs in disordered superconductors. *Nature Physics* 7(3): 239–244. ISSN: 1745-2481. https://doi.org/10.1038/nphys1892.

Sakano M, Okawa K, Kanou M, Sanjo H, Okuda T, Sasagawa T, and Ishizaka K (2015) Topologically protected surface states in a centrosymmetric superconductor β-$PdBi_2$. *Nature Communications* 6(1): 8595. ISSN: 2041-1723. https://doi.org/10.1038/ncomms9595.

Sakata H, Oosawa M, Matsuba K, Nishida N, Takeya H, and Hirata K (2000) Imaging of a vortex lattice transition in YNi_2B_2C by scanning tunneling spectroscopy. *Physical Review Letters* 84(7): 1583–1586. https://doi.org/10.1103/PhysRevLett.84.1583.

Schnyder AP, Ryu S, Furusaki A, and Ludwig AWW (2008) Classification of topological insulators and superconductors in three spatial dimensions. *Physical Review B* 78(19): 195125. https://doi.org/10.1103/PhysRevB.78.195125.

Senkpiel J, Dambach S, Etzkorn M, Drost R, Padurariu C, Kubala B, Belzig W, Yeyati AL, Cuevas JC, Ankerhold J, Ast CR, and Kern K (2020) Single channel Josephson effect in a high transmission atomic contact. *Communications Physics* 3(1): 131. ISSN: 2399-3650. https://doi.org/10.1038/s42005-020-00397-z.

Senkpiel J, Drost R, Klöckner JC, Etzkorn M, Ankerhold J, Cuevas JC, Pauly F, Kern K, and Ast CR (2022) Extracting transport channel transmissions in scanning tunneling microscopy using superconducting excess current. *Physical Review B* 105(16): 165401. https://doi.org/10.1103/PhysRevB.105.165401.

Sherman D, Kopnov G, Shahar D, and Frydman A (2012) Measurement of a superconducting energy gap in a homogeneously amorphous insulator. *Physical Review Letters* 108(17): 177006. https://doi.org/10.1103/PhysRevLett.108.177006.

Shibauchi T, Hanaguri T, and Matsuda Y (2020) Exotic superconducting states in FeSe-based materials. *Journal of the Physical Society of Japan* 89(10): 102002. https://doi.org/10.7566/JPSJ.89.102002.

Sigrist M (2005) Review on the chiral p-wave phase of Sr_2RuO_4. *Progress of Theoretical Physics Supplement* 160: 1–14. ISSN: 0375-9687. https://doi.org/10.1143/PTPS.160.1.

Sigrist M and Ueda K (1991) Phenomenological theory of unconventional superconductivity. *Reviews of Modern Physics* 63(2): 239–311. https://doi.org/10.1103/RevModPhys.63.239.

Song C-L, Wang Y-L, Cheng P, Jiang Y-P, Li W, Zhang T, Li Z, He K, Wang L, Jia J-F, Hung H-H, Wu C, Ma X, Chen X, and Xue Q-K (2011) Direct observation of nodes and twofold symmetry in FeSe superconductor. *Science* 332(6036): 1410–1413. https://doi.org/10.1126/science.1202226.

Sprau PO, Kostin A, Kreisel A, Böhmer AE, Taufour V, Canfield PC, Mukherjee S, Hirschfeld PJ, Andersen BM, and Davis JCS (2017) Discovery of orbital-selective cooper pairing in FeSe. *Science* 357(6346): 75–80. https://doi.org/10.1126/science.aal1575.

Stolyarov VS, Pervakov KS, Astrakhantseva AS, Golovchanskiy IA, Vyalikh DV, Kim TK, Eremeev SV, Vlasenko VA, Pudalov VM, Golubov AA, Chulkov EV, and Roditchev D (2020) Electronic structures and surface reconstructions in magnetic superconductor $RbEuFe_4As_4$. *The Journal of Physical Chemistry Letters* 11(21): 9393–9399. https://doi.org/10.1021/acs.jpclett.0c02711. PMID: 33095988.

Suderow H, Martinez-Samper P, Luchier N, Brison JP, Vieira S, and Canfield PC (2001) Tunneling spectroscopy in the magnetic superconductor $TmNi_2B_2C$. *Physical Review B* 64(2): 020503. https://doi.org/10.1103/PhysRevB.64.020503.

Suderow H, Bascones E, Izquierdo A, Guinea F, and Vieira S (2002) Proximity effect and strong-coupling superconductivity in nanostructures built with an STM. *Physical Review B* 65(10): 100519. https://doi.org/10.1103/PhysRevB.65.100519.

Suderow H, Crespo V, Guillamon I, Vieira S, Servant F, Lejay P, Brison JP, and Flouquet J (2009) A nodeless superconducting gap in Sr_2RuO_4 from tunneling spectroscopy. *New Journal of Physics* 11(9): 093004. https://doi.org/10.1088/1367-2630/11/9/093004.

Suderow H, Guillamón I, Rodrigo JG, and Vieira S (2014) Imaging superconducting vortex cores and lattices with a scanning tunneling microscope. *Superconductor Science and Technology* 27(6): 063001. https://doi.org/10.1088/0953-2048/27/6/063001.

Tafuri F (2023) Josephson junctions. In: Tafuri F (ed.) *Encyclopedia of Condensed Matter Physics*. Oxford: Elsevier.

Tersoff J and Hamann DR (1983) Theory and application for the scanning tunneling microscope. *Physical Review Letters* 50(25): 1998–2001. https://doi.org/10.1103/PhysRevLett.50.1998.

Tersoff J and Hamann DR (1985) Theory of the scanning tunneling microscope. *Physical Review B* 31(2): 805–813. https://doi.org/10.1103/PhysRevB.31.805.

Tonnoir C, Kimouche A, Coraux J, Magaud L, Delsol B, Gilles B, and Chapelier C (2013) Induced superconductivity in graphene grown on Rhenium. *Physical Review Letters* 111(24): 246805. https://doi.org/10.1103/PhysRevLett.111.246805.

Valencia-Ibáñez S, Jiménez-Guerrero D, Salcedo-Pimienta JD, Vega-Bustos K, Cárdenas-Chirivi G, López-Manrique L, Herrera-Vasco E, Galvis JA, Hernández Y, and Giraldo-Gallo P (2022) Raman spectroscopy of few-layers TaS_2 and Mo-doped TaS_2 with enhanced superconductivity. *Advanced Electronic Materials* 8(10): 2200457. https://doi.org/10.1002/aelm.202200457.

Valles JM, Dynes RC, and Garno JP (1989) Temperature dependence of the two-dimensional electronic density of states in disordered metal films. *Physical Review B* 40(11): 7590–7593. https://doi.org/10.1103/PhysRevB.40.7590.

Vinokur V (2023) Superinsulators. In: Vinokur V, Diamantini C, and Trugenberger CA (eds.) *Encyclopedia of Condensed Matter Physics*. Oxford: Elsevier.

Vinokur VM, Baturina TI, Fistul MV, Mironov AY, Baklanov MR, and Strunk C (2008) Superinsulator and quantum synchronization. *Nature* 452(7187): 613–615. ISSN: 1476-4687. https://doi.org/10.1038/nature06837.

Wang F, Kivelson SA, and Lee D-H (2015) Nematicity and quantum paramagnetism in FeSe. *Nature Physics* 11(11): 959–963. ISSN: 1745-2481. https://doi.org/10.1038/nphys3456.

Wang Z, Walkup D, Derry P, Scaffidi T, Rak M, Vig S, Kogar A, Zeljkovic I, Husain A, Santos LH, Wang Y, Damascelli A, Maeno Y, Abbamonte P, Fradkin E, and Madhavan V (2017) Quasiparticle interference and strong electron-mode coupling in the quasi-one-dimensional bands of Sr_2RuO_4. *Nature Physics* 13(8): 799–805. ISSN: 1745-2481. https://doi.org/10.1038/nphys4107.

Wang Y, Edkins SD, Hamidian MH, Davis JCS, Fradkin E, and Kivelson SA (2018) Pair density waves in superconducting vortex halos. *Physical Review B* 97(17): 174510. https://doi.org/10.1103/PhysRevB.97.174510.

Wang Q, Fanfarillo L, and Böhmer AE (2022) Editorial: Nematicity in iron-based superconductors. *Frontiers in Physics* 10. ISSN: 2296-424X. https://doi.org/10.3389/fphy.2022.1038127.

Watson MD, Kim TK, Haghighirad AA, Davies NR, McCollam A, Narayanan A, Blake SF, Chen YL, Ghannadzadeh S, Schofield AJ, Hoesch M, Meingast C, Wolf T, and Coldea AI (2015) Emergence of the nematic electronic state in FeSe. *Physical Review B* 91(15): 155106. https://doi.org/10.1103/PhysRevB.91.155106.

Yu R and Si Q (2015) Antiferroquadrupolar and Ising-nematic orders of a frustrated bilinear-biquadratic heisenberg model and implications for the magnetism of FeSe. *Physical Review Letters* 115(11): 116401. https://doi.org/10.1103/PhysRevLett.115.116401.

Yu R, Zhu J-X, and Si Q (2018) Orbital selectivity enhanced by nematic order in FeSe. *Physical Review Letters* 121(22): 227003. https://doi.org/10.1103/PhysRevLett.121.227003.

Zhang P, Yaji K, Hashimoto T, Ota Y, Kondo T, Okazaki K, Wang Z, Wen J, Gu GD, Ding H, and Shin S (2018) Observation of topological superconductivity on the surface of an iron-based superconductor. *Science* 360(6385): 182–186. https://doi.org/10.1126/science.aan4596.

Zhao B, Shen D, Zhang Z, Lu P, Hossain M, Li J, Li B, and Duan X (2021) 2D Metallic transition-metal dichalcogenides: Structures, synthesis, properties, and applications. *Advanced Functional Materials* 31(48): 2105132. https://doi.org/10.1002/adfm.202105132.

Ziman JM (1972) *Principles of the Theory of Solids*, second ed. Cambridge University Press. https://doi.org/10.1017/CBO9781139644075.

Josephson junctions

Francesco Tafuri, Dipartimento di Fisica “E.Pancini", Università di Napoli Federico II, Napoli, Italy

© 2024 Elsevier Ltd. All rights reserved.

Introduction **616**
The coupling between macroscopic quantum systems and the equations of the Josephson effect **617**
From tunnel barriers to transparent interfaces 617
More transparent barriers and the Josephson effect derived from Quasi-particle Andreev Bound States 620
Essential parameters of a Josephson junction 620
Properties of a Josephson junction and imprints of macroscopic quantum phenomena **621**
Current-Voltage (I–V) characteristics: From the washboard potential to macroscopic quantum phenomena 621
Hamiltonian of a Josephson junction 623
Temperature and magnetic dependence of the critical current and of I–V curves 623
Temperature dependence of I_c 623
Magnetic dependence of the critical current 624
Emerging trends: From qubits to hybrid JJs **626**
Low temperature Josephson junctions for qubits, quantum circuits and superconducting electronics 626
Hybrid Josephson junctions uncovering emergent phenomena: from semiconducting and ferromagnetic barriers to topological insulators and Van der Waals crystals 627
The semiconducting barrier 627
Topological insulators 627
The ferromagnetic barrier 628
vdW crystals integration into JJs and Twisted HTS JJs 628
Conclusion **628**
References **629**

Abstract

A Josephson junction has the unique capability of transferring quantum mechanics rules to macroscopic systems and is at the same time a versatile component of all superconducting electronics with its key feature of carrying a dissipationless phase-driven current. Progress in materials science and nanotechnology consolidates expectations for a series of challenging applications, including the realization of multi-qubit quantum processors, while unconventional hybrid and high critical temperature superconductor Josephson junctions keep disclosing novel problems at the frontier of our knowledge. The diversity in Josephson junctions opens ‘horizons’. Much is happening and partly needs to be consolidated. Much remains to do.

Introduction

In these 50 years since its discovery (Josephson, 1962), the Josephson effect has played a key role for advances in physics both on fundamental aspects and applications. The key feature is a dissipationless current driven by a phase difference of the macroscopic wavefunction between the two superconducting electrodes. A Josephson junction (JJ) has thus the ability to manipulate and measure this phase difference transferring on a macroscopic circuit the quantum mechanics approach commonly applied on microscopic entities. Quantum tunneling takes place at a macroscopic scale in a JJ. A macroscopic superconducting circuit incorporating JJs will be described by a Hamiltonian built on the charge and phase operators. The states of the circuit will correspond to the eigenfunctions of the Hamiltonian associated to the specific circuit. The Josephson junction is an extremely versatile component of all superconducting circuits providing a series of unique properties and the required nonlinear behavior necessary for a wide range of applications (Barone and Paternò, 1982; Likharev, 1986). The Josephson junction is the main block of the superconducting qubit and thus of the emerging field of superconducting quantum computation engineering.

Josephson coupling is not confined to junctions using artificial barriers, but it extends to intrinsic junctions that may naturally build up across superconducting planes or grains or between coherent islands of size characteristic of the material. The Josephson coupling keeps being a formidable tool to disclose new fundamental physics (Barone and Paternò, 1982; Likharev, 1986; Tafuri, 2019). Since the discovery of high-temperature superconductivity in cuprates, for instance, Josephson junction-based phase-sensitive experiments are believed and have been used to provide the most convincing evidence for determining the pairing symmetry (Tsuei et al., 1994; Wollman et al., 1995; Van Harlingen, 1995; Tsuei and Kirtley, 2000). Hybrid systems offer special opportunities by combining the potentials of the superconducting electrodes with those of the barriers, as for instance topological materials, semiconducting nanowires, ferromagnets, graphene. These barriers and the related interfaces are considered as triggers of Majorana fermions, triplet superconductivity and fancy physics. We will give an account of the meaning of the Josephson effect, also

https://doi.org/10.1016/B978-0-323-90800-9.00145-1

through its formalism, and of the methods used to demonstrate its nature and to establish its codes. These are indispensable references to be used in recent explorations on the Josephson effect. Much has to be expected in the future.

The coupling between macroscopic quantum systems and the equations of the Josephson effect

From tunnel barriers to transparent interfaces

Brian Josephson discovered that tunneling effect is not limited to quasi-particles and that also Cooper pairs can tunnel through a thin insulating layer (I) when the electrodes are composed of two superconductors S_R and S_L (Josephson, 1962). Cooper pair tunneling carries information on the phase difference of the macroscopic wavefunctions of the two superconductors. The Josephson effect is expressed by the two following equations, originally derived for an S_R-I-S_L junction:

$$I_s = I_c sin\varphi \tag{1}$$

$$d\varphi/dt = 2eV/\hbar \tag{2}$$

where $\varphi = \varphi_R - \varphi_L$ is the phase difference between the two superconducting electrodes φ_R and φ_L, e and $\hbar$ are the electron charge and the reduced Planck constant respectively. I_C is the maximum critical current and depends on the temperature and the magnetic field. Josephson supercurrent survives as long as the macroscopic wave functions of the superconducting electrodes overlap in the barrier region (Fig. 1a).

The first tunnel Josephson junctions used soft superconductors as Sn, In, Pb, and thermal oxidation for the barrier. Later on, the "lead-alloy technology" was the first to use self-limiting sputter-oxidation process. A key advance was the development of devices

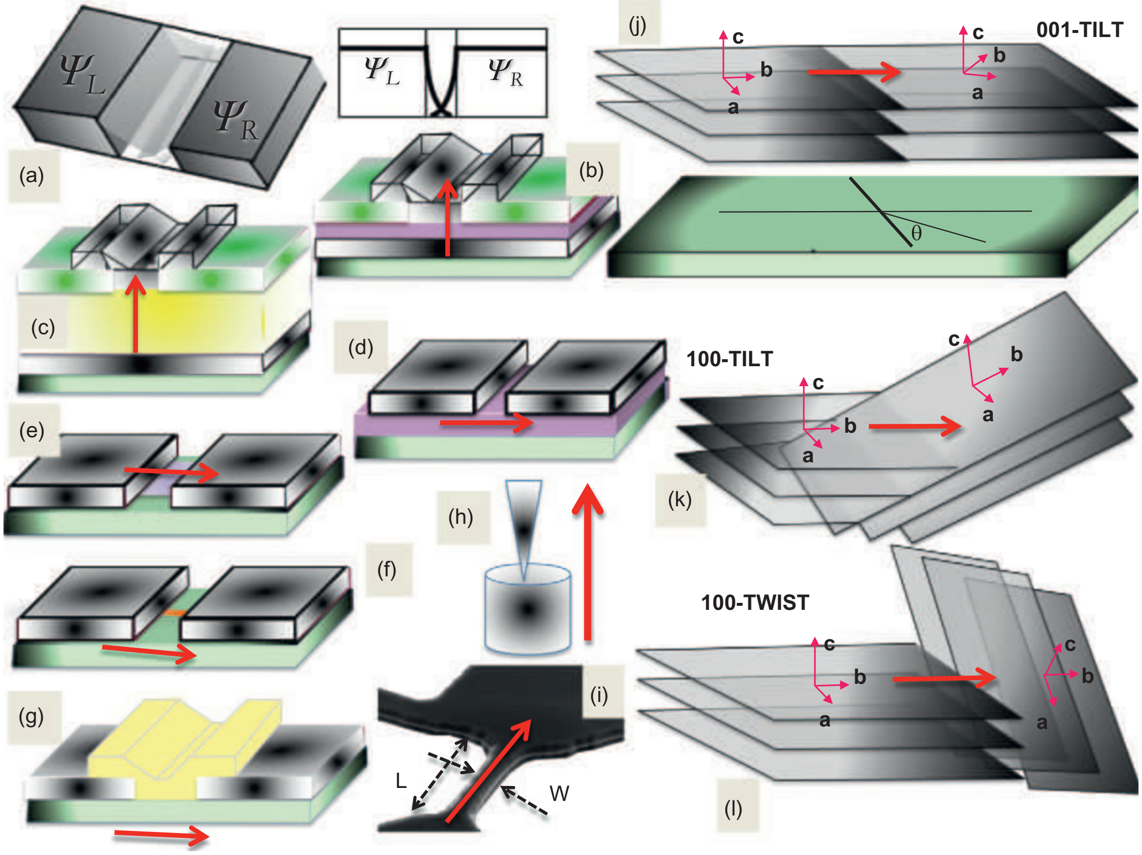

Fig. 1 (a) Spatial dependence of the macroscopic wave functions of the two electrodes in a Josephson junction in a 3-d and 2-d view. Different junction configurations: window-type geometry for a sandwich junction with (b) insulating or (c) normal metal or semiconducting or ferromagnet barrier. (d) Coplanar variable-thickness bridge; the barrier is grown before the deposition of the superconductor; the barrier can be a flake of graphene or of topological insulator (e) or a nanowire (f). The coplanar can also have an inverted structure where the barrier is deposited on the top of the barrier afterwards, as shown in (g). In (h) the scheme of a point contact junction is shown. In all these graphs we use grey/black for a superconductor, yellow for a metal or a semiconductor or a ferromagnet. Thin insulating barrier is in violet, while thick insulating layers are in green, and they serve to completely isolate the electrodes. The red arrow approximately indicates the current direction. In (i) scheme of microbridge. L refers to the length of the barrier, while W is the width of the weak link. Tri-dimensional view of a 001 tilt (j), 100 tilt (k) and 100 twist (l) grain boundary junction. In (j) it is also reported the bicrystal substrate, which in the most common technique determines the growth of the thin superconducting layer.

based on "rigid" superconductors as Nb, with the use of artificial barriers replacing the native Nb oxide barriers. Al turned to be the perfect material solution forming a natural, self-limiting, high quality, insulating oxide (Gurvitch et al., 1983). Other rigid superconductors such as NbN, Nb_3Sn, V_3Si and Nb_3Ge were later used (Wolf et al., 2017). The impact of high critical temperature superconductors (HTS) was also impressive for the development of activities on Josephson devices and to use these properties at unprecedented values of temperature and magnetic fields (Koelle et al., 1999; Tsuei and Kirtley, 2000; Hilgenkamp and Mannhart, 2002; Tafuri and Kirtley, 2005).

For a finite voltage $V \neq 0$ the phase φ varies in time $\varphi = \varphi_o + 2e/\hbar\, V\, t$, as derived from Eq. (2), and an alternating current $I = I_c$ $sin\, (\varphi_o + 2e/\hbar\, V\, t)$ appears with an angular frequency $\omega = 2eV/\hbar$. This is called the a.c. Josephson effect, and the ratio between frequency and voltage is given by: $v/V = 483.6\ MHz/\mu V$, of the order of 10^9–10^{13} Hz at typical voltages 10^{-3}—10 mV. A direct manifestation of the a.c. Josephson effect is the presence of current steps at constant voltages: $V_n = nh/(2e)$ where $n = \pm 1, \pm 2, \ldots$ in presence of microwave irradiation at a frequency v_o. The steps are the direct consequence of an interaction between the a.c. Josephson current and the applied microwave signal. These steps first observed by Shapiro (Shapiro, 1963) are commonly reported as Shapiro steps. The a.c. Josephson effect can be also derived from the very general arguments of spontaneous breakdown of electromagnetic gage invariance (Weinberg, 1986; Anderson, 1997). The high precision predictions about superconductors, and for the a.c. Josephson effect the frequency of the alternating current in terms of the fundamental constant e/h, derive from spontaneous breakdown of electromagnetic gage invariance in a S (Weinberg, 1986; Thouless, 1998).

The Josephson effect is not restricted to tunnel junctions (Fig. 1b), but it occurs in junctions with more transmissive barriers where the I layer is replaced by a metallic N layer (see for instance Fig. 1c). The Josephson supercurrent will flow in the resulting S_L-N-S_R structure as far as the thickness of the barrier is comparable with the coherence length $\xi_N = \sqrt{\hbar D_{diff}/(k_B T)}$ induced in the barrier (de Gennes, 1964) (T is the temperature and $D_{diff} = v_F \ell/3$ is the normal metal diffusion constant, being v_F the Fermi velocity, ℓ the electron mean free path and k_B the Boltzmann's constant respectively). ξ_N can be in some cases even of the order of a few microns. A barrier composed by a normal metal dramatically reduces the normal state junction resistance (R_N) and significantly modifies the junction capacitance (C). New physical "processes" replace tunneling, and they all fall in the category of effects induced by the proximity effect (PE), which will be specific of the junction configuration depending on the material, the type of barrier, the geometry, the boundary conditions. PE expresses the mutual influence between the superconducting electrode and the adjacent barrier layer, other than insulating (Clarke, 1971,de Gennes, 1964, de Gennes, 1966). The barrier is not limited to a normal metal but can be for instance a semiconductor, a ferromagnet, a topological insulator and so on, with novel effects related to the intrinsic nature of the barrier and of the interfaces. The various materials and their properties influence the geometry and the layout of the junction inspiring alternative ways of placing a barrier as reported in Fig. 1d–g, respectively. An accurate description of systems based on S/N interfaces can be also given in terms of Andreev reflection (AR) (Andreev, 1964), the microscopic process in which a dissipative electrical current is converted at an S/N interface into dissipationless supercurrent. AR is the scattering mechanism describing how an electron excitation slightly above the Fermi level in the normal metal is reflected at the interface as a hole excitation slightly below the Fermi level (Andreev, 1964). In Fig. 2a the energy representation of AR is sketched. The missing charge of 2e is removed as a Cooper pair. This is a branch-crossing process which converts electrons into holes and vice versa, and therefore changes the net charge in the excitation distribution. The reflected hole (or electron) has a shift in phase compared to the incoming electron (or hole) wave-function: $\varphi_{hole} = \varphi_{elect} + \varphi_{superc} \pm \arccos(E/\Delta)$, $\varphi_{elect} = \varphi_{hole} - \varphi_{superc} \pm \arccos(E/\Delta)$where Δ and φ_{superc} are the gap value and the superconducting phase of the S respectively. φ_{superc} is equivalent to φ_L or φ_R used in all previous expressions. The macroscopic phase of the S and the microscopic phase of the quasi-particles are therefore mixed through AR. The Andreev-reflected holes operate as a parallel conduction channel to the initial electron current. The normal state conductance of the S/N interface is doubled for applied voltages less than the superconducting gap $eV < \Delta$ (Blonder et al., 1982). Blonder et al. (1982) (BTK) introduced the dimensionless parameter Z, proportional to the potential barrier at the interface, to describe the barrier transparency. This allows the continuous passage from the tunnel limit to a transmissive barrier since the barrier transparency is defined as $D = 1/(1 + Z^2)$. An exact expression for the tunneling current has been also obtained, using standard, many-body, nonequilibrium Green's function techniques (Arnold, 1985). The Landauer conductance expression has been extended to the case of an S-N interface through scattering matrix theory (Beenakker, 1997) $G_{NS} = 2e^2/(\pi\hbar)\sum_{n=1}^{N} t_n^2/(2 - t_n)^2$, where the t_n values are the transmission eigenvalues for the n channel, and N is the total number of channels. In a S_L-N-S_R structure multiple Andreev reflections occur (see Fig. 2b) (see below).

The modern era of Josephson devices is thus strongly influenced by the combined continuous progress in material science and nanotechnologies applied to superconductivity. These aspects are tightly connected. Progress in material science means new materials and new superconductors, and novel abilities in building interfaces and in the precise control of heterostructure in the growth process. Barriers of classical tunnel junctions (employing well-established low critical temperature superconductors (LTS)) benefit as well of the general technological progress and are designed and fabricated with unprecedented precision, opening the route to more performing devices. Advances in nanotechnologies applied to superconductivity is a necessary tool towards the practical implementation of Josephson devices using advanced materials, since they allow to suitably scale the size of the barrier and to handle pre-built barriers as for instance nanowires (NWs) and flakes. Hybrid junctions are an obvious consequence of the combined progress of material science and nanotechnology.

Another practical way to form a Josephson junction is through a point contact (Fig. 1h) or by creating a micro-restriction in a superconducting thin film (Fig. 1i). Scanning Tunnel Microscopy and atomic point contacts represent advanced versions of the original point contact technique (Wolf, 1985). For widths of the order of a few times the coherence length of the superconductor ξ_S, the microbridge will behave as a Josephson weak link (Likharev, 1979). This type of junction depends very critically on the dimensions of the microbridge and its characteristic lengths, ranging from a Josephson junction to a bridge hosting phase slip events

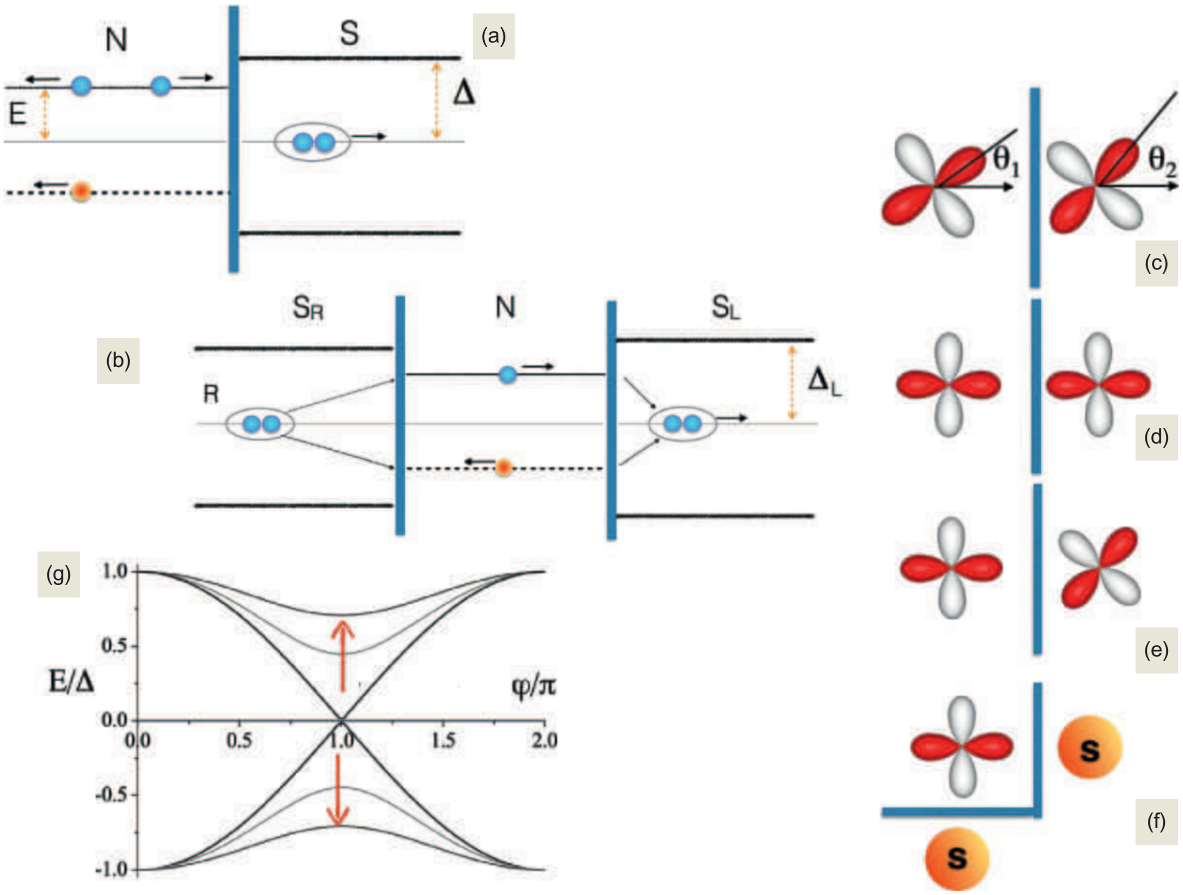

Fig. 2 (a) Energy representation of AR process: an electron excitation slightly above the Fermi level in the normal metal is reflected at the interface as a hole excitation slightly below the Fermi level. The electron is reflected as a hole with the same momentum and opposite velocity. The missing charge of 2e is absorbed as a Cooper pair by the superconducting condensate. (b) Energy representation of Andreev reflections in SNS junctions. (c) The d-wave OP symmetry configuration is reported for a 001 tilt GB for two generic misorientation angles θ_1 and θ_2. Maximum coupling (maximum I_c) happens for lobes facing each other ($\theta_1 = \theta_2 = 0°$) (d), while minimal coupling (minimal I_c) occurs for a lobe facing a node ($\theta_1 = 0°$, $\theta_2 = 45°$) (e). (f) "Corner" junction between an HTS d-wave electrode and an ordinary s-wave counter-electrode. (g) Andreev bands for different values of the D parameter: curve a D = 1, curve b D = 0.8; curve c D = 0.5; an opening of a gap in the Andreev band is evident in the presence of a potential barrier.

or Abrikosov vortex motion respectively. A kind of 'phase diagram' can be derived as a function of their dimensions (width W, length L) (Likharev, 1979). The Josephson effect only takes place for $L < 3.5\ \xi_S$ independently of the width W (Likharev, 1979). Phenomena associated to phase slips ($W < \xi_S$) or to the motion of Abrikosov vortices ($W > \xi_S$) will take place for $L > 3.5\ \xi_S$ (Likharev, 1979). In the limit of long microbridges, Josephson behavior substantially disappears in favor of a regime of strong superconductivity, where the critical current is controlled by standard depairing processes (Tinkham, 2004).

Josephson coupling can also take place at grain boundaries (GBs) and this property has been widely used to produce HTS JJs (Hilgenkamp and Mannhart, 2002; Tafuri and Kirtley, 2005). Any GB can be considered as the result of three fundamental operations as shown in Fig. 1j–l (Chaudari et al., 1988; Dimos et al., 1990): one electrode can be tilted with respect to the other electrode around the c-axis (001 tilt), or tilted around the a or b direction (tilt of the c-axis, 100 tilt) or twisted along the junction interface (100 twist). GBs can realize quite special atomically flat interface configurations. In HTS the d-wave order parameter (OP) symmetry generates quite unconventional features. In Fig. 2c the d-wave OP symmetry configuration is reported for a 001 tilt GB for two generic misorientation angles θ_1 and θ_2 (Hilgenkamp and Mannhart, 2002; Tsuei and Kirtley, 2000, Tafuri and Kirtley, 2005). Maximum coupling (maximum I_c) happens for lobes facing each other ($\theta_1 = \theta_2 = 0°$) (Fig. 2d), while minimal coupling (minimal I_c) occurs for a lobe facing a node ($\theta_1 = 0°$, $\theta_2 = 45°$) (Fig. 2e). D-wave effects are visible in the whole class of HTS Josephson junctions in opportune conditions. In Fig. 2f for instance a "corner" junction between an HTS d-wave electrode and an ordinary s-wave counter-electrode is depicted. Here it is possible to measure the effects generated by the contemporary presence of two channels probing both lobes of the OP in the k_x and k_y directions respectively (Wollman et al., 1995; Van Harlingen, 1995). The angular dependence of the Josephson critical currents of c-axis tilt biepitaxial GB YBCO junctions has been measured in remarkable agreement with predictions based on d-wave OP symmetry (Lombardi et al., 2002; Tafuri and Kirtley, 2005; Kirtley, 2019b). On bicrystal GB JJs it is also based the powerful demonstration of the spontaneous generation of half-flux quantum vortices in the appropriate geometry for the cuprates, observed by a scanning SQUID (superconducting quantum interference device) microscope at the tricrystal point for an optimally doped YBCO (Tsuei et al., 1994; Tsuei and Kirtley, 2000). Finally in the layered crystal structure of cuprate superconductors (especially in the most anisotropic compounds such as $Bi_2Sr_2CaCu_2O_8$), the current-flow of Cooper pairs from the CuO_2 sheets across the blocking layer is of Josephson type and, thus, a single crystal forms a natural stack of Josephson junctions (Kleiner et al., 1992; Kleiner and Wang, 2019).

In conclusions, we have never had so many different families of superconducting materials and so many different types of Josephson junctions as nowadays (Tafuri, 2019), with so many fundamental open questions on their nature and on the prevalent mechanisms they exchange phase information.

More transparent barriers and the Josephson effect derived from Quasi-particle Andreev Bound States

A more transparent barrier, as occurring for barriers composed of normal metals, modifies the critical current-phase $I_S(\varphi)$ relation (CPR):

$$I_S(\varphi) = \sum\nolimits_{n\geq 1} (I_n \, sin\,(n\varphi) + J_n \, cos\,(n\varphi)) \tag{3}$$

The d.c. Josephson Eq. (1) represents a particular case of this general expression. The I_n contribution depends on the barrier transparency D as a D^n power-law. The J_n vanish if time-reversal symmetry is not broken. The expression above may include effects related to possible anisotropic OP symmetry as previously mentioned (Tsuei and Kirtley, 2000). In this case I_n and J_n would depend on the angles θ_1 and θ_2 of the crystallographic axes with respect to the junction interface of the left and right electrodes respectively (Tsuei and Kirtley, 2000). The CPR is the major Josephson 'code' and is the input to calculate most of *dynamical* junction properties. Deviations due to higher harmonics occur in JJs with highly transparent barriers also at the meso- and nano-scale. In atomic point contacts single Andreev processes have been counted (Chauvin et al., 2007).

Quasi-particle Andreev bound states (ABSs) provide a natural framework to describe the Josephson effect in a large variety of systems traceable to S_L-N-S_R structures. The electron obtains an extra phase of $\varphi_L - \varphi_R + \pi$ in each period (see Fig. 2b). The spectrum of the elementary excitations of a N layer in contact with S on both sides is quantized for $E < \Delta$. The expression of the bound state energy in the S_L-N-S_R one-dimensional system in the short junction limit $L \ll \xi_N$ is (Kulik, 1969): $E = \pm\Delta\sqrt{1 - D\ sin^2(\varphi/2)}$, as shown in Fig. 2g.

There is a general relation between the current through the Andreev state and the phase dispersion of the energy of the Andreev state, $I_S = \frac{2e}{\hbar}\frac{dE}{d\varphi}$ (Beenakker, 1992; Beenakker, 1997; Golubov et al., 2004; Lofwander et al., 2001). The d.c. Josephson current is a resonant effect, where the Josephson current flows through resonant Andreev levels. Surfaces may hybridize and form bound states in JJs, and Andreev reflection may lead to the formation of zero energy quasi-particle bound states, as for instance in d-wave superconductors (Hu, 1994; Sigrist, 1998; Kashiwaya and Tanaka, 2000; Lofwander et al., 2001). The existence of midgap states enhances the Josephson current at low temperatures. ABSs may have special features in hybrid junctions with unconventional barriers as for instance graphene (G) and topological insulator (TI). Differently from the usual case, where the electron and hole both lie in the conduction band, at a G/S interface for instance specular AR happens if an electron in the conduction band is converted into a hole in the valence band (Beenakker, 2008).

Essential parameters of a Josephson junction

The energy associated with the phase difference φ across the Josephson junction depends on the critical current I_c and is:

$$E = E_J(1 - cos\varphi) \tag{4}$$

where $E_J = \Phi_o I_c/(2\pi)$ indicates the Josephson energy, being $\Phi_o = h/(2e) \approx 2.07\ 10^{-15}$ Weber the flux quantum. This represents the energy stored in the junction in the superconducting state and comes from the kinetic energy of the charge carriers. The other relevant scaling energy of a JJ is associated to the charge Q which can accumulate on the capacitor C formed by the junction, giving rise to an electrostatic Coulomb energy $E_c = Q^2/(2C)$.

From the fundamental Josephson relations, it results that a change in the supercurrent modifies the Josephson phase, thus determining a nonzero voltage state. The junction thus acts like an effective nonlinear inductance

$$L_J = \frac{\hbar}{2eI_c cos\varphi}$$

as it can be inferred by differentiating Eq. (1) and then using Eq. (2) (Barone and Paternò, 1982; Likharev, 1986). L_J has the unusual property of taking negative values in opportune intervals of the phase φ. A variable inductance is particularly relevant for quantum information manipulation (Clarke and Wilhelm, 2008; McDermott, 2009; Martinis, 2009; Oliver and Welander, 2013; Devoret and Schoelkopf, 2013; Kjaergaard et al., 2020). The maximum critical current I_c, the normal state resistance R_n and the capacitance C of the junctions define the characteristic energy scales of a JJ, the Josephson inductance L_J, the plasma frequency ω_J and the whole phase dynamics as it will be described in the next section. They also determine the spatial scale of the magnetic response of the junction by setting the Josephson penetration depth λ_J.

Properties of a Josephson junction and imprints of macroscopic quantum phenomena

Current-Voltage (I–V) characteristics: From the washboard potential to macroscopic quantum phenomena

In Fig. 3 we report I–V curves when changing the transparency of the junction barrier. The shape of the I–V curves are the very first fingerprints of the nature of a JJ. If we keep constant the cross section of the barrier, a change in the transparency implies a variation of the critical current density J_c. As a reference we also include an I–V curve with a characteristic downward bending (Fig. 3a) measured in microbridges, nanowires and HTS GBs with small misorientation. In a junction with higher J_c, as occurring for S-N-S JJs the bending is in the upward direction (Fig. 3b). This behavior is characteristic of low capacitance junctions and is commonly reported as overdamped regime. At lower values of J_c, I–V curves present hysteresis directly associated to the dielectric nature of the barrier and its capacitance (underdamped regime) (Fig. 3c). Switching events from the S to the R branch (see inset of Fig. 3c) as a function of the bias current are a manifestation of a stochastic process that is fully codified in switching current distributions (SCDs) (see below). Hysteresis can be incomplete with finite retrapping currents depending on dissipation (see for example Fig. 3d).

The Resistively Shunted Junction (RSJ) model, first introduced by Mc-Cumber and Stewart (Stewart, 1986; McCumber, 1968) gives an account of the I–V phenomenology in a variety of weak links (Barone and Paternò, 1982; Likharev, 1986). Representing the displacement current by a capacitor C and the sum of the quasi-particle and insulator leakage current by a resistance R, the current conservation for the equivalent circuit of the junction gives the following equation:

$$I + I_F = I_c \sin\varphi + \frac{V}{R} + C dV/\mathrm{d}t$$

The noise source I_F is associated with its shunt resistance. In the following we will confine to the case $R = R_n$ (Devoret et al., 1985; Martinis et al., 1987; Massarotti and Tafuri, 2019a). By using Josephson relations, it can be transformed in:

$$\left(\frac{\Phi_o}{2\pi}\right)^2 C\frac{\partial^2\varphi}{\partial t^2} + \left(\frac{\Phi_o}{2\pi}\right)^2 \frac{1}{R}\frac{\partial\varphi}{\partial t} + \frac{\partial U}{\partial\varphi} = 0 \tag{5}$$

where

$$U = -\Phi_o/(2\pi)(I_c\cos\varphi + I\varphi) \tag{6}$$

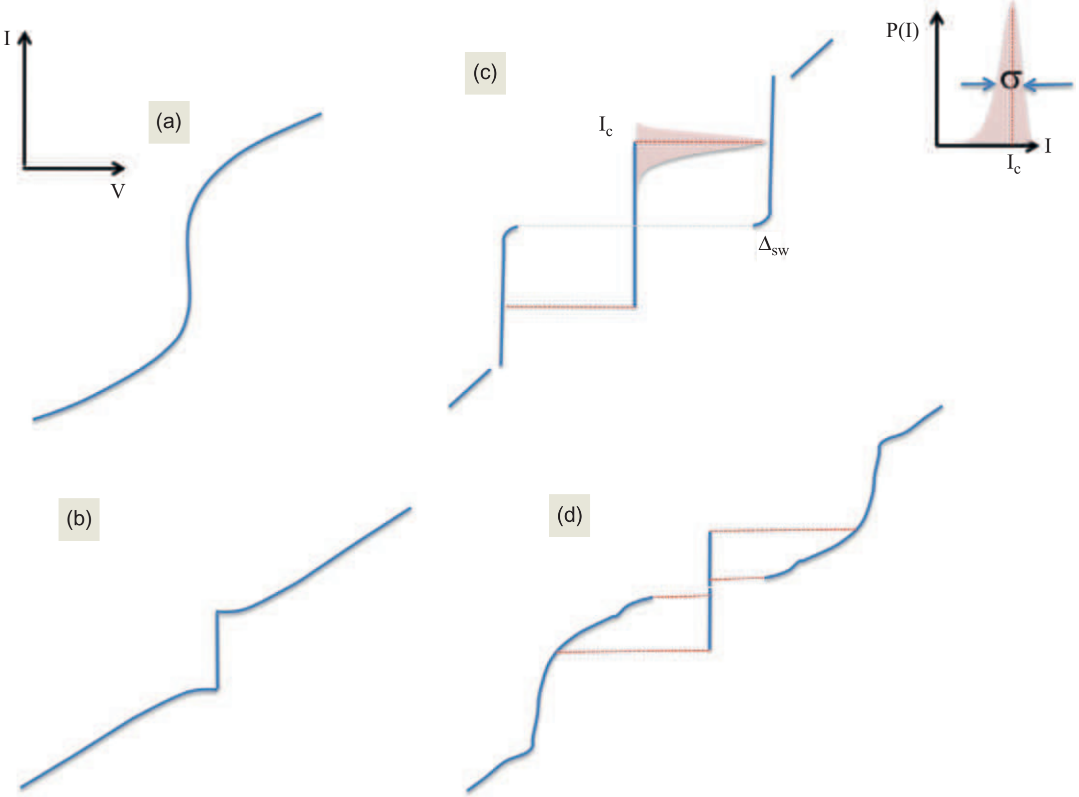

Fig. 3 At very high J_c, as occurring in microbridges and nanowires or in GBs with small misorientation angles (a), the I–V curves present a characteristic down-ward bending. (b) I–V characteristics of overdamped junctions. (c) I–V characteristics of underdamped junctions. This behavior is characteristic of tunnel junctions, and hysteresis is directly associated to the dielectric nature of the barrier. The switch from the S to the R branch is a stochastic process with a peculiar distribution. Hysteresis can be incomplete with finite retrapping currents and the presence of leakage currents (d).

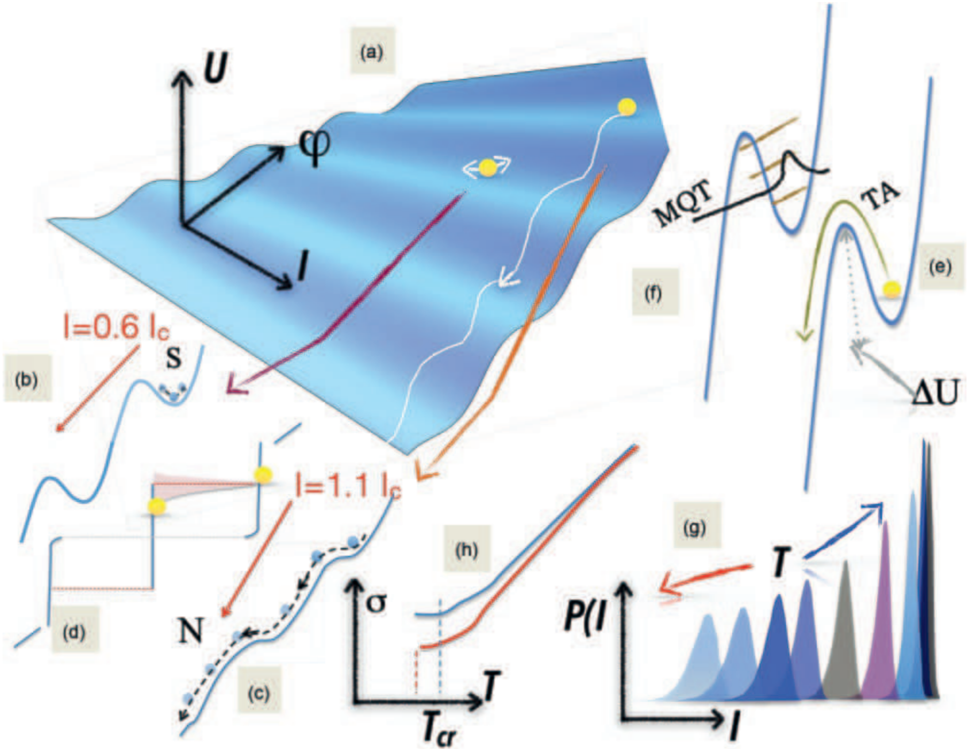

Fig. 4 (a) Washboard potential for different values of the bias current for the standard sinusoidal $I_s(\varphi)$ relation. In (b) and (c) two dimensional projections for two different values of the current (0.6 I_c and 1.1 I_c) are given as examples This phase representations correspond to the yellow points in the I–V curve reported in (d). The particle/phase overcomes the barrier in the washboard potential (e) by Thermal Activation (TA) or by Macroscopic Quantum Tunneling (MQT) (f), then it rolls in the running state. The SCDs are reported as a function of temperature in (g). The standard deviation σ of the distributions are plotted as a function of the temperature in (h). T_{cr} signals the crossover between the TA the MQT regimes and is tuned by the magnetic field. Blue curve and red curve sketch measurements in absence and in presence of an externally applied magnetic field respectively. The magnetic field reduces I_c and thus ω_J, changing finally T_{cr}.

This equation describes the motion of a ball moving on the *tilted washboard* potential U (Stewart, 1986, McCumber, 1968) and allows a direct understanding of the junction non-linear dynamics. The term involving C represents the mass of the particle, the 1/R term represents the damping of the motion, φ the position of the particle and the average "tilt" of the washboard is proportional to I. A tridimensional view of U as a function of φ and I is shown in Fig. 4a.

When ramping the bias current I, the tilt of the energy potential increases and the height $\Delta U = \sqrt{2}/3\ E_J(1 - I/I_c)^{3/2}$ of the energy barrier between consecutive wells decreases. For values of $I < I_c$, the particle is confined to one of the potential wells, where it oscillates back and forth at the plasma frequency $\omega_J(I) = (2\pi I_c/(C\Phi_o))^{1/2}(1 - (I/I_c)^2)^{1/4}$ (see Fig. 4b). For $I < I_c$ the average voltage across the junction is zero. When the current I exceeds I_c, the particle rolls down the washboard (see Fig. 4c); in this case a voltage appears across the junction (see Fig. 4d). Due to effects induced by thermal fluctuations and quantum tunneling, the junction may switch to the finite voltage state for values of $I < I_c$. The relative weight of these two escape processes depends on the temperature of the system (Kramers, 1940; Caldeira and Leggett, 1981; Devoret et al., 1985; Martinis et al., 1987).

A wide variety of I–V characteristics can be described through an opportune choice of parameters within the RSJ model and its variants. The McCumber-Stewart parameter $\beta_c = 2\pi I_c R^2 C/\Phi_o$ is a practical way to estimate the amount of damping of the junction (Barone and Paternò, 1982, Likharev, 1986). The strength of the friction can be also expressed through the junction damping parameter $Q = \omega_J RC$. Underdamped junctions have hysteretic I–V curves for $\beta_c > 1$ and are hence latching. For $\beta_c < 1$ overdamped junctions have non-hysteretic I–V curves and are non-latching. Apart from an obvious capacitive effect, the shape of the subgap currents is very indicative of the dissipative effects (Massarotti and Tafuri, 2019b), which are also strongly influenced by the environment, i.e., the circuitry connected to the junction. Both the nonlinear-Resistive (RSJN) model and the Tunnel-Junction-Microscopic (TJM) model attempt to include dissipative effects for a better account of subgap leakage currents (Scott, 1970; Likharev, 1986; Massarotti and Tafuri, 2019b).

The washboard potential offers a very intuitive picture even on macroscopic quantum phenomena (Leggett, 1980; Caldeira and Leggett, 1983). In the resistive state the particle is rolling down the washboard potential, it is escaping from a generic well by thermal activation following the very general Arrhenius law (Kramers, 1940) (Fig. 4e). In underdamped junctions and at very low temperatures, the dominant contribution to phase escape from the well is due to quantum tunneling (see Fig. 4f) (Caldeira and Leggett, 1981). A study of the distribution of switching events as a function of bias current and obviously of the temperature is the appropriate tool to quantify contributions to escape due to thermal activation (TA) and macroscopic quantum tunneling (MQT), respectively. The SCDs (Fig. 4g) (Fulton and Dunkleberger, 1974) and their first and second momenta (the mean $\bar{I}$ and the standard deviation σ) (Fig. 4h) are neat codes of the junction phase dynamics (Devoret et al., 1985, Martinis et al., 1987). SCD is extracted by repeating the measurement several times (typically 10,000 events). All SCDs are measured at different temperatures as shown in the sketch reported in Fig. 4g. The width σ of each SCD is finally reported as a function of T in Fig. 4h. $T_{cr} = \hbar\omega_J/(2\pi k_B)$ indicates the crossover temperature from the thermal to the quantum regime (Devoret et al., 1985, Martinis et al., 1987). In the quantum regime σ does not depend on T (blue curve). To rule out the possibility that the saturation is due to noise or other spurious effects, the same measurements are realized in presence of an externally applied magnetic field (red curve). The magnetic field reduces I_c and thus ω_J, changing finally T_{cr}. The tuning of T_{cr} demonstrates that the saturation of σ is not due to extrinsic effects (Devoret et al., 1985, Martinis et al., 1987). A collection of experiments on the transition from TA to MQT is reviewed in (Massarotti and Tafuri, 2019b), including those on unconventional JJs. MQT and energy level quantization have been observed in YBCO biepitaxial GB JJs (Bauch et al., 2005; Bauch et al., 2006). The observation of MQT even for junctions with a lobe of the OP facing a node demonstrates that the quality factor Q of high critical temperature superconductor grain boundary JJs is however high enough to observe macroscopic quantum behaviors and that low energy quasi-particles in d-wave JJs are less harmful and dissipative than expected (Bauch et al., 2005, Bauch et al., 2006). In later studies (Longobardi et al., 2012), junction parameters have been finely tuned to explore phase dynamics in YBCO JJs in the moderately damped regime, where phase diffusion regime can also occur in an opportune range of temperatures. After the first escape process, the particle can be retrapped in one of the next wells and then released again, and this will be visible through distinctive features in SCDs measurements. This effect has been first clearly observed in low critical temperature superconductor JJs (Kivioja et al., 2005; Männik et al., 2005; Massarotti and Tafuri, 2019b).

Hamiltonian of a Josephson junction

The passage from the classical to the quantum description of a Josephson junction or of a superconducting electrical circuit is obtained by replacing classical variables with corresponding quantum operators. The Hamiltonian function is replaced by a function of operators. Operatively, the circuit Hamiltonian will be built by adding the kinetic energy associated with the charging energy of the capacitive elements $K = CV^2/2$ and the potential energy associated with the Josephson inductance $U_J = -E_J \cos\varphi$ and with the inductance of the superconducting leads $U_L = \Phi^2/(2L)$, where Φ is the magnetic flux (Devoret and Martinis, 2004; Wendin and Shumeiko, 2007; Wendin, 2017; Kockum and Nori, 2019; Kjaergaard et al., 2020). All these quantities have to be expressed in terms of φ for a given circuit element, which are connected to V and Φ by the Josephson Eq. (2) and by the relation $\Phi = \Phi_o\varphi$ respectively. The commutation relation commonly reported in literature is $[\Phi, q] = 2i\hbar$ where Φ and q are conjugate operators (Likharev, 1986), or more simply $[\varphi, n] = i$, where n the induced charge on the capacitor measured in units of 2e (Cooper pairs). The charge n and phase φ operators do not commute, which means that their expectation values cannot be measured simultaneously. The circuit Hamiltonian is finally constructed by summing up the energies of all circuit elements: $H = \sum K(n_j) + U(\varphi_j)$ (Wendin and Shumeiko, 2007; Kjaergaard et al., 2020). If several circuit elements are connected in a closed loop, the flux quantization equation imposes a constraint on the phases of these elements: $\sum\varphi_i + \varphi_e = 2\pi n$, where $\varphi_e = 2e/\hbar\, \Phi_e$ and Φ_e is the phase associated with the applied magnetic flux.

The Hamiltonian of a current-biased Josephson junction will be therefore expressed as:

$$H = E_{co}n^2 - E_J cos\varphi - \hbar I\varphi/(2e) \tag{7}$$

where $E_{co} = (2e)^2/(2C)$ is the charging energy and I is the applied current. Quantum Josephson junctions with either a well-defined charge or phase variable will depend on the relative magnitude of $E_c = E_{co}n^2$ and E_J (phase for $E_J \gg E_c$, charge for $E_J \ll E_c$ respectively) (Clarke and Wilhelm, 2008).

The Hamiltonian of the Josephson junction can be part of a more general Hamiltonian describing a generic circuit (Devoret and Martinis, 2004; Wendin and Shumeiko, 2007; Wendin, 2017; Kockum and Nori, 2019; Krantz et al., 2019; Kjaergaard et al., 2020). The Cooper pair box, which consists of a superconducting island connected to a superconducting reservoir through a small junction, has been the first superconducting qubit whose quantum state was manipulated coherently (Nakamura et al., 1999). Its Hamiltonian is:

$$H = E_{co}\left(n - n_g\right)^2 - E_J \ \cos\ \varphi \tag{8}$$

where $n_g = -C_g V_g/(2e)$ plays the role of external controlling parameter, and C_g is the gate capacitance. Similar expressions describe other quantum circuits, from phase to flux qubits, from the transmon and the quantronium to the fluxonium (Devoret and Martinis, 2004; Koch et al., 2007; Martinis, 2009; Wendin, 2017). Solving the Hamiltonian for each specific circuit will allow to find the energy-level structure of the system.

Temperature and magnetic dependence of the critical current and of I–V curves

Temperature dependence of I_c

The temperature dependence of I–V curves is a standard key reference to understand the nature of the junction. Accurate predictions exist to evaluate deviations of the I_cR_n vs T dependence from the tunnel limit represented by the Ambegaokar-Baratoff (AB) regime valid for the SIS configuration (Ambegaokar and Baratoff, 1963). In point contacts in the dirty (KO1), where the mean free path l is

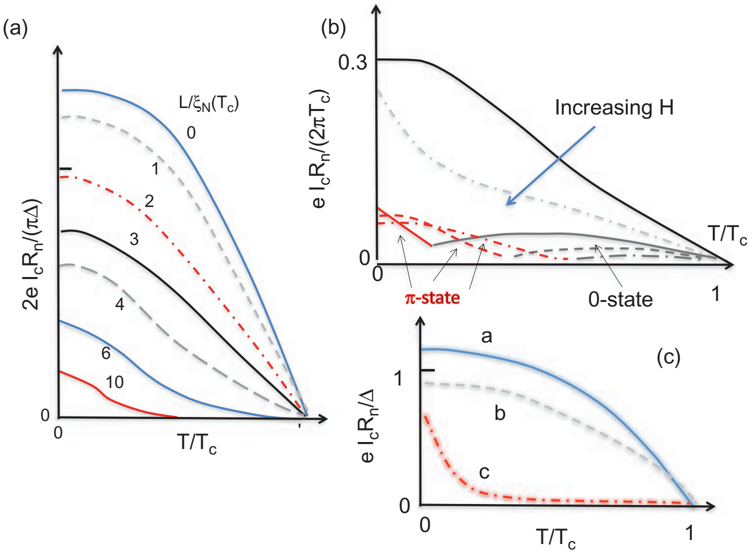

Fig. 5 (a) I_cR_n (T) is reported in units normalized to the gap value Δ as a function of the temperature T, for different values of the ratio between the barrier length L and ξ_n. (b) In a S-F-S junction I_cR_n is reported in units normalized to the critical temperature T_c as a function of T/ T_c, for different values of the exchange field H. Above a critical field an additional minimum in I_cR_n signals the 0-π transition. (c) I_cR_n (T) is calculated for different misorientation angles in HTS d-wave GB JJs: curve a d_0/d_0; curve b $d_0/d_{\pi/8}$ and curve c $d_0/d_{\pi/4}$. (a) Adapted from Ref. Likharev KK (1979) Superconducting weak links. *Reviews of Modern Physics* **51**: 101; (b) Adapted from Ref. Golubov AA, Kupriyanov MY and Il'ichev E (2004) The current-phase relation in Josephson junctions. *Reviews of Modern Physics* **76**: 411; (c) Adapted from Ref. Tanaka Y and Kashiwaya S (1997) Theory of Josephson effects in anisotropic superconductors. *Physical Review B* **56**: 892

shorter than the length of the weak link L, ($l < L$) (Kulik and Omelyanchuk, 1975) and clean (KO2), where ($l > L$) (Kulik and Omelyanchuk, 1977) limits, the values of I_c at $T = 0$ K are higher than AB value. If a metallic barrier N replaces the insulator I, the I_cR_n (T) is quite different and even changes concavity (Likharev, 1986). In Fig. 5a a variety of qualitatively different behaviors, including the transition from the short ($L < <\xi_n$) to the long ($L> > \xi_n$) regime, is reported (Likharev, 1979; Delin and Kleinsasser, 1996; Golubov et al., 2004). The tail in the exponential growth and the width of the intermediate region substantially depends on L/ξ_n (Barone and Paternò, 1982; Likharev, 1979; Golubov et al., 2004). Finer quantitative deviations depend on details of the proximity effect and on boundary conditions.

Radically different I_cR_n(T) curves are measured, when a 0-π transition is induced by changing the temperature with a characteristic non-monotonous dependence of the I_cR_n(T). This is visible in Fig. 5b when the exchange field H is increased above a certain threshold in a S-F-S junction (Ryazanov et al., 2001; Golubov et al., 2004; Buzdin, 2005). A peculiar 1/T scaling of the I_cR_n has been predicted for ideal interfaces in HTS d-wave GB JJs (Barash et al., 1996; Tanaka and Kashiwaya, 1997; Riedel and Bagwell, 1998; Kashiwaya and Tanaka, 2000; Lofwander et al., 2001). This is due to the change in the dispersion relation for the ABSs, and the corresponding angle integrated current-phase relation, which is particularly relevant for high misorientation angles in GB JJs. In the resonant case, the splitting of the levels, and consequently the width of the Andreev band, will be particularly large, proportional to $D^{1/2}$. The (maximum) I_cR_n is proportional to $D^{1/2}$, and is much larger than the AB value in conventional s-wave tunnel junctions, which is proportional to D (Likharev, 1979; Tanaka and Kashiwaya, 1997). This is shown in Fig. 5c, where I_cR_n(T) is calculated for different misorientation angles in HTS d-wave GB JJs. Using the notation $d_{\theta 1}/d_{\theta 2}$, by increasing the misorientation angle from d_0/d_0 (curve a) to $d_0/d_{\pi/8}$ (curve b) and finally $d_0/d_{\pi/4}$ (curve c), dramatic changes occur in the shape of the I_cR_n(T). In (c) I_cR_n (T) does not saturate (Golubov et al., 2004).

Magnetic dependence of the critical current

The phase variation induced by an externally applied magnetic field has been since early times an invaluable and unambiguous tool to demonstrate the Josephson effect and a key fingerprint for plenty of sensor applications. This is widely documented in all textbooks and especially in (Barone and Paternò, 1982). Geometry of the junction, nature of the electrodes or of the barrier and their possible inhomogeneities determine specific space-dependent phase variations across the barrier, inducing Meissner screening magnetic interference effects, vortex formation and trapping, shielding and spontaneous supercurrents. All these effects cooperate to induce a distinctive spatial distribution of the critical current density across the junction barrier, and thus special features in the magnetic dependence of the I_c and of the I–V curves.

The final expression of the dependence of the critical current on the external magnetic flux for an ideal rectangular geometry is:

$$I_s(\Phi) = J_s WL \left| \frac{\sin\left(\pi \frac{\Phi}{\Phi_o}\right)}{\pi \frac{\Phi}{\Phi_o}} \right| \tag{9}$$

In Eq. (10) the product $W{\cdot}L$ represents the junction magnetic area. The curve is reported in Fig. 6a.

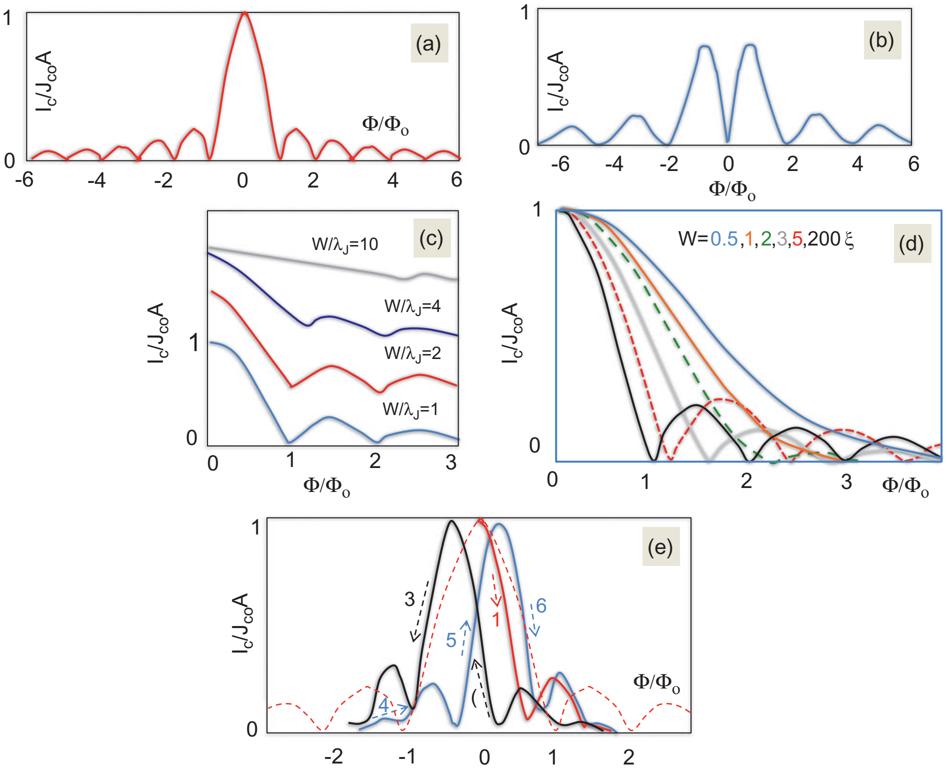

Fig. 6 (a) Magnetic field dependence of the maximum Josephson current for 'ideal' JJ; (b) Dependence of the I_S on the magnetic field for a d-wave corner junction composed of Pb and YBCO electrodes, two symmetric maxima appear at finite magnetic fields. In (c) self-field effects induced by non-uniform distribution of the critical current occurring in long junctions, are visible in the magnetic pattern for ordinary junctions. The reduction and then the fading of the secondary lobes accompanied by a shift in the position of the minima of I_S also occurs in diffusive SNS junctions (d). In spin filter SFS JJs the I_S keeps memory of the history of how the magnetic field has been applied (e). The sequence of how the magnetic field is applied in the experiments is: red curve, black curve, blue curve. (b) Adapted from Wollman DA, Van Harlingen DJ, Giapintzakis J, Ginsberg DM (1995) Evidence for d-wave pairing from the magnetic field modulation of in $YBa_2Cu_3O_{7-\delta}$ -Pb Josephson junctions. Physical Review Letters 74, 797–800; (c) adapted from Kirtley JR, Moler KA and Scalapino DJ (1997) Spontaneous flux and magnetic-interference patterns in 0-π Josephson junctions. *Physical Review B* **56**: 886; (d) Adapted from Bergeret FS and Cuevas JC (2008) The vortex state and Josephson critical current of diffusive SNS junction. *Journal of Low Temperature Physics* **153**: 304–324; (e) Adapted from Massarotti D, Pal A, Rotoli G, Longobardi L, Blamire MG and Tafuri F (2015) Macroscopic quantum tunnelling in spin filter ferromagnetic Josephson junctions. *Nature Communications* **6**: 7376.

It can be derived the one-dimensional time-independent sine-Gordon equation combining Maxwell's equation and the d.c. Josephson relation:

$$\frac{\partial^2\varphi}{\partial x^2} = \frac{\sin\varphi}{\lambda_J^2} \tag{10}$$

where $\lambda_J = \sqrt{\Phi_o/(2\pi d\mu_o J_c)}$ is the Josephson penetration depth and gives a measure of the distance from the edge where d.c. Josephson currents are confined, being $d = t + \lambda_R + \lambda_L$, with t the barrier thickness, $\lambda_{R(L)}$ the London penetration depth in the R(L) electrode and μ_o the magnetic permeability of vacuum respectively.

We refer to textbooks and extensive reviews for a detailed account of theory and all deviations (Barone and Paternò, 1982; Kirtley, 2019a; Kirtley, 2019b). The magnetic patterns shown in Fig. 6 give finally a brief overview on some of the most significant deviations from the standard patterns. In all figures on y-axis I_c is always reported. On the x-axis depending on the origin of the curves (simulations or experiments) magnetic flux or magnetic field is reported, respectively. In a d-wave corner junction composed of Pb and YBCO electrodes, two symmetric maxima appear at finite magnetic fields (Fig. 6b) (Wollman et al., 1995). If the d-wave junction has more than the two facets of the corner junction, relative maxima in I_S appear between the two absolute maxima (for an applied magnetics flux $\Phi_{max} = N\Phi_o/2$) (Smilde et al., 2002). The vanishing I_S at $\Phi = 0$ occurs for an even number of facets N. In Figs. 6c self-field effects induced by non-uniform distribution of I_S occurring in long junctions, are briefly sketched for ordinary junctions (Kirtley et al., 1997; Barone and Paternò, 1982). When increasing the width W of the junction with respect to the Josephson penetration depth λ_J, lobes at higher fields tend to be smeared out and the characteristic interferometric behavior is even lost when W is larger than 10 λ_J.

The reduction and then the fading of the secondary lobes accompanied by a shift in the position of the minima of I_S also occurs in diffusive SNS junctions (see 6d) (Bergeret and Cuevas, 2008). For W comparable or smaller than $\xi_H = \sqrt{\Phi_o/H}$ the formation of a linear array of vortices is not favored and the field acts as a strong pair-breaking mechanism monotonically suppressing I_S. The monotonic suppression of I_c is also obtained while increasing L, even for fixed W to about ξ_H (Bergeret and Cuevas, 2008). The presence of higher harmonics in the current-phase relation also affects the magnetic response (Goldobin et al., 2007; Kirtley, 2019a; Kirtley, 2019b). A distinctive feature is the appearance of oscillations of I_S with twice shorter period in H when increasing the intensity of the second harmonic. SFS JJs are expected to generate several anomalous magnetic behaviors due to the magnetic nature of the barrier itself (Ryazanov et al., 2001; Buzdin, 2005). I_S keeps memory of the history of how the magnetic field has been applied and the magnetic pattern is hysteretic (see Fig. 6e) (Senapati et al., 2011; Massarotti et al., 2015).

Hybrid junctions using almost bi-dimensional flakes are posing new questions also on the magnetic dependence of I_S. In addition to extrinsic features as those for instance induced by the way contacts are placed in a typical coplanar junction configuration, the intrinsic nature of the barrier may add special fingerprints. A recent example in a Ti/Al-InAs/GaSb-Ti/Al junction is given by the influence of edge states (Pribiag et al., 2015). Here gate-tuning between edge-dominated and bulk-dominated regimes of superconducting transport is demonstrated through superconducting quantum interference. The edge-dominated regime arises only under conditions of high-bulk resistivity, which has been associated with the two-dimensional topological phase. For wide barriers, supercurrents will flow along distant edges resembling the typical response of a SQUID (Pribiag et al., 2015).

Emerging trends: From qubits to hybrid JJs

The new frontiers of the Josephson effect are currently developing along a few exciting and challenging directions.

Low temperature Josephson junctions for qubits, quantum circuits and superconducting electronics

JJs are the fundamental cells for quantum bits and quantum circuits with a variety of functionalities.

Superconducting qubits encode information in the energy eigenstates of Josephson junction-based electronic circuits (Clarke and Wilhelm, 2008; McDermott, 2009; Martinis, 2009; Oliver and Welander, 2013; Devoret and Schoelkopf, 2013; Krantz et al., 2019; de Leon et al., 2021).

The first cornerstone was the experiment in 1999 where time-resolved coherent oscillations in a superconducting qubit were observed (Nakamura et al., 1999). Further key steps were the observation of coherent oscillations in coupled superconducting qubits (Pashkin et al., 2003; Yamamoto et al., 2003) and the significant improvements of the coherence times of these devices (Clarke and Wilhelm, 2008; Vion et al., 2002; Devoret and Schoelkopf, 2013, Krantz et al., 2019; Kjaergaard et al., 2020). There are currently several types of superconducting qubits with different circuit construction. The highly anharmonic Josephson potential allows to selectively excite the states used as basis of the qubit, and to avoid contributions from other energy levels. Thermal energy must be sufficiently low to avoid incoherent mixing of eigenstates ($k_BT < < \omega_{01}$, where ω_{01} is energy quantum associated with the transition between the ground state $|0\rangle$ and the first excited state $|1\rangle$ of the qubit), and the macroscopic degree of freedom must be sufficiently decoupled from other degrees of freedom for the lifetime of the quantum states to be long on the characteristic time scale of the system. From the requirements $k_BT < < \omega_{01}$ and $\omega_{01} < < \Delta$ junctions need to be fabricated with materials with a $T_c > 1$ K. Aluminum JJs guarantee long coherence times T_1 (T_1 is the time required for a qubit to relax from $|1\rangle$ to $|0\rangle$) (Clarke and Wilhelm, 2008; Martinis, 2009). The transmon (Koch et al., 2007) and x-mon (Barends et al., 2013) consist of a capacitively shunted JJ where the junction acts as a nonlinear inductor. The fluxonium qubit (Manucharyan et al., 2009) is an inductively shunted JJ. By applying a magnetic flux through a superconducting loop, its potential well structure can be controllably modified. The capacitively shunted flux qubit (You et al., 2007; Steffen et al., 2010) is a SQUID loop with three JJs, shunted by a large capacitor where the qubit state is an energy eigenstate of the persistent current in the SQUID loop. The gatemon uses a voltage-tunable semiconductor weak-link barrier for the Josephson junction (Larsen et al., 2015). In all these devices, the JJs act as nonlinear elements, providing anharmonicity to the energy levels of the circuit. Most of these superconducting qubits were strongly coupled to photons stored in high-quality coplanar waveguide resonators, that would protect qubits from decoherence and promote techniques both for read out of their state and for their coupling in a quantum computer architecture (Blais et al., 2021; Blais et al., 2021). The first experimental realization of a circuit QED system achieving the strong- coupling regime of light-matter interaction was realized in 2004 (Chiorescu et al., 2004; Krantz et al., 2019; Wallraff et al., 2004).

Currently reference fidelity is on a single-qubit gate 99.97%, on readout 99.8%, and on two-qubit gate operations 99.5% (Jurcevic et al., 2021), respectively. T_1 times are typically about 100 μs (Krantz et al., 2019, Kjaergaard et al., 2020). For fixed-frequency transmon qubits, the time interval within which information stored in a single qubit is lost, generally referred to as the coherence time T_2, can be increased to about $\approx T_1 \approx 100\ \mu s$ with opportune sequences of multiple pulses. Typical gate times are around a few hundred nanoseconds (Sheldon et al., 2016; Paik et al., 2016). Tunable transmons or capacitively shunted flux qubits can allow for much faster gate times, around tens of nanoseconds, but their tunability also renders them more susceptible to flux noise (Kjaergaard et al., 2020). Circuit QED is paving the way to the development of quantum-limited amplifiers (Clerk et al., 2010; Roy and Devoret, 2016; Siddiqi et al., 2004; Vijay et al., 2011) and single-microwave photon detectors (Besse et al., 2018; Kono et al., 2018; Lescanne et al., 2020). The generation and routing of control pulses involve a substantial experimental overhead in the form of room-temperature and cryogenic electronics hardware. An attractive candidate for the control of large-scale qubit arrays is the single flux quantum (SFQ) digital logic family (Opremcak et al., 2018). In SFQ digital logic, classical bits of information are encoded in fluxons (Mukhanov et al., 2019).

Both bulk materials and surface and interfaces induce decoherence affecting the final qubit performances. Progress in material science is fundamental to face issues related to substrate dielectric loss, excess quasiparticles in superconducting metal causing dissipation and dephasing, the presence of uncontrolled oxides and contaminants at interfaces hosting two-level systems, surface spins and charges causing flux noise and charge noise, respectively. Better quality junction is an important issue to improve qubit performances (Clarke and Wilhelm, 2008; McDermott, 2009; Martinis, 2009; Oliver and Welander, 2013; Devoret and Schoelkopf, 2013; de Leon et al., 2021), also to contribute to overcome the main intrinsic limitation on the coherence of superconducting qubits resulting from low-frequency noise, notably 1/f noise. This raises from a uniform distribution of two-state defects. Each defect produces random telegraph noise, and a superposition of such uncorrelated processes leads to a 1/f power spectrum. Recognized sources of 1/f noise are (Clarke and Wilhelm, 2008): (1) critical-current fluctuations, which arise from fluctuations in the transparency of the junction caused by the trapping and untrapping of electrons in the tunnel barrier (van Harlingen et al., 2004); (2) charge fluctuations, which arise from the hopping of electrons between traps on the surface of the superconducting film or the surface of the substrate and this motion induces charges onto the surface of nearby superconductors; (3) magnetic-flux fluctuations. Despite the successful use of Al junctions, two-level defects (TLDs) in AlO_x tunnel barrier remain one of the major sources of decoherence in superconducting qubits (Martinis et al., 2003; McDermott, 2009; Oliver and Welander, 2013; Grabovskij et al., 2012).

Hybrid Josephson junctions uncovering emergent phenomena: from semiconducting and ferromagnetic barriers to topological insulators and Van der Waals crystals

Hybrid Josephson junctions are driving research in other relevant directions. Here "hybrid" stands for a barrier which, differently from a simple insulator or a normal metallic layer, can add novel functionalities to the Josephson coupling, transferring the specific features of the barrier to the coherent flow of the carriers such as topological states, ferroelectricity, magnetoelectricity, non-collinear magnetism and emergent properties from twisted heterostructures. Barriers leading to hybrid JJs are for instance ferromagnets, semiconductors, topological insulators (TI), graphene (G), nanotubes. Van der Waals (vdW) crystals can be superconducting and can work as electrodes and as barriers as well. Barriers for hybrid junctions are frequently two-dimensional (2D) sheets or nanowires. Some of the above-mentioned barriers are also commonly reported as "quantum materials". The coplanar junction configuration is particularly convenient for hybrid junctions because it avoids the extremely challenging critical step of the barrier deposition on the superconducting film. The components can be obviously inverted when the superconductor has more critical conditions to be deposited as occurring for instance in HTS JJs. Nowadays, among the barriers listed above only ferromagnets are easily integrated into trilayers and not necessarily use coplanar layout.

The semiconducting barrier

In S-Sm-S systems, interface effects and boundary conditions will eventually tune the superconducting proximity effect and the capability of transferring coherence from the electrodes to the barrier (Barone and Paternò, 1982). An intuitive picture can be derived by standard proximity arguments by investigating the induced coherence length in the semiconducting barrier ξs_m. ξs_m depends on the carrier density through the diffusion constant and can be tuned, for instance, through a gate voltage for high transmittance S-Sm interface (Barone and Paternò, 1982; Kleinsasser and Jackson, 1990; Takayanagi et al., 1995; Tafuri, 2019). These barriers commonly are schematized as two-dimensional electron gas (2DEG) systems and their properties can be tuned through the gate from the weak localization to the strongly localized regime, thus tuning I_c and R_n values and I–V curves (Takayanagi et al., 1995). One of the ultimate targets for this type of device with Sm barrier has always been the challenging realization of a superconducting Josephson field-effect transistor (Jo-FET) (Mannhart, 1996).

Topological insulators

The fractional Josephson effect is known to be a characteristic phenomenon of topological Josephson junctions hosting Majorana zero modes (MZMs), where the Josephson current has a 4π (rather than a 2π) periodicity in the phase difference between the two topological superconductors (Kitaev, 2001; Fu and Kane, 2008; Mourik et al., 2012; Beenakker, 2015; Alicea, 2012). Topological phases of matter have attracted much attention in condensed matter physics. One of the characteristic features of topological phases of matter is the presence of symmetry-protected gapless boundary states that are robust against weak perturbations respecting relevant symmetry. The robustness is related to topology of wave functions and is important from the perspective of device applications as well as fundamental physics. Interesting ballistic and mesoscopic transport effects are also expected implementing materials with a Dirac dispersion such as TI and G. These phenomena can be investigated by tuning the electron concentration of the Dirac material at the Dirac point. Despite claims on the observation of signatures of Majorana fermions so far, a decisive and unambiguous evidence of the existence of MZMs is still missing (Sumita and Furusaki, 2021; Galaktionov and Zaikin, 2021). It is widely believed that superconducting junctions involving topological insulators and hosting Majorana-like bound states may exhibit an unusual "fractional" (4π-periodic) ac Josephson effect. The 4π-periodic CPR stays as a quite unusual and characteristic feature not occurring in a standard JJ. Inner properties of any weak link between two conventional superconductors may influence its critical current and the form of CPR but not its periodicity in φ, which is fundamentally determined by the periodicity of the charge space reciprocal to the phase one (Galaktionov and Zaikin, 2021; Sumita and Furusaki, 2021). In 4π-CPR, the charge transfer between superconducting condensates on both sides of the junction should be provided by quasiparticles with charge e rather than by Cooper pairs with charge 2e.

Pronounced Shapiro steps at fractional frequencies have been detected in a number of microwave experiments performed with HgTe- and BiSb-based superconducting junctions (see for instance Wiedenmann et al., 2016 and references therein). Multiple

Andreev reflection (MAR) are also expected to play an important role in experiments with junctions involving topological insulators (Galaktionov and Zaikin, 2021). Electrodynamics of these junctions is poorly understood because of difficulties in modeling effective capacitance and dissipation of the junctions. Here heating effects may have more dramatic effects because of the lower dimensionality of the system. Within this framework, junctions of more than two superconducting terminals have gained renewed interest with the perspective of multiple supercurrents simultaneously transiting across the junction (de Bruyn Ouboter et al., 1995; Amin et al., 2002a; Amin et al., 2002b; van Heck et al., 2014; Riwar et al., 2016; Pankratova et al., 2020).

The ferromagnetic barrier

In a ferromagnetic JJ, exchange energy (E_{ex}) in magnets imposes a finite momentum to Cooper pairs, leading to a modulation of spatially damped oscillations of the OP when penetrating the ferromagnetic barrier over the decay length scale. Depending on the JJ barrier thickness, the ground state can either be a 0-junction with equal superconducting phases on both sides or a π-junction. Experiments have shown the presence of 0-π transitions by tuning the F-layer thickness in metallic or alloyed magnets. (Buzdin, 2005; Bergeret et al., 2005; Linder and Robinson, 2015; Eschrig, 2015). Magnetic insulators barriers in JJs are also fascinating for their spin filtering tunnel properties (Senapati et al., 2011); also in these junctions macroscopic quantum tunneling has been observed (Massarotti et al., 2015). A vdW ferromagnetic JJ has been recently obtained by inserting a few-layer ferromagnetic insulator $Cr_2Ge_2Te_6$ into two layers of the layered dichalcogenide 2H-$NbSe_2$ superconductor. With atomically flat and magnetically sharp interfaces, these type of functional nanodevices may potentially serve as critical components for superconducting quantum circuits or memories (Ai et al., 2021).

vdW crystals integration into JJs and Twisted HTS JJs

This last experiment falls in a series of recent studies, where 2D vdW crystals have been integrated into JJs. vdW heterostructures are a promising material platform for quantum devices. Cleaved from pure bulk crystals, the surfaces of these heterostructures are pristine and atomically flat. When assembled into stacks, the layers are held together by weak bonds that do not strain the crystals. Weak vdW bonding between neighboring atomic layers also offers a unique opportunity for engineering atomic interfaces with controlled twist angles (Ribeiro-Palau et al., 2018). Careful adjustment of the twist angle can create the spatial periodicity of a moire´ superlattice (Yoo et al., 2019) with narrow electronic bands and topological structure (Carr et al., 2020). Realizations of such 'twistronics' host a plethora of emergent electronic states, at the twisted interface of various vdW materials. This technique has been extended also to HTS (Frank Zhao et al., 2021). Twisted interfaces between stacked van der Waals cuprate crystals enable tunable Josephson coupling between in-plane anisotropic superconducting order parameters between nodal superconducting order parameters (SOP) across a twisted vdW interface (Frank Zhao et al., 2021). Employing a novel cryogenic assembly technique, Josephson junctions with an atomically sharp twisted interface between $Bi_2Sr_2CaCu_2O_{8+x}$ (BSCCO) crystals have been realized. In $Bi_2Sr_2CaCu_2O_{8+x}$ (BSCCO), superconducting CuO_2 bilayers are Josephson-coupled through insulating [SrO-BiO] bilayers, where the crystal can be mechanically cleaved into atomically flat crystals. J_c sensitively depends on the twist angle, reaching the maximum value comparable to that of the intrinsic junctions at small twisting angles and is suppressed by almost two orders of magnitude close to 45° twist angle. The J_c dependence on the twist angle is consistent with d-wave expectations, in agreement with what was observed on grain boundary YBcCuO biepitaxial Josephson junctions (Lombardi et al., 2002). Twisted bilayers of high-T_c cuprate superconductors have renewed arguments on topological phases with spontaneously broken time reversal symmetry (T) for certain twist angles with the key outstanding challenge to identify unambiguous signatures of these topological phases in experiments (Tummuru et al., 2022). A detection of the π-periodic term is by itself not sufficient to identify the topological phase. These more controlled heterostructures may give the opportunity to investigate fundamental issued raised since early time on HTS JJs. Another study on twisted ultrathin $Bi_2Sr_2CaCu_2O_{8+x}$ substantially confirms that experimental results are extremely sensitive to atomic details of the junction structures (Zhu et al., 2021; Li et al., 1999), that can cause artifacts even for these very sophisticated techniques (Zhu et al., 2021).

Conclusion

We have gone through the concepts and the phenomenology of the Josephson effect guided by the key feature of a dissipationless current driven by a phase difference of the macroscopic wavefunction between the two superconducting electrodes. To this unique capability of transferring quantum mechanics rules to macroscopic objects and circuits, a Josephson junction adds the ability of being a versatile component of all superconducting circuits providing a series of unique properties including the nonlinear behavior used in all current qubit architectures. Progress in materials science and nanotechnology has allowed to enlarge the 'parameter space' of operation for Josephson junctions to unprecedented values and control. The continuous progress in realizing high quality LTS-based JJs consolidates expectations for a series of challenging applications, including the realization of multi-qubit quantum processors. Unconventional junctions keep opening novel problems, confirming a series of predictions and promoting the study of novel physical processes. This impressive experimental progress is accompanied by a formidable capability of handling theoretical problems of significant complexity. Diversity in Josephson junctions opens breath-taking 'horizons', also because of its unique capability to transfer quantum to the macroscopic real. Much remains to do.

References

Ai L, Zhang E, Yang J, Xie X, Yang Y, Jia Z, Zhang Y, Liu S, Li Z, Leng P, Cao X, Sun X, Zhang T, Kou X, Han Z, Xiu F, and Dong S (2021) Van der Waals ferromagnetic Josephson junctions. *Nature Communications* 12: 6580.

Alicea J (2012) New directions in the pursuit of Majorana fermions in solid state systems. *Reports on Progress in Physics* 75: 076501–076536.

Ambegaokar V and Baratoff A (1963) Tunneling between Superconductors. *Physical Review Letters* 10: 486. Errata *Phys. Rev. Lett.* 11: 104.

Amin MHS, Omelyanchouk AN, and Zagoskin AM (2002a) Dc squid based on the mesoscopic multiterminal Josephson junction. *Physica C: Superconductivity* 372: 178–180.

Amin M, Omelyanchouk AN, Blais A, van den Brink AM, Rose G, Duty T, and Zagoskin AM (2002b) Multi-terminal superconducting phase qubit. *Physica (Amsterdam)* 368C: 310.

Anderson PW (1997) *Basic Notions of Condensed Matter Physics*. Boston: Westview Press/Addison-Wesley.

Andreev AF (1964) The thermal conductivity of the intermediate state in superconductors. Zh. Esker. Teor. Fiz. 46, 1823-1828 *Soviet Physics Journal of Experimental and Theoretical Physics* 19: 1228–1231.

Arnold GB (1985) Superconducting tunneling without the tunneling Hamiltonian. *Journal of Low Temperature Physics* 59: 143–183.

Barash YS, Burkhardt H, and Rainer D (1996) Low-temperature anomaly in the Josephson critical current of junctions in d-wave superconductors. *Physical Review Letters* 77: 4070.

Barends R, et al. (2013) Coherent Josephson qubit suitable for scalable quantum integrated circuits. *Physical Review Letters* 111: 080502.

Barone A and Paternò G (1982) *Physics and Applications of the Josephson Effect*. New York: John Wiley & Sons, Inc.

Bauch T, Lombardi F, Tafuri F, Barone A, Rotoli G, Delsing P, and Claeson T (2005) Macroscopic quantum tunneling in d-wave$YBa_2Cu_3O_{7-x}$ Josephson junctions. *Physical Review Letters* 94: 087003.

Bauch T, Lindström T, Tafuri F, Rotoli G, Delsing P, Claeson T, and Lombardi F (2006) Quantum dynamics of a d-wave Josephson junction. *Science* 311: 57–60.

Beenakker CWJ (1992) Quantum transport in semiconductor-superconductor microjunctions. *Physical Review B* 46: 12841.

Beenakker CWJ (1997) Random-matrix theory of quantum transport. *Reviews of Modern Physics* 69: 731.

Beenakker CWJ (2008) Andreev reflection and Klein tunneling in graphene. *Reviews of Modern Physics* 80: 1337.

Beenakker CWJ (2015) Random-matrix theory of Majorana fermions and topological superconductors. *Reviews of Modern Physics* 87: 1037.

Bergeret FS and Cuevas JC (2008) The vortex state and Josephson critical current of diffusive SNS junction. *Journal of Low Temperature Physics* 153: 304–324.

Bergeret FS, Volkov AF, and Efetov KB (2005) Odd triplet superconductivity and related phenomena in superconductor/ferromagnet structures. *Reviews of Modern Physics* 77: 1321–1373.

Besse J-C, Gasparinetti S, Walter T, Kurpiers P, Pechal M, Eichler C, and Wallraff A (2018) Single-shot quantum nondemolition detection of individual itinerant microwave photons. *Physical Review X* 8: 021003.

Blais A, Arne L, Grimsmo AL, Girvin SM, and Wallraff A (2021) Circuit quantum electrodynamics. *Reviews of Modern Physics* 93: 025005-1.

Blonder GE, Tinkham M, and Klapwijk TM (1982) Transition from metallic to tunneling regimes in superconducting microconstrictions: Excess current, charge imbalance, and supercurrent conversion. *Physical Review B* 25: 4515.

Buzdin AI (2005) Proximity effects in superconductor-ferromagnet heterostructures. *Reviews of Modern Physics* 77: 935.

Caldeira AO and Leggett AJ (1981) Influence of dissipation on quantum tunneling in macroscopic systems. *Physical Review Letters* 46: 211.

Caldeira AO and Leggett AJ (1983) Quantum tunnelling in a dissipative system. *Annals of Physics* 149: 374–456.

Carr S, Fang S, and Kaxiras E (2020) Electronic-structure methods for twisted moire layers. *Nature Reviews Materials* 5: 748–763.

Chaudari P, Mannhart J, Dimos D, Tsuei CC, Chi CC, Oprysko MM, and Scheuermann M (1988) Direct measurement of the superconducting properties of single grain boundaries in $YBa_2Cu_3O_{7-\delta}$. *Physical Review Letters* 60: 1653–1656.

Chauvin M, vom Stein P, Esteve D, Urbina C, Cuevas JC, and Levy YA (2007) Crossover from Josephson to multiple Andreev reflection currents in atomic contacts. *Physical Review Letters* 99: 067008-067011.

Chiorescu I, Bertet P, Semba K, Nakamura Y, Harmans CJPM, and Mooij JE (2004) Coherent dynamics of a flux qubit coupled to a harmonic oscillator. *Nature* 159: 4317005.

Clarke J (1971) Finite-voltage behavior of lead-copper-lead junctions, Phys. Rev. B 4, 2963; 1969, Supercurrents in lead-copper-lead sandwiches. *Proceedings of the Royal Society A* 308: 447–471.

Clarke J and Wilhelm FK (2008) Superconducting quantum bits. *Nature* 453: 1031–1042.

Clerk AA, Devoret MH, Girvin SM, Marquardt F, and Schoelkopf RJ (2010) Introduction to quantum noise, measurement, and amplification. *Reviews of Modern Physics* 82: 1155.

de Bruyn Ouboter R, Omelyanchouk AN, and Vol ED (1995) Multi-terminal squid controlled by the transport current. *Physica (Amsterdam)* 205B: 153.

de Gennes PG (1964) Boundary effects in superconductors. *Reviews of Modern Physics* 36: 225–237.

de Gennes PG (1966) *Superconductivity of Metals and Alloys*. New York: Benjamin.

de Leon NP, Itoh KM, Kim D, Mehta KK, Northup TE, Paik H, Palmer BS, Samarth N, Sangtawesin S, and Steuerman DW (2021) Materials challenges and opportunities for quantum computing hardware. *Science* 372: 2823.

Delin KA and Kleinsasser AW (1996) Stationary properties of high-critical-temperature proximity effect Josephson junctions. *Superconductor Science and Technology* 9: 227–269.

Devoret MH and Martinis JM (2004) Superconducting qubits. In: Esteve D, Raimond JM, and Dalibard J (eds.) *Quantum Entanglement and Information Processing, volume 79 of Les Houches Summer School Session, Les Houches Session 79th on Quantum Entanglement and Information Processing* 443–485.

Devoret MH and Schoelkopf RJ (2013) Superconducting circuits for quantum information: An outlook. *Science* 339: 1169–1174.

Devoret MH, Martinis JM, and Clarke J (1985) Measurements of macroscopic quantum tunneling out of the Zero-Voltage state of a current-biased Josephson junction. *Physical Review Letters* 55: 1908.

Dimos D, Chaudhari P, and Mannhart J (1990) Superconducting transport properties of grain boundaries in $YBa_2Cu_3O_{7-\delta}$ bicrystals. *Physical Review B* 41: 4038.

Eschrig M (2015) Spin-polarized supercurrents for spintronics: A review of current progress. *Reports on Progress in Physics* 78: 104501.

Frank Zhao SY, Poccia N, Cui X, Volkov PA, Yoo H, Engelke R, Ronen Y, Zhong R, Gu G, Plugge S, Tummuru T, Franz M, Pixley JH, and Kim P (2021) Emergent interfacial superconductivity between twisted cuprate superconductors. *Condensed Matter.* 2108.13455v1.

Fu L and Kane CL (2008) Superconducting proximity effect and majorana fermions at the surface of a topological insulator. *Physical Review Letters* 100: 096407.

Fulton TA and Dunkleberger LN (1974) Lifetime of the zero-voltage state in Josephson tunnel junctions. *Physical Review B* 9: 4760.

Galaktionov AV and Zaikin AD (2021) Fractional Shapiro steps without fractional Josephson effect. *Physical Review B* 104: 054521.

Goldobin E, Koelle D, Kleiner R, and Buzdin A (2007) Josephson junctions with second harmonic in the current-phase relation: Properties of π junctions. *Physical Review B* 76: 224523.

Golubov AA, Kupriyanov MY, and Il'ichev E (2004) The current-phase relation in Josephson junctions. *Reviews of Modern Physics* 76: 411.

Grabovskij GJ, Peichl T, Lisenfeld J, Weiss G, and Ustinov A (2012) Strain tuning of individual atomic tunnelling systems detected by a superconducting qubit. *Science* 338: 232–234.

Gurvitch M, Washington MA, and Huggins HA (1983) High quality refractory Josephson tunnel junctions utilizing thin aluminum layers. *Applied Physics Letters* 42: 472–474.

Hilgenkamp H and Mannhart J (2002) Grain boundaries in high-T_c superconductors. *Reviews of Modern Physics* 74: 485.

Hu C-R (1994) Midgap surface states as a novel signature for d-wave superconductivity. *Physical Review Letters* 72: 1526.

Josephson BD (1962) Possible new effects in superconductive tunnelling. *Physics Letters* 7: 251–253.

Jurcevic P, et al. (2021) Demonstration of quantum volume 64 on a superconducting quantum computing system. *Quantum Science and Technology* 6: 025020.

Kashiwaya S and Tanaka Y (2000) Tunnelling effects on surface bound states in unconventional superconductors. *Reports on Progress in Physics* 63: 1641–1724.

Kirtley JR (2019a) Chapter 6: Magnetic field effects in Josephson junctions. In: Tafuri (ed.) *Fundamentals and Frontiers of the Josephson Effect*. Berlin: Springer.

Kirtley JR (2019b) Chapter 9: Pairing symmetry effects. In: Tafuri (ed.) *Fundamentals and Frontiers of the Josephson Effect*. Berlin: Springer.

Kirtley JR, Moler KA, and Scalapino DJ (1997) Spontaneous flux and magnetic-interference patterns in 0-π Josephson junctions. *Physical Review B* 56: 886.

Kitaev A (2001) Unpaired Majorana fermions in quantum wires. *Physics-Uspekhi* 44: 131.

Kivioja JM, Nieminen TE, Claudon J, Buisson O, Hekking FWJ, and Pekola JP (2005) Observation of transition from escape dynamics to underdamped phase diffusion in a Josephson junction. *Physical Review Letters* 94: 247002.

Kjaergaard M, Schwartz ME, Braumüller J, Krantz P, Wang J, Gustavsson S, and Oliver WD (2020) Superconducting qubits: Current state of play. *Annual Review of Condensed Matter Physics* 11: 369–395.

Kleiner R and Wang H (2019) Chapter 10: Intrinsic Josephson junctions in high temperature superconductors. In: Tafuri (ed.) *Fundamentals and Frontiers of the Josephson effect*. Berlin: Springer.

Kleiner R, Steinmeyer F, Kunkel G, and Müller P (1992) Intrinsic Josephson effects in$Bi_2Sr_2CaCu_2O_8$ single crystals. *Physical Review Letters* 68: 2394–2397.

Kleinsasser AW and Jackson TN (1990) Critical currents of superconducting metal-oxide-semiconductor field-effect transistors. *Physical Review B* 42: 8716.

Koch J, Yu TM, Gambetta J, Houck AA, Schuster DI, Majer J, Blais A, Devoret MH, Girvin SM, and Schoelkopf RJ (2007) Charge insensitive qubit design from optimizing the cooper-pair box. *Physical Review A* 76: 042319.

Kockum AF and Nori F (2019) Chapter 17: Quantum Bits with Josephson Junctions. In: Tafuri (ed.) *Fundamentals and Frontiers of the Josephson Effect*. Berlin: Springer.

Koelle D, Kleiner R, Ludwig F, Dantsker E, and Clarke J (1999) High-transition-temperature superconducting quantum interference devices. *Reviews of Modern Physics* 71: 631.

Kono S, Koshino K, Tabuchi Y, Noguchi A, and Nakamura Y (2018) Quantum non-demolition detection of an itinerant microwave photon. *Nature Physics* 14: 546.

Kramers HA (1940) Brownian motion in a field of force and the diffusion model of chemical reactions. *Physica* 7: 284–304.

Krantz P, Kjaergaard M, Yan F, Orlando TP, Gustavsson S, and Oliver WD (2019) A quantum engineer's guide to superconducting qubits. *Applied Physics Reviews* 6: 021318. 58 pages.

Kulik IO (1969) Macroscopic quantization and the proximity effect in S-N-S junctions. Zh. Esker. Teor. Fiz. 57, 1745-1759 *Soviet Physics Journal of Experimental and Theoretical Physics* 30: 944–950.

Kulik IO and Omelyanchuk AN (1975) Contribution to the microscopic theory of the Josephson effect in superconducting bridges. Pis'ma v Zh. Eksp. Teor. Fiz. 21, 216–217 *JETP Letters* 21: 96–97.

Kulik IO and Omelyanchuk AN (1977) Properties of superconducting microbridges in the pure limit. Fiz. Nizk.-Temp. 4,945-946 *Soviet Journal of Low Temperature Physics* 3: 459–460.

Larsen TW, Petersson KD, Kuemmeth F, Jespersen TS, Krogstrup P, Nygård J, and Marcus CM (2015) Semiconductor-nanowire-based superconducting qubit. *Physical Review Letters* 115: 127001.

Leggett AJ (1980) Macroscopic quantum systems and the quantum theory of measurement. *Progress of Theoretical Physics Supplement* 69: 80–100.

Lescanne R, Deleglise S, Albertinale E, Reglade U, Capelle T, Ivanov E, Jacqmin T, Leghtas Z, and Flurin E (2020) Irreversible qubit-photon coupling for the detection of itinerant microwave photons. *Physical Review X* 10: 021038.

Li Q, Tsay YN, Suenaga M, Klemm RA, Gu GD, and Koshizuka N (1999) $Bi_2Sr_2CaCu_2O_{8-\delta}$ Bicrystal c-Axis twist Josephson junctions: A new phase-sensitive test of order parameter symmetry. *Physical Review Letters* 83: 4160.

Likharev KK (1979) Superconducting weak links. *Reviews of Modern Physics* 51: 101.

Likharev KK (1986) *Dynamics of Josephson Junctions and Circuits*. New York: Gordon and Breach.

Linder J and Robinson WA (2015) Superconducting spintronics. *Nature Physics* 11: 307–315.

Lofwander T, Shumeiko VS, and Wendin G (2001) Andreev bound states in high- T_c superconducting junctions. *Superconductor Science and Technology* 14: R53–R77.

Lombardi F, Tafuri F, Ricci F, Miletto GF, Barone A, Testa G, Sarnelli E, Kirtley JR, and Tsuei CC (2002) Intrinsic d-wave effects in $YBa_2Cu_3O_{7-\delta}$ grain boundary Josephson junctions. *Physical Review Letters* 89: 207001.

Longobardi L, Massarotti D, Stornaiuolo D, Galletti L, Rotoli G, Lombardi F, and Tafuri F (2012) Direct transition from quantum escape to a phase diffusion regime in YBaCuO biepitaxial Josephson junctions. *Physical Review Letters* 109: 050601-050604.

Mannhart J (1996) High-T_c transistors. *Superconductor Science and Technology* 9: 49.

Männik J, Li S, Qiu W, Chen W, Patel V, Han S, and Lukens JE (2005) Crossover from Kramers to phase-diffusion switching in moderately damped Josephson junctions. *Physical Review B* 71: 220509.

Manucharyan VE, Koch J, Glazman LI, and Devoret MK (2009) Fluxonium: Single cooper-pair circuit free of charge offsets. *Science* 326: 113–116.

Martinis JM (2009) Superconducting phase qubits. *Quantum Information Processing* 8: 81–103.

Martinis JM, Devoret MH, and Clarke J (1987) Experimental tests for the quantum behavior of a macroscopic degree of freedom: The phase difference across a Josephson junction. *Physical Review B* 35: 4682.

Martinis JM, Nam S, Aumentado J, Lang KM, and Urbina C (2003) Decoherence of a superconducting qubit due to bias noise. *Physical Review B* 67: 094510.

Massarotti D and Tafuri F (2019a) Chapter 7: Current–voltage characteristics. In: Tafuri (ed.) *Fundamentals and Frontiers of the Josephson Effect*. Berlin: Springer.

Massarotti D and Tafuri F (2019b) Chapter 11: Phase Dynamics and Macroscopic Quantum Tunneling. In: Tafuri (ed.) *Fundamentals and Frontiers of the Josephson Effect*. Berlin: Springer.

Massarotti D, Pal A, Rotoli G, Longobardi L, Blamire MG, and Tafuri F (2015) Macroscopic quantum tunnelling in spin filter ferromagnetic Josephson junctions. *Nature Communications* 6: 7376.

McCumber DE (1968) Effect of ac impedance on dc voltage-current characteristics of superconductor Weak-Link junctions. *Journal of Applied Physics* 39: 3113–3118.

McDermott R (2009) Materials origins of decoherence in superconducting qubits. *IEEE Transactions on Applied Superconductivity* 19: 2–13.

Mourik V, Zuo K, Frolov SM, Plissard SR, Bakkers EPAM, and Kouwenhoven LP (2012) Signatures of Majorana fermions in hybrid superconductor-semiconductor nanowire devices. *Science* 336: 1003–1007.

Mukhanov O, Yoshikawa N, Nevirkovets IP, and Hidaka M (2019) Chapter 16: Josephson Junctions for Digital Applications: Single Flux Quantum Logic. In: Tafuri (ed.) *Fundamentals and Frontiers of the Josephson Effect*. Berlin: Springer.

Nakamura Y, Pashkin YA, and Tsai JS (1999) Coherent control of macroscopic quantum states in a single Cooper pair box. *Nature* 398: 786–788.

Oliver WD and Welander PB (2013) Materials in superconducting quantum bits. *MRS Bulletin* 38: 816–825.

Opremcak A, Pechenezhskiy IV, Howington C, Christensen BG, Beck MA, Leonard E Jr., Suttle J, Wilen C, Nesterov K, Ribeill GJ, Thorbeck T, Schlenker F, Vavilov MG, Plourde BLT, and McDermott R (2018) Measurement of a superconducting qubit with a microwave photon counter. *Science* 361: 1239–1242.

Paik H, et al. (2016) Experimental demonstration of a resonator- induced phase gate in a multiqubit circuit-QED system. *Physical Review Letters* 117: 250502.

Pankratova N, Lee H, Kuzmin R, Wickramasinghe K, Mayer W, Yuan J, Vavilov MG, Shabani J, and Manucharyan VE (2020) Multiterminal Josephson Effect. *Physical Review X* 10: 031051.

Pashkin YA, Yamamoto T, Astafiev O, Nakamura Y, Averin DV, and Tsai JS (2003) Quantum oscillations in two coupled charge qubits. *Nature* 421: 823–826.

Pribiag VS, Beukman AJA, Qu F, Cassidy MC, Charpentier C, Wegscheider W, and Kouwenhoven LP (2015) Edge-mode superconductivity in a two-dimensional topological insulator. *Nature Nanotechnology* 10: 593.

Ribeiro-Palau R, Zhang C, Watanabe K, Taniguchi T, Hone J, and Dean CR (2018) Twistable electronics with dynamically rotatable heterostructures. *Science* 361: 690–693.

Riedel RA and Bagwell PF (1998) Low-temperature Josephson current peak in junctions with d-wave order parameters. *Physical Review B* 57: 6084.

Riwar R-P, Houzet M, Meyer JS, and Nazarov YV (2016) Multi-terminal Josephson junctions as topological matter. *Nature Communications* 7: 11167.

Roy A and Devoret M (2016) Introduction to parametric amplification of quantum signals with Josephson circuits. *Comptes Rendus Physique* 17: 740–755.

Ryazanov VV, Oboznov VA, Rusanov AY, Veretennikov AV, Golubov AA, and Aarts J (2001) Coupling of two superconductors through a ferromagnet: Evidence for a π junction. *Physical Review Letters* 86: 2427.

Scott WC (1970) Hysteresis in the dc switching characteristics of Josephson junctions. *Applied Physics Letters* 17: 166–168.

Senapati K, Blamire MG, and Barber ZH (2011) Spin-filter Josephson junctions. *Nature Materials* 10: 849–852.

Shapiro S (1963) Josephson currents in superconducting tunneling: The effect of Microwaves and other observations. *Physical Review Letters* 11: 80.

Sheldon S, Magesan E, Chow JM, and Gambetta JM (2016) Procedure for systematically tuning up cross-talk in the cross-resonance gate. *Physical Review A* 93: 060302.

Siddiqi I, Vijay R, Pierre F, Wilson CM, Metcalfe M, Rigetti C, Frunzio L, and Devoret MH (2004) RF-driven Josephson bifurcation amplifier for quantum measurement. *Physical Review Letters* 93: 207002–207005.

Sigrist M (1998) Time-reversal symmetry breaking states in high-temperature superconductors. *Progress in Theoretical Physics* 99: 899–929.

Smilde HJH, Ariando DHA, Blank GJ, Gerritsma H, Hilgenkamp H, and Rogalla H (2002) d-wave-induced josephson current counterflow YBCO/Nb Zigzag junctions. *Physical Review Letters* 88: 57004–57007.

Steffen M, Kumar S, DiVincenzo DP, Rozen JR, Keefe GA, Rothwell MB, and Ketchen MB (2010) High-coherence hybrid superconducting qubit. *Physical Review Letters* 105: 100502.

Stewart WC (1986) Current-voltage characteristics of Josephson junctions. *Applied Physics Letters* 12: 277–280.

Sumita S and Furusaki A (2021) Superconductor/normal-metal/superconductor junction of topological superconductors revisited: Fractional Josephson current, fermion parity, and oscillating wave functions. *Physical Review B* 104: 205431.

Tafuri F (2019) *Fundamentals and Frontiers of the Josephson Effect*. Berlin: Springer.

Tafuri F and Kirtley JR (2005) Weak links in high critical temperature superconductors. *Reports on Progress in Physics* 68: 2573–2663.

Takayanagi H, Bindslev HJ, and Nitta J (1995) Mesoscopic fluctuations of the critical current in a superconductor/normal-conductor/superconductor. *Physical Review Letters* 74: 166.

Tanaka Y and Kashiwaya S (1997) Theory of Josephson effects in anisotropic superconductors. *Physical Review B* 56: 892.

Thouless DJ (1998) *Topological Quantum Numbers in Nonrelativistic Physics*. Singapore: World Scientific.

Tinkham M (2004) *Introduction to Superconductivity*, 2nd edn Dover Publications.

Tsuei CC and Kirtley JR (2000) Pairing symmetry in cuprate superconductors. *Reviews of Modern Physics* 72: 969.

Tsuei CC, Kirtley JR, Chi CC, Yu-Jahnes LS, Gupta A, Shaw T, Sun JZ, and Ketchen MB (1994) Pairing symmetry and flux quantization in a tricrystal superconducting ring of $YBa_2Cu_3O_{7-\delta}$. *Physical Review Letters* 73: 593–596.

Tummuru T, Plugge S, and Franz M (2022) Josephson effects in twisted cuprate bilayers. *Physical Review B* 105: 064501.

Van Harlingen DJ (1995) Phase-sensitive tests of the symmetry of the pairing state in the high-temperature superconductors: Evidence for d-wave symmetry. *Reviews of Modern Physics* 67: 515.

van Harlingen DJ, Robertson TL, Plourde BLT, Reichardt PA, Crane TA, and Clarke J (2004) Decoherence in Josephson-junction qubits due to critical-current fluctuations. *Physical Review B* 70: 064517.

van Heck B, Mi S, and Akhmerov AR (2014) Single fermion manipulation via superconducting phase differences in multiterminal Josephson junctions. *Physical Review B* 90: 155450.

Vijay R, Slichter DH, and Siddiqi I (2011) Observation of quantum jumps in a superconducting artificial atom. *Physical Review Letters* 106: 110502–110505.

Vion D, Aassimea A, Cottet A, Joyez P, Pothier C, Urbina C, Esteve D, and Devoret MH (2002) Manipulating the quantum state of an electrical circuit. *Science* 296: 886–889.

Wallraff A, Schuster DI, Blais A, Frunzio L, Huang R-S, Majer J, Kumar S, Girvin SM, and Schoelkopf RJ (2004) Strong coupling of a single photon to a superconducting qubit using circuit quantum electrodynamics. *Nature* 431: 162–167.

Weinberg S (1986) Superconductivity for particular theorists. *Progress of Theoretical Physics Supplement* 86: 43–53.

Wendin G (2017) Quantum information processing with superconducting circuits: A review. *Reports on Progress in Physics* 80: 106001.

Wendin G and Shumeiko VS (2007) Quantum bits with Josephson junctions. *Journal of Low Temperature Physics* 33: 724–744.

Wiedenmann J, Bocquillon E, Deacon RS, Hartinger S, Herrmann O, Klapwijk TM, Maier L, Ames C, Brüne C, Gould C, Oiwa A, Ishibashi K, Tarucha S, Buhmann H, and Molenkamp LW (2016) 4π-periodic Josephson supercurrent in HgTe-based topological Josephson junctions. *Nature Communications* 7: 10303.

Wolf E (1985) *Principles of Electron Tunneling Spectroscopy*. Oxford University Press.

Wolf E, Arnold G, Gurvitch M, and Zasadzinski J (2017) *Josephson Junctions History, Devices, and Applications*. Singapore: Pan Stanford Publishing.

Wollman DA, Van Harlingen DJ, Giapintzakis J, and Ginsberg DM (1995) Evidence for d-wave pairing from the magnetic field modulation of in $YBa_2Cu_3O_{7-\delta}$ -Pb Josephson junctions. *Physical Review Letters* 74: 797–800.

Yamamoto Y, Pashkin YA, Astafiev O, Nakamura Y, and Tsai (2003) Demonstration of conditional gate operation using superconducting charge qubits. *Nature* 425: 941–944.

Yoo H, Engelke R, Carr S, Fang S, Zhang K, Cazeaux P, Sung SH, Hovden R, Tsen AW, Taniguchi T, Watanabe K, Yi G-C, Kim M, Luskin M, Tadmor EB, Kaxiras E, and Kim P (2019) Atomic and electronic reconstruction at the van der Waals interface in twisted bilayer graphene. *Nature Materials* 18: 448–453.

You JQ, Hu X, Ashhab S, and Nori F (2007) Low-decoherence flux qubit. *Physical Review B* 75: 140515.

Zhu Y, Liao M, Zhang Q, Xie H-Y, Meng F, Liu Y, Bai Z, Ji S, Zhang J, Jiang K, Zhong R, Schneeloch J, Gu G, Gu L, Ma X, Zhang D, and Xue Q-K (2021) Presence of s-Wave pairing in Josephson Junctions made of twisted ultrathin $Bi_2Sr_2CaCu_2O_{8+x}$ flakes. *Physical Review X* 11: 031011.

Superconductivity: Electronic mechanisms

Andrey V Chubukov, School of Physics and Astronomy and William I. Fine Theoretical Physics Institute, University of Minnesota, Minneapolis, MN, United States

© 2024 Elsevier Ltd. All rights reserved.

Introduction **632**
Superconductivity due to electron-electron interaction **633**
A brief history 633
Modern studies—Applications to lattice systems **633**
Fe-pnictides 633
Cuprates 635
Doped graphene 637
Chiral superconductivity 637
Twisted bilayer graphene 638
s-wave superconductivity from repulsion 638
Superconductivity at strong coupling **639**
Renormalization group analysis 639
Pairing by spin and charge fluctuations 640
Superconductivity near a quantum-critical point 641
Strong coupling limit 642
Conclusion **643**
Acknowledgments **643**
References **643**

Abstract

Superconductivity is a fascinating subject, which remains at the forefront of research in condensed matter physics in the 21st century. In this Chapter I review several directions of the research over the last two decades, with emphasis on unconventional superconductivity of strongly correlated electrons.

Key points

- Unconventional superconductivity of strongly correlated electrons can emerge from nominally repulsive electronelectron interaction. A static screening of electronelectron repulsion often gives rise to attraction in non-swave spatial channels, like *d*-wave, where the gap function changes sign along the Fermi surface. A dynamical screening reduces the repulsion at smaller frequencies and may give rise to spatially uniform *s*-wave superconductivity, where the gap function has a non-trivial phase winding between small and large frequencies.

Introduction

Superconductivity (SC) is one of most remarkable aspects of quantum physics of interacting electrons. Discovered in 1911 by Kamerlingh Onnes and his team of technicians, it preoccupied the minds of the most prominent physicists of the 20th century and remains at the forefront of condensed-matter physics in the 21st century. Many ideas that emerged from the study of superconductivity were extended to other fields of physics, famously serving as paradigms to explain the generation of a Higgs mass generation of the electroweak W and Z gauge bosons in particle physics.

In simple words, superconductivity is the ability of fermions to carry electric current without dissipation. In quantum physics such phenomenon is associated with the appearance of a macroscopic condensate, i.e., a quantum state in which 10^{23} particles “hold together” at the lowest quantum level and do not allow individual members to get swiped away by impurities, interactions with boundaries, etc. Bosons are capable to do this because any number of them can occupy a single quantum level, and the appearance of a macroscopic condensate of bosons is a well-known phenomenon of Bose-Einstein condensation. Fermions, on the other hand, are “lone wolves”—by Pauli principle, only two of them (with opposite spins) can occupy a single quantum level, others are expelled. However, if fermions form bound pairs, quantum mechanics teaches us that each pair has spin $S = 0$ or 1, i.e., it is a boson. Paired fermions then condense and behave as one monolithic object, i.e., if they are forced to move in one direction by an applied electric field, they will continue moving even after the field is turned off.

https://doi.org/10.1016/B978-0-323-90800-9.00059-7

Bardeen, Cooper, and Schrieffer (BCS) attributed pair formation to attractive interaction between electrons and phonons. Electron-phonon mechanism of SC has been successfully applied to explain the pairing in a large variety of materials, from *Hg* and *Al* to MgB_2 with $T_c = 39\ K$. The discovery of SC in the cuprates and, later, in iron-pnictides signaled the beginning of the new era of "high-temperature superconductivity." The vast majority of researchers believe that superconductivity in these systems, as well in ruthenates, heavy-fermion, and organic materials, does not come from electron-phonon interaction, by one reason of the other. This leaves a nominally repulsive electron-electron interaction as a potential pairing glue. In this Chapter I review some basic aspects of superconductivity due to electron-electron interaction (Basov and Chubukov, 2011; Chubukov and Hirschfeld, 2015; Tremblay and Chubukov, 2017; Armitage et al., 2010), discuss recent applications to several classes of materials (Basov and Chubukov, 2011; Chubukov and Hirschfeld, 2015; Tremblay and Chubukov, 2017; Armitage et al., 2010; Lee et al., 2006; Keimer et al., 2015) and strong coupling effects, including the interplay with non-Fermi liquid behavior near a quantum-critical point (Abanov and Chubukov, 2020).

Superconductivity due to electron-electron interaction

A brief history

The study of the pairing due to nominally repulsive electron-electron interaction started in 1960th, when it was realized that the pairing problem decouples between different angular momenta l, and bound pairs develop even if the interaction has a single attractive partial component $U_{l0} < 0$ with some l_0. Quantum mechanics tells that partial components with large l come from large distances, where a screened Coulomb potential has the long range oscillatory tail $\cos(2k_F r + \varphi_0)/r^3$ in 3D, where k_F is the Fermi momentum, (these are called Friedel oscillations). Hence, in some ranges of r a screened Coulomb interaction gets over-screened and becomes negative, i.e., attractive.

A bold step in this analysis has been made by Kohn and Luttinger (KL) in 1965 (Kohn and Luttinger, 1965; Fay and Layzer, 1968; Baranov et al., 1992). They obtained U_l at large l by separating non-analytic $2k_F$ screening and regular screening from other momenta. They argued that the first contribution to U_l scales as $1/l^4$, while the second one behave at large l as e^{-l}, i.e., is much smaller. Neglecting these regular terms, KL found that U_l with large odd l are definitely attractive, hence any rotationally invariant system with repulsive Coulomb interaction is unstable against pairing.

The situation at smaller l is less definite as one no longer can separate the non-analytic $2k_F$ contribution to the irreducible pairing vertex and regular contributions from other momenta. In this situation, one can only do perturbation theory to second order in some bare $U(q)$. For momentum-independent (Hubbard) interaction $U(q) = U$, KL attraction survives down to $l = 1$, which by far is the largest attractive component.

Modern studies—Applications to lattice systems

For lattice systems, the situation is more complex because angular components with different l no longer decouple. There is a partial decoupling between different irreducible representations, however their number is finite, and within each representation there is an infinite number of pairing channels, which do not decouple in the analysis of the pairing (Maiti and Chubukov, 2014; Kiesel et al., 2012). Nevertheless, the very idea that the electron-electron interaction, relevant to the pairing, differs from a regularly screened electron-electron repulsion (e.g., the Hubbard interaction at strong screening) due to "$2k_F$" renormalizations from low-energy fermions turned out to be rather fruitful and allowed one to understand in simple terms the gap symmetry in various superconductors. I illustrate this on three examples below.

Fe-pnictides

Fe-pnictides are binary compounds of pnictogens, which are the elements from the 5th group: N, P, As, Sb, Bi. Superconductivity in these materials has been discovered in 2008 by Hosono and his collaborators. Later, superconductivity has been found also in Fe-chalcogenides—Fe-based compounds with elements from the 16th group: S, Se, Te. The family of *Fe*-based superconductors (FeSCs) includes 1111 systems RFeAsO (R = rare earth element), 122 systems like XFe_2As_2(B = Ba,Na, K) and AFe_2Se_2 (A = K, Rb, Cs), 111 systems like LiFeAs, and 11 systems, like FeSe. Parent compounds of most of FeSCs are metallic antiferromagnets. Because electrons, which carry magnetic moments, can travel relatively freely from site to site, antiferromagnetic order is often termed as a "spin-density-wave" (SDW), by analogy with, e.g., magnetism in *Cr*, rather than "Heisenberg antiferromagnetism"—the latter term is reserved for systems in which electrons are "nailed down" to particular lattice sites by very strong Coulomb repulsion. In some parts of the phase diagram a lattice rotational symmetry is spontaneously broken. Such a state is called a nematic. Superconductivity emerges upon either hole or electron doping (see Fig. 1), but can also be induced by pressure or by isovalent replacement of one pnictide element by another, e.g., As by P. In some systems, like LiFeAs and FeSe, superconductivity emerges already at zero doping, instead of a magnetic order, but in FeSe it is preceded by a nematic order (Basov and Chubukov, 2011; Chubukov and Hirschfeld, 2015; Tremblay and Chubukov, 2017; Armitage et al., 2010).

The electronic structure of FeSCs is fairly complex, with multiple Fermi surfaces (FS's), as evidenced by ARPES and quantum oscillations measurements. In most systems, there are two or three near-cylindrical hole FS's, centered at $k_x = k_y = 0$, and two electron FS's centered at (π,π). For electron pockets, states inside the pockets are occupied, for hole pockets, states inside the pockets are empty.

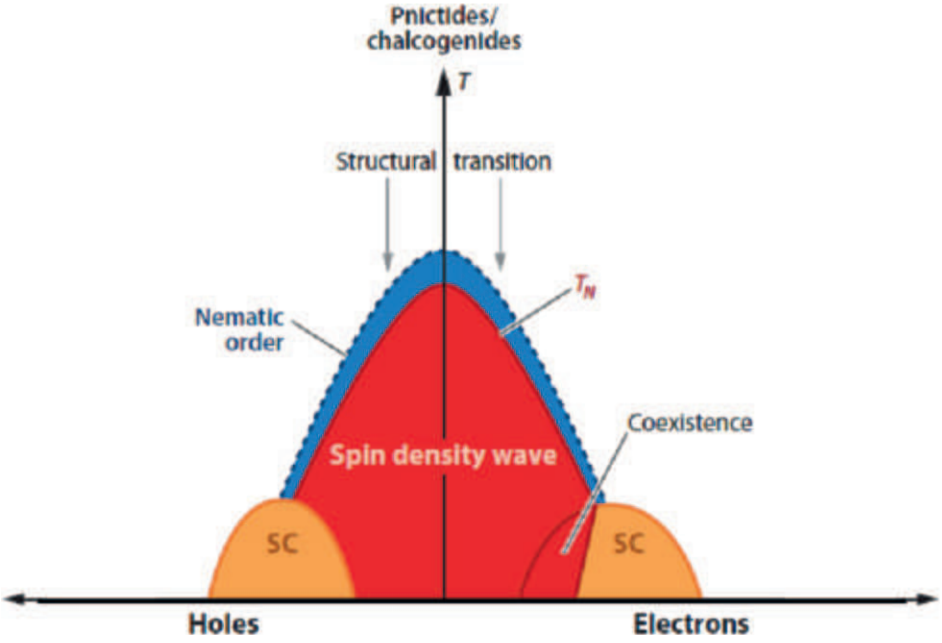

Fig. 1 Schematic phase diagram of Fe-based pnictides upon hole or electron doping. In the shaded region, superconductivity and antiferromagnetism co-exist. Not all details/phases are shown. Superconductivity can be initiated not only by doping but also by pressure and/or isovalent replacement of one pnictide element by another. From Basov D.N., Chubukov A.V. (2011) *Nature Physics* 7: 273.

For proof-of-concept we consider a simpler problem: a 2D two-pocket model with one hole and one electron FS, both circular and of equal size (see Fig. 2 left). The free-fermion Hamiltonian is the sum of kinetic energies of holes and electrons:

$$H_2 = \sum_{k,\sigma} \varepsilon_c c^{\dagger}_{k,\sigma} c_{k,\sigma} + \varepsilon_f f^{\dagger}_{k,\sigma} f_{k,\sigma} \tag{1}$$

where c stands for holes, f stands for electrons, and $\varepsilon_{c,f}$ stand for their respective dispersions with the property the $\varepsilon_c(k) = -\varepsilon_f(k + Q)$, where $\mathbf{Q}$ is the momentum vector which connects the centra of the two FS's.

The two interactions that contribute to the pairing are intra-pocket density-density interaction G_4 and pair hopping G_3, in which two fermions from one pocket transform into two fermions from the other pocket:

$$\begin{aligned} H_{\text{int}} = \; & \sum_{[k,\ \sigma]} \frac{G_3}{2} \left(c^{\dagger}_{k1,\sigma 1} c^{\dagger}_{k2,\sigma 2} f_{k3,\sigma 2} f_{k4,\sigma 1} + \text{h.c} \right) \\ & + \sum_{[k,\ \sigma]} \left(\frac{G_4}{2} c^{\dagger}_{k1,\sigma 1} c^{\dagger}_{k2,\sigma 2} c_{k3,\sigma 2} c_{k4,\sigma 1} + c \leftrightarrow f \right) \end{aligned} \tag{2}$$

where $^{\mathrm{P}}{}_{[k,\sigma]}$ is short for the sum over the spins and the sum over all the momenta constrained to $k_1 + k_2 = k_3 + k_4$ modulo a reciprocal lattice vector. Both interactions are positive, i.e., repulsive, but they are include all renormalizations from particle-hole channel, including "$2k_F$" renormalizations. These interactions are often called *irreducible* particle-particle vertices to emphasize that they are considered "bare" interactions for particle-particle channel, but at the same time incorporate all renormalizations from the particle-hole channel (Maiti and Chubukov, 2014; Kiesel et al., 2012).

To analyze the pairing, one has to consider vertex functions for fermions on the FS for zero total incoming momentum (i.e., for fermions with momenta $\mathbf{k}$ and $-\mathbf{k}$) and finite frequency Ω. If a pairing instability develops at some $T_c > 0$, then at $T = 0$ the fully renormalized vertex function has a pole in the upper hap-plane of complex Ω, implying that perturbations above the normal state grow exponentially with time.

Because there are two pockets, there are three relevant vertices: $\Gamma_{hh}(\mathbf{k}_F, -\mathbf{k}_F, \mathbf{p}_F, -\mathbf{p}_F) = \Gamma_{ee}(\mathbf{k}_F, -\mathbf{k}_F, \mathbf{p}_F, -\mathbf{p}_F)$, where $\mathbf{k}_F$ and $\mathbf{p}_F$ belong to the same pocket, and $\Gamma_{he}(\mathbf{k}_F, -\mathbf{k}_F, \mathbf{p}_F, -\mathbf{p}_F)$, where $\mathbf{k}_F$ and $\mathbf{p}_F$ belong to different pockets. The renormalizations of irreducible $\Gamma_{hh} = \Gamma_{ee}$ and Γ_{he} come from the particle-particle-channel, like in BCS theory. The result is

$$\begin{aligned} \Gamma^{full}_{hh} &= -\frac{1}{2} \left(\frac{G_4 + G_3}{1 + (G_4 + G_3)\Pi_{pp}} + \frac{G_4 - G_3}{1 + (G_4 - G_3)\Pi_{pp}} \right) \\ \Gamma^{full}_{he} &= -\frac{1}{2} \left(\frac{G_4 + G_3}{1 + (G_4 + G_3)\Pi_{pp}} - \frac{G_4 - G_3}{1 + (G_4 - G_3)\Pi_{pp}} \right), \end{aligned} \tag{3}$$

where $\Pi_{pp} = \Pi_{pp}(\Omega) = N_0(\log|\omega_c/\Omega| + i\pi/2)$, where N_0 is the density of states at the FS.

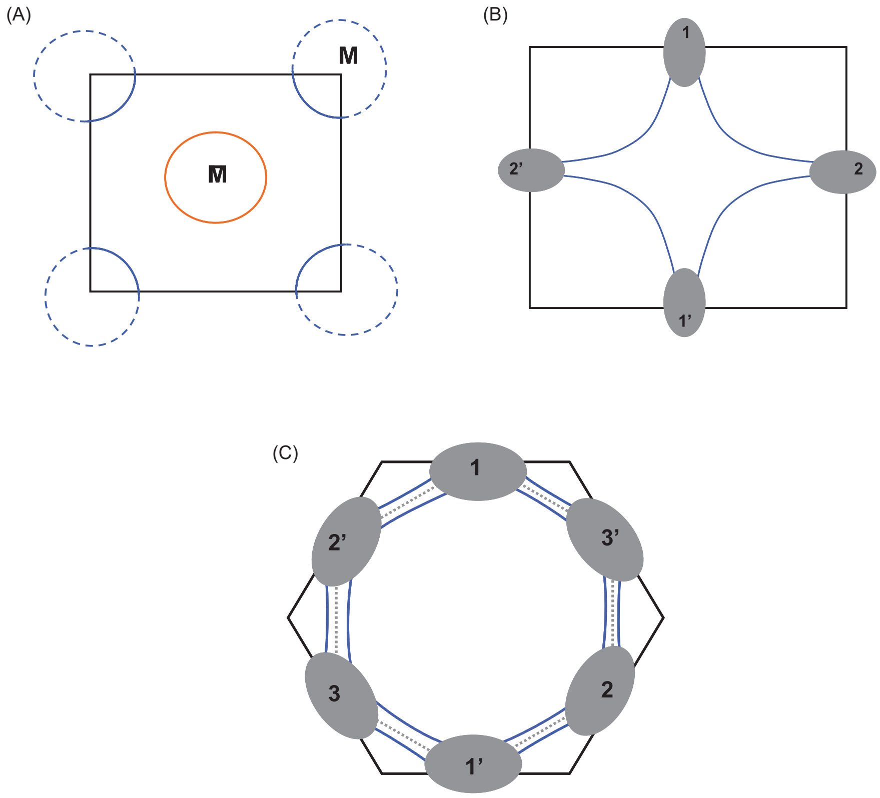

Fig. 2 FS topologies for a 2-pocket model for FeSCs (left), for hole-overdoped cuprate (center) and doped graphene (right). In pnictides there are hole and electron FS's (blue and orange circles, respectively). For cuprates and graphene one can have disconnected pieces or a singly-connected FS's, depending on the doping. The doping at which an open FS transforms into a closed one is called the Van-Hove doping. At this doping the density of states is logarithmically singular near the saddle points, marked by gray patches. From Maiti S., Chubukov A.V. (2014) In: Bennemann, Ketterson (eds.) *"Novel Superfluids", Chapter 15.* Oxford Press.

The pole in Γ^{full} is in the upper half-plane when $G_4 - G_3$ is negative. How to get it? It is customary to model regular screening by replacing the Coulomb $U(r)$ by Hubbard U. If we do this, we get $G_3 = G_4 = U$, hence no instability. Let's now include $2k_F''$ renormalizations. They come from intra-pocket density-density and exchange interactions. The result is

$$\begin{aligned} G_3 &= U\left(1 + 2U\Pi_{ph}(Q)\right), \\ G_4 &= U\left(1 + 2U\Pi_{ph}(0)\right), \end{aligned} \tag{4}$$

where $\Pi_{ph}(q)$ is a particle-hole bubble at momentum Q. The condition $G_3 > G_4$ then reduces to $\Pi_{ph}(Q) > \Pi_{ph}(0)$. For fermions with one circular FS, $\Pi_{ph}(q)$ either stays constant or decreases with q, then this condition is not satisfied. However, in our case, there are two FS's, separated by $\mathbf{Q}$, one of hole type and the other of electron type. One can easily verify that, in this situation, $\Pi_{ph}(Q)$ is logarithmically enhanced comparable to $\Pi_{ph}(0)$, hence irreducible G_3 is necessary larger than irreducible G_4. This is lattice analog of KL scenario.

What kind of the pairing state we get? Both Γ^{full}_{hh} and Γ^{full}_{he} do not depend on the direction along each of the two pockets, hence the pairing state is necessary s-wave.

At the same time, near the pole $\Gamma^{full}_{hh} = -\Gamma^{full}_{he}$, which implies that the two-fermion pair wave function changes sign between hole and electron pockets. Such an s-wave state is often call s^{+-}.

The majority of researchers believe that s_{+-} is the correct gap symmetry for FeSCs. It is consistent with STM and neutron scattering data. Nevertheless, a conventional s-wave gap due to phonons and a d-wave gap symmetry for strongly hole doped 111 materials have also been proposed.

Cuprates

Cuprates are layered materials with one or more crystal planes consisting of Cu and O atoms (two O per Cu), and charge reservoirs between them. Superconductivity is widely believed to originate from electron-electron interactions in these CuO_2 planes. The undoped parent compounds are Mott insulators/Heisenberg antiferromagnets due to very strong Coulomb repulsion which prevents electron hopping from Cu to Cu and therefore localizes electrons near lattice sites (Lee et al., 2006; Keimer et al., 2015). Doping these insulating CuO_2 layers with carriers (by adding/removing electrons from/to charge reservoir) leads to a (bad) metallic behavior and to the appearance of high-temperature superconductivity. A schematic phase diagram of doped cuprates is shown in Fig. 3.

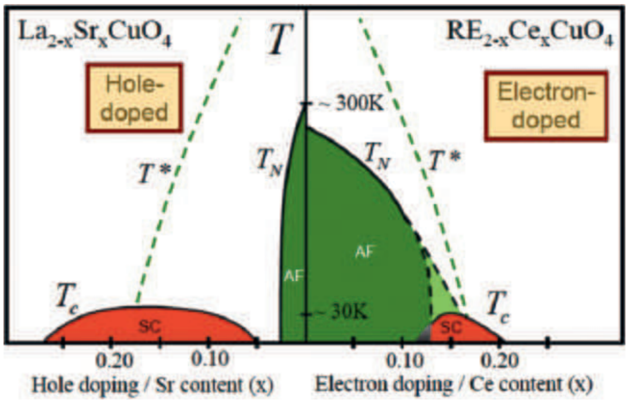

Fig. 3 The phase diagram for the cuprates. In similarity with FeSCs, parent compounds are antiferromagnets. Among differences, the most important one is that antiferromagnetism is of Heisenberg type, and is a part of Mott behavior In the region below T^*, the system displays pseudogap behavior. *d*-wave symmetry of superconducting state holds for both hole and electron dopings. From Armitage N.P., Fournier P., Greene R.L. (2010) *Reviews of Modern Physics* 82: 2421.

There are several features in the phase diagram, like the pseudogap in hole-doped cuprates, which are still not fully understood, although a substantial progress has been made over the last few years (Basov and Chubukov, 2011; Chubukov and Hirschfeld, 2015; Tremblay and Chubukov, 2017; Armitage et al., 2010; Lee et al., 2006; Keimer et al., 2015).

By all accounts, the symmetry of the superconducting state does not change between small doping, where pseudogap physics is relevant, and doping above the optimal one. For these larger dopings, ARPES and quantum oscillation experiments show a large FS, consistent with Luttinger count for fermionic states. In this doping range, it is natural to expect that the pairing symmetry can be at least qualitatively understood by performing the same analysis as for Fe-based systems.

The FS for hole-doped cuprates is an is open electron FS shown in Fig. 2 (center). The fermionic density of states is the largest near the points $(0,\pm\pi)$ and $(\pm\pi,0)$, where two FS lines come close to each other (the density of states is logarithmically enhanced and actually diverges when the two FS lines merge at $(0,\pm\pi)$ and $(\pm\pi,0)$—this is termed as Van Hove singularity). The FS regions with the largest DOS mostly contribute to superconductivity, and, to first approximation, one can consider the FS in Fig. 2 (center) as consisting of four patches. Experiments clearly indicate that bound fermionic pairs are spin singlets. A spin-singlet pair wave function is an even function of momentum. This leaves two non-equivalent patches, which for definiteness we choose to be near $(0,\pi)$ and $(\pi,0)$.

The resulting two-patch model is in many respects similar to the two-pocket model for Fe-pnictides, only instead of hole-hole, electron-electron, and hole-electron interaction we now have intra-patch and inter-patch interactions for two patches, which we label as 1 and 2. Introducing as before inter-patch repulsion G_4 and inter-patch pair-hopping interaction G_3, we obtain, in full analogy with (3),

$$\begin{aligned}\Gamma_{11}^{full} &= -\frac{1}{2}\left(\frac{G_4+G_3}{1+(G_4+G_3)\Pi_{pp}}+\frac{G_4-G_3}{1+(G_4-G_3)\Pi_{pp}}\right)\\ \Gamma_{12}^{full} &= -\frac{1}{2}\left(\frac{G_4+G_3}{1+(G_4+G_3)\Pi_{pp}}-\frac{G_4-G_3}{1+(G_4-G_3)\Pi_{pp}}\right),\end{aligned} \tag{5}$$

and

$$G_3-G_4=2U^2\left(\Pi_{ph}(Q)-\Pi_{ph}(0)\right) \tag{6}$$

The two particle-hole polarization bubbles can be straightforwardly calculated for the lattice model of fermionic dispersion with hopping t (t^0) between nearest (next-nearest) neighbors The result is that $\Pi_{ph}(Q)>\Pi_{ph}(0)$, hence irreducible G_3 again exceeds irreducible G_4, and superconductivity develops. Near the pole, $\Gamma_{11}^{full}\approx -\Gamma_{12}^{full}$.

Now, in the two-pocket model for FeSCs, the sign changing pair wave-function changes sign between different FS pockets, but preserves the same sign along a given pocket. In two-patch model for the cuprates, the sign-changing wave function changes sign between the two ends of the same "arc" of the FS, i.e., it changes sign under $\pi/2$ rotation from x to y axis and necessary passes through zero in between. The prototype wave function for such a state is $\cos k_x-\cos k_y$. According to a standard classification scheme, such a wave function belongs to B_{1g} representation and is often called d-wave because it changes sign 4 times along the full FS.

The *d*-wave symmetry of superconducting order parameter (often called gap function) in the cuprates has been firmly established by a number of experiments. In 2011, Juan Carlos Campuzano from Argonne National Laboratory, P. Johnson from Brookhaven National Laboratory, and Z.X. Shen from Stanford University were awarded the prestigious Oliver E. Buckley Condensed Matter Prize by the American Physical Society for innovative ARPES experiments, which established *d*-wave gap symmetry.

Doped graphene

The same logics can be applied to a system of fermions of a hexagonal lattice, at a so-called van Hove doping, when the system is about to undergo a topological transition between a singly connected large FS and a set of disconnected small FS's (Gonzalez, 2008; Nandkishore et al., 2012). Such a situation holds in a single-layer graphene at a doping when six separate Fermi pockets that emerge out of Dirac points, merge (Fig. 4). A van Hove doping of a single layer graphene has been achieved by placing *Ca* and *K* dopants above and below a graphene layer.

Near van Hove instability, low-energy physics is again described by a patch model, but now there are three non-equivalent patches, labeled 1,2 and 3 in Fig. 2 (right). We introduce intra-patch and inter-patch vertices Γ_{ij}, $i, j \in (1,2,3)$ with $\Gamma_{ij} = \Gamma_{ji}$. Because the three patches are fully symmetric, the number of independent vertices is just two:

$$\begin{aligned}\Gamma_{11} &= \Gamma_{22} = \Gamma_{33}\\ \Gamma_{12} &= \Gamma_{13} = \Gamma_{23}\end{aligned}, \tag{7}$$

and there are two irreducible pairing interactions, which like before we call G_3 and G_4. Summing up ladder diagrams in the particle-particle channel, one obtains the result similar, but not identical to (5):

$$\begin{aligned}\Gamma_{11}^{full} &= -\frac{1}{3}\left(\frac{G_4 + 2G_3}{1 + (G_4 + 2G_3)\Pi_{pp}} + 2\frac{G_4 - G_3}{1 + (G_4 - G_3)\Pi_{pp}}\right)\\ \Gamma_{12}^{full} &= -\frac{1}{3}\left(\frac{G_4 + 2G_3}{1 + (G_4 + 2G_3)\Pi_{pp}} - \frac{G_4 - G_3}{1 + (G_4 - G_3)\Pi_{pp}}\right).\end{aligned} \tag{8}$$

For Hubbard interaction the bare $G_3^0 = G_4^0 = U$ are again equal, i.e., at this level there is no superconductivity, but irreducible interactions are

$$G_4 = U\left(1 + 3U\Pi_{ph}(0)\right), G_3 = U\left(1 + 2U\Pi_{ph}(Q)\right) \tag{9}$$

where now Q is the momenta between van Hove points. Superconductivity develops when $\Pi_{ph}(Q) > (3/2)\Pi_{ph}(0)$. Computations of the polarization bubble shows that $\Pi_{ph}(Q)$ is again logarithmically singular and well exceeds $\Pi_{ph}(0)$. Then superconductivity does develop.

What is the symmetry of a pair wave function? Near the instability the ratio of inter-patch Γ_{ij}^{full} and intrapatch Γ_{ii}^{full} is $-1/2. = -\frac{D}{2}$ for $i \neq j$. If we view Γ_{ii}^{full} as the modulus square of the superconducting order parameter $|\Delta_i|^2$ and Γ_{ij}^{full} as $Re[\Delta_i \Delta_j^*]$, we find that the phase of complex Δ must change by $\pm\frac{2\pi}{3}$ between each pair of patches $\left(\cos\frac{2\pi}{3} = -\frac{1}{2}\right)$. In other words, if the order parameter in patch 1 is Δ_1, then $\Delta_2 = \Delta_1 e^{\pm 2\pi i/3}$ and $\Delta_3 = \Delta_1 e^{\pm 4\pi i/3}$. The two resulting structures of Δ are shown in Fig. 5. Each of the two candidate order parameters has *d*-wave symmetry, because if we extend it to the whole FS, we find that it changes sign 4 times.

Chiral superconductivity

The two order parameters in Fig. 5 represent counter clockwise and clockwise phase winding by 4π along the full FS. These order parameters are completely equivalent, i.e., there is an additional Z_2 symmetry of a superconducting wave function, which is different from a conventional $U(1)$ phase symmetry. The analysis of the Landau functional in the superconducting state shows that Z_2 symmetry gets broken, i.e., the system spontaneously chooses counter clockwise or clockwise phase winding. Such a state is called $d + id$ or $d - id$. It breaks time reversal and inversion symmetries and is called a chiral superconductor. The nontrivial topology of the $d \pm id$ state manifests itself in exceptionally rich phenomenology, including a quantized spin and thermal Hall conductance, and a quantized boundary current in magnetic field (Gonzalez, 2008; Nandkishore et al., 2012). Theoretical analysis of such

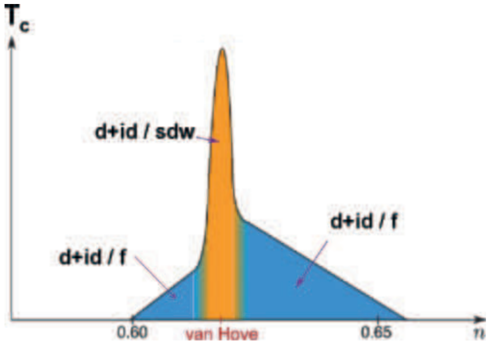

Fig. 4 Schematic phase diagram of doped graphene. T_c is the instability temperature toward spin singlet $d + id$ or spin triplet *f*-wave SC states, or SDW state. T_c is plotted against doping (*n*). Doped Graphene is expected to be mostly superconducting with competition with the SDW phase near the Van-Hove region. Modified from Kiesel M.L., et al. (2012) *Physical Review B* 86: 020507(R).

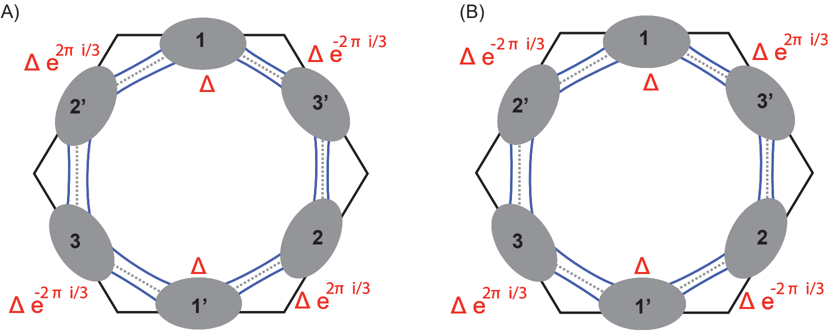

Fig. 5 The phases of the pair-wave functions at the patches (regions with enhanced density of states). The left and right represent the two Z_2 breaking *d*-wave solutions $d + id$ or $d - id$. From Maiti S., Chubukov A.V. (2014) In: Bennemann, Ketterson (eds.) *"Novel Superfluids", Chapter 15.* Oxford Press.

superconductors and a search for their practical realizations are integral parts of modern studies of superconductivity. The most frequently discussed example is spin-triplet $p + ip$ superconductivity, which has multiple applications for quantum computation (Sato and Ando, 2017). In practical applications, $p + ip$ gap symmetry has been discussed in the context of superfluidity in ^{3}He. It was proposed for Sr_2RuO_4, but recent experiments cast doubt on this explanation. Understanding of the pairing symmetry in Sr_2RuO_4, which by all accounts, falls into a weak coupling category, is another actively explored area of modern research on superconductivity.

Twisted bilayer graphene

Superconductivity with highest $T_c \sim 3\ K$ and strongly correlated behavior around it have been recently discovered in a twisted bilayer graphene (TBG), consisting of two graphene sheets rotated by a "magic" angle (Cao et al., 2018; Stepanov et al., 2020) (Fig. 6). STM data for TBG show sharp van Hove peaks, and several researchers argued that superconductivity in TBG emerges by the same reason as in a single graphene sheet, and has a chiral *d*-wave symmetry. Others, however, argued that superconductivity may come from electron-phonon interaction and is likely *s*-wave. Another proposal is that superconductivity is ultimately a fundamentally novel phenomenon, related to insulating states nearby (Khalaf et al., 2021). Another potential novel feature of superconductivity in TBG is suggested breaking of lattice-rotational symmetry below T_c, in which case the ordered state becomes a nematic superconductor. Theoretical understanding of nematic superconductivity here and in other systems is another rapidly developing field of research, along with the studies of partially melted superconducting states, in which fluctuating Cooper pairs do not establish phase coherence, but already break Z_2 time-reversal symmetry or symmetry associated with a rotational invariance.

s-wave superconductivity from repulsion

Another issue, first discussed in early studies of superconductivity, but revisited recently in the context of superconductivity in strontium titanate and related systems, is whether one can potentially get an ordinary *s*-wave superconductivity with momentum-independent order parameter from repulsion. This question has been raised for electron-phonon superconductivity

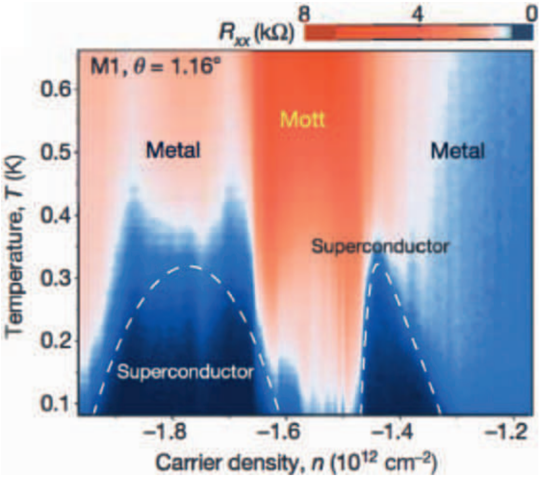

Fig. 6 The phase diagram of TBG. Reproduced from Cao Y., et al. (2018) *Nature* 556: 43; Stepanov P., et al. (2020) *Nature* 583: 375, with permission from Springer Nature.

as Coulomb repulsion is present in systems, which are believed to be *s*-wave electron-phonon superconductors, and is larger than electron-phonon attraction. A frequently cited explanation is that in cases where the Fermi energy E_F is much larger than the Debye frequency ω_D, there is a wide range of frequencies where the repulsive Coulomb repulsion is logarithmically renormalized down dy ladder series in the same particle-particle channel that would give rise to pairing in case of attraction (the Tyablikov-McMillan logarithm). If this range is wide enough, the renormalized Coulomb repulsion becomes smaller than the electron-phonon attraction at energies below ω_D.

Upon closer examination, this explanation appears incomplete as Tyablikov-McMillan renormalization holds for the full interaction, i.e., for the sum of electronelectron and electron-phonon interactions. Under the renormalization this full interaction decreases, but does not change sign, i.e., remains repulsive. How one can get superconductivity in this situation?

It has been originally discussed quite some time ago for large E_F/ω_D and has been re-analyzed recently in the context of superconductivity in systems with small Fermi energy, like $SrTiO_3$, $Pb_{1-x}Tl_xTe$, half-Heusler compounds, where E_F and ω_D are comparable and Tyablikov-McMillan reasoning does not work.

It has been realized that the actual reason why electron-phonon superconductivity holds despite larger Coulomb interaction, is that the full interaction on the Matsubara axis (where it is real) is a dynamical one, $V(\Omega_m)$, and although a phonon-mediated attraction does not invert the sign of $V(\Omega_m)$, it nevertheless reduces it at frequencies below the Debye energy. A convenient way to model $V(\Omega_m)$ is to treat it as a sum of two parts: a constant Hubbard repulsion U, and a frequency-dependent attractive part due to electron-phonon interaction:

$$V(\Omega_m) \propto U - \frac{U_{el-ph}}{1 + (\Omega_m/\Omega_1)^2}, \tag{10}$$

where Ω_1 is of order of the Debye energy and Ω_m is a bosonic Matsubara frequency. A similar model has been recently used for dynamically screened electron-electron interaction in single-crystal Bi, where Ω_1 is of the order of plasma frequency.

For $U > U_{el-ph}$, $V(\Omega_m) > 0$ for all frequencies. Yet, because the interaction is dynamical, one can, to first approximation, replace it by a step-like function, with different values at small at large frequencies (regions 1 and 2) and solve a set of coupled equations for Γ_{11}, Γ_{22}, and Γ_{12}. The set is qualitatively the same as in (3), (5), (8), and the analogs of G_3 and G_4 are approximately U and $U - U_{el-ph}$ Without electron-phonon attraction, $G_3 = G_4 = U$. Once electron-phonon attraction is added, G_3 becomes larger than G_4, and superconductivity develops. Like in previous cases, this order parameter necessary changes sign, but here it does this as a function of frequency, i.e., the signs of the gap function at small and large ω_m are different. The McMillan formula $T_c \sim \Omega_1 e^{-1/(N_F U - \lambda^*)}$, where $\lambda^* \sim 1/\log E_F/\Omega_1$ is reproduced for $E_F \gg \Omega_1$ once one integrate out fermions with high-frequencies and obtain an effective interaction between low-energy fermions. This interaction is attractive when $N_F U > \lambda^*$, but it incorporates the fact that the sign of the order parameter at large frequencies is opposite to that at small frequencies.

Superconductivity at strong coupling

The weak coupling approach, based on second-order renormalization of the Hubbard interaction, is highly useful for the understanding of the symmetry of the superconducting order parameter for a particular material, but at the same time is incomplete as it is based on the assumptions that the bare interaction in the relevant pairing channel is zero, and that fermions are weakly interacting quasiparticles. These assumptions work for the case of a weak Hubbard interaction, but not beyond it. Indeed, a generic screened Coulomb interaction is larger at small momentum transfer, hence, in the notations used above, a bare G_4 is larger than a bare G_3. To get an attraction, the "$2k_F$" screening must overcome this difference, and to verify this one necessary has to go beyond weak coupling.

Modern studies of superconductivity beyond weak coupling can be broadly divided into three classes: (i) The analysis of "$2k_F$" screening beyond second order in perturbation, but still at weak coupling. This is most often done using some version of renormalization group (RG) analysis; (ii) The analysis of the pairing in a metal, mediated by a soft collective boson in either spin or charge channel. The most studied examples here are pairing by spin fluctuations and by Ising-nematic fluctuations. This is valid for an intermediate coupling strength, when on one hand interaction is strong enough to bring the system close to an instability in spin or charge channel, and on the other the carriers retain their itinerant character; (iii) The analysis of the pairing in the truly strong coupling regime, when interaction is strong enough to localize most of the carriers. The most studied example here is pairing of a doped Mott insulator, extensively discussed for the cuprates, and pairing of a doped Chern insulator, recently suggested in the studies of TBG.

Renormalization group analysis

The RG approach is an attempt to go beyond the lowest order in perturbation already for weak coupling, when dimensionless $g_3 = N_F G_3$ and $g_4 = N_F G_4$ are small. A good starting point here is the BCS approach, in which one assumes that the bare dimensionless pairing interaction g^0 is small and neglects all regular corrections in powers of g^0, but sums up series of corrections in $g^0 L$, where $L = logW/T$ is a Cooper logarithm. Within BCS approximation, the series in $g^0 L$ are geometrical, and the dressed $g = g^0/(1 - g^0 L)$ (The dressed vertex $\Gamma = \Gamma^0 (g/g^0) \propto /(1 - gL)$). The flow of the dressed g with running L (i.e., with changing temperature) can be cast into the differential equation $dotg = g^2$, where $g^{\bullet} = dg/dL$ and BCS result about the pairing instability at weak coupling can be reformulated as the divergence of the running g as the temperature approaches T_c (or, equivalently, as the divergence of the running vertex Γ).

This reasoning has been extended in the last two decade to extend the analysis of the irreducible vertex beyond second order in perturbation. In all three cases discussed in Sec. III the particle-hole polarization $\Pi_{ph}(Q)$ is logarithmically enhanced by one reason or the other. The idea is then to treat logarithmic terms in the particle-hole channel on equal footing with logarithmic renormalizations in the particle-particle channel and detect the flow of irreducible g_3 and g_4 simultaneously with their renor-malizations in the particle-particle channel. As long as g_i are small and $g_i L \leq 1$, this can be done rigorously. The corresponding RG procedure is called it parquet RG as logarithmic renormalizations are extended simultaneously into two particle-hole and particle-particle channels, which can be viewed as the two "perpendicular" directions. A similar but somewhat more involved *functional RG* has also be applied for this purpose. There are two goals of parquet/functional RG analysis. First to verify whether in the flow the running g_3 becomes larger than g_4, even if bare g_4 was larger. If so, then the system self-generates attraction below some upper cutoff, determined by the system. Second, to understand the interplay between superconductivity and particle-hole orders, which can also develop under RG flow.

As an illustration, consider the 2-pocket model for FeSCs. For the RG analysis, we need to add two other interactions between low-energy fermions: interaction between fermionic densities in the two pockets, g_1, and intra-pocket density-density interaction g_2 ($c_\alpha c_\alpha f_\beta f_\beta$ and $c_\alpha f_\alpha f_\beta c_\beta$ terms, respectively). At second order, these two interaction renormalize the irreducible g_3 and g_4. Beyond second order, they also flow with L and can give rise to SDW, charge-density-wave (CDW), nematic and other orders. The full set of parquet RG equations is

$$
\begin{aligned}
\dot{g}_1 &= g_1^2 + g_3^2 \\
\dot{g}_2 &= 2g_2(g_1 - g_2) \\
\dot{g}_3 &= 2g_3(2g_1 - g_2 - g_4) \\
\dot{g}_4 &= -g_3^2 - g_4^2.
\end{aligned}
$$

The solution is shown in Fig. 7. We see that g_3 does become larger than g_4 above some L, even if its bare value was smaller. The competition between superconductivity and other orders is determined by the behavior of different g_i near the fixed trajectory, where all $g_i \propto 1/(L_{cr} - L)$ and $L_{cr} = logW/T_{cr}$, where T_{cr} is the highest instability temperature.

Pairing by spin and charge fluctuations

When g_i are not small, neglecting regular corrections in g_i is not an option. Because no controlled calculations are possible in this case (except for specific extensions to, e.g., large number of fermionic flavors) one frequently discussed option is to adopt a semi-phenomenological approach based on the experimental phase diagram. Many materials, in which superconductivity is believed to be of electronic origin, the phase diagram shows some other ordered phases close to where superconductivity exists: undoped cuprates display antiferromagnetic order, parent compounds of FeSCs show either SDW or nematic order, in doped graphene there are strong SDW and CDW correlations, etc. In this situation, it is tempting to consider the propagator of a soft boson in either spin or charge channel as a pairing glue for superconductivity, i.e., consider pairing mediated by spin or charge fluctuations.

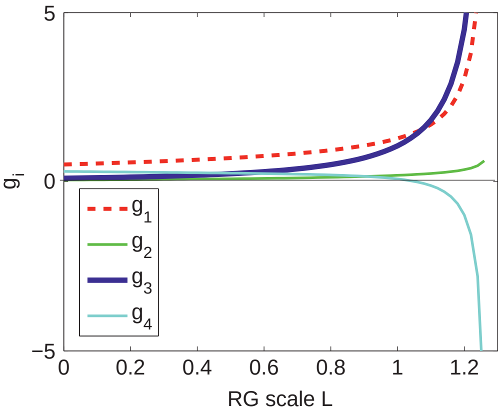

Fig. 7 The flow of dimensionless couplings $g_{1,2,3,4}$. g_3 grows and eventually crosses g_4, which becomes negative at a large enough RG scale. From Maiti S., Chubukov A.V. (2014) In: Bennemann, Ketterson (eds.) *"Novel Superfluids", Chapter 15.* Oxford Press.

From theory viewpoint, in this approach one extends the computation of the irreducible vertex functions in the particle-particle channel by restricting to a particular set of diagrams beyond second order. The vertex function can be generally split into spin and charge components: $\Gamma\alpha\beta;\gamma\delta = \Gamma_c\ \delta_{\alpha\gamma}\delta_{\beta\delta} + \Gamma_s\ \sigma_{\alpha\gamma}\sigma_{\beta\delta}$, here σi are Pauli matrices. A re-examination of second order results in Sec. III shows that for a repulsive interaction, the "$2k_F$" screening enhances the spin component of the interaction at momentum **Q**. Collecting ladder series of the same renormalizations, one further enhances Γ_s. If the enhancement is strong enough, one can keep only this term and neglect the interaction at small momentum transfer and the charge component of the interaction near **Q**. Then one arrives at the effective 4-fermion spin-spin interaction with momentum transfer near **Q**. For the 1-band cuprate case

$$H_{eff} = \sum_{k,q,p} \Gamma_s(q) c^{\dagger}_{k,\alpha} \sigma_{\alpha\gamma} c_{k+q,\gamma} c^{\dagger}_{p^{\prime},\beta} \sigma_{\beta\delta} c_{p\ -q^{\prime},}\delta \tag{11}$$

By construction, this interaction is attractive in the corresponding spatial channel (*d*-wave for the cuprates, s^{+-} and, in special cases, *d*-wave for FeSCs, $d \pm id$ for doped graphene. We illustrate this in Fig. 8. The attractive component has the same spatial structure as in 2nd order calculations, so in this respect the difference between the second order analysis and spin fluctuation approach is only in the magnitude of the attractive interaction. It is customary to use the Ornstein-Zernike form $\Gamma_s = \Gamma/(\xi^{-2} + (\mathbf{q} - \mathbf{Q})^2)$, where ξ is a magnetic correlation length. For large ξ, Γ_s is large for **q** near **Q**. The same strategy has been used to obtain the interaction mediated by SDW or nematic fluctuations.

Superconductivity near a quantum-critical point

At a first glance, the attraction mediated by a soft boson can be made as large as possible by focusing on $\mathbf{q} \approx \mathbf{Q}$ and making ξ larger, i.e., bringing the system closer to a magnetic instability. This is not completely true, however, as in most cases of interest a collective boson can decay into a particle-hole pair, that is the bosonic propagator contains the Landau damping term $|\Omega_m|/v_F q$. This leads to new physics, which attracted a substantial interest in recent years (Abanov and Chubukov, 2020; Chubukov et al., 2020; Esterlis and Schmalian, 2019; Wang, 2020). Namely, when projected into the particle-hole channel, boson-mediated interaction gives rise to dynamical self-energy, $\Sigma(k,\omega_m)$. At $\xi = \infty$ and in dimension $D \leq 3$, this self-energy at $k = {}_F$ acquires a non-Fermi liquid form $|\omega_m|^a \mathrm{sign}\omega_m$ with $a < 1$ at small frequencies. In other words, the same interaction that gives rise to the pairing, also gives rise to incoherent non-Fermi liquid (NFL) behavior. Whether or not superconductivity occurs in this situation depends on the outcome of the interplay between strong dynamical pairing interaction and strong fermionic incoherence, which acts again pairing. From

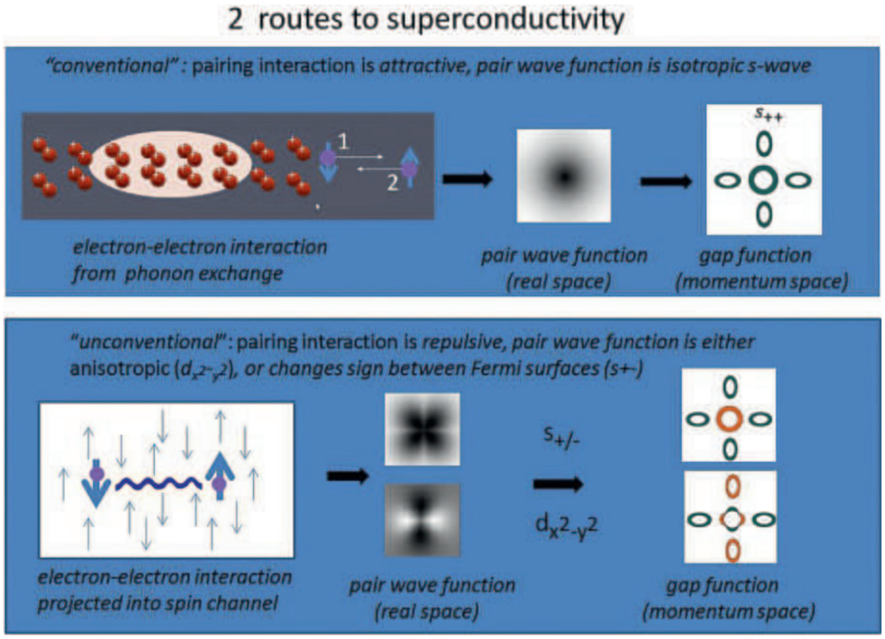
2 routes to superconductivity
"conventional": pairing interaction is attractive, pair wave function is isotropic s-wave
1
2
s_{++}
electron-electron interaction from phonon exchange
pair wave function (real space)
gap function (momentum space)
"unconventional": pairing interaction is repulsive, pair wave function is either anisotropic ($d_{x^2-y^2}$), or changes sign between Fermi surfaces (s+-)
$s_{+/-}$
$d_{x^2-y^2}$
electron-electron interaction projected into spin channel
pair wave function (real space)
gap function (momentum space)

Fig. 8 *Two routes to superconductivity* (a)—Two electrons attract each other when the 1st polarizes the lattice, and the second is attracted to this region. The *pair wave function* $\Psi(\mathbf{r})$ of the relative electronic coordinate **r**, has the full symmetry of the crystal and gives rise to a *gap function* $\triangle_{\mathbf{k}}$ of the same sign for all momenta **k** on the FeSC Fermi surface (green = +). (b) Electrons interact with each other via Coulomb interaction. Shown is an example where the dominant interaction is the magnetic exchange arising between opposite spin electrons due to Coulomb forces. The first electron polarizes the conduction electron gas antiferromagnetically, and an opposite spin electron can lower its energy in this locally polarized region. In this case $\Psi(\mathbf{r})$ has a node at the origin, helping to avoid the Coulomb interaction, and can have either $s_{+/-}$ or $d_x2_{-y}2$ form, as shown. These two possibilities lead to gap functions of opposite sign on the Fermi surface (orange = –). From Chubukov A.V., Hirschfeld P.J. (2015) *Physics Today.*

theory perspective, fermionic incoherence destroys Cooper logarithm and reduces the tendency to pairing, while the opening of a superconducting gap eliminates scattering at low energies and renders a Fermi liquid behavior. Because incoherence and pairing come from the same interaction, they are intertwined, and in general their characteristic scales comparable.

This issue recently attracted strong interest among both condensed-matter and high-energy theorists. Itinerant quantum-critical systems, analyzed analytically in recent years, include fermions in spatial dimensions $D \leq 3$, two-dimensional (2D) fermions near a SDW and CDW instabilities, $2k_F$ density-wave instability, pair-density-wave instabilities, $q = 0$ instabilities toward a Pomeranchuk order and toward a state with circulating currents, 2D fermions at a half-filled Landau level, generic quantum-critical models with varying critical exponents, Sachdev-Ye-Kitaev (SYK) and SYK-Yukawa models, extensively studied in recent years, strong coupling limit of electron-phonon superconductivity, and even color superconductivity of quarks, mediated by gluon exchange. These problems have also been studied using various numerical techniques (see literature in Abanov and Chubukov, 2020; Chubukov et al., 2020; Esterlis and Schmalian, 2019; Wang, 2020).

To find the outcome of the interplay between SC and NFL, one needs to analyze the set of coupled integral equations for the fermionic self-energy and the pairing vertex., In most metallic quantum-critical models, the dressed low-energy fermions are fast excitations compared to soft bosons for one reason of another. In this situation, which bears parallels with the Eliashberg theory for electron-phonon interaction, the momentum integration can be carried out exactly, after projecting the pairing interaction into the proper irreducible channel, and to resolve the competition between NFL and superconductivity, one has to solve one-dimensional non-linear integral equation for the gap function $\triangle(\omega_m)$:

$$\Delta(\omega_m) = \pi T \sum_{m'} \frac{\Delta(\omega_{m'}) - \Delta(\omega_m)\frac{\omega_{m'}}{\omega_m}}{\sqrt{(\omega_{m'})^2 + \Delta^2(\omega_{m'})}} V(\omega_m - \omega_{m'}) \tag{12}$$

where $V(\Omega_m)$ is an effective "local" interaction with singular frequency dependence $1/|\Omega_m|^\gamma$. The exponent $\gamma > 0$ depends on the microscopic realization. A small $\gamma = O()$ holds for models in $D = 3$—and for pairing of quarks, mediated by gluon exchange, $\gamma = 1/3$ for 2D models at the onset of a nematic or Ising-ferromagnetic order, and for fermions at a half-filled Landau level, $\gamma \approx 1/2$ for 2D models at the onset of SDW or CDW order, $\gamma \approx 0.68$ for pairing in SYK-type modes with equal number of fermion and boson flavors, $\gamma = 1$ for the pairing mediated by 2D propagating bosons, $\gamma \approx 1.2$ has been suggested for Fe-pnictides, and $\gamma = 2$ describes pairing mediated by an Einstein phonon, in the (properly defined) limit of vanishing Debye frequency.

The analysis of (12) shows that NFL in the normal state does not prevent pair formation below a certain T_p, whose value depends on γ, but in a non-critical way (Fig. 9). It is less certain whether T_p is a true superconducting transition temperature or onset temperature for pairing of still incoherent fermions. In the latter case, the actual T_c is smaller than T_p, and in between T_c and T_p the system displays preformed pair behavior.

Strong coupling limit

Superconductivity in the strong coupling limit have been mostly studied for fermions doped into a Mott insulator. These doped fermions form a small Fermi surface, whose area scales as doping x rather than $1 - x$ expected for a metal with the same number of fermions. A highly non-trivial superconductivity mediate by topological skirmion excitations has been proposed in the context of superconductivity near Chern insulating regime in TBG (Khalaf et al., 2021). Another research direction is superconductivity near the boundary to the Mott phase in systems like C_{60}.

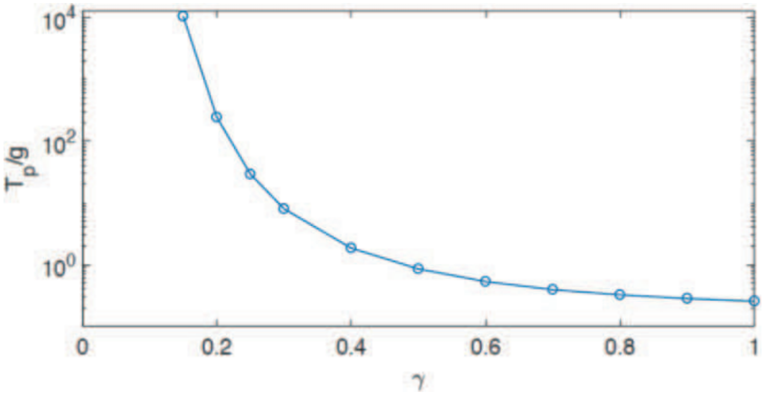

Fig. 9 The onset temperature of the pairing, T_p, as a function of γ. From Abanov A.R., Chubukov A. V. (2020) *Physical Review B* 102: 024524 (and references therein).

Conclusion

Superconductivity is a fascinating subject, which remains at the forefront of research in condensed matter physics in the 21st century. In this Chapter I described several directions of the research over the last two decades, with emphasis on unconventional superconductivity of strongly correlated electrons. Other exciting developments in the field of superconductivity are recent works on Higgs excitations in superconductors, on feedback from superconductivity on electronic spectrum, particularly for strongly correlated electrons (neutron resonance and related stuff), on highly non-trivial superconducting order parameters, which preserve the Fermi surface (called Bogolyubov Fermi surface for this purpose), on odd-frequency superconductivity, and on the interplay between pair formation and a true superconductivity (often called BCS-BEC crossover). Another rapidly growing area of research is the analysis of topological aspects of superconductivity. This last area includes the analysis of topological aspects of the pairing near a quantum-critical point.

Acknowledgments

This work was supported by US Department of Energy, Office of Science, Basic Energy Sciences, under Award No. DE-SC0014402.

References

Abanov AR and Chubukov AV (2020) *Physical Review B* 102: 024524. (and references therein).
Armitage NP, Fournier P, and Greene RL (2010) *Reviews of Modern Physics* 82: 2421.
Baranov M, Chubukov AV, and Kagan MY (1992) *International Journal of Modern Physics* 6: 2471.
Basov DN and Chubukov AV (2011) *Nature Physics* 7: 273.
Cao Y, et al. (2018) *Nature* 556: 43.
Chubukov AV and Hirschfeld PJ (2015) *Physics Today* 68(6): 46.
Chubukov AV, Abanov AR, Esterlis I, and Kivelson SA (2020) *Annals of Physics* 417: 168190.
Esterlis I and Schmalian J (2019) *Physical Review B* 100: 115132.
Fay D and Layzer A (1968) *Physical Review Letters* 20: 187.
Gonzalez J (2008) *Physical Review B* 78: 205431.
Keimer B, Kivelson SA, Norman MR, Uchida S, and Zaanen J (2015) *Nature* 518: 179.
Khalaf E, Chatterjee S, Bultinck N, Zaletel MP, and Vishwanath A (2021) *Science Advances* 7(19).
Kiesel ML, et al. (2012) *Physical Review B* 86: 020507(R).
Kohn W and Luttinger JM (1965) *Physical Review Letters* 15: 524.
Lee PA, Nagaosa N, and Wen X-G (2006) *Reviews of Modern Physics* 78: 17.
Maiti S and Chubukov AV (2014) In: Bennemann and Ketterson (eds.) *"Novel Superfluids",* Chapter 15. Oxford Press.
Nandkishore R, Levitov L, and Chubukov A (2012) *Nature Physics* 8: 158–163.
Sato M and Ando Y (2017) *Reports on Progress in Physics* 80: 076501.
Stepanov P, et al. (2020) *Nature* 583: 375.
Tremblay A-M and Chubukov AV (2017) *CERN Courier*. Aug. 11.
Wang Y (2020) *Physical Review Letters* 124: 017002.

Electrodynamics of superconductors[☆]

Vladimir Kozhevnikov, Tulsa Community College, Tulsa, Oklahoma, United States; KU Leuven, Leuven, Belgium

© 2024 Elsevier Ltd. All rights reserved.

Introduction **644**
Meissner state **645**
Definitions 645
Cooper pairs 646
Microscopic whirls 651
Penetration depth 652
Temperature 652
Flux quantization **653**
Total current **655**
Conclusion **655**
Acknowledgments **656**
References **656**
Further reading **656**

Abstract

Electrodynamics of superconductors is primarily the electrodynamics of the Meissner state, a state characterized by zero magnetic induction of a superconducting fraction of conduction electrons. Simultaneously, the Meissner state is characterized by zero resistivity and zero entropy of these electrons. The latter means that the temperature of an ensemble of superconducting electrons is zero as well. Understanding properties of the Meissner state provides a key to understand and predict these and other equilibrium and non-equilibrium properties of superconductors, e.g., properties of the intermediate and mixed states, flux quantization, resistanceless transport current, etc. The reader will see that all these properties have a single and very simple origin: quantization of the angular momentum of the conduction electrons combined into Cooper pairs, and that the electrodynamics of superconductors and superconductivity as a whole is a magnificent manifestation of the boundless ingenuity of Nature and of the power of Physics laws.

Key points

- The electromagnetic and thermal properties of superconductors are dictated by Cooper pairs. On this reason, the electrodynamics of superconductors is primarily the electrodynamics of an ensemble of Cooper pairs.
- By definition of Cooper pairs, the paired electrons orbit their center of mass. The stability of Cooper pairs means that the pairs obey the Bohr-Sommerfeld quantization condition.
- In the Meissner phase (the phase of a superconducting sample with zero magnetic induction B) the magnetic field intensity H is equal to or greater than the intensity of the applied field H_0.
- The properties of superconductors (zero resistivity, zero magnetic induction, zero entropy, flux quantization, etc.) are governed by the precession of Cooper pairs with quantized angular momentum.
- Due to zero entropy, the temperature of an ensemble of Cooper pairs equal to zero regardless of the temperature of the sample.

Introduction

Superconductivity was discovered in the laboratory of Kameringh Onnes as a phenomenon of a sharp drop of electrical resistance in a high purity mercury wire at temperature T below 4.2 K (Kamerlingh Onnes, 1911). An original estimate of the resistance drop was 10^4 times compare to the resistance just above the transition temperature, called the critical temperature T_c, a constant of the superconducting (S) material. Fairly soon it became clear that resistance of a superconductor is not merely a small, but zero. Namely, the current in a closed S circuit represents a persistent current like that caused by electrons bound in atoms.[1] It was also found that the S state exists up to a certain temperature-dependent critical magnetic field $H_c(T)$, which is another characteristic of

---

[☆] *Change History*: July 2022. V Kozhevnikov updated the chapter.

[1] Persistent current is a current running in a closed circuit without both thermal and radiation losses.

https://doi.org/10.1016/B978-0-323-90800-9.00036-6

the material. While number of superconductors was (and is) steadily growing, at an early stage it seemed that zero resistivity is the only property distinguishing superconductors from the so-called normal (N) metals.

The second hallmark of superconductivity, the disappearance of thermoelectric effects, was discovered by Walter Meissner (Meissner, 1927). Lack of thermo-e.m.f. suggests that entropy of the S fraction of conduction electrons (called "superconducting electrons") is zero. If so, then superconductivity can be a previously unknown thermodynamic state of matter characterized by complete ordering of superconducting electrons. Gorter and Casimir used zero entropy as the base postulate of their two-fluid model (Gorter and Casimir, 1934), a seminal thermodynamic theory addressing properties of superconductors in zero field. On the other hand, a non-zero thermo-e.m.f. looks incompatible with zero resistivity of the S state, since otherwise it would lead to an infinite current and therefore to an instantaneous restoration of the N state.

The idea of the new thermodynamic state was brilliantly confirmed in a so-called Meissner effect independently discovered by Meissner and Ochsenfeld[2] (Meissner and Ochsenfeld, 1933) and Ryabinin and Shubnikov (Rjabinin and Shubnikow, 1934). It was found that, apart from zero resistivity and zero entropy, superconductivity is also characterized by zero magnetic induction B regardless on the history of the field application. Hence, a sample in the Meissner state (MS) represents a perfect diamagnetic, i.e., its magnetic susceptibility χ and permeability $\mu_m(=1+4\pi\chi)$ are equal to $-1/4\pi$ and zero, respectively. Important to note that (i) like in regular diamagnetics, in the MS χ and therefore μ_m do not depend on the sample temperature T and the applied field H_0; and (ii) if the first two "big zeroes" of superconductivity take place in samples of any shape, connectivity and purity, the third zero ($B=0$ or the Meissner effect) is observed only with sufficiently pure singly connected samples of an ellipsoidal shape.

It was found that there are two kinds of superconductors distinguishing by the sign of the S/N interphase energy also called surface tension. Materials with positive and negative surface tension are referred to as type-I and type-II superconductors, respectively. All type-I superconductors are elementary metals, while type-II materials, with very few exceptions, are alloys and multicomponent compounds. A sample of type-I material can be made behaving like type-II superconductor by introducing impurities and/or reducing the sample size, e.g., by decreasing the thickness of a film sample. However, the opposite is not possible. Other really astonishing properties, such as the flux quantization, Josephson effect and others, were discovered in 1960s and later.

A search for the source of the superconductivity phenomenon culminated in a ground braking theoretical discovery of Leon Cooper (1956), who shown that even a weak attraction can lead to formation of stable electron pairs called Cooper pairs. The origin of attraction lays in the medium polarization occurring due to electron-lattice interaction, as it was first suggested by Fröhlich (1950) and discussed in the BCS theory (Bardeen, Cooper, Schrieffer, 1957). Cooper's prediction was irrefutably confirmed in experiments (Deaver and Fairbank, 1961 and many others).

Cooper pairs profoundly alter the medium electrodynamics. The physics behind these alterations is the subject of this chapter.

The chapter consists of three sections: Meissner state, Flux quantization and Total current, and a brief summary. References to literature for further reading are given at the end. The cgs units are used because these units are the most appropriate for discussing electrodynamics of continuous media.[3] In view of the space limit only key references are provided.

Meissner state

Definitions

The MS is an equilibrium S state defined as the state with $B=0$ throughout the sample volume V. Alike, the MS can be defined as the state with $\mu_m=0$ or $\chi=-1/4\pi$ all over V.

The MS takes place in sufficiently pure massive and simply connected samples of an ellipsoidal shape in the applied field $H_0<H_{c1}(1-\eta)$. Here H_{c1} is the lower critical field of type-II superconductors equal to the thermodynamic critical field H_c in the type-I counterparts, and η is the demagnetizing factor[4] with respect to an ellipsoidal axis parallel to $\mathbf{H}_0$. A sample is considered as massive if its minimal size significantly exceeds a so-called penetration depth λ, a width of the surface layer where B decays from the induction of external field near the sample surface B_{ext} to zero in the sample interior.

A unique feature of the ellipsoidal bodies in a static magnetic field is uniformity of the field intensity $\mathbf{H}$ (also called the magnetizing force, field strength, etc.) throughout their volume, as it was first shown by Poisson (Poisson, 1824) and discussed by Maxwell (Maxwell, 1873). The intensity $\mathbf{H}$ is responsible for magnetization $\mathbf{I}(=\chi\mathbf{H})$. Depending on a demagnetizing field $\mathbf{H}_d(=4\pi\eta\mathbf{I})$, in diamagnetics $\mathbf{H}(=\mathbf{H}_0-\mathbf{H}_d)$ is greater than or equal to $\mathbf{H}_0$ in magnitude, and its direction can differ from that of the applied field. $\mathbf{H}$ is the field acting on "native" (belonging to the body) charges, whereas the induction $\mathbf{B}$ is the field acting on a "foreign" (extraneous) charges.[5] Contrarily to $\mathbf{B}(=\mathbf{H}+4\pi\mathbf{I})$, the average of microscopic fields caused by all native charges, $\mathbf{H}$ does not include the field due to the charge in question.[6] Respectively, in any medium $\mathbf{H}$ differs from $\mathbf{B}$. On the contrary, in a free space (vacuum) $\boldsymbol{I}=0$ and, consequently, $\mathbf{H}=\mathbf{B}$.[7]

---

[2] An active promoter of this experiment was von Laue.

[3] Different dimensions of the induction **B** and the intensity **H** of the magnetic field in the SI unit system, make this system in its current form inapplicable for this purpose.

[4] The demagnetizing factors are determined by relationship of the ellipsoidal axes. Respectively, η-s are defined only for the ellipsoidal bodies.

[5] On that reason the field measured by a prob charge, e.g., in μSR, is B, whereas in magnetic resonances the measured or controlling field is H.

[6] Here, the charge should be understood as the current caused by all types of microscopic movement, including the spinning one, of a given charge.

[7] Important that this is not just a mathematical coincidence, but a physical identity. This implies that in any system of physical units the dimensions of **B** and **H** must be the same.

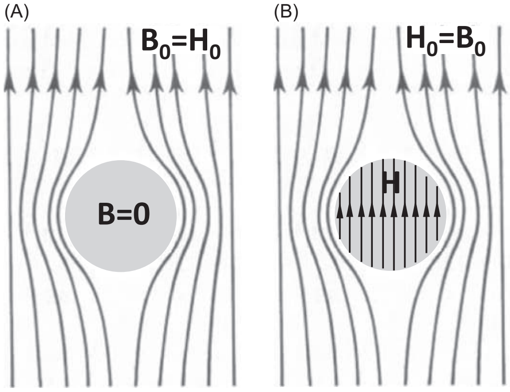

Fig. 1 Induction **B** (A) and intensity **H** (B) of the magnetic field inside and outside of a long cylindrical sample in the Meissner state when the field $\mathbf{H}_0$ is applied transversely to its longitudinal axis. For this sample/field configuration $\eta = 1/2$. Inside the sample $\mathbf{B} = 0$ and $\mathbf{H} = \mathbf{H}_0/(1 - \eta) = 2\mathbf{H}_0$; outside it $\mathbf{H} = \mathbf{B}$ and far away $\mathbf{H}_0 = \mathbf{B}_0$. Shadowed circle is a cross-section of the sample oriented perpendicular to the page.

At the sample boundary the normal component of the intensity H_n undergoes a discontinuity $\Delta H_n = 4\pi I_n$, where I_n is the magnitude of the normal component of magnetization **I**. Correspondingly, the intensity can be viewed as a potential field created by magnetic charges sitting on the boundary and having a surface density I_n. On the other hand, the intensity inside the sample, i.e. in any volume element dV not crossed by the sample boundary, represents a solenoidal or divergenceless field, which, therefore, can be described by a vector potential. As an example, Fig. 1 schematically shows the induction **B** and the intensity **H** of the magnetic field in and out of a sample with $\eta = 1/2$ when it is in the MS.[8]

If $\mathbf{H}_0$ is parallel to an axis of the ellipsoidal sample in the MS, $\mathbf{H} = \mathbf{H}_0/(1 - \eta)$, where η is the demagnetizing factor about this axis. If $\mathbf{H}_0$ is not parallel to either axis, **H** is the vector sum of the intensities relative to each axis. At any orientation of $\mathbf{H}_0$ with respect to the sample in the MS, inside it the magnitude of intensity **H** is less than H_{c1}.

After all, a very important property of the MS follows from the Law of the symmetry of time reversal, mandatory for any (either classical or quantum) equilibrium state. According to this Law, no total current can occur in the equilibrium state[9] and therefore all currents in the MS must be compensated.

In samples with $\eta = 0$, referred to as the samples of cylindrical geometry, the outer field due to the magnetized sample is absent and respectively $\mathbf{H} = \mathbf{H}_0$ both inside and outside the sample. Such samples can be, e.g., long cylinders, infinite slabs or wide ribbon-like foils in $\mathbf{H}_0$ parallel to their generating line.[10] Here our discussion of the MS will be limited by the cylindrical samples.

In this case the magnetic moment M of the sample is

$$\mathbf{M} \equiv \chi V \mathbf{H} = -\frac{V}{4\pi}\mathbf{H}_0 \tag{1}$$

and the sample magnetic energy E_m is

$$E_m \equiv -\int \mathbf{M} \cdot d\mathbf{H}_0 = -\frac{\mathbf{M} \cdot \mathbf{H}_0}{2} = \frac{VH_0^2}{8\pi}. \tag{2}$$

By virtue of the energy conservation, in the cylindrical samples $E_m = \Delta T$, where the latter is the field-induced change of the kinetic energy of electrons. As an example, graphs for **M** vs $\mathbf{H}_0$ for a type-I superconductor with $\eta = 0$ are shown in Fig. 2.

Cooper pairs

The Cooper pairs are defined as a correlated state of two conduction electrons with zero net kinetic linear momentum with respect to their center of mass and zero net spin. The latter condition stems from the requirement of thermodynamics since the free energy of a system of units with zero spin is lesser than it would be if the spin is not zero. The same condition justifies the thermodynamic advantage of the electron pairing since it allows to null the spin.

Zero net kinetic linear momentum and stability of the pairs mean that the paired electrons orbit their center of mass like, e.g., stars in a binary star. Therefore, each Cooper pair possesses the angular momentum $\boldsymbol{\iota}$ and the magnetic moment $\boldsymbol{\mu} = \gamma\boldsymbol{\iota}$, where γ is the gyromagnetic ratio. As measured by Kikoin and Goobar, 1938, γ in superconductors equals its classical value $e/2mc$. Here m and e are mass and charge of one electron, respectively, and c is the electromagnetic constant of the cgs unit system equal to speed of light. This confirms that the "superconducting" electrons are effectively spinless.

---

[8] The London theory, adopted for description of the MS in the Ginzburg-Landau and BCS theories, is based on an assumption that in superconductors the magnetic susceptibility μ_m and the dielectric permittivity ε_e are unity and therefore$\mathbf{B} = \mathbf{H}$. However, this is only true in a vacuum.

[9] The time transformation $t \rightarrow -t$ changes the direction of magnetic moment of a system with total current and therefore such a system can not be in the equilibrium state by definition.

[10] Any sample with $\eta = 0$ can be broken for a large number of identical thin circular cylinders parallel to $\mathbf{H}_0$.

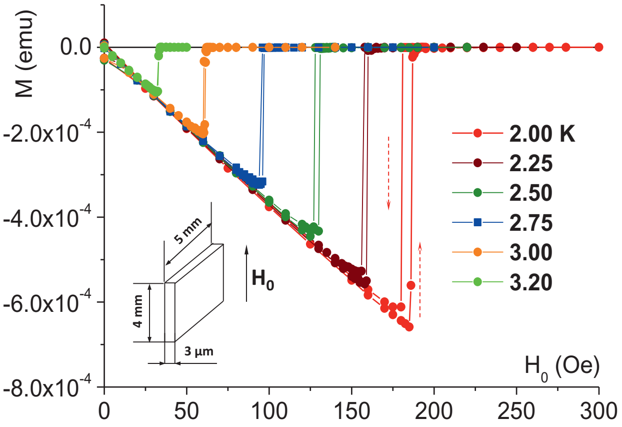

Fig. 2 Magnetic moment of a 2.9 – μm thick indium film in the parallel field $\mathbf{H}_0$ measured at constant temperatures, as indicated. For this sample $\eta = 0$ and $\mathbf{H} = \mathbf{H}_0$. The data were taken with the sample cooled in zero field (arrow up for 2.0 K) and in the field exceeding H_c (arrow down for 2.0 K). Hysteresis at the S/N transition is the supercooling effect caused by the positive S/N surface tension. The film geometry is shown in the insert. After Kozhevnikov V, Suter A, Prokscha T, and Van Haesendonck C (2020) *Journal of Superconductivity and Novel Magnetism* 33: 3361; reprinted with permission from Springer Nature.

Stability of the pairs also means that the orbital motion of the paired electrons occurs without energy dissipation. Therefore they must obey the Bohr-Sommerfeld quantization condition. At the same time, one should bear in mind that to meet the law of momentum conservation, in a magnetic field the linear momentum should be taken in a generalized form. Hence, the quantization condition for the single Cooper pair is

$$\oint \tilde{\mathbf{p}}_{cp}\cdot d\mathbf{l} = 2\pi R\tilde{p}_{cp} = 2\pi\tilde{\imath}_{cp} = nh, \tag{3}$$

where $\tilde{p}_{cp}$ and $\tilde{\imath}_{cp}$ are the generalized linear and angular momentum of the pair, respectively, R is the radius of orbital motion of paired electrons, h is the Planck constant, and n is a non-negative integer ($n = 0,1,2, \ldots$).

By definition of $\tilde{\mathbf{p}}$, the generalized linear momentum of the paired electrons $\tilde{\mathbf{p}}_{cp}$ is

$$\tilde{\mathbf{p}}_{cp} = \tilde{\mathbf{p}}_1 + \tilde{\mathbf{p}}_2 = \left(m\mathbf{v}_1 + \frac{e\mathbf{A}_1}{c}\right) + \left(m\mathbf{v}_2 + \frac{e\mathbf{A}_2}{c}\right) \tag{4}$$

where $\mathbf{v}$ is the electron velocity and $\mathbf{A}$ is the vector potential of the field acting on the electron, i.e. of the intensity $\mathbf{H}$; subscripts 1 and 2 denote the quantities related to the first and second electron in the pair.

In the ground state, i.e. at zero field and temperature, n in Eq. (3) takes the lowest value $n = 0$ and $\tilde{\mathbf{p}}_{cp}$ is the sum of kinetic linear momentums $\mathbf{p}(=m\mathbf{v})$ of electrons. Hence,

$$\left(\tilde{\mathbf{p}}_{cp}\right)_0 = \left(\mathbf{p}_{cp}\right)_0 = \mathbf{p}_{10} + \mathbf{p}_{20} = 0 \tag{5}$$

where subscript 0 denotes the zero field.

The last part of Eq. (5) is identical to the definition of Cooper pair. The first part of this equation $\left[\left(\tilde{\mathbf{p}}_{cp}\right)_0 = 0\right]$ is a modified London's rigidity, originally formulated for a single superconducting electron (London, 1960). Also, Eq. (5) implies that the center of mass of the pair is at rest with respect to the sample.

The motion of electrons in one Cooper pair at zero field and temperature is schematically shown in Fig. 3. The orbit diameter $2R_0$ corresponds to the coherence length ξ_0 of the BCS theory and ξ of the Ginzburg-Landau (GL) theory (Ginzburg and Landau, 1950), which are close to each other at these conditions.

One more important property at zero field is related to the ensemble of Cooper pairs: due to symmetry, the total magnetic moment of all pairs (the magnetic moment of the sample) is zero, i.e.

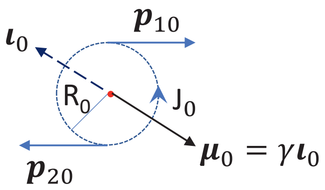

Fig. 3 Schematics of a single Cooper pair at zero field and temperature. $\boldsymbol{\iota}_0$ and $\boldsymbol{\mu}_0$ are the angular momentum and the magnetic moment of the pair, respectively; γ is the gyromagnetic ratio; p_{10} and p_{20} are the kinetic linear momentums of electrons; J_0 is the current caused by the orbital motion of electrons round their center of mass; R_0 is the orbit radius; red dot designates the center of mass of the pair.

$$\mathbf{M}_0 = \sum \boldsymbol{\mu}_0 = 0 \tag{6}$$

where summation is taken over all pairs.[11]

In view of uniformity of the bulk properties of the MS, Eq. (6) holds for the unit volume as well as for a physically infinitesimal volume element dV. The latter in superconductors is defined as a volume, which size is much smaller than the size of the volume taken by the S phase and much larger than the spatial inhomogeneity of microscopic currents, i.e. R_0. We remind that Cooper pairs are heavily overlap, but it affects neither stability, no mobility of the pairs. Taking into account the wave side of the electron nature, this fact is similar as the overlapping of myriads of electromagnetic waves does not prevent us from seeing objects or enjoying music broadcast from the other side of the globe.

Now it is rather obvious what happens when the magnetic field is turned on: Cooper pairs precess. Let us see how does it go.

In the field, each of the paired electrons (as well as all other charges constituting the sample) experiences the action of the Lorentz force.[12] In absence of the applied electric field,[13] this force is

$$\mathbf{F} \equiv \frac{d\mathbf{p}}{dt} = -\frac{e}{c}\left(\frac{\partial \mathbf{A}}{\partial t}\right) + \frac{e}{c}\mathbf{v} \times \mathbf{H} = -\frac{e}{c}\left(\frac{\partial \mathbf{A}}{\partial t}\right) + \frac{e}{c}\mathbf{v} \times (\nabla \times \mathbf{A}) \tag{7}$$

Here t is time, $\mathbf{A}$ is the vector potential of the field $\mathbf{H}(=\nabla \times \mathbf{A})$, and $\mathbf{v}$ is the electron velocity, which magnitude is about the same as the Fermi velocity v_F (the maximum difference between v and v_F is on the order of a percent).

Important to note that since inside real bodies $\mathbf{B}$ and $\mathbf{H}$ are different, one has to distinguish the vector potential for $\mathbf{H}$ and for $\mathbf{B}$. In our notations $\mathbf{A}$ is the vector potential of the intensity $\mathbf{H}$ inside the sample. Below we will see how $\mathbf{A}$ is related to the vector potential $\mathbf{A}_B$ defined by the relationship $\mathbf{B} = \nabla \times \mathbf{A}_B$. As usual, the supplementary condition $\nabla \cdot \mathbf{A} = 0$ is presumed.

The first term in the right-hand side of Eq. (7) is an electric force $\mathbf{F}_E$ caused by the changing magnetic field.

Corresponding vortex electric field $\mathbf{E}$ is defined as

$$\mathbf{E} \equiv \frac{\mathbf{F}_E}{e} = -\frac{1}{c}\left(\frac{\partial \mathbf{A}}{\partial t}\right). \tag{8}$$

As with bound electrons in conventional materials, the electric field $\mathbf{E}$ (existing while the magnetic field is changing) does the work resulting in a change of kinetic energy of electrons and in the appearance of an induced magnetic moment in each pair.

Specifically, when the vector potential changes from zero to $\mathbf{A}$, which corresponds to the intensity change from zero to $\mathbf{H}$, the velocity of electrons in the pair is changed from $\mathbf{v}_0$ to $\mathbf{v}'$. The difference $\mathbf{v}_i = \mathbf{v}' - \mathbf{v}_0$ is the velocity induced due to the applied magnetic field. Integrating Eq. (8) over time, one obtains

$$\mathbf{v}_i = -e\frac{\mathbf{A}}{cm}. \tag{9}$$

This is a very important formula. It shows that $\mathbf{v}_i$ is parallel to $\mathbf{A}$. Therefore, since by definition $\mathbf{A}$ lies in the plane perpendicular to $\mathbf{H}$, $\mathbf{v}_i$ and therefore the induced current also lies in the plane transverse to $\mathbf{H}$. On the other hand, the induced current makes a closed loop (it cannot leave the sample) and the loop must be circular due to rotational symmetry stemming from uniformity of $\mathbf{H}$ (all directions in the transverse plane are equivalent); therefore lines of the vector potential make the circular loops either. Hence, an appropriate gauge for the vector potential of $\mathbf{H}$ is the circular one, namely $\mathbf{A} = \mathbf{H} \times \mathbf{r}/2$. The lines of this vector potential are shown in Fig. 4.

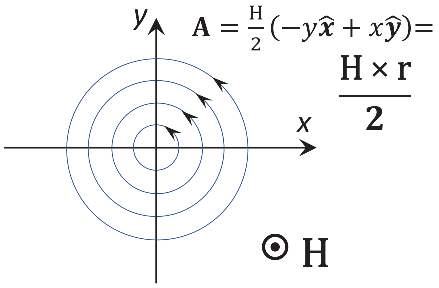
y
$\mathbf{A} = \frac{\mathrm{H}}{2}(-y\hat{\boldsymbol{x}} + x\hat{\boldsymbol{y}}) = \frac{\mathbf{H} \times \mathbf{r}}{2}$
x
⊙ H

Fig. 4 Lines of the vector potentials **A** of the circular gauge for a uniform magnetic field **H** directed toward the reader (along the z-axis); $\hat{x}$ and $\hat{y}$ are unit vectors along x and y axes, respectively. **r** is a radius vector lying in xy plane. As for all vector fields, the line of **A** is the directional line tangential to the vector **A** in each of its point.

---

[11] Note that Eq. (6) resembles the definition of a diamagnetic atom, where each electron has a non-zero orbital momentum, while the momentum of the atom is zero.

[12] The action of a magnetic field on atomic electrons and nuclei results in the usual diamagnetic response; its action on unpaired conduction electrons causes a weak Landau diamagnetism.

[13] A static electric field does not penetrate the superconducting sample due to the screening effect of always present "normal" electrons.

Thus, since $e < 0$, Eq. (9) indicates that the current induced in each Cooper pair creates a magnetic moment directed opposite to **H**, i.e. the induced moment is always diamagnetic, in accord with requirements of thermodynamics and the time reversal symmetry. This also means that diamagnetism (both in normal and superconducting materials) results from the changing magnetic field in full consistency with the laws of the classical physics.

Next, like in regular diamagnetics, in Eq. (9) the time has dropped out implying that the induced velocity $\mathbf{v}_i$ is indifferent to the rate of the field change.

After all, Eq. (9) implies that the vector potential in superconductors is not gauge-invariant since a change in **A** changes the induced moment and because **A** of any but the circular gauge does not possess the necessary rotational symmetry. However, this is not surprising,[14] since the gauge invariance is inapplicable to quantities defined by the vector potential in explicit form. Non-fulfillment of the gauge-invariance in superconductors is an additional confirmation of the fact that the vector potential is a real and primary characteristics of the magnetic field, as demonstrated by the Aharonov-Bohm effect (Ehrenberg and Siday, 1949; Aharonov and Bohm, 1959).

The second term in the right hand side of Eq. (7) is termed the magnetic force $\mathbf{F}_M$. It is perpendicular to the electron velocity and therefore does no work. Hence, $\mathbf{F}_M$ does not affect the electron kinetic energy and the magnitude of its magnetic moment. On the other hand, since the uniform magnetic field cannot change position of the pair's center of mass, $\mathbf{F}_{M1} = -\mathbf{F}_{M2}$ (those are the magnetic forces acting on the 1st and 2nd electron in the pair), and also $\mathbf{F}_{M1}$ and $\mathbf{F}_{M2}$ are non-central forces. Hence, they make a couple resulting, due to non-zero $\boldsymbol{\iota}_0$, in precession of $\boldsymbol{\mu}_0$ relative to the vector **H**, as schematically shown in Fig. 5.

The angular velocity of precession, referred to as Larmor frequency, is

$$\mathbf{o} = -\gamma\mathbf{H} = -\frac{eg_L}{2mc}\mathbf{H}, \tag{10}$$

where g_L is the Lande factor. As mentioned, in superconductors γ takes the classical value, i.e. $g_L = 1$.

As follows from the Larmor theorem, if $v_i \ll v_0$, precession of the electron orbit is equivalent to the undisturbed orbital motion at the field absence (i.e. with fixed $\boldsymbol{\mu}_0$ and R_0) plus an additional (field induced) circular motion with the angular velocity $\boldsymbol{o}$ and radius r proportional to R_0, which leads to appearance of the diamagnetic moment $\boldsymbol{\mu}_{cp}$. On the other hand, the invariability of $\boldsymbol{\mu}_0$ means that Eq. (6) is valid both in the absence and presence of the magnetic field. This can be also understood basing on the fact that precession is an inertia-free motion and therefore all pairs precess synchronously,[15] i.e. without changing their mutual orientation.

Thus, we arrive to conclusion (following both from consideration of the action of Lorentz force Eq. (7) and from the Larmor theorem) that the net effect of the magnetic field is the induced circular motion of the paired electrons in the planes transverse to **H**. On the other hand, as it is known for any kind of cyclic motion in magnetic field, the changing $|\mathbf{H}|$ changes the magnitude of $\mathbf{v}_i$ only, i. e. the radius of the induced motion r does not depend of the field provided that $v_i \ll v_0$.

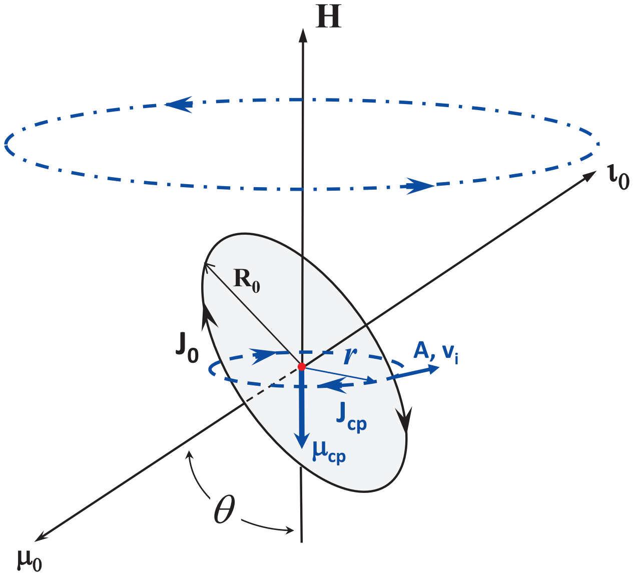

Fig. 5 Schematics of the Cooper pair precession in the magnetic field **H**. Vectors $\boldsymbol{\iota}_0$ and $\boldsymbol{\mu}_0$, current J_0 and radius R_0 are the same quantities as those at zero field shown in Fig. 3. A dot-dashed circle designates the path of the tip of the precessing $\boldsymbol{\iota}_0$. A dashed blue circle depicts the field-induced current J_{cp}; it is also a line of the vector potential directed opposite to the current J_{cp}. **A** and $\mathbf{v}_i$ designate the vector potential and the induced velocity of one electron, respectively; r is the radius of the induced current; μ_{cp} is the induced magnetic moment of the pair. Designated by a single arrow **A** and $\mathbf{v}_i$ are proportional but not equal. After Kozhevnikov V (2021) *Journal of Superconductivity and Novel Magnetism* 34: 1979; reprinted with permission from Springer Nature.

---

[14] Recall that the gauge-invariance does not hold in the London and BCS theories.

[15] Also, as it is shown below, the induced circular motion of the paired electrons occurs in phase.

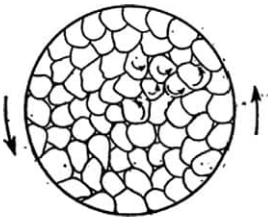

Fig. 6 A cross sectional view of a conventional diamagnetic sample showing induced bound currents caused by precession of the atomic electron orbits; the field is directed into the page. This picture is similar to the induced currents caused by precession of Cooper pairs in a superconducting sample in the Meissner state. After the textbook of Tamm IE, *Fundamentals of the Theory of Electricity*, 9th edn. Moscow: Mir, 1979, reprinted with permission from Mirtitles.

One can also show that $\tilde{\mathbf{p}}_{cp}$ does not depend on the magnetic field either, namely

$$\tilde{\mathbf{p}}_{cp} = \tilde{\mathbf{p}}_1 + \tilde{\mathbf{p}}_2 = \tilde{\mathbf{p}}_{10} + \tilde{\mathbf{p}}_{20} = 0. \tag{11}$$

Hence, the modified London's rigidity holds both in zero and non-zero field. Below we will see that it also holds at non-zero temperature.

The induced currents in superconductors in the MS (and in other equilibrium S states) are qualitatively identical to the induced bound currents in regular diamagnetics schematically shown in Fig. 6. In our case, like in the normal materials, the induced currents mutually compensate each other in the sample bulk, leaving an uncompensated surface current caused by electrons bound in Cooper pairs with resting centers of inertia. Then the magnetic moment of the sample is exactly the same as the moment produced by a continuous (circumferential) surface current.

Now we are ready to calculate magnetic proprieties of our cylindrical sample in the MS.

After turning on the applied field $\mathbf{H}_0$, the field intensity and the vector potential inside the sample after a short relaxation time become $\mathbf{H}$ and $\mathbf{A}$, respectively. Then, using Eq. (9), we write.

$$m\mathbf{v}_i = -\frac{e}{c}\mathbf{A} = -\frac{e}{2c}\mathbf{H}\times\mathbf{r}. \tag{12}$$

Hence,

$$m\boldsymbol{\omega} = -\frac{e}{2c}\mathbf{H}, \tag{13}$$

where $\boldsymbol{\omega} = (\mathbf{r}\times\mathbf{v}_i)/r^2$ is the angular velocity of the induced circular motion of the paired electrons.

Taking into account that $e < 0$, Eq. (13) reads that $\boldsymbol{\omega}$ is parallel to $\mathbf{H}$ and its magnitude is

$$\omega = \frac{v_i}{r} = \frac{e}{2mc}H. \tag{14}$$

Comparing with Eq. (10) we see that ω equals the classical Larmor frequency ($g_L = 1$). This confirms that we really deal with the precession of paired electrons with zero total spin, since non-paired electrons (as any other charge) in a magnetic field circulate with a so-called cyclotron frequency $\omega_c = (e/mc)H$..

The induced current per one electron in the pair J_i is

$$J_i = \frac{e}{2\pi}\omega = \frac{e^2}{4\pi mc}H. \tag{15}$$

As follows from Eqs. (14) and (15), neither induced angular velocity ω, nor the induced current J_i depend on r. However, this is not the case for the induced magnetic moment and the corresponding change of kinetic energy of the paired electrons: they both depend on r^2. On the other hand, r for Cooper pairs with different orientation of $\boldsymbol{\mu}_0$ is different. So what we want to know is the mean square $\langle r^2\rangle$, which we will denote as r_i^2.

Using Eq. (15), the magnitude of an average induced magnetic moment per one electron in Cooper pairs is

$$\mu_i = \frac{1}{c}J_i\pi r_i^2 = \frac{e^2 r_i^2}{4mc^2}H = \frac{e^2 n_s 4\pi}{mc^2}\left(\frac{r_i}{2}\right)^2\frac{H}{4\pi n_s} = \frac{(r_i/2)^2}{\lambda_L^2}\frac{H}{4\pi n_s}. \tag{16}$$

where n_s is a number density of superconducting (i.e. paired) electrons and λ_L is so-called London penetration depth defined as

$$\lambda_L = \left(\frac{mc^2}{4\pi n_s e^2}\right)^{1/2} = \left(\frac{m_{cp}c^2}{4\pi n_{cp} q_{cp}^2}\right)^{1/2}, \tag{17}$$

where $m_{cp} = 2m$, $q_{cp} = 2e$ and $n_{cp} = n_s/2$ are the mass, charge and number density of Cooper pairs, respectively.

Since induced magnetic moments in all Cooper pairs are parallel, the magnitude of the magnetic moment of our sample is

$$M = n_{cp}V\mu_{cp} = \frac{(r_i/2)^2}{\lambda_L^2}\frac{V}{4\pi}H = \frac{(r_i/2)^2}{\lambda_L^2}\frac{V}{4\pi}H_0. \tag{18}$$

Comparing this result with Eq. (1), we see that the rms radius of the induced motion of the paired electrons is

$$r_i = 2\lambda_L. \tag{19}$$

Since r does not depend on the field, r_i and therefore λ_L do not depend on the field either.

Next, basing on Eq. (6) one can show that, like in regular diamagnetics, the change of kinetic energy of the superconducting electrons ΔT is the sum of the field-induced kinetic energies of each of these electrons, i.e.

$$\Delta T = E_k = \varepsilon_i n_s V = \varepsilon_{cp} n_{cp} V, \tag{20}$$

where $\varepsilon_{cp} = 2\varepsilon_i$ is the average kinetic energy of the induced motion of electrons in one pair.

Using Eq. (14), we write

$$\varepsilon_i = \frac{mv_i^2}{2} = \frac{e^2H^2r_i^2}{8c^2m} = \left(\frac{(r_i/2)}{\lambda_L}\right)^2 \frac{H^2}{8\pi n_s}. \tag{21}$$

Thus, taking into account Eq. (19), the change of kinetic energy of the paired electrons is

$$\Delta T = \varepsilon_i n_s V = \left(\frac{(r_i/2)}{\lambda_L}\right)^2 \frac{H^2}{8\pi} V = \frac{H^2}{8\pi} V. \tag{22}$$

In our sample $H = H_0$ and, according to the energy conservation, $\Delta T = E_m = H_0{}^2 V/8\pi$ (see Eq. 2). Hence, our description meets the Law of energy conservation.

Next, we calculate the gyromagnetic ratio coming from its definition. Using Eqs. (14) and (16) we write

$$\gamma \equiv \frac{M_i}{L_i} = \frac{\mu_i n_s V}{\iota_i n_s V} = \frac{\mu_i}{m v_i r_i} = \frac{e^2 r_i^2 H}{4mc^2}\,\frac{2c}{e r_i^2 H} = \frac{e}{2mc}, \tag{23}$$

where M_i and L_i are magnitudes of the induced magnetic moment and of the induced angular momentum of the sample, respectively; and ι_i is an average field-induced angular momentum per one electron.

We see that γ is fully consistent with the experimental result of I. Kikoin and Goobar.

After all, calculate the induction in the sample interior. Using Eqs. (16) and (19), and the fact that μ_i is negative, we obtain

$$\mathbf{B} = \mathbf{H} + 4\pi\mathbf{I} = \mathbf{H} + 4\pi(\boldsymbol{\mu}_i n_s) = \mathbf{H} - 4\pi\frac{\mathbf{H}}{4\pi n_s} n_s = 0, \tag{24}$$

in agreement with the result of Meissner and Ochsenfeld and of Rjabinin and Shubnikov.

Correspondingly, the magnetic permittivity $\mu_m \equiv B/H$ and susceptibility per unit volume χ of the S phase are zero and $-1/4\pi$, respectively.

Naturally, due to microscopic character of the induced currents, there is no problem in establishing the Meissner condition ($B=0$) in samples/domains of any shape, as soon as the field **H** is uniform. The latter is indeed so in ellipsoidal samples, regardless whether they are in the MS or in the inhomogeneous equilibrium states, i.e., in the mixed state of type-II and in the intermediate state of type-I superconductors.

This explains why the Meissner state is observed only in the ellipsoidal bodies, as well as the plenty domain shapes observed in the intermediate state.

The above consideration applies to the samples cooled in zero field (ZFC), whereas the Meissner effect is about both the ZFC and FC (field-cooled) samples. So, what happens in the latter case?

Upon lowering temperature below $T_c(H_0)$ in the fixed field $H_0 < H_{c1}(1 - \eta)$, a temperature dependent fraction of conduction electrons condenses forming stable Cooper pairs. This means that speed of these electrons drops from v_F to v_0, each pair starts orbiting its center of mass and, being in the field, the pairs precess. Like in regular diamagnetics, the latter leads to establishing magnetization **I**, the field intensity $\mathbf{H} = \mathbf{H}_0 - 4\pi\eta\mathbf{I}$ and the induction $\mathbf{B} = \langle\mathbf{h}\rangle = \mathbf{H} + 4\pi\mathbf{I}$, where $\langle\mathbf{h}\rangle$ is the average microscopic field. Hence, after the short relaxation time needed to establish the intensity **H**, the environment inside the FC sample becomes the same as that in the ZFC sample. Thus, the given description meets the Meissner effect indeed.[16]

One more remark. As mentioned above, radius of the electron orbit R_0 in precessing Cooper pairs is fixed (i.e. it does not depend on the field) and the Larmor theorem is exact if $v_i \ll v_0$. Taking typical value of $H_{c1} \sim 100$ Oe and $\lambda_L \sim 10^{-6}$ cm, from Eq. (12) one finds $v_i \sim 10^2$cm/s, which is six orders of magnitude less than $v_0 \approx v_F \sim 10^8$ cm/s. So, there is no doubt that R_0 does not depend on the field. On the other hand, since r_i and R_0 are quantities of the same or close order of magnitude, this estimate implies that $\omega \ll \omega_0 \equiv v_0/R_0$, i.e. the precession is very slow.

Microscopic whirls

Now, let us reconstruct the current structure of the MS. We understand that all induced currents form identical circular loops with the rms radius r_i laying in parallel planes transverse to **H**. How these currents are arranged with respect to each other?

---

[16] The standard description of the Meissner effect is based on the London theory in which this effect is achieved by postulating $B = 0$.

Coming from symmetry, one can expect either complete chaos or complete order. Since the system of the ordered currents has lesser free energy, the second option prevails. This is consistent with experimental results of Keesom and Kok (1934) that entropy of the sample in the S state is less than that in the N state.

An ordered structure of identical circular currents laying in the planes transverse to **H** possesses the maximum symmetry if the currents form a 2D hexagonal lattice of cylindrical micro-whirls resembling densely packed and tightly "wound" micro-solenoids parallel to each other and to **H**. Length of each whirl/solenoid equals the sample size along direction of **H** and its rms diameter is $2r_i = 4\lambda_L$. Since the solenoids are parallel, they do not interact. In addition, since the currents are given by the field-induced circular motion of the paired electrons, the complete ordering implies that in all Cooper pairs this motion is in phase.[17]

Just a few facts supporting this statement. (i) The internal energy of the cylindrical sample in the MS is just the sum of kinetic energies ε_i (Eq. 22) and it does not contain the term(s) responsible for interaction. (ii) In pure type-II superconductors Abrikosov vortices[18] make the hexagonal lattice, as was first observed by Essmann and Träuble (Essmann and Träuble, 1967). (iii) An experimental evidence showing that the Abrikosov vortices do not interact with each other in pure samples (Kozhevnikov et al., 2018).

Naturally, the complete ordering of the field-induced currents together with Eq. (6) mean that entropy of the ensemble of Cooper pairs S_{cp} is zero, exactly as it takes place for the magnetic part of entropy in regular diamagnetics. Therefore the given theoretical interpretation, referred to as a micro-whirls (MW) model, is consistent with the absence of the thermoelectric effects in superconductors and justifies the postulate of zero entropy of superconducting electrons of the two-fluid model of Gorter and Casimir.

One more detail about the micro-whirls. A spacing between current loops Δ along the whirl axis is a universal quantity[19] equal to

$$\Delta = \frac{2e^2}{mc^2} = 5.6 \cdot 10^{-13}\ cm \approx 6\ fm. \tag{25}$$

So Δ is about a tripled size of a proton ($1.7\ fm$) and therefore the whirls are similar to very tightly wound solenoids indeed.

An important feature of a single whirl is that it is characterized by two microscopic quantities with dimension of length. Those are the radius of the orbital motion R_0 and the radius of the field-induced circular motion r_i. As mentioned, r_i is proportional to R_0, both radii do not depend on the field and the ratio r_i/R_0 is a constant of superconducting material. However, if vector $\mathbf{r}_i$ always lays in the transverse plane, $\mathbf{R}_0$ is symmetrically distributed over 3D space as follows from Eq. (6). So, like in the Langevin theory of diamagnetism, a mean squared projection of $\mathbf{R}_0$ on the transverse plane ${R_\perp}^2$ equals $2{R_0}^2/3$. In other words, $R_\perp$ is an rms radius of a cylinder coaxial to the cylinder with radius r_i and filled by orbiting Cooper pairs. Hence, an individual whirl can be viewed as a "double wall" cylinder with radii $R_\perp$ and r_i.

A parameter of material in the MW model is $\aleph$ (aleph) defined as

$$\aleph = \frac{r_i}{R_\perp}. \tag{26}$$

In materials with $\aleph < 1$ the S/N surface tension is positive and correspondingly such materials represent type-I superconductors. In type-II superconductors the S/N interphase energy is negative and $\aleph > 1$. The cross section of the whirl structure in type-I and type-II superconductors is shown in Fig. 7.

Penetration depth

Another important property of the MS is the penetration depth λ, a width of the surface layer where B decades from $B_{ext}(=B_0 = H_0$ for the cylindrical samples) to zero in the sample interior.

According to the London theory, in a sample with a plane boundary (i.e., in the massive cylindrical samples), the induction $B(z)$, where z is the distance from the surface, decays exponentially with the decay constant λ_L. Correspondingly, λ is infinite and an effective penetration depth $\lambda_{eff} = \lambda_L$.[20] What is λ in the MW model?

To answer this question one needs to know the angular distribution of $\boldsymbol{\mu}_0$, which is beyond the scope of the semiclassical consideration employed in the model. One can estimate λ assuming that the boundary of the blue cylinders in Fig. 7 is sharp or the induced current J_i is linear. Then for the plane sample boundary $\lambda = r_i = 2\lambda_L$ and $\lambda_{eff} = \lambda_L/2$. This is, of course, an oversimplified estimate, however in any case in the MW model λ is finite and close to λ_L.

Temperature

All properties discussed so far are related to those for the samples at $T = 0$. However, it is quite obvious that nothing will change if $T \neq 0$.

---

[17] Note the direct analogy with the phase of the quantum-mechanical wave function. The wave functions of all Cooper pairs must be in phase since otherwise there would be a total current forbidden by the time reversal symmetry.

[18] The Abrikosov vortices represent holes in the network of the ordered currents of the MS.

[19] Since ${r_i}^2 = (2\lambda_L)^2 \sim 1/n_{cp}$, the universality of Δ is a necessary condition that the whirls, i.e., ordered Cooper pairs, fill the entire volume of the sample in the MS at any change of n_{cp} (occurring when T changes) regardless of the specific material of the sample.

[20] λ_{eff} is such a depth over which the flux of the penetrating field is the same as the flux of the real field and the flux density B is constant and equal to B_{ext}.

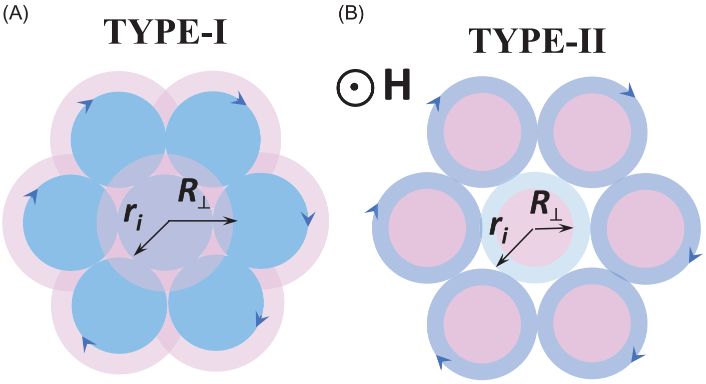

Fig. 7 Schematics of the micro-whirl structure in the transverse cross section of type-I (A) and type-II (B) superconductors. In (A) $r_i < R_\perp$ or $\aleph < 1$; in (B) $r_i > R_\perp$ or $\aleph > 1$. The induced currents (all are in phase with each other) are designated by arrows. Areas filled with Cooper pairs are colored in pink; the cross-sectional areas of the induced currents are colored in blue. $R_\perp$ is the rms projection of the pairs radius R_0 onto the plane perpendicular to **H**; r_i is the rms radius of the induced motion of the paired electrons. Boundaries of all cylinders are diffuse (unsharp), the cylinders overlap without leaving voids. The field **H** is directed toward the reader. After Kozhevnikov V (2021) *Journal of Superconductivity and Novel Magnetism* 34: 1979; reprinted with permission from Springer Nature.

Indeed, we have seen that entropy of the ensemble of Cooper pairs S_{cp} is zero. Therefore, according to the Third law (Nernst's theorem), the temperature of the ensemble of Cooper pairs T_{cp} is zero as well, regardless on the sample temperature T. Hence, all results obtained in this section hold in the whole temperature range of the existence of Cooper pairs. In other words, the paired electrons are in the ground state in the entire temperature and field range of the S state.

However, $T_{cp} = 0$ does not mean that the sample temperature has no effect on the properties of paired electrons, since otherwise T_c would be infinite. The sample temperature affects the lattice polarization responsible for the electron pairing. Correspondingly, it changes $n_s(=2n_{cp})$, as shown in the two-fluid model. Therefore, the change of T leads to the change of λ_L and, correspondingly, to the change of r_i, the rms radius of the field-induced motion of electrons in the pairs. On the other hand, r_i is proportional to R_0 with the proportionality coefficient $\aleph$ (more strictly $\sqrt{2/3}\aleph$) determined by the superconducting material. In its turn, $\aleph$ does not depend on T due to the constancy of $T_{cp}(=0)$.

Flux quantization

Let us consider a closed macroscopic loop l located inside a sample in the MS away from its surface. For simplicity, take a cylindrical sample and the loop lying in the transverse plane as shown in Fig. 8A. Now, calculate the circulation of the linear momentum $\tilde{\mathbf{p}}_{cp}$ over this loop.

Moving along the loop, we will pass through lots of pairs, so we should consider the average momentum $\left\langle \tilde{p}_{cp} \right\rangle$ and the average quantum number $\langle n \rangle$. Since all Cooper pairs are in identical conditions $\langle n \rangle = n$. Therefore, the Bohr-Sommerfeld quantization condition for this case is

$$\oint_l \left\langle \tilde{\mathbf{p}}_{cp} \right\rangle \cdot d\mathbf{l} = nh, \tag{27}$$

where l is the loop length.

Now, open $\left\langle \tilde{\mathbf{p}}_{cp} \right\rangle$ and take into account that in the MS $n = 0$. Then, Eq. (27) becomes

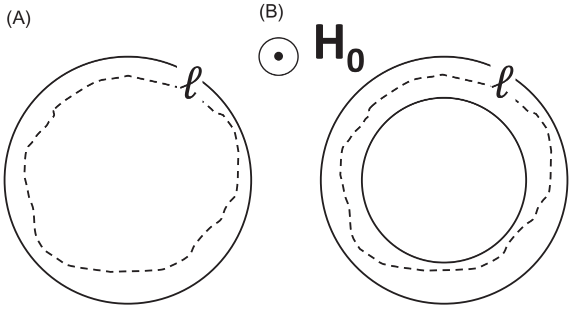

Fig. 8 Cross section of solid (A) and hollow (B) cylindrical samples in a field $\mathbf{H}_0$ parallel to the long axis of the samples. l is a loop lying away from the wall(s) of the cylinders.

$$\oint_l \left\langle \tilde{\mathbf{p}}_{cp} \right\rangle \cdot d\mathbf{l} = \oint_l \langle m\mathbf{v}_{i1}\rangle \cdot d\mathbf{l} + \oint_l \langle m\mathbf{v}_{i2}\rangle \cdot d\mathbf{l} + \frac{2e}{c}\oint_l \langle \mathbf{A}\rangle \cdot d\mathbf{l} = 0. \tag{28}$$

The first two integrals are zero due to mutual compensation of the induced kinetic linear momentums of electrons in neighboring pairs, similar as it takes place in the regular diamagnetics.

Now, what is $\langle \mathbf{A}\rangle$, the average of the vector potential of the intensity $\mathbf{H}$? To answer, we apply Stokes' theorem; then Eq. (28) is rewritten as

$$\frac{2e}{c}\oint_l \langle \mathbf{A}\rangle \cdot d\mathbf{l} = \frac{2e}{c}\int_{F_l} (\nabla \times \langle \mathbf{A}\rangle) \cdot d\mathbf{f} = 0 \tag{29}$$

where F_l is the area of a surface bounded by the loop l and $d\mathbf{f}$ is a vector element of this surface.

From Eq. (29) we see that the integral over the area F_l is the flux of a vector $[\nabla \times \langle \mathbf{A}\rangle]$ and this flux equals zero. Therefore, since $\nabla \times \mathbf{A} \equiv \mathbf{H} \neq 0$, $\langle \mathbf{A}\rangle \neq \mathbf{A}$.

On the other hand, inside our sample the induction $\mathbf{B}$ and therefore its flux is zero (Eq. (39)). Therefore, Eq. (29) suggests that $\langle \mathbf{A}\rangle$ is the vector potential of the magnetic flux density (induction) $\mathbf{A}_B$ defined as $\mathbf{B} = \nabla \times \mathbf{A}_B$. In other words, the vector potential of the flux density $\mathbf{A}_B$ is a macroscopic average of the vector potential $\mathbf{A}$ determining the field induced microscopic currents J_i. This is an exact match with the classical definition of $\mathbf{A}_B$ as a macroscopic mean of the vector potentials caused by the microscopic currents. So, putting $\langle \mathbf{A}\rangle = \mathbf{A}_B$, we rewrite Eq. (29) as

$$\frac{2e}{c}\int_{F_l} (\nabla \times \langle \mathbf{A}\rangle) \cdot d\mathbf{f} = \frac{2e}{c}\int_{F_l} \mathbf{B} \cdot d\mathbf{f} = \frac{2e}{c}\Phi = 0, \tag{30}$$

where ϕ is the magnetic flux through the area F_l.

Now, take a hollow (tube-like) thick-wall long cylinder shown in Fig. 8B, apply the field $H_0(<H_{c1})$ parallel to its longitudinal axis and cool the cylinder below T_c. The loop l encircles the opening of the cylinder and lies inside the wall far (compare to λ) from the inner and outer cylinder surfaces. The induction inside the wall is zero, implying that, as in Eq. (28), $\langle m\mathbf{v}_i\rangle = 0$. On the other hand, the flux ϕ inside the hollow cylinder is frozen and therefore it is not zero. Then Eq. (27) yields

$$\oint_l \left\langle \tilde{\mathbf{p}}_{cp} \right\rangle \cdot d\mathbf{l} = \frac{2e}{c}\oint_l \langle \mathbf{A}\rangle \cdot d\mathbf{l} = \frac{2e}{c}\int_{F_l} \nabla \times \langle \mathbf{A}\rangle \cdot d\mathbf{f} = \frac{2e}{c}\int_{F_l} \mathbf{B} \cdot d\mathbf{f} = \frac{2e}{c}\Phi = nh. \tag{31}$$

Hence, the magnetic flux passing through the opening (plus surrounding it penetration area) in a multiply connected superconductor is

$$\Phi = \frac{c}{2e}nh. \tag{32}$$

This is the famous London's flux quantization but for the paired electrons. Hence, the origin of the superconducting flux quantization is the Bohr-Sommerfeld quantization condition, which also justifies existence of the field induced persistent currents in the MS.

Eq. (32) implies that the flux quantum and therefore the flux passing through each so-called Abrikosov vortex in type-II superconductors in the mixed state is

$$\Phi_0 = \frac{c}{2e}h = \frac{\pi c\hbar}{e}. \tag{33}$$

As well known, the flux quantization Eq. (32) and the single flux quantum in the Abrikosov vortices Eq. (33) are in full agreement with experiment.

Thus, inside the S phase the vector potential $\mathbf{A}_B = \langle \mathbf{A}\rangle$, where $\mathbf{A}$ is the vector potential of the field $\mathbf{H}$. Now, what is the value of $\mathbf{A}_B$ inside the sample in the MS?

In the plane perpendicular to $\mathbf{H}$ we have uniformly distributed identical induced circular currents, i.e. in-plane currents with the same magnitude J_{cp} and the same rms radius r_i circulating clockwise relative to $\mathbf{H}$. Therefore, exactly as it takes place in regular diamagnetics, equal amount of electricity flows in opposite directions throughout an out-of-plane cross section of an arbitrary chosen volume element dV. Hence, an average current density $\langle \mathbf{j}\rangle = en_s\langle \mathbf{v}_i\rangle$ is zero in any volume element of the sample interior or inside the S phase. So, taking into account Eq. (9), we write

$$\mathbf{A}_B \equiv \langle \mathbf{A}\rangle = \langle \mathbf{v}_i\rangle = \langle \mathbf{j}\rangle = 0. \tag{34}$$

Thus, inside the sample in the MS, or in general inside the S phase, in spite of non-zero $\mathbf{H}$, an average of its vector potential $\langle \mathbf{A}\rangle$, as well as the average induced velocity $\langle \mathbf{v}_i\rangle$, and the average induced current $\langle \mathbf{j}\rangle$ are all equal zero. Out of these three equalities the last one $[\langle \mathbf{j}\rangle = 0]$ is the most important: it shows that all currents in the S phase are mutually compensated, as required by the Law of the time reversal symmetry.

Total current

As we have seen, the equilibrium magnetic properties of superconductors are qualitatively similar to the properties of conventional diamagnetics. In both cases these properties are due to magnetization arising from precession of the microscopic magnetic moments caused by the orbital motion of electrons bound either in atoms (conventional diamagnetics) or in Cooper pairs (superconductors). A colossal quantitative difference in the magnetic susceptibilities in these materials (up to 5 orders of magnitude!) is due to the differences in the size of the orbits and correspondingly in the radii of the induced microscopic currents of the bound electrons.

However, there is also an important qualitative difference in these induced currents. Namely, in conventional diamagnetics the orbiting electrons are bound in motionless atoms (fixed in the crystal lattice), while in superconductors - in movable Cooper pairs. The pairs mobility allows them to compose the whirl structure with zero entropy. On the other hand, since the pairs have electric charge, they can form an electric current, referred to as the total current. It includes the transport current and the field-induced current encircling the openings in multiply connected bodies. In the latter case, as was for the first time observed by Deaver and Fairbank (1961), the total current is quantized due to the flux quantization.

The total current in superconductors plays a role similar to that of the transport current in conventional metals, where it is executed by conduction electrons. The latter obey Fermi-Dirac statistics and their energy equals the Fermi energy E_F. This implies that the carriers of the transport current in normal metals, or in the N phase of superconductors, are “very hot”: their temperature, the temperature of the ensemble of conduction electrons, equals the Fermi temperature $T_F = E_F/k_B \sim 10^4$ K (k_B is the Boltzmann constant), i.e., it is about the same as the sun surface temperature.

In striking contrast, the charge carriers (Cooper pairs) of the total current in the S phase are “deadly cold.” Since their spins are zero, the pairs obey Bose-Einstein statistics and, since the temperature of the ensemble of the paired electrons T_{cp} is zero, they form the Bose-Einstein condensate (BEC). This (zero temperature) leads to the disappearance of the thermoelectric effects, as observed in experiments. The amazing transformation of the “very hot” single electrons to the “zero-temperature” electron pairs can be compared with the fact known from the relativity theory: two flying apart massless photons form a massive pair located in their center of mass.

Therefore, the total current in superconductors represents the transport current in BEC, known on the properties of superfluid helium. Correspondingly, the total current set in a closed superconducting circuit continues running without energy dissipation provided speed of the charge carriers (density of the total current) is lesser of a definite critical value (Landau, 1941; Feynman, 1955).

Thus, in the MW model the electromagnetic properties of superconductors caused by the total current[21] resemble the properties of hypothetical perfect conductors.

The hell-mark of the perfect conductors is irreversibly of the sample magnetic moment induced by the changing applied magnetic field; its direction is determined by the Lenz law whereas the magnetic moment caused by magnetization is always diamagnetic. On this reason the multiply connected bodies can never be in thermodynamic equilibrium and therefore neither the principal of the free energy minimum nor the time reversal symmetry can be applied to them.

However, it should be stressed that even in the presence of the total current, magnetic properties of superconductors in the MW model are different from those of the perfect conductors. Since the total current is accompanied by its own magnetic field, it represents a combination of the whirl and translational motion of the paired electrons regardless of the presence or absence of the applied field. This explains the observation reported by Meissner and Ochsenfeld in their fundamental paper of 1933 (Meissner and Ochsenfeld, 1933): “When the parallel superconductors are connected end-to-end in series and an external current is connected to flow through them above the critical temperature the magnetic field between the superconductors is increased below the transition temperature the external current being unchanged.”

Conclusion

In this chapter we presented the basics of the micro-whirls model of superconductivity and a description of main electrodynamic properties as it follows from the model. It is important to underline, that the “big zeroes” of superconductivity listed in the abstract, as well as the zero generalized linear momentum (modified London’s rigidity), the zero average vector potential and the zero average current in the sample bulk, all rise from a single root: quantization of the angular momentum of electrons combined into Cooper pairs. It will not be redundant to note that the fact of zero temperature of Cooper pairs regardless of the sample temperature means that there is no fundamental limit in the critical temperature of superconductors, as it is really observed after the discovery of high-temperature superconductors by Bednorz and Müller in 1986 (Bednorz and Müller, 1986).

---

[21] We are talking about the dc total current. Consideration of the ac current must include contribution of the unpaired electrons, which is significant at frequencies $\gtrsim 10^3$MHz.

Acknowledgments

The author is deeply grateful to Prof. Vladimir Kresin and Prof. Orest Simko for valuable comments after reading the manuscript. After the submission of this chapter, tragic news came: on July 28, Professor Kresin passed away. Vladimir Kresin was a brilliant physicist and real gentleman. This chapter is dedicated to his blessed memory.

References

Aharonov Y and Bohm D (1959) *Physical Review* 115: 485.
Bardeen J, Cooper LN, and Schrieffer JR (1957) *Physics Review* 108: 1175.
Bednorz JG and Müller KA (1986) *Zeitschrift für Physik B* 64: 189.
Cooper LN (1956) *Physics Review* 104: 1189.
Deaver BS Jr. and Fairbank WM (1961) *Physical Review Letters* 7: 43.
Ehrenberg W and Siday RE (1949) *Proceedings of the Physical Society B* 62: 8.
Essmann U and Träuble H (1967) *Physics Letters* 24A: 526.
Feynman RP (1955) *Progress in Low Temperature Physics*. vol. I, Amsterdam: Elsevier, 17.
Fröhlich H (1950) *Physics Review* 79: 845.
Ginzburg VL and Landau LD (1950) *Journal of Experimental and Theoretical Physics* 20(1064).
Gorter CJ and Casimir HBG (1934) *Physikalishce Zeitschrift* 35: 963.
Kamerlingh Onnes H (1911) *KNAW Proceedings* 13: 1274. 14: 113 (1911).
Keesom WH and Kok JA (1934) *Physica* I: 503.
Kikoin IK and Goobar SV (1938) *C. R. Academy of Sciences USSR* 19: 249. Journal of Physics USSR 3: 333 (1940); reprinted in “I. K. Kikoin - Physics and Fate”, Ed. S. S. Yakimov, p. 145, Nauka, Moscow, 2008.
Kozhevnikov V, Valente-Feliciano A-M, Curran PJ, Richter G, Volodin A, Suter A, Bending SJ, and Van Haesendonck C (2018) *Journal of Superconductivity and Novel Magnetism* 31: 3433.
Landau LD (1941) *Journal of Physics/Academy of Sciences of the USSR* 5: 71.
London F (1960) *Superfluids*. vol. I. N.Y: Dover.
Maxwell JC (1873) *A Treatise on Electricity and Magnetism*, 2nd edn. vol. II. Oxford: Clarendon Press.
Meissner WZ (1927) *Ges. Kältenindustr.* 34: 197.
Meissner W and Ochsenfeld R (1933) *Naturwissenschaften* 21: 787.
Poisson M (1824) *Memoire sur La Theorie Du Magnetisme*. Lu a l’Academie Royale des Sciences. 2 Fevrier.
Rjabinin GN and Shubnikow LW (1934) *Nature* 134: 286.

Further reading

Details of the micro-whirls model with necessary references to experimental and theoretical works, and a broader description of the superconducting properties are is available in
Kozhevnikov V (2021) Meissner effect: History of development and novel aspects. *Journal of Superconductivity and Novel Magnetism* 34: 1979–2009.

A perfect review of experimental and theoretical works up to 1952 is available in
Shoenberg D (1962) *Superconductivity*, 2nd. edn. Cambridge: University Press.

For fundamentals of electrodynamics we recommend (these textbooks complement but not replace one another)
Landau LD, Lifshitz EM, and Pitaevskii LP (1984) *Electrodynamics of Continuous Media*, 2nd edn. Oxford: Elsevier.
Purcell EM (1985) *Electricity and Magnetism*, 2nd edn. Boston: McGraw-Hill.
Griffiths DJ (2017) *Introduction to Electrodynamics*, 4th edn. Cambridge: University Press.
Tamm IE (1979) *Fundamentals of the Theory of Electricity*, 9th edn. Moscow: Mir (available online).

Thermodynamics of superconductors is discussed in
Kozhevnikov V (2019) *Thermodynamics of Magnetizing Materials and Superconductors*. Boca Raton: CRC Press.

Superconductivity: BCS theory

KH Bennemann, Physics Department, FU-Berlin, Berlin, Germany

© 2024 Elsevier Ltd. All rights reserved.

This is an update of K.H. Bennemann, Superconductivity: BCS Theory, Editor(s): Franco Bassani, Gerald L. Liedl, Peter Wyder, Encyclopedia of Condensed Matter Physics, Elsevier, 2005, Pages 72–81, ISBN 9780123694010, https://doi.org/10.1016/B0-12-369401-9/00701-4.

Introduction 657
BCS theory 660
Novel superconductors 665
Summary and outlook 665
Conclusion 668
Acknowledgments 669
References 669
Further reading 669

Abstract

Since the discovery by Kamerlingh Onnes in 1911 superconductivity has remained an important phenomenon in solid state physics with continuing discoveries. The explanation of the superconductivity phenomenon was given by the most elegant BCS theory of Bardeen, Cooper, and Schrieffer in 1957. The formation of Cooper pairs results from an effective attractive phonon-mediated interaction between two electrons with opposite spin near the Fermi surface. The BCS theory provided justification to the successful phenomenological Ginzburg–Landau theory from 1950. We discuss the BCS theory, Josephson tunneling of Cooper pairs between tunnel junctions, and the McMillan equation for the superconducting transition temperature and use this for its pressure dependence and for superconductivity in amorphous metals. We also discuss the Eliashberg theory treating electrons and phonons in superconductors on the same footing. Furthermore, we also discuss the high transition temperature (cuprate) superconductors for which the Cooper pair glue is still debated and for which the repulsive coupling yields an order parameter of d-symmetry. Interesting behavior of various superconducting nanostructures (e.g., system of quantum dots) is discussed. This is a corrected and extended version of the chapter (Bennemann, 2005).

Key points

- The BCS theory provided the most elegant microscopic explanation of the superconductivity phenomenon.
- Formation of Cooper pairs results from an effective attractive phonon-mediated interaction between two electrons with opposite spin near the Fermi surface.
- The BCS theory provided a justification to the successful phenomenological Ginzburg–Landau theory.
- Josephson tunneling of Cooper pairs between tunnel junctions is discussed.
- The McMillan equation for the superconducting transition temperature is used for description of its pressure dependence and for explaining superconductivity in amorphous metals.
- The Eliashberg theory treats electrons and phonons in superconductors on the same footing.
- In the high transition temperature (cuprate) superconductors, the Cooper pair glue is still debated and the repulsive coupling yields a d-symmetry of the order parameter.
- Behavior of various superconducting nanostructures (e.g., system of quantum dots) is discussed.

Introduction

For many years, superconductivity has remained one of the most interesting phenomena in physics. After its discovery by Kamerlingh Onnes in 1911, many superconductors have been found, see Fig. 1. The discovery of MgB_2 as a superconductor with a transition temperature $T_c = 39$ K suggests that further surprises can be expected in the future. The basic interdependence of superconductivity and lattice structure still needs to be understood. Fig. 2 shows the transition temperature of some interesting metals.

Some of the cornerstones in the history of superconductivity were the observation of (1) a vanishing electrical DC resistivity $\rho(T)$ at T_c, (2) the magnetic behavior exhibiting type-I superconductors expelling magnetic flux (Meissner–Ochsenfeld), and type-II superconductors where quantized magnetic flux can penetrate in filaments, (3) the isotope effect, $T_c \propto M^{-\alpha}$, for example, $\alpha \approx 0.5$ for Hg, suggesting that the electron–phonon coupling might be responsible for superconductivity, and (4) Josephson tunneling with an electronic current $j = j_0 + j_1 \sin[\Delta\phi - (2eV_{21}/\hbar)t]$, where $\Delta\phi$ is the phase difference and V_{21} the voltage between two superconductors 1 and 2. There are many additional interesting observations including the occurrence of a gap in the electronic density of states (DOS),

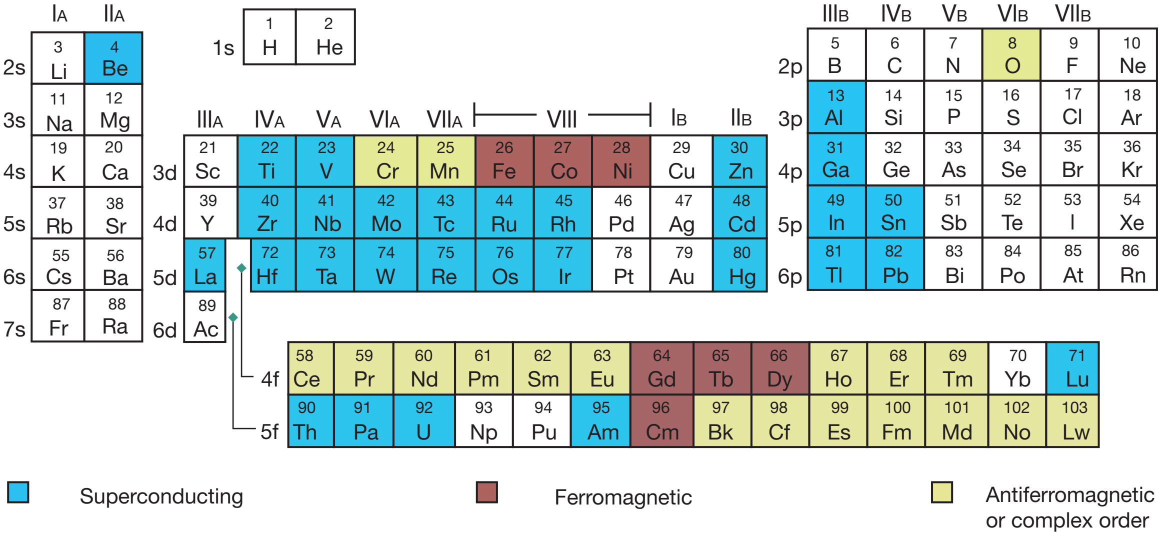

Fig. 1 The occurrence of superconductivity in the periodic table is illustrated. As the history of superconductivity shows, alloys and compounds of the elements play an important role. From Bennemann KH (2005) Superconductivity: BCS theory. In: Encyclopedia of Condensed Matter Physics, 1st edn., pp. 72–81. Amsterdam: Elsevier.

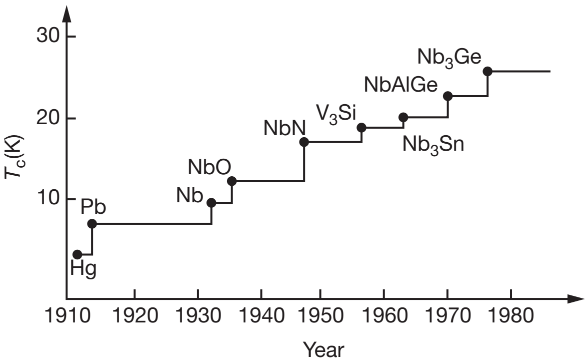

Fig. 2 History of the transition temperature T_c for the first 70 years following the discovery of superconductivity in 1911. The A-15 compounds were of particular interest in the search for higher T_c superconductors. From Bennemann KH (2005) Superconductivity: BCS theory. In: Encyclopedia of Condensed Matter Physics, 1st edn., pp. 72–81. Amsterdam: Elsevier.

gapless superconductors, and the interdependence of atomic structure and T_c, seen in particular in layered structures, and granular superconductors.

Most important theories developed for a physical understanding of the superconductivity phenomena were: (1) the London theory in 1935 explaining the Meissner–Ochsenfeld effect by using for the superconducting current driven by the vector potential the expression $\boldsymbol{j}_s = -(c/4\pi\Lambda_L^2)\boldsymbol{A}$, with the penetration depth, $\lambda_L = (mc^2/4\pi e^2 n_s)^{1/2}$, where n_s is the superfluid density (Abrikosov et al., 1963). (2) the Ginzburg–Landau theory in 1950, which extended the London theory by writing the free energy in terms of an order parameter $\psi(\boldsymbol{r}, t) = |\psi| e^{i\varphi(\boldsymbol{r})}$ as,

$$F = F_0 + \int d^3r \left\{ a|\psi|^2 + \frac{b}{2}|\psi|^4 + \frac{\hbar^2}{2m^*}\left|\left(\nabla - i\frac{e^*}{\hbar c}\boldsymbol{A}\right)\psi\right|^2 + \frac{h^2}{8\pi}\right\}, \tag{1}$$

yielding the current via minimization with respect to ψ (or ψ^*):

$$\boldsymbol{j} = -i\frac{\hbar e^*}{2m^*}(\psi^*\nabla\psi - \psi\nabla\psi^*) - \frac{e^{*2}}{m^*c}|\psi|^2\boldsymbol{A}. \tag{2}$$

In 1957, the Bardeen–Cooper–Schrieffer (BCS) theory (Bardeen et al., 1957) [see also Parks (1969) and Schrieffer (1964)] derived superconductivity from an electronic Hamiltonian $H = H_0 + H_{\mathrm{eph}}$, where H_{eph} describes the electron–phonon interaction. It is to be noted that Eq. (2) immediately yields the Meissner effect, by assuming that the superconducting wave function is rigid and is not affected by an electromagnetic field (thus, the first term in Eq. (2) is zero), and for $\psi = |\psi| e^{i\phi(\mathrm{r})}$ ($\psi\psi* \sim n_s$ and ϕ are conjugate variables). The Josephson tunnel current between two superconductors 1 and 2 (with phase and voltage difference $\Delta\phi$, ΔV) is given by

$$j_J = j_0 \sin\left(\Delta\phi - \frac{e^*}{\hbar}\Delta V t\right) \tag{3}$$

Here,

$$\begin{aligned} \Delta\phi &= \varphi_1 - \varphi_2 + \frac{2\pi}{\phi_0}\int_1^2 \boldsymbol{dl}\cdot\boldsymbol{A} \\ j_0 &= \frac{e^*\hbar}{m^* d}|\psi|^2, \qquad (m^* = 2m, \quad e^* = 2e) \end{aligned}$$

and d is a parameter referring to the tunnel junction, $\phi_0 = hc/2e$. Assuming the single-valuedness of ψ, one obtains the quantization of flux trapped (in a filament) in a superconductor (see gauge transformation ψ):

$$\phi = n\phi_0, \qquad n = 0, \pm 1, \ldots \tag{4}$$

These are remarkable general results that hold for different possible mechanisms causing condensation of a Fermi liquid into a superconducting state.

The BCS theory is one of the most elegant theories in physics; it effectively explains superconductivity resulting from Cooper pairs ($\boldsymbol{k}\uparrow$, $-\boldsymbol{k}\downarrow$) for electrons with opposite spin and momentum $\boldsymbol{k}$ at the Fermi surface. As illustrated in Fig. 3, the exchange of virtual phonons yields an attractive interaction and thus a singlet Cooper pairing. This pairing causes a gap in the single-electron DOS, reflecting the binding energy of the Cooper pairs, $\Delta = \Delta(T, h, \ldots)$. The theory correctly predicts the behavior and some other thermodynamical and electrodynamical quantities.

Following the BCS theory, the quantum field theory using the Green's function method, in particular by Gor'kov et al., gave the theory of superconductivity a very elegant form. In general, for phase transitions (ferromagnetism, etc.), the superconducting state cannot be obtained from the normal state by using the perturbation theory. That the electron–phonon interaction described in second-quantization notation by

$$H_{\mathrm{eph}} = \sum_{\boldsymbol{k},\boldsymbol{k}',\lambda} g_{\boldsymbol{k}\boldsymbol{k}'\lambda} c^+_{\boldsymbol{k}'} c_{\boldsymbol{k}} \left(d_\lambda(\boldsymbol{q}) + d^+_\lambda(-\boldsymbol{q})\right) + \cdots \tag{5}$$

is responsible for superconductivity was suggested earlier by Fröhlich and others and explains, for example, the isotope effect. Here $c_{\boldsymbol{k}}$ and $c^+_{\boldsymbol{k}}$ represent the electron annihilation and creation operators, while $d_\lambda(\boldsymbol{q})$ and $d^+_\lambda(\boldsymbol{q})$ are the corresponding annihilation and creation operators for phonons of momenta $\boldsymbol{q} = \boldsymbol{k}' - \boldsymbol{k}$. The electron–phonon coupling constant is given by

$$g_{\boldsymbol{k}\boldsymbol{k}'\lambda} = \sum_{i,\alpha}\left(\frac{\hbar N_\alpha}{2\omega_{\boldsymbol{q}\lambda} M_\alpha}\right)\langle \boldsymbol{k}'|\nabla_i U_{i\alpha}|\boldsymbol{k}\rangle \mathcal{E}_\lambda(\alpha) e^{i\boldsymbol{q}\cdot\boldsymbol{\rho}^0_\alpha} \tag{6}$$

where $U_{i\alpha}$ is the potential of the ion i, α and $\mathcal{E}_{q\lambda}$ are the lattice polarization vectors. Since, as illustrated in Fig. 3, emission and absorption of phonons by electrons at the Fermi surface can lead to an effective attractive interaction, it seemed possible that Cooper pairing ($\boldsymbol{k}\uparrow$, $-\boldsymbol{k}\downarrow$) occurs for electrons within an energy shell of $2\omega_D$, where ω_D is the Debye frequency. On general grounds, one expects, for an attractive potential with a range of the order of the interatomic distance ($a \sim p_F^{-1}$), due to the Pauli principle, singlet pairing and pairing of $\boldsymbol{k}$ and $-\boldsymbol{k}$ electrons to avoid kinetic energy of the Cooper pairs and thus to obtain maximal condensation energy. To avoid the destructive repulsive electron–electron interaction, the pairing results from a retarded potential.

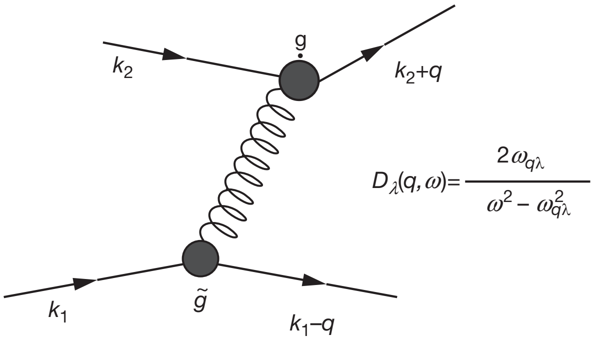
g
k_2
k_2+q
$D_\lambda(q,\omega) = \frac{2\omega_{q\lambda}}{\omega^2 - \omega^2_{q\lambda}}$
$\tilde{g}$
k_1
k_1-q

Fig. 3 Illustration of the interaction between electrons with k_1 and k_2 via exchange of a phonon with polarization λ, wave vector $\boldsymbol{q}$ and energy $\omega_{\boldsymbol{q}\lambda}$; $\omega_{\boldsymbol{q}\lambda} \simeq \varepsilon_{\boldsymbol{k}_1-\boldsymbol{q}} - \varepsilon_{\boldsymbol{k}_1}$; then an attractive effective electron–electron interaction $g^2 D < 0$ results, if $\omega < \omega_{\boldsymbol{q}\lambda}$, $\widetilde{g} = g\Gamma$, where Γ denotes many-body corrections to the electron–phonon coupling. From Bennemann KH (2005) Superconductivity: BCS theory. In: Encyclopedia of Condensed Matter Physics, 1st edn., pp. 72–81. Amsterdam: Elsevier.

The electron $\boldsymbol{k}\uparrow$ polarizes the lattice for a time of the order of $t \sim \omega_D^{-1}$, which is slower than the electron motion, and then the other electron $-\boldsymbol{k}\downarrow$, arriving at the polarized lattice within that time might feel an effective attractive electron–electron interaction due to over-screening. The resultant binding energy 2Δ causes a correlation and coherence length of the order of $\xi \sim v_F/2\Delta$. It is to be noted that Coulomb fields are screened at a distance of the order of the interatomic distance. This analysis and the study by Cooper, showing that for electrons at the Fermi surface the pair wave function $\psi = \sum_{k\sim k_F} a_k e^{i\boldsymbol{k}\cdot\boldsymbol{\rho}}$, $\boldsymbol{\rho} = \boldsymbol{r}_1 - \boldsymbol{r}_2$ lowers the energy $((H_0 + V)\psi = E\psi$ and $V < 0)$, gave a more definite clue that the Cooper pairing of the electrons within an energy shell of the order of $2\hbar\omega_D$ causes superconductivity.

Cooper pairing is the essence of the electronic BCS theory, also for the novel superconductivity of the cuprates like YBCO and HgBCCO, which gives the microscopic justification of the phenomenological Ginzburg–Landau theory. Its formulation was achieved with the help of quantum field-theoretical methods (Tinkham, 1975).

BCS theory

The BCS theory begins by using the Hamiltonian

$$H = \sum_{k,\sigma} \xi_k n_{k\sigma} + \sum_{k,k'} V_{kk'} a^+_{k\uparrow} a^+_{-k\downarrow} a_{-k'\downarrow} a_{k'\uparrow} \tag{7}$$

with excitation energies $\xi_{\boldsymbol{k}} = \varepsilon_{\boldsymbol{k}} - \mu$ for electrons near the Fermi energy (μ is the chemical potential) and the effective interaction $V_{\boldsymbol{kk'}}$ between electrons with wave vectors $\boldsymbol{k}$ and $-\boldsymbol{k}$, and spin ↑ and ↓. Note that the remaining interactions between the electrons are assumed to be included in the energies $\xi_{\boldsymbol{k}}$. $a^+_{\boldsymbol{k}\sigma}$ and $a_{\boldsymbol{k}\sigma}$ are the usual creation and annihilation operators for fermions with momentum $\boldsymbol{k}$ and spin σ, and $n_{\boldsymbol{k}\sigma}$ is the particle number occupation operator. The BCS theory uses the wave function,

$$\begin{aligned} |\psi\rangle &= \prod_{k} (u_k + v_k a^+_{k\uparrow} a^+_{-k\downarrow}) |\psi_0\rangle, \\ |u_k|^2 &+ |v_k|^2 = 1, \end{aligned} \tag{8}$$

to calculate the free energy. The ground state is $|\psi_0\rangle$. $|v_{\boldsymbol{k}}|^2$ gives the probability of a pair $(\boldsymbol{k}\uparrow, -\boldsymbol{k}\downarrow)$. The diagonalization of H is most elegantly achieved by the Bogoliubov and Valatin canonical transformations

$$\begin{gathered} b_{-k+} = u_k a_{-k\downarrow} + v_k a^+_{k\uparrow}, \qquad b_{k-} = u_k a_{k\uparrow} - v_k a^+_{-k\downarrow}, \\ u_k^2 + v_k^2 = 1, \end{gathered} \tag{9}$$

which introduce new fermion operators $b_{\boldsymbol{k}\sigma}$ and $b^+_{\boldsymbol{k}\sigma}$. Due to isotropy, the coefficients $u_{\boldsymbol{k}}$ and $v_{\boldsymbol{k}}$ depend only on k and can be chosen to be real and such that, for a given entropy, the electronic energy E is minimal. Then one gets straightforwardly (with $V_{\boldsymbol{kk'}} = -g/V$),

$$E = \sum_{k} \xi_k \left[2v_k^2 + \left(u_k^2 - v_k^2\right) \sum_{\sigma=\pm} N_{k\sigma} \right] - \frac{g}{V} \left[\sum_{k} u_k v_k \left(1 - \sum_{\sigma=\pm} N_{k\sigma} \right) \right]^2, \tag{10}$$

where $N_{\boldsymbol{k}\sigma} = b^+_{\boldsymbol{k}\sigma} b_{\boldsymbol{k}\sigma}$ and, from $\partial E/\partial u_{\boldsymbol{k}}$, the result,

$$2\xi_k u_k v_k = \Delta_k \left(u_k^2 - v_k^2\right). \tag{11}$$

Here, using $u_{\boldsymbol{k}}^2 + v_{\boldsymbol{k}}^2 = 1$ and Eq. (9), the order parameter $(\Delta_{\boldsymbol{k}} \propto \langle a_{-\boldsymbol{k}\downarrow} a_{\boldsymbol{k}\uparrow} \rangle)$,

$$\Delta_k = \frac{g}{V} \sum_{k} u_k v_k \left(1 - \sum_{\sigma=\pm} N_{k\sigma} \right) \tag{12}$$

has been introduced. The order parameter can be expressed as

$$\begin{aligned} \Delta_k &= \frac{g}{V} \sum_{k'} \frac{\Delta_{k'}}{2\mathcal{E}_{k'}} \tanh\left(\frac{\mathcal{E}_{k'}}{2k_B T} \right) \\ \mathcal{E}_k &= \sqrt{\xi_k^2 + \Delta_k^2}. \end{aligned} \tag{13}$$

It is of interest to note that Eq. (13) has solutions not only for attractive interaction (with $g > 0$) but possibly also for repulsive ones with $g < 0$. Then the $\boldsymbol{k}$-dependence of $\Delta_{\boldsymbol{k}}$ is important.

The new quasiparticle energies are $\mathcal{E}_{\boldsymbol{k}} = (dE/dN_{\boldsymbol{k}})_{u_k,v_k} = \sqrt{\xi_{\boldsymbol{k}}^2 + \Delta_{\boldsymbol{k}}^2}$. Their distribution function is $N_{\boldsymbol{k}} = \left(e^{\mathcal{E}_k/k_B T} + 1\right)^{-1}$. These quasiparticles contribute to the energy the term $\sum_{\boldsymbol{k},\sigma} \mathcal{E}_{\boldsymbol{k}} N_{\boldsymbol{k}\sigma}$. It is to be noted that $2\Delta_{\boldsymbol{k}}$ is the binding energy of the correlated electrons. Thus, the coherence length $\xi = \hbar v_F/2\Delta$ yields the correlation distance, for most conventional superconductors, a much larger value than the interatomic distance $\hbar/p_F$.

Note that for an isotopic gap $\Delta_{\boldsymbol{k}} = \Delta$ one gets

$$1 = \frac{g}{V}\sum_{\boldsymbol{k}} \frac{1}{2\sqrt{\xi_{\boldsymbol{k}}^2 + \Delta^2}} \tanh\left(\frac{\sqrt{\xi_{\boldsymbol{k}}^2 + \Delta^2}}{2k_BT}\right). \tag{14}$$

and from this, for $\Delta(T)$, the expression

$$\Delta(T) = 3.2k_BT_c\left(1 - \frac{T}{T_c}\right)^{1/2}. \tag{15}$$

The superconducting transition temperature T_c follows from $\Delta(T_c)$. Thus, $\left(\sum_{\boldsymbol{k}} \to \int_{-\omega_D}^{\omega_D} d\varepsilon\right)$,

$$\begin{aligned} T_c &\simeq 1.14\hbar\omega_D e^{-1/(N(0)g)} \propto M^{-1} \\ \frac{2\Delta(0)}{k_BT_c} &= 3.52. \end{aligned} \tag{16}$$

As shown by McMillan (1968), Bennemann and Garland (1972), and others, Eq. (16) needs to be improved to calculate realistic T_c values for simple metals, transition metals, A-15 compounds, alloys, etc., and to understand the interdependence of superconductivity and atomic structure better. Taking into account more details of the electron–phonon coupling, the phonon spectrum, the retardation of the pairing potential, and the remaining repulsive electron–electron interaction ($\propto \mu*$, pseudo-Coulomb potential), one gets the McMillan equation (McMillan, 1968):

$$\begin{aligned} T_c &\simeq \frac{\omega_D}{1.45}\exp\left[-\frac{1.04(1+\lambda)}{\lambda - \mu^*(1+0.62\lambda)}\right] \\ \lambda &= 2\int_0^\infty d\omega \frac{\alpha^2(\omega)F(\omega)}{\omega}. \end{aligned} \tag{17}$$

Here, the effective coupling constant λ depends on the DOS, $N(0)$. First, $\lambda \propto N(0)$, then λ saturates and decreases again as $N(0)$ increases such as in transition metals. Note that $\lambda = (m^*/m) - 1$. Typically $\mu^* \approx 0.1$, but μ^* may also change strongly near magnetic instabilities.

The DOS for the quasiparticles is given by

$$N_s(\varepsilon) = N_n(\varepsilon)\frac{\varepsilon}{\sqrt{\varepsilon^2 - \Delta^2}}. \tag{18}$$

This follows from the one-to-one correspondence of old and new quasiparticles, $N_s(\varepsilon)d\varepsilon = N_n(\xi)d\xi$. For the thermodynamic potential Ω, which is the appropriate function for a system with given μ, all thermodynamic properties can be calculated using the formulas,

$$\begin{aligned} \left.\frac{\partial\Omega}{\partial g}\right|_{T,V,\mu} &= -V\frac{\Delta^2}{g^2} \\ \Omega_s - \Omega_n &= \int_0^\Delta d\Delta'\Delta'^2\frac{d(1/g)}{d\Delta'} \end{aligned} \tag{19}$$

This gives, in particular at T_c, the specific heat (Fig. 4),

$$c_s - c_n \simeq \frac{4mp_F}{7\zeta(3)\hbar^3}T_c, \qquad c_s(T) \propto e^{-\Delta_0/k_BT}, \tag{20}$$

where $\zeta(x)$ is the Riemann–Zeta function, $V = 1$. To obtain the behavior in electromagnetic fields, one uses the recipe $\boldsymbol{p} \to \boldsymbol{p} - (e/c)\boldsymbol{A}$, $\boldsymbol{p} \to -i\hbar\nabla$, where $\boldsymbol{A}$ denotes the vector potential ($\boldsymbol{A} = \sum_{\boldsymbol{q}} a_{\boldsymbol{q}} e^{i\boldsymbol{q}\cdot\boldsymbol{r}}$). This yields the coupling,

$$\begin{aligned} H_{\text{int}} &= i\frac{e\hbar}{2mc}\sum_{\boldsymbol{k}}(\boldsymbol{v_k}\cdot\boldsymbol{A} + \boldsymbol{A}\cdot\boldsymbol{v_k}) \\ &= -\frac{e\hbar}{mc}\sum_{\boldsymbol{k},\boldsymbol{q}}\boldsymbol{k}\cdot\boldsymbol{a_q}c^+_{\boldsymbol{k}+\boldsymbol{q},\sigma}c_{\boldsymbol{k}\sigma}. \end{aligned} \tag{21}$$

Here, the spin is unchanged since $\boldsymbol{A}$ couples dominantly to the orbital motion of pairing electrons. (Note that $\boldsymbol{q} \cdot \boldsymbol{a} = 0$ for tranversal fields.) Thus, one obtains, as in the Ginzburg–Landau theory for the electric current due to $\boldsymbol{A}$ ($\boldsymbol{j} = en\boldsymbol{v}$) for Cooper pairs ($m \to 2m$, $e \to 2e$),

$$\boldsymbol{j} = -\frac{ne^2}{mc}\boldsymbol{A} + \boldsymbol{j}_2, \tag{22}$$

where the paramagnetic current is $\boldsymbol{j}_2 = e\hbar/m\sum_{\boldsymbol{k},\boldsymbol{q}}\boldsymbol{k}a^+_{\boldsymbol{k}-\boldsymbol{q}}a_{\boldsymbol{k}}$, which would vanish if the superconducting wave function ψ is rigid, that is, not affected by $\boldsymbol{A}$.

It is to be noted that, since n_s is the density of Cooper pairs, the first term gives the famous London equation

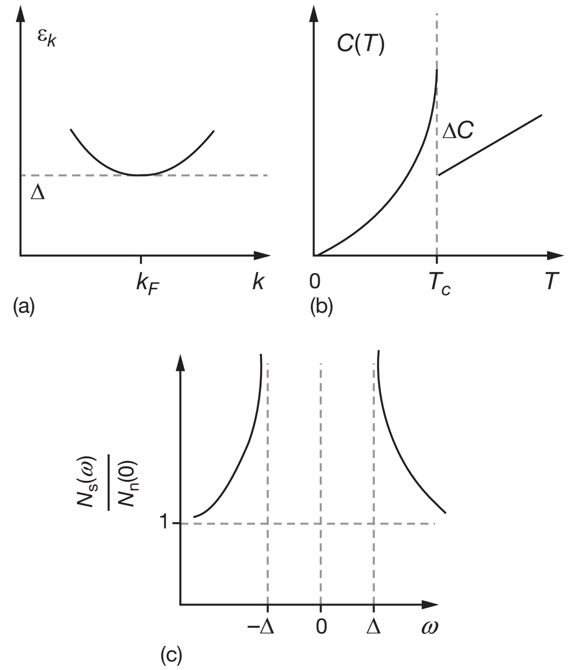

Fig. 4 Illustration of (A) the gap Δ in the elementary excitation spectrum, (B) the jump $(C_s/C_n)T_c = 2.43$ in the specific heat, and (C) the electronic DOS. From Bennemann KH (2005) Superconductivity: BCS theory. In: Encyclopedia of Condensed Matter Physics, 1st edn., pp. 72–81. Amsterdam: Elsevier.

$$\begin{aligned} \boldsymbol{j}_1 &= -\frac{n_s e^2}{mc}\boldsymbol{A} = -\frac{c}{4\pi\lambda^2}\boldsymbol{A} \\ \lambda^2 &= \frac{mc^2}{4\pi e^2 n_s}. \end{aligned} \tag{23}$$

Hence, by determining the penetration depth λ of an external magnetic field $\boldsymbol{h}$ into a superconductor, one may calculate the superfluid density n_s, an important quantity reflecting whether all electrons at the Fermi surface pair. Evidently, if $\xi > \lambda$, Eq. (22) gives the Meissner effect. Using the response theory,

$$\boldsymbol{j}_q = -\frac{c}{4\pi}K_q \boldsymbol{a}_q, \tag{24}$$

where $K_q = \lambda^{-2}(1 + \lambda^2 K'_q)$ and K'_q is calculated within the BCS theory.

The two characteristic length scales ξ and λ suggest that there exist two types of superconductors characterized by $\kappa = \lambda/\xi$. As shown by Abrikosov, they correspond to types I ($\kappa < 1/\sqrt{2}$) and II ($\kappa > 1/\sqrt{2}$). Superconductors of type I repel an external magnetic field, which however may penetrate via an array of quantized flux filaments into type-II ones. For these, one expects vortex lines with $\Delta \simeq 0$ around them. The superconductor compromises both effects in order to profit from the Cooper-pair condensation energy and the magnetic field energy. It is to be noted that the formation of a vortex costs an energy of the order $(\xi h^2/8\pi)$ due to a variation of $\Delta(\boldsymbol{r})$ or the wave function ψ, and reduces the (diamagnetic) field energy by about $(\lambda h^2/8\pi)$. Fig. 5 characterizes the behavior of superconductors in an external magnetic field. From the general formula for the free energy,

$$F_s = F_n - \frac{h^2}{8\pi}, \tag{25}$$

assuming no field penetration into the superconductor, one gets a critical magnetic field, H_{c1} below which a pure Meissner superconductor is present. Above H_{c1}, the magnetic flux ϕ may penetrate until $H_{c1} = \phi/\pi\xi^2$ (ϕ = flux of area $\pi\xi^2$). As already noted, the flux ϕ is quantized due to the macroscopic phase of the superconductor as a whole. Note that for fields h such that $H_{c1} < h < H_{c2}$ one gets a mixed state, with $H_{c2} = \sqrt{2}\kappa H_{c1}$. Surfaces may favor Cooper-pair condensation. Then there exists another critical field H_{c3} above which superconductivity at the surface is destroyed ($H_{c3} \simeq 1.7H_{c2}$).

Obviously, strong magnetic fields may also affect Cooper pairing by destroying the singlet state. This is of relevance for the interdependence of superconductivity and magnetism in antiferromagnets or ferromagnets. As a result of internal molecular fields acting on the electron spins, one may get a spatially inhomogeneous superconducting state, $\Delta = \Delta(\boldsymbol{k}, \boldsymbol{r})$, and then again a compromise to profit from both Cooper pairing energy and magnetic energy.

The spin–orbit coupling and scattering by local spins (paramagnetic impurities) also affect the singlet pairing. Scattering by paramagnetic impurities with spins via exchange coupling (J), $H_{\text{ex}} = -J\sum_i \boldsymbol{S}_i \cdot \boldsymbol{\sigma}$, will, of course, weaken the singlet Cooper pairing. The interesting analysis by Abrikosov and Gor'kov yields

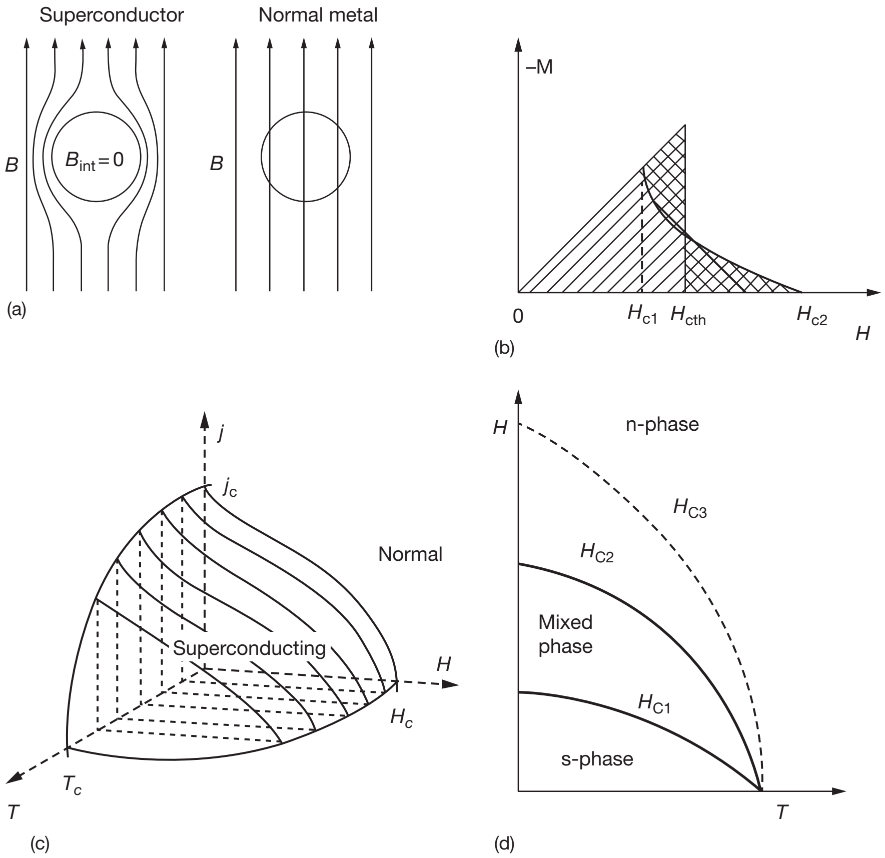

Fig. 5 (A) Meissner effect for type-I superconductors where, below the superconducting transition temperature T_c, the magnetic flux B is abruptly expelled; (B) Typical behavior of type-II superconductors, where, below B_{c2}, the flux penetrates, and perfect Meissner effect behavior occurs below B_{c1}; (C) dependence of type-I superconductor on B and j and (D) temperature dependence of critical magnetic fields. At H_{c3}, surface superconductivity disappears, $B = H + 4\pi M$. From Bennemann KH (2005) Superconductivity: BCS theory. In: Encyclopedia of Condensed Matter Physics, 1st edn., pp. 72–81. Amsterdam: Elsevier.

$$\ln\left(\frac{T_c}{T_{c0}}\right) = \psi\left(\frac{1}{2}\right) - \psi\left(\frac{1}{2} + \frac{\hbar}{4\pi\tau}\frac{1}{T_c}\right), \tag{26}$$

where τ is spin scattering time and $\psi(x) = \Gamma'(x)/\Gamma(x)$ is the digamma function. The discovery of gapless elementary excitations was unexpected. The effects on the singlet superconducting state due to spin-mixing via spin–orbit coupling and spin-flip scattering via exchange interaction are observed through the temperature dependence of the Knight shift $K(T)$, for example, and cause $K > 0$ for $T \to 0$. Clearly, the spin splitting of the Fermi surface for spin $\uparrow$ and $\downarrow$ electrons also weakens pairing of $\boldsymbol{k}$ and $-\boldsymbol{k}$ electrons.

For a better understanding of the phonon and electron dynamics due to H_{eph}, one can use the Hamiltonian $H = H_0 + H_{\mathrm{eph}} + H_{\mathrm{el}}$, where H_0 refers to phonons and electrons in the absence of H_{eph}, and H_{el} to the electron–electron interactions. The dynamic field operators ψ, ψ^+, and φ (in this context φ represents the phonon field, which is $\propto d + d^+$ introduced earlier) are treated on the same level. This yields renormalizations of both phonon and electron excitations. The physical situation is illustrated in Fig. 6. Then one obtains a frequency-dependent complex superconducting order parameter $\Delta(\omega)$ and, for the DOS (see Fig. 7),

$$N_T(\omega) \sim \mathrm{Re}\frac{\omega}{\sqrt{\omega^2 - \Delta^2(\omega)}}. \tag{27}$$

Using matrix Green's functions, the Nambu notation $\psi_{\boldsymbol{k}}^+ = \left(c_{\boldsymbol{k}\uparrow}^+ \;\; c_{-\boldsymbol{k}\downarrow}\right)$, and Matsubara frequencies, one gets for $\mathcal{G}_{\boldsymbol{k}}(\tau) = -\langle T_\tau \psi_{\boldsymbol{k}}(\tau)\psi_{\boldsymbol{k}}^+(0)\rangle$, and similarly for $\mathcal{D}(\boldsymbol{q},\tau)$, the Dyson equations shown in Fig. 6 where

$$\mathcal{G} = \begin{pmatrix} G & F \\ F^+ & \tilde{G} \end{pmatrix}, \qquad \mathcal{G}_0 = \begin{pmatrix} G_0 & 0 \\ 0 & \tilde{G}_0 \end{pmatrix}, \qquad \mathcal{G}_0 = \begin{pmatrix} D & 0 \\ 0 & \tilde{D} \end{pmatrix}$$

One gets (for $D = (i\omega_n Z)^2 - (\varepsilon_{\boldsymbol{k}} + \xi)^2 - \phi^2$, $\omega_n = (2n+1)\pi T$)

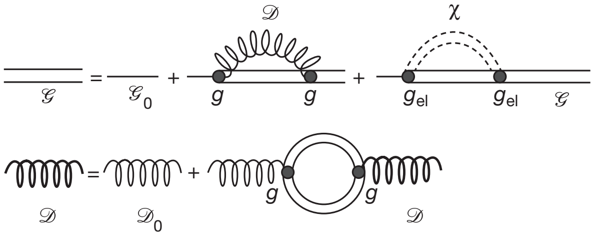

Fig. 6 Illustration of the dynamics of the coupled electron and phonon systems using Feynman diagrams and thermodynamic matrix Green's functions G, D (Eliashberg-type theory (McMillan, 1968)). The graph(===)refers to an additional electron–electron interaction and also to spin excitations (and impurity scattering) (g = eph., g_{el} = el–el.). From Bennemann KH (2005) Superconductivity: BCS theory. In: Encyclopedia of Condensed Matter Physics, 1st edn., pp. 72–81. Amsterdam: Elsevier.

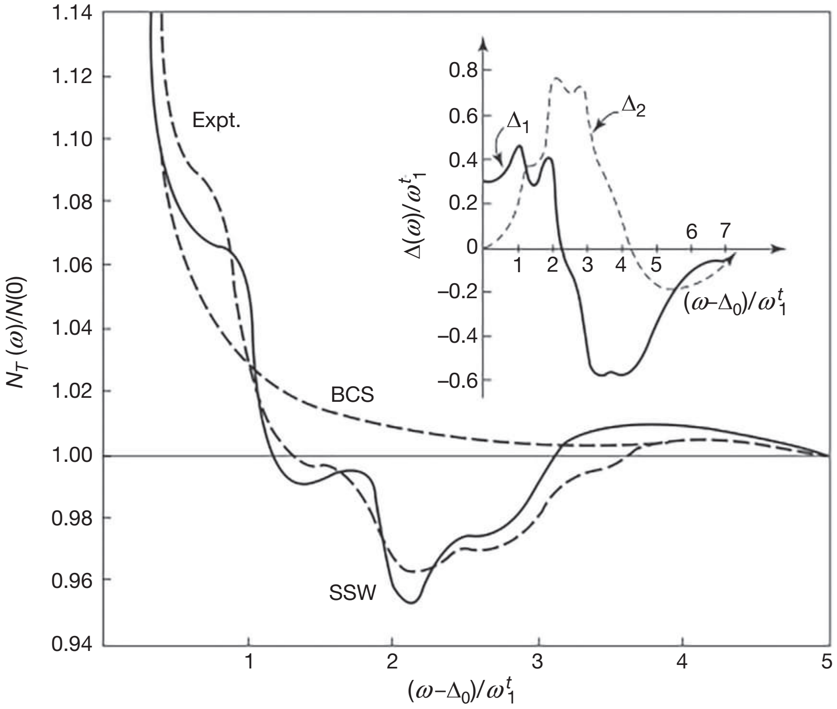

Fig. 7 Tunneling DOS with structure due to electron–phonon interaction. Also $\Delta(\omega) = \Delta_1 + i\Delta_2$ is given (ω^t: phonon frequency). From Bennemann KH (2005) Superconductivity: BCS theory. In: Encyclopedia of Condensed Matter Physics, 1st edn., pp. 72–81. Amsterdam: Elsevier.

$$G(\boldsymbol{k}, i\omega_n) = \frac{i\omega_n + \varepsilon_{\boldsymbol{k}} + \xi}{D}, \qquad F(\boldsymbol{k}, i\omega_n) = \frac{\phi(\boldsymbol{k}, i\omega_n)}{D}, \tag{28}$$

for the electron (G) and Cooper pair Green's function (F), respectively. Note that $D = 0$ yields the elementary excitations and $\Delta = \phi/Z$ the order parameter with $Z \simeq 1$. After continuation to the real axis, one obtains

$$\Delta(\omega) = \frac{N(0)}{Z(\omega)} \int_{\Delta_0}^{\omega_c} d\omega' \mathrm{Re} \frac{\Delta(\omega')}{\sqrt{\omega'^2 - \Delta^2}}, \tag{29}$$

with $U_c = V_c/(1/N(0)V_c \ln(\omega_m/\omega_0)$ due to electron–electron interactions, ($\omega_m \sim \varepsilon_F$, ω_0—cutoff parameter) and (from phonon spectrum $B_\alpha(q, z)$),

$$\begin{aligned} K_{\text{ph}} = \sum_\alpha \int_0^{2k_F} \frac{dgq}{2k_F^2} \int_0^\infty dz B_\alpha(q, z) |g_{q\alpha}|^2 \\ \times \left(\frac{1}{\omega' + \omega + z - i\delta} + \frac{1}{\omega' - \omega + z - i\delta} \right). \end{aligned} \tag{30}$$

These equations are the essence of the Eliashberg-type theory (McMillan, 1968) and produce, for a simplified phonon spectrum, the results obtained by Scalapino, Schrieffer, and Wilkins (SSW) (Scalapino et al., 1966)) shown in Fig. 7. This analysis is of utmost significance since it shows definitely that for BCS-type superconductors the electron–phonon coupling causes Cooper pairing. Note that phase-coherent Cooper pairs occur at T_c. The phonon frequencies are

$$\omega_q^2 \simeq \left(\omega_q^0\right)^2 + 2\omega_q^0 \frac{|g_q|^2}{V_c(q)} \left[\frac{1}{\varepsilon(q, \omega)} - 1\right], \tag{31}$$

where $\varepsilon(q, \omega)$ is the dielectric function. Presumably, the Dyson equation illustrated in Fig. 6 also applies if $\mathcal{D}$ is replaced by the Green's function of spin excitations, the dynamical spin susceptibility $\chi(q, \omega)$, or of other modes that possibly cause Cooper pairing. Fig. 6 describes not only singlet but also triplet Cooper pairing such as in He^3, and also suppression of Cooper pairing due to magnetic interactions; see "Further reading" section. Superconductivity in different materials, for example, isotropic lattices, layered lattice structures, nanostructures, and amorphous metals can be described adequately by taking into account details of the coupling constant $g_{kk'\lambda}$ and its renormalization due to vertex corrections (Ward identities) (Table 1).

Novel superconductors

The essence of novel superconductivity in cuprates like LBCO, YBCO, and HgBCCO is the presence of singlet Cooper pairs with d-wave symmetry. Such a symmetry is expected for repulsive coupling g, see the discussion by Manske et al. (2000), as implied by the experimental results for the high superconducting transition temperatures ranging from 100 to 130 K and higher. Manske et al. (2000) have discussed in detail the phase diagram for the high transition temperature cuprates assuming spin fluctuation induced Cooper pairing and including their phase fluctuations expected for underdoped cuprates. Also for positive interaction g, it is argued how the gap equation provides a solution of the d-wave symmetry (Bennemann and Ketterson, 2003, 2014).

Summary and outlook

Both BCS theory and its extension, including dynamical effects yielding the Abrikosov–Gor'kov and Eliashberg theory, explain superconductivity resulting from electron–phonon coupling. It still remains a challenge to calculate T_c from first principles and its dependence on atomic structure, lattice instabilities, and magnetic activity. The results shown in Table 1 were obtained by Garland et al. (1968) using the McMillan equation and assuming phonon softening. A very good agreement with experiment by Buckel and Hilsch (1954) was achieved.

Changes in the atomic structure affect the phonon spectrum and the coupling constant $g_{q\lambda}$ and T_c, Δ, etc., as observed for disordered and amorphous metals. In transition metals and alloys thereof with large $N(0)$, one may attempt to relate T_c to the cohesive energy, since $g \sim \langle \nabla t_{ij} \rangle \sim t$, where t_{ij} is the hopping integral for electrons (see also studies by Labbé et al. (1967)). For a study of pressure-induced superconductivity in narrow band metals (Bennemann and Garland, 1972) both changes in the phonon spectrum and coupling constant g may be important. Similarly, for transition metal alloys A_xB_{1-x}, the different bonds (AA, AB, and BB) may play a role in determining $\Delta(x)$ and $T_c(x)$. For this, the BCS theory has been extended by Bennemann and coworkers (see Kerker and Bennemann, 1974), using the coherent-potential approximation. In case of strong anisotropy of the lattice structure as in layered structures, one may expect approximately two coupling constants g_i ($g_i \sim \nabla t_i \cdot e$), different critical fields H_{c2}^{a-b} and H_{c2}^{c}, and two gaps ($i \simeq \pi$, σ, $a - b$ in plane, $c \perp a - b$)

$$\Delta_i Z_i \simeq \pi T \sum_{l,m} \frac{\lambda_{il} - \mu_{il}^*}{\sqrt{\omega_m^2 + \Delta_l^2(m)}} \Delta_l(m). \tag{32}$$

Fig. 8 shows the results for MgB_2. Note that hybridization of π and σ electrons gives a common T_c.

The interplay of magnetism and superconductivity suggested already by the occurrence of superconductivity in the periodic table is, for several reasons, of utmost interest. This has, for example, been studied for (film) structures $N_1 \, |N_2 \mid N_3$. Results are given in Fig. 9.

Organic superconductors display, in particular, interesting dimensional structural effects and those due to charge-wave and magnetic instabilities. Also, astonishingly, superconductivity may be induced by strong magnetic fields. In Fig. 10, the interesting phase diagram of κ-$(BEDT\text{-}TTF)_2$-$Cu[N(CN)_2]Br$, a typical composition of a charge-transfer salt, is shown. Such molecules are stacked into layers. Planes of $Cu[N(CN)_2]Br$ anions separate these layers. Within these layers, the molecules form dimers and

Table 1 Estimates of the superconducting transition temperature T_c in disordered and amorphous metals.

Material	$(T_c/T_{c0})_{expt.}$	$(T_c/T_{c0})_{calc.}$
Al	~ 5	4.9
Pb	~0	0
Ga	~ 8	8
Sn	~ 1.3	2
In	~ 1.3	1.2

Courtesy of W. Buckel et al.

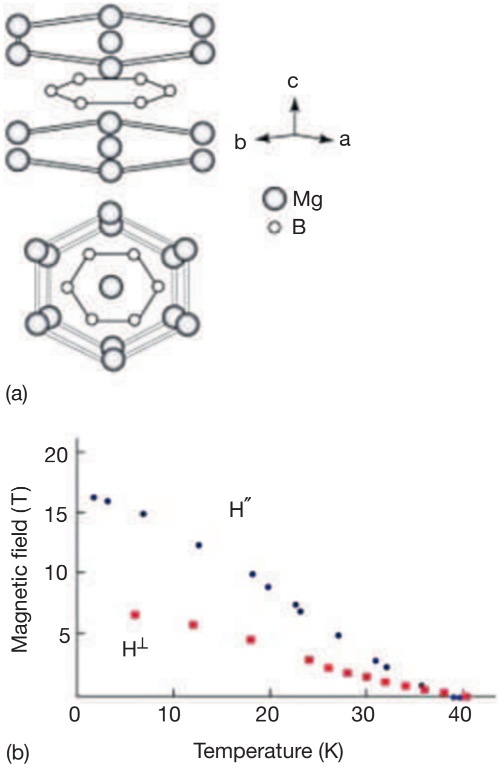

Fig. 8 (A) Structure of MgB_2 (AlB_2, etc.). The boron planes seem to play an important role regarding superconductivity and Cooper pairing. The Mg–B bonds are softer than the B–B ones. (B) Critical upper magnetic fields $H_{c2}^{\parallel}$ and $H_{c2}^{\perp}$ referring to the B-planes and direction perpendicular to it, respectively. The anisotropic behavior of $H_{c2}(T)$ suggests two-gap behavior. From Bennemann KH (2005) Superconductivity: BCS theory. In: Encyclopedia of Condensed Matter Physics, pp. 72–81. first ed., Amsterdam: Elsevier.

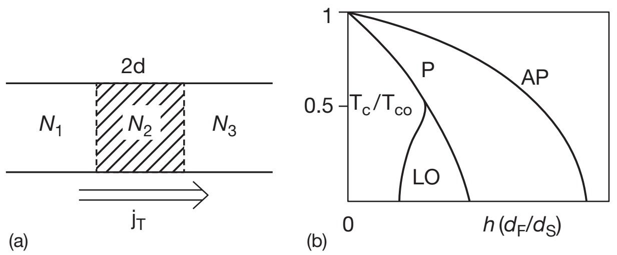

Fig. 9 (A) Illustration of a tunnel junction $N_1/N_2/N_3$, where N_i may refer to singlet and triplet superconductors and to normal-state metals, including ferromagnets. The tunnel current j_T may refer to single electrons or Cooper pairs and transport of charge and spin. Depending on the thickness, $2d$, of the tunnel medium proximity effect and Andreev reflection at S/N interfaces plays a role. (B) Phase diagram of a ($F_1/S/F_3$) sandwich. S refers to a singlet superconductor and F_1, F_3 to ferromagnets with parallel (P) or antiparallel (AP) orientation of their magnetization. LO is the Larkin–Ovchinnikov phase, h the exchange field and T_c and T_{co}, the superconducting transition temperature in the presence and absence, respectively, of the exchange field. d_F and d_S refer to the thickness of the ferromagnetic and superconducting film, respectively. From Bennemann KH (2005) Superconductivity: BCS theory. In: Encyclopedia of Condensed Matter Physics, 1st edn., pp. 72–81. Amsterdam: Elsevier.

electrons or holes can then hop easily from one molecule to the next one, but not perpendicular to the layers. The salts consist of conducting layers separated by a nonconducting environment (anions). Clearly, bond-length changes, also due to pressure, will sensitively change the electrical properties. Also, a magnetic field perpendicular to the layers (along the c-axis) affects the system due to the formation of Landau levels, which will pass the Fermi energy as the external magnetic field varies (cf. de Haas–van Alphen oscillations). In stronger magnetic fields quantum mechanical interband tunneling also occurs. Note that superconductivity occurs at relatively low temperatures, usually upon applying pressure. Experiments indicate unconventional Cooper pairing ($2\Delta_0 \sim 7k_BT_c$, non-s-symmetry of Δ_k). Whether phonons are involved in Cooper pairing must be clarified by further analysis.

In an external magnetic field, interesting behavior, such as Landau-level formation and spin-split bands, may result due to the layered structure. Possibly, Cooper pairs ($(\boldsymbol{k}\uparrow, -\boldsymbol{k}+\boldsymbol{q}\downarrow)$) may form. A Larkin–Ovchinnikov (LO) state with $\Delta_k \sim \cos(\boldsymbol{k}\cdot\boldsymbol{r})$ may occur. In general, the response to an external magnetic field is highly anisotropic. Furthermore, it is interesting that superconductivity may

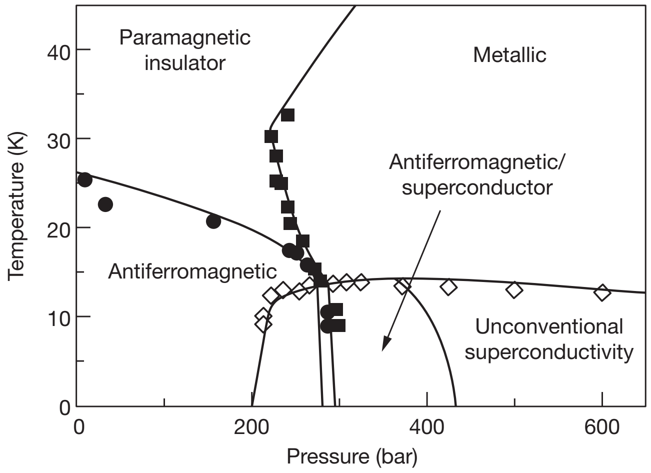

Fig. 10 Phase diagram of κ-(BEDT-TTF)$_2$ Cu[N(CN)$_2$]Br, an organic superconductor, from AC susceptibility and nuclear magnetic resonance. From Bennemann KH (2005) Superconductivity: BCS theory. In: Encyclopedia of Condensed Matter Physics, 1st edn., pp. 72–81. Amsterdam: Elsevier.

be induced in λ-(BETS)$_2$FeCl$_4$ by a magnetic field h, which destroys long-range magnetic order of the Fe^{3+}. Field-induced superconductivity may also occur in α-(BEDT-TTF)$_2$KHg(SCN)$_4$ by affecting the charge density wave (CDW) with the external magnetic field h. Further experiments are needed; however, rich behavior may be expected in general since CDW and SDW excitations, Landau levels, and 2D properties are present.

Superconductivity in small particles (radius R) due to electronic level discretization ($\delta_2 \approx \varepsilon_F/n \approx (\hbar v_F/R)(k_F R)^{-2}$, $\xi \sim (R\delta/kT_c)(Rk_F)^2$), and charge fluctuations, $Q = en \Leftrightarrow Q \pm e$, as a result of single electron and Cooper pair hopping, exhibit interesting behavior.

The charging of small particles is controlled by electrostatic energy. The change of the charge $Q = en \rightarrow Q \pm e$ causes an energy change $e^2/2C$, where C is the capacitance of the small particle, leading to a Coulomb blockade (in tunneling, for example). At temperatures $T \simeq 0$, due to the electrostatic energy, it is ($\Delta Q = e\Delta n$)

$$E_n = \frac{Q^2}{2C} - \frac{Q}{C}C'V, \tag{33}$$

(C and C' are capacitances of a system including voltage contact and V is the external potential), and the blockade is periodically lifted as a function of n and V ($E_{n+1} = E_n$). In the superconducting state, one has for $T \simeq 0$ that $\Delta > e^2/2C$. The situation is illustrated in Fig. 11. From $E_{n+1} + \Delta = E_n$ and $E_{n+2} = E_n$, n even and large sea of Cooper pairs, a period doubling results, with respect to the normal state. Note that the equation $E_{n+2} = E_n$ might not hold for smaller density of Cooper pairs. In view of the strong quantum-mechanical behavior of small particles, structures consisting of a larger number of small particles seem very interesting (mesoscopic systems).

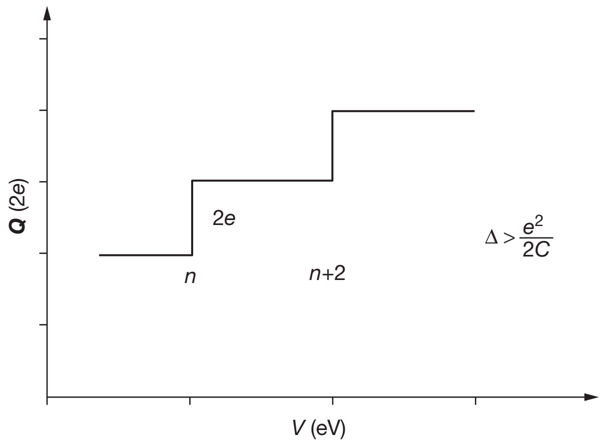

Fig. 11 Charging-up behavior of a small superconductor with capacitance C and charge $Q = en$, n even, in a potential V ($\Delta > e^2/2C$). This behavior follows from $E_n = E_{n+2}$ and reflects Cooper pair formation. One also has $E_n = E_{n+1} + \Delta$, where E_{n+1} refers to a state with one unpaired electron. Then Q changes by e at $\Delta V \propto (2n + 1)$. From Bennemann KH (2005) Superconductivity: BCS theory. In: Encyclopedia of Condensed Matter Physics, 1st edn., pp. 72–81. Amsterdam: Elsevier.

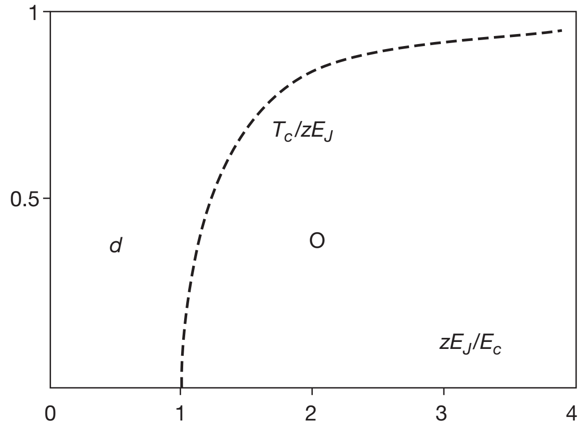

Fig. 12 Transitions in an ensemble of superconducting quantum dots controlled by the Josephson-energy E_J and the Coulomb-energy $E_c = e^2/2C$. T_c refers to the global superconducting transition temperature of the ensemble. Phase O refers to a globally ordered superconducting state of the ensemble and phase *d* to superconducting grains with no global Cooper pair phase coherence, *z* is the coordination number. From Bennemann KH (2005) Superconductivity: BCS theory. In: Encyclopedia of Condensed Matter Physics, 1st edn., pp. 72–81. Amsterdam: Elsevier.

An ensemble of grains for illustration may exhibit transitions to superconductivity at T_{c1}, where the single grains get superconducting, and at T_{c2}, where the whole ensemble becomes superconducting ($T_{c2} \leq T_{c1}$) globally and phase coherently; see Fig. 12. Generally, an ensemble of grains may resemble an alloy-like array of S/S and S/N junctions (S = superconducting, N = normal state grains). The behavior of an ensemble of grains depends, of course, on the coupling and electron hopping between the grains. Also the structural order of the grains plays a role. A regular lattice-like arrangement of the grains (one-dimensional or two-dimensional topology) is of particular interest. For small distances between the cluster particles, electron tunneling and inelastic Cooper pair tunneling (Josephson coupling) occur. Hence, charge fluctuations are present in such granular superconductors. The resultant interesting Josephson effect can be described by

$$\begin{aligned} H = H_T - \sum_{i,j} E_g(i,j)\cos\Phi_{ij} \\ + \frac{2e^2}{C}\sum_{i,j}(N_i - N_j)^2 + \cdots \end{aligned} \tag{34}$$

The first term refers to normal electron hopping between the grains, the second term to Cooper pairs tunneling between neighboring superconducting grains (Josephson effect), and the last term is the electrostatic energy due to different charges of neighboring grains i, j. For simplicity, the same capacitances C and E_J (Josephson energy) are used. The phase difference $\Phi_{ij} = \Phi_i - \Phi_j$ refers to the phases Φ_i of the superconducting order parameter $\Delta_i = |\Delta_i|e^{i\Phi_i}$ of grain i. It is important to note that $[\Phi, N] = i$, where N is the Cooper-pair number operator.

Conclusion

In conclusion, BCS superconductivity has been overviewed. While the basis of the BCS theory is well developed, details of the physics may have interesting consequences that have not been understood yet. New important discoveries can be expected. The relationship of phase-coherent and, in particular, phase-incoherent Cooper pairing with the Bose–Einstein condensation (BEC) is of fundamental interest. One expects, in particular, for more local pairing, perfect Boson behavior of the two paired electrons and thus an intimate relationship between Cooper pairing and BEC. Meissner-type superconductivity and BEC should result only for phase-coherent Cooper pairing.

The size of the Cooper pairs is of the order of the coherence length. For small superconductivity density, one may reach a state (also possibly achieved geometrically, e.g., in narrow pipes, granular superconductors, etc.) where the singulet Cooper pairs do not overlap and behave like Bosons and a BEC transition is expected (Bennemann and Ketterson, 2014). Near the crossover transition, anomalous behavior may occur, for example, in cuprate underdoped superconductors due to phase fluctuations. Applying the Heisenberg uncertainty relation, one gets that the product of phase and occupation is $\sim h$ (Bennemann and Ketterson, 2014).

While for the cuprates the glue for Cooper pairing Phonons or Spin fluctuations is still debated, it seems that the essential structure of BCS theory is valid (namely Cooper pairs, Josephson current, order parameter equation with g positive or negative) (Bennemann, 2005).

Various properties of conventional and unconventional superconductors have been discussed. The general calculation of the superconducting transition temperature remains a problem. Also a discussion of other Cooper pairing mechanisms (spin fluctuation besides phonon-induced superconductivity) as well as triplet pairing like in He-3 is an open issue.

Acknowledgments

The author is grateful to F. Nogueira, J. W. Garland, J. Ketterson, W. Buckel, M. Avignon, L. Tewordt, M. Peter, R. Parks, D. Manske, I. Eremin, J. Schmalian, R. Schrieffer, J. Bardeen, and many more for helping him in understanding superconductivity. A helpful visit at the Aspen Institute of Physics is also gratefully acknowledged. The author is grateful to V. M. Fomin and F. Nogueira, who prepared this Chapter for publication.

References

Abrikosov AA, Gor'kov LP, and Dzyaloshinski IE (1963) *Quantum Field Theory in Statistical Physics Englewood Cliffs*. NJ: Prentice-Hall Inc.
Bardeen J, Cooper LN, and Schrieffer JR (1957) *Physical Review* 106: 162–164. Physical Review 108, 1175–1204.
Bennemann KH (2005) Superconductivity: BCS theory. In: *Encyclopedia of Condensed Matter Physics*, 1st edn., pp. 72–81. Amsterdam: Elsevier.
Bennemann KH and Garland JW (1972) In: Douglass DH (ed.) *Superconductivity in d- and f-Band Metals, AIP Conference Proceedings*, vol. 4, pp. 103–137.
Bennemann KH and Ketterson JB (2003) *The Physics of Superconductors*. Berlin: Springer.
Bennemann KH and Ketterson JB (2014) *Novel Superfluids*. Oxford: Oxford Science Publications.
Buckel W and Hilsch R (1954) *Zeitschrift für Physik* 138: 109–120.
Garland JW, Bennemann KH, and Mueller FM (1968) *Physical Review Letters* 21: 1315–1319.
Kerker G and Bennemann KH (1974) *Solid State Communications* 14: 399–401.
Labbé J, Barišić S, and Friedel J (1967) *Physical Review Letters* 19: 1039–1041.
Manske D, Eremin I, and Bennemann KH (2000) *Physical Review B* 62: 13922.
McMillan WL (1968) *Physical Review* 167: 331–344.
Parks RD (1969) *Superconductivity*. New York: Marcel Dekker.
Scalapino DJ, Schrieffer JR, and Wilkins JW (1966) *Physical Review* 148: 263–279.
Schrieffer JR (1964) *Theory of Superconductivity*. New York: Benjamin.
Tinkham M (1975) *Introduction to Superconductivity*. New York: McGraw-Hill.

Further reading

General literature on: Magnetism, history of; Quantum Mechanics: Methods; statistical mechanics: Classical; superconductivity: General aspects; superconductivity: Ginzburg-Landau theory and vortex lattice; superconductivity: Tunneling; superconductors, high Tc. Bassani, F., Liedl, G. L., Wyder, P. (Eds.) Encyclopedia of Condensed Matter Physics. 1st edn., Elsevier, Amsterdam.
Brandt EH (2023) Superconductivity: Ginzburg-Landau theory and vortex lattice. In: *Encyclopedia of Condensed Matter Physics, 2nd edn*. Oxford: Elsevier.
Chubukov A (2023) Superconductivity: electronic mechanisms. In: *Encyclopedia of Condensed Matter Physics*, 2nd edn. Oxford: Elsevier.
Gurevich A (2023) Superconductivity: Critical currents. In: *Encyclopedia of Condensed Matter Physics, 2nd edn*. Oxford: Elsevier.
Kozhevnikov V (2023) Electrodynamics of superconductors. In: *Encyclopedia of Condensed Matter Physics, 2nd edn*. Oxford: Elsevier.
Mazin I (2023) Superconductors, conventional vs unconventional. In: *Encyclopedia of Condensed Matter Physics*, 2nd edn. Oxford: Elsevier.

Quantum fluctuations in superconducting nanowires

Andrei D Zaikin[a] **and IE Tamm**[b,c], [a]Institute for Quantum Materials and Technologies, Karlsruhe Institute of Nanotechnology (KIT), Karlsruhe, Germany; [b]Department of Theoretical Physics, P.N. Lebedev Physical Institute, Moscow, Russia; [c]National Research University Higher School of Economics, Moscow, Russia

© 2024 Elsevier Ltd. All rights reserved.

Introduction 670
Superconducting fluctuations 671
Quantum phase slips 672
Quantum phase transition 674
Phase-charge duality 675
“Superconducting” regime: Dissipative transport and noise 676
“Insulating” regime: Localization of Cooper pairs 678
Conclusion 680
References 681

Abstract

Low temperature properties of superconducting nanowires are determined by quantum fluctuations. Both Gaussian fluctuations of the superconducting phase—associated with plasma modes propagating along the wire—and non-Gaussian fluctuations of the order parameter—quantum phase slips—are equally important being responsible, e.g., for a “superconductor-insulator” quantum phase transition governed by the wire diameter. Thicker (“superconducting”) nanowires demonstrate non-vanishing resistance and shot noise of the voltage caused by quantum phase slips. Thinner (“insulating”) nanowires become truly insulating only at scales exceeding a non-perturbative localization length for Cooper pairs, whereas at shorter length scales they still exhibit superconducting properties.

Key points

- Microscopic theory of superconducting fluctuations, proliferation of quantum phase slips in superconducting nanowires, description of quantum properties of “superconducting” and “insulating” phases.

Introduction

A vast majority of properties of bulk conventional superconductors is perfectly described by the standard Bardeen-Cooper-Schrieffer (BCS) theory operating with complex order parameter $\Delta = |\Delta| \exp(i\varphi)$ within the mean field approach (Tinkham, 1996). Superconducting fluctuations play little role here and, hence, macroscopic phase coherence usually remains well preserved over the whole sample.

Unlike in bulk superconductors, fluctuations become far more important in lower dimension where—according to the well known Mermin-Wagner-Hohenberg theorem—fluctuations of the superconducting phase φ should destroy the long-range order, i.e., long-range phase coherence. Fortunately, this formal observation does not yet imply that low dimensional systems cannot exhibit superconducting properties. This is because any generic superconducting system has a finite size in which case phase coherence can survive at least to a certain extent. For instance, two-dimensional (2D) superconducting films are known to undergo Berezinskii-Kosterlitz-Thouless (BKT) topological phase transition. As a result, the decay of superconducting correlations in such films changes from exponential at higher temperatures T to power law at lower ones, implying that at low enough T long range phase coherence remains essentially preserved in samples of a finite size. Hence, generic 2D metallic films can and do turn superconducting.

Does superconductivity also survive in quasi-one-dimensional (1D) wires or do phase fluctuations disrupt supercurrent in such systems? The answer to this question is of both fundamental interest and practical importance due to rapidly progressing miniaturization of superconducting circuits employed in a broad range of applications, such as, e.g., quantum nanoelectronics, quantum information and metrology. As we will see below, superconducting fluctuations play a crucial role in 1D wires and essentially determine both their transport and ground state properties. The behavior of superconducting nanowires turns out to be rich, complex and highly interesting.

https://doi.org/10.1016/B978-0-323-90800-9.00151-7

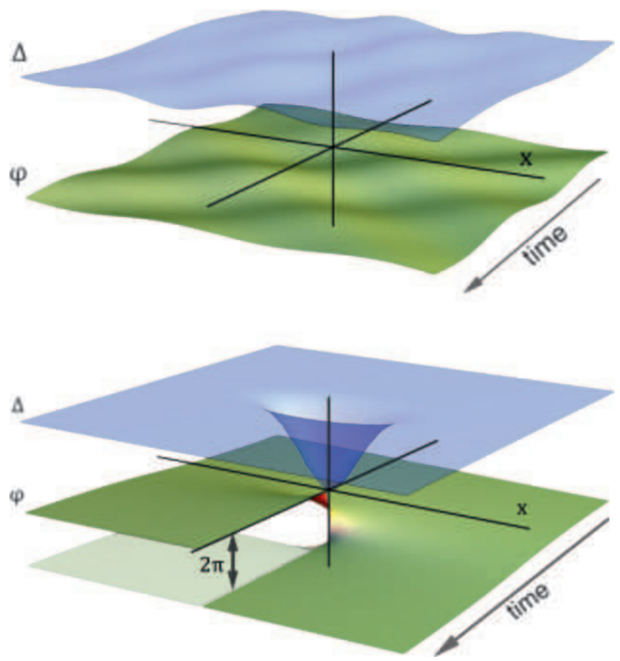

Fig. 1 Schematics of small fluctuations of the order parameter (upper panel) and the phase slip process (lower panel) in superconducting nanowires. During the latter process the absolute value of the order parameter Δ gets locally and temporarily suppressed due to thermal and/or quantum fluctuations while its phase φ suffers a jump by 2π. Adapted from Semenov AG and Zaikin AD (2022) Superconducting quantum fluctuations in one dimension. *Physics-Uspekhi* 65: 945–983.

Superconducting fluctuations

Thermal and quantum fluctuations may cause deviations of both the modulus and the phase of the superconducting order parameter $\Delta(x)$ (with x being the coordinate along the wire) from their mean field values. One can distinguish (i) small (Gaussian) fluctuations of the order parameter and (ii) non-Gaussian fluctuations, i.e., the so-called *phase slips* (Arutyunov et al., 2008; Bezryadin, 2013; Zaikin, 2010; Zaikin and Golubev, 2019). These two kinds of fluctuations are schematically illustrated in Fig. 1.

The strength of fluctuation effects in superconducting nanowires is essentially controlled by two different parameters, dimensionless conductance g_ξ and dimensionless admittance g_Z. These parameters are defined as

$$g_\xi = R_q/R_\xi, \quad g_Z = R_q/Z_\mathrm{w}, \tag{1}$$

where $R_q = 2\pi/e^2 \simeq 25.8\ \mathrm{K\Omega}$ is the quantum resistance unit, R_ξ is the normal state resistance of the wire segment of length equal to the superconducting coherence length ξ,$Z_\mathrm{w} = \sqrt{\mathcal{L}/\mathcal{C}}$ is the wire impedance, $\mathcal{L} = 1/(\pi\sigma_N\Delta_0 s)$ and $\mathcal{C}$ are respectively the kinetic wire inductance (times length) and the geometric wire capacitance (per length), σ_N is the normal state Drude conductance of the wire and s is the wire cross section. Both parameters (1) scale with the wire cross section as $g_\xi \propto s$ and $g_Z \propto \sqrt{s}$. Note that here and below for simplicity and compactness we set the Planck constant $\hbar$, the Boltzmann constant k_B and the speed of light c equal to unity. If necessary, these parameters can easily be restored at any stage of our analysis.

In generic metallic nanowires the dimensionless conductance g_ξ typically strongly exceeds unity. In this case one can demonstrate that small (Gaussian) fluctuations of both the absolute value and the phase of the order parameter yield only a small ($\propto 1/g_\xi$) fluctuation correction to the BCS (mean field) value of this parameter Δ_0. In particular, at $T \to 0$ one has (Zaikin, 2010; Zaikin and Golubev, 2019)

$$\Delta = \Delta_0 - \delta\Delta_0, \quad \frac{\delta\Delta_0}{\Delta_0} \sim \frac{1}{g_\xi} \sim Gi_{1\mathrm{D}}^{3/2}. \tag{2}$$

Here $Gi_{1\mathrm{D}}$ is the so-called Ginzburg number (Larkin and Varlamov, 2005) which controls the fluctuation region in the immediate vicinity of the BCS critical temperature T_C. Eq. (2) demonstrates that at low T the order parameter suppression due to Gaussian fluctuations may become significant only in extremely thin nanowires with $Gi_{1\mathrm{D}} \sim 1$ and $g_\xi \sim 1$.

It turns out that in the limit $g_\xi \gg 1$ Gaussian phase fluctuations in superconducting wires are practically decoupled from those of $|\Delta|$. Such phase fluctuations are controlled by the parameter g_Z (1) and are intimately related to sound-like plasma modes (the so-called Mooij-Schön modes) propagating along superconducting wires with the velocity $v = 1/\sqrt{\mathcal{LC}}$. As we will see below, the presence of such plasma modes is crucially important and to a large extent determines the physics of superconducting nanowires at low temperatures.

Turning to non-Gaussian fluctuations of the order parameter illustrated in lower panel of Fig. 1, we observe that the phase slip process corresponds to temporal suppression of $|\Delta(x)|$ down to zero in some point $x = x_0$ inside the wire. As soon as the modulus of the order parameter $|\Delta(x_0)|$ vanishes, the phase $\varphi(x_0)$ becomes unrestricted and can jump by 2π. After that $|\Delta(x_0)|$ gets restored, the phase becomes single valued again and the system returns to its initial state accumulating the net phase shift 2π.

According to the Josephson relation each such phase jump—depending on its sign—implies positive or negative voltage pulse $\delta V = \dot{\varphi}/2e$. In the absence of any bias current the average number of "positive" voltage pulses is exactly equal to that of the "negative" ones. Hence, the net voltage drop across the wire remains zero. Applying the current $I \propto |\Delta|^2 \nabla \varphi$ one creates nonzero phase gradient along the wire, thereby breaking the symmetry between "positive" and "negative" phase slips and making the former to prevail over the latter (or vice versa). As a result, the net voltage drop V across the wire now differs from zero. Hence, phase slips should cause non-zero resistance $R = V/I$ of 1D superconducting wires at temperatures below T_C.

At T just slightly below T_C phase slips occur predominantly due to thermal fluctuations of the order parameter. Creation rate of such thermally activated phase slips (TAPS) and, hence, the wire resistance R below T_C are determined by the activation exponent, i.e.,

$$R(T) \propto \exp\left(-\delta F/T\right), \quad \delta F \sim \frac{N_0 \Delta_0^2(T)}{2} s\xi(T), \tag{3}$$

where the free energy difference δF plays the role of an effective potential barrier for TAPS determined by the superconducting condensation energy $N_0{\Delta_0}^2/2$ (N_0 being the normal electron density of states) within the volume $\sim s\xi(T)$ of the wire segment where superconductivity is destroyed by thermal fluctuations. At temperatures close to T_C Eq. (3) yields appreciable resistivity which was indeed detected in experiments performed on small superconducting whiskers with typical diameters $\sim 0.5\,\mu$m. However, as the temperature is lowered considerably below T_C the TAPS rate decreases exponentially and no measurable wire resistance is predicted by Eq. (3) in the limit of low T.

In this limit quantum fluctuations of the order parameter should take over. As we already indicated, significant non-Gaussian quantum fluctuations in such wires are quantum phase slips (QPS). Each QPS event involves suppression of the order parameter in the phase slip core and a winding of its phase around this core. This configuration describes quantum tunneling of the order parameter field $\Delta(x)$ through an effective potential barrier $\sim \delta F$. The probability of such tunneling process turns out to be negligible for thicker wires. However, recent progress in nanolithographic technique allowed to fabricate samples with much smaller diameters down to—and even below—10 nm. In this case the potential barrier $\delta F \propto s$ becomes much lower and the QPS tunneling rate increases dramatically enabling quantum phase slips to dominate low temperature behavior of superconducting nanowires.

Quantum phase slips

While the TAPS rate at T close to T_C can be estimated employing just a simple Ginzburg-Landau-type of approach, theoretical analysis of QPS effects requires a much more complicated theory describing full quantum dynamics of the superconducting order parameter field at any temperature down to $T = 0$. This theory is constructed in the spirit of the celebrated Feynman-Vernon-Caldeira-Leggett influence functional technique (Zaikin, 2010; Zaikin and Golubev, 2019).

The starting point is the microscopic Hamiltonian $\widehat{H}$ for electrons in a superconductor that includes a short range attractive BCS and a long range repulsive Coulomb interactions as well as electromagnetic fields. With the aid of the Hubbard-Stratonovich transformations one decouples these interaction terms and introduces the fluctuating order parameter field Δ and the fluctuating scalar potential V. Integrating out all electronic degrees of freedom, one arrives at the grand partition function $\mathcal{Z}$ expressed in terms of the path integral

$$\mathcal{Z} = \operatorname{Tr} \exp\left(-\hat{H}/T\right) = \int \mathcal{D}^2\Delta \mathcal{D}V \mathcal{D}\mathbf{A}\, e^{-S_{\text{eff}}}. \tag{4}$$

The gauge invariant effective action reads

$$S_{\text{eff}} = -\operatorname{Tr} \ln \mathcal{G}^{-1} + S_0[V, \mathbf{A}, \Delta]. \tag{5}$$

Here $\mathbf{A}$ is the electromagnetic vector potential and

$$\mathcal{G}^{-1} = \begin{pmatrix} \partial_\tau + \xi(\nabla) - \mathrm{i}e\Phi + \frac{m\mathbf{v}_s^2}{2} - \frac{\mathrm{i}}{2}\{\nabla,\ \mathbf{v}_s\} & |\Delta| \\ |\Delta| & \partial_\tau - \xi(\nabla) + \mathrm{i}e\Phi - \frac{m\mathbf{v}_s^2}{2} - \frac{\mathrm{i}}{2}\{\nabla,\ \mathbf{v}_s\} \end{pmatrix},$$

where $\xi(\nabla) \equiv -\nabla^2/2m - \mu + U(x)$ describes a single conduction band with quadratic dispersion and also includes an arbitrary impurity potential $U(x)$ and the curly brackets denote the anticommutator. We also introduce the gauge invariant linear combinations

$$\Phi = V - \frac{\dot{\varphi}}{2e}, \quad \mathbf{v}_s = \frac{1}{2m}\left(\nabla\varphi - \frac{2e}{c}\mathbf{A}\right), \tag{6}$$

which define the so-called chemical potential of Cooper pairs Φ and the superconducting velocity v_s.

Quantum phase slip configuration represents a nontrivial saddle point of the action (5). It is a formidable task to explicitly find this saddle point for the full nonlinear effective action S_{eff}. Obviously, this task can hardly be accomplished in practice. On the other hand, the problem becomes simpler provided one is interested in estimating the QPS effective action $S_{\rm qps}$ up to a numerical prefactor of order one. For that purpose we can resort to several approximations.

Specifically, we perform a perturbative expansion of the action up to the second order in Φ, $\mathbf{v}_s$ and the fluctuating part of the order parameter $\delta\Delta(x,\tau) = |\Delta(x,\tau)| - \Delta_0$ around its equilibrium value Δ_0. In addition, we average over the random potential of impurities. After this step the effective action becomes translationally invariant both in space and in time. Integrating out V-and $\mathbf{A}$-fields we identically rewrite our partition function and the effective action only in terms of the fluctuating variables $\delta\Delta$ and φ. Then performing the Fourier transformation with respect to both x and τ, expanding the action in powers of ω and q^2 up to terms $\sim\omega^2 q^2$ and rewriting the action again in the space-time domain, we obtain

$$\begin{aligned} S_{\rm eff} \simeq \int dx d\tau \bigg\{ & \frac{\mathcal{C}}{8e^2}\left(\frac{\partial\varphi}{\partial\tau}\right)^2 + \frac{1}{8e^2\mathcal{L}}\left(\frac{\partial\varphi}{\partial x}\right)^2 \\ & + \frac{\pi\sigma_N s}{64e^2\Delta_0}\left(\frac{\partial^2\varphi}{\partial x\partial\tau}\right)^2 + sN_0\delta\Delta^2 \\ & + \frac{sN_0}{12\Delta_0^2}\left(\frac{\partial\delta\Delta}{\partial\tau}\right)^2 + \frac{\pi s N_0 D}{8\Delta_0}\left(\frac{\partial\delta\Delta}{\partial x}\right)^2 \bigg\}, \end{aligned} \tag{7}$$

where D is the normal state diffusion constant. The first two terms under the integrals of Eq. (7) describe phase fluctuations corresponding to Mooij-Schön plasma modes, the third term $\sim\sigma_N(\nabla\dot{\varphi})^2$ has to do with "gapped" dissipation inside the wire and is reminiscent of that describing capacitance renormalization due to retardation effects in Josephson junctions, while the last three terms account for the loss of the condensation energy due to fluctuations of $|\Delta|$.

It is convenient to separate the action for a single QPS $S_{\rm qps}$ into a core part $S_{\rm core}$ and that originating from outside the core $S_{\rm out}$, which depends on the hydrodynamics of the electromagnetic fields, i.e.,

$$S_{\rm qps} = S_{\rm core} + S_{\rm out}. \tag{8}$$

Let us denote the QPS core size as x_0 and the (imaginary) time duration of the QPS event as τ_0. At this stage both these parameters are not yet known and remain to be determined from our subsequent analysis.

We first evaluate the hydrodynamic part $S_{\rm out}$. Outside the QPS core only the phase variable φ fluctuates both in space and in time while $|\Delta| = \Delta_0$ does not. Then the saddle point solution $\tilde{\varphi}(x,\tau)$ corresponding to a single QPS event should satisfy the identity

$$\partial_x\partial_\tau\tilde{\varphi} - \partial_\tau\partial_x\tilde{\varphi} = 2\pi\delta(\tau, x) \tag{9}$$

implying that after a wind around the QPS center (assumed to be located at $\tau = 0$ and $x = 0$) the phase should change by 2π. We observe that QPS is just equivalent to a vortex in space-time with the phase distribution $\varphi(x,\tau)$ described by the saddle point solution

$$\tilde{\varphi}(x,\tau) = -\arctan(x/v\tau). \tag{10}$$

Substituting the solution (10) into the action (7), we obtain

$$S_{\rm out} = \lambda \ln[\min(L, v/T)/\max(x_0, v\tau_0)], \tag{11}$$

where the parameter $\lambda = g_Z/8$ sets the scale for the hydrodynamic part of the QPS action, L is the wire length.

Let us now turn to the core term $S_{\rm core}$. As we are anyway aiming at evaluating this term up to a numerical prefactor of order one, without loss of generality we may approximate the order parameter field inside the QPS core by two simple functions

$$\delta\Delta(x,\tau) = \Delta_0 \exp\left(-x^2/2x_0^2 - \tau^2/2\tau_0^2\right), \tag{12}$$

$$\varphi(x,\tau) = -(\pi/2)\tanh(x\tau_0/x_0\tau). \tag{13}$$

These functions obey all necessary requirements, the most important of which are: (i) the magnitude of the order parameter $\Delta(x,\tau)$ vanishes at $x = 0$ and $\tau = 0$ and coincides with the mean field value Δ_0 outside the QPS core at $|x| \gtrsim x_0/2$, $|\tau| \gtrsim \tau_0/2$ and (ii) the phase $\varphi(x,\tau)$ flips at $x = 0$ and $\tau = 0$ in a way to provide the change of the net phase difference across the wire by 2π. Note that the choice of the trial functions (12), (13) is by no means restrictive for our purposes, almost any other sufficiently smooth function obeying the above requirements can be used to estimate $S_{\rm core}$ within the required accuracy.

Substituting the functions (12), (13) into the action (7), setting $\sigma_N = 2e^2N_0D$ and minimizing the resulting expression for $S_{\rm core}$ with respect to x_0 and τ_0, we arrive at the final results both for the core parameters

$$x_0 \sim \xi = \sqrt{D/\Delta_0}, \quad \tau_0 \sim 1/\Delta_0 \tag{14}$$

and for the core action

$$S_{\rm core} = a g_\xi \sim N_0 s\sqrt{D\Delta_0}. \tag{15}$$

Note that during this minimization procedure we neglected the contribution $S_{\rm out}$ (11) to the total QPS action $S_{\rm qps}$ (8). This is appropriate because the two contributions to the QPS action depend differently on the wire thickness, i.e., $S_{\rm core} \propto \mathcal{N}$ and $S_{\rm out} \propto \sqrt{\mathcal{N}}$, where $\mathcal{N} = p_F^2 s/4\pi$ defines the total number of conducting channels in the wire and p_F is the Fermi momentum. Hence, for generic metallic wires with $\mathcal{N} \gg 1$ one usually has $S_{\rm core} \gg S_{\rm out}$. In addition, one can verify that the results (14) and (15) hold for not too long wires with lengths $L \lesssim \xi\mathcal{N}$. The latter condition is satisfied in a vast majority of experiments with superconducting nanowires.

We also point out that minimization of the "condensation energy" contribution $\sim\delta\Delta^2$ (the last three terms in Eq. (7)) alone already yields the correct estimate for $S_{\rm core} \sim N_0 s\sqrt{D\Delta_0}$. This observation, however, by no means implies that phase fluctuations terms in Eq. (7) can be neglected. Just on the contrary, phase fluctuations yield exactly the same order-of-magnitude estimate for $S_{\rm core}$ provided one keeps "gapped" dissipation term $\sim \sigma_N(\nabla\dot{\varphi})^2$ with the Drude expression $\sigma_N = 2e^2N_0D$. At the same time, e.g., ignoring this term by formally setting $\sigma_N \to 0$ in Eq. (7) during our minimization procedure would immediately yield meaningless results for x_0 and τ_0 as well as the QPS action parametrically different from that in Eq. (15).

The result (15) allows to recover the QPS tunneling amplitude $\gamma_{\rm qps}$ within the exponential accuracy. Evaluating the contribution of fluctuations around the QPS saddle point one gets (Zaikin and Golubev, 2019)

$$\gamma_{\rm qps} \sim (g_\xi\Delta_0/\xi)\exp(-ag_\xi), \tag{16}$$

where g_ξ is supposed to be much larger than one and the prefactor $a \sim 1$ can be regarded as a fit parameter, which can be extracted, e.g., from the available experimental data. The QPS amplitude (16) will play a prominent role in our subsequent analysis.

Quantum phase transition

Although the hydrodynamic part of the action (11) and the parameter λ do not enter directly into the expression for the QPS amplitude $\gamma_{\rm qps}$(16), they also plays an important role, as they determine interactions between different quantum phase slips mediated by plasmon modes propagating along the wire.

Consider the configuration of n phase slips essentially equivalent to n vortices in space-time with the corresponding core coordinates (x_n, τ_n). Provided the phase slip cores do not overlap with each other the core contributions are independent and simply add up. In order to evaluate the hydrodynamic part we substitute the superposition of the saddle point solutions for n quantum phase slips $\varphi = \sum_i^n \tilde{\varphi}_i(x - x_i, \tau - \tau_i)$ into the action. Then we get $S_{QPS}^{(n)} = nS_{\rm core} + S_{\rm int}^{(n)}$, where

$$S_{\rm int}^{(n)} = -\lambda\sum_{i\neq j}\nu_i\nu_j\ln\left(\frac{\rho_{ij}}{x_0}\right) + \frac{\Phi_0}{c}I\sum_i \nu_i\tau_i. \tag{17}$$

Here $\rho_{ij} = (v^2(\tau_i - \tau_j)^2 + (x_i - x_j)^2)^{1/2}$ defines the distance between the i-th and j-th QPS in the (x,τ) plane and $\nu_i = \pm 1$ are QPS topological charges which fix the sign of the phase change after a wind around the QPS center. In Eq. (17) for simplicity we assumed $x_0 \sim v\tau_0$ and included an additional term which keeps track of the total current I possibly flowing across the wire. We observe that different quantum phase slips interact logarithmically in space-time attracting (repelling) each other in the case of opposite (equal) topological charges.

The grand partition function of the wire $\mathcal{Z}$ is represented as a sum over all possible QPS configurations:

$$\begin{aligned}\mathcal{Z} = &\sum_{n=0}^{\infty}\frac{1}{2n!}\left(\frac{y}{2}\right)^{2n}\int_{x_0}^{L}\frac{dx_1}{x_0}\cdots\int_{x_0}^{L}\frac{dx_{2n}}{x_0}\\ &\times\int_{\tau_0}^{1/T}\frac{d\tau_1}{\tau_0}\cdots\int_{\tau_0}^{1/T}\frac{d\tau_{2n}}{\tau_0}\sum_{\nu_i=\pm1}e^{-S_{\rm int}^{(2n)}},\end{aligned} \tag{18}$$

where $y = x_0\tau_0\gamma_{\rm qps}$ is an effective QPS fugacity. The sum in Eq. (18) runs over neutral QPS configurations with $\sum_i^{2n}\nu_i = 0$, which is a direct consequence of the boundary condition $\varphi(x,\tau) = \varphi(x, \tau + 1/T)$ in the corresponding path integral for $\mathcal{Z}$.

In the limit $I \to 0$ Eqs. (17) and (18) define the standard model for a 2D gas of logarithmically interacting charges ν_i. Making use of the standard BKT renormalization group (RG) analysis of logarithmically interacting 2D Coulomb gas we arrive at the scaling equations for the interaction parameter λ and the charge fugacity y:

$$\partial_\Lambda\lambda = -4\pi^2\lambda^2y^2, \quad \partial_\Lambda y = (2 - \lambda)y. \tag{19}$$

Here $\Lambda = \ln(\rho/x_0)$ is the scaling parameter.

Following the standard line of reasoning we immediately conclude that a quantum phase transition (QPT) for phase slips occurs in a long superconducting wire at $T \to 0$ and

$$\lambda = 2 + 4\pi y \simeq 2. \tag{20}$$

This is nothing but BKT-like phase transition for topological charges ν_i in space-time (Zaikin and Golubev, 2019). The difference from the standard BKT transition in 2D superconducting films is that in our case the transition is driven by the interaction parameter $\lambda = g_Z/8 \propto \sqrt{s}$ and not by temperature.

For thicker wires with $\lambda > 2$ (corresponding to the "ordered" phase) QPS with opposite topological charges are bound in pairs (dipols) thereby limiting the effect of quantum fluctuations, whereas in thinner ones with $\lambda < 2$ ("disordered" phase) the density of free (unbound) QPS always remains nonzero implying that long range phase coherence gets destroyed in this case. Below we will demonstrate that this QPT can be interpreted as a superconductor-insulator phase transition with rather non-trivial features of both "superconducting" and "insulating" phases.

Phase-charge duality

Before we turn to this issue let us establish an important property of superconducting nanowires which is the so-called phase-charge duality.

To begin with, we note that duality between the phase and the charge variables is a well known property of Josephson junctions. In particular, under a certain duality transformation the effective actions for Josephson tunnel junctions in the phase and in the charge representations are exactly transformed onto each other (Schön and Zaikin, 1990). Furthermore, in the absence of an external circuit the Josephson junction can be described in terms of an effective Hamiltonian for a "quantum particle" in the periodic potential in the (quasi)-charge space. Within this picture, the charge Q and the flux Φ are canonically conjugate variables fully analogous to the momentum and coordinate variables in quantum mechanics.

Similar duality ideas can be worked out and applied to superconducting nanowires (Semenov and Zaikin, 2022). To this end, let us for simplicity assume that our superconducting wire is isolated from any external circuit and ignore for a moment all kinds of fluctuations of the absolute value of the order parameter including, of course, quantum phase slips. In this case only phase fluctuations remain and the wire effective action with a high accuracy can be described by the terms in the first line of Eq. (7). Then the effective Hamiltonian of the wire reduces to that of a transmission line

$$\hat{H}_{\text{TL}} = \int_0^L dx \left[\frac{\hat{Q}^2(x)}{2\mathcal{C}} + \frac{1}{2\mathcal{L}} \left(\frac{\partial_x \hat{\varphi}(x)}{2e} \right)^2 \right], \tag{21}$$

where $\hat{Q}(x)$ and $\hat{\varphi}(x)$ are canonically conjugate local charge and phase operators obeying the commutation relations

$$\left[\hat{Q}(x), \hat{\varphi}(x') \right] = -2ie\delta(x - x'). \tag{22}$$

These operators can also be expressed as

$$\hat{Q}(x) = \frac{1}{\Phi_0} \partial_x \hat{\chi}(x), \quad \partial_x \hat{\varphi}(x) = 2e\hat{\Phi}(x), \tag{23}$$

where $\hat{\chi}(x)$ and $\hat{\Phi}(x)$ represent some new (dual) operators. Combining Eqs. (21) and (23), we obtain

$$\hat{H}_{\text{TL}} = \int_0^L dx \left[\frac{\hat{\Phi}^2(x)}{2\mathcal{L}} + \frac{1}{2\mathcal{C}} \left(\frac{\partial_x \hat{\chi}(x)}{\Phi_0} \right)^2 \right]. \tag{24}$$

The physical meaning of both dual operators is transparent from Eqs. (23) and (24), i.e., $\hat{\Phi}(x)$ is the local flux operator, while $\hat{\chi}(x)$ is proportional to the operator for electric charge passed through the point x.

Let us now include quantum phase slips into our consideration. With the aid of a rigorous calculation one can demonstrate that the total effective wire Hamiltonian in the presence of QPS takes the form

$$\hat{H}_{\text{wire}} = \hat{H}_{\text{TL}} - \gamma_{\text{qps}} \int_0^L dx \, \cos\left(\hat{\chi}(x)\right), \tag{25}$$

where $\hat{H}_{\text{TL}}$ is defined in Eq. (24). Evaluating the partition function $\mathcal{Z} = \operatorname{Tr} \exp\left(-\hat{H}_{\text{wire}}/T\right)$ with the Hamiltonian (25) and expanding in powers of γ_{qps} one immediately recovers Eq. (18).

Let us now take a look at Fig. 2 displaying two complementary superconducting devices. One of them is an arbitrarily long superconducting nanowire surrounded by the vacuum or an insulator (upper part of the figure). In the device depicted in the lower part of the figure the superconductor is interchanged with the vacuum/insulator, thus forming a spatially extended Josephson junction between two superconductors. A superconducting nanowire in Fig. 2 is described by the Hamiltonian (25), whereas the Hamiltonian corresponding to a Josephson junction (of length L) in Fig. 2 has the well known form

$$\hat{H}_{\text{JJ}} = \int_0^L dx \left[\frac{\hat{\mathcal{Q}}^2(x)}{2C_J} + \frac{1}{2\mathcal{L}_J} \left(\frac{\partial_x \hat{\phi}(x)}{2e} \right)^2 \right] - \frac{j_C}{2e} \int_0^L dx \, \cos\hat{\phi}(x), \tag{26}$$

where $\hat{\mathcal{Q}}(x)$ and $\hat{\phi}(x)$ are the local charge and phase difference operators, C_J and $\mathcal{L}_J$ represent respectively the Josephson junction capacitance and inductance per unit junction length and, finally, j_C is the Josephson critical current density. Under the transformation of the operators

$$\hat{\Phi}(x) \leftrightarrow \hat{\mathcal{Q}}(x), \quad \hat{\chi}(x) \leftrightarrow \hat{\phi}(x) \tag{27}$$

the Hamiltonians $\hat{H}_{\text{wire}}$ and $\hat{H}_{\text{JJ}}$ are *exactly dual* to each other provided we interchange

$$\Phi_0 \leftrightarrow 2e, \quad \gamma_{QPS} \leftrightarrow \frac{j_C}{2e}, \quad \mathcal{L} \leftrightarrow C_J, \quad \mathcal{C} \leftrightarrow \mathcal{L}_J. \tag{28}$$

The above duality transformations—on one hand—interchange magnetic and charging energies in these two Hamiltonians and—on the other hand—establish the correspondence between the last term in Eq. (25) describing the effect of QPS and the Josephson coupling energy in the second line in Eq. (26) that accounts for Cooper pair tunneling across the junction.

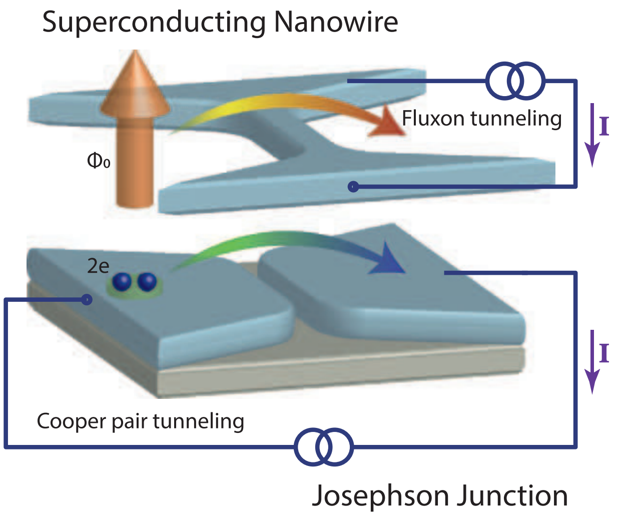

Fig. 2 Dual tunneling processes for a quantum fluxon (that tunnels through a superconducting nanowire) and for a Cooper pair (which tunnels across a Josephson junction). Reproduced from Arutyunov KYu, Lehtinen JS, Radkevich A, Semenov AG, and Zaikin AD (2021) Superconducting insulators and localization of Cooper pairs. *Communications Physics* 4: 146. This work is licensed under a Creative Commons Attribution 4.0 International License, http://creativecommons.org/licenses/by/4.0/.

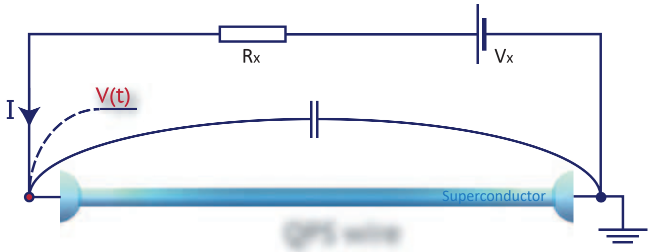

Fig. 3 The system under consideration. Adapted from Semenov AG and Zaikin AD (2022) Superconducting quantum fluctuations in one dimension. *Physics-Uspekhi* 65: 945–983.

Hence, tunneling of a Cooper pair with charge $2e$ between two superconductors is a dual process to a QPS event that can also be viewed as tunneling of a flux quantum Φ_0 across a superconducting wire. Indeed, the last term in the Hamiltonian (25) contains a linear combination of creation $\left(e^{i\hat{\chi}}\right)$ and annihilation $\left(e^{-i\hat{\chi}}\right)$ operators for the flux quantum Φ_0. Each QPS event corresponds to the net phase jump by 2π associated with voltage pulse $\delta V = \dot{\varphi}/2e$ and magnetic flux $\int |\delta V(t)|\, dt = \Phi_0$ passing through the wire in the direction normal to its axis, as it is illustrated in Fig. 2.

"Superconducting" regime: Dissipative transport and noise

Let us examine the properties of superconducting nanowires in the "ordered" phase $\lambda > 2$ where QPS are bound in pairs and, hence, phase fluctuations are largely suppressed. These properties turn out to differ drastically from those of bulk superconductors (Semenov and Zaikin, 2022; Zaikin and Golubev, 2019).

Let us consider the circuit depicted in Fig. 3. It consists of a superconducting nanowire, an external capacitance C switched in parallel to this wire and the voltage source V_x applied via resistor R_x. The voltage $V(t)$ at the left end of the wire $x = 0$ fluctuates and can be measured by a detector while its right end $(x = L)$ is grounded.

An effective Hamiltonian for this system can be written in the form

$$\hat{H} = \hat{H}_{\mathrm{wire}} - I\varphi/2e + \frac{1}{2C}\left(-i\frac{\partial}{\partial(\varphi/2e)} + Q\right)^2, \tag{29}$$

where the term $\hat{H}_{\mathrm{wire}}$ is defined in Eqs. (24) and (25) and describes the superconducting wire, whereas the second and third terms in the right-hand side of Eq. (29) account respectively for the potential energy tilt produced by an external current $I = V_x/R_x$ and for the charging energy. The variable $\varphi(t) \equiv \varphi(0,t)$ represents the phase of the order parameter field $\Delta(x,t)$ at $x = 0$ and the charge Q equals to $Q(t) = \chi(0,t)/\Phi_0$. Here we also set $\varphi(L,t) \equiv 0$.

In order to proceed it is convenient to make use of the Keldysh path integral technique, thus defining our variables of interest on the forward (F) and backward (B) time branches of the Keldysh contour, i.e., we now have $\varphi_{F,B}(t)$ and $\chi_{F,B}(x,t)$. We also introduce "classical" and "quantum" variables, respectively $\varphi_+(t) = (\varphi_F(t) + \varphi_B(t))/2$ and $\varphi_-(t) = \varphi_F(t) - \varphi_B(t)$ (and similarly for the χ-fields). Making use of the Josephson relation between the voltage and the phase one can formally express the expectation value for the (symmetrized with respect to time moments) product of n voltage operators in the form

$$\langle V(t_1)V(t_2)\ldots V(t_n)\rangle = \frac{\left\langle \dot{\varphi}_+(t_1)\dot{\varphi}_+(t_2)\ldots\dot{\varphi}_+(t_n)e^{iS_{\mathrm{qps}}}\right\rangle_0}{(2e)^n}, \tag{30}$$

where

$$S_{\mathrm{qps}} = -2\gamma_{\mathrm{qps}}\int dt\int_0^L dx \sin(\chi_+)\sin(\chi_-/2) \tag{31}$$

and

$$\langle\ldots\rangle_0 = \int \mathcal{D}^2\varphi(t)\mathcal{D}^2\chi(x,t)(\ldots)e^{iS_0[\varphi,\chi]} \tag{32}$$

implies averaging with the Keldysh effective action S_0 corresponding to the Hamiltonian $\hat{H}$ (29) with $\gamma_{\mathrm{qps}} = 0$. The above formally exact expressions describe complete statistics of voltage fluctuations across superconducting nanowires.

Provided $\lambda > 2$ the expectation values (30) can be evaluated perturbatively in γ_{qps}. In the zero order in γ_{qps} all averages can be handled exactly. Expanding Eq. (30) up to the second order in γ_{qps} and performing all necessary averages we arrive at the results for voltage correlators of an arbitrary order.

In particular, for the expectation value of the voltage operator we obtain

$$\langle V\rangle = \frac{\Phi_0 L v\gamma_{\mathrm{qps}}^2}{4}\varsigma^2\left(\frac{\Phi_0 I}{2}\right)\sinh\left(\frac{\Phi_0 I}{2T}\right), \tag{33}$$

where

$$\varsigma(\omega) = \tau_0^{\lambda}(2\pi T)^{\lambda-1}\frac{\Gamma\left(\frac{\lambda}{2} - \frac{i\omega}{2\pi T}\right)\Gamma\left(\frac{\lambda}{2} + \frac{i\omega}{2\pi T}\right)}{\Gamma(\lambda)} \tag{34}$$

and $\Gamma(x)$ is the Euler Gamma-function. Evaluating the wire resistivity ρ from the above equations we get

$$\rho = \langle V\rangle/(IL) \propto \begin{cases} \gamma_{\mathrm{qps}}^2 T^{2\lambda-3}, & T \gg \Phi_0 I, \\ \gamma_{\mathrm{qps}}^2 I^{2\lambda-3}, & T \ll \Phi_0 I. \end{cases} \tag{35}$$

These results imply that due to QPS effects charge transport across our nanowires remains *dissipative* even in the "superconducting" phase $\lambda > 2$: The linear wire resistance tends to zero only at $T \to 0$, whereas its nonlinear resistance remains non-zero down to $T = 0$. This effect remains weak only for sufficiently thick nanowires with very large values of g_ξ (in which case γ_{qps} is vanishingly small) but becomes progressively more important for thinner nanowires. It is also worth pointing out that the key dissipation mechanism in this case is associated with Mooij-Schön plasma modes playing the role of an effective quantum bath for electrons inside the wire.

Quantum phase slips cause not only non-vanishing wire resistance but also voltage fluctuations. In order quantify our description of such fluctuations we will analyze the voltage-voltage correlation function which can also be recovered from Eqs. (30)–(32) within the framework of the same perturbative in γ_{qps} approach. Let us define the noise power spectrum S_Ω which perturbative expression consists of three different contributions:

$$S_\Omega = \int dt e^{i\Omega t}\langle V(t)V(0)\rangle = S_\Omega^{(0)} + S_\Omega^r + S_\Omega^a. \tag{36}$$

The first of these contributions $S_\Omega^{(0)}$ has nothing to do with QPS and just defines equilibrium voltage noise for a transmission line. The other two terms are due to QPS effects. In the zero bias limit $I \to 0$ the term S_Ω^a vanishes, and the equilibrium noise spectrum $S_\Omega = S_\Omega^{(0)} + S_\Omega^r$ is determined from the fluctuation-dissipation theorem.

At non-zero bias values the QPS noise turns non-equilibrium. In the zero frequency limit $\Omega \to 0$ the terms $S_\Omega^{(0)}$ and S_Ω^r tend to zero, and the voltage noise $S_{\Omega\to 0} \equiv S_0$ is determined solely by S_Ω^a which yields

$$S_0 = \Phi_0 \coth\left(\frac{\Phi_0 I}{2T}\right)\langle V\rangle, \tag{37}$$

where $\langle V\rangle$ is specified in Eqs. (33) and (34). Hence, we obtain

$$S_0 \propto \begin{cases} T^{2\lambda-2}, & T \gg \Phi_0 I, \\ I^{2\lambda-2}, & T \ll \Phi_0 I. \end{cases} \tag{38}$$

At higher temperatures $T \gg \Phi_0 I$ Eq. (38) reduces to equilibrium voltage noise $S_0 = 2TR$ of a linear Ohmic resistor $R = \rho L$. In the opposite low temperature limit $T \ll \Phi_0 I$ it accounts for QPS-induced *shot noise* $S_0 = \Phi_0\langle V\rangle$ obeying *Poisson statistics* with an effective "charge" equal to the flux quantum Φ_0.

This result sheds light on the physical origin of shot noise in superconducting nanowires: It is produced by coherent tunneling of magnetic flux quanta Φ_0 across the wire. As we have already learned, such flux quanta can be viewed as charged quantum "particles" (fluxons) passing through (and being scattered at) an effective spatially extended "tunnel" barrier which role is played by a nanowire.

It is also interesting to analyze voltage noise produced by QPS at non-zero frequencies. In the limit of sufficiently high frequencies and/or long wires $v/L \ll \Omega \ll \Delta_0$ we obtain

$$S_\Omega^{(0)} = \frac{\lambda}{8\pi e^2} \frac{\Omega \coth\left(\frac{\Omega}{2T}\right)}{(\Omega/2E_C)^2 + (\lambda/\pi)^2}. \tag{39}$$

This contribution does not depend on the wire length L. At low T and $\Omega/\lambda \gtrsim E_C = e^2/2C$ we have $S_\Omega^{(0)} \propto 1/\Omega$, i.e., in this regime the wire may generate $1/f$ voltage noise. Evaluating the QPS terms S_Ω^r and S_Ω^a we observe that the latter scales linearly with the wire length L whereas the former does not. Hence, the term S_Ω^r can be safely neglected in the long wire limit. For the remaining QPS term S_Ω^a we get

$$\begin{aligned} S_\Omega^a = {} & \frac{L\lambda^2 v\gamma_{\mathrm{qps}}^2}{4e^2}\left[\varsigma\left(\frac{\Phi_0 I}{2} - \Omega\right) - \varsigma\left(\frac{\Phi_0 I}{2} + \Omega\right)\right] \\ & \times \frac{\sinh\left(\frac{\Phi_0 I}{2T}\right)\varsigma\left(\frac{\Phi_0 I}{2}\right)}{\left((\Omega/2E_C)^2 + (\lambda/\pi)^2\right)\sinh\left(\frac{\Omega}{2T}\right)}. \end{aligned} \tag{40}$$

At $T \to 0$ from Eq. (40) we find

$$S_\Omega^a \propto \begin{cases} I^{\lambda-1}(I - 2\Omega/\Phi_0)^{\lambda-1}, & \Omega < \Phi_0 I/2, \\ 0, & \Omega > \Phi_0 I/2. \end{cases} \tag{41}$$

In order to interpret this result we note that at $T = 0$ each QPS event excites (at least) two plasmons with total energy $E = \Phi_0 I$ propagating in the opposite directions along the wire. One of those plasmons (with energy $E/2$) gets dissipated at the grounded end of the wire while another one (also with energy $E/2$) reaches its opposite end causing voltage fluctuations (emits a photon) with frequency Ω measured by a detector. Obviously, at $T = 0$ this process is only possible at $\Omega < E/2$ in the agreement with Eq. (41).

In order to complete our analysis of voltage fluctuations we remark that Eqs. (30)–(32) allow to also recover all higher order correlators (cumulants) of the voltage operator, thus enabling one to construct full counting statistics of quantum phase slips. In the zero frequency limit this statistics is Poissonian, and it becomes very complicated beyond this limit.

To conclude, already in the "superconducting" regime $\lambda > 2$ the nanowires exhibit physical properties dramatically different from those of bulk superconductors. Such unusual behavior includes not only non-vanishing resistance of superconducting nanowires down to $T = 0$ but also coherent voltage fluctuations generated by quantum phase slips. In the presence of a current bias I quantum tunneling of magnetic fluxons across the wire causes Poissonian shot noise with a non-trivial power law dependence of its spectrum on both I and frequency Ω.

"Insulating" regime: Localization of Cooper pairs

Let us now turn to the analysis of quantum fluctuations in superconducting nanowires in the "insulating" regime $\lambda < 2$. For simplicity we start by considering two somewhat different configurations displayed in Fig. 4. One of them (left plot) corresponds to a nanowire in the form of a ring with a perimeter $L = 2\pi R$. For brevity in what follows we will denote it as a QPS ring meaning that

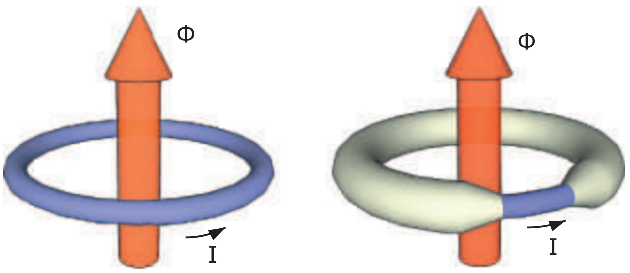

Fig. 4 Left: Quantum phase slip ring, i.e., an ultrathin superconducting ring threaded by an external magnetic flux. Right: Quantum phase slip junction embedded in a thick superconducting ring. Reproduced from Semenov AG and Zaikin AD (2013) Persistent currents in quantum phase slip rings. *Physical Review B* 88: 054505.

the nanowire remains thin enough for QPS effects to be pronounced there. Another configuration (right plot) also corresponds to a superconducting ring which now has thicker and thinner parts. Quantum fluctuations of the order parameter are negligible in the bulk part of the ring but proliferate inside its thinner part (a nanowire of length L) which we will call a QPS junction. In both cases the superconducting ring is pierced by an external magnetic flux Φ_x.

For the sake of definiteness below we will only consider the case of a QPS ring, exactly the same results will also apply to a QPS junction. We first assume that the QPS ring perimeter L is small enough enabling us to disregard the coordinate dependence of our fluctuating variables of interest. Specifically, it implies that we can ignore the last term in the Hamiltonian (24). In this limit the effective Hamiltonian of our QPS ring that follows from Eqs. (24) and (25) takes the form.

$$\hat{H} = \frac{E_{\mathcal{L}}}{2}\left(\hat{\phi} - \phi_x\right)^2 - \gamma_{\text{qps}} L \cos\hat{\chi}, \tag{42}$$

where $E_{\mathcal{L}} \sim g_\xi \Delta\xi/L$, $\hat{\phi} = \hat{\Phi}/\Phi_0$ and $\phi_x = \Phi_x/\Phi_0$.

The Hamiltonian (42) describes a fictitious quantum particle on a ring in the presence of a cosine external potential. The solution of this problem is well known from any standard course in quantum mechanics. One can distinguish two different regimes by comparing the "kinetic" and "potential" energies $E_{\mathcal{L}}$ and $\gamma_{\text{qps}}L$ or, equivalently, by comparing the ring perimeter L and the parameter (Zaikin, 2010)

$$L_{c0} \sim \xi \exp\left(a g_\xi/2\right). \tag{43}$$

For smaller rings with $L \ll L_c$ the flux-dependent ground state energy of the problem reads $E_0(\phi_x) \simeq (E_{\mathcal{L}}/2)\min_n(n + \phi_x)^2$ except in the vicinity of the crossing points $\phi_x = 1/2 + n$ where the gap to the first excited energy band $\delta E_{01} = \gamma_{\text{qps}}L$ opens up due to level repulsion. Evaluating the supercurrent I flowing around the ring at $T \to 0$ by means of the formula

$$I = \frac{e}{\pi}\frac{\partial E_0(\phi_x)}{\partial \phi_x}, \tag{44}$$

one recovers the standard sawtooth-like dependence which—not too close to the points $\phi_x = 1/2 + n$—is not affected by QPS.

For larger ring perimeters $L \gtrsim L_{c0}$ the bandwidth shrinks while the gaps become bigger. Then, combining the corresponding solution for the ground state energy $E_0(\phi_x)$ with Eq. (44), at $T \to 0$ we obtain

$$I = I_0 \sin\left(2\pi\phi_x\right), \quad I_0 \sim e g_\xi \Delta\sqrt{\frac{L}{\xi}} e^{-\frac{3a}{4}g_\xi} e^{-L/L_{c0}}. \tag{45}$$

This equation demonstrates that quantum phase slips yield exponential suppression of the supercurrent even at $T = 0$ provided the ring perimeter L exceeds the critical value L_{c0} (43).

As we already pointed out, the above analysis holds only for sufficiently small values of the ring perimeter L. In a general case it is necessary to employ the full sine/Gordon Hamiltonian (24), (25) instead of the reduced one (42). This amounts to taking into account logarithmic interactions between quantum phase slips, cf., e.g., Eq. (17). This task can be accomplished by means of the RG approach employing (19).

As before, assuming for simplicity that $v/\Delta x_0 \sim \xi$ and starting renormalization at the shortest scale $\Lambda \sim \xi$ we proceed to bigger scales. Ignoring weak renormalization of the parameter λ we obtain the solution of Eq. (19) in the form $\gamma_{\text{qps}}(\Lambda) = \gamma_{\text{qps}}(\xi/\Lambda)^\lambda$. Our RG procedure should be stopped at the scale corresponding to the ring perimeter $\Lambda \sim L$. As a result, we arrive at the renormalized QPS amplitude

$$\tilde{\gamma}_{\text{qps}} = \gamma_{\text{qps}}(\xi_c/L)^\lambda. \tag{46}$$

This result allows to conclude that inter-QPS interaction effects remain weak and can be disregarded only for very small values of $\lambda \ll 1/\ln(L/\xi)$ or, equivalently, for ring perimeters obeying the inequality

$$L \ll \xi \exp\left(\frac{1}{\lambda}\right). \tag{47}$$

This inequality naturally restricts both the wire length and cross section values at which it can be treated as a zero-dimensional object described by the Hamiltonian (42).

Substituting the renormalized QPS amplitude (46) instead of the bare one and extracting the correlation length L_c from the condition $E_{\mathcal{L}} \sim \tilde{\gamma}_{QPS}L$, we get (Semenov and Zaikin, 2022)

$$L_c \sim \xi \exp\left(\frac{a g_\xi}{2 - \lambda}\right), \tag{48}$$

where λ is supposed not to exceed 2. We observe that the correlation length L_c (48) increases with increasing λ and eventually diverges at the quantum phase transition point $\lambda = 2$. In the limit of small $\lambda \ll 1/\ln(L/\xi)$ the parameter L_c reduces to L_{c0} (43).

As before, for smaller rings with $L \ll L_c$ and at $T \to 0$ the supercurrent I is almost insensitive to QPS, whereas in the opposite limit $L \gg L_c$ we again reproduce Eq. (45) for I, where now

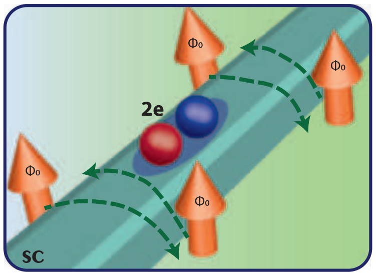

Fig. 5 Localization of Cooper pairs in the ground state of a uniform superconducting nanowire due to strong zero-point fluctuations of magnetic flux. Reproduced from Arutyunov KYu, Lehtinen JS, Radkevich A, Semenov AG, and Zaikin AD (2021) Superconducting insulators and localization of Cooper pairs. *Communications Physics* 4: 146. This work is licensed under a Creative Commons Attribution 4.0 International License, http://creativecommons.org/licenses/by/4.0/.

$$I_0 \sim e g_\xi \Delta \left(\frac{R}{\xi}\right)^{1/2-3\lambda/4} e^{-\frac{3a}{4}g_\xi} e^{-(L/L_c)^{\frac{1}{1-\lambda/2}}}. \tag{49}$$

We observe that the supercurrent gets essentially suppressed by quantum fluctuations as soon as L exceeds L_c.

The same conclusions hold also for superconducting nanowires displayed, e.g., in Fig. 3. For such wires we again apply the sine-Gordon Hamiltonian (24), (25) but, unlike in the case of a ring geometry of Fig. 4, we do not anymore impose any periodic boundary conditions at the wire ends. It is well established that for $\lambda < 2$ the relevant excitations of our sine-Gordon theory are kinks and anti-kinks (as well as their bound states) with an effective gap in the spectrum $\tilde{\Delta} \propto \gamma_{\mathrm{qps}}^{\frac{1}{2-\lambda}}$. This gap, in turn, gives rise to the same correlation length $L_c \propto 1/\tilde{\Delta}$ defined in Eq. (48).

The appearance of this fundamental length scale in our problem is directly related to the flux-charge duality. It can be interpreted as a result of spontaneous tunneling of magnetic fluxons Φ_0 back and forth across the wire, as it is illustrated in Fig. 5. These strong quantum fluctuations of magnetic flux wipe out phase coherence at distances $\gtrsim L_c$ and yield effective *localization of Cooper pairs* at such length scales. Accordingly, one may interpret the energy $\sim \xi\Delta g_\xi/L_c \propto \tilde{\Delta}$ as an effective Coulomb gap for the wire segment of length $\sim L_c$.

To conclude, the properties of the "insulating" phase realized at $T \to 0$ in thinnest wires and rings with $\lambda < 2$ turn out to be highly non-trivial. In this phase, quantum phase slips remain unbound and determine a nonperturbative localization length of Cooper pairs L_c beyond which the supercurrent gets suppressed by quantum fluctuations. Accordingly, for $T \to 0$ such nanowires turn insulating only at length scales exceeding L_c, whereas at shorter length scales they may still exhibit superconducting properties.

Conclusion

In a sharp contrast to bulk superconductors, low temperature properties of quasi-one-dimensional nanowires are essentially determined by quantum fluctuations which are, in turn, controlled by two different parameters, the dimensionless normal state conductance of the wire segment g_ξ and the dimensionless wire admittance g_Z. Both these parameters (1) decrease with decreasing wire diameter, thus making quantum fluctuations progressively more pronounced.

Provided g_ξ remains very large, the low temperature behavior of the system is determined by small (Gaussian) quantum fluctuations of the phase of the order parameter controlled by the parameter g_Z. Such fluctuations are directly related to sound-like plasma modes propagating along superconducting nanowires. As soon as the dimensionless conductance g_ξ becomes not too large quantum phase slips come into play forming a logarithmically interacting "gas" in 1 + 1 (space + time) dimensions. Such interactions between different QPS are mediated by plasma modes and cause a "superconductor-insulator" quantum phase transition at $T \to 0$ and $\lambda \equiv g_Z/8 \simeq 2$.

The "superconducting" phase $\lambda > 2$ is characterized by bound QPS pairs and weaker decay of superconducting correlations in space-time. Nevertheless, even in this regime current-biased superconducting nanowires acquire a non-zero resistance and exhibit shot noise of the voltage. These phenomena can be interpreted in terms of tunneling of quantum fluxons across the nanowire. In the context of flux-charge duality, such fluxons ("charged" by the flux quantum Φ_0) can be treated as effective quantum "particles" exactly dual to Cooper pairs with charge $2e$. Such "particles" obey complicated full counting statistics which reduces to Poissonian one in the zero frequency limit.

In thinner nanowires with $\lambda < 2$ quantum phase slips remain unbound and superconducting correlations decay exponentially at length scales exceeding the size of a "superconducting domain" $\sim L_c$ (48). At such length scales and at $T \to 0$ superconducting nanowires exhibit an insulating behavior, whereas at shorter length scales they may demonstrate superconducting properties albeit possibly affected by quantum fluctuations of the phase. Hence, the correlation length L_c may be interpreted as an effective *localization length for Cooper pairs.*

These and other non-trivial quantum properties of superconducting nanowires remain under intensive investigation and also form a basis for a variety of applications of such nanowires in quantum information technology, metrology and nanoelectronics.

References

Arutyunov KY, Golubev DS, and Zaikin AD (2008) Superconductivity in one dimension. *Physics Reports* 464: 1–70.

Bezryadin A (2013) *Superconductivity in Nanowires.* Weinheim: Wiley-VCH.

Larkin AI and Varlamov AA (2005) *Theory of Fluctuations in Superconductors.* Oxford: Clarendon.

Schön G and Zaikin AD (1990) Quantum coherent effects, phase transitions, and the dissipative dynamics of ultra small tunnel junctions. *Physics Reports* 198: 237–412.

Semenov AG and Zaikin AD (2022) Superconducting quantum fluctuations in one dimension. *Physics-Uspekhi* 65: 945–983.

Tinkham M (1996) *Introduction to Superconductivity.* New York: McGraw-Hill.

Zaikin AD (2010) uperconducting nanowires and nanorings. In: Sattler KD (ed.) *Handbook of Nanophysics: Nanotubes and Nanowires*, pp. 40-1–40-24. Boca Raton: CRC Press.

Zaikin AD and Golubev DS (2019) *Dissipative Quantum Mechanics of Nanostructures: Electron Transport, Fluctuations and Interactions.* Singapore: Jenny Stanford.

Superconductor-ferromagnet hybrid structures

F Sebastian[a,b] **and Stefan Ilić**[a], [a]Centro de Física de Materiales (CFM-MPC), Centro Mixto CSIC-UPV/EHU, Donostia-San Sebastián, Spain; [b]Donostia International Physics Center (DIPC), Donostia-San Sebastián, Spain

© 2024 Elsevier Ltd. All rights reserved.

Introduction **682**
Metallic S/F structures **683**
Manifestations of oscillatory condensate function in observables 684
Odd-frequency triplet superconductivity in S/F structures **686**
The role of spin-orbit coupling 687
Magnetic proximity effect **687**
Superconductor-ferromagnetic insulator structures 688
F/S/F spin valves 689
Non-equilibrium properties of S/F structures **689**
Conclusion **691**
References **691**

Abstract

This chapter presents an overview of the physics of superconductor-ferromagnet (S/F) hybrid structures. In addition to the important role in the development of superconducting spintronics, topological superconductors, and radiation detectors, these structures present a variety of exciting effects resulting from the interaction between superconductivity and magnetism. The superconducting proximity effect produces an oscillatory electron pair wave function inside the ferromagnet. This has several striking consequences, such as non-monotonic dependence of the critical temperature on the thickness of the ferromagnet and the "π" Josephson effect. Moreover, an odd-frequency triplet component of the superconducting condensate is generated in such systems. Since it is also even in momentum, the triplet is insensitive to non-magnetic disorder. When the magnetization of the ferromagnet is non-homogeneous, the triplets can penetrate over large distances in a ferromagnet even with a strong exchange field. We also discuss the inverse proximity effect in S/F structures, which induces a finite magnetic moment in the superconductor and may lead to spin-splitting of the density of states. We finish the chapter with an overview of the non-equilibrium properties of S/F structures.

Key points

- The superconductor/ferromagnet (S/F) structures provide a platform to explore the interplay and coexistence of two antagonistic phenomena - ferromagnetism and superconductivity.
- The proximity effect at the S/F interface produces an oscillatory electron-pair wave-function inside the ferromagnet. This leads to several striking phenomena, such as non-monotonic dependence of the critical temperature on the thickness of the ferromagnet, and the "π" Josephson effect.
- An odd-frequency triplet component of the superconducting condensate is generated in S/F structures. Since it is also even in momentum, the triplet is insensitive to non-magnetic disorder. In the case when magnetization of the ferromagnet is non-homogeneous, the triplets can penetrate across large distances in the ferromagnet and are not suppressed even by strong exchange fields.
- Magnetism may be induced in a superconductor in a S/F structure - the magnetic proximity effect. This manifests as suppression of the critical temperature and the spin-splitting of the density of states of the superconductor.
- S/F structures also provide a good platform to explore novel non-equilibrium phenomena related to the coupling of different electronic degrees of freedom.

Introduction

The interplay between superconductivity and exchange fields has been a topic of interest practically since the publication of the BCS theory in 1957. In a very early work, Abrikosov and Gor'kov (1960) demonstrated how a small amount of random magnetic impurities suppresses superconductivity, by breaking the local time-inversion symmetry due to the exchange field between impurities and conduction electrons. If the impurities are ferromagnetically aligned the situation is even more detrimental for conventional superconductivity, since the effective exchange field generated by the impurities tries to align the spins of the Cooper pair, which are in a singlet state. This leads to a pair-breaking mechanisms and hence suppression of the superconducting state.

https://doi.org/10.1016/B978-0-323-90800-9.00130-X

An interesting consequence of the interplay between superconductivity and an exchange field was predicted separately by Fulde and Ferrell (1964) and Larkin and Ovchinnikov (1965), who showed that the exchange field in a superconductor can lead to an inhomogeneous superconducting state, the so called FFLO state. This state is very sensitive to disorder and therefore very difficult to observe in conventional superconductors.

There is, however, another platform that allows the study of the interplay between superconductivity and exchange fields at the mesoscopic scale: the hybrid superconductor/ferromagnet S/F structures, which show interesting emerging states. In the case of S/F metallic structures, the superconducting *proximity effect* allows superconducting pair correlations to penetrate into the ferromagnet, in analogy to the proximity effect in superconductor/normal metal systems. The difference with the latter is that the electrons of the pair, which in conventional superconductors are in a singlet state, in the ferromagnet experience a different potential depending on their spin. This means that at the Fermi level, each electron in the pair acquires a different momentum, and the total momentum of the pair is no longer zero. Quantitatively, in an ideal 1D case, the momentum at the Fermi level for spin-up (down) electrons is $p_\pm = p_F \pm h/v_F$, where h is the exchange field in the ferromagnet, and v_F and p_F are the Fermi velocity and momentum, respectively. Thus, the total momentum acquired by the electron pair is $Q \equiv p_+ - p_- = 2h/v_F$, which determines the oscillation period of the superconducting correlations in the ferromagnet, in a sense analogous to the FFLO state.

In real metallic S/F structures, the oscillations of the superconducting correlations in the F layer is accompanied by an exponential decay away from the S/F interface. Specifically, the electron pair wave function has the form

$$\Psi(x) \sim e^{-x/\xi_F}, \tag{1}$$

where x is the spatial coordinate normal to the S/F interface and ξ_F is a complex length defined in a metallic system by

$$\xi_F \sim \sqrt{\frac{D_F}{2(\pi T + ih)}}. \tag{2}$$

Here D_F is the diffusion coefficient of the F metal, T the temperature, and we use the units where $\hbar = k_B = 1$. In a non-magnetic metal (N), $h = 0$ and the decay of Ψ into N is over the thermal length $\sim \sqrt{D_N/T}$, which at low temperature is only limited by inelastic scattering [see Fig. 1A].

In a ferromagnet h is finite and the pair correlation function oscillates and decays in space according to Eqs. (1), (2), see Fig. 1B. This results in a several remarkable phenomena discussed in detail in Section "Metallic S/F structures": non-monotonic dependence of the critical temperature on the thickness of the F layers in S/F bilayers, oscillation of the local electronic density of states in S/F bilayers, and a phase shift of π in the current-phase relation of a S/F/S Josephson junctions, for certain thicknesses of the F-layer.

Metallic S/F structures

Most of the experimental research on S/F structures is done on metallic systems. Typical superconductors are Al, Nb, V, whereas F layers consist of Fe, Ni, Co, Py, Ho, etc. All these materials can be well described using the diffusion equation, which in the case of superconductivity was derived by Usadel (1970). For a qualitative description of the proximity effect and calculation of observables, such as the critical current or the density of states, it is most often sufficient to consider the linearized Usadel equation. It is an equation determining the anomalous quasiclassical Green's function, $\hat{f}$, describing the superconducting pair condensate in the F layer:

$$-D_F \nabla^2 \hat{f} + \left\{ |\omega_n| + i\mathbf{h} \cdot \boldsymbol{\sigma} \operatorname{sgn} \omega_n, \hat{f} \right\} = 0. \tag{3}$$

Here $\omega_n = \pi T(2n + 1)$ are the Matsubara frequencies, $\mathbf{h}$ the exchange field in the ferromagnet, and $\boldsymbol{\sigma} = (\sigma_x, \sigma_y, \sigma_z)$ is the vector of spin Pauli matrices. The condensate function depends on the spatial coordinate and the frequency, $\hat{f}(\mathbf{r}, \omega_n)$, and it is a matrix in spin space. Eq. (3) is valid when superconducting correlations in F are weak, which is true at large temperatures $T \gg \Delta$, as well as for the case of a weak proximity effect due to non-ideal S/F interfaces. If these conditions are not met, the non-linear Usadel equation must be used.

In order to determine the function $\hat{f}$, Eq. (3) needs to be supplemented with a boundary condition at the S/F interface

$$\partial_x \hat{f} = -\gamma f_{BCS}. \tag{4}$$

Here, γ is a parameter describing the transparency of the interface ($\gamma = 0$ corresponds to infinitely resistive interface, whereas $\gamma \to \infty$ describes a fully transparent interface), x is the direction perpendicular to the interface, and $f_{BCS} = \Delta/\sqrt{\omega_n^2 + \Delta^2}$..

One can solve Eq. (3) for the case of an homogeneous magnetization and a very long F layer ($d_F \gg \xi_F$), where we set $\mathbf{h} \cdot \boldsymbol{\sigma} = h\sigma_z$ without loss of generality. $\hat{f}$ is then a diagonal matrix with elements

$$f_\pm = \gamma f_{BCS} \xi_\pm e^{-x\xi_r/|\xi_+|^2} e^{ix\xi_i/|\xi_+|^2}, \tag{5}$$

where $\xi_\pm = \sqrt{D_F/(2|\omega_n| \mp 2ih\operatorname{sgn}\omega_n)} = \xi_r \pm i\operatorname{sgn}\omega_n \xi_i$, and

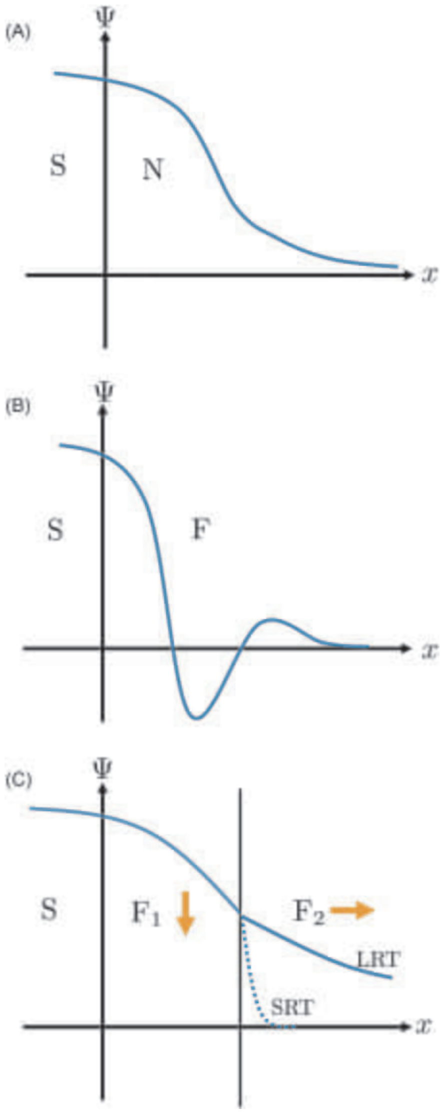

Fig. 1 Schematic representation of the spatial dependence of the pair correlation function Ψ in a (A) S/N structure, (B) S/F structure with homogeneous magnetization, and (C) S/F structure with inhomogeneous magnetization. In panel (C) SRT and LRT stand for short-range and long-range triplets, respectively.

$$\xi_{r,i} = \sqrt{D_F \frac{\sqrt{|\omega_n|^2 + h^2} \pm |\omega_n|^2}{4\left(|\omega_n|^2 + h^2\right)}}. \tag{6}$$

Eq. (5) confirms the decay and oscillations of the condensate function in the F layer. For a strong ferromagnet with $h \gg \Delta$, the decaying length and oscillation period is $\xi_F \sim \sqrt{D_F/h}$, which for usual ferromagnets (Fe, Co) corresponds to a sub-nanometer scale. This length scale is too short to be probed in an experiment, and therefore, one needs to use weaker ferromagnets with $h \lesssim \Delta$, or as we discuss below, to create pair correlations with equal spin projection.

Manifestations of oscillatory condensate function in observables

The oscillations of the condensate function in the ferromagnet lead to several theoretical predictions successfully tested in experiments. For example, the critical temperature T_c of the S/F bilayer shows non-monotonic behavior as a function of the thickness d_F of the ferromagnetic layer (Buzdin and Kupriyanov, 1990; Radović et al., 1991). Furthermore, T_c can be calculated by combining the solution of the linearized Usadel equation with the self-consistency condition for the order parameter Δ. Fig. 2A shows the measurement of T_c by Lazar et al. (2000), which is in good agreement with theoretical predictions.

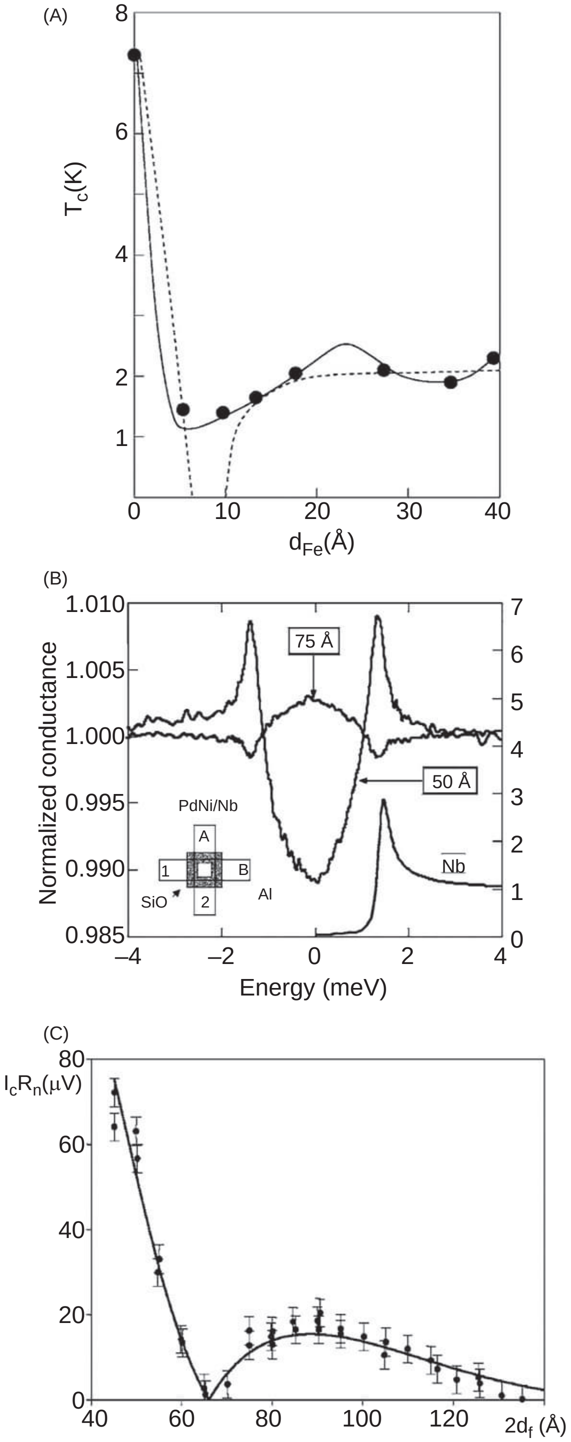

Fig. 2 Main results of several experiments on S/F structures. (A) Measurement of non-monotonic critical temperature in Pb/Fe bilayers as a function of ferromagnet thickness d_F. The solid and dashed lines are fits to the theory assuming a perfect and imperfect interface, respectively. (B) Measurements of the differential conductance in PdNi/Nb bilayer for different thicknesses of the ferromagnet PdNi, illustrating oscillating density of states. (C) Critical current of a S/F/S Josephson junction as a function of the thickness of the ferromagnet PdNi. The point where critical current vanishes ($d_F \sim 65$Å) corresponds to the transition from "0" to "π" phase. (A) Adapted with permission from Lazar L, Westerholt K, Zabel H, Tagirov L, Goryunov YV, Garif'yanov N, and Garifullin I (2000) Superconductor/ferromagnet proximity effect in Fe/Pb/Fe trilayers. *Physical Review B* 61(5): 3711. Copyright (2000) by the American Physical Society. (B) Reproduced with permission from Kontos T, Aprili M, Lesueur J, and Grison X (2001) Inhomogeneous superconductivity induced in a ferromagnet by proximity effect. *Physical Review Letters* 86(2): 304. Copyright (2001) by the Americal Physical Society. (C) Adapted with permission from Kontos T, Aprili M, Lesueur J, Genêt F, Stephanidis B, and Boursier R (2002) Josephson junction through a thin ferromagnetic layer: Negative coupling. *Physical Review Letters* 89(13): 137007. Copyright (2002) by the American Physical Society.

Another example are the oscillations of the local quasi-particle density of states (DoS) $N(\epsilon)$ (Buzdin, 2000), which can be calculated using Eq. (5) as $N(\epsilon) = N_0 + \delta N(\epsilon)$, where

$$\delta N(\epsilon) = \frac{N_0}{4}\,\mathrm{Re}\left(f_+^2 + f_-^2\right)\Big|_{i\omega_n \to \epsilon}. \tag{7}$$

Here, N_0 is the DoS in the normal state of the F layer, δN is the correction due to the superconducting proximity effect, and ϵ is the energy. In S/N structures, induced superconductivity suppresses the density of states around the Fermi level, $\epsilon = 0$. In other words, $\delta N < 0$. If one goes beyond the linearized limit, such suppression can be significant and induce a gap in the density of states of the N layer. In contrast, the spatial oscillations of the condensate in S/F structures can lead to different signs of δN, and hence to a situation where the DoS of S/F is *higher* than F alone at $\epsilon = 0$ for some d_F. This has been seen in the tunneling spectroscopy experiment by Kontos et al. (2001) [see Fig. 2B].

The oscillations of the superconducting condensate also manifest in the Josephson effect of S/F/S junctions. The Josephson effect establishes that the supercurrent can flow in the junction of two superconductors in the presence of a phase difference φ between them

$$I_S = I_c \sin\varphi. \tag{8}$$

Eq. (8) is known as the current-phase relation, where I_c is the critical current of the junction. The ground state of the junction corresponds to a zero-current state, which is either at $\varphi = 0$ or $\varphi = \pi$. In conventional tunneling or S/N/S Josephson junctions, $\varphi = 0$ corresponds to a minimum of energy; therefore, it is the ground state of the junction. Moreover, in an S/N/S junction, I_c monotonically decreases as the N thickness increases. In a S/F/S junction, because of the oscillation of the condensate function, I_c has an oscillatory behavior. In the case of large exchange field $h \gg T$ and large temperatures the critical current is given by

$$I_c \sim e^{-d_F/\xi_F}\cos(d_F/\xi_F), \tag{9}$$

where $\xi_F \sim \sqrt{D_F/h}$. Therefore, depending on the thickness d_F, I_c may change its sign. If $I_c < 0$, then $\varphi = 0$ corresponds to a maximum of the Josephson energy, which is now minimized by $\varphi = \pi$. Junctions with positive and negative I_c are called "0" and "π" junctions, respectively. The "0-π" transition in S/F/S junctions was first predicted by Buzdin, Bulaevskii, and Panyukov in 1982 (Buzdin, 2005; Buzdin et al., 1982) and observed in several experiments (see e.g. Ryazanov et al. (2001), Kontos et al., (2002)). In the former experiment, a ferromagnet $\mathrm{Cu}_x\mathrm{Ni}_{1-x}$ has been used, whose exchange field is weak, $h \sim T_c$. In this case, the penetration of the condensate function in the F region is long-range. The complex length ξ_+ depends on temperature and leads to oscillations of I_c as a function of the temperature, as observed in the experiment. Oscillations of I_c as a function of d_F have also been reported in experiments [see Fig. 2C].

Odd-frequency triplet superconductivity in S/F structures

In 2001, the same year that the 0-π transition was experimentally verified, Bergeret, Volkov, and Efetov (Bergeret et al., 2001, 2005; Kadigrobov et al., 2001) predicted the existence of a long-range triplet component of the superconducting condensate in S/F structures with inhomogeneous magnetization. Such component corresponds to equal-spin Cooper pairs, which are insensitive to the exchange field. To understand how this component appears it is sufficient to consider the linearized theory of the previous section.

If the magnetization is homogeneous there is a single spin quantization axis, and the condensate matrix $\hat{f}$ is diagonal with components $f_\pm$, see Eq. (5). If the magnetization of the F layer is inhomogeneous, for instance due to magnetic domains and domain walls, the condensate matrix can be decomposed into singlet and triplet components:

$$\hat{f} = f_s\sigma_0 + \mathbf{f}_t\cdot\boldsymbol{\sigma}, \tag{10}$$

where $\mathbf{f}_t = (f_x, f_y, f_z)$ is the triplet condensate vector. In the previous example of a homogeneously magnetized ferromagnet, only the singlet and f_z component are finite, with $f_s = (f_+ + f_-)/2$ and $f_z = (f_+ - f_-)/2$. The latter corresponds to the triplet component with zero total spin projection, i.e. to the Cooper pair state $(\uparrow\downarrow + \downarrow\uparrow)$.

It follows from Eq. (3) that:

(i) The exchange field term always leads to singlet-triplet conversion.

(ii) The singlet component is an even function of the Matsubara frequency, whereas the triplet component is odd in frequency. This is a consequence of the Pauli exclusion principle. Namely, the components of $\mathbf{f}_t$ are even in momentum (*s*-wave symmetry) and even in spin (triplet state), and therefore they need to be odd in frequency. This type of superconductivity is denoted as odd-frequency triplet superconductivity.

(iii) Since these odd-frequency triplets are even in momentum, they are insensitive to non-magnetic disorder (Anderson theorem). This is in contrast to triplets associated with unconventional superconductivity with *p*-wave symmetry, which are suppressed by disorder.

(iv) Components of the triplet vector $\mathbf{f}_t$ orthogonal to the local exchange field $\mathbf{h}$ are not affected by it. Namely, those components decay in F without oscillating, over the thermal length $\xi_T = \sqrt{D_F/(2|\omega_n|)}$. In a ferromagnet with a strong exchange field, ξ_T is much larger than the magnetic length defined in Eq. (5). Thus, this component is long-range [see the sketch in Fig. 1C].

Long-range triplets correspond to Cooper pairs in a triplet state with finite spin projection, i.e. combination of (↑↑) and (↓↓). Because the spins of the electron pairs are parallel, they induce spin-polarized supercurrents in a S/F/S junction.

Observation of long-range Josephson coupling attributed to triplet supercurrents has been reported in a wide variety of magnetic materials, including half-metals (Keizer et al., 2006; Singh et al., 2015), multilayered F-structure (Khaire et al., 2010), and magnets with conical magnetic texture such as Ho (Robinson et al., 2010).

The role of spin-orbit coupling

The physical picture described above may be modified in an S/F system with spin-orbit coupling (SOC). Namely, SOC in diffusive systems leads to spin relaxation, which in the superconducting state manifests as an additional relaxation of the triplet component of the condensate. Specifically, the characteristic length over which the long-range triplet component of the condensate decays in a ferromagnet is given by (Demler et al., 1997)

$$\xi_t^{-1} = \sqrt{\frac{2}{D_F}\left(|\omega_n| + \frac{4}{\tau_{so}}\right)}, \tag{11}$$

where τ_{so} is the scattering time between collisions at spin-orbit impurities.

In S/F systems with a lack of inversion symmetry, due to either non-centrosymmetric materials, or hybrid interfaces, SOC can be of the Rashba type. In such a case the effect of SOC can be introduced in the diffusion equation, Eq. (3), as a SU(2) vector potential, $\widehat{\mathcal{A}}$, by substituting the derivatives by SU(2)-covariant ones: $\nabla \rightarrow \widetilde{\nabla} = \nabla - i\left[\widehat{\mathcal{A}}, \cdot\right]$. This substitution leads to new terms describing precession and relaxation of the triplet component. In particular, the precession term may convert the short-range triplet component into a long-range one. Moreover, Rashba-like SOC in superconducting structures may lead to an additional source of singlet-triplet conversion.

The SOC-mediated singlet-triplet conversion in combination with a finite magnetization leads to a variety of magnetoelectric phenomena in S/F structures, meaning that a spin response can be achieved by passing a current and vice-versa. Some prominent examples of such phenomena are the anomalous Josephson effect, where an arbitrary phase shift φ_0 can appear in the current-phase relation, and the supercurrent diode effect, where the critical current depends on the direction of current flow.

Magnetic proximity effect

While the superconducting proximity effect is responsible for the effects described above, the inverse proximity effect, or magnetic effect, is also important. Namely, magnetism may be induced in a superconductor in an S/F structure. The first manifestation of this phenomenon is the strong suppression of the superconducting critical temperature of thin S films in contact with F metal with a strong exchange field. However, superconductivity survives if the superconductor is thick enough or the exchange field is not particularly strong. The triplet correlations induced in the F layer may penetrate the S layer and change its spectrum. Indeed, as predicted by Bergeret et al. (2004) and verified experimentally by Xia et al. (2009), the triplet correlations induce a magnetic moment in the superconductor opposite to the average magnetization of the itinerant electrons in the ferromagnet. For example, the magnetic moment of an F particle embedded in a superconductor is screened via the inverse proximity effect, as illustrated in Fig. 3.

Such screening can be understood by recalling the paramagnetic response of a superconductor. In the pure paramagnetic case a magnetic field **B** induces in a superconductor a magnetic moment:

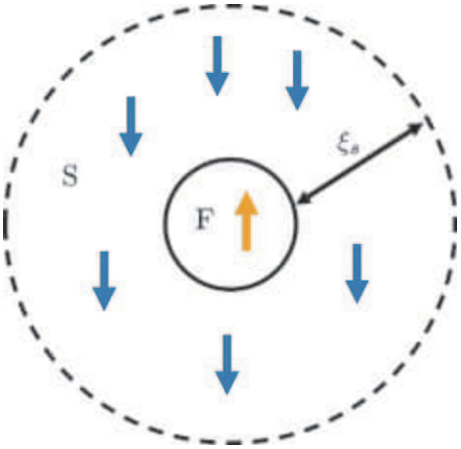

Fig. 3 Ferromagnetic grain embedded in a superconductor. The magnetic moment of the grain is screened by the superconductor due to the magnetic proximity effect.

$$\mathbf{S} = \chi_0 \mathbf{B} + \delta \mathbf{S}(T). \tag{12}$$

The first term is the usual Pauli paramagnetic term, with $\chi_0 = -2\mu_B N_0$ and μ_B being the Bohr magneton. The second term is the deviation from the Pauli paramagnetic response due to the superconducting correlations. In a homogeneous case and at zero temperature $\delta\mathbf{S}(T) = -\chi_0\mathbf{B}$, which reflects the fact that superconductors exhibit zero paramagnetic response at $T = 0$. In the presence of SOC $\delta\mathbf{S}(0) \neq -\chi_0\mathbf{B}$, and the superconductor may exhibit a finite paramagnetic susceptibility at $T = 0$.

In a hybrid S/F structure, the ferromagnet is usually described by free electrons in an effective exchange field $\mathbf{h}$ acting as a paramagnetic field. It is only finite in the F region and induces a local magnetic moment equivalent to the Pauli term in Eq. (12), proportional to $N_0\mathbf{h}(\mathbf{r})$. The second term on the right-hand side of Eq. (12) describes the response of the superconductor to the exchange field. It is a non-local magnetic moment with an opposite sign extending over a distance of the order of the superconducting coherence length away from the F region (see Fig. 3). While the local magnetic moment is finite, after spatial integration, the total one is zero at $T = 0$, as in the homogeneous case. The local magnetic moment can be probed using the polar Kerr effect or low-energy muons.

Superconductor-ferromagnetic insulator structures

Beside all-metallic S/F structures, the magnetic proximity effect can also be observed in ferromagnetic insulator/superconductor structures (FI/S) (Hijano et al., 2021; Meservey and Tedrow, 1994). Ferromagnetic insulators, such as EuS, EuO, or GdN, when put in contact with a thin superconducting film, such as Al or Nb, may induce in the latter a spin-split BCS density of states. This is equivalent to the Zeeman splitting induced in a thin superconducting film in a large in-plane magnetic field [see Fig. 4A]. At the same time, since the electrons from S cannot penetrate the insulating FI, there is no superconducting proximity effect. In other

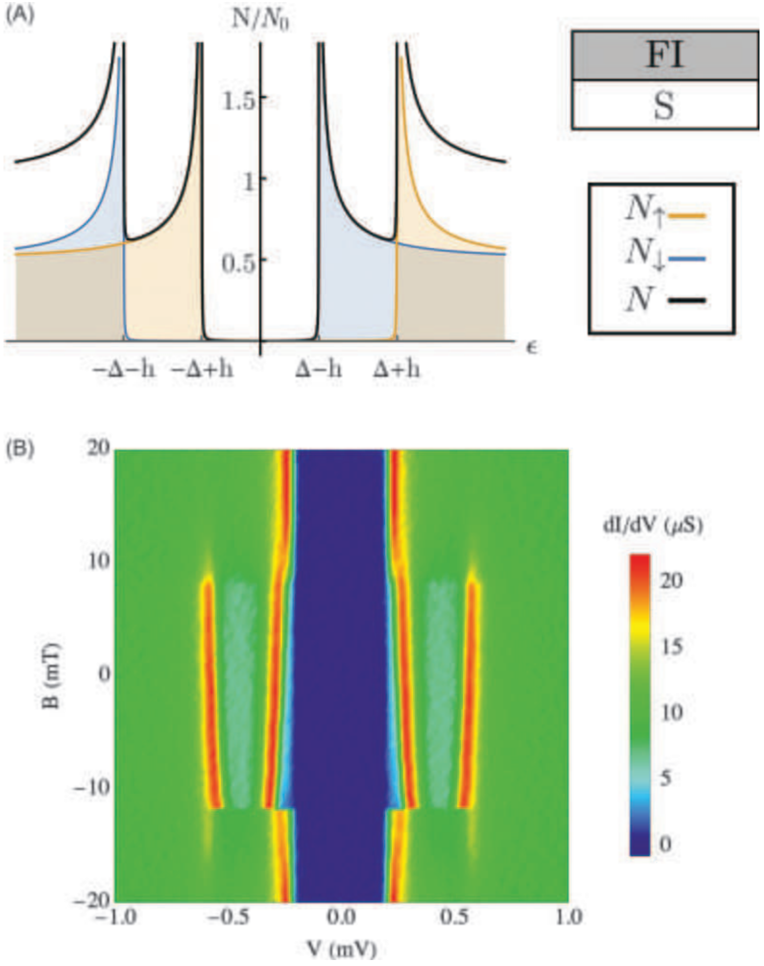

Fig. 4 (A) Spin-split density of states in a FI/S structure. (B) Measurements of the differential conductance of a EuS/Al structure, as a function of externally applied magnetic field *B* and voltage, from Hijano et al., (2021). Well defined spin-splitting can be observed even at $B = 0$. Adapted from Hijano A, Ilić S, Rouco M, González-Orellana C, Ilyn M, Rogero C, Virtanen P, Heikkilä T, Khorshidian S, Spies M. et al. (2021) Coexistence of superconductivity and spin-splitting fields in superconductor/ferromagnetic insulator bilayers of arbitrary thickness. *Physical Review Research* 3(2): 023131. This work is licensed under a Creative Commons Attribution 4.0 International License, http://creativecommons.org/licenses/by/4.0/.

words, the Cooper pairs do not "leak" from S to FI, resulting in robust superconductivity in S and sharp coherence peaks in the density of states.

The origin of spin-splitting is the interfacial effective exchange coupling between the localized magnetic moments of the FI and the conduction electrons of the S layer. If the thickness of the latter is smaller than the coherence length, then the density of states can be assumed to be homogeneous in space and given by $N(\epsilon) = \frac{1}{2}\left[N_\uparrow(\epsilon) + N_\downarrow(\epsilon)\right]$, with

$$N_{\uparrow,\downarrow}(\epsilon) = \operatorname{Re} \frac{\epsilon \pm h_{eff}}{\sqrt{\left(\epsilon \pm h_{eff}\right)^2 - \Delta^2}}, \tag{13}$$

where $N_{\uparrow,\downarrow}$ is the density of states for spin-up and -down. The effective spin-splitting field h_{eff} is given by the interfacial exchange field multiplied by a/d_S, where a is an atomic length scale over which the exchange interaction takes place, and d_S the thickness of the superconducting layer.

Since the end of the 1980s, numerous spectroscopy experiments on EuS/Al have demonstrated large spin-split density of states even at zero magnetic field [see Fig. 4]. Recently, interest in these systems has been renewed because of their potential for application in detectors, spintronics, and topological superconducting qubits.

For some of these applications, an important feature of FI is that it can also act as a spin-filtering tunneling barrier, as spin-filtering combined with spin-splitting leads to electron-hole (e-h) symmetry breaking. Namely, the total DoS $N(\epsilon)$ is e-h symmetric, $N(\epsilon) = N(-\epsilon)$, however if one spin species is filtered-out the symmetry is broken, $N_{\uparrow,\downarrow}(\epsilon) \neq N_{\uparrow,\downarrow}(-\epsilon)$, as seen from Eq. (13). Such spin-dependent transport leads to several interesting phenomena in FI/S structures, such as thermoelectric effects and rectification of AC currents which can be used for detectors or thermometers.

F/S/F spin valves

Another manifestation of the magnetic proximity effect is the change of the critical temperature of F/S/F structures, called spin-valves, when the relative magnetization of the two F layers changes between parallel (P) and antiparallel (AP) configurations (see Fig. 5). The effective exchange field in the superconducting layer is an average of the exchange fields induced at each S/F interface. In the P configuration the averaged exchange field induced in the superconductor is larger as in the AP case, and therefore leads to lower critical temperature.

This behavior was theoretically predicted by De Gennes (1966) on the example of FI/S/FI structures and verified in experiments by Hauser (1969). In later works, these claims were extended to metallic samples: theoretically by Buzdin et al. (1999) and Tagirov (1999), and experimentally by Gu et al. (2002) and Moraru et al., (2006). Another type of spin valve, namely S/F/F/S junctions, has been used to accurately control the 0-π transition by Gingrich et al. (2016).

Non-equilibrium properties of S/F structures

So far we considered the spectral and equilibrium properties of S/F hybrid structures. There is also a large experimental and theoretical activity on the transport properties of such structures under non-equilibrium conditions (Beckmann, 2016; Bergeret et al., 2018; Heikkilä et al., 2019). A typical experimental setup is sketched in Fig. 6: a superconducting wire is contacted to various

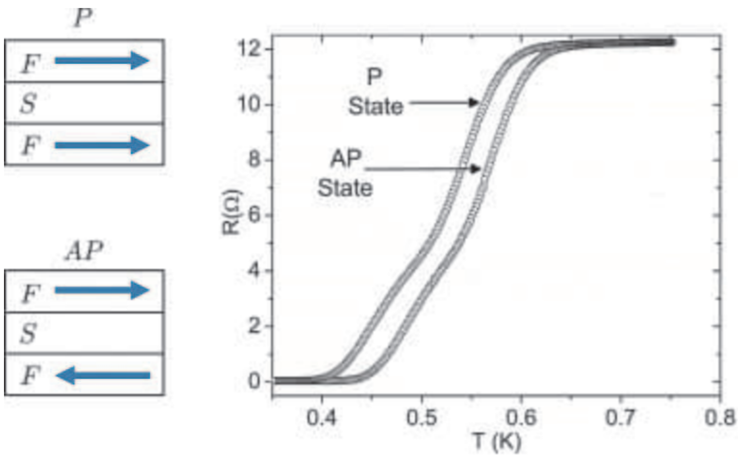

Fig. 5 Resistance measurement by Moraru IC, Pratt W Jr, and Birge NO (2006) in a Ni/Nb/Ni spin-valve, showing that the superconducting transition temperatures in the AP state is higher than in the P state. Adapted with permission from Moraru IC, Pratt W Jr, and Birge NO (2006) Magnetization-dependent T_c shift in ferromagnet/superconductor/ferromagnet trilayers with a strong ferromagnet. *Physical Review Letters* 96(3): 037004. Copyright (2006) by the American Physical Society.

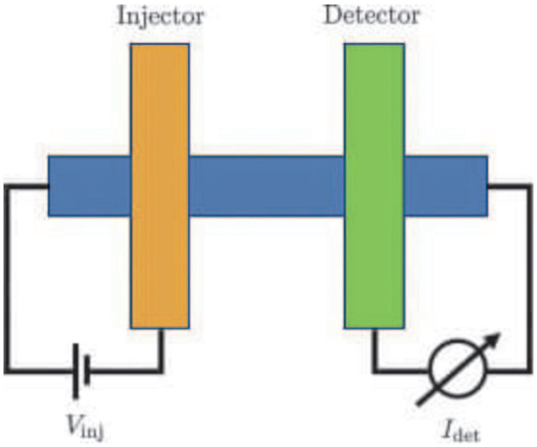

Fig. 6 Sketch of a setup for detection of the non-equilibrium modes in a superconductor (blue wire) via transport measurements. Injector and detector are normal or ferromagnetic metals.

electrodes, which can be non-magnetic or ferromagnets. One can, for example, inject a current from the injector by applying a voltage V_{inj}, and measure the current I_{det} in the detector circuit at zero bias (Hübler et al., 2012). The injected current drives the superconductor to a nonequilibrium state. Then, the current in the detector is given by the expression

$$I_{\text{det}} = G_{\text{det}}(\mu + P_{\text{det}}\mu_s), \tag{14}$$

where G_{det} is the tunneling conductance and P_{det} is the effective spin polarization of the detector. The charge imbalance μ and spin accumulation μ_s are related to the different components of the distribution function matrix via [see Silaev et al., 2015]:

$$\mu = -\frac{1}{2}\int_0^\infty d\epsilon(N_+F_T + N_-F_{Ls}), \tag{15}$$

$$\mu_s = -\frac{1}{2}\int_0^\infty d\epsilon\left[N_+F_{Ts} + N_-\left(F_L - F_{eq}\right)\right], \tag{16}$$

where $N_\pm = N_\uparrow \pm N_\downarrow$, and $F_{eq}(\epsilon) = \tanh(\epsilon/2T)$ is the equilibrium distribution function. The different functions F describe the different non-equilibrium modes. We use here the conventional notation denoting by the label T/L the transverse/longitudinal modes, which are symmetric/antisymmetric functions of the energy ϵ. F_T describes the charge imbalance mode, which quantifies the imbalance between quasiparticles above and below the Fermi surface. This mode can be excited by charge injection from a normal electrode to the superconductor. The mode F_L describes local changes in the effective temperature. Any heating mechanism can generally generate it. In the absence of ferromagnets, only these two modes can be excited and have been widely studied in the 70s and 80s. In the presence of ferromagnetic injectors/detectors, or spin-splitting fields in the superconductor, another two modes appear. The spin imbalance mode, F_{Ts}, describes the spin accumulation induced, for example, by a spin-polarized current injected from a ferromagnetic electrode. And finally the spin-energy mode, F_{Lj}, describes a non-equilibrium state with antisymmetric differences in the electron-hole and spin-up/down distributions. Nonequilibrium modes are determined by the Keldysh-Usadel kinetic equations presented in Silaev et al. (2015).

Fig. 7A shows the calculated non-local conductance defined as $g_{\text{nl}} = dI_{\text{det}}/dV_{\text{inj}}$ for different values of the spin-splitting field h. At zero field, only the terms proportional to N_+ in Eqs. (15) and (16) contribute to the detector current, Eq. (14). The contribution from the spin accumulation, Eq. (16), decays over the spin relaxation length. Therefore, if the distance between injector and detector is much larger than this length, the signal is dominated by the charge imbalance. This explains the almost symmetric signal, $g_{\text{nl}}(V_{\text{inj}}) \approx g_{\text{nl}}(-V_{\text{inj}})$, observed in experiments on charge imbalance (Hübler et al., 2012; Quay et al., 2013).

In the case of a finite spin-splitting field $N_- \neq 0$, so the second terms in Eqs. (15) and (16) also contribute to g_{nl}. If the spin-splitting is caused by an external magnetic field, the latter suppresses the charge imbalance via the orbital depairing effect. The non-local signal is then dominated by the energy mode F_L, the second term in Eq. (16). This results in almost antisymmetric $g_{\text{nl}}(V_{\text{inj}})$ curves, as shown in Fig. 7A. This contribution is independent of the elastic spin-dependent scattering, since the F_L mode relaxes only by inelastic scattering. At low temperatures, inelastic scattering becomes weak and therefore the spin accumulation can be long-range, as observed in experiments by Hübler et al. (2012), Wolf et al. (2013) and Quay et al. (2013). The comparison between theory and the experiment by Hübler et al. (2012), Fig. 7B, shows a very good agreement.

Interestingly, according to the theory one can also generate a spin accumulation even if the injector is a nonmagnetic metal. The simple injection of a current at voltages larger than the superconducting gap generates energy imbalance F_L. If the spin-splitting field is finite, a long-range contribution from the second term of Eq. (16) appears. This is also in accordance with the observations of Wolf et al. (2013). Long-range spin-dependent signals can have direct applications in the field of spintronics (Eschrig, 2011; Linder and Robinson, 2015).

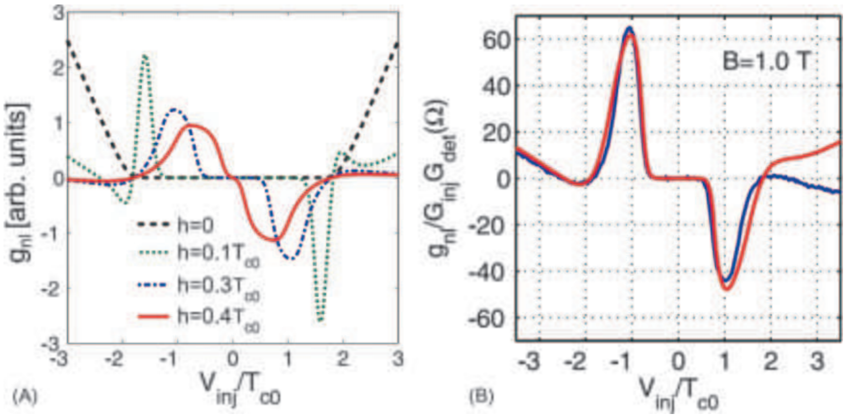

Fig. 7 (A) Calculated non-local conductance for different values of the spin-splitting field. (B) Comparison between theory (red curve) and experiment of Hübler et al. (2012) (blue curve). Adapted with permission from Silaev M, Virtanen P, Bergeret F, and Heikkilä T (2015) Long-range spin accumulation from heat injection in mesoscopic superconductors with Zeeman splitting. *Physical Review Letters* 114(16): 167002. Copyright (2015) by the American Physical Society.

Finally, the spin-energy mode, F_{Ls}, has been recently detected by Kuzmanović et al. (2020) in a setup as the one sketched in Fig. 6. The experiment did not use ferromagnetic materials and hence only the charge imbalance, Eq. (15), contributes to the non-local signal, Eq. (14). Using the kinetic theory developed by Silaev et al. (2015) and Heikkilä et al. (2019), Kuzmanović et al. (2020) could unambiguously identify the spin energy mode F_{Ls}.

Conclusion

The S/F structures provide an opportunity to study the interplay and coexistence of two antagonistic phenomena - ferromagnetism and superconductivity. As such, they have been a subject of vigorous investigation in the last few decades, both on the experimental and theoretical front. In this chapter we summarized the main results of these efforts, using a simple diffusion-like Usadel equation to qualitatively illustrate the main points.

The interest in these structures persists to this day, as they have been identified as a building block for many applications ranging from superconducting spintronics, topological superconductivity, to radiation detectors. Recent advances in sample preparation even allow to build atomically thin S/F structures in Wan der Vaals heterostructures, using monolayer ferromagnets such as $NiBr_2$.

References

Abrikosov AA and Gor'kov LP (1960) Contribution to the theory of superconducting alloys with paramagnetic impurities. *Zhurnal Eksperimental'noi i Teoreticheskoi Fiziki* 39.

Beckmann D (2016) Spin manipulation in nanoscale superconductors. *Journal of Physics: Condensed Matter* 28(16): 163001.

Bergeret F, Volkov A, and Efetov K (2001) Long-range proximity effects in superconductor-ferromagnet structures. *Physical Review Letters* 86(18): 4096.

Bergeret F, Volkov AF, and Efetov K (2004) Induced ferromagnetism due to superconductivity in superconductorferromagnet structures. *Physical Review B* 69(17): 174504.

Bergeret F, Volkov AF, and Efetov KB (2005) Odd triplet superconductivity and related phenomena in superconductor-ferromagnet structures. *Reviews of Modern Physics* 77(4): 1321.

Bergeret FS, Silaev M, Virtanen P, and Heikkilä TT (2018) Colloquium: Nonequilibrium effects in superconductors with a spin-splitting field. *Reviews of Modern Physics* 90(4), 041001.

Buzdin A (2000) Density of states oscillations in a ferromagnetic metal in contact with a superconductor. *Physical Review B* 62(17): 11377.

Buzdin AI (2005) Proximity effects in superconductorferromagnet heterostructures. *Reviews of Modern Physics* 77(3): 935.

Buzdin AI and Kupriyanov MY (1990) Transition temperature of a superconductor-ferromagnet superlattice. *JETP Letters* 52: 1089.

Buzdin AI, Bulaevskii L, and Panyukov S (1982) Critical-current oscillations as a function of the exchange field and thickness of the ferromagnetic metal (F) in an SFS Josephson junction. *JETP Letters* 35(4): 178–180.

Buzdin AI, Vedyayev A, and Ryzhanova N (1999) Spin-orientation–dependent superconductivity in F/S/F structures. *Europhysics Letters* 48(6): 686.

De Gennes P (1966) Coupling between ferromagnets through a superconducting layer. *Physics Letters* 23(1): 10–11.

Demler EA, Arnold G, and Beasley M (1997) Superconducting proximity effects in magnetic metals. *Physical Review B* 55(2): 15174.

Eschrig M (2011) Spin-polarized supercurrents for spintronics. *Physics Today* 64(1): 43.

Fulde P and Ferrell RA (1964) Superconductivity in a strong spin-exchange field. *Physical Review* 135(A): A550.

Gingrich E, Niedzielski BM, Glick JA, Wang Y, Miller D, Loloee R, Pratt W Jr., and Birge NO (2016) Controllable 0–π josephson junctions containing a ferromagnetic spin valve. *Nature Physics* 12(6): 564–567.

Gu J, You C-Y, Jiang J, Pearson J, Bazaliy YB, and Bader S (2002) Magnetization-orientation dependence of the superconducting transition temperature in the ferromagnet-superconductor-ferromagnet system: CuNi/Nb/CuNi. *Physical Review Letters* 89(26): 267001.

Hauser J (1969) Coupling between ferrimagnetic insulators through a superconducting layer. *Physical Review Letters* 23(7): 374.

Heikkilä TT, Silaev M, Virtanen P, and Bergeret FS (2019) Thermal, electric and spin transport in superconductor/ferromagnetic-insulator structures. *Progress in Surface Science* 94(3): 100540.

Hijano A, Ilić S, Rouco M, González-Orellana C, Ilyn M, Rogero C, Virtanen P, Heikkilä T, Khorshidian S, Spies M, et al. (2021) Coexistence of superconductivity and spin-splitting fields in superconductor/ferromagnetic insulator bilayers of arbitrary thickness. *Physical Review Research* 3(2): 023131.

Hübler F, Wolf M, Beckmann D, Löhneysen H, and v. (2012) Long-range spin-polarized quasiparticle transport in mesoscopic Al superconductors with a Zeeman splitting. *Physical Review Letters* 109(20): 207001.
Kadigrobov A, Shekhter R, and Jonson M (2001) Quantum spin fluctuations as a source of long-range proximity effects in diffusive ferromagnet-super conductor structures. *Europhysics Letters* 54(3): 394.
Keizer RS, Gönnenwein ST, Klapwijk TM, Miao G, Xiao G, and Gupta A (2006) A spin triplet supercurrent through the half-metallic ferromagnet CrO_2. *Nature* 439(7078): 825–827.
Khaire TS, Khasawneh MA, Pratt W Jr., and Birge NO (2010) Observation of spin-triplet superconductivity in Co-based Josephson junctions. *Physical Review Letters* 104(13), 137002.
Kontos T, Aprili M, Lesueur J, and Grison X (2001) Inhomogeneous superconductivity induced in a ferromagnet by proximity effect. *Physical Review Letters* 86(2): 304.
Kontos T, Aprili M, Lesueur J, Genêt F, Stephanidis B, and Boursier R (2002) Josephson junction through a thin ferromagnetic layer: negative coupling. *Physical Review Letters* 89(13): 137007.
Kuzmanović M, Wu B, Weideneder M, Quay C, and Aprili M (2020) Evidence for spin-dependent energy transport in a superconductor. *Nature Communications* 11(1): 1–7.
Larkin A and Ovchinnikov YN (1965) Nonuniform state of superconductors. *Soviet Physics - JETP* 20(3): 762.
Lazar L, Westerholt K, Zabel H, Tagirov L, Goryunov YV, Garif'yanov N, and Garifullin I (2000) Superconductor/ferromagnet proximity effect in Fe/Pb/Fe trilayers. *Physical Review B* 61(5): 3711.
Linder J and Robinson JW (2015) Superconducting spintronics. *Nature Physics* 11(4): 307–315.
Meservey R and Tedrow P (1994) Spin-polarized electron tunneling. *Physics Reports* 238(4): 173–243.
Moraru IC, Pratt W Jr., and Birge NO (2006) Magnetization-dependent T_c shift in ferromagnet/superconductor/ferromagnet trilayers with a strong ferromagnet. *Physical Review Letters* 96(3): 037004.
Quay C, Chevallier D, Bena C, and Aprili M (2013) Spin imbalance and spin-charge separation in a mesoscopic superconductor. *Nature Physics* 9(2): 84–88.
Radović Z, Ledvij M, Dobrosavljević-Grujić L, Buzdin AI, and Clem JR (1991) Transition temperatures of superconductor-ferromagnet superlattices. *Physical Review B* 44(2): 759.
Robinson J, Witt J, and Blamire M (2010) Controlled injection of spin-triplet supercurrents into a strong ferromagnet. *Science* 329(5987): 59–61.
Ryazanov V, Oboznov V, Rusanov AY, Veretennikov A, Golubov AA, and Aarts J (2001) Coupling of two superconductors through a ferromagnet: Evidence for a π junction. *Physical Review Letters* 86(11): 2427.
Silaev M, Virtanen P, Bergeret F, and Heikkilä T (2015) Long-range spin accumulation from heat injection in mesoscopic superconductors with Zeeman splitting. *Physical Review Letters* 114(16): 167002.
Singh A, Voltan S, Lahabi K, and Aarts J (2015) Colossal proximity effect in a superconducting triplet spin valve based on the half-metallic ferromagnet CrO_2. *Physical Review X* 5(2): 021019.
Tagirov L (1999) Low-field superconducting spin switch based on a superconductor/ferromagnet multilayer. *Physical Review Letters* 83(10): 2058.
Usadel KD (1970) Generalized diffusion equation for superconducting alloys. *Physical Review Letters* 25(8): 507–509.
Wolf MJ, Hübler F, Kolenda Sv, Löhneysen Hv, and Beckmann D (2013) Spin injection from a normal metal into a mesoscopic superconductor. *Physical Review B* 87(2): 024517.
Xia J, Shelukhin V, Karpovski M, Kapitulnik A, and Palevski A (2009) Inverse proximity effect in superconductor-ferromagnet bilayer structures. *Physical Review Letters* 102(8): 087004.

Superconductivity: Ginzburg-Landau theory and vortex lattice[☆]

EH Brandt[*], Max-Planck-Institut fur Metallforschung, Stuttgart, Germany

© 2024 Elsevier Ltd. All rights reserved.

This is an update of E.H. Brandt, Superconductivity: Ginzburg–Landau Theory and Vortex Lattice, Editor(s): Franco Bassani, Gerald L. Liedl, Peter Wyder, Encyclopedia of Condensed Matter Physics, Elsevier, 2005, Pages 98–105, ISBN 9780123694010, https://doi.org/10.1016/B0-12-369401-9/00702-6.

Introduction 693
Ginzburg-Landau theory 694
Critical fields 694
Vortex lattice 695
London theory 697
Vortices near surfaces and in films 698
Elasticity of the vortex lattice 699
Conclusion 701
References 701

Abstract

Some properties of the flux-line lattice in conventional and high-T_c superconductors are reviewed, with particular emphasis on phenomenological theories, nonlocal elasticity, irreversible magnetization curves, and influence of the specimen shape on the electromagnetic response.

Key points

- Main concepts and results of Ginzburg-Landau and London theories
- Description of vortex lattices in type-II superconductors within the Ginzburg Landau and London theories
- Elasticity of the vortex lattice in type-II superconductors

Introduction

After the discovery of superconductivity in 1912 by Heike Kamerlingh-Onnes in Leiden, it took almost 50 years until this fascinating phenomenon was understood microscopically, when in 1957 Bardeen, Cooper, and Schrieffer established their BCS theory. But long before this electron-pairing theory, there were powerful phenomenological theories which were able to explain most electromagnetic and thermodynamic observations on superconductors, and which are very useful today also (Brandt, 1995; De Gennes, 1966; Tinkham, 1975). The London theory, conceived by Fritz and Heinz London in 1935, is particularly useful for the description of the high-T_c superconductors, which were discovered in 1987 by Bednorz and Muller in Zurich. Perhaps the most useful and elegant phenomenological theory of superconductors was established by Vitalii Ginzburg and Lew Landau in 1951. The Ginzburg-Landau (GL) theory generalizes Landau's theory of second-order phase transitions to spatially varying charged systems in a magnetic field and should thus be applicable near the superconducting transition temperature T_c, but in many cases it yields a qualitatively correct behavior also at lower temperatures. The GL theory can be derived from the microscopic BCS theory, and it reduces to the London theory in situations when the GL function (the superconducting order parameter) has nearly constant magnitude. The theory of Ginzburg and Landau was also generalized to the cases of multiband and unconventional superconductors (Orlova et al., 2013; Sigrist and Ueda, 1991).

The GL theory has high predictive power. It predicts that superconductors can be of type-I (with positive energy of the wall between normal conducting and superconducting domains) or of type-II (with negative wall energy, pointing to an instability) and that superconductivity can be suppressed by a high magnetic field and by a high current density, namely, by the depairing current which breaks the Cooper pairs. Its most spectacular success was the prediction of spontaneous nucleation and penetration of magnetic vortices in type-II superconductors by Alexei Abrikosov in 1957. The properties of these Abrikosov vortices (or fluxons, flux lines, carrying one quantum of magnetic flux $\Phi_0 = h/2e = 2.07 \times 10^{-15}\mathrm{Tm}^2$) and their motion and pinning by material inhomogeneities, are important topics both in research and in the practical application of superconductors. Most applications

---

[☆] *Change History*: September 2022. B Grigorii Mikitik added two new references to Introduction. Updated abstract, conclusions, composed the list of references, and corrected misprints.

Deceased. The present version has been redrafted by Grigorii Mikitik, B. Verkin Institute for Low Temperature Physics and Engineering of the NAS of Ukraine.

require type-II superconductors with high critical magnetic fields and currents, but high loss-free supercurrents require that the vortices are pinned so that they cannot move under the action of this current and dissipate energy.

Ginzburg-Landau theory

The GL theory introduces a complex, spatially varying order parameter $\psi(\mathbf{r})$ in addition to the magnetic field $\mathbf{B}(\mathbf{r}) = \nabla \times \mathbf{A}(\mathbf{r})$ or vector potential $\mathbf{A}$. The GL function $\psi(\mathbf{r})$ later turned out to be proportional to the BCS energy-gap function $\Delta(\mathbf{r})$, and its square $|\psi(\mathbf{r})|^2$ to the density of Cooper pairs. It defines two characteristic lengths: the superconducting coherence length ξ sets the scale over which $\psi(\mathbf{r})$ can vary, while λ governs the variation of the magnetic field as in the London theory. Both λ and ξ diverge at the superconducting transition temperature T_c according to $\lambda \propto \xi \propto (T_c - T)^{-1/2}$, but their ratio, the GL parameter $\kappa = \lambda/\xi$, is nearly independent of the temperature T. The GL theory reduces to the London theory (which is valid down to $T = 0$) in the limit $\xi \ll \lambda$, which means constant magnitude $|\psi(\mathbf{r})| = \text{const}$ (except in the vortex cores, where ψ vanishes, see below). The GL equations are obtained by minimizing a free-energy functional $F\{\psi, \mathbf{A}\}$ with respect to the GL function $\psi(\mathbf{r})$ and the vector potential $\mathbf{A}(\mathbf{r})$. With the length unit λ and magnetic field unit $\sqrt{2}B_c\left(B_c = \Phi_0/\left(\sqrt{8}\pi\xi\lambda\right)\right.$ is thermodynamic critical field), the GL functional reads

$$F\{\Psi, \mathbf{A}\} = \frac{B_c^2}{\mu_0}\int_V \left[-|\Psi|^2 + \frac{1}{2}|\Psi|^4 + \left|\left(-\frac{i\nabla}{\kappa} - \mathbf{A}\right)\Psi\right|^2 + (\nabla \times \mathbf{A})^2\right] d^3r. \tag{1}$$

Here the integral is over the volume V of the superconductor. The first two terms are the superconducting condensation energy, which is minimum when $|\psi|^2 = 1$. The third term is the energy cost of the spatial variation of ψ; this gauge-invariant gradient also introduces $\mathbf{A}$ and thus the magnetic field. The last term is the magnetic energy density $B^2/2\mu_0$.

The GL functional and the resulting GL equations may be expressed in terms of the real-valued function $|\psi|$ and the gauge-invariant supervelocity $\nabla\varphi/\kappa - \mathbf{A}$, where $\varphi(r)$ is the phase of $\psi = |\psi| \exp(i\varphi)$. From the variation $\delta F/\delta\psi = 0$ follows the first GL equation determining the amplitude and phase of ψ. From the variation $\delta F/\delta \mathbf{A} = 0$ follows the supercurrent density $J = \mu_0^{-1}\lambda^2[(\Phi_0/2\pi)\nabla\varphi - \mathbf{A}]|\psi|^2$, which has to be supplemented by the Maxwell equation $J = \mu_0^{-1}\,\text{curl}\,\text{curl}\,\mathbf{A}$ to obtain an equation for $\mathbf{A}$ or $\mathbf{J}$ alone. The minimization of F yields not only the functions $\psi(\mathbf{r})$ and $\mathbf{A}(\mathrm{r})$, but also the boundary condition that the current density and supervelocity do not have a component perpendicular to the free surface of the superconductor.

In an external field H_a, one has to minimize not the free energy F but the Gibbs free energy $G = F - \overline{B}H_a$, where $\overline{B}$ is the spatial average of the magnetic induction B in the superconductor. The condition $\partial G/\partial\overline{B} = 0$ yields the equilibrium field $H_a = \partial F/\partial\overline{B}$. In sufficiently low H_a, the superconductor expels the applied magnetic field completely, that is, one has $B = 0$ inside the superconductor (Meissner state). More precisely, the parallel applied field penetrates into a thin surface layer of thickness λ. In a superconductor filling the half space $x \geq 0$, one has $B(x) = \mu_0 H_a \exp(-x/\lambda)$. This screening of H_a is caused by a surface current of density $j(x) = (H_a/\lambda)\exp(-x/\lambda)$ flowing perpendicular to H_a. Such an exponential screening, strictly spoken, occurs only for London superconductors with large GL-parameter $\kappa \gg 1$, while for smaller κ values both $|\psi|$ and B vary near the surface and have to be obtained by solving the GL equations. Moreover, for superconductors of realistic shape, such as short cylinders or rectangular plates, the penetration of a magnetic field into the surface layer has to be calculated numerically; only for spheres and long cylinders with $\kappa \gg 1$, analytical solutions were obtained by London.

Critical fields

In type-I superconductors (defined by $\kappa < 1/\sqrt{2}$), complete screening occurs when the applied magnetic field H_a is less than the thermodynamic critical field $H_c = \mu_0^{-1}B_c$; in larger fields $H_a \geq H_c$, these superconductors are normal conducting. For type-II superconductors (defined by $\kappa \geq 1/\sqrt{2}$), full screening occurs up to the lower critical field $H_{c1} = \mu_0^{-1}B_{c1}$ where penetration of Abrikosov vortices begins. With a further increasing of H_a, more vortices penetrate in the form of a more or less regular flux-line

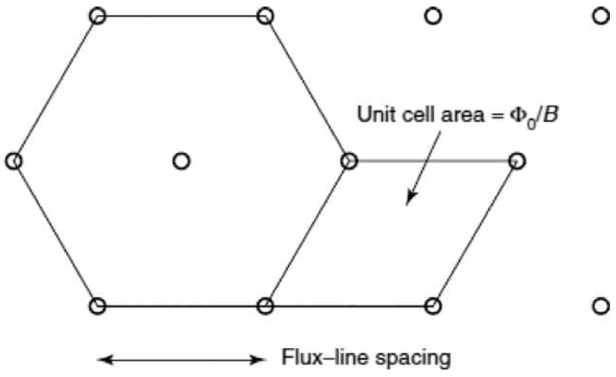

Fig. 1 The triangular vortex lattice. The dots mark the positions of vortex cores. From Brandt E.H. (2005) Superconductivity: Ginzburg-Landau theory and vortex lattice. *Encyclopedia of Condense Matter Physics*, 1st edn., pp. 98–105. Elsevier.

lattice (Fig. 1), which has an average induction $\overline{B} = n\Phi_0$, where n is the area-density of vortices and $\Phi_0 = 2.07 \times 10^{-15}\mathrm{Tm}^2$ is the quantum of magnetic flux. When H_a reaches the upper critical field $H_{c2} = \mu_0^{-1}B_{c2}$, the vortex cores overlap so strongly that the superconductor turns normal and one has $\overline{B} = \mu_0 H_a > B_{c2}$. The GL theory yields

$$B_{c1} = \frac{\Phi_0(\ln\kappa + \alpha)}{4\pi\lambda^2}, \quad B_c = \frac{\Phi_0}{\sqrt{8}\pi\lambda\xi}, \quad B_{c2} = \frac{\Phi_0}{2\pi\xi^2} \tag{2}$$

with $\alpha(\kappa) \approx 0.5 + (1 + \ln 2)/\left(2\kappa - \sqrt{2} + 2\right)$ (Brandt, 2003). At $\kappa = 1/\sqrt{2}$, one has exactly $B_{c1} = B_c = B_{c2}$, and for type-II superconductors $B_{c1} \le B_c \le B_{c2}$. In both types of superconductors, B_c determines the area under the magnetization curve $\mu_0 M(H_a)$; this area equals the superconducting condensation energy B_c^2/μ_0. For ideal pin-free superconductors, the magnetization is $M = \mu_0^{-1}\overline{B} - H_a \le 0$, see Fig. 2. For type-II superconductors with an ideal planar surface, H_c is also the field up to which the so-called Bean-Livingston surface barrier may prevent a vortex penetration ("overheating"). Interestingly, as discovered theoretically by De Gennes in 1963, even above B_{c2}, a thin surface sheath of thickness ξ remains superconducting up to a third critical field, $B_{c3} = 1.695B_{c2}$ (De Gennes, 1966).

The above scenario applies to long superconductors in the parallel magnetic field H_a. In realistic samples like spheres, platelets, or films, demagnetization effects lead to flux penetration at lower fields. In ideal ellipsoids, the penetration fields, H_c or H_{c1}, are reduced by a factor $1-N$, where N is the demagnetization factor. For spheres, one has $N = 1/3$, and for long cylinders, $N = 0$ in a parallel field and $N = 1/2$ in a perpendicular field, while for thin plates in a perpendicular field, one has $1 - N \ll 1$, and thus very small fields will force flux penetration from the edges.

In type-I superconductors with $N > 0$, demagnetization effects lead to partial penetration of flux in the form of planar domains or more complicated structures, while in type-II superconductors they just shear the magnetization curve, but the vortex lattice remains uniform if the specimen is an ellipsoid. For other shapes such as platelets, strips, or disks with constant thickness, the demagnetization effects are more complicated and lead to a geometrical barrier for flux penetration, with a penetration field which is approximately H_{c1} times the square root of the aspect ratio thickness/width (Brandt et al., 2013; Zeldov et al., 1994). For specimens much larger than λ, this result can be derived by the continuum theory without considering individual vortex lines. But for small mesoscopic superconductors with size comparable to or smaller than λ, the full GL theory has to be solved numerically to see the detailed pattern of penetrated flux lines and the shape of the magnetization curve $M(H_a)$ that may exhibit jumps at certain values of H_a.

Vortex lattice

Abrikosov (1957) found a solution of the GL theory that exhibits a two-dimensional (2D) regular lattice of zeros in the order parameter $\psi(x,y)$ and a periodic magnetic field $B(x, y)$. This solution describes a lattice of parallel vortex lines along z. The ideal lattice is triangular, that is, each vortex has six nearest neighbors, see Fig. 1. The vortices start penetrating at $H_a = H_{c1}$. The profiles $|\psi(r)|^2$ and $B(r)$ of one isolated vortex line are shown in Fig. 3 (r is the radial coordinate). As H_a is increased, more vortices penetrate and form a vortex lattice as shown in Fig. 4. First, the magnetic fields of the flux lines overlap, such that the amplitude of the periodic $B(x, y)$ decreases. Then, the cores also overlap, such that the amplitude of the order parameter $|\psi|^2$ decreases until it vanishes at $H_a = H_{c2}$. For $b = \overline{B}/B_{c2} > 0.5$, good approximations are (Brandt, 1995)

$$|\Psi(\mathbf{r})|^2 = \frac{1-\overline{B}/B_{c2}}{[1-1/(2\kappa^2)]\beta_A + 1}\sum_{\mathbf{K}} a_K \cos\mathbf{Kr}, \tag{3}$$

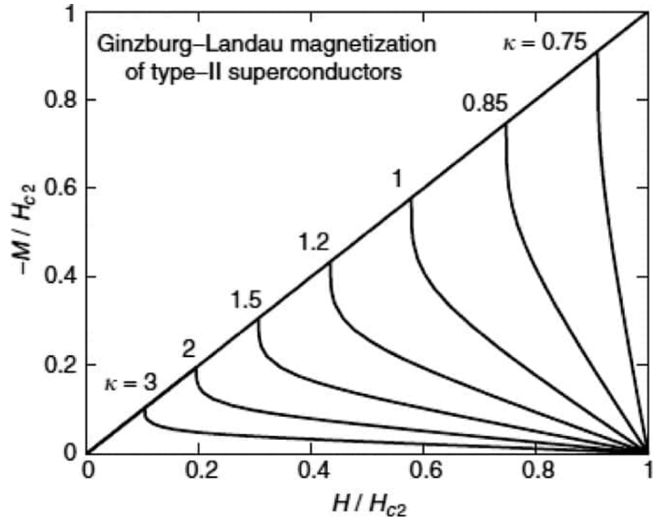

Fig. 2 Magnetization curves $M(H)$ of long type-II superconductors in parallel magnetic field $H = H_a$ (demagnetization factor $N = 0$) calculated from Ginzburg-Landau theory for various Ginzburg-Landau parameters $\kappa = 0.75\ldots3$. For $\kappa = 1/\sqrt{2}$, $-M$ jumps vertically from $-M = H$ to $M = 0$ at $H = H_{c1} = H_{c2}$.

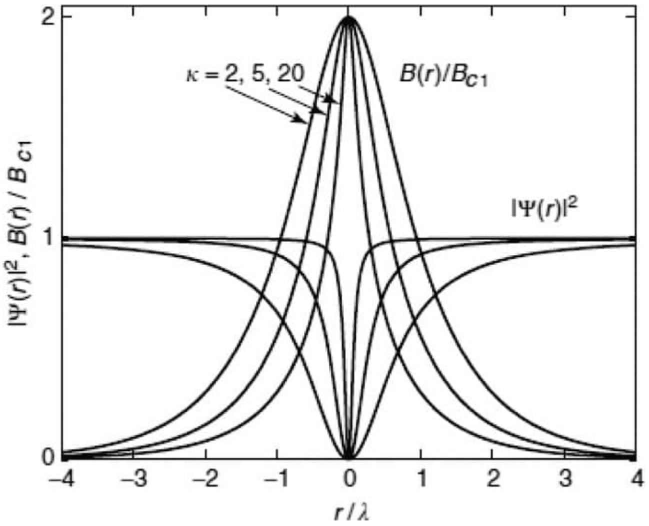

Fig. 3 Magnetic field $B(r)$ and order parameter $|\psi(r)|^2$ of an isolated flux line calculated from the Ginzburg-Landau theory for Ginzburg-Landau parameters $\kappa = 2$, 5, and 20.

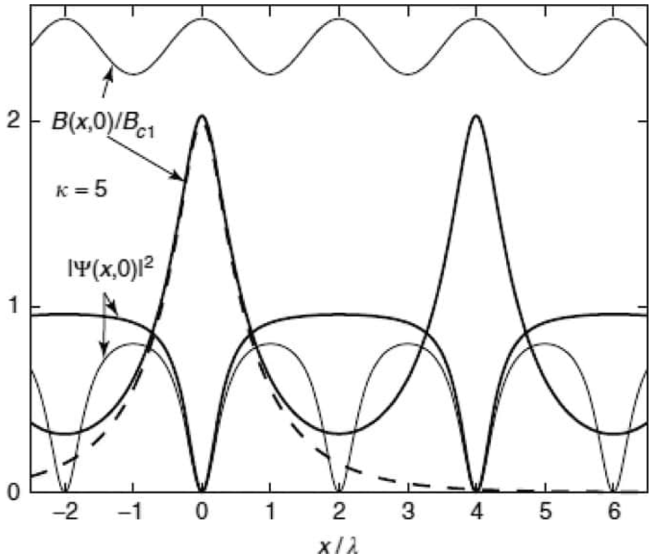

Fig. 4 Two profiles of the magnetic field $B(x, y)$ and order parameter $|\Psi(x, y)|^2$ along the x-axis (a nearest-neighbor direction) for flux-line lattices with lattice spacing $a = 4\lambda$ (bold lines) and $a = 2\lambda$ (thin lines). The dashed line shows the magnetic field of an isolated flux line from Fig. 3. Calculations from the Ginzburg-Landau theory for $\kappa = 5$.

$$B(\mathbf{r}) = \mu_0 H_a - \frac{\Phi_0}{4\pi\lambda^2}|\Psi(\mathbf{r})|^2. \tag{4}$$

Here $\mathbf{r} = (x, y)$ and the sum is over all reciprocal lattice vectors $K_{mn} = (2\pi/x_1y_2)(my_2; -mx_2 + nx_1)$ of the periodic flux-line lattice (FLL) with fluxline positions $R_{mn} = (mx_1 + nx_2; ny_2)$ $(m, n = \text{integer})$. The unit-cell area x_1y_2 yields the mean induction $\overline{B} = \Phi_0/x_1y_2$. The first Brillouin zone has the area πk_{BZ}^2 with $k_{BZ}^2 = 4\pi\overline{B}/\Phi_0$. For general lattice symmetry, the Fourier coefficients a_K and the Abrikosov parameter β_A are:

$$a_K = (-1)^{m+mn+n}\exp\left(-K_{mn}^2 x_1 y_2/8\pi\right), \tag{5}$$

$$\beta_A = \frac{<|\Psi|^4>}{<|\Psi|^2>^2} = \sum_{\mathbf{K}} a_K^2. \tag{6}$$

From $\psi(\mathbf{r} = 0) = 0$ follows $\sum_{\mathbf{K}} a_K = 0$, or with $a_{K=0} = 1$, $\sum_{\mathbf{K}\neq 0} a_K = -1$. In particular, for the triangular vortex lattice with spacing $a = \left(2\Phi_0/\sqrt{3}\overline{B}\right)^{1/2}$, one has $x_1 = a, x_2 = a/2, y_2 = \sqrt{3}a/2, \overline{B} = 2\Phi_0/\left(\sqrt{3}a^2\right), a_K = (-1)^p \exp\left(-\pi p/\sqrt{3}\right)$ with $p = m^2 + mn + n^2 = R_{mn}^2/R_{10}^2$. This yields $\beta_A = 1.15960$ (the reciprocal-lattice sum converges very rapidly) and the useful relationships

$K_{10} = 2\pi/y_2, K_{10}^2 = 16\pi^2/3a^2 = 8\pi^2\overline{B}/\sqrt{3}\Phi_0$. For square vortex lattice, one has $x_1 = y_2 = a, x_2 = 0, \overline{B} = \Phi_0/a^2$, and $\beta_A = 1.18034$. This means the energy of the square vortex lattice is only slightly larger than that of the triangular lattice, by 2% at most. A vortex lattice with square symmetry has been observed experimentally, for example, when the underlying square symmetry of the atomic lattice couples to the vortex lattice such that the square vortex lattice has lower energy, but also other effects may stabilize the square lattice, for example, an anisotropic Fermi surface or a deviation from the GL theory.

The free energy $F(\overline{B})$ per unit volume and the negative magnetization $-M = H_a - \mu_0^{-1}\overline{B} \geq 0$ with $H_a = \partial F/\partial \overline{B}$ are (still for $\overline{B}/B_{c2} > 0.5$ and from the GL theory):

$$F(\overline{B}) = \frac{\overline{B}^2}{2\mu_0} - \frac{\left(B_{c2} - \overline{B}\right)^2/2\mu_0}{(2\kappa^2 - 1)\beta_A + 1}, \tag{7}$$

$$-\mu_0 M(\overline{B}) = \frac{\left(B_{c2} - \overline{B}\right)}{(2\kappa^2 - 1)\beta_A + 1} = \frac{\Phi_0}{4\pi\lambda^2} < |\Psi|^2 > . \tag{8}$$

For the periodic field $B(\mathbf{r}) = \sum_{\mathbf{K}} B_K \cos \mathbf{K}\mathbf{r}$, the Fourier coefficients are $B_{K\neq 0} = \mu_0 M a_K, B_{K=0} = \bar{B}$, and $<|\psi|^2> = (4\pi\lambda^2/\Phi_0)\mu_0 \mid M|$.

At lower induction $\overline{B}/B_{c2} < 0.5$, the vortex lattice and its magnetization curve have to be computed from the GL theory numerically, see Figs. 2–4. However, when $\kappa \gg 1$, one may also use the London theory, which is a good approximation for small inductions $\overline{B}/B_{c2} < 0.2$.

London theory

The London theory follows from the GL theory by putting $|\psi| = 1$, but it may also be obtained by minimizing the sum F of the energy of the magnetic field $B(\mathbf{r})$ and the kinetic energy of the supercurrent density $\mathbf{J}(\mathbf{r}) = \mu_0^{-1} \nabla \times \mathbf{B}(\mathbf{r})$. This yields the London energy functional

$$F(B) = \frac{1}{2\mu_0} \int_V \left[B^2 + \lambda^2 (\nabla \times \mathbf{B})^2\right] d^3 r. \tag{9}$$

Minimizing this with respect to $\mathbf{B} = \nabla \times \mathbf{A}$, one obtains the homogeneous London equation $\mathbf{B} - \lambda^2 \nabla^2 \mathbf{B} = 0$ or $\mathbf{J} = -\mu_0^{-1}\lambda^{-2}\mathbf{A}$ where the Maxwell equations $\nabla \cdot \mathbf{B} = 0$ and $\nabla \times \mathbf{B} = \mu_0 \mathbf{J}$ were used, and the vector potential $\mathbf{A}$ was chosen in the "London gauge," which requires that $\nabla \cdot \mathbf{A} = 0$ and $\mathbf{A}$ is parallel to the surface everywhere. In presence of vortices, one has to add singularities that describe the vortex core, which may be straight or curved.

For straight parallel vortex lines along the unit vector $\mathbf{z}$, one gets the modified London equation

$$\mathbf{B} - \lambda^2 \nabla^2 \mathbf{B} = \mathbf{z}\Phi_0 \sum_v \delta_2(\mathbf{r} - \mathbf{r}_v). \tag{10}$$

Here $\mathbf{r}_v = (x_v, y_v)$ are the 2D vortex positions, which now do not have to form a periodic lattice, and $\delta_2(\mathbf{r}) = \delta(x)\delta(y)$ is the 2D delta function. This linear equation may be solved by Fourier transform using the relations $\int \exp(i\mathbf{kr}) d^2k = 4\pi^2 \delta_2(\mathbf{r})$ and $\int \exp(i\mathbf{kr}) (k^2 + \lambda^{-2})^{-1} d^2k = 2\pi K_0(|\mathbf{r}|/\lambda)$. Here, $K_0(x)$ is a modified Bessel function with the limits $K_0(x) \approx \ln(1.123/x)$ for $x \ll 1$ and $K_0(x) \approx (\pi/2x)^{1/2} \exp(-x)$ for $x \gg 1$. The resulting magnetic field of any arrangement of parallel vortices is the sum of individual London vortex fields centered at the positions $\mathbf{r}_v$,

$$\mathbf{B}(\mathbf{r}) = \mathbf{z}\frac{\Phi_0}{2\pi\lambda^2} \sum_v K_0\left(\frac{|\mathbf{r} - \mathbf{r}_v|}{\lambda}\right). \tag{11}$$

The energy F_{2D} of this 2D arrangement of vortex lines with length L (the specimen height) is obtained by inserting Eq. (10) into Eq. (9). Integrating over the delta function, one finds that the London energy is determined by the magnetic field values at the vortex positions,

$$F_{2D} = L\frac{\Phi_0}{2\mu_0} \sum_\mu B(\mathbf{r}_\mu) = L\frac{\Phi_0^2}{4\pi\mu_0\lambda^2} \sum_\mu \sum_v K_0\left(\frac{|\mathbf{r}_\mu - \mathbf{r}_v|}{\lambda}\right). \tag{12}$$

This expression shows that the energy is composed of the pairwise interaction energy (terms $\mu \neq v$) and the self-energy of the vortices (terms $\mu = v$). To avoid the divergence of the self-energy, one has to cut off the logarithmic infinity of B at the vortex centers $\mathbf{r}_v$ by introducing a finite radius of the vortex core of order ξ, the coherence length of the GL theory. This cutoff may be achieved by replacing, in Eqs. (11) and (12), the distance $r_{\mu v} = |\mathbf{r}_\mu - \mathbf{r}_v|$ by $\tilde{r}_{\mu v} = \left(r_{\mu v}^2 + 2\xi^2\right)^{1/2}$, and multiplying B by a normalization factor ≈ 1 to conserve the flux Φ_0 of the vortex. This analytical expression suggested by John Clem for a single vortex and later generalized to the vortex lattice (Hao et al., 1991), is an excellent approximation, as was shown numerically by solving the GL equation for the periodic FLL in the entire ranges of $\overline{B}$ and κ for $0 \leq \overline{B} \leq B_{c2}$ and $\kappa \geq 1/\sqrt{2}$ (Brandt, 1997).

For curved vortices at arbitrary positions $\mathbf{r}_v(z) = [x_v(z), y_v(z), z]$, the 3D modified London equation reads

$$\mathbf{B}-\lambda^2\nabla^2\mathbf{B} = \Phi_0\sum_\nu \int d\mathbf{r}_\nu \delta_3(\mathbf{r}-\mathbf{r}_\nu). \tag{13}$$

Here, the integral is along the vortex lines and $\delta_3(\mathbf{r}) = \delta(x)\delta(y)\delta(z)$. The resulting magnetic field and energy are, with $\tilde{r}_{\mu\nu} = \left[\left|\mathbf{r}_\mu - \mathbf{r}_\nu\right|^2 + 2\xi^2\right]^{1/2}$,

$$\mathbf{B}(\mathbf{r}) = \frac{\Phi_0}{4\pi\lambda^2}\sum_\nu \int d\mathbf{r}_\nu \frac{\exp\left[-\tilde{r}_{\mu\nu}\left(\mathbf{r}_\mu = \mathbf{r}\right)/\lambda\right]}{\tilde{r}_{\mu\nu}\left(\mathbf{r}_\mu = \mathbf{r}\right)}, \tag{14}$$

$$F_{3D} = \frac{\Phi_0}{2\mu_0}\sum_\mu \int d\mathbf{r}_\mu B\left(\mathbf{r}_\mu\right) = \frac{\Phi_0^2}{8\pi\mu_0\lambda^2}\sum_\mu\sum_\nu \int d\mathbf{r}_\mu \int d\mathbf{r}_\nu \frac{\exp\left(-\tilde{r}_{\mu\nu}/\lambda\right)}{\tilde{r}_{\mu\nu}}.$$

This means all the vortex segments interact with each other similar to magnetic dipoles or tiny current loops, but the magnetic long-range interaction $\propto 1/r$ is screened by a factor $\exp\left(-\tilde{r}_{\mu\nu}/\lambda\right)$. The 3D interaction between curved vortices is visualized in Fig. 5.

Vortices near surfaces and in films

The above London solutions apply to vortices in the bulk. Near the surface of the superconductor, these expressions have to be modified. In simple geometries, for example, for superconductors with one or two planar surfaces surrounded by vacuum, the magnetic field and energy of a given vortex arrangement is obtained by adding the field of appropriate images (in order to satisfy the boundary condition that no current crosses the surface) and a magnetic stray field which is caused by a fictitious surface layer of magnetic monopoles. This stray field makes the total magnetic field $B(\mathbf{r})$ continuous across the surface. Fig. 6 shows an example for this.

The magnetic field and interaction of straight vortices oriented perpendicular to a superconducting film of arbitrary thickness was calculated by Carneiro and Brandt (2000) from the London theory and by Brandt (2005) from the GL theory. In films of thickness $d \ll \lambda$ in a perpendicular magnetic field, the short vortices interact mainly via their magnetic stray field outside the superconductor over an effective penetration depth $\Lambda = 2\lambda^2/d$. With decreasing thickness d, the Fourier transform of the 2D vortex interaction $V(r) = \int\left(d^2k/4\pi^2\right)\tilde{V}(k)\exp\left(i\mathbf{k}\mathbf{r}\right)$ changes from $\tilde{V}(k) = E_0\left(k^2 + \lambda^{-2}\right)^{-1}$ for $d \gg \lambda$ to $\tilde{V}(k) = E_0\left(k^2 + k\Lambda^{-1}\right)^{-1}$ for $d \ll \lambda$, where $E_0 = d\Phi_0^2/\left(\mu_0\lambda^2\right)$.

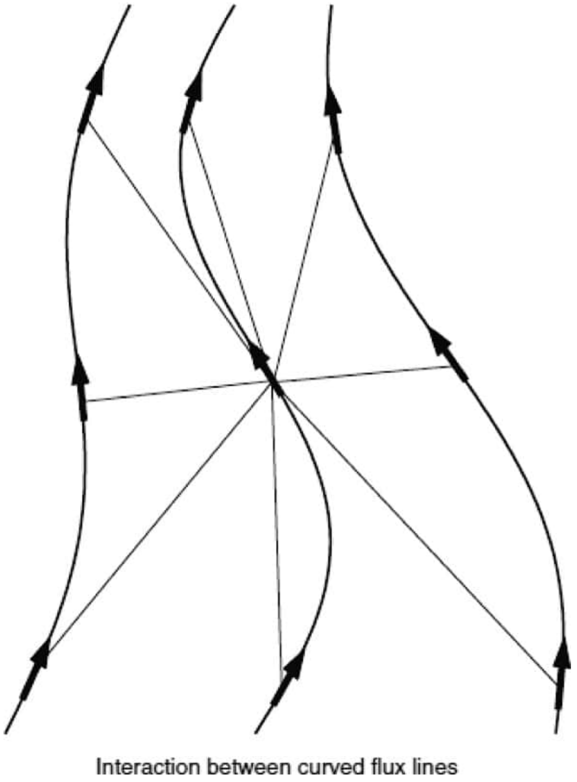

Fig. 5 Pairwise interaction between all line elements (arrows) of curved flux lines within the London theory (schematic).

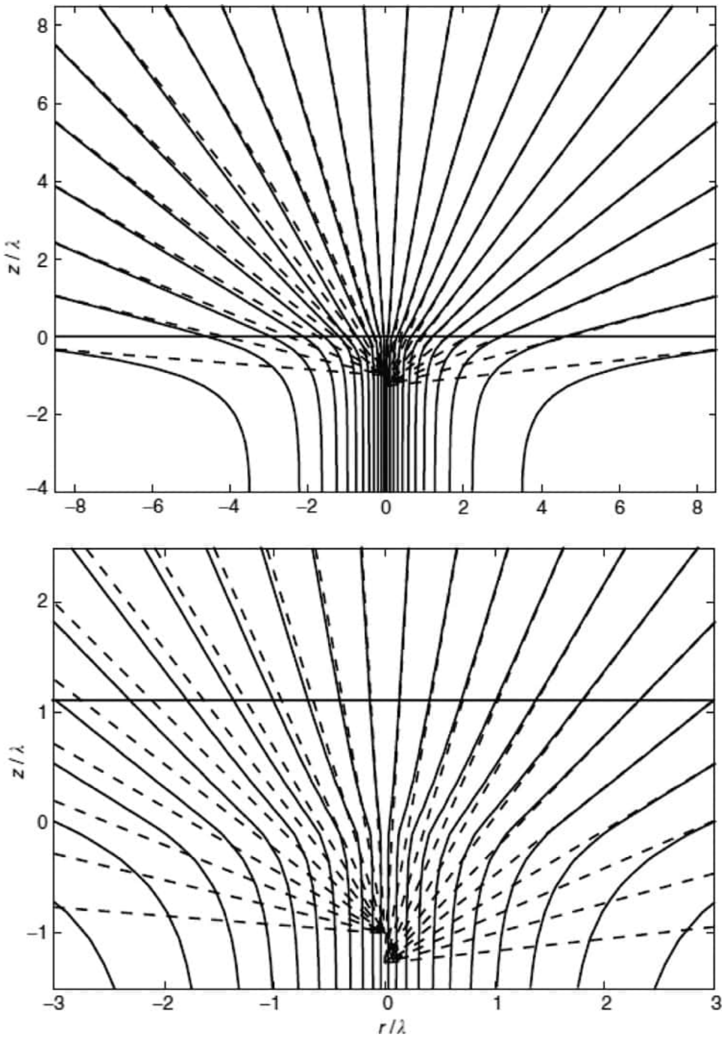

Fig. 6 Magnetic field lines of a straight vortex in and near a superconducting half space. From the London theory, for $\kappa = 20$. The dashed lines give the radial field lines of a magnetic charge of size $2\Phi_0$ positioned on the vortex axis at a depth $-z_0 = \lambda$ (left half, the far field) and $-z_0 = 1.27\lambda$ (right half), which gives a better fit to the near field. The lower plot enlarges the center of the upper plot.

As shown by Clem (1991), a similar (but 3D) magnetic interaction exists between the 2D "pancake vortices" in the superconducting Cu-O layers of high-T_c superconductors, $\tilde{V}(k) = E_0 d k_3^2 k_2^{-2} \left(\lambda^{-2} + k_3^2\right)^{-1}$, where now d is the distance between the layers, $k_2^2 = k_x^2 + k_y^2$, $k_3^2 = k_2^2 + k_z^2$, and $\lambda = \lambda_{ab}$ is the penetration depth for the supercurrents flowing in these layers.

Elasticity of the vortex lattice

Small flux-line displacements caused by pinning forces or by thermal fluctuations may be calculated using the linear elasticity theory of the vortex lattice. Fig. 7 visualizes the three basic distortions of the triangular vortex lattice: shear γ, uniaxial compression ε, and tilt α, defining the three elastic moduli c_{66}, c_{11}, and c_{44} and the naive (local) elastic energy

$$F_{\text{elast}} = \frac{V}{2}\left[c_{11}\varepsilon^2 + c_{66}\gamma^2 + c_{44}\alpha^2\right]. \tag{15}$$

The linear elastic energy F_{elast} of the vortex lattice is obtained by expanding its free energy F with respect to small displacements $\mathbf{u}_\nu(z) = \mathbf{r}_\nu(z) - \mathbf{R}_\nu = (u_{\nu x}, u_{\nu y})$ of the vortices from their ideal parallel lattice positions $\mathbf{R}_\nu$ and keeping only the quadratic terms. This yields (Brandt, 1995)

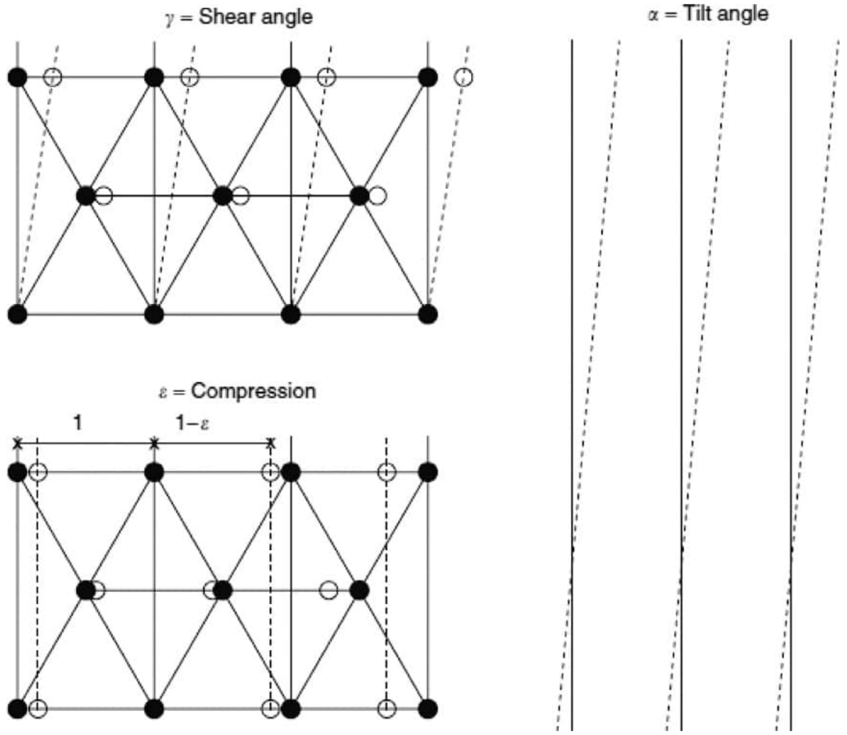

Fig. 7 The three basic homogeneous elastic distortions of the triangular vortex lattice. The full dots and solid lines mark the ideal lattice, and the hollow dots and dashed lines the distorted lattice.

$$F_{\text{elast}} = \frac{1}{2}\int_{\text{BZ}} \frac{d^3k}{8\pi^3} u_\alpha(\mathbf{k})\Phi_{\alpha\beta}(\mathbf{k})u^*_\beta(\mathbf{k}), \tag{16}$$

where $u(\mathbf{k})$ is the Fourier transform of the displacement field $u_\nu(z)$, $(\alpha, \beta) = (x, y)$, and $\mathbf{k} = (k_x, k_y, k_z)$. The k-integral in Eq. (16) is over the Brillouin zone (BZ) of the FLL since the "elastic matrix" $\Phi_{\alpha\beta}(\mathbf{k})$ is periodic in the k_x, k_y plane; the finite vortex core radius restricts the k_z integration to $|k_z| \le \xi^{-1}$. For an elastic medium with uniaxial symmetry, the elastic matrix reads

$$\Phi_{\alpha\beta}(\mathbf{k}) = (c_{11}-c_{66})k_\alpha k_\beta + \delta_{\alpha\beta}\left[\left(k_x^2 + k_y^2\right)c_{66} + k_z^2 c_{44}\right]. \tag{17}$$

Here the coefficients c_{11}, c_{66}, and c_{44} are the elastic moduli of uniaxial compression, shear, and tilt, respectively. For the vortex lattice, $\Phi_{\alpha\beta}(\mathbf{k})$ was calculated from the GL and London theories. The result, a sum over reciprocal lattice vectors, should coincide with expression (17) in the continuum limit, that is, for small $|\mathbf{k}| \ll k_{\text{BZ}}$, where $k_{\text{BZ}} = \left(4\pi\overline{B}/\Phi_0\right)^{1/2}$ is the radius of the circularized (actually hexagonal) Brillouin zone of the triangle vortex lattice with area πk_{BZ}^2. In the London limit, one finds for isotropic superconductors, the elastic moduli (Blatter et al., 1994; Brandt, 1995)

$$c_{11}(k) \approx \frac{\overline{B}^2/\mu_0}{1 + k^2\lambda^2}, \quad c_{66} \approx \frac{\overline{B}\Phi_0/\mu_0}{16\pi\lambda^2},$$

$$c_{44}(\mathbf{k}) \approx \frac{\overline{B}^2/\mu_0}{1 + k^2\lambda^2} + \frac{\overline{B}\Phi_0/\mu_0}{8\pi\lambda^2}\ln\frac{\kappa^2}{1 + k_z^2\lambda^2}. \tag{18}$$

The GL theory yields an additional factor $\left(1-\overline{B}/B_{c2}\right)^2$ in c_{66}, that is, $c_{66} \propto \bar{B}(\bar{B}-B_{c2})^2$, and replaces λ in c_{11} and c_{44} (first term) by $\lambda' = \lambda/\left(1-\overline{B}/B_{c2}\right)^{1/2}$ (Brandt, 1995).

The k dependence (dispersion) of the compression and tilt moduli $c_{11}(k)$ and $c_{44}(\mathbf{k})$ means that the elasticity of the vortex lattice is nonlocal, that is, strains with short wavelengths, $2\pi/k \ll 2\pi\lambda$, have a much lower elastic energy than a homogeneous compression or tilt (corresponding to $k \to 0$) with the same amplitude. This elastic nonlocality comes from the fact that the magnetic interaction between the flux lines typically has a range λ much longer than the flux-line spacing a_0; therefore, each flux line interacts with many other flux lines. Note that a large λ causes a small shear stiffness since $c_{66} \propto \lambda^{-2}$, and a smaller $c_{11}(k > \lambda^{-1})$ at short wavelengths, but the uniform compressibility $c_{11}(k = 0)$ is independent of λ.

As a consequence of nonlocal elasticity, vortex displacement $\mathbf{u}_\nu(z)$ caused by local pinning forces, and also the space- and time-averaged thermal fluctuations of the vortex positions, $<u_\nu(z)^2>$, are much larger than they would be if $c_{44}(\mathbf{k})$ had no dispersion, that is, if it were replaced by $c_{44}(0) = \overline{B}H_a \approx \overline{B}^2/\mu_0$. The maximum vortex displacement $u(0) \propto f$ caused at $\mathbf{r} = 0$ by a point force of density $f\delta_3(\mathbf{r})$, and the thermal fluctuations $<u^2> \propto k_B T$, are given by similar expressions (Brandt, 1995),

$$\frac{2u(0)}{f} \approx \frac{<u^2>}{k_B T} \approx \int_{BZ} \frac{d^3k}{8\pi^3} \frac{1}{\left(k_x^2 + k_y^2\right)c_{66} + k_z^2 c_{44}(\mathbf{k})} \approx \frac{k_{BZ}^2 \lambda}{8\pi[c_{66}c_{44}(0)]^{1/2}}. \tag{19}$$

In this result, a large factor $[c_{44}(0)/c_{44}(k_{BZ})]^{1/2} \approx k_{BZ}\lambda \approx \pi\lambda/a \gg 1$ originates from the elastic nonlocality. In anisotropic superconductors with $B \parallel c$ (the crystalline c axis), the thermal fluctuations, Eq. (19), are enhanced by an additional factor $\Gamma = \lambda_c/\lambda_{ab} \gg 1$, where λ_{ab} and λ_c are the two penetration depths of uniaxially anisotropic superconductors.

Conclusion

The phenomenological London and Ginzburg-Landau theories are effective tools for investigating both low-T_c and high-T_c superconductors. These theories permit one to understand the thermodynamic properties of superconducting materials and to describe the vortex lattice in type-II superconductors even without any information on the microscopic mechanism of the superconductivity. In particular, the lattices of straight and curved vortices, the vortices in films, and the vortex-lattice elasticity, which is a necessary constituent of an analysis of the vortex pinning, have been considered in the framework of this approach.

References

Abrikosov AA (1957) On the magnetic properties of superconductors of the second group. *Soviet Physics—JETP* 5: 1174–1182.

Blatter G, Feigel'man MV, Geshkenbein VB, Larkin AI, and Vinokur VM (1994) Vortices in high-temperature superconductors. *Reviews of Modern Physics* 66: 1125–1388.

Brandt EH (1995) The flux-line lattice in superconductors. *Reports on Progress in Physics* 58: 1465–1594.

Brandt EH (1997) Precision Ginzburg-Landau solution of ideal vortex lattices for any induction and symmetry. *Physical Review Letters* 78: 2208–2211.

Brandt EH (2003) Properties of the ideal Ginzburg-Landau vortex lattice. *Physical Review B* 68(054506): 1–11.

Brandt EH (2005) Ginzburg-Landau vortex lattice in superconducting films of finite thickness. *Physical Review B* 71(014521): 1–21.

Brandt EH, Mikitik GP, and Zeldov E (2013) Two regimes of vortex penetration into platelet-shaped type-II superconductors. *Journal of Experimental and Theoretical Physics* 117: 439–448.

Carneiro GM and Brandt EH (2000) Vortex lines in films: Fields and interactions. *Physical Review B* 61: 6370–6376.

Clem JR (1991) Two-dimensional vortices in a stack of thin superconducting films: A model for high-temperature superconducting multilayers. *Physical Review B* 43: 7837–7846.

De Gennes PG (1966) *Superconductivity of Metals and Alloys*. New York: Benjamin.

Hao Z, Clem JR, Mc Elfresh MW, Civale L, Malozemov AP, and Holtzberg F (1991) *Physical Review B* 43: 2844–2852.

Orlova NV, Shanenko AA, Milocevic MV, Peeters FM, Vagov AV, and Axt VM (2013) Ginzburg-Landau theory for multiband superconductors: Microscopic derivation. *Physical Review B* 87(134510): 1–8.

Sigrist M and Ueda K (1991) Phenomenological theory of unconventional superconductivity. *Reviews of Modern Physics* 63: 239–311.

Tinkham M (1975) *Introduction to Superconductivity*. New York: McGraw-Hill.

Zeldov E, Larkin AI, Geshkenbein VB, Konczykowski M, Majer D, Khaykovich B, Vinokur VM, and Shtrikman H (1994) Geometrical barriers in high-T_c superconductors. *Physical Review Letters* 73: 1428–1431.

Nanodimensional superconducting quantum interference devices

MI Faley, ER-C-1(Physics of Nanoscale Systems) Forschungszentrum Jülich, Jülich, Germany

© 2024 Elsevier Ltd. All rights reserved.

Introduction	702
Overview	703
Key issues	708
Conclusion	709
References	710

Abstract

The fabrication methods, principle of operation, microstructural, and electron transport properties, as well as the application of nanoscale superconducting quantum interference devices (nanoSQUIDs) are considered. NanoSQUIDs by definition have a submicrometer loop size, which limits dimensions of Josephson junctions to about 100 nm or less. This makes the use of tunnel junctions problematic, but encourages the use of nanobridges and other types of Josephson junctions with high critical current densities. The use of nitride superconductors helps to optimize the superconducting parameters and enhances the corrosion resistance of the nanobridge Josephson junctions and nanoSQUIDs. Additional passivation by a Si layer improves thermal sink and protects against the mechanical and electrical fragility of the devices. Nanosculpturing of cantilevers makes it possible to position the nanoSQUID at a distance of 10–100 nm from the objects under study in the nanoSQUID scanning measurement system. Several promising applications of nanoSQUIDs are briefly reviewed.

Key points

- NanoSQUIDs with a sub-micrometer loop size and dimensions of Josephson junctions to about 100 nm or less.
- The use of nanobridges and other types of Josephson junctions with high critical current densities.
- The use of nitride superconductors to optimize the superconducting parameters and to enhance the corrosion resistance of the Josephson junctions and nanoSQUIDs.
- Passivation by a Si layer to improve thermal sink and protect against the mechanical and electrical fragility of the devices.
- Nanosculpturing of cantilevers makes it possible to position the nanoSQUID at a distance of 10–100 nm from the objects under study in the nanoSQUID scanning system.
- Several promising applications of nanoSQUIDs are considered.

Introduction

A nanoscale Superconducting QUantum Interference Device (nanoSQUID) is defined as a submicron loop of superconducting material that is interrupted by at least one Josephson junction. Josephson junctions are weak links connecting two superconducting leads. These weak links can be made by many different methods: using tunnel barriers, normal conducting or semiconducting interlayers, by superconducting interlayer with lower T_c as in the electrodes, or using short narrow constrictions (nanobridges).

NanoSQUIDs are among the most sensitive tools for measuring very weak magnetic fields with high spatial resolution down to a few nanometers (Anahory et al., 2020; Granata and Vettoliere, 2016; Foley and Hilgenkamp, 2009). The submicron size of the nanoSQUID loop imposes serious limitations on the size of Josephson junctions: Typical Josephson junction sizes for implementation in nanoSQUIDs are around 300 nm, or more often below 100 nm when better spatial resolution is required. This makes the use of tunnel junctions problematic, but encourages the use of single layer short narrow constrictions (nanobridges) and other types of Josephson junctions with high critical current densities. Tunnel types of Josephson junction are traditionally used in superconducting electronics and currently also in superconducting quantum bits (qubits). The resistively shunted tunnel Josephson junctions, which have been designed for most applications in superconducting electronics, are typically a few micrometers in size (together with the shunt resistor) and do not fit inside nanoSQUIDs. In the case of submicron junctions, the realization of the three-layer structure with internally shunted junctions in the form of thinner tunnel junctions that are used for qubits or with a normal or a semiconductor conductor barrier is technologically relatively complex and associated with an increasing scattering of the junction parameters. An exceptional example is a nanosculpturing of tunnel junctions using a focused ion beam (FIB) that makes it possible to achieve high critical current modulation depth, non-hysteretic $I(V)$-characteristics at 4.2 K and a record energy resolution of about 1.3 h, where h is Planck's constant (Schmelz et al., 2017). The renaissance of nanobridge Josephson junctions (nJJs) is observed in the case of nanoSQUIDs after more than 40 years of dominance of tunneling Josephson junctions for other applications in superconducting electronics. The great advantage of nJJs especially for preparation of planar nanoSQUIDs is

https://doi.org/10.1016/B978-0-323-90800-9.00161-X

that their size is limited only by the spatial resolution of the single layer patterning methods, and the possibility to achieve the highest critical current density that approaches the depairing current densities in the superconducting films.

The operating temperature of nanoSQUIDs is lower than the superconducting transition temperature T_c of the superconducting material, and it is typically liquid helium temperature 4.2 K or lower for low-temperature superconductors such as Nb, NbN, TiN, etc., or liquid nitrogen temperature 77.4 K or lower for high-temperature superconductor $YBa_2Cu_3O_{7-x}$. The use of nitride superconductors helps to optimize the superconducting parameters and enhances the corrosion resistance of the Josephson junctions and nanoSQUIDs. Additional passivation by a Si layer can improve thermal sink and protect against the mechanical and electrical fragility of the devices. Nanosculpturing of cantilevers makes it possible to position the nanoSQUID at a distance of 10–100 nm from the objects under study in the nanoSQUID scanning system. Attocube's low temperature positioning and scanning system allows extremely large scanning of areas up to 5 × 5 mm with sub-nm spatial resolution at 4.2 K.

NanoSQUIDs are designed to study small magnetic systems like magnetic nanoparticles or current distribution at low temperatures with nanoscale spatial resolution down to ~40 nm and high sensitivity to tiny magnetic moments that is expressed in the units of spin sensitivity $\mu_B/\sqrt{Hz}$, where $\mu_B \cong 9.27 \times 10^{-24}$ J/T is Bohr magneton. Currently, the best nanoSQUIDs are able to measure distribution of magnetic fields of single atomic spins with spin sensitivity $<1\ \mu_B/\sqrt{Hz}$ (Vasyukov et al., 2013; Anahory et al., 2020). NanoSQUID microscopy competes with diamond microscopy, which is based on negatively charged nitrogen vacancy (NV) centers in diamond, and demonstrated nanoscale magnetic imaging of a single electron spin when operated at room temperature. Low operation temperatures of nanoSQUIDs can be useful in studying properties of small magnetic systems at low temperatures, transition edge detectors for single photon, macromolecule detection and for applications in superconducting quantum technologies, such as quantum metrology and low dissipation readout of quantum bits (qubits).

Overview

NanoSQUID is a nanoscale subtype of a superconducting quantum interference device (SQUID) that represents a superconducting loop interrupted by at least one Josephson junction. SQUID uses the amplitude and phase of wave function of Cooper pairs to detect small magnetic fluxes treading the SQUID loop. Contrary to uninterrupted superconducting loop, magnetic flux through the SQUID loop can take arbitrary values because a part of phase difference can be accommodated on the Josephson junctions and be measured using Josephson's current-phase relation that is periodic with a magnetic flux quantum $\Phi_0 = h/2e \cong 2.068\ \mathrm{fT\ m}^2$. In the case of only one Josephson contact, no leads are attached to the SQUID and the coupling to the readout electronics takes place inductively at a radio frequency. Such single Josephson junction SQUID is called an RF SQUID. In some cases also SQUIDs containing several Josephson junctions are inductively coupled to RF readout electronics and operate as RF SQUIDs (Zhang et al., 1993). As the size of the SQUID circuit is reduced, the inductive coupling becomes weaker, but this can be partially compensated by galvanic coupling and a corresponding resonant circuit. The smallest pickup loops of RF SQUIDs implemented for SQUID microscopy have a diameter of ~1 μm (Foroughi et al., 2018). Direct current SQUID (DC SQUID) has a parallel connection of at least two Josephson junctions between two superconducting electrodes on a closed superconducting loop. It can be biased by a current above the critical current of the transitions to their voltage state, which is easier compared to controlling the operation of RF SQUIDs, especially at submicron SQUID sizes. This explains the exclusive use of the DC SQUID in the design of nanoSQUIDs, and only these will be described later in this review.

The superconducting loop of the DC-SQUID contains two or more Josephson junctions and galvanic connections to the readout electronics that allow the DC-SQUID to be biased to a voltage state. DC SQUIDs act as magnetic flux to voltage converters because they convert the magnetic flux penetrating the DC SQUID loop to voltage on the DC SQUID. Operation of DC SQUIDs is based on the dependence of the canonical momentum of charged particles on the vector potential of magnetic field $\vec{p} = m\vec{v} + q\vec{A}$, where the charge $q = -2e$ for the case of Cooper pairs in superconducting electrodes of a DC SQUID: see Fig. 1. Consequently, de Broglie wavelength of the Cooper pairs $\lambda = h/|\vec{p}|$ and their wave vector $\vec{k} = 2\pi\vec{p}/h$ are dependent on the local values of the vector potential. As a result, phase shift $\delta\varphi = \int \vec{k}d\vec{l}$ of Cooper pair's wave function acquired when moving Cooper pairs around the hole in the SQUID loop is determined by the magnetic flux Φ penetrating through the loop. The Cooper pairs travel inside superconductors that in ideal case shields completely from magnetic field. Nevertheless, the vector potential of magnetic field is present inside superconductor and it changes the de Broglie wavelength and the wave vector of the Cooper pairs. The total phase shift acquired by the Cooper pair when moving along the SQUID loop is determined only by the magnetic flux through the loop and does not

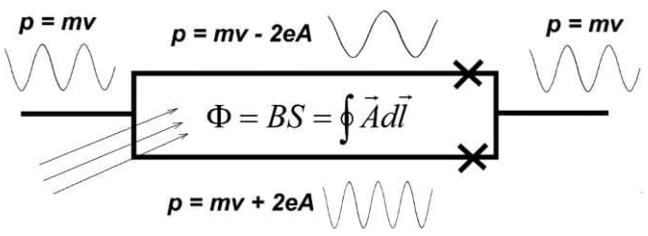

Fig. 1 Schematic representation of a DC SQUID loop with values of the impulse p of Cooper pairs and magnetic flux Φ through the loop.

depend on the shape of the loop. This is a type of Berry phase, similar to the phase that a single electron receives in the -Aharonov-Bohm effect used in modified for electron holography measurements transmission electron microscopes (Dunin-Borkowski, 1998).

Maximal superconducting current $I_s(\max)$ of DC SQUID is a periodical function of the magnetic flux Φ penetrating through the loop:

$$I_s = 2I_C\left|\cos\frac{\pi\Phi}{\Phi_0}\right|, \tag{1}$$

where $\Phi_0 = h/2e \cong 2.068$ fT m^2 is a magnetic flux quantum.

Josephson junctions convert the phase shift into voltage when the DC-SQUID is biased with a bias current I_B slightly higher than the sum of the critical currents $2I_c$ of the Josephson junctions in the absence of magnetic field. Above I_c voltage $U(t)$ across a Josephson junction oscillates in the form of periodic pulses (Josephson oscillations). At bias currents $I_B > 2I_C$ similar voltage pulses $U(\Phi,t)$ proceed on DC SQUID but they depend also on magnetic flux Φ passing through the SQUID loop due to the phase difference between the Josephson oscillations on individual junctions. Averaging of $U(\Phi,t)$ over the period τ of the Josephson oscillations results in the DC voltage V across the DC SQUID:

$$V = \frac{1}{\tau}\int_0^\tau U(\Phi,t)dt \approx \frac{R_N I_B}{2}\sqrt{1 - \left(\frac{2I_C}{I_B}\cos\frac{\pi\Phi}{\Phi_0}\right)}, \tag{2}$$

where R_N is the normal state resistance of the individual Josephson junction in the DC SQUID. The DC voltage V across the DC SQUID is thus a periodic function of the magnetic flux Φ passing through the SQUID loop.

Eq. (2) was obtained under the assumption of a negligible inductance of nanoSQUIDs. The non-zero inductance L_s reduces modulation of critical current of DC SQUID to $\Delta I_s(\max) \sim \Phi_0/L_s$. By increasing L_s, the optimal modulation parameter $\beta_L = 2L_sI_c/\Phi_0 \cong 1$ for DC SQUIDs corresponds to still large modulation of critical current and already good magnetic coupling to the measured signal. Responsible for magnetic coupling, geometrical inductance of nanoSQUID is typically below 0.5 pH and typical critical current is limited to $I_c \sim 20$ μA even for nJJs in order to avoid hysteretic $I(V)$-characteristics. Taking into account only the geometrical inductance corresponds to the modulation parameter $\beta_L \cong 0.01$. On the other hand, kinetic inductance of the nanoSQUID loop $L_{kS} \cong 2\pi\mu_0\lambda_L{}^2R/A \cong 60$ pH, where (for example) $R \cong 300$ nm is the nanoSQUID's loop radius, $\lambda_L \cong 500$ nm is London penetration depth in superconducting film of the loop and $A \cong 0.01$ μm^2 is the estimated cross sectional area of the loop. This corresponds to the boundary value of the modulation parameter $\beta_L \cong 1.1$. The task of optimizing nanoSQUIDs includes taking into account its kinetic inductance, limiting it, and finding ways to reduce it through the correct design, technology, and choice of material. The theoretical expectation for kinetic inductance of a nanobridge $L_{kn} \cong \gamma\frac{l}{w}\frac{\hbar R}{k_BT_c}$, where ℓ and w are length and width of nanobridge, $\gamma \cong 0.2$ and $R_{\blacksquare}$ is the normal-state sheet resistance of the superconducting film.

The Josephson current-phase relation $I_s = I_c\sin(\Delta\varphi)$ is realized in Josephson junctions made by different methods in spite of variety of used electron-transport mechanisms: tunneling effect in insulator barrier, proximity effect in normal conducting and semiconducting barriers or spatially constricted superconducting current in nJJs. Operation principle of tunnel and proximity effect Josephson junctions is well described in many current textbooks and handbooks (see, for example, (Mangin and Kahn, 2017) and (Ruggiero, 2015)) as a standard explanation of Josephson effect because such 3-layer junctions are the most widely used type of Josephson junction in conventional superconducting electronics. Tunnel junctions are currently also effectively used in qubits (e.g., flux qubits and transmons) thanks to their low dissipation levels and large subgap resistances.

NanoSQUID are in most cases based on nJJs because nJJs provide the highest critical current density and a better reproducibility in the sub-100 nm size range as compared with three-layer junctions. Description of the operation principle of nJJ can be made according to the theory of (Aslamazov and Larkin, 1968) that is using the Ginzburg–Landau (GL) equation. The GL equation describes Josephson effect in nJJs and it is valid only at temperatures T sufficiently close to the electrode critical temperature T_c: $0.9\ T < T < T_c$. In a one-dimensional approximation the GL equation can be written in the form:

$$\xi^2\frac{d^2\Psi}{dx^2} + \Psi - \Psi|\Psi|^2 = 0, \tag{3}$$

where ξ is the coherence length and Ψ is the order parameter. When nanobridge length l is shorter than coherence length, ideally $\ell << \xi$, the first term dominates and the Eq. (3) is reduced to the Laplace equation $\frac{d^2\Psi}{dx^2} = 0$, for which the solution is the linear function $\Psi = a + bx$, with x ranging from 0 to l:

$$\Psi = \left(1 - \frac{x}{l}\right)\Psi_\infty + \left(\frac{x}{l}\right)e^{i\Delta\varphi}\Psi_\infty, \tag{4}$$

where $\Delta\varphi$ is the phase difference between the wave functions in the electrodes and Ψ_∞ is the order parameter in the electrodes. Insertion of the latter equation for Ψ into the GL equation for the superconducting current $I_s \sim \mathrm{Im}(\Psi^*\nabla\Psi)$ results in the Josephson current-phase dependence $I_s = I_c\sin(\Delta\varphi)$.

The coherence length diverges at T_c according to the temperature dependence $\xi(T) \propto \left(1 - \frac{T}{T_c}\right)^{-1/2}$ that simplifies the condition $\ell << \xi(T)$ for the ideal Josephson effect in nJJs. However, small values of $\xi(0) \leq 10$ nm in the superconducting films of Nb, Pb, NbN, TiNbN, and MoRe with $T_c > 4.2$ K represent a challenge for the structuring of the nJJs using these materials. The current-phase relationship becomes multivalued when the length ℓ of nJJ exceeds the value $3.49\xi(T)$, for example, at temperatures $T << T_c$. The dependence of the maximum superconducting current density J_s on the phase drop $\Delta\varphi$ is described by the Likharev and Yakobson expression:

$$J_s(\Delta\varphi) = \frac{\Phi_0}{2\pi\mu_0\xi\lambda^2}\left[\frac{\xi\Delta\varphi}{l} - \left(\frac{\xi\Delta\varphi}{l}\right)^3\right]. \tag{5}$$

The *I(V)*-characteristics of nanoSQUIDs and nJJs made from Nb, Pb, NbN, TiNbN, or MoRe are often hysteretic at 4.2 K due to thermal hysteresis in the nJJs (Skocpol et al., 1974). Usually observed hysteresis of *I(V)*-characteristics of DC SQUIDs due to Stewart-McCumber parameter $\beta_L > 1$ is unlikely in the case of nanoSQUIDs because nJJs have negligible capacitance when compared with tunnel JJs. The non-hysteretic *I(V)*-characteristics are required for the use of conventional readout techniques to operate the nanoSQUID as a magnetic flux to voltage converter. In the case of $T << T_c$, the *I(V)*-characteristics become hysteretic, but if the critical current I_c is determined by phenomena of Josephson oscillations, phase-slip, or a creep of Abrikosov vortices it is still possible to use the nanoSQUID for point-by-point measurements of magnetic fields using the dependence of the critical current I_c on the magnetic field that was realized for NbN (Russo et al., 2017) and Nb (Shishkin et al., 2020) nanoSQUIDs. Demonstration of microwave-induced Shapiro steps on hysteretic *I(V)*-characteristic shows presence of Josephson oscillations in the dissipative branch of such nJJ (Shelly et al., 2020) that can be due to the local overheating of nJJ to the narrow temperature range below T_c where the I(V) characteristics of the nJJs are non-hysteretic. More practical is the realization of non-hysteretic *I(V)*-characteristics at low temperatures by partial suppression of the critical current using bias magnetic fields ~1 T (Anahory et al., 2020). Much below T_c, nJJs in such nanoSQUIDs have a lower Johnson current noise $I_n = (4k_BT/R_N)^{1/2}$, which likely results in lower intrinsic noise and better spin sensitivity of the nanoSQUID. In the case of the potential application of nanoSQUIDs for quantum computers at temperatures ~10 mK influence of quantum fluctuations on the operation of nanoSQUIDs cannot be neglected. At temperatures below ~100 mK the quantum fluctuations would lead to saturation of the noise on the level $S_{\Phi Q}^{1/2} = \sqrt{\hbar L_S}$, where L_S is the nanoSQUID loop inductance.

Thermal hysteresis is a result of overheating of nJJ when its superconducting current exceeds the critical current and the dissipated energy will heat the nJJ above T_c so that the nanobridge enters the normal conducting state (Skocpol et al., 1974). The resulting Joule heat dissipated by the normally conducting nanobridge raises additionally its temperature, which in turn reduces the retrapping critical current I_r. The ratio of I_c and I_r depends on the thermal coupling between nJJ and the substrate and it is larger in the case of poor heat removal (for example, in the case of free-standing nJJs or nJJs on membranes). The pure thermal hysteresis is observed at a bias current of the order of depairing current of superconducting film that is typically greater than the sum of the critical currents of nJJs in nanoSQUID does not depend on the magnetic flux through the nanoSQUID loop and therefore cannot be used to measure magnetic fields (Faley et al., 2022).

Eq. (4) is an approximation in which the entire change in the phase of the wave function occurs inside the nJJs. This is a simplified theoretical model that is not suitable for Dayem-type nJJs consisting of electrodes and a nanobridge of the same thickness: the spatial phase change propagates inside the electrodes, almost doubling the effective length of the nJJ (Faley et al., 2021a). A much better approximation to the theory is realized in a variable-thickness nJJ that include a nanobridge thinner than its electrodes. A 3D design of nJJs and nanoSQUIDs using a multilayer technology were successfully realized (Chen et al., 2016). Such nJJs also provide the nanoSQUID with a lower kinetic inductance, thereby improving its voltage swings and the spin sensitivity. Realization of variable-thickness nJJs at nanoscale is also possible within the framework of a single-layer technology using many different tricks: (1.) Directed deposition on 3D-shaped substrate that was used, for example, in construction of elegant SQUID-on-tip cantilevers (Vasyukov et al., 2013), (Anahory et al., 2020); (2.) Oblique incidence evaporation through an electron beam resist shadow mask; (3.) Using undercut during isotropic reactive ion etching (Faley et al., 2021b and Faley et al., 2022); (4.) Using different etch times during patterning of nJJs by FIB etching (Faley and Dunin-Borkowski, 2022); (5.) Using different etch rates in open areas and inside narrow slits in electron beam resist ("grooved Dayem nanobridges") (Trabaldo et al., 2019); etc. As an example, Fig. 2 shows SEM image of a 20-nm-wide variable-thickness TiN nJJ with approximately 100 nm thick electrodes recorded at a 45° sample tilt angle. The remains of the electron beam resist were removed with warm acetone heated to 70 °C. The TiN

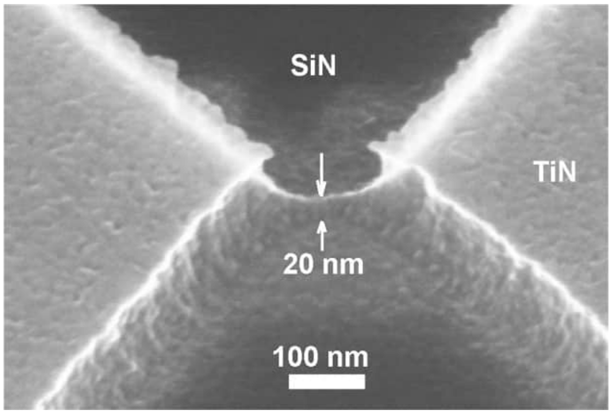

Fig. 2 SEM image of a 20-nm-wide variable-thickness TiN nJJ recorded at a 45° sample tilt angle. The TiN electrodes are approximately 100 nm thick.

films sputtered at high temperatures in an Ar-N_2 atmosphere on Si substrates show domain epitaxy and have advantages for the implementation in nanoSQUIDs due to their large coherence length >100 nm at 4.2 K and their high corrosion resistance (Faley et al., 2021b).

Spin sensitivity of nanoSQUID′ measurement system at sufficiently high frequencies has a white noise spectrum and is determined by: (1.) Johnson current noise i_n of the nJJs (Voss et al., 1980); (2.) Preamplifier noise of the readout electronics; and (3.) Size of the nanoSQUID loop and its distance to the magnetic nanosize dipole. The Johnson current noise of each nJJ has a white spectrum at the level $i_n = (4k_BT/R_N)^{1/2}$, where R_N is the normal state resistance of the nJJs. The total current noise of the nanoSQUID is $I_n = i_n\sqrt{2}$ and the voltage noise $V_n = R_dI_n$, where R_d is the differential resistance of the nanoSQUID at a bias current slightly above the critical current. The intrinsic flux noise of the nanoSQUID is $\sqrt{S_\Phi} \cong V_n/(\partial V/\partial\Phi)$, where the maximum slope of the transfer function $\partial V/\partial\Phi$ in the approximation of sinusoidal $V(\Phi)$ dependence is determined by the expression (Enpuku et al., 1995):

$$\frac{\partial V}{\partial \Phi} \approx \frac{4}{\Phi_0}\,\frac{I_cR_n}{\left(1+\frac{2L_sI_c}{\Phi_0}\right)}\exp\left(-3.5\pi^2\frac{k_BTL_s}{\Phi_0^2}\right). \tag{6}$$

Decrease of temperature below $\sim 0.9T_c$ leads to increase of energy gap in superconducting films reflected in increase of I_cR_n product in the nJJs, increase of I_c and deviation of $V(\Phi)$ dependence from sinusoidal. The $I(V)$-characteristics of the nJJs approach hysteresis, which manifests itself in an increase in R_d and V_n at a bias current slightly above $2I_c$. In the flux noise $\sqrt{S_\Phi}$ the changes of V_n and $\partial V/\partial\Phi$ partially compensate each other, but the contribution of noise of the readout electronics decreases. By using the SQUID array preamplifier similar to that demonstrated in Hao (2008), it is possible to further reduce the noise of the readout electronics by a factor of more than 10.

In addition to the white noise, the 1/f noise is often observed in nanoSQUIDs at frequencies below 10 kHz and associated with critical current fluctuation in the Josephson junctions (see, for example, (Martínez-Pérez et al., 2017) and (Schmelz et al., 2017)).

The magnetic field resolution $B_n = (\partial B/\partial\Phi)\sqrt{S_\Phi} = \sqrt{S_\Phi}/A_{eff}$, where A_{eff} is an effective area of the nanoSQUID. The spin sensitivity $\sqrt{S_n}$ measured using nanoSQUID of radius r placed on the same axis as a magnetic dipol (electron spin) at the distance h from it is given by the equation:

$$\sqrt{S_n} = \sqrt{S_\Phi}\left(1+\frac{h^2}{r^2}\right)^{3/2}\frac{r}{r_e}, \tag{7}$$

where $r_e = 2.82 \times 10^{-15}$ m is the classical electron radius. At $h << r$ the spin sensitivity $\sqrt{S_n} = \sqrt{S_\Phi}\,(r/r_e)$. For a better spin sensitivity it is important to make smaller size of nanoSQUID and place it closer to the nanoscale magnetic object. Bulk nanomachining of silicon substrates for nanoSQUID′ cantilevers can be performed with submicrometer precision using RIE (Faley et al., 2021a). Fig. 3a and Fig. 3b show scanning electron microscopy (SEM) images of a planar (a) 2 nJJs nanoSQUID that was structured using RIE and (b) 4 nJJs nanoSQUID that was structured using FIB (Faley and Dunin-Borkowski, 2022). Both nanoSQUIDs were placed within (a) 200 nm and (b) 300 nm from the corners of $2 \times 2 \times 0.05$ mm^3 cantilevers using FIB and aluminum sacrificial layers. Such nanoSQUID cantilevers belong to NanoElectroMechanical System (NEMS) are a class of devices integrating electrical and mechanical functionality on the nanoscale. In a scanning nanoSQUID measurement system the cantilever can be placed on a quartz tuning fork at a small angle ~10° with respect to the surface of the studied magnetic object, while its corner serves as the tip of an atomic force microscope. In this case the distance between the nanoSQUID and surface of the studied magnetic object would be only ~10 nm that is much smaller than the sizes of all currently available planar nanoSQUIDs. The nanoSQUIDs are typically fixed on attocube's positioning and scanning stages that allow extremely large specified measurement scanning range up to 5 mm with sub-nm spatial resolution at 4.2 K.

The maximum of the nanoSQUID voltage response on magnetic flux $\partial V/\partial\Phi$ occurs at a $\Phi_0/4$ magnetic flux bias, which corresponds to 1.5 mT for the nanoSQUID shown in Fig. 2a. Such a flux bias can be achieved without an external magnetic field, but with the help of a direct injection of current through the third (middle) electrode of this nanoSQUID. The flux biasing current,

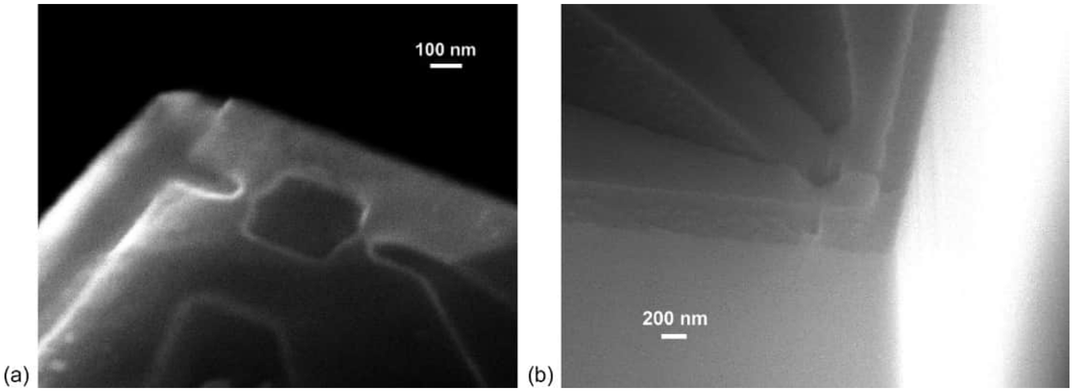

Fig. 3 (a) SEM image of a planar 2nJJs nanoSQUID structured using RIE. (b) SEM image of a planar 4nJJs nanoSQUID structured using FIB. Both nanoSQUIDs were placed within (a) 200 nm and (b) 300 nm from the corners of 2 × 2 × 0.05 mm cantilevers using FIB and aluminum sacrificial layers.

approaching the depairing current in the superconducting film, is necessary because of the relatively small geometric inductance $L_g \approx 0.14$ pH of the part of the nanoSQUID loop between the left and middle electrodes of the nanoSQUID shown in Fig. 3. Such method of the $\Phi_0/4$ flux bias does not work for smaller nanoSQUIDs: to squeeze $\Phi_0/4$ into the nanoSQUID loop of effective area $A_{eff} < (100\text{ nm})^2$ the required magnetic field $B > \Phi_0/4A_{eff} \sim 50$ mT. The geometric inductances of the nJJs and the nanoSQUID loop become negligible. The kinetic inductance L_k is much larger, but it cannot be used to generate the constant flux bias. Instead, another method does not require external magnetic fields or injection of additional current in the nanoSQUID loop and based on the phase drops at additional nJJs can be used.

An example of the new flux bias method was demonstrated in the self-flux-biased four-JJ-nanoSQUID (Faley and Dunin-Borkowski, 2022). The effect of self-flux-biasing in such nanoSQUID can be explained when all nJJs are still in zero voltage state. Let us consider nanoSQUID with 4 nJJs of which 2 nJJs have each phase drop φ_1 and the smallest critical current I_{c1} while 2 other nJJs have larger cross-sections, each has a smaller phase drop φ_2 and the largest critical current $I_{c2} > I_{c1}$ (see Fig. 4). The optimal phase drop $2\varphi_2$ on the largest nJJs is equivalent to the required flux bias $\Phi_0/4$.

The relation between the net magnetic flux Φ and the phase drops φ_1 and φ_2 across the nJJs is given by the flux quantization equation in the nanoSQUID' loop: $2\varphi_1 + 2\varphi_2 + 2\pi\Phi/\Phi_0 = 2\pi n$, where n is an integer. At the operation conditions $\Phi = \Phi_0/4$ the bias current of the nanoSQUID $I_b = 2I_{c1}$ that means that the phase drop on these nJJs has the maximal for the zero voltage state value $\varphi_1 = \pi/2$. Each of the other two junctions have phase drop φ_2 determined by their maximal current limited by the critical current of the smallest junctions I_{c1} and its critical current I_{c2}: $\varphi_2 = \arcsin(I_{c1}/I_{c2})$. This maximal current is reached at the magnetic flux Φ passing through the loop of the nanoSQUID $\Phi = (\pi/2 - \varphi_2)\Phi_0/\pi$ at $n = 1$. The maximum responsivity point in zero external magnetic field will be when at the magnetic flux $\Phi = \Phi_0/4$: $2\pi/2 + 2\varphi_2 + 2\pi/4 = 2\pi n$, or: $\varphi_2 = \pi/4$ at $n = 1$. This last equation determines in the first approximation the relation between the critical currents: $I_{c2} = I_{c1}/\sin(\pi/4) = I_{c1}\sqrt{2}$. The real optimal critical current I_{c2} is closer to I_{c1} because the geometrical inductances of the nJJs are not zero and should be also taken into account.

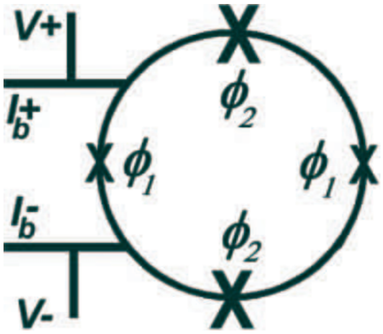

Fig. 4 Schematic representation of 4-nJJs-nanoSQUID. Two nJJs with larger critical current I_{c2} and smaller phase drop $\phi_2 < \pi/2$ are shown by larger crosses.

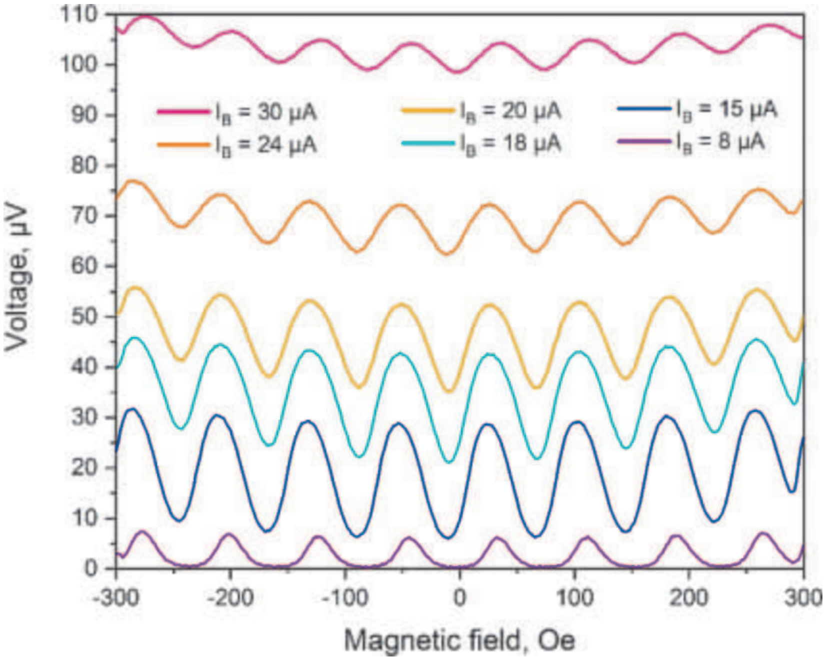

Fig. 5 NanoSQUID' $V(\Phi)$ dependences measured using a Quantum Design PPMS for different bias currents at 4.2 K. The uppermost curve was measured at the highest bias current and the bottom curve was measured at the lowest bias current.

Using the third electrode for injection of current through one of the largest nJJs will allow modulation of the flux bias via modulation of φ_2 that is much more effective as compared with the modulation of the external magnetic field or the use of current injection into a part of SQUID loop.

Fig. 5 shows the $V(\Phi)$ dependence of a nanoSQUID′ that was measured using a Quantum Design Physical Property Measurement System (PPMS) for different nanoSQUID bias currents close to $I_B \cong 2I_c$ at 4.2 K. The uppermost curve was measured at the highest bias current of 30 μA and the bottom curve corresponds to the lowest bias current of 8 μA. The bias current of the lower curve is slightly below $2I_c$, so almost half of the curve is in the zero voltage state. Increasing of the bias current changes shape of the $V(\Phi)$ dependence to sinusoidal and leads to a non-zero voltage bias at all points of the $V(\Phi)$ curves. At the bias current 15 μA the amplitude of the voltage modulation of the $V(\Phi)$ dependence is maximal as well as its derivative $\partial V/\partial \Phi$ at the optimal for operation bias of the flux $\Phi = \Phi_0/4$. By decreasing of temperature the amplitude of modulation increasing due to increase of the I_cR_n product and the derivative $\partial V/\partial \Phi$ is increasing proportionally to the differential resistance R_d but the shape of the $V(\Phi)$ dependence changes from sinusoidal to rectangular and the range of bias currents where there is any modulation of $V(\Phi)$ dependence is decreasing.

NanoSQUIDs are promising sensors for non-destructive and low noise detection of magnetic fields at low temperatures with submicrometer spatial resolution for study of nanoscale magnetism of condensed matter systems and measure any physical quantity that can be converted into magnetic flux. These mesoscopic-scale, low-temperature conditions are of particular interest because they are in a largely unexplored zone between the quantum world and the normal world. NanoSQUIDs can provide readout of magnetic signals of individual nucleons and electrons and track their quantum interactions while creation of tiny magnetic domains and/or magnetic nanoparticles. In the ideal case, the zero voltage and the magnetic field of the superconducting body of the nanoSQUID ensure lossless measurements that do not destroy the quantum state of the examined objects: Cooper pairs within the superconducting body of nanoSQUID acquire a phase shift due to the presence of only a vector potential of the magnetic field, ideally without any dissipation and in a zero magnetic field. The phase change results in the change in the non-linear inductance of the nanoSQUID, which stays in the zero-voltage state without Johnson noise and can be used in a resonant circuit of a parametric amplifier.

The applications of nanoSQUIDs can be divided into two areas: (1.) "Stationary," where nanoSQUID and the object under investigation are fixed relatively each other on the same substrate; (2.) "Scanning nanoSQUID microscopy," where nanoSQUID is fixed on a cantilever near tip of scanning system. The "Stationary" method is the simplest and it is the mostly used now to study, for example, magnetization of ferromagnetic nanoparticles (Martínez-Pérez et al., 2017). The magnetic nanoparticles can be deposited from a very much diluted solution over the nanoSQUID and the magnetic response of one of them that is occasionally fixed in the vicinity of the nanoSQUID or, better, one on the nJJs, is detected by the nanoSQUID. The magnetic nanoparticle can be exposed to different magnetic fields from zero to high fields >1 T to investigate its behavior, for example, during magnetization of ferromagnetic nanoparticles or to study their high frequency ferromagnetic resonance. The superconductors like Nb, NbN and, especially, $\mathrm{YBa_2Cu_3O_{7-x}}$ have critical magnetic fields $H_{c2} >> 1$ T. Another nanoSQUID without magnetic nanoparticle as a reference can be placed on the same chip for subtraction of parasitic background signals. To the prospective "Stationary" applications of nanoSQUIDs belong among other things also readout of qubits, ultra-high frequency detection of nanoscale magnetic fields in combination with single photon detection as a trigger and the detectors for the motion of resonators made from NEMS. At low temperatures, NEMS resonators exhibit quantum behavior.

"Scanning nanoSQUID microscopy" is a type of scanning probe microscopy and a method for imaging magnetic fields on a nanoscale using nanoSQUID as a sensor. A nanoSQUID is mounted on a cantilever tip, which is then scanned over a sub-micron distance from the surface of the sample to be measured. The nanoSQUID cantilevers were realized in the form of: (1.) "SQUID-on-tip" 3D configuration of a nanoSQUID deposited at three different tilt angles on apex of a very sharp pipette that was pulled from a hollow quartz tube (Vasyukov et al., 2013; Anahory et al., 2020) or (2.) A "planar nanoSQUID" fabricated using e-beam lithography on a standard Si wafer, which is then nanosculptured so that the nanoSQUID is within ~1 μm proximity of the corner of the cantilever that serves as the cantilever′ tip (Faley et al., 2021a; Faley and Dunin-Borkowski, 2022). In both cases the cantilever is fixed on a quartz tuning fork that in a Tapping Mode provides a contactless atomic force feedback for the nanoscale proximity of nanoSQUID to the surface of the investigated object. The mainly van der Waals forces acting on the cantilever as the tip approaches the surface cause the amplitude and frequency of the vibration of the tuning fork to change as the tip approaches the sample. Another scanning mode is also possible, similar to that used in the case of a magnetic force microscope: nanoSQUID can scan at a certain distance from the surface of the sample. The sensitivity and spatial resolution will be worse in this case, but this mode will be safer (non-destructive) for both the nanoSQUID and the sample. Any touching of the sample surface poses a risk of destroying nanoSQUID in the SQUID-on-tip configuration, which requires special care during operation. Planar nanoSQUIDs in this case are still at a controlled safe distance from the object and can be used also in Contact Mode.

Key issues

To date, the SQUID-on-tip configuration has demonstrated the possibility to realize the smallest size of nanoSQUIDs ~40 nm, and the best spatial resolution ~40 nm and the best spin sensitivity of down to <0.3 $\mu_B/\sqrt{\mathrm{Hz}}$ (Anahory et al., 2020). However, flexibility in choice of superconducting materials and design of nanoSQUIDs, their reproducibility and long-term stability are the advantages of cantilevers with planar nanoSQUIDs that were fabricated by e-beam lithography and nanosculpturing techniques. As an example, Fig. 6a shows a photograph of a 100 mm diameter silicon wafer pre-etched in KOH to fabricate 132 nanoSQUID cantilevers (Fig. 6b). For example, epitaxial growth of nitrides or the high-T_c superconductor $\mathrm{YBa_2Cu_3O_{7-x}}$ on molten quartz capillaries would be a problem. The reproducibility of both types of nanoSQUIDs is limited by the relative scatter of the sizes $\delta x/x$ due to local variations of material properties, which strongly increases with decreasing nanostructure size $x < 100$ nm.

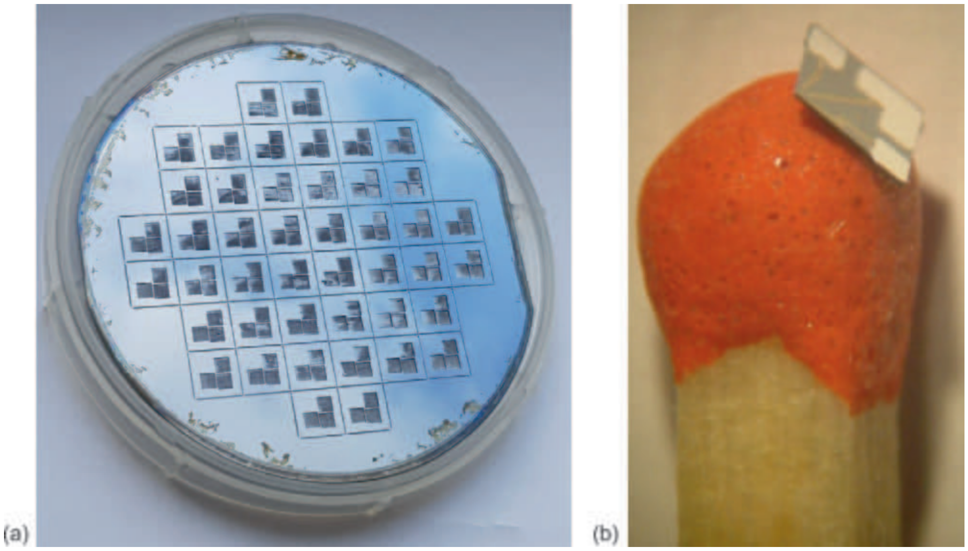

Fig. 6 (a) Photograph of a 100 mm diameter silicon wafer pre-etched in KOH to make 132 nanoSQUID cantilevers. (b) Photograph of a 2 × 2 × 0.05 mm cantilever with a nanoSQUID placed on an ordinary match as a scale.

The long-term stability of nanoSQUIDs is an important issue related to the corrosion resistance of the superconducting materials used. Up to ~10 nm nanometers from the surface of Nb are oxidizing very fast but exactly such thickness would be optimal because the coherence length in Nb films is ~10 nm. Moreover, niobium films react with water and oxygen in laboratory air: in columnar-grown polycrystalline films of niobium oxygen penetrates along grain boundaries through the whole film and produces Nb_2O_5 crystallites that expand and crack the Nb films and the nJJs. Pb films are unstable to degradation during thermal cycling from room temperature to an operating temperature of 4.2 K: this leads to the formation of bumps and cavities on the films, which also destroy the nJJs. Films of the high-temperature superconductor $YBa_2Cu_3O_{7-x}$ decompose in air with the formation of carbonates.

Various methods of film surface passivation are used with varying degrees of efficiency. Coating of Nb films by a protective layer of NbN significantly suppress their oxidation: NbN is resistant to O_2, H_2, CO_2, and air. The passivating Si protective layer improves heat dissipation and protect against the mechanical and electrical fragility of the devices: prevents nJJ from being destroyed by electrostatic discharges. Devices made from $YBa_2Cu_3O_{7-x}$ films usually require vacuum-tight encapsulation or can be partially protected by epitaxial films of $SrTiO_3$.

Epitaxial films of TiN and NbN nitrides have excellent corrosion resistance, which contributes to the long-term stability of nJJ and nanoSQUID. Unlike NbN films, TiN films have only recently begun to be used to fabricate nJJ and nanoSQUID. Thanks to the large coherence length $\xi(0) > 100$ nm at 4.2 K of the TiN films, the non-hysteretic variable-thickness TiN nJJs were realized using e-beam lithography and reactive ion etching. The TiN nJJs with smaller cross-section operate at mK temperatures and can be combined with high quality resonators made from the same material. Multilayers of NbN/TiN have even better mechanical, anticorrosion, and superconducting properties when compared with single-layer NbN and TiN films. MoRe is another corrosion-resistant superconducting material that has been used for the preparation of nanoSQUIDs. Thin films of NbN and MoRe have relatively large energy gaps $2\Delta \sim 5$ meV. However, their T_c values of up to ~16 K and their very short coherence lengths ξ of ~5 nm lead to difficulties in the realization of non-hysteretic nanoSQUIDs with nJJs at an operation temperature of 4.2 K. A combination of TiN nanobridge with NbN electrodes was realized using a double layer of NbN/TiN, so creating an S-S′-S nJJ, where the S′ superconductor TiN has $T_c \leq 6$ K that is smaller than T_c of the S superconductor NbN. of By optimization of deposition parameters and relative thickness of these nitride superconductors it is possible to optimize the superconducting parameters of the corrosion resistant nJJs and nanoSQUIDs.

Conclusion

The fabrication methods, principle of operation, microstructural and electron transport properties, as well as the application of nanoSQUIDs are considered. NanoSQUIDs by definition have a submicrometer loop size, which limits dimensions of Josephson junctions to about 100 nm or less. This makes the use of tunnel junctions problematic, but encourages the use of nanobridges and other types of nJJs with high critical current densities. The use of nitride superconductors helps to optimize the superconducting parameters and enhances the corrosion resistance of the Josephson junctions and nanoSQUIDs. Additional passivation by, for instance, an amorphous Si layer can improve thermal sink of the nJJs and protect against the mechanical and electrical fragility of the devices. Nanosculpturing of cantilevers makes it possible to position the nanoSQUID at a distance of 10–100 nm from the objects under study in the nanoSQUID scanning system. Several promising applications of nanoSQUIDs are briefly reviewed.

With the development of research and applications in mesoscopic quantum systems ("nanoworld"), nanoSQUIDs will play an important role in their niche of low-temperature low-noise measurements and detectors. Planar nanoSQUIDs should reach spin sensitivities that were so far demonstrated only in SQUID-on-tip 3D configuration. The reproducibility, long-term stability of planar nanoSQUIDs, and the possibility of their fabrication on standard silicon wafers in large quantities should facilitate their market acceptance and mass production by commercial companies. Ideally, cantilevers with nanoSQUIDs should become as accessible as cantilevers for atomic force microscopes. The submicron distance between the nanoSQUID and the tip of the cantilever should be the standard. The tip can be a cantilever corner or a pin that can be grown on the surface of the cantilever, for example, by local electron beam assisted carbon, tungsten or platinum deposition inside the SEM or FIB.

The issues of structuring thin films of various superconducting materials for nanoSQUIDs are being further developed. So far, nanoSQUIDs were realized with Nb, NbN, Pb, $YBa_2Cu_3O_{7-x}$, MoRe, MgB_2, doped diamond, Ti, and TiN. The variety of superconducting materials used in the nanoSQUIDs matches the many different applications in which these nanoSQUIDs will be used. For example, nanoSQUIDs designed to measure the magnetization of nanoparticles must be able to operate in strong magnetic fields $H_{c2} > 1$ T that corresponds to superconducting coherence length $\xi < 18$ nm. Films of Nb ($\xi(0) \cong 10$ nm), NbN ($\xi(0) \cong 6$ nm) and $YBa_2Cu_3O_{7-x}$ ($\xi(0) \cong 1$ nm) satisfy this criteria. NbN-based nanoSQUIDs have demonstrated sustainability to fields below 8 T parallel to the plane of the nanoSQUID's loop. The theoretical estimate of the corresponding coherence length $\xi \sim \sqrt{\frac{\hbar}{2e\mu_0 H_{c2}}}.\sim 6$ nm is well suited for the NbN films. If a strong magnetic field is not essential, a more comfortable operating temperature of 4.2 K can be realized using TiN films. With the help of TiN films, it is also possible to realize completely TiN nJJ for qubits and their readout based on nanoSQUIDs operating at temperatures of ~10 mK thanks to the large coherence length ξ_{TiN} in TiN films and possibility to create TiN-nJJs of a size much smaller than ξ_{TiN}. In this case, the temperature dependence of the critical current TiN nJJ saturates at low temperatures (Faley et al., 2022), similarly to the temperature dependence of tunneling Josephson junctions.

New promising potential applications for planar and/or 3D nanoSQUIDs are expected to be developed. To give just a couple of examples, nanoSQUIDs can be also used in: (a) cryogenic transmission electron microscopes (Cryo-TEM) and (b) for reading the results of calculations of adiabatic quantum annealing in arrays of quantum bits using a nanoSQUID scanning system:

(a) TEM sample holders cooled with liquid nitrogen or helium are now commercially available. Superconducting nanostructures, such as narrow lines or Josephson junctions in the form of nanobridges, are quite thin and can be fabricated on electron transparent SiN membranes for use in TEM. Superconducting circuits have extremely low energy dissipation, which is of great advantage when they operate on a thin membrane under ultrahigh vacuum TEM conditions. Josephson radiation from nJJ can be used to excite magnetic resonances in magnetic nanoparticles or coplanar lines, while nanoSQUIDs can detect their net magnetization.

(b) Quantum calculations based on adiabatic quantum annealing lead to a two-dimensional distribution of magnetic moments stored in individual quantum bits in their final classical (non-entangled) mode. The reading of these results can be performed non-destructively using the nanoSQUID scanning system and clearly represented in the form of a 2D magnetic image. This would drastically reduce number of wires needed for operation of superconducting quantum computer. Exposure of the nJJs to FIB can provide controlled suppression of their T_c and this can help optimize the operation of nanoSQUIDs at the millikelvin temperatures.

References

Anahory Y, et al. (2020) SQUID-on-tip with single-electron spin sensitivity for high-field and ultra-low temperature nanomagnetic imaging. *Nanoscale* 12: 3174–3182.

Aslamazov LG and Larkin AI (1968) Josephson effect in superconducting point contacts. *Pis′ ma v Zhurnal Èksperimental′ noy i Teoreticheskoy Fiziki* 9(2): 150–154.

Chen L, Hao Wang H, Liu X, Wu L, and Wang Z (2016) A high-performance Nb nano-superconducting quantum interference device with a three-dimensional structure. *Nano Letters* 16: 7726–7730.

Dunin-Borkowski RE, et al. (1998) Magnetic Microstructure of Magnetotactic Bacteria by Electron Holography. *Science* 282(5395): 1868–1870.

Enpuku K, Tokita G, Maruo T, and Minotani T (1995) Parameter dependencies of characteristics of a high-T_c dc superconducting quantum interference device. *Journal of Applied Physics* 78: 3498–3503.

Faley MI and Dunin-Borkowski RE (2022) A self-flux-biased nanoSQUID with four NbN-TiN-NbN nanobridge Josephson junctions. *Electronics* 11: 1704.

Faley MI, Bikulov T, Bosboom V, Golubov AA, and Dunin-Borkowski RE (2021a) Bulk nanomachining of cantilevers with Nb nanoSQUIDs based on nanobridge Josephson junctions. *Superconductor Science and Technology* 34: 035014.

Faley MI, Liu Y, and Dunin-Borkowski RE (2021b) Titanium nitride as a new prospective material for nanoSQUIDs and superconducting nanobridge electronics. *Nanomaterials* 11: 466.

Faley MI, Fiadziushkin H, Frohn B, Schüffelgen P, and Dunin-Borkowski RE (2022) TiN nanobridge Josephson junctions and nanoSQUIDs on SiN-buffered Si. *Superconductor Science and Technology* 35: 065001.

Foley CP and Hilgenkamp H (2009) Why nanoSQUIDs are important: An introduction to the focus issue. *Superconductor Science and Technology* 22: 064001.

Foroughi F, Mol J-M, Mueller T, Kirtley J, Moler KA, and Bluhm H (2018) A micro-SQUID with dispersive readout for magnetic scanning microscopy. *Applied Physics Letters* 112: 252601.

Granata C and Vettoliere A (2016) Nano Superconducting Quantum Interference device: A powerful tool for nanoscale investigations. *Physics Reports* 614: 1–69.

Hao L, et al. (2008) Measurement and noise performance of nano-superconducting-quantum interference devices fabricated by focused ion beam. *Applied Physics Letters* 92: 192507.

Mangin P and Kahn R (2017) *Superconductivity: An Introduction*, 1st edn. Springer. 2017 edition. ISBN-10: 9783319505251. ISBN-13: 978-3319505251.

Martínez-Pérez MJ, Müller B, Schwebius D, Korinski D, Kleiner R, Sesé J, and Koelle D (2017) NanoSQUID magnetometry of individual cobalt nanoparticles grown by focused electron beam induced deposition. *Superconductor Science and Technology* 30: 024003.

Ruggiero ST (2015) Tunneling and superconductivity. In: Seidel P (ed.) *Applied Superconductivity: Handbook on Devices and Applications*. vol. 1, pp. 66–75. Weinheim: Wiley.

Russo R, Esposito E, Crescitelli A, Di Gennaro E, Granata C, Vettoliere A, Cristiano R, and Lisitskiy M (2017) NanoSQUIDs based on niobium nitride films. *Superconductor Science and Technology* 30: 024009.

Schmelz M, Vettoliere A, Zakosarenko V, De Leo N, Fretto M, Stolz R, and Granata C (2017) 3D nanoSQUID based on tunnel nano-junctions with an energy sensitivity of 1.3 h at 4.2 K. *Applied Physics Letters* 111: 032604.

Shelly CD, See P, Rungger I, and Williams JM (2020) Existence of shapiro steps in the dissipative regime in superconducting weak links. *Physical Review Applied* 13: 024070.
Shishkin AG, Skryabina OV, Gurtovoi VL, Dizhur SE, Faley MI, Golubov AA, and Stolyarov VS (2020) The planar MoRe-based dc nanoSQUID. *Superconductor Science and Technology* 33(6): 065005.
Skocpol WJ, Beasley MR, and Tinkham M (1974) Self-heating hotspots in superconducting thin-film microbridges. *Journal of Applied Physics* 45: 4054–4066.
Trabaldo E, et al. (2019) Grooved dayem nanobridges as building blocks of high-performance $YBa_2Cu_3O_{7-\delta}$ SQUID magnetometers. *Nano Letters* 19: 1902–1907.
Vasyukov D, et al. (2013) A scanning superconducting quantum interference device with single electron spin sensitivity. *Nature Nanotechnology* 8: 639–644.
Voss RF, Laibowitz RB, and Broers AN (1980) Niobium nanobridge dc SQUID. *Applied Physics Letters* 37: 656–658.
Zhang Y, et al. (1993) High temperature RF SQUIDS for biomedical applications. *Physiological Measurement* 14: 113–119.

Perspective in the twistronics of high-temperature superconductors

Giuseppe Serpico[a,b] **and Nicola Poccia**[b], [a]Department of Physics, University of Naples Federico II, Naples, Italy; [b]Leibniz Institute for Solid State and Materials Science Dresden, Dresden, Germany

© 2024 Elsevier Ltd. All rights reserved.

Introduction 712
Van der Waals nature of high-temperature superconductors and their chemical complexity 714
The role of oxygen dopants in cuprates 714
Twistronics of $Bi_2Sr_2Ca_n$-$1Cu_nO_{4+2n+x}$ 716
Josephson effects in twisted $Bi_2Sr_2Ca_n$-$1Cu_nO_{4+2n+x}$ 717
Introducing twisted high-temperature superconductors in quantum circuits 719
Conclusion 721
Acknowledgments 721
References 721

Abstract

Van der Waals heterostructures formed by mechanically stacking layers of 2-Dimensional (2D) materials possess unique properties and new functionalities, not seen in standard materials, that make them an irreplaceable platform for emergent electronics. What hinders the progress in utilizing van der Waals' attractive features in technology is the fact that many of them, especially the novel topological quantum states and related phenomena, are restricted to low temperatures. This poses the challenge of creating van der Waals heterostructures harboring novel topological quantum matter physics at elevated temperatures. This challenge is met by employing high-temperature superconductors-based 2D films, which offer the most advantageous route to increase the temperature range in which the topological states and phenomena associated with van der Waals devices can be used. Realizing this daunting task requires understanding the microscopic mechanisms underlying their properties as well as the developing technologies for their engineering and manipulation. This article addresses the use of $Bi_2Sr_2Ca_n$-$1Cu_nO_{4+2n+x}$ films. Its chemical complexity is analyzed by studying the role of the oxygen dopants and incommensurate lattice modulation, which is a key element for understanding the electrical properties of cuprates. Utilizing solvent- and polymer-free nanofabrication advances makes it possible to create Josephson junctions based on high-temperature superconductors. This article describes the fundamental properties of such a junction and discusses the possibility of introducing twisted high-temperature superconductors in quantum circuits.

Key points

- An introduction to the state of quantum technologies and challenges is given.
- Complexity of the cuprate materials is reviewed by giving special attention to the role of the oxygen ordering and the incommensurate superlattice modulations.
- Fabrication methodologies for the realization of van der Waals twisted cuprate heterostructures are reviewed. Special attention is given to the cryogenic stacking technique.
- Topological superconductivity in twisted cuprate heterostructures is introduced.
- A prospective outlook for the microwave quantum circuit integration in twisted cuprate heterostructures is given.

Introduction

Quantum mechanics is a fundamental theory in physics that explains phenomena found in nature at the scale of atoms and subatomic particles. Modern technologies operate at a scale where quantum effects like quantum entanglement (Horodecki et al., 2009), quantum superposition, and quantum tunneling are significant. For this reason, in the last few decades, an emerging field of physics and engineering encompassing technologies that rely on the properties of quantum mechanics is born. Understanding the laws of quantum physics in order to build new and exciting applications is the purpose of Quantum Technology. Famous examples of emerging quantum technologies are quantum computing (Gyongyosi and Imre, 2019), sensors (Degen et al., 2017), cryptography (Pirandola et al., 2020), and simulation (Georgescu et al., 2014). These technologies are studied today in laboratories all over the world and are waiting to be turned into applications, marking the beginning of a second quantum revolution (Durakiewicz and Greene, 2018). The development of these kinds of quantum technologies will in fact heavily impact established fields like cybersecurity, financial modeling, machine learning, and pharmaceutical and chemical industries. In order to create such a

https://doi.org/10.1016/B978-0-323-90800-9.00248-1

revolution, manifold platforms have been developed because there is no ubiquitous way to exploit the properties of quantum physics to build quantum devices. Ultra-cold atoms (Langen et al., 2015), ion traps (Bruzewicz et al., 2019), and photonics (Slussarenko and Pryde, 2019) are just a few examples of the possible ways to build quantum applications. However, one of the most promising platforms that are mostly used in the world of quantum devices is superconductivity.

In these last years, a lot of successes have been achieved exploiting the properties of superconducting materials, and some of their technological applications include sensitive magnetometers (superconducting quantum interference device) (Fagaly, 2006), fast digital circuits like rapid single flux quantum (RSFQ) technology (Bunyk et al., 2001), Qubits (Kjaergaard et al., 2020), high sensitivity particle detectors like kinetic inductance detector (mKID) (Ulbricht et al., 2021), and superconducting nanowire single-photon detector (SNSPD) (You, 2020). Nevertheless, even if the achievements of the superconductive devices are impressive and their performances are surprising, it is also true that the materials employed are monoatomic, like Niobium or Germanium, or at most diatomic like AlO (Kjaergaard et al., 2020; Scappucci et al., 2021). Then, currently, the activities regarding superconductivity rely on these materials which become superconductive at temperatures far below ambient (T_c of a few Kelvin) and therefore require elaborated cooling systems. On the other hand, high-temperature superconductors (HTSs) show a higher resistance to more "disadvantage conditions" for superconductivity like higher critical temperature and pressure. However, high-temperature superconductivity, under pressure ambient conditions, cannot be achieved with monatomic or diatomic materials. It has already been shown that the lattice complexity plays a key role in defining the critical temperature of a superconductive material (Poccia et al., 2012b). In fact, the critical temperature increases with the number of atomic elements in the lattice proving that HTSs require an intrinsic complexity of the lattice and consequentially of the phase diagram (Keimer et al., 2015; Poccia et al., 2010). This realization initiated new efforts with respect to material science, which has developed into fascinating fields of research and has discovered several families of HTS.

A remarkable and promising class of HTSs are the cuprate families (Bednorz and Müller, 1988; Chu et al., 2015), called like that since CuO_2 (cuprous oxide) plane is the common component in all these new HTS. Common traits of all the cuprates are their layered structure, consisting of CuO_2 layers separated by insulating layers, and the difficulty to handle them due to their ceramic nature. There are five main classes of superconducting cuprates: lanthanum-based, yttrium-based, bismuth-based, thallium-based, and mercury-based. A special place in the cuprate families is held by the bismuth-based compound Bi-Sr-Ca-Cu-O (Fig. 1), which is held together by van der Waals (vdW) bond in between BiO layers and can be realized in three crystallographic phases, Bi-2201, Bi-2212, and Bi-2223, forming a homologous series as $Bi_2Sr_2Ca_n\text{-}1Cu_nO_{4+2n+x}$, with $n = 1$, 2, and 3, each one of them with different superconducting critical temperature properties.

The unique nodal Fermi surface investigated with a variety of spectroscopic techniques (Saleem and Hussain, 2013) and the emerging strange metallic properties (Božović et al., 2017), different from those of monoatomic and diatomic superconductors, not only have made these Bismuth-based cuprates important for our fundamental understanding of HTSs, but are also considered as key advantages for future circuit quantum electrodynamics (cQED) in HTSs. In the later sections, the BSCCO vdW heterostructures and properties are introduced. Finally, the perspective and flexibility of these heterostructures in the field of superconductive technologies are discussed.

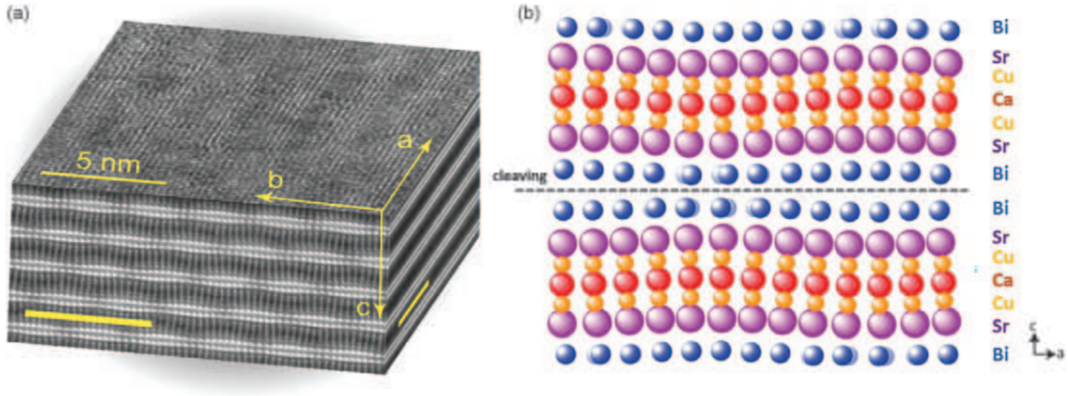

Fig. 1 Atomic structure of the incommensurate supermodulation of the BSCCO crystal. (A) Scanning transmission electron microscopy (STEM) image of the BSCCO showing the crystallographic planes. (B) Sketch of the displacements of all non-O atoms in a Bi-2212 unit cell. (A) Adapted from Poccia N, Zhao SYF, Yoo H, Huang X, Yan H, Chu YS, Zhong R, Gu G, Mazzoli C, Watanabe K, Taniguchi T, Campi G, Vinokur VM, and Kim P (2020) Spatially correlated incommensurate lattice modulations in an atomically thin high-temperature $Br_{2.1}Sr_{1.9}CaCu_{2.0}O_{8+y}$ superconductor. *Physical Review Materials* 4(11). https://doi.org/10.1103/physrevmaterials4.114007. (B) Adapted from Slezak JA, Lee J, Wang M, McElroy K, Fujita K, Andersen BM, Hirschfeld PJ, Eisaki H, Uchida S, and Davis JC (2008) Imaging the impact on cuprate superconductivity of varying the interatomic distances within individual crystal unit cells. *Proceedings of the National Academy of Sciences* 105(9): 3203–3208. https://doi.org/10.1073/pnas.0706795105.

Van der Waals nature of high-temperature superconductors and their chemical complexity

Practical applications of HTSs are steadily improving every year and count a variety of systems going from the large scale (e.g., superconducting bearings for motors, fault current limiters for energy storage devices) (MacManus-Driscoll and Wimbush, 2021) to the small scale (e.g., superconducting quantum interference devices for magnetometry, superconducting and bolometers for astronomy) (Stornaiuolo and Tafuri, 2019). Grain Boundaries (GBs) have been used to create JJs in cuprate HTSs and have had a significant impact on our understanding of the macroscopic properties of these complex materials (Hilgenkamp and Mannhart, 2002). One of the main experimental evidence of oscillatory supercurrent density following a d-wave pairing symmetry was found in biepitaxial GB made of $YBa_2Cu_3O_{7-x}$ (YBCO) HTSs (Lombardi et al., 2002). A conclusive proof for the d-wave order in HTS JJs was demonstrated in tricrystal ring experiments with YBCO (Tsuei et al., 2004). Here the GBs angles were adjusted so that one segment could show a π phase shift with the consequence that a spontaneous circulating current could be detected by scanning quantum interference device microscope images. However, GBs interfaces can only be realized in-plane and can form multifaceted interfaces that may result in unusual magnetic interference patterns and spontaneous flux generation (Hilgenkamp et al., 1996). Moreover, the predicted quasiparticle suppression (important for quantum hardware, Kawabata et al., 2004) in vertical JJs near 45 degrees cannot be realized in in-plane GBs JJ. Although experimental evidence pointed out that quantization of JJs might be possible in YBCO GBs, enabling the prospect for quantum devices using these systems, the same author pointed out that improvement of the interface is necessary to fully exploit HTS in quantum hardware (Bauch et al., 2006).

In recent years, an alternative road exploits the isolation of atomically thin Bi-2212 vdW crystals without degrading the superconducting transition temperature compared to bulk crystals (Yu et al., 2019; Zhao et al., 2019). This experimental progress has encouraged theoretical predictions for a second-order co-tunneling effect in twisted Bi-2212 bilayers, facilitating a coherent superposition of d-wave orders (Can et al., 2021; Volkov et al., 2020). The energetically favorable configuration is characterized by a finite superconducting gap for all momenta, and more importantly, corresponds to a phase with a spontaneously broken time-reversal symmetry (TRS) (Volkov et al., 2021; Tummuru et al., 2022b; Song et al., 2022). Employing HTSs based on 2D films for manufacturing vdW heterostructures, therefore, offers the most advantageous route to increase the temperature range in which the topological states and phenomena associated with vdW devices can be studied and used.

However, stacking Bi-2212 is a great challenge, and many attempts have been realized over the years. Previously, Bi-2212 twist junctions required high-temperature oxygen annealing to restore interfacial superconductivity (Li et al., 1999; Latyshev et al., 2004; Zhu et al., 2021; Takano et al., 2002; Lee et al., 2021), often at the cost of a significant interfacial structural reconstruction, suppressed T_c, low critical current density J_c at zero twist angle, and pronounced anomalies in the resistance–temperature R(T) curves. In the coming subsections, we will discuss the origin and the role of the oxygen and the complexity in the fabrication of mesoscale devices based on thin cuprate crystals.

The role of oxygen dopants in cuprates

The structure of bulk Bi-2212 (BSCCO), as presented in Fig. 1A, consists of alternately stacked superconducting CuO_2 bilayers, and insulating SrO-BiO layers. This insulating layer creates a tunnel-type Josephson coupling between two superconducting CuO_2 bilayers and this special atomic arrangement determines the intrinsic Josephson coupling in between the layers experimentally measured (Kleiner et al., 1992; Yurgens, 2000). The coexistence of such high T_c (nitrogen temperatures) at ambient pressure and at the same time naturally forming intrinsic Josephson junctions along the c-axis already is enough to make the BSCCO unique among the cuprate materials, but more generally among all the HTSs families. The wonder and complexity of the BSCCO materials are well visible by looking also at the structure.

The differences between CuO_2 layers and the insulating layers indeed give rise to intriguing crystallographic patterns up to the mesoscale, which can control superconducting properties (Bianconi et al., 1998; Gao et al., 2009; Triscone et al., 1990; Yamamoto et al., 1990). The percolative process has subtle effects in the superconducting properties of the system, determined by a spatial interplay between k-space and r-space orders as probed by several experiments and discussed in theory works (Fratini et al., 2010; Campi et al., 2015; Poccia et al., 2014a, b; De Mello and Dias, 2007; Pelc et al., 2019; Kugel et al., 2008). Furthermore, BSCCO, as a cuprate superconductor, displays startling nanoscale inhomogeneity in essential properties such as the spectral gap (Howald et al., 2001; Pan et al., 2001) and the pairing temperature (Gomes et al., 2007). Lattice strains control this electronic inhomogeneity since they have been empirically linked with electronic structure. The largest source of strain in Bi-2212 is an incommensurate structural buckling (see Fig. 1B) known as the ILMs (Petricek et al., 1990; Le Page et al., 1989). The 1D incommensurate modulation has been recently modeled as mismatched CuO_2 bilayers (Sboychakov et al., 2022). The authors here intriguingly point out the remarkable similarity of the complex Van Hove Singularity (VHS) splitting with VHS due to the moiré lattice as it is in strained twisted bilayer graphene. A tiny variation in the oxygen disposition in the ILM may change the Fermi level at these VHS, dramatically changing the properties of the system. The ILM along the b-axis in BSCCO is known experimentally to produce weak-diffuse and sharp-intense satellite diffraction peaks up to high temperatures (Castellan et al., 2006; Izquierdo et al., 2006; Comes et al., 2007) and it is correlated with the distribution of oxygen interstitials in the SrO (Zeljkovic et al., 2014, 2012b) and BiO layers (Zeljkovic et al., 2012a). Furthermore, ILM is also correlated with the Fermi surface reconstruction (Valla et al., 2019), and the inhomogeneous distribution of the ILM can change the spatial variation of the superconducting gaps (Slezak et al., 2008) and percolative electronic orders (Carlson and Dahmen, 2011; Carlson et al., 2015).

The previous discussion should therefore make clear to the reader that BSCCO is a complex material and in order to integrate it in mesoscale devices novel methodologies of fabrication are required. Indeed, the methodologies of fabrication need to be developed in order to keep the complexity of the BSCCO intact, especially for what concerns the r-k space orders of oxygen dopants. To get a glimpse of this complexity, the reader is referred to the STM studies, which can be used to analyze the dopants' arrangements in BSCCO highlighting that the oxygen dopants are periodically distributed in correlation with local strain. There are two sources of strain: the previously introduced incommensurate lattice modulation known as the "supermodulation" and the commensurate orthorhombic distortion that shifts two sublattices in opposite directions primarily in the BiO plane (Zeljkovic et al., 2012a; Subramanian et al., 1988). On the other hand there are three species of dopants:

- The interstitial oxygen dopants called "type-A," which are likely to be in the SrO layer (Zeljkovic et al., 2012b; Zhou et al., 2007).
- The interstitial oxygen dopants called "type-B," which are likely to be in the BiO layer (McElroy et al., 2005).
- The apical oxygen vacancies, which are thought to donate electrons to the CuO_2 plane (Zeljkovic et al., 2012b).

Then the STM can locate the three species of dopants with picoscale precision in Bi-2212. In particular, it turns out that the type-B oxygen dopant and the apical oxygen vacancies are correlated with the supermodulation, suggesting the potential utility of the supermodulation as a scaffold for such dopant arrangements. Furthermore, this expresses the importance of oxygen dopants in cuprates because the gap is locally controlled by dopants alone.

As previously mentioned, the superconducting properties are therefore retained only if the configuration of the oxygens is intact after any fabrication process. Nevertheless, the oxygens present high mobility at temperatures higher than 200 K (Poccia et al., 2011b, 2012a; Littlewood, 2011). In this experiment, it is shown that oxygen can be regulated by X-ray light in staged, ordered structures only above 200 K and below 300 K. However, the X-ray continuous manipulation of the cuprate material is not possible anymore if the temperature is below 200 K because below this temperature the oxygens are frozen and the X-ray exposition cannot induce the ordering of the oxygen interstitials. Furthermore, the volatility of oxygen interstitials in the crystals increases as the thickness is decreased and as a result, the lattice becomes more unstable. Given that most of the cuprates are oxygen ion conductors (Skinner and Kilner, 2003), thin BSCCO crystals reduce the thermal activation gap of the oxygen interstitials, which become freer to roam in the lattice. However, oxygen interstitials diffusion can also introduce cracks in the lattice and therefore detrimental disorder in the system. One of the main goals in device technology with BSCCO is therefore to slow down the deterioration of the flakes during the nanofabrication. But the oxygens are not the only factor to consider because, although it has been observed that some layered materials are vertically bonded together by weak vdW bonds that can be cleaved by a simple scotch tape exfoliation, the softness and structural modulation nature of the compound make the synthesis of the ultra-thin film of BSCCO a real challenge (Sandilands et al., 2014). The early attempts to stamp the BSCCO crystal on a substrate using a scotch tape indeed produced atomically thin crystals that were, unfortunately, insulating (Novoselov et al., 2005).

By analyzing the principal properties in the bulk BSSCO using micro X-rays (Poccia et al., 2011a), one may wonder if these properties, including ILM, would change in the 2D limit since the elastic properties of the atomically thin crystals can differ from those in the bulk (Poccia et al., 2020) due to the higher elasticity of thin crystal compared with the bulk. The answer lies in the comparison of the ILM in the bulk BSCCO crystal and a thin film of BSCCO (Fig. 2). This can be done using the X-ray diffraction technique. In particular, the spatial distribution of the ILMs can be visualized using X-ray diffraction at the bulk (Yamamoto et al., 1990; Bianconi et al., 1996; Castellan et al., 2006; Izquierdo et al., 2006). Using this technique, the 1D ILM has been reported to have both diffuse short-range order (SRO) satellites and long-range order (LRO) satellites around Bragg peaks.

The experiment shows that the incommensurate lattice modulation distribution forms puddles of different wavevectors in real space for the bulk crystal. As the crystal is reduced down to 6 nm of thickness, the wavevector of the incommensurate lattice modulation remains basically constant, with some minimal variation in real space given that the thin flakes were realized at room temperature and the system was, therefore, more unstable. Indeed, the puddles spatial correlation changes in the atomically thin limit even in the case the fabrication is realized in an inert atmosphere and the system is encapsulated. The puddles organization has a subtle influence on the electronic properties of the system (Velasco and Neto, 2023; Tromp et al., 2023) and its synchronization. The lattice degradation is observed also in transmission electron microscopy pictures (Zhao et al., 2019) even though the superconductivity in the same arrangement of the materials was preserved down to the atomically thin limit and the Hall-effect measured with the advanced methodology of the stencil mask applied in inert environment and metallic evaporation performed in situ. It is therefore made apparent from these measurements that a 0.5 u.c. of the surface of any BSCCO crystals is extremely complex to preserve and keep intact during a fabrication process. An encouraging result showed that 0.5 u.c. crystals can be realized and superconductivity preserved intact if the BSCCO crystals are exfoliated below room temperature and the electrical contacts realized cold (Yu et al., 2019). Both the Hall measurements in atomically thin BSCCO (Zhao et al., 2019) and the 0.5 u.c. BSCCO superconductor (Yu et al., 2019) had clear advantages and disadvantages in terms of fabrication. Both the experiments nevertheless showed that atomically thin BSCCO crystals were indeed superconducting, setting up the stage for the search of new methodologies in order to integrate the advantages in fabrication discovered in Zhao et al. (2019) and Yu et al. (2019) in new fabrication procedures, which could enable more complex mesoscale devices with atomically thin BSCCO crystals. These are the topics of the next two sections.

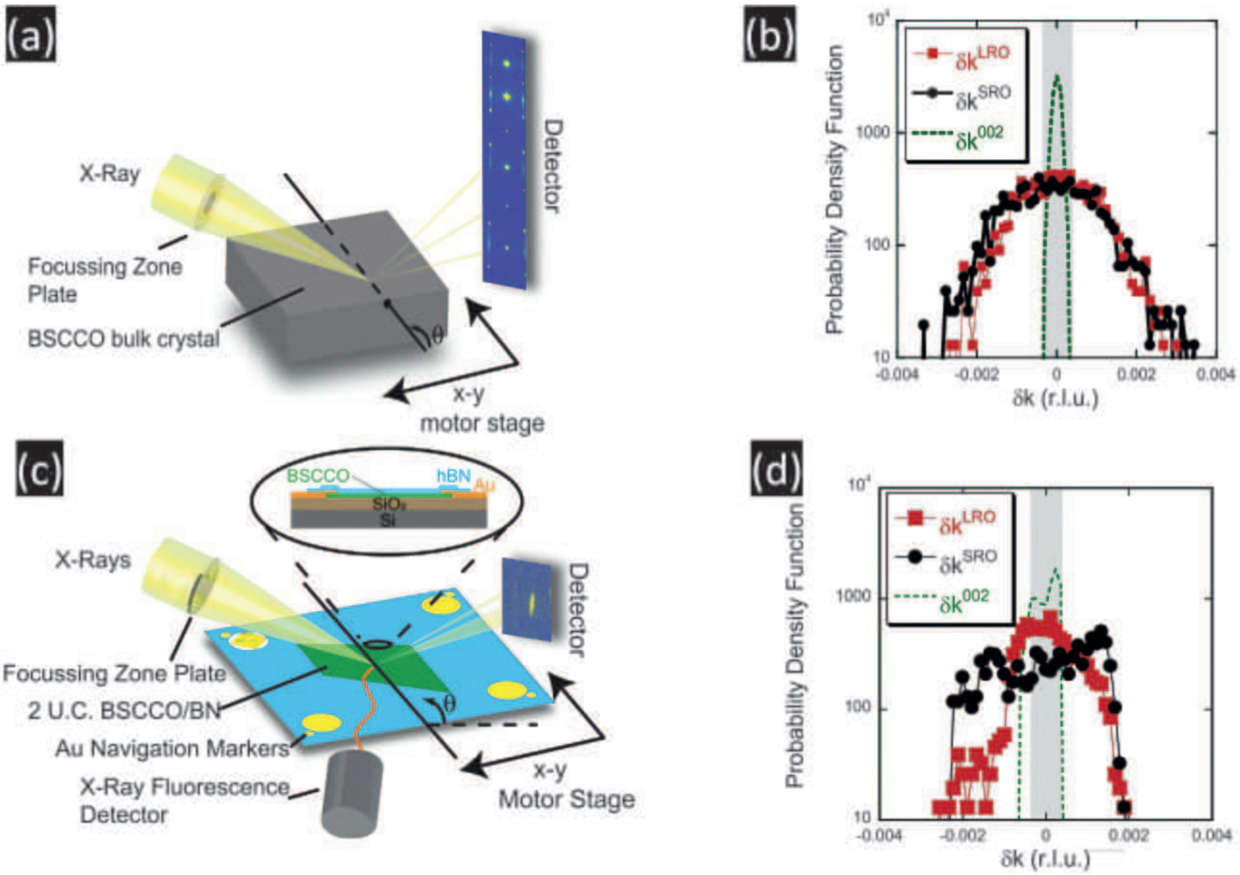

Fig. 2 (A) Schematic diagram of the scanning nano X-ray diffraction of a BSCCO bulk single crystal. The diffracted beam is collected by a 2D detector whose image is integrated from a wide-range angular scan. (B) The probability density function of δk is calculated from the LRO and SRO maps. Furthermore, in order to characterize and map the lattice strain, the wave–vector fluctuations δk for the [002] Bragg peak have been plotted. The experimental resolution is indicated by the *shadowed rectangle*. (C) Scanning nano X-ray diffraction of a thin VdW BSCCO heterostructure. (D) Probability density function of δk calculated from the LRO, the SRO, and the [002] peak maps of the thin film. In this case, the variation of the [002] peak exceeds the experimental resolution. Adapted from Poccia N, Zhao SYF, Yoo H, Huang X, Yan H, Chu YS, Zhong R, Gu G, Mazzoli C, Watanabe K, Taniguchi T, Campi G, Vinokur VM, and Kim P (2020) Spatially correlated incommensurate lattice modulations in an atomically thin high-temperature $Br_{2.1}Sr_{1.9}CaCu_{2.0}O_{8+y}$ superconductor. *Physical Review Materials* 4(11). https://doi.org/10.1103/physrevmaterials4.114007.

Twistronics of $Bi_2Sr_2Ca_n\text{-}1Cu_nO_{4+2n+x}$

But there is more to the BSCCO. The terminating layer is an insulating BiO layer, and usually mechanical cleavage occurs between BiO double layers (see Fig. 1B) due to the weaker vdW bonding (Shaw et al., 1988; Sunshine et al., 1988; Tarascon et al., 1988). For this reason, as introduced in the previous section, the BSCCO can form a tunneling junction along the *c*-axis without the insertion of an insulating layer. Previous experiments on twisted Bi-2212 can be categorized based on the starting crystals used to construct the junction (Li et al., 1999; Latyshev et al., 2004; Zhu et al., 2021; Takano et al., 2002). One experiment utilized bulk single crystals—the only experiment to match the bulk T_c. Structurally, the crystal layers next to the twist junction interface were thicker than the rest and were identified as $Bi_2Sr_2Ca_2Cu_3O_{10+x}$ (Bi-2223) layers (Li et al., 1999). However, due to the large twist interface area, accurate measurements of the coupling between crystals were difficult, and no angular dependence was observed. Two experiments relied on Bi-2212 whiskers, either placed atop one another or naturally fused during growth (Latyshev et al., 2004; Takano et al., 2002). In both cases, the interfaces had to be annealed at 850°C to become superconducting. The resulting devices had a high T_c (~73 K vs. 65 K) and a critical current density J_c (1.17 kA/cm^2 vs. 0.05 kA/cm^2). However, even in these high-quality junctions, structural reconstruction was visible. The second crystal layer from the interface appeared to be 22% thinner than the rest, and the junctions' Fraunhofer patterns were poorly defined. The Shapiro step at 45 degrees also showed integer steps.

In all these experiments, the crystallinity and chemical composition of the surface forming the twist junction are uncontrolled due to air exposure and/or the whiskers' growth environment. From the experience with atomically thin Bi-2212 crystals, however, it became clear that the resulting junction is no more superconducting after a brief (~10 minutes) exposures to air, even when covered by boron nitride crystals (Zhao et al., 2019; Yu et al., 2019). So, it is not surprising that the re-annealed twist interfaces in these experiments are structurally distinct from the bulk.

Among the experiments using vdW fabrication techniques, one method involved cleaving the crystals in argon at 100–200°C and exfoliating the two copies without touching the interface area (Zhu et al., 2021; Lee et al., 2021). The molten transfer polymer had to be subsequently washed off in acetone. In contrast, in another experiment, researchers exfoliated their crystals onto Gel-Pak polymer stamps (Lee et al., 2021) and placed two crystals atop one another onto pre-patterned electrodes to form the twist junction. This procedure was done at room temperature and in argon, but Gel-Pak is known to leave visible residues in optical microscopes, and this polymer stamp was placed directly in contact with the bottom crystal's interfacial region. Furthermore, twist junction transport characteristics often degrade when the interfacial region has been exposed to argon for more than a few minutes as it happens for a 0.5 u.c. atomically thin Bi-2212 crystal. Therefore, the junctions required annealing before becoming superconducting. However, even after the annealing procedure, the contributions reported a prominent structural reconstruction at the interface, a prominent two-step superconducting transition versus temperature, and a large spread in both T_c (<60 K at best) and J_c (smaller than intrinsic JJs values). In this regard, an alternative approach for transferring atomically thin Bi-2212 crystals has been developed based on a cryogenic pick-and-place technique used to create intrinsic JJs (Zhao et al., 2019; Lee et al., 2023; Martini et al., 2023).

This technique consists of cleaving a sequential pair of fresh surfaces of the Bi-2212 from a pre-exfoliated single crystal and stacking the two resulting flakes on top of each other. First, the Bi-2212 crystals are mechanically exfoliated with scotch tape on SiO_2/Si substrates. Next, we cover the Bi-2212 flake with an edge of a PDMS stamp placed on a glass slide (mounted on a micromanipulator), and we let the assembly thermalize. At a temperature slightly above the glass transition of PDMS ($T_g = -120$°C), the stamp becomes very adhesive. By quickly detaching the stamp from the substrate, we can cleave the crystal along an atomically flat plane between BiO planes, obtaining two thinner flakes. The flake standing on the PDMS stamp is aligned and placed back onto the bottom flake on the substrate within 90 s. The time between cleaving and stacking makes a big impact on the junction's quality.

Finally, the stage is slowly heated up to −30°C and the top flake is released on the bottom one (the PDMS loses its adhesive properties). The control over the adhesion of the PDMS stamp allows us to fabricate the junctions using a dry and solvent-free transfer at low temperatures. Additionally, the interfaces can be protected from water molecules by placing an encapsulating hexagonal boron nitride (hBN) flake on top of the stacked flakes immediately after stacking. This improves the interfaces' survival when they are transferred to a cryogenic measurement system (Lee et al., 2023; Martini et al., 2023). Electrical contacts can be deposited in two steps using a chemical-free stencil mask technique in an evaporation chamber, directly connected to the glovebox cluster. The T_c of the JJs is close to that of a bulk crystal, indicating the high uniformity of oxygen dopants. In Fig. 3, there is a sketch of a single flake cleaved by the stinky PDMS stamp.

Josephson effects in twisted $Bi_2Sr_2Ca_n$-$1Cu_nO_{4+2n+x}$

Exploiting this fabrication process is possible to create a two-dimensional BSCCO assembled into bilayers with a twist between individual layers. In Fig. 4A, an example of 42.6 degrees twisted junction is reported. Measurements of Current-voltage characteristics ad normalized differential resistance are presented in Fig. 4B.

The twist angle modulates interfacial Josephson coupling between twisted nodal d-wave superconductors (Klemm, 2005). At exactly $\theta = 45$ degrees, only the second-order co-tunneling of Cooper pairs is allowed (Can et al., 2021; Sigrist, 1998; Goldobin et al., 2007) while direct Cooper pair tunneling is forbidden due to the complete mismatch between the $d_{x^2-y^2}$ symmetric superconducting order parameters (SOPs) across the interface (Klemm, 2005). This is expected to support topological, time-reversal symmetry-breaking superconducting phases persisting up to the junction superconducting transition temperature T_c (Can et al., 2021; Yang et al., 2018). At $\theta = 0$ degree, electronic characteristics similar to single-crystal intrinsic junctions are shown by the BSCCO junction (Zhao et al., 2021; Lee et al., 2023, 2021). The encapsulation is realized to prolongate the lifetime of the junctions in ambient conditions, moreover, it becomes essential in order to realize intrinsic junctions if the thermal evaporation of the electrical contacts is done in a high vacuum chamber (10^{-6} bar) (Lee et al., 2023; Martini et al., 2023) in comparison to a more

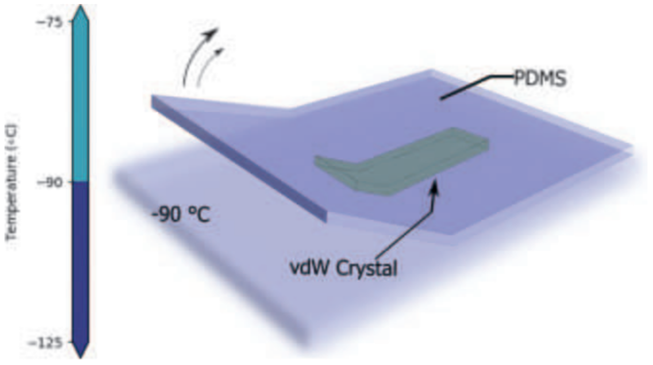

Fig. 3 A polymer called polydimethylsiloxane is used to exfoliate a BSCCO crystal at −90°C. The stacking process of a BSCCO flake on to another is done at −90°C because as previously mentioned, the oxygens are frozen under 200 K preserving the ILM and the electronic properties. The interface creation is done therefore in less than one minute with each flake oriented to each other at the desired angle.

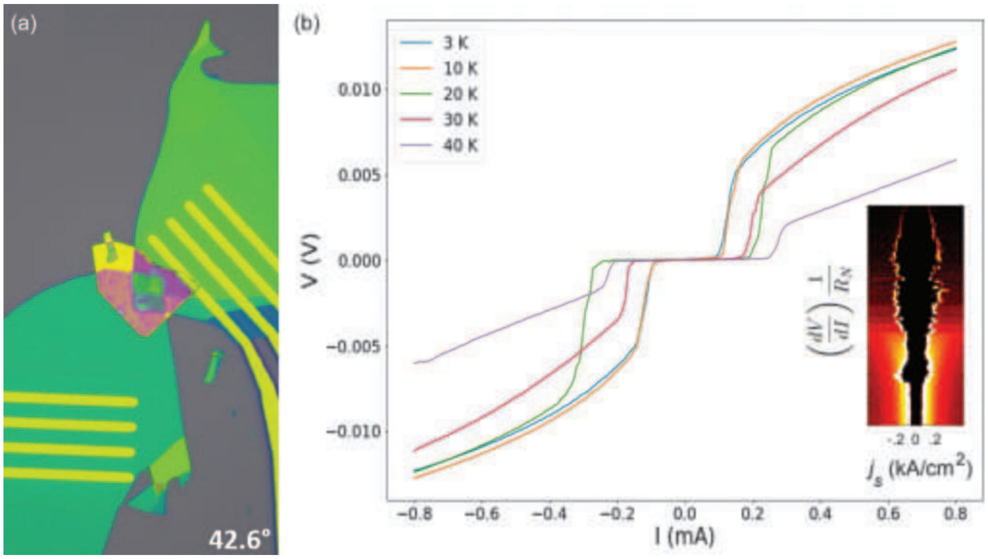

Fig. 4 (A) Optical micrographs of a twisted JJs device with a twist angle of 42.6 degrees. (B) Current–voltage characteristics of JJ are measured by sweeping the current at different temperatures. In the insert the normalized differential resistance [dV/dI]/R_N as a function of $I_C R_N$ and temperature T from 2 to 80 K has been shown. The lowest values of the normalized differential resistance are *black* while the highest values are *yellow*. Adapted from Lee Y, Martini M, Confalone T, Shokri S, Saggau CN, Wolf D, Gu G, Watanabe K, Taniguchi T, Montemurro D, Vinokur VM, Nielsch K, and Poccia N (2023) Encapsulating hightemperature superconducting twisted van der Waals heterostructures blocks detrimental effects of disorder. *Advanced Materials* 35(15): 2209135. https://doi.org/10.1002/adma.202209135.

expensive ultra-high vacuum evaporator (10^{-8} bar) (Zhao et al., 2021). These experimental observations indicate that for $\theta = 0$ degree the JJ reaches electronic quality comparable to intrinsic JJ in single-crystal BSCCO as observed in bulk crystals (Kleiner et al., 1992). Normalizing the bias current with the junction normal resistance R_N, the transport characteristics of different twisted JJs can be compared. Since I_C and R_N^{-1} are proportional to the area of the junction, the product $I_C R_N$ is independent of the junction area. It comes out that the magnitude of $I_C R_N$ becomes smaller closer to 45 and 135 degrees where the JJs also appear less hysteretic (Zhao et al., 2021). In particular, $I_C R_N(\theta)$ has a behavior similar to the angular dependence of junction voltage just above the critical current $V\,(I_C)$ because it behaves like $|\cos 2\theta|$, which is expected for somewhat incoherent Cooper pair tunneling between d-wave superconductors (Klemm, 2005). Further insight into the pairing symmetry of the Cooper pairs in BSCCO is provided by the temperature dependence of Josephson coupling in the twisted junctions (Zhao et al., 2021; Martini et al., 2023; Lee et al., 2023). For $\theta \sim 0$, $I_C(T)R_N$ monotonically decreases as T increases, approximately following the theory curve for nearly incoherent tunneling between d-wave superconductors. However, a nonmonotonic behavior of $I_C(T)R_N$ appears when θ increases. For example, for $\theta = 29$ and 39 degrees, the $I_C(T)R_N$ increases alongside T, reaching a maximum value and then decreases as T approaches T_c (Zhao et al., 2021). For $\theta = (44.9 \pm 0.1)$ degrees junction, the $I_C R_N$ is about two orders of magnitude smaller than the 0 degree value. The origin of the finite supercurrent near 45 degrees is encoded in the Josephson current-phase relation (CPR) (Can et al., 2021; Sigrist, 1998; Goldobin et al., 2007). Using the Ginzburg–Landau theory on each layer it is possible to write the following CPR:

$$I(\phi) = I_{c1}\sin(\phi) - I_{c2}\sin(2\phi), \tag{1}$$

in which I_{C1} depends on the twisting angle θ according to the relation $I_{C1} \sim \cos(2\theta)$. The competition between the first and second terms in the previous equation underlies the emergence of the spontaneously broken time-reversal symmetry phase near the 45 degrees twist. In fact, When θ is close to zero, the conventional Josephson tunneling term I_{C1} dominates and the corresponding free energy minimum occurs at $\phi = 0$. However, $I_{C1} \sim \cos(2\theta)$ decreases when increasing the twist. Eventually, for a twist angle approaching 45 degrees, the I_{C2} term begins to dominate and the free energy develops two minima. This means that tunneling one by one of Cooper pairs across the junction is suppressed and a stronger link between the layers enables the transfer of multiple Cooper pairs in a single act of tunneling (Goldobin et al., 2007). The co-tunneling of Cooper pairs is predicted to support an interfacial SOP with emergent $d_{x^2-y^2} + id_{xy}$ symmetry (Sigrist, 1998; Yang et al., 2018; Can et al., 2021). The signature of the strong second-order harmonic $I_C \sim \sin(2\phi)$ can be experimentally probed by measuring the Fraunhofer pattern (Barone and Paterno, 1982) or microwave-induced Shapiro steps (Shapiro et al., 1964) in the I–V characteristic, which are both sensitive to the 4e charge of co-tunneling Cooper pairs across the junction (Sigrist, 1998; Yang et al., 2018; Goldobin et al., 2007).

Fraunhofer interference occurs when a JJ is subjected to an external magnetic field parallel to the junction plane. When θ approaches 45 degrees, the current-phase relation changes and the period of the Fraunhofer pattern becomes halved (Tummuru et al., 2022b). This period-halved contribution in the Fraunhofer pattern is rapidly lost when moving to θ under 40 degrees signaling the field dependence of the critical current can be tested to probe for spontaneous broken TRS.

Shapiro steps occur when the junction is continuously irradiated with microwaves at frequency f. The resonance between microwave and ac Josephson frequency resulted in quantized voltage steps, with a step height of $hf/2e$, in the I–V characteristic curve. When θ approaches 45 degrees, additional steps appear at fractional values $V_n/2$ because the second harmonic becomes dominant in the current-phase relation. Then the Shapiro steps are a manifestation of the tunneling of Cooper pairs across the barrier while the fractional steps, on the other hand, coincide with two Cooper pairs tunneling across the junction. In both cases whenever the potential energy across the junction is equal to the photon energy, or a multiple thereof, one or two Cooper pairs can absorb photons from the radiation field. Both the prediction for the Shapiro and the Fraunhofer have been confirmed in experiments (Zhao et al., 2021).

Although these experiments are hard to realize given the described fragility of these interfaces, the tantalizing perspective provided by the previous experimental fabrication advancements and observations encourages theory to propose novel architectures. Theoretically, the induced superconducting topological gap at the interface can be manipulated by controlling the 3D architecture of the material. Indeed, the twist degree of freedom of each layer can be tuned independently. Cuprate-twisted multilayers admit several inequivalent arrangements, which can improve the size of the topological superconducting gap and the superconducting region in the phase diagram (twist angle vs. temperature) where broken TRS broken states can be created and detected. As a function of the angle, two (three) Dirac cones merge to form a quadratic (cubic) band touching dispersion. This results in an alternated (chiral) twist symmetry, which can exhibit chiral topological superconductivity in an extended region of the twist-angle phase diagram (Tummuru et al., 2022a). In the chiral case, the angle of twisted trilayer cuprate heterostructures is predicted to exhibit a power-law divergent density of states. States that break TRS host chiral edge modes that always come in pairs and therefore do not require the inclusion of a zero-energy state, such as the Majorana fermions. However, we can create a topological phase with odd chiral edge modes by introducing a topological insulator with strong spin–orbit coupling as a substrate or as an encapsulation layer. The interface of a twisted cuprate bilayer can yield a topological phase with odd chiral edge modes (Margalit et al., 2022). The expected chiral mode can include a single chiral Majorana zero mode at each vortex if a perpendicular magnetic field is applied to the system (Mercado et al., 2022). Early work on interfacing topological insulators with (untwisted) Bi-2212 has already produced encouraging results (Zareapour et al., 2012). Although an additional study failed to detect a proximity-induced measurable gap (Xu et al., 2014), the research underscores the interest in twisted cuprate/topological insulators heterostructures fabrication.

Introducing twisted high-temperature superconductors in quantum circuits

As introduced before, the possibility to twist the BSCCO monolayers introduces a new degree of tunability which paves the way for superconducting technologies. JJ-based superconducting circuits are at the vanguard in many areas of microwave quantum circuits (Devoret and Schoelkopf, 2013; Devoret and Martinis, 2004) and they are used as state-of-the-art not only for qubits but also for readout amplifiers, cavities, detectors, circulators, and amplifiers (Bergeal et al., 2008; Frattini et al., 2018; Clarke and Braginski, 2006). In order to take advantage of these extraordinary properties explained previously, a promising pathway is to integrate the 2D twisted JJ composed of BSCCO flakes into conventional 3D superconducting circuits. Obviously, one of the most challenging parts is the creation of reliable superconducting contact between the 2D and 3D materials allowing the use of standard microwave readout and drive techniques. Once this aspect is overcome, there is the possibility of fabricating microwave resonant circuits allowing for high-quality hybrid circuits.

Microwave resonators are an indispensable element in the field of microwave quantum circuits. For example, they are the building blocks of superconducting photon detectors like SNSPD (Natarajan et al., 2012) or mKID (Day et al., 2003; Baselmans et al., 2008). In this sense, hybrid circuits incorporating a twisted BSCCO vdW heterostructure can be used as a novel inductive detector capable of detecting single photons in the low frequency (THz) regime, with micron spatial resolution given by the size of the flake. A photon hitting the superconductor generates quasiparticles above the gap, which are detected either via the resistive response (in SNSPDs) or via the reactive phase response (in mKIDs). Such a device can be used as a novel inductive detector capable of detecting single photons in the low frequency (THz) regime, with micron spatial resolution given by the size of the flake. Such a device is also useful for the basic study of superconductivity, as the superconducting circuit can probe the superfluid density of the BSCCO flake and explore its superconducting gap structure.

Furthermore, microwave superconducting resonators are widely used to build qubits. Since the first realization of the Cooper-pair box (Koch et al., 2007), superconducting qubit technology has evolved to become a leading modality for quantum computation (Bravyi et al., 2022). Employing other materials or devices with alternative electronic or degrees of freedom paves the way for novel and exotic qubits realizations. In this sense, integrating the resonator with the 2D BSCCO junction could be possible to create a platform toward qubits with unique properties and a new degree of tunability proper of this junction.

But hybrid superconducting circuits are interesting platforms not only for quantum computing technologies but also for fundamental sciences. The coupling between the superconducting resonator and the 2D BSCCO junction can be used to investigate, through a radio frequency measurement, the fundamental properties of the junction such as the CPR and the free energy. A hybrid device of such kind is a valuable tool to evaluate the contribution of the second harmonic in Eq. (1) for different twisting angles (Tummuru et al., 2022b). In particular, to perform this measurement, a superconducting resonator should be galvanically coupled with the Junction, which is embedded in a SQUID loop as shown in the Fig. 5A.

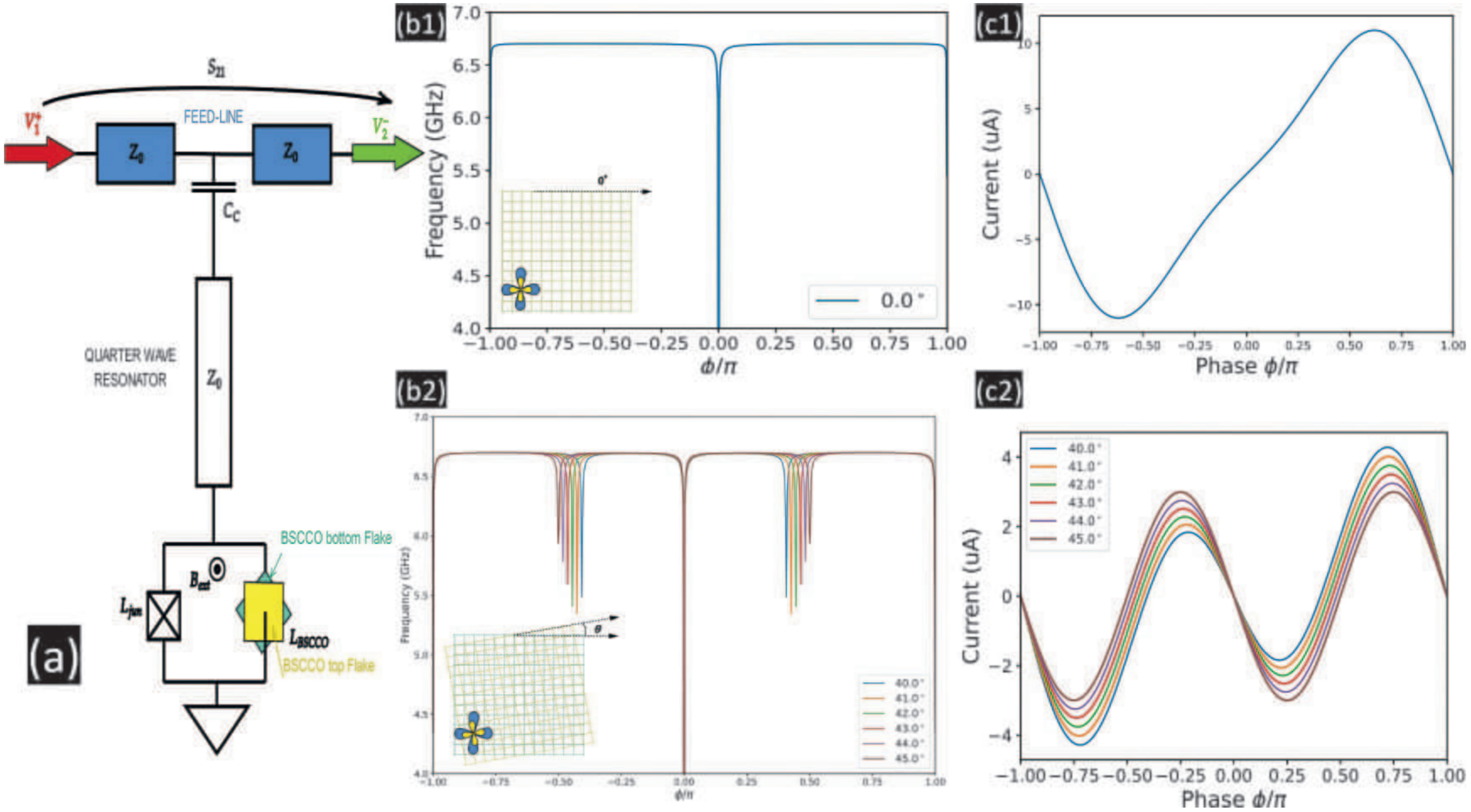

Fig. 5 (A) Sketch of the proposed device able to measure the CPR of a junction. The twisted junction is embedded in a SQUID loop which is galvanically coupled to the resonator. (B1) Resonance deep produced by a 0 degree twist junction and (C1) the corresponding current phase relation. (B2) The same analysis has been done for θ near 45 degrees and (C2) additional shifts appear thanks to the dominance of the second harmonic contribution.

Applying a magnetic field in the superconducting loop, the phenomenon of flux quantization arises changing the Josephson inductance of the junction and consequently the resonance frequency of the device which is expressed as

$$f_{res} = \frac{1}{4l_{res}\sqrt{L_{tot}C_{cpw}}}, \tag{2}$$

where L_{tot} is the total inductance of the device containing the resonator inductance and the resulting inductance of the two junctions in the loop. Then, by probing the resonator in the radio frequency range, a direct measurement of the resonance shift for different twisting angles can be done. As shown in Fig. 5B1 and B2 additional shifts of the resonance frequency appear when the twisting angle approaches 45 degrees. From the behavior of the resonance frequency, by reconstructing the CPR, the second harmonic contribution in the JJ is evaluated as presented in Fig. 5C1 and C2. In this sense, the superconducting resonator could be a powerful tool to analyze the fundamental properties of the junction. Furthermore, it is important to underline that even though a lot of DC transport measurements have been performed on vdW heterostructures only in a few recent experiments, they have been integrated into cQED (Wang et al., 2019; Sinko et al., 2021). For this reason, this device could be the first important step toward the integration of vdW heterostructures in the field of quantum technologies.

Conclusion

By introducing new materials and experimental approaches, hybrid superconducting circuits can make a great contribution to quantum technologies and fundamental research. The unique electronic properties of these heterostructures make vdW BSCCO-based devices a promising alternative for constructing key elements of novel solid-state quantum computing platforms. Materials science is becoming an important element in the world of quantum circuits and soon may make significant contributions to the already thriving cQED sector. Given the promising results, in the near future, an integration of these novel materials in superconducting circuits is desirable in order to harness the properties of BSCCO heterostructures for use in the cQED architecture.

Acknowledgments

The experiment presented in Fig. 4 is the result of the work of Yejin Lee, Mickey Martini, Sanaz Shokri, Christian Saggau, and Tommaso Confalone. The crystals were provided by Genda Gu, Kenji Watanabe, and Takashi Taniguchi. The experiments were partially supported by the Deutsche Forschungsgemeinschaft (DFG 452128813, DFG 512734967, DFG 492704387, DFG 460444718). The work was supported by the Terra Quantum AG. K.W. and T.T. acknowledge support from the JSPS KAKENHI. The work at BNL was supported by the US Department of Energy, office of Basic Energy Sciences. The authors are grateful to Heiko Reith and Nicolas Perez for providing access to cleanroom and cryogenic facilities, respectively. The authors are also grateful to S. Y. Frank Zhao, Philip Kim, Francesco Tafuri, Giampiero Pepe, Uri Vool, Kornelius Nielsch, Valerii M. Vinokur, Domenico Montemurro, Davide Massarotti, Naurang L. Saini, Gaetano Campi, Axel Lubk, Carlo di Castro, Valentina Brosco, and Pavel A. Volkov for illuminating and fruitful discussions.

References

Barone A and Paterno G (1982) *Physics and Applications of the Josephson Effect*, vol. 1. Wiley Online Library.

Baselmans JJA, Yates S, Barends R, Lankwarden Y, Gao JR, Hoevers H, and Klapwijk TM (2008) Noise and sensitivity of aluminum kinetic inductance detectors for sub-mm astronomy. *Journal of Low Temperature Physics* 151: 524–529. https://doi.org/10.1007/s10909-007-9684-3.

Bauch T, Lindström T, Tafuri F, Rotoli G, Delsing P, Claeson T, and Lombardi F (2006) Quantum dynamics of a d-wave Josephson junction. *Science* 311(5757): 57–60.

Bednorz JG and Müller KA (1988) Perovskite-type oxides—The new approach to high-T_c superconductivity. *Reviews of Modern Physics* 60(3): 585.

Bergeal N, Vijay R, Manucharyan VE, Siddiqi I, Schoelkopf RJ, Girvin SM, and Devoret MH (2008) *Analog information processing at the quantum limit with a Josephson ring modulator*. https://doi.org/10.48550/ARXIV.0805.3452.

Bianconi A, Lusignoli M, Saini NL, Bordet P, Kvick A, and Radaelli PG (1996) Stripe structure of the CuO_2 plane in $Bi_2Sr_2CaCu_2O_{8+y}$ by anomalous x-ray diffraction. *Physical Review B, Condensed Matter* 54(6): 4310–4314. https://doi.org/10.1103/PhysRevB.54.4310.

Bianconi A, Valletta A, Perali A, and Saini NL (1998) Superconductivity of a striped phase at the atomic limit. *Physica C: Superconductivity* 296(3): 269–280. ISSN: 0921-4534. https://doi.org/10.1016/S0921-4534(97)01825-X.

Božović I, He X, Wu J, and Bollinger A (2017) What is strange about high-temperature superconductivity in cuprates? *International Journal of Modern Physics B* 31(25): 1745005.

Bravyi S, Dial O, Gambetta JM, Gil D, and Nazario Z (2022) *The future of quantum computing with superconducting qubits*. https://doi.org/10.48550/ARXIV.2209.06841.

Bruzewicz CD, Chiaverini J, McConnell R, and Sage JM (2019) Trapped-ion quantum computing: Progress and challenges. *Applied Physics Reviews* 6(2): 021314. https://doi.org/10.1063/1.5088164.

Bunyk P, Likharev K, and Zinoviev D (2001) RSFQ technology: Physics and devices. *International Journal of High Speed Electronics and Systems* 11(01): 257–305. https://doi.org/10.1142/S012915640100085X.

Campi G, Bianconi A, Poccia N, Bianconi G, Barba L, Arrighetti G, Innocenti D, Karpinski J, Zhigadlo ND, Kazakov SM, et al. (2015) Inhomogeneity of charge-density-wave order and quenched disorder in a high-T_c superconductor. *Nature* 525(7569): 359–362.

Can O, Tummuru T, Day RP, Elfimov I, Damascelli A, and Franz M (2021) High-temperature topological superconductivity in twisted double-layer copper oxides. *Nature Physics* 17(4): 519–524. https://doi.org/10.1038/s41567-020-01142-7.

Carlson EW and Dahmen KA (2011) Using disorder to detect locally ordered electron nematics via hysteresis. *Nature Communications* 2(1): 1–6.

Carlson EW, Liu S, Phillabaum B, and Dahmen KA (2015) Decoding spatial complexity in strongly correlated electronic systems. *Journal of Superconductivity and Novel Magnetism* 28(4): 1237–1243.

Castellan JP, Gaulin BD, Dabkowska HA, Nabialek A, Gu G, Liu X, and Islam Z (2006) Two- and three-dimensional incommensurate modulation in optimally-doped $Bi_2Sr_2CaCu_2O_{8+\delta}$. *Physical Review B* 73(17): 174505. https://doi.org/10.1103/PhysRevB.73.174505.

Chu CW, Deng LZ, and Lv B (2015) Hole-doped cuprate high temperature superconductors. *Physica C: Superconductivity and its Applications* 514: 290–313.

Clarke J and Braginski AI (2006) *The SQUID Handbook Fundamentals and Technology of SQUIDs and SQUID Systems*, vol. 1. Weinheim: Wiley-VCH.

Comes R, Izquierdo M, Megtert S, Albouy PA, Avila J, Valbuena MA, Gu G, Abell JS, and Asensio MC (2007) X-ray diffuse scattering experiments on bismuth based high T_c superconductors. *Physica C: Superconductivity* 460–462: 730–731. https://doi.org/10.1016/j.physc.2007.03.154. Proceedings of the 8th International Conference on Materials and Mechanisms of Superconductivity and High Temperature Superconductors.

Day PK, Leduc HG, Mazin BA, Vayonakis A, and Zmuidzinas J (2003) A broadband superconducting detector suitable for use in large arrays. *Nature* 425: 817–821.

De Mello EVL and Dias DHN (2007) Phase separation and the phase diagram of cuprate superconductors. *Journal of Physics: Condensed Matter* 19(8): 086218.

Degen CL, Reinhard F, and Cappellaro P (2017) Quantum sensing. *Reviews of Modern Physics* 89(3): 035002. https://doi.org/10.1103/RevModPhys.89.035002.

Devoret M and Martinis J (2004) Implementing qubits with superconducting integrated circuits: Experimental aspects of quantum computing. *Quantum Information Processing* 3: 163–203. https://doi.org/10.1007/s11128-004-3101-5.

Devoret MH and Schoelkopf RJ (2013) Superconducting circuits for quantum information: An outlook. *Science* 339(6124): 1169–1174. https://doi.org/10.1126/science.1231930.

Durakiewicz T and Greene L (2018) Commentary: Enabling a quantum leap. *Physics Today* 71(9): 10–11.

Fagaly RL (2006) Superconducting quantum interference device instruments and applications. *Review of Scientific Instruments* 77(10): 101101. https://doi.org/10.1063/1.2354545.

Fratini M, Poccia N, Ricci A, Campi G, Burghammer M, Aeppli G, and Bianconi A (2010) Scale-free structural organization of oxygen interstitials in La_2CuO_{4+y}. *Nature* 466(7308): 841–844.

Frattini NE, Sivak VV, Lingenfelter A, Shankar S, and Devoret MH (2018) Optimizing the nonlinearity and dissipation of a SNAIL parametric amplifier for dynamic range. *Physical Review Applied* 10(5): 054020. https://doi.org/10.1103/PhysRevApplied.10.054020.

Gao WB, Liu QQ, Yang LX, Yu Y, Li FY, Jin CQ, and Uchida S (2009) Out-of-plane effect on the superconductivity of $Sr_{2-x}Ba_xCuO_{3+\delta}$ with T_c up to 98 K. *Physical Review B* 80(9): 094523. https://doi.org/10.1103/PhysRevB.80.094523.

Georgescu IM, Ashhab S, and Nori F (2014) Quantum simulation. *Reviews of Modern Physics* 86(1): 153–185. https://doi.org/10.1103/revmodphys.86.153.

Goldobin E, Koelle D, Kleiner R, and Buzdin A (2007) Josephson junctions with second harmonic in the current-phase relation: Properties of φ junctions. *Physical Review B* 76(22): 224523. https://doi.org/10.1103/PhysRevB.76.224523.

Gomes KK, Pasupathy AN, Pushp A, Ono S, Ando Y, and Yazdani A (2007) Visualizing pair formation on the atomic scale in the high-T_c superconductor $Bi_2Sr_2CaCu_2O_{8+\delta}$. *Nature* 447 (7144): 569–572.

Gyongyosi L and Imre S (2019) A survey on quantum computing technology. *Computer Science Review* 31: 51–71. ISSN: 1574-0137. https://doi.org/10.1016/j.cosrev.2018.11.002.

Hilgenkamp H and Mannhart J (2002) Grain boundaries in high-T_c superconductors. *Reviews of Modern Physics* 74(2): 485.

Hilgenkamp H, Mannhart J, and Mayer B (1996) Implications of $d_{x_2-y_2}$ symmetry and faceting for the transport properties of grain boundaries in high-T_c superconductors. *Physical Review B* 53(21): 14586.

Horodecki R, Horodecki P, Horodecki M, and Horodecki K (2009) Quantum entanglement. *Reviews of Modern Physics* 81(2): 865–942. https://doi.org/10.1103/RevModPhys.81.865.

Howald C, Fournier P, and Kapitulnik A (2001) Inherent inhomogeneities in tunneling spectra of $Bi_2Sr_2CaCu_2O_{8-x}$ crystals in the superconducting state. *Physical Review B* 64(10): 100504. https://doi.org/10.1103/PhysRevB.64.100504.

Izquierdo M, Megtert S, Albouy JP, Avila J, Valbuena MA, Gu G, Abell JS, Yang G, Asensio MC, and Comes R (2006) X-ray diffuse scattering experiments from bismuth-based high-T_c superconductors. *Physical Review B* 74(5): 054512. https://doi.org/10.1103/PhysRevB.74.054512.

Kawabata S, Kashiwaya S, Asano Y, and Tanaka Y (2004) Macroscopic quantum tunneling and quasiparticle dissipation in d-wave superconductor Josephson junctions. *Physical Review B* 70(13): 132505.

Keimer B, Kivelson SA, Norman MR, Uchida S, and Zaanen J (2015) From quantum matter to high-temperature superconductivity in copper oxides. *Nature* 518(7538): 179–186.

Kjaergaard M, Schwartz ME, Braumüller J, Krantz P, Wang JI-J, Gustavsson S, and Oliver WD (2020) Superconducting qubits: Current state of play. *Annual Review of Condensed Matter Physics* 11(1): 369–395. https://doi.org/10.1146/annurev-conmatphys-031119-050605.

Kleiner R, Steinmeyer F, Kunkel G, and Müller P (1992) Intrinsic Josephson effects in $Bi_2Sr_2CaCu_2O_8$ single crystals. *Physical Review Letters* 68(15): 2394.

Klemm RA (2005) The phase-sensitive c-axis twist experiments on $Bi_2Sr_2CaCu_2O_{8+\delta}$ and their implications. *Philosophical Magazine* 85(8): 801–853. https://doi.org/10.1080/14786430412331314573.

Koch J, Yu TM, Gambetta J, Houck AA, Schuster DI, Majer J, Blais A, Devoret MH, Girvin SM, and Schoelkopf RJ (2007) Charge-insensitive qubit design derived from the Cooper pair box. *Physical Review A* 76(4): 042319. https://doi.org/10.1103/physreva.76.042319.

Kugel KI, Rakhmanov AL, Sboychakov AO, Poccia N, and Bianconi A (2008) Model for phase separation controlled by doping and the internal chemical pressure in different cuprate superconductors. *Physical Review B* 78(16): 165124.

Langen T, Geiger R, and Schmiedmayer J (2015) Ultracold atoms out of equilibrium. *Annual Review of Condensed Matter Physics* 6(1): 201–217. https://doi.org/10.1146/annurev-conmatphys-031214-014548.

Latyshev YI, Orlov AP, Nikitina AM, Monceau P, and Klemm RA (2004) c-axis transport in naturally grown $Bi_2Sr_2CaCu_2O_{8+\delta}$ cross-whisker junctions. *Physical Review B* 70(9): 094517.

Le Page Y, McKinnon WR, Tarascon J-M, and Barboux P (1989) Origin of the incommensurate modulation of the 80-K superconductor $Bi_2Sr_2CaCu_2O_{8.21}$ derived from isostructural commensurate $Bi_{10}Sr_{15}Fe_{10}O_{46}$. *Physical Review B* 40(10): 6810–6816. https://doi.org/10.1103/PhysRevB.40.6810.

Lee J, Lee W, Kim G-Y, Choi Y-B, Park J, Jang S, Gu G, Choi S-Y, Cho GY, Lee G-H, et al. (2021) Twisted van der Waals Josephson junction based on a high-T_c superconductor. *Nano Letters* 21(24): 10469–10477.

Lee Y, Martini M, Confalone T, Shokri S, Saggau CN, Wolf D, Gu G, Watanabe K, Taniguchi T, Montemurro D, Vinokur VM, Nielsch K, and Poccia N (2023) Encapsulating high-temperature superconducting twisted van der Waals heterostructures blocks detrimental effects of disorder. *Advanced Materials* 35(15): 2209135. https://doi.org/10.1002/adma.202209135.

Li Q, Tsay YN, Suenaga M, Klemm RA, Gu GD, and Koshizuka N (1999) $Bi_2Sr_2CaCu_2O_{8+\delta}$ bicrystal *c*-axis twist Josephson junctions: A new phase-sensitive test of order parameter symmetry. *Physical Review Letters* 83(20): 4160–4163. https://doi.org/10.1103/PhysRevLett.83.4160.

Littlewood P (2011) An X-ray oxygen regulator. *Nature Materials* 10(10): 726–727.

Lombardi F, Tafuri F, Ricci F, Granozio FM, Barone A, Testa G, Sarnelli E, Kirtley JR, and Tsuei CC (2002) Intrinsic d-wave effects in $YBa_2Cu_3O_{7-\delta}$ grain boundary Josephson junctions. *Physical Review Letters* 89(20): 207001.

MacManus-Driscoll JL and Wimbush SC (2021) Processing and application of high-temperature superconducting coated conductors. *Nature Reviews Materials* 6(7): 587–604.

Margalit G, Yan B, Franz M, and Oreg Y (2022) Chiral majorana modes via proximity to a twisted cuprate bilayer. *Physical Review B* 106(20): 205424.

Martini M, Lee Y, Confalone T, Shokri S, Saggau CN, Wolf D, Gu G, Watanabe K, Taniguchi T, Montemurro D, Vinokur VM, Nielsch K, and Poccia N (2023) Twisted cuprate van der Waals heterostructures with controlled Josephson coupling. *arXiv:2303.16029*.

McElroy K, Lee J, Slezak JA, Lee D-H, Eisaki H, Uchida S, and Davis JC (2005) Atomic-scale sources and mechanism of nanoscale electronic disorder in $Bi_{2.1}Sr_{1.9}CaCu_{2.0}O_{8+\delta}$. *Science* 309(5737): 1048–1052. https://doi.org/10.1126/science.1113095.

Mercado A, Sahoo S, and Franz M (2022) High-temperature Majorana zero modes. *Physical Review Letters* 128(13): 137002.

Natarajan CM, Tanner MG, and Hadfield RH (2012) Superconducting nanowire single-photon detectors: Physics and applications. *Superconductor Science and Technology* 25(6): 063001. https://doi.org/10.1088/0953-2048/25/6/063001.

Novoselov KS, Jiang D, Schedin F, Booth TJ, Khotkevich VV, Morozov SV, and Geim AK (2005) Two-dimensional atomic crystals. *Proceedings of the National Academy of Sciences* 102 (30): 10451–10453.

Pan SH, O'Neal J, Badzey R, Chamon C, Ding H, Engelbrecht J, Wang Z, Eisaki H, Uchida S-i, Gupta A, Ng K-W, and Hudson E (2001) Microscopic electronic inhomogeneity in the high-T_c superconductor $Bi_2Sr_2CaCu_2O_{8+x}$. *Nature* 413: 282–285. https://doi.org/10.1038/35095012.

Pelc D, Popčević P, Požek M, Greven M, and Barišić N (2019) Unusual behavior of cuprates explained by heterogeneous charge localization. *Science Advances* 5(1): eaau4538.

Petricek V, Gao Y, Lee P, and Coppens P (1990) X-ray analysis of the incommensurate modulation in the 2:2:1:2 Bi-Sr-Ca-Cu-O superconductor including the oxygen atoms. *Physical Review B* 42(1): 387–392. https://doi.org/10.1103/PhysRevB.42.387.

Pirandola S, Andersen UL, Banchi L, Berta M, Bunandar D, Colbeck R, Englund D, Gehring T, Lupo C, Ottaviani C, Pereira JL, Razavi M, Shaari JS, Tomamichel M, Usenko VC, Vallone G, Villoresi P, and Wallden P (2020) Advances in quantum cryptography. *Advances in Optics and Photonics* 12(4): 1012. https://doi.org/10.1364/aop.361502.

Poccia N, Ricci A, Bianconi A, et al. (2010) Misfit strain in superlattices controlling the electron-lattice interaction via microstrain in active layers. *Advances in Condensed Matter Physics* 2010: 261849.

Poccia N, Campi G, Fratini M, Ricci A, Saini NL, and Bianconi A (2011a) Spatial inhomogeneity and planar symmetry breaking of the lattice incommensurate supermodulation in the high-temperature superconductor $Bi_2Sr_2CaCu_2O_{8+y}$. *Physical Review B* 84(10): 100504.

Poccia N, et al. (2011b) Evolution and control of oxygen order in a cuprate superconductor. *Nature Materials* 10(10): 733–736. https://doi.org/10.1038/nmat3088.

Poccia N, Bianconi A, Campi G, Fratini M, and Ricci A (2012a) Size evolution of the oxygen interstitial nanowires in La_2CuO_{4+y} by thermal treatments and x-ray continuous illumination. *Superconductor Science and Technology* 25(12): 124004.

Poccia N, Ricci A, Campi G, Fratini M, Puri A, Gioacchino DD, Marcelli A, Reynolds M, Burghammer M, Saini NL, Aeppli G, and Bianconi A (2012b) Optimum inhomogeneity of local lattice distortions in La_2CuO_{4+y}. *Proceedings of the National Academy of Sciences* 109(39): 15685–15690. https://doi.org/10.1073/pnas.1208492109.

Poccia N, Chorro M, Ricci A, Xu W, Marcelli A, Campi G, and Bianconi A (2014a) Percolative superconductivity in $La_2CuO_{4.06}$ by lattice granularity patterns with scanning micro x-ray absorption near edge structure. *Applied Physics Letters* 104(22): 221903.

Poccia N, Lankhorst M, and Golubov AA (2014b) Manifestation of percolation in high temperature superconductivity. *Physica C: Superconductivity and its Applications* 503: 82–88.

Poccia N, Zhao SYF, Yoo H, Huang X, Yan H, Chu YS, Zhong R, Gu G, Mazzoli C, Watanabe K, Taniguchi T, Campi G, Vinokur VM, and Kim P (2020) Spatially correlated incommensurate lattice modulations in an atomically thin high-temperature $Br_{2.1}Sr_{1.9}CaCu_{2.0}O_{8+y}$ superconductor. *Physical Review Materials* 4(11). https://doi.org/10.1103/physrevmaterials.4.114007.

Saleem A and Hussain S (2013) Review the High Temperature Superconductor (HTSC) Cuprates-Properties and Applications. *Journal of Surfaces and Interfaces of Materials* 1: 97–119. https://doi.org/10.1166/jsim.2013.1025.

Sandilands LJ, Reijnders AA, Su AH, Baydina V, Xu Z, Yang A, Gu G, Pedersen T, Borondics F, and Burch KS (2014) Origin of the insulating state in exfoliated high-T_c two-dimensional atomic crystals. *Physical Review B* 90(8): 081402. https://doi.org/10.1103/PhysRevB.90.081402.

Sboychakov AO, Kugel KI, and Bianconi A (2022) Moiré-like superlattice generated van hove singularities in a strained CuO_2 double layer. *Condensed Matter* 7(3): 50.

Scappucci G, Kloeffel C, Zwanenburg FA, Loss D, Myronov M, Zhang J-J, De Franceschi S, Katsaros G, and Veldhorst M (2021) The germanium quantum information route. *Nature Reviews Materials* 6(10): 926–943.

Shapiro S, Janus AR, and Holly S (1964) Effect of microwaves on Josephson currents in superconducting tunneling. *Reviews of Modern Physics* 36(1): 223–225. https://doi.org/10.1103/RevModPhys.36.223.

Shaw TM, Shivashankar SA, La Placa SJ, Cuomo JJ, McGuire TR, Roy RA, Kelleher KH, and Yee DS (1988) Incommensurate structure in the Bi-Sr-Ca-Cu-O 80-K superconductor. *Physical Review B* 37(16): 9856–9859. https://doi.org/10.1103/PhysRevB.37.9856.

Sigrist M (1998) Time-reversal symmetry breaking states in high-temperature superconductors. *Progress of Theoretical Physics* 99(6): 899–929. https://doi.org/10.1143/PTP.99.899.

Sinko MR, de la Barrera SC, Lanes O, Watanabe K, Taniguchi T, Tan S, Pekker D, Hatridge M, and Hunt BM (2021) Superconducting contact and quantum interference between two-dimensional van der Waals and three-dimensional conventional superconductors. *Physical Review Materials* 5(1): 014001. https://doi.org/10.1103/PhysRevMaterials.5.014001.

Skinner SJ and Kilner JA (2003) Oxygen ion conductors. *Materials Today* 6(3): 30–37.

Slezak JA, Lee J, Wang M, McElroy K, Fujita K, Andersen BM, Hirschfeld PJ, Eisaki H, Uchida S, and Davis JC (2008) Imaging the impact on cuprate superconductivity of varying the interatomic distances within individual crystal unit cells. *Proceedings of the National Academy of Sciences* 105(9): 3203–3208. https://doi.org/10.1073/pnas.0706795105.

Slussarenko S and Pryde GJ (2019) Photonic quantum information processing: A concise review. *Applied Physics Reviews* 6(4): 041303. https://doi.org/10.1063/1.5115814.

Song X-Y, Zhang Y-H, and Vishwanath A (2022) Doping a moiré mott insulator: A $t-J$ model study of twisted cuprates. *Physical Review B* 105(20): L201102.

Stornaiuolo D and Tafuri F (2019) High critical temperature superconductor Josephson junctions and other exotic structures. In: *Fundamentals and Frontiers of the Josephson Effect*, pp. 275–337. Springer.

Subramanian MA, Torardi CC, Calabrese JC, Gopalakrishnan J, Morrissey KJ, Askew TR, Flippen RB, Chowdhry U, and Sleight AW (1988) A new high-temperature superconductor: $Bi_2Sr_{3-x}Ca_xCu_2O_{8+y}$. *Science* 239(4843): 1015–1017. https://doi.org/10.1126/science.239.4843.1015.

Sunshine SA, Siegrist T, Schneemeyer LF, Murphy DW, Cava RJ, Batlogg B, van Dover RB, Fleming RM, Glarum SH, Nakahara S, Farrow R, Krajewski JJ, Zahurak SM, Waszczak JV, Marshall JH, Marsh P, Rupp LW, and Peck WF (1988) Structure and physical properties of single crystals of the 84-K superconductor $Bi_{2.2}Sr_2Ca_{0.8}Cu_2O_{8+\delta}$. *Physical Review B* 38(1): 893–896. https://doi.org/10.1103/PhysRevB.38.893.

Takano Y, Hatano T, Fukuyo A, Ishii A, Ohmori M, Arisawa S, Togano K, and Tachiki M (2002) d-like symmetry of the order parameter and intrinsic Josephson effects in $Bi_2Sr_2CaCu_2O_{8+\delta}$ cross-whisker junctions. *Physical Review B* 65(14): 140513.

Tarascon JM, Le Page Y, Barboux P, Bagley BG, Greene LH, McKinnon WR, Hull GW, Giroud M, and Hwang DM (1988) Crystal substructure and physical properties of the superconducting phase $Bi_4(Sr,Ca)_6Cu_4O_{16+x}$. *Physical Review B* 37(16): 9382–9389. https://doi.org/10.1103/PhysRevB.37.9382.

Triscone J-M, Fischer O, Brunner O, Antognazza L, Kent AD, and Karkut MG (1990) $YBa_2CU_3O_7/PrBa_2Cu_3O_7$ superlattices: Properties of ultrathin superconducting layers separated by insulating layers. *Physical Review Letters* 64(7): 804–807. https://doi.org/10.1103/PhysRevLett.64.804.

Tromp WO, Benschop T, Ge J-F, Battisti I, Bastiaans KM, Chatzopoulos D, Vervloet AH, Smit S, van Heumen E, Golden MS, et al. (2023) Puddle formation and persistent gaps across the non-mean-field breakdown of superconductivity in overdoped $(Pb, Bi)_2Sr_2CuO_{6+\delta}$. *Nature Materials* 22(6): 703–709.

Tsuei CC, Kirtley JR, Hammerl G, Mannhart J, Raffy H, and Li ZZ (2004) Robust $d_{x^2-y^2}$ pairing symmetry in hole-doped cuprate superconductors. *Physical Review Letters* 93(18): 187004.

Tummuru T, Lantagne-Hurtubise É, and Franz M (2022a) Twisted multilayer nodal superconductors. *Physical Review B* 106(1): 014520.

Tummuru T, Plugge S, and Franz M (2022b) Josephson effects in twisted cuprate bilayers. *Physical Review B* 105(6): 064501.

Ulbricht G, Lucia MD, and Baldwin E (2021) Applications for microwave kinetic induction detectors in advanced instrumentation. *Applied Sciences* 11(6): 2671. https://doi.org/10.3390/app11062671.

Valla T, Pletikosić I, Drozdov IK, and Gu GD (2019) Reconstruction of the $Bi_2Sr_2CaCu_2O_{8+\delta}$ fermi surface. *Physical Review B* 100(24): 241112. https://doi.org/10.1103/PhysRevB.100.241112.

Velasco V and Neto MBS (2023) Disorder-induced finite center-of-mass momentum cooper pairing and its consequences to the critical temperature and superconducting gap of overdoped cuprates. *arXiv:2301.02892.*

Volkov PA, Wilson JH, and Pixley JH (2020) *Magic angles and current-induced topology in twisted nodal superconductors.* https://doi.org/10.48550/ARXIV.2012.07860.

Volkov PA, Zhao SYF, Poccia N, Cui X, Kim P, and Pixley JH (2021) Josephson effects in twisted nodal superconductors. *arXiv:2108.13456.*

Wang J, Rodan-Legrain D, Bretheau L, Campbell D, Kannan B, Kim D, Kjaergaard M, Krantz P, Samach G, Yan F, Yoder J, Watanabe K, Taniguchi T, Orlando T, Gustavsson S, Jarillo-Herrero P, and Oliver W (2019) Coherent control of a hybrid superconducting circuit made with graphene-based van der Waals heterostructures. *Nature Nanotechnology* 14: 120–125. https://doi.org/10.1038/s41565-018-0329-2.

Xu S-Y, Liu C, Richardella A, Belopolski I, Alidoust N, Neupane M, Bian G, Samarth N, and Hasan MZ (2014) Fermi-level electronic structure of a topological-insulator/cuprate-superconductor based heterostructure in the superconducting proximity effect regime. *Physical Review B* 90(8): 085128.

Yamamoto A, Onoda M, Takayama-Muromachi E, Izumi F, Ishigaki T, and Asano H (1990) Rietveld analysis of the modulated structure in the superconducting oxide $Bi_2(Sr,Ca)_3Cu_2O_{8+x}$. *Physical Review B* 42(7): 4228–4239. https://doi.org/10.1103/PhysRevB.42.4228.

Yang Z, Qin S, Zhang Q, Fang C, and Hu J (2018) $\pi/2$-Josephson junction as a topological superconductor. *Physical Review B* 98(10): 104515. https://doi.org/10.1103/PhysRevB.98.104515.

You L (2020) Superconducting nanowire single-photon detectors for quantum information. *Nanophotonics* 9(9): 2673–2692. https://doi.org/10.1515/nanoph-2020-0186.

Yu Y, Ma L, Cai P, Zhong R, Ye C, Shen J, Gu GD, Chen XH, and Zhang Y (2019) High-temperature superconductivity in monolayer $Bi_2Sr_2CaCu_2O_{8+\delta}$. *Nature* 575(7781): 156–163.

Yurgens AA (2000) Intrinsic Josephson junctions: Recent developments. *Superconductor Science and Technology* 13(8): R85.

Zareapour P, Hayat A, Zhao SYF, Kreshchuk M, Jain A, Kwok DC, Lee N, Cheong S-W, Xu Z, Yang A, et al. (2012) Proximity-induced high-temperature superconductivity in the topological insulators Bi_2Se_3 and Bi_2Te_3. *Nature Communications* 3(1): 1056.

Zeljkovic I, Main EJ, Williams TL, Boyer M, Chatterjee K, Wise W, Yin Y, Zech M, Pivonka A, Kondo T, et al. (2012a) Scanning tunnelling microscopy imaging of symmetry-breaking structural distortion in the bismuth-based cuprate superconductors. *Nature Materials* 11(7): 585–589.

Zeljkovic I, Xu Z, Wen J, Gu G, Markiewicz RS, and Hoffman JE (2012b) Imaging the impact of single oxygen atoms on superconducting $Bi_{2+y}Sr_{2-y}CaCu_2O_{8+x}$. *Science* 337(6092): 320–323. https://doi.org/10.1126/science.1218648.

Zeljkovic I, Nieminen J, Huang D, Chang T-R, He Y, Jeng H-T, Xu Z, Wen J, Gu G, Lin H, Markiewicz RS, Bansil A, and Hoffman JE (2014) Nanoscale interplay of strain and doping in a high-temperature superconductor. *Nano Letters* 14(12): 6749–6753. https://doi.org/10.1021/nl501890k.

Zhao SYF, Poccia N, Panetta MG, Yu C, Johnson JW, Yoo H, Zhong R, Gu GD, Watanabe K, Taniguchi T, Postolova SV, Vinokur VM, and Kim P (2019) Sign-reversing hall effect in atomically thin high-temperature $Bi_{2.1}Sr_{1.9}CaCu_{2.0}O_{8+\delta}$ superconductors. *Physical Review Letters* 122(24): 247001. https://doi.org/10.1103/PhysRevLett.122.247001.

Zhao SYF, Poccia N, Cui X, Volkov PA, Yoo H, Engelke R, Ronen Y, Zhong R, Gu G, Plugge S, Tummuru T, Franz M, Pixley JH, and Kim P (2021) *Emergent interfacial superconductivity between twisted cuprate superconductors*. https://doi.org/10.48550/ARXIV.2108.13455.

Zhou S, Ding H, and Wang Z (2007) Correlating off-stoichiometric doping and nanoscale electronic inhomogeneity in the high-T_c superconductor $Bi_2Sr_2CaCu_2O_{8+\delta}$. *Physical Review Letters* 98(7): 076401. https://doi.org/10.1103/PhysRevLett.98.076401.

Zhu Y, Liao M, Zhang Q, Xie H-Y, Meng F, Liu Y, Bai Z, Ji S, Zhang J, Jiang K, et al. (2021) Presence of s-wave pairing in Josephson junctions made of twisted ultrathin $Bi_2Sr_2CaCu_2O_{8+x}$ flakes. *Physical Review X* 11(3): 031011.

Critical current fluctuations in Josephson junctions

Davide Massarotti, Department of Electrical Engineering and Information Technologies, University Federico II of Naples, Napoli, Italy

© 2024 Elsevier Ltd. All rights reserved.

Introduction 725
Phase dynamics in the underdamped regime 726
Moderately damped regime 728
The very high critical current density regime 730
Conclusion 732
References 733

Abstract

The novel opportunities offered by nanotechnologies and materials science have enlarged the physical conditions of occurrence of the Josephson effect. Semiconducting, ferromagnetic, topological-insulator, and graphene barriers lead to unconventional and anomalous aspects of the Josephson coupling, which might be useful to respond to some issues on key problems of solid-state physics. However, the complexity of the layout and the competing physical processes occurring in the junctions pose novel questions on the interpretation of their phenomenology. Measurements of critical current fluctuations have turned to be imaging tools of different dissipation processes, whose origin may depend on the type of the barrier, the nature of the interface, the geometry and dimensionality of the device. In this chapter, we classify some significant behaviors of unconventional junctions in terms of the temperature properties of the critical current fluctuations, thus providing accurate arguments to distinguish and understand physical processes occurring in quite different dynamical regimes. These notions are universal and apply to all kinds of junctions.

Key points

- Phase dynamics of a Josephson junction.
- Observation of macroscopic quantum phenomena through measurements of switching current distributions.
- Underdamped regime and moderately damped regime: the role of dissipation.
- Heating events in Josephson junctions characterized by high values of the critical current density.
- Capability to distinguish different dissipation sources in unconventional Josephson junctions: fingerprints of the switching current distributions.

Introduction

The possibility that a macroscopic system could behave quantum mechanically if it was suitably decoupled from its environment (Caldeira and Leggett, 1981; Clarke and Wilhelm, 2008; Devoret and Schoelkopf, 2013; Kockum and Nori, 2019) was somehow the start of an intense research activity aimed at investigating the boundary between the microscopic quantum and macroscopic classical worlds. Anthony J. Leggett immediately emphasized the importance of distinguishing macroscopic quantum phenomena originating in the superposition of a large number of microscopic variables (such as superfluidity and superconductivity) from those displayed by a single macroscopic degree of freedom (Caldeira and Leggett, 1981).

Because of their design scalability and their flexibility in controlling the level of damping, Josephson devices have proven to be a fantastic test bench for studying fundamental physics problems such as quantum coherence in macroscopic systems, taking advantage from the anharmonicity deriving from the Josephson equations (Josephson, 1962). In the 1980s, the macroscopic quantum tunneling (MQT), and therefore the macroscopic quantum nature of the phase difference φ across a Josephson junction (JJ), has been demonstrated (Voss and Webb, 1981; Jackel et al., 1981; der Boer and de Bruyn Ouboter, 1980; Prance et al., 1981; Dmitrenko et al., 1985; Washburn et al., 1985; Devoret et al., 1984, 1985; Clarke et al., 1988). These MQT experiments established that, although a JJ contains a large number of atomic constituents, it is atom-like in the sense that it has a macroscopic single degree of freedom behaving quantum mechanically (Clarke and Wilhelm, 2008; Devoret and Schoelkopf, 2013; Kockum and Nori, 2019). Thermal energy must be sufficiently low to avoid incoherent mixing of eigenstates, and the macroscopic degree of freedom must be sufficiently decoupled from other degrees of freedom for the lifetime of the quantum states to be long on the characteristic time scale of the system (Clarke et al., 1988).

Advances in materials science and in the application of nanotechnologies to superconducting devices are leading to novel and promising devices in view of quantum systems and superconducting quantum technologies (Koshino, 2023; Tafuri, 2023; Zaikin, 2023; Bergeret and Ilic, 2023), whose complete competitiveness has to be evaluated along with a possible impact on the fundamental themes of coherence and dissipation. Measurements of switching current distributions (SCDs) have turned to be

https://doi.org/10.1016/B978-0-323-90800-9.00230-4

standard tools to investigate phase dynamics and dissipation phenomena in unconventional and hybrid systems and nanostructures (Massarotti and Tafuri, 2019). In the present Chapter, we look at phase dynamics aware that materials science is not only offering a variety of novel interfaces and junctions, but also radically new solutions of synthesizing hybrid Josephson devices taking advantage at the same time of the progress registered in using nanotechnologies in superconducting electronics and quantum circuits. In the following sections, the phenomenology of the switching current measurements will be addressed in most of the regimes interested by unconventional nano-devices and hybrid JJs.

Phase dynamics in the underdamped regime

A JJ consists of two superconducting electrodes separated by an insulating barrier of appropriate thickness, typically few nanometers, through which Cooper pairs can tunnel coherently. Josephson (1962) showed that the supercurrent I through the barrier is related to the gage-invariant phase difference φ between the phases of the two superconductors by the current–phase relationship

$$I = I_{c0}\sin\varphi \tag{1}$$

where I_{c0} is the critical current of the junction in the absence of thermal fluctuations. In the presence of a potential difference V between the two electrodes, the phase difference evolves in time as

$$\frac{\partial\varphi}{\partial t} = \frac{2eV}{\hbar} \tag{2}$$

Eqs. (1) and (2) are the so-called Josephson equations. The more general case of barriers other than an insulating layer or with unconventional superconducting electrodes, such as high critical temperature superconductors (HTS), is discussed in Tafuri (2023).

In a quantum-mechanical picture, the two relevant operators are the phase difference φ, which is associated with the Josephson coupling energy $E_J = I_{c0}\hbar/2e$, and the Cooper-pair number difference N across the junction capacitance C, which is associated to the charging energy $E_c = e^2/2C$. Therefore, in the absence of dissipation, the behavior of a JJ can be described by an Hamiltonian $\mathcal{H}$, which is a function of the phase difference φ and of the charge Q transferred between the electrodes (Iansiti et al., 1987; Tinkham, 1996; Kockum and Nori, 2019):

$$\mathcal{H}(\varphi, Q) = E_c(Q/e)^2 - E_J\cos\varphi \tag{3}$$

As in the case of position and momentum operators x and p_x, the operators for φ and for the charge on the capacitor Q are canonically conjugate. The fact that φ and Q are subject to Heisenberg's uncertainty principle has important consequences. When $E_J \gg E_c$, φ is well defined and Q has large quantum fluctuations; therefore, the Josephson nature of the junction dominates. On the other hand, when $E_J \ll E_c$, N is well defined and φ has large quantum fluctuations; therefore, the charging nature of the capacitor is dominating. More details can be found in Chapter (Tafuri, 2023).

In this chapter we will consider the more standard condition $E_J \gg E_c$ and dissipation arising from the environment will be discussed. If the condition $E_J \gg, E_c$ is satisfied, the charging energy in Eq. (3) can be disregarded. Therefore, the phase difference φ is well defined and governs the dynamics of a current-biased JJ. In the framework of the Resistively and Capacitively Shunted Junction (RCSJ) model (Barone and Paternò, 1982; Likharev, 1979), according to which a real junction is modeled as an ideal JJ in parallel to the junction capacitance C, which arises from the dielectric nature of the barrier, and a dissipative resistor R (inset of Fig. 1A), the phase dynamics is equivalent to the motion of a particle in a washboard potential $U = -E_J(\cos\varphi + \varphi I/I_{c0})$ (see Fig. 1A):

$$\left(\frac{\Phi_0}{2\pi}\right)^2 C\frac{\partial^2\phi}{\partial t^2} + \left(\frac{\Phi_0}{2\pi}\right)^2 \frac{1}{R}\frac{\partial\phi}{\partial t} + \frac{\partial}{\partial\phi}U = 0, \tag{4}$$

where $\Phi_0 = h/2e$ is the flux quantum and the tilt of the washboard potential is given by the bias current I. The term involving the capacitance C represents the mass of the particle and the $1/R$ term represents the damping of the motion. For $I < I_{c0}$, the potential U has local minima where the phase particle is trapped and oscillates at the plasma frequency $\omega_p = \omega_0\left(1 - i^2\right)^{1/4} = \sqrt{2eI_{c0}/\hbar C}\left(1 - i^2\right)^{1/4}$, where $i = I/I_{c0}$. The strength of the friction can be expressed through the junction quality factor $Q = \omega_p RC$, which depends on the junction capacitance C, on the dissipative element R and on the critical current, which in turn is proportional to the Josephson coupling energy E_J. According to the mechanical analogy provided by the RCSJ model, low damping corresponds to $Q \gg 1$, while the junction is overdamped for $Q < 1$. When ramping the bias current I, the tilt of the energy potential increases and the height $\Delta U(i) = 4\sqrt{2}/3{\cdot}E_J(1 - i)^{3/2}$ of the energy barrier between consecutive wells decreases. In absence of thermal fluctuations, for $I = I_{c0}$ the phase will escape from the well and roll down the washboard potential. Therefore a voltage will appear at the junction's edges. Decreasing the bias current, the potential tilt will be reduced and for $I = I_R$, the particle will be retrapped in a well, returning to the zero voltage state. Therefore I_R is known as the retrapping current. In the case of underdamped junctions, hysteresis is present in the current–voltage (I–V) characteristic and the voltage will switch abruptly from the zero voltage state to about twice the superconducting gap Δ/e (see Fig. 1B).

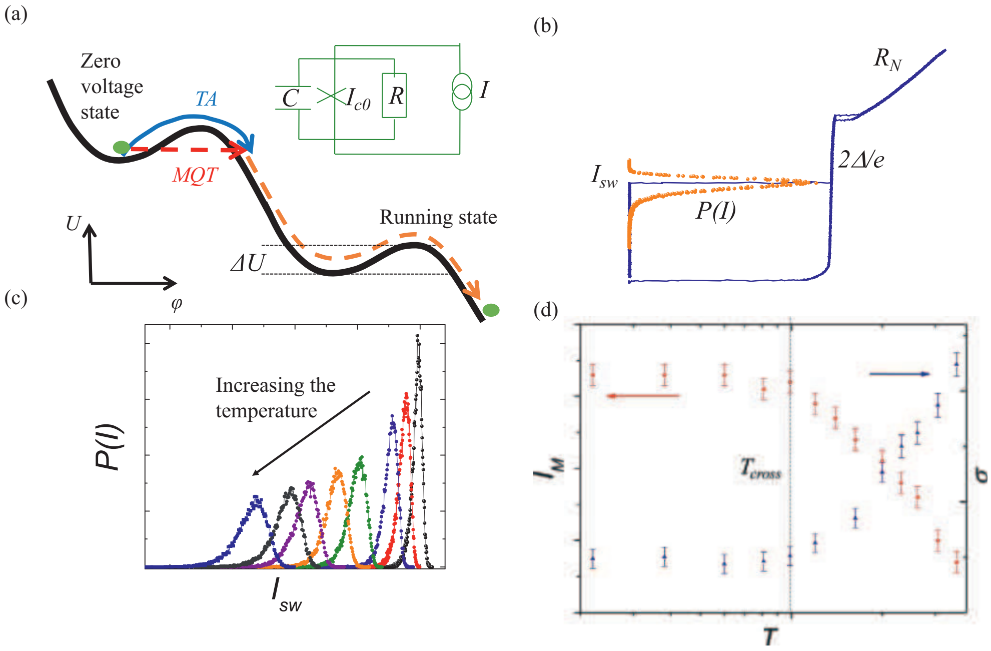

Fig. 1 (A) Phase dynamics of an underdamped current biased JJ. The equivalent RCSJ circuit is shown as the inset of panel (A). In the superconducting state (zero voltage state) the phase particle is confined to one well of the washboard potential where it oscillates back and forth and the average voltage is zero. The phase particle can escape from the well either by thermal activation (TA) (*blue arrow*) or macroscopic quantum tunnelling (MQT) (*red dashed arrow*) and the system switches to the running state (*orange dashed arrow*). (B) The escape is a stochastic phenomenon; thus the distribution of the switching events can be measured by repeatedly sweeping the bias current (orange points superimposed on a typical *I–V* characteristic of an underdamped JJ). (C) Measurements of SCDs as a function of the temperature: by increasing *T* the histograms move to lower currents and their standard deviation σ increases, according to the TA regime. The temperature dependence of σ (*blue up triangles*) and of the mean switching current I_M (*red points*) are both reported in panel (D): below the crossover temperature T_{cross} the histograms overlap and both I_M and σ saturate.

Due to the effects of thermal fluctuations and quantum tunneling, the junction may switch to the finite voltage state for values of $I < I_{c0}$. The bias current at which the transition to the finite voltage state occurs is the switching current I_{sw}, depicted in Fig. 1B along with a typical SCD. Such a transition corresponds to the particle escaping from the well either by a thermally activated process (Kramers, 1940) (*blue arrow* in Fig. 1A) or by tunneling through the barrier potential, the MQT process (*red dashed arrow* in Fig. 1A) or the quantum decay of the macroscopic phase difference φ from a metastable state (Caldeira and Leggett, 1981). The relative weight of these two escape processes depends on the temperature of the system and on the junction plasma frequency. For $k_BT \gg \hbar\omega_p$, the escape process is dominated by TA with a rate given by the Arrhenius law (Kramers, 1940):

$$\Gamma_T(i) = a_T \frac{\omega_p}{2\pi} \exp\left(-\frac{\Delta U(i)}{k_B T}\right), \tag{5}$$

where $a_T = 4/[(1+Qk_BT/1.8\Delta U)^{1/2}+1]^2$. The escape rate will be dominated by MQT at low enough temperature (Caldeira and Leggett, 1981): for i close to one and to the lowest order in $1/Q$, it is approximated by

$$\Gamma_q(i) = a_q \frac{\omega_p}{2\pi} \exp\left[-7.2 \frac{\Delta U(i)}{\hbar\omega_p}\left(1 + \frac{0.87}{Q}\right)\right], \tag{6}$$

where $a_q = \left(864\pi\Delta U/\hbar\omega_p\right)^{1/2}$. The MQT rate is affected by dissipation, the irreversible energy transfer between the system and the environment, described by the junction quality factor Q (Caldeira and Leggett, 1981).

The crossover temperature T_{cross} between the thermal and quantum regimes is given by (Grabert et al., 1987)

$$T_{cross} = \left(\hbar\omega_p/2\pi k_B\right)\left[\left(1 + 1/4Q^2\right)^{1/2} - 1/2Q\right] \tag{7}$$

The behavior of the phase difference φ is deduced from measurements of the escape rate Γ from the zero-voltage state. To determine the escape rate, 10^4–10^5 switching events are typically collected at fixed temperature. In order to investigate the phase dynamics of Josephson devices, the bias current of the junction is ramped at a constant sweep rate, the voltage is measured using a low noise differential amplifier and is usually fed into a threshold detector which is set to generate a pulse signal when the junction switches from the superconducting state to the finite voltage state. This signal is used to trigger a fast voltmeter to record the value of the bias current I_{sw} at which the transition to the running state occurs (Massarotti and Tafuri, 2019). The resulting distribution of the switching probability $P(I)$ is used to compute the escape rate out of the zero-voltage state as a function of the bias current I (Fulton and Dunkleberger, 1974):

$$\Gamma(I) = \frac{1}{\Delta I}\frac{dI}{dt} ln \left(\frac{\sum_{i \geq I} P(I)}{\sum_{i \geq I + \Delta I} P(I)} \right) \tag{8}$$

where dI/dt is the current ramp rate and ΔI is the channel width of the analog-to-digital converter.

The first experiments on the transition from the thermal to the quantum regime in a JJ were carried out by Voss and Webb (1981) and by Jackel et al. (1981), while related experiments on a junction inserted in a superconducting loop were realized by der Boer and de Bruyn Ouboter (1980), Prance et al. (1981), and Dmitrenko et al. (1985). The temperature dependence and the effect of damping on the tunneling have been addressed by later experiments (Washburn et al., 1985). Devoret et al. (1985) have established a detailed conceptual and experimental protocol to follow to prove the macroscopic quantum nature of the phase difference across a JJ and the crossover to the thermal regime, used in most of later experiments. The problem of the impedance presented to the junction at microwave frequencies by the wires directly connected to it has been clearly addressed, and classical phenomena have been used to measure all relevant parameters of the junction in situ (Devoret et al., 1984, 1985). In particular, the magnetic field has been used as a knob to tune the crossover temperature by changing the critical current and therefore the plasma frequency. This represents a crucial test to distinguish macroscopic quantum phenomena from classical effects related to heating or spurious noise in the measurement setup (Devoret et al., 1985; Clarke et al., 1988).

In underdamped JJs, the typical behavior of the SCDs is reported in Fig. 1C and presents a characteristic temperature behavior: by reducing the temperature T the mean value of the switching histogram I_M moves to higher currents and their standard deviation σ scales with the temperature down to T_{cross}, which is defined as the temperature below which the histograms overlap and do not depend any more on the temperature. For $T < T_{cross}$, both the mean value I_M and the standard deviation σ of the switching histograms saturate, indicating the transition to the MQT regime, as schematically shown in Fig. 1D.

Moderately damped regime

In underdamped junctions, a single escape event is enough for the junction to switch to the running state. This occurs since the kinetic energy gained by the phase particle running down in the tilted washboard potential is not all dissipated, but enough energy remains to carry the phase over the next well. In the case of moderately damped regime (MDR) ($1 < Q < 5$), following an event of escape, the particle may travel down the potential for few wells and then is retrapped in one of the following minima of the potential, as shown by the *green dashed arrow* in Fig. 2A. At low bias the process of escape and retrapping occurs multiple times, thus

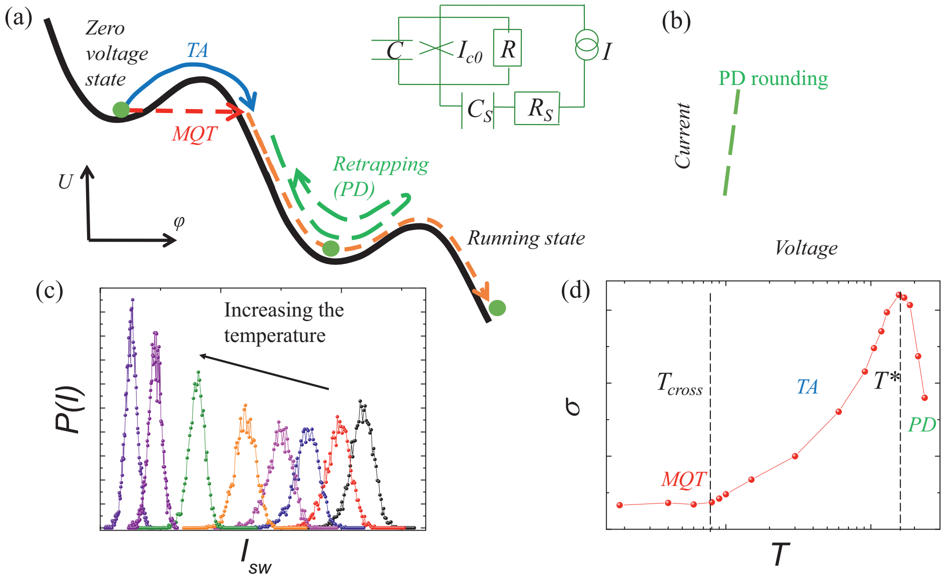

Fig. 2 (A) The equivalent circuit in the framework of frequency dependent RCSJ model is shown as the inset. Due to onset of multiple escape (TA or MQT, *blue* and *red dashed arrows*, respectively) and retrapping processes (*green dashed arrow*), at low bias the phase particle diffuses along the tilted washboard potential, until an increase of the tilt raises the velocity and the phase particle can switch to the running state. (B) *I*–*V* characteristics display both hysteresis and a PD branch (signaled by the *green dashed line*) at small voltages. (C) SCD histograms are schematized as a function of the temperature in the moderately damping regime, with a clear nonmonotonic behavior when increasing *T*. (D) Temperature dependence of σ. Its behavior is qualitatively quite different when compared to the underdamped case, providing distinct signatures of the phase dynamics.

inducing a diffusive motion of the phase particle until an increase of the tilt of the potential, due to a change in the bias current, raises the velocity of the particle and the transition to the running state occurs.

If the Josephson energy E_J is of the order of the thermal energy k_BT, the competition between multiple escape and retrapping processes prevents the access to the running state and leads to the appearance of a non zero voltage, manifesting as a phase diffusion (PD) branch in the I–V characteristic (Barone and Paternò, 1982; Iansiti et al., 1987; Kautz and Martinis, 1990; Vion et al., 1996), as schematically reported in Fig. 2B. The analytical expression for the retrapping rate from the resistive to the superconducting state is given by (Stewart, 1968; Ben-Jacob et al., 1982)

$$\Gamma_R(I) = \omega_p \frac{I - I_{R0}}{I_{c0}} \sqrt{\frac{E_J}{2\pi k_B T}} \exp\left[\frac{-E_J Q^2}{2k_B T}\left(\frac{I - I_{R0}}{I_{c0}}\right)^2\right], \tag{9}$$

where I_{R0} is the fluctuation-free retrapping current. Kautz and Martinis (1990), following the works by Ono et al. (1987), have shown both experimentally and theoretically that hysteresis and PD can coexist, within the RCSJ model, if frequency-dependent damping is taken into account. In a typical experimental setup, the junction is also capacitively (C_S) and resistively (R_S) shunted by the leads attached to the junction itself. A more realistic equivalent circuit of the junction is reported in the inset of Fig. 2A rather than the simple RCSJ model of Fig. 1A.

At low frequencies, the dissipation is mostly determined by the junction resistance R, but at high frequencies (usually ω_p is of the order of 10 GHz) the impedance is typically small because C_s acts as a short and R_s is small compared to R. In the zero voltage state, the phase oscillates in a well at the plasma frequency and it may transit from one well to another in a time which is of the order of the inverse of the plasma frequency. In this case, dissipation is thus characterized by $R(\omega \approx \omega_p)$. Without a specially designed environmental circuit, this high frequency dissipation is usually of the order of the impedance of the leads ($\approx 100\ \Omega$). After the switching to the running state, dissipation takes place at low frequencies ($\omega \approx 0$) so that junctions are overdamped at high frequencies but are in the underdamped limit at low frequencies (Kautz and Martinis, 1990; Vion et al., 1996; Massarotti and Tafuri, 2019).

PD phenomena are typical of the MDR, characterized by values of Q ranging from 1 to 5. It represents the technological result of the application of nanotechnology to more standard Josephson devices based on conventional low temperature superconductors (LTS) (Kautz and Martinis, 1990; Männik et al., 2005; Kivioja et al., 2005; Krasnov et al., 2005; Massarotti and Tafuri, 2019), and of the implementation of novel types of hybrid systems. For LTS systems, once the barrier thickness and the critical current density J_c have been fixed, a reduction in its size unavoidably leads to a lowering of the critical current and determines a quite different phase dynamics (Iansiti et al., 1987; Kautz and Martinis, 1990; Vion et al., 1996; Männik et al., 2005; Kivioja et al., 2005; Yu et al., 2011). Lower critical currents result in lower Josephson energies, and higher levels of dissipation are expected. The same regime can be controllably induced in larger junctions in case of low J_c (Longobardi et al., 2011a, b; Massarotti et al., 2012), or with lower reproducibility in junctions with larger intrinsic dissipation levels, as occurring in HTS systems (Krasnov et al., 2005; Bauch et al., 2005, 2006; Inomata et al., 2005; Bae et al., 2009). The low J_c limit seems to be characteristic also of all futuristic nano-hybrid devices incorporating nanowires, and the MDR is intrinsically more common than it could be expected (Zhang et al., 2008; Borzenets et al., 2011).

In the MDR, I_c usually ranges from a few hundred nA to a few μA, thus satisfying the condition $E_J \gg k_BT$. The I–V characteristics are hysteretic and the transition to the running state is a stochastic phenomenon. In addition to the usual crossover between MQT and TA behavior, measurements of SCDs (reference temperature behavior is reported in Fig. 2C) have shown the transition from TA to the PD regime, indicated by a characteristic dependence of σ, as the appearance of an anticorrelation between the temperature and the width of the switching distributions (Männik et al., 2005; Kivioja et al., 2005; Krasnov et al., 2005; Bae et al., 2009; Longobardi et al., 2011a, b; Massarotti et al., 2012). After the MQT saturation at the lowest temperatures, σ follows the expected $T^{2/3}$ dependence, deviations are evident in proximity and above a transition temperature T^* that is defined as the temperature at which the width σ of the SCD reaches the maximum value, as shown in Fig. 2D. A decrease of the Josephson energy E_J and of the quality factor Q enhances the retrapping probability Γ_R, as shown by Eq. (9), causing multiple retrapping phenomena in the switching dynamics. Above T^* histograms shrink rather than broaden with a consequent increase of their maximum (see Fig. 2C). The decreasing behavior of σ when increasing the temperature and a modification of the shape of the distributions at around T^* turn to be distinctive signatures of the PD regime. Such an anomalous behavior can be explained by considering the competition between thermal escape and multiple retrapping processes in the switching dynamics (Fenton and Warburton, 2008; Zonda et al., 2015). For $T < T^*$, thermal escape dominates on the retrapping rate, differently from the case $T > T^*$.

The symmetrization of the switching distribution due to the interplay between escape and retrapping events can be clearly measured by considering the skewness of the distributions γ as a function of the temperature. γ is the ratio m_3/σ^3 where m_3 is the third central moment of the distribution. In the MQT and TA regimes, where retrapping processes are negligible, $\gamma = -1$, which is consistent with a typical escape rate which follows the Arrhenius law (Massarotti and Tafuri, 2019; Longobardi et al., 2011a; Fenton and Warburton, 2008; Murphy et al., 2013). As the temperature increases and the junction falls in the PD regime, the distributions become more and more symmetric as γ tends to zero. Therefore, the switching events on the left side of the distribution (ascending side), which occur for lower values of the bias current, are prevented by phase retrapping, with a consequent symmetrization of the SCDs (Massarotti and Tafuri, 2019; Longobardi et al., 2011a; Fenton and Warburton, 2008; Murphy et al., 2013).

The possibility to have extremely low I_c can be functional to investigate phase dynamics at extreme conditions. In recent experiments on submicron Nb/AlOx/Nb junctions (Yu et al., 2011) an anomalous $\sigma(T)$ dependence with a negative $d\sigma/dT$ over the entire temperature range has been observed. This regime can be achieved by engineering junctions with lower critical current and junction capacitance such that the ratio I_{c0}/C, which regulates T_{cross}, is constant and the transition temperature T^*, which scales with the Josephson energy (Krasnov et al., 2005), is lower or comparable to the quantum crossover temperature T_{cross}. Another example is given by the work by Yoon et al. (2011). They have engineered Al/AlOx/Al JJs in order to obtain low critical currents, of about 400 nA, and low capacitance, of about 40 fF, at the same time. In this way they have observed that TA is completely suppressed since T^* is lower than T_{cross}. On the other hand, TA regime is recovered by adding a shunting capacitance in the device circuit, and this demonstrates that the capacitance can be used in order to tune the phase dynamics.

Similar phenomenology of the SCDs, as reported in Fig. 3A and B, can be achieved by using unconventional HTS Josephson devices, such as YBCO grain boundary (GB) biepitaxial JJs (Bauch et al., 2005, 2006; Stornaiuolo et al., 2013). In particular, it is possible to engineer devices with $T^* < T_{cross}$ (Longobardi et al., 2012), to which correspond a direct transition from MQT to the PD regime, and TA is completely suppressed. For temperatures well below T_{cross}, MQT contributions to escape rates are larger than those coming from both thermal escape and retrapping processes (see Fig. 3C), while above T_{cross} the retrapping rate dominates over thermal and quantum escape rates (see Fig. 3D).

The typical temperature behavior of σ in this regime is shown in Fig. 3A. Below T_{cross}, histograms overlap and σ saturates, which is a typical signature of a quantum activation regime. In analogy to what commonly done to prove MQT in underdamped junctions (Devoret et al., 1985; Clarke et al., 1988; Massarotti and Tafuri, 2019), the magnetic field can be used to tune in situ T_{cross} to unambiguously prove MQT as source of the saturation of σ. In the presence of magnetic field, a lower value of T_{cross} and lower values of σ are observed, as schematically sketched in Fig. 3C and expected from the theory (see Eq. 7). In Fig. 3A, increasing the temperature above T_{cross}, the switching current histograms shrink rather than broaden, which corresponds to the negative temperature derivative of σ in Fig. 3B. This behavior is consistent with a diffusive motion due to multiple escape and retrapping processes in the potential wells.

The experimental results and the numerical outcomes can be condensed in a phase diagram, which includes the various activation regimes (Kivioja et al., 2005; Longobardi et al., 2012). The phase diagram is a function of the characteristic scaling energies E_J and k_BT and of the dissipation parameter Q; therefore it is valid in a large range of dissipation conditions and constitutes a functional guide to classify the switching behavior of a JJ. Moreover, it is a reference for phase dynamics of novel types of junctions and systems for which the nature of the current-induced transition from the superconducting to the normal state has not been completely clarified.

The very high critical current density regime

The temperature behaviors of critical current fluctuations reported in the previous sections are typical of JJs characterized by critical current density J_c in the range 10–10^3 A/cm^2. Recently, measurements of SCD have been performed on a series of different nanostructures (Murphy et al., 2013; Li et al., 2011; Sahu et al., 2009; Murphy et al., 2015; Massarotti et al., 2015b; Baumans et al., 2017; Ejrnaes et al., 2019; Salvoni et al., 2022; Zgirski et al., 2020, 2021; Zhang et al., 2022). Some of them are junctions and they can be classified in the schemes described in the previous sections. Some of them are simple nanowires (Zaikin, 2023). A subtle path exists between these different systems with analogies and distinctive features. When considering that a micro-bridge of width of the order of the coherence length behaves as a JJ (Barone and Paternò, 1982; Likharev, 1979), measurements of SCDs will turn to be a direct

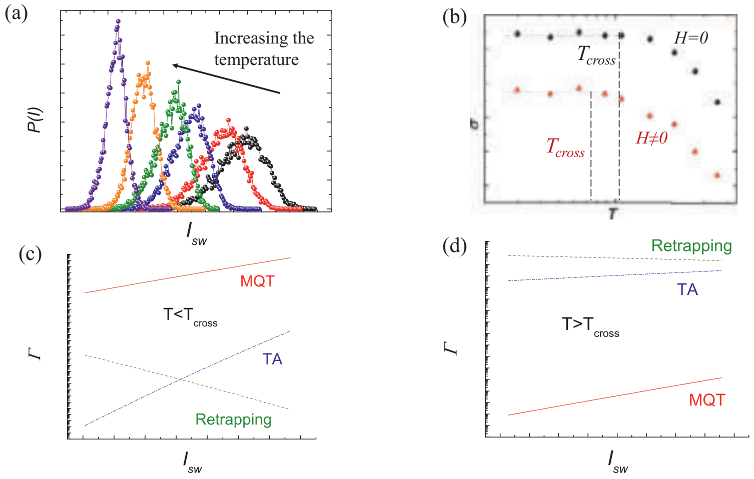

Fig. 3 (A) SCDs as a function of T when the PD transition temperature T^* is lower than the quantum crossover T_{cross} and TA is suppressed. (B) Temperature behavior of σ for $H = 0$ (*black points*) and in the presence of magnetic field (*red triangles*): the magnetic field reduces both T_{cross} and the values of σ, thus confirming that spurious noise can be disregarded as the origin of σ saturation. Schematic escape rates of MQT, TA, and retrapping processes at $T < T_{cross}$ (panel (C), MQT escape rate dominates) and at $T > T_{cross}$ (panel D, retrapping processes dominate).

way of discriminating the phase dynamics and the transport in nontrivial cases, which are going to be more and more common with advances in nano-patterning superconductors at extreme scales.

Recent experiments on superconducting nanowires have shown an anticorrelation between the bath temperature and the width of the switching distributions (Li et al., 2011; Sahu et al., 2009; Murphy et al., 2015; Baumans et al., 2017; Ejrnaes et al., 2019; Salvoni et al., 2022). A numerical model in order to study the stochastic aspects of the switching dynamics in these devices has been developed by Shah et al. (2008). The model is based on a freestanding wire of effective length L and cross-sectional area A, the ends of which are at the bath temperature T_b. All heat generated locally in the wire can be taken away only through the ends. The stochasticity inherent in the switching process is based on the fact that the resistive fluctuations of the superconducting nanowire consist of discrete phase-slip events that occur at random instants and are centered at random spatial locations along the wire (Little, 1967; Zaikin, 2023). Given that edge effects favor phase-slip locations away from the wire ends, the source term is restricted to the region at the center of the wire of length W (Shah et al., 2008). Stochastic phase slips that heat the wire and heat dissipation that cools the wire are the dominating mechanisms. Since the phase-slip rate depends on the local temperature of the wire, heating by phase slips can create a runaway cascade that eventually overheats the wire. More details can be found in Massarotti and Tafuri (2019).

The stochastic phase-slip dynamics is reduced to the following ordinary differential equation for the time evolution of the temperature of the central segment (Shah et al., 2008):

$$\frac{dT}{dt} = -\alpha(T,T_b)(T-T_b) + \eta(T,I)\sum_i \delta(t-t_i) \tag{10}$$

The relaxation coefficient $\alpha(T, T_b)$ depends on the thermal conductivity $K(T)$, on the thermal capacity $C_v(T)$ of the phase slip volume, and on T_b (Shah et al., 2008). The second term on the right-hand side corresponds to stochastic heating by phase slips, whose rate $\Gamma(I, T)$ is temperature and current dependent and follows the Arrhenius law:

$$\Gamma(I,T) = \Omega(I,T)\ \exp\ -\frac{\Delta F(I,T)}{k_B T} \tag{11}$$

where $\Omega(I, T)$ is the attempt frequency (Shah et al., 2008; Massarotti et al., 2015b) and $\Delta F(I, T)$ is the free energy barrier given by (Little, 1967):

$$\Delta F(I,T) = \left[\frac{\sqrt{6}\phi_0 I_c(T)}{k_B T}\ (1-I/I_{c0})^{5/4}\right], \tag{12}$$

If T_i and T_f are the temperatures before and after a phase slip, respectively, the temperature jump $\eta(I, T)$ due to a phase slip can be expressed as

$$A\cdot W\int_{T_i}^{T_f=T_i+\eta} C_v(y)dy = hI/2e. \tag{13}$$

The first term in Eq. (10) represents the cooling mechanism as a result of conduction of heat from the central segment to the external bath via the two end segments, each of length $(L - W)$. The temperature-dependent cooling rate is given by

$$\alpha(T,T_b) = \frac{4}{W(L-W)C_v(T)}\,\frac{1}{T-T_b}\int_{T_b}^{T} dyK(y) \tag{14}$$

In addition to restrictions on length scales, in the equations above the time for a phase slip and the quasiparticle thermalization time are both assumed to be smaller than the heat diffusion time (Shah et al., 2008).

Solutions of Eq. (10) have been performed numerically by Shah et al. (2008) in a wide range of temperature and current. At low temperatures the occurrence of just one phase-slip is sufficient to cause the nanowire to switch from the superconducting to the resistive state. In this temperature range, the width of the switching histograms increases when increasing the temperature, following the usual TA expressed by the Arrhenius law.

Such a broadening in the distribution width is indeed obtained up to a crossover temperature. At higher temperatures, the distribution width shows an anomalous decrease since histograms begin to shrink rather than broaden. Therefore, one phase slip is not sufficient to induce switching and multiple phase slips are needed. Such striking behavior of the distribution width may be understood by the following argument: the larger the number of phase slips in the sequence inducing the transition from the superconducting to the resistive state, the smaller the stochasticity in the switching process and, hence, the sharper the distribution of switching currents (Shah et al., 2008; Sahu et al., 2009; Murphy et al., 2015; Baumans et al., 2017; Ejrnaes et al., 2019). As in the case of moderately damped JJs, the change in the sign of the derivative of $\sigma(T)$ is related to a change in the phase-slips dynamics from single to multiple phase-slips fluctuations in the wire.

Typical measurements of SCDs on high J_c JJ are reported in Fig. 4A (Massarotti et al., 2015b). In this case, the critical current of the junction is about 50 μA and the junction width is about 200 nm; thus the resulting J_c is of the order 10^5 A/cm^2, from one to two orders of magnitude larger than the junctions analyzed in the previous sections, thus J_c high values close to those observed in nanowires (Li et al., 2011; Sahu et al., 2009; Murphy et al., 2015). For high values of J_c, the phase dynamics is radically different

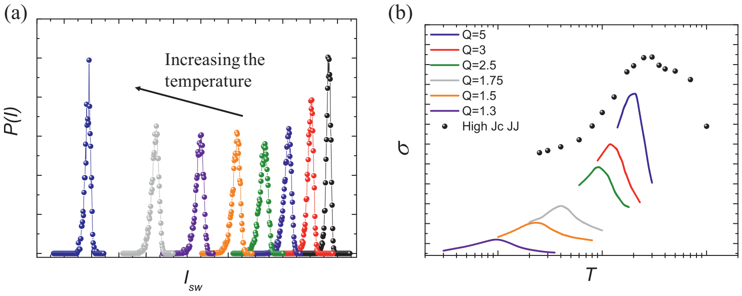

Fig. 4 (A) SCDs measured on high J_c JJ in a wide range of temperatures. (B) Temperature dependence of σ of high J_c JJ (*black circles*) is compared to those calculated through numerical simulations within the RCSJ model based on different values of Q (the lines are a guide for the eye). The transition temperature T^* and the shape of $\sigma(T)$ in the PD regime are both affected by the junction quality factor Q, while the temperature behavior of σ of high J_c JJ cannot be reproduced within the RCSJ model.

above the transition temperature, defined as the maximum of $\sigma(T)$. In particular, the rate of decrease of $\sigma(T)$ above its maximum value turns to be a distinctive marker of the phase dynamics. In the high J_c JJ, the slope of $\sigma(T)$ is much smaller when compared to those of moderately damped JJs, as shown in Fig. 4B where the temperature behavior of σ is reported as a result of numerical simulations for different values of the Q factor. The smooth decrease of $\sigma(T)$ cannot be described in terms of the intermediate dissipation regime: according to the RCSJ model, keeping all the other junction parameters fixed, an increase of J_c leads to an enhancement of I_c and Q. The increase of Q moves T^* to higher values, and the negative slope of $\sigma(T)$ above T^* becomes steeper and steeper, as shown by the numerical simulations for Q ranging between 1 and 5 reported in Fig. 4B.

The switching dynamics of JJs in the J_c interval 10^4–10^5 A/cm^2 can be consistently reproduced by considering a transition driven by local heating events, as shown in Massarotti et al. (2015b) and Baumans et al. (2017) possibly induced by intrinsic inhomogeneous composition unavoidable for high J_c junctions. Large values of Joule power density deposited in the weak link can induce a self-heating process during the switch to the resistive branch (Courtois et al., 2008). The absence of a set of self-consistent electrodynamics parameters to describe the temperature behavior of the SCDs is a strong indication of the failure of the standard Josephson dynamics. For larger values of J_c, heating driven mechanisms become dominant with a transition to the normal state locally in the junction area. These events can be modeled as heating events, as confirmed by the details of the simulations which are reported by Massarotti et al. (2015b), Baumans et al. (2017), and Shah et al. (2008), in the sense that they are local processes, break the coherence of the phase information, and are described by a heat diffusion-like equation.

As it occurs in superconducting nanowires, the temperature jump $\eta(T)$ depends on temperature because the specific heat is strongly temperature-dependent. At low temperatures, the specific heat is quite low; thus with each heating event there is a considerable increase in the temperature. In addition, the thermal conductivity and the thermal capacity are both quite low as the system is deeply into the superconducting phase. The junction is rather isolated from the environment and the heating event is destructive for the superconducting state. For this reason a single heating event can induce a direct jump to the resistive state at low temperatures: it induces a large local heating that is difficult to dissipate (Massarotti and Tafuri, 2019; Massarotti et al., 2015b). At high temperatures, the temperature jump $\eta(T)$ per heating event is rather small. In addition both the thermal conductivity and the thermal capacity increase with increasing temperature as well. Thermal diffusion and contact with the environment is more effective and multiple heating events are required for switching. This occurs at higher temperatures, where the derivative $d\sigma/dT$ is negative.

Therefore, it turns out that SCDs allow to distinguish different dissipation processes: a JJ cannot sustain an unlimited increase in the critical current I_c, and thus in the quality factor Q, through larger critical current density J_c while still preserving all the properties of the Josephson effect and all the features of the underdamped regime (Massarotti and Tafuri, 2019). The classical Josephson phase dynamics, which takes place in junctions characterized by lower critical current densities J_c, is replaced at high J_c values by a regime driven by local heating events where phase information is lost. Nonequilibrium phenomena produce hysteretic I–V characteristics and modify the influence of dissipation, thus becoming measurable through modeling of the SCDs in terms of heating modes (Shah et al., 2008; Massarotti et al., 2015a, b)

Conclusion

Every experiment or application using a superconducting weak link is based on how the phase difference φ between the electrodes evolves in time and space. The large variety of barriers now available between the superconducting electrodes offer novel functionalities and efficient tuning of physical processes occurring at the nanoscale and at different interfaces. Measurements of SCDs focus on the moment at which resistance originates in superconducting weak links; thus they constitute a direct way of discriminating the phase dynamics and the transport also in nontrivial cases of Josephson nanodevices and hybrid systems (Feofanov et al., 2010; Inomata et al., 2005; Massarotti et al., 2015a; Goldobin et al., 2007; Sickinger et al., 2012; Goldobin et al., 2013; Ahmad et al., 2020). These junctions are going to be more and more common with advances in nanopatterning superconductors and in materials science; thus the range of the energy dynamical parameters is significantly enlarged. In this chapter we have represented well-defined criteria to identify different regimes of the phase dynamics. We believe that further progress in the field will lead to novel insights and a wide vision on macroscopic quantum phenomena in a variety of complementary systems, thus promoting novel arguments on the interplay of coherence and dissipation in solid state systems. Issues on a more detailed understanding of coherence, dissipation, and noise in the various devices play a significant role in the progress of quantum circuits (Larsen et al., 2015; de Lange et al., 2015; Wiedenmann et al., 2016; Ahmad et al., 2022).

References

Ahmad H, Caruso R, Pal A, Rotoli G, Pepe GP, Blamire M, Tafuri F, and Massarotti D (2020) *Physical Review Applied* 13: 014017.

Ahmad HG, Brosco V, Miano A, Di Palma L, Arzeo M, Montemurro D, Lucignano P, Pepe GP, Tafuri F, Fazio R, and Massarotti D (2022) *Physical Review B* 105: 214522.

Bae MH, Sahu M, Lee HJ, and Bezryadin A (2009) *Physical Review B* 79: 104509.

Barone A and Paternò G (1982) *Physics and Applications of the Josephson Effect*. John Wiley and Sons.

Bauch T, Lombardi F, Tafuri F, Barone A, Rotoli G, Delsing P, and Claeson T (2005) *Physical Review Letters* 94: 087003.

Bauch T, Lindstrom T, Tafuri F, Rotoli G, Delsing P, Claeson T, and Lombardi F (2006) *Science* 311: 56.

Baumans XDA, Zharinov VS, Raymenants E, Alvarez SB, Scheerder JE, Brisbois J, Massarotti D, Caruso R, Tafuri F, Janssens E, Moshchalkov VV, Van de Vondel J, and Silhanek AV (2017) *Scientific Reports* 7: 44569.

Ben-Jacob E, Bergman DJ, Matkowsky BJ, and Schuss Z (1982) *Physical Review A* 26: 2805.

Bergeret FS and Ilic S (2023) *ECMP*, 2nd ed. Oxford: Elsevier.

Borzenets IV, Coskun UC, Jones SJ, and Finkelstein G (2011) *Physical Review Letters* 107: 137005.

Caldeira AO and Leggett AJ (1981) *Physical Review Letters* 46: 211.

Clarke J and Wilhelm FK (2008) *Nature (London)* 453: 1031.

Clarke J, Cleland AN, Devoret MH, Esteve D, and Martinis JM (1988) *Science* 239: 992.

Courtois H, Meschke M, Peltonen JT, and Pekola JP (2008) *Physical Review Letters* 101: 067002.

de Lange G, van Heck B, Bruno A, van Woerkom DJ, Geresdi A, Plissard SR, Bakkers EPAM, Akhmerov AR, and Di Carlo L (2015) *Physical Review Letters* 115: 127002.

der Boer W and de Bruyn Ouboter R (1980) *Physica B: Condensed Matter* 98: 185.

Devoret MH and Schoelkopf RJ (2013) *Science* 339: 1169.

Devoret MH, Martinis JM, Esteve D, and Clarke J (1984) *Physical Review Letters* 53: 1260.

Devoret MH, Martinis JM, and Clarke J (1985) *Physical Review Letters* 55: 1908.

Dmitrenko IM, Khlus VA, Tsoi GM, and Shnyrkov VI (1985) *Fizika Nizkikh Temperatur* 11: 146 (Sov. J. Low Temp. Phys. 11, 77 (1985)).

Ejrnaes M, Salvoni D, Parlato L, Massarotti D, Caruso R, Tafuri F, Yang XY, You LX, Wang Z, Pepe GP, and Cristiano R (2019) *Scientific Reports* 9: 8053.

Fenton JC and Warburton PA (2008) *Physical Review B* 78: 054526.

Feofanov AK, Oboznov VA, Bol'ginov VV, Lisenfeld J, Poletto S, Ryazanov VV, Rossolenko AN, Khabipov M, Balashov D, Zorin AB, Dmitriev PN, Koshelets VP, and Ustinov AV (2010) *Nature Physics* 6: 593–597.

Fulton TA and Dunkleberger LN (1974) *Physical Review B* 9: 4760.

Goldobin E, Koelle D, Kleiner R, and Buzdin AI (2007) *Physical Review B* 76: 224523.

Goldobin E, Kleiner R, Koelle D, and Mints RG (2013) *Physical Review Letters* 111: 057004.

Grabert H, Olschowski P, and Weiss U (1987) *Physical Review B* 36: 1931.

Iansiti M, Johnson AT, Smith WF, Rogalla H, Lobb CJ, and Tinkham M (1987) *Physical Review Letters* 59: 489.

Inomata K, Sato S, Nakajima K, Tanaka A, Takano Y, Wang HB, Nagao M, Hatano H, and Kawabata S (2005) *Physical Review Letters* 95: 107005.

Jackel LD, Gordon JP, Hu EL, Howard RE, Fetter LA, Tennant DM, Epworth RW, and Kurkijarvi J (1981) *Physical Review Letters* 47: 697.

Josephson BD (1962) *Physics Letters* 1: 251.

Kautz RL and Martinis JM (1990) *Physical Review B* 42: 9903.

Kivioja JM, Nieminen TE, Claudon J, Buisson O, Hekking FWJ, and Pekola JP (2005) *Physical Review Letters* 94: 247002.

Kockum AF and Nori F (2019) *Quantum Bits With Josephson Junctions*, pp. 703–741. Cham: Springer International Publishing.

Koshino M (2023) *ECMP*, 2nd ed. Oxford: Elsevier.

Kramers HA (1940) *Physica (Utrecht)* 7: 284.

Krasnov VM, Bauch T, Intiso S, Hürfeld E, Akazaki T, Takayanagi H, and Delsing P (2005) *Physical Review Letters* 95: 157002.

Larsen TW, Petersson KD, Kuemmeth F, Jespersen TS, Krogstrup P, Nygard J, and Marcus CM (2015) *Physical Review Letters* 115: 127001.

Li P, Wu PM, Bomze Y, Borzenets IV, Finkelstein G, and Chang AM (2011) *Physical Review Letters* 107: 137004.

Likharev KK (1979) *Reviews of Modern Physics* 51: 101.

Little WA (1967) *Physics Review* 156: 396.

Longobardi L, Massarotti D, Rotoli G, Stornaiuolo D, Papari G, Kawakami A, Pepe GP, Barone A, and Tafuri F (2011a) *Physical Review B* 84: 184504.

Longobardi L, Massarotti D, Rotoli G, Stornaiuolo D, Papari G, Kawakami A, Pepe GP, Barone A, and Tafuri F (2011b) *Applied Physics Letters* 99: 062510.

Longobardi L, Massarotti D, Stornaiuolo D, Galletti L, Rotoli G, Lombardi F, and Tafuri F (2012) *Physical Review Letters* 109: 184504.

Männik J, Li S, Qiu W, Chen W, Patel V, Han S, and Lukens JE (2005) *Physical Review B* 71: 220509.

Massarotti D and Tafuri F (2019) Phase Dynamics and Macroscopic Quantum Tunneling, vol. 286. Cham: Springer.

Massarotti D, Longobardi L, Galletti L, Stornaiuolo D, Montemurro D, Pepe GP, Rotoli G, Barone A, and Tafuri F (2012) *Journal of Low Temperature Physics* 38: 263.

Massarotti D, Pal A, Rotoli G, Longobardi L, Blamire MG, and Tafuri F (2015a) *Nature Communications* 6: 7376.

Massarotti D, Stornaiuolo D, Lucignano P, Galletti L, Born D, Rotoli G, Lombardi F, Longobardi L, Tagliacozzo A, and Tafuri F (2015b) *Physical Review B* 92: 054501.

Murphy A, Weinberg P, Aref T, Coskun U, Vakaryuk V, Levchenko A, and Bezryadin A (2013) *Physical Review Letters* 110: 247001.

Murphy A, Semenov A, Korneev A, Korneeva Y, Gol'tsman G, and Bezryadin A (2015) *Scientific Reports* 5: 10174.

Ono RH, Cromar MW, Kautz RL, Soulen RJ, Colwell JH, and Fogle WE (1987) *IEEE Transactions on Magnetics* MAG-23: 1670.

Prance RJ, Long AP, Clarke TD, Widom A, Mutton JE, Sacco J, Potts MW, Negaloudis G, and Goodall F (1981) *Nature* 289: 543.

Sahu M, Bae MH, Rogachev A, Pekker D, Wei TC, Shah N, Goldbart PM, and Bezryadin A (2009) *Nature Physics* 5: 503.

Salvoni D, Ejrnaes M, Gaggero A, Mattioli F, Martini F, Ahmad HG, Di Palma L, Satariano R, Yang XY, You L, Tafuri F, Pepe GP, Massarotti D, Montemurro D, and Parlato L (2022) *Physical Review Applied* 18: 014006.

Shah N, Pekker D, and Goldbart PM (2008) *Physical Review Letters* 101: 207001.

Sickinger H, Lipman A, Weides M, Mints RG, Kohlstedt H, Koelle D, Kleiner R, and Goldobin E (2012) *Physical Review Letters* 109: 107002.

Stewart WC (1968) *Applied Physics Letters* 12: 277.

Stornaiuolo D, Rotoli G, Massarotti D, Carillo F, Longobardi L, Beltram F, and Tafuri F (2013) *Physical Review B* 87: 134517.

Tafuri F (2023) *ECMP*, 2nd ed. Oxford: Elsevier.

Tinkham M (1996) *Introduction to Superconductivity*. New York: McGraw-Hill.

Vion D, Gotz M, Joyez P, Esteve D, and Devoret MH (1996) *Physical Review Letters* 77: 3435–3438.

Voss RF and Webb RA (1981) *Physical Review Letters* 47: 265.

Washburn S, Webb RA, Voss RF, and Farris SM (1985) *Physical Review Letters* 54: 2712.

Wiedenmann J, Bocquillon E, Deacon RS, Hartinger S, Herrmann O, Klapwijk TM, Maier L, Ames C, Brüne C, Gould C, Oiwa A, Ishibashi K, Tarucha S, Buhmann H, and Molenkamp LW (2016) *Nature Communications* 7(1): 10303.

Yoon Y, Gasparinetti S, Mottonen M, and Pekola JP (2011) *Journal of Low Temperature Physics* 163: 164.

Yu HF, Zhu XB, Peng ZH, Tian Y, Cui DJ, Chen GH, Zheng DN, Jing XN, Lu L, Zhao SP, and Han S (2011) *Physical Review Letters* 107: 067004.

Zaikin A (2023) *ECMP*, 2nd ed. Oxford: Elsevier.

Zgirski M, Foltyn M, Savin A, Naumov A, and Norowski K (2020) *Physical Review Applied* 14: 044024.

Zgirski M, Foltyn M, Savin A, Naumov A, and Norowski K (2021) *Physical Review B* 104: 014506.

Zhang Y, Liu G, and Lau CN (2008) *Nano Research* 1: 145–151.

Zhang B, Zhang L, Chen Q, Guan Y, He G, Fei Y, Wang X, Lyu J, Tan J, Li H, Dai Y, Li F, Wang H, Yu S, Tu X, Zhao Q, Jia X, Kang L, Chen J, and Wu P (2022) *Physical Review Applied* 17: 014032.

Zonda M, Belzig W, and Novotny T (2015) *Physical Review B* 91: 134305.

Fast dynamics of vortices in superconductors

Oleksandr V Dobrovolskiy, Faculty of Physics, Nanomagnetism and Magnonics, Superconductivity and Spintronics Laboratory, University of Vienna, Vienna, Austria

© 2024 Elsevier Ltd. All rights reserved.

Introduction **736**
Flux-flow instability models **737**
Flux-flow instability mechanisms 737
Quasiparticle scattering mechanisms 737
Larkin-Ovchinnikov model of FFI 737
Refinements of the Larkin-Ovchinnikov model 738
Quasiparticle relaxation in dirty and clean regimes 739
High-T_c superconductors and ultraclean regime 739
Pinning effects on the flux-flow instability **739**
Effects of uncorrelated disorder on FFI 739
Low-field crossover in the instability velocity 740
Pinning effects on self-heating and FFI 740
Vortex lattice commensurability effects on FFI 741
Fast dynamics of guided magnetic flux quanta 741
From global to local instability models **741**
Local FFI model for thin films near Tc 741
Rearrangement of vortices in the TDGL model 742
Edge-controlled FFI in the weak-pinning regime 743
Edge barrier effects on the fluxon speed limits 743
Edge defects as gates for fast-moving fluxons 743
Fast vortex dynamics under a microwave ac stimulus **744**
Enhancement of superconductivity at microwaves 744
Condensate and quasiparticles under dc/ac biasing 744
Microwave stimulation in the vortex state 745
Braking of instabilities by a microwave stimulus 746
Future directions **747**
Superconductivity in curved 3D nanoarchitectures 747
Cryogenic magnonics and magnon fluxonics 748
Conclusion **748**
Acknowledgments **748**
References **748**

Abstract

The last decade has been marked by great interest in the dynamics of vortices moving at high (>10 km/s) velocities in superconductors. However, the flux-flow instability (FFI) prevents its exploration and sets practical limits for the use of vortices in various applications. Even so, FFI has turned into a valuable tool for studying the quasiparticle energy relaxation in superconductors, with the view of enhancement of the single-photon detection capability of micrometer-wide strips operated at large bias currents. In this context, the failure of "global" FFI models for materials with strong intrinsic and edge vortex pinning has urged the elaboration of "local" FFI models. This chapter outlines the recent advances in the research on FFI and highlights superconductors with perfect edges and weak volume pinning as prospective materials for studying fast vortex dynamics and nonequilibrium superconductivity.

Key points

- Flux-flow instability at high vortex velocities.
- Pinning effects on the flux-flow instability.
- Paradigm shift from global to local instability models.
- Fast vortex motion at a microwave ac stimulus.

https://doi.org/10.1016/B978-0-323-90800-9.00015-9

Introduction

Fast vortex dynamics and related nonequilibrium phenomena are essential subjects of research in modern superconductivity (Bezuglyj et al., 2019; Budinska et al., 2022; Buh et al., 2015; Cherpak et al., 2014; Dobrovolskiy et al., 2020a; Dobrovolskiy et al., 2019a; Dobrovolskiy et al., 2020c; Embon et al., 2017; Grimaldi et al., 2015; Gurevich, 2014; Kogan and Nakagawa, 2021; Kogan and Nakagawa, 2022; Kogan and Prozorov, 2020; Lara et al., 2017; Lyatti et al., 2020; Madan et al., 2018; Pathirana and Gurevich, 2021; Puica et al., 2012; Sheikhzada and Gurevich, 2017; Sheikhzada and Gurevich, 2020; Wördenweber et al., 2012). High velocities of magnetic flux quanta (Abrikosov vortices or fluxons) attract great interest because of the fundamental questions regarding their stability as topological excitations of the superconducting order parameter ψ and the ultimate speed limits for magnetic flux transport via vortices at intense transport currents. Furthermore, fast dynamics of fluxons determines the vortex-assisted mechanism of the initial dissipation of superconducting microstrip single-photon detectors (Korneeva et al., 2020; Vodolazov, 2017) and makes accessible novel phenomena in hybrid superconductor-based systems, such as the generation of sound (Bulaevskii and Chudnovsky, 2005; Ivlev et al., 1999) and spin (Bespalov et al., 2014; Dobrovolskiy et al., 2021) waves, as well as emerging functionalities, e.g., in microwave radiation/detection (Bulaevskii and Chudnovsky, 2006; Dobrovolskiy et al., 2018; Dobrovolskiy et al., 2020b; Lösch et al., 2019).

Probing the upper speed limits for vortices represents a valuable approach for studying the energy relaxation processes in superconductors (Attanasio and Cirillo, 2012; Knight and Kunchur, 2006; Leo et al., 2011; Leo et al., 2020a). This method allows one to quantify the lifetimes of quasiparticles (unpaired electrons) when their energy distribution is out of equilibrium. The physical phenomenon underlaying this approach is termed *flux-flow instability* (FFI) (Bezuglyj and Shklovskij, 1992; Kunchur, 2002; Larkin and Ovchinnikov, 1975; Larkin and Ovchinnikov, 1986). In the current-voltage (I–V) curve of superconductors, FFI becomes apparent as a discontinuous jump to a highly resistive state at some instability current I^* which corresponds to the instability voltage V^*, see Fig. 1A. Note that I^* is usually smaller than the maximal current a superconductor can carry without dissipation—the *depairing current* I_d, thereby setting the actual limit for the use of superconductors in applications. The instability

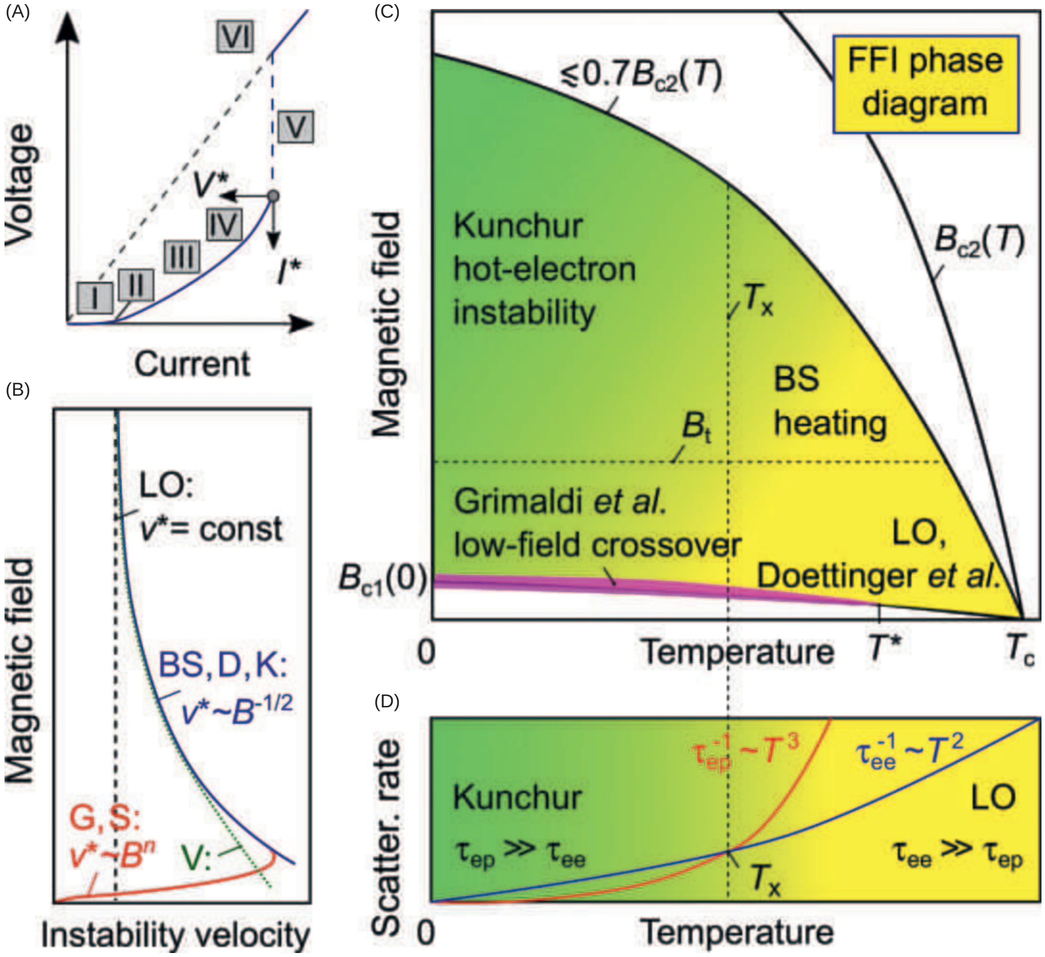

Fig. 1 (A) Typical I–V curve of a superconductor in the mixed state, with the indicated instability current I^* and instability voltage V^*, and the regimes of pinned vortices (I), depinning transition (II), flux flow (III), nonlinear conductivity (IV), flux-flow instability (V), and highly-resistive state (VI). (B) Predictions of different FFI models for $v^*(B)$. LO: (Larkin and Ovchinnikov, 1975), BS: (Bezuglyj and Shklovskij, 1992), D: (Doettinger et al., 1995), K: (Kunchur et al., 2001), G: (Grimaldi et al., 2010), S: (Shklovskij, 2017), V: (Vodolazov, 2019). (C) Different FFI regimes on the B-T plane. B_t: overheating field in the BS model (Bezuglyj and Shklovskij, 1992). (D) Temperature dependences of the inelastic electron-electron and electron-photon scattering rates. T_x: crossover temperature.

voltage allows one to quantify the maximal vortex velocity (instability velocity) v^* by using the standard relation $v^* = V^*/(BL)$, where B is the magnitude of the applied magnetic field and L the distance between the voltage leads. The understanding of the microscopic mechanisms determining the maximal vortex velocities and the behavior of $v^*(B)$ is an essential task in the FFI research, see Fig. 1B.

Reviews and discussions of FFI and nonlinear effects occurring during fast vortex motion are given in Attanasio and Cirillo (2012), Dean and Kunchur (2018), Huebener (2019), Kunchur and Knight (2003), Misko et al. (2007) and Vodolazov (2020). This chapter presents (i) a summary of the different FFI models with emphasis on the links between them, (ii) an outline of the vortex-pinning effects on FFI and the associated *paradigm shift* from *global* (Bezuglyj and Shklovskij, 1992; Larkin and Ovchinnikov, 1975; Larkin and Ovchinnikov, 1986) to *local* (Bezuglyj et al., 2019; Vodolazov, 2019) FFI models, and (iii) some of the prospective directions in the fast dynamics research.

Flux-flow instability models

Flux-flow instability mechanisms

Theoretical foundations for understanding of the electronic nonequilibrium effects were laid by Eliashberg (1970) and Eliashberg and Ivlev (1986). Due to external energy input, the quasiparticle energy distribution is modified with respect to equilibrium, which affects the superconducting parameters such as critical temperature T_c, critical current I_c, and superfluid density, and can even result in their enhancement (Wyatt et al., 1966). For instance, the quasiparticle energy distribution can be modified via irradiation with light, microwaves, phonons, injection of quasiparticles, etc. (Gray, 1981).

Experimental studies of the photon absorption response and the effects of high-frequency irradiation of superconductors are usually performed at zero external magnetic field (Natarajan et al., 2012; Zolochevskii, 2013). By contrast, nonequilibrium effects in the mixed state and the vortex motion under intense transport currents and FFI are studied in the presence of external magnetic fields (Gray, 1981).

The FFI mechanisms are distinct at high ($T \approx T_c$) and low ($T \ll T_c$) temperatures, see Fig. 1C. Close to T_c, FFI can be described by the Larkin-Ovchinnikov (LO) theory (Larkin and Ovchinnikov, 1975; Larkin and Ovchinnikov, 1986). In the LO theory, FFI is associated with a shrinking of the moving vortex and a reduction of the viscosity of the superconducting medium due to the diffusion of quasiparticles from the vortex core to the surroundings. Well below T_c, the LO mechanism is ineffective since in this case the superconducting energy gap Δ does not depend strongly on small changes of the electron distribution function.

At $T \ll T_c$, FFI is described within the framework of the Kunchur (K) hot-electron model in which the electronic temperature T_e is elevated due to dissipation. The higher T_e stipulates the creation of additional quasiparticles, which diminishes Δ. This leads to an expansion of the vortex core (Kunchur et al., 2001; Kunchur et al., 2002), which has the effect of reducing the viscous drag because of the softening of gradients of the vortex profile (Kunchur, 2002).

The LO model (Larkin and Ovchinnikov, 1975) is justified when the inelastic electron-electron scattering time τ_{ee} is much larger than the electron-photon scattering time τ_{ep}, $\tau_{ee} \gg \tau_{ep}$, which ensures a *non-thermal* electron energy distribution. By contrast, $\tau_{ee} \ll \tau_{ep}$ in the K model implies a *thermal-like* electron distribution so that the electronic ensemble exhibits a shift of the electronic temperature T_e with respect to the phonon temperature T_p (Kunchur et al., 2001).

Quasiparticle scattering mechanisms

Standard estimates (Abrikosov, 1988; Kaplan et al., 1976) for the scattering rates $\tau_{ee}^{-1} = k_B T^2/r\hbar\varepsilon_F$ and $\tau_{ep}^{-1} = k_B T^3/r^3\hbar T_D^2$ [ε_F: Fermi energy, T_D: Debye temperature] give a crossover temperature $T_x = r^2 k_B T_D^2/\varepsilon_F$. Here, $r < 1$ is the phonon reflection coefficient at the film-substrate interface, arising from their acoustic mismatch. Thus, one has $\tau_{ee} > \tau_{ep}$ above T_x which can be viewed as a crossover temperature between the K and LO models, see Fig. 1D.

For the classical superconductors, the electron-phonon interaction is usually dominant compared to the electron-electron interaction (Aronov and Spivak, 1978). By contrast, the electron-electron interaction is more important in materials with a high T_D and in high-T_c superconductors (Doettinger et al., 1997). For instance, $T_x \simeq 1$ K for Nb makes accessible both K and LO regimes (Leo et al., 2011). By contrast, $T_x \simeq 100$ K for YBCO points to the dominating electron-electron scattering in the entire temperature range of the superconducting state (Knight and Kunchur, 2006). Finally, $T_x \simeq 0.5$ K for amorphous superconductors like MoGe (Liang and Kunchur, 2010) suggests that the LO mechanism dominates in a broad range of temperatures of the superconducting state.

Larkin-Ovchinnikov model of FFI

The key point of the LO theory (Larkin and Ovchinnikov, 1975; Larkin and Ovchinnikov, 1986) is illustrated in Fig. 2A. At high vortex velocities, the quasiparticles within the vortex core are accelerated toward the core boundary, where they undergo Andreev reflection (Andreev, 1964; Blonder et al., 1982; Octavio et al., 1983) and alternate between electrons and holes. As a result, their energy increases and they eventually escape from the vortex core. This leads to a shrinking of the vortex core and the vortex viscosity η becomes a nonmonotonic function of the velocity v, namely $\eta(v) = \eta(0)/[1 + (v/v^*)^2]$ (Larkin and Ovchinnikov, 1975; Larkin and Ovchinnikov, 1986), so that the viscous force $F_v = \eta(v)v$ has a maximum at v^*. At velocities exceeding v^*, F_v decreases, leading to an even further increase of v, causing an instability in the vortex motion.

The nontrivial nature of the LO effect should be emphasized especially. If one uses the Bardeen-Stephen expression (Bardeen and Stephen, 1965) for $\eta = \Phi_0^2/(2\pi\xi^2\rho_n)$ [Φ_0: magnetic flux quantum, ξ: coherence length, ρ_n: resistivity in the normal state], one finds that it actually *increases* if the size of the vortex core ($\sim 2\xi$) decreases. By contrast, in the LO model, the vortex core shrinks and this

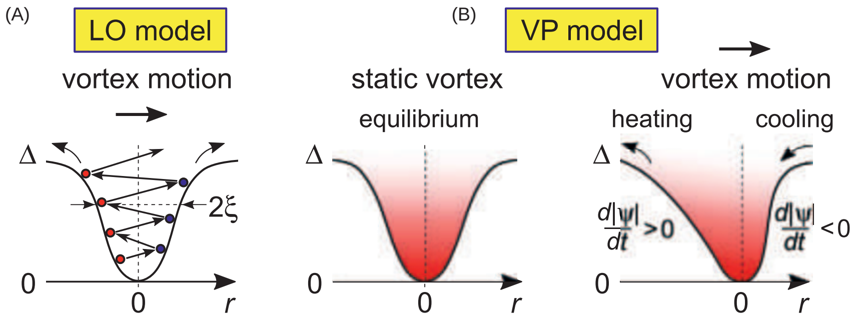

Fig. 2 Schematics of the vortex core shapes in the LO (Klein et al., 1985; Larkin and Ovchinnikov, 1975) and VP (Vodolazov and Peeters, 2007) models assuming spatially uniform and nonuniform nonequilibrium quasiparticle distributions, respectively. (A) The electric field generated by fast vortex motion raises the energy of the quasiparticles trapped in the core. During this process the particle character alternates between electron-like and hole-like due to Andreev reflections. The vortex core shrinks in consequence of the quasiparticle escape. (B) Deformation of the vortex core due to vortex motion. The color depth indicates the density of the quasiparticles. In case the quasiparticle diffusion length is smaller than ξ, diffusion of the quasiparticles is not strong and locally there is an effective cooling and heating of the quasiparticles.

results in a *decrease* of η. This contradiction can be explained by the failure of the Bardeen-Stephen model for the vortex as a normal cylinder with radius of the order of ξ when the vortex is moving with a high enough velocity v.

The essential assumption of the LO theory is a *spatially uniform* nonequilibrium quasiparticle distribution function $f(E)$ in the superconductor. Accordingly, while the vortex core shrinks as the vortex is accelerated to high velocities, its shape remains *axially symmetric* in the LO model, see Fig. 2A. Moreover, FFI nucleates at all points of the superconductor at the same time and this leads to a *field-independent* v^* at which FFI occurs, see Fig. 1B. Thus, all refinements of the LO model dealing with the spatially uniform nucleation of FFI can be termed *global* FFI models.

Refinements of the Larkin-Ovchinnikov model

Early experiments on low-T_c superconductors confirmed the LO prediction of FFI (Klein et al., 1985; Musienko et al., 1980; Volotskaya et al., 1992). It was revealed that FFI occurs at magnetic fields $B \lesssim 0.7B_{c2}$ (Babic et al., 2004), where B_{c2} is the upper critical field of the superconductor. From the good quantitative agreement between theory and experiment in large magnetic fields, it was concluded (Klein et al., 1985; Musienko et al., 1980) that the condition of spatially uniform $f(E)$ is well satisfied when the distance between vortices $a(B) \simeq \sqrt{\Phi_0/B} \ll L_\varepsilon \equiv v^* \tau_\varepsilon$ [L_ε: quasiparticle diffusion length, τ_ε: quasiparticle energy relaxation time].

However, at $B \ll B_{c2}$, $v^*(B) \sim \sqrt{1/B}$ was observed in many experiments (Doettinger et al., 1994; Doettinger et al., 1995; Lefloch et al., 1999), see Fig. 1B. The observed dependence was explained as a consequence of the crossover from a uniform to a *nonuniform* distribution of nonequilibrium quasiparticles when $L_\varepsilon = \sqrt{D\tau_\varepsilon}$ [D: electron diffusion coefficient] becomes comparable with the intervortex distance, $v^* \tau_\varepsilon \simeq a(B)$. Doettinger et al suggested (Doettinger et al., 1995) that at smaller fields the system can be recovered to a spatially homogeneous state by allowing v^* to grow accordingly to the increase of a with decrease of the applied magnetic field, $a = \left(2\Phi_0/\sqrt{3}B\right)^{1/2}$. The LO expression was complemented (Doettinger et al., 1995) with the term $a/\sqrt{D\tau_\varepsilon}$, yielding

$$v^* = \left[\frac{(1-t)^{1/2} D[14\zeta(3)]^{1/2}}{\pi\tau_\varepsilon}\right]^{1/2}\left(1 + \frac{a}{\sqrt{D\tau_\varepsilon}}\right), \qquad (1)$$

where $t = T/T_c$ and $\zeta(x)$ is the Riemann function. Note that a $v^*(B) \propto 1/\sqrt{B}$ dependence appears in other FFI models as well.

In the original LO theory, the nonlinear flux-flow behavior is due only to the *electric field-induced* change in $f(E)$ and not Joule heating. Bezuglyj and Shklovskij (BS) extended the LO theory in the thin-film configuration by taking into account *Joule heating* effects (Bezuglyj and Shklovskij, 1992). BS found that even if the Joule heating of the lattice is negligible, quasiparticles can still experience an overheating due to the finite heat removal rate of the power dissipated in the sample which can trigger FFI. Thus, in the BS model, $f(E)$ depends on the *vortex density* and the *rate of heat removal* from the film to the substrate. BS used the electronic temperature approximation, i.e. the assumption that the quasiparticles temperature T_e is uniform throughout the film thickness due to a high electron thermal conductivity. Thus, if the film thickness d is much smaller than the electron-phonon scattering length (that usually occurs in thin films), the nonequilibrium phonons can escape from the film without re-absorption leading to the electron overheating (Bezuglyj and Shklovskij, 1992).

BS introduced a transition magnetic field B_t, see Fig. 1C, which depends on the heat transfer coefficient between the film and the substrate (Bezuglyj and Shklovskij, 1992). At fields $B < B_t$ the hypothesis of a uniform quasiparticles distribution in the LO model remains justified. By contrast, at $B \gg B_t$ dissipation during the flux flow raises the electronic temperature T_e and the onset of FFI is governed by thermal effects. The BS model yields $v^*(B) \propto B^{-1/2}$, see Fig. 1B. Note just the same dependence $v^*(B) \propto B^{-1/2}$ is found in the K model (Kunchur et al., 2001) at $T \ll T_c$ in which thermal effects diminish the superconducting order parameter and lead to an expansion of the vortex cores. However, in the low-temperature regime, the quasiparticles heating reduces B_{c2} to $B_{c2}(T_e) < B_{c2}$.

Quasiparticle relaxation in dirty and clean regimes

The schematics of the vortex core in Fig. 2A allows one to consider distinct quasiparticle energy relaxation processes for dirty and clean superconductors (Peroz and Villard, 2005). When the mean electron free path l is shorter than the coherence length (dirty limit, $l < \xi$), the energy relation occurs via the *scattering process inside the vortex core*. In the opposite case (clean limit, $l > \xi$) the quasiparticles can relax their energy by *recombination outside the vortex core* only after covering a distance within the core equivalent to several ξ.

In the microscopic picture where the quasiparticle energy rise comes from Andreev reflections (Andreev, 1964; Blonder et al., 1982; Octavio et al., 1983) at the vortex core boundary, see Fig. 2A, an increase of the quasiparticles energy occurs well below v^* in clean samples so that v^* values in the clean limit are noticeably smaller than in the dirty limit (Peroz and Villard, 2005). Indeed, in the dirty limit, more energy is needed to induce the depletion of quasiparticles of the core. The shrinking of the vortex core occurs at higher energy and τ_ε is substantially *temperature independent*. In the clean limit, the quasiparticle distribution function is influenced by the recombination of quasiparticles to Cooper pairs. This means that in the clean limit τ_ε is strongly *temperature dependent* since the quasiparticles recombination mechanism obeys an *exponential law* (Doettinger et al., 1997; Liang and Kunchur, 2010; Peroz and Villard, 2005).

High-T_c superconductors and ultraclean regime

FFI was also extensively investigated for high-temperature superconductors (HTSs). These studies were performed for epitaxial (Cherpak et al., 2014; Doettinger et al., 1994; Doettinger et al., 1995; Xiao and Ziemann, 1996), vicinal (Puica et al., 2012) and He ion-irradiated (Xiao et al., 1996) $YBa_2Cu_3O_{7-\delta}$ films, MgB_2 (Kunchur et al., 2003), $Bi_2Sr_2CaCu_2O_{8+\delta}$ (Xiao et al., 1998), $La_{1.85}Sr_{0.15}CuO_{4-x}$ (Doettinger et al., 1997), $Nd_{2-x}Ce_xCuO_y$ (Huebener et al., 1999; Stoll et al., 1999; Stoll et al., 1998) films and $YBa_2Cu_3O_{7-\delta}$ nanowires (Lyatti et al., 2018; Rouco et al., 2018). The distinct effects of intrinsic (nonequilibrium) and extrinsic (thermal runaway) mechanisms driving FFI were discussed for $YBa_2Cu_3O_{7-\delta}$ films (Maza et al., 2008) and for iron based superconductors (Leo et al., 2016). Signatures of FFI in the anisotropic FeSeTe have allowed for its treatment halfway between low-T_c and high-T_c superconductors.

In the dirty limit, the energy distribution of the quasiparticles in the vortex core is strongly smeared out due to their high scattering rate. The separation between the quasiparticles energy levels and between the Fermi energy ξ_F and the lowest bound state in the vortex core is proportional to ξ^{-2} (Huebener, 2019). With an estimate $\xi \lesssim 10$ nm for disordered low-temperature superconductors (Córdoba et al., 2019; Korneeva et al., 2020; Porrati et al., 2019), the core can be treated as an energy continuum of quasiparticles. By contrast, the extremely small $\xi \lesssim 1$ nm in the HTS cuprates makes the *electron quantum structure* of the vortex core essential. For its experimental observation, the energy smearing $\delta\varepsilon = \hbar/\tau$ due to the mean electronic scattering time τ must be sufficiently small, $\delta\varepsilon \ll \Delta^2/\varepsilon_F$, corresponding to the ultraclean superconducting limit. Such a regime has been experimentally realized in Huebener et al. (1999), Stoll et al. (1999) and Stoll et al. (1998). Proceeding from an isolated vortex to the vortex lattice, the discrete energy levels within the vortex core interact between neighboring vortices and broaden into *mini-bands* (Huebener, 2019). In this case, vortex motion at high velocities is accompanied by emerging phenomena, such as Bloch oscillations of the quasiparticles, negative differential resistance, and multi-step instabilities (Huebener, 2019; Huebener et al., 1999; Stoll et al., 1999; Stoll et al., 1998).

Pinning effects on the flux-flow instability

Effects of uncorrelated disorder on FFI

The LO model considered a moving vortex lattice in an infinite superconductor in the Wigner-Seitz approximation and ignored collective effects related to vortex pinning and lattice transformations. The assumption of no pinning corresponds to a δ-functional velocity distribution in the vortex ensemble and a free flux flow with zero critical current (Liang et al., 2010). In this case, an increase of current produces a shift of the velocity distribution to higher mean values $\langle v \rangle$ until the vortex instability occurs at v^* for all vortices *simultaneously*. Note, it is the *mean value* $\langle v \rangle$ which is deduced from the dc voltage measured experimentally.

In disordered systems, a rather narrow distribution of vortex velocities, see Fig. 3A, can be realized in a *weak-pinning* regime or at high enough fields and currents such that the vortex-vortex interaction is stronger than the vortex-pinning interaction (Blatter et al., 1994). In particular, an increase of the current I above I_c produces a shift of the velocity distribution toward higher mean values $\langle v \rangle$ and progressively *narrows* the distribution peak in consequence of the enhanced long-range order in the moving vortex lattice (Koshelev and Vinokur, 1994). The FFI jump occurs at the end of the quasilinear flux-flow regime, see Fig. 3B. The commonly occurring vortex dynamics regimes are indicated in Fig. 1A.

The introduction of *strong pinning* by *uncorrelated disorder* substantially modifies the previous picture (Leo et al., 2010; Ruck et al., 2000; Shklovskij et al., 2017; Silhanek et al., 2012). As pointed out by Silhanek et al. (2012), on the one hand, the presence of disorder broadens the velocity distribution and extends the nonlinear regime for currents above the critical value I_c (Grimaldi et al., 2009b). This is schematically shown in Fig. 3C and D. On the other hand, strong pinning increases I_c and causes FFI to occur within the depinning-mediated nonlinear section of the I–V curve. Importantly, the broadening of the velocity distribution implies a *sizable separation between* $\langle v \rangle$ and the maximal attainable vortex velocity v^*. This means that it is the vortices which move faster than other vortices in the ensemble which actually trigger FFI. Once FFI is triggered in the regions of faster-moving vortices it is then spread over the entire volume of the superconductor.

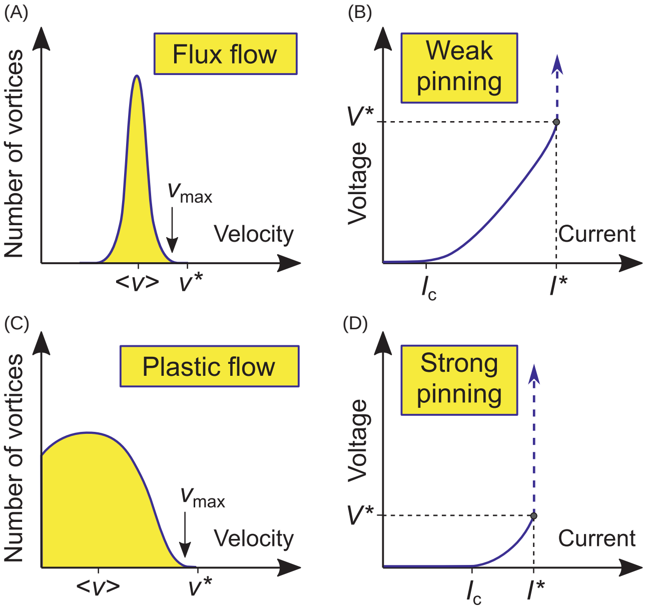

Fig. 3 Schematic representation of different dynamic regimes after Silhanek et al. (2012). Velocity distribution for the case of flux flow (A) and plastic flow (C). Expected I–V curves for weak (B) and strong (D) pinning strengths. The critical current density I_c indicates the onset of dissipation. The instability current I^* and voltage V^* indicate where FFI takes place.

Thus, in this plastic vortex flow regime, the system reaches the instability point at a *lower* vortex velocity than expected, practically when $v_{max} \simeq v^*$. In this case, the LO assumption of homogeneous quasiparticle distribution in the whole sample has to be dropped and instead homogeneous quasiparticle distribution only along the paths where the vortices move has to be considered (Silhanek et al., 2012). As the magnetic field increases, the distance between the vortices decreases and the vortex-vortex interaction increases, which in turn effectively diminishes the role of pinning. This narrows the vortex velocity distribution so that v^* increases. With a further increase of the magnetic field, the assumption of homogeneous quasiparticle distribution becomes justified again, and the LO scenario is retained. This gives rise to qualitatively different dependences of $v^*(B)$, see Fig. 1B, and enables controlling the flux-flow dissipation via vortex pinning engineering in superconductors (Grimaldi et al., 2012; Ruck et al., 2000).

Low-field crossover in the instability velocity

A crossover to a different behavior of $v^*(B)$ at magnetic fields $B < B_{cr1}$ was reported by Grimaldi et al. (2009a) and Grimaldi et al. (2010) for Nb films with moderately strong intrinsic pinning. This field B_{cr1} corresponds to a crossover from the regime where v^* *increases* with increasing magnetic field to the regime $v^* \propto B^{-1/2}$, see Fig. 1B. Magneto-optical imaging of the flux penetration into the films at $B \ll B_{cr1}$ revealed that the flux does not penetrate with a smooth advancing front, but instead as a series of irregularly shaped protrusions. This causes the formation of an inhomogeneous magnetic field distribution and induces preferential stationary channels for the moving vortices with a total effective width l (Grimaldi et al., 2010). An inspection of the films by field emission scanning electron microscopy revealed that these channels are grouped together in clusters along the strip (Grimaldi et al., 2010). This means that the voltages measured across the distance L between the voltage leads are actually produced across an *effective distance* $l < L$, so that in the low-field range $B < B_{cr1}$, the flux-flow channels fill only parts of the whole strip length.

On the contrary, when the flux penetration becomes smooth, above some threshold temperature T^* ($\simeq 0.75T_c$ for the films studied in (Grimaldi et al., 2010)), the pinning strength decreases so the vortex flow becomes uniform as well. In this way, below T^*, the decreasing low-field dependence $v^*(B)$ is preserved, whereas above T^*, the crossover field disappears, leading to a monotonous decrease of $v^*(B) \propto B^{-1/2}$, see Fig. 1B and C. Herewith, B_{cr1} corresponds to a crossover from the channel-like vortex motion to a uniform flux-flow state with increase of the magnetic field. Accordingly, at $T < T^*$, the flux-flow resistance ρ_{ff} assumes lower values than the Bardeen-Stephen prediction while the expected linear $\rho_{ff}(B) \propto B$ is retained at $T > T^*$ (Grimaldi et al., 2010).

Pinning effects on self-heating and FFI

The effects of pinning and self-heating on FFI in thin films were considered theoretically by Shklovskij et al for the cases $T \ll T_c$ (Shklovskij, 2017) and $T \approx T_c$ (Shklovskij et al., 2017). The problem was considered in the single-vortex approximation, upon the nonlinear I–V curves derived for a saw-tooth (Shklovskij and Dobrovolskiy, 2006) and cosine (Shklovskij and Dobrovolskiy, 2008) pinning potentials.

In the low-temperature regime, within the framework of the K model (Kunchur, 2002), the presence of pinning has been revealed (Shklovskij, 2017) to not modify the magnetic field dependences of the electric field $E^*(B)$, current density $j^*(B)$ and resistivity ρ^* at the instability point, which remain monotonic. By contrast, the derivative of the instability velocity dv^*/dB may *change its sign twice*, as observed in experiments (Dobrovolskiy et al., 2017b; Grimaldi et al., 2009a; Grimaldi et al., 2011; Grimaldi et al., 2012; Grimaldi et al., 2010; Leo et al., 2010; Leo et al., 2020b; Silhanek et al., 2012). In particular, experiments on weak-pinning 5 μm-wide Mo_3Ge thin films (Leo et al., 2020b) revealed that the observed nonmonotonic $v^*(B)$ dependence can be described well with the theoretical dependences of Shklovskij (2017). For wider films, that is in the absence of the surface pinning caused by the mesoscopic geometry, the experimentally observed (Leo et al., 2020b) dependence $v^*(B) \propto B^{-1/2}$ fits the K model (Kunchur et al., 2001).

In the high-temperature regime, within the framework of the LO theory (Larkin and Ovchinnikov, 1975) and its generalization by BS (Bezuglyj and Shklovskij, 1992), the increase of the pinning strength does not change the field dependences of the electric field strength $E^*(B)$ and the current density $j^*(B)$ qualitatively. At a fixed magnetic field value, E^* and v^* *decrease* while j^* *increases* with increasing magnetic field. In this way, the theoretical analysis of Shklovskij (2017) and Shklovskij et al. (2017) corroborates that the *presence of pinning* leads to a *reduction* of v^*, with exception of highly-correlated, periodic pinning-induced regimes in the vortex dynamics as outlined next.

Vortex lattice commensurability effects on FFI

In the presence of a periodic pinning, the spatial commensurability between the vortex lattice with the pinning landscape leads to magnetoresistance minima and critical current maxima (Cuadra-Solis et al., 2014; Dobrovolskiy et al., 2020a; Dobrovolskiy et al., 2012; Dobrovolskiy et al., 2018; Dobrovolskiy et al., 2017b; Jaque et al., 2002; Lu et al., 2007; Villegas et al., 2003). In this regime, v^* attains a *maximum* when the spacing between the rows of vortices driven across an array of nanogrooves is commensurate with the distance between them (Dobrovolskiy et al., 2017b). The location of this matching peak can be tuned through the nanostructure period variation.

The considered case can be realized for nanopatterned superconductors at the fundamental matching field when vortex dynamics is in a coherent regime, i.e., the entire vortex ensemble behaves as a vortex crystal (Cuadra-Solis et al., 2014; Dobrovolskiy et al., 2020a; Lu et al., 2007; Villegas et al., 2003). At the same time, the background pinning due to undesired random disorder must be weak to ensure the long-range order in the vortex lattice in the vicinity of the depinning transition. This condition can be realized, e.g., in weak-pinning amorphous Mo_3Ge (Grimaldi et al., 2015), Nb_7Ge_3 (Babic et al., 2004), MoSi (Budinska et al., 2022), nanocrystalline Nb–C (Dobrovolskiy et al., 2020c), as well as Al (Silhanek et al., 2012) and epitaxial Nb films in the clean superconducting limit (Dobrovolskiy and Huth, 2012).

Fast dynamics of guided magnetic flux quanta

An interesting possibility to enhance the long-range order in the moving vortex lattice is offered by the vortex guiding effect (Dobrovolskiy et al., 2010; Niessen and Weijsenfeld, 1969; Shklovskij and Dobrovolskiy, 2006). This effect consists in the noncollinearity of the velocity of vortices with the driving force exerted on them by the transport current. In the regime of guiding under the action of the driving Lorentz-type force F_L directed at a small tilt angle α with respect to linearly extended "pinning sites", see Fig. 4A, all vortices move along the pinning channels and the distribution of their velocities is close to the δ-functional shape. The small angle α ensures that the normal component of the driving force $F_L \sin \alpha$ is not large enough to let vortices overcome the potential troughs, while the tangential component $F_L \cos \alpha$ is large enough to drive the vortices at a few km/s velocities (Dobrovolskiy et al., 2019a).

The presence of the vortex velocity component *along* the sample length in the guiding regime leads to the appearance of a *transverse* voltage. This voltage vanishes upon a transition from the vortex guiding regime to a regime in which vortices start overcoming the pinning potential barriers (Reichhardt and Reichhardt, 2008; Shklovskij and Dobrovolskiy, 2006). By guiding magnetic flux quanta at a tilt angle of 15 degrees with respect to Co nanostripe arrays deposited on top of Nb films, a fivefold enhancement of v^* (up to 5 km/s at low magnetic fields) was observed experimentally (Dobrovolskiy et al., 2019a). In a different experiment, I–V measurements on tracks perpendicular to the vicinal (8 degrees) step direction of $YBa_2Cu_3O_{7-\delta}$ films (current crossed between *ab* planes) provided evidence for the sliding motion along the *ab* planes (vortex channeling) at velocities exceeding 8 km/s (Puica et al., 2012).

From global to local instability models

Local FFI model for thin films near Tc

Distinct from the nonlinear conductivity regime considered by LO, FFI jumps were also observed in linear I–V sections (Grimaldi et al., 2011; Volotskaya et al., 1992). A broad distribution of vortex velocities caused by the presence of regions with different pinning strengths is a likely cause for such a regime. Namely, on average, an essentially larger number of slowly moving vortices can make a larger contribution to the measured voltage as compared to the contribution of a much smaller number of faster moving vortices, allowing the I–V curve to maintain a linear shape up to the instability point. The respective *local* FFI theory was developed

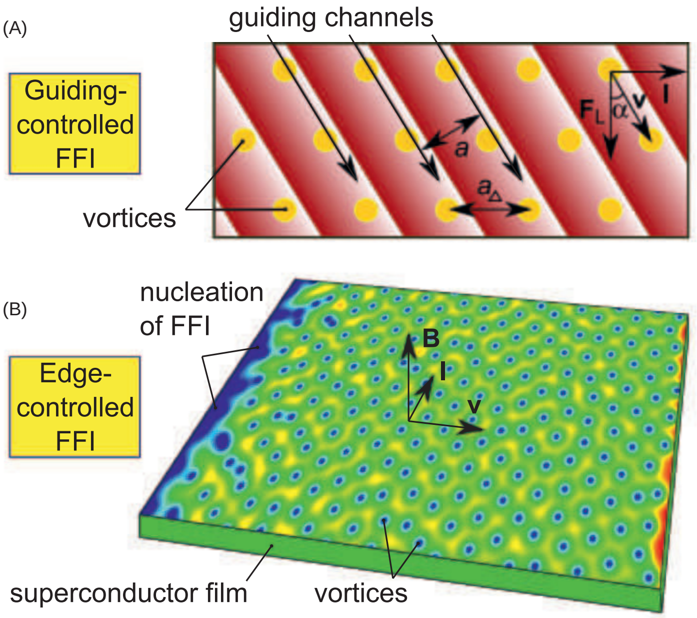

Fig. 4 (A) Schematic of a vortex lattice which is commensurate with a periodic washboard pinning landscape. When the vortices are guided at some tilt angle α with respect to the pinning channels, the long-range order in the vortex lattice is enhanced (Dobrovolskiy et al., 2020a; Dobrovolskiy et al., 2019a). (B) The combination of a weak intrinsic pinning, close-to-depairing critical current and fast relaxation of nonequilibrium allows for ultra-high vortex velocities (Dobrovolskiy et al., 2020c). The nucleation of FFI occurs at the film edge of the film and is decisively controlled by its quality (Budinska et al., 2022; Vodolazov, 2019).

by Bezuglyj et al. (2019), based on the assumption that FFI occurs upon reaching I^* not in the entire superconducting film but in a narrow strip with weak pinning across the film width in which vortices move much faster than outside it.

As a consequence of the overheating of the local areas with faster moving vortices, *normal domains* can be formed *across* the superconducting film. Once the current density exceeds some threshold current density (determining the equilibrium of the non-isothermal normal/superconducting boundary) (Bezuglyj and Shklovskij, 1984; Gurevich and Mints, 1984) these domains begin to grow and the whole sample transits to the normal state (Bezuglyj et al., 2019). In this case, the standard relation $v^* = V^* /(BL)$ can no longer yield the instability velocity quantitatively. Nevertheless, the functional relations between the LO instability parameters in the case of a local FFI remain the same as in the case of a global FFI, but require *renormalization* of the sample length (Bezuglyj et al., 2019).

Rearrangement of vortices in the TDGL model

The LO model assumes that the vortex lattice does not exhibit any structural changes upon the transition of the superconductor to a state with a resistance close to the normal value. However, experiments on low- and high-temperature superconductors suggested that some kind of phase transition may occur in the fast-moving vortex lattice and regions with fast and slow vortex motions may appear in the sample (Adami et al., 2015; Grimaldi et al., 2015).

An alternative view of the moving vortex at high velocities, in which it loses the shape of a rigid cylinder, was used by Vodolazov and Peeters (2007). Reducing the problem to a two-dimensional one, VP solved *numerically* the generalized time-dependent Ginzburg-Landau (TDGL) equations (Kramer and Watts-Tobin, 1978; Watts-Tobin et al., 1981) which take into account the spatially *nonuniform* distribution of quasiparticles as the longitudinal (odd in energy E) part $f_L(E) = f(-E) - f(E)$ of the nonequilibrium $f(E)$ distribution is localized only in the region where the time derivative $\partial|\psi|/\partial t$ is finite, that is only near the moving vortex core, see Fig. 2B.

Indeed, the motion of a vortex implies a suppression of the order parameter ψ in front of the vortex and its recovery behind it. If the vortex velocity is large enough, $v \simeq \xi/\tau_\varepsilon$, the number of quasiparticles in front of the vortex becomes smaller than the equilibrium value and it becomes larger behind the vortex due to the finite relaxation time of $f(E)$. Effectively, this can be viewed as *cooling* of the quasiparticles in front of the vortex and *heating* behind the vortex. Since the relaxation time of ψ depends on temperature as $\tau|\psi|\sim 1/(T_c - T)$, the healing time of the order parameter behind the vortex is long while the time of the order parameter suppression in front of the vortex is short. This leads to an *elongated shape* of the vortex core with a point where $|\psi| = 0$ displaced in the direction of the vortex motion.

The elongated shape of the core of a fast-moving vortex is in line with the field distribution around it as derived *analytically* based on the time-dependent London (TDL) equation (which ignores the vortex core) (Kogan and Prozorov, 2020). The flux quantum of a moving vortex is redistributed: The back-side part of the flux is enhanced, whereas the in-front part is depleted (Kogan and Nakagawa, 2021). Distortions of the field distribution of single moving vortices lead to distorted intervortex interactions and therefore to a change in the vortex lattice structure (Kogan, 2018). At large velocities, the moving vortex lattice adopts the structure with one of the lattice vectors along the velocity, the same result as obtained within TDGL (Li et al., 2004; Vodolazov and Peeters, 2007).

Edge-controlled FFI in the weak-pinning regime

In the Knight and Kunchur (2006), Kunchur (2002), Shklovskij (2017), Bezuglyj and Shklovskij (1992) and Shklovskij et al. (2017) models the temperature of the electrons T_e was calculated from the balance between the spatially- and time-averaged Joule dissipation and the heat removal to the substrate, which ignores the discrete nature of the moving vortices. Vodolazov (2019) solved the TDGL equation in conjunction with the heat conductance equation for T_e and the energy balance equation to find the phonon temperature T_p, which were derived from the *kinetic equations* for the electron and phonon distribution functions (Vodolazov, 2017).

In the V model, in the low-resistive state, there is a temperature gradient across the width of the strip with maximal local temperature near the edge where vortices enter the sample (Vodolazov, 2019). The higher temperature at the edge is caused by the larger current density in the near-edge area due to the presence of the *edge barrier* for vortex entry and, hence, the locally larger Joule dissipation. With increase of the current, there is a series of *transformations* of the moving vortex lattice in the V model.

At $I \lesssim I^*$, localized areas with strongly suppressed superconductivity and closely spaced vortices appear near the hottest edge (left edge in Fig. 4B). Upon reaching I^*, these areas begin to grow in the direction of the opposite edge and form highly resistive Josephson SNS-like links—*vortex rivers*—along which the vortices move. Such vortex rivers were observed experimentally by scanning local probes (Embon et al., 2017; Silhanek et al., 2010). Due to the increasing dissipation, vortex rivers evolve into normal domains which then expand along the strip (Dobrovolskiy et al., 2020c).

Distinct from the modified LO model (Doettinger et al., 1995), in the V model $v^* \sim B^{-1/2}$ only at comparatively large magnetic fields (see Fig. 1B), when the intervortex distance at $I \simeq I_c$ and $I \simeq I^*$ is almost the same despite the transformations in the moving vortex lattice. By contrast, at relatively small magnetic fields, a in the vortex rows is smaller than $(2\Phi_0/B\sqrt{3})^{1/2}$ at $I \simeq I^*$ and the number of vortices n is smaller than follows from $n\Phi_0 = BS$ [S: sample area]. This leads to a weaker dependence $v^*(B)$ than $v^* \sim B^{-1/2}$ following from "global" instability models. This behavior is confirmed experimentally (Dobrovolskiy et al., 2020c).

Edge barrier effects on the fluxon speed limits

The prediction (Vodolazov, 2017) and experimental confirmation (Charaev et al., 2020; Chiles et al., 2020; Korneeva et al., 2020; Korneeva et al., 2018) of the single-photon detection capability of micrometer-wide strips has turned FFI into a widely used method for judging whether a superconducting material could be potentially suitable for single-photon detection (Caputo et al., 2017; Cirillo et al., 2021; Dobrovolskiy et al., 2020c; Lin et al., 2013). This assessment is based on the deduction of the quasiparticle relaxation times from FFI. However, while many dirty superconductors (NbN (Korzh et al., 2020), MoSi (Korneeva et al., 2020), NbRe (Cirillo et al., 2020), NbReN (Cirillo et al., 2021), etc.) possess good single-photon detection capability, v^* and τ_ε deduced from FFI are not always consistent with the fast relaxation processes implied by photon-counting experiments (Budinska et al., 2022).

The edge quality turns out to be decisive for the nucleation of FFI and, hence, quantification of the relaxation times from the I–V measurements (Budinska et al., 2022). By investigating FFI in wide MoSi strips differing only by the edge quality, a factor of 3 larger critical currents I_c, a factor of 20 higher maximal vortex velocities of 20 km/s, and a factor of 20 shorter τ_ε have been revealed for MoSi films with perfect edges. Thus, for the deduction of the intrinsic τ_ε of the material from the I–V curves, utmost care should be taken regarding the edge and sample quality, and such a deduction is justified only if the field dependence of I_c points to the dominating edge pinning of vortices (Budinska et al., 2022).

Edge defects as gates for fast-moving fluxons

The requirement of close-to-depairing critical currents I_c in superconductor strips is related to blocking of the penetration of vortices via the strip edges and knowledge of the effects of various edge defects on the penetration and patterns of Abrikosov vortices (Aladyshkin et al., 2001; Glazman, 1986; Sivakov et al., 2018; Vodolazov et al., 2015; Vodolazov et al., 2003). Once the Lorentz force exerted on a vortex by the transport current exceeds the force of attraction of the vortex to the sample edge, the edge barrier is suppressed. This suppression can be local in the case of a local increase of the current density—*current-crowding* effect (Adami et al., 2013), and it can be realized, e.g., in strips with an edge defect (Budinska et al., 2022; Dobrovolskiy et al., 2020c). In this case, the defect acts as a gate (Aladyshkin et al., 2001) for vortices entering into the superconductor strip and crossing it under the competing action of the Lorentz and vortex-vortex interaction forces.

If the size of the defect is much larger than ξ, the defect can serve as a nucleation point for several vortex chains (Budinska et al., 2022; Embon et al., 2017). Such chains form a *vortex jet* with the apex at the defect and expanding due to the repulsion of vortices as they move to the opposite film edge. If the defect size is $\simeq \xi$, the vortices enter into the strip consequentially. However, in the presence of fluctuations and inhomogeneities in the strip, the vortex chain evolves into a diverging jet because of the intervortex repulsion.

Vortices penetrating into a superconducting Pb film at rates of tens of GHz and moving with velocities of up to tens of km/s were observed by scanning SQUID-on-tip (SOT) microscopy (Embon et al., 2017). Though these vortices move faster than the perpendicular current superflow which drives them, no excessive changes in the structure of the Abrikosov vortex core has been revealed even at velocities of the order of 10 km/s (Embon et al., 2017). Because of the large current density gradient across the constriction with narrowing, a vortex chain splits up into a fan-like pattern of slipstreaming vortices. The TDGL modeling suggested that the slipstreaming vortices could further evolve to Josephson-like vortices moving with velocities as high as $\sim$100 km/s (Embon et al., 2017). Spatial modulation of the order parameter between these vortices is rather weak and the channel behaves effectively as a self-induced Josephson junction, which appears without materials weak links. Such flux channels in thin films can be interpreted as phase-slip lines (Sivakov et al., 2003).

Vortex jet shapes have recently been analyzed based on the dynamic equation (Bezuglyj et al., 2022). For wide strips (width w much larger than the penetration depth λ), the analytically calculated vortex jet shapes reproduce qualitatively the experiment (Embon et al., 2017). For narrow strips ($\xi \ll w < \lambda$), the discrete TDGL approach reveals dynamic transitions from a vortex chain to a vortex jet and, at $I \lesssim I^* \simeq I_d$, from the vortex jet to a vortex river (Bezuglyj et al., 2022).

Fast vortex dynamics under a microwave ac stimulus

Enhancement of superconductivity at microwaves

Microwave irradiation is being used to control the quantum properties of different systems, ranging from supercurrents in superconductors to mechanical oscillators (Barzanjeh et al., 2022; Bergeret et al., 2010; Clerk et al., 2020; McIver et al., 2012; Palomaki et al., 2013). Nowadays, using nonequilibrium pumping for cooling is a hot topic (Bhadrachalam et al., 2014; Fornieri and Giazotto, 2017; José Martínez-Pérez and Giazotto, 2014; Maillet et al., 2020; Schneider et al., 2020; Uroš et al., 2020). In 1966, microwave stimulated superconductivity (MSSC) was discovered in superconducting bridges (Wyatt et al., 1966) and later confirmed for different type I superconducting systems (Beck et al., 2013; Dayem and Wiegand, 1967; de Visser et al., 2014; Heslinga and Klapwijk, 1993; Pals and Dobben, 1979; Pals and Dobben, 1980; Tolpygo and Tulin, 1983). It was later found that also acoustic waves (Tredwell and Jacobsen, 1975) and tunneling injection currents may, under certain conditions, cause an increase of the gap in the excitation spectrum, the order parameter, the critical current and the critical temperature T_c (Gray, 1981).

The phenomenon of MSSC was explained by Eliashberg (1970) as a consequence of an irradiation-induced redistribution of quasiparticles away from the gap edge. Namely, in the BCS theory, there is a fundamental connection between the gap value Δ and the occupation of the quasiparticle states (Bardeen et al., 1957; Tinkham, 2004). When the temperature is increased from zero, more and more quasiparticles are excited blocking states which were previously available for Cooper pair formation. Ultimately this process leads to the disappearance of superconductivity at T_c. Extraction of quasiparticles leads to enhancement of superconductivity but is elusive to realize. However, there is another possibility. Electron states near the Fermi surface are more important to Cooper pair formation than states further away from it. If a quasiparticle in a state near ε_F is removed to a state with higher energy, the energy gap increases, although the total number of quasiparticles remains constant. This is the essential basis of the E mechanism. In a microwave field, the quasiparticles are "pumped up", away from the gap. Even if the average energy of the quasiparticles increases, the gap is enhanced. Recent reviews on MSSC are given in Klapwijk and de Visser (2020) and Tikhonov et al. (2020).

Condensate and quasiparticles under dc/ac biasing

The vortex state is characterized by a spatially modulated superconducting order parameter which vanishes in the vortex cores and attains a maximal value between them. Accordingly, a type II superconductor can be regarded as a continuum medium consisting of bunches of quasiparticles in the vortex cores surrounded by a bath of the superconducting condensate formed by the superfluid of Cooper pairs. So far there is no available theory addressing the complex interaction of the superimposed dc and microwave currents with the quasiparticles and the condensate at the same time. However, the essential ingredients of this interaction have been studied separately.

The effect of a dc current on the superconducting condensate is well known (Anthore et al., 2003). With an increase of a dc current, the absolute value of the order parameter is decreasing and the peak in the density of states at the edge of the superconducting gap is smeared, see Fig. 5A. This is because of gaining a finite momentum by the Cooper pairs that form a coherent excited state that plays a central role in the explanation of the gauge invariance of the Meissner effect (Anderson, 1958). A general theory of depairing by a microwave field has been formulated recently (Semenov et al., 2016), under the condition of rather small ac

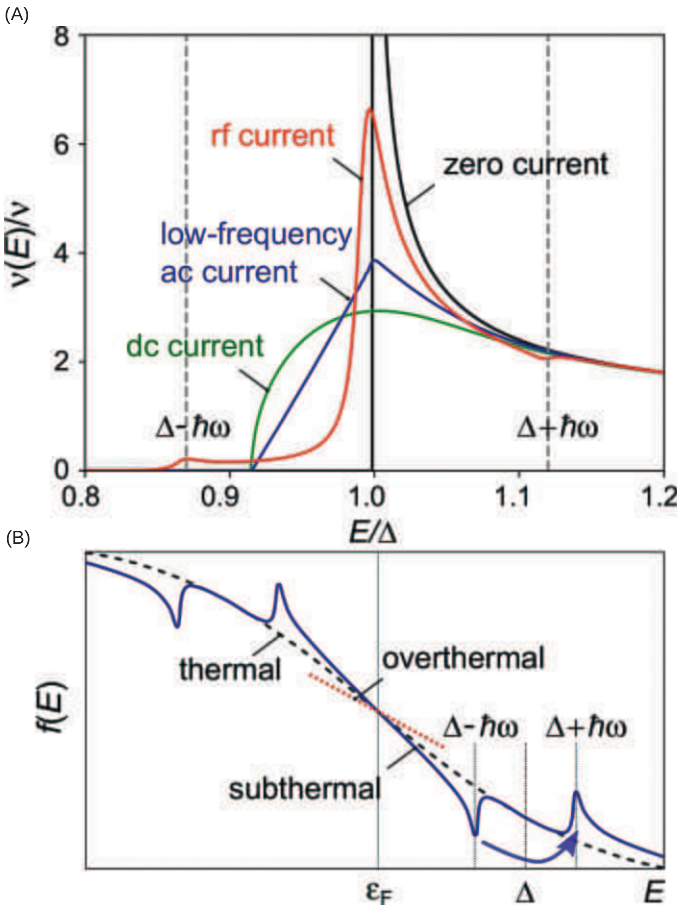

Fig. 5 (A) Schematics of the modification of the electronic distribution function $f(E)$ in the presence of a microwave excitation after (Tikhonov et al., 2018). The redistribution of the quasiparticles between the $\Delta-\hbar\omega$ and $\Delta+\hbar\omega$ states leads to a higher inclination of $f(E)$ at the Fermi energy level ε_F, which can be viewed as an effective "cooling". (B) Time-averaged density of states in a dirty superconductor at low temperature ($T \ll T_c$) under different biasing after (Semenov et al., 2016; Tikhonov et al., 2020). The value of the current or its amplitude is $0.25I_c$.

field amplitudes. It has been shown that the ground state of a superconductor is altered qualitatively in analogy to the depairing due to a dc current. However, in contrast to dc depairing, the density of states acquires steps at multiples of the microwave photon energy and shows an exponential-like tail in the subgap regime (Semenov et al., 2016). Additionally, depending on temperature, one can consider two regimes in which the response of a superconductor is dominated either by the response of the superfluid ($T \leq T_c$) or by the quasiparticles ($T \approx T_c$). It is also known that at $T \approx T_c$, microwave radiation can be absorbed by quasiparticles, leading to a nonequilibrium distribution over the energies (Eliashberg, 1970), see Fig. 5B.

In general, the response of the condensate to an external microwave field becomes apparent via a change of the kinetic impedance (imaginary part of the complex resistivity) while the quasiparticles give rise to the microwave loss (real part of the complex resistivity). The known effects of stimulation of superconductivity by a microwave stimulus in the absence of an external magnetic field include an enhancement of the Ginzburg-Landau depairing current (in narrow channels) implying a transition to a resistive state due to the formation of phase-slip centers (Zolochevskii, 2013) or the Aslamazov-Lempitskii maximum current (in wide films) at which the vortex structure induced by the self-field evolves into the first phase-slip line (Aslamazov and Lempitskii, 1982). In the presence of an external magnetic field inducing vortices in the superconductor, the vortex-induced microwave losses dominate the response of the superconductor (Pompeo and Silva, 2008).

Microwave stimulation in the vortex state

From Fig. 5A it follows that a dc current leads to a smearing of the BCS peak at the gap edge. Further, the presence of vortices leads to a strongly spatially non-uniform order parameter (with normal-state regions inside the vortex cores). Moreover, the motion of current-driven vortices leads to dissipation (Brandt, 1995; Pompeo and Silva, 2008). All together, these circumstances diminish the stimulation effect of the microwave excitation. Nonetheless, in the regime of low vortex densities and for superconductors with rather slow relaxation of nonequilibrium quasiparticles, the stimulation of superconductivity under a microwave ac stimulus can be observed in the presence of vortices (Dobrovolskiy et al., 2019b; Lara et al., 2015).

Note, the dynamics of vortices under a microwave ac stimulus differs qualitatively from the dc-driven vortex motion. Namely, while a moderately strong dc transport current (i.e., when the current-induced Lorentz-type force exceeds the pinning force (Brandt, 1995)) causes a *translational* motion of vortices, a microwave ac current *shakes* the vortices. Accordingly, in the presence of pinning sites, one can distinguish between the low-frequency and high-frequency regimes in the vortex dynamics. Namely, when the ac half-period is long enough, a vortex can move over *many* pinning sites, while in the high-frequency regime a vortex is shaken in vicinity of *one* pinning site. The crossover between the two regimes occurs at the so-called *depinning frequency* f_d (Coffey and Clem, 1991; Dobrovolskiy et al., 2015; Gittleman and Rosenblum, 1966; Pompeo and Silva, 2008; Shklovskij and Dobrovolskiy, 2008; Shklovskij et al., 2014). In the low-frequency regime, the pinning forces dominate and the vortex response is weakly dissipative. By contrast, in the high-frequency regime, the oscillating vortices cease to feel the detail of the pinning potential, the frictional forces prevail, and the response is strongly dissipative. Note, this consideration is justified for short vortices in thin films and it is inapplicable to thick films where long vortices can get elastically distorted extending over many pinning sites (Pathirana and Gurevich, 2021).

The depinning frequency depends on temperature $f_\mathrm{d}(T, H, I) \simeq f_\mathrm{d}(0, H, I)[1-(T/T_c)^4]$ (Alimenti et al., 2020; Zaitsev et al., 2003), magnetic field $f_\mathrm{d}(T, H, I)-f_\mathrm{d}(T, 0, I)[1-(H/H_{c2})^2]$ (Alimenti et al., 2020; Janjušević et al., 2006) and the dc current as $f_\mathrm{d}(T, H, I) \simeq f_\mathrm{d}(T, H, 0)[1-(I/I_\mathrm{d})^m]^n$ with the exponents m between 3/2 and 4 and n between 1/4 and 2/3, depending on the details of the pinning potential (Dobrovolskiy et al., 2017a). At relatively low excitation power levels, for a commensurate vortex lattice in a periodic pinning landscape, ac losses due to ac-driven vortex oscillations are minimal because of the enhanced efficiency of the pinning (Dobrovolskiy et al., 2020a; Dobrovolskiy and Huth, 2015). By contrast, a qualitatively different behavior is observed when the microwave power increases beyond a certain, frequency-dependent power level: the microwave losses are maximal for pinned vortices, and they are minimal for depinned vortices (Dobrovolskiy et al., 2019b; Lara et al., 2015). In this nonlinear regime, the vortices act as "relaxators" rather than rigid "oscillators". Since quasiparticles escape from the vortex cores, their escape can be seen as an effective decrease of the amplitude of the vortex oscillations with increase of the ac frequency.

Braking of instabilities by a microwave stimulus

The FFI onset can be advanced or delayed in the presence of superimposed dc and ac current drives (Cherpak et al., 2014; Dobrovolskiy et al., 2020b). Namely, in the presence of a dc current, an abrupt transition to a high-loss state occurs at lower microwave power levels (Cherpak et al., 2014). The addition of an ac stimulus on top of a dc current allows for tuning the FFI onset (Dobrovolskiy et al., 2020b), see Fig. 6A, depending on the ac power P and frequency f. Thus, when the ac power exceeds some threshold value P_st, at high enough (GHz) ac frequencies the quasilinear flux-flow regime can be extended up to a higher current I^*_mw, whereas the FFI occurs at a smaller I^*_mw in the presence of a low-frequency ac current (Dobrovolskiy et al., 2020b). With a

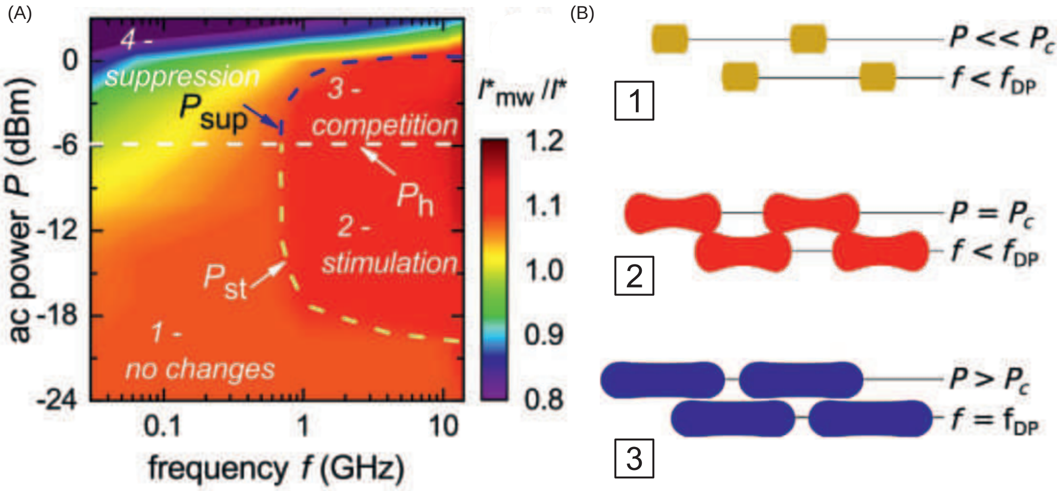

Fig. 6 (A) Evolution of the instability current $f \lesssim f_\mathrm{d}$ for a Nb film at $T = 0.998T_c$ and $H = 10$ mT in a broad range of frequencies and power levels of the ac stimulus. I^*: instability current value without microwave stimulus. (B) The sketch illustrates the overlap of the regions where vortices move under a microwave ac field of different powers and frequencies. As the vortices move, their radii change. This could lead the heated zones to overlap and produce avalanches.
(A) Adapted under the terms of the CC-BY Creative Commons Attribution 4.0 International license Dobrovolskiy OV, González-Ruano C, Lara A, Sachser R, Bevz VM, Shklovskij VA, Bezuglyj AI, Vovk RV, Huth M and Aliev FG (2020b) Moving flux quanta cool superconductors by a microwave breath. *Communications on Physics* **3**(1): 64. doi: 10.1038/s42005-020-0329-z. Copyright 2020, The Authors, published by Springer Nature; (B) Lara A, Aliev FG, Moshchalkov VV and Galperin YM (2017) Thermally driven inhibition of superconducting vortex avalanches. *Physical Review Applied* **8**: 034027. doi: 10.1103/PhysRevApplied.8.034027. Copyright 2017, American Physical Society.

further increase of the ac power, the heating will dominate the cooling effect and the FFI will occur at a smaller I^{*}_{mw}. This behavior can be explained, qualitatively, based on a model of "breathing mobile hot spots", implying a competition of heating and cooling of quasiparticles along the trajectories of moving fluxons whose core sizes vary in time. This breathing mode appears owing to the variation of the vortex core sizes in time due to the periodically modulated quasiparticle escape from the cores. Accordingly, the strong oscillations of vortices lead to the formation of "clouds" of quasiparticles around the vortex cores, whose relaxation takes place in a larger volume as compared to the non-excited case. Thus, dissipation is decreasing due to the combined effects of the redistribution of quasiparticles away from the gap edge via the Eliashberg mechanism and the relaxation of the quasiparticles in larger volumes around the vortex cores. A theory of MSSC at high vortex velocities is yet to be elaborated.

Instabilities can also occur in superconductors when the flux is getting redistributed upon temperature or magnetic field variation (Altshuler and Johansen, 2004; Aranson et al., 2005; Colauto et al., 2021; Mints and Rakhmanov, 1981). Herewith, vortex penetration may occur either smoothly or in sudden bursts, giving rise to *thermomagnetic instabilities*. In the case of smooth penetration, the flux density inside the superconductor changes gradually, being described by a *critical state model* (Bean, 1962; Kim et al., 1963; Zeldov et al., 1994). However, when the penetration is abrupt, narrow branches of flux, in the form of dendrites, invade the sample. The critical state model is no longer appropriate to describe this case.

In a typical critical state type of flux distribution, millions of vortices self-organize, under the competing vortex-vortex repulsion, Lorentz and pinning forces. This delicate balance results in metastable states between which sudden flux redistributions occur. These *flux avalanches* occur typically during a slow ramping of the applied magnetic field, and at temperatures below a certain fraction of T_{c}. The flux patterns are never reproduced when experiments are repeated, thus ruling out possible explanations based on material defects guiding the flux motion (Colauto et al., 2021). The thermomagnetic instability or flux jumping arises because of two fundamental reasons (Denisov et al., 2006): (i) motion of magnetic flux releases energy, and hence increases the local temperature; (ii) the temperature rise decreases flux pinning, and hence facilitates the flux motion. This positive feedback can result in thermal runaways and global flux redistributions jeopardizing superconducting devices.

According to the model based on thermomagnetic instabilities (Rakhmanov et al., 2004), an avalanche is triggered by a thermal fluctuation (hot spot), which facilitates more flux motion toward the hot place, with a subsequent heat release. Under quasi-equilibrium conditions, the avalanches can also be triggered by microwave pulses (Cuadra-Solis et al., 2013) or ac signals at near resonant frequencies of superconducting cavities (Ghigo et al., 2007). Under a broadband microwave field sweep, flux avalanches are triggered at different depinning frequencies due the distribution in strength of individual vortex pinning sites (Awad et al., 2011).

At I^{*}_{mw}, flux avalanches exhibit a thermally driven behavior since higher temperatures facilitate the entrance of magnetic flux and enhance the vortex mobility. Accordingly, the critical microwave power P_{c} for triggering an avalanche monotonously decreases with approaching T_{c}. However, at $f \simeq f_{\mathrm{d}}$, the behavior of $P_{\mathrm{c}}(T)$ inverts, demonstrating a thermally driven avalanche *inhibition* (Lara et al., 2017). This effect can be understood as a consequence of the dependence of the vortex core size on P and f. Namely, at $f \lessapprox f_{\mathrm{d}}$, the LO effect manifests itself only in the regions of maximal velocity (i.e., close to displacement minima), see panel 1 in Fig. 6B. On the other hand, at $f \simeq f_{\mathrm{d}}$, the vortices become more mobile. As a result, the LO reduction of the vortex core manifests itself during the whole displacement cycle, see panel 2 in Fig. 6B. Below f_{d} and at low P, local "normal" regions created by the driven vortices do not overlap and are not sufficient to trigger the avalanche process.

Increasing the microwave power below f_{d} enhances the absolute changes in the vortex core size, inducing the overlap between different extended core areas and triggering the avalanche at $P \simeq P_{\mathrm{c}}$, see panel 3 in Fig. 6B. This process is thermally activated since the vortex diameter strongly increases as $T \to T_{\mathrm{c}}$. However, at $f \simeq f_{\mathrm{d}}$ and in the temperature region where vortices become depinned, the LO effect reduces the vortex core ending up in only a small variation in the vortex core size during periodically driven motion. This reduces the probability of the overlap between normal regions and, therefore, the avalanche is triggered at higher microwave powers for a given temperature (Lara et al., 2017).

Future directions

Superconductivity in curved 3D nanoarchitectures

3D nanoarchitectures have become of increasing importance across various domains of science and technology (Fomin, 2018; Fomin, 2021; Makarov et al., 2022), including magnetism (Fernández-Pacheco et al., 2017; Skjærvø et al., 2020), photonics (von Freymann et al., 2010), magnonics (Gubbiotti, 2019) and plasmonics (Winkler et al., 2017). From the applications viewpoint, the extension of nanoscale superconductors into the third dimension allows for the full-vector-field sensing in quantum interferometry (Martínez-Pérez et al., 2018), noise-equivalent power reduction in bolometry (Lösch et al., 2019) and reduction of footprints of fluxonic devices (Fourie et al., 2011). Extending quasi-1D or -2D superconductor manifolds into the third dimension allows for their thermal decoupling from the substrate and the development of multi-terminal devices and circuits with complex interconnectivity. Herewith, curved geometries bring about the smoothness of conjunctions, which allows for avoiding undesired weak links at sharp turns (Porrati et al., 2019) and minimizing current-crowding effects (Clem and Berggren, 2011). The complex interplay between Meissner screening currents, Abrikosov vortices and slips of the phase of the superconducting order parameter in curved 3D nanoarchitectures gives rise to topological modes which do not occur in planar 2D films (Fomin and Dobrovolskiy, 2022). Nowadays, topological transitions between the different regimes in the vortex and phase-slip dynamics in curved 3D nanoarchitectures are a subject of extensive investigations (Córdoba et al., 2019; Fomin et al., 2022; Fomin et al., 2012; Fomin et al., 2020). The stability of these regimes under intense dc transport currents and high ac frequencies requires experimental and theoretical exploration.

Cryogenic magnonics and magnon fluxonics

The interplay between the fundamental excitations in superconducting and magnetic systems has recently given birth to the research domains of cryogenic magnonics and magnon fluxonics (Dobrovolskiy and Chumak, 2022; Dobrovolskiy et al., 2019c; Golovchanskiy et al., 2019; Golovchanskiy et al., 2018). Magnonics is one of the most rapidly growing research fields in modern magnetism (Barman et al., 2021). It is concerned with the dynamics of spin waves (and their quanta—magnons), which are precessional excitations of ordered spins in magnetic materials, and their use for wave-based information processing (Chumak et al., 2022). In this regard, Meissner screening currents offer interesting possibilities to control the magnetization dynamics in superconductor-based hybrids at low temperatures (Golovchanskiy et al., 2019; Golovchanskiy et al., 2018). Furthermore, the periodic modulation of the local magnetic field emanating from the vortex cores induces Bloch-like bandgaps in the magnon frequency spectrum while a current-driven vortex lattice acts as a moving Bragg grating (Barnes et al., 1996), leading to Doppler shifts of the magnon bandgap frequencies (Dobrovolskiy and Chumak, 2022; Dobrovolskiy et al., 2019c).

The fast motion of the vortex lattice opens up new prospects for the magnon-fluxon interaction: the phenomenon of Cherenkov radiation of magnons (Bespalov et al., 2014; Bulaevskii et al., 2005; Shekhter et al., 2011), when the vortex lattice velocity reaches the phase velocity of the spin wave. The experimentally observed magnon emission is unidirectional (spin wave propagates in the direction of motion of the vortex lattice), monochromatic (magnon wavelength is equal to the vortex lattice parameter), and coherent (spin-wave phase is self-locked due to quantum interference with eddy currents in the superconductor) (Dobrovolskiy et al., 2021). The magnon radiation is accompanied by a magnon Shapiro step in the I–V curve of the superconductor, reduces the dissipation (Bespalov et al., 2014; Bulaevskii et al., 2005; Shekhter et al., 2011), and inhibits the FFI onset (Dobrovolskiy et al., 2021). Thus, the generation of collective modes by a fast-moving vortex lattice can be viewed as an interesting approach for the inhibition of FFI and studies of fast vortex dynamics. Further research should address magnetic flux transport mechanisms in trancient Abrikosov-Josephson vortex regimes (Embon et al., 2017) and ultra-fast vortex motion in systems exhibiting a superconductor-insulator transition (Porrati et al., 2022).

Conclusion

Summing up, the exploration of ultrafast vortex dynamics in superconductors has recently turned into a major research avenue. These studies are motivated by the enhancement of current-carrying capacity of superconductors, reduction of microwave loss therein, and improvement of superconducting single-photon detectors. From the viewpoint of basic research, the fast-moving ensemble of quantized magnetic flux lines entails emerging nonequilibrium phenomena and complex interactions, and it allows for the generation of collective modes in superconductor-based systems. It is anticipated that in the years to come, research along these lines will fuel the domain of vortex matter under nonequilibrium conditions and will lead to the development of novel applications.

Acknowledgments

This work is based on the research funded by the German Research Foundation (DFG) through Grant Nos. DO1511/2-1, DO1511/2-4, DO1511/3-1 and the Austrian Science Fund (FWF) through Grant Nos. I 4889 (CurviMag) and I 6079 (FluMag). Further, support by the European Cooperation in Science and Technology via COST Actions CA16218 (NANOCOHYBRI), CA19108 (HiSCALE), and CA21144 (SUPERQUMAP) is acknowledged.

References

Abrikosov AA (1988) *Fundamentals of the Theory of Metals*, North-Holland, Amsterdam.

Adami O-A, Cerbu D, Cabosart D, Motta M, Cuppens J, Ortiz WA, Moshchalkov VV, Hackens B, Delamare R, Van de Vondel J, and Silhanek AV (2013) Current crowding effects in superconducting corner-shaped Al microstrips. *Applied Physics Letters* 102(5): 052603 1–5. https://doi.org/10.1063/1.4790625.

Adami O-A, Jelic ZL, Xue C, Abdel-Hafiez M, Hackens B, Moshchalkov VV, Milosevic MV, Van de Vondel J, and Silhanek AV (2015) Onset, evolution, and magnetic braking of vortex lattice instabilities in nanostructured superconducting films. *Physical Review B* 92: 134506. https://doi.org/10.1103/PhysRevB.92.134506.

Aladyshkin A, Mel'nikov AS, Shereshevsky IA, and Tokman ID (2001) What is the best gate for vortex entry into type-II superconductor? *Physica C* 361(1): 67–72.

Alimenti A, Pompeo N, Torokhtii K, Spina T, Flükiger R, Muzzi L, and Silva E (2020) Microwave measurements of the high magnetic field vortex motion pinning parameters in Nb_3Sn. *Superconductor Science and Technology* 34(1): 014003. https://doi.org/10.1088/1361-6668/abc05d.

Altshuler E and Johansen TH (2004) Colloquium: Experiments in vortex avalanches. *Reviews of Modern Physics* 76: 471–487. https://doi.org/10.1103/RevModPhys.76.471.

Anderson PW (1958) Coherent excited states in the theory of superconductivity: Gauge invariance and the Meissner effect. *Physics Review* 110: 827–835. https://doi.org/10.1103/PhysRev.110.827.

Andreev AF (1964) Thermal conductivity of the intermediate state of superconductors. *Soviet Physics - JETP* 19: 1228.

Anthore A, Pothier H, and Esteve D (2003) Density of states in a superconductor carrying a supercurrent. *Physical Review Letters* 90: 127001. https://doi.org/10.1103/PhysRevLett.90.127001.

Aranson IS, Gurevich A, Welling MS, Wijngaarden RJ, Vlasko-Vlasov VK, Vinokur VM, and Welp U (2005) Dendritic flux avalanches and nonlocal electrodynamics in thin superconducting films. *Physical Review Letters* 94: 037002. https://doi.org/10.1103/PhysRevLett.94.037002.

Aronov AG and Spivak BZ (1978) *Soviet Physics - JETP* 50: 328.

Aslamazov LG and Lempitskii SV (1982) Superconductivity stimulation by a microwave field in superconductor-normal metal-superconductor junctions. *Zhurnal Eksperimental'noi i Teoreticheskoi Fiziki* 82: 1671–1678.

Attanasio C and Cirillo C (2012) Quasiparticle relaxation mechanisms in superconductor/ferromagnet bilayers. *Journal of Physics. Condensed Matter* 24(8), 083201. http://stacks.iop.org/0953-8984/24/i=8/a=083201.

Awad AA, Aliev FG, Ataklti GW, Silhanek A, Moshchalkov VV, Galperin YM, and Vinokur V (2011) Flux avalanches triggered by microwave depinning of magnetic vortices in Pb superconducting films. *Physical Review B* 84: 224511. https://doi.org/10.1103/PhysRevB.84.224511.

Babic D, Bentner J, Sürgers C, and Strunk C (2004) Flux-flow instabilities in amorphous Nb$_{0.7}$Ge$_{0.3}$ microbridges. *Physical Review B* 69: 092510 1–4. https://doi.org/10.1103/PhysRevB.69.092510.

Bardeen J and Stephen MJ (1965) Theory of the motion of vortices in superconductors. *Physics Review* 140: A1197–A1207. https://doi.org/10.1103/PhysRev.140.A1197.

Bardeen J, Cooper LN, and Schrieffer JR (1957) Microscopic theory of superconductivity. *Physics Review* 106: 162–164. https://doi.org/10.1103/PhysRev.106.162.

Barman A, et al. (2021) The 2021 magnonics roadmap. *Journal of Physics. Condensed Matter* 33(41): 413001. https://doi.org/10.1088/1361-648x/abec1a.

Barnes SE, Cohn JL, and Zuo F (1996) The possibility of flux flow spectroscopy. *Physical Review Letters* 77: 3252–3255. https://doi.org/10.1103/PhysRevLett.77.3252.

Barzanjeh S, Xuereb A, Gröblacher S, Paternostro M, Regal CA, and Weig EM (2022) Optomechanics for quantum technologies. *Nature Physics* 18(1): 15–24. https://doi.org/10.1038/s41567-021-01402-0.

Bean CP (1962) Magnetization of hard superconductors. *Physical Review Letters* 8: 250–253. https://doi.org/10.1103/PhysRevLett.8.250.

Beck M, Rousseau I, Klammer M, Leiderer P, Mittendorff M, Winnerl S, Helm M, Gol'tsman GN, and Demsar J (2013) Transient increase of the energy gap of superconducting NbN thin films excited by resonant narrow-band terahertz pulses. *Physical Review Letters* 110: 267003. https://doi.org/10.1103/PhysRevLett.110.267003.

Bergeret FS, Virtanen P, Heikkilä TT, and Cuevas JC (2010) Theory of microwave-assisted supercurrent in quantumpoint contacts. *Physical Review Letters* 105: 117001. https://doi.org/10.1103/PhysRevLett.105.117001.

Bespalov AA, Mel'nikov AS, and Buzdin AI (2014) Magnon radiation by moving Abrikosov vortices in ferromagnetic superconductors and superconductor-ferromagnet multilayers. *Physical Review B* 89: 054516. https://doi.org/10.1103/PhysRevB.89.054516.

Bezuglyj AI and Shklovskij VA (1984) Thermal domains in inhomogeneous current-carrying superconductors. current-voltage characteristics and dynamics of domain formation after current jumps. *Journal of Low Temperature Physics* 57(3): 227–247. https://doi.org/10.1007/BF00681190.

Bezuglyj A and Shklovskij V (1992) Effect of self-heating on flux flow instability in a superconductor near T_c. *Physica C* 202(314): 234. http://www.sciencedirect.com/science/article/pii/0921453492901659.

Bezuglyj AI, Shklovskij VA, Vovk RV, Bevz VM, Huth M, and Dobrovolskiy OV (2019) Local flux-flow instability in superconducting films near T_c. *Physical Review B* 99: 174518. https://doi.org/10.1103/PhysRevB.99.174518.

Bhadrachalam P, Subramanian R, Ray V, Ma L-C, Wang W, Kim J, Cho K, and Koh SJ (2014) Energy-filtered cold electron transport at room temperature. *Nature Communications* 5(1): 4745. https://doi.org/10.1038/ncomms5745.

Blatter G, Feigel'man MV, Geshkenbein VB, Larkin AI, and Vinokur VM (1994) Vortices in high-temperature superconductors. *Reviews of Modern Physics* 66: 1125–1388. https://doi.org/10.1103/RevModPhys.66.1125.

Blonder GE, Tinkham M, and Klapwijk TM (1982) Transition from metallic to tunneling regimes in superconducting microconstrictions: Excess current, charge imbalance, and supercurrent conversion. *Physical Review B* 25: 4515–4532. https://doi.org/10.1103/PhysRevB.25.4515.

Brandt EH (1995) The flux-line lattice in superconductors. *Reports on Progress in Physics* 58(11): 1465–1594. http://stacks.iop.org/0034-4885/58/i=11/a=003.

Budinska B, Aichner B, Vodolazov DY, Mikhailov MY, Porrati F, Huth M, Chumak AV, Lang W, and Dobrovolskiy OV (2022) Rising speed limits for fluxons via edge-quality improvement in wide MoSi thin films. *Physical Review Applied* 17: 034072. https://doi.org/10.1103/PhysRevApplied.17.034072.

Buh J, Kabanov V, Baranov V, Mrzel A, Kovic A, and Mihailovic D (2015) Control of switching between metastable superconducting states in d-MoN nanowires. *Nature Communications* 6: 10250. https://doi.org/10.1038/ncomms10250.

Bulaevskii LN and Chudnovsky EM (2005) Sound generation by the vortex flow in type-II superconductors. *Physical Review B* 72: 094518. https://doi.org/10.1103/PhysRevB.72.094518.

Bulaevskii LN and Chudnovsky EM (2006) Electromagnetic radiation from vortex flow in type-II superconductors. *Physical Review Letters* 97: 197002. https://doi.org/10.1103/PhysRevLett.97.197002.

Bulaevskii LN, Hruška M, and Maley MP (2005) Spectroscopy of magnetic excitations in magnetic superconductors using vortex motion. *Physical Review Letters* 95: 207002. https://doi.org/10.1103/PhysRevLett.95.207002.

Caputo M, Cirillo C, and Attanasio C (2017) NbRe as candidate material for fast single photon detection. *Applied Physics Letters* 111(19), 192601. https://doi.org/10.1063/1.4997675.

Charaev I, Morimoto Y, Dane A, Agarwal A, Colangelo M, and Berggren KK (2020) Large-area microwire MoSi single-photon detectors at 1550 nm wavelength. *Applied Physics Letters* 116(24), 242603. https://doi.org/10.1063/5.0005439.

Cherpak NT, Lavrinovich AA, Gubin AI, and Vitusevich SA (2014) Direct-current-assisted microwave quenching of YBa$_2$Cu$_3$O$_{7-x}$ coplanar waveguide to a highly dissipative state. *Applied Physics Letters* 105(2), 022601. https://doi.org/10.1063/1.4890123.

Chiles J, Buckley SM, Lita A, Verma VB, All-maras J, Korzh B, Shaw MD, Shainline JM, Mirin RP, and Nam SW (2020) Superconducting microwire detectors based on WSi with single-photon sensitivity in the near-infrared. *Applied Physics Letters* 116(24), 242602. https://doi.org/10.1063/5.0006221.

Chumak AV, et al. (2022) Roadmap on spin-wave computing. In: *IEEE Transactions on Magnetics xx, xx* .

Cirillo C, Chang J, Caputo M, Los JWN, Dorenbos S, Esmaeil Zadeh I, and Attanasio C (2020) Superconducting nanowire single photon detectors based on disordered NbRe films. *Applied Physics Letters* 117(17), 172602. https://doi.org/10.1063/5.0021487.

Cirillo C, Granata V, Spuri A, Di Bernardo A, and Attanasio C (2021) NbReN: A disordered superconductor in thin film form for potential application as superconducting nanowire single photon detector. *Physical Review Materials* 5: 085004. https://doi.org/10.1103/PhysRevMaterials.5.085004.

Clem JR and Berggren KK (2011) Geometry-dependent critical currents in superconducting nanocircuits. *Physical Review B* 84: 174510. https://doi.org/10.1103/PhysRevB.84.174510.

Clerk AA, Lehnert KW, Bertet P, Petta JR, and Nakamura Y (2020) Hybrid quantum systems with circuit quantum electrodynamics. *Nature Physics* 16(3): 257–267. https://doi.org/10.1038/s41567-020-0797-9.

Coffey MW and Clem JR (1991) Unified theory of effects of vortex pinning and flux creep upon the rf surface impedance of type-II superconductors. *Physical Review Letters* 67: 386–389. https://doi.org/10.1103/PhysRevLett.67.386.

Colauto F, Motta M, and Ortiz WA (2021) Controlling magnetic flux penetration in low-Tc superconducting films and hybrids. *Superconductor Science and Technology* 34(1), 013002. https://doi.org/10.1088/1361-6668/abac1e.

Córdoba R, Mailly D, Rezaev RO, Smirnova EI, Schmidt OG, Fomin VM, Zeitler U, Guillamón I, Suderow H, and De Teresa JM (2019) Three-dimensional superconducting nanohelices grown by He$^+$-focused-ion-beam direct writing. *Nano Letters* 19: 8597.

Cuadra-Solis P-D-J, Hernandez JM, García-Santiago A, Tejada J, Vanacken J, and Moshchalkov VV (2013) Avalanche-like vortex penetration driven by pulsed microwave fields in an epitaxial LaSrCuO thin film. *Journal of Applied Physics* 114(23), 233902. https://doi.org/10.1063/1.4848997.

Cuadra-Solis P-D-J, Garcia-Santiago A, Hernandez JM, Tejada J, Vanacken J, and Moshchalkov VV (2014) Observation of commensurability effects in a patterned thin superconducting Pb film using microwave reflection spectrometry. *Physical Review B* 89: 054517. https://doi.org/10.1103/PhysRevB.89.054517.

Dayem AH and Wiegand JJ (1967) Behavior of thin-film superconducting bridges in a microwave field. *Physics Review* 155: 419–428. https://doi.org/10.1103/PhysRev.155.419.

de Visser PJ, Goldie DJ, Diener P, Withington S, Baselmans JJA, and Klapwijk TM (2014) Evidence of a nonequilibrium distribution of quasiparticles in the microwave response of a superconducting aluminum resonator. *Physical Review Letters* 112: 047004. https://doi.org/10.1103/PhysRevLett.112.047004.

Dean CL and Kunchur MN (2018) Dissipative-regime measurements as a tool for confirming and characterizing near-room-temperature superconductivity. *Quantum Studies: Mathematics and Foundations* 5(1): 111–121. https://doi.org/10.1007/s40509-017-0123-0.

Denisov DV, Shantsev DV, Galperin YM, Choi E-M, Lee H-S, Lee S-I, Bobyl AV, Goa PE, Olsen AAF, and Johansen TH (2006) Onset of dendritic flux avalanches in superconducting films. *Physical Review Letters* 97: 077002 1–4. https://doi.org/10.1103/PhysRevLett.97.077002.

Dobrovolskiy OV and Chumak AV (2022) Nonreciprocal magnon fluxonics upon ferromagnet/superconductor hybrids. *Journal of Magnetism and Magnetic Materials* 543: 168633. https://www.sciencedirect.com/science/article/pii/S0304885321008726.

Dobrovolskiy OV and Huth M (2012) Crossover from dirty to clean superconducting limit in dc magnetron-sputtered thin Nb films. *Thin Solid Films* 520: 5985–5990. http://www.sciencedirect.com/science/article/pii/S0040609012005718.

Dobrovolskiy OV and Huth M (2015) Dual cut-off direct current-tunable microwave low-pass filter on superconducting Nb microstrips with asymmetric nanogrooves. *Applied Physics Letters* 106: 142601 1–5. https://doi.org/10.1063/1.4917229.

Dobrovolskiy OV, Huth M, and Shklovskij VA (2010) Anisotropic magnetoresistive response in thin Nb films decorated by an array of Co stripes. *Superconductor Science and Technology* 23(12): 125014 1–5. https://doi.org/10.1088/0953-2048/23/12/125014.

Dobrovolskiy OV, Begun E, Huth M, and Shklovskij VA (2012) Electrical transport and pinning properties of Nb thin films patterned with focused ion beam-milled washboard nanostructures. *New Journal of Physics* 14: 113027 1–27. http://stacks.iop.org/1367-2630/14/i=11/a=113027.

Dobrovolskiy OV, Huth M, and Shklovskij VA (2015) Alternating current-driven microwave loss modulation in a fluxonic metamaterial. *Applied Physics Letters* 107: 162603 1–5. http://scitation.aip.org/content/aip/journal/apl/107/16/10.1063/1.4934487.

Dobrovolskiy OV, Huth M, Shklovskij V, and Vovk RV (2017a) Mobile fluxons as coherent probes of periodic pinning in superconductors. *Scientific Reports* 7: 13740. https://doi.org/10.1038/s41598-017-14232-z.

Dobrovolskiy OV, Shklovskij VA, Hanefeld M, Zörb M, Köhs L, and Huth M (2017b) Pinning effects on flux flow instability in epitaxial Nb thin films. *Superconductor Science and Technology* 30(8): 085002. http://stacks.iop.org/0953-2048/30/i=8/a=085002.

Dobrovolskiy OV, Bevz VM, Mikhailov MY, Yuzephovich OI, Shklovskij VA, Vovk RV, Tsindlekht MI, Sachser R, and Huth M (2018) Microwave emission from superconducting vortices in Mo/Si superlattices. *Nature Communications* 9(1): 4927. https://doi.org/10.1038/s41467-018-07256-0.

Dobrovolskiy OV, Bevz VM, Begun E, Sachser R, Vovk RV, and Huth M (2019a) Fast dynamics of guided magnetic flux quanta. *Physical Review Applied* 11: 054064. https://doi.org/10.1103/PhysRevApplied.11.054064.

Dobrovolskiy OV, Sachser R, Bevz VM, Lara A, Aliev FG, Shklovskij VA, Bezuglyj A, Vovk RV, and Huth M (2019b) Reduction of microwave loss by mobile fluxons in grooved Nb films. *Physica Status Solidi (RRL)* 13: 1800223. https://doi.org/10.1002/pssr.201800223.

Dobrovolskiy OV, Sachser R, Brächer T, Böttcher T, Kruglyak VV, Vovk RV, Shklovskij VA, Huth M, Hillebrands B, and Chumak AV (2019c) Magnon-fluxon interaction in a ferromagnet/superconductor heterostructure. *Nature Physics* 15: 477. https://www.nature.com/articles/s41567-019-0428-5.

Dobrovolskiy O, Begun E, Bevz V, Sachser R, and Huth M (2020a) Upper frequency limits for vortex guiding and ratchet effects. *Physical Review Applied* 13: 024012. https://doi.org/10.1103/PhysRevApplied.13.024012.

Dobrovolskiy OV, González-Ruano C, Lara A, Sachser R, Bevz VM, Shklovskij VA, Bezuglyj AI, Vovk RV, Huth M, and Aliev FG (2020b) Moving flux quanta cool superconductors by a microwave breath. *Communications on Physics* 3(1): 64. https://doi.org/10.1038/s42005-020-0329-z.

Dobrovolskiy OV, Vodolazov DY, Porrati F, Sachser R, Bevz VM, Mikhailov MY, Chumak AV, and Huth M (2020c) Ultra-fast vortex motion in a direct-write Nb-C superconductor. *Nature Communications* 11(1): 3291. https://doi.org/10.1038/s41467-020-16987-y.

Dobrovolskiy OV, Wang Q, Vodolazov DY, Budinska B, Sachser R, Chumak A, Huth M, and Buzdin AI (2021) Cherenkov radiation of spin waves by ultra-fast moving magnetic flux quanta. *arXiv:2103.10156* https://arxiv.org/abs/2103.10156.

Doettinger SG, Huebener RP, Gerdemann R, Kühle A, Anders S, Träuble TG, and Villégier JC (1994) Electronic instability at high flux-flow velocities in high-T_c superconducting films. *Physical Review Letters* 73: 1691–1694. https://doi.org/10.1103/PhysRevLett.73.1691.

Doettinger S, Huebener R, and Kühle A (1995) Electronic instability during vortex motion in cuprate superconductors regime of low and high magnetic fields. *Physica C* 251(3): 285–289. http://www.sciencedirect.com/science/article/pii/0921453495004114.

Doettinger SG, Kittelberger S, Huebener RP, and Tsuei CC (1997) Quasiparticle energy relaxation in the cuprate superconductors. *Physical Review B* 56: 14157–14162. https://doi.org/10.1103/PhysRevB.56.14157.

Eliashberg GM (1970) Film superconductivity stimulated by a high-frequency field. *JETP Letters* 11: 186. http://www.jetpletters.ac.ru/ps/1716/article_26086.pdf.

Bezuglyj AI, Shklovskij VA, Budinska B, Aichner B, Bevz VM, Mikhailov MY, Vodolazov DY, Lang W, and Dobrovolskiy OV (2022) Vortex jets generated by edge defects in current-carrying superconductor thin strips. *Physical Review B* 105: 214507. https://doi.org/10.1103/PhysRevB.105.214507.

Eliashberg GM and Ivlev BI (1986) *Nonequilibrium superconductivity, North-Holland, Amsterdam*. p. 211.

Embon L, Anahory Y, Jelic ZL, Lachman EO, Myasoedov Y, Huber ME, Mikitik GP, Silhanek AV, Milosevic MV, Gurevich A, and Zeldov E (2017) Imaging of super-fast dynamics and flow instabilities of superconducting vortices. *Nature Communications* 8(1): 85. https://doi.org/10.1038/s41467-017-00089-3.

Fernández-Pacheco A, Streubel R, Fruchart O, Hertel R, Fischer P, and Cowburn RP (2017) Three-dimensional nanomagnetism. *Nature Communications* 8: 15756. https://doi.org/10.1038/ncomms15756.

Fomin VM (2018) *Topology-Driven Effects in Advanced Nanoarchitectures*. Springer International Publishing195–220. https://doi.org/10.1007/978-3-319-90481-8-10.

Fomin VM (2021) *Self-Rolled Micro- and Nanoarchitectures: Effects of Topology and Geometry*. Berlin/Boston: De Gruyter.

Fomin VM and Dobrovolskiy OV (2022) A perspective on superconductivity in curved 3D nanoarchitectures. *Applied Physics Letters* 120(9): 090501. https://doi.org/10.1063/5.0085095.

Fomin VM, Rezaev R, and Dobrovolskiy OV (2022) Topological transitions in ac/dc-driven superconductor nanotubes. *Scientific Reports* 12: 10069. https://doi.org/10.1038/s41598-022-13543-0.

Fomin VM, Rezaev RO, and Schmidt OG (2012) Tunable generation of correlated vortices in open superconductor tubes. *Nano Letters* 12: 1282. https://doi.org/10.1021/nl203765f.

Fomin VM, Rezaev RO, Smirnova EI, and Schmidt OG (2020) Topological transitions in superconductor nanomembranes in a magnetic field with submicron inhomogeneity under a strong transport current. *Communications on Physics* 3: 144. https://www.nature.com/articles/s42005-020-00411-4.

Fornieri A and Giazotto F (2017) Towards phase-coherent caloritronics in superconducting circuits. *Nature Nanotechnology* 12(10): 944–952. https://doi.org/10.1038/nnano.2017.204.

Fourie CJ, Wetzstein O, Ortlepp T, and Kunert J (2011) Three-dimensional multi-terminal superconductive integrated circuit inductance extraction. *Superconductor Science and Technology* 24(12): 125015. https://doi.org/10.1088/0953-2048/24/12/125015.

Ghigo G, Laviano F, Gozzelino L, Gerbaldo R, Mezzetti E, Monticone E, and Portesi C (2007) Evidence of RF-driven dendritic vortex avalanches in MgB_2 microwave resonators. *Journal of Applied Physics* 102(11): 113901. https://doi.org/10.1063/1.2816257.

Gittleman JI and Rosenblum B (1966) Radio-frequency resistance in the mixed state for subcritical currents. *Physical Review Letters* 16: 734–736. https://doi.org/10.1103/PhysRevLett.16.734.

Glazman LI (1986) Vortex induced transverse voltage within film. *Journal of Low Temperature Physics* 12: 389.

Golovchanskiy IA, Abramov NN, Stolyarov VS, Bolginov VV, Ryazanov VV, Golubov AA, and Ustinov AV (2018) Ferromagnet/superconductor hybridization for magnonic applications. *Advanced Functional Materials* 28(33): 1802375. https://doi.org/10.1002/adfm.201802375.

Golovchanskiy IA, Abramov NN, Pfirrmann M, Piskor T, Voss JN, Baranov DS, Hovhannisyan RA, Stolyarov VS, Dubs C, Golubov AA, Ryazanov VV, Ustinov AV, and Weides M (2019) Interplay of magnetization dynamics with a microwave waveguide at cryogenic temperatures. *Physical Review Applied* 11: 044076. https://doi.org/10.1103/PhysRevApplied.11.044076.

Gray KE (ed.) (1981) *Nonequilibrium Superconductivity, Phonons, and Kapitza Boundaries*. New York/London: Plenum Press.

Grimaldi G, Leo A, Cirillo C, Attanasio C, Nigro A, and Pace S (2009a) Magnetic field and temperature dependence of the critical vortex velocity in type-II superconducting films. *Journal of Physics: Condensed Matter* 21(25): 254207. http://stacks.iop.org/0953-8984/21/i=25/a=254207.

Grimaldi G, Leo A, Nigro A, Pace S, and Huebener RP (2009b) Dynamic ordering and instability of the vortex lattice in Nb films exhibiting moderately strong pinning. *Physical Review B* 80: 144521 1–10 https://doi.org/10.1103/PhysRevB.80.144521.

Grimaldi G, Leo A, Zola D, Nigro A, Pace S, Laviano F, and Mezzetti E (2010) Evidence for low-field crossover in the vortex critical velocity of type-II superconducting thin films. *Physical Review B* 82: 024512. https://doi.org/10.1103/PhysRevB.82.024512.

Grimaldi G, Leo A, Cirillo C, Casaburi A, Cristiano R, Attanasio C, Nigro A, Pace S, and Huebener R (2011) Non-linear flux flow resistance of type-II superconducting films. *Journal of Superconductivity and Novel Magnetism* 24(1–2): 81–87. https://doi.org/10.1007/s10948-010-0902-x.

Grimaldi G, Leo A, Nigro A, Silhanek AV, Verellen N, Moshchalkov VV, Milosevic MV, Casaburi A, Cristiano R, and Pace S (2012) Controlling flux flow dissipation by changing flux pinning in superconducting films. *Applied Physics Letters* 100(20). http://scitation.aip.org/content/aip/journal/apl/100/20/10.1063/1.4718309.

Grimaldi G, Leo A, Sabatino P, Carapella G, Nigro A, Pace S, Moshchalkov VV, and Silhanek AV (2015) Speed limit to the Abrikosov lattice in mesoscopic superconductors. *Physical Review B* 92: 024513. https://doi.org/10.1103/PhysRevB.92.024513.

Gubbiotti G (ed.) (2019) *Three-Dimensional Magnonics: Layered, Micro- and Nanostructures*. Jenny Stanford Publishing.

Gurevich A (2014) Reduction of dissipative nonlinear conductivity of superconductors by static and microwave magnetic fields. *Physical Review Letters* 113: 087001. https://doi.org/10.1103/PhysRevLett.113.087001.

Gurevich AV and Mints RG (1984) *Soviet Physics Uspekhi* 27: 19.

Heslinga DR and Klapwijk TM (1993) Enhancement of superconductivity far above the critical temperature in double-barrier tunnel junctions. *Physical Review B* 47: 5157–5164. https://doi.org/10.1103/PhysRevB.47.5157.

Huebener RP (2019) The abrikosov vortex lattice: Its discovery and impact. *Journal of Superconductivity and Novel Magnetism* 32(3): 475–481. https://doi.org/10.1007/s10948-018-4916-0.

Huebener RP, Stoll OM, and Kaiser S (1999) Electronic vortex structure and quasiparticle scattering in the cuprate superconductor $Nd_{2-x}Ce_xCuO_y$. *Physical Review B* 59: R3945–R3947. https://doi.org/10.1103/PhysRevB.59.R3945.

Ivlev BI, Mejía-Rosales S, and Kunchur MN (1999) Cherenkov resonances in vortex dissipation in superconductors. *Physical Review B* 60: 12419–12423. https://doi.org/10.1103/PhysRevB.60.12419.

Janjušević D, Grbíí MS, Požek M, Dulčić A, Paar D, Nebendahl B, and Wagner T (2006) Microwave response of thin niobium films under perpendicular static magnetic fields. *Physical Review B* 74: 104501 1–7 https://doi.org/10.1103/PhysRevB.74.104501.

Jaque D, Gonzalez EM, Martin JI, Anguita JV, and Vicent JL (2002) Anisotropic pinning enhancement in Nb films with arrays of submicrometric Ni lines. *Applied Physics Letters* 81: 2851–2854. http://link.aip.org/link/?APL/81/2851/1.

José Martínez-Pérez M and Giazotto F (2014) A quantum diffractor for thermal flux. *Nature Communications* 5(1): 3579. https://doi.org/10.1038/ncomms4579.

Kaplan SB, Chi CC, Langenberg DN, Chang JJ, Jafarey S, and Scalapino DJ (1976) Quasiparticle and phonon lifetimes in superconductors. *Physical Review B* 14: 4854–4873. https://doi.org/10.1103/PhysRevB.14.4854.

Kim YB, Hempstead CF, and Strnad AR (1963) Magnetization and critical supercurrents. *Physics Review* 129: 528–535. https://doi.org/10.1103/PhysRev.129.528.

Klapwijk TM and de Visser PJ (2020) The discovery, disappearance and re-emergence of radiation-stimulated superconductivity. *Annals of Physics* 417: 168104. https://www.sciencedirect.com/science/article/pii/S0003491620300373.

Klein W, Huebener RP, Gauss S, and Parisi J (1985) Nonlinearity in the flux-flow behavior of thin-film superconductors. *Journal of Low Temperature Physics* 61(5): 413–432. https://doi.org/10.1007/BF00683694.

Knight JM and Kunchur MN (2006) Energy relaxation at a hot-electron vortex instability. *Physical Review B* 74: 064512. https://doi.org/10.1103/PhysRevB.74.064512.

Kogan VG (2018) Time-dependent London approach: Dissipation due to out-of-core normal excitations by moving vortices. *Physical Review B* 97: 094510. https://doi.org/10.1103/PhysRevB.97.094510.

Kogan VG and Nakagawa N (2021) Current distributions by moving vortices in superconductors. *Physical Review B* 103: 134511. https://doi.org/10.1103/PhysRevB.103.134511.

Kogan VG and Nakagawa N (2022) Dissipation of moving vortices in thin films. *Physical Review B* 105: L020507. https://doi.org/10.1103/PhysRevB.105.L020507.

Kogan VG and Prozorov R (2020) Interaction between moving Abrikosov vortices in type-II superconductors. *Physical Review B* 102: 024506. https://doi.org/10.1103/PhysRevB.102.024506.

Korneeva YP, Vodolazov DY, Semenov AV, Florya IN, Simonov N, Baeva E, Korneev AA, Goltsman GN, and Klapwijk TM (2018) Optical single-photon detection in micrometer-scale NbN bridges. *Physical Review Applied* 9: 064037. https://doi.org/10.1103/PhysRevApplied.9.064037.

Korneeva YP, Manova N, Florya I, Mikhailov MY, Dobrovolskiy O, Korneev A, and Vodolazov DY (2020) Different single-photon response of wide and narrow superconducting Mo_xSi_{1-x} strips. *Physical Review Applied* 13: 024011. https://doi.org/10.1103/PhysRevApplied.13.024011.

Korzh B, Zhao Q-Y, Allmaras JP, Frasca S, Autry TM, Bersin EA, Beyer AD, Briggs RM, Bumble B, Colangelo M, Crouch GM, Dane AE, Gerrits T, Lita AE, Marsili F, Moody G, Peña C, Ramirez E, Rezac JD, Sinclair N, Stevens MJ, Velasco AE, Verma VB, Wollman EE, Xie S, Zhu D, Hale PD, Spiropulu M, Silverman KL, Mirin RP, Nam SW, Kozorezov AG, Shaw MD, and Berggren KK (2020) Demonstration of sub-3 ps temporal resolution with a superconducting nanowire single-photon detector. *Nature Photonics* 14(4): 250–255. https://doi.org/10.1038/s41566-020-0589-x.

Koshelev AE and Vinokur VM (1994) Dynamic melting of the vortex lattice. *Physical Review Letters* 73: 3580–3583. https://doi.org/10.1103/PhysRevLett.73.3580.

Kramer L and Watts-Tobin RJ (1978) Theory of dissipative current-carrying states in superconducting filaments. *Physical Review Letters* 40: 1041–1044. https://doi.org/10.1103/PhysRevLett.40.1041.

Kunchur MN (2002) Unstable flux flow due to heated electrons in superconducting films. *Physical Review Letters* 89: 137005. https://doi.org/10.1103/PhysRevLett.89.137005.

Kunchur MN and Knight JM (2003) Hot-electron instability in superconductors. *Modern Physics Letters B* 17(10 – 12): 549–558. https://doi.org/10.1142/S0217984903005573.

Kunchur MN, Ivlev BI, and Knight JM (2001) Steps in the negative-differential-conductivity regime of a superconductor. *Physical Review Letters* 87: 177001. https://doi.org/10.1103/PhysRevLett.87.177001.

Kunchur MN, Ivlev BI, and Knight JM (2002) Shear fragmentation of unstable flux flow. *Physical Review B* 66: 060505. https://doi.org/10.1103/PhysRevB.66.060505.

Kunchur MN, Wu C, Arcos DH, Ivlev BI, Choi E-M, Kim KHP, Kang WN, and Lee S-I (2003) Critical flux pinning and enhanced upper critical field in magnesium diboride films. *Physical Review B* 68: 100503. https://doi.org/10.1103/PhysRevB.68.100503.

Lara A, Aliev FG, Silhanek AV, and Moshchalkov VV (2015) Microwave-stimulated superconductivity due to presence of vortices. *Scientific Reports* 5: 9187. https://doi.org/10.1038/srep09187.

Lara A, Aliev FG, Moshchalkov VV, and Galperin YM (2017) Thermally driven inhibition of superconducting vortex avalanches. *Physical Review Applied* 8: 034027. https://doi.org/10.1103/PhysRevApplied.8.034027.

Larkin AI and Ovchinnikov YN (1975) Nonlinear conductivity of superconductors in the mixed state. *Journal of Experimental and Theoretical Physics* 41: 960. http://jetp.ras.ru/cgi-bin/e/index/e/41/5/p960?a=list.

Larkin AI and Ovchinnikov YN (1986) *Nonequilibrium Superconductivity*. Amsterdam: Elsevier493.

Lefloch F, Hoffmann C, and Demolliens O (1999) Nonlinear flux flow in TiN superconducting thin film. *Physica C* 319(3): 258–266. http://www.sciencedirect.com/science/article/pii/S092145349900297X.

Leo A, Grimaldi G, Nigro A, Pace S, Verellen N, Silhanek A, Gillijns W, Moshchalkov V, Metlushko V, and Ilic B (2010) Pinning effects on the vortex critical velocity in type-ii superconducting thin films. *Physica C* 470(19): 904–906. http://www.sciencedirect.com/science/article/pii/S0921453410001607.

Leo A, Grimaldi G, Citro R, Nigro A, Pace S, and Huebener RP (2011) Quasiparticle scattering time in niobium superconducting films. *Physical Review B* 84: 014536 1–7 https://doi.org/10.1103/PhysRevB.84.014536.

Leo A, Marra P, Grimaldi G, Citro R, Kawale S, Bellingeri E, Ferdeghini C, Pace S, and Nigro A (2016) Competition between intrinsic and extrinsic effects in the quenching of the superconducting state in fe(se,te) thin films. *Physical Review B* 93: 054503. https://doi.org/10.1103/PhysRevB.93.054503.

Leo A, Nigro A, Braccini V, Sylva G, Provino A, Galluzzi A, Polichetti M, Ferdeghini C, Putti M, and Grimaldi G (2020a) Flux flow instability as a probe for quasiparticle energy relaxation time in Fe-chalcogenides. *Superconductor Science and Technology* 33(10): 104005. https://doi.org/10.1088/1361-6668/abaec1.

Leo A, Nigro A, and Grimaldi G (2020b) Critical phenomenon of vortex motion in superconductors: Vortex instability and flux pinning. *Low Temperature Physics* 46(4): 375–378. https://doi.org/10.1063/10.0000870.

Li D, Malkin AM, and Rosenstein B (2004) Structure and orientation of the moving vortex lattice in clean type-II superconductors. *Physical Review B* 70: 214529. https://doi.org/10.1103/PhysRevB.70.214529.

Liang M and Kunchur MN (2010) Vortex instability in molybdenum-germanium superconducting films. *Physical Review B* 82: 144517. https://doi.org/10.1103/PhysRevB.82.144517.

Liang M, Kunchur MN, Hua J, and Xiao Z (2010) Evaluating free flux flow in low-pinning molybdenum-germanium superconducting films. *Physical Review B* 82: 064502 1–5. https://doi.org/10.1103/PhysRevB.82.064502.

Lin S-Z, Ayala-Valenzuela O, McDonald RD, Bulaevskii LN, Holesinger TG, Ronning F, Weisse-Bernstein NR, Williamson TL, Mueller AH, Hoff-bauer MA, Rabin MW, and Graf MJ (2013) Characterization of the thin-film NbN superconductor for single-photon detection by transport measurements. *Physical Review B* 87: 184507. https://doi.org/10.1103/PhysRevB.87.184507.

Lösch S, Alfonsov A, Dobrovolskiy OV, Keil R, Engemaier V, Baunack S, Li G, Schmidt OG, and Bürger D (2019) Microwave radiation detection with an ultra-thin free-standing superconducting niobium nanohelix. *ACS Nano* 13: 2948–2955. https://doi.org/10.1021/acsnano.8b07280.

Lu Q, Reichhardt CJO, and Reichhardt C (2007) Reversible vortex ratchet effects and ordering in superconductors with simple asymmetric potential arrays. *Physical Review B* 75: 054502. https://doi.org/10.1103/PhysRevB.75.054502.

Lyatti M, Wolff MA, Savenko A, Kruth M, Ferrari S, Poppe U, Pernice W, Dunin-Borkowski RE, and Schuck C (2018) Experimental evidence for hotspot and phase-slip mechanisms of voltage switching in ultrathin $YBa_2Cu_3O_{7-x}$ nanowires. *Physical Review B* 98: 054505. https://doi.org/10.1103/PhysRevB.98.054505.

Lyatti M, Wolff MA, Gundareva I, Kruth M, Ferrari S, Dunin-Borkowski RE, and Schuck C (2020) Energy-level quantization and single-photon control of phase slips in $YBa_2Cu_3O_{7-x}$ nanowires. *Nature Communications* 11(1): 763. https://doi.org/10.1038/s41467-020-14548-x.

Madan I, Buh J, Baranov VV, Kabanov VV, Mrzel A, and Mihailovic D (2018) Nonequilibrium optical control of dynamical states in superconducting nanowire circuits. *Science Advances* 4(3). http://advances.sciencemag.org/content/4/3/eaao0043.

Maillet O, Subero D, Peltonen JT, Golubev DS, and Pekola JP (2020) Electric field control of radiative heat transfer in a superconducting circuit. *Nature Communications* 11(1): 4326. https://doi.org/10.1038/s41467-020-18163-8.

Makarov D, Volkov OM, Kákay A, Pylypovskyi OV, Budinská B, and Dobrovolskiy OV (2022) New dimension in magnetism and superconductivity: 3D and curvilinear nanoarchitectures. *Advanced Materials* 34: 2101758. https://doi.org/10.1002/adma.202101758.

Martínez-Pérez MJ, Pablo-Navarro J, Müller B, Kleiner R, Magén C, Koelle D, de Teresa JM, and Sesé J (2018) NanoSQUID magnetometry on individual as-grown and annealed Co nanowires at variable temperature. *Nano Letters* 18(12): 7674–7682. https://doi.org/10.1021/acs.nanolett.8b03329.

Maza J, Ferro G, Veira JA, and Vidal F (2008) Transition to the normal state induced by high current densities in YBCO thin films: A thermal runaway account. *Physical Review B* 78: 094512. https://doi.org/10.1103/PhysRevB.78.094512.

McIver JW, Hsieh D, Steinberg H, Jarillo-Herrero P, and Gedik N (2012) Control over topological insulator photocurrents with light polarization. *Nature Nanotechnology* 7(2): 96–100. https://doi.org/10.1038/nnano.2011.214.

Mints RG and Rakhmanov AL (1981) Critical state stability in type-II superconductors and superconducting-normal-metal composites. *Reviews of Modern Physics* 53: 551–592. https://doi.org/10.1103/RevModPhys.53.551.

Misko VR, Savel'ev S, Rakhmanov AL, and Nori F (2007) Negative differential resistivity in superconductors with periodic arrays of pinning sites. *Physical Review B* 75: 024509. https://doi.org/10.1103/PhysRevB.75.024509.

Musienko LE, Dmitrenko IM, and Volotskaya VG (1980) Nonlinear conductivity of thin films in a mixed state. *JETP Letters* 31: 567.

Natarajan CM, Tanner MG, and Hadfield RH (2012) Superconducting nanowire single-photon detectors: Physics and applications. *Superconductor Science and Technology* 25(6), 063001. http://stacks.iop.org/0953-2048/25/i=6/a=063001.

Niessen AK and Weijsenfeld CH (1969) Anisotropic pinning and guided motion of vortices in type-II superconductors. *Journal of Applied Physics* 40(1): 384–393. http://link.aip.org/link/?JAP/40/384/1.

Octavio M, Tinkham M, Blonder GE, and Klapwijk TM (1983) Subharmonic energy-gap structure in superconducting constrictions. *Physical Review B* 27: 6739–6746. https://doi.org/10.1103/PhysRevB.27.6739.

Palomaki TA, Harlow JW, Teufel JD, Simmonds RW, and Lehnert KW (2013) Coherent state transfer between itinerant microwave fields and a mechanical oscillator. *Nature* 495(7440): 210–214. https://doi.org/10.1038/nature11915.

Pals JA and Dobben J (1979) Measurements of microwave-enhanced superconductivity in aluminum strips. *Physical Review B* 20: 935–944. https://doi.org/10.1103/PhysRevB.20.935.

Pals JA and Dobben J (1980) Observation or order-parameter enhancement by microwave irradiation in a superconducting aluminum cylinder. *Physical Review Letters* 44: 1143–1146. https://doi.org/10.1103/PhysRevLett.44.1143.

Pathirana WPMR and Gurevich A (2021) Effect of random pinning on nonlinear dynamics and dissipation of a vortex driven by a strong microwave current. *Physical Review B* 103: 184518. https://doi.org/10.1103/PhysRevB.103.184518.

Peroz C and Villard C (2005) Flux flow properties of niobium thin films in clean and dirty superconducting limits. *Physical Review B* 72: 014515 1–6. https://doi.org/10.1103/PhysRevB.72.014515.

Pompeo N and Silva E (2008) Reliable determination of vortex parameters from measurements of the microwave complex resistivity. *Physical Review B* 78: 094503 1–10. https://doi.org/10.1103/PhysRevB.78.094503.

Porrati F, Barth S, Sachser R, Dobrovolskiy OV, Seybert A, Frangakis AS, and Huth M (2019) Crystalline niobiumcarbide superconducting nanowires prepared by focused ion beam direct writing. *ACS Nano* 13(6): 6287–6296. https://doi.org/10.1021/acsnano.9b00059.

Porrati F, Jungwirth F, Barth S, Gazzadi G C, Frabboni S, Dobrovolskiy O V, and Huth M (2022) Highly-packed proximity-coupled DC-Josephson junction arrays by a direct-write approach. *Advanced Functional Materials*. 2203889. https://doi.org/10.1002/adfm.202203889.

Puica I, Lang W, and Durrell JH (2012) High velocity vortex channeling in vicinal YBCO thin films. *Physica C* 479: 88–91. https://www.sciencedirect.com/science/article/pii/S0921453411005594.

Rakhmanov AL, Shantsev DV, Galperin YM, and Johansen TH (2004) Finger patterns produced by thermomagnetic instability in superconductors. *Physical Review B* 70: 224502. https://doi.org/10.1103/PhysRevB.70.224502.

Reichhardt C and Reichhardt CJO (2008) Moving vortex phases, dynamical symmetry breaking, and jamming for vortices in honeycomb pinning arrays. *Physical Review B* 78: 224511. https://doi.org/10.1103/PhysRevB.78.224511.

Rouco V, Massarotti M, Stornaiuolo D, Papari GP, Obradors X, Puig T, Tafuri F, and Palau A (2018) Vortex lattice instabilities in $YBa_2Cu_3O_{7-x}$ nanowires. *Materials* 11: 211.

Ruck BJ, Trodahl HJ, Abele JC, and Gesel-bracht MJ (2000) Dynamic vortex instabilities in ta/ge-based multilayers and thin films with various pinning strengths. *Physical Review B* 62: 12468–12476. https://doi.org/10.1103/PhysRevB.62.12468.

Schneider M, Brächer T, Breitbach D, Lauer V, Pirro P, Bozhko DA, Musiienko-Shmarova HY, Heinz B, Wang Q, Meyer T, Heussner F, Keller S, Papaioannou ET, Lägel B, Löber T, Dubs C, Slavin AN, Tiberkevich VS, Serga AA, Hille-brands B, and Chumak AV (2020) Bose-Einstein condensation of quasiparticles by rapid cooling. *Nature Nanotechnology* 15(6): 457–461. https://doi.org/10.1038/s41565-020-0671-z.

Semenov AV, Devyatov IA, de Visser PJ, and Klapwijk TM (2016) Coherent excited states in superconductors due to a microwave field. *Physical Review Letters* 117: 047002. https://doi.org/10.1103/PhysRevLett.117.047002.

Sheikhzada A and Gurevich A (2017) Dynamic transition of vortices into phase slips and generation of vortex-antivortex pairs in thin film josephson junctions under dc and ac currents. *Physical Review B* 95: 214507. https://doi.org/10.1103/PhysRevB.95.214507.

Sheikhzada A and Gurevich A (2020) Dynamic pair-breaking current, critical superfluid velocity, and nonlinear electromagnetic response of nonequilibrium superconductors. *Physical Review B* 102: 104507. https://doi.org/10.1103/PhysRevB.102.104507.

Shekhter A, Bulaevskii LN, and Batista CD (2011) Vortex viscosity in magnetic superconductors due to radiation of spin waves. *Physical Review Letters* 106: 037001. https://doi.org/10.1103/PhysRevLett.106.037001.

Shklovskij VA (2017) Pinning effects on hot-electron vortex flow instability in superconducting films. *Physica C* 538: 20–26. http://www.sciencedirect.com/science/article/pii/S0921453417300953.

Shklovskij VA and Dobrovolskiy OV (2006) Influence of pointlike disorder on the guiding of vortices and the Hall effect in a washboard planar pinning potential. *Physical Review B* 74: 104511 1–14. https://doi.org/10.1103/PhysRevB.74.104511.

Shklovskij VA and Dobrovolskiy OV (2008) AC-driven vortices and the Hall effect in a superconductor with a tilted washboard pinning potential. *Physical Review B* 78: 104526. https://doi.org/10.1103/PhysRevB.78.104526.

Shklovskij VA, Sosedkin VV, and Dobrovolskiy OV (2014) Vortex ratchet reversal in an asymmetric washboard pinning potential subject to combined dc and ac stimuli. *Journal of Physics. Condensed Matter* 26(2), 025703. http://stacks.iop.org/0953-8984/26/i=2/a=025703.

Shklovskij VA, Nazipova AP, and Dobrovolskiy OV (2017) Pinning effects on self-heating and flux-flow instability in superconducting films near T_c. *Physical Review B* 95: 184517. https://doi.org/10.1103/PhysRevB.95.184517.

Silhanek AV, Milošević MV, Kramer RBG, Berdiyorov GR, Van de Vondel J, Luccas RF, Puig T, Peeters FM, and Moshchalkov VV (2010) Formation of stripelike flux patterns obtained by freezing kinematic vortices in a superconducting Pb film. *Physical Review Letters* 104: 017001. https://doi.org/10.1103/PhysRevLett.104.017001.

Silhanek AV, Leo A, Grimaldi G, Berdiyorov GR, Milosevic MV, Nigro A, Pace S, Verellen N, Gillijns W, Metlushko V, Ilić B, Zhu X, and Moshchalkov VV (2012) Influence of artificial pinning on vortex lattice instability in superconducting films. *New Journal of Physics* 14(5), 053006. http://stacks.iop.org/1367-2630/14/i=5/a=053006.

Sivakov AG, Glukhov AM, Omelyanchouk AN, Koval Y, Müller P, and Ustinov AV (2003) Josephson behavior of phase-slip lines in wide superconducting strips. *Physical Review Letters* 91: 267001 1–4. https://doi.org/10.1103/PhysRevLett.91.267001.

Sivakov AG, Turutanov OG, Kolinko AE, and Pokhila AS (2018) Spatial characterization of the edge barrier in wide superconducting films. *Low Temperature Physics* 44(3): 226–232. https://doi.org/10.1063/1.5024540.

Skjærvø SH, Marrows CH, Stamps RL, and Heyderman LJ (2020) Advances in artificial spin ice. *Nature Reviews Physics* 2(1): 13–28. https://doi.org/10.1038/s42254-019-0118-3.

Stoll OM, Kaiser S, Huebener RP, and Naito M (1998) Intrinsic flux-flow resistance steps in the cuprate superconductor $Nd_{2-x}Ce_xCuO_y$. *Physical Review Letters* 81: 2994–2997. https://doi.org/10.1103/PhysRevLett.81.2994.

Stoll OM, Huebener RP, Kaiser S, and Naito M (1999) Magnetic field and temperature dependence of the intrinsic resistance steps in the mixed state of the cuprate superconductor $Nd_{2-x}Ce_xCuO_y$. *Physical Review B* 60: 12424–12428. https://doi.org/10.1103/PhysRevB.60.12424.

Tikhonov KS, Skvortsov MA, and Klapwijk TM (2018) Superconductivity in the presence of microwaves: Full phase diagram. *Physical Review B* 97: 184516. https://doi.org/10.1103/PhysRevB.97.184516.

Tikhonov KS, Semenov AV, Devyatov IA, and Skvortsov MA (2020) Microwave response of a superconductor beyond the eliashberg theory. *Annals of Physics* 417: 168101. https://www.sciencedirect.com/science/article/pii/S0003491620300348.

Tinkham M (2004) *Introduction to Superconductivity*. Mineola, New York.

Tolpygo SK and Tulin VA (1983) Influence of microwave irradiation on high-frequency absorption by thin superconducting films (superconductivity stimulation). *Soviet Physics - JETP* 57: 123.

Tredwell TJ and Jacobsen EH (1975) Phonon-induced enhancement of the superconducting energy gap. *Physical Review Letters* 35: 244–247. https://doi.org/10.1103/PhysRevLett.35.244.

Uroš D, Manuel R, Kahan D, David G, Vladan V, Nikolai K, and Markus A (2020) Cooling of a levitated nanoparticle to the motional quantum ground state. *Science* 367(6480): 892–895. https://doi.org/10.1126/science.aba3993.

Villegas JE, Savel'ev S, Nori F, Gonzalez EM, Anguita JV, Garcia R, and Vicent JL (2003) A superconducting reversible rectifier that controls the motion of magnetic flux quanta. *Science* 302(5648): 1188–1191. http://www.sciencemag.org/content/302/5648/1188.abstract.

Vodolazov DY (2017) Single-photon detection by a dirty current-carrying superconducting strip based on the kinetic-equation approach. *Physical Review Applied* 7: 034014. https://doi.org/10.1103/PhysRevApplied.7.034014.

Vodolazov DY (2019) Flux-flow instability in a strongly disordered superconducting strip with an edge barrier for vortex entry. *Superconductor Science and Technology* 32(11): 115013. https://doi.org/10.1088/1361-6668/ab4168.

Vodolazov DY (2020) Flux flow instability in type II superconducting strips: Spatially uniform versus nonuniform transition. *Low Temperature Physics* 46(4): 372–374. https://doi.org/10.1063/10.0000869.

Vodolazov DY and Peeters FM (2007) Rearrangement of the vortex lattice due to instabilities of vortex flow. *Physical Review B* 76: 014521. https://doi.org/10.1103/PhysRevB.76.014521.

Vodolazov DY, Maksimov IL, and Brandt EH (2003) Vortex entry conditions in type-II superconductors: Effect of surface defects. *Physica C* 384(1): 211–226. https://www.sciencedirect.com/science/article/pii/S0921453402018774.

Vodolazov DY, Ilin K, Merker M, and Siegel M (2015) Defect-controlled vortex generation in current-carrying narrow superconducting strips. *Superconductor Science and Technology* 29(2): 025002. https://doi.org/10.1088/0953-2048/29/2/025002.

Volotskaya VG, Dmitrenko IM, Koretskaya OA, and Musienko LE (1992) A study of the effect of superheating on the Larkin-Ovchinmkov instability evolution in thin Sn films. *Fizika Nizkikh Temperatur* 18: 973.

von Freymann G, Ledermann A, Thiel M, Staude I, Essig S, Busch K, and Wegener M (2010) Three-dimensional nanostructures for photonics. *Advanced Functional Materials* 20(7): 1038–1052. https://doi.org/10.1002/adfm.200901838.

Watts-Tobin RJ, Krähenbühl Y, and Kramer L (1981) Nonequilibrium theory of dirty, current-carrying superconductors: Phase-slip oscillators in narrow filaments near Tc. *Journal of Low Temperature Physics* 42(5): 459–501. https://doi.org/10.1007/BF00117427.

Winkler R, Schmidt F-P, Haselmann U, Fowlkes JD, Lewis BB, Kothleitner G, Rack PD, and Plank H (2017) Direct-write 3d nanoprinting of plasmonic structures. *ACS Applied Materials & Interfaces* 9(9): 8233–8240. https://doi.org/10.1021/acsami.6b13062.

Wördenweber R, Hollmann E, Schubert J, Kutzner R, and Panaitov G (2012) Regimes of flux transport at microwave frequencies in nanostructured high-T_c films. *Physical Review B* 85: 064503 1–6 https://doi.org/10.1103/PhysRevB.85.064503.

Wyatt AFG, Dmitriev VM, Moore WS, and Sheard FW (1966) Microwave-enhanced critical supercurrents in constricted tin films. *Physical Review Letters* 16: 1166–1169. https://doi.org/10.1103/PhysRevLett.16.1166.

Xiao ZL and Ziemann P (1996) Vortex dynamics in YBCO superconducting films: Experimental evidence for an instability in the vortex system at high current densities. *Physical Review B* 53: 15265–15271. https://doi.org/10.1103/PhysRevB.53.15265.

Xiao ZL, Häring J, Heinz B, and Ziemann P (1996) Influence of He ion bombardment at medium energies on the vortex instability at high current densities observed in YBaCuO films. *Journal of Low Temperature Physics* 105(5): 1159–1164. https://doi.org/10.1007/BF00753856.

Xiao ZL, Andrei EY, and Ziemann P (1998) Coexistence of the hot-spot effect and flux-flow instability in high-T_c superconducting films. *Physical Review B* 58: 11185–11188. https://doi.org/10.1103/PhysRevB.58.11185.

Zaitsev AG, Schneider R, Linker G, Ratzel F, Smithey R, and Geerk J (2003) Effect of flux flow on microwave losses in $YBa_2Cu_3O_{7-x}$ superconducting films. *Physical Review B* 68: 104502. https://doi.org/10.1103/PhysRevB.68.104502.

Zeldov E, Larkin AI, Geshkenbein VB, Konczykowski M, Majer D, Khaykovich B, Vinokur VM, and Shtrikman H (1994) Geometrical barriers in high-temperature superconductors. *Physical Review Letters* 73: 1428–1431. https://doi.org/10.1103/PhysRevLett.73.1428.

Zolochevskii IV (2013) Stimulation of superconductivity by microwave radiation in wide tin films. *Low Temperature Physics* 39: 571.

Non-Abelian anyons and non-Abelian vortices in topological superconductors

Yusuke Masaki[a,b], **Takeshi Mizushima**[c], **and Muneto Nitta**[b,d,e], [a]Department of Physics, Tohoku University, Sendai, Miyagi, Japan; [b]Research and Education Center for Natural Sciences, Keio University, Yokohama, Kanagawa, Japan; [c]Department of Materials Engineering Science, Osaka University, Toyonaka, Osaka, Japan; [d]Department of Physics, Keio University, Hiyoshi, Japan; [e]International Institute for Sustainability with Knotted Chiral Meta Matter (SKCM^2), Hiroshima University, Higashi-Hiroshima, Hiroshima, Japan

© 2024 Elsevier Ltd. All rights reserved.

Introduction 756
Non-Abelian anyons 757
Braid group and quantum statistics 757
Non-Abelian anyons 758
Ising anyons 759
Fibonacci anyons 759
Yang-Lee anyons 760
Vortex anyons 760
Non-Abelian anyons in topological SCs 761
Majorana zero modes as Ising anyons 761
Majorana zero modes 761
Braiding Majorana zero modes 762
Platforms for Majorana zero modes 763
HQVs with Majorana zero modes in SF ^{3}He 763
HQVs in SCs 765
Superconducting nanowires 767
Vortices in Fe(Se,Te) 768
Topological quantum computation 768
Symmetry-protected non-Abelian anyons 768
Mirror and unitary symmetries 769
Multiple Majorana zero modes and Coxeter group 770
Non-Abelian vortex anyons 771
Non-Abelian vortices 771
Examples of non-Abelian vortices 772
Nematic liquid crystals 772
UN liquid crystals 773
D_2-BN liquid crystals (Poenaru and Toulouse, 1977; Volovik and Mineev, 1977; Mermin, 1979; Balachandran et al., 1984) 773
D_4-BN liquid crystals 774
Spinor BECs 774
BN phases in spin-2 BEC (Song et al., 2007; Uchino et al., 2010; Kobayashi et al., 2012; Borgh and Ruostekoski, 2016) 774
Cyclic phase in spin-2 BEC (Semenoff and Zhou, 2007; Kobayashi et al., 2009, 2012) 775
Other examples 776
Fusion rules for non-Abelian vortex anyons 776
Non-Abelian vortex anyons in D_2-BN 776
Non-Abelian vortex anyons in spin-2 BECs 777
$^3P_2$ Topological SFs 778
Overview of $^3P_2$ topological SFs 778
Nematic state 779
Cyclic state 780
Ferromagnetic state 780
Magnetized nematic state 780
Vortices in $^3P_2$ SFs 780
Half quantum vortex in D_4-BN state 781
Vortices in D_4-BN state 781
Axisymmetric singly quantized vortex 782
Nonaxisymmetric singly quantized vortex 782
HQVs 782
Isolated HQV $(\kappa,n) = (1/2, +1/4)$ 784
Isolated HQV $(\kappa,n) = (1/2, -1/4)$ 785
Molecule of HQVs (stability) 785
Non-Abelian anyon in non-Abelian vortex 785
Existence of zero energy states 785
Discrete symmetry of vortices 786

https://doi.org/10.1016/B978-0-323-90800-9.00225-0

Topology of the vortex-bound states 787
Conclusion 788
Acknowledgments 788
References 788

Abstract

Anyons are particles obeying statistics of neither bosons nor fermions. Non-Abelian anyons, whose exchanges are described by a non-Abelian group acting on a set of wave functions, are attracting a great attention because of possible applications to topological quantum computations. Braiding of non-Abelian anyons corresponds to quantum computations. The simplest non-Abelian anyons are Ising anyons which can be realized by Majorana fermions hosted by vortices or edges of topological superconductors, $\nu = 5/2$ quantum Hall states, spin liquids, and dense quark matter. While Ising anyons are insufficient for universal quantum computations, Fibonacci anyons present in $\nu = 12/5$ quantum Hall states can be used for universal quantum computations. Yang-Lee anyons are nonunitary counterparts of Fibonacci anyons. Another possibility of non-Abelian anyons (of bosonic origin) is given by vortex anyons, which are constructed from non-Abelian vortices supported by a non-Abelian first homotopy group, relevant for certain nematic liquid crystals, superfluid ^{3}He, spinor Bose-Einstein condensates, and high density quark matter. Finally, there is a unique system admitting two types of non-Abelian anyons, Majorana fermions (Ising anyons) and non-Abelian vortex anyons. That is $^3P_2$ superfluids (spin-triplet, *p*-wave paring of neutrons), expected to exist in neutron star interiors as the largest topological quantum matter in our universe.

Key points

- Unlike fermions and bosons, the exchange of non-Abelian anyons is described by unitary transformations that operate on topologically protected degenerate ground states. The adiabatic exchanges of two or more non-Abelian anyons manipulate quantum information stored in a set of degenerate ground states, leading to topological quantum computations.
- The simplest non-Abelian anyons are Ising anyons which are predicted to exist as Majorana zero modes in topological superconductors, fractional quantum Hall states, Kitaev materials, and dense quark matter.
- Another non-Abelian anyons are vortex anyons, which are constructed from non-Abelian vortices supported by a non-Abelian first homotopy group. Such vortex anyons exist in liquid crystals, superfluid ^{3}He, spinor Bose-Einstein condensates, and high-density quark matter.
- $^3P_2$ superfluids, which are expected to be realized in neutron stars, provide unique systems simultaneously admitting two kinds of non-Abelian anyons, that is, Ising anyons and vortex anyons.

Introduction

In three spatial dimensions, all particles are either bosons or fermions in quantum physics, that is, a wave function of multiparticle states is symmetric (antisymmetric) under the exchanges of two bosons (fermions). On contrary, in two spatial dimensions, there exist exotic particles classified to neither bosons nor fermions, *anyons*. A wave function of two anyons receives a nontrivial phase factor under their exchanges (Leinaas and Myrheim, 1977; Wilczek, 1982). Such exotic particles play essential roles in fractional quantum Hall states (Halperin, 1984; Arovas et al., 1984), and have been experimentally observed for $\nu = 1/3$ fractional quantum Hall states (Bartolomei et al., 2020; Nakamura et al., 2020).

Recently, yet exotic particles attracted great attention, that is, *non-Abelian anyons*. Non-Abelian anyons are described by a set of multiple wave functions, and the exchanges of two non-Abelian anyons lead to unitary matrix operations on a set of wave functions. They have been theoretically predicted to exist in $\nu = 5/2$ fractional quantum Hall states (Moore and Read, 1991; Nayak and Wilczek, 1996), topological superconductors (SCs) and superfluids (SFs) (Read and Green, 2000; Ivanov, 2001; Kitaev, 2001), and spin liquids (Kitaev, 2006; Motome and Nasu, 2020), and experimental observation is pursued. Non-Abelian anyons are attracting significant interests owing to the possibility to offer a platform of topologically protected quantum computations realized by braiding of non-Abelian anyons (Kitaev, 2003; Kitaev and Laumann, 2008; Nayak et al., 2008; Pachos, 2012; Sarma et al., 2015; Field and Simula, 2018). Since the Hilbert space and braiding operations are topologically protected, they are robust against noises in contrast to the conventional quantum computation methods. Recently, it has been reported that non-Abelian braiding and fusions have been experimentally realized in a superconducting quantum processor, where the fusion and braiding protocols are implemented using a quantum circuit on a superconducting quantum processor (Andersen et al., 2022), thereby opening a significant step to realize topological quantum computations.

One of the main routes to realize non-Abelian anyons is based on Majorana fermions in topological SCs (Ivanov, 2001; Kitaev, 2001; Alicea, 2012; Leijnse and Flensberg, 2012; Beenakker, 2013; Silaev and Volovik, 2014; Elliott and Franz, 2015; Sato and

Fujimoto, 2016; Mizushima et al., 2016; Sato and Ando, 2017; Beenakker, 2020; Marra, 2022). Majorana fermions were originally proposed in high energy physics to explain neutrinos; they are particles that coincide with their own antiparticles (Majorana, 1937). In condensed matter physics, Majorana fermions are localized at vortices or edge of materials for which several protocols of non-Abelian braiding were proposed. Non-Abelian anyons constructed from Majorana fermions are so-called Ising anyons. They are not enough for universal quantum computations, and thus some nontopological process should be included (Nayak et al., 2008). In contrast, another type of anyons called Fibonacci anyons (Trebst et al., 2008) can offer a promising platform for universal topological quantum computation that all quantum gates are implemented by braiding manipulation in a topologically protected way (Preskill, 2004; Bonesteel et al., 2005; Hormozi et al., 2007). Such Fibonacci anyons are proposed to exist in $\nu = 12/5$ quantum Hall states, a junction made of a conventional SC and a $\nu = 2/3$ fractional quantum Hall state (Mong et al., 2014), interacting Majorana fermions realized in a septuple-layer structure of topological SCs (Hu and Kane, 2018), and Rydberg atoms in a lattice (Lesanovsky and Katsura, 2012). Yang-Lee anyons are also proposed as nonunitary counterparts of Fibonacci anyons, obeying nonunitary non-Abelian statistics (Ardonne et al., 2011; Freedman et al., 2012; Sanno et al., 2022).

The aforementioned anyons are all quasiparticle excitations composed of fermions. On the other hand, a different type of non-Abelian anyons can be composed of bosons in certain ordered states accompanied with symmetry breakings $G \to H$. They are called non-Abelian vortex anyons, whose exchange statistics are non-Abelian due to non-Abelian vortices, that is quantum vortices supported by a non-Abelian first homotopy (fundamental) group of order parameter manifolds, $\pi_1(G/H)$ (Bais, 1980; Wilczek and Wu, 1990; Bucher, 1991; Brekke et al., 1993; Lo and Preskill, 1993; Lee, 1994; Brekke et al., 1997).[1] Such non-Abelian vortices exist in liquid crystals (Poenaru and Toulouse, 1977; Volovik and Mineev, 1977; Mermin, 1979; Lavrentovich and Kleman, 2001), ^{3}He SFs (Balachandran et al., 1984; Salomaa and Volovik, 1987; Volovik, 2003), spinor Bose-Einstein condensates (BECs) (Semenoff and Zhou, 2007; Kobayashi et al., 2009, 2012; Borgh and Ruostekoski, 2016), and high-density quark (QCD) matter (Fujimoto and Nitta, 2021a, b, c; Eto and Nitta, 2021). Non-Abelian braiding of vortex anyons in spinor BECs and its application to quantum computations were proposed (Mawson et al., 2019).

In addition to these systems admitting one type of non-Abelian anyons, there is the unique system simultaneously admitting two kinds of non-Abelian anyons, Ising anyons based on Majorana fermions and non-Abelian vortex anyons. It is a $^3P_2$ SF, spin-triplet and p-wave pairing with the total angular momentum two (Hoffberg et al., 1970; Tamagaki, 1970; Takatsuka and Tamagaki, 1971; Takatsuka, 1972; Richardson, 1972). Such $^3P_2$ SFs are expected to be realized by neutrons, relevant for neutron star interiors (Sedrakian and Clark, 2018). $^3P_2$ SFs are the largest topological SFs in our universe (Mizushima et al., 2017) and admit non-Abelian vortices (Masuda and Nitta, 2020). Non-Abelian vortices host Majorana fermions in their cores (Masaki et al., 2022), thus behaving as non-Abelian anyons.

The purpose of this article is to summarize these non-Abelian anyons of various types. After introducing basics of non-Abelian anyons in Section "Non-Abelian anyons," we describe non-Abelian anyons in fermionic and bosonic systems, based on Majorana fermions and non-Abelian first homotopy group in Sections "Non-Abelian anyons in topological SCs" and "Non-Abelian vortex anyons," respectively. In Section "$^3P_2$ Topological SFs," we introduce $^3P_2$ SFs as the unique system simultaneously admitting two kinds of non-Abelian anyons. We summarize this article in Section "Summary."

Non-Abelian anyons

Braid group and quantum statistics

Here we consider pointlike topological defects (e.g., vortices in two-dimensional *spinless* SCs), which behave as identical particles in a two-dimensional plane. The exchange of n particles in three or higher dimension is described by the symmetric group S_n (Leinaas and Myrheim, 1977). There are two one-dimensional representations of S_n, ± 1, due to even or odd permutation and $+1$ (-1) corresponds the Bose (Fermi) statistics. Two dimension is special and the exchange of particles is given by the braid group B_n (Wu, 1984). The braid of particles is expressed as a set of operators $T_k (1 \leq k \leq n-1)$ that exchange the neighboring kth and $(k+1)$th particles in an anticlockwise direction. The operators obey the relations (see Fig. 1)

$$T_i T_j T_i = T_j T_i T_j, \quad \text{for } |i-j| = 1, \tag{1}$$

$$T_i T_j = T_j T_i, \quad \text{for } |i-j| \geq 2. \tag{2}$$

The exotic statistics of particles represented by the braid group stems from the relation $T_i^{-1} \neq T_i$. In the one-dimensional representation, the generator of T_i is given by a phase factor that a wave function under the exchange of particles acquires, $\tau_j \equiv \tau(T_j) = e^{i\theta_j}$ $(0 \leq \theta_j < 2\pi)$. The relation in Eq. (1) implies that the exchange operation of any two particles induces the same phase factor $\tau_1 = \tau_2 = \cdots = \tau_{n-1} = e^{i\theta}$. The phase factor characterizes the quantum statistics of particles (Wu, 1984), and the absence of the relation $T_i^2 = 1$ allows for the fractional (anyon) statistics with neither $\theta = 0$ (bosons) nor $\theta = \pi$ (fermions). In addition to the one-dimensional representation, the braid group has non-Abelian representations. In Section "Non-Abelian anyons in topological

---

[1] The term "non-Abelian" on vortices depends on the context. In the other contexts (in particular in high energy physics), vortices in a symmetry breaking $G \to H$ with non-Abelian magnetic fluxes are often called non-Abelian even though $\pi_1(G/H)$ the first homotopy group is Abelian (Hanany and Tong, 2003; Auzzi et al., 2003; Eto et al., 2006; Shifman and Yung, 2007; Eto et al., 2014). In condensed matter physics, vortices with Majorana fermions in their cores are also sometimes called non-Abelian vortices (because they are non-Abelian anyons). In this article, the term "non-Abelian" on vortices is used only for vortices with non-Abelian first homotopy group π_1.

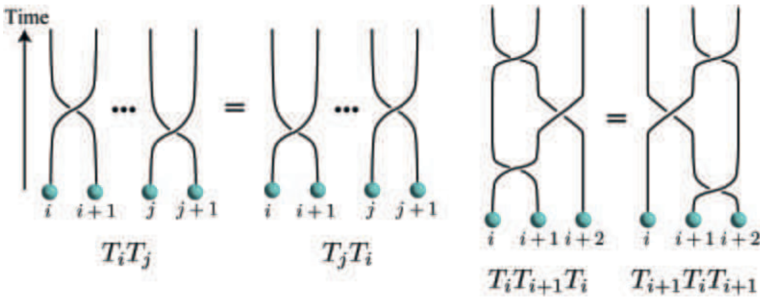

Fig. 1 Schematic of the braid relations in Eqs. (1) and (2): $T_iT_j = T_jT_i$ for $|i - j| \geq 2$ (left) and $T_iT_jT_i = T_jT_iT_j$ for $|i - j| = 1$ (right).

SCs," we will show that the generators of the braid of Majorana zero modes are noncommutative as $[\tau_i, \tau_j] \neq 0$ for $|i - j| = 1$ and the pointlike defects hosting Majorana modes behave as non-Abelian anyons.

Although the braid group is trivial in three dimensions, a three-dimensional model with pointlike topological defects, which host Majorana modes and obey the non-Abelian statistics, has been proposed (Teo and Kane, 2010a). The non-Abelian statistics of the defects, which behave as hedgehogs, can be interpreted as the projective ribbon permutation statistics (Freedman et al., 2011b, a). Such non-Abelian statistics enables to construct three-dimensional networks of topological superconducting wires supporting Majorana modes.

Non-Abelian anyons

In three spatial dimensions, the statistics of particles is determined by their intrinsic spins. According to the spin statistics theorem, all particles with integer (half-integer) spin are bosons (fermions). A pair formed by two fermions with the spin 1/2 behaves as a boson, and the spin of the composite particle obeys the "fusion rule" $\frac{1}{2} \otimes \frac{1}{2} = 0 \oplus 1$, where 0 and 1 denote the spin singlet and triplet states, respectively. When particles are trapped in a two-dimensional plane, however, there is another possibility that is neither fermions nor bosons, that is, anyons. In general, anyons can be characterized by the topological charge, the fusion rule (N_{ab}^c), the associative law (the F-matrix), and the braiding operation (the R-matrix) (Preskill, 2004; Nayak et al., 2008; Pachos, 2012).

Let $\mathbf{1}$ and $\{a, b, \ldots\}$ be the vacuum and the different species of particles, respectively. Consider the anyon model spanned by $M = \{\mathbf{1}, a, b, \ldots\}$ and bring two anyons a and b together. The fused particle also belongs to M. The fusion rule is represented by

$$a \otimes b = \sum_{c \in M} N_{ab}^c c, \tag{3}$$

where fusion coefficients N_{ab}^c are nonnegative integers. Fig. 2A shows the diagrammatic expression of the fusion of two anyons with topological charges a and b to an anyon with charge c. When N_{ab}^c is not zero for only one value of c, the fusion of paired a and b anyons is uniquely determined and the anyon is called the Abelian anyon. The non-Abelian anyons are characterized by two or more coefficients that satisfy $N_{ab}^c \neq 0$. In the context of quantum computation, the fusion rule determines the Hilbert space that encodes quantum information, and quantum computation is implemented by the braiding manipulation of non-Abelian anyons in a topologically protected way. Fig. 2B shows the diagrammatic expression of the R-matrix. When one anyon moves around the other, the pairwise anyons acquire a phase. As mentioned below, the R-matrix describes a phase resulting from the exchange of anyons a and b which fuse to a anyon c. Let us also consider the fusion of three anyons a, b, and c into an anyon d. The outcome of

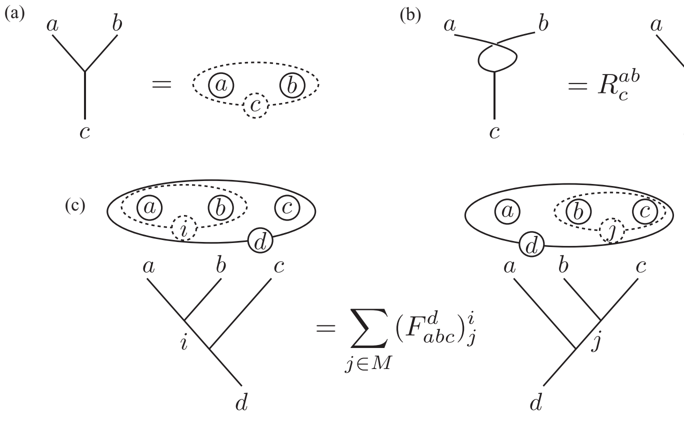

Fig. 2 (A) Diagram of the fusion of two anyons a and b to an anyon c. Diagrammatic expressions of the R-matrix (B) and the F-matrix (C).

the fusion process is independent of order in which the anyons are to be fused. This implies that the fusion process obeys the associative law, $(a \otimes b) \otimes c = a \otimes (b \otimes c)$, which is characterized by the F-matrix. The F matrix represents the transformation between different fusion bases or the choice of order of fusion, which is expressed as shown in Fig. 2C. The R-matrix and the F-matrix are the building blocks for constructing the braid group in multiple anyon systems (Preskill, 2004).

Ising anyons

An example of the non-Abelian anyons is the Ising anyon (Kitaev, 2006; Nayak et al., 2008; Pachos, 2012). The Ising anyon model consists of the vacuum $\mathbf{1}$, Ising anyons σ, and Dirac (complex) fermions ψ, which obey the fusion rules

$$\sigma \otimes \sigma = \mathbf{1} \oplus \psi, \ \sigma \otimes \psi = \sigma, \ \psi \otimes \psi = \mathbf{1}, \ \mathbf{1} \otimes x = x, \tag{4}$$

where $x \in \{\mathbf{1}, \sigma, \psi\}$. Consider three Ising anyons, where the two left-most anyons fuse into either $\mathbf{1}$ or ψ (see Fig. 2C with $(a, b, c) \to \sigma$ and $i, j = \{\mathbf{1}, \psi\}$). The R-matrix and the F-matrix are given, respectively, by

$$R = \begin{pmatrix} R_{\mathbf{1}}^{\sigma\sigma} & 0 \\ 0 & R_{\psi}^{\sigma\sigma} \end{pmatrix} = e^{-i\pi/8} \begin{pmatrix} 1 & 0 \\ 0 & i \end{pmatrix}, \tag{5}$$

$$F_{\sigma\sigma\sigma}^{\sigma} = \frac{1}{\sqrt{2}} \begin{pmatrix} 1 & 1 \\ 1 & -1 \end{pmatrix}. \tag{6}$$

The diagonal components of the R-matrix are the phases resulting from the counterclockwise exchange of two left-most Ising anyons (σ) fusing to $\mathbf{1}$ or ψ while the twice exchange operation of two right-most Ising anyons is represented by the unitary matrix, $F^{-1}R^2F = e^{-i\pi/4}\sigma_x$. Hence, braiding two anyons corresponds to the implementation of the quantum gates acting on the quantum states spanned by $\mathbf{1}$ and ψ.

In general, the anyons are described by conformal field theory, corresponding to gapless edge states residing in the boundary of two-dimensional gapped topological phases. For Ising anyons, the theory is the conformal field theory with the central charge $c = 1/2$, which describes critical Ising models such as the two-dimensional Ising model at the point of second-order phase transition (Di Francesco et al., 1997).

The Moore-Read state in the fractional quantum Hall state at the filling factor $\nu = 5/2$ supports this type of non-Abelian anyons (Nayak et al., 2008). The Ising anyons can also be realized in the Kitaev's honeycomb model, which is an exactly solvable model of quantum spin liquid states (Kitaev, 2006). In this model, the spins are fractionalized to Majorana fermions coupled to $\mathbb{Z}_2$ gauge fields. The Ising anyons appear as Majorana zero modes bound to the $\mathbb{Z}_2$ flux. Materials including 4d or 5d atoms with a strong spin–orbit coupling have been proposed as candidates of Kitaev magnets, and the half-integer thermal Hall effect was reported in α-RuCl$_3$ (Kasahara et al., 2018; Yamashita et al., 2020; Yokoi et al., 2021; Bruin et al., 2022), which is a signature of Majorana fermions in the chiral quantum spin liquid phase (Vinkler-Aviv and Rosch, 2018; Ye et al., 2018). Apart from materials, Google team reported the demonstration of fusion and braiding rules of non-Abelian Ising anyons on a superconducting quantum processor, where the fusion and braiding protocols are implemented using a quantum circuit on a superconducting quantum processor (Andersen et al., 2022). Another platform to realize Ising anyons is a topological SC. In the context of topological SCs, the Ising anyons (σ) appear as Majorana zero modes bound at their boundaries or topological defects, such as the surface, interface, and vortices (Read and Green, 2000; Kitaev, 2001; Nayak et al., 2008; Alicea, 2012; Sato and Fujimoto, 2016; Mizushima et al., 2016). Pairwise Majorana zero modes form a complex fermion that can define either the unoccupied state ($\mathbf{1}$) or the occupied state (ψ) of the zero energy eigenstate, implying $\sigma \otimes \sigma = \mathbf{1} \oplus \psi$. The vacuum $\mathbf{1}$ corresponds to a condensate of Cooper pairs, while ψ represents a Bogoliubov quasiparticle which can pair into a condensate, that is, $\psi \otimes \psi = \mathbf{1}$. The detailed properties and realization of Majorana zero modes in topological SCs are described in Sections "Majorana zero modes as Ising anyons" and "Platforms for Majorana zero modes."

Fibonacci anyons

Another example is the Fibonacci anyons (Trebst et al., 2008). The Fibonacci anyon model consists of the vacuum $\mathbf{1}$ and the nontrivial anyon τ, which obey the fusion rules

$$\tau \otimes \tau = \mathbf{1} \oplus \tau, \quad \mathbf{1} \otimes x = x, \tag{7}$$

where $x = \mathbf{1}, \tau$. The first rule implies that the fusion of two anyons may result in either annihilation or creation of a new anyon, and thus the Fibonacci anyon may be its own antiparticle. Repeated fusions of the $n + 1$ τ-anyons result in either the vacuum or the τ anyon as $\tau \otimes \tau \otimes \cdots \otimes \tau = a_n \cdot \mathbf{1} \oplus b_n \tau$, where $a_n = 1$ for $n = 2$ and $a_n = n - 2$ for $n \geq 3$. The coefficient b_n grows as the Fibonacci series, and the first few values in the sequence are $b_2 = 1$, $b_3 = 2$, $b_4 = 3$, $b_5 = 5$, ... The R-matrix and the F-matrix are given, respectively, by

$$R = \begin{pmatrix} R_{\mathbf{1}}^{\tau\tau} & 0 \\ 0 & R_{\tau}^{\tau\tau} \end{pmatrix} = \begin{pmatrix} e^{i4\pi/5} & 0 \\ 0 & -e^{i2\pi/5} \end{pmatrix}, \tag{8}$$

$$F^{\tau}_{\tau\tau\tau} = \begin{pmatrix} \phi^{-1} & \phi^{-1/2} \\ \phi^{-1/2} & -\phi^{-1}, \end{pmatrix} \tag{9}$$

where $\phi = (1 + \sqrt{5})/2$ is the golden ratio. The Fibonacci anyons are described by the level-1 G_2 Wess–Zumino–Witten theory with the central charge $c = 14/5$ (Mong et al., 2014), where G_2 is the simplest exceptional Lie group. While Ising anyons are not sufficient for universal quantum computation, the Fibonacci anyon systems can offer a promising platform for universal topological quantum computation that all quantum gates are implemented by braiding manipulation in a topologically protected way (Preskill, 2004; Bonesteel et al., 2005; Hormozi et al., 2007).

The existence of the Fibonacci anyons is predicted in the $\nu = 12/5$ fractional quantum Hall state that is described by the Read-Rezayi state (Read and Rezayi, 1999). It is also proposed that a junction made of a conventional SC and the $\nu = 2/3$ fractional quantum Hall state supports the Fibonacci anyons (Mong et al., 2014). Fibonacci anyons can also be made from interacting Majorana fermions realized in a septuple-layer structure of topological SCs (Hu and Kane, 2018) and from Rydberg atoms in a lattice (Lesanovsky and Katsura, 2012).

Yang-Lee anyons

There are nonunitary counterparts of Fibonacci anyons, which are referred to as Yang-Lee anyons. The conformal field theory corresponding to Yang-Lee anyons is nonunitary and Galois conjugate to the Fibonacci conformal field theory (Ardonne et al., 2011; Freedman et al., 2012). Because of nonunitarity, the central charge and the scaling dimension for the one nontrivial primary field are negative, $c = -22/5$ and $\Delta = -2/5$, respectively. As shown in Eq. (9), the F-matrix for Fibonacci anyons is given by the golden ratio ϕ, that is, one solution of the equation $x^2 = 1 + x$, which is an algebraic analog of the fusion rule. The F-matrix for Yang-Lee anyons is obtained from Eq. (9) by replacing $\phi \to -1/\phi$ as

$$F^{\tau}_{\tau\tau\tau} = \begin{pmatrix} -\phi & i\sqrt{\phi} \\ i\sqrt{\phi} & \phi \end{pmatrix}, \tag{10}$$

as $-1/\phi$ is the other solution of the equation $x^2 = 1 + x$. In Eq. (10), the bases of the F-matrix are spanned by the vacuum state **1** and a Yang-Lee anyon τ. The R-matrix are given by

$$R = \begin{pmatrix} R^{\tau\tau}_{1} & 0 \\ 0 & R^{\tau\tau}_{\tau} \end{pmatrix} = \begin{pmatrix} e^{i2\pi/5} & 0 \\ 0 & e^{i\pi/5} \end{pmatrix}. \tag{11}$$

Unlike the Fibonacci anyons, braiding two Yang-Lee anyons is represented by a combination of the R-matrix and the nonunitary matrix, $F^{-1}RF$. While Yang-Lee anyons obey the same fusion rule as that of Fibonacci anyons given by Eq. (7), the F-matrix in Eq. (10) is the nonunitary and the Yang-Lee anyons obey the nonunitary non-Abelian statistics.

The nonunitary conformal field theory with $c = -22/5$ describes the nonunitary critical phenomenon known as the Yang-Lee edge singularity (Cardy, 1985). Let us consider the Ising model with an imaginary magnetic field ih ($h \in \mathbb{R}$). For temperatures above the critical temperature, the zeros of the partition function in the thermodynamic limit, which are referred to as the Lee-Yang zeros, accumulate on the line $h > h_c$ and the edge of the Lee-Yang zeros corresponds to the critical point h_c (Lee and Yang, 1952). As h ($> h_c$) approaches the edge, the density of zeros has a power-law behavior as $|h - h_c|^{\sigma}$, which characterizes the critical phenomenon (Kortman and Griffiths, 1971; Fisher, 1978). For instance, the magnetization exhibits singular behavior with the same critical exponent σ. The Yang-Lee edge singularity is also realized by the quantum Ising model with a real transverse field and a pure-imaginary longitudinal field (von Gehlen, 1991).

The quantum Ising model with an imaginary longitudinal field, which supports the Yang-Lee anyons, can be constructed from Majorana zero modes in a network of topological superconducting wires coupled with dissipative electron baths (Sanno et al., 2022). The Majorana modes bound at the end points of one-dimensional topological SCs constitute spin 1/2 operators. A coupling of Majorana zero modes with electrons in a metallic substrate plays a role of the pure-imaginarily longitudinal field, while the tunneling of Majorana zero modes between neighboring superconducting wires induces a transverse magnetic field. Schemes for the fusion, measurement, and braiding of Yang-Lee anyons are also proposed in Sanno et al. (2022). As mentioned above, the Yang-Lee anyons obey the nonunitary non-Abelian statistics. The nonunitary evolution of quantum states has been discussed in connection with measurement-based quantum computation (Terashima and Ueda, 2005; Usher et al., 2017; Piroli and Cirac, 2020; Zheng, 2021). Although the Yang-Lee anyons with the nonunitary F-matrix are not suitable for application to unitary quantum computation, they can be the building blocks for the construction of measurement-based quantum computation. In addition, as the nonunitary quantum gates can be implemented by braiding manipulations, the Yang-Lee anyon systems may offer a quantum simulator for nonunitary time evolution of open quantum systems in a controllable way.

Vortex anyons

In this article, we also discuss non-Abelian anyons made of bosonic (topological) excitations in ordered states. The nontrivial structure of the order parameter manifold appears in the liquid crystals, spin-2 BECs, the A phase of SF ^{3}He, dense QCD matter, and $^3P_2$ SFs. The line defects in such ordered systems, such as vortices, are represented by non-Abelian first homotopy group and their topological charges are noncommutative. Such topological defects with noncommutative topological charges behave as non-Abelian anyons, called the non-Abelian vortex anyons. In Section "Non-Abelian vortex anyons," we demonstrate that order parameter manifolds in nematic liquid crystals and spin-2 BECs admit the existence of non-Abelian vortices and show the fusion rules of such non-Abelian vortex anyons.

Non-Abelian anyons in topological SCs

Majorana zero modes as Ising anyons

Majorana zero modes

An elementary excitation from superconducting ground states is a Bogoliubov quasiparticle that is a superposition of the electron and hole. The quasiparticle excitations are described by the Bogoliubov-de Gennes (BdG) Hamiltonian

$$H = \sum_{ij} \left(\boldsymbol{\psi}_i^\dagger, \ \boldsymbol{\psi}_i \right) \mathcal{H}_{ij} \begin{pmatrix} \boldsymbol{\psi}_j \\ \boldsymbol{\psi}_j^\dagger \end{pmatrix}, \tag{12}$$

$$\mathcal{H}_{ij} = \begin{pmatrix} h_{ij} & \Delta_{ij} \\ \Delta_{ij}^\dagger & -h_{ij}^* \end{pmatrix}. \tag{13}$$

Here, $\boldsymbol{\psi}_j$ is the N-component vector of the electron field operator and $\mathcal{H}$ is the $2N \times 2N$ Hermitian matrix, where N is the sum of the spin degrees of freedom and the number of the lattice sites and so on. The $N \times N$ Hermitian matrix h describes the normal state Hamiltonian and the superconducting pair potential Δ obeys $\Delta^{\mathrm{t}} = -\Delta$ because of the Fermi statistics, where a^{t} denotes the transpose of a matrix a. The BdG Hamiltonian naturally holds the particle-hole symmetry

$$\mathcal{C}\mathcal{H}\mathcal{C}^{-1} = -\mathcal{H}, \tag{14}$$

where the particle-hole operator $\mathcal{C} = \Theta K$ is an antiunitary operator composed of the unitary operator Θ and the complex conjugation operator K. The self-conjugate Dirac fermions are called Majorana fermions, where the quantized field $\boldsymbol{\Psi} \equiv (\boldsymbol{\psi}, \boldsymbol{\psi}^\dagger)^{\mathrm{t}}$ obeys

$$\boldsymbol{\Psi} = \mathcal{C}\boldsymbol{\Psi}, \quad \mathcal{C}^2 = +1. \tag{15}$$

We expand the quantized field $\boldsymbol{\Psi}$ in terms of the energy eigenstates. The energy eigenstates are obtained from the BdG equation,

$$\sum_j \mathcal{H}_{ij} (\boldsymbol{\varphi}_E)_j = E(\boldsymbol{\varphi}_E)_i, \tag{16}$$

which describes the quasiparticle with the energy E and the wave function $\boldsymbol{\varphi}_E$. Eq. (14) guarantees that the quasiparticle state with $E > 0$ and $\boldsymbol{\varphi}_E$ is accompanied by the negative energy state with $-E$ and $\boldsymbol{\varphi}_{-E} = \mathcal{C}\boldsymbol{\varphi}_E$. Thus, the negative energy states are redundant as long as the particle-hole symmetry is maintained. Let η_E be the quasiparticle operator which satisfies the anticommutation relations, $\{\eta_E, \eta_{E'}^\dagger\} = \delta_{E,E'}$ and $\{\eta_E, \eta_{E'}\} = \{\eta_E^\dagger, \eta_{E'}^\dagger\} = 0$ $(E, E' > 0)$. The self-charge conjugation relation (15) then implies that the quasiparticle annihilation operator with a positive energy is equivalent to the creation with a negative energy as $\eta_E = \eta_{-E}^\dagger$, and $\boldsymbol{\Psi}$ is expanded only in terms of positive energy states as $\boldsymbol{\Psi}(\boldsymbol{r}) = \sum_{E>0} [\boldsymbol{\varphi}_E \eta_E + \mathcal{C}\boldsymbol{\varphi}_E \eta_E^\dagger]$. The condition (15) can be fulfilled by odd-parity SCs. In the absence of spin–orbit coupling, the spin-singlet pair potential is always invariant under the spin rotation, and the particle-hole exchange operator is given by $\mathcal{C}^2 = -1$ in each spin sector. Hence, spin-singlet SCs cannot satisfy Eq. (15). Spin–orbit coupling, however, enables even spin singlet SCs to host Majorana fermions (Sato and Ando, 2017; Alicea, 2012; Sato and Fujimoto, 2016).

Now, let us suppose that a single zero-energy state exists, and $\boldsymbol{\varphi}_0$ is its wave function. Then, we can rewrite the quantized field to

$$\boldsymbol{\Psi} = \boldsymbol{\varphi}_0 \gamma + \sum_{E>0} \left[\boldsymbol{\varphi}_E \eta_E + \mathcal{C}\boldsymbol{\varphi}_E \eta_E^\dagger \right]. \tag{17}$$

We have introduced γ, instead of $\eta_{E=0}$, to distinguish the zero mode from other energy eigenstates. Owing to Eq. (14), the zero-energy quasiparticle is composed of equal contributions from the particle-like and hole-like components of quasiparticles, that is, $\mathcal{C}\boldsymbol{\varphi}_0 = \boldsymbol{\varphi}_0$. The self-conjugate constraint in Eq. (15) imposes the following relations:

$$\gamma^\dagger = \gamma, \tag{18}$$

and $(\gamma)^2 = 1$ and $\{\gamma, \eta_{E>0}\} = \{\gamma, \eta_{E>0}^\dagger\} = 0$. The quasiparticle obeying this relation is called the Majorana zero mode. The zero energy states appear in a topological defect of topological SCs, such as chiral SCs. In Fig. 3A, we show the spectrum of Andreev bound states bound at a vortex in a chiral SC, where the level spacing between the zero mode and the lowest excitation state is $\Delta E \sim \Delta_0^2/\varepsilon_{\mathrm{F}}$ (Kopnin and Salomaa, 1991; Volovik, 1999; Read and Green, 2000; Matsumoto and Heeb, 2001). In many vortices, the hybridization between neighboring Majorana modes gives rise to the formation of the band structure with the width $\Delta E_{\mathrm{M}} \sim e^{-D/\xi}$ (Cheng et al., 2009; Mizushima and Machida, 2010), where D and ξ are the mean distance of neighboring vortices and superconducting coherence length, respectively (see Fig. 3B).

The Majorana zero modes exhibit the non-Abelian anyonic behaviors (Ivanov, 2001). To clarify this, we start with two Majorana zero modes residing in an SC. Using two Majorana operators, γ^1 and γ^2, we define the new fermion operators c and $c^\dagger$ as

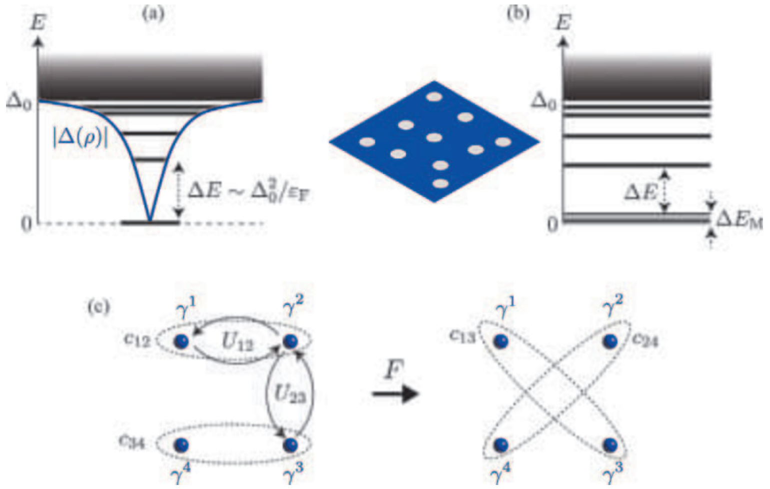

Fig. 3 Schematic of the quasiparticle states bound at a single vortex (A) and energy spectrum of many vortices (B) in a *spinless* SC, where the level spacing of vortex bound states is $\Delta E \sim \Delta_0^2/\varepsilon_F$ and ΔE_M denotes the band width of Majorana states bound at each core. (C) Operations of the braiding matrices U_{12} and U_{23} and the *F*-matrix in four Majorana modes.

$$c = \frac{1}{2}(\gamma^1 + i\gamma^2), \quad c^\dagger = \frac{1}{2}(\gamma^1 - i\gamma^2), \tag{19}$$

which obey the anticommutation relations, $\{c, c^\dagger\} = 1$ and $\{c, c\} = \{c^\dagger, c^\dagger\} = 0$. The two degenerate ground states are defined as the vacuum $|0\rangle$ and the occupied state of the zero energy state $|1\rangle = c^\dagger|0\rangle$, respectively, where the former (latter) state is the even (odd) fermion parity. We note that as the BdG Hamiltonian for superconducting states is generally commutable with the parity operator, the fermion parity remains as a good quantum number. For the even (odd) parity sector, the Hilbert space is spanned by using $|0\rangle$ ($|1\rangle$) and excited states that are constructed as $\eta^\dagger_E\eta^\dagger_{E'}\eta^\dagger_{E''}\cdots|0\rangle$ ($\eta^\dagger_E\eta^\dagger_{E'}\eta^\dagger_{E''}\cdots|1\rangle$). The Majorana operators, γ^1, γ^2, and $i\gamma^1\gamma^2$, act on the Hilbert space as the Pauli matrices σ_x, σ_y, and σ_z, respectively. The eigenstates of the Majorana operators γ^1 and γ^2 are given by the superposition of the degenerate states with different fermion parity, $|0\rangle$ and $|1\rangle$. Hence, the eigenstate of a single Majorana zero mode cannot be a physical state.

Consider $2N$ Majorana zero modes denoted by γ^j ($j = 1, \cdots, 2N$), where N complex fermions are constructed by the fusion of ith and jth Majorana zero modes as $c_{ij} = (\gamma^i + i\gamma^j)/2$. We define the occupation number operator of the complex fermion,

$$n_{ij} \equiv c^\dagger_{ij}c_{ij} = \frac{1}{2}(1 + i\gamma^i\gamma^j). \tag{20}$$

In a basis that diagonalizes paired Majorana modes $i\gamma^i\gamma^j$, two eigenvalues of the complex fermion, $n_{ij} = 0$ and 1, correspond to the fusion channels **1** and ψ, respectively. Hence, the Majorana zero mode is referred to as the Ising anyon. 2^N degenerate ground states are expressed in terms of the occupation numbers as $|n_{12}, n_{34}, \cdots\rangle$, which are separated to the sectors of the even/odd fermion parity. Here we assume that the temperature of the system is much lower than the level spacing (ΔE) between the Majorana zero mode and the lowest excitation (non-Majorana) state. Then, the 2^{N-1} degenerate ground states in each fermion parity sector can be utilized as topological qubits, where quantum information is stored in a topologically protected way.

Braiding Majorana zero modes

Here we discuss the braiding statistics of Majorana zero modes γ^i and γ^j and show the non-Abelian statistics of Majorana zero modes (Ivanov, 2001; Alicea et al., 2011; Clarke et al., 2011). While we consider the exchange of Majorana zero modes residing in vortices, the theory is also applicable to Majorana zero modes bound at the end points of one-dimensional topological SCs.

Let T_{ij} be the braid operators that satisfy Eqs. (1) and (2) and transform γ^i and γ^j to $e^{\theta_i}\gamma^j$ and $e^{i\theta_j}\gamma^i$, respectively. The unitary time evolution of Majorana zero modes is governed by the Heisenberg equation, $i\frac{d}{dt}\gamma^j(t) = [\gamma^j(t), \mathcal{H}(t)]$. The positions of two Majorana modes are adiabatically exchanged in the time interval $[0, T]$. The adiabatic condition defines the lower bound for the time scale of the braiding operation, T, so that T is much longer than the inverse of the level spacing between the Majorana zero mode and the lowest excitation (non-Majorana) state, ΔE. In addition, the upper bound is associated with the band width of Majorana modes $\Delta E_M \sim e^{-D/\xi}$ (see Fig. 3B), that is, $\Delta E^{-1} \ll T \ll \Delta E_M^{-1}$. Within the adiabatic condition, the braiding dynamics of Majorana zero modes can be regarded as the unitary time evolution, $\gamma^j(t) = U^\dagger_{ij}(t)\gamma^j(0)U_{ij}(t)$. After the braiding operation, γ^i (γ^j) changes to γ^j (γ^i) with an additional phase shift. Then, the braiding operation is represented by

$$U^\dagger_{ij}\gamma^i U_{ij} = e^{i\theta_i}\gamma^j, \quad U^\dagger_{ij}\gamma^j U_{ij} = e^{i\theta_j}\gamma^i, \tag{21}$$

where $U_{ij} \equiv U_{ij}(T)$ is the unitary operator which describes the exchange operation of two Majorana zero modes γ^i and γ^j, that is, the representation of T_{ij}. According to the conditions, $(e^{i\theta_i}\gamma^j)^2 = \left(U^\dagger_{ij}\gamma^i U_{ij}\right)^2 = 1$ and $(\gamma^j)^2 = 1$, the phase shifts obey $\theta_i = n\pi$ and $\theta_j = m\pi$, where $n, m \in \mathbb{Z}$. The braiding operations must not change the parity of the occupation number defined in Eq. (20) and thus satisfy $U^{\dagger}_{ij} n_{ij} U_{ij} = n_{ij}$, which imposes the condition, $\theta_1 + \theta_2 = (2n+1)\pi$, on the phase shift. As a result, the exchange operation of two Majorana zero modes obtains the following braiding rules:

$$U^{\dagger}_{ij}\gamma^i U_{ij} = \gamma^j, \quad U^{\dagger}_{ij}\gamma^j U_{ij} = -\gamma^i. \tag{22}$$

Consider four Majorana zero modes denoted by γ^1, γ^2, γ^3, and γ^4, which form two complex fermions as $c_{12} \equiv (\gamma^1 + i\gamma^2)/\sqrt{2}$ and $c_{34} \equiv (\gamma^3 + i\gamma^4)/\sqrt{2}$ (Fig. 3C). When the Majorana mode "3" adiabatically encircles the Majorana mode "2," both Majorana modes operators acquire the π phase shift, $\gamma^2 \mapsto -\gamma^2$ and $\gamma^3 \mapsto -\gamma^3$, corresponding to the twice operation of Eq. (22). Therefore, the braiding operation changes the occupation numbers of the complex fermion $n_{12} \equiv c^{\dagger}_{12}c_{12}$ and $n_{34} \equiv c^{\dagger}_{34}c_{34}$. For example, the above braiding generates a pair of the complex fermions $|11\rangle$ from their vacuum $|00\rangle$. Here these two states are orthogonal, $\langle 11|00\rangle = 0$. The braiding rule can be generalized to $2N$ Majorana modes. The $2N$ Majorana modes are fused to N complex fermions, leading to the 2^{N-1}-fold degeneracy of ground states while preserving fermion parity. As discussed above, when the ith and jth Majorana modes are exchanged with each other, their operators behave as $\gamma_i \mapsto \gamma_j$ and $\gamma_j \mapsto -\gamma_i$. The representation of the braid operator T_{ij} that satisfies Eq. (22) is given in terms of the zero mode operators as (Ivanov, 2001)

$$U_{ij} = e^{i\theta}\exp\left(\frac{\pi}{4}\gamma_j\gamma_i\right) = e^{i\theta}\frac{1}{\sqrt{2}}\left(1 + \gamma_j\gamma_i\right). \tag{23}$$

From now on, we omit the overall Abelian phase factor $e^{i\theta}$ as it is not important for quantum computation. Eq. (23) also holds in the case of the Moore-Read state (Nayak and Wilczek, 1996). For $N = 1$, there is only a single ground state in each sector with definite fermion parity, and the exchange of two vortices results in the global phase of the ground state by $e^{i\pi/4}$. One can easily find that for $N \geq 2$, the exchange operators U_{ij} and U_{jk} do not commute to each other, $[U_{ij}, U_{jk}] \neq 0$, implying the non-Abelian anyon statistics of the Majorana zero modes.

For four Majorana zero modes ($N = 2$), twofold degenerate ground states exist in each fermion-parity sector: $|00\rangle \equiv |\mathrm{vac}\rangle$ and $|11\rangle = c^{\dagger}_{12}c^{\dagger}_{34}|\mathrm{vac}\rangle$ in the sector of even fermion parity, and $|10\rangle = c^{\dagger}_{12}|\mathrm{vac}\rangle$ and $|01\rangle = c^{\dagger}_{34}|\mathrm{vac}\rangle$ in the sector of odd fermion parity. For the even-parity sector, the representation matrix for the exchange of 1 ↔ 2 and 3 ↔ 4 (Fig. 3C) is given by

$$U_{12} = U_{34} = e^{-i\frac{\pi}{4}}|00\rangle\langle 00| + e^{i\frac{\pi}{4}}|11\rangle\langle 11|. \tag{24}$$

This merely rotates the phase of the ground state as in the $N = 1$ case. In contrast, the representation matrix for the intervortex exchange (2 ↔ 3 in Fig. 3C) has the mixing terms of the two degenerate ground states $|00\rangle$ and $|11\rangle$,

$$U_{23} = \frac{1}{\sqrt{2}}[|00\rangle\langle 00| - i|00\rangle\langle 11| + |11\rangle\langle 11| - i|11\rangle\langle 00|]. \tag{25}$$

We note that the choice of the pairing to form the complex fermion is arbitrary. The change of the fused Majorana modes corresponds to the change of the basis from one which diagonalizes $i\gamma^1\gamma^2$ and $i\gamma^3\gamma^4$ to another which diagonalizes $i\gamma^1\gamma^3$ and $i\gamma^2\gamma^4$. The basis transformation is represented by the F-matrix as

$$F = \frac{1}{\sqrt{2}}\begin{pmatrix} 1 & 1 \\ 1 & -1 \end{pmatrix}. \tag{26}$$

The braiding matrix in Eq. (24) implies that the exchange of two Majorana zero modes fusing to ψ ($|11\rangle$) acquires an additional $\pi/2$ phase compared to the fusion channel to $\mathbf{1}$ ($|00\rangle$). Hence, Eq. (24) satisfies the property of the R-matrix in Eq. (5), that is, $R^{\sigma\sigma}_{\mathbf{1}} = -iR^{\sigma\sigma}_{\psi}$.

Platforms for Majorana zero modes

The realization of non-Abelian anyons requires to freeze out the internal degrees of freedom of Majorana modes. The simplest example is *spinless* p-wave SCs/SFs, which emerge from the low-energy part of spinful chiral p-wave SCs. To clarify this, we start with spin-triplet SCs, whose pair potential is given by a 2 × 2 spin matrix (Leggett, 1975)

$$\hat{\Delta}(\boldsymbol{k}) = \begin{pmatrix} \Delta_{\uparrow\uparrow}(\boldsymbol{k}) & \Delta_{\uparrow\downarrow}(\boldsymbol{k}) \\ \Delta_{\downarrow\uparrow}(\boldsymbol{k}) & \Delta_{\downarrow\downarrow}(\boldsymbol{k}) \end{pmatrix} = i\sigma_\mu\sigma_y d_\mu(\boldsymbol{k}) = i\sigma_\mu\sigma_y A_{\mu i}\hat{k}_i, \tag{27}$$

where $\hat{k}_i \equiv k_i/k_{\mathrm{F}}$ is scaled with the Fermi momentum k_{F}, and the repeated Greek/Roman indices imply the sum over x, y, z. Here we omit the spin-singlet component. Owing to the Fermi statistics, the spin-triplet order parameter, $\boldsymbol{d}(\boldsymbol{k})$, obeys $\boldsymbol{d}(\boldsymbol{k}) = -\boldsymbol{d}(-\boldsymbol{k})$. For spin-triplet p-wave pairing, the most general form of the order parameter is given by a 3 × 3 complex matrix, $A_{\mu i} \in \mathbb{C}$, where the components are labelled by $\mu, i \in \{x, y, z\}$.

HQVs with Majorana zero modes in SF ^{3}He

We consider the Anderson-Brinkman-Morel (ABM) state (Anderson and Morel, 1961; Anderson and Brinkman, 1973), as a prototypical example of chiral p-wave states hosting Majorana zero modes. The ABM state is realized in the A-phase of the SF

^{3}He, which appears in high pressures and high temperatures (Vollhardt and Wölfle, 1990; Volovik, 2003). At temperatures above the SF transition temperature, $T > T_c \approx 1$–2 mK, the normal Fermi liquid ^{3}He maintains a high degree of symmetry

$$G = SO(3)_L \times SO(3)_S \times U(1), \tag{28}$$

where $SO(3)_L$, $SO(3)_S$, and $U(1)$ are the rotation symmetry in space, the rotational symmetry of the nuclear spin degrees of freedom, and the global gauge symmetry, respectively. The tensor $A_{\mu i}$ transforms as a vector with respect to index μ under spin rotations, and, separately, as a vector with respect to index i under orbital rotations. The order parameter of the ABM state is then given by the complex form

$$A_{\mu j} = \Delta e^{i\varphi} \hat{d}_\mu (\hat{m}_j + i\hat{n}_j). \tag{29}$$

The ABM state is the condensation of Cooper pairs with the "ferromagnetic" orbital, and spontaneously breaks the time-reversal symmetry. The orbital part of the order parameter is characterized by a set of three unit vectors forming the triad $(\hat{\boldsymbol{m}}, \hat{\boldsymbol{n}}, \hat{\boldsymbol{l}})$, where $\hat{\boldsymbol{l}} = \hat{\boldsymbol{m}} \times \hat{\boldsymbol{n}}$ denotes the orientation of the orbital angular momentum of Cooper pairs. The remaining symmetry in the ABM state is $H_A = SO(2)_{S_z} \times SO(2)_{L_z - \varphi} \times \mathbb{Z}_2$, where $SO(2)_{S_z}$ is the two-dimensional rotation symmetry in the spin space. The ABM state is also invariant under $SO(2)_{L_z - \varphi}$ which is the combined gauge-orbital symmetry, where the $U(1)$ phase rotation, $\varphi \to \varphi + \delta\varphi$, is compensated by the continuous rotation of the orbital part about $\hat{\boldsymbol{l}}$, $\hat{m}_j + i\hat{n}_j \to e^{-i\delta\varphi}(\hat{m}'_j + i\hat{n}'_j)$. In addition, $\mathbb{Z}_2$ is the mod-2 discrete symmetry $(\hat{\boldsymbol{d}}, \hat{\boldsymbol{m}}, \hat{\boldsymbol{n}}) \to (-\hat{\boldsymbol{d}}, -\hat{\boldsymbol{m}}, -\hat{\boldsymbol{n}})$. The manifold of the order parameter degeneracy is then given by

$$R_A \simeq G/H_A \simeq S^2_S \times SO(3)_{L_z, \varphi}/\mathbb{Z}_2. \tag{30}$$

The two-sphere, S^2_S, is associated with the variation of $\hat{\boldsymbol{d}}$. The degeneracy space has an extra $\mathbb{Z}_2$ symmetry that the change from $\hat{\boldsymbol{d}}$ to $-\hat{\boldsymbol{d}}$ can be compensated by the phase rotation $\varphi \to \varphi + \pi$.

The topologically stable linear defects in the ABM state are characterized by the group of the integers modulo 4 (Vollhardt and Wölfle, 1990; Volovik, 1992; Salomaa and Volovik, 1987; Volovik, 2003),

$$\pi_1(R_A) \simeq \pi_1(SO(3)/\mathbb{Z}_2) \simeq \mathbb{Z}_4. \tag{31}$$

There exist four different classes of topologically protected linear defects in the dipole-free case. The four linear defects can be categorized by the fractional topological charge,

$$N_A = 0, \ \frac{1}{2}, \ 1, \ \frac{3}{2}, \tag{32}$$

where $N_A = 3/2$ is topologically identical to $N_A = -1/2$. The representatives of $N_A = 0$ and $N_A = 1/2$ classes include continuous vortex such as the Anderson-Toulouse vortex and half quantum vortex (HQV), respectively. Owing to $N_A = 2 = 0$, a pure phase vortex with winding number 2 is continuously deformed into a nonsingular vortex without a core, that is, the Anderson-Toulouse vortex (Anderson and Toulouse, 1977). The $N_A = 1/2$ vortex is a combination of the half-wound $\hat{\boldsymbol{d}}$-disgyration with a half-integer value of the $U(1)$ phase winding (Fig. 4). The extra $\mathbb{Z}_2$ symmetry allows us to take the half-integer value of the topological charge, because the π-phase jump arising from the half-winding of the $U(1)$ phase ($\varphi = \theta/2$) can be canceled out by the change in the orientation of $\hat{\boldsymbol{d}}$ ($\hat{\boldsymbol{d}} \to -\hat{\boldsymbol{d}}$). The $N_A = 1$ class includes a pure phase vortex with odd winding number and the radial/tangential disgyrations without phase winding. The latter was originally introduced by de Gennes as $\boldsymbol{l}$-textures with a singularity line (De Gennes, 1973; Ambegaokar et al., 1974).

The vortex with the fractional charge $N_A = 1/2$ is a harbor for spinless Majorana zero modes. We introduce the center-of-mass coordinate of Cooper pairs, $\boldsymbol{R} = (\rho, \theta, z)$, as $\hat{\Delta}(\boldsymbol{k}) \to \hat{\Delta}(\boldsymbol{k}, \boldsymbol{R})$, where $\rho = \sqrt{x^2 + y^2}$. The vortex core is located at $\rho = 0$. The vortex state is subject to the boundary condition at $\rho \to \infty$ where the orbital angular momentum of the Cooper pair is aligned to the z-axis ($\hat{\boldsymbol{l}} \parallel \hat{\boldsymbol{z}}$) and the $U(1)$ phase φ continuously changes from 0 to $2\pi\kappa$ along the azimuthal (θ) direction,

$$A_{\mu i}(\rho = \infty, \theta) = \Delta e^{i\kappa\theta} \hat{d}_\mu(\theta)(\hat{x}_j + i\hat{y}_j). \tag{33}$$

Owing to the spontaneous breaking of the gauge-orbital symmetry, there are two classes for the vorticity κ: Integer quantum vortices with $\kappa \in \mathbb{Z}$ and HQVs with $\kappa \in \mathbb{Z}/2$. In the HQVs, both the $U(1)$ phase and $\hat{\boldsymbol{d}}$ rotate by π about the vortex center (see Fig. 4). In general, the $\hat{\boldsymbol{d}}$-texture for HQVs is obtained as

$$\hat{\boldsymbol{d}}(\theta) = \cos(\kappa^{\rm sp}\theta)\hat{\boldsymbol{x}} + \sin(\kappa^{\rm sp}\theta)\hat{\boldsymbol{y}}, \tag{34}$$

where $\kappa^{\rm sp}$ denotes the winding of $\hat{\boldsymbol{d}}$. The HQV is characterized by $(\kappa, \kappa^{\rm sp}) = (1/2, \pm 1/2)$ while the integer quantum vortex has $(\kappa, \kappa^{\rm sp}) = (1, 0)$. It is remarkable to notice that since the ABM state is the equal spin pairing state, the order parameter for the HQV is recast into the representation in the spin basis as

$$\hat{\Delta} = \Delta\left[e^{i(\kappa - \kappa^{\rm sp})\theta}|\uparrow\uparrow\rangle + e^{i(\kappa + \kappa^{\rm sp})\theta}|\downarrow\downarrow\rangle\right]. \tag{35}$$

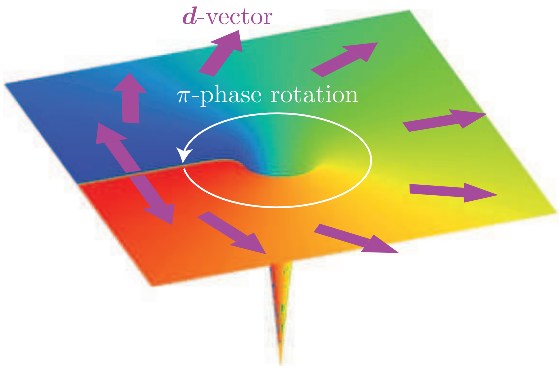

Fig. 4 Schematic of the HQV realized in the ABM state. The color map shows the U(1) phase winding from $\varphi = 0$ (*red*) at θ to π (*blue*) at $\theta = 2\pi$, and the *arrows* represent the texture of the $\hat{\boldsymbol{d}}$-vectors shown in Eq. (34) with $\kappa^{\rm sp} = 1/2$.

For the HQV with $(\kappa, \kappa^{\rm sp}) = (1/2, 1/2)$ the $|\uparrow\uparrow\rangle$ Cooper pair possesses the spatially uniform phase while the $|\downarrow\downarrow\rangle$ pair has the phase winding of 2π around the vortex as in a conventional singly quantized vortex. Thus, the vortex-free state in the ↑ spin sector exhibits fully gapped quasiparticle excitations, while the low-lying structures in HQV are effectively describable with a singly quantized vortex in the ↓ spin sector, that is, the spin-polarized chiral p-wave SC. An odd-vorticity vortex in the spin-polarized chiral system hosts a single *spinless* Majorana zero mode that obeys non-Abelian statistics. The existence of non-Abelian anyonic zero modes in half quantum vortices was first revealed by Ivanov, who developed the non-Abelian braiding statistics of vortices with spinless Majorana zero modes (Ivanov, 2001).

In the bulk A-phase of the SF ^{3}He, an obstacle to realizing the HQVs is the formation of continuous vortices with the $\hat{\boldsymbol{l}}$-texture, which are characterized by the topological charge $N = 0$. As the orientation of the $\hat{\boldsymbol{l}}$-vector is associated with the orbital motion of the Cooper pair, the $\hat{\boldsymbol{l}}$-texture can be uniformly aligned in a parallel plate geometry with thickness D. The motion of Cooper pairs is confined in the two-dimensional plane and $\hat{\boldsymbol{l}}$ is locked perpendicular to the plates. Applying a magnetic field further restricts the orientation of $\hat{\boldsymbol{d}}$ to the two-dimensional plane perpendicular to the applied field, which is a favorable situation to stabilize the HQVs. In the parallel plate geometry with $D = 12.5\mu$m, the measurements of NMR frequency shift observed that the $\hat{\boldsymbol{d}}$-vectors are confined to the two-dimensional plane perpendicular to $\hat{\boldsymbol{l}}$ (Yamashita et al., 2008). The experiment was performed in a rotating cryostat at ISSP, University of Tokyo. The parallel plates are rotated at the angular velocity $\lesssim 12$ rad/s but no conclusive evidence of HQVs was observed (Yamashita et al., 2008). Although the SF ^{3}He-A thin film provides an ideal platform for HQVs with Majorana zero modes, the realization of HQVs remains as a challenging task. We also note that point-like solitons in a superfluid ^{3}He film, such as spin disclinations, were shown to behave as anyons with fractional charges (Volovik and Yakovenko, 1989).

Another promising route to realize HQVs with Majorana zero modes is to artificially introduce well-controlled disorders with high-porosity aerogel. In particular, the polar phase was observed in anisotropic aerogels consisting of uniaxially ordered alumina strands, called the nematic aerogels (Dmitriev et al., 2015; Halperin, 2019) (see Fig. 5A). The order parameter of the polar phase is given by $A_{\mu i} = \Delta e^{i\varphi}\hat{d}_\mu \hat{z}_i$, where the orbital state of the Cooper pair $(\hat{z}_i)$ is confined by the uniaxially anisotropic disorders. As in the ABM state in the bulk ^{3}He, the texture of the $\hat{\boldsymbol{d}}$-vector concomitant with the half-integer vorticity can realize HQVs in the polar phase. In the polar phase, HQVs are energetically preferable to integer quantum vortices at zero magnetic fields and magnetic fields applied along the uniaxial anisotropy (Nagamura and Ikeda, 2018; Mineev, 2014; Regan et al., 2021). Indeed, the HQVs were experimentally observed in nematic aerogels under rotation (Autti et al., 2016). The HQVs were also created by temperature quench via the Kibble-Zurek mechanism (Rysti et al., 2021). As shown in Fig. 5A, the superfluid phase diagram in nematic aerogels is drastically changed from that of the bulk ^{3}He without disorders, where the polar-distorted A and B (PdA and PdB) phases are stabilized in addition to the polar phase. The NMR measurements performed in Mäkinen et al. (2019) observed that the HQVs survive across the phase transition to the PdA phase. As shown in Fig. 4, the HQV is accompanied by the $\hat{\boldsymbol{d}}$-soliton in which the $\hat{\boldsymbol{d}}$ orientation rotates. Fig. 5B shows the observed NMR spectra which have satellite peaks in addition to the main peak around the Larmor frequency. The main peak is a signal of the bulk PdA phase. The satellite peak originates from the spin excitation localized at the $\hat{\boldsymbol{d}}$-solitons connecting pairs of HQVs. The order parameter of the PdA phase is given by $A_{\mu i} = \Delta e^{i\varphi}\hat{d}_\mu(\hat{\boldsymbol{m}} + i\varepsilon\hat{\boldsymbol{n}})_i$, where $\hat{\boldsymbol{m}}$ is aligned along the axis of nematic aerogels and $\varepsilon \in (0, 1)$ is the temperature- and pressure-dependent parameter on the distortion of Eq. (29) by nematic aerogels. Although the HQVs in the polar phase host no Majorana zero modes, the low energy structure of the HQVs in the PdA phase is essentially same as that of HQVs in the ABM state and each core may support the existence of *spinless* Majorana zero modes (Mäkinen et al., 2019; Mäkinen et al., 2022). Hence, the survival of the HQVs in the PdA phase is important as a potential platform for topological quantum computation. The elucidation of the nature of the fermionic excitations bound to the HQVs remains as a future problem.

HQVs in SCs

In contrast to the SF ^{3}He, it is difficult to stabilize HQVs in SCs. The difficulty is attributed to the fact that the mass (charge) current is screened exponentially in the length scale of the penetration depth λ, while such a screening effect is absent in the spin current

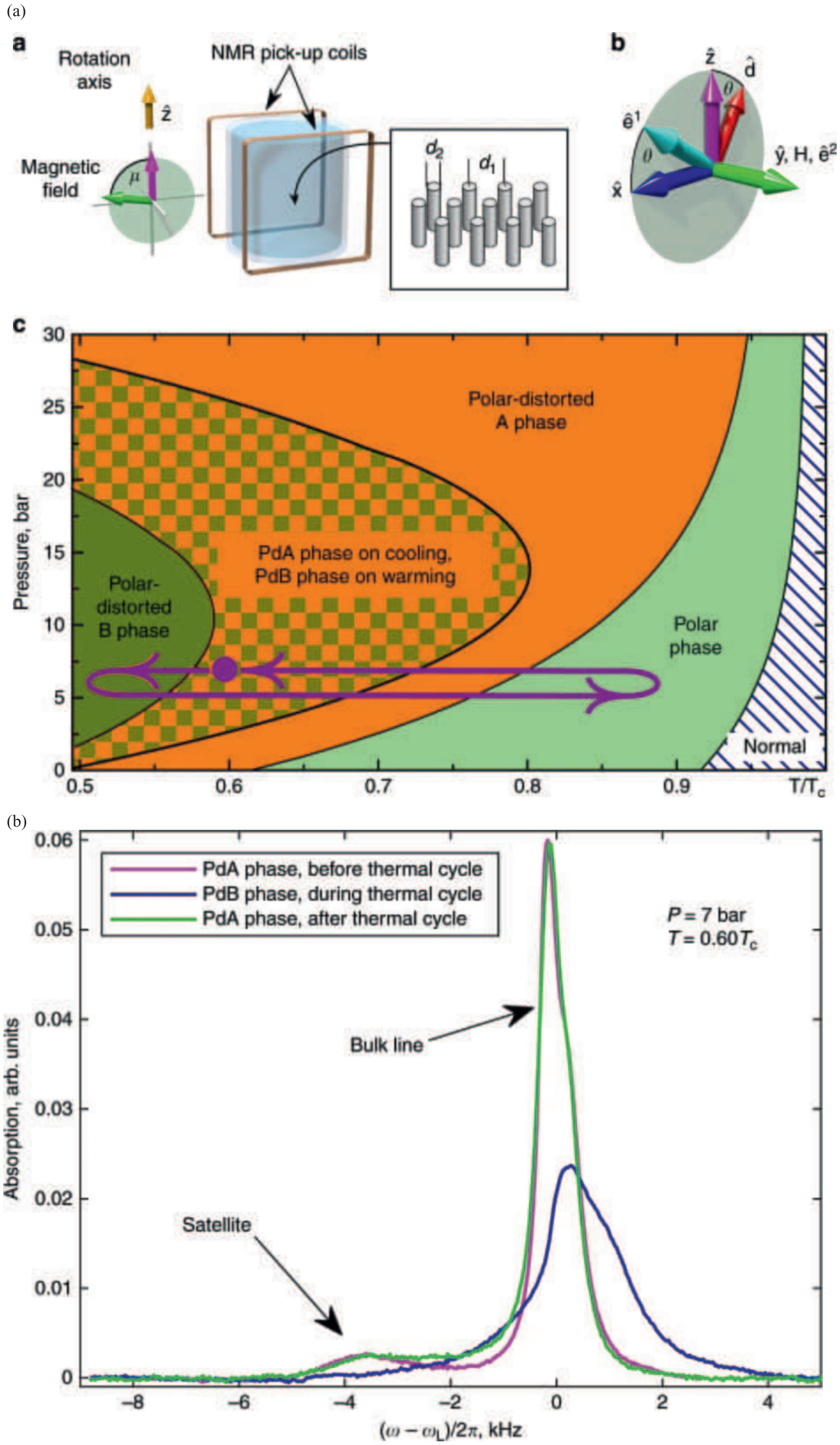

Fig. 5 (A) The experimental setup and the phase diagram in the liquid ^{3}He with nematic disorders and (B) NMR spectra at pressure $P = 7$ bar and $T = 0.60T_c$ in the presence of a magnetic field perpendicular to the anisotropy direction of nematic disorders (Mäkinen et al., 2019), where T_c is the critical temperature of the bulk SF ^{3}He without disorders. The disorders consist of nearly parallel Al_2O_3 strands, where the diameter and mean distance are $d_2 \approx 8$nm and $d_1 \approx 50$nm, respectively. In (B), the main peaks with *green* and *magenta* colors correspond to the signal of the bulk PdA phase while the satellite peaks originate from the spin excitation bound to the $\hat{\boldsymbol{d}}$-solitons connecting pairs of HQVs. The satellite peak remains unchanged after the thermal cycling illustrated by *purple arrows* in (A). Taken from Mäkinen JT, Dmitriev VV, Nissinen J, Rysti J, Volovik GE, Yudin AN, Zhang K, and Eltsov VB (2019) Half-quantum vortices and walls bounded by strings in the polar-distorted phases of topological superfluid ^{3}He. Nature Communications 10 (1): 237. https://doi.org/10.1038/s41467-018-08204-8

(Chung et al., 2007). The HQV is accompanied by the spin current in addition to the mass current, while in the integer quantum vortex, the integer vorticity ($\kappa \in \mathbb{Z}$) and uniform $\hat{\boldsymbol{d}}$-texture in Eq. (33) induce no spin current. Therefore, the absence of the screening effect on the spin current is unfavorable for the stability of the HQVs relative to the integer quantum vortices, where the later may host spin-degenerate Majorana zero modes. It has also been proposed that configurational entropy at finite temperatures drives the fractionalization of the integer quantum vortices into pairwise HQVs (Chung and Kivelson, 2010). However, no firm experimental evidence for HQVs has been reported in SCs.

Superconducting nanowires

Here we briefly mention recent progress on the search of Majorana zero modes bound at the end points of superconducting nanowires, although we mainly focus on non-Abelian anyons emergent in vortices in this article.

The first idea was proposed by Kitaev that a spinless one-dimensional SC is a platform to host a Majorana zero mode (Kitaev, 2001). Although it was initially thought to be a toy model, it was recognized that a system with the same topological properties can be realized by a semiconductor/SC heterostructure (Alicea, 2012; Sato and Ando, 2017). The key ingredients are a semiconductor nanowire and a large Zeeman magnetic field in addition to the proximitized superconducting gap Δ (Sato et al., 2009, 2010). Consider the Hamiltonian of the semiconductor nanowire under a magnetic field B, $h(p) = p^2/2m - \mu + \lambda p\sigma_y - B\sigma_z$, which appears in the diagonal part of Eq. (13), where m is the mass of an electron and λ is the strength of the spin–orbit coupling. The spin–orbit coupling is not only a source of nontrivial topology, but is also necessary to realize spinless electronic systems together with the large Zeeman field ($B > \mu$). In fact, if the proximitized superconducting gap is taken into account, a combination of spin–orbit coupling with the superconducting gap induces topological odd-parity superconductivity. The topological phase with the spinless Majorana zero mode appears in the higher magnetic field satisfying $B > B_{\rm c} = \sqrt{\Delta^2 + \mu^2}$.

A direct signature of Majorana zero mode is the quantization of a zero-bias peak in differential conductance, where the height of the zero-bias peak stemming from the Majorana zero mode is predicted to be quantized to the universal conductance value of $2e^2/h$ at zero temperature (Akhmerov et al., 2011; Fulga et al., 2011). Consider a charge-transfer process through a normal metal–SC junction. When an electron with the incident energy E enters from the normal metal to the SC, it forms the Cooper pair with an electron in the Fermi sea at the interface and a hole is created in the normal side as a consequence of momentum conservation. Such a process in which electrons are retroreflected as holes is called Andreev reflection. Let $\phi_E^{\rm in,out} = [u_E, v_E]^{\rm t}$ be the two-component wavefunctions of the incident and reflected particles, respectively, where u_E (v_E) accounts for the electron (hole) component. We now consider the scattering problem $\phi_E^{\rm out}(\boldsymbol{x}) = S(E)\phi_E^{\rm in}(\boldsymbol{x})$. The S-matrix is defined in the particle-hole space as

$$S(E) = \begin{pmatrix} r^{\rm ee}(E) & r^{\rm eh}(E) \\ r^{\rm he}(E) & r^{\rm hh}(E) \end{pmatrix}, \tag{36}$$

which is a unitary matrix $S \in U(2)$. The coefficient $r^{\rm ee}$ ($r^{\rm eh}(E)$) is the amplitude of the normal (Andreev) reflection, and the others are the reflection coefficients of incident holes.

The conductance $G(E)$ at the normal/SC interface is obtained with the conductance quantum $G_0 = e^2/h$ per spin as $G(E) = 2G_0|r^{\rm eh}(E)|^2$. The particle-hole symmetry imposes on the S matrix the constraint, $\mathcal{C}S(E)\mathcal{C}^{-1} = S(-E)$, leading to $\det S(0) = |r^{\rm ee}(0)|^2 - |r^{\rm eh}(0)|^2$ at $E = 0$. Let V be the unitary matrix defined by $V\,\phi_0 = ({\rm Re}u, {\rm Im}u)$. In this basis, the scattering matrix $S(0)$ is transformed as $S'(0) = V\,S(0)V^{\dagger}$, where $S'(0) \in O(2)$ is an orthogonal matrix satisfying $S'^{\dagger} = S'^{-1} = S'^{\rm tr}$ and $\det S(0) = \det S'(0) = \pm 1$. Hence, there are two different processes, a perfect normal reflection process ($\det S(0) = +1$) and a perfect Andreev reflection process ($\det S(0) = -1$). This discrete value, $\det S(0) = \pm 1$, is a topological invariant representing the parity of the number of Majorana zero modes residing at the interface. When $\det S(0) = -1$, there exists at least one Majorana zero mode, which involves the perfect Andreev reflection process and the quantized conductance,

$$G(0) = \frac{2e^2}{h}. \tag{37}$$

The analytical expression of the conductance is obtained by solving the BdG equation and quasiclassical Usadel equation at an interface of the normal metal and unconventional SCs (e.g., p- and d-wave SCs) (Tanaka and Kashiwaya, 1995; Kashiwaya and Tanaka, 2000; Tanaka et al., 2004, 2005), where the conductance per spin reaches $2e^2/h$. The quantized conductance is also related to the Atiyah–Singer index when the Hamiltonian holds the chiral symmetry (Ikegaya et al., 2016).

The conductance has recently been measured in a junction system of InSb-Al hybrid semiconductor-SC nanowire devices. The differential conductance yields the plateau behavior where the peak height reaches values $2e^3/h$ (Zhang et al., 2021). In the device used in the experiment, the tunnel barrier is controlled by applying a gate voltage to the narrow region between the electrode and the region where the proximity effect occurs in the semiconductor wire. In the vicinity of the barrier, the unintentionally formed quantum dot or nonuniform potential formed in the vicinity of the interface gives rise to the formation of nearly zero-energy Andreev bound states. Such Andreev bound states mimic the plateau of $G(0) = 2e^2/h$ even in the topologically trivial region of the magnetic field ($B < B_c$) (Liu et al., 2017; Prada et al., 2020; Cayao and Burset, 2021; Yu et al., 2021; Valentini et al., 2021). From the plateau of $G(0)$, it is not possible to identify whether the observed $G(0) \sim 2e^2/h$ is due to Majorana zero mode or the effect of accidentally formed s bound states. Alternative experimental schemes to distinguish the trivial and topological bound states have been proposed (Liu et al., 2018; Ricco et al., 2019; Yavilberg et al., 2019; Awoga et al., 2019; Zhang and Spånslätt, 2020; Schulenborg and Flensberg, 2020; Pan et al., 2021; Liu et al., 2021; Ricco et al., 2021; Thamm and Rosenow, 2021; Chen et al., 2022; Sugeta et al., 2022).

Vortices in Fe(Se,Te)

The iron-based SC Fe(Se,Te) is a candidate of topologically nontrivial superconducting state supporting Majorana zero modes. In the parent material FeSe, the $3d$ electrons of Fe near the Fermi level mainly contribute to superconductivity, and the p_z orbitals of Se appear on the higher energy. Substitution of Se with Te causes a band inversion between the p_z and $3d$ orbitals. As a result of the band inversion, the normal state of $\mathrm{FeTe}_{1-x}\mathrm{Se}_x$ is topologically nontrivial, and accompanied by the surface Dirac fermions (Zhang et al., 2018). Below the superconducting critical temperature, the superconducting gap is proximitized to the surface Dirac states. It was theoretically pointed out that the topological phase with a spinless Majorana zero mode can be realized when the superconducting proximity effect occurs in the Dirac fermion system (Sato, 2003; Fu and Kane, 2008). Therefore, the surface state of Fe(Se,Te) is a topological superconducting state. When a magnetic field is applied to Fe(Se,Te), the vortex lines penetrate to the surface state and the zero energy state appears. The wave function of the zero mode is tightly bound at the intersection of the vortex line and the surface (Hosur et al., 2011; Kawakami and Hu, 2015).

When a magnetic field is applied to an SC, a quantized vortex penetrates. The magnetic flux is accompanied by the $2\pi m$ winding of the $U(1)$ phase and the superconducting gap vanishes. In other words, a quantized vortex can be regarded as a quantum well with a radius of ξ and a height of Δ. Hence, the Andreev bound states are formed and the level spacing between them is on the order of Δ^2/ε_F, where the level spacing is about 100–200 μeV in Fe(Se,Te). In the topological phase, the lowest level has the exact zero energy, and the quasiparticle behaves as Majorana fermion. Ultra-low temperature STM/STS with high energy resolution observed a pronounced zero-bias conductance peak (Machida et al., 2019). If a Majorana zero mode is bound to the vortex, the conductance should be quantized to the universal value $2e^2/h$ independent of tunnel barriers. In the tunneling spectroscopy performed while changing the distance between the sample surface and the STM tip, the height of the zero-bias conductance peak is approximately 0.6 times as large as the universal value stemming from the Majorana zero mode (Zhu et al., 2020). Although $2e^2/h$ has not been reached, this plateau structure strongly suggests the existence of Majorana zero modes because it cannot be explained by non-Majorana vortex bound states.

Topological quantum computation

Quantum computation based on the braiding of Majorana zero modes is basically along the two directions: implementation of quantum gates and measurement based quantum computation. The unitary evolution of the qubits is controlled by a set of discrete unitary operations, that is, quantum gates. The simple example of the quantum gates acting on a single qubit is the set of the Pauli gates, which are given by the three Pauli matrices $X \equiv \sigma_x$, $Y \equiv \sigma_y$, and $Z \equiv \sigma_z$. The multiqubit gate operation can be implemented by a combination of a set of single-qubit gates and the controlled-NOT (CNOT) gate. According to the Solovay–Kitaev theorem (Nielsen and Chuang, 2010), an arbitrary single-qubit gate can be approximated by a sequence of the discrete gate operations (H, S, T), where $H = (X + Z)/\sqrt{2}$, $S = \sqrt{Z}$, and $T = \sqrt{S}$ are the Hadamard gate, the single-qubit 4π rotation, and the T-gate ($\pi/8$-gate), respectively. Universal quantum computation can be implemented by a sequence of the single-qubit gates (H, S, T) and the CNOT gate.

In Majorana qubits, the Pauli gates are expressed in terms of the braiding operations as $X = iU_{23}^2$, $Y = iU_{31}^2$, and $Z = iU_{12}^2$, and the Hadamard and S gates are implemented by a combination of such operations as $H = iU_{12}U_{23}U_{12}$ and $S = e^{i\pi/4}U_{12}$. In addition, the CNOT gate can be implemented by a combination of the measurement and braiding operations in two Majorana qubits (i.e., 8 Majorana zero modes) with a single ancilla Majorana qubit (Bravyi, 2006). All the Clifford gates (H, S, CNOT) are realized as a composition of braiding operators in a topologically protected way. According to the Gottesman–Knill theorem, however, quantum circuits only using the elements of Clifford group can be efficiently simulated in polynomial time on a classical computer (Nielsen and Chuang, 2010). Indeed, degenerate quantum states composed of multiple Ising anyons offer tolerant storage of quantum information, and their braiding operations provide all necessary quantum gates in a topologically protected way, except for the non-Clifford T-gate. The T-gate can be implemented only in a topologically unprotected way. For instance, Karzig et al. proposed a scheme to implement the T-gate in a Y-shaped junction accompanied by 4 Majorana zero modes (Karzig et al., 2016).

As mentioned in Section "Non-Abelian anyons," Fibonacci anyon systems can offer a platform for universal topological quantum computation, where all the single-qubit gates (H, S, T) and the CNOT gate are implemented by the braiding manipulations of the anyons in a topologically protected way (Preskill, 2004; Bonesteel et al., 2005; Hormozi et al., 2007).

Another way to realize universal quantum computation in Majorana qubits is measurement-based quantum computation. It was realized that all braiding manipulations can be implemented in a topologically protected manner by the measurements of topological charges of pairwise anyons (Bonderson et al., 2008, 2009). The process of the quantum information encoded to Majorana qubits can take place by a series of simple projective measurements without braiding Majorana modes. The building block is a Coulomb-blockaded Majorana box which is made from even numbers of Majorana modes in a floating topological SC (Plugge et al., 2017; Karzig et al., 2017; Oreg and von Oppen, 2020).

Symmetry-protected non-Abelian anyons

Symmetry-protected non-Abelian anyons in spinful SCs and SFs were discussed for class D (Ueno et al., 2013; Sato et al., 2014; Fang et al., 2014) and for class DIII (Liu et al., 2014; Gao et al., 2016). In the former (latter) case, mirror reflection symmetry (time reversal symmetry) plays an essential role in the topological protection of non-Abelian nature. In addition, unitary symmetry protected non-Abelian statistics has been theoretically proposed (Hong et al., 2022). The non-Abelian statistics of vortices supporting multiple Majorana zero modes has also been discussed in Yasui et al. (2011) and Hirono et al. (2012) in the context of high-energy physics.

Mirror and unitary symmetries

As the simple example of symmetry protected non-Abelian anyons, we consider integer quantum vortices in chiral p-wave SCs and ^{3}He-A (Sato et al., 2014), where each vortex core supports spinful Majorana zero modes. Contrary to the standard wisdom, a pair of Majorana zero modes in integer quantum vortices can be protected by the mirror symmetry and obey the non-Abelian statistics (Ueno et al., 2013; Sato et al., 2014).

Let us consider two-dimensional superconducting film and assume that the normal state holds the mirror symmetry with respect to the xy-plane, $M_{xy}h(\boldsymbol{k})M_{xy}^{\dagger} = h(\boldsymbol{k})$, where $\boldsymbol{k} = (k_x, k_y)$ is the two-dimensional momentum and the mirror operator is defined as $M_{xy} = i\sigma_z$. The nontrivial topological properties are characterized by the first Chern number in each mirror subsector. When $\Delta(\boldsymbol{k})$ obeys $M_{xy}\Delta(\boldsymbol{k})M_{xy}^{\mathrm{t}} = \eta\Delta(\boldsymbol{k})$ $(\eta = \pm)$, the BdG Hamiltonian is commutable with the mirror reflection operator in the particle-hole space, $\mathcal{M}^{\eta}$, as

$$[\mathcal{M}^{\eta}, \mathcal{H}(\boldsymbol{k})] = 0, \quad \mathcal{M}^{\eta} = \begin{pmatrix} M_{xy} & 0 \\ 0 & \eta M_{xy}^{*} \end{pmatrix}. \tag{38}$$

Thus, the eigenstates of $\mathcal{H}(\boldsymbol{k})$ are the simultaneous eigenstates of $\mathcal{M}^{\eta}$. Let $|u_n^{(\lambda)}(\boldsymbol{k})\rangle$ and $E_n^{(\lambda)}$ be the wavefunction and eigenenergy of the Bogoliubov quasiparticles in each mirror subsector, where the $\lambda = \pm i$ are the eigenvalues of $\mathcal{M}^{\eta}$. Then, the first Chern number is defined in each mirror subsector,

$$\mathrm{Ch}_1^{(\lambda)} = \frac{i}{2\pi}\int \mathcal{F}^{(\lambda)} \in \mathbb{Z}, \tag{39}$$

where $\mathcal{F}^{(\lambda)} = d\mathcal{A}^{(\lambda)}$ is the Berry curvature in each mirror subsector and $\mathcal{A}_{\mu}^{(\lambda)}(\boldsymbol{k}) = \sum_{E_n^{(\lambda)}<0} \langle u_n^{(\lambda)}(\boldsymbol{k})|\partial_{k_\mu} u_n^{(\lambda)}(\boldsymbol{k})\rangle$. The nonzero value ensures the existence of the zero energy state in the λ subsector. For the ^{3}He-A thin film and chiral p-wave SCs, $|\mathrm{Ch}_1^{(\lambda)}| = 1$ in each mirror subsector, implying that integer quantum vortices support two Majorana zero modes per each core.

Multiple Majorana zero modes behave as non-Abelian anyons only when the mirror subsector holds the particle-hole symmetry, which are referred to as mirror Majorana zero modes. The condition for each mirror subsector to maintain the particle-hole symmetry is given by (Ueno et al., 2013; Sato et al., 2014)

$$\{\mathcal{C}, \mathcal{M}^{\eta}\} = 0. \tag{40}$$

For integer quantum vortices, the condition depends on the orientation of the $\boldsymbol{d}$-vector. For $\hat{\boldsymbol{d}} \parallel \hat{\boldsymbol{z}}$, the mirror subsector supports its own particle-hole symmetry, but otherwise the subsector does not maintain the particle-hole symmetry and belongs to class A.

Now let us clarify the non-Abelian statistics of spin-degenerate Majorana modes. Consider $2N$ integer quantum vortices. Two Majorana zero modes bound at the ith vortex are denoted by γ_{λ}^{i} with mirror eigenvalues $\lambda = \pm i$. The Majorana zero modes satisfy the self-conjugate condition $\gamma_{\lambda}^{i} = (\gamma_{\lambda}^{i})^{\dagger}$ and the anticommutation relation, $\{\gamma_{\lambda}^{i}, \gamma_{\lambda'}^{j}\} = 2\delta_{i,j}\delta_{\lambda,\lambda'}$. In contrast to spinless Majorana zero modes, there are two possibilities to form a complex fermion: (i) intervortex pairs, $c_{ij}^{\lambda} \equiv (\gamma_{\lambda}^{i} + i\gamma_{\lambda}^{j})/2$ and (ii) intravortex pairs, $\psi_i \equiv (\gamma_{\lambda=i}^{i} + i\gamma_{\lambda=-i}^{i})/2$ (see Fig. 6A and B). In the former case (i), the exchange operators of the ith and jth vortices are defined in a manner similar to that for spinless Majorana zero modes as

$$U_{ij}^{\lambda\dagger}\gamma_{\lambda}^{i}U_{ij}^{\lambda} = \gamma_{\lambda}^{j}, \quad U_{ij}^{\lambda\dagger}\gamma_{\lambda}^{j}U_{ij}^{\lambda} = -\gamma_{\lambda}^{i}. \tag{41}$$

The above transformation is realized by the unitary operator,

$$U_{ij}^{\lambda} = \exp\left(\frac{\pi}{4}\gamma_{\lambda}^{j}\gamma_{\lambda}^{i}\right) = \frac{1}{\sqrt{2}}\left(1 + \gamma_{\lambda}^{j}\gamma_{\lambda}^{i}\right), \tag{42}$$

Similarly to U_{ij} and U_{jk} in spinless Majorana zero modes, the exchange operators U_{ij}^{λ} and U_{jk}^{λ} defined in each mirror subsector do not commute to each other, which implies the non-Abelian anyon statistics of integer quantum vortices hosting mirror Majorana zero modes.

In the case (ii) (Fig. 6B), a complex fermion is formed as a local pair of two mirror Majorana modes, which also obeys the non-Abelian statistics (Yasui et al., 2012; Sato et al., 2014). The expression of the exchange operator is obtained as $U_{ij} = 1 + \psi_j\psi_i^{\dagger} + \psi_j^{\dagger}\psi_i - \psi_i^{\dagger}\psi_i - \psi_j^{\dagger}\psi_j + 2\psi_j^{\dagger}\psi_j\psi_i^{\dagger}\psi_i$. In general, the exchange operators are not commutable with each other, $[U_{ij}, U_{jk}] \neq 0$. As the operator preserves the fermion number $N_{\mathrm{f}} = \sum_i \psi_i^{\dagger}\psi_i$, the degenerate ground states are expressed in terms of the occupation number of the complex fermion in each vortex. For example, let us consider the four-vortex state $|1100\rangle$ where the first and second vortices are accompanied by the Dirac zero modes, while the third and fourth are not. Up to a phase factor, this state changes under U_{12} and U_{34} as $|1100\rangle \rightarrow |1100\rangle$ and $|1100\rangle \rightarrow |1010\rangle$, respectively. The complete representations of the exchange operators U_{ij} are presented in Yasui et al. (2012). The extension to non-Abelian statistics of multiple complex fermions was discussed in Yasui et al. (2013).

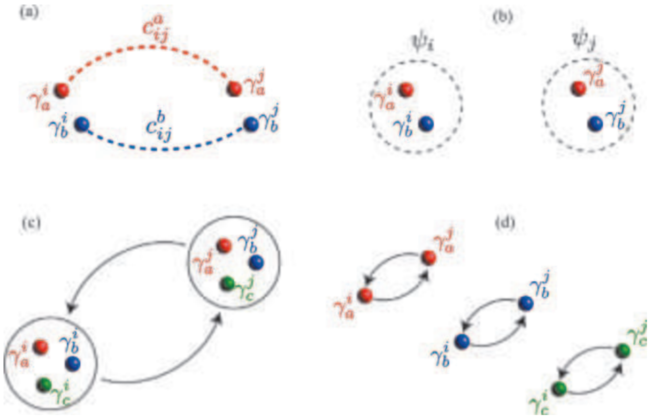

Fig. 6 Complex fermions formed by intervortex pairs (A) and intravoretx pairs (B), where γ_a^j denotes a Majorana zero mode with internal degrees of freedom *a* (e.g., spin) bound at the *i*th vortex. (C) Schematic of the exchange of two vortices with multiple Majorana zero modes. (D) When the system holds a unitary symmetry such as the mirror symmetry in Eq. (38), the operation (C) is equivalent to the exchange of two Majorana zero modes in each sector.

When the BdG Hamiltonian maintains the mirror symmetry in Eq. (38), as mentioned above, the braiding of vortices supporting spinful Majorana modes is decomposed into two individual exchanges between Majorana zero modes γ_λ^i and γ_λ^j in each mirror subsector (see also Fig. 6C and D) and the exchange matrices are represented by Eqs. (41) and (42). This argument is applicable for the systems hosting multiple Majorana modes protected by unitary symmetries (Hong et al., 2022), where the couplings between Majorana zero modes in each core are excluded by the unitary symmetries. The braiding of two vortices with n unitary-symmetry-protected multiple Majorana modes generically reduces to the n independent braiding operations in each sector as

$$U_{ij} = \prod_a U_{ij}^a, \tag{43}$$

where a denotes the internal degrees of freedom of Majorana zero modes. The unitary time evolution representing the braiding process does not dynamically break the unitary symmetry, which prohibits the coupling between Majorana modes in different subsectors labeled by a. The mirror reflection symmetry in Eq. (38) is an example of such symmetry-protected non-Abelian anyons. Another example is the non-Abelian vortices in dense QCD matter which trap multiple Majorana zero modes in each core (Yasui et al., 2010; Fujiwara et al., 2011). As discussed below, such vortices with multiple Majorana zero modes obey the non-Abelian statistics and the braiding matrices are identical with the elements in the Coxeter group (Yasui et al., 2011; Hirono et al., 2012).

Contrary to unitary symmetries, the braiding process, characterized as a unitary evolution, may dynamically break antiunitary symmetry such as the time-reversal symmetry. We note that in contrast to time reversal-broken topological SCs such as superconducting nanowires, topological superconductors with time reversal symmetry do not require an external magnetic field for realizing the topological phase and can keep the topological gap close to the proximity-induced superconducting gap (Haim and Oreg, 2019; Wong and Law, 2012; Zhang et al., 2013). Hence, the Majorana-Kramers pairs leads to longer decoherence time of the stored quantum information (Liu et al., 2014). As mentioned above, however, the braiding process of the Majorana-Kramers pairs may dynamically break the antiunitary symmetry. Such dynamical symmetry breaking gives rise to the local mixing of the Majorana-Kramers pairs (Wölms et al., 2014, 2016; Knapp et al., 2020). Gao et al. proposed the conditions to protect the non-Abelian statistics of the Majorana-Kramers pairs (Gao et al., 2016). In addition, Tanaka et al. examined by numerical simulations the tolerance of non-Abelian braidings of Majorana-Kramers pairs against two types of perturbations which may cause decoherence of Majorana-Kramers quits (Tanaka et al., 2022): (i) Applied magnetic fields and (ii) the effect of a gate-induced inhomogeneous potential at junctions of superconducting nanowires. The former break time reversal symmetry and generate the energy gap of Majorana states while the latter gives rise to non-Majorana low-energy Andreev bound states (Kells et al., 2012; Liu et al., 2017; Moore et al., 2018b, a; Pan et al., 2020; Pan and Das Sarma, 2020). The numerical simulation revealed that the non-Abelian braiding is successful when the direction of the applied magnetic field preserves the chiral symmetry in the initial and final states of a braiding process, where the chiral symmetry is a combination of time reversal symmetry and mirror symmetry (Tanaka et al., 2022). Remarkably, this tolerance is preserved even when the intermediate states of the braiding process breaks this symmetry. As for (ii), non-Majorana-bound states emergent in gate-induced inhomogeneous potentials make Majorana-Kramers qubits vulnerable to quasiparticle poisoning and disturb the braiding protocol. However, the influence can be ignored when the width of the gate-induced potential is sufficiently smaller than the superconducting coherence length.

Multiple Majorana zero modes and Coxeter group

It has been demonstrated that the non-Abelian statistics of vortices hosting three Majorana zero modes has a novel structure, when the Majorana modes have additional $SO(3)$ symmetry (Yasui et al., 2011; Hirono et al., 2012). The representation of braiding operations in four vortices is given by a tensor product of two matrices, where one is identical to the matrix for the braiding of spinless Majorana zero modes, and the other is a generator of the Coxeter group.

Let γ_a^i ($a = 1, 2, 3$) be the operators of three Majorana zero modes in the ith vortex, belonging to the triplet of $SO(3)$. Consider four vortices hosting three Majorana zero modes in each core. The braiding of these vortices is decomposed into the three individual exchanges between Majorana zero modes γ_a^i and γ_a^j (see Fig. 6C and D). For each component a, Majorana zero modes γ_a^i and γ_a^j under braiding manipulations transform in the same way as Eq. (41) and the exchange matrices, U_{ij}^a, are obtained by $U_{ij}^{\lambda} \to U_{ij}^a$ in Eqs. (41) and (42). Then, the representations of U_{ij} for vortices with triplet Majorana zero modes are obtained by the 64×64 matrix, $U_{ij} = \prod_{a=1,2,3} U_{ij}^a$, as in Eq. (43).

We now introduce the complex fermion operators as the nonlocal pairs of Majorana zero modes, $c_{ij}^a = (\gamma_a^i + i\gamma_a^j)/2$. For two vortices (i.e., six Majorana modes), this leads to the 2^3-fold degenerate ground states and the Hilbert space is spanned by the four basis sets: singlet-even $|\mathbf{1}_0\rangle \equiv |0\rangle$ (vacuum) and triplet-even $|\mathbf{3}_2\rangle \equiv \frac{1}{2!}\varepsilon^{abc} c_{ij}^{b\dagger} c_{ij}^{c\dagger}|0\rangle$ (occupied by two fermions) for even fermion parity and singlet-odd $|\mathbf{1}_3\rangle \equiv \frac{1}{3!}\varepsilon^{abc} c_{ij}^{a\dagger} c_{ij}^{b\dagger} c_{ij}^{c\dagger}|0\rangle$ (occupied by three fermions) and triplet-odd $|\mathbf{3}_1\rangle \equiv c_{ij}^{a\dagger}|0\rangle$ (occupied by single fermion). In the case of four vortices, the ground-state degeneracy is $2^6 = 64$ and the bases of the Hilbert space are singlet ($\mathbf{1}$), triplet ($\mathbf{3}$), and quintet ($\mathbf{5}$) states, which are further divided in terms of the fermion parity. The exchange operator is expressed as a product of two $SO(3)$ invariant unitary operators,

$$U_{ij} = \prod_{a=1,2,3} U_{ij}^a = \sigma_{ij} h_{ij} \tag{44}$$

where both matrices are given in terms of γ_i^a as

$$\sigma_{ij} = \frac{1}{2}\left(1 - \gamma_j^1\gamma_j^2\gamma_i^1\gamma_i^2 - \gamma_j^2\gamma_j^3\gamma_i^2\gamma_i^3 - \gamma_j^3\gamma_j^1\gamma_i^3\gamma_i^1\right), \tag{45}$$

and

$$h_{ij} = \frac{1}{\sqrt{2}}\left(1 - \gamma_j^1\gamma_j^2\gamma_j^3\gamma_i^1\gamma_i^2\gamma_i^3\right). \tag{46}$$

While the matrices h_{ij} are a natural extension of that originally introduced in Ivanov (2001), the matrices σ_{ij} are proper to vortices with three or more Majorana zero modes. It was demonstrated that the matrices σ_{ij} are identified with the elements in the Coxeter group which satisfies the relations

$$(\sigma_{ij})^2 = 1, \; (\sigma_{ij}\sigma_{jk})^3 = 1, \; (\sigma_{ij}\sigma_{kl})^2 = 1. \tag{47}$$

The Coxeter group is a symmetry group of polytopes in high dimensions such as a triangle and a tetrahedron. The exchange operators acting on the singlet ($\mathbf{1}$) and triplet ($\mathbf{3}$) are identified with the elements in the Coxeter group, such as a 2-simplex (triangle) under the reflections for the singlet and a 3-simplex (tetrahedron) under the reflections for the triplet (Yasui et al., 2011). The decomposition of the braiding operators U_{ij} in the $SO(3)$ triplet was generalized to the Majorana zero modes of arbitrary odd $n_{\mathrm{M}} \geq 3$ with $SO(n_{\mathrm{M}})$ symmetry (Hirono et al., 2012).

Such multiple Majorana zero modes were first found in Yasui et al. (2010) and Fujiwara et al. (2011) inside the cores of color flux tubes ("non-Abelian" vortices) (Balachandran et al., 2006; Nakano et al., 2008; Eto and Nitta, 2009; Eto et al., 2014) in QCD matter (Alford et al., 2008). They were also discussed in edges of a topological superconducting wire coupled to a normal lead (Kashuba and Timm, 2015).

Non-Abelian vortex anyons

Here we introduce non-Abelian anyons made of bosonic excitations, which are non-Abelian vortices obeying a non-Abelian statistics (Bais, 1980; Wilczek and Wu, 1990; Bucher, 1991; Brekke et al., 1993; Lo and Preskill, 1993; Lee, 1994; Brekke et al., 1997; Mawson et al., 2019). These non-Abelian vortices are sometime called fluxons.[2]

Non-Abelian vortices

When a symmetry G, that is either global or local, is spontaneously broken into its subgroup H, there appears an order parameter space

$$M \simeq G/H \tag{48}$$

---

[2] Here, the term "flux" originally comes from the fact that they were proposed in gauge theory where non-Abelian symmetry is gauged in the context of high energy physics (Bais, 1980). In this article, we consider only global non-Abelian symmetry relevant for condensed matter physics and they do not carry non-Abelian fluxes.

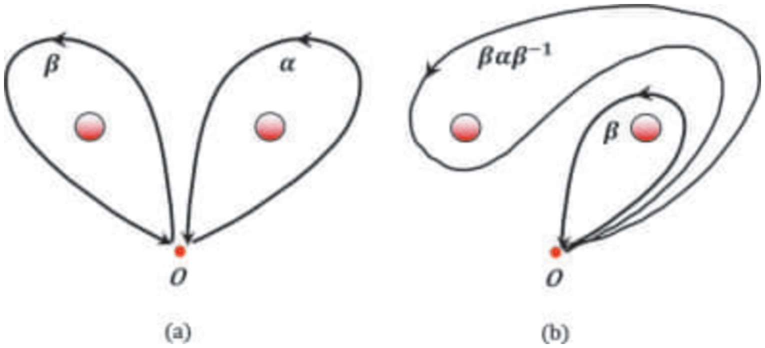

Fig. 7 Exchange of two vortices. (A) Two closed paths α and β encircle two vortices. (B) Exchange them counterclockwisely.

parameterized by Nambu-Goldstone modes. The first homotopy group of the order parameter space

$$\pi_1(G/H) \simeq \pi_0(H) \tag{49}$$

is responsible for the existence of quantum vortices, where we have assumed that G is semisimple. We further have

$$\pi_0(H) \simeq H/H_0 (\simeq H \text{ for a discrete group } H) \tag{50}$$

with a normal subgroup H_0 of H. When $\pi_1(G/H)$ is Abelian (and thus H/H_0 (for semisimple G) is Abelian), vortices are Abelian, while when it is non-Abelian, vortices are non-Abelian (Balachandran et al., 1984; Alford et al., 1990, 1991, 1992).

One of characteristic features of non-Abelian vortices is that H is not globally defined (or multivalued): the unbroken symmetry H_θ depends on the azimuthal angle θ around a non-Abelian vortex as $H_\theta = g(\theta)H_{\theta=0}g^{-1}(\theta)$ with $g(\theta) \in G$, $g(0) = \mathbf{1}$ and $g(2\pi)$ taking a disconnected component of H/H_0, see Eq. (50). Then, after an adiabatic transport along a loop encircling the non-Abelian vortex, the unbroken symmetry at $\theta = 2\pi$ does not have to come back: $H_{\theta=2\pi} \neq H_{\theta=0}$. This is called *topological obstruction*, and the symmetry H is topologically broken down to a subgroup $K \equiv \{h|[h, g(2\pi)] = 0, h \in H\}$ which is single-valued and globally defined (Balachandran et al., 1984; Alford et al., 1990). This is also called *topological symmetry breaking*. When G and H are local gauge symmetries, it gives a non-Abelian Aharonov–Bohm effect (Bais, 1980; Wilczek and Wu, 1990; Bucher, 1991; Alford et al., 1990, 1991, 1992). Another related feature is the existence of nonlocal charges, called Cheshire charges, existing among separated vortices (Preskill and Krauss, 1990; Alford et al., 1990; Bucher et al., 1992).

Let $\alpha, \beta \in \pi_1(G/H)$ being closed passes enclosing two vortices. Then, if one adiabatically transports the vortex α around the vortex β counterclockwisely, the vortex α transforms as (see Fig. 7B)

$$\alpha \to \beta\alpha\beta^{-1}. \tag{51}$$

Therefore, when one exchanges a pair (α, β) counterclockwisely, they transform as

$$(\alpha, \beta) \to (\beta, \beta\alpha\beta^{-1}). \tag{52}$$

The first homotopy group π_1 is a based fundamental group for which every loop starts from a fixed point O. Instead of it, the conjugacy classes

$$[\alpha] = \beta\alpha\beta^{-1}, \ \forall \beta \in \pi_1(G/H) \tag{53}$$

characterize individual vortices as can be seen from Eqs. (51) and (52). Two vortices corresponding to two different elements in the same conjugacy class are *indistinguishable* even though they are not the same.

Non-Abelian first homotopy groups significantly control the dynamics of vortices. In two spatial dimensions, scattering of such non-Abelian vortices was discussed in the case that G and H are local gauge symmetries (Wilczek and Wu, 1990; Bucher, 1991; Lo and Preskill, 1993). In three spatial dimensions, vortices are lines. When two vortex lines collide in three spatial dimensions, the fate is determined by corresponding elements of the first homotopy group. When these elements commute, the two vortices pass through or reconnect each other if these elements are identical. On the other hand, when these elements are noncommutative, the third vortex bridging them must be created (Poenaru and Toulouse, 1977; Mermin, 1979; Kobayashi et al., 2009).

Examples of non-Abelian vortices

Nematic liquid crystals

Let us start from nematic liquid crystals focusing on uniaxial nematics (UNs), and D_2- and D_4-biaxial nematics (BNs).

UN liquid crystals

The order parameter of UNs is an unoriented rod. The rotational symmetry $G = SO(3)$ is spontaneously broken down to $H \simeq O(2)$, which implies the order parameter manifold

$$\frac{G}{H} = \frac{SO(3)}{O(2)} \simeq \frac{SU(2)}{Pin(2)} \simeq S^2/\mathbb{Z}_2 \simeq \mathbb{R}P^2, \tag{54}$$

which is a real projective space of two dimensions, where $SU(2)$ and $Pin(2)$ are double covering groups of $SO(3)$ and $O(2)$, respectively. Since the fundamental group $\pi_1(\mathbb{R}P^2) = \mathbb{Z}_2$ is Abelian, this does not admits non-Abelian vortices. These vortices are called Alice strings (when G and H are local gauge symmetries) (Schwarz, 1982). Around the Alice string, $SO(2) \subset H$ is not globally defined and H is topologically broken to $K \simeq \mathbb{Z}_2$.

D_2-BN liquid crystals (Poenaru and Toulouse, 1977; Volovik and Mineev, 1977; Mermin, 1979; Balachandran et al., 1984)

Cholesteric liquid crystals (chiral nematic liquid crystals) can also have the same order parameter space with D_2-BN liquid crystals (Lavrentovich and Kleman, 2001) and all the following discussions hold. The order parameter of BNs is a set of two unoriented rods of different lengths orthogonal to each other. The (unbroken) symmetry is the dihedral group D_2 keeping a rectangular invariant. Thus, the rotational symmetry $G = SO(3)$ is spontaneously broken down to

$$H \simeq D_2 = \left\{ \mathbf{1}_3, I_x = \begin{pmatrix} +1 & 0 & 0 \\ 0 & -1 & 0 \\ 0 & 0 & -1 \end{pmatrix}, I_y = \begin{pmatrix} -1 & 0 & 0 \\ 0 & +1 & 0 \\ 0 & 0 & -1 \end{pmatrix}, I_z = \begin{pmatrix} -1 & 0 & 0 \\ 0 & -1 & 0 \\ 0 & 0 & +1 \end{pmatrix} \right\}. \tag{55}$$

Note that $D_2 \simeq \mathbb{Z}_2 \times \mathbb{Z}_2$ is Abelian. The order parameter manifold is

$$G/H = SO(3)/D_2 \simeq SU(2)/\mathbb{Q}, \tag{56}$$

where the quaternion group $\mathbb{Q}$ are universal (double) covering group of D_2:

$$\mathbb{Q} = \{\pm \mathbf{1}_2, \pm i\sigma_x, \pm i\sigma_y, \pm i\sigma_z\}. \tag{57}$$

Note that $H^* \simeq \mathbb{Q}$ is a non-Abelian group while $H \simeq D_2$ is an Abelian group. This breaking can occur for instance by five real-scalar order parameters belonging to spin-2 representation of $SO(3)$, which is a traceless symmetric 3×3 tensor A with real components, taking a form of

$$A = \mathrm{diag}(1, r, -1-r). \tag{58}$$

The first homotopy group is isomorphic to the quaternion group $\mathbb{Q}$ in Eq. (57)

$$\pi_1(SU(2)/\mathbb{Q}) \simeq \mathbb{Q}. \tag{59}$$

The elements in Eq. (57) correspond to the ground state ($\mathbf{1}_2$), spin vortices of 2π rotation ($-\mathbf{1}_2$), and spin vortices of $\pm\pi$ rotation about the x, y, z-axes ($\pm i\sigma_{x,\,y,\,z}$). These vortex configurations at the large distance can be asymptotically written as

$$A \sim O(\theta) A_{\theta=0} O^T(\theta), \quad O(\theta) \in SO(3) \tag{60}$$

with the azimuthal angle θ. The concrete forms of $O(\theta)$'s are given in Table 1. Corresponding $SU(2)$ elements $g(\theta)$ can be defined as a double covering of $SO(3)$ with $g(2\pi) \in \pi_1(G/H)$. A spin vortex of 2π rotation ($-\mathbf{1}_2$) and a spin vortex of π rotation ($\pm i\sigma_a$) ($a = x, y, z$) are given by

$$\begin{aligned} g(\theta) &= \exp\left(\pm i \frac{\theta}{2} \sigma \cdot \mathbf{n}\right) = \cos\frac{\theta}{2} \mathbf{1}_2 \pm i\sigma \cdot \mathbf{n} \sin\frac{\theta}{2}, \\ g(\theta) &= \exp\left(\pm i \frac{\theta}{4} \sigma_a\right) = \cos\frac{\theta}{4} \mathbf{1}_2 \pm i\sigma_a \sin\frac{\theta}{4}, \end{aligned} \tag{61}$$

respectively, with a unit three-vector $\mathbf{n}$, giving the elements of $\pi_1(G/H)$ at $\theta = 2\pi$: $g(2\pi) = -\mathbf{1}_2$ and $g(2\pi) = \pm i\sigma_a$, respectively. While the former is Abelian because $[g(2\pi), H^*] = 0$ (even though $g(2\pi) \neq g(0)$), the latter is non-Abelian because $[g(2\pi), H^*] \neq 0$ with the universal covering $H^* \simeq SU(2)$,[3] and H^* is topologically broken to $K^*_a = \{\pm \mathbf{1}_2, \pm i\sigma_a\}$.

---

[3] Note that $[O(2\pi), H] = 0$, and thus the criterion of non-Abelian property should be considered in the universal covering group H^* but not in H.

Table 1 Asymptotic configurations of spin vortices in D_2-BNs: the fundamental group elements $g(2\pi) \in \pi_1(G/H)$, the $SU(2)$ elements $g(\theta) \in SU(2)$, $O(2\pi)$, and the $SO(3)$ group elements $O(\theta) \in SO(3)$, acting on the order parameter A as Eq. (60). The group actions $O(\theta)$ and $g(\theta)$ for a spin vortex of 2π rotation ($-\mathbf{1}_2$) can be a rotation around any axis along the unit vector $\mathbf{n}$. L_i are 3×3 spin-1 matrices $[L_i]_{jk} = -i\varepsilon_{ijk}$.

$g(2\pi) \in \pi_1(G/H)$	$\mathbf{1}_2$	$-\mathbf{1}_2$	$\pm i\sigma_x$	$\pm i\sigma_y$	$\pm i\sigma_z$
$g(\theta)$	$\mathbf{1}_2$	$\exp\left(i\frac{\theta}{2}\mathbf{n}\cdot\sigma\right)$	$\exp\left(\pm i\frac{\theta}{4}\sigma_x\right)$	$\exp\left(\pm i\frac{\theta}{4}\sigma_y\right)$	$\exp\left(\pm i\frac{\theta}{4}\sigma_z\right)$
$O(2\pi)$	$\mathbf{1}_3$	$\mathbf{1}_3$	I_x	I_y	I_z
$O(\theta)$	$\mathbf{1}_3$	$\exp(i\theta\mathbf{n}\cdot\mathbf{L})$	$\exp\left(\pm i\frac{\theta}{2}L_x\right)$	$\exp\left(\pm i\frac{\theta}{2}L_y\right)$	$\exp\left(\pm i\frac{\theta}{2}L_z\right)$

The elements in Eq. (57) are grouped to the conjugacy classes, Eq. (53), consisting of five elements:

$$\{\mathbf{1}_2\}, \{-\mathbf{1}_2\}, \{\pm i\sigma_x\}, \{\pm i\sigma_y\}, \{\pm i\sigma_z\}. \tag{62}$$

This follows for instance from $(i\sigma_y)^{-1}(i\sigma_x)(i\sigma_y) = -i\sigma_x$, implying that a vortex corresponding to $i\sigma_x$ becomes $-i\sigma_x$ when it travels around a vortex corresponding to $i\sigma_y$. Thus, the vortices corresponding to $i\sigma_x$ and $-i\sigma_x$ are *indistinguishable* although they are not the same. From $(i\sigma_a)(-i\sigma_a) = \mathbf{1}_2$ $(a = x, y, z)$, vortices belonging to the same conjugacy class are antiparticles of each other, and thus they are similar to Majorana fermions discussed in the last section.

In three spatial dimensions, this phenomenon of noncommutativity appears as follows: when two vortex lines corresponding to $i\sigma_x$ and $i\sigma_y$ collide in three spatial dimensions, the third vortex bridging them is created (Poenaru and Toulouse, 1977; Mermin, 1979).

D_4-BN liquid crystals

The order parameter of D_4 BNs is a set of two unoriented indistinguishable rods of the *same* lengths orthogonal to each other. In this case, the (unbroken) symmetry is a dihedral group D_4 keeping a square invariant:

$$G/H = SO(3)/D_4 \simeq SU(2)/D_4^*, \tag{63}$$

where M^* denotes a universal covering group of M. The fundamental group is given by

$$\pi_1(SU(2)/D_4^*) \simeq D_4^* \tag{64}$$

with the sixteen elements

$$\left\{\pm\mathbf{1}_2, \pm i\sigma_x, \pm i\sigma_y, \pm i\sigma_z, \pm C_4, \pm C_4^{-1}, \pm i\sigma_x C_4, \pm i\sigma_x C_4^{-1}\right\} \tag{65}$$

with $C_4 \equiv e^{i\frac{\pi}{4}\sigma_z} = (1/\sqrt{2})(\mathbf{1}_2 + i\sigma_z)$. Note $(C_4)^2 = i\sigma_z$ and $(C_4)^4 = -\mathbf{1}_2$. The conjugacy classes consist of the following seven elements

$$\{\mathbf{1}_2\}, \{-\mathbf{1}_2\}, \{\pm i\sigma_x, \pm i\sigma_y\}, \{\pm i\sigma_z\}, \{C_4, C_4^{-1}\}, \{-C_4, -C_4^{-1}\}, \{\pm i\sigma_x C_4, \pm i\sigma_x C_4^{-1}\}. \tag{66}$$

Since $-C_4 = C_4^3$ $(-C_4^{-1} = C_4^{-3})$, vortices of these elements have more energy than those of C_4 and C_4^{-1}. This symmetry breaking of D_4 nematics can be realized by a higher rank tensor order parameter (Mietke and Dunkel, 2022), in which more generally D_n nematic liquid crystals were also discussed.

Spinor BECs

Next we provide examples of spinor BECs (Kawaguchi and Ueda, 2012). The order parameter of spin-2 BECs is a traceless symmetric 3×3 tensor A with *complex* components transforming under the symmetry $G = U(1) \times SO(3)$ as

$$A \to e^{i\theta} g A g^T, \quad e^{i\theta} \in U(1), \quad g \in SO(3). \tag{67}$$

Phases of condensations with total angular momentum two are classified by Mermin (Mermin, 1974). They are nematic, cyclic, and ferromagnetic phases. All phases are theoretically possible in the case of spin-2 BECs. The spin-2 BECs are experimentally realized by ^{87}Rb atoms for which the phase is around the boundary between cyclic phase and ferromagnetic phase, see for example, Tojo et al. (2009). Here, we discuss nematic and cyclic phases which host non-Abelian vortex anyons. In the next section, we discuss $^3P_2$ SF which is in the nematic phase.

BN phases in spin-2 BEC (Song et al., 2007; Uchino et al., 2010; Kobayashi et al., 2012; Borgh and Ruostekoski, 2016)

The nematic phase consists of three degenerate phases: the UN, D_2- and D_4-BN phases. The order parameters of the UN, D_2-, and D_4-BN phases are given by

$$\begin{aligned} &\mathrm{UN}: A \sim \mathrm{diag}(1,\ -1/2,\ -1/2),\\ &D_2\text{-BN}: A \sim \mathrm{diag}(1, r,\ -1-r),\\ &D_4\text{-BN}: A \sim \mathrm{diag}(1,\ -1, 0), \end{aligned} \tag{68}$$

respectively, where $r \in \mathbb{R}$ and $-1 < r < -1/2$. In the D_2-BN phase, the limits $r \to -1/2, -1$ correspond to UN and D_4-BN phases, respectively. The symmetry breaking patterns and the order parameter manifolds are

$$\begin{aligned} &\mathrm{UN}: \frac{G}{H} = U(1) \times \frac{SO(3)}{O(2)} \simeq U(1) \times \mathbb{R}P^2,\\ &D_2\text{-BN}: \frac{G}{H} = U(1) \times \frac{SO(3)}{D_2} \simeq U(1) \times \frac{SU(2)}{\mathbb{Q}},\\ &D_4\text{-BN}: \frac{G}{H} = \frac{U(1) \times SO(3)}{D_4} \simeq \frac{U(1) \times SU(2)}{D_4^*}. \end{aligned} \tag{69}$$

These phases are continuously connected by the parameter r interpreted as a quasi-Nambu-Goldstone mode. The degeneracy is lifted by quantum effects and either of these phases remains as the ground state (Uchino et al., 2010).

The D_2-BN and D_4-BN admit non-Abelian vortices. The order parameters of the UN and D_2-BN phases of spin-2 BECs are merely products of the $U(1)$ phonon and the order parameters of the corresponding nematic liquids. Thus, we concentrate on the D_4-BN phase hereafter. The fundamental group of the D_4-BN phase is given by

$$\pi_1\left(\frac{U(1) \times SU(2)}{D_4^*}\right) \cong \mathbb{Z} \times_h D_4^* \tag{70}$$

where $\times_h$ is defined in Kobayashi et al. (2012). This consists of the following sixteen elements

$$\begin{aligned} &\{(N, \pm \mathbf{1}_2), (N, \pm i\sigma_x), (N, \pm i\sigma_y), (N, \pm i\sigma_z),\\ &\left(N + \frac{1}{2}, \pm C_4\right), \left(N + \frac{1}{2}, \pm i\sigma_x C_4\right), \left(N + \frac{1}{2}, \pm C_4^{-1}\right), \left(N + \frac{1}{2}, \pm i\sigma_x C_4^{-1}\right)\} \end{aligned} \tag{71}$$

where the first and second elements of a pair $(\cdot, \cdot)$ denote the circulation κ ($U(1)$ winding number) and an $SU(2)$ element, respectively with $N \in \mathbb{Z}$. Here $C_4 \equiv e^{i\frac{\pi}{4}\sigma_z} = (1/\sqrt{2})(\mathbf{1}_2 + i\sigma_z)$ satisfying $C_4^4 = -\mathbf{1}_2$. The conjugacy classes of Eq. (71) are composed of seven elements for each N:

$$\begin{array}{ll} \text{(I)} & \{(N, \mathbf{1}_2)\},\\ \text{(II)} & \{(N, -\mathbf{1}_2)\},\\ \text{(III)} & \{(N, \pm i\sigma_x), (N, \pm i\sigma_y)\},\\ \text{(IV)} & \{(N, \pm i\sigma_z)\},\\ \text{(V)} & \left\{\left(N + \frac{1}{2}, C_4\right), \left(N + \frac{1}{2}, C_4^{-1}\right)\right\},\\ \text{(VI)} & \left\{\left(N + \frac{1}{2}, -C_4\right), \left(N + \frac{1}{2}, -C_4^{-1}\right)\right\},\\ \text{(VII)} & \left\{\left(N + \frac{1}{2}, \pm i\sigma_x C_4\right), \left(N + \frac{1}{2}, \pm i\sigma_x C_4^{-1}\right)\right\}. \end{array} \tag{72}$$

They describe (I) integer vortices ($N = 0$ corresponds to the vacuum), (II) spin vortices of 2π rotation, (III),(IV) spin vortices of π rotation around the x, y, and z axes, and (V)–(VII) non-Abelian HQVs.

In Section "${}^3P_2$ Topological SFs," we see that ${}^3P_2$ SFs are in the D_4-BN phase in a strong magnetic field. There, a singly quantized vortex $(1, \mathbf{1})$ splits into two HQVs $(1/2, C_4)$ and $(1/2, C_4^{-1})$ both in the conjugacy class (V).[4] When they fuse, they go back to the singly quantized vortex $(1, \mathbf{1})$. However, one of them, for example, $(1/2, C_4^{-1})$ can transform to the other $(1/2, C_4)$ once some other vortex passes through between them because they belong to the same conjugacy class. If they fuse after that, they become $(1, i\sigma_z)$ because $C_4^2 = i\sigma_z$ which is a composite belonging to (IV), of a singly quantized vortex and a spin vortex of π rotation.

Cyclic phase in spin-2 BEC (Semenoff and Zhou, 2007; Kobayashi et al., 2009, 2012)

The order parameter of the cyclic phase is

$$A \sim \mathrm{diag}(1, e^{2\pi i/3}, e^{4\pi i/3}), \tag{73}$$

---

[4] Topologically a decay into a pair $(1/2, -C_4)$ and $(1/2, -C_4^{-1})$ in the conjugacy class (VI) is also possible, but energetically disfavored.

yielding the symmetry breaking to the tetrahedral group $H \simeq T$ and the order parameter manifold, given by

$$\frac{G}{H} = \frac{U(1) \times SO(3)}{T} \simeq \frac{U(1) \times SU(2)}{T^*} \tag{74}$$

with the universal covering group T^* of T. The fundamental group in the cyclic phase is given by

$$\pi_1\left(\frac{U(1) \times SU(2)}{T^*}\right) \cong \mathbb{Z} \times_h T^* \tag{75}$$

with the 24 elements

$$\begin{aligned}
&\{(N, \pm \mathbf{1}_2), (N, \pm i\sigma_x), (N, \pm i\sigma_y), (N, \pm i\sigma_z),\\
&\left(N + \frac{1}{3}, \pm C_3\right), \left(N + \frac{1}{3}, \pm i\sigma_x C_3\right), \left(N + \frac{1}{3}, \pm i\sigma_y C_3\right), \left(N + \frac{1}{3}, \pm i\sigma_z C_3\right),\\
&\left(N - \frac{1}{3}, \pm C_3^2\right), \left(N - \frac{1}{3}, \pm i\sigma_x C_3^2\right), \left(N - \frac{1}{3}, \pm i\sigma_y C_3^2\right), \left(N - \frac{1}{3}, \pm i\sigma_z C_3^2\right)\Big\},
\end{aligned} \tag{76}$$

with the same notation with Eq. (71). Here $C_3 \equiv (1/2)(\mathbf{1}_2 + i\sigma_x + i\sigma_y + i\sigma_z)$ satisfying $(C_3)^3 = -\mathbf{1}_2$. The conjugacy classes of Eq. (76) are composed of the following seven elements for each N (Semenoff and Zhou, 2007):

$$\begin{array}{ll}
\text{(I)} & \{(N, \mathbf{1}_2)\},\\
\text{(II)} & \{(N, -\mathbf{1}_2)\},\\
\text{(III)} & \{(N, \pm i\sigma_x), (N, \pm i\sigma_y), (N, \pm i\sigma_z)\},\\
\text{(IV)} & \left\{\left(N + \frac{1}{3}, C_3\right), \left(N + \frac{1}{3}, -i\sigma_x C_3\right), \left(N + \frac{1}{3}, -i\sigma_y C_3\right), \left(N + \frac{1}{3}, -i\sigma_z C_3\right)\right\},\\
\text{(V)} & \left\{\left(N + \frac{1}{3}, -C_3\right), \left(N + \frac{1}{3}, i\sigma_x C_3\right), \left(N + \frac{1}{3}, i\sigma_y C_3\right), \left(N + \frac{1}{3}, i\sigma_z C_3\right)\right\},\\
\text{(VI)} & \left\{\left(N - \frac{1}{3}, C_3^2\right), \left(N - \frac{1}{3}, i\sigma_x C_3^2\right), \left(N - \frac{1}{3}, i\sigma_y C_3^2\right), \left(N - \frac{1}{3}, i\sigma_z C_3^2\right)\right\},\\
\text{(VII)} & \left\{\left(N - \frac{1}{3}, -C_3^2\right), \left(N - \frac{1}{3}, -i\sigma_x C_3^2\right), \left(N - \frac{1}{3}, -i\sigma_y C_3^2\right), \left(N - \frac{1}{3}, -i\sigma_z C_3^2\right)\right\}.
\end{array} \tag{77}$$

They describe (I) integer vortices ($N = 0$ corresponds to the vacuum), (II) spin vortices of 2π rotation, (III) spin vortices of π rotation around the x, y, z axes, and (IV)–(VII) 1/3-quantum vortices.

Other examples

Another example in condensed matter physics can be found in vortex lines in the dipole-free A-phase of SF ^{3}He (Balachandran et al., 1984; Salomaa and Volovik, 1987). An example in high energy physics can be found in color flux tubes ("non-Abelian" vortices) in high-density QCD matter (Fujimoto and Nitta, 2021a, b, c; Eto and Nitta, 2021).

Fusion rules for non-Abelian vortex anyons

Two non-Abelian vortices belonging to the same conjugacy class are indistinguishable even if they are not identical. For instance, a vortex $a \in \pi_1(G/H)$ and a vortex $b = cac^{-1}$ with $c \in \pi_1(G/H)$ are not the same and thus a and antivortex of b cannot pair annihilate. Nevertheless they are indistinguishable with a help of c. This leads a class of non-Abelian statistics (Brekke et al., 1993; Lo and Preskill, 1993; Lee, 1994; Brekke et al., 1997). Such non-Abelian anyons are called non-Abelian vortex anyons.

In order to discuss non-Abelian vortex anyons, first we define anyons $\{\mathbf{1}, \sigma, \tau\}$ appropriately by conjugacy classes of non-Abelian vortices. Then, the fusion rule (3) for non-Abelian vortex anyons can be written as (Mawson et al., 2019)

$$\begin{aligned}
&\tau \otimes \tau = N_{\tau\tau}^{\mathbf{1}} \mathbf{1} \oplus N_{\tau\tau}^{\sigma} \sigma \oplus N_{\tau\tau}^{\tau} \tau,\\
&\tau \otimes \sigma = \tau, \quad \sigma \otimes \sigma = \mathbf{1}, \quad x \otimes \mathbf{1} = x,
\end{aligned} \tag{78}$$

with $x \in \{\mathbf{1}, \sigma, \tau\}$.

Non-Abelian vortex anyons in D_2-BN

Let us discuss the simplest case. For D_2-BN liquid crystals or D_2-BN phases of spin-2 BECs, the conjugacy class is given in Eq. (62). We then define

$$\mathbf{1} = \{+\mathbf{1}_2\}, \quad \sigma = \{-\mathbf{1}_2\}, \quad \tau = \{\pm i\sigma_a\} \tag{79}$$

with a being either x, y, or z. The coefficient N_{ab}^{c} counts how many ways anyons a and b fuse to an anyon c. The relations $(-i\sigma_a)(+i\sigma_a) = (+i\sigma_a)(-i\sigma_a) = +\mathbf{1}_2$ and $(-i\sigma_a)(-i\sigma_a) = (+i\sigma_a)(+i\sigma_a) = -\mathbf{1}_2$ lead $N_{\tau\tau}^{\mathbf{1}} = 2$ and $N_{\tau\tau}^{\sigma} = 2$, respectively. Furthermore, τ anyons do not fuse to τ in this case and then $N_{\tau\tau}^{\tau} = 0$. We thus reach

$$\begin{aligned} &\tau \otimes \tau = 2\mathbf{1} \oplus 2\sigma, \\ &\tau \otimes \sigma = \tau, \quad \sigma \otimes \sigma = \mathbf{1}, \quad x \otimes \mathbf{1} = x, \end{aligned} \tag{80}$$

with $x \in \{\mathbf{1}, \sigma, \tau\}$. Since two τ-anyons fuse to two different anyons $\mathbf{1}$ and σ, τ anyons are non-Abelian anyons. Comparing this fusion rule with that of the Ising anyons in Eq. (4), we find that these non-Abelian vortex anyons are similar to the Ising anyons. In fact, a τ anynon coincide with its antiparticle, and so similar to a Majorana fermion.

Gathering all $\tau_a = \{\pm i\sigma_a\}$ $(a = x, y, z)$ together, we obtain the following fusion formula from the relation $(i\sigma_a)(i\sigma_b) = -\delta_{ab} + \varepsilon_{abc}(-i\sigma_c)$:

$$\begin{aligned} &\tau_a \otimes \tau_b = 2\delta_{ab}\mathbf{1} \oplus 2\delta_{ab}\sigma \oplus 2\varepsilon_{abc}\tau_c \\ &\tau_a \otimes \sigma = \tau_a, \quad \sigma \otimes \sigma = \mathbf{1}, \quad x \otimes \mathbf{1} = x, \end{aligned} \tag{81}$$

with $x \in \{\mathbf{1}, \sigma, \tau_x, \tau_y, \tau_z\}$. In this case, there are the three non-Abelian anyons τ_a coupled to each other.

Non-Abelian vortex anyons in spin-2 BECs

Non-Abelian vortex anyons in spin-2 BECs were studied in Mawson et al. (2019). For the cyclic phase in a spin-2 BEC, $\{\mathbf{1}, \sigma, \tau\}$ are defined by the conjugacy classes (I), (II) and (III) with $N = 0$ in Eq. (77). Then, we have (see Table 2) $N_{\tau\tau}^{\mathbf{1}} = 6,\ N_{\tau\tau}^{\sigma} = 6,\ N_{\tau\tau}^{\tau} = 4$:

$$\begin{aligned} &\tau \otimes \tau = 6\mathbf{1} \oplus 6\sigma \oplus 4\tau, \\ &\tau \otimes \sigma = \tau, \quad \sigma \otimes \sigma = \mathbf{1}, \quad x \otimes \mathbf{1} = x, \end{aligned} \tag{82}$$

with $x \in \{\mathbf{1}, \sigma, \tau\}$. The non-Abelian 1/3-quantum vortices in (IV)–(VII) are also non-Abelian anyons but one cannot restrict to the $N = 0$ sector, and needs infinite numbers of anyons for a closed algebra.

The fusion rule for vortex anyons in the D_4-BN phase of a spin-2 BEC was also obtained by the conjugacy classes (I)–(IV) in Eq. (72) (Mawson et al., 2019). In this case, τ in the cyclic phase is split into $\tau_1 = \mathrm{III}_0$ and $\tau_2 = \mathrm{IV}_0$. Then, we have $N_{\tau_1\tau_1}^{\mathbf{1}} = 4,\ N_{\tau_1\tau_1}^{\sigma} = 4,\ N_{\tau_1\tau_1}^{\tau_1} = 4,\ N_{\tau_2\tau_2}^{\mathbf{1}} = 2,\ N_{\tau_2\tau_2}^{\sigma} = 2$ with the other components zero:

$$\begin{aligned} &\tau_1 \otimes \tau_1 = 4\mathbf{1} \oplus 4\sigma \oplus 4\tau_1, \\ &\tau_2 \otimes \tau_2 = 2\mathbf{1} \oplus 2\sigma, \\ &\tau_i \otimes \sigma = \tau_i, \quad \sigma \otimes \sigma = \mathbf{1}, \quad x \otimes \mathbf{1} = x, \end{aligned} \tag{83}$$

with $i = 1, 2$ and $x \in \{\mathbf{1}, \sigma, \tau_i\}$. See Table 3. The non-Abelian HQVs in (V)–(VII) are also non-Abelian anyons, but again infinite numbers of anyons are necessary for a closed algebra. The same fusion rule in Eq. (83) should hold for a D_4-BN liquid crystal, as seen in Eq. (66).

Including Bogoliubov modes, the algebra of vortex anyons is extended to a quantum double (Koornwinder et al., 1999; Mawson et al., 2019). An application to quantum computation was also proposed in Génetay Johansen and Simula (2022).

Table 2 Fusion rule for vortex anyons in a cyclic spin-2 BEC (Mawson et al., 2019). The subscript on the conjugacy class denotes the $U(1)$ winding number N.

	I_0	II_0	III_0	IV_0	V_0	VI_{-1}	VII_{-1}
$\mathbf{1} = \mathrm{I}_0$	I_0	II_0	III_0	IV_0	V_0	VI_{-1}	VII_{-1}
$\sigma = \mathrm{II}_0$	II_0	I_0	III_0	V_0	IV_0	VII_{-1}	VI_{-1}
$\tau = \mathrm{III}_0$	III_0	III_0	$6\mathrm{I}_0 \oplus 6\mathrm{II}_0 \oplus 4\mathrm{III}_0$	$3\mathrm{IV}_0 \oplus 3\mathrm{V}_0$	$3\mathrm{IV}_0 \oplus 3\mathrm{V}_0$	$3\mathrm{VI}_{-1} \oplus 3\mathrm{VII}_{-1}$	$3\mathrm{VI}_{-1} \oplus 3\mathrm{VII}_{-1}$
IV_0	IV_0	V_0	$3\mathrm{IV}_0 \oplus 3\mathrm{V}_0$	$3\mathrm{VI}_0 \oplus \mathrm{VII}_0$	$\mathrm{VI}_0 \oplus 3\mathrm{VII}_0$	$4\mathrm{I}_0 \oplus 3\mathrm{III}_0$	$4\mathrm{II}_0 \oplus 2\mathrm{III}_0$
V_0	V_0	IV_0	$3\mathrm{IV}_0 \oplus 3\mathrm{V}_0$	$\mathrm{VI}_0 \oplus 3\mathrm{VII}_0$	$3\mathrm{VI}_0 \oplus \mathrm{VII}_0$	$4\mathrm{II}_0 \oplus 2\mathrm{III}_0$	$4\mathrm{I}_0 \oplus 2\mathrm{III}_0$
VI_{-1}	VI_{-1}	VII_{-1}	$3\mathrm{VI}_{-1} \oplus 3\mathrm{VII}_{-1}$	$4\mathrm{I}_0 \oplus 2\mathrm{III}_0$	$4\mathrm{II}_0 \oplus 2\mathrm{III}_0$	$3\mathrm{IV}_{-1} \oplus \mathrm{V}_{-1}$	$\mathrm{IV}_{-1} \oplus 3\mathrm{V}_{-1}$
VII_{-1}	VII_{-1}	VI_{-1}	$3\mathrm{IV}_{-1} \oplus 3\mathrm{VII}_{-1}$	$4\mathrm{II}_0 \oplus 2\mathrm{III}_0$	$4\mathrm{I}_0 \oplus 2\mathrm{III}_0$	$\mathrm{IV}_{-1} \oplus 3\mathrm{V}_{-1}$	$3\mathrm{IV}_{-1} \oplus 2\mathrm{V}_{-1}$

Table 3 Fusion rule for vortex anyons in a D_4-BN spin-2 BEC (Mawson et al., 2019). The subscript on the conjugacy class denotes the $U(1)$ winding number N.

	I_0	II_0	III_0	IV_0	V_0	VI_0	VII_0
$\mathbf{1} = \mathrm{I}_0$	I_0	II_0	III_0	IV_0	V_0	VI_0	VII_0
$\sigma = \mathrm{II}_0$	II_0	I_0	III_0	IV_0	VI_0	V_0	VII_0
$\tau_1 = \mathrm{III}_0$	III_0	III_0	$4\mathrm{I}_0 \oplus 4\mathrm{II}_0 \oplus 4\mathrm{IV}_0$	$2\mathrm{III}_0$	$2\mathrm{VII}_0$	$2\mathrm{VII}_0$	$4\mathrm{V}_0 \oplus 4\mathrm{VI}_0$
$\tau_2 = \mathrm{IV}_0$	IV_0	IV_0	$2\mathrm{III}_0$	$2\mathrm{I}_0 \oplus 2\mathrm{II}_0$	$\mathrm{V}_0 \oplus \mathrm{VI}_0$	$\mathrm{V}_0 \oplus \mathrm{VI}_0$	$2\mathrm{VII}_0$
V_0	V_0	VI_0	$2\mathrm{VII}_0$	$\mathrm{V}_0 \oplus \mathrm{VI}_0$	$2\mathrm{I}_1 \oplus \mathrm{IV}_1$	$2\mathrm{II}_1 \oplus \mathrm{IV}_1$	$2\mathrm{III}_1$
VI_0	VI_0	V_0	$2\mathrm{VII}_0$	$\mathrm{V}_0 \oplus \mathrm{VI}_0$	$2\mathrm{II}_1 \oplus \mathrm{IV}_1$	$2\mathrm{I}_1 \oplus \mathrm{IV}_1$	$2\mathrm{III}_1$
VII_0	VII_0	VII_0	$4\mathrm{IV}_0 \oplus 4\mathrm{V}_0$	$2\mathrm{VII}_0$	$2\mathrm{III}_1$	$2\mathrm{III}_1$	$4\mathrm{I}_1 \oplus 4\mathrm{II}_1 \oplus 4\mathrm{IV}_1$

$^3P_2$ Topological SFs

Finally we discuss the twofold non-Abelian object in a novel topological SF called a $^3P_2$ SF: The twofold non-Abelian nature is attributed to the fermionic part (Section "Non-Abelian anyons in topological SCs") and the vortex part (Section "Non-Abelian vortex anyons"). The $^3P_2$ SF is a condensate of spin-triplet ($S = 1$) p-wave ($L = 2$) Cooper pairs with total angular momentum $J = 2$. In the following, we briefly review $^3P_2$ SFs in Section "Overview of $^3P_2$ topological SFs." In Section "Half quantum vortex in D_4-BN state," the stability of a pair of HQVs compared with a singly quantized vortex is discussed. In Section "Non-Abelian anyon in non-Abelian vortex," we show that a Majorana fermion, a non-Abelian Ising anyon, exists in the core of each HQV.

Overview of $^3P_2$ topological SFs

Study of $^3P_2$ SFs was initiated since 1970s (Hoffberg et al., 1970; Tamagaki, 1970; Takatsuka and Tamagaki, 1971; Takatsuka, 1972; Richardson, 1972; Sedrakian and Clark, 2018). On the basis of the analysis of the phase shifts from nucleon-nucleon scattering in a free space, spin-singlet s-wave $^1S_0$ symmetry is a dominant attractive channel in the inner crust region ($\rho \lesssim 0.5\rho_0$, where $\rho_0 = 0.17\text{fm}^{-3}$ is called the nuclear density) (Tamagaki, 1970). The critical temperature was estimated as 10^8–10^{10} K, which is two orders of magnitude smaller than the Fermi energy. For further increase in density $0.7\rho_0 \lesssim \rho \lesssim 3\rho_0$ in the inner core region, the $^1S_0$ superfluidity is suppressed, and instead the attractive channel of the $^3P_2$ grows. Because of the attractively strong spin–orbit force, the $^3P_2$ Cooper pair channels with high angular momentum become more attractive than other ^3P pairing symmetry in contrast to the atomic physics where the lower total angular momentum state is favored as in the SF ^{3}He-B phase. The anisotropic form of the Cooper pair is thought to affect the Cooling rate of neutron stars. Extreme conditions of neutron stars are not only high density but also rapid rotation, and a strong magnetic field. Especially, neutron stars accompanied by magnetic field ranging from 10^{15} to 10^{18} G are called magnetars. Rich structures of exotic condensates and vortices explained below may be the origin of the observed *pulser glitches*, that is, the sudden increase of the angular momentum of neutron stars. Among them, the existence of non-Abelian HQVs in high magnetic fields is responsible for the scaling law of the glitches without any fitting parameters (Marmorini et al., 2020).

In terms of the symmetry point of view, $^3P_2$ SFs spontaneously break the global gauge symmetry $U(1)_\varphi$ and the simultaneous rotational symmetry in the spin-momentum space $SO(3)_J$ which originally exist in the normal state inside neutron stars. The order parameter of $^3P_2$ SFs is spanned by 3 by 3 traceless symmetric tensor $A_{\mu i}$, where the 2 by 2 gap function in momentum space can be given by $\hat{\Delta}(\boldsymbol{k}) = A_{\mu i}\bar{k}_i\hat{\sigma}_\mu i\hat{\sigma}_y$. For later convenience, we introduce a representation based on the total angular momentum along the quantization axis, $M = -2, \cdots, 2$:

$$A_{\mu i} = \sum_{M=-2}^{2} \gamma_M [\Gamma_M]_{\mu i}, \tag{84}$$

where γ_M is a complex wave function of the Cooper pair in the angular momentum sector M. A basis set Γ_M is given for the quantization axis $\hat{w}$ by

$$[\Gamma_{\pm 2}]_{\mu i} = \frac{(\hat{u} \pm i\hat{v})_\mu (\hat{u} \pm i\hat{v})_i}{2}, \tag{85}$$

$$[\Gamma_{\pm 1}]_{\mu i} = \mp \frac{(\hat{u} \pm i\hat{v})_\mu \hat{w}_i + \hat{w}_\mu (\hat{u} \pm i\hat{v})_i}{2}, \tag{86}$$

$$[\Gamma_0]_{\mu i} = \frac{-\hat{u}_\mu \hat{u}_i - \hat{v}_\mu \hat{v}_i + 2\hat{w}_\mu \hat{w}_i}{\sqrt{6}}, \tag{87}$$

where $\hat{u}$, $\hat{v}$, and $\hat{w}$ constitute the orthonormal triad.

From a phenomenological aspect, the Ginzburg-Landau (GL) energy functional invariant under the $SO(3)_J$ and $U(1)_\varphi$ symmetry was obtained for $^3P_2$ SFs as (Richardson, 1972; Fujita and Tsuneto, 1972; Sauls and Serene, 1978; Muzikar et al., 1980; Sauls et al., 1982)

$$\mathcal{F} = \alpha \text{tr}[AA^*] + \beta_1 |\text{tr}A^2|^2 + \beta_2 (\text{tr}[AA^*])^2 + \beta_3 \text{tr}[A^2 A^{*2}]. \tag{88}$$

It should be remarked that spin-2 spinor BECs ($L = 0$, $S = 2$) and d-wave superconductivity ($L = 2$, $S = 0$) have similar order parameter structures. The GL functional for the $^3P_2$ Cooper pairs was minimized by Sauls and Serene by using the correspondence to the $L = 2$ GL functional which was solved by Mermin (Sauls and Serene, 1978; Mermin, 1974). The ground-state solutions are classified into three types of phases determined by $\beta_{i=1,\,2,\,3}$, as shown in Fig. 8A: nematic phases with time reversal symmetry and the cyclic and ferromagnetic phases as nonunitary state. The microscopic derivation of the GL parameters clarifies that the ground state is the nematic phases in the weak coupling limit (Sauls and Serene, 1978; Sauls, 1980). The order parameter tensor of a nematic phase is given by $A_{\mu i} = \Delta[\hat{u}_\mu \hat{u}_i + r\hat{v}_\mu \hat{v}_i - (1 + r)\hat{w}_\mu \hat{w}_i]$ with a real number $r \in [-1, -1/2]$ (see also Eq. 68). The nematic phase has a continuous degeneracy which is lifted by either a magnetic field or sixth-order terms in the GL free energy. For the GL parameters derived from the microscopic model, the UN phase for $r = -1/2$ is favored at zero magnetic field while D_2-BN ($-1 < r < -1/2$) and D_4-BN $r = -1$ phases are favored for moderate and strong magnetic fields, respectively (Masuda and Nitta, 2016),

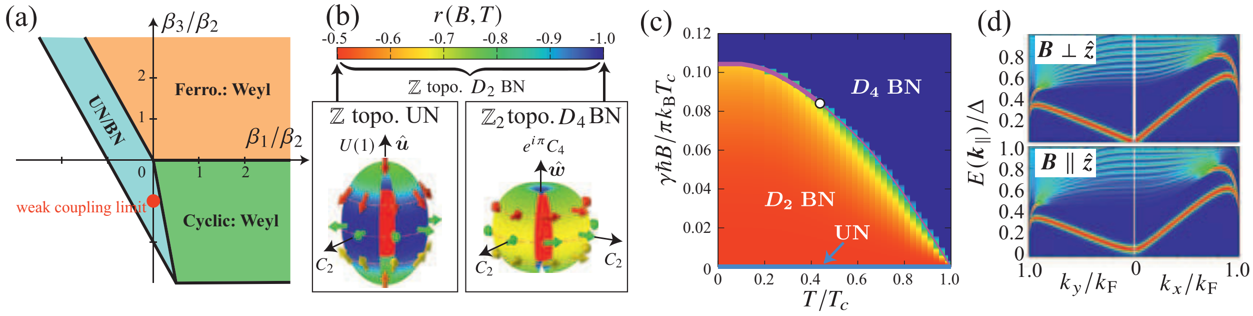

Fig. 8 (A) Phase diagram without magnetic field based on the GL theory. (B) Gap structure of the nematic state. (C) Phase diagram with magnetic field in the weak coupling limit. (D) The momentum resolved local density state at the surface perpendicular to the $\hat{z}$-axis. The magnetic field is applied parallel (perpendicular) to the surface [top (bottom) panel]. Adapted from Mizushima T, Masuda K, and Nitta M (2017) $^3P_2$ Superfluids are topological. Physical Review B 95 (14): 140503. https://doi.org/10.1103/PhysRevB.95.140503. ©2022 American Physical Society.

relevant for magnetars. The schematic images of the gap structures for the UN and D_4-BN states are shown in Fig. 8B, where the arrows account for the momentum-dependent direction of the d-vector, defined by $d_\mu(\boldsymbol{k}) = \sum_i A_{\mu i} k_i$. We will discuss other possible states later in the context of the fermionic topology.

The microscopic model of $^3P_2$ SFs in terms of the fermion degrees of freedom was constructed by Richardson (1972), Tamagaki (1970), Takatsuka and Tamagaki (1971), and Takatsuka (1972): The starting microscopic Hamiltonian is composed of the one-body term H_1 and the interaction term H_2 given, respectively, in the following forms:

$$H_1 = \int \mathrm{d}\boldsymbol{r} \vec{\psi}^\dagger(\boldsymbol{r})[\hat{h}_N(-i\nabla)]\vec{\psi}(\boldsymbol{r}), \tag{89}$$

$$H_2 = -\int \mathrm{d}\boldsymbol{r} \sum_{\alpha\beta=x,y,z} \frac{g}{2} T^\dagger_{\alpha\beta}(\boldsymbol{r}) T_{\alpha\beta}(\boldsymbol{r}). \tag{90}$$

In the first line, $[\vec{\psi}(\boldsymbol{r})]_\sigma = \psi_\sigma(\boldsymbol{r})$ and $[\hat{h}_N(-i\nabla)]_{\sigma,\sigma'}$ is the sum of the kinetic energy $h_0(-i\nabla)\delta_{\sigma,\sigma'} = (-\nabla^2/2m - \mu)\delta_{\sigma,\sigma'}$ measured from the chemical potential μ, and the Zeeman energy $-\boldsymbol{B}\cdot\hat{\boldsymbol{\sigma}}$ for a magnetic field $\boldsymbol{B} = B\boldsymbol{n}$. The $^3P_2$ force with coupling strength $g > 0$ is represented by H_2 with the pair-annihilation operator T defined by $T_{\alpha\beta}(\boldsymbol{r}) = \sum_{\sigma\sigma'}[t_{\alpha\beta,\sigma\sigma'}(-i\bar{\nabla})\psi_{\sigma'}(\boldsymbol{r})]\psi_\sigma(\boldsymbol{r})$, where $\bar{\nabla} \equiv k_F^{-1}\nabla$. We have introduced a spin–momentum coupling in the pair force via the 2 × 2 matrix in spin space $\hat{t}_{\alpha\beta}$ defined by $\hat{t}_{\alpha\beta}(-i\bar{\nabla}) = i\hat{\sigma}_y\left\{\left[\hat{\sigma}_\alpha(-i\bar{\nabla}_\beta)+\hat{\sigma}_\beta(-i\bar{\nabla}_\alpha)\right]/2\sqrt{2} - \delta_{\alpha\beta}\hat{\boldsymbol{\sigma}}\cdot(-i\bar{\nabla})/3\sqrt{2}\right\}$. Within the mean field approximation, the BdG equation is derived as

$$\check{\mathcal{H}}(-i\nabla, \boldsymbol{R})\vec{u}_\nu(\boldsymbol{R}) = \varepsilon_\nu \vec{u}_\nu(\boldsymbol{R}), \tag{91}$$

$$\check{\mathcal{H}}(-i\nabla, \boldsymbol{R}) = \begin{pmatrix} \hat{h}_N(-i\nabla) & \hat{\Delta}(-i\nabla, \boldsymbol{R}) \\ -[\hat{\Delta}(-i\nabla, \boldsymbol{R})]^* & -[\hat{h}_N(-i\nabla)]^* \end{pmatrix}, \tag{92}$$

where the gap matrix is given by $\hat{\Delta}(-i\nabla, \boldsymbol{R}) = \sum_{\alpha,\beta} \frac{i\hat{\sigma}_\alpha\hat{\sigma}_y}{2k_F}\{2A_{\alpha\beta}(\boldsymbol{R})(-i\nabla_\beta) + [(-i\nabla_\beta)A_{\alpha\beta}(\boldsymbol{R})]\}$. This model was also used to determine the aforementioned GL parameters in the weak coupling limit and was directly investigated within a quasiclassical approximation recently in Mizushima et al. (2017). Even in the presence of the magnetic field, the quasiclassical approximation, where the size of the Fermi surface is treated as an infinite one, predicts that a nematic state is the most stable with parameter r determined by the strength of the magnetic field as in the GL theory. The T-B phase diagram is shown in Fig. 8C. As explained later, the ferromagnetic state appears near T_c when the finite-size correction of the Fermi surface is taken into account. The microscopic analysis reveals the existence of the tricritical point on the phase boundary between the D_4-BN and D_2-BN states in the T-B phase diagram shown in Fig. 8C: at temperatures below the tricritical point, the phase transition becomes discontinuous (Mizushima et al., 2017). The existence of the tricritical point was later confirmed in Mizushima et al. (2020) also in the GL theory with higher order terms (up to the eighth order (Yasui et al., 2019a)). In addition to such drastic change in critical phenomena, the advantage of the microscopic model lies in studies of the fermionic topology of the superfluidity. In the following, we explain the fermionic topology of the possible phases of the $^3P_2$ SFs.

Nematic state

In the weak coupling limit without a magnetic field, the UN state is the ground state. The order parameter tensors of the UN state and the BN state under a magnetic field are already explained above. On the basis of the symmetry of the BdG Hamiltonian, the nematic state is revealed as a topological SF with time reversal symmetry (a class DIII in the classification of topological insulators and SCs). The analysis of the BdG equation in the presence of the boundary clarifies the existence of the gapless surface bound Majorana fermion, the hallmark character of the topological states. The surface Majorana fermion has an Ising spin character

(Chung and Zhang, 2009; Nagato et al., 2009; Volovik, 2010; Mizushima and Machida, 2011), that is, the only external field coupled to the Ising spin gives a mass gap to the Majorana fermion as shown in Fig. 8D. The magnetic field direction giving the gap to the Majorana fermion is the direction perpendicular to the surface, denoted by $\boldsymbol{n}_\perp$. This is because the surface Majorana fermion is protected not only by the time reversal symmetry but also another key symmetry, which is the magnetic π-rotation symmetry about $\boldsymbol{n}_\perp$. The magnetic π-rotation symmetry is also called the $\bar{P}_3$ symmetry.[5] The magnetic π-rotation is the combined operation of the time-reversal and the π rotation. The chiral operator, defined by the combination of particle-hole operation $\mathcal{C}$ and the magnetic π-rotation $\bar{P}_3$ as $\Gamma = \mathcal{C}\bar{P}_3$, commutes with the Hamiltonian $\mathcal{H}(\boldsymbol{k}_\perp)$ with magnetic field $\boldsymbol{B}\cdot\boldsymbol{n}_\perp = 0$ and the chiral symmetric momentum $\boldsymbol{k}_\perp = k_\perp \boldsymbol{n}_\perp$ such that $\Gamma : \boldsymbol{k}_\perp \to \boldsymbol{k}_\perp$. Using this commutation relation, a one-dimensional winding number can be introduced as $w_{1\mathrm{d}} = -\frac{1}{4\pi i}\int dk_\perp \mathrm{Tr}[\Gamma\mathcal{H}(\boldsymbol{k}_\perp)\partial_{k_\perp}\mathcal{H}(\boldsymbol{k}_\perp)] = 2$, which is unchanged unless the symmetry is broken or the bulk gap is closed. The P_3 symmetry and thus the chiral symmetry is broken by the magnetic filed $\boldsymbol{B}\cdot\boldsymbol{n}_\perp \neq 0$ which gives a mass gap to the Majorana fermion (the bottom panel of Fig. 8D, where $\boldsymbol{n}_\perp \parallel \hat{z}$).

Cyclic state

For $-6\beta_1 < \beta_3 < 0$ based on the basis of $SO(3)_J$ invariant GL functional, the cyclic state is the ground state. The order parameter tensor has a form of $A_{\mu i} = \Delta[\hat{u}_\mu\hat{u}_i + \omega\hat{v}_\mu\hat{v}_i + \omega^2\hat{w}_\mu\hat{w}_i]$ with $\omega = e^{2\pi i/3}$ [see also Eq. (73)], which is unique except for trivial $SO(3)_J$ and $U(1)_\varphi$ rotations. In the absence of magnetic field, the quasiparticle excitation energy consists of two branches $E_\pm(\boldsymbol{k}) = [h_0(\boldsymbol{k})^2 + |\boldsymbol{d}(\boldsymbol{k})|^2 \pm |\boldsymbol{d}(\boldsymbol{k})\times\boldsymbol{d}^*(\boldsymbol{k})|]^{1/2}$, where $E_+(\boldsymbol{k})$ is full gap and $E_-(\boldsymbol{k})$ has eight nodal points $\pm\boldsymbol{k}_{\alpha=1,\cdots,4}$, each of which is a Weyl point. The subscript α denotes the four vertices of a tetrahedron, and $\pm$ represents the monopole charge of the Weyl point. Because of the topological nature of Weyl SCs/SFs, there exist surface zero energy states which connect two oppositely charged Weyls points on the projected momentum space normal to the surface direction.

Ferromagnetic state

For $|\beta_1| - \beta_1 < \beta_3$, the ferromagnetic state described by $A_{\mu i} = \Delta(\hat{u}_\mu + i\hat{v}_\mu)(\hat{u}_i + i\hat{v}_i)$ minimizes the GL functional. This nonunitary state is also unique except for trivial $SO(3)_J$ and $U(1)_\varphi$ rotations. The order parameter is equivalent to the A_1 state of the SF ^{3}He. The bulk quasiparticle spectrum consists of two parts: one is a normal fluid and the other is a Weyl SF with a pair of oppositely charged Weyl fermions. The ferromagnetic state is also realized in the limit of a strong magnetic field or the vicinity of the critical temperature even in the weak coupling limit owing to the finite-size correction of the Fermi surface.

Magnetized nematic state

Recently, even in the weak coupling limit, nonunitary states are predicted in a magnetic field (Mizushima et al., 2021). As mentioned above, quasiclassical approximation, which treats the size of the Fermi surface as infinity, allows only the nematic states, which is unitary. By contrast, in the presence of the finite-size correction of the Fermi surface, a magnetic field along the $\hat{w}$ -direction induces the nonunitary component into the nematic state with $r \in (-1, -1/2)$ as $A_{\mu i} = \Delta[\hat{u}_\mu\hat{u}_i + r\hat{v}_\mu\hat{v}_i + i\kappa(\hat{u}_\mu\hat{v}_i + \hat{v}_\mu\hat{u}_i) - (1+r)\hat{w}_\mu\hat{w}_i]$ or equivalently

$$A_{\mu i} = \Delta\begin{pmatrix} 1 & i\kappa & 0 \\ i\kappa & r & 0 \\ 0 & 0 & -(1+r) \end{pmatrix}. \tag{93}$$

For simplicity, Mizushima et al. (2021) studied the case of $r = -1$, that is, in a strong magnetic field. In the quasiclassical limit, $\kappa = 0$ and the D_4-BN state is realized. The order parameter tensor in the angular momentum representation is reduced to $A_{\mu i} = \Delta[\Gamma_2 + \Gamma_{-2}]_{\mu i}$, which shows the same gap amplitudes for $M = \pm 2$. The finite size correction of the Fermi surface induces a finite κ. In the angular momentum representation, the order parameter tensor becomes $A_{\mu i} = \Delta[(1+\kappa)\Gamma_2 + (1-\kappa)\Gamma_{-2}]_{\mu i}$. Thus, κ represents the imbalance between the $M = \pm 2$ sectors. In terms of the gap matrix in the spin basis, the Cooper pairs are decomposed into two spin polarized sectors $|\uparrow\uparrow\rangle$ and $|\downarrow\downarrow\rangle$ with different gap amplitudes. Each spin sector has a polarized orbital angular momentum state, and thus, a pair of the Weyl fermions appears at the north pole and the south pole in each spin sector. The orbital angular momentum between these two spin states is opposite, which means that two Weyl fermions with opposite helicity at each pole. This is in contrast to the A_2 phase proposed for the SF ^{3}He. In the limit of a strong magnetic field or the vicinity of the critical temperature, $\kappa \to 1$, the ferromagnetic state is realized. However, we note that this imbalance originates from the finite size effect of the Fermi surface. The effect is parametrized by $\Delta/\varepsilon_{\mathrm{F}}$, which is usually small for conventional neutron stars, and thus the imbalance κ is also expected to be small.

Vortices in ^{3}P$_2$ SFs

The vortices admitted in $^3P_2$ SFs are basically the same as those in spin-2 BECs, which are discussed in Section "Examples of non-Abelian vortices." Table 4 summarizes remaining symmetry, order parameter manifold, and fundamental group of the topological defects of the above-discussed possible phases. Non-Abelian vortex anyons are included in the D_2- and D_4-BN states and the cyclic state as discussed in Section "Fusion rules for non-Abelian vortex anyons." Non-Abelian vortex anyons in the D_2-BN states are spin vortices of π rotation, as shown in Eq. (81). The D_4-BN states admit HQVs (V)–(VII) in Eq. (72) in addition to spin vortices (III) and

---

[5] Here we use the bar to distinguish the magnetic π-rotation about the x-axis introduced later.

Table 4 Summary of order parameters (r, κ in Eq. (93)), remaining symmetry (H), ($R \simeq G/H$), and topological vortices $\pi_1(R)$ in possible phases.

Phase	r & κ in Eq. (93)	H	$R \simeq G/H$	$\pi_1(R)$
UN	$r = -1/2$ & $\kappa = 0$	$D_\infty \simeq O(2)$	$U(1) \times \mathbb{R}P^2$	$\mathbb{Z} \oplus \mathbb{Z}_2$
D_2-BN	$r \in (-1, -1/2)$ & $\kappa = 0$	D_2	$[U(1) \times SO(3)]/D_4$	$\mathbb{Z} \oplus \mathbb{Q}$
D_4-BN	$r = -1$ & $\kappa = 0$	D_4	$[U(1) \times SO(3)]/D_4$	$\mathbb{Z} \times_h D_4^*$
Cyclic	$r = e^{i2\pi/3}$ & $\kappa = 0$	T	$[U(1) \times SO(3)]/T$	$\mathbb{Z} \times_h T^*$
Mag. D_2-BN	$r \in (-1, -1/2)$ & $\kappa \in (0, 1)$	0	$U(1) \times SO(3)$	$\mathbb{Z} \oplus \mathbb{Z}_2$
Mag. D_4-BN	$r = -1$ & $\kappa = -1$	C_4	$[U(1) \times SO(3)]/\mathbb{Z}_4$	$\mathbb{Z} \times_h C_4^*$
FM	$r = -1$ & $\kappa = 1$	$U(1)_{J_z+2\Phi}$	$SO(3)_{J_z-2\Phi}/\mathbb{Z}_2$	$\mathbb{Z}_4$

Source: Taken from Mizushima T, Yasui S, Inotani D, and Nitta M (2021) Spin-polarized phases of $^3P_2$ superfluids in neutron stars. Physical Review C 104 (4): 045803. ISSN 2469-9985. https://doi.org/10.1103/PhysRevC.104.045803. See also the references therein.

(IV) in Eq. (72) as non-Abelian vortex anyons (see also Table 3). The cyclic states admit 1/3-quantum vortices (IV)–(VII) in Eq. (77) as well as spin vortices (III) in Eq. (77) as non-Abelian vortex anyons (see also Table 2).

Especially, the non-Abelian vortex in the D_4-BN state is the main target in the remaining part. We explain the vortices in the D_4-BN state in the beginning of the next subsection.

Half quantum vortex in D_4-BN state

Vortices in D_4-BN state

The D_4-BN state, which can be thermodynamically stabilized by a large magnetic field, has a pair of point nodes at the north and south poles along the direction of the magnetic field (Masuda and Nitta, 2016; Mizushima et al., 2017; Yasui et al., 2019b; Mizushima et al., 2020). Hereafter, we focus on the D_4-BN state with a pair of point node along $\hat{w} = \hat{z}$. The homogeneous order parameter tensor has a diagonal form (Sauls and Serene, 1978): $A = \Delta\text{diag}(1, -1, 0)$ (Eq. 68), which is invariant under a D_4 group. (A similar order parameter form is taken in the planar state of SF ^{3}He (Makhlin et al., 2014; Silaev and Volovik, 2014), but different topological defects are resulted from different order parameter manifolds.)

As already discussed in Section "Non-Abelian vortex anyons," the order parameter manifold in the D_4-BN state is then characterized by the broken symmetry, $R \simeq [U(1) \times SO(3)]/D_4$, see Eq. (69). The topological charges of line defects are characterized by the first homotopy group, Eq. (75)

$$\pi_1(R) \simeq \mathbb{Z} \times_h D_4^* \tag{94}$$

where $\times_h$ denotes a product defined in Kobayashi et al. (2012). This ensures two different classes of topological line defects: Vortices with commutative topological charges and vortices with noncommutative topological charges. The former includes integer vortices (I) in Eq. (72) with or without internal structures, while an example of the latter is the non-Abelian HQV, (V)–(VII) in Eq. (72). Integer vortices are characterized by vorticity quantized to an integer number because of the singlevaluedness of the order parameter. Fractionally quantized case such as a HQV usually has a phase jump (π-phase jump for a HQV) along the contour surrounding the vortex. In the D_4-BN state, however, the phase discontinuity is compensated by the phase originating from the discrete rotation of the D_4 symmetry. Thereby HQVs are topologically allowed. Here, we particularly focus on the case where the vorticity is along the $\hat{z}$-direction accompanying the π-phase jump compensated by the C_4 rotation about the $\hat{z}$-axis, as indicated in Figs. 8B, 10A and F, and 11A. Such HQVs belong to the group (V) or (VI) in Eq. (72).

Hereafter, we review possible vortices when the vorticity and the point nodes of the D_4-BN state are along the $\hat{z}$-direction. As a basis set of the order parameter tensor $A_{\mu i}$, the eigenstates of the z component of the total angular momentum, denoted by $J_z\Gamma_M = M\Gamma_M$, are convenient: $A_{\mu i}(\rho, \theta) = \sum_{M=-2}^{2} \gamma_M(\rho, \theta)[\Gamma_M]_{\mu i}$, where the cylindrical coordinate system $\boldsymbol{R} = (\rho, \theta)$ is introduced with assumption of uniformity along the z-direction. In the region far from the vortex core $\rho \to \infty$, there is no radial dependence, and the order parameter modulation is described by the $U(1)$ phase rotation characterized by vorticity κ and the simultaneous rotation in the spin–orbit space of Cooper pairs. For the latter rotation by angle φ about the $\hat{z}$-axis, the other components of the triad, $\hat{x}$, and $\hat{y}$, are transformed as

$$R(\varphi) : \hat{x} \to \cos\varphi\hat{x} + \sin\varphi\hat{y}, \tag{95}$$

$$R(\varphi) : \hat{y} \to -\sin\varphi\hat{x} + \cos\varphi\hat{y}. \tag{96}$$

Using Γ_M, the $U(1)$ phase winding and the spin–orbit rotation for nonzero bulk components (i.e., $\rho \to \infty$) are expressed as

$$A_{\mu i}(\theta) = \sum_{M=-2}^{2} \gamma_{M,\infty} e^{i\kappa\theta - M\varphi} [\Gamma_M]_{\mu i} \equiv \sum_{M=-2}^{2} \gamma_{M,\infty} e^{i(\kappa - nM)\theta} [\Gamma_M]_{\mu i}. \tag{97}$$

Table 5 Internal structures of axisymmetric vortices. The second and third columns show order parameters of the core structure. The fourth column is coreless (singular) whether the vortex core is occupied (unoccupied) by some SF components. The last column accounts for the preserved symmetry.

Vortex	$\gamma_{M=0}(\rho)$	$\gamma_{M=\pm 1}(\rho)$	Core	Symmetry
o vortex	Real	Zero	Singular	P_1, P_2, P_3
u vortex	Complex	Zero	Singular	P_1
v vortex	Real	Real	Coreless	P_2
w vortex	Real	Imaginary	Coreless	P_3
uvw vortex	Complex	Complex	Coreless	–

Especially, in the D_4-BN state with the point nodes along the $\hat{z}$-axis, $|\gamma_{2,\infty}| = |\gamma_{-2,\infty}|$ and $\gamma_{\pm 1,\infty} = \gamma_{0.\infty} = 0$. Here in the second line, we parametrize $\varphi = n\theta$ along the contour surrounding the vortex, where the spin–orbit rotation can be regarded as the n-fold J-disgyration.[6] Note that n is not necessarily an integer. The boundary condition of a vortex characterized by (κ, n) is given by Eq. (97).

Axisymmetric singly quantized vortex

The integer vortices belong to a class $\kappa \in \mathbb{Z}$. Even in the singly quantized case $\kappa = \pm 1$, however, there are many possibilities because of differences in the internal structure and the disgyration in the spin–orbit space. As a simple case, the axisymmetric vortex can be described as $A_{\mu i}(\rho, \theta) = \sum_{M=-2}^{2} \gamma_M(\rho) e^{i(\kappa - M)\theta} [\Gamma_M]_{\mu i}$ in a whole region, which includes complex radial functions $\gamma_M(\rho)$ to be determined. The disgyration of the axisymmetric vortex is one-fold ($n = 1$ in Eq. 97), that is, the 2π rotation of the triad around the vortex. Thus, the axisymmetric vortex belongs to the conjugacy class (II) in Eq. (72).[7] Although the loss in the kinetic energy becomes large because of the J-disgyration, there is a nice analogy with vortices in SF ^{3}He-B phase. As in the SF ^{3}He-B phase, the symmetry of the vortices can be characterized by three discrete symmetries called $P_{1,2,3}$ symmetries (Salomaa and Volovik, 1985b, 1987), which are discussed in the next subsection.[8] The internal structures $\gamma_{-1,0,1}(\rho)$ characterize a classification based on these discrete symmetries, which allows several vortices as summarized in Table 5. Within an axisymmetric condition, only *o* vortex or *v* vortex is realized as a self-consistent solution. The *o* vortex has a singular core and is the most symmetric one so that it meets all the discrete symmetries. By contrast, the core of the axisymmetric *v* vortex is occupied by the SF component $\gamma_{\pm 1}$ for $\kappa = \pm 1$, and it has the P_2 (magnetic mirror reflection) symmetry, but does not have the P_1 (inversion) or P_3 (magnetic π-rotation about the x-axis) symmetries. Energetically, the *v* vortex is more stable than the *o* vortex because of a gain in the condensation energy in the core region. However, the induced component of the *v* vortex which occupies the core is suppressed by a magnetic field .

Nonaxisymmetric singly quantized vortex

Without the axisymmetric condition, the lower energy condition for a singly quantized vortex is given by $(\kappa, n) = (\pm 1, 0)$ to reduce the loss of the gradient energy. Such a vortex belongs to the conjugacy class (I) in Eq. (72). In this case, so-called double-core vortex (*d* vortex) can be a self-consistent solution (Masaki et al., 2022) as in the SF ^{3}He-B phase (Thuneberg, 1986; Salomaa and Volovik, 1986). The *d* vortex is also called the nonaxisymmetric *v* vortex because it has the P_2 symmetry but does not have the P_1 and P_3 symmetries (Tsutsumi et al., 2015). Note that the axial symmetry is spontaneously broken for the *d* vortex in the SF ^{3}He-B phase, while the symmetry is broken by the boundary condition for the *d* vortex in a $^3P_2$ SF. Fig. 9 shows the order parameter structure of the *d* vortex in the D_4-BN state for $T = 0.4T_c$ and $B = 0.5T_c$ with critical temperature T_c. In the panels, the unit of length is the coherence length defined by $\xi_0 = v_F/2\pi T_c$ with Fermi velocity v_F, where $\langle \cdots \rangle_F$ accounts for the Fermi surface average. The bulk components $\gamma_{\pm 2}$ have a conventional vortex structure with a single phase winding [see panels (A) and (B)]. The double core structure can be clearly observed in the total amplitude defined by $\left[\frac{3}{2}\mathrm{Tr}\langle \hat{\Delta}^\dagger \hat{\Delta} \rangle_F\right]^{1/2}$ in panel (F). Such a structure is due to the occupations of the core by $\gamma_{M=\pm 1}$ as shown in panels (C) and (D). As can be seen below, the *d* vortex is not the lowest energy state among the vortex states with $(\kappa, n) = (\pm 1, 0)$ in the D_4-BN state and it splits into two HQVs. The *d* vortex in the SF ^{3}He-B phase is the most stable vortex solution in the low pressure region (Kasamatsu et al., 2019; Regan et al., 2019). A *d* vortex is realized as the lowest energy state in the UN and the D_2-BN states.

HQVs

The HQVs can be characterized by $\kappa = \pm 1/2$. The possibility of the half-quantized vortex in the D_4-BN state was pointed out long back in 1980 (Sauls, 1980) on the basis of the topological consideration of the form of $A_{\mu i}$. Since κ is a half odd integer, the $U(1)$ phase part gives the minus sign under the spatial rotation $\theta \to \theta + 2\pi$. By rotating the triad by angle $\pm\, \pi/2$ while going around the vortex, which is denoted by $n = \pm 1/4$ in Eq. (97), the above minus sign can be compensated by the other minus sign stemming from the disgyration. This topological consideration is represented by the boundary condition Eq. (97) with $(\kappa, n) = (\pm 1/2, \pm 1/4)$, which

---

[6] The term "J-disgyration" accounts for a singularity in the spin–orbit space, that is, the total angular momentum (J) space. Spin disgyrations and orbital disgyrations are introduced after Eq. (32).

[7] In Section "Examples of non-Abelian vortices," we discuss the spin vortex of 2π rotation in spin-2 BECs.

[8] The P_3 symmetry is already introduced when defining the one-dimensional winding number in the bulk nematic state.

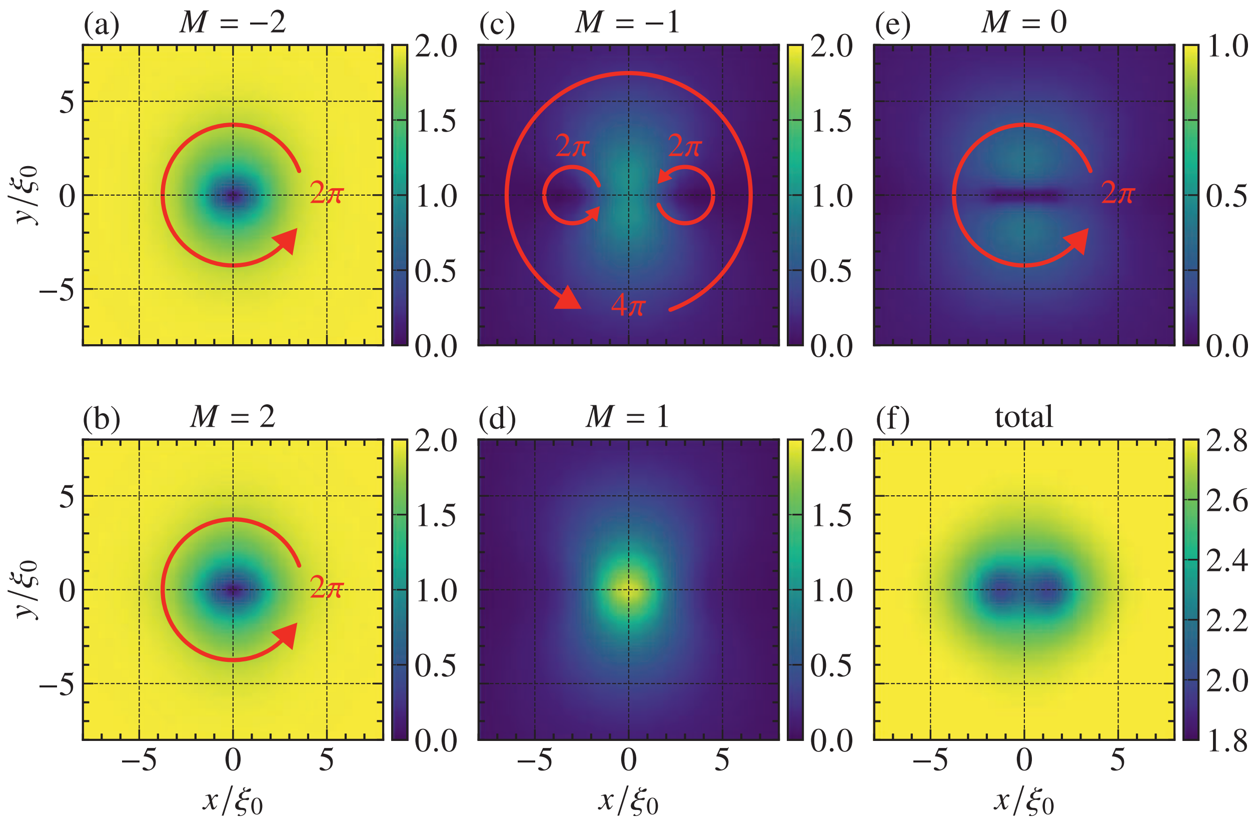

Fig. 9 Gap structure of the *d* vortex in the D_4-BN state ($T = 0.4T_c$ and $B = 0.5T_c$). (A)–(E) Amplitude of each angular momentum sector. *Red arrows* indicate the phase winding structures. (F) Total amplitude of the order parameter defined by $\left[\frac{3}{2}\mathrm{Tr}\langle\hat{\Delta}^{\dagger}\hat{\Delta}\rangle_{\mathrm{F}}\right]^{1/2}$.

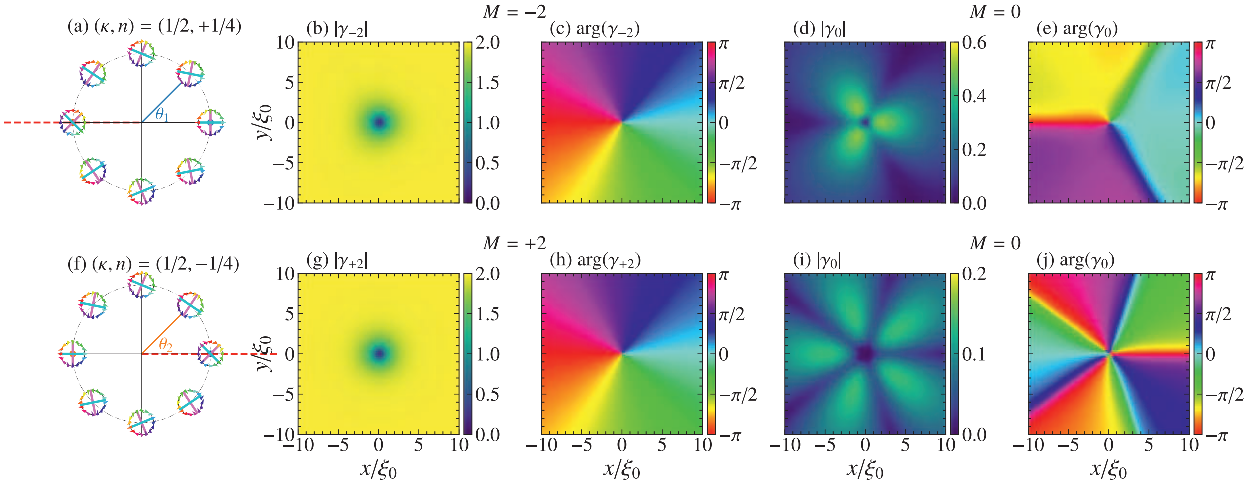

Fig. 10 HQV with $(\kappa, n) = (1/2, +1/4)$ [(A)–(E)] and $(\kappa, n) = (1/2, -1/4)$ [(F)–(J)]. The boundary conditions are sketched in (A) and (F). The amplitudes of γ_M for $M = -2$ and 0 (+ 2 and 0) are shown in (B) and (D) [(G) and (I)], respectively. The phases of γ_M for $M = -2$ and 0 (+ 2 and 0) are shown in (C) and (E) [(H) and (J)], respectively. Adapted from Masaki Y, Mizushima T, and Nitta M (2022) Non-Abelian half-quantum vortices in $^3P_2$ topological superfluids. Physical Review B 105 (22): L220503. ISSN 2469-9950. https://doi.org/10.1103/PhysRevB.105.L220503. ©2022 American Physical Society.

belongs to the conjugacy class (V) or (VI) in Eq. (72). The gradient energy of an isolated HQV far from the core is a half of that of an singly quantized vortex described by $(\kappa, n) = (\pm 1, 0)$, namely, the energy of two HQVs is the same as that of the singly quantized vortex except for contributions from the vortex cores. In other words, whether the singly quantized vortex can be split into two HQVs depends on the energy of their internal structures and the interaction energy between two HQVs.

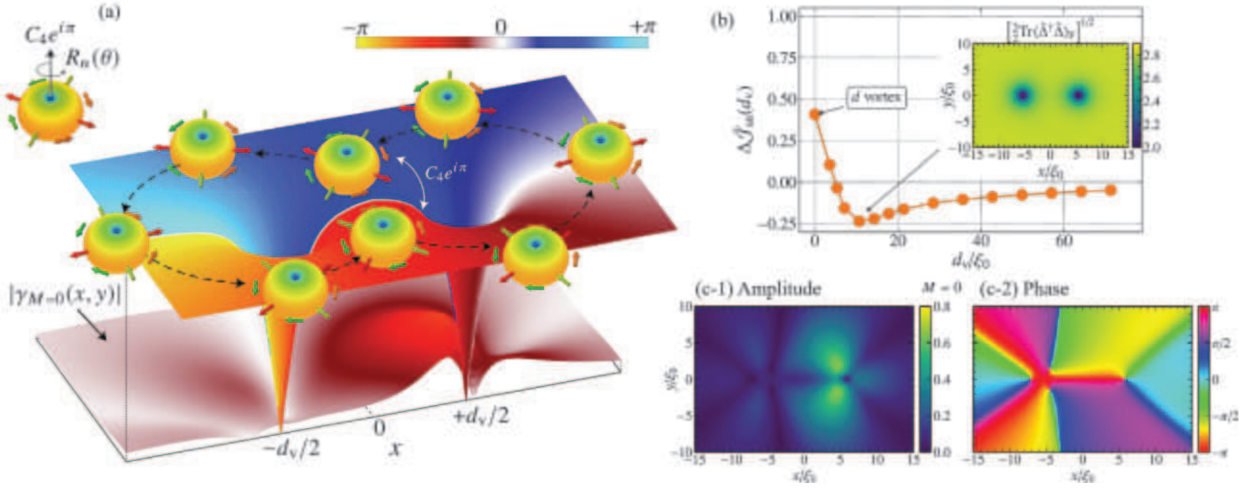

Fig. 11 (A) Schematic image of a molecule of non-Abelian HQVs in a D_4-BN state at a cross section perpendicular to the two parallel vortex lines, characterized by $(\kappa, n) = (1/2, +1/4)$ at $x = d_v/2$ and $(1/2, -1/4)$ at $x = -d_v/2$. Its spin-momentum structure is shown by objects with *color arrows* representing *d* vectors. The *color map* on the surface shows the $U(1)$ phase, and the bottom plot shows the induced component also shown in panel (C-1). (B) Interaction energy of two HQVs as a function of their separation d_v. The inset shows the total amplitude of the order parameter for the HQV molecule whose intervortex distance is indicated by the *arrow*. The free energy is scaled as $\bar{J}_{sn} = J_{sn}/(\nu_n T_c^2 \xi_0^2 \Omega_z)$, where Ω_z is the length of the system in the *z* direction, and ν_n is the density of states at the Fermi energy in the normal state. The energy at $d_v = 0$ is the free energy of the *d* vortex shown in Fig. 9. (C-1) and (C-2) The amplitude and the phase of the induced component γ_0. The intervortex distance d_v is the same as that in the inset of panel (B). Adapted from Masaki Y, Mizushima T, and Nitta M (2022) Non-Abelian half-quantum vortices in $^3P_2$ topological superfluids. Physical Review B 105 (22): L220503. ISSN 2469-9950. https://doi.org/10.1103/PhysRevB.105.L220503. ©2022 American Physical Society.

Although the above topological consideration does not take into account the core structure, recently, the whole structures of isolated HQVs were studied using the phenomenological GL theory (Masuda and Nitta, 2020; Kobayashi and Nitta, 2022a, b) and the microscopic quasiclassical theory (Masaki et al., 2022). It is proposed that an integer vortex with $\kappa = 1$ can split into two HQVs with $(\kappa, n) = (1/2, 1/4)$ and $(\kappa, n) = (1/2, -1/4)$ (Masuda and Nitta, 2020). Here we assume that $\kappa > 0$ without loss of generality. The configuration of the two HQVs given as one for $n_1 = +1/4$ with its core at $\boldsymbol{R}_1$ and the other for $n_2 = -1/4$ with its core at $\boldsymbol{R}_2$ has the following boundary condition at $\boldsymbol{R}$:

$$A(\boldsymbol{R}) \sim \sum_{M=\pm 2} e^{i(\kappa - n_1 M)\theta_1 + i(\kappa - n_2 M)\theta_2}\gamma_M \Gamma_M, \tag{98}$$

where θ_1 (θ_2) is the angle of $\boldsymbol{R} - \boldsymbol{R}_1$ $(\boldsymbol{R} - \boldsymbol{R}_2)$. Since the difference between θ_1 and θ_2 is negligible for $|\boldsymbol{R}| \to \infty$, the phase part behaves as $\exp(2i\kappa\theta)$ $[\theta \simeq (\theta_1 + \theta_2)/2]$, which means the boundary conditions for the two HQVs and the singly quantized vortex are equivalent in the limit $\rho \to \infty$. In the following, we explain the internal structure of each HQV, and the interaction energy of the two HQV vortex through the comparison of the singly quantized vortex (Masaki et al., 2022). Particularly, the nonaxisymmetric internal structure of each HQV is important to the interaction energy.

Isolated HQV (κ,n) = (1/2, +1/4)

The two disgyrations of the triads, given by $n = \pm 1/4$, are inequivalent because one is parallel to the vorticity while the other is antiparallel. Here we first explain the antiparallel case $(n, \kappa) = (1/2, 1/4)$. In the above notation, by setting $\boldsymbol{R}_1 = (0, 0)$ and $\boldsymbol{R}_2 = (-\infty, 0)$, and thus setting $\theta_2 \to 0$, the boundary condition is obtained from Eq. (98). In this case, the relative phase of $\gamma_{\pm 2}$ is zero, and the schematic image of the disgyration is drawn in Fig. 10A. Each circular object shows the directions of *d*-vectors by *colored arrows*, whose color bar is the same as in panel (C). There are also the *cyan* and *magenta lines*, which represent the directions of the eigenvalues +1 and −1 of the order parameter *A*, respectively. This HQV is $(1/2, C_4)$ in the conjugacy class (V) in Eq. (72). The self-consistent solutions of the nontrivial components are shown in panels (B)–(E). Here γ_2, not shown, is almost uniform without phase winding, as expected from the boundary condition $\kappa - n_1 M = 1/2 - 1/4 * 2 = 0$. The other bulk component γ_{-2} is a conventional singular vortex with the single-phase winding shown in panel (C). The amplitude and the phase of the internal structure of γ_0 are, respectively, shown in panels (D) and (E). The phase of the internal structure is oppositely winding against γ_{-2}, which can be understood by analogy with a vortex in a spinless chiral *p*-wave SC. We assume, for simplicity, $\bar{k}_z = 0$, and then write $\bar{k}_\chi = (k_x + i\chi k_y)/k_F = e^{i\chi\alpha}$ with the sign of the angular momentum $\chi = \pm$. With this notation, the gap function is written as

$$\hat{\Delta}(\boldsymbol{k}_F, \boldsymbol{R}) = [-\gamma_2(\boldsymbol{R})\bar{k}_+ + \gamma_0(\boldsymbol{R})/\sqrt{6}\bar{k}_-]|\uparrow\uparrow\rangle + [\gamma_{-2}(\boldsymbol{R})\bar{k}_- - \gamma_0(\boldsymbol{R})/\sqrt{6}\bar{k}_+]|\downarrow\downarrow\rangle. \tag{99}$$

In each spin sector, two opposite orbital-angular-momenta, $\bar{k}_\pm$, are mixed owing to the induced component γ_0. In a spinless chiral p-wave SC, the induced component has the opposite angular momentum relative to the component which has a nonzero order parameter far from the vortex core, that is, $\chi_i = -\chi_b$ (Heeb and Agterberg, 1999; Matsumoto and Heeb, 2001). Here we call the latter component the *bulk component*, and χ_b (χ_i) represents the sign of the angular momentum for the bulk (induced) component. The vorticity of the induced component, κ_i, is given by $\kappa_i = \kappa_b + \chi_b - \chi_i$, where κ_b is the vorticity of the bulk component. Here the $\chi_b - \chi_i$ accounts for the angular momentum difference between the bulk and induced components, and is reduced to $2\chi_b$. For the $(1/2, +1/4)$-HQV, the bulk component γ_{-2} has the vorticity $\kappa_b = \kappa - n(-2) = 1$, and $\chi_b = -1$. Thereby $\kappa_i = \kappa_b + 2\chi_b = -1$ successfully explains the vorticity of the induced component shown in panel (E). More striking feature is the three-fold symmetry in the amplitude of the induced component $|\gamma_0|$. Reflecting this discrete symmetry, the phase evolution of the induced component surrounding the vortex is nonlinear. As seen from Eq. (99), the main structure of this HQV is in the spin-down sector.

Isolated HQV (κ,n) = (1/2, −1/4)

The other HQV, characterized by $(1/2, -1/4)$, at $\boldsymbol{R}_2 = (0, 0)$, is obtained by $\boldsymbol{R}_1 \to (+\infty, 0)$, that is, $\theta \to \pi$ in Eq. (98), in which the relative phase of $\gamma_{\pm 2}$ is opposite because of the phase factor $\exp[i(1/2 + M/4)\pi]$ from the $(1/2, +1/4)$ HQV. This HQV is $(1/2, C_4^{-1})$ in the conjugacy class (V) in Eq. (72), and its disgyration is schematically drawn in Fig. 10F. In contrast to the previous case, a conventional vortex structure appears in the $M = +2$ sector shown in panels (G) and (H), while an almost uniform structure without phase winding is in the $M = -2$ sector. In panel (J) the phase winding of the induced component is +3, which can be understood as in the previous case: $\kappa_i = \kappa_b + 2\chi_b = 3$ for $\kappa_b = \kappa + M/4 = 1$ and $\chi_b = +1$. The phase evolution surrounding the vortex is again nonlinear reflecting the discrete symmetry of the amplitude $|\gamma_0|$, which is fivefold as shown in panel (H). The major vortex structure of this HQV is in the spin-up sector.

Molecule of HQVs (stability)

The two types of internal structures in the $M = 0$ component induced for the HQVs with $n = \pm 1/4$ are modulated by the connection of these two HQVs. This modulation causes an interaction between the two HQVs. The interaction energy of the two HQVs is defined by $\Delta\mathcal{J}_{\rm sn}(d_{\rm v}) = \mathcal{J}_{\rm sn}(\boldsymbol{R}_1, \boldsymbol{R}_2) - \mathcal{J}^+_{\rm sn}(\boldsymbol{R}_1) - \mathcal{J}^-_{\rm sn}(\boldsymbol{R}_2)$ based on the Luttinger–Ward energy functional $\mathcal{J}_{\rm sn}$ (Vorontsov and Sauls, 2003). Here the two HQVs are at $\boldsymbol{R}_1 = (d_{\rm v}/2, 0)$ and $\boldsymbol{R}_2 = (-d_{\rm v}/2, 0)$, schematically shown in Fig. 11A, whose energy is denoted by $\mathcal{J}_{\rm sn}(\boldsymbol{R}_1, \boldsymbol{R}_2)$. The energies of the isolated HQVs $(\kappa, n) = (1/2, +1/4)$ at $\boldsymbol{R}_1$ and $(1/2, -1/4)$ at $\boldsymbol{R}_2$ are denoted by $\mathcal{J}^+_{\rm sn}(\boldsymbol{R}_1)$ and $\mathcal{J}^-_{\rm sn}(\boldsymbol{R}_2)$, respectively.

Fig. 11B shows the interaction energies of the two HQVs as a function of intervortex distance $d_{\rm v}$. When $d_{\rm v} = 0$, the d vortex (the singly quantized vortex with double core structure) is realized. The gap structure is shown in Fig. 9. Importantly, the positive energy of the d vortex means that two isolated HQVs ($d_{\rm v} \to \infty$) are more stable than the d vortex. The actual interaction energy takes the minimum at finite $d_{\rm v}$, indicating the instability of the d vortex into a bound state of the two HQVs like a molecule. As discussed in Section "Examples of non-Abelian vortices," a singly quantized vortex $(\kappa, n) = (1, 0)$ in the conjugacy class (I) in Eq. (72) splits into two HQVs $(1/2, +1/4)$ and $(1/2, -1/4)$ in the class (V).

The stabilization mechanism in this molecule state is a deformation in the nonaxisymmetric-induced component γ_0, as shown in Fig. 11C-1 and C-2, realized in the strongly spin–orbit-coupled Cooper pairs (Masaki et al., 2022). This mechanism is purely intrinsic and possible even in the weak coupling limit, different from those in other systems such as the SF ^{3}He (Salomaa and Volovik, 1985a) and unconventional SCs (Chung et al., 2007): In the SF ^{3}He-A phase, Volovik and Salomaa phenomenologically introduced some corrections in spin mass to stabilize the HQV (Salomaa and Volovik, 1985a); This correction might be regarded as a kind of strong coupling effect through the Fermi liquid correction, but another strong coupling effect is known to destabilize the HQV (Kawakami et al., 2009, 2010, 2011; Mizushima et al., 2016). Vakaryuk and Leggett unveiled that the HQVs in equal spin pairing states, such as ^{3}He-A and D_4-BN, are accompanied by a nonzero spin polarization even in the absence of external Zeeman coupling (Vakaryuk and Leggett, 2009). The coupling of such spin polarization to external magnetic fields may affect the stability of HQVs. Another example of the stabilization mechanism is an extrinsic one in the polar and polar-distorted phases of the SF ^{3}He because of strongly anisotropic impurities, as discussed in Section "Platforms for Majorana zero modes."

Non-Abelian anyon in non-Abelian vortex

In this section, first the zero energy-bound states in above-discussed HQVs are demonstrated. Second we summarize the discrete symmetries in the presence of vortices, and finally discuss the topological protection of the zero energy states and their non-Abelian nature.

Existence of zero energy states

To investigate fermionic bound states at discrete energy levels, it is necessary to solve the BdG Eq. (92). By assuming the spatial uniformity along the z-direction, the quantum number is labeled as $\nu = (\alpha, k_z)$, and only the $k_z = 0$ sector is focused on to seek for zero energy bound states. The direct numerical calculation gives us a spectral function including the discrete bound states around the HQV-cores, as shown in Fig. 12A. There are two zero energy states localized in both of the cores. Here, the molecule state of the

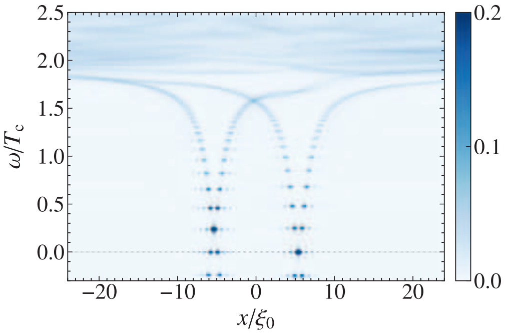

Fig. 12 Local density of states $\nu_{k_z=0}(\boldsymbol{R};\omega)$ at $k_z = 0$ and $y = 0$ for a pair of HQVs located at $(x, y) = (\pm d_v/2, 0)$ with $d_v \simeq 10.7\xi_0$. The spatial distributions of the two zero energy states are different. Adapted from Masaki Y, Mizushima T, and Nitta M (2022) Non-Abelian half-quantum vortices in $^3P_2$ topological superfluids. Physical Review B 105 (22): L220503. ISSN 2469-9950. https://doi.org/10.1103/PhysRevB.105.L220503. ©2022 American Physical Society.

two HQVs with $d_v \simeq 10.7\xi_0$ is used for a gap function in the BdG equation, and the spectral function, also known as the local density of state, is defined as $\nu_{k_z=0}(\boldsymbol{R};\omega) = \sum_{\alpha,\sigma}|u_{\alpha,k_z=0,\sigma}(\boldsymbol{R})|^2\delta(\omega - \varepsilon_{\alpha,k_z=0})$ along $\boldsymbol{R} = (x, 0)$, where $u_{\alpha,k_z,\sigma}(\boldsymbol{R})$ is the particle component with spin σ of the eigenfunction $\vec{u}_{\alpha,k_z}(\boldsymbol{R})$. In the calculation, the parameter $k_F\xi_0$, characterizing the discreteness of the bound states, is set to 5. The Majorana condition, $u_{\alpha,k_z=0,\sigma}(\boldsymbol{R}) = [v_{\alpha,k_z=0,\sigma}(\boldsymbol{R})]^*$, for the wave functions of the zero energy state can be confirmed (Masaki et al., 2022).

Discrete symmetry of vortices

We utilize the semiclassical approximation to clarify the symmetry and topology of vortices, following Tsutsumi et al. (2015), Mizushima et al. (2016), and Shiozaki and Sato (2014). In the semiclassical approximation, the spatial modulation due to a vortex line is treated as adiabatic changes as a function of the real-space coordinate surrounding the defect with the angle θ. Then, the BdG Hamiltonian in the base space, $(\boldsymbol{k}, \theta)$, is obtained from Eq. (92) as

$$\check{\mathcal{H}}(\boldsymbol{k},\theta) = \begin{pmatrix} \hat{h}_N(\boldsymbol{k}) & \hat{\Delta}(\boldsymbol{k},\theta) \\ \hat{\Delta}^\dagger(\boldsymbol{k},\theta) & -\hat{h}_N^*(\boldsymbol{k}) \end{pmatrix}, \tag{100}$$

where the $^3P_2$ pair potential within a semiclassical approximation is given by

$$\hat{\Delta}(\boldsymbol{k},\theta) = i\hat{\sigma}_\mu A_{\mu i}(\theta)k_i/k_F\hat{\sigma}_y. \tag{101}$$

Let us now summarize the discrete symmetries of the BdG Hamiltonian in Eq. (100). In the presence of vortex, the BdG Hamiltonian breaks the time-reversal symmetry $\hat{\mathcal{T}} = -i\hat{\sigma}_y K$, but holds the particle-hole symmetry

$$\check{\mathcal{C}}\check{\mathcal{H}}(\boldsymbol{k},\theta)\check{\mathcal{C}}^{-1} = -\check{\mathcal{H}}(-\boldsymbol{k},\theta), \tag{102}$$

where $\check{\mathcal{C}} = \check{\tau}_x K$ and K is the complex conjugation operator. In addition to the particle-hole symmetry, three discrete symmetries, the $\{P_1, P_2, P_3\}$, are pointed out to be relevant to vortices of the SF ^{3}He-B phase (Salomaa and Volovik, 1985b, 1987). Their representations are given by

$$\hat{P}_1 = PU_\pi\hat{1}, \ \hat{P}_3 = \hat{\mathcal{T}}\hat{C}_{2,x}, \tag{103}$$

and $\hat{P}_2 = \hat{P}_1\hat{P}_3$. Here, P, $U_\pi = e^{i(\kappa+1)\pi}$, $\hat{C}_{2,x} = e^{-i\hat{J}_x\pi}$ are the spatial inversion, the discrete phase rotation, and the π-rotation in the spin–orbit space about the x-axis. The physical meanings of P_1, P_2, and P_3 symmetries are the inversion, magnetic reflection, and magnetic π-rotation symmetries, respectively. From the definition, $P_1P_2P_3 = 1$. Under these symmetry operations, a momentum $\boldsymbol{k}$ and a spin $\boldsymbol{\sigma}$ are transformed as

$$P_1 : \boldsymbol{k} \to (-k_x, -k_y, -k_z), \ \boldsymbol{\sigma} \to (\sigma_x, \sigma_y, \sigma_z), \tag{104}$$

$$P_2 : \boldsymbol{k} \to (k_x, -k_y, -k_z), \ \boldsymbol{\sigma} \to (-\sigma_x, \sigma_y, \sigma_z), \tag{105}$$

$$P_3 : \boldsymbol{k} \to (-k_x, k_y, k_z), \ \boldsymbol{\sigma} \to (-\sigma_x, \sigma_y, \sigma_z). \tag{106}$$

Under these transformation, the order parameters are transformed as

$$P_1 : \gamma_M(\rho,\theta) \to -\gamma_M(\rho,\theta+\pi), \tag{107}$$

$$P_2 : \gamma_M(\rho, \theta) \to (-1)^{\kappa+M}[\gamma_M(\rho, \pi-\theta)]^*, \tag{108}$$

$$P_3 : \gamma_M(\rho, \theta) \to (-1)^{M}[\gamma_M(\rho, -\theta)]^*. \tag{109}$$

For axisymmetric vortices, we confirm the nonzero components of $\gamma_M(\rho)$ summarized in Table 5 by using the relation $\gamma_M(\rho, \theta) = \gamma_M(\rho)e^{i(\kappa-M)\theta}$. For example, $P_2 : \gamma_M(\rho)e^{i(\kappa-M)\theta} \to \gamma^*_M(\rho)e^{i(\kappa-M)\theta}$, and when the P_2 symmetry is preserved, $\gamma_M(\rho) = \gamma^*_M(\rho)$ can be obtained. In the case of the *d* vortex, the P_3 symmetry is broken because of the nonzero $\gamma_{\pm 1}$ components, and the P_2 symmetry is the only preserved symmetry among these three. In the case of isolated HQVs, even though $\gamma_{\pm 1} = 0$, because of the threefold, and fivefold symmetry in the gap amplitude of γ_0, the P_1 and P_2 symmetries are broken, but the P_3 symmetry is preserved.

Another discrete symmetry is the mirror reflection symmetry about the plane perpendicular to the vortex line, that is, the *xy*-plane, which is already discussed in Section "Symmetry-protected non-Abelian anyons." The mirror refection symmetry M_{xy} transforms the momentum and the spin as

$$M_{xy} : \boldsymbol{k} \to (k_x, k_y, -k_z),\ \boldsymbol{\sigma} \to (-\sigma_x, -\sigma_y, \sigma_z), \tag{110}$$

and thus the order parameter is transformed as

$$M_{xy} : \gamma_M(\rho, \theta) \to (-1)^{M+1}\gamma_M(\rho, \theta). \tag{111}$$

Therefore, in the presence of M_{xy}, even M and odd M cannot be mixed. In the case of the D_4-BN state with the point nodes along the *z*-direction, $\gamma_{M=\pm 2} \neq 0$, and the only possible mirror operation that commutes with the BdG Hamiltonian at the mirror invariant momentum $\boldsymbol{k}_M = (k_x, k_y, 0)$ is $\eta = -$ in Eq. (38) when $\gamma_{\pm 1} = 0$. The above-discussed vortices of a ${}^3P_2$, SF which preserve the M_{xy} symmetry, are the axisymmetric *o* and *u* vortices, and the HQVs.

Topology of the vortex-bound states

On the basis of the above-discussed discrete symmetries, the zero energy state of each HQV is shown to be protected by two topological numbers: one based on the chiral symmetry, a combined symmetry between the particle-hole symmetry and the P_3 symmetry, and the other based on the mirror reflection symmetry.

When the P_3 symmetry is preserved, the semiclassical BdG Hamiltonian is transformed under the combined symmetry operation $\Gamma = \mathcal{C}P_3$ with $\Gamma^2 = +1$ as

$$\check{\Gamma}\check{\mathcal{H}}(\boldsymbol{k}, \theta)\check{\Gamma}^{-1} = -\check{\mathcal{H}}(k_x, -k_y, -k_z, -\theta). \tag{112}$$

Particularly, for $k_y = k_z = 0$ and $\theta = 0$ or π, the BdG Hamiltonian anticommutes with Γ, which can be regarded as chiral symmetry (Sato et al., 2011; Mizushima et al., 2012; Tsutsumi et al., 2013; Shiozaki and Sato, 2014; Tsutsumi et al., 2015; Masaki et al., 2020; Mizushima et al., 2016). As in the bulk nematic state, as long as the chiral symmetry is preserved, one can define the one-dimensional winding number for $\boldsymbol{k}_x = (k_x, 0, 0)$ and $\theta = 0$ or π as

$$w_{1\mathrm{d}}(\theta) = -\frac{1}{4\pi i}\int dk_x \mathrm{tr}\left[\check{\Gamma}\check{\mathcal{H}}^{-1}(\boldsymbol{k}_x, \theta)\partial_{k_x}\check{\mathcal{H}}(\boldsymbol{k}_x, \theta)\right]. \tag{113}$$

The vortices that preserve the P_3 symmetry are *o* and *w* vortices, and the non-Abelian HQVs. Among them, the winding numbers $(w_{1\mathrm{d}}(0), w_{1\mathrm{d}}(\pi))$ of *o* and *w* vortices are (2, –2), and thus the topological invariant $w_{1\mathrm{d}} = (w_{1\mathrm{d}}(0) - w_{1\mathrm{d}}(\pi))/2 = 2$ ensures the existence of two zero energy states. In the case of non-Abelian HQVs, $(w_{1\mathrm{d}}(0), w_{1\mathrm{d}}(\pi))$ is (2, 0) for $(\kappa, n) = (1/2, +1/4)$ and (0, –2) for (1/2, –1/4).[9] In both cases, the topological invariant $w_{1\mathrm{d}}$ becomes 1, which ensures the existence of one zero energy state in each HQV core.

Next we explain the topological invariant based on the mirror reflection symmetry M_{xy}. As discussed above, the BdG Hamiltonian $\mathcal{H}(\boldsymbol{k}_M, \theta)$ for the mirror invariant momentum $\boldsymbol{k}_M$ commutes with the mirror operator $\check{\mathcal{M}}^{\eta}$ for $\eta = -$ in Eq. (38). Thus, $\mathcal{H}(\boldsymbol{k}_\mathrm{M}, \theta)$ can be block diagonalized with respect to the mirror eigenstates with eigenvalues $\lambda = \pm i$ as

$$\check{\mathcal{H}}(\boldsymbol{k}_\mathrm{M}, \theta) = \bigoplus_{\lambda} \tilde{\mathcal{H}}_\lambda(\boldsymbol{k}_\mathrm{M}, \theta). \tag{114}$$

Significantly, even for the BdG Hamiltonian in each mirror subsector, $\tilde{\mathcal{H}}_\lambda$, the reduced particle-hole symmetry $\tilde{\mathcal{C}}$ is preserved, though it is not for the other mirror symmetry operator $\check{\mathcal{M}}^{\eta=+}$. Therefore, $\tilde{H}_\lambda$ belongs to the class D as well as spinless chiral SCs (Schnyder et al., 2008), and the $\mathbb{Z}_2$ invariant, ν_λ can be constructed in each mirror subsector (Teo and Kane, 2010b; Qi et al., 2008). Nontrivial (odd) value of ν_λ ensures that the vortex has a single Majorana zero mode which behaves as a non-Abelian (Ising) anyon (Ueno et al., 2013; Sato et al., 2014; Tsutsumi et al., 2013).

The $\mathbb{Z}_2$ invariant ν_λ is defined on the base space $(S^2 \times S)$ composed of the two dimensional mirror invariant momentum space $\boldsymbol{k}_\mathrm{M}$ and the angle in the real space surrounding the vortex θ, and constructed by the dimensional reduction of the second Chern number defined in the four-dimensional base space $(S^3 \times S)$ composed of $\boldsymbol{k}$ and θ. The $\mathbb{Z}_2$ invariant in each mirror subsector is given by the integral of the Chern–Simons form:

---

[9] The choice of the relative phase between $\gamma_{\pm 2}$ as π by $\theta_1 \to \pi$ leads to $(w_{1\mathrm{d}}(0), w_{1\mathrm{d}}(\pi)) = (0, -2)$ rather than (2, 0) for the HQV of $(\kappa, n) = (1/2, -1/4)$.

$$\nu_\lambda = \left(\frac{i}{\pi}\right)^2 \int_{S^2\times S^1} \tilde{Q}_{3,\lambda} \mod 2, \tag{115}$$

$$\tilde{Q}_{3,\lambda} = \mathrm{tr}[\tilde{\mathcal{A}}_\lambda \wedge d\ \ \tilde{\mathcal{A}}_\lambda + \frac{2}{3}\tilde{\mathcal{A}}_\lambda \wedge \tilde{\mathcal{A}}_\lambda \wedge \tilde{\mathcal{A}}_\lambda]. \tag{116}$$

A non-Abelian Berry connection $\tilde{\mathcal{A}}_\lambda$ is given by

$$i[\tilde{\mathcal{A}}_\lambda]_{nm} = \sum_\alpha \langle \tilde{\mathrm{u}}_{\lambda,\mathrm{n}}(\boldsymbol{k}_\mathrm{M},\theta)|\partial_\alpha \tilde{\mathrm{u}}_{\lambda,\mathrm{m}}(\boldsymbol{k}_\mathrm{M},\theta)\rangle \mathrm{d}\alpha, \tag{117}$$

where α denotes (k_x, k_y, θ), and $|\tilde{u}_{\lambda,m}(\boldsymbol{k}_\mathrm{M},\theta)\rangle$ is the mth eigenstate of $\tilde{\mathcal{H}}_\lambda(\boldsymbol{k},\theta)$. Within the semiclassical approximation in the D_4-BN state, the $\mathbb{Z}_2$ invariant is calculated as

$$\nu_\lambda = \ell_\lambda \kappa_\lambda \mod 2, \tag{118}$$

where ℓ_λ and κ_λ are the first Chern number and the vorticity in the mirror subsector λ. The former characterizes the bulk topology and $\ell_{\lambda=\pm i} = \pm 1$. The latter is given by $\kappa_\lambda = \kappa - nM$ for the bulk component M in the λ subsector. In the case of the isolated HQVs, $(\nu_{+i}, \nu_{-i}) = (0, -1)$ $[(+1, 0)]$ for $(\kappa, n) = (1/2, +1/4)$ $[(1/2, -1/4)]$. The two HQVs host Majorana fermions in different mirror sectors, and thus the $\mathbb{Z}_2$ invariant of the molecule state is given by $(\nu_{+i}, \nu_{-i}) = (+1, -1)$. The $\mathbb{Z}_2$ invariant of the o vortex has the same one, and the pairwise Majorana fermions are localized at the same core (Masaki et al., 2020).

The zero energy state bound in each HQV core is protected by the two topological invariants based on the mirror reflection symmetry and the chiral symmetry, and it is identified as non-Abelian (Ising) anyon of the Majorana fermion. Therefore, the HQV in the D_4-BN state has twofold non-Abelian nature: one from the non-Abelian Ising anyon and the other from non-Abelian first homotopy group.

Conclusion

We have presented various types of non-Abelian anyons in topological SCs/SFs and other systems. Non-Abelian anyons are attracting a great attention because of possible applications to topological quantum computations, where quantum computations are realized by braiding of non-Abelian anyons. The simplest non-Abelian anyons are Ising anyons realized by Majorana fermions hosted by vortices (or edges) of topological superconductors, $\nu = 5/2$ quantum Hall states, spin liquids, and QCD matter. These are, however, insufficient for universal quantum computations. The other anyons that can be used for universal quantum computations are given by Fibonacci anyons, which exist in $\nu = 12/5$ quantum Hall states. There are also Yang-Lee anyons, which are nonunitary counterparts of Fibonacci anyons. Another class of non-Abelian anyons of the bosonic origin can be given by non-Abelian vortex anyons realized by non-Abelian vortices supported by a non-Abelian first homotopy group. These vortex anyons exist in BN liquid crystals, cholesteric liquid crystals, spin-2 spinor BECs, and QCD matter. There is a unique system simultaneously admitting two kinds of non-Abelian anyons, which is the Majorana fermions (Ising anyons) and non-Abelian vortex anyons. That is $^3P_2$ SFs, spin-triplet, p-wave paring of neutrons, expected to exist in neutron star interiors as the largest topological quantum matter in universe.

Acknowledgments

This work was supported by a Grant-in-Aid for Scientific Research on Innovative Areas "Quantum Liquid Crystals" (Grant No. JP22H04480) from JSPS of Japan and JSPS KAKENHI (Grants No. JP18H01217, No. JP19K14662, No. JP20K03860, No. JP20H01857, No. JP21H01039, and No. JP22H01221), and the WPI program "Sustainability with Knotted Chiral Meta Matter (SKCM^2)" at Hiroshima University.

References

Akhmerov AR, Dahlhaus JP, Hassler F, Wimmer M, and Beenakker CWJ (2011) Quantized conductance at the Majorana phase transition in a disordered superconducting wire. *Physical Review Letters* 106(5): 057001. https://doi.org/10.1103/PhysRevLett.106.057001.

Alford MG, Benson K, Coleman SR, March-Russell J, and Wilczek F (1990) The interactions and excitations of nonabelian vortices. *Physical Review Letters* 64: 1632. https://doi.org/10.1103/PhysRevLett.64.1632 [Erratum: Phys.Rev.Lett. 65, 668 (1990)].

Alford MG, Benson K, Coleman SR, March-Russell J, and Wilczek F (1991) Zero modes of nonabelian vortices. *Nuclear Physics B* 349: 414–438. https://doi.org/10.1016/0550-3213(91)90331-Q.

Alford MG, Lee K-M, March-Russell J, and Preskill J (1992) Quantum field theory of non-Abelian strings and vortices. *Nuclear Physics B* 384: 251–317. https://doi.org/10.1016/0550-3213(92)90468-Q. hep-th/9112038.

Alford MG, Schmitt A, Rajagopal K, and Schäfer T (2008) Color superconductivity in dense quark matter. *Reviews of Modern Physics* 80: 1455–1515. https://doi.org/10.1103/RevModPhys.80.1455.

Alicea J (2012) New directions in the pursuit of Majorana fermions in solid state systems. *Reports on Progress in Physics* 75(7): 76501.

Alicea J, Oreg Y, Refael G, von Oppen F, and Fisher MPA (2011) Non-Abelian statistics and topological quantum information processing in 1D wire networks. *Nature Physics* 7: 412. https://doi.org/10.1038/nphys1915.

Ambegaokar V, deGennes PG, and Rainer D (1974) Landau-Ginsburg equations for an anisotropic superfluid. *Physical Review A* 9(6): 2676–2685. https://doi.org/10.1103/PhysRevA.9.2676.

Andersen TI, et al. (2022) Observation of non-Abelian exchange statistics on a superconducting processor. *arXiv:2210.10255.*

Anderson PW and Brinkman WF (1973) Anisotropic superfluidity in ^{3}He: A possible interpretation of its stability as a spin-fluctuation effect. *Physical Review Letters* 30(22): 1108–1111. https://doi.org/10.1103/PhysRevLett.30.1108.

Anderson PW and Morel P (1961) Generalized Bardeen-Cooper-Schrieffer states and the proposed low-temperature phase of liquid He^3. *Physical Review* 123(6): 1911–1934. https://doi.org/10.1103/PhysRev.123.1911.

Anderson PW and Toulouse G (1977) Phase slippage without vortex cores: Vortex textures in superfluid ^{3}He. *Physical Review Letters* 38(9): 508–511. https://doi.org/10.1103/PhysRevLett.38.508.

Ardonne E, Gukelberger J, Ludwig AWW, Trebst S, and Troyer M (2011) Microscopic models of interacting Yang-Lee anyons. *New Journal of Physics* 13(4): 045006. https://doi.org/10.1088/1367-2630/13/4/045006.

Arovas D, Schrieffer JR, and Wilczek F (1984) Fractional statistics and the quantum Hall effect. *Physical Review Letters* 53: 722–723. https://doi.org/10.1103/PhysRevLett.53.722.

Autti S, Dmitriev VV, Mäkinen JT, Soldatov AA, Volovik GE, Yudin AN, Zavjalov VV, and Eltsov VB (2016) Observation of half-quantum vortices in topological superfluid ^{3}He. *Physical Review Letters* 117(25): 255301. https://doi.org/10.1103/PhysRevLett.117.255301.

Auzzi R, Bolognesi S, Evslin J, Konishi K, and Yung A (2003) NonAbelian superconductors: Vortices and confinement in N=2 SQCD. *Nuclear Physics B* 673: 187–216. https://doi.org/10.1016/j.nuclphysb.2003.09.029. hep-th/0307287.

Awoga OA, Cayao J, and Black-Schaffer AM (2019) Supercurrent detection of topologically trivial zero-energy states in nanowire junctions. *Physical Review Letters* 123(11): 117001. https://doi.org/10.1103/PhysRevLett.123.117001.

Bais FA (1980) Flux Metamorphosis. *Nuclear Physics B* 170: 32–43. https://doi.org/10.1016/0550-3213(80)90474-5.

Balachandran AP, Lizzi F, and Rodgers VGJ (1984) Topological symmetry breakdown in cholesterics, nematics, and ^{3}He. *Physical Review Letters* 52: 1818–1821. https://doi.org/10.1103/PhysRevLett.52.1818.

Balachandran AP, Digal S, and Matsuura T (2006) Semi-superfluid strings in high density QCD. *Physical Review D* 73: 074009. https://doi.org/10.1103/PhysRevD.73.074009.

Bartolomei H, Kumar M, Bisognin R, Marguerite A, Berroir J-M, Bocquillon E, Plaçais B, Cavanna A, Dong Q, Gennser U, Jin Y, and Fève G (2020) Fractional statistics in anyon collisions. *Science* 368(6487): 173–177. https://doi.org/10.1126/science.aaz5601.

Beenakker CWJ (2013) Search for Majorana fermions in superconductors. *Annual Review of Condensed Matter Physics* ISSN: 1947-5454. 4(1): 113–136. https://doi.org/10.1146/annurev-conmatphys-030212-184337.

Beenakker CWJ (2020) Search for non-Abelian Majorana braiding statistics in superconductors. *SciPost Physics Lecture Notes* ISSN: 2590-1990. 15: 15. https://doi.org/10.21468/SciPostPhysLectNotes.15.

Bonderson P, Freedman M, and Nayak C (2008) Measurement-only topological quantum computation. *Physical Review Letters* 101(1): 010501. https://doi.org/10.1103/PhysRevLett.101.010501.

Bonderson P, Freedman M, and Nayak C (2009) Measurement-only topological quantum computation via anyonic interferometry. *Annals of Physics* ISSN: 0003-4916. 324(4): 787–826. https://doi.org/10.1016/j.aop.2008.09.009.

Bonesteel NE, Hormozi L, Zikos G, and Simon SH (2005) Braid topologies for quantum computation. *Physical Review Letters* 95(14): 140503. https://doi.org/10.1103/PhysRevLett.95.140503.

Borgh MO and Ruostekoski J (2016) Core structure and non-Abelian reconnection of defects in a biaxial nematic Spin-2 Bose-Einstein condensate. *Physical Review Letters* 117(27): 275302. https://doi.org/10.1103/PhysRevLett.117.275302 [Erratum: Physical Review Lett. 118, 129901 (2017)].

Bravyi S (2006) Universal quantum computation with the $\nu = 5/2$ fractional quantum Hall state. *Physical Review A* 73(4): 042313. https://doi.org/10.1103/PhysRevA.73.042313.

Brekke L, Imbo TD, Dykstra H, and Falk AF (1993) Novel spin and statistical properties of nonabelian vortices. *Physics Letters B* 304: 127–133. https://doi.org/10.1016/0370-2693(93)91411-F. hep-th/9210131.

Brekke L, Collins SJ, and Imbo TD (1997) Non-Abelian vortices on surfaces and their statistics. *Nuclear Physics B* 500: 465–485. https://doi.org/10.1016/S0550-3213(97)00409-4. hep-th/9701056.

Bruin JAN, Claus RR, Matsumoto Y, Kurita N, Tanaka H, and Takagi H (2022) Robustness of the thermal Hall effect close to half-quantization in α-RuCl3. *Nature Physics* 18: 401. https://doi.org/10.1038/s41567-021-01501-y.

Bucher M (1991) The Aharonov-Bohm effect and exotic statistics for nonabelian vortices. *Nuclear Physics B* 350: 163–178. https://doi.org/10.1016/0550-3213(91)90256-W.

Bucher M, Lee K-M, and Preskill J (1992) On detecting discrete Cheshire charge. *Nuclear Physics B* 386: 27–42. https://doi.org/10.1016/0550-3213(92)90174-A. hep-th/9112040.

Cardy JL (1985) Conformal invariance and the Yang-Lee edge singularity in two dimensions. *Physical Review Letters* 54(13): 1354–1356. https://doi.org/10.1103/PhysRevLett.54.1354.

Cayao J and Burset P (2021) Confinement-induced zero-bias peaks in conventional superconductor hybrids. *Physical Review B* 104(13): 134507. https://doi.org/10.1103/PhysRevB.104.134507.

Chen W, Wang J, Wu Y, Qi J, Liu J, and Xie XC (2022) Non-Abelian statistics of Majorana zero modes in the presence of an Andreev bound state. *Physical Review B* 105(5): 054507. https://doi.org/10.1103/PhysRevB.105.054507.

Cheng M, Lutchyn RM, Galitski V, and Das Sarma S (2009) Splitting of Majorana-fermion modes due to intervortex tunneling in a $p_x + ip_y$ superconductor. *Physical Review Letters* 103(10): 107001. https://doi.org/10.1103/PhysRevLett.103.107001.

Chung SB and Kivelson SA (2010) Entropy-driven formation of a half-quantum vortex lattice. *Physical Review B* 82(21): 214512. https://doi.org/10.1103/PhysRevB.82.214512.

Chung SB and Zhang S-C (2009) Detecting the Majorana fermion surface state of ^{3}He$-B$ through spin relaxation. *Physical Review Letters* ISSN: 0031-9007. 103(23): 235301. https://doi.org/10.1103/PhysRevLett.103.235301.

Chung SB, Bluhm H, and Kim E-A (2007) Stability of half-quantum vortices in $p_x + ip_y$ superconductors. *Physical Review Letters* 99: 197002. https://doi.org/10.1103/PhysRevLett.99.197002.

Clarke DJ, Sau JD, and Tewari S (2011) Majorana fermion exchange in quasi-one-dimensional networks. *Physical Review B* 84(3): 035120. https://doi.org/10.1103/PhysRevB.84.035120.

De Gennes PG (1973) Long range distortions in an anisotropic superfluid. *Physics Letters A* ISSN: 0375-9601. 44(4): 271–272. https://doi.org/10.1016/0375-9601(73)90916-X.

Di Francesco PD, Mathieu P, and Sénéchal. (1997) *Conformal Field Theory.* New York: Springer-Verlag.

Dmitriev VV, Senin AA, Soldatov AA, and Yudin AN (2015) Polar phase of superfluid ^{3}He in anisotropic aerogel. *Physical Review Letters* 115(16): 165304. https://doi.org/10.1103/PhysRevLett.115.165304.

Elliott SR and Franz M (2015) Colloquium: Majorana fermions in nuclear, particle, and solid-state physics. *Reviews of Modern Physics* ISSN: 0034-6861. 87(1): 137–163. https://doi.org/10.1103/RevModPhys.87.137.

Eto M and Nitta M (2009) Color magnetic flux tubes in dense QCD. *Physical Review D* 80: 125007. https://doi.org/10.1103/PhysRevD.80.125007.

Eto M and Nitta M (2021) Chiral non-Abelian vortices and their confinement in three flavor dense QCD. *Physical Review D* 104(9): 094052. https://doi.org/10.1103/PhysRevD.104.094052. 2103.13011.

Eto M, Isozumi Y, Nitta M, Ohashi K, and Sakai N (2006) Solitons in the Higgs phase: The moduli matrix approach. *Journal of Physics A: Mathematical and General* 39: R315–R392. https://doi.org/10.1088/0305-4470/39/26/R01. hep-th/0602170.

Eto M, Hirono Y, Nitta M, and Yasui S (2014) Vortices and other topological solitons in dense quark matter. *Progress of Theoretical and Experimental Physics* 2014(1): 012D01. https://doi.org/10.1093/ptep/ptt095. 1308.1535.

Fang C, Gilbert MJ, and Bernevig BA (2014) New class of topological superconductors protected by magnetic group symmetries. *Physical Review Letters* 112(10): 106401. https://doi.org/10.1103/PhysRevLett.112.106401.

Field B and Simula T (2018) Introduction to topological quantum computation with non-Abelian anyons. *Quantum Science and Technology* 3: 045004.

Fisher ME (1978) Yang-Lee edge singularity and ϕ^3 field theory. *Physical Review Letters* 40(25): 1610–1613. https://doi.org/10.1103/PhysRevLett.40.1610.

Freedman M, Hastings MB, Nayak C, and Qi X-L (2011a) Weakly coupled non-Abelian anyons in three dimensions. *Physical Review B* 84(24): 245119. https://doi.org/10.1103/PhysRevB.84.245119.

Freedman M, Hastings MB, Nayak C, Qi X-L, Walker K, and Wang Z (2011b) Projective ribbon permutation statistics: A remnant of non-abelian braiding in higher dimensions. *Physical Review B* 83(11): 115132. https://doi.org/10.1103/PhysRevB.83.115132.

Freedman MH, Gukelberger J, Hastings MB, Trebst S, Troyer M, and Wang Z (2012) Galois conjugates of topological phases. *Physical Review B* 85(4): 045414. https://doi.org/10.1103/PhysRevB.85.045414.

Fu L and Kane CL (2008) Superconducting proximity effect and Majorana fermions at the surface of a topological insulator. *Physical Review Lett.* 100(9): 096407. https://doi.org/10.1103/PhysRevLett.100.096407.

Fujimoto Y and Nitta M (2021a) Non-Abelian alice strings in two-flavor dense QCD. *Physical Review D* 103: 054002. https://doi.org/10.1103/PhysRevD.103.054002. 2011.09947.

Fujimoto Y and Nitta M (2021b) Topological confinement of vortices in two-flavor dense QCD. *Journal of High Energy Physics* 09: 192. https://doi.org/10.1007/JHEP09(2021)192. 2103.15185.

Fujimoto Y and Nitta M (2021c) Vortices penetrating two-flavor quark-hadron continuity. *Physical Review D* 103(11): 114003. https://doi.org/10.1103/PhysRevD.103.114003. 2102.12928.

Fujita T and Tsuneto T (1972) The Ginzburg-Landau equation for 3P2 pairingsuperfluidity in neutron stars. *Progress in Theoretical Physics* 48(3): 766–782. https://doi.org/10.1143/PTP.48.766.

Fujiwara T, Fukui T, Nitta M, and Yasui S (2011) Index theorem and Majorana zero modes along a non-Abelian vortex in a color superconductor. *Physical Review D* 84: 076002. https://doi.org/10.1103/PhysRevD.84.076002. 1105.2115.

Fulga IC, Hassler F, Akhmerov AR, and Beenakker CWJ (2011) Scattering formula for the topological quantum number of a disordered multimode wire. *Physical Review B* 83(15): 155429. https://doi.org/10.1103/PhysRevB.83.155429.

Gao P, He Y-P, and Liu X-J (2016) Symmetry-protected non-Abelian braiding of Majorana Kramers pairs. *Physical Review B* 94(22): 224509. https://doi.org/10.1103/PhysRevB.94.224509.

Génetay Johansen E and Simula T (2022) Prime number factorization using a spinor Bose–Einstein condensate-inspired topological quantum computer. *Quantum Information Processing* 21(1): 31. https://doi.org/10.1007/s11128-021-03366-9.

Haim A and Oreg Y (2019) Time-reversal-invariant topological superconductivity in one and two dimensions. *Physics Reports* ISSN: 0370-1573. 825: 1–48. https://doi.org/10.1016/j.physrep.2019.08.002. Time-reversal-invariant topological superconductivity in one and two dimensions.

Halperin BI (1984) Statistics of quasiparticles and the hierarchy of fractional quantized Hall states. *Physical Review Letters* 52: 1583–1586. https://doi.org/10.1103/PhysRevLett.52.1583 [Erratum: Phys.Rev.Lett. 52, 2390 (1984)].

Halperin WP (2019) Superfluid 3He in aerogel. *Annual Review of Condensed Matter Physics* 10(1): 155–170. https://doi.org/10.1146/annurev-conmatphys-031218-013134.

Hanany A and Tong D (2003) Vortices, instantons and branes. *Journal of High Energy Physics* 07: 037. https://doi.org/10.1088/1126-6708/2003/07/037. hep-th/0306150.

Heeb R and Agterberg DF (1999) Ginzburg-Landau theory for a *p*-wave Sr_2RuO_4 superconductor: Vortex core structure and extended London theory. *Physical Review B* ISSN: 0163-1829. 59(10): 7076–7082. https://doi.org/10.1103/PhysRevB.59.7076. http://arxiv.org/abs/cond-mat/9811190.

Hirono Y, Yasui S, Itakura K, and Nitta M (2012) Non-Abelian statistics of vortices with multiple Majorana fermions. *Physical Review B* 86: 014508. https://doi.org/10.1103/PhysRevB.86.014508.

Hoffberg M, Glassgold AE, Richardson RW, and Ruderman M (1970) Anisotropic superfluidity in neutron star matter. *Physical Review Letters* 24(14): 775. https://doi.org/10.1103/PhysRevLett.24.775.

Hong J-S, Poon T-FJ, Zhang L, and Liu X-J (2022) Unitary symmetry-protected non-Abelian statistics of Majorana modes. *Physical Review B* 105(2): 024503. https://doi.org/10.1103/PhysRevB.105.024503.

Hormozi L, Zikos G, Bonesteel NE, and Simon SH (2007) Topological quantum compiling. *Physical Review B* 75(16): 165310. https://doi.org/10.1103/PhysRevB.75.165310.

Hosur P, Ghaemi P, Mong RSK, and Vishwanath A (2011) Majorana modes at the ends of superconductor vortices in doped topological insulators. *Physical Review Letters* 107(9): 097001. https://doi.org/10.1103/PhysRevLett.107.097001.

Hu Y and Kane CL (2018) Fibonacci topological superconductor. *Physical Review Letters* 120(6): 066801. https://doi.org/10.1103/PhysRevLett.120.066801.

Ikegaya S, Suzuki S-I, Tanaka Y, and Asano Y (2016) Quantization of conductance minimum and index theorem. *Physical Review B* 94(5): 054512. https://doi.org/10.1103/PhysRevB.94.054512.

Ivanov DA (2001) Non-abelian statistics of half-quantum vortices in p-wave superconductors. *Physical Review Letters* 86(2): 268. https://doi.org/10.1103/PhysRevLett.86.268.

Karzig T, Oreg Y, Refael G, and Freedman MH (2016) Universal geometric path to a robust Majorana magic gate. *Physical Review X* 6(3): 031019. https://doi.org/10.1103/PhysRevX.6.031019.

Karzig T, Knapp C, Lutchyn RM, Bonderson P, Hastings MB, Nayak C, Alicea J, Flensberg K, Plugge S, Oreg Y, Marcus CM, and Freedman MH (2017) Scalable designs for quasiparticle-poisoning-protected topological quantum computation with Majorana zero modes. *Physical Review B* 95(23): 235305. https://doi.org/10.1103/PhysRevB.95.235305.

Kasahara Y, Ohnishi T, Mizukami Y, Tanaka O, Ma S, Sugii K, Kurita N, Tanaka H, Nasu J, Motome Y, Shibauchi T, and Matsuda Y (2018) Majorana quantization and half-integer thermal quantum Hall effect in a Kitaev spin liquid. *Nature* 559: 227. https://doi.org/10.1038/s41586-018-0274-0.

Kasamatsu K, Mizuno R, Ohmi T, and Nakahara M (2019) Effects of a magnetic field on vortex states in superfluid $^3\mathrm{He}-B$. *Physical Review B* 99(10): 104513. https://doi.org/10.1103/PhysRevB.99.104513.

Kashiwaya S and Tanaka Y (2000) Tunnelling effects on surface bound states in unconventional superconductors. *Reports on Progress in Physics* 63(10): 1641–1724. https://doi.org/10.1088/0034-4885/63/10/202.

Kashuba O and Timm C (2015) Topological Kondo effect in transport through a superconducting wire with multiple Majorana end states. *Physical Review Letters* 114(11): 116801. https://doi.org/10.1103/PhysRevLett.114.116801.

Kawaguchi Y and Ueda M (2012) Spinor Bose-Einstein condensates. *Physics Reports* 520: 253–381. https://doi.org/10.1016/j.physrep.2012.07.005.

Kawakami T and Hu X (2015) Evolution of density of states and a spin-resolved checkerboard-type pattern associated with the Majorana bound state. *Physical Review Letters* 115(17): 177001. https://doi.org/10.1103/PhysRevLett.115.177001.

Kawakami T, Tsutsumi Y, and Machida K (2009) Stability of a half-quantum vortex in rotating superfluid $^3\mathrm{He}-A$ between parallel plates. *Physical Review B* ISSN: 1098-0121. 79(9): 092506. https://doi.org/10.1103/PhysRevB.79.092506.

Kawakami T, Tsutsumi Y, and Machida K (2010) Singular and half-quantum vortices and associated Majorana particles in superfluid 3 He-A between parallel plates. *Journal of the Physical Society of Japan* ISSN: 0031-9015. 79(4): 044607. https://doi.org/10.1143/JPSJ.79.044607.

Kawakami T, Mizushima T, and Machida K (2011) Zero energy modes and statistics of vortices in spinful chiral p-wave superfluids. *Journal of the Physical Society of Japan* ISSN: 0031-9015. 80(4): 044603. https://doi.org/10.1143/JPSJ.80.044603.

Kells G, Meidan D, and Brouwer PW (2012) Near-zero-energy end states in topologically trivial spin-orbit coupled superconducting nanowires with a smooth confinement. *Physical Review B* 86(10): 100503. https://doi.org/10.1103/PhysRevB.86.100503.

Kitaev AY (2001) Unpaired Majorana fermions in quantum wires. *Physics-Uspekhi* 44(10S): 131–136. https://doi.org/10.1070/1063-7869/44/10S/S29.

Kitaev AY (2003) Fault tolerant quantum computation by anyons. *Annals of Physics* 303: 2–30. https://doi.org/10.1016/S0003-4916(02)00018-0.

Kitaev A (2006) Anyons in an exactly solved model and beyond. *Annals of Physics (New York)* ISSN: 00034916. 321(1): 2–111. https://doi.org/10.1016/j.aop.2005.10.005.

Kitaev A and Laumann C (2008) Topological Phases and Quantum Computation. *Lecture Notes of the Les Houches Summer School. No. 89.* , pp. 101–125. Oxford University Press, ISBN: 0-19-957461-8.

Knapp C, Chew A, and Alicea J (2020) Fragility of the fractional Josephson effect in time-reversal-invariant topological superconductors. *Physical Review Letters* 125(20): 207002. https://doi.org/10.1103/PhysRevLett.125.207002.

Kobayashi M and Nitta M (2022a) Core structures of vortices in Ginzburg-Landau theory for neutron $^3P_2$ superfluids. *Physical Review C* 105(3): 035807. https://doi.org/10.1103/PhysRevC.105.035807. 2203.09300.

Kobayashi M and Nitta M (2022b) Proximity effects of vortices in neutron $^3P_2$ superfluids in neutron stars: Vortex core transitions and covalent bonding of vortex molecules. *arXiv:2209.07205.*

Kobayashi M, Kawaguchi Y, Nitta M, and Ueda M (2009) Collision dynamics and rung formation of non-Abelian vortices. *Physical Review Letters* 103: 115301. https://doi.org/10.1103/PhysRevLett.103.115301.

Kobayashi S, Kobayashi M, Kawaguchi Y, Nitta M, and Ueda M (2012) Abe homotopy classification of topological excitations under the topological influence of vortices. *Nuclear Physics B* 856: 577–606. https://doi.org/10.1016/j.nuclphysb.2011.11.003.

Koornwinder TH, Schroers BJ, Slingerland JK, and Bais FA (1999) Fourier transform and the Verlinde formula for the quantum double of a finite group. *Journal of Physics A: Mathematical and General* 32: 8539–8549. https://doi.org/10.1088/0305-4470/32/48/313. math/9904029.

Kopnin NB and Salomaa MM (1991) Mutual friction in superfluid ^{3}He: Effects of bound states in the vortex core. *Physical Review B* 44(17): 9667–9677. https://doi.org/10.1103/PhysRevB.44.9667.

Kortman PJ and Griffiths RB (1971) Density of zeros on the Lee-Yang circle for two Ising ferromagnets. *Physical Review Letters* 27(21): 1439–1442. https://doi.org/10.1103/PhysRevLett.27.1439.

Lavrentovich OD and Kleman M (2001) Cholesteric liquid crystals: Defects and topology. In: Kitzerow H-S and Bahr C (eds.) *Chirality in Liquid Crystals*, pp. 115–158. New York, NY: Springer New York.

Lee K-M (1994) Vortices on higher genus surfaces. *Physical Review D* 49: 2030–2040. https://doi.org/10.1103/PhysRevD.49.2030. hep-th/9307139.

Lee TD and Yang CN (1952) Statistical theory of equations of state and phase transitions. II. Lattice gas and Ising model. *Physical Review* 87(3): 410–419. https://doi.org/10.1103/PhysRev.87.410.

Leggett AJ (1975) A theoretical description of the new phases of liquid ^{3}He. *Reviews of Modern Physics* 47(2): 331–414. https://doi.org/10.1103/RevModPhys.47.331.

Leijnse M and Flensberg K (2012) Introduction to topological superconductivity and Majorana fermions. *Semiconductor Science and Technology* 27(12): 124003. http://stacks.iop.org/0268-1242/27/i=12/a=124003.

Leinaas JM and Myrheim J (1977) On the theory of identical particles. *Nuovo Cimento B* 37: 1–23. https://doi.org/10.1007/BF02727953.

Lesanovsky I and Katsura H (2012) Interacting Fibonacci anyons in a Rydberg gas. *Physical Review A* 86(4): 041601. https://doi.org/10.1103/PhysRevA.86.041601.

Liu X-J, Wong CLM, and Law KT (2014) Non-Abelian Majorana doublets in time-reversal-invariant topological superconductors. *Physical Review X* 4(2): 021018. https://doi.org/10.1103/PhysRevX.4.021018.

Liu C-X, Sau JD, Stanescu TD, and Das Sarma S (2017) Andreev bound states versus Majorana bound states in quantum dot-nanowire-superconductor hybrid structures: Trivial versus topological zero-bias conductance peaks. *Physical Review B* 96(7): 075161. https://doi.org/10.1103/PhysRevB.96.075161.

Liu C-X, Sau JD, and Das Sarma S (2018) Distinguishing topological Majorana bound states from trivial Andreev bound states: Proposed tests through differential tunneling conductance spectroscopy. *Physical Review B* 97(21): 214502. https://doi.org/10.1103/PhysRevB.97.214502.

Liu D, Cao Z, Liu X, Zhang H, and Liu DE (2021) Topological Kondo device for distinguishing quasi-Majorana and Majorana signatures. *Physical Review B* 104(20): 205125. https://doi.org/10.1103/PhysRevB.104.205125.

Lo H-K and Preskill J (1993) Non-Abelian vortices and non-Abelian statistics. *Physical Review D* 48: 4821–4834. https://doi.org/10.1103/PhysRevD.48.4821.

Machida T, Sun Y, Pyon S, Takeda S, Kohsaka Y, Hanaguri T, Sasagawa T, and Tamegai T (2019) Zero-energy vortex bound state in the superconducting topological surface state of Fe(Se,Te). *Nature Materials* 18: 811. https://doi.org/10.1038/s41563-019-0397-1.

Majorana E (1937) Teoria simmetrica dell'elettrone e del positrone. *Nuovo Cimento* 14: 171–184. https://doi.org/10.1007/BF02961314.

Makhlin Y, Silaev M, and Volovik GE (2014) Topology of the planar phase of superfluid ^{3}He and bulk-boundary correspondence for three-dimensional topological superconductors. *Physical Review B* 89(17): 174502. https://doi.org/10.1103/PhysRevB.89.174502.

Mäkinen JT, Dmitriev VV, Nissinen J, Rysti J, Volovik GE, Yudin AN, Zhang K, and Eltsov VB (2019) Half-quantum vortices and walls bounded by strings in the polar-distorted phases of topological superfluid ^{3}He. *Nature Communications* 10(1): 237. https://doi.org/10.1038/s41467-018-08204-8.

Mäkinen JT, Zhang K, and Eltsov VB (2022) Vortex-bound solitons in topological superfluid ^{3}He. *arXiv:2211.17117.*

Marmorini G, Yasui S, and Nitta M (2020) Pulsar glitches from quantum vortex networks. *arXiv:2010.09032.*

Marra P (2022) Majorana nanowires for topological quantum computation. *Journal of Applied Physics* 132: 231101.

Masaki Y, Mizushima T, and Nitta M (2020) Microscopic description of axisymmetric vortices in $^3P_2$ superfluids. *Physical Review Research* 2(1): 013193. https://doi.org/10.1103/PhysRevResearch.2.013193.

Masaki Y, Mizushima T, and Nitta M (2022) Non-Abelian half-quantum vortices in $^3P_2$ topological superfluids. *Physical Review B* ISSN: 2469-9950. 105(22): L220503. https://doi.org/10.1103/PhysRevB.105.L220503.

Masuda K and Nitta M (2016) Magnetic properties of quantized vortices in neutron $^3P_2$ superfluids in neutron stars. *Physical Review C* 93(3): 035804. https://doi.org/10.1103/PhysRevC.93.035804.

Masuda K and Nitta M (2020) Half-quantized non-Abelian vortices in neutron $^3P_2$ superfluids inside magnetars. *Progress of Theoretical and Experimental Physics* 2020(1): 013D01. https://doi.org/10.1093/ptep/ptz138.

Matsumoto M and Heeb R (2001) Vortex charging effect in a chiral $p_x \pm ip_y$-wave superconductor. *Physical Review B* ISSN: 0163-1829. 65(1): 014504. https://doi.org/10.1103/PhysRevB.65.014504.

Mawson T, Petersen TC, Slingerland JK, and Simula TP (2019) Braiding and fusion of non-Abelian vortex anyons. *Physical Review Letters* 123(14): 140404. https://doi.org/10.1103/PhysRevLett.123.140404.

Mermin ND (1974) d-Wave pairing near the transition temperature. *Physical Review A* 9: 868–872. https://doi.org/10.1103/PhysRevA.9.868.

Mermin ND (1979) The topological theory of defects in ordered media. *Reviews of Modern Physics* 51: 591–648. https://doi.org/10.1103/RevModPhys.51.591.

Mietke A and Dunkel J (2022) Anyonic defect braiding and spontaneous chiral symmetry breaking in dihedral liquid crystals. *Physical Review X* 12(1): 011027. https://doi.org/10.1103/PhysRevX.12.011027. 2011.04648.

Mineev VP (2014) Half-quantum vortices in polar phase of superfluid ^{3}He. *Journal of Low Temperature Physics* 177: 48. https://doi.org/10.1007/s10909-014-1189-2.

Mizushima T and Machida K (2010) Splitting and oscillation of Majorana zero modes in the *p*-wave BCS-BEC evolution with plural vortices. *Physical Review A* 82(2): 023624. https://doi.org/10.1103/PhysRevA.82.023624.

Mizushima T and Machida K (2011) Effects of Majorana edge fermions on dynamical spin susceptibility in topological superfluid 3He-B. *Journal of Low Temperature Physics* ISSN: 00222291. 162(3-4): 204–211. https://doi.org/10.1007/s10909-010-0297-x.

Mizushima T, Sato M, and Machida K (2012) Symmetry protected topological order and spin susceptibility in superfluid ^{3}He$-B$. *Physical Review Letters* 109(16): 165301. https://doi.org/10.1103/PhysRevLett.109.165301.

Mizushima T, Tsutsumi Y, Kawakami T, Sato M, Ichioka M, and Machida K (2016) Symmetry-protected topological superfluids and superconductors-from the basics to ^{3}He-. *Journal of the Physical Society of Japan* 85(2): 022001. https://doi.org/10.7566/JPSJ.85.022001.

Mizushima T, Masuda K, and Nitta M (2017) $^3P_2$ superfluids are topological. *Physical Review B* 95(14): 140503. https://doi.org/10.1103/PhysRevB.95.140503.

Mizushima T, Yasui S, and Nitta M (2020) Critical endpoint and universality class of neutron $^3P_2$ superfluids in neutron stars. *Physical Review Research* 2: 013194. https://doi.org/10.1103/PhysRevResearch.2.013194.

Mizushima T, Yasui S, Inotani D, and Nitta M (2021) Spin-polarized phases of $^3P_2$ superfluids in neutron stars. *Physical Review C* ISSN: 2469-9985. 104(4): 045803. https://doi.org/10.1103/PhysRevC.104.045803.

Mong RSK, Clarke DJ, Alicea J, Lindner NH, Fendley P, Nayak C, Oreg Y, Stern A, Berg E, Shtengel K, and Fisher MPA (2014) Universal topological quantum computation from a superconductor-Abelian quantum Hall heterostructure. *Physical Review X* 4(1): 011036. https://doi.org/10.1103/PhysRevX.4.011036.

Moore GW and Read N (1991) Nonabelions in the fractional quantum Hall effect. *Nuclear Physics B* 360: 362–396. https://doi.org/10.1016/0550-3213(91)90407-O.

Moore C, Stanescu TD, and Tewari S (2018a) Two-terminal charge tunneling: Disentangling Majorana zero modes from partially separated Andreev bound states in semiconductor-superconductor heterostructures. *Physical Review B* 97(16): 165302. https://doi.org/10.1103/PhysRevB.97.165302.

Moore C, Zeng C, Stanescu TD, and Tewari S (2018b) Quantized zero-bias conductance plateau in semiconductor-superconductor heterostructures without topological Majorana zero modes. *Physical Review B* 98(15): 155314. https://doi.org/10.1103/PhysRevB.98.155314.

Motome Y and Nasu J (2020) Hunting Majorana fermions in Kitaev magnets. *Journal of the Physical Society of Japan* ISSN: 0031-9015. 89(1): 012002. https://doi.org/10.7566/JPSJ.89.012002.

Muzikar P, Sauls JA, and Serene JW (1980) $^3P_2$ pairing in neutron star matter: Magnetic field effects and vortices. *Physical Review D* 21: 1494–1502. https://doi.org/10.1103/PhysRevD.21.1494.

Nagamura N and Ikeda R (2018) Stability of half-quantum vortices in equal-spin pairing states of ^{3}He. *Physical Review B* ISSN: 2469-9950. 98(9): 094524. https://doi.org/10.1103/PhysRevB.98.094524.

Nagato Y, Higashitani S, and Nagai K (2009) Strong anisotropy in spin susceptibility of superfluid 3 He-B film caused by surface bound states. *Journal of the Physical Society of Japan* ISSN: 0031-9015. 78(12): 123603. https://doi.org/10.1143/JPSJ.78.123603.

Nakamura J, Liang S, Gardner GC, and Manfra MJ (2020) Direct observation of anyonic braiding statistics. *Nature Physics* 16: 931–936. https://doi.org/10.1038/s41567-020-1019-1.

Nakano E, Nitta M, and Matsuura T (2008) Non-Abelian strings in high density QCD: Zero modes and interactions. *Physical Review D* 78: 045002. https://doi.org/10.1103/PhysRevD.78.045002.

Nayak C and Wilczek F (1996) 2^n-Quasihole states realize 2^{n-1}-dimensional spinor braiding statistics in paired quantum Hall states. *Nuclear Physics B* ISSN: 0550-3213. 479(3): 529–553. https://doi.org/10.1016/0550-3213(96)00430-0.

Nayak C, Simon SH, Stern A, Freedman M, and Das Sarma S (2008) Non-Abelian anyons and topological quantum computation. *Reviews of Modern Physics* 80: 1083–1159. https://doi.org/10.1103/RevModPhys.80.1083.

Nielsen M and Chuang I (2010) *Quantum Computation and Quantum Information.* Cambridge University Press.

Oreg Y and von Oppen F (2020) Majorana zero modes in networks of Cooper-Pair boxes: Topologically ordered states and topological quantum computation. *Annual Review of Condensed Matter Physics* 11(1): 397–420. https://doi.org/10.1146/annurev-conmatphys-031218-013618.

Pachos JK (2012) *Introduction to Topological Quantum Computation.* Cambridge: Cambridge University Press. https://doi.org/10.1017/CBO9780511792908.

Pan H and Das Sarma S (2020) Physical mechanisms for zero-bias conductance peaks in Majorana nanowires. *Physical Review Research* 2(1): 013377. https://doi.org/10.1103/PhysRevResearch.2.013377.

Pan H, Cole WS, Sau JD, and Das Sarma S (2020) Generic quantized zero-bias conductance peaks in superconductor-semiconductor hybrid structures. *Physical Review B* 101(2): 024506. https://doi.org/10.1103/PhysRevB.101.024506.

Pan H, Sau JD, and Das Sarma S (2021) Three-terminal nonlocal conductance in Majorana nanowires: Distinguishing topological and trivial in realistic systems with disorder and inhomogeneous potential. *Physical Review B* 103(1): 014513. https://doi.org/10.1103/PhysRevB.103.014513.

Piroli L and Cirac JI (2020) Quantum cellular automata, tensor networks, and area laws. *Physical Review Letters* 125(19): 190402. https://doi.org/10.1103/PhysRevLett.125.190402.

Plugge S, Rasmussen A, Egger R, and Flensberg K (2017) Majorana box qubits. *New Journal of Physics* 19: 012001. https://doi.org/10.1088/1367-2630/aa54e1.

Poenaru V and Toulouse G (1977) The crossing of defects in ordered media and the topology of 3-manifolds. *Journal de Physique (Paris)* 38: 887. https://doi.org/10.1051/jphys:01977003808088700.

Prada E, San-Jose P, de Moor MWA, Geresdi A, Lee EJH, Klinovaja J, Loss D, Nygård J, Aguado R, and Kouwenhoven LP (2020) From Andreev to Majorana bound states in hybrid superconductor-semiconductor nanowires. *Nature Reviews Physics* 2: 575. https://doi.org/10.1038/s42254-020-0228-y.

Preskill J (2004) *Lecture Notes for Physics 219: Quantum Computation*. http://www.theory.caltech.edu/preskill/ph219/ph219_2004.html.

Preskill J and Krauss LM (1990) Local discrete symmetry and quantum mechanical hair. *Nuclear Physics B* 341: 50–100. https://doi.org/10.1016/0550-3213(90)90262-C.

Qi X-L, Hughes TL, and Zhang S-C (2008) Topological field theory of time-reversal invariant insulators. *Physical Review B* 78(19): 195424. https://doi.org/10.1103/PhysRevB.78.195424.

Read N and Green D (2000) Paired states of fermions in two-dimensions with breaking of parity and time reversal symmetries, and the fractional quantum Hall effect. *Physical Review B* 61: 10267. https://doi.org/10.1103/PhysRevB.61.10267.

Read N and Rezayi E (1999) Beyond paired quantum Hall states: Parafermions and incompressible states in the first excited Landau level. *Physical Review B* 59(12): 8084–8092. https://doi.org/10.1103/PhysRevB.59.8084.

Regan RC, Wiman JJ, and Sauls JA (2019) The vortex phase diagram of rotating superfluid ^{3}He-B. *Physical Review B* ISSN: 2469-9950. 101(2): 024517. https://doi.org/10.1103/PhysRevB.101.024517.

Regan RC, Wiman JJ, and Sauls JA (2021) Half-quantum vortices in nematic and chiral phases of ^{3}He. *Physical Review B* 104(2): 024513. https://doi.org/10.1103/PhysRevB.104.024513.

Ricco LS, de Souza M, Figueira MS, Shelykh IA, and Seridonio AC (2019) Spin-dependent zero-bias peak in a hybrid nanowire-quantum dot system: Distinguishing isolated Majorana fermions from Andreev bound states. *Physical Review B* 99(15): 155159. https://doi.org/10.1103/PhysRevB.99.155159.

Ricco LS, Sanches JE, Marques Y, de Souza M, Figueira MS, Shelykh IA, and Seridonio AC (2021) Topological isoconductance signatures in Majorana nanowires. *Scientific Reports* 11: 17310. https://doi.org/10.1038/s41598-021-96415-3.

Richardson RW (1972) Ginzburg-Landau theory of anisotropic superfluid neutron-star matter. *Physical Review D* 5: 1883–1896. https://doi.org/10.1103/PhysRevD.5.1883.

Rysti J, Mäkinen JT, Autti S, Kamppinen T, Volovik GE, and Eltsov VB (2021) Suppressing the Kibble-Zurek mechanism by a symmetry-violating bias. *Physical Review Letters* 127(11): 115702. https://doi.org/10.1103/PhysRevLett.127.115702.

Salomaa MM and Volovik GE (1985a) Half-quantum vortices in superfluid ^{3}He-A. *Physical Review Letters* 55(11): 1184–1187. https://doi.org/10.1103/PhysRevLett.55.1184.

Salomaa MM and Volovik GE (1985b) Symmetry and structure of quantized vortices in superfluid ^3B. *Physical Review B* 31(1): 203–227. https://doi.org/10.1103/PhysRevB.31.203.

Salomaa MM and Volovik GE (1986) Vortices with spontaneously broken axisymmetry in ^3B. *Physical Review Letters* ISSN: 0031-9007. 56(4): 363–366. https://doi.org/10.1103/PhysRevLett.56.363.

Salomaa MM and Volovik GE (1987) Quantized vortices in superfluid ^{3}He. *Reviews of Modern Physics* 59(3): 533–613. https://doi.org/10.1103/RevModPhys.59.533.

Sanno T, Yamada MG, Mizushima T, and Fujimoto S (2022) Engineering Yang-Lee anyons via Majorana bound states. *Physical Review B* 106(17): 174517. https://doi.org/10.1103/PhysRevB.106.174517.

Sarma SD, Freedman M, and Nayak C (2015) Majorana zero modes and topological quantum computation. *npj Quantum Information* 1(1): 15001. https://doi.org/10.1038/npjqi.2015.1. http://www.nature.com/articles/npjqi20151.

Sato M (2003) Non-Abelian statistics of axion strings. *Physics Letters B* ISSN: 0370-2693. 575(1): 126–130. https://doi.org/10.1016/j.physletb.2003.09.047.

Sato M and Ando Y (2017) Topological superconductors: A review. *Reports on Progress in Physics* 80(7): 076501. https://doi.org/10.1088/1361-6633/aa6ac7.

Sato M and Fujimoto S (2016) Majorana fermions and topology in superconductors. *Journal of the Physical Society of Japan* ISSN: 0031-9015. 85(7): 072001. https://doi.org/10.7566/JPSJ.85.072001.

Sato M, Takahashi Y, and Fujimoto S (2009) Non-Abelian topological order in *s*-wave superfluids of ultracold fermionic atoms. *Physical Review Letters* 103(2): 020401. https://doi.org/10.1103/PhysRevLett.103.020401.

Sato M, Takahashi Y, and Fujimoto S (2010) Non-Abelian topological orders and Majorana fermions in spin-singlet superconductors. *Physical Review B* 82(13): 134521. https://doi.org/10.1103/PhysRevB.82.134521.

Sato M, Tanaka Y, Yada K, and Yokoyama T (2011) Topology of Andreev bound states with flat dispersion. *Physical Review B* 83(22): 224511. https://doi.org/10.1103/PhysRevB.83.224511.

Sato M, Yamakage A, and Mizushima T (2014) Mirror Majorana zero modes in spinful superconductors/superfluids non-Abelian anyons in integer quantum vortices. *Physica E* 55: 20.

Sauls, J. A., 1980. Anisotropic Superfluidity in Neutron Stars and Strong Coupling Effect in Superfluid 3He (Ph.D. thesis). SUNY Stony Brook.

Sauls JA and Serene JW (1978) $^3P_2$ Pairing near the transition temperature in neutron-star matter. *Physical Review D* 17(6): 1524–1528. https://doi.org/10.1103/PhysRevD.17.1524.

Sauls JA, Stein DL, and Serene JW (1982) Magnetic vortices in a rotating $^3P_2$ neutron superfluid. *Physical Review D* 25(4): 967–975. https://doi.org/10.1103/PhysRevD.25.967.

Schnyder AP, Ryu S, Furusaki A, and Ludwig AWW (2008) Classification of topological insulators and superconductors in three spatial dimensions. *Physical Review B* 78(19): 195125. https://doi.org/10.1103/PhysRevB.78.195125.

Schulenborg J and Flensberg K (2020) Absence of supercurrent sign reversal in a topological junction with a quantum dot. *Physical Review B* 101(1): 014512. https://doi.org/10.1103/PhysRevB.101.014512.

Schwarz AS (1982) Field theories with no local conservation of the electric charge. *Nuclear Physics B* 208: 141–158. https://doi.org/10.1016/0550-3213(82)90190-0.

Sedrakian A and Clark JW (2018) Superfluidity in nuclear systems and neutron stars. *arXiv:1802.00017.*

Semenoff GW and Zhou F (2007) Discrete symmetries and 1/3-quantum vortices in condensates of F=2 cold atoms. *Physical Review Letters* 98: 100401. https://doi.org/10.1103/PhysRevLett.98.100401.

Shifman M and Yung A (2007) Supersymmetric solitons and how they help us understand non-Abelian gauge theories. *Reviews of Modern Physics* 79: 1139. https://doi.org/10.1103/RevModPhys.79.1139. hep-th/0703267.

Shiozaki K and Sato M (2014) Topology of crystalline insulators and superconductors. *Physical Review B* 90(16): 165114. https://doi.org/10.1103/PhysRevB.90.165114.

Silaev MA and Volovik GE (2014) Andreev-Majorana bound states in superfluids. *Journal of Experimental and Theoretical Physics* ISSN: 1063-7761. 119(6): 1042–1057. https://doi.org/10.1134/S1063776114120097.

Song JL, Semenoff GW, and Zhou F (2007) Quantum fluctuation-induced uniaxial and biaxial spin nematics. *Physical Review Letters* 98: 160408. https://doi.org/10.1103/PhysRevLett.98.160408. cond-mat/0702052.

Sugeta M, Mizushima T, and Fujimoto S (2022) *Enhanced 2π-periodic Aharonov-Bohm effect as a signature of Majorana bound states probed by nonlocal measurements.* https://doi.org/10.48550/ARXIV.2205.07506.

Takatsuka T (1972) Superfluid state in neutron star matter. III tensor coupling effect in 3P2 energy gap. *Progress in Theoretical Physics* 47(3): 1062–1064. https://doi.org/10.1143/PTP.47.1062.

Takatsuka T and Tamagaki R (1971) Superfluid state in neutron star matter. II properties of anisotropic energy gap of 3P2 pairing. *Progress in Theoretical Physics* 46(1): 114–134. https://doi.org/10.1143/PTP.46.114.

Tamagaki R (1970) Superfluid state in neutron star matter. I generalized Bogoliubov transformation and existence of 3P2 gap at high density. *Progress in Theoretical Physics* 44(4): 905–928. https://doi.org/10.1143/PTP.44.905.

Tanaka Y and Kashiwaya S (1995) Theory of tunneling spectroscopy of *d*-wave superconductors. *Physical Review Letters* 74(17): 3451–3454. https://doi.org/10.1103/PhysRevLett.74.3451.

Tanaka Y, Nazarov YV, Golubov AA, and Kashiwaya S (2004) Theory of charge transport in diffusive normal metal/unconventional singlet superconductor contacts. *Physical Review B* 69(14): 144519. https://doi.org/10.1103/PhysRevB.69.144519.

Tanaka Y, Kashiwaya S, and Yokoyama T (2005) Theory of enhanced proximity effect by midgap Andreev resonant state in diffusive normal-metal/triplet superconductor junctions. *Physical Review B* 71(9): 094513. https://doi.org/10.1103/PhysRevB.71.094513.

Tanaka Y, Sanno T, Mizushima T, and Fujimoto S (2022) Manipulation of Majorana-Kramers qubit and its tolerance in time-reversal invariant topological superconductor. *Physical Review B* 106(1): 014522. https://doi.org/10.1103/PhysRevB.106.014522.

Teo JCY and Kane CL (2010a) Majorana fermions and non-Abelian statistics in three dimensions. *Physical Review Letters* 104(4): 046401. https://doi.org/10.1103/PhysRevLett.104.046401.

Teo JCY and Kane CL (2010b) Topological defects and gapless modes in insulators and superconductors. *Physical Review B* 82(11): 115120. https://doi.org/10.1103/PhysRevB.82.115120.

Terashima H and Ueda M (2005) Nonunitary quantum circuit. *International Journal of Quantum Information* 3(4): 633. https://doi.org/10.1142/S0219749905001456.

Thamm M and Rosenow B (2021) Transmission amplitude through a Coulomb blockaded Majorana wire. *Physical Review Research* 3(2): 023221. https://doi.org/10.1103/PhysRevResearch.3.023221.

Thuneberg EV (1986) Identification of vortices in superfluid ^{3}He*B*. *Physical Review Letters* 56(4): 359–362. https://doi.org/10.1103/PhysRevLett.56.359.

Tojo S, Hayashi T, Tanabe T, Hirano T, Kawaguchi Y, Saito H, and Ueda M (2009) Spin-dependent inelastic collisions in spin-2 Bose-Einstein condensates. *Physical Review A* 80(4): 042704. https://doi.org/10.1103/PhysRevA.80.042704.

Trebst S, Troyer M, Wang Z, and Ludwig AWW (2008) A short introduction to Fibonacci anyon models. *Progress of Theoretical Physics Supplement* ISSN: 0375-9687. 176: 384–407. https://doi.org/10.1143/PTPS.176.384.

Tsutsumi Y, Ishikawa M, Kawakami T, Mizushima T, Sato M, Ichioka M, and Machida K (2013) UPt3 as a topological crystalline superconductor. *Journal of the Physical Society of Japan* 82(11): 113707. https://doi.org/10.7566/JPSJ.82.113707.

Tsutsumi Y, Kawakami T, Shiozaki K, Sato M, and Machida K (2015) Symmetry-protected vortex bound state in superfluid ^{3}He−*B* phase. *Physical Review B* 91(14): 144504. https://doi.org/10.1103/PhysRevB.91.144504.

Uchino S, Kobayashi M, Nitta M, and Ueda M (2010) Quasi-Nambu-goldstone modes in Bose-Einstein condensates. *Physical Review Letters* 105: 230406. https://doi.org/10.1103/PhysRevLett.105.230406.

Ueno Y, Yamakage A, Tanaka Y, and Sato M (2013) Symmetry-protected Majorana fermions in topological crystalline superconductors: Theory and application to Sr_2RuO_4. *Physical Review Letters* 111(8): 087002. https://doi.org/10.1103/PhysRevLett.111.087002.

Usher N, Hoban MJ, and Browne DE (2017) Nonunitary quantum computation in the ground space of local hamiltonians. *Physical Review A* 96(3): 032321. https://doi.org/10.1103/PhysRevA.96.032321.

Vakaryuk V and Leggett AJ (2009) Spin polarization of half-quantum vortex in systems with equal spin pairing. *Physical Review Letters* 103(5): 057003. https://doi.org/10.1103/PhysRevLett.103.057003.

Valentini M, Peñaranda F, Hofmann A, Brauns M, Hauschild R, Krogstrup P, San-Jose P, Prada E, Aguado R, and Katsaros G (2021) Nontopological zero-bias peaks in full-shell nanowires induced by flux-tunable Andreev states. *Science* 373(6550): 82–88. https://doi.org/10.1126/science.abf1513.

Vinkler-Aviv Y and Rosch A (2018) Approximately quantized thermal Hall effect of chiral liquids coupled to phonons. *Physical Review X* 8(3): 031032. https://doi.org/10.1103/PhysRevX.8.031032.

Vollhardt D and Wölfle P (1990) *The Superfluid Phases of Helium 3*. London: Taylor & Francis, ISBN: 9780850664126. https://books.google.co.jp/books?id=t0Rw75gMuwIC.

Volovik GE (1992) *Exotic Properties of Superfluid ^{3}He*. Singapore: World Scientific.

Volovik GE (1999) Fermion zero modes on vortices in chiral superconductors. *JETP Letters* 70: 609. https://doi.org/10.1134/1.568223.

Volovik GE (2003) *The Universe in a Helium Droplet*. Oxford, U.K.: Clarendon.

Volovik GE (2010) Topological superfluid 3He-B in magnetic field and Ising variable. *JETP Letters* ISSN: 0021-3640. 91(4): 201–205. https://doi.org/10.1134/S0021364010040090.

Volovik GE and Mineev VP (1977) Investigation of singularities in superfluid He3 and in liquid crystals by the homotopic topology methods. *Zhurnal Eksperimental'noi i Teoreticheskoi Fiziki* 72: 2256 [Sov. Phys. JETP 45, 1186 (1977)].

Volovik GE and Yakovenko VM (1989) Fractional charge, spin and statistics of solitons in superfluid 3He film. *Journal of Physics. Condensed Matter* 1(31): 5263. https://doi.org/10.1088/0953-8984/1/31/025.

von Gehlen G (1991) Critical and off-critical conformal analysis of the Ising quantum chain in an imaginary field. *Journal of Physics A: Mathematical and General* 24(22): 5371. https://doi.org/10.1088/0305-4470/24/22/021.

Vorontsov AB and Sauls JA (2003) Thermodynamic properties of thin films of superfluid ^{3}He-A. *Physical Review B* 68(6): 064508. https://doi.org/10.1103/PhysRevB.68.064508.

Wilczek F (1982) Quantum mechanics of fractional spin particles. *Physical Review Letters* 49: 957–959. https://doi.org/10.1103/PhysRevLett.49.957.

Wilczek F and Wu Y-S (1990) Space-time approach to holonomy scattering. *Physical Review Letters* 65: 13–16. https://doi.org/10.1103/PhysRevLett.65.13.

Wölms K, Stern A, and Flensberg K (2014) Local adiabatic mixing of Kramers pairs of Majorana bound states. *Physical Review Letters* 113(24): 246401. https://doi.org/10.1103/PhysRevLett.113.246401.

Wölms K, Stern A, and Flensberg K (2016) Braiding properties of Majorana Kramers pairs. *Physical Review B* 93(4): 045417. https://doi.org/10.1103/PhysRevB.93.045417.

Wong CLM and Law KT (2012) Majorana Kramers doublets in $d_{x^2-y^2}$-wave superconductors with Rashba spin-orbit coupling. *Physical Review B* 86(18): 184516. https://doi.org/10.1103/PhysRevB.86.184516.

Wu Y-S (1984) General theory for quantum statistics in two dimensions. *Physical Review Letters* 52(24): 2103–2106. https://doi.org/10.1103/PhysRevLett.52.2103.

Yamashita M, Izumina K, Matsubara A, Sasaki Y, Ishikawa O, Takagi T, Kubota M, and Mizusaki T (2008) Spin wave and vortex excitations of superfluid ^{3}He-A in parallel-plate geometry. *Physical Review Letters* 101(2): 025302. https://doi.org/10.1103/PhysRevLett.101.025302.

Yamashita M, Gouchi J, Uwatoko Y, Kurita N, and Tanaka H (2020) Sample dependence of half-integer quantized thermal Hall effect in the Kitaev spin-liquid candidate $\alpha-$RuCl$_3$. *Physical Review B* 102(22): 220404. https://doi.org/10.1103/PhysRevB.102.220404.

Yasui S, Itakura K, and Nitta M (2010) Fermion structure of non-Abelian vortices in high density QCD. *Physical Review D* 81: 105003. https://doi.org/10.1103/PhysRevD.81.105003. 1001.3730.

Yasui S, Itakura K, and Nitta M (2011) Majorana meets coxeter: Non-Abelian Majorana fermions and non-Abelian statistics. *Physical Review B* 83: 134518. https://doi.org/10.1103/PhysRevB.83.134518.

Yasui S, Itakura K, and Nitta M (2012) Dirac returns: Non-abelian statistics of vortices with dirac fermions. *Nuclear Physics B* 859: 261. https://doi.org/10.1016/j.nuclphysb.2012.02.007.

Yasui S, Hirono Y, Itakura K, and Nitta M (2013) Non-Abelian statistics of vortices with non-Abelian dirac fermions. *Physical Review E* 87(5): 052142. https://doi.org/10.1103/PhysRevE.87.052142. 1204.1164.

Yasui S, Chatterjee C, Kobayashi M, and Nitta M (2019a) Reexamining Ginzburg-Landau theory for neutron $^3P_2$ superfluidity in neutron stars. *Physical Review C* 100(2): 025204. https://doi.org/10.1103/PhysRevC.100.025204.

Yasui S, Chatterjee C, and Nitta M (2019b) Phase structure of neutron $^3P_2$ superfluids in strong magnetic fields in neutron stars. *Physical Review C* 99(3): 035213. https://doi.org/10.1103/PhysRevC.99.035213.

Yavilberg K, Ginossar E, and Grosfeld E (2019) Differentiating Majorana from Andreev bound states in a superconducting circuit. *Physical Review B* 100(24): 241408. https://doi.org/10.1103/PhysRevB.100.241408.

Ye M, Halász GB, Savary L, and Balents L (2018) Quantization of the thermal hall conductivity at small Hall angles. *Physical Review Letters* 121(14): 147201. https://doi.org/10.1103/PhysRevLett.121.147201.

Yokoi T, Ma S, Kasahara Y, Kasahara S, Shibauchi T, Kurita N, Tanaka H, Nasu J, Motome Y, Hickey C, Trebst S, and Matsuda Y (2021) Half-integer quantized anomalous thermal Hall effect in the Kitaev material candidate α-RuCl$_3$. *Science* 373(6554): 568–572. https://doi.org/10.1126/science.aay5551.

Yu P, Chen J, Gomanko M, Badawy G, Bakkers EPAM, Zuo K, Mourik V, and Frolov SM (2021) Non-Majorana states yield nearly quantized conductance in proximatized nanowires. *Nature Physics* 17: 482. https://doi.org/10.1038/s41567-020-01107-w.

Zhang G and Spånslätt C (2020) Distinguishing between topological and quasi Majorana zero modes with a dissipative resonant level. *Physical Review B* 102(4): 045111. https://doi.org/10.1103/PhysRevB.102.045111.

Zhang F, Kane CL, and Mele EJ (2013) Time-reversal-invariant topological superconductivity and Majorana Kramers pairs. *Physical Review Letters* 111(5): 056402. https://doi.org/10.1103/PhysRevLett.111.056402.

Zhang P, Yaji K, Hashimoto T, Ota Y, Kondo T, Okazaki K, Wang Z, Wen J, Gu GD, Ding H, and Shin S (2018) Observation of topological superconductivity on the surface of an iron-based superconductor. *Science* 360(6385): 182. https://doi.org/10.1126/science.aan4596.

Zhang H, de Moor MWA, Bommer JDS, Xu D, Wang G, van Loo N, Liu C-X, Gazibegovic S, Logan JA, Car D, het Veld RLMO, van Veldhoven PJ, Koelling S, Verheijen MA, Pendharkar M, Pennachio DJ, Shojaei B, Lee JS, Palmstrøm CJ, Bakkers EPAM, Das Sarma S, and Kouwenhoven LP (2021) Large zero-bias peaks in InSb-Al hybrid semiconductor-superconductor nanowire devices. *arXiv:2101.11456*.

Zheng C (2021) Universal quantum simulation of single-qubit nonunitary operators using duality quantum algorithm. *Scientific Reports* 2021: 3960. https://doi.org/10.1038/s41598-021-83521-5.

Zhu S, Kong L, Cao L, Chen H, Papaj M, Du S, Xing Y, Liu W, Wang D, Shen C, Yang F, Schneeloch J, Zhong R, Gu G, Fu L, Zhang Y-Y, Ding H, and Gao H-J (2020) Nearly quantized conductance plateau of vortex zero mode in an iron-based superconductor. *Science* 367(6474): 189. https://doi.org/10.1126/science.aax0274.

Topological superconductors

Shinsei Ryu, Department of Physics, Princeton University, Princeton, NJ, United States

© 2024 Elsevier Ltd. All rights reserved.

Introduction **795**
Overview **796**
One-dimensional topological superconductors 796
Two-dimensional topological superconductors 798
Three-dimensional topological superconductors 798
Key issues **799**
Periodic table of topological insulators and superconductors 799
Bulk-boundary correspondence and the effect of disorder 800
The effect of interactions 801
Conclusion **801**
Acknowledgments **802**
References **802**

Abstract

This article provides a concise description of topological superconductors. After reviewing representative examples of fully gapped topological superconductors in various dimensions, we discuss the basic concepts including the symmetry classification scheme of generic fermionic systems and topological classifications. The bulk-boundary correspondence, one of the hallmarks of topological superconductors, is also discussed, addressing disorder and interaction effects.

Key points

- Topological superconductors are quantum phases of matter that cannot continuously be deformable to trivial states of matter, such as a collection of atoms without any interatomic interaction.
- Topological superconductors host exotic Andreev bound states at their boundaries and vortex cores. They are stable against perturbations and disorder. In some cases, the boundary states are zero-energy Majorana modes. The close-knit relation between the bulk topological properties and protected boundary states is called the bulk-boundary correspondence.
- Examples of topological superconductors include one-dimensional topological superconductors (the Kitaev chain), two-dimensional chiral *p*-wave superconductors, and the B phase of ^{3}He in three dimensions. Topological superconductors in different dimensions and symmetry classes can be summarized in the periodic table of topological insulators and superconductors.

Introduction

The concept of topology has prevailed in condensed matter physics to date. The quantum Hall effect (both integer and fractional ones) is one of the first examples that made us realize the pivotal role played by topology in many-body quantum physics (Prange and Girvin, 1990). Since then, the topological concepts in condensed matter physics have been developed in great depth and breadth. The list of topological phenomena and topological systems has also been expanding vastly. In particular, the discovery of topological insulators fueled the development of topological condensed matter physics (Hasan and Kane, 2010; Qi and Zhang, 2011; Bernevig and Hughes, 2013).

Topology is a branch of mathematics that deals with properties that do not change under a continuous deformation of objects (which can be large as long as tearing and gluing are avoided). Likewise, quantum phenomena that have a topological origin or that occur within topological phases of matter can be robust against perturbations such as disorder and interactions. Furthermore, topological phenomena in many-body quantum systems are of purely quantum mechanical origin and go beyond what we expect from classical physics.

Topological concepts can be applied to superconductors (and superfluids). In fact, at the mean-field level, topological superconductors can be thought of as a close cousin of (integer) quantum Hall states and topological band insulators. Within the mean-field theory, superconductors are described in terms of (almost noninteracting) fermionic Bogoliubov quasiparticles and bosonic Cooper pairs. From the point of view of quasiparticles, Cooper pairs can be viewed as a nondynamical background. We can

https://doi.org/10.1016/B978-0-323-90800-9.00239-0

then discuss the band structure of quasiparticles using the Bogoliubov-de Gennes (BdG) Hamiltonian. In the quantum Hall effect and topological insulators, single-particle (Bloch) wave functions below the energy gap have certain topological properties that are characterized by some topological invariants, such as the Chern number (quantized Hall conductivity). Similarly, in topological superconductors, wave functions of fermionic quasiparticles have topological characters. Furthermore, like their nonsuperconducting cousins, topological superconductors support gapless modes at their boundaries. These are Andreev bound states that appear within the superconducting gap.

For certain types of topological superconductors, the Andreev bound states are Majorana fermion modes—one of the reasons why topological superconductors have become the subject of intense research. Majorana fermions are emergent excitations in condensed matter systems and are known for the fact that they are their own antiparticles. While Majorana fermions have appeared in various branches of physics, such as Neutrino physics, the recent surge of interest came from their promise for robust quantum computation. Due to their topological origin, Majorana fermions can be used as stable qubits (Nayak et al., 2008; Alicea, 2012; Beenakker, 2013).

Overview

Some of the defining properties of gapped topological (ground) states are:

(i) Topological states are not adiabatically connected to trivial states. Here, by trivial states, we mean states that can be written as a product state, which does not have spatial correlations and entanglement, such as a collection of atoms without any interatomic interactions. In other words, in the phase diagram, topological phases are necessarily separated from trivial phases by quantum phase transitions.

(ii) Topological states are characterized by quantized topological invariants. These topological invariants are often related to quantized responses of topological systems to an external background. For example, for particle number-conserving systems, an external electromagnetic field can be used to detect, for example, the quantized Hall conductivity. It can also take the form of an unoriented spacetime topology that can detect topological phases protected by symmetry that reverses the orientation of spacetime, such as time-reversal symmetry (TRS). Quantized topological invariants should be contrasted with local order parameters that can detect and characterize more conventional phases of matter with (spontaneous) symmetry-breaking.

(iii) In the presence of a spatial boundary, d-dimensional topological systems necessarily support excitations localized at the boundary. The appearance of these $(d-1)$-dimensional boundary states is a direct manifestation of the bulk topological properties (topological invariants). These boundary states are said to be anomalous in the sense that they cannot exist on their own as $(d-1)$-dimensional isolated systems, that is, they cannot be realized as $(d-1)$-dimensional isolated lattice systems. This close-knit relation between bulk topological properties and anomalous boundary states is called the bulk-boundary correspondence.

As alluded to in (ii), all these can be discussed in the presence of proper symmetry, such as TRS. For example, the adiabatic (dis) continuity of ground states can be discussed in the presence of symmetry. Because of the symmetry, states that are otherwise connected to trivial states can be made nontrivial. We say that these states are symmetry-protected (from being trivial).

We note that while we focused above on fully gapped topological phases, gapless topological states are also possible, and need to be discussed separately. Also, there is the concept of topologically ordered states (phases), examples of which include fractional quantum Hall states (Wen, 2007). While the above descriptions apply to topologically ordered phases, they require further characterizations such as topological ground-state degeneracy and exotic anyonic excitations.

The above descriptions (i–iii) apply to a broad class of topological systems and topological superconductors are no exceptions. To illustrate the concept of topological superconductors, we will discuss three representative examples: one-dimensional topological superconductivity realized in the so-called Kitaev chain, two-dimensional chiral p-wave superconductors, and the three-dimensional topological superconductivity (superfluidity) realized in the B-phase of ^{3}He. (In the following, we will work with the natural unit $\hbar = c = 1$ unless otherwise stated.)

One-dimensional topological superconductors

First, let us discuss a one-dimensional topological superconductor using the Kitaev chain (Kitaev, 2001). The Kitaev chain is defined by the Hamiltonian

$$\begin{aligned}\hat{H} &= \frac{t}{2}\sum_i \left(\hat{c}_i^\dagger \hat{c}_{i+1} + \hat{c}_{i+1}^\dagger \hat{c}_i\right) - \mu \sum_i \left(\hat{c}_i^\dagger \hat{c}_i - 1/2\right) \\ &+ \frac{1}{2}\sum_i \left(\Delta^* \hat{c}_i^\dagger \hat{c}_{i+1}^\dagger - \Delta \hat{c}_i \hat{c}_{i+1}\right),\end{aligned} \tag{1}$$

where $\hat{c}_i^\dagger$ ($\hat{c}_i$) is a fermion creation (annihilation) operator at site i on the one-dimensional lattice, and t, Δ, and μ are parameters representing hopping amplitude, pairing potential, and chemical potential, respectively. Note that we here consider spinless fermions. This type of BdG Hamiltonian may arise in proximity-induced superconductivity in a quantum wire with strong spin–orbit coupling, and ferromagnetic atomic chains on a superconductor (Lutchyn et al., 2010; Oreg et al., 2010; Nadj-Perge et al., 2014). For simplicity, we set $t = \Delta \in \mathbb{R}$ in the following. The Kitaev chain in momentum space is written as

$$\hat{H} = \frac{1}{2}\sum_k \left[\hat{c}_k^\dagger, \hat{c}_{-k}\right] \mathcal{H}(k) \begin{bmatrix} \hat{c}_k \\ \hat{c}_{-k}^\dagger \end{bmatrix}, \qquad \text{where} \quad \mathcal{H}(k) = (t\cos k - \mu)\tau_3 - t\sin k\,\tau_2, \tag{2}$$

where $k \in [-\pi, \pi)$ is the one-dimensional wave number, and $\tau_{1,2,3}$ are the Pauli matrices acting on the particle-hole space.

From the quasiparticle band structure, $\varepsilon_\pm(k) = \pm\sqrt{(t\cos k - \mu)^2 + t^2\sin^2 k}$, we see that there are two gapped phases realized in this model, for $\mu > t$ and $\mu < t$. At $\mu = t$, the gap in the quasiparticle band structure closes (quantum phase transition). These two gapped phases are topologically distinct. Namely, there is no adiabatic path connecting these two phases. This can be checked explicitly for the above Hamiltonian. No matter how we change t, Δ, and μ; there is no way to connect these two phases without going through a quantum phase transition. This turns out to be true even when we consider a more generic class of deformations of the Hamiltonian. This can be argued at least in two ways.

First, we can construct a (bulk) quantized topological invariant. It is given by a Wilson loop of the Berry connection for the lower quasiparticle band,

$$W = \exp\left[i\oint_{-\pi}^{\pi} dk\, A^-(k)\right]. \tag{3}$$

Here, $A^-(k)$ is the Berry connection constructed from the quasiparticle wave function for the lower band, $\mathcal{H}(k)|u_-(k)\rangle = \varepsilon_-(k)|u_-(k)\rangle$, as $A^-(k) = i\langle u_-(k)|\frac{\partial}{\partial k}|u_-(k)\rangle$. It can be shown that the topological invariant is quantized and takes only two possible values, $W = +1$ and $W = -1$. The quantization follows from the condition

$$\tau_1\mathcal{H}(-k)^T\tau_1 = -\mathcal{H}(k), \tag{4}$$

that is satisfied for generic BdG Hamiltonians. For the above model, $W = +1$ for $\mu > t$ while $W = -1$ for $\mu < t$. The above formula for the topological invariant can properly be generalized when there are more than one quasiparticle band for negative quasiparticle energy. Also, it can be written in different forms, for example, by using the Pfaffian of the BdG Hamiltonian (Kitaev, 2001; Chiu et al., 2016).

The topological invariant can also be formulated in terms of the fermion number parity of the many-body ground state $|GS\rangle$; when periodic boundary condition is imposed, $|GS\rangle$ is fermion number parity odd/even, $\langle GS|(-1)^{\hat{N}}|GS\rangle = \mp 1$ when we are in the topological/trivial superconducting phase, respectively. Here, $(-1)^{\hat{N}} = (-1)^{\sum_i \hat{c}_i^\dagger \hat{c}_i}$ is the total fermion number parity operator. This is the quantized response of one-dimensional topological superconductors to the twisted boundary condition.

Second, in the presence of boundaries (open boundary condition), the topological superconducting phase supports Majorana fermion modes localized at the boundaries. These states appear within the bulk quasiparticle energy gap, and are exactly at zero energy (in the limit where the ratio between the bulk correlation length and the system size goes to zero). To see this, let us introduce Majorana fermion operators as

$$\hat{\lambda}_j := \hat{c}_j^\dagger + \hat{c}_j, \quad \hat{\lambda}_j' := (\hat{c}_j - \hat{c}_j^\dagger)/i, \tag{5}$$

which correspond to the "real" and "imaginary" parts of the complex fermion operators $\hat{c}_j$ and $\hat{c}_j^\dagger$. They satisfy $\{\hat{\lambda}_j, \hat{\lambda}_k\} = \{\hat{\lambda}_j', \hat{\lambda}_k\} = 2\delta_{jk}$, $\{\hat{\lambda}_j, \hat{\lambda}_k'\} = 0$. In particular, $(\hat{\lambda}_j)^2 = (\hat{\lambda}_j')^2 = 1$. In the Majorana basis,

$$\hat{H} = -\frac{it}{2}\sum_j \hat{\lambda}_j'\hat{\lambda}_{j+1} - \frac{i\mu}{2}\sum_j \hat{\lambda}_j\,\hat{\lambda}_j'. \tag{6}$$

Deep inside the topological superconductor phase, $\mu = 0$, $\hat{H} = \frac{-it}{2}\sum_j \hat{\lambda}_j'\hat{\lambda}_{j+1}$. If we consider the Kitaev chain with L sites and with open boundary conditions, $\hat{H}$ does not include Majorana operators $\hat{\lambda}_1 = \hat{c}_1 + \hat{c}_1^\dagger$ and $\hat{\lambda}_L' = (-i)(\hat{c}_L - \hat{c}_L^\dagger)$. Hence, trivially, we have $[\hat{H}, \hat{\lambda}_1] = [\hat{H}, \hat{\lambda}_L'] = 0$. This means that the modes $\hat{\lambda}_1$ and $\hat{\lambda}_L'$ correspond to zero-energy eigenstates of the single-particle BdG Hamiltonian localized at $j = 1$ and $j = L$, respectively. They exist within the bulk quasiparticle energy gap. Due to these zero-energy modes, there is a twofold degeneracy for the many-body ground states. They are characterized by the fermion number of the fermion operators, $\hat{f} := (\hat{\lambda}_1 + i\hat{\lambda}_L')/2$ and $\hat{f}^\dagger := (\hat{\lambda}_1 - i\hat{\lambda}_L')/2$, $\hat{f}^\dagger\hat{f} - 1/2 = -i\hat{\lambda}_1\hat{\lambda}_L'/2 = \pm 1/2$.

Two-dimensional topological superconductors

As a second example, let us consider a two-dimensional spinless chiral p-wave superconductor (Read and Green, 2000). The BdG Hamiltonian is given by

$$\begin{aligned} \hat{H} &= \frac{1}{2}\int d^2k \left[\hat{c}^\dagger_{\mathbf{k}}, \hat{c}_{-\mathbf{k}}\right]\mathcal{H}(\mathbf{k})\begin{bmatrix}\hat{c}_{\mathbf{k}}\\ \hat{c}^\dagger_{-\mathbf{k}}\end{bmatrix}, \\ \text{where}\quad \mathcal{H}(\mathbf{k}) &= \begin{bmatrix}\xi_{\mathbf{k}} & \Delta_{\mathbf{k}}\\ \Delta^*_{\mathbf{k}} & -\xi_{\mathbf{k}}\end{bmatrix}, \\ \xi_{\mathbf{k}} &= \frac{k^2}{2m} - \mu, \quad \Delta_{\mathbf{k}} = |\Delta|(k_x - ik_y). \end{aligned} \tag{7}$$

Here, $\mathbf{k} = (k_x, k_y)$ is two-dimensional momentum, and m, μ, $|\Delta|$, representing the mass of fermions (electrons), chemical potential, and the amplitude of pairing potential, respectively, are real parameters. As we can see from the quasiparticle band structure, there are two phases in this model for $\mu > 0$ and $\mu < 0$ (the so-called weak and strong pairing phases). These two phases are topologically distinct. As before, this can be argued in two different ways. First, we can define a bulk topological invariant. To this end, we define a three-dimensional vector $\boldsymbol{R}(\mathbf{k})$ as $\mathcal{H}(k) = \boldsymbol{R}(k)\cdot\boldsymbol{\tau}$. We can further normalize $\boldsymbol{R}$, $\hat{\boldsymbol{R}}(\mathbf{k}) = \boldsymbol{R}(\mathbf{k})/|\boldsymbol{R}(\mathbf{k})|$. Deep inside the strong pairing phase, $\mu \gg 1$, the vector $\hat{\boldsymbol{R}}(\mathbf{k})$ is localized around the $\hat{R}_z$ axis. On the other hand, in the weak pairing phase, the trajectory or the surface swept by the vector $\hat{\boldsymbol{R}}(\mathbf{k})$ is more nontrivial; as $\mathbf{k}$ changes in the two-dimensional momentum space, $\hat{\boldsymbol{R}}(\mathbf{k})$ wraps the unit sphere once. The topological invariant (the Chern number) is then defined by

$$Ch = \int \frac{d^2k}{4\pi}\, \hat{\boldsymbol{R}}\cdot\left(\partial_x\hat{\boldsymbol{R}} \times \partial_y\hat{\boldsymbol{R}}\right), \tag{8}$$

where $\partial_i = \partial_{k_i}$. It can be shown that the Chern number is quantized to be integral values as far as there is a gap in the quasiparticle band structure. From the direct calculation, $Ch = 1$ for $\mu > 0$ and $Ch = 0$ for $\mu < 0$. These values reflect the nontrivial/trivial behavior of the $\hat{\boldsymbol{R}}$ vector mentioned before. For generic quasiparticle band structures with more than two quasiparticle bands, we can use the Thouless-Kohmoto-Nightingale-den Nijs (TKNN) formula to define and calculate the topological invariant,

$$Ch = \frac{1}{2\pi}\int d^2k \sum_a \varepsilon_{ij}\partial_i A^a_j(\mathbf{k}), \tag{9}$$

where the sum runs over all quasiparticle bands below zero energy and $A^a_i(\mathbf{k})$ is the Berry connection for the eigenfunction $|u_a(\mathbf{k})\rangle$ of the a-th quasiparticle band, $A^a_i(\mathbf{k}) = i\langle u_a(\mathbf{k})|\partial_i|u_a(\mathbf{k})\rangle$. The nontrivial topological character is also reflected in the many-body ground-state wave function. In the weak pairing phase, the ground-state wave function (projected to a sector with a fixed number of particles) is given by the Pfaffian, $\sim\text{Pf}\,(z_i - z_j)^{-1}$, where $z_i = x_i + iy_i$ is the complexified real-space coordinate of the i-th fermion. The wave function decays algebraically for the distance between fermions. On the other hand, in the strong pairing phase, the many-body ground-state wave function is short-ranged.

Second, in the topologically nontrivial phase, the system supports a chiral edge state. At low energies, the dispersion of the edge state is linear—it is a chiral Majorana (Majorana-Weyl) fermion. At finite temperatures (T), the chiral edge state carries nonzero thermal current, $I = \frac{Ch}{2}\frac{\pi^2 k_B^2}{6h}T^2$. This leads to the thermal Hall conductivity

$$\kappa_{xy} = \frac{Ch}{2}\frac{\pi^2 k_B^2}{3h}T, \tag{10}$$

where we restored the Planck constant h and the Boltzmann constant k_B. This quantization is an analog of the quantized electrical Hall conductivity in the quantum Hall effect. The universal coefficient $Ch/2$ is called chiral central charge. The chiral central charge is an integer for noninteracting fermion systems (e.g., integer quantum Hall states). The fractional value of the central charge is indicative of electron fractionalization and nontrivial topological order. Similarly, a midgap zero-energy state appears in the presence of a superconducting vortex. Similar to the end state of the one-dimensional topological superconductor discussed above, this zero-energy state is a Majorana state.

Three-dimensional topological superconductors

Besides the above examples, there are other kinds of topological superconductors. First, topological superconductors may exist in the presence of symmetries. In the above examples, the only relevant symmetry is the conservation of the fermion number parity. (Here, the fermion number parity conservation simply means Hamiltonians must be bosonic operators. Quite often in the literature, this is not phrased or regarded as symmetry.) We can have other symmetries such as time reversal, spin rotation, and crystallographic symmetries. In some cases, some symmetry is necessary to have a topological distinction between different quantum ground states—they may belong to a symmetry-protected phase. Second, topological superconductors are possible other than one and two dimensions discussed above. For example, topological superconductors protected by TRS can exist in three spatial dimensions. The B phase of ^{3}He is an example (the so-called Balian-Werthamer (BW) state). It is described by the BdG Hamiltonian

$$\hat{H} = \frac{1}{2}\int d^3k \left[\hat{c}^\dagger_{\mathbf{k}\uparrow}, \hat{c}^\dagger_{\mathbf{k}\downarrow}, \hat{c}_{-\mathbf{k}\uparrow}, \hat{c}_{-\mathbf{k}\downarrow}\right] \mathcal{H}(\mathbf{k}) \begin{bmatrix} \hat{c}_{\mathbf{k}\uparrow} \\ \hat{c}_{\mathbf{k}\downarrow} \\ \hat{c}^\dagger_{-\mathbf{k}\uparrow} \\ \hat{c}^\dagger_{-\mathbf{k}\downarrow} \end{bmatrix},$$

$$\text{where} \quad \mathcal{H}(\mathbf{k}) = \begin{bmatrix} \xi_\mathbf{k} & \Delta_\mathbf{k} \\ \Delta^\dagger_\mathbf{k} & -\xi_\mathbf{k} \end{bmatrix},$$

$$\xi_\mathbf{k} = \frac{k^2}{2m} - \mu, \quad \Delta_\mathbf{k} = |\Delta|(i\sigma_y)\mathbf{k}\cdot\boldsymbol{\sigma}, \tag{11}$$

where the Pauli matrices $\sigma_{1,2,3}$ act on spin degrees of freedom. In addition to the particle-hole condition (4), the BdG Hamiltonian also satisfies $\sigma_2\mathcal{H}(-\mathbf{k})^*\sigma_2 = \mathcal{H}(\mathbf{k})$, that is, TRS. Combined together, we see that the BdG Hamiltonian (11) anticommutes with $\Gamma \equiv \sigma_2 \otimes \tau_1$, $\Gamma\mathcal{H}(\mathbf{k})\Gamma = -\mathcal{H}(\mathbf{k})$—we say $\mathcal{H}(k)$ has chiral symmetry (CS). This implies, in the basis where Γ is diagonal, the Hamiltonian takes a block off-diagonal form,

$$\mathcal{H}(\mathbf{k}) = \begin{pmatrix} 0 & D(\mathbf{k}) \\ D^\dagger(\mathbf{k}) & 0 \end{pmatrix}. \tag{12}$$

We note that CS pairs up (nonzero) eigenvalues and eigenvectors of $\mathcal{H}(\mathbf{k})$: It is straightforward to see that when $\boldsymbol{w}_a(\mathbf{k})$ is an eigenvector with eigenvalue $\varepsilon_a(\mathbf{k})$, $\mathcal{H}(\mathbf{k})\boldsymbol{w}_a(\mathbf{k}) = \varepsilon_a(\mathbf{k})\boldsymbol{w}_a(\mathbf{k})$, $\Gamma\boldsymbol{w}_a(\mathbf{k})$ is another eigenvector with eigenvalue $-\varepsilon_a(\mathbf{k})$. CS and the off-diagonal structure are also useful to introduce the topological invariant of the three-dimensional, time-reversal symmetric topological superconductor (superfluid). We first note that $\mathcal{H}(\mathbf{k})^2 = \text{diag}\,(DD^\dagger, D^\dagger D)$, and hence the eigenvalues of $\mathcal{H}(\mathbf{k})$, $\pm\,\varepsilon_a(\mathbf{k})$, are obtained by solving

$$DD^\dagger\boldsymbol{u}_a = \varepsilon_a^2\boldsymbol{u}_a, \quad D^\dagger D\boldsymbol{v}_a = \varepsilon_a^2\boldsymbol{v}_a. \tag{13}$$

We then introduce a $\mathbf{k}$-dependent matrix, $q(\mathbf{k}) := \sum_a \boldsymbol{u}_a(\mathbf{k})\boldsymbol{v}_a^\dagger(\mathbf{k})$ (where $\boldsymbol{u}_a(\mathbf{k})$ and $\boldsymbol{v}_a^\dagger(\mathbf{k})$ are column and row vectors, respectively). The topological invariant is then given by (Schnyder et al., 2008)

$$\nu = \int \frac{d^3k}{24\pi^2}\,\varepsilon^{ijk}\,\text{Tr}\left[(q^{-1}\partial_i q)(q^{-1}\partial_j q)(q^{-1}\partial_k q)\right] \in \mathbb{Z},$$

$$i, j, k = x, y, z, \quad \partial_i = \partial_{k_i}. \tag{14}$$

For $\mu > 0$, the topological invariant is $\nu = 1$ while for $\mu < 0$, it is zero.

Key issues

Periodic table of topological insulators and superconductors

A systematic way to discuss topological superconductors (and topological insulators) in different dimensions and with different symmetries is to utilize the Altland–Zirnbauer symmetry classification (Altland and Zirnbauer, 1997). In this classification, quadratic fermionic Hamiltonians (including the BdG Hamiltonians) are classified in terms of the presence/absence of time-reversal and particle-hole symmetries (spin rotation symmetry also plays a role).

The Altland–Zirnbauer classification concerns BdG Hamiltonians given in the following form:

$$\mathcal{H} = \begin{bmatrix} h & \Delta \\ -\Delta^* & -h^T \end{bmatrix},$$

$$h^\dagger = h, \quad \Delta = -\Delta^T. \tag{15}$$

Here, h is a normal part (e.g., lattice tight-binding Hamiltonian), and Δ represents superconducting order parameters. For single-particle (BdG) Hamiltonians, we can consider three discrete symmetries, time-reversal, particle-hole, and chiral symmetries. (When the total Hamiltonian $\mathcal{H}$ is invariant under unitary symmetry (e.g., spin-rotation symmetry) and block-diagonalizable, we focus on each irreducible block of $\mathcal{H}$.) TRS is defined by

$$U_T\,\mathcal{H}^*\,U_T^\dagger = \mathcal{H}, \tag{16}$$

where U_T is a unitary matrix. For example, using the y component of the spin operator S^y, U_T is given by $U_T = \exp(i\pi S^y)$. Note that, when the time-evolution of a state ψ is given by $i\partial\psi(t)/\partial t = \mathcal{H}\psi(t)$, $\psi' = U_T\psi^*$ obeys the time-reversed Schrödinger equation, $-i\partial\psi'(t)/\partial t = \mathcal{H}\psi'(t)$, if $\mathcal{H}$ satisfies (16). Next, particle-hole symmetry (PHS) is defined by

$$U_C\, \mathcal{H}^T\, U_C^\dagger = -\mathcal{H}, \tag{17}$$

where U_C is a unitary matrix. We note that if we have an eigenstate ψ with eigenvalue ε, $\psi' = U_C\psi^*$ is also an eigenstate with energy $-\varepsilon$.

When $\mathcal{H}$ is invariant under both time-reversal and particle-hole, there is a unitary matrix that anticommutes with $\mathcal{H}$,

$$\mathcal{H}\,\Gamma = -\Gamma\,\mathcal{H}, \quad \Gamma = U_T U_C^\dagger. \tag{18}$$

(See the previous example presented around (12).) When such a unitary matrix exists, we say $\mathcal{H}$ is chiral symmetric. It is however possible that a Hamiltonian is chiral symmetric without having time-reversal and particle-hole symmetries.

Furthermore, time-reversal and particle-hole symmetries can be typified into two classes. As well known, time reversal for integer spin particles squares to +1 while that for half-odd integer particles squares to −1. We can make a similar distinction for particle-hole transformations—those that square to +1 and −1. To summarize, by considering the presence/absence of time-reversal and particle-hole symmetries, and when they exist, their types, we have $3 \times 3 = 9$ possible cases. Adding the case where we have neither time-reversal nor PHS, we have 10 different cases in total. These 10 symmetry classes were identified by Altland and Zirnbauer around 1996 in the context of disordered BdG Hamiltonians and random matrix theory.

The 10 symmetry classes are summarized in Table 1. In the leftmost column of the table, A, AI, etc., are nomenclature for the symmetry classes. This is based on the fact that the symmetry classes of Hamiltonians are in one-to-one correspondence with the classification of symmetric spaces by Cartan. The ensemble of generic BdG Hamiltonians satisfying (4) is called symmetry class D. By imposing various symmetries, BdG Hamiltonians can realize five other symmetry classes: DIII, A, AIII, C, and CI. First, imposing TRS leads to symmetry class DIII. If we impose the conservation of S_z, we realize symmetry class A, and, with further requiring TRS, symmetry class AIII. On the other hand, if we impose $SU(2)$ spin rotation symmetry, we realize symmetry class C (without TRS) and CI (with TRS).

For the 10 Altland–Zirnbauer symmetry classes, and a given spatial dimension d, Table 1 summarizes the presence/absence of topological insulators and superconductors, and when they exist, the type of topological invariants (Schnyder et al., 2008; Ryu et al., 2010; Kitaev, 2009). Here, $\varnothing$ means that there are no topological insulators and superconductors, while $\mathbb{Z}$, $\mathbb{Z}_2$, and $2\mathbb{Z}$ mean topological invariants are integer-valued, $\mathbb{Z}_2$ valued, and even integer-valued, respectively. The Kitaev chain and chiral p-wave examples both belong to class D, in $d = 1$ and $d = 2$, respectively. The BW state is a topological superconductor (superfluid) in symmetry class DIII in $d = 3$ dimensions.

Bulk-boundary correspondence and the effect of disorder

In all the three examples we have discussed, the topological superconductors in $d = 1, 2, 3$ spatial dimensions, gapless states (zero-energy Majorana mode for the case of 1d topological superconductor) appear when the system is terminated by a boundary. These states localize near the boundary and are stable against gap-opening by perturbations that respect the symmetries of the system—they are said to be ingappable or ungappable. The presence of these stable boundary states near a boundary is a direct consequence of nontrivial bulk topology.

Furthermore, these boundary states are anomalous in the sense that they cannot be realized on their own in an isolated $(d - 1)$-dimensional lattice system. In this sense, topological bulk and anomalous boundary systems are inseparable. The close

Table 1 Classification of topological insulators and superconductors.

class	*TRS*	*PHS*	*CS*	d = *1*	d = *2*	d = *3*
A	0	0	0	$\emptyset$	$\mathbb{Z}$	$\emptyset$
AIII	0	0	1	$\mathbb{Z}$	$\emptyset$	$\mathbb{Z}$
AI	+ 1	0	0	$\emptyset$	$\emptyset$	$\emptyset$
BDI	+ 1	+ 1	1	$\mathbb{Z}$	$\emptyset$	$\emptyset$
D	0	+ 1	0	$\mathbb{Z}_2$	$\mathbb{Z}$	$\emptyset$
DIII	− 1	+ 1	1	$\mathbb{Z}_2$	$\mathbb{Z}_2$	$\mathbb{Z}$
AII	− 1	0	0	$\emptyset$	$\mathbb{Z}_2$	$\mathbb{Z}_2$
CII	− 1	− 1	1	$2\mathbb{Z}$	$\emptyset$	$\mathbb{Z}_2$
C	0	− 1	0	$\emptyset$	$2\mathbb{Z}$	$\emptyset$
CI	+ 1	− 1	1	$\emptyset$	$\emptyset$	$2\mathbb{Z}$

The leftmost column (A, AIII, . . ., CI) represents 10 symmetry classes of single-particle Hamiltonians classified in terms of the presence or absence of time-reversal symmetry (TRS) and particle-hole symmetry (PHS), as well as chiral symmetry (CS). In the table, the absence of symmetries is denoted by 0. The presence of these symmetries is denoted either by +1 or −1, depending on whether the (antiunitary) operator implementing the symmetry at the level of the single-particle Hamiltonian squares to + 1 or − 1. *d* is the spatial dimension. The symbols $\mathbb{Z}_2$, $\mathbb{Z}$ and $2\mathbb{Z}$ indicate the relevant topological invariant is $\mathbb{Z}_2$-valued, integral-valued, or even integral-valued, respectively [$\emptyset$ means there is no topological invariant (no topologically-nontrivial state)]. The table is partitioned into two groups, classes A and AIII ("complex classes") which do not preserve TRS and PHS, and the rest ("real classes"). If we extend the classification table to arbitrary spatial dimension *d*, the complex (real) classes exhibit two (eight)-fold periodicity in *d*.

relation between them is known as bulk-boundary correspondence. Some of the salient features of the bulk-boundary correspondence are as follows. First, as mentioned already, a boundary of a topological bulk system cannot be trivially gapped (while preserving symmetries). For noninteracting systems, this means boundary modes have to be gapless. (In interacting systems and when $(d - 1) = 2$, boundary systems can be topologically ordered instead of being gapless (Vishwanath and Senthil, 2013).) Also, boundary states avoid the so-called fermion doubling theorem (the Nielsen-Ninomiya theorem and its variants), which claims that, in lattice systems, Weyl points should always appear in pairs with zero net chirality. Finally, when the topological properties of a bulk system are protected by some symmetry, the symmetry is not strictly preserved on its boundary. Even though the boundary system may look symmetric classically (i.e., at the level of Hamiltonian or Lagrangian), the symmetry is violated through quantum mechanical effects. This type of symmetry breaking is called quantum anomaly in quantum field theory. All in all, these features of boundary states are not compatible with isolated (fully-regularized) quantum many-body systems, and they have to be realized on a boundary of a higher-dimensional (topological) system.

We have so far assumed that perturbations and deformations in boundary systems are spatially homogeneous. The bulk-boundary correspondence however holds even in the presence of disorder—Gapless boundary states on a boundary of topological systems are stable against disorder. That is, the boundary modes do not Anderson localize even in the presence of disorder, as long as symmetry conditions (if any) are preserved or enforced, and as long as disorder does not alter the bulk topological properties. This is in sharp contrast with regular (lattice) systems, where Anderson localization is ubiquitous and inevitable when disorder is strong enough (as shown originally by Anderson (Anderson, 1958)). The lack of Anderson localization indicates the absence of atomic limit, and, once again, that the boundary system cannot be realized as a $(d - 1)$-dimensional lattice system. See, for example, Nomura et al. (2007) which demonstrates the lack of Anderson localization on the surface of a $d = 3$-dimensional topological insulator. In Schnyder et al. (2008) and Ryu et al. (2010), the lack of Anderson localization at boundaries was hypothesized to be the defining property of topological insulators and superconductors and used as a guiding principle to search and classify topological insulators and superconductors.

The effect of interactions

All of the aforementioned examples can be understood in terms of noninteracting or mean-field Hamiltonians. With interactions, some (noninteracting) topological superconductors are stable, while others cease to be topological, that is, once interaction effects are included, they are adiabatically connected to trivial states. Interactions can also give rise to new topological phases that do not exist without interactions. For example, the topological superconductor phase in the Kitaev chain and the weak paring phase of the chiral p-wave superconductor turn out to be stable even with interactions. On the other hand, the topological classification in symmetry class BDI in $d = 1$ dimension is altered in the presence of interactions. The topological classification at the noninteracting level is $\mathbb{Z}$ (c.f. Table 1). A simple example of topological superconductors in this class is obtained from the Kitaev chain by imposing TRS. This classification, however, in the presence of interactions is known to be modified to $\mathbb{Z}_8$ (Fidkowski and Kitaev, 2010, 2011). Namely, noninteracting topological superconductors with topological invariant being an integer multiple of 8 can be turned into a topologically trivial state by turning on interactions. We say the integral topological classification collapses or is reduced to $\mathbb{Z}_8$.

Beyond the above one-dimensional example, a similar reduction of topological classifications has been established in other symmetry classes in various spatial dimensions. For example, the integer classification of three-dimensional time-reversal symmetric topological superconductors is reduced to $\mathbb{Z}_{16}$. This has been argued, following the spirit of the bulk-boundary correspondence, by studying surface states of 3d topological superconductors (Fidkowski et al., 2013; Wang and Senthil, 2014; Metlitski et al., 2014; You and Xu, 2014; Kitaev, 2015; Morimoto et al., 2015). Furthermore, topological quantum field theory approaches have been developed (along with the developments of symmetry-protected topological phases in general) (Kapustin et al., 2015; Witten, 2016; Freed and Hopkins, 2021).

Conclusion

Topological superconductors have become an active field of research, with exciting new discoveries being made constantly. In this article, we mainly focused on fully gapped ones within the BdG (mean-field) formalism. The theory of topological superconductors and related topological systems has been vastly expanding, and there are many topics that we cannot discuss in this article.

One notable omission is the topic of gapless topological superconductors. Nodal systems, such as semimetals and nodal superconductors, can exhibit nontrivial band topology, even though the bulk gap closes at certain points in the Brillouin zone. The Fermi surfaces (superconducting nodes) of these gapless materials are topologically protected by topological invariants, which are defined in terms of an integral along a surface enclosing the gapless points. Similar to fully gapped topological systems, the topological characteristics of nodal materials manifest themselves at the surface in terms of gapless boundary modes. Depending on the symmetry properties and the dimensionality of the bulk Fermi surface, these gapless boundary modes form Dirac cones, Fermi arcs, or flat bands. Topological nodal systems can be protected by nonspatial symmetries (i.e., time-reversal or PHS) as well as spatial lattice symmetries, or a combination thereof. Examples of gapless topological superconductors include two-dimensional $d_{x^2-y^2}$-wave superconductors (Hu, 1994) and the A phase of superfluid ^{3}He (Volovik, 2011, 2003).

Other topics that we did not have space to discuss include, for instance, topological classification in the presence of crystalline symmetries (topological crystalline superconductors), higher-order topology (Benalcazar et al., 2017), and topological superconductors that can emerge in dynamical settings such as topological Floquet superconductors (Jiang et al., 2011).

In terms of material realization, a variety of systems have been discussed in search of topological superconductors and Majorana fermions. Despite the abundance of examples of topological insulators, topological superconductors remain rare, and to conclude decisively the realization of topological superconductors has been more subtle and difficult. This is partly because an unconventional pairing symmetry is required for a topologically nontrivial state. However, zero-energy Majorana bound states have also been explored in heterostructures involving *s*-wave superconductors. Examples of this type of setup are a superconductor-magnet domain wall along the edge of a two-dimensional quantum spin Hall insulator (Fu and Kane, 2009), or a Chern insulator interface (Qi et al., 2010; Cheng, 2012; Lindner et al., 2012; Vaezi, 2013; Clarke et al., 2013; Barkeshli et al., 2013; Mong et al., 2014). Another example is a flux vortex across a superconducting interface between three-dimensional topological and trivial insulators (Fu and Kane, 2008). In these examples, *s*-wave superconductors are not topological. Nevertheless, these systems still support zero-energy Majorana bound states, and nontrivial topological invariants can be defined for the heterostructures (defects) themselves (Teo and Kane, 2010). In an even broader context, beyond the regular superconductors, the physics of topological superconductors and Majorana fermions are relevant to $\nu = 5/2$ fractional quantum Hall states (paired states of composite fermions) (Moore and Read, 1991; Greiter et al., 1992), and the Kitaev spin liquid (Kitaev, 2006).

Acknowledgments

SR is supported by a Simons Investigator Grant from the Simons Foundation (Award No. 566116).

References

Alicea J (2012) New directions in the pursuit of Majorana fermions in solid state systems. *Reports on Progress in Physics* 75(7): 076501. https://doi.org/10.1088/0034-4885/75/7/076501. 1202.1293.

Altland A and Zirnbauer MR (1997) Nonstandard symmetry classes in mesoscopic normal-superconducting hybrid structures. *Physical Review B* 55(2): 1142–1161. https://doi.org/10.1103/PhysRevB.55.1142. cond-mat/9602137.

Anderson PW (1958) Absence of diffusion in certain random lattices. *Physical Review* 109: 1492–1505. https://doi.org/10.1103/PhysRev.109.1492.

Barkeshli M, Jian C-M, and Qi X-L (2013) Twist defects and projective non-Abelian braiding statistics. *Physical Review B* 87(4): 045130. https://doi.org/10.1103/PhysRevB.87.045130. 1208.4834.

Beenakker CWJ (2013) Search for majorana fermions in superconductors. *Annual Review of Condensed Matter Physics* 4: 113. https://doi.org/10.1146/annurev-conmatphys-030212-184337.

Benalcazar WA, Bernevig BA, and Hughes TL (2017) Quantized electric multipole insulators. *Science* 357(6346): 61–66. https://doi.org/10.1126/science.aah6442. 1611.07987.

Bernevig BA and Hughes T (2013) *Topological Insulators and Topological Superconductors*. Princeton University Press.

Cheng M (2012) Superconducting proximity effect on the edge of fractional topological insulators. *Physical Review B* 86(19): 195126. https://doi.org/10.1103/PhysRevB.86.195126. 1204.6084.

Chiu C-K, Teo JCY, Schnyder AP, and Ryu S (2016) Classification of topological quantum matter with symmetries. *Reviews of Modern Physics* 88(3): 035005. https://doi.org/10.1103/RevModPhys.88.035005. 1505.03535.

Clarke DJ, Alicea J, and Shtengel K (2013) Exotic non-Abelian anyons from conventional fractional quantum Hall states. *Nature Communications* 4: 1348. https://doi.org/10.1038/ncomms2340. 1204.5479.

Fidkowski L and Kitaev A (2010) Effects of interactions on the topological classification of free fermion systems. *Physical Review B* 81(13): 134509. https://doi.org/10.1103/PhysRevB.81.134509. 0904.2197.

Fidkowski L and Kitaev A (2011) Topological phases of fermions in one dimension. *Physical Review B* 83(7): 075103. https://doi.org/10.1103/PhysRevB.83.075103. 1008.4138.

Fidkowski L, Chen X, and Vishwanath A (2013) Non-Abelian topological order on the surface of a 3D topological superconductor from an exactly solved model. *Physical Review X* 3(4): 041016. https://doi.org/10.1103/PhysRevX.3.041016. 1305.5851.

Freed DS and Hopkins MJ (2021) Reflection positivity and invertible topological phases. *Geometry and Topology* 25: 1165–1330. https://doi.org/10.2140/gt.2021.25.1165. 1604.06527.

Fu L and Kane CL (2008) Superconducting proximity effect and Majorana fermions at the surface of a topological insulator. *Physical Review Letters* 100(9): 096407. https://doi.org/10.1103/PhysRevLett.100.096407. 0707.1692.

Fu L and Kane CL (2009) Josephson current and noise at a superconductor/quantum-spin-Hall-insulator/superconductor junction. *Physical Review B* 79(16): 161408. https://doi.org/10.1103/PhysRevB.79.161408. 0804.4469.

Greiter M, Wen XG, and Wilczek F (1992) On paired Hall states. *Nuclear Physics B* 374: 567–614. https://doi.org/10.1016/0550-3213(92)90401-V.

Hasan MZ and Kane CL (2010) Colloquium: Topological insulators. *Reviews of Modern Physics* 82: 3045–3067. https://doi.org/10.1103/RevModPhys.82.3045. 1002.3895.

Hu C-R (1994) Midgap surface states as a novel signature for d^2_{xa}-x^2_b-wave superconductivity. *Physical Review Letters* 72: 1526–1529. https://doi.org/10.1103/PhysRevLet-72-1526.

Jiang L, Kitagawa T, Alicea J, Akhmerov AR, Pekker D, Refael G, Cirac JI, Demler E, Lukin MD, and Zoller P (2011) Majorana fermions in equilibrium and in driven cold-atom quantum wires. *Physical Review Letters* 106(22): 220402. https://doi.org/10.1103/PhysRevLett.106.220402. 1102.5367.

Kapustin A, Thorngren R, Turzillo A, and Wang Z (2015) Fermionic symmetry protected topological phases and cobordisms. *Journal of High Energy Physics* 2015: 52. https://doi.org/10.1007/JHEP12(2015)052. 1406.7329.

Kitaev AY (2001) 6. QUANTUM COMPUTING: Unpaired Majorana fermions in quantum wires. *Physics Uspekhi* 44(10S): 131. https://doi.org/10.1070/1063-7869/44/10S/S29. cond-mat/0010440.

Kitaev A (2006) Anyons in an exactly solved model and beyond. *Annals of Physics* 321(1): 2–111. https://doi.org/10.1016/j.aop.2005.10.005. cond-mat/0506438.

Kitaev A (2009) Periodic table for topological insulators and superconductors. In: Lebedev V and Feigel'Man M (eds.). *Advances in Theoretical Physics: Landau Memorial Conference*, vol. 1134, *American Institute of Physics Conference Series*, pp. 22–30. 0901.2686.

Kitaev A (2015) *Homotopy-theoretic approach to SPT phases in action: Z16 classification of three-dimensional superconductors*. http://www.ipam.ucla.edu/abstract/?tid=12389&pcode=STQ2015.

Lindner NH, Berg E, Refael G, and Stern A (2012) Fractionalizing Majorana fermions: Non-Abelian statistics on the edges of Abelian quantum Hall states. *Physical Review X* 2(4): 041002. https://doi.org/10.1103/PhysRevX.2.041002. 1204.5733.

Lutchyn RM, Sau JD, and Das Sarma S (2010) Majorana fermions and a topological phase transition in semiconductor-superconductor heterostructures. *Physical Review Letters* 105 (7): 077001. https://doi.org/10.1103/PhysRevLett.105.077001. 1002.4033.

Metlitski MA, Fidkowski L, Chen X, and Vishwanath A (2014) Interaction effects on 3D topological superconductors: Surface topological order from vortex condensation, the 16 fold way and fermionic Kramers doublets. *arXiv e-prints.* arXiv:1406.3032.

Mong RSK, Clarke DJ, Alicea J, Lindner NH, Fendley P, Nayak C, Oreg Y, Stern A, Berg E, Shtengel K, and Fisher MPA (2014) Universal Topological Quantum Computation from a Superconductor-Abelian Quantum Hall Heterostructure. *Physical Review X* 4(1): 011036. https://doi.org/10.1103/PhysRevX.4.011036. 1307.4403.

Moore GW and Read N (1991) Nonabelions in the fractional quantum Hall effect. *Nuclear Physics B* 360: 362–396. https://doi.org/10.1016/0550-3213(91)90407-O.

Morimoto T, Furusaki A, and Mudry C (2015) Breakdown of the topological classification Z for gapped phases of noninteracting fermions by quartic interactions. *Physical Review B* 92(12): 125104. https://doi.org/10.1103/PhysRevB.92.125104. 1505.06341.

Nadj-Perge S, Drozdov IK, Li J, Chen H, Jeon S, Seo J, MacDonald AH, Bernevig BA, and Yazdani A (2014) Observation of Majorana fermions in ferromagnetic atomic chains on a superconductor. *Science* 346(6209): 602–607. https://doi.org/10.1126/science.1259327. 1410.0682.

Nayak C, Simon SH, Stern A, Freedman M, and Das Sarma S (2008) Non-Abelian anyons and topological quantum computation. *Reviews of Modern Physics* 80: 1083–1159. https://doi.org/10.1103/RevModPhys.80.1083.

Nomura K, Koshino M, and Ryu S (2007) Topological delocalization of two-dimensional massless dirac fermions. *Physical Review Letters* 99(14): 146806. https://doi.org/10.1103/PhysRevLett.99.146806. 0705.1607.

Oreg Y, Refael G, and von Oppen F (2010) Helical liquids and Majorana bound states in quantum wires. *Physical Review Letters* 105(17): 177002. https://doi.org/10.1103/PhysRevLett.105.177002. 1003.1145.

Prange RE and Girvin SM (1990) *The Quantum Hall effect.* Springer-Verlag, ISBN: 9780387971773.

Qi X-L and Zhang S-C (2011) Topological insulators and superconductors. *Reviews of Modern Physics* 83(4): 1057–1110. https://doi.org/10.1103/RevModPhys.83.1057. 1008.2026.

Qi X-L, Hughes TL, and Zhang S-C (2010) Chiral topological superconductor from the quantum Hall state. *Physical Review B* 82(18): 184516. https://doi.org/10.1103/PhysRevB.82.184516. 1003.5448.

Read N and Green D (2000) Paired states of fermions in two dimensions with breaking of parity and time-reversal symmetries and the fractional quantum Hall effect. *Physical Review B* 61(15): 10267–10297. https://doi.org/10.1103/PhysRevB.61.10267. cond-mat/9906453.

Ryu S, Schnyder AP, Furusaki A, and Ludwig AWW (2010) Topological insulators and superconductors: Tenfold way and dimensional hierarchy. *New Journal of Physics* 12(6): 065010. https://doi.org/10.1088/1367-2630/12/6/065010. 0912.2157.

Schnyder AP, Ryu S, Furusaki A, and Ludwig AWW (2008) Classification of topological insulators and superconductors in three spatial dimensions. *Physical Review B* 78(19): 195125. https://doi.org/10.1103/PhysRevB.78.195125. 0803.2786.

Teo JCY and Kane CL (2010) Topological defects and gapless modes in insulators and superconductors. *Physical Review B* 82(11): 115120. https://doi.org/10.1103/PhysRevB.82.115120. 1006.0690.

Vaezi A (2013) Fractional topological superconductor with fractionalized Majorana fermions. *Physical Review B* 87(3): 035132. https://doi.org/10.1103/PhysRevB.87.035132. 1204.6245.

Vishwanath A and Senthil T (2013) Physics of three-dimensional bosonic topological insulators: Surface-deconfined criticality and quantized magnetoelectric effect. *Physical Review X* 3(1): 011016. https://doi.org/10.1103/PhysRevX.3.011016. 1209.3058.

Volovik GE (2003) *Universe in a Helium Droplet.* Oxford, UK: Oxford University Press, ISBN: 0521670535.

Volovik GE (2011) *JETP Letters* 93: 66.

Wang C and Senthil T (2014) Interacting fermionic topological insulators/superconductors in three dimensions. *Physical Review B* 89(19): 195124. https://doi.org/10.1103/PhysRevB.89.195124. 1401.1142.

Wen XG (2007) *Quantum Field Theory of Many-Body Systems: From the Origin of Sound to an Origin of Light and Electrons.* Oxford: Oxford University Press.

Witten E (2016) Fermion path integrals and topological phases. *Reviews of Modern Physics* 88(3): 035001. https://doi.org/10.1103/RevModPhys.88.035001. 1508.04715.

You Y-Z and Xu C (2014) Symmetry-protected topological states of interacting fermions and bosons. *Physical Review B* 90(24): 245120. https://doi.org/10.1103/PhysRevB.90.245120. 1409.0168.

Superinsulation

MC Diamantini[a], **CA Trugenberger**[b], **and VM Vinokur**[c], [a]NiPS Laboratory, INFN and Department of Physics and Geology, University of Perugia, Perugia, Italy; [b]SwissScientific Technologies SA, Geneva, Switzerland; [c]Terra Quantum AG, Terra Quantum AG, St. Gallen, Switzerland

© 2024 Elsevier Ltd. All rights reserved.

Introduction **804**
Gauge theories of planar superconductors **806**
Superconducting films 807
Josephson junction arrays 808
The quantum phases in the vicinity of the SIT **808**
Quantum phase diagram at $T = 0$ 808
Finite temperature phase diagram 809
The nature of the superinsulator **809**
Asymptotic freedom and size effects 811
Electric Meissner effect and its manifestation in the $I(V)$ characteristics 811
Dynamical exponents and the linear potential 813
Oblique superinsulators in 3D **813**
The role of disorder **814**
Conclusion **815**
References **815**

Abstract

Superinsulation is a state of matter in which the electrical conductivity vanishes in the finite-temperature range between zero and the superinsulating transition temperature. This state is dual to superconductivity, where the resistance vanishes within a similar finite-temperature interval. The phenomenon of superinsulation arises in certain quantum materials possessing either inherent or self-induced granularity. In these materials the effective electromagnetic action contains magnetic monopoles. When these proliferate, the Coulomb interactions dominate magnetic interactions. In two dimensions (2D), magnetic monopole instantons turn the Coulomb interaction between two charges of the opposite signs into a linear attractive potential causing the same charge confinement that holds quarks together in hadrons and, therefore, leading to an infinite electric resistance even at finite temperatures. In three dimensions (3D), a superinsulator harbors a condensate of magnetic monopoles resulting in a similar charge confinement. The phenomenon of superinsulation has been experimentally discovered and studied in nearly 2D thin superconducting films of materials with a large normal-state dielectric permittivity and in generic granular superconductors.

Key points

The article gives an introductory description of the superinsulation, specifically focusing on:

- The role of magnetic monopoles in materials
- Showing that planar superconductors are governed by a topological gage field theory
- Deriving the quantum and thermal phase structure of planar superconductors
- Illustrating the magnetic–electric duality between the superconducting and superinsulating phases, with zero and infinite electric resistance, respectively
- Discussing the nature of superinsulators and showing that they realize an Abelian version of the confinement that holds quarks together in hadrons
- Proposing that an oblique version of superinsulation may be realized in the pseudogap state of high temperature superconductors
- Discussing the role of disorder

Introduction

Superinsulation, a state of matter mirror dual to superconductivity, refers to the complete disappearance of the electrical conductivity in certain materials when they are cooled below a certain critical transition temperature. Superconductivity is a phenomenon whereby an electric current flows through a material, called superconductor, even in the absence of applied voltage hence without resistance. Accordingly, a superinsulator is a material that does not conduct electricity despite applied voltage, hence having infinite resistance.

https://doi.org/10.1016/B978-0-323-90800-9.00220-1

Superinsulation emerges because of the electric–magnetic symmetry of laws of nature. To place electric and magnetic fields on equal footing, one has to introduce magnetic charges q_g as a dual mirror of electric charges q_e. Then electric–magnetic symmetry manifests as a symmetry under simultaneous interchange of electric and magnetic fields, $\mathbf{E} \to \mathbf{B}$, $\mathbf{B} \to -\mathbf{E}$, and electric and magnetic charges, $q_e \Leftrightarrow q_g$. Magnetic charges are perfectly consistent in a quantum theory of electromagnetism, provided the product of electric and magnetic charges is quantized, as shown in a seminal work by Dirac in the 1930s (Dirac, 1931). Magnetic charges, called magnetic monopoles, appear naturally in the most grand-unified theories (GUTs) of particle interactions (Goddard and Olive, 1978) and are a cornerstone of the superinsulation phenomenon. Despite good 40 years of intensive search, however, they have never been detected in any high-energy experiment.

While the GUT monopoles are elusive, other Abelian U(1) monopoles can lead to notable effects. As Polyakov pointed out (Polyakov, 1975), there are two possible kinds of electromagnetism, the noncompact one, with gage group $\mathbb{R}$ and the compact one, with the gage group U(1). In classical physics, where only equations of motion matter, there is no real distinction between the two. At the quantum level, however, things become different: it is the compact quantum electrodynamics (QED) that admits magnetic monopoles, see Polyakov (1987). There are two ways of obtaining compact QED: either one considers it as a surviving low-energy theory after spontaneous symmetry breaking of a larger compact group, or one formulates it on a lattice. Either way, compact QED is an effective theory, with an ultraviolet (UV) cutoff.

Already in the 1970s it was realized that dual superconductivity and related Abelian magnetic monopoles in the $U(1)^{N-1}$ subgroup of SU(N) offer a model for quark confinement via the dual Meissner effect that squeezes color-electric fields into thin tubes, strings, linearly binding quarks into hadrons (Mandelstam, 1976; Nambu, 1974; 't Hooft, 1978). This mechanism can also take place in other settings. Integrating out the matter degrees of freedom, the nonrelativistic Maxwell action becomes the effective action for insulators. If this effective action is compact, it admits magnetic monopoles, which can lead to confinement, see Greensite (2011) of electric charges by squeezing electric flux into thin tubes as shown in Fig. 1. This is a new, superinsulating phase of insulators.

The idea that the electric–magnetic duality, resulting in charge confinement, is realized in condensed matter physics was first proposed in 1996 in the context of Josephson junction arrays (JJAs) (Diamantini et al., 1996) and the ensuing new state of matter was called *superinsulator* since it is characterized by an infinite electrical resistance (Diamantini et al., 1996). The duality in terms of charges and vortices was subsequently surmised in numerical simulations (Krämer and Doniach, 1998). In 2008, superinsulation was independently proposed as a new state of matter emerging in thin superconducting films (Vinokur et al., 2008; Baturina and Vinokur, 2013) as a manifestation of the uncertainty principle relating amplitude and phase of the superconducting order parameter. Experimentally, superinsulation has been detected in TiN (Baturina et al., 2007; Vinokur et al., 2008) and NbTiN (Mironov et al., 2018) films and in InO (Sambandamurthy et al., 2005) and NbSi (Humbert et al., 2021) films.

The superinsulating state, detected again later in InO (Ovadia et al., 2015), was referred there as "finite-temperature insulator" and was associated with charge carriers overheating (Basko et al., 2007; Altshuler et al., 2009). Here, however we would like to dispel the view that overheating is a "description of the nature" of this new state of matter. It is most certainly not. Overheating is a possible model of how this state is destroyed in a dynamical phase transition when a sufficiently strong applied voltage is applied. A model of the new state must explain why the charges become immobile below a transition temperature in the first place. The idea behind overheating is that this is due to many-body localization (MBL) (Altshuler et al., 2006), a model that has been studied in 1D but for which there is no established support in 2D, let alone for the essentially 3D InO films, in which the coherence length is quite smaller than the thickness. In the section below dedicated to the role of disorder, we show how recent experimental data essentially rule out this idea.

Superinsulation appears as an inherent feature of the superconductor–insulator transition (SIT) at low temperatures. In superconducting films with a large normal-state dielectric permittivity, the Coulomb interaction becomes logarithmic over the entire system and competes with the magnetic interaction between vortices (Baturina and Vinokur, 2013). When two interactions are

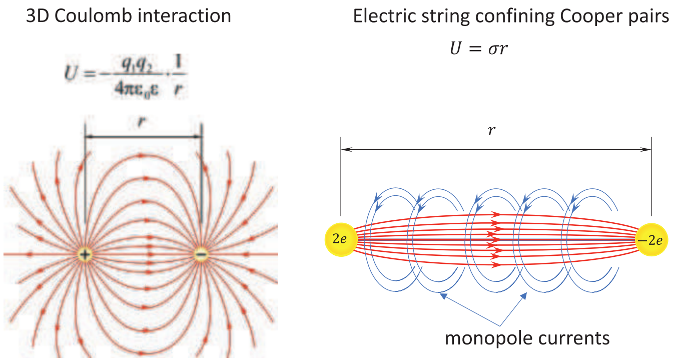
3D Coulomb interaction
$U = -\frac{q_1 q_2}{4\pi\varepsilon_0\varepsilon} \cdot \frac{1}{r}$
r
+
−
Electric string confining Cooper pairs
$U = \sigma r$
r
2e
−2e
monopole currents

Fig. 1 Confinement of Cooper pairs by a magnetic monopole condensate. Left panel illustrates the usual 3D Coulomb interaction between two charges q_1 and q_2 of opposite signs. Right panel illustrates that, in full analogy with the charge condensate currents squeezing magnetic field into thin filaments, Abrikosov vortices, the magnetic condensate currents squeeze electric field lines into electric strings with the linear tension σ. As a result, the attracting interaction between charges grows linearly with the separation distance r. Reproduced from Baturina TI and Vinokur VM (2013) Superinsulator-superconductor duality in two dimensions. Annalen der Physik 331: 236–257.

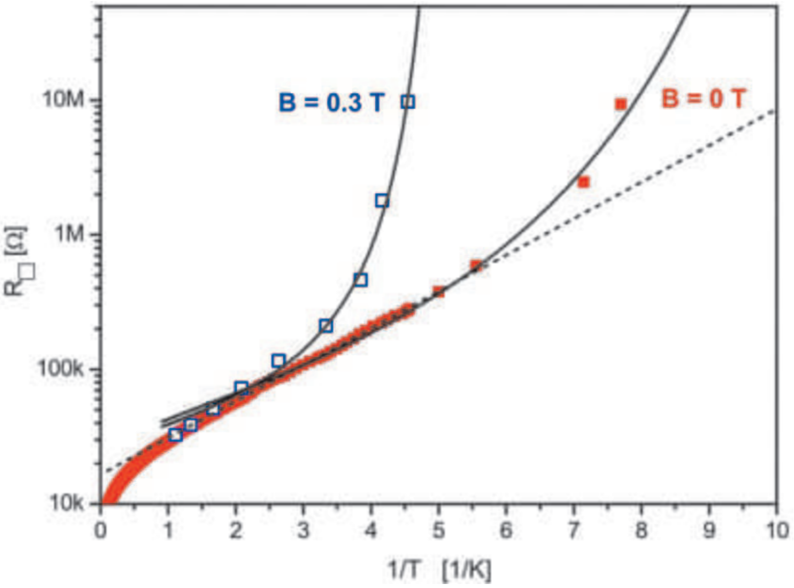

Fig. 2 Sheet resistance as a function of temperature for a TiN film (Diamantini et al., 2019). The *dashed straight line* in this logarithmic scale is the activated Arrhenius behavior typical of insulators. The deviation at very low temperatures shows the hyperactivated behavior indicating superinsulation. The deviation becomes stronger when a magnetic field is applied. Reproduced from Diamantini MC et al. (2019) The superconductor-superinsulator transition: S-duality and the QCD on the desktop. Journal of Superconductivity and Novel Magnetism 32: 47–51.

comparable, the superconducting condensate breaks down into separate superconducting granules connected via Josephson links. This granular array hosts superconducting islands (Sacépé et al., 2008, 2011; Kowal and Ovadyahu, 1994; Fistul et al., 2008) intertwined with the coreless Josephson vortices (Diamantini et al., 2020a, 2021b). Superinsulation arises due to instability of these vortices upon further increase of the 2D Coulomb interaction. Magnetic monopole instantons (Polyakov, 1987), corresponding to vortex tunneling events, cause the Coulomb interaction between charges to become linear (Diamantini et al., 2018), see Fig. 1 so that only neutral "electric pions" survive at large distances and charge transport is suppressed (Diamantini et al., 2020b). The result is the *hyperactivated* behavior of the sheet resistance as function of temperature, the exemplary $R_\square(1/T)$ dependence being shown in Fig. 2.

In the following exposition, we use natural units $c = 1$, $\hbar = 1$, $\varepsilon_0 = 1$.

Gauge theories of planar superconductors

The vicinity of the SIT is governed by the interplay of two topological phenomena, mutual statistics Aharonov–Bohm–Casher (ABC) interactions (Aharonov and Bohm, 1959; Aharonov and Casher, 1984) between Cooper pairs and Josephson vortices and their Berezinskii–Kosterlitz–Thouless (BKT) (Berezinskii, 1971; Kosterlitz and Thouless, 1972, 1973) topological phase transitions. In the critical vicinity of the SIT the films acquire a self-induced electronic granular structure, and they have to be viewed as arrays of superconducting condensate droplets with the characteristic size $\ell \simeq \mathcal{O}(\xi)$, where ξ is the superconducting coherence length, coupled via Josephson links, that is, as a JJA. The vortices in the system are Josephson vortices which, unlike Abrikosov vortices, do not have a normal core. Above the vortex–BKT transition, that is, above the vortex unbinding temperature T_{VBKT}, the Josephson vortices have topological mutual statistics interactions with the out-of-condensate Cooper pairs that emerge there. Moreover, as Josephson vortices do not have normal cores, their dynamics acquires ballistic character (van Otterlo et al., 1994; van der Zant et al., 1992). As a consequence, the description of the SIT and planar superconductivity is achieved by the topological gage theory presented below.

En passant we remark that the XY model, adapted to describe 2D superfluids and viewed as an equivalent to the Coulomb gas picture (Minnhagen, 1987), is often applied also to charged superconductors. However, although it captures several experimental features fairly well, it does not account for the mutual statistics topological interactions and ballistic dynamics of Josephson vortices, hence misses topological aspects of 2D superconductivity that are essential near the SIT.

The ABC topological interactions are encoded in the phase acquired by the wave function of one of the types of the excitation, say a charge, when it encircles the other, say a vortex, Aharonov–Bohm effect (Aharonov and Bohm, 1959), and vice versa, Aharonov–Casher effect (Aharonov and Casher, 1984). These interactions (Wilczek, 1990) are infrared (IR)-dominant since they have an infinite interaction range. In the Euclidean partition function describing point charges and vortices they must be accounted for by the topological Gauss linking number of their trajectories. This topological invariant is nonlocal, but, as noted by Wilczek (1992), can be turned local by coupling the point charge and vortex currents, Q_μ and M_μ to two fictitious gage fields a_μ and b_μ with mixed Chern–Simons term (Jackiw and Templeton, 1981; Deser et al., 1982a, b), resulting in the Euclidean partition function

$$Z = \sum_{\{Q_\mu, M_\mu\}} \int \mathcal{D}a_\mu \mathcal{D}b_\mu \, e^{-S},$$
$$S = \int d^3x \frac{i}{2\pi} a_\mu \varepsilon^{\mu\alpha\nu} \partial_\alpha b_\nu + i a_\mu Q_\mu + i b_\mu M_\mu. \tag{1}$$

This same model can also be derived from another point of view. Following Wen and Zee (1992) in their derivation of the long-distance effective field theories of incompressible quantum Hall states, one can define topologically conserved charge and vortex currents in terms of the curl of a fictitious pseudovector field b_μ and a fictitious vector field a_μ, a_μ:

$$j^\mu = \frac{1}{2\pi} f^\mu = \frac{1}{2\pi} \varepsilon^{\mu\alpha\nu} \partial_\alpha b_\nu,$$
$$\phi^\mu = \frac{1}{2\pi} g^\mu = \frac{1}{2\pi} \varepsilon^{\mu\alpha\nu} \partial_\alpha a_\nu. \tag{2}$$

The fields a_μ and b_μ are gauge fields, since physical currents are left invariant under the gauge transformations $a_\mu \to a_\mu + \partial_\mu \Upsilon$ and $b_\mu \to b_\mu + \partial_\mu \Psi$, where Υ and Ψ are arbitrary scalar functions. The effective action involving charges and vortices must therefore be a gauge theory. The IR-dominant gauge invariant term which preserves the parity ($\mathcal{P}$) and time-reversal ($\mathcal{T}$) symmetries is the mixed Chern–Simons term. If the gauge group is U(1), the gauge fields are compact. In a lattice formulation, as appropriate for a granular system of the typical size ℓ, the gauge functions are angular variables defined in the domain $[-\pi, +\pi]$. To enforce this periodicity we must introduce integer-valued link variables Q_μ and M_μ, and we are back to Eq. (1).

The Chern–Simons term describes only the topological interactions. To include the dynamics of both charges and vortices, one adds all the possible local gauge invariant terms. This results in the most general (Euclidean) effective action which encodes all the physics of a 2D system of interacting charges and vortices (Diamantini et al., 1996, 2020a)

$$S = \sum_x i \frac{\ell_0 \ell^2}{2\pi} a_\mu k_{\mu\nu} b_\nu + \frac{\ell_0 \ell^2}{2 e_v^2 \mu} f_0^2 + \frac{\ell_0 \ell^2 \varepsilon}{2 e_v^2} \mathbf{f}^2 + \frac{\ell_0 \ell^2}{2 e_q^2 \mu} g_0^2 + \frac{\ell_0 \ell^2 \varepsilon}{2 e_q^2} \mathbf{g}^2 + \sum_{x,i} i \ell_0 a_0 Q_0 + i \ell a_i Q_i + i \ell_0 b_0 M_0 + i \ell b_i M_i, \tag{3}$$

where $\ell_0 = \ell / v$ is the lattice spacing in the Euclidean time direction, v is the speed of light in the material, and $k_{\mu\nu}$ is the lattice version of the Chern–Simons term (Diamantini et al., 1996), whose exact form is not of importance for what follows.

There are four phenomenological parameters in this action. The couplings e_v^2 and e_q^2 distinguish between the electric and magnetic sectors of the theory and have canonical dimension [1/length]. The dimensionless parameters ε and μ distinguish between "electric" and "magnetic" components within the sector and represent the relative dielectric permittivity and magnetic permeability. Correspondingly, $v = 1/\sqrt{\mu\varepsilon}$ is the light velocity in the material. In materials that manifest superinsulating behavior $v \ll 1$ so that the "magnetic" components are suppressed with respect to "electric" ones. The two extreme cases, $\mu = 1$, $\varepsilon \gg 1$ and $\varepsilon = 1$, $\mu \gg 1$ correspond to superconducting thin films and to fabricated JJAs respectively (Fazio and van der Zant, 2001). In this latter case the effective field theory (3) becomes exact in the limit $\mu \to \infty$ when the ballistic term for vortices is included with a particular mass that makes the model self-dual.

Superconducting films

Superconducting films are characterized by two spatial scales, the thickness, d, and the London penetration depth, λ_L, of the material. The couplings of the effective gage theory are expressed in terms of these two scales,

$$e_q^2 = \mathcal{O}\left(\frac{e^2}{2\pi d}\right),$$
$$e_v^2 = \mathcal{O}\left(\frac{\pi}{e^2 \lambda_\perp}\right) = \mathcal{O}\left(\frac{\pi d}{e^2 \lambda_L^2}\right), \tag{4}$$

where $\lambda_\perp = \lambda_L^2 / d$ is the so-called Pearl length (Tinkham, 1996) and represents the electric and magnetic energies of a fundamental granule. The topological interaction induces a spectrum gap (Jackiw and Templeton, 1981; Deser et al., 1982a, b). Both charge and vortex fluctuations acquire the dispersion relation

$$E = \sqrt{m^2 v^4 + v^2 p^2}, \tag{5}$$

with the topological mass

$$m = \frac{e_q e_v}{2\pi v} = \mathcal{O}\left(\frac{1}{v \lambda_L}\right), \tag{6}$$

The parameters e_q^2 and e_v^2 can be traded for this topological mass $m = e_q e_v / 2\pi v$ and one dimensionless parameter $g = e_v / e_q = \mathcal{O}(d / (\alpha \lambda_L))$, where $\alpha = e^2 / 4\pi$ is the fine structure constant. The parameter g plays the role of a dimensionless conductivity.

Josephson junction arrays

The Hamiltonian for an exemplary square JJA comprising superconducting islands with spacing ℓ and characterized by phases φ, voltages V and nearest-neighbor Josephson coupling of strength E_J is given by (Fazio and Schön, 1991)

$$H = \sum_{\mathbf{x}} \frac{C_0}{2} V_{\mathbf{x}}^2 + \sum_{<\mathbf{xy}>} \frac{C}{2} \left(V_{\mathbf{y}} - V_{\mathbf{x}}\right)^2 + E_J\left(1 - \cos\left(\varphi_{\mathbf{y}} - \varphi_{\mathbf{x}}\right)\right). \tag{7}$$

Here each island has a self-capacitance C_0 and C are mutual capacitances to its nearest neighbors. This Hamiltonian can be also expressed in terms of the integer number $q_{\mathbf{x}}$ of Cooper pairs on the islands

$$H = \sum_{\mathbf{x}} 4E_C\, q_{\mathbf{x}} \frac{1}{C_0/C - \nabla^2} q_{\mathbf{x}} + \sum_{\mathbf{x},i} E_J(1 - \cos(\Delta_i \varphi_{\mathbf{x}})), \tag{8}$$

where $E_C = e^2/2C$ is the scale of the charging energy and Δ_i denotes the finite difference operator in direction i. In the self-capacitance limit $C_0 \to 0$, and adding the vortex kinetic term with the topological mass of Eq. (6) (Diamantini et al., 1996), one finds that the zero-temperature partition function corresponding to this Hamiltonian has precisely the action of the effective gage theory (3) in the limit $\varepsilon = 1$, $\mu \to \infty$, with the substitutions

$$\begin{aligned} ve_v^2 &\to 4\pi^2 E_J, \\ ve_q^2 &\to 8E_C, \end{aligned} \tag{9}$$

so that

$$\begin{aligned} g &\to \sqrt{\frac{\pi^2 E_J}{2E_C}}, \\ \Delta_{\mathrm{top}} = mv^2 = \frac{ve_v e_q}{2\pi} &\to \sqrt{8E_C E_J} = \omega_P, \end{aligned} \tag{10}$$

where ω_P is the plasma frequency of the array. Again, the dimensionless coupling governing the phase structure of the array is the ratio of the two magnetic and electric energy scales in the problem. Here, it becomes explicit that this parameter indeed governs the conductivity of the array. The role of the topological energy gap, Δ_{top}, is taken by the plasma frequency, describing small phase oscillations at the superconducting islands of the array.

The quantum phases in the vicinity of the SIT

Quantum phase diagram at $T = 0$

Given that e_q^2 and e_v^2 have the canonical dimension [1/length] and, correspondingly, the two kinetic terms in (3) are IR-irrelevant, one might be tempted to leave them out and consider only the IR-dominant mixed Chern–Simons theory. Unfortunately, this leads to wrong results and the origin of the problem lies exactly in the role of the quantized charges and vortices associated with the compactness of the two gage groups. The important point is that the "topological limit" $e_q^2 \to \infty$ and $e_v^2 \to \infty$ is not well defined without specifying the value of g in this limit. The behavior of quantized charges and vortices depends crucially on this value and, as a consequence one obtains very different ground states when g is varied, typically by changing the film thickness, applying a magnetic field or gate voltages, as shown in Fig. 3.

In the framework of the gauge theory, the SIT is a material realization of the field-theoretic S-duality which expresses the above mentioned invariance of Maxwell's equation under the exchange of electric and magnetic fields and charges. The structure of the phase diagram is governed by the dimensionless conductivity g and the additional dimensionless parameter η describing the strength of quantum fluctuations. Near the SIT, where $e_q \approx e_v$, η acquires the form (in physical cgs units)

$$\eta = \frac{1}{\alpha} \frac{\pi \ell}{\mu_e \lambda_\perp}\, G\left(\frac{\ell}{2\alpha\lambda_\perp}\right), \tag{11}$$

where $\alpha = e^2/\hbar c \approx 1/137$ is the fine structure constant, $\mu_e = \mathcal{O}(1)$ is the positional entropy contribution to the free energy of the system, and G is the diagonal element of the 3D Green function describing electromagnetic interactions screened by the CS mass:

$$G(m\ell v) = \frac{1}{(2\pi)^3} \int_{-\pi}^{\pi} d^3k \frac{1}{(m\ell v)^2 + \sum_{i=0}^{2} 4\sin\left(\frac{k^i}{2}\right)^2}. \tag{12}$$

Identifying the UV cutoff with the superconducting coherence length ξ yields the geometric factor as $d/(\kappa\lambda_L)$, where $\kappa = \lambda_L/\xi$ is the Landau–Ginzburg parameter.

The parameter η plays the role analogous to the role of the inverse of the Ginzburg–Landau parameter of 3D superconductors. For $\eta < 1$, there is a direct transition from a superconductor to a superinsulator, whose exact nature is the subject of the next section. This direct phase transition is the first-order quantum transition in the sense that it goes via a region of coexistence of both states

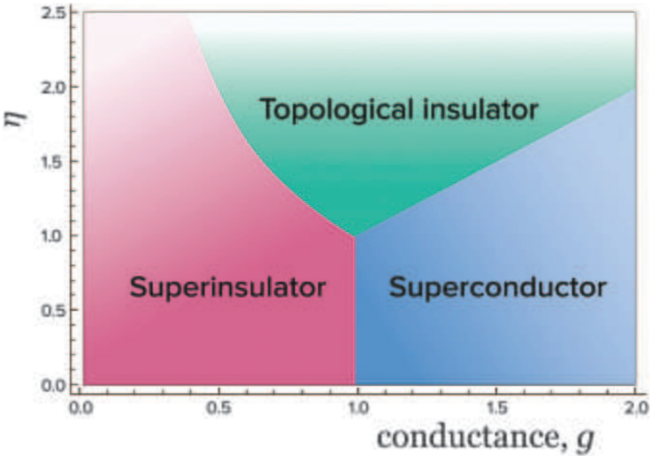

Fig. 3 The possible quantum phases ($T = 0$) of an interacting system of charges and vortices as a function of the dimensionless conductance g which controls the relative strength of the vortex interaction with respect to the Coulomb interaction. The parameter η is a function of the ratio ℓ/λ_L of the granule size to the penetration depth of the bulk superconductor and controls the presence/absence of an intermediate state in the transition.

around the value $g = 1$. At this self-dual point $g = 1$, the system is a universal metal with exactly the quantum of sheet resistance, $R_\square = R_Q = h/4e^2$ (Fisher and Grinstein, 1988; Fisher, 1990a; Fisher et al., 1990b; Girvin et al., 1992). For $\eta > 1$, which is realized when the granule size and the London penetration depths are comparable, quantum fluctuations destroy both Cooper pairs and monopole condensates and the universal metal point opens up to a full fledged metal phase made of bosons (Diamantini et al., 1996), the so-called Bose metal (Das and Doniach, 1999, 2001; Dalidovich and Phillips, 2002; Phillips and Dalidovich, 2003), see for a review (Kapitulnik et al., 2019). This Bose metal is nothing else but the bosonic topological insulator (Lu and Vishwanath, 2012; Yang and Senthil, 2013; Chen et al., 2013), with a bulk frozen by the topological gap caused by the mutual statistics interactions and symmetry-protected edge states giving rise to the metallic behavior (Diamantini et al., 2020a). The two quantum transitions between superconductor and bosonic topological insulator and between bosonic topological insulator and superinsulator are quantum BKT transitions (Diamantini et al., 2020a). The point where all three transitions meet is a quantum tri-critical point. In the vicinity of this tri-critical point, the geometric scales of the problem satisfy the relation $\ell = d/\alpha$. This indicates that the transition from superconducting to superinsulating behavior is caused by strong quantum fluctuations.

Finite temperature phase diagram

Fig. 4 shows the finite-temperature phase diagram for $\eta > 1$. Both the phase transitions are BKT transitions, one corresponding to vortex unbinding (for the superconductor) and one to charge unbinding (for the superinsulator) (Mironov et al., 2018). The two critical conductances satisfy the self-dual relation $g_1 g_2 = 1$ around the quantum resistance value $g = 1$.

In the phase diagram presented in Fig. 4 we have sketched the behavior of the topological gap $\Delta(g)$ in the bosonic topological insulator phase (*red dashed line*) and we have marked by horizontal dashed lines what experiments, necessarily done at various finite temperatures, would see. For temperatures sufficiently above the topological gap, charges are essentially free in the intermediate state and we have the usual superconductor-to-metal transition. When the temperature is below the topological gap, an experiment would detect simply the transition from a superconductor to an activated insulator. This is the origin of the by now paradigmatic name “superconductor-to-insulator” transition (SIT) (Fazio and Schön, 1991; Fisher and Grinstein, 1988; Fisher, 1990a; Efetov, 1980; Haviland et al., 1989; Hebard and Paalanen, 1990). At extremely low temperatures the bulk becomes effectively frozen and the Bose metal (Kapitulnik et al., 2019) conduction by edge modes starts to be detected. This behavior is seen also in fabricated devices (Bøttcher et al., 2018). However, only at temperatures and conductivities g low enough can the transition to a superinsulator be detected. At $T = 0$ the full quantum regime is realized and an experiment would record a transition from a superconductor to a superinsulator with a Bose metal intermediate phase (Diamantini et al., 2020a).

The nature of the superinsulator

Describing quark interactions within hadrons, ‘t Hooft (1978) put forth an appealing confinement mechanism and coined the term “superinsulator” for the confined quark matter with infinite chromo-electric resistance (‘t Hooft, 1978). Polyakov showed (Polyakov, 1987) that this confinement mechanism occurs also in Abelian gage theories, provided they are compact and hence support topological excitations and magnetic monopoles, which are instantons in 2D and solitons in 3D.

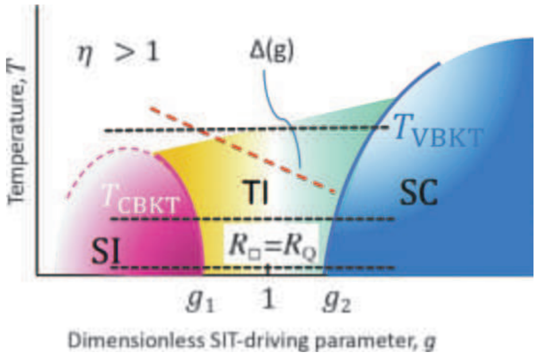

Fig. 4 The finite-temperature phase diagram of an interacting charge–vortex system for the case $\eta > 1$. The transitions are vortex and charge BKT transitions with critical temperatures T_{VBKT} and T_{CBKT}, respectively. The *red dashed line* marks the behavior of the topological gap $\Delta(g)$ in the bosonic topological insulator phase while the horizontal *black dashed lines* sketch the transitions seen by an experiment done at the respective temperatures. Reproduced from Trugenberger CA et al. (2020) Magnetic monopoles and superinsulation in Josephson junction arrays. Quantum Reports 2: 388–399.

Remarkably, this Abelian confinement emerges in a condensed matter realization of superinsulators. These electric superinsulators constitute a state of matter with infinite resistance at finite temperatures due to electric strings binding Cooper pairs into "electric mesons." Coupling the matter charge current j^μ to the real electromagnetic gauge potential A_μ, $S \to S + i\sum_x \ell_0 \ell^2 A_\mu j_\mu$ in the Euclidean action (with ℓ_0 being the minimal length along the time axis), and integrating out all matter variables, one obtains the effective action describing the electromagnetic response of a system. For the bosonic topological insulator, this is

$$S_{\mathrm{eff}}(A_\mu) = \frac{1}{2e_{\mathrm{eff}}^2} \sum_x \mathbf{E}_x^2, \tag{13}$$

with the effective coupling constant

$$e_{\mathrm{eff}}^2 = \mathcal{O}\left(\frac{1}{g}\right) = \mathcal{O}\left(\frac{e^2 \lambda_{\mathrm{L}}}{d}\right), \tag{14}$$

This is the electromagnetic response of a Mott insulator with high dielectric permittivity so that the electric field $\mathbf{E}$ dominates the action. The effective coupling e_{eff}^2 characterizes the strength of the Coulomb interaction, which grows with decreasing g, in particular, with decreasing film thickness d.

In the superinsulating phase the effective action becomes

$$S_{\mathrm{eff}}(A_\mu) = \frac{1}{2e_{\mathrm{eff}}^2} \sum_x \mathbf{E}_x^2 + \frac{2\pi^2}{e_{\mathrm{eff}}^2} \sum_x m_x \frac{1}{-\nabla^2} m_x, \tag{15}$$

where m_x are dynamic magnetic monopole instantons, as shown in Fig. 5, over which one has also to sum in the partition function.

Contrary to charges, whose conservation is ensured by the Noether theorem, Josephson vortices are topological excitations, characterized by the topological quantum number labeled by the homotopy group $\Pi_1(\mathrm{U}(1)) = \mathbb{Z}$, which in this case is the winding number of the longitudinal component of the gauge field. Such topological quantum numbers can vary in local tunneling events, called instantons, which appear as particles in the Euclidean space-time lattice (Coleman, 1985). These Euclidean particles are (nonrelativistic) magnetic monopoles (Polyakov, 1975). In the relativistic limit, magnetic monopoles interact via the 3D Euclidean Coulomb potential and are, thus, always in a plasma phase (Polyakov, 1975). In the present case, since only electric fields enter the game, the interaction is the logarithmic 2D Coulomb potential (Trugenberger et al., 2020), to which the standard treatment of the 2D Coulomb gas (Minnhagen, 1987) with the temperature replaced by the effective coupling e_{eff}^2 applies. In particular, at small e_{eff}^2, that is, large g, the monopoles are confined and the electromagnetic response of the system coincides with the electromagnetic response of the bosonic topological insulator. However, monopoles unbind if e_{eff}^2 is sufficiently large, that is, if g is sufficiently small, and the Coulomb interaction becomes stronger than its critical value. The resulting monopoles' "endogenous disorder" squeezes electric fields created by neighboring electric charges of opposite signs into thin electric flux tubes, Polyakov's electric strings, dual to superconducting Abrikosov vortices, see, for example, Tinkham (1996). This induces a linear electric potential $V_{\mathrm{string}} = \sigma L$ between the two probe charges at distance L. Hence, the charges can be viewed as bound by a string with the tension (Diamantini et al., 2020b)

$$\sigma = \frac{\sqrt{8} e_{\mathrm{eff}}}{\pi \ell_0 \ell} e^{-\frac{\pi^2}{e_{\mathrm{eff}}^2} G_2(0)}, \tag{16}$$

where $G_2(0)$ is the IR-regularized 2D lattice Coulomb potential at the coinciding points.

When the two probe charges are separated by distances larger than the typical string length $d_s = 1/\sqrt{\sigma}$ on which the tension starts to be felt, a couple Cooper pair-Cooper hole emerges out of the vacuum to form two short strings replacing the long one. This is the

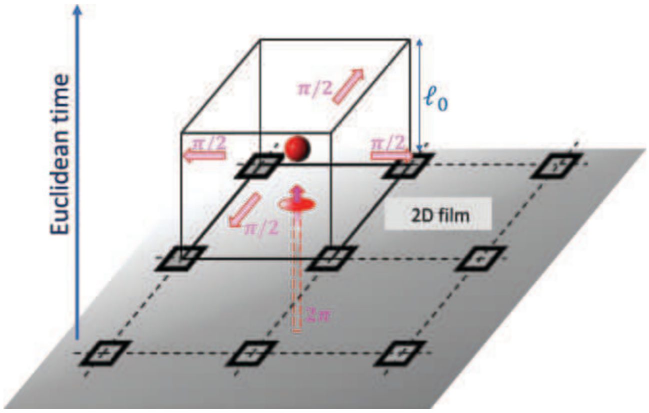

Fig. 5 A (nonrelativistic) magnetic monopole instanton. The flux 2π on a plaquette formed by 4 granules disappears in a tunneling event between times t and $t+\ell_0$. . Reproduced from Diamantini MC et al. (2020b) Direct probe of the interior of an electric pion in a Cooper pair superinsulator. Communications on Physics 3: 142

property of *confinement*, the mechanism holding quarks together in color-neutral hadrons (Greensite, 2011). This, of course, assumes dynamical matter but indeed, confinement by U(1) monopoles survives when dynamical matter is coupled to the gage fields, at least for one species of relativistic fermions (Nogueira and Kleinert, 2008). Confinement means that, on large scales, the spectrum of the theory does not contain charged Cooper pairs anymore but only neutral electric "pions." As a consequence, the system, if large enough, acquires infinite resistance, which holds up to the temperature of the charge BKT transition, T_{CBKT}.

Asymptotic freedom and size effects

Confining strings are characterized by two scales, the typical length after which tension is felt, d_s, and the width, w. The latter is set by the photon mass, the gap characterizing the superinsulating phase, $w = 1/m_{\mathrm{ph}}$ (Polyakov, 1975, 1987). Contrary to strings in quantum chromodynamics, the width and length of these Abelian strings scale differently with the coupling constant (Caselle et al., 2016) so that in the physical regime, the Abelian strings are thin and long.

The confinement scale $d_s = 1/\sqrt{\sigma}$ sets the dimension of the neutral bound states. In quantum chromodynamics, the strong interaction binding quarks implies that mesons and hadrons are extremely small and it is impossible to "look inside" them. Quarks can be observed only indirectly, by smashing hadrons in colliders and observing the jets formed in these collisions. The electric forces in superinsulators are much weaker than the strong interactions; hence electric pions are much larger than their elementary particle cousins and it is conceivable that one can measure their interior simply by experimenting on small enough samples.

What would one expect in this interior? Non-Abelian gage theories are characterized by the phenomenon of asymptotic freedom (Gross, 1999), the coupling constant, and thus the strength of the interaction, flows to zero at short scales. While this is the original point of view from the vicinity of the Gaussian UV fixed point, asymptotic freedom can be understood also from the point of view of the IR string theory, where gauge interactions become nonperturbative. This is the statement that the string tension decreases, and eventually vanishes, when approaching short scales, where perturbative gauge interactions take over. This is particularly important in the present case, where we have two clearly distinct scales. At intermediate observation scales $w = 1/m_{\mathrm{ph}} < r_{\mathrm{obs}} < d_s$, Cooper pairs feel neither the string tension nor the standard Coulomb potential, which is screened by the photon mass on scales larger than w. One can thus expect that the hyperactivated resistance behavior caused by the string should give way directly to a saturated metallic resistance when the sample size decreases below the critical threshold d_s. This is fully confirmed in experiment (Diamantini et al., 2020b), as shown in Fig. 6.

Electric Meissner effect and its manifestation in the *I*(*V*) characteristics

Exactly as superconductivity can be destroyed by the application of a strong enough magnetic field, superinsulation does not survive the application of a sufficiently strong electric field, that is, an external voltage. An electric field E decreases the effective linear potential of Cooper pairs separated by the distance L to $U_{\mathrm{eff}} = (\sigma - 2eE)L$. Below the critical value $V_{c1} = \sigma(T)L/2e$, however, the effective string tension $\sigma_{\mathrm{eff}}(T)$ remains positive and the $I(V)$ characteristics is given by (Diamantini et al., 2020b)

$$I \propto V \exp\left(-\frac{\sigma_{\mathrm{eff}}(T)L}{T}\right), \quad V < V_{c1} = \frac{\sigma(T)L}{2e}, \tag{17}$$

which, in the thermodynamic limit $L \to \infty$, implies an infinite resistance. This is the electric Meissner state of the superinsulator. When the applied voltage V reaches the critical value $V_{c1} = \sigma(T)L/2e$, the effective tension vanishes. This, however, does not entail complete destruction of the superinsulating state, the photon mass gap is still present. This means that, above this threshold, thin, long electric strings can penetrate the sample from one end to the other and current starts to pass. This is the transition from the

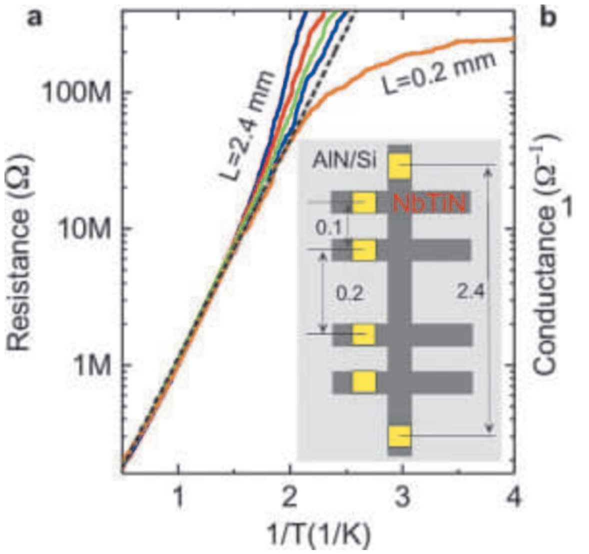

Fig. 6 Size dependence of the sheet resistance of a NbTiN film. In this logarithmic plot the *dashed straight line* corresponds to the usual activated behavior of a normal insulator. The largest samples show the hyperactivated behavior characteristic of superinsulation. The resistance of the shortest sample size 0.2 mm, however, saturates at the lowest temperatures, denoting a metallic behavior. For comparison, the string scale in this experiment was estimated as $d_s \approx 0.13$ mm. Reproduced from Diamantini MC et al. (2020b) Direct probe of the interior of an electric pion in a Cooper pair superinsulator. Communications on Physics 3: 142

electric Meissner state of a superinsulator, in which electric fields are completely expelled, to the mixed state in which electric flux tubes penetrate the sample. In this regime, the $I(V)$ characteristics acquire a power law form (Diamantini et al., 2020b),

$$\begin{aligned} I &\propto (V - \sigma(T)L/2e)^{1+T_{\mathrm{CBKT}}/16T}, \\ \text{at} \quad V_{c1} &< V < V_{c2} \equiv \frac{L}{2e}\left[\sigma(T) + \frac{T_{\mathrm{CBKT}}}{2.718 r_0}\right], \end{aligned} \tag{18}$$

where T_{CBKT} is the charge BKT transition temperature. Above the second critical threshold V_{c2}, the photon mass vanishes, superinsulation is completely destroyed, and the system becomes a normal insulator.

The three possible states, Meissner state, mixed state, and normal insulator, are separated by two kinks in the $I(V)$ characteristics of a superinsulating material (Diamantini et al., 2020b), as shown in Fig. 7. For an infinite sample, the current $I(V)$ vanishes identically in the Meissner state, realized for $V < V_{c1}$.

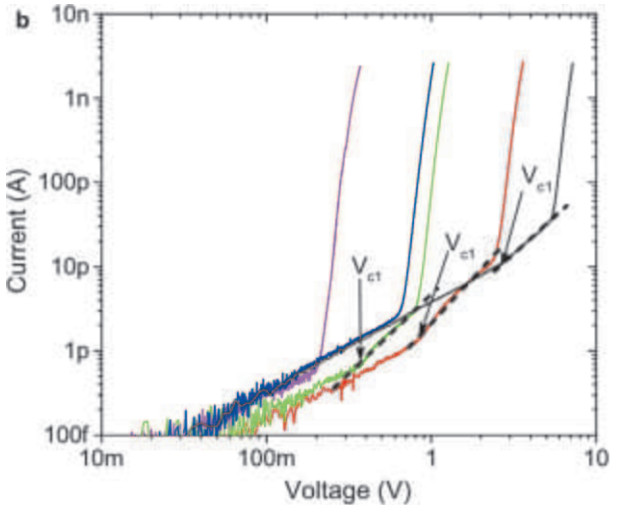

Fig. 7 The two kinks in the $I(V)$ characteristics of a NbTiN film. For an infinite sample the $I(V)$ curve vanishes identically for $V < V_{c1}$, reflecting the electric Meissner state.

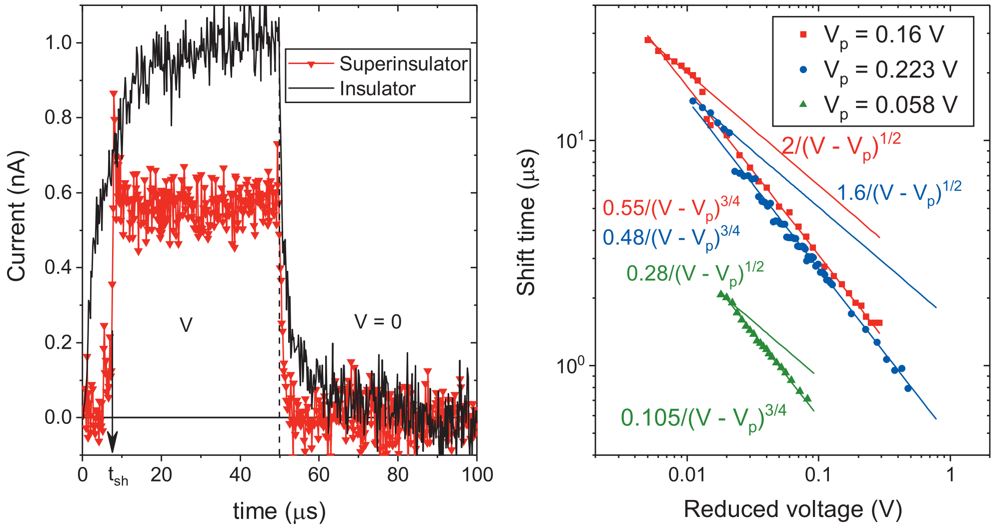

Fig. 8 Characteristic current time dependence upon application of a rectangular voltage pulse with amplitude $V = 0.155$ V and duration 50 μs (left panel) to a NbTiN film at the temperature of 20 mK. In the superinsulating state as compared to the same response of the normal insulator at 300 mK. The right panel displays the log–log plot of the current response time t_{sh} as function of the amplitude of the rectangular voltage pulse. The experimental data are shown by symbols. The *solid lines* present the fitting functions revealing the power law scaling of $t_{sh}(V - V_p)$ dependence. Reproduced from Mironov A-Y et al. (2022) Relaxation electrodynamics of superinsulators. Scientific Reports 12: 19918.

Dynamical exponents and the linear potential

The charge-hole potential in the superinsulating state can be measured directly by applying a voltage pulse and measuring the delay for current passage (Mironov et al., 2022). The results are presented in Fig. 8, in which the scaling of the current response time as a function of the pulse strength $(V - V_{c1})$ (here denoted as V_p) is shown for a rectangular pulse of strength V and duration 50 μs applied to a NbTiN film at 20 mK in the superinsulating state, and compared to the current response for the normal insulator at 300 mK.

The two kinks described in the previous section are again clearly visible and correspond to two different dynamical exponents μ in the scaling

$$t_{sh} \propto (V - V_{c1})^{-\mu}. \tag{19}$$

Consider two charges $\pm 2e$ of mass m bound by the linear potential $V(\mathbf{x}_1, \mathbf{x}_2) = \sigma|\mathbf{x}_1 - \mathbf{x}_2|$, where σ is the string tension of the confining electric string and $\mathbf{x}_i$ are the coordinates of the two particles. The critical value of the potential when current starts to pass is $V_{c1} = \sigma L$, with L being the sample length, corresponding to a configuration in which the two opposite charges reach the sample boundaries. In the center of mass coordinates, one can reduce the problem to a single particle of reduced mass $m/2$ at the origin, subject to the potential energy $\mathrm{U}(r) = 2e\sigma r$, with r denoting the separation distance. A positive linear potential results in an attractive constant force $F_a = 2e\sigma = 2eV_{c1}/L$. An external potential V amounts to an additional repulsive force $F_r = 2eV/L$. The total acceleration of separation is thus $a = (2/m)F_{tot} = (4e/mL)(V - V_{c1})$. The corresponding equation of motion describing the separation distance of the charge-hole system is

$$r(t) = \frac{2e}{mL}(V - V_{c1})t^2. \tag{20}$$

Current starts to pass when charges of opposite sign reach the sample boundaries, that is when $r(t_{c1}) = L$. The delay for current passage is thus given by inverting Eq. (20),

$$t_{cr} = \sqrt{\frac{mL^2}{2e}}(V - V_{c1})^{-1/2}. \tag{21}$$

The observed dynamical exponent $\mu = 1/2$ is thus a direct confirmation of the linear potential binding charges of opposite sign.

Oblique superinsulators in 3D

Superconductors with emergent granularity also arise in three dimensions (Diamantini et al., 2021a). Similarly to their 2D counterparts, they are natural hosts for quantized Josephson vortices that comprise supercurrent rings spanning over adjacent granules in the same plane. The difference is that now since the current rings pile on top of each other to minimize the interaction energy, these Josephson vortices become 1D extended excitations. Since the resulting liner tension is low, nothing prevents the vortex cores to tear making them open and having magnetic monopole-antimonopole pairs at their ends. In the 3D case, magnetic monopoles are no more instantons but become real, particle-like excitations. If the vortex tension vanishes, the quantized vortices turn into the unobservable Dirac strings (Dirac, 1931; Goddard and Olive, 1978): there is no energy price to pay to make one vortex go from one monopole to infinity and then return back to antimonopole. In this case magnetic monopoles form a Bose condensate, that is, 3D superinsulator (Diamantini et al., 2021c).

All the described properties of superinsulators, including the confining electric string between Cooper pairs, the Meissner state, and the nonlinear $I(V)$ curves can be derived, mutatis mutandis, as in the 2D case. The 3D superinsulators are characterized by dual London equations for the magnetic monopole current $\mathbf{j}_{\mathrm{m}}$,

$$\begin{aligned} \partial_t \frac{\pi}{e} \mathbf{j}_{\mathrm{m}} &= \frac{1}{\lambda_{\mathrm{E}}^2} \mathbf{B}, \\ \nabla \wedge \frac{\pi}{e} \mathbf{j}_{\mathrm{m}} &= \frac{1}{\lambda_{\mathrm{e}}^2} \mathbf{E}. \end{aligned} \tag{22}$$

where the electric penetration depth is set by the photon mass, $\lambda_{\mathrm{E}} = 1/m_{\mathrm{ph}}$.

The new effect, arising exclusively in 3D, is the possible presence of the topological θ-term (Treiman et al., 1985)

$$S_\theta = \frac{\theta}{4\pi^2} \int d^4x \, \mathbf{E} \cdot \mathbf{B}. \tag{23}$$

in the electromagnetic action, giving rise to the so-called axion electrodynamics (Wilczek, 1987). If the gauge group is compact, the new parameter θ is an angle. The correct periodicity is 2π for fermionic systems and 4π for bosonic ones (Metlitski et al., 2013; Vishwanath and Senthil, 2013). The θ-term changes the character of superinsulators since it induces the electric charge $\theta/2\pi$ on magnetic monopoles (Witten, 1979) which become *dyons*, the particles carrying both electric and magnetic charge (Goddard and Olive, 1978). In the presence of the θ-term one arrives at the *oblique superinsulator*, a Bose condensate of both electric and magnetic charges, in which the corresponding oblique London equations hold:

$$\begin{aligned} \partial_t \frac{\pi}{e} \mathbf{j}_{\mathrm{m}} &= \frac{\Lambda^2}{4e^2} \left(\mathbf{B} + \frac{2e^2}{\pi} \frac{\theta}{2\pi} \mathbf{E} \right), \\ \nabla \wedge \frac{\pi}{e} \mathbf{j}_{\mathrm{m}} &= \frac{\Lambda^2}{4e^2} \left(\mathbf{E} - \frac{2e^2}{\pi} \frac{\theta}{2\pi} \mathbf{B} \right). \end{aligned} \tag{24}$$

Here, Λ denotes the gap energy scale. Combining these equations with the (static) Ampère equations in the presence of the magnetic charge

$$\begin{aligned} \nabla \wedge \mathbf{B} &= 2e \, \mathbf{j}_{\mathrm{e}}, \\ \nabla \wedge \mathbf{E} &= -\frac{\pi}{e} \mathbf{j}_{\mathrm{m}}, \end{aligned} \tag{25}$$

and using the fact that the electric current is $\mathbf{j}_{\mathrm{e}} = (\theta/2\pi)\mathbf{j}_{\mathrm{m}}$ since it is carried by charged magnetic monopoles one obtains (for sourceless currents)

$$\left(\nabla^2 - \frac{1}{\lambda_\theta^2} \right) \mathbf{j}_{\mathrm{e}} = 0, \tag{26}$$

where

$$\lambda_\theta = \frac{\pi}{e\Lambda} \frac{1}{\sqrt{\left(\frac{\pi}{2e^2}\right)^2 + \left(\frac{\theta}{2\pi}\right)^2}}. \tag{27}$$

Currents are screened in the interior of the dyon condensate and survive only in the surface strips of the width set by the oblique penetration depth λ_θ. While in normal superinsulators the penetration depth increases in the strong coupling limit, the contrary is true for oblique superinsulators, where for $e \to \infty$ we have $\lambda_\theta \to 0$. One can show that in this limit, oblique superinsulators form a topological state of matter in which only edge states survive while the bulk charges are frozen by the diverging gap (Diamantini et al., 2021b). The θ-term residing on closed manifolds is equivalent to the Chern–Simons term on the boundary (Treiman et al., 1985). This induces statistical transmutations for the surviving edge states (Wilczek, 1990). In particular, for $\theta = 2\pi$, the edge states become symmetry-protected charge $2e$ fermions and thus are expected to behave as an ideal Fermi liquid, with the resistance scaling as the square of temperature. The experiments reported precisely this $R \propto T^2$ resistance behavior in the pseudogap state of high-T_{c} superconductors (Zhou, 2021). This observation in conjunction with the nematicity and magnetoelectric effects observed in the pseudogap state, set the base for putting forth the proposal that the pseudogap state, proclaimed in Zhou (2021) as an unanswered issue, is actually the oblique superinsulator (Diamantini et al., 2021b).

The role of disorder

The first quantitative descriptions of the superinsulating state were derived in the context of JJAs (Diamantini et al., 1996; Fistul et al., 2008) and revealed that, in this context, the tuning parameter driving the SIT is $g \simeq E_{\mathrm{J}}/E_{\mathrm{C}}$ that is, the relative strength of the Josephson coupling and the Coulomb interaction. At the same time, experimentally, superinsulation was discovered

(Baturina et al., 2007) by driving a TiN film across the SIT via tuning the room temperature sheet resistance $R_{\square}(T_{\mathrm{Room}})$, which is a measure of disorder. Indeed, disorder enhances the Coulomb interaction by reducing the charge screening (Finkel'shtein, 1987). The main parameter driving the SIT is the relative strength of the Coulomb interaction: disorder is indeed one of the possible ways to affect this strength, as is the thickness of the film or an applied magnetic field.

A widespread view at the dawn of SIT studies was that disorder plays also another role, governing the structure of the phase diagram near the SIT via Anderson localization of the Cooper pairs (Fisher, 1990a; Fisher et al., 1990b) or its interacting version, referred to as many-body localization (Altshuler et al., 2006; Basko et al., 2007; Altshuler et al., 2009), see Sacépé et al. (2020) for a review. A consistent theory of the SIT (Diamantini et al., 2020a, 2021a) demonstrates, however, that localization does not play a role in the critical vicinity of the SIT because, on one hand, of the dominance of topological interactions in the intermediate Bose metal state and, on the other hand, the presence of long range linear Coulomb interactions in the superinsulating state. Exactly as in the quantum Hall effect (QHE), localization can help to pin the quasi-particles forming around the topological ground state (Pu et al., 2021) corresponding to the Bose metal, although, strictly speaking not even this is necessary, neither for the formation of plateaus in the QHE (Kim and Kivelson, 2021) nor for the emergence of the topological Bose metal phase (Diamantini et al., 2021a). On the other side, many-body localization does not survive linear interactions, not even in 1D, where they are kinematic (Nandkishore and Sondhi, 2017; Akhtar et al., 2018), and may become effective when only short-range interactions are present. Only after one has identified the correct neutral physical states in the spectrum and only short-range interactions are left, can one even speak of localization.

The observation of two kinks (rather than only one), see Fig. 6, in the $I(V)$ curves in the superinsulating state (Diamantini et al., 2020b), is a strong experimental evidence that Cooper pairs are confined by Polyakov's strings, rather than localized by disorder. Localization by disorder is further strongly disfavored by the measurement of a linear potential between charges of opposite sign in the superinsulating state (Mironov et al., 2022). Notably, the confinement by this linear potential induces breaking of thermalization and ergodicity. These phenomena are typically associated with many-body localization in the presence of disorder (James et al., 2019; Mazza et al., 2019). Note that while the many-body localization phenomenon is far from being established in 2D and 3D, the phenomena associated with it are straightforward and typical consequences of the established existence of the confinement phase. Therefore, while disorder may appear as an important tuning parameter for the SIT, it is irrelevant in the renormalization group sense in the critical vicinity of the SIT, since it does not influence the character of the phases emerging near the superconductor-superinsulator transition. The interpretation of this effect as a finite-temperature insulating behavior due to many-body localization proposed in Ovadia et al. (2015) is thus disfavored by recent experimental evidences.

Conclusion

We have shown that condensed matter systems that admit magnetic monopoles lead to a material realization of the S duality under exchange of electric and magnetic fields and charges. Under this duality, a superconductor is mapped into a superinsulator, a phase in which the system exhibits an infinite electric resistance (even at finite temperatures). Contrary to the superconducting phase, where vortices experience logarithmic interactions, in superinsulators charges are bound into neutral pairs by linear potentials due to the "endogenous disorder" created by the monopoles. Superinsulation has been experimentally detected in TiN, InO, NbTiN, and NbSi films. In bulk materials, a particular, "oblique" version of superinsulation may be realized in the pseudogap state of high-temperature superconductors.

References

Aharonov Y and Bohm D (1959) Significance of electromagnetic potentials in quantum theory. *Physics Review* 115: 485–491.

Aharonov Y and Casher A (1984) Topological quantum effects for neutral particles. *Physical Review Letters* 53: 319–321.

Akhtar AA, et al. (2018) Symmetry breaking and localization in a random Schwinger model with commensuration. *Physical Review B* 98: 115109.

Altshuler BL, et al. (2006) Metal-insulator transition in a weakly interacting many-electron system with localized single-particle states. *Annals of Physics* 321(5): 1126–1205.

Altshuler BL, et al. (2009) Jumps in current-voltage characteristics in disordered films. *Physical Review Letters* 102: 176803.

Basko DM, et al. (2007) Possible experimental manifestations of the many-body localization. *Physical Review B* 76: 052203.

Baturina TI and Vinokur VM (2013) Superinsulator-superconductor duality in two dimensions. *Annalen der Physik* 331: 236–257.

Baturina TI, et al. (2007) Localized superconductivity in the quantum-critical region of the disorder-driven superconductor-insulator transition in TiN thin films. *Physical Review Letters* 99: 257003.

Berezinskii VL (1971) Destruction of long-range order in one-dimensional and two-dimensional systems having a continuous symmetry group I. Classical systems. *Soviet Physics–JETP* 32: 493–500.

Bøttcher CGL, et al. (2018) Superconducting, insulating and anomalous metallic regimes in a gated two-dimensional semiconductor-superconductor array. *Nature Physics* 14: 1138–1144.

Caselle M, et al. (2016) Width of the flux tube in compact U(1) gauge theory in three dimensions. *Journal of High Energy Physics* 02: 180.

Chen X, et al. (2013) Symmetry protected topological orders and the group cohomology of their symmetry group. *Physical Review B* 87: 155114.

Coleman S (1985) *Aspects of Symmetry*. Cambridge: Cambridge University Press.

Dalidovich D and Phillips P (2002) Phase glass is a Bose metal: A new conducting state in two dimensions. *Physical Review Letters* 89: 27001.

Das D and Doniach S (1999) Existence of a Bose metal at $T = 0$. *Physical Review B* 60: 1261–1275.

Das D and Doniach S (2001) Bose metal: Gauge field fluctuations and scaling for field-tuned quantum phase transitions. *Physical Review B* 64: 134511.

Deser S, et al. (1982a) Three-dimensional massive gauge theories. *Physical Review Letters* 48: 975–978.

Deser S, et al. (1982b) Topologically massive gauge theories. *Annals of Physics* 140: 372–411.

Diamantini MC, et al. (2021c) Quantum magnetic monopole condensate. *Communications on Physics* 4: 25.

Diamantini MC, et al. (1996) Gauge theories of Josephson junction arrays. *Nuclear Physics B* 474: 641–677.

Diamantini MC, et al. (2018) Confinement and asymptotic freedom with Cooper pairs. *Communications on Physics* 1: 77.
Diamantini MC, et al. (2019) The superconductor-superinsulator transition: S-duality and the QCD on the desktop. *Journal of Superconductivity and Novel Magnetism* 32: 47–51.
Diamantini MC, et al. (2020a) Bosonic topological intermediate state in the superconductor-insulator transition. *Physics Letters A* 384: 126570.
Diamantini MC, et al. (2020b) Direct probe of the interior of an electric pion in a Cooper pair superinsulator. *Communications Physics* 3: 142.
Diamantini MC, et al. (2021a) Superconductor-to-insulator transition in absence of disorder. *Physical Review B* 103: 174516.
Diamantini MC, et al. (2021b) Topological nature of high-temperature superconductivity. *Advanced Quantum Technologies* 4: 2000135.
Dirac PAM (1931) Quantized singularities in the electromagnetic field. *Proceedings of the Royal Society of London A* 133: 60–72.
Efetov KB (1980) Phase transition in granulated superconductors. *Soviet Physics–JETP* 51: 1015–1022.
Fazio R and Schön G (1991) Charge and vortex dynamics in arrays of tunnel junctions. *Physical Review B* 43: 5307–5320.
Fazio R and van der Zant H (2001) Quantum phase transitions and vortex dynamics in superconducting networks. *Physics Reports* 355: 235–334.
Finkel'shtein AM (1987) Superconducting transition temperature in amorphous films. *JETP Letters* 45: 46–49.
Fisher MPA (1990a) Quantum phase transitions in disordered two-dimensional superconductors. *Physical Review Letters* 65: 923–926.
Fisher MPA and Grinstein G (1988) Quantum critical phenomena in charged superconductors. *Physical Review Letters* 60: 208–211.
Fisher MPA, et al. (1990b) Presence of quantum diffusion in two dimensions: Universal resistance at the superconductor-insulator transition. *Physical Review Letters* 64: 587–590.
Fistul MV, et al. (2008) Collective Cooper-pair transport in the insulating state of Josephson-junction arrays. *Physical Review Letters* 100: 086805.
Girvin SM, et al. (1992) Universal conductivity as the superconductor-insulator transition in two dimensions. *Progress of Theoretical Physics Supplement* 107: 135–144.
Goddard P and Olive DI (1978) Magnetic monopoles in gauge field theories. *Reports on Progress in Physics* 41: 1357–1437.
Greensite J (2011) *An Introduction to the Confinement Problem*. Berlin: Springer-Verlag.
Gross D (1999) Twenty five years of asymptotic freedom. *Nuclear Physics B, Proceedings Supplements* 74: 426–446.
Haviland D, et al. (1989) Onset of superconductivity in the two-dimensional limit. *Physical Review Letters* 62: 2180–2183.
Hebard A and Paalanen MA (1990) Magnetic-field-tuned superconductor-insulator transition in two-dimensional films. *Physical Review Letters* 65: 927–930.
Humbert V, et al. (2021) Overactivated transport in the localized phase of the superconductor-insulator transition. *Nature Communications* 12: 6733.
Jackiw R and Templeton S (1981) How super-renormalizable interactions cure infrared divergences. *Physical Review D* 23: 2291–2304.
James AJA, et al. (2019) Nonthermal states arising from confinement in one and two dimensions. *Physical Review Letters* 122: 130603.
Kapitulnik A, et al. (2019) Anomalous metals–failed superconductors. *Reviews of Modern Physics* 91: 011002.
Kim K-S and Kivelson S-A (2021) The quantum Hall effect in the absence of disorder. *Quantum Matter* 6: 22.
Kosterlitz J-M and Thouless D-J (1972) Long range order and metastability in two dimensional solids and superfluids. (Application of dislocation theory). *Journal of Physics C: Solid State Physics* 5: L124.
Kosterlitz J-M and Thouless D-J (1973) Ordering, metastability and phase transitions in two-dimensional systems. *Journal of Physics C: Solid State Physics* 6: 1181–1203.
Kowal D and Ovadyahu Z (1994) Disorder induced granularity in an amorphous superconductor. *Solid State Communications* 90: 783–786.
Krämer A and Doniach S (1998) Superinsulator phase of two-dimensional superconductors. *Physical Review Letters* 81: 3523–3526.
Lu Y-M and Vishwanath A (2012) Theory and classification of interacting integer topological phases in two dimensions: A Chern-Simons approach. *Physical Review B* 86: 125119.
Mandelstam S (1976) Vortices and quark confinement in non-Abelian gauge theories. *Physics Reports* 23: 245–249.
Mazza P, et al. (2019) Suppression of transport in non-disordered quantum spin chains due to confined excitations. *Physical Review B* 99: 180302.
Metlitski M-A, et al. (2013) Bosonic topological insulator in three dimensions and the statistical Witten effect. *Physical Review B* 88: 035131.
Minnhagen P (1987) The two-dimensional coulomb gas, vortex unbinding and superfluid-superconducting films. *Reviews of Modern Physics* 59: 1001–1066.
Mironov A-Y, et al. (2018) Charge Berezinskii-Kosterlitz-Thouless transition in superconducting NbTiN films. *Scientific Reports* 8: 408.
Mironov A-Y, et al. (2022) Relaxation electrodynamics of superinsulators. *Scientific Reports* 12: 19918.
Nambu Y (1974) Strings, monopoles and gauge fields. *Physical Review D* 10: 4262–4268.
Nandkishore R-M and Sondhi S-L (2017) Many-body localization with long-range interactions. *Physical Review X* 7: 041021.
Nogueira F-S and Kleinert H (2008) Compact quantum electrodynamics in 2+1 dimensions and spinon confinement: A renormalization group analysis. *Physical Review B* 77: 045107.
Ovadia M, et al. (2015) Evidence for a finite-temperature insulator. *Scientific Reports* 5: 13503.
Phillips P and Dalidovich D (2003) The elusive Bose metal. *Science* 302: 243–247.
Polyakov A-M (1975) Compact gauge fields and the infrared catastrophe. *Physics Letters* 59: 82–84.
Polyakov A-M (1987) *Fields and Strings*. Chur, Switzerland: Harwood Academic Publisher.
Pu S, et al. (2021) Anderson localization in fractional quantum Hall effect. *arXiv.2109.00362*.
Sacépé B, et al. (2008) Disorder-induced inhomogeneities of the superconducting state close to the superconductor-insulator transition. *Physical Review Letters* 101: 157006.
Sacépé B, et al. (2011) Localization of preformed Cooper pairs in disordered superconductors. *Nature Physics* 7: 239–244.
Sacépé B, et al. (2020) Quantum breakdown of superconductivity in low-dimensional materials. *Nature Physics* 16: 734–746.
Sambandamurthy G, et al. (2005) Experimental evidence for a collective insulating state in two-dimensional superconductors. *Physical Review Letters* 94: 017003.
't Hooft G (1978) On the phase transition towards permanent quark confinement. *Physical Review B* 138: 1–25.
Tinkham M (1996) *Introduction to Superconductivity*. New York: Dover Publications.
Treiman SB, et al. (1985) *Current Algebra and Anomalies*. Singapore: World Scientific.
Trugenberger CA, et al. (2020) Magnetic monopoles and superinsulation in Josephson junction arrays. *Quantum Reports* 2: 388–399.
van der Zant H, et al. (1992) Ballistic motion of vortices in Josephson junction arrays. *Europhysics Letters* 18: 343–512.
van Otterlo A, et al. (1994) Quantum vortex dynamics in Josephson junction arrays. *Physica B* 203: 504–512.
Vinokur VM, et al. (2008) Superinsulator and quantum synchronization. *Nature* 452: 613–615.
Vishwanath A and Senthil T (2013) Physics of three-dimensional Bosonic topological insulators: Surface-deconfined criticality and quantized magnetoelectric effect. *Physical Review X* 3: 011016.
Wen XG and Zee A (1992) Classification of Abelian quantum Hall states and matrix formulation of topological fluids. *Physical Review B* 46: 2290–2301.
Wilczek F (1987) Two applications of axion electrodynamics. *Physical Review Letters* 58: 1799–1802.
Wilczek F (1990) *Fractional Statistics and Anyon Superconductivity*. Singapore: World Scientific.
Wilczek F (1992) Disassembling anyons. *Physical Review Letters* 69: 132–135.
Witten E (1979) Dyons of charge $\theta/2\pi$. *Physics Letters* 86: 283–287.
Yang C and Senthil T (2013) Boson topological insulators: A window into highly entangled quantum phases. *Physical Review B* 87: 235122.
Zhou X (2021) High-temperature superconductivity. *Nature Review Physics* 3: 462–465.

Encyclopedia of
Condensed Matter Physics

Second Edition

EDITOR-IN-CHIEF:
Tapash Chakraborty
University of Manitoba, Winnipeg, Manitoba, Canada

SECTION EDITORS:
Ana M. Sanchez
Department of Physics, University of Warwick, Coventry, United Kingdom

Hideo Aoki
Department of Physics, University of Tokyo, Tokyo, Japan

Robert H. Blick
Center for Hybrid Nanostructures, University of Hamburg & DESY, Hamburg, Germany

Roberto Raimondi
Mathematics and Physics Department, Roma Tre University, Rome, Italy

Rudolf A. Roemer
Department of Physics, University of Warwick, Coventry, United Kingdom

Vladimir Mihajlovic Fomin
Leibniz Institute for Solid State and Materials Research (IFW), Dresden, Germany

ELSEVIER
ACADEMIC PRESS
An imprint of Elsevier
elsevier.com/books-and-journals

Volume ISBN
ISBN 978-0-443-21824-8
9 780443 218248

Set ISBN
ISBN 978-0-323-90800-9
9 780323 908009

ENCYCLOPEDIA OF CONDENSED MATTER PHYSICS

SECOND EDITION

This page intentionally left blank

ENCYCLOPEDIA OF CONDENSED MATTER PHYSICS

SECOND EDITION

EDITOR-IN-CHIEF

Tapash Chakraborty[*]
Professor, Tier-I Canada Research Chair, University of Manitoba, Winnipeg, MB, Canada

VOLUME 3

ELSEVIER

---

[*] Retired.

Elsevier
Radarweg 29, PO Box 211, 1000 AE Amsterdam, Netherlands
The Boulevard, Langford Lane, Kidlington, Oxford OX5 1GB, United Kingdom
50 Hampshire Street, 5th Floor, Cambridge MA 02139, United States

Copyright © 2024 Elsevier Ltd. All rights reserved

No part of this publication may be reproduced or transmitted in any form or by any means, electronic or mechanical, including photocopying, recording, or any information storage and retrieval system, without permission in writing from the publisher. Details on how to seek permission, further information about the Publisher's permissions policies and our arrangements with organizations such as the Copyright Clearance Center and the Copyright Licensing Agency, can be found at our website: www.elsevier.com/permissions.

This book and the individual contributions contained in it are protected under copyright by the Publisher (other than as may be noted herein).

Notices
Knowledge and best practice in this field are constantly changing. As new research and experience broaden our understanding, changes in research methods, professional practices, or medical treatment may become necessary.

Practitioners and researchers may always rely on their own experience and knowledge in evaluating and using any information, methods, compounds, or experiments described herein. In using such information or methods they should be mindful of their own safety and the safety of others, including parties for whom they have a professional responsibility.

To the fullest extent of the law, neither the Publisher nor the authors, contributors, or editors, assume any liability for any injury and/or damage to persons or property as a matter of products liability, negligence or otherwise, or from any use or operation of any methods, products, instructions, or ideas contained in the material herein.

Library of Congress Cataloging-in-Publication Data
A catalog record for this book is available from the Library of Congress

British Library Cataloguing-in-Publication Data
A catalogue record for this book is available from the British Library

ISBN 978-0-32-390800-9

For information on all publications visit our website at http://store.elsevier.com

ELSEVIER
Book Aid International
Working together to grow libraries in developing countries
www.elsevier.com • www.bookaid.org

Publisher: Oliver Walter
Acquisitions Editor: Oliver Walter
Content Project Manager: Naman Negi
Associate Content Project Manager: Nandhini Mahendran
Designer: Mark Rogers

EDITOR-IN-CHIEF BIOGRAPHY

Tapash Chakraborty is a retired professor of physics from the University of Manitoba, Canada, where he was also the Canada Research Chair in Nanoscale Physics (2003–17). His research focus has been on many-body theories of various quantum materials, such as nuclear matter, helium liquids, and electron-hole liquids, that he studied under the tutelage of late Professor Manfred Ristig, at the University of Köln (1979–81). Just a year after the discovery of the fractional quantum Hall effect, he (working with his coworkers) demonstrated that electron–electron interactions could actually lead to quantum Hall states with nontrivial spin configurations, and that the low-lying excitations could be described as "spin-reversed quasiparticles." This prediction motivated much experimental work from laboratories around the world, as a result of which the concept of spin-reversed quasi-particles was established.

Similarly, his work on the quantum Hall states in double layer systems has received much attention from the community. Furthermore, Dr. Chakraborty (working with Dr. P. Maksym and others) made pioneering contributions to the many-electron theory of quantum dots. Dr. Chakraborty has also contributed to the theory of electronic properties of various nanoscale systems, such as spin-orbit coupled quantum dots, quantum rings, and single- and double-layer graphene (primarily with Dr. V. Apalkov). He has authored many books and reviews: the book with Dr. Pietiläinen on the quantum Hall effect and the single-authored book on quantum dots have become standard references in their respective fields.

This page intentionally left blank

EDITORIAL ADVISORY BOARD

Ana M. Sanchez
Department of Physics, University of Warwick, Coventry, United Kingdom

Hideo Aoki
Department of Physics, University of Tokyo, Tokyo, Japan

Robert H. Blick
Center for Hybrid Nanostructures, University of Hamburg & DESY, Hamburg, Germany

Roberto Raimondi
Mathematics and Physics Department, Roma Tre University, Rome, Italy

Rudolf A. Roemer
Department of Physics, University of Warwick, Coventry, United Kingdom

Vladimir Mihajlovic Fomin
Leibniz Institute for Solid State and Materials Research (IFW), Dresden, Germany

This page intentionally left blank

INTRODUCTION

> Electrons in orbits contained by the quantum,
> And atoms conjoined by the dipolar force,
> Gravity balanced by pressure
> And flap of a wing.
> Here, I remember the angles and curves,
> Calculus, I learned it all –
> Each bird bit and moon fracture
> Fixed by the symmetries,
> Airborne and airless, aloft.
>
> – Alan Lightman: *Song of Two Worlds*

Condensed matter physics (CMP) is the largest discipline in physics, involving a wide variety of interesting concepts and challenges. To quote Leggett (1992), CMP embraces topics "as diverse as traditional solid-state physics, neutron stars and the physics of biological matter." He further added that, by a liberal definition "just about all of physics outside atomic, nuclear and particle physics and cosmology" fall in this vast enterprise[1]. One of the primary goals of CMP is to explore the fundamental properties of matter—solids, liquids or gasses—comprising a large number of *interacting* constituent particles (Laughlin and Pines, 2000). The quantum-mechanical nature of these many-body systems makes condensed-matter highly nontrivial, sometimes counterintuitive and even astonishing. Superconductivity and the fractional quantum Hall effect (FQHE) naturally fall within that category. In fact, for the past four decades, the quantum Hall effects (QHEs) have been the epitome of elegant CMP (von Klitzing et al., 2020). Our fundamental system of units has been redefined following the discovery of the QHE when the "von Klitzing constant" $R_\mathrm{K} = 25,\ 812.8074593045\ \Omega$ came into being (von Klitzing, 2019; Nawrocki, 2019). Observation of the QHE in graphene[2] was crucial in determining the Dirac nature of charge carriers there (see for example, Jiang et al., 2007).

Another effect that outwardly resembles the QHE but is conceptually quite different is the FQHE, which is a quintessential manifestation of electron correlations governed by the Coulomb interaction (Störmer, 1992; Eisenstein and Stormer, 1990). To explain this fascinating effect, Laughlin (1983) introduced his eponymous wave function that not only provided the foundation for understanding the effect but also triggered a new wave of ideas with impact far beyond the realm of CMP[3]. Who would have imagined that a large collection of interacting electrons confined on a plane in a perpendicular magnetic field would result in elementary excitations (quasiholes and quasiparticles) (Chakraborty and Pietiläinen, 1988, 1995; Halperin, 1983; Clark and Maksym, 1989) carrying fractional electron charge and obeying the exotic exchange statistics of anyons (Halperin, 1984; Arovas et al., 1984)? These quasiparticles and quasiholes of the Laughlin state still remain an enigma (Laughlin, 1984; Chakraborty, 1985; Morf and Halperin, 1986). Fractional statistics is a truly path-breaking concept in CMP that was introduced by Leinaas and Myrheim (1977), and has been recently confirmed experimentally (Bartolomei et al., 2020; Nakamura et al., 2020).

Much of the history of CMP can be viewed as a series of paradigm shifts[4]. The field evolved rapidly through frequent ground-breaking discoveries that challenged existing paradigms and opened up new applications, and this evolution is expected to continue (Leggett, 2018; Cohen, 2008). For example, our current understanding of

the FQHE required deep mathematical analysis and a wide range of experimental exploration, which revealed a treasure trove of unique phenomena that are yet to be fully understood or explained. Other studies of electron correlations in low spatial dimensions have ushered in many groundbreaking notions, such as Pfaffian states, Majorana fermions in condensed matter, Chern insulators, and topological quantum materials that promise a fault tolerant means to perform quantum computation. The presence of incompressible FQHE states in monolayer graphene (Apalkov and Chakraborty, 2006), bilayer graphene (Apalkov and Chakraborty, 2010, 2011), and double-layer graphene (Liu et al., 2019) has demonstrated the robustness of the effect, and provides invaluable insight into the nature of this effect.

---

[1] Interestingly, some similarities do exist between the mathematical frameworks that describe low-temperature CMP and early-universe cosmology. See Kibble and Srivastava (2013).

[2] An isolated single layer of graphite consisting of carbon atoms bonded together in a hexagonal structure. See, e.g., Abergel et al. (2010).

[3] For example, an important aspect of Laughlin's theory is its seamless concinnity of classical plasma physics and the planar electron gas that has inspired others to use a similar approach to quark-gluon plasma (Lu, 2022).

[4] A detailed exposition of the meaning and examples of "paradigm shifts" (Kuhn-type) can be found in Leggett (2018).

The dynamics of an electron in a periodic potential subjected to a perpendicular magnetic field has been an intriguing problem for more than half a century (Obermair and Wannier, 1976; Osadchy and Avron, 2001)[5]. Within the nearest neighbor tight-binding description of the periodic potential the electron energy spectrum is described by the Harper equation (Harper, 1955). Numerical solution of this equation (Hofstadter, 1976) has revealed that the applied field splits the Bloch bands into subbands and gaps. As the field is varied, the splitting of band continues indefinitely, leading to bands within bands within bands. When plotted as a function of the magnetic flux per lattice cell, the energy spectrum depicts a *fractal* pattern (a self-similar pattern that repeats at every scale) and is known in the literature as Hofstadter's butterfly because of the resemblance of the pattern to butterflies[6]. Observation of the butterfly spectra in real systems is an arduous task. For example, in ordinary crystalline lattices, the required magnetic field to see the butterflies exceeds 1000 Tesla, which is far beyond the reach of present-day technology. Graphene seems to be the ideal system in the quest of those fractal butterflies (Weiss, 2013). It is interesting to note that a mathematical solution of the Harper equation, in contrast to the numerical solution mentioned above, remained a challenging problem (the so-called Ten Martini Problem) for mathematicians until it was solved (Avila and Jitomirskaya, 2006) in 2006.

Magnetism has been known to mankind since ancient times, and it remains a major topic in CMP. The road to understanding magnetism has been long and tortuous. At various times in history, magnets were claimed to have the healing power to cure a myriad of ailments that included epilepsy, arthritis, gout, and baldness. Magnets were the prime ingredients for the "elixir of life" by Paracelsus (1493–1541). Then there was the healing process of "animal magnetism" proposed by Franz Anton Mesmer (1734–1815) (mesmerism)[7], which was famously mocked in Mozart's *Così fan tutte* (Steptoe, 1986). Our current understanding of magnetism is deeply rooted in quantum mechanics as Van Vleck explained (Van Vleck, 1978): "Quantum mechanics is the key to understand magnetism. When one enters the first room with this key there are unexpected rooms beyond, but it is always the master key that unlocks each door." For centuries, the magnetism of certain rocks and metallic iron was only used for the practical purposes of direction finding, particularly navigation with a compass. Motors, generators, and electrical distribution networks appeared only in the 19th century after the discovery of the deep connection between electricity and magnetism. Magnetic order is a collective phenomenon akin to superconductivity and superfluidity that involves a very large number of particles. The rich variety of magnetically ordered states in solids, not only ferromagnetism but also antiferromagnetism, ferrimagnetism, and a range of noncollinear structures, was confirmed only in the middle of the 20th century, with the availability of neutron beams in research reactors. A range of new magnetic materials are taking their place as active layers in thin film sensors and memory devices (Baltz et al., 2018). Besides information storage (Blundell, 2001), important technical applications include magnetic resonance imaging (MRI) and the use of magnetic nanoparticles in medicine.

Many outstanding discoveries in magnetism and magnetic materials have resulted in rapid advances in information storage technology. Over the last two decades spintronics has emerged as an important field of research both from the point of view of fundamental science and advanced technological applications (Yamaguchi et al., 2021; Pinarbasi and Kent, 2022). The giant magnetoresistance (GMR) effect, the spin Hall effect, and the spin galvanic effects are typical examples of developments in the field. Spintronics aims at understanding how the spin degree of freedom of the electrical carriers can be controlled in order to obtain devices with new functionalities and better performance. This endeavor often combines concepts from different aspects of condensed matter systems, giving the topic a fascinating interdisciplinary flavor. Spintronic phenomena are now being studied in an impressive range of different materials ranging from metals to half-metals to semiconductors, graphene and other two-dimensional systems such as transition metal dichalcogenides.

---

[5] For a recent review on butterflies in graphene, see for example Chakraborty and Apalkov (2015).

[6] However, as one of the authors of this Encyclopedia has (somewhat humorously) pointed out, this butterfly has Lebesgue measure zero, that is, it cannot fly!.

[7] A wonderful account of the use of magnetism in medicine since ancient times can be found in Mourino (1991).

The GMR effect and the related tunnel magnetoresistance effect (TMR) found their first commercial use in magnetic field sensors for hard-disk read-heads, before broadening their field of application to include magnetic sensors for the automobile industry, solid-state compasses, biosensors, and nonvolatile magnetic memory (Hartmann, 2000). The ability to manipulate the magnetic state of ferromagnetic structures led to initial developments in spintronics, where the spin direction was controlled by externally applied magnetic fields. However, the push for downscaling and faster timescales has prompted research advances in the past decade where the manipulation of magnetic configurations is achieved by local electric currents (the spin torque effect) (Brataas et al., 2012; Locatelli et al., 2014). In recent years, various novel concepts, such as chiral spintronics, skyrmionic spin textures, and magnetic domain walls in spintronics, have been actively pursued. The rate of progress in spintronics is truly astounding (Editorial, 2022).

In the past century, superconductivity has raised many theoretical challenges and triggered numerous technical developments. Discovered in mercury in 1911, this unique phenomenon occurs when the electrical resistance of many metals and alloys drops to zero when cooled below about 4 K, the temperature of liquid helium. More significantly, the material expels magnetic flux and becomes perfectly diamagnetic. Superconductivity has been adopted or evaluated for a wide range of technical applications (Rogalla and Kes, 2012). These include electric power generation, electric power transmission, high-speed maglev transportation, and ultra-strong magnetic field generation in high-resolution MRI and other nuclear magnetic resonance (NMR) systems. Interestingly, it took almost 50 years after the original discovery for the phenomena to be explained by the BCS theory (Tinkham, 2004) of reciprocal-space electron pairing, via the electron–phonon interaction. This electron–phonon mediated superconductivity became known as "conventional superconductivity" after the discovery of "high-temperature superconductivity" (Müller and Bednorz, 1987) at liquid nitrogen temperatures in tetragonal copper oxides in 1986. This threw open a new challenge to explain the properties of strongly correlated *anisotropic* electronic systems. Further new classes of superconductors that remain to be properly understood include the iron-based pnictides discovered in 2008 (Hosono et al., 2018). Recently, a two-dimensional superlattice made from a twisted bilayer of "magic angle" graphene was found to exhibit unconventional superconductivity (Cao et al., 2018), driven by electron–electron interactions.

The phenomenon of spontaneous symmetry breaking (SSB) is ubiquitous in physics, and plays a fundamental role in CMP, particle physics, and even in cosmology. A classic illustration of SSB being Heisenberg's 1928 paper on ferromagnetism (Heisenberg, 1928). It is responsible for various collective modes, such as the famous Nambu-Goldstone (NG) and Higgs modes. Named by Baker and Glashow (Baker and Glashow, 1962), SSB corresponds to the case where the ground or lowest-energy state does not have the symmetry of the underlying dynamics. Instead, multiple degenerate ground states are available and the symmetry breaking is *spontaneous* because it is not clear, a priori, which one of those ground states will be chosen. In this well-trodden territory a simple analogy of this abstruse concept given by A. Salam is illuminating (CERN, 1977): "Imagine a banquet where guests sit at round tables. A bird's eye view of the scene presents total symmetry, with serviettes alternating with people around each table. A person could equally well take a serviette from his right or from his left. The symmetry is spontaneously broken when one guest decides to pick up from his left and everyone else follows suit." Over the years, development of the concept of SSB has taken a circuitous route (Gaudenzi, 2022): "from the land of particle physics to the physics of many bodies (solids and nuclei), from there to the province of superconductivity, and from the latter back to particle physics ... ." SSB's significance extends beyond the physics of the Higgs boson to the study of low-energy phenomena such as superconductivity, superfluidity, magnetism, and others. Historically, the particle physics community has been guided by this exploration in their quest to understand and discover particles like the Higgs boson. More to the point, when a continuous symmetry is spontaneously broken, a gapless mode, the NG mode, appears which governs the low-energy behavior of the system. As an example, in a solid, the acoustic phonon is the NG mode associated with translational symmetry breaking and determines the behavior of the specific heat at low temperature (the Debye T^3 law). Recently, signatures of Higgs and Goldstone modes have been proposed to exist in a perovskite oxide (Marthinsen et al., 2018), in other crystalline structures (Vallone, 2019), and also in various other quantum systems (Léonard et al., 2017). On a lighter note, it is the symmetry breaking that is claimed to have prevented the fabled donkey (Weintraub, 2012) in the parable by Jean Buridan (1300–50) from dying of starvation (Fubini, 1974).

Common to the theoretical descriptions of these phenomena across CMP and high-energy physics is Quantum field theory (QFT). QFT was originally developed to describe the fundamental processes in high-energy physics, but has now become a valuable tool to address problems across physics, in particular, in CMP (Fradkin, 2013; see also, Mustafa, 2023), statistical physics, modern quantum chemistry, and even in

pure mathematics (Folland, 2008). Advances in our understanding of strongly correlated electron systems in CMP such as high-temperature superconductivity and the FQHE have been aided by the QFT. It has facilitated the treatment of spontaneous symmetry broken states, such as superfluids. Interestingly, many of the conceptual developments in CMP have, in return, had a reciprocal impact in QFT. A spectacular example being Nambu's work in dynamical symmetry breaking (Weinberg, 1986; Nambu, 2009) in particle physics, based on the BCS theory of superconductivity.

A glass is a noncrystalline solid obtained by quenching a liquid. It has a liquid-like structure, but a transition from liquid to solid behavior occurs on cooling. It may have one of a continuum of possible ground states that exhibit frozen-in liquid-like disorder. The term "spin glass" was coined by B.R. Coles (Mydosh, 1993) in 1970 for a diluted magnetic material with frozen-in paramagnetic-like spin disorder where the magnetic moments interact with randomly varying positive or negative exchange interactions leading to a multitude of possible ground states with different, random orientations of the spins. As in a normal glass, the energy barriers between the continuum of metastable states prevent it from ever reaching equilibrium. This phase of condensed matter has been an important and productive area of research. Spin-glass models are conceptually simple, but embody sophisticated physics. These models have become a paradigm for the solution of complex optimization problems (Mézard, 2022): much like the undulating flight patterns of starlings around the skies over Rome (Parisi, 2023). After cooling from the paramagnetic phase, the spin glass remains out of equilibrium, and it slowly evolves. This aging phenomenon corresponds to the growth of a "spin-glass order" parameter, whose correlation length can be measured (Joh et al., 1999). A cooling temperature step during aging causes a partial "rejuvenation," while the "memory" of previous aging is stored and can be retrieved (Refregier et al., 1987; Bouchaud et al., 2001). Many glassy materials present aging, and rejuvenation and memory effects can be found in other cases, but they are usually less pronounced. Numerical simulations of these phenomena are under active investigation using custom-built computers (Baity-Jesi et al., 2023; Vincent, 2023). A general understanding of glassy systems, to which spin glasses bring some special insight, is being pursued. It was realized decades ago that the physics of spin glasses has deep connections with the behavior of complex biological systems. In fact, spin-glass type states in neural network models offer interesting insights into states of high and low brain activity, as observed in mammals (Recio and Torres, 2016). These analogies are potentially useful for applications in fields such as robotics and artificial intelligence (AI) (Andriuschenko et al., 2022).

One of the most spectacular phenomena in CMP, discovered in the last century, was Bose-Einstein condensation (BEC). This macroscopic quantum phenomenon had its genesis in the work of Satyendra Nath Bose (Bose, 1924; Blanpied, 1972; Tomczyk, 2022) (whose name is forever associated with bosons), and has fascinated physicists for decades, ever since the first observation of this exotic state of matter in an ultracold gas of rubidium atoms (Georgescu, 2020). Among the advances made in this field, we highlight only a few: simulation of correlated electron states, such as the FQHE state and a bosonic analog of the Laughlin state, and the famous BEC-BCS crossover from a BEC to a BCS superfluid of weakly bound Cooper pairs, as the interparticle interaction strength is varied. Noteworthy is the recent measurement of the dynamic structure factor in an ultracold Fermi gas of lithium-6 atoms in the "unitary" limit, where a linear phonon mode for low momentum transfer can be clearly discerned (Biss et al., 2022). Perhaps such a method might one day shed light on the Laughlin quasiparticle gap and the collective modes that are still largely unresolved (Chakraborty and Pietiläinen, 1988, 1995; Halperin, 1983; Clark and Maksym, 1989).

Liquid helium, ^{4}He, and the less common isotope ^{3}He are unique quantum systems (Volovik, 2009). They remain liquid even at absolute zero temperature, a direct manifestation of Heisenberg's uncertainty principle and zero-point energy. The light mass of helium atoms and their weak interatomic attraction leads to a substantial zero-point kinetic energy and the system remains in the liquid state at ambient pressure. Solidification occurs when a pressure of about 25 MPa is applied. The different quantum statistics of the two helium isotopes (^{4}He is a boson while ^{3}He is a fermion) are responsible for the different physical characteristics of the two systems. Microscopic approaches to understand the ground state and low-energy excitations of the liquid state have occupied researchers for many decades (see for example, Ristig and Clark, 1976; Lam et al., 1977). These highly correlated quantum fluids have been established as systems where the efficacies of different many-body theories can be tested (Kallio and Smith, 1977; Lantto et al., 1977). These systems have been described as Ariadne's thread in this Encyclopedia, where the strongly interacting constituent particles are treated by a variety of ingenious theoretical and experimental approaches. Interestingly, liquid helium has been proposed to be a medium to design multiexcitation detectors to probe *dark matter* (Schutz and Zurek, 2016) in the keV mass limit. Although this looks far afield from CMP, the interface between CMP and high-energy particle physics could inspire new horizons in CMP, as discussed earlier.

CMP also has an enormous impact on our daily lives with unceasing technological innovation stemming directly from the advances in CMP research. It is also closely associated with the progress of our understanding of materials science and mechanical, chemical, and electrical engineering that deals with properties of novel materials and devices. As some authors have very aptly pointed out (Chaikin and Lubensky, 1995): The use and understanding of matter in its condensed (liquid or solid) state have gone hand in hand with the advances of civilization and technology since the first use of primitive tools. So important has the control of condensed matter been to man that prehistoric ages—the Stone Age, the Bronze Age, the Iron Age—are named after the material dominating the technology of the time. In fact, modern civilization is entirely dependent on our deep understanding and practical use of materials, old and new: Steel, glass, and concrete have shaped our modern living with comfort, health, longevity, and material wealth. All around us, from a tiny paper clip to giant skyscrapers, from jet planes to modern medicines, and the ubiquitous plastics that are integrated into nearly all aspects of human life, are testaments to our control over the myriad behavior of materials (Miodownik, 2014). Today, a large number of materials are designed by using principles of quantum mechanics (Freeman, 2002).

The Silicon chip that launched the information age is a great example of the effect of CMP on our daily lives. The scaling of transistors down to the nanometer range has enabled them to be embedded in greater numbers in the all-pervasive electronic devices that have transformed every facet of life all around the world. The transition from room-size to pocket-size computers with ever increasing computational power and memory, that occurred in only a few decades, epitomizes the unrelenting progress made in this direction. Advances in nanoscale research have opened the door to exploration of the natural world at the ultra-small scale (Chakraborty, 2022), with the potential to shape our future world.

Quantum dots (QDs), the quasi-zero-dimensional electron systems, are one of the most extensively studied nanostructures in the past three decades. They represent the ultimate reduction in dimensionality of a semiconductor device. Here the electrons are confined (either electrostatically or structurally) in all three directions and occupy spectrally sharp energy levels similar to those found in atoms (Chakraborty, 1999), hence the popular moniker *artificial atoms* (Maksym and Chakraborty, 1990). QDs and other similar nanostructures (Chakraborty, 2003) offer a rich variety of fundamental phenomena that result from manipulation of single electrons (single electronics) or single spins at the nanoscale. The study of interacting electrons in a QD requires large-scale numerical computations involving matrices of dimensions in the millions ("monster matrices") (Chakraborty and Pietiläinen, 2005; Pietiläinen and Chakraborty, 2006). QDs are also thought to have vast potential for future technological applications. One prominent example being quantum cryptography where the QDs are used in single photon emitters (Nowak et al., 2014), and in single photon detectors (Shields et al., 2000). Quantum cryptography, in turn, forms the basis of the *quantum Internet* (Liao et al., 2018). Other applications include lasers, and spintronics in quantum computing, entertainment industry (Bourzac, 2013), and even in biology (Bruchez and Holz, 2007).

Research in recent years has increasingly revealed that quantum phenomena are also ubiquitous in the natural world (Ball, 2011). They govern how birds are able to navigate around the globe using Earth's magnetic field or how plants use photosynthesis to harvest sunlight for conversion to chemical energy. All depend on subtle quantum effects that are now coming to light, thereby ushering the topic of quantum biology into CMP. Deoxyribonucleic acid (DNA), the molecule responsible for storage of genetic information in the cells of all living organism, is entrusted with the task of preserving, copying, and transmitting information that are necessary for living beings to grow and function. It is often referred to as the body's hereditary material as DNA is replicated and transmitted from parents to their offspring. This "molecule of life" was discovered in 1869 by Friedrich Miescher in Tübingen, Germany, who called it "nuclein," as it was isolated from the nucleus of white blood cells (Dahm, 2005; Thess et al., 2021). It took more than eighty years from that momentous event, to discover that DNA has a right-handed double-helix structure with appropriate base pairing (Watson and Crick, 1953; Klug, 2004). That discovery was so important that it has been compared with the discovery of the atomic nucleus in physics (Frank-Khamenetskii, 1997). Understanding the structure of the atom heralded quantum physics, while understanding of the structure of DNA brought forth the field of molecular biology.

DNA has several remarkable properties that make this molecule a prime candidate for nano-electronic materials (Chakraborty, 2007). These include molecular recognition and the ability to self-assemble via the complementarity of the base sequences on the two strands, which means that DNA can be integrated error-free in current semiconductor technology. DNA can also detect information about its own integrity that can trigger its eventual repair mechanism. All these properties are perfectly suitable for developing nanoscale electronics involving DNA

(Taniguchi and Kawai, 2006). Despite the promise of harnessing biology to realize integrated molecular electronics remains fascinating, much work remains to be done to make it a reality (Braun and Keren, 2004).

Protein molecules play a vital role in all living organisms. They are described as Nature's robots (Tanford and Reynolds, 2001) because for every imaginable task required in a living organism, and for every step of that task, there is a protein designed to carry it out. These proteins are even programmed to know when to turn on or off. Just as the twenty-six letters in the alphabet can spell out hundreds of thousands of words, there are twenty different naturally occurring amino acids that can be combined into many more different proteins than there are atoms in the known universe! Protein's biological function is determined by its unique and native three-dimensional structures that are characteristic of individual proteins (Gomes and Faísca, 2019; Echenique, 2007). The question of how proteins fold to their unique, compact, and highly organized functional states has remained an enduring challenge ("The protein-folding problem") (Chan and Dill, 1993; Dill and MacCallum, 2012; Wolynes and Eaton, 1999). Recently, there has been a tremendous development in this area of research. In November 2020, an AI program called AlphaFold, designed to tackle the problem of protein folding, predicted the three-dimensional structures of almost every protein known to science—about 200 millions in all (Jumper et al., 2021). AlphaFold uses a machine learning methodology to bring together information from preexisting knowledge of protein structures, and other geometric and physical constraints to predict protein structures. While this has been heralded a watershed moment in structural biology (Perrakis and Sixma, 2021), there are many key questions that AlphaFold cannot address yet. These include aspects of protein behavior that cannot be understood from a static structure, such as how proteins respond to their environment or how intrinsically disordered proteins actually are organized. Some authors (Nasser et al., 2021) have likened it to solving a crime story: while AlphaFold presents a snapshot in time, the question about how we get there remains unanswered. Biological systems have developed elaborate mechanisms to ensure that proteins fold correctly, or otherwise, they are detected and degraded before any serious harm can result to the host organism. However, protein misfolding does happen and that misfolding in the cell is linked to an array of diseases, including cancers, cardiovascular disease, type II diabetes, and numerous neurodegenerative diseases, such as Alzheimer's, Parkinson's, and Huntington's disease. NMR spectroscopy has been an important technique to study protein folding where valuable insights are gained into many aspects of the folding process (Jane Dyson and Wright, 1996).

In this Encyclopedia, we strive to present a taste of all the developments in CMP described above (and much more), written by experts in the field. We are keenly aware that many important and interesting topics are not covered here. However, that is not for want of trying. As some authors had rightly pointed out (Hoddeson, 1992): The field is huge and varied and lacks the unifying features beloved of historians, neither a single hypothesis or set of basic equations underpin the field, as in quantum mechanics or relativity theory, nor a single spectacular and fundamental discovery such as uranium fission for nuclear technology or the structure of DNA for molecular biology. CMP owes what unity it has simply to a common concern with solid and liquid materials. This encompasses such a large range of theories and methods that the field resembles a confederation of interest groups rather than a single entity. Clearly, the task of collecting everything in one place is a monumental endeavor, but we do hope that our compilation of a large number of chapters in this five-volume work, covering a broad range of in-depth descriptions of varied phenomena in CMP will be a treasured source of facts and ideas for the community.

It is undeniably true that there would have been no Encyclopedia without the extraordinary contributions of the large number of authors whose valuable time and efforts brought this project to fruition. My sincere thanks to all of them. I also wish to extend my deep appreciation to the staff at Elsevier for their skillful handling of this huge project. The cover image was created by Hong-Yi Chen from National Taiwan Normal University. The image below was created by Elisabetta Collini, one of the authors. My deepest appreciation to them for taking the time to do this work. Finally, my sincere thanks to the Section editors, Vladimir Fomin, Ana Sanchez, Roberto Raimondi, Hideo Aoki, Rudolf Römer, and Robert Blick for the effort they all expended, that has contributed to the success of this venture. Special thanks go to Vladimir Fomin and Ana Sanchez for securing a large share of the chapters and for their enduring help in providing valuable advice and support to bring the project to fruition. Thanks are also due to many of my friends and colleagues, in particular, Michael Coey, Jürg Fröhlich, Sinéad Griffin, Peter Maksym, Eric Vincent, and Jakob Yngvason for their careful and critical reading of the introduction.

Tapash Chakraborty
St. Catharines
Ontario, Canada

References

Abergel DSL, Apalkov V, Berashevich J, Ziegler K, and Chakraborty T (2010) Properties of graphene: A theoretical perspective. *Advances in Physics* 59: 261. https://doi.org/10.1080/00018732.2010.487978.

Andriuschenko P, Kapitan D, and Kapitan V (2022) A new look at the spin glass problem from a deep learning perspective. *Entropy* 24: 697. https://doi.org/10.3390/e24050697.

Apalkov VM and Chakraborty T (2006) Fractional quantum Hall states of Dirac electrons in graphene. *Physical Review Letters* 97: 126801. https://doi.org/10.1103/PhysRevLett.97.126801.

Apalkov VM and Chakraborty T (2010) Controllable driven phase transitions in fractional quantum Hall states in bilayer graphene. *Physical Review Letters* 105: 036801. https://doi.org/10.1103/PhysRevLett.105.036801.

Apalkov VM and Chakraborty T (2011) Stable pfaffian state in bilayer graphene. *Physical Review Letters* 107: 186803. https://doi.org/10.1103/PhysRevLett.107.186803.

Arovas D, Schrieffer JR, and Wilczek F (1984) Fractional statistics and the quantum Hall effect. *Physical Review Letters* 53: 722. https://doi.org/10.1103/PhysRevLett.53.722.

Avila A and Jitomirskaya S (2006) Solving the ten martini problem. *Lecture Notes in Physics* 690: 5. https://doi.org/10.1007/3-540-34273-7_2.

Baity-Jesi M, et al. (2023) Memory and rejuvenation effects in spin glasses are governed by more than one length scale. *Nature Physics* 19: 978–985. https://doi.org/10.1038/s41567-023-02014-6.

Baker M and Glashow SL (1962) Spontaneous breakdown of elementary particle symmetries. *Physics Review* 128: 2462. https://doi.org/10.1103/PhysRev.128.2462.

Ball P (2011) Physics of life: The dawn of quantum biology. *Nature* 474: 272. https://doi.org/10.1038/474272a.

Baltz V, et al. (2018) Antiferromagnetic spintronics. *Reviews of Modern Physics* 90: 015005. https://doi.org/10.1103/RevModPhys.90.015005.

Bartolomei H, et al. (2020) Fractional statistics in anyon collisions. *Science* 368: 173. https://doi.org/10.1126/science.aaz5601.

Biss H, et al. (2022) Excitation spectrum and superfluid gap of an ultracold Fermi gas. *Physical Review Letters* 128: 100401. https://doi.org/10.1103/PhysRevLett.128.100401.

Blanpied WA (1972) Satyendranath Bose: Co-founder of quantum statistics. *American Journal of Physics* 40: 1212. https://doi.org/10.1119/1.1986805.

Blundell S (2001) *Magnetism in Condensed Matter*. New York: Oxford U.P.

Bose SN (1924) Plancks gesetz und lichtquantenhypothese. *Zeitschrift für Physik* 26: 178. https://doi.org/10.1007/BF01327326.

Bouchaud J-P, Dupuis V, Hammann J, and Vincent E (2001) Separation of time and length scales in spin glasses: Temperature as a microscope. *Physical Review B* 65: 024439. https://doi.org/10.1103/PhysRevB.65.024439.

Bourzac K (2013) Quantum dots go on display. *Nature* 493: 283. https://doi.org/10.1038/493283a.

Brataas A, Kent AD, and Ono H (2012) Current-induced torques in magnetic materials. *Nature Materials* 11: 372. https://doi.org/10.1038/nmat3311.

Braun E and Keren K (2004) From DNA to transistors. *Advances in Physics* 53: 441. https://doi.org/10.1080/00018730412331294688.

Bruchez MP and Holz CZ (2007) *Quantum Dots: Applications in Biology*. New Jersey: Humana Press. https://doi.org/10.1385/1597453692.

Cao Y, et al. (2018) Unconventional superconductivity in magic-angle graphene superlattices. *Nature* 556: 43. https://doi.org/10.1038/nature26160.

CERN. (1977) Gauge theories with the lid, partially, off. *CERN Courier* 17: 271. https://cds.cern.ch/record/1730245/files/vol17-issue9-p271-e.pdf.

Chaikin PM and Lubensky TC (1995) *Principles of Condensed Matter Physics*. Cambridge University Press. https://doi.org/10.1017/CBO9780511813467.

Chakraborty T (1985) Elementary excitations in the fractional quantum Hall effect. *Physical Review B* 31: 4026. https://doi.org/10.1103/PhysRevB.31.4026.

Chakraborty T (1999) *Quantum Dots: A Survey of the Properties of Artificial Atoms*. Amsterdam: North-Holland. https://doi.org/10.1016/B978-0-444-50258-2.X5000-7.

Chakraborty T (2003) Nanoscopic quantum rings: A new perspective. *Advances in Solid State Physics* 43: 79. https://doi.org/10.1007/978-3-540-44838-9_6.

Chakraborty T (ed.) (2007) *Charge Migration in DNA*. Springer. https://doi.org/10.1007/978-3-540-72494-0.

Chakraborty T (2022) *Nanoscale Quantum Materials: Musings on the Ultra-Small World*. CRC Press. https://doi.org/10.1201/9781003090908.

Chakraborty T and Apalkov VM (2015) Fractal butterflies of Dirac fermions in monolayer and bilayer graphene. *IET Circuits, Devices and Systems* 9: 19. https://doi.org/10.1049/iet-cds.2014.0275.

Chakraborty T and Pietiläinen P (1988) *The Fractional Quantum Hall Effect*. Springer Verlag. https://doi.org/10.1007/978-3-642-97101-3.

Chakraborty T and Pietiläinen P (1995) *The Quantum Hall Effects*, 2nd. Springer. https://doi.org/10.1007/978-3-642-79319-6.

Chakraborty T and Pietiläinen P (2005) Optical signatures of spin-orbit interaction effects in a parabolic quantum dot. *Physical Review Letters* 95: 136603. https://doi.org/10.1103/PhysRevLett.95.136603.

Chan HS and Dill KA (1993) The protein folding problem. *Physics Today* 46: 24. https://doi.org/10.1063/1.881371.

Clark R and Maksym P (1989) Fractional quantum Hall effect in a spin. *Physics World* 2: 39. https://doi.org/10.1088/2058-7058/2/9/23.

Cohen ML (2008) Fifty years of condensed matter physics. *Physical Review Letters* 101: 250001. https://doi.org/10.1103/PhysRevLett.101.250001.

Dahm R (2005) Friedrich miescher and the discovery of DNA. *Developmental Biology* 278: 274. https://doi.org/10.1016/j.ydbio.2004.11.028.

Dill KA and MacCallum JL (2012) The protein-folding problem, 50 years on. *Science* 338: 1042. https://doi.org/10.1126/science.1219021.

Echenique P (2007) Introduction to protein folding for physicists. *Contemporary Physics* 48: 81. https://doi.org/10.1080/00107510701520843.

Editorial (2022) New horizons in spintronics. Nature Materials 21: 1. https://doi.org/10.1038/s41563-021-01184-z.

Eisenstein JP and Stormer HL (1990) The fractional quantum Hall effect. *Science* 248: 1510. https://doi.org/10.1126/science.248.4962.1510.

Folland GB (2008) *Quantum Field Theory: A tourist guide for Mathematicians*. American Mathematical Society. https://doi.org/10.1090/surv/149.

Fradkin E (2013) *Field Theories of Condensed Matter Physics*. Cambridge University Press. https://doi.org/10.1017/CBO9781139015509.

Frank-Khamenetskii MD (1997) *Unraveling DNA: The Most Important Molecule of life*. Basic Books.

Freeman AJ (2002) Materials by design and the exciting role of quantum computation/simulation. *Journal of Computational and Applied Mathematics* 149: 27. https://doi.org/10.1016/S0377-0427(02)00519-8.

Fubini S (1974) Present trends in particle physics. In: *Proc. Intl. Conf. on High Energy Physics*. Didcot, England: Rutherford Laboratory. https://cds.cern.ch/record/417271/files/CM-P00060491.pdf.

Gaudenzi R (2022) *Historical Roots of Spontaneous Symmetry Breaking: Steps Towards an Analogy*. Springer. https://doi.org/10.1007/978-3-030-99895-0.

Georgescu I (2020) 25 Years of BEC. *Nature Reviews Physics* 2: 396. https://doi.org/10.1038/s42254-020-0211-7.

Gomes CM and Faísca PFN (2019) *Protein Folding: An Introduction*. Springer. https://doi.org/10.1007/978-3-319-00882-0_1.

Halperin BI (1983) Theory of the quantized Hall conductance. *Helvetica Physica Acta* 56: 75. https://doi.org/10.5169/seals-115362.

Halperin BI (1984) Statistics of quasiparticles and the hierarchy of fractional quantized Hall states. *Physical Review Letters* 52: 1583. https://doi.org/10.1103/PhysRevLett.52.1583.

Harper PG (1955) Single band motion of conduction electrons in a uniform magnetic field. *Proceedings of the Physical Society. Section A* 68: 874. https://doi.org/10.1088/0370-1298/68/10/304.

Hartmann U (2000) *Magnetic Multilayers and Giant Magnetoresistance: Fundamentals and Industrial Applications*. Berlin: Springer Verlag. https://doi.org/10.1007/978-3-662-04121-5.

Heisenberg W (1928) Zur theorie des ferromagnetismus. *Zeitschrift für Physik* 49: 619. https://doi.org/10.1007/BF01328601.

Hoddeson L (1992) *Out of the Crystal Maze: Chapters From the History of Solid-State Physics*. N.Y.: Oxford University Press.

Hofstadter D (1976) Energy levels and wave functions of Bloch electrons in rational and irrational magnetic fields. *Physical Review B* 14: 2239. https://doi.org/10.1103/PhysRevB.14.2239.

Hosono H, et al. (2018) Recent advances in iron-based superconductors toward applications. *Materials Today* 21: 278. https://doi.org/10.1016/j.mattod.2017.09.006.

Jane Dyson H and Wright PE (1996) Insights into protein folding from NMR. *Annual Review of Physical Chemistry* 47: 369. https://doi.org/10.1146/annurev.physchem.47.1.369.

Jiang Z, et al. (2007) Quantum Hall effect in graphene. *Solid State Communications* 143: 14. https://doi.org/10.1016/j.ssc.2007.02.046.

Joh YG, Orbach R, Wood JJ, Hammann J, and Vincent E (1999) Extraction of the spin glass correlation length. *Physical Review Letters* 82: 438. https://doi.org/10.1103/PhysRevLett.82.438.

Jumper J, et al. (2021) Highly accurate protein structure prediction with alphafold. *Nature* 596: 583. https://doi.org/10.1038/s41586-021-03819-2.

Kallio A and Smith RA (1977) How simple can HNC be and still be right? *Physics Letters B* 68: 315. https://doi.org/10.1016/0370-2693(77)90483-X.

Kibble T and Srivastava A (2013) Condensed matter analogues of cosmology. *Journal of Physics. Condensed Matter* 25: 400301. https://doi.org/10.1088/0953-8984/25/40/400301.

Klug A (2004) The discovery of the DNA double helix. *Journal of Molecular Biology* 335: 3. https://doi.org/10.1016/j.jmb.2003.11.015.

Lam PM, Clark JW, and Ristig ML (1977) Density matrix and momentum distribution of helium liquids and nuclear matter. *Physical Review B* 16: 222. https://doi.org/10.1103/PhysRevB.16.222.

Lantto LJ, Jackson AD, and Siemens PJ (1977) HNC variational calculations of boson matter. *Physics Letters B* 68: 311. https://doi.org/10.1016/0370-2693(77)90482-8.

Laughlin RB (1983) Anomalous quantum Hall effect: An incompressible quantum fluid with fractionally charged excitations. *Physical Review Letters* 50: 1395. https://doi.org/10.1103/PhysRevLett.50.1395.

Laughlin RB (1984) Primitive and composite ground states in the fractional quantum Hall effect. *Surface Science* 142: 163. https://doi.org/10.1016/0039-6028(84)90301-7.

Laughlin RB and Pines D (2000) The theory of everything. *Proceedings of the National Academy of Sciences of the United States of America* 97: 28. https://doi.org/10.1073/pnas.97.1.28.

Leggett A (1992) On the nature of research in condensed-state physics. *Foundations of Physics* 22: 221. https://doi.org/10.1007/BF01893613.

Leggett A (2018) Reflections on the past, present and future of condensed matter physics. *Science Bulletin* 63: 1019. https://doi.org/10.1016/j.scib.2018.07.004.

Leinaas JM and Myrheim J (1977) On the theory of identical particles. *Il Nuovo Cimento B* 37: 1. https://doi.org/10.1007/BF02727953.

Léonard J, et al. (2017) Monitoring and manipulating higgs and goldstone modes in a supersolid quantum gas. *Science* 358: 1415. https://doi.org/10.1126/science.aan2608.

Liao S-K, et al. (2018) Satellite-relayed intercontinental quantum network. *Physical Review Letters* 120: 030501. https://doi.org/10.1103/PhysRevLett.120.030501.

Liu X, Hao Z, Watanabe K, Taniguchi T, Halperin BI, and Kim P (2019) Interlayer fractional quantum Hall effect in a coupled graphene double layer. *Nature Physics* 15: 893. https://doi.org/10.1038/s41567-019-0546-0.

Locatelli N, Cros V, and Grollier J (2014) Spin-torque building blocks. *Nature Materials* 13: 11. https://doi.org/10.1038/nmat3823.

Lu W (2022) Quark-gluon plasma and nucleons à la Laughlin. *International Journal of Geometric Methods in Modern Physics* 19: 2250061. https://doi.org/10.1142/S021988782250061X.

Maksym P and Chakraborty T (1990) Quantum dots in a magnetic field: Role of electron-electron interactions. *Physical Review Letters* 65: 108. https://doi.org/10.1103/PhysRevLett.65.108.

Marthinsen A, et al. (2018) Goldstone-like phonon modes in a (111)-strained perovskite. *Physical Review Materials* 2: 014404. https://doi.org/10.1103/PhysRevMaterials.2.014404.

Mézard M (2022) Spin glasses and optimization in complex systems. *Europhysics News* 53: 15. https://doi.org/10.1051/epn/2022105.

Miodownik M (2014) *Stuff Matters: Exploring the Marvelous Materials That Shape Our Man-Made World*. N.Y.: Houghton Mifflin Harcourt.

Morf R and Halperin BI (1986) Monte Carlo evaluation of trial wave functions for the fractional quantized Hall effect: Disk geometry. *Physical Review B* 33: 2221. https://doi.org/10.1103/PhysRevB.33.2221.

Mourino MR (1991) From thales to lauterbur, or from the loadstone to MR imaging: Magnetism and medicine. *Radiology* 180: 593. https://doi.org/10.1148/radiology.180.3.1871268.

Müller KA and Bednorz JG (1987) The discovery of a class of high-temperature superconductors. *Science* 237: 1133. https://doi.org/10.1126/science.237.4819.1133

Mustafa MG (2023) An introduction to thermal field theory and some of its application. *The European Physical Journal Special Topics* 232: 1369–1457. https://doi.org/10.1140/epjs/s11734-023-00868-8.

Mydosh JA (1993) *Spin Glasses: An Experimental Introduction*. CRC Press.

Nakamura J, et al. (2020) Direct observation of anyonic braiding statistics. *Nature Physics* 16: 931. https://doi.org/10.1038/s41567-020-1019-1.

Nambu Y (2009) Nobel lecture: Spontaneous symmetry breaking in particle physics: A case of cross fertilization. *Reviews of Modern Physics* 81: 1015. https://doi.org/10.1103/RevModPhys.81.1015.

Nasser R, Dignon GL, Razban RM, and Dill KA (2021) The protein folding problem: The role of theory. *Journal of Molecular Biology* 433: 167126. https://doi.org/10.1016/j.jmb.2021.167126.

Nawrocki W (2019) *Introduction to Quantum Metrology*, 2nd. Springer. https://doi.org/10.1007/978-3-030-19677-6.

Nowak AL, et al. (2014) Deterministic and electrically tunable bright single-photon source. *Nature Communications* 5: 3240. https://doi.org/10.1038/ncomms4240.

Obermair GM and Wannier GH (1976) Bloch electrons in magnetic fields: Rationality, irrationality, degeneracy. *Physica Status Solidi (B)* 76: 217. https://doi.org/10.1002/pssb.2220760122.

Osadchy D and Avron JE (2001) Hofstadter butterfly as quantum phase diagram. *Journal of Mathematical Physics* 42: 5665. https://doi.org/10.1063/1.1412464.

Parisi G (2023) *In a Flight of Starlings: The Wonders of Complex Systems*. Penguin Press.

Perrakis A and Sixma TK (2021) Ai revolutions in biology. *EMBO Reports* 22: e54046. https://doi.org/10.15252/embr.202154046.

Pietiläinen P and Chakraborty T (2006) Energy levels and magneto-optical transitions in parabolic quantum dots with spin-orbit coupling. *Physical Review B* 73: 155315. https://doi.org/10.1103/PhysRevB.73.155315.

Pinarbasi M and Kent AD (2022) Perspectives on spintronics technology: Giant magnetoresistance to spin transfer torque magnetic random access memory. *APL Materials* 10: 020901. https://doi.org/10.1063/5.0075945.

Recio I and Torres JJ (2016) Emergence of low noise frustrated states in E/I balanced neural networks. *Neural Networks* 84: 91. https://doi.org/10.1016/j.neunet.2016.08.010.

Refregier P, Vincent E, Hammann J, and Ocio M (1987) Ageing phenomena in a spin-glass: Effect of temperature changes below Tg. *Journal of Physics (France)* 48: 1533. https://doi.org/10.1051/jphys:019870048090153300.

Ristig ML and Clark JW (1976) Density matrix of quantum fluids. *Physical Review B* 14: 2875. https://doi.org/10.1103/PhysRevB.14.2875.

Rogalla H and Kes PH (2012) *100 Years of Superconductivity*. Boca Raton: Taylor & Francis Group. https://doi.org/10.1201/b11312.

Schutz K and Zurek KM (2016) Detectability of light dark matter with superfluid helium. *Physical Review Letters* 117: 121302. https://doi.org/10.1103/PhysRevLett.117.121302.

Shields AJ, et al. (2000) Detection of single photons using a field-effect transistor gated by a layer of quantum dots. *Applied Physics Letters* 103: 3673. https://doi.org/10.1063/1.126745.

Steptoe A (1986) Mozart, mesmer and ‘cosi fan tutte’. *Musics and Letters* 67: 248. https://doi.org/10.1093/ml/67.3.248.

Störmer HL (1992) Two-dimensional electron correlation in high magnetic fields. *Physica B: Condensed Matter* 177: 401. https://doi.org/10.1016/0921-4526(92)90138-I.

Tanford C and Reynolds J (2001) *Nature’s Robots: A History of Proteins*. Oxford University Press.

Taniguchi M and Kawai T (2006) Dna electronics. *Physica E: Low-dimensional Systems and Nanostructures* 33: 1. https://doi.org/10.1016/j.physe.2006.01.005.

Thess A, et al. (2021) Historic nucleic acids isolated by Friedrich Miescher contain RNA beside DNA. *Biological Chemistry* 402: 1179. https://doi.org/10.1515/hsz-2021-0226.

Tinkham M (2004) *Introduction to Superconductivity*. N.Y.: Dover.

Tomczyk H (2022) Did Einstein predict Bose-Einstein condensation? *Studies in History and Philosophy of Science* 93: 30. https://doi.org/10.1016/j.shpsa.2022.02.014.

Vallone M (2019) Higgs and goldstone modes in crystalline solids. *Physica Status Solidi* 257: 1900443. https://doi.org/10.1002/pssb.201900443.

Van Vleck JH (1978) Quantum mechanics—The key to understanding magnetism. *Reviews of Modern Physics* 50: 181. https://doi.org/10.1103/RevModPhys.50.181.

Vincent E (2023) Rejuvenated but remembering. *Nature Physics* 19: 926–927. https://doi.org/10.1038/s41567-023-02097-1.

Volovik GE (2009) *The Universe in a Helium Droplet*. Oxford University Press. https://doi.org/10.1093/acprof:oso/9780199564842.001.0001.

von Klitzing K (2019) Essay: Quantum Hall effect and the new international system of units. *Physical Review Letters* 122: 200001. https://doi.org/10.1103/PhysRevLett.122.200001.

von Klitzing K, Chakraborty T, Kim P, Madhavan V, Dai X, McIver J, Tokura Y, Savary L, Smirnova D, Rey AM, Felser C, Gooth J, and Qi X (2020) 40 years of the quantum Hall effect. *Nature Reviews Physics* 2: 397. https://doi.org/10.1038/s42254-020-0209-1.

Watson JD and Crick FHC (1953) Molecular structure of nucleic acids. *Nature* 171: 737. https://doi.org/10.1038/171737a0.

Weinberg S (1986) Superconductivity for particular theorists. *Progress of Theoretical Physics Supplement* 86: 43. https://doi.org/10.1143/PTPS.86.43.

Weintraub R (2012) What can we learn from Buridan’s ass? *Canadian Journal of Philosophy* 42: 281. https://doi.org/10.1353/cjp.2012.0013.

Weiss D (2013) The butterfly emerges. *Nature Physics* 9: 395. https://doi.org/10.1038/nphys2680.

Wolynes PG and Eaton WA (1999) The physics of protein folding. *Physics World* 12: 39. https://doi.org/10.1088/2058-7058/12/9/24.

Yamaguchi A, Hirohata A, and Stadler BJH (2021) *Nanomagnetic Materials: Fabrication, Characterization and Application*. Elsevier. (Chapter 5). https://doi.org/10.1016/C2018-0-05445-6.

This page intentionally left blank

LIST OF CONTRIBUTORS FOR VOLUME 3

Kyosuke Adachi
RIKEN Center for Biosystems Dynamics Research, Kobe, Japan; RIKEN InterdisciplinaryTheoretical and Mathematical Sciences Program, Wako, Japan

Jimmie Adriazola
Department of Physics, New Jersey Institute of Technology, Newark, NJ, United States

M Agio
Università degli Studi di Pavia, Pavia, Italy

Farzin Akbar
Micro- and NanoBiomedical Engineering Group (MNBE), Institute for Integrative Nanosciences, Leibniz Institute for Solid State and Materials Research (IFW), Dresden, Germany

M-C Amann
Technische Universität Munchen, Garching, Germany

LC Andreani
Università degli Studi di Pavia, Pavia, Italy

SN Aqida
Automotive Engineering Centre, Universiti Malaysia Pahang, Pekan, Pahang, Malaysia

Giorgio Baccarani
Department of Electrical Electronic and Information Engineering (DEI), and Advanced Research Center on Electronic Systems E. de Castro (ARCES), University of Bologna, Bologna, Italy

M Basini
Department of Physics, Stockholm University, Stockholm, Sweden

J Bass
Michigan State University, East Lansing, MI, United States

K Behnia
Ecole Supérieure de Physique et de Chimie Industrielles, Paris, France

Antonio Bianconi
Institute of Crystallography, CNR, Rome, Italy; RICMASS Rome International Center for Materials Science, Rome, Italy

Christopher Bolton
Department of Physics, New Jersey Institute of Technology, Newark, NJ, United States

D Bossini
Department of Physics and Center for Applied Photonics, University of Konstanz, Konstanz, Germany

K Bowman
Purdue University, West Lafayette, IN, USA

Stéphane Brûlé
Aix-Marseille Université, CNRS, Centrale Marseille, Institut Fresnel, Marseille, France

Gaetano Campi
Institute of Crystallography, CNR, Rome, Italy

A Cano
Université Grenoble Alpes, CNRS, Institut Néel, Grenoble, France

David Castellanos Robles
Micro- and NanoBiomedical Engineering Group (MNBE), Institute for Integrative Nanosciences, Leibniz Institute for Solid State and Materials Research (IFW), Dresden, Germany

Tapash Chakraborty
Department of Physics, Brock University, St. Catharines, ON, Canada; Department of Physics and Astronomy, University of Manitoba, Winnipeg, MB, Canada

JR Chelikowsky
University of Texas at Austin, Austin, TX, USA

Kikuo Cho
Emeritus of Osaka University, Kobe, Japan

Alexander T Clark
Department of Physics, New Jersey Institute of Technology, Newark, NJ, United States

John W Clark
Department of Physics, Washington University, St. Louis, MI, United States; Centro de Investigação em Matemática e Aplicações, University of Madeira, Funchal, Portugal

Rosa Córdoba
Institute of Molecular Science, University of Valencia, Paterna, Spain

Francisco AG de Lira
Department of Physics, Federal University of Maranhão, São Luís, Maranhão, Brazil

Alexander L Efros
Center for Computational Material Science, Naval Research Laboratory, Washington, DC, United States

Christoph Eigen
Cavendish Laboratory, University of Cambridge, Cambridge, United Kingdom

NG Einspruch
University of Miami, Coral Gables, FL, USA

SR Elliott
University of Cambridge, Cambridge, United Kingdom

Stefan Enoch
Aix-Marseille Université, CNRS, Centrale Marseille, Institut Fresnel, Marseille, France

Leonardo Fallani
Department of Physics and Astronomy, University of Florence, Florence, Italy; LENS European Laboratory for Nonlinear Spectroscopy, Firenze, Italy

John F Federici
Department of Physics, New Jersey Institute of Technology, Newark, NJ, United States

AM Finkel'stein
Department of Condensed Matter Physics, The Weizmann Institute of Science, Rehovot, Israel; Department of Physics and Astronomy, Texas A&M University, College Station, TX, United States

Paola Gallo
Dipartimento di Matematica e Fisica, Università "Roma Tre", Roma, Italy

Jorge M García
Instituto de Micro y Nanotecnología, IMN-CNM, CSIC, (CEI UAM+CSIC), Isaac Newton, Madrid, Spain

Ian Gatley
Department of Physics, New Jersey Institute of Technology, Newark, NJ, United States

Samuel Gatley
Department of Physics, New Jersey Institute of Technology, Newark, NJ, United States

Elena Gnani
Department of Electrical Electronic and Information Engineering (DEI), and Advanced Research Center on Electronic Systems E. de Castro (ARCES), University of Bologna, Bologna, Italy

M Goerdeler
Institut für Metallkunde und Metallphysik, Aachen, Germany

H Julian Goldsmid
School of Physics, University of New South Wales, Sydney, NSW, Australia

G Gottstein
Institut für Metallkunde und Metallphysik, Aachen, Germany

M Grundmann
Universität Leipzig, Leipzig, Germany

Sébastien Guenneau
The Blackett Laboratory, Department of Physics, Imperial College, London, United Kingdom

Ralf Hielscher
Fakultät für Mathematik, Technische Universität Chemnitz, Chemnitz, Germany

Y Hirayama
NTT Basic Research Laboratories, Kanagawa, Japan

Massimo Inguscio
LENS European Laboratory for Nonlinear Spectroscopy, Firenze, Italy; Campus Bio-Medico University of Rome, Rome, Italy

Hajime Ishihara
Department of Materials Engineering Science, Osaka University, Osaka, Japan; Center for Quantum Information and Quantum Biology, Osaka University, Osaka, Japan

EL Ivchenko
Ioffe Institute, Russian Academy of Sciences, St. Petersburg, Russia

Yoshihiro Iwasa
Department of Applied Physics and Quantum-Phase Electronics Center, The University of Tokyo, Tokyo, Japan; RIKEN Center for Emergent Matter Science, Wako, Japan

Wataru Izumida
Tohoku University, Sendai, Japan

Alexey Kavokin
International Center for Polaritonics, School of Science, Westlake University, Hangzhou, Zhejiang Province, China; Russian Quantum Center, Skolkovo, Moscow Region, Russia; Moscow Institute of Physics and

Technology, Institutskiy Pereulok, Dolgoprudny, Moscow Oblast, Russia

AV Kimel
Institute for Molecules and Materials, Radboud University, Nijmegen, The Netherlands

Albert Kirakosyan
Department of Solid State Physics, Yerevan State University, Yerevan, Armenia

D Klenam
Academic Development Unit & School of Chemical and Metallurgical Engineering, University of the Witwatersrand, Johannesburg, South Africa

Alexander M Korsunsky
Trinity College, Oxford, United Kingdom

EE Krasovskii
Donostia International Physics Center DIPC, P. Manuel de Lardizabal 4, San Sebastián, Spain; Departamento de Polímeros y Materiales Avanzados: Física, Química y Tecnología, Universidad del Pais Vasco/Euskal Herriko Unibertsitatea, Donostia-San Sebastián, Spain; IKERBASQUE, Basque Foundation for Science, Bilbao, Spain

Wolfgang Lang
Faculty of Physics, University of Vienna, Vienna, Austria

Fabrice P Laussy
Faculty of Science and Engineering, University of Wolverhampton, Wolverhampton, United Kingdom; Russian Quantum Center, Skolkovo, Moscow Region, Russia

Jean-Pierre Leburton
University of Illinois at Urbana-Champaign, Urbana, IL, United States

AP Levanyuk
Department of Physics, University of Washington, Seattle, WA, United States

A-M Leventi-Peetz
Federal Office for Information Security (BSI), Bonn, Germany

R Livi
Dipartimento di Fisica e Astronomia, Università di Firenze and Sezione INFN di Firenze, Sesto Fiorentino, Italy; ISC-CNR, Sesto Fiorentino, Italy

AC Lund
Massachusetts Institute of Technology, Cambridge, MA, USA

Wenchen Luo
School of Physics and Electronics & Hunan Key Laboratory of Nanophotonics and Devices, Central South University, Changsha, China

LB Ma
Institute for Integrative Nanosciences, Leibniz IFW Dresden, Dresden, Germany

J Maier
Physical Chemistry of Solids, Max Planck Institute for Solid State Research, Stuttgart, Germany

Aram Manaselyan
Department of Solid State Physics, Yerevan State University, Yerevan, Armenia

Euclydes Marega Jr
Instituto de Física de São Carlos, Universidade de São Paulo, São Carlos, SP, Brazil

G Mattei
CNR, Istituto dei Sistemi Complessi, Rome, Italy

JD Maynard
The Pennsylvania State University, University Park, PA, United States

F McBagonluri
Department of Mechanical Engineering, Academic City University College, Accra, Ghana

Mariana Medina-Sánchez
Micro- and NanoBiomedical Engineering Group (MNBE), Institute for Integrative Nanosciences, Leibniz Institute for Solid State and Materials Research (IFW), Dresden, Germany; Chair of Micro- and NanoSystems, Center for Molecular Bioengineering (B CUBE), Dresden University of Technology, Dresden, Germany

Vram Mughnetsyan
Department of Solid State Physics, Yerevan State University, Yerevan, Armenia

Yuli V Nazarov
Department of QuantumNanoscience, Kavli Institute of Nanoscience, Delft University of Technology, The Netherlands

David Neilson
CMT Group, Department of Physics, University of Antwerp, Antwerp, Belgium; ARC Centre of Excellence for Future Low Energy Electronics Technologies, School of Physics, The University of New South Wales, Sydney, NSW, Australia

Jessy Nemati
Department of Physics, New Jersey Institute of Technology, Newark, NJ, United States

Yoji Ohashi
Department of Physics, Keio University, Yokohama, Japan

Michael O'Donovan
Photonics Theory Group, Tyndall National Institute, Cork, Ireland; School of Physics, University College Cork, Cork, Ireland

Eoin P O'Reilly
Photonics Theory Group, Tyndall National Institute, Cork, Ireland; School of Physics, University College Cork, Cork, Ireland

J M Parker
Department of Materials Science and Engineering, Sheffield University, Sheffield, United Kingdom

G Pastore
Dipartimento di Fisica, Università di Trieste, Trieste, Italy

Shenglin Peng
School of Information Science and Technology, Northwest University, Xi'an, China

Luís Fernando C Pereira
Department of Physics, Federal University of Maranhão, São Luís, Maranhão, Brazil

Jan Petzelt
Institute of Physics, Czech Academy of Sciences, Prague, Czech Republic

GVSS Prasad
Institut für Metallkunde und Metallphysik, Aachen, Germany

Nick P Proukakis
Joint Quantum Centre (JQC) Durham–Newcastle, School of Mathematics, Statistics and Physics, Newcastle University, Newcastle upon Tyne, United Kingdom

Alessio Recati
Pitaevskii BEC Center, CNR-INO and Department of Physics, University of Trento, Trento, Italy

Gregory S Rohrer
Department of Materials Science and Engineering, Carnegie Mellon University, Pittsburgh, PA, United States

Rudolf A Römer
Department of Physics, University of Warwick, Coventry, West Midlands, United Kingdom

Mauro Rovere
Dipartimento di Matematica e Fisica, Università "Roma Tre", Roma, Italy

Ivan Rychetský
Institute of Physics, Czech Academy of Sciences, Prague, Czech Republic

W Schattke
Donostia International Physics Center DIPC, P. Manuel de Lardizabal 4, San Sebastián, Spain; Institut für Theoretische Physik und Astrophysik der Christian-Albrechts-Universität, Leibnizstraße 15, Kiel, Germany

CA Schuh
Massachusetts Institute of Technology, Cambridge, MA, USA

Stefan Schulz
Photonics Theory Group, Tyndall National Institute, Cork, Ireland; School of Physics, University College Cork, Cork, Ireland

G Schwiete
Department of Physics and Astronomy, The University of Alabama, Tuscaloosa, AL, United States

Armen Sedrakian
Frankfurt Institute for Advanced Studies, Frankfurt am Main, Germany; Institute of Theoretical Physics, University of Wroclaw, Wroclaw, Poland

F Seitz
Rockefeller University, New York, NY, USA

V Silkin
Donostia International Physics Center DIPC, P. Manuel de Lardizabal 4, San Sebastián, Spain; Departamento de Polímeros y Materiales Avanzados: Física, Química y Tecnología, Universidad del Pais Vasco/Euskal Herriko Unibertsitatea, Donostia-San Sebastián, Spain; IKERBASQUE, Basque Foundation for Science, Bilbao, Spain

Edilberto O Silva
Department of Physics, Federal University of Maranhão, São Luís, Maranhão, Brazil

Robert P Smith
Clarendon Laboratory, University of Oxford, Oxford, United Kingdom

W Soboyejo
Department of Mechanical Engineering, Worcester Polytechnic Institute, Worcester, MA, United States

EB Sonin
Racah Institute of Physic, Hebrew University of Jerusalem, Jerusalem, Israel

Sandro Stringari
Pitaevskii BEC Center, CNR-INO and Department of Physics, University of Trento, Trento, Italy

BA Strukov
Department of Physics, Lomonosov Moscow State University, Moscow, Russia

T Takahashi
University of Tokyo, Tokyo, Japan

Yoshiro Takahashi
Department of Physics, Graduate School of Science, Kyoto University, Kyoto City, Japan

EV Thuneberg
QTF Centre of Excellence, Department of Applied Physics, Aalto University, Espoo, Finland

V Yu Timoshenko
Faculty of Physics, Lomonosov Moscow State University, Moscow, Russia

MP Tosi
Scuola Normale Superiore, Pisa, Italy

V Unikandanunni
Department of Physics, Stockholm University, Stockholm, Sweden

M Van Rossum
IMEC, Leuven, Belgium

JW Wang
School of Electronic and Information Engineering, Harbin Institute of Technology (Shenzhen), Shenzhen, China

Nickolas Warholak
Department of Physics, New Jersey Institute of Technology, Newark, NJ, United States

Stuart I Wright
EDAX, St George, UT, United States

Michihisa Yamamoto
RIKEN Center for Emergent Matter Science, Wako, Japan

Kosuke Yoshioka
Photon Science Center, School of Engineering, The University of Tokyo, Tokyo, Japan

This page intentionally left blank

CONTENTS OF VOLUME 3

Superfluidity 1
EV Thuneberg

BEC-BCS crossover in ultracold atomic gases and neutron stars 10
Yoji Ohashi

Superconductivity and superfluidity in neutron stars 22
Armen Sedrakian and John W Clark

BEC-BCS crossover, condensed matter experiments 31
Kyosuke Adachi and Yoshihiro Iwasa

Excitonic superfluidity in electron-hole bilayer systems 38
David Neilson

Spin superfluidity 51
EB Sonin

Bose–Einstein condensation 68
Leonardo Fallani, Massimo Inguscio, Alessio Recati, and Sandro Stringari

Universality of Bose–Einstein condensation and quenched formation dynamics 84
Nick P Proukakis

Interacting Bose-condensed gases 124
Christoph Eigen and Robert P Smith

Cold-atom systems as condensed matter physics emulation 135
Yoshiro Takahashi

Ionic and mixed conductivity in condensed phases 145
J Maier

Electronic structure of liquids 161
G Pastore and MP Tosi

Supercooled liquids 171
Paola Gallo and Mauro Rovere

Glasses 181
J M Parker

Disordered solids and glasses, electronic structure of 191
SR Elliott

Acoustics: Physical principles and applications to condensed matter physics 200
JD Maynard

Numerical methods for localization 212
Rudolf A Römer

Disordered electron liquid with interactions: Theoretical aspects 220
AM Finkel'stein and G Schwiete

Basics of simulations and carrier localization effects in semiconductor materials 236
Eoin P O'Reilly, Michael O'Donovan, and Stefan Schulz

Conductivity, electrical 251
J Bass

Coulomb blockade 260
Yuli V Nazarov

Conductivity, thermal 273
K Behnia

Transport properties: Mass transport 278
R Livi

Ferroelectricity 284
AP Levanyuk, BA Strukov, and A Cano

Planar quantum dots: Theoretical approaches 297
Aram Manaselyan, Vram Mughnetsyan, and Albert Kirakosyan

Quantum dots: Optical properties 308
V Yu Timoshenko

The physics of quantum dots 325
Jean-Pierre Leburton

Self-organized semiconductor nanostructures (quantum dots, quantum rings and their arrays) 337
Euclydes Marega Jr

Optical properties in rolled-up structures 354
JW Wang and LB Ma

Nanostructured superconductors 368
Wolfgang Lang

Kondo effects in quantum dots: Theory 381
Wataru Izumida

Kondo effects in quantum dots: Experiment 388
Michihisa Yamamoto

Spin textures in quantum dots and quantum rings 400
Wenchen Luo, Shenglin Peng, and Tapash Chakraborty

Quantum rings: Electronic properties 415
Luı́s Fernando C Pereira, Francisco AG de Lira, and Edilberto O Silva

Aharonov-Bohm effect in self-assembled InAs/GaAs Quantum Rings: Fabrication, formation mechanism and optical characterization 426
Jorge M García

Superstripes landscape in perovskites high Tc superconductors 437
Gaetano Campi and Antonio Bianconi

Additive nanofabrication using focused ion and electron beams 448
Rosa Córdoba

Microstucture and macrostructure 465
Gregory S Rohrer

Structures: Orientation texture 481
Stuart I Wright and Ralf Hielscher

Nanostructures, Electronic Structure of 500
JR Chelikowsky

THz light and manipulations of matter 509
M Basini and V Unikandanunni

The importance of full-scale experiments for the study of seismic metamaterials 519
Stéphane Brûlé, Stefan Enoch, and Sébastien Guenneau

Quantum devices of reduced dimensionality 529
M Grundmann

Thermoelectric energy conversion devices 534
H Julian Goldsmid

Geometry matters: Gamete transport using magnetic microrobots 540
David Castellanos Robles, Farzin Akbar, and Mariana Medina-Sánchez

Memory devices—Non-volatile memories 552
Elena Gnani and Giorgio Baccarani

Memory devices – Volatile memories 576
Elena Gnani and Giorgio Baccarani

Residual stress and strain evaluation across the scales 592
Alexander M Korsunsky

Terahertz nondestructive evaluation of additively manufactured and multilayered structures 601
Alexander T Clark, Jessy Nemati, Christopher Bolton, Nickolas Warholak, Jimmie Adriazola, Ian Gatley, Samuel Gatley, and John F Federici

Excitons in nanoscale semiconductor structures 629
Alexander L Efros

Bose-Einstein Condensation of Excitons in a bulk semiconductor 644
Kosuke Yoshioka

Nonlocal optical response of nanostructures 653
Hajime Ishihara and Kikuo Cho

Optical properties of dielectrics and semiconductors 665
EL Ivchenko

Polarizability and its generalization 683
Kikuo Cho

Ultrafast spectroscopy of correlated materials 694
D Bossini and AV Kimel

Excitons in crystals 706
Fabrice P Laussy and Alexey Kavokin

Optical properties of surface enhanced Raman scattering 728
G Mattei and SN Aqida

Photonic Bandgap Materials, Electronic States of 739
M Agio and LC Andreani

Integrated Circuits 748
M Van Rossum

Semiconductor Devices 757
T Takahashi

Semiconductor Lasers 770
M-C Amann

Transistors 781
Y Hirayama

Silicon, History of 791
F Seitz and NG Einspruch

Local field effects 802
A-M Leventi-Peetz, EE Krasovskii, V Silkin, and W Schattke

Dielectric function 812
Jan Petzelt and Ivan Rychetský

Mechanical properties: Fatigue 818
D Klenam, F McBagonluri, and W Soboyejo

Mechanical Properties: Elastic Behavior 838
K Bowman

Mechanical Properties: Plastic Behavior 844
G Gottstein, M Goerdeler, and GVSS Prasad

Mechanical Properties: Strengthening Mechanisms in Metals 853
AC Lund and CA Schuh

Superfluidity

EV Thuneberg, QTF Centre of Excellence, Department of Applied Physics, Aalto University, Espoo, Finland

© 2024 Elsevier Ltd. All rights reserved.

This is an update of E.V. Thuneberg, Superfluidity, Editor(s): Franco Bassani, Gerald L. Liedl, Peter Wyder, Encyclopedia of Condensed Matter Physics, Elsevier, 2005, Pages 128–133, ISBN 9780123694010, https://doi.org/10.1016/B0-12-369401-9/00710-5.

Introduction 1
Occurrence 1
Microscopic origin 3
Hydrodynamics 5
Quantization of circulation 6
Rotating superfluid and vortex lines 7
Phase slip, Josephson effect and critical velocity 8
Conclusion 9
References 9

Abstract

This chapter gives an introduction to basic properties of superfluids. After defining the subject, we list systems where it occurs: liquid ^{4}He, liquid ^{3}He, dilute atomic gases, neutron stars and superconducting metals. The microscopic basis for the formation of the superfluid phase is considered in boson and fermion systems. The two-fluid model is introduced and some consequences are discussed. The quantization of circulation is presented. Quantized vortex lines are introduced and they are used to explain the structure of a rotating superfluid. Phase slip, Josephson effect and critical velocity are discussed.

Key points

- Definition of superfluidity
- Occurrence of superfluidity
- Microscopic basis of superfluidity
- Two-fluid model
- Quantized circulation, vortices and rotating superfluid
- Phase slip, Josephson effect and critical velocity

Introduction

Fluids (gases and liquids) are distinguished from solids by the property that they can flow. In almost all cases there is viscosity associated with the flow. Due to viscosity, the flow energy is gradually dissipated into heat. Contrary to this common situation, there is a special class of fluids, which can flow without viscosity. These are called superfluids and the phenomenon is called superfluidity (London, 1954; Tilley and Tilley, 1990; Guénault, 2003; Annett, 2004; Leggett, 2006; Bennemann and Ketterson, 2013; Barenghi and Parker, 2016). As a concrete example, consider a ring-shaped container filled with superfluid, see Fig. 1. Once the fluid is put into circular motion, it will continue to circulate and no energy is dissipated. The flow can continue as long as the external conditions remain unchanged, in particular the temperature is kept low enough.

Superfluids show many spectacular phenomena, which are discussed in Sections "Hydrodynamics," "Quantization of circulation," "Rotating superfluid and vortex lines," "Phase slip, Josephson effect and critical velocity." Before going into these we discuss the systems where superfluidity occurs (Section Occurrence) and the microscopic basis of superfluidity (Section Microscopic origin). While Section Microscopic origin gives deeper insight, it is not absolutely necessary for discussing the phenomena in Sections "Hydrodynamics," "Quantization of circulation," "Rotating superfluid and vortex lines," "Phase slip, Josephson effect and critical velocity."

Occurrence

Superfluidity occurs only in certain substances under special conditions. Superfluidity occurs at temperatures T below a transition temperature T_c, which strongly depends on the substance.

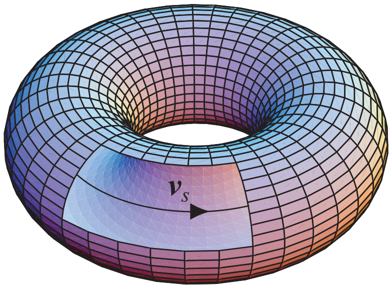

Fig. 1 Once generated, the circulation of a superfluid (with velocity v_s) persists as long as the experiment can be continued.

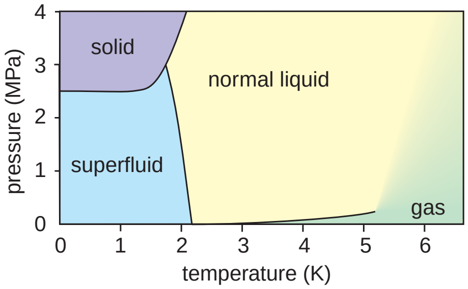

Fig. 2 Phase diagram of ^{4}He at low temperatures. ^{4}He remains liquid at zero temperature if the pressure is below 2.5 MPa (approximately 25 atm). The liquid has a phase transition to a superfluid phase, also known as He-II, at the temperature of 2.17 K (at vapor pressure).

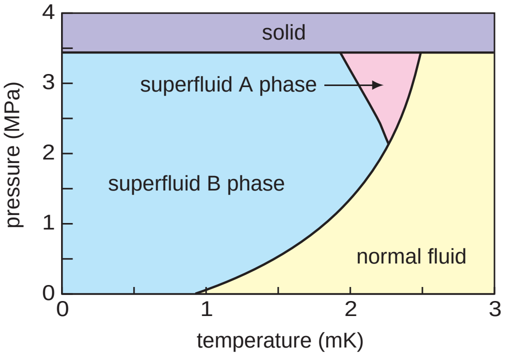

Fig. 3 The phase diagram of ^{3}He at low temperatures. Note that the temperature is in units of millikelvin, in contrast to Fig. 2. Two superfluid phases, A and B, are shown. The figure is based on data by Greywall (1986).

As a first case we discuss liquid helium. Under standard pressure and temperature helium is a gas. It liquifies at temperatures around 4 K. Cooling further down, it enters the *superfluid phase* at temperatures around 2 K, depending on pressure (Wilks, 1967). The phase diagram of natural helium at low temperatures is shown in Fig. 2. Natural helium consists essentially of isotope ^{4}He. A ^{4}He atom is a *boson* since both the electronic spin and the nuclear spin vanish. Helium was first liquefied in 1908 and the superfluid phase was discovered in 1938.

Helium has another stable isotope, ^{3}He. A ^{3}He atom is a *fermion* because the nuclear spin is 1/2. At temperatures below a few kelvin, its behavior is radically different from the isotope ^{4}He. It also becomes superfluid, but at temperatures that are a factor of one thousand smaller than for ^{4}He (Wheatley, 1975; Leggett, 1975; Vollhardt and Wölfle, 1990; Dobbs, 2001). The phase diagram of ^{3}He at low temperatures is shown in Fig. 3. ^{3}He has three different superfluid phases, A, A1, and B. The A1 phase only appears in magnetic field, and therefore is not visible in Fig. 3. Recently, also the polar phase has been demonstrated by adding dilute impurity, aerogel, into the liquid (Dmitriev et al., 2015). The superfluid phases A and B of ^{3}He were found in 1972.

With laser cooling it is possible cool certain dilute atomic gases like ^{1}H, ^{6}Li, ^{7}Li, ^{23}Na, ^{40}Ka, ^{87}Rb to very low temperatures. These gases condense to superfluid state at temperatures on the order of 1 μK, depending on the density and on atomic interactions (Pethick and Smith, 2002; Pitaevskii and Stringari, 2003; Leggett, 2006; Bloch et al., 2008). This state shows many properties that are similar to the helium superfluids, although it is not a thermodynamically stable state, and therefore the flow cannot last for ever. Most of the discussion in this article applies also to condensed gases. An important difference is that instead of container walls for helium liquids, one has to consider the confining potential of the gas, which can be generated either magnetically (by field gradients) or optically (by laser beams). The gas atoms ^{1}H, ^{7}Li, ^{23}Na, ^{87}Rb are bosons while ^{6}Li and ^{40}Ka are fermions. Superfluid condensation in a gas was first found in ^{87}Rb in 1995.

Superfluidity is expected to occur also in astrophysical objects. The neutron liquid in a neutron star is believed to be in a superfluid state (Page et al., 2014; Gezerlis et al., 2014; Chamel, 2017). Also protons in a neutron star are expected to condense to a superfluid state. Both neutrons and protons are fermions. The superfluidity has been suggested as an explanation for the observed sudden changes in the rotation velocity of pulsars.

Superfluidity is closely related to *superconductivity* (Tinkham, 1996; Bennemann and Ketterson, 2008). Superconductivity means that electric current can flow without resistance. This phenomenon appears in several elemental metals like Al, Sn, and Nb at temperatures on the order of 10 K or below. It also appears in several alloys and compounds. Superconductivity arises from resistanceless motion of the conduction electrons in a metal. Therefore, superconductivity can be understood as Superfluidity of the conduction electrons, which are fermions. Part of the discussion in this article applies also to superconductivity, but there are differences caused mainly by two reasons. (a) Electrons have electric charge and therefore their motion is essentially coupled with magnetic field. (b) The crystal lattice of the ions constitutes a preferred frame of reference, which does not exist for helium liquids. Superconductivity was first found in Mercury in 1911.

Microscopic origin

In short, superfluidity can be explained as a quantum mechanical effect that shows up on a macroscopic scale.

Quantum mechanics is crucial in understanding the microscopic world. It explains that electrons in atoms have only discrete energies. There is no friction on the atomic scale, and the electrons can circulate the nucleus without losing energy.

We know that quantum mechanics rarely shows up on macroscopic scale. Instead of quantum mechanics, macroscopic objects obey the rules of classical physics. The reason is that a macroscopic sample consists of large number of particles and, instead of individual particles, one can only observe their average behavior. Usually the particles are in different quantum states, and an average over them obeys classical laws of physics. Examples of these laws are the Navier-Stokes equations for fluids and Ohm's law for electrical conduction.

Superfluidity is an exception to this general rule. In superfluids a macroscopic number of particles is in the same quantum state. It follows that summing over particles does not lead to averaging, but produces a *macroscopic wave function*.

Consider a free particle with mass m and momentum p. Its kinetic energy is $E = p^2/2\,m$. Its state is represented by the single-particle wave function

$$\psi(\boldsymbol{r}) = \frac{1}{\sqrt{V}} \exp\left(\frac{i}{\hbar}\boldsymbol{p}\cdot\boldsymbol{r}\right), \tag{1}$$

where V is the volume of the system and $h = 2\pi\hbar$ the Planck constant. Below we also use the wave vector $\boldsymbol{k}$ so that $\boldsymbol{p} = \hbar\boldsymbol{k}$. The wave function of a many body system $\Psi\ (\boldsymbol{r}_1, \boldsymbol{r}_2, \ldots)$ is more general and depends on the coordinates $\boldsymbol{r}_i$ of all particles, $i = 1, 2, \ldots, N$, where N is the number of particles.

Further analysis depends essentially whether the particles are bosons or fermions. We now assume the particles are bosons. This means that the total wave function must be symmetric when exchanging any pair of particles. In the case of two particles this means $\Psi\ (\boldsymbol{r}_1, \boldsymbol{r}_2) = \Psi\ (\boldsymbol{r}_2, \boldsymbol{r}_1)$. Further we assume that there is no interaction between the bosons. It can be shown that the occupation of the lowest energy state becomes macroscopic, if the temperature T is less than

$$T_{BE} = \frac{h^2}{2\pi m k_B}\left(\frac{N}{2.612V}\right)^{2/3} \tag{2}$$

Here k_B the Boltzmann constant. This is known as *Bose-Einstein condensation* (BEC). The wave function (1) of the lowest energy state (p = 0) becomes macroscopic. At zero temperature, all particles are in this state. While the ideal gas model explains Bose-Einstein condensation, it is quite insufficient in other respects. The interactions between particles are essential for the system to show superfluidity (see Section "Phase slip, Josephson effect and critical velocity"). In interacting system the macroscopically occupied state $\psi(\boldsymbol{r})$ need not be the lowest energy state, and thus the macroscopic wave function can be nontrivial. In Bose gases (^{87}Rb, etc.) the interactions are weak, and a quantitative description can be achieved by the relatively simple Gross-Pitaevskii equation. In liquid ^{4}He the interactions are much stronger, and a quantitative theory is not easily achieved. But even in that case, formula (2) gives 3.1 K, which is not too far from the measured value. A simple phenomenological description of ^{4}He superfluid is obtained by considering its elementary excitations, see Fig. 4A. The excitation spectrum is liner, $E(p) = cp$ at small momenta, where c is the velocity of sound. These excitations are known as phonons. At larger momenta $E(p)$ starts to decrease and it attains a minimum. The excitations near this minimum are known as rotons. In Bose gases only phonon excitations are visible because of weaker interactions.

Let us now turn to fermions. The fermions have spin, which has to be described by an additional index σ. Here we consider only spin-half particles, where the spin projection σ takes two values, $\sigma = \pm\frac{1}{2}$. The wave function of a fermion system is $\Psi\ (\boldsymbol{r}_1, \sigma_1, \boldsymbol{r}_2, \sigma_2, \ldots)$, and it has to be antisymmetric in the exchange of any pair of particles. For a two-particle state this means

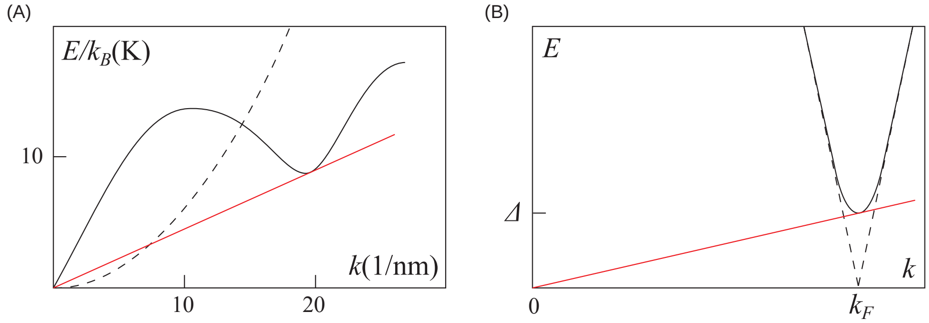

Fig. 4 The energy of elementary excitations as a function of the wave number, $E(k)$. (A) Elementary excitations in liquid ^{4}He at vapor pressure (black solid line). The free atom kinetic energy is given by dashed line. The figure is based on neutron-scattering data by Henshaw and Woods (1961). (B) Sketch of elementary excitations of a degenerate fermion system. The excitation energy in the normal state (dashed lines) vanishes at the Fermi surface, $k = k_F$. The excitations are particle type at $k > k_F$ and hole type at $k < k_F$. In the superfluid state (black solid line) an energy gap Δ opens up. For visibility of the figure, the scales are far from those ones in superconducting metals and liquid ^{3}He. In both panels the sloped straight lines (red) correspond the critical velocity according to Landau criterion (17).

$$\Psi(\boldsymbol{r}_1, \sigma_1, \boldsymbol{r}_2, \sigma_2) = -\Psi(\boldsymbol{r}_2, \sigma_2, \boldsymbol{r}_1, \sigma_1). \tag{3}$$

This implies that the occupation of any single-particle state only can be zero or one. This is known as the *Pauli exclusion principle*. Thus macroscopic occupation of a single-particle state (1) is not possible.

Superfluidity in a fermion system can appear as a result of an attractive interaction between particles. Such an interaction can cause formation of pairs. Each pair has to satisfy the antisymmetry condition (3). However, a pair is a unit that behaves like a boson. In particular, it is not excluded that several pairs are in the same pair state. Superfluidity in fermion systems can be understood as a macroscopic occupation of a single pair state. Thus superfluidity can be understood as Bose condensation of pairs.

The spin part of the pair wave function has four different possibilities. These can be classified as a singlet state

$$\uparrow\downarrow - \downarrow\uparrow \tag{4}$$

(which is a compact notation for $\delta_{\sigma 1,1/2}\,\delta_{\sigma 2,-1/2} - \delta_{\sigma 1,-1/2}\,\delta_{\sigma 2,1/2}$) and three triplet states, which can be chosen as

$$-\uparrow\uparrow + \downarrow\downarrow,\ i(\uparrow\uparrow + \downarrow\downarrow),\ \uparrow\downarrow + \downarrow\uparrow\ . \tag{5}$$

Let us first study the case of spin singlet (4). The pair wave function in this case is assumed to be of the form

$$\Psi(\boldsymbol{r}_1, \sigma_1, \boldsymbol{r}_2, \sigma_2) = \psi\left(\frac{\boldsymbol{r}_1 + \boldsymbol{r}_2}{2}\right)\chi(\boldsymbol{r}_1 - \boldsymbol{r}_2)(\uparrow\downarrow - \downarrow\uparrow) \tag{6}$$

where we have separated the orbital wave function to a center of mass part ψ and a relative part χ. The singlet spin state (4) is antisymmetric in the exchange of the two spins. In order to satisfy pair antisymmetry (3), the corresponding orbital part $\chi(\boldsymbol{r}_1 - \boldsymbol{r}_2)$ has to be symmetric, $\chi(\boldsymbol{r}) = \chi(-\boldsymbol{r})$. In most superconductors the pair wave function is of the form (6). In majority of them (Al, Sn, Nb, . . .) χ is approximately independent of the direction of $\boldsymbol{r}_1 - \boldsymbol{r}_2$. This is called s-wave pairing in analogy with *s, p, d*, etc., atomic orbitals. In high-T_c superconductors there is strong evidence of *d*-wave symmetry of χ. In Fermi gases s-wave pairing has been observed with the spin being pseudo spin formed by two atomic hyperfine states (Zwierlein, 2014).

Another alternative is that the spin state of a pair is triplet (5). This case is realized in ^{3}He and possibly in some superconductors. In ^{3}He the orbital wave function is of *p* type. There are three degenerate *p*-wave states p_x, p_y and p_z. The pair wave function can be written as

$$\Psi(\boldsymbol{r}_1, \sigma_1, \boldsymbol{r}_2, \sigma_2) = \sum_{j=1}^{3}\sum_{\mu=1}^{3}\psi_{\mu j}\left(\frac{\boldsymbol{r}_1 + \boldsymbol{r}_2}{2}\right)p_j(\boldsymbol{r}_1 - \boldsymbol{r}_2)i\hat{\sigma}_\mu\hat{\sigma}_2. \tag{7}$$

Here $i\hat{\sigma}_\mu\hat{\sigma}_2$ denotes the same three spin states as in Eq. (5), but expressed using Pauli spin matrices $\hat{\sigma}_i$.

The macroscopic wave function of bosons is called *order parameter*, since it describes ordering of the particles and it vanishes in the normal fluid phase. For fermions the same role is played by the center of mass part of the pair function. This is the soft degree of freedom, which can change as a function of time and location, whereas the other parts in the pair wave function (6)–(7) are fixed. We see that the order parameter in ^{4}He and in most superconductors is a complex-valued scalar ψ, but in ^{3}He it is a 3×3 matrix $\psi_{\mu j}$. The order parameter in condensed boson gases is a scalar in the simplest case, but including atoms in different hyperfine states allows more complicated forms. In neutron stars both spin singlet and triplet pairing has been predicted to occur.

An important energy scale in a Fermi system is *Fermi energy*. It is the energy up to which all noninteracting single particle states would be filled at zero temperature. It is $E_F = p_F^2/2m$, where the Fermi momentum p_F is related to the particle density by

$N/V = p_F^3/3\pi^2\hbar^3$. Compared with thermal energy k_BT, it corresponds to Fermi temperature $T_F = E_F / k_B$. For ^{3}He $T_F \sim 1$ K and for elemental superconductors $T_F \sim 10^4$ K. We see that for both ^{3}He and superconductors, the transition temperature is small compared to the Fermi temperature, $T_c / T_F \sim 10^{-3}$ or less. This implies that only excitations that have low energy ($\ll E_F$) close to the Fermi surface $p = p_F$ play role in Superfluidity. Such excitations are described by Landau's *Fermi liquid theory*. The normal state excitations are quasiparticles which are free-particle like and weakly interacting, see Fig. 4B. In the superfluid state pairs are formed. They are weakly bound and called Cooper pairs. The pair condensation opens an energy gap in the excitation spectrum. Quantitative theory of fermion superfluids is based on the Bardeen-Cooper-Schrieffer (BCS) theory of superconductivity (Bardeen et al., 1957). The extension to cover superfluid ^{3}He is discussed by Serene and Rainer (1983).

Above we have discussed the boson and fermion cases separately. But in fact, one can think to go continuously from one case to the other. By increasing the attractive interaction of the fermions in a Cooper pair, one could transform it to a strongly bound pair, which could be considered as a single Bose particle. This BCS-BEC crossover has been experimentally studied in fermion gases.

Hydrodynamics

Many properties of superfluids can be understood in terms of the *two-fluid* model. The basic assumption is that the liquid consists of two parts. These are called the *superfluid* and *normal components*. The current density $\boldsymbol{j}$ can be represented as a sum

$$\boldsymbol{j} = \rho_s \boldsymbol{v}_s + \rho_n \boldsymbol{v}_n. \tag{8}$$

Here ρ_s and $\boldsymbol{v}_s$ are the density and velocity of the superfluid component and ρ_n and $\boldsymbol{v}_n$ are the corresponding quantities for the normal component. The liquid density is the sum of the two densities, $\rho = \rho_s + \rho_n$. The superfluid component can flow without viscosity and it carries no heat or entropy. Moreover it is curl free,

$$\nabla \times \boldsymbol{v}_s = 0. \tag{9}$$

(This is valid only in uncharged superfluids.) The normal component behaves more like a usual viscous fluid.

The two-fluid model can be justified from the microscopic theory discussed in Section Microscopic origin. The superfluid component corresponds to particles in the macroscopic wave function, and the normal component to particles in the excited states. The densities of the two components depend on temperature. At zero temperature all particles are in the condensate, $\rho_n = 0$ and $\rho_s = \rho$. With increasing temperature more particles are excited out of the condensate to the excited states. Thus $\rho_n(T)$ grows and $\rho_s(T)$ drops, see Fig. 5. The superfluid transition T_c is the temperature at which the condensate ceases to exist, and corresponds to $\rho_s = 0$ and $\rho_n = \rho$.

In application of the two-fluid model we can distinguish two cases. Consider first the case that only the superfluid component moves, $v_n = 0$. This can be realized in the ring-shaped container (Fig. 1). Once the superfluid component is set into motion, it can

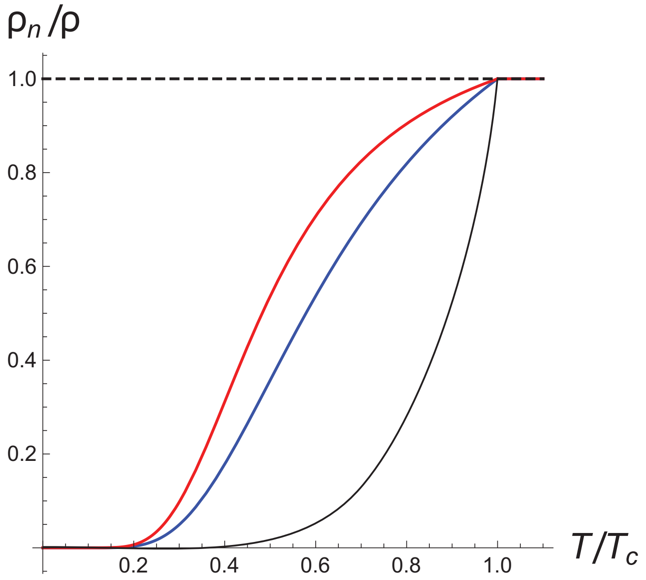

Fig. 5 The normal fluid fraction ρ_n/ρ as a function of temperature relative to T_c. The lowest curve is for superfluid ^{4}He at vapor pressure and is based on data in Peshkov (1946). The other curves are for superfluid ^{3}He-B at melting pressure (upper curve) and vapor pressure (middle curve) according to weak coupling theory (BCS theory generalized to triplet *p*-pairing and including Fermi-liquid interactions). The superfluid fraction $\rho_s/\rho = 1-\rho_n/\rho$.

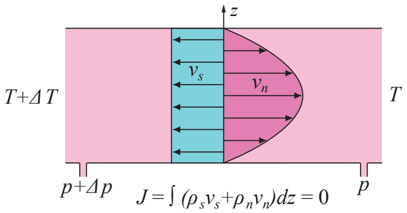

Fig. 6 A difference in temperature ΔT generates flow of normal and superfluid components in opposite directions, and a pressure difference Δp appears. The viscosity of the normal component causes v_n to vanish at walls. The superfluid velocity $v_s(z)$ has to be constant in order to be curl free (9). In a channel with closed ends the total mass flow J has to vanish.

persists because flow is ideal with no viscosity. This explains that superfluid can flow through narrow pores or as a thin film in response to small or vanishing pressure difference.

The other type of motion is that also the normal component participates in it. This takes place, for example, when an object moves in the liquid. Because of motion of the normal component, viscous forces and dissipation appear. This explains that nonvanishing viscosity is measured with a viscometer, where the superfluid is placed between two plates or coaxial cylinders that move at different velocities. The measured viscosity can still be small at low temperatures, where the normal component density is vanishingly small.

Superfluids show peculiar mixing of thermal and mechanical properties. Consider superfluid in a channel which is heated at one end, see Fig. 6. The superfluid component is attracted to the hot region because the chemical potential is lower there. As a consequence a pressure difference appears. This drives the normal component in the direction of decreasing temperature and convects the heat away from the source. Assuming the geometry does not allow net mass transfer, the mass transported by the normal and superfluid components in opposite directions are equal in magnitude. Such *counter flow* can lead to exceptionally large heat conductance.

In addition to usual sound wave, superfluids have another propagating mode. This *second sound* is an oscillation where normal and superfluid components move in opposite directions. This leads to oscillation of temperature whereas the density remains nearly constant. Second sound can be generated by heating the superfluid periodically, and standing waves of temperature have been demonstrated experimentally.

In addition to the mass current $\boldsymbol{j}$, there can be persistent spin currents. This is possible in superfluids whose order parameter is more complicated than scalar (^{3}He). Spin current is described by a tensor $j_{\mu j}{}^{\text{spin}}$ The index $\mu = x, y, z$ indicates the direction of spin angular momentum that is flowing, and $j = x; y; z$ indicates the direction of the flow. Even in equilibrium the order parameter of ^{3}He has nontrivial spatial variation called *texture*. This is associated with persistent spin currents and, in case of ^{3}He-A, also with persistent mass currents.

Quantization of circulation

Consider a superfluid with order parameter ψ. (Assume an uncharged superfluid, ψ can be either scalar or matrix.) The superfluid velocity $\boldsymbol{v}_s$ can be expressed as a function of the order parameter as

$$\boldsymbol{v}_s = \frac{\hbar}{M}\nabla\phi. \tag{10}$$

Here $\phi(\boldsymbol{r})$ is the phase of the order parameter, $\psi(\boldsymbol{r}) = Ae^{i\phi(\boldsymbol{r})}$, and the amplitude A is assumed constant. M is the boson mass, i.e., the mass of a particle in a boson superfluid and the mass of a pair in a fermion superfluid. Eq. (10) can be justified starting from the expression of current in quantum mechanics.

An alternative form of Eq. (10) is obtained by taking line integral along a closed path,

$$\oint \boldsymbol{v}_s \cdot d\boldsymbol{l} = N\frac{h}{M}. \tag{11}$$

Here we have used the property that ϕ is defined modulo 2π, and N is an integer. Eq. (11) is known as *quantization of circulation*. The curl-free condition (9) is a direct consequence of Eq. (10) or (11).

Consider again superfluid in a ring-shaped container (Fig. 1). We can apply Eq. (11) to a path in the ring. We see that, in addition to being persistent, the superfluid velocity can only have discrete values. A similar phenomenon in superconductors is *flux quantization*. It says that magnetic flux through a ring shaped superconductor is an integral multiple of flux quantum $\Phi_0 = h/2e$, where e is the elementary charge.

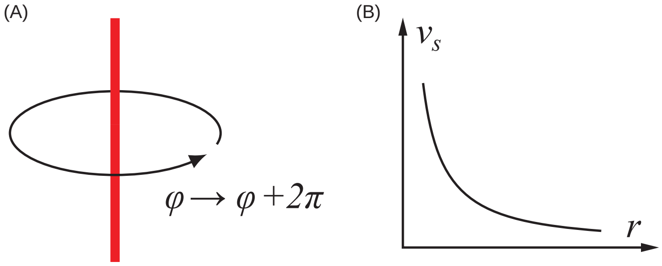

Fig. 7 (A) Schema of a vortex line, where the phase of the order parameter changes by 2π when encircling the line. (B) Dependence of the azimuthal velocity field (12) on the distance r from the vortex line.

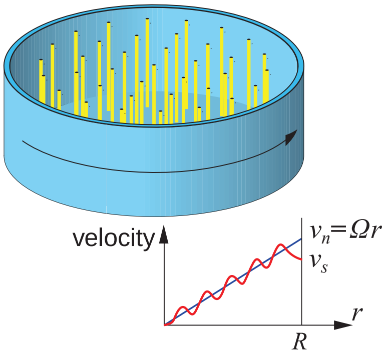

Fig. 8 In a rotating container the vortex lines form a regular array so that the superfluid and normal fluid velocities, $\boldsymbol{v}_s$ and $\boldsymbol{v}_n$, are equal on the average. In equilibrium the vortex array rotates rigidly with the container.

Rotating superfluid and vortex lines

Let us consider superfluid in a container that is rotated with angular velocity Ω. The normal component will follow this motion because of its viscosity. In equilibrium it rotates uniformly with the container, $\boldsymbol{v}_n = \boldsymbol{\Omega} \times \boldsymbol{r}$. This is not possible for the superfluid component because it has to be curl free (9). [Eq. (9) should be compared to $\nabla \times \boldsymbol{v}_n = 2\,\boldsymbol{\Omega}$.]

The rotating state of a superfluid is most commonly realized by *vortex lines* (Andronikashvili and Mamaladze, 1966; Donnelly, 1991). On a path around the vortex line, the phase ϕ changes by 2π (or an integral multiple of it). This is illustrated in Fig. 7. Equivalently, the circulation of superfluid velocity (11) around the vortex line is h/M. Assuming cylindrical symmetry, the phase ϕ is the same as the azimuthal angle in the cylindrical coordinate system (r, ϕ, z). The velocity field can be calculated from Eq. (10):

$$\boldsymbol{v}_s = \frac{\hbar}{Mr}\hat{\boldsymbol{\phi}}, \tag{12}$$

where $\widehat{\phi}$ is a unit vector in the azimuthal direction.

The structure of the rotating state is determined by minimum of free energy. The rotation of the container is taken into account by minimizing $F = F_0 - \boldsymbol{L}\cdot\boldsymbol{\Omega}$, where F_0 is the free energy functional in the stationary case and $\boldsymbol{L}$ the angular momentum. In the two-fluid model this reduces to

$$F = \int d^3r \frac{1}{2}\rho_s(\boldsymbol{v}_s - \boldsymbol{v}_n)^2 + \text{constant}. \tag{13}$$

Thus the optimal solution corresponds to $\boldsymbol{v}_s$ as equal as possible to $\boldsymbol{v}_n = \boldsymbol{\Omega} \times \boldsymbol{r}$, but subject to condition (10). This is achieved by a regular array of vortex lines, see Fig. 8. The number of vortex lines n per unit area is determined by the condition that the circulations of normal and superfluid velocities are the same over an area containing many vortex lines. This yields

$$n = \frac{2M\Omega}{h}. \tag{14}$$

There are approximately 1000 vortex lines in a circular container of radius 1 cm that is rotating 1 round per minute.

Vortex lines in an uncharged superfluid are analogous to *flux lines*, which occur in type II superconductors. Flux lines of superconductors appear in magnetic field, which is analogous to rotation of an uncharged superfluid.

The velocity field (12) of a vortex diverges at the vortex line. Thus there must be a *vortex core*, where the two-fluid description is insufficient. A finite energy in the vortex core is achieved if the amplitude of the order parameter vanishes at the vortex line. This is the case for a scalar order parameter. For a matrix order parameter it is not necessary that all components of the matrix vanish at the line. Such vortex lines are realized in superfluid ^{3}He-B.

The quantization of the superfluid velocity (11) is not always true for uncharged superfluids. This happens when there is an additional contribution to the superfluid velocity (10) coming from the matrix form of the order parameter. Such a case is realized in superfluid ^{3}He-A, and careful reanalysis of the rotating state is needed. It turns out that, in addition to one-dimensional vortex lines, the vorticity may be arranged as two-dimensional vortex sheets and three-dimensional textures. All these have been confirmed experimentally (Lounasmaa and Thuneberg, 1999). In any case, a homogeneous rotation of the superfluid is excluded. Many more topological objects in quantum liquids and their parallels in particle physics and cosmology are discussed by Volovik (2003).

Besides rotating superfluid, vortex lines appear also in other circumstances. Vortices are important in limiting the maximal flow velocity, as will be discussed in the following section. By strong mechanical driving or by large thermal counterow (Fig. 6) one can generate a large number of vortices. This is the quantum version of turbulence (Skrbek et al., 2021). In three dimensions the energy of vortex lines is high relative to the quasiparticle excitations, and therefore they are not important for thermodynamics. This changes in a thin liquid film, which forms essentially a two-dimensional system. The transition from superfluid to normal state can be seen as formation of free vortices that destroy the superfluid coherence, which is known as Kosterlitz-Thouless transition.

Phase slip, Josephson effect and critical velocity

Let us study superow in a channel under thermal equilibrium ($v_n = 0$). The maximum supercurrent is determined by a process called *phase slip*. Consider that a short piece of vortex line is nucleated at a surface on one side of the channel. This vortex expands, goes through the whole cross section of the channel, and finally disappears on the other side. As a result of this process, the phase difference $\Delta\phi$ between the ends of the channel has changed by 2π. Part of the superfluid kinetic energy is dissipated in the motion of the vortex. This means that the flow ceases to be dissipationless above a critical velocity for phase slips. Phase slips preferentially take place in constrictions of the flow channel, where the superfluid velocity has its maximum value.

A special type of phase slip takes place in very short constrictions, where Eq. (10) ceases to be valid. An ideally short constriction shows the *Josephson effect*, where the supercurrent J_s depends on the phase difference $\Delta\phi$ as

$$J_s = J_c \sin\,(\Delta\phi), \tag{15}$$

and J_c is a constant. Moreover, the time derivative of $\Delta\phi$ is proportional to the difference of the chemical potential $\Delta\mu$ on the two sides of the constriction,

$$\frac{d\Delta\phi}{dt} = -\frac{2\Delta\mu}{\hbar}. \tag{16}$$

Combining the two equations, one sees that a constant $\Delta\mu$ generates an oscillating current at the frequency $2\Delta\mu/h$.

The Josephson effect takes place in all superfluids. It has extensively been studied in superconductors, where it is straightforward to fabricate barriers through which electrons can tunnel. For helium one has to use sufficiently small constrictions. Josephson effect in ^{3}He has been discussed by Davis and Packard (2002).

Let us consider a macroscopic moving object in a stationary superfluid. As discussed above, there generally is viscous drag from the normal component, but restricting to low temperatures, say below $0.2T_c$, the normal fraction is vanishingly small. In this case the motion is nearly dissipationless as long as the object does not generate new excitations. The creation of excitations is limited by energy and momentum conservation. A simple calculations shows that no excitations are generated below the velocity

$$v_c = \min\frac{E(p)}{p}, \tag{17}$$

which means the minimum of $E(p)/p$ over all excitations. In connection of superfluidity, the velocity (17) is known as Landau velocity. It is more general, however, because the condition $v < v_c = \min\,\omega(k)/k$ means relatively low dissipation in any system, where the medium has waves with angular frequency ω and wave number k. The critical velocity (17) can also be derived from the condition that the waves generated by the object are stationary in the frame where the object is at rest. This is familiar to us, for example, from waves generated by a ship on the surface of water.

When the object velocity exceeds the Landau velocity v_c, a steep increase of the drag force is expected. Let us examine this in special cases. For ^{4}He the critical velocity is determined by the roton minimum [sloped line in Fig. 4A]. This gives $v_c \approx 60$ m/s. Landau critical velocity has been observed for ions moving in superfluid ^{4}He under pressure. In most experiments, the measured critical velocity is much lower. This is commonly interpreted to be caused by vortices, which are hard to avoid in a macroscopic set up.

For ^{3}He-B the Landau velocity $v_c = \Delta/p_F$, which corresponds to 27 mm/s at vapor pressure. Again, critical velocity of this magnitude has been seen with moving ions. For macroscopic objects the measured critical velocity is smaller than this. However, a recent experiment observes very little dissipation up to velocity $\sim 2v_c$ (Bradley et al., 2016). At the time of writing, this is not understood theoretically (Kuorelahti et al., 2018).

Landau velocity has also been applied to cases where only the superfluid component is in motion. For example, in ideal boson gas and in normal state fermions (dashed lines in Fig. 4) it gives vanishing critical velocity, $v_c = 0$. This is consistent with other arguments that these systems are not superfluids. However, for non-s-wave pairing of fermions, it is possible that the energy gap Δ depends on the point on the Fermi surface, and can have nodes, leading to $v_c = 0$. Such a case appears ^{3}He-A. In this case the vanishing of the Landau velocity does not imply absence of superfluidity.

Conclusion

We have given introduction to the basic properties of superfluids. Several more advanced topics are mentioned, but all details of them are left to be read from the given references and other literature.

References

Andronikashvili EL and Mamaladze YG (1966) Quantization of macroscopic motions and hydrodynamics of rotating helium II. *Reviews of Modern Physics* 38: 567–625. https://doi.org/10.1103/RevModPhys.38.567.

Annett JF (2004) *Superconductivity, Superfluids, and Condensates*. Oxford: Oxford.

Bardeen J, Cooper LN, and Schrieffer JR (1957) Theory of superconductivity. *Physical Review* 108: 1175–1204. https://doi.org/10.1103/PhysRev.108.1175.

Barenghi CF and Parker NG (2016) *A Primer on Quantum Fluids*. Springer.

Bennemann KH and Ketterson JB (eds.) (2008) *Superconductivity*. In: vol. I–II. Heidelberg: Springer.

Bennemann KH and Ketterson JB (eds.) (2013) *Novel Superfluids*. In: vol. I. Oxford: Oxford.

Bloch I, Dalibard J, and Zwerger W (2008) Many-body physics with ultracold gases. *Reviews of Modern Physics* 80: 885–964. https://doi.org/10.1103/RevModPhys.80.885.

Bradley DI, Fisher SN, Guénault AM, Haley RP, Lawson CR, Pickett GR, Schanen R, Skyba M, Tsepelin V, and Zmeev DE (2016) Breaking the superfluid speed limit in a fermionic condensate. *Nature Physics* 12: 1017–1021. https://doi.org/10.1038/nphys3813.

Chamel N (2017) Superfluidity and superconductivity in neutron stars. *Journal of Astrophysics and Astronomy* 38: 43. https://doi.org/10.1007/s12036-017-9470-9.

Davis JC and Packard RE (2002) Superfluid ^{3}He Josephson weak links. *Reviews of Modern Physics* 74: 741–773. https://doi.org/10.1103/RevModPhys.74.741.

Dmitriev VV, Senin AA, Soldatov AA, and Yudin AN (2015) Polar phase of superfluid ^{3}He in anisotropic aerogel. *Physical Review Letters* 115: 165304. https://doi.org/10.1103/PhysRevLett.115. 165304.

Dobbs ER (2001) *Helium Three*. Oxford: Oxford.

Donnelly RJ (1991) *Quantized Vortices in Helium II*. Cambridge: Cambridge.

Gezerlis A, Pethick CJ, and Schwenk A (2014) Pairing and superfluidity of nucleons in neutron stars. In: Bennemann KH and Ketterson JB (eds.) *Novel Superfluids*. vol. 2, pp. 580–615. Oxford: Oxford. (chapter 22).

Greywall DS (1986) ^{3}He specific heat and thermometry at millikelvin temperatures. *Physical Review B* 33: 7520–7538. https://doi.org/10.1103/PhysRevB.33.7520.

Guénault T (2003) *Basic Superfluids*. London: Taylor & Francis.

Henshaw DG and Woods ADB (1961) Modes of atomic motions in liquid helium by inelastic scattering of neutrons. *Physical Review* 121: 1266–1274. https://doi.org/10.1103/PhysRev. 121.1266.

Kuorelahti JA, Laine SM, and Thuneberg EV (2018) Models for supercritical motion in a superfluid Fermi liquid. *Physical Review B* 98: 144512. https://doi.org/10.1103/PhysRevB.98.144512.

Leggett AJ (1975) A theoretical description of the new phases of liquid ^{3}He. *Reviews of Modern Physics* 47: 331–414. https://doi.org/10.1103/RevModPhys.47.331.

Leggett AJ (2006) *Quantum Liquids: Bose Condensation and Cooper Pairing in Condensed-Matter Systems*. Oxford: Oxford.

London F (1954) *Superfluids*. vol. II. New York: Wiley.

Lounasmaa OV and Thuneberg E (1999) Vortices in rotating superfluid ^{3}He. *Proceedings of the National Academy of Sciences of the United States of America* 96: 7760–7767. https://doi.org/10.1073/pnas.96.14.7760. arXiv:https://www.pnas.org/content/96/14/7760.full.pdf.

Page D, Lattimer JM, Prakash M, and Steiner AW (2014) Stellar superfluids. In: Bennemann KH and Ketterson JB (eds.) *Novel Superfluids*. volume 2, pp. 505–579. Oxford: Oxford. chapter 21.

Peshkov VP (1946) Determination of the velocity of propagation of the second sound in helium II. *Journal of Physics (Moscow)* 10: 389.

Pethick CJ and Smith H (2002) *Bose-Einstein Condensation in Dilute Gases*. Cambridge: Cambridge.

Pitaevskii L and Stringari S (2003) *Bose-Einstein condensation*. Oxford: Oxford.

Serene J and Rainer D (1983) The quasiclassical approach to superfluid ^{3}He. *Physics Reports* 101: 221–311. https://doi.org/10.1016/0370-1573(83)90051–0.

Skrbek L, Schmoranzer D, Midlik S, and Sreenivasan KR (2021) Phenomenology of quantum turbulence in superfluid helium. *Proceedings of the National Academy of Sciences of the United States of America* 118. https://doi.org/10.1073/pnas.2018406118. arXiv:https://www.pnas.org/content/118/16/e2018406118. full.pdf.

Tilley DR and Tilley J (1990) *Superfluids*. vol. II. Bristol: IOP Publishing.

Tinkham M (1996) *Introduction to Superconductivity*, 2nd ed. New York: McGraw-Hill.

Vollhardt D and Wölfle P (1990) *The Superfluid Phases of Helium 3*. London: Taylor & Francis.

Volovik GE (2003) *The Universe in a Helium Droplet*. Oxford: Clarendon.

Wheatley JC (1975) Experimental properties of superfluid ^{3}He. *Reviews of Modern Physics* 47: 415–470. https://doi.org/10.1103/RevModPhys. 47.415.

Wilks J (1967) *The Properties of Liquid and Solid Helium*. Oxford: Clarendon.

Zwierlein MW (2014) Superfluidity in ultracold atomic fermi gases. In: Bennemann KH and Ketterson JB (eds.) *Novel Superfluids*. volume 2, pp. 269–422. Oxford: Oxford. chapter 18.

BEC-BCS crossover in ultracold atomic gases and neutron stars

Yoji Ohashi, Department of Physics, Keio University, Yokohama, Japan

© 2024 Elsevier Ltd. All rights reserved.

Introduction 10
Overview of BEC-BCS crossover physics 11
CFB model and BCS model 11
BEC-BCS crossover at $T=0$ 13
BEC-BCS crossover at T_c 14
Nambu-Goldstone mode 16
Tan's contact 17
Unitary Fermi gas and universal thermodynamics 18
Neutron superfluid in the crust regime of neutron star 19
Conclusion 20
Acknowledgments 20
References 20

Abstract

This chapter reviews how the BCS-type Fermi superfluid discussed in superconductivity continuously changes to the Bose-Einstein condensation of tightly bound molecules, as the strength of a pairing interaction between fermions increases. Theoretical treatment and basic properties of this quantum many-body phenomenon are explained. Realization in ultracold ^{40}K and ^{6}Li Fermi gases with a Feshbach resonance, as well as a similar phenomenon predicted in the low-density crust regime of neutron stars, are also addressed.

Key points

- The BEC-BCS crossover provides a unified description of the Fermi and the Bose superfluids.
- This phenomenon has been realized in ^{40}K and ^{6}Li Fermi atomic gases, by using a tunable pairing interaction associated with a Feshbach resonance.
- A similar phenomenon is predicted in the low-density crust regime of a neutron star. In this system, the increase of the neutron number density as one goes inside the star effectively tunes the strength of a pairing interaction.
- The mean-field BCS theory can describe the BEC-BCS crossover at $T=0$, when strong-coupling corrections to the Fermi chemical potential are taken into account.
- To evaluate T_c in the BEC-BCS crossover region, one needs to include pairing fluctuations, going beyond the mean-field BCS theory.

Introduction

The BEC (Bose-Einstein condensation)-BCS (Bardeen-Cooper-Schrieffer) crossover is a quantum many-body phenomenon, where the character of a Fermi superfluid continuously changes from the weak-coupling BCS-type (which is discussed in superconductivity) to the BEC of tightly bound molecules, as one increases the strength of a pairing interaction between fermions. Here, 'crossover' means the absence of any phase transition during the change from the BCS to BEC region. The BEC-BCS crossover was originally proposed in the field of superconductivity in 1960s (Eagles, 1969); however, since the experimental tuning of interaction strength was not easy, no one could realize this crossover phenomenon in the 20th century.

This situation drastically changed in 2004, when the superfluid phase transition was experimentally achieved in an ultracold ^{40}K Fermi atomic gas (Regal et al., 2004). Soon later, a superfluid ^{6}Li Fermi gas was also realized (Zwierlein et al., 2004; Kinast et al., 2004; Bartenstein et al., 2004). These Fermi atomic gases are experimentally prepared by trapping vaporized atoms in a harmonic potential produced by magnetic/optical manner, and then cooling the system down to below micro-Kelvin by using laser cooling, as well as evaporative cooling. While the pairing interaction in conventional *s*-wave superconductivity (such as Al) is medicated by phonon (Fig. 1(a)), superfluid ^{40}K and 6Li Fermi gases use a pairing interaction associated with a Feshbach resonance (Chin et al., 2010) (Fig. 1(b)). This pairing mechanism has the unique property that one can tune the interaction strength by adjusting an external magnetic field. Indeed, by using this advantage, the superfluid phase transition and the BEC-BCS crossover were simultaneously realized in ^{40}K and ^{6}Li Fermi gases with a Feshbach resonance.

In the low-density crust regime of a neutron star, neutron liquid is considered to be in the *s*-wave superfluid state (Gandolfi et al., 2015) by an attractive interaction with the *s*-wave scattering length $a_s \simeq -18.5$ fm (Stoks et al., 1993). Using the typical value of the

https://doi.org/10.1016/B978-0-323-90800-9.00100-1

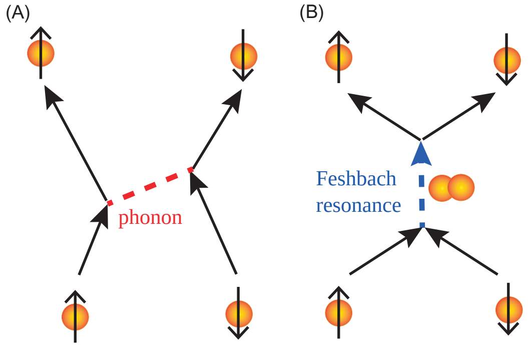

Fig. 1 Illustration of pairing mechanism. (a) Phonon-mediated pairing interaction in superconductivity, working between spin-↑ and spin-↓ electrons. (b) Feshbach-induced tunable pairing interaction in ultracold Fermi atomic gases. Pseudospin-↑, ↓ represent two atomic hyperfine states contributing to the Cooper-pair formation.

Fermi momentum $k_{\rm F} \sim 1\ {\rm fm}^{-1}$ in the neutron-stare crust, the scaled interaction strength is estimated as $(k_{\rm F}a_s)^{-1} \ll 1$, indicating that the system is close to the unitary limit ($(k_{\rm F}a_s)^{-1} = 0$). Before 2004, any experiment could not access such a strong-coupling superfluid state, because all the conventional superconductors were in the weak-coupling BCS regime ($(k_{\rm F}a_s)^{-1} \ll -1$). However, since the superfluid ^{40}K and ^{6}Li Fermi gases can widely cover various interaction strengths, ranging from $(k_{\rm F}a_s) \lesssim -1$ to $(k_{\rm F}a_s) \gtrsim +1$, we can now experimentally examine physical properties of a nearly unitary Fermi superfluid. In addition, although the value of the neutron s-wave scattering is fixed, the scaled interaction strength $(k_{\rm F}a_s)^{-1}$ varies as one goes inside the neutron star, due to the increase of the neutron number density $\rho_{\rm N} \propto k_{\rm F}^3$. Thus, the tunable pairing interaction associated with a Feshbach resonance is also convenient to simulate this situation in terrestrial experiments.

In the followings, we overview the BEC-BCS crossover physics discussed in ^{40}K and ^{6}Li Fermi gases, as well as its application to the s-wave neutron superfluid predicted in the crust regime of a neutron star. For simplicity, we set $\hbar = k_{\rm B} = 1$ and the system volume V is taken to be unity.

Overview of BEC-BCS crossover physics

CFB model and BCS model

A two-component ultracold Fermi gas with a Feshbach resonance is described by the following coupled fermion-boson (CFB) model Hamiltonian (Holland et al., 2001; Ohashi and Griffin, 2002):

$$
\begin{aligned}
H_{\rm CFB} = & \sum_{\boldsymbol{p},\sigma} \xi_{\boldsymbol{p}} c^\dagger_{\boldsymbol{p},\sigma} c_{\boldsymbol{p},\sigma} + \sum_{\boldsymbol{q}} \xi^{\rm B}_{\boldsymbol{q}} b^\dagger_{\boldsymbol{q}} b_{\boldsymbol{q}} \\
& + g \sum_{\boldsymbol{p},\boldsymbol{q}} \left[b^\dagger_{\boldsymbol{q}} c_{-\boldsymbol{p}+\boldsymbol{q}/2,\downarrow} c_{\boldsymbol{p}+\boldsymbol{q}/2,\uparrow} + {\rm h.c.} \right] \\
& -U \sum_{\boldsymbol{p},\boldsymbol{p}',\boldsymbol{q}} c^\dagger_{\boldsymbol{p}'\boldsymbol{q}/2,\uparrow} c^\dagger_{-\boldsymbol{p}+\boldsymbol{q}/2,\downarrow} c_{-\boldsymbol{p}'+\boldsymbol{q}/2,\downarrow} c_{\boldsymbol{p}'+\boldsymbol{q}/2,\uparrow}.
\end{aligned}
\tag{1}
$$

Here, $c^\dagger_{\boldsymbol{p},\sigma}$ is the creation operator of a Fermi atom with pseudospin $\sigma = \uparrow, \downarrow$, describing two atomic hyperfine states forming Cooper pairs. $\xi_{\boldsymbol{p}} = \varepsilon_{\boldsymbol{p}} - \mu = \boldsymbol{p}^2/(2m) - \mu$ is the kinetic energy of a Fermi atom with an atomic mass m, measured from the Fermi chemical potential μ. $b_{\boldsymbol{q}}$ describes a molecular boson appearing in the intermediate state of a Feshbach resonance shown in Fig. 1(b). The molecular kinetic energy is given by

$$
\xi^{\rm B}_{\boldsymbol{q}} = \varepsilon^{\rm B}_{\boldsymbol{q}} - \mu_{\rm B} = \frac{\boldsymbol{q}^2}{2M} + 2\nu - \mu_{\rm B}, \tag{2}
$$

where 2ν is the threshold energy of a Feshbach resonance, and $\mu_{\rm B}$ is the Bose chemical potential. Since one Feshbach molecule consists of two Fermi atoms, we take $M = 2m$ and $\mu_{\rm B} = 2\mu$. The second line in Eq. (1) describes a Feshbach resonance with the coupling constant g, where two Fermi atoms form a quasi-molecular boson and it dissociates into two Fermi atoms again. $-U$ is a residual weak inter-atomic interaction which has nothing to do with the Feshbach resonance.

The CFB Hamiltonian in Eq. (1) makes us expect two kinds of superfluid states: One is characterized by the BEC order parameter, $\phi_{\rm m} \equiv \langle b_{\boldsymbol{q}=0} \rangle$, and the other is characterized by the BCS superfluid order parameter,

$$
\Delta \equiv U \sum_{\boldsymbol{p}} \langle c_{-\boldsymbol{p},\downarrow} c_{\boldsymbol{p},\uparrow} \rangle. \tag{3}
$$

However, imposing the condition that the Bose order parameter ϕ_m has no time dependence in the thermal equilibrium state ($\partial \phi_m / \partial t = 0$), one exactly obtains the following relation (Ohashi and Griffin, 2003):

$$\phi_m = -\frac{g}{2\nu - 2\mu}\frac{\Delta}{U}. \tag{4}$$

Thus, only the superfluid phase with $\phi_{\rm m} \neq 0$ and $\Delta \neq 0$ is actually possible.

Introducing the composite order parameter $\tilde{\Delta} \equiv \Delta - g\phi_{\rm m}$, one finds that the mean-field gap equation to determine $\tilde{\Delta}$ has the form,

$$1 = \left[U_{\rm res} + \frac{g^2}{2\nu - 2\mu}\right]\sum_{\boldsymbol{p}}\frac{1}{2E_{\boldsymbol{p}}}\tanh\frac{E_{\boldsymbol{p}}}{2T}, \tag{5}$$

where

$$E_{\boldsymbol{p}} = \sqrt{(\varepsilon_{\boldsymbol{p}} - \mu)^2 + |\tilde{\Delta}|^2} \tag{6}$$

describes Bogoliubov single-particle excitations in the superfluid phase. From the comparison of Eq. (5) with the ordinary BCS gap equation (see Eq. (9)), we find that the Feshbach-induced pairing interaction ($\equiv U_{\rm FR}$) is the second term in [. . .] in Eq. (5), that is,

$$U_{\rm FR} = -\frac{g^2}{2\nu - 2\mu}. \tag{7}$$

Since the threshold energy 2ν of a Feshbach resonance depends on an external magnetic field B, Eq. (7) is tunable by adjusting B. We briefly note that this tuning mechanism uses the fact that hyperfine states of Fermi atoms confined in a Feshbach molecule (closed channel) are different from those of the incident and the outgoing atoms (open channel) shown in Fig. 1(b) (Chin et al., 2010). Their Zeeman energies then become different from each other. Because the threshold energy 2ν is directly related to the energy difference between the open channel and the closed channel, B-dependent 2ν is realized.

In the current experiments on superfluid ^{40}K and ^{6}Li Fermi gases, the so-called broad Feshbach resonance is always used. This resonance type is characterized by a large coupling constant g. In this case, the pairing interaction $U_{\rm FR}$ in Eq. (7) can be strong even when $2\nu \gg 2\mu$. Then, while a molecular boson virtually appears in the intermediate state of the Feshbach resonance (see Fig. 1(b)), the occupation number of the Feshbach-molecular band $\varepsilon_{\boldsymbol{q}}^{\rm B} = \boldsymbol{q}^2/(2M) + 2\nu$ ($\gg 2\mu$), which is located much higher than the bottom energy of the atomic band $\varepsilon_{\boldsymbol{p}}$, is negligibly small, as far as we consider the interesting BEC-BCS crossover region (Partridge et al., 2005). As a result, for the study of ^{40}K and ^{6}Li Fermi gases with a broad Feshbach resonance, one may use the simpler BCS model Hamiltonian,

$$\begin{aligned} H_{\rm BCS} = &\sum_{\boldsymbol{p},\sigma}\xi_{\boldsymbol{p}}c^\dagger_{\boldsymbol{p},\sigma}c_{\boldsymbol{p},\sigma} \\ &-U\sum_{\boldsymbol{p},\boldsymbol{p}',\boldsymbol{q}}c^\dagger_{\boldsymbol{p}+\boldsymbol{q}/2,\uparrow}c^\dagger_{-\boldsymbol{p}+\boldsymbol{q}/2,\uparrow}c_{-\boldsymbol{p}'+\boldsymbol{q}/2,\uparrow}c_{\boldsymbol{p}'+\boldsymbol{q}/2,\uparrow}, \end{aligned} \tag{8}$$

instead of the CFB model in Eq. (1). In Eq. (8), $-U$ is *not* the fixed residual weak interaction involved in Eq. (1), but a *tunable* pairing interaction associated with a broad Feshbach resonance. Then, the superfluid state is characterized by the ordinary BCS order parameter Δ in Eq. (3). In the mean-field approximation, it obeys the BCS gap equation (Schrieffer, 1964),

$$1 = U\sum_{\boldsymbol{p}}\frac{1}{2E_{\boldsymbol{p}}}\tanh\frac{E_{\boldsymbol{p}}}{2T}, \tag{9}$$

where $E_{\boldsymbol{p}}$ is given in Eq. (6) where the composite order parameter $\tilde{\Delta}$ is replaced by the ordinary BCS one Δ.

The above simplification is not valid for a narrow Feshbach resonance, being characterized by a small coupling g. In this case, in order for the Feshbach-induced interaction $U_{\rm FR}$ to be strong, one needs to lower the threshold energy 2ν down to be close to $2\,\mu$ so that the denominator in Eq. (7) is much smaller than g^2. Such a situation naturally brings about the sizable occupation of the molecular band, so that one must deal with the CFB model.

The momentum summation in the gap equation (9) exhibits ultraviolet divergence without a cutoff, because the contact-type interaction $-U$ is used in Eq. (8). Regarding this, in conventional s-wave superconductivity, the phonon-mediated pairing interaction works only near the Fermi surface within the energy range $\sim[\varepsilon_{\rm F} - \omega_{\rm D}, \varepsilon_{\rm F} + \omega_{\rm D}]$, where $\varepsilon_{\rm F}$ is the Fermi energy and $\omega_{\rm D}$ ($\ll \varepsilon_{\rm F}$) is related to the Debye frequency. Thus, one actually does not need to worry about this divergence, because the momentum summation in Eq. (9) is physically restricted to this energy range (which is also referred to as the BCS window in the literature).

On the other hand, such a physical cutoff is absent, or at least unclear, in the case of the Feshbach-induced pairing interaction. In this case, to remove the ultraviolet divergence from the gap equation (9), it is convenient to measure the interaction strength in terms of the observable s-wave scattering length a_s, which is related to the bare interaction $-U$ as (Randeria, 1995)

$$\frac{4\pi a_s}{m} = -\frac{U}{1 - U\sum_{\boldsymbol{p}}\frac{1}{2\varepsilon_{\boldsymbol{p}}}}. \tag{10}$$

Although the momentum summation in Eq. (10) diverges without a cutoff, we actually do not explicitly evaluate this equation, but 'borrow' the observed value of a_s. In this scale, the weak-coupling BCS regime and the strong-coupling BEC regime are specified as $(k_{\rm F}a_s)^{-1} \lesssim -1$ and $1 \lesssim (k_{\rm F}a_s)^{-1}$, respectively. The region, $-1 \lesssim (k_{\rm F}a_s)^{-1} \lesssim 1$, is called the BCS-BEC crossover region. Using a_s, we obtain the *renormalized* gap equation,

$$1 = -\frac{4\pi a_s}{m}\sum_{\boldsymbol{p}}\left[\frac{1}{2E_{\boldsymbol{p}}}\tanh\frac{E_{\boldsymbol{p}}}{2T} - \frac{1}{2\varepsilon_{\boldsymbol{p}}}\right]. \tag{11}$$

The momentum summation in Eq. (11) now converges without a cutoff.

BEC-BCS crossover at $T = 0$

The BCS gap equation (11) was originally derived for the weak-coupling superconducting state. However, it can also describe the BEC-BCS crossover phenomenon at $T = 0$, at least qualitatively, if one solves Eq. (11) together with the equation for the number N of fermions in the BCS approximation,

$$N = \sum_{\boldsymbol{p}}\left[1 - \frac{\xi_{\boldsymbol{p}}}{E_{\boldsymbol{p}}}\tanh\frac{E_{\boldsymbol{p}}}{2T}\right], \tag{12}$$

to self-consistently determine Δ and μ for a given interaction strength. This approach is sometimes referred to as the BCS-Leggett theory (Leggett, 2006).

In the weak-coupling BCS limit ($(k_{\mathrm{F}}a_s)^{-1} \ll -1$), Eqs. (11) and (12) give (Pethick and Smith, 2008)

$$\mu(T = 0) = \varepsilon_{\mathrm{F}}(> 0), \tag{13}$$

$$\Delta(T = 0) = \frac{8}{e^2}\varepsilon_{\mathrm{F}}e^{\frac{\pi}{2k_{\mathrm{F}}a_s}}(\ll \varepsilon_{\mathrm{F}}). \tag{14}$$

In the strong-coupling BEC limit ($(k_{\mathrm{F}}a_s)^{-1} \gg +1$), on the other hand, we obtain

$$\mu(T = 0) = \frac{1}{2}E_{\mathrm{bound}}^{2\mathrm{b}}(< 0), \tag{15}$$

$$\Delta(T = 0) = \sqrt{\frac{16}{3\pi}}|\mu|^{1/4}\varepsilon_{\mathrm{F}}^{3/4}(\ll |\mu|). \tag{16}$$

Here,

$$E_{\mathrm{bound}}^{2\mathrm{b}} = -\frac{1}{ma_s^2} \tag{17}$$

is the energy of a two-body bound state, obtained from the following two-particle Schrödinger equation when $a_s > 0$:

$$\left[-\frac{\nabla_{\mathbf{r}_1}^2}{2m} - \frac{\nabla_{\mathbf{r}_2}^2}{2m} - U\delta(\boldsymbol{r}_1 - \boldsymbol{r}_2)\right]\Psi(\boldsymbol{r}_1 - \boldsymbol{r}_2, \sigma_1, \sigma_2) = E_{\mathrm{bound}}^{2\mathrm{b}}\Psi(\boldsymbol{r}_1 - \boldsymbol{r}_2, \sigma_1, \sigma_2). \tag{18}$$

In Eq. (18), the bound-state wavefunction $\Psi(\boldsymbol{r}_1 - \boldsymbol{r}_2, \sigma_1, \sigma_2)$ has the form,

$$\Psi(\boldsymbol{r}_1 - \boldsymbol{r}_2, \sigma_1, \sigma_2) = \frac{1}{\sqrt{2\pi a_2}}\frac{1}{|\boldsymbol{r}_1 - \boldsymbol{r}_2|}e^{-|\boldsymbol{r}_1 - \boldsymbol{r}_2|a_s}|0, 0 > , \tag{19}$$

where $|0, 0\rangle$ is the spin-singlet state. Since the contact interaction $-U\,\delta\,(\boldsymbol{r}_1 - \boldsymbol{r}_2)$ works only when two fermions come to the same spatial position, the spin-triplet bound state is not obtained from Eq. (18).

Since the chemical potential physically means the energy to add one fermion to the system, Eq. (13) reasonably indicates the presence of a Fermi sphere in the weak-coupling limit. We also find from Eq. (15) that, when *two* fermions are added to the system deep inside the BEC regime, they immediately form a two-body bound state given in Eq. (19), so that the system energy is lowered by $2 \times \mu = E_{\mathrm{bound}}^{2\mathrm{b}}$ (<0). That is, this regime may be viewed as a gas of two-body bound molecules, as expected in the BEC-BCS crossover phenomenon. The BCS-Leggett theory can really describe this feature.

Because of the sign change of the chemical potential in the BEC-BCS crossover seen in Eqs. (13) and (15), the threshold energy ($\equiv E_{\mathrm{th}}$) of Bogoliubov single-particle excitations given in Eq. (6) changes from $E_{\mathrm{th}} = |\Delta|$ to $E_{\mathrm{th}} = \sqrt{\mu^2 + |\Delta|^2}$, as one moves from the BCS regime to the BEC regime. Equations (15)–(17) indicate that $|\mu| \gg |\Delta|$ in the extreme BEC limit, so that the threshold energy is eventually reduced to $E_{\mathrm{th}} \to |\mu| = |E_{\mathrm{bound}}^{2\mathrm{b}}|/2$ there. Since $2 \times E_{\mathrm{th}}$ physically means the energy to break up a Cooper pair, this result in the BEC limit is consistent with the above-mentioned picture of a gas of two-body bound molecules.

The Schrödinger equation (18) does not have a bound state solution when $a_s < 0$, which means that the interaction strength is not strong enough to form a *two-body* bound state there. As clarified by Cooper (1956), the Cooper pair in this weak-coupling regime is a *many-body* bound state, in the sense that this pair formation is assisted by the presence of a Fermi surface (Cooper instability): $E_{\mathrm{th}} = 2|\Delta|$ physically means the binding energy of such a Fermi-surface-assisted bound state. Thus, the change, $E_{\mathrm{th}} = |\Delta| \to |\mu|$, in the BEC-BCS crossover reflects the change of the character of a Cooper pair, from a many-body bound state to a two-body one.

BEC-BCS crossover at T_{c}

The mean-field based coupled gap equation (11) with the number equation (12) can also be applied to the system at non-zero temperatures in the weak-coupling BCS regime. Particularly at the superfluid phase transition temperature T_{c} in this regime, the number equation simply gives $\mu(T_{\mathrm{c}}) \simeq \varepsilon_{\mathrm{F}}$. T_{c} is obtained from the gap equation (11) with $\Delta = 0$ as (Pethick and Smith, 2008)

$$T_{\mathrm{c}} = \frac{8\gamma}{\pi e^2} e^{\frac{\pi \quad 1}{2k_{\mathrm{F}} a_s}}, \tag{20}$$

where $\gamma = 1.78$ is the Euler constant. The ratio of Eq. (14) to Eq. (20),

$$\frac{2\Delta(T=0)}{T_{\mathrm{c}}} = \frac{2\pi}{\gamma} \simeq 3.54, \tag{21}$$

is known as the BCS universal constant. While Eq. (21) was historically used to confirm the correctness of the BCS theory, this ratio also tells us that the magnitude of T_{c} is comparable to the binding energy $2|\Delta(T=0)|$ of a Cooper pair at $T = 0$. This physically means that the superfluid phase transition in the weak-coupling BCS regime is caused by the thermal dissociation of Cooper pairs when the temperature increases. Because of this, T_{c} in this regime increases with increasing the interaction strength, reflecting the increase of the binding energy of a Cooper pair.

In the strong-coupling BEC regime, most Fermi atoms form two-body bound states with the binding energy $|E_{\mathrm{bound}}^{\mathrm{2b}}| = 1/(ma_s^2)$, so that the resulting system may be viewed as a gas of $N_{\mathrm{B}} \simeq N/2$ Bose molecules with a molecular mass $m_{\mathrm{B}} = 2\,m$. Thus, the superfluid phase transition temperature in this regime should approach the BEC phase transition temperature T_{BEC} of such a molecular Bose gas, given by

$$T_{\mathrm{BEC}} = \frac{2\pi}{\varsigma(3/2)^{2/3}} \frac{N_{\mathrm{B}}^{2/3}}{m_{\mathrm{B}}} \simeq 0.218 T_{\mathrm{F}}, \tag{22}$$

where $\zeta(3/2) \simeq 2.612$ is the zeta-function.

However, the mean-field based BCS-Leggett theory cannot describe this situation: While the gap equation (11) with $\Delta = 0$,

$$1 = -\frac{4\pi a_s}{m} \sum_{\boldsymbol{p}} \left[\frac{1}{2\xi_{\boldsymbol{p}}} \tanh \frac{\xi_{\boldsymbol{p}}}{2T} - \frac{1}{2\varepsilon_{\boldsymbol{p}}} \right], \tag{23}$$

gives the expected result, $\mu(T_{\mathrm{c}}) = E_{\mathrm{bound}}^{\mathrm{2b}}/2$ (<0), deep inside the BEC regime ($(k_{\mathrm{F}} a_s)^{-1} \gg +1$), Eq. (12) at T_{c} is simply reduced to the number equation in a *free Fermi gas*,

$$N = 2\sum_{\boldsymbol{p}} f(\xi_{\boldsymbol{p}}), \tag{24}$$

where $f(\xi_{\boldsymbol{p}}) = 1/[e^{\xi_{\boldsymbol{p}}/T} + 1]$ is the Fermi distribution function. Obviously, Eq. (24) cannot give T_{BEC} in Eq. (22).

This problem was solved by Nozières and Schmit-Rink (NSR) (Nozières and Schmitt-Rink, 1985). They corrected the number equation (24) by including effects of pairing fluctuations, that are completely ignored in the mean-field scheme. On the other hand, the T_{c}-equation (23) remained unchanged in their theory. In this so-called NSR theory, the corrected number equation is derived from the thermodynamic identity,

$$N = -\left(\frac{\partial \Omega}{\partial \mu} \right)_{T,V}, \tag{25}$$

where the thermodynamic potential Ω involves fluctuation corrections $\delta\Omega$ which is diagrammatically given in Fig. 2(a). The resulting NSR number equation is given by Nozières and Schmitt-Rink (1985) and Ohashi et al. (2020)

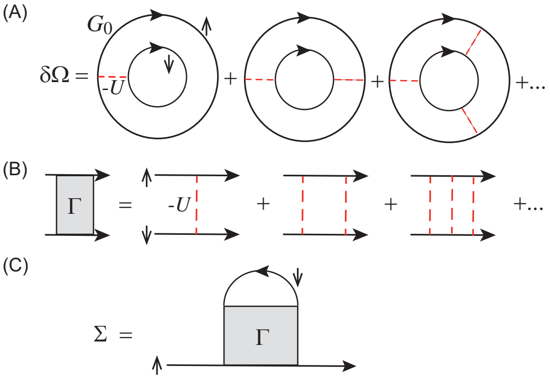

Fig. 2 (a) Fluctuation correction $\delta\Omega$ to the thermodynamic potential Ω in the NSR theory. The solid line is the bare single-particle thermal Green's function G_0, and the dashed line denotes the pairing interaction $-U$. (b) Diagrammatic representation of the particle-particle scattering matrix $\Gamma(\boldsymbol{q}, i\nu_n)$ in Eq. (27). (c) Self-energy Σ in a T-matrix approximation.

$$N = 2\sum_{\boldsymbol{p}} f(\xi_{\boldsymbol{p}}) - T\sum_{\boldsymbol{q},\nu_n} \Gamma(\boldsymbol{q}, i\nu_n) \frac{\partial \Pi(\boldsymbol{q}, i\nu_n)}{\partial \mu} e^{i\delta\nu_n}. \tag{26}$$

Here, $\nu_n = 2n\pi T$ is the boson Matsubara frequency (where $n = 0, \pm 1, \pm 2, \ldots$) and δ is an infinitesimally small positive number. In Eq. (26), the particle-particle scattering matrix $\Gamma\ (\boldsymbol{q}, i\nu_n)$, which is given by the sum of the ladder diagrams in Fig. 2(b), describe pairing fluctuations. Summing up these diagrams, we obtain

$$\Gamma(\boldsymbol{q}, i\nu_n) = \frac{\frac{4\pi a_s}{m}}{1 + \frac{4\pi a_s}{m}\left[\Pi(\boldsymbol{q}, i\nu_n) - \sum_{\boldsymbol{q}} \frac{1}{2\varepsilon_{\boldsymbol{p}}}\right]}, \tag{27}$$

where

$$\Pi(\boldsymbol{q}, i\nu_n) = \sum_{\boldsymbol{p}} \frac{1 - f\left(\xi_{\boldsymbol{p}+\boldsymbol{q}/2}\right) - f\left(\xi_{-\boldsymbol{p}+\boldsymbol{q}/2}\right)}{\xi_{\boldsymbol{p}+\boldsymbol{q}/2} + \xi_{-\boldsymbol{p}+\boldsymbol{q}/2} - i\nu_n} \tag{28}$$

is the lowest-order pair correlation function in terms of the pairing interaction.

When pairing fluctuations are weak in the weak-coupling BCS regime ($(k_F a_s)^{-1} \lesssim -1$), the last term in Eq. (26) may be safely ignored. In this case, T_c in Eq. (20) and $\mu(T_c) \simeq \varepsilon_F$ are again obtained.

In the strong-coupling BEC regime ($(k_F a_s)^{-1} \gg +1$), Eq. (23) gives,

$$\mu(T_c) \simeq \frac{1}{2} E_{\text{bound}}^{2\text{b}} (< 0). \tag{29}$$

Because of this negative chemical potential, the NSR number equation (26) is dominated by the second term in this regime. Deep inside the BEC regime ($(k_F a_s)^{-1} \gg +1$), Eq. (26) is reduced to

$$\frac{N}{2} = \sum_{\boldsymbol{q}} \frac{1}{e^{\left(\frac{q^2}{4m}\right)/T} - 1}. \tag{30}$$

This is just the condition for the BEC phase transition of an ideal gas of $N/2$ bosons with a Bose mass $2\ m$, giving the expected BEC phase transition temperature T_{BEC} in Eq. (22). By numerically solving the T_c-equation (23) together with the NSR number equation (26), the NSR theory is found to smoothly connect these two extreme results, as schematically shown in Fig. 3.

The molecular picture in the BEC regime at T_c is also valid for the normal state above T_c, because Eq. (29) indicates that molecular bosons still remain to exist even at T_c. This situation is quite different from that in the weak-coupling BCS regime, where Cooper pairs are destroyed thermally to disappear above T_c. Thus, in the strong-coupling BEC regime, single-particle excitations in the normal state near T_c are still accompanied by molecular dissociations. This situation leads to the opening of the energy gap $E_{\text{gap}} \simeq |E_{\text{bound}}^{2\text{b}}|$ in the Fermi single-particle density of states (DOS) (Stewart, 2008), although the superfluid order parameter Δ vanishes above T_c. This gapped DOS gradually changes to the ordinary gapless one, as one passes through the BEC-BCS crossover region to approach the BCS regime. Thus, around the unitary limit ($(k_F a_s)^{-1} = 0$), DOS in the normal state exhibits a pseudogap structure near T_c, being characterized by a dip structure around the Fermi level (Tsuchiya et al., 2008).

The particle-particle scattering matrix $\Gamma(\boldsymbol{q}, i\nu_n)$ in Eq. (27) has a pole at $\boldsymbol{q} = \nu_n = 0$, when Eq. (23) is satisfied at T_c. This is a direct consequence of the appearance of the gapless Nambu-Goldstone mode below T_c. However, the divergence of $\Gamma(\boldsymbol{q} = 0, i\nu_n = 0)$ itself does not remain after the $\boldsymbol{q}$-summation is taken in Eq. (26) in three dimension, leading to non-zero T_c. In one and two dimensions, on the other hand, the second term in Eq. (26) diverges when the gap equation (23) is satisfied, leading to the vanishing T_c. This is consistent with the Hohenberg-Mermin-Wagner theorem (Hohenberg, 1967; Mermin and Wagner, 1966).

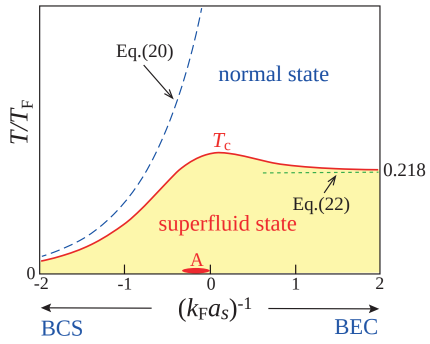

Fig. 3 Illustration of BEC-BCS crossover behavior of T_c. The region-A is considered similar to the s-wave neutron superfluid predicted in the low density crust regime of a neutron star.

The idea of NSR theory was later applied to the Green's function theory, to produce various T-matrix type BEC-BCS crossover theories (Haussmann, 1999; Kashimura, 2012; Perali et al., 2002). In these theories, the self-energy Σ having the diagrammatic structure shown in Fig. 3(c) are commonly used. For example, when the bare single-particle thermal Green's function,

$$G_0(\boldsymbol{p}, i\omega_n) = \frac{1}{i\omega_n - \xi_{\boldsymbol{p}}}, \tag{31}$$

(where $\omega_n = \pi(2n+1)T$ is the fermion Matsubara frequency, with $n = 0, \pm 1, \pm 2, \ldots$) is used to construct this self-energy diagram, it is called the T-matrix approximation (TMA) (Perali et al., 2002). On the other hand, the self-consistent T-matrix approximation (SCTMA) (Haussmann, 1999) uses the dressed Green's function,

$$G(\boldsymbol{p}, i\omega_n) = \frac{1}{i\omega_n - \xi_{\boldsymbol{p}} - \Sigma(\boldsymbol{p}, i\omega_n)}, \tag{32}$$

to construct the self-energy. The intermediate version between the two also exists, which is sometimes referred to as the extended TMA (ETMA) (Kashimura, 2012). Apart from details, all these strong-coupling theories can describe the BEC-BCS crossover behavior of T_c shown in Fig. 3. These strong-coupling theories at T_c have also been extended to the superfluid phase below T_c (Fukushima et al., 2007; Haussmann, 2008), where phase and amplitude fluctuations of the superfluid order parameter Δ are taken into account.

Nambu-Goldstone mode

A characteristic superfluid phenomenon below T_c is the appearance of the Nambu-Goldstone mode. It is a collective phase oscillation of the superfluid order parameter Δ, and has a linear dispersion, $\omega_{\boldsymbol{q}} = v_\phi q$, in the low-momentum region. Since the Bogoliubnov single-particle excitations have non-zero energy gap (see Eq. (6)), the low-energy properties of the superfluid state are dominated by this *gapless* collective mode.

Treating the Nambu-Goldstone mode at $T = 0$ within the BCS-Leggett theory, the mode energy $\omega_{\boldsymbol{q}}$ is obtained from the pole of the analytic continued particle-particle scattering matrix $\Gamma(\boldsymbol{q}, i\nu \to \omega_{\boldsymbol{q}} + i\delta)$ in Eq. (27) extended to the superfluid phase below T_c (Ohashi et al., 2020). In the weak-coupling BCS regime ($(k_F a_s)^{-1} \lesssim -1$), this so-called BCS-GRPA (generalized random phase approximation) theory gives the velocity of the Anderson-Bogoliubov mode in the neutral Fermi superfluid (Anderson, 1958),

$$v_\phi = \frac{1}{\sqrt{3}} v_F, \tag{33}$$

where v_F is the Fermi velocity. In the strong-coupling BEC regime ($(k_F a_s)^{-1} \gtrsim 1$), on the other hand, one obtains

$$v_\phi = \sqrt{\frac{U_B N_B}{m_B}}, \tag{34}$$

which is just the velocity of the collective Bogoliubov phonon in a weakly interacting Bose superfluid with $N_B = N/2$ bosons and mass $m_B = 2\,m$. In Eq. (34),

$$U_B = \frac{4\pi a_B}{m_B} \tag{35}$$

is an effective Bose-Bose interaction. For the value of the s-wave Bose scattering length a_B, the BCS-GRPA scheme gives $a_B = 2a_s$ (Ohashi et al., 2020), which is larger than the exact value $a_B = 0.6a_s$ obtained by solving a four-particle problem (Petrov et al., 2004). These results ($a_B > 0$) indicate that molecular bosons in the BEC regime *repulsively* interact each other, although the interaction between Fermi atoms is *attractive*. With increasing the strength of a pairing interaction, the velocity v_ϕ of the Nambu-Goldstone mode gradually decreases from Eq. (33), to eventually vanishes in the extreme BEC limit ($(k_F a_s)^{-1} \to +\infty$), where the system is simply described by an ideal molecular Bose gas.

In the weak-coupling BCS regime, when the mode energy $\omega_{\boldsymbol{q}}$ approaches the excitation threshold $2|\Delta|$ of the two-particle continuum (which physically describe the dissociations of Cooper pairs), level repulsion occurs between them, which makes the mode dispersion a convex upward function. Deep inside the BEC regime ($\mu < 0$), on the other hand, the threshold energy $\left(= 2\sqrt{\mu^2 + |\Delta|^2} \to 2|\mu|\right)$ of the two-particle continuum is very high, so that the Nambu-Goldstone mode is not affected by this threshold energy. As a result, the mode dispersion in the BEC regime has the same form as that of the Bogoliubov phonon (Pethick and Smith, 2008),

$$\omega_{\boldsymbol{q}} = \sqrt{\frac{\boldsymbol{q}^2}{2m_B}\left[\frac{\boldsymbol{q}^2}{2m_B} + 2U_B N_B\right]}, \tag{36}$$

which is a convex downward function. Thus, starting from the weak-coupling BCS regime, the dispersion of the Nambu-Goldstone mode changes from a *convex upward* function to a *convex downward* one, as one passes through the BEC-BCS crossover region. Such a change of the mode dispersion in the BEC-BCS crossover region has been observed in a superfluid ^{6}Li Fermi gas (Biss et al., 2022).

Since the low-energy excitations in the superfluid state is dominated by the gapless Nambu-Goldstone mode, the fact that it always has a linear dispersion around $\boldsymbol{q} = 0$ in the whole BEC-BCS crossover region is crucial for the *superfluidity* of the system: According to the Landau criterion, the supercurrent state is stable, when the current velocity $\boldsymbol{V}_{\rm sc}$ satisfies

$$|\mathbf{V}_{\rm SC}||\boldsymbol{q}| < \omega_{\boldsymbol{q}}. \tag{37}$$

Indeed, Eq. (37) guarantees non-zero critical velocity of the supercurrent state in the case when $\omega_{\boldsymbol{q}}$ has a linear dispersion around $\boldsymbol{q} = 0$, unless $\omega_{\boldsymbol{q}}$ vanishes at a non-zero $\boldsymbol{q}$. We briefly note that Eq. (37) is obtained from the condition that the supercurrent state is stable against a low-energy excitation with the energy $\omega_{\boldsymbol{q}}$ and the momentum $\boldsymbol{q}$ (Ohashi et al., 2020). That is, the energy $E_{\rm sc} = M_{\rm sys}V_{\rm sc}^2/2$ in this supercurrent state (where $M_{\rm sys}$ the total mass of the system) must be always lower than the energy in the excited state as

$$\frac{1}{2}M_{\rm sys}\boldsymbol{V}_{\rm sc}^2 < \frac{1}{2}M_{\rm sys}\overline{\boldsymbol{V}}_{\rm sc}^2 + \omega_{\boldsymbol{q}} \tag{38}$$

where the current velocity $\overline{\boldsymbol{V}}_{\rm sc}$ in the excited state satisfies the momentum conservation,

$$M_{\rm sys}\boldsymbol{V}_{\rm sc} = M_{\rm sys}\overline{\boldsymbol{V}}_{\rm sc} + \boldsymbol{q}. \tag{39}$$

Under the assumption that the system mass $M_{\rm sys}$ is huge, Eq. (38) immediately gives Eq. (37).

We note that the Nambu-Goldstone mode with a linear dispersion does not exist in the ground state of metallic superconductivity. In this case, the long-range Coulomb interaction between electrons pushes this gapless mode up to the gapped plasma mode (Anderson-Higgs mechanism) (Anderson, 1963),

$$\omega_{\rm p1} = \sqrt{\frac{4\pi N e^2}{m}}. \tag{40}$$

Just below T_c, however, the gapless collective mode revives even in superconductivity, because quasi-particles excited thermally (that are actually Bogoliubov single-particle excitations) screen the long-range Coulomb interaction between superconducting electrons, so that the Anderson-Higgs mechanism no longer works. This revived Nambu-Goldstone mode in superconductivity is known as the Carlson-Goldman mode (Carlson and Goldman, 1975; Ohashi and Takada, 1997).

Tan's contact

When the system is described by the BCS Hamiltonian in Eq. (8) with no high-momentum cutoff, Tan proved that the internal energy E can be written as (Tan, 2008a)

$$E = 2\sum_{\boldsymbol{p}} \varepsilon_{\boldsymbol{p}}\left[n_{\boldsymbol{p}} - \frac{C}{p^4}\right] + \frac{C}{4\pi m a_s}, \tag{41}$$

where C is called the Tan's contact, which is obtained from the high momentum behavior of the momentum distribution $n_{\boldsymbol{p}} = \langle c_{\boldsymbol{p},\sigma}^{\dagger} a_{\boldsymbol{p},\sigma}\rangle$ as

$$n_{\boldsymbol{p}} \xrightarrow[p\to\infty]{} \frac{C}{p^4}. \tag{42}$$

The Tan's contact C vanishes in a free Fermi gas, because $n_{\boldsymbol{p}}$ is just the Fermi distribution function in this case. Thus, C is related to correlation effects. Since ^{40}K and ^{6}Fermi gases with a broad Feshbach resonance are well described by the BCS model in Eq. (8), this quantity in the BEC-BCS crossover region has attracted much attention in cold Fermi gas physics.

Although the BCS-Leggett theory is an approximate theory, it still satisfies the exact expression in Eq. (41): In the mean-field BCS approximation, one finds,

$$n_{\boldsymbol{p}} = 1 - \frac{\xi_{\boldsymbol{p}}}{E_{\boldsymbol{p}}} \xrightarrow[p\to\infty]{} \frac{m^2\Delta^2}{p^4}, \tag{43}$$

which immediately gives

$$C = m^2|\Delta|^2. \tag{44}$$

It can be shown that the BCS ground state energy,

$$E = \sum_{\boldsymbol{p}}\left[\xi_{\boldsymbol{p}} - E_{\boldsymbol{p}} + \frac{\Delta^2}{2\varepsilon_{\boldsymbol{p}}}\right] + \mu N - \frac{m}{4\pi a_s}|\Delta|^2, \tag{45}$$

can be rewritten as Eq. (41), when Eq. (44) is used.

In the unitary limit ($(k_{\rm F}a_s)^{-1} = 0$) at $T = 0$, Eq. (44) gives $C \simeq 0.12k_{\rm F}^4$ (Ohashi et al., 2020), which is close the experimental result, $C \simeq 0.1k_{\rm F}^4$, observed in a ^{6}Li superfluid Fermi gas (Horikoshi et al., 2017).

Tan also derived the following *adiabatic sweep theorem* (Tan, 2008b),

$$\left(\frac{\partial E}{\partial a_s^{-1}}\right)_N = -\frac{C}{4\pi m}, \tag{46}$$

as well as the *pressure relation*,

$$P = \frac{2}{3}E + \frac{C}{12\pi m a_s}. \tag{47}$$

These exact equations are also satisfied in the BCS-Leggett theory, when Eq. (44) is used (Ohashi et al., 2020).

Unitary Fermi gas and universal thermodynamics

The unitary limit, which is characterized by the diverging scattering length $a_s \to \pm\infty$ (or $(k_{\rm F}a_s)^{-1} = 0$), is located just in the center of the BEC-BCS crossover phase diagram shown in Fig. 3. Since this regime is dominated by strong pairing fluctuations cause by the strong attractive interaction, various interacting many-body phenomena, such as the pseudogap, have been discussed (Zwerger, 2012).

At this special interaction strength ($a_s^{-1} = 0$), we can no longer use the scattering length a_s as a length scale of the system. The remaining relevant length scales are the thermal de Broglie length,

$$\lambda_T(T) = \sqrt{\frac{2\pi}{mT}}, \tag{48}$$

and the inter-particle distance $l \propto \rho(\mu)^{-1/3}$, where

$$\rho(\mu) = \frac{(2m\mu)^{3/2}}{3\pi^2} \tag{49}$$

is the number density of an assumed free Fermi gas with the Fermi energy μ. Using these, Ho proposed the hypothesis that the thermodynamic potential Ω in a unitary Fermi gas may be scaled by these parameters as (Ho, 2004), for example,

$$\Omega(T, \mu, V) = \mu V \rho(\mu) g_\mu\left(\frac{\mu}{T}\right), \tag{50}$$

and

$$\Omega(T, \mu, V) = T\frac{V}{\lambda_T^3(T)} g_T\left(\frac{\mu}{T}\right), \tag{51}$$

where $g_\mu(x)$ and $g_T(x)$ are dimensionless functions. Using Eq. (51), one obtains the particle number N and the entropy S as, respectively,

$$N = -\left(\frac{\partial\Omega}{\partial\mu}\right)_{T,V} = -\frac{V}{\lambda_T^3}\left(\frac{\partial g_T(x)}{\partial x}\right)_{x=\mu/T}, \tag{52}$$

$$\begin{aligned} S &= -\left(\frac{\partial\Omega}{\partial T}\right)_{\mu,V} \\ &= -\frac{5}{2}\frac{V}{\lambda_T^3} g_T\left(\frac{\mu}{T}\right) + \frac{\mu}{T}\frac{V}{\lambda_T^3}\left(\frac{\partial g_T(x)}{\partial x}\right)_{x=\mu/T}. \end{aligned} \tag{53}$$

Substituting Eqs. (51)–(53) into the thermodynamic identity,

$$\Omega = -PV = E - TS - \mu N, \tag{54}$$

we obtain the well-known expression in a free Fermi gas,

$$E = \frac{2}{3}PV, \tag{55}$$

in spite of the fact that we are considering a strongly interacting unitary Fermi gas. Equation (55) is universal in the sense that it holds at arbitrary temperatures in the unitary limit, irrespective of whether the system is in the superfluid state or in the normal state. Equation (55) also agrees with the exact pressure relation in Eq. (47) when $a_s^{-1} \to 0$.

At $T = 0$, using Eq. (54) with $S(T = 0) = 0$, we also obtain

$$E = \frac{3}{5}N\mu \equiv \frac{3}{5}\xi_{\rm B} N \varepsilon_{\rm F}, \tag{56}$$

where $\xi_B = \mu/\varepsilon_F$ is called the Bertsch parameter, describing correlation effects in the ground state of a unitary Fermi gas. The BCS-Leggett theory gives $\xi_B \simeq 0.6$, which is larger than the experimental result, $\xi_B \simeq 0.375$, on a ^{6}Li unitary Fermi gas (Horikoshi et al., 2017). The T-matrix theories give better results, $\xi_B = 0.36$–0.45, depending on detailed approximations (Ohashi et al., 2020).

Neutron superfluid in the crust regime of neutron star

It is expected that the region-A in Fig. 3 ($(k_F a_s)^{-1} \ll 1$ and $T \ll T_c$) is similar to the s-wave neutron superfluid state predicted in the low-density crust regime of a neutron star. Since the neutron number density ($\rho_N \propto k_F^3$) increases as one goes inside the neutron star, the scaled interaction $(k_F a_s)^{-1}$ varies, in spite of the fixed value of the neutron s-wave scattering length $a_s \simeq -18.5$ fm. This is the reason why the region-A in Fig. 3 extends laterally.

However, we cannot immediately employ the results obtained in this regime of superfluid ^{40}K and ^{6}Li Fermi gases for the study of the neutron superfluid, because the importance of the effective range $r_{\rm eff}$ is different between the two systems: While it is negligibly small in ^{40}K and ^{6}Li Fermi gases, it cannot be ignored in the neutron superfluid, because $r_{\rm eff} \simeq 2.7$ fm there (which gives $(k_F r_{\rm eff}) \simeq 2.7$ for the typical value $k_F = 1\ {\rm fm}^{-1}$ in the crust regime). Thus, in order to study the latter nuclear matter, we need to extend the strong-coupling theories developed in cold Fermi gas physics to the case with $r_{\rm eff} \neq 0$.

To deal with the effective range $r_{\rm eff}$, it is convenient to replace the contact-type pairing interaction $-U$ involved in Eq. (8) by a momentum dependent one $-\tilde{U}(\boldsymbol{p} - \boldsymbol{p}')$. Within the effective range theory, $r_{\rm eff}$ can conveniently be incorporated into the theory by approximating $-\tilde{U}(\boldsymbol{p} - \boldsymbol{p}')$ to the following separable form in considering the Cooper channel:

$$-\tilde{U}(\boldsymbol{p} - \boldsymbol{p}') \to -\tilde{U}(\boldsymbol{0})\gamma_{\boldsymbol{p}}\gamma_{\boldsymbol{p}'}. \tag{57}$$

Here, the basis function $\gamma_{\boldsymbol{p}}$ has the form,

$$\gamma_{\boldsymbol{p}} = \frac{1}{\sqrt{1 + (p/p_c)^2}}. \tag{58}$$

The relation between the s-wave scattering length a_s and the BCS coupling constant $-U$ in Eq. (10) is replaced by

$$\frac{4\pi a_s}{m} = -\frac{\tilde{U}(\boldsymbol{0})}{1 - \tilde{U}(\boldsymbol{0})\sum_{\boldsymbol{p}} \frac{\gamma_{\boldsymbol{p}}^2}{2\varepsilon_{\boldsymbol{p}}}} = -\frac{\tilde{U}(\boldsymbol{0})}{1 - \tilde{U}(\boldsymbol{0})\frac{m p_c}{4\pi}}. \tag{59}$$

In the two-particle limit, setting

$$P_c = \frac{1}{r_{\rm eff}}\left[\sqrt{1 - \frac{2r_{\rm eff}}{a_s}} + 1\right], \tag{60}$$

we obtain the ordinary expression for the s-wave scattering amplitude $f_s(p)$ in the effective range theory (van Wyk et al., 2018),

$$f_s(p) = \frac{1}{-\frac{1}{a_s} + \frac{1}{2}r_{\rm eff}p^2 - ip}. \tag{61}$$

When the pairing interaction is replaced by Eq. (57) in the BCS-Leggett theory, the number equation (12) remains unchanged, except that superfluid order parameter Δ involved in $E_{\boldsymbol{p}} = \sqrt{\xi_{\boldsymbol{p}}^2 + |\Delta|^2}$ is replaced by the momentum-dependent one,

$$\Delta_{\boldsymbol{p}} = \gamma_{\boldsymbol{p}}\Delta. \tag{62}$$

The gap equation (11) is replaced with

$$1 = \tilde{U}(\boldsymbol{0})\sum_{\boldsymbol{p}} \frac{\gamma_{\boldsymbol{p}}^2}{2E_{\boldsymbol{p}}}. \tag{63}$$

In the case of Eq. (10) where the momentum summation diverges, the strength of the bare interaction strength $-U$ should be considered infinitesimally small. Because of this, in the BCS-Leggett theory explained in Sec. II·B has no Hartree term. On the other hand, Eq. (59) gives $-\tilde{U}(0) \neq 0$, leading to non-zero Hartree energy $\Sigma_H = -\tilde{U}(\boldsymbol{0})N_{\rm MF}/2$ (where $N_{\rm MF}$ is the number of Fermi atoms in the mean-field approximation). When this effect is taken into account, the Fermi chemical potential μ involved in the gap equation (63) and the number equation (12) is replaced by $\tilde{\mu} = \mu - \Sigma_H$.

The gap equation (63) indicates that $r_{\rm eff}$ effectively gives a (smooth) momentum cutoff, above which the pairing interaction is weak. Regarding this, we note that, while the cutoff ω_D in conventional superconductivity determines the region where the phonon-mediated pairing interaction works *around the Fermi level* $\sim [\varepsilon_F - \omega_D, \varepsilon_F + \omega_D]$, the present cutoff coming from the effective range $r_{\rm eff}$ does not depend on the Fermi level. As a result, when $p_c \gg k_F$ in the low density region, the situation is close to the case of ultracold Fermi gases (where $p_c \to \infty$, see also Eq. (10)). On the other hand, the pairing interaction around the Fermi level becomes weak, when $p_c \ll k_F$ in the high-density region. In this case, we cannot ignore effects of the effective range on the pairing phenomenon.

In the *s*-wave neutron superfluid ($a_s \simeq -18.5$ fm and $r_{\rm eff} \simeq 2.7$ fm), Eq. (60) is evaluated as

$$p_c \simeq 0.79 \text{ fm}^{-1}. \tag{64}$$

Thus, we expect that the cold Fermi gas system can be used as a quantum simulator for the study of the neutron superfluid in the low-density region satisfying $p \lesssim 0.79\text{fm}^{-1}$ Indeed, it has been shown that the superfluid NSR theory including the effective range well reproduces the equation of states of a neutron star predicted by using realistic nucleon-nucleon interactions, up to $k_{\rm F} \simeq 1$ fm^{-1} (van Wyk et al., 2018).

When one goes deeper inside a neutron star ($k_{\rm F}$ ⊠ 1fm^{-1}), the *s*-wave interaction gradually becomes less dominant. Instead, mole complicated interactions, such as a *p*-wave and a *d*-wave ones, appear. At this stage, the simplest *s*-wave superfluid state has been realized in ultracold Fermi gases. Thus, it seems difficult to simulate the deeper inside a neutron star in the current stage of cold Fermi gas physics.

Conclusion

The BEC-BCS crossover phenomenon enables us to study how a Fermi superfluid continuously changes to a Bose superfluid, as the strength of a Fermi-Fermi attractive interaction increases. In a sense, this many-body phenomenon provides a unified description of these superfluids that are usually discussed in different physical systems. A tunable pairing interaction associated with a Feshbach resonance is a crucial key in realizing this phenomenon in ultracold ^{40}K and ^{6}Li Fermi gases.

Although the mean-field BCS theory was originally invented to describe weak-coupling superconductivity, it can actually cover the whole BEC-BCS crossover region at $T = 0$, when strong-coupling corrections to the Fermi chemical potential is taken into account. At non-zero temperatures, especially at $T_{\rm c}$, however, we need to include effects of pairing fluctuations beyond the mean-field level.

The *s*-wave neutron superfluid predicted in the low-density crust regime of a neutron star is considered to be close to a unitary Fermi superfluid far below $T_{\rm c}$. Thus, although the importance of the effective range is different between this neutron superfluid and superfluid ^{40}K and ^{6}Li Fermi atomic gases, the latter atomic system may be used as a quantum simulator for the study of the former nuclear matter in the low density region ($k_{\rm F} \lesssim 1$ fm^{-1}).

We finally list some future directions:

1. At present, the simplest *s*-wave superfluid has only been realized in ultracold Fermi gases. Since various non *s*-wave Fermi superfluids are known in superconductivity, liquid ^{3}He, as well as deep inside neutron stars, the realization of unconventional pairing states is an important challenge in cold Fermi gas experiment. Once an unconventional superfluid Fermi atomic gas is realized by using a non *s*-wave Feshbach resonance, we would again be able to examine properties of this state from the weak-to strong-coupling regime, as in the *s*-wave case.
2. Although we now have various strong-coupling theories that can describe the BEC-BCS crossover phenomenon, their treatments of the correlation between Cooper pairs in the strong coupling BEC regime have still room for improvement (Petrov et al., 2004). In addition, when we simply extend the NSR theory and *T*-matrix theories to the superfluid phase below $T_{\rm c}$, it is known that they unphysically give the first-order phase transition in the strong-coupling BEC regime (Fukushima et al., 2007). These remain to be solved in BEC-BCS crossover theory.
3. Recently, the BEC-BCS crossover has experimentally been discussed in various metallic superconductors (Kasahara et al., 2014; Nakagawa et al., 2022; Suzuki et al., 2022). The possibility of crossover phenomenon has also been discussed in non-equilibrium exciton-polariton condensate (Yamaguchi et al., 2012). It would also be an crucial issue to explore how to use the highly tunable ultracold Fermi gas system as a quantum simulator for the studies of these newly developing BEC-BCS crossover systems.

Acknowledgments

I thank Prof. Tapash Chakraborty for giving me the opportunity of preparing this chapter.

References

Anderson PW (1958) Random-phase approximation in the theory of superconductivity. *Physics Review* 112: 1900–1916.
Anderson PW (1963) Plasmons, gauge invariance, and mass. *Physics Review* 130: 439–442.
Bartenstein M, et al. (2004) Crossover from a molecular Bose-Einstein condensate to a degenerate fermi gas. *Physical Review Letters* 92: 120401. (1-4).
Biss H, et al. (2022) Excitation spectrum and superfluid gap of an ultracold fermi gas. *Physical Review Letters* 128: 100401. (1-7).
Carlson RV and Goldman AM (1975) Propagating order-parameter collective modes in superconducting films. *Physical Review Letters* 34: 11–15.
Chin C, et al. (2010) Feshbach resonances in ultracold gases. *Reviews of Modern Physics* 82: 1225–1286.
Cooper L (1956) Bound electron pairs in a degenerate fermi gas. *Physics Review* 104: 1189–1190.
Eagles DM (1969) Possible pairing without superconductivity at low carrier concentrations in bulk and thin-film superconducting semiconductors. *Physics Review* 186: 456–463.

Fukushima N, et al. (2007) Superfluid density and condensate fraction in the BCS-BEC crossover regime at finite temperatures. *Physical Review A* 75: 033609. (1-10).

Gandolfi S, et al. (2015) Neutron matter from low to high density. *Annual Review of Nuclear and Particle Science* 65: 303–328.

Haussmann R (1999) *Self-Consistent Quantum-Field Theory and Bozonization for Strongly Correlated Electron Systems*. Berlin: Springer.

Haussmann R (2008) Thermodynamics of the BCS-BEC crossover. *Physical Review A* 75: 023610. (1-22).

Ho TL (2004) Universal thermodynamics of degenerate quantum gases in the unitarity limit. *Physical Review Letters* 92: 090402. (1-4).

Hohenberg PC (1967) Existence of long-range order in one and two dimensions. *Physics Review* 158: 383–386.

Holland M, et al. (2001) Resonance superfluidity in a quantum degenerate fermi gas. *Physical Review Letters* 87: 120406. (1-4).

Horikoshi M, et al. (2017) Ground-state thermodynamic quantities of homogeneous spin-1/2 fermions from the BCS region to the unitarity limit. *Physics Review X* 7: 041004. (1-15).

Kasahara S, et al. (2014) Field-induced superconducting phase of FeSe in the BCS-BEC cross-over. *PNAS* 111: 16309–16313.

Kashimura T (2012) Spin susceptibility and fluctuation corrections in the BCS-BEC crossover regime of an ultracold Fermi gas. *Physical Review A* 86: 043622. (1-8).

Kinast J, et al. (2004) Evidence for superfluidity in a resonantly interacting fermi gas. *Physical Review Letters* 92: 150402. (1-4).

Leggett AJ (2006) *Quantum Liquid*. New York: Oxford.

Mermin ND and Wagner H (1966) Absence of ferro-magnetism or antiferromagnetism in one- or two-dimensional isotropic heisenberg models. *Physical Review Letters* 17: 1133–1136.

Nakagawa Y, et al. (2022) Gate-controlled BCS-BEC crossover in a two-dimensional superconductor. *Science* 372: 190–195.

Nozières P and Schmitt-Rink S (1985) Bose condensation in an attractive fermion gas: From weak to strong coupling superconductivity. *Journal of Low Temperature Physics* 59: 195–211.

Ohashi Y and Griffin A (2002) BCS-BEC crossover in a gas of fermi atoms with a Feshbach resonance. *Physical Review Letters* 89: 130402. (1-4).

Ohashi Y and Griffin A (2003) Superfluidity and collective modes in a uniform gas of Fermi atoms with a Feshbach resonance. *Physical Review A* 67: 063612. (1-24).

Ohashi Y and Takada S (1997) Goldstone mode in charged superconductivity: Theoretical studies of Carlson-Goldman mode and effects of landau damping in the superconducting state. *Journal of the Physical Society of Japan* 66: 2437–2458.

Ohashi Y, et al. (2020) BCS-BEC crossover in cold atomic and in nuclear systems. *Progress in Particle and Nuclear Physics* 111: 103739. (1-54).

Partridge GB, et al. (2005) Molecular probe of pairing in the BEC-BCS crossover. *Physical Review Letters* 95: 020404. (1-4).

Perali A, et al. (2002) Pseudogap and spectral function from superconducting fluctuations to the bosonic limit. *Physical Review B* 66: 024510. (1-16).

Pethick CJ and Smith H (2008) *Bose-Einstein Condensation in Dilute Gases*. Cambridge: Cambridge University Press.

Petrov D, et al. (2004) Weakly bound dimers of fermionic atoms. *Physical Review Letters* 93: 090404. (1-4).

Randeria M (1995) Crossover from BCS Theory to Bose-Einstein Condensation. In: Griffin A, et al. (ed.) *Bose-Einstein Condensation*, pp. 355–392. New York: Cambridge University Press.

Regal CA, et al. (2004) Observation of resonance condensation of fermionic atom pairs. *Physical Review Letters* 92: 040403. (1-4).

Schrieffer JR (1964) *Theory of Superconductivity*. New York: Addison-Wesley.

Stewart JT (2008) Using photoemission spectroscopy to probe a strongly interacting Fermi gas. *Nature* 454: 744–747.

Stoks VGJ, et al. (1993) Partial-wave analysis of all nucleon-nucleon scattering data below 350 MeV. *Physical Review C: Nuclear Physics* 48: 792–815.

Suzuki Y, et al. (2022) Mott-driven BEC-BCS crossover in a doped spin liquid candidate κ-(BEDT-TTF)$_4$H$_{g2.89}$B$_{r8}$. *Physical Review X* 12: 011016. (1-9).

Tan S (2008a) Energetics of a strongly correlated Fermi gas. *Ann. Phys.* 323: 2952–2970.

Tan S (2008b) Large momentum part of a strongly correlated Fermi gas. *Annals of Physics* 323: 2971–2986.

Tsuchiya S, et al. (2008) Single-particle properties and pseudogap effects in the BCS-BEC crossover regime of an ultracold Fermi gas above Tc. *Physical Review A* 80: , 033613. (1-9).

van Wyk P, et al. (2018) Superfluid Fermi atomic gas as a quantum simulator for the study of the neutron-star equation of state in the low-density region. *Physical Review A* 97: 013601. (1-13).

Yamaguchi M, et al. (2012) BEC-BCS-laser crossover in Coulomb-correlated electron-hole-photon systems. *New Journal of Physics* 14: 065001. (1-33).

Zwerger W (ed.) (2012) *The BCS-BEC Crossover and the Unitary Fermi Gas*. New York: Springer.

Zwierlein MW, et al. (2004) Condensation of pairs of fermionic atoms near a feshbach resonance. *Physical Review Letters* 92: 120403. (1-4).

Superconductivity and superfluidity in neutron stars

Armen Sedrakian[a,b] **and John W Clark**[c,d], [a]Frankfurt Institute for Advanced Studies, Frankfurt am Main, Germany; [b]Institute of Theoretical Physics, University of Wroclaw, Wroclaw, Poland; [c]Department of Physics, Washington University, St. Louis, MI, United States; [d]Centro de Investigação em Matemática e Aplicações, University of Madeira, Funchal, Portugal

© 2024 Elsevier Ltd. All rights reserved.

Introduction 22
Overview 23
Microscopic theories 23
Imbalanced pairing 24
Quantized vorticity and rotation of neutron superfluids 25
Flux tubes and domains in the proton superconductor 26
Thermal evolution: Effects of superfluidity 27
Selected key issues 27
Neutron gap, induced interactions, non-adiabatic effects 27
The Proton gap and the role of the environment 27
Higher-spin pairing 28
Superfluid fraction in neutron star crusts 28
Conclusion 28
References 29

Abstract

Neutron and proton components of matter in neutron stars become superfluid and superconducting respectively, by forming Cooper pairs. In this contribution, we provide a concise overview of the current state and open questions in the area of superfluidity and superconductivity in neutron stars, including the microscopic quantum many-body theories and their methods, physics at the meso-scale associated with the quantum vorticity and, finally, the effects of superfluidity on the macroscopic manifestations in neutron stars.

Key points

- Neutron star internal structure, superconducting and superfluid phases.
- Many-body methods of solving the Cooper pairing problem.
- Quantum vortices and flux tubes in rotating and magnetized neutron stars.
- Some open problems from the micro- to macro-scales and interpretations of observations.

Introduction

Neutron stars are often viewed as low-temperature laboratories for studies of phenomena in strongly interacting quantum many-particle systems, which are encountered in a variety of terrestrial condensed matter systems. In reviewing their physics below we will emphasize the key milestones, the recent developments, and the open issues. For a more comprehensive coverage of the topic see our recent review (Sedrakian and Clark, 2019), as well as earlier alternatives which place emphasis on varied aspects of pairing phenomena (Lombardo and Schulze, 2001; Dean and Hjorth-Jensen, 2003; Takatsuka and Tamagaki, 1993). Among the many parallels between neutron stars and condensed matter systems, one could highlight the formation of quantized vortices in neutron matter in response to stellar rotation (Ginzburg, 1969; Baym et al., 1969b) in analogy to rotating liquid Helium-II (Khalatnikov, 1989; Hall and Vinen, 1956), emergence of quantized flux-tubes in the proton superconductor (Baym et al., 1969a) in analogy to the type-II superconductors in metals (Abrikosov, 1988), spin-1 pairing in high-density neutron matter (Takatsuka and Tamagaki, 1971) in analogy to the A-phase of liquid ^{3}He (Volovik, 2009), and mutual entrainment of neutron-proton condensates (Sedrakian and Shakhabasian, 1980; Alpar et al., 1984) in analogy to the mixtures of superfluid ^{3}He and ^{4}He (Andreev and Bashkin, 1976).

Nucleonic Fermi liquids of neutrons (n) and protons (p) can be found in a neutron star's inner crust and outer core, where neutrons and a small fraction ($\lesssim$10%) of protons and electrons coexist under the conditions of charge neutrality and β equilibrium with respect to neutron decay $n \to p + e + \bar{\nu}$ and electron-capture processes $p + e \to n + \nu$. Here, e, ν, and $\bar{\nu}$ stand for electrons, neutrinos, and anti-neutrinos; see Fig. 1 for an illustration. Due to the attractive component of the nuclear force, neutrons and protons form Cooper pairs on their respective Fermi surfaces in analogy to the Bardeen-Cooper-Schrieffer (BCS) mechanism of superconductivity. While the induced interaction is an important factor in determining the magnitude of the gap in the neutron and

https://doi.org/10.1016/B978-0-323-90800-9.00124-4

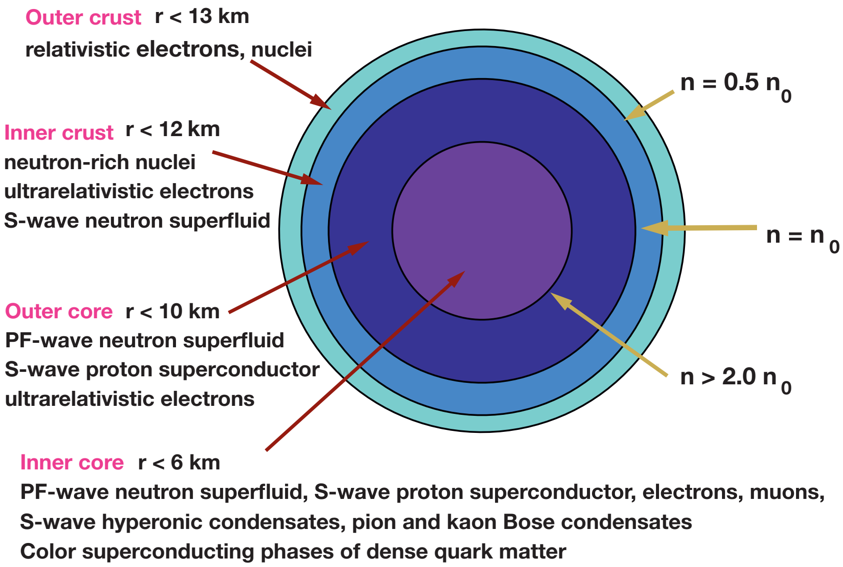
Outer crust r < 13 km
relativistic electrons, nuclei
Inner crust r < 12 km
neutron-rich nuclei
ultrarelativistic electrons
S-wave neutron superfluid
Outer core r < 10 km
PF-wave neutron superfluid
S-wave proton superconductor
ultrarelativistic electrons
Inner core r < 6 km
PF-wave neutron superfluid, S-wave proton superconductor, electrons, muons,
S-wave hyperonic condensates, pion and kaon Bose condensates
Color superconducting phases of dense quark matter
n = 0.5 n0
n = n0
n > 2.0 n0

Fig. 1 Schematic interior of a neutron star of mass $M = 1.4M_\odot$ with its four basic regions: outer and inner crusts and outer and inner cores. The four shells are identified along with the values of their respective outer radii r. Also indicated are the corresponding transition densities in units of n_0, as well as the particle content and condensates that may exist within each shell. Note that the figure is not to scale, low-n/large-r domains being strongly expanded.

proton quasiparticle spectra, its role is less crucial compared to the situation in metals, because of the attractive interaction between nucleons in the free space as opposed to e–e repulsion. Neutron-proton pairing is strongly suppressed by the large difference in the Fermi energies of neutrons and protons. The nucleon-nucleon potentials are analyzed in terms of their partial-wave components: in the low density (low energy) regime the dominant attractive interaction among neutrons, as well as protons, is in the $^1S_0$ partial-wave channel. This remains the case roughly up to the saturation density of nuclear matter, $n_0 \simeq 0.16$ fm^{-3}. At higher densities the most attractive channel is the coupled $^3P_2$–$^3F_2$ channel. It is worth noting that in isospin-symmetric nuclear matter with equal number of protons and neutrons, the dominant interaction channels in free space are the $^3S_1$–$^3D_1$ and $^3D_2$ channels at low and high energies. The characteristic scale of pairing gaps is of the order of 1 MeV, which is much larger than the characteristic temperature of mature neutron stars ($T \simeq 10^8$ K, 1 MeV $= 1.16\ 10^{10}$ K). Accordingly, neutron and proton superfluids can be treated effectively in the low-temperature limit. Fig. 1 shows schematically the structure of a neutron star and the location of various superfluid and superconducting phases.

There exists significant observational evidence for superfluidity of nucleonic components in neutron stars. The pulsed emission of pulsars (with periods of from milliseconds to several seconds) is caused by the periodic rotation of the star. This makes them nearly perfect clocks, but energy losses increase the rotational periods of pulsars over secular timescales. However, some pulsars undergo abrupt increases (glitches) in their rotation and spin-down rates that are followed by slow relaxation toward their pre-glitch values (in some cases with some permanent shift of either sign in the asymptotic values). These relaxations take place on a time scale of order weeks to years. A regularly glitching pulsar is the Vela pulsar, with typical changes in the spin $\Delta\nu/\nu \simeq 10^{-6}$ and spin-derivative $\Delta\dot{\nu}/\dot{\nu} \simeq 10^{-2}$. Another prominent pulsar in the Crab nebula shows smaller glitches with $\Delta\nu/\nu \simeq 10^{-8}$ (Espinoza et al., 2011). The long relaxations after glitches are commonly attributed to components within the star that are only weakly coupled to the rigidly rotating non-superfluid component, to which the emission of pulsed radiation is locked. Candidates for such a phase are various neutron superfluid components the core or in the crust (Haskell and Melatos, 2015; Haskell and Sedrakian, 2018; Andersson, 2021). Another (indirect) source of evidence for superfluidity of neutron star interiors is their cooling evolution over long time-scales of order of millions of years. Modeling of this process shows that the suppression of the specific heat of the nucleonic component by the gaps in the neutron and proton quasiparticle spectra and additional neutrino emission due to Cooper pair-breaking processes are necessary for a proper account of the available data on the surface temperatures of neutron stars (Yakovlev et al., 2001; Page et al., 2013; Sedrakian, 2007; Schmitt and Shternin, 2018).

Natural units $\hbar = c = k_B = 1$ will be used throughout.

Overview

Microscopic theories

The main challenge of computation of parameters of nucleonic superfluids and superconductors lies in the fact that nucleons form a strongly interacting system. Variety of microscopic methods have been employed to compute, most notably, the gap in the quasiparticle spectrum. At the *mean-field BCS level* and in the energy range where the interactions are well constrained by the elastic nucleon-nucleon scattering data, i.e., for laboratory energies $E_{\rm lab.} < 350$ MeV, the gap can be computed from the interaction in a given partial wave (Sedrakian and Clark, 2019). In the case of an S-wave interaction $v_0(p, p')$, where p and p' are the magnitudes of the relative incoming and outgoing momenta of the particles, the gap equation reads

$$\Delta(p) = -\frac{1}{V}\sum_{p'} v_0(p,p')\frac{\Delta(p')}{2E(p')}[1-2f(p')], \tag{1}$$

where V is the volume, $E(p) = \sqrt{\varepsilon(p)^2 + \Delta(p)^2}$ is the quasiparticle energy, composed of the gap $\Delta(p)$ and the particle energy $\varepsilon(p)$ in the unpaired state, while $f(p) = (e^{E(p)/T} + 1)^{-1}$ is the Fermi distribution function at temperature T. Mean-field computations of the gap with high-precision nuclear potentials lead to identical results for the gap function in the low-density S-wave paired superfluid and for wave superfluids up to the energy at which the elastic phase-shifts are accurate. Apart from these, effective interactions such as the so-called Skyrme and Gogny forces have been employed with similar results (Su et al., 1987; Sedrakian et al., 2003; Allard and Chamel, 2022).

Computation beyond mean-field level has focused mainly on two issues (i) Inclusion of correlations beyond mean-field in the self-energies of the nucleons, which are often encompassed in their effective masses, accounting for the momentum and energy dependence of the self-energy. The momentum dependence of the interaction leads to an effective mass in the range $m^*/m \simeq 0.8 - 0.6$ for neutron matter at low and intermediate densities ($n/n_0 \sim 0.5$–2), with similar values also for the dilute proton component at somewhat higher densities. The energy-dependent effective mass (inverse of wave-function renormalization) is close to unity and has less dramatic effect on the gap (Cao et al., 2006; Baldo and Schulze, 2007). (ii) Inclusion of the long-range correlations in the effective pairing interaction, which typically requires summation of polarization graphs; hence these corrections are often called "polarization" effects (Clark et al., 1976). They have been found to significantly reduce the gap by factors 50% and more (Cao et al., 2006; Rios et al., 2017; Urban and Ramanan, 2020).

The theories beyond mean field have been formulated using various many-body theories, which we sketch briefly below. The early work concentrated on the correlated basis function (CBF) theory (Clark, 2013). In this theory the correlations are built in the normal-state description of a strongly interacting Fermi system through the action of a correlation operator on the mean-field state. Pairing correlations are then superimposed on the correlated normal ground state, utilizing the BCS theory approach. This method allows one to sum up and include, in a parquet manner (Jackson et al., 1982, 1985) large classes of cluster diagrams in both particle-particle and particle-hole channels, albeit this requires some averaging procedure. In recent years this approach has been applied to low-density neutron matter (Fan and Krotscheck, 2019; Krotscheck and Wang, 2021; Krotscheck and Wang, 2022).

Various Monte Carlo approaches to the problem have focused mainly on finding the correlated ground state of the normal state. In practice, an infinite system is simulated in a finite box containing a fixed number of particles subject to periodic boundary conditions. The pairing gap is then obtained from the energy difference between systems with odd and even particle numbers. These computations typically involve solutions of the non-relativistic Schrödinger equation using stochastic sampling of configurations, as the system is advanced in imaginary time. Recent work has concentrated on the Green Function Monte Carlo (GFMC) and Auxiliary Field Diffusion Monte Carlo (AFDMC) algorithms (Carlson et al., 2012; Gandolfi et al., 2022). The latest GFMC computations of bulk energy and pairing gaps in nuclear matter have been performed for systems of 60 nucleons. The self-consistent Green functions (SCGF) method (Ding et al., 2016; Rios et al., 2017) solves for the spectral function of a strongly interacting Fermi system in the normal state, thus taking into account the full off-shell features of the real and imaginary parts of the nucleon self-energy. The spectral functions are then also inserted into the BCS-type gap equation, which can be re-written in terms of normal and anomalous Greens functions featuring the normal-state spectral function. It should be noted that when detailed comparisons are appropriate, there is satisfactory agreement between the most recent CBF gap calculations (Fan and Krotscheck, 2019; Krotscheck and Wang, 2021; Krotscheck and Wang, 2022) and the $^1S_0$ gap in pure neutron matter and corresponding Monte Carlo results (Carlson et al., 2012, Gandolfi et al., 2022).

Fermi-liquid methods have been employed for several decades to assess the important effect of polarization of the medium on the value of the gap. Various studies have converged to the assessment that the mean-field gap in neutron matter, which is of the order of 1 MeV, is reduced by factors of the order of 2–3. (Wambach et al., 1993; Schulze et al., 2001; Urban and Ramanan, 2020).

Imbalanced pairing

Imbalanced pairing has been studied in metals since shortly after the formulation of the BCS theory in 1956. A new class of superconductors and superfluids arises when the pairing is between fermions that are on different Fermi surfaces. This is a generic situation in many contexts. In condensed matter systems, a superconductor placed in a spin-polarizing magnetic field, causing an imbalance between the number of spin-up and spin-down electrons is a good example. (Note that in fact the magnetic field mimics the polarizing effect of magnetic impurities in a metal). In nuclear physics, imbalanced pairing occurs, for example, for neutron-proton Cooper pairs in isospin asymmetric matter (i.e., for unequal numbers of protons and neutrons). Similar physics governs the pairing when neutrons (or protons) are placed in a strong magnetic field and the pairing is among spin-up and spin-down neutrons (or protons) (Stein et al., 2016). In condensed-matter systems, imbalanced pairing has been considered in the weak-coupling formalism, where the back-reaction of the pairing on the chemical potentials of particles is ignored. The imbalance was found to suppress pairing, the maximal value of the shift in the chemical potentials of two species being $\Delta(0)/\sqrt{2}$, where $\Delta(0)$ is the pairing gap in a balanced system. This limit is known as the Chandrasekhar-Clogston limit (Abrikosov, 1988). In the context of neutron-proton pairing, this back-reaction has been taken into account, leading notably to a continuous change in the gap as a function of density asymmetry (Stein et al., 2014). The ground state of an imbalanced superfluid can break translational or rotational symmetries if the imbalance is large enough. Breaking of translational invariance was first proposed and studied independently by Fulde and Ferrell (1964) and Larkin and Ovchinnikov (1965), (FFLO) who discovered that the superconducting state where the Cooper pairs carry a finite center of mass momentum can sustain imbalances beyond those given by

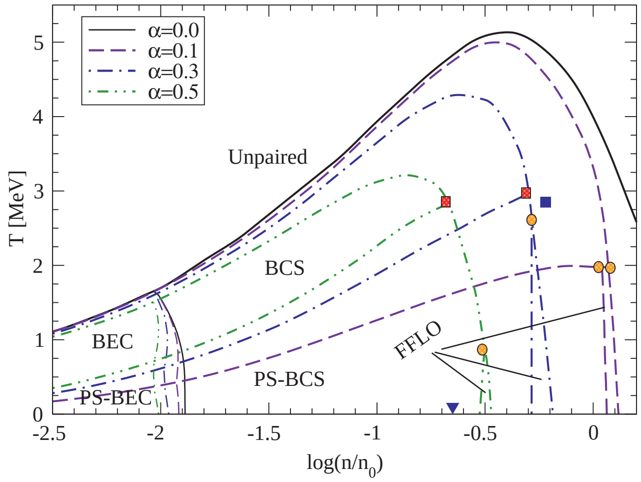

Fig. 2 Phase diagram of dilute nuclear matter in the temperature-density plane for several isospin asymmetries $\alpha = (n_n - n_p)/(n_n + n_p)$, where $n_{n/p}$ are the neutron and proton densities (Stein et al., 2014). The density is normalized by the nuclear saturation density n_0. For each fixed value of α there are two tri-critical points, the point bordering the FFLO phase always being a Lifshitz point. In a special case the tri-critical points merge into a tetra-critical point (square dot). The FFLO phase disappears in the low-density regime (the limiting value being shown by a triangle). The transition from BCS pairing to BEC occurs on the vertical lines located around $\log_{10}(n/n_0) = -2$.

Chandrasekhar-Clogston limit. An alternative to the FFLO phase invokes deformations of the Fermi surfaces of the fermion species from spherically symmetric to ellipsoidal form (Müther and Sedrakian, 2002, 2003). Another possibility is the separation of phases, originally suggested in the context of cold atomic gases (Bedaque et al., 2003) and studied thereafter in infinite nuclear matter under isospin asymmetry (Stein et al., 2014). When these various phases are studied simultaneously, it turns out that the phase diagram of dilute nuclear matter features BCS type pairing at temperatures close to the critical one, but develops various types of symmetry-broken phases at lower temperatures: the phase diagram then features tri-critical points, with at least one being a Lifshitz point (Stein et al., 2014), as seen in Fig. 2. Finally, let us note that nuclear systems may feature a transition from BCS pairing to Bose-Einstein condensation (BEC) as the system transitions from high to low density (Lombardo et al., 2001). The interplay between the BCS-BEC transition and imbalanced pairing demonstrates that the low-density and low-temperature limit features only a phase-separated imbalanced phase, whereas the phases with broken symmetries, as genuinely Fermi-surface phenomena, disappear (Stein et al., 2014). In closing, we note that imbalanced superfluids have been studied experimentally in ultracold atomic gases (Schunck et al., 2007). These systems allow for an unprecedented control over the parameters of the system, including the strength of the interaction via Feshbach resonance, size of the system, relative number of spin-up and -down particles, etc.

Quantized vorticity and rotation of neutron superfluids

Neutron stars contain an array of quantum vorticity in the neutron superfluid which emerges in response to the stellar rotation, in full analogy to terrestrial superfluids such as the Bose-condensed superfluid ^{4}He, fermionic superfluid ^{3}He, or dilute Bose or Fermi quantum gases. The rotational frequencies of neutron stars (pulsars) are well within the range between the lower and upper critical velocities for the formation and destruction of vorticity. Therefore we expect that the neutron fluid is generically threaded by an array of vortices with number density per unit area and triangular lattice basis vector given by

$$n_n^{(V)} = \frac{2\Omega}{\kappa}, \qquad d_n = \left(\frac{\kappa}{\sqrt{3}\Omega}\right)^{1/2}, \tag{2}$$

where $\kappa = \pi/m_n$ is the quantum of circulation, m_n is the neutron mass, and Ω is the angular velocity. The inter-vortex distance is of the order of $d_n \sim 10^{-4}$ cm for rotation periods of the order of a fraction of second. This characteristic scale is much larger than the microscopic length scales associated with the nuclear interaction and nuclear clusters (of the order 10 fm), but are much smaller than the macroscopic scales characterizing the sizes of the various regions (of the order of km). Thus the quantum vorticity defines a new *mesoscopic scale* for the description of neutron-star superfluids. Note that the macroscopic hydrodynamics requires an averaging over a large number of vortices. Interestingly, the vortex core size given by the coherence length $\xi \sim 10$ fm of the superfluid is microscopic. In the range $r \leq \xi$, where r is the radial cylindrical coordinate, the order parameter of the superfluid is suppressed linearly for $r \to 0$, vanishing at its center.

Microscopically, the core of a vortex contains specific excitations – a quasiparticle bound state described by the microscopic Bogolyubov-De Gennes (BdG) theory (de Gennes, 1999; Caroli et al., 1964; Yu and Bulgac, 2003). The solutions of these equations, in the simplest case of an S-wave superfluid in the cylindrical symmetry, show that their states are plane waves along the vortex circulation, but are quantized in the orthogonal direction. In the case of a P-wave superfluid, the vortex solutions have been studied within the Ginzburg-Landau theory, suitably generalized to spin-1 pairing. The solutions in the case have quite complex features, which include not only vortices but also domain walls (Masaki et al., 2022; Kobayashi and Nitta, 2022).

The rotational dynamics of neutron stars, notably their short-term behavior during glitches and post-glitch relaxation is controlled, to a large extent, by the dynamics of neutron vortices and their interactions with the ambient matter (Haskell and Sedrakian, 2018). Much attention has been paid to the idea of pinning of neutron vortices to nuclei in the inner crust, as seen in Fig. 1, and to their dissipative motion through it due to their quantum and thermally activated creep in analogy with the resistive state of type-II superconducting metals (Anderson and Itoh, 1975). Under a stationarity assumption, a first estimate of the pinning energy can be obtained by comparing the energy difference between a configuration where nucleus and vortex are well separated, with a configuration in which they intersect. More sophisticated approaches are based on microscopic solutions of the BdG equations (Wlazlowski et al., 2016; Bulgac, 2019).

Independent of the nature of the friction between the vortices and the normal fluid(s), a generic model of two-component star can be developed with a single superfluid and normal component, which provides qualitative understanding of the post-glitch relaxations of pulsars (Sedrakyan and Sedrakyan, 1995). The model is valid as long as the friction is linear in the velocity differences between the superfluid and the normal components (this may not be the case in some pinning models). More sophisticated models can be built upon assuming several superfluid shells with different moments of inertia and friction coefficients (Sedrakian et al., 1995). The fits to the post-glitch data allow one to fix these parameters in a model-independent manner (again assuming forces linear in velocities).

In the core of the star, the coexistence of the neutron and proton superfluids leads to their mutual entrainment (Sedrakian and Shakhabasian, 1980; Alpar et al., 1984; Allard and Chamel, 2022), in analogy to the mixtures of liquid ^{3}He and ^{4}He (Andreev and Bashkin, 1976), which implies that the motion of neutron fluid is accompanied by the motion of proton condensate and vice-versa. Mathematically, this arises from the off-diagonal elements of the matrix of densities which relates the fluid velocities to mass currents. As a result, the neutron circulation indues proton flow around the vortex, which in turn induces magnetization. Thus, neutron vortices acquire a non-quantized flux (Sedrakian and Shakhabasian, 1980; Alpar et al., 1984)

$$\phi^* = k_{\rm ent}\phi_0, \quad k_{\rm ent} = \frac{m_p^*}{m_p}, \tag{3}$$

where $\phi_0 = \pi/e$ is the flux quantum, while m_p^* and m_p are the effective and bare masses of protons.

An entrainment-like effect also takes place in the neutron star's inner crust consisting of neutron superfluid and plasma of crustal nuclei and electrons (Carter et al., 2006; Chamel, 2012, 2013, 2017; Watanabe and Pethick, 2017; Martin and Urban, 2016; Pethick et al., 2010; Kobyakov and Pethick, 2013). In this case also, the hydrodynamical mass current of each fluid is associated with the motion of the other. This has significant implications for the phenomenology of the neutron star glitches, through a reduction of the effective moment of inertia of the neutron superfluid, which rotates at a rate different from the crustal plasma that is locked to the rotation of the star.

Flux tubes and domains in the proton superconductor

Neutron stars are highly magnetized objects with typical field values in the range $B \sim 10^{12}$–10^{13} G. Along with the main population there are weak-field neutron stars, notably the millisecond pulsars with fields of the order $B \sim 10^8$–10^9 G and highly magnetized stars, known as magnetars, having $B \sim 10^{14}$–10^{15} G. Proton superconductors respond to this magnetic field depending on the local value of the Ginzburg-Landau parameter $\kappa_{\rm GL} = \lambda^*/\xi_p$, where ξ_p is the proton coherence length and λ^* is the penetration depth of the magnetic field in superconductor.

In a wide range of densities in neutron star's core (and pasta phases of the inner crusts) one has $\kappa_{\rm GL} > 1/\sqrt{2}$, indicating that the proton superconductor is type II. This implies that electromagnetic vortices are formed with a density (Sedrakian et al., 1995)

$$n_p^{(V)} = \frac{B}{\phi_0}, \qquad \phi_0 = \frac{\pi}{e}, \tag{4}$$

where $\phi_{\rm O}$ is the flux quantum and B is the mean magnetic-field induction. As in metallic type II superconductors, the B-field will penetrate the proton superconductor if the field strength is between a lower critical field H_{c1} and an upper critical field H_{c2}. However, since neutron stars are expected to feature a magnetic field before proton superconductivity sets in and the timescales for the expulsion of the magnetic field from the star are very long, the flux remains frozen in the matter (Baym et al., 1969a). This implies that local regions of with high-intensity magnetic field can be formed with $H > H_{c1}$, which will allow quantum flux tubes to form. Computations show that in the high-density regime $\kappa_{\rm GL} < 1/\sqrt{2}$, which implies a type I superconductivity (Bruk, 1973; Sedrakian et al., 1997; Wood and Graber, 2022). As known from condensed matter systems, flux tubes are unstable in this case. The field is then arranged in superconducting and normal domains. The size of the domains depends on the mesoscopic physics, but is expected to be significantly larger than the size of a flux tube, which is of the order of $\lambda^* \sim 100$ fm.

In magnetars the fields are so strong that their characteristic energy can be of the order of the gap. Indeed, we note that interior fields of magnetars could be of the order of $B \sim 10^{16}$–10^{17} G without affecting the hydrostatic stability of the star. The interaction between the nucleon spin and the magnetic field is given by the term $\mu_N B$, where $\mu_N = e\hbar/2m_p$ is the nuclear magneton. Because this interaction will induce an imbalance in the numbers of spin-up and spin-down particles, one can anticipate that imbalance pairing patterns will arise in strongly magnetized superfluids in neutron stars. The fields at which the Chandrasekhar-Clogston limit is achieved are of the order $H_{c2} \sim 10^{16}$–10^{17} G for neutrons (Stein et al., 2016) and $H_{c2} \sim 10^{15}$ G for protons (Sinha and Sedrakian, 2015). Microscopic calculations show that the proton pairing gap and H_{c2} depend substantially on the density and it is plausible to expect that in some regions of the star the condition $B \leq H_{c2}$ will be fulfilled, i.e., the superconductivity will be quenched by the field. It should be noted that the mechanism described above does not work in the case of spin-parallel *P*-wave pairing (Mizushima et al., 2021).

The protonic superconductor will form quantum vortex arrays which are much more dense than those in the neutron superfluid for typical fields of the order of 10^{12} G and typical rotation frequencies of neutron stars. The number of flux tubes per unit area of a single neutron vortex is of the order of 10^{13}. There exist several scenarios on how the networks of neutron and proton vortices interact, and evolve in time. The "frozen-in" scenario assumes that the proton vortex array is tightly bound to the global field of the star and neutron vortices move through pinning barriers formed by proton flux-tubes. This resistive flow would then determine the rate at which the superfluid will react to the changes in the rotational rate of the star. The problem is complicated by the fact that (a) the topology of the magnetic field could be quite complicated (e.g., poloidal, toroidal, etc. fields) and therefore the structure of the flux-tube networks may be intricate; (b) the force between neutron and proton vortices strongly depends on their relative orientation, therefore their coupled dynamics will depend on the assumed configurations.

As a consequence of the entrainment, a neutron vortex may carry a whole cluster of proton flux tubes colinear with it (Sedrakian et al., 1995). The reason is that in the vicinity of the core of the neutron vortex the field intensity is larger than H_{c1} (ignoring for the moment any "primordial" field), so the proton superconductor is inevitably forced to create flux tubes. A cluster "dressing" a neutron vortex provides a much more effective scattering target than a single neutron vortex magnetized by entrainment. This has interesting implications for the response time scales of the superfluid core to sudden glitches (Sedrakian and Cordes, 1999).

The interaction between neutron and proton components in the case of type-I superconductivity of protons is complicated due to a number of factors. In some cases, when simplifying assumptions about the structure of the domains are made, one can compute the dynamics of a neutron vortex embedded in a type-I superconductor. In this case the coupling of the superfluid to the normal matter turns out to be less efficient (Sedrakian, 2005).

Thermal evolution: Effects of superfluidity

The thermal evolution of neutron stars can be tentatively divided into three stages: (a) An initial fast transient of 100 years during which the star's temperature drops to about 10^8 K at which the star's core becomes isothermal. (b) The following $t \lesssim 10^5$ yr are characterized by neutrino emission from the star's interior. This stage determines the subsequent evolution of the star and is important for interpretation of the X-ray data obtained from the observations by the satellites. (c) The last stage is characterized by the dominance of the photon emission from the surface of the star (Page et al., 2006).

The pairing of nucleonic components has significant effect on the cooling evolution of neutron stars and, therefore, the values of the gaps are crucial input in the simulations. Firstly, the pairing reduces the specific heat of nucleonic component in full analogy with the reduction of the specific heat of a superconductor as observed under terrestrial conditions. This reduces the "thermal inertia" of the star, which makes it easier to change its thermal content for a given energy loss mechanism. Secondly, because pairing blocks fermion excitations with energies smaller than twice the gap value, the neutrino radiation processes are exponentially suppressed for temperatures $T \ll \Delta$. This is quite analogous to the disappearance of resistivity in an ordinary superconductor due to the suppression of scattering by the gap. Thirdly, close to the critical temperature of pairing, close to which a star spends substantial time, pair-breaking and formation bremsstrahlung processes occur, in which Cooper pairs are thermally broken and recombined, with emission of neutrino-anti-neutrino pairs (Leinson and Pérez, 2006; Kolomeitsev and Voskresensky, 2008, 2010; Sedrakian, 2012).These processes are analogs of the condensed-matter processes of radio-frequency absorption by superconductors, which allow one to measure the magnitude of the gap in a variety of systems, including ultracold gases. Thus, one of the aims of research on thermal evolution of neutron stars is to place constraints on the pairing patterns and magnitudes of the gaps through a comparison of theoretical cooling curves with the observed surface temperature of neutron stars.

Selected key issues

Neutron gap, induced interactions, non-adiabatic effects

As should be clear from the discussion above, the magnitude of the pairing gap in neutron superfluid and proton superconductor is of crucial importance for modeling an array of problems in compact stars, including rotational dynamics (glitches, post-glitch relaxations), thermal evolution (specific heats, pair-breaking radiation rates), etc. While there is a convergence in the literature with regard to the mean-field and low-density behavior of the neutron gap, and some consensus about the suppression of the gap by the polarization effects, the ultimate role of various medium *effects* such as the polarization, off-shell contributions from the self-energy, and short-range correlations are still unsettled. Neutron pairing at subnuclear densities thus remains a topical issue where sophisticated many-body methods are called for. Non-adiabatic effects, well-known from the strong-coupling Eliashberg theories in condensed matter have rarely been considered in the case of nucleonic matter, but may offer an avenue to assess the impact of the induced interactions on the pairing gap beyond the Fermi-surface approximation.

The Proton gap and the role of the environment

The unbound proton component is commonly embedded in a much denser neutron component, whose effects on the proton pairing may be more significant than in the case of neutrons. For example, the polarization of the medium in this case and the contribution from the induced interaction may be larger than in the case of neutron matter. Short-range correlations and non-Fermi liquid effects are expected to be more pronounced for protons, which fill a much smaller Fermi-sphere than neutrons. It is plausible that protons cannot be approximated, in a reasonable manner, as well-defined quasiparticles.

Higher-spin pairing

The *P*-wave superfluidity of neutrons at high densities is uncertain for several reasons. Firstly, the interactions are not fixed by phase-shifts above a certain density, so the results can vary widely. Secondly, the gap has many components characterized by various quantum numbers and, in addition, there is an important tensor coupling of the *P* to the *F*-wave. Thus, an accurate solution of the pairing problem even at the mean-field level poses a significant problem.

Superfluid fraction in neutron star crusts

The fraction of neutron superfluid in the crust can be reduced if some of it is entrained by the lattice component. The resulting reduction of the superfluid moment of inertia can be prohibitive for explanation of glitches by crust-based models only. There is an ongoing debate about the actual amount of entrained neutrons, the key issue being the inclusion of pairing effects in the band structure calculations (Watanabe and Pethick, 2017; Chamel, 2017; Kashiwaba and Nakatsukasa, 2019).

Conclusion

We have briefly reviewed some topics related to nucleonic superfluidity in neutron stars. It is evident that there are profound parallels to condensed matter systems, in particular to cold atomic gases where many features discussed can be studied experimentally under controlled conditions. At the same time, a closer look demonstrates that the physics of neutron stars requires answers to questions that have not been or in the future may not be in the focus of condensed matter theory.

At the microscopic scale, it can be stated that the pairing problem at the level of mean-field BCS theory, with the pairing interaction extracted directly from free-space nuclear interactions, is essentially solved within the density range corresponding to energies where the scattering phase shifts are known. Various microscopic many-body calculation predict pairing properties that vary to certain degree, specifically with regard to the issue of suppression of *S*-wave pairing in neutron matter by long-range collective fluctuations in the nuclear medium. Recent progress has been in the area of treating fluctuation corrections and the effects of short-range correlations due to the repulsion of the two-nucleon potential at short distances. The ultimate goal of achieving a convergent result at least in the low-density regime is within reach. More challenging problems include the studies of pairing at higher densities, in particular pairing gaps in the $^3P_2$–$^3F_2$ channel, where the increasingly role of the three-nucleon forces cannot be neglected. Furthermore, the non-adiabatic effects (through the frequency dependence of the gap) and their impact on the phenomenology of neutron stars remains unexplored.

At meso-scales, it has been well established that the neutron superfluid rotates by forming a lattice of neutron vortices, protons are mostly type-II superconductors with characteristic critical fields within the range encountered in neutron stars, and pinning effects may play a prominent role both in the crust (vortex-nucleus pinning) and in the core (vortex-flux-tube) pinning. It has been shown that neutron vortices which are embedded in a proton superconductor acquire a non-quantized magnetic flux due to the entrainment effect; interestingly this observation does not have analogs in condensed matter theory to date. Open questions at the meso-scale involve (a) the structure of the pairing matrix for the $^3P_2$–$^3F_2$ paired condensate and its vortex solutions, (b) type-I superconductivity in the deep core of a neutron stars, in its domain structure and dynamics, (c) the spatial form and structure of proton vortex flux tubes, their possible clustering, and their interaction with neutron vortices; (d) the mutual friction coefficients in each specific scenario of neutron pairing and type of superconductivity, (e) the amount of entrainment in the crust, which remains a significant problem for crust-only glitch models in spite of convergent results for pinning forces that have emerged in recent years.

At the macroscopic scales, modeling of neutron-star thermal evolution and dynamics and comparison with available and emerging data is needed to gain control over the physics at smaller scales. Open questions include the location of glitches (crust vs. core vs. mixed location models), the components of the star responsible for post-glitch relaxation, and understanding the diversity of post-glitch behavior in theoretical models. Accounting for the wide diversity of measured temperatures of neutron stars remains a challenge to theory, and the role played by pairing is far from being explored exhaustively, although our understanding of the basic process and their effects on cooling are solid.

In closing, we can be confident that a significant number of observational programs in the electromagnetic spectrum and in gravitational waves—those planned and those already operating—will provide the community with new information on neutron stars, which is so crucial for the feedback and development of the theory.

This work was supported by the Deutsche Forschungsgemeinschaft (DFG) grant No. SE1836/5-2, and the Polish National Science Centre (NCN) grant 2020/37/B/ST9/01937. The authors acknowledge the support of the European COST Action PHAR0S(CA16214).

References

Abrikosov A (1988) *Fundamentals of the Theory of Metals*. North-Holland, Amsterdam: Courier Dover Publications.

Allard V and Chamel N (2022) $^1S_0$ pairing gaps, chemical potential and entrainment matrix in superfluid neutron-star cores for the Brussels-Montreal functionals. *arXiv e-prints,* art. arXiv:2203.08778.

Alpar MA, Langer SA, and Sauls JA (1984) Rapid postglitch spin-up of the superfluid core in pulsars. *ApJ* 282: 533–541.

Anderson PW and Itoh N (1975) Pulsar glitches and restlessness as a hard superfluidity phenomenon. *Nature* 256(5512): 25–27.

Andersson N (2021) A superfluid perspective on neutron star dynamics. *Universe* 7(1): 17.

Andreev AF and Bashkin EP (1976) Three-velocity hydrodynamics of superfluid solutions. *Soviet Physics - JETP* 42: 164.

Baldo M and Schulze HJ (2007) Proton pairing in neutron stars. *Physical Review C* 75(2): 025802.

Baym G, Pethick C, and Pines D (1969a) Superfluidity in neutron stars. *Nature* 224: 673–674.

Baym G, Pethick C, Pines D, and Ruderman M (1969b) Spin up in neutron stars: The future of the Vela pulsar. *Nature* 224: 872–874.

Bedaque PF, Caldas H, and Rupak G (2003) Phase separation in asymmetrical fermion superfluids. *Physical Review Letters* 91(24): 247002.

Bruk YM (1973) The intermediate state in a superconducting neutron star. *Astrofizika* 9: 237–256.

Bulgac A (2019) Time-dependent density functional theory for fermionic Superfluids: From cold atomic gases—To nuclei and neutron stars crust. *Physica Status Solidi B: Basic Research* 256(7): 1800592.

Cao LG, Lombardo U, and Schuck P (2006) Screening effects in superfluid nuclear and neutron matter within Brueckner theory. *Physical Review C* 74(6): 064301.

Carlson J, Gandolfi S, and Gezerlis A (2012) Quantum Monte Carlo approaches to nuclear and atomic physics. *Progress of Theoretical and Experimental Physics* 2012(1): 01A209.

Caroli C, De Gennes PG, and Matricon J (1964) Bound Fermion states on a vortex line in a type II superconductor. *Physics Letters* 9: 307–309.

Carter B, Chachoua E, and Chamel N (2006) Covariant Newtonian and relativistic dynamics of (magneto)-elastic solid model for neutron star crust. *General Relativity and Gravitation* 38: 83–119.

Chamel N (2012) Neutron conduction in the inner crust of a neutron star in the framework of the band theory of solids. *Physical Review C* 85(3): 035801.

Chamel N (2013) Crustal entrainment and pulsar glitches. *Physical Review Letters* 110(1): 011101.

Chamel N (2017) Entrainment in Superfluid Neutron-Star Crusts: Hydrodynamic Description and Microscopic Origin. *Journal of Low Temperature Physics* 189: 328–360.

Clark JW (2013) CBF in BCS. In: Broglia RA and Zelevinsky V (eds.) *Fifty Years of Nuclear BCS: Pairing in Finite Systems*, pp. 360–375. Singapore: World Scientific Publishing.

Clark JW, Källman C-G, Yang C-H, and Chakkalakal DA (1976) Effect of polarization on superfluidity in low density neutron matter. *Physics Letters A* 61: 331–334.

de Gennes P-G (1999) *Superconductivity of Metals and Alloys*. New York, NY: Advanced Book Program, Perseus Books.

Dean DJ and Hjorth-Jensen M (2003) Pairing in nuclear systems: From neutron stars to finite nuclei. *Reviews of Modern Physics* 75: 607–656.

Ding D, Rios A, Dussan H, Dickhoff WH, Witte SJ, Carbone A, and Polls A (2016) Pairing in high-density neutron matter including short- and long-range correlations. *Physical Review C* 94(2): 025802.

Espinoza CM, Lyne AG, Stappers BW, and Kramer M (2011) A study of 315 glitches in the rotation of 102 pulsars. *MNRAS* 414(2): 1679–1704.

Fan HH and Krotscheck E (2019) Variational and parquet-diagram theory for strongly correlated normal and superfluid systems. *Physics Reports* 823: 1–59.

Fulde P and Ferrell RA (1964) Superconductivity in a strong spin-exchange field. *Physics Review* 135: 550–563.

Gandolfi S, Palkanoglou G, Carlson J, Gezerlis A and Schmidt KE (2022) The $^1S_0$ pairing gap in neutron matter. *arXiv e-prints,* art. arXiv:2201.01308.

Ginzburg VL (1969) Superfluidity and superconductivity in the universe. *Journal of Statistical Physics* 1572-96131(1): 3–24.

Hall HE and Vinen WF (1956) The rotation of liquid Helium II. II. The theory of mutual friction in uniformly rotating Helium II. *Proceedings of the Royal Society of London Series A* 238: 215–234.

Haskell B and Melatos A (2015) Models of pulsar glitches. *International Journal of Modern Physics D: Gravitation; Astrophysics and Cosmology* 24: 1530008.

Haskell B and Sedrakian A (2018) Superfluidity and superconductivity in neutron stars. *Astrophysics and Space Science Library* 457: 401–454.

Jackson AD, Lande A, and Smith RA (1982) Variational and perturbation theories made planar. *Physics Reports* 86: 55–111.

Jackson AD, Lande A, and Smith RA (1985) Planar theory made variational. *Physical Review Letters* 54: 1469–1471.

Kashiwaba Y and Nakatsukasa T (2019) Self-consistent band calculation of the slab phase in the neutron-star crust. *Physical Review C* 100(3): 035804.

Khalatnikov I (1989) *An Introduction to the Theory of Superfluidity. Advanced Books Classics Series*Addison-Wesley Publishing Company. ISBN: 9780201095050.

Kobayashi M and Nitta M (2022) Core structures of vortices in Ginzburg-Landau theory for neutron $^3P_2$ superfluids. *Physical Review C* 105(3): 035807.

Kobyakov D and Pethick CJ (2013) Dynamics of the inner crust of neutron stars: Hydrodynamics, elasticity, and collective modes. *Physical Review C* 87(5): 055803.

Kolomeitsev EE and Voskresensky DN (2008) Neutrino emission due to Cooper-pair recombination in neutron stars reexamined. *Physical Review C* 77(6): 065808.

Kolomeitsev EE and Voskresensky DN (2010) Neutral weak currents in nucleon superfluid Fermi liquids: Larkin-Migdal and Leggett approaches. *Physical Review C* 81(6): 065801.

Krotscheck E and Wang J (2021) Variational and parquet-diagram calculations for neutron matter. III. S-wave pairing. *Physical Review C* 103(3): 035808.

Krotscheck E and Wang J (2022) Variational and parquet-diagram calculations for neutron matter. IV. Spin-orbit interactions and linear response. *Physical Review C* 105: 034345.

Larkin AI and Ovchinnikov Y (1965) Inhomogenous superconductivity. *Soviet Physics - JETP* 20: 762.

Leinson LB and Pérez A (2006) Vector current conservation and neutrino emission from singlet-paired baryons in neutron stars. *Physics Letters B* 638: 114–118.

Lombardo U and Schulze H-J (2001) Superfluidity in neutron star matter. In: Blaschke D, Glendenning NK, and Sedrakian A (eds.) *Physics of Neutron Star Interiors*. vol. 578, p. 30. Berlin: Springer Verlag.

Lombardo U, Nozières P, Schuck P, Schulze H-J, and Sedrakian A (2001) Transition from BCS pairing to Bose-Einstein condensation in low-density asymmetric nuclear matter. *Physical Review C* 64(6): 064314.

Martin N and Urban M (2016) Superfluid hydrodynamics in the inner crust of neutron stars. *Physical Review C* 94(6): 065801.

Masaki Y, Mizushima T, and Nitta M (2022) Non-Abelian half-quantum vortices in $^3P_2$ topological superfluids. *Physical Review B* 105(22): L220503.

Mizushima T, Yasui S, Inotani D, and Nitta M (2021) Spin-polarized phases of $^3P_2$ superfluids in neutron stars. *Physical Review C* 104(4): 045803.

Müther H and Sedrakian A (2002) Spontaneous breaking of rotational symmetry in superconductors. *Physical Review Letters* 88(25): 252503.

Müther H and Sedrakian A (2003) Phases of asymmetric nuclear matter with broken space symmetries. *Physical Review C* 67(1): 015802.

Page D, Geppert U, and Weber F (2006) The cooling of compact stars. *Nuclear Physics A* 777: 497–530.

Page D, Lattimer JM, Prakash M, and Steiner AW (2013) Pairing and superfluidity of nucleons in neutron stars. In: Bennemann KH and Ketterson JB (eds.) *Novel Superfluids, International Series of Monographs on Physics*, p. 505. Oxford: Oxford University Press.

Pethick CJ, Chamel N, and Reddy S (2010) Superfluid dynamics in neutron star crusts. *Progress of Theoretical Physics Supplement* 186: 9–16.

Rios A, Polls A, and Dickhoff WH (2017) Pairing and short-range correlations in nuclear systems. *Journal of Low Temperature Physics* 189(5–6): 234–249.

Schmitt A and Shternin P (2018) Reaction Rates and Transport in Neutron Stars. In: Rezzolla L, Pizzochero P, Jones DI, Rea N, and Vidaña I (eds.) *Astrophysics and Space Science Library*, *Volume 457 of Astrophysics and Space Science Library,* p. 455.

Schulze H-J, Polls A, and Ramos A (2001) Pairing with polarization effects in low-density neutron matter. *Physical Review C* 63(4): 044310.

Schunck CH, Shin Y, Schirotzek A, Zwierlein MW, and Ketterle W (2007) Pairing without superfluidity: The ground state of an imbalanced Fermi mixture. *Science* 316(5826): 867.

Sedrakian A (2005) Type-I superconductivity and neutron star precession. *Physical Review D* 71(8): 083003.

Sedrakian A (2007) The physics of dense hadronic matter and compact stars. *Progress in Particle and Nuclear Physics* 58: 168–246.

Sedrakian A (2012) Vertex renormalization of weak interactions in compact stars: Beyond leading order. *Physical Review C* 86(2): 025803.

Sedrakian A and Clark JW (2019) Superfluidity in nuclear systems and neutron stars. *European Physical Journal A* 55(9): 167.
Sedrakian A and Cordes JM (1999) Vortex-interface interactions and generation of glitches in pulsars. *MNRAS* 307(2): 365–375.
Sedrakian DM and Shakhabasian KM (1980) On a mechanism of magnetic field generation in pulsars. *Astrofizika* 16: 727–736.
Sedrakian AD, Sedrakian DM, Cordes JM, and Terzian Y (1995) Superfluid core rotation in pulsars. II. Postjump relaxations. *ApJ* 447: 324.
Sedrakian DM, Sedrakian AD, and Zharkov GF (1997) Type I superconductivity of protons in neutron stars. *MNRAS* 290(1): 203–207.
Sedrakian A, Kuo TTS, Müther H, and Schuck P (2003) Pairing in nuclear systems with effective Gogny and V_{low-k} interactions. *Physics Letters B* 576: 68–74.
Sedrakyan AD and Sedrakyan DM (1995) Dynamics of rotating superfluid systems with pinning. *Soviet Journal of Experimental and Theoretical Physics* 81(2): 341–346.
Sinha M and Sedrakian A (2015) Magnetar superconductivity versus magnetism: Neutrino cooling processes. *Physical Review C* 91(3): 035805.
Stein M, Sedrakian A, Huang X-G, and Clark JW (2014) BCS-BEC crossovers and unconventional phases in dilute nuclear matter. *Physical Review C* 90(6): 065804.
Stein M, Sedrakian A, Huang X-G, and Clark JW (2016) Spin-polarized neutron matter: Critical unpairing and BCS-BEC precursor. *Physical Review C* 93(1): 015802.
Su RK, Yang SD, and Kuo TTS (1987) Liquid-gas and superconducting phase transitions of nuclear matter calculated with real time Green's function methods and Skyrme interactions. *Physical Review C* 35: 1539–1550.
Takatsuka T and Tamagaki R (1971) Superfluid state in neutron star matter. II—Properties of anisotropic energy gap of $^3P_2$ pairing. *Progress of Theoretical Physics* 46(1): 114–134.
Takatsuka T and Tamagaki R (1993) Chapter II. Superfluidity in neutron star matter and symmetric nuclear matter. *Progress of Theoretical Physics Supplement* 112: 27–65.
Urban M and Ramanan S (2020) Neutron pairing with medium polarization beyond the Landau approximation. *Physical Review C* 101(3): 035803.
Volovik G (2009) *The Universe in a Helium Droplet. International Series of Monographs on Physics*Oxford: Oxford University Press. ISBN: 9780199564842.
Wambach J, Ainsworth TL, and Pines D (1993) Quasiparticle interactions in neutron matter for applications in neutron stars. *Nuclear Physics A* 555: 128–150.
Watanabe G and Pethick CJ (2017) Superfluid density of neutrons in the inner crust of neutron stars: New life for pulsar glitch models. *Physical Review Letters* 119(6): 062701.
Wlazlowski G, Sekizawa K, Magierski P, Bulgac A, and Forbes MM (2016) Vortex pinning and dynamics in the neutron star crust. *Physical Review Letters* 117(23): 232701.
Wood TS and Graber V (2022) Superconducting phases in neutron star cores. *Universe* 8(4): 228.
Yakovlev DG, Kaminker AD, Gnedin OY, and Haensel P (2001) Neutrino emission from neutron stars. *Physics Reports* 354: 1–155.
Yu Y and Bulgac A (2003) Spatial structure of a vortex in low density neutron matter. *Physical Review Letters* 90(16): 161101.

BEC-BCS crossover, condensed matter experiments

Kyosuke Adachi[a,b] **and Yoshihiro Iwasa**[c,d], [a]RIKEN Center for Biosystems Dynamics Research, Kobe, Japan; [b]RIKEN InterdisciplinaryTheoretical and Mathematical Sciences Program, Wako, Japan; [c]Department of Applied Physics and Quantum-Phase Electronics Center, The University of Tokyo, Tokyo, Japan; [d]RIKEN Center for Emergent Matter Science, Wako, Japan

© 2024 Elsevier Ltd. All rights reserved.

Introduction 31
Density-controlled BCS-BEC crossover 33
New materials 34
Graphene-based systems 34
Iron-based systems 34
Organic systems 35
Conclusion 36
References 36

Abstract

The BCS-BEC crossover indicates the qualitative change in physical properties of Fermions with attractive interactions from the weakly to strongly interacting regime, offering an important guideline for maximizing T_c with given interactions. Though Uemura et al. (1991) pointed out that high-T_c cuprates and other exotic superconductors can be close to the crossover regime, the superconducting gap, Δ, is typically more than two orders of magnitude smaller than the Fermi energy, E_F. This suggests that these materials are still far from the crossover regime. Recently, several classes of new superconductors with comparable Δ and E_F have been discovered. Furthermore, the density-controlled BCS-BEC crossover has been achieved in gate-controlled two-dimensional superconductors. We review the recent progress of superconductor research from the viewpoint of the BCS-BEC crossover.

Key points

- With the development of experimental techniques, the BCS-BEC crossover has been investigated in several classes of new superconductors.
- Material research substantiated by theoretical approaches should be essential in exploring new physical properties in the BCS-BEC crossover.

Introduction

Fermions with attractive interactions, like electrons in a superconductor, show qualitatively different collective properties depending on the interaction strength. The BCS-BEC crossover indicates the change in physical properties from weak to strong interaction regions, and several classes of superconductors have recently been investigated in the context of the BCS-BEC crossover. In the Introduction, we review the concept of the BCS-BEC crossover, a short history on the experimental side, and a simple theoretical expectation. Then we move to the subsequent sections that focus on the recent material research.

We first explain the basic concept of the BCS-BEC crossover using Fig. 1 (Randeria and Taylor, 2014). For Fermions with weak attractive interactions (left side in Fig. 1), the formation and condensation of pairs with opposite spins occur at the same temperature ($T^* = T_c$), and superconductivity (or superfluidity for electrically neutral Fermions) appears below T_c. In such a weak-coupling region, which is known as the BCS regime, superconductivity can be described by the BCS theory. In contrast, in the strong-coupling region called the BEC regime (right side in Fig. 1), pair formation temperature T^* is much higher than condensation temperature T_c, and superconductivity is regarded as BEC of tightly bound pairs. The superconducting states in the BCS and BEC regimes are connected without any phase transition through a crossover, which is called the BCS-BEC crossover. Typically, the crossover appears around the unitarity, which is the threshold for the creation of a two-body bound state in the vacuum. Importantly, T_c could be maximized around the unitarity, and thus approaching from the BCS to the BEC regime possibly provides us with some hint toward room temperature superconductivity.

The history of research on the BCS-BEC crossover is rather old. Early on, researchers had superconductors (Eagles, 1969; Nozières and Schmitt-Rink, 1985) or liquid helium (Leggett, 1980) in mind, but since the BEC and BCS-BEC crossover were experimentally discovered in ultracold atoms of ^{40}K (Regal et al., 2004) and ^{6}Li (Zwierlein et al., 2004), the major target was changed to ultracold Fermion atoms. The biggest experimental advantage of ultracold atoms is that the interaction between two Fermions can be tuned

https://doi.org/10.1016/B978-0-323-90800-9.00259-6

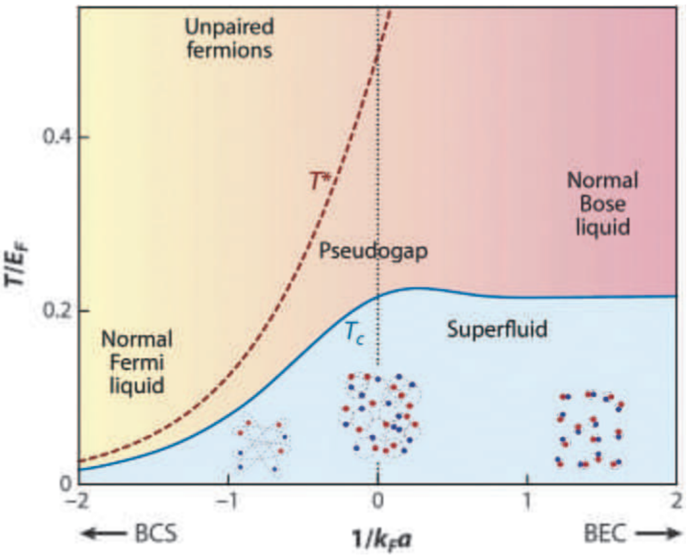

Fig. 1 Typical phase diagram for the BCS-BEC crossover (Randeria and Taylor, 2014). The horizontal axis represents the interaction strength measured by $1/k_{\mathrm{F}}a$, where k_{F} and a are the Fermi wavenumber and s-wave scattering length, respectively. From Randeria M and Taylor E (2014) Crossover from Bardeen-Cooper-Schrieffer to Bose-Einstein condensation and the unitary Fermi gas. *Annual Review of Condensed Matter Physics* 5: 209.

by the application of an external magnetic field through the Feshbach resonance. This allows the ultracold atom systems to access the crossover regime from the BEC side. For example, recent experimental techniques have enabled direct measurements of the excitation spectrum of Fermions through the BCS-BEC crossover (Biss et al., 2022).

The BCS-BEC crossover was first discussed from the material viewpoint by Uemura et al. (1991). They found that many new superconductors discovered in the 1980s, including high-T_c cuprates, organics, heavy Fermions, and even fullerenes, have low carrier density and are positioned rather close to the BCS-BEC crossover regime with $k_BT_c/E_F \sim 0.05$, where E_F is the Fermi energy, as shown in the well-known Uemura plot. However, the superconducting temperatures of these superconductors do not reach the BEC temperature estimated from statistical mechanics, and reaching this BEC regime remained a challenge for the material science of superconductors in the last century.

In contrast to the ultracold atom experiments, systematic control of the Fermion interaction strength is usually difficult in experiments of superconductors. Instead, carrier density can be tuned by doping or in more sophisticated ways explained in the next section, and thus the carrier density-induced BCS-BEC crossover is the realistic target in superconductors in contrast to the case of ultracold atoms. Here we briefly discuss the importance of dimensionality in inducing the BCS-BEC crossover by the change in carrier density. In Fig. 2, we show the ground-state superconducting gap divided by the Fermi energy, Δ/E_F, as a function of the Fermion density, which is calculated by the mean-field theory for (Fig. 2A) two-dimensional (2D) and (Fig. 2B) three-dimensional (3D) Fermion gas models with contact attractive interactions. Here, we roughly regard the regions with $\Delta/E_F < 0.1$ and $\Delta/E_F > 1$ as the BCS and BEC regimes, respectively. For the 3D case (Fig. 2B), we show the curves for positive, negative, and zero inverse scattering lengths, corresponding to different interaction strengths. We can see the qualitative difference

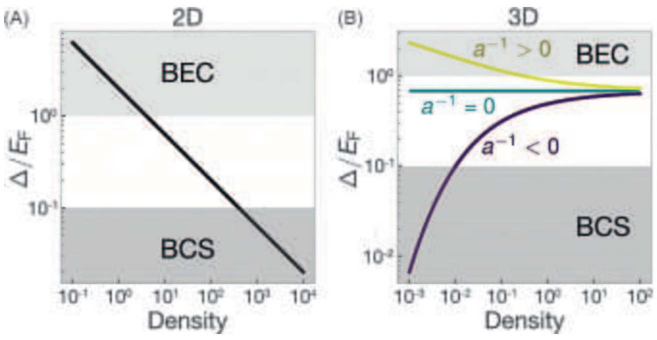

Fig. 2 Ratio of the superconducting gap to the Fermi energy, Δ/E_F, as a function of density for the (A) 2D and (B) 3D Fermion gas models with contact attractive interactions, calculated by the mean-field theory. For (A), density is normalized by $mE_B/2\pi$, where m is the particle mass and E_B is the two-particle bound-state energy. For (B), a is the s-wave scattering length, where the unitarity corresponds to $a^{-1} = 0$; density is normalized by $|a|^{-3}$ and k_F^3 for $a^{-1} \neq 0$ and $a^{-1} = 0$, respectively, where k_F is the Fermi wavenumber.

between the 2D and 3D systems: reducing the density in the 2D system can induce the crossover from the BCS regime to the BEC regime, whereas the change of density in the 3D system can only achieve either the BCS or BEC side, depending on the interaction parameter a. This notable difference indicates that the unitarity limit (i.e., $a^{-1} = 0$) is moved to the BCS limit in the 2D case, suggesting that 2D systems have a great advantage for the experimental realization of the density-controlled BCS-BEC crossover in superconductors.

Density-controlled BCS-BEC crossover

Following the considerations above, it is natural for experimentalists to choose 2D or layered materials to realize the carrier density-induced BCS-BEC crossover in superconductors. The field effect transistor, or more broadly, the "gating" technique has been utilized in this direction since it is a powerful tool for controlling the carrier density in superconductors, especially in the low carrier density regime. Recently, the gate-controlled BCS-BEC crossover has been reported on two different materials. One is the twisted bi- or tri-layer graphene (Cao et al., 2018; Park et al., 2021), and the other is the Li-intercalated ZrNCl (Nakagawa et al., 2021; Heyl et al., 2022). The former graphene systems are well-known 2D superconductors, where superconductivity appears in the extremely low carrier density regime owing to its moire superlattice. The carrier density is continuously controlled by the gate voltage. The latter ZrNCl is a band insulator and a van der Waals layered material, which consists of double honeycomb ZrN layers sandwiched by Cl layers. Intercalated Li ions go into the van der Waals gap between the Cl layers and supply electrons to the ZrN layer, which leads to conducting and superconducting properties. The carrier density is changed through the amount of the Li ions, which were controlled by an ionic gating device with $LiClO_4$/polyethylene glycol as an electrolyte.

Fig. 3 displays an electronic phase diagram for Li_xZrNCl. Here, Li amount x is supposed to be identical to the carrier density. In the high-density region, T_c is basically insensitive to the carrier density, whereas it forms a peak at $x \sim 0.01$. An important feature is that the pseudogap phase, detected by the tunneling spectroscopy, appears below $x = 0.1$, and its onset temperature T^* keeps increasing as x is decreased. The open triangles in Fig. 3 are the data obtained from the experiments on bulk polycrystalline samples, where $x = 0.05$ has been the limit (Kasahara et al., 2009). The ionic gating device has allowed us to go below this limit and reach the BCS-BEC crossover, as shown with the blue diamonds. Here we note that Li_xZrNCl is a layered material, and thus the system is highly two dimensional. Indeed, the resistive transitions exhibit the Berezinskii-Kosterliz-Thouless (BKT) behavior with the BKT transition temperature T_{BKT} slightly lower than T_c. However, the difference between T_{BKT} and T_c is small and negligible in the scale of Fig. 3.

Fig. 4 is the so-called Uemura plot, which shows the relation between T_c and Fermi temperature T_F, as mentioned in the Introduction. The important feature of Li_xZrNCl is that it starts from the deep inside of the BCS regime and traverses all the way to the theoretical BEC line for 2D systems by reducing the carrier density by almost two orders of magnitude. When compared with the phase diagram in Fig. 3, one realizes that the region on the left side of the peak of T_c reaches the theoretical limit for 2D systems. This behavior is a clear demonstration of the density-induced BCS-BEC crossover.

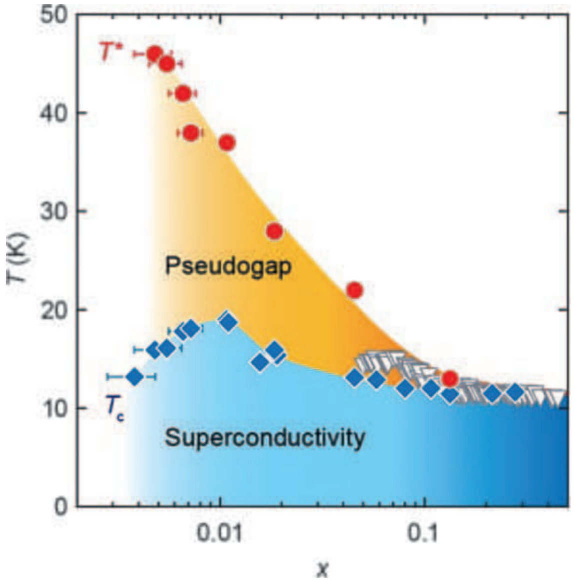

Fig. 3 Electronic phase diagram of Li_xZrNCl (Nakagawa et al., 2021). Blue triangles show the superconducting transition temperature T_c defined by the half resistance. Red circles show the gap-opening temperature T^* from the tunneling spectroscopy.

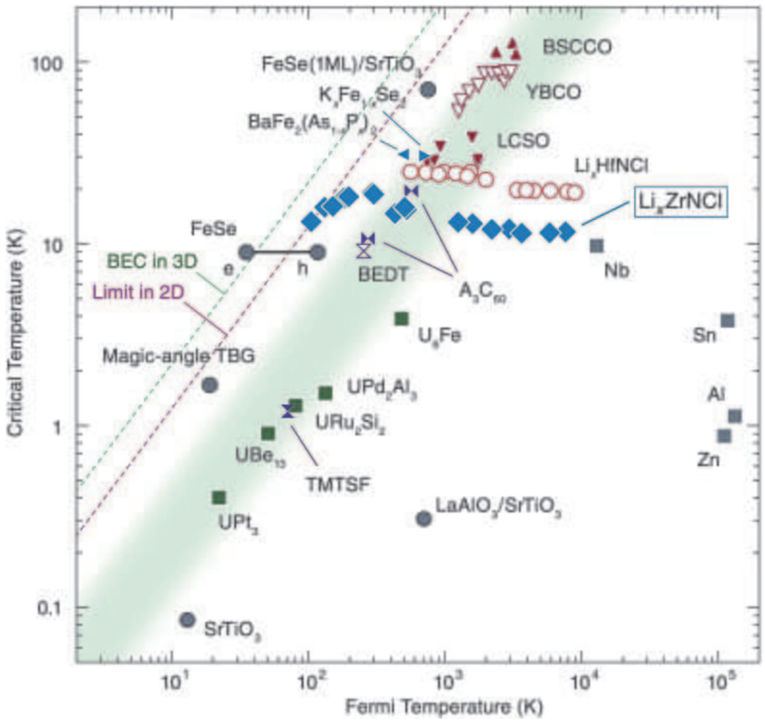

Fig. 4 Uemura plot. The magenta and green dashed lines are the theoretical predictions for the BEC limits in 2D and 3D systems, respectively. Two plots designated by e and h for FeSe show the points for the electron and hole pockets, respectively. From Nakagawa Y, Kasahara Y, Nomoto T, Arita R, Nojima T, and Iwasa Y (2021) Gate-controlled BCS-BEC crossover in a two-dimensional superconductor. *Science* 372: 190.

Furthermore, comparing the experimental (Fig. 3) and theoretical (Fig. 1) phase diagrams, we find that these two show qualitatively the same behavior by appropriately exchanging the horizontal axis. The pseudogap phase disappears in the BCS regime of Fig. 3, whereas it rapidly grows as the carrier density is reduced. Presumably, the layered structure of Li_xZrNCl shifts the unitarity toward the BCS side and enables the density-controlled BCS-BEC crossover, just like the 2D case in Fig. 2A.

Uemura et al. (1991) pointed out that many exotic superconductors discovered in the 1980s and 1990s fell on the green belt in Fig. 4, but the value of T_c/T_F was still one order of magnitude smaller than the theoretical predictions for the BEC limit. However, new materials discovered in the past decades are indeed very close to the limit for 2D systems. In Fig. 4, we can find FeSe systems and twisted bilayer graphene. Interestingly, these are 2D or quasi-2D systems, but we should point out that the BCS-BEC crossover in 3D is not prohibited, but only the density-controlled crossover in purely 3D systems with fixed interaction strength is prohibited by the theory. In the following, we briefly address such newly emerging superconductors.

New materials

Graphene-based systems

The BCS-BEC crossover was first pointed out in the discovery paper of superconductivity in magic-angle twisted bilayer graphene (Cao et al., 2018). The twisted bilayer graphene is also a 2D system and the crossover was approached also by the gating technique, but in this case, by the standard solid gate dielectric of exfoliated hexagonal BN. Amazingly, superconductivity appeared at the extreme carrier density of 1.5×10^{11} cm^{-2} as optimal, which was determined by the quantum oscillation. This carrier density is more than two orders of magnitude smaller than the optimal value in Li_xZrNCl. They realized the value of $T_c/T_{BEC} = 0.37$, where the 3D value for the BEC limit ($T_{BEC} = 0.218T_F$) was used for comparison. This means that they have achieved $T_c/T_F = 0.08$, which is close enough to the BEC limit for 2D systems ($T_{BEC} = 0.125T_F$), as seen in Fig. 4. In Park et al. (2021), the same group reported that the twisted trilayer graphene also exhibits the BCS-BEC crossover and reaches $T_c/T_F = 0.125$, the limiting value for 2D systems.

Iron-based systems

Fig. 4 indicates that two groups of FeSe are placed near the 2D BEC line. One is the FeSe single crystal with $T_c = 9$ K, and the other is the monolayer FeSe on the $SrTiO_3$ substrate. The former is a semimetal with a small carrier density, whereas, for the latter, many electrons are doped possibly from the $SrTiO_3$. Despite the big difference in T_c, which is around 9 K (Hsu et al., 2008) for the single crystal and 100 K for the monolayer (Ge et al., 2015), T_c/T_F is close to the 2D BEC limit of 0.125 for both systems. Since T_c in FeSe/$SrTiO_3$ has not been reproduced since the first paper and remains controversial, we focus on the superconductivity of the FeSe single crystal in the following.

One of the distinctive features common in iron-based superconductors is the multiband electronic structure. In FeSe, the cylindrical hole and electron bands contribute to the Fermi surface and the low-energy excitations (Terashima et al., 2014). According to the ARPES and STS experiments (Kasahara et al., 2014; Hashimoto et al., 2020), the values of T_c/T_F are around 0.05 and 0.1 for the hole and electron bands, respectively, and $\Delta/E_F > 0.1$ for both the hole and electron bands, suggesting that FeSe undergoes superconductivity between the BCS and BEC regimes. Despite the large values of T_c/T_F and Δ/E_F, the pseudogap has not been observed in the STS measurements, which may be explained by the theoretically expected suppression of the pseudogap region due to the nature of compensated semimetal (Chubukov et al., 2016).

In the BCS-BEC crossover, since the pairing interaction energy becomes comparable to the kinetic energy, the effect of superconducting fluctuation is expected to be significant. In FeSe, enhancement of the diamagnetic susceptibility has been observed well above T_c (Kasahara et al., 2016). Fig. 5 shows the temperature dependence of the diamagnetic susceptibility in FeSe (light-blue and red points), compared with the prediction of the Gaussian fluctuation theory (blue line), which is applicable to superconductors in the BCS regime with small fluctuation effects. The large gap between the observed susceptibility and the theoretical prediction has been attributed to the enhanced superconducting fluctuation in the crossover regime, though a smaller fluctuation effect has also been reported on FeSe using a different measurement technique (Takahashi et al., 2019).

The multiband features in the BCS-BEC crossover have also been studied using the S-doped FeSe systems (Hashimoto et al., 2020). As the S doping is increased, the orthorhombic-tetragonal structural transition is known to occur, and the pseudogap has been observed in the tetragonal phase in ARPES experiments. In addition, the Bogoliubov quasiparticles show a relatively flat dispersion relation in the S-doped systems, which may be attributed to the interband coupling between multiple hole bands near the Γ point. A comprehensive understanding of the multiband effects in the BCS-BEC crossover will require further experimental and theoretical investigations.

Organic systems

Suzuki et al. (2022) announced the discovery of pressure-driven BCS-BEC crossover in an organic superconductor, κ-$(BEDT\text{-}TTF)_4Hg_{2.89}Br_8$ (κ-HgBr hereafter). In this compound, dimers of BEDT-TTF molecules constitute a nearly isotropic triangular lattice, separated by insulating $Hg_{2.89}Br_8$ layers. The nonstoichiometry of Hg arises from its sublattice incommensurate with the host lattice formed by BEDT-TTF and Br. The triangular lattice structure is almost identical to that of the Mott-insulating spin liquid candidate κ-$(BEDT\text{-}TTF)_2Cu_2(CN)_3$, in which the spin-1/2 localized on each BEDT-TTF dimer interacts with its neighbors through an antiferromagnetic exchange energy of 250 K but does not order down to 30 mK. Due to the nonstoichiometry in κ-HgBr, this compound is regarded as a hole-doped Mott insulator and exhibits superconductivity at $T_c \sim 5$ K under pressure above 0.24 GPa.

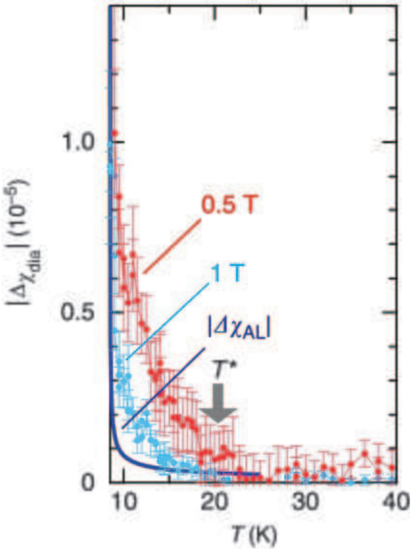

Fig. 5 Temperature dependence of the diamagnetic susceptibility above T_c (around 9K) for two values of the external magnetic field in FeSe (Kasahara et al., 2016). The vertical axis represents the difference between the *ab*-plane and *c*-axis susceptibilities with the subtraction of the corresponding value at a high field (7T). The blue line is the prediction of the Gaussian (Aslamasov-Larkin) fluctuation theory. T^* is the temperature at which the temperature derivative of resistivity takes the minimum, and the field dependence of the susceptibility is significant below T^*. From Kasahara S et al. (2016) Giant superconducting fluctuations in the compensated semimetal FeSe at the BCS-BEC crossover. *Nature Communications* 7: 12843.

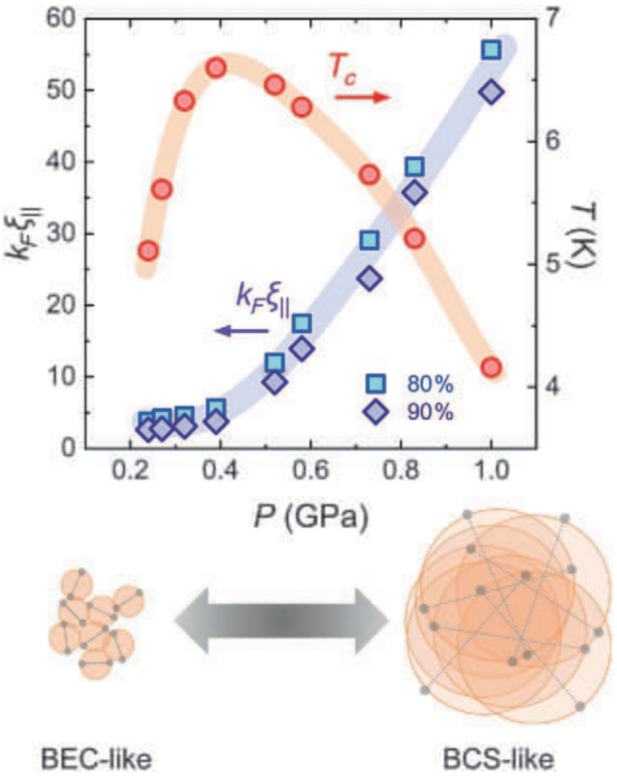

Fig. 6 Pressure dependence of T_c and $k_F\xi_{||}$ for κ-(BEDT-TTF)$_4$Hg$_{2.89}$Br$_8$ (Suzuki et al., 2022). Regarding the points indicated by 80% and 90% in the $k_F\xi_{||}$ plot, $\xi_{||}$ is the coherence length derived from the out-of-plane upper critical field, which is defined by the magnetic field showing 80% and 90% of the normal-state resistivity, respectively. From Suzuki Y, Wakamatsu K, Ibuka J, Oike H, Fujii T, Miyagawa K, Taniguchi H, and Kanoda K (2022) Mott-driven BEC-BCS crossover in a doped spin liquid candidate kappa-(BEDT-TTF)4Hg2.89Br8. *Physical Review X* 12: 011016.

Fig. 6 shows the pressure evolution of T_c and $k_F\xi_{||}$, where $\xi_{||}$ is the in-plane coherence length. $k_F\xi_{||}$ was estimated as 3 at low pressure, indicating that the material is already in the BCS-BEC crossover regime. As pressure is increased, $k_F\xi_{||}$ increases by a factor of 20 associated with the peaking of T_c, which indicates the crossover from the BEC to the BCS regime. According to the analysis, the pressure-induced change in $k_F\xi_{||}$ is dominated by the change in $\xi_{||}$, which indicates that the crossover is predominantly driven by the interaction strength. This poses an interesting contrast with the density-controlled BCS-BEC crossover in Li$_x$ZrNCl and graphene systems.

Conclusion

In this chapter, we have reviewed recent studies on the BCS-BEC crossover in materials. According to a simple theory on Fermion gas systems, 2D materials are expected to have the advantage of realizing the BCS-BEC crossover by tuning the carrier density. Indeed, the density-controlled crossover has been found in 2D-like ZrNCl and graphene-based systems using the gating technique. More broadly, several kinds of materials have been reported as candidates in the crossover or even BEC regime. From the viewpoint of the BCS-BEC crossover, we have explained the essential features of graphene-based, iron-based, and organic systems. Material research supported by theoretical approaches will be crucial in elucidating the guiding principles for realizing the BCS-BEC crossover and exploring new physical properties.

References

Biss H, Sobirey L, Luick N, Bohlen M, Kinnunen JJ, Bruun GM, Lompe T, and Moritz H (2022) Excitation spectrum and superfluid gap of an ultracold fermi gas. *Physical Review Letters* 128: 100401.

Cao Y, Fatemi V, Fang S, Watanabe K, Taniguchi T, Kaxiras E, and Jarillo-Herrero P (2018) Unconventional superconductivity in magic-angle graphene superlattices. *Nature* 556: 43.

Chubukov AV, Eremin I, and Efremov DV (2016) Superconductivity versus bound-state formation in a two-band superconductor with small Fermi energy: Applications to Fe pnictides/chalcogenides and doped SrTiO$_3$. *Physical Review B* 93: 174516.

Eagles DM (1969) Possible pairing without superconductivity at low carrier concentrations in bulk and thin-film superconducting semiconductors. *Physics Review* 186: 456.

Ge J-F, Liu Z-L, Liu C, Gao C-L, Qian D, Xue Q-K, Liu Y, and Jia J-F (2015) Superconductivity above 100 K in single-layer FeSe films on doped SrTiO$_3$. *Nature Materials* 14: 285.

Hashimoto T, et al. (2020) Bose-Einstein condensation superconductivity induced by disappearance of the nematic state. *Science Advances* 6: eabb9052.

Heyl M, Adachi K, Itahashi YM, Nakagawa Y, Kasahara Y, List-Kratochvil EJW, Kato Y, and Iwasa Y (2022) Vortex dynamics in the two-dimensional BCS-BEC crossover. *Nature Communications* 13: 6986.

Hsu F-C, et al. (2008) Superconductivity in the PbO-type structure α-FeSe. *Proceedings of the National Academy of Sciences of the United States of America* 105: 14262.

Kasahara Y, Kishiume T, Takano T, Kobayashi K, Matsuoka E, Onodera H, Kuroki K, Taguchi Y, and Iwasa Y (2009) Enhancement of pairing interaction and magnetic fluctuations toward a band insulator in an electron-doped Li_xZrNCl Superconductor. *Physical Review Letters* 103: 077004.

Kasahara S, et al. (2014) Field-induced superconducting phase of FeSe in the BCS-BEC cross-over. *Proceedings of the National Academy of Sciences of the United States of America* 111: 16309.

Kasahara S, et al. (2016) Giant superconducting fluctuations in the compensated semimetal FeSe at the BCS-BEC crossover. *Nature Communications* 7: 12843.

Leggett AJ (1980) In: Pekalski A and Przystawa JA (eds.) *Modern Trends in the Theory of Condensed Matter*, pp. 13–27. Berlin, Heidelberg: Springer Berlin Heidelberg.

Nakagawa Y, Kasahara Y, Nomoto T, Arita R, Nojima T, and Iwasa Y (2021) Gate-controlled BCS-BEC crossover in a two-dimensional superconductor. *Science* 372: 190.

Nozières P and Schmitt-Rink S (1985) Bose condensation in an attractive fermion gas: From weak to strong coupling superconductivity. *Journal of Low Temperature Physics* 59: 195.

Park JM, Cao Y, Watanabe K, Taniguchi T, and Jarillo-Herrero P (2021) Tunable strongly coupled superconductivity in magic-angle twisted trilayer graphene. *Nature* 590: 249.

Randeria M and Taylor E (2014) Crossover from Bardeen-Cooper-Schrieffer to Bose-Einstein condensation and the unitary Fermi gas. *Annual Review of Condensed Matter Physics* 5: 209.

Regal CA, Greiner M, and Jin DS (2004) Observation of resonance condensation of fermionic atom pairs. *Physical Review Letters* 92: 040403.

Suzuki Y, Wakamatsu K, Ibuka J, Oike H, Fujii T, Miyagawa K, Taniguchi H, and Kanoda K (2022) Mott-driven BEC-BCS crossover in a doped spin liquid candidate kappa-(BEDT-TTF) 4Hg2.89Br8. *Physical Review X* 12: 011016.

Takahashi H, Nabeshima F, Ogawa R, Ohmichi E, Ohta H, and Maeda A (2019) Superconducting fluctuations in FeSe investigated by precise torque magnetometry. *Physical Review B* 99: 060503.

Terashima T, et al. (2014) Anomalous Fermi surface in FeSe seen by Shubnikov-de Haas oscillation measurements. *Physical Review B* 90: 144517.

Uemura YJ, et al. (1991) Basic similarities among cuprate, bismuthate, organic, chevrel-phase, and heavy-fermion superconductors shown by penetration-depth measurements. *Physical Review Letters* 66: 2665.

Zwierlein MW, Stan CA, Schunck CH, Raupach SMF, Kerman AJ, and Ketterle W (2004) Condensation of pairs of fermionic atoms near a Feshbach resonance. *Physical Review Letters* 92: 120403.

Excitonic superfluidity in electron-hole bilayer systems

David Neilson[a,b], [a]CMT Group, Department of Physics, University of Antwerp, Antwerp, Belgium; [b]ARC Centre of Excellence for Future Low Energy Electronics Technologies, School of Physics, The University of New South Wales, Sydney, NSW, Australia

© 2024 Elsevier Ltd. All rights reserved.

Introduction 39
Theory of electron-hole superfluidity 39
Superfluid equations 40
Screening in a superfluid 40
Superfluid crossover physics 41
Superfluid gap and superfluid onset density 42
Superfluid transition temperature 42
Identifying superfluidity 43
Systems 44
Gallium arsenide double quantum wells 44
Double monolayer graphene 44
Double bilayer graphene 45
Double transition metal dichalcogenide monolayers 46
Indium arsenide–gallium antimonide double quantum wells 46
Future systems 46
Other quantum wells 46
Silicon-germanium double quantum wells 46
Other atomically thin layers 47
Double monolayer graphene in a periodic magnetic field 47
Nanoribbons from double monolayer graphene 47
Hybridization of double bilayer graphene 47
Double trilayer and quadlayer graphene 48
Double van der Waals layers with Type-III interfaces 48
Superlattice of transition metal dichalcogenide monolayers 48
Conclusion 48
Acknowledgments 48
References 48

Abstract

There is accumulating evidence for the existence of quantum condensation of excitons in double layer semiconductor heterostructure devices, with the electrons and holes spatially separated in adjacent parallel conducting layers. This has sparked a lot of interest in excitonic superfluidity at equilibrium. The electron-hole pairing attraction is strong, promising high transition temperatures. Because the attraction is long-ranged, screening controls many superfluid properties. The systems offer the exciting prospect of a tunable electronic device that can sweep across the superfluid BCS-BEC crossover regimes. Pros and cons of different candidate heterostructures are discussed, accompanied by a brief overview of the current experimental status.

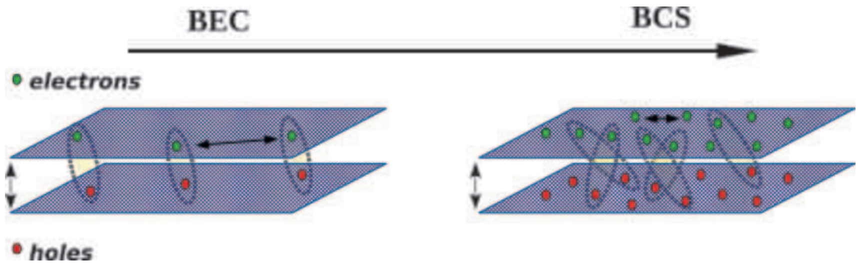

https://doi.org/10.1016/B978-0-323-90800-9.00138-4

Key points

- How to generate equilibrium excitonic superfluidity and Bose Einstein condensation
- Systems are double conducting-layer semiconductor electronic devices
- Electrons and holes are separated in adjacent layers to avoid recombination
- Electron-hole pairing attraction is strong
- Pairing attraction is long-ranged so screening controls many superfluid properties
- Systems can be tuned across all the superfluid BCS-BEC crossover regimes
- Advantages and disadvantages of different material configurations
- Current experimental status

Introduction

The electrons and holes in semiconductors can form bound pairs called excitons. The attraction between the charged electrons and holes is Coulombic, with strong exciton binding energies that can exceed thermal energies even at room temperature.

In the phenomenon of conventional superconductivity, weakly bound pairs of electrons quantum condense into a single quantum state. This allows the condensate to flow through the metallic conductor without resistance. The electron pairs are bound by a residual attraction that is weak, so the dissipation-less flow of electrical current is generally limited to very low temperatures.

Based on the strong electron-hole Coulomb attraction, Keldysh and Kopaev (1965) predicted many years ago that, not only should excitons quantum condense, but the energy gap of the resulting superfluid should be large. However, realization of superfluidity was blocked by the very short exciton lifetimes, as the electrons and holes recombine and destroy the exciton. The short lifetimes make it difficult for the excitons to quantum condense in bulk semiconductors. One workaround is to couple the excitons to light confined in a cavity. Hybrid exciton-polaritons can be formed with long enough lifetimes to quantum condense (Kasprzak et al., 2006). However, to maintain a constant exciton-polariton population it must be optically pumped, leading to a non-equilibrium steady-state. Lozovik and Yudson (1975, 1976) and Shevchenko (1976) proposed instead to generate equilibrium electron-hole superfluidity by separating the electrons and holes in a semiconductor heterostructure, confining them in two adjacent quantum wells. This suppresses electron-hole recombination and stabilizes the exciton lifetimes indefinitely. This article focuses on realizations of this idea.

Implementation of the idea remained technically unfeasible for many years. The quantum well subbands form quasi two-dimensional conducting layers with typical average interparticle spacings $r_0 \sim 10$ nm. To generate a population of excitons with strong electron-hole attraction and weak screening, the quantum wells must be fabricated no more than a perpendicular distance r_0 apart (Neilson et al., 1993; Liu et al., 1996, 1998). This is no mean task.

When the layer separation is less than the effective Bohr radius typical of semiconductors, the exciton binding energies can approach $\sim$1000 K, leading to large superfluid energy gaps, $\sim$300 K (Perali et al., 2013). However in two-dimensional systems, large superfluid gaps do not in general translate into high transition temperatures. The reason is that strong fluctuations, together with the topological nature of the two-dimensional Berezinskii-Kosterlitz-Thouless transition (Berezinsky, 1972; Kosterlitz and Thouless, 1973), make the transition temperature only dependent on the density. The transition temperature does not depend on the strength of the pairing interaction.

A further major challenge in electron-hole superfluidity is screening of the long range pairing attraction. We recall that most superconductors and superfluids involve contact or short-range pairing interactions, so screening is not important. With the pair interaction for electron-hole superfluidity that is Coulombic and long-range, screening effects are unavoidable and strong. In fact, screening can weaken the pairing attraction to such a degree that superfluidity would occur only at impractically low temperatures (Kharitonov and Efetov, 2008). However at low enough densities, the existence of a large superfluid gap in the excitation energy spectrum can block low-lying single-particle excitations near the Fermi surface sufficiently to allow strong-coupled superfluidity (Lozovik et al., 2012; Perali et al., 2013). But even when strong-coupled superfluidity does stabilize, the maximum transition temperature is in general capped at low values. This is because of the joint effect of the transition temperature being determined by the density and the superfluidity being restricted to low densities.

Theory of electron-hole superfluidity

The electron-hole bilayer system consists of an n-doped and a p-doped conducting layer separated by a thin insulating layer of thickness d and dielectric constant κ (Fig. 1). V^{eh} is the electron-hole attractive screened interaction between the layers, and $V^{ee}(V^{hh})$ are the repulsive Coulomb interactions for the electrons (holes) interacting within their layers. Voltages applied to the top and bottom metal gates, V_{TG} and V_{BG}, and a voltage across the layers, V_{BB}, are used to adjust the electron and hole densities n (Lee et al., 2014; Zeng and MacDonald, 2020). Changing the densities, changes the average strength of the electron-electron (hole-hole) Coulomb interactions, $\langle V^{ee}(V^{hh})\rangle = e^2/\kappa r_0 = e^2\sqrt{\pi n}/\kappa$. The most favorable condition for superfluidity is an equilibrium exciton gas with equal electron and hole densities (Pieri et al., 2007).

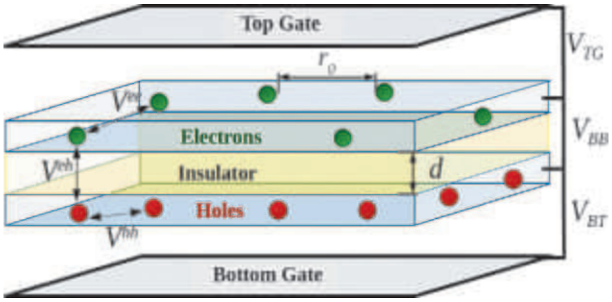

Fig. 1 Schematic representation of double electron-hole layer system. An upper conducting layer of electrons and a lower conducting layer of holes are separated a distance d by a thin insulating layer. Average interparticle spacing within each layer is r_0. The interactions are electron-hole between the layers, V^{eh}, and electron-electron (hole-hole) within the layers, $V^{ee}(V^{hh})$. The potentials V_{TG} and V_{BG} are from top and bottom metal gates which, together with the bias between the layers V_{BB}, tune the electron and hole densities.

Superfluid equations

At zero temperature, a BCS mean-field description is a good approximation for strong-coupling superfluidity as well as for the familiar weak-coupling case (Nozières and Pistolesi, 1999). For the p-doped bilayer, the standard particle-hole transformation is used to map the negative-energy valence band to a positive-energy conduction band, with positively charged holes filling their conduction band states up to a Fermi level $E_F > 0$.

The BCS normal Green function $\mathcal{G}(\mathbf{k}, \mathrm{i}\varepsilon_n)$ and anomalous Green function $\mathcal{F}(\mathbf{k}, \mathrm{i}\varepsilon_n)$ for symmetric electron and hole bands with dispersion $\varepsilon_{\mathbf{k}}$ are given by (Lozovik and Sokolik, 2010),

$$\begin{aligned} \mathcal{G}(\mathbf{k}, \mathrm{i}\varepsilon_n) &= \frac{u_k^2}{\mathrm{i}\varepsilon_n - E_k} + \frac{v_k^2}{\mathrm{i}\varepsilon_n + E_k} \\ \mathcal{F}(\mathbf{k}, \mathrm{i}\varepsilon_n) &= \frac{u_k v_k}{\mathrm{i}\varepsilon_n - E_k} - \frac{u_k v_k}{\mathrm{i}\varepsilon_n + E_k}, \end{aligned} \tag{1}$$

with energies $E_{\mathbf{k}} = \sqrt{\xi_{\mathbf{k}}^2 + \Delta_{\mathbf{k}}^2}$, $\xi_{\mathbf{k}} = \varepsilon_k - \mu$, and Bogoliubov factors, $v_k = \sqrt{\frac{1}{2}(1 - \xi_k/E_k)}$ and $u_k = \sqrt{\frac{1}{2}(1 + \xi_k/E_k)}$. For a given value of the chemical potential in the superfluid, $\mu \le E_F$, the equations for the momentum-dependent electron-hole superfluid energy gap $\Delta_{\mathbf{k}}$ and density n are,

$$\Delta_{\mathbf{k}} = -\sum\nolimits_{\mathbf{k}'} \frac{1}{2} \mathcal{F}^{eh}_{\mathbf{k}-\mathbf{k}'} V^{eh}_{\mathbf{k}-\mathbf{k}'} \frac{\Delta_{\mathbf{k}'}}{2E_{\mathbf{k}'}}; \qquad n = 2g_v \sum\nolimits_{\mathbf{k}} v_{\mathbf{k}}^2. \tag{2}$$

$V^{eh}_{\mathbf{k}-\mathbf{k}'}$ is a screened interaction between the electrons and holes that depends on the momentum exchange in the scattering process. This gives the superfluid gap its momentum dependence. The form factor $\mathcal{F}^{eh}_{\mathbf{k}-\mathbf{k}'}$ accounts for the overlap between the electron and hole single-particle wave functions. g_v is the valley degeneracy.

There have been extensions of the mean-field approach to non-symmetric electron and hole bands and to unequal densities (Pieri et al., 2007; Subasi et al., 2010; Conti et al., 2021a).

Screening in a superfluid

When there is a superfluid energy gap, the screened interaction $V^{eh}_{\mathbf{k}-\mathbf{k}'}$ in Eq. (2) must be determined self-consistently. In the static limit, it is given by the linear-response expression (Lozovik and Sokolik, 2010),

$$V^{eh}_{\mathbf{q}} = \frac{V_0^{eh}(q)}{1 - 2V_0^{ee}(q)\Pi_0(q) + \left[\left(V_0^{ee}(q)\right)^2 - \left(V_0^{eh}(q)\right)^2\right](\Pi_0(q))^2} \tag{3}$$

where $V_0^{eh}(q) = -2\pi e^2 e^{-qd}/(\kappa q)$ is the bare electron-hole Coulomb attraction, and $V_0^{ee}(q)\,(V_0^{hh}(q)) = 2\pi e^2/(\kappa q)$ the bare electron-electron (hole-hole) Coulomb repulsion within a layer. For Fermi liquids the linear-response polarizability $\Pi_0(q)$ is the static Lindhard function for a two-dimensional layer (Stern, 1967), but in a superfluid, $\Pi_0(q) = \Pi_0^{(n)}(q) + \Pi_0^{(a)}(q)$, a sum of the normal ($n$) and anomalous ($a$) linear response polarizabilities (Lozovik et al., 2012; Perali et al., 2013).

The polarizabilities $\Pi_0^{(n)}(q)$ and $\Pi_0^{(a)}(q)$ for the superfluid are constructed from the normal and anomalous Green functions (Fig. 2). Summing the fermionic Matsubara frequencies ε_n of the particle-hole loop, and taking the static limit (Lozovik et al., 2012),

$$\Pi_0^{(n)}(q) = -2g_v \sum_{\mathbf{k}} \mathcal{F}^{ee}_{\mathbf{q}} \frac{u_{\mathbf{k}}^2 v_{\mathbf{k}-\mathbf{q}}^2 + v_{\mathbf{k}}^2 v_{\mathbf{k}-\mathbf{q}}^2}{E_{\mathbf{k}} + E_{\mathbf{k}-\mathbf{q}}} \tag{4}$$

$$\Pi_0^{(a)}(q) = 2g_v \sum_{\mathbf{k}} \mathcal{F}^{eh}_{\mathbf{q}} \frac{2u_{\mathbf{k}} v_{\mathbf{k}} u_{\mathbf{k}-\mathbf{q}} v_{\mathbf{k}-\mathbf{q}}}{E_{\mathbf{k}} + E_{\mathbf{k}-\mathbf{q}}}. \tag{5}$$

$\mathcal{F}^{ee}_{\mathbf{q}}$ is the electron-electron form factor.

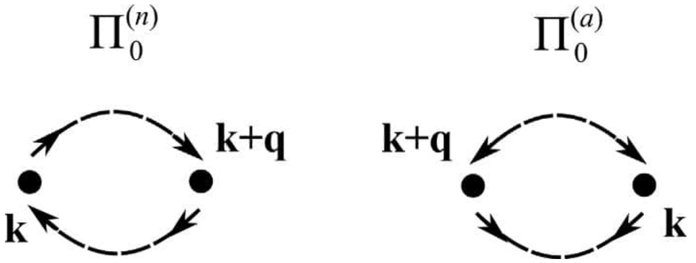

Fig. 2 Normal and anomalous polarizabilities $\Pi_0^{(n)}(q)$ and $\Pi_0^{(a)}(q)$ made up of two normal and two anomalous Green functions, respectively.

$\Pi_0^{(n)}(q)$ and $\Pi_0^{(a)}(q)$ in the superfluid state are suppressed for small momentum transfers q for two reasons. The presence of a superfluid gap in the excitation energy spectrum increases the magnitude of the energy denominators in the polarizabilities, which weakens the screening. In addition, for any non-zero energy gap, there is an exact cancelation of the sum $\Pi_0^{(n)}(q) + \Pi_0^{(a)}(q)$ at $q = 0$, rigorously eliminating screening in the long-wave limit (Lozovik et al., 2012). Increasing the strength of the superfluid gap expands the range of q over which the screening is suppressed. When $\Delta \gg E_F$, screening in the superfluid state is completely suppressed by Δ. The physical picture is that, with such strong coupling, the electron-hole pairs are compact relative to their spacing, quasi-neutral excitons which mutually interact through weak dipole repulsion. Since the pairs closely resemble weakly interacting bosons, screening is negligible (Perali et al., 2013).

Nilsson and Aryasetiawan (2021) have extended the self-consistent approach to include dynamic screening (see also Sodemann et al., 2012). Intralayer interaction contributions to the quasiparticle self-energies, and hence to E_k, have been considered by Debnath et al. (2017). These generalizations introduce corrections that renormalize the coupling strength and the superfluid gap.

Superfluid crossover physics

Eagles (1969), Leggett (1980), and Nozières and Schmitt-Rink (1985) developed a formalism for the BCS–BEC crossover, in which the spontaneous symmetry broken Bardeen–Cooper–Schrieffer (BCS) (Bardeen et al., 1957) superfluidity smoothly connects with Bose–Einstein condensation (BEC) (Schafroth et al., 1957) through a continuous reduction in the spatial size of the fermion pairs, here electron-hole pairs. As the pair coupling interaction is strengthened, the electron-hole pairs evolve from weakly-coupled, diffuse, interpenetrating Cooper pairs, the BCS regime, to pairs comparable in diameter to their spacing in the layers, the BCS-BEC crossover regime, and finally to pairs that are compact, non-overlapping composite bosons, the BEC regime. For a review, see Strinati et al. (2018).

An important feature of a semiconductor bilayer heterostructure is that the average coupling strength $\langle V^{ee}\rangle/E_F$ can be tuned by changing the density. In the example of parabolic bands, the Fermi energy $E_F \sim 1/r_0^2$, so $\langle V^{ee}\rangle/E_F \sim r_0$. Thus the electron-hole layers can be swept continuously across the BCS-BEC crossover regimes of the superfluid, starting from the weak coupled BCS regime at high densities (small r_0) to the strong-coupled BEC regime at low densities (large r_0) (Pieri et al., 2007; Perali et al., 2013; Liu et al., 2022).

The nature of the superfluidity in each of the regimes can be characterized by the dependence on k of the superfluid gap Δ_k. These properties are illustrated in Fig. 3, showing Δ_k in the three BCS to BEC crossover regimes. The regimes have been identified independently using the superfluid condensate fraction CF (Guidini and Perali, 2014). For the weak-coupled BCS limit, corresponding to $CF \leq 0.2$, the $\Delta_k \ll E_F$ is narrowly peaked at $k = k_F$, reflecting the interpenetrating nature of the Cooper pairs.

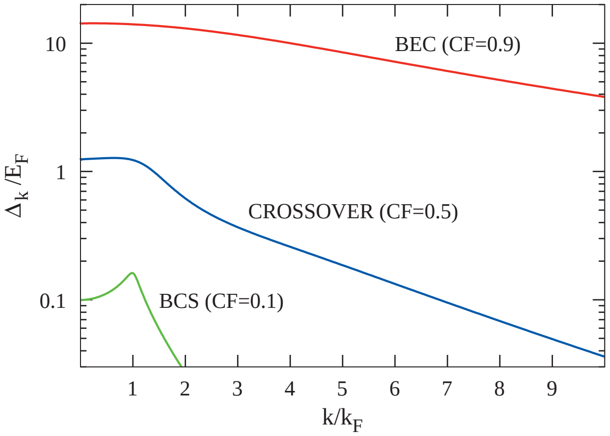

Fig. 3 Contrasting momentum dependence of the superfluid gap Δ_k for the different BCS-BEC crossover regimes as labeled, with the corresponding value of the condensate fraction CF. Δ_k is scaled with the Fermi energy E_F, k with the Fermi momentum k_F.

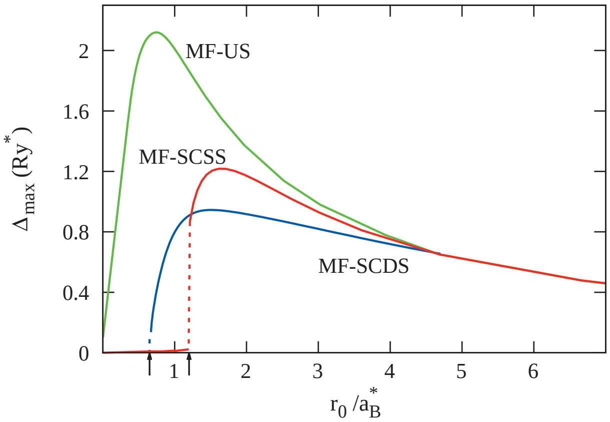

Fig. 4 Superfluid gap $\Delta_{\rm max}$, the maximum of Δ_k, in effective Rydbergs Ry* as a function of the average interparticle distance r_0. a_B^* is the effective Bohr radius. The curves compare the mean-field results for self-consistent static screening (MF-SCSS), for self-consistent dynamic screening (MF-SCDS), and in the absence of screening (MF-US). With self-consistent screening, there is a superfluid onset density (small arrows) at which $\Delta_{\rm max}$ drops by orders of magnitude.

In the BCS-BEC crossover regime, $0.2 < CF < 0.8$, the maximum in Δ_k is of the order of E_F and has shifted to $k < k_F$, with a broad peak. In the BEC regime, $CF \geq 0.8$, the maximum is at $k = 0$, and $\Delta_k \gg E_F$ is almost constant out to $k \gg k_F$, corresponding to pairs that are compact in real space compared with the interparticle spacing.

Superfluid gap and superfluid onset density

Fig. 4 demonstrates a central rôle played by screening for the long-range pair interaction. The system is double bilayer graphene with a 1 nm thick hexagonal boron nitride insulating barrier. $\Delta_{\rm max}$ is the maximum of Δ_k. In the weak-coupled regime at high densities, small r_0, the value of $\Delta_{\rm max}$ calculated without screening (MF-US) is much larger than $\Delta_{\rm max}$ calculated with self-consistent screening, both static (MF-SCSS) and dynamic (MF-SCDS). While this difference is to be expected, the figure reveals a striking additional result: in the presence of screening there exists a superfluid onset density n_0, above which there is a sharp orders of magnitude decrease in $\Delta_{\rm max}$. For densities $n > n_0$, the superfluidity is negligible, with the superfluid gap lying in the mKelvin energy range (Kharitonov and Efetov, 2008). In real systems, residual disorder would more than likely destroy such weakly bound pairs.

While screening is responsible for completely suppressing superfluidity at high densities, by contrast in the strong-coupled region at low densities, $r_0/a_B^* > 4$, it is the superfluidity that suppresses the effect of screening. In this case, $\Delta_{\rm max}$ calculated with or without screening is the same. This occurs because $\Delta_{\rm max} \gg E_F$, blocking the low-lying states that are responsible for screening.

Fig. 4 also shows the effect of dynamics on the screening (Nilsson and Aryasetiawan, 2021). At low densities, screening is unimportant. However, at higher densities the magnitude of the superfluid gap is increased by the dynamic corrections to static screening and the onset density is higher.

The results shown in Figs. 3 and 4 were determined within the mean-field approximation with self-consistent screening. Effects such as self-energy insertions, vertex corrections, etc., are not considered. For this reason, it is useful to compare these results with results determined from a full diffusion quantum Monte-Carlo calculation which includes all these additional effects. Fig. 5 compares results calculated using diffusion quantum Monte-Carlo (López Ríos et al., 2018), with a mean-field calculation for the same system using the static self-consistent screened pairing interaction (Neilson et al., 2014). The system is the same as for Fig. 4.

Fig. 5(a) shows that the superfluid gap $\Delta_{\rm max}$ from mean-field with self-consistent screening is substantially in agreement with the full quantum Monte Carlo result. This demonstrates that the mean-field calculation with self-consistent screening captures the essence of the phenomenon, including the remarkable existence and the location of an onset density.

Fig. 5(b) characterizes the BCS-BEC crossover regimes, comparing the diffusion quantum Monte-Carlo superfluid condensate fraction CF with the condensate fraction from mean-field. In most of what should be the BCS regime, the density is already above the onset density, so in most of the BCS regime the weak superfluidity cannot overcome the strong screening (Perali et al., 2013).

Superfluid transition temperature

The binding energies of the pairs in these double layer systems can be very large, resulting in large superfluid gaps $\Delta_{\rm max} > 300$ K, but disappointingly, these huge values do not usually translate into room temperature superfluidity. This is because in two-dimensional systems, transition temperatures are tightly capped by the Mermin-Wagner theorem (Mermin and Wagner, 1966; Hohenberg, 1967). The maximum transition temperature is limited by the topological properties of the Berezinskii-Kosterlitz-Thouless (BKT) transition (Kosterlitz and Thouless, 1973). The transition temperature T_c^{BKT} is, up to a constant, equal to the superfluid stiffness $\rho_S(T)$. It depends only on the density and it is not affected by the coupling strength. For parabolic bands, it is linearly proportional to the density, $T_c^{BKT} = \left[\frac{\pi}{2}\frac{\hbar^2}{2M}\right]n$, where M is the mass of the electron-hole pair. Consequently, the maximum transition temperature $T_c^{\rm max}$ occurs at the superfluid onset density, $n = n_0$.

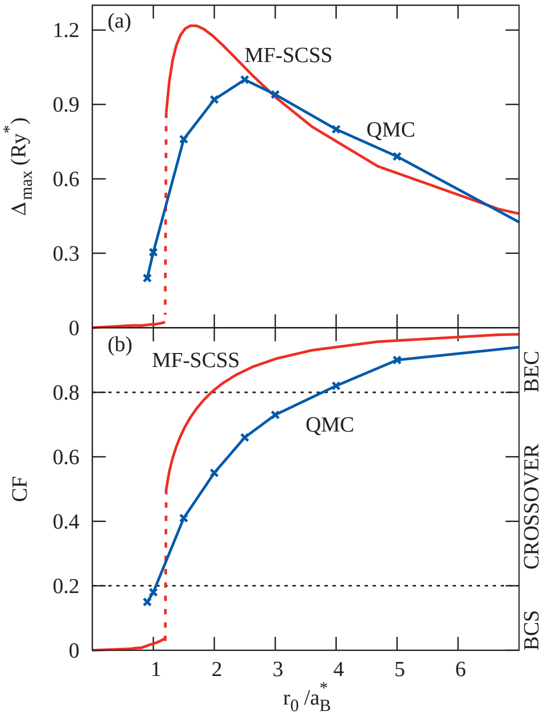

Fig. 5 Comparison of (a) superfluid gap Δ_{max} in effective Rydbergs Ry* and (b) superfluid condensate fraction CF, calculated within mean-field using self-consistent static screening (MF-SCSS) and by a full diffusion quantum Monte Carlo (QMC) calculation. r_0/a_B^* is the average interparticle distance scaled with the effective Bohr radius. In (b) the BCS-BEC crossover regimes are indicated on the right axis.

The complete phase diagram is shown in Fig. 6. Above the onset density $n > n_0$, the superfluid transition temperature is in the mKelvin range, above which the system is a Fermi liquid. For $n < n_0$ and temperatures above T_c^{BKT}, signatures of the superfluid state should persist arising from the pseudogap. The pseudogap arises from localized dynamic fluctuations of the pairing field (Franz, 2007), and is a precursor of the superfluid gap in the normal degenerate electron gas. It extends up to the degeneracy temperature T_D (Butov, 2004). As it can be significant up to temperatures $T \sim \Delta_{max}$ (Perali et al., 2002; Gaebler et al., 2010), in the present case the pseudogap could survive to room temperature.

Identifying superfluidity

To identify clear signatures of electron-hole superfluidity remains a major challenge. Although the superfluid current is neutral, nevertheless because the charged electrons and holes are spatially separated, an electrical current can be generated by passing counterflow currents in the two layers in opposite directions (Sivan et al., 1992; Su and MacDonald, 2008). Since in a superfluid

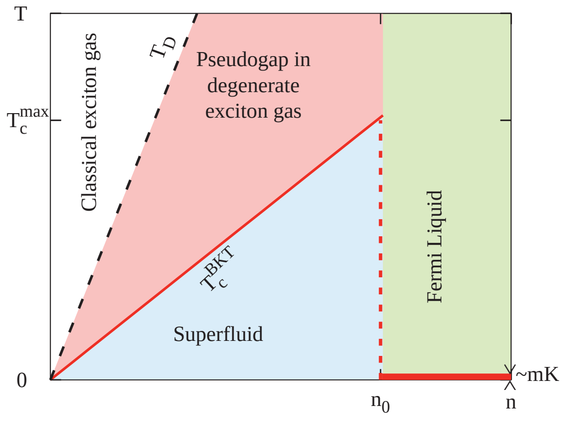

Fig. 6 Temperature-density T-n phase diagram. T_c^{BKT} is the superfluid transition temperature. n is the equal density of electrons and holes. The maximum transition temperature T_c^{max} occurs at the onset density n_0. For densities $n > n_0$, the superfluid transition temperature is in the mKelvin range. T_D is the degeneracy temperature for the exciton gas.

the counter-currents will couple to the dissipationless neutral exciton current, the counter-currents are expected also to be dissipationless (Eisenstein and MacDonald, 2004; Fil and Shevchenko, 2018).

Properties of the electron-hole drag resistance, the bilayer transresistivity, is another signature of condensation (Conti et al., 1998; Hu, 2000). The transresistivity is directly related to the interlayer scattering rate (Narozhny and Levchenko, 2016), and using a minimum dissipation principle for the superfluid current, Vignale and MacDonald (1996) showed that superfluidity can be characterized by a discontinuous jump in the drag resistance at the transition temperature. As the temperature is further decreased, the drag resistance diverges for temperatures approaching zero.

Enhanced electron-hole tunneling between the layers is a further indicator of spontaneous interlayer phase coherence (Eisenstein and MacDonald, 2004; Efimkin et al., 2020). However, Zeng and MacDonald (2020) showed that a strong interlayer tunneling current between the layers influences the transport and can lead to a steady state that is not in equilibrium.

Josephson junction-like behavior across a weak link could also be used in identifying superfluidity (Zenker et al., 2015; Pascucci et al., 2022).

Systems

Although the electron-hole double layer system is a multiband system, with a hole band and an electron band, it is possible to have just a single condensate with the one gap parameter. This is diametrically opposite to multiband superconductors like magnesium diboride in which the pairing occurs within the bands and for which multiple coupled condensates must appear, each condensate with a gap parameter associated with a different band (Komendová et al., 2012).

Gallium arsenide double quantum wells

Electron-hole superfluidity and BCS-BEC crossover physics was first proposed for an excitonic system in a conventional semiconductor heterostructure of double quantum wells in gallium arsenide (Comte and Nozières, 1982). Technical advances in the early 1990s in the fabrication of double quantum wells in III–V semiconductors offered an apparently unobstructed path (Balatsky et al., 2004) to experimentally realize superfluidity in a double layer semiconductor system (Sivan et al., 1992; Kane et al., 1994; Pohlt et al., 2002). Charge-separated excitons were produced by confining electrons and holes in adjacent quantum wells consisting of two disconnected thin slabs of gallium arsenide, with a very thin slab of aluminum gallium arsenide between them as an insulating barrier (Butov et al., 2002).

Superfluidity in gallium arsenide double quantum wells differs in important ways from superfluidity in coupled atomically flat layers like graphene (Section "Double monolayer graphene"). Advantages include a large bandgap, and low-energy bands that are insensitive to gate potentials. Pieri et al. (2007) showed that the large difference in the electron and hole effective masses in gallium arsenide, $m_h^*/m_e^* \sim 5$, as well as any density imbalance, have further intriguing consequences. The large mass difference should lead to the existence of the exotic superfluid phases, Fulde-Ferrel-Larkin-Ovchinnikov (FFLO) (Fulde and Ferrell, 1964; Larkin and Ovchinnikov, 1965) and Sarma (Sarma, 1963).

However, a significant drawback of gallium arsenide is that in double quantum wells, the electron–hole pairing interactions are weak since it is difficult to fabricate the wells sufficiently close to each other. A limitation with transport in quantum wells is that the wells must not be fabricated too narrow (<12 nm for gallium arsenide), otherwise interface roughness scattering increases rapidly when the well is made narrower, resulting in samples with very low mobilities. This restriction places tight limits on minimum effective electron-hole separations (Saberi-Pouya et al., 2020), and the formation of excitons is exponentially suppressed when the thickness of the insulating barrier exceeds the effective Bohr radius, $a_B^* = 13$ nm in gallium arsenide.

Bose-Einstein condensation of excitons has been reported in gallium arsenide double quantum wells using optical pumping (Butov, 2004; High et al., 2012). Because of the fast recombination of the photoexcited excitons, the condensate was not in equilibrium.

With transport measurements, there have been independent reported observations at low temperature of strong nonmonotonic deviations of the Coulomb drag on the hole layer away from the $\sim T^2$ behavior expected for a Fermi-liquid (Croxall et al., 2008; Seamons et al., 2009; Das Gupta et al., 2011). However no clear, consistent signature has emerged that the deviations are associated with a superfluid transition. This is consistent with theoretical predictions. For the smallest quantum well separations fabricated to date, the pairing interactions are still too weak and the lowest densities currently attained remain a little above the predicted superfluid onset density (Saberi-Pouya et al., 2020). At such low densities, charge-carrier freeze-out occurs and the conducting layers become insulators. Disconnected puddles of superfluidity might survive, randomly distributed along the quantum well interfaces. These could be detected using capacitance spectroscopy.

Double monolayer graphene

The fabrication of graphene atomic monolayers (Novoselov et al., 2004) opened up new possibilities by replacing the finite width quantum wells of the III–V semiconductors with atomically-thin layers of graphene. The discovery of the extraordinarily efficient insulating properties of hexagonal boron nitride (Britnell et al., 2012), reduced separations between the layers to unprecedentedly small values (Min et al., 2008; Lozovik and Sokolik, 2008). A hexagonal boron nitride barrier has a much larger bandgap, ~5 eV, than the gallium aluminum arsenide barrier in gallium arsenide double quantum wells (~0.5 eV), and just three monolayers of hexagonal boron nitride, of total thickness 1 nm between two monolayers of graphene are sufficient to eliminate the electron-hole tunneling current between the layers. Such a barrier is thin on the scale of the effective Bohr radius in graphene ($a_B^* \sim 10$ nm).

Because the energy bands in monolayer graphene are symmetric and have zero bandgap, the Dirac cone, the superfluidity would be inherently multicomponent with intraband pairing of electrons and holes that come from the same band, as well as crosspairing between the conduction and valence bands (Shanenko et al., 2012). The mean-field formalism for electron-hole superfluidity was generalized to multicomponents by Lozovik and Sokolik (2010).

Unfortunately however, since the energy bands follow a linear dispersion, $\varepsilon(k) = \pm \hbar v_F k$, with v_F the constant Fermi velocity, the kinetic energy decreases linearly with the inter-particle spacing r_0, making $\langle V\rangle/E_F$, the ratio of the average Coulomb energy to Fermi energy, independent of density. Lozovik et al. (2012) showed that only when $\langle V\rangle/E_F > 2.35$ is the pair coupling strong enough for a superfluid gap to suppress the screening, allowing the superfluidity to exist. For the band parameters in graphene, $\langle V\rangle/E_F \sim 0.7$, so the pair coupling strength would always be too weak. Thus at any density in monolayer graphene, superfluidity is suppressed by screening. Because the electrons and holes are massless, localized excitons cannot form (Lozovik and Sokolik, 2008). If any remnant superfluidity survived in the presence of such strong screening, its transition temperature T_c would be impractically low (Kharitonov and Efetov, 2008). Lozovik and Sokolik (2010) and Sodemann et al. (2012) generalized the static screening theory to dynamic screening. Dynamic screening did not alter the key conclusion that superfluidity is not to be expected in double monolayer graphene.

Electron-hole Coulomb drag measurements of Gorbachev et al. (2012) bear this conclusion out. No jump or divergence in the drag resistance was observed, and the T^2 temperature behavior of the drag resistance across the full density and temperature range was consistent with Fermi liquid properties.

Double bilayer graphene

With the difficulties faced by double monolayer graphene, Perali et al. (2013) proposed an alternate strategy: to substitute two graphene bilayers for the two graphene monolayers while retaining the hexagonal boron nitride insulating barrier. In graphene bilayers, the energy bands $\varepsilon(k)$ resemble the bands of conventional semiconductors and are approximately parabolic. Then, as in the semiconductors, reducing the density increases $\langle V\rangle/E_F$ and strengthens the pair coupling.

With strong electron-hole coupling, the superfluidity can overcome the screening. The suppression of screening is more dramatic for the quadratic bands of bilayer graphene than for linear bands of monolayer graphene. This is because with the larger density of states for quadratic bands, the corresponding gaps from Eq. (2) are larger, while at the same time E_F is smaller. A larger Δ/E_F ratio is more effective at suppressing the screening.

The bandgap for bilayer graphene is very small and tunable, typically $E_g \sim 5-100$ meV, up to a maximum $E_g \sim 250$ meV. The bandgap is determined by the gate voltages. For such small bandgaps, the valence band provides a second superfluid gap, and the superfluid is multicomponent.

The two superfluid components are coupled through Josephson-like transfers of electron-hole pairs between the valence and conduction band condensates (Conti et al., 2017). This should reinforce the superfluid gaps, but with small bandgaps there are additional interband contributions to the screening coming from valence to conduction band excitations (Conti et al., 2019). These two effects act in opposing directions. In the end, the effect of the additional screening that weakens the superfluid gaps turns out to be the stronger effect, making Josephson-like transfers negligible (Conti et al., 2019). The reason is the following. These transfers would leave in their trail a population of free vacancies in the valence-band, adding to the screening. This makes the resulting superfluid gaps always smaller than the bandgap, so Josephson-like pair transfers are suppressed. Without the pair transfer, the net result is that the conduction and valence band condensates are decoupled, with the conduction band condensate dominant. For small bandgaps, the conduction band condensate is weakened by the additional interband screening arising from single-particle excitations out of the valence band. As the bandgaps get bigger, interband screening weakens and the conduction band superfluid gap becomes stronger.

A further advantage of large bandgaps comes from the fact that the bilayer graphene conduction band is flatter than a parabolic band for low energies (Castro et al., 2010). This results in a larger density of states, so the Fermi energy E_F at a given density is reduced, thus permitting a superfluid gap of a given magnitude to block a wider range of low-lying excitations. This more efficiently suppresses the screening, and the superfluid gap is increased.

In summary, in double bilayer graphene the superfluid onset density is sensitive to the variable bandgap. When the bandgap $E_g < E_F$, the interband contributions reinforce the screening, and the onset density is low. Conversely, when $E_g \gg E_F$ the onset density is larger. For a separation between the bilayers $d = 1$ nm and bandgap $E_g \gtrsim 35$ meV, the onset density $n_0 \gtrsim 2 \times 10^{11}$ cm^{-2}. This puts strong-coupled superfluidity in the BCS-BEC crossover and BEC regimes within experimental reach in double bilayer graphene.

Burg et al. (2018) observed strongly enhanced interlayer tunneling at equal electron and hole densities in double bilayer graphene separated by a $d = 1.4$ nm tungsten diselenide insulating barrier. Below a temperature $T_c \sim 1.5$ K, the interlayer tunneling current had a vertical onset as a function of interlayer voltage, suggesting a transition to a coherent state at that temperature. Such tunneling enhancement is a strong indicator of exciton condensation. The interlayer current I_{int} was measured as a function of the interlayer voltage V_{BB}, at fixed top and back gate voltages, V_{TG} and V_{BG} (see Fig. 1).

The vertical onset of the interlayer tunneling current and the tunneling enhancement were observed at densities only below an onset density $n_0 = 8 \times 10^{11}$ cm^{-2}, a value consistent with theory (Perali et al., 2013; López Ríos et al., 2018; Nilsson and Aryasetiawan, 2021).

Double transition metal dichalcogenide monolayers

To circumvent the detrimental effect of the valence band screening encountered in double bilayer graphene, Conti et al. (2020b) suggested double monolayers from the transition metal dichalcogenide (TMD) family, specifically, molybdenum disulfide, molybdenum diselenide, tungsten disulfide, and tungsten diselenide. This group have large bandgaps, $E_g \gtrsim 1$ eV (Mak et al., 2010; Jiang, 2012).

The conduction bands in this class of transition metal dichalcogenides are split by spin-orbit coupling, leading to two condensates in the conduction bands and hence multicomponent superfluidity. The two superfluid components reinforce the superfluidity in this case (Conti et al., 2017). In addition, the electron and hole effective masses are large, increasing the binding energies compared to bilayer graphene. This further strengthens the electron-hole pairing interactions (Fogler et al., 2014). Lagoin and Dubin (2021) pointed out that the presence of moiré potentials in transition metal dichalcogenides heterobilayers will further enhance the effective masses.

As a result of the large bandgaps, the reinforcing multicomponent effects, and the large effective masses, the superfluid onset densities in double layer transition metal dichalcogenides are high, with a 1 nm barrier, $n_0 \sim 1 \times 10^{13}$ cm^{-2} (Conti et al., 2020b). These are much larger than in double bilayer graphene, $n_0 \sim 8 \times 10^{11}$ cm^{-2} (Burg et al., 2018; Conti et al., 2019), phosphorene, $n_0 \sim 4 \times 10^{12}$ cm^{-2} (Saberi-Pouya et al., 2018), and gallium arsenide, $n_0 \sim 5 \times 10^{10}$ cm^{-2} (Saberi-Pouya et al., 2020). With such high onset densities, the transition metal dichalcogenides hold great promise for exciton superfluids at high-temperature, with transition temperatures predicted as high as $T_c^{BKT} \sim 100$ K (Conti et al., 2020b).

This family of materials hosts additional curious possibilities. Conti et al. (2020a) showed that by exploiting a change in the energy band alignments, certain combinations of transition metal dichalcogenides can provide a doping-dependent switch, to switch from one-component to two-component superfluidity (Conti et al., 2020b). The switch in doping also affects the spin alignment of the electron-hole pairs, leading to an intriguing possibility of tuning from a system purely of dark excitons to a system purely of bright excitons (Combescot et al., 2017).

Enhanced interlayer tunneling and enhanced electroluminescence intensity have been observed in molybdenum diselenide–tungsten diselenide separated by 1–2 nm of hexagonal boron nitride (Wang et al., 2019; Chaves and Neilson, 2019; Ma et al., 2021). Again there was an onset density, below which a large tunneling current was observed between the monolayers. At exactly equal electron–hole densities, the electroluminescence intensity from electron–hole recombination triggered by inter-layer tunneling was strongly enhanced, a property again consistent with exciton condensation. The tunneling enhancement and the electroluminescence intensity shared the same onset density, and the properties persisted up to remarkably high temperatures, $T_c \sim 100$ K (Fogler et al., 2014).

Indium arsenide–gallium antimonide double quantum wells

Indium arsenide–gallium antimonide double quantum wells have an inverted band structure with finite overlap of the conduction and valence bands. With electrons in the indium arsenide well and holes in the gallium antimonide well, the electrons and holes are in equilibrium without photoexcitation, and they are spatially separated without the need for a barrier.

Du et al. (2017) reported optical spectroscopic and electronic transport evidence for the formation of an excitonic insulator gap in this system at relatively high densities. Terahertz transmission spectra exhibited two absorption lines which are quantitatively consistent with predictions from the pair-breaking excitation dispersion, calculated based on the BCS superfluid gap equation (Eq. 2). Transport measurements show an insulating gap of $\Delta \sim 25$ K, with a transition temperature of $T_c \sim 10$ K which, with quantized edge conductance, suggests the existence of a topological excitonic insulator phase.

Future systems

Other quantum wells

Silicon-germanium double quantum wells

Conti et al. (2021b) have proposed electron-hole quantum wells in a strained silicon-germanium double layer heterostructure as an interesting alternative system for superfluidity. Because of the Type-II band alignment of the silicon-germanium interface (Virgilio and Grosso, 2006), there is no requirement for an insulating barrier to keep the electrons and holes apart, as is needed in gallium arsenide double quantum wells. The resultant close proximity of the electrons and holes greatly enhances the electron-hole pair interaction, leading to much higher onset densities than in gallium arsenide. A compressively strained 3 nm epitaxial germanium layer and tensile strained 3 nm epitaxial silicon layer ensures that the layers are lattice matched. The low-lying bands result in a double quantum well structure, with the electrons confined in the silicon well and the holes in the germanium well. In the presence of the strain, the effective mass imbalance is large, $m_h^*/m_e^* = 0.26$ (Lodari et al., 2021; Schäffler, 1997; Zwanenburg et al., 2013).

The system offers some unique advantages. One is the ability to independently contact the layers since there exists no quantum well for holes in the silicon layer and there is no quantum well for electrons in the germanium layer that is energetically accessible. This makes it straightforward with a simple and robust process, to independently electrically contact just one layer and not the other. In contrast, to fabricate independent contacts for the systems already discussed requires painstaking multi-stage processing.

A second distinct advantage is scalability. The silicon-germanium heterostructures would be grown on 300 mm silicon wafers using mainstream chemical vapor deposition (Pillarisetty, 2011). In this way, these heterostructures can take advantage of state-of-the-art semiconductor manufacturing, promising high device yield and integration. A silicon-germanium bilayer is readily integrated with advanced quantum technologies (Scappucci et al., 2020), including long-lived electron spin qubits in silicon (Watson et al., 2018), hole spin qubit arrays in germanium (Hendrickx et al., 2020), and superconducting contacts to holes (Vigneau et al., 2019).

By contrast, device fabrication for double graphene bilayers and double transition metal dichalcogenide bilayers involves layer by layer assembly using pick and transfer techniques. These are prone to layer wrinkling, contamination, and misorientation (Frisenda et al., 2018). Device yields tend to be low and prospects for scalability limited. III–V semiconductor based devices such as gallium arsenide, offer more promise for scalability, but the molecular beam epitaxy growth technique is not compatible with standard complementary metal-oxide semiconductor technology, thus limiting the prospects for advanced manufacturing and large scale device integration.

Other atomically thin layers

Double monolayer graphene in a periodic magnetic field

To boost the value of the ratio $\langle V\rangle/E_F$, Dell'Anna et al. (2015) proposed applying a periodically modulated external magnetic field perpendicular to the two graphene monolayers. The magnetic field preserves the linear dispersion of the graphene monolayer energy bands, but it reduces the constant Fermi velocity v_F, flattening the gradient of the bands. This reduces E_F, increases $\langle V\rangle/E_F$, and strengthens the superfluid pair coupling. A magnetic field $B_\perp \gtrsim 1$ T with a periodicity $\lesssim$10 nm, would boost $\langle V\rangle/E_F$ above 2.35 (see Section "Double monolayer graphene"). The resulting superfluid gaps are large, of the order of hundreds of Kelvin.

There is an upper limit $B_\perp^{\max}$ on the magnetic field strength. At $B_\perp^{\max}$, the Fermi energy passes through the top of the band of the magnetic field. Once the Fermi energy is in the bandgap, the assumption that the spectrum is linear is no longer valid.

Nanoribbons from double monolayer graphene

Zarenia et al. (2016) predicted strong electron-hole superfluidity in coupled monolayer graphene armchair-edge terminated nanoribbons, separated by a hexagonal boron nitride insulating barrier (Fig. 7). The nanoribbons would be independently contacted, with top and bottom metal gates to tune the densities.

In contrast to graphene monolayers, the bands of the nanoribbons are parabolic at low energies and there is a bandgap. As a result, the screening of the electron-hole pairing interaction is much weaker compared with coupled graphene monolayers. The one-dimensional quantum confinement of the electrons and holes further enhances the pairing attraction. The one-dimensional van Hove enhancement of the density of states magnifies superfluid shape resonances from the confinement (see (Perali et al., 1996; Bianconi et al., 1997, 1998)), acting non-linearly through the superfluid gap equation to enhance the magnitude of the gaps. The resulting superfluidity is strong-coupled with very large superfluid gaps that can be in excess of $\Delta \sim 1000$ K. The superfluidity is multicomponent, with different condensates for the multiple subbands of the nanoribbon.

Hybridization of double bilayer graphene

In double bilayer graphene with separations between the bilayers less than $d = 1$ nm, the electron-hole pairing interaction would become very strong, potentially increasing superfluid onset densities and hence transition temperatures. However, for separations $d < 1$ nm, electron-hole recombination rates will be extremely rapid, thus making equilibration uncertain. When the separation

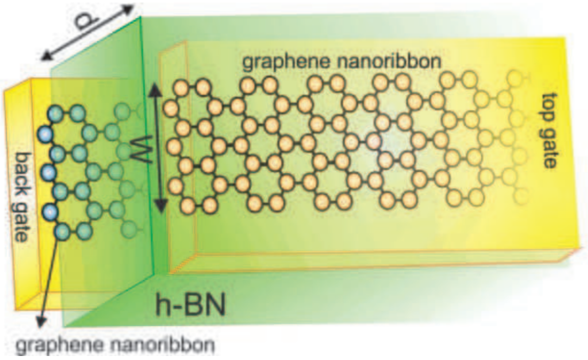

Fig. 7 Electron-doped and hole-doped armchair-edge terminated graphene nanoribbons of width *W* separated by a hexagonal boron nitride insulator (h-BN) of thickness *d*. Top and back metal gates tune the densities.

between the graphene bilayers is comparable to the thickness of each bilayer (0.37 nm (Nilsson et al., 2008)), strong hybridization will occur across all four monolayers making up the double graphene bilayer system. Su and MacDonald (2017) demonstrated that there could exist a rich diagram of novel phases, including spin-density-wave states and mixed excitonic and spin order states. In practice, with tunneling rates that grow exponentially as the bilayer separations decrease, whether these new phases could be realized is unclear.

Double trilayer and quadlayer graphene

Zarenia et al. (2014) extended the idea of increasing the density of states, and thus reducing the Fermi energy for a given density, to double trilayer and double quadlayer graphene. The additional layers depress the Fermi energy at a given density, which further strengthens the coupling in the superfluid. The strong coupling increases the onset density and hence the maximum transition temperature. For double quadlayer graphene, transition temperatures as high as $T_c^{BKT} \sim 40$ K are predicted.

Double van der Waals layers with Type-III interfaces

Gupta et al. (2020) identified lattice-matched van der Waals double monolayer heterostructures with broken-gap Type-III interface band alignment, in which the top of the valence band in the upper layer lies above the bottom of the conduction band in the lower layer. This band alignment permits electrons to spontaneously transfer from the top of the upper-layer valence band to the bottom of the lower-layer conduction band, leaving a hole behind in the upper-layer valence band. In this way, the Type-III interface spontaneously generates without gate voltages, spatially separated densities of electrons and holes that are in equilibrium. As with Type-II interfaces, Type-III interfaces need no insulating barrier to separate the electrons and holes, leading to strong electron-hole pairing interactions. The density range, $10^{11}-10^{13}$ cm^{-2}, is experimentally accessible. To sweep across the different BCS-BEC crossover regimes, the densities can be tuned with gate voltages or with strain.

Superlattice of transition metal dichalcogenide monolayers

Van der Donck et al. (2020) proposed overcoming the topological limitations on the Berezinskii-Kosterlitz-Thouless transition temperature, by replacing the double electron-hole layers with a superlattice of alternating electron-doped and hole-doped layers. Since a superlattice is a three-dimensional structure, the transition is no longer topological, opening a new way for the strong electron-hole pairing interactions and the correspondingly large superfluid gaps to be exploited, so as to drive the transition to much higher temperatures. A superlattice of alternating tungsten disulfide and tungsten diselenide monolayers, was demonstrated to be optimal, with transition temperatures close to room temperature, $T_c \sim 270$ K.

Conclusion

This chapter has presented an overview to a phenomenon that recently has received impetus from accumulating experimental evidence that equilibrium electron-hole superfluidity, encompassing Bose-Einstein condensation of excitons and BCS-BEC crossover physics, is realizable in semiconductor heterostructure devices in which electrons and holes are kept spatially separated in adjacent parallel conducting layers. The electron-hole pairing attraction is strong, promising high transition temperatures. Because the attraction is long-ranged, screening determines many superfluid properties. Heterostructures currently receiving much attention include gallium arsenide and indium arsenide–gallium antimonide double quantum wells, and graphene and transition metal dichalcogenide double layers. Advantages, disadvantages, and the current experimental status of these and other promising systems have been discussed. To identify clear signatures of electron-hole superfluidity remains a major challenge. Current efforts focus on searching for dissipationless counterflow currents in the two layers, electron-hole drag resistance, and enhanced electron-hole tunneling between the layers combined with electroluminescence from the ensuing recombination. An ability to investigate crossover physics in electronic devices at equilibrium offers exciting prospects for the future.

Acknowledgments

I am grateful to Dr. Sara Conti for a great deal of assistance in the preparation of this article.

References

Balatsky AV, Joglekar YN, and Littlewood PB (2004) Dipolar superfluidity in electron-hole bilayer systems. *Physical Review Letters* 93: 266801.

Bardeen J, Cooper LN, and Schrieffer JR (1957) Theory of superconductivity. *Physics Review* 108(5): 1175.

Berezinsky VL (1972) Destruction of long-range order in one-dimensional and two-dimensional systems possessing a continuous symmetry group. II. Quantum systems. *Soviet Physics—JETP* 34: 610. (Zh. Eksp. Teor. Fiz. 61, 1144 (1972)).

Bianconi A, Valletta A, Perali A, and Saini N (1997) High T_c superconductivity in a superlattice of quantum stripes. *Solid State Communications* 102(5): 369–374.

Bianconi A, Valletta A, Perali A, and Saini NL (1998) Superconductivity of a striped phase at the atomic limit. *Physica C* 296: 269–280.

Britnell L, Gorbachev RV, Jalil R, Belle BD, Schedin F, Mishchenko A, Georgiou T, Katsnelson MI, Eaves L, Morozov SV, Peres NMR, Leist J, Geim AK, Novoselov KS, and Ponomarenko LA (2012) Field-effect tunneling transistor based on vertical graphene heterostructures. *Science* 335(6071): 947–950.

Burg GW, Prasad N, Kim K, Taniguchi T, Watanabe K, MacDonald AH, Register LF, and Tutuc E (2018) Strongly enhanced tunneling at total charge neutrality in double-bilayer graphene-WSe$_2$ heterostructures. *Physical Review Letters* 120: 177702.

Butov LV (2004) Condensation and pattern formation in cold exciton gases in coupled quantum wells. *Journal of Physics. Condensed Matter* 16(50): R1577–R1613.

Butov LV, Lai CW, Ivanov AL, Gossard AC, and Chemla DS (2002) Towards Bose–Einstein condensation of excitons in potential traps. *Nature* 417(6884): 47–52.

Castro EV, Novoselov KS, Morozov SV, Peres NMR, Dos Santos JMBL, Nilsson J, Guinea F, Geim AK, and Castro Neto AH (2010) Electronic properties of a biased graphene bilayer. *Journal of Physics. Condensed Matter* 22(17): 175503.

Chaves A and Neilson D (2019) Two-dimensional semiconductors host high-temperature exotic state. *Nature (London)* 574(7776): 39.

Combescot M, Combescot R, and Dubin F (2017) Bose-Einstein condensation and indirect excitons: A review. *Reports on Progress in Physics* 80(6): 066501.

Comte C and Nozières P (1982) Exciton Bose condensation: The ground state of an electron-hole gas. I. Mean field description of a simplified model. *Journal de Physique* 43: 1069.

Conti S, Vignale G, and MacDonald AH (1998) Engineering superfluidity in electron–hole double layers. *Physical Review B* 57: R6846–R6849.

Conti S, Perali A, Peeters FM, and Neilson D (2017) Multicomponent electron-hole superfluidity and the BCS-BEC crossover in double bilayer graphene. *Physical Review Letters* 119: 257002.

Conti S, Perali A, Peeters FM, and Neilson D (2019) Multicomponent screening and superfluidity in gapped electron-hole double bilayer graphene with realistic bands. *Physical Review B* 99: 144517.

Conti S, Neilson D, Peeters FM, and Perali A (2020a) Transition metal dichalcogenides as strategy for high temperature electron-hole superfluidity. *Condensed Matter* 5: 22.

Conti S, Van der Donck M, Perali A, Peeters FM, and Neilson D (2020b) Doping-dependent switch from one- to two-component superfluidity in coupled electron-hole van der Waals heterostructures. *Physical Review B* 101: 220504(R).

Conti S, Perali A, Peeters FM, and Neilson D (2021a) Effect of mismatched electron-hole effective masses on superfluidity in double layer solid-state systems. *Condensed Matter* 6(2).

Conti S, Saberi-Pouya S, Perali A, Virgilio M, Peeters FM, Hamilton AR, Scappucci G, and Neilson D (2021b) Electron-hole superfluidity in strained Si/Ge type II heterojunctions. *npj Quantum Materials* 6(1): 1–7.

Croxall AF, Das Gupta K, Nicoll CA, Thangaraj M, Beere HE, Farrer I, Ritchie DA, and Pepper M (2008) Anomalous Coulomb drag in electron-hole bilayers. *Physical Review Letters* 101: 246801.

Das Gupta K, Croxall AF, Waldie J, Nicoll CA, Beere HE, Farrer I, Ritchie DA, and Pepper M (2011) Experimental progress towards probing the ground state of an electron-hole bilayer by low-temperature transport. *Advances in Condensed Matter Physics* 2011: 727958.

Debnath B, Barlas Y, Wickramaratne D, Neupane MR, and Lake RK (2017) Exciton condensate in bilayer transition metal dichalcogenides: Strong coupling regime. *Physical Review B* 96: 174504.

Dell'Anna L, Perali A, Covaci L, and Neilson D (2015) Using magnetic stripes to stabilize superfluidity in electron-hole double monolayer graphene. *Physical Review B* 92: 220502.

Du L, Li X, Lou W, Sullivan G, Chang K, Kono J, and Du R-R (2017) Evidence for a topological excitonic insulator in InAs/GaSb bilayers. *Nature Communications* 8(1): 1971.

Eagles DM (1969) Possible pairing without superconductivity at low carrier concentrations in bulk and thin-film superconducting semiconductors. *Physics Review* 186: 456–463.

Efimkin DK, Burg GW, Tutuc E, and MacDonald AH (2020) Tunneling and fluctuating electron-hole Cooper pairs in double bilayer graphene. *Physical Review B* 101: 035413.

Eisenstein JP and MacDonald AH (2004) Bose–Einstein condensation of excitons in bilayer electron systems. *Nature* 432(7018): 691.

Fil DV and Shevchenko SI (2018) Electron-hole superconductivity. *Low Temperature Physics* 44(9): 867–909.

Fogler MM, Butov LV, and Novoselov KS (2014) High-temperature superfluidity with indirect excitons in van der Waals heterostructures. *Nature Communications* 5: 4555.

Franz M (2007) Importance of fluctuations. *Nature Physics* 3: 686.

Frisenda R, Navarro-Moratalla E, Gant P, Pérez De Lara D, Jarillo-Herrero P, Gorbachev RV, and Castellanos-Gomez A (2018) Recent progress in the assembly of nanodevices and van der Waals heterostructures by deterministic placement of 2D materials. *Chemical Society Reviews* 47: 53–68.

Fulde P and Ferrell RA (1964) Superconductivity in a strong spin-exchange field. *Physics Review* 135: A550.

Gaebler JP, Stewart JT, Drake TE, Jin DS, Perali A, Pieri P, and Strinati GC (2010) Observation of pseudogap behaviour in a strongly interacting Fermi gas. *Nature Physics* 6: 569.

Gorbachev RV, Geim AK, Katsnelson MI, Novoselov KS, Tudorovskiy T, Grigorieva IV, MacDonald AH, Morozov SV, Watanabe K, Taniguchi T, and Ponomarenko LA (2012) Strong Coulomb drag and broken symmetry in double-layer graphene. *Nature Physics* 8(12): 896.

Guidini A and Perali A (2014) Band-edge BCS–BEC crossover in a twoband superconductor: Physical properties and detection parameters. *Superconductor Science and Technology* 27(12): 124002.

Gupta S, Kutana A, and Yakobson BI (2020) Heterobilayers of 2D materials as a platform for excitonic superfluidity. *Nature Communications* 11(1): 1–7.

Hendrickx NW, Franke DP, Sammak A, Scappucci G, and Veldhorst M (2020) Fast two-qubit logic with holes in germanium. *Nature* 577(7791): 487–491.

High AA, Leonard JR, Remeika M, Butov LV, Hanson M, and Gossard AC (2012) Condensation of excitons in a trap. *Nano Letters* 12(5): 2605.

Hohenberg PC (1967) Existence of long-range order in one and two dimensions. *Physics Review* 158: 383.

Hu BY-K (2000) Prospecting for the superfluid transition in electron-hole coupled quantum wells using Coulomb drag. *Physical Review Letters* 85: 820.

Jiang H (2012) Electronic band structures of molybdenum and tungsten dichalcogenides by the GW approach. *Journal of Physical Chemistry C* 116(14): 7664.

Kane BE, Eisenstein JP, Wegscheider W, Pfeiffer LN, and West KW (1994) Separately contacted electron–hole double layer in a GaAs/Al$_x$Ga$_{1-x}$ As heterostructure. *Applied Physics Letters* 65(25): 3266–3268.

Kasprzak J, Richard M, Kundermann S, Baas A, Jeambrun P, Keeling JMJ, Marchetti FM, Szymańska MH, André R, Staehli JL, Savona V, Littlewood PB, Deveaud B, and Dang LS (2006) Bose–Einstein condensation of exciton polaritons. *Nature* 443(7110): 409–414.

Keldysh LV and Kopaev YV (1965) Possible instability of semimetallic state toward Coulomb interaction. *Soviet Physics—Solid State USSR* 6(9): 2219. (Fizika Tverdogo Tela, 6, 2791-2798 (1964)).

Kharitonov MY and Efetov KB (2008) Electron screening and excitonic condensation in double-layer graphene systems. *Physical Review B* 78: 241401.

Komendová L, Chen Y, Shanenko AA, Milošević MV, and Peeters FM (2012) Two-band superconductors: Hidden criticality deep in the superconducting state. *Physical Review Letters* 108(20): 207002.

Kosterlitz JM and Thouless DJ (1973) Ordering, metastability and phase transitions in two-dimensional systems. *Journal of Physics C: Solid State Physics* 6: 1181–1203.

Lagoin C and Dubin F (2021) Key role of the moiré potential for the quasi-condensation of interlayer excitons in van der Waals heterostructures. *Physical Review B* 103: L041406.

Larkin AI and Ovchinnikov YN (1965) Quantum theory of defects in crystals. *Soviet Physics—JETP* 20: 762–770. (Zh. Eksp. Teor. Fiz. 47, 1136 (1964)).

Lee K, Fallahazad B, Xue J, Dillen DC, Kim K, Taniguchi T, Watanabe K, and Tutuc E (2014) Chemical potential and quantum Hall ferromagnetism in bilayer graphene. *Science* 345(6192): 58.

Leggett AJ (1980) Diatomic molecules and Cooper pairs. In: *Modern Trends in the Theory of Condensed Matter*, pp. 13–27. Springer.

Liu L, Świerkowski L, Neilson D, and Szymański J (1996) Static and dynamic properties of coupled electron-electron and electron–hole layers. *Physical Review B* 53: 7923–7931.

Liu L, Świerkowski L, and Neilson D (1998) Exciton and charge density wave formation in spatially separated electron–hole liquids. *Physica B: Condensed Matter* 249-251: 594–597.

Liu X, Li JIA, Watanabe K, Taniguchi T, Hone J, Halperin BI, Kim P, and Dean CR (2022) Crossover between strongly coupled and weakly coupled exciton superfluids. *Science* 375(6577): 205–209.

Lodari M, Hendrickx NW, Lawrie WIL, Hsiao T-K, Vandersypen LMK, Sammak A, Veldhorst M, and Scappucci G (2021) Low percolation density and charge noise with holes in germanium. *Materials for Quantum Technology* 1(1): 011002.

López Ríos P, Perali A, Needs RJ, and Neilson D (2018) Evidence from quantum Monte Carlo simulations of large-gap superfluidity and BCS-BEC crossover in double electron-hole layers. *Physical Review Letters* 120: 177701.

Lozovik YE and Sokolik AA (2008) Coherent phases and collective electron phenomena in graphene. *Journal of Physics Conference Series* 129(1): 012003.

Lozovik YE and Sokolik A (2010) Ultrarelativistic electron-hole pairing in graphene bilayer. *European Physical Journal B* 73(2): 195.

Lozovik YE and Yudson VI (1975) Feasibility of superfluidity of paired spatially separated electrons and holes. *JETP Letters (USSR)* 22(11): 274–276. (Pis'ma Zh. Eksp. Teor. Fiz. 22, 556-559 (1975)).

Lozovik YE and Yudson VI (1976) A new mechanism for superconductivity: Pairing between spatially separated electrons and holes. *Soviet Physics—JETP* 44: 389–397. (Zh. Eksp. Teor. Fiz. 71, 738-753 (1976)).

Lozovik YE, Ogarkov SL, and Sokolik AA (2012) Condensation of electron-hole pairs in a two-layer graphene system: Correlation effects. *Physical Review B* 86: 045429.

Ma L, Nguyen PX, Wang Z, Zeng Y, Watanabe K, Taniguchi T, MacDonald AH, Mak KF, and Shan J (2021) Strongly correlated excitonic insulator in atomic double layers. *Nature* 598(7882): 585–589.

Mak KF, Lee C, Hone J, Shan J, and Heinz TF (2010) Atomically thin MoS_2: A new direct-gap semiconductor. *Physical Review Letters* 105(13): 136805.

Mermin ND and Wagner H (1966) Absence of ferromagnetism or antiferromagnetism in one- or two-dimensional isotropic Heisenberg models. *Physical Review Letters* 17: 1133.

Min H, Bistritzer R, Su J-J, and MacDonald AH (2008) Room-temperature superfluidity in graphene bilayers. *Physical Review B* 78(12): 121401.

Narozhny BN and Levchenko A (2016) Coulomb drag. *Reviews of Modern Physics* 88: 025003.

Neilson D, Świerkowski L, Szymański J, and Liu L (1993) Excitations of the strongly correlated electron liquid in coupled layers. *Physical Review Letters* 71: 4035–4038.

Neilson D, Perali A, and Hamilton AR (2014) Excitonic superfluidity and screening in electron-hole bilayer systems. *Physical Review B* 89: 060502(R).

Nilsson F and Aryasetiawan F (2021) Effects of dynamical screening on the BCS-BEC crossover in double bilayer graphene: Density functional theory for exciton bilayers. *Physical Review Materials* 5: L050801.

Nilsson J, Castro Neto AH, Guinea F, and Peres NMR (2008) Electronic properties of bilayer and multilayer graphene. *Physical Review B* 78: 045405.

Novoselov KS, Geim AK, Morozov SV, Jiang D, Zhang Y, Dubonos SV, Grigorieva IV, and Firsov AA (2004) Electric field effect in atomically thin carbon films. *Science* 306(5696): 666.

Nozières P and Pistolesi F (1999) From semiconductors to superconductors: A simple model for pseudogaps. *European Physical Journal B* 10(4): 649.

Nozières P and Schmitt-Rink S (1985) Bose condensation in an attractive fermion gas: From weak to strong coupling superconductivity. *Journal of Low Temperature Physics* 59(3): 195.

Pascucci F, Conti S, Neilson D, Tempere J, and Perali A (2022) Josephson effect as signature of electron-hole superfluidity in bilayers of van der Waals heterostructures. *Physical Review B*. In press.

Perali A, Bianconi A, Lanzara A, and Saini N (1996) The gap amplification at a shape resonance in a superlattice of quantum stripes: A mechanism for high T_c. *Solid State Communications* 100(3): 181–186.

Perali A, Pieri P, Strinati GC, and Castellani C (2002) Pseudogap and spectral function from superconducting fluctuations to the bosonic limit. *Physical Review B* 66: 024510.

Perali A, Neilson D, and Hamilton AR (2013) High-temperature superfluidity in double-bilayer graphene. *Physical Review Letters* 110: 146803.

Pieri P, Neilson D, and Strinati GC (2007) Effects of density imbalance on the BCS-BEC crossover in semiconductor electron-hole bilayers. *Physical Review B* 75(11): 113301.

Pillarisetty R (2011) Academic and industry research progress in germanium nanodevices. *Nature* 479(7373): 324–328.

Pohlt M, Lynass M, Lok JGS, Dietsche W, Klitzing KV, Eberl K, and Mühle R (2002) Closely spaced and separately contacted two–dimensional electron and hole gases by in situ focused–ion implantation. *Applied Physics Letters* 80(12): 2105–2107.

Saberi-Pouya S, Zarenia M, Perali A, Vazifehshenas T, and Peeters FM (2018) High-temperature electron-hole superfluidity with strong anisotropic gaps in double phosphorene monolayers. *Physical Review B* 97(17): 174503.

Saberi-Pouya S, Conti S, Perali A, Croxall AF, Hamilton AR, Peeters FM, and Neilson D (2020) Experimental conditions for the observation of electron-hole superfluidity in GaAs heterostructures. *Physical Review B* 101: 140501(R).

Sarma G (1963) On the influence of a uniform exchange field acting on the spins of the conduction electrons in a superconductor. *Journal of Physics and Chemistry of Solids* 24(8): 1029.

Scappucci G, Kloeffel C, Zwanenburg FA, Loss D, Myronov M, Zhang J-J, De Franceschi S, Katsaros G, and Veldhorst M (2020) The germanium quantum information route. *Nature Reviews Materials* 1–18.

Schäffler F (1997) High-mobility Si and Ge structures. *Semiconductor Science and Technology* 12(12): 1515–1549.

Schafroth MR, Butler ST, and Blatt JM (1957) Quasichemical equilibrium approach to superconductivity. *Helvetica Physica Acta* 30: 93–134.

Seamons JA, Morath CP, Reno JL, and Lilly MP (2009) Coulomb drag in the exciton regime in electron-hole bilayers. *Physical Review Letters* 102: 026804.

Shanenko AA, Croitoru MD, Vagov AV, Axt VM, Perali A, and Peeters FM (2012) Atypical BCS-BEC crossover induced by quantum-size effects. *Physical Review A* 86(3): 033612.

Shevchenko SI (1976) Theory of superconductivity of systems with pairing of spatially separated electrons and holes. *Soviet Journal of Low Temperature Physics* 2(4): 251. (Fiz. Nizk. Temp. 2, 505 (1976)).

Sivan U, Solomon PM, and Shtrikman H (1992) Coupled electron-hole transport. *Physical Review Letters* 68: 1196.

Sodemann I, Pesin DA, and MacDonald AH (2012) Interaction-enhanced coherence between two-dimensional Dirac layers. *Physical Review B* 85: 195136.

Stern F (1967) Polarizability of a two-dimensional electron gas. *Physical Review Letters* 18: 546–548.

Strinati GC, Pieri P, Röpke G, Schuck P, and Urban M (2018) The BCS–BEC crossover: From ultra-cold Fermi gases to nuclear systems. *Physics Reports* 738: 1–76.

Su J-J and MacDonald AH (2008) How to make a bilayer exciton condensate flow. *Nature Physics* 4(10): 799–802.

Su J-J and MacDonald AH (2017) Spatially indirect exciton condensate phases in double bilayer graphene. *Physical Review B* 95: 045416.

Subasi AL, Pieri P, Senatore G, and Tanatar B (2010) Stability of Sarma phases in density imbalanced electron-hole bilayer systems. *Physical Review B* 81: 075436.

Van der Donck M, Conti S, Perali A, Hamilton AR, Partoens B, Peeters FM, and Neilson D (2020) Three-dimensional electron-hole superfluidity in a superlattice close to room temperature. *Physical Review B* 102: 060503.

Vignale G and MacDonald AH (1996) Drag in paired electron-hole layers. *Physical Review Letters* 76: 2786.

Vigneau F, Mizokuchi R, Zanuz DC, Huang X, Tan S, Maurand R, Frolov S, Sammak A, Scappucci G, Lefloch F, and Franceschi SD (2019) Germanium quantum-well Josephson field-effect transistors and interferometers. *Nano Letters* 19(2): 1023–1027.

Virgilio M and Grosso G (2006) Type-I alignment and direct fundamental gap in SiGe based heterostructures. *Journal of Physics. Condensed Matter* 18(3): 1021–1031.

Wang Z, Rhodes DA, Watanabe K, Taniguchi T, Hone JC, Shan J, and Mak KF (2019) Evidence of high-temperature exciton condensation in two-dimensional atomic double layers. *Nature (London)* 574(7776): 76–80.

Watson TF, Philips SGJ, Kawakami E, Ward DR, Scarlino P, Veldhorst M, Savage DE, Lagally MG, Friesen M, Coppersmith SN, Eriksson MA, and Vandersypen LMK (2018) A programmable two-qubit quantum processor in silicon. *Nature* 555(7698): 633–637.

Zarenia M, Perali A, Neilson D, and Peeters F (2014) Enhancement of electron-hole superfluidity in double few-layer graphene. *Scientific Reports* 4: 7319.

Zarenia M, Perali A, Peeters FM, and Neilson D (2016) Large gap electron-hole superfluidity and shape resonances in coupled graphene nanoribbons. *Scientific Reports* 6(1): 24860.

Zeng Y and MacDonald AH (2020) Electrically controlled two-dimensional electron-hole fluids. *Physical Review B* 102: 085154.

Zenker B, Fehske H, and Beck H (2015) Excitonic Josephson effect in double-layer graphene junctions. *Physical Review B* 92: 081111.

Zwanenburg FA, Dzurak AS, Morello A, Simmons MY, Hollenberg LCL, Klimeck G, Rogge S, Coppersmith SN, and Eriksson MA (2013) Silicon quantum electronics. *Reviews of Modern Physics* 85: 961–1019.

Spin superfluidity

EB Sonin, Racah Institute of Physic, Hebrew University of Jerusalem, Jerusalem, Israel

© 2024 Elsevier Ltd. All rights reserved.

Introduction 51
Concept of superfluidity 52
Spin superfluidity in ferromagnets 56
Spin superfluidity in antiferromagnets 59
Superfluid spin transport without spin conservation law 62
Long-distance superfluid spin transport 63
Experiments on detection of spin superfluidity 64
Conclusion 65
References 66

Abstract

The phenomenon of superfluidity (superconductivity) is a possibility of transport of mass (charge) on macroscopical distances without essential dissipation. In magnetically ordered media with easy-plane topology of the order parameter space the superfluid transport of spin is also possible despite the absence of the strict conservation law for spin. The article addresses three key issues in the theory of spin superfluidity: topology of the order parameter space, Landau criterion for superfluidity, and decay of superfluid currents via phase slip events, in which magnetic vortices cross current streamlines. Experiments on detection of spin superfluidity are also surveyed.

Key points

- Spin superfluidity is the possibility to transport spin with essentially suppressed dissipation on long distances.
- Spin superfluidity is possible if the magnetic order parameter space has the topology of a circumference.
- The necessary topology is provided by easy-plane anisotropy in ferromagnets or by magnetic field in antiferromagnets.
- Metastability of spin superfluid current states is restricted by the Landau criterion.
- Decay of spin superfluid currents is realized via phase slips, in which magnetic vortices cross current streamlines.

Introduction

The phenomenon of superfluidity (superconductivity in the case of charged fluids) is known more than a hundred years. Its analog for spin (spin superfluidity) occupies minds of condensed matter physicists from 70s of the last century. The term *superfluidity* is used in the literature to cover a broad range of phenomena in superfluid ^{4}He and ^{3}He, Bose-Einstein condensates of cold atoms, and solids. In this article superfluidity means only the possibility to transport a physical quantity (mass, charge, spin, ...) without dissipation (more accurately, with essentially suppressed dissipation). This corresponds to the original hundred-years old meaning of the term from the times of Kamerlingh Onnes and Kapitza.

The superfluidity is conditioned by the special topology of the order parameter space (vacuum manifold). Namely, this topology is that of a circumference in a plane. The angle of rotation around this circumference is the order parameter phase describing all degenerate ground states. In superfluids the phase is the phase of the macroscopic wave function. In magnetically ordered systems (ferro- and antiferromagnets) the necessary topology is provided by easy-plane magnetic anisotropy, and the phase is the angle of rotation around the axis (further the axis *z*) normal to the easy plane. Currents of mass (charge) or spin are proportional to phase gradients and are called supercurrents.

In early discussions of the spin supercurrent it was considered as a counterflow of superfluid currents of particles with different spins in superfluid ^{3}He (Vuorio, 1974), i.e., spin was transported by itinerant spin carriers. Later it was demonstrated that spin superfluidity is a universal phenomenon, which does not require mobile spin carriers and is possible in magnetic insulators (Sonin, 1978a, 1982). It can be described within the framework of the standard Landau–Lifshitz–Gilbert (LLG) theory. However, the publications conditioning spin superfluid transport by the presence of mobile carriers of spin continued to appear in the literature (Bunkov, 1995; Shi et al., 2006). According to Shi et al. (2006), it is a critical flaw of spin-current definition if it predicts spin currents in insulators.

Strictly speaking the analogy of spin superfluidity with superfluids is complete only if there is invariance with respect to any rotation in the spin space around the axis *z*. Then according to Noether's theorem the spin component along the axis *z* is conserved.

https://doi.org/10.1016/B978-0-323-90800-9.00170-0

But there is always some magnetic anisotropy, which breaks the rotational invariance. Correspondingly, there is no strict conservation law for spin, while in superfluids the gauge invariance is exact, and the conservation law of mass (charge) is also exact.

In the past there were arguments about whether superfluidity is possible in the absence of the conservation law. This dispute started at discussion of superfluidity of electron-hole pairs or excitons. The number of electron-hole pairs can vary due to interband transitions, and the degeneracy with respect to the phase of the pair condensate is lifted. Guseinov and Keldysh (1972) called this effect "fixation of phase." They demonstrated that spatially *homogeneous* stationary current states are impossible, and concluded that there is no analogy with superfluidity. However, later it was demonstrated that phase fixation does not rule out the existence of weakly *inhomogeneous* stationary current states analogous to superfluid current states (Kulik and Shevchenko, 1976; Lozovik and Yudson, 1977; Sonin, 1977). This analysis was extended on spin superfluidity (Sonin, 1978a,b, 1982). In magnetism violation of the spin conservation law usually is rather weak because it is related with relativistically small (inversely proportional to the speed of light) processes of spin-orbit interaction. In fact, the LLG theory itself is based on the assumption of weak spin-orbit interaction (Landau and Lifshitz, 1980).

Above we discussed supercurrents generated in the equilibrium (ground state) of the magnetically ordered medium with easy plane topology. But in magnetically ordered system this topology is possible also in non-equilibrium coherent precession states, when spin pumping supports spin precession with fixed spin component along the magnetic field. Such non-equilibrium coherent precession states, which are called nowadays magnon BEC, were experimentally investigated in the *B* phase of superfluid ^{3}He and in yttrium-iron-garnet (YIG) films (Bunkov, 1995; Demokritov et al., 2006).

Spin superfluid transport is possible as long as the spin phase gradient does not exceeds the critical value determined by the Landau criterion. The Landau criterion checks stability of supercurrent states with respect to elementary excitations of all collective modes. The Landau criterion determines a threshold for the current state instability, but it tells nothing about how the instability develops. The decay of the supercurrent is possible only via phase slips. In a phase slip event a magnetic vortex crosses current streamlines decreasing the phase difference along streamlines. Below the critical value of supercurrent phase slips are suppressed by energetic barriers. The critical value of the supercurrent at which barriers vanish is of the same order as that estimated from the Landau criterion. This leads to a conclusion that the instability predicted by the Landau criterion is a precursor of the avalanche of phase slips not suppressed by any activation barrier.

The superfluid spin transport on macroscopical distances is possible only if the spin phase performs a large number of full 2π rotations along current streamlines (large winding number), and phase slips are suppressed by energetic barriers. On the other hand, small phase variations less than 2π are ubiquitous in magnetism. They emerge in any spin wave, any domain wall, or due to disorder. Their existence is confirmed by numerous experiments in the past. Spin currents generated by these small phase differences transport spin only on small distances and oscillate in space or time, or both. Their existence is not a manifestation of spin superfluidity.

In last decades the interest to spin superfluidity was revived (Bunkov and Volovik, 2013; Chen and MacDonald, 2017; Evers and Nowak, 2020; Iacocca et al., 2017; Qaiumzadeh et al., 2017; Sonin, 2010, 2017, 2019b, 2020; Sun et al., 2016; Takei et al., 2014; Takei and Tserkovnyak, 2014; Tserkovnyak and Kläui, 2017) in connection with the emergence of spintronics. The present article reviews the three essentials of the spin superfluidity concept: topology, Landau criterion, and phase slips. The article focuses on the qualitative analysis avoiding details of calculations, which can be found in original papers. After the theoretical analysis the experiments searching for spin superfluidity are shortly discussed.

Concept of superfluidity

Let us remind the concept of superfluidity for the transport of mass (charge). In superfluid hydrodynamics there are the Hamilton equations for the pair of the canonically conjugate variables "phase-particle density":

$$\hbar\frac{d\varphi}{dt} = -\frac{\delta\mathcal{H}}{\delta n}, \qquad \frac{dn}{dt} = \frac{\delta\mathcal{H}}{\hbar\delta\varphi}. \tag{1}$$

Here

$$\frac{\delta\mathcal{H}}{\delta n} = \frac{\partial\mathcal{H}}{\partial n} - \nabla\cdot\frac{\partial\mathcal{H}}{\partial\nabla n}, \qquad \frac{\delta\mathcal{H}}{\delta\varphi} = \frac{\partial\mathcal{H}}{\partial\varphi} - \nabla\cdot\frac{\partial\mathcal{H}}{\partial\nabla\varphi} \tag{2}$$

are functional derivatives of the Hamiltonian

$$\mathcal{H} = \frac{\hbar^2 n}{2m}\nabla\varphi^2 + E_0(n), \tag{3}$$

φ is the phase of the wave function describing the Bose-Einstein condensate (BEC) in Bose liquids or the Cooper pair condensate in Fermi liquids, and $E_0(n)$ is the energy of the superfluid at rest, which depends only on the particle density n. Taking into account the gauge invariance [$U(1)$ symmetry] $\partial H/\partial\varphi = 0$, the Hamilton equations are reduced to the equations of hydrodynamics for an ideal liquid:

$$m\frac{d\boldsymbol{v}}{dt} = -\nabla\mu, \tag{4}$$

$$\frac{dn}{dt} = -\nabla\cdot\boldsymbol{j}. \tag{5}$$

In these expressions

$$\mu = \frac{\partial E_0}{\partial n} + \frac{\hbar^2}{2m}\nabla\varphi^2 \tag{6}$$

is the chemical potential, and

$$\boldsymbol{j} = n\boldsymbol{v} = \frac{\partial\mathcal{H}}{\hbar\partial\nabla\varphi} \tag{7}$$

is the particle current. We consider the zero-temperature limit, when the superfluid velocity coincides with the center-of-mass velocity of the whole liquid:

$$\boldsymbol{v} = \frac{\hbar}{m}\nabla\varphi. \tag{8}$$

The continuity equation Eq. (5) satisfies the conservation law of mass (charge), which follows from the gauge invariance.

A collective mode of the ideal liquid is a plane sound wave $\propto e^{i\boldsymbol{k}\cdot\boldsymbol{r}-i\omega t}$ with the wave vector $\boldsymbol{k}$, the frequency ω, and the linear spectrum $\omega = u_s k$. The sound velocity is

$$u_s = \sqrt{\frac{n}{m}\frac{\partial^2 E_0}{\partial n^2}}. \tag{9}$$

In the sound wave the phase varies in space, i.e., the wave is accompanied by mass currents [Fig. 1(a)]. An amplitude of the phase variation is small, and currents transport mass on distances of the order of the wavelength. A real superfluid transport on macroscopic distances is possible in current states, which are stationary solutions of the hydrodynamic equations with finite constant currents, i.e., with constant nonzero phase gradients. In the current state the phase rotates through a large number of full 2π-rotations along streamlines of the current [Fig. 1(b)]. These are supercurrents or persistent currents.

The crucial point of the superfluidity theory is why the supercurrent in Fig. 1(b) is a metastable state and does not decay a long time. The first explanation of the supercurrent metastability was the well known Landau criterion (Landau, 1941). According to this criterion, the current state is stable as far as *any quasiparticle* in a moving liquid has a positive energy in the laboratory frame and therefore its creation requires an energy input. Let us suppose that elementary quasiparticles of the liquid at rest have an energy $\varepsilon(\boldsymbol{p}) = \hbar\omega(\boldsymbol{k})$, where $\boldsymbol{p} = \hbar\boldsymbol{k}$ is the quasiparticle momentum. If the liquid moves with the velocity $\boldsymbol{v}$ the quasiparticle energy in the laboratory frame becomes $\tilde{\varepsilon}(\boldsymbol{p}) = \varepsilon(\boldsymbol{p}) + \boldsymbol{p}\cdot\boldsymbol{v}$. This is the Doppler effect in the Galilean invariant fluid. The current state is stable if the energy $\tilde{\varepsilon}$ is never negative. This condition is the Landau criterion:

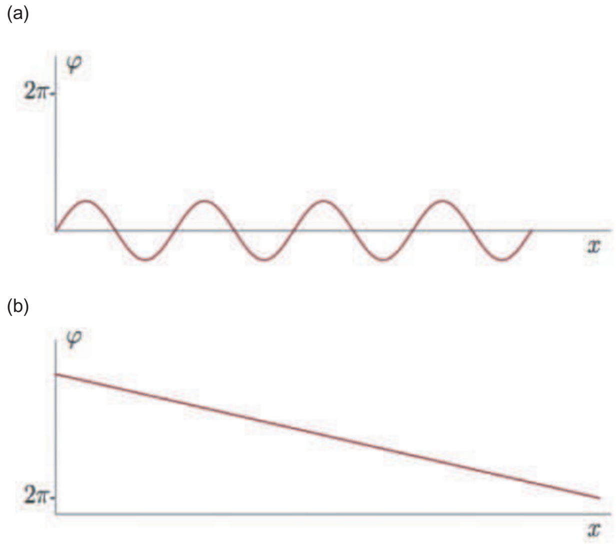

Fig. 1 Phase (in-plane rotation angle) variation in space at the presence of mass (spin) currents. (a) Oscillating currents in a sound (spin) wave. (b) Stationary mass (spin) supercurrent. From Sonin EB (2010) Spin currents and spin superfluidity. *Advances in Physics* 59: 181–255.

$$v < v_L = \min \frac{\varepsilon(\boldsymbol{p})}{p} = \min \frac{\omega(\boldsymbol{k})}{k}. \tag{10}$$

If quasiparticles are phonons (quanta of sound waves) the Landau critical velocity v_L is the sound velocity u_s. In superfluid ^{4}He the Landau critical velocity v_L is determined by the roton part of the spectrum. It is a few times less than the sound velocity.

The Landau criterion checks the stability with respect to elementary microscopic perturbations of the current state, but does not provide an information how the instability would develop. The whole process of the supercurrent decay is connected with generation of macroscopic perturbations. These perturbations are quantum vortices. If the vortex axis (vortex line) coincides with the z axis, the phase gradient around the vortex line is given by

$$\boldsymbol{v}_v = \frac{\hbar}{m}\nabla\varphi_v = \frac{\kappa\,[\hat{z}\times\boldsymbol{r}]}{2\pi r^2}, \tag{11}$$

where $\boldsymbol{r}$ is the position vector in the xy plane and $\kappa = h/m$ is the velocity circulation quantum.

Creation of the vortex requires some energy. The vortex energy per unit length (line tension) is determined mostly by the kinetic (gradient) energy in the area not very close to the vortex axis where the particle density does not differ essentially from its equilibrium value n_0 (the London region):

$$\varepsilon_v = n_0 \int d^2\boldsymbol{r}\,\frac{\hbar^2(\nabla\varphi_v)^2}{2m} = \frac{\pi\hbar^2 n_0}{m}\ln\frac{r_m}{r_c}. \tag{12}$$

The upper cut-off r_m of the logarithm is determined by geometry. For the vortex shown in Fig. 2(a) it is the distance of the vortex line from a sample border. The lower cut-of r_c is the vortex-core radius. It determines the distance r at which the phase gradient is so high that the density n starts to decrease compared to the equilibrium density n_0 at large r. The energy $E_0(n)$ of the resting superfluid at small $n - n_0$ is determined by the fluid compressibility:

$$E_0(n) = E_0(n_0) + \frac{m\,(n_0 - n)^2 u_s^2}{2n_0}. \tag{13}$$

At the distance r_c from the vortex axis the energy $mn\,\nabla\,\varphi_v^2/2$ becomes of the order of the compressibility energy at $n_0 - n \sim n_0$. This happens when the velocity $v_v(r)$ induced by the vortex becomes of the order of the sound velocity u_s. This yields $r_c \sim \kappa/u_s$. Inside the core the density vanishes at the vortex axis eliminating the singularity in the kinetic energy. For the weakly non-ideal Bose-gas r_c is on the order of the coherence length.

Phase slips are impeded by energy barriers determined by topology of the order parameter space (vacuum manifold). The order parameter of a superfluid is a complex wave function $\psi = \psi_0 e^{i\varphi}$, where the modulus ψ_0 of the wave function is a positive constant determined by minimization of the energy and the phase φ is a degeneracy parameter. Any degenerate ground state in a closed annular channel (torus) with some constant phase φ maps on some point at the circumference $|\psi| = \psi_0$ in the complex plane ψ, while a current state with the phase change $2\pi N$ around the torus maps onto a path [Fig. 3(a)] winding around the circumference N times. The integer winding number N is a topological charge. The current can relax if it is possible to change the topological charge.

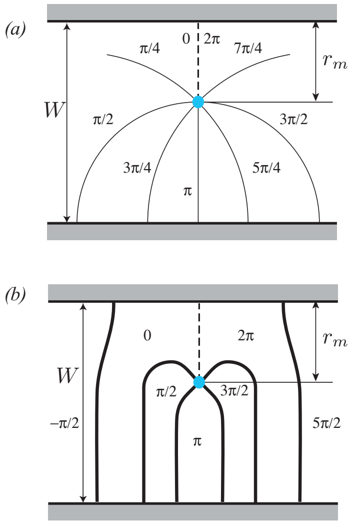

Fig. 2 Mass and magnetic vortices. (a) Vortex in a superfluid or magnetic vortex in an easy-plane ferromagnet without in-plane anisotropy. (b) magnetic vortex at small average spin currents ($\langle\nabla\varphi\rangle \ll 1/l$) for fourfold inplane symmetry. The vortex line is a confluence of four 90° domain walls (solid lines). From Sonin EB (2010) Spin currents and spin superfluidity. *Advances in Physics* 59: 181–255.

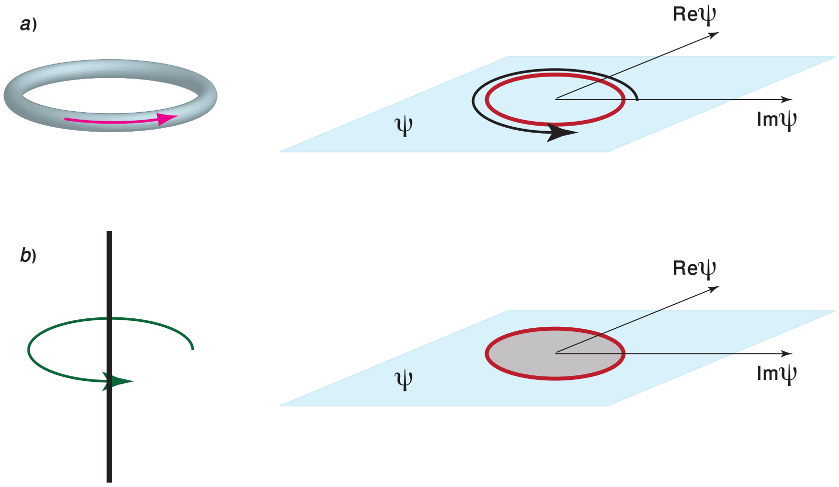

Fig. 3 Topology of the uniform mass current and the vortex states. (a) The current state in a torus maps onto the circumference $|\psi| = \psi_0$ in the complex ψ—plane, where ψ_0 is the modulus of the equilibrium order parameter wave function in the uniform state. (b) The current state with a vortex maps onto the circle $|\psi| \leq \psi_0$. From Sonin EB (2010) Spin currents and spin superfluidity. *Advances in Physics* 59: 181–255.

A change of the topological charge from N to $N - 1$ is possible, if a vortex generated at one border of a channel with a moving superfluid moves across current streamlines "cutting" the channel cross-section, and annihilates at another border as shown in Fig. 2 (a). This is a phase slip. In the phase slip event the distance r_m of the vortex from a border varies from zero to the width W of the channel. The energy of the vortex in a moving superfluid is determined by a sum of the constant gradient $\nabla\varphi_0$, which determines the supercurrent, and the phase gradient $\nabla\varphi_v$ induced by the vortex. The vortex energy consists of the energy of the vortex in a resting fluid given by Eq. (12) and of the energy from the cross terms of the two gradient fields $\nabla\varphi_0$ and $\nabla\varphi_v$:

$$\tilde{\varepsilon}_v = \frac{\pi\hbar^2 n_0}{m} L \ln\frac{r_m}{r_c} - \frac{2\pi\hbar^2 n_0}{m} S\nabla\varphi_0, \tag{14}$$

where L is the length of the vortex line and S is the area of the cut, at which the phase jumps by 2π. For the 2D case shown in Fig. 2 (a) (a straight vortex in a slab of thickness L normal to the picture plane) $S = Lr_m$. The vortex motion across the channel (growth of r_m) is impeded by the barrier determined by the maximum of the energy $\tilde{\varepsilon}_v$ as a function r_m. The height of the barrier is the vortex energy at $r_m = 1/2 \nabla \varphi_0$:

$$\varepsilon_b \approx \frac{\pi\hbar^2 n}{m} L \ln\frac{2}{r_c\nabla\varphi_0}. \tag{15}$$

The barrier disappears at gradients $\nabla\varphi_0 \sim 1/r_c$, which are of the same order as the critical gradient determined from the Landau criterion. On the other hand, in the limit of small velocity $v \propto \nabla\varphi_0$ the barrier height grows and at very small velocity $v \sim \hbar/mW$ reaches the value

$$\varepsilon_m \approx \frac{\pi\hbar^2 n}{m} L \ln\frac{W}{r_c}. \tag{16}$$

Thus, in the thermodynamic (macroscopic) limit $W \to \infty$ the barrier height becomes infinite. Since the phase slip probability exponentially decreases on the barrier height (whether the barrier is overcome due to thermal fluctuations or via quantum tunneling) the life time of the current state in conventional superfluidity diverges when the velocity (phase gradient) decreases. This justifies calling superfluidity macroscopic quantum phenomenon.

In the 3D geometry the phase slip is realized with expansion of vortex rings. For the ring of radius R the vortex-length and the area of the cut are $L = 2\pi R$ and $S = \pi R^2$ respectively, and the barrier disappears at the same critical gradient $\sim 1/r_c$ as in the 2D case.

The state with the vortex in a moving superfluid maps on the full circle $|\psi| \leq \psi_0$ [Fig. 3(b)]. The area outside the vortex core maps on the circumference $|\psi| = \psi_0$, while the core maps on the interior of the circle. In a weakly interacting Bose-gas the structure of the core is determined by solution of the Gross—Pitaevskii equation (Pitaevskii and Stringari, 2003; Sonin, 2016). The details of the core structure are not important for the content of the present article.

For better understanding of the superfluidity phenomenon it is useful to consider a mechanical analog of superfluid current (Sonin, 1982). Let us twist a long elastic rod so that a twisting angle at one end of the rod with respect to an opposite end reaches values many times 2π. Bending the rod into a ring and connecting the ends rigidly, one obtains a ring with a circulating persistent angular-momentum flux (Fig. 4). The flux is proportional to the gradient of twisting angle, which plays the role of the phase gradient in the supercurrent. The deformed state of the ring is not the ground state of the ring, but it cannot relax to the ground state

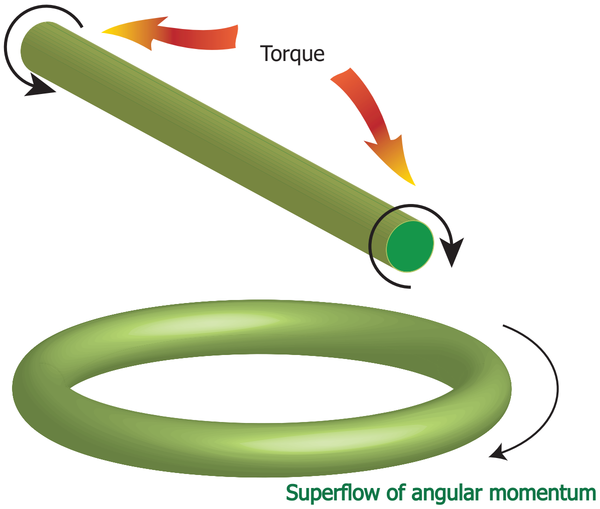

Fig. 4 Mechanical analog of a persistent current: A twisted elastic rod bent into a closed ring. There is a persistent angular-momentum flux around the ring. From Sonin EB (2010) Spin currents and spin superfluidity. *Advances in Physics* 59: 181–255.

via any elastic process, because it is topologically stable. The only way to relieve the strain inside the rod is *plastic displacements*. This means that dislocations start to move across rod cross-sections. The role of dislocations in the twisted rod is similar to the role of vortices in the superfluid.

Spin superfluidity in ferromagnets

For a ferromagnet with magnetization density $\boldsymbol{M}$ the LLG equation is (Landau and Lifshitz, 1980)

$$\frac{\partial \boldsymbol{M}}{\partial t} = \gamma\left[\boldsymbol{H}_{\mathrm{eff}} \times \boldsymbol{M}\right], \tag{17}$$

where γ is the gyromagnetic ratio between the magnetic and mechanical moment. The effective magnetic field is determined by the functional derivative of the Hamiltonian $\mathcal{H}$:

$$\boldsymbol{H}_{\mathrm{eff}} = -\frac{\delta\mathcal{H}}{\delta\boldsymbol{M}} = -\frac{\partial\mathcal{H}}{\partial\boldsymbol{M}} + \nabla_i \frac{\partial\mathcal{H}}{\partial\nabla_i\boldsymbol{M}} \tag{18}$$

According to the LLG equation, the absolute value M of the magnetization does not vary. The evolution of $\boldsymbol{M}$ is a precession around the effective magnetic field $\boldsymbol{H}_{\mathrm{eff}}$.

If spin-rotational invariance is broken and there is uniaxial crystal magnetic anisotropy the phenomenological Hamiltonian is

$$\mathcal{H} = \frac{A}{2}\nabla_i\boldsymbol{M}\cdot\nabla_i\boldsymbol{M} + \frac{GM_z^2}{2M^2} - \boldsymbol{H}\cdot\boldsymbol{M}. \tag{19}$$

The parameter A is stiffness of the spin system determined by exchange interaction. If the anisotropy parameter G is positive, it is the "easy plane" anisotropy, which keeps the magnetization in the xy plane. If the external magnetic field $\boldsymbol{H}$ is directed along the z axis, the z component of spin is conserved because of invariance with respect to rotations around the z axis. For the sake of simplicity we ignore the magnetostatic energy, which depends on sample shape.

Since the absolute value M of magnetization is fixed, the magnetization vector $\boldsymbol{M}$ is fully determined by the z magnetization component M_z and the angle φ showing the direction of $\boldsymbol{M}$ in the easy plane xy:

$$M_x = M_\perp \cos\varphi, \quad M_y = M_\perp \sin\varphi, \quad M_\perp = \sqrt{M^2 - M_z^2}. \tag{20}$$

In the new variables the Hamiltonian is

$$\mathcal{H} = \frac{AM_\perp^2(\nabla\varphi)^2}{2} + \frac{M_z^2}{2\chi} - HM_z. \tag{21}$$

Here we neglected gradients of M_z. The magnetic susceptibility $\chi = M^2/G$ along the z axis is determined by the easy-plane anisotropy parameter G. The LLG equation reduces to the Hamilton equations for a pair of canonically conjugate continuous variables "angle–moment":

$$\frac{1}{\gamma}\frac{d\varphi}{dt} = -\frac{\delta\mathcal{H}}{\delta M_z} = -\frac{\partial\mathcal{H}}{\partial M_z}, \tag{22}$$

$$\frac{1}{\gamma}\frac{dM_z}{dt} = \frac{\delta\mathcal{H}}{\delta\varphi} = -\nabla\cdot\frac{\partial\mathcal{H}}{\partial\nabla\varphi}, \tag{23}$$

where functional derivatives are taken from the Hamiltonian Eq. (21). Using the expressions for functional derivatives the Hamilton equations are

$$\frac{1}{\gamma}\frac{d\varphi}{dt} = AM_z(\nabla\varphi)^2 - \frac{M_z - \chi H}{\chi}, \tag{24}$$

$$\frac{1}{\gamma}\frac{dM_z}{dt} + \nabla\cdot\boldsymbol{J}_s = 0, \tag{25}$$

where

$$\boldsymbol{J}_s = -\frac{\partial\mathcal{H}}{\partial\nabla\varphi} = -AM_\perp^2\nabla\varphi \tag{26}$$

is the spin current. Although our equations are written for magnetization, but not for the spin density, $\boldsymbol{J}_s$ is defined as a current of spin with the spin density M_z/γ.

There is an evident analogy of Eqs. (24) and (25) with the hydrodynamic equations (4) and (5) for the superfluid. This analogy of magnetodynamics with hydrodynamics was pointed out by Halperin and Hohenberg (1969) for spin waves in antiferromagnets. The analogy is also important for spin superfluidity.

There are linear solutions of Eqs. (24) and (25) describing the plane spin-wave mode $\propto e^{i\boldsymbol{k}\cdot\boldsymbol{r}-i\omega t}$ with the sound-like spectrum:

$$\omega = c_{sw}k, \tag{27}$$

where

$$c_{sw} = \gamma M_\perp\sqrt{\frac{A}{\chi}} \tag{28}$$

is the spin-wave velocity in the ground state. The variation of the phase in the space is the same as in the sound mode propagating in the superfluid and shown in Fig. 1(a).

However, as well as the mass current in a sound wave, the small oscillating spin current in the spin wave does not lead to long-distance superfluid spin transport, which this article addresses. Spin superfluid transport on long distances is realized in current states with spin performing a large number of full 2π-rotations in the easy plane as shown in Fig. 1(b). In the current state with a constant gradient of the spin phase $\boldsymbol{K} = \nabla\varphi$, there is a constant magnetization component along the magnetic field (the axis z):

$$M_z = \frac{\chi H}{1 - \chi AK^2}. \tag{29}$$

Like in superfluids, the stability of current states is connected with topology of the order parameter space. In isotropic ferromagnets ($G = 0$) the order parameter space is a spherical surface of radius equal to the absolute value of the magnetization vector $\boldsymbol{M}$ [Fig. 5(a)]. All points on this surface correspond to the same energy of the ground state. Suppose we created the spin current state with monotonously varying phase φ in a torus. This state maps on the equatorial circumference in the order parameter space. The topology allows to continuously shift the circumference and to reduce it to a point (the northern or the southern pole). During this process shown in Fig. 5(a) the path remains in the order parameter space all the time, and therefore, no energetic barrier resists to the transformation. Thus, in isotropic ferromagnets the metastable current state are not expected.

In a ferromagnet with easy-plane anisotropy ($G > 0$) the order parameter space reduces from the spherical surface to a circumference parallel to the xy plane. It is shown in Fig. 5(b) for zero magnetic field when the circumference is the equator. This order parameter space is topologically equivalent to that in superfluids. Now the transformation of the circumference to the point costs the anisotropy energy. This allows to expect metastable spin currents (supercurrents). The magnetic field along the anisotropy axis z shifts the easy plane either up [Fig. 5(d)] or down away from the equator.

In order to check the Landau criterion, one should know the spectrum of spin waves in the current state with the constant value of the spin phase gradient $\boldsymbol{K} = \nabla\varphi$ and with the longitudinal (along the magnetic field) magnetization given by Eq. (29). The spectrum is determined by solving the Hamilton equations Eqs. (24) and (25) linearized with respect to weak perturbations of the current state. We skip the standard algebra given elsewhere (Sonin, 2019b). Finally one obtains (Iacocca et al., 2017; Sonin, 2019b) the spectrum of plane spin waves:

$$\omega + \boldsymbol{w}\cdot\boldsymbol{k} = \tilde{c}_{sw}k. \tag{30}$$

Here

$$\tilde{c}_{sw} = \sqrt{1 - \chi AK^2}c_{sw} \tag{31}$$

is the spin-wave velocity in the current state, and the spin wave velocity c_{sw} in the ground state is given by Eq. (28). The velocity

$$\boldsymbol{w} = 2\gamma M_z A\boldsymbol{K} \tag{32}$$

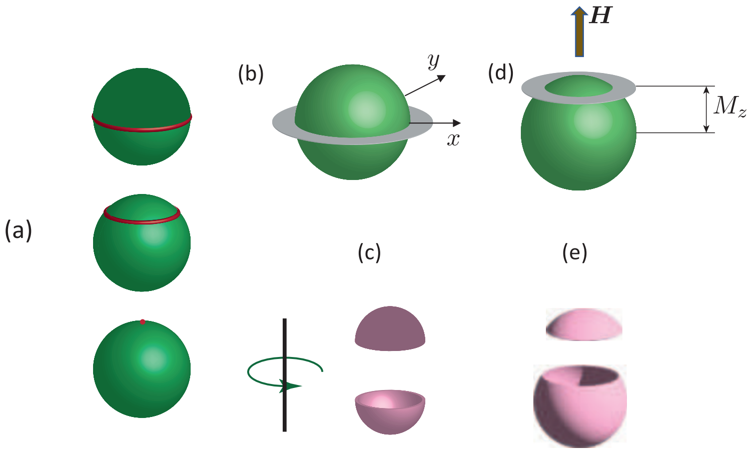

Fig. 5 Mapping of spin current states on the order parameter space of the ferromagnet. (a) Spin current in an isotropic ferromagnet. The current state in torus maps on an equatorial circumference on the sphere of radius *M* (top). Continuous shift of mapping on the surface of the sphere (middle) reduces it to a point at the northern pole (bottom), which corresponds to the ground state without currents. (b) Spin current in an easy-plane ferromagnet at $M_z = 0$. The easy-plane anisotropy reduces the order parameter space to an equatorial circumference in the *xy* plane topologically equivalent to the order parameter space in superfluids. (c) Spin current state with a magnetic vortex in an easy-plane ferromagnet at $M_z = 0$. The states map on the surface of the upper or the lower hemisphere. (d) Spin current in an easy-plane ferromagnet at $M_z \neq 0$. Spin is confined in the plane parallel to the *xy* plane but shifted closer to the northern pole. A nonzero M_z appears either in the equilibrium due to a magnetic field parallel to the axis *z*, or due to spin pumping. (e) Spin current state with a magnetic vortex in an easy-plane ferromagnet at $M_z \neq 0$. The state maps on the surface of the upper or the lower parts of the sphere. Two options of mapping are not degenerate, and the phase slip with the magnetic vortex of a smaller energy (a smaller area of mapping) is more probable. From Sonin EB (2020) Superfluid spin transport in magnetically ordered solids (review article). *Fizika Nizkikh Temperatur* 46: 523–535, [Low Temp. Phys. 46, 436 (2020)].

can be called Doppler velocity because its effect on the frequency is similar to the Doppler effect in a Galilean invariant fluid [see the text before Eq. (10)]. However, our system is not Galilean invariant (Iacocca et al., 2017), and this is the pseudo Doppler effect. Because of it, the gradient K proportional to w is present also on the right-hand side of the dispersion relation Eq. (30).

We obtained the gapless Goldstone mode with the sound-like linear in $\boldsymbol{k}$ spectrum. The current state becomes unstable when at $\boldsymbol{k}$ antiparallel to $\boldsymbol{w}$ the frequency ω becomes negative. This happens at the gradient K equal to the Landau critical gradient

$$K_L = \frac{M_\perp}{\sqrt{4M^2 - 3M_\perp^2}}\,\frac{1}{\sqrt{\chi A}}. \tag{33}$$

In the limit of weak magnetic fields when $M_z \ll M$ the Landau critical gradient is

$$K_L = \frac{1}{\sqrt{\chi A}} = \frac{\gamma M}{\chi c_{sw}}. \tag{34}$$

In this limit the pseudo-Doppler effect is not important, and at the Landau critical gradient K_L the spin-wave velocity $\tilde{c}_{sw}$ in the current state vanishes.

In the opposite limit $M_z \to M$ ($M_\perp \to 0$) the Landau critical gradient,

$$K_L = \frac{M_\perp}{2M}\,\frac{1}{\sqrt{\chi A}}, \tag{35}$$

decreases, and the spin superfluidity becomes impossible at the phase transition to the easy-axis anisotropy ($M_\perp = 0$).

Deriving the sound-like spectrum of the spin wave we neglected in the Hamiltonian terms dependent on gradients ∇M_z. One should take into account these terms at the wavelength on the order of the coherence length

$$\xi_0 = \frac{M}{M_\perp}\sqrt{\chi A} = \frac{M^2}{M_\perp}\sqrt{\frac{A}{G}}. \tag{36}$$

The Landau critical gradient K_L is on the order of the inverse coherence length $1/\xi_0$.

The current states relax to the ground state via phase slips events, in which magnetic vortices cross spin current streamlines. At $M_z = 0$ the current state with a magnetic vortex maps on a surface of a hemisphere of radius M either above or below the equator (Nikiforov and Sonin, 1983) as shown in Fig. 5(c). The vortex core has a structure of a skyrmion. The skyrmion mapping on a hemisphere is called meron. At $M_z = 0$ two magnetic vortices with opposite spin polarizations have the same energy, and both can participate in phase slips. But at $M_z \neq 0$ the magnetic vortex with a smaller mapping area [Fig. 5(e)] has a smaller energy, and phase slips with its participation are more frequent. Since inside the core the gradients ∇M_z cannot be ignored, the core radius is on the order of the coherence length ξ_0. Variation of the magnetization direction in space inside the skyrmion core is schematically shown

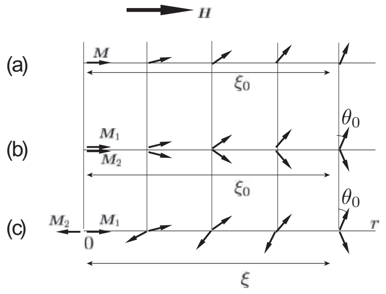

Fig. 6 Skyrmion cores of magnetic vortices. Variation of magnetization vectors (***M*** in a ferromagnet, ***M***$_1$ and ***M***$_2$ in an antiferromagnet) in the vortex core as a function of the distance *r* from the vortex axis is shown schematically. Horizontal directions of magnetizations correspond to the direction of the *z* axis in the spin space. (a) The magnetic vortex in the ferromagnet corresponding to the gapless Goldstone spin wave mode with the coherence length ξ_0 given by Eq. (36). (b) The magnetic vortex in the antiferromagnet corresponding to the Goldstone spin wave mode with the coherence length ξ_0 given by Eq. (59). (c) The magnetic vortex in the antiferromagnet corresponding to the gapped spin wave mode with the coherence length ξ given by Eq. (61). From Sonin EB (2019a) Interplay of spin and mass superfluidity in antiferromagnetic spin-1 Bose–Einstein condensates and bicirculation vortices. *Physical Review Research* 1: 033103.

in Fig. 6(a). One can find more details and numerical calculations of the structure of skyrmion cores of magnetic vortices in ferromagnets elsewhere (Sonin, 2018).

The estimation of barriers for phase slips in spin-superfluid ferromagnets is similar to that in the case of mass superfluidity. The spin phase gradient in the current state with a straight magnetic vortex parallel to the axis z is

$$\nabla\varphi = \frac{[\hat{z}\times \boldsymbol{r}]}{r^2} + \boldsymbol{K}. \tag{37}$$

We consider a 2D problem of the straight magnetic vortex at the distance r_m from the plane border. The gradient $\boldsymbol{K}$ is parallel to the border. Substituting the phase gradient field Eq. (37) into the kinetic energy and integrating the energy over the London region, where $M_\perp$ is close to its value in the ground state, one obtains the energy of the magnetic vortex per unit length:

$$\tilde{\varepsilon}_v = \pi A M_\perp^2\left(\ln\frac{r_m}{r_c} - 2Kr_m\right). \tag{38}$$

The magnetic vortex energy has a maximum at $r_m = 1/2K$. The energy at the maximum is a barrier preventing phase slips:

$$\varepsilon_b = \pi A M_\perp^2 \ln\frac{1}{2Kr_c}. \tag{39}$$

The barrier vanishes if the gradient K becomes of the order of the inverse vortex core radius r_c. This gradient is on the order of the Landau critical gradient K_L.

Considering mapping of current states with nonzero magnetization M_z [Fig. 5(d) and (e)], we had in mind the equilibrium magnetization $M_z = \chi H$ produced by an external magnetic field $\boldsymbol{H}$. In the equilibrium there is no precession of the magnetization $\boldsymbol{M}$ around the axis z. However, non-equilibrium states with non-equilibrium magnetization M_z, which makes the magnetization (spin) to coherently precess, are also possible. One can create them by pumping of magnons, which bring spin and energy into the system. Spin pumping compensates inevitable losses of spin due to spin relaxation. However, usually the process of spin relaxation is weak, and one may treat the coherent precession state as a quasi-equilibrium state at fixed M_z. The coherent precession state does not requires the crystal easy-plane anisotropy for its existence. The easy-plane topology of Fig. 5(d) is provided dynamically, and, as a result, metastable spin current states are also possible.

Spin superfluidity in the quasi-equilibrium coherent precession state was investigated theoretically and experimentally in the B phase of superfluid ^{3}He (Bunkov, 1995). Later the coherent precession state in ^{3}He was rebranded as magnon BEC (Bunkov and Volovik, 2013). Coherent spin precession state (also under the name of magnon BEC) was revealed also in YIG magnetic films (Demokritov et al., 2006). Spin superfluidity in YIG was discussed by Sun et al. (2016, 2017) and Sonin (2017). In the quasi-equilibrium coherent precession state demonstration of the long-distance superfluid spin transport is problematic (see Section "Experiments on detection of spin superfluidity"). Semantic dilemma "coherent precession state, or magnon BEC" was discussed by Sonin (2010).

Spin superfluidity in antiferromagnets

The dynamics of a bipartite antiferromagnet can be described by the LLG equations for two spin sublattices coupled via exchange interaction (Keffer and Kittel, 1951):

$$\frac{d\boldsymbol{M}_i}{dt} = \gamma[\boldsymbol{H}_i \times \boldsymbol{M}_i]. \tag{40}$$

Here the subscript $i = 1, 2$ indicates to which sublattice the magnetization $\boldsymbol{M}_i$ belongs, and

$$\boldsymbol{H}_i = -\frac{\delta \mathcal{H}}{\delta \boldsymbol{M}_i} = -\frac{\partial \mathcal{H}}{\partial \boldsymbol{M}_i} + \nabla_j \frac{\partial \mathcal{H}}{\partial \nabla_j \boldsymbol{M}_i} \tag{41}$$

is the effective field for the ith sublattice determined by the functional derivative of the Hamiltonian $\mathcal{H}$. For an isotropic antiferromagnet the Hamiltonian is

$$\begin{aligned}\mathcal{H} = \frac{\boldsymbol{M}_1\cdot\boldsymbol{M}_2}{\chi} + \frac{A(\nabla_i\boldsymbol{M}_1\cdot\nabla_i\boldsymbol{M}_1 + \nabla_i\boldsymbol{M}_2\cdot\nabla_i\boldsymbol{M}_2)}{2} \\ + A_{12}\nabla_j\boldsymbol{M}_1\cdot\nabla_j\boldsymbol{M}_2 - \boldsymbol{H}\cdot\boldsymbol{m}.\end{aligned} \tag{42}$$

The total magnetization is

$$\boldsymbol{m} = \boldsymbol{M}_1 + \boldsymbol{M}_2, \tag{43}$$

and the staggered magnetization

$$\boldsymbol{L} = \boldsymbol{M}_1 - \boldsymbol{M}_2 \tag{44}$$

is normal to $\boldsymbol{m}$.

In the LLG theory absolute values of sublattice magnetizations $\boldsymbol{M}_1$ and $\boldsymbol{M}_2$ are equal to constant M, and in the uniform state without gradients the Hamiltonian is

$$\mathcal{H} = -\frac{M^2}{\chi} + \frac{m^2}{2\chi} - Hm_z. \tag{45}$$

Here and later on we assume that the magnetic field is applied along the z axis. The constant term M^2/χ can be ignored. In the ground state the total magnetization $\boldsymbol{m}$ is directed along the magnetic field (the z axis), and the staggered magnetization $\boldsymbol{L}$ is confined to the xy plane.

The order parameter for an antiferromagnet is the unit Néel vector $\boldsymbol{l} = \boldsymbol{L}/L$. The order parameter space for the isotropic antiferromagnet in the absence of the external magnetic field is a surface of a sphere, as for isotropic ferromagnets. But in ferromagnets the magnetic field produces an easy axis for the magnetization, while in the antiferromagnet the magnetic field produces the easy plane for the order parameter vector $\mathbf{l}$. Thus, the easy-plane topology necessary for the spin superfluidity in antiferromagnets does not require the crystal easy-plane anisotropy.

In the analogy to the ferromagnetic case, one can describe the vectors of sublattice magnetizations $\boldsymbol{M}_i$ with the constant absolute value M by the two pairs of the conjugate variables (M_{iz}, φ_i), which are determined by the two pairs of the Hamilton equations:

$$\frac{1}{\gamma}\frac{d\varphi_i}{dt} = -\frac{\delta \mathcal{H}}{\delta M_{iz}} = -\frac{\partial \mathcal{H}}{\partial M_{iz}}, \tag{46}$$

$$\frac{1}{\gamma}\frac{dM_{iz}}{dt} = \frac{\delta \mathcal{H}}{\delta \varphi_i} = \frac{\partial \mathcal{H}}{\partial \varphi_i} - \nabla\cdot\frac{\partial \mathcal{H}}{\partial \nabla \varphi_i}. \tag{47}$$

Let us consider the magnetization distribution with axial symmetry around the axis z:

$$\begin{gathered}M_{1z} = M_{2z} = \frac{m_z}{2} = M\sin\theta_0, \quad m_x = m_y = 0, \\ M_{1x} = -M_{2x} = \frac{L}{2}\cos\varphi, \\ M_{1y} = -M_{2y} = \frac{L}{2}\sin\varphi, \quad L_z = 0.\end{gathered} \tag{48}$$

Here $\varphi = \varphi_1 = \pi - \varphi_2$ is the angle of rotation of $\boldsymbol{L}$ around the z axis, $L = \sqrt{4M^2 - m_z^2} = 2M\cos\theta_0$, and θ_0 is the canting angle. The Hamiltonian Eq. (42) for the axisymmetric case becomes the Hamiltonian

$$\mathcal{H} = \frac{m_z^2}{2\chi} - Hm_z + \frac{A_- L^2(\nabla\varphi)^2}{4} \tag{49}$$

for the pair of the canonically conjugate variables (m_z, φ). The Hamilton equations for this pair are

$$\frac{1}{\gamma}\frac{d\varphi}{dt} = \frac{A_- m_z(\nabla\varphi)^2}{2} - \frac{m_z - \chi H}{\chi}, \tag{50}$$

$$\frac{1}{\gamma}\frac{dm_z}{dt} + \nabla\cdot\boldsymbol{J}_s = 0. \tag{51}$$

Here $A_- = A - A_{12}$, and

$$J_s = -\frac{A_- L^2}{2}\nabla\varphi \tag{52}$$

is the superfluid spin current. These equations are identical to Eqs. (24)–(26) for the ferromagnet after replacing the spontaneous magnetization component M_z by the total magnetization component m_z, A by $A_-/2$, and $M_\perp$ by L.

In the stationary spin current state there is a constant gradient $\boldsymbol{K} = \nabla\varphi$ of the spin phase and a constant total magnetization

$$m_z = \frac{\chi H}{1 - \chi A_- K^2/2}. \tag{53}$$

For checking the Landau criterion we must know the spectrum of all collective modes. Solution of Eqs. (50) and (51) linearized with respect to plane wave perturbations $m' \propto e^{i\boldsymbol{k}\cdot\boldsymbol{r}-i\omega t}$ and $\varphi' \propto e^{i\boldsymbol{k}\cdot\boldsymbol{r}-i\omega t}$ of the stationary spin current state yield the spectrum of the Goldstone gapless mode:

$$\omega + \boldsymbol{w}\cdot\boldsymbol{k} = \tilde{c}_{sw}k. \tag{54}$$

Here the spin-wave velocity $\tilde{c}_{sw}$ in the current state and the Doppler velocity $\boldsymbol{w}$ are

$$\tilde{c}_{sw} = c_{sw}\sqrt{1 - \frac{\chi A_- K^2}{2}}, \quad \boldsymbol{w} = \gamma m_z A_- \boldsymbol{K}, \tag{55}$$

while

$$c_{sw} = \gamma L\sqrt{\frac{A_-}{2\chi}} = 2\gamma M\ \cos\theta_0\sqrt{\frac{A_-}{2\chi}} \tag{56}$$

is the spin-wave velocity in the ground state without spin currents. The difference between gapless modes in a ferromagnet and an antiferromagnet is that in the former the total magnetization precesses around the z axis, while in the latter there is the precession of the staggered magnetization. Oscillations of sublattice magnetizations $\boldsymbol{M}_1$ and $\boldsymbol{M}_2$ in the gapless mode are illustrated in Fig. 7(a).

In antiferromagnets there is another mode in which the total magnetization $\boldsymbol{m}$ and the staggered magnetization $\boldsymbol{L}$ perform rotational oscillations around the axis normal to the axis z. Without spin supercurrents this axis does not vary in space, and one can choose it to be the axis y. The oscillations of the sublattice magnetizations are illustrated in Fig. 7(b). In the spin current state $\boldsymbol{L}$ rotates around the axis, which itself rotates in the easy-plane xy along the current streamlines. The magnetic field breaks invariance with respect to rotations around axes normal to the field, and the mode spectrum is

$$\omega + \boldsymbol{w}\cdot\boldsymbol{k} = \sqrt{\omega_0^2 + c_{sw}k^2}, \tag{57}$$

where the gap is given by

$$\omega_0 = \sqrt{\frac{\gamma^2 m_z^2}{\chi^2} - c_{sw}^2 K^2}. \tag{58}$$

More details of the derivation are given by Sonin (2019b).

Applying the Landau criterion to the gapless mode at small canting angles θ_0 (weak magnetic fields), one obtains the critical gradient K_L and the correlation length ξ_0,

$$K_L = \frac{1}{\xi_0}, \quad \xi_0 = \sqrt{\frac{\chi A_-}{2}}, \tag{59}$$

similar to those obtained for a ferromagnet [Eqs. (35) and (36)]. However, in contrast to a ferromagnet where the susceptibility χ is connected with weak anisotropy energy, in an antiferromagnet the susceptibility χ is determined by a much larger exchange energy

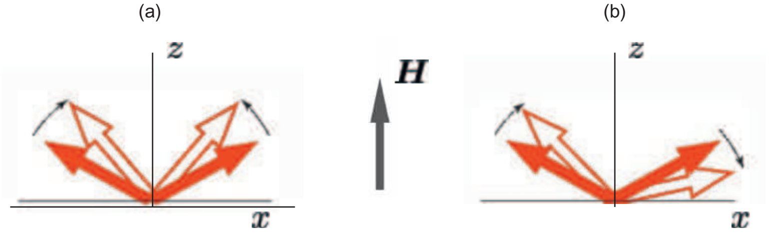

Fig. 7 The schematic picture of the two spin wave modes in the bipartite antiferromagnet in the plane *xz*. (a) The gapless Goldstone mode. There are oscillations of the canting angle determining the magnetization component m_z and rotational oscillations around the axis *z*. (b) The gapped mode. There are rotational oscillations of the two magnetizations around the axis *y*. From Sonin EB (2020) Superfluid spin transport in magnetically ordered solids (review article). *Fizika Nizkikh Temperatur* 46: 523–535, [Low Temp. Phys. 46, 436 (2020)].

and is rather small. As a result, in the antiferromagnet the gapped mode loses its stability at much lower values of K than the gapless mode. This happens at the Landau critical gradient

$$K_L = \frac{1}{\xi} \tag{60}$$

when the gap given by Eq. (58) vanishes and the mode frequency becomes complex. Here we introduced a new correlation length

$$\xi = \frac{c_s}{\gamma H} = \frac{\chi c_s}{\gamma m_z}. \tag{61}$$

As usual, the instability with respect to phase slips with magnetic vortices starts at the gradients of the same order as the Landau critical gradient. Two modes in antiferromagnets have different correlation lengths, and, correspondingly, there are two types of magnetic vortices with different structure and size of the skyrmion core. Fig. 6(b) shows schematically spatial variation of the sublattice magnetizations in the skyrmion core of a magnetic vortex connected with the Goldstone gapless mode. The core radius is of the order of the correlation length ξ_0 given by Eq. (59). Inside the core the canting angle θ_0 grows and reaches $\pi/2$ at the vortex axis. This transforms an antiferromagnet to a ferromagnet with the magnetization $2M$. The transformation increases the exchange energy, and at weak magnetic fields creation of magnetic vortices connected with the gapped mode starts earlier. Its core size is determined by the larger correlation length ξ determined by the Zeeman energy and given by Eq. (61). The skyrmion core connected with the gapped mode is illustrated in Fig. 6(c).

Superfluid spin transport without spin conservation law

Though processes violating the spin conservation law are relativistically weak, their effect is of principal importance and cannot be ignored in general. Here we consider the effect of broken rotational symmetry in the easy plane in ferromagnets. Its extension on antiferromagnets requires insignificant modifications. One should add the s-fold in-plane anisotropy energy $\propto G_{in}$ to the Hamiltonian (21), which becomes

$$\mathcal{H} = \frac{M_z^2}{2\chi} - \gamma M_z H + \frac{AM_\perp^2(\nabla\varphi)^2}{2} + G_{in}[1 - \cos(s\varphi)]. \tag{62}$$

Then the spin continuity equation (25) becomes

$$\frac{dM_z}{dt} = -\nabla\cdot\boldsymbol{J}_s + sG_{in}\sin(s\varphi) = AM_\perp^2\left[\nabla^2\varphi - \frac{\sin(s\varphi)}{l^2}\right], \tag{63}$$

where

$$l = \sqrt{\frac{AM_\perp^2}{sG_{in}}} \tag{64}$$

is the thickness of the wall separating domains with s equivalent easiest directions in the easy plane. In the stationary spin current states $dM_z/dt = 0$, and the phase φ is a periodical solution of the sine-Gordon equation parametrized by the average phase gradients $\langle\nabla\varphi\rangle$. At small $\langle\nabla\varphi\rangle \ll 1/l$ the spin structure constitutes the chain of domains with the period $2\pi/s\langle\nabla\varphi\rangle$. Spin currents (gradients) inside domains are negligible but there are spin currents inside domain walls. The spin current has a maximum in the center of the domain wall equal to

$$J_l = \sqrt{\frac{2}{s}}\frac{A}{l}. \tag{65}$$

The spin transport in the case $\langle\nabla\varphi\rangle \ll 1/l$ hardly reminds the superfluid transport on macroscopic scales: spin is transported over distances on the order of the domain-wall thickness $\mathbf{l}$. With increasing $\langle\nabla\varphi\rangle$ the density of domain walls grows, and at $\langle\nabla\varphi\rangle \gg 1/l$ the domains coalesce. Deviations of the gradient $\nabla\varphi$ from the constant average gradient $\langle\nabla\varphi\rangle$ become negligible. This restores the analogy with the superfluid transport in superfluids (Sonin, 1978a,b, 1982), and spin non-conservation can be ignored. The transformation of the domain wall chain into a weakly inhomogeneous current state at growing $\langle\nabla\varphi\rangle$ is illustrated in Fig. 8. According to the Landau criterion, spin current states become unstable at $\nabla\varphi \sim 1/\xi_0$, where the correlation length ξ_0 is given by Eq. (36). Thus, one can expect metastable nearly uniform current states at $1/l \ll \langle\nabla\varphi\rangle \ll 1/\xi_0$. This is possible if the easy plane anisotropy energy G essentially exceeds the in-plane anisotropy energy G_{in}.

In the limit $\nabla\varphi \ll 1/l$ of strongly nonuniform current states the decay of the current is also possible only via phase slips, but the structure of magnetic vortices is essentially different from that in the opposite limit $\nabla\varphi \gg 1/l$. The magnetic vortex is a line defect at which s domain walls end. The phase slip with the magnetic vortex crossing the streamlines in the channel leads to annihilation of s domain walls. This process is illustrated in Fig. 2(b) for the fourfold in-plane symmetry ($s = 4$).

An important difference with conventional mass superfluidity is that while the existence of conventional superfluidity is restricted only from above by the Landau critical gradients, the spin superfluidity is restricted also from below: gradients should

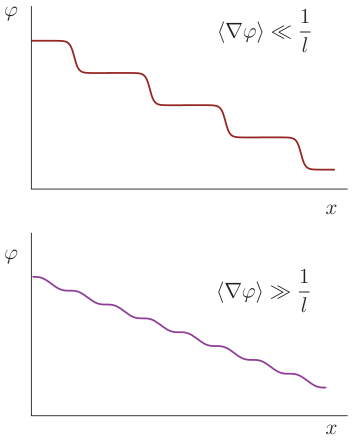

Fig. 8 The nonuniform spin-current states with $\langle\nabla\varphi\rangle \ll 1/l$ and $\langle\nabla\varphi\rangle \gg 1/l$. From Sonin EB (2010) Spin currents and spin superfluidity. *Advances in Physics* 59: 181–255.

not be less than the value $1/l$. Thus, the gradient $K = \langle\nabla\varphi\rangle$ in the expression Eq. (39) barrier height cannot be less than $1/l$, and the height of the barrier cannot exceed

$$\varepsilon_m = \pi A M_\perp^2 \ln \frac{l}{r_c}. \tag{66}$$

In contrast to the maximal phase slip barrier Eq. (16) in mass superfluidity, in spin superfluidity the maximal phase slip barrier does not become infinite in the macro-scopic limit $W \to \infty$ (König et al., 2001; Sonin, 1978a,b, 1982).

Long-distance superfluid spin transport

The absence of the strict spin conservation law also leads to the dissipative process, which is impossible in the mass superfluidity and very important for long-distance superfluid spin transport (Sonin, 1978a, 2010; Takei et al., 2014; Takei and Tserkovnyak, 2014): longitudinal spin relaxation characterized in the magnetism theory by the Bloch time T_1. Taking the Bloch relaxation into account, the equation for the non-equilibrium magnetization $M_z' = M_z - \chi H$ becomes.

$$\frac{1}{\gamma}\frac{dM_z'}{dt} = -\nabla\cdot\boldsymbol{J} - \frac{M_z'}{\gamma T_1}. \tag{67}$$

Here the total current $\boldsymbol{J} = \boldsymbol{J}_s + \boldsymbol{J}_d$ includes not only the spin supercurrent $\boldsymbol{J}_s$ given by Eq. (26), but also the spin diffusion current

$$\boldsymbol{J}_d = -\frac{D}{\gamma}\nabla M_z. \tag{68}$$

In the absence of spin superfluidity ($\boldsymbol{J}_s = 0$) Eq. (67) describes pure spin diffusion [Fig. 9(a)]. Its solution, with the boundary condition that the spin current J_0 is injected at the interface $x = 0$, is

$$J_d = J_0 e^{-x/L_d}, \quad M_z' = \gamma J_0 \sqrt{\frac{T_1}{D}} e^{-x/L_d}, \tag{69}$$

where

$$L_d = \sqrt{DT_1} \tag{70}$$

is the spin-diffusion length. Thus, the effect of spin injection exponentially decays at the scale of the spin-diffusion length, and the density of spin accumulated at the other border of the medium decreases exponentially with growing distance d.

However, if spin superfluidity is possible, the spin precession equation Eq. (24) becomes relevant. According to this equation, in a stationary state the magnetization M_z' cannot vary in space [Fig. 9(b)] since the gradient $\nabla M_z'$ leads to the linear in time growth of the gradient $\nabla\varphi$. The right-hand side of Eq. (24) is an analog of the chemical potential, and the requirement of constant in space magnetization M_z is similar to the requirement of constant in space chemical potential in superfluids, or the electrochemical potential in superconductors. As a consequence of this requirement, spin diffusion current is impossible in the bulk since it is simply "short-circuited" by the superfluid spin current. The bulk spin diffusion current can appear only in AC processes.

If the spin superfluidity is possible, the spin current can reach the spin detector at the plane $x = d$ opposite to the border where spin is injected. As a boundary condition at $x = d$, one can use a phenomenological relation $J_s(d) = M_z'(d)v_d$ connecting the spin

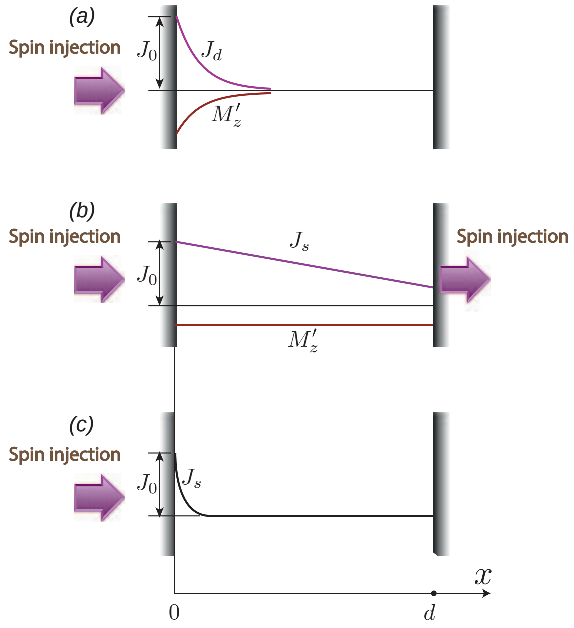

Fig. 9 Long distance spin transport. (a) Injection of the spin current J_0 into a spin-non-superfluid medium. (b) Injection of the strong spin current $J_0 \gg J_l$ into a spin-superfluid medium. (c) Injection of the weak spin current $J_0 < J_l$ into a spin-superfluid medium. From Sonin EB (2010) Spin currents and spin superfluidity. *Advances in Physics* 59: 181–255.

current with the non-equilibrium magnetization at the border with a non-magnetic medium. Here v_d is a phenomenological constant. This boundary condition (Sonin, 1978a) was confirmed by the microscopic theory of Takei and Tserkovnyak (2014). Together with the boundary condition $J_s(0) = J_0$ at $x = 0$ this yields the solution of Eqs. (24) and (67):

$$M_z' = \frac{T_1}{d + v_d T_1}\gamma J_0, \quad J_s(x) = J_0\left(1 - \frac{x}{d + v_d T_1}\right). \tag{71}$$

Thus, the spin accumulated at large distance d from the spin injector slowly decreases with d as $1/(d + C)$ [Fig. 9(b)], in contrast to the exponential decay $\propto e^{-d/L_d}$ in the spin diffusion transport [Fig. 9(a)]. The constant C is determined by the boundary condition at $x = d$.

The long-distance superfluid spin transport is possible only if the injected spin current is not too small. If the injection spin current J_0 is less than the current J_l determined by Eq. (65) the superfluid spin current penetrates into the medium only at distances not longer than the width l of a domain wall in a non-uniform spin current state at a very small average gradient $\langle \nabla\varphi \rangle \ll 1/l$ [Fig. 9(c)]. This threshold for the long-distance spin superfluid transport is connected with the absence of the strict conservation law for spin (Section "Superfluid spin transport without spin conservation law").

Experiments on detection of spin superfluidity

Experimental detection of spin superfluidity does not reduce to experimental evidence of the existence of spin supercurrents proportional to gradients of spin phase. As pointed out in Introduction (Section "Introduction"), such supercurrents produced by spin phase difference smaller than 2π emerge in any non-uniform spin structure. Numerous observations of spin waves and domain structures during the more than half-a-century history of modern magnetism cannot be explained without these microscopic spin currents. Only detection of macroscopical spin supercurrents produced by the phase difference many times larger than 2π is evidence of spin superfluidity.

The experimental evidence of macroscopical spin supercurrents was obtained in the past in the B phase of superfluid ^{3}He (Borovik-Romanov et al., 1987). A spin current was generated in a long channel connecting two cells filled by ^{3}He - B. The quasi-equilibrium state of the coherent spin precession was supported by spin pumping. The magnetic fields applied to the two cells were slightly different, and therefore, the spins in the two cells precessed with different frequencies. A small difference in the frequencies leads to a linear growth of difference of the precession phases in the cells and a phase gradient in the channel. When the gradient reached the critical value, 2π phase slips were detected. This was evidence of non-trivial spin supercurrents.

This experiment was done in the dynamical state of coherent spin precession (non-equilibrium magnon BEC). The states require pumping of spin in the whole bulk for their existence. In the geometry of the experiment on long-distance spin transport (Section "Long-distance superfluid spin transport") this would mean that spin is permanently pumped not only by a distant

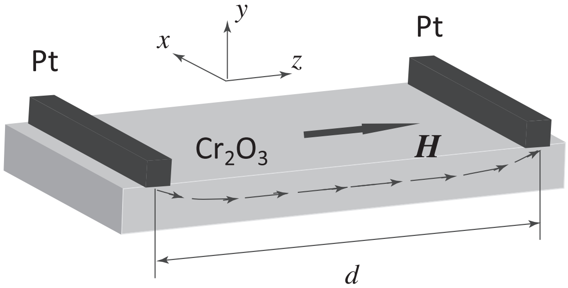

Fig. 10 Long distance spin transport in the experiment by Yuan et al. (2018). Spin is injected from the left Pt wire and flows along the Cr_2O_3 film to the right Pt wire, which serves as a detector. The arrowed dashed line shows a spin-current streamline. From Sonin EB (2020) Superfluid spin transport in magnetically ordered solids (review article). *Fizika Nizkikh Temperatur* 46: 523–535, [Low Temp. Phys. 46, 436 (2020)].

injector but also all the way up to the place where its accumulation is probed. Thus, the spin detector measures not only spin coming from the distant injector but also spin pumped close to the detector. Therefore, the experiment cannot demonstrate the existence of long-distance superfluid spin transport, but can provide, nevertheless, indirect evidence that long-distance superfluid spin transport is possible in principle.

The experiment on detection of long-distance superfluid spin transport (Section "Long-distance superfluid spin transport") was recently done by Yuan et al. (2018) in antiferromagnetic Cr_2O_3. The spin was injected from a Pt injector by heating [the Seebeck effect (Seki et al., 2015)] on one side of the Cr_2O_3 film and spin accumulation was probed on another side of the film by the Pt detector via the inverse spin Hall effect (Fig. 10). In agreement with the theoretical prediction, they observed spin accumulation inversely proportional to the distance from the interface where spin was injected.

In the experiment of Yuan et al. (2018) spin injection required heating of the Pt injector, and the spin current to the detector is inevitably accompanied by a heat flow. Lebrun et al. (2018) argued that Yuan et al. (2018) detected a signal not from spin coming from the distant injector but from spin generated by the Seebeck effect at the interface between the heated antiferromagnet and the Pt detector. If true, Yuan et al. (2018) observed not long-distance spin transport but long-distance heat transport. A resolution of this controversy requires further experimental and theoretical investigations. In particular, one could check long-distance heat transport scenario by replacing the Pt spin injector in the experiment of Yuan et al. (2018) by a heater, which produces heat but no spin.

Observation of the long-distance superfluid spin transport was also reported by Stepanov et al. (2018) in a graphene quantum Hall antiferromagnet. However, the discussion of this report requires an extensive theoretical analysis of the $\nu = 0$ quantum Hall state of graphene, which goes beyond the scope of the present article. A reader can find this analysis in Takei et al. (2016).

Conclusion

The article addressed the basics of the spin superfluidity concept: topology, Landau criterion, and phase slips. Metastable (persistent) superfluid current states are possible if the order parameter space (vacuum manifold) has the topology of a circumference like in conventional superfluids. In ferromagnets it is the circumference on the spherical surface of the spontaneous magnetizations $\boldsymbol{M}$, and in antiferromagnets it is the spherical surface of the unit Néel vector $\boldsymbol{L}/L$, where $\boldsymbol{L}$ is the staggered magnetization. The topology necessary for spin superfluidity requires the magnetic easy-plane anisotropy in ferromagnets, while in antiferromagnets this anisotropy is provided by the Zeeman energy, which confines the Néel vector in the plane normal to the magnetic field.

The Landau criterion was checked for the spectrum of elementary excitations, which are spin waves in our case. In ferromagnets there is only one gapless Goldstone spin wave mode. In bipartite antiferromagnets there are two modes: the Goldstone mode in which spins perform rotational oscillations around the symmetry axis and the gapped mode with rotational oscillations around the axis normal to the symmetry axis. At weak magnetic fields the Landau instability starts not in the Goldstone mode, but in the gapped mode. In contrast to superfluid mass currents in conventional superfluids, metastable spin superfluid currents are restricted not only by the Landau criterion from above but also from below. The restriction from below is related to the absence of the strict conservation law for spin.

The Landau instability with respect to elementary excitations is a precursor for the instability with respect to phase slips. The latter instability starts when the spin phase gradient reaches the value of the inverse vortex core radius. This value is on the same order of magnitude as the Landau critical gradient. Magnetic vortices participating in phase slips have skyrmion cores, which map on the upper or lower part of the spherical surface in the space of spontaneous magnetizations in ferromagnets, or in the space of the unit Néel vectors in antiferromagnets.

It is worthwhile to note that in reality it is not easy to reach the critical gradients discussed in the present article experimentally. The decay of superfluid spin currents is possible also at subcritical spin phase gradients since the barriers for phase slips can be overcome by thermal activation or macroscopic quantum tunneling. This makes the very definition of the real critical gradient rather ambiguous and dependent on duration of observation of persistent currents. Calculation of real critical gradients requires a detailed dynamical analysis of processes of thermal activation or macroscopic quantum tunneling through phase slip barriers, which is beyond the scope of the present article. One can find examples of such analysis for conventional superfluids with mass supercurrents in Sonin (2016).

Experimental evidence of the existence of metastable superfluid spin currents in the B phase of superfluid ^{3}He was reported long ago (Borovik-Romanov et al., 1987). The experiment was done in the non-equilibrium state of coherent spin precession, which requires permanent spin pumping in whole bulk for its existence. This does not allow to check true long-distance superfluid spin transport without any additional spin injection on the way from an injector to a detector of spin. The experiment demonstrating the long-distance transport of spin in the solid antiferromagnet was reported recently (Yuan et al., 2018). But the interpretation of this experiment in the terms of spin superfluidity was challenged (Lebrun et al., 2018), and experimental verification of the long-distance superfluid spin transport in magnetically ordered solids convincing many (if not all) in the community is still wanted.

Mechanical analogy of the mass superfluidity discussed in the end of Section "Concept of superfluidity" is valid also for spin superfluidity. The "superfluid" flux of the angular momentum in a twisted elastic rod is similar to the superfluid spin current in magnetically ordered solids. Of course, it is not obligatory to discuss the twisted rod in terms of angular-momentum flux. More usual is to discuss it in the terms of the elasticity theory: deformations, stresses, and elastic stiffness. On the same grounds, one can avoid to use the terms "spin current" and "spin superfluidity" and consider the spin current states as metastable helicoidal spin structures determined by "phase stiffness." This stance was quite popular in early disputes about spin superfluidity. Nowadays in the era spintronics the terms "spin supercurrents" and "spin superfluidity" are widely accepted.

In this article the essentials of spin superfluidity were discussed for simpler cases of a ferromagnet and of a bipartite antiferromagnet at zero temperature. Spin superfluidity was also investigated in antiferromagnets with a more complicated magnetic structure (Li and Kovalev, 2021). At finite temperates the presence of the gas of incoherent magnons was taken into account in the two-fluid theory (Flebus et al., 2016) similar to the two-fluid theory in the theory of mass superfluidity.

The present article focused on spin superfluidity in magnetically ordered solids. In superfluid ^{3}He spin superfluidity coexists with mass superfluidity. Recently investigations of spin superfluidity were extended to spin-1 BEC, where spin and mass superfluidity also coexist and interplay (Armaitis and Duine, 2017; Lamacraft, 2017; Sonin, 2018, 2019a). This interplay leads to a number of new nontrivial features of the phenomenon of superfluidity. The both types of superfluidity are restricted by the Landau criterion for the softer collective modes, which usually are the spin wave modes. As a result, the presence of spin superfluidity diminishes the possibility of the conventional mass superfluidity. Another consequence of the coexistence of spin and mass superfluidity is phase slips with bicirculation vortices characterized by two topological charges (winding numbers) (Sonin, 2019a).

References

Armaitis J and Duine RA (2017) Superfluidity and spin superfluidity in spinor Bose gases. *Physical Review A* 95: 053607.

Borovik-Romanov AS, Bunkov YM, Dmitriev VV, and Mukharskii YM (1987) Observation of phase slippage during the flow of a superfluid spin current in ^{3}He-b. *Pis′ma v Zhurnal Èksperimental′noy i Teoreticheskoy Fiziki* 45: 98–101. [JETP Lett. 45, 124–128 (1987)].

Bunkov YM (1995) Spin supercurrent and novel properties of NMR in ^{3}He. *Progress of Low Temperature Physics* 14: 68. edited by W. P. Halperin (Elsevier).

Bunkov YM and Volovik GE (2013) Spin superfluidity and magnon Bose-Einstein condensation. In: Bennemann KH and Ketterson JB (eds.) *Novel Superfluids. International Series of Monographs on Physics*, vol. 1, pp. 253–311. Oxford University Press. Chap. IV.

Chen H and MacDonald AH (2017) Spin–superfluidity and spin–current mediated nonlocal transport. In: Proukakis NP, Snoke DW, and Littlewood PB (eds.) *Universal Themes of Bose–Einstein Condensation*, pp. 525–548. Cambridge University Press. Chap. 27. arXiv:1604.02429.

Demokritov SO, Demidov VE, Dzyapko O, Melkov GA, Serga AA, Hillebrands B, and Slavin AN (2006) Bose–Einstein condensation of quasi-equilibrium magnons at room temperature under pumping. *Nature* 443: 430–433.

Evers M and Nowak U (2020) Transport properties of spin superfluids: Comparing easy-plane ferromagnets and antiferromagnets. *Physical Review B* 101: 184415.

Flebus B, Bender SA, Tserkovnyak Y, and Duine RA (2016) Two-fluid theory for spin superfluidity in magnetic insulators. *Physical Review Letters* 116: 117201.

Guseinov RR and Keldysh LV (1972) Nature of the phase transition under the conditions of an "exitonic" instability in the electronic spectrum of a crystal. *Zhurnal Eksperimental'noi i Teoreticheskoi Fiziki* 63: 2255. [Sov. Phys.–JETP 36, 1193 (1972)].

Halperin BI and Hohenberg PC (1969) Hydrodynamic theory of spin waves. *Physics Review* 188: 898–918.

Iacocca E, Silva TJ, and Hoefer MA (2017) Breaking of Galilean invariance in the hydrodynamic formulation of ferromagnetic thin films. *Physical Review Letters* 118: 017203.

Keffer F and Kittel C (1951) Theory of antiferrornagnetic resonance. *Physics Review* 85: 329–337.

König J, Bønsager MC, and MacDonald AH (2001) Dissipationless spin transport in thin film ferromagnets. *Physical Review Letters* 87: 187202.

Kulik IO and Shevchenko SI (1976) Exciton pairing and superconductivity in layered systems. *Fizika Nizkikh Temperatur* 2: 1405–1426. [Sov. J. Low Temp. Phys. 2, 687 (1976)].

Lamacraft A (2017) Persistent currents in ferromagnetic condensates. *Physical Review B* 95: 224512.

Landau LD (1941) Theory of superfluidity of helium II. *Journal of Physical (USSR)* 5: 71.

Landau LD and Lifshitz EM (1980) *Statistical Physics. Part II*. Pergamon Press.

Lebrun R, Ross A, Bender SA, Qaiumzadeh A, Baldrati L, Cramer J, Brataas A, Duine RA, and Kläui M (2018) Tunable long-distance spin transport in a crystalline antiferromagnetic iron oxide. *Nature* 561: 222–225.

Li B and Kovalev AA (2021) Spin superfluidity in noncollinear antiferromagnets. *Physical Review B* 103: L060406.

Lozovik YE and Yudson VI (1977) Interband transitions and the possibility of current states in systems with electron-hole pairing. *Pis'ma v Zhurnal Eksperimental'noi i Teoreticheskoi Fiziki* 25: 18–21. [JETP Lett. 25, 14–17 (1977)].

Nikiforov AV and Sonin EB (1983) Dynamics of magnetic vortices in a planar ferromagnet. *Zhurnal Eksperimental'noi i Teoreticheskoi Fiziki* 85: 642–651. [Sov. Phys.–JETP 58, 373 (1983)].

Pitaevskii L and Stringari S (2003) *Bose–Einstein Condensation*. Oxford University Press.

Qaiumzadeh A, Skarsvåg H, Holmqvist C, and Brataas A (2017) Spin superfluidity in biaxial antiferromagnetic insulators. *Physical Review Letters* 118: 137201.

Seki S, Ideue T, Kubota M, Kozuka Y, Takagi R, Nakamura M, Kaneko Y, Kawasaki M, and Tokura Y (2015) Thermal generation of spin current in an antiferromagnet. *Physical Review Letters* 115: 266601.

Shi J, Zhang P, Xiao D, and Niu Q (2006) Proper definition of spin current in spin-orbit coupled systems. *Physical Review Letters* 96: 076604.

Sonin EB (1977) On superfuidity of Bose condensate of electron-hole pairs. *Pis'ma v Zhurnal Eksperimental'noi i Teoreticheskoi Fiziki* 25: 95–98. [JETP Lett. 25, 84–87 (1977)].

Sonin EB (1978a) Analogs of superfluid currents for spins and electron-hole pairs. *Zhurnal Eksperimental'noi i Teoreticheskoi Fiziki* 74: 2097–2111. [Sov. Phys.–JETP, 47, 1091–1099 (1978)].

Sonin EB (1978b) Phase fixation, exitonic and spin superfluidity of electron-hole pairs and antiferromagnetic chromium. *Solid State Communications* 25: 253–255.

Sonin EB (1982) Superflows and superfluidity. *Uspekhi Fiziologicheskikh Nauk* 137: 267. [Sov. Phys.–Usp., 25, 409 (1982)].

Sonin EB (2010) Spin currents and spin superfluidity. *Advances in Physics* 59: 181–255.

Sonin EB (2016) *Dynamics of Quantised Vortices in Superfluids*. Cambridge University Press.

Sonin EB (2017) Spin superfluidity and spin waves in YIG films. *Physical Review B* 95: 144432.

Sonin EB (2018) Spin and mass superfluidity in ferromagnetic spin-1 BEC. *Physical Review B* 97: 224517. Although the subject of the paper is the BEC of cold atoms with spin 1, Sec. VII of the paper investigates vortices in a solid ferromagnet in order to compare them with vortices in the spin-1 BEC.

Sonin EB (2019a) Interplay of spin and mass superfluidity in antiferromagnetic spin-1 Bose–Einstein condensates and bicirculation vortices. *Physical Review Research* 1: 033103.

Sonin EB (2019b) Superfluid spin transport in ferro- and antiferromagnets. *Physical Review B* 99: 104423.

Sonin EB (2020) Superfluid spin transport in magnetically ordered solids (review article). *Fizika Nizkikh Temperatur* 46: 523–535. [Low Temp. Phys. 46, 436 (2020)].

Stepanov P, Che S, Shcherbakov D, Yang J, Chen R, Thilahar K, Voigt G, Bockrath MW, Smirnov D, Watanabe K, Taniguchi T, Lake RK, Barlas Y, MacDonald AH, and Lau CN (2018) Long-distance spin transport through a graphene quantum Hall antiferromagnet. *Nature Physics* 14(9): 907–911.

Sun C, Nattermann T, and Pokrovsky VL (2016) Unconventional superfluidity in yttrium iron garnet films. *Physical Review Letters* 116: 257205.

Sun C, Nattermann T, and Pokrovsky VL (2017) Bose–Einstein condensation and superfluidity of magnons in yttrium iron garnet films. *Journal of Physics D: Applied Physics* 50(14), 143002.

Takei S and Tserkovnyak Y (2014) Superfluid spin transport through easy-plane ferromagnetic insulators. *Physical Review Letters* 112: 227201.

Takei S, Halperin BI, Yacoby A, and Tserkovnyak Y (2014) Superfluid spin transport through antiferromagnetic insulators. *Physical Review B* 90: 094408.

Takei S, Yacoby A, Halperin BI, and Tserkovnyak Y (2016) Spin superfluidity in the $\nu = 0$ quantum Hall state of graphene. *Physical Review Letters* 116: 216801.

Tserkovnyak Y and Kläui M (2017) Exploiting coherence in nonlinear spin-superfluid transport. *Physical Review Letters* 119: 187705.

Vuorio M (1974) Condensate spin currents in helium-3. *Journal of Physics C: Solid State Physics* 7(1): L5–L8.

Yuan W, Zhu Q, Tang S, Yao Y, Xing W, Chen Y, Ma Y, Lin X, Shi J, Shindou R, Xie XC, and Han W (2018) Experimental signatures of spin superfluid ground state in canted antiferromagnet Cr_2O_3 via nonlocal spin transport. *Science Advances* 4(4): eaat1098.

Bose–Einstein condensation

Leonardo Fallani[a,b], **Massimo Inguscio**[b,c], **Alessio Recati**[d], **and Sandro Stringari**[d], [a]Department of Physics and Astronomy, University of Florence, Florence, Italy; [b]LENS European Laboratory for Nonlinear Spectroscopy, Firenze, Italy; [c]Campus Bio-Medico University of Rome, Rome, Italy; [d]Pitaevskii BEC Center, CNR-INO and Department of Physics, University of Trento, Trento, Italy

© 2024 Elsevier Ltd. All rights reserved.

This is an update of M. Inguscio, S. Stringari, Bose–Einstein Condensation, Editor(s): Franco Bassani, Gerald L. Liedl, Peter Wyder, Encyclopedia of Condensed Matter Physics, Elsevier, 2005, Pages 131–141, ISBN 9780123694010, https://doi.org/10.1016/B0-12-369401-9/00759-2.

Introduction **68**
How to reach BEC in dilute atomic gases **70**
Imaging the new macroscopic quantum state **71**
Role of interactions **72**
Fermi gases **73**
Coherence and superfluidity **75**
Quantum mixtures of ultracold atomic gases **78**
Further directions **79**
Optical lattices 79
Disorder 79
Synthetic fields and synthetic matter 80
Low-dimensional physics 81
Long-range interactions 81
Supersolidity 81
Conclusion **82**
References **82**

Abstract

Bose–Einstein condensation embodies some of the most fascinating aspects of quantum mechanics. Predicted 100 years ago, its experimental realization in 1995 opened up unexpected directions in both fundamental and applied quantum physics. This chapter describes the main features of Bose–Einstein condensation, focusing on its experimental realization in ultracold atomic gases. We will present the theoretical description of the effect and the main laboratory techniques used to produce and probe ultracold quantum gases, discussing both milestone experiments and emerging research directions that the theoretical and experimental investigation of Bose–Einstein condensation has opened in the recent past.

Key points

- Describe the phenomenon of Bose–Einstein condensation (BEC).
- Illustrate the experimental techniques to achieve BEC in ultracold atomic gases.
- Explain the role of atom–atom interactions in BEC.
- Discuss the connection between BEC and fundamental phenomena such as superfluidity and quantum coherence.
- Show how BEC and superfluidity can be achieved for interacting spin mixtures of ultracold Fermi gases.
- Show seminal experiments that highlighted the main properties of atomic BECs.
- Discuss emerging research directions stemming from the experimental realization of BEC in ultracold gases.

Introduction

At room temperature the behavior of a gas is governed by the laws of classical mechanics. In fact the thermal de Broglie wavelength

$$\lambda_T = \sqrt{\frac{2\pi\hbar^2}{mk_BT}}, \tag{1}$$

which describes the smearing of the position of the atoms due to the Heisenberg uncertainty principle ($\hbar$ is the Planck's constant divided by 2π, k_B is the Boltzmann constant, m is the atomic mass, and T is the temperature of the gas), is much smaller than the average spacing between atoms, which then behave as classical objects. As the gas is cooled, however, the smearing increases and the wavefunctions of adjacent atoms overlap, causing the atoms to lose their identity. If the overlap is large, the effects of quantum mechanics cannot be ignored any longer.

When quantum effects become important, it is crucial to distinguish between Bose and Fermi statistics. Bosons are particles with even total spin, and their many-body wave function is symmetric with respect to the exchange of two particles. As a consequence, bosons like to occupy the same state. Conversely fermions (particles with odd spin) are described by an antisymmetric wave function and cannot occupy the same state due to the Pauli exclusion principle. At very low temperatures, bosons and fermions behave quite differently (see Fig. 1), giving rise to distinct dynamic and thermodynamic behaviors.

Bosons are known to undergo a phase transition below a critical temperature T_c. This transition is characterized by the macroscopic occupation of a single particle state and is called *Bose–Einstein condensation*. A unique peculiarity of the transition is that it can occur even in the absence of interactions, being driven by genuine quantum statistical effects. Albert Einstein predicted the occurrence of this transition in 1924 (Einstein, 1924), on the basis of a paper of the Indian physicist S. N. Bose (Bose, 1924), devoted to the statistical description of the quanta of light. For a long time, Einstein's predictions had no practical impact and only after the discovery of superfluidity in liquid helium in 1938, the phenomenon of Bose–Einstein condensation became again the object of theoretical investigation, with the pioneering works by London, Bogoliubov, Landau, Lifshitz, Penrose, Onsager, and Feynman.

When the temperature is low enough, all interacting systems, with the exception of helium, undergo a phase transition to the solid phase. This behavior is illustrated in Fig. 2, where we show a typical pressure–temperature phase diagram. In the figure we also draw the pressure–temperature line characterizing the BEC phase transition of an ideal gas. Above this line, a dilute gas would be Bose–Einstein condensed. However, this configuration is unstable since thermodynamic equilibrium would correspond to the solid

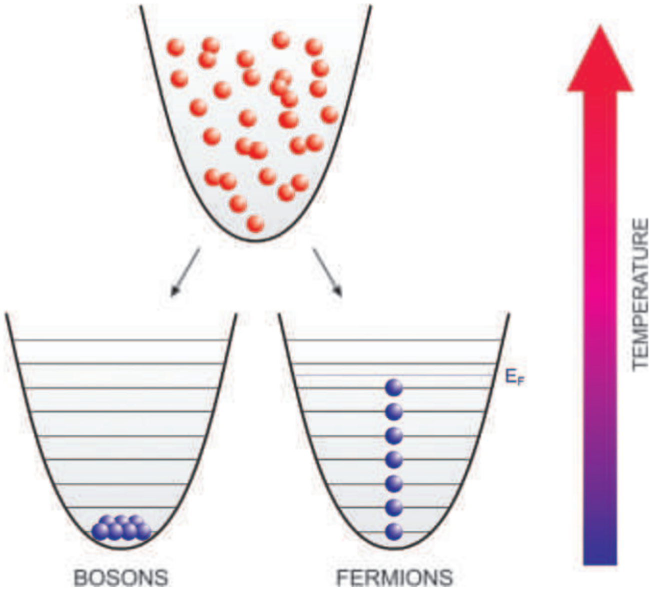

Fig. 1 Schematics of the level occupancy for a harmonically trapped gas at ultralow temperature. The ground state of the many-body system is completely determined by the quantum statistics. At zero temperature bosons (even-spin particles) all occupy the same single-particle ground state, forming a Bose–Einstein condensate. Fermions (odd-spin particles), obeying the Pauli exclusion principle, pile up until they reach the Fermi energy E_F.

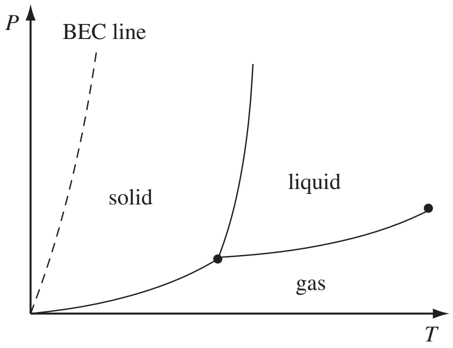

Fig. 2 A typical pressure–temperature phase diagram. The *dashed line* corresponds to the BEC phase transition for an ideal gas.

phase for such values of pressure and temperature. This shows that BEC can be actually achieved only in conditions of metastability and that the density of the gas should be small enough in order to suppress the collisional processes (three-body collisions) responsible for bringing the system into the thermodynamically stable solid phase. In practice, typical densities reached in the BEC phase are 10^{13} – 10^{15} cm^{-3}, so the predicted values of T_c are extremely low (a few microKelvin or even less). This explains why Bose–Einstein condensation was experimentally realized in atomic gases only seventy years after Einstein's historical paper.

Bose–Einstein condensation was achieved for the first time in ultracold gases of alkali atoms in 1995 and was recognized with the Nobel Prize for Physics in 2001 to E. A. Cornell, W. Ketterle, and C. E. Wieman (Cornell and Wieman, 2002; Ketterle, 2002). This achievement is the result of extraordinary efforts made in atomic physics during the two last decades of 1900s (Inguscio and Fallani, 2013; Inguscio et al., 1999), through the development of advanced techniques of laser cooling and atom trapping, which were recognized with the award of the Nobel Prize for Physics in 1997. At present BEC has been achieved in atomic gases made by isotopes of a variety of different chemical elements: alkali atoms (Li, Na, K, Rb, and Cs), alkaline-earth atoms (Ca and Sr) and other two-electron atoms (Yb) including metastable Helium (He*), inner-shell transition metals and lanthanide atoms (Cr, Dy, and Er), and in atomic hydrogen (H) as well.

How to reach BEC in dilute atomic gases

The first experimental studies on BEC were focused on spin-polarized hydrogen, which was considered the most natural candidate because of its light mass, which naturally leads to a more pronounced quantum behavior (see Eq. 1). To this purpose cryogenic and evaporative cooling techniques were developed since the early 1970s. Eventually, BEC was first realized in alkali atoms, despite their relatively large masses, because of their suitability to be cooled with laser techniques.

Indeed, all the experimental realization of BECs in atomic gases (except hydrogen) do involve some form of laser cooling, where the radiation pressure force, arising from the exchange of momentum between the photons of a laser field and the atoms, is used to reduce the atomic velocity (Inguscio and Fallani, 2013; Inguscio et al., 1999). The most common configuration is that of a magneto-optical trap (MOT), where three pairs of orthogonal, counterpropagating laser beams, red-detuned with respect to an atomic transition, result in a viscous force (also called "optical molasses") slowing the motion of the atoms. In addition, the presence of a magnetic field gradient allows the atoms to be spatially confined around the point where the magnetic field vanishes. In the case of rubidium, one can typically trap $\sim 10^9$ atoms with a temperature of $\sim$10 μK in a region of $\sim$1 cm^3.

The density and temperature achievable in a MOT are far from the values required for Bose–Einstein condensation, mostly because of laser-induced collisions between the atoms, which limit the maximum density achievable in a MOT. The next stage consists in transferring the laser-cooled sample from the MOT to a conservative trap, either a magnetic trap or an optical dipole trap, as shown in Fig. 3. In both the cases the trapping potential arises from the interaction of an atomic dipole moment with a spatially varying field: magnetic traps are based on the Zeeman interaction $-\boldsymbol{\mu} \cdot \mathbf{B}(\mathbf{r})$ between the magnetic dipole moment $\boldsymbol{\mu}$ (proportional to the angular momentum of the atom) and an inhomogeneous magnetic field $\mathbf{B}(\mathbf{r})$; optical dipole traps are based on the optical dipole potential $-\mathbf{d} \cdot \mathbf{E}(\mathbf{r})$ which arises when a far-detuned laser field with electric field amplitude $\mathbf{E}(\mathbf{r})$ induces an electric dipole

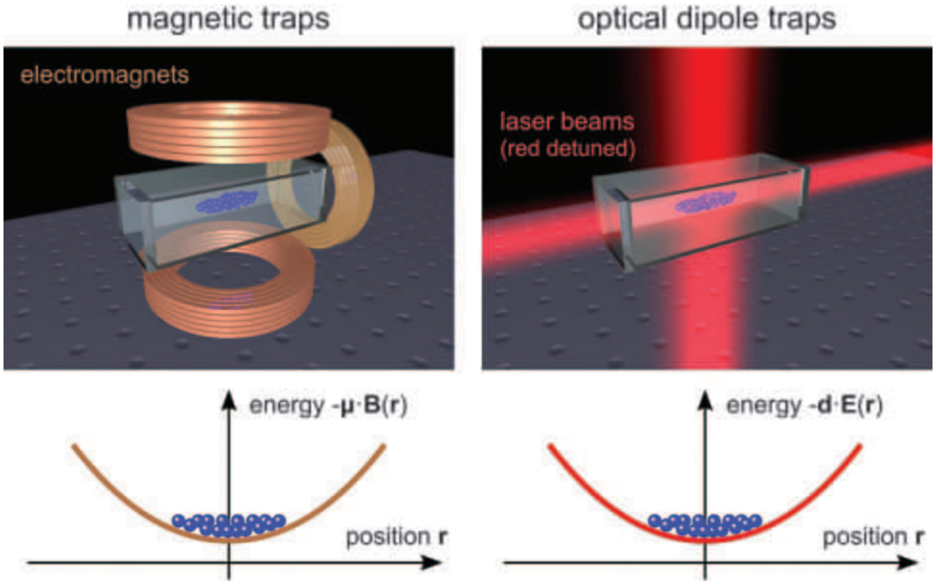

Fig. 3 Atom trapping. In a magnetic trap the atoms are trapped in a local minimum of the magnetic field $B(\mathbf{r})$ created by sets of electromagnets. In an optical dipole trap the atoms are trapped in local minima or maxima of the laser intensity $I(\mathbf{r}) \propto |E(\mathbf{r})|^2$ (maxima, for red-detuned optical traps).

moment **d** (proportional to the electric field) in the atom. In both the cases the atoms are trapped in a local minimum of the confining potential, corresponding to a magnetic field minimum for magnetic traps or to a minimum/maximum of light intensity (according to the sign of the laser detuning) for optical dipole traps.

Despite the intrinsic robustness of magnetic traps (typically created with arrangements of electromagnets), optical dipole traps have become increasingly popular over the last 20 years, as they allow for a much larger variety of trapping potentials. Exploiting the interference between counterpropagating laser beams, it is possible to produce for example, *optical lattices*, that is, periodic arrays of microscopic optical dipole traps corresponding to the antinodes of the laser standing wave (see Section "Further directions"). Furthermore, by shaping the trapping laser with spatial light modulators, it is possible to create almost any trapping configuration, including "box-like potentials" where BEC in a uniform gas can be studied.

The final cooling stage is the so called *evaporative cooling*, that consists in the selective removal of the most energetic atoms from the trap. This process, allowing a reduction of the average energy per atom, can be accomplished either by using frequency-selective radiofrequency/microwave transitions toward spin states that are untrapped by magnetic traps, or by lowering the trap depth in optical dipole traps. If this forced evaporation is slow enough the remaining atoms have time to collide and restore a thermodynamic equilibrium at lower temperatures. At the end of this process, if the density of the sample is high enough, the phase transition to a Bose–Einstein condensate can take place (typical values for rubidium are $n \sim 10^{14}\ \mathrm{cm}^{-3}$ and $T \sim 100$ nK). Bose–Einstein condensation in a trap occurs both in momentum and coordinate space, with the atomic density distribution reflecting the shape of the trapping potential.

All these cooling stages are performed in a ultra-high-vacuum environment (typical background pressure $\sim 10^{-11}$ torr), in order to ensure an optimal thermal isolation and a long lifetime ($\sim$1 min) of the trapped atomic samples against collisions with the room-temperature background gas.

Imaging the new macroscopic quantum state

Images of the ultracold atomic sample can be obtained by shining a resonant laser beam. The absorption of light by the atoms creates a shadow that is recorded by a CCD camera. The typical size of a condensate is of the order of a few micrometers and a very high resolving power is hence necessary for *in situ* imaging. Most frequently, images are taken by switching the trap off and allowing the gas to expand to larger sizes. Typical images obtained after expansion are shown in Fig. 4. At temperatures higher than T_c (left), the sample expands ballistically and quickly reaches an isotropic distribution, well described by a Maxwellian distribution, from which the temperature of the gas can be measured. At the onset of the BEC transition (center), the shape of the cloud is characterized by a pronounced increase of the density in the center and by a characteristic bimodal distribution: the non condensed atoms determine the wings of the distribution, still given by a Maxwellian form, while the condensed atoms give rise to a narrow central peak, which becomes more and more pronounced as the temperature is lowered (right). The shape of the central peak is no longer a

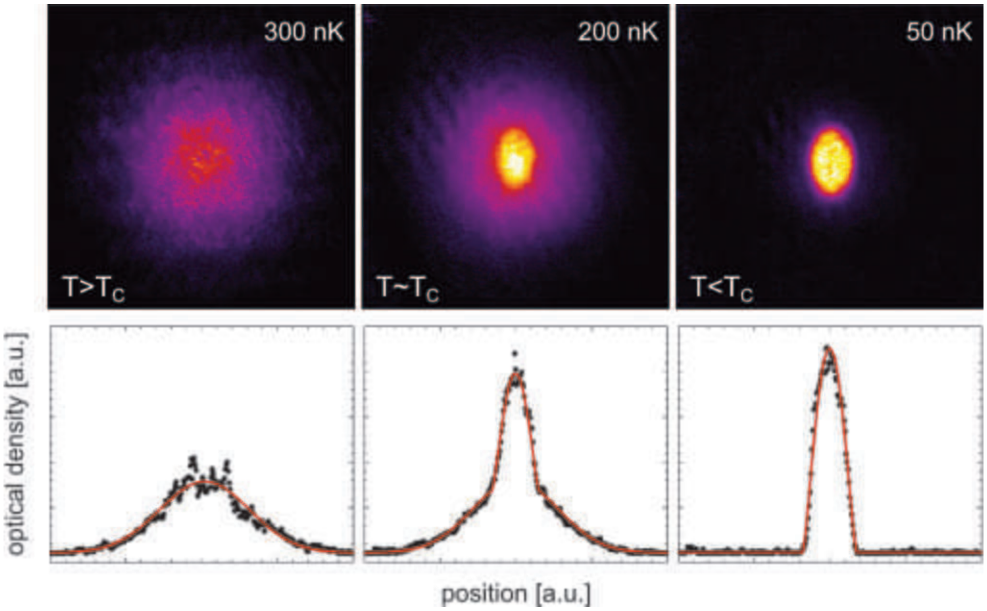

Fig. 4 (Top) Absorption images of an expanded cloud of ^{87}Rb bosons recorded at LENS by varying the temperature T across the BEC transition at T_C. From left to right, the images show a thermal cloud, a partially condensed cloud and a pure BEC. (Bottom) Cross sections of the density distributions. The lines are fits of the experimental points with a gaussian, a bimodal distribution and an inverted parabola, respectively.

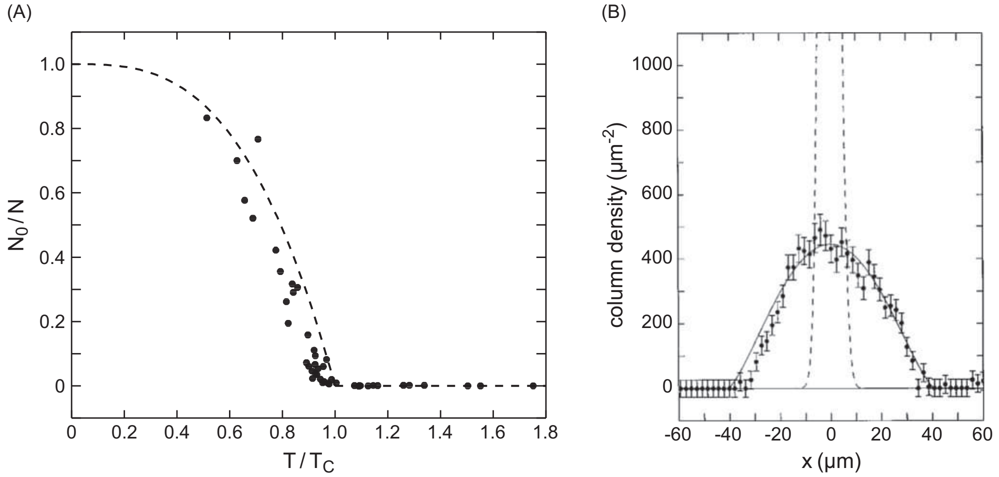

Fig. 5 (A) Condensate fraction N_0/N as a function of T/T_C: *circles* are early experimental results from JILA, while the *dashed line* is the theoretical prediction of Eqs. (2) and (3). (B) BEC density profile: *circles* are experimental results from Harvard University while the *dashed line* is the theoretical prediction for a noninteracting BEC. Reproduced from Ensher JR, Jin DS, Matthews MR, Wieman CE, and Cornell EA (1996) Bose-Einstein condensation in a dilute gas: Measurement of energy and ground-state occupation. Physical Review Letters 77: 4984 and Hau LV, Busch BD, Liu C, Dutton Z, Burns MM, and Golovchenko JA (1998) Near-resonant spatial images of confined Bose-Einstein condensates in a 4-Dee magnetic bottle. Physical Review A 58: R54 with permission from the authors.

Maxwellian and depends on the properties of the confining potential: in the most common experimental realization, the trap can be approximated as harmonic and the shape of the condensate is an inverted parabola, as predicted by the Gross–Pitaevskii theory (see Section "Role of interactions"). The analysis of the images also provides the number N of atoms in the sample and the condensed fraction.

In the presence of harmonic confinement, theory predicts precise values for both the critical temperature T_c and the fraction of condensed atoms for $T \leq T_c$. For an ideal gas trapped by a harmonic potential one finds (Dalfovo et al., 1999)

$$k_B T_c \simeq 0.94 \hbar \omega_0 N^{1/3} \tag{2}$$

and

$$\frac{N_0}{N} = 1 - \left(\frac{T}{T_c}\right)^3 \tag{3}$$

where ω_0 is the geometric average of the trapping frequencies and N_0 is the number of atoms in the condensate. One of the first theory–experiment comparisons (Ensher et al., 1996) is shown in Fig. 5A, where the value of T_c is a few hundreds of nanoKelvin. Despite the relatively small number of atoms used in this experiment ($\sim 10^4$) the evidence for the phase transition is very clear. The good agreement with the predictions of the ideal gas model indicates that the effects of atom–atom interactions on the condensate fraction and on the value of T_c are small. This is the consequence of the extreme diluteness of the trapped gas.

Role of interactions

Interactions between atoms play an important role in the experimental realization of ultracold atomic gases. Most importantly, they are responsible for the thermalization of the gas following the selective removal of the hottest atoms in evaporative cooling. As discussed in the previous section, this is a crucial step for the achievement of the low temperatures that are required for the realization of Bose–Einstein condensation.

Besides their importance in the cooling process, interactions play a crucial role in determining some of the equilibrium properties of the Bose–Einstein condensed gas (Dalfovo et al., 1999; Pethick and Smith, 2002; Pitaevskii and Stringari, 2016). For example, the size of the condensate, which, in the absence of interactions, is fixed by the harmonic-trap oscillator length, can become dozens of times larger as a consequence of the repulsion between atoms, as shown in Fig. 5B (Hau et al., 1998). Interactions also affect other dynamic properties, like the propagation of collective excitations and the expansion of the BEC after the removal of the confining potential. Both the equilibrium and the dynamic properties of interacting dilute Bose–Einstein condensed gases are well described by the Gross–Pitaevskii equation, which then provides the basic theoretical framework to describe several many-body features of these systems,

$$i\hbar \frac{\partial \psi}{\partial t} = \left(-\frac{\hbar^2}{2m} \nabla^2 + V(\mathbf{r}) + \frac{4\pi \hbar^2 a}{m} |\psi|^2 \right) \psi \tag{4}$$

where ψ is the BEC wavefunction and $V(\mathbf{r})$ is the external confining potential. The last term in parenthesis, leading to a nonlinear character of the equation, describes atom–atom interactions in a mean-field approximation. Remarkably, interactions in ultracold dilute gases are described by a single parameter a, which fixes the most relevant many-body properties of the system and whose sign characterizes the nature of the system in a unique way: when $a > 0$ interactions have a repulsive character, when $a < 0$ they are attractive. In the case of Bose gases $a \geq 0$ is required to ensure the stability of large Bose–Einstein condensed gases against collapse. When a becomes negative the nonlinearity in the Gross–Pitaevskii equation is also responsible for solitonic solutions (bright solitons) which propagate without dispersion in 1D configurations.

An exciting feature of ultracold-atom experiments is the possibility to control the scattering length by taking advantage of the so-called *Feshbach resonances* (see Fig. 6A). This phenomenon occurs when the energy of two colliding atoms in a given spin configuration (open channel) is quasiresonant with the energy of a molecular state that can be formed by those atoms in a different spin configuration (closed channel). The resonance condition can be controlled by tuning the energy separation $\Delta(B)$ between the two channels thanks to the differential Zeeman shift induced by an external magnetic field B. When the resonance condition is met, the scattering length exhibits a divergence and changes sign from one resonance side to the other, eventually crossing a point where it can be zeroed, as shown in Fig. 6B (Inouye et al., 1998). This magnetic tuning of the scattering length allows for unique possibilities in the physics of interacting ultracold gases, as described further in the next sections.

Fermi gases

Differently from the case of bosons, an ideal Fermi gas does not exhibit a phase transition at low temperature. The system, however, is still characterized by important quantum phenomena originating from the Pauli exclusion principle. This is well illustrated in Fig. 1, where one sees that at very low temperatures the gas exhibits single occupancy of the single-particle states up to a maximum energy, called *Fermi energy*.

The experimental procedure to reach quantum degeneracy in Fermi gases requires an additional effort compared to the case of bosons. As a matter of fact, in a Fermi gas of identical particles, the antisymmetrization requirement forbids s-wave collisions, which is the only collisional channel available at low temperature, and this causes the absence of those thermalization processes which are crucial for the mechanism of evaporative cooling. This difficulty can be overcome by cooling mixtures of fermions in two spin states, which are distinguishable and thus can interact also at low temperature. Alternatively, one can use mixtures of fermions and bosons, either of the same chemical species or of different species: bosons are cooled down with the standard evaporative cooling technique and then fermions thermalize sympathetically. Fig. 7 shows this second type of approach, achieved with mixtures of potassium and rubidium (Roati et al., 2002).

Despite the complication of the cooling procedure, the absence of interactions in a gas of spin-polarized fermions can provide important advantages. An example is given by the application of polarized Fermi gases to accurate measurements, that is, in atom interferometry, or in high-precision spectroscopy, where the absence of atom–atom interactions prevents unwanted decoherence effects or interactions shifts, respectively.

On the other side, the possibility of trapping fermions in different spin states has opened new perspectives related to the physics of interacting systems. In the first decade of 2000s, experimentalists were able to realize superfluid configurations in interacting Fermi gases, profiting of the possibility of tuning the interaction between pairs of atoms in different spin states in proximity of

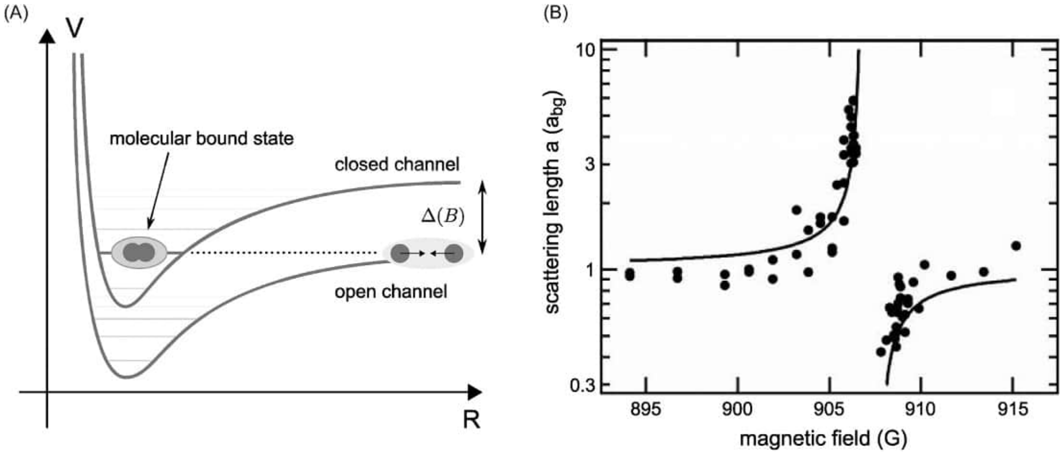

Fig. 6 (A) A Feshbach resonance occurs when the energy of two colliding atoms (open channel) matches the energy of a molecular bound state for the same atoms in a different spin configuration (closed channel), and can be tuned by applying a magnetic field that shifts the two molecular potentials $V(R)$, where R is the interatomic distance. (B) First observation of a Feshbach resonance in a ^{23}Na Bose–Einstein condensate reported in 1998 at MIT. Reproduced from Inouye S, Andrews MR, Stenger J, Miesner H-J, Stamper-Kurn DM, and Ketterle W (1998) Observation of Feshbach resonances in a Bose-Einstein condensate. Nature 392: 151 with permission from the authors.

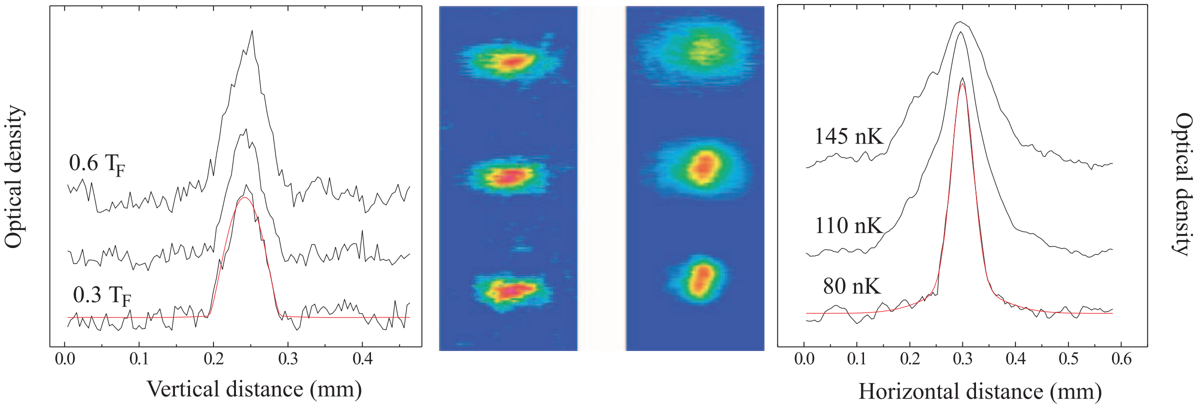

Fig. 7 Sympathetic cooling of fermionic ^{40}K with bosonic ^{87}Rb, as first reported at LENS in 2002. The bosons are directly cooled with standard evaporative cooling techniques and the fermions thermalize sympathetically at lower temperatures via collisions with the bosons. The figure shows the simultaneous onset of Fermi degeneracy for ^{40}K (left) and of Bose–Einstein condensation for ^{87}Rb (right). The absorption images are taken for decreasing temperatures (from top to bottom) and the sections show the correspondent momentum distributions. Figure reproduced from Roati G, Riboli F, Modugno G, and Inguscio M (2002) Fermi-Bose quantum degenerate 40K-87Rb mixture with attractive interaction. Physical Review Letters 89: 150403.

Feshbach resonances (see Inguscio et al. (2007) for a review of the first years of investigations). In the case of Fermi gases, thanks to the repulsive effect of the Fermi pressure, the system can support $a < 0$ values. At zero temperature, dilute Fermi gases interacting with small and negative scattering length exhibit a superfluid phase described by the traditional BCS theory, which was first developed to describe the phenomenon of superconductivity. If the scattering length becomes large or positive, new scenarios for fermionic superfluidity take place. In particular, by adjusting the scattering length from $a < 0$ to $a > 0$ across a Feshbach resonance, it is possible to produce ultracold molecules made by two fermions in different spin states. Since these molecules have a bosonic nature, being composed of an even number of fermions, they can undergo a phase transition to BEC, similar to that exhibited by a gas of bosonic atoms. Molecular BECs were first demonstrated in 2003 starting from ^{6}Li and ^{40}K fermionic atoms (see Fig. 8 for the realization of a molecular ^{40}K$_2$ BEC reported in Greiner et al. (2003)).

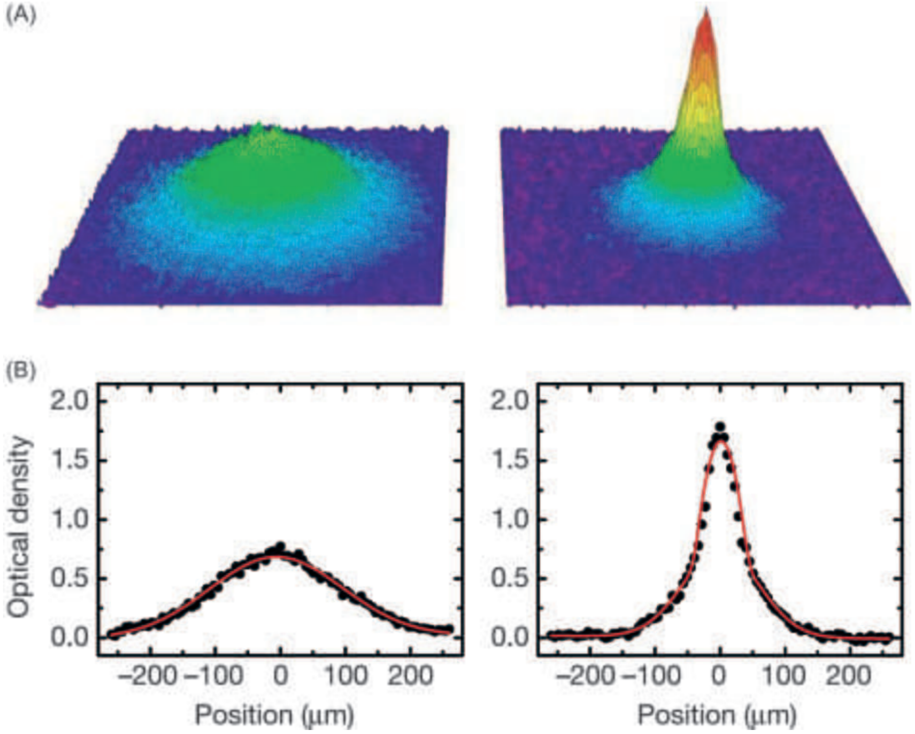

Fig. 8 Bose Einstein condensation of ^{40}K$_2$ molecules, as reported in 2003 at JILA. The (bosonic) dimers are produced starting with quantum degenerate ^{40}K fermions in two spin states and sweeping the value of an applied magnetic field across a Feshbach resonance. (A) Absorption images of the molecular density distribution after expansion. When the initial temperature of the fermionic cloud is lowered across a critical value (from left to right) a narrow peak appears in the momentum distribution. (B) Cross section and fit with a bimodal distribution. The change in the density profile is a signature that a BEC of molecules has formed. Reproduced from Greiner M, Regal CA, and Jin DS (2003) Emergence of a molecular Bose-Einstein condensate from a Fermi gas. Nature 426: 537 with permission from the authors.

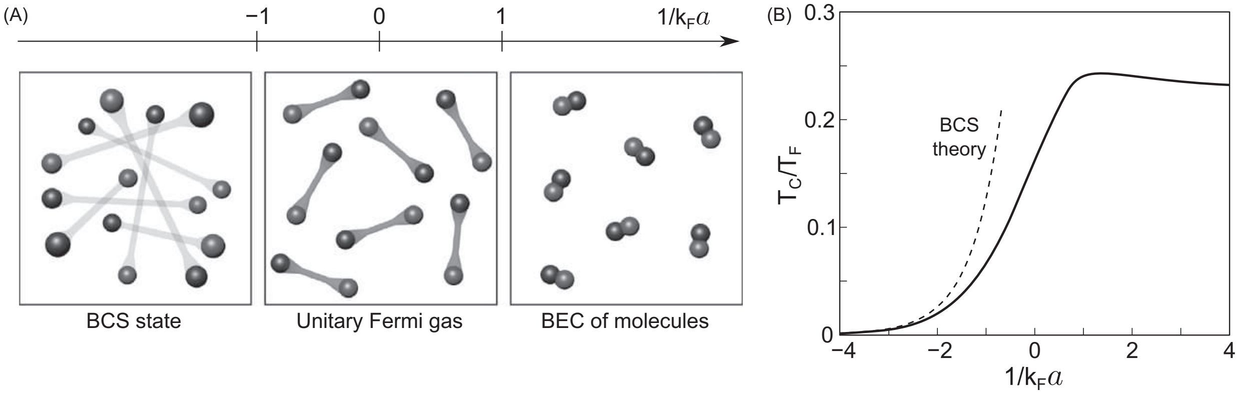

Fig. 9 BEC–BCS crossover. (A) Changing the value of the scattering length a across a Feshbach resonance, a binary mixture of fermions in two spin states evolves from the condensation of tightly bound bosonic molecules (on the BEC side $a > 0$) to the formation of weakly bound Cooper pairs with a size much larger than the interparticle distance (on the BCS side $a < 0$). (B) Dependence of the critical temperature on the interaction parameter. (A): Reproduced from Inguscio M, Ketterle W, and Salomon C (eds.) (2007) Ultracold fermi gases. In: Proceedings of the International School of Physics "Enrico Fermi", Varenna (Italy)-Course CLXIV. IOS Press (chapter by W. Ketterle and M. Zwierlein) with permission from the authors.

In the following years, important efforts led to the first experimental investigations of the BEC-BCS crossover (see Fig. 9A), which occurs by varying continuously the scattering length a across a Feshbach resonance from positive to negative values (Zwerger, 2014). In particular, at resonance, where the scattering length becomes much larger than the average distance between atoms, the system exhibits new challenging features and acquires a universal behavior which is independent from the actual value of the scattering length. This is the so called *unitary Fermi gas*, of special interest also in other domains of physics like in neutron matter and characterized by peculiar superfluid features. In particular, the value of the critical temperature at unitarity, characterizing the transition from the normal to the superfluid phase, is a significant fraction of the Fermi temperature (see Fig. 9B), much higher than in the case of the presently available high-Tc superconductors. The theoretical investigation of the unitary regime cannot be simply described using the theory of weakly interacting gases and requires the use of more advanced many-body approaches.

Coherence and superfluidity

Bose–Einstein condensates are characterized by a complex order parameter (the so called *wavefunction* of the condensate)

$$\Phi = \sqrt{n_0} e^{iS}. \tag{5}$$

The modulus is fixed by the condensate density n_0, which, in dilute gases and at temperatures much smaller than T_c, practically coincides with the density of the sample. The phase S of the order parameter is at the origin of important properties of the system, both concerning coherence and superfluid effects.

Coherence phenomena make the physics of these systems similar to that of a laser, if one replaces photons with atoms. Indeed, the laser field can be described in terms of photons all occupying the same mode of the electromagnetic field, similarly to the atoms of a BEC all sharing the same wavefunction. Bright sources of atoms, the so called *atom lasers*, can be obtained outcoupling the atoms from the condensate, that is the analog of the laser cavity in which coherent photons are stored, with the eventual demonstration of atom lasers operating in continuous-wave mode (Chen et al., 2022). Another example of this analogy is revealed by the interference phenomena observed with Bose–Einstein condensates. In Fig. 10 we show the interference fringes produced by two separate condensates overlapping after expansion (Andrews et al., 1997). This experiment, which first demonstrated the coherence of the condensed state, is the analog of the most famous double slit experiment with light.

An important consequence of the complex order parameter and of the presence of interactions concerns the phenomenon of superfluidity. In fact the gradient of the phase S is proportional to the superfluid velocity:

$$\mathbf{v}_s = \frac{\hbar}{m} \nabla S \tag{6}$$

Before 1995, superfluid phenomena had been observed only in dense liquids, like ^{4}He. The possibility of investigating superfluidity in dilute gases has allowed a better understanding of its microscopic origin and its relationship to the phenomenon of BEC (Pitaevskii and Stringari, 2016). Among the various manifestations of superfluidity, it is worth mentioning the rich variety of collective oscillations exhibited by these confined systems, which have been the object of intense theoretical and experimental work in the last decades. The images in Fig. 11 show the shape oscillation of a Bose–Einstein condensate, from which one can extract the frequency of the collective modes with high precision. The dynamic behavior of the condensate is well described by the hydrodynamic equations of superfluids, which predict values for collective frequencies in excellent agreement with the experiment.

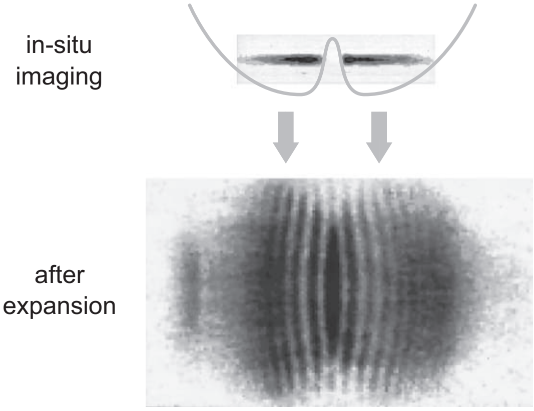

Fig. 10 Interference of two BECs overlapping after expansion. In the central region, one clearly sees interference fringes, similar to the ones observed in optics in the famous Young experiment. This image was recorded in 1997 at MIT in the first experiment where interference of two BECs was observed. Reproduced from Andrews MR, Townsend CG, Miesner HJ, Durfee DS, Kurn DM, and Ketterle W (1997) Observation of interference between two Bose condensates. Science 275: 637 with permission from the authors.

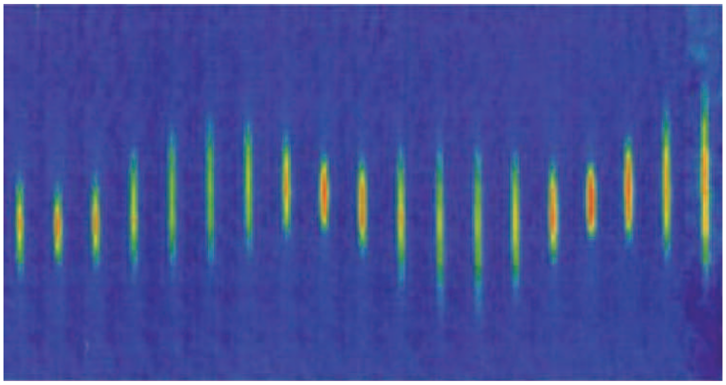

Fig. 11 Collective excitations of a Bose–Einstein condensate, as detected in early MIT experiments. The excitations were produced by modulating the magnetic field used to trap the condensate and then letting the cloud evolve freely. The field of view in the vertical direction is about 600 μm and the time step is 5 ms per frame. The measured frequency of these collective excitations is a clear signature of the BEC superfluidity. From D. Stamper-Kurn and W. Ketterle (private communication), reproduced from Dalfovo F, Giorgini S, Pitaevskii LP, and Stringari S (1999) Theory of Bose-Einstein condensation in trapped gases. Reviews of Modern Physics 71: 463.

An even more spectacular prediction of superfluidity concerns the rotational properties of ultracold atomic gases. Superfluids cannot rotate like classical objects because of the irrotationality constraint imposed by Eq. (6). A striking consequence is that angular momentum can be carried only by quantized vortices. If the confining trap rotates slowly, vortices cannot be formed because they are energetically unfavorable and the sample does not carry any angular momentum. However, when the angular velocity increases, quantized vortices are formed (see Fig. 12A). Eventually, at high angular velocities, one can generate a vortex lattice of regular geometrical shape. Quantized vortices have been observed also across the BCS–BEC crossover of an interacting Fermi gas, reflecting the universality of the superfluid behavior exhibited by interacting quantum gases (see Fig. 12B).

Another important manifestation of coherence is given by the Josephson oscillations characterized by the coherent tunnelling of atoms through the barriers generated by external double-well (Albiez et al., 2005) or many-well potentials (Cataliotti et al., 2001), as shown in Fig. 13. This peculiar effect is associated with an oscillating behavior of the relative phase between the two condensates occupying the wells and has been observed also through the interference patterns measured after expansion. The Josephson effect plays a crucial role also in the coherent oscillation between condensates in two different internal state (so-called *internal* Josephson effect), where all the atoms of the cloud oscillate in sync between the two states.

The Josephson effect was originally predicted for superconductors, where Cooper pairs can move by coherent tunnelling through a small insulating region. Recently, at LENS, such fascinating phenomenon has been studied in superfluid Fermi gases across the BEC–BCS crossover, allowing for the observation of effects beyond the perturbative BCS theory.

Collective modes of Josephson-like nature have been investigated also by exciting the center of mass oscillations of a BEC gas confined in the combined potential created with a harmonic trap and an optical lattice produced by laser fields. Fig. 13 (right) shows that only the superfluid condensed component is able to tunnel coherently while the thermal component is localized. Theoretically one can predict the frequency of the oscillation, which turns out to be in good agreement with the experiment.

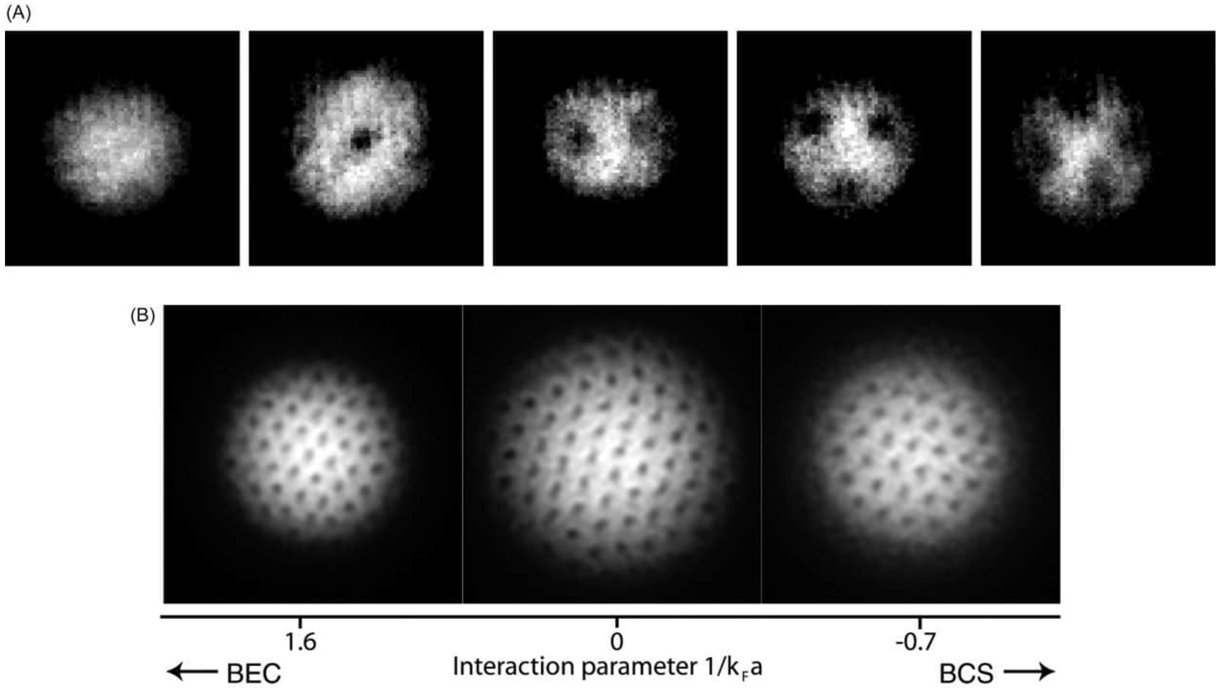

Fig. 12 (A) Formation of vortices in a Bose–Einstein condensate, as observed in 2000 at LKB-ENS: as the rotation frequency of the trap increases (from left to right), a higher number of vortices is formed (Madison et al., 2000). (B) Vortex arrays in two-component strongly interacting Fermi gases, demonstrating a superfluid behavior all the way from the BCS to the BEC limit, as first observed in 2005 at MIT. Reproduced from Madison KW, Chevy F, Wohlleben W, and Dalibard J (2000) Vortex formation in a stirred Bose-Einstein condensate. Physical Review Letters 84: 806 and Inguscio M, Ketterle W, and Salomon C (eds.) (2007) Ultracold fermi gases. In: Proceedings of the International School of Physics "Enrico Fermi", Varenna (Italy)-Course CLXIV. IOS Press (chapter by W. Ketterle and M. Zwierlein) with permission from the authors.

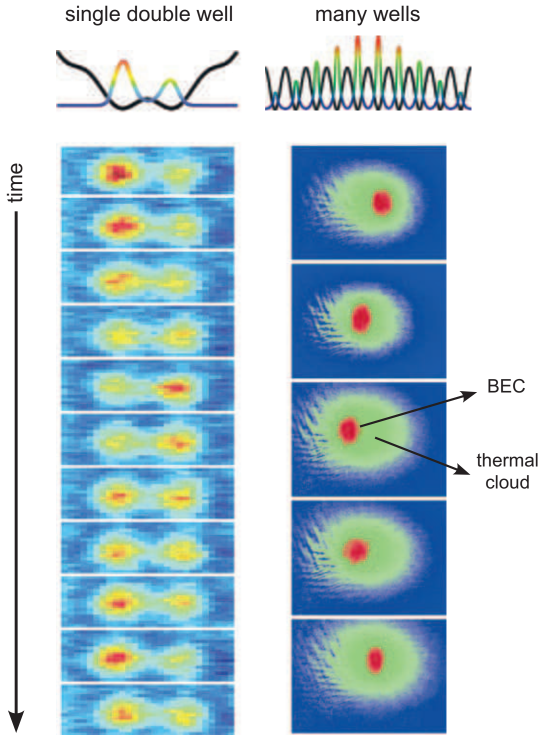

Fig. 13 Josephson effect in atomic superfluids. (Left) Josephson oscillations induced by tunnelling in a double-well potential, as reported in 2005 at Heidelberg University. (Right) Josephson dynamics in an optical lattice made by many potential wells, as reported in early experiments at LENS: while the BEC performs coherent oscillations, in analogy with the double-well Josephson effect, the center of mass of the thermal cloud is stuck in the initial position. Left: Reproduced from Albiez M, Gati R, Fölling J, Hunsmann S, Cristiani M, and Oberthaler MK (2005) Direct observation of tunneling and nonlinear self-trapping in a single Bosonic Josephson junction. Physical Review Letters 95: 010402 with permission from the authors.

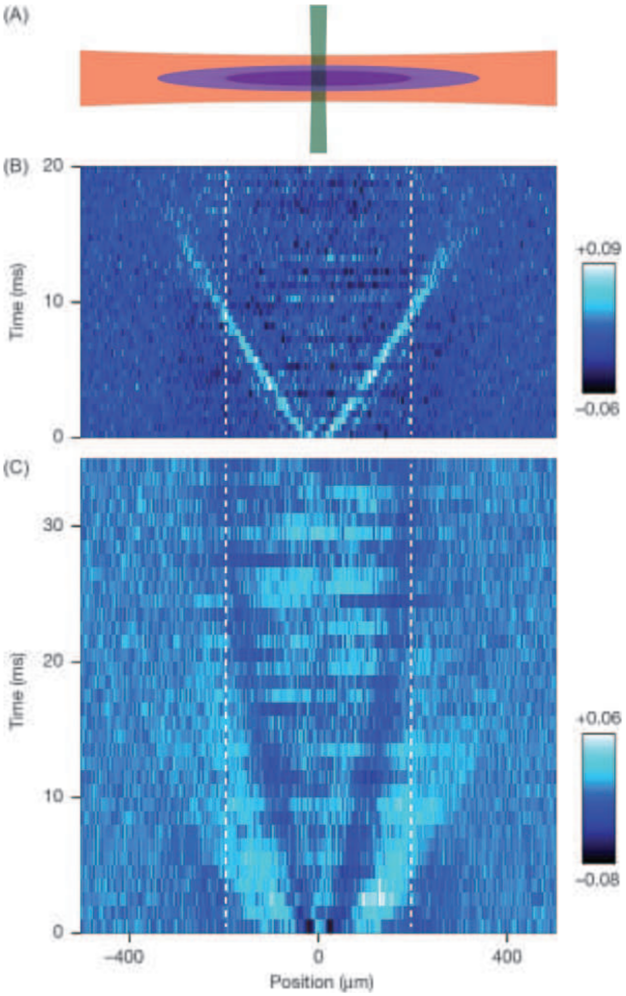

Fig. 14 Propagation of sound modes in a fermionic ^{6}Li superfluid, as reported in 2013 at Innsbruck University. (A) A focused laser beam creates an excitation in a localized region of the superfluid. (B) Propagation of density waves (ordinary sound). (C) Propagation of entropy/temperature waves (second sound). The two sounds clearly propagate at a different speed. Reproduced from Sidorenkov LA, Tey MK, Grimm R, Hou Y-H, Pitaevskii L, and Stringari S (2013) Second sound and the superfluid fraction in a Fermi gas with resonant interactions. Nature 498: 78.

Important superfluid phenomena take place also at finite temperature, where Landau's theory predicts the occurrence of peculiar dynamic features described by two-fluid hydrodynamics. The most spectacular manifestation is the propagation of a new type of sound, the so-called *second sound*, that was extensively investigated in superfluid helium. Differently from usual sound, which corresponds to a pressure wave, second sound can be regarded as an entropy wave and the corresponding velocity is intimately related to the superfluid density of the system. Second sound was measured in a strongly interacting Fermi gas close to unitarity (Fig. 14) allowing for the first determination of the temperature dependence of the superfluid fraction of a Fermi superfluid (Sidorenkov et al., 2013). More recently, second sound was also measured in two-dimensional Bose gases.

Quantum mixtures of ultracold atomic gases

The possibility of reaching ultracold temperatures in both Bose and Fermi gases and in a variety of different atomic species has opened an exciting development of experimental and theoretical activities in the field of the so called *quantum mixtures*, where gases of different atomic species can co-exist and interact in the quantum degenerate limit, giving rise to novel phenomena (Grimm et al., 2023). This possibility was long sought in the past in the case of mixtures of liquid ^{4}He and ^{3}He, where, however, the possibility of obtaining two interacting superfluids is inhibited by the lack of miscibility of the two helium fluids at very low temperature. New possibilities have now become available in the case of ultracold atomic gases, both with Bose–Bose and Bose–Fermi superfluid mixtures, including the interdisciplinary topic of *polarons*, which corresponds to extreme population unbalanced mixtures, where essentially only one or few impurities of a certain atomic species are immersed in a bath formed by the other component.

The studies of polarons in a clean ultracold-gases setup has already allowed for a better understanding and direct measurement of the concept of dressed particles by the bath excitations, as well as the back action of the impurities on the bath itself.

The phenomenology specific of a certain mixture is very rich and very diverse depending on the "ingredients" of the selected mixture. In particular for Bose mixtures, one can distinguish between mixtures where the number of atoms of each species is conserved and those in which only the total number of atoms is conserved. To the first class belong mixtures of different atomic species while the second class concerns mixtures of hyperfine levels where, due to either spin-changing collisions or external fields, the number conservation of the single components is broken.

Among the most interesting effects in mixtures we can count the existence of a collisionless drag between the two superfluid components and, even more remarkably, of self-bound droplets and of a liquid-like (incompressible) phase. The description of the above-mentioned phenomena is not included in a simple two-component Gross–Pitaevskii equation and requires the inclusion of the so-called quantum fluctuations.

For non-number-conserving mixtures, it is remarkable the presence of magnetic-like quantum phase transitions (i.e., phase transitions that occur at zero temperature), where the magnetic language is used to describe the spinor or vector order parameter of the system. It is therefore possible to study magnetic superfluids and the interplay between superfluidity and magnetism. In the same framework, it was possible to realize condensates with spin–orbit coupling, allowing for new states of matter, complementary to the electronic states in solid-state physics.

Further directions

The possibility of tuning the interactions among atoms and the large variety of trapping conditions reachable by combing magnetic and optical methods has allowed for the realization of a number of configurations involving Bose and/or Fermi gases (see Bloch et al. (2008) and Inguscio et al. (2016) for a review of major developments). The resulting scenarios are still evolving and cover topics of high interdisciplinary interest, as briefly listed below.

Optical lattices

Optical lattices can be used to provide perfect periodic potentials where the atoms can be trapped, in very close analogy to what happens in the solid state, where the electrons are bound to the periodic arrangement of atoms of the crystalline structure.

Since the first years of this century, optical lattices have been used as a powerful instrument to probe the coherence and superfluid properties of Bose–Einstein condensates: notable examples are the observation of many-BEC interference with long-range coherence or the realization of Josephson junctions arrays (Cataliotti et al., 2001). Optical lattices are also an ideal tool to study key aspects of quantum transport in defect-free solid-state analogs, such as the modification of the transport properties caused by the emerging band structure (Fallani et al., 2003), according to Bloch theorem (Fig. 15A). Fundamental effects of solid-state physics were cleanly observed in this setting, the most prominent one being the occurrence of undamped Bloch oscillations activated by a constant force (Fig. 15B), which are also a valuable resource for precision measurements in the context of atom interferometry (Roati et al., 2004).

This analogy with the solid state has been exploited intensively to provide the first realizations of the idea of *quantum simulation* pioneered by R. Feynman in the 1980s. Optical lattices were used to provide a clean realization of bosonic and fermionic Hubbard models, originally introduced in condensed-matter physics to describe interacting quantum particles hopping between the sites of a deep lattice. By an accurate experimental control of the coupling constants of the Bose–Hubbard model, a quantum phase transition between a superfluid state and a Mott insulator was observed (Greiner et al., 2002), as shown in Fig. 16: when the depth of the optical lattice is small, interactions effects are weak and the system exhibits long-range coherence, which is witnessed by the sharp peaks in the matter-wave interference; when the lattice depth is increased above a critical value, repulsive interactions between particles dominate over the hopping and the system localizes in a Mott state with no particle number fluctuations and no coherence, and the peaks in the matter-wave interference disappear. Experimental studies of the Fermi-Hubbard model have also evidenced the antiferromagnetic ordering of the Mott localized phase for a mixture of spin-up/spin-down fermions, which is believed to provide a key mechanism for the explanation of high-Tc superconductivity in cuprates, also opening new paths for the exploration of spin lattice models.

Disorder

Not only light can be used to create optical lattices where solid-state models can be simulated in a defect-free way. It can also be used to realize controllable disordered or quasi-disordered potentials, via the use of speckle patterns or multichromatic optical lattices, respectively. In this settings, Anderson localization of matter waves was first observed by studying the expansion of a Bose–Einstein condensate in a disordered potential (Billy et al., 2008; Roati et al., 2008): when the amount of disorder was strong enough, the BEC stopped its free expansion in the disordered potential, in correspondence with the transition of the eigenstates from extended to localized (see Fig. 17). Since the first observations of localization in disordered BECs, the interplay between disorder and interactions has been studied extensively, also in the context of the topic of many-body localization, where localization is accompanied by nontrivial quantum effects concerning thermodynamics and equilibrium.

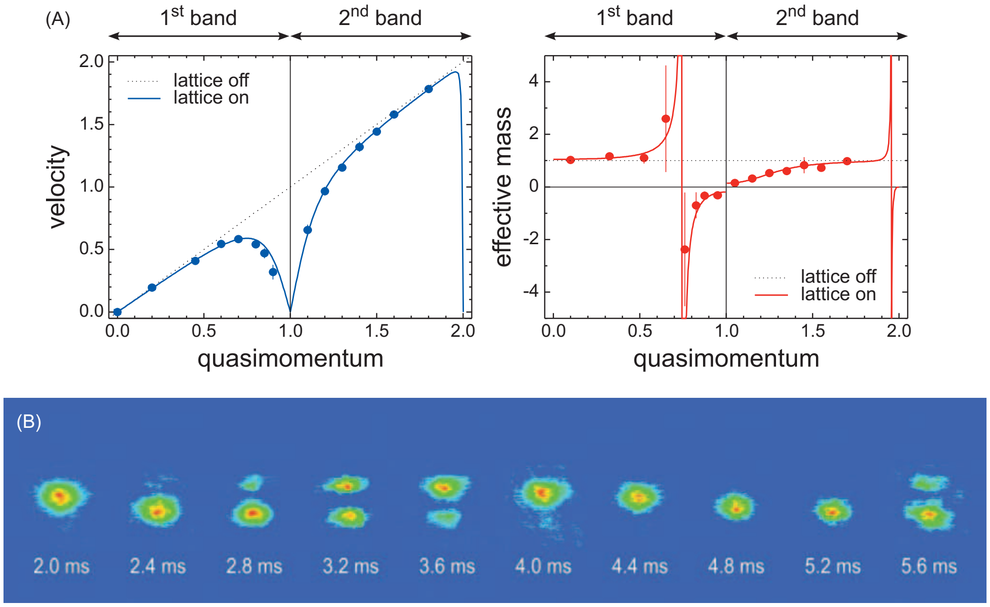

Fig. 15 Quantum transport in an optical lattice, as studied in early experiments at LENS: (A) Experimental measurements of the velocity and effective mass of a BEC in an optical lattice as a function of its quasimomentum, compared with the predictions of the Bloch theory describing electrons in a crystal lattice. (B) Ultracold fermions trapped in a vertical optical lattice, performing long-lived Bloch oscillations under the effect of gravity: measuring the frequency of the oscillation allows an accurate determination of the local gravity acceleration *g* and can be used for high-precision measurements of forces on a short distance scale. Reproduced from Fallani L, Cataliotti FS, Catani J, Fort C, Modugno M, Zawada M, and Inguscio M (2003) Optically induced lensing effect on a Bose-Einstein condensate expanding in a moving lattice. Physical Review Letters 91: 240405 and Roati G, De Mirandes E, Ferlaino F, Ott H, Modugno G, and Inguscio M (2004) Atom interferometry with trapped Fermi gases. Physical Review Letters 92: 230402.

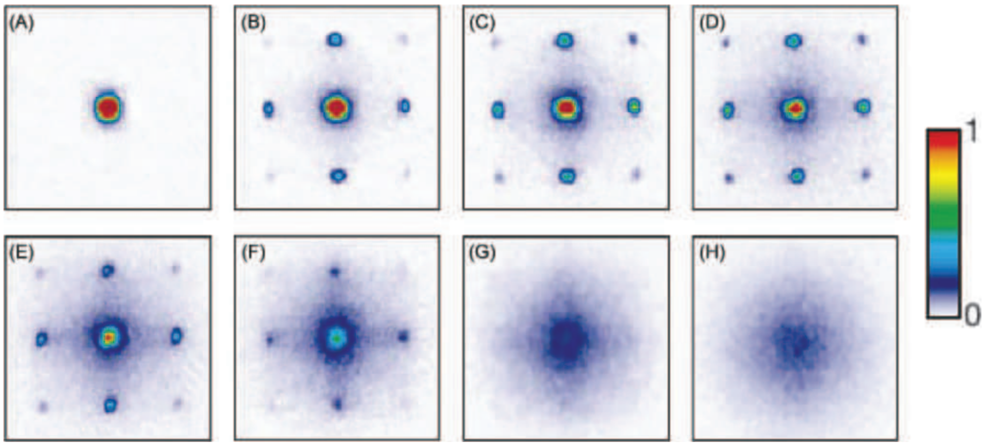

Fig. 16 Quantum phase transition from a superfluid to a Mott insulator for ultracold bosons in a 3D optical lattice, as first observed in 2002 at MPQ. In the Mott phase, the atoms are localized in the lattice sites, phase fluctuations increase and the long-range coherence of the superfluid phase is lost. This is evidenced by the disappearance of the matter-wave interference pattern when the lattice depth is increased (from A to H). Reproduced from Greiner M, Mandel O, Esslinger T, Hänsch TW, and Bloch I (2002) Quantum phase transition from a superfluid to a Mott insulator in a gas of ultracold atoms. Nature 415: 39 with permission from the authors.

Synthetic fields and synthetic matter

Starting from the 2010s new experimental approaches involving the manipulation of BECs with laser light have allowed researchers to engineer new kind of interactions for quantum simulation experiments. Pioneering experiments performed at JQI/NIST demonstrated the possibility of realizing light-induced spin–orbit interactions, by which the motion of the atoms is coupled to their spin, or synthetic magnetic fields, in which the phase imprinted by the interaction with the lasers emulates a magnetic vector potential, thus mimicking the effect of a synthetic magnetic field on atoms with a synthetic charge (see Goldman et al. (2014) for a review). These first demonstrations triggered a new field of research, in which BECs and Fermi gases are used to study novel quantum phases and topological states of matter.

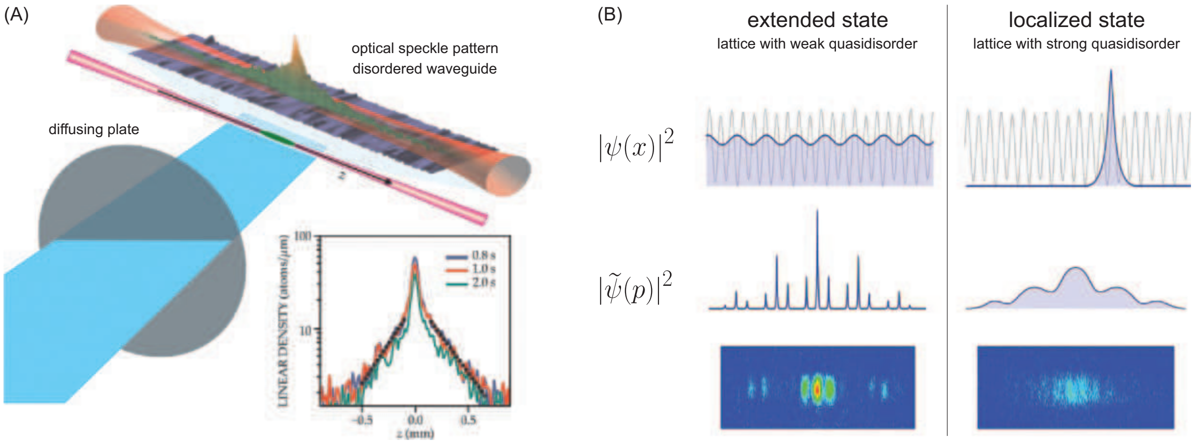

Fig. 17 Evidences of Anderson localization with ultracold atoms, as first reported in 2008 at Institut d'Optique and LENS. (A) The wavefunction of a weakly interacting ^{87}Rb BEC expanding in a speckle potential shows exponentially decreasing tails. (B) The momentum distribution $|\widetilde{\Psi}(p)|^2$ of a noninteracting ^{39}K BEC in an incommensurate bichromatic lattice becomes broad as the wavefunction $\Psi(x)$ changes from extended to Anderson-localized when the amplitude of the quasidisorder is above a localization threshold. Reproduced from Billy J, Josse V, Zuo Z, Bernard A, Hambrecht B, Lugan P, Clément D, Sanchez-Palencia L, Bouyer P, and Aspect A (2008) Direct observation of Anderson localization of matter waves in a controlled disorder. Nature 453: 891 and Roati G, D'Errico C, Fallani L, Fattori M, Fort C, Zaccanti M, Modugno G, Modugno M, and Inguscio M (2008) Anderson localization of a noninteracting Bose-Einstein condensate. Nature 453: 895. with permission from the authors.

Low-dimensional physics

Since the first realizations of optical lattices, it was clear that the strong confinement of the atoms in the lattice sites also represented a practical tool to study BEC in low-dimensional settings. As a matter of fact, a strong 1D optical lattice can be used to restrict the atomic motion on a 2D plane while a strong 2D lattice can create quantum wires, where the motion of the atoms is restricted along 1D only. The dimensionality of space has important consequences on the collective properties of many-body quantum systems, with dramatic effects that emerge from the interplay of interactions and reduced dimensionality. In an interacting 2D Bose gas superfluidity can arise even in the absence of Bose–Einstein condensation, as a result of a Berezinskii–Kosterlitz–Thouless (BKT) transition. The collective excitations of an interacting 1D Bose gas can be described in terms of the theory of Luttinger liquids and the system can even realize a "fermionized" Tonks–Girardeau gas, where the strong repulsion between the bosons force them to acquire a fermionic behavior, playing the role of an effective Pauli repulsion.

Long-range interactions

The vast majority of experimental and theoretical works on ultracold gases deals with atoms whose interaction—at the energy and temperatures of interest—can be described as contact-like and described by *s*-wave scattering lengths. More recently it has been possible to trap and manipulate gases where the dipolar interaction is strong enough to give rise to new phenomena, due to its long-range and anisotropic nature. A first approach to make the dipolar interaction relevant for the phenomenology of the system is to consider atoms with a relatively large dipolar interaction, as rare-earth atoms, and reduce the strength of the contact interaction by exploiting Feshbach resonances. In this way physicists were able to obtain the quantum equivalent of ferrofluids, to measure roton-like spectra, and, for Fermi gases, to characterize Fermi sphere deformations, just to mention a few. In particular it was observed that, when the dipolar interaction becomes large enough, the gas can break into a matrix of self-bound droplets (Kadau et al., 2016), as shown in Fig. 18. The nature of these droplets is very similar to that of the droplets found in Bose–Bose mixtures, since they are both stabilized by quantum fluctuations. Even more importantly, such droplets can be made coherent among each other, allowing for the very first observation of the so-called supersolid state (see below).

Magnetic dipolar atomic gases are not the only platforms where long-range interaction can play a major role in the context of ultracold gases. Another possibility is to exploit the electric dipole moment of heteronuclear binary molecules. In this case the dipole–dipole interaction can be very strong and much attention has been devoted to long-range interaction effects in molecular gases loaded in deep optical lattices, with the realization of important solid-state Hamiltonians. Other approaches to synthesize effective long-range interactions include atoms in optical cavities, Rydberg atoms, and trapped ions. The latter platforms are considered to be good candidates also for the realization of atom-based quantum computers.

Supersolidity

In the last few years supersolidity has emerged as an exciting and active frontier of research in the field of ultracold atoms. Supersolidity is an intriguing phenomenon, where both superfluid and crystalline properties coexist as a consequence of the simultaneous breaking of phase and translational symmetry. After unsuccessful attempts in solid helium, supersolidity was

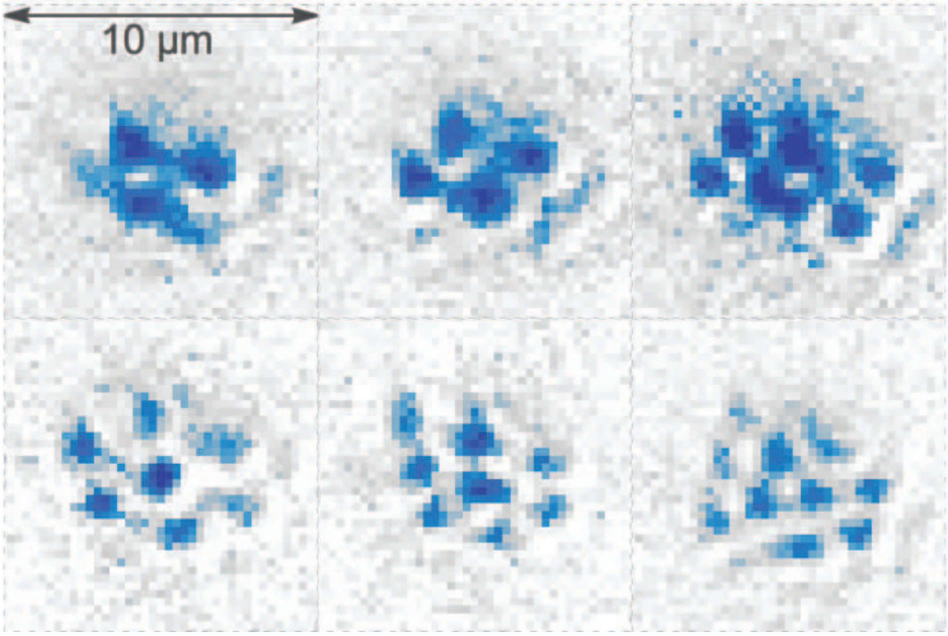

Fig. 18 Observation of self-bound quantum droplets in a dipolar gas of ^{164}Dy, as observed in 2016 at University of Stuttgart. Reproduced from Kadau H, Schmitt M, Wenzel M, Wink C, Maier T, Ferrier-Barbut I, and Pfau T (2016) Observing the Rosensweig instability of a quantum ferrofluid. Nature 530: 194 with permission from the authors.

experimentally reported in 2017 in Bose–Einstein condensates with spin–orbit coupling (MIT) and inside optical resonators (ETH). Remarkably, in 2019 the supersolid state was realized in dipolar Bose gases almost at the same time in three different laboratories (at LENS-Pisa, Innsbruck and Stuttgart). The experimental and the theoretical research activity has then become particularly rich (see Recati and Stringari (2023)) for a review). In particular in the case of dipolar gases, phase coherence, the spatial modulations of the density profile, and the superfluid rotational properties, as well as the emergence of the Goldstone modes associated with the superfluid and crystal behavior, were observed.

Conclusion

The experimental realization of Bose–Einstein condensation in ultracold atomic gases in 1995 opened completely new research directions that were inconceivable before then. BEC experiments have become “quantum laboratories,” where quantum theories can be tested for the first time “on demand,” providing a natural embodiment of the “quantum simulation” approach envisioned by R. Feynman. Almost three decades of exciting research have led us to a much better understanding of fundamental physical effects, in a continuous synergy between theoretical studies and experimental investigations, always going hand-in-hand, one prompting each other in a virtuous circle. What could the developments of the next three decades be? In the last chapter we have identified some of the major trending topics, but the list is far from conclusive and it is difficult to foresee what the next breakthroughs will be. What we can certainly say is that a growing, enthusiastic community of scientists will keep working, trying to achieve a better understanding of the quantum world, also with the aim of translating this knowledge into new quantum-based technologies for the benefit of society at large.

References

Albiez M, Gati R, Fölling J, Hunsmann S, Cristiani M, and Oberthaler MK (2005) Direct observation of tunneling and nonlinear self-trapping in a single Bosonic Josephson junction. *Physical Review Letters* 95: 010402.

Andrews MR, Townsend CG, Miesner HJ, Durfee DS, Kurn DM, and Ketterle W (1997) Observation of interference between two Bose condensates. *Science* 275: 637.

Billy J, Josse V, Zuo Z, Bernard A, Hambrecht B, Lugan P, Clément D, Sanchez-Palencia L, Bouyer P, and Aspect A (2008) Direct observation of Anderson localization of matter waves in a controlled disorder. *Nature* 453: 891.

Bloch I, Dalibard J, and Zwerger W (2008) Many-body physics with ultracold gases. *Reviews of Modern Physics* 80: 885.

Bose SN (1924) Plancks Gesetz und Lichtquantenhypothese. *Zeitschrift für Physik* 26: 178.

Cataliotti FS, Burger S, Fort C, Maddaloni P, Minardi F, Trombettoni A, Smerzi A, and Inguscio M (2001) Josephson junction arrays with Bose-Einstein condensates. *Science* 293: 843.

Chen C-C, Escudero RG, Minář J, Pasquiou B, Bennetts S, and Schreck F (2022) Continuous Bose-Einstein condensation. *Nature* 606: 683.

Cornell EA and Wieman CE (2002) Nobel lecture: Bose-Einstein condensation in a dilute gas, the first 70 years and some recent experiments. *Reviews of Modern Physics* 74: 875.

Dalfovo F, Giorgini S, Pitaevskii LP, and Stringari S (1999) Theory of Bose-Einstein condensation in trapped gases. *Reviews of Modern Physics* 71: 463.

Einstein A (1924) Quantentheorie des einatomigen idealen gases. *Sitzungsberichte der Preuischen Akademie der Wissenschaften*: 261. (1925) Quantentheorie des einatomigen idealen Gases. Sitzber. Kgl. Preuss. Akad. Wiss. 3.

Ensher JR, Jin DS, Matthews MR, Wieman CE, and Cornell EA (1996) Bose-Einstein condensation in a dilute gas: Measurement of energy and ground-state occupation. *Physical Review Letters* 77: 4984.

Fallani L, Cataliotti FS, Catani J, Fort C, Modugno M, Zawada M, and Inguscio M (2003) Optically induced lensing effect on a Bose-Einstein condensate expanding in a moving lattice. *Physical Review Letters* 91: 240405.

Goldman N, Juzeliūnas G, Öhberg P, and Spielman IB (2014) Light-induced gauge fields for ultracold atoms. *Reports on Progress in Physics* 77: 126401.

Greiner M, Mandel O, Esslinger T, Hänsch TW, and Bloch I (2002) Quantum phase transition from a superfluid to a Mott insulator in a gas of ultracold atoms. *Nature* 415: 39.

Greiner M, Regal CA, and Jin DS (2003) Emergence of a molecular Bose-Einstein condensate from a Fermi gas. *Nature* 426: 537.

Grimm R, Inguscio M, Stringari S, and Lamporesi G (eds.) (2023) *Proceedings of the International School of Physics "Enrico Fermi", Varenna (Italy)–Course 211. Quantum Mixtures With Ultracold Atoms*. IOS Press. In press.

Hau LV, Busch BD, Liu C, Dutton Z, Burns MM, and Golovchenko JA (1998) Near-resonant spatial images of confined Bose-Einstein condensates in a 4-Dee magnetic bottle. *Physical Review A* 58: R54.

Inguscio M and Fallani L (2013) *Atomic Physics: Precise Measurements and Ultracold Matter*. Oxford University Press.

Inguscio M, Stringari S, and Wieman CE (eds.) (1999) *Proceedings of the International School of Physics "Enrico Fermi", Varenna (Italy)–Course CXL. Bose-Einstein Condensation in Atomic Gases*. IOS Press.

Inguscio M, Ketterle W, and Salomon C (eds.) (2007) *Proceedings of the International School of Physics "Enrico Fermi", Varenna (Italy)–Course CLXIV. Ultracold Fermi gases*. IOS Press.

Inguscio M, Ketterle W, Stringari S, and Roati G (eds.) (2016) *Proceedings of the International School of Physics "Enrico Fermi", Varenna (Italy)–Course CXCI. Quantum Matter at Ultralow Temperatures*. IOS Press.

Inouye S, Andrews MR, Stenger J, Miesner H-J, Stamper-Kurn DM, and Ketterle W (1998) Observation of Feshbach resonances in a Bose-Einstein condensate. *Nature* 392: 151.

Kadau H, Schmitt M, Wenzel M, Wink C, Maier T, Ferrier-Barbut I, and Pfau T (2016) Observing the Rosensweig instability of a quantum ferrofluid. *Nature* 530: 194.

Ketterle W (2002) Nobel lecture: When atoms behave as waves: Bose-Einstein condensation and the atom laser. *Reviews of Modern Physics* 74: 1131.

Madison KW, Chevy F, Wohlleben W, and Dalibard J (2000) Vortex formation in a stirred Bose-Einstein condensate. *Physical Review Letters* 84: 806.

Pethick CJ and Smith H (2002) *Bose-Einstein Condensation in Dilute Gases*. Cambridge University Press.

Pitaevskii LP and Stringari S (2016) *Bose-Einstein Condensation and Superfluidity*. Oxford University Press.

Recati A and Stringari S (2023) Supersolidity in ultra-cold dipolar gases. *Nature*. In press.

Roati G, Riboli F, Modugno G, and Inguscio M (2002) Fermi-Bose quantum degenerate 40K-87Rb mixture with attractive interaction. *Physical Review Letters* 89: 150403.

Roati G, De Mirandes E, Ferlaino F, Ott H, Modugno G, and Inguscio M (2004) Atom interferometry with trapped Fermi gases. *Physical Review Letters* 92: 230402.

Roati G, D'Errico C, Fallani L, Fattori M, Fort C, Zaccanti M, Modugno G, Modugno M, and Inguscio M (2008) Anderson localization of a non-interacting Bose-Einstein condensate. *Nature* 453: 895.

Sidorenkov LA, Tey MK, Grimm R, Hou Y-H, Pitaevskii L, and Stringari S (2013) Second sound and the superfluid fraction in a Fermi gas with resonant interactions. *Nature* 498: 78.

Zwerger W (2014) *The BCS-BEC Crossover and the Unitary Fermi Gas*. Berlin, Heidelberg: Springer.

Universality of Bose–Einstein condensation and quenched formation dynamics

Nick P Proukakis, Joint Quantum Centre (JQC) Durham–Newcastle, School of Mathematics, Statistics and Physics, Newcastle University, Newcastle upon Tyne, United Kingdom

© 2024 Elsevier Ltd. All rights reserved.

Introduction **85**
"Universality" of Bose–Einstein condensation 85
Dynamical phase transition stages 88
Relevant coherence measures 89
Correlation functions 89
Penrose–Onsager condensation vs. quasi-condensation 90
Workhorse model of Bose–Einstein condensation 92
Universality during phase transition crossing: The Kibble–Zurek scaling law **93**
Early ideas 93
Numerical phase transition model 94
Criticality at equilibrium 95
Criticality in a dynamical setting 95
The Kibble–Zurek scaling law 97
Analyzing Kibble–Zurek in an elongated ultracold atomic system 99
Beyond homogeneous Kibble–Zurek considerations 102
Universality during phase-ordering dynamics **104**
Scaling hypothesis and late-time coarsening 104
Evolution around nonthermal fixed points 106
Relation of quenched turbulence dynamics to "controlled" turbulence experiments 108
Selected further considerations **109**
Beyond continuous single-component atomic gases 109
Driven-dissipative condensation in exciton-polariton systems 110
Bose–Einstein condensation on astrophysical/cosmological scales? 114
Conclusion **117**
Acknowledgments **117**
References **117**

Abstract

The emergence of macroscopic coherence in a many-body quantum system is a ubiquitous phenomenon across different physical systems and scales. This chapter reviews key concepts characterizing such systems (correlation functions, condensation, and quasi-condensation) and applies them to the study of emerging nonequilibrium features in the dynamical path toward such a highly coherent state: particular emphasis is placed on emerging universal features in the dynamics of conservative and open quantum systems, their equilibrium or nonequilibrium nature, and the extent that these can be observed in current experiments with quantum gases. Characteristic examples include symmetry-breaking in the Kibble-Zurek mechanism, coarsening and phase-ordering kinetics, and universal spatiotemporal scalings around nonthermal fixed points and in the context of the Kardar–Parisi–Zhang equation; the chapter concludes with a brief review of the potential relevance of some of these concepts in modeling the large-scale distribution of dark matter in the universe.

Key points

- Demonstration of ubiquitous nature of Bose–Einstein condensation and key observables characterizing it.
- Unified overview of the dynamical phase transition crossing from an incoherent initial condition to a (highly/fully) coherent final state, introducing key universal scaling laws applicable during such process.
- Detailed explanation of the Kibble–Zurek mechanism for a driven dynamical phase transition crossing through an external time-dependent parameter.
- Discussion of phase-ordering process and universal scaling at late evolution times following an instantaneous quench from an incoherent state.
- Applications of above frameworks to the dynamics of ultracold atoms and exciton-polaritons, with concrete examples and experimental observations.

https://doi.org/10.1016/B978-0-323-90800-9.00253-5

- Discussion of other highly nonequilibrium features of quantum gases originally stemming from cosmology (nonthermal fixed points) and classical systems (Kardar–Parisi–Zhang).
- Review of cosmological condensation model for dark matter, and its analogies to laboratory condensates.

Introduction

Bose–Einstein condensation (BEC), first predicted nearly 100 years ago, is a phenomenon associated with the emergence of a highly coherent state which manifests itself across vastly different physical systems: Interestingly, not only the existence of the effect but also the manner in which it emerges dynamically across such systems can exhibit the same characteristic features (Proukakis et al., 2017). This chapter reviews such universality of the existence and the dynamical emergence of a Bose–Einstein condensate starting from an incoherent (or thermal) state: in particular, attention is paid to universal scaling laws and (dynamical) self-similarity associated with the initial growth stages when the system breaks the Hamiltonian symmetry to randomly choose phase domains in a potentially "turbulent" manner, and with the subsequent relaxation of such a nonequilibrium state to the corresponding final equilibrium state (or steady state). The main aim of this chapter is to give an overview of key concepts of (selected) universal scaling laws which have developed over decades across distinct branches of physics, and focus on those with recent applications to experimentally controlled quantum gases; as such, this chapter is only intended to give a "flavor" and not a thorough overview of such topics across other systems, for which the reader is referred to suitable review articles. Nonetheless, before concluding, I also briefly discuss a less widely known emerging new example characterizing the interplay between condensed matter physics, nonequilibrium statistical physics and cosmology/high-energy physics, in the context of how quasi-condensation, BEC and turbulence, characterized through relevant correlation functions, could potentially relate to our understanding of large-scale cosmological structures.

"Universality" of Bose–Einstein condensation

BEC is a fundamental manifestation of many-particle coherence in a quantum system, occurring when a system of many particles acquires wave-like properties. Such behavior emerges when the de Broglie wavelength $\lambda \sim h/p$ (where h is Planck's constant and p is momentum) of the underlying particles becomes comparable to, or exceeds, the typical interparticle separation in the medium (Fig. 1). The textbook discussion of this effect (Huang, 1987; Dalfovo et al., 1999; Pitaevskii and Stringari, 2016; Pethick and Smith, 2002; Ueda, 2010) typically focusses on the case of a three-dimensional (3D) system of bosonic particles (i.e., particles of integer spin obeying Bose–Einstein statistics), for which such condensation emerges when the dimensionless phase-space density $n\lambda^3 \gtrsim O(1)$ (where $n = N/V$ is the number density of particles in the system) exceeds a value of order 1 (in a 3D noninteracting system, the exact value is $\zeta(3/2) \approx 2.612$). This occurs at a characteristic, or critical, value (ϵ_c) of the relevant external parameter, ϵ, which varies across, and thus induces, the transition. For example, in the well-studied case of particles being cooled (and noting that for such systems $\lambda \sim (mT)^{-1/2}$), BEC emerges at a critical temperature, T_c—a well-known characteristic in superfluidity/condensation phase diagrams of liquid helium and ultracold quantum gases.

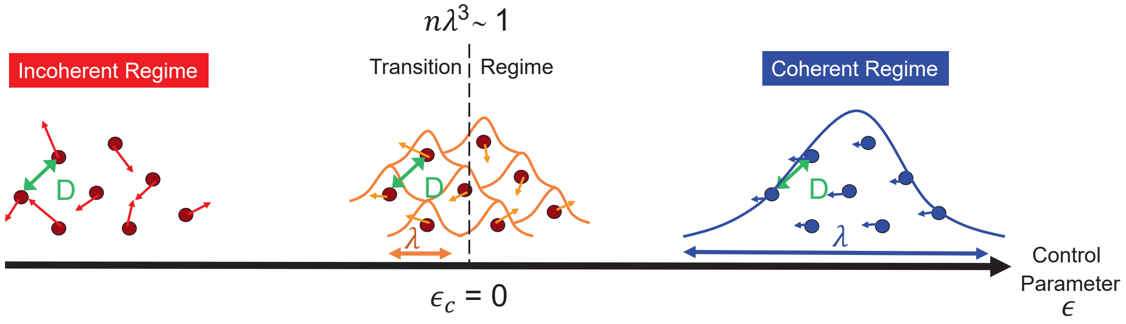

Fig. 1 Schematic of the transition from a system of incoherent, distinguishable (potentially composite) bosonic particles having a mean interparticle distance $D \sim n^{-1/3}$ (left), through the critical region in which the de Broglie wavelength, λ, becomes comparable to D (when $n\lambda^3 \sim 1$) (middle), to the quantum-degenerate (highly coherent) regime in which the typical wavelength much exceeds the mean interparticle distance (right) in terms of an external control parameter ϵ (e.g., corresponding to decreasing system temperature). Depicted *arrows* indicate particle velocities, which typically start aligning in the transition region (when the external control parameter, ϵ acquires a critical value ϵ_c, which is typically set to zero for convenience) eventually forming a coherent matter wave, known as a Bose–Einstein condensate, with a unique (randomly chosen) direction; the reduced vector magnitudes shown here indicate cooling.

However, in general, the role of the critical external control parameter could be played by many different physical variables (Snoke et al., 2017): for example, for the systems considered in this chapter, beyond a critical temperature or a critical density, such a phenomenon could also arise in terms of a critical interaction—whose magnitude can also be controlled by the system confinement/dimensionality—or a critical pumping rate, although more broadly a system could be induced to criticality through a critical magnetic field or pressure.

The bosonic particle undergoing such change of state can be fundamental (e.g., photons (Klaers et al., 2010)), or composite—noting that an even number of fermions also acquires integer spin, thus behaving bosonically. The simplest example of a composite bosonic particle is that of a Hydrogen ^{1}H atom, which comprises two fermions: a proton in the core, surrounded by a single electron. As it turns out, significant success in laser cooling and trapping (Chu, 1998; Cohen-Tannoudji, 1998; Phillips, 1998) has facilitated BEC to be achieved in a range of dilute (and thus typically weakly interacting) alkali gases (Cornell and Wieman, 2002; Ketterle, 2002): in fact the first observations of a *weakly interacting* BEC across any physical system were made in ultracold atomic gases of ^{87}Rb and ^{23}Na (prior to its observation in spin-polarized ^{1}H, which followed a few years later (Fried et al., 1998; Greytak and Kleppner, 2017)). Helium is the first known superfluid (and the only one known to exist in thermodynamic equilibrium). Although the well-studied bosonic ^{4}He, which is also a composite boson, exhibits a clear transition at some characteristic temperature and reaches 100% superfluidity at $T = 0$, the fraction of condensed particles in such a system nonetheless remains under 10% due to the relatively strong atomic interactions. Composite bosonic quasiparticles can also be formed from an even number of fermions: the most striking example is that of electron-hole Cooper pairs in superconductors or pairs of fermionic ^{3}He atoms exhibiting superfluidity. Although the detailed microscopic mechanism here is different (the well-known Bardeen–Cooper–Schrieffer, or BCS, mechanism (Cooper and Feldman, 2010)), ultimately the composite bosonic quasiparticle still effectively undergoes a BEC-type transition to a state of macroscopic coherence (Leggett, 2006). In fact, the exquisite controlled setting of ultracold atomic gases enables one to probe, even experimentally, the transition from a BEC to a BCS coherent system (Zwerger, 2011). Another example receiving significant current attention over the past 15 years is the condensation of a composite half-matter-half-light quasiparticle known as an exciton-polariton condensate, which manifests itself in pumped semiconductor microcavities (Sanvitto and Timofeev, 2012; Deng et al., 2010; Carusotto and Ciuti, 2013).

Signatures of BEC (and macroscopic coherence in general) in fact arise across an immensely broad range of length and energy/temperature scales (see Fig. 2), spanning from nuclear and atomic physics, through optical and condensed matter systems to astrophysical (neutron star cores) and even cosmological (fuzzy dark matter) settings (Proukakis and Burnett, 2013)—a more extended discussion on such diverse manifestations can be found in Proukakis et al. (2017).

Although BEC was initially discussed in the context of a homogeneous, noninteracting 3D system, realistic systems are in fact of finite size and do exhibit some interactions—which can mask the effects of BEC, as in the case of superfluid ^{4}He. This led to a many-decade-long search for experimentally controllable weakly interacting systems which could exhibit BEC: ultracold atomic experiments have provided a natural setting for achieving and observing nearly pure condensates, despite their (typically) inhomogeneous nature and finite system size. Current experiments in such systems in fact facilitate a detailed understanding of the modifications to both equilibrium coherence properties and dynamical formation induced by inhomogeneous/trapped and finite-size configurations, the influence of (realistic) weak interactions, the transition to more strongly interacting settings, and the confinement to lower effective dimensionalities, alongside studies of mixtures, superfluid turbulence, quantum phase transitions and even long-range interactions and supersolidity. Moreover, the last 2 decades have facilitated another well-controlled system, namely that of exciton-polaritons, which additionally offer glimpses to nonequilibrium phase transition features.

Beyond a classification of equilibrium properties of such systems, a fascinating generic underlying question with a history of significant contributions spanning many decades and across diverse physical settings concerns the fundamental question of how such systems form, and what common—or universal—features may exist during such a process.

In this chapter, I discuss in a broad sense the main aspects of the dynamical path toward such a highly coherent state, focusing primarily on the context of trapped ultracold (bosonic) atomic gases, with some emphasis on realistic inhomogeneous settings that facilitate direct links to controlled experiments: applicability and extension of such concepts to other physical settings and systems—most notably exciton-polariton condensates—are also discussed at relevant points within this chapter. The presentation is kept at a broad introductory level, geared to a nonexpert audience, with the intention to give a flavor of such rich questions—for a more complete picture, and historical overview, the reader is referred to a number of excellent reviews on such topics (Proukakis et al., 2017; del Campo and Zurek, 2014; del Campo et al., 2013; Bray, 1994; Rutenberg and Bray, 1995a; Schmied et al., 2019; Chantesana et al., 2019; Jos, 2013; Bloch et al., 2022).

This chapter is structured as follows: The rest of Section "Introduction" gives a unified qualitative overview of the dynamical stages in the transition process from an initial incoherent state to the emerging final equilibrium or steady-state of the system (Section "Dynamical phase transition stages"), discussing the key physical quantities used to characterize such a system (Section "Relevant coherence measures"), with a brief introduction to the basic phenomenological description of a BEC (Section "Workhorse model of Bose–Einstein condensation"). Section "Universality during phase transition crossing: The Kibble–Zurek scaling law," which forms the core of this chapter, addresses how coherence grows dynamically during an external parameter quench through spontaneous symmetry breaking and defect formation in the context of the so-called Kibble–Zurek mechanism giving rise to universal scaling laws: after giving a brief historical introduction (Section "Early ideas") and presenting a minimal numerical model capturing such effects (Section "Numerical phase transition model"), the key underlying principles and scaling law of Kibble–Zurek are described mathematically by extending the ideas of equilibrium criticality (which are thus also briefly reviewed here in Section "Criticality at equilibrium") to dynamical transition crossing (Section "Criticality in a dynamical setting" and

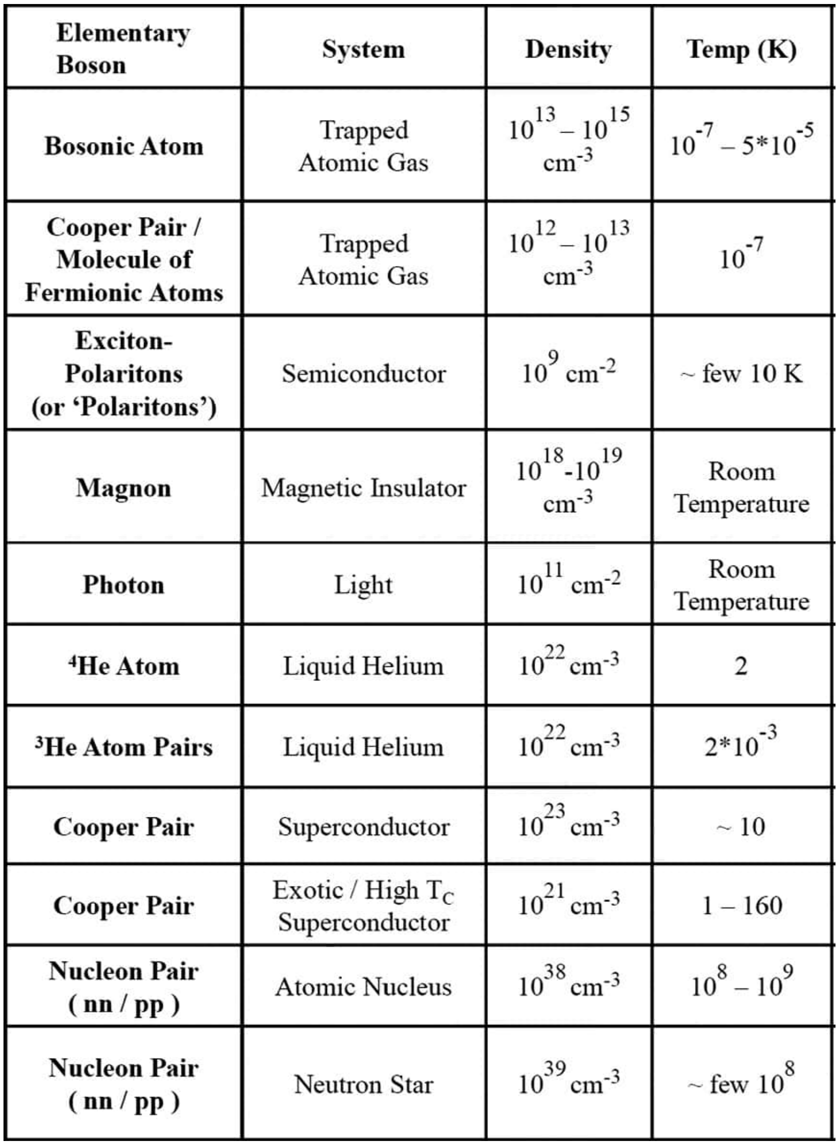

Elementary Boson	System	Density	Temp (K)
Bosonic Atom	Trapped Atomic Gas	$10^{13} – 10^{15}$ cm^{-3}	$10^{-7} – 5*10^{-5}$
Cooper Pair / Molecule of Fermionic Atoms	Trapped Atomic Gas	$10^{12} – 10^{13}$ cm^{-3}	10^{-7}
Exciton-Polaritons (or 'Polaritons')	Semiconductor	10^{9} cm^{-2}	~ few 10 K
Magnon	Magnetic Insulator	10^{18}-10^{19} cm^{-3}	Room Temperature
Photon	Light	10^{11} cm^{-2}	Room Temperature
^{4}He Atom	Liquid Helium	10^{22} cm^{-3}	2
^{3}He Atom Pairs	Liquid Helium	10^{22} cm^{-3}	$2*10^{-3}$
Cooper Pair	Superconductor	10^{23} cm^{-3}	~ 10
Cooper Pair	Exotic / High T_C Superconductor	10^{21} cm^{-3}	1 – 160
Nucleon Pair (nn / pp)	Atomic Nucleus	10^{38} cm^{-3}	$10^{8} – 10^{9}$
Nucleon Pair (nn / pp)	Neutron Star	10^{39} cm^{-3}	~ few 10^{8}

Fig. 2 Examples of very different systems exhibiting macroscopic quantum coherence and Bose–Einstein condensation, facilitated through a high dimensionless phase-space density $n\lambda^d \sim 1$ (where d the system dimensionality). For a more extended discussion of typical control parameters, probes, observables, and related characteristic properties and dimensionalities across such diverse systems, see Snoke et al. (2017). Adapted with permission from Proukakis NP and Burnett K (2013) Quantum gases: Setting the scene. In: Proukakis NP, Snoke DW, and Littlewood PB (eds.) Quantum Gases: Finite Temperature and Non-Equilibrium Dynamics: 1 (Cold Atoms), London: Imperial College Press

"The Kibble–Zurek scaling law") and then applying them to recent experiments (Section "Analyzing Kibble–Zurek in an elongated ultracold atomic system") which highlight the need for a more extended framework to account for inhomogeneous systems and their interplay with causality, which is also presented here (Section "Beyond homogeneous Kibble–Zurek considerations"). Section "Universality during phase-ordering dynamics" discusses universal phase-ordering dynamics following an instantaneous quench, demonstrating the emergence of universal scaling of the spatial correlation function in characteristic late-time evolution stages of a relaxing quantum gas (Section "Scaling hypothesis and late-time coarsening"), with particular emphasis on highly nonequilibrium quenches giving rise to "turbulent" states evolving in the vicinity of nonthermal fixed points (Section "Evolution around nonthermal fixed points"). Section "Selected further considerations" presents a highly-relevant (but heuristic) selection of applications of such concepts to other systems, briefly mentioning for completeness other effects and manifestations in ultracold quantum gases not discussed here (Section "Beyond continuous single-component atomic gases"). Section "Driven-dissipative condensation in exciton-polariton systems" focuses on the emergence of dynamical features discussed in Sections "Universality during phase transition crossing: The Kibble–Zurek scaling law" and "Universality during phase-ordering dynamics" and the related spatiotemporal scaling according to a (quantum) mapping of phase evolution in an open, driven-dissipative, quantum gas of exciton-polaritons to the well-known (classical) Kardar–Parisi–Zhang equation characterizing interfacial growth. Section "Bose–Einstein condensation on astrophysical/cosmological scales?" discusses the potential relevance of some of the discussed characterizations to the context of a cosmological-scale BEC, which is shown to exhibit many characteristics similar to harmonically confined ultracold quantum gases. General concluding remarks and outlook are given in Section "Conclusion."

Dynamical phase transition stages

Condensate formation is a fundamental nonequilibrium problem with a very long history dating over many decades (see, e.g., selected influential early works (Kagan, 1995; Stoof, 1995, 1999), discussions (Gardiner et al., 1998; Bijlsma et al., 2000) of the first quantitative ultracold atomic growth experiments (Miesner et al., 1998; Köhl et al., 2002), and the review (Davis et al., 2017), which contains many more highly relevant references). The main question to be addressed here is how a system, originally in a disordered/incoherent state, transitions—through the breaking of a continuous symmetry—to an equilibrium state (or steady state) exhibiting a high degree of macroscopic coherence, the extent of which is set by the particular system under consideration (e.g., system geometry and dimensionality, nature and strength of interactions between constituent particles, mass of constituent boson). A schematic of the main steps during such a process is shown in Fig. 3 in terms of the external control parameter ϵ.

From an equilibrium perspective, such a transition can be visualized as a gradual passage through different equilibrium states, with a well-identified critical region (around $\epsilon \sim \epsilon_c \sim 0$) separating purely incoherent from emerging coherent states. But how is such a picture affected when the external control parameter is dynamically varied, that is, $\epsilon \longrightarrow \epsilon(t)$? Let us consider here by means of an example the specific case of a temperature quench, for which $\epsilon = (T_c - T)/T_c$.

During the first stage of cooling, and while the system is still (sufficiently) above the critical temperature, particle dynamics can be described in the usual (classical) phase-space picture, based on a Boltzmann equation with collisions (Lifshitz and Pitaevskii, 1995). Under continuous cooling toward the critical point, particles are gradually redistributed into lower energy states (with elastic collisions typically occurring on a much faster timescale than that governing the variation of the external control parameter, thus providing the required thermalization).

The second, and arguably most interesting, stage in the evolution addresses the question of how the system dynamically crosses the phase transition, and what the nature of the nonequilibrium state generated in this vicinity of the critical point is. This is discussed in detail in Section "Universality during phase transition crossing: The Kibble–Zurek scaling law": for now, it suffices to say that this leads to a delay in the crossing of the phase transition, and the emergence of interesting (potentially "chaotic," or "turbulent-like") nonequilibrium states displaying a (potential) abundance of phase defects and relevant universal properties: such emerging transient states depend, in general, on both the dimensionality/geometry of the system and the rate of crossing of the phase transition (e.g., adiabatically vs. instantaneously).

The final stage in the equilibration/thermalization of the system is intricately related to the subsequent relaxation of such phase defects, and the related emergence of (a certain degree of) macroscopic coherence across the system: universal behavior is again

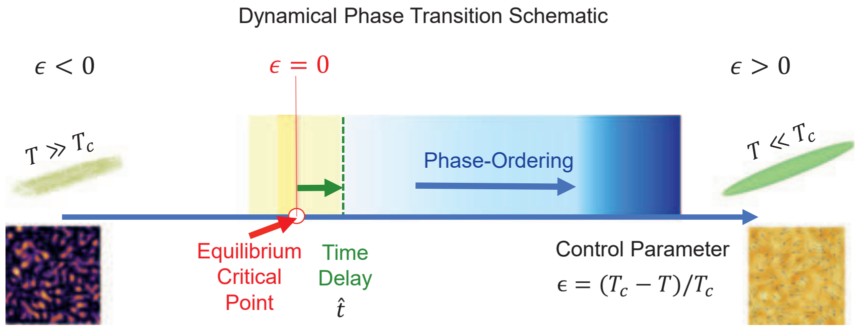
Dynamical Phase Transition Schematic
$\epsilon < 0$
$\epsilon = 0$
$\epsilon > 0$
$T \gg T_c$
Phase-Ordering
$T \ll T_c$
Equilibrium Critical Point
Time Delay $\hat{t}$
Control Parameter $\epsilon = (T_c - T)/T_c$

Fig. 3 Dynamical phase transition schematic: As the external control parameter, ϵ, is dynamically varied across the transition (i.e., $\epsilon \longrightarrow \epsilon(t)$), the system exhibits a delayed response compared to the corresponding equilibrium critical point at $\epsilon = \epsilon_c$ (corresponding, for example, to $T = T_c$), with ϵ_c typically set to 0, thus separating the incoherent ($\epsilon < 0$) from the coherent ($\epsilon > 0$) side of the phase transition. As soon as $\epsilon(t)$ dynamically crosses to a positive value, and still within the critical regime (i.e., $\epsilon(t) \longrightarrow 0^+$), it acquires (in general) a chaotic, turbulent nonequilibrium configuration containing phase defects: such physics is dominated by a universal Kibble–Zurek scaling law governing the dynamical phase transition. The subsequent gradual relaxation of such defects leads to the emergence of macroscopic coherence over much longer timescales; this includes a self-similar "phase ordering" process obeying universal scaling laws. Other universal features discussed in this chapter (such as spatio-temporal evolution around nonthermal fixed points and Kardar–Parisi–Zhang scaling) may also appear at appropriate scales and evolutionary stages during the extended process, depending on the particular system, initial state preparation, and quenching protocol. Specific equilibrium density snapshots shown here sufficiently before/after the transition are for the specific cases of an elongated inhomogeneous 3D, and a homogeneous 2D, ultracold atomic gas—both analyzed within this chapter.

expected to emerge here in some dynamical scenarios/regimes (e.g., for homogeneous systems, or very rapidly quenched, highly nonequilibrium states), but the specific system details can potentially also leave their imprint on this process, thus masking (or even potentially modifying the details of) such universality.

Such discussion can be formulated in terms of two commonly considered types of quenched regimes: instantaneous quenches, where the system is prepared, or induced, into a highly nonequilibrium state, and finite-duration (i.e., noninstantaneous) quenches starting from an incoherent equilibrium configuration, in which the system is typically modeled on the basis of a smoothly varying external parameter inducing such transition. Both such cases lead to interesting universal physical laws, associated with the dynamical phase transition crossing and the subsequent phase-ordering process, as discussed in more detail below (Sections "Universality during phase transition crossing: The Kibble–Zurek scaling law" and "Universality during phase-ordering dynamics"), starting from the finite-duration phase transitions.

Relevant coherence measures

Classification of the system equilibrium and dynamical properties is intricately related to appropriate characterization of the degree of system coherence.

Correlation functions

For a quantum system described by Bose field operators $\hat{\Psi}(\mathbf{r}, t)$ and $\hat{\Psi}^\dagger(\mathbf{r}, t)$, a classification of the coherence in both the spatial and temporal domains can be obtained through the n^{th}-order correlation function

$$\begin{aligned} &G^{(n)}\left(\mathbf{r}_1, \mathbf{r}'_1, \mathbf{r}_2, \mathbf{r}'_2, \cdots, t_1, t'_1, t_2, t'_2, \cdots\right) \\ &= \langle \hat{\Psi}^\dagger(\mathbf{r}_1, t_1)\hat{\Psi}^\dagger(\mathbf{r}_2, t_2)\cdots\hat{\Psi}^\dagger(\mathbf{r}_n, t_n)\hat{\Psi}(\mathbf{r}'_n, t'_n)\cdots\hat{\Psi}(\mathbf{r}'_2, t'_2)\hat{\Psi}(\mathbf{r}'_1, t'_1)\rangle \end{aligned} \tag{1}$$

measured across n different spatial locations and at n different times (with ... intended to reflect remaining terms such that there are n pairs of $\hat{\Psi}^*(\mathbf{r}_n, t_n)\ \hat{\Psi}(\mathbf{r}'_n, t'_n)$ contained within the above expectation value expression).

In practice, the most elementary—and thus most commonly discussed—correlation functions are those associated with spatial and temporal one-body correlations, respectively defined as

$$\text{Fixed } t: \quad C(\mathbf{r}, \mathbf{r}') = C(\mathbf{r}, \mathbf{r}', t, t) = \langle \hat{\Psi}^\dagger(\mathbf{r}, t)\hat{\Psi}(\mathbf{r}', t)\rangle \tag{2}$$

$$\text{Fixed } \mathbf{r}: \quad C(t, t') = C(\mathbf{r}, \mathbf{r}, t, t') = \langle \hat{\Psi}^\dagger(\mathbf{r}, t)\hat{\Psi}(\mathbf{r}, t')\rangle, \tag{3}$$

as these contain the primary information about spatial and temporal coherence.

The typical definition of equilibrium BEC is in the form of so-called off-diagonal-long-range order (ODLRO), associated with the nonvanishing asymptotic (spatial) behavior of the one-body density matrix $\rho(\mathbf{r}, \mathbf{r}', t) = \langle \hat{\Psi}^\dagger(\mathbf{r}, t)\ \hat{\Psi}(\mathbf{r}', t)\rangle$ (Pitaevskii and Stringari, 2016; Ueda, 2010; Leggett, 2006). In particular, ODLRO is defined by

$$\text{Lim}_{|\mathbf{r}-\mathbf{r}'|\to\infty}\langle \hat{\Psi}^\dagger(\mathbf{r}, t)\hat{\Psi}(\mathbf{r}', t)\rangle \neq 0, \tag{4}$$

with its value tending to some nonzero constant limit $\psi^*(r, t)\ \psi(r', t)$, consistent with the existence of off-diagonal correlations in the one-body density matrix. This introduces the quantity $\psi(r,\ t)$ as the so-called order parameter of the system. To highlight the existence of a nonzero value, this is usually expressed as $\psi = |\psi|e^{i\theta}$, a form that facilitates an analogy to classical fluids through the mass density $\rho = m|\psi|^2$ and superfluid velocity $v = (\hbar/m)\nabla\theta$ (Pitaevskii and Stringari, 2016).

Moreover, one often connects the BEC order parameter with the expectation value of the Bose field operator through $\psi(\mathbf{r}, t) = \langle \hat{\Psi} \rangle$. Such an argument is motivated by the analogous classical description of the electromagnetic field, in which one introduces a complex "classical" electric field as the expectation value of the corresponding (quantum-mechanical) electric field operator. While somewhat useful, there are some subtleties in following such procedure for massive particles, like atoms, which (unlike photons) cannot be created/destroyed from the vacuum by single-particle creation/annihilation operators: an insightful discussion of this issue, and the definition of BEC can be found in the book by Leggett (2006). While models explicitly maintaining the quantum-mechanical nature of the operator also exist, it is not essential to discuss such an extension here, with the reader instead referred to recent reviews (Proukakis and Jackson, 2008; Proukakis et al., 2013). For the purposes of this discussion, we approximate the actual field operator by a fluctuating classical field (obeying a classical probability distribution in phase space), thus accommodating both density and phase fluctuations into the subsequent description in a manner which significantly simplifies the direct numerical modeling (see later). All discussion, from this point onwards are thus expressed in terms of the complex/multimode classical field, which in this work will be denoted by $\Phi(\mathbf{r},\ t)$ and also referred to occasionally as the order parameter.

When studying the correlation in a given system, it is often useful to deal with appropriately normalized correlation functions, denoted by $g^{(n)}$: for example, the above general expression (Eq. 1) (written now in terms of the classical field $\Phi(\mathbf{r},\ t)$) can be normalized by the product $\Pi_i\sqrt{\langle|\Phi(\mathbf{r}_i,t_i)|^2\rangle\langle|\Phi(\mathbf{r}_i',t_i')|^2\rangle}$. This is useful as it implies that the same-location (all $\mathbf{r}_i$, $\mathbf{r}_i'$ the same), equal-time (all t_i, t_i' the same) normalized correlation function $g^{(n)}(0)$ has the elegant limiting cases (Cohen-Tannoudji and Robilliard, 2001)

$$g^{(n)}(\mathbf{r}_i\cdots\mathbf{r}_i;t_i\cdots t_i)=\left\{\begin{matrix}1 & \text{(Purely Coherent)}\\ n! & \text{(Incoherent)}\end{matrix}\right\}. \tag{5}$$

In what follows, I will use interchangeably the (unnormalized) correlation functions $C(\mathbf{r}, \mathbf{r}')$ and $C(t, t')$, or their normalized versions respectively defined by

$$g^{(1)}(\mathbf{r},\mathbf{r}')=\frac{\langle\Phi^*(\mathbf{r},t)\Phi(\mathbf{r}',t)\rangle}{\sqrt{\langle|\Phi(\mathbf{r},t)|^2\rangle}\sqrt{\langle|\Phi(\mathbf{r}',t)|^2\rangle}}, \tag{6}$$

and

$$g^{(1)}(t,t')=\frac{\langle\Phi^*(\mathbf{r},t)\Phi(\mathbf{r},t')\rangle}{\sqrt{\langle|\Phi(\mathbf{r},t)|^2\rangle}\sqrt{\langle|\Phi(\mathbf{r},t')|^2\rangle}}. \tag{7}$$

Note that although Eqs. (6) and (7) are often considered independently, a combined analysis of these two quantities can provide further crucial information about the extent of the "equilibrium" (or "nonequilibrium") nature of the system, or the emerging spatiotemporal scaling relations (see subsequent discussion on exciton-polaritons in Section "Driven-dissipative condensation in exciton-polariton systems").

As previously mentioned, the hallmark of BEC in a 3D system is the striking emergence of ODLRO, signifying that (some degree of) coherence is maintained across all space, that is, $g^{(1)}(\mathbf{r}, \mathbf{r}'; t)$ tends to a nonzero-valued plateau (having a value between 0 and 1) as $|\mathbf{r} - \mathbf{r}'| \to \infty$: for a finite-size system, it is of course only meaningful to study the dependence of $g^{(1)}$ on $|\mathbf{r} - \mathbf{r}'|$ over the spatial extent of the (coherent part of the) system. In fact, the extent of deviation of the plateau value from the starting value of 1 (taken at $\mathbf{r} = \mathbf{r}'$) provides information about the fraction of incoherent particles coexisting with the condensed part (Cohen-Tannoudji and Robilliard, 2001).

Key emerging concepts utilized throughout this chapter, and described in more detail later, are those of self-similarity and scaling hypothesis. In a nutshell, the underlying idea is that under appropriate conditions (e.g., in a restricted spatial and/or temporal window) the microscopic details of the system are not relevant, with the physical description of key system observables acquiring a universal description in terms of appropriately rescaled variables and a specific functional form. Elimination of nonessential details at short scales (times) in favor of emphasizing large-scale (long-time) features—a key step in the universal description of a physical system associated with the analysis of critical phenomena and the concept of renormalization group theory (see, e.g., Nishimori and Ortiz, 2011; Binney et al., 1992; Bruce and Wallace, 1992)—is possible when there exists a characteristic lengthscale (timescale), which is much larger (longer) than all other relevant system scales (but smaller than the system size/evolution time). This in turn allows us to express relevant correlation functions over a limited spatial and/or temporal range in terms of a unique (but not *a priori* known) functional form whose arguments are appropriately rescaled spatial (temporal) variables, combined with a small number of critical exponents characterizing such behavior (Nishimori and Ortiz, 2011; Binney et al., 1992). Details of such scalings will become more apparent at relevant points throughout this chapter.

Given the existence of both density and phase fluctuations in a realistic system, it is natural to examine their interplay and relative importance. In general, as a system approaches quantum degeneracy from the incoherent regime, density fluctuations start becoming suppressed at an earlier point (larger value of $|\epsilon|$) than phase fluctuations. In the specific context of cooling (thermal phase transition), this implies the emergence of two distinct characteristic temperatures for suppression of density and phase fluctuations. This is particularly pronounced in lower effective dimensionalities (i.e., in quasi-1D and quasi-2D geometries) (Petrov et al., 2004), but such effect is still present in 3D geometries, even if largely obscured (and so, subdominant).

In order to also investigate the emergence of density fluctuations, we thus introduce here the second-order, or density–density correlation function (taken here for simplicity at equal times)

$$g^{(2)}(\mathbf{r},\mathbf{r}',t)=\frac{\langle\Phi^*(\mathbf{r},t)\Phi^*(\mathbf{r}',t)\Phi(\mathbf{r}',t)\Phi(\mathbf{r},t)\rangle}{\langle|\Phi(\mathbf{r},t)|^2\rangle\langle|\Phi(\mathbf{r}',t)|^2\rangle}=\frac{\langle n(\mathbf{r},t)\ n(\mathbf{r}',t)\rangle}{\langle n(\mathbf{r},t)\rangle\ \langle n(\mathbf{r}',t)\rangle}, \tag{8}$$

with local density–density correlations accessible by evaluating such quantity at $r' = r$.

As a direct consequence of Eq. (5), a pure BEC can be identified through $g^{(1)}(\mathbf{r}, \mathbf{r}, t) = g^{(2)}(\mathbf{r}, \mathbf{r}, t) = 1$, whereas an incoherent (thermal) field has $g^{(2)}(\mathbf{r}, \mathbf{r}, t) = 2$: this simple identification provides a further probe for testing the degree of coherence of a system at a given time t.

Penrose–Onsager condensation vs. quasi-condensation

The above discussion has introduced the concept of ODLRO for characterizing a condensate at equilibrium: However, one is typically dealing with a finite-size system, and so such discussion has to be necessarily limited to within the spatial extent of the system (which should much exceed all other characteristic system lengthscales to make this nontrivial), and as limiting behavior in the thermodynamic limit.

In practice, for a finite-sized interacting system, one can instead proceed with a different characterization, following a seminal contribution by Penrose and Onsager (1956). In particular, one can diagonalize the off-diagonal one-body density matrix $\rho(\mathbf{r}, \mathbf{r}', t)$ to calculate its eigenvalues N_n through $\rho(\mathbf{r}, \mathbf{r}', t) = \sum_n N_n(t)\phi_n^*(\mathbf{r}, t)\phi_n(\mathbf{r}', t)$, where $\phi_n(\mathbf{r}, t)$ denotes the corresponding n-th eigenfunction. If in doing so one finds a macroscopically dominating eigenvalue, which is on the *same order* as the total particle number, then one can identify the mode corresponding to such eigenvalue with the Bose–Einstein condensate mode (Leggett, 2006). Mathematically, a dominant eigenvalue (if one exists) and corresponding eigenfunction of the density matrix can be identified from the solution of

$$\int \mathrm{d}\mathbf{r}' \varrho(\mathbf{r}, \mathbf{r}')\phi_n(\mathbf{r}') = N_n \phi_n(\mathbf{r}). \tag{9}$$

In practice one often uses a slightly relaxed criterion associated with the existence of a single eigenvalue which is much larger than all other eigenvalues of the system, but does not necessarily need to be on the same order as the total number of particles in the system. Such a mode is nowadays routinely referred to as the Penrose–Onsager mode of the system (and the above condition known as the Penrose–Onsager criterion) (Blakie et al., 2008).

In the context of numerical simulations of a fluctuating classical field, it is often numerically prohibitive to perform such a calculation by means of an ensemble/trajectory averaging. Thus, for purely practical reasons, one often resorts to time-averaging of a single trajectory as a numerical trick to achieve the same effect: the idea here is to compute the off-diagonal density matrix by averaging over a large number of samples spread over a timescale which is both longer than that governing the evolution of intrinsic fluctuations and shorter than any typical evolution of interest in the system (e.g., collective mode, large-scale motion of defects): in such a scenario, fluctuations in the field quickly randomize a single trajectory, thus making an average over different time evolutions of a single trajectory statistically analogous to averaging over many different independent trajectories: in other words, with careful choice of parameters, averaging over different time samples can also mimic the effect of averaging over different trajectories not only in a dynamical steady state in which the order parameter fluctuates about some mean value but also in a dynamical setting (Blakie et al., 2008). Note that global observables depending critically on the dynamical path additionally require averaging over (at least) a small number of trajectories to ensure the result is indeed statistically independent (and does not contain information about the system history): this is for example the case when probing correlation functions and defect numbers later in the context of quenched (Kibble–Zurek) dynamics in an inhomogeneous geometry (Section "Analyzing Kibble–Zurek in an elongated ultracold atomic system").

At this stage it is important to also comment on the role of system dimensionality: As well known, ODLRO—and so BEC—is strictly speaking restricted to 3D (or higher) configurations, with corresponding homogeneous ideal 2D systems (for all $T \neq 0$) only exhibiting a reduced degree of coherence, known as quasi-long-range (or topological) order; such distinction arises despite the fact that both systems exhibit superfluidity (Pitaevskii and Stringari, 2016; Ueda, 2010). Reduced coherence in 2D arises as a result of the dominant role of long-wavelength excitations destroying the overall phase coherence of the system, according to the well-known Hohenberg–Mermin–Wagner theorem. In such a case, the system exhibits a distinct phase transition, known as the Berezinskii–Kosterlitz–Thouless (BKT) transition (Kosterlitz, 2017; Jos, 2013): this is associated for $\epsilon \gtrsim 0$ with the binding of the free vortices which typically proliferate above the critical temperature ($\epsilon > 0$)—and whose presence randomizes the system phase—into vortex–antivortex pairs; such binding effectively screens their existence, which can be visualized as annihilation. Thermal fluctuations in 2D at any nonzero temperature reduce the coherence of the system compared to the corresponding 3D case, with the corresponding spatial profile of the correlation exhibiting instead in 2D a power-law decay and quasi-long-range order (as opposed to ODLRO).

Given that the dominant factor in the behavior of the spatial correlation function $g^{(1)}(\mathbf{r}, \mathbf{r}')$ is the distance between the two points, that is, $|\mathbf{r} - \mathbf{r}'|$, and to simplify the expressions, here I arbitrarily choose to label one of these points as $\mathbf{0}$, and the distance between them as $\mathbf{r}$, such that the relevant normalized spatial correlation function takes the form $g^{(1)}(\mathbf{r}) = g^{(1)}(\mathbf{0}, \mathbf{r})$. Below the critical temperature ($\epsilon \to 0^+$)—and in the specific context of an infinite homogeneous system—this takes in the $r \to \infty$ limit the dimensionality-dependent form

$$g^{(1)}(0, \mathbf{r})|_{0<T<T_c} = \left\{ \begin{matrix} \text{constant} & (3\text{D}) \\ r^{-\alpha(T)} & (2\text{D}) \end{matrix} \right\}, \tag{10}$$

with the value of the constant being temperature-dependent and lying between 0 and 1. In the above expression $\alpha(T) = 1/n_s\lambda^2$ is a temperature-dependent exponent characterizing the rate at which the correlation function decays to zero in a 2D system, which is inversely proportional to the superfluid density n_s. In an *equilibrium* 2D system, $\alpha(T) \lesssim 1/4$, with equality reached at the critical point $T = T_c$. Since no ODLRO can emerge in an infinite homogeneous 2D system (except for the specific case of $T = 0$), such a system cannot possess a condensate in the infinite limit. (Of course experimental systems are finite in nature, and so in confined atomic condensates one still often speaks of a "condensate" in the sense of significant coherence over the system size.) In that case one instead introduces a quasi-condensate, n_{qc}, which corresponds to that part of the density n which exhibits (relatively) suppressed density fluctuations, but whose phase is still largely fluctuating—this is possible due to the previously mentioned decoupling of the characteristic temperatures for the onset of phase and density fluctuations.

The quasi-condensate is defined as (Prokof'ev and Svistunov, 2002; Proukakis, 2006)

$$n_{qc}(\mathbf{r}) = n(\mathbf{r}) \quad \sqrt{2 - g^{(2)}(\mathbf{r})}, \tag{11}$$

where $g^{(2)}(\mathbf{r}) = g^{(2)}(\mathbf{r}, \mathbf{r}; t, t)$. From a density matrix perspective, a quasi-condensate corresponds to a state with many relatively large eigenvalues of (broadly) comparable values. Put differently, a quasi-condensate arises when the system has multiple modes exhibiting relatively enhanced macroscopic occupation, but there is no single mode which can be identified as dominant. Although a quasi-condensate is thus a more natural state to consider in a lower dimensional setting (both in 2D and, for weakly interacting systems, also in 1D), it is important to note that such a state also plays a crucial (transient) role even in 3D systems during the formation stage of a true Bose–Einstein condensate: in a nutshell, the transition from an incoherent 3D system to a coherent 3D BEC precedes through states of quasi-condensation (Kagan et al., 1992; Proukakis et al., 2017; Berloff and Svistunov, 2002), which simply implies that, as the system occupation is redistributed toward lower momenta, there is initially some competition of various low-lying modes before one ultimately dominates and forms the Bose–Einstein condensate (in the sense of the dominant Penrose–Onsager mode).

The Penrose–Onsager mode exhibits both suppressed density and suppressed phase fluctuations. As such, this mode can also be (approximately numerically) reconstructed from the two lowest order correlation functions. For example, for the specific case of a harmonically trapped condensate which provides a natural peak in the condensate density at the trap center $\mathbf{r} = 0$, one can approximate (Al Khawaja et al., 2002; Cockburn et al., 2011) (for a fixed time t, suppressed here)

$$n_c(\mathbf{r}) = g^{(1)}(\mathbf{r}) \quad n_{qc}(\mathbf{r}) = g^{(1)}(\mathbf{r}) \quad \sqrt{2 - g^{(2)}(\mathbf{r})} \quad n(\mathbf{r}). \tag{12}$$

Notwithstanding the above, I note that for finite systems trapped in inhomogeneous potentials, such as harmonic traps, the system maintains sizeable coherence over its spatial extent, as the trap sets a lower limit for the momenta of the elementary excitations, thus suppressing the extent of phase fluctuations. As a result, in the limit of relatively low temperatures (much below T_c), one can still identify the equilibrium state of the system as a "true" BEC (Petrov et al., 2004; Al Khawaja et al., 2002; Ueda, 2010).

Workhorse model of Bose–Einstein condensation

The usual (and simplest) textbook description of a continuous phase transition is in terms of a phenomenological Ginzburg-Landau model, whose free energy functional takes the general form (Leggett, 2006)

$$F[\Phi(\mathbf{r})] = \int d^3\mathbf{r} \left[F_0 + \alpha|\Phi|^2 + \frac{\beta}{2}|\Phi|^4 + \gamma|\nabla\Phi|^2 \right], \tag{13}$$

for an appropriate (system-specific) choice of parameters α, β and γ. The usefulness of such a model is that it supports a phase transition from a symmetric state with a global minimum of the free energy when $\Phi = 0$, to a Mexican-hat style potential exhibiting a minimum at a $\Phi \neq 0$ value (see illustration in subsequent Fig. 6): in other words, it facilitates—under appropriate conditions—the emergence of a nonzero order parameter of the system.

In the context of BEC, such a model is cast in terms of a nonlinear Schrödinger equation—known as the Gross–Pitaevskii (GP) equation—which takes the form (Pethick and Smith, 2002; Pitaevskii and Stringari, 2016; Ueda, 2010; Dalfovo et al., 1999)

$$i\hbar \frac{\partial \Phi}{\partial t} = -\frac{\hbar^2}{2m}\nabla^2\Phi + V\Phi + g|\Phi|^2\Phi. \tag{14}$$

Here m is the mass of the (composite) boson, V is the external potential, and g is the effective interaction strength between constituent bosons, assumed here for simplicity to be local [i.e., $V(\mathbf{r} - \mathbf{r}') = g\delta(\mathbf{r} - \mathbf{r}')$], based on the lowest order (or s-wave) scattering process. This equation is often explicitly written with an additional $-\mu\Phi$ term on the right-hand-side, where μ is the system chemical potential.

This equation arises both as (trivially) the lowest order equation for the symmetry-broken field $\Phi = \langle \hat{\Psi} \rangle$, and as the effective (low-energy) field equation for a semi-classical field (or order parameter) Φ—the latter applicable for all highly-occupied modes in the system (i.e., those with occupation exceeding one particle per mode): for more information, see recent reviews (Proukakis and Jackson, 2008; Proukakis et al., 2013; Berloff et al., 2014; Blakie et al., 2008).

Beyond ultracold atomic gases, an appropriately modified form of this equation, which takes account of specific system details (e.g., nonlocal interactions, pumping, dissipation, rotation, gravitational effects), is applicable (with some limitations) to a range of diverse systems including liquid helium (Berloff, 1999), photon (Klaers et al., 2010) and exciton-polariton condensates (Carusotto and Ciuti, 2013), neutron star superfluidity (Warszawski et al., 2012; Drummond and Melatos, 2017; Verma et al., 2022), and fuzzy dark matter (FDM) (Marsh, 2016; Hui, 2021; Ferreira, 2021)—many of which are more explicitly discussed in subsequent sections. Specifically to account for a coupling to a heat bath (e.g., providing pumping, and/or dissipation), and the associated dynamical stochasticity, one often further supplements the above picture with further pumping/dissipation terms and an associated (typically additive) noise contribution, thus generalizing the "basic" Ginzburg-Landau model of Eq. (13) to a stochastic complex Ginzburg-Landau equation (see also subsequent Eqs. (15) and (32)).

Having identified the relevant physical systems, key considerations, and quantities useful in their description, I proceed to discuss features of universal dynamics emerging during the phase transition crossing (Section "Universality during phase transition crossing: The Kibble–Zurek scaling law") and the subsequent system phase-ordering and relaxation to the final (equilibrium) state (Section "Universality during phase-ordering dynamics")—with some emphasis on ultracold atomic gases as the physical system. Further remarks in the context of driven-dissipative quantum gases and other related features are then discussed in Section "Selected further considerations," with some overall concluding remarks in Section "Conclusion."

Key to the subsequent discussion is the idea of a scaling hypothesis in the spatial—and, by extension, also the temporal—domain, that is, the idea that correlation functions acquire in some limited "universal" regime the same functional form, in terms of a limited set of parameters—with the obvious example being that of a time-dependent lengthscale—and a specific set of exponents describing such dependence. Interestingly, the concepts discussed below are interdisciplinary, benefiting from cross-fertilization of ideas between (among other fields) condensed-matter theory, statistical physics, elementary particle theory, and cosmology.

Universality during phase transition crossing: The Kibble–Zurek scaling law

Early ideas

The concepts of spontaneous symmetry breaking and order formation at a critical temperature in ferromagnets and superconductors have found analogs in the context of the hot big bang model, with the universe transiting from a symmetric, to a symmetry-broken phase. Building on such (mathematical/notional) analogies, Tom Kibble wrote a seminal paper discussing the formation, topology, and evolution of domains emerging during a dynamical (second-order) continuous phase transition in the context of early-universe cosmology (Kibble, 1976). In such work, Kibble noted the initial chaotic formation of small quasi-ordered localized regions, or "protodomains," between which the system expectation value would vary randomly from region to region as the system breaks its $U(1)$ symmetry, and starts choosing a preferred phase. In particular, Kibble raised the question of whether any residue of such protodomains may remain detectable—in the form of a long-lived topologically stable structure such as monopole, string, or domain wall—as the overall system coherence grows: such a structure would form naturally at the interface of two spatially separated regions of different phase. This question has since been appropriately reformulated, finding significant applications in diverse lab-based condensed-matter systems (including liquid helium, liquid crystals, superconductors, and trapped ions), owing to the intuition of Wojciech Zurek who later discussed the analogy between such cosmological strings and vortex lines in a superfluid in 1985 (Zurek, 1985), and thus proposed schemes for its experimental study.

For completeness, I briefly note here that analogies between superfluids and the early universe are abundant, with liquid helium having been proposed as a system in which to study a range of different phenomena of relevance to the physics of the universe (Zurek, 1996; Volovik, 2009; Pickett, 2017), considerations which have since been extended to other controlled quantum gases (ultracold atomic systems and exciton-polariton condensates) in which aspects such as analog gravity (Jacquet et al., 2020), false vacuum decay (Fialko et al., 2015; Billam et al., 2022), and hydrodynamic QCD plasma analogs (Adams et al., 2012) are currently under investigation.

A schematic from the pioneering work of Zurek is shown in Fig. 5A, depicting a quench in a very thin (so effectively one-dimensional) doughnut-shaped (annular) helium superfluid of radius R (Fig. 5A) (Zurek, 1985, 1996): Building on the idea of "protodomains," let us consider that—at the time the system crosses the phase transition dynamically—the typical correlation length of the system takes a characteristic value $\hat{\xi}$; in other words, the system density around the ring circumference is divided into a number of regions, of effective mean length $\hat{\xi}$, each of which exhibits a constant phase, but such phase is chosen independently, and thus randomly, across different locations around the ring with no causal connection between them. Assuming a random walk of the phase between regions, a net (nonzero) phase gradient can emerge from the phase mismatch $\Delta\theta$ around the ring, which is in turn translated into a superfluid velocity via $v_s = \hbar/m\nabla(\Delta\theta)$. Zurek thus concluded that a rapid phase transition quench (pressure quench in the case of liquid helium) could leave the superfluid rotating around the annulus, that is, a (random) nonzero circulation. By the structure of the order parameter $\Phi = |\Phi|e^{i\theta}$, such circulation would then be in the form of integer multiples of 2π, corresponding to persistent currents around the ring—with the value of the integer multiple characterizing the so-called winding number. The emergence of such persistent currents was predicted to occur stochastically with the most likely outcome being the absence of a persistent current.

Stochastic formation of persistent currents through a quenched phase transition of a condensed matter system in the specific context of such a (single) annulus has been experimentally studied in a single superconducting ring (Monaco et al., 2009) (see also related earlier references therein), and, more recently, in an ultracold atomic gas ring (Corman et al., 2014)—the latter briefly discussed in the next section. However, it is important to note at this stage—as will become clearer later—that the proposed Kibble–Zurek mechanism is very general and, as such, has been observed in a range of controlled quench experiments across different systems, such as liquid helium (Hendry et al., 1994; Bäuerle et al., 1996), superconductors (Carmi et al., 2000), liquid crystals (Chuang et al., 1991), multiferroics (Chae et al., 2012), trapped ions (Ulm et al., 2013), and single-component trapped ultracold atoms (Weiler et al., 2008; Lamporesi et al., 2013; Corman et al., 2014; Chomaz et al., 2015; Navon et al., 2015; Donadello et al., 2016; Aidelsburger et al., 2017; Ko et al., 2019)—see recent reviews (del Campo and Zurek, 2014; del Campo et al., 2013; Beugnon and Navon, 2017) for more details.

Numerical phase transition model

Although interesting nonequilibrium properties of the system can be studied by the Gross–Pitaevskii equation (Eq. 14) for classical field subject to appropriate initial choice of nonequilibrium states (see discussion in subsequent Section "Evolution around nonthermal fixed points"), a commonly used alternative, which further introduces the element of (dynamical) stochasticity to the system, is a slightly generalized version in the form of the so-called Stochastic Gross–Pitaevskii equation (Stoof and Bijlsma, 2001; Gardiner and Davis, 2003; Proukakis and Jackson, 2008; Blakie et al., 2008; Proukakis et al., 2013; Berloff et al., 2014)

$$i\hbar\frac{\partial\Phi}{\partial t}=\mathcal{P}\left\{(1-i\gamma)\left[-\frac{\hbar^2}{2m}\nabla^2\Phi+V\Phi+g|\Phi|^2\Phi-\mu\Phi\right]+\eta\right\}. \tag{15}$$

This is a nonlinear Langevin equation corresponding to an effective field theory for the low-energy modes of a system: implicit in this model is that such modes are driven by their coupling to higher lying modes (representing a bath of purely thermal particles having an effective chemical potential μ and temperature T) through the dissipation strength γ, which—together with T—sets the mean strength of the fluctuations; the latter are treated as Gaussian noise with δ-correlations in both space and time, that is, $\langle\eta^\star(\mathbf{r},t)\eta(\mathbf{r}',t')\rangle=\overline{\eta}^2\delta(\mathbf{r}-\mathbf{r}')\delta(t-t')$, where $\overline{\eta}=\sqrt{2\hbar\gamma k_BT}$. A projector $\mathcal{P}$ has also been included in Eq. (15) to ensure numerical consistency, by restricting dynamics within the same low-energy band of modes (Bradley et al., 2008; Blakie et al., 2008; Berloff et al., 2014).

Based on such simple techniques, one can numerically visualize phase evolution within Zurek's original annular ring-trap setting in the context of ultracold quantum gases: this was beautifully demonstrated for the (effectively 1D) case of a very narrow annulus in Das et al. (2012). Corresponding results, generalized to a 2D setting such that the annulus width, w is also explicitly taken into consideration, thus facilitating also radial phase gradient and dynamics are shown in Fig. 4B. During such evolution, the dynamical noise η can drive an initial random phase into distinct regimes, having either zero net circulation (the most likely outcome, top right plot in Fig. 4B) or a nonzero phase winding of an integer multiple of $\pm 2\pi$ around the loop: in this particular example, the nonzero winding number generated is $n_w=1$ (bottom right plot in Fig. 4B).

Such features were explicitly verified experimentally in ultracold atomic gases in Corman et al. (2014), finding a spread of winding numbers around a zero mean value. The detection was done by removing the ring potential and allowing the annular condensate to expand and interfere with an independent (reference) condensate formed in the center of the ring: a nonzero

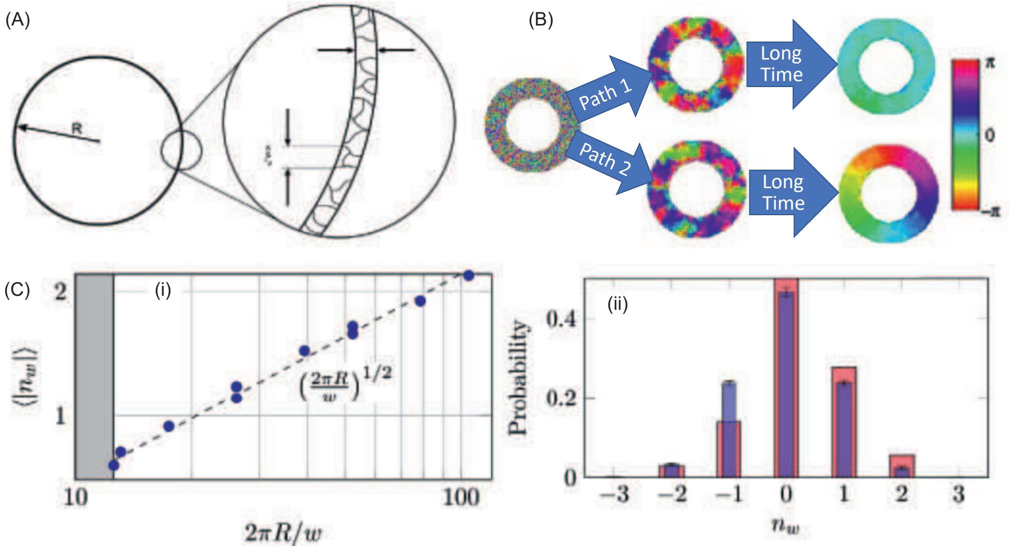

Fig. 4 Phase evolution in an annular geometry (ring trap). (A) Original thought experiment of Zurek about an ultra-thin, effectively 1D ring in which the crossing of the phase transition induces typical domains of mean size $\hat{\xi} \ll R$, where R is the ring radius. (B) Typical phase profile evolution in a 2D ultracold atomic gas based on SPGPE simulations of Eq. (15): a truly random, incoherent, initial state whose phase varies wildly within the ring (left) can follow under external parameter quenching different random paths of establishing larger regions of constant, but random, phase (middle), with this ultimately leading—for example—to the establishment of essentially constant phase across the ring (right, top), or a variation of 2π (right, bottom), that is, respectively a winding number n_W, or "charge" of 0, or 1. (C) (i) Dependence of mean winding number modulus $\langle|n_W|\rangle$ on mean ring radius R and ring width w through their ratio (R/w) (*blue points*) and corresponding prediction based on Zurek's random region formation scenario (*dashed line*). (ii) Probability of occurrence of different winding number outcomes, n_W, in the quenched experiment of Corman et al. (2014) (*red bars*) and corresponding SPGPE predictions (*blue bars*) (Bland et al., 2020): the asymmetry in the experimental measurements is likely due to a smaller number of trajectory averaging over numerical simulations. (A) Reprinted with permission from Zurek WH (1985) Cosmological experiments in superfluid helium? Nature 317(6037): 505–508. Copyright (1985) by the Nature Publishing Group. (C) Reprinted with permission from Bland T, et al. Persistent current formation in double-ring geometries, Journal of Physics B: Atomic, Molecular and Optical Physics 53(2): 033183. Copyright (2020) by the Institute of Physics

circulation could then be inferred from spiral distributions in the density, detected destructively through absorption imaging. A numerical confirmation (based on Eq. (15)) of the anticipated mean winding number scaling in terms of the ring radius R and width w, namely $\langle |n_w| \rangle = \sqrt{2\pi R/w}$, and a comparison demonstrating excellent agreement of numerically generated and observed winding numbers in the experimental set-up are respectively shown in Fig. 4C(i)–(ii) (Bland et al., 2020).

Zurek's original analysis and extensive follow-on work have led to the establishment of what is now known as the universal Kibble–Zurek scaling law of defect formation in a quenched quantum liquid. In order to be in a position to discuss such dynamical crossing of a phase transition more explicitly, I should first comment on equilibrium features around a critical point, ideas which will subsequently be appropriately extended to provide a universal description of nonequilibrium phase transition dynamics.

Criticality at equilibrium

As the system is probed on the incoherent side through different equilibrium states of decreasing temperature, the coherence length of a system, characterizing the spatial variation of the first-order correlation function, increases. Standard statistical physics considerations and critical phenomena theory enable us to describe the system correlations in terms of universal scaling relations, independent from the microscopic details of the system, and specified in terms of the distance to criticality, in a manner specified by a set of critical exponents and a scaling function (Binney et al., 1992; Nishimori and Ortiz, 2011): such considerations are a key aspect of the present discussion.

A striking example of the universal approach to criticality is the divergence of the system coherence length L at the actual system critical point: on the incoherent side of the phase transition, such approach is characterized via $g^{(1)}(\mathbf{r}) \sim e^{-r/L}$; this is in fact a very useful observable in order to identify the precise location of a critical point (either experimentally or numerically within a given model); such points will in general be slightly shifted due to quantum fluctuations, interaction, and finite-size effects (Dalfovo et al., 1999; Holzmann et al., 2004). One generally quantifies this by defining a "distance to criticality" parameter ϵ, which is measured as the difference of the value of ϵ in a given configuration from the critical value ϵ_c which signifies the transition point (the latter typically taken as $\epsilon_c = 0$).

Although the existence of a divergence at criticality is broadly applicable, the way that such a divergence manifests itself depends sensitively on the system dimensionality and symmetry and interaction properties of the underlying system Hamiltonian (which, in turn, define the corresponding order parameter for the particular phase transition being considered) (Binney et al., 1992). Systems whose approach to criticality (for a continuous phase transition) obey the same scaling functions and the same diverging behaviors in terms of $|\epsilon|$ are said to belong to the same universality class (Nishimori and Ortiz, 2011): the Bose gas (ultracold bosonic atoms, λ transition in ^{4}He) belongs to the XY universality class, and thus its critical properties are expected to exhibit the same behavior as the XY model. However, as should be anticipated from the preceding discussion, 3D and 2D systems do not exhibit the same behavior near criticality (they have distinct critical behavior/exponents), and this is also related to the very different nature of the phase transition: BEC vs. BKT.

Once the approach to criticality has been identified, one can specify the relevant information for the transition in terms of the values of the relevant critical exponents characterizing such divergence as a function of $|\epsilon|$: systems having the same dimensionality and the same critical exponents are said to belong to the same universality class . To make this more specific, let us consider the correlation length ξ in an infinite 3D system undergoing BEC through cooling, for which the distance to criticality, ϵ, is defined according to $\epsilon = (T_c - T)/T$. In the $\epsilon \lesssim 0$ limit (corresponding to $T > T_c$) this is expected to diverge in the vicinity of the critical point, that is, at $\epsilon \to 0^-$, as

$$\xi = \xi_0 |\epsilon|^{-\nu} = \xi_0 \left| \frac{T - T_c}{T_c} \right|^{-\nu}, \tag{16}$$

where ξ_0 is a nonuniversal parameter depending on the specific system microphysics (which is thus not considered further here) and ν is the static critical exponent. In the case of ultracold atoms, ν has been measured as $\nu \approx 0.67$ (Donner et al., 2007) (consistent with expectations of the 3D XY model). An example of such behavior is shown in Fig. 5A. Note that in a 2D system, the behavior of the coherence length near criticality takes a more stringent form $\xi \sim \exp(b|\epsilon|^{-\nu})$ (where $b \sim O(1)$ is a constant) (Jelić and Cugliandolo, 2011), with the exact form still under discussion.

Criticality in a dynamical setting

Generalizing to a dynamical setting, it should be noted that the relaxation dynamics of a system, that is, the process by which the system equilibrates in a given configuration (i.e., for a fixed value of ϵ) from a nonequilibrium initial condition, is dramatically slowed down near the transition point; this is intricately related to the fact that the correlation length of the system, that is, the distance over which the system has to achieve phase coherence, is—as previously discussed—rapidly increasing in the vicinity of the critical point. The associated increase (divergence) in time required for the relaxation process is known as critical slowing down (Nishimori and Ortiz, 2011). In fact, the relaxation time (in the 3D BEC system under discussion), also known as correlation, time, diverges according to [see Fig. 5B]

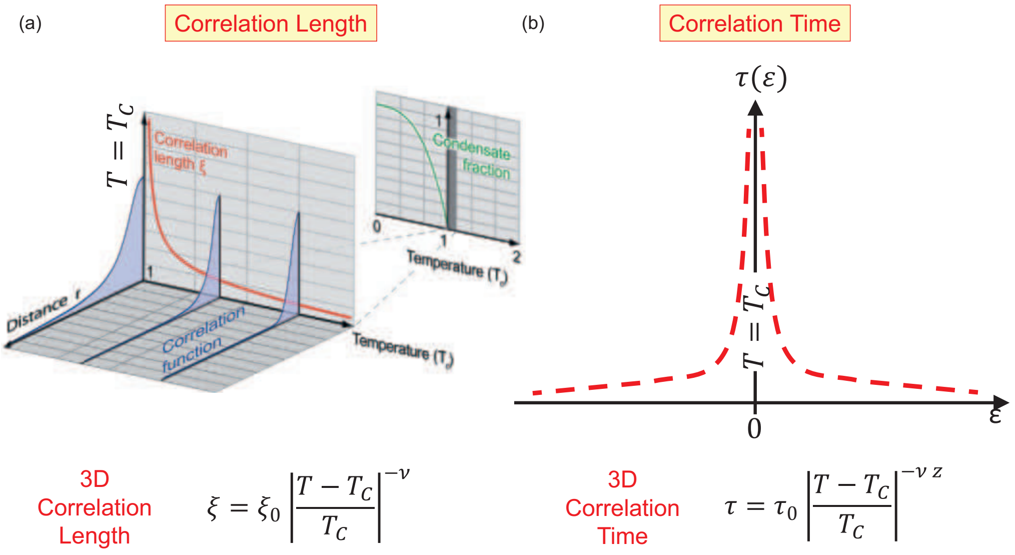

Fig. 5 Divergence of (A) equilibrium correlation length and (B) correlation time in the vicinity of a phase transition occurring at $T = T_c$ (or $\epsilon = 0$): (A) Main plot shows the diverging correlation length ξ (*red line*) as the system approaches criticality from higher temperatures (i.e., from the right); characteristic snapshots of the unnormalized first-order spatial correlation function $G^{(1)}(\mathbf{r})$, which decays as $1/r$ with the distance from the trap center, are shown at three different temperatures, that is, at different values of ϵ (*filled blue curves*). Inset: Temperature dependence of the overall system condensate fraction (*green curve*), with the *gray band* in the immediate vicinity of, and specifically above, the critical point depicting the temperature region probed in the main plot. (B) Divergence of correlation time assumed symmetric on both sides of the transition, and plotted here in terms of $\epsilon = (T_c - T)/T$ for ease of comparison with subsequent time-dependent discussion. Expressions quoted in each case summarize our understanding of equilibrium criticality as a function of temperature T, demonstrating the relation $\tau \sim \xi^z$. (A) Reprinted with permission from Donner T, Ritter S, Bourdel T, Ottl A, Köhl M, and Esslinger T (2007) Critical behavior of a trapped interacting Bose gas. Science 315(5818): 1556–1558. https://doi.org/10.1126/science.1138807. Reprinted with permission from the Science Publishing Group

$$\tau = \tau_0 \, |\epsilon|^{-\nu z} \sim \xi^z. \tag{17}$$

This additionally introduces the dynamical critical exponent z governing intrinsic system evolution at a fixed value of $|\epsilon|$: note that τ_0 appearing here is a nonuniversal time containing details of microscopic properties.

Having discussed the path to equilibration for a given value of ϵ, one can now proceed to consider the dynamical quench scenario, and thus address the question of the system dynamics when the distance to criticality is itself tuned in a dynamical manner, that is, $\epsilon \to \epsilon(t)$. The simplest, and standard, scenario considered is that of a linear variation of the distance to criticality with evolution time, which is assumed to occur over a characteristic quench timescale τ_Q, that is,

$$\epsilon(t) = \frac{t}{\tau_Q}. \tag{18}$$

As such, τ_Q controls the effective quench rate: small τ_Q implies the system is moving rapidly through different regimes along the ϵ axis, that is, small τ_Q corresponds to rapid quenches; conversely, the adiabatic crossing of the phase transition (through equilibrium states) is achieved in the limit $\tau_Q \to \infty$.

The evolution of the system from an (incoherent) state without symmetry-breaking (left) to a broken-symmetry one [which supports the formation of a phase-coherent state] (right) is shown schematically in Fig. 6 in terms of the time-dependent distance to criticality, with $\epsilon(t) = 0$ indicating the equilibrium critical point (del Campo and Zurek, 2014). Shown in this figure are two curves: the diverging correlation time (*dashed black lines*) and an instantaneous system-adjustment timescale constructed from the rate of quenching across the phase transition (i.e., the rate of change of the distance to criticality $\dot{\epsilon}$) through the relation $t = \epsilon/\dot{\epsilon}$. By convention, during the dynamical crossing of the phase transition, the time of the transition corresponds to $t = 0$, with $t < 0$ (corresponding to $\epsilon < 0$) labeling the incoherent side of the transition, and $t > 0$ the coherent side. Our understanding of the dynamics of the phase transition can be cast in terms of the relative magnitude of these two times (correlation time and system-adjustment timescale).

As the system moves toward the critical point (starting from an incoherent equilibrium state), the time taken for the system to adjust to its new instantaneous equilibrium solution grows, and starts doing so very rapidly as it approaches closer to the (equilibrium) critical point (where it diverges). Thus, necessarily, as the system is dynamically induced through the phase transition, the situation will arise, in which the rate at which the system is driven through the phase transition parameter space is so fast that its corresponding inverse timescale is shorter than the time required for the system to equilibrate over an increasing lengthscale; this happens when the correlation time τ becomes (in the vicinity of the critical point) larger than the magnitude of the instantaneous timescale $|\epsilon/\dot{\epsilon}|$, associated with the rate of quenching. Beyond such time, the system no longer has enough time to adjust as a whole

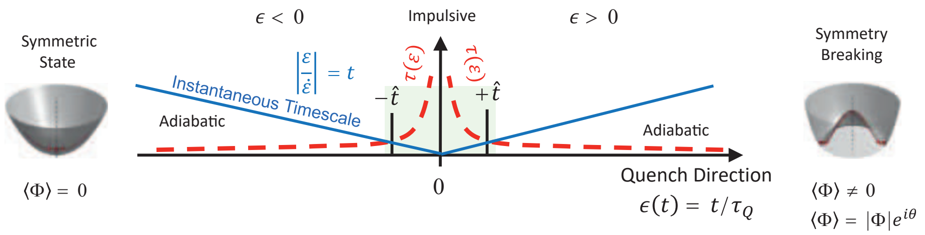

Fig. 6 Schematic of the "cartoon" Kibble–Zurek scenario, describing the phase transition from an incoherent to a coherent state through a dynamically induced linear crossing of the distance to criticality $\epsilon(t)$ in time. Shown in terms of $\epsilon(t)$ are the correlation time, which diverges from both sides as $\epsilon(t) \to 0$ [*dashed red line*] and an instantaneous timescale $\epsilon/\dot{\epsilon}$ set by the rate at which the quench is induced. Regarding the latter, I note here that when plotting things in terms of $\epsilon(t)$, slower quenches have a steeper slope of $|\epsilon/\dot{\epsilon}|$, thus allowing the system to reach, in principle, arbitrarily close to the critical point before it can no longer adiabatically follow equilibrium states in its crossing through the phase transition. During its crossing, the system can only adiabatically follow corresponding equilibrium states for as long as $|\tau| < |\epsilon/\dot{\epsilon}|$; otherwise, the characteristic correlation length setting the size of the domains becomes frozen to its value, $\hat{\xi} = \xi(\hat{\epsilon})$ evaluated at $\hat{\epsilon} = \epsilon(-\hat{t}\,)$ and the system behaves impulsively between $-\hat{t}$ and $\hat{t}$. The symmetry of the prequench (symmetric, $\langle\Phi\rangle = 0$) and postquench (symmetry-broken, $\langle\Phi\rangle \neq 0$) equilibria of the system are depicted in terms of the thermodynamic potential with the radial direction depicting the absence (left) or existence (right) of a nonzero order parameter: in the latter case, and while the azimuthal angle in this "Mexican hat" potential can in principle take any value with equal probability, the merging dynamics of domains of spontaneously generated random phases ultimately leave the system at sufficiently large values of $\epsilon > 0$ (and in this case at sufficiently late, or asymptotically long, times such that all critical transient dynamics have died out) with a particular spontaneously chosen direction, or phase θ (whose gradient sets the superfluid velocity).

to the external quench, and so different parts of the system necessarily evolve independently of each other, no longer controlled by the external drive (e.g., cooling ramp); in other words, the system is allowed to evolve independently on a local scale, and so the global symmetry is broken. This implies that the thermodynamic potential of the system transitions suddenly from a single minimum at the origin corresponding to the absence of any identified order parameter, that is, $\langle\Phi\rangle = 0$, to a typical "Mexican-hat" potential with $\langle\Phi\rangle \neq 0$ (see Fig. 6); in such a potential, the radial location of the minima indicates a nonzero expectation value of the system order parameter Φ, which thus acquires a meaning on this side of the phase transition while the azimuthal direction contains information about the phase of Φ. Note that, at this stage, all minima in such a potential, corresponding to different azimuthal orientation (at fixed radial distance), become equally probable, that is, all local phase choices are equally likely; this in turn implies that the phase varies randomly (following a random walk) between different domains, the size of which is (typically much) smaller than the system size. In fact, the typical size of such domains is set by the equilibrium correlation length of the system evaluated at the distance to criticality ϵ corresponding to the time when the symmetry is broken.

The Kibble–Zurek scaling law

Having introduced the key concepts, one can now formulate the fundamental equations governing the Kibble–Zurek mechanism of quenched phase transitions. The underlying idea is to use the equilibrium behavior of the system near criticality to make specific predictions regarding the nonequilibrium consequences of the dynamics of symmetry breaking. Mathematically, this relies on identifying the characteristic time at which the instantaneous quench timescale $|\epsilon/\dot{\epsilon}|$ [diagonal lines in Fig. 6] becomes equal to the diverging relaxation timescale τ: such time, typically denoted by $\mp\hat{t}$, signifies the so-called freeze-out time, that is, the time during the quench when the system behavior seizes being identified by parameters adiabatically following the equilibrium properties of the system as a whole (at a rate set by the quench rate). The typical size of subsequent independent domains—which have (in this simplistic scenario) no causal connection between them—is then set by the instantaneous value of the system correlation length at the freeze-out time. The discussion below follows closely the review articles (del Campo et al., 2013; del Campo and Zurek, 2014) based on the considerations by Kibble and Zurek.

Mathematically, one equates the diverging relaxation time τ, evaluated at the freeze-out time $-\hat{t}$, to the time $|-\hat{t}\,|$ set by $|\epsilon(-\hat{t})/\dot{\epsilon}(-\hat{t})|$. The fundamental Kibble–Zurek relation can thus be written as

$$\tau(-\hat{t}\,) = |-\hat{t}\,|, \tag{19}$$

As the above equation simply labels the two points of intersection of the *solid* and *dashed lines* in Fig. 6, which are the same in this (presumed symmetric) schematic across both sides of the phase transition, one often quotes this as the more "memorable" and algebraically equivalent form $\tau(\hat{t}) = \hat{t}$. Since the quench rate $\epsilon(t)$ depends on the quench timescale, τ_Q, then so do the above-mentioned intersection points, thus characterizing the dependence of correlation time—and, by extension, of correlation length (during the quenched evolution)—on τ_Q.

In its most basic (and most commonly presented) form (discussed here), the Kibble–Zurek scenario considers the system dynamics as being "frozen" between $-\hat{t}$ and $+\hat{t}$ (i.e., when $\tau > |\hat{t}|$), with such temporal window—during which the system remains fragmented into a number of smaller domains, exhibiting no correlation between them—labeled as the "impulsive" regime.

To understand the implications of such relation further, let us now consider a specific case—namely the example of a 3D homogeneous system, known to obey the equilibrium critical scalings of Eqs. (16) and (17). In that case, one can re-express Eq. (19) [or its equivalent relation $\tau(\hat{t}) = \hat{t}$] as

$$\tau(\hat{t}) = \tau_0 |\epsilon(\hat{t})|^{-\nu z} = \tau_0 \left| \left(\frac{\hat{t}}{\tau_Q} \right) \right|^{-\nu z} = \hat{t}. \tag{20}$$

Such a relation allows us to obtain a characteristic scaling of the freeze-out time, $\hat{t}$, in terms of τ_Q, with a corresponding relation for $\hat{\xi}$ obtained through $\hat{t} = \hat{\xi}^z$. Ignoring microscopic prefactors, which are not relevant for the universal system dynamics, one thus deduces that (for a homogeneous 3D system)

$$\hat{t} \sim \tau_Q^{\nu z/(1+\nu z)}, \tag{21}$$

and correspondingly

$$\hat{\xi} = \xi(\epsilon(\hat{t})) = \xi_0 |\epsilon(\hat{t})|^{-\nu} \sim \tau_Q^{\nu/(1+\nu z)}. \tag{22}$$

Although the Kibble–Zurek relation (Eq. 19) will always specify a characteristic scaling for $\hat{t}$ and $\hat{\xi}$ in terms of τ_Q around criticality, the exact form (and arising exponents) of such emerging relations will depend on the dimensionality and universality class of the system—with these results requiring revisiting in an inhomogeneous context (see later).

We have thus identified the timescale $\hat{t}$ and length scale $\hat{\xi}$, as the dominant relevant scales in the system in the critical region. As such, within such limited regime, one can formulate the temporal and spatial dependence of physical variables in the system in a universal manner by a simple rescaling of the form

$$\begin{array}{rl} \text{Time} & t \to t/\hat{t} \\ \text{Distance} & \mathbf{r} \to \mathbf{r}/\hat{\xi} \\ \text{Wavevector} & \mathbf{k} \to \mathbf{k}\hat{\xi} \end{array}$$

Having identified the relevant scales in the system allows us to formulate the corresponding scaling hypothesis for the system correlations (applicable in the long-wavelength, low-frequency limit); in the discussion below I also ignore for simplicity the anomalous critical exponent (denoted by η), as its value is typically zero or very close to it (Nishimori and Ortiz, 2011; Binney et al., 1992). The Kibble–Zurek scaling hypothesis thus states that in the critical region $[-\hat{t}\ ,\ \hat{t}\,]$, the correlation function can be cast in the form

$$C(\mathbf{r}, t) \sim \frac{1}{\hat{\xi}^{d-2}} F\left(\frac{t}{\hat{t}}, \ \frac{\mathbf{r}}{\hat{\xi}} \right), \tag{23}$$

where F is some system-specific function, and d is the system dimensionality. In general, this implies that the correlation function is dynamically evolving in a manner that changes both its shape and its range. However, the discussion so far has been focused on the (adiabatic-impulsive-adiabatic) "cartoon" Kibble–Zurek scenario of Fig. 6; it is thus pertinent to note here that while such a "cartoon" picture is indeed consistent with the scaling function of Eq. (23), it nonetheless further constraints it by implying a particular (time-independent) form for F.

Setting this aside for now, I note that the Kibble–Zurek relation of Eq. (19) enables us to predict the scaling of the number of defects spontaneously generated within such system during the linearly quenched phase transition crossing with the quench timescale τ_Q. Based on the typical size of independent domains $\hat{\xi}$ in the broken-symmetry phase (set by the equilibrium correlation length ξ evaluated at the freeze-out time $-\hat{t}$), and information about the system dimensionality, d, and defect dimensionality, $\mathcal{D}$, this takes the form (del Campo et al., 2013)

$$n_{\text{defect}} \sim \left(\frac{\hat{\xi}^{\mathcal{D}}}{\hat{\xi}^{d}} \right) \sim (\tau_Q)^{-\alpha}, \tag{24}$$

where the exponent $\alpha > 0$ in general depends on the critical exponents (ν, z) and the system/defect dimensionalities (d, $\mathcal{D}$). For example, $(d - \mathcal{D}) = 1$ for a 2D planar soliton in a 3D system or a point-like solitonic defect in a 1D system, while $(d - \mathcal{D}) = 2$ in both cases of a linear vortex filament in a 3D system, or a point-like vortex defect in a 2D system, because two dimensions are needed to accommodate the phase profile around such a vortex. As expected, one finds that—compared to slow quenches—faster quenches (i.e., small τ_Q) for which $|\epsilon/\dot{\epsilon}|$ has a smaller slope, and thus yields a smaller value of $\hat{\xi}$, lead to the generation of more defects; this is because more independent regions of smaller size can be accommodated in a given system size. In the specific 3D homogeneous example, $\alpha = (d - \mathcal{D})\nu/(1 + \nu z)$, whereas this becomes modified in the presence of harmonic confinement (see later). The power of the presented "cartoon" Kibble–Zurek mechanism is that it predicts the correct *scalings* with τ_Q for a linearly quenched homogeneous system. Nonetheless, an immediate shortcoming of such adiabatic-impulsive-adiabatic scenario, which can be identified, is that it ignores the temporal growth of correlations within the critical region; moreover, realistic experiments (besides being performed in finite-size systems) are often conducted in spatially varying potentials, thus requiring the extension of such mechanism to inhomogeneous settings. Both these issues are addressed in Sections "Analyzing Kibble–Zurek in an elongated ultracold atomic system" and "Beyond homogeneous Kibble–Zurek considerations."

In the context of ultracold atom experiments, beyond the previously-mentioned ring-trap geometry (Corman et al., 2014; Aidelsburger et al., 2017), the Kibble–Zurek phenomenon across a thermal phase transition has also been studied in different settings, including box-like geometries in 3D (Navon et al., 2015) and 2D (Chomaz et al., 2015), elongated 3D (Lamporesi et al., 2013; Donadello et al., 2016; Liu et al., 2018; Wolswijk et al., 2022) and oblate (pancake-like) (Goo et al., 2021, 2022; Kim et al., 2022) inhomogeneous traps, and even in the context of strongly interacting fermionic superfluids (Ko et al., 2019) (Tuning the interactions across the BEC-BCS crossover through the unitarity limit in a strongly-interacting superfluid revealed a near-constant, that is, interaction-strength-independent, critical exponent α.).

The insightful experiment at Cambridge in a 3D box-like geometry (Navon et al., 2015) probed the system spatial correlation function at different times, by interfering the system with a displaced copy of itself: they used such measurements to explicitly demonstrate the existence of critical slowing down; by determining the scaling of the correlation length with τ_Q—and using the expected (and previously experimentally extracted (Donner et al., 2007) value of $\nu \approx 2/3$ discussed earlier)—they were able to show that the dynamical critical exponent $z = 3/2$, consistent with the expectation for the 3D XY model universality class. Many of these early ultracold experiments also probed the number of generated vortices during a controlled quench, and its dependence on the quench timescale τ_Q (Corman et al., 2014; Chomaz et al., 2015; Donadello et al., 2016) (see subsequent discussions for more recent works). On the whole, good overall agreement with the expected behavior was obtained for sufficiently slow quenches as long as other appropriate factors, such as dimensionality and type of confinement (e.g., harmonic, ring-trap), were taken into account; however, a common potential limitation in such cases arises from the fact that experimental defect counting is typically only possible at times significantly longer than $+\hat{t}$ (which can generally be rather restrictive for most defect types due to their relatively short lifetimes), or after allowing the system to relax and/or expand for some time to make defect detection easier; such aspects are further discussed below.

Analyzing Kibble–Zurek in an elongated ultracold atomic system

To gain further direct microscopic insight into the complex system dynamics over all timescales and physical observables, and probe the physics beyond the "cartoon" Kibble–Zurek picture presented so far, I briefly review here key results obtained in the context of a particular sequence of experiments conducted at Trento in an elongated 3D harmonic geometry (Lamporesi et al., 2013; Donadello et al., 2016; Liu et al., 2018; Wolswijk et al., 2022). In such experiments, the system was cooled through the phase transition at different rates $\dot{T}$, with approximately fixed initial and final states.

A schematic of such process—based on extensive numerical simulations (Liu et al., 2018) via Eq. (15)—is shown in Fig. 7. An initially incoherent gas is dynamically quenched through the critical point (which is itself shifted by the combination of fluctuations and mean-field effects). As predicted, the system reacts ("unfreezes" its dynamics) with a certain delay time $+\hat{t}$ after crossing the equilibrium critical point, at which point the highly symmetry-broken state looks rather "chaotic": here the randomly distributed and tangled *purple lines* of variable lengths and orientations depict spontaneously generated defects in the form of highly excited vortices in a strongly turbulent state. Notice that the defects only emerge within an elliptical volume—consistent with the

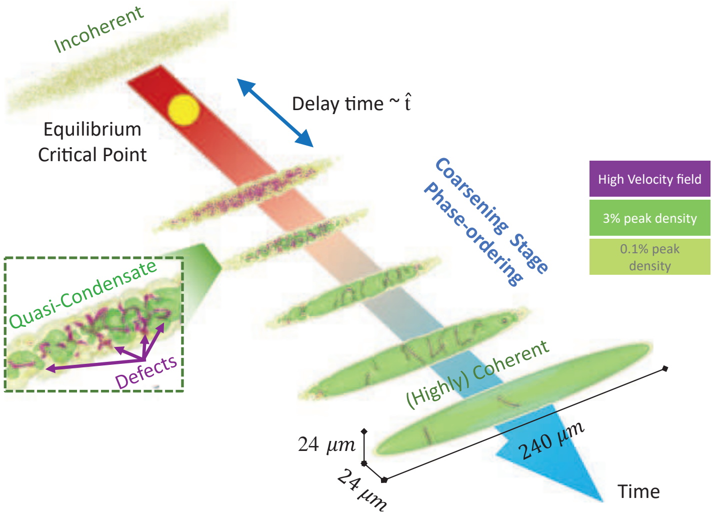

Fig. 7 Schematic of entire condensate growth process during a driven cooling quench from an initial equilibrium thermal configuration: Shown are density isosurfaces of the most populated (Penrose–Onsager) mode based on numerical simulations of Eq. (15) for the parameters of a recent elongated 3D harmonic trap experiment of Lamporesi et al. (2013), Donadello et al. (2016), as discussed in Liu et al. (2018). After the characteristic Kibble–Zurek delay time of $\sim \hat{t}$, one sees the spontaneous emergence of a "turbulent" quasi-condensate state (*green*) containing a large number of spontaneously generated defects (shown in *purple*) whose density decreases as one moves away from the trap center: these tangled defects gradually decay to a small number of well-formed vortices which are rather long-lived and become trapped in the growing macroscopically occupied condensate mode. During such evolution, the relative weight of the dominant eigenvalue (compared to the next largest one) increases significantly, revealing clear evidence of the transition from a quasi-condensate exhibiting multiple equally likely populated modes (around $\hat{t}$) to a pure BEC (with one dominant eigenvalue) in the latter density snapshots, in which the relative volume occupied by the defects has significantly decreased.

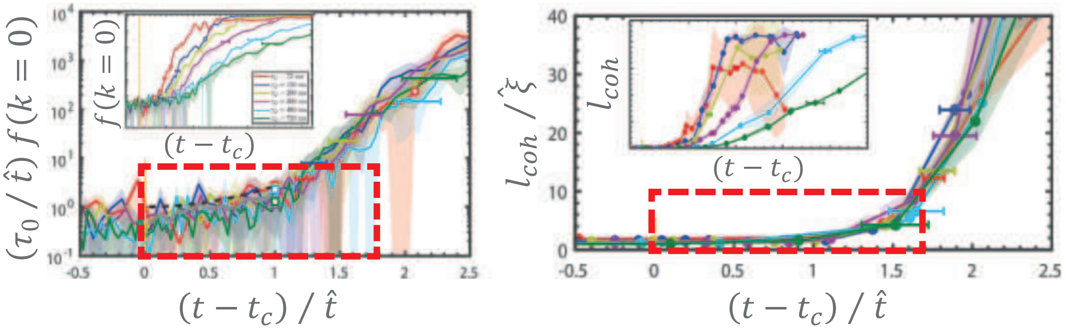

Fig. 8 Numerical demonstration of the Kibble–Zurek scaling hypothesis revealing self-similar evolution for the parameters of Fig. 7 in terms of appropriately rescaled (i) zero-momentum mode occupation $f(k=0)$, and (ii) coherence length l_{coh} for a range of different τ_Q. Main plots show rescaled evolution of insets, with time measured in terms of $(t - t_c)$ (where $t_c = t(\epsilon = 0)$) and scaled to $\hat{t}$. Rescaled vertical axes respectively plot (i) $(\tau_0/\hat{t})f(k=0)$ (where τ_0 is a nonuniversal constant time) and (ii) $l_{coh}/\hat{\xi}$. In the unscaled insets (plotted in terms of $(t - t_c)$, the value of the quench timescale τ_Q decreases from the lower (slower quench, *green*) to the upper (faster quench, *red*) curves. Adapted with permission from Liu I-K, Dziarmaga J, Gou S-C, Dalfovo F, and Proukakis NP (2020) Kibble-Zurek dynamics in a trapped ultracold Bose gas. Physical Review Research 2: 033183. https://doi.org/10.1103/PhysRevResearch.2.033183. Copyright (2020) by the American Physical Society.

imposed anisotropic harmonic confinement—and that the defect density is highest at the trap center, where the particle density is also highest: I will comment later on the significance of such observations.

Based on the Kibble–Zurek scaling hypothesis, all system observables become universal during the time interval $t \in [-\hat{t}, \hat{t}]$, thus uniquely specifying the temporal window during which one should be investigating universal Kibble–Zurek scaling effects for constant-rate cooling quenches $\tau_Q = T_c/|\dot{T}|$.

The emergence of such universal features can be seen in Fig. 8 which showcases the unscaled (insets) and appropriately rescaled dynamical evolution of (i) the zero-momentum mode occupation $f(k=0)$ [left], and (ii) the evolving system correlation length l_{coh} [right]. Unscaled images are plotted in terms of the time $(t - t_c)$ lapsed since crossing the equilibrium phase transition, whereas such shifted time has been additionally scaled by $\hat{t}$ in the rescaled plots [main plots]. Moreover, in the rescaled plots, the vertical-axis variables have been respectively rescaled as $\tau_0/\hat{t}f(k=0)$ and $l_{coh}/\hat{\xi}$. These simulations (Liu et al., 2020) reveal universal features up to a timescale of $\sim \hat{t}$ after the system crosses the equilibrium critical point. Although a delayed response was also found in more recent experiments with the same system, at such early times there was neither direct access to the spatially resolved density distribution nor the vortex number, with such delay instead attributed to other factors masking the ability to extract $\hat{t}$ directly (Wolswijk et al., 2022).

As the system is further cooled (i.e., $\epsilon > 0$ increases), one obtains a clear glimpse of its quasi-condensate characteristics: in particular, one sees the emergence of scattered localized regions of randomly selected near-constant phase (and so high coherence *locally*), separated by chaotically evolving and highly excited defects (vortices): at this stage there are many highly occupied modes competing against each other, and such information is revealed by the study of the largest, approximately equally dominant, eigenvalues (Liu et al., 2018)—providing direct evidence of quasi-condensation. The state of the system can also be thought of as "turbulent" (in the broad interpretation of the word).

As time evolves, and the system is further externally cooled (at the same constant rate), the random quasi-coherent regions grow in size, with the defects separating such regions interacting with other defects, thus dissipating their energy and shrinking in size. Naturally, the process of defect generation through the symmetry-breaking process and defect decay through coarsening coexist temporally, making it hard to isolate the relative importance of such competing mechanisms. However, at sufficiently late times after the dynamical phase transition crossing (i.e., for $\epsilon(t) \gg 0$), and within a specific temporal window, such dynamics are generally expected to exhibit a new set of self-similar (universal) scaling behavior associated with the phase-ordering process (Bray, 1994; Damle et al., 1996). The complicated inhomogeneous and anharmonic elongated 3D geometry of this system largely conceals such features, which are therefore discussed in more detail later on in the "cleaner" context of a homogeneous 2D quantum gas in Section "Scaling hypothesis and late-time coarsening." The net effect of this lengthy process is the gradual establishment of domains of increased volume and coherence, and thus the gradual transition from a state of "quasi-condensation" to that of true condensation, with properties set by the external system parameters (T and μ).

During such dynamics, the tight transverse direction rapidly constrains the system evolution, and dictates the specific type of defect preferentially forming in such a system; this corresponds to the macroscopic excitation with the lowest energy in the given geometry (In this case, such defect is a so-called "solitonic vortex" which exhibits a 2π phase winding characteristic of quantized vorticity, but with a nonuniform gradient, such that its phase profile resembles the characteristic planar jump of a dark soliton from larger distances (Donadello et al., 2014).). As the defect density gradually decreases, one sees the emergence of a phase-coherent condensate within which are embedded few long-lived defects; this is in fact a very clear dynamical demonstration of the trapping of defects emerging as relics of the phase transition in the growing highly coherent system. The particular geometrical set-up constrains their interactions such that they only interact rather infrequently when few defects remain. However, when they do, the defects can reconnect and dissipate away further energy (Serafini et al., 2017). After significant such evolution, the system eventually expels all of its defects: at this point, the competition between the various quasi-condensate modes is complete, and one arrives at a fully

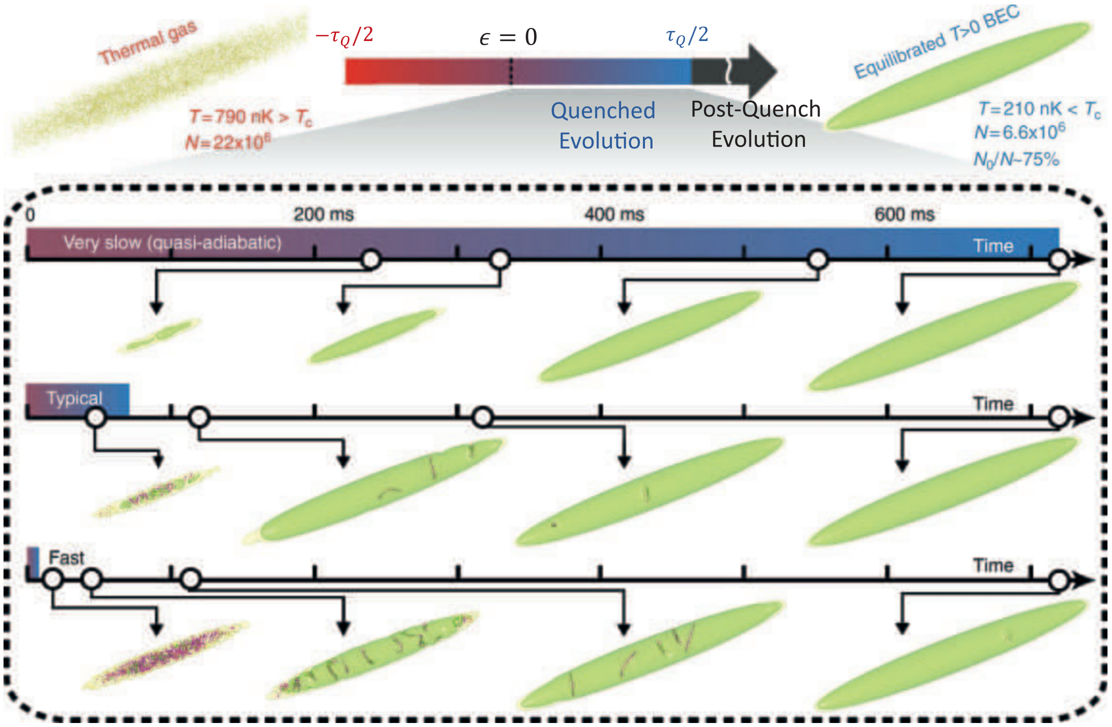

Fig. 9 Dependence of dynamical growth on quench rate for the parameters of Fig. 7 based on characteristic single-trajectory temporal evolution from a fixed initial (thermal) to a fixed final state (with a $\sim 75\%$ BEC fraction) for three different values of τ_Q: schematic at the top shows symmetric quench protocol from a $\mu < 0$, $T > T_c$ initial thermal state to one with $\mu > 0$, $T < T_c$ indicating corresponding temperatures and atom numbers characteristic of such controlled quench experiment. The quench rate increases from quasi-adiabatic (top) to fast (bottom), with middle trajectory showcasing a typical case where Kibble–Zurek scaling is expected to be fully applicable. Remarkably, faster quenches (bottom) contain (on average) more defects at a very late evolution time that slower quenches. Adapted with permission from Liu I-K, Donadello S, Lamporesi G, Ferrari G, Gou S-C, Dalfovo F, and Proukakis NP (2018) Dynamical equilibration across a quenched phase transition in a trapped quantum gas. Communications Physics 1(1): 24. ISSN 2399-3650. https://doi.org/10.1038/s42005-018-0023-6. Copyright (2018) by the Nature Publishing Group

phase-coherent Bose–Einstein condensate. Such a transition is further confirmed by a study of the ratio of the largest to second-largest eigenvalue of the system as a function of time (Liu et al., 2018, 2020). Density profiles (*green*) in Figs. 7 and 9 showcase the evolution of the spatial distribution of the most populated eigenstate, even though one only becomes genuinely dominant (the Penrose–Onsager mode) at late times.

Obviously, details of such process are heavily dependent on the quench protocol (e.g., temperature quench, interaction quench, geometry/phase-space quench), system geometry and dimensionality and interaction strength (which respectively set the typical number, type, and size of the defects). A characteristic illustration of how the quenching rate (which for given initial and final states is simply a function of the inverse quench timescale τ_Q) affects the dynamics can be found in Fig. 9, which displays the system evolution over an extended fixed total evolution time for three different quench rates (Liu et al., 2018). As evident, more defects are generated *on average* early on for more rapid quenches (bottom); moreover, because of this—and despite rapid defect annihilation and expulsion—typically more defects remain visible at a later absolute time when performing rapid cooling (i.e., for systems that cross the equilibrium critical point $\epsilon = 0$ faster), than in more gradual cooling schemes. For completeness, I note that while the example trajectories chosen to be displayed here are characteristic of the average behavior, each single cooling realization (for a fixed value of τ_Q) can lead to some variation in the number (and distribution) of generated defects; therefore, one needs to perform a number of distinct numerical/experimental realizations to appropriately extract relevant averaged parameters (e.g., defect number evolution).

Performing such averaging over different realizations, both experiments (Donadello et al., 2016) and simulations (Liu et al., 2018) found a power law decay in the defect number with τ_Q, with an exponent broadly consistent with the analytically predicted exponent α for this setting (del Campo and Zurek, 2014); while such features/measurements were only experimentally accessible at rather late evolution times, much exceeding $\hat{t}$, numerical simulations demonstrated that the actual overall scaling behavior was rather insensitive to evolution time; this is presumably because after defects have formed, they primarily propagate "freely" in the confining potentials for significant fractions of time, thus being rather long-lived; this is particularly true when the number of defects is not too large and they are spread over a large volume, as is the case for not-very-fast quenches. Importantly—and rather intuitively—such Kibble–Zurek scaling was not however seen for very fast quenches ($\tau_Q \sim O(\hat{t})$): this arises when the maximum number of defects that can be accommodated in the system volume (or the maximum number that can be experimentally, or numerically, detected) has been reached in a given geometry, thus giving rise to a plateau in the defect number for small τ_Q; this was clearly observed experimentally (at late times) (Donadello et al., 2016), and found to be consistent both with a simple model and with numerical simulations (Liu et al., 2018). We also note that the decay of fluctuations was found to obey a universal power law, with a distinct exponent to that corresponding to the growth of condensation (Liu et al., 2018; Wolswijk et al., 2022).

The quenching of defect number for very rapid quenches (i.e., the deviation from the Kibble–Zurek scaling law $n_{\text{defect}} \sim (\tau_Q)^{-\alpha}$) was also observed in strongly interacting fermionic superfluids (Ko et al., 2019) and in more recent bosonic experiments in an oblate geometry (Goo et al., 2021, 2022; Kim et al., 2022). The latter series of experiments also reported observational evidence for universal coarsening dynamics during the early stages of defect formation. Moreover, they were able to observe spatial variations in the generated defect number: both these features are in qualitative agreement with the presented numerical simulations (Liu et al., 2018).

All above features indicate that—rather unsurprisingly—there is more to driven phase transition crossing than the simple (but still very elegant and powerful) adiabatic-impulsive-adiabatic Kibble–Zurek model of Fig. 6. Below I address more systematic extensions of such a model, as highly relevant in light of such recent experimental developments.

Beyond homogeneous Kibble–Zurek considerations

The preceding discussion has highlighted two limitations of the adiabatic-impulsive-adiabatic Kibble–Zurek scenario of Fig. 6 which I address here.

The first one, concerns the "freezing" of the correlation length ξ during the entire evolution $t \in [-\hat{t},\ \hat{t}\,]$, to a constant (time-independent) value corresponding to its instantaneous value at the time $-\hat{t}$ when symmetry-breaking occurs; in other words $\xi \to \hat{\xi} = \xi(\epsilon(-\hat{t}\,))$, which would imply a constant size of domains during $[-\hat{t},\ \hat{t}\,]$, which is somewhat counter-intuitive. In fact, during such a temporal period, causality implies the existence of a characteristic velocity for the growth of correlations which—in this context—can be defined as (Dziarmaga et al., 1999; Zurek, 2009; Sadhukhan et al., 2020)

$$\hat{v} = \frac{\hat{\xi}}{\hat{t}}. \tag{25}$$

Given that the typical locally coherent regions grow with such a velocity even during $t \in [-\hat{t},\ \hat{t}]$, the emerging effective size of domains at $\hat{t}$ is in fact larger than previously suggested, with $\xi(+\hat{t})$ typically a few times its corresponding value at $-\hat{t}$ (Sadhukhan et al., 2020); a schematic of such enhanced picture is shown in Fig. 10. Although such considerations evidently decrease the total number of spontaneously generated defects, rather remarkably they do not actually invalidate the previous arguments in terms of the existence of *scalings* of the defect number with quench timescale (Eq. 24), provided of course that the system inhomogeneity determining the shape of the region of increasing density is appropriately accounted for in the exponent α.

In this context, it should be noted that the "cartoon" Kibble–Zurek scenario discussed in Section "The Kibble–Zurek scaling law" (Fig. 6) was formulated for a homogeneous system and thus assumed that the system reacts, in a statistical sense, in the same way irrespective of which part of the system one looks at. However, as clearly visible from Fig. 7—and commented upon earlier—the density is highest at the center of a harmonically confined gas, implying that coherence grows from the trap center radially outwards. As a result, both the critical temperature of the system and hence the distance to criticality ϵ become position-dependent (Zurek, 2009; del Campo et al., 2011, 2013; del Campo and Zurek, 2014), that is, $T_c \to T_c(\mathbf{r})$ and $\epsilon(t) \to \epsilon(\mathbf{r}, t)$. A natural question then arises, as to the extent to which the previous "cartoon" picture holds under inhomogeneous trapping, and how to appropriately generalize this.

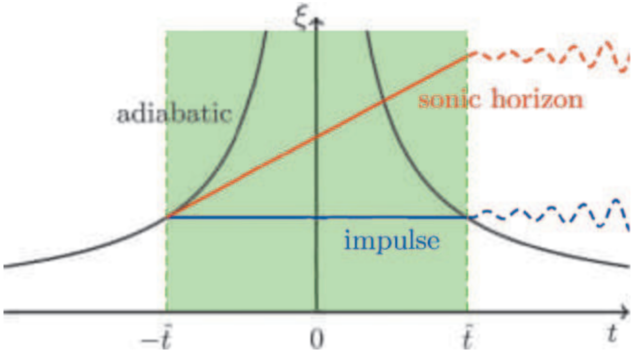

Fig. 10 Extended view of the Kibble–Zurek mechanism explicitly accounting for a sonic horizon propagation with a critical speed of $\hat{\xi}/\hat{t}$. Unlike the "cartoon" regime of impulsive dynamics for $t \in [-\hat{t},\ \hat{t}]$ shown in Fig. 6, during which the correlation length is assumed to remain frozen to its value at $-\hat{t}$, this improved picture allows the "sonic cone" to grow during such time window by a constant rate set by the instantaneous slope of $\xi(-\hat{t})/\hat{t}$. As a result, the typical radius of the region over which broken symmetry emerges grows from $\hat{\xi}$ to few $\hat{\xi}$. Reprinted with permission from Sadhukhan D, Sinha A, Francuz A, Stefaniak J, Rams MM, Dziarmaga J, and Zurek WH (2020) Sonic horizons and causality in phase transition dynamics. Physical Review B 101: 144429. https://doi.org/10.1103/PhysRevB.101.144429. Copyright (2020) by the American Physical Society.

In the context of the homogeneous Gross–Pitaevskii equation (with repulsive interactions $g > 0$), symmetry-breaking is induced simultaneously across the entire system when the chemical potential transitions from negative values (corresponding to a purely thermal cloud) to positive values. Due to the presence of the trap, one can instead define an effective spatially dependent chemical potential $\mu(\mathbf{r}, t) = (\mu(t) - V(\mathbf{r}))$; thus outlining at any given time the region with $\mu(\mathbf{r}, t) > 0$ where symmetry-breaking takes place. Such region grows radially outwards from the trap center (here in an elliptical manner), thus defining a phase transition front which propagates in the system with a characteristic speed

$$v_F(\mathbf{r}) = \frac{T_c(0)}{\tau_Q}\left(\frac{dT_c(\mathbf{r})}{d\mathbf{r}}\right). \tag{26}$$

As such, the simultaneous emergence of symmetry breaking in a homogeneous system can be described in terms of an infinite phase transition front velocity v_F, and this is also (locally) the case at the center of a harmonic trap where local evolution mimics that of a homogeneous system. The extent to which the emerging symmetry-breaking features in the phase transition of a system have a global or a local character thus depends on the competition between the characteristic velocity $\hat{v}$ for the growth of correlations set by causality and the velocity v_F for the growth of the critical front as determined by the system geometry, thus also accounting for the shape of the growing volume of the coherent density front. The generalization of the Kibble–Zurek effect, which accounts for such spatial variations and local features, is known as the inhomogeneous Kibble–Zurek mechanism, and is extensively discussed in Zurek (2009), del Campo et al. (2011), del Campo et al. (2013), del Campo and Zurek (2014), Sadhukhan et al. (2020), and Dziarmaga et al. (1999).

As a result, the previously discussed "cartoon" picture of Section "The Kibble–Zurek scaling law," known as the *homogeneous* Kibble–Zurek picture remains *qualitatively* valid as long as (and within the regions where)

$$v_F > \hat{v}, \tag{27}$$

that is, the growth of the critical front happens on a faster rate than such causality-induced coherence growth associated with the sonic horizon. In such a regime, the phase of each newly formed domain is chosen locally. As explained above, this is always the case in the center of the harmonic trap, and in a region near the propagating front (due to critical slowing down) (del Campo et al., 2013). As a result, defects can in general only form spontaneously over a restricted volume in an inhomogeneous system, thus leading to a reduced number of emerging defects in comparison to the homogeneous predictions. In the opposite limit of $v_F < \hat{v}$, the growing condensate can rapidly communicate its choice of phase to the neighboring domains, and so no further defect formation can occur. For an evolving system to enter a regime where it can probe its true inhomogeneous nature, the sonic horizon should be growing faster than the evolution of the critical front.

This, in turn, places constraints on the values of τ_Q required in a given system for a quench to allow the inhomogeneous nature of the phase transition to be fully probed; applying such simple arguments to the above elongated 3D experiment suggested the need for significantly slower quenches, thus also requiring longer evolution times and enhanced system stability. Although such a regime was not reached in the experiments of Donadello et al. (2016), it should nonetheless be noted that (i) the corresponding numerical simulations discussed in Section "Analyzing Kibble–Zurek in an elongated ultracold atomic system" clearly demonstrated the spatial dependence of spontaneous defect generation over a restricted volume, and that (ii) both observed and numerically computed scalings of the defect density with τ_Q were found to be consistent with predictions based on critical exponents for a harmonic trap (Donadello et al., 2016; Liu et al., 2018) (leading to an amended power $\alpha = (d - \mathcal{D})(1 + 2\nu)/(1 + \nu z)$ (del Campo et al., 2011; del Campo and Zurek, 2014) when such geometrical features of the growth were taken into account).

Furthermore, it has been noted that a quasi-2D geometry may be a more favorable setting for observing such spatial signatures of the inhomogeneous nature of the dynamical phase transition. This was indeed shown in very recent experiments in a quasi-2D geometry; specifically, following experiments highlighting the anticipated importance of coarsening dynamics during the early stages of spontaneous defect formation (Goo et al., 2021, 2022) observations of the spatial distribution of defects in such a geometry found (after allowing the system to relax further and expand) a local suppression of spontaneous defect generation with τ_Q, which was more pronounced in the outer region (Kim et al., 2022). In other words, the local value of the power law exponent $\alpha(r)$ dictating the defect number through the power law $n_{\text{defect}} \sim \tau_Q^{-\alpha(r)}$ was inferred after expansion to increase locally as one moves away from the trap center. While such an observation is consistent with the interplay of causality and inhomogeneity, they consistently found higher exponents than might be anticipated. Although various factors could be at play here, associated with the fact that observations were made after relaxation and expansion (and so not at $\hat{t}$), the ongoing defect dynamics and coarsening, and intricate details of the trapping potential; this does also pose interesting questions meriting further investigation regarding the applicability of the inhomogeneous Kibble–Zurek effect.

Irrespective of the precise details just discussed of corrections to the basic Kibble–Zurek scheme, which allow for evolution of the characteristic lengthscale and the interplay between inhomogeneity and causality, as the system exits the critical region in the $\epsilon > 0$ side of the phase transition at $t = +\hat{t}$, it will be left in a rather nonequilibrium state (the faster the quench, the more nonequilibrium the state is likely to be—see Fig. 9); such a nonequilibrium state features a random mosaic of domains of of different, near-constant, phase, separated by defects of variable length, orientation, and curvature, in a way which accounts for the differences in phase between the establishing micro-domains. The relaxation of such a state through the gradual decay of the number/length of defects will ultimately lead to the final coherent state for the given system parameters. Here, one can distinguish two cases: Either one continues driving the system to the final desired equilibrium and studies its relaxation in an "open" (driven) environment or one leaves the system in such a highly chaotic/turbulent state and observes its dynamical evolution toward relaxation in a "closed" manner: the fundamental dynamics governing these two cases are different. Nonetheless, in both cases, universal laws can (and do, in general) emerge in certain temporal (and momentum) windows. Below I discuss the general concept of self-ordering by means of a scaling hypothesis, paying attention to nonequilibrium features, particularly in terms of universal late-time dynamics and other more general nonequilibrium features facilitating a bidirectional dynamic scaling, both of which can leave a significant imprint in the decay of superfluid turbulence.

Although very distinct dynamical regimes with different scaling laws, the dynamically evolving $\hat{\xi}$ discussed above does bear some notional analogy to the dynamically growing lengthscale $L_c(t)$ emerging in the scaling regime discussed below.

Universality during phase-ordering dynamics

So far, I have discussed the role of finite-duration quenches in a system, focusing on an incoherent to coherent thermal phase transition. We have discussed a broad dynamical range from quasi-adiabatic to near-instantaneous transitions, and explained how universal Kibble–Zurek dynamics emerges in the critical region provided the quench is not too fast. As discussed, the relaxation process in the system is governed by the decay of defects giving rise to growing regions of constant phase, with the quasi-condensate giving way to a macroscopic condensate (Witkowska et al., 2011; Liu et al., 2018), a process known as phase-ordering.

In order to present the key features of such process in its most pure form, it is convenient to consider the idealized limit of instantaneous quenches. Moreover, based on the above findings on the role of inhomogeneous trapping, and in order to suppress transversal (e.g., Kelvin-wave-like) excitations on the defects, I initially restrict the discussion to two-dimensional homogeneous systems, before returning to more general nonequilibrium settings.

Scaling hypothesis and late-time coarsening

The dynamics through which the system expels all defects and orders its phase is known as phase-ordering kinetics, and has a long history. Here I do not attempt to give a full account—referring the reader to excellent reviews (Bray, 1994; Rutenberg and Bray, 1995b, a)—but rather to discuss its features in the specific context of quenched quantum gases.

Naturally, even when quenched instantaneously, the system requires some time to order itself: as argued before, defects—which emerge at the interfaces across regions of different phases—gradually disappear, thus allowing adjacent regions of particular (randomly chosen) phases to merge, leading to the temporal growth of the typical domain size. A key point to note here is that this is also a scaling phenomenon. From a statistical point of view, the distribution of such domains—each with a constant phase, yet no phase coherence between them—looks at late times remarkably similar to the one at earlier times, with the growth of the typical domain size fully accommodated through a (simple) global change of scale.

We recall at this stage that a dynamical scaling hypothesis was previously considered in the context of the Kibble–Zurek scenario [Eq. (23), Section "The Kibble–Zurek scaling law"]. The scaling function was generally argued to change in time both in terms of its shape (through its explicit dependence on $t/\hat{t}$) and its spatial extent. In stark contrast to this, I note here that during the late-time self-similar dynamics and in the scaling limit $r \gg \xi$, the shape of the correlation function remains unchanged (i.e., there is no explicit dependence on time), with its spatial range changing in time only through a dynamically growing domain size $L_c(t)$, that is, through a dependence of the form $r/L_c(t)$; such an increase in the characteristic length scale is consistent with the number of independent domains and defect number decreasing.

The existence of a single (dynamical) dominant lengthscale in the system allows us to formulate the correlation function in the form (Bray, 1994)

$$C(\mathbf{r}, t) \sim F\left(\frac{r}{L_c(t)}\right) \tag{28}$$

with the corresponding momentum distributions taking the form

$$n(k, t) \sim [L_c(t)]^d G(kL_c(t)). \tag{29}$$

Here, F is an (unspecified) universal function and G is its Fourier transform, with temporal variation fully accounted for by the change in scale.

To calculate how such a characteristic lengthscale varies for a nonconserved field (i.e., in the presence of external dissipation), one can utilize energetic considerations, taking into account the system symmetries and the fact that the defects are not isolated (thus introducing a lengthscale beyond which a defect becomes screened by other defects). By estimating a critical velocity for the growth of such domains $u = dL_c(t)/dt$ and integrating, one can obtain the functional form of $L_c(t)$, as explicitly discussed in Bray (1994). This is generally found to exhibit a power law scaling of the form $L_c(t) \sim t^{\beta}$, with the critical exponent β related to the dynamical critical exponent z through $\beta = 1/z$. We note that in the special case of point vortices in a purely 2D geometry the presence of external dissipation (e.g., through coupling the system to an external bath) leads to well-known logarithmic corrections such that $L_c(t) \sim (t/\log(t))^{1/z}$.

The topic of phase-ordering has been extensively discussed in the literature (see, e.g., Yurke et al., 1993; Rutenberg and Bray, 1995a; Damle et al., 1996; Jelić and Cugliandolo, 2011; Nam et al., 2012; Karl and Gasenzer, 2017; Groszek et al., 2021). To make this point clear, I briefly discuss here recent extended numerical simulations (Groszek et al., 2021) in a 2D box with periodic boundary conditions in the context of both the conservative and the dissipative Gross–Pitaevskii equations, respectively via Eqs. (14) and (15).

In both cases, phase-ordering during the postquench evolution takes place through the annihilation of vortex-antivortex pairs (*white/black squares* in temporal evolution snapshots shown in Fig. 11A–C). Spatial correlations at a general time t are probed in terms of the equilibrium correlation function $g_{eq}^{(1)}(r,t)$—the latter obtained after very lengthy numerical propagation—through the generic relation

$$\frac{g^{(1)}(\mathbf{r},t)}{g_{eq}^{(1)}(\mathbf{r},t)} = F\left(\frac{\mathbf{r}}{L_c(t)}\right). \tag{30}$$

Correlation functions in terms of the scaled time-dependent variable $\mathbf{r}/L_c(t)$ are found to collapse perfectly onto a single function (Fig. 11D) within a certain time window, which thus identifies both the evolutionary stage when the scaling hypothesis (Eq. 28) holds and the manner in which $L_c(t)$ grows, directly confirming an evolution of the form $L_c(t) \sim t^{\beta}$. Correspondingly, directly counting the decay in the vortex number, one confirms a scaling for the vortex density of the form $n_V \sim 1/L_c^2 \sim t^{-2\beta}$. Identifying $\beta = 1/z$ allows the extraction of the dynamical critical exponent z through these fits during the scaling interval. The behavior shown in Fig. 11 is generic, broadly applicable to both the conservative and the dissipative Gross–Pitaevskii equations.

Nonetheless, a detailed numerical comparison of the predictions between the conserved and dissipative regimes leads to slightly different behavior and modifications in the precise value of the critical exponent. This can be traced back to the fundamental question of "isolated" (conservative) vs. 'open' (dissipative) quantum systems (Hohenberg and Halperin, 1977); in the purely dissipative limit (i.e., Eq. (15) without the 1 in $(1 - i\gamma)$), the existence of vortices leads to logarithmic corrections to the system dynamics, such that $L_c(t) \sim (t/\log(t))^{1/z}$ with $z = 2$ exactly, and such behavior is explicitly reproduced in the simulations [see also subsequent discussion in the context of instantaneously quenched driven-dissipative exciton-polariton condensate systems (Section "Driven-dissipative condensation in exciton-polariton systems")]. However, in the purely conservative limit (and without

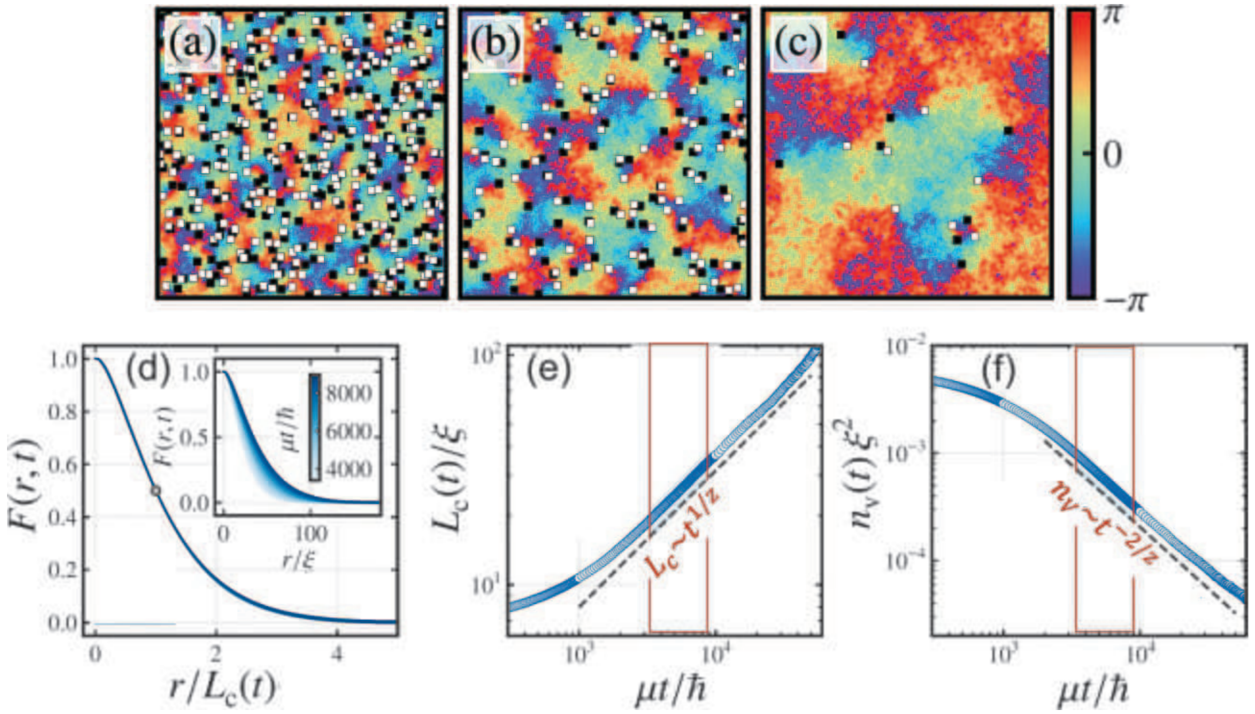

Fig. 11 Phase-ordering kinetics of a 2D homogeneous Bose gas following an instantaneous quench across the BKT phase transition: (A)–(C) Evolutionary snapshots of the phase, showing the reduction in the number of vortices/antivortices (*white/black squares* respectively). (D) Self-similarity through the collapse (main plot) of the spatial correlation functions evaluated at different times t within the "collapse window," scaled to $\hbar/\mu$ (inset) onto a universal scaling function F in terms of the scaled variable $r/L_c(t)$ according to Eq. (28). (E) Postquench growth of the characteristic lengthscale $L_c(t)$, clearly highlighting the time window when all self-similar correlation functions perfectly collapse onto one another. (F) Corresponding decreasing evolution of the vortex number density n_V. Although both (E) and (F) plot the variation across the entire temporal domain, note that the very late-time evolution is somewhat sensitive to numerical boundary effects (as can be seen from the slight deviation of both behaviors at very late times). Adapted with permission from Groszek AJ, Comaron P, Proukakis NP, and Billam TP (2021) Crossover in the dynamical critical exponent of a quenched two-dimensional Bose gas. Physical Review Research 3: 013212. https://doi.org/10.1103/PhysRevResearch. (3.013212). Copyright (2021) by the American Physical Society.

including such logarithmic corrections), the value of z was found to lie approximately 15–20% below the $z = 2$ value (Groszek et al., 2021). While a possible explanation for such a change in z is likely to arise from a power-law vortex mobility due to vortex-sound interactions, a detailed understanding of such subtleties (as well as its extension to inhomogeneous systems) is still lacking.

Evolution around nonthermal fixed points

At this point, the reader is briefly reminded (in rather basic terms) of the notion of "fixed points" in renormalization group theory—for more details the reader is referred to Nishimori and Ortiz (2011), Binney et al. (1992), and Bruce and Wallace (1992). In such a language, one typically scales out microscopic details in favor of global features of macroscopic observables; as such, one deals with a parameter space of available many-body configurations of the system expressed in terms of a limiting set of relevant "coupling" parameters: long-time evolution between possible many-body system configurations is then modeled through flowing trajectories within such space, in a manner governed by the system Hamiltonian. Such a picture can be characterized by a small number of fixed points, which define the nature of the system evolution for different configurations. Specifically, flow around (toward/away from) such points qualitatively indicates the system evolution in parameter space. Naively, one can think of a fixed point as arising when a change of the scaling parameter, for example, $L_c(t)$, leaves the correlation function unchanged (Binney et al., 1992). For example, for a system undergoing a single-phase transition, one can directly identify certain fixed points: in the common case of a thermal phase transition, one identifies a low-temperature fixed point (denoting the system equilibrium at $T = 0$, e.g., in the fully coherent state, or more generally in the $\epsilon \to +\infty$ limit) and a high-temperature fixed point (denoting the system in the $T \to \infty$, or $\epsilon \to -\infty$ limit); ultimately the system flows to either of those, with all equilibria below/above the critical point formally mapping onto the former (condensed), or latter (thermal) by an appropriate rescaling of relevant parameters. Such trajectories are separated by a critical line/surface, which contains a "mixed" critical fixed point, such that it is attractive along all the directions within the critical surface, and repulsive along those pointing away from the critical surface (Binney et al., 1992). Note that exactly at the critical point, the system exhibits fluctuations at all lengthscales, making it impossible to eliminate (as argued above) short-scale behavior through a sequence of transformations, thus implying that a critical point is a fixed point. More generally, a fixed point is characterized by a pure scaling form and a coupling which no longer changes under a rescaling. The previously discussed phase-ordering dynamics is a simple example of a scaling phenomenon controlled by a (strong coupling) fixed point (Bray, 1994).

In general, various different classes of fixed points may exist. In particular, some attention is currently being devoted to the context of so-called 'nonthermal' fixed points, which arise as a fixed point in a typical far-from-equilibrium scenario: as such, they can be thought of as nonequilibrium configurations exhibiting scaling in both space and time, in terms of a limited number of properties. These were originally introduced by Berges and coworkers in the context of reheating after early-universe inflation (Berges et al., 2008; Berges and Hoffmeister, 2009; Piñeiro Orioli et al., 2015; Berges, 2016), and have been increasingly investigated across different physical systems, including heavy-ion collisions (Berges et al., 2015, 2021) and quantum gases (Nowak et al., 2011, 2012, 2014; Karl and Gasenzer, 2017; Chantesana et al., 2019; Schmied et al., 2019), also finding applications in a range of experiments (Prüfer et al., 2018; Erne et al., 2018; Glidden et al., 2021; García-Orozco et al., 2022; Madeira and Bagnato, 2022). The emergence of such points builds upon the concepts of self-similarity and critical behavior, generalizing them to far from equilibrium dynamics. Under appropriate conditions, a system may spend a significant amount of time around such a nonthermal fixed point. The discussion below is largely based on recent reviews (Chantesana et al., 2019; Schmied et al., 2019; Madeira and Bagnato, 2022).

In a nutshell, the dynamics of a system in the vicinity of a nonthermal fixed point acquires a generalized evolution according to

$$n(k,t) = \left(\frac{t}{t_0}\right)^{\alpha} \, n\left(\left(\frac{t}{t_0}\right)^{\beta} k, \quad t_0\right), \tag{31}$$

where α and β are two scaling parameters which are, in general, distinct and which, combined, identify the universality class of the system. The relation between α and β is in fact set by the relevant conservation laws of the system. Essentially, these define—within a broad momentum range—how particles are redistributed in the self-similar regimes, and relate the scaling exponents α and β. In the simplest case of particle number conservation (and for a particle with quadratic dispersion relation), this leads to $\alpha = \beta d$ (in the long-wavelength, or infrared, regime), where d is the system dimensionality. Further noting that the characteristic lengthscale $L_c(t) \approx t^{\beta}$, and $\beta = 1/z$ practically reduces such expression to that of Eq. (29) governing the self-similar phase-ordering kinetics previously discussed. As such the preceding discussion of Section "Scaling hypothesis and late-time coarsening" can be seen as a special case of nonthermal fixed points under total particle number conservation.

However, the concept of nonthermal fixed points is more general. In particular, I note that the scaling function (Eq. 31) can behave differently in different momentum limits, namely, the previously discussed "inverse" particle transfer toward lower momenta arises from the conservation of particle number in the infrared (low-momentum) limit. Scalings due to energy conservation instead affect the ultraviolet (high-momentum) limit, leading to energy transport toward higher momenta and $\alpha = (d + z)\beta$. As a result, evolution around a nonthermal fixed point leads to a bidirectional flow (see Fig. 12).

As a highly nonequilibrium feature, it is not surprising that the potential emergence of a nonthermal fixed point following a thermal quench would require a rather specific engineered nonequilibrium set of initial conditions. In this context, I note the seminal numerical work of Berloff and Svistunov (2002). They considered a quench in a 3D box, starting with a strongly nonequilibrium initial condition (Svistunov, 1991; Kagan et al., 1992; Kagan and Svistunov, 1994, 1997) $\Phi(\mathbf{r}, t = 0) = \sum_k a_k e^{i\mathbf{k}\cdot\mathbf{r}}$, for which the magnitudes of the complex amplitude a_k were obtained from the self-similar solution of the (wave/semiclassical)

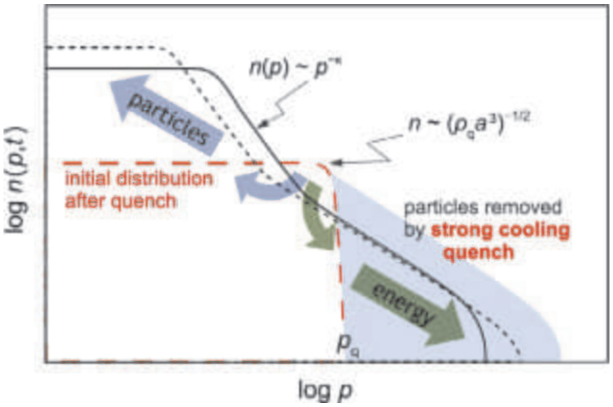
$n(p) \sim p^{-\kappa}$
$n \sim (\rho_Q a^3)^{-1/2}$
particles
initial distribution after quench
particles removed by strong cooling quench
energy
p_Q
$\log n(p,t)$
$\log p$

Fig. 12 Schematic of the bidirectional flow exhibited by the spectrum $n(k, t)$ vs. k [shown here in terms of $p = \hbar k$] around a nonthermal fixed point: A highly nonequilibrium initial distribution with equal population across all modes up to a cutoff, and random phases—shown here by the *dashed red lines*—evolves in a manner such that particles flow in an inverse manner toward lower k (through conservation of particle number: $\alpha, \beta > 0$), while energy flows toward higher k ($\alpha, \beta < 0$), carried by few particles in a manner which conserves total system energy. Reprinted with permission from Chantesana I, Orioli AP, and Gasenzer T (2019) Kinetic theory of nonthermal fixed points in a Bose gas. Physical Review A 99(4): 043620. https://doi.org/10.1103/PhysRevA.99.043620. Copyright (2019) by the American Physical Society

Boltzmann equation describing the system dynamics sufficiently before the critical phase transition region, and their phases were uniformly distributed between 0 and 2π. Evolving by means of the classical field Eq. (14), they observed, as would be expected, particle build-up toward lower momenta, with most particles restricted to modes below a certain cutoff. This is a direct indication of the gradual build-up of a quasicondensate, arising from the macroscopic occupation of, and competition between, numerous low-momentum modes. Significantly, however, filtering out higher momentum modes revealed a tangle of vortices, a characteristic of a "strongly" turbulent state.

As the governing equation (Eq. 14) is conservative, this tangle was found to gradually decay, following the relaxation process of superfluid turbulence in a nondriven system through the generation of sound waves and shrinking/annihilation of defects via a typical energy cascade. Similar features, revealing also information about the vortex structure and its decay products, were found when doing a limited time averaging, thus connecting to the previous discussion on the application of short-time averaging during evolutionary dynamics (Section "Penrose–Onsager condensation vs. quasi-condensation"). We also note here that probing the state of an initially nonequilibrium system after very long classical field evolution in a separate numerical work revealed the existence of vortex tangles, with the total vortex linelength increasing significantly as the system energy, and thus temperature, was increased (Davis et al., 2002). Considering a similar scenario, Nowak et al. (2014) studied the system evolution following a sudden thermal quench by removing high-momentum particles from the distribution. When a relatively small amount of energy was removed through the quench, they also found the system to evolve toward a coherent condensate, with clear evidence of a tangle of vortices after filtering short-wavelength fluctuations. However, when a stronger quench was performed by instantaneously removing all the particles above some momentum cutoff value, they found a long-standing strong wave turbulence inverse cascade toward lower energies, with a rather distinct power law power spectrum $n(k) \sim k^{-5}$; such behavior, which is consistent with so-called "Porod" high-momentum tails $n(k) \sim 1/k^{d+2}$ (Schmied et al., 2019; Bray, 1994) corresponds to the case of randomly distributed vortices at momenta exceeding the inverse lengthscale corresponding to the distance between defects, a feature that is a direct consequence of the velocity field ($\mathbf{v} \sim (1/r)\,\hat{\boldsymbol{\phi}}$) around a vortex line. Nonetheless, excitations in the high-momentum part of the spectrum still revealed $n(k) \sim k^{-2}$, leading to a bimodal spectrum. Importantly, the above-discussed features were now found to become observable without the need to filter out short-wavelength fluctuations. Ultimately, the overall momentum distribution takes the form $n(k) \sim k^{-2}$, leading to the relaxation of the system—but this now happens on a much longer timescale. This was considered as evidence of the system spending significant time around a nonthermal fixed point.

This example clearly shows the distinct features that a thermal phase transition can exhibit depending on the nature and details of the strength of the cooling quench, that is, in this case on the initial nonequilibrium conditions for the classical field evolution. Further evidence of the emergence and decay of the arising vortex tangle and properties of the order parameter were also discussed in Kobayashi and Cugliandolo (2016b), Kobayashi and Cugliandolo (2016a), and Stagg et al. (2016).

Dynamical properties of evolution consistent with Eq. (31) were recently observed in experiments in an isolated quench-cooled atomic gas (Glidden et al., 2021). By removing a significant fraction of the atoms and energy of a system initially just above the critical temperature and doing this process with interactions switched off, the experiment was able to generate a highly nonequilibrium state, and observe its relaxational dynamics, thus verifying the expected distinct scaling relations across the ultraviolet and infrared limits, corresponding to different conservation laws (Glidden et al., 2021) (see Fig. 13). Moreover, this experiment was also able to confirm the emergence of a quasicondensate in the early evolution stages, with the coherence across the system gradually growing to span the whole system, in a manner consistent with the system equilibrium for the given atom number and total energy.

For completeness, I note here that manifestations of evolution consistent with Eq. (31) have also been reported (prior to the above experiment) in a quasi-one-dimensional spin-1 BEC (Prüfer et al., 2018), and a single-component BEC (Erne et al., 2018) while also bearing close analogies to the inverse cascade evolutions observed in 2D experiments (Johnstone et al., 2019; Gauthier

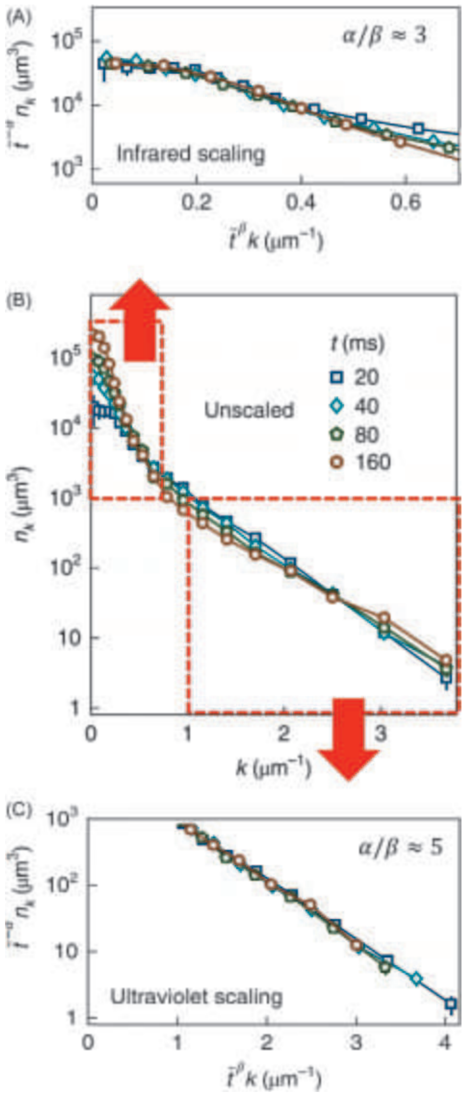

Fig. 13 Experimental demonstration of bidirectional flow according to Eq. (31) in an isolated $d = 3$ ultracold atomic gas in a box quenched from just above the critical temperature to a highly nonequilibrium situation by removing significant fractions of atoms and energy such that the system ultimately relaxes to a state with an $\approx 40\%$ BEC fraction: The unscaled momentum distribution shown in (B) at different evolution times following the nonequilibrium quench is scaled differently in the limiting (A) infrared case (for which one finds α, $\beta > 0$, with $\alpha/\beta \approx 3$, consistent with the condition $\alpha/\beta = d$ for particle-conserving transport), and (C) ultraviolet case (for which one finds $\alpha/\beta \approx 5$ with α, $\beta < 0$ consistent with the prediction $\alpha/\beta = d + 2$ for energy-conserving transport). Adapted with permission from Glidden JAP, Eigen C, Dogra LH, Hilker TA, Smith RP, and Hadzibabic Z (2021) Bidirectional dynamic scaling in an isolated Bose gas far from equilibrium. Nature Physics 17: 457–461. Copyright (2021) by the Nature Publishing Group

et al., 2019). We refer the reader to these works and excellent recent reviews on nonthermal fixed points—which also address in some detail the relation of nonthermal fixed points to weak-wave turbulence and strong turbulence (Schmied et al., 2019; Chantesana et al., 2019)—and their experimental study in ultracold quantum matter (Madeira and Bagnato, 2022).

Relation of quenched turbulence dynamics to "controlled" turbulence experiments

In this chapter, I have focused on the emergence of "turbulent" features through the instantaneous (Section "Universality during phase-ordering dynamics") or driven (Section "Universality during phase transition crossing: The Kibble–Zurek scaling law") cooling across a thermal phase transition, starting from an incoherent state, that is, quenching from $\epsilon < 0$ to $\epsilon > 0$, and studying the relaxation of the emerging nonequilibrium states generated, which typically include some type of vortex tangle. As well known (Tsatsos et al., 2016; Barenghi et al., 2014; Tsubota et al., 2017), an open, dynamically driven, system can reach a steady state under continuous driving, subject to a dissipation mechanism at a different scale from that where energy is being injected, thus acquiring a momentum spectrum exhibiting universal features in a certain "inertial" range. On the other hand, a closed turbulent nonequilibrium system will gradually see its vorticity decay in a manner which can also display universal scaling laws; for completeness, I briefly consider both these cases below.

First, if the system is left isolated shortly after its quench into such a turbulent state, one could also compare its subsequent relaxation evolution to studies characterizing the decay of superfluid turbulence. The topic of superfluid turbulence has a rich history (Barenghi et al., 2001; Vinen and Niemela, 2002), with an extensive body of literature on liquid helium supplemented by recent work on ultracold quantum gases which gives access to different lengthscales (Barenghi et al., 2014; Tsatsos et al., 2016; Tsubota et al., 2017). The relaxation dynamics can be different, depending on whether the system is primarily a superfluid, or has a significant (potentially dominant) thermal fraction.

Current studies, based on experimental observations (Walmsley and Golov, 2008; Bradley et al., 2006) and detailed numerical simulations (Baggaley et al., 2012; Barenghi et al., 2016), make a distinction between two types of superfluid turbulence at relatively low temperatures when a well-formed condensate exists (see also recent reviews (Barenghi et al., 2014; Tsatsos et al., 2016)). The most common form of turbulence discussed is that of Kolmogorov, or “quasi-classical” turbulence, which can exhibit (under continuous injection of energy) a cascade of kinetic energy from large to small eddies, thus giving rise to the well-known classical Kolmogorov spectrum $E_k \sim k^{-5/3}$ for $k \ll 1/l$ (where l is the typical intervortex spacing); this form of turbulence—which is thus a property of the motions at lengthscales larger than the intervortex spacing—is now understood to be associated with the existence of turbulent bundles of vortices. Once the injection of energy is discontinued, this leads to a total vortex linelength decay (characterizing the intensity of turbulence), which scales as $L_V \sim t^{-3/2}$.

On the other hand, some systems can exhibit a (potentially transient) turbulent state, somewhat similar to random flow, which is dominated by the presence of individual randomly oriented tangled vortices (with most of the energy contained in the intermediate scales): in such a regime, known as “ultraquantum,” or “Vinen” turbulence, the vortex linelength decays instead according to $L_V \sim t^{-1}$.

Early controlled low-temperature turbulence experiments with ultracold atoms focused on the generation of tangled vorticity through either shaking across two distinct axes (Henn et al., 2009) or intense periodic driving (Navon et al., 2016) in both cases starting from a $T \approx 0$ pure condensate. As such dynamics are generated by initiating the dynamical quenching from the coherent side, it is clearly a very distinct excitation process to the thermal quenches starting from an incoherent system discussed in this chapter. Among other findings, this has led to the observation of the expected power-law spectrum $n(k) \sim k^{-\gamma}$ in a box geometry, consistent with (Kolmogorov-Zakharov) weak-wave turbulence of compressible superfluids (Navon et al., 2016); further characterization of the flux of such a cascade through dissipation, has enabled the probing of the propagation of the cascade front in momentum space at both short- and long-time evolution (Navon et al., 2019); very recent experiments from the same group have also facilitated a direct measurement of the equation of state in experiments. The concept or reversibility was also probed in such quenches. Experiments in a box revealed that when such a turbulent system was left undriven for a significant period, it would reform into a near-pure condensate consistent with the initial state, that is, the process was found to be fully reversible (Navon et al., 2016).

Nonetheless, I also note here a recent related experiment (García-Orozco et al., 2022) studying the evolution of $n(k, t)$ from a nonequilibrium initial state generated by the application of a misaligned sinusoidally varying magnetic field on an initial highly coherent harmonically confined BEC. The excitation was performed in such a manner so as to perturb the system through dynamical rotations and distortions. Rather interestingly, such an experiment observed a behavior broadly consistent with the scaling relation of Eq. (31), but in this case both α and β exponents were found to be negative (beyond the expected $\alpha, \beta < 0$ values in the ultraviolet regime) also in the infrared regime: this should be contrasted to the previously discussed dynamics observed following a strong nonequilibrium quench in a box-like geometry (Glidden et al., 2021) for which in the infrared regime both $\alpha, \beta > 0$. For completeness, I mention also here related studies of such an inverse excitation process starting from a coherent equilibrium BEC and leading to a strongly nonequilibrium symmetric state, proceeding through a sequence of states with spontaneously arising topological defects: while this effect has been loosely named an “inverse Kibble–Zurek” scenario (Yukalov et al., 2015)—in the sense of dynamics in the opposite direction to the established (and previously discussed) Kibble–Zurek mechanism—this is simply a qualitative analogy, as no corresponding detailed scaling laws have been obtained.

Although a detailed understanding of all above dynamical issues is still an open matter, the ongoing experiments evidence the important role that an inhomogeneous geometry can play, and the richness of the dynamical features it can generate, which may have a nonnegligible impact on the types of turbulence generated and their subsequent relaxation. Moreover, differences in the dynamical properties of turbulent states generated starting from a well-formed superfluid, or an incoherent thermal cloud also highlight the important role that the thermal cloud can play on such dynamics.

For a more in-depth discussion of the current understanding of the relation between nonthermal fixed points, weak-wave turbulence and strong turbulence, and the relevance of such fixed points to other dynamical aspects, such as prethermalization (Berges et al., 2004; Gring et al., 2012), the reader is referred to the review articles (Schmied et al., 2019; Chantesana et al., 2019).

Selected further considerations

Beyond continuous single-component atomic gases

The properties of ultracold atomic gases can be controlled experimentally by a range of different tunable parameters. In this chapter, I have focused on the role of temperature in inducing a transition across criticality between two single-component thermalized states with very different characteristic properties. Relevant comments have also been made regarding the role of geometry and dimensionality in single atomic species confined in continuous potentials, such as harmonic traps and box-like potentials.

The exquisite control offered in experiments with ultracold atoms has opened up the way for a plethora of other types of quenches—with, no doubt, new physics yet to be explored in them, although significant progress toward various probes of universality have already been performed. While this section cannot do justice to such exciting developments, for completeness I note in passing a few such areas of relevance below.

A transition across criticality can also be engineered at fixed temperature by changing the interaction energy, which can also control the type of emerging equilibrium phase transition. In this vein, Smith et al. (2011) demonstrated the smooth crossover from an interaction-driven BKT transition to a BEC transition in the limit of vanishing interactions. Such issues are further discussed in Smith (2017). For example, the interaction energy can be tuned by changing either the atom number/density or the effective strength g of contact interactions appearing in the Gross–Pitaevskii equation—which provides another exciting knob for probing universal physics.

Moreover, one can also control the dominant type and range of interactions in dipolar atomic condensates, which offer tuneability in the relative strength of local and long-range interactions (Chomaz et al., 2022). Furthermore, degenerate Fermi gas settings provide an added "dimension" to such topics through control of the interaction strength, as they encompass different physical regimes depending on the value of $(k_F\, a)^{-1}$, where k_F is the Fermi wavevector and a the s-wave scattering length. In particular, such systems facilitate a study of the BEC limit (in the sense of atoms pairing up to form closely bound molecules which then Bose-condense), the BCS limit (where the formation of Cooper pairs of atoms in momentum space leads to familiar BCS-like effects), and—even more interestingly—the unitarity regime between these two, exhibiting infinite-range interactions. The physics of the unitarity limit is however also accessible in Bose gases. Moreover, the coexistence of mixtures of quantum-degenerate gases and components with a spin degree of freedom (or, so-called, spinor gases) enable such studies to be generalized to quantum mixtures.

In the vein of the main topics covered in this chapter, I note a significant (but not exhaustive) body of literature on Kibble–Zurek-type quenches, including, for example, through interaction-induced quenches in mixtures (Sabbatini et al., 2011) and spinor condensates (Sadler et al., 2006; Saito et al., 2007; Świsłocki et al., 2013; Witkowska et al., 2013; Williamson and Blakie, 2016; Anquez et al., 2016; Jiménez-García et al., 2019), prethermalization quenches in 1D (Langen and Schmiedmayer, 2017; Gring et al., 2012), superfluid quenches across unitarity (Eigen et al., 2018, 2017), and quantum quenches (Dziarmaga, 2010; Polkovnikov et al., 2011) in periodic potentials (optical lattices) (Greiner et al., 2002; Chen et al., 2011; Braun et al., 2015; Clark et al., 2016), which could facilitate applications in quantum simulations (Bloch et al., 2012; Gardas et al., 2018; Bando et al., 2020), or in the presence of disorder (Meldgin et al., 2016), with open realms for studying Kibble–Zurek physics in systems such as dipolar gases and photon condensates. An important feature of quantum quenches is that they are performed under conditions of negligible thermal dissipation, thus potentially facilitating better control and cleaner scalings while allowing for the possibility of the emergence of new interesting physical regimes.

Clearly these, and other settings not mentioned here, demonstrate the power of controlled quantum gas experiments with ultracold atomic gases. Nonetheless, new physics corresponding to the dynamics in an open quantum system can be probed in another experimentally well-controlled quantum gas platform, namely that of exciton-polariton systems, which I discuss next.

Driven-dissipative condensation in exciton-polariton systems

A somewhat distinct physical system, that of exciton-polariton condensates, can be studied by embedding a 2D quantum well in a semiconductor microcavity driven by external pumping (laser) (Deng et al., 2010). The presence of the cavity allows the emergence of a new type of quasiparticle, which is a mixture of a photon and a matter excitation; under sufficiently strong pumping, this leads to "hybridization" and a new dressed-state bosonic quasiparticle whose spectrum facilitates the emergence of a quasi-ordered state with a high degree of coherence (Kasprzak et al., 2006; Carusotto and Ciuti, 2013; Bloch et al., 2022). As this is a strictly 2D system, technically one should not speak of "condensation," but rather of a "BKT"-type phase transition to a "quasi-condensate" state exhibiting quasi-long-range order, as discussed in more detail below. Experimentally, there are various distinct pumping schemes that can be used to generate such an exciton-polariton system; one of these used rather commonly is that of incoherent pumping, which allows the quasi-ordered state to form spontaneously, through relaxation in the hybridized energy spectrum (relaxation in the so-called "lower polariton" branch).

Under the assumption that the exciton bath can be adiabatically eliminated—which is valid in many experimental set-ups—the fundamental equation describing such a scenario can take the form of a generalized Gross–Pitaevskii equation already alluded to in Section "Workhorse model of Bose–Einstein condensation" (Wouters and Carusotto, 2007; Keeling and Berloff, 2008). When further adding stochastic noise to this (and in the usual convention of setting $\hbar = 1$), this takes the form of a stochastic complex Ginzburg–Landau equation (Chiocchetta and Carusotto, 2013; Carusotto and Ciuti, 2013; Gladilin et al., 2014; Comaron et al., 2018):

$$i\frac{\partial\Phi}{\partial t} = -\frac{\nabla^2}{2m} + g|\Phi|^2 + \frac{i}{2}\left(\frac{P}{1+|\Phi|^2/n_s} - \gamma\right)\Phi + dW \tag{32}$$

where m is the polariton mass (which is many orders of magnitude smaller than the electron mass), P is the strength of the homogeneous external drive, g is the polariton–polariton interaction strength, n_s is a (phenomenological) saturation density, and dW a complex-valued noise term satisfying $\langle dW^*(\mathbf{r},t)dW(\mathbf{r}',t)\rangle = [(P+\gamma)/2]\delta_{\mathbf{r},\mathbf{r}'}$, where γ here is the inverse of the polariton lifetime.

I note here that, despite the decaying nature of the quasiparticle, the system does nonetheless enter a nonequilibrium steady-state (provided external pumping is maintained). Different variants of this equation exist in the literature, including extensions that account for a frequency-selective pumping mechanism favoring relaxation to low-energy modes (Chiocchetta and Carusotto, 2013; Wouters et al., 2010; Comaron et al., 2018).

For such systems, the control parameter is not temperature, but pumping; in fact the quasi-coherent regime sets in when pumping exceeds a threshold "critical pumping" value. In other words, $\epsilon = (P - P_c)/P_c$ such that $\epsilon > 0$ occurs in the high pumping limit $P > P_c$ (recall that in the case of cold quantum matter $\epsilon > 0$ labeling the coherent side is a low-temperature case $T < T_c$). In the mean-field limit, when $\epsilon > 0$, Eq. (32) supports a nontrivial steady-state solution in the form of $|\Phi|^2 = n_s(P/\gamma - 1)$.

Based on the previous discussion, one would expect a BKT transition associated with vortex–antivortex binding with increasing pumping strength; however the driven-dissipative nature of the system can modify such picture of "equilibrium condensation" previously discussed in the context of ultracold atomic gases (For the sake of clarity, I note here that while ultracold atomic condensates can be thought of as equilibrium, that is, fully-relaxed, during their probed long timescale, the true thermodynamic equilibrium of such systems is in fact a solid, facilitated by three-body loss processes which are not usually dominant during experimentally-probed timescales in most cold atom settings, thus enabling "long" lifetimes of up to a few minutes), and this has led to significant discussion in the community about the nature of the phase transition (Altman et al., 2015; Dagvadorj et al., 2015; Keeling et al., 2017).

In effect, the extent that the phase transition from disordered to (quasi-)ordered state is an "equilibrium" phase transition or not—and the nature of the arising correlation functions on the quasi-ordered state—depend on the system parameters, which can be controlled by the quality of the sample on which experiments are performed (i.e., the polariton lifetime), but also by the spatial pump profile, details of the pumping scheme, and any engineered anisotropy in the effective polariton mass. Depending on such parameters, these systems can also exhibit a broader range of universal behavior, as discussed below.

We start with revisiting the universal dynamics during a gradual driven transition (Kibble–Zurek) and the late-time phase-ordering for parameters corresponding to recent exciton-polariton experiments (Nitsche et al., 2014). The equilibrium criticality phase diagram can be characterized by looking at the divergence of the characteristic coherence length, ξ on the incoherent (here below threshold) pumping side $\epsilon < 0$ and the corresponding behavior of the exponent α_s of the spatial coherence power law decay on the $\epsilon > 0$ (quasi)ordered side (Eq. (10) with $\alpha(T) \rightarrow \alpha_s$). Such behavior is shown in Fig. 14A as a function of the ratio of the pumping power to the corresponding critical value predicted by mean-field theory (respectively by *green* and *red lines*) (Comaron et al., 2021). First, it should be noted here that due to the inclusion of fluctuations (via the noise term), the transition is in fact shifted from the predicted mean-field value by a few %. It is instructive to also consider the decay of the temporal correlations as one approaches the critical region from the $\epsilon > 0$ (quasi-)ordered side; these are shown by the red line. The diverging behavior on the (quasi)ordered side is the same qualitatively for spatial and temporal correlations. However, it clearly becomes evident (see also inset) that $\alpha_s = 2\alpha_t$ (Comaron et al., 2021), with such a relation between their respective exponents giving the transition a genuine *nonequilibrium* flavor (Szymańska et al., 2006, 2007). Moreover, various experiments observed the universal scaling exponent characteristic of the spatial correlation function decay on the (quasi)ordered side to exceed the expected *equilibrium* value of (1/4) at the critical point (Roumpos et al., 2012; Nitsche et al., 2014): although this has also been seen in numerical simulations (Dagvadorj et al., 2015), the results presented here—while broadly consistent with such a picture—cannot provide a conclusive answer because the precise value is also expected to be somewhat sensitive to finite-size effects (Comaron et al., 2021).

Having identified the precise location of the critical point, one can now consider the dependence of the system properties as a function of the distance to criticality ϵ, the first step toward performing and characterizing linear quenches across the phase transition. As expected the number of vortices in this 2D system at equilibrium decreases very dramatically in the vicinity of $\epsilon = 0$ (*dashed red line* in Fig. 14B). Quenching across the transition at different rates leads to such vortices surviving for significant amounts of time after the system parameters have been quenched to the (quasi-)ordered side (Zamora et al., 2020); this is here visible by the slower decay of vortices with ϵ, where $\epsilon = \epsilon(t) = t/\tau_Q$ following the quenched system evolution through the externally imposed parameter. The slower decay of vortices in time as the system adapts to the external quench across the phase transition leads to the expected divergence in the relaxation time (*red line*, $\tau(\epsilon)$, in bottom left inset to Fig. 14B). The faster one quenches across the phase transition (i.e., the smaller that τ_Q is), the deeper into $\epsilon(t) > 0$ values that the vortices can be observed on the (quasi)ordered side. Of course, ultimately such vortices will decay to the corresponding equilibrium value at such value of ϵ, marked by the *dashed red line*. I recall here that the quench rate affects the slope of $\epsilon(t)/\dot{\epsilon}(t)$ (*dashed blue line* in bottom left inset to Fig. 14B), and so the exact location of the intersection point of these two curves which, according to the fundamental Kibble–Zurek equation, defines the timescale $-\hat{t}$. Numerical simulations (Zamora et al., 2020) have confirmed the validity of the Kibble–Zurek scenario, by revealing the expected proportionality between the observed relaxation time of vortex dynamics (essentially the time when the quenched *solid lines* in Fig. 14B deviate from the equilibrium *dashed red line*) and the time predicted by matching $\tau(-\hat{t})$ to $\epsilon(-\hat{t})/\dot{\epsilon}(-\hat{t})$ (up to some irrelevant microscopic nonuniversal prefactor); such proportionality can be seen in the top right inset.

In the long-time limit, the vortices decay. As discussed in Section "Scaling hypothesis and late-time coarsening," this decay (following instantaneous quenching into the (quasi-)ordered state) is expected to enter another scaling window, associated with phase-ordering (Jelić and Cugliandolo, 2011). Already from Fig. 14B one can see that the vortex decay slows down as their number decreases for a given value of τ_Q, that is, along a particular curve shown in Fig. 14B. This is because vortices move (on average) further and further apart; thus the frequency of their annihilations slows down. Then, at some late time, when there are only relatively few vortices left in the system, the behavior changes drastically. Such behavior (following now an instantaneous quench) has been mapped out in Fig. 14C; after a very rapid decay in the number of vortices (*blue*) and corresponding increase in the

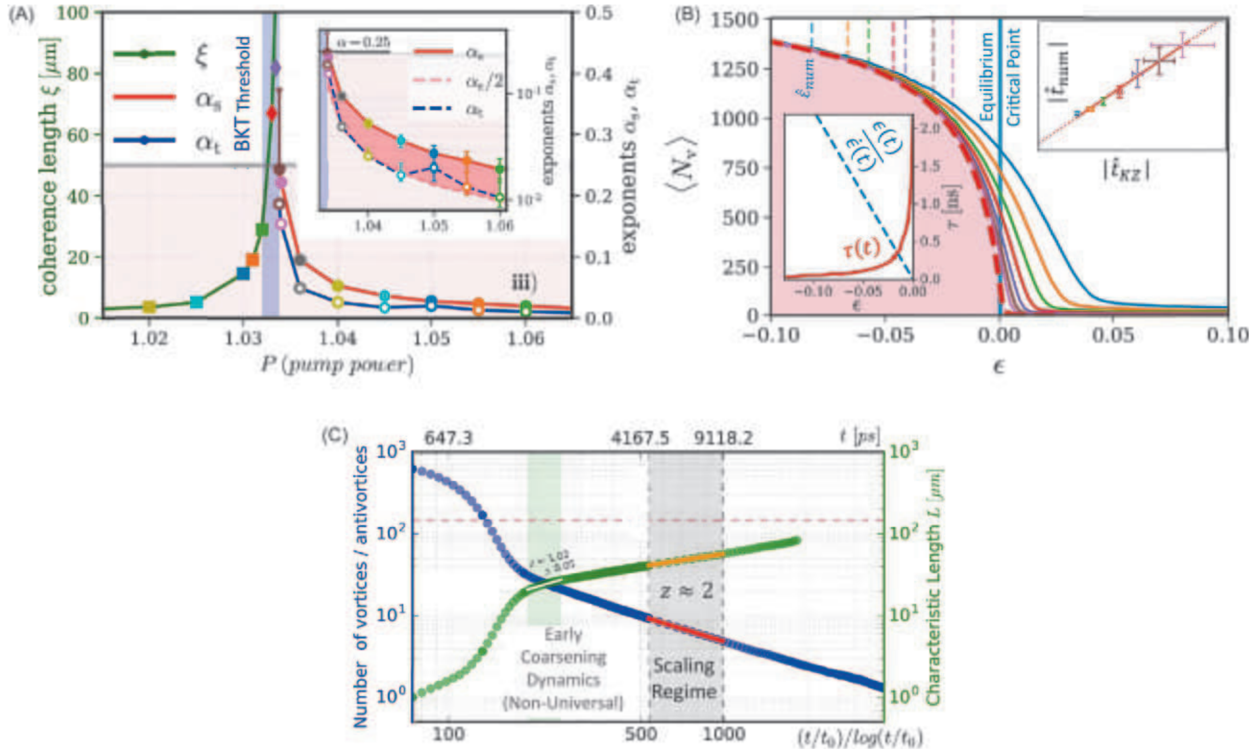

Fig. 14 Universal features of a nonequilibrium driven-dissipative exciton-polariton condensate for typical experimental parameters. (A) Dependence of the coherence length, ξ, defined by $g^{(1)}(\mathbf{r}) \sim e^{-r/\xi}$ on the incoherent side of the phase transition, and of the spatial (temporal) exponents α_s (α_t) defined on the quasi-ordered side by $g^{(1)}(\mathbf{r}) = r^{-\alpha_s}$ ($g^{(1)}(t) = t^{-\alpha_t}$). Horizontal axis depicts the external pump power in units of the critical value predicted by mean-field theory, with the transition occurring above the critical pump threshold (here $P_{cr} \sim 1.033$); fluctuations clearly shift this by (up to) a few %, toward a higher pump value. *Inset*: zoomed-in version clearly revealing $\alpha_s = 2\alpha_t$, as direct evidence of the nonequilibrium nature of the phase transition in such parameter regime. (B) Demonstration of validity of the Kibble–Zurek relation (Eq. 19). Main panel shows the dependence of vortex number on $\epsilon = (P - P_c)/P_c$ for the equilibrium case (*dashed red line*) and the corresponding dependence for $\langle N_v(t) \rangle$ in terms of $\epsilon(t)$ for a linear external quench in the pump via $\epsilon(t) = t/\tau_Q$, with τ_Q decreasing between curves as one moves from left to right. For each τ_Q, there is a corresponding value of $\epsilon = \epsilon(\hat{t}_{num})$ at which the (dynamical) curve determining the postquench number of vortices (*solid*) as a function of ϵ deviates from the corresponding equilibrium one (*dashed red*)—these values are shown by the *dashed vertical lines*, and yield the numerical estimate $\hat{t}_{num}$. Insets: (bottom left) Relation between diverging relaxation time τ and characteristic timescale $\epsilon(t)/\dot{\epsilon}(t)$ in the vicinity of the critical point, with their intersection defining the freeze-out time $-\hat{t}_{KZ}$. (top right) Demonstration of $|\hat{t}_{num}| \sim |\hat{t}_{KZ}|$ validating the expected Kibble–Zurek proportionality relation (up to some microscopic, nonuniversal prefactor). (C) Evolution of decreasing number of vortices/antivortices (*blue curve*) and growing characteristic lengthscale (*green curve*) highlighting the dramatic early postquench coarsening evolution, and their corresponding dependence on time in the scaling regime, allowing us to extract the dynamical critical exponent $z = 2$. Note that all axes are plotted on logarithmic scale, with the temporal axis also including the anticipated logarithmic correction to the system evolution. (A) Adapted with permission from Comaron P, Carusotto I, Szymańska, MH, and Proukakis NP (2021) Non-equilibrium Berezinskii-Kosterlitz-Thouless transition in driven-dissipative condensates(a). Europhysics Letters 133(1): 17002. https://doi.org/10.1209/0295-5075/133/17002. Copyright (2021) by the Institute of Physics. (B) Adapted with permission from Zamora A, Dagvadorj G, Comaron P, Carusotto I, Proukakis NP, and Szymańska MH (2020) Kibble-Zurek mechanism in driven dissipative systems crossing a nonequilibrium phase transition. Physical Review Letters 125: 095301. https://doi.org/10.1103/PhysRevLett.125.095301. Copyright (2020) by the American Physical Society. (C) Adapted with permission from Comaron P, Dagvadorj G, Zamora A, Carusotto I, Proukakis NP, and Szymańska MH (2018) Dynamical critical exponents in driven-dissipative quantum systems. Physical Review Letters 121 (9): 095302. Copyright (2018) by the American Physical Society

characteristic lengthscale describing the typical size of the emerging quasi-ordered regions (*green*), the system enters the scaling regime (Comaron et al., 2018). In this regime, properties of the system can be characterized by a single growing lengthscale and thus all correlation functions collapse onto a single function, in terms of such an appropriately rescaled variable $L_c(t)$ (see Eq. 30). Interestingly, one now sees very clearly both the existence of the expected logarithmic corrections in the presence of external coupling (dissipation) (previously discussed in Section "Scaling hypothesis and late-time coarsening"), and the anticipated value of the dynamical critical exponent ($z = 2$) (Jelić and Cugliandolo, 2011). While this behavior is expected to continue at later times, finite size effects make it harder to obtain concrete predictions of $L_c(t)$ from the spatial correlation function.

The above results have painted the picture of a "nonequilibrium" BKT phase transition, and an anticipated late-time phase-ordering law, with significant discussion in the literature addressing the nature of this phase transition (Dagvadorj et al., 2015; Altman et al., 2015; Keeling et al., 2017). Parallel to this, there has been quite some interest in searching for a different kind of universal behavior on the quasi-ordered ($\epsilon > 0$) side of the transition, associated with a so-called Kardar–Parisi–Zhang (KPZ) universality class (Kardar et al., 1986).

The KPZ equation describes the stochastic growth of the height of an interface and is established in diverse (classical) physical settings, including, for example, polymer growth, and spreading of wildfires. In the present context, I note that the KPZ equation arises as an equation modeling the phase of the superfluid θ, obtained from $\Phi(\mathbf{r}, t) = \sqrt{n(\mathbf{r}, t)}e^{i\theta(\mathbf{r},t)}$ in the presence of a momentum-dependent damping rate under the assumption that the density fluctuations ($\delta n(\mathbf{r}, t) = n(\mathbf{r}, t) - \langle n(\mathbf{r}, t)\rangle$) vary slowly both in space ($\nabla\delta n \approx 0$) and in time ($\partial n/\partial t \approx 0$). Such an assumption makes the KPZ physics more relevant in regimes characterized by weak-phase fluctuations, namely, deep in the quasi-ordered phase $\epsilon > 0$. In that case, one obtains the KPZ equation in the form (Altman et al., 2015; Gladilin et al., 2014; Ji et al., 2015; Wachtel et al., 2016; He et al., 2015; Squizzato et al., 2018; Deligiannis et al., 2021)

$$\frac{\partial\theta}{\partial t} = \nu\nabla^2\theta + \frac{\lambda}{2}(\nabla\theta)^2 + \sqrt{D}\,\eta. \tag{33}$$

The terms on the right-hand side describe the diffusion leading to smoothening, a nonlinear contribution leading to critical roughening, and a stochastic noise term, with the constants ν, λ, and D depending on microscopic system parameters. This equation maps the evolution of the phase of the polariton mean field to a growing interface with the same internal dimension.

Let us consider the general normalized first-order correlation functions in space and time in the form $g^{(1)}(\mathbf{r}, \mathbf{r} + \boldsymbol{\Delta}\mathbf{r}, t, t + \Delta t)$ and denote this by the short-hand notation $g^{(1)}(\boldsymbol{\Delta}\mathbf{r}, \Delta t)$. In general (upon neglecting density–density and density–phase correlations), one can show that (Fontaine et al., 2022)

$$g^{(1)}(\boldsymbol{\Delta}\mathbf{r}, \Delta t) = \langle \exp(i\Delta\theta(\boldsymbol{\Delta}\mathbf{r}, \Delta t))\rangle \tag{34}$$

where $\Delta\theta$ denotes the change in phase from some reference value. To lowest order in the fluctuations, this would thus give the dominant behavior that

$$\begin{aligned} \text{Fixed}\ \ \Delta t_0:\ |g^{(1)}(\boldsymbol{\Delta}\mathbf{r},\ \Delta t_0)| &\sim \exp\left(-\frac{1}{2}\left(\frac{\Delta r}{\lambda}\right)^{2\chi}\right) \\ \text{Fixed}\ \ \Delta r_0:\ |g^{(1)}(\boldsymbol{\Delta}\mathbf{r}_0,\ \Delta t)| &\sim \exp\left(-\frac{1}{2}\left(\frac{\Delta t}{\tau}\right)^{2\beta}\right) \end{aligned} \tag{35}$$

thus introducing the two KPZ critical exponents χ and β for space and time, respectively, denoting the roughness and growth critical exponents (with λ and τ, the corresponding nonuniversal parameters). As a result, KPZ scaling would show up as "stretched exponential" decay in the correlation functions in the limit of a relatively well-formed mean field, that is, for "sufficiently large" $\epsilon > 0$ values (such behavior is termed "stretched exponential" here because 2χ, $2\beta \neq 1$ as would be the case in a "normal" exponential). In order to unequivocally observe such behavior, one would generally need to observe very large systems (and for very long times) because of the existence of a characteristic minimum lengthscale for the onset of KPZ physics (Altman et al., 2015).

Notwithstanding the earlier comments about a possible *nonequilibrium* BKT phase transition, an experiment conducted with high-quality samples (and so longer polariton lifetimes, thus facilitating a less nonequilibrium regime) found two interesting results (Caputo et al., 2018) (see Fig. 15A); first, although spatial and temporal correlation functions could be fitted by both stretched exponential and power-law decays in the vicinity of the critical region, the power-law decay always fits better on the quasi-ordered side of the phase transition, thus explicitly verifying BKT-type correlations—consistent with BKT being the transition mechanism. Second, unlike the previous discussion, the power-law exponents for the spatial and temporal decay on the quasi-ordered side were found to exactly match each other, both having a value clearly below 0.25. All this corroborated to an *equilibrium* BKT phase transition in this particular experimental setting, demonstrating that exciton-polariton condensates can control the extent of the "equilibrium" or "nonequilibrium" nature of the phase transition through the sample quality characterizing the polariton lifetime.

From a theoretical point of view, the universal scaling function for KPZ takes the form (Deligiannis et al., 2021)

$$\begin{aligned} C(\boldsymbol{\Delta}\mathbf{r},\ \Delta t) &= \langle(\Delta\theta(\boldsymbol{\Delta}\mathbf{r}, \Delta t))^2\rangle - \langle\Delta\theta(\boldsymbol{\Delta}\mathbf{r}, \Delta t)\rangle^2 \\ &= -2\ln\left(\left|g^{(1)}(\boldsymbol{\Delta}\mathbf{r},\ \Delta t)\right|\right) \\ &= C_0(\Delta t)^{2\beta}\ \ F\left(\gamma_0\frac{|\boldsymbol{\Delta}\mathbf{r}|}{\Delta t^{1/z}}\right), \end{aligned} \tag{36}$$

where $F(\gamma)$ is a universal scaling function (whose asymptotics are known), $z = \chi/\beta$ and C_0 and γ_0 are nonuniversal constants.

Such emergence of KPZ scaling was conclusively demonstrated in an appropriately engineered (discrete) 1D setting (Fontaine et al., 2022), constituting the first realization of KPZ scaling in a quantum system. In addition to identifying a spatial/temporal region where Eqs. (35) hold (Fig. 15B(i)–(ii)), they were able to convincingly demonstrate the emergence of a universal spatiotemporal KPZ scaling function by plotting $C(\Delta r,\ \Delta t)/(\Delta t)^{2\beta}$ as a function of $\Delta r/\Delta t^{1/z}$, for the particular exponent values of $\beta = 1/3$ and $z = 3/2$, thus corresponding to $\chi = 1/2$.

Extending such analysis to the 2D limit, the same team also managed to numerically demonstrate—sufficiently above threshold so that vortices do not overwhelm KPZ effects (Deligiannis et al., 2022)—the emergence of scaling according to Eq. (35), with critical exponents consistent with those anticipated in the 2D KPZ universality class. This opens up the possibility of observing—for the first time—2D KPZ physics in an experiment, a long-standing goal in nonequilibrium statistical physics. The above brief discussion highlights driven-dissipative exciton-polaritons as ideal systems for tuning both the extent of equilibrium (or nonequilibrium) nature of the BKT phase transition, and the prevailing universality class through carefully engineered experiments (Zamora et al., 2017; Diessel et al., 2022).

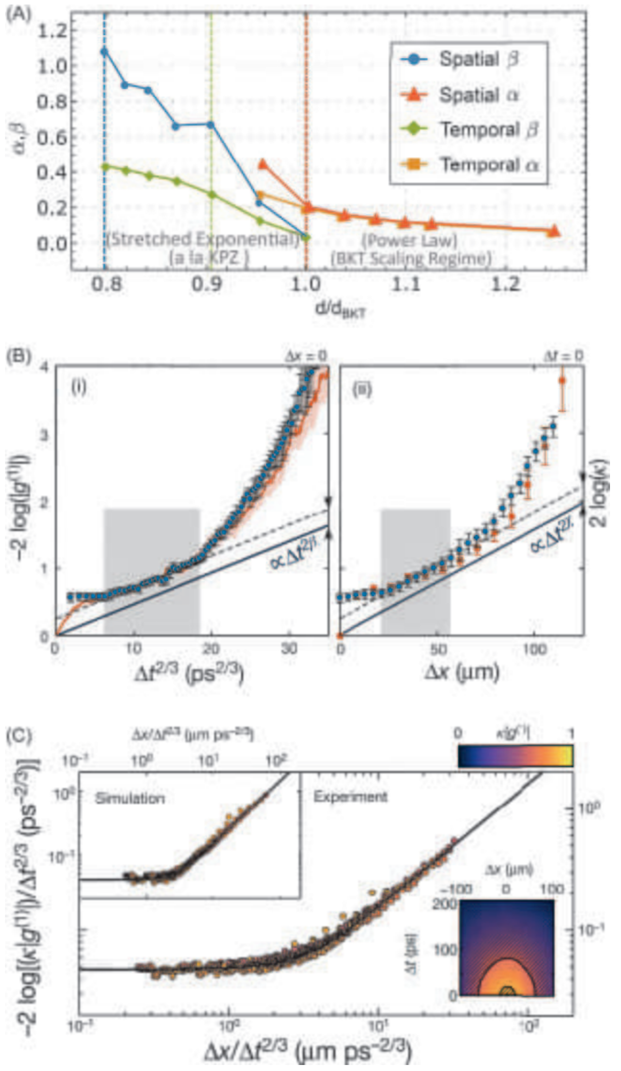

Fig. 15 (A) Regime of 2D equilibrium BKT. Dependence of the spatial and temporal correlation function exponents as a function of the pumping (here d) scaled to the critical value (d_{BKT}) for the experimental parameters of Caputo et al. (2018). Depicted values correspond to exponents labeling correlation decay in the form of either stretched exponentials (left part of plot) or algebraic decay (right part of plot) according to which one of these fits works best in each regime. Here one sees clearly that algebraic decay (characteristic of the 2D XY model) dominates (overstretched exponential decay) for all points above threshold, and that, importantly, the emerging spatial (α) and temporal (β) exponents are equal and do not exceed the value of 0.25 at the critical point. (B) and (C) Experimental demonstration of nonequilibrium KPZ scaling in 1D. (B)(i)–(ii) Identification of spatiotemporal regime where both spatial and temporal correlations exhibit their expected stretched exponential scalings of Eq. (35) on the quasi-ordered side. (C) Appropriately rescaled plot confirming the KPZ picture of Eq. (36) for all data points in (B)(i)–(ii) within the corresponding scaling regimes for which $|g^{(1)}|$ takes the values shown within the annulus in the bottom right inset. Note that such scaling function shows a plateau at small $y = y_0\Delta r/(\Delta t)^{2/3}$ and linear growth at large y. Insets: (top left) Corresponding analysis by means of numerical simulations; (bottom right) Coherence map showing value of $|g^{(1)}|$ (see colorbar) in terms of Δr (denoted here by Δx) and Δt. (A) Adapted with permission from Caputo D, Ballarini, D, Dagvadorj G, Munoz CS, de Giorgi M, Dominici L, West, K, Pfeiffer LN, Gigli G, Laussy FP, Szymanska MH, and Sanvitto D (2018) Topological order and thermal equilibrium in polariton condensates. Nature Materials 17: 145–151. Copyright (2018) by the Nature Publishing Group. (B) Adapted with permission from Fontaine Q, Squizzato D, Baboux F, Amelio I, Lemaître A, Morassi M, Sagnes I, Gratiet L, Harouri A, Wouters M, Carusotto I, Amo A, Richard M, Minguzzi A, Canet L, Ravets S, and Bloch J (2022) Kardar-Parisi-Zhang universality in a one-dimensional polariton condensate. Nature 608: 687–691. Copyright (2022) by the Nature Publishing Group

Bose–Einstein condensation on astrophysical/cosmological scales?

Due to its universal nature, BEC has even been hypothesized to be at play across very different astrophysical/cosmological settings. Perhaps the most broadly known example is that of neutron stars (Pethick et al., 2017), whose core is expected to exhibit both superfluidity and superconductivity. However, various other forms of condensation have been discussed in the literature (see, e.g., early discussions in Griffin et al., 1995), including rather interestingly condensation of gravitons (Dvali and Gomez, 2017). Below I briefly outline an alternative idea gaining increasing attention currently in the literature in the context of dark matter modeling.

The possibility of the existence of a cosmological-scale gravitating BEC of axionic particles has been proposed as a plausible alternative picture of the nature of dark matter (Hu et al., 2000) (see also the related scenario of thermalizing QCD axions (Banik and Sikivie, 2017)). More recently, the focus of such theoretical ideas appears to be in the context of ultralight axion-like particles of mass 10^{-22} eV/c^2: due to their low mass, these can give rise to galactic-size de Broglie wavelengths (recall that $\lambda \sim 1/\sqrt{m}$), thus facilitating condensation on such unprecedented scales. While such systems cannot be controlled in any way (and so the question of phase transition crossing becomes less relevant), nonetheless, predictions of such models in the current (late-time, virialized) state could ultimately be related to cosmological observations.

As well known, there is currently an established model of cold dark matter (CDM), which explains the large-scale structures of the universe very well through N-body numerical simulations (Frenk and White, 2012). Nonetheless, some discrepancies have been recently noted in relation to the small-scale structure (Weinberg et al., 2015; Bullock and Boylan-Kolchin, 2017; Del Popolo and Le Delliou, 2017) (most notably the inferred distribution of the dark matter density at the very center of galaxies). One very elegant way (but admittedly not the only one) to resolve such discrepancies is to describe such features through BEC in the context of the so-called FDM model (Schive et al., 2014; Mocz et al., 2017; Marsh, 2016; Hui, 2021; Ferreira, 2021). The underlying idea here is that dark matter consists of ultralight axionic particles, of mass 10^{-22}eV/c^2. Due to their high density and low mass, such particles would have a very high phase-space density allowing the emergence of BEC on galactic scales. The power of such an approach is that it describes "short-range" (on cosmological scales) features by the emergence of a so-called gravitationally self-bound soliton of dark matter while still reproducing the very successful large-scale predictions of the usual CDM model—most notably the Navarro-Frenk-White (NFW) radial density profiles at large distances from the galactic core (Navarro et al., 1996).

The equation governing such cosmological condensates is a Schrödinger equation, embedded within the gravitational field (Widrow and Kaiser, 1993; Seidel and Suen, 1990; Schive et al., 2014; Mocz et al., 2017). In general, one could also envisage the existence of interactions between such axionic particles (although some constraints on their maximum strength do exist) (Chavanis, 2011; Desjacques et al., 2018; Mocz et al., 2023; Delgado and Muñoz Mateo, 2022), giving rise to the following system of coupled equations, loosely termed the Gross–Pitaevskii–Poisson equations:

$$i\hbar\frac{\partial\Phi(\mathbf{r},t)}{\partial t} = \left[-\frac{\hbar^2\nabla^2}{2m} + g\rho(\mathbf{r},t)+mV(\mathbf{r},t)\right]\Phi(\mathbf{r},t) \tag{37}$$

where the Newtonian potential $V(\mathbf{r}, t)$ follows the Poisson equation,

$$\nabla^2 V(\mathbf{r},t) = 4\pi G(\rho(\mathbf{r},t) - \overline{\rho}) \tag{38}$$

with the mass density $\rho(\mathbf{r}, t) = |\Phi(\mathbf{r}, t)|^2$, and $\overline{\rho}$ its spatially averaged constant value (and G denotes the gravitational constant). (Interestingly this same set of equations has also been recently used to model glitches in pulsars (Verma et al., 2022).)

While the validity of the FDM model has yet to be tested, even in the absence of interactions (and we may still be a long way away before some of the emerging predictions can be directly tested against observational data), there is a rapidly growing body of work (see, e.g., recent reviews (Marsh, 2016; Hui, 2021; Ferreira, 2021)) addressing the model's predictions both on the cosmological large scale (Fig. 16A) (Schive et al., 2014; Mocz et al., 2017; May and Springel, 2021) and on the level of a single (isolated) cored-halo regime corresponding to the distribution of dark matter on the level of a typical galaxy (Fig. 16B and C) (Mocz et al., 2017; Schwabe et al., 2016; Chan et al., 2022; Liu et al., 2023). The important new contribution from the FDM picture discussed in the above works (and many references therein) is that the density at the center of the galaxy behaves very differently to CDM predictions, with the emergence of a well-formed soliton whose density remains finite as $\mathbf{r} \to 0$. Essentially this leads to a bimodal profile of a central soliton surrounded by fluctuating dark matter density satisfying the NFW profile; this is somewhat reminiscent of the density profiles of ultracold atomic gases in harmonic traps, with gravitational attraction in the galactic case playing a role analogous to the harmonic confinement of ultracold atomic gases—such an important and interesting analogy has been explicitly discussed in Liu et al. (2023).

Addressing the coherent properties of such a (virialized) cored-halo system, Liu et al. (2023) demonstrated that the discussed solitonic core is in fact fully coherent in the sense of a dominant Penrose–Onsager mode, with a nearly constant spatial correlation function in the central solitonic region exhibiting $g^{(1)}(\mathbf{r}) \approx g^{(2)}(\mathbf{r}) \approx 1$ for $r \lesssim r_c$, where r_c labels a typical soliton radius. Beyond this, there is an intermediate region of gradually decreasing coherence spatially, with global-phase coherence across the soliton core lost between the soliton core and an outer "transition" region r_t, at which point $g^{(1)}(\mathbf{r}) \approx 0$ and $g^{(2)}(\mathbf{r}) \approx 2$, consistent with a chaotic field. Nonetheless, closer inspection demonstrates that the outer halo region ($r > r_t$) contains randomly distributed regions of near constant density, which locally feature enhanced phase coherence. Such domains are separated by randomly oriented vortices that scramble the phase between them; in the cosmological context, such regions are termed "granules." Such a picture closely resembles a cosmological-size quasi-condensate, as shown schematically—based on actual numerical data—in Fig. 16C (Liu et al., 2023); as such vortices are randomly oriented/distributed and move around (albeit on rather cosmologically-slow timescales), there is no overall phase coherence after radial, or temporal averaging. Moreover—at least in the absence of self-interactions—this system exhibits familiar scaling laws of (ultraquantum) turbulence, with such states in fact rather similar qualitatively to the early dynamical phases of condensate formation discussed in Section "Analyzing Kibble–Zurek in an elongated ultracold atomic system" (Liu et al., 2023); interestingly recent works have shown such a structure to be very long-lived, unlike the rapidly decaying turbulent states generated in nondriven ultracold atomic systems.

The predictions of the FDM model may end up not having a direct bearing on real-world observables. Nonetheless, the mere fact that a cosmological model of a BEC can actually generate features seemingly consistent with our current understanding of large-scale structure in the universe is truly remarkable in its own right, and demonstrates the power and universality of such a physical phenomenon.

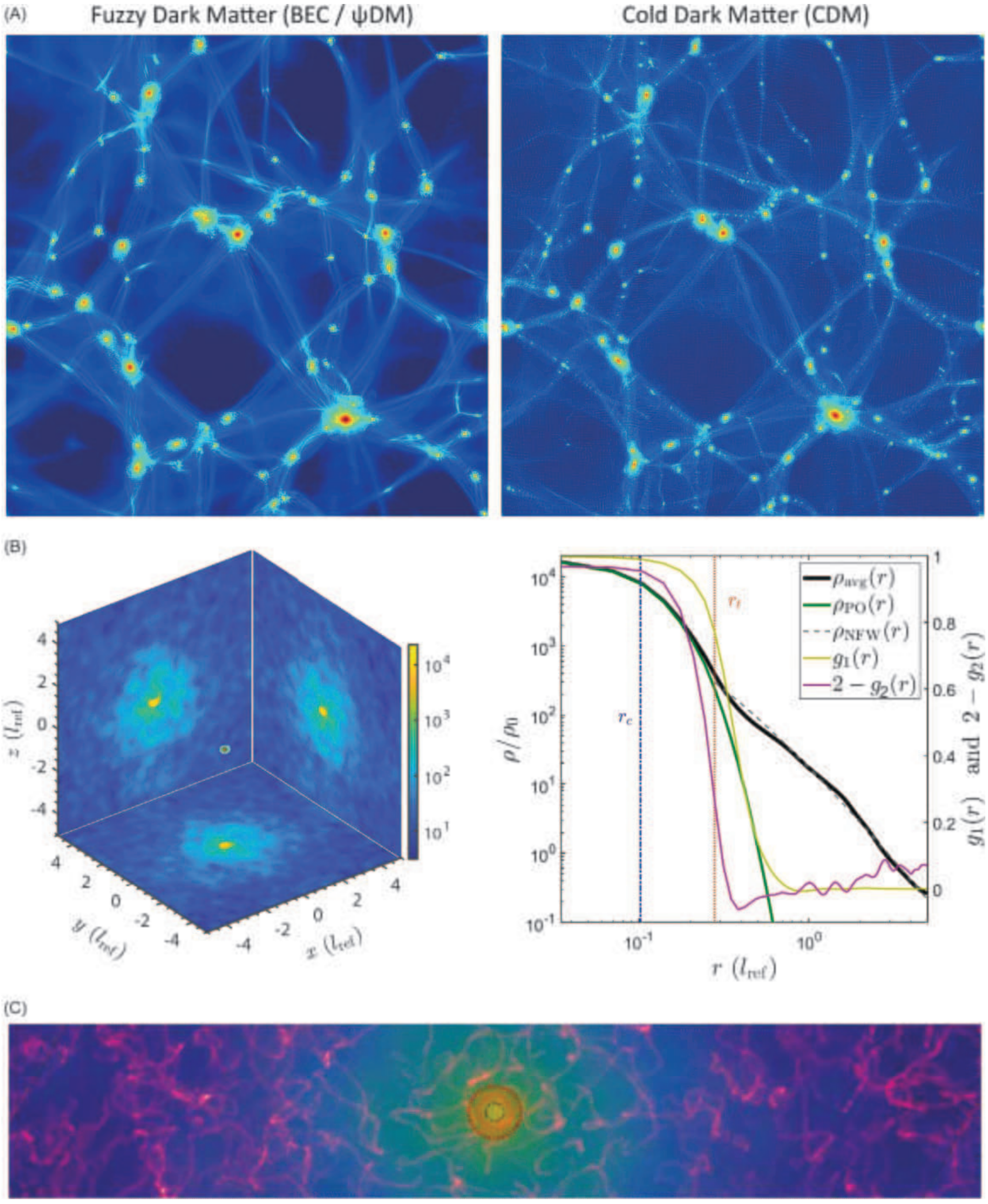

Fig. 16 Cosmological condensation in the fuzzy dark matter (FDM) model (also known as ψDM in Schive et al. (2014)): (A) Large-scale comparison of FDM predictions (left) to the established cold dark matter (CDM) model based on N-body simulations (right) from a given set of initial cosmological conditions; large-scale features are excellently reproduced. (B) FDM simulations focusing on an isolated (single) galactic halo, which in the FDM model contains a characteristic solitonic core at its center (left image), reveal a number of interesting features shown in the right image; first, the radial density profile (*black line*) both exhibits a core at the center (unlike the CDM model predictions that lead to an "unphysical" $1/r$ divergence as $r \to 0$, which is not shown here) and reproduces the expected NFW profiles (*dashed brown line*) at larger distances ($r > r_t$); importantly, the solitonic core exhibits near-perfect coherence $g^{(1)}(\mathbf{r}) \approx g^{(2)}(\mathbf{r}) \approx 1$ for $r \le r_c$, with coherence only gradually lost with increasing radial distance up to r_t, at which point the NFW density profile sets in; in fact, the solitonic core can be fully described as a Penrose–Onsager condensate mode (*green line*) all the way up to r_t, with the remaining (incoherent) density concentrated primarily outside the solitonic region, but with a nonzero (albeit small) component still present at smaller radii; this is directly analogous to the condensate-thermal cloud bimodal distribution of Hartree-Fock theories for ultracold atomic gases (see, e.g., Proukakis and Jackson, 2008) and the corresponding experimentally obtained density distributions. (C) Example schematic of the density distribution of the solitonic core (*yellow core*—with both r_c and r_t radii shown to give a sense of scale) surrounded by regions of decreasing density filled with random vortices (*purple lines*) which scramble the phase between different domains of locally similar phase—constituting a galactic-size example of a quasi-condensate state. (A) Reprinted with permission from Schive H-Y, Chiueh T, and Broadhurst T (2014) Cosmic structure as the quantum interference of a coherent dark wave. Nature Physics 10(7): 496–499. https://doi.org/10.1038/nphys2996.1406.6586. Copyright (2014) by the Nature Publishing Group. (B) and (C) Adapted with permission from Liu I-K, Proukakis NP, and Rigopoulos G (2023) Coherent and incoherent structures in fuzzy dark matter haloes. Monthly Notices of the Royal Astronomical Society 521(3): 3625–3647. ISSN 0035-8711. https://doi.org/10.1093/mnras/stad591. Copyright (2023) by Oxford University Press.

Conclusion

In this chapter, I have given a broad overview of manifestations of macroscopic coherence across a diverse range of physical systems, spanning from the very tiny (exciton-polaritons, atoms) to the very large (cosmological). While the specific physical manifestation across such systems might be different, with BEC associated with a single macroscopic observable and off-diagonal long-range order giving way—in some limits—to related behavior in terms of a Berezinskii–Kosterlitz–Thouless transition to a quasi-ordered state, or even to a state exhibiting stretched exponential correlation functions consistent with those of the Kardar–Parisi–Zhang model over a restricted spatiotemporal regime, such systems nonetheless exhibit evidence of universal behavior in appropriate temporal domains and/or spatial regions, with some common observable features. This facilitates an exciting cross-fertilization of ideas, which have borne out of seemingly distinct fields such as low-temperature physics; statistical physics; condensed matter; and atomic, molecular, and optical physics. Interestingly, many of the ideas discussed in this chapter have their origins in cosmological or theoretical physics studies, even if perhaps some of those features are now becoming more the playground of controlled quantum matter experiments.

For example, the concept of defects arising during a dynamical phase transition becoming embedded into, and thus observable within, the long-time evolution of the system—first proposed in the context of a hot Big Bang model—has not only found significant validation in a diverse range of coherent quantum systems but also led to exciting studies pushing new frontiers in quantum gas experiments conducted with an unprecedented flexibility and accuracy—such as experiments with ultracold atoms. In this context, one is now investigating the modifications to this Kibble–Zurek scenario of driven quenching across the phase transitions imposed by inhomogeneities and the interplay with causality.

Moreover, the concept of highly nonequilibrium scenarios, associated with the dynamics around nonthermal fixed points emerged initially from studies of reheating after early universe inflation, but recent years have seen a number of distinct experiments with ultracold atoms revealing evidence of dynamics consistent with predicted scalings around such nonthermal-fixed points. Such nonequilibrium scenarios have a close connection with the emergence of (strong) turbulence, in a generalized manner, that is, with the state of a system filled with random tangled defects, which can also exhibit various types of universal scaling laws in appropriate regimes. Beyond the familiar and already observed direct energy cascade Kolmogorov turbulence of a driven system and associated decay of bundles of vortices once driving is removed, experiments with liquid helium and ultracold atomic systems have revealed a new “type” of turbulence, known as “ultraquantum” (or “Vinen”) turbulence, which is dominated by the tangling and relaxation of individual vortices. The rapid quenching of a phase transition creates a strongly “turbulent” state with broadly similar features qualitatively, whose subsequent evolution ultimately follows universal scaling laws—whether in the context of spatially self-similar solutions during phase-ordering, the stronger spatiotemporal evolution around nonthermal-fixed points, or even evolution related to the Kardar–Parisi–Zhang spatiotemporal self-similarity. Interestingly, such features also connect the driven or instantaneous breaking of a continuous symmetry with phenomena investigated in fluids, including classical fluids and growth of interfaces.

As such, systems exhibiting macroscopic quantum coherence in controlled quantum matter experiments give access to a range of different universal types of behaviors, and the emergence of a range of scaling laws having wide applicability to very different physical systems across both the classical and the quantum realm. Combined with the enhanced quantum control in these systems, which facilitates the on-demand construction of system Hamiltonians—thus making them ideal systems for quantum simulations—such systems collectively open up a very exciting, highly interdisciplinary realm for a deeper understanding of the nonequilibrium physical world.

Acknowledgments

The unified presentation given here has been made possible through collaborations (or extended discussions) on these topics with many excellent colleagues and friends over a period of years, including specifically for the presented context and concepts Tom Billam, Tom Bland, Jerome Beugnon, Iacopo Carusotto, Paolo Comaron, Leticia Cugliandolo, Franco Dalfovo, Jacek Dziarmaga, Jean Dalibard, Piotr Deuar, Gabriele Ferrari, Andrew Groszek, Giacomo Lamporesi, Fabrizio Larcher, Rob Smith, Henk Stoof, Marzena Szymanska, and Alex Zamora, to whom I am grateful. In such a context, I would particularly like to highlight Dr I-Kang (Gary) Liu and Dr Paolo Comaron who have been pivotal to my respective understanding of Kibble–Zurek physics and polariton condensation, as well as Dr Gerasimos Rigopoulos and Dr I-Kang Liu for our recent collaboration into coherent cosmological endeavors. During the preparation of this chapter, I have benefited enormously from discussions with, and direct feedback on this manuscript from, Vanderlei Bagnato, Carlo Barenghi, Paolo Comaron, Jacek Dziarmaga, Thomas Gasenzer, Gary Liu, Gerasimos Rigopoulos, and Marzena Szymanska. I also thank Jacek Dziarmaga, Thomas Gasenzer, Anna Minguzzi, Hsi-Yu Schive, Rob Smith, and Wojciech Zurek for explicit permissions to reprint key figures from their earlier works, and the UK EPSRC, Leverhulme Trust, and the Horizon-2020 framework for funding—with particular note to the Quantera grant “Nonequilibrium dynamics in Atomic systems for QUAntum Simulation” (NAQUAS) which refocused my interest on such topics.

References

Adams A, Carr LD, Schäfer T, Steinberg P, and Thomas JE (2012) Strongly correlated quantum fluids: Ultracold quantum gases, quantum chromodynamic plasmas and holographic duality. *New Journal of Physics* 14(11): 115009. https://doi.org/10.1088/1367-2630/14/11/115009.

Aidelsburger M, Ville JL, Saint-Jalm R, Nascimbène S, Dalibard J, and Beugnon J (2017) Relaxation dynamics in the merging of *n* independent condensates. *Physical Review Letters* 119: 190403. https://doi.org/10.1103/PhysRevLett.119.190403.

Al Khawaja U, Andersen JO, Proukakis NP, and Stoof HTC (2002) Low dimensional Bose gases. *Physical Review A* 66(1): 013615. https://doi.org/10.1103/PhysRevA.66.013615.

Altman E, Sieberer LM, Chen L, Diehl S, and Toner J (2015) Two-dimensional superfluidity of exciton polaritons requires strong anisotropy. *Physical Review X* 5: 011017. https://doi.org/10.1103/PhysRevX.5.011017.

Anquez M, Robbins BA, Bharath HM, Boguslawski M, Hoang TM, and Chapman MS (2016) Quantum Kibble-Zurek mechanism in a spin-1 Bose-Einstein condensate. *Physical Review Letters* 116: 155301. https://doi.org/10.1103/PhysRevLett.116.155301.

Baggaley AW, Barenghi CF, and Sergeev YA (2012) Quasiclassical and ultraquantum decay of superfluid turbulence. *Physical Review B* 85: 060501. https://doi.org/10.1103/PhysRevB.85.060501.

Bando Y, Susa Y, Oshiyama H, Shibata N, Ohzeki M, Gómez-Ruiz FJ, Lidar DA, Suzuki S, del Campo A, and Nishimori H (2020) Probing the universality of topological defect formation in a quantum annealer: Kibble-Zurek mechanism and beyond. *Physical Review Research* 2: 033369. https://doi.org/10.1103/PhysRevResearch.2.033369.

Banik N and Sikivie P (2017) Cosmic axion Bose-Einstein condensation. In: Proukakis NP, Snoke DW, and Littlewood PB (eds.) *Universal Themes of Bose-Einstein Condensation*. Cambridge: Cambridge University Press.

Barenghi CF, Donnelly RJ, and Vinen WF (2001) Quantized Vortex Dynamics and Superfluid Turbulence. *Lecture Notes in Physics.* , 571. Berlin: Springer.

Barenghi CF, Skrbek L, and Sreenivasan KR (2014) Introduction to quantum turbulence. *Proceedings of the National Academy of Sciences of the United States of America* 111: 4647–4652. supplement 1.

Barenghi CF, Sergeev YA, and Baggaley AW (2016) Regimes of turbulence without an energy cascade. *Scientific Reports* 6: 35701.

Bäuerle C, Bunkov YM, Fisher SN, Godfrin H, and Pickett GR (1996) Laboratory simulation of cosmic string formation in the early Universe using superfluid 3He. *Nature* 382(6589): 332–334. https://doi.org/10.1038/382332a0.

Berges J (2016) Nonequilibrium quantum fields: From cold atoms to cosmology. In: *Strongly Interacting Quantum Systems out of Equilibrium. Lecture Notes of the Les Houches Summer School: Volume 99, August 2012*. Oxford University Press. https://eur03.safelinks.protection.outlook.com/?url=https%3A%2F%2Fdoi.org%2F10.1093%2Facprof%3Aoso%2F9780198768166.003.0002&data=05%7C01%7Cnikolaos.proukakis%40newcastle.ac.uk%7C90a05c0408694589ee1f08db0b714766%7C9c5012c9b61644c2a91766814fbe3e87%7C1%7C0%7C638116353390136069%7CUnknown%7CTWFpbGZsb3d8eyJWIjoiMC4wLjAwMDAiLCJQIjoiV2luMzIiLCJBTiI6Ik1haWwiLCJXVCI6Mn0%3D%7C3000%7C%7C%7C&sdata=0gz0T2ycHAJ1uYfQ1hcBciuW2C%2BvomBpm5gk7OyAN%2F8%3D&reserved=0.

Berges J and Hoffmeister G (2009) Nonthermal fixed points and the functional renormalization group. *Nuclear Physics* B813: 383. https://doi.org/10.1016/j.nuclphysb.2008.12.017. 0809.5208.

Berges J, Borsanyi S, and Wetterich C (2004) Prethermalization. *Physical Review Letters* 93: 142002. https://doi.org/10.1103/PhysRevLett.93.142002. hep-ph/0403234.

Berges J, Rothkopf A, and Schmidt J (2008) Non-thermal fixed points: Effective weak-coupling for strongly correlated systems far from equilibrium. *Physical Review Letters* 101: 041603. https://doi.org/10.1103/PhysRevLett.101.041603. 0803.0131.

Berges J, Boguslavski K, Schlichting S, and Venugopalan R (2015) Universality far from equilibrium: From superfluid Bose gases to heavy-ion collisions. *Physical Review Letters* 114: 061601. https://doi.org/10.1103/PhysRevLett.114.061601.

Berges J, Heller MP, Mazeliauskas A, and Venugopalan R (2021) Qcd thermalization: Ab initio approaches and interdisciplinary connections. *Reviews of Modern Physics* 93: 035003. https://doi.org/10.1103/RevModPhys.93.035003.

Berloff NG (1999) Nonlocal nonlinear Schrödinger equations as models of superfluidity. *Journal of Low Temperature Physics* 116: 359–380.

Berloff NG and Svistunov BV (2002) Scenario of strongly nonequilibrated Bose-Einstein condensation. *Physical Review A* 66(1): 013603. https://doi.org/10.1103/PhysRevA.66.013603.

Berloff NG, Brachet M, and Proukakis NP (2014) Modeling quantum fluid dynamics at nonzero temperatures. *Proceedings of the National Academy of Sciences of the United States of America* 111(supplement 1): 4675–4682. https://doi.org/10.1073/pnas.1312549111.

Beugnon J and Navon N (2017) Exploring the Kibble-Zurek mechanism with homogeneous Bose gases. *Journal of Physics B: Atomic, Molecular and Optical Physics* 50(2): 022002. https://doi.org/10.1088/1361-6455/50/2/022002.

Bijlsma MJ, Zaremba E, and Stoof HTC (2000) Condensate growth in trapped Bose gases. *Physical Review A* 62: 063609. https://doi.org/10.1103/PhysRevA.62.063609.

Billam TP, Brown K, and Moss IG (2022) False-vacuum decay in an ultracold spin-1 Bose gas. *Physical Review A* 105: L041301. https://doi.org/10.1103/PhysRevA.105.L041301.

Binney J, Dowrick NJ, Fisher AJ, and Newman MEJ (1992) The Theory of Critical Phenomena: An Introduction to the Renormalization Group. *Oxford Science Publ.* Clarendon Press, ISBN: 9780198513933. https://books.google.co.uk/books?id=lvZcGJI3X9cC.

Blakie PB, Bradley AS, Davis MJ, Ballagh RJ, and Gardiner CW (2008) Dynamics and statistical mechanics of ultra-cold Bose gases using c-field techniques. *Advances in Physics* 57(5): 363–455. https://doi.org/10.1080/00018730802564254. 0809.1487.

Bland T, Marolleau Q, Comaron P, Malomed B, and Proukakis NP (2020) Persistent current formation in double-ring geometries. *Journal of Physics B: Atomic, Molecular and Optical Physics* 53: 115301. http://iopscience.iop.org/10.1088/1361-6455/ab81e9.

Bloch I, Dalibard J, and Nascimbène S (2012) Quantum simulations with ultracold quantum gases. *Nature Physics* ISSN: 1745-2473. 8(4): 267–276. https://doi.org/10.1038/nphys2259. http://www.nature.com.ezproxy.lib.monash.edu.au/nphys/journal/v8/n4/abs/nphys2259.html?foxtrotcallback=true.

Bloch J, Carusotto I, and Wouters M (2022) Non-equilibrium Bose-Einstein condensation in photonic systems. *Nature Reviews Physics* 4: 470–488.

Bradley DI, Clubb DO, Fisher SN, Guénault AM, Haley RP, Matthews CJ, Pickett GR, Tsepelin V, and Zaki K (2006) Decay of pure quantum turbulence in superfluid ^{3}He-B. *Physical Review Letters* 96: 035301. https://doi.org/10.1103/PhysRevLett.96.035301.

Bradley AS, Gardiner CW, and Davis MJ (2008) Bose-Einstein condensation from a rotating thermal cloud: Vortex nucleation and lattice formation. *Physical Review A* 77: 033616. https://doi.org/10.1103/PhysRevA.77.033616.

Braun S, Friesdorf M, Hodgman SS, Schreiber M, Ronzheimer JP, Riera A, del Rey M, Bloch I, Eisert J, and Schneider U (2015) Emergence of coherence and the dynamics of quantum phase transitions. *Proceedings of the National Academy of Sciences of the United States of America* ISSN: 0027-8424. 112(12): 3641–3646. https://doi.org/10.1073/pnas.1408861112.

Bray AJ (1994) Theory of phase-ordering kinetics. *Advances in Physics* ISSN: 0001-8732. 43: 357–459. https://doi.org/10.1080/00018730110117433.

Bruce A and Wallace D (1992) Critical point phenomena: Universal physics at large length scales. In: Davies P (ed.) *The New Physics*. Cambridge: Cambridge University Press.

Bullock JS and Boylan-Kolchin M (2017) Small-Scale Challenges to the ΛCDM Paradigm. *Annual Review of Astronomy and Astrophysics* 55(1): 343–387. https://doi.org/10.1146/annurev-astro-091916-055313. 1707.04256.

Caputo D, Ballarini D, Dagvadorj G, Munoz CS, de Giorgi M, Dominici L, West K, Pfeiffer LN, Gigli G, Laussy FP, Szymanska MH, and Sanvitto D (2018) Topological order and thermal equilibrium in polariton condensates. *Nature Materials* 17: 145–151.

Carmi R, Polturak E, and Koren G (2000) Observation of spontaneous flux generation in a multi-Josephson-junction loop. *Physical Review Letters* 84: 4966–4969. https://doi.org/10.1103/PhysRevLett.84.4966.

Carusotto I and Ciuti C (2013) Quantum fluids of light. *Reviews of Modern Physics* 85(1): 299.

Chae SC, Lee N, Horibe Y, Tanimura M, Mori S, Gao B, Carr S, and Cheong S-W (2012) Direct observation of the proliferation of ferroelectric loop domains and vortex-antivortex pairs. *Physical Review Letters* 108: 167603. https://doi.org/10.1103/PhysRevLett.108.167603.

Chan HYJ, Ferreira EGM, May S, Hayashi K, and Chiba M (2022) The diversity of core-halo structure in the fuzzy dark matter model. *Monthly Notices of the Royal Astronomical Society* ISSN: 0035-8711. 511(1): 943–952. https://doi.org/10.1093/mnras/stac063.

Chantesana I, Orioli AP, and Gasenzer T (2019) Kinetic theory of nonthermal fixed points in a Bose gas. *Physical Review A* 99(4): 043620. https://doi.org/10.1103/PhysRevA.99.043620.

Chavanis P-H (2011) Mass-radius relation of Newtonian self-gravitating Bose-Einstein condensates with short-range interactions. I. Analytical results. *Physical Review D* 84: 043531. https://doi.org/10.1103/PhysRevD.84.043531.

Chen D, White M, Borries C, and DeMarco B (2011) Quantum quench of an atomic Mott insulator. *Physical Review Letters* 106: 235304. https://doi.org/10.1103/PhysRevLett.106.235304.

Chiocchetta A and Carusotto I (2013) Non-equilibrium quasi-condensates in reduced dimensions. *EPL (Europhysics Letters)* 102(6): 67007.

Chomaz L, Corman L, Bienaimé T, Desbuquois R, Weitenberg C, Nascimbène S, Beugnon J, and Dalibard J (2015) Emergence of coherence via transverse condensation in a uniform quasi-two-dimensional Bose gas. *Nature Communications* 6(1): 6162. https://doi.org/10.1038/ncomms7162.

Chomaz L, Ferrier-Barbut I, Ferlaino F, Laburthe-Tolra B, Lev BL, and Pfau T (2022) Dipolar physics: A review of experiments with magnetic quantum gases. *Reports on Progress in Physics* 86(2): 026401. https://doi.org/10.1088/1361-6633/aca814.

Chu S (1998) Nobel lecture: The manipulation of neutral particles. *Reviews of Modern Physics* 70: 685–706. https://doi.org/10.1103/RevModPhys.70.685.

Chuang I, Durrer R, Turok N, and Yurke B (1991) Cosmology in the laboratory: Defect dynamics in liquid crystals. *Science* 251(4999): 1336–1342. https://doi.org/10.1126/science.251.4999.1336.

Clark LW, Feng L, and Chin C (2016) Universal space-time scaling symmetry in the dynamics of bosons across a quantum phase transition. *Science* 354(6312): 606–610. https://doi.org/10.1126/science.aaf9657.

Cockburn SP, Negretti A, Proukakis NP, and Henkel C (2011) Comparison between microscopic methods for finite-temperature Bose gases. *Physical Review A* 83: 043619. https://doi.org/10.1103/PhysRevA.83.043619.

Cohen-Tannoudji CN (1998) Nobel lecture: Manipulating atoms with photons. *Reviews of Modern Physics* 70: 707–719. https://doi.org/10.1103/RevModPhys.70.707.

Cohen-Tannoudji C and Robilliard C (2001) Wave functions, relative phase and interference for atomic Bose-Einstein condensates. *Comptes Rendus Physique* 2: 445.

Comaron P, Dagvadorj G, Zamora A, Carusotto I, Proukakis NP, and Szymańska MH (2018) Dynamical critical exponents in driven-dissipative quantum systems. *Physical Review Letters* 121(9): 095302.

Comaron P, Carusotto I, Szymańska MH, and Proukakis NP (2021) Non-equilibrium Berezinskii-Kosterlitz-Thouless transition in driven-dissipative condensates(a). *Europhysics Letters* 133(1): 17002. https://doi.org/10.1209/0295-5075/133/17002.

Cooper LN and Feldman D (2010) *Bcs: 50 Years*. World Scientific Publishing Company, ISBN: 9789814360869. https://books.google.co.uk/books?id=spnFCgAAQBAJ.

Corman L, Chomaz L, Bienaime T, Desbuquois R, Weitenberg C, Nascimbene S, Dalibard J, and Beugnon J (2014) Quench-induced supercurrents in an annular Bose gas. *Physical Review Letters* 113: 135302.

Cornell EA and Wieman CE (2002) Nobel lecture: Bose-Einstein condensation in a dilute gas, the first 70 years and some recent experiments. *Reviews of Modern Physics* 74: 875–893. https://doi.org/10.1103/RevModPhys.74.875.

Dagvadorj G, Fellows JM, Matyjaśkiewicz S, Marchetti FM, Carusotto I, and Szymańska MH (2015) Nonequilibrium phase transition in a two-dimensional driven open quantum system. *Physical Review X* 5: 041028. https://doi.org/10.1103/PhysRevX.5.041028.

Dalfovo F, Giorgini S, Pitaevskii LP, and Stringari S (1999) Theory of Bose-Einstein condensation in trapped gases. *Reviews of Modern Physics* 71: 463–512.

Damle K, Majumdar SN, and Sachdev S (1996) Phase ordering kinetics of the Bose gas. *Physical Review A* 54: 5037–5041. https://doi.org/10.1103/PhysRevA.54.5037.

Das A, Sabbatini J, and Zurek WH (2012) Winding up superfluid in a torus via Bose Einstein condensation. *Scientific Reports* 2: 352.

Davis MJ, Morgan SA, and Burnett K (2002) Simulations of thermal Bose fields in the classical limit. *Physical Review A* 66: 053618. https://doi.org/10.1103/PhysRevA.66.053618.

Davis MJ, Wright TM, Gasenzer T, Gardiner SA, and Proukakis NP (2017) Formation of Bose-Einstein condensates. In: Proukakis NP, Snoke DW, and Littlewood PB (eds.) *Universal Themes of Bose-Einstein Condensation*. Cambridge: Cambridge University Press.

del Campo A and Zurek WH (2014) Universality of phase transition dynamics: Topological defects from symmetry breaking. *International Journal of Modern Physics A* ISSN: 0217-751X. 29(08): 1430018. https://doi.org/10.1142/S0217751X1430018X.

del Campo A, Retzker A, and Plenio MB (2011) The inhomogeneous Kibble-Zurek mechanism: Vortex nucleation during Bose-Einstein condensation. *New Journal of Physics* 13(8): 083022. https://doi.org/10.1088/1367-2630/13/8/083022.

del Campo A, Kibble TWB, and Zurek WH (2013) Causality and non-equilibrium second-order phase transitions in inhomogeneous systems. *Journal of Physics. Condensed Matter* 25(40): 404210. https://doi.org/10.1088/0953-8984/25/40/404210.

Del Popolo A and Le Delliou M (2017) Small scale problems of the ΛCDM model: A short review. *Galaxies* 5(1): 17. https://doi.org/10.3390/galaxies5010017. 1606.07790.

Delgado V and Muñoz Mateo A (2022) Self-interacting superfluid dark matter droplets. *Monthly Notices of the Royal Astronomical Society* ISSN: 0035-8711. 518(3): 4064–4072. https://doi.org/10.1093/mnras/stac3386.

Deligiannis K, Squizzato D, Minguzzi A, and Canet L (2021) Accessing Kardar-Parisi-Zhang universality sub-classes with exciton polaritons(a). *Europhysics Letters* 132(6): 67004. https://doi.org/10.1209/0295-5075/132/67004.

Deligiannis K, Fontaine Q, Squizzato D, Richard M, Ravets S, Bloch J, Minguzzi A, and Canet L (2022) Kardar-Parisi-Zhang universality in discrete two-dimensional driven-dissipative exciton polariton condensates. *Physical Review Research* 4: 043207. https://doi.org/10.1103/PhysRevResearch.4.043207.

Deng H, Haug H, and Yamamoto Y (2010) Exciton-polariton Bose-Einstein condensation. *Reviews of Modern Physics* 82(2): 1489. https://doi.org/10.1103/RevModPhys.82.1489.

Desjacques V, Kehagias A, and Riotto A (2018) Impact of ultralight axion self-interactions on the large scale structure of the universe. *Physical Review D* 97: 023529. https://doi.org/10.1103/PhysRevD.97.023529.

Diessel OK, Diehl S, and Chiocchetta A (2022) Emergent Kardar-Parisi-Zhang phase in quadratically driven condensates. *Physical Review Letters* 128: 070401. https://doi.org/10.1103/PhysRevLett.128.070401.

Donadello S, Serafini S, Tylutki M, Pitaevskii LP, Dalfovo F, Lamporesi G, and Ferrari G (2014) Observation of Solitonic Vortices in Bose-Einstein Condensates. *Physical Review Letters* 113(6): 065302. https://doi.org/10.1103/PhysRevLett.113.065302.

Donadello S, Serafini S, Bienaimé T, Dalfovo F, Lamporesi G, and Ferrari G (2016) Creation and counting of defects in a temperature-quenched Bose-Einstein condensate. *Physical Review A* 94(2): 023628.

Donner T, Ritter S, Bourdel T, Ottl A, Köhl M, and Esslinger T (2007) Critical behavior of a trapped interacting Bose gas. *Science* 315(5818): 1556–1558. https://doi.org/10.1126/science.1138807.

Drummond LV and Melatos A (2017) Stability of interlinked neutron vortex and proton flux tube arrays in a neutron star: Equilibrium configurations. *Monthly Notices of the Royal Astronomical Society* ISSN: 0035-8711. 472(4): 4851–4869. https://doi.org/10.1093/mnras/stx2301.

Dvali G and Gomez C (2017) Graviton BECs: A new approach to quantum gravity. In: Proukakis NP, Snoke DW, and Littlewood PB (eds.) *Universal Themes of Bose-Einstein Condensation*. Cambridge: Cambridge University Press.

Dziarmaga J (2010) Dynamics of a quantum phase transition and relaxation to a steady state. *Advances in Physics* 59(6): 1063–1189.

Dziarmaga J, Laguna P, and Zurek WH (1999) Symmetry breaking with a slant: Topological defects after an inhomogeneous quench. *Physical Review Letters* 82: 4749–4752. https://doi.org/10.1103/PhysRevLett.82.4749.

Eigen C, Glidden JAP, Lopes R, Navon N, Hadzibabic Z, and Smith RP (2017) Universal scaling laws in the dynamics of a homogeneous unitary Bose gas. *Physical Review Letters* 119: 250404. https://doi.org/10.1103/PhysRevLett.119.250404.

Eigen C, Glidden JAP, Lopes R, Cornell EA, Smith RP, and Hadzibabic Z (2018) Universal prethermal dynamics of Bose gases quenched to unitarity. *Nature* 563: 221–224.

Erne S, Bücker R, Gasenzer T, Berges J, and Schmiedmayer J (2018) Universal dynamics in an isolated one-dimensional Bose gas far from equilibrium. *Nature* 563: 225–229.

Ferreira EGM (2021) Ultra-light dark matter. *Astronomy and Astrophysics Review* 29: 7.

Fialko O, Opanchuk B, Sidorov AI, Drummond PD, and Brand J (2015) Fate of the false vacuum: Towards realization with ultra-cold atoms. *Europhysics Letters* 110(5): 56001. https://doi.org/10.1209/0295-5075/110/56001.

Fontaine Q, Squizzato D, Baboux F, Amelio I, Lemaître A, Morassi M, Sagnes I, Gratiet L, Harouri A, Wouters M, Carusotto I, Amo A, Richard M, Minguzzi A, Canet L, Ravets S, and Bloch J (2022) Kardar-Parisi-Zhang universality in a one-dimensional polariton condensate. *Nature* 608: 687–691.

Frenk CS and White SDM (2012) Dark matter and cosmic structure. *Annalen der Physik* 524(9-10): 507–534. https://doi.org/10.1002/andp.201200212. 1210.0544.

Fried DG, Killian TC, Willmann L, Landhuis D, Moss SC, Kleppner D, and Greytak TJ (1998) Bose-Einstein condensation of atomic hydrogen. *Physical Review Letters* 81: 3811.

García-Orozco AD, Madeira L, Moreno-Armijos MA, Fritsch AR, Tavares PES, Castilho PCM, Cidrim A, Roati G, and Bagnato VS (2022) Universal dynamics of a turbulent superfluid Bose gas. *Physical Review A* 106: 023314. https://doi.org/10.1103/PhysRevA.106.023314.

Gardas B, Dziarmaga J, Zurek WH, and Zwolak M (2018) Defects in quantum computers. *Scientific Reports* 8: 4539. https://doi.org/10.1038/s41598-018-22763-2.

Gardiner CW and Davis MJ (2003) The stochastic Gross-Pitaevskii equation: II. *Journal of Physics B: Atomic, Molecular and Optical Physics* ISSN: 0953-4075. 36(23): 4731. https://doi.org/10.1088/0953-4075/36/23/010.

Gardiner CW, Lee MD, Ballagh RJ, Davis MJ, and Zoller P (1998) Quantum kinetic theory of condensate growth: Comparison of experiment and theory. *Physical Review Letters* 81: 5266.

Gauthier G, Reeves MT, Yu X, Bradley AS, Baker MA, Bell TA, Rubinsztein-Dunlop H, Davis MJ, and Neely TW (2019) Giant vortex clusters in a two-dimensional quantum fluid. *Science* 364(6447): 1264–1267. https://doi.org/10.1126/science.aat5718.

Gladilin VN, Ji K, and Wouters M (2014) Spatial coherence of weakly interacting one-dimensional nonequilibrium bosonic quantum fluids. *Physical Review A* 90: 023615. https://doi.org/10.1103/PhysRevA.90.023615.

Glidden JAP, Eigen C, Dogra LH, Hilker TA, Smith RP, and Hadzibabic Z (2021) Bidirectional dynamic scaling in an isolated Bose gas far from equilibrium. *Nature Physics* 17: 457–461.

Goo J, Lim Y, and Shin Y (2021) Defect saturation in a rapidly quenched Bose gas. *Physical Review Letters* 127: 115701. https://doi.org/10.1103/PhysRevLett.127.115701.

Goo J, Lee Y, Lim Y, Bae D, Rabga T, and Shin Y (2022) Universal early coarsening of quenched Bose gases. *Physical Review Letters* 128: 135701. https://doi.org/10.1103/PhysRevLett.128.135701.

Greiner M, Mandel MO, Esslinger T, Hänsch T, and Bloch I (2002) Quantum phase transition from a superfluid to a mott insulator in a gas of ultracold atoms. *Nature* 415: 39.

Greytak T and Kleppner D (2017) A history of Bose-Einstein condensation of atomic hydrogen. In: Proukakis NP, Snoke DW, and Littlewood PB (eds.) *Universal Themes of Bose-Einstein Condensation.* Cambridge: Cambridge University Press.

Griffin A, Snoke DW, and Stringari S (1995) *Bose-Einstein Condensation.* Cambridge: Cambridge University Press.

Gring M, Kuhnert M, Langen T, Kitagawa T, Rauer B, Schreitl M, Mazets I, Smith DA, Demler E, and Schmiedmayer J (2012) Relaxation and prethermalization in an isolated quantum system. *Science* 337(6100): 1318. https://doi.org/10.1126/science.1224953.

Groszek AJ, Comaron P, Proukakis NP, and Billam TP (2021) Crossover in the dynamical critical exponent of a quenched two-dimensional Bose gas. *Physical Review Research* 3: 013212. https://doi.org/10.1103/PhysRevResearch.3.013212.

He L, Sieberer LM, Altman E, and Diehl S (2015) Scaling properties of one-dimensional driven-dissipative condensates. *Physical Review B* 92: 155307. https://doi.org/10.1103/PhysRevB.92.155307.

Hendry PC, Lawson NS, Lee RAM, McClintock PVE, and Williams CDH (1994) Generation of defects in superfluid 4He as an analogue of the formation of cosmic strings. *Nature* 368: 315–317.

Henn EAL, Seman JA, Roati G, Magalhães KMF, and Bagnato VS (2009) Emergence of turbulence in an oscillating Bose-Einstein condensate. *Physical Review Letters* 103: 045301. https://doi.org/10.1103/PhysRevLett.103.045301.

Hohenberg PC and Halperin BI (1977) Theory of dynamic critical phenomena. *Reviews of Modern Physics* 49: 435–479. https://doi.org/10.1103/RevModPhys.49.435.

Holzmann M, Fuchs J-N, Baym GA, Blaizot J-P, and Laloë F (2004) Bose-Einstein transition temperature in a dilute repulsive gas. *Comptes Rendus Physique* ISSN: 1631-0705. 5(1): 21–37. https://doi.org/10.1016/j.crhy.2004.01.003. Bose-Einstein condensates: Recent advances in collective effects.

Hu W, Barkana R, and Gruzinov A (2000) Fuzzy cold dark matter: The wave properties of ultralight particles. *Physical Review Letters* ISSN: 00319007. 85(6): 1158–1161. https://doi.org/10.1103/PhysRevLett.85.1158.

Huang K (1987) *Statistical Mechanics.* New York: Wiley.

Hui L (2021) Wave dark matter. *Annual Review of Astronomy and Astrophysics* 59: 247–289. https://doi.org/10.1146/annurev-astro-120920-010024. 2101.11735.

Jacquet MJ, Weinfurtner S, and König F (2020) The next generation of analogue gravity experiments. *Philosophical Transactions of the Royal Society A* 378: 20190239.

Jelić A and Cugliandolo LF (2011) Quench dynamics of the 2d XY model. *Journal of Statistical Mechanics: Theory and Experiment* 2011(2): P02032.

Ji K, Gladilin VN, and Wouters M (2015) Temporal coherence of one-dimensional nonequilibrium quantum fluids. *Physical Review B* 91: 045301. https://doi.org/10.1103/PhysRevB.91.045301.

Jiménez-García K, Invernizzi A, Evrard B, Frapolli C, Dalibard J, and Gerbier F (2019) Spontaneous formation and relaxation of spin domains in antiferromagnetic spin-1 condensates. *Nature Communications* 10: 1422.

Johnstone SP, Groszek AJ, Starkey PT, Billington CJ, Simula TP, and Helmerson K (2019) Evolution of large-scale flow from turbulence in a two-dimensional superfluid. *Science* 364 (6447): 1267–1271. https://doi.org/10.1126/science.aat5793.

Jos JV (2013) 40 Years of Berezinskii-Kosterlitz-Thouless Theory. *EBL-Schweitzer.* World Scientific, ISBN: 9789814417648. https://books.google.co.uk/books?id=roO6CgAAQBAJ.

Kagan Y (1995) Kinetics of Bose-Einstein condensate formation in an interacting Bose gas. In: Griffin A, Snoke DW, and Stringari S (eds.) *Bose-Einstein Condensation*, p. 202. Cambridge: Cambridge University Press.

Kagan Y and Svistunov BV (1994) Kinetics of the onset of long-range order during Bose condensation in an interacting gas. *Soviet Physics–JETP* 78: 187.

Kagan Y and Svistunov BV (1997) Evolution of correlation properties and appearance of broken symmetry in the process of Bose-Einstein condensation. *Physical Review Letters* 79: 3331.

Kagan Y, Svistunov BV, and Shlyapnikov GV (1992) Kinetics of Bose condensation in an interacting Bose gas. *Soviet Physics–JETP* 75: 387.

Kardar M, Parisi G, and Zhang Y-C (1986) Dynamic scaling of growing interfaces. *Physical Review Letters* 56: 889–892. https://doi.org/10.1103/PhysRevLett.56.889.

Karl M and Gasenzer T (2017) Strongly anomalous non-thermal fixed point in a quenched two-dimensional Bose gas. *New Journal of Physics* 19(9): 093014. https://doi.org/10.1088/1367-2630/aa7eeb.

Kasprzak J, et al. (2006) Bose-Einstein condensation of exciton polaritons. *Nature (London)* 443(7110): 409–414. https://doi.org/10.1038/nature05131.

Keeling J and Berloff NG (2008) Spontaneous rotating vortex lattices in a pumped decaying condensate. *Physical Review Letters* 100: 250401. https://doi.org/10.1103/PhysRevLett.100.250401.

Keeling J, Sieberer LM, Altman E, Chen L, Diehl S, and Toner J (2017) Superfluidity and phase correlations of driven dissipative condensates. In: Proukakis N, Snoke DW, and Littlewood PB (eds.) *Universal Themes of Bose-Einstein Condensation.* Cambridge: Cambridge University Press.

Ketterle W (2002) Nobel lecture: When atoms behave as waves: Bose-Einstein condensation and the atom laser. *Reviews of Modern Physics* 74: 1131–1151. https://doi.org/10.1103/RevModPhys.74.1131.

Kibble TWB (1976) Topology of cosmic domains and strings. *Journal of Physics A: Mathematical and General* 9(8): 1387.

Kim M, Rabga T, Lee Y, Goo J, Bae D, and Shin Y (2022) Suppression of spontaneous defect formation in inhomogeneous Bose gases. *Physical Review A* 106: L061301. https://doi.org/10.1103/PhysRevA.106.L061301.

Klaers J, Schmitt J, Vewinger F, and Weitz M (2010) Bose-Einstein condensation of photons in an optical microcavity. *Nature* 468: 545–548.

Ko B, Park JW, and Shin Y (2019) Kibble-Zurek universality in a strongly interacting Fermi superfluid. *Nature Physics* 15: 1227–1231. https://doi.org/10.1038/s41567-019-0650-1.

Kobayashi M and Cugliandolo LF (2016a) Quench dynamics of the three-dimensional U(1) complex field theory: Geometric and scaling characterizations of the vortex tangle. *Physical Review E* 94: 062146. https://doi.org/10.1103/PhysRevE.94.062146.

Kobayashi M and Cugliandolo LF (2016b) Thermal quenches in the stochastic Gross-Pitaevskii equation: Morphology of the vortex network. *Europhysics Letters* 115(2): 20007. https://doi.org/10.1209/0295-5075/115/20007.

Köhl M, Davis MJ, Gardiner CW, Hänsch TW, and Esslinger T (2002) Growth of Bose-Einstein condensates from thermal vapor. *Physical Review Letters* 88: 080402. https://doi.org/10.1103/PhysRevLett.88.080402.

Kosterlitz JM (2017) Nobel lecture: Topological defects and phase transitions. *Reviews of Modern Physics* 89: 040501. https://doi.org/10.1103/RevModPhys.89.040501.

Lamporesi G, Donadello S, Serafini S, Dalfovo F, and Ferrari G (2013) Spontaneous creation of Kibble-Zurek solitons in a Bose-Einstein condensate. *Nature Physics* 9(10): 656.

Langen T and Schmiedmayer J (2017) Quenches, relaxation and prethermalization in an isolated quantum system. In: Proukakis NP, Snoke DW, and Littlewood PB (eds.) *Universal Themes of Bose-Einstein Condensation*. Cambridge: Cambridge University Press.

Leggett AJ (2006) *Quantum Liquids*. Oxford University Press.

Lifshitz EM and Pitaevskii LP (1995) Physical Kinetics. *Course of Theoretical Physics.* , vol. 10. Elsevier Science, ISBN: 9780750626354. https://books.google.co.uk/books?id=h7LgAAAAMAAJ.

Liu I-K, Donadello S, Lamporesi G, Ferrari G, Gou S-C, Dalfovo F, and Proukakis NP (2018) Dynamical equilibration across a quenched phase transition in a trapped quantum gas. *Communications Physics* ISSN: 2399-3650. 1(1): 24. https://doi.org/10.1038/s42005-018-0023-6.

Liu I-K, Dziarmaga J, Gou S-C, Dalfovo F, and Proukakis NP (2020) Kibble-Zurek dynamics in a trapped ultracold Bose gas. *Physical Review Research* 2: 033183. https://doi.org/10.1103/PhysRevResearch.2.033183.

Liu I-K, Proukakis NP, and Rigopoulos G (2023) Coherent and incoherent structures in fuzzy dark matter haloes. *Monthly Notices of the Royal Astronomical Society* ISSN: 0035-8711. 521(3): 3625–3647. https://doi.org/10.1093/mnras/stad591.

Madeira L and Bagnato VS (2022) Non-thermal fixed points in Bose gas experiments. *Symmetry* 678: 14.

Marsh DJE (2016) Axion cosmology. *Physics Reports* 643: 1–79. https://doi.org/10.1016/j.physrep.2016.06.005. 1510.07633.

May S and Springel V (2021) Structure formation in large-volume cosmological simulations of fuzzy dark matter: Impact of the non-linear dynamics. *Monthly Notices of the Royal Astronomical Society* 506(2): 2603–2618. https://doi.org/10.1093/mnras/stab1764. 2101.01828.

Meldgin C, Ray U, Russ P, Chen D, Ceperley DM, and DeMarco B (2016) Probing the Bose glass-superfluid transition using quantum quenches of disorder. *Nature Physics* 12: 646–649. https://doi.org/10.1038/nphys3695.

Miesner H-J, Stamper-Kurn DM, Andrews MR, Durfee DS, Inouye S, and Ketterle W (1998) Bosonic stimulation in the formation of a Bose-Einstein condensate. *Science* 279(5353): 1005–1007. https://doi.org/10.1126/science.279.5353.1005.

Mocz P, Vogelsberger M, Robles VH, Zavala J, Boylan-Kolchin M, Fialkov A, and Hernquist L (2017) Galaxy formation with BECDM - I. Turbulence and relaxation of idealized haloes. *Monthly Notices of the Royal Astronomical Society* 471(4): 4559–4570. https://doi.org/10.1093/mnras/stx1887. 1705.05845.

Mocz P, Fialkov A, Vogelsberger M, Boylan-Kolchin M, Chavanis P-H, Amin MA, Bose S, Dome T, Hernquist L, Lancaster L, Notis M, Painter C, Robles VH, and Zavala J (2023) Cosmological structure formation and soliton phase transition in fuzzy dark matter with axion self-interactions. *Monthly Notices of the Royal Astronomical Society* ISSN: 0035-8711. 521(2): 2608–2615. https://doi.org/10.1093/mnras/stad694.

Monaco R, Mygind J, Rivers RJ, and Koshelets VP (2009) Spontaneous fluxoid formation in superconducting loops. *Physical Review B* 80: 180501. https://doi.org/10.1103/PhysRevB.80.180501.

Nam K, Baek W-B, Kim B, and Lee SJ (2012) Coarsening of two-dimensional XY model with Hamiltonian dynamics: Logarithmically divergent vortex mobility. *Journal of Statistical Mechanics: Theory and Experiment* 2012(11): P11023. https://doi.org/10.1088/1742-5468/2012/11/P11023.

Navarro JF, Frenk CS, and White SDM (1996) The structure of cold dark matter Halos. *The Astrophysical Journal* 462: 563.

Navon N, Gaunt AL, Smith RP, and Hadzibabic Z (2015) Critical dynamics of spontaneous symmetry breaking in a homogeneous Bose gas. *Science* 347(6218): 167–170. https://doi.org/10.1126/science.1258676.

Navon N, Gaunt A, Smith R, and Hadzibabic Z (2016) Emergence of a turbulent cascade in a quantum gas. *Nature* 539: 72–75.

Navon N, Eigen C, Zhang J, Lopes R, Gaunt AL, Fujimoto K, Tsubota M, Smith RP, and Hadzibabic Z (2019) Synthetic dissipation and cascade fluxes in a turbulent quantum gas. *Science* 366(6463): 382–385. https://doi.org/10.1126/science.aau6103.

Nishimori H and Ortiz G (2011) Elements of Phase Transitions and Critical Phenomena. *Oxford Graduate Texts.* OUP Oxford, ISBN: 9780199577224. https://books.google.co.uk/books?id=qiEUDAAAQBAJ.

Nitsche WH, Kim NY, Roumpos G, Schneider C, Kamp M, Höfling S, Forchel A, and Yamamoto Y (2014) Algebraic order and the Berezinskii-Kosterlitz-Thouless transition in an exciton-polariton gas. *Physical Review B* 90(20): 205430. https://doi.org/10.1103/PhysRevB.90.205430.

Nowak B, Sexty D, and Gasenzer T (2011) Superfluid turbulence: Nonthermal fixed point in an ultracold Bose gas. *Physical Review B* 84: 020506. https://doi.org/10.1103/PhysRevB.84.020506.

Nowak B, Schole J, Sexty D, and Gasenzer T (2012) Nonthermal fixed points, vortex statistics, and superfluid turbulence in an ultracold Bose gas. *Physical Review A* 85: 043627. https://doi.org/10.1103/PhysRevA.85.043627.

Nowak B, Schole J, and Gasenzer T (2014) Universal dynamics on the way to thermalization. *New Journal of Physics* 16(9): 093052. https://doi.org/10.1088/1367-2630/16/9/093052.

Penrose O and Onsager L (1956) Bose-Einstein condensation and liquid helium. *Physical Review* 104: 576.

Pethick CJ and Smith H (2002) *Bose-Einstein Condensation in Dilute Gases.* Cambridge University Press.

Pethick CJ, Schafer T, and Schwenk A (2017) Bose-Einstein condensates in neutron stars. In: Proukakis NP, Snoke DW, and Littlewood PB (eds.) *Universal Themes of Bose-Einstein Condensation.* Cambridge: Cambridge University Press.

Petrov DS, Gangardt DM, and Shlyapnikov GV (2004) Low-dimensional trapped gases. *Journal de Physique IV* 116: 5–44.

Phillips WD (1998) Nobel lecture: Laser cooling and trapping of neutral atoms. *Reviews of Modern Physics* 70: 721–741. https://doi.org/10.1103/RevModPhys.70.721.

Pickett GR (2017) A simulated cosmological metric: The superfluid ^{3}he condensate. In: Proukakis NP, Snoke DW, and Littlewood PB (eds.) *Universal Themes of Bose-Einstein Condensation.* Cambridge: Cambridge University Press.

Piñeiro Orioli A, Boguslavski K, and Berges J (2015) Universal self-similar dynamics of relativistic and nonrelativistic field theories near nonthermal fixed points. *Physical Review D* 92(2): 025041. https://doi.org/10.1103/PhysRevD.92.025041. 1503.02498.

Pitaevskii L and Stringari S (2016) *Bose-Einstein Condensation and Superfluidity.* Oxford: Oxford University Press.

Polkovnikov A, Sengupta K, Silva A, and Vengalattore M (2011) Colloquium: Nonequilibrium dynamics of closed interacting quantum systems. *Reviews of Modern Physics* 83: 863–883. https://doi.org/10.1103/RevModPhys.83.863.

Prokof'ev N and Svistunov B (2002) Two-dimensional weakly interacting Bose gas in the fluctuation region. *Physical Review A* 66: 043608. https://doi.org/10.1103/PhysRevA.66.043608.

Proukakis NP (2006) Spatial correlation functions of one-dimensional Bose gases at equilibrium. *Physical Review A* 74(5): 053617. https://doi.org/10.1103/PhysRevA.74.053617. cond-mat/0606617.

Proukakis NP and Burnett K (2013) Quantum gases: Setting the scene. In: Proukakis NP, Snoke DW, and Littlewood PB (eds.) *Quantum Gases: Finite Temperature and Non-Equilibrium Dynamics: 1 (Cold Atoms).* London: Imperial College Press.

Proukakis NP and Jackson B (2008) Finite-temperature models of Bose-Einstein condensation. *Journal of Physics B: Atomic, Molecular and Optical Physics* ISSN: 0953-4075. 41(20): 203002. https://doi.org/10.1088/0953-4075/41/20/203002.

Proukakis N, Gardiner S, Davis M, and Szymańska M (2013) *Quantum Gases: Finite Temperature and Non-Equilibrium Dynamics: 1 (Cold Atoms).* ICP.

Proukakis NP, Snoke DW, and Littlewood PB (2017) *Universal Themes of Bose-Einstein Condensation.* Cambridge University Press.

Prüfer M, Kunkel P, Strobel H, Lannig S, Linnemann D, Schmied C-M, Berges J, Gasenzer T, and Oberthaler MK (2018) Observation of universal dynamics in a spinor Bose gas far from equilibrium. *Nature* 563: 217–220.

Roumpos G, et al. (2012) Power-law decay of the spatial correlation function in exciton-polariton condensates. *Proceedings of the National Academy of Sciences* 109(17): 6467–6472. https://doi.org/10.1073/pnas.1107970109.

Rutenberg AD and Bray AJ (1995a) Energy-scaling approach to phase-ordering growth laws. *Physical Review E* 51(6): 5499–5514. https://doi.org/10.1103/PhysRevE.51.5499.

Rutenberg AD and Bray AJ (1995b) Phase ordering of two-dimensional XY systems below the Kosterlitz-Thouless transition temperature. *Physical Review E* 51(3): R1641. https://doi.org/10.1103/PhysRevE.51.R1641.

Sabbatini J, Zurek WH, and Davis MJ (2011) Phase separation and pattern formation in a binary Bose-Einstein condensate. *Physical Review Letters* 107: 230402. https://doi.org/10.1103/PhysRevLett.107.230402.

Sadhukhan D, Sinha A, Francuz A, Stefaniak J, Rams MM, Dziarmaga J, and Zurek WH (2020) Sonic horizons and causality in phase transition dynamics. *Physical Review B* 101: 144429. https://doi.org/10.1103/PhysRevB.101.144429.

Sadler LE, Higbie JM, Leslie SR, Vengalattore M, and Stamper-Kurn DM (2006) Spontaneous symmetry breaking in a quenched ferromagnetic spinor Bose-Einstein condensate. *Nature* 443: 312–315.

Saito H, Kawaguchi Y, and Ueda M (2007) Kibble-Zurek mechanism in a quenched ferromagnetic Bose-Einstein condensate. *Physical Review A* 76(4): 043613.

Sanvitto D and Timofeev V (2012) Exciton Polaritons in Microcavities: New Frontiers. *Springer Series in Solid-State Sciences.* Springer Berlin Heidelberg, ISBN: 9783642241864. https://books.google.co.uk/books?id=3ybfbv8d3NUC.

Schive H-Y, Chiueh T, and Broadhurst T (2014) Cosmic structure as the quantum interference of a coherent dark wave. *Nature Physics* 10(7): 496–499. https://doi.org/10.1038/nphys2996. 1406.6586.

Schmied C-M, Mikheev AN, and Gasenzer T (2019) Non-thermal fixed points: Universal dynamics far from equilibrium. *International Journal of Modern Physics A* ISSN: 0217-751X. 34(29): 1941006. https://doi.org/10.1142/S0217751X19410069.

Schwabe B, Niemeyer JC, and Engels JF (2016) Simulations of solitonic core mergers in ultralight axion dark matter cosmologies. *Physical Review D* 94(4): 043513. https://doi.org/10.1103/PhysRevD.94.043513. 1606.05151.

Seidel E and Suen W-M (1990) Dynamical evolution of Boson stars: Perturbing the ground state. *Physical Review D* 42(2): 384–403. https://doi.org/10.1103/PhysRevD.42.384.

Serafini S, Galantucci L, Iseni E, Bienaimé T, Bisset RN, Barenghi CF, Dalfovo F, Lamporesi G, and Ferrari G (2017) Vortex reconnections and rebounds in trapped atomic Bose-Einstein condensates. *Physical Review X* 7: 021031. https://doi.org/10.1103/PhysRevX.7.021031.

Smith RP (2017) Effects of interactions on Bose-Einstein condensation. In: Proukakis NP, Snoke DW, and Littlewood PB (eds.) *Universal Themes of Bose-Einstein Condensation.* Cambridge: Cambridge University Press.

Smith RP, Campbell RLD, Tammuz N, and Hadzibabic Z (2011) Effects of interactions on the critical temperature of a trapped Bose gas. *Physical Review Letters* 106: 250403. https://doi.org/10.1103/PhysRevLett.106.250403.

Snoke DW, Proukakis NP, Giamarchi T, and Littlewood PB (2017) Universality and Bose-Einstein condensation: Perspectives on recent work. In: Proukakis NP, Snoke DW, and Littlewood PB (eds.) *Universal Themes of Bose-Einstein Condensation.* Cambridge: Cambridge University Press.

Squizzato D, Canet L, and Minguzzi A (2018) Kardar-Parisi-Zhang universality in the phase distributions of one-dimensional exciton-polaritons. *Physical Review B* 97: 195453. https://doi.org/10.1103/PhysRevB.97.195453.

Stagg GW, Parker NG, and Barenghi CF (2016) Ultraquantum turbulence in a quenched homogeneous Bose gas. *Physical Review A* 94: 053632. https://doi.org/10.1103/PhysRevA.94.053632.

Stoof HTC (1995) Condensate formation in a Bose gas. In: Griffin A, Snoke DW, and Stringari S (eds.) *Bose-Einstein Condensation*, pp. 226–245. Cambridge: Cambridge University Press.

Stoof HTC (1999) Coherent versus incoherent dynamics during Bose-Einstein condensation in atomic gases. *Journal of Low Temperature Physics* 114(1/2): 11.

Stoof HTC and Bijlsma MJ (2001) Dynamics of fluctuating Bose-Einstein condensates. *Journal of Low Temperature Physics* 124: 431–442. https://doi.org/10.1023/A:1017519118408.

Svistunov BV (1991) Highly nonequilibrium Bose condensation in a weakly interacting gas. *Journal of the Moscow Physical Society* 1: 373–390.

Świsłocki T, Witkowska E, Dziarmaga J, and Matuszewski M (2013) Double universality of a quantum phase transition in spinor condensates: Modification of the Kibble-żurek mechanism by a conservation law. *Physical Review Letters* 110: 045303. https://doi.org/10.1103/PhysRevLett.110.045303.

Szymańska MH, Keeling J, and Littlewood PB (2006) Nonequilibrium quantum condensation in an incoherently pumped dissipative system. *Physical Review Letters* 96: 230602. https://doi.org/10.1103/PhysRevLett.96.230602.

Szymańska MH, Keeling J, and Littlewood PB (2007) Mean-field theory and fluctuation spectrum of a pumped decaying Bose-Fermi system across the quantum condensation transition. *Physical Review B* 75: 195331. https://doi.org/10.1103/PhysRevB.75.195331.

Tsatsos MC, Tavares PES, Cidrim A, Fritsch AR, Caracanhas MA, dos Santos FEA, Barenghi CF, and Bagnato VS (2016) Quantum turbulence in trapped atomic Bose-Einstein condensates. *Physics Reports* ISSN: 0370-1573. 622: 1–52. https://doi.org/10.1016/j.physrep.2016.02.003. Quantum turbulence in trapped atomic Bose-Einstein condensates.

Tsubota M, Fujimoto K, and Yui S (2017) Numerical studies of quantum turbulence. *Journal of Low Temperature Physics* 188: 119–189.

Ueda M (2010) *Fundamentals and New Frontiers of Bose-Einstein Condensation.* World Scientific, ISBN: 9789812839596. https://books.google.co.uk/books?id=iix3_pqy6ysC.

Ulm S, Roßnagel J, Jacob G, Degünther C, Dawkins ST, Poschinger UG, Nigmatullin R, Retzker A, Plenio MB, Schmidt-Kaler F, et al. (2013) Observation of the Kibble-Zurek scaling law for defect formation in ion crystals. *Nature Communications* 4: 2290.

Verma AK, Pandit R, and Brachet ME (2022) Rotating self-gravitating Bose-Einstein condensates with a crust: A model for pulsar glitches. *Physical Review Research* 4: 013026. https://doi.org/10.1103/PhysRevResearch.4.013026.

Vinen WF and Niemela JJ (2002) Quantum turbulence. *Journal of Low Temperature Physics* 128: 167–231.

Volovik GE (2009) The Universe in a Helium Droplet. *International Series of Monographs on Physics.* Oxford University Press. https://books.google.co.uk/books?id=VuLJrQEACAAJ.

Wachtel G, Sieberer LM, Diehl S, and Altman E (2016) Electrodynamic duality and vortex unbinding in driven-dissipative condensates. *Physical Review B* 94: 104520. https://doi.org/10.1103/PhysRevB.94.104520.

Walmsley PM and Golov AI (2008) Quantum and quasiclassical types of superfluid turbulence. *Physical Review Letters* 100: 245301. https://doi.org/10.1103/PhysRevLett.100.245301.

Warszawski L, Melatos A, and Berloff NG (2012) Unpinning triggers for superfluid vortex avalanches. *Physical Review B* 85: 104503. https://doi.org/10.1103/PhysRevB.85.104503.

Weiler CN, Neely TW, Scherer DR, Bradley AS, Davis MJ, and Anderson BP (2008) Spontaneous vortices in the formation of Bose-Einstein condensates. *Nature* 455: 948–951. https://doi.org/10.1038/nature07334. 0807.3323.

Weinberg DH, Bullock JS, Governato F, Kuzio de Naray R, and Peter AHG (2015) Cold dark matter: Controversies on small scales. *Proceedings of the National Academy of Science* 112 (40): 12249–12255. https://doi.org/10.1073/pnas.1308716112. 1306.0913.

Widrow LM and Kaiser N (1993) Using the Schrodinger equation to simulate collisionless matter. *Astrophysical Journal Letters* 416: L71. https://doi.org/10.1086/187073.

Williamson LA and Blakie PB (2016) Universal coarsening dynamics of a quenched ferromagnetic spin-1 condensate. *Physical Review Letters* 116(2): 025301. https://doi.org/10.1103/PhysRevLett.116.025301.

Witkowska E, Deuar P, Gajda M, and RząŻewski K (2011) Solitons as the early stage of quasicondensate formation during evaporative cooling. *Physical Review Letters* 106: 135301. https://doi.org/10.1103/PhysRevLett.106.135301.

Witkowska E, Dziarmaga J, Świsłocki T, and Matuszewski M (2013) Dynamics of the modified Kibble-żurek mechanism in antiferromagnetic spin-1 condensates. *Physical Review B* 88: 054508. https://doi.org/10.1103/PhysRevB.88.054508.

Wolswijk L, Mordini C, Farolfi A, Trypogeorgos D, Dalfovo F, Zenesini A, Ferrari G, and Lamporesi G (2022) Measurement of the order parameter and its spatial fluctuations across Bose-Einstein condensation. *Physical Review A* 105: 033316. https://doi.org/10.1103/PhysRevA.105.033316.

Wouters M and Carusotto I (2007) Excitations in a nonequilibrium Bose-Einstein condensate of exciton polaritons. *Physical Review Letters* 99: 140402. https://doi.org/10.1103/PhysRevLett.99.140402.

Wouters M, Liew TCH, and Savona V (2010) Energy relaxation in one-dimensional polariton condensates. *Physical Review B* 82: 245315. https://doi.org/10.1103/PhysRevB.82.245315.

Yukalov VI, Novikov AN, and Bagnato VS (2015) Realization of inverse Kibble-Zurek scenario with trapped Bose gases. *Physics Letters A* ISSN: 0375-9601. 379(20): 1366–1371. https://doi.org/10.1016/j.physleta.2015.02.033.

Yurke B, Pargellis AN, Kovacs T, and Huse DA (1993) Coarsening dynamics of the XY model. *Physical Review E* 47: 1525–1530. https://doi.org/10.1103/PhysRevE.47.1525.

Zamora A, Sieberer LM, Dunnett K, Diehl S, and Szymańska MH (2017) Tuning across universalities with a driven open condensate. *Physical Review X* 7: 041006. https://doi.org/10.1103/PhysRevX.7.041006.

Zamora A, Dagvadorj G, Comaron P, Carusotto I, Proukakis NP, and Szymańska MH (2020) Kibble-Zurek mechanism in driven dissipative systems crossing a nonequilibrium phase transition. *Physical Review Letters* 125: 095301. https://doi.org/10.1103/PhysRevLett.125.095301.

Zurek WH (1985) Cosmological experiments in superfluid helium? *Nature* 317(6037): 505–508.

Zurek WH (1996) Cosmological experiments in condensed matter systems. *Physics Reports* 276(4): 177–221.

Zurek WH (2009) Causality in condensates: Gray solitons as relics of BEC formation. *Physical Review Letters* 102: 105702. https://doi.org/10.1103/PhysRevLett.102.105702.

Zwerger W (2011) The BCS-BEC Crossover and the Unitary Fermi Gas. *Lecture Notes in Physics.* Springer Berlin Heidelberg, ISBN: 9783642219771. https://books.google.co.uk/books?id=VjdUd5JbRooC.

Interacting Bose-condensed gases

Christoph Eigen[a] **and Robert P Smith**[b], [a]Cavendish Laboratory, University of Cambridge, Cambridge, United Kingdom; [b]Clarendon Laboratory, University of Oxford, Oxford, United Kingdom

© 2024 Elsevier Ltd. All rights reserved.

Introduction **124**
Noninteracting Bose gases **125**
Weak repulsive contact interactions **126**
Excitations and sound 126
Quantum depletion 127
Interaction effects near T_c 128
Unitary contact interactions **129**
Attractive contact interactions and dipolar interactions **130**
Attractive contact interactions 130
Interacting Bose mixtures 131
Dipolar interactions 131
Conclusion **132**
Acknowledgments **132**
References **133**

Abstract

We provide an overview of the effects of interactions in Bose-condensed gases. We focus on phenomena that have been explored in ultracold atom experiments, covering both tuneable contact interactions and dipolar interactions. Our discussion includes: modifications to the ground state and excitation spectrum, critical behavior near the Bose–Einstein condensation temperature, the unitary regime where the interactions are as strong as allowed by quantum mechanics, quantum droplets in mixtures, and supersolids in dipolar gases.

Key objectives

- Summarize ideal-gas Bose–Einstein condensation.
- Review the consequences of weak repulsive contact interactions on the ground state, excitations, and thermodynamics of Bose condensed gases.
- Showcase recent work on the unitary Bose gas.
- Highlight novel effects in condensates that experience attractive or dipolar interactions, including the formation of quantum droplets and supersolids.

Introduction

Bose–Einstein condensation (BEC) plays an important role across a variety of quantum systems and phenomena, from superconductivity (Onnes, 1911), and exciton (Deng et al., 2002, 2006; Kasprzak et al., 2006; Balili et al., 2007) and magnon (Demokritov et al., 2006) condensation in the solid state, to superfluidity in liquid helium (Kapitza, 1938; Allen and Misener, 1938), to photon condensates in optically pumped dye-filled mircocavities (Klaers et al., 2010), and to its most direct demonstration in ultracold dilute gases (Anderson et al., 1995; Davis et al., 1995). A unique aspect of the Bose condensed state is that the (phase) order it displays is not primarily the result of interparticle interactions, but can occur in an ideal (noninteracting) gas solely due to quantum statistics.

In this article we discuss how the interplay of interparticle interactions with the underlying phase order affects the Bose-condensed state, and the host of fascinating phenomena that ensue. While such questions first arose in the context of liquid helium (a strongly interacting fluid), here we focus our discussion on dilute ultracold atomic gases. In these systems the interaction strength can readily be tuned, allowing controlled access to both subtle and dramatic interaction effects. This enables tests of fundamental many-body theories and the progressive exploration toward strong interactions, where a first principles description is intractable.

We further restrict our discussion to continuous Bose gases in three dimensions (3D), leaving aside fermionic systems where BEC can occur as a consequence of pairing (Inguscio et al., 2007; Zwerger, 2011; Zwierlein, 2014), Bose gases confined in optical lattices (Bloch, 2005; Morsch and Oberthaler, 2006), and lower-dimensional systems where the enhanced role of fluctuations often precludes BEC (Cazalilla et al., 2011; Hadzibabic and Dalibard, 2011). Note that we provide only a brief overview here; many of the topics are covered in much greater detail elsewhere (see, e.g., Pethick and Smith, 2002; Pitaevskii and Stringari, 2016). We also refer the reader to

https://doi.org/10.1016/B978-0-323-90800-9.00156-6

other related articles within this volume; Stringari (2023) gives a more general introduction to BEC in ultracold atom systems, and while here we focus mainly on equilibrium systems Proukakis (2023) explores non-equilibrium effects on BEC formation.

The article is organized as follows. In "Noninteracting Bose gases" we briefly review Bose–Einstein condensation in a gas of noninteracting particles, before exploring the effect of different interparticle interactions on the Bose condensed state: "Weak repulsive contact interactions" and "Unitary contact interactions" consider repulsive contact interactions in, respectively, the weak and strong limit. "Attractive contact interactions and dipolar interactions" explores phenomena which occur due to either attractive or dipole-dipole interactions. Finally, we conclude and provide a brief outlook in "Conclusion."

Noninteracting Bose gases

BEC is a phase transition associated with the onset of long-range phase order, which results from the macroscopic occupation of a single-particle state. This is a consequence of Bose–Einstein statistics and occurs at a critical temperature T_c far above the single-particle energy-level spacing.

Qualitatively, the transition can be understood by considering lengthscales in a quantum gas (see Fig. 1(a)). The two relevant lengthscales are the interparticle spacing, $n^{-1/3}$, set by the gas density n, and the (quantum-mechanical) thermal wavelength $\lambda = [2\pi\hbar^2/(mk_B T)]^{1/2}$ set by the temperature T and the mass m of the gas particles. Condensation occurs when the thermal wavelength is large enough to be comparable to the interparticle spacing ($\lambda \gtrsim n^{-1/3}$).

More quantitatively, we consider the occupation of a momentum state $\mathbf{p}$ in a homogeneous ideal (noninteracting) gas, which is given by the Bose distribution

$$f_B = \frac{1}{e^{(\varepsilon-\mu)/(k_B T)} - 1}, \tag{1}$$

where μ is the chemical potential and $\varepsilon = p^2/(2m)$ the energy of the state. The total number of particles in the gas is found by summing over all possible states:

$$N = \sum_{\varepsilon} \frac{g_\varepsilon}{e^{(\varepsilon-\mu)/(k_B T)} - 1}, \tag{2}$$

where the degeneracy factor g_ε accounts for the number of states with a given ε. Demanding all terms in the sum to be real positive numbers requires $\mu \le \varepsilon_0$, where ε_0 is the ground-state energy. As μ approaches ε_0 from below (practically achieved by, e.g., increasing N) the ground-state occupation can become arbitrarily large (see Eq. (1)), whereas the occupation of all the other states (the excited states) sums to a finite (critical) number in 3D. This statistical saturation of excited states (graphically demonstrated in Fig. 1(b)) is, in essence, the mechanism for BEC. At fixed temperature, as particles are added to a Bose gas they populate the excited states until their population saturates at the critical atom number. From this point on, any additional particles must enter the ground state, which thus becomes macroscopically occupied.

In the thermodynamic limit, in which both N and the volume of the system V are large, while the particle density n is finite, we may (semiclassically) approximate the sum over excited states by an integral. The density of excited states n' (also known as the thermal density), is given by:

$$n' = \int \frac{d\mathbf{p}}{(2\pi\hbar)^3} \frac{1}{e^{(p^2/(2m)-\mu)/(k_B T)} - 1} = \frac{g_{3/2}\left(e^{\mu/(k_B T)}\right)}{\lambda^3}, \tag{3}$$

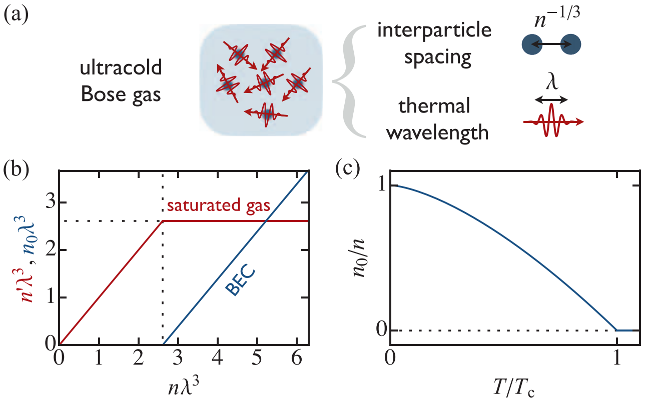

Fig. 1 Ideal Bose gases. (a) Noninteracting ultracold Bose gases feature two relevant lengthscales: the interparticle spacing $n^{-1/3}$ and the thermal wavelength λ. (b) Excited- and ground-state phase space densities vs. total phase space density. Above a critical D_c (dotted vertical line), $n'\lambda^3$ saturates and $n_0\lambda^3$ grows. (c) Condensed fraction n_0/n vs. T/T_c (Eq. (5)).

where the polylogarithm $g_{3/2}(x) = \sum_{l=1}^{\infty} x^l/l^{3/2}$. We can re-express this result in terms of the phase space density $n'\lambda^3 = g_{3/2}(\mathrm{e}^{\mu/(k_\mathrm{B}T)})$, which reaches a maximum (critical) value when $\mu = 0$ (which is allowed as $\varepsilon_0 \to 0$), such that, $n'\lambda^3 = \mathcal{D}_\mathrm{c} = g_{3/2}(1) \equiv \zeta(3/2) \approx 2.612$, where ζ is the Riemann function.

For a fixed n, the BEC transition temperature is given by

$$k_\mathrm{B}T_\mathrm{c} = \frac{2\pi\hbar^2}{m}\left(\frac{n}{\zeta(3/2)}\right)^{2/3}, \tag{4}$$

and the condensed fraction

$$n_0/n = 1 - (T/T_\mathrm{c})^{3/2}, \tag{5}$$

where n_0 is the condensate density (see Fig. 1(c)).

In the following section we discuss how this picture changes in the presence of weak repulsive *contact* interactions, a regime readily accessible in ultracold-gas experiments.

Weak repulsive contact interactions

For a dilute atomic gas the effective low-energy interaction between two atoms at $\mathbf{r}$ and $\mathbf{r}'$ can be approximated as a contact interaction $g\delta(\mathbf{r} - \mathbf{r}')$ with $g = 4\pi\hbar^2 a/m$, where a is the s-wave scattering length. The interactions are thus quantified by a single lengthscale a, which can be tuned experimentally using so-called Feshbach resonances (Chin et al., 2010). The consequences of interactions are often grouped into mean-field (MF) and beyond-mean-field (BMF) effects.

Simplistically speaking, MF effects result from the effective potential felt by a particle due to the average local particle density. Within the Hartree–Fock approximation (Dalfovo et al., 1999) the excited-state atoms feel an effective potential $V_\mathrm{int}{}' = g(2n_0 + 2n')$ and, owing to the lack of the exchange interaction for particles in the same state, the ground-state atoms experience a different interaction potential $V_{\mathrm{int},0} = g(n_0 + 2n')$. In a homogeneous system, these interaction potentials lead to a uniform energy offset, i.e., $\varepsilon = p^2/2m + V_\mathrm{int}$ in Eq. (1). This is accompanied by a simple shift of the chemical potential such that it is only the factor of two difference between the condensate-condensate and condensate-thermal interaction potentials that leads to non-trivial interaction effects at the MF level. By contrast, in inhomogeneous systems the entire interaction potential is important as it effectively modifies the form of the trap. This often results in MF effects being more prominent in inhomogeneous systems; see Smith (2017) for a detailed discussion. Note that, at the MF level, the condensate behavior can be described by a macroscopic wavefunction that obeys the Gross–Pitaevski equation (see Pitaevskii and Stringari, 2016), a nonlinear Schrödinger equation.

Beyond-mean-field effects arise due to changes of the many-body wavefunction, sometimes referred to as quantum fluctuations. These effects become significant if the interaction energy $\sim gn$ is no longer negligible compared to the relevant (kinetic) energy. In particular, significant effects occur whenever low-energy (long-wavelength) excitations play a central role.

We now consider the effect of interactions on the elementary excitations of a Bose-condensed system, on its ground state, and on its behavior near T_c.

Excitations and sound

In a homogeneous system, at the MF-level the excitation spectrum is simply given by $\varepsilon(k) = p^2/(2m) + V_\mathrm{int}{}' - V_{\mathrm{int},0} = \hbar^2k^2/(2m) + gn_0$, where $k = p/\hbar$ is the excitation wavenumber.

For low-energy (low-k) excitations this MF approach is no longer adequate; to next order the effect of interactions can be calculated using the Bogoliubov transformation (Bogoliubov, 1947), which enables a description in terms of noninteracting quasiparticles; this approach predicts an excitation spectrum

$$\varepsilon(k) = \sqrt{\frac{\hbar^2k^2}{2m}\left(\frac{\hbar^2k^2}{2m} + 2gn\right)}. \tag{6}$$

Now at low-k there are collective excitations with a sound-like form $\varepsilon/\hbar = c_0k$, where $c_0 = \sqrt{gn/m}$. This is crucial for superfluidity in Bose condensed systems, as it ensures (unlike in an ideal gas) a nonzero superfluid critical velocity (according to the Landau criterion). The sound-like excitation spectrum was first seen in liquid ^{4}He (Nozières and Pines, 1990). In ultracold atomic gases, following initial studies of collective excitations (Jin et al., 1996; Mewes et al., 1996; Andrews et al., 1997), a direct comparison to Eq. (6) was made possible by using Bragg spectroscopy on an ultracold Bose–Einstein condensate (see Steinhauer et al., 2002, Kozuma et al., 1999, Stenger et al., 1999 and Fig. 2(a)).

At finite temperature the situation is further complicated by the presence of thermal excitations, which lead to two distinct sound modes, the (faster) first and (slower) second sound. The two modes can be understood, in the hydrodynamic limit, within the two-fluid model (Landau, 1941), which separately considers the normal and superfluid components. The nature of the sound modes changes depending on how compressible the Bose fluid is. In the almost incompressible liquid helium, first and second sound are, respectively, density and temperature (or entropy) waves. Instead, in a dilute Bose fluid (which is highly compressible) the two modes are excitations of mainly the normal and superfluid components (see Hilker et al., 2022 and Fig. 2(b)).

Quantized vortices are another important type of excitation that feature in interacting Bose-condensed gases. Such vortices carry angular momentum quantized in units of $\hbar/m$ and have vanishing density along the vortex core over a healing length $1/\sqrt{8\pi na}$ (see Madison et al., 2000 and Fig. 2(c)). In a system containing many vortices the interactions between them can result in the

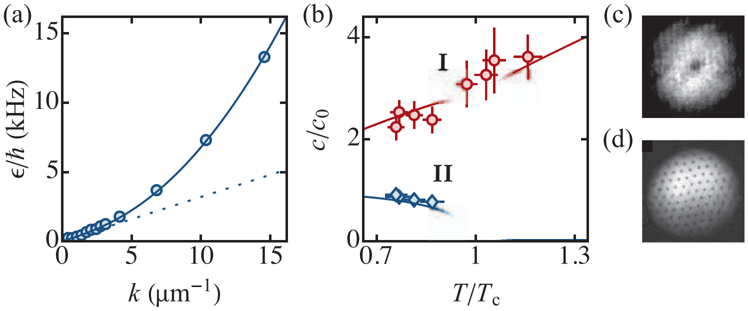

Fig. 2 Excitations in interacting degenerate Bose gases. (a) Excitation spectrum of a weakly interacting Bose–Einstein condensate, measured in a harmonic trap (Steinhauer et al., 2002). The solid line shows the fitted Bogoliubov form, with a linear spectrum at low momenta (dotted line), the slope of which gives the speed of sound. (b) At finite temperature a Bose fluid supports two sound modes, here measured in a box-trapped ultracold gas (Hilker et al., 2022); the speeds are normalized by the Bogoliubov speed and the solid lines show the two-fluid model predictions. (c) Vortices are another important type of excitation; the image shows a single vortex generated via stirring a Bose–Einstein condensate with a laser beam (Madison et al., 2000). (d) When large numbers of vortices are generated the interactions between them lead to the formation of an Abrikosov lattice (Abo-Shaeer et al., 2001). Panels adapted from: (a) Steinhauer, R Ozeri, N Katz, and N Davidson (2002) Excitation spectrum of a Bose–Einstein condensate, *Physical Review Letters* 88:120407, (b) Hilker, LH Dogra, C Eigen, JAP Glidden, RP Smith, and Z Hadzibabic (2022) First and second sound in a compressible 3D Bose fluid, *Physical Review Letters* 128:223601, (c) Madison, F Chevy, W Wohlleben, and J Dalibard (2000) Vortex formation in a stirred Bose–Einstein condensate, *Physical Review Letters* 84:806, (d) Abo-Shaeer, C Raman, JM Vogels, and W Ketterle (2001) Observation of vortex lattices in Bose–Einstein condensates, *Science* 292:476.

formation of vortex lattices (see Abo-Shaeer et al., 2001 and Fig. 2(d)). Note that these lattices are closely related to those that occur in type-II superconductors in the presence of a magnetic field; rotation can be thought of as an artificial magnetic field, which is an example of a synthetic gauge field (see, e.g., Goldman et al., 2014; Zhai, 2015; Aidelsburger et al., 2018).

Quantum depletion

In addition to modifying the excitation spectrum, interparticle interactions also modify the ground state, an effect known as quantum depletion. This entails the coherent expulsion of particles from the single particle ($p = 0$) ground state, even at $T = 0$; in essence, it is energetically favorable for some higher momentum states to be occupied.

The most striking example of quantum depletion occurs in liquid ^{4}He, where even though at $T = 0$ the system is 100% superfluid, the condensed fraction n_0/n is only around 10%. However, liquid ^{4}He is a strongly interacting fluid, and so theoretical predictions are challenging. Instead, for a weakly interacting gas $[(na^3)^{1/2} \ll 1]$, a theoretical description is more tractable, with $T = 0$ Bogoliubov theory predicting (Lee et al., 1957)

$$\frac{n_0}{n} = 1 - \frac{8}{3\sqrt{\pi}}\left(na^3\right)^{1/2}. \tag{7}$$

This famous prediction was experimentally verified in a box-trapped (homogeneous) ultracold gas (see Lopes et al., 2017 and Fig. 3). Within the same theoretical framework, the ground-state energy is also modified, as first measured by Navon et al. (2011).

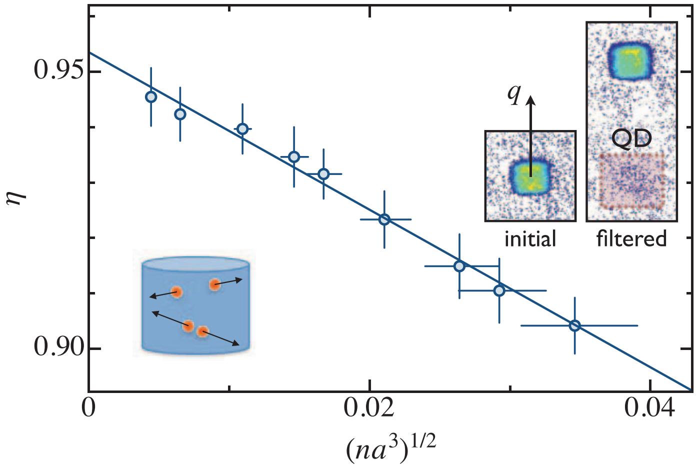

Fig. 3 Measurement of quantum depletion. The maximal diffracted fraction η vs. the interaction parameter $(na^3)^{1/2}$; here a Bragg filtering technique was used to spatially separate the condensate from the high-k components of the gas (including the quantum depletion; see top inset). Assuming both perfect k-space separation and filtering, η corresponds to the condensed fraction. A linear fit (solid line) gives a slope $\gamma = 1.5(2)$, quantitatively confirming the Bogoliubov prediction $\gamma = 8/(3\pi^{1/2}) \approx 1.5$. The fact that the intercept is only close to unity, arises from an imperfect k-space separation and a non-zero initial temperature. The cartoon (bottom inset) depicts the coherent excitations out of the (blue) condensate, which occur as pairs of atoms with opposite momenta. Figure adapted from Lopes, C Eigen, N Navon, D Clément, RP Smith, and Z Hadzibabic (2017) Quantum depletion of a homogeneous Bose–Einstein condensate, *Physical Review Letters* 119:190404.

Interaction effects near T_c

We now turn to the effect of interactions on the thermodynamics of a Bose condensed gas, focusing on the behavior close to T_c; these effects are summarized in Figs. 4(a, b).

First, in the (partially) condensed phase, interactions cause $n'\lambda^3$ to no longer be saturated at $\mathcal{D}_c$ (*cf.* Figs. 1(b) and 4(a)), but instead it decreases for increasing $n\lambda^3$. This effect comes about (at the MF level) because an atom can reduce its interaction energy by entering the condensate. Note that for a harmonically trapped gas the opposite effect occurs, with the excited-state population increasing as the system goes more deeply into the condensed state (Tammuz et al., 2011).

Secondly, condensation occurs at $\mathcal{D}_c < \mathcal{D}_c^0$ (or equivalently for $T_c > T_c^0$ at fixed n); here the superscript ^{0} denotes the ideal-gas results. This effect can only be understood at the BMF level, as long-wavelength fluctuations become increasingly important close to T_c. Calculating the shift was a significant theoretical challenge and it took several decades to reach a consensus (see Andersen, 2004; Arnold and Moore, 2001; Baym et al., 2001; Holzmann et al., 2004 for a review); the shift is predicted to be (Arnold and Moore, 2001; Kashurnikov et al., 2001)

$$\frac{\Delta T_c}{T_c^0} \approx 1.8\,\frac{a}{\lambda}, \tag{8}$$

but this result has yet to be confirmed experimentally.

In a harmonic trap, a relatively simple geometric (MF) effect results in a negative T_c shift, with the more interesting BMF effects expected to be pushed to higher order in a/λ. As shown in Fig. 4(c), measurements in a harmonic trap (Smith et al., 2011) did show an upward shift from the MF prediction (dashed line), but making a quantitative comparison with Eq. (8) (dotted line) was not possible.

Thirdly, interactions modify the critical exponents of the BEC transition, changing the universality class to that of the 3D XY model. In particular, the correlation length critical exponent is predicted to change from $\nu = 1$ to $\nu \approx 0.67$ (Burovski et al., 2006a); see Fig. 4(b). This exponent has been measured by locally probing a harmonically trapped ultracold gas (see Donner et al., 2007 and Fig. 4(d)), and also with much higher precision in ^{4}He (see Burovski et al., 2006b).

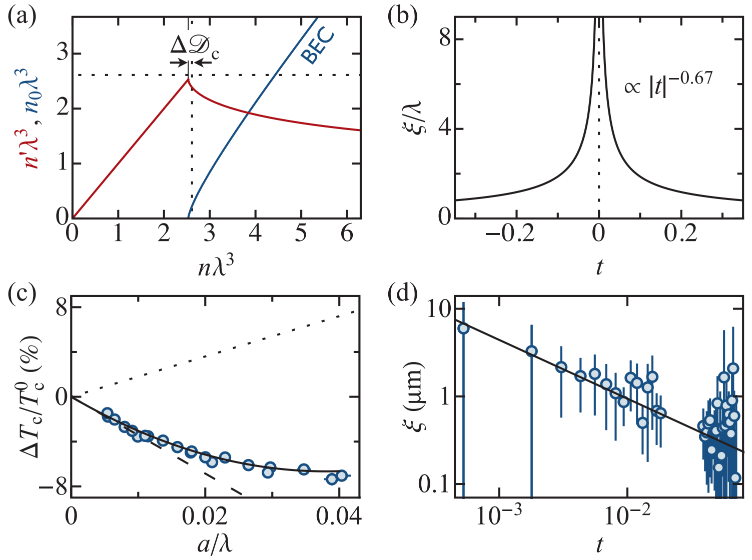

Fig. 4 Thermodynamics near T_c. In (a) and (b) we illustrate the effects of interactions near T_c in a homogeneous system, while (c) and (d) highlight related experimental results. (a) Excited- and ground-state phase-space densities as a function of the total phase-space density for an interacting Bose gas (*cf.* Fig. 1(b)). For $n\lambda^3 > D_c, n'\lambda^3$ is no longer saturated at D_c, but decreases as $n\lambda^3$ increases. The critical phase-space density also undergoes a small shift. (b) The correlation length ξ vs. reduced temperature $t = (T - T_c)/T_c$ near the BEC transition. The interacting Bose gas is in the 3D XY Model universality class, which has $\xi \sim t^{-\nu}$ with $\nu \approx 0.67$. (c) Measured T_c shift vs. interaction strength for a harmonically trapped Bose gas Smith et al. (2011); an upward shift from the predominant MF geometric effect (dashed line) is seen, but quantitatively comparing this to the homogeneous system result (dotted line) was not possible.
(d) Measurement of the correlation length critical exponent in a ultracold Bose gas Donner et al. (2007); the line is a fit to the data, which gives $\nu = 0.67(13)$ consistent with the 3D XY Model. Panels adapted from: (c) Smith, RLD Campbell, N Tammuz, and Z Hadzibabic (2011) Effects of interactions on the critical temperature of a trapped Bose gas, *Physical Review Letters* 106:250403, (d) Donner, S Ritter, T Bourdel, A Ottl, M Köhl, and T Esslinger (2007) Critical behavior of a trapped interacting Bose gas, *Science* 315:1556.

Unitary contact interactions

Here we consider Bose-condensed systems in the strongly interacting limit ($na^3 \gg 1$), experimentally accessible at a Feshbach resonance, where a diverges. In this so-called unitary regime, the interactions between particles are as strong as allowed by quantum mechanics. The fact that the value of the diverging a can no longer matter leads to the universality hypothesis, in which the interparticle spacing $n^{-1/3}$ is the only relevant lengthscale for a degenerate gas (see Cowell et al., 2002, Ho, 2004 and Fig. 5(a)). This also sets the natural momentum, energy, and time scales:

$$\hbar k_n = \hbar\left(6\pi^2 n\right)^{1/3}, E_n = \hbar^2 k_n^2/(2m), \text{and } t_n = \hbar/E_n. \tag{9}$$

In contrast to their widely studied Fermi counterparts (Inguscio et al., 2007; Zwerger, 2011; Zwierlein, 2014), unitary Bose gases feature dramatically enhanced particle loss[1] and associated heating, which makes their study an inherently dynamical problem and raised the question whether such a gas can ever exist in equilibrium.

The experimental approach has been to forsake equilibrium and quench into the unitary regime (by rapidly increasing a), to then observe the ensuing dynamics. These experiments have shown a remarkable degree of universality (see Makotyn et al., 2014, Eigen et al., 2017, 2018, Klauss et al., 2017 and Fig. 5(b, c)). The post-quench dynamics also revealed that the gas, even though it is not in true thermal equilibrium, does attain a quasi-equilibrium (prethermal) state (Berges et al., 2004; Makotyn et al., 2014; Yin and Radzihovsky, 2016; Eigen et al., 2018). Eventually, the gas decays and heats, ultimately following the dimensionless loss rate for a thermal unitary gas $-t_n\dot{n}/n \propto (E_n/E)^2$, where E is the kinetic energy per particle (dashed line in Fig. 5(b); see also thermal unitary-gas measurements Rem et al., 2013, Fletcher et al., 2013, Eismann et al., 2016).

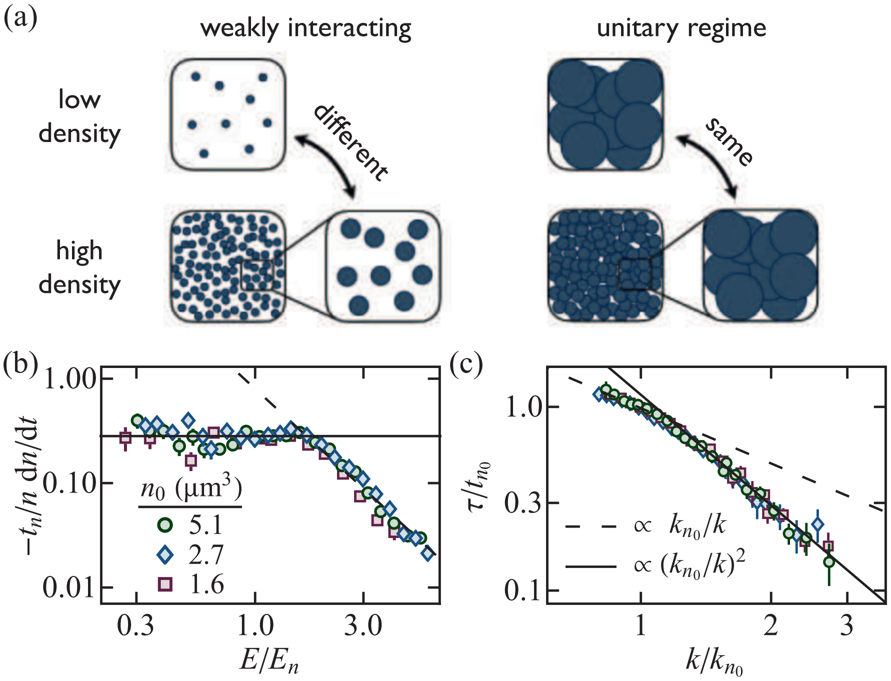

Fig. 5 Universal behavior in unitary Bose gases. (a) In a weakly interacting Bose gas (left) the interactions, characterized by a, set the relevant lengthscale (size of the circles in the cartoon), so that when "zooming in" on a high-density gas it looks different to a low-density gas. In the unitary regime (right), upon zooming in, the high-density gas instead looks the same as the low-density one, exhibiting scale invariance. (b, c) Examples of experimental verification of the universality hypothesis. For initially degenerate Bose gases of initial density n_0 quenched to unitarity, both (b) the dimensionless loss rate vs. E/E_n (Eigen et al., 2017) and (c) the momentum-dependent prethermal relaxation timescale τ/t_{n_0} (Eigen et al., 2018) are universal functions that depend solely on the density. Panels adapted from: (b) Eigen, JAP Glidden, R Lopes, N Navon, Z Hadzibabic, and RP Smith (2017) Universal scaling laws in the dynamics of a homogeneous unitary Bose gas, *Physical Review Letters* 119:250404, (c) Eigen, JAP Glidden, R Lopes, EA Cornell, RP Smith, and Z Hadzibabic (2018) Universal prethermal dynamics of Bose gases quenched to unitarity, *Nature* 563:221.

---

[1] For i-body loss, dimensional analysis gives $\dot{n}/n \propto \hbar/ma^{3i-5}n^{i-1}$ (Thøgersen et al., 2008; Mehta et al., 2009), which for $na^3 \gg 1$ gives $\dot{n}/n \propto 1/t_n$ for all i. Also note that in Bose gases Efimov physics further modulates the atom loss (Efimov, 1970; Braaten and Hammer, 2007; Naidon and Endo, 2017).

Intriguingly, the observed post-quench prethermal state featured: (1) a momentum-dependent relaxation timescale approximately given by $\hbar/\varepsilon(k)$ (see Eq. (6)) with gn replaced by E_n (see Fig. 5(c)), and (2) a universal momentum distribution, which implies a non-zero condensed fraction. This hints at the possibility of a novel superfluid state consisting of Efimov trimers,[2] which has also been theoretically predicted (Piatecki and Krauth, 2014; Musolino et al., 2022).

Attractive contact interactions and dipolar interactions

So far, we have only discussed the effect of repulsive contact interactions on a single component Bose gas, which for $na^3 \ll 1$ leads to relatively modest changes (see "Weak repulsive contact interactions").

We now turn to scenarios where the interactions are (at least partially) attractive. This can lead to far more dramatic consequences and also to situations where BMF effects play a critical role. In the following, we in turn discuss: single component condensates with weak attractive contact interactions, quantum mixtures, and situations in which the atoms interact via both contact and dipolar interactions.

Attractive contact interactions

For attractive contact interactions ($a < 0$) in the thermodynamic limit, Bose–Einstein condensates are not stable, and are susceptible to collapse. This can be seen by examining the Bogoliubov excitation spectrum (Eq. (6)) and noting that negative values of g lead to imaginary excitation energies at low k, signifying unstable (exponentially growing) modes; this is sometimes referred to as a phonon instability.

Trapped (finite-sized) 3D condensates can be stabilized by the ground-state kinetic energy (quantum pressure), such that for a given atom number N, collapse only occurs above a critical attractive $|a_c|$. Note that in lower-dimensional systems the situation is somewhat different, e.g., in 1D the balance of kinetic and interaction energy permits the formation of solitons (Strecker et al., 2002; Khaykovich et al., 2002).

Condensate collapse was originally explored for atoms confined in harmonic traps (Gerton et al., 2000; Roberts et al., 2001; Donley et al., 2001) and later also for those in 3D box potentials (Eigen et al., 2016). In Fig. 6(a, b) we show, respectively, experimental images of the collapse in harmonically and box-trapped gases. In both cases, the critical point is given by $Na_c \propto L$, where L is the linear size of the single-particle ground state (see Gerton et al., 2000, Roberts et al., 2001, Donley et al., 2001, Eigen et al., 2016 and Fig. 6(c)). The basic picture can again be understood from Eq. (6): Equating $2gn$ to $\hbar^2k^2/(2m)$ with (the minimum) $k \sim \pi/L$ (using $n \approx N/L^3$) predicts a critical value of $Na_c/L \approx -0.2$ (*cf.* Fig. 6(c)). More quantitatively, the collapse of such matter waves can be well described using the Gross–Pitaevskii equation.

In single-component condensates with attractive contact interactions, the BMF effects are typically negligible as a is close to zero. However, in situations where two (potentially) large MF effects cancel, BMF effects can become important and even lead to qualitatively new effects; examples of such scenarios are explored in the two following sections.

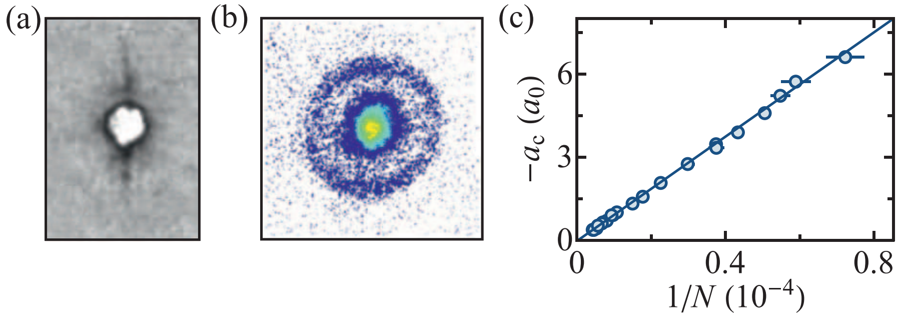

Fig. 6 Condensate collapse. (a, b) Absorption images of ultracold quantum gases following wave collapse for (a) a harmonically trapped (Donley et al., 2001) and (b) a box-trapped (Eigen et al., 2016) cloud. (c) Measured critical a_c (in units of the Bohr radius a_0) vs. $1/N$ for collapse of a condensate confined in a cylindrical box trap of size L (length equal to diameter) (Eigen et al. (2016)). The solid line shows a fit to the data, which gives $-a_c = 0.16(4)L/N$ consistent with the Gross–Pitaevskii equation prediction $-a_c = 0.17L/N$. Panels adapted from: (a) Donley, NR Claussen, SL Cornish, JL Roberts, EA Cornell, and CE Wieman (2001) Dynamics of collapsing and exploding Bose–Einstein condensates, *Nature* 412:295, (b, c) Eigen, AL Gaunt, A Suleymanzade, N Navon, Z Hadzibabic, and RP Smith (2016) Observation of weak collapse in a Bose–Einstein condensate, *Physical Review X* 6:041058.

---

[2] The Efimov effect is a quantum three-body effect first discussed in nuclear physics (Efimov, 1970).

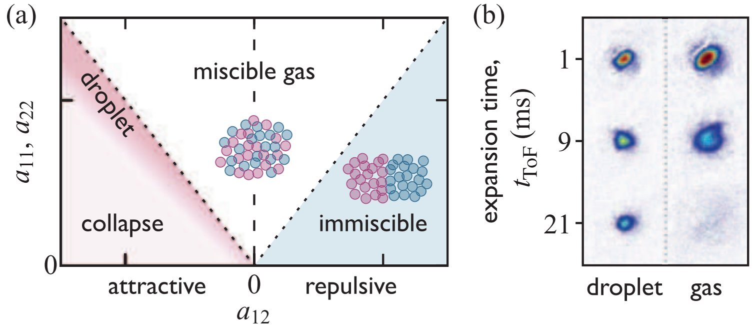

Fig. 7 Realizing quantum droplets in Bose mixtures. (a) Illustrative phase diagram for $a_{11} = a_{22} > 0$ showing the miscible, immiscible, collapse, and droplet regimes. At the MF level for a homogeneous gas, the miscible region is given by $-\sqrt{a_{11}a_{22}} < a_{12} < \sqrt{a_{11}a_{22}}$ (between the dotted lines). Quantum droplets can be formed in a sliver of the phase diagram near $\delta a = a_{12} + \sqrt{a_{11}a_{22}} = 0$, where BMF effects can become important (see text). (b) Images demonstrating the existence of a droplet phase (Cabrera et al., 2018); for $\delta a = -3.2a_0$ (left) the cloud remains self-bound after release from the trap, compared to $\delta a = 1.2a_0$ (right), which shows the typical expansion of a miscible gas. Panel (b) adapted from Cabrera, L Tanzi, J Sanz, B Naylor, P Thomas, P Cheiney, and L Tarruell (2018) Quantum liquid droplets in a mixture of Bose–Einstein condensates, *Science* 359:301.

Interacting Bose mixtures

In a two-component quantum mixture with contact interactions between the constituents, there are three relevant scattering lengths: two intrastate ones (a_{11} and a_{22}), and an interstate one (a_{12}). A sketch of the zero-temperature phase diagram of such a mixture is shown in Fig. 7(a) for the case $a_{11} = a_{22} > 0$.

At the MF level, for $a_{12} > \sqrt{a_{11}a_{22}}$ the interstate repulsion causes the two components to separate (the system is immiscible), whereas for $a_{12} < -\sqrt{a_{11}a_{22}}$ the interstate attraction overwhelms the intrastate repulsion, leading to collapse. In between, the two components are miscible—forming overlapping condensates. The miscible-immiscible transition has been studied since the early days of atomic-gas condensates (see, e.g., Hall et al., 1998; Stenger et al., 1998; Papp et al., 2008).

At the collapse boundary, where the MF terms (almost) cancel, the residual mean-field interaction, $\delta a = a_{12} + \sqrt{a_{11}a_{22}}$, is small. However, in contrast to a single-component gas near the collapse boundary, the BMF effects are not necessarily negligible. The BMF effects are typically repulsive in nature and scale more strongly with density than the MF effects that drive the collapse, opening the possibility of quantum liquid droplets where (at an appropriate density) the attractive MF attraction can be balanced by BMF repulsion (Petrov, 2015). Such droplets were realized in 2018 (see Cabrera et al., 2018, Semeghini et al., 2018 and Fig. 7(b)). The "liquid" label refers to the fact that, in principle, the droplets are stabilized at a fixed density and are self bound; in practice, the high densities involved lead to (three-body) losses that limit the droplet lifetime. In the special case where $\delta a \approx 0$, a so-called "LHY fluid" is formed, which only features BMF interactions (Skov et al., 2021).

Dipolar interactions

In this section we briefly review novel effects of dipole-dipole interactions on Bose-condensed gases (see, e.g., Lahaye et al., 2009, Norcia and Ferlaino, 2021, Chomaz et al., 2023 for a more detailed treatment). Such interactions, which arise for particles with a permanent dipole moment, are long-range and anisotropic; the interaction potential for two polarized dipoles a distance $r = |\mathbf{r}|$ apart is given by

$$V_{\mathrm{dd}} = \frac{C_{\mathrm{dd}}}{4\pi}\,\frac{1 - 3\cos^2\theta}{r^3}, \tag{10}$$

where θ is the angle between $\mathbf{r}$ and the polarization axis, and C_{dd} the dipole coupling constant, which is given by $\mu_0\mu^2$ (d^2/ε_0) for magnetic (electric) dipoles. The strength of dipolar interactions are also commonly captured by the dipolar length $a_{\mathrm{dd}} = C_{\mathrm{dd}}m/(12\pi\hbar^2)$.

For a homogeneous gas with both contact and dipole-dipole interactions, the Bogoliubov excitation spectrum (Eq. (6)) is modified such that

$$\varepsilon(\mathbf{k}) = \sqrt{\frac{\hbar^2k^2}{2m}\left(\frac{\hbar^2k^2}{2m} + 2gn + 2C_{\mathrm{dd}}\left(\cos^2\alpha - \frac{1}{3}\right)n\right)}, \tag{11}$$

where α is the angle between $\mathbf{k}$ and the polarization direction. Several consequences of dipolar interactions can directly be inferred from Eq. (11).

Even for weak dipolar interactions the excitation spectrum is anisotropic, which leads to anisotropic sound waves (Bismut et al., 2012). Moreover, for $C_{\mathrm{dd}}/3 > g$ (or equivalently $a_{\mathrm{dd}} > a$) unstable phonon modes exist and (at least from a MF perspective) the gas

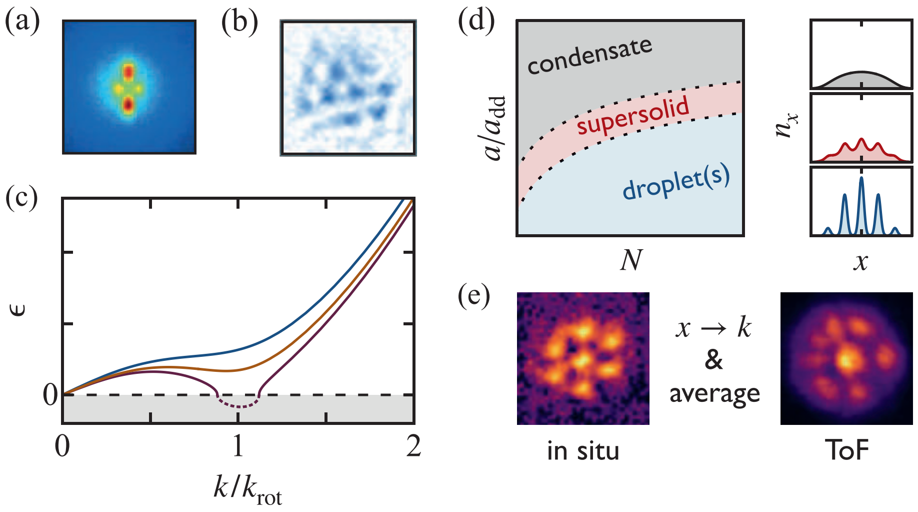

Fig. 8 Dipolar Bose gases. (a) Absorption image revealing the effects of dipolar interactions following the collapse and subsequent explosion of a condensate (Lahaye et al., 2008). (b) Observation of dipolar quantum droplets (Kadau et al., 2016). (c) Sketch of the roton excitation spectrum seen in dipolar gases that are confined along their polarization direction. As the relative strength of dipole-dipole interactions increases the roton minimum deepens and then triggers (red line) an instability near $k_{\rm rot}$. (d) Cartoon of the phase diagram of a dipolar gas in a cigar-shaped trap. Starting with a condensate, reducing $a/a_{\rm dd}$ triggers the roton instability resulting in an array of droplets. For a sliver of the phase diagram a supersolid state exists, in which the droplets are phase coherent (Tanzi et al., 2019; Böttcher et al., 2019; Chomaz et al., 2019). (e) Observation of a 2D supersolid (Norcia et al., 2021; Bland et al., 2022); (left) an in-situ image revealing a hexagonal density modulationand (right) a time-of-flight (ToF) image, averaged over multiple realizations, which demonstrates the global phase coherence of the system. Panels adapted from: (a) Lahaye, J Metz, B Fröhlich, T Koch, M Meister, A Griesmaier, T Pfau, H Saito, Y Kawaguchi, and M Ueda (2008) d-Wave collapse and explosion of a dipolar Bose–Einstein condensate, *Physical Review Letters* 101:080401, (b) Kadau, M Schmitt, M Wenzel, C Wink, T Maier, I Ferrier-Barbut, and T Pfau (2016) Observing the Rosensweig instability of a quantum ferrofluid, *Nature* 530:194,, (e) Bland, E Poli, C Politi, L Klaus, MA Norcia, F Ferlaino, L Santos, and RN Bisset (2022) Two-dimensional supersolid formation in dipolar condensates, *Physical Review Letters* 128:195302.

can undergo collapse, with the angular dependence of the interactions leading to spectacular collapse dynamics (see Lahaye et al., 2007 and Fig. 8(a)). As in the case of a Bose mixture, collapse occurs at a nonzero g, opening up the possibility of the collapse being arrested by BMF effects, which again can result in the formation of quantum droplets (see Kadau et al., 2016, Schmitt et al., 2016, Ferrier-Barbut et al., 2016, Chomaz et al., 2016 and Fig. 8(b)).

The presence of a trap tends to stabilize the system. A particularly interesting situation arises when a dipolar gas is tightly confined along the polarization direction, which leads to the development of an in-plane roton-like excitation spectrum (see Petter et al., 2019 and Fig. 8(c)). Note that although similar to the roton excitation spectrum originally seen in liquid ^{4}He (see, e.g., Donnelly et al., 1981), its microscopic origin is different, occurring as the consequence of both confinement and long-range anisotropic interactions. When the roton gap closes, an instability occurs at finite $k = k_{\rm rot}$, such that without any stabilization mechanism a runaway density modulation would ensue. However, the collapse can yet again be halted by BMF effects, leading to the formation of a droplet array. For a narrow range of parameters close the stability boundary, these droplets remain phase coherent, signaling the existence of a supersolid state—a state with both long-range phase order (and hence superfluidity) and long-range spatial order (the density modulation) (see Tanzi et al., 2019; Böttcher et al., 2019; Chomaz et al., 2019; Norcia et al., 2021; Bland et al., 2022 and Fig. 8(d, e)).

Conclusion

In summary, we have reviewed effects of both contact and dipolar interactions on Bose-condensed gases. Many of the observed phenomena have been long predicted, if only more recently confirmed in ultracold gases, while others, such as the observation of supersolidity, were largely unexpected. Looking forward, further breakthroughs in both categories are within reach. A major longstanding task is to experimentally resolve the simple question of how weak interactions shift the BEC transition temperature. On the more exploratory side, the realms of strong contact and dipolar interactions offer the possibility of novel many-body physics.

Acknowledgments

We thank Zoran Hadzibabic for comments on the manuscript. C. E. acknowledges support from Jesus College (Cambridge).

References

Abo-Shaeer JR, Raman C, Vogels JM, and Ketterle W (2001) Observation of vortex lattices in Bose–Einstein condensates. *Science* 292: 476.

Aidelsburger M, Nascimbene S, and Goldman N (2018) Artificial gauge fields in materials and engineered systems. *Comptes Rendus Physique* 19: 394.

Allen JF and Misener AD (1938) Flow of liquid helium II. *Nature* 141: 75.

Andersen JO (2004) Theory of the weakly interacting Bose gas. *Reviews of Modern Physics* 76: 599.

Anderson MH, Ensher JR, Matthews MR, Wieman CE, and Cornell EA (1995) Observation of Bose–Einstein condensation in a dilute atomic vapor. *Science* 269: 198.

Andrews MR, Kurn DM, Miesner H-J, Durfee DS, Townsend CG, Inouye S, and Ketterle W (1997) Propagation of sound in a Bose–Einstein condensate. *Physical Review Letters* 79: 553.

Arnold P and Moore G (2001) BEC transition temperature of a dilute homogeneous imperfect Bose gas. *Physical Review Letters* 87: 120401.

Balili R, Hartwell V, Snoke D, Pfeiffer L, and West K (2007) Bose-Einstein condensation of microcavity polaritons in a trap. *Science* 316: 1007.

Baym G, Blaizot J-P, Holzmann M, Laloë F, and Vautherin D (2001) Bose–Einstein transition in a dilute interacting gas. *European Physical Journal B: Condensed Matter and Complex Systems* 24: 107.

Berges J, Borsányi S, and Wetterich C (2004) Prethermalization. *Physical Review Letters* 93: 142002.

Bismut G, Laburthe-Tolra B, Maréchal E, Pedri P, Gorceix O, and Vernac L (2012) Anisotropic excitation spectrum of a dipolar quantum Bose gas. *Physical Review Letters* 109: 155302.

Bland T, Poli E, Politi C, Klaus L, Norcia MA, Ferlaino F, Santos L, and Bisset RN (2022) Two-dimensional supersolid formation in dipolar condensates. *Physical Review Letters* 128: 195302.

Bloch I (2005) Ultracold quantum gases in optical lattices. *Nature Physics* 1: 23.

Bogoliubov NN (1947) On the theory of superfluidity. *Journal of Physics (USSR)* 11(23).

Böttcher F, Schmidt J-N, Wenzel M, Hertkorn J, Guo M, Langen T, and Pfau T (2019) Transient supersolid properties in an array of dipolar quantum droplets. *Physical Review X* 9: 011051.

Braaten E and Hammer H-W (2007) Efimov physics in cold atoms. *Ann. Phys.* 322: 120.

Burovski E, Machta J, Prokof'ev N, and Svistunov B (2006a) High-precision measurement of the thermal exponent for the three-dimensional xy universality class. *Physical Review B* 74: 132502.

Burovski E, Prokof'ev N, Svistunov B, and Troyer M (2006b) Critical temperature and thermodynamics of attractive fermions at unitarity. *Physical Review Letters* 96: 160402.

Cabrera CR, Tanzi L, Sanz J, Naylor B, Thomas P, Cheiney P, and Tarruell L (2018) Quantum liquid droplets in a mixture of Bose–Einstein condensates. *Science* 359: 301.

Cazalilla MA, Citro R, Giamarchi T, Orignac E, and Rigol M (2011) One dimensional bosons: From condensed matter systems to ultracold gases. *Reviews of Modern Physics* 83: 1405.

Chin C, Grimm R, Julienne P, and Tiesinga E (2010) Feshbach resonances in ultracold gases. *Reviews of Modern Physics* 82: 1225.

Chomaz L, Baier S, Petter D, Mark MJ, Wächtler F, Santos L, and Ferlaino F (2016) Quantum-fluctuation-driven crossover from a dilute Bose–Einstein condensate to a macrodroplet in a dipolar quantum fluid. *Physical Review X* 6: 041039.

Chomaz L, Ferrier-Barbut I, Ferlaino F, Laburthe-Tolra B, Lev BL, and Pfau T (2023) Dipolar physics: A review of experiments with magnetic quantum gases. *Rep. Prog. Phys.* 86: 026401.

Chomaz L, Petter D, Ilzhöfer P, Natale G, Trautmann A, Politi C, Durastante G, van Bijnen RMW, Patscheider A, Sohmen M, Mark MJ, and Ferlaino F (2019) Long-lived and transient supersolid behaviors in dipolar quantum gases. *Physical Review X* 9: 021012.

Cowell S, Heiselberg H, Mazets IE, Morales J, Pandharipande VR, and Pethick CJ (2002) Cold Bose gases with large scattering lengths. *Physical Review Letters* 88: 210403.

Dalfovo F, Giorgini S, Pitaevkii LP, and Stringari S (1999) Theory of Bose–Einstein condensation in trapped gases. *Reviews of Modern Physics* 71: 463.

Davis KB, Mewes MO, Andrews MR, van Druten NJ, Durfee DS, Kurn DM, and Ketterle W (1995) Bose–Einstein condensation in a gas of sodium atoms. *Physical Review Letters* 75: 3969.

Demokritov SO, Demidov VE, Dzyapko O, Melkov GA, Serga AA, Hillebrands B, and Slavin AN (2006) Bose–Einstein condensation of quasi-equilibrium magnons at room temperature under pumping. *Nature* 443: 430.

Deng H, Weihs G, Santori C, Bloch J, and Yamamoto Y (2002) Condensation of semiconductor microcavity exciton polaritons. *Science* 298: 199.

Deng H, Press D, Götzinger S, Solomon GS, Hey R, Ploog KH, and Yamamoto Y (2006) Quantum degenerate exciton-polaritons in thermal equilibrium. *Physical Review Letters* 97: 146402.

Donley EA, Claussen NR, Cornish SL, Roberts JL, Cornell EA, and Wieman CE (2001) Dynamics of collapsing and exploding Bose–Einstein condensates. *Nature* 412: 295.

Donnelly RJ, Donnelly JA, and Hills RN (1981) Specific heat and dispersion curve for helium II. *Journal of Low Temperature Physics* 44: 471.

Donner T, Ritter S, Bourdel T, Ottl A, Köhl M, and Esslinger T (2007) Critical behavior of a trapped interacting Bose gas. *Science* 315: 1556.

Efimov V (1970) Energy levels arising from resonant two-body forces in a three-body system. *Physics Letters B* 33: 563.

Eigen C, Gaunt AL, Suleymanzade A, Navon N, Hadzibabic Z, and Smith RP (2016) Observation of weak collapse in a Bose–Einstein condensate. *Physical Review X* 6: 041058.

Eigen C, Glidden JAP, Lopes R, Navon N, Hadzibabic Z, and Smith RP (2017) Universal scaling laws in the dynamics of a homogeneous unitary Bose gas. *Physical Review Letters* 119: 250404.

Eigen C, Glidden JAP, Lopes R, Cornell EA, Smith RP, and Hadzibabic Z (2018) Universal prethermal dynamics of Bose gases quenched to unitarity. *Nature* 563: 221.

Eismann U, Khaykovich L, Laurent S, Ferrier-Barbut I, Rem BS, Grier AT, Delehaye M, Chevy F, Salomon C, Ha L-C, and Chin C (2016) Universal loss dynamics in a unitary BOSE gas. *Physical Review X* 6: 021025.

Ferrier-Barbut I, Kadau H, Schmitt M, Wenzel M, and Pfau T (2016) Observation of quantum droplets in a strongly dipolar BOSE gas. *Physical Review Letters* 116: 215301.

Fletcher RJ, Gaunt AL, Navon N, Smith RP, and Hadzibabic Z (2013) Stability of a unitary BOSE gas. *Physical Review Letters* 111: 125303.

Gerton JM, Strekalov D, Prodan I, and Hulet RG (2000) Direct observation of growth and collapse of a Bose–Einstein condensate with attractive interactions. *Nature* 408: 692.

Goldman N, Juzeliūnas G, Öhberg P, and Spielman IB (2014) Light-induced gauge fields for ultracold atoms. *Reports on Progress in Physics* 77: 126401.

Hadzibabic Z and Dalibard J (2011) Two-dimensional Bose fluids: An atomic physics perspective. *Rivista del Nuovo Cimento della Societa Italiana di Fisica* 34: 389.

Hall DS, Matthews MR, Ensher JR, Wieman CE, and Cornell EA (1998) The dynamics of component separation in a binary mixture of Bose–Einstein condensates. *Physical Review Letters* 81: 4531.

Hilker TA, Dogra LH, Eigen C, Glidden JAP, Smith RP, and Hadzibabic Z (2022) First and second sound in a compressible 3D Bose fluid. *Physical Review Letters* 128: 223601.

Ho T-L (2004) Universal thermodynamics of degenerate quantum gases in the unitarity limit. *Physical Review Letters* 92: 090402.

Holzmann M, Fuchs JN, Baym G, Blaizot JP, and Laloë F (2004) Bose–Einstein transition temperature in a dilute repulsive gas. *Comptes Rendus Physique* 5: 21.

Inguscio M, Ketterle W, and Salomon C (2007) *Ultracold Fermi Gases, Proceedings of the International School of Physics "Enrico Fermi", Course CLXIV*.

Jin DS, Ensher JR, Matthews MR, Wieman CE, and Cornell EA (1996) Collective excitations of a Bose–Einstein condensate in a dilute gas. *Physical Review Letters* 77: 420.

Kadau H, Schmitt M, Wenzel M, Wink C, Maier T, Ferrier-Barbut I, and Pfau T (2016) Observing the Rosensweig instability of a quantum ferrofluid. *Nature* 530(194): 1508.05007.

Kapitza P (1938) Viscosity of liquid helium below the λ - Point,. *Nature* 141: 74.

Kashurnikov VA, Prokof'ev NV, and Svistunov BV (2001) Critical temperature shift in weakly interacting Bose gas. *Physical Review Letters* 87: 120402.

Kasprzak J, Richard M, Kundermann S, Baas A, Jeambrun P, Keeling JMJ, Marchetti FM, Szymanska MH, Andre R, Staehli JL, Savona V, Littlewood PB, Deveaud B, and Dang LS (2006) Bose–Einstein condensation of exciton polaritons. *Nature* 443: 409.

Khaykovich L, Schreck F, Ferrari G, Bourdel T, Cubizolles J, Carr LD, Castin Y, and Salomon C (2002) Formation of a matter-wave bright soliton. *Science* 296: 1290.

Klaers J, Schmitt J, Vewinger F, and Weitz M (2010) Bose–Einstein condensation of photons in an optical microcavity. *Nature* 468: 545.

Klauss CE, Xie X, Lopez-Abadia C, D'Incao JP, Hadzibabic Z, Jin DS, and Cornell EA (2017) Observation of Efimov molecules created from a resonantly interacting Bose gas. *Physical Review Letters* 119: 143401.

Kozuma M, Deng L, Hagley EW, Wen J, Lutwak R, Helmerson K, Rolston SL, and Phillips WD (1999) Coherent splitting of Bose–EINSTEIN condensed atoms with optically induced bragg diffraction. *Physical Review Letters* 82: 871.

Lahaye T, Koch T, Frohlich B, Fattori M, Metz J, Griesmaier A, Giovanazzi S, and Pfau T (2007) Strong dipolar effects in a quantum ferrofluid. *Nature* 448: 672.

Lahaye T, Metz J, Fröhlich B, Koch T, Meister M, Griesmaier A, Pfau T, Saito H, Kawaguchi Y, and Ueda M (2008) *d*-Wave collapse and explosion of a dipolar Bose–Einstein condensate. *Physical Review Letters* 101: 080401.

Lahaye T, Menotti C, Santos L, Lewenstein M, and Pfau T (2009) The physics of dipolar bosonic quantum gases. *Reports on Progress in Physics* 72: 126401.

Landau LD (1941) The theory of superfluidity of helium II. *Journal of Physics (USSR)* 5(71).

Lee TD, Huang K, and Yang CN (1957) Eigenvalues and eigenfunctions of a Bose system of hard spheres and its low-temperature properties. *Physics Review* 106: 1135.

Lopes R, Eigen C, Navon N, Clément D, Smith RP, and Hadzibabic Z (2017) Quantum depletion of a homogeneous BOSE–EINSTEIN condensate. *Physical Review Letters* 119: 190404.

Madison KW, Chevy F, Wohlleben W, and Dalibard J (2000) Vortex formation in a stirred Bose–Einstein condensate. *Physical Review Letters* 84: 806.

Makotyn P, Klauss CE, Goldberger DL, Cornell EA, and Jin DS (2014) Universal dynamics of a degenerate unitary Bose gas. *Nature Physics* 10: 116.

Mehta NP, Rittenhouse ST, D'Incao JP, von Stecher J, and Greene CH (2009) General theoretical description of *n*-body recombination. *Physical Review Letters* 103: 153201.

Mewes M-O, Andrews MR, van Druten NJ, Kurn DM, Durfee DS, Townsend CG, and Ketterle W (1996) Collective excitations of a Bose–Einstein condensate in a magnetic trap. *Physical Review Letters* 77: 988.

Morsch O and Oberthaler M (2006) Dynamics of Bose–Einstein condensates in optical lattices. *Reviews of Modern Physics* 78: 179.

Musolino S, Kurkjian H, Van Regemortel M, Wouters M, Kokkelmans SJJMF, and Colussi VE (2022) Bose–Einstein condensation of EFIMOVIAN triples in the unitary BOSE gas. *Physical Review Letters* 128(020401).

Naidon P and Endo S (2017) Efimov physics: A review. *Reports on Progress in Physics* 80: 056001.

Navon N, Piatecki S, Günter K, Rem B, Nguyen TC, Chevy F, Krauth W, and Salomon C (2011) Dynamics and Thermodynamics of the low-temperature strongly interacting Bose gas. *Physical Review Letters* 107: 135301.

Norcia MA and Ferlaino F (2021) Developments in atomic control using ultracold magnetic lanthanides. *Nature Physics* 17: 1349.

Norcia MA, Politi C, Klaus L, Poli E, Sohmen M, Mark MJ, Bisset RN, Santos L, and Ferlaino F (2021) Two-dimensional supersolidity in a dipolar quantum gas. *Nature* 596: 357.

Nozières P and Pines D (1990) *The Theory of Quantum Liquids*. Westview Press.

Onnes HK (1911) Further Experiments With Liquid Helium. D. On the Change of Electrical Resistance of Pure Metals at Very Low Temperatures, etc. V. The Disappearance of the Resistance of Mercury. *Proc. K. Ned. Akad. Wet.* , Vol. 14, p. 113.

Papp SB, Pino JM, and Wieman CE (2008) Tunable miscibility in a dual-species Bose–Einstein condensate. *Physical Review Letters* 101: 040402.

Pethick CJ and Smith H (2002) *Bose–Einstein Condensation in Dilute Gases*. Cambridge University Press.

Petrov DS (2015) Quantum mechanical stabilization of a collapsing Bose-Bose mixture. *Physical Review Letters* 115: 155302.

Petter D, Natale G, van Bijnen RMW, Patscheider A, Mark MJ, Chomaz L, and Ferlaino F (2019) Probing the roton excitation spectrum of a stable dipolar BOSE gas. *Physical Review Letters* 122: 183401.

Piatecki S and Krauth W (2014) Efimov-driven phase transitions of the unitary Bose gas. *Nature Communications* 5: 3503.

Pitaevskii L and Stringari S (2016) *Bose–Einstein Condensation and Superfluidity*. Oxford University Press.

Proukakis NP (2023) Universality of Bose-Einstein condensation and quenched formation dynamics. *Encyclopedia of Condensed Matter Physics*. 2nd ed. Elsevier.

Rem BS, Grier AT, Ferrier-Barbut I, Eismann U, Langen T, Navon N, Khaykovich L, Werner F, Petrov DS, Chevy F, and Salomon C (2013) Lifetime of the Bose gas with resonant interactions. *Physical Review Letters* 110: 163202.

Roberts JL, Claussen NR, Cornish SL, Donley EA, Cornell EA, and Wieman CE (2001) Controlled collapse of a BOSE–EINSTEIN condensate. *Physical Review Letters* 86: 4211.

Schmitt M, Wenzel M, Böttcher F, Ferrier-Barbut I, and Pfau T (2016) Self-bound droplets of a dilute magnetic quantum liquid. *Nature* 539: 259.

Semeghini G, Ferioli G, Masi L, Mazzinghi C, Wolswijk L, Minardi F, Modugno M, Modugno G, Inguscio M, and Fattori M (2018) Self-bound quantum droplets of atomic mixtures in free space. *Physical Review Letters* 120: 235301.

Skov TG, Skou MG, Jørgensen NB, and Arlt JJ (2021) Observation of a Lee-Huang-Yang fluid. *Physical Review Letters* 126: 230404.

Smith RP (2017) Effects of interactions on Bose–Einstein condensation. In: Proukakis N, Snoke D, and Littlewood P (eds.) *Universal Themes of Bose–Einstein Condensation*. Cambridge University Press.

Smith RP, Campbell RLD, Tammuz N, and Hadzibabic Z (2011) Effects of interactions on the critical temperature of a trapped Bose gas. *Physical Review Letters* 106: 250403.

Steinhauer J, Ozeri R, Katz N, and Davidson N (2002) Excitation spectrum of a Bose–Einstein condensate. *Physical Review Letters* 88: 120407.

Stenger J, Inouye S, Stamper-Kurn DM, Miesner H-J, Chikkatur AP, and Ketterle W (1998) Spin domains in ground-state Bose–Einstein condensates. *Nature* 396: 345.

Stenger J, Inouye S, Chikkatur AP, Stamper-Kurn DM, Pritchard DE, and Ketterle W (1999) Bragg spectroscopy of a Bose–Einstein condensate. *Physical Review Letters* 82: 4569.

Strecker KE, Partridge GB, Truscott AG, and Hulet RG (2002) Formation and propagation of matter-wave soliton trains. *Nature* 417: 150.

Stringari S (2023) Bose–Einstein condensation. *Encyclopedia of Condensed Matter Physics*. 2nd ed. Elsevier.

Tammuz N, Smith RP, Campbell RLD, Beattie S, Moulder S, Dalibard J, and Hadzibabic Z (2011) Can a Bose gas be saturated? *Physical Review Letters* 106: 230401.

Tanzi L, Lucioni E, Famà F, Catani J, Fioretti A, Gabbanini C, Bisset RN, Santos L, and Modugno G (2019) Observation of a dipolar quantum gas with metastable supersolid properties. *Physical Review Letters* 122: 130405.

Thøgersen M, Fedorov DV, and Jensen AS (2008) N-body EFIMOV states of trapped bosons. *EPL (Europhysics Letters)* 83(30012).

Yin X and Radzihovsky L (2016) Postquench dynamics and prethermalization in a resonant Bose gas. *Physical Review A* 93: 033653.

Zhai H (2015) Degenerate quantum gases with spin–orbit coupling: A review. *Reports on Progress in Physics* 78: 026001.

Zwerger W (2011) *BCS-BEC Crossover and the Unitary Fermi Gas*. Springer.

Zwierlein MW (2014) Superfluidity in ultracold atomic Fermi gases. In: Bennemann K-H and Ketterson JB (eds.) *Novel Superfluids: Volume 2*. Oxford University Press.

Cold-atom systems as condensed matter physics emulation

Yoshiro Takahashi, Department of Physics, Graduate School of Science, Kyoto University, Kyoto City, Japan

© 2024 Elsevier Ltd. All rights reserved.

Introduction	**135**
Key issues	**136**
Overview	**136**
Optical lattice minimum	**137**
Controllability of parameters	137
Measurement methods	137
Quantum gas microscopy	138
Ultracold Fermions as Fermi-Hubbard-Model emulation	**138**
Cold atom SU(N) fermion system	138
Cold atom realization of dissipative Hubbard model as open quantum system emulation	**139**
Open quantum system	139
Dissipation in cold atom experiment	139
Cold atom realization of Thouless pump as topological physics emulation	**139**
Thouless pump in cold atom experiments	140
Two-orbital cold atom system as quantum transport emulation	**140**
Two-orbital two-electron atom system as Kondo-effect emulation	140
Cold atom system as mesoscopic quantum transport emulation	141
Non-standard optical lattice system as novel energy-band emulation	**141**
Optical Lieb lattice system as novel flat-band emulator	141
Conclusion	**142**
Acknowledgments	**142**
References	**142**

Abstract

Ultracold-atom systems are an ideal quantum simulator or emulator of condensed matter physics, providing a unique approach to study strongly correlated quantum many body physics. In particular, a system of ultracold atoms loaded into an optical lattice is well described by a Hubbard model, an important minimal model in the study of condensed matter physics. High controllability of system parameters is a key to this new approach. In this chapter, we describe in detail the basic techniques as well as the recent developments of this rapidly growing field.

Key points

- Ultracold atom systems, especially those loaded into an optical lattice are an ideal quantum emulation platform of condensed matter physics, enabling the exploration of quantum many-body problems.
- Quantum emulation of a Fermi-Hubbard model as well as its SU(N) extension made possible by the use of two-electron atom system is important since classical computer cannot efficiently solve these models.
- Open quantum system can be studied with cold-atom quantum emulators by introducing the dissipation in a well-controlled manner.
- Quantum emulator of ultracold atom systems can be utilized to study topological phenomena, Thouless pump being a representative example.
- Quantum transport phenomena are studied by exploiting the state-of-the-art technologies of cold-atom systems.
- The flexibility of optical lattice setups for cold atoms enables the study of novel phenomena originating from unique band dispersions.

Introduction

Recently, atomic physicists can prepare ultracold atoms in a trap formed by a laser beam or a magnetic field in a high vacuum condition. Cooling to quantum degenerate regimes like a Bose-Einstein condensates or Fermi degenerate gases at a temperature of nano kelvin is achieved by laser cooling and evaporative cooling techniques (Ketterle and Druten, 1996). They are a closed quantum system, well isolated from the environment. Ultracold atom systems are regarded as an ideal quantum emulator or simulator of quantum many body systems owing to the high controllability of system parameters (Bloch et al., 2008). In particular, among many, an inter-atomic interaction can be finely and widely controlled by a Feshbach resonance technique, which is not available by condensed matter systems. This leads to the realization of the Bardeen-Cooper-Schrieffer to Bose-Einstein condensate (BCS-BEC) crossover, for example. Other illustrative examples of quantum emulation studies using ultracold atoms include the physics of universal few body bound states like Efimov trimers (Naidon and Endo, 2017).

Of particular importance and interest in the study of quantum emulation of condensed matter systems is a system of ultracold atoms loaded into a periodic potential with lattice constant of the order of the laser wavelength, called an optical lattice (Bloch et al., 2008, 2012; Gross and Bloch, 2017; Schäfer et al., 2020). It is well described by a Hubbard model, which is crucially important in condensed matter physics, and is regarded as an important minimal model in the study of strongly-correlated quantum many body systems like high-temperature cuprate superconductors (Lee et al., 2006). Although only the nearest neighbor hopping t and on-site interaction U are involved, the Hubbard model captures the essence and provides the explanation of diverse phenomena observed in condensed-matter physics. Quantitative understandings that can be obtained from the quantum emulation of strongly correlated many-body systems will offer unique guidelines for synthesis of novel materials.

Key issues

Here, we note that it is obvious that experiments using ultracold atoms are not always regarded as quantum emulation. Then, in what conditions should the experiments performed using cold atoms be termed as quantum emulation? Here, we provide a brief comment on the requisite for quantum emulation using ultracold atoms (Qiu et al., 2020). We think that, at least, the Hamiltonian or model of the target system should be clearly defined with reasonable grounds, and only the difficulty to describe an observed behavior by a mean-field theory, or the complexity to calculate static or dynamic properties of the system, for example, should be insufficient. One illustrative example of quantum emulation research from the engineering point of view is the computationally hard problem of Fermi-Hubbard model (FHM) where the sign-problem prevents the efficient numerical approach with quantum Monte-Carlo methods. From the viewpoints of scientific importance, on the other hand, one can target the conceptually important phenomena like topological quantum phenomena, no matter how computationally hard or not.

One of the important advantages of quantum emulation approach of condensed matter physics using ultracold atoms is rich varieties of interesting research topics. Fig. 1 illustrates some examples of interesting optical lattice quantum emulation research topics. These include non-equilibrium dynamics, potential disorder, SU(N) spin symmetry, non-standard lattice, topological physics, open quantum dynamics, quantum mixtures, quantum transport, synthetic gauge field, and so on.

Overview

In this article, we describe in detail the basic techniques as well as several interesting research topics of optical lattice quantum emulation research. In Section "Optical lattice minimum," the basic knowledges and techniques required to understand the optical lattice system are summarized. In particular, we pay special attention to a powerful technique of quantum gas microscopy. The following sections are devoted to the focused discussion on the selected topics. In Section "Ultracold Fermions as Fermi-Hubbard-Model emulation," we describe in detail a system of ultracold fermions as Fermi-Hubbard-model emulator, with the special emphasis on the unique possibility of studying SU(N) Fermi-Hubbard model. Section "Cold atom realization of dissipative Hubbard model as open quantum system emulation" describes the cold-atom realization of dissipative Hubbard model as an open quantum system emulator, which is of recent interest. In Section "Cold atom realization of Thouless pump as topological physics emulation," we describe the cold-atom realization of Thouless pump as an illustrative example from the viewpoint of the

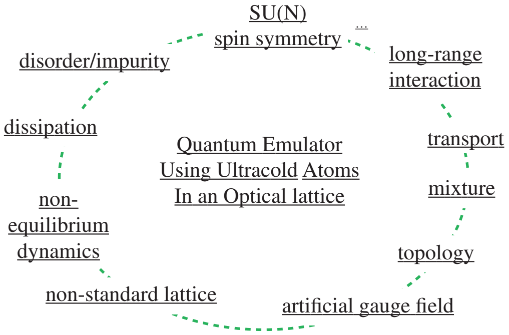

Fig. 1 Few examples of interesting optical lattice quantum emulation research topics.

emulation of topological physics which is intensively and extensively studied in condensed matter physics. Section "Two-orbital cold atom system as quantum transport emulation" is devoted to the discussion on the quantum transport emulation of the Kondo effect as well as mesoscopic quantum transport. The final focused topic described in Section "Non-standard optical lattice system as novel energy-band emulation" is a non-standard optical-lattice system as novel-energy-band emulation, with special emphasis on a Lieb lattice. We conclude this article by describing the summary and future directions in the final Section "Conclusion."

Optical lattice minimum

Fig. 2 shows the schematic view of an optical lattice. A variety of atomic species have been successfully cooled to quantum-degenerate regimes, such as rather standard alkali-metal, alkali-earth-like, and magnetic lanthanide atoms (Schäfer et al., 2020). These ultracold atoms are first prepared in a weak harmonic trap. Then, adiabatic ramping-up of an optical lattice potential results in a successful loading of the ultracold atoms into an optical lattice with no significant heating effect. Sufficiently deep optical lattice potential enables us to treat the atoms in an optical lattice by the tight-binding model where an atom is localized on each lattice site and undergoes hopping between adjacent lattice sites. A single-band Hubbard model, then, describes the behavior of the atoms by a tunneling term characterized by a tunneling energy t and an on-site interaction term characterized by an energy U when more than two particles occupy the same lattice site. In addition, a weak external confinement is superimposed to a periodic optical lattice potential and is described as a site-dependent energy offset ε_i where i represents the site index. Multiple occupancy sites are created, depending on the total number of atoms and the external confinement.

Controllability of parameters

As is mentioned, the Hubbard model is characterized by important parameters of a tunneling energy t and an on-site interaction energy U. Different from the ordinary condensed matter system, the ratio of these two parameters is precisely controlled experimentally by tuning the depth of the optical lattice potential. Individual control of these two is also possible. Feshbach resonances (Chin et al., 2010) provide the novel possibility of controlling the strength as well as sign of the on-site interaction, while the strength, sign, and even the complex phases (Peierls phases) of the tunneling energy t can also be controlled by lattice shaking and Raman-assisted tunneling methods. As in the condensed matter system, filling factor, temperature, and the total atom number can be finely controlled.

Measurement methods

Here, we review some basic measurement methods. The time-of-flight (TOF) method, in which the optical lattice potential is suddenly turned off and the atom imaging is taken after a certain time, TOF, provides the information of atomic coherence over the lattice sites, which is the key for the observation of the superfluid-to-Mott insulator transition of the Bose-Hubbard model, where the sharp interference peaks of TOF images is an important signature of superfluid phase and the vanishing of the interference Mott-insulator (Greiner et al., 2002). In the slight modification of TOF method, known as band-mapping method, TOF images are taken after adiabatic ramp-down of the optical lattice, enabling the measurement of quasi-momentum distributions of the atoms (Bloch et al., 2008). In addition, the application of a spin-dependent potential gradient just before TOF measurement enables the spin-resolving imaging through a Stern-Gerlach effect.

High-resolution spectroscopy using radio-frequency and optical clock transition resolves the spectra from different occupancies (Schäfer et al., 2020). Spin correlation is the observable of great interest in the study of quantum magnetism. Similar to the solid-state quantum dot systems, a singlet-triplet-oscillation protocol is developed for cold atom systems to reveal the spin correlation between nearest-neighbor sites by combining the methods of superlattice, photo-association, Feshbach resonance, or a band mapping (Trotzky et al., 2010; Greif et al., 2013; Ozawa et al., 2018). Long-range coherences of a superfluid phase of bosons are successfully detected by exploiting the Talbot effect incorporating the in-trap atom expansion (Santra et al., 2017). Berry curvature

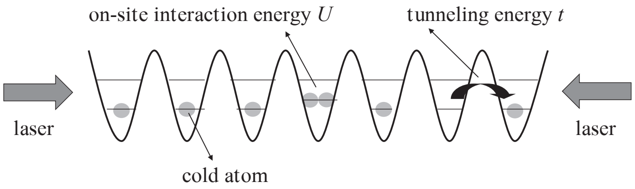

Fig. 2 Schematic view of an optical lattice.

and topological invariants are successfully measured through the excitation rate measurement to higher bands after amplitude modulation, revealing a quantum geometric tensor or through a shift of an atom cloud in the case of Thouless pump, for example.

Quantum gas microscopy

Ultimately, the atom distribution in a 2D optical lattice is measured by single-site resolving imaging of quantum gas microscopy (QGM), enabling the study of a quantum many-body system in a direct manner (Gross and Bloch, 2017). The QGM method is first developed for a bosonic atom of ^{87}Rb by utilizing the favorable features of cooling and imaging. The quantum phase transition of superfluid to Mott insulator states has been successfully demonstrated from the spatial distribution of atoms. In particular, the density plateau is directly confirmed as well as the particle-hole correlations in the Mott insulating state. The ability to observe the single-site resolving imaging is also utilized to a single-atom addressing technique, enabling the studies of non-equilibrium dynamics like a quantum walks, spin wave propagations, quantum thermalization, and quantum many-body localization. From the quantum information research perspective, entanglement entropy is directly measured. The QGM is also applied to fermionic atoms by developing efficient cooling methods, which is described in the next section.

Ultracold Fermions as Fermi-Hubbard-Model emulation

In the context of condensed matter physics emulation, ultracold fermions in an optical lattice play a fundamental role, as strongly correlated many-body systems of fermionic particles of electrons do in condensed-matter physics (Auerbach, 2012). A new approach made possible by using ultracold fermionic atoms in optical lattices will give important insights for strongly correlated electron systems. Here, we describe in more detail the recent experiments using ultracold fermions as Fermi-Hubbard-Model emulation.

As is mentioned, a system of ultracold fermions in an optical lattice is well described by the Fermi-Hubbard model (FHM),

$$H^{\mathrm{FHM}} = -t\sum_{\langle i,j\rangle,\sigma} c_{i,\sigma}^{\dagger}c_{j,\sigma} + U\sum_{i} n_{i,\uparrow}n_{i,\downarrow} + \varepsilon_i\sum_{i,\sigma} n_{i,\sigma} \tag{1}$$

where $c_{i,\sigma}$ is fermionic annihilation operator for site i and spin $\sigma = +1/2(\uparrow)$ or $-1/2(\downarrow)$, $n_{i,\sigma} = c_{i,\sigma}^{\dagger}c_{i,\sigma}$ is the number operator, and ε_i represents the weak potential offset superimposed to the optical lattice potential.

In this case of two-component or SU(2) FHM, similar to the electrons, as a higher temperature phase, a paramagnetic Mott insulator state emerges when the interaction is strongly repulsive. However, at a lower temperature below the Néel temperature, quantum magnetism manifests itself as an antiferromagnetic ordered state, as a result of the super-exchange interaction (Moriya and Ueda, 2003). Quantum emulation of the Fermi Hubbard model is especially important since the understanding of the behaviors of doped 2D SU(2) FHM at low temperatures, key for high-Tc superconductivity, still escapes complete understanding in spite of intensive studies in both condensed matter theory and experiments (Lee et al., 2006).

Mott insulating phases of cold atom FHM have been realized and studied by various techniques. In particular, the QGM is quite useful for studying the cold atom FHM, and especially QGM with a spin resolving ability is a powerful method for the short- as well as long-range spin correlation measurements of FHM. In fact, the QGM method enables the observation of an antiferromagnetic correlation and ordered phase (Mazurenko et al., 2017). More recent studies explore the doped region of Fermi-Hubbard model, revealing the non-local correlations of string orders. Toward the goal of realization of the *d*-wave superfluidity of FHM, further cooling of fermions in optical lattices is crucially important. Local manipulation of the optical lattice potential using elaborate spatial light modulating devices enables the successful demonstration of powerful strategy of entropy redistribution, leading to the temperature of $0.25(2)/\mathrm{k_B}\times t$ (Mazurenko et al., 2017). Here $\mathrm{k_B}$ is the Boltzmann constant.

Cold atom SU(N) fermion system

Beyond the scope of the emulation of traditional condensed matter systems, a new state of matter can be realized by utilizing novel possibilities available in ultracold atomic systems. As one illustrative example, we can here describe in detail the realization of SU(N) Fermi Hubbard model. Originally, the study of SU(N) Hubbard model has started from a purely theoretical interest as an extension of the conventional SU(2) Fermi Hubbard model (Affleck, 1985), and now reveals rich quantum phases (Wu et al., 2003; Cazalilla and Rey, 2014). The enhancement of quantum fluctuation causes qualitatively different behaviors from those of SU(2) model. The SU(N) FHM is described by the following Hamiltonian Eq. (2)

$$H^{\mathrm{SU(N)FHM}} = -t\sum_{\langle i,j\rangle,\sigma} c_{i,\sigma}^{\dagger}c_{j,\sigma} + U\sum_{i,\sigma\neq\sigma'} n_{i,\sigma}n_{i,\sigma'} + \varepsilon_i\sum_{i,\sigma} n_{i,\sigma} \tag{2}$$

where $\sigma = 1, 2, \ldots \mathrm{N}$. Note that the hopping matrix element t and on-site interaction U do not depend on the spin σ, which assures the SU(N) symmetry.

Implementation of SU(N) Fermi Hubbard model is realized by using fermionic isotopes of alkali-earth-like atoms, such as ytterbium (^{173}Yb) and strontium (^{87}Sr). In these atoms, the electron and nuclear spin angular momenta are decoupled in the ground $^1S_0$ and metastable $^3P_0$ states. This results in the independence of the inter-atomic interaction with respect to the spin degrees of freedom σ, here corresponding to the nuclear spin I, which is key for realizing the SU($N = 2I + 1$) FHM.

A high temperature phase of a paramagnetic SU(N) Mott insulator is realized by loading the SU(N) fermions into an optical lattice. This is confirmed by several signatures like the charge excitation gap, suppressed compressibility $\partial n/\partial \mu$, low temperature estimated by doubloon-production-rate measurement (Taie et al., 2012) and in situ observation of a Mott plateau (Hofrichter et al., 2016).

Quantum magnetism or spin correlation expected at a lower temperature phase is studied for various lattice geometries including 1D, 2D, 3D, and a dimerized lattice. An STO technique, first developed for quantum-dot system and later applied to cold atom system of bosons (Trotzky et al., 2010) and fermions (Greif et al., 2013), is successfully applied to observe the nearest-neighbor antiferromagnetic spin correlations of SU(N) fermions of ^{173}Yb (Ozawa et al., 2018). In particular, the experimental data for a system of SU(6) fermions in a 1D lattice is compared with the theoretical calculations based on exact diagonalization and determinantal quantum Monte-Carlo methods, indicating the achieved temperature of about 0.1 of the tunneling energy t (Taie et al., 2022). This corresponds to the lowest temperature ever achieved for ultracold fermions. The observed significant cooling effect for the SU(6) system is attributed to the enhanced Pomeranchuk cooling effect, first observed in solid ^{3}He. Note that even the state-of-the-art theoretical calculations are not powerful to quantitatively explain the data for higher dimensions, illustrating the importance of the SU(N) fermion system as quantum emulator.

Cold atom realization of dissipative Hubbard model as open quantum system emulation

Open quantum system

One of the recent considerable interests in condensed matter physics, especially in theory, is the study of open quantum systems. This is reasonable because the dissipation is ubiquitous in real condensed matter systems. Theoretically, an introduction of coupling between a closed quantum system with the environment calls the necessity to describe the system dynamics by Liouvillian dynamics, which is qualitatively different from a unitary dynamics of an isolated, closed quantum mechanical system. The novel role of the dissipation as a tool for preparation of certain quantum states is recently discussed (Daley, 2014; Müller et al., 2012).

As an example, here we consider the case of a dissipative Bose-Hubbard model with two-body dissipation. The master equation for density operator ρ describing this system is given as,

$$\hbar \frac{d}{dt}\rho = -i\left[H^{\mathrm{BHM}}, \rho\right] + L_2(\rho), \tag{3}$$

$$H^{\mathrm{BHM}} = -t\sum_{\langle i,j\rangle} b_i^\dagger b_j + U\sum_i n_i(n_i - 1)/2, \tag{4}$$

$$L_2(\rho) = \frac{\hbar\Gamma}{4}\sum_i \left(-b_i^\dagger b_i^\dagger b_j b_j \rho - \rho b_i^\dagger b_i^\dagger b_j b_j + 2 b_j b_j \rho b_i^\dagger b_i^\dagger\right), \tag{5}$$

where b_j represents boson annihilation operator and Γ denotes the strength of the two-body dissipation.

Dissipation in cold atom experiment

Ultracold atoms in an optical lattice is in itself a well-defined closed quantum many-body system, isolated in a vacuum chamber. Therefore, when one artificially introduces dissipation processes in a well-controlled manner, one has a novel possibility of realizing open quantum system with engineered dissipation. In fact, various types of dissipation, such as a one-body dissipation via an electron beam (Labouvie et al., 2015) and well-controlled photon scattering process (Patil et al., 2015; Takasu et al., 2020), two-body loss via a molecular inelastic collision (Syassen et al., 2008; Yan et al., 2013) and photo-association (Tomita et al., 2017), and three-body loss via a Feshbach resonance (Mark et al., 2012) are successfully introduced to a cold atom system. The successful implementation of dissipation process reveals the novel behaviors due to the dissipation, such as the localization of particle, quantum Zeno effect, stabilization of the Mott insulator, realization of PT-symmetric state, formation of ferromagnetic spin correlation indicating the negative spin temperature (Honda et al., 2023), and so on.

Cold atom realization of Thouless pump as topological physics emulation

Another example of the research topics of considerable interests in condensed matter physics is topological physics. Especially in recently years, there has been impressive progress in topological solid-state material synthesis. The theoretical backgrounds of these recent studies can be found in the seminal paper (Thouless et al., 1982) by Thouless, Kohmoto, Nightigale, and den Nijs (TKNN) in which the quantization of the Hall conductance for the integer quantum Hall effect is revealed as a topological invariant known as a

Chern number. High controllability of ultracold atoms in optical lattices enables the researchers to realize various topologically-non-trivial systems (Goldman et al., 2016).

In another seminal 1983's Thouless paper (Thouless, 1983), the quantization of the charge transferred in each pumping cycle for a periodically driven electron gas in an infinite one-dimensional periodic potential is revealed as a topological invariant. Importantly, these seemingly different phenomena share the same topological origin. Topological robustness inherent in these phenomena are also crucially important from the viewpoints of the application to the standard: the quantized Hall conductance and Thouless pump can serve as very accurate standards for electric resistance and electric current, respectively.

Thouless pump in cold atom experiments

Successful demonstration of the Thouless charge pump (Nakajima et al., 2016; Lohse et al., 2016) is achieved by constructing a controllable one-dimensional periodic potential consisting of an optical superlattice and loading ultracold bosonic or fermionic atoms. These experiments are based on the specific lattice model of a Rice-Mele model given in Eq. (6),

$$H^{\mathrm{RM}} = \sum_i \left(-(J+\delta) a_i^\dagger b_i - (J-\delta) a_i^\dagger b_{i+1} + \mathrm{h.c.} + \Delta\left(a_i^\dagger a_i - b_i^\dagger b_i \right) \right), \tag{6}$$

where a_i and b_i are annihilation operators of an atom in the two sublattices of the i-th unit cell, $J \pm \delta$ is the tunneling amplitude within and between unit cells, and Δ denotes a staggered on-site energy offset. Temporal periodic change of the dimerized hopping amplitude δ and staggered energy Δ, forming a particular trajectory in the δ-Δ parameter space, drives Thouless pumping, the topology of which is determined by the trajectory that encircles the degeneracy point of $\delta = \Delta = 0$. The quantization of Thouless pumping manifests itself as the quantized shift of the atomic cloud. In particular, the experiments with various pumping sequences reveal the topological natures of this pumping: relevance on the winding number of the trajectory around the degeneracy point as well as the irrelevance on the details of the trajectory.

Two-orbital cold atom system as quantum transport emulation

From the viewpoints of quantum emulation of condensed matter physics, two-electron atoms, or alkali-earth-like atoms are unique in that their long-lived metastable states like the $^3\mathrm{P}_0$ and $^3\mathrm{P}_2$ electronic states, combined with the ground state $^1\mathrm{S}_0$ enables the study of the multi-orbital physics. These metastable states are accessible from the $^1\mathrm{S}_0$ state through a coherent excitation utilizing very stable lasers with a Hz-level linewidth, which also attracts much attention for the application to an optical frequency standard. In addition to the inter-orbital spin-exchange interaction for nuclear spin degrees of freedom, the existence of a magnetic (orbital) Feshbach resonance between the ground $^1\mathrm{S}_0$ and $^3\mathrm{P}_2$ ($^3\mathrm{P}_0$) states offers the powerful control of the interatomic interaction between the atoms in these states.

Among the spin-orbital-related physics so far studied in condensed matter physics, the Kondo effect (Kondo, 1964), arising from an antiferromagnetic spin-exchange interaction between conduction electrons and magnetic impurities, is quite important, since it is one of the central problems of the strongly-correlated quantum many-body physics. In the case of periodically aligned localized spins, the corresponding system is described by the Kondo lattice model, exhibiting rich quantum phases like a paramagnetic phase and the Ruderman-Kittel-Kasuya-Yoshida ordered phase in a Doniach phase diagram (Doniach, 1977). The system is described by the following Hamiltonian H^{KLM},

$$H^{\mathrm{KLM}} = -t_c \sum_{\langle i,j\rangle,\sigma} c_{i,c,\sigma}^\dagger c_{j,c,\sigma} + V^{ex} \sum_{i,\sigma\neq\sigma'} c_{i,c,\sigma}^\dagger c_{i,l,\sigma'}^\dagger c_{i,c,\sigma'} c_{i,l,\sigma}, \tag{7}$$

where t_c is the tunneling amplitude in the conduction band, V^{ex} the spin-exchange energy between the conduction electron and localized impurity, and the symbols c and l the conduction and localized orbitals, respectively. We note that, for a system of alkali atoms, there are also several proposals of cold atom quantum emulator of the Kondo effect.

Two-orbital two-electron atom system as Kondo-effect emulation

Owing to the existence of two-orbital as well as spin degrees of freedom, as is mentioned, it is quite natural to consider a system of two-electron atoms as an experimental platform of Kondo-effect or Kondo lattice model emulator (Gorshkov et al., 2010). We can expect that the application of a quantum gas microscope technique for two-electron atoms will reveal the Kondo screening behavior, for example. However, this does not mean that any two-electron atoms can be used for this emulation. In order to study the Kondo effect, the interorbital spin-exchange interaction should be antiferromagnetic, which makes only a fermionic isotope of ^{171}Yb a natural candidate (Ono et al., 2019), while an interesting possibility of controllability of spin-exchange interaction is theoretically proposed and experimentally demonstrated for ^{173}Yb atoms with a ferromagnetic spin-exchange interaction. Toward this goal, progresses are obtained like a construction of localization-itinerant mixed-dimensional two-orbital optical lattice system and a successful observation of the spin-exchange dynamics between ^{171}Yb atoms in the $^1\mathrm{S}_0$ and $^3\mathrm{P}_0$ states (Ono et al., 2021a).

Cold atom system as mesoscopic quantum transport emulation

In solid state mesoscopic materials, there have been extensive studies on quantum transport of electrons between terminals through narrow channels (Ihn, 2010; Imry, 2002). The quantized conductance, predicted by the Landauer formula, is one illustrative example.

High controllability and state-of-the-art optical trapping technique enable the realization of narrow conduction channels for quantum transport experiments using ultracold atoms (Krinner et al., 2017). This quantum emulator using ultracold atoms, extended to mesoscopic quantum transport research, is called atomtronics. A series of elaborate experiments have established a cold-atom analog of mesoscopic quantum point contact, verifying conductance quantization, for example (Krinner et al., 2015). More recently, a novel scheme of a quantum transport emulation using the spin degrees of freedom is proposed (You et al., 2019, and Nakada et al., 2020), and experimentally realized (Ono et al., 2021b). In particular, the use of a multicomponent spin system enables the realization of a multiterminal quantum point contact system.

Non-standard optical lattice system as novel energy-band emulation

Recent advance of highly sophisticated laser technologies makes not only standard but also various types of optical lattice geometries available for quantum emulation experiments. In fact, various geometries of optical lattices are realized (Windpassinger and Sengstock, 2013). In addition to standard 1D, 2D, or 3D lattices, non-standard lattices of superlattices (Fölling et al., 2007), triangular lattices (Becker et al., 2010), Kagomé lattices (Jo et al., 2012), Lieb lattices (Taie et al., 2015), honeycomb lattices (Tarruell et al., 2012), quasi-crystal potentials (Viebahn et al., 2019) are successfully formed, for example, enabling the study of geometric frustration, topology, and so on.

Novel geometries of lattice structures lead to interesting energy bands which will play crucial roles in the manifestation of the novel quantum phases. For example, a honeycomb lattice shows a linear dispersion of Dirac cone, and the Kagomé lattice structure exhibits a totally vanishing dispersion, called a flat band with the macroscopic degeneracy.

Optical Lieb lattice system as novel flat-band emulator

Here, we describe in detail a Lieb lattice as an illustrative example of optical-lattice realization of interesting non-standard lattice structure. Cold-atom systems provide the possibility to study exotic phases like supersolids using bosons loaded into a Lieb lattice as a result of interplay between frustrated kinetic energy and inter-atomic interactions, as well as the ferromagnetism using fermions based on the Lieb's theorem.

The Lieb lattice supports the flat band as well as the Dirac cone, and is also called a *d-p* model since it is identical to the lattice structure of the CuO_2 plane of high-T_c superconductors. The lattice structure of the Lieb lattice involves three sublattices A, B, and C, in which A-sites forms a square lattice and B- and C-sites are located on every line of the square lattice. Taking only the nearest-neighbor tunneling t into consideration and considering the quasi-momentum eigenstates $|\boldsymbol{q}, A\rangle$, $|\boldsymbol{q}, B\rangle$, and $|\boldsymbol{q}, C\rangle$ as basis sets, the tight-binding Hamiltonian can be described by transfer matrix M, given by

$$M = \begin{pmatrix} 0 & -2t\cos(q_x d/2) & -2t\cos\left(q_y d/2\right) \\ -2t\cos(q_x d/2) & 0 & 0 \\ -2t\cos\left(q_y d/2\right) & 0 & 0 \end{pmatrix}, \tag{8}$$

where d denote the lattice constant. The diagonalization of this transfer matrix gives the energy-bands and the eigenvalues. Importantly, the second energy-band of the Lieb lattice exhibits the flat band with no energy dispersion, with the eigenstates given by a superposition of only the B- and C- sites,

$$|\boldsymbol{q}, \mathrm{FB}\rangle = \cos\theta_{\boldsymbol{q}} |\boldsymbol{q}, \mathrm{B}\rangle - \sin\theta_{\boldsymbol{q}} |\boldsymbol{q}, \mathrm{C}\rangle \tag{9}$$

where $\tan\theta_{\boldsymbol{q}} = \cos(q_x d/2)/\cos(q_y d/2)$. Note that the flat band structure is not originated from a zero hopping energy but from the destructive interference between the hopping from B- to A- sites and that from C- to A- sites.

Optical-lattice realization of the Lieb lattice is done by superimposing three different kinds of optical lattices by exploiting the high flexibility of laser phases and wavelengths. The controllability of the optical lattice parameters enables the direct observation of the localization of a matter wave within the B- and C- sites in the flat band, different from the delocalization in a usual dispersive band. In addition, the structure of the transfer matrix M suggests the analogy between the phenomenon of Stimulated Raman Adiabatic Passage (STIRAP) process (Bergmann et al., 1998), studied both theoretically and experimentally in quantum optics, and the Lieb lattice, studied in condensed matter physics. In fact, this is the nice example in which the phenomena discussed in different fields of physics can be understood on the same grounds. This close analogy provides the interesting manner of understanding of the flat band. Namely, the eigenstate of the flat band is nothing but a dark state which does not couple with electromagnetic fields applied in the STIRAP process.

This analogy between the Lieb lattice and laser-coupled three-level system considered in a STIRAP process not only provides the deeper understanding but also the novel possibility of realization of a matter-wave analog of the STIRAP, called spatial adiabatic passage, or transport without transit (Rab et al., 2008). According to this analogy, we can consider novel quantum transport of a quantum-mechanical particle between well-separated positions of B- and C- sites in real space, with no possibility of finding the atoms at the intermediate position of A-site. In fact, this novel transport is realized experimentally (Taie et al., 2020).

Conclusion

In summary, after the basic techniques of an optical lattice are introduced, we described several interesting research topics of quantum emulation of condensed matter physics. The discussed topics include quantum emulation of Fermi-Hubbard-model, dissipative Hubbard model, Thouless pump, quantum transport, and a Lieb lattice model.

Here, we briefly mention other important topics which are not involved in the former sections. The first is the study of the nonequilibrium dynamics of a quantum many-body system. It is noted that an optical lattice quantum emulator is ideal for this purpose, owing to the high controllability, especially for the lattice potential and interatomic interaction in a time-dependent manner, allowing for the study of Kibble-Zurek mechanism across phase transitions (Braun et al., 2015) and the dynamical spreading of quantum information and the Lieb-Robinson bound (Cheneau et al., 2012). This is particularly important since the long-term dynamics of quantum many-body system after quantum quench is in general quite hard to simulate with classical computers, and thus the experimental results can serve as a versatile benchmark for developing a new numerical technique.

In addition to the regular periodic lattice potentials, introducing disorder potentials enables the quantum emulation of disorder-induced phenomenon such as Anderson localization (Billy et al., 2008; Roati et al., 2008), many-body localization (Abanin et al., 2019), and so on. Disordered potentials are introduced by a number of ways like imprinting speckle patterns, superpositions of optical lattices at incommensurable lattice spacings, and introducing atomic impurities.

In spite of the fact that ultracold atoms are neutral in charge, recent developments of cold-atom quantum emulation technologies successfully introduce artificial gauge fields, spin-orbit coupling and topologically non-trivial bands in optical lattices (Cooper et al., 2019). The notion of synthetic dimensions (Ozawa and Price, 2019) is also actively applied to the study of quantum emulation of condensed matter physics. A rich variety of parameter spaces spanned by time, internal degrees of freedom of atoms, and well-defined atomic momentum are available in a cold-atom system. Note that already explained example of Thouless pump utilizes the time as one of the two dimensions required for defining the Chern number. Furthermore, Raman-coupling of internal states can implement spin-orbit coupling in cold atom systems, enabling the various research related with condensed matter physics.

Here, we also briefly note on the recent development of the novel optical trapping system, called an atom tweezer array system (Saffman et al., 2010; Kaufman and Ni, 2021), which offers rather complementary possibilities with the optical lattice platform. By tightly focusing laser beams created by spatial light modulating devices with a high-numerical aperture objective lens, single atoms are trapped in defect-free atomic arrays with spacings of about a few micrometer with rather arbitrary geometries in one, two, and three dimensions. Moreover, Rydberg state excitation can induce strong interaction between the atoms in neighboring sites of a tweezer array. The Rydberg atom tweezer array system is now extensively used for quantum emulation of Ising spin model and reveals quantum thermalization problem like a quantum many-body scar, for example.

The final remark is on an interesting future possibility of performing remote quantum emulation experiment (Heck et al., 2018) by anyone, including condensed matter theorists, who is not an expert of cold-atom experiments that require the knowledge and experience to operate very complicated machines. Such a remote quantum emulation system will enhance the development of new numerical calculations.

Acknowledgments

We greatly thank many experimental and theoretical collaborators to understand the works described in this article. Especially, we thank Y. Takasu, S. Taie, S. Nakajima, H. Ozawa, R. Yamamoto, Y. Takata, N. Kitamura, K. Honda, Y. Nakamura, T. Kusano, K. Ono, T. Ishiyama, and T. Takano, for experiment, and I. Danshita, S. Goto, M. Yamashita, K. Inaba, Y. Kuno, S. Uchino, Y. Nishida, L. Wang, K. Hazzard, R. T. Scalettar, and E. Ibarra-García-Padilla for theory. The work was partially supported by the Grant-in-Aid for Scientific Research of JSPS (Nos. JP17H06138, JP18H05405, and JP18H05228), the Impulsing Paradigm Change through Disruptive Technologies (ImPACT) program, JST CREST (No. JP-MJCR1673), MEXT Quantum Leap Flagship Program (MEXT Q-LEAP) Grant No. JPMXS0118069021, and JST Moonshot R&D – MILLENNIA Program (Grant No. JPMJMS2269).

References

Abanin DA, Altman E, Bloch I, and Serbyn M (2019) Colloquium: Many-body localization, thermalization, and entanglement. *Reviews of Modern Physics* 91: 021001.
Affleck I (1985) Large-N limit of SU(N) quantum "spin" chains. *Physical Review Letters* 54: 966.
Auerbach A (2012) Interacting Electrons and Quantum Magnetism. *Graduate Texts in Contemporary Physics.* Springer New York.

Becker C, et al. (2010) Ultracold quantum gases in triangular optical lattices. *New Journal of Physics* 12: 065025.

Bergmann K, Theuer H, and Shore BW (1998) Coherent population transfer among quantum states of atoms and molecules. *Reviews of Modern Physics* 70: 1003–1025.

Billy J, et al. (2008) Direct observation of Anderson localization of matter waves in a controlled disorder. *Nature* 453: 891–894.

Bloch I, Dalibard J, and Zwerger W (2008) Many-body physics with ultracold gases. *Reviews of Modern Physics* 80: 885–964.

Bloch I, Dalibard J, and Nascimbène S (2012) Quantum simulations with ultracold quantum gases. *Nature Physics* 8: 267–276.

Braun S, et al. (2015) Emergence of coherence and the dynamics of quantum phase transitions. *Proceedings of the National Academy of Sciences of the United States of America* 112: 3641–3646.

Cazalilla MA and Rey AM (2014) Ultracold Fermi gases with emergent SU(N) symmetry. *Reports on Progress in Physics* 77: 124401.

Cheneau M, et al. (2012) Light-cone-like spreading of correlations in a quantum many-body system. *Nature* 481: 484–487.

Chin C, Grimm R, Julienne P, and Tiesinga E (2010) Feshbach resonances in ultracold gases. *Reviews of Modern Physics* 82: 1225.

Cooper NR, Dalibard J, and Spielman IB (2019) Topological bands for ultracold atoms. *Reviews of Modern Physics* 91: 015005.

Daley AJ (2014) Quantum trajectories and open many-body quantum systems. *Advances in Physics* 63: 77–149.

Doniach S (1977) The Kondo lattice and weak antiferromagnetism. *Physica B+ C* 91: 231.

Fölling S, et al. (2007) Direct observation of second-order atom tunnelling. *Nature* 448: 1029–1032.

Goldman N, Budich JC, and Zoller P (2016) Topological quantum matter with ultracold gases in optical lattices. *Nature Physics* 12: 639–645.

Gorshkov AV, Hermele M, Gurarie V, Xu C, Julienne PS, Ye J, Zoller P, Demler E, Lukin MD, and Rey AM (2010) Two-orbital SU(N) magnetism with ultracold alkaline-earth atoms. *Nature Physics* 6: 289–295.

Greif D, Uehlinger T, Jotzu G, Tarruell L, and Esslinger T (2013) Short-range quantum magnetism of ultracold fermions in an optical lattice. *Science* 340: 1307–1310.

Greiner M, Mandel O, Esslinger T, Hansch TW, and Bloch I (2002) Quantum phase transition from a superfluid to a Mott insulator in a gas of ultracold atoms. *Nature* 415: 39–44.

Gross C and Bloch I (2017) Quantum simulations with ultracold atoms in optical lattices. *Science* 357: 995–1001.

Heck R, Vuculescua O, Sørensena JJ, Zoller J, Andreasena MG, Basone MG, Ejlertsena P, Elíassona O, Haikkaa P, Laustsena JS, Nielsena LL, Maoa A, Mullera R, Napolitanoa M, Pedersena MK, Thorsena AR, Bergenholtza C, Calarcoc T, Montangeroc S, and Shersona JF (2018) Remote optimization of an ultracold atoms experiment by experts and citizen scientists. *Proceedings of the National Academy of Sciences of the United States of America* 115: E11231–E11237.

Hofrichter C, Riegger L, Scazza F, Höfer M, Rio Fernandes D, Bloch I, and Fölling S (2016) Direct probing of the mott crossover in the SU(N) Fermi-Hubbard model. *Physical Review X* 6: 021030.

Honda K, Taie S, Takasu Y, Nishizawa N, Nakagawa M, and Takahashi M (2023) Observation of the sign reversal of the magnetic correlation in a driven-dissipative fermi gas in double wells. *Physical Review Letters* 130: 063001.

Ihn T (2010) *Semiconductor Nanostructures: Quantum States and Electronic Transport*. Oxford: Oxford University Press.

Imry Y (2002) *Introduction to Mesoscopic Physics*. Oxford: Oxford University Press.

Jo G-B, Guzman J, Thomas CK, Hosur P, Vishwanath A, and Stamper-Kurn DM (2012) Ultracold atoms in a tunable optical Kagome lattice. *Physical Review Letters* 108: 045305.

Kaufman AM and Ni K-K (2021) Quantum science with optical tweezer arrays of ultracold atoms and molecules. *Nature Physics* 17: 1324–1333.

Ketterle W and Druten NJV (1996) Evaporative cooling of trapped atoms. In: Bederson B and Walther H (eds.) *Advances In Atomic, Molecular, and Optical Physics*, vol. 37, pp. 181–236. Academic Press.

Kondo J (1964) Resistance minimum in dilute magnetic alloys. *Progress of Theoretical Physics* 32: 37.

Krinner S, Stadler D, Husmann D, Brantut J-P, and Esslinger T (2015) Observation of quantized conductance in neutral matter. *Nature* 517: 64–67.

Krinner S, Esslinger T, and Brantut J-P (2017) Two-terminal transport measurements with cold atoms. *Journal of Physics: Condensed Matter* 29: 343003.

Labouvie R, Santra B, Heun S, Wimberger S, and Ott H (2015) Negative differential conductivity in an interacting quantum gas. *Physical Review Letters* 115: 050601.

Lee PA, Nagaosa N, and Wen X-G (2006) Doping a Mott insulator: Physics of high-temperature superconductivity. *Reviews of Modern Physics* 78: 17–85.

Lohse M, Schweizer C, Zilberberg O, Aidelsburger M, and Bloch I (2016) A Thouless quantum pump with ultracold bosonic atoms in an optical superlattice. *Nature Physics* 12: 350–354.

Mark MJ, Haller E, Lauber K, Danzl JG, Janisch A, Büchler HP, Daley AJ, and Nägerl H-C (2012) Preparation and spectroscopy of a metastable mott-insulator state with attractive interactions. *Physical Review Letters* 108: 215302.

Mazurenko A, Chiu CS, Ji G, Parsons MF, Kanász-Nagy M, Schmidt R, Grusdt F, Demler E, Greif D, and Greiner M (2017) A cold-atom Fermi–Hubbard antiferromagnet. *Nature* 545: 462–466.

Moriya T and Ueda K (2003) Antiferromagnetic spin fluctuation and superconductivity. *Reports on Progress in Physics* 66: 1299–1341.

Müller M, Diehl S, Pupillo G, and Zoller P (2012) Engineered open systems and quantum simulations with atoms and ions. *Advances in Atomic, Molecular, and Optical Physics* 61: 1–80.

Naidon P and Endo S (2017) Efimov physics: A review. *Reports on Progress in Physics* 80(056001): 1–78.

Nakada S, Uchino S, and Nishida Y (2020) Simulating quantum transport with ultracold atoms and interaction effects. *Physical Review A* 102: 031302.

Nakajima S, Tomita T, Taie S, Ichinose T, Ozawa T, Wang L, Troyer M, and Takahashi Y (2016) Topological Thouless pumping of ultracold fermions. *Nature Physics* 12: 296–300.

Ono K, Kobayashi J, Amano Y, Sato K, and Takahashi Y (2019) Antiferromagnetic interorbital spin-exchange interaction of ^{171}Yb. *Physical Review A* 99: 032707.

Ono K, Amano Y, Higomoto T, Saito Y, and Takahashi Y (2021a) Observation of spin-exchange dynamics between itinerant and localized ^{171}Yb atoms. *Physical Review A* 103: L041303.

Ono K, Higomoto T, Saito Y, Uchino S, Nishida Y, and Takahashi Y (2021b) Observation of spin-space quantum transport induced by an atomic quantum point contact. *Nature Communications* 12: 6724.

Ozawa T and Price HM (2019) Topological quantum matter in synthetic dimensions. *Nature Reviews Physics* 1: 349–357.

Ozawa H, Taie S, Takasu Y, and Takahashi Y (2018) Antiferromagnetic spin correlation of SU(N) Fermi gas in an optical superlattice. *Physical Review Letters* 121: 225303.

Patil YS, Chakram S, and Vengalattore M (2015) Measurement-induced localization of an ultracold lattice gas. *Physical Review Letters* 115: 140402.

Qiu X, Zou J, Qi X, and Li X (2020) Precise programmable quantum simulations with optical lattices. *npj Quantum Information* 87: 1–8.

Rab M, Cole JH, Parker NG, Greentree AD, Hollenberg LCL, and Martin AM (2008) Spatial coherent transport of interacting dilute Bose gases. *Physical Review A* 77: 061602.

Roati G, et al. (2008) Anderson localization of a non-interacting Bose–Einstein condensate. *Nature* 453: 895–898.

Saffman M, Walker TG, and Mølmer K (2010) Quantum information with Rydberg atoms. *Reviews of Modern Physics* 82: 2313–2363.

Santra B, et al. (2017) Measuring finite-range phase coherence in an optical lattice using Talbot interferometry. *Nature Communications* 8: 15601.

Schäfer F, Fukuhara T, Sugawa S, Takasu Y, and Takahashi Y (2020) Tools for quantum simulation with ultracold atoms in optical lattices. *Nature Reviews Physics* 2: 411–425.

Syassen N, Bauer DM, Lettner M, Volz T, Dietze D, García-Ripoll JJ, Cirac JI, Rempe G, and Dürr S (2008) Strong dissipation inhibits losses and induces correlations in cold molecular gases. *Science* 320: 1329–1331.

Taie S, Yamazaki R, Sugawa S, and Takahashi Y (2012) An SU(6) Mott insulator of an atomic Fermi gas realized by large-spin Pomeranchuk cooling. *Nature Physics* 8: 825–830.

Taie S, Ozawa H, Ichinose T, Nishio T, Nakajima S, and Takahashi Y (2015) Coherent driving and freezing of bosonic matter wave in an optical Lieb lattice. *Science Advances* 1: e1500854.

Taie S, Ichinose T, Ozawa H, and Takahashi Y (2020) Spatial adiabatic passage of massive quantum particles in an optical Lieb lattice. *Nature Communications* 11: 257.

Taie S, Ibarra-García-Padilla E, Nishizawa N, Takasu Y, Kuno Y, Wei H-T, Scalettar RT, Hazzard KRA, and Takahashi Y (2022) Observation of antiferromagnetic correlations in an ultracold SU(N) Hubbard model. *Nature Physics* 18: 1356–1361.

Takasu Y, Yagami T, Ashida Y, Hamazaki R, Kuno Y, and Takahashi Y (2020) PT-symmetric non-Hermitian quantum many-body system using ultracold atoms in an optical lattice with controlled dissipation. *Progress of Theoretical and Experimental Physics* 2020: 12A110.

Tarruell L, Greif D, Uehlinger T, Jotzu G, and Esslinger T (2012) Creating, moving and merging Dirac points with a Fermi gas in a tunable honeycomb lattice. *Nature* 483: 302–305.

Thouless DJ (1983) Quantization of particle transport. *Physical Review B* 27: 6083–6087.

Thouless DJ, Kohmoto M, Nightingale MP, and den Nijs M (1982) Quantized Hall conductance in a two-dimensional periodic potential. *Physical Review Letters* 49: 405–408.

Tomita T, Nakajima S, Danshita I, Takasu Y, and Takahashi Y (2017) Observation of the Mott insulator to superfluid crossover of a driven-dissipative Bose-Hubbard system. *Science Advances* 3: e1701513.

Trotzky S, Chen Y-A, Schnorrberger U, Cheinet P, and Bloch I (2010) Controlling and detecting spin correlations of ultracold atoms in optical lattices. *Physical Review Letters* 105: 265303.

Viebahn K, Sbroscia M, Carter E, Yu J-C, and Schneider U (2019) Matter-wave diffraction from a quasicrystalline optical lattice. *Physical Review Letters* 122: 110404.

Windpassinger P and Sengstock K (2013) Engineering novel optical lattices. *Reports on Progress in Physics* 76: 086401.

Wu C, Hu J-P, and Zhang S-C (2003) Exact SO(5) symmetry in the spin 3/2 fermionic system. *Physical Review Letters* 91: 186402.

Yan B, Moses SA, Gadway B, Covey JP, Hazzard KRA, Rey AM, Jin DS, and Ye J (2013) Observation of dipolar spin-exchange interactions with lattice-confined polar molecules. *Nature* 501: 521–525.

You J-S, Schmidt R, Ivanov DA, Knap M, and Demler E (2019) Atomtronics with a spin: Statistics of spin transport and nonequilibrium orthogonality catastrophe in cold quantum gases. *Physical Review B* 99: 214505.

Ionic and mixed conductivity in condensed phases☆

J Maier, Physical Chemistry of Solids, Max Planck Institute for Solid State Research, Stuttgart, Germany

© 2024 Elsevier Ltd. All rights reserved.

This is an update of J. Maier, Ionic and Mixed Conductivity in Condensed Phases, Editor(s): Franco Bassani, Gerald L. Liedl, Peter Wyder, Encyclopedia of Condensed Matter Physics, Elsevier, 2005, Pages 9–21, ISBN 9780123694010, https://doi.org/10.1016/B0-12-369401-9/00432-0.

Introduction: Hopping process 145
Charge carrier concentrations in pure compounds and dilute bulk 146
Doping effects 149
High charge carrier concentrations—Interactions 152
Boundary layers (Heterogeneous doping) 153
Nano-Ionics 154
Partial equilibrium—Bridge between high-temperature and low-temperature situation 156
Mobility: From low to high concentrations 156
Chemical diffusion in mixed conductors and battery storage 157
Ion transport in biology 159
Conclusion 159
References 160

Abstract

Ion transport plays a key role in solid state science. It is not only conceptually important, it is also key to solid state devices in energy research. Moreover, the kinetics of solid state chemical processes typically rely on it. If electron transport is involved as well, redox processes can occur, e.g., storage processes in lithium or sodium batteries. Of particular significance are ionic and mixed conductivity processes in interfacially dominated and/or confined systems (Nanoionics). The latter establishes natural ties to biology. The article traces back all these phenomena to the respective mechanistic centers (e.g., point defects in ionic solids) and to the basic thermodynamic and kinetic relations.

Key points

- Basics and mechanisms of ion transport.
- Ionic charge carriers in pure, doped and partially frozen states.
- Transport in bulk, at interfaces, and in confined systems.
- Ion transport enabling electrolyte function and nerve signals.
- Mixed conductivity and ambipolar transport enabling electrode storage and compositional changes.

Introduction: Hopping process

While a quantum mechanical particle such as quasi-free-electron can tunnel through a barrier by interference of the states on both sides of the barrier (denoted by x and x'), that is, by seizing the hindrance in a wave-like way, the transport of a heavy particle such as an ion has to rely on the ensemble fraction with energy high enough to reach the final state (hopping) (Allnatt and Lidiard, 1993; Maier, 2004). On the one hand, under favorable circumstances protons may also tunnel, while on the other hand electrons that strongly polarize their environment (large polarons) behave almost classically as ions. In most cases of interest (consider A as an ion with charge z_A), the hopping of A from x to x' ($x' = x + \triangle x$) may be written as.

$$\mathrm{A}(x) + \mathrm{V}'(x') \rightleftharpoons \mathrm{V}(x) + \mathrm{A}'(x') \tag{1}$$

(The dash takes account of the possibility for A to have a different structural environment at x'). In cases where A denotes an ion on a regular site in a crystal, V is the vacancy that serves as a jump partner, while in cases where A refers to an excess ion sitting on interstitial sites, V denotes the vacant interstitial site. In crystals, V (in the first case) or A (in the second case) are usually diluted with the energy levels of these sites being well defined. The concentration of the respective reaction partner is then approximately constant and the corresponding rate equation for the hopping process is pseudo-monomolecular. In amorphous solids, the sites are

---

☆*Change History*: September 2022. J Maier updated sections Nano-Ionics, Chemical diffusion in mixed conductors and battery storage, Ion transport in biology, Summary and Figures 16 and 17.

less defined, which also holds for the spatial energy distribution; in polymers, melts or liquids, these sites and energy distributions fluctuate. In these cases, one would better speak of smeared-out density of states, as far as thermal excitations are concerned. The rate constant for the hopping rate equation is decisively influenced by the activation free enthalpy. The parameters k and $\Delta G^{\neq}$, for example, for the forward reaction (index$\rightharpoonup$) related through (prefactor k_0 is proportional to the attempt frequency Γ_0)

$$\overrightarrow{k} = k_0 \exp\left(\frac{\Delta \overrightarrow{G}^{\neq}}{RT}\right) \tag{2}$$

refer to the built-in part of the forward rate constant and its activation free energy, respectively. This expression has to be complemented by the factor $\exp\left(-\overrightarrow{\alpha}\Delta\phi F/RT\right)$ in order to take account of the applied electric field. The parameter $\Delta\phi$ is that part of the external voltage that drops from x to x' and the term $\overrightarrow{\alpha}\,\Delta\phi$ measures the portion of $\Delta\phi$ that is relevant for the forward reaction (distance between saddle point and initial state).

The relations for the backward reaction are analogous $\left(\overrightarrow{\alpha} + \overleftarrow{\alpha} = 1\right)$. This leads to the Butler-Volmer equation which describes the charge transfer from x to x' for an asymmetric free-energy profile. In the homogeneous bulk region (and also in the space charge region sufficiently far from the interface, i.e., $\mathrm{A} = \mathrm{A}'$), the built-in profile is symmetrical, that is, $(\overleftarrow{k} = \overrightarrow{k} = k,\ \overrightarrow{\alpha} = \overleftarrow{\alpha} = 1/2)$ and $\Delta\overrightarrow{G} = \Delta\overleftarrow{G}$. The result for the rate represented by the current density i_j of carrier j in x-direction

$$\begin{aligned} i_j = & -2k_j c_j z_j F \sinh\frac{z_j F \Delta\phi}{2RT} \\ \simeq & -\sigma_j \frac{\Delta\phi}{\Delta x} \end{aligned} \tag{3}$$

can be simplified to Ohm's law (bottom part) for $\Delta\phi \ll RT/z_jF$; the conductivity σ_j of the carrier is proportional to its mobility $u_j (u_j \propto k_j)$, (molar) concentration (c_j) and (molar) charge (z_jF) and given as

$$\sigma_j = z_j F u_j c_j \tag{4}$$

Allowing also for a concentration variation during the process and generalizing to three dimensions, but restricting to small effects the Nernst-Planck equation is arrived at

$$i_j = -D_j z_j F \nabla c_j - \sigma_j \nabla\phi \tag{5}$$

where the diffusion coefficient (D) and conductivity (σ) are related through the Nernst-Einstein equation. Close to equilibrium, this equation corresponds to the result obtained by linear irreversible thermodynamics,

$$i_j = \frac{\sigma_j}{z_j F}\nabla\tilde{\mu}_j \tag{6}$$

which assumes the current to be proportional to the gradient in the electrochemical potential $\tilde{\mu} = \mu + zF\phi$ (chemical potential + (molar charge x electrical potential)). The latter relation is more general concerning the concentration range, while the former (as regards the diffusion term) is a little more general as far as the magnitude of this driving force is concerned. In cases where the current of a given species is also generated by secondary driving forces (e.g., by $\nabla\tilde{\mu}$ of a different particle), cross terms occur for which the Onsager-Casimir symmetry relations are valid. Also Eq. (6) can be generalized towards higher driving forces. Maier (2004) and Riess and Maier, 2008 give a symmetrized relation in terms of the electrochemical potential drop over the jump distance appearing as exponent in a sinh-function (similar as in Eq. (3)). As regards the determination of the conductivity, the first task is to determine the carrier concentration as a function of the control parameters. This is feasible by solving the defect model for the system under consideration.

Charge carrier concentrations in pure compounds and dilute bulk

Fig. 1 displays the fundamental charge carrier formation reaction in an "energy level" diagram for a fluid (H_2O) and an ionic crystal (AgCl) (Maier, 1993a). These levels refer to effective standard (electro) chemical potentials or—in the case of the "Fermi levels" that are positioned within the gap—full (electro) chemical potentials. (As long as the bulk is considered, $zF\phi$ can be neglected and one can refer to μ instead of $\tilde{\mu}$.) As long as—in pure materials—the gap remains large compared to RT, the Boltzmann form of the chemical potential of the respective charge carrier (defect) is valid which has the form

$$\mu_j = \mu_j^{\circ} + RT\ln\left(\frac{c_j}{c_j^{\circ}}\right) \tag{7}$$

As outlined below, this relation holds largely independent of the charge carrier situation and the form of the energy level distribution. If the levels are smeared out or if there is a band of levels, μ_j° refers to an effective level (i.e., band edges in nondegenerate semiconductors or an appropriately averaged energy when dealing with fluids or disordered solids). The coupling of the ionic level picture and the electronic level picture for AgCl (Fig. 2) is established via the thermodynamic relation

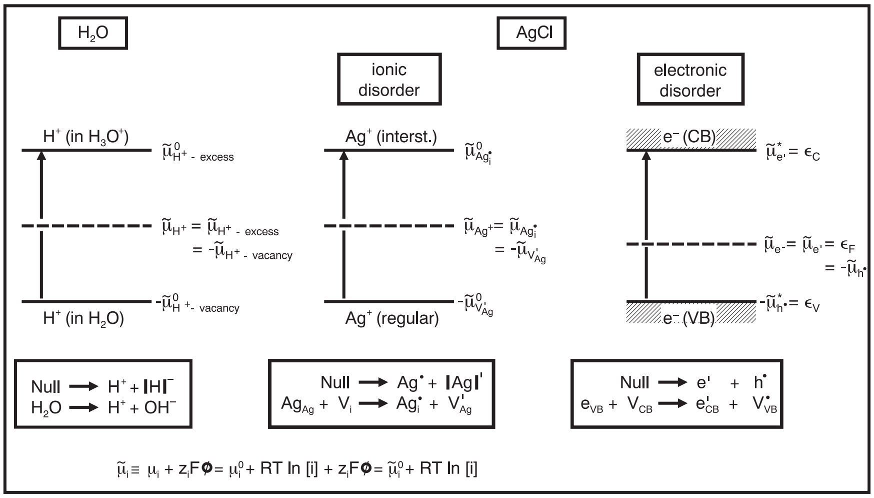
H_2O
AgCl
ionic disorder
electronic disorder
H^+ (in H_3O^+)
$\tilde{\mu}^0_{H^+\text{ - excess}}$
$\tilde{\mu}_{H^+} = \tilde{\mu}_{H^+\text{ - excess}}$
$= -\tilde{\mu}_{H^+\text{ - vacancy}}$
$-\tilde{\mu}^0_{H^+\text{- vacancy}}$
H^+ (in H_2O)
Ag^+ (interst.)
$\tilde{\mu}^0_{Ag_i^\bullet}$
$\tilde{\mu}_{Ag^+} = \tilde{\mu}_{Ag_i^\bullet}$
$= -\tilde{\mu}_{V'_{Ag}}$
$-\tilde{\mu}^0_{V'_{Ag}}$
Ag^+ (regular)
e^- (CB)
$\tilde{\mu}^*_{e'} = \epsilon_C$
$\tilde{\mu}_{e^-} = \tilde{\mu}_{e'} = \epsilon_F$
$= -\tilde{\mu}_{h^\bullet}$
$-\tilde{\mu}^*_{h^\bullet} = \epsilon_V$
e^- (VB)
$\text{Null} \longrightarrow H^+ + |H|^-$
$H_2O \longrightarrow H^+ + OH^-$
$\text{Null} \longrightarrow Ag^\bullet + |Ag|'$
$Ag_{Ag} + V_i \longrightarrow Ag_i^\bullet + V'_{Ag}$
$\text{Null} \longrightarrow e' + h^\bullet$
$e_{VB} + V_{CB} \longrightarrow e'_{CB} + V^\bullet_{VB}$
$\tilde{\mu}_i \equiv \mu_i + z_iF\phi = \mu_i^0 + RT\ln[i] + z_iF\phi = \tilde{\mu}_i^0 + RT\ln[i]$

Fig. 1 Electronic and ionic disorder in ionic solids and water in "physical" (top) and "chemical" language (bottom).

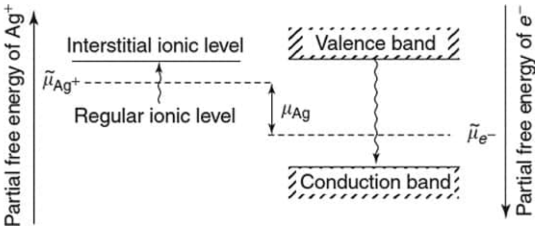
Partial free energy of Ag^+
Interstitial ionic level
$\tilde{\mu}_{Ag^+}$
Regular ionic level
μ_{Ag}
Valence band
$\tilde{\mu}_{e^-}$
Conduction band
Partial free energy of e^-

Fig. 2 Coupling of ionic and electronic levels in AgCl.

$\tilde{\mu}_{Ag+} + \tilde{\mu}_{e-} = \mu_{Ag}$, and hence via the component potential which reflects the precise position in the phase diagram. The meaning of μ° becomes obvious, if for simplicity one considers an elemental crystal (with defect j). For the formation of N_j identical defects (among N regular positions), a local free enthalpy of $N_j \Delta g_j^\circ$ is required in the interaction-free case; including also the configurational contribution, the Gibbs energy of the defective crystal (G_P refers to the perfect crystal) reads

$$G = G_p + N_j \Delta g_j^\circ - k_B T \ln \binom{N}{N_j} \tag{8}$$

The configuration term describes the number of combinations of N_j elements out of N choices without repetition. The calculation of Δg°, the free energy to form a single defect, requires an atomistic consideration (Allnatt and Lidiard, 1993; Kröger, 1964).

If one refers to ionic defects in crystals, it is essentially composed of lattice energy, polarization energy, and vibrational entropy terms. In more general terms, N_j is the number of defects and N the number of particles that can be made defective. Owing to the

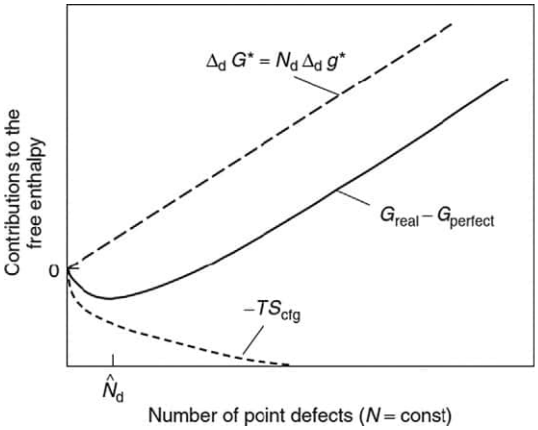

Fig. 3 Contributions to the free enthalpy of the solid by defect formation with a constant total number of sites. From Maier J (2004) Physical chemistry of ionic materials. In: *Ions and Electrons in Solids*. John Wiley & Sons, Ltd: Chichester.

infinitely steep decrease of the configurational term with N_j, a minimum in $G(N_j)$ (see Fig. 3) is observed in the elemental crystal; here the chemical potential of j, that is, $\mu_j \equiv \partial G/\partial(N_j/N_m)$, vanishes. Generally it holds that

$$\begin{aligned} \mu_j &= \mu_j^\circ + RT\ln\frac{N_j}{N - N_j} \\ &\simeq \mu_j^\circ + RT\ln\frac{N_j}{N} \\ &\mu_j^\circ + RT\ln\frac{n_j}{n} \end{aligned} \tag{9}$$

($n \equiv N/N_m, n_j \equiv N_j/N_m, N_m =$ Avogadro's number; $\mu_j^\circ = N_m\Delta g_j^\circ$). It is noteworthy that the strict result (top) which is formally valid for higher concentrations also is of the Fermi-Dirac type. This is due to the fact that one refers to combinations without repetition, that is, double occupancy is excluded and hence the sites are exhaustible similarly as it is the case for quantum states in electronic problems (Maier, 2005; Kirchheim, 1988). (Combinations with repetitions lead to Bose-Einstein distribution.) In a situation in which the levels are broadened to a more or less continuous zone (e.g., electrons in semiconductors and ions in fluids), the parameters N_j and μ_j° of the Fermi-Dirac form have to be attributed to an infinitely small level interval. Denoting the partial free energy level by ε, this integral ranges from ε_j to $\varepsilon_j + \mathrm{d}\varepsilon_j$ and the total (molar) concentration follows from integration:

$$n_j = \int_{\text{zone}} \frac{D(\in_j)\mathrm{d}\in_j}{1 + \exp\left(|\in_j - \mu_j|/RT\right)} \tag{10}$$

whereby the molar density of states $D(\varepsilon_j)$ appears in the integrand. At equilibrium, μ_j is independent of ε_j. Considering without restriction of generality, the almost empty zone and the lower edge of this zone designated as ε_j, one can neglect the unity in the denominator of the above equation for all levels more distant from μ_j than ε_j' which leads to the Boltzmann expression $n_j \simeq \overline{n}_j(T)\exp\left(-\left|\in_j' - \mu_j\right|/RT\right)$. The effective value $\overline{n}_j$ is given by

$$\overline{n}_j(T) = \int_{\text{zone}} \mathrm{d}\in_j \left[D(\in_j)\exp\left(\frac{\left|\in_j - \in_j'\right|}{RT}\right)\right] \tag{11}$$

$\overline{n}_j$ being usually weakly temperature dependent. It is worth noting that, owing to the high dilution, changes of the parameters with occupation have been ignored (for electrons in semiconductors, this is called the "rigid band model"). As anticipated above, the Boltzmann form of the chemical potential results with μ° representing an effective value. If n is identified with $\overline{n}_j$, the effective value μ_j° is given by ε_j'. As long as one refers to dilute conditions, considerable freedom of normalization is left with respect to the concentration measure. In ionic compounds, charged defects occur pairwise, the formation of which is subject to disorder reactions (and electroneutrality conditions). Then, only the reaction combination of chemical potential vanishes, that is $\sum_j v_{rj}\mu_j = 0$ (identical to $\sum_j v_{rj}\tilde{\mu}_j = 0$ since $\sum_j v_{rj}z_j = 0$), where v_{rj} is the stoichiometric coefficient of j in the respective disorder reaction r (cf. Fig. 1, bottom). Boltzmann expressions can be written for the individual carriers, if the formation energies and the configuration entropies are considered to be independent. The application of chemical thermodynamics elegantly permits treatment of a variety of ionic and electronic disorder processes that simultaneously occur in a given solid. This is not only possible for the internal disorder equations (such as Schottky, Frenkel, anti-Frenkel, anti-Schottky, electron-hole formation) but also for external reactions such as the interaction of an oxide with the oxygen partial pressure and hence the stoichiometric variation. Under Boltzmann (i.e., dilute) and Brouwer (i.e., two majority carriers) conditions (Kröger, 1964), an adequate expression is arrived at for any charge carrier concentration as a function of the control parameters (temperature T, doping content, component partial pressure P), namely

$$c_j(T, P) = \alpha_j^{\beta_j} P^{N_j} \prod_r K_r(T)^{\gamma_{rj}} \tag{12}$$

(($N_j, \gamma_{rj}, \alpha_j, \beta_j$) being characteristically simple rational numbers; the total pressure is assumed to be constant.) For multinary compounds (i.e., m components) at complete equilibrium ($m-1$) component partial pressures are to be considered. This solution is only a sectional solution with a window in which the majority carriers situation (Brouwer condition) does not change. The power-law equation defines van't Hoff diagrams characterized by

$$-\frac{\partial \ln c_j}{\partial 1/RT} = \sum_r \gamma_{rj}\Delta_r H^\circ \tag{13}$$

according to which, for not too extended T-ranges (i.e., $\Delta_r H^\circ$, the reaction enthalpy of the defect reaction γ, is constant), straight lines are observed in the ln c_j versus $1/T$ representation, as well as Kröger-Vink diagrams characterized by straight lines in the plots ln c_j versus ln$P$ with slopes

$$\frac{\partial \ln c_j}{\partial \ln P} = N_j \tag{14}$$

Fig. 4 displays the defect chemistry within the phase width of the oxide MO. At low oxygen partial pressure (P_{O_2}), vacant oxygen ions (V_O) and reduced states (e') are in the majority ($2[V_O] \simeq [e'] \gg 2[O_i''], [h^\cdot]$) ($N$ – regime) whilst oxygen interstitials (O_i'') and oxidized states ($h^\cdot$) dominate for very high P_{O_2}($2[O_i''] \simeq [h^\cdot] \gg [e'],[V_O^{\cdot\cdot}]$) ($P$-regime). At intermediate P_{O2}, usually ionic disorder

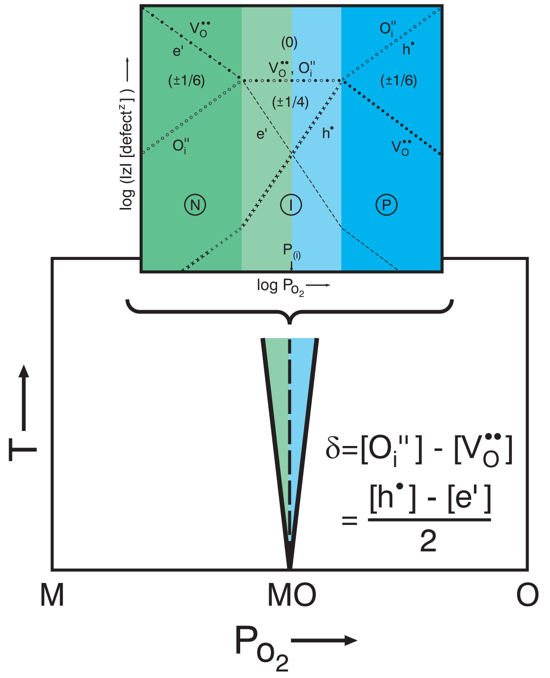

Fig. 4 Internal redox and acid-base chemistry in a solid $MO_{1+\delta}$ within the phase width at a given temperature *T* (disorder in the *M*-sublattice assumed to be negligible).

prevails ($[V_O^{\cdot\cdot}] \simeq [O_i''] \gg [e'],[h^{\cdot}]$) (*I*-regime); the alternative situation that electronic disorder predominates ($[e'] \simeq [h^{\cdot}] \gg [V_O^{\cdot\cdot}], [O_i'']$) is usually scarce. Exactly at the Dalton composition (i.e., at $P_{O_2}^{(i)}$ where $2[O''_i] = 2[V_O^{\cdot\cdot}] = [e'] = [h^{\cdot}]$), the "nonstoichiometry" δ in $MO_{1+\delta}$ (i.e.,$[O''_i] - [V_O^{\cdot\cdot}] = \frac{1}{2}[h^{\cdot}] - \frac{1}{2}[e']$) is precisely zero. For $\delta \gg 0$, *p*-conductors (mobility of $h^{\cdot}$ usually much greater than for O''_i) are referred to, for $\delta \ll 0$, one refers (mobility of e' is usually much greater than for $V_O^{\cdot\cdot}$) to *n*-conductors, while at $\delta \simeq 0$, mixed conduction is expected (only if the ionic concentrations are much larger than the electric ones, pure ion conduction results). Usually, the entire diagram is not observed, as there are limits of experimentally realizing extreme P_{O_2} values as well as limits with respect to the phase stability (formation of higher oxides or lower oxides, if not of the elemental metal). Fig. 5 gives three examples: SnO_2 as an oxygen-deficient material, La_2CuO_4 as an example of a *p*-type conductor, and PbO as an example of *I*-regime exhibiting mixed conduction. (In PbO, most probably, the counter defect to O_i'' is Pbi rather than $V_O^{\cdot\cdot}$, the results, however, are not different then.) The slopes directly follow from simple mass action considerations

The model example of AgCl shall be considered in more detail. It also exhibits predominant ionic disorder, but now the decisive disorder reaction is the Frenkel reaction of the Ag sublattice (i.e., the formation of silver ion vacancy, V_{Ag}', and interstitial silver ion, $Ag_i^{\cdot}$). The role of P_{O_2} is played by the chlorine partial pressure. The mass action law for the interaction with Cl_2 reads $[Ag_i^{\cdot}] P_{Cl_2}{}^{+1/2}[e']=$ constant, the mass action constant for the Frenkel reaction being $[Ag_i^{\cdot}][V_{Ag}'] = K_F$ and that for the band-band transfer $[e'][h^{\cdot}] = K_B$. Since $[Ag_i^{\cdot}] \simeq [V_{Ag}'] \gg [e'], [h^{\cdot}]$, it follows as solution $\left[V_{Ag}{}'\right] = \left[Ag_i{}^{\cdot}\right] = \sqrt{K_F}$, $\left[e'\right] \propto P_{Cl_2}^{-1/2}$, $[h^{\cdot}] \propto P_{Cl_2}^{+1/2}$.

Doping effects

Dopants, i.e. irreversibly introduced structure elements as Cd^{2+} substituting Ag^+ to form the defect $Cd_{Ag}^{\cdot}$, do not significantly influence the relevant mass action laws, but appear in the electroneutrality relation, here

$$[Ag_i^{\cdot}] + \left[Cd_{Ag}^{\cdot}\right] \simeq \left[V_{Ag}'\right] \tag{15}$$

Coupling the above relation with the Frenkel equation $[Ag_i^{\cdot}][V_{Ag}'] = K_F$ leads to

$$\left[V_{Ag}'\right] = \frac{C}{2} + \sqrt{\frac{C^2}{4} + K_F} \tag{16}$$

$$[Ag_i^{\cdot}] = -\frac{C}{2} + \sqrt{\frac{C^2}{4} + K_F} \tag{17}$$

where C stands for $[Cd_{Ag}]$. Consider the Brouwer conditions again. For $C \ll \sqrt{K_F}$, the intrinsic result $[V_{Ag}'] = [Ag_i^{\cdot}] = \sqrt{K_F}$ is obtained. For $C \gg \sqrt{K_F}$, one arrives at

$$\left[V_{Ag}\right] = C \tag{18}$$

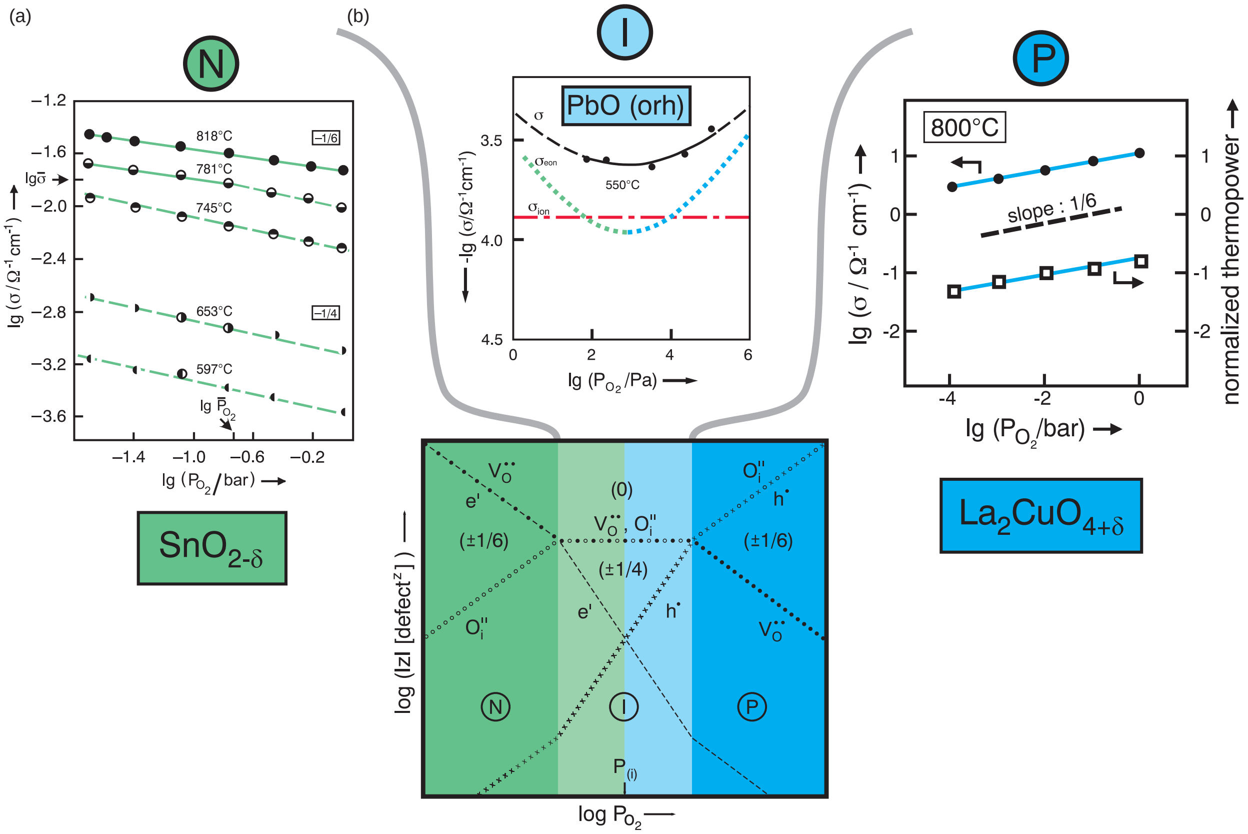

Fig. 5 Three experimental examples of Kroeger-Vink diagrams in a pure oxide MO with ideal defect chemistry. (a) SnO_2 as an *n*-type conductor, (b) PbO as a mixed conductor, and (c) La_2CuO_4 as a *p*-type conductor. Reproduced with permission from Maier J (2003a) Ionic and mixed conductors for electrochemical devices. *Radiation Effects and Defects in Solids* **158**: 1–10; © Taylor and Francis.

$$[\mathrm{Ag}^{\cdot}_{\mathrm{i}}] = K_{\mathrm{F}}\mathrm{C}^{-1} \tag{19}$$

which are immediately obtained by neglecting [$\mathrm{Ag}_\mathrm{i}^\cdot$] from the electroneutrality relation. Power-law equations are then also valid for the electronic minority carriers in AgCl.

Fig. 6 refers to AgCl and displays the solutions for the ionic defect arrived at by the more accurate equations for both concentrations and conductivities. The different behaviors of defect concentrations and conductivities stem from the fact that the interstitials are more mobile than the vacancies. The introduction of the dopant increases the concentration of the oppositely charged defect and depresses the concentration of the counterdefect according to electroneutrality and mass action. This leads to a decreased ionic conductivity, before the counter defect starts defining the overall conductivity. The conductivity minimum lies approximately at $\sqrt{K_\mathrm{F}u_\mathrm{i}/u_\mathrm{v}}$. Figs. 7 and 8 display the dependence of conductivity on temperature in pure samples and on the doping concentration at given *T* with regard to positive and negative doping. While the response to Cd^{2+} doping ($\mathrm{Cd}^{\cdot}_{\mathrm{Ag}}$) follows exactly the predictions (see Figs. 7 and 8), the effect of S^{2-} doping ($\mathrm{S}_{\mathrm{Cl}}'$) suffers from interaction effects (see below, the absence of a minimum in Fig. 8, LHS, is in qualitative agreement with the fact that [$\mathrm{Ag}_\mathrm{i}^\cdot$] is increased).

It is clear that for doped samples under Brouwer and Boltzmann conditions, the concentration of any carrier is not only a function of *P*, *T* but also of C, and reads (Maier, 2004)

$$c_j(T, P, C) = \alpha_j^{\beta_j}\left(\prod_p P_p^{N_{pi}}\right)C^{M_j}\left(\prod_r K_r(T)^{\gamma_{rj}}\right) \tag{20}$$

(p^{Nj} is replaced by $\Pi_p\, P_p^{N_{pi}}$ in order to allow for multinary equilibria labeled by *p*). Since.

unlike (the in situ parameters) *P* and *T*, the variation of C requires a new high temperature preparation, C is designated as an ex situ parameter.

Now this also predicts sectionally constant slopes in diagrams of the type log c_j versus log C according to

$$\frac{\partial \ln c_j}{\partial \ln \mathrm{C}} = M_j \tag{21}$$

For a simple defect chemistry, the sign of M_j is determined by ("rule of heterogeneous doping")

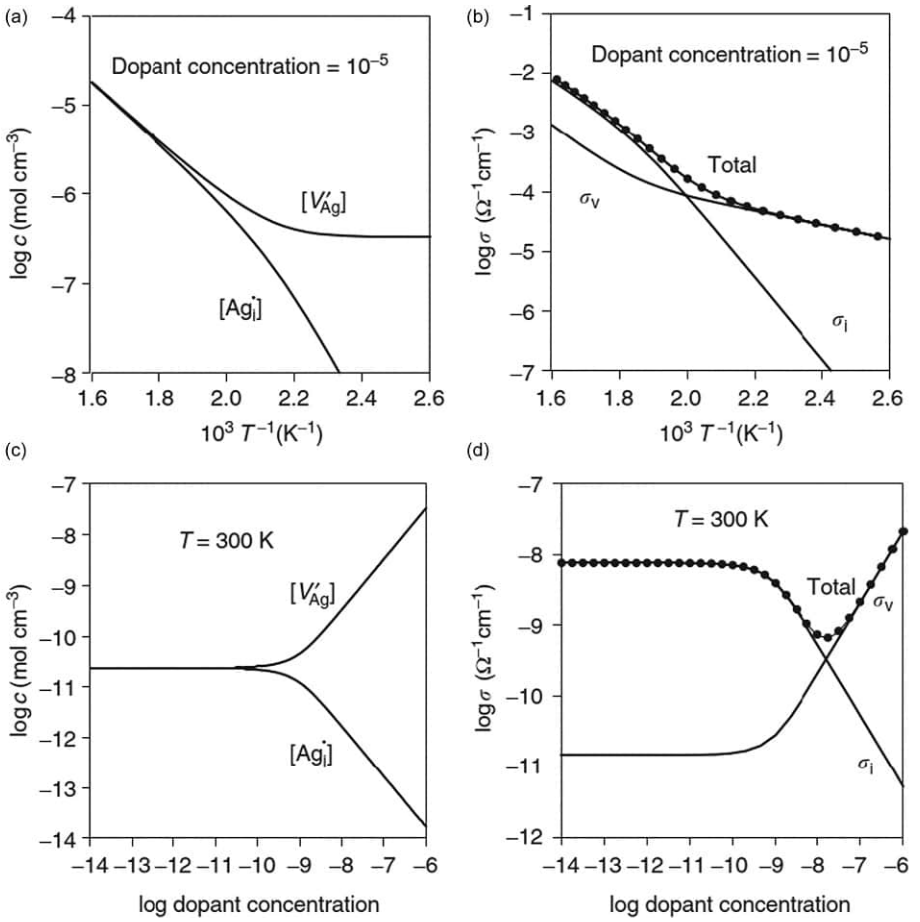

Fig. 6 Defect concentrations and conductivities as a function of temperature for a fixed Cd-content (a) and (b) and as a function of Cd-content for a fixed temperature (c) and (d).

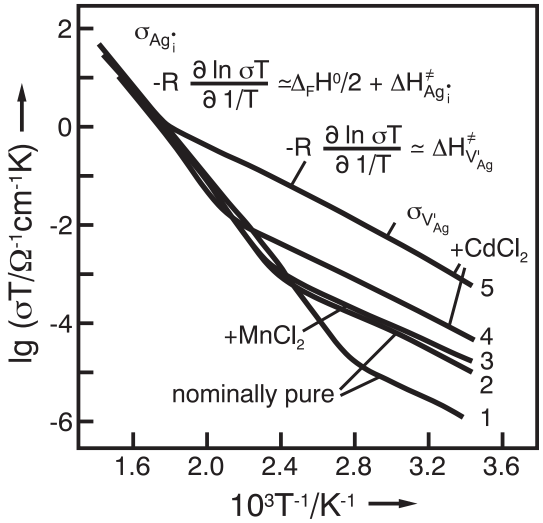

Fig. 7 Experimental conductivity data for nominally pure and doped AgCl as a function of 1/*T*. Here log(σT) is plotted instead of log σ to take account of the slight *T*-dependence of the prefactor. However, this does not alter the slope noticeably ($\Delta_F H^0$: formation enthalpy of Frenkel defects; $\Delta H_j^{\neq}$: migration enthalpy). Reproduced from Corish J, Jacobs PWM (1972) Ionic conductivity of silver-chloride single-crystals. *Journal of Physics and Chemistry of Solids* **33**: 1799–1818, with permission from Elsevier.

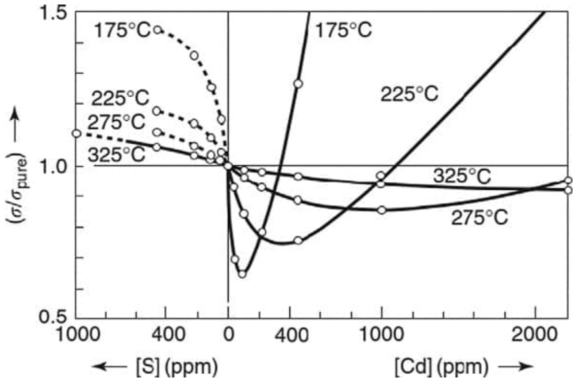

Fig. 8 The dependence of the conductivity increase brought about by the impurities on the S and Cd content of AgBr. The RHS solid curves are calculated according to the ideal defect chemistry. Reproduced with permission from Teltow J (1949) Zur Ionenleitung und Fehlordnung von Silberbromid mit Zusätzen zweiwertiger Kationen. I. Leitfähigkeitsmessungen und Zustandsdiagramme. *Annalen der Physik* **6**: 63–70; © WileyVCH.; Teltow J (1950) Zur Ionen-, Elektronenleitung und Fehlordnung von Silberbromid mit Zusätzen von Silber-, Cadmium- und Bleisulfid. *Zeitschrift für Physikalische Chemie* **1**95: 213–224; & Oldenbourg Wissenschaftsverlag; © Wiley-VCH.

$$\frac{z_j M_j}{z_d} < 0 \tag{22}$$

which means that, for a positive (negative) doping, the concentration of all negative (positive) defects is increased and all positive (negative) defects are decreased (z_d: charge number of dopant defect). A negative doping is also the reason for the change in the slope from the intrinsic value −1/6 to the extrinsic value −1/4, in Fig. 5a for SnO$_2$, which directly results from the mass action law for oxygen incorporation, that is, $P_{O_2}{}^{1/2}[V_O^{\cdot\cdot}][e']^2 = \text{constant}$ (for $2[V_O^{\cdot\cdot}] \simeq C$, one obtains $\sigma \simeq \sigma_n \propto [e'] \propto P_{O_2}{}^{-1/4}$ whereas for $2[V_O] = [e']$, the result is $\sigma \propto P_{O_2}{}^{-1/6}$).

High charge carrier concentrations—Interactions

The above solutions are valid for ionic and electronic carrier concentrations but require low concentrations. One way of correcting interactions is to introduce associates, that is, novel particles formed as the result of these interactions and responding differently to electrical fields or other driving forces. In this way, the scheme of defects is rescaled with the consequence of writing ideal chemical potentials (i.e., interaction free) for these to a better approximation. Examples are interactions of dopants with electronic or ionic carriers (these states appear as midgap states in Fig. 1), associates between electronic carriers (excitons, Cooper-pairs), or between ionic carriers (such as vacancy pairs, interstitial pairs, and Frenkel associates). As an example, the association between $\mathrm{Cd}_{\mathrm{Ag}}^{\cdot}$ and V_{Ag}' is mentioned that leads to a thermally activated process at low temperatures in the case of CdCl$_2$-doped AgCl (lower than those shown in Fig. 7). The more general approach is to include interactions via analytical corrections in the chemical potentials (μ^{ex}) of the charge carriers. (On the level of the concentration, this leads to the activity coefficient as a correction factor.) If the high carrier concentration is a consequence of the high temperatures, such a procedure is indispensable. If it is a consequence of a high doping content, it may be replaced by or better combined with the association procedure. Interactions lead to entropic corrections as well. One of them is obviously due to the exhaustibility of sites (Fermi-Dirac correction). The more detailed account of derivations from a random distribution owing to interactions leads to very complex expressions (e.g., Mayer theory for real gases). Fortunately in the case of weak interactions, the neglect of such entropic corrections is a tolerable approximation. Then, besides possible local vibrational entropies, only energetic nonideality corrections need to be considered. The Debye-Hückel theory (considering each central ion embedded into a diffusive cloud of counter ions, the size being characterized by λ) leads, in the first approximation, to an expression of the form (Allnatt and Lidiard, 1993)

$$\mu_j^{\mathrm{ex}} = RT\ln f_j = -\frac{z_j^2 \mathrm{F}^2}{8\pi\varepsilon N_m\lambda} \propto c_j^{1/2} \tag{23}$$

that reasonably corrects the chemical potential for low defect concentration. The Debye-Hückel theory proved particularly helpful for electrolytic solutions. At higher concentrations, the corrections become not only complicated but also individual. Here, an ad hoc model that is able to describe interactions in some simple binary crystals and estimate these interactions by assuming that the interaction energy (viz. the structure) can be assessed by a virtual Madelung-superlattice of defects (Hainovsky and Maier, 1995) of the mean lattice constant $\propto c^{1/3}$ is briefly discussed. The prefactor J in $\mu^{\mathrm{ex}} = -Jc^{1/3}$ is determined by Madelung constants of lattice defect, and ground lattice as well as the dielectric constant. The attractive interaction of oppositely charged carriers has the consequence that the formation becomes increasingly easier at high temperatures as soon as the carriers perceive each other in ionic crystals. The conductivity increases in an over-Boltzmann fashion (premelting) and eventually the avalanche effect leads to a phase transformation into the superionic (or molten) state. The order of the transition can be calculated by comparing the

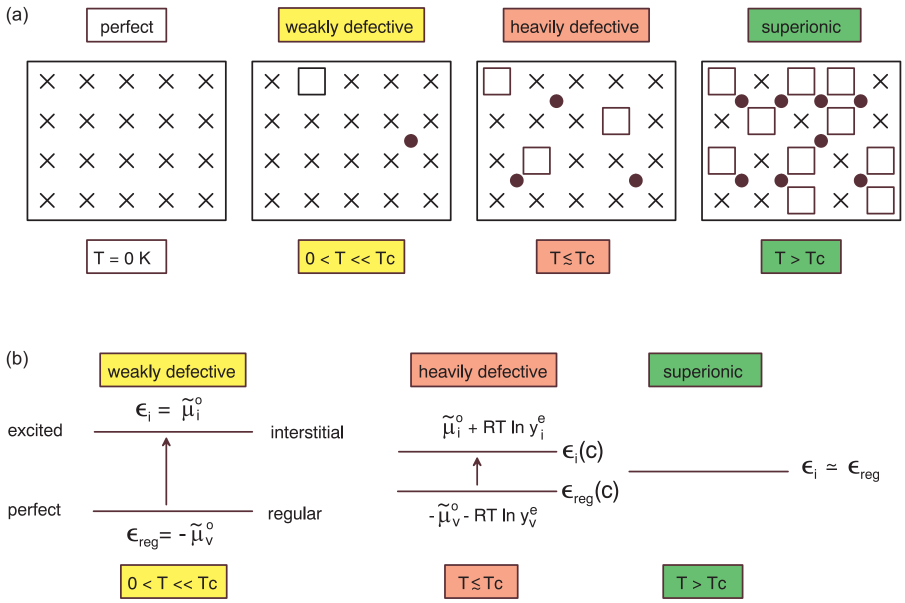

Fig. 9 The “thermal destiny” of an ionic crystal above absolute zero: a progressive development from a perfect to a superionic phase via an ideally defective and a heavily defective state. (a) Crystallographic defect picture and (b) corresponding “energy level” schemes. The indices *v* and *i* refer to the vacant regular and interstitial sites. Reproduced with permission from Maier J, Münch W (2000) Thermal destiny of an ionic crystal. *Zeitschrift für Anorganische und Allgemeine Chemie* **626**: 264; © Wiley-VCH.

formation enthalpy, the formation entropy, and the interaction strength. Fig. 9 shows the “thermal destiny” of a pure Frekel disordered binary crystal from the perfect state at low *T* to the superionic state at high *T*.

Boundary layers (Heterogeneous doping)

At boundary layers, electroneutrality is no longer fulfilled and space charge regions (width ~ Debye length) occur. The reason for this is the adjustment of structurally different regions. Not only are the electronic concentrations modified, but the mobile ionic charge carriers are also distributed according to the space charge field (both “Fermi levels” are positionally constant). Effects on the ionic conductivity can be immense (Maier, 1995). Double layers formed by the contact of the electrolyte solution to an electrode or charged membrane surfaces in electrophysiology are well-established examples.

Fig. 10 depicts four prototype cases involving solid electrolyte: (1) the contact of an ionic conductor to an insulator, the surface of which is able to trap (internally absorb) ions, leading to the concept of heterogeneous doping (influencing of conductivity by dispersing fine insulator particles is characterized by a similar rule of heterogeneous doping as given above for homogeneous doping obtained ; one just has to replace the concentration and charge of the dopant defect by the surface charge density and its sign); (2) the contact of two ionic conductors leading to a charge transfer of ions from one conductor to the other (cf. “*p-n* junctions”); (3) charge can also be stored within that core of the boundary, that is, in a grain boundary which joins two chemically identical grains (the effects can be tuned by chemical modification of the boundary or by varying the misfit) and (4) the contact to a fluid, for example, gas phase, acid-base active gases may cause attractive or repelling interactions with mobile ions) Since in many mixed, even in predominantly electronic conductors, ionic charge carriers may be in majority, the ionic redistribution effect may "enslave" the overall electronic boundary concentrations (fellow-traveler effect).

Fig. 11 shows the bending of ionic and electronic energy levels and their interrelation. The determination of the bending effect requires treatment of the chemical thermodynamics of the contact problem and hence a knowledge of energy levels in the interfacial core. In the case of a strong interfacial effect (c_o: carrier concentration in the first layer adjacent to interface),

$$\Delta\sigma_{\mathrm{m}}^{||} = \frac{u}{L}\sqrt{2\varepsilon RT c_o} \tag{24}$$

describes the excess mean conductivity of the mobile majority defect in a Gouy-Chapmann accumulation layer, and

$$\Delta\varrho_{\mathrm{m}}^{\perp} = \frac{1}{L}\sqrt{\frac{\varepsilon RT}{2u^2 c_\infty F^4 c_{\mathrm{o}}^2 \ln\left(c_\infty/c_0\right)}} \tag{25}$$

the excess mean resistivity of the mobile majority carriers across a single Mott-Schottky depletion layer situation (dopant with molar charge *F* and concentration c_∞). *L* is the distance perpendicular to the interface over which the measurement averages. Here and in the following we assume for simplicity that all charges are ±1.

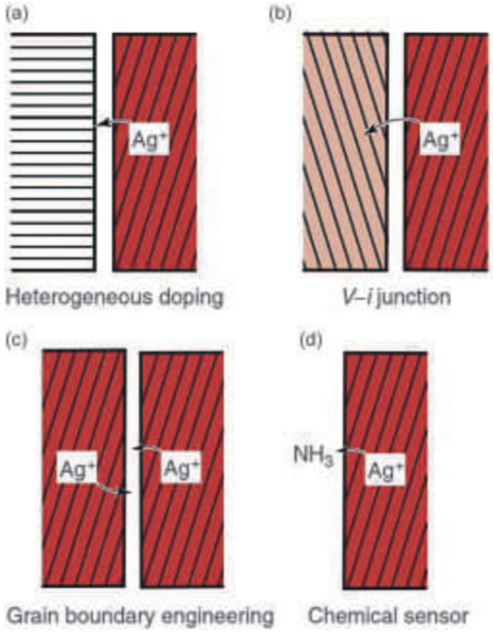
(a)
Ag+
Heterogeneous doping
(b)
Ag+
V–i junction
(c)
Ag+
Ag+
Grain boundary engineering
(d)
NH3
Ag+
Chemical sensor

Fig. 10 Four basic charge situations involving ionic conductors (here silver ion conductor): (a) contact with an insulator, (b) contact with a second ion conductor, (c) grain boundary, and (d) contact with a fluid phase. Reproduced with permission from Maier J (2002a) Nanoionics and soft materials science. In: Knauth P. and Schoonman J. (eds.) *Nanocrystalline Metals and Oxides. Selected Properties and Applications, Kluwer International Series in Electronic Materials: Science & Technology*, vol. 7, pp. 81–110. Boston: Kluwer Academic; © Kluwer Academic/Plenum Publishers.

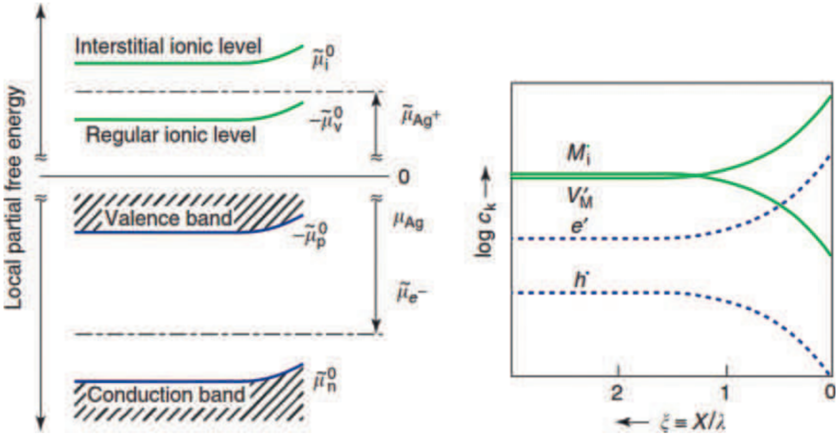
Local partial free energy
Interstitial ionic level
$\tilde{\mu}_i^0$
Regular ionic level
$-\tilde{\mu}_v^0$
$\tilde{\mu}_{Ag^+}$
0
Valence band
$-\tilde{\mu}_p^0$
μ_{Ag}
$\tilde{\mu}_{e^-}$
Conduction band
$\tilde{\mu}_n^0$
log c_k
$M_i^{\cdot}$
V_M'
e'
$h^{\cdot}$
2
1
0
$\xi = X/\lambda$

Fig. 11 Bending of "energy levels" and concentration profiles in space charge zones ($\zeta = 0$ refers to the interfacial edge). Reproduced with permission from Maier J (2002b) Nano-sized mixed conductors (Aspects of nano-ionics. Part III). *Solid State Ionics* **148**: 367–374, with permission from Elsevier.; Maier J (2003b) Defect chemistry and ion transport in nanostructured materials. Part II. Aspects of nanoionics. *Solid State Ionics* **157**: 327, with permission from Elsevier.

Fig. 12 shows heterolayers of CaF_2 and BaF_2 and the effect of the concentration of interfaces on the overall parallel conductance. In a polycrystalline material, bulk and boundary conductivities have to be superimposed according to the microstructural situation. An approximate relation that takes into account the conductivities across ($\perp$) and along ($\|$) grain boundaries ($\widehat{\sigma}$: complex conductivity; $\widehat{\sigma}^{\|,\perp}$ refer to the local mean values) is

$$\widehat{\sigma}_m = \frac{\widehat{\sigma}_\infty \widehat{\sigma}_{gb}^{\perp} + \beta_{gb}^{\|} \varphi_{gb} \widehat{\sigma}_{gb}^{\|} \widehat{\sigma}_{gb}^{\perp}}{\widehat{\sigma}_{gb}^{\perp} + \beta_{gb}^{\perp} \varphi_{gb} \widehat{\sigma}_\infty} \tag{26}$$

($\beta^{\|}$, $\beta^{\perp}$ refer to the portions of the volume fraction φ that contribute to the path; in the simplest approach, $\beta^{\|} = 2/3$, $\beta^{\perp} = 1/3$.)

Nano-Ionics

Nano-sized conductors can provide large ionic conductivity anomalies owing to the high concentration of interfaces. Moreover, the spacing of interfaces may be so narrow that they perceive each other (Hainovsky and Maier, 1995; Maier, 2005). Fig. 13a shows the

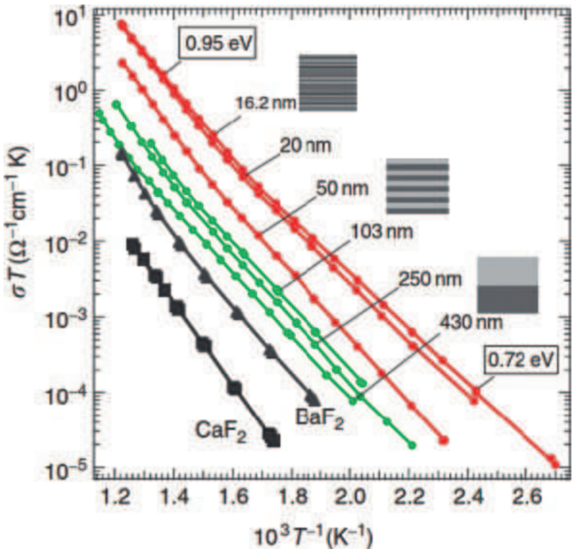

Fig. 12 Variation of the parallel ionic conductivity of CaF_2-BaF_2 heterolayers as a function of temperature for different periods (spacings). Reproduced with permission from Sata N, Eberman K, Eberl K, Maier J (2000) Mesoscopic fast ion conduction in nanometer-scale planar heterostructures. *Nature* **408**: 946–949; © Nature Publishing.

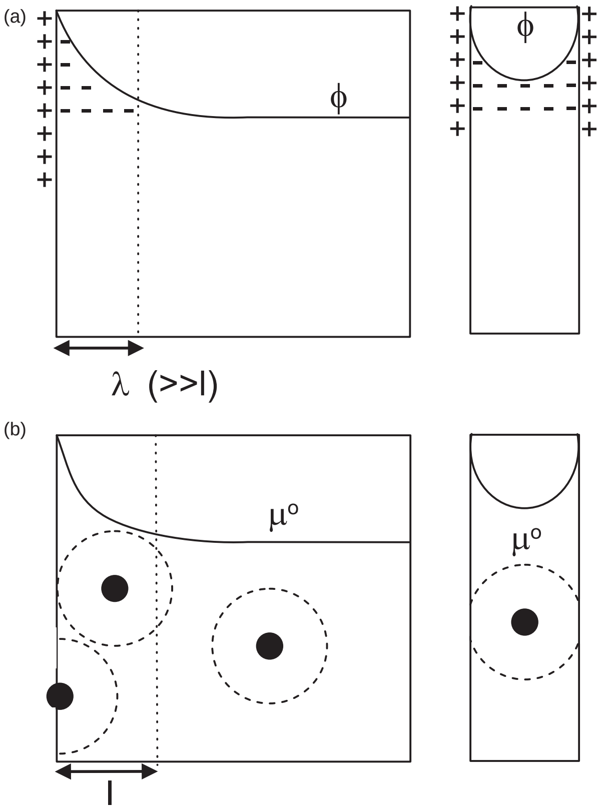

Fig. 13 (a) Space charge effects decaying with λ. (b) Structural effects which decay rapidly in the bulk, Within the indicated distance (l); the structurally perturbed core (not shown, extension s) is perceived by the defects as far as μ° is concerned. Reproduced with permission from Maier J (2003c) Nano-ionics: Trivial and non-trivial size effects on ion conduction in solids. *Zeitschrift für Physikalische Chemie* **217**: 415–436; © Oldenbourg Wissenschaftsverlag.

space charge overlap occurring in materials when the distance of neighboring interfaces becomes smaller than the Debye length, with the structure being invariant (cf. also Fig. 12). The additional conductivity effects can be described by nano-size factors (Maier, 2005).

If the distance is smaller than the effective thickness of the point defect (i.e., point defect including the sphere of influence in which the structure is perceptibly modified), then the local standard chemical potential changes (Fig. 13b). In the case of delocalized electrons, this may happen at much larger distances. These are only two examples of nanosize effects on ion conduction. Among others, the effects of particle geometry of curvature are mentioned, by which approximately a Gibbs-Kelvin term ($\propto \overline{\gamma}/\overline{r}$; $\overline{\gamma}$: mean surface tension, $\overline{r}$: mean radius) is introduced into the chemical potential if we assume fluid thermodynamics. Such effects do not only affect transport properties, they are also interesting as far as mass storage is concerned.

Partial equilibrium—Bridge between high-temperature and low-temperature situation

Arbitrary deviations from equilibrium require a detailed kinetic treatment. The situations in which some carriers behave reversibly while others are completely frozen are briefly considered here. Such considerations are helpful when the bridge has to be spanned from high-temperature equilibrium (during preparation) to a low operational temperature. In fact, such a partial equilibrium situation was already tacitly assumed when doping effects were studied. At high enough temperatures, dopants become reversible and segregation equilibria become active. Generally speaking, freezing of carriers leads to a reshuffling of in situ to ex situ parameters (i.e., from the P-term to the C-term in the power-law Eq. (20)) (Maier, 2003). The discrepancy between the equilibrium concentration (usually fulfilled at high temperatures under preparation temperatures) and the partially frozen situation becomes apparent in the application of the electroceramics (e.g., high-temperature superconductors and dielectrics) that are used at room temperature. Two aspects are important: (1) a reproducible preparation and (2) a detailed understanding of defect chemistry. For a systematic treatment of these complex problems, the reader is referred to the literature.

Mobility: From low to high concentrations

For dilute concentrations, the mobility in ionic crystals is usually taken to be independent of the concentration. According to the hopping equation ($u_j \propto k_j$), it follows

$$u_j \propto \Gamma_{0j} (\Delta x)^2 \exp\left(+ \frac{\Delta S_j^{\neq}}{R} \right) \exp\left(- \frac{\Delta H_j^{\neq}}{RT} \right) \tag{27}$$

(Γ_0 is the attempt frequency (cf. k_0, i.e., the prefactor ok k), Δx is the hopping distance; $\Delta H^{\neq}$ and $\Delta S^{\neq}$ denote activation enthalpy and entropy, respectively.)

Fig. 14 displays three fundamental hopping mechanisms (Maier, 1993a). While the treatment of the ionic carrier concentrations is, in essence, very similar for liquids or solids, this is less so in the case of mobility. In solids, the activation thresholds of hopping transport are usually substantial (approximately several 100 meV at least), while in dilute liquid electrolytes, temperature effects act on carrier mobilities mainly through changes in in the viscosity. At high concentrations, the jump partners in the hopping processes are important which formally leads to the appearance of a concentration factor $(1 - (c/c_{\max}))$ in the mobility. Higher concentrations, however, affect carrier transport in such an individual way that no universal relation can be given and even the decomposition into charge carrier concentration and mobility becomes questionable. For not too strong interactions, a fairly general interaction effect is to be considered. Defect interactions lead to relaxation phenomena in that a particle that has made a jump from x to x' does not directly create its equilibrium environment and has a higher tendency to jump back again. It is, in particular, the rearrangement of the other defects that determines the finite relaxation time. This mismatch situation causes back-jumps to be more likely, making the rate constants of the hopping equation time dependent and hence the conductivity frequency dependent (Funke, 1993). In liquids too, relaxation or better rearrangement effects occur (Onsager, 1927; Barthel et al., 1998). Since the formation of the ion cloud does not immediately follow the mobile ion under regard, the charge cloud becomes asymmetrical and acts as a brake. The relaxation time is proportional to the viscosity. The occurrence of counter transport of differently charged ions which carry along these solvation spheres lead to friction, that is, to a second defect that diminishes the mobility, the so-called electrophoretic effect. These phenomena explain the Kohlrausch's $\sqrt{c}$ law, which is well established for strong electrolytes, and reads

$$\Lambda_c = \Lambda_o \left[\frac{A}{(\varepsilon T)^{3/2}} \Lambda_o + \frac{B}{(\varepsilon T)^{1/2}} \right] \sqrt{c} \tag{28}$$

(A and B are constants, $\Lambda_O \equiv \Lambda_c$ $(c = 0)$, ε is the dielectric constant and Λ_c the equivalent conductivity, that is, conductivity per equivalent salt concentration.) (Bockris and Reddy, 1970) Fig. 15 gives some examples of the above phenomena.

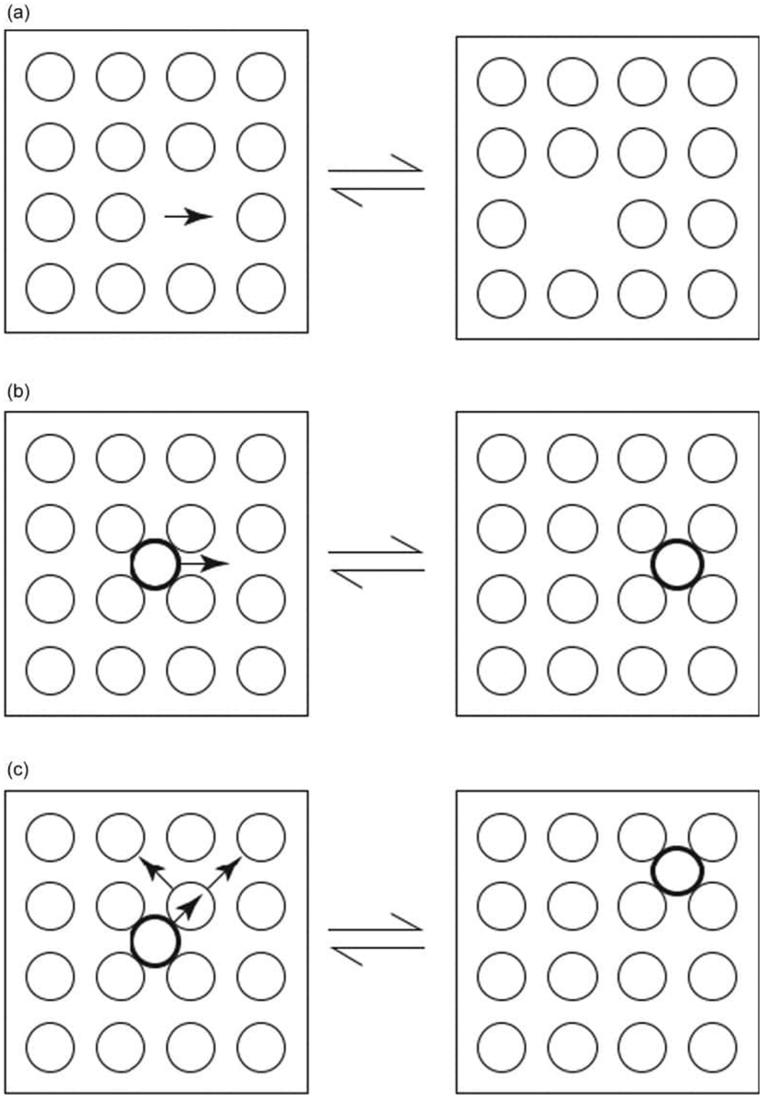

Fig. 14 Elementary jump mechanisms in crystals: (a) vacancy mechanism, (b) direct interstitial mechanism, and (c) (collinear or noncollinear), indirect interstitial mechanism (interstitialcy mechanism).

Chemical diffusion in mixed conductors and battery storage

The simultaneous presence of ionic and electronic carriers in so-called mixed conductors leads to the phenomenon of chemical diffusion (coupled transport of ions and electrons) and the possibility of changing stoichiometry (Wagner, 1975). Technologically important examples for which this phenomenon plays a decisive role are insertion electrodes, electrochemical windows, permeation membranes, and conductivity sensors; more generally, chemical diffusion is important for all electroceramics, for their preparation (Schmalzried, 1981, 1995) as well as for their performance that depends on the detailed stoichiometry (such as in dielectrics or superconductors). Stoichiometry changes also occur, if the electrodes applied in the electrochemical measurements are not completely reversible for both ions and electrons; in this case, the partial current density is given by

$$i_j = \left(\frac{\sigma_j}{\sigma}\right) i + z_j F D^{\delta} \nabla c_j \tag{29}$$

D^{δ} being the chemical diffusion coefficient that is determined by mobilities and the concentrations of all charge carriers involved in the transport (i: total current density). If different internal reactions such as valence state changes occur for the conducting species, the equation has to be modified (Maier, 1993b). The use of selectively blocking electrodes leads to the suppression of the current of one carrier type at the expense of a concentration polarization. This allows the separation of ionic and electronic conductivities and of the chemical diffusion coefficient. A major application of ion conductors is their use as electrolytes which nullifies gradients in the electrochemical potential of ions but supports gradients in the electrochemical potential of electrons. This gives rise to a cell voltage (e.m.f) which is consequently proportional to the integrated gradient of the neutral component (cf. distance Fig. 2) and

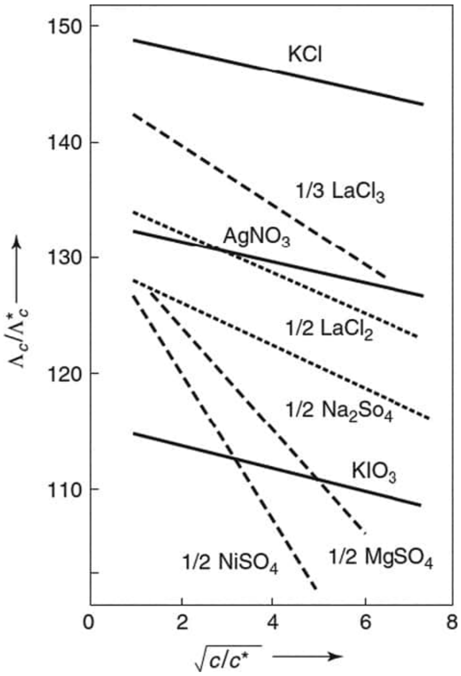

Fig. 15 Equivalent conductivity for a variety of aqueous salt solutions vs. concentration (Λ_c^* and c^* denote unit values). Reproduced with permission from Kortüm G (1972) *Lehrbuch der Elektrochemie*, 5th edn. VCH; Weinheim; © Wiley-VCH.

corresponds to the Nernst equation. In other words, differences in the chemical component potentials can be transformed into an electrical voltage (such as exploited in batteries, fuel cells, and sensors). In mixed conductors, a partial internal short-circuit occurs, causing a nonzero gradient in the electrochemical potential of the ions, which is proportional to the gradient in the electronic Fermi level. Hence, the cell voltage is diminished by a factor (transport number) that depends on the proportion of electronic conductivity and consequently allows for its determination (Maier, 2004; Wagner, 1975; Rickert, 1982).

The kinetics of reaching such a steady state is—if diffusion controlled—determined by the above mentioned chemical diffusion coefficient D^δ. Together with the diffusion distance (L) this value determines the relaxation time of the transients (τ^δ)

$$\tau^\delta \propto \frac{L^2}{D^\delta} \propto R^\delta C^\delta. \tag{30}$$

Writing the product in terms of a chemical resistance R^δ and a chemical capacitance C^δ (Maier, 2004), it becomes obvious that not only the ionic and electronic conductivities are important for the kinetics but also the parameters that determine how much is internally stored. For dilute interaction-free conditions C^δ is determined by the defect concentrations. An important extension refers to including internal reactions as this can change the picture qualitatively. Hence in solids a counter diffusion of two ions that are identical but exhibit different charges (different redox states) translates into an implicit electronic current; in liquids the ambipolar diffusion of ions and their aggregates can pretend (and effectively establish) a diffusion of counter-ions. If the internal reactions are fast, this can be treated within the concept of "conservative ensembles" (Maier, 1993b, 2014). Chemical diffusion also typically describes the kinetics of storage in intercalation batteries (Maier, 2013; Usiskin and Maier, 2018). Unlike usual chemical diffusion processes where a common diffusion source for the component is present, in batteries, ions and electrons are provided from different sites (current collector providing the electrons; electrolyte providing the ions). If this diffusion problem is adequately considered, recipes of how to optimally place these contacts can be derived (see Fig. 16). These so-called optimum wiring lengths (L_{ion}^*,L_{eon}^*) complement the particle size as decisive parameter and allow one to tackle morphological questions in batteries.

Besides intercalation in single-phases, storage e.g., of Li in solid electrodes may involve two- or multi-phase reactions. For the treatment of such phenomena the reader is referred to the literature (Maier, 2013). A conceptually interesting mode concerns interfacial storage in two-phase systems: Space charge effects enable storage at abrupt junctions even in cases where the bulks of the two-phases are not electro-inactive. Here the ion is stored in one and the electron in the other phase. The detailed treatment brings about worthwhile insight (Chen and Maier, 2017; Chen et al., 2016) in terms of: (a) unexpected excess storage, (b) generalization of bulk and boundary storage in that the storage is discussed as a function of position coordinate, and (c) unification of bulk and supercapacitive storage with the possibility of generating artificial electrodes.

As far as the kinetics are considered, bulk pathways become important but also diffusion along the space charge zones. The latter is characterized by "heterogeneous" chemical diffusion coefficients which may exhibit extremely high values.

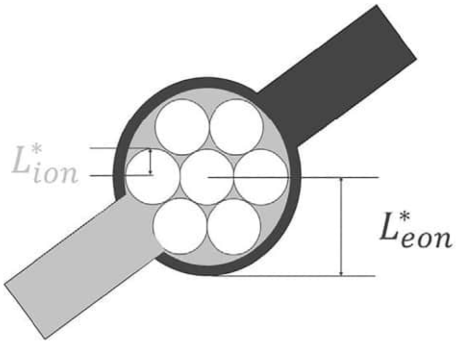

Fig. 16 In the case of Li-storage the ions are delivered by the electrolyte and the electrons by the current collector. The particles should be small to enable fast storage. How intimate the electronic or ionic contacts have to be, can be deduced from the partial conductivities. Here predominantly electronically conducting electrode particles are assumed. After Zhu C, Usiskin RE, Yu Y, Maier J (2017) The nanoscale circuity of battery electrodes. *Science* **358**: eaao2808, (1–8).

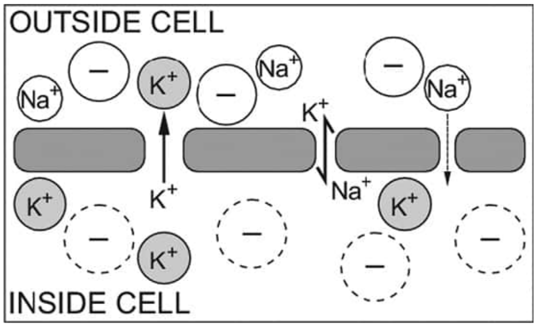

Fig. 17 Sketch of a membrane. Its electric potential derives from the charge imbalance stemming from osmotic effects. Its selective permeability relies on the functions of ion channels and ion pumps and sensitively depends on the membrane potential itself.

Ion transport in biology

Ion transport is also crucial in biology (Kandel et al., 2000). In relevant cells channels and pumps lead to ion leakage, or active transport of ions by using biological energy conversion (ADP/ATP). These functional elements are important e.g., in the process of photosynthesis but in particular for the generation and transmission of nerve signals. The fundamental process is the generation of a membrane potential. This membrane potential is due to the membrane's selectivity. The membrane allows the transport of a given ion but precludes the transport of others. Hence an electric potential is generated if the membrane separates two chambers of different salt concentrations. (It is revealing to compare this with the generation of a battery potential). Here the electrolyte shows selectivity concerning transport of ions versus transport of electrons. The latter is precluded and a voltage generated if the electrolyte membrane separates two chambers of different chemical component potentials. What distinguishes such biological systems from usual electrochemical systems is the chemical complexity and—not independent from it—the non-linearity of the flux-force relation. The latter is achieved by the variation of the membrane conductivity (selectivity) on varying the stimulus, e.g., the voltage. Applying a certain electric potential results e.g., in opening or closing of specific ion channels which eventually leads to what is called an action potential. Fig. 17 refers to a typical situation at a membrane of a nerve cell.

The non-linearity is also responsible for the nerve-signal transmission within the neuron. The transmission from one neuron to the next occurs via synapses. The "plasticity" of the synaptic action is highly important for learning effects in the brain.

In physics mostly electronic transfer and transport is considered. The sheer concentration on it, i.e., ignoring ion transport forbids a proper treatment of mass transport in ionic materials, compositional changes and electrode storage phenomena. The article traces ion transport back to the basic mechanistic centers as well as to the basic phenomenological relations. It deals with bulk as well as interfacial phenomena. Reducing the size co-ordinate leads to phenomena in the realm of nanoionics which is expected to be of similar importance for basic research and application as nanoelectronics. Taking seriously the chemistry allows one also to get a hold on the complexity co-ordinate, and thus also to achieving a better understanding of electrophysiological processes.

Conclusion

The significance of ion transport in condensed matter is threefold:

(1) It is key to the understanding of electrochemical processes ranging from battery research to nerve-signal propagation.

(2) The combination with electron transport enables compositional changes. Typical examples are stoichiometric changes within the condensed phases as a consequence of the interaction with ambient phases.
(3) Even if one concentrates on electronic effects such as electronic resistance or electron redistribution at interfaces, the role of ion motion ions is very often decisive and may even dictate the electronic situation.

The contribution summarizes the fundamentals of ionic charge carriers with emphasis on the solid crystalline state; it reveals isomorphicities and differences between ionic and electronic charge carriers on one side and between solid and liquid state situations on the other.

References

Allnatt AR and Lidiard AB (1993) *Atomic Transport in Solids*. Cambridge: Cambridge University Press.
Barthel JMG, Krienke H, and Kunz W (1998) *Physical Chemistry of Electrolyte Solutions*. New York: Springer.
Bockris JO'M and Reddy AKV (1970) *Modern Electrochemistry*. New York: Plenum Press.
Chen C-C, Fu L-J, and Maier J (2016) Synergistic, ultrafast mass storage and removal in artificial mixed conductors. *Nature* 536: 159–164.
Chen C-C and Maier J (2017) Space charge storage in composites: Thermodynamics. *Physcial Chemistry Chemical Physics* 19: 6379–6396.
Funke K (1993) Jump relaxation in solid electrolytes. *Progress in Solid State Chemistry* 22: 111–195.
Hainovsky J and Maier J (1995) Simple phenomenological approach to premelting and sublattice melting in Frenkel disordered ionic crystals. *Physical Review B* 51: 15789–15797.
Kandel ER, Schwartz JH, and Jessell TM (2000) *Principle of Neural Science*. New York: McGraw-Hill.
Kirchheim R (1988) Hydrogen solubility and diffusivity in defective and amorphous metals. *Progress in Materials Science* 32: 261.
Kröger FA (1964) *Chemistry of Imperfect Crystals*. Amsterdam.
Maier J (1993a) Defect chemistry: Composition, transport, and reactions in the solid state; Part I: Thermodynamics. *Angewandte Chemie, International Edition* 32: 313–335.
Maier J (1993b) Mass transport in the presence of internal defect reactions—Concept of conservative ensembles: I, Chemical diffusion in pure compounds. *Journal of the American Ceramic Society* 76: 1212–1217.
Maier J (1995) Ionic Conduction in Space Charge Regions. *Progress in Solid State Chemistry* 23: 171–263.
Maier J (2003) Complex oxides: High temperature defect chemistry vs. low temperature defect chemistry. *Physcial Chemistry Chemical Physics* 5: 2164–2173.
Maier J (2004) Physical chemistry of ionic materials. In: *Ions and Electrons in Solids*. Chichester: John Wiley & Sons, Ltd.
Maier J (2005) Chemical potential of charge carriers in solids. *Zeitschrift für Physikalische Chemie* 219: 35–46.
Maier J (2013) Thermodynamics of electrochemical lithium storage. *Angewandte Chemie, International Edition* 51: 49985026.
Maier J (2014) Salt concentration polarization of liquid electrolytes and determination of transport properties of cations, anions, ion pairs and ion triples. *Electrochimica Acta* 129: 21–27.
Onsager L (1927) On the theory of electrolytes II. *Physikalishce Zeitschrift* 28: 277–298.
Rickert H (1982) *Electrochemistry of Solids*, 1st edn. Berlin: Springer.
Riess I and Maier J (2008) Symmetrized general hopping current equation. *Physical Review Letters* 100: 205901. (1-4).
Schmalzried H (1981) *Solid State Reactions*, 1st edn. Weinheim: VCH.
Schmalzried H (1995) *Chemical Kinetics of Solids*, 1st edn. Weinheim: VCH.
Usiskin RE and Maier J (2018) Guidelines for optimizing the architecture of battery insertion electrodes based on the concept of wiring lengths. *Physical Chemistry Chemical Physics* 20: 16449–16462.
Wagner C (1975) Equations for transport in solid oxides and sulfides of transition metals. *Progress in Solid State Chemistry* 10: 3–16.

Electronic structure of liquids☆

G Pastore[a] and **MP Tosi**[b],*, [a]Dipartimento di Fisica, Università di Trieste, Trieste, Italy; [b]Scuola Normale Superiore, Pisa, Italy

© 2024 Elsevier Ltd. All rights reserved.

This is an update of M.P. Tosi, Liquids, Electronic Structure of, Editor(s): Franco Bassani, Gerald L. Liedl, Peter Wyder, Encyclopedia of Condensed Matter Physics, Elsevier, 2005, Pages 120–126, ISBN 9780123694010, https://doi.org/10.1016/B0-12-369401-9/00465-4.

Introduction **162**
Experimental and theoretical methods **163**
Metallic liquids **164**
Simple metals 164
Polyvalent metals 165
Expanded liquid metals and M/NM transition 166
Metallic alloys 166
Electron–ion correlations **167**
Liquid semiconductors and insulators **168**
Molten semiconductors 168
Molten salts 168
Excess electrons, molecular liquids, and metallization under pressure 168
Conclusion **169**
References **169**

Abstract

This article provides an overview of and general introduction to the present understanding of the electronic structure of liquids. Special emphasis is laid on the role played in recent years by ab-initio simulation methods to get insight into the strong interplay between electronic and structural properties typical of the liquid state. Discussion of physical systems is organized around the illustration of few selected results for prototype classes of liquid systems corresponding to the five types of electronic bonds: metallic, covalent, ionic, hydrogen, and van der Waals.

Key points

- The electronic structure of liquids is strongly linked to the average atomic positions in a self-consistent way.
- Classification of the electronic properties of crystalline solids can be directly adapted to the case of liquids by eliminating the features more related to spatial periodicity.
- Key quantities for describing the properties of electronic structure are the space-dependent electronic density and the electronic density of states (e-DOS).
- The electronic density directly controls interatomic interactions.
- Recent advances in ab-initio numerical simulation methods allow a description of the electronic structure of liquids equivalent to that of solids.
- This chapter aims to provide an overview of the present understanding of the electronic structure of liquids by focusing on a few selected results for prototype classes of liquid systems.

☆*Change History*: May 2023. Author involved in preparing the update G Pastore. All the sections and the figures of the articles have been updated, although the original organization of the article around the different types of binding in condensed matter has been kept. Relatively minor changes have been introduced in the sections on Simple metals, Expanded liquid metals, M/NM transition, Excess electrons, molecular liquids, and metallization under pressure.

*Deceased.

Nomenclature

e	electron charge
e-DOS	electronic density of states the number of one-electron states per unit energy and volume
$\hbar$	Planck constant h-crossed (h divided by 2π
k_B	Boltzmann constant
k_F	Fermi wavenumber
m	electron mass
M/NM	metal nonmetal
$V_{ij}(k)$	product of the electron–ion pseudopotentials of two ions of species i and j
x_i	concentration of the species i
z	ionic valence
Δ	nonadditivity parameter
ε_0	vacuum dielectric constant
$\varepsilon(k)$	static dielectric function
κ	thermal conductivity
ρ_e	electric resistivity
σ_i	effective diameter of an ion of species i
$\phi_{ps}(k)$	Fourier component of the electron–ion pseudopotential
$\phi(r)$	effective ion–ion pair potential

Introduction

The electron distribution in a material directly controls interatomic forces, and thus the atomic structure of a material. At laboratory temperatures and pressures, part of the electronic structure, the innermost atomic shells in a one-electron description, is practically unaffected by changes in interatomic distances and chemical environment. Another part, the valence electrons, is directly involved in forming bonds, and then it plays a double-face role. At the same time, it affects, and it is affected by the nuclear positions in a self-consistent way.

In the case of crystalline solids, such a link between structure and interactions can be partially broken by exploiting the simplified description of the atomic positions in periodically repeated units. Liquids, with their intrinsic high atomic mobility, present a broader range of possibilities for atomic positions, inducing dramatic modifications of the average electronic configuration as a function of a pressure, temperature, and composition. Distinct features of liquid phases, important for their role in determining the electronic properties are highly individual and collective ionic mobility, a time scale of ionic dynamics much shorter than the time scale of electronic relaxation, the absence of long-range order but the presence of short-range order with a continuous distribution of interatomic distances and angles.

From the experimental and theoretical side, studying the electronic structure of liquids does not introduce fundamental differences with the case of amorphous solids, while we have to renounce to many of the solid-state techniques directly related to the translational symmetry of crystalline structures. However, the evolution of experimental and numerical simulation techniques has provided a partial compensation, resulting in a much more accurate description of disordered phases than in the past. Still, some concepts play a central role for all condensed systems. An example is the electronic density of states (e-DOS; the number of one-electron states per unit energy and volume). Although based on the introduction of approximate one-particle wavefunctions, it is a quantity of primary interest for discussing electronic properties in many condensed systems. Other examples include the dipole-moment distribution or the local net charges around ions, helpful to razionalize experimental results.

The differences between disordered and ordered phases should not make us forget that a previous knowledge of the properties of crystalline phases may be useful to understand the disordered phases. Indeed, at a local level, there are some important similarities between liquid and solid phases. The reason is the relatively small difference in the coexisting solid and liquid density, usually not larger than a few tens of percent. Thus, the resulting variation of the interatomic distances at melting is usually small. Thus, a useful way to open an overview on the electronic structure of liquids is to recall the five types of crystal binding: metallic, covalent, ionic, hydrogen, and van der Waals bonding.

It stands to reason that the electronic structure of a metal is essentially unchanged on melting. In metallic liquids, the e-DOS, although blurred due to the lack of long-range order, still has significant values at the Fermi energy, providing a mechanism for typical metallic conduction. In parallel with the case of metallic crystals, the e-DOS of liquid metals goes from a recognizable modification of the uniform electron gas behavior in the case of the alkali metals, to more significant deviations for polyvalent sp-bonded metals, to the qualitative modifications due to the contributions of the d and f states in transition metals and rare earths.

As a consequence of density changes or by varying the composition in mixtures, a rapid departure from a purely metallic behavior up to the catastrophic metal/nonmetal (M/NM) transition may appear, with the system always remaining in the fluid phase.

In contrast to metals, dramatic changes in the electronic structure occur on melting in some covalent elemental systems such as B, Si, Ge, and 13–15 (III–V) compounds: the covalent bonds collapse into a metallic state, though with some peculiarities of its own. These elemental melts can be brought into an amorphous state by rapid quenching, just as those of other covalent compounds such as SiO_2 or $GeSe_2$ whose liquid structure is best described as a disordered covalent network.

Pure covalent binding is characterized by a gap in the e-DOS between occupied and empty states, and by a higher localization of valence electrons between ions. The resulting interatomic interactions have a quite strong dependence on the mutual orientation of neighbor ionic pairs as measured by the angle between triples of atoms. Therefore, the resulting interactions cannot be reduced to pairwise force fields, and three-body or four-body terms are required.

A typical example of ionic binding in liquids is the case of molten salts. Typical gaps between occupied and empty states in the e-DOS are higher than in covalent systems, but their distinguishing feature is the presence of at least two atomic species with a great difference in electronegativity. Electrons from the less electronegative atom move toward the more electronegative and, in the limiting case of alkali halides, the topmost s electron of the alkali is almost entirely transferred to the halide ion. Such a feature clearly visible in experimental measurements of the electronic density in the solid remains when the solid melts, although the larger range of distances in the liquid induces some deformation effect (polarization) of the electronic density around the ions. In some cases, the state of aggregation of the ions may drastically change. For example, $AlCl_3$ melts from a layer structure where the Al ions are sixfold coordinated into a liquid of Al_2Cl_3 molecular dimers showing fourfold coordination of Al. The presence of chemical order in these melts can favor the acceptance of foreign electrons inside the liquid structure, as in mixtures with metals that may be stable over a wide range of concentrations.

The cases of van der Waals interactions are not only typical of rare gases but are also typical of closed-shell molecules and of the hydrogen bond. They share with the stronger ionic binding the characteristic of being only marginally perturbed on melting, requiring only, as a first approximation, to take into account polarization effects. The reason for such stability can be traced to the stability of closed shell structures, for van der Waals fluids, to the special role of the hydrogen cation (a proton) in polarizing the shell of valence electrons of near atoms in the case of hydrogen-bonded fluids.

In addition to the characteristic electronic structures of the above-mentioned classes of liquids we will briefly mention the case of localized states of excess electrons, historically one of the oldest topics in the electronic structure of liquids. The article ends with a brief section of conclusions and an outlook.

Experimental and theoretical methods

Before discussing recent progress in the understanding of the electronic structure of different classes of systems, it is worthwhile to briefly recall how such properties can be measured and what are the main theoretical tools and their recent evolution.

On the experimental side, photoemission spectroscopy remains one of the main techniques to directly probe the e-DOS of condensed phases, liquids included. Information on the atomic positions is usually obtained from scattering experiments. In the case of bulk liquids, mainly X-ray and elastic neutron scattering are routinely employed. The resulting information is encoded in the atomic pair radial distribution functions or their Fourier transforms, the atomic structure factors. Such quantities provide only statistical information about atomic positions, constraining them but not providing explicitly three-dimensional atomic coordinates. In combination with X-ray absorption spectroscopy (XAS) and theory and simulations, elastic scattering data may provide quite a detailed description of the average local structure in disordered phases.

In recent years, new methods have appeared, in particular, ultrafast spectroscopy, specially tailored for typical transient phenomena in the liquid state. An example of the potentialities of such techniques is the recent study of the possible liquid–liquid phase transition in silicon (Beye et al., 2010).

On the theoretical side, approximate theories of the electronic structure of liquids have evolved, mainly during the nineties, to a stage where at least for sp-bonded liquids, it is possible to get quite accurate self-consistent calculations of the atomic structure and e-DOS at the same time (Stratt, 1990). One interesting approach is based on a combination of a tight-binding description of the electronic interactions and the Ornstein-Zernike (OZ) integral equation description of the pair correlations in the atomic structure (Hansen and McDonald, 2013). The resulting theory, formally similar to the integral equation theory for the liquid structure, allows the numerical calculation of reliable and accurate e-DOS as compared with simulation results for s- and sp-bonded liquids (López-Martín et al., 1997).

Probably, the most important progress in the last decades has come from simulation methods with the progressive establishment of Ab-initio Molecular Dynamics (AIMD) techniques, like Car-Parrinello (Car and Parrinello, 1985) or Born-Oppenheimer algorithms (Hutter, 2012) as a standard for numerical calculations of equilibrium properties for liquids. AIMD simulations are currently based on the Density Functional Theory (DFT) of the electrons (Martin, 2020), thus shifting the focus from wavefunctions to electronic density. The main idea behind AIMD, introduced for the first time by Car and Parrinello is to combine the numerical integration of classical equations of motions for the atoms with a calculation on-the-fly of the interatomic forces, based on an efficient updating of the DFT-based electronic density at each time step. A key ingredient of many AIMD calculations is the introduction of ab-initio electron–ion pseudopotentials designed to reproduce with the maximum accuracy the scattering properties of the frozen-core ions in a suitable interval of energies. Introduction of pseudopotentials dramatically reduces the number of dynamical variables of the simulations without introducing uncontrolled approximations.

Classical trajectories of the atoms resulting from forces due to ionic cores and quantum electrons can be evaluated, and used to compute time averages of physical properties. At variance with Molecular Dynamics based on empirical force fields, AIMD methods do not introduce additional approximations on the interactions beyond the Born-Oppenheimer partial decoupling between ionic and electronic components, the frozen core approximation for electrons, and the classical treatment of ionic dynamics. Moreover, based on the solution of the quantum electronic problem, AIMD provides direct and self-consistent information on the electronic structure. At the one-electron theory behind the usual Kohn-Sham implementation of DFT, the one-electron energy spectrum can be used to evaluate the time-averaged e-DOS.

Using more ambitious techniques like time-dependent DFT (TDDFT) (Marques et al., 2006) and Quantum Monte Carlo algorithms (Becca and Sorella, 2017) is progressively increasing, even though they are at a less mature stage as general-purpose simulation methods, and do not allow direct calculations of atomic dynamical properties.

Metallic liquids

Simple metals

The simplest liquid metals are one-component systems made of atoms with only s and p valence electrons. In correspondence with the first column of the periodic tables (alkali metals) the interaction between the ionic cores and valence electrons is relatively weak, and this is reflected in weak pseudopotentials. For such systems, second-order perturbation theory of the uniform electron gas in powers of the electron–ion pseudopotential provides good results for electronic and structural properties, in quantitative agreement with more precise calculations.

By introducing the Fourier component of a local (i.e., independent of the angular momentum value) electron–ion pseudopotential $v_{ps}(k)$, and perturbing with it a homogeneous, interacting electron gas, characterized by a static dielectric function $\varepsilon(k)$, we can obtain an effective pairwise interatomic potential from second-order perturbation theory (March, 1990)

$$\phi(r) = \frac{z^2 e^2}{4\pi\varepsilon_0 r} + \frac{1}{2\pi^2}\int_0^{+\infty} \frac{\sin(kr)}{kr}\hat{\phi}_{ps}(k)k^2 \mathrm{d}k$$

where

$$\hat{\phi}_{ps}(k) = \frac{1}{\frac{e^2}{\varepsilon_0 k^2}}\left(\frac{1}{\varepsilon(k)} - 1\right)v_{ps}^2(k).$$

Here, z is the ionic valence, e is the electronic charge, and $\varepsilon(k)$ is the static dielectric function of the interacting electron gas. The qualitative behavior of such pairwise interaction is shown in Fig. 1. The characteristic oscillations of wavenumber $2k_F$ are related to the nonanalytic behavior of the dielectric function of the ideal Fermi gas at the Fermi momentum. The atomic structure factors obtained from these interactions are in excellent agreement with elastic scattering experiments.

The adequacy of a perturbative approach in the case of alkali metals is also confirmed by the success of the simple diffraction theory by Ziman (Ziman, 1961) to account for electric resistivity, dominated in the metals by the electronic contribution. Ziman's theory allows us to calculate the electric resistivity within the same linear response theory used to account for the electronic density, interatomic interactions, and Thermodynamic properties. The electronic contribution is also dominant in the thermal conductivity κ of the metals. Indeed, the Wiedemann–Franz law asserts that the quantity $\rho_e\kappa/T$, where ρ_e is the electric resistivity and T is the absolute temperature, is a universal constant, the Lorenz number, $L = \pi^2 k_B^2/3e^2$ where k_B is the Boltzmann constant. Empirically, this law is satisfied by many liquid metals near freezing, within a scatter of about ± 10%. The electronic contribution is minor in simple liquid metals' shear and bulk viscosities.

A more demanding case for perturbation theory is the calculation of the properties of alkali metal alloys. They can be satisfactorily described by perturbation theory only in the case of the simplest case of Na-K alloys. An example is provided by the results of the calculation of the electric resistivity using the extension of Ziman's theory to the alloys, resulting in the following approximate formula

$$\rho_e = \frac{12\pi m^2}{\hbar^3 n e^2 k_F^2}\int_0^1\left[\sum_{ij} x_i x_j |V_{ij}(k)|^2 S_{ij}(k)\right]\cdot\left(\frac{k}{2k_F}\right)^3 \mathrm{d}\left(\frac{k}{2k_F}\right).$$

A comparison of theoretical and experimental results for the isothermal variation of resistivity with the concentrations is shown in Fig. 2 (Pastore et al., 1981).

The excellent agreement obtained in this case progressively degrades in other binary alkali metal alloys. The reason for such a failure of the perturbation approach can easily be understood. Sodium and potassium pseudopotentials are the closest among the

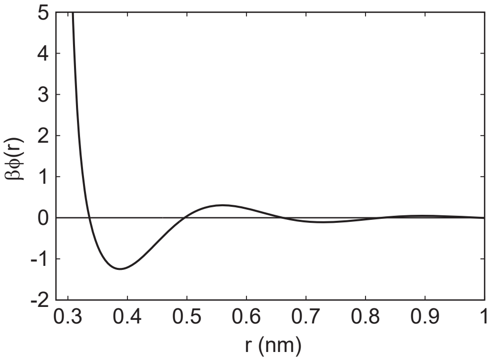

Fig. 1 Qualitative behavior of the effective pair potential (multiplied by $\beta = (k_B T)^{-1}$). Notice the damped Friedel oscillations related to the non analyticity of the electronic dielectric function at the Fermi wavenumber.

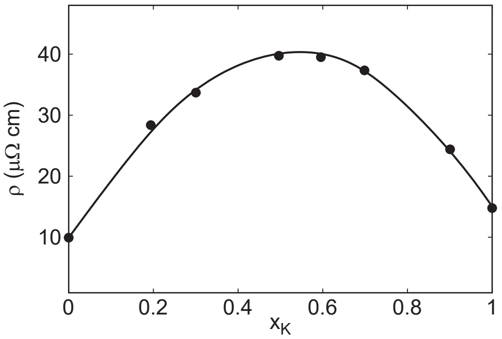

Fig. 2 Electric resistivity of the Na-K liquid alloy at 100°C versus potassium concentration. Full curve: theoretical results from perturbation theory and Faber-Ziman formula (see text); dots:experimental results from Hennephof et al. (1978).

alkalis. The increasing difference in electro–ion interactions in other alkalis makes the local environment of an atom in a mixture farther from that in pure liquids. Such a difference would require more transferrable pseudopotentials, but a higher transferability is accompanied by an increase in the strength, making second-order perturbation less accurate.

Polyvalent metals

Moving away from the first column elements, increasingly stronger deviations from the free-electron approximation are also a consequence of stronger electron–ion pseudopotentials. Moreover, in the case of transition metals, the presence of incomplete 3d, 4d, and 5d shells introduces sharp features in the broad sp bands. Taking into account the limitations of perturbation theory, AIMD was expedient in shading light on the ionic and electronic properties of polyvalent liquid metals and their alloys in disordered phases.

As an example, in Fig. 3, we can see the contour plot of the electronic density in a plane containing three magnesium atoms in a single configuration of an AIMD simulation for pure liquid magnesium at 1000 K (De Wijs et al., 1995).

The contour plot of the total valence density in the left panel of the figure shows a spatial modulation with a maximum gradient around the ions. The apparent plateau of density close to the nuclear position is the effect of plotting the valence density only. If included, the contribution to the electronic density from the core states density would dominate the region around nuclei. The right panel nicely illustrates the poly-center nature of the metallic bond. Part of the atomic density has been transferred to the interstitial region between the ionic cores without a strong localization.

The general agreement between experimental values and AIMD calculations of physical properties of polyvalent liquid metals, including transition metals, is in general excellent.

In the case of the heaviest elements, relativistic effects play an essential role and should be taken into account in DFT calculations. Not only are such effects responsible for important changes in the gap values of the e-DOS, therefore modifying the optical properties with respect to nonrelativistic calculations, but, as it has been recently shown, they play an essential role in ionic and thermodynamic properties. As an example, AIMD calculations have shown that the melting point of Mercury at normal pressure would be more than 150 K higher, making this metal a solid at room temperature (Steenbergen et al., 2017).

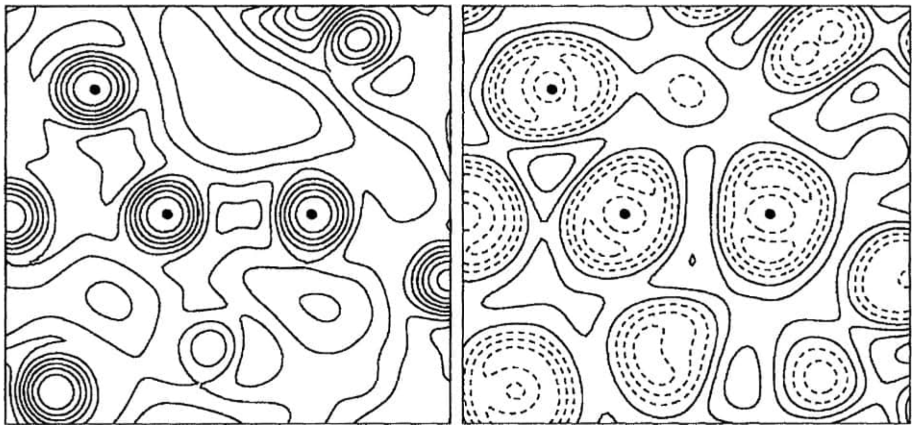

Fig. 3 Left panel: contour plots of the electronic density in liquid Mg at 1000 K from a single configuration of an AIMD simulation (De Wijs et al., 1995). The three black dots indicate the position of three Mg atoms. The iso-density lines are drawn at a density spacing of 13.5 electrons/nm^3. Right panel: difference between the self-consistent ground state density shown in the left panel and the superposition of isolated atom densities. Dashed lines indicate negative values. Contours are traced at a spacing of 6.75 electrons/nm^3.

As a general rule, relativistic effects on the electronic structure act at two different levels. On the one hand, spin-orbit effects tend to increase the gaps in the e-DOS, like in the solid phases. Moreover, a different effect is related to the contraction of the core shells, with an indirect effect on the valence electrons via the pseudopotentials. Notice that such effects are not limited to metallic systems.

Expanded liquid metals and M/NM transition

Extensive work done in the past (Hensel and Warren, 2014) and also recently (Pilgrim et al., 2018) on expanded mercury and liquid alkali metals (the metallic elements with the most accessible critical point) has shown how closely the electric transport properties of expanded liquid metals depend on the properties of the electron gas as a function of density. By decreasing density, the screening is weakened, and electrons are more easily localized in a scenario consistent with Mott's model. A typical variation of electric resistivity with the density in such systems is shown in Fig. 4. Data are plotted as a function of the reduced density $\phi = \frac{\rho - \rho_2}{\rho_1 - \rho_2}$, where ρ_1 and ρ_2 are the density of the metallic and nonmetallic phases, respectively. Data from Ruland and Hensel (2010).

A density threshold is evident, separating a high conductivity phase, at higher densities, from a low (but not zero) conductivity at low densities. The present experimental evidence indicates that the M/NM transitions occur with a decomposition of the metallic liquid into a two-component mixture of conducting and nonconducting domains. Such a decomposition seems to accompany the liquid–vapor coexistence in the case of liquid alkali metals. The coordination number of a Cs atom that is obtained from the data by extrapolation to the critical density approaches the value 2. This suggests that, as the metallic fluid is driven toward a metal-insulator transition, chainlike structures are stabilized by chemical bonding and probably coexist with small clusters such as ionized dimers. On the gas side of the critical point, one finds a large number of diamagnetic units such as Cs_2 molecules and probably larger clusters.

Different scenarios are possible, accordingly to the hypotheses proposed initially by Landau and Zeldovich (discussed in Hensel (2010)). A first-order M/NM phase transition could occur wholly in the liquid or vapor phase or on the continuation of the coexistence line above the critical temperature and pressure. Although a definite conclusion is still missing, work on such a topic is in progress.

Metallic alloys

Metallic liquid alloys show a much larger variety of behaviors than pure components. Differences of electronegativity, with the resulting partial electron transfer from one species to another, allow a vast set of possibilities for electronic and, consequently, ionic configurations. Almost all the metallic binary alloys show a clear indication of nonadditivity of the excluded volumes around the ions. This is visible on the partial radial distribution functions $g_{ij}(r)$ obtained from the Fourier transform of the k –dependent cross-section from the elastic scattering of X-rays or thermal neutrons.

If we quantify the radius σ_{ij} of the volume around a particle of species i excluded for particles of species j by using the position of the first peaks or from other reasonable estimates like the distance where each $g_{ij}(r) = 1$, in general we can write

$$\sigma_{12} = \frac{\sigma_{11} + \sigma_{22}}{2}(1 + \Delta).$$

with a nonadditivity parameter (Δ) positive or negative. Positive values of Δ imply a local tendency toward homo-coordination and the possibility of a demixing phase transition as a function of the state. Negative values correspond to a tendency toward etherocoordination and enhanced stability of the mixed phase. Such a local tendency may be increased or decreased by long-range interactions. Therefore, for many liquid alloys, a parallel study of the size nonadditivity, and the charge transfer due to the electronegativity differences may help to predict their solubility properties.

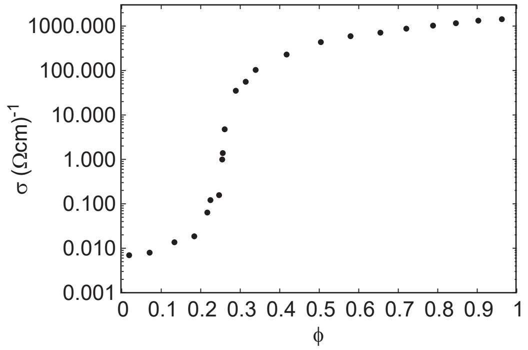

Fig. 4 Experimental behavior of electrical conductivity of expanded fluid mercury as a function of the reduced density ϕ (see text for definition). Data from Ruland W and Hensel F (2010) Critical region and metal-nonmetal transition in expanded fluid mercury: Advanced evaluation of small-angle X-ray scattering data. Journal of Applied Crystallography 43 (2): 244249.

In some cases, the analysis of the corresponding solid phases has suggested the persistence in the liquid phase of some peculiar atomic structures stabilized by the electronic structure.

An interesting example of this can be found in the case of the so-called Zintl phases. In the 1930s, the inorganic chemist Zintl proposed a powerful interpretation principle for a class of intermetallic compounds. The principle can be applied to ionic alloys with a large difference in electronegativity, like alkali-group 14 (IV) elements. In such alloys, each alkali cation loses its valence electron, while negatively charged anions become isoelectronic to P or As, which form in the gas phase, tetrahedral P_4 and As_4 clusters. Indeed, negative anions form ionic tetrahedra clearly identified in the crystalline phases. All the crystalline phases of equimolar alloys show isomorph or closely related atomic structures. In the liquid phase, these alloys exhibit special behaviors, like the resistivity maximum and dips in the alkali Knight shift as a function of composition, suggesting the presence of such clusters in the liquid phase, causing a depletion of electrons at the Fermi level. A piece of indirect evidence was obtained from the analysis of the partial structure factors of the liquid. In particular, the presence of a prepeak in the total structure factor is usually a signal of intermediate-range ordering due to the clusters.

Only after the development of AIMD methods was it possible to validate the Zint model based on a careful analysis of the ionic configurations obtained from a consistent treatment of the electronic states. Numerical simulations of these alloys have provided evidence for the correlation between preferred atomic configurations and electronic properties of the model, albeit with more complex details. In the solid structures of equimolar alloys, the separation between bonding and antibonding states is reflexed by a minimum or a gap in the e-DOS. AIMD calculations have shown that even if perfect tetrahedra are destroyed by the thermal ionic motion, tetrahedral coordination and angle distribution remain close to the tetrahedral values. Thus, the naïve model with perfect tetrahedral Zintl ions should be modified into a more complex scenario characterized by the presence of fluctuating clusters of fourfold coordinate atoms, coexisting and merging with other clusters, still keeping an electronic e-DOS qualitatively amenable to the ideal e-DOS of a structure made of perfect tetrahedra. Indeed, the analysis of the electronic ground state of an s-p tetrahedral cluster like P_4 shows that the p levels, quite far from the s levels, are split into four full low-lying bonding states and two empty high-lying antibonding states. The e-DOS averaged over many ionic configurations is consistent with the analysis of the energy levels of the isolated cluster and calculations on crystals. The case of CsPb is shown in Fig. 5.

Three bands are visible. The lowest lying band is due only to the Cs 5s states. The double peak band around – 10 eV is due to hybridized Cs 5p states (the peak on the left) and Pb 6s states (a broad peak from – 11 to – 6 eV, with an absolute maximum at the position of the subpeak on the right). The third visible band, starting below – 2 eV, has a local minimum close to the Fermi energy (E_F) with an essential contribution from the d states of Cs. Such a minimum of the e-DOS is consistent with a semiconductor-like behavior of the electric resistivity.

Zintl ions are not the only example of characteristic electronic structures due to the presence of complexes in the liquid. Anomalies in all the electronic properties related to compound formation have been reported at the electronic octet composition, in the case of Li_4Pb and Li_4Sn, or at equimolar composition for CsAu.

Electron–ion correlations

In a crystalline solid, X-ray scattering can directly provide information about the electronic density distribution around the nuclei. In a liquid, the atomic motion does not allow a direct measurement. However, looking at the system as a two-component system of ions and conduction electrons, and following a quite old proposal by Egelstaff, it should be possible to combine different scattering techniques to obtain separate contributions coming from the electron–electron, electro–ion, and ion–ion correlations.

Takeda’s group carried out some pioneering efforts in such direction for several liquid metals combining neutron and X-ray scattering with theoretical results for the electron-electron correlations (Takeda et al., 1996).

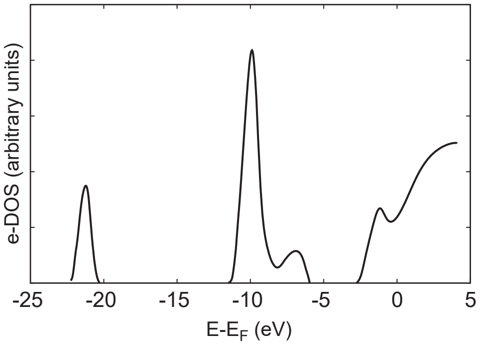

Fig. 5 e-DOS of CsPb liquid alloy at 1050 K. Data from 10 liquid configurations have been averaged and smoothed.

AIMD provided a computational tool for studying electron–ion correlations. An early attempt in this direction was made for liquid Mg and Bi, and additional studies have demonstrated the feasibility of such computational approach. The combination of experiments and AIMD could be instrumental to get insight into the electronic distribution and, indirectly, to assess the quality of different density functionals and pseudopotentials. However, the present status of such an approach (Anta et al., 1998) is that the quantitative discrepancies exist between simulation and experimental results, suggesting the need for improvements in the corrections in data analysis of both neutron and x-ray scattering measurements.

Liquid semiconductors and insulators

Molten semiconductors

A sharp distinction between liquid metals and liquid semiconductors is difficult. In practice, an arbitrary border is conventionally put at values of the electrical conductivity σ larger than 2000 $\Omega^{-1}\text{cm}^{-1}$, corresponding to the threshold where, in the free electron model, the mean free path of the electrons becomes comparable with the interatomic distances. However, no sharp transition is observed experimentally, if it is not accompanied by significant structural rearrangements. Semiconducting group-14 (IV) elements and 13–15 (III–V) compounds, at their melting point under normal pressure, increase both density and coordination numbers, thus going to more compact structures characterized by metallic conductivity.

Such a general scenario is declined differently in different systems. Crystalline archetypal semiconductors like Silicon and Germanium are found in the open fourfold coordinated diamond structure up to their melting point. The corresponding liquids have coordination between 6 and 7 and are metallic. Therefore, melting is accompanied by a partial release of the valence electrons from interatomic bonds into less localized conducting states. Liquid silicon was the subject of one of the first applications of AIMD to the liquid state. Analyses of the electronic density between nearest neighbors strongly suggested a continuous change of bonding character as a function of the atomic distance.

Just below their melting point, Selenium and Tellurium are semiconductors in hexagonal crystalline structures where atoms are arranged in infinite helical chains. After melting, liquid Selenium remains a semiconductor with a structure characterized by the persistence of long chains (about 10^5 atoms) with coordination close to two. On the contrary, liquid Tellurium is metallic. Surprisingly, it shares with water a few anomalies, notwithstanding the entirely different kind of binding: covalent bonds in Te, and hydrogen bonds in the case of water. Below the melting point, extrema are present in specific heat, isothermal compressibility, and thermal expansion coefficient of Tellurium. Close to the melting point ($T = 722$), there is a density maximum. DFT calculations have shown that disruption of Te chains requires less energy than Se chains. As an effect, the liquid structure of Te and then its electronic properties are strongly affected by a rapid change in the chain length and by the presence of two-fold and threefold coordinated atoms, rings, and cavities.

Molten salts

The simplest molten salts are represented by the alkali halides, where the large electronegativity difference is responsible for the almost complete transfer of the unpaired s electron of the alkali to the anion. We have direct evidence of that from experiments in the solid state, and an indirect evidence by the good performances of purely ionic models for energy and structural properties of the solid and molten phases. Still, the agreement is not complete, and the polarization effects of the ionic electronic shells are deemed to account for about 10% of the cohesive energy and turn out essential to bring numerical calculations in quantitative agreement with structural data from scattering experiments.

The liquid structure of alkali halides characterized by strong short-range chemical order: each ion is surrounded by a well-definite screening shell of oppositely charged first neighbors.

Moving toward a smaller difference in electronegativity, polarization effects (mainly in the anions) become increasingly important, and become the key ingredient to understand local order and its variation with the thermodynamic state in many molten salts.

Like in the case of intermetallic compounds, many molecules with a strong ionic character show a persistence of their molecular properties in the molten salt phase. The main questions about the electronic structure in such ionic conductors are about the modifications of the electronic states induced by the disordered condensed phase and, in particular, the possible modifications of the electronic and structural properties under pressure. Again, combining experimental techniques and AIMD methods allows us to gain insight into this fascinating subject (Brazhkin et al., 2007).

Excess electrons, molecular liquids, and metallization under pressure

A problem that has garnered interest for its relevance for many radiation chemistry problems and for many applications, for example the high-energy particle detectors, is the description of the electronic states of excess electrons in dielectric liquids. Recent research agrees on a general scenario where electrons relax to localized cavity-like structures. The study of the relaxation process and the possibilities of reaction of the solvated electron in the host liquid strongly depend on the material and research in this field could recently take advantage of developments in experimental (Herbert and Coons, 2017) and simulation (Marsalek et al., 2012) techniques.

Molecular liquids maintaining the presence of stable closed-shell molecular units are insulators. Their electronic properties are mainly related to dipole moments and electric polarizability. The range of the observed behavior is quite broad, from molecular liquids of apolar diatomic molecules to the case of strongly polar molecules, including hydrogen-bonded molecules. From the point of view of the electronic structure, an interesting problem is understanding the mechanism underlying molecular unit evolution and its consequences on the physical properties under pressure. In a way, it is the high-pressure-side counterpart of the M/NM transition.

Recent high-pressure studies have reached several hundred gigapascals, corresponding to free-energy variations larger than 10 eV, exceeding the binding energy of the strongest covalent bonds. Thus, under very high pressure, significant bond changes may appear, affecting almost all physical properties. For such reasons, High-pressure Physics has become an important laboratory for studying the variation of electronic structure and its consequences.

Not all materials behave in the same way under pressure. Alkali metals are deemed to undergo a dimerization, forming an insulating phase under pressure before a final metallization at even larger pressures. Some molecules remain stable under relatively high pressures. For example, liquid iodine shows an increase in the bond length under pressure and indications of molecular dissociation close to 4.5 GPa and 1000 K. The metallization in the liquid phase shows some puzzling features. The most important is its appearance in the liquid phase at a lower pressure than in the solid phase. In both phases, the abrupt drop in electric resistivity with increasing pressure occurs before the molecular dissociation.

Probably the most challenging case of metallization of a molecular liquid is the case of hydrogen, both for its unique behavior making it more similar to halides than alkali metals and for the relevance of results for many astrophysical problems. Hydrogen has a very rich phase diagram, notwithstanding the simplest structure of the atom. In standard laboratory conditions, cooling the gas of diatomic molecules brings it into a liquid of weakly coupled molecules and then into a crystal, in which the molecules are rotating with weak hindrances from each other. Compression at low temperatures brings the crystal into a new phase, in which the molecular rotations are hindered and ultimately into a further crystal phase whose strong infrared activity indicates a mainly dipolar distortion of the electronic distribution. Molecular dissociation can occur as hydrogen is brought into the regions of high temperatures and densities relevant to astrophysics. Dynamic experiments under pressure have provided evidence of a transition from semiconducting to a metallic state around 3000 K and 140 GPa. The possibility of a first-order phase transition has been studied with the best numerical techniques. However, a definite conclusion about such a scenario is still missing.

The dissociation transformation revealed by these studies in which molecular hydrogen transforms, not directly into a fully ionized plasma but first into a partially ionized atomic fluid, is also relevant to modeling the interior of giant planets such as Jupiter or Saturn. However, the situation there is more complex because hydrogen and helium coexist as main components. It is estimated that these two elements are at pressures of up to 4500 GPa, and temperatures up to 24,000 K in Jupiter, and about 1000 GPa and 10,000 K in Saturn. The planet is thought to consist of three main layers: an outer layer of molecular hydrogen and atomic helium, a middle layer of metalized atomic hydrogen and helium, and a rocky core compressed to as high as 104 GPa at the center of Jupiter. In Saturn, an internal energy source has been proposed, from demixing and gravitational separation of the hydrogen–helium fluid at pressures below 1000 GPa.

Conclusion

Almost four decades of progress in theoretical, computational, and experimental techniques have brought the study of the electronic structure of liquids from an initial pioneering stage to the present state where it is possible to investigate the electronic properties of liquids almost at the same level of accuracy than in the case of crystalline solids.

It is difficult to overestimate the role played by AIMD, although we have to recall that the underlying DFT has not yet reached a completely mature state (Burke, 2012). In particular, the case of strongly correlated systems remains an active research topic. Efficient application to the liquid state of alternatives to DFT like Diffusion Monte Carlo, domain-based local pair natural orbital coupled cluster, the time-dependent formulation of DFT, and the GW method (Per and Cleland, 2020), remains an active field of investigation.

References

Anta JA, Jesson BJ, and Madden PA (1998) Ion-electron correlations in liquid metals from orbital-free *ab initio* molecular dynamics. *Physical Review B* 58(10): 6124.

Becca F and Sorella S (2017) *Quantum Monte Carlo Approaches for Correlated Systems.* Cambridge: Cambridge University Press. https://doi.org/10.1017/9781316417041.

Beye M, Sorgenfrei F, Schlotter WF, Wurth W, and Föhlisch A (2010) The liquid-liquid phase transition in silicon revealed by snapshots of valence electrons. *Proceedings of the National Academy of Sciences* 107(39): 16772–16776.

Brazhkin VV, Lyapin AG, Popova SV, Katayama Y, Saitoh H, and Utsumi W (2007) Molecular-network-ionic structure transitions in liquid $AlCl_3$ and $ZnCl_2$ halogenides under pressure. *Journal of Physics: Condensed Matter* 19(24): 246104.

Burke K (2012) Perspective on density functional theory. *The Journal of Chemical Physics* 136(15): 150901.

Car R and Parrinello M (1985) Unified approach for molecular dynamics and density-functional theory. *Physical Review Letters* 55(22): 2471–2474.

De Wijs GA, Pastore G, Selloni A, and Van Der Lugt W (1995) Electron-ion correlation in liquid metals from first principles: Liquid Mg and liquid Bi. *Physical Review Letters* 75(24): 4480.

Hansen J-P and McDonald IR (2013) *Theory of simple liquids: With applications to soft matter.* Academic Press.

Hennephof J, Van der Marel C, and Van der Lugt W (1978) The electrical resistivity of liquid potassium-rubidium, rubidium-caesium and sodium-potassium alloys. *Physica B+C* 94(1): 101–104.

Hensel F (2010) The metal-nonmetal transition in fluid mercury: Landau-zeldovich revisited. In: Redmer R, Holst B, and Hensel F (eds.) *Metal-to-Nonmetal Transitions*, vol. 132, pp. 23–35. Springer.

Hensel F and Warren WW (2014) *Fluid Metals*. Princeton University Press.

Herbert JM and Coons MP (2017) The hydrated electron. *Annual Review of Physical Chemistry* 68(1): 447–472.

Hutter J (2012) Car-parrinello molecular dynamics. *Wiley Interdisciplinary Reviews: Computational Molecular Science* 2(4): 604–612.

López-Martín JL, Lomba E, Kahl G, Winn MD, and Rassinger M (1997) An integral-equation approach to the electronic structure of liquid silicon. *Journal of Physics: Condensed Matter* 9(16): 3321.

March NH (1990) *Liquid Metals - Concepts and Theory*. Cambridge: Cambridge University Press.

Marques MAL, Ullrich CA, Nogueira F, Rubio A, Burke K, and Gross EKU (2006) *Time-Dependent Density Functional Theory*, vol. 706. Springer Science & Business Media.

Marsalek O, Uhlig F, Vandevondele J, and Jungwirth P (2012) Structure, dynamics, and reactivity of hydrated electrons by ab initio molecular dynamics. *Accounts of Chemical Research* 45(1): 23–32.

Martin RM (2020) *Electronic structure: Basic theory and practical methods*. Cambridge University Press.

Pastore G, Senatore G, and Tosi MP (1981) Electric resistivity and structure of liquid alkali metals and alloys as electron-ion plasmas. *Physica B+C* 111(2-3): 283–290.

Per MC and Cleland DM (2020) Roadmap on post-dft methods for nanoscience. *Nano Futures* 4(3): 032004.

Pilgrim W-C, Szubrin D, Demmel F, Orecchini A, Rols S, Laloni A, and De Francesco A (2018) New perspectives onto the metal-to-non-metal transition in expanded liquid metals. *EPL (Europhysics Letters)* 122(3): 36005.

Ruland W and Hensel F (2010) Critical region and metal-nonmetal transition in expanded fluid mercury: Advanced evaluation of small-angle X-ray scattering data. *Journal of Applied Crystallography* 43(2): 244–249.

Steenbergen KG, Pahl E, and Schwerdtfeger P (2017) Accurate, large-scale density functional melting of Hg: Relativistic effects decrease melting temperature by 160 K. *The Journal of Physical Chemistry Letters* 8(7): 1407–1412.

Stratt RM (1990) The electronic structure of liquids. *Annual Review of Physical Chemistry* 41(1): 175–205.

Takeda S, Kawakita Y, Inui M, Maruyama K, Tamaki S, and Waseda Y (1996) Electron-ion correlation in liquid metals. *Journal of Non-Crystalline Solids* 205: 365–369.

Ziman JM (1961) A theory of the electrical properties of liquid metals. I: The monovalent metals. *Philosophical Magazine* 6(68): 1013–1034.

Supercooled liquids

Paola Gallo and Mauro Rovere, Dipartimento di Matematica e Fisica, Università "Roma Tre", Roma, Italy

© 2024 Elsevier Ltd. All rights reserved.

Introduction 171
Overview of metastable states: From supercooled liquid to glass 172
Dynamics of supercooled liquids 173
Diffusion 173
Fragile and strong liquids 174
Slow dynamics 175
Supercooled water 177
No man's land and glassy states of water 177
The second critical point and two forms of liquid water 178
Dynamics of supercooled liquid water 179
Conclusion 180
Further reading 180

Abstract

We consider the phenomenology of a liquid rapidly quenched below its melting point. The metastable state obtained is called supercooled liquid and its behavior shows many interesting and peculiar features. The supercooled liquid can be further quenched to approach the transition to the glassy state. Glasses are amorphous solids with a disordered structure, they are relevant in many applications. The glass transition takes place in a metastable region and it is characterized by a very interesting phenomenology. In approaching the glassy state supercooled liquids show a slowing down of the dynamics and a rapid increase of the viscosity of many order of magnitude. We will discuss how the interplay between thermodynamics and dynamical behavior in the metastable region represents a very challenging problem for statistical mechanics and experiments. As an example of a very important system we consider the supercooled liquid state of water. The experiments are limited by difficulties in avoiding crystallization. For this reason computer simulation has played a very important role in the study of supercooled water. This is still a topic of a large amount of research both for experiments and theories with many open questions.

Key points

- Consider substances kept liquid below the melting point to obtain supercooled liquids.
- Consider the thermodynamics and dynamical properties of supercooled liquids.
- Describe the transition to the glassy state.
- Consider the classification of glass formers materials in terms of fragile and strong materials.
- Describe the slow dynamics of the supercooled liquids in approaching the glass transition.
- Assume as an important example the case of supercooled liquid water.
- Show the peculiar behavior of water in approaching the glass transition with the presence of a second critical point connected to a fragile to strong transition.

Introduction

In the area of condensed matter physics the systems under study are composed by many interacting atoms. These systems are present in our life in different forms, for instance we are accustomed to see water at ambient conditions as a liquid, upon heating it becomes vapor (gas) and after some time in a freezer it becomes ice. Normally the phase diagram of a single component system is characterized by the three equilibrium phases gas, liquid and solid. The solid equilibrium phase is the crystalline structure. From the microscopic point of view in the gas and liquid phases the atoms are in disordered configurations, they move continuously while in the crystal the atoms are located on precise positions in the space. However in our everyday activities we have to deal sometimes with materials that are not in an equilibrium state. The most well known are the sheets of glass in our window panels. Glass is a particular state of matter, it is a solid characterized by a disordered arrangement of the atoms. For this reason the glasses are called amorphous solids to distinguish them from the crystalline solids. Glassy materials are not in equilibrium but they persist in their state for very long time and for this reason it is usual to consider the glassy state as metastable. It is important in physics to understand the phenomenon of transition from a liquid to a glass. In order to reach the glassy state from the liquid the substance must be kept liquid below its melting point upon cooling. Such liquid is called supercooled liquid. Experimental methods, theoretical approaches, and computer simulations gave important insight in studying the phenomenon. In experiments special

https://doi.org/10.1016/B978-0-323-90800-9.00146-3

techniques can be applied to a system in the liquid phase to avoid the crystallization below the melting point. The supercooled liquid is an important metastable state of matter and its study sheds light on the mechanism of formation of glasses and on other relevant phenomena that are observed in different materials of interest in technological application, in biology and in medicine.

Overview of metastable states: From supercooled liquid to glass

The values of temperature, pressure and number of moles, considered as the external constraint variables, usually determine the state of a substance. According to Thermodynamics, equilibrium states are defined by the conditions of minimum of the appropriate thermodynamic potential for the given external constraints. For instance at constant pressure p, temperature T and fixed number of moles the thermodynamic potential to consider is the Gibbs free energy

$$G = U - TS + pV \tag{1}$$

where U is the internal energy, S the entropy and V the volume.

The lifetime of an equilibrium state is infinite and only changes in the external variables can induce a transition to another state. It is well known for instance that a liquid can be transformed in a crystal upon decreasing the temperature. The temperature of the transition changes by varying the pressure. The liquid and solid phases coexist along a freezing/melting line defined in the T, p plane.

Upon cooling the process of formation of the crystalline phase is not rapid in terms of microscopic time scales. It starts with the formation of a nucleus where the atoms are ordered in a regular pattern. In order to form a crystal the nucleus must diffuse and grow. But as long as the crystalline pattern grows, the viscosity increases slowing down the diffusion. The consequence is an increase of the relaxation time τ_{relax} to equilibrium. With a fast enough quenching procedure the crystalline growth can be frustrated and the system remains in the liquid state. Eventually with appropriate quenching rate the supercooled liquid can be driven in an amorphous solid state. The quenching rate necessary to bypass crystallization depends on the chemical composition of the material. For instance it can be estimated of the order of 10^{-2} K/s, for system like SiO_2 or GeO_2 and it increases up to 10^9 K/s for metallic glasses.

To understand why a glass can remain as such for a long time we must consider that below melting the free energy has a minimum at the stable crystalline state but it is possible under some conditions the existence of other local minima located at higher levels. If a local minimum is separated from the stable state by a very high barrier, see Fig. 1, the system remains trapped in the metastable state. To be more precise it results that the lifetime of the state is such that $\tau_{life} > \tau_{obs}$, where τ_{obs} is the typical observation time of experiments.

The transition from liquid to glass is not a conventional phase transition between equilibrium states, however as long as the condition $\tau_{life} > \tau_{obs}$ is satisfied it is possible to use thermodynamic concepts, as we will see below.

Many systems show a transition from the supercooled liquid to a glassy state. In a glass the atoms are not located in precise positions but the local arrangement of the atoms, called short range structure, sometimes resembles that of the corresponding crystal. The terms amorphous solid is often used as synonymous of glass. There are also systems, like water, where it is difficult to drive directly the supercooled liquid to the glassy state, the amorphous ice. Given the importance of water we will discuss its case later.

In Fig. 2 it is represented the behavior of the enthalpy $H = U + pV$ as function of temperature. This thermodynamic potential is the most used in experiment on melting that are performed at constant pressure since it gives a measure of the work required for changing volume. As usual in the liquid phase the enthalpy decreases at decreasing temperature and at the melting point T_m there is a change ΔH related to the latent heat of fusion (or solidification). If the system is maintained in the supercooled liquid state the

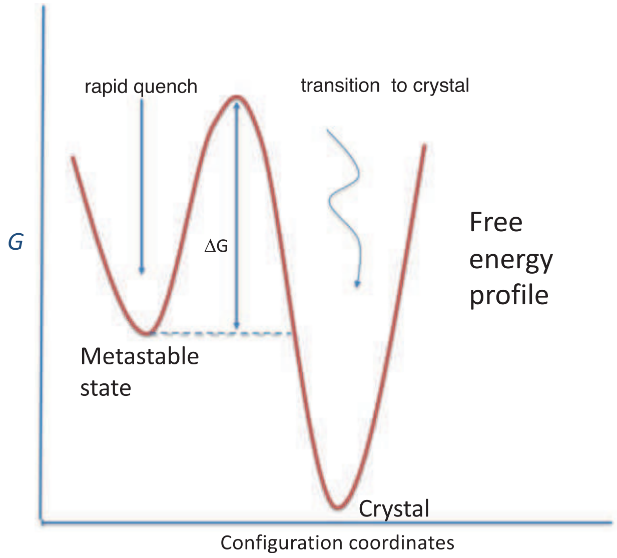

Fig. 1 Schematic representation of a possible Gibbs free energy profile below melting as determined by the system configuration. From the upper stable liquid state it is possible upon cooling to reach the crystal stable state but with a very rapid quench the system can be driven to a metastable state. The higher the barrier ΔG between the higher and the lower minima the more the lifetime of the metastable state is increased.

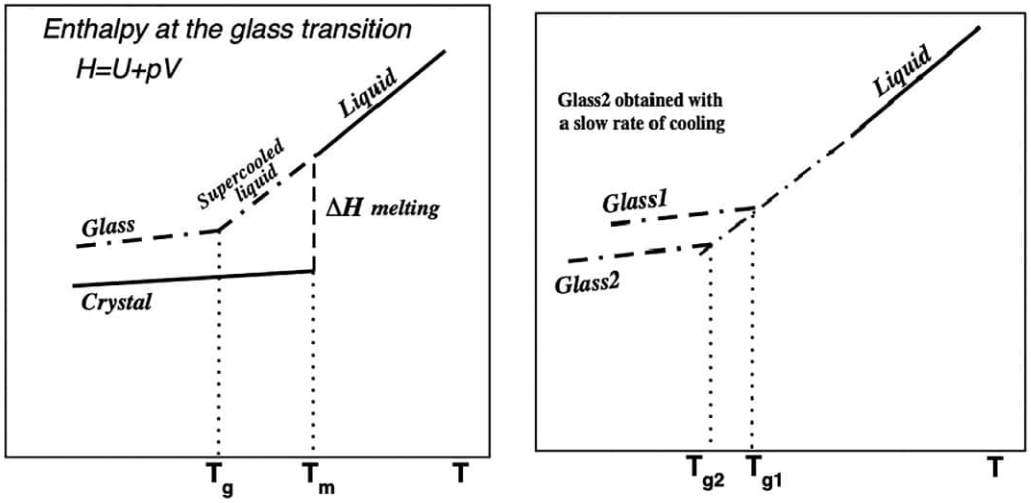

Fig. 2 Enthalpy change upon cooling. On the left T_m is the melting temperature. T_g is the glass transition temperature. On the right side the transitions to *Glass1* takes place at a higher temperature with respect to *Glass2* due to the different quenching rate.

enthalpy keeps to decrease as a continuous function. At the transition to the glassy state, $T = T_g$, it is usually observed a change in the slope and the enthalpy decreases in similar way as in the crystalline phase.

It has to be noted that while the melting temperature has a fixed value, since the liquid-glass transition does not occur between two equilibrium phases the glass transition temperature T_g depends on the quenching rate. By slowing down the cooling rate it is found a lower glass transition temperature. A schematic example is shown in the right side of Fig. 2.

So by slowing down the quenching rate it is possible to decrease T_g. Kauzmann explored the possibility of predicting an asymptotic glass transition temperature. He observed from the phenomenology that the entropy of the supercooled liquid decreases more rapidly than the entropy of the crystal and he deduced that it could exists a temperature where the entropy of the supercooled liquid could reach and cross the curve of the crystal entropy. The temperature T_K, that we call now Kauzmann temperature, is defined as the temperature where

$$S_l(T_K) - S_{cr}(T_K) = 0. \tag{2}$$

where S_l and S_{cr} are respectively the liquid and crystal entropy. Kauzmann realized that for $T < T_K$ the more disordered liquid state would have an entropy lower with respect to the ordered crystal. In order to avoid this paradox Kauzmann suggested that a crystallization would occur in approaching T_K. Estimations of T_K require extrapolations of experimental data well below T_g. The Kauzmann hypothesis has been widely discussed in literature. It has been suggested that the Kauzmann temperature would correspond to a limit of very slow supercooling process with the liquid attaining an ideal glass transition.

Dynamics of supercooled liquids

Diffusion

The motion of the atoms in a liquid is characterized by different regimes of diffusion. Each atom is surrounded by nearest neighbor but in the initial time it moves freely. This is called ballistic regime. After a period of time the atom starts to collide with the others and the diffusion enters in a more complex regime. This type of motion with frequent collisions is related to the old studies performed by the botanist Robert Brown in 1827 on the motion of pollen suspended in water. In 1905 Einstein reconsidered the work done by Brown and he developed a more general theory of the diffusion based on statistical mechanics. The diffusion of atoms can be studied by considering the displacement of an atom $r(t)$ from the initial position at $t = 0$. Since the motion is completely random the average on the time indicated with $\langle \ldots \rangle$ will give $\langle r(t) \rangle = 0$. For this reason to study the phenomenon we must consider the mean square displacement(MSD). The average on the time obtained in experiments is replaced in the theoretical approach by the statistical mechanics average, realized by averaging on a great number of trajectories.

The MSD is one of the important quantities that connects directly our macroscopic measure to the microscopic behavior. Einstein introduced the diffusion coefficient D as a phenomenological parameter and he found that along each direction in the long time limit $\langle x^2(t) \rangle \rightarrow 2Dt$. So the MSD increases linearly with the time following in three dimensions the Einstein relation

$$< r^2(t) > = 6Dt. \tag{3}$$

The diffusion of atoms in the liquid can be studied by experiments and simulations. It is observed that the diffusion is strongly determined by the thermodynamic conditions as represented in Fig. 3. In a liquid above melting after the ballistic regime for the frequent collisions the diffusion process enters in the Brownian regime described by the Einstein relation. From the long time slope the diffusion coefficient can be determined.

Upon supercooling it is observed a strong modification. After the ballistic regime it appears a plateau. Below melting, even if it is avoided the transition to a crystalline structure, there is a formation of a cage of nearest neighbors around each atom. At variance

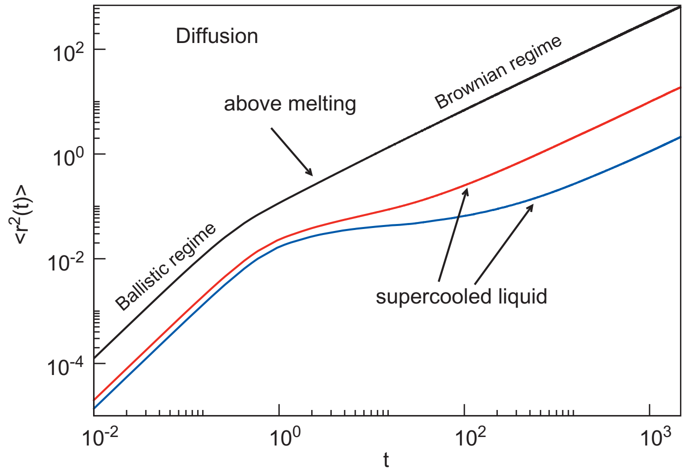

Fig. 3 Mean square displacement as function of time for decreasing temperatures.

with crystal the cage persists for a short time, but the region of the plateau corresponds to the period in which the atom is trapped in the cage. This is called cage effect. After a certain amount of time the cage relaxes and the diffusion starts again in the Brownian regime. The length of the plateau increases upon decreasing temperature.

Fragile and strong liquids

Related to the diffusion in liquid it is also the viscosity, indicated as η. The viscosity is intended as the friction due to the collisions that slows down the velocity of the moving particles. An higher viscosity reduces the diffusion. For spherical particles of radius r_0 they are related through the Stokes-Einstein formula

$$D = \frac{k_B T}{6\pi r_0 \eta}. \tag{4}$$

It is well known that a large increase of the viscosity is observed in approaching a transition to a solid state. By collecting the experimental measures of a large number of glass formers Angell found evidence that the viscosity increases of many order of magnitude in the supercooled liquid and it reaches a common value at the glass transition. He proposed as definition of T_g the temperature at which the viscosity η is found to be

$$\eta = 10^{13} \text{ poise} \tag{5}$$

By considering the behavior of the viscosity in approaching the common value at T_g Angell introduced a precise classification of the glass former materials. Two types of phenomenology are found, as shown schematically in Fig. 4.

There are systems, classified as strong glass formers, where *log*(η) increases linearly. This behavior is called *à la* Arrhenius and it is the most simple to explain

$$\eta(T) = \eta_0 e^{E_A/k_B T} \tag{6}$$

where E_A is the activation energy and η_0 is the limit at high temperature. In an Arrhenius process it is considered that a particle can move by overcoming a potential barrier with E_A the energy required.

In the category of strong liquids there are systems like SiO_2 and GeO_2. This glass formers are characterized by a tetrahedral local order that does not change going to the glassy state. As a consequence it is found a small change in the specific heat across T_g.

Other systems, called fragile, show a so called super Arrhenius behavior. η approximately follows the Vogel-Fulcher-Tamman (VFT) phenomenological formula

$$\eta = \eta_0 \exp\left[\frac{BT_0}{T - T_0}\right] \tag{7}$$

where T_0 is an hypothetical temperature below T_g where η would diverge. The parameter B is related to the degree of fragility, since smaller values of B correspond to higher fragility.

Fragile liquids, as for instance glycerol or ethanol, show a complete change in their local structure with a large change in the specific heat across T_g. The motion of the particles in fragile liquids upon supercooling is determined by a sequence of overcoming barriers in a configurational space more complex with respect to the case of strong liquids.

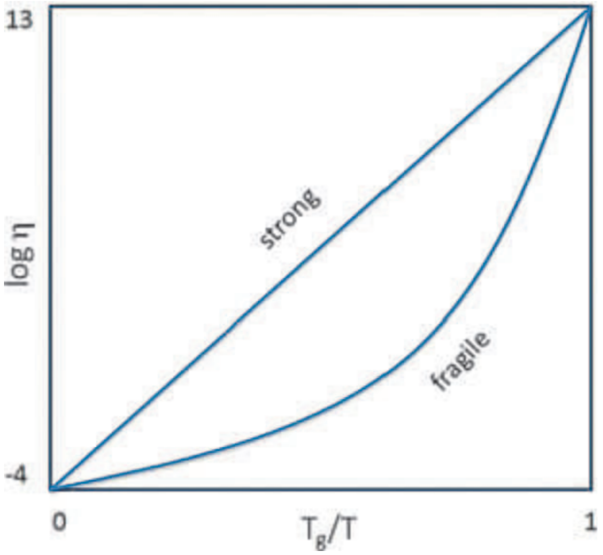

Fig. 4 Behavior of log η as function of T_g/T: strong behavior as Eq. (6), fragile behavior as Eq. (7).

Slow dynamics

The thermodynamic conditions determine the macroscopic density of the fluid ρ_0. At the microscopic level the atoms move continuously. The local density of the particles $\rho(r, t)$ fluctuates around the equilibrium value ρ_0. During fluctuations the particles usually move from a zone at higher density to a zone with lower density to partially restore the equilibrium. In order to study more in details the density fluctuations we have to consider that the microscopic fluctuation in a position r at time t

$$\delta\rho(r, t) = \rho(r, t) - \rho_0$$

is correlated to the fluctuation in another position r' at a different time t' of another or the same particle. In the study of the diffusion we follow the motion of a single particle. In similar way we can follow the fluctuations of the density of a single particle $\rho_s(r, t)$ and look how the fluctuation at a certain time and position is related to a previous fluctuation in a different position and time. For this purpose we can introduce the statistical average of the product of the single particle fluctuations

$$C_s\ (r - r',\ t - t') = \langle \delta\rho_s(r,\ \ t)\,\delta\rho_s(r',\ \ t')\rangle \tag{8}$$

This is the self correlation function that in an homogeneous system depends from the differences $r—r'$ and $t—t'$.

The Fourier transforms of density correlation functions are accessible to neutron scattering experiments. By considering the Fourier transform of the single particle density fluctuations $\delta\rho_s(k, t)$ it is possible to define the self intermediate scattering function as

$$F_s(k,\ t) = \frac{1}{N}\langle \delta\rho_s(k,\ \ t)\,\delta\rho_s(-k,\ \ 0)\rangle \tag{9}$$

From its definition $F_s(k, t = 0) \to 1$.

In liquids above melting the behavior of the $F_s(k, t)$ is represented in Fig. 5 (black curve) for a wave vector $k = k_0$ where $k_0 \approx 2\pi/r_0$ with r_0 the nearest neighbor distance between the atoms, the most interesting distance to explore for this phenomenon.

After a short period corresponding to the ballistic regime, the function decays exponentially with the Debye equation

$$F_s(k,\ t) = e^{-t/\tau} \tag{10}$$

where it is introduced the relaxation time τ, that measures the time needed to the system to reach the equilibrium. So τ is connected to diffusion and viscosity. In particular it results that

$$\tau = cost\frac{T}{D} \propto \eta \tag{11}$$

according to Eq. (4) τ is proportional to η.

In the supercooled liquid it is observed a change in the behavior of $F_s(k, t)$ due to the cage effects. As shown in Fig. 5, a plateau appears in correspondence to the period in which the atom is trapped in the cage. The long time decay is modified in the form of a stretched exponential

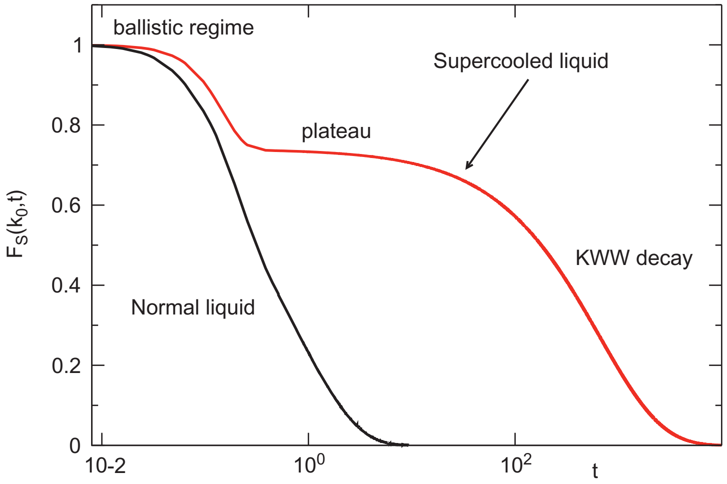

Fig. 5 Behavior of $F_s(k_0, t)$ for a liquid above melting and for a supercooled liquid. In the normal liquid (black curve) after the ballistic regime the function decays exponentially. In the supercooled liquid (red curve) after the ballistic regime the function shows a plateau and it decays with the KWW function.

$$F_s(k,\ t) \approx e^{-(t/\tau)^{\beta}} \tag{12}$$

where it is found that the exponent $\beta < 1$. This type of decay is called Kohlrausch-Williams-Watts (KWW) function. The relaxation time τ increases of orders of magnitude with decreasing temperature with a different behavior expected for fragile and strong liquids since from Eq. (11) $\tau \propto \eta$.

The dynamical behavior of supercooled liquids has been studied and interpreted by several theories and models.

One of the most famous theoretical approach is the Mode Coupling Theory for the evolution of glassy dynamics (MCT). The MCT is a microscopic theory that provides an unified description of the dynamical properties of supercooled liquids. The cage effect and the long time decay of the correlation functions are derived from first principles starting from the only input of the static structure of the liquid. The glass transition is interpreted in terms of a transition from an ergodic regime where the system can reach an equilibrium state after the cages are dissolved to a non ergodic regime where the dynamic of the liquid is arrested. In particular the plateau in both the case of the diffusion and the dynamic correlation functions extends to infinity. The crossover would take place at a specific temperature T_C. The relaxation time τ introduced above will become infinite with a power law

$$\tau \sim (T - T_C)^{-\gamma}\ . \tag{13}$$

where γ is an exponent related to the microscopic properties of the liquid. According to MCT, by considering Eq. (11) the diffusion constant goes asymptotically to zero for $T \rightarrow T_C$. In summary the MCT predicts the glass transition in terms of an ideal ergodic to non ergodic cross over taking place at a temperature T_C that results higher with respect to the conventional glass transition temperature T_g. The MCT predictions can be tested by experiments in terms of asymptotic behavior of the diffusion and the long time decay of the density correlation functions.

Often MCT works only in the regime of mild supercooling where extended structural relaxation drives the system toward ergodicity. In the deep supercooled region for many glass formers when the structural relaxations are frozen hopping (activated) processes restore ergodicity. In this regime the system explores the valley of the free energy landscape.

Adam and Gibbs connected the relaxation to equilibrium of supercooled liquid in the deep supercooled regime with the entropy of the system. In particular they consider the role of the configurational entropy S_c that is approximately identified as the difference between the liquid entropy and the crystal entropy. S_c is related to the number of available glassy states at the given temperature and pressure conditions. Adam and Gibbs found for the relaxation time the equation

$$\tau \propto \exp\left[\frac{\alpha}{TS_c(T)}\right]. \tag{14}$$

In the supercooled liquid approaching the glassy state S_c decreases, as consequence of the decrease of the possible configurations for the system. S_c can be derived from phenomenological observations of quantities like the specific heat in approaching the glass transition, in particular the configurational part of the heat capacity can be approximated as proportional to the inverse temperature

$$C_c \approx \frac{c}{T}, \tag{15}$$

this can be integrated to obtain S_c. By assuming that it exists a temperature T_0 for which $S_c\ (T \rightarrow T_0) = 0$ the configurational entropy can be calculated as

$$S_c(T) = \int_{T_0}^{T} \frac{c}{(T')^2}\, dT', \tag{16}$$

and substituting in Eq. (14) we obtain

$$\tau = \tau_0 \exp\left[\frac{BT_0}{(T - T_0)}\right]. \tag{17}$$

the VFT formula introduced before as obtained from experimental data.

Supercooled water

Among all glass formers water singles out because its behavior is characterized by anomalous properties in comparison with other substances. The most well known anomaly is the fact that ice is less dense than liquid water. Upon decreasing temperature the density of liquid water increases as usual but at a temperature of 4 °C at ambient pressure the density starts to decrease. The change of slope of the density vs. temperature defines a temperature of maximum density (TMD). The line of the TMD as function of pressure extends just above the melting line. At melting it is found that the density of the crystalline phase ρ_{crys} is less than the density of ρ_{liq}. The reason is connected to the particular structure of liquid water and ice. The structure is based on the formation of hydrogen bond (HB) between water molecules. As shown in Fig. 6 the water molecule is formed by the bond of an oxygen and two hydrogens. In the H_2O molecule the oxygen remains with two lone pairs of electrons and it has an effective negative charge while each hydrogen in the bond with the oxygen results to have a positive charge. The negative lone pair can attract the positive hydrogen of another molecule to form the so called hydrogen bond (HB). If enough molecules are present each molecule results to be connected to other four as shown in the figure. The pentamer shown in the figure is the nucleus of the crystalline structure of ice.

No man's land and glassy states of water

Because of its strongly stable pentameric structure water has a very strong tendency to crystallize. Even the ice cubes contained in our freezer are polycrystalline and made of small single crystal grains of hexagonal ice, which is the stable state of ice at ambient pressure. As a consequence the quenching of liquid water below melting to enter in the supercooled region is more difficult than in other liquids. Beside, the presence of impurities favors the formation of ice nuclei and the crystallization. By appropriate experimental techniques the concentration of impurities can be restricted, in this way the temperature of the onset of crystallization can be reduced. By extrapolating, it is possible to define for any pressure a limiting value for the temperature of supercooling. This temperature is called the homogeneous nucleation temperature, indicated with T_H. The curve of T_H as function of pressure has been for many years the lowest limit for performing experiments on supercooled water. In particular they were left without explanation the experimental observations of the anomalous increase of quantities like the isothermal compressibility K_T and the isobaric specific heat C_p upon supercooling in approaching the T_H line, as shown in Fig. 7.

This type of strong increase of K_T and C_p is observed when a liquid approaches the liquid-gas transition as a precursor effect of the divergence of those quantities at the critical point.

New more recent methods have been successful in supercooling below the homogeneous nucleation temperature. Amorphous ice systems can be obtained by overtaking the region of supercooled liquid for instance by rapid quenching directly from the vapor. Two different amorphous ice states have been found, see Fig. 8. At lower pressure the low density amorphous (LDA) that coexists with the high density amorphous (HDA) at higher pressure. The coexistence line is close to 200 MPa and a first order transition is observed between the two states with changes in volume and enthalpy. LDA and HDA are characterized by different local structures. LDA shows a more ordered short range structure similar to a tetrahedral network, while in HDA the molecules are arranged in a more disordered structure where the tetrahedral short range order is lost.

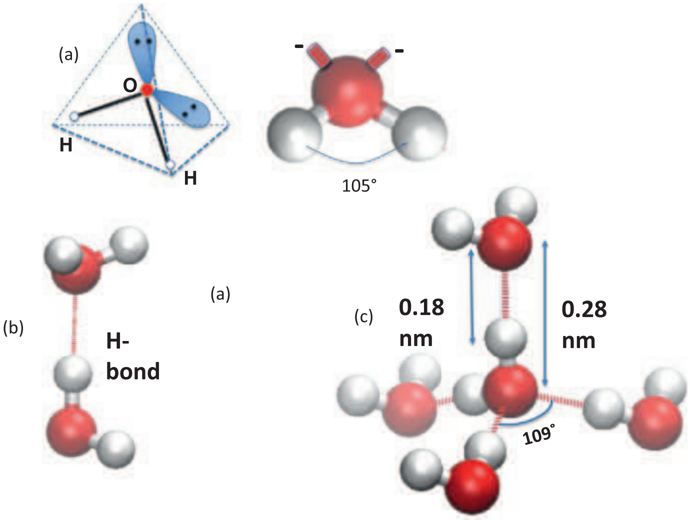

Fig. 6 (a) water molecule, (b) H-bond between two molecules, (c) HB between four water molecules.

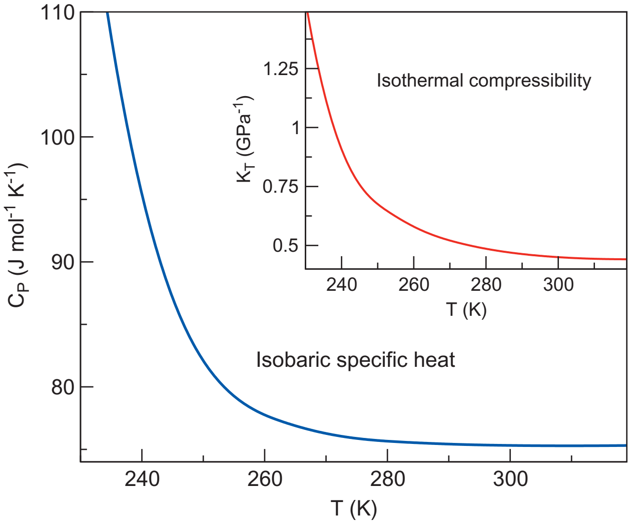

Fig. 7 Isobaric specific heat and isothermal compressibility of water upon supercooling.

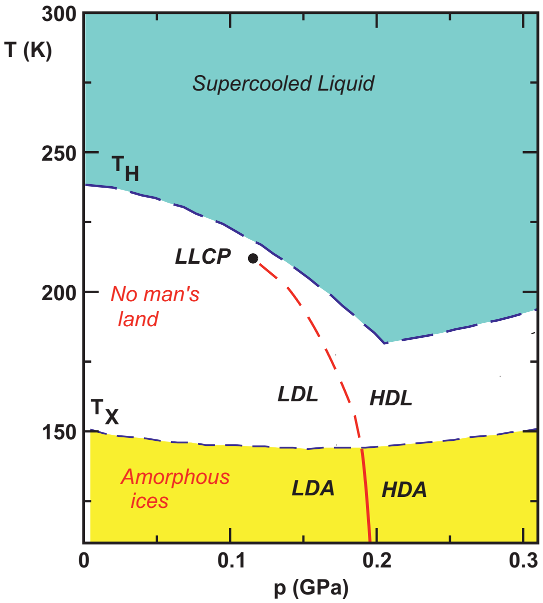

Fig. 8 Phase diagram of supercooled liquid water and amorphous ice states. The LDA/HDA coexistence evolves in the LDL/HDL coexistence in the no man's land, where it would be present a liquid-liquid critical point (LLCP).

LDA and HDA undergo a glass transition at around 136 K, above 136 K it is found an high viscous liquid that at ambient pressure crystallizes in a cubic ice at 150 K. In analogy with the definition of the homogeneous nucleation line T_H it is possible to define a temperature of spontaneous crystallization T_X. The lines of T_H and T_X as function of pressure delimit from above and below respectively the so called *no man's land*, where supercooled water is very difficult to study by experiments.

The second critical point and two forms of liquid water

In the *no man's land* region recent extensive computer simulations and experiments gave access to a rich phenomenology, see Fig. 8. The LDA and HDA upon increasing temperature above the line T_H undergo a transition to two forms of liquid, called for analogy with the glassy states, low density liquid (LDL) and high density liquid (HDL). LDL and HDL keep local structures very similar to the corresponding glassy states. The great difference is that the coexistence line LDL/HDL would terminate in a critical point, called liquid-liquid critical point (LLCP), hypothesized by Poole, Sciortino, Essmann, and Stanley in 1992. On the basis of results of computer simulations and extrapolation of experiments the LLCP was estimated to be in the *no man's land* at around 220 K at a pressure of 100 MPa approximately. The presence of this second critical point could explain the experimental observations of the anomalous increase of the isothermal compressibility K_T and the isobaric specific heat C_p in approaching the border of the no man's land.

It is found that the LDL configuration is characterized by a lower entropy and energy with respect to the HDL structure. In LDL in fact the short range order is similar to the tetrahedral arrangement observed in ice. In the HDL structure instead there is a collapse of the tetrahedral structure making possible to reach an higher density.

We have already seen that in a fluid the microscopic fluctuation of the density in a position r is correlated to the fluctuation in another position r'. In normal thermodynamic conditions the density fluctuations in different points are correlated in a range determined by the correlation length ξ. Upon approaching the critical point the correlation length increases and it diverges at the transition. This induces the large increase and the divergence of K_T and C_p since they become proportional to powers of ξ.

As in the case of the liquid-gas transition also for the LLCP we can consider more in details the behavior of the system in approaching the critical point from the single phase region. It is found that both the isothermal compressibility and the specific heat start to show maxima along lines that finally collapse on the so called Widom line, the locus of the maxima of the correlation length that extends from the critical point toward the single phase region. In the case of the liquid-gas transition the Widom line close enough to the critical point separates liquid-like states from gas-like states in the single phase region.

In computer simulations the Widom line can be located by searching the maxima of the specific heat or the isothermal compressibility in the single phase region. At the crossing of the critical point the Widom line will be connected to the coexistence line in the two phase region. We will show below that the Widom line has an important role in the classification of the dynamical behavior of supercooled water.

In order to validate the results obtained with different water models in computer simulations, the liquid-liquid transition in supercooled water has been studied also with very refined methods of calculation of the free energy already typically used for the analysis of the second order phase transitions. The free energy was considered as function of two order parameters: the density and also a bond orientational order parameter that indicates the degree of crystalline order to exclude the formation of ice upon cooling.

Recent interpretations of experiments and computer simulations start to consider liquid water as a mixture of the two competing states with different short range order HDL and LDL. With refined numerical analysis it is possible to evidence that water show a bimodal distribution of the two components. At ambient conditions the HDL component prevails but upon supercooling the LDL component appears and at low enough temperature starts to prevails. The liquid behaves similarly to a non ideal binary mixtures dominated by an interplay between energy and entropy. In this respect the critical point will be determined by an entropy driven unmixing process.

A number of recent experiments evidenced the presence of LDL/HDL states in agreement with the theoretical predictions.

A clear support to the two state model and the liquid-liquid transition derives also from the study of the dynamical behavior of supercooled water.

Dynamics of supercooled liquid water

If we want to study the dynamics of translational motion of the water molecules we have to consider the diffusion and the density fluctuations of the center of mass of the molecules that corresponds approximately to the position of the oxygen. Supercooled water show a dynamical behavior very similar to the other supercooled liquids but with a very important peculiarity related to the presence of the LDL/HDL components.

The self intermediate scattering function of the oxygen's obtained by computer simulation upon supercooling, shows a long time KWW decay characterized by the stretched exponential

$$F_s^{OO}(k, \quad t) \approx e^{-(t/\tau)^\beta} \tag{18}$$

In a range of temperature below melting the relaxation time τ follows the MCT prediction of a power law divergence, Eq. (13). However at given pressure in a range of density by going down in temperature it is found a crossover to an Arrhenius behavior, by recalling Eq. (6) and that $\tau \sim \eta$

$$\tau(T) = \tau_0 e^{E_A/k_B T} \tag{19}$$

In Fig. 9 it is shown the data obtained in the simulation of supercooled water with the use of the TIP4P/2005 model. The data can be fitted with the MCT until a certain temperature then it appears a clear deviation and the remaining points follow an Arrhenius behavior.

According to the classification introduced above this crossover from a fragile (MCT type) to a strong (Arrhenius type) behavior can be interpreted by considering that HDL and LDL have a more fragile and a more strong character respectively.

A detailed analysis in all the range of the supercooled region shows that the fragile to strong crossover (FSC) takes place at the crossing of the Widom line as shown in the scheme in Fig. 10.

These phenomenologies were observed with quasi elastic neutron scattering and optical Kerr effect measurements.

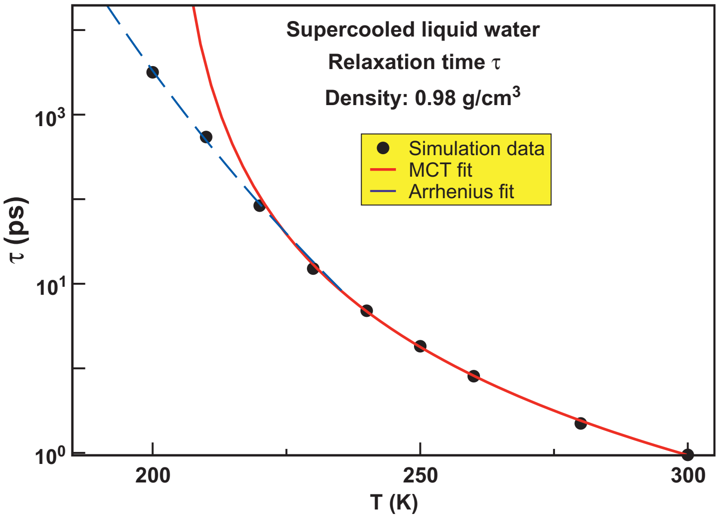

Fig. 9 Relaxation time of water (in logarithmic scale) at the indicated density. The black points are the data from computer simulation with the TIP4P/2005 model, the MCT fit is obtained with Eq. (13) by assuming T_C as a fitting parameter, the Arrhenius fit is obtained with Eq. (19).

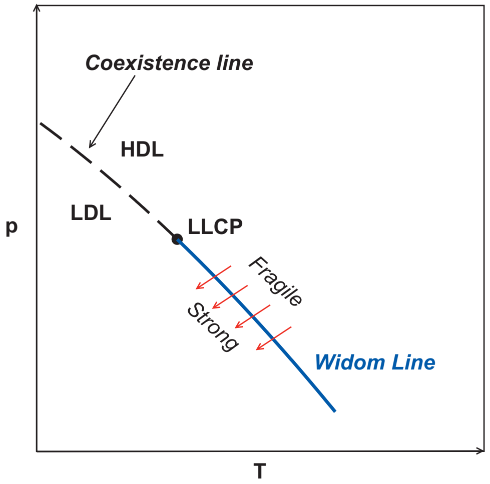

Fig. 10 Schematic representation of the phase diagram of supercooled water close to the LLCP. The coexistence line separates the LDL and HDL forms of water. The Widom line in the single phase region separates the HDL like from the LDL like regions.

Conclusion

Supercooled liquids represents an important metastable state characterized by very peculiar connections between thermodynamics and dynamical properties. The microscopic processes that produce the slowing down of dynamics and the corresponding increase of viscosity in approaching the glassy state are widely studied with various techniques in experiment and in computer simulation. Supercooled liquids are in fact important for applications, developing technologies and development of new materials.

Further reading

Debenedetti PG (1996) *Metastable Liquids. Concepts and Principles*. Princeton: Princeton University Press.
Debenedetti PG and Stillinger FH (2001) Supercooled liquids and the glass transition. *Nature* 410: 259–267.
Gallo P and Rovere M (2021) *Physics of Liquid Matter*. Cham, Switzerland: Springer International Publishing.
Gallo P, et al. (2016) Water: A Tale of Two Liquids. *Chemical Reviews* 116: 7463–7500.
Götze WG (2009) *Dynamics of Glass-Forming Liquids: A Mode-Coupling Theory*. Oxford: Oxford University Press.
Poole PH, Sciortino F, Essmann U, and Stanley HE (1992) Phase behaviour of metastable water. *Nature* 360: 324–328.

Glasses

J M Parker, Department of Materials Science and Engineering, Sheffield University, Sheffield, United Kingdom

© 2024 Elsevier Ltd. All rights reserved.

This is an update of J.M. Parker, Glasses, Editor(s): Franco Bassani, Gerald L. Liedl, Peter Wyder, Encyclopedia of Condensed Matter Physics, Elsevier, 2005, Pages 273–280, ISBN 9780123694010, https://doi.org/10.1016/B0-12-369401-9/00538-6.

Introduction 181
What is a glass? 182
How are glasses made? 182
Glass structure 182
Short-range order 182
Medium-range order 183
Defects 185
Nonsilicate glass-forming systems 185
Crystal growth and phase separation 185
Phase separation 186
Glass formation 186
Viscosity 186
Processing 187
Transformation range effects 187
Thermal properties 187
Mechanical behavior 188
Optical properties 188
Diffusion and electrical behavior 189
Conclusion 190
Further reading 190

Abstract

This overview of glassy materials begins with production methods, highlighting how the homogeneity achieved, the creation of flat surfaces and the elimination of bubbles leads to their inherent transparency. The links between composition, structure and behavior are explained, leading on to an extended discussion of the main properties, ranging from mechanical and chemical durability through thermal, optical, diffusion and electrical characteristics. These properties are linked to common applications.

Key points

- What differentiates glasses from other materials?
- How are they made?
- What are their compositions and structures
- Their thermal, chemical and mechanical properties
- Their optical properties
- Diffusion and electrical behavior

Introduction

Glasses feature widely in everyday life and also in science. Their transparency and chemical durability, combined with ease of fabrication, ensure a role in windows, containers, table- and laboratory-ware; they are key components in optical instrumentation, for example, microscopes, cameras, telescopes and optical fibers. Some devices utilize specific interactions between light and glass, for example, lasers. Other applications use their electrical and magnetic behavior, strength, and thermal characteristics, including crystallization and phase separation. The range and flexibility of known glass compositions allow different properties to be independently tailored. Combining glasses with other materials or modifying their behavior by coating has extended their use further. Understanding glass structure and its consequences is also challenging the boundaries of condensed matter physics.

What is a glass?

Glasses have been defined as inorganic products of fusion cooled to a solid without crystallizing. This encapsulates key properties: glasses have a liquid-like structure, but cooling has caused a transition from liquid to solid behavior. It also implies features that are now disputed: organic glasses exist, and melting is not the only route for glass making. A characteristic implicit in the definition is that crystallization rates are low; this is often associated with high melt viscosities below the liquidus (T_L). Glasses differ from amorphous solids, in that they can be reheated to the liquid state; the latter crystallize on heating before melting (Doremus, 1994; Scholze, 1988; Uhlman and Kreidl, 1990; Varshneya, 1994; Zarzycki, 1991; Ossi, 2003).

How are glasses made?

Often glasses are made from solids by heating until fully melted, bubbles have dissipated, and the melt is homogeneous. Commercially, temperatures may reach 1600 °C and melting may take days. Laboratory melts need a few hours. Density separation of batch components, differential melting rates, contamination by the container, and volatilization losses can limit the glass quality. High melt viscosities limit diffusion and militate against homogeneity; mechanical or convection-driven stirring may be necessary. The oxidation state of any multivalent ions depends on the atmosphere around the batch during initial melting; subsequently, equilibrium with the furnace atmosphere is achieved only slowly. Rapid quenching may be needed, for example, roller quenching, splat cooling onto a rotating copper wheel, or fiber pulling.

Alternative production routes include: condensation of vapor phase reaction products on cold substrates; hydrolysis of organic derivatives of silicon (e.g., $Si(OC_2H_5)_4$) or other components to give a gel that is dried and sintered to a fully dense product; and extended grinding or applying pressure to crystals.

Glass structure

Short-range order

Glass structures have been studied by X-ray or neutron diffraction, various spectroscopic techniques, and computer modeling. Their short-range structure often mirrors that of corresponding crystalline compounds, particularly higher temperature phases. Zachariasen postulated that single-component glass-forming systems have cations with low coordination numbers (3 or 4) surrounded by bridging anions, each linking two coordination polyhedra at corners rather than edges. SiO_2 consists of a matrix of SiO_4 tetrahedra (Fig. 1) that defines its low thermal expansion coefficient (TEC), high viscosity at T_L, and high melting point. Other single-component glass-forming systems include GeO_2, BeF_2, B_2O_3, and As_2O_3.

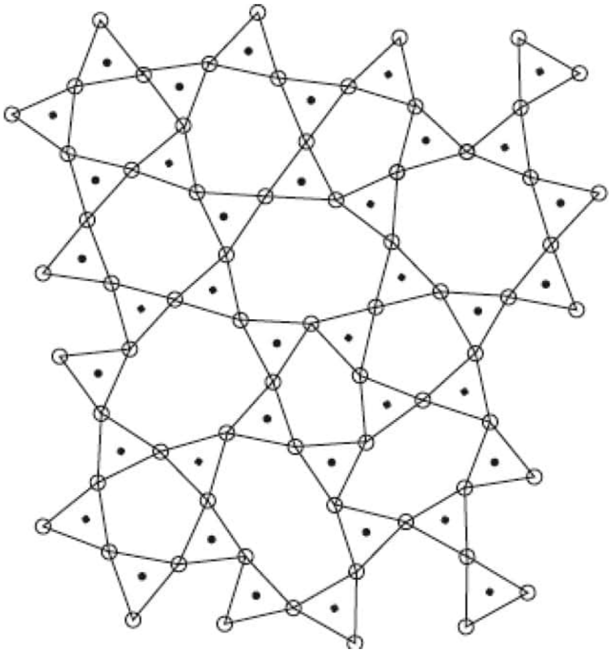

Fig. 1 A schematic representation of the structure of vitreous silica. The tetrahedral SiO_4 units in silica are represented by triangular units.

A second component can extend glass formation, for example, to 58 mol% Na_2O in the Na_2O–SiO_2 system. Each oxygen added breaks one corner linkage in the network, creating two nonbridging oxygens (Fig. 2). Silicons are called "network formers" and sodiums, which enter interstices surrounded by bridging and nonbridging oxygens are termed "network modifiers." A silicon linked to three bridging and one nonbridging oxygen is denoted by Q_3; the spread of Q_n species depends on composition and is generally narrow. Adding soda (Na_2O) increases the TEC and reduces viscosity by depolymerizing the network, while increasing density by filling interstices. Various cations adopt a network-forming role (e.g., Ge, P, Pb). The melt structure, being flexible, can accommodate many modifier ions despite different radii and preferred coordination, for example, Li^+, K^+, Rb^+, Mg^{2+}, Ca^{2+}, Fe^{2+}. Intermediate ions (Al^{3+}, Fe^{3+}) can take either role in the structure. Some oxide combinations form glasses even though the components do not—the network-forming ion is called a "conditional" glass former, for example, Al in CaO–Al_2O_3 glasses. The oxygens can also be (partially) replaced by other anions, for example, F, S, N (Scholze, 1988).

Properties can often be modeled using expressions that are linear functions of composition and the viscosity of industrial glasses is usually calculated rather than measured. Anomalies occur if a cation changes role with composition (e.g., B coordination depends on alkali content); the TECs of M_2O–B_2O_3 glasses display a minimum with composition (the "boric oxide anomaly"), requiring a $[B_2O_3]^2$ term in composition models. Liquidus temperatures, which are discontinuous across phase boundaries, are best modeled using the underlying free energy functions. Components can also interact: Na_2O decreases network connectivity, while Al_2O_3 is a network former at low concentrations and, being oxygen deficient, removes nonbridging oxygens. If Na_2O:Al_2O_3 = 1, a highly connected, viscous system results; excess Na_2O or Al_2O_3 decreases viscosity, in the latter case because Al coordination changes from [4] (former) to [6] (modifier).

Medium-range order

Diffraction experiments give structural data in the form of radial distribution functions, representing the summed distribution of atoms with distance around all species present (Fig. 3); network-forming ions sit in remarkably regular sites but longer distance correlations are harder to resolve because of peak overlap. Extended X-ray absorption fine structure (EXAFS) experiments allow study of the environment of individual species and suggest that network modifiers also sit within polyhedra of notable regularity, that is, all cations optimize their local structure. Such distribution functions show that the network-forming polyhedra can also form extended structures, for example, vitreous B_2O_3 consists of BO_3 triangles, that form planar groupings, termed boroxol rings (B_3O_6),

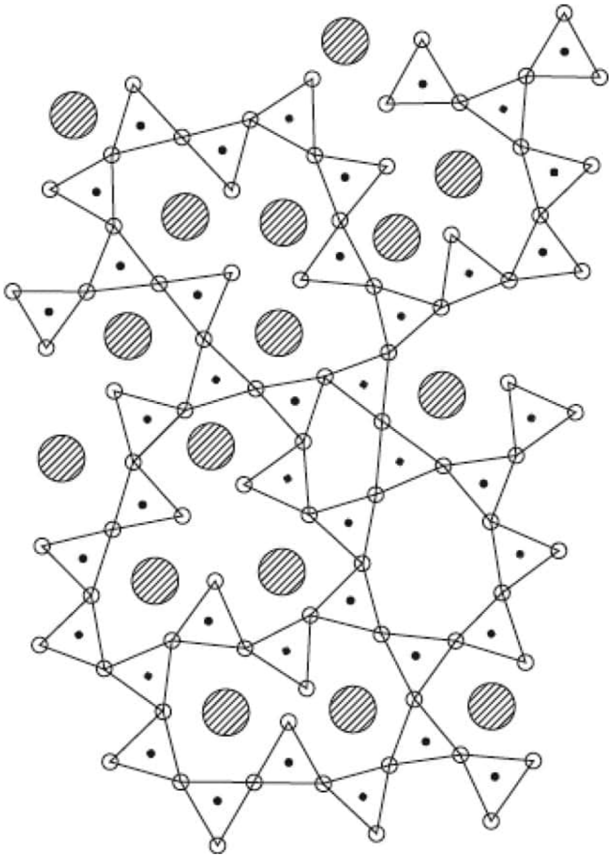

Fig. 2 A schematic representation of the structure of an Na_2O–SiO_2 glass illustrating the break-up of the network by the introduction of nonbridging oxygens (linked to only one Si), and the sites taken by the sodium ions.

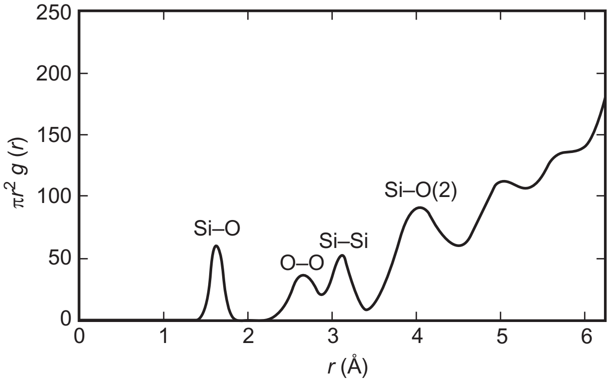

Fig. 3 An idealized radial distribution function for SiO_2. The first four peaks give the distribution of nearest neighbor Os around Si, the Si–Si distribution, the O–O distribution, and the distribution of second nearest neighbor oxygens around Si. The peak areas give coordination numbers and the breadths indicate thermal and structural disorder. A random distribution would give a parabolic curve. Experimental curves show some ripple at low r caused by data termination errors. Many authors now plot correlation functions ($\pi r\, g(r)$) rather than r.d.f.s.

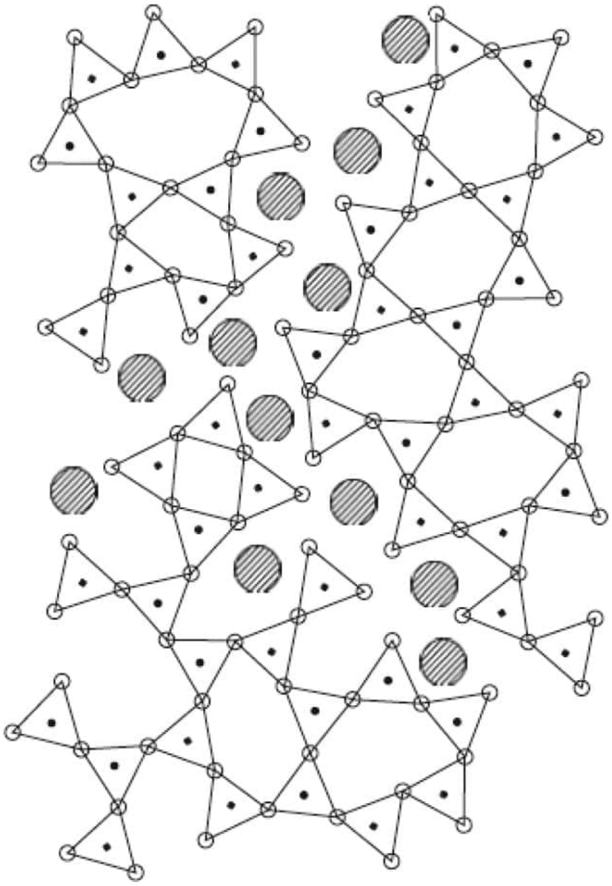

Fig. 4 A schematic representation of the modified random network model for an Na_2O–SiO_2 glass showing the tendency for modifier ions to segregate.

not found in B_2O_3 crystals. The modified random network model for alkali silicate glasses is based on segregation of network modifying atoms into layers surrounding SiO_2-rich regions (Fig. 4). The diffraction patterns for many glasses have a relatively sharp low-angle first diffraction peak, consistent with extended ordering, as confirmed by modeling and electron microscopy. IR spectroscopy supports such structural models by accounting for the network vibrational modes. In Raman and Brillouin scattering experiments, glasses have, as a common feature, a boson peak at 100 cm^{-1} that provides additional insight into nanometer-scale inhomogeneities. Models incorporating medium-range order are distinct from older microcrystallite theories of glass, discounted by the lack of small angle X-ray or neutron scattering beyond that predicted from incipient random fluctuations in density. These conclusions underpin the thermodynamic modeling of glass properties based on contributions from components with appropriate compositions in defined proportions (Zarzycki, 1991).

Defects

Glasses can contain bonding and electronic defects induced by radiation or high temperatures. Their concentrations are low but they influence optical properties by introducing visible or ultraviolet (UV) absorptions and causing refractive index (r.i.) changes. Defects may involve unpaired electrons (*), e.g., the nonbridging oxygen hole center, $\equiv$Si—O*; E′ center, $\equiv$Si*; peroxy radical, $\equiv$Si$_2$—O—O*; or species such as Zr^{3+}, F_2^-. Some defects can be eliminated by optical or thermal bleaching, while others survive for years under normal conditions.

Nonsilicate glass-forming systems

Silicate glasses have three-dimensional (3D) network structures with intermediate ionic/covalent bonds. Alkali phosphate glasses have similar bonding but are often better described as chains (Ropp, 1992) Chalcogenide glasses are largely covalent and based on networks, sheets, chains, and rings. Hydrogen-bonded molecular glasses are common in organic systems (e.g., sugars), while some highly ionic or metallic systems adopt almost random close-packed structures. Various salts (nitrates, sulfates, acetates) also form glasses. Even crystals can show glassy behavior. Spin glasses may form in magnetic systems, based on disordered arrangements of unpaired electron spins, or molecules may have random orientations on a regular lattice as in KBr–KCN. Polymers usually consist of covalently bonded chains, which may have irregular monomer unit sequences or cross-link randomly along their lengths, giving glassy materials at low temperatures that cannot untangle into crystalline forms. In extreme cases, oxide glass melts have been described with two or more configurations that transform only slowly from one to the other or may coexist in equilibrium (Ropp, 1992).

Crystal growth and phase separation

Once a melt is cooled below T_L, crystal growth is possible. The driving force (difference in free energy between crystalline and liquid state) increases with undercooling and initially growth rates rise as temperature falls (Fig. 5). Subsequently kinetic factors, for example diffusion through the melt to the growing crystal and atomic rearrangement at the interface, limit growth. In stable glass-forming systems, growth rates may be only mm h^{-1} but may reach m s^{-1} in glassy metals. For large undercoolings the fastest growing phase is not necessarily the primary phase defined by the phase diagram; metastable phases also often form. Crystallization requires a nucleation step. Homogeneous nucleation is an intrinsic property. The free energy gain on producing a crystalline nucleus

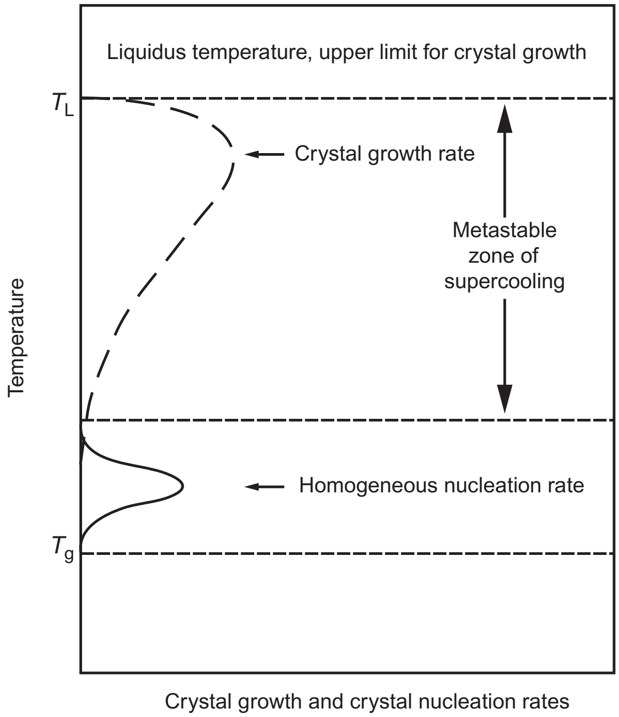
Liquidus temperature, upper limit for crystal growth
T_L
Crystal growth rate
Metastable zone of supercooling
Temperature
Homogeneous nucleation rate
T_g
Crystal growth and crystal nucleation rates

Fig. 5 A schematic representation of the crystal growth and nucleation curves for a single phase precipitating from a glass-forming melt. In reality other phases may also appear at different temperatures with their own growth rate curves.

must balance the energy penalty of generating its surface. Surface effects dominate for small particles and so nuclei must exceed a critical size before they are viable. Small undercoolings require a large critical nucleus whose spontaneous formation is improbable, so melts can exist metastably for long periods just below T_L. At lower temperatures, the critical nucleus size decreases and nucleation rates rise rapidly to a maximum just above T_g, subsequently falling as kinetic factors dominate. Homogeneous nucleation is, however, rare. Nucleation starts more easily from pre-existing discontinuities, for example, "dirty" surfaces or container walls. Nucleation can be engineered by dissolving at high temperatures a component that becomes insoluble on cooling and precipitates (by homogeneous nucleation or phase separation). Examples include halides (NaF, CaF_2, CuCl), oxides (TiO_2, ZrO_2, P_2O_5), or metals (Ag, Au). If homogeneous nucleation rates are high, two-step heat treatment in the nucleation and growth regions can give a finely crystalline structure. The resulting "glass ceramics" are made by standard melting and forming technology but, once crystallized, can have enhanced properties, while lacking the porosity intrinsic to conventional ceramics. Glass ceramics can remain transparent if the crystals are smaller than the wavelength of light and r.i. differences are minimized (Bach, 1995; Lewis, 1989).

Phase separation

Phase separation is the chemical segregation of a melt into two liquids, driven by an associated reduction in free energy, for example, Na_2O–SiO_2 melts, with $Na_2O < 20$ mol%, separate into SiO_2 and sodium silicate; the SiO_2 structure is relatively intolerant to impurities. The minor phase may occur as droplets or a continuously connected phase, whose scale depends on heat treatment time and whose microstructure can be preserved by quenching. The initial step may involve homogeneous nucleation or spinodal decomposition (no energy barrier). Borosilicate glasses also phase separate; the connected phase can be removed by solution, allowing manufacture of finely porous SiO_2.

Glass formation

First, the flexibility of linkages in network systems results in only small energy differences between glassy and crystalline states (cf. the many SiO_2 polymorphs). This is a key thermodynamic factor in glass formation. Second, the network connectivity and bond strength cause the high melt viscosity and slow crystallization rates. Finally, the high melting temperatures destroy, by reaction or solution, foreign particles that might otherwise catalyze crystallization. Mathematical models, based on crystal growth and nucleation behavior, and their degree of overlap with temperature, can predict critical cooling rates for glass formation. They suggest that many systems, including some metal alloys, can form glasses. Cooling rates of $10^6\,°C\,s^{-1}$ may be needed, so heat transfer limits their production to thin artifacts, for example, ribbons or wires. New glass-forming systems have been identified, based on TeO_2, Al_2O_3, Ga_2O_3, ZrF_4, InF_3, by using faster quenching, smaller samples, and purer materials melted under clean conditions to eliminate nucleating agents. Glasses are often associated with eutectics where liquidus temperatures are low and the melts differ most in composition (and structure) from crystalline compounds. Adding more components can also improve glass-forming ability—the so-called "confusion" or "garbage-can" principle (Doremus, 1994; Uhlman and Kreidl, 1990; Varshneya, 1994; Babcock, 1977; Rawson, 1991).

Viscosity

Melt viscosities (η) typically follow the Vogel–Tammann–Fulcher equation (VTF) with temperature: $\log\eta = A + B/(T - T_0)$ where A, B, and T_0 are fitted constants. At the temperature where $\eta = 10^{12}$ Pa s^{-1}, deformation rates are slow, the material is effectively solid over short times ($\sim 10^2$s), and this provides one definition of the "glass transition temperature, T_g." By the strain point ($\eta = 10^{13.6}$ Pa s^{-1}), stress release takes hours. First-order thermodynamic properties such as volume are continuous through the glass transition, in contrast to phase changes such as crystallization, but second-order thermodynamic properties (specific heat (C_p) or TEC) are stepped (Fig. 6). T_g can therefore also be measured from C_p or length changes using a differential scanning calorimeter or

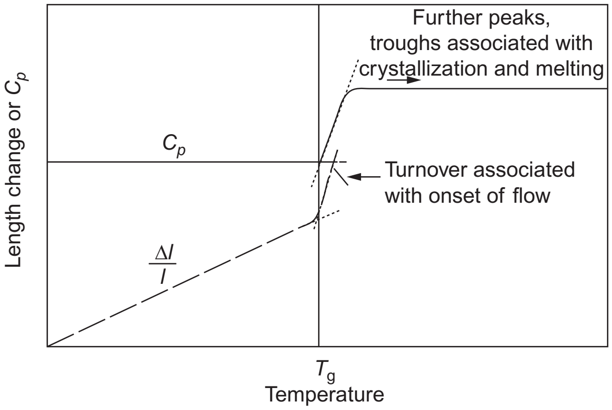

Fig. 6 An idealized graph of the specific heat of a glass as a function of temperature during a constant heating rate experiment and the length of a glass specimen as a function of temperature under similar heating conditions. There is a step in C_p at T_g and a change of slope (corresponding to a step in the TEC) in the specimen length.

a dilatometer, but the values depend on the heating rate used, since the transition is kinetically defined, and are not necessarily equal for different properties. Some have concluded that glass flows at room temperature, it being a liquid, and have perpetuated a myth that old windows are thicker at their base. Neither measurements nor calculations substantiate such conclusions, flow having become immeasurably slow. Where old panes are thicker at one edge, it is a manufacturing defect.

A glass artifact, cooled quickly, will solidify with large temperature gradients present; the differential contraction on reaching room temperature can induce significant stresses. These stresses depend on cooling rate, TEC, elastic properties, and thickness; bulk articles are therefore annealed, by equilibration above T_g, followed by slow cooling to the strain point. Angell has compared glass-forming systems using normalized plots of log η against T_g/T; those displaying Arrhenius behavior most closely he termed "strong" glasses while those with large deviations he termed "fragile." Fragility implies cooperative breakdown of the melt structure into increasingly small units above T_g. The VFT formalism predicts $\eta = \infty$ at $T - T_0$. Some studies have attached physical significance to T_0, relating it to the temperature where extrapolation of experimental data predicts that the entropy of a glass becomes equal to that of the corresponding crystal, that is, the configurational entropy falls to zero, a concept underpinning the "Kauzmann paradox" (Varshneya, 1994).

Processing

High melt viscosities, along with gravity and surface tension, aid shaping as the melt cools. Sheet glass achieves optical flatness by gravity-driven flow, while floating on a molten tin bath with a 7 mm equilibrium thickness defined by surface tension and density. Optical fibers maintain their r.i. profiles during drawing. Containers and laboratory ware are blown and pressed by complex machinery to give the desired glass distribution. Strain rates may be high. A few glasses display non-Newtonian flow by structural alignment during forming (Cable and Parker, 1992).

Transformation range effects

Glass structure does not depend only on composition but also on thermal history; densities may vary by 1%. Fast quenching freezes in a structural state corresponding to equilibrium at a higher temperature than slow cooling. The effective quenched-in equilibrium temperature is called the "fictive temperature." Control of cooling through the transformation range allows fine tuning of an optical glass r.i., and low cooling rates ensure the whole sample has the same thermal history (and minimum stress). Optical glass manufacturers recommend that their products should not be heated above $T_g = 150\ ^\circ C$ because of potential property changes. Similar considerations apply to the processing of glass sheets for LCD displays. The electronic circuitry used to address individual pixels is printed at high temperatures in several layers; precise registry demands dimensional stability. A glass heated in the transformation range may, after an initial instantaneous change, relax exponentially to a new equilibrium state (Maxwell spring and dashpot model). Stress release rates can be measured and accurate data as f(t, T) are needed for high-precision fabrication. Detailed analysis suggests a stretched exponential formulation: $S_t = S_0 \exp. (-[t/\tau]^n)$ where S_t is the stress at time t, S_0 the initial stress, and τ is proportional to viscosity, n ranges typically from 0.5 near T_g to 1. Many other properties behave similarly although not necessarily with the same constants for a given glass. Study of relaxation behavior and structural dynamics has given fruitful insights into the nature of the glass transition. At lower temperatures, bulk flow ceases but atoms can slide into new relative positions corresponding to different local energy minima, associated with the disordered structure. Such effects are manifest in internal friction experiments, for example, measurement of the damping of a pendulum suspended from a glass fiber under torsion. Damping involves transfer of mechanical energy to thermal energy and is observed down to room temperature in silicate glasses. Different mechanisms, termed α and β relaxations, dominate as temperature rises. These are attributed to mechanisms from modifier ion motion and relative movement of nonbridging oxygens, to motion of whole structural units.

A related phenomenon is semipermanent densification of v-SiO_2 at high pressures (GPa). Deformations of several percent do not fully relax on return to normal atmospheric conditions. Kinetic studies of relaxation suggest a low activation energy process, which is therefore not bond breakage; Raman spectroscopy confirms this. Early mercury-in-glass thermometers also displayed delayed elasticity. After calibration at 100 °C, the mercury failed to return immediately to its 0 °C calibration point on cooling. This relaxation behavior was minimized in mixed alkali glasses. Similar effects have been observed in rare-earth doped glasses; optical pumping into particular excited states, and the consequent energy transfer to the lattice, has excited structural changes that only recover at raised temperatures. The associated r.i. changes allow holographic image storage (Brawer, 1985).

Thermal properties

Specific heats are consistent with Dulong and Petit's law near T_g but show a positive step at T_g, the size of which indicates the level of structural breakdown occurring. Thermal conductivities are lower than for equivalent crystalline phases and decrease with falling temperature, consistent with the short phonon mean free paths associated with structural disorder. At high temperatures, heat transport by photons becomes significant—glass is semitransparent in the near infrared allowing absorption and re-emission as a heat transport mechanism, termed radiation conductivity. Radiation conductivity varies as T^3 and is significant in commercial glass melting (Babcock, 1977).

Mechanical behavior

Glasses are brittle, with strengths dominated by their surface state. In microhardness tests, they exhibit limited flow under compression, attributed to densification and faulting. No flow occurs under tensile stress however; surface flaws remain atomically sharp at high loads and are effective stress raisers (stress at crack tip is enhanced by $(r/\rho)^{1/2}$ where r is crack length and r tip radius). Flaws are induced by impact, friction, adhering particles of different TEC, and devitrification. Strengths of several GPa in undamaged fibers can fall to <50 MPa. Water attack at flaw tips under stress causes static and dynamic fatigue, which is maximized in glasses of poor chemical durability; conversely, v-SiO_2 is unusually strong because of its excellent durability. The stress intensity factor, K_{1c}, allows isolation of compositional factors by eliminating the effects of flaw size. Variations between glasses are small and related to bond strengths or atomic packing densities. Strengths are improved by protective coating or surface compressive stresses induced by rapid cooling or ion exchange, where large cations replace smaller cations. Many glass ceramics have enhanced strengths, the crystals impeding crack growth (Lewis, 1989).

Optical properties

Glasses are intrinsically transparent because they lack internal structure (e.g., grain boundaries) where r.i. changes would scatter light. Transparency also requires the absence of absorption mechanisms. UV photons can excite bonding electrons into empty molecular orbitals, limiting transparency. v-SiO_2 and phosphate glasses have strongly bound electrons and are transparent to <200 nm, but nonbridging oxygens, with their more weakly bound electrons, reduce transmission. IR photons can excite atomic vibrations and SiO_2 is opaque beyond 4.5 μm; OH absorptions usually limit transmission near 3 μm. Transmission can be extended by reducing the natural vibrational frequencies using heavier ions and weaker bonding. Fluoride glasses based on singly charged anions and heavy cations (Zr, La, In, Hf) will transmit to 7.5 μm and chalcogenide glasses (based on S, Se, Te) can transmit to 20 μm (France et al., 1989).

The UV and IR absorptions in glass are responsible for its r.i., *n*, and wavelength dispersion, *v*, as implicit in the semi-empirical fitting formula of Helmholtz–Ketteler: $n^2\text{-}1 = A + \Sigma_i c_i \lambda^2/(\lambda_{0i}^2 - \lambda^2)$ with λ_{0i} = wavelength of absorption bands and c_i a weighting factor related to band strength. SiO_2 has a low n because its strong bonding gives short λ_{0i} values, whereas PbO-rich glasses have longer λ_{0i}, and correspondingly higher n and ν values. The UV absorption is associated with the 6 s → 6p transition of the lone pair electrons in Pb^{2+}. These weakly bonded, highly polarizable electrons also increase the second-order coefficient of optical nonlinearity (n_2). $d^2n/d\lambda^2 = 0$ near 1.5 μm for SiO_2 because of the competing effects of UV and IR absorptions, minimizing materials-based signal dispersion in fibers.

Transition metal and rare-earth ions introduce weak absorptions, which are broader than in crystals because of the inherent structural disorder. Such species color glass. The matrix composition can strongly influence excited state lifetimes, and affects absorption and emission peak shapes. Halide and chalcogenide glasses are often preferred hosts because their low phonon energy lattices increase excited state lifetimes. Crystallization, where dopant ions segregate into the crystal phase, can offer similar advantages but with more tightly defined dopant ion environments. Both glassy and transparent glass–ceramic materials make efficient lasers (in fiber form for telecommunications).

Color can result from precipitated particles, for example, Au, Cu, and Ag color glass red or yellow and Cu(Cl,Br), Cd(S,Se), or PbTe give sharp absorption edges in the UV, visible, or IR, depending on their bandgap. If particles exceed 20 nm, light scattering can become excessive. The electronic energy levels of these precipitates are influenced by particle size via quantum confinement effects, giving rise to enhanced optical nonlinearities.

Such materials require dissolution of an appropriate compound at high temperatures that will precipitate on cooling. Metals are dissolved as ions, reduced to atoms on cooling by a redox process (e.g., $Au^+ + Ce^{3+} \rightarrow Au^0 + Ce^{4+}$), and subsequently agglomerate. Electron transfer can be catalyzed by UV photons. Thus, regions of high metallic particle concentrations, capable of nucleating bulk crystallization, can be engineered. The crystallized regions can display differential HF etching rates, and finely structured products for fluidics or replacement bones for the ear can be made (Bamford, 1977; Paul, 1990).

Glasses are rarely birefringent being intrinsically isotropic, but anisotropy can be induced temporarily by stress, or permanently by shearing melts with chain-like structures or showing phase separation, while cooling through T_g.

The Faraday effect involves rotation of the plane of polarization of a light beam by a magnetic field. Applications include optical devices requiring rapid switching or protection against back-reflected light. The plane of polarization is rotated in one sense by diamagnetic materials and in the reverse by paramagnetic materials. Large diamagnetic effects occur in $PbO–Bi_2O_3–Ga_2O_3$ glasses because of the polarizable Pb and Bi ions, while typical paramagnetic materials contain rare-earth ions with unpaired 4*f* electrons, for example, Tb^{3+}, Pr^{3+}, and Dy^{3+}. The equivalent effect for electrical fields is named after Kerr.

Energetic photons can form point defects or re-arrange bonds, causing density and r.i. changes that may be used for laser writing; Bragg reflecting gratings, for telecoms signal demultiplexing or stress sensors, are written in Ge-doped SiO_2 optical fibers by two interfering beams from an excimer laser. Light-induced differential etching rates in chalcogenide glasses allow manufacture of photo-diffractive elements (Cable and Parker, 1992).

Diffusion and electrical behavior

SiO_2 has an open structure allowing solution of small molecules (e.g., He, H_2) and significant diffusion rates, even at 20 °C. Modifier ions block the diffusion paths but, being weakly bonded, may themselves diffuse below T_g. Some surface modification technologies, for example, chemical toughening or planar waveguide manufacture, use this. At room temperature, most glasses are insulators but ion motion can cause significant AC dielectric loss; consequently glass ceramics are often preferred substrates in the electronics industry. Glasses become ionic conductors at higher temperatures (~100 °C) for silicate glasses with significant modifier ion content; larger ions and higher charge reduce conductivity). The phenomenon of fast ion conduction, observed in some crystalline ceramics, also occurs in glasses (Varshneya, 1994).

The mixed alkali effect is a characteristic of ionic conduction and diffusion. Fig. 7 plots the conductivity of glasses containing Na and K against concentration; a pronounced minimum occurs where Na:K = 50:50, explained by the different sites the two ions occupy. Sodiums hop easily between equivalent sodium sites but mixed sites create an energy barrier. The loss of vibrational coupling between adjacent ions may also reduce coordinated hopping. The mixed alkali effect is most pronounced below T_g, the cation sites being unable to relax (Doremus, 1994).

Both crystalline and glassy semiconductors display valence and conduction bands, and a bandgap. Interband states exist even in undoped glasses however, particularly near the band edge. Chalcogenide glasses, based on S, Se, Te with, for example, Ge, Si, As, Sb, Ga, and glasses with high concentrations of transition metals in mixed valence states (e.g., V, Fe) can be semiconducting, electrons hopping between adjacent ions in different oxidation states in the latter case. Chalcogenide glasses have typical semiconductor characteristics, for example, photoconductivity and xerography; a-Si is a common component of solar cells. They also display switching behavior. Low voltages give small currents but higher voltages can induce crystalline filaments of higher conductivity. If crystallization is reversible, a memory switch results (Rawson, 1991).

See also: Ceramics, History of; Disordered Solids and Glasses, Electronic Structure of; Insulators, Optical Properties of; Ionic and Mixed Conductivity in Condensed Phases; Optical Instruments; Optical Properties of Materials; Phases and Phase Equilibrium.

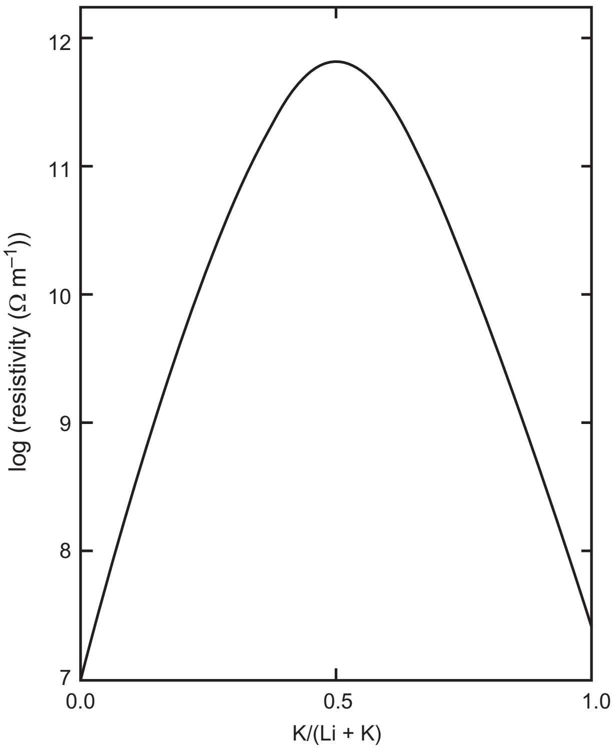

Fig. 7 An idealized graph of resistivity against the concentration of K as a fraction of total alkali content [K/(Li + K)] for an M_2O–$2SiO_2$ glass. The peak in resistivity is a result of the mixed alkali effect.

Conclusion

Because of their unique properties, glassy materials are widely used as containers and in architecture, in instrumentation, telecommunications, clean water production and as biomaterials. They are infinitely recyclable and so can be produced sustainably. They can be manufactured with a zero carbon footprint and are widely used in energy generation as well as for energy saving.

Further reading

Babcock CL (1977) *Silicate Glass Technology Methods*. New York: Wiley.
Bach H (1995) *Low Thermal Expansion Glass Ceramics*. Berlin: Springer.
Bamford CR (1977) *Colour Generation and Control in Glass*. Amsterdam: Elsevier.
Brawer S (1985) *Relaxation in Viscous Liquids and Glasses*. Columbus: American Ceramic Society.
Cable M and Parker JM (1992) *High Performance Glasses*. Glasgow: Blackie.
Doremus RH (1994) *Glass Science*. New York: Wiley.
France PW, Drexhage MG, Parker JM, Moore MW, Carter SF, et al. (1989) *Fluoride Glass Optical Fibres*. Glasgow: Blackie.
Lewis MH (1989) *Glass and Glass-Ceramics*. London: Chapman and Hall.
Ossi PM (2003) *Disordered Materials*. Berlin: Springer.
Paul A (1990) *Chemistry of Glass*. London: Chapman and Hall.
Pulker HK (1984) *Coatings on Glass*. Amsterdam: Elsevier.
Rawson H (1991) *Glasses and Their Applications*. London: Institute of Materials, Minerals and Mining.
Ropp RC (1992) *Inorganic Polymeric Glasses*. Amsterdam: Elsevier.
Scholze H (1988) *Glas: Natur, Struktur und Eigenschaften*. Berlin: Springer.
Uhlman DR and Kreidl NJ (1990) Glass science and technology. *Vol 4A: Structure, Microstructure and Properties*. Boston: Academic Press.
Varshneya AK (1994) *Fundamentals of Inorganic Glasses*. San Diego: Academic Press.
Zarzycki J (1991) *Glasses and the Vitreous State*. Cambridge: Cambridge University Press.

Disordered solids and glasses, electronic structure of☆

SR Elliott, University of Cambridge, Cambridge, United Kingdom

© 2024 Elsevier Ltd. All rights reserved.

This is an update of S.R. Elliott, Disordered Solids and Glasses, Electronic Structure of, Editor(s): Franco Bassani, Gerald L. Liedl, Peter Wyder, Encyclopedia of Condensed Matter Physics, Elsevier, 2005, Pages 457–463, ISBN 9780123694010, https://doi.org/10.1016/B0-12-369401-9/00466-6.

Introduction 192
Nature of disorder 192
Effects of disorder on the electronic structure 194
General aspects 194
The electronic density of states 195
The electronic wavefunction 198
Conclusion 199
References 199
Further reading 199

Abstract

The presence of atomic-structural (topological) disorder, as in amorphous/glassy materials, has significant effects on the character and behavior of electron states, particularly in disordered semiconductors/insulators. All electron states in perfectly crystalline solids are spatially delocalized; such Bloch states, characterized by well-defined values of electron wavevectors, reflect the underlying crystal symmetries. However, structural disorder destroys the long-range atomic-translational symmetry of crystals, and hence the electron wavevector is no longer a unique characteristic of electron wavefunctions in amorphous/glassy materials. Moreover, the sharp features (van Hove singularities) appearing in the electronic density of states of crystalline materials are broadened out in amorphous/glassy solids, due to disorder. But the key difference in the characteristics of the electronic-structure behavior between crystals and amorphous/glassy materials is in the nature of the electronic wavefunction: in crystals, the (Bloch) electron wavefunctions are all spatially delocalized, whereas in amorphous/glassy semiconductors and insulators, the electronic wavefunctions are spatially localized, due to potential-energy disorder, at the edges of the valence and conduction bands, and also in the bandgap between valence and conduction bands where the localized electron states are associated with atomic-coordination defects.

Key points

- Electronic states in amorphous/glassy materials are very different from those in corresponding crystalline solids, due to the presence of atomic-structural (topological) disorder
- In crystals, electronic wavefunctions are characterized by well-defined values of electron wavevector, whereas in amorphous/glassy materials, electron wavevectors are much less well-defined due to the effects of structural disorder
- The electronic density of states (EDOS) as a function of energy is more featureless in amorphous/glassy materials than in corresponding crystals—sharp "van Hove singularity" features in the EDOS of crystalline materials are absent in the EDOS of amorphous/glassy solids
- Amorphous/glassy semiconductors/insulators contain spatially-localized electron states, arising from atomic topological disorder, at the top of the valence band (VB) and at the bottom of the conduction band (CB) in the EDOS, as well as in the bandgap between VB and CB, the latter being associated particularly with atomic-coordination defects, such as over-coordinated atomic configurations and under-coordinated geometries ("dangling bonds")

Nomenclature

a	unit-cell parameter
C_i^α	chalcogen atom with atomic coordination i (=1 – 3) and electric charge α(– ,0, +)
$D(E)$	EDOS (per energy per volume) = $g(E)/V$
E	electron energy
E_g	bandgap energy
$g(E)$	electronic density of states (per energy) = $D(E) \times V$

☆*Change History*: November 2022. SR Elliott updated Fig. 6.

$\boldsymbol{k}$	electron wave vector magnitude
k	electron wavevector
r	real-space position vector
S_{E}	constant-energy surface of electron states in $\boldsymbol{k}$-space
$\boldsymbol{u_k(r)}$	function having periodicity of crystal lattice (in Bloch function)
$\boldsymbol{V}$	volume
$\boldsymbol{V_1}$	intrasite electron interaction
$\boldsymbol{V_2}$	intersite electron interaction
$\boldsymbol{\alpha}$	inverse localization length of envelope of a localized state
$\boldsymbol{\alpha_{\mathrm{I}}}$	inverse localization length of island state within a localized state
$\boldsymbol{\delta(E)}$	Dirac delta function (of energy)
$\nabla_k \boldsymbol{E}$	gradient of electron energy with respect to wavevector
$\boldsymbol{\theta}$	bond angle
$\boldsymbol{\rho_e(r)}$	electron charge density
$\boldsymbol{\psi}(r)$	electron wavefunction

Introduction

In this article, the term "electronic structure" is taken to mean a description of the details of the solution, in its totality, of the Schrödinger equation for electrons in solids. Two quantities characterize the Schrödinger eigen-equation solution, namely the eigenvalue (or electron energy, E) and eigenvector (or electron wavefunction, $\psi(r)$).

In the simple case of electron states in perfect single-crystalline materials, that is, those considered in most textbooks on the electronic theory of solids (Elliott, 1998), the term electronic structure is often restricted to a description solely of the electronic energy since, for translationally periodic systems, the electronic states themselves always have the same character and generic functional form. The electronic wavefunction is always spatially extended throughout the volume of the crystalline sample, and has the functional form of the "Bloch" function, that is, a product of a spatially extended plane-wave state and a function, $u_k(r)$, having the periodicity of the underlying crystal lattice:

$$\psi_k(r) = u_k(r)\mathrm{e}^{\mathrm{i}k\cdot r} \tag{1}$$

where $\boldsymbol{k}$ is the (quantized) wavevector of the plane-wave component and is used as a label for the eigenstate. (This is not the case for disordered systems, as will be seen.)

Thus, for perfect single crystals, the electronic structure, characteristic of a particular material, is taken to refer to either the four-dimensional **(4D)** quantity, the electronic band structure, $E(\boldsymbol{k})$, or its **2D** derivative, the electronic density of states **(EDOS)**, $g(\boldsymbol{E})$, where generally

$$g(E) = \sum_i \delta(E - E_i). \tag{2}$$

The EDOS in this representation is simply a sum of Dirac delta functions at all allowed, quantized electron-energy eigenvalues, $\boldsymbol{E_i}$; it is the number of electron states at a particular energy in unit energy interval, and $g(\boldsymbol{E})$, therefore, has the units of inverse energy. Alternatively, for a single crystal, the EDOS can be obtained as a surface integral in $\boldsymbol{k}$-space over the Brillouin zone of a constant-energy surface $\boldsymbol{S_E}$ of the electronic band structure, that is,

$$D(E) = \frac{2}{(2\pi)^3}\int_{E(k)=\mathrm{const}} \frac{\mathrm{d}S_{\mathrm{E}}}{\nabla_k E}. \tag{3}$$

Here, $D(E) = g(E)/V$, where $\boldsymbol{V}$ is the volume of the sample, and hence this form of the EDOS has units of inverse energy times volume.

One special feature of the EDOS of crystalline solids is the presence of van Hove singularities, that is, sharp features in the density of states corresponding to flat regions of the band structure, for which $\nabla_k E = 0$ (cf. Eq. 3), that is, regions where there are a large number of electron states with different $\boldsymbol{k}$-values in a very small energy interval.

It will be seen that the introduction of disorder in a solid can have dramatic effects on the above simple picture of electron states in single-crystal materials.

Nature of disorder

The translational periodicity characteristic of perfect single crystals can be disrupted in a number of ways. Although, in a given disordered material, a glass for instance, several different types of disorder may occur together, nevertheless it is instructive to consider such possible forms of disorder separately. Perhaps, the simplest form is substitutional disorder in which a different type of atom is substituted for another in the crystalline lattice of the host material. The simplest example of substitutional disorder is the inclusion of one type of atom in the structure consisting entirely of another type, for example, the electrical dopants, n-type phosphorus or p-type boron, in crystalline silicon (Fig. 1a). A related substitutional defect is the so-called antisite defect, for

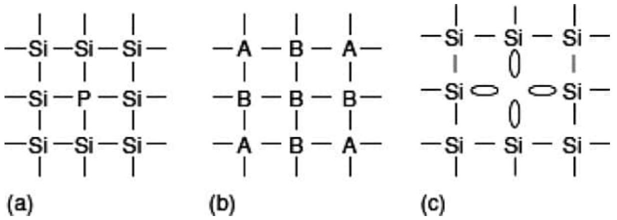

Fig. 1 Schematic illustration of different types of substitutional disorder associated with point defects in solid (crystalline) materials: (a) a phosphorus donor atom in crystalline silicon; (b) an antisite defect in a binary crystal, AB, the central B atom substituting for an A atom; and (c) an atomic vacancy (e.g., in crystalline silicon, showing four dangling-bond orbitals pointing into the vacancy).

example, in a binary crystalline compound, **AB**, where only heteropolar (**A–B**) bonding occurs in the completely ordered case. The replacement of an **A** atom, for example, by a **B** atom leads to the formation of homopolar (**B–B** in this case) nearest-neighbor bonds (Fig. 1b). A related defect is the atomic vacancy, where an atom is missing at a lattice-related site (Fig. 1c). This type of disorder involves point (or zero-dimensional) defects.

A somewhat related **2D** defect is the so-called antiphase boundary in a binary crystal, **AB**, where an entire plane of atoms is missing (i.e., a stacking fault exists): in this case, like atoms face each other across the antiphase boundary (Fig. 2).

Another type of disorder prevalent in crystalline materials is positional disorder, characteristic of vibrational motion: atoms are instantaneously displaced randomly from their equilibrium, lattice-related crystallographic sites, according to a Gaussian (normal) distribution in the case of thermal vibrational disorder (Fig. 3). Positional disorder in crystals due to vibrational motion is dynamic in nature: the time-averaged atomic positions are simply the equilibrium, lattice-related sites. However, for the case of noncrystalline (e.g., amorphous or glassy) materials, the positional disorder is static in nature, that is, the equilibrium atomic positions do not correspond to a crystalline lattice.

What really distinguishes an amorphous material from its crystalline counterpart, however, is the presence of topological disorder (Elliott, 1990). This can involve, for example, the presence of noncrystalline ring orders in (covalent) network materials, even though the nearest-neighbor atomic coordination remains the same (Fig. 4), or for amorphous metals, the presence of a distribution of nearest-neighbor coordination numbers, rather than a single coordination polyhedron as in the corresponding crystal (e.g., 12-fold coordination in face-centered-cubic (fcc) crystals). In this case, the disorder is more profound, and there is no simple displacement relationship between noncrystalline and crystalline structures, as there is for positional disorder, for example.

The presence of topological disorder also permits the existence of other types of defective structures, unique to the amorphous phase and not found in the crystalline state. For instance, in materials with strongly directed covalent bonds, isolated dangling-bond (under-coordinated) coordination defects can occur instead of the clusters of dangling bonds that always occur at the site of atomic vacancies in crystals of such materials, for example, the four (unreconstructed) dangling bonds pointing into the vacancy in the tetrahedral crystalline material, c-Si (Fig. 1c). In addition, isolated homopolar-bond defects can occur in amorphous compound materials (where in the stoichiometric composition, only heteropolar bonds would otherwise be expected), instead of the clusters of homopolar-bond defects that exist around an antisite defect (Fig. 1b) or along an antiphase boundary (Fig. 2) in the corresponding crystalline materials.

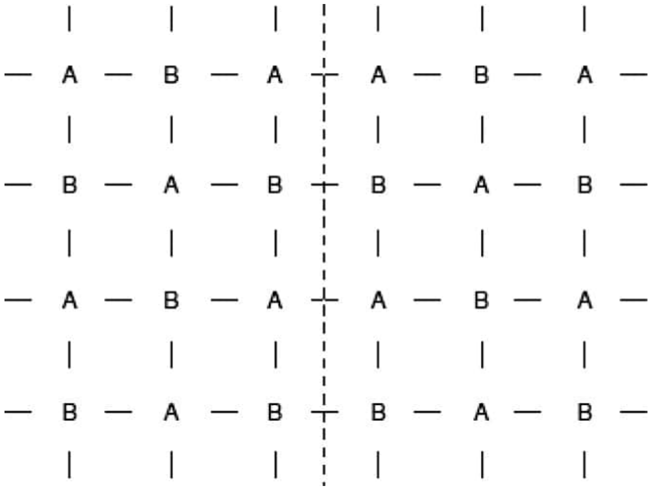

Fig. 2 Schematic illustration of a two-dimensional stacking fault (missing layer) or antiphase boundary (dashed line) in a binary crystal, AB.

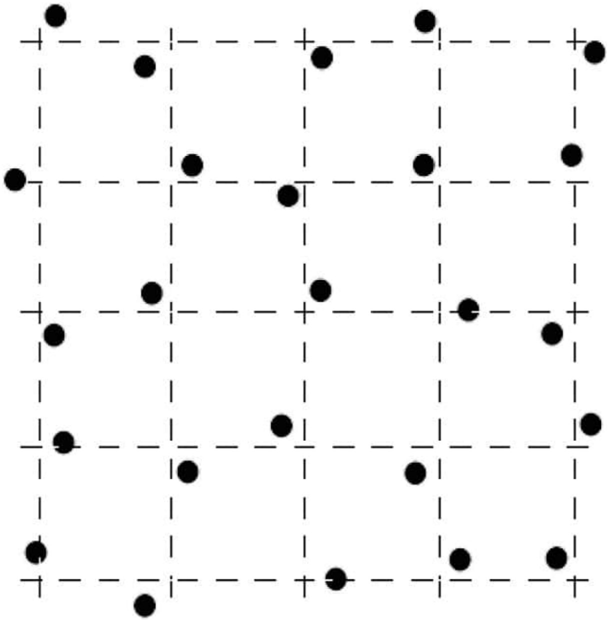

Fig. 3 Schematic illustration of positional (e.g., vibrational) disorder.

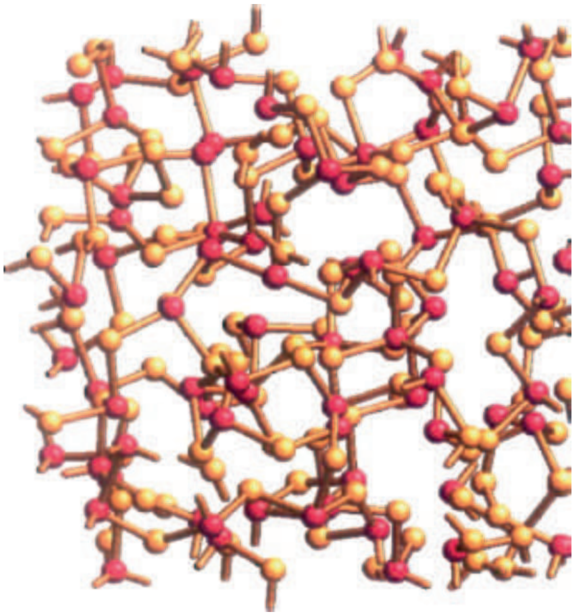

Fig. 4 Illustration of topological disorder in a computer-simulated model of amorphous As_2S_3, created by density-functional-based tight-binding molecular dynamics: As atoms are colored pink and S atoms are yellow. From SI Simdyankin and SR Elliott, unpublished data. See: Simdyankin SI, Elliott SR, Hajnal Z, Niehaus TA and Frauenheim TH (2004) Simulation of the physical properties of the chalcogenide glass As_2S_3 using a density-functional-based tight-binding method. *Physical Review B*, 69: 144202.

Effects of disorder on the electronic structure

General aspects

In the case of a perfect crystal, the allowed values of the quantized electron wave vector, $\boldsymbol{k}$, are set by the periodicity of the lattice: for example, for a **1D** crystal with a unit-cell parameter a, and with N atoms in the sample, there are correspondingly N discrete k-states, equally spread in $k(= |\boldsymbol{k}|)$ in the first Brillouin zone, that is, for the range of k-values $-\pi/a < \boldsymbol{k} < \pi/a$. Each electron eigenvalue (energy) is associated with a particular $\boldsymbol{k}$-value, which shows that the electronic band structure, $E(\boldsymbol{k})$, is a well-defined quantity (see Fig. 5).

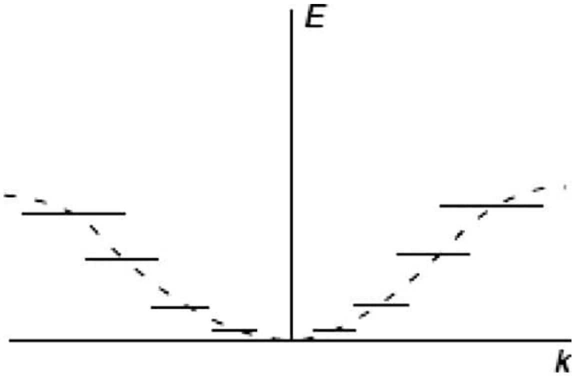

Fig. 5 Schematic illustration of a one-dimensional electronic band structure for a 1D crystal (dashed line) and an amorphous solid (solid lines, illustrating the uncertainty in electron wave vector ***k*** for a given eigenenergy).

The presence of a single defect (or a surface) is sufficient to break the infinitely ranged translational invariance characteristic of ideal single crystals. In the case of a disordered material with no translational periodicity, there is no crystalline unit cell and hence the electron wavevector becomes an ill-defined quantity and no longer is useful as a label for electron states. Although at low electron energies corresponding to small $\boldsymbol{k}$ (the electron wavelength being long compared to characteristic atomic-structural distances, for example, the nearest-neighbor bond length), the uncertainty in $\boldsymbol{k}$ is rather small, it rapidly increases with increasing energy (Fig. 5). In other words, the electron wave function for a disordered material can no longer be expressed in terms of a single plane wave, characterized by one particular $\boldsymbol{k}$-value, as in the case for Bloch states in single-crystalline materials (Eq. (1)). Instead, in a disordered material, electronic wave functions can be regarded as comprising an increasing number of Fourier components with increasing energy.

In the light of the above discussion, evidently the electronic band structure, $E(\boldsymbol{k})$, is not an appropriate description of electron states for disordered materials. However, since the electron energy remains a well-defined quantity, even in the presence of strong disorder, the EDOS (as defined as a sum of delta functions by Eq. (2), but not in terms of the band structure, Eq. (3)) remains a valid form of description for the electron states of disordered materials.

The electronic density of states

The effect of disorder on the EDOS is varied: some changes are striking; others are more subtle. Perhaps, the most striking effect of the loss of translational symmetry is in the destruction (broadening) of the van Hove singularities in the EDOS that are a signature of the presence of flat electron-energy surfaces in k-space, characteristic of crystals (see Fig. 6).

However, van Hove singularities apart, the EDOS of many amorphous materials is often similar to that of their crystalline counterparts (see Fig. 6 for the case of silicon). This is particularly true for covalently bonded semiconductors/insulators, where the similarity in the electronic structure arises from marked similarities in the short-range atomic structural order between the two phases. In the case of amorphous and crystalline silicon, for example, the short-range structural motif is the $SiSi_4$ tetrahedron in both cases: the average nearest-neighbor bond length and bond angle are practically the same, although the amorphous phase is characterized by having an $\sim \pm$ 10% variation in bond angle from the average tetrahedral value, $\theta = 109°28'$. (The translational periodicity of the crystalline phase is destroyed in the amorphous material, not so much by this bond-angle disorder as by the disorder in dihedral angles, that is, the angle of twist between pairs of corner-sharing connected tetrahedra.)

The reason for the overall similarity in EDOS between amorphous and crystalline states, for example, of silicon, can be seen from a simple tight-binding description of the origin of the electron states, and the similarity in the short-range order in both cases. Only two types of local electronic interactions are assumed to be operative, namely a nearest-neighbor intersite interaction, V_2, between orbitals emanating from pairs of nearest-neighbor atoms and forming common bonds, and an intrasite interaction, V_1 between orbitals emanating from the same atom (Fig. 7). In the case of silicon, for example, atomic s- and p-orbitals hybridize to give the sp^3-hybrid basis orbitals. The intersite interaction, V_2, is responsible for a gap of magnitude $2V_2$ occurring between occupied and unoccupied electron states (i.e., the bonding–antibonding splitting). The intrasite interaction, V_1, in this model, is responsible for the broadening of bonding and antibonding levels into, respectively, the valence and conduction bands, each of width $4V_1$ (Fig. 7), since it couples orbitals together in such a way that, together with the intersite interaction, an electron may hop from any given orbital on one atom to any other orbital on any other atom, thereby becoming delocalized (extended) throughout the sample volume. It should be noted that both V_1 and V_2 are negative quantities. In this model, a bandgap occurs between filled valence and empty conduction bands as long as the bonding–antibonding splitting is sufficiently large to overcome the opposing effect of the band broadening, that is, for

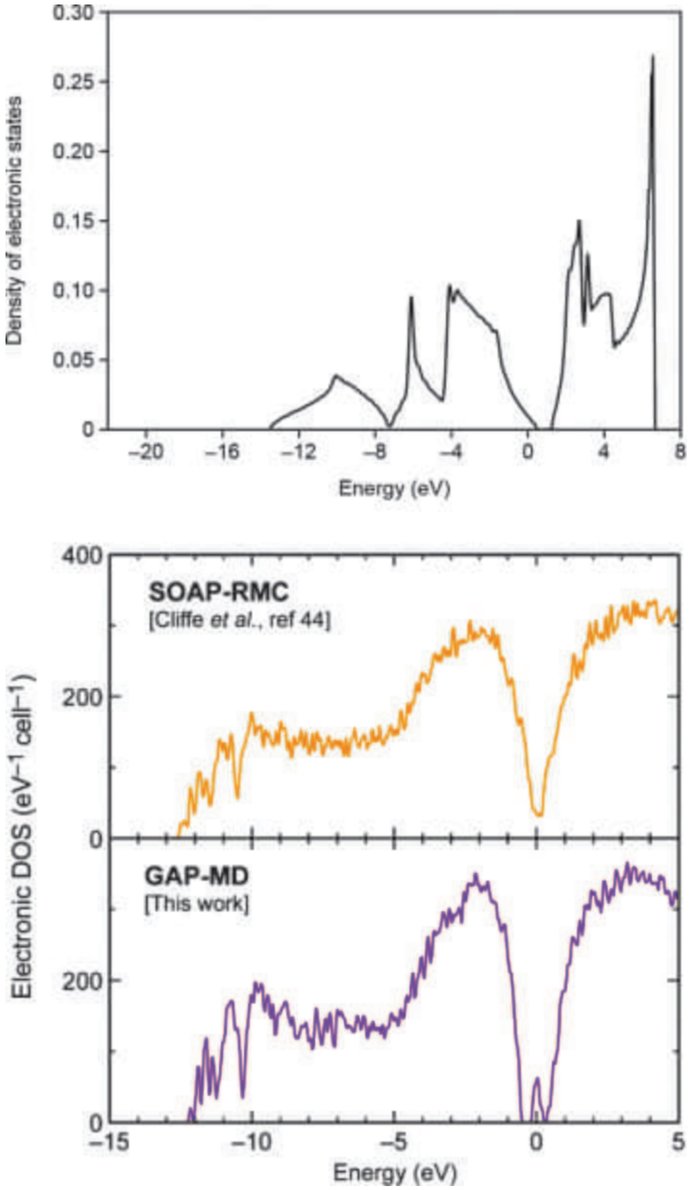

Fig. 6 Computed EDOS curves for: (a) a 2,097,172-atom model of diamond-cubic crystalline Si calculated using a tight-binding procedure; (b) two 512-atom models of amorphous Si, one generated by a reverse-Monte Carlo (RMC) method, the other by use of a machine-learned Gaussian Approximation Potential (GAP) used in an MD simulation. From Panel (a) Deringer VL, Bernstein N, Csányi G, Ben Mahmoud C, Ceriotti M, Wilson M, Drabold DA and Elliott SR (2021) Origins of structural and electronic transitions in disordered silicon. *Nature* 589: 59. Panel (b) Cliffe MJ, Bartók AP, Kerber RN, Grey CP, Csányi G and Goodwin, AL (2017) Structural simplicity as a restraint on the structure of amorphous silicon. *Physical Review B*, 95: 224108. Panel (c) Deringer VL, Bernstein N, Bartok AP, Cliffe MJ, Kerber RN, Marbella LE, Grey CP, Elliott SR and Csányi G (2018) Realistic atomistic structure of amorphous silicon from machine-learning-driven molecular dynamics. *Journal of Physical Chemistry Letters*, 9: 2879.

$$|V_2| > 2|V_1| \tag{4}$$

and the bandgap, therefore, has the value

$$E_g = 2|V_2 - 2V_1| \tag{5}$$

Since the average nearest-neighbor bond lengths and angles in amorphous and crystalline silicon are very similar, the magnitude of the electron-hopping interactions V_1 and V_2 are also expected to be very similar, and hence, for example, the width and shape of the valence band, and the magnitude of the bandgap between valence and conduction bands, is expected to be very similar for the two phases (see Fig. 6 for the case of Si).

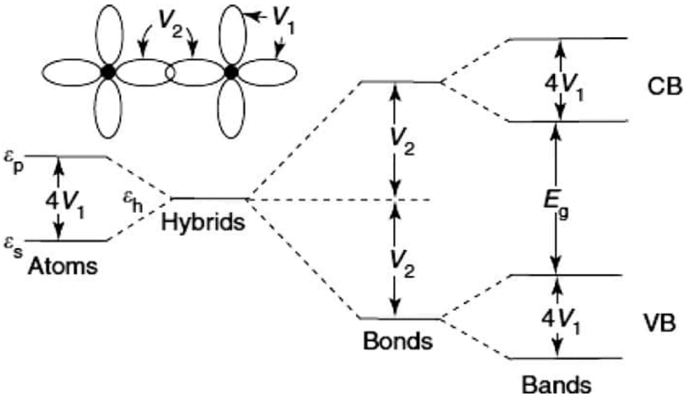

Fig. 7 Illustration of the origin of the bandgap between valence and conduction bands for a tetrahedrally coordinated material, such as silicon. The successive sections show the atomic *s*- and *p*-levels, the sp^3-hybrid level, the bonding-antibonding splitting resulting from the intersite electron interaction, V_2, and the formation of bands resulting from the intrasite interaction, V_1. The origins of the interactions V_1 and V_2 are shown in the inset.

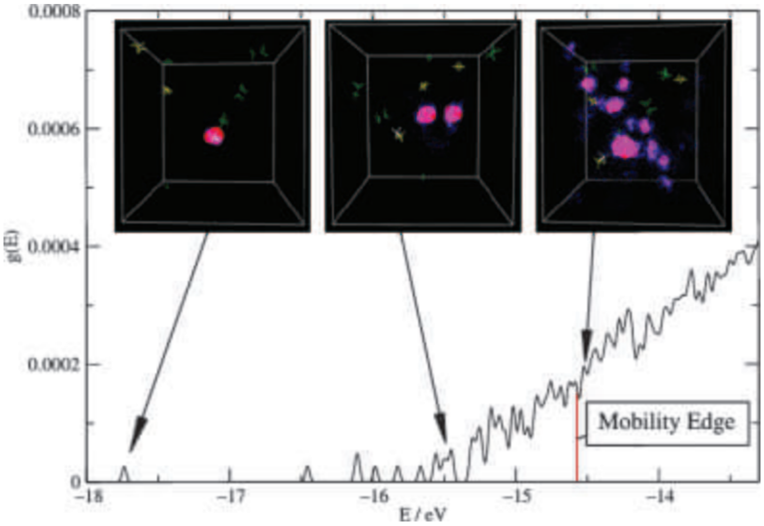

Fig. 8 The density of states for the (lower-energy) valence-band tail calculated for a 10,000-atom model of amorphous silicon, showing the computed position of the LD transition energy ("mobility edge"). Visualizations of three representative spatially-localized electron eigenstates are also shown: a highly localized near-mid-gap state associated with a dangling bond; a localized tail state; and a critical state at the LD transition energy, each showing constituent island states, the number of which increase on approaching the LD transition. From Ludlam JJ, Taraskin SN, Elliott SR and Drabold DA (2005) Universal features of localized eigenstates in disordered systems. *Journal of Physics. Condensed Matter*, 17: L321

However, subtle changes in the EDOS can be caused by disorder. Since the bandwidth in this tight-binding picture is governed by the intrasite interaction, V_1, and this interaction (as well as the degree of orbital hybridization) depends on the angle, θ, between (hybrid) orbitals at a site (Fig. 7), the fluctuations in θ will lead correspondingly to variations in the bandwidth, that is, a tailing of states at the band edges into the gap region (see Fig. 8). It appears, on the basis of experimental data, that these band tails in amorphous semiconductors generally have an exponential energy dependence:

$$g(E) = \frac{N_0}{E_0} \exp\left(E/E_0\right) \tag{6}$$

where N_0 is the total number of tail states, and E_0 is the energy decay parameter.

Substitutional disorder, for example, phosphorus donor dopants in silicon, that is, Si:P (Fig. 1a), also gives rise to electron states lying outside the bands of the perfect crystal; in the case of Si:P, these are donor levels just below the conduction-band edge. (Acceptor states associated with substitutional acceptors, for example, boron in silicon, Si:B, correspondingly lie just above the valence-band edge.) Substitutional defects comprising atoms having a greater electronegativity difference with the atoms in the host material correspondingly give rise to electron states lying deeper within the bandgap.

Although relatively small levels of disorder, for example, bond-angle deviations in covalent amorphous semiconductors, produce relatively small changes in the EDOS, that is, moderate band tailing into the bandgap, larger degrees of disorder can cause correspondingly larger changes in the EDOS. For instance, electron states associated with gross instances of disorder (e.g., coordination defects such as dangling bonds in amorphous network materials) have energy levels deeper in the bandgap than the bond-angle-fluctuation-induced band tails. The reason why (singly occupied) dangling-bond orbitals should have an electron energy lying near midgap in the case of a-Si can be seen from the simple tight-binding hybrid–orbital picture illustrated in Fig. 7: the dangling-bond orbital is a nonbonding state and hence should lie at the level corresponding to that of the sp^3-hybrids (i.e., at midgap in this model). Such singly occupied, electrically neutral dangling-bond defects in silicon can be represented by the symbol Si_3^0, where the subscript denotes the coordination number at the defect, and the superscript denotes the electrical charge state of the defect. Such Si_3^0 defects are electron-spin resonance (ESR) active because of the unpaired electron spin in the dangling-bond orbital.

Not all dangling-bond defects in amorphous semiconductors are paramagnetic, as they are in a-Si or a-Ge, however. In chalcogenide glasses, which contain the chalcogen (C) elements, S, Se, or Te, alloyed with neighboring elements (e.g., As, Ge, Sb, and B), bond reconstruction can make electron pairing at dangling-bond defects energetically favorable. An electron, transferred between two C_1^0 paramagnetic (Mott et al., 1975) chalcogen dangling-bond defects to create a C_1^+, C_1^- defect pair, can be energetically stabilized by the formation of a dative bond between the empty p-orbital on C_1^+ and the filled nonbonding, lone-pair p-π orbital on a neighboring, normally bonded chalcogen (i.e., C_2^0), thereby forming an over-coordinated defect, C_3^+, with the overall defect reaction being

$$2\mathrm{C}_2^0 \rightarrow \mathrm{C}_3^+ + \mathrm{C}_1^- \tag{7}$$

The so-called valence-alternation pair (VAP) of defects, C_3^+, C_1^-, is spin-paired and hence diamagnetic, and has energy levels closer to the band edges than the near mid-gap position of C_1^0.

The electronic wavefunction

Disorder in a material can cause a qualitative change in the nature of the electron wavefunctions compared with the Bloch form (Eq. (1)) characteristic of perfectly crystalline solids. Instead of all wavefunctions being spatially extended (delocalized) as in the case of single crystals, the presence of disorder can cause some electron states instead to become spatially localized: (Kramer and MacKinnon, 1993) the envelope of the magnitude of the wavefunction then decays exponentially with distance away from the center of localization (or the site of maximum magnitude of the electron charge density, $\rho_e(r)$, or $|\psi(r)|^2$) as

$$\psi(r) = Ae^{-\alpha r} \tag{8}$$

where α^{-1} is the localization length.

An isolated substitutional impurity, for example, a P donor in c-Si (Fig. 1a), also shows clearly the disorder-induced localized nature of the associated electron wave function: the isolated donor state can be represented reasonably accurately by a 1s-like hydrogenic orbital having an exponential envelope, the extra donor electron being bound to the positively charged P^+ donor atom by the Coulomb interaction, screened by the dielectric constant of the Si host, resulting in the effective Bohr radius of the electron orbit (equivalent to the localization length) being several tens of unit-cell lengths in size.

The isolated dangling-bond electron state lying near mid-gap in topologically disordered amorphous semiconductors is more strongly exponentially localized, with the localization length being comparable to the nearest-neighbor bond length, $\alpha^{-1} \cong r_1$. It is generally true that, the deeper the energy level of an electron state in the bandgap, away from the valence-or conduction-band edges, the stronger the degree of spatial localization (i.e., the smaller the value of α^{-1}) of the associated electron wave function.

A remarkable feature of the nature of electron states in disordered materials, such as amorphous solids, is that there are critical energies in the tails of the bands, at which the character of the eigenstates changes from being spatially extended (but non-Bloch-like, and having a dispersion of $\boldsymbol{k}$-values), for states nearer the band center, to being spatially (exponentially) localized, for states nearer the gap. The localization length, α^{-1}, of the envelope of the localized states diverges at the localization-delocalization (LD) transition. Fig. 8 shows this LD transition energy, sometimes called the (electron) mobility edge, because the electron transport changes there from being high-mobility diffusive for extended states to being low mobility involving thermal hopping for localized states, calculated for a structural model of a-Si with a realistic tight-binding electron-interaction Hamiltonian. Also shown in this figure are visualizations of the computed localized electron wavefunction for different representative energies in the gap and the band tail. A dangling-bond state deep in the bandgap is very strongly localized at a coordination defect, the localized wavefunction consisting of a single region of charge density having an exponential envelope. However, localized electron states in the band tail, especially with energies approaching the LD transition, do not consist of single uniform regions of charge density with ever-increasing localization length, α^{-1}. Instead, discrete "islands" of charge density occur within the overall exponential envelope of the localized wave function; these individual islands are also exponentially localized, but their localization length, α_I^{-1}, increases only very gradually, and the number of islands also increases significantly, as their energy moves toward the LD transition. The electron eigenstate at the LD transition itself is a multifractal state consisting of a dense collection of the individual island states (see Fig. 8).

Conclusion

The effects of disorder on electron states in solids are fourfold: (1) the electron wavevector is no longer a good quantum number; (2) sharp features in the density of states are destroyed; (3) bands broaden, creating band tails having an exponential energy dependence; and (4) electron states in band tails and in the bandgap region, lying below a critical energy and corresponding to very disordered sites, are exponentially spatially localized.

References

Elliott SR (1990) *Physics of Amorphous Materials*, 2nd edn, Harlow: Longman.
Elliott SR (1998) *The Physics and Chemistry of Solids*. Chichester: Wiley.
Kramer B and MacKinnon A (1993) Localization: Theory and experiment. *Reports of Progress in Physics* 56: 1469.
Mott NF, Davis EA, and Street RA (1975) States in the gap and recombination in amorphous semiconductors. *Philosophical Magazine* 32: 961–996.

Further reading

Brandes T and Kettemann S (eds.) (2003) *Anderson Localization and its Ramifications: Disorder, Phase Coherence and Electron Correlations*. Berlin, New York: Springer.
Elliott SR (1990) *Physics of Amorphous Materials*, 2nd edn, Harlow: Longman.
Elliott SR (1998) *The Physics and Chemistry of Solids*. Chichester: Wiley.
Kamimura H and Aoki H (1989) *The Physics of Interacting Electrons in Disordered Systems*. Oxford: Clarendon Press.
Kugler S and Shimakawa K (2015) *Amorphous Semiconductors*. Cambridge: Cambridge University Press.
Morigaki K (1999) *Physics of Amorphous Semiconductors*. London: Imperial College Press.
Singh J and Shimakawa K (2003) *Advances in Amorphous Semiconductors*. London: Taylor and Francis.
Tanaka K and Shimakawa K (2021) *Amorphous Chalcogenide Semiconductors and Related Materials*, 2nd edn, Berlin, New York: Springer.

Acoustics: Physical principles and applications to condensed matter physics[☆]

JD Maynard, The Pennsylvania State University, University Park, PA, United States

© 2024 Elsevier Ltd. All rights reserved.

This is an update of J.D. Maynard, Acoustics: Physical Principles and Applications to Condensed Matter Physics, Editor(s): Franco Bassani, Gerald L. Liedl, Peter Wyder, Encyclopedia of Condensed Matter Physics, Elsevier, 2005, Pages 1–8, ISBN 9780123694010, https://doi.org/10.1016/B0-12-369401-9/01129-3.

Introduction 200
Basic acoustic theory 201
Acoustic theory for fluids 202
Acoustic theory for solids and piezoelectrics 203
Application of acoustics to liquids 205
Determination of the equation of state 205
Viscosity 206
Colloids 206
Liquid crystals 206
Containerless confinement of liquids 207
Application of acoustics to solids 207
Diamond 207
Plutonium 207
Thermoelectric devices employing clathrates 207
Piezoelectrics 208
The search for a supersolid 208
Another application of acoustics 209
Conclusion 209
References 209

Abstract

When a system, composed of some substance, is displaced from equilibrium, the forces which were maintaining equilibrium will bring the system back toward equilibrium. Because of the mass of the substance, the system will overshoot equilibrium, then have to return, and subsequently the system will oscillate about equilibrium. This is the essence of acoustics, and it applies to virtually everything, from molecules to galaxies. In acoustic experiments, measurements of acoustic motion and damping, over a wide range of conditions, can be made to high precision and accuracy, and significant information may be obtained about the thermodynamics and interatomic forces involved in condensed matter physics.

Key points

- Provide a detailed theoretical basis for the physics of acoustics
- Discuss precise and accurate experimental acoustic measurement techniques
- Review acoustic measurements on basic liquids and solids
- Review acoustic measurements on exotic liquids and solids
- Present some special applications of acoustics

Introduction

For many materials, acoustic measurements provide a crucial probe of important and fundamental physics of the material. In the case of solids, acoustic data determine derivatives of the free energy with respect to atomic positions (the elastic constants), and can provide information about the environment for electronic phenomena, including piezoelectric, electron-phonon and magnetic effects, and about energy dissipation pathways. Involving tensor quantities, acoustics can probe anisotropic properties of crystals. For both solids and liquids, the measurement of acoustic properties, when taken as functions of temperature, pressure, etc., can be related to other fundamental thermodynamic quantities such as the equation of state, specific heat, Debye temperature and the Gruneisen parameter, and they can be used to check theoretical models. Acoustic measurements are a sensitive probe of first and

---

[☆] *Change History*: July 2022. JD Maynard updated the chapter.

https://doi.org/10.1016/B978-0-323-90800-9.00037-8

second order phase transitions and critical phenomena, including structural transitions in solids, the superconducting transition and the superfluid transition. The application of acoustics in condensed matter physics is a vast field, so only some topics can be covered here. Fortunately, there exist comprehensive accounts in books and review articles; such accounts include the topics of experimental methods (Truell et al., 1969; Goodwin and Trusler, 2003; Leisure, 2017), acoustics for liquids (Levy et al., 2001a), for solids (Levy et al., 2001b; Luthi, 2005; Leisure, 2017), for piezoelectrics (Cady, 1946; Rosen et al., 1992; Yang, 2018), for superfluids (Rudnick, 1970; Kojima, 2001) and for superconductors (Schrieffer, 1964; Levy, 1992), and for acoustic studies of phase transitions and critical phenomena (Ahlers, 1980; Leisure, 2017; Luthi, 2005; Rudnick, 1970, 1978) and damping mechanisms in solids (Bhatia, 1967; Leisure, 2017). Before discussing the principles of acoustics for condensed matter, it would be worthwhile to present some fundamentals of acoustic measurements, because this would elucidate the connections between acoustic theory and experiment.

Most of the early acoustic measurements on materials were made using the time-of-flight of pulses. For solid crystals, this could require re-orienting samples and re-mounting transducers, but analyzing the results to obtain material properties required relatively little computation. However, with the advent of powerful computers, more information can be obtained with a single, simpler measurement. In this case, acoustic resonators are most appropriate, for the following reasons: In introductory physics, it is shown that for a mass on a spring with damping, driven by an oscillating force, the amplitude of the motion of the mass as a function of frequency is a tuning curve, with a peak at the resonance frequency and a defined width. The quality factor Q of the resonance is the resonance frequency divided by the width. Assuming the mass is known, the spring constant may be determined from the resonance frequency and the damping may be determined from the Q. Furthermore, if the system is driven not by an oscillating force on the mass, but by an oscillating displacement at the end of the spring, then at resonance the amplitude of the mass motion is Q times larger than the amplitude of the drive. Thus using a resonator to make measurements has two advantages: first, information is obtained from frequency, which the easiest quantity to measure accurately, and second, one may take advantage of a natural, noise-free amplifier with a gain equal to the Q. Acoustic resonators may be fashioned for condensed matter samples ranging in three-dimensional size from a few hundred microns to meters, as well as samples in the form of thin films or filaments.

In an acoustic resonance measurement, the resonator is designed to minimize damping and avoid any extraneous perturbations of the resonance frequency (or frequencies). One or more tuning curves are recorded and fitted so as to obtain precise resonance frequencies and quality factors. These, along with information about the resonator, are entered into a computer program which then determines the material properties. In the next sections, the theories for fluids and solids will include discussion of the connection between material properties and acoustic resonances and quality factors.

Basic acoustic theory

A condensed matter material is taken to be a large collection of atoms, and within the collection an arbitrary volume V inside a closed surface $\mathscr{A}$ is considered. It is assumed that the volume is just large enough so that a sum of a quantity over the atoms inside may be replaced by an integral of a field over the volume. The motion of the volume is taken to be that of its center-of-mass; the motion of the atoms inside the volume about the center-of-mass is accounted for with thermodynamics. The volume may be defined for only a short time, from t to $t + dt$, sufficient to determine equations governing the dynamics of the fields.

The force acting on the volume is due to the interaction of the atoms just outside the surface with the atoms just inside the surface. For a patch of area $d\mathscr{A}$ with a unit outward normal $\widehat{n}$, the force would be proportional to $d\mathscr{A}$ and in a direction which may be written as a rotation of $\widehat{n}$: $d\vec{F} = \overleftrightarrow{\sigma} \cdot \widehat{n} d\mathscr{A}$, where $\overleftrightarrow{\sigma} = \{\sigma_{ij}\}$ (with i, j = 1,2,3 indexing Cartesian coordinate axes, having unit vectors $\widehat{x}_i$) is referred to as the stress tensor. The force per unit area $d\vec{F}/d\mathscr{A} = \overleftrightarrow{\sigma} \cdot \widehat{n}$ is called the traction.

Net stresses occur when the relative distance between atoms change, which may be determined from a displacement field $\vec{\Psi}\left(\vec{r}, t\right)$, defined so that a point in the material originally at $\vec{r}$ is displaced to $\vec{r} + \vec{\Psi}\left(\vec{r}, t\right)$. For a nearby point $\vec{r} + d\vec{r}$, its displaced position is $\vec{r} + d\vec{r} + \vec{\Psi}\left(\vec{r} + d\vec{r}, t\right)$. The change in the distance between the two points is found from $\vec{\Psi}\left(\vec{r} + d\vec{r}, t\right) - \vec{\Psi}\left(\vec{r}, t\right) = \widehat{x}_i(\partial\Psi_i/\partial x_j)dx_j$ (using the convention that indices repeated in a term indicate summing over those indices). Noting that rotations do not change distances, the change in displacements between nearby points is expressed with a tensor which is symmetric (thereby excluding rotations): $\widehat{x}_i e_{ij} dx_j$, *where* $e_{ij}\left(\vec{r}, t\right) = (1/2)\left(\partial\Psi_i/\partial x_j + \partial\Psi_j/\partial x_i\right)$.

Other fields include the mass density ρ, the velocity $\overrightarrow{\mathscr{U}} = \partial\vec{\Psi}/\partial t$, the entropy per unit mass S, and temperature T (not necessarily constant). All fields may be functions of position $\vec{r}$ and time t. Other quantities usually assumed to be constants include the shear viscosity η, the bulk viscosity ζ and the thermal conductivity κ. Defining a streaming derivative as $D/Dt = \partial/\partial t + \overrightarrow{\mathscr{U}} \cdot \vec{\nabla}$, the constitutive equations (Huang, 1987) are conservation of mass, Newton's law and conservation of energy:

$$\frac{D\rho}{Dt} + \rho\vec{\nabla} \cdot \overrightarrow{\mathscr{U}} = 0 \tag{1}$$

$$\rho\frac{D\overrightarrow{\mathscr{U}}}{Dt} = \vec{\nabla} \cdot \overleftrightarrow{\sigma} + \eta\nabla^2\overrightarrow{\mathscr{U}} + \left(\frac{1}{3}\eta + \zeta\right)\vec{\nabla}\left(\vec{\nabla} \cdot \overrightarrow{\mathscr{U}}\right) \tag{2}$$

$$\rho\frac{DS}{Dt} = \frac{2\eta}{T}\left[\frac{\partial e_{ij}}{\partial t} - \frac{1}{3}\left(\vec{\nabla} \cdot \overrightarrow{\mathscr{U}}\right)\delta_{ij}\right]^2 + \frac{\zeta}{T}\left(\vec{\nabla} \cdot \overrightarrow{\mathscr{U}}\right)^2 + \frac{1}{T}\vec{\nabla} \cdot \left(\kappa\vec{\nabla}T\right) \tag{3}$$

where δ_{ij} is the Kroniker delta. Counting the three components of Newton's law as three independent equations, there are five constitutive equations. The fields $\overrightarrow{\mathscr{U}}$ and e_{ij} are determined from the displacement field $\vec{\Psi}$, and the stress tensor σ_{ij} may be determined from e_{ij}. In thermodynamics, the temperature T, in theory, may be written as a function of the entropy S and the mass density ρ. Thus there are five independent fields: ρ, S and the three components of the displacement field $\vec{\Psi}$, and these are governed by the five constitutive equations.

For piezoelectric and piezomagnetic materials, electric and magnetic fields must be included, along with more constitutive equations. However, it can be shown that magnetic effects are smaller that electric effects by a factor given by the speed of sound divided by the speed of light (Auld, 1990), which has a maximum value of $\sim 10^{-5}$. Thus piezomagnetic effects are small and will not be considered here. For piezoelectric effects, it is sufficient to add just one field, the electric potential Φ, which gives the electric field $\vec{E} = -\vec{\nabla}\Phi$, and from $\vec{E}$ the electric displacement $\vec{D}$ may be determined. Noting that piezoelectric materials cannot have free charges (otherwise their displacement would cancel any piezoelectric field), then a Maxwell equation gives $\vec{\nabla}\cdot\vec{D} = 0$. Thus for piezoelectrics, there is one additional field, Φ, and one additional constitutive equation.

For acoustics, it is assumed that a material undergoes only small deviations from equilibrium. Applying just this to the constitutive equations still results in mathematically difficult and nonlinear equations, so some further assumptions may be made to obtain basic results. First, nonlinear acoustics is an extensive subject on it own, so only first order approximations will be treated here. Second, effects of viscosity and thermal conductivity are small and may be treated perturbatively after basic acoustic equations are solved, so initially η, ζ and κ are set to zero. Finally, it is assumed that in equilibrium, all fields are constant in time and space.

The assumptions above have some immediate consequences. It is assumed that in equilibrium, $\overrightarrow{\mathscr{U}} = 0$, so that $\overrightarrow{\mathscr{U}}$ itself is small. Since only small deviations depend on position, then $\vec{\nabla}$ operates only on small quantities. Thus, in the streaming derivative, $\overrightarrow{\mathscr{U}}\cdot\vec{\nabla}$ is second order, and can be dropped, so that $D/Dt \simeq \partial/\partial t$. With this, and dropping viscosity and thermal conductivity, Eq. (3) becomes $\partial S/\partial t = 0$, so that for basic acoustics, entropy is constant.

In the next section, the acoustic theory for fluids will be presented, followed by a section on acoustic theory for solids and piezoelectrics.

Acoustic theory for fluids

Fluids, by definition, cannot support shear stress, so that $\sigma_{ij} = -P\delta_{ij}$, where $P\left(\vec{r}, t\right)$ is the pressure field in the fluid. For small deviations from equilibrium, $\rho = \bar{\rho} + \rho'\left(\vec{r}, t\right)$ and, $P = \bar{P} + P'\left(\vec{r}, t\right)$, where $\bar{\rho}$ and $\bar{P}$ are the constant, equilibrium values of mass density and pressure. Eqs. (1) and (2) become

$$\frac{\partial \rho'}{\partial t} = -\bar{\rho}\vec{\nabla}\cdot\overrightarrow{\mathscr{U}} \tag{4}$$

$$\bar{\rho}\frac{\partial \overrightarrow{\mathscr{U}}}{\partial t} = -\vec{\nabla}P' \tag{5}$$

Since entropy is constant, thermodynamic derivatives at constant entropy S can be used to relate small quantities (also defining a quantity c_s): $P' = (\partial P/\partial \rho)_S \rho' = c_s^2\rho'; c_s^2 = (\partial P/\partial \rho)_S = \gamma/\mathscr{K}_T$ where γ is the ratio of the specific heat at constant pressure to the specific heat at constant volume, c_p/c_V, and $\mathscr{K}_T = (1/\rho)(\partial\rho/\partial P)_T$ is the isothermal compressibility. Taking two time derivatives of $P' = c_s{}^2\rho'$ and using Eqs. (4) and (5), one obtains

$$\frac{\partial^2 P'}{\partial t^2} = c_s^2\frac{\partial}{\partial t}\left[\frac{\partial \rho'}{\partial t}\right] = c_s^2\frac{\partial}{\partial t}\left[-\bar{\rho}\vec{\nabla}\cdot\overrightarrow{\mathscr{U}}\right] = c_s^2\vec{\nabla}\cdot\left[-\bar{\rho}\frac{\partial\overrightarrow{\mathscr{U}}}{\partial t}\right] = c_s^2\vec{\nabla}\cdot\left[\vec{\nabla}P'\right] = c_s^2\nabla^2 P' \tag{6}$$

This is the wave equation with a speed of sound $c_s = \sqrt{(\partial P/\partial \rho)_S}$. A sound wave in a fluid also has a temperature oscillation, with an amplitude relative to the pressure amplitude given by $T_0' = P_0'(\gamma - 1)/\bar{\rho}c_s^2\beta_p$, where β_p is the thermal expansion coefficient.

At this point, acoustic energy dissipation (losses) due to viscous and thermal conductivity effects may be addressed. As discussed earlier, the quality factor Q accounts for damping in a resonance, and may be determined experimentally as the resonance frequency f divided by the width of the resonance. The Q may also be expressed with a theoretical formula; in this case the$Q$ is $2\pi f$ times the acoustic energy stored in the resonator divided by the rate at which energy is dissipated. The energy stored may be expressed as the kinetic energy plus the potential energy of the acoustic field, expressed in terms of the first order fields found for the resonator. The rate of energy dissipated is equal to the rate at which heat is generated, which is just the temperature T times $\partial S/\partial t$, which is given by Eq. (3). The theoretical formula for the quality factor is found to be

$$\mathcal{Q} = \frac{\bar{\rho}c_s^2}{4\pi^2 f^2}\left[\left(\frac{4}{3}\eta + \zeta\right) + \frac{\kappa}{\gamma c_V}(\gamma - 1)\right]^{-1} \tag{7}$$

The effects of bulk viscosity are usually small and will not be considered here. Eq. (7) is for dissipation only within the volume of fluid; there may be other losses at the interface between the fluid and the walls of the resonator. In particular, shear viscous loss as fluid oscillates back and forth next to a wall usually dominates the dissipation. However, this loss may be completely eliminated with the use of a spherical resonator (Goodwin and Trusler, 2003; Leonard, 1946). In such a resonator, some of the modes involve only radial motion of the fluid, so that there is no motion of the fluid parallel to the wall, and thus there are no wall shear viscous losses. Another advantage of the spherical resonator is that, for a fixed volume, deviations from perfect sphericity have only second order effects on the resonance frequencies. Yet another advantage is that an electrically conducting spherical resonator can also measure microwave resonances, which may be used to calibrate the sphere; in this case, measured sound speeds may be referenced to the speed of light, which is a defined constant. The only intrinsic limitation is that the walls of the resonator usually have a relatively high heat capacity, and remain at constant temperature. In this case, the temperature oscillations in the fluid result in thermal conductivity losses. In any case, the use of different resonators and/or different modes of resonance can enable an accurate determination of c_s, η and κ from measured resonance frequencies and quality factors.

Usually acoustic resonance in fluids corresponds to fitting an integral number of half-wavelengths into a relevant linear dimension. With the wavelength being the speed of sound divided by the frequency, then a study at a low frequency could require a large resonator. This inconvenience can be avoided with the use of a Helmholtz resonator, which is a fluid version of a mass on a spring. This resonator consists of a volume of fluid inside a rigid-walled vessel which opens through a neck to a large (assumed infinite) reservoir of fluid. The volume acts as a spring, the fluid in the neck acts as a mass, and the shear viscous losses at the walls of the neck act as damping. The resonance frequency may be low without requiring that the resonator size be on the order of a wavelength. However, a drawback is that it is difficult to accurately account for the radiation of sound out of the neck into a reservoir which is not infinite. This drawback is eliminated with the double Helmholtz resonator, for which the neck connects two (usually identical) volumes; there is no opening out to a reservoir.

Acoustic theory for solids and piezoelectrics

Before discussing acoustic theory for solids and piezoelectrics, it would be worthwhile to introduce some details about resonance measurements for solids, particularly for a technique referred to as resonant ultrasound spectroscopy (RUS) (Maynard, 1996; Migliori and Sarrao, 1997; Leisure, 2017). A RUS apparatus measures resonance frequencies and quality factors, and this is typically done by contacting the sample with two transducers, a drive and a receiver; the drive provides an oscillating force, and as the drive frequency is swept, the receiver records a tuning curve when the frequency passes through a resonance of the sample. For a sample of solid material, the acoustic resonances depend on the shape and boundary conditions of the sample. It is usually assumed that the sample may be supported in such a manner that the boundaries (surfaces) of the sample are virtually stress free (i.e. the traction at all points on the sample surfaces is zero). A useful sample shape is a rectangular parallelepiped, which has two advantages: one, crystalline samples may be oriented and polished into accurate rectangular parallelepipeds; and two, the sample may be supported at opposite corners, which are mechanically weak, with the result that the transducer contact has minimal effect on the resonance. An example of a RUS apparatus is shown in Fig. 1; this apparatus was designed for small samples, with sample edge lengths of only a few hundred microns. The transducers consist of 0.5 mm wide ribbons of piezoelectric film, only 9μm thick.

As mentioned in the introduction, measured resonance frequencies and quality factors, along with information about the resonator, are entered into a computer program which then determines the material properties. Such a computer program typically has two components. One component assumes likely values for the material properties and then calculates the resonance frequencies; this is referred to as the forward program. In the other component, the program adjusts the values of the material properties in the forward program so that the calculated frequencies and quality factors least-squares fit the measured frequencies and quality factors; this is referred to as the inverse program. In the section below, acoustic theory for solids and piezoelectrics is presented in a manner to address the forward problem.

The forward problem is essentially a boundary value problem, and a convenient method for solving such a problem is to minimize a Lagrangian. The minimization procedure should recover the constitutive equations for the solid as well as the boundary conditions, and the solutions would provide the resonance frequencies (eigenvalues) as well as the normal modes of vibration

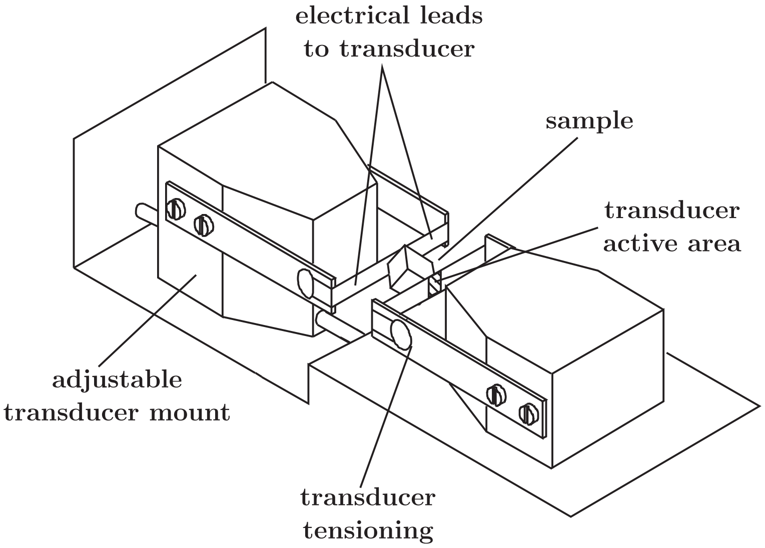

Fig. 1 An apparatus for measuring elastic constants and acoustic attenuation with resonant ultrasound spectroscopy. The transducers are fashioned from 0.5 mm wide ribbons of 9μm thick piezoelectric film. The rectangular parallelepiped sample is supported with two opposing corners lightly touching the transducers.

(eigenfunctions). The constitutive equations are Eqs. (1) through (3), along with $\vec{\nabla}\cdot\vec{D} = 0$ for piezoelectrics. As for fluids, it is assumed that there are small displacements from equilibrium and that η, ζ and κ are zero, so that $D/Dt \simeq \partial/\partial t$ and entropy is constant. The possible boundary conditions for a piezoelectric must be stated: for a point $\vec{r}_{\mathscr{A}}$ on a bare surface of a piezoelectric, $\hat{n}\cdot\vec{D}\left(\vec{r}_{\mathscr{A}}, t\right) = 0$; if a portion of the surface $(\mathscr{A}')$ of the piezoelectric has an electrically conducting film, then the boundary condition is $\Phi\left(\vec{r}_{\mathscr{A}'}, t\right) = 0$.

In the basic theory, it was stated that for piezoelectrics, there were six constitutive equations and six fields: ρ, $\vec{\Psi}$, S and Φ, but this required that σ_{ij} and $\vec{D}$ be known functions of $e_{ij} = (1/2)(\partial\Psi_i/\partial x_j + \partial\Psi_j/\partial x_i)$ and $\vec{E}\left(\text{or } -\vec{\nabla}\Phi\right)$. Since, as a result of small displacements from equilibrium, the constitutive equations have been made linear, then it may be assumed that the required functions are linear. The linear equations, with constant coefficients, are

$$\sigma_{ij} = c_{ijkl}e_{kl} - d_{kij}E_k = c_{ijkl}\frac{\partial\Psi_k}{\partial x_l} + d_{kij}\frac{\partial\Phi}{\partial x_k} \tag{8}$$

$$D_k = d_{kij}e_{ij} + \varepsilon_{ki}E_i = d_{kij}\frac{\partial\Psi_i}{\partial x_j} - \varepsilon_{ki}\frac{\partial\Phi}{\partial x_i} \tag{9}$$

where the c_{ijkl} are the elastic constants, the d_{kij} are the piezoelectric constants and the ε_{ij} are the dielectric constants. The duplication of the d_{kij} in the two equations is the consequence of a thermodynamic Maxwell relation.

To proceed, it is assumed that all acoustic fields have a time dependence $e^{i\omega t}$, where $\omega = 2\pi f : \Psi\left(\vec{r}, t\right) = \psi\left(\vec{r}\right)e^{i\omega t}$ and $\Phi\left(\vec{r}, t\right) = \Phi\left(\vec{r}\right)e^{i\omega t}$. In this case, two time derivatives can be replaced with ω^2, and the Lagrangian is found to be (Holland, 1968, Holland and Eer Nisse, 1968)

$$\begin{aligned}\mathscr{L} = &\iiint \frac{1}{2}\left[\bar{\rho}\omega^2(\psi_i)^2 - \frac{\partial\psi_i}{\partial x_j}c_{ijkl}\frac{\partial\psi_k}{\partial x_l} - 2\frac{\partial\Phi}{\partial x_l}d_{lij}\frac{\partial\psi_i}{\partial x_j} + \frac{\partial\Phi}{\partial x_i}\varepsilon_{ij}\frac{\partial\Phi}{\partial x_j}\right]dV \\ &+ \iint_{\mathscr{A}'}\frac{1}{2}\left[2(\Phi n_i)d_{ikl}\frac{\partial\psi_k}{\partial x_l} - (\Phi n_i)\varepsilon_{ij}\frac{\partial\Phi}{\partial x_j} - \frac{\partial\Phi}{\partial x_i}\varepsilon_{ij}\left(\Phi n_j\right)\right]d\mathscr{A}'\end{aligned} \tag{10}$$

where the volume integral is over the entire sample and the $\mathscr{A}'$ integral is over the portion of the sample's surface which has an electrically conducting film.

In order to solve the Lagrangian minimization problem numerically, the fields ψ_i and Φ must be expanded in series of basis functions, such as $\psi_i = \mathscr{C}_{im}\mathcal{F}_m\left(\vec{r}\right)$, $\psi_j = \mathscr{C}_{jn}\mathcal{F}_n\left(\vec{r}\right)$, where the $\mathscr{C}_{im}$ are coefficients to be determined by minimizing the Lagrangian. Eventually a matrix eigenvalue problem will emerge, and this would be facilitated if $\mathscr{C}_{im}$ had only one index. Thus a single index will be defined for different pairs, e.g. *im* becomes ι, *jn* becomes ς. In this case, the indices i, j, m, n become functions of ι, ς, e.g. $i(\iota)$, $m(\iota)$, etc. The field expansions become

$$\psi_i(x_1, x_2, x_3) = \delta_{ii(\xi)}\mathscr{C}_{\xi}\mathcal{F}_{m(\xi)}(x_1, x_2, x_3) \tag{11}$$

$$\Phi(x_1, x_2, x_3) = \mathscr{D}_{\kappa}\mathscr{F}_{n(\kappa)}(x_1, x_2, x_3) \tag{12}$$

where in Eq. (11) there is no sum over i. The Lagrangian becomes

$$\mathcal{L} = \frac{1}{2}\left[\omega^2\mathscr{C}_{\iota}B_{\iota\zeta}\mathscr{C}_{\varsigma} - \mathscr{C}_{\iota}A_{\iota\zeta}\mathscr{C}_{\varsigma} - 2\mathscr{D}_{\kappa}D_{\kappa\iota}\mathscr{C}_{\iota} + \mathscr{D}_{\kappa}E_{\kappa\xi}\mathscr{D}_{\xi}\right] \tag{13}$$

where

$$A_{\iota\varsigma} = \iiint c_{i(\iota)kj(\varsigma)l}\frac{\partial\mathcal{F}_{m(\iota)}}{\partial x_k}\frac{\partial\mathcal{F}_{n(\varsigma)}}{\partial x_l}dV \tag{14}$$

$$B_{\iota\varsigma} = \delta_{i(\iota)j(\varsigma)}\iiint \overline{\rho}\mathcal{F}_{m(\iota)}\mathcal{F}_{n(\varsigma)}dV \tag{15}$$

$$E_{\kappa\xi} = \iiint \varepsilon_{ij}\frac{\partial\mathcal{F}_{m(\kappa)}}{\partial x_i}\frac{\partial\mathcal{F}_{n(\xi)}}{\partial x_j}dV - \iint_{\mathscr{A}'}\left[\mathcal{F}_{m(\kappa)}n_i\varepsilon_{ij}\frac{\partial\mathcal{F}_{n(\xi)}}{\partial x_j} + \frac{\partial\mathcal{F}_{m(\kappa)}}{\partial x_i}\varepsilon_{ij}\mathcal{F}_{n(\xi)}n_j\right]d\mathscr{A}' \tag{16}$$

$$D_{\kappa\iota} = \iiint d_{li(\iota)j}\frac{\partial\mathcal{F}_{m(\kappa)}}{\partial x_l}\frac{\partial\mathcal{F}_{n(\iota)}}{\partial x_j}dV - \iint_{\mathscr{A}'}\mathcal{F}_{m(\kappa)}n_i d_{ik(\iota)l}\frac{\partial\mathcal{F}_{n(\iota)}}{\partial x_l}d\mathscr{A}' \tag{17}$$

$A_{\iota\zeta}$ is referred to as the stiffness matrix, $B_{\iota\zeta}$ is the mass matrix, $E_{\kappa\xi}$ is the dielectric matrix and $D_{\kappa\iota}$ is the piezoelectric-elastic coupling matrix. To minimize the matrix version of L, Eq. (13), first take a derivative of Eq. (13) with respect to $\mathscr{C}_{\iota}$ and set the result equal to zero:

$$\frac{\partial\mathcal{L}}{\partial\mathscr{C}_{\iota}} = \omega^2B_{\iota\zeta}\mathscr{C}_{\varsigma} - A_{\iota\zeta}\mathscr{C}_{\varsigma} - \mathscr{D}_{\kappa}D_{\kappa\iota} = \omega^2B_{\iota\zeta}\mathscr{C}_{\varsigma} - A_{\iota\zeta}\mathscr{C}_{\varsigma} - \left(D^T\right)_{\iota\xi}\mathscr{D}_{\xi} = 0 \tag{18}$$

where D^T is the transpose of the matrix D. Taking the derivative of Eq. (13) with respect to $\mathscr{D}_{\kappa}$ and setting the result equal to zero gives

$$\frac{\partial \mathcal{L}}{\partial \mathscr{D}_\kappa} = -D_{\kappa\iota}\mathscr{C}_\iota + E_{\kappa\xi}\mathscr{D}_\xi = 0 \tag{19}$$

By inverting the $E_{\kappa\xi}$ matrix, Eq. (19) can be used to solve for the $\mathscr{D}_\xi$ coefficients in terms of the $\mathscr{C}_\iota$ coefficients:

$$\mathscr{D}_\xi = \left(E^{-1}\right)_{\xi\kappa} D_{\kappa\varsigma}\mathscr{C}_\varsigma \tag{20}$$

Substituting for $\mathscr{D}_\xi$ in Eq. (18) gives:

$$0 = \omega^2 B_{\iota\varsigma}\mathscr{C}_\varsigma - A_{\iota\zeta}\mathscr{C}_\varsigma - \left(D^T\right)_{\iota\xi}\left(E^{-1}\right)_{\xi\kappa} D_{\kappa\varsigma}\mathscr{C}_\varsigma \tag{21}$$

This can be re-written to give the piezoelectric generalized eigenvalue problem:

$$\left[A_{\iota\varsigma} + \left(D^T\right)_{\iota\xi}\left(E^{-1}\right)_{\xi\kappa} D_{\kappa\varsigma}\right]\mathscr{C}_\varsigma = \omega^2 B_{\iota\varsigma}\mathscr{C}_\varsigma \tag{22}$$

A computer can solve this equation to yield the resonance frequencies $f_v = \omega_v/2\pi$; for a non-piezoelectric solid, one solves Eq. (22) with $D_{\kappa\iota} = 0$. This constitutes the forward problem for the resonance frequencies, with the matrices containing the material properties. The inverse program for the frequencies could be a standard data-fitting algorithm, such as the genetic algorithm. The quality factors are treated separately, as follows:

The use of $e^{i\omega t}$ in acoustics has two consequences in regard to energy dissipation. From an experimental point of view, the width of the tuning curve may be accounted for by giving each resonance frequency the complex form $f_v(1 + i/2Q_v)$. From a microscopic point of view, the acoustic energy loss in a solid material may be accounted for by giving the elastic constants an imaginary part: $c_{ijkl}(1 + i\varepsilon_{ijkl})$, where ε_{ijkl} is a (usually small) dimensionless loss factor corresponding to the elastic constant c_{ijkl}. Noting that the resonance frequencies f_v of a sample are given by a function of the elastic constants, then if the elastic constants are given an imaginary part, then the resonances frequencies will also acquire an imaginary part, and this must be the same as the experimental form. If the function giving the resonance frequencies in terms of the elastic constants is made complex and expanded to first order in small quantities, then the result is

$$\frac{1}{2Q_v} = \left(\frac{c_{ijkl}}{f_v}\frac{\partial f_v}{\partial c_{ijkl}}\right)\varepsilon_{ijkl} \tag{23}$$

In Eq. (23) there are sums over i, j, k and l, but not over v. The normalized derivatives in Eq. (23) may be determined numerically using the RUS forward program: the elastic constants c_{ijkl} are each in turn given a small change, and the small changes in f_v are calculated; the normalized derivatives are given by the ratios indicated in Eq. (23). A computer program can use Eq. (23) to find the values of the ε_{ijkl} which best fit the measured quality factors.

In the application of RUS to piezoelectrics, the dielectric constants ε_{ij} are usually not adjusted to fit the resonance frequencies; these parameters are easily and accurately determined by sandwiching the piezoelectric in a capacitor of known dimensions and measuring its electrical impedance.

Application of acoustics to liquids

Determination of the equation of state

When the speed of sound of a liquid is measured over an appropriate range of temperature and pressure and combined with measurements of the mass density and isobaric specific heat along one isobar, then relatively stable numerical integration can determine all other thermodynamic properties. Of particular value is the equation of state (EoS) which relates the mass density ρ, the pressure P and the temperature T. In this process, the thermodynamic Maxwell relation

$$\gamma = \frac{c_p}{c_v} = 1 + \frac{T\beta_p^2 c_s^2}{c_p} \tag{24}$$

is used. Even without complete T and P coverage, the speed of sound, as a derivative of density with respect to pressure, provides a sensitive test of a theoretical EoS.

The EoS is of particular importance for reference liquids; an example is water, which can be highly purified and its properties are standardized by the Internation Association for the Properties of Water and Steam (IAPWS). The current water EoS gets the speed of sound to 0.005%, with relative uncertainties of ±10 ppm (Wagner and Pruss, 2002; Benedetto et al., 2005; Scalabrin et al., 2007; Bollengier et al., 2019).

The EoS of liquids are needed for general chemical engineering data and for the design of efficient industrial processes, and speed of sound measurements have contributed to the EoS for many important liquids. Liquid n-hexane (Scholz and Richter, 2021) is a working fluid in geothermal, biodiesel and food processing plants, and n-heptane is an extractant and solvent in chemical and food industries. Methanol (Scholz and Span, 2021b) is important as an energy storage liquid for renewable energy sources; during periods of high supply, methanol can be manufactured, and during times of insufficient supply, the methanol may be burned to cover demand. Liquid (mono)-ethanolamine and diethanolamine (Scholz and Span, 2021c) are used to mitigate climate change by capturing and storing carbon dioxide. Other liquids having numerous important applications and having an EoS developed with acoustics include isobutane (El Hawary and Meier, 2018), ethane (El Hawary and Meier, 2016a), n-butane (El Hawary and Meier, 2016b), propane (Meier and Kabelac, 2012), methane (Cavuoto et al., 2020), toluene (Dhakal et al., 2021), cyclopentane (Gedanitz et al., 2015), propylene glycol (Eisenbach et al., 2021), octamethyltrisiloxane and decamethyltetrasiloxane (Thol et al., 2017).

The EoS for liquids under extreme conditions are needed for research in geophysics (Ghiorso and Kress, 2004), planetary sciences and astrophysics, for the understanding of shock waves (McCoy et al., 2017), and for heat transfer in nuclear reactors. In the case for nuclear reactors, the liquids require high heat of vaporization, high thermal conductivity, low viscosity and a wide range of liquid densities, and liquid metals typically satisfy these requirements. Speed of sound measurements at high temperatures and pressures have been performed on liquid alkali metals (Ramasama and Karuppannan, 2019), liquid lead (Kozyrev and Gordeev, 2021), liquid tin (Humrickhouse, 2019) and liquid bismuth (Su et al., 2017). Sound velocity measurements at extreme pressures are made typically in a diamond anvil cell.

Liquid mercury is of special interest; it has a metal-to-non-metal transition which involves inter-atomic pseudo-potentials, and the variation of the speed of sound with pressure and temperature can provide important information. Normally, the sound velocity reflects the long-range electron screened interaction, but at large mercury mass densities, the sound velocity probes the repulsive part of the potential (Ayrinhac et al., 2014).

Viscosity

The measurement of shear viscosity (as well as mass density) of a liquid is often accomplished with a "quartz microbalance", which is a resonator with a flat surface oscillating back and forth in the plane of the surface. If a bulk liquid, film of liquid or drop of liquid is in contact with the surface, then the frequency of the resonator is decreased by an amount which can be used to determine the mass density of the liquid, and the quality factor of the resonance is decreased by an amount which can be used to determine the shear viscosity of the liquid (Crane and Fischer, 1979). Typically the resonator is a quartz crystal cut so as to have a thickness shear mode which has the least temperature dependence (in order to facilitate measuring the temperature dependence of the shear viscosity). Longitudinal mode resonators for measuring liquid bulk viscosity may also be used (Taskoprulu et al., 1961), and piezoelectrics other than quartz may be used (Bannai and Wakatsuki, 2003).

With the advent of microelectromechanical systems, atomic force microscopes and other devices made with microelectronic fabrication techniques, other resonator-based viscometers have been devised. Typically a quartz tuning fork is used, either completely immersed in the liquid (Voglhuber-Brunnmaier et al., 2019; Zhang et al., 2020), or with a needle appendage extended through a liquid surface (Fernandez et al., 2018). A variation employs a cantilever vibrator with a needle which immerses a small sphere in the liquid (Patois et al., 2000). These viscometers require complicated analyses, and it is not clear if there are advantages over the microbalance resonator.

As discussed earlier, a particularly useful device in acoustics is the double Helmholtz resonator, which consists of two volumes connected by a neck. If the neck is an appropriately sized capillary, then such a resonator is a "Greenspan viscometer" (Gillis et al., 2003); the resonance frequency and quality factor can be used to determine the mass density or adiabatic bulk modulus, and the shear viscosity of the fluid. The Greenspan viscometer is a standard for determining viscosity for gases. Inexplicably, only single Helmholtz resonators have been used for liquids (Ehlers, 1960; Chen and Park, 2019).

Colloids

Sound waves experience novel effects when propagating in colloids, which are liquids containing insoluble particles of a particular size (typically 1–1000 nm) and density. If the wavelength of longitudinal sound is about the same as the size of the particle, then the sound will experience maximum scattering, and with sufficient interaction, an acoustic shear wave can propagate (Forrester et al., 2016). If the density of particles is sufficiently large so that the particles can touch and undergo a percolation transition, then the sound wave will exhibit a significant change in speed and indicate power law behavior as a function of particle density (Ye et al., 1993). Measurements of the attenuation of sound can provide information about the interactions between the particles (Lebedev-Stepanov and Rybak, 2011), and acoustic measurements as a function of temperature can indicate that at low temperatures particles may agglomerate and form larger particles (Blaudez et al., 1994). Since longitudinal sound waves modulate the density of the particles, and since the scattering of light by a colloid depends on the density of particles, then the combined effect (the photo-acoustic effect) can be used to further probe and image effects in a colloid (Fuentes-Oliver et al., 2021).

Liquid crystals

Acoustic measurements have a number of ways of obtaining information about liquid crystals, which are liquids composed of elongated, rod-like molecules. In such liquids, the molecules may be unaligned and disordered in position, aligned and disordered in position, or aligned with various patterns in position, and there can be phase transitions between the different possibilities. The modes of acoustic propagation and attenuation are numerous, and it will not be possible to provide a comprehensive treatment here; however, there are review texts (de Gennes, 1993; Yang and Wu, 2015; Larionov et al., 2017). Some representative acoustics research includes anisotropic wave propagation (Biscari et al., 2014), the effect of lattice defects in a cubic crystal-like phase (Fujii and Henrich, 2021), viscoelastic effects (Turzi, 2016) and relaxation effects near a phase transition (Balcerzak, 2005).

Containerless confinement of liquids

One of the problems with measurements on liquids, particularly in undercooled metastable states, is that the walls of a container may have a significant effect on the phenomenon under study. This can be overcome with "containerless" measurements made possible with acoustic levitation and confinement; these are nonlinear acoustic effects which may be explained as follows:

In an acoustic standing wave, fluid particles at a node are motionless while fluid particles at an antinode are oscillating back and forth with a maximum amplitude. If one time averages, then the averaged velocity of the fluid is zero everywhere. However, if one time averages the square of the velocity, U^2, then one gets zero at a node and a maximum value at an antinode. Bernoulli's law states that where U^2 is large, then pressure is diminished; the result is that there is a pressure gradient from nodes to antinodes. A gas (possibly inert) resonator may be fabricated so that a vertical standing wave can levitate a liquid mass, and horizontal standing waves, with pressure minima, can hold the liquid in a selected position. If the horizontal standing waves are driven 90 degrees out of phase, then the liquid mass may be made to rotate. In a microgravity application, the levitating wave may become a vertical positioning wave. When providing a containerless environment for liquids, acoustics in not the probe; the probe may be light, synchrotron radiation or a neutron beam (Kohara et al., 2018).

Application of acoustics to solids

The use of acoustics to determine elastic constants and piezoelectric constants is a vast enterprise, and review books and articles have been mentioned in the introduction. Only a few representative examples will be mentioned here.

Diamond

RUS was used to measure, at unprecedented precision, all of the elastic constants for a single crystal of diamond over the temperature range from 10 K to 322 K (Migliori et al., 2008). The published paper shows in detail how the results can be used to determine the phonon distribution function, the Debye temperature parameter (used in the Debye-Einstein model for the specific heat and the Bardeen-Cooper-Schreifer theory for superconductivity), parameters related to interatomic potentials, and the Gruneisen parameter which reflects anharmonic and finite temperature effects.

Plutonium

Plutonium is one of the most complicated and puzzling materials in condensed matter physics. It has six different crystal structures, extreme elastic anisotropy, negative thermal expansion, large volume changes during structural transitions, a relatively incomprehensible electronic structure and aging effects (defect formation) resulting from its own nuclear radiation. During the time when a satisfactory explanation of the physics was not available, it was feared that aging could make old nuclear weapons unreliable, so that fresh nuclear weapons had to be manufactured. Fortunately, RUS measurements on old and new plutonium under a comprehensive array of conditions significantly changed the situation (Mairov et al., 2017; Keppens et al., 2010). The vastly enhanced understanding of aging has improved the confidence in nuclear weapons, and this has supported a considerable reduction of the stockpile of nuclear weapons. The plutonium research has been a notable benefit of acoustics to society as well as to condensed matter physics.

Thermoelectric devices employing clathrates

Thermoelectric materials could make very useful devices: by passing an electrical current through them, they could provide cooling with no moving parts; by delivering heat to them (possibly waste heat from an engine or industrial process) they could generate electricity. However, there is a difficulty, because for large heat transport, large electrical currents would be involved, so that a thermoelectric material should have high electrical conductivity. However, a general property of solids is that a large electrical conductivity is almost always accompanied by a large thermal conductivity, and this conductivity would "short out" any desired temperature gradient across the thermoelectric device. What is needed is some unusual material which has a large electrical conductivity (meaning low scattering of electrons) and a small thermal conductivity (meaning high scattering of thermal lattice vibrations, or phonons). Materials which have possibilities are the clathrates; these materials are semiconductors (which can have satisfactory electrical conductivity) with voids in their lattice structure which can hold foreign "guest" atoms. Through spring-like interactions with the host atoms at the surface of the void, the guest atoms can have several modes of vibration and can provide a relatively large scattering cross-section for thermal phonons, thereby reducing the thermal conductivity. These guest vibrators also have a dramatic effect on the temperature dependence of the clathrate's elastic constants, as illustrated in Fig. 2. The solid line in the figure shows the behavior an elastic constant for nearly all materials (excluding phase transitions); the dashed line is taken from a RUS measurement on a clathrate, showing a radical deviation. (Zerec et al., 2004).

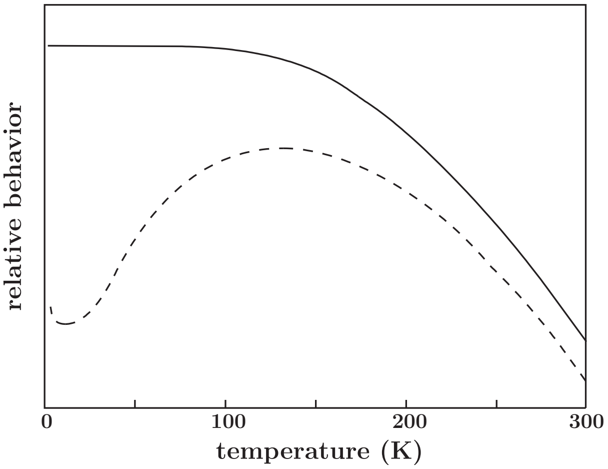

Fig. 2 Illustration of the temperature behavior of most elastic constants (solid line), and the dramatically different behavior of clathrates (dashed line). The acoustics of these materials make them potential candidates for high performance thermoelectrics.

Piezoelectrics

Measurements of elastic and piezoelectric constants have been undertaken for decades. However, early measurements required that samples be re-cut, re-polished, have transducers re-attached, and have conducting films re-deposited, sometimes as many as five times. There was so much bother that measurements were often made at room temperature only, and because measurements were made under so many different conditions, the results were often inconsistent. With RUS, one sample can be mounted once, held at a controlled temperature, and have a spectrum of frequencies measured in a matter of minutes; the measurement can then be repeated with only the temperature (or other external field) changed. For each temperature, the spectrum of frequencies may be used to determine a complete and self-consistent set of elastic and piezoelectric constants.

Such measurements have been made for classic piezoelectrics, including quartz (Ogi et al., 2006), lithium niobate and lithium tantalate (Tarumi et al., 2012). potassium titanyl phosphate (Zhang et al., 2016), tourmaline (Pandey and Schreuer, 2012) and lead-zirconate-titanate (Li et al., 2019; Zhang et al., 2017) Measurements have been made on exotic materials showing giant piezoelectric effects (relaxor-based ferroelectric single crystals) including lead-magnesium-niobium-lead-titanate and lead-indium-niobium-lead-titinate (Schreuer, 2002; Delaunay et al., 2008; Chen et al., 2019) For promising practical applications, measurements have been mode on high-temperature piezoelectrics, including langstate (Davulis and da Cunha, 2013) and langasite (Ogi et al., 2003). RUS has also been used to study symmetry breaking in crystals which normally would not be piezoelectric (Aktas et al., 2021).

The search for a supersolid

In 2004, an experiment indicating the probable observation of a supersolid phase of helium four was reported (Kim and Chan, 2004). The experiment involved measuring the temperature dependence of the resonance frequency of a torsional oscillator, which consisted of a torsion rod connected to a cylindrical "bob"; solid helium was confined inside the bob. An elementary model of the oscillator was that of a torsional spring connected to a rigid-body bob, so that the resonance frequency was simply related to the torsional spring constant divided by the moment of inertia of the bob. Such a model was used with great success in the study of superfluid helium; the principle was that when the helium became superfluid (or supersolid), then the helium would decouple from the rest of the bob and no longer fully contribute to the moment of inertia, and the resonance frequency would increase. While this elementary model is satisfactory for liquid helium, it is insufficient for solid helium. The problem is that there is no such thing as a rigid body, and as indicated in the theory section for acoustics in solids, the proper model for the resonance frequency of the torsional oscillator requires knowing the mass density and shear modulus throughout the entire apparatus. There are two reasons why the elementary model was satisfactory for liquid helium but not for the solid: one, the shear modulus of a liquid is always zero and has no temperature dependence; and two, it was already known that the shear viscosity of liquid helium changed abruptly at the superfluid transition temperature. By contrast, solid helium has a shear modulus which could change with temperature regardless of a supersolid transition, but at the time its temperature dependence was unknown. In 2007 the temperature dependence of the shear modulus was measured with an independent acoustic method (Day and Beamish, 2007), and it was found that it did change in an anomalous fashion in the temperature range of the supersolid observations and could account for the change in the torsional oscillator resonance frequency. While the temperature dependence of the solid helium shear modulus was not related to a supersolid, it was interesting in its own right, involving the thermally activated depinning of helium three impurities from lattice defects in a quantum solid (Day and Beamish, 2007).

Another application of acoustics

In condensed matter theory, one might determine material properties by using the energies (quantum or classical) of individual atoms and calculating averages over a large collection. Experimentally, one cannot measure the energies of individual atoms, but one can measure the temperature and then determine averages with a distribution function. In order to make the connection between energies in the theory and temperatures in the experiment, one needs the Boltzmann constant, which has been one of the least accurately known of the fundamental physical constants. This has changed because of acoustic measurements in spherical resonators, where a speed of sound was measured to high accuracy, and by calibrating the resonator with microwaves, the measured speed was related to the speed of light, a defined physical constant. The fluid in the spherical resonator was low density helium gas, for which the theoretical status had become so advanced that its speed of sound could be calculated to high accuracy. By comparing the experimental and theoretical results, the Boltzmann constant could be determined to such high accuracy that it could be made a defined fundamental constant (Pitre et al., 2017). Furthermore, the acoustic method is now the standard for measuring temperature. While the measurements do not involve a liquid or solid, they are certainly a notable contribution from acoustics to condensed matter physics.

Conclusion

Acoustic measurements are being made easier, over a wider scope of materials, and under a broader range of conditions. The results are increasingly more precise, accurate and self-consistent. Information obtained from acoustic measurements about condensed matter physics has led to improved a priori calculations and predictions of behavior in conditions not readily available for study. It is anticipated that this process will continue and grow in the future.

References

Ahlers G (1980) Critical phenomena at low temperature. *Reviews of Modern Physics* 52: 489–503.

Aktas O, Kangama M, Linyu G, Catalan G, and Ding X (2021) Piezoelectricity in nominally centrosymmetric phases. *Physical Review Research* 3(043221): 1–13.

Auld BA (1990) *Acoustic fields and waves in solids*. Florida: Krieger.

Ayrinhac S, Gauthier M, Bove LE, Morand M, Le Marchand G, Bergame F, Philippe J, and Decremps F (2014) Equation of state of liquid mercury to 520 K and 7 GPa from acoustic velocity measurements. *The Journal of Chemical Physics* 140(244201): 1–11.

Balcerzak A (2005) Relaxation phenomena in the nematic phase of liquid crystal near phase transition. *Molecular and Quantum Acoustics* 26: 7–13.

Bannai M and Wakatsuki N (2003) A study on shear wave $LiTaO_3$ resonators for viscosity sensor. *Japanese Journal of Applied Physics* 42: 3093–3097.

Benedetto G, Gavioso RM, Albo PAG, Lago S, Ripa DM, and Spagnolo R (2005) Speed of sound in pure water at temperatures between 274 and 395 K and at pressures up to 90 MPa. *International Journal of Thermophysics* 26: 1667–1680.

Bhatia AB (1967) *Ultrasonic Absorption*. Oxford: Oxford University Press.

Biscari P, DiCarlo A, and Turzi SS (2014) Anisotropic wave propagation in nematic liquid crystals. *Soft Matter* 10: 8296–8307.

Blaudez D, Lombardo D, Mallamace F, and Micali N (1994) Sound propagation and viscosity in water short-chain amphiphiles solutions, evidence of percolation phenomena. *Il Nuovo Cimento* 16D: 1619–1625.

Bollengier O, Brown JM, and Shaw GH (2019) Thermodynamics of pure liquid water: Sound speed measurements tp 700 MPa down to the freezing point, and an equation of state to 2300 MPa from 240 to 500 K. *The Journal of Chemical Physics* 151(054501): 1–17.

Cady WG (1946) *Piezoelectricity*. New York: McGraw-Hill.

Cavuoto G, Lago S, Albo PAG, and Serazio D (2020) Speed of sound measurements in liquid methane (CH_4) at cryogenic temperatures between 130 and 162 K and at pressures up to 10 MPa. *The Journal of Chemical Thermodynamics* 142(106007): 1–11.

Chen Y and Park Y-H (2019) Measurement of an analyte concentration in test solution by using Helmholtz resonator for biosensor applications. *Sensors* 19(1127): 1–9.

Chen C, Liu S, Tan X, Tang L, and Cao W (2019) Accurate characterization of complete set constants of single domain $0.72Pb(Mg_{1/3}Nb_{2/3})O_3 - 0.28PbTiO_3$ single crystal by resonant ultrasound spectroscopy using only one sample. *Journal of Applied Physics* 125(064102): 1–11.

Crane RA and Fischer G (1979) Analysis of a quartz crystal microbalance with coatings of finite viscosity. *Journal of Physics D: Applied Physics* 12: 2019–2026.

Davulis PM and da Cunha MP (2013) A full set of langatate high-temperature acoustic wave constants: elastic, piezielectric, dielectric constants up to 900 C. *IEEE Transactions on Ultrasonics, Ferroelectrics, and Frequency Control* 60: 824–833.

Day J and Beamish J (2007) Low-temprature shear modulus changes in solid He and connection to supersolidity. *Nature Letters* 450: 853–856.

de Gennes PG (1993) *The Physics of Liquid Crystals*. Oxford: Clarendon Press.

Delaunay TD, Le Clezio E, Guennou M, Dammak H, Thi MP, and Feuillard G (2008) Full tensorial characterization of PZN-12%PT single crystal by resonant ultrasound spectroscopy. *IEEE Transactions on Ultrasonics, Ferroelectrics, and Frequency Control* 55: 476–488.

Dhakal S, Tay WJ, Al Ghafri SZS, Rowland D, Mullins SP, May EF, Trusler JPM, and Stanwix PL (2021) Thermodynamic properties of liquid toluene from speed-of-sound measurements at temperatures from 283.15 to 473.15 K and at pressures up to 390 MPa. *International Journal of Thermophysics* 42, 169: 1–40.

Ehlers FE (1960) Method for measuring bulk modulus of a liquid using a Helmholtz resonator. *The Journal of the Acoustical Society of America* 32: 538–546.

Eisenbach T, Scholz C, Span R, Cristabcho D, and Lemmon EW (2021) Speed-of-sound measurements and a fundamental equation of state for propylene glycol. *Journal of Physical and Chemical Reference Data* 50(023105): 1–26.

El Hawary A and Meier K (2016a) Measurements of the Speed of sound in liquid and supercritical ethane. *Fluid Phase Equilibria* 418: 125–132.

El Hawary A and Meier K (2016b) Measurements of the Speed of sound in liquid n-butane. *Journal of Chemical & Engineering Data* 61: 3858–3867.

El Hawary A and Meier K (2018) Speed-of-sound measurements and derived thermodynamic properties of liquid isobutane. *Journal of Chemical Engineering* 63: 3684–3703.

Fernandez R, Brockman T, Bai J, and La Rosa AH (2018) Confined fluid analyzed with near-field acoustic detection. *Journal of Physics Conference Series* 1143(012017): 1–10.

Forrester DM, Huang J, and Pinfeld VJ (2016) Characterisation of colloidal dispersions using ultrasound spectroscopy and multiple-scattering theory inclusive of shear wave effects. *Chemical Engineering Research and Design* 114: 69–78.

Fuentes-Oliver EI, Moock VM, Quispe-Sicca RM, Fernandez-Bienes A, and Garcia-Segundo C (2021) Analysis of the photoacoustic spectral dispersion in dielectric colloids. *Physica Scripta* 96(125510): 1–13.

Fujii S and Henrich O (2021) Shear-enhanced elasticity in the cubic blue phase I. *Physical Review E* 103(052704): 1–11.

Gedanitz H, Davila MJ, and Lemmon E (2015) Speed of sound measurements and a fundamental equation of state for cyclopentane. *Journal of Chemical & Engineering Data* 60: 1331–1337.

Ghiorso MS and Kress VC (2004) An equation of state for silicate melts II. Calibration of volumetric properties at 10^5 Pa. *American Journal of Science* 304: 679–751.

Gillis KA, Mehl JB, and Moldover MR (2003) Theory of the Greenspan viscometer. *The Journal of the Acoustical Society of America* 114: 166–173.

Goodwin ARH and Trusler JPM (2003) Measurement of the speed of sound. In: Goodwin ARH, Marsh KN, and Wakeham WA (eds.) *Measurement of the Thermodynamic Properties of Single Phases*, pp. 237–323. Amsterdam: Elsevier.

Holland R (1968) Resonant properties of piezoelectric ceramic rectangular parallelepipeds. *The Journal of the Acoustical Society of America* 43: 988–997.

Holland R and Eer Nisse EP (1968) Variational evaluation of admittances of multi-electrided three-dimensional piezoelectric structures. *IEEE Transactions on Sonics and Ultrasonics* SU-15: 119–132.

Huang K (1987) *Statistical Mechanics*. New York: John Wiley and Sons, 96–113.

Humrickhouse PW (2019) An equation of state and compendium of thermophysical properties of liquid tin, a prospective plasma-facing material. *IEEE Transactions on Plasma Science* 47: 3374–3379.

Keppens VM, Maynard JD, and Migliori A (2010) Listening to materials: From auto safety to reducing the nuclear arsenal. *Acoustics Today* 6: 6–13.

Kim E and Chan MHW (2004) Probable observation of a supersolid helium phase. *Nature* 427: 225–227.

Kohara S, Ohara K, Ishikawa T, Tamaro H, and Weber R (2018) Investigation of structure and dynamics in disordered materials using containerless techniques with in-situ quantum beam and thermophysical property measurments. *Quantum Beam Science* 2(2010005): 1–23.

Kojima H (2001) In: Levy M, Bass HE, Stern RR, Raspet R, and Sinha DN (eds.) *Velocity and absorption of sound waves in superfluid He, in: Handbook of Elastic Properties of Solids, Liquids and Gases, Volume IV Elastic Properties of Fluids: Liquids and Gases*. San Diego: Academic Press.

Kozyrev NV and Gordeev VV (2021) Thermodynamic characterization and equation of state for solid and liquid lead. *Metals* 2022(12): 1–19.

Larionov AN, Polivaev OI, Larionova NN, Kunetsov AN, and Gorban LK (2017) Acoustic researches of liquid crystals and prospects of their application in electronic devices of automobile transport. *Materials Science and Engineering* 327(042060): 1–6.

Lebedev-Stepanov PV and Rybak SA (2011) Sound absorption in a colloidal solution of interacting particles. *Acoustical Physics* 57: 786–791.

Leisure RG (2017) *Ultrasonic Spectroscopy*. Cambridge University Press.

Leonard RW (1946) The attenuation of ultrasonic sound waves in water by a reverberation method. *The Journal of the Acoustical Society of America* 18: 252.

Levy M (1992) *Ultrasonics of High- T_c and Other Unconventional Superconductors, Physical Acosutics*. vol. XX. Boston: Academic Press.

Levy M, Bass HE, Stern RR, and Keppens V (2001a) Handbook of elastic properties of solids, liquids and gases, volume II elastic properties of solids. In: *Theory, Elements and Compounds, Technological Materials, Alloys and Building Materials*. San Diego: Academic Press.

Levy M, Bass HE, Stern RR, Raspet R, and Sinha DN (2001b) *Handbook of Elastic Properties of Solids, Liquids and Gases. Elastic Properties of Fluids: Liquids and Gases*, vol. IV. San Diego: Academic Press.

Li H, Ma Y, Zhou Z, Yan T, Wu Y, Tang L, Liu S, and Wu X (2019) Characterizing elastic and piezoelectric constants of piezoelectric materials from one sample using resonant ultrasonic spectroscopy. *Journal of Materials Science* 54: 6786–6798.

Luthi B (2005) *Physical Acoustics in the Solid State*. Springer.

Mairov B, Betts JB, Soderlind P, Landa A, Hernandez SC, Saleh TA, Freibert FJ, and Migliori A (2017) Elastic moduli of δ-Pu^{239} reveal aging in real time. *Journal of Applied Physics* 121(125107): 1–9.

Maynard JD (1996) Resonant ultrasound spectroscopy. *Physics Today* 49: 26–31.

McCoy CA, Knudsen MD, and Root S (2017) Absolut measurement of the Hugoniot and sound velocity of liquid copper at multimegabar pressures. *Physical Review B* 96(174109): 1–8.

Meier K and Kabelac S (2012) Thermodynamics properties of propane. IV. Speed of sound in the liquid and supercritical regions. *Journal of Chemical & Engineering Data* 57: 3391–3398.

Migliori A and Sarrao JL (1997) *Resonant Ultrasound Spectroscopy*. New York: John Wiley & Sons.

Migliori A, Ledbetter H, Leisure R, Pantea C, and Betts JB (2008) Diamond's elastic stiffness from 322 to 10 K. *Journal of Applied Physics* 104(053512): 1–4.

Ogi H, Nakamura N, Sato K, Hirao M, and Uda S (2003) Elastic, anelastic and piezoelectric coefficients of langsite: Resonance ultrasound spectroscopy with laser-doppler interferometry. *IEEE Transactions on Ultrasonics, Ferroelectrics, and Frequency Control* 50: 533–560.

Ogi H, Ohmori T, Nakamura N, and Hirao M (2006) Elastic, anelastic and piezoelectric coefficients of α-quartz determined by resonance ultrasound spectroscopy. *Journal of Applied Physics* 100(053511): 1–7.

Pandey CS and Schreuer J (2012) Elastic and piezoelastic constants of tourmaline single crystals at non-ambient temperatures determined by resonant ultrasound spectroscopy. *Journal of Applied Physics* 111(013516): 1–7.

Patois R, Vairac P, and Cretin B (2000) Near-field acoustic densimeter and viscosimeter. *The Review of Scientific Instruments* 71: 3860–3863.

Pitre L, Sparasci F, Risegari L, Guianvarc'h C, Martin C, Himbert ME, Plimmer MD, Allard A, Marty B, Giuliano Albo PA, Gao B, Moldover MR, and Mehl JB (2017) New measurement of the Boltzmann constant k by acoustic thermometry of helium-4 gas. *Metrologia* 54: 856–873.

Ramasama B and Karuppannan R (2019) Sound speed in fluid alkali metals. *American Journal of Chemistry and Materials Science* 6: 44–51.

Rosen CZ, Hiremath BV, and Newnham RE (1992) *Piezoelectricity*. New York: American Institute of Physics.

Rudnick I (1970) Selected problems in sound propagation in liquid helium. In: *Proceedings of the Batsheva Conference, Technion, Haifa, Isreal. Gordon Breach*, 251–283.

Rudnick I (1978) Critical surface density of the superfluid component in He films. *Physical Review Letters* 40: 1454–1455.

Scalabrin G, Concion MG, Marchi P, and Lago S (2007) Development of a fundamental equation of state for the liquid region of a pure fluid from speed of sound measurements. Application to water. *Experimental Thermal and Fluid Science* 31: 539–549.

Scholz CW and Richter M (2021) Speeds of sound in n-hexane and n-heptane at temperatures from 233.33 to 353.21 K and pressures up to 20 MPa. *International Journal of Thermophysics* 42(18): 1–23.

Scholz CW and Span R (2021b) Speeds of sound in methanol at at temperatures from 233.33 to 353.21 K at pressures up to 20 MPa. *International Journal of Thermophysics* 42(65): 1–13.

Scholz, C. W. and Span, R., 2021c. Measurements of the (p,ρ,T) behavior of liquid MEA and DEA at temperatures from 293.15 to 423.15 K at pressures up to 90 MPa. International Journal of Thermophysics, **42**:70, 1–26. (sales pitch only)

Schreuer J (2002) Elastic and piezoelectric properties of $La_3Ga_5SiO_{14}$ and $La_3Ga_{5.5}Ta_{0.5}O_{14}$: An application of resonant ultrasound spectroscopy. *IEEE Transactions on Ultrasonics, Ferroelectrics, and Frequency Control* 49: 1474–1479.

Schrieffer JR (1964) *Theory of Superconductivity*. New York: W. A. Benjamin.

Su C, Liu Y, Wang Z, Song W, Asimow PD, Tang H, and Xie H (2017) Equation of state of liquid bismuth and its melting curve from ultrasonic investigation at high pressure. *Physica B* 524: 154–162.

Tarumi R, Matsuhisa T, and Shibutani Y (2012) Low temperature elastic constants and piezoelectric coefficients of $LiNbO_3$ and $LiTaO_3$: Resonant ultrasound spectroscopy measurement and lattice dynamics analysis. *Japanese Journal of Applied Physics* 51: 1–6. 07GA02.

Taskoprulu NS, Barlow AJ, and Lamb J (1961) Ultrasonic and visco-elastic relaxation in a lubricating oil. *The Journal of the Acoustical Society of America* 33: 278–285.

Thol M, Dubberke FH, Baumhogger E, Vrabec J, and Span R (2017) Speed of sound measurements and fundamental equations of state for octamethyltrisiloxane and decamethyltetrasiloxane. *Journal of Chemical & Engineering Data* 62: 2633–2648.

Truell R, Elbaum C, and Chick BB (1969) *Ultrasonic Methods in Solid State Physics*. New York: Academic Press.

Turzi SS (2016) Viscoelastic nematodynamics. *Physical Review E* 94(062705): 1–9.

Voglhuber-Brunnmaier T, Niedermayer AO, Feichtinger F, and Jakoby B (2019) Fluid sensing using quartz tuning forks - Measurement technology and applications. *Sensors* 19(2336): 1–15.

Wagner W and Pruss A (2002) The IAPWS formulation 1995 for the thermodynamic properties of ordinary water substance for general and scientific use. *Journal of Physical and Chemical Reference Data* 31: 387–535.

Yang J (2018) *An Introduction to the Theory of Piezoelectricity*. Springer.

Yang D-K and Wu S-T (2015) *Fundamentals of liquid crystal devices*. UK: John Wiley and Sons.

Ye L, Liu J, Sheng P, Huang JS, and Weitz DA (1993) Sound propagation in colloidal systems. *Journal de Physique* 3: 183–196.

Zerec I, Keppens V, McGuire MA, Mandrus D, Sales BC, and Thalmeier P (2004) Four-well tunneling states and elastic response of clathrates. *Physical Review Letters* 92(185502): 1–4.

Zhang Y, Tang L, Ji N, Liu G, Wang J, and Jiang H (2016) Temperature dependence of full set tensor properties of $KTiOPO_4$ single crystal measured from one sample. *Journal of Applied Physics* 119(124104): 1–7.

Zhang Y, Tang L, Tian H, Wang J, and Cao W (2017) Determination of temperature dependence of full matrix material constants of PZT-8 piezoceramics using only one sample. *Journal of Alloys and Compounds* 714: 20–25.

Zhang M, Chen D, He X, and Wang X (2020) A hydrodynamic model for measuring fluid density and viscosity by using quartz tuning forks. *Sensors* 20(198): 1–12.

Numerical methods for localization

Rudolf A Römer, Department of Physics, University of Warwick, Coventry, West Midlands, United Kingdom

© 2024 Elsevier Ltd. All rights reserved.

Introduction 212
Exact diagonalization 213
Quasi 1D methods 213
Renormalization and decimation methods 214
Energy-level statistics 215
Wavefunction statistics and multi-fractal analysis 215
Finite-size scaling 216
Localization and many-body interactions 216
Machine learning 217
Conclusion 217
Acknowledgments 217
References 217

Abstract

Anderson localization provides a challenge to numerical approaches due to the inherent randomness, and hence absence of simple symmetries, in its discrete Hamiltonian representation. Numerous algorithmic approaches have been developed or adopted from other fields and have been collected in this encyclopedia entry. In the discussions below, the emphasis is on the numerical algorithms for localization, while the discussion of the physics of localization is referred to in companion entries by Elgart and Oganesyan in this encyclopedia.

Key points

- The article reviews existing numerical algorithms used when studying Anderson localization and gives relevant references
- algorithms for data generation
  1. diagonalization strategies such as exact methods, sparse-matrix methods, kernel-polynomial methods
  2. iterative/quasi-1D algorithms such as the transfer-matrix and the Green function method
  3. renormalization-inspired numerical approaches
- data analysis algorithms
  1. energy-level and -ratio statistics
  2. wave function statistics and multi-fractal analysis
  3. finite-size scaling algorithms, with and without assuming a scaling form
- current challenges
  1. numerical algorithms in use for data generation and analysis of interacting disordered systems
  2. algorithms based on machine learning strategies

Introduction

Anderson localization, as reviewed in this encyclopedia in other entries, cannot be solved analytically in dimensions two and above (Stollmann, 2001). Hence much effort has been focused on developing efficient numerical tools. In its usual form, the discrete Anderson Hamiltonian (Anderson, 1958) is given by the matrix elements

$$H_{\mathbf{ab}} = \varepsilon_{\mathbf{a}}\delta_{\mathbf{ab}} - t_{\mathbf{ab}}\delta_{\langle \mathbf{a},\, \mathbf{b}\rangle}, \tag{1}$$

where $\varepsilon_{\mathbf{a}}$ is the potential onsite disorder and $\delta_{\mathbf{ab}}$ the Kronecker delta, while $t_{\mathbf{ab}}$ denotes the kinetic hopping energy with $\delta_{\langle \mathbf{a},\mathbf{b}\rangle}$ non-zero when lattice sites $\mathbf{a} = (a_1, a_2, \ldots, a_d)$, $\mathbf{b} = (b_1, \ldots, b_d)$ are within a defined distance relationship on a discrete, d-dimensional lattice $\mathcal{L}_d$ — usually the nearest-neighbor separation on $\mathcal{L}_d$. With $|\mathcal{L}_d|$ counting the number of lattice sites, $H_{\mathbf{ab}}$ is an $|\mathcal{L}_d| \times |\mathcal{L}_d|$ matrix. The time-independent single-particle Schrödinger equation can then be written as

$$\varepsilon_{\mathbf{a}}\Psi_{\mathbf{a}} - \sum_{\mathbf{b}\in\mathcal{L}} t_{\mathbf{ab}}\delta_{\langle \mathbf{a},\, \mathbf{b}\rangle}\Psi_{\mathbf{b}} = E\Psi_{\mathbf{a}} \tag{2}$$

with $\Psi_{\mathbf{a}} = \Psi_{a_1, \ldots, a_d}$ the coefficients of the wave function $\Psi = \sum_{\mathbf{a}\in\mathcal{L}_d}\Psi_{\mathbf{a}} \,|\, \mathbf{a}\rangle$ in a suitable basis $|\mathbf{a}\rangle$ and E the energy.

https://doi.org/10.1016/B978-0-323-90800-9.00099-8

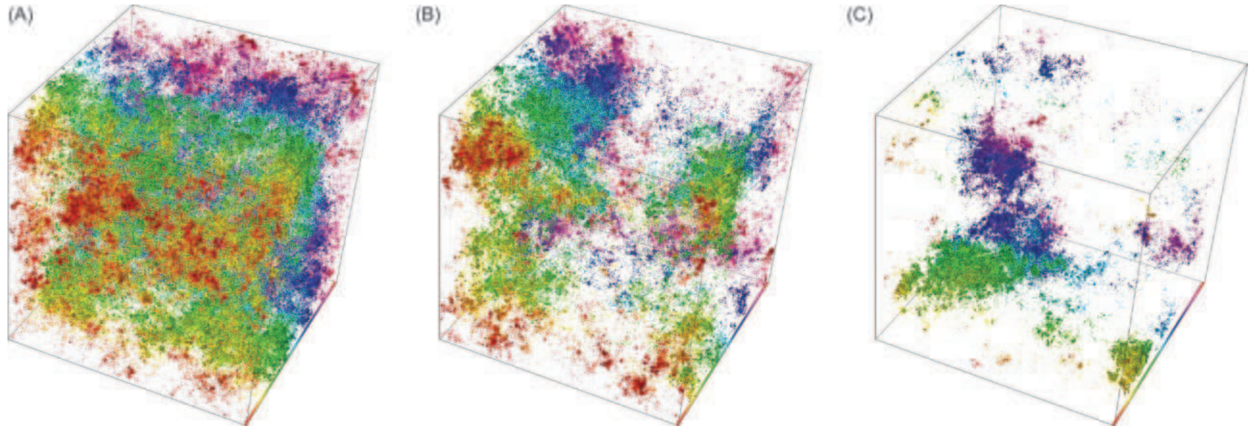

Fig. 1 (A) Extended, (B) critical and (C) localized wave function probabilities for the three-dimensional Anderson model with periodic boundary conditions at $E \approx 0$ with $N = 200^3$ and $W = 15$, 16.5 and 18, respectively. Every site a with probability $|\psi_{\mathbf{a}}|^2$ larger than the average $1/|\mathcal{L}_3|$ is shown as a box with volume $|\psi_{\mathbf{a}}|^2 |\mathcal{L}_3|$. Boxes with $|\psi_{\mathbf{a}}|^2 |\mathcal{L}_3| > \sqrt{1000}$ are plotted with black edges. The color scale along the bottom right edge distinguishes between different slices of the system. The eigenstates have been computed with JADAMILU (Bollhöfer and Notay, 2007) as described by Schenk et al. (2008).

In its simplest form, the Hamiltonian (1) is studied on a d-cubic lattice with $t_{\mathbf{ab}} = t_{\mathbf{ba}} = t = 1$ for all nearest-neighbors **a**, **b** and $\varepsilon_{\mathbf{a}}$ independent and identically distributed random numbers $\in [-W/2, W/2]$. Hence the parameter W/t expresses the strength of the disorder. See Fig. 1 for examples of Ψ in $d = 3$. Since numerical studies of Anderson localization began to emerge in the late 1970s, this set-up has of course been much varied to include more complicated situations (Kramer and MacKinnon, 1993). Examples include variations in d from 1 to ∞, changes in the lattice structure, symmetry and topology, changes to and additional disorder or correlations in the $\varepsilon_{\mathbf{a}}$ and $t_{\mathbf{ab}}$, as well as inclusion of spin-, external field and interaction effects (Brandes and Kettemann, 2003). The common theme unifying all the studies is the absence of symmetries in H due to the disorder which in turn prevents a simple restructuring of the matrix into much smaller irreducible blocks (Evers and Mirlin, 2008). Connecting the properties of such a single large-block matrix with the physics of Anderson localization is the challenge taken on by the numerical algorithms listed in this encyclopedia entry.

Exact diagonalization

Given an invertible matrix (1), the most straightforward approach is to use standard *full* matrix methods to compute eigenvalues and eigenvectors such as given by the LAPACK library routines (Anderson et al., 1999) and their many highly optimized implementations. At the time of writing this entry, matrices of sizes up to $\sim 10^4 \times 10^4$ can be readily studied with this method. However, as an average over many different disorder realizations is always necessary to find physically reliable results, already such matrix sizes can lead to many weeks of computing. Many of the algorithms mentioned below were conceived to allow for faster availability of results, while at the same time leading to a more limited set of computed information.

When $\delta_{\langle \mathbf{a},\mathbf{b} \rangle}$ is sufficiently short-ranged, many of the matrix elements $H_{\mathbf{ab}}$ are equal to 0. In this case, it can be advantageous to use *sparse* matrix methods. Such methods construct selected regions of the eigenspectra using repeats of an optimized matrix-vector product computation for $H_{\mathbf{ab}}\Psi_{\mathbf{b}}$ following the classic power series algorithm (Horn and Johnson, 1985). For the Anderson problem, the implementation of the Lanczos variant by Cullum and Willoughby (2002) is particularly useful since the disorder removes spectral degeneracies such that the "ghost eigenvalues" coming from the implementation can be readily identified. Polynomial convergence acceleration can often further improve convergence Elsner et al. (1999). Coupling the sparse-matrix approach with advantages in iteratively solving coupled systems of equations, Schenk et al. (2008) found that a Jacobi-Davidson approach coupled with shift-and-invert techniques Parlett (1980) can construct eigenstates of size up to $350^3 \times 350^3$ in the numerically most demanding region around the center of the spectrum within a reasonable time. Weiße et al. (2006) showed that similar sizes can be reached using kernel-polynomial methods when coupled with efficient recursive polynomial expansion techniques. The method is particularly efficient in determining a change in the *distribution* of the local density of states as a criterion for Anderson localization.

Quasi 1D methods

Repeated matrix-vector computations also underlie the celebrated transfer-matrix method (TMM) (Pichard and Sarma, 1981; MacKinnon and Kramer, 1983). The main idea is that it is often possible for a suitable $\mathcal{L}_d$ to rewrite (2) as

$$\begin{pmatrix} \psi_{n+1} \\ \psi_n \end{pmatrix} = \begin{pmatrix} \tau^{-1}_{\langle n+1,\, n \rangle}(E\mathbf{1} - \mathbf{H}_{\mathbf{d}-1}) & -\tau^{-1}_{\langle n+1,\, n \rangle}\tau_{\langle n,\, n-1 \rangle} \\ \mathbf{1} & \mathbf{0} \end{pmatrix} \begin{pmatrix} \psi_n \\ \psi_{n-1} \end{pmatrix}. \tag{3}$$

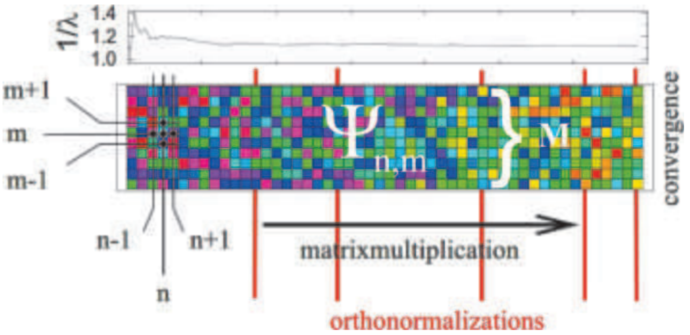

Fig. 2 Schematic diagram of the TMM method for the example of a $d = 2$ Anderson model. At slice n and position m, one needs to know the (past) $\psi_{n-1,m}$ value, the (present) values of $\psi_{n,m}$ and $\psi_{n,m\pm1}$ and then compute the (future) value of $\psi_{n+1,m}$. The red lines indicate the orthogonalizations for ψ needed for numerical stability. The diagram at the top shows the behavior of the typical convergence for a Lyapunov exponent measured after each reorthonormalization, the actual number of reorthonormalization used here exceeds 10^4. The colors of $\psi_{n,m}$ are chosen such that they indicate the eventual convergence for $n \to \infty$.

Here, $\psi_n = (\psi_{n,\ 1}, \ldots, \psi_{n,|\mathcal{L}_{d-1}|})$ are transfer states along a single spatial coordinate in $\mathcal{L}_d$ while $\mathbf{H_{d-1}}$ is the $|\mathcal{L}_{d-1}| \times |\mathcal{L}_{d-1}|$ Hamiltonian along the remaining d–1 directions and $\tau_{\langle n+1,n\rangle}$ denotes the connectivity matrices along the transfer direction (cp. Fig. 2). The advantage of singling out a special direction along which to study wave function progression lies in the fact that 1D localization is mathematically known to be very strong which usually translates into fast algorithmic convergence.

With T_n the $2\,|\,\mathcal{L}_{d-1}\,|\ \times 2\,|\,\mathcal{L}_{d-1}|$ (local transfer) matrix in (3), we define the global transfer matrix $\mathcal{T}_{\mathcal{L}_{d-1}}(|\mathcal{L}_1|) = \prod_{n=1}^{|\mathcal{L}1|} T_n$. Then $\lim_{|\mathcal{L}_1|\to\infty}(\mathcal{T}\mathcal{T}^\dagger) = \exp\left[2\,\mathrm{diag}(\gamma_1,\ \ldots,\ \gamma_{2\mathcal{L}_{d-1}})|\mathcal{L}_1|\right]$ with Lyapunov decay exponents $\gamma_1,\ \ldots,\ \gamma_{2|\mathcal{L}_{d-1}|}$, ordered $\gamma_1 > \gamma_2 > \ldots > \gamma_{|\mathcal{L}_{d-1}|} > 0 > -\gamma_{|\mathcal{L}_{d-1}|} > \ldots > -\gamma_1$, i.e. the Lyapunov exponents come in pairs $\pm\gamma_m$, $m = 1,\ \ldots,\ |\,\mathcal{L}_{d-1}|$ due to the symplectic structure of the T_n. The positive $\gamma_{\mathcal{L}_{d-1}}$ indicates the largest extend of the states along the transfer direction, leading to the definition of the (largest) localization length as $\lambda_{\mathcal{L}_{d-1}} = 1/\gamma_{\mathcal{L}_{d-1}}$. Implicit in the convergent construction of the $\lambda_m = 1/\gamma_m$ is the self-averaging over the disorder along the transfer direction. An error analysis in the *statistical* changes of the λ_m has to be made when computing the stopping criterion of the TMM (MacKinnon and Kramer, 1983). The $|\mathcal{L}_d\ -1|$ dependence of $\lambda|\mathcal{L}_d\ -1|$ lends itself to finite-size scaling and can hence be used to characterize universal properties of Anderson localization. A direct connection to the typical conductance is also known Pichard and Sarma (1981).

Generalizations of the TMM include different lattice structures (Schreiber and Ottomeier, 1992; Eilmes et al., 2008) as well as non-standard transfer directions (Frahm et al., 1995). For disorder distributions for whom self-averaging is not applicable, a forward/backward variant of the TMM has been given as well (Frahm et al., 1995; Ndawana et al., 2004). A recent reevaluation of the idea of self-averaging has also led to the first efficient implementation of TMM on massively-parallel computing architectures (Slevin and Ohtsuki, 2018).

Computing matrix elements of the resolvent $(E\mathbf{1} - \mathbf{H_{d-1}})^{-1}$ leads to a conceptually very similar recursion setup compared to (3). This so-called Green function method (MacKinnon and Kramer, 1981) again provides access to localization lengths and conductivity for chosen values of $\mathcal{L}_{d-1}$. An implementation of the method along a non-standard transfer direction has been given by Von Oppen et al. (1996).

Renormalization and decimation methods

Real-space renormalization approaches provide another starting point for studying Anderson localized systems. Here the idea is that an individual lattice site **a** can be" removed" from $\mathcal{L}$, leading to a modified $H_{\mathbf{ab}}$. For example, the decimation method (Aoki, 1982;

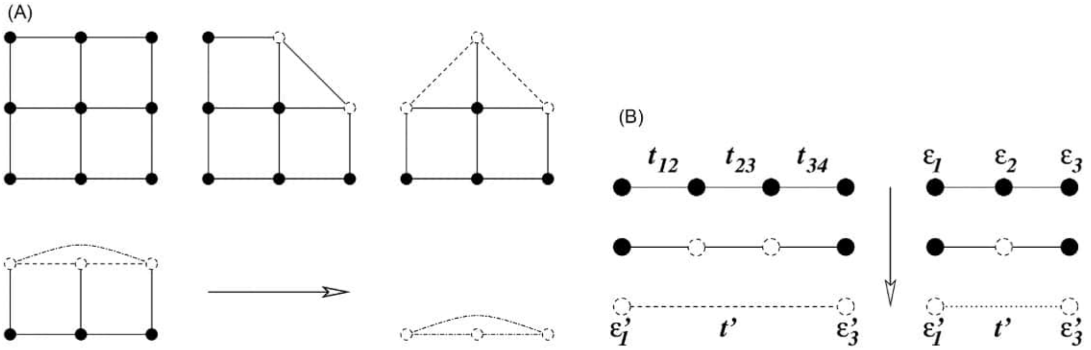

Fig. 3 Schematic of real-space decimation procedures using (A) Green function renormalization in $d = 2$ and (B) local energy renormalization for hopping (left of ↓) and onsite terms (right of ↓) in, e.g., $d = 1$. In both schematics, solid lines and circles indicate unrenormalized hopping (t_{12}, t_{23}, t_{34}) and onsite energies (ε_1, ε_2, ε_3), respectively, while the dashed and dotted lines and circles represent renormalized values (t' and ε_1', ε_3'). The (A) horizontal and (B) vertical arrows represent to renormalization progression in both schemes.

Leadbeater et al., 1999), finds $H_{\mathbf{ab},}{}' = H_{\mathbf{a},\ \mathbf{b}} + (H_{\mathbf{a},\ |\mathcal{L}_d|} H_{|\mathcal{L}_d|,\ \mathbf{b}})/(E - H_{|\mathcal{L}_d|,\ |\mathcal{L}_d|})$ after removal of the site $(|\mathcal{L}_d|, |\mathcal{L}_d|)$ while the Green function remains unchanged. In this way, the decimation of lattice sites can proceed until a sufficiently small Hamiltonian has been constructed to use the exact diagonalization routines reviewed above (cp. Fig. 3A). Another recent variant of real-space normalization makes use of the information encoded in the $\varepsilon_{\mathbf{a}}$ and $t_{\mathbf{a,b}}$ values. By recursively elimination those sites with the largest local energy scale $\Omega = \max_{\mathbf{a,b}} \{|\varepsilon_{\mathbf{a}}|, |t_{\mathbf{a,b}}|\}$, (Mard et al., 2014, 2017) continue until only a single renormalized link $\varepsilon_\alpha{}' - t_{\alpha,\ \beta}{}' - \varepsilon_\beta{}'$ is left. This last link can then be used to compute transport properties, including their disorder W dependence and the scaling behavior (cp. Fig. 3B). The method is applicable for $1 \leq d < \infty$. In $d = 2$, the approach is similar in spirit to the real-space renormalization approach used for localization in a magnetic field (Cain and Römer, 2005).

Energy-level statistics

The distribution of energy-level spacings $\delta_n = E_{n+1} - E_n$ in the eigen-spectra $\{E_n\}$ of Anderson-type systems has long been known to provide a marker able to distinguish between extended and localized eigenstates Ψ (Altshuler and Shklovskii, 1986; Evangelou and Economou, 1992; Shklovskii et al., 1993) with distribution functions $P(\delta)$ of the spacing following the three Dyson ensembles — e.g. with the Gaussian orthogonal ensemble (GOE) corresponding to real-symmetric matrices invariant under orthogonal transformations — (Dyson, 1962; Shklovskii et al., 1993) and generalizations thereof (Altland and Zirnbauer, 1997). Often, the integrated distribution function $I(\delta) = \int_0^\delta P(\delta')d\delta'$ is a numerically more stable indicator (Zhong et al., 1998). More detailed tests of the spectral properties such as the Δ_3 and Σ_2 statistics have also been employed (Mehta, 2004; Hofstetter and Schreiber, 1993). As usual, the $|\mathcal{L}_d|$ dependence of these quantities can be used for scaling; convenient estimates of $P(\delta)$, etc., have been given based on Wigner surmises (Shklovskii et al., 1993).

However, before a detailed comparison with predictions of random matrix theory is possible, the region of the spectrum under investigation has to be *unfolded* so that the unfolded density-of-states is constant Hofstetter and Schreiber (1993). This adds a possible source of numerical uncertainty for systems with large fluctuations in the density-of-states. Recently, it has been suggested to study ratios of level spacings such as $0 \leq r_n = \min\{\delta_n, \delta_{n-1}\}/\max\{\delta_n, \delta_{n-1}\} \leq 1$ (Oganesyan and Huse, 2007) and others (Luo et al., 2021) and their distributions instead (cp. Fig. 4A). For such ratios, the unfolding procedure is no longer necessary, while mean and moments are still accessible via surmises and even exact results exist (Atas et al., 2013; Giraud et al., 2022). A recent application of r-value statistics to characterize the Anderson transition can be found in (Šuntajs et al., 2021).

Wavefunction statistics and multi-fractal analysis

Unsurprisingly, the characteristics of the eigenstates of (1) are also useful when studying the localization properties. In the simplest situation, the participation number $\mathcal{P} = \left(\sum_{\mathbf{a}\in\mathcal{L}_d} |\Psi_{\mathbf{a}}|^4\right)^{-1}$ (Wegner, 1980) measures how many sites in $\mathcal{L}_d$ *participate* in the spatial extend of a given Ψ. E.g. for a localized Ψ, $\mathcal{P} \sim 1$, whereas for an extended Ψ, $\mathcal{P} \sim |\mathcal{L}_d|$. The universal statistical properties of Ψ can

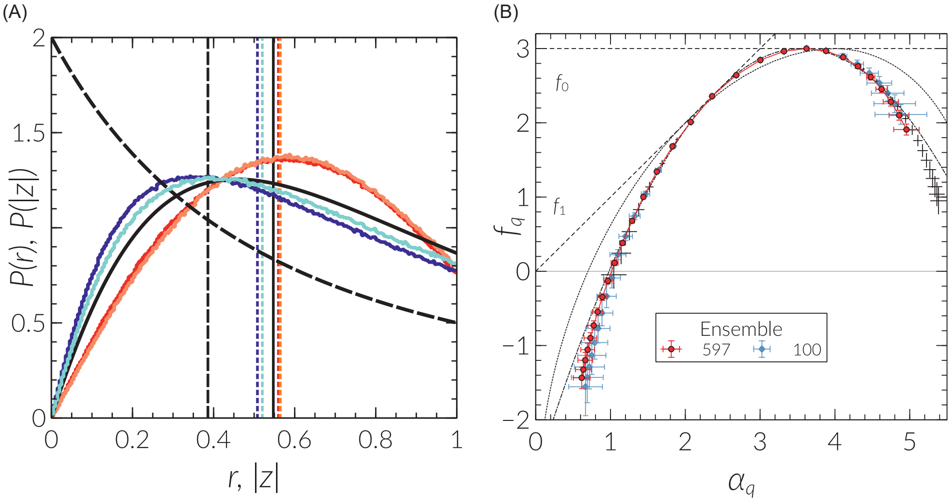

Fig. 4 (A) Distributions of the energy level ratios r (dark and light blue) and $|z|$ (dark and light red) for a $d = 3$ Lieb model with 44^3 sites (Liu et al., 2020) and averaged over $\sim 8 \times 10^6$ ratios for each curve. Darker colors denote slightly larger disorders. The black dashed and solid lines indicate the exact $P_{\text{Poisson}}(r)$ and a surmise for $P_{\text{GOE}}(r)$. No such predictions are yet known for $P(|z|)$ (Luo et al., 2021). (B) Ensemble-averaged singularity spectrum $f_q(\alpha_q)$, parameterized by q-moments, for Kohn-Sham wave functions computed via density-functional theory of Si:P with 22^3 atoms of which 140 are P impurities (Carnio et al., 2019a). The spectrum has been sampled for values of $q = 5, 4.75, \ldots, -1.75, -2$ (decreasing from left to right) in the bulk of the impurity band at 0.2495 eV below the Fermi energy. Blue diamonds show the results for the ensemble of the first 100 disorder realizations, while red circles indicate the results from all 597 available realizations. Simple error bars, without data point, indicate the symmetrized spectrum of the full ensemble. Dashed lines indicate $f_0 \equiv 3$ and $f_1(\alpha) = \alpha$. The dotted line represents the spectrum for the standard cubic 3D Anderson model at criticality, reproduced from Rodriguez et al. (2011), while the dot-dashed line shows the fit to a parabolic approximation (Evers and Mirlin, 2008). The two horizontal lines are guides to $f = 0$ and 3.

be computed as well, with the Porter-Thomas distributions capturing the behavior at weak disorder while the systematic corrections at larger disorder have been calculated in a series of works (Mirlin, 1999). Directly at the Anderson metal-insulator transition, e.g. in three-dimensions, Ψ has the scaling properties of a multifractal (Janssen, 1998). The full multifractal spectrum can be shown to be system-size independent and the moments of the multifractal distributions can be used to characterize the critical properties of the transition (Rodriguez et al., 2011), via finite-size scaling. A typical multi-fractal $f(\alpha)$ spectrum is shown in Fig. 4B.

Finite-size scaling

The finite-size scaling approach to second order phase transitions has been well documented by now (Abrahams et al., 1979; Belitz and Kirkpatrick, 1994; Slevin and Ohtsuki, 1999). Roughly speaking, finite-size scaling implies the collapse of data for different parameters such as E and W onto a single scaling curve when their system size $|\mathcal{L}_d|$ dependence is adjusted as well (Slevin and Ohtsuki, 1999).

For the Anderson localization problem, there exist two different numerical approaches. In the absence of a phase transition, i.e. in $d \leq 2$, or when the functional form of the transition is not known, one can attempt to simply construct the data collapse of a suitably chosen quantity, such as the localization length $\lambda_{|\mathcal{L}_d|}$ or a multifractal moment τ_q, by minimization of the overlap between curves. In this approach, the shift needed to achieve this minimal overlap defines a scaling parameter ξ and its parameter dependence on E or W. For the Anderson transition in three dimensions, the behavior should be a good approximation of $\xi \propto |E - E_c|^{-\nu}$ or $\xi \propto |W - W_c|^{-\nu}$. This defines the critical transition points E_c, W_c as well as the critical exponent ν.

The second, more modern approach, starts by assuming a scaling form for $\xi_{|\mathcal{L}_d|}$, say

$$\xi_{|\mathcal{L}_d|}(F) = a_{00} + a_{01}(F/F_c - 1)|\mathcal{L}_d|^{1/\nu} + |\mathcal{L}_d|^{-y}\left[a_{10} + a_{11}(F/F_c - 1)|\mathcal{L}_d|^{1/\nu}\right], \tag{4}$$

and then fits the parameters a_{ij}, ν and y to allow the best possible fit to the accumulated data points by a non-linear regression (Slevin and Ohtsuki, 1999) for either energy ($F = E$) or disorder ($F = W$) dependence (cp. Fig. 5). This more systematic approach allows the inclusion of the irrelevant scaling exponent $y > 0$ as shown in the example. The accuracy of a fit is quantified via χ^2 analysis. When constructing the scaling function ξ in powers of relevant and irrelevant corrections, one has to take care that the fit with the best χ^2 statistics is also robust with respect to changes in the range of energies and disorders considered as well as stable within the computed accuracy when increasing the complexity of the fit function. It is this second finite-size scaling approach, together with high accuracy data computed by the TMM or sparse matrix diagonalization coupled with multifractal analysis as outlined above, which currently gives the accepted best-fit estimates of the critical properties at the Anderson transition (Slevin and Ohtsuki, 1999).

Localization and many-body interactions

The possibility of including the influence of interactions on the Anderson localization problem has always intrigued the community and was mentioned already by Anderson (1958). Numerically, the problem becomes much harder since the number of states in Hilbert space grows from $\propto |\mathcal{L}_d|^d$ to $\propto \exp |\mathcal{L}_d|$ while the requirement to perform the disorder averaging remains. Early investigations concentrated on studying the influence of disorder on the ground states of interacting systems (Giamarchi, 2003; Schuster et al., 2002). Mostly, progress was based on numerical methods adopted from clean interacting systems with methods such as the density-matrix renormalization group approach (White, 1992; Schollwöck, 2005) and exact diagonalization most commonly used. For the many-body localization problem (see article in this encyclopedia), the complete spectrum is often of more interest, so

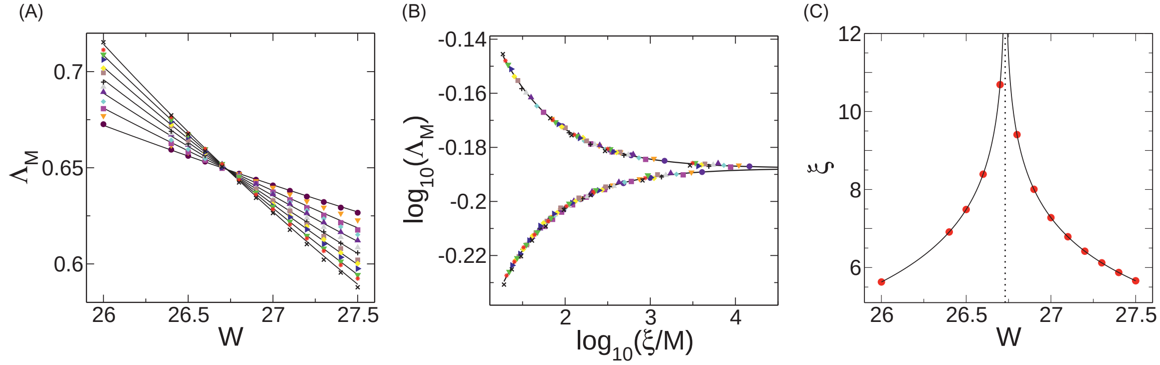

Fig. 5 Reduced localization lengths $\Lambda_M = \lambda_{|\mathcal{L}_2|}/M$, with $M = |\mathcal{L}_2|$ the size of the TMM bar, versus (A) W or (B) $\xi(W)/M$ for $E = 0$ of a $d = 3$ Anderson model defined on an fcc lattice (Eilmes et al., 2008). Different symbols and colors denote increasing $M = 3$(●), . . ., 15(×). Panel (C) shows the constructed $\xi(W)$ scaling parameter function (black line) with divergence at $W_c = 26.73(1)$ (vertical dotted line) and the computed $\xi(W_i)$ values for $W_i = 26, \ldots, 27.5$ (circles).

exact diagonalization is often the method of choice, severely restricting the spatial size of systems while still retaining a relatively large Hilbert space (Oganesyan and Huse, 2007). Recently, applications of shift-and-invert (Pietracaprina et al. (2018) as well as polynomial convergence acceleration Sierant et al. (2020) (cp. Section "Exact diagonalization") have further increased the available system size and modern Hilbert-space renormalization schemes known as tensor network methods are becoming more main stream (Montangero (2018). Renormalization schemes adaptive to the disorder, such as implementations of the strong-disorder renormalization group (Hikihara et al., 1999; Goldsborough and Römer, 2014) already mentioned above for the non-interacting case, might also provide a way forward.

Approximate methods such as the time-honored Hartee-Fock (Weidinger et al., 2018; Oswald and Römer, 2020) as well as density-functional-theory methods (Harashima and Slevin, 2014; Carnio et al., 2019b) have also begun to be applied to the localization problem. Particularly the latter offer the exciting possibility of providing a material-specific approach to studies of Anderson localization (Carnio et al., 2019a). In this context, one should also mention the typical medium dynamical cluster approximation for disordered electronic systems (Aguiar et al., 2009) which can now also be used to incorporate density-functional-theory-derived potentials, the effect of multiple bands, non-local disorder, and electron-electron interactions (Terletska et al., 2018). Another approximate method that incorporates the full spatial variations of wave functions and *local* interactions effects is the statistical dynamical mean field theory (Dobrosavljević and Kotliar, 1997; Miranda and Dobrosavljević, 2012). Local interactions are included self-consistently through effective correlated single-impurity problems (CSIP) (Georges et al., 1996). In the disordered context, each site defines a different CSIP whose local self-energy is fed back into the lattice self-consistent loop. In the non-interacting limit the formulation is exact. It has been used to study the disordered Mott transition (Miranda and Dobrosavljević, 2012; Suárez-Villagrán et al., 2020) and disordered heavy fermion systems (Miranda and Dobrosavljevic, 2001), where a distribution of Kondo temperatures is a conceptually useful byproduct.

Machine learning

A seemingly new approach has become available to the numerical study of Anderson localization with the emergence of the machine learning paradigm. Instead of specifying in detail which physical aspects of data to concentrate on, say transport properties such as λ, conductivity or multifractal moments τ_q, the data-driven machine learning approach can be used to find Anderson transitions for variants of the model Hamiltonian (1) when training deep learning networks on, e.g., the standard cubic Anderson model (Ohtsuki and Ohtsuki, 2016). With this form of *supervised* machine learning of Anderson localization, Ohtsuki and Mano (2020) found that one can determine phase diagrams in other disordered systems such as topological insulators and disordered Weyl semimetals (see corresponding entries in the encyclopedia). How other machine learning strategies such as unsupervised and reinforcement learning might add to the numerical approaches for Anderson localization is curerently under much investigation.

Conclusion

In this entry to the encyclopedia, I have attempted to provide a very brief review of the rich variety of numerical algorithms developed to study Anderson localization. Due to brevity requirements appropriate for such an entry, details had to be mostly neglected. Still, with citations provided to hopefully the original publications as well as some recent examples, I hope that the reader can find enough information to get started with each approach and that seeing them in context allows for a considered choice of which method to use.

Acknowledgments

I am grateful for constructive suggestions on the manuscript by H. Fehske, E. Miranda, A. Rodriguez, T. Ohtsuki, L. Vidmar and J. Zakrzewski. Special thanks to E. Carnio for help with Fig. 4.

References

Abrahams E, Anderson PW, Licciardello DC, and Ramakrishnan TV (1979) Scaling theory of localization: Absence of quantum diffusion in two dimensions. *Physical Review Letters* 42(10): 673–676. ISSN 0031-9007. https://doi.org/10.1103/PhysRevLett.42.673.

Aguiar MCO, Dobrosavljević V, Abrahams E, and Kotliar G (2009) Critical behavior at the Mott-Anderson transition: A typical-medium theory perspective. *Physical Review Letters* 102(15). ISSN 00319007. https://doi.org/10.1103/PhysRevLett.102.156402.

Altland A and Zirnbauer MR (1997) Nonstandard symmetry classes in mesoscopic normal-superconducting hybrid structures. *Physical Review B* 55(2): 1142. ISSN 1550235X. https://doi.org/10.1103/PhysRevB.55.1142.

Altshuler BL and Shklovskii BI (1986) Repulsion of energy levels and conductivity of small metal samples. *Zhurnal Eksperimentalnoi I Teoreticheskoi Fiziki* 91(July): 220–234.

Anderson PW (1958) Absence of diffusion in certain random lattices. *Physical Review* 109(5): 1492–1505. ISSN 0031-899X. https://doi.org/10.1103/PhysRev.109.1492.

Anderson E, Bai Z, Bischof C, Blackford LS, Demmel J, Dongarra J, Du Croz J, Greenbaum A, Hammarling S, McKenney A, and Sorensen D (1999) LAPACK Users' Guide. *Society for Industrial and Applied Mathematics* 1. ISBN 978-0-89871-447-0. https://doi.org/10.1137/1.9780898719604.

Aoki H (1982) Decimation method of real-space renormalization for electron systems with application to random systems. *Physica A: Statistical Mechanics and its Applications* 114(1-3): 538–542. ISSN 03784371. https://doi.org/10.1016/0378-4371(82)90345-4.

Atas YY, Bogomolny E, Giraud O, Vivo P, and Vivo E (2013) Joint probability densities of level spacing ratios in random matrices. *Journal of Physics A: Mathematical and Theoretical* 46(35): 355204. https://doi.org/10.1088/1751-8113/46/35/355204. ISSN 1751-8113.

Belitz D and Kirkpatrick TR (1994) The Anderson-Mott transition. *Reviews of Modern Physics* 66(2): 261–380. https://doi.org/10.1103/RevModPhys.66.261. ISSN 0034-6861.

Bollhöfer M and Notay Y (2007) JADAMILU: A software code for computing selected eigenvalues of large sparse symmetric matrices. *Computer Physics Communications* 177(12): 951–964. https://doi.org/10.1016/j.cpc.2007.08.004. ISSN 00104655.

Brandes T and Kettemann S (2003) Anderson localization and its ramifications. *Lecture Notes in Physics*. vol. 630. Berlin Heidelberg, Berlin, Heidelberg: Springer. ISBN: 978-3-540-40785-0https://doi.org/10.1007/b13139.

Cain P and Römer RA (2005) Real-space renormalization-group approach to the integer quantum Hall effect. *International Journal of Modern Physics B* 19(13): 2085–2119. https://doi.org/10.1142/S0217979205029742. ISSN 0217-9792.

Carnio EG, Hine ND, and Römer RA (2019a) Multifractality of ab initio wave functions in doped semiconductors. *Physica E: Low-dimensional Systems and Nanostructures* 111: 141–147. https://doi.org/10.1016/j.physe.2019.02.020. ISSN 13869477.

Carnio EG, Hine NDM, and Römer RA (2019b) Resolution of the exponent puzzle for the Anderson transition in doped semiconductors. *Physical Review B* 99(8): 081201(R). https://doi.org/10.1103/PhysRevB.99.081201. ISSN 2469-9950.

Cullum JK and Willoughby RA (2002) Lanczos algorithms for large symmetric eigenvalue computations. In: *Society for Industrial and Applied Mathematics*, ISBN: 978-0-89871-523-1. https://doi.org/10.1137/1.9780898719192.

Dobrosavljević V and Kotliar G (1997) Mean field theory of the Mott-Anderson transition. *Physical Review Letters* 78(20): 3943–3946. https://doi.org/10.1103/PhysRevLett.78.3943. ISSN 0031-9007.

Dyson FJ (1962) Statistical theory of the energy levels of complex systems. I. *Journal of Mathematical Physics* 3(1): 140–156. https://doi.org/10.1063/1.1703773. ISSN 0022-2488.

Eilmes A, Fischer AM, and Römer RA (2008) Critical parameters for the disorder-induced metal-insulator transition in fcc and bcc lattices. *Physical Review B* 77(24): 245117. https://doi.org/10.1103/PhysRevB.77.245117. ISSN 1098-0121.

Elsner U, Mehrmann V, Milde F, Römer RA, and Schreiber M (1999) The Anderson model of localization: A Challenge for modern eigenvalue methods. *SIAM Journal on Scientific Computing* 20(6): 2089–2102. https://doi.org/10.1137/S1064827598332217. ISSN 1064-8275.

Evangelou SN and Economou EN (1992) Spectral density singularities, level statistics, and localization in a sparse random matrix ensemble. *Physical Review Letters* 68(3): 361. https://doi.org/10.1103/PhysRevLett.68.361. ISSN 00319007.

Evers F and Mirlin AD (2008) Anderson transitions. *Reviews of Modern Physics* 80(4): 1355–1417. https://doi.org/10.1103/RevModPhys.80.1355. ISSN 00346861.

Frahm K, Müller-Groeling A, Pichard J-L, and Weinmann D (1995) Scaling in interaction-assisted coherent transport. *Europhysics Letters (EPL)* 31(3): 169–174. https://doi.org/10.1209/0295-5075/31/3/008. ISSN 0295-5075.

Georges A, Kotliar G, Krauth W, and Rozenberg MJ (1996) Dynamical mean-field theory of strongly correlated fermion systems and the limit of infinite dimensions. *Reviews of Modern Physics* 68(1): 13–125. https://doi.org/10.1103/RevModPhys.68.13. ISSN 0034-6861.

Giamarchi T (2003) Disordered systems. In: *Quantum Physics in One Dimension*, pp. 270–302. Oxford University Press. https://doi.org/10.1093/ACPROF:OSO/9780198525004.003.0009.

Giraud O, Macé N, Vernier E, and Alet F (2022) Probing symmetries of quantum many-body systems through gap ratio statistics. *Physical Review X* 12(1): 011006. https://doi.org/10.1103/PHYSREVX.12.011006/FIGURES/9/MEDIUM. ISSN 21603308.

Goldsborough AM and Römer RA (2014) Self-assembling tensor networks and holography in disordered spin chains. *Physical Review B* 89(21): 214203. https://doi.org/10.1103/PhysRevB.89.214203. ISSN 1098-0121.

Harashima Y and Slevin K (2014) Critical exponent of metal-insulator transition in doped semiconductors: The relevance of the Coulomb interaction. *Physical Review B* 89: 205108. https://doi.org/10.1103/PhysRevB.89.205108. ISSN 1098-0121.

Hikihara T, Furusaki A, and Sigrist M (1999) Numerical renormalization-group study of spin correlations in one-dimensional random spin chains. *Physical Review B* 60(17): 12116–12124. https://doi.org/10.1103/PhysRevB.60.12116. ISSN 0163-1829.

Hofstetter E and Schreiber M (1993) Statistical properties of the eigenvalue spectrum of the three-dimensional Anderson Hamiltonian. *Physical Review B* 48(23): 16979. https://doi.org/10.1103/PhysRevB.48. ISSN 01631829.

Horn RA and Johnson CR (1985) *Matrix Analysis*, 2nd edn. Cambridge University Press.

Janssen M (1998) Statistics and scaling in disordered mesoscopic electron systems. *Physics Reports* 295(1-2): 1–91. https://doi.org/10.1016/S0370-1573(97)00050-1. ISSN 03701573.

Kramer B and MacKinnon A (1993) Localization: Theory and experiment. *Reports on Progress in Physics* 56(12): 1469–1564. https://doi.org/10.1088/0034-4885/56/12/001. ISSN 0034-4885.

Leadbeater M, Römer R, and Schreiber M (1999) Interaction-dependent enhancement of the localisation length for two interacting particles in a one-dimensional random potential. *The European Physical Journal B* 8(4): 643–652. https://doi.org/10.1007/s100510050732. ISSN 1434-6028.

Liu J, Mao X, Zhong J, and Römer RA (2020) Localization, phases, and transitions in three-dimensional extended Lieb lattices. *Physical Review B* 102(17): 174207. https://doi.org/10.1103/PhysRevB.102.174207. ISSN 2469-9950.

Luo X, Ohtsuki T, and Shindou R (2021) Universality classes of the Anderson transitions driven by Non-Hermitian disorder. *Physical Review Letters* 126(9): 90402. https://doi.org/10.1103/PhysRevLett.126.090402. ISSN 10797114.

MacKinnon A and Kramer B (1981) One-parameter scaling of localization length and conductance in disordered systems. *Physical Review Letters* 47(21): 1546. https://doi.org/10.1103/PhysRevLett.47. ISSN 00319007.

MacKinnon A and Kramer B (1983) The scaling theory of electrons in disordered solids: Additional numerical results. *Zeitschrift für Physik B Condensed Matter* 53(1): 1–13. https://doi.org/10.1007/BF01578242. ISSN 0722-3277.

Mard HJ, Hoyos JA, Miranda E, and Dobrosavljević V (2014) Strong-disorder renormalization-group study of the one-dimensional tight-binding model. *Physical Review B* 90(12): 125141. https://doi.org/10.1103/PhysRevB.90.125141. ISSN 1098-0121.

Mard HJ, Hoyos JA, Miranda E, and Dobrosavljević V (2017) Strong-disorder approach for the Anderson localization transition. *Physical Review B* 96(4): 045143. https://doi.org/10.1103/PhysRevB.96.045143. ISSN 2469-9950.

Mehta ML (2004) *Random Matrices*. Academic Press. p. 706. http://store.elsevier.com/product.jsp?isbn=9780120884094&_requestid=513396.

Miranda E and Dobrosavljevic V (2001) Localization-induced Griffiths phase of disordered Anderson lattices. *Physical Review Letters* 86(2): 264. https://doi.org/10.1103/PhysRevLett.86.264. ISSN 00319007.

Miranda E and Dobrosavljević V (2012) Dynamical mean-field theories of correlation and disorder. In: Dobrosavljević V, Trivedi N, and Valles JM (eds.) *Conductor-Insulator Quantum Phase Transitions*, 1st edn, pp. 161–243. Oxford, UK: Oxford University Press.. volume 9780199592. ISBN 9780191741050.

Mirlin AD (1999) Correlations of wave functions in disordered systems. In: Lerner I, Keating J, and Khmelnitskii D (eds.) *Supersymmetry and Trace Formulae*, nato asi s edition, pp. 245–260. Boston, MA: Springer. https://doi.org/10.1007/978-1-4615-4875-1_12.

Montangero S (2018) *Introduction to Tensor Network Methods*. Cham: Springer International Publishing. ISBN: 978-3-030-01408-7. https://doi.org/10.1007/978-3-030-01409-4.

Ndawana ML, Römer RA, and Schreiber M (2004) The Anderson metal-insulator transition in the presence of scale-free disorder. *Europhysics Letters (EPL)* 68(5): 678–684. https://doi.org/10.1209/epl/i2004-10267-5. ISSN 0295-5075.

Oganesyan V and Huse DA (2007) Localization of interacting fermions at high temperature. *Physical Review B* 75(15): 155111. https://doi.org/10.1103/PhysRevB.75.155111. ISSN 1098-0121.

Ohtsuki T and Mano T (2020) Drawing phase diagrams of random quantum systems by deep learning the wave functions. *Journal of the Physical Society of Japan* 89(2): 022001. https://doi.org/10.7566/JPSJ.89.022001. ISSN 0031-9015.

Ohtsuki T and Ohtsuki T (2016) Deep learning the quantum phase transitions in random two-dimensional electron systems. *Journal of the Physical Society of Japan* 85(12). https://doi.org/10.7566/JPSJ.85.123706. ISSN 13474073.

Oswald J and Römer RA (2020) Microscopic details of stripes and bubbles in the quantum Hall regime. *Physical Review B* 102(12): 121305. https://doi.org/10.1103/PhysRevB.102.121305. ISSN 2469-9950.

Parlett BN (1980) *The Symmetric Eigenvalue Problem.* Englewood Cliffs, NJ: Prentice-Hall.

Pichard JL and Sarma G (1981) Finite size scaling approach to Anderson localisation. *Journal of Physics C: Solid State Physics* 14(6). https://doi.org/10.1088/0022-3719/14/6/003. ISSN 00223719.

Pietracaprina F, Macé N, Luitz DJ, and Alet F (2018) Shift-invert diagonalization of large many-body localizing spin chains. *SciPost Physics* 5(5): 045. https://doi.org/10.21468/SciPostPhys.5.5.045.

Rodriguez A, Vasquez LJ, Slevin K, and Römer RA (2011) Multifractal finite-size scaling and universality at the Anderson transition. *Physical Review B* 84(13): 134209. https://doi.org/10.1103/PhysRevB.84.134209.

Schenk O, Bollhöfer M, and Römer RA (2008) On large-scale diagonalization techniques for the Anderson model of localization. *SIAM Review* 50(1): 91–112. https://doi.org/10.1137/070707002. ISSN 0036-1445.

Schollwöck U (2005) The density-matrix renormalization group. *Reviews of Modern Physics* 77(1): 259–315. https://doi.org/10.1103/RevModPhys.77.259. ISSN 0034-6861.

Schreiber M and Ottomeier M (1992) Localization of electronic states in 2D disordered systems. *Journal of Physics: Condensed Matter* 4(8): 1959–1971. https://doi.org/10.1088/0953-8984/4/8/011. ISSN 0953-8984.

Schuster C, Römer RA, and Schreiber M (2002) Interacting particles at a metal-insulator transition. *Physical Review B* 65(11): 115114. https://doi.org/10.1103/PhysRevB.65.115114.

Shklovskii BI, Shapiro B, Sears BR, Lambrianides P, and Shore HB (1993) Statistics of spectra of disordered systems near the metal-insulator transition. *Physical Review B* 47(17): 11487. https://doi.org/10.1103/PhysRevB.47.11487. ISSN 01631829.

Sierant P, Lewenstein M, and Zakrzewski J (2020) Polynomially filtered exact diagonalization approach to many-body localization. *Physical Review Letters* 125(15): 156601. https://doi.org/10.1103/PhysRevLett.125.156601. ISSN 0031-9007.

Slevin K and Ohtsuki T (1999) Corrections to scaling at the Anderson transition. *Physical Review Letters* 82(2): 382–385. https://doi.org/10.1103/PhysRevLett.82.382.

Slevin K and Ohtsuki T (2018) Critical exponent of the Anderson transition using massively parallel supercomputing. *Journal of the Physical Society of Japan* 87(9): 094703. https://doi.org/10.7566/JPSJ.87.094703. ISSN 0031-9015.

Stollmann P (2001) *Caught by Disorder*. Boston, MA: Birkhäuser Boston. ISBN: 978-1-4612-6644-0. https://doi.org/10.1007/978-1-4612-0169-4.

Suárez-Villagrán MY, Mitsakos N, Lee TH, Dobrosavljević V, Miller JH, and Miranda E (2020) Two-dimensional disordered Mott metal-insulator transition. *Physical Review B* 101(23): 235112. https://doi.org/10.1103/PHYSREVB.101.235112/FIGURES/14/MEDIUM. ISSN 24699969.

Šuntajs J, Prosen T, and Vidmar L (2021) Spectral properties of three-dimensional Anderson model. *Annals of Physics* 435: 168469. https://doi.org/10.1016/j.aop.2021.168469. ISSN 00034916.

Terletska H, Zhang Y, Tam K-M, Berlijn T, Chioncel L, Vidhyad-hiraja N, and Jarrell M (2018) Systematic quantum cluster typical medium method for the study of localization in strongly disordered electronic systems. *Applied Sciences* 8(12): 2401. https://doi.org/10.3390/app8122401. ISSN 2076-3417.

Von Oppen F, Wettig T, and Müller J (1996) Interaction-induced delocalization of two particles in a random potential: Scaling properties. *Physical Review Letters* 76(3): 491. https://doi.org/10.1103/PhysRevLett.76.491. ISSN 10797114.

Wegner F (1980) Inverse participation ratio in 2 + ε? dimensions. *Zeitschrift für Physik B Condensed Matter and Quanta* 36(3): 209–214. https://doi.org/10.1007/BF01325284. ISSN 0340-224X.

Weidinger SA, Gopalakrishnan S, and Knap M (2018) Self-consistent Hartree-Fock approach to many-body localization. *Physical Review B* 98(22): 224205. https://doi.org/10.1103/PHYSREVB.98.224205/FIGURES/11/MEDIUM. ISSN 24699969.

Weiße A, Wellein G, Alvermann A, and Fehske H (2006) The kernel polynomial method. *Reviews of Modern Physics* 78(1): 275–306. https://doi.org/10.1103/RevModPhys.78.275. ISSN 0034-6861.

White SR (1992) Density matrix formulation for quantum renormalization groups. *Physical Review Letters* 69(19): 2863. https://doi.org/10.1103/PhysRevLett.69.2863. ISSN 00319007.

Zhong JX, Grimm U, Römer RA, and Schreiber M (1998) Level-spacing distributions of planar quasiperiodic tight-binding models. *Physical Review Letters* 80(18): 3996–3999. https://doi.org/10.1103/PhysRevLett.80.3996. ISSN 0031-9007.

Disordered electron liquid with interactions: Theoretical aspects

AM Finkel'stein[a,b] **and G Schwiete**[c], [a]Department of Condensed Matter Physics, The Weizmann Institute of Science, Rehovot, Israel; [b]Department of Physics and Astronomy, Texas A&M University, College Station, TX, United States; [c]Department of Physics and Astronomy, The University of Alabama, Tuscaloosa, AL, United States

© 2024 Elsevier Ltd. All rights reserved.

Introduction: Fermi-liquid in the presence of disorder 220
Beyond Fermi-liquid theory: Non-linear sigma model and scale-dependent theory of the disordered electron liquid 223
Scaling theory of the metal-insulator transition in d = 2 + ϵ; role of the parameter z 226
Tunneling density of states 228
The MIT in a two-dimensional system 229
Thermal conductivity 231
Conclusion 234
Acknowledgments 234
References 234
Further reading 235

Abstract

Physics of itinerant electrons is governed by the combined effect of disorder and e-e interactions. Such systems display singular corrections in transport and thermodynamics and can be described in terms of a scale-dependent Fermi liquid. The metal-insulator transition (MIT) in the presence of interactions is a non-trivial example of a quantum phase transition. The dynamical exponent characterizing this transition is determined by a renormalization group equation. In two dimensions, the MIT can be discussed in terms of a flow in the disorder-interaction phase plane. The Wiedemann-Franz law holds for short range interactions, but is violated by the long-range Coulomb interactions.

Key points

- The analysis of the electron liquid in the presence of disorder focuses on diffusing electron-hole pairs.
- At low enough temperatures the resistance and the e–e scattering amplitudes acquire singular corrections, which are the more significant the stronger disorder is.
- The scheme most suitable for the analysis of the singular corrections arising in the system of diffusing electrons is the Renormalization Group (RG).
- The RG-analysis of the disordered electron liquid can efficiently be performed using the matrix Non-Linear Sigma Model (NLSM), which is a minimal functional that incorporates all essential degrees of freedom and symmetries.
- The metal-insulator transition (MIT) in a system of interacting electrons is an example of a quantum phase transition (QPT). The value of the dynamical scaling exponent which connects the spatial and energy scales in this QPT has to be calculated using a special RG-equation.
- The RG-flow captures both quantitatively and qualitatively the physics of the disordered two-dimensional electron liquid including the MIT.
- Similar to the electric conductivity, the thermal conductivity acquires a pronounced temperature-dependence at low temperatures, which can be analyzed with the NLSM extended to include gravitational potentials.

Introduction: Fermi-liquid in the presence of disorder

The original Fermi-liquid theory has been formulated by Landau (1956,1957) in terms of quasiparticles labeled with momenta $\mathbf{p}$, see in Lifshitz and Pitaevskii (1980). The most distinctive feature of a clean Fermi-liquid is a jump in the occupation number $n(\mathbf{p})$ at the Fermi-surface. Since in the presence of disorder the Fermi-surface is smeared, it may look as if the Fermi-liquid theory loses its applicability. This is, however, not completely correct. Elastic impurity scattering by itself does not generate electron-hole pairs and, therefore, some elements of the Fermi-liquid description are preserved even in the presence of disorder. The focus, however, shifts from quasiparticles toward diffusing electron-hole pairs. In Landau's microscopic theory of the clean Fermi-liquid the combination $\omega/(\omega - v_F\mathbf{nk})$ is used as the dynamic part of the propagator of an electron-hole pair. This expression describes propagation of the pair along the direction $\mathbf{n}$, when the momentum difference of the two quasiparticles is $\mathbf{k}$, and the frequency difference is ω.

For large times, $t \gg \tau_{el}$, electrons have undergone many collisions with impurities; here, τ_{el} is the elastic mean free time for scattering from static impurities. Then, after averaging over the directions $\mathbf{n}$, the dynamical part of the electron-hole pair propagator acquires a diffusive form that after the analytical continuation to the imaginary frequency axis looks as follows:

https://doi.org/10.1016/B978-0-323-90800-9.00078-0

$$\frac{\omega}{\omega - v_F\mathbf{nk}} \Rightarrow \frac{\omega_n}{\omega_n + iv_F\mathbf{nk}} \Rightarrow \frac{\omega_n}{\omega_n + Dk^2}, \tag{1}$$

where $D = v_F^2\tau_{el}/d$ is the diffusion coefficient for the spatial dimension d; it is assumed that $1/\tau_{el} > D\mathbf{k}^2, \omega, T$. The resulting term in Eq. (1) describes the free diffusion of electron-hole pairs between acts of rescattering induced by the e–e interaction amplitude Γ^k. (Index k in Γ^k means that in the singular amplitude $\Gamma(\mathbf{k},\omega)$ one first takes the limit $\omega = 0$ and only afterwards the limit $k \to 0$, i.e., Γ^k is static). In clean Fermi-liquids, because of the angular dependence of $\mathbf{nk}$ in the denominator of the combination on the left hand side of Eq. (1), different angular harmonics Γ_l^k of the interaction amplitudes are coupled. On the contrary, in the presence of disorder only the zeroth harmonic of the interaction amplitude, $\Gamma_{l=0}^k$, is relevant for the rescattering of diffusing electron-hole pairs. All other harmonics with $l \neq 0$ are eliminated by random scattering of electrons caused by impurities. (This implies that the zero-sound modes predicted by Landau cease to exist in the presence of disorder.) As a result, the calculation of $\Gamma(\mathbf{k},\omega)$ does not require the solution of an equation for the harmonics, but instead reduces to a simple summation of a geometric series. The process of rescattering is illustrated in Fig. 1.

The two-particle amplitude $\Gamma_{l=0}^k$ can be split into parts which can be classified according their spin structure:

$$\Gamma^{k\,\alpha_1\alpha_2}_{l=0\,\alpha_3\alpha_4} = \frac{1}{2}\left[2\tilde{\Gamma}_\rho\delta_{\alpha_1,\alpha_3}\delta_{\alpha_2,\alpha_4} + \Gamma_\sigma\vec{\sigma}_{\alpha_1,\alpha_3}\vec{\sigma}_{\alpha_2,\alpha_4}\right]. \tag{2}$$

Here, the singlet-channel amplitude $\tilde{\Gamma}_\rho$ controls propagation of the particle-number density $\rho(\mathbf{k},\omega)$ in the singlet channel, $S = 0$, while Γ_σ controls the spin density, i.e., the triplet channel, $S = 1$.

A key point in studies of the true electron liquid, i.e., a quantum liquid with charged fermions, is the long-range character of the Coulomb interaction which requires special care. With this in mind, one has to identify terms in the interaction amplitude $\tilde{\Gamma}_\rho$ that carry information about the singular behavior of the Coulomb interaction at small momenta. (Graphically, these terms can be disconnected by cutting a single Coulomb interaction line, see Fig. 2.) The resulting amplitude of this part of the e–e interaction will be denoted as Γ_ρ^0, while the remaining part of the interaction amplitude, which is irreducible with respect to the Coulomb interaction, will be denoted as Γ_ρ. The latter part describes the short-ranged part of the e–e interaction in the singlet channel that is not sensitive to the Coulomb singularity at small momenta. As a result, the amplitude $\tilde{\Gamma}_\rho$ has been split into two terms, $\tilde{\Gamma}_\rho = \Gamma_\rho^0 + \Gamma_\rho$.

To include dynamics in the ρ- and σ-density channels, one has to consider a ladder of either Γ_ρ- or Γ_σ-amplitudes alternating with dynamical electron-hole propagators. The resulting amplitudes $\Gamma_\rho(\mathbf{k},\omega)$ and $\Gamma_\sigma(\mathbf{k},\omega)$ acquire the form:

$$\Gamma_\alpha(\mathbf{k},\omega) = \Gamma_\alpha\frac{Dk^2 + \omega_n}{Dk^2 + (1 - \Gamma_\alpha)\omega_n}, \quad \alpha = \rho,\sigma. \tag{3}$$

The position of the diffusion pole in $\Gamma_{\rho,\,\sigma}(\mathbf{k},\omega)$ shifts as a result of re-scattering. This shift is the origin of the renormalization of the diffusion coefficients that is different in the ρ- and σ channels. The amplitudes $\Gamma_{\rho,\,\sigma}$ are related to the standard Landau parameters of Fermi liquid theory as $1 - \Gamma_\alpha = 1/(1 + F_0{}^\alpha)$.

In the analysis of the density-density correlation functions for a charged liquid, the focus of attention has to be directed toward the polarization operator $\Pi(k,\omega_n)$, which is the density-density correlation function *irreducible* with respect to the Coulomb interaction. The dynamical part of the polarization operator contains two "triangle" vertices γ^ρ separated by a ladder of dynamical

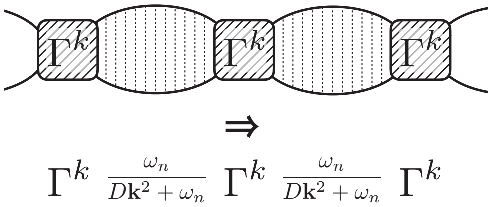
Γ^k
Γ^k
Γ^k
$\Rightarrow$
$\Gamma^k \frac{\omega_n}{D\mathbf{k}^2 + \omega_n} \Gamma^k \frac{\omega_n}{D\mathbf{k}^2 + \omega_n} \Gamma^k$

Fig. 1 Disordered Fermi-liquid: geometric series leading to Eq. (3) for $\Gamma(\mathbf{k},\omega)$. Dashed lines symbolize the impurity scattering after averaging over a random disorder realization. In the framework of Fermi liquid theory only ladder-like processes are kept.

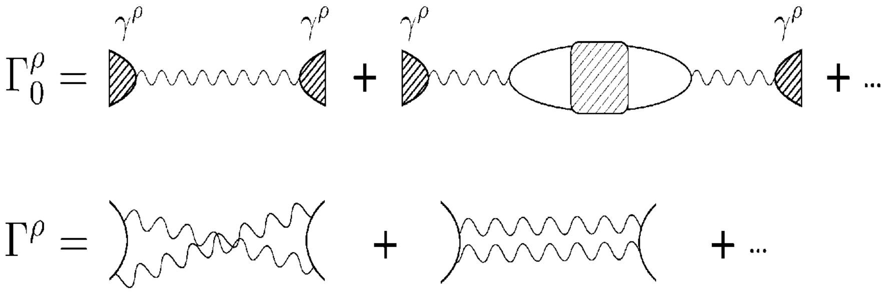

Fig. 2 On top: the screened Coulomb interaction. The triangular vertices γ^ρ are attached to the ending points of the interaction line. On the bottom: the short-range interaction amplitude in the singlet channel.

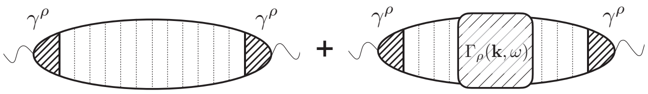

Fig. 3 Disordered Fermi-liquid: dynamical part of the polarization operator $\Pi(k,\omega_n)$.

electron-hole pair propagators, see Fig. 3. Both the left and right vertices γ^ρ are irreducible with respect to the dynamical sections. Collecting the static and dynamical parts of the polarization operator, one obtains Eq. (4b)

$$\Pi(k,\,\omega_n) = \Pi_{st} - 2\nu(\gamma^\rho)^2\left[\frac{\omega_n}{Dk^2 + (1 - \Gamma_\rho)\omega_n}\right] \tag{4a}$$

$$\Rightarrow \Pi_{st}\frac{Dk^2}{Dk^2 + (1 - \Gamma_\rho)\omega_n}. \tag{4b}$$

In Eq. (4b), we have arrived at the canonical form for a correlation function of the density of a conserved quantity which must vanish in the limit $k \to 0$ when $\omega_n \neq 0$. This property must hold for any *conserved* quantity, as can be seen from the general form of a retarded correlation function

$$\chi(\mathbf{k},\,\omega) = i\int_0^\infty dt e^{i\omega t}\langle[x(t),\;x(0)]\rangle_{\mathbf{k}}. \tag{5}$$

In the limit $k \to 0$ the densities $x(t)$ and $x(0)$ transform into the quantities $X(t)$ and $X(0)$, that are integrated over space. In the case when $X(t)$ is conserved in time, it obviously commutes with $X(0)$ at any moment. Consequently, $\chi(k \to 0, \omega)$ should vanish at any frequency.

One may rewrite the expression given in Eq. (4b) in a more conventional form corresponding to diffusion:

$$\Pi(k,\,\omega_n) = \Pi_{st}\frac{D_\rho k^2}{D_\rho k^2 + \omega_n}, \quad D_\rho = \frac{D}{1 - \Gamma_\rho}. \tag{6}$$

Here D_ρ is the diffusion coefficient of the particle-number density ρ. The next step which allows to find the electric conductivity is to relate $\Pi(k,\omega_n)$ to the current-current correlation function through the continuity equation $\partial\rho/\partial t + \nabla \cdot \mathbf{j} = 0$. Then, with the help of the Kubo formula, one can obtain the Fermi-liquid expression for the electric conductivity (e is electron charge):

$$\frac{\sigma_{charge}}{e^2} = \lim_{k\to 0}\frac{\omega_n}{k^2}\Pi(k,\,\omega_n) = \frac{\partial n}{\partial\mu}D_\rho = 2\nu D. \tag{7}$$

The above equation is nothing else but the Einstein relation for the electric conductivity $\sigma \equiv \sigma_{\text{charge}}$. It is worth emphasizing that the conductivity is determined by the product $(\partial n/\partial\mu)D_\rho$ (which is unquestionably positive) rather than a naïve $(\partial n/\partial\mu)D$. This point is very important in view of experimental measurements in heterostructures hosting a two-dimensional ($2d$) electron gas. In these systems, the electron gas is often under conditions when $\partial n/\partial\mu = (1 - \Gamma_\rho)$ becomes negative. However, for the conductivity the two negative renormalizations cancel each other out.

It remains to comment why the *irreducible* part of the density-density correlation function, $\Pi(k,\omega_n)$, rather than the full correlation function, has been used to find the conductivity. The terms that can be disconnected by cutting a single Coulomb line describe the rearrangement of the system in response to the external perturbation. The point here is that conductivity is a response to a resulting field acting on a charged electron. This resulting field is measured by a voltmeter as the difference in the electro-chemical potential. Thus, by keeping only terms that are irreducible with respect to the Coulomb interaction the rearrangement has been taken into account, and one can obtain the electric current in response to the actual field.

In the case when the total spin of conducting electrons is conserved, the scheme outlined above can be straightforwardly applied for the analysis of the spin-density correlation function. In the case of the spin density, the external vertices contain a spin operator $\sigma^x/2$ that corresponds to a probing magnetic field directed along the x-axis. These vertices are renormalized by the e–e interactions, and the corresponding renormalization factor is denoted below as γ^σ. In spite of this modification, all formulas for the spin-density correlation function $\chi_s^{xx}(k,\omega_n)$ are similar to those obtained in the case of $\Pi(k,\omega_n)$. The only change is the substitution of Γ_ρ by Γ_σ in the above expressions (correspondingly, one should replace $\gamma^\rho \to \gamma^\sigma$ and $\Gamma_\rho \to \Gamma_\sigma$ in Fig. 3).

The spin susceptibility χ_s determines the static limit of the spin-density correlation function $\chi_s^{xx}(k,\omega_n)$, just like $\partial n/\partial\mu$ determines the static limit of the polarization operator. As a result of the Fermi liquid corrections, $\chi_s \equiv \chi_s^{xx}(k \to 0, \omega_n = 0)$ is modified by the factor $(1 - \Gamma_\sigma)$ compared to $\chi_s^0 = (g_L\mu_B/2)^2 2\nu$ for the clean Fermi gas (where g_L is the g-factor for the charge carriers), so that $\chi_s = \chi_s^0(1 - \Gamma_\sigma)$. In the standard Fermi-liquid notation, $1 - \Gamma_\sigma = 1/(1 + F_0^\sigma)$. Usually, F_0^σ is negative. Then, $(1 - \Gamma_\sigma)$ describes the Stoner enhancement of the spin susceptibility.

In the absence of magnetic impurities, i.e., when the total spin of conducting electrons is conserved, the sum of the static and dynamical parts acquires the structure already familiar from the calculation of $\Pi(k,\omega_n)$:

$$\chi_s^{xx}(k,\omega)=\chi_s\frac{D_\sigma k^2}{\omega_n+D_\sigma k^2}, \tag{8}$$

where $D_\sigma=D/(1-\Gamma_\sigma)$. Hence, $(1-\Gamma_\sigma)$ describes not only the Stoner enhancement of the spin susceptibility due to the *e*–*e* interaction, but also the suppression of the spin-diffusion coefficient $D_\sigma=D/(1-\Gamma_\sigma)$.

In the case when the spin of conducting electrons is conserved, one may derive the Einstein-like relation for the spin conductivity following the route outlined previously for the electric conductivity, see Eq. (7):

$$\frac{\sigma_{spin}}{(g_L^0\mu_B/2)^2}=\frac{1}{(g_L^0\mu_B/2)^2}\lim_{k\to 0}\frac{\omega_n}{k^2}\chi_s^{xx}(k,\omega_n)=2\nu D. \tag{9}$$

Taken together, Eqs. (7) and (9) reflect the fact that both the charge and the spin are carried by the same particles.

Up to now, averaging over disorder has been performed in a very particular fashion: within the framework of the Fermi-liquid theory, disorder has been considered only in the dynamical blocks describing diffusive propagation of electron-hole pairs interrupted by rescattering induced by the *e*–*e* interaction. This separation of the *e*–*e* interaction and disorder is the main approximation of the disordered Fermi-liquid theory. The content of this Section is a byproduct of a more general theory of the *e*–*e* interactions in disordered conductors developed by Finkel'stein (1983a, 1984a).

Beyond Fermi-liquid theory: Non-linear sigma model and scale-dependent theory of the disordered electron liquid

Matrix elements determining amplitudes of the *e*–*e* interaction, in fact, could be strongly modified by disorder, especially for states that are close in energy. Two examples showing how it works for effective amplitudes are presented in Fig. 4. The amplitudes are decorated by ladders of dashed lines which result *after averaging* over impurity scattering. Each of these ladders generates a diffusion propagator $1/(Dq^2+\omega_n)$ and, consequently, is called "diffuson" (when the frequency is on the real axis, the retarded diffuson is equal to $1/(Dq^2-i\omega)$); see Fig. 5. Diffusons, being singular, play a special role in modifying (renormalizing) the interaction amplitudes. As a result of the interplay of the interaction amplitudes and diffusons, the effective *e*–*e* interaction amplitudes in the diffusive regime, $1/\tau_{el}>T$, acquire corrections that are non-analytic in temperature T.

Besides the diffuson there is another mode, called the Cooperon, which also generates non-analytic corrections of *various* kinds (Gor'kov et al., 1979). This mode is a "cousin" of the diffuson, and it has the same diffusion propagator. The Cooperon represents a particle-particle pair with small total momentum propagating in a disordered environment, see Fig. 6. It is called the Cooperon, because of its relevance for the Cooper channel in which the superconducting instability develops.

The electric conductivity and, correspondingly, the diffusion constant D also acquire corrections that in the diffusive regime are non-analytic in temperature. Two diagrams illustrating the origin of corrections to D are shown in Fig. 7. In $d=2$, *all* corrections both to the diffusion coefficient (electric conductivity) and the interaction amplitudes are logarithmically divergent in temperature, i.e., proportional to $\ln 1/T\tau_{el}$. Logarithmic corrections to the conductivity caused by the *e*–*e* interaction were first obtained by Altshuler et al. (1980) and, conversely, to the interaction amplitudes themselves by Finkel'stein (1983a). In higher

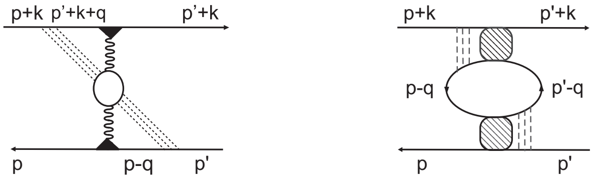

Fig. 4 Examples of the *e*–*e* interaction amplitudes modified by disorder.

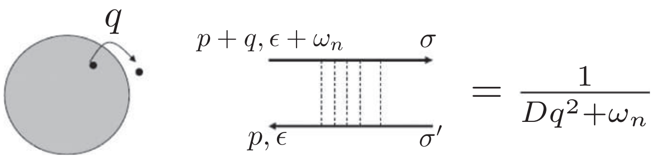

Fig. 5 Diffuson: propagators that capture the diffusive propagation of the electron-hole pairs at large time and length scales are called "diffusons".

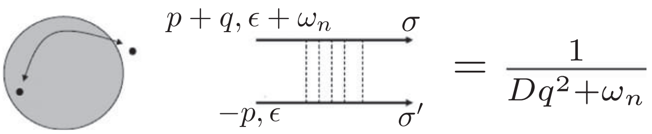

Fig. 6 Cooperon: disorder-averaged propagator of a particle-particle pair with small total momentum. The Cooperons capture the effects of quantum interference which lead to the weak localization corrections.

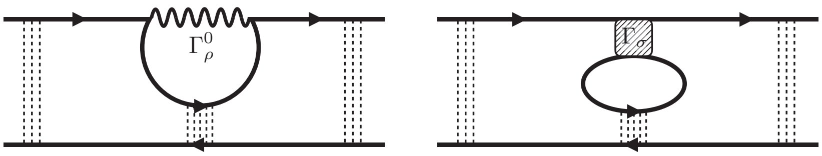

Fig. 7 Diagrams illustrating the origin of corrections to the diffusion constant D due to combined action of the e–e interactions and disorder.

dimensions, the problem becomes logarithmic near the MIT, Finkel'stein (1983b, 1984b), and Castellani et al. (1984a). (In the ballistic region, $T > 1/\tau_{el}$, non-analytic corrections due to the interplay of interaction and disorder also exist, Clarke et al. (2008). In $2d$, they are linear in temperature, when the disorder scattering is short-range.)

The divergent corrections signal the breakdown of the Fermi-liquid theory presented above. There is a need for resummation of the divergent terms using the Renormalization Group (RG) technique but, most importantly, there is a need to clarify the general structure of the theory. Objectives for RG analysis are as follows: At low enough energies, the e–e scattering amplitudes Γ_ρ and Γ_σ acquire corrections, which are the more significant the stronger disorder is. Conversely, resistivity - which is a measure of the effective strength of disorder - also acquires corrections which depend on the value of the interaction amplitudes. Hence, this problem calls for a scheme that can account for both effects in a consistent fashion. The RG-analysis is precisely such a scheme.

The RG-analysis for disordered conducting fermions can most efficiently be performed using the technique of the matrix Non-Linear Sigma Model (NLSM) originally introduced for non-interacting particles by Wegner (1979) and Efetov et al. (1980). In matrix terms, the disorder-averaged N-replica partition function of interacting electrons reads as follows:

$$\langle Z_N \rangle = \int dQ e^{-S[Q]}, \tag{10}$$

$$\begin{aligned} S[Q] = \frac{\pi\nu}{8} \int d^d r \mathrm{Tr}\left[D\left(\nabla\hat{Q}\right)^2 - 4z\left(\hat{\varepsilon}\hat{Q}\right)\right] \\ -\frac{\pi\nu}{16} \int d^d r \left\{\hat{Q}\left(\hat{\Gamma}_\rho^0 + \hat{\Gamma}_\rho\right)\hat{Q} + \hat{Q}\hat{\Gamma}_\sigma\hat{Q} + \hat{Q}\hat{\Gamma}_c\hat{Q}\right\}. \end{aligned} \tag{11}$$

This functional is usually referred to as Finkel'stein's model, Finkel'stein (1983a, 1984a). The functional integration has to be performed over a matrix field $\hat{Q}$ within the manifold limited by the constraints: $\hat{Q}^2 = 1, \hat{Q} = \hat{Q}^\dagger$, and $\mathrm{Tr}\hat{Q} = 0$. These constraints make the problem non-linear and also very non-trivial. The components of the matrix $\hat{Q}$ are defined as $Q_{n_1,n_2}^{ij,\alpha\beta}$, where n_1, n_2 are the Matsubara fermionic frequency indices with $\varepsilon_n = (2n + 1)\pi T$; i, j are the replica indices, and α, β include the spin and quaternion indices. The quaternion indices are needed to incorporate both the diffusons and Cooperons within one scheme. The replica limit, $N \to 0$, should be taken in order to perform the averaging over different realizations of disorder. The frequency matrix is $(\hat{\varepsilon})_{nm}^{ij,\alpha\beta} = \varepsilon_n \delta_{nm} \delta_{ij} \delta_{\alpha\beta}$. All the interaction terms are restricted by the energy and momentum conservation laws. (After averaging over disorder realizations, the resulting effective system is translation invariant: the scattering of the diffusion modes obeys the momentum conservation law.) The interaction terms are written symbolically, omitting such important details as the Pauli matrices acting in the spin and quaternion spaces which unify diffuson and Cooperon degrees of freedom in the Q matrices. Note that the ρ-term is split into two pieces as discussed above in connection with the polarization operator. The additional term $\hat{\Gamma}_c$ describes the e–e interaction in the Cooper channel.

The last point to be commented on is the parameter z introduced in front of the frequency matrix in the action $S[Q]$. For free electrons $z = 1$; also within the Fermi-liquid analysis of disordered electrons it remains equal to 1. When the theory is extended beyond the limits of the disordered Fermi-Liquid theory, z starts to acquire renormalization corrections. The parameter z gives the frequency renormalization in the propagators of the diffusons and Cooperons. Precisely owing to this parameter, the output of the RG-procedure is compatible with the charge- and spin-conservation laws. Moreover, z determines the relative scaling of the frequency with respect to the length scale and, thereby, it plays a central role in the critical region of the metal-insulator transition.

The saddle-point value of the matrix $\hat{Q}$, which is usually denoted as $\hat{\Lambda}$, is fixed by the frequency term $\left(\hat{\varepsilon}\hat{Q}\right)$ in the above action; $\Lambda_{nm}^{ij,\alpha\beta} =$ sign $(n)\delta_{nm}\delta_{ij}\delta_{\alpha\beta}$. It is clear that for small ε_n the fluctuating matrix $\hat{Q}$ is only weakly fixed to its equilibrium position and, correspondingly, fluctuations away from the equilibrium position are strong. To get some intuition, one may look on the NLSM for non-interacting electrons as a sort of the Heisenberg functional used in the theory of magnetism. Then, the frequency term in $S[Q]$ that breaks the symmetry with respect to the sign of the frequency is the counterpart of the external magnetic field. In this analogy, the diffusons and Cooperons are the counterparts of the magnons. The fluctuations of the $\hat{Q}$-field are nothing else but the diffusons and Cooperons. The propagators of these two diffusion modes acquire the modified form $1/(Dk^2 + z\omega_n)$. They can be obtained by expanding the first two terms in $S[Q]$ up to quadratic order in $\delta\hat{Q} = \left(\hat{Q} - \hat{\Lambda}\right)$.

The functional $S[Q]$ describes disordered interacting electrons with energies smaller than $1/\tau_{el}$. One may observe that the Fermi-liquid description of the disordered electron liquid presented in the previous Section can be reproduced by the quadratic expansion of the action $S[Q]$ in deviations of $\hat{Q}$ from its equilibrium value. Systems that principally differ from the disordered Fermi-liquid, e.g., electrons under the conditions of the quantum Hall effect, topological insulator surface states, graphene in the absence of the intervalley scattering, etc., contain a term in the action which leads to a topological protection. The coefficients in the action $S[Q]$, e.g., the single-particle density ν, incorporate the Fermi-liquid renormalizations of the clean liquid as the input parameters. The RG-analysis covers energies between $1/\tau_{el}$ and the temperature. The disorder-averaged interaction amplitudes, the diffusion coefficient D as well as the parameter z are all scale-dependent at energies $\lesssim 1/\tau_{el}$. The renormalization corrections are determined by non-quadratic (i.e., anharmonic) terms in the action S. Note that the decoupling of different interaction channels occurs only on the level of the quadratic form of the action. During the course of the RG-procedure different channels, $\alpha = \rho, \sigma, c$, interfere. For example, in the diagram presented on the left side of Fig. 4, the amplitude Γ_ρ^0 is converted into Γ_σ as a result of scattering induced by disorder.

With the frequency renormalization parameter z included, the action $S[Q]$ preserves its form during the course of RG-transformations. With this at hand, the analysis of density-correlation functions of conserved quantities based on $S[Q]$ includes several steps: one needs to find (i) the RG-modified static part of the correlation function, and (ii) the renormalized triangle vertex, and then to obtain (iii) the dynamical part of the correlation function with the use of the quadratic expansion of the already renormalized action $S[Q]$. Performing these steps, one may observe that it is sufficient to substitute in all Fermi liquid expressions, starting from Eq. (3) till Eq. (8), the standard combinations $(1 - \Gamma_a)$ by the factors $(z - \Gamma_a)$ that also incorporate the renormalized values of the amplitudes Γ_a, Finkel'stein (1984a) and Castellani et al. (1984b):

$$\chi_a(k, \omega) = \chi_a^{static} \frac{D_a k^2}{\omega_n + D_a k^2}, \quad a = \rho, \sigma. \tag{12}$$

Here, $\chi_\rho^{static} = 2\nu(z - \Gamma_\rho)$ for the static part of the polarization operator, and $\chi_\sigma^{static} = \chi_\sigma^0(z - \Gamma_\sigma)$; the diffusion coefficients are both defined as $D_a = D/(z - \Gamma_a)$. It follows from Eq. (12) that the relation $\sigma/e^2 = 2\nu D$, see Eq. (7), still holds albeit with the value of D obtained from the RG procedure. The observation about equality of the charge and spin conductivities, $\sigma_{charge}/e^2 = \sigma_{spin}/(g_L^0 \mu_B/2)^2$, also remains valid.

In the important case of the Coulomb interaction, the amplitude of the screened long-range interaction, Γ_ρ^0, the shortrange part of the interaction amplitude, Γ_ρ, and the parameter z are all renormalized in such a way that the resulting interaction amplitude acting in the ρ-channel is equal to z:

$$\Gamma_\rho^0 + \Gamma_\rho = z. \tag{13}$$

This result is of fundamental importance. It manifests that the theory of the electron gas interacting via the Coulomb interaction displays a high degree of internal symmetry. Pruisken and his coauthors connected this symmetry to a global symmetry of the problem which they called $\mathcal{F}$-invariance (Pruisken et al., 1999), and which is intimately related to the gauge invariance.

Finally, it is useful to regroup the parameters of the functional S_Q by combining the frequency renormalization parameter z together with ν, Finkel'stein (1984a). Then, z acquires the physical meaning of a parameter renormalizing the density of states of the diffusion modes, while $D_Q = D/z$ can be interpreted as their diffusion coefficient:

$$\nu \Rightarrow z\nu, \quad D \Rightarrow D_Q = D/z. \tag{14}$$

As a result of regrouping, the interaction amplitudes always appear as Γ_a/z. Combining z with ν allows one to use dimensional arguments for expressions involving this parameter. It is natural to link $z\nu$ to the coefficient determining the specific heat c, Castellani and DiCastro (1986). Furthermore, the Einstein relation, the renormalized susceptibilities, as well as the diffusion coefficients describing the evolution of the charge- and spin-densities, all take a Fermi-liquid form albeit with renormalized coefficients which depend on the running scale of the RG procedure. For thermodynamics one gets

$$\chi_a^{static} = z\nu(1 - \Gamma_a/z)(\chi_a^0/\nu); \tag{15}$$

$$c/T = z\nu(c_0/T\nu); \tag{16}$$

and for transport quantities

$$D_a = D_Q/(1 - \Gamma_a/z), \quad a = \rho, \sigma; \tag{17}$$

$$\sigma/e^2 = 2(\nu z) D_Q = 2\nu D. \tag{18}$$

Here, χ_a^0/ν and $c_0/T\nu$ are constants, e.g., for the specific heat, $c_0/(\nu T) = 2\pi^2/3$.

Thus, the effective theory that adequately describes the problem of electrons diffusing in the random field of impurities is the NLSM with interactions. In fact, it is not a model, like the Landau's Fermi liquid theory is not a model. Independent of the assumptions used for the microscopical derivation of S_Q, it is a *minimal functional* which incorporates all essential degrees of freedom and symmetries of the disordered electron liquid. Magnetic impurities, external magnetic field, or spin-orbit scattering induce additional terms in the action $S[Q]$. These terms make some of the diffusion modes gapped. Then, a possible strategy is to preserve the general form of $S[Q]$ as given by Eq. (11), but to reduce the auxiliary matrix field $\hat{Q}$ to such a manifold that only singular diffusion modes remain, while all gapped modes will be excluded. Systems with different sets of singular fluctuation propagators (i.e., when the $\hat{Q}$-fields are elements of different manifolds) belong to different universality classes. When only the fluctuations of density are important, such a system belongs to the so-called unitary class. The richest case is the orthogonal class in which fluctuations of the charge- and spin- densities as well as different kind of Cooperons are relevant. A system where spin-orbit interaction reduces singular fluctuations to the charge-density mode and the singlet Cooperon belongs to the symplectic class. Naturally, the number of the e–e interaction terms involved in the action $S[Q]$ is different for different classes.

The symmetries encoded in the functional S_Q ensure its renormalizability. Correspondingly, during the course of the RG-procedure, the resulting theory of the disordered electron liquid preserves the structure of the Fermi-liquid theory, albeit with renormalized coefficients.

Scaling theory of the metal-insulator transition in $d = 2 + \epsilon$; role of the parameter z

In the dimension $d = 2 + \epsilon$ each *momentum integration* involving the diffusion propagators (see e.g., examples presented in Figs. 4 and 7) generates the dimensionless parameter

$$\rho = \frac{r_d(\lambda)}{2\pi^2/e^2} \propto \frac{e^2}{\sigma}\lambda^{d-2}. \tag{19}$$

Here ρ is equal to the resistance r_d of a d-dimensional cube of side length $\sim 2\pi/\lambda$ measured in units of $2\pi^2/e^2$; compared to the standard definition of the quantum resistance, this unit contains an additional factor π; λ is the momentum cutoff which decreases during the renormalization; decreasing λ corresponds to enlarging blocks in the real-space renormalization procedure. Eq. (19) corresponds to Ohm's law with the conductivity σ depending on the scale λ.

It follows from the structure of the action $S[Q]$, when written with the help of Eqs. (13) and (14), that the RG-procedure can be performed in terms of the dimensionless resistance ρ and the reduced interaction amplitudes

$$\gamma_2 = -\Gamma_\sigma/z = \Gamma_2/z, \tag{20a}$$

(for repulsive interaction, $\gamma_2 > 0$) and

$$\gamma_c = \Gamma_c/z. \tag{20b}$$

With these variables, the set of the RG equations takes the general form:

$$d\ln\rho/dy = -\frac{\epsilon}{2} + \rho\beta_\rho(\rho;\gamma_2,\gamma_c;\epsilon), \tag{21a}$$

$$d\gamma_2/dy = \rho\beta_{\gamma_2}(\rho;\gamma_2,\gamma_c;\epsilon), \tag{21b}$$

and also

$$d\gamma_c/dy = -\gamma_c^2 + \rho\beta_{\gamma_c}(\rho;\gamma_2,\gamma_c;\epsilon). \tag{22}$$

The right hand side of Eq. (22) starts from the γ_c^2-term which describes the rescattering in the Cooper channel. In the case of attraction, $\gamma_c < 0$, this term is responsible for the superconducting instability at low temperatures. Generally, there is a competition between the γ_c^2-term and β_{γ_c}, which describes the suppression of the temperature of the superconducting transition by disorder. In amorphous films superconductivity can be *totally suppressed* by a moderate resistance per square, Finkel'stein (1987a).

The parameter z is described by a separate equation:

$$d\ln z/dy = \rho\beta_z(\rho;\gamma_2,\gamma_c;\epsilon). \tag{23}$$

The function β_z, as well as β_ρ and $\beta_{\gamma_2,\gamma_c}$ are all independent of z. In the above set of RG equations the logarithmic variable $y = \ln 1/[\max(D\lambda^2/z,\omega_n)\tau]$ has been used. This choice of the logarithmic variable is convenient because it allows us to take T as a natural lower cutoff; the upper cutoff is $1/\tau$. The explicit factor ϵ in the equation determining ρ originates from λ^{d-2} entering the definition of the RG-charge ρ. The concrete form of the functions $\beta_{\rho,\,\gamma_2,\,\gamma_c,\,\gamma_z}$ depends on the universality class (i.e., the symmetry) of the system. In reality, the MIT in $3d$ is a difficult issue for analysis, because on its way to the MIT (e.g., as the temperature is lowered) the system may pass through a number of *crossovers* from one universality class to another.

In the case of a MIT, in Eq. (21a) the quantum corrections induced by the Cooperons (weak localization) and the ones appearing as a result of the interplay of the e–e interaction and disorder lead to an increase of the resistance as temperature decreases (i.e., $\beta_\rho > 0$, thus favoring localization), while the geometric factor ϵ competes with these corrections for $d > 2$. As a result, there is an unstable fixed point, $\rho = \rho_c$, which determines the critical behavior of the conductivity near the MIT.

Recall that while ρ is a constant at the point of the MIT, exactly at this point the conductivity vanishes at $T \to 0$. As it follows from Eq. (19), in the vicinity of the transition

$$\sigma(\lambda)/e^2 \propto \lambda^{d-2}. \tag{24}$$

In the $3d$ case, for example, on the metallic side of the transition the critical behavior develops in the region for which $1 \gg \lambda \gg \sigma(T = 0)/e^2$. At non-zero temperature, in the critical regime of the MIT, the process of renormalization ceases at a scale where

$$D(\lambda)\lambda^2/z(\lambda)\sim T \quad \underset{using\ Eq.(18)}{\Rightarrow} \quad \lambda^d/\nu \sim zT. \tag{25}$$

For the electric conductivity measured at external frequency $\omega \gg T$, the renormalization is cut off by ω rather than T. The above relations are a consequence of (i) the form of the diffusion propagator $\mathcal{D}(k,\omega_n)=1/\left(Dk^2+z\omega_n\right)$, and (ii) the definition of the RG-parameter g which exhibits a fixed point at the MIT. In addition, these relations take into account the result discussed in the previous section that (iii) all the renormalizations in between σ and D are canceled out: $\sigma/e^2=2\nu D$.

Thus, in order to find the temperature or frequency behavior of σ at the MIT, one has to connect the momentum and energy scales in the critical region, $\lambda \sim (z \max[\omega,T])^{1/d}$. However, z itself is a scaling parameter, see Eq. (23). Therefore, one needs to know the critical behavior of the parameter z at the transition, which is determined by the value of $\rho\beta_z$ at the critical point:

$$\tilde{\zeta} = -(\rho\beta_z)_{critical\ point}. \tag{26}$$

Correspondingly, the dynamical critical exponent connecting energy and momentum scales at the point of the MIT is

$$z_{en/m} = \frac{d}{1+\tilde{\zeta}}. \tag{27}$$

For free electrons z is not renormalized, $\tilde{\zeta}=0$, and at zero temperature $\sigma(\omega)\propto\omega^{1/3}$ for $d=\ 3$. The e–e interaction modifies this critical behavior of the conductivity through ξ which results in $z_{en/m}\neq d$ for the critical exponent, and

$$\sigma(\omega,T)\propto(\max[\omega,\ T])^{\frac{d-2}{z_{en/m}}}\propto(\max[\omega,\ T])^{\frac{d-2}{d}\left(1+\tilde{\zeta}\right)}. \tag{28}$$

If $\omega \lesssim T$, the RG flow is cut off by the temperature, and

$$\sigma(T)\propto T^{\frac{d-2}{d}\left(1+\tilde{\zeta}\right)}. \tag{29}$$

The scaling behavior described above suggests that the dependence of the conductivity on frequency and temperature can be described by a single function

$$\sigma(T,\omega)_{critical}\propto T^x f(\omega/T), \tag{30}$$

where $f(r)\rightarrow$ const when $r\rightarrow 0$, and $f(r)\propto r^x$ when $r\rightarrow\infty$, with $x=\frac{d-2}{z_{e/m}}=\frac{d-2}{d}\left(1+\tilde{\zeta}\right)$. This is a typical behavior near a quantum phase transition for which the MIT is, perhaps, a primary example. The outcome of the above discussion is quite general, and it does not depend on the specific details of the ϵ-expansion or any other approximation: the frequency or temperature behavior of the conductivity in the critical region of the MIT is determined by the right-hand side of the separate Eq. (23) at the fixed point of the transition, Finkel'stein (1983b, 1984b).

Experimentally, the study of the critical behavior of the MIT is a difficult task. A comprehensive discussion of experiments is beyond the scope of this article. Still a few comments seem to be appropriate here: (i) The dependence of σ on temperature in the critical region can be determined with a limited accuracy only. For the analysis of the critical behavior, the data should be taken outside the region of perturbative corrections, $\sigma(T)-\sigma(T=0)\gtrsim\sigma(T=0)$. On the other hand, one should remain within the quantum transport region, $\sigma(T)<\sigma_{\min}$. (The Mott minimal conductivity $\sigma_{\min}$ is a scale separating regions where transport is dominated by classical or quantum mechanisms.) These two inequalities leave a limited window of $\sigma(T)$ appropriate for the analysis of the truly critical region of the MIT. (ii) The true critical behavior may be obscured by the so-called rounding of the transition, caused by an inhomogeneous distribution of dopants. Rounding may noticeably change the critical behavior, van Schaijk et al. (2000). (iii) It appears that "canonical" Si:P is not very suitable for studying the critical behavior at the MIT. The critical region is very narrow, and several different mechanisms interfere, Löneysen (2011). (iv) In measurements on the magnetic-field-induced MIT in GaAs and InSb semiconductors the critical behavior $\sigma(T)\sim T^{1/3}$ has been observed, Newson and Pepper (1986). In a persistent photoconductor, where the carrier concentration can be controlled very neatly, Katsumoto et al. (1987), $\sigma(T)\sim T^{1/2}$ at the transition, i.e., $x=1/2$; this corresponds to $\tilde{\zeta}=1/2$.

On the theoretical side, the problematic feature of the flow equations given by Eqs. (21a) and (21b) is that the amplitude γ_2 in the absence of spin scattering (i.e., in the case of the orthogonal class) diverges at a finite scale, Finkel'stein (1984c), and thereafter the RG-calculation becomes uncontrolled. The peculiar point here is that together with the divergency of γ_2 the diffusion coefficient $D_\sigma=D/(z+\Gamma_2)\rightarrow 0$. This allows to suggest that on the metallic side of the MIT there is a finite region of concentrations where the fluctuations of the spin density are already localized, while the charge density fluctuations remain itinerant. There is a number of scenarios related to the divergence of γ_2. In particular, the question of a possible transmutation of the spin diffusion modes into local ones near the MIT in 3d still remains unresolved. An interesting observation here is that the width of the Electron Spin Resonance line $\Delta H_{1/2}$ (i.e., the rate of relaxation) in uncompensated Si:P with $n/n_c=1.09$ and 1.25 appears to be *exactly proportional* to the spin susceptibility χ when the temperature is below 1 K, Paalanen et al. (1986). Presumably, the MIT in uncompensated Si:P differs from that in the compensated semiconductors by generating local spin modes at low enough energies in a region near the transition, Finkel'stein (1987b). The discussed divergence in the spin-density channel at a finite scale may well be a driving force for the formation of local spin modes at the corresponding scale. Whether they will reveal themselves as the Kondo effect or somehow differently remains unclear, and it may depend on whether the semiconductor is compensated or not.

The conductivity is usually fitted by

$$\sigma(T)_{critical} \propto T^x f_t(|t/t_c - 1|/T^y), \tag{31}$$

where t is the tuning parameter. It is assumed that in the limit $u \to 0$, the function $f_t(u) \to const$, and $\sigma(T) \propto T^x$ at the transition. In the opposite limit $u \to \infty$, i.e., at lowest temperatures, $f_t(u) \propto u^{x/y}$. This implies that $\sigma \to |t/t_c - 1|^{x/y}$ and, thereby, the critical exponent $\mu = x/y$. In this analysis, a fit with the same parameters x and y can be performed on both sides of the MIT, metallic and insulating. As a byproduct of such a study, the fact that the MIT is indeed a quantum phase transition can be confirmed.

As a tuning parameter t, the concentration of dopants, magnetic field (Khmel'nitskii and Larkin, 1981), or intensity of light in the case of persistent photoconductor can be used. The neutron-transmutation-doping (NTD) method allows researchers to fabricate samples with completely homogeneous doping in order to avoid rounding of the transition. Studies of the disorder driven MIT in NTD Ge:Ga uncompensated and compensated semiconductors reveal a very interesting and rich picture, Itoh et al. (2004). It was found that in non-compensated Ge:Ga at $B = 0$ in a very narrow region of dopant concentrations, $(n_c - n)/n_c \lesssim 1\%$, the critical exponent is $x = 0.38$. However, when the MIT was tuned by a magnetic field, $B \neq 0$, a successful fit with the exponent $x = 0.5$ can be performed in a broad region of magnetic fields. Finally, for the compensated samples in the absence of a magnetic field, $B = 0$, the exponent is $x = 0.33$.

Measurements of the AC conductivity, $\sigma(\omega)$, are, unfortunately, very rare. For example, the temperature and frequency dependences were studied simultaneously in amorphous niobium-silicon alloys (Nb:Si). The one-to-one correspondence between the T- and ω-dependent conductivities was observed at compositions near the MIT, Lee et al. (2000), thus confirming the above picture of the MIT as a quantum phase transition. The critical exponent x has been found to be equal to 1/2 for this system which corresponds to $z_{en/m} = 2$, i.e., $\sigma(T, \omega)_{critical} \propto T^{1/2} f(\omega/T)$, see Eq. (30).

Another important consequence of the general structure of the RG-equations which describe the critical region of the MIT concerns thermodynamics. From the very fact that the critical region is determined by the fixed point of Eqs. (21a), (21b), and (22), it follows that the only parameter which continues to evolve when changing the scale during the course of the RG is the parameter z. Since z is directly related to the renormalization of the effective density of states of the diffusion modes, it follows immediately from Eqs. (15) and (16) that the critical temperature dependence of thermodynamic quantities at the MIT is described by the same dynamical critical exponent $z_{en/m}$. For the specific heat, for example, $c \propto T^{d/z_{en/m}}$.

The content of this section may look like a simple dimensional analysis. In fact, it heavily relies on the structure of the theory described by the NLSM with interaction terms. In this context, the parameter z plays a special role. Since this parameter is responsible for the frequency renormalization of the diffusion propagators, it is of particular importance for finding the correct form of the density and spin-density correlation functions. Furthermore, the form of the density correlation function dictated by the particle number conservation allows one to obtain the Einstein relation for the electric conductivity. Only with the information about the structure of the theory at hand, the critical behavior near the MIT can be found by a straightforward dimensional analysis.

In conclusion, the metal-insulator transition in a system of diffusing electrons is an example of a *quantum phase transition*, Sachdev (2011), with a dynamical scaling exponent $z_{en/m}$ controlled by the parameter z. Precisely the same parameter describes the scaling behavior of both the conductivity and thermodynamic quantities in the critical region of the MIT. In the critical region, the scaling dependence of the parameter z on the temperature or frequency is described by the critical exponent ξ. The structure of the theory is very general and is not related to the ϵ-expansion which can be used for the approximate calculation of the value of ξ for different classes of universality. The appearance of a finite critical exponent $\tilde{\zeta} \neq 0$ is a direct consequence of the *e–e* interaction, and it takes different values for systems belonging to different universality classes. The value of ξ and, correspondingly, of the dynamical scaling exponent $z_{en/m}$ cannot be postulated from general principals, but has to be calculated based on Eq. (26) at the fixed point controlling the MIT.

Tunneling density of states

The tunneling density of states (TDOS) or, as it is also called, the single-particle density of states, $\nu(\varepsilon)$, exhibits a rather pronounced critical behavior in the vicinity of the MIT. This quantity can be obtained by measuring the differential conductance $G_j(V)$ of a tunneling junction at a finite voltage bias $V: G_j(V) \propto \nu(\varepsilon = V)$. In the early theory of the MIT by McMillan (1981), when the parameter z was yet not identified, the TDOS was erroneously treated as the parameter connecting the length and energy (or frequency) scales that provides a dynamic critical exponent. In fact, the TDOS is not a part of the RG-scheme. The TDOS is defined as

$$\nu(\varepsilon) = -\frac{1}{\pi}\mathrm{Im}\int \mathcal{G}^R(\varepsilon, \mathbf{p})\frac{d\mathbf{p}}{(2\pi)^d}. \tag{32}$$

As such, this quantity is not gauge invariant, and it can be changed by a time-dependent gauge transformation. Thereby, it cannot enter the RG-scheme which operates only with truly gauge-invariant quantities. Moreover, with the use of the $\hat{Q}$-technique, $\nu(\varepsilon)$ can be expressed as a diagonal component of the averaged product of the two matrices:

$$\nu(\varepsilon)/\nu = \left\langle \hat{\Lambda}\hat{Q} \right\rangle_{\varepsilon\varepsilon}, \tag{33}$$

However, the presence of $\hat{\Lambda}$ in its explicit form (rather than as in the form of matrix $\hat{Q}$) indicates that the corresponding quantity has potential complications related to gauge-invariance.

The combined effect of Coulomb interaction and disorder leads to a strong suppression of the TDOS. This observation explains the so-called zero-bias anomaly in the tunneling spectra of disordered systems (Altshuler and Aronov, 1979). Compared to other effects related to the interplay of the *e–e* interaction and disorder, corrections to the TDOS are the strongest. In particular, in two-dimensions the *perturbative correction* obtained in the lowest order in ρ appears to be log-squared rather than just logarithmic:

$$\nu(\varepsilon)/\nu = 1 - \frac{\rho}{4} \ln\left(1/|\varepsilon|\tau\right) \ln\left(\tau\omega_0^2/|\varepsilon|\right). \tag{34}$$

Here $\omega_0 = D\kappa_{scr}^2$, while κ_{scr} is the inverse of Thomas-Fermi screening radius.

It follows from Eq. (33), that by measuring the TDOS one studies how an ε-component of the matrix $\hat{Q}$ fluctuates around its equilibrium position as a consequence of the *e–e* interaction. In the absence of the *e–e* interaction, there are no such fluctuations, and the TDOS $\nu(\varepsilon)$ is equal to ν. To go beyond the perturbative correction, a comparison with the physics of phonons is instructive. Measurement of a tunneling current is a kind of "*Mössbauer experiment*" which determines the effect of the zero-point fluctuations of the electromagnetic field on the effectiveness of tunneling. Indeed, it has been recognized already in the early studies (Finkel'stein, 1983a) that the calculation of $\nu(\varepsilon)$ is very similar to the calculation of the Debye-Waller factor, and can be reduced to a *Gaussian integration* with respect to the fields describing deviations of the matrix $\hat{Q}$ from $\hat{\Lambda}$. Correspondingly, in order to obtain a non-perturbative result, the perturbative correction to the TDOS should be exponentiated:

$$\nu(\varepsilon)/\nu \propto \exp\left[-\frac{\rho}{4} \ln\left(1/|\varepsilon|\tau\right) \ln\left(\tau\omega_0^2/|\varepsilon|\right)\right]. \tag{35}$$

The presence of the log-square corrections to $\nu(\varepsilon)$ when $d = 2$ leads to the fact that the ϵ-expansion of the critical exponent of the TDOS starts from a constant, Finkel'stein (1984b). The reason is that at $d = 2 + \epsilon$ in the exponent of Eq. (35), the factor $1/\epsilon$ replaces one of the two logs and cancels a factor ϵ coming from the charge $\rho_c \propto \epsilon$.

The log-square corrections in the TDOS are specific for the long-range Coulomb interaction only. In a model description, when the dynamically screened Coulomb interaction $V_C(k, \omega_n)$ is replaced by a constant, such corrections cannot arise. Furthermore, the log-squared corrections cancel out when calculating any other physical quantities, except the TDOS.

The TDOS is often erroneously considered as the effective density of states in the presence of the *e–e*-interaction. In fact, the TDOS is a very peculiar quantity: by fabricating a counter-electrode for the tunneling junction, one creates a reference point which allows to study the effect of long-range fluctuations of the electric potential on the tunneling conductivity. While giving rise to log-squared corrections to the TDOS, these fluctuations do not contribute to other physical quantities. For example, this type of correction does not influence the temperature of the superconducting transition T_c (i.e., a quantity, which is very sensitive to the density of states at the Fermi energy ν). All log-squared corrections to T_c are canceled out, Finkel'stein (1988).

The MIT in a two-dimensional system

In the 2*d*-geometry, extensive measurements can be performed using the same sample. By applying a gate voltage, it is possible to vary broadly the density of electrons confined within the 2*d*-channel inside a MOSFET device. When the density of electrons is high, the level of disorder is, effectively, small. Conversely, when the density is low, the electrons are at a strong level of disorder. Thus, one can pass from a metallic to an insulating behavior by varying the gate voltage, which is a big advantage of working with 2*d* systems. It has been found in Si-MOSFETs that on the metallic side of the transition the resistance $\rho(T)$ at low enough temperatures drops noticeably as the temperature is lowered further. Since (i) the resistance for a moderate strength of disorder drops at low temperatures, while (ii) the resistance indisputably increases when disorder is strong, it is therefore *unavoidable* that the MIT exists somewhere in-between, at least in *n*-(001) silicon inversion layers.

An important observation in Si-MOSFETs is that in a relatively broad region on the metallic side of the MIT $\rho(T)$ is non-monotonic; it increases before dropping down as the temperature is lowered. The non-monotonic behavior of $\rho(T)$ points toward the existence of a *competition* between different mechanisms. Any "universal" theory of the MIT in dilute 2*d* electron systems that employs only one parameter cannot succeed in describing a system with a non-monotonic temperature dependence. The value of the critical resistance at which the transition occurred was found to be the same for devices fabricated even from different wafers, although the critical density at the MIT was sample dependent, see Fig. 3 in Kravchenko and Sarachik (2004). This fact points toward universality. One, therefore, has some reasons to apply the approach based on the RG-analysis of the NLSM, if the conducting electrons are degenerate and within the diffusive regime, i.e., $T \ll 1/\tau_{el} \lesssim \varepsilon_{\mathrm{F}}$. The 2*d* electron gas in Si-MOSFETs, which in fact is only a moderately high-mobility system, is *unique* in the sense that the scattering is mostly short-range, so that the MIT indeed occurs in the diffusive regime. (The smoothness of the disorder may drive a system with a high-mobility directly from the ballistic regime to the insulating phase.)

The boundary of the diffusive regime can be determined from measurements of the in-plane magnetoconductivity. The spin-splitting induced by the in-plane magnetic field suppresses the effectiveness of the spin-density fluctuations that results in a negative magnetoconductivity, Lee and Ramakrishnan (1982). In the diffusive regime, for $b = g_L\mu_B B/k_B T \ll 1$

$$\Delta\sigma = -\left(e^2/\pi h\right)K_v C_{ee}(\gamma_2, \rho)b^2. \tag{36}$$

Here $K_v = n_v^2$; the conduction band in an n-(001) silicon inversion layer has two almost degenerate valleys, i.e., in Si-MOSFET $n_v = 2$. At not too strong disorder C_{ee} depends only on the interaction amplitude, $C_{ee} = 0.091\gamma_2(\gamma_2 + 1)$. By contrast, at higher temperatures, or at higher density, when electrons are ballistic, $\Delta\sigma \propto (T\tau)b^2$. Thus, by studying the temperature dependence of the magnetoconductivity, one may chart the region where the electrons are diffusive and, furthermore, extract the temperature dependence of the amplitude γ_2 which appears as a result of the logarithmic corrections. Proceeding in this way, it has been found that the diffusive regime in Si-MOSFETs extends up to a few Kelvin in a density range around the critical density of the MIT. The corresponding Fermi temperature is of the order of 10 K and, therefore, electrons are already degenerate at temperatures convenient for measurements.

In the one-loop order, the pair of coupled RG equations describing the evolution of the resistance and the amplitude γ_2 with temperature takes the form, Punnoose and Finkel'stein (2002):

$$\frac{d\ln\rho}{dy} = \rho\left[n_v + 1 - \left(4n_v^2 - 1\right)\Phi(\gamma_2)\right], \tag{37}$$

$$\frac{d\gamma_2}{dy} = \rho\,\frac{(1+\gamma_2)^2}{2}. \tag{38}$$

These equations obtained in the lowest order in ρ incorporate the full dependence on the e–e amplitudes. In the first equation, the combination $(4n_v^2 - 1)$ is the number of spin-valley multiplet channels, while the standard combination $\Phi(\gamma_2) = \frac{1+\gamma_2}{\gamma_2}\ln(1+\gamma_2) - 1$ was first time obtained by Finkel'stein (1983a) for $n_v = 1$. The factor n_v in the square brackets corresponds to the weak-localization (Cooperon) corrections and, finally, the factor 1 entering the square brackets is the contribution of the long-ranged Coulomb singlet-amplitude (after dynamical screening) and is, therefore, universal. Next, it should be noted that the factor 1 appearing in Eq. (38) for γ_2 also originates from the Coulomb singlet-amplitude combined with scattering induced by disorder.

The following salient features of the RG-flow described by Eqs. (37) and (38) should be noted: While the amplitude γ_2 increases monotonically as the temperature is reduced, the resistance has a very special non-monotonic form changing from insulating behavior ($d\rho/dT < 0$) at high temperatures to metallic behavior ($d\rho/dT > 0$) at low temperatures. The non-monotonic behavior of the resistance as a function of the temperature results from a competition between the charge-density diffusion modes and the Cooperons, on the one hand, and the fluctuations of the spin- (and valley-) degrees of freedom, on the other hand. The former favor localization, while the latter act against it, thus stabilizing the metallic state at low enough temperatures, with a change of the trend in $\rho(T)$ at an intermediate temperature. The two equations act in a tandem: resistance increases the amplitude γ_2. This increasing amplitude in its turn changes the trend in $\rho(T)$.

For $n_v = 1$ the change in the slope of $\rho(T)$ occurs at $\gamma_2 = 2.08$, whereas for $n_v = 2$ the combination $(4n_v^2 - 1)$ considerably increases the effectiveness of anti-localization, so that passing through the maximum in $\rho(T)$ happens at a considerably smaller value $\gamma_2 = 0.45$. It follows from the general form of Eqs. (37) and (38), that the ratio $\rho(T)/\rho_{\max}$ is equal to a universal function, once the logarithmic variable η_T is introduced: $\rho(T)/\rho_{\max} = R(\eta_T)$, where the logarithmic variable $\eta_T = \rho_{\max}\ln(T/T_{\max})$, and $\rho_{\max}$ is the value of $\rho(T)$ at its maximum.

The description provided by the RG equations (37) and (38) has been confirmed by the analysis of the experimental data for a moderate strength of disorder i.e., in the region of applicability of the one-loop approximation. The fit of the resistance curves with a single universal function $R(\eta)$ captured in the correct temperature intervals the non-monotonic behavior of $\rho(T)$ together with its drop by a factor of five and the subsequent flattening, Punnoose and Finkel'stein, 2002. The full temperature dependence of the resistance is completely controlled by its value $\rho_{\max}$ at the maximum; there are no other fitting parameters. Not too close to the MIT, the extracted values of $\gamma_2(T_{max})$ at which $\rho(T)$ passes through the maximum was found (Anissimova et al., 2007) equal to 0.45 as predicted by the theory for $n_v = 2$. A similar analysis of the data obtained in devices fabricated from another wafer was given by Knyazev et al. (2006).

Since the one-loop calculation, which is valid for a moderate strength of disorder, gives a *drop* of the resistance at low temperatures, and the localization at strong disorder is indisputable, the conclusion about the existence of the MIT can be justified even within the one-loop approximation. Starting from the 1980s, it had been commonly assumed that electrons in $2d$ are "eventually" (i.e., at $T = 0$ always localized, Abrahams et al. (1979). In view of the anti-localization effect of the e–e interactions, this point of view had to be radically altered.

As it has been already discussed in connection with Eqs. (21a) and (21b), the problematic feature of the flow equations given by Eqs. (37) and (38) is that the amplitude γ_2 diverges at a finite temperature T^* and thereafter the RG-calculation becomes uncontrolled. Fortunately, the scale T^* decreases very rapidly with n_v as $\ln\ln(1/\tau T^*) \sim (2n_v)^2$, making the problem of the divergence of γ_2 irrelevant for all practical purposes even for $n_v = 2$. At $n_v \to \infty$, the theory becomes internally consistent: $T^* \to 0$.

Obviously, in spite of the success in the description of Si-MOSFETs at a moderate disorder, the *single-curve* (universal) solution $R(\eta)$ cannot provide a description of the MIT. To approach the critical region of the MIT, the disorder has to be treated beyond the lowest order in ρ, while adequately retaining the effects of the interaction. A theory of the MIT, based on a two-loop calculation, was

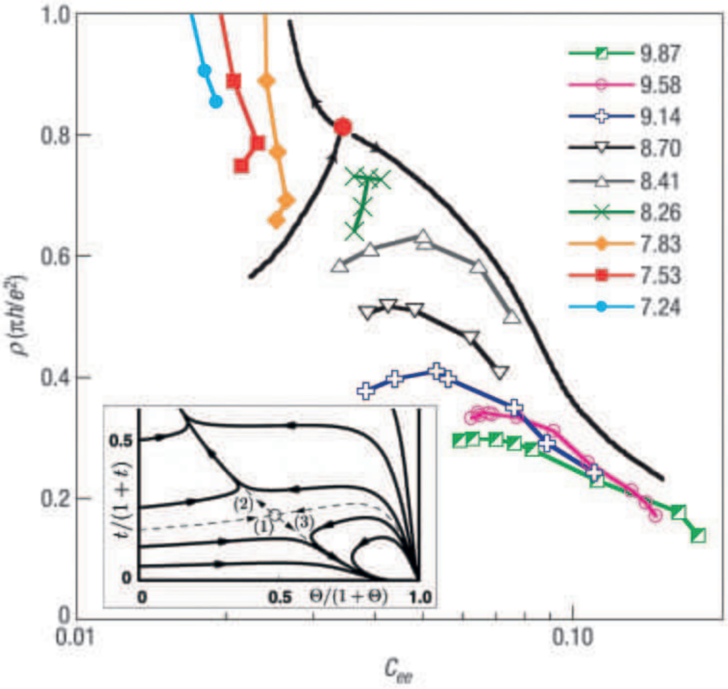

Fig. 8 The resistance-interaction flow diagram of 2*d* electrons in a Si-MOSFET device. The circle indicates the location of the quantum critical point from which the three separatrices emanate. The arrows shown on the separatrices indicate the direction of the flow as the temperature is lowered. The electron densities are given in units of 10^{10} cm^{-2}. The interaction amplitude in the spin-density channel is represented by the coefficient C_{ee}, which was extracted from the magnetoresistance. *Inset*: The resistance-interaction ($t - \Theta$) flow diagram obtained in the two-loop calculations. Area (1) is the metallic phase, which is stabilized by the interaction. Area (2) is the insulating phase where disorder prevails. Area (3) is the region of strong spin correlations (not accessible in this device).

developed by Punnoose and Finkel'stein (2005) using the number of identical valleys as a large parameter, $n_v \to \infty$. The valley degrees of freedom are akin to flavors in standard field-theoretic models. It is natural, working in the large-n_v approximation, to introduce the amplitudes $\Theta = 2n_v\gamma_2$ together with the resistance parameter $t = n_v\rho$. The parameter t is thus the resistance per valley, $t = 1/[(2\pi)^2\nu D]$. Both quantities Θ and t remain finite in the large-n_v limit.

The resulting resistance-interaction ($t - \Theta$) flow diagram is plotted as an inset in Fig. 8. It contains the quantum critical point, which corresponds to the fixed point of the equations describing the evolution of t and Θ. Crossing the attractive separatrix by changing the initial values of t and Θ (e.g., by changing the carrier density) leads to the MIT. In the main panel of Fig. 8 the two-parameter scaling theory has been verified experimentally by Anissimova et al. (2007). In this plot, the coefficient C_{ee} effectively represents the interaction amplitude in the spin-density channel. It has been extracted by fitting $\Delta\sigma(B,T)$ to Eq. (36), which allows to obtain the RG-evolution of C_{ee} as a function of temperature. A number of curves with a non-monotonous temperature dependence of $\rho(T)$ in the metallic region are clearly visible there. The flow diagram presented in Fig. 8 confirms all the qualitative features of the theoretical predictions. The possibility of presenting the data as a flow diagram gives a very strong argument in favor of the two-parameter scaling theory in Si-MOSFETs.

To conclude, the high-mobility samples of Si-MOSFETs provide an ideal playground to study the properties of a 2*d* disordered electron liquid and, in particular, Anderson localization in the presence of the *e*–*e* interactions. The RG-theory gives not only a qualitative but (within the region of its applicability) also a quantitative description of the experimental data in these systems. The two-parameter RG-theory of the disordered electron liquid captures both quantitatively (for moderate disorder) and qualitatively the physics of the two-dimensional disordered liquid in the diffusive regime. A quantum critical point separates the metallic phase, which is stabilized by electronic interactions, from the insulating phase, where disorder prevails over the electronic interactions. The possibility of presenting the data as a flow diagram is a strong argument in favor of the applicability of the two-parameter scaling theory in Si-MOSFETs.

Thermal conductivity

The thermal conductivity κ characterizes the heat current $\mathbf{j}_Q$ flowing through a material in response to a temperature gradient, $\mathbf{j}_Q = -\kappa\nabla T$. In a Fermi liquid at low enough temperatures, the inelastic scattering rate for particles near the Fermi energy is small, the thermal conductivity is primarily determined by disorder scattering, and the Wiedemann-Franz law (WFL) $\kappa = \mathcal{L}_0\sigma T$ with $\mathcal{L}_0 = \pi^2/3e^2$ holds. In the disordered electron liquid, disorder scattering and interactions become strongly intertwined. Their interplay leads to renormalizations of transport coefficients and thermodynamic susceptibilities. A question of fundamental importance for understanding the scale-dependent Fermi liquid theory addressed in this Section is how the renormalizations affect the thermal conductivity, and if they can lead to a violation of the WFL.

It is convenient to discuss the thermal conductivity using the NLSM formalism in the Keldysh technique, rather than in the Matsubara formalism. In the Keldysh technique, the action is defined on the Keldysh contour which contains the forward (+) and backward (−) paths, see e.g., Kamenev (2011). The thermal conductivity can be extracted from the retarded heat density correlation function defined as $\chi_k(x_1, x_2) = -i\theta(t_1 - t_2)\left\langle\left[\hat{k}(x_1),\ \hat{k}(x_2)\right]\right\rangle_T$, where $\hat{k} = \hat{h} - \mu\hat{n}$ is the heat density operator, $\hat{h}$ is the Hamiltonian density operator, $x = (\mathrm{r}, t)$, and the angular brackets denote thermal averaging.

Introducing fields on the forward (+) and backward (−) paths of the Keldysh contour, one may define the classical (cl) and quantum components (q) of the heat density symmetrized over the two branches of the contour, $k_{cl/q} = \frac{1}{2}(k_+ \pm k_-)$. The RG-analysis, including effects of the spin density fluctuations, has been reproduced in the Keldysh technique by Schwiete and Finkel'stein (2014a). For thermal transport, this scheme has to be extended by adding the source term $S_\eta = 2\int_x[\eta_2(x)k_{cl}(x) + \eta_1(x)k_q(x)]$ to the microscopic action, where η_1 and η_2 are the so-called gravitational potentials, Luttinger (1964). With these terms, one can find χ_k by differentiation the partition function, $\chi_k(x_1, x_2) = (i/2)\delta^2\mathcal{Z}/\delta\eta_2(x_1)\delta\eta_1(x_2)$. Finally, the thermal conductivity κ can be extracted from the disorder-averaged correlation function $\langle\chi_k(x_1, x_2)\rangle_{dis} = \chi_k(x_1 - x_2)$ (Castellani et al., 1987) as follows:

$$\kappa = -\frac{1}{T}\lim_{\omega\to 0}\ \lim_{k\to 0}\left[\frac{\omega}{k^2}\mathrm{Im}\ \chi_k(k,\ \omega)\right]. \tag{39}$$

A serious complication arises when working with the gravitational potentials introduced via term $S_\eta : \eta_{1,\ 2}$ couple (among other terms) to the random disorder potential u_{dis}. Fortunately, one can release the disorder term from the explicit dependence on the gravitational fields with the transformation $\psi \to \hat{\lambda}^{1/2}\psi, \overline{\psi} \to \overline{\psi}\hat{\lambda}^{1/2}$, where $\hat{\lambda} = 1/(1 + \eta_1\hat{\sigma}_0 + \eta_2\hat{\sigma}_1)$ and $\hat{\sigma}_0$ and $\hat{\sigma}_1$ are Pauli matrices in Keldysh space. From here on, the NLσM in terms of the Keldysh $\hat{Q}$-matrices can be derived along standard lines. In the Keldysh NLSM, $\hat{Q}_{\varepsilon\varepsilon'}$ generally depends on both frequency arguments. The metallic saddle point $\hat{Q}_{sp} = \hat{\sigma}_3$, where $\hat{\sigma}_3$ is also Pauli matrix in the Keldysh space. The temperature of electrons enters through the distribution function encoded in $\hat{u}$,

$$\hat{u}_\varepsilon = \begin{pmatrix} 1 & \mathcal{F}_\varepsilon \\ 0 & -1 \end{pmatrix}, \quad \mathcal{F}_\varepsilon = \tanh\left(\frac{\varepsilon}{2T}\right). \tag{40}$$

Matrices $\hat{u}$ decorates the $\hat{Q}$-matrices as follows: $\hat{Q}(\varepsilon\varepsilon') = \hat{u}_\varepsilon\hat{Q}_{\varepsilon\varepsilon'}\hat{u}_{\varepsilon'}$.

The static part of the heat density correlation function is related to the specific heat c as $\chi_k^{static} = -cT$, while the specific heat can be found from the average heat density as $c = \partial_T\left\langle\hat{k}\right\rangle_T$. The average value of $\left\langle\hat{k}\right\rangle_T$ can be obtained by differentiating the partition function with respect to the gravitation source η_2. Then, the analysis of the diffusion modes part of the specific heat together with the fermionic part c_0 allows to reproduce the conclusion (Castellani and DiCastro, 1986) that in the disordered electron liquid as a result of renormalizations $c = zc_0$.

For finding the thermal conductivity, it is enough to know the dynamical part of the heat density correlation function χ_k^{dyn}, see Eq. (39). For the analysis of χ_k^{dyn}, it suffices to keep terms up to linear order in the gravitation potentials in the NLSM action by expanding $\hat{\lambda} \approx 1 - \eta_1\hat{\sigma}_0 - \eta_2\hat{\sigma}_1$. Since the RG flow for D, z, and the interaction amplitudes Γ_ρ and Γ_σ is known, it remains to determine vertex corrections by studying the renormalization of the gravitation source field $\hat{\eta}$. The NLSM *extended* by the gravitational potentials has the following (symbolic) form, Schwiete and Finkel'stein (2014b):

$$\begin{aligned} S_\zeta = \ & \frac{\pi\nu i}{4}\int d^d r \mathrm{Tr}\left[D\left(1 + \hat{\zeta}_D\right)\left(\nabla\underline{\hat{Q}}\right)^2 + 2iz\left\{\hat{\varepsilon},\ 1 + \hat{\zeta}_z\right\}\underline{\delta\hat{Q}}\right] \\ & -\frac{\pi\nu}{8}\sum_{n=1}^{2}\int d^d r\nu\left\{\underline{\delta\hat{Q}}\left(1 + \hat{\zeta}_{\Gamma_n}\right)\hat{\Gamma}_n\underline{\delta\hat{Q}}\right\}, \end{aligned} \tag{41}$$

where $\hat{\zeta}_X(\mathbf{r}, \varepsilon + \omega, \varepsilon) = \zeta_X(\mathbf{r}, \omega)$ for $X \in \{D, z, \Gamma_1, \Gamma_2\}$ represent the gravitational potentials (it is convenient here to work with the interaction amplitudes $\Gamma_1 = (\Gamma_\rho - \Gamma_\sigma)/2$ and $\Gamma_2 = -\Gamma_\sigma$); here, $\delta\hat{Q} = \hat{Q} - \hat{\sigma}_3$ and $\underline{\delta\hat{Q}} = \hat{u}\delta\hat{Q}\hat{u}$. The initial conditions for the gravitation potential are: $\zeta_z = \zeta_{\Gamma_1} = \zeta_{\Gamma_2} = -\eta_1, \quad \zeta_D = 0$. We see from Eq. (41), that there are vertices related to frequency and interactions. Besides, the potential ζ_D was introduced to anticipate the possibility that the sources ζ_X with $X \neq D$ migrate to the D-term during the RG procedure.

The final result of the RG-analysis acquires a very compact form, Schwiete and Finkel'stein (2014b, 2014c):

$$\Delta\left(X_{i_0}\zeta_{i_0}\right) = \sum_{j=1}^{4}\zeta_j\frac{\partial}{\partial X_j}\left(\Delta X_{i_0}\right), \tag{42}$$

where ΔX symbolizes a logarithmic correction to X. The result holds for all $X \in \{D, z, \Gamma_1, \Gamma_2\}$ (In Eq. (42), the notation ζ_i and X_i with $i = 1\ldots4$ is used). The result presented in Eqs. (42) bears a certain resemblance with the multiplicative RG (Bogoliubov and Shirkov, 1959), because the source terms enter in combination with the charges X in a multiplicative way. One can show, using Eqs. (42) in combination with the known structure of the RG equations that the parameters ζ_X do not flow, provided that initially $\zeta_D = 0$ holds

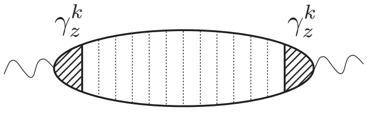

Fig. 9 The dynamical part of the heat density-heat density correlation function. As discussed in the main text, no additional rescattering induced by the *e–e* interactions occurs.

and all remaining $\zeta_{X\neq D}$ are equal to each other. Thus, there exists a fixed point for the gravitational potentials in the multi-parametric RG-flow of the functional S_ζ. This remarkable balance between the different terms in S_ζ ensures the conservation of energy during the course of the RG-procedure.

After all renormalizations, the dynamical part χ_{kk}^{dyn} is determined by the averaged product of η_1- and η_2-frequency terms that can be calculated in the ladder approximation, see Fig. 9. The interaction vertices are not effective at this final stage, because such contributions have already been accounted for during the RG procedure. Finally, the dynamical part of the correlation function takes the form $\chi^{dyn}(k,\omega) = -c_0T(\gamma_z^k)^2 i\omega/(Dk^2 - iz\omega)$. Overall, the heat density correlation function is obtained by adding the static and dynamical parts as

$$\chi_k(k,\,\omega) = -cT - c_0Tz^2\frac{i\omega}{Dk^2 - iz\omega} = -cT\frac{D_Qk^2}{D_Qk^2 - i\omega}. \tag{43}$$

In these equations, the relation $c = zc_0$ for the renormalization of the specific heat has been used. With the help of Eq. (39), the thermal conductivity is found as $\kappa = cD_k = c_0D$. While the diffusion of heat is governed by the heat diffusion coefficient $D_Q = D/z$, the frequency renormalization z cancels out when calculating the thermal conductivity. As an immediate consequence of this observation in combination with the RG-result for the conductivity, $\sigma = 2e^2\nu D$, the WFL $\kappa/\sigma = \pi^2T/3e^2 = \mathcal{L}_0T$ holds even in the scale dependent disordered electron liquid, Castellani et al. (1987) and Schwiete and Finkel'stein (2014b).

So far, the calculation of the thermal conductivity described above is based on a model with Fermi-liquid type interactions. The inclusion of Coulomb interactions into the RG analysis affects the results for both electric and thermal conductivities, but leaves the Wiedemann-Franz ratio $\kappa/\sigma T$ unchanged. However, the long-range character of the Coulomb interaction and the constraints imposed by gauge invariance require special care, Catelani and Aleiner (2005) and Schwiete and Finkel'stein (2016a). For example, in the case of $2d$ conducting electrons, while electrons are confined within a conducting plane or thin film, the electric field and its energy density extend over the whole $3d$ space.

Owing to long range part of the Coulomb interaction, *additional* logarithmic corrections to the thermal conductivity without analog for the electric conductivity arise in $2d$ from a *sub-temperature* energy range. Consequently, the WFL is violated in the presence of Coulomb interactions. Because of the additional logarithmic corrections, the calculation of thermal conductivity demands a two-stage procedure: the leading logarithmic corrections originating from energies in the RG-interval $(1/\tau, T)$ can be absorbed into the scale-dependent RG charges of the *extended* NLσM. Once all RG-corrections are taken into account, one may find the sub-temperature correction using parameters determined by the current scale of the RG procedure. The structure of the heat density correlation function, Eq. (43), remains intact. The only modification is the diffusion coefficient, $D \to \tilde{D} = D + \delta D$, where D includes the RG-corrections and δD originates from the sub-thermal processes. The correction to the thermal conductivity from sub-thermal energies is equal to

$$\delta\kappa = \frac{T}{12}\log\frac{D\kappa_{scr}^2}{T}. \tag{44}$$

The correction $\delta\kappa$ presented in Eq. (44) was obtained perturbatively by various techniques (Raimondi et al., 2004; Niven and Smith, 2005; and Catelani and Aleiner, 2005). The two-stage procedure described above generalized these calculations by showing that all Fermi-liquid and RG renormalizations (including the parameter z) drop out when calculating, Schwiete and Finkel'stein (2016b).

The correction $\delta\kappa$ causes a violation of the WFL. For a detailed discussion of the violation of the WFL, it is useful to introduce the "thermal resistance" $\rho_k \equiv (\mathcal{L}_0T/\kappa)e^2/2\pi^2$, for which the relation $\rho_k = \rho$ holds as long as the WFL is satisfied. The dimensionless function $R_k(\eta_T) = \rho_k(\eta_T)/\rho_{max}$ is the thermal analog of universal function $R(\eta_T)$ discussed in the previous section. While the solution of the RG equations (37) and (38) depends on n_ν, the number of valleys does not affect the correction. Hence, the relative weight of the WFL-violating correction is n_ν-dependent. For an arbitrary n_ν, $R_k(\eta_T)$ can be parametrized as (Schwiete and Finkel'stein, 2016b)

$$R_k(\eta_T) = \frac{R(\eta_T)}{1 + R(\eta_T)\left(P_{max} - \frac{1}{2}\eta_T\right)}, \tag{45}$$

where $P_{max} \equiv (1/2)\rho_{max}\log\left(D\kappa_{scr}^2/T_{max}\right) = [\rho_{max} - \rho_k(0)]/\rho_k(0)$ is a measure for the violation of the WFL law at the temperature T_{max}. Remarkably, the maximum of $R_k(\eta_T)$ is positioned at a universal value (independent of P_{max}), determined by the condition $(\partial_{\eta_T}R)/R^2 = 1/2$. For $n_\nu = 2$, this gives $\eta_{T,\,k}^{max} \approx -0.0785$; examples of curves with $P_{max} = 0.2$,0.3 and 0.4 are shown in Fig. 10.

To conclude, for short-range interactions of the Fermi liquid-type, the WFL displays a remarkable robustness, and the low-temperature corrections to thermal conductivity are parallel to those for the electric conductivity. In contrast, for a generic electron liquid with long-range Coulomb interactions, there exist *delocalizing* contributions to the thermal conductivity that do not

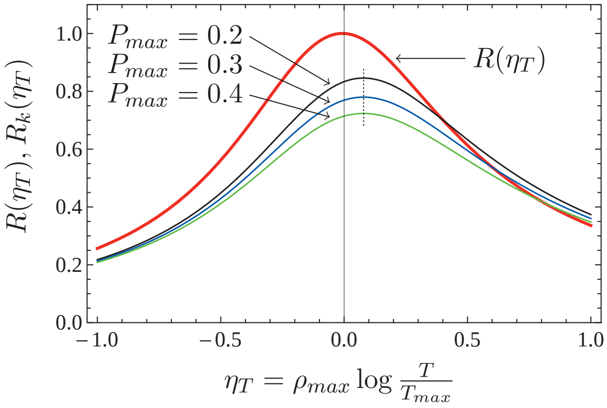

Fig. 10 "Thermal resistance" R_k and resistance R in dimensionless units for $n_v = 2$. R_k coincides with R if the WFL holds. The parameter P_{max} is a measure for the violation of the WFL law at the temperature T_{max}. In the discussed theory, the maxima of R_k are shifted from the maximum of R by a value that is independent on P_{max}. The high temperature-regime for which $R_k > R$ is unphysical.

have any analog for the electric conductivity. They are beyond the RG approach, originate from scattering processes with very low energy-transfer of the order of the temperature, and lead to a violation of the WFL.

Conclusion

The physics of itinerant electrons is determined by the combined effect of disorder and *e–e* interactions. Together, they generate a rich set of non-trivial phenomena. There are singular corrections to various quantities, both in transport and thermodynamics, which need to be summed in order to obtain the resulting behavior. The metal-insulator transition (MIT) gives a non-trivial example of a quantum phase transition (QPT). The dynamical scaling exponent needs to be found from a separate RG equation, rather than being postulated heuristically. In two-dimensional systems, the physics is determined by the RG-flow in the disorder-interaction plane. The flow is governed by a fixed point and associated separatrices. Crossing the separatrix implies the MIT. In thermal transport, the long-range part of the Coulomb interaction causes a violation of the Wiedeman-Franz law.

On the methodological side, the problem of disordered interacting electrons is an impressive example of the effectiveness of field-theoretical methods in condensed matter physics. In particular, the effect of correlations in the originally fermionic problem is entirely described in terms of fluctuations of the Q-matrices in the NLSM functional.

Acknowledgments

The authors acknowledge valuable discussions with David Khmelnitskii, Alex Punnoose, Karen Michaeli and the late Konstantin Efetov on topics related to this work. G. S. would like to thank the National Science Foundation for financial support under Grant No. DMR-1742752.

References

Abrahams E, et al. (1979) Scaling theory of localization: Absence of quantum diffusion in two dimensions. *Physical Review Letters* 42: 673.
Altshuler BL and Aronov AG (1979) Contribution to the theory of disordered metals in strongly doped semiconductors. *Zhurnal Eksperimental'noi i Teoreticheskoi Fiziki* **77**: 2028. [*Sov. Phys. JETP* **50**, 968 (1979)].
Altshuler BL, Aronov AG, and Lee PA (1980) Interaction effects in disordered fermi systems in two dimensions. *Physical Review Letters* 44: 1288.
Anissimova S, et al. (2007) Flow diagram of the metalinsulator transition in two dimensions. *Nature Physics* 3: 707.
Bogoliubov NN and Shirkov DV (1959) *Introduction to the Theory of Quantized Fields.* Interscience.
Castellani C and DiCastro C (1986) Effective Landau theory for disordered interacting electron systems: Specific-heat behavior. *Physical Review B* 34: 5935.
Castellani C, et al. (1984a) Interaction-driven metalinsulator transitions in disordered fermion systems. *Physical Review B* 30: 527.
Castellani C, et al. (1984b) Spin fluctuations in disordered interacting electrons. *Physical Review B* 30: R1596.
Castellani C, et al. (1987) Thermal conductivity in disordered interacting-electron systems. *Physical Review Letters* 59: 447.
Catelani G and Aleiner IL (2005) Interaction corrections to thermal transport coefficients in disordered metals: The quantum kinetic equation approach. *Journal of Experimental and Theoretical Physics* 100: 331.
Clarke WR, et al. (2008) Impact of long- and short-range disorder on the metallic behaviour of two-dimensional systems. *Nature Physics* 4: 55.
Efetov KB, Larkin AI, and Khmelnitskii DE (1980) Diffusion mode interaction in the theory of localization. *Zhurnal Eksperimental'noi i Teoreticheskoi Fiziki* **79**: 1120. [*Sov. Phys. JETP* **52**, 568 (1980)].
Finkel'stein AM (1983a) The influence of Coulomb interaction on the properties of disordered metals. *Zhurnal Eksperimental'noi i Teoreticheskoi Fiziki* **84**: 168. [*Sov. Phys. JETP* **57**, 97 (1983)].

Finkel'stein AM (1983b) On the Frequency and Temperature dependence of the conductivity near a Metal-Insulator Transition. *Pis'ma ZhETF* **37**: 436. [*Sov. Phys. JETP Lett.* **37**, 517(1983)].

Finkel'stein AM (1984a) Weak-localization and Coulomb interactions in disordered systems. *Zeitschrift fuer Physik B: Condensed Matter* 56: 189.

Finkel'stein AM (1984b) Metal-insulator transition in a disordered system. *Zhurnal Eksperimental'noi i Teoreticheskoi Fiziki* **86**: 367. [*Sov. Phys. JETP* **59**, 212(1984)].

Finkel'stein AM (1984c) Spin fluctuations in disordered systems near the metal-insulator transition. *Pis'ma ZhETF* **40**: 63. [*Sov. Phys. JETP Lett.* **40**, 796 (1984)].

Finkel'stein AM (1987a) Superconducting transition temperature in amorphous films. *Pis'ma ZhETF* 45: 37. [*Sov. Phys. JETP Lett.* **45**, 63 (1987)].

Finkel'stein AM (1987b) ESR near a metal-insulator transition. *Pis'ma ZhETF* **46**: 407. [*Sov. Phys. JETP Lett.* **46**, 513 (1987)].

Finkel'stein AM (1988) The temperature of the superconducting transition in amorphous films. In: Ando T and Fukuyama H (eds.) Proc. Int. Symp. on Anderson Localization, Springer Proc. in Physics, vol. 28, p. 230. Berlin: Springer-Verlag.

Gor'kov LP, Larkin LP, and Khmel'nitskii DE (1979) Particle conductivity in a two-dimensional random potential. *Pis'ma ZhETF* **30**: 248. [*Sov. Phys. JETP Lett.* **30**, 228 (1979)].

Itoh KM, et al. (2004) Complete scaling analysis of the metal-insulator transition in Ge:Ga: Effects of doping compensation and magnetic field. *Journal of the Physical Society of Japan* 73: 173–183.

Kamenev A (2011) *Non-Equilibrium Systems.* Cambridge University Press.

Katsumoto S, et al. (1987) Fine tuning of metal-insulator transition in $Al_{0.3}Ga_{0.7}$ As using persistent photoconductivity. *Journal of the Physical Society of Japan* 56: 2259–2262.

Khmel'nitskii DE and Larkin AI (1981) Mobility edge shift in external magnetic field. *Solid State Communications* 39: 10691070.

Knyazev DA, et al. (2006) Critical behavior of transport and magnetotransport in 2D electron system in Si in the vicinity of the metal-insulator transition. *Pis'ma ZhETF* **84**: 780. [*JETP Lett.* **84**, 662 (2006)].

Kravchenko SV and Sarachik MP (2004) Metal-insulator transition in two-dimensional electron systems. *Reports on Progress in Physics* 67: 1.

Lee PA and Ramakrishnan TV (1982) Magnetoresistance of weakly disordered electrons. *Physical Review B* 26: 4009+.

Lee HL, et al. (2000) Quantum-critical conductivity scaling for a metal-insulator transition. *Science* 287: 633.

Lifshitz EM and Pitaevskii LP (eds.) (1980) *Course of Theoretical Physics*. In: *Statistical Physics, Part 2*, vol. 9. Oxford: Pergamon Press.

Löneysen HV (2011) Electron-electron interactions and the metal-insulator transition in heavily doped silicon. *Annals of Physics (Berlin)* 523: 599–611.

Luttinger JM (1964) Theory of Thermal Transport Coefficients. *Physics Review* **135**: A1505–A1514.

McMillan WL (1981) Scaling theory of the metal-insulator transition in amorphous materials. *Physical Review B* 24: 2739.

Newson DJ and Pepper M (1986) Critical conductivity at the magnetic field induced metal-insulator transition in n − GaAs and n-InSb. *Journal of Physics C* 19: 3983–3990.

Niven DR and Smith RA (2005) Electron-electron interaction corrections to the thermal conductivity in disordered conductors. *Physical Review B* 71: 035106.

Paalanen MA, et al. (1986) Spin dynamics of nearly localized electrons. *Physical Review Letters* 57: 2061.

Pruisken AMM, Baranov MA, and Skoric' B (1999) (Mis-)handling gauge invariance in the theory of the quantum Hall effect. II. Perturbative results. *Physical Review B* 60: 16821.

Punnoose A and Finkel'stein AM (2002) Dilute electron gas near the metal-insulator transition: Role of valleys in silicon inversion layers. *Physical Review Letters* 88: 016802.

Punnoose A and Finkel'stein AM (2005) Metal-insulator transition in disordered two-dimensional electron systems. *Science* 310: 289.

Raimondi R, et al. (2004) Electronic thermal conductivity of disordered metals. *Physical Review B* 70: 155109.

Sachdev (2011) *Quantum Phase Transitions*. Cambridge: Cambridge University Press.

Schwiete G and Finkel'stein AM (2014a) Keldysh approach to the renormalization group analysis of the disordered electron liquid. *Physical Review B* 89: 075437.

Schwiete G and Finkel'stein AM (2014b) Thermal transport and Wiedemann-Franz law in the disordered Fermi liquid. *Physical Review B* 90: 060201.

Schwiete G and Finkel'stein AM (2014c) Renormalization group analysis of thermal transport in the disordered Fermi liquid. *Physical Review B* 90.

Schwiete G and Finkel'stein AM (2016a) Heat diffusion in the disordered electron gas. *Physical Review B* 93: 115121.

Schwiete G and Finkel'stein AM (2016b) Theory of thermal conductivity in the disordered electron liquid. *Journal of Experimental and Theoretical Physics* 122: 567.

van Schaijk RTF, et al. (2000) Probing the plateau insulator quantum phase transition in the quantum hall regime. *Physical Review Letters* 84: 1567.

Wegner FJ (1979) The mobility edge: Continuous symmetry and a conjecture. *Zeitschrift fuer Physik B: Condensed Matter* 35: 207.

Further reading

Abrahams E, Kravchenko SV, and Sarachik MP (2001) Metallic behavior and related phenomena in two dimensions. *Reviews of Modern Physics* 73: 251.

Altshuler BL and Aronov AG (1985) Electron-electron interactions in disordered systems. In: Efros AL and Pollak M (eds.) *Modern Problems in Condensed Matter Physics*, p. 1. North Holland: Elsevier.

Belitz D and Kirkpatrick TR (1994) The Anderson-Mott transition. *Reviews of Modern Physics* 66: 261.

Belitz D, Kirkpatrick TR, and Vojta T (2005) How generic scale invariance influences quantum and classical phase transitions. *Reviews of Modern Physics* 77: 579.

Burmistrov IS (2017) Transport in a two-dimensional disordered electron liquid with isospin degrees of freedom. In: Kravchenko SV (ed.) *Strongly Correlated Electrons in Two Dimensions*, pp. 65–116. Pan Stanford Publishing.

Burmistrov IS (2019) Finkel'stein nonlinear sigma model: interplay of disorder and interaction in 2D electron systems. *Zhurnal Eksperimental'noi i Teoreticheskoi Fiziki* **156**: 724–737. [*Sov. Phys. JETP* **129**, pp. 669–679 (2019)].

Di Castro C and Raimondi R (2003) Disordered electron systems. In: Giuliani GF and Vignale G (eds.) Proceedings of the International School of Physics "Enrico Fermi"*: Varenna, Italy, 29 July-8 August 2003 - Amsterdam .*

Evers F and Mirlin AD (2008) *Reviews of Modern Physics* 80: 1355.

Finkel'stein AM (1990) Electron liquid in disordered conductors. *Soviet Scientific Reviews Section A, Physics Reviews* **14**(part 2): 1.

Finkel'stein AM (1994) Suppression of superconductivity in homogeneously disordered systems. *Physica B* 197: 636.

Finkel'stein AM (2010) Disordered electron liquid with interactions. *International Journal of Modern Physics B* **24**(12 − 13): 1855–1894. [50 Years of Anderson Localization, Ed. by E. Abrahams, World Scientific, 385–424 (2010)].

Pruisken AMM (1987) Field theory, scaling and the localization problem. In: Prange RE and Girvin SM (eds.) *The Quantum Hall Effect*. Berlin: Springer-Verlag.

Spivak B, Kravchenko SV, Kivelson SA, and Gao XPA (2010) Transport in strongly correlated two-dimensional electron fluids. *Reviews of Modern Physics* 82: 1743.

Basics of simulations and carrier localization effects in semiconductor materials

Eoin P O'Reilly, Michael O'Donovan, and Stefan Schulz, Photonics Theory Group, Tyndall National Institute, Cork, Ireland;
School of Physics, University College Cork, Cork, Ireland

© 2024 Elsevier Ltd. All rights reserved.

Introduction to basics of simulations and carrier localization effects in semiconductor materials **236**
Introduction 236
Theoretical approaches to address carrier localization effects in semiconductor alloys and related heterostructures 237
Density functional theory 238
Continuum-based approaches 239
Semi-empirical atomistic approaches 242
Overview of carrier localization effects in (In,Ga)N, (Al,In)N and (Al,Ga)N systems: Similarities and differences 243
(In,Ga)N alloys and heterostructures 244
(Al,In)N systems 245
(Al,Ga)N systems 246
Conclusion **247**
References **248**

Abstract

Semiconductor alloys are at the heart of many optoelectronic devices. Among these alloys there are many prominent materials in which the virtual crystal approximation breaks down, including both highly-mismatched alloys such as $GaAs_{1-x}N_x$, and also the III-N alloys, (Al,Ga, In)N, where the difference in energy gap between InN and AlN is more than twice that between any of the more conventional III-V alloys. For such alloys one needs to describe the electronic structure taking atomic-scale disorder effects explicitly into account. Density functional theory can give some insight, but the limited supercell size that can be treated imposes artificial long-range ordering that can give misleading results. This has mandated the development of predictive empirical atomistic methods such as tight-binding and empirical pseudopotential models for large-scale calculations to quantitatively predict electronic and optical properties. Such atomistic models are, however, computationally too expensive for full device simulation, which then requires continuum models. But conventional continuum models are not sufficiently accurate for many disordered systems. Various quantum approaches have therefore been developed to overcome this challenge. These include explicitly incorporating random composition fluctuations into one- or multi-band $\boldsymbol{k}\cdot\boldsymbol{p}$ models, or the explicit introduction of localized states in the Hamiltonian, giving a band-anticrossing model to describe, e.g., the impact of N resonant defect levels on the band structure of $GaAs_{1-x}N_x$. Device simulations based, e.g., on the drift-diffusion model require semi-classical approaches that quantitatively treat disorder. We describe how the recently developed localization landscape method is addressing this question. Having overviewed the impact of disorder, we exemplify its effects by considering III-N alloys and heterostructures, where disorder effects play an increasingly important role as one moves from (Al,Ga)N to (In,Ga)N and then to (Al,In)N.

Key points

- Disorder effects are critical for the electronic and optical properties of key semiconductor alloys.
- Different scales of calculation—from *ab-initio* quantum to disordered semi-classical—required to analyze material and device properties.
- Localized defect states can strongly impact in extreme alloys.
- Novel approaches such as the localization landscape method allow quantitative simulation of disordered alloy systems.

Introduction to basics of simulations and carrier localization effects in semiconductor materials

Introduction

Advanced optoelectronic devices rely on the epitaxial growth of heterostructures, utilizing a combination of different semiconductor materials. Using ternary or even quaternary alloys in the active region of a device, one of the main aims is to tune the emission wavelength of the system to the desired region. For many III-V alloys, formation of an alloy only introduces weak disorder, and it remains possible to describe the band structure using what is referred to as the *virtual crystal approximation* (VCA), where for instance one treats each group III atom in gallium aluminum arsenide ($Ga_{1-x}Al_xAs$) as a weighted average of a Ga and an Al atom. However,

https://doi.org/10.1016/B978-0-323-90800-9.00243-2

when bringing different materials together in an alloy, the electronic structure might be more dramatically changed than one would expect from a simple linear interpolation of the material parameters of the involved components. From a fundamental physics viewpoint, this is often related to the fact that the replaced anion or cation species is much bigger or smaller in size than its "substitute". Also, differences in electronegativity have to be considered when predicting electronic and optical properties of the alloy. A well-known example in which a simple electronic structure description fails is the dilute nitride (N) system $GaAs_xN_{1-x}$ (O'Reilly et al., 2009). When a single N atom replaces an As atom in GaAs, it forms a resonant defect level (localized state) above the conduction band edge of GaAs (Wolford et al., 1984a; Liu et al., 1990). Conventional alloy models cannot describe the electronic structure of such an *extreme alloy*, and other approaches must be employed. To account at least in part for some of the localization effects, simplified *band-anticrossing (BAC) models* have been established to capture key features in the electronic structure of such systems (O'Reilly et al., 2009).

Carrier localization effects can be observed in many systems. For instance, when looking at (In, Ga)N alloys, one is replacing Ga atoms by much larger In atoms. The situation is even more extreme for (Al, In)N alloys in terms of the atomic sizes. In analogy to the dilute N case, one could expect carrier localization effects in III-N systems. Experimental observations give clear indications of localization effects in III-N alloys. For example, using positron annihilation measurements, Chichibu et al. (2006) demonstrated the presence of carrier localization effects in nitride-based alloys. Further clear experimental evidence of localization phenomena has been given by optical measurements, such as photoluminescence (PL) spectroscopy studies (Chichibu et al., 1999; Morel et al., 2003; Graham et al., 2005; Hammersley et al., 2012; Marcinkeviˇcius et al., 2013).

Here, we focus our attention on theoretical methods to describe quantitatively carrier localization effects in semiconductor materials and heterostructures, taking as example both dilute nitride and III-N alloys. We overview advantages and shortcomings of some of the different approaches used to address this question. Furthermore, we highlight some of the outcomes of these theoretical studies, confirming for instance the presence of localized states in nitride-based alloys and their importance for an accurate modeling of their electronic and optical properties. Overall, it is important to note that while on the experimental side, localization features in semiconductor alloys have been observed and discussed widely, a detailed theoretical investigation of these effects started only recently.

We therefore present here an overview of different theoretical approaches to address the electronic structure of semiconductor materials, describing how these different models can account for alloy fluctuations and thus carrier localization effects. Key models include density functional theory, continuum-based models and semi-empirical atomistic frameworks. In general, several features and aspects of disordered alloys and related heterostructures are still not well understood and here we point out some of these open questions taking as primary example localization features in (In, Ga)N, (Al, In)N and (Al,Ga)N systems. We conclude with a summary of our analysis and key perspectives for the future.

Theoretical approaches to address carrier localization effects in semiconductor alloys and related heterostructures

Despite clear experimental evidence, potential carrier localization effects due to alloy fluctuations have been widely ignored in the theoretical modeling of III-V and III-N alloys, heterostructures and devices. Systems such as wurtzite (In, Ga)N/GaN-based quantum wells (QWs) have been largely treated as homogenous, one-dimensional structures which can be described by averaged material parameters. It is only in the last few years that more sophisticated theoretical studies have been performed. Several approaches have been taken to gain insight into electronic and optical properties of disordered semiconductor alloys, related heterostructures and optoelectronic devices. These include first-principle density functional theory, (modified) continuum-based approaches, and semi-empirical atomistic models. Modified continuum approaches include the band-anticrossing model used to describe extreme alloys such as $GaAs_xN_{1-x}$, as well as the localization landscape approach employed to take account of disorder effects when undertaking semi-classical simulations of disordered structures, and in particular for understanding the impact of alloy fluctuations on the carrier transport in light-emitting diodes (LEDs).

However, before focusing on the different approaches in detail, we consider some of the particularities of III-N alloys, to highlight why one faces considerably different challenges in the modeling of such disordered systems when compared to other more "classical" III-V materials, e.g. (In,Ga)As or (Al,Ga)As alloys. One of the main differences between, for instance, (In,Ga)As and III-N systems is that the latter is usually grown in the hexagonal wurtzite phase; (In,Ga)As preferentially growths in the cubic zincblende phase. This change in the crystal structure has a range of relevant consequences. For example, it leads to the situation that wurtzite III-N systems exhibit a so-called *spontaneous built-in electric polarization vector field* (Bernardini et al., 1997). This quantity, due to the symmetry of the underlying zincblende lattice, is not present in (In,Ga)As systems (Bernardini et al., 1997). This spontaneous polarization vector field is a constant field along the wurtzite *c*-axis, which is usually the standard growth direction of III-N heterostructures. Thus, when growing heterostructures where in general the involved materials exhibit different spontaneous polarization vector fields, from basic electrostatics one expects an electrostatic built-in field in these systems. Consequently, in a GaN/(Al,Ga)N QW system polarization charge densities at the interfaces between the material systems GaN and (Al,Ga)N are expected. These polarization charges result in an electrostatic built-in field (Im et al., 1998). A schematic illustration of the situation is given in Fig. 1 (left) where it can be seen that the field gives rise to a spatial separation of the charge carriers in a QW structure, with

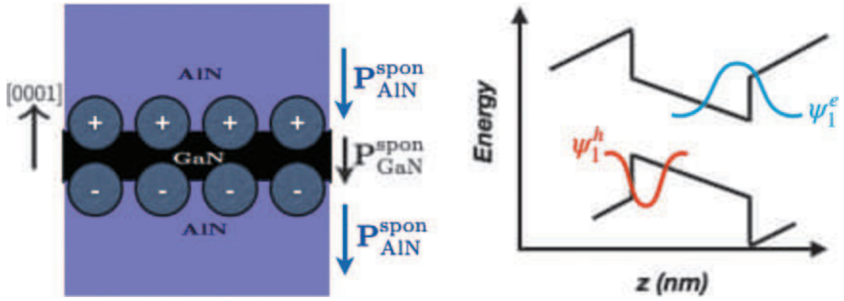
[0001]
AlN
+
GaN
-
AlN
$\mathbf{P}^{spon}_{AlN}$
$\mathbf{P}^{spon}_{GaN}$
$\mathbf{P}^{spon}_{AlN}$
Energy
ψ_1^e
ψ_1^h
z (nm)

Fig. 1 (left) Schematic illustration of the spontaneous polarization vector fields ($\mathbf{P}^{spon}$) and the connected interface polarization charges in a *c*-plane GaN/AlN quantum well. (b) Consequence of the electrostatic built-in field for electron (ψ_1^e) and hole (ψ_1^h) ground states; Solid black lines indicate conduction and valence band edges in a *c*-plane system.

electrons pulled to the upper interface of the heterostructure and holes to the lower interface in Fig. 1 (right). This built-in field does not directly lead to localization effects, but, as we discuss below, can have impact on the analysis of localization effects.

In addition to the spontaneous polarization vector field, there is also a strain induced, so-called *piezoelectric polarization vector field* present in III-N materials (Bernardini et al., 1997). This feature is further enhanced by the large lattice mismatch between the binary materials InN, GaN and AlN. For instance, the lattice mismatch between InN and GaN is approximately 10–11%; between InN and AlN it is around 14–15%. Taking all these aspects into account, electrostatic built-in fields of the order of MV/cm have been reported in the literature (Im et al., 1998; Simon et al., 2003).

Additionally, the large lattice mismatch and thus strain fields also give rise to the question how local strain effects and connected built-in potential contributions affect the electronic structure. Further, given the big difference in atom size for example between In, Ga and N atoms, the question arises as to how local In—N—In chains embedded in GaN affect the electronic structure of (In,Ga)N alloys. Similar questions are relevant when considering the substitution, e.g., of As atoms by N atoms in $\mathrm{GaAs}_x\mathrm{N}_{1-x}$.

Taking all these effects into account, an accurate theoretical modeling of the electronic structure of disordered III-V and III-N materials presents significant challenges, especially when compared to more conventional (In,Ga)As systems. Thus, in general one faces in a first step the question of how to calculate the electronic structure of disordered systems. To this end we will introduce methods that range from first-principle calculations up to semi-empirical models. We start in the next section with the "exact" solution of the Schrödinger equation to predict the band structure of a semiconductor material, which leads us to *density functional theory*.

Density functional theory

When looking at the number of valence electrons that contribute to the bonding in each cubic centimeter of a material, one ends up with around 10^{23} valence electrons. Thus, when calculating the electronic structure of a solid, in general a complex many-body problem must be solved, given that the energy and the wave function of each electron depends on those of all other electrons. To find for instance the ground state energy, E_{GS}, of the electronic system under consideration, the full *time-independent Schrödinger equation* of a complex N-particle many-body system needs to be solved. Obviously, this is a highly non-trivial problem. The basic idea of *density functional theory (DFT)* is now, instead of calculating the antisymmetric ground state wave function $\psi_{GS}(\mathbf{r}_1, \ldots, \mathbf{r}_N)$, one investigates the corresponding electron charge density $\rho_{GS}(\mathbf{r})$. The benefit of studying $\rho_{GS}(\mathbf{r})$ instead of $\psi_{GS}(\mathbf{r}_1, \ldots, \mathbf{r}_N)$ is that, while $\psi_{GS}(\mathbf{r}_1, \ldots, \mathbf{r}_N)$ depends on three spatial coordinates per particle, $\rho_{GS}(\mathbf{r})$ depends only on three spatial variables since it is a collective quantity.

Hohenberg and Kohn (1964) were able to prove that the ground state energy E_{GS} of a many-particle system is an unambiguous functional of the ground state electron density $\rho_{GS}(\mathbf{r})$. But even though the Hohenberg-Kohn approach provides a general framework, it does not immediately give the form of the different functionals, e.g., how the kinetic energy depends on $\rho_{GS}(\mathbf{r})$. This was solved in a second step by Kohn and Sham in 1965 by introducing a scheme that gave rise to an effective single-particle equation in which a particular part of the effective potential, namely the *exchange-correlation part*, requires approximations (Kohn and Sham, 1965). The derived effective single-particle Schrödinger equation is known as the *Kohn-Sham equation*.

For practical calculations within the framework of the Kohn-Sham equations, information about the form of the exchange-correlation functional is required. For this quantity one must rely on approximations. One of these approximations, which is still widely used, is the so-called *local density approximation (LDA)* (Kohn and Sham, 1965; Martin, 2011), whereby an inhomogeneous system is locally described by a homogenous electron gas. While this is a crude approximation, it works remarkably well for many systems and properties but systematically fails for others (Perdew, 1985; Cohen et al., 2012). The underestimation of the band gap energy of semiconductors and insulators is probably one of the best-known problems of LDA (Perdew, 1985). Looking at the III-N systems, LDA fails completely for InN with its small band gap (Moses et al., 2011), and predicts it to be a metal. Therefore, when interested in optical properties of narrow gap systems, LDA-DFT suffers from significant shortcomings.

For this reason, modified and improved DFT approaches have been used by different groups around the world to overcome the shortcomings of the LDA-DFT approach. One scheme that has become very popular is the use of *screened hybrid functional approaches*, for instance, the *Heyd-Scuseria-Ernzerhof (HSE)* ansatz (Heyd et al., 2003). In such an ansatz, Hartree-Fock theory is combined with local exchange correlation functionals in which the so-called *exact exchange mixing parameter* α can also be used as an adjustable parameter (Moses et al., 2011; Heyd et al., 2003). These hybrid functionals are a step forward in comparison to local functionals and have been widely used for semiconductor materials since they can provide, in contrast to LDA-DFT, very good descriptions of the bulk band gaps. For instance, with standard settings of HSE-DFT calculations (HSE06 functionals), the band gap of InN is 0.66 eV, which is in good agreement with experimental data (0.6–0.7 eV) (Moses et al., 2011).

Such a DFT approach allows in general for an accurate description of the electronic band structure over the entire *first Brillouin zone*. Additionally, it can treat semiconductor alloys on a microscopic level, allowing therefore to study any given alloy on an atomistic level. However, this high accuracy, first-principle approach comes also at the cost of high computational demands. Compared to LDA-DFT, the computational demands of hybrid-functional calculations are significantly higher (Pela et al., 2015). Thus, within these *ab-initio* approaches, supercells of a several hundred up to a few 1000 atoms can be treated. Standard calculations rely probably on 64–128 atom supercells. Therefore, with these methods fundamental bulk properties of alloys can ideally be studied. But, when it comes to carrier localization features in realistic QW systems, where not only the active region (e.g. (In,Ga)N) has to be considered but also the barrier material (e.g., GaN), the simulation system size can reach easily several tens of thousands of atoms. This is beyond most of the current DFT implementations. Thus, more empirical methods are required.

Given that many alloy systems are direct band gap materials, of particular interest for optoelectronic devices is the band structure around $\mathbf{k} = \mathbf{0}$, the Γ-point. The behavior of the highest valence and lowest conduction bands at the boundaries of the first Brillouin zone is of secondary importance for the optical properties of these systems. Building on the aspect that only a particular part of the first Brillouin zone is relevant for optical properties, more empirical methods have been developed over the years to describe the band structure accurately in the region of interest. These models are computationally less demanding and due to their semi-empirical nature, they can overcome for instance the band gap problem of standard LDA-DFT calculations. Obviously, given that they are computationally relatively cheap, these methods are highly attractive for calculations of electronic and optical properties of semiconductor heterostructures and devices. In the next sections the basic concepts of these methods are reviewed, starting with the so-called *(multi-band)* $\boldsymbol{k}\cdot\boldsymbol{p}$*-method*, which can be classified in general as a continuum-based approach.

Continuum-based approaches

When modeling the electronic structure of electronic and optical devices, one is generally interested in the region near the band gap E_g, which is defined as the energetic separation between the highest filled valence (bonding) band state and the lowest empty conduction (anti-bonding) band state. Fig. 2 shows schematically the band structure of GaN close to the energy gap, where the lowest energy state in the conduction band, E_c, is at the Γ-point ($\mathbf{k} = \mathbf{0}$). Since E_c is directly above the highest energy state in the valence band, E_v, GaN is called a *direct band gap semiconductor*. To provide a continuum description of the band structure of a system

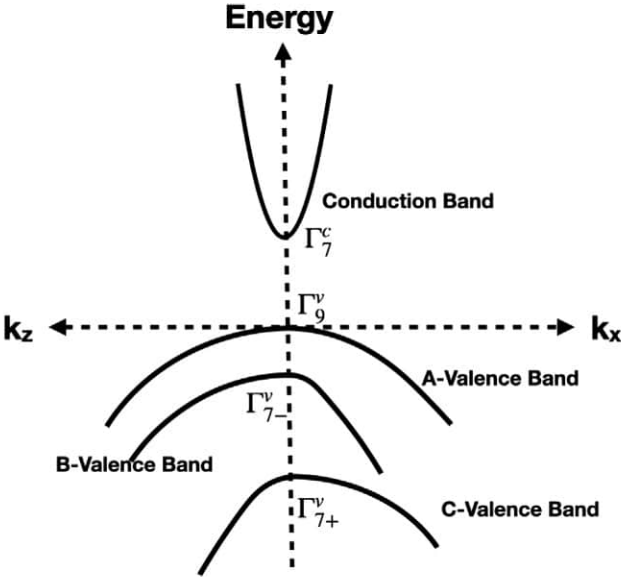

Fig. 2 Schematic illustration of a bulk band structure in III-N nitride materials, including group theoretical classification of the different conduction (Γ^c) and valence (Γ^v) bands.

near $\mathbf{k} = \mathbf{0}$ for direct band gap materials, the $\mathbf{k}{\cdot}\mathbf{p}$ approach is a widely used ansatz (Chuang and Chang, 1996; Winkelnkemper et al., 2006; Marquardt et al., 2012; Yang et al., 2014). In general this method is based on perturbation theory and requires the exact energy levels to be known near $\mathbf{k} = \mathbf{0}$. More details about the underlying theory can be found in several books, for instance, in Refs. Lew Yan Voon and Willatzen (2009) and O'Reilly (2002) and we will not give here all the mathematical aspects.

To establish a $\mathbf{k}{\cdot}\mathbf{p}$ model, it requires an accurate description of the lowest conduction band and the highest valence bands. A similar approach is taken for zincblende and wurtzite structures. It can be seen from Fig. 2 that the valence band structure presents a more complicated situation compared to the conduction band. This stems from the fact that from an atomistic point of view the conduction band is mainly described by an *s*-like state while the valence band states in both wurtzite and zincblende structures are mainly *p*-like in character near the valence band edge. Therefore, in the case of the valence band, the "Bloch" wave functions are made up of p_x-, p_y- and p_z-like atomic orbitals which all contribute to the valence band states. Fig. 2 consequently shows three bands near the valence band maximum. The first two bands are so-called *heavy-hole (HH)* and *light-hole (LH)* bands, or sometimes *A*- and *B*-bands. They receive their names from the fact that the energy of the HH band varies at a slower rate when moving away from $\mathbf{k} = \mathbf{0}$ than in the case of the LH band. The third band in a wurtzite structure is usually denoted as the *crystal field split-off (CF)* or *C-band*. The energetic position of this band with respect to the *A*- and *B*-bands is dependent on the nitride material in question. For InN and GaN, the *C*-band lies energetically *below* the *A*- and *B*-band (Vurgaftman and Meyer, 2003). For AlN the *C*-band sits energetically *above* the other two bands (Vurgaftman and Meyer, 2003). The position of the band is connected to the so-called *crystal field splitting energy*, which is positive in InN and GaN and negative in AlN (Vurgaftman and Meyer, 2003). The valence band ordering has implications for the polarization properties of the emitted light.

$\mathbf{k}{\cdot}\mathbf{p}$ methods can be at different levels of sophistication, basically depending on the number of bands included in the description. The number of explicitly included bulk bands in the model also gives the name of the multi-band Hamiltonian (Harrison, 2005). One of the most widely used models for analyzing the band structure of wurtzite III-N systems is the 8-band model by Chuang and Chang introduced in Ref. Chuang and Chang (1996). It accounts for the three valence bands and the (energetically lowest) conduction band. Since the model takes the electron spin into account, each band is two-fold degenerate. Thus, eight bands are considered in the description. Likewise, an 8-band $\mathbf{k}{\cdot}\mathbf{p}$ model can be used to describe the doubly degenerate lowest conduction and three highest valence bands in zincblende materials. However, it should be noted that often reduced versions of this approach are employed for studying the band structure of wurtzite or zincblende heterostructures. An example is the single-band effective mass approximation, where only the conduction and the *A*-band are included in the calculation for GaN, for instance. These bands are then even separately treated, thus neglecting valence band conduction band coupling effects. A detailed overview of different types of multi-band $\mathbf{k}{\cdot}\mathbf{p}$ models is given for example in the textbook by Lew Yan Voon and Willatzen (2009).

These models are extremely popular to describe the electronic and optical properties of semiconductor heterostructures. Overall, the benefit of this approach is that it is computationally extremely cheap, at least when compared to DFT. Thus, QW and quantum dot (QD) structures of realistic size and shape can be addressed. Additionally, these models are parameterized in terms of bulk material parameters such as effective masses, band gaps, etc. near the Γ-point for instance. So once the composition dependence of the different quantities is established, the model can be easily applied to different systems. However, here the drawback of the method becomes apparent. Since the whole approach relies on macroscopic bulk parameters, the method, at least in its standard 1-,4-,6- or 8-band description, is not sensitive to the underlying microscopic crystal structure in terms of different atomic positions in an alloy. Thus, when looking for example at (In,Ga)N/GaN QW structures with 25% In content, the QW region is described by a Hamiltonian *H* with effective parameters, which have been interpolated between the parameters of GaN and InN in a particular way (linearly, quadratic, etc.). Thus, QWs are in general described as an ideal one-dimensional problem along the growth direction. In the in-plane direction, the QW is still perfectly periodic and thus states can be characterized by an in-plane wave vector $\mathbf{k}_{||}$. But, if carrier localization effects are introduced by random alloy fluctuations, the continuum-based $\mathbf{k}{\cdot}\mathbf{p}$ method intrinsically is not designed to address this question, at least on a microscopic level and in its "standard" form described above. Nevertheless, different groups have introduced modified continuum-based models to account for alloy fluctuations and thus connected carrier localization effects as we will see below.

Band-anticrossing model

One of the most useful modified models is the band-anticrossing (BAC) model to describe the electronic structure of extreme alloys such as $GaAs_xN_{1-x}$. It is well-established that when a single N atom replaces an As atom in GaAs, it forms a resonant defect level above the conduction band edge (CBE) of GaAs (Liu et al., 1990; Wolford et al., 1984b). This defect level arises because of the large difference in electronegativity and atomic size between N and As (Vogl, 1984; Hjalmarson et al., 1980; Lindsay and O'Reilly, 2003). The BAC model introduced by Walukiewicz and co-workers explains the extreme band gap bowing observed in $Ga_{1-y}In_yN_xAs_{1-x}$ in terms of an interaction between two levels, one at energy E_N associated with these localized N impurity states ψ_N, and the other at energy E_c associated with the extended CBE state ψ_{c0} of the (Ga, In)As matrix, with the two states linked by a matrix element V_{Nc} describing the interaction between them (Shan et al., 1999). The conduction band dispersion of (Ga, In)N_xAs_{1-x} is then given in the BAC model by the lower eigenvalue of the determinant

$$\begin{vmatrix} E_N - E & V_{Nc} \\ V_{Nc} & E_c + \dfrac{\hbar^2 k^2}{2m_c^*} - E \end{vmatrix} \tag{1}$$

where m_c^* is an appropriately chosen band edge effective mass for the (Ga,In)As host matrix material. The measured variation of band gap with N composition, x, is then very well described using the BAC. The BAC model has therefore proved very useful in the design and analysis of optoelectronic devices containing (Ga,In)(N,As) and other extreme alloys.

In practice however, replacing As by N introduces a range of N-related defect levels, associated with isolated N atoms, N-N pairs and larger clusters of N atoms. The effect of such defect levels on the alloy conduction band structure is strongly dependent on the relative energy of the distribution of defect levels and the host CBE. Overall, the BAC model therefore provides a good qualitative explanation of the electronic properties of dilute nitride and other extreme alloys. However, it is in many cases necessary to include detail of the distribution of N-related defect levels to obtain a quantitative understanding of the conduction band structure and of localization effects in dilute nitride alloys.

Composition fluctuations and localization landscape approach

For III-N systems, probably one of the first works into the direction of treating carrier localization effects was that of Watson-Parris et al. (2011). Their starting point was a one-band effective mass model for electrons and holes. However, instead of treating the QW problem as an ideal one-dimensional problem, a full three-dimensional representation of the QW was considered. Thus, at each grid point in the three-dimensional supercell, used to solve the Schrödinger equation, different material compositions have been considered. In other words, the grid points inside the (In,Ga)N QW region can be either InN or GaN. The number of InN grid points inside the QW region determines then the InN content of the QW system. This method can also account for strain and piezoelectric effects, again using the material parameters corresponding to InN or GaN at each grid point. Thus, insight can be gained into the effect of carrier localization due to variations in the InN content employing a modified continuum-based approximation. However, this method requires full solution of the Schrödinger equation $H\psi = E\psi$ for the random potential, which becomes computationally expensive if included e.g., in a self-consistent solution to carrier transport in a heterostructure.

To address this issue, a very interesting method has recently been proposed and used in the literature. Filoche et al. (2017) have introduced a new approach, the so-called *localization landscape theory*. In this approach, instead of solving the Schrödinger equation, one deals with the problem $Hu = 1$. It can be shown that u is connected to the ground state energy and wave function. For square wells this method is in excellent agreement with the formal solution of the Schrödinger equation. Furthermore, it also turns out that $1/u$ describes an effective potential which, when compared to the results from a full Schrödinger equation of a disordered system, gives a very good indication in which regions the wave functions are localized. Since $W = 1/u$ is related to an effective potential and describes regions in which the carriers are localized, it is called *localization landscape theory*. Overall, the benefit of this method is that instead of solving a large (sparse) eigenvalue problem, one is left with solving a set of linear equations, which is computationally significantly cheaper. Furthermore, the effective potential W is also extremely useful for treating disorder and localization effects in drift-diffusion-based transport calculations (Li et al., 2017; O'Donovan et al., 2021). Here, W can be included in these calculations to treat composition fluctuations and to mimic effects such as tunneling that are not intrinsically accounted for in standard drift-diffusion simulations. This approach is sometimes called a quantum corrected transport model. More details can be found in Refs. Li et al. (2017) and O'Donovan et al. (2021).

However, in comparison to the modified continuum-based model described above, for instance used by Watson-Parris et al. (2011) to address alloy fluctuations and carrier localization features, it is not obvious how to treat multi-band models within localization landscape theory. This makes the method problematic to apply to extreme alloys such as $\mathrm{GaN}_x\mathrm{As}_{1-x}$, where the BAC model is intrinsically a multi-band approach. By contrast, it is straightforward to include multiple bands in the approach used by Watson-Parris et al. (2011). Additionally, to obtain reliable results from $Hu = 1$, the energy zero must be chosen carefully. Especially when dealing with (In,Ga)N/GaN multi-QW (MQW) systems, where one is left with a triangular shaped conduction and valence band profile, which also varies between the wells due to the built-in potential, attention has to be paid to the aspect of the zero of energy choice. Here, the system may be partitioned in smaller sub-systems and the energy zero of each of these sub-systems is adjusted (O'Donovan et al., 2022). Additionally, and in contrast to solving Schrödinger's equation, the solution of $Hu = 1$ gives initially only access to ground state energies. However, here also approaches can be chosen to obtain the densities of states within this method (Piccardo et al., 2017).

Motivated by the interest in the localization landscape approach, and by the challenges associated both with choosing a zero of energy and determining the densities of states, other approaches have recently been proposed to provide robust quantum-corrected models for simulation of disordered systems. Detailed analysis has shown that application of the Hamiltonian H recursively to random wave functions (RWF) or application of a universal low-pass filter (ULF) to the random potential can provide a more accurate quasi-classical description of the temperature-dependent carrier density, $n(\mathbf{r}, T)$ in an effective potential (Gebhard et al., 2023; Nenashev et al., 2023). While both of these approaches look very promising, they have not, at the time of writing, been used yet to analyze a realistic disordered semiconductor structure.

Overall, given that these different approaches are numerically cheap compared to DFT, they can treat disordered QWs of realistic sizes and dimensions and give first insight into carrier localization effects. But they have the drawback that they do not allow for an atomistic, microscopic description of the system. The question here is then, is it justified to assume that one uses the bulk material parameters e.g., for pure InN or GaN at neighboring sites without modifications? This asks also the question what grid size should be chosen so that this becomes a good approximation? From a fundamental point of view, these modified continuum-based approximations cannot provide any insight into the question of how important for instance In—N—In chains are for carrier localization effects in (In,Ga)N or to what extent neighboring N atoms will modify the electronic structure of Ga(N, As).

As discussed above, DFT can give insight into such questions, but due to its computational expense, this can only be done for small supercells. Consequently, DFT might fail to shed light onto connected carrier localization features.

Thus, theoretical models are desirable which provide insight into these questions on an atomistic, microscopic level, while at the same time being able to deal with large supercells, and so treat realistically sized heterostructures. Two methods which meet these criteria are the so-called *(semi-) empirical pseudo-potential method (EPM)* and the *(semi-)empirical tight-binding model (ETBM)*. These approaches can then also provide benchmarks and or further inputs into e.g., a localization landscape treatment of alloy induced carrier localization effects in semiconductor QWs. The following sub-sections briefly review ETBM and EPM.

Semi-empirical atomistic approaches

Having motivated the need for empirical atomistic electronic structure theories, we now briefly introduce the basic concepts of (empirical) tight-binding and empirical pseudopotential theory. For more details we refer to textbooks (O'Reilly, 2002; Harrison, 2005).

Empirical tight-binding theory

The basic idea underlying the tight-binding (TB) model is that the electronic band structure can be described by starting from the limit of isolated atoms. Thus, localized orbitals at the different atoms in the unit cell or for bigger systems in the supercell form the basis states of the TB approach. The TB model offers a transparent approach since the involved matrix elements are described in the language of overlaps of (localized) atomic-like orbitals. Therefore, this method has a simple physical interpretation.

Two main assumptions are made in every TB model, namely (i) the bulk band structure can be accurately described by a small number of basis states per unit cell and (ii) with increasing distance between atom positions, the overlap of the strongly localized atomic-like orbitals decreases rapidly. Popular TB approaches are the so-called nearest neighbor sp^3, sp^3s^* or $sp^3d^5s^*$ models (Caro et al., 2013; Vogl et al., 1983; Jancu et al., 2002; Schulz et al., 2015a). For instance, in the case of a nearest neighbor sp^3 TB model one takes one *s*- and three *p*-orbitals (p_x, p_y, p_z) per lattice site into account.

One of the main tasks to establish a TB model is the calculation/determination of the overlap matrix elements between different orbitals at different sites. The matrix elements are generally obtained by treating them as fitting parameters. This leads to the so-called *empirical TB model (ETBM)*. Here parameters are fitted to characteristic bulk band structure features such as band gaps and effective masses. The ETBM provides a microscopic description of the solid since in the underlying picture, interactions between for example an *s*-orbital on an In atom with a p_x-orbital on a N atom are accounted for.

So far, we have discussed the ETBM method only for bulk systems. However, a few extra ingredients are required to describe alloys on a microscopic level. We illustrate the general procedure here on the basis of a wurtzite *c*-plane (In,Ga)N/GaN QW. Also, since most of the ETBMs applied to III-V systems are nearest neighbor models, we will assume a nearest neighbor model in the following. As a first step, it is necessary to have parameters suitable for each of the constituent materials, in this case GaN and InN. Next it is necessary to choose a suitable averaging approach for the self-energy parameters of atoms such as N which can have differing numbers of In and Ga atoms.

Due to the lattice mismatch between InN and GaN, also strain effects need to be accounted for in the model. To do this, it is required to first establish the new equilibrium positions of the different atoms in an atomistic picture of the alloy. This is generally achieved using so called *valence force field (VFF) models* (Keating, 1966; Martin, 1970). In general these models are parameterized in terms of bond-bending and bond-stretching contributions with free adjustable parameters. VFF models with different levels of complexity on the level of interactions accounted for can be found in the literature (Schulz et al., 2015a; Keating, 1966; Martin, 1970; Camacho and Niquet, 2010). Once such a VFF model is developed and established, the new equilibrium positions of the In, N, and Ga atoms in an alloy or heterostructure can be found by minimizing the total elastic energy of the simulation cell. With the relaxed atomic positions being determined, the original bulk TB matrix elements must be adjusted to account for the strain in the system (Caro et al., 2013; Vogl et al., 1983; Jancu et al., 2002; Schulz et al., 2015a).

The last ingredient to a TB model describing the electronic properties of $In_xGa_{1-x}N$ systems is the (local) built-in potential arising from the spontaneous and strain-induced piezoelectric polarization response discussed already above. To include the built-in potential $\phi(\mathbf{r})$ in the ETBM description, the widely used ansatz is a site-diagonal correction to the Hamiltonian. In general, the built-in potential can be obtained from solving Poisson's equation. However, for an underlying wurtzite lattice plus the fact that the underlying lattice is even further modified by the presence of (local) strain fields, solving Poisson's equation is non-trivial. As example, the bond distances in InN are much larger (by about 10%) when compared to GaN. Thus, in (In,Ga)N large local strains can be present around In, N or Ga atoms. Given that the piezoelectric response is strain dependent, local piezoelectric polarization can play an important role and might affect carrier localization effects significantly on a microscopic level. To take effects arising from local strain and disorder on piezoelectric polarization and thus the local built-in potential into account, a local theory of polarization was developed (Caro et al., 2013). The theory relies on decoupling the macroscopic and local contributions to the total polarization; the latter can be evaluated at each atomic site. The connected (local) built-in potential can be calculated from a point-dipole model. More details of the whole method and an in-depth discussion are given in Ref. Caro et al. (2013).

In summary, within this framework an atomistic description of the electronic structure of III-N alloys and heterostructures of realistic size can now be achieved. This approach accounts for the underlying microscopic alloy structure, such as In—N—In chains. It is a multi-band approach, thus includes band mixing effects and, due to its semi-empirical nature, very large supercells can be studied. A schematic illustration of the typical workflow is given in Fig. 3.

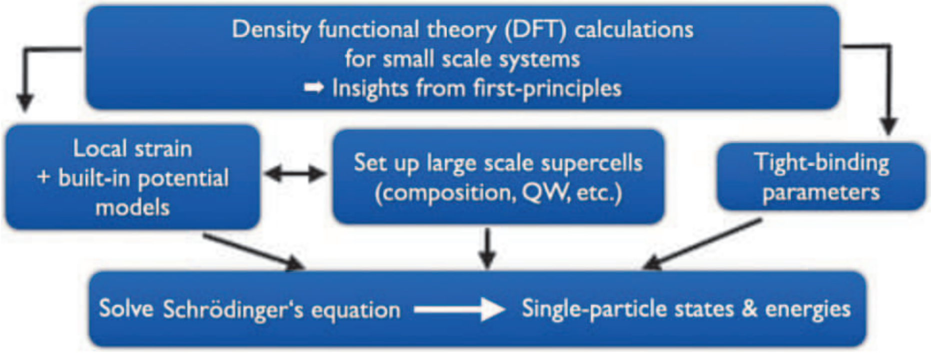
Density functional theory (DFT) calculations
for small scale systems
➡ Insights from first-principles
Local strain
+ built-in potential
models
Set up large scale supercells
(composition, QW, etc.)
Tight-binding
parameters
Solve Schrödinger's equation
Single-particle states & energies

Fig. 3 Schematic visualization of the workflow using empirical tight-binding theory for modeling the electronic structure of wurtzite III-N alloys and heterostructures. A similar workflow can be applied for zincblende alloys, often without the need to include local polarization potential fluctuations.

Another way to achieve an atomistic description of the electronic structure of semiconductor alloys or nanostructures is the *empirical pseudo-potential method (EPM)*. This method requires basically the same ingredients (VFF model, local polarization theory, etc.) as the ETBM. The main difference between the two methods is the electronic structure theory, thus how the underlying Hamiltonian is constructed.

Empirical pseudo-potential method

We review here the basic idea underlying electronic structure calculations within the framework of the EPM. We focus here on bulk systems since transferring this approach to a nanostructure is basically following the same steps as in the ETBM case. For more details on this aspect, we refer to the literature (Bester, 2009).

In general, the EPM approach is similar to the TB ansatz. This means in the EPM the time-independent Schrödinger equation for a bulk system is solved without knowing the exact potential in which the electrons are moving. Here one relies on an effective potential (Harrison, 2005; Cohen and Chelikowski, 1989). The EPM also starts from the idea that core electrons are tightly bound to the nuclei. Furthermore, the assumption is that they contribute only very little to conduction and valence band states and thus to the electronic properties near the band edges. Additionally, the assumption is made that the core electrons are unaffected by the change in environment of a solid (frozen core approximation). Within this frame the basic task is to find a scheme that removes the core electron contributions from the total wave function. Compared to the behavior of the wave function outside the core, the wave function changes rapidly (oscillates) inside the core region. A large number of plane waves would be required to describe this behavior, making such a calculation numerically heavy. However, as already discussed above, the behavior of the wave function in the core region is of secondary importance for the states around the conduction and valence band edge. The basic idea now is to find a pseudo-potential that results in a slowly varying wave function in the core region but reproduces at the same time the 'original' wave function outside the core region. Therefore, one is left with the problem of determining such a pseudo-potential.

To address now a nanostructure based on for instance (In,Ga)N, similar to the ETBM, the empirical pseudo-potentials are constructed from independent binaries (e.g., InN and GaN). Thus, one faces here also the problem of describing the pseudo-potentials of the common anion species (i.e., N) in (In,Ga)N since the empirical pseudo-potentials for N in InN and GaN are most likely to be different. In general, here also weighted averaging procedures for the empirical pseudo-potentials are employed (Bester, 2009). Once the empirical pseudo-potentials are derived, a similar work flow applies as in the ETBM approach (cf. Fig. 3), meaning that the equilibrium atomic positions and the connected built-in potentials are required, which form then input for solving Schrödinger's equation in the frame of the EPM. A detailed overview of the method can be found in Ref. Bester (2009), for instance.

Having discussed different theoretical methods to address carrier localization effects in III-V bulk alloys and heterostructures, we now turn to present some of the theoretical conclusions that have been drawn on the basis of these approaches.

Overview of carrier localization effects in (In,Ga)N, (Al,In)N and (Al,Ga)N systems: Similarities and differences

Equipped with knowledge of the basic concepts and ingredients of the different theoretical models to describe the electronic and optical properties of semiconductor systems, we give a brief overview of carrier localization effects in the III-N alloys (In,Ga)N, (Al,In)N and (Al,Ga)N. It is well established that localization effects play a key role in each of these three systems. Comparing the similarities and differences between the three alloys allows us to draw useful overall conclusions. We will focus on both bulk systems and heterostructures, here in particular on QWs.

Overall, it should be noted that, despite its importance, the impact of carrier localization and its consequences for electronic and optical properties of III-N structures has been widely neglected in the theoretical analysis of these systems and only recently a strong focus has been placed on this aspect. On the one hand this is surprising. Experimental studies gave clear indications that carrier localization effects can dominate the fundamental properties of, for instance, (In,Ga)N/GaN QW systems. However, as we have seen above, the theoretical description of these systems requires a far more complex modeling procedure when compared to other III-V alloys such as (In,Ga)As/GaAs systems. We start the overview here with (In,Ga)N/GaN systems. In a second step, we turn our attention to (Al,In)N before finally discussing (Al,Ga)N-based structures.

(In,Ga)N alloys and heterostructures

Different experimental features gave clear indications of carrier localization effects in (In,Ga)N systems. For instance, blue emitting (In,Ga)N-based devices exhibit high quantum efficiencies, even though they display extremely high defect densities (Dawson et al., 2016). The widely accepted explanation for the defect insensitivity is that the carriers are spatially localized due to alloy fluctuations, preventing them from diffusing to defects (Nakamura and Chichibu, 2000; Humphreys, 2008).

Probably one of the first theoretical studies on carrier localization in (In,Ga)N alloys was performed by Bellaiche et al. (1999) using the EPM. These calculations on large, bulk zincblende supercells, assuming a random distribution of In atoms in the alloy, revealed hole localization near In atoms. Wang (2001) performed an analysis similar to Bellaiche et al. (1999) but this time for a wurtzite system, which also revealed hole localization around In—N—In chains in the alloy. Calculations based on DFT within the LDA framework further supported the EPM results (Schulz et al., 2015b). Overall, these empirical atomistic and also DFT-based calculations revealed a strong asymmetry in the localization behavior of electrons and holes in (In,Ga)N bulk systems.

All the above discussed calculations and conclusions were based on bulk systems. However, in a wurtzite (In,Ga)N/GaN *QW* system several new factors contribute. For instance, given that the (In,Ga)N QW is grown on GaN, the QW is strained to the GaN barrier. Furthermore, due to the interfaces between (In,Ga)N and GaN in (In,Ga)N/GaN QWs grown along the polar *c*-axis, strong electrostatic built-in fields are present, which lead to a spatial separation of the carriers along the growth direction (*c*-axis), as already discussed above. This macroscopic built-in field is not present when dealing with bulk systems. Additionally, the combination of built-in field and (In,Ga)N—GaN interfaces also gives rise to the question how interface roughness, e.g., well width fluctuations, affects electronic and optical properties of these heterostructures. Again, this factor does not contribute in the bulk situation.

The first theoretical work to shed light on the question of carrier localization in realistically sized wurtzite *c*-plane (In,Ga)N/GaN QWs was performed by Watson-Parris et al. (2011) using the modified single-band effective mass approximation discussed above. Their calculations showed that random alloy effects are sufficient to localize holes. Additionally, when including well width fluctuations in the form of disk-like structures at the interface between the (In,Ga)N well and the GaN barrier, as indicated in experiment (Watson-Parris et al., 2011), they also found that these structural inhomogeneities can localize electron wave functions. Thus, both types of carriers (electrons and holes) are localized in *c*-plane (In,Ga)N/GaN QWs at opposite interfaces due to the presence of the built-in field. This result was later also confirmed by Schulz et al. (2015a) in the framework of atomistic ETBM calculations. Fig. 4 shows results of such a calculation. The effect of the Coulomb interaction between the carriers may modify the

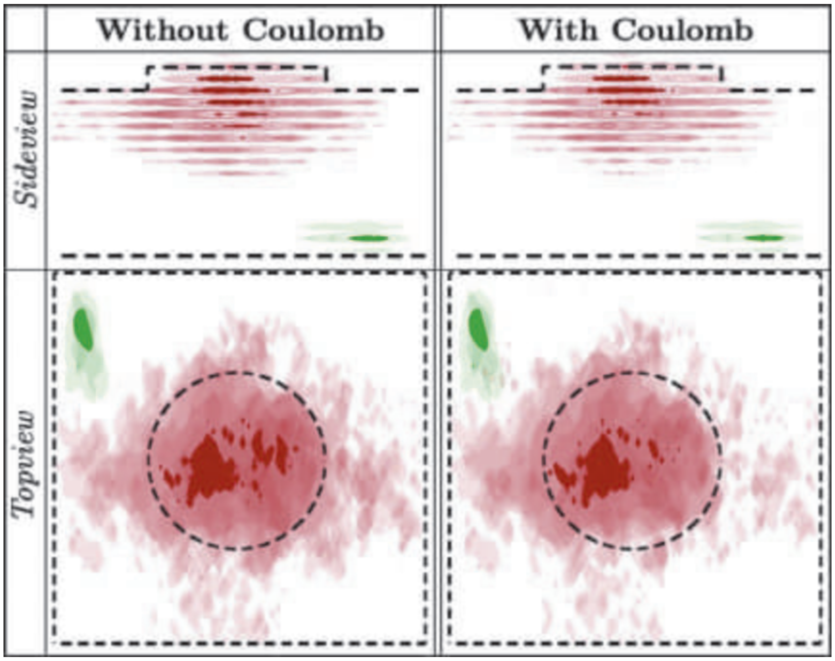

Fig. 4 Calculated isosurfaces of the electron (red) and hole (green) ground state charge densities in a *c*-plane $In_{0.15}Ga_{0.85}N$/GaN quantum well. The results are shown in the absence ("Without Coulomb"; left) and in the presence of Coulomb effects ("With Coulomb"; right). The isosurfaces are depicted at 10% and 50% of the respective maximum charge densities. The quantum well interfaces are indicated by the dashed lines. The "Topview" shows a view parallel to the *c*-axis while "Sideview" is a view perpendicular to the *c*-axis. The in-plane dimensions of the cell are 10 nm × 9 nm and along the *c*-axis the cell dimension is 10 nm. The quantum well width is approximately 3.4 nm. A well width fluctuation with a diameter of 5 nm and height of 2 monolayers has been included in the calculations. A random distribution of In atoms has been assumed here.

picture of independently localized carriers. Schulz et al. (2015a) thus extended the atomistic ETBM analysis and accounted for Coulomb effects (excitonic effects) and their analysis revealed that the combination of carrier localization due to (i) built-in fields, (ii) alloy fluctuations and (iii) structural inhomogeneities (well width fluctuations) dominate over the attractive Coulomb interaction between the carriers, at least for the systems studied. Further studies (Tanner et al., 2018; David and Weisbuch, 2022) also focused on the impact of the well width and how the picture is changed when well width fluctuations are absent. For narrower wells the interplay of well width, carrier localization and Coulomb effects is more involved and less clear cut. Nevertheless, carrier localization effects play a dominant role so that the wave function overlap is still strongly dependent on the alloy microstructure.

In addition to *c*-plane (In,Ga)N/GaN QWs, (In,Ga)N/GaN QWs grown on so-called *non-* or *semipolar planes* have attracted considerable interest (Schwarz and Kneissl, 2007; Waltereit et al., 2000). This originates from the fact that these structures ideally promise reduced (semipolar) or even the complete absence (nonpolar) of macroscopic electrostatic built-in fields. Clear experimental evidence has been given that alloy disorder induced carrier localization effects also play a significant role for understanding the electronic and optical properties of such heterostructures (Sutherland et al., 2015; Mounir et al., 2016).

The first theoretical, atomistic analysis of these systems, in conjunction with atom probe tomography (APT) and time resolved PL measurements, revealed that, when neglecting Coulomb effects, the hole wave function is localized by the random alloy fluctuations while the electron charge density is less affected by the local effects and to a first approximation spreads out over the entire QW region. An example of this situation is given in Fig. 5 (left) for the electron and hole ground state charge densities in a *m*-plane $In_{0.17}Ga_{0.83}N$/GaN QW. However, when combining the ETBM with configuration interaction calculations to account for the attractive electron hole Coulomb interaction, the theoretical studies revealed that the electron localizes about the hole, which is still localized by the random alloy fluctuations. An example of the situation is given in Fig. 5 (right). Thus, the theoretical analysis predicted exciton localization effects in *m*-plane (In,Ga)N/GaN QWs, consistent with the experimentally observed single-exponential PL decay curves (Marcinkeviˇcius et al., 2013; Sutherland et al., 2015; Schulz et al., 2015c). Thus the situation in a non-polar *m*-plane system is very different from a *c*-plane system where one is basically left with independently localized carriers (or strongly varying wave function overlaps in narrower wells).

In summary, it can be seen that electron wave functions are far less affected by random alloy fluctuations, at least when compared to holes in (In,Ga)N bulk and (In,Ga)N/GaN QW systems. For holes already the presence of an In—N—In chain is sufficient to introduce strong localization effects. Even though these localization effects are very strong in (In,Ga)N systems and can dominate their optical properties, we will see in the next sub-section that localization features can be even more dramatic in (Al,In)N, reflecting the greater difference in size and electronegativity between In and Al compared to In and Ga.

(Al,In)N systems

The III-N alloy (Al,In)N has attracted significant research interest given its potential for electronic and optoelectronic devices such as high-electron-mobility transistors, high-frequency and high-power microwave devices (Pandey et al., 2012), and for devices operating in the deep UV spectral region (Tan et al., 2016). This interest originates from the fact that AlN has a band gap (6.0–6.25 eV) that is even larger than the band gap of GaN (3.5 eV) (Moses et al., 2011; Vurgaftman and Meyer, 2003). Thus, by replacing Al by In in AlN, emission in the UV spectral region can, in principle, be tailored to specific applications. However, compared to (Al,In)N, (In,Ga)N looks like a well characterized system in terms of its fundamental properties. For instance, the band

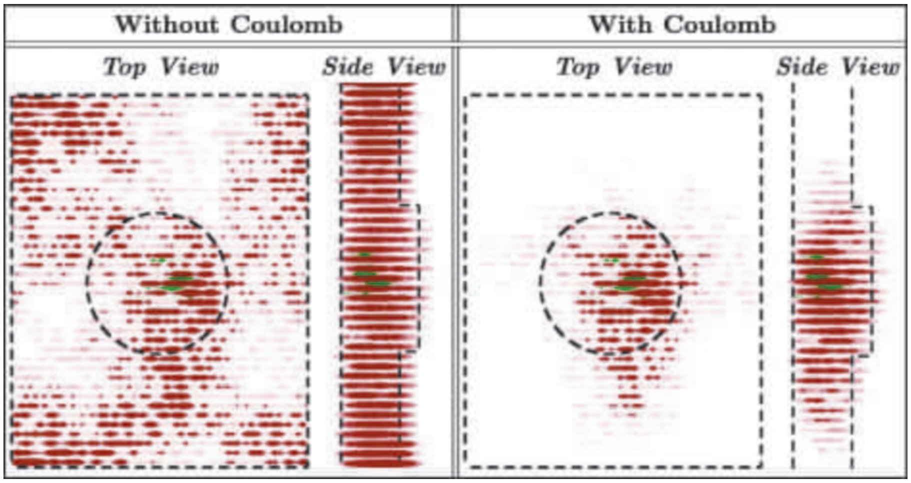

Fig. 5 Isosurfaces of the electron (red) and hole (green) ground state charge densities in a *m*-plane $In_{0.17}Ga_{0.83}N$/GaN quantum well. The isosurfaces are plotted at 10% and 25% of the respective maximum charge density values. The quantum well width is 2 nm and a disk-like well width fluctuation with a diameter of 5 nm and height of 2 monolayers has been considered here. The quantum well interfaces are schematically indicated by the dashed lines. The overall cell dimensions are 10 nm × 9 nm × 10 nm. The "Top View" displays a view along the *m*-axis, while "Side View" corresponds to a view perpendicular to the *m*-axis. Data in the absence of Coulomb effects are shown in the left panel ("Without Coulomb"); in the presence of Coulomb effects the results are depicted in the right panel of the figure ("With Coulomb"). More information about the calculations can be found in Ref. (Schulz et al., 2015c).

gap variation of (Al,In)N alloys with In content is key when designing optoelectronic devices operating in the UV spectral region utilizing these alloys. For most other III-V materials, it is found that the band gap of an alloy $A_{1-x}B_xC$ varies approximately linearly with composition x. Cations of the alloy in question are denoted by A and B while C denotes the anion. Any deviation from this linear behavior is usually accounted for by a small quadratic term, $-b \cdot x \cdot (1-x)$ (Vurgaftman et al., 2001). The quantity b is the so-called *band gap bowing parameter*. This approximation is sometimes called the *virtual crystal approximation* (VCA) since the material parameters can be smoothly interpolated between the binary materials AC and BC. However, the alloy microstructure change is not taken into account. Both experimentally and theoretically clear indications are given that (Al,In)N is not a "standard III-V alloy" and that VCA breaks down. For instance, Sakalauskas et al. (2010) extracted, based on their experimental data over the full composition range, a *composition dependent* bowing parameter $b(x)$, with values of $b(x)$ as large as 6.4 eV for the *A*-valence band transition at small In composition x, e.g., 5% In. Similarly, DFT calculations based on small supercells revealed a *composition dependent* bowing parameter (Pela et al., 2011). While both results pointed in the direction of a composition dependent bowing parameter, the fundamental physics origin of this behavior was unclear.

To understand further the fundamental properties of (Al,In)N alloys, Schulz and co-workers performed large scale DFT based calculations for this system (Schulz et al., 2014). Their analysis revealed that a single, isolated In atom results in a strongly localized state above the conduction band edge (CBE). They found also that this localized state hybridizes with and modifies the CBE state. In other words, the CBE state in (Al,In)N is a linear combination of the AlN CBE state and the localized state (CBE+1) introduced by the single In atom. Thus, these studies gave clear evidence of a cation-based (In-based) *band-anticrossing* (*BAC)* and localization in the conduction band of (Al,In)N alloys. Furthermore, Schulz et al. extended the DFT based analysis to higher In contents. Here special attention was again paid to the impact of In—N—In chains on the electronic structure (Schulz et al., 2014). From the review above of carrier localization in (In,Ga)N alloys, one knows already that In—N—In chains can effectively localize hole wave functions: a similar effect was found by Schulz et al. in (Al,In)N (Schulz et al., 2014).

Overall, carrier localization effects in (Al,In)N alloys are therefore even more pronounced when compared to (In,Ga)N systems. This originates from the strong difference in size and electronegativity of In and Al atoms, so that even a single In atom in an AlN host matrix leads to a localized state in the conduction band. Perhaps uniquely for a III-V semiconductor, localization effects are found in both the conduction and valence band, leading to a strong reduction in band gap energy of the alloy and consequently to a composition dependent bowing parameter, consistent with several experimental studies (Sakalauskas et al., 2010; Schulz et al., 2013). Since (Al,In)N systems are potential candidates for light sources in the UV spectral region, a detailed understanding of the band gap energy variation with composition and of carrier localization effects are key for designing such emitters. Additionally, theoretical studies not only revealed that the band gap variation but also light polarization characteristics of (Al,In)N alloys are significantly affected by carrier localization effects (Schulz et al., 2013), again an important aspect especially for designing light emitters operating in the deep UV spectral region.

(Al,Ga)N systems

As a final example, we consider wurtzite $Al_{1-x}Ga_xN$ alloys, which are also of major interest for light emitters operating in the UV spectral range (Humphreys, 2008). Because Al and Ga are more similar to each other than either is to In, carrier localization effects are more subtle but still remain important in (Al,Ga)N bulk alloys and heterostructures, and so the impact of these effects should also be included for describing their electronic and optical properties accurately.

Overall, experimental and theoretical data on (Al,Ga)N *bulk* systems indicate that in comparison to (In,Ga)N or (Al,In)N systems, carrier localization effects are less pronounced but still present. In heterostructures, the electrostatic built-in fields and possible QW widths or (barrier) alloy fluctuations can come into play. Thus, even though the active region in a GaN/(Al,Ga)N QW or QD system is pure GaN, the barrier material is (Al,Ga)N. Furthermore, given that the built-in potential in *c*-plane structures forces the wave functions of electrons and holes to the GaN/(Al,Ga)N interfaces, alloy fluctuations may become important. While experimental data give indications of carrier localization in (Al,Ga)N QW systems (Leroux et al., 1998; Sabooni et al., 2007; Frankerl et al., 2020), theoretical studies have only recently been employed that take potential carrier localization effects in these systems into account. Calculations in the framework of modified continuum-models ($\mathbf{k}\cdot\mathbf{p}$) targeted the question of the importance of alloy fluctuations in the barrier material for the optical properties of GaN/(Al,Ga)N QWs (Rigutti et al., 2016; Roble et al., 2019). These studies revealed that the combined effect of built-in field and alloy fluctuations lead to hole localization and a much weaker electron localization; when accounting for excitonic effects the hole wave function is still localized by alloy fluctuations, while the electron tends to localize about the hole wave function due to the attractive Coulomb interaction (Roble et al., 2019). Studies on the impact of alloy disorder in (Al,Ga)N QWs with AlN barriers (Finn et al., 2022) further supported the observation of hole localization effects in (Al,Ga)N heterostructures; this finding was independent of the Al content in the well. These atomistic studies indicated also that at higher Al (>50%) contents electron localization may become relevant as the effective electron masses of AlN and GaN are significantly higher when compared to InN.

All these considerations and results highlight that carrier localization can also play a role in (Al,Ga)N heterostructures. On the theoretical side and compared to (In,Ga)N or even (Al,In)N systems, far less attention has been directed towards these effects in (Al, Ga)N structures. However, given the importance of (deep) UV light emitters for a wide range of applications, and building on the model development already carried out for instance for (In,Ga)N systems, studies of the impact of alloy disorder and carrier localization effects on the properties of (Al,Ga)N heterostructures has recently gained strong momentum and continues to grow.

Conclusion

In this chapter an overview of different theoretical methods to study the electronic structure of disordered alloys and heterostructures has been presented. These methods were discussed with respect to their capability of treating alloy fluctuations and potentially connected carrier localization effects. The starting point here was density functional theory (DFT). While this method provides insight into carrier localization features due to alloy fluctuations on a microscopic level, it is in its standard implementation only applicable to small supercells. This presents especially a problem when looking at heterostructures such as quantum wells (QWs), where not only the active region of the system (QW) but also the barrier material must be treated explicitly. Empirical atomistic models, e.g., empirical tight-binding or empirical pseudopotential methods, allow for a description that treats explicitly hundreds of thousands of atoms. However, in these empirical atomistic methods the parameter extraction is more complicated, and the cost of calculations in general remains too high to treat device simulations self-consistently.

This issue can be circumvented by using continuum-based approximations, e.g., multi-band $\mathbf{k}\cdot\mathbf{p}$ models. The impact of localized states in extreme alloys such as $GaAs_{1-x}N_x$ can also be treated by adding additional bands associated with the localized states to the conventional $\mathbf{k}\cdot\mathbf{p}$ Hamiltonian, in what is referred to as a band-anticrossing (BAC) model. However, the drawback here is that both conventional and BAC $\mathbf{k}\cdot\mathbf{p}$ models, in general, treat the system as a continuum which is described by average material parameters. To address this issue, modified continuum-based approaches have been established where at different grid points of the simulation cell different alloy compositions are considered. While this gives then a three-dimensional description of the system and the alloy fluctuations, it still remains computationally expensive for device simulations.

To avoid full solution of the Schrödinger equation $H\psi = E\psi$ for a random potential, a very interesting approach has recently been proposed and used in the literature, the so-called *localization landscape theory*. In this approach, instead of solving the Schrödinger equation, one deals with a one-band problem $Hu = 1$. It can be shown that $1/u$ describes an effective potential, W, which, when compared to the results from a full Schrödinger equation, gives a very good indication in which regions the wave functions are localized. Furthermore, the effective potential W is then extremely useful for treating disorder and localization effects in self-consistent drift-diffusion-based transport calculations, giving what is sometimes called a quantum corrected transport model.

The localization landscape approach has challenges associated e.g., with choosing a zero of energy and determining the densities of states. Other approaches have therefore recently been proposed to provide robust quantum-corrected models. Detailed analysis has shown that application of the Hamiltonian H recursively to random wave functions (RWF) or application of a universal low-pass filter (ULF) to the random potential can provide a more accurate quasi-classical description of the temperature-dependent carrier density, $n(\mathbf{r},T)$ in an effective potential. While both of these approaches look promising, they have, at the time of writing, still to be applied to analyze a realistic disordered semiconductor structure.

Overall, given that these different continuum approaches are numerically cheap compared to the atomistic DFT and empirical tight-binding and pseudopotential approaches, they can treat disordered QWs of realistic sizes and dimensions and give valuable insight into carrier localization effects. But they have the drawback that they do not allow for an atomistic, microscopic description of the system. The question here is then, is it justified to assume that one uses the bulk material parameters e.g., for pure InN or GaN at neighboring sites without modifications? This asks also the question what grid size should be chosen so that this becomes a good approximation? From a fundamental point of view, these modified continuum-based approximations cannot provide any insight into the question of how important for instance In—N—In chains are for carrier localization effects in (In,Ga)N or to what extent neighboring N atoms will modify the electronic structure of Ga(N,As).

Thus, theoretical models which provide insight into these questions on an atomistic, microscopic level, while at the same time being able to deal with large supercells remain essential. The *(semi-) empirical pseudo-potential method (EPM)* and the *(semi-)empirical tight-binding model (ETBM)* both meet these criteria. These approaches are often benchmarked against DFT calculations but can then serve to provide benchmarks and or further inputs into e.g., a localization landscape treatment of alloy induced carrier localization effects in semiconductor QWs. Overall, we conclude that calculations across different length scales remain essential for a reliable description of localization effects in disordered semiconductors and thus their electronic, optical and transport properties.

Having reviewed the advantages and disadvantages of the different methods, we overviewed their application by taking III-N alloys as exemplar materials and addressing the similarities and differences between carrier localization features in (In,Ga)N, (Al,In)N and (Al,Ga)N systems. Starting with (In,Ga)N systems, calculations on both bulk alloys and QWs revealed strong hole localization effects. Here already random alloy fluctuations and the introduction of In—N—In chains are sufficient to lead to hole localization features. For electrons the situation is different. In bulk systems, and in comparison to hole states, random alloy fluctuations have a much weaker effect on electron wave functions. Similar effects are seen in *non-polar* (In,Ga)N/GaN QW systems when assuming a random distribution of In atoms in the active region. However, in a *polar c*-plane QW system, due to the presence of the strong electrostatic built-in field, well width fluctuations can act as localization centers for electron wave functions.

Turning to (Al,In)N systems, localization effects are even more pronounced when compared to (In,Ga)N alloys, reflecting the larger difference between AlN and InN than between GaN and InN. Here, already a single In atom in a large AlN host matrix gives rise to electron localization effects in the conduction band, with their impact on the conduction band edge being well described using a BAC model. In addition to this, when two In atoms share a N atom, strong hole localization effects are observed, similar to (In,Ga)N. These localized states in the conduction and valence band of (Al,In)N alloys are manifested by a composition dependent band gap bowing parameter.

Studies on (Al,Ga)N *bulk* systems indicate that carrier localization features are less pronounced, at least compared to (In,Ga)N or (Al,In)N alloys, in line with the fact that Al and Ga are more similar to each other than either is to In. Despite this, some localization effects can be observed in *c*-plane GaN/(Al,Ga)N QW and QD structures. Although the active region is mainly pure GaN, at the QW-barrier interface alloy fluctuations become important due to the presence of the electrostatic built-in field in these systems and the connected spatial separation of electron and hole wave functions. Here, calculations again reveal hole localization effects while the electron wave functions are only slightly perturbed by the presence of the random alloy fluctuations at least when compared to the hole. Similar observations have been made in (Al,Ga)N QWs with pure AlN barriers.

Overall, even though significant progress has been made in the theoretical description and understanding of electronic and optical properties of semiconductor alloys and heterostructures over the last few years, there still remain several open questions and challenges related to the impact of disorder. For instance, the question of how radiative recombination rates in III-N QWs are affected by random alloy fluctuations in comparison to virtual crystal type calculations is still under discussion. Additional questions are related to *non-radiative recombination processes* such as *Auger recombination*. In (In,Ga)N/GaN QW systems the widely used approximation to determine Auger coefficients builds on continuum-based models neglecting carrier localization effects. This means that these studies apply *k*-selection rules for transitions between different states. However, due to the presence of intrinsic alloy fluctuations and associated carrier localization effects, these symmetries/selection rules are no longer applicable given that the translational symmetry of the system is broken. A first work by Jones et al. (2017), using a modified single-band continuum approach, started to look at this problem. These calculations revealed that for (In,Ga)N/GaN QWs, Auger coefficients involving two holes and one electron (hole-hole-electron) are larger in magnitude than the coefficient related to processes involving two electrons and one hole (electron-electron-hole). A similar conclusion was derived in a recent atomistic investigation (McMahon et al., 2022) of Auger effects that accounted for alloy disorder and temperature effects, but performed calculations at fixed carrier density, thus focusing on the thermal rather than the current "droop". Experimental and theoretical studies (Jones et al., 2017; McMahon et al., 2022; Nirschl et al., 2016) of Auger recombination give non-conclusive answers to which of the different processes (electron-electron-hole or hole-hole-electron) dominate, and may contradict each other. All this indicates that further studies are still required to fully understand the impact of carrier localization effects on the electronic and optical properties of semiconductor alloys and connected heterostructures, in order to ultimately exploit their full potential for future novel and energy efficient device applications.

References

Bellaiche L, Mattila T, Wang LW, Wei SH, and Zunger A (1999) Resonant hole localization and anomalous optical bowing in InGaN alloys. *Applied Physics Letters* 74: 1842.

Bernardini F, Fiorentini V, and Vanderbilt D (1997) Spontaneous polarization and piezoelectric constants of III-V nitrides. *Physical Review B* 56: R10024.

Bester G (2009) Electronic excitations in nanostructures: An empirical pseudopotential based approach. *Journal of Physics: Condensed Matter* 21: 023202.

Camacho D and Niquet YM (2010) Application of Keating's valence force field model to non-ideal wurtzite materials. *Physica E* 42: 1361.

Caro MA, Schulz S, and O'Reilly EP (2013) Theory of local electric polarization and its relation to internal strain: Impact on the polarization potential and electronic properties of group-III nitrides. *Physical Review B* 88: 214103.

Chichibu SF, Abare AC, Mack MP, Minsky MS, Deguchi T, Cohen D, Kozodoy P, Fleischer SB, Keller S, Speck JS, Bowers JE, Hu E, Mishra UK, Coldren LA, DenBaars SP, Wada K, Sota T, and Nakamura S (1999) Optical properties of InGaN quantum wells. *Materials Science and Engineering B* 59: 298.

Chichibu SF, Uedono A, Onuma T, Haskell BA, Chakraborty A, Koyama T, Fini PT, Keller S, DenBaars SP, Speck JS, Mishra UK, Nakamura S, Yamaguchi S, Kamiyama S, Amano H, Akasaki I, Han J, and Sota T (2006) Origin of defect-insensitive emission probability in in-containing (Al,In,Ga)N alloy semiconductors. *Nature Materials* 5: 810.

Chuang SL and Chang CS (1996) $\mathbf{k} \cdot \mathbf{p}$ method for strained wurtzite semiconductors. *Physical Review B* 54: 2491.

Cohen ML and Chelikowski JR (1989) *Electronic Structure and Optical Properties of Semiconductors*, 2nd edn. *Series in Solid-State Sciences*, 2nd edn., vol. 75. Berlin: Springer.

Cohen AJ, Mori-Sanchez P, and Yang W (2012) Challenges for density functional theory. *Chemical Reviews* 112: 289.

David A and Weisbuch C (2022) Excitons in a disordered medium: A numerical study in InGaN quantum wells. *Physical Review Research* 4: 043004.

Dawson P, Schulz S, Oliver RA, Kappers MJ, and Humphreys CJ (2016) The nature of carrier localisation in polar and nonpolar InGaN/GaN quantum wells. *Journal of Applied Physics* 119: 181505.

Filoche M, Piccardo M, Wu Y-R, Li C-K, Weisbuch C, and Mayboroda S (2017) Localization landscape theory of disorder in semiconductors. I. Theory and modeling. *Physical Review B* 95: 144204.

Finn R, Schulz S, and S. (2022) Impact, of random alloy fluctuations on the electronic and optical properties of (Al,Ga)N quantum wells: Insights from tight-binding calculations. *The Journal of Chemical Physics* 157: 244705.

Frankerl C, Nippert F, Hoffmann MP, Wang H, Brandl C, Lugauer H-J, Zeisel R, Hoffmann A, and Davies MJ (2020) Strongly localized carriers in Al-rich AlGaN/AlN single quantum wells grown on sapphire substrates. *Journal of Applied Physics* 127: 095701.

Gebhard F, Nenashev AV, Meerholz K, and Baranovskii SD (2023) Quantum states in disordered media I. Low-pass filter approach. *Physical Review B* 95: 144205.

Graham DM, Soltani-Vala A, Dawson P, Godfrey MJ, Smeeton TM, Barnard JS, Kappers MJ, Humphreys CJ, and Thrush EJ (2005) Optical and microstructural studies of InGaN/GaN single-quantum-well structures. *Journal of Applied Physics* 97: 103508.

Hammersley S, Watson-Parris D, Dawson P, Godfrey MJ, Badcock TJ, Kappers MJ, McAleese C, Oliver RA, and Humphreys CJ (2012) The consequences of high injected carrier densities on carrier localization and efficiency droop InGaN/GaN quantum well structures. *Journal of Applied Physics* 111: 083512.

Harrison P (2005) *Quantum Wells, Wires and Dots: Theoretical and Computational Physics of Semiconductor Nanostructures*. New York: Wiley & Sons.

Heyd J, Scuseria GE, and Ernzerhof M (2003) Hybrid functionals based on a screened coulomb potential. *The Journal of Chemical Physics* 118: 8207.

Hjalmarson HP, Vogl P, Wolford DJ, and Dow JD (1980) Theory of substitutional deep traps in covalent semiconductors. *Physical Review Letters* 44: 810.

Hohenberg P and Kohn W (1964) Inhomogeneous electron gas. *Physics Review* 136: B864.

Humphreys CJ (2008) Solid-state lighting. *MRS Bulletin* 33: 459.

Im JS, Kollmer H, Off J, Sohmer A, Scholz F, and Hangleiter A (1998) Reduction of oscillator strength due to piezoelectric fields in GaN/AlGaN quantum wells. *Physical Review B* 57: R9435.

Jancu J-M, Bassani F, Salla FD, and Scholz R (2002) Transferable tight-binding parametrization for the group-III nitrides. *Applied Physics Letters* 81: 4838.

Jones CM, Teng C-H, Yan Q, Ku P-C, and Kioupakis E (2017) Impact of carrier localization on recombination in InGaN quantum wells and the efficiency of nitride lightemitting diodes: Insights from theory and numerical simulations. *Applied Physics Letters* 111: 113501.

Keating PN (1966) Effect of invariance requirements on the elastic strain energy of crystals with application to the diamond structure. *Physics Review* 145: 637.

Kohn W and Sham LJ (1965) Self-consistent equations including exchange and correlation effects. *Physics Review* 140: A1133.

Leroux M, Grandjean N, Laugt M, Massies J, Gil B, Lefebvre P, and Bigenwald P (1998) Quantum confined stark effect due to built-in internal polarization fields in (Al,Ga)N/GaN quantum wells. *Physical Review B* 58: R13371.

Lew Yan Voon LC and Willatzen M (2009) *The $\mathbf{k}\cdot\mathbf{p}$ Method: Electronic Properties of Semiconductors*. Heidelberg: Springer.

Li C-K, Piccardo M, Lu L-S, Mayboroda S, Martinelli L, Peretti J, Speck JS, Weisbuch C, Filoche M, and Wu Y-R (2017) Localization landscape theory of disorder in semiconductors. iii. Application to carrier transport and recombination in light emitting diodes. *Physical Review B* 95: 144206.

Lindsay A and O'Reilly EP (2003) A universal model for trends in A_1-type defects states in zincblende and diamond semiconductor structures. *Physica B* 340–342: 434.

Liu X, Pistol ME, Samuelson L, Schwetlick S, and Seifert W (1990) Nitrogen pair luminescence in GaAs. *Applied Physics Letters* 56: 1451.

Marcinkevi˘cius S, Kelchner KM, Kuritzky LY, Nakamura S, DenBaars SP, and Speck JS (2013) Photoexcited carrier recombination in wide m-plane InGaN/GaN quantum wells. *Applied Physics Letters* 103: 111107.

Marquardt O, Schulz S, Freysoldt C, Boeck S, Hickel T, O'Reilly EP, and Neugebauer J (2012) A flexible, plane-wave based multiband model. *Optical and Quantum Electronics* 44: 183.

Martin RM (1970) Elastic properties of ZnS structure semiconductors. *Physical Review B* 1: 4005.

Martin RM (2011) *Electronic Structure: Basic Theory and Practical Methods*. Cambridge: Cambridge University Press.

McMahon JM, Kioupakis E, and Schulz S (2022) Atomistic analysis of auger recombination in c-plane (In,Ga)N/GaN quantum wells: Temperature dependent competition between radiative and nonradiative recombination. *Physical Review B* 105: 195307.

Morel A, Lefebvre P, Kalliakos S, Taliercio T, Bretagnon T, and Gil B (2003) Donor-acceptor-like behavior of electron-hole pair recombinations in low-dimensional (Ga,In)N/GaN systems. *Physical Review B* 68: 045331.

Moses PG, Miao M, Yan Q, and Van de Walle CG (2011) Hybrid functional investigations of band gaps and band alignments for AlN, GaN, InN, and InGaN. *The Journal of Chemical Physics* 134: 084703.

Mounir C, Schwarz UT, Koslow IL, Kneissl M, Wernicke T, Schimpke T, and Strassburg M (2016) Impact of inhomogeneous broadening on optical polarization of high-inclination semipolar and nonpolar $In_xGa_{1-x}N$/GaN quantum wells. *Physical Review B* 93: 235314.

Nakamura S and Chichibu S (2000) *Introduction to Nitride Semiconductor Blue Lasers and Light Emitting Diodes*. London: Taylor & Francis.

Nenashev AV, Baranovskii SD, Meerholz K, and Gebhard F (2023) Quantum states in disordered media II. Spatial charge distribution. *Physical Review B* 95: 144205.

Nirschl A, Binder M, Schmid M, Pietzonka I, Lugauer H-J, Zeisel R, Sabathil M, Bougeard D, and Galler B (2016) Towards quantification of the crucial impact of Auger recombination for the efficiency droop in (AlInGa)N quantum well structures. *Optics Express* 24: 2971.

O'Donovan M, Chaudhuri D, Streckenbach T, Farrell P, Schulz S, and Koprucki T (2021) From atomistic tight-binding theory to macroscale drift–diffusion: Multiscale modeling and numerical simulation of uni-polar charge transport in (In,Ga)N devices with random fluctuations. *Journal of Applied Physics* 130: 065702.

O'Donovan M, Farrell P, Streckenbach T, Koprucki T, and Schulz S (2022) Multiscale simulations of uni-polar hole transport in (In,Ga)N quantum well systems. *Optical and Quantum Electronics* 54: 23.

O'Reilly EP (2002) *Quantum Theory of Solids. Masters Series in Physics and Astronomy*. London: Taylor & Francis.

O'Reilly EP, Lindsay A, Klar PJ, Polimeni A, and Capizzi M (2009) Trends in the electronic structure of dilute nitride alloys. *Semiconductor Science and Technology* 24: 033001.

Pandey S, Cavalcoli D, Fraboni B, Cavallini A, Brazzini T, and Calle F (2012) Role of surface trap states on two-dimensional electron gas density in AlInN/AlN/GaN heterostructures. *Applied Physics Letters* 100: 152116.

Pela RR, Caetano C, Marques M, Ferreira LG, Furthmüller J, and Teles LK (2011) Accurate band gaps of AlGaN, InGaN, and AlInN alloys calculations based on LDA-1/2 approach. *Applied Physics Letters* 98: 151907.

Pela RR, Marques M, and Teles LK (2015) Comparing LDA-1/2, HSE03, HSE06 and G_0W_0 approaches for band gap calculations of alloys. *Journal of Physics: Condensed Matter* 27: 505502.

Perdew JP (1985) Density functional theory and the band gap problem. *International Journal of Quantum Chemistry* 28: 497.

Piccardo M, Li C-K, Wu Y-R, Speck JS, Bonef B, Farrell RM, Filoche M, Martinelli L, Peretti J, and Weisbuch C (2017) Localization landscape theory of disorder in semiconductors. II. Urbach tails of disordered quantum well layers. *Physical Review B* 95: 144205.

Rigutti L, Mancini L, Lefebvre W, Houard J, Hernandez-Maldonado D, Russo ED, Giraud E, Butte R, Carlin J-F, Grandjean N, Blavette D, and Vurpillot F (2016) Statistical nanoscale study of localised radiative transitions in GaN/AlGaN quantum wells and AlGaN epitaxial layers. *Semiconductor Science and Technology* 31: 095009.

Roble AA, Patra SK, Massabuau F, Frentrup M, Leontiadou MA, Dawson P, Kappers MJ, Oliver RA, Graham DM, and Schulz S (2019) Impact of alloy fluctuations and Coulomb effects on the electronic and optical properties of c-plane GaN/AlGaN quantum wells. *Scientific Reports* 9: 1.

Sabooni M, Esmaeili M, Haratizadeh H, Monemar B, Paskov P, Kamiyama S, Iwaya M, Amano H, and Akasaki I (2007) Exciton localization behaviour in different well width undoped GaN/$Al_{0.07}Ga_{0.93}N$ nanostructures. *Opto-Electronics Review* 15: 163.

Sakalauskas E, Behmenburg H, Hums C, Schley P, Rossbach G, Giesen C, Heuken M, Kalisch H, Jansen RH, and Bl¨asing, J., Dadgar, A., Krost, A. and Goldhahn, R. (2010) Dielectric function and optical properties of Al-rich AlInN alloys pseudomorphically grown on GaN. *Journal of Physics D: Applied Physics* 43: 365102.

Schulz S, Caro MA, Tan L-T, Parbrook PJ, Martin RW, and O'Reilly EP (2013) Composition-dependent band gap and band-edge bowing in AlInN: A combined theoretical and experimental study. *Applied Physics Express* 6: 121001.

Schulz S, Caro MA, and O'Reilly EP (2014) Impact of cation-based localized electronic states on the conduction and valence band structure of AlInN alloys. *Applied Physics Letters* 104: 172102.

Schulz S, Caro MA, Coughlan C, and O'Reilly EP (2015a) Atomistic anaylsis of the impact of alloy and well width fluctuations on the electronic and optical properties of InGaN/GaN quantum wells. *Physical Review B* 91: 035439.

Schulz S, Marquardt O, Coughlan C, Caro MA, Brandt O, and O'Reilly EP (2015b) Atomistic description of wave function localization effects in $In_xGa_{1-x}N$ alloys and quantum wells. In: Witzigmann B, Osinski M, Henneberger F, and Arakawa Y (eds.) *Proceedings of SPIE, Physics and Simulation of Optoelectronic Devices XXIII*, p. 93570C. SPIE.

Schulz S, Tanner DP, O'Reilly EP, Caro MA, Martin TL, Bagot PAJ, Moody MP, Tang F, Griffiths JT, Oehler F, Kappers MJ, Oliver RA, Humphreys CJ, Sutherland D, Davies MJ, and Dawson P (2015c) Structural, electronic, and optical properties of *m*-plane InGaN/GaN quantum wells: Insights from experiment and atomistic theory. *Physical Review B* 92: 235419.

Schwarz UT and Kneissl M (2007) Nitride emitters go nonpolar. *Physica Status Solidi (RRL)* 1: A44.

Shan W, Walukiewicz W, Ager JW III, Haller EE, Geisz JF, Friedman DJ, Olson JM, and Kurtz SR (1999) Band anitcrossing in GaInNAs. *Physical Review Letters* 82: 1221.

Simon J, Pelekanos NT, Adelmann C, Martinez-Guerrero E, Andre R, Daudin B, Dang LS, and Mariette H (2003) Direct comparison of recombination dynamics in cubic and hexagonal GaN/AlN quantum dots. *Physical Review B* 68: 035312.

Sutherland D, Zhu T, Griffiths JT, Tang F, Dawson P, Kundys D, Oehler F, Kappers MJ, Humphreys CJ, and Oliver RA (2015) Optical studies of nonpolar *m*-plane (1-100) InGaN/GaN multi-quantum wells grown on freestanding bulk GaN. *Physica Status Solidi B* 252: 965.

Tan C-K, Sun W, Borovac D, and Tansu N (2016) Large optical gain AlInN-Delta-GaN quantum well for deep ultraviolet emitters. *Scientific Reports* 6: 22983.

Tanner DSP, McMahon JM, and Schulz S (2018) Interface roughness, carrier localization, and wave function overlap in c-plane (In,Ga)N/GaN quantum wells: Interplay of well width, alloy microstructure, structural inhomogeneities, and Coulomb effects. *Physical Review Applied* 10: 034027.

Vogl P (1984) Prediction of deep-impurity level energies in semiconductors. *Advances in Electronics and Electron Physics* 62: 101.

Vogl P, Hjalmarson HP, and Dow JD (1983) A semi-empirical tight-binding theory of the electronic structure of semiconductors. *Journal of Physics and Chemistry of Solids* 44(5): 365.

Vurgaftman I and Meyer JR (2003) Band parameters for nitrogen-containing semiconductors. *Journal of Applied Physics* 94: 3675.

Vurgaftman I, Meyer JR, and Ram-Mohan LR (2001) Band parameters for III-V compound semiconductors and their alloys. *Journal of Applied Physics* 89: 5815.

Waltereit P, Brandt O, Trampert A, Grahn HT, Menniger J, Ramsteiner M, and Ploog KH (2000) Nitride semiconductors free of electrostatic fields for efficient white light-emitting diodes. *Nature* 406: 865.

Wang L-W (2001) Calculations of carrier localization in $In_xGa_{1-x}N$. *Physical Review B* 63: 245107.

Watson-Parris D, Godfrey MJ, Dawson P, Oliver RA, Galtrey MJ, Kappers MJ, and Humphreys CJ (2011) Carrier localization mechanisms in $In_xGa_{1-x}N$/GaN. *Physical Review B* 83: 115321.

Winkelnkemper M, Schliwa A, and Bimberg D (2006) Interrelation of structural and electronic properties in $In_xGa_{1-x}N$/GaN quantum dots using an eight-band $\mathbf{k}\cdot\mathbf{p}$ model. *Physical Review B* 74: 155322.

Wolford DJ, Bradley JA, Fry K, and Thompson J (1984a) The nitrogen isoelectric trap in GaAs. In: Proceedings of the 17th International Conference on the Physics of Semiconductors, New York: Springer.

Wolford DJ, Bradley JA, Fry K, and Thompson J (1984b) The nitrogen isoelectric trap in GaAs. In: Proceedings of the 17th International Conference on the Physics of Semiconductors, p. 627. New York: Springer.

Yang T-J, Shivaraman R, Speck JS, and Wu Y-R (2014) The influence of random indium alloy fluctuations in indium gallium nitride quantum wells on the device behavior. *Journal of Applied Physics* 116: 113104.

Conductivity, electrical[☆]

J Bass, Michigan State University, East Lansing, MI, United States

© 2024 Elsevier Ltd. All rights reserved.

This is an update of J. Bass, Conductivity, Electrical, Editor(s): Franco Bassani, Gerald L. Liedl, Peter Wyder, Encyclopedia of Condensed Matter Physics, Elsevier, 2005, Pages 219–225, ISBN 9780123694010, https://doi.org/10.1016/B0-12-369401-9/00722-1.

Introduction 251
Measurements 251
Theoretical background 252
Experimental temperature and impurity-concentration dependence 254
Pressure 258
Size effects (mean free path) 258
Some related phenomena outside the purview of this chapter 259
Magnetoresistance 259
Kondo effect 259
Mesoscopic effects 259
Further reading 259

Abstract

One important way to characterize a material is in terms of its electrical conductivity (or the inverse, its electrical resistivity). A metal conducts electricity well, and its resistivity usually increases with increasing temperature. Most elements (82 of the 104 naturally occurring ones) are metals. A semiconductor conducts electricity less well, and its resistivity usually decreases with increasing temperature. An insulator hardly conducts electricity at all; its resistivity is very large. This article deals with the electrical resistivity of pure metals and alloys. The focus is mainly on nonmagnetic metals—magnetic metals are covered elsewhere. References to both the theory of the electrical resistivity of metals, and to data on the resistivities of pure metals and alloys, are given in the Further reading section.

Introduction

Formally, the electrical conductivity tensor σ (and its inverse—the resistivity tensor ρ) are defined by Ohm's law:

$$\boldsymbol{J} = \sigma \cdot E \tag{1}$$

and

$$E = \boldsymbol{\rho} \cdot \boldsymbol{J} \tag{2}$$

where $\boldsymbol{J}$ is the current density and $\boldsymbol{E}$ is the electric field (both vectors). In the general case, $\boldsymbol{\rho}$ is the inverse of the tensor $\boldsymbol{\sigma}$. However, if no magnetic field is present, and if the crystal structure of the metal is cubic -simple cubic (s.c.), face-centered cubic (f.c.c.), or body-centered cubic (b.c.c.)—then $\boldsymbol{\sigma}$ and $\boldsymbol{\rho}$ reduce to scalars, and $\rho = 1/\sigma$. Since many of the most common metals have cubic structures, the focus is on the case where ρ and σ are scalars, in which case it suffices to consider ρ, because σ is simply its inverse. Where appropriate, noncubic metals are discussed.

Near room temperature ($\sim$295 K), convenient units for ρ are micro-ohm cm (μΩ cm), since the resistivities of all pure elemental metals at 295 K range from $\sim$1.6 μΩ cm for Ag to somewhat over 100 μΩ cm for Mn, Gd, and Tb.

Measurements

The resistivity ρ at temperature T, $\rho(T)$, of a given metal or alloy is derived from a "four-probe" measurement of the electrical resistance $R = V/I$ of a long thin wire of known cross-sectional area $A = \pi r^2$, or a long, narrow film of area $A = Wt$, as shown schematically in Fig. 1. Here r is the radius of the wire, W and t are the width and thickness of the film, and the voltage leads are made long and thin to minimize perturbing the current flow. These geometries minimize end effects, thereby ensuring that the current density $J = I/A$ is uniform across A, and contact effects by eliminating current flow into the voltage contacts. In such a case, measuring the voltage V across a well-defined length L of the sample gives $\rho = RA/L = VA/IL$.

[☆] *Change History*: October 2022. J Bass updated the chapter.

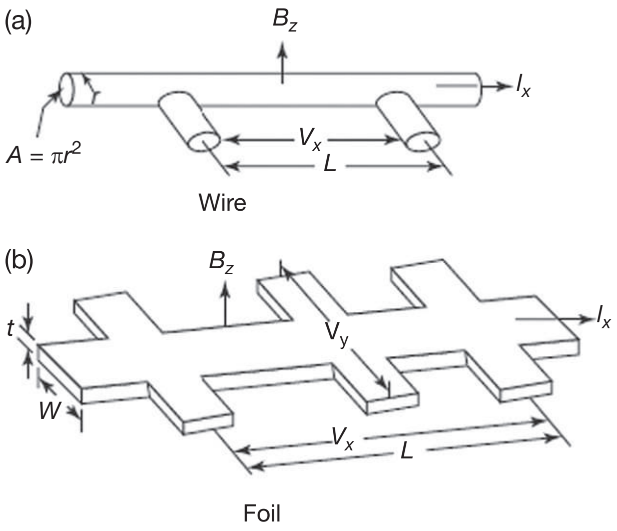

Fig. 1 Schematic drawings of (a) Wire and (b) film geometries for measuring resistivities so that complications due to nonuniform current flow and contact resistances are minimal.

Strictly, as noted above, a unique value of $\rho(T)$ can be determined for either a single crystal or a polycrystal line sample of a cubic metal, but only for a single crystal of a noncubic metal that is oriented along a symmetry axis. Even in these cases, it will be seen below that $\rho(T)$ can depend upon the size of the sample if r or t are very small, and upon the content of impurities or other defects such as grain boundaries or dislocation.

Theoretical background

The first derivation of Ohm's law and σ was made by Drude in 1900, who used the classical kinetic theory to treat an assumed gas of free electrons in a metal. His result can be obtained by assuming that an electron of charge e and mass m is accelerated by an electric field E and is subject to a frictional retarding force proportional to its velocity v and inversely proportional to a relaxation time τ (a measure of the average time between scattering events). Then, at steady state, the electron is not accelerated, and

$$m\,\mathrm{d}v/\mathrm{d}t = 0 = eE - mv/\tau \rightarrow v = eE\tau/m \tag{3}$$

Taking

$$J = nev \tag{4}$$

(where e is the electron's charge and n is the number of electrons per unit volume), Ohm's law is obtained:

$$J = nev = \left(ne^2\tau/m\right)E \tag{5}$$

with

$$\sigma = ne^2\tau/m \tag{6}$$

The Bohr-Sommerfeld analysis of a quantum free-electron gas gives a similar expression, but with τ evaluated at the Fermi energy. If a mean free path λ between scattering events is defined as $\lambda = v$, Eq. (6) can be rewritten as

$$\sigma = ne^2\lambda/mv_\mathrm{F} \tag{7}$$

Inverting Eq. (7) then gives

$$\rho\lambda = mv_\mathrm{F}/ne^2 \tag{8}$$

For a given metal or alloy at temperature T, Eq. (7) shows that $\sigma \propto \lambda$, and Eq. (8) shows that the product $\rho\lambda$ is a constant for a given metal, depending upon the particular metal only through n and v_F. Eq. (8) can be used to estimate λ for a given value of ρ.

To generalize Eqs. (7) and (8) to real (as opposed to free-electron) metals, with real Fermi surfaces, one must turn to a more general analysis, such as the Boltzmann transport equation. Here, one defines an electron distribution function $f(\boldsymbol{k}, \boldsymbol{r}, t)$ such that $(4\pi^3)^{-1} f(\boldsymbol{k}, \boldsymbol{r}, t)\,\mathrm{d}\boldsymbol{k}\,\mathrm{d}\boldsymbol{r}$ gives the number of electrons of wave vector $\boldsymbol{k}$ (or crystal momentum $\hbar\boldsymbol{k}$, where $\hbar$ is Planck's constant divided by 2π) at point $\boldsymbol{r}$ within an element $\mathrm{d}\boldsymbol{r}$ in real space and $\mathrm{d}\boldsymbol{k}$ in wave vector space at time t. $f(\boldsymbol{k}, \boldsymbol{r}, t) = 1$ if all states with $\boldsymbol{k}$ and $\boldsymbol{r}$ are filled and 0 if all such states are empty. If the electron gas is at thermal equilibrium at a temperature T,

$$f_0 = 1/\left(\mathrm{e}^{(\varepsilon - \varepsilon_\mathrm{F})/k_\mathrm{B}T} + 1\right) \tag{9}$$

is the usual Fermi-Dirac distribution function. The Boltzmann transport equation for $f(\boldsymbol{k}, \boldsymbol{r}, t)$ is then

$$\partial f/\partial t + (\partial f/\partial \boldsymbol{r})(\partial \boldsymbol{r}/\partial t) + (\partial f/\partial k)(\partial k/\partial t) = (\partial f/\partial t)_{\mathrm{scatt}} \tag{10a}$$

where $(\partial f/\partial t)_{\mathrm{scatt}}$ is the rate of change of f due to scattering from defects, quantized lattice vibrations (phonons), or the sample surface. Since $(\partial \boldsymbol{r}/\partial t) = v$, and $\hbar(\partial k/\partial t) = \boldsymbol{F}$, any external force $\boldsymbol{F}$, Eq. (10a) may be rewritten as

$$\partial f/\partial t + v(\boldsymbol{k})(\partial f/\partial \boldsymbol{r}) + (1/\hbar)\boldsymbol{F}(\partial f/\partial \boldsymbol{k}) = (\partial f/\partial t)_{\mathrm{scatt}} \tag{10b}$$

If both an electric field $\boldsymbol{E}$ and a magnetic field $\boldsymbol{B}$ are present, $\boldsymbol{F} = e\boldsymbol{E} + v \times \boldsymbol{B}$. In the absence of a magnetic field, Eq. (10b) can be rewritten as

$$\partial f/\partial t + v(k)(\partial f/\partial \boldsymbol{r}) + (e/\hbar)\boldsymbol{E}(\partial f/\partial k) = (\partial f/\partial t)_{\mathrm{scatt}} \tag{10c}$$

If the focus is only upon the electrical conductivity σ of the bulk material, the temperature can be taken as constant across the sample, any changes in f with $\boldsymbol{r}$ can be neglected, and only the steady-state solution can be considered. Eq. (10c) then reduces to

$$(e/\hbar)\boldsymbol{E}(\partial f/\partial k) = (\partial f/\partial t)_{\mathrm{scatt}} \tag{10d}$$

Because changes in f with $\boldsymbol{r}$ are neglected, this equation will not allow one to treat scattering at the sample surface (size effects). Such effects are discussed briefly below.

Finally, for the physics of present interest, the deviations of $f(\boldsymbol{k})$ from $f_0(\boldsymbol{k})$ will be small. These deviations can be considered by writing $f(\boldsymbol{k}) = f_0(\boldsymbol{k}) + g(\boldsymbol{k})$. In order to obtain Ohm's law, Eq. (10d) must then be linearized (i.e., drop terms of higher order in $\boldsymbol{E}$), giving

$$(e/\hbar)\boldsymbol{E}(\partial f_0/\partial k) = (\partial f/\partial t)_{\mathrm{scatt}} \tag{11}$$

Eq. (11) is the linearized Boltzmann transport equation in the absence of temperature gradients, magnetic fields, and size effects. In introductory and intermediate texts, it is usually simplified one more time by making the "relaxation time approximation," that is by taking

$$(\partial f/\partial t)_{\mathrm{scatt}} = -g_k/\tau_k \tag{12}$$

where τ_k is called the relaxation time. Since f_0 (see Eq. (9)) is only a function of the energy ε_k, and $v = (1/\hbar)\partial\varepsilon/\partial \boldsymbol{k}$, Eq. (11) can be rewritten in the final form

$$e\boldsymbol{E}v_k(\partial f_0/\partial \varepsilon_k) = -g_k/\tau_k \tag{13}$$

Generalizing Eq. (4) gives $J = \int \mathrm{d}\boldsymbol{k}^3 e g_k v_k$ and some manipulation of Eq. (13) leads to the relation

$$\sigma = (1/12\pi)\left(e^2/\hbar\right)\int \lambda_k \,\mathrm{d}S_k \tag{14}$$

where λ_k is the mean free path of electrons of wave vector $\boldsymbol{k}$, and $\mathrm{d}\boldsymbol{S_k}$ is a differential area on the Fermi surface around wave vector $\boldsymbol{k}$. Eq. (14) is the generalization of Eq. (7).

For the present purposes, only one more result (the Bloch-Gruneisen equation for the temperature-dependent electrical resistivity of a free-electron gas (i.e., a spherical Fermi surface), in which the electrons are scattered only by phonons and with no participation of reciprocal lattice vectors (i.e., no Umklapp scattering)) is needed. The result, taken as their approximation for the resistivity of an ideally pure metal, ρ_{P}, is

$$\rho_{\mathrm{P}} = (K/\vartheta)(T/\vartheta)(T/\vartheta)^4 \int_0^{\vartheta/T} 4z^4 \,\mathrm{d}z/(\mathrm{e}^z - 1) \tag{15}$$

Since the interest here is only in the Bloch-Gruneisen prediction for the temperature dependence of ρ_{P}, several constants and parameters have been collected together into K, and only scaling parameter, ϑ, is left with the units of temperature.

At high temperatures, where $T \gg \vartheta$, the term $\mathrm{e}^z - 1$ in the denominator of the integral reduces to just z, leaving four powers of z inside the integral. The lower limit of the integral then gives zero, and the upper limit is proportional to $(\vartheta/T)^4$, which cancels the $(T/\vartheta)^4$ outside the integral, leaving just (T/ϑ). In this limit, ρ_{P} is proportional to T.

At low temperatures, where $T \ll \vartheta$, the upper limit can be approximated as infinity, turning the integral into just a number. The temperature dependence in this limit is then just that outside the integral, or T^5.

The Bloch-Gruneisen calculation thus predicts that ρ_{P} should be proportional to T at high T, and to T^5 at low T. A linear variation with T is often seen at high T (but not necessarily extrapolating to $\rho_{\mathrm{P}} = 0$ at $T = 0$ as would be predicted by Bloch-Gruneisen). A strict T^5 variation is rarely, if ever, seen at low T. Deviations from the simple prediction occur for a variety of reasons, including: real Fermi surface effects such as Umklapp scattering; electron-electron scattering (which can give a T^2 variation); deviations from Matthiessen's rule; and the onset of superconductivity.

Experimental temperature and impurity-concentration dependence

From Bloch's theorem, the resistivity of a perfectly periodic metal should be zero. Resistivity results from scattering of conduction electrons by deviations from perfect periodicity, either due to the presence of defects at atomic sites (e.g., impurities, vacancies, dislocations, grain boundaries) or due to vibrations of the atoms of the lattice away from their equilibrium sites (quantized lattice vibrations are called phonons).

In a high-purity metal, scattering by phonons dominates at all but the lowest temperatures. As noted above, for a free-electron metal, the Bloch-Gruneisen model of $\rho(T)$ predicts a linear dependence upon T at high temperatures, and a more rapid decrease at lower temperatures, eventually reaching T^5 at cryogenic temperatures. Figs. 2–4 illustrate some of the behaviors of $\rho(T)$ at higher temperatures, using data for the simple f.c.c. metal Cu, which looks qualitatively like the expectation from Bloch-Gruneisen, the f.c.c. metal Ni, which undergoes a ferromagnetic phase transition at 630 K, and the hexagonal close-packed (h.c.p.) metal Gd, which undergoes magnetic phase transitions at 240 and 293 K. In the simplest case, Cu, at temperatures above ~100 K, $\rho(T)$ is approximately linear in T. At cryogenic temperatures, $\rho(T)$ decreases more rapidly than linearly with T. If the metal was perfectly pure, $\rho(T)$ would approach 0 as $T \to 0$ K, either smoothly if the metal remains "normal" (i.e., nonsuperconducting), or abruptly at a characteristic temperature, Tc, if the metal becomes superconducting. Fig. 5 shows an example of a superconductor, Pb, both in the zero magnetic field (open circles) where it becomes superconducting (resistance drops to zero) at $T_c = 7.2$ K and in magnetic fields (triangles and filled circles) large enough to keep it normal down to at least 2 K. In this article, the concentration is on nonsuperconducting behavior. Below ~8 K, the normal resistivity of Pb in a magnetic field decreases more rapidly than linearly with temperature, and then saturates to a constant value at the lowest temperatures. Fig. 6 shows, in Pd, a more complex low-temperature resistivity than just the Bloch-Gruneisen form; here $\rho(T)$ contains two terms, a term arising from electron-electron scattering, plus an approximately T^5 Bloch-Gruneisen-like term. As T decreases, Figs. 5 and 6 show that the

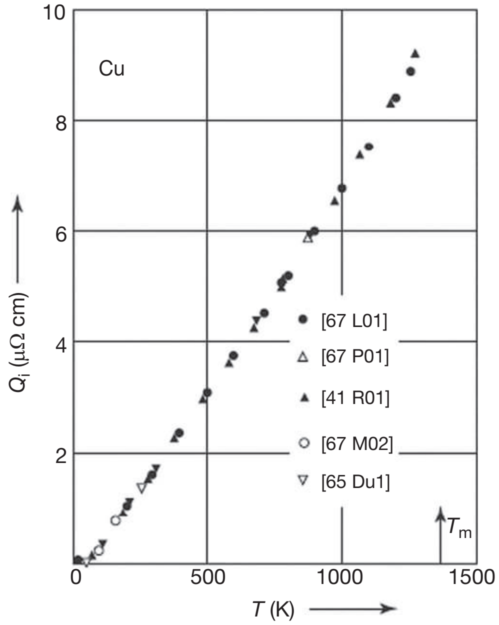

Fig. 2 Resistivity as a function of temperature for Cu, a metal where the form of the resistivity is similar to that predicted by the Bloch-Gruneisen model.

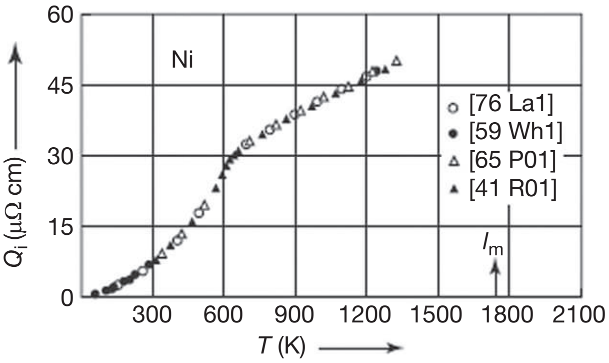

Fig. 3 Resistivity as a function of temperature for Ni, a metal that becomes ferromagnetic below its Curie temperature of ~650 K.

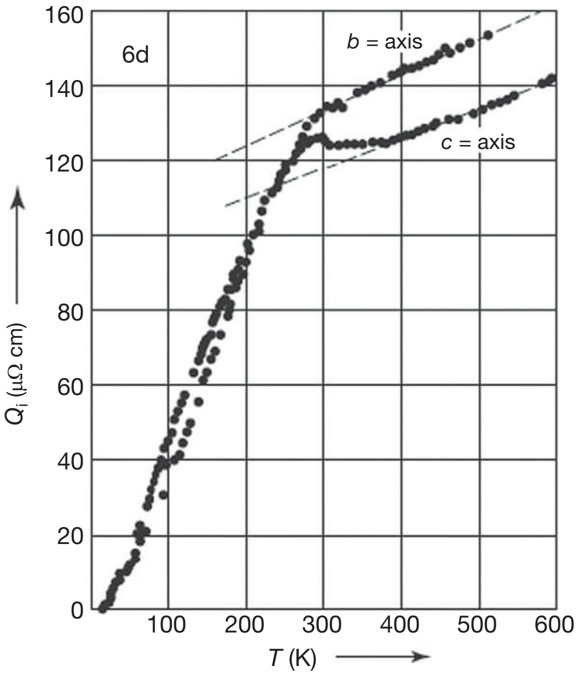

Fig. 4 Resistivity as a function of temperature for a single-crystal sample of Gd, which has a noncubic crystal structure.

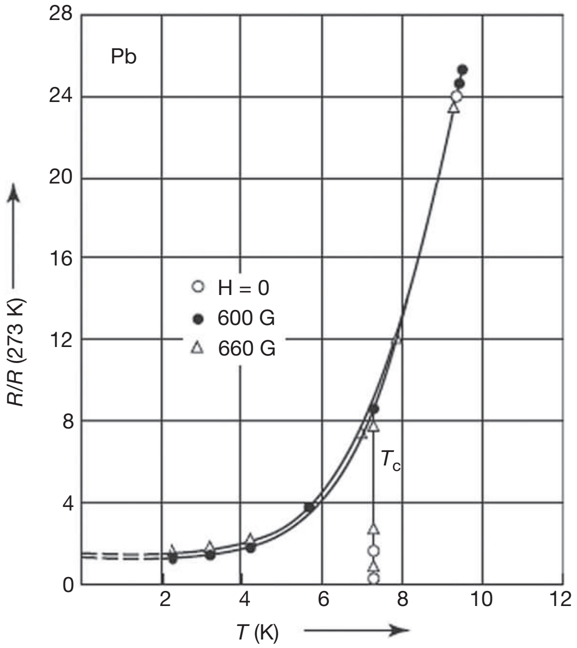

Fig. 5 Low-temperature resistivity of Pb, which becomes superconducting (the resistivity drops to zero) in zero magnetic field at ~7.2 K. In a magnetic field of 600 Oe, Pb remains normal to the lowest temperature measured in this figure, and the resistivity at the lowest temperatures becomes constant, at a value determined by residual impurities.

temperature-dependent part of $\rho(T)$ eventually becomes smaller than the resistivity due to residual defects, and the measured resistivity (designated as residual resistivity, ρ_0) becomes closely independent of temperature (constant) at a value determined by the nature and concentration of these defects.

If a concentration c of a given defect is added to a "pure" metal, the resulting total resistivity $\rho_T(c, T)$ can often be approximated by simply summing the temperature-dependent resistivity, $\rho_P(T)$, of the ideally pure host metal and a temperature-independent term, $\rho_0(c)$, due to the presence of the defect. This result is called Matthiessen's rule:

$$\rho_T(c, T) \approx \rho_0(c) + \rho_P(T) \tag{16}$$

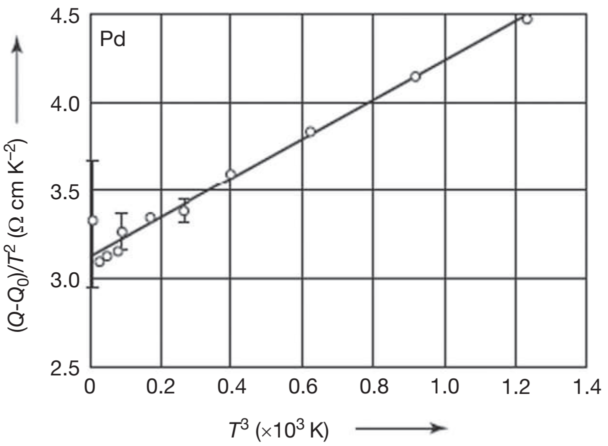

Fig. 6 $(\rho - \rho_0)/T^2$ vs T^3 for the transition metal Pd at low temperatures, where ρ_0 is the (constant) residual resistivity. In addition to an approximately T^5 Bloch-Gruneisen-like term, the data contain also a T^2 term due to electron-electron scattering.

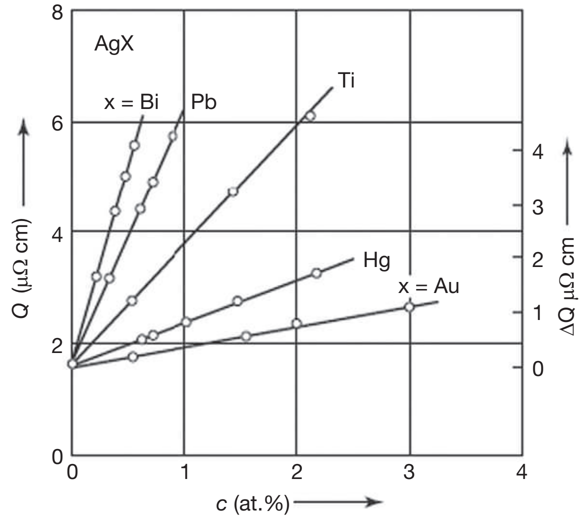

Fig. 7 Resistivity vs concentration (c in at.%) for Bi, Pb, Tl, Hg, and Au impurities in Ag, showing the expected linear variation with *c*, for small *c*.

The content of Eq. (16) is twofold: (1) the most important feature of the defects is simply their presence, rather than that they vibrate differently from the host atoms; and (2) scattering of electrons from the defects is independent of scattering from the phonons. In practice, Eq. (16) is used to define $\rho_P(T)$, by subtracting the low temperature constant limit of the data, ρ_0, from the measured $\rho(T)$ for the highest-purity samples available.

For small c, $\rho_0(c)$ is proportional to c, $\rho_0(c) = Kc$. The scale for K is μΩ cm at.%$^{-1}$, with values ranging from 0.1 μΩ cm (at.%)$^{-1}$ to 10 μΩ cm (at.%)$^{-1}$ for different impurities in different host metals. Fig. 7 shows examples of linear variations of $\rho_0(c)$ with c for dilute Ag-based alloys. Note that K increases with increasing difference between the number of "conduction electrons" for the impurity (Au = 1, Hg = 2, Tl = 3, Pb = 4, and Bi = 5) and for the host metal, Ag = 1. If the values of K for impurity A in host B and for impurity B in host A are closely the same, then the relation between $\rho_0(c)$ and c can be approximated over the whole range of alloy concentrations as

$$\rho_0(c) = Kc(1 - c) \tag{17}$$

In practice, the K values for different pairs of metals are usually different enough that Eq. (17) is only a very rough approximation to reality. Fig. 8 shows an example of experimental data for PdAu alloys.

Careful measurements of $\rho_T(c, T)$ show that Matthiessen's rule is never exact. The resulting deviations from Matthiessen's rule (DMR) are defined by the relation

$$\Delta(c, T) = \rho_T(c, T) - \rho_0(c) - \rho_P(T) \tag{18}$$

Such deviations have been studied for a variety of impurities and host metals. $\Delta(c, T)$ usually consists of a low-temperature peak followed by a linear component at high T that can have positive, negative, or zero slope. Figs. 9 and 10 illustrate the forms seen.

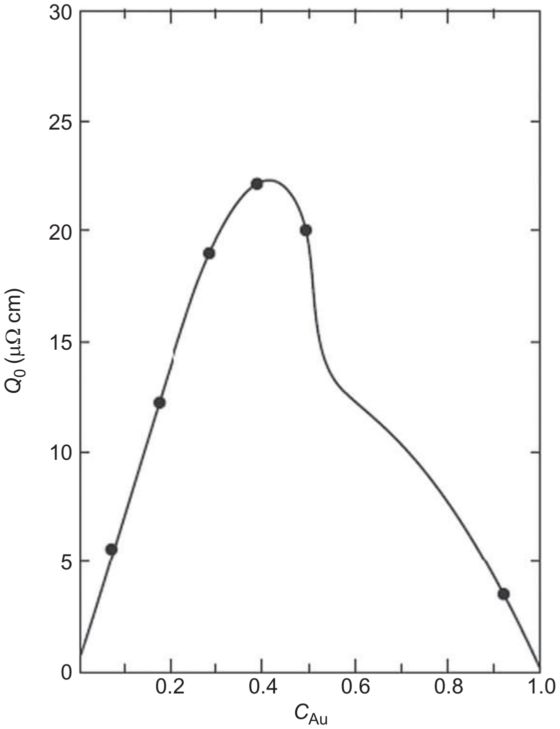

Fig. 8 Residual resistivity vs Au concentration C_{Au} for PdAu alloys, showing that the residual resistivity need not be a symmetric function of C_{Au}.

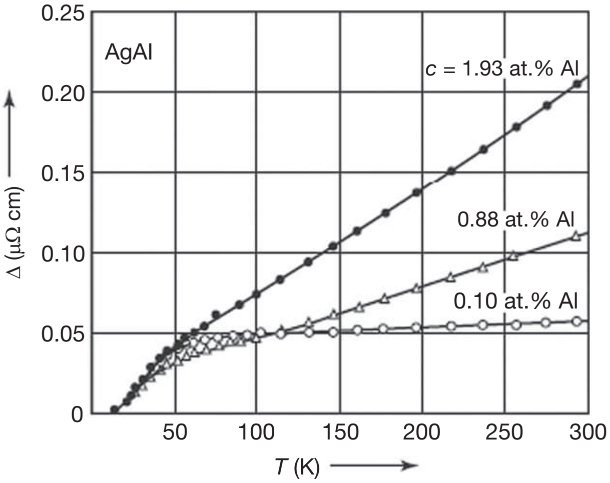

Fig. 9 Deviation from Matthiessen's rule, **Δ**, vs temperature for three alloys of Al in Ag.

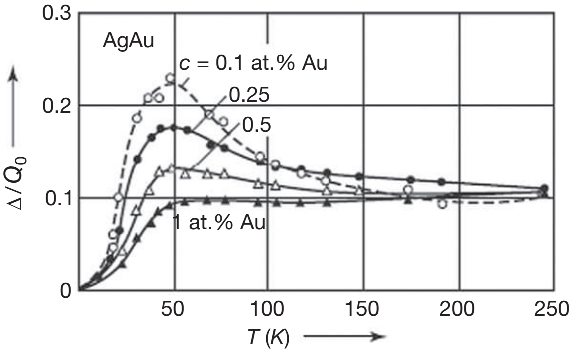

Fig. 10 Normalized deviation from Matthiessen's rule, $\mathbf{\Delta}/\rho_0$, for a series of alloys of Au in Ag.

Pressure

Measurements of ρ are almost invariably made at constant pressure P, usually at atmospheric pressure or in vacuum. Calculations of ρ, in contrast, are normally made by assuming constant volume V. Thus, to compare measurements and calculations, knowledge of how ρ changes with P is required. Studies of $\rho(P)$ are useful for providing such corrections (which are usually small) and also because measuring R is often the easiest way to study phenomena induced by an application of pressure, such as pressure-induced phase transitions. The relative ease of measuring R also makes it one of the properties of choice for studying phase transitions induced by temperature.

Size effects (mean free path)

If a sample wire or film is made so thin that there is a significant probability of electrons being scattered by the sample surface, and if such scattering is at least partly diffuse (i.e., with the final momentum of the scattered electron randomized in direction), then the resistance of the sample will increase due to such scattering. In the simplest case of a thin cylindrical wire of a free-electron metal of diameter d and completely diffuse scattering (i.e., the component of the electron's momentum along the wire or film is randomized by each collision), the total resistance $\rho_T(d)$ can be approximated by the relation

$$\rho_T(d) = \rho_B + (\rho\lambda)/d \tag{19}$$

Here, ρ_B is the resistivity of the bulk material, and $\rho\lambda$ is a constant representative of the particular metal involved, as shown in Eq. (8). If one replaces ρ by the experimental resistivity of the metal at a particular temperature, then λ would be the experimental "mean free path" for free electrons in that metal at that temperature—that is, λ is the typical distance moved between scattering events that significantly change the direction of the electron's momentum. A qualitative insight into Eq. (19) can be obtained by analogy with Matthiessen's rule, wherein the second term of Eq. (19) represents the increas in resistivity when the sample diameter is equal to its mean free path. For partially specular scattering (mirror-like, in which the momentum component along the wire or film remains unchanged), or for the different geometry of a film, the equations are more complex, and the interested reader is referred to the Further reading section. Fig. 11 shows examples of the applicability of Eq. (19) for samples with different amounts of surface specularity.

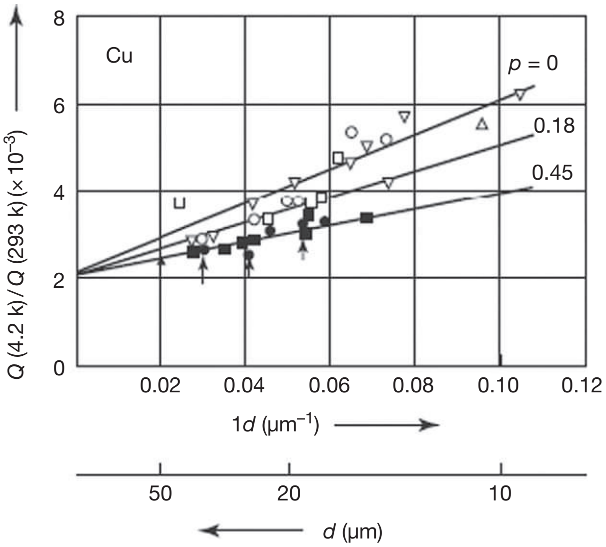

Fig. 11 ρ(4.2 K)/ρ(293 K) vs inverse wire diameter, 1/d, for a series of Cu wires with surfaces giving different amounts of diffuse scattering ($\rho = 0$ indicates estimated completely diffuse scattering).

Some related phenomena outside the purview of this chapter

Magnetoresistance

The standard quasiclassical treatment of electrical conduction in metals outlined above can also be used to describe the phenomenon of magnetoresistance in nonmagnetic metals and alloys, as well as the changes in electrical resistivity that occur upon application of an external magnetic field.

Kondo effect

In contrast, this standard quasiclassical analysis always yields, as a low-temperature limit, a constant resistivity, corresponding to the scattering of the conduction electrons by residual impurities. It could, thus, not explain observed deviations from this prediction for some magnetic impurities in nonmagnetic hosts, where the resistivity increases with decreasing temperature. This phenomenon was dubbed the "Kondo effect" when it was explained many years later by Kondo as arising from an anomalous scattering by a dilute concentration of localized magnetic moments in a metallic host. This phenomenon is described elsewhere in this encyclopedia.

Mesoscopic effects

The standard quasiclassical analysis of metallic transport is also unable to explain mesoscopic effects in metallic samples with at least one dimension less than the phase coherence (or dephasing) length, which can be microns or more at cryogenic temperatures. These effects include weak localization in highly disordered metals, and oscillations with the magnetic field in multiply connected samples of size comparable to the dephasing length. To properly treat both the temperature dependence of transport in highly disordered metals, and the oscillatory response to magnetic fields of metallic rings with dimensions smaller than the dephasing length, one must take account of the interference between waves of electrons that follow different trajectories between two points in the sample.

Further reading

Ashcroft NW and Mermin ND (1976) *Solid State Physics*. Philadelphia: Saunders College.
Bass J (1982/1985) *Electrical Resistivity of Pure Metals and Alloys. Landolt-Bornstein, New Series, Group III, V15a, 1; V15b, 1*, Berlin: Springer.
Bass J, Pratt WP Jr., and Schroeder PA (1990) The temperature dependent electrical resistivities of the alkali metals. *Reviews of Modern Physics* 62: 645–744.
Dugdale JS and Myers A (1985) *Electrical Resistivity of Pure Metals and Alloys: Pressure Effects. Landolt-Bornstein, New Series, Group III, V15b, 13*, Berlin: Springer.
Meaden GT (1965) *Electrical Resistance of Metals*. New York: Plenum Press.
Rossiter PL (1987) *The Electrical Resistivity of Metals and Alloys*. Cambridge: Cambridge University Press.
Rossiter P and Bass J (1992) Electronic transport properties of normal metals. In: Cahn R, Haasen P, and Kramer EJ (eds.) *Materials Science and Technology*. vol. 3A, pp. 257–320. Weinheim: VCH.
Schroder K (1983) *Handbook of Electrical Resistivities of Binary Metallic Alloys*. Boca Raton, FL: CRC Press.
Ziman JM (1964) *Principles of the Theory of Solids*. Cambridge: Cambridge University Press.

Coulomb blockade

Yuli V Nazarov, Department of QuantumNanoscience, Kavli Institute of Nanoscience, Delft University of Technology, The Netherlands

© 2024 Elsevier Ltd. All rights reserved.

Introduction 260
Charge quantization and charging energy 261
Single electron box 262
Single electron transistor 262
Coulomb oscillations and staircase 265
Quantum effects 267
Co-tunneling 268
Applications 270
Conclusion 271
References 271

Abstract

Coulomb blockade is a universal phenomenon in electron transport in artificially made nanostructures. It can be understood by a simple and closed reasoning given in this article. We concentrate on big normal Coulomb islands omitting superconductivity and discreteness of electron spectrum. We review the basic concepts of Coulomb blockade, consider the work of generic devices—SEB en SET, master equation approach for single electron transfer. We outline quantum effects and co-tunneling, and shortly review the applications of the phenomenon.

Key points

- The concepts of charge quantization and charging energy
- Single electron box to store quantized charge
- Tunneling rates and master equation to describe the Coulomb-blockaded transport
- The simplest device: Single Electron Transistor
- The typical manifestations of Coulomb blockade phenomenon
- Co-tunneling: a quantum altertative to single-charge tunneling
- Weak Coulomb blockade: if quantum effects are significant
- Possible applications of Coulomb blockade

Notations and acronyms

SEB	Single-electron box
SET	Single-electron transistor

Introduction

In fact, it is paradoxical that interacting electrons are commonly regarded as non-interacting particles in solid state physics of bulk materials. Doing so, we satisfy the human want for simplification that fortunately can be justified in many cases by physical reasons. The most common physical argument is that in conductors we are not dealing with electrons. Rather, we call "electrons" the quasi-electrons: Landau quasiparticles, charged elementary excitations on the background of a ground state formed by original interacting electrons. The quasi-electrons indeed interact very weakly provided their energies are sufficiently close to the Fermi surface, this is in contrast to the original electrons. The interaction renormalizes their velocities at the Fermi surface, yet this change is not qualitative one. This is why our use of a model of non-interacting electrons usually goes unpunished. The model of non-interacting electrons ceases to work only in isolated cases, that are notoriously difficult to comprehend and quantify. Some of them, like Mott insulator transition, are known for almost a century, yet the progress in this direction remains moderate. Importantly, the progress is restricted to particular cases—the understanding of strongly interacting electrons does not match the universality of noninteracting model.

Surprisingly, the role of interaction in quantum transport is in contrast with that in solid state physics. There is a very common and universal regime where interaction is dominant and non-interacting model makes no sense. This regime is also simple: relevant

https://doi.org/10.1016/B978-0-323-90800-9.00076-7

and non-trivial predictions can be derived from an unbelievably short, self-contained and closed reasoning that takes charge quantization and associated charging energy as the starting point. This is the Coulomb blockade regime outlined in this article. It occurs in any nanostructure where a place to store an electron—an island—is sufficiently isolated from the leads and/or other islands.

In this article, we concentrate on Coulomb blockade in sufficiently big normal islands. Coulomb blockade is also crucial for quantum dots, where islands are sufficiently small to manifest the discreteness of electron spectrum, as well as for superconducting structures, where the combination of Coulomb blockade and Josephson effect provides a base for modern sophisticated quantum technologies.

Charge quantization and charging energy

To comprehend these concepts, let us consider a many-atom isolated metallic island hanging in vacuum—a setup similar to that of seminal oil drop experiment (Millikan, 1913). The bulk properties of the island should be well described with the non-interacting electron model: the electron-electron interaction suppose to result in a velocity renormalization. Let us however note that the total charge of the island may be non-zero. Since number of elementary particles in the island—protons and electrons—must be integer, this charge is *quantized* amounting to an integer number of elementary charges, $Q = Ne$. Owing to screening, the actual charge is concentrated in a thin layer near the surface of the island not affecting its bulk properties. Abeit the charge Q produces electric field $\boldsymbol{E}$ outside the island, and this costs energy. According to the laws of electrostatics, this energy is readily be expressed via capacitance C of the island,

$$E = \frac{Q^2}{2C} = \frac{e^2}{2C}N^2 \equiv E_C N^2. \tag{1}$$

So if we charge a neutral island with an extra electron, we have to pay the *charging energy* E_C. This energy cost is rising if we put more electrons: we have to supply $E_C N^2 - E_C(N-1)^2 = E_C(2N-1)$ extra energy to add the Nth electron. The same goes for the electron extraction. The fact that the addition energy depends on number of particles added is in contradiction with the non-interacting model: Charging energy presents electron-electron interaction. The capacitance scales with the linear size of the island. Owing to this, the charging energy $\propto 1/C$ vanishes in common limit of big number of particles when the energies are counted per particle. However, the charging energy is finite for any finite island.

The addition energy is also contributed by a non-interaction effect: The electron levels in a finite island are quantized with a finite mean level spacing δ_S, and the electron added would go to the first unoccupied level separated by δ_S from an occupied one (Fig. 1b). Let us compare these two contributions: charging energy E_C and the mean level spacing δ_S. Let us take an island of the typical size L It consists of $N_{at} \simeq (L/a)^3$ atoms, a being the interatomic distance. Since there are several valence electron states per atom and they fill up the energy band $\simeq E_F$, the mean level spacing is estimated as $\delta_S \simeq E_F/N_{at}$. Since the charge e is spread over the size L, Coulomb law delivers the estimate for the charging energy of $e^2/(4\pi\varepsilon_0 L)$. We notice that $e^2/(4\pi\varepsilon_0 a) \simeq E_F$ for typical metals to arrive at

$$\frac{\delta_S}{E_C} \simeq \frac{E_F L}{e^2 N_{at}} = \frac{E_F a}{e^2}\frac{4\pi\varepsilon_0 L}{a N_{at}} \simeq \frac{1}{N_{at}^{2/3}}$$

Thus Coulomb interaction dominates the addition energy provided the island consists of many atoms, $E_C \gg \delta_S$. This discreteness becomes important only for nanostructures consisting of several natural atoms, like a molecule, or comprising an artificial atom, like a quantum dot in a semiconductor heterostructure. To give several numbers, for $L = 100$ nm $E_C \simeq 1$meV, while $\delta_S \simeq 10^{-8}$eV: five orders of magnitude difference. In the rest of the article we neglect the discreteness of electron spectrum.

The electron transport to the island is blocked unless the energy of the order of E_C is supplied either by an external voltage source or by a thermal fluctuation. This explains the term *Coulomb blockade*.

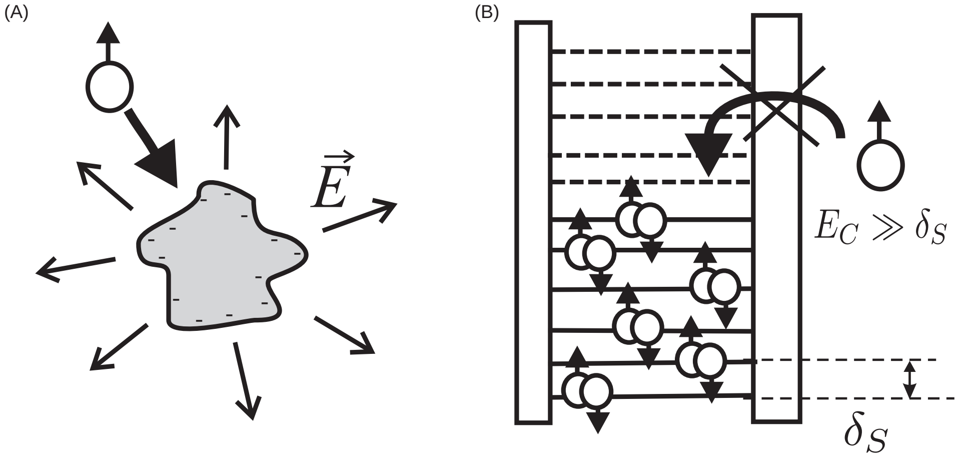

Fig. 1 (a) Excess charge in an isolated metallic island produces electric field outside, this costs charging energy. (b) The energy required to put an electron into the island is not just a typical level spacing δ_S: it includes charging energy $E_C \gg \delta_S$.

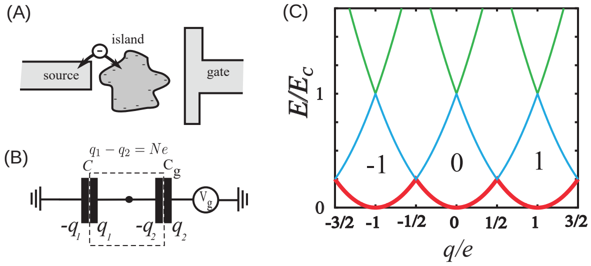

Fig. 2 Single Electron Box. (a) Setup. (b) Equivalent capacitance circuit (dashed box includes capacitance plates that belong to the island) (c) The charging energy of the single electron box vs. $q = -C_gV_g$. Each parabola corresponds to a charge state with N excess charges. Lowest segments of the parabolas give the minimum energy of the setup and the actual charge state.

Single electron box

The concepts outlined above have been put forward by Kulik and Shekhter (1975) to understand the transport in granular materials composed of a plenty of random and uncontrolled metallic islands. They did not get much popularity till the advance of nano-fabrication permitted realization of controllable setups with a single or several islands of submicrometer size. The basic setup of this kind is called a Single Electron Box (SEB) and has been realized in Lafarge et al. (1991). It consists of a single island and two bulk metallic electrodes: Source and gate. One places the island close to the source electrode to enable electron transfer, while the transfer is not possible between the island and the gate electrode (2 a). The advantage of the setup is the possibility to tune the number of extra electrons in the island changing the potential V_g of the gate electrode with respect to the source (so that $V_s = 0$). Physically, V_g shifts the electrostatic potential of the island with respect to the source, this drives electrons to/from the island. In other words, the gate potential induces charge in the island.

To quantify, note that in a stationary state the number of electrons in the island corresponds to the minimum electro-static energy. The equivalent electrostatic circuit of the setup is given in Fig. 2b. It consists of two capacitors: C, which is in between the island and the source, and C_g, which is in between the island and the gate. The charges at the plates of these capacitors are $\pm q_{1,\ 2}$ respectively. The total charge of the island is $eN = q_1 - q_2$. The electrostatic energy consists of the energy accumulated in these capacitors and the work done by the voltage source to transfer the charge q_2 to the gate electrode, $-q_2V_g$. Minimization in q_2 yields

$$E_{el} = E_C\left(N - \frac{q}{e}\right)^2; E_C \equiv \frac{e^2}{2(C + C_g)} \qquad (2)$$

where we skip terms not depending on N and introduce a handy notation: a charge induced in the island by the gate, $q \equiv -C_gV_g$. This *induced charge* is a continuous variable in contrast to the quantized charge eN of the island. If N were continuous, the charge of the island would have been q corresponding to $E_{el} = 0$.

To reveal the effect of charge quantization, we plot in Fig. 2c the energy vs. q for various discrete N. Each N gives a parabola that reaches zero minimum at $q_N = eN$. The ground state energy is defined by lowest segments of the parabolas. The minimum energy thus occurs at different discrete $N(q) = [q/e + 1/2]$, where the square brackets denote the floor of a continuous number. $N(q)$ is thus a steplike function of q. step-like function of q (or V_g). We note e-periodicity: The minimum energy along with all system properties is periodic in q with a period e.

Let us understand the requirements on the connection between the island and the source electrode for charge quantization to occur. It is clear that even a thinnest metallic shortcut connecting the two would kill the effect: in this case, the charge in the island does not have to take integer values since there is no natural separation between electron states in the island and in the electrode and an electron has to be localized neither in the island nor in the electrode. In practice, the sufficient isolation can only be provided if the two are separated by an insulating layer the electrons can tunnel through. If this layer is thick exceeding by far the typical electron wave length, the tunneling is exponentially slow and the resulting currents are too small to measure. The thicknesses of the insulating layers should be of the order of the wave length, that is, for good metals, several interatomic distances. The native oxide layers at aluminum provide most frequent practical solution. However, it is not a thickness of the layer that is relevant for the absence or presence of charge quantization. Rather, it is the total conductance G of the resulting tunnel junction in units of conductance quantum $G_Q \equiv e^2/\pi\hbar$. This follows from a simple qualitative reasoning that combines classical and quantum approaches. The Heisenberg uncertainty relation $\Delta E\Delta t$ ⊠ $\hbar$ implies that the energy difference is well-defined provided the typical time scale at which it is acquired is sufficiently long. For our situation, $\Delta E \simeq E_C$, while the time scale is a typical RC time of capacitor discharge through the junction, $\Delta t \simeq C/G$. Substituting this into the uncertainty relation, we obtain that the well-defined charge quantization requires $G \ll G_Q$. We will assume this to be fulfilled till the Sections "Coulomb oscillations and staircase" and "Quantum effects" of this article where we discuss the effects of quantum fluctuations on Coulomb blockade: weak Coulomb blockade and co-tunneling.

Single electron transistor

The appeal of Coulomb blockade systems is that the electrons under most general circumstances are transferred one by one: Most of the time the islands of a system are in a well-defined charge state, the most probable change of its state involves a single electron

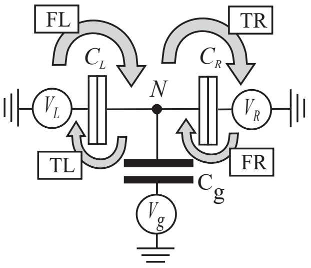

Fig. 3 Single Electron Transistor(SET). The electron transport from *L* to *R* requires change of the charging state *N* and is influenced by the gate voltage V_g. The arrows give four possible single-electron transfers in SET (from/to left/right).

transfer in one of the tunnel junctions. We exemplify the notion of single electron transfers describing in detail the simplest and by far most popular Coulomb blockade device, single electron transistor (SET). It is. The concepts outlined—the energetics of the transfers, master equation approach to their dynamics, the energy dependence of the tunneling rates—are straightforwardly applied to more complex Coulomb blockade systems.

The design of the SET (Averin and Likharev, 1986; Fulton and Dolan, 1987, Fig. 3) is very similar to that of the SEB with an important distinction: an extra transport electrode contacting the island. Like any transistor, SET has three electrodes. Two electrodes, ***R*** and ***L***, source and drain, are the transport ones: an electric current from ***R*** to ***L*** if there is a voltage difference between those. This current is affected by the potential of the gate electrode. The electrostatic energy for a given charge configuration involves all the capacitances C_R, C_L, C_g and voltages V_R, V_L, V_g being present and is given by an expression similar to that of SEB.

$$E_{el} = E_C(N - q/e)^2; E_C = \frac{e^2}{2C_\Sigma}. \tag{3}$$

where the total capacitance of the island $C_\Sigma = C_R + C_L + C_g$ is contributed by all capacitors as well as the induced charge $q = C_R V_R + C_L V_L + C_g V_g$.

Let us list all possible processes of single electron transfer in a SET given it is in the charge state *N*. The number of charges can change in four ways (Fig. 3): Extra electron can jump into the island either from the left (FL) or from the right (FR) electrode, with *N* changing to *N* + 1. Alternatively, an electron can also leave the island either to the left (TL) or to the right (TR), with the change $N \to N - 1$. Each process at a given *N* is characterized by an energy difference between final and initial state. This energy difference involves the difference of electrostatic energy given by Eq. (3)as well as the energy cost associated with addition/extraction of an electron $\pm eV_i$ to/from the corresponding electrode. Let us list the energy differences associated with all four processes,

$$\begin{aligned}
FL &: \Delta E_{FL}(N) = E_{el}(N+1) - E_{el}(N) - eV_L;\\
TL &: \Delta E_{TL}(N) = E_{el}(N-1) - E_{el}(N) + eV_L;\\
FR &: \Delta E_{FR}(N) = E_{el}(N+1) - E_{el}(N) - eV_R;\\
TR &: \Delta E_{TR}(N) = E_{el}(N-1) - E_{el}(N) + eV_R.
\end{aligned}$$

Here, the electrostatic energy change reads

$$E_{el}(N \pm 1) - E_{el}(N) = 2(\pm N + 1/2 \mp q/e)E_C.$$

Let us concentrate at zero temperature limit where the tunneling electron can gain no energy from heat. In this case, an electron transfer can only occur if the corresponding energy difference is negative, $\Delta E < 0$: Indeed, the energy can only be dissipated, and not gained. This simple inequality governs the transport in Coulomb blockade systems and defines the regions of parameters—gate and transport voltages—where the electron transport proceeds in a certain way, that is, the regions of different transport regimes.

The simplest, and the most important transport regime is the Coulomb blockade itself. In this case, in the given charge state *N* all four single-electron processes are forbidden. This requires all four energy differences to be positive,

$$\Delta E_{TL,FL,TR,FR}(N) > 0. \tag{4}$$

Since the charge state does not change and no electron transfers take place, no current is expected in Coulomb blockade regime at zero temperature.

To sketch the parameter regions where Coulomb blockade takes place, we assume symmetric capacitors $C_R = C_L$ and antisymmetric bias voltage $V_L = -V_R = V/2$ (in such setup, the induced charge *q* conveniently does not depend on bias voltage). For $N = 0$, the four conditions (4) become $2E_C(\pm + q/e) \pm eV/2 > 0$. In the *V*–*q* plane, each condition corresponds to a slanted straight line. Four such lines crave a diamond in *V*–*q* plane where all four conditions are fulfilled. For $N = \pm 1, \pm 2, \ldots$ the corresponding diamond is shifted by $\pm e, \pm 2e, \ldots$ along *q*-axis (Fig. 4) representing the *e*-periodicity in induced charge *q*. Such periodic diamond pattern of a suppressed current is typical for various systems and nanostructures exhibiting Coulomb blockade.

Another example transport regime is when the electrons go one by one from the left to the right. Two transfers are allowed: one from the left at *N*, and one to the right at *N* + 1, and thus have negative energy differences,

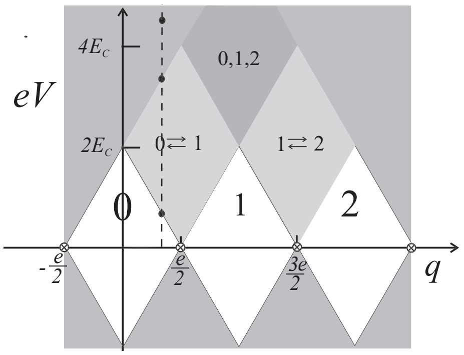

Fig. 4 Coulomb diamonds in SET. The transport is blocked inside white diamonds corresponding to. Light gray: the region where the one-by-one transport cycle takes place.

$$\Delta E_{FL}(N) < 0; \Delta E_{TR}(N+1) < 0.$$

while all other possible processes at N and $N+1$ are blocked and thus have positive energy differences. In particular,

$$\Delta E_{FL}(N+1) > 0.$$

assures that the electrons really go one-by-one: the second electron cannot enter the island while the extra electron is there. This regime is realized in light-gray diamonds in Fig. 4. They have the same shape as the Coulomb diamond and are shifted in such a way that a diamond where N, $N+1$ states participate in the transport is adjacent to the Coulomb diamonds with N and $N+1$. This pattern repeats itself for higher diamonds: a diamond inherits the participating charging states from the lower diamonds adjacent to it. This sets various transport regimes in V–q plane.

The electron transport in Coulomb blockade system can be accurately quantified within the master equation approach. For a SET, one can assume that at any given moment of time it is in a given charge state N. This is a classical state rather than a quantum one, no quantum superpositions are permitted. The transitions between the states proceed by means of electron transfers. A certain transfer is a stochastic event that happens with the probability per unit time given by the corresponding rate *rate* Γ that depends on the charging state. The probability per unit time for this transfer. Since the dynamics are random, the approach has to be probabilistic. The SET is described by probability $\mathrm{p}(N)$ to be in the state N. The probability is obtained from the master equation:

$$\begin{aligned}\frac{d}{dt}p_N(t) = &-(\Gamma_F(N) + \Gamma_T(N))p_N(t) + \\ &\Gamma_F(N-1)p_{N-1}(t) + \Gamma_T(N+1)p_{N+1}(t).\end{aligned} \tag{5}$$

Here, $\Gamma_{F,\,L}$ are the total rates to go from/to the island,

$$\Gamma_F = \Gamma_{FL} + \Gamma_{FR}; \Gamma_T = \Gamma_{TL} + \Gamma_{TR}.$$

Here, the probability change per unit time is given by the time derivative at the l.h.s. and is contributed by two groups of terms: Outgoing and incoming. Outgoing terms are due to transfers from the state N to any other states. For a SET, these states can be either $N-1$ or $N+1$, the corresponding rates adding up. The contribution to the derivative is negative and proportional to the probability to be in the initial state p_N: The system must be in this state for the process to occur. Incoming terms are due to transfers any initial state to the state N. Their contribution to the derivative is positive and proportional to the probabilities to be in the initial states and the corresponding rates: for initial states $N+1$ and $N-1$ the rates are respectively $\Gamma_F(N+1)$ and $\Gamma_T(N-1)$.

For stationary conditions (stationary voltages) a stationary solution of the master equation, $p_N^{(0)}$ is readily obtained from the master equation with zero l.h.s. and the condition that the probability to be in any state must total to 1, $\sum_N p_N = 1$.

The currents are also obtained from the probability balance. For instance, the current through the left junction is contributed by "from the left" processes with positive sign and by "to the left" processes with negative sign, so that

$$I_L = e\sum_N [\Gamma_{FL}(N) - \Gamma_{TL}(N)]p_N. \tag{6}$$

Similarly, for the current through the right junction we obtain

$$I_R = e\sum_N [\Gamma_{TR}(N) - \Gamma_{FR}(N)]p_N.$$

By virtue of charge conservation, the stationary currents $I_L = I_R$. This is automatically fulfilled if p_N is the stationary solution of the master equation, $p_N = p_N^{(0)}$.

To use the master equation for the quantitative description of single-electron transport, we must know the rates at given setting of the gate and bias voltages. The rates could be computed from the tunneling Hamiltonian, but in fact could be derived from the following elementary reasoning. Let us consider a tunnel junction between two leads and forget about Coulomb blockade for a moment. If a voltage difference at $k_BT = 0$ is applied to the leads, the electrons in the energy strip of the width eV can go from the left to the right. The number of electron transfers per unit time is given by the transfer rate Γ so it is related to the current simply by $\Gamma = I/e$. From the other hand, $I = GV$ by definition of the junction conductance G. Therefore $\Gamma = eVG/e^2$, provided eV is positive. Note that $eV = -\Delta E$, the energy difference associated with this transfer that determines the energy strip available for tunneling. If Coulomb blockade is present, the tunneling electron must perform some extra work to charge the capacitors of the SET, so $\Delta E \neq -eV$ yet still determines the width of the relevant energy strip. So that the rate of a single electron transfer in a junction of conductance G accompanied by the energy change ΔE is generally given by

$$\Gamma = \frac{G}{e^2}(-\Delta E)\Theta(-\Delta E) \tag{7}$$

at $k_BT = 0$. At finite temperature this is modified to

$$\Gamma = \frac{G}{e^2}\frac{\Delta E}{\exp\left(\frac{\Delta E}{k_BT}\right) - 1}. \tag{8}$$

That is, the thermal fluctuations provide a finite rate even for $\Delta E > 0$. This rate is exponentially small provided $\Delta E \gg k_BT$.

The concepts discussed in this Section—energy differences in capacitive networks, the transfer rates determined by these differences, the master equation incorporating the rates—form a closed scheme that can be readily applied to quantify the transport in any arbitrary complex Coulomb blockade system.

Coulomb oscillations and staircase

Here, we discuss the two common and prominent transport signatures that manifest Coulomb blockade in SET. The first one called *Coulomb oscillations* is observed in zerovoltage conductance of the device. At zero bias voltage and $k_BT \ll E_C$ the SET is in Coulomb blockade regime except the points $q/e = 1/2 + N$ where diamonds corresponding to charging states N and $N + 1$ touch each other at $V = 0$ line (crossed circles in Fig. 4). In these points, the energies of two charging states are the same and the minimum addition energy $\Delta_{\min} = 2E_C(1/2 - |q|/e)$ vanishes enabling the electron transport at $k_BT \simeq \Delta_{\min}$, and the conductance peaks. The peak shape near the degeneracy point is given by $G(q) = G_{\max}(\Delta_{\min}/k_BT)/\sinh(\Delta_{\min}/k_BT)$, where $G_{\max} = (1/2)G_LG_R/(G_L + G_R)$. One thus observes a periodic (oscillating) pattern of equidistant peaks, with a period e along q axis. With increasing temperature, the peaks first become wider and then merge at $k_BT \approx 0.15E_C$ (Fig. 5). However, the periodic modulation—Coulomb oscillations—remains visible up to $k_BT \simeq 0.7E_C$. At $k_BT \gg E_C$ charging energy becomes irrelevant, and Ohm's law is restored with the conductance $G_\infty = G_LG_R/(G_L + G_R)$ Note that $G_\infty = 2G_{\max}$. This is because at the peak the electrons tunnel one-byone, an extra electron blocks further transfers, while at high temperatures no blocking takes place. This implies there is a temperature range where typical conductance changes from $G_{\max}$ Indeed, in the temperature range $1.5 < k_BT/E_C < 4$ the conductance looses sensitivity to the gate

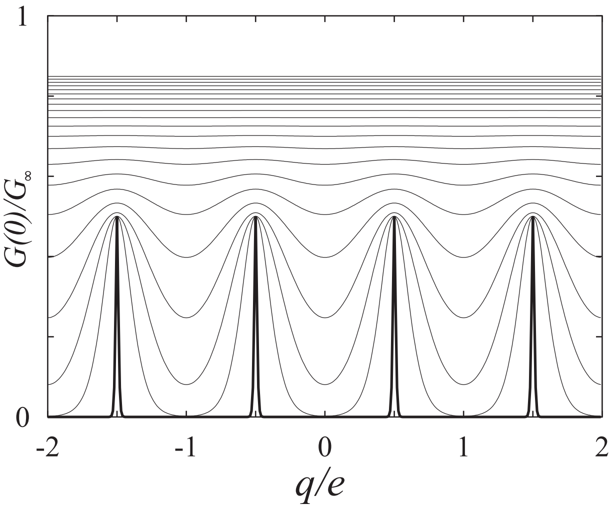

Fig. 5 Coulomb osicllations. A periodic pattern of zerovoltage conductance of a symmetric SET vs. the charge induced at different temperatures. $k_BT/E_C = 0.01$ for the thick curve and ranges from 0.1 to 2.0 with step 0.1 for subsequent curves.

voltages remaining sensitive to temperature (Fig. 5). Thus, the SET, and the Coulomb blockade systems in general, can be used as a precise thermometer (Meschke et al., 2016) in this temperature range.

Another signature of Coulomb blockade is observed upon increasing the bias voltage at fixed gate voltage. As seen in Fig. 4, the number of charge states available for transport at $k_BT \ll$ eV increases with increasing the voltage. Any time a new state becomes available, the differential conductance $G(V)$ exhibits a jump—this pattern is called *Coulomb staircase*. There are two equidistant series of the voltage values at which a new state becomes available, special voltages

$$eV_{\text{special}} = 4E_C\left(M + \frac{1}{2} \pm \frac{q}{e}\right), \tag{9}$$

M being integer and ± corresponding to a new transfer through the right (left) junction. These values are given by black circles in Fig. 4 at a dashed line corresponding to $q = 0.3$.

There is a cusp in the current—jump in the differential conductance—at any special voltage for any SET. However, if the conductances of two tunnel junctions are comparable, the cusps are hardly visible in a I–V curve while sufficiently pronounced in the differential conductance(Fig. 6, upper pane).

The Coulomb staircase comes into full beauty if the junction conductances differ by more than an order of magnitude, as illustrated in Fig. 6, lower pane. The cusps are clearly visible in I–V curve and develop into characteristic smooth steps separated by $4E_C/e$ in voltage. Only one cusp series is visible, corresponding to new transfers via the most conducting junction. The current jumps are explained by the fact that the charging state is set by the most conducting junction while the current is determined by the transfers through the least conducting junction. The change of the charging state thus gives a jump in ΔE and the step in the current. The step is rounded at the voltage scale $e\Delta V/E_C \simeq G_{\text{small}}/G_{\text{big}}\cdot$.

In any case, at bigger voltages, above E_C/e, the current tends to Ohm's law $I = G_\infty V$ since the big voltage drops involved mask any manifestation of single-charging phenomena. It is interesting to note that the best fit is provided by an off-set Ohm's law $I = G_\infty(V - 2E_C/esgn(V))$. This is used for estimations of the charging energy for concrete devices.

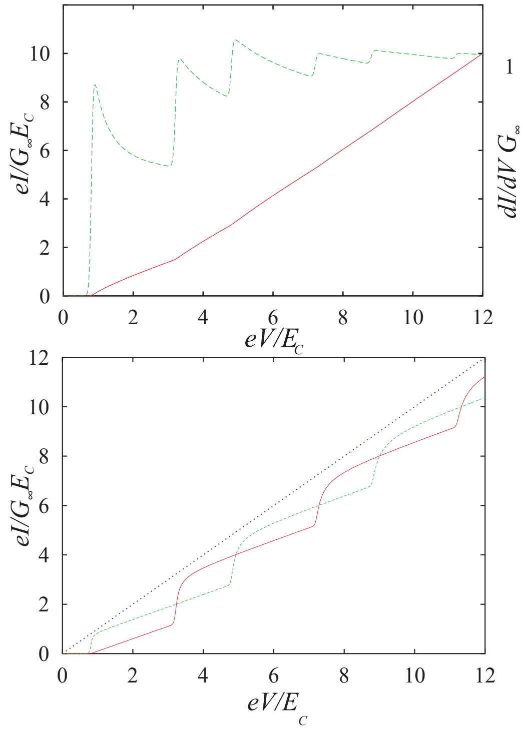

Fig. 6 Coulomb staircase. Upper pane: $G_L = G_R$, $q = 0.3e$. Solid: I–V curve. Dashed: the corresponding differential conductance gives a jump at special values of the bias voltage. The jumps are slightly rounded by finite temperature ($k_BT = 0.01E_C$). Lower pane: Coulomb staircases with $G_L = 100G_R$ and $G_L = 0.01G_R(q = 0.3e)$. Each cusp in the current is followed by a the step-like increase. Only one series of special voltages is visible for each curve. Dotted line: Ohm's law.

Quantum effects

As outlined, the concept of Coulomb blockade is classical in nature involving single-electron transitions between well-defined charge states. This concept is valid in the limit of low tunneling conductances $G \ll G_Q$. The concept does not fit the reality precisely at any finite G: the quantum effects mix up the charge states so that the ground state of a Coulomb blockade system does not have a definite charge, and provide the collective electron transfers in Coulomb blockade regime, so-called co-tunneling events.

Let us consider quantum effects in a SEB that is in the ground state with $N = 0$. An electron transfer between the island and would bring the system to a state with $N = \pm 1$ and an electron-hole pair whose components are in the lead and in the island, respectively. This state has a higher energy $E^{(\pm)} \pm + \xi \simeq E_C$, $E^{(\pm)}$ being the chargin addition/extraction energy, ξ being the energy of the electron-hole pair. Therefore, the transfer cannot actually occur. Nevertheless, by virtue of Heisenberg uncertainly principle, the SEB can enter this state for a short time $t_H \simeq \hbar/E_C$ with the rate Γ. This implies that the true ground state of the single electron box is not an eigenstate of charge anymore: there is a finite probability to catch the SEB in an excited charging state $N = \pm 1$, $p_{\pm 1} \simeq \Gamma t_H \simeq G/G_Q$. Second-order perturbation calculation yields

$$p_{\pm 1} = \frac{\hbar}{2\pi}\int \frac{\Gamma(-\xi)d\xi}{\left(E^{(\pm)} + \xi\right)^2} = \frac{G}{2\pi^2 G_Q}\int_0^\infty \frac{\xi d\xi}{\left(E^{(\pm)} + \xi\right)^2}, \tag{10}$$

the integration is over the energies of all possible electronhole pairs, $\Gamma(E)$ is given by Eq. (7). We give the expression for average charge representing a smoothing quantum correction to the classical step-like N–q relation,

$$\delta\langle N\rangle = p_1 - p_{-1} = \frac{G}{2\pi^2 G_Q}\ln\left(\frac{1/2 + q/e}{1/2 - q/e}\right) \tag{11}$$

(see Fig. 7) A special feature is that the integral diverges at low energies provided $E^{\pm} \to 0$, this corresponds to $q \to \pm e/2$. Indeed, the correction to average charge formally diverges at $q \to \pm e/2$, at the degeneracy of two charging states. This indicates that the perturbation theory is no good at tiny energy scale $E^{\pm} \simeq E_C \exp\{-G/(2\pi^2 G_Q)\}$. This energy range has been inspected in Matveev (1991) where the similarity with a Kondo-like complex many-body problem has been revealed. The Coulomb blockade Kondo has been experimentally investigated in Iftikhar et al. (2015).

To fully understand the Coulomb blockade phenomenon, it is constructive to access the opposite limit of large conductances $G \gg G_Q$—the limit of weak Coulomb blockade. Here, it becomes important that a connector between the island and the lead does not have to be a tunnel junction as in the opposite limit. Rather, the connector is characterized by a set of transmission coefficients T_p in its spinsplit transport channels. The influence of the connector on Coulomb blockade in the island depends on the details of the transmission coefficients rather than on the total conductance $G = \frac{G_Q}{2}\sum_p T_p$ only. A simple signature of Coulomb blockade in the ground state of a SEB is the e-periodic q dependent part of the ground state energy. As we have seen, in the limit of vanishing conductance, this part is $\simeq E_C$. The analysis (Nazarov, 1999) shows that a typical spread $\tilde{E}_C$ of the q -dependent part is suppressed by transmission and is estimated as

$$\frac{\tilde{E}_C}{E_C} = \prod_p \sqrt{1 - T_p} \tag{12}$$

This shows that Coulomb blockade, although weakened, survives at any connector, unless one of the transmission is ideal, $T_p = 1$. At a given transmission distribution, $\tilde{E}_C$ is exponentially suppressed. For a tunnel junction where all $T_p \ll 1, \tilde{E}_C/E_C \simeq \exp(-G/G_Q)$, while for a diffusive connector of the same conductance $\tilde{E}_C/E_C \simeq \exp(-\pi^2 G/4G_Q)$.

The above expression gives only a leading order estimate of the q -dependent part of the ground state energy. To get the details, and in particular the form of the q -dependence, one needs the full solution of a complex many-body problem. That had been sought for almost 20 years and has been found in Lukyanov (2007). According to Lukyanov (2007), the q dependence is cos-like in the leading order in G,

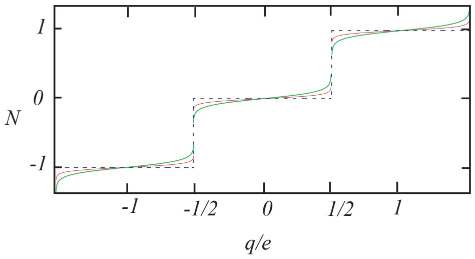

Fig. 7 Quantum fluctuations—virtual transitions to other charge states—smoothen the step-like features in N–q relation. Dashed line is $G = 0$ limits, two solid curves correspond to $G = 0.5$ and $0.25G_Q$.

$$E(q) = 4E^*(1 - \cos(q/e)); \quad E^* = \tilde{E}_C(G/\pi G_Q)^2. \tag{13}$$

The weak Coulomb blockade is a manifestation of a many-body virtual tunneling process called Korshunov instanton (Korshunov, 1987). This process is a phase slip whereby the total wave function of the island is shifted by 2π shift. It is worth noting that the number N of the particles is a canonically conjugated quantum variable to this phase. This becomes especially relevant in superconducting context where it enables quantum applications of superconducting Coulomb blockade devices. However, it is also manifested for normal metal islands, see Jezouin et al. (2016) for experimental verification.

The Korshunov instanton is a close relative of a real process producing so-called leviton excitations (Keeling et al., 2006) The levitons are generated when a carefully engineered voltage pulse, corresponding to a 2π phase shift, is applied to a quantum connector. The levitons have been confirmed experimentally in Dubois et al. (2013). Whereas the leviton is an excitation of electron systems, the Korshunov instanton is a virtual process governing the charge quantization.

Co-tunneling

An old joke likens classical physics to a totalitarian regime where every detail is unambiguously determined by the regulations—physical laws. Quantum physics in this joke presents a more liberal society where everybody is free to get around the regulations—unless those are not fundamental laws. The tunnel processes involving many electrons—co-tunneling processes (Averin and Nazarov, 1990)—under Coulomb blockade conditions provide a rather explicit illustration of this joke.

Let us concentrate on a SET in Coulomb blockade regime at vanishing temperature with a small bias voltage. On a classical level of single electron transfers, the current cannot flow since the transfers are forbidden by energy conservation. On a quantum level, one envisages a combined process where the tunneling of an electron from the left is immediately followed by the tunneling of another electron to the right. In the resulting state, the island charge does not change. However, one electron charge has been transferred from the left to the right producing a current: two electrons have successfully co-operated to get around an energy restriction imposed on single electron transfers. Let us start with a cartoon which will give us an order-of value estimations of such co-tunneling rates. Electrons want to get from the left to the right (Fig. 8a). They would do it with a typical rate Γ_{FL}. They can not tunnel by virtue of energy conservation: They have to pay charging energy E_C which they do not possess. The cartoon is that the energy conservation is not imposed instantly: the electron may stay in the island during Heisenberg uncertainty time $t_H \simeq \hbar E_C$ even if the energy conservation forbids a permanent stay. This gives a small but finite chance for the co-tunneling: jump the right junction. This intermediate state is virtual jump the right junction. This intermediate state is virtual rate to the right in this virtual state is thus Γ_{TR}. The chance to realize co-tunneling during the short stay is therefore $\Gamma_{TR} t_H \ll 1$. Multiplying the chances, we get the following estimation,

$$\Gamma_{cot} \simeq \Gamma_{FL}\Gamma_{TR}\frac{\hbar}{E_C}$$

Since a typical estimation of single-electron rate is $\Gamma_{se} \simeq G/C \simeq GE_C/e^2$, we can present this as

$$\Gamma_{cot} \simeq \Gamma_{se}\frac{G}{G_Q}. \tag{14}$$

so that the co-tunneling is essentially less probable than single-electron tunneling provided $G \ll G_Q$, the same condition that assures the presence of Coulomb blockade. At $G \simeq G_Q$ the co-tunneling and similar multi-particle processes become as important as single-electron ones, resulting in corruption and vanishing of Coulomb blockade.

We can make a better cartoon if we take into account the details of the virtual and the final state. Each transfer produces an electron-hole pair as shown in Fig. 8b with positive energies $\xi_L = \varepsilon_1 + \varepsilon_2$, $\xi_R = \varepsilon_3 + \varepsilon_4$. After two electron transfers, the SET is in the final state with four excitations: a hole in the left electrode, an electron and a hole in the island, and an electron in the right electrode. We count the energies of these excitations from the corresponding Fermi levels, so that all $\varepsilon_i > 0$. The energy conservation dictates

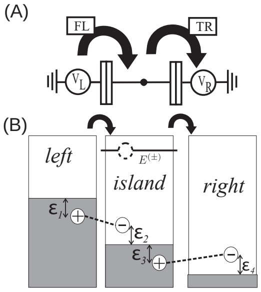

Fig. 8 Co-tunneling in SET. (a) Co-tunneling in SET: simultaneous transfer of two electrons in two junctions is not forbidden by energy conservation. (b) Energy diagram for inelastic co-tunneling: two electron-hole pairs left in the final state. Gray: filled electron states.

that $\xi_L + \xi_R = \sum \varepsilon_i = eV$, so each $\varepsilon_i < eV$. Since the number of electron states in an energy strip is proportional to the width of the strip, the number of states available is reduced by a factor $\simeq (eV/E_C)^2$. The same factor reduces the rate in comparison with the estimation (14)

$$\Gamma_{cot} \simeq \frac{G_L}{G_Q}\frac{G_R}{G_Q}\left(\frac{eV}{E_C}\right)^2 eV. \tag{15}$$

This consideration is relevant at vanishing temperature $k_BT \ll eV$. In the opposite case $k_BT \gg eV$, the excitations can appear in the energy strip of the width of k_BT, this gives the rate of thermally activated co-tunneling,

$$\Gamma_{cot} \simeq \frac{G_L}{G_Q}\frac{G_R}{G_Q}\left(\frac{k_BT}{E_C}\right)^2 k_BT. \tag{16}$$

The thermally-activated processes can proceed in both directions, from the left to the right as well as from the right to the left. The rates in both directions differ only by a small factor $\simeq eV/k_BT$. Therefore the current can be estimated as $I_{cot} \simeq V(G/G_Q)^2(k_BT/E_C)^2$. Two-electron co-tunneling is an inelastic process, and leads to non-linear and/or temperature-dependent I–V curves.

Let us quantify the co-tunneling rates in a SET setup. General rules of quantum mechanics imply that the transition rate between initial state i and final state f is given by the Fermi Golden rule the square of transition matrix element M_{if}, or amplitude, between the states. In our case, the amplitude involves the tunneling matrix elements of both transfers and the inverse energies of the virtual states,

$$M_{if} = \sum_{v}\frac{H^{(int)}_{iv}H^{(int)}_{vf}}{E_i - E_v}. \tag{17}$$

Note that each final state can be reached via two possible virtual states that differ in the order of two single-electron transfers. If the tunneling through the left junction comes first, the charge of the island changes from N to $N+1$. The energy of the resulting virtual state v_+ with respect to initial one is $E^{(+)} + \xi_L$. Alternatively, the transfer through the right junction happens first changing the charge of the island to $N-1$ so the energy of alternative state v_- reads $E^{(-)} + \xi_L$ The resulting amplitude is thus the sum of these two possibilities. Squaring the amplitudes and implementing Eq. (7) for the single-electron rate yields

$$\Gamma_{cot} = \frac{\hbar}{2\pi}\int d\xi_L d\xi_R \Gamma_L(-\xi_L)\Gamma_R(-\xi_R) \times \left(\frac{1}{E^{(+)}+\xi_L} + \frac{1}{E^{(-)}+\xi_R}\right)^2 \delta(\xi_R + \xi_L - eV). \tag{18}$$

This gives the co-tunneling from the left to the right, the cotunneling in opposite direction is obtained by the replacement $eV \to -eV$.

Let us elaborate on two simple limits. For $eV \gg k_BT$, the co-tunneling proceeds only in the energetically favorable direction. The integration domain is restricted by $\xi_{L,R} > 0$ and the expression is valid in the whole Coulomb diamond restricted by $E^{(\pm)} > 0$. The single-electron rates in this situation read $\Gamma_{L,R}(-\xi) = G_{L,R}/e^2\xi$, and the integration can be performed analytically to give

$$I_{cot}(V) = \frac{\hbar G_L G_R V}{2\pi e^2}\left[\left(1 + \frac{2}{eV}\frac{E^{(+)}E^{(-)}}{E^{(+)}+E^{(-)}+eV}\right) \times \ln\left(1 + eV/E^{(+)}\right)\left(1 + eV/E^{(-)}\right) - 2\right]. \tag{19}$$

Another significant limit is that of relatively small voltage $eV \simeq k_BT \ll E^{(\pm)}$. To integrate, we disregard the dependence of energy denominators on $\xi_{L,R}$, so the rate reduces to

$$\Gamma^{LR}_{cot} = \frac{\hbar G_L G_R}{12\pi e^4}\left(\frac{1}{E^{(+)}} + \frac{1}{E^{(-)}}\right)^2 \frac{(eV)\left((eV)^2 + (2\pi k_BT)^2\right)}{1 - \exp(-eV/k_BT)},$$

and $\Gamma^{RL}_{cot}(V) = \Gamma^{RL}_{cot}(-V)$. The co-tunneling current is the difference of these two rates,

$$\begin{aligned} I(V) = e\left(\Gamma^{LR} - \Gamma^{RL}\right) = {} & \frac{\hbar G_L G_R}{12\pi e^2}\left(\frac{1}{E^{(+)}} + \frac{1}{E^{(-)}}\right)^2 \\ & \times V\left((eV)^2 + (2\pi k_BT)^2\right), \end{aligned} \tag{20}$$

in full accordance with the above qualitative estimations. The typical V^3 dependence of co-tunneling current has been experimentally verified rather early (Geerligs et al., 1990b). However, the observed current was roughly a factor of two larger than one predicted by Eq. (20). This discrepancy was explained in Laakso et al. (2010) by overheating of the SET island to effective temperatures $k_BT \simeq eV$.

There are more interesting and complex co-tunneling processes. To protect the Coulomb blockade in devices against undesired multi-electron processes, one can replace a SET with a 1 d array of N junctions and $N-1$ islands (Fig. 9a) To transfer a charge across an array of N junctions, N electrons should co-operate jumping simultaneously. Such process creates $2N$ excitations in the final state. Multiplying rate suppression factors for each junction and for each excitation brings us to the following estimate (with the energy available for co-tunneling being $\Delta E \simeq \max(eV, k_BT)$)

$$\Gamma_{cot} \simeq \left(\frac{G}{G_Q}\right)^N E_C/\hbar, \Delta E \simeq E_C; \tag{21}$$

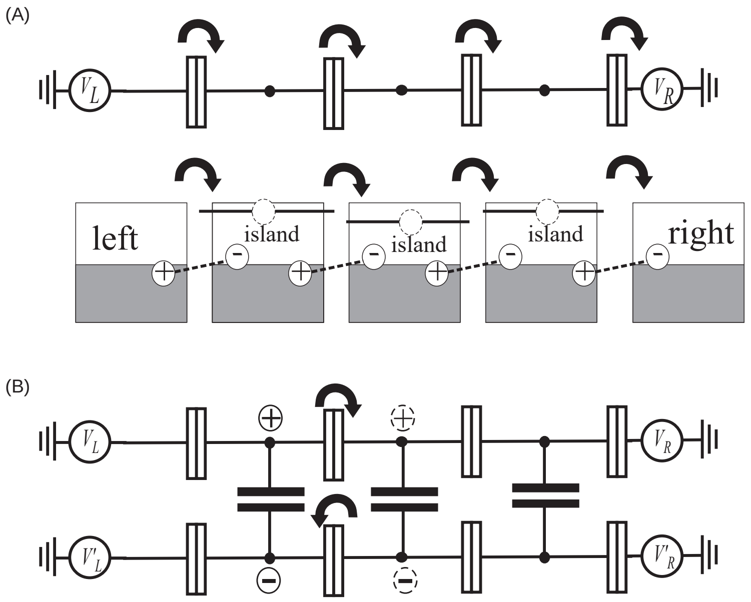

Fig. 9 Complex co-tunneling processes. (a) A charge transfer in a four-junction array under Coulomb blockade conditions. Four electron-hole pairs are left in the final state. (b) Cotunneling enables transport of artificial excitons—electronhole pairs in capacitively coupled arrays.

$$\Gamma_{cot} \simeq \left(\frac{G}{G_Q}\right)^N \left(\frac{\Delta E}{E_C}\right)^{2N-2} \frac{\Delta E}{\hbar}, \Delta E \ll E_C \tag{22}$$

As far as $G \ll G_Q$, the rate of N -electron co-tunneling is much smaller than that of two-electron one.

Co-tunneling not only spoils Coulomb blockade: it may provide novel device functionalities. To demonstrate this, let us place two 1D Coulomb arrays close to each other making a substantial capacitive coupling between neighboring islands of opposite arrays (Fig. 9b). There is no electric connection between the arrays, and each of them is connected to its own transport electrodes. With proper gate voltages, one induces charges of opposite polarities in these opposite arrays. The Coulomb attraction between these charges of opposite sign forms artificial excitons: bound states of electron and hole (Averin et al., 1991). To set these artificial excitons into motion, small bias voltages are applied to the arrays. The exciton moves in this double array as a whole by means of a co-tunneling process made of two simultaneous electron transfers in opposite directions and opposite arrays. In a wide window of bias voltages, the currents in both electric circuits are therefore same in amplitude and opposite in direction. This is a current copier experimentally realized in Matters et al. (1997).

Until now we assumed that at least two electrons participate in a co-tunneling process. However, there is a chance that the same electron that enters the island from the left tunnels out to the right thereby completing the co-tunneling process without creating an electron-hole pair in the island. The chance for this seems negligible: it must be smaller than the inelastic cotunneling rate by a factor of number of states in the energy window of the order of E_C. The electron states in the island are discrete with average spacing $\delta_S \ll E_C$. Thus, the same-electron rate is estimated as $\Gamma_{el-cot} \simeq \Gamma_{cot}(\delta_S/E_C)$. However, the process involving the same electron is elastic: no excitations are there in the island in the final state, and the electron transferred to the right has the same energy as the incoming electron. This lifts the extra factor $(eV/E_C)^2$ which suppresses the inelastic co-tunneling at small bias,

$$\Gamma_{el-cot} \simeq G_{el}V/e; G_{el} \simeq \frac{G_L G_R}{G_Q}\frac{\delta_S}{E_C}. \tag{23}$$

Comparing this with Eq. (15), we find that the elastic cotunneling dominates at sufficiently low energies $\Delta E \leq \sqrt{\delta_S E_C}$. This has been confirmed experimentally (Hanna et al., 1992). The elastic cotunneling is important for quantum dots where $\delta_S \simeq E_C$.

Applications

Before discussing the applications of Coulomb blockade, let us mention the major obstacle hindering those: background charges. From the above discussion, one can get an impression that the charge state is unambiguously defined by gate voltages. However, the gate electrodes is not the only source of the induced charge. In a realistic nanostructure, there are always some stray charges located in insulating parts of the structure: either in tunnel barriers of the junctions or in the substrate. Usually, these charges are ionized impurities inevitably present in any material. All together, these random sources produce a background charge q_i that adds to the charge induced by the gate electrode in the island i. The absolute amount of the excess charges does not matter, since the charging energy is periodic in N, q/e. Therefore one can regard the q_i to be uniformly distributed in the interval $(-|e|/2, |e|/2)$. In principle, the background charge can be always compensated by the proper shift of the gate voltage, and this goes almost automatically for a single-island SET. However, N-island system requires a complex and hardly practical tuning on N independent gate voltages. Another aspect is that the configuration of the background charges changes spontaneously at some large time scale related to the motion of these charged impurities. This produces a low-frequency charge noise affecting the work of Coulomb blockade devices.

The most successful and promising application of Coulomb blockade concerns the artificial quantum systems for quantum information processing made in superconducting nanostructures and based on combination of Josephson effect and Coulomb blockade (Wendin, 2017) This topic is bulky and certainly beyond the scope of the present article. Let us however spend several lines to explain how this works (Nazarov and Blanter, 2009) taking a SEB as an example. Superconductivity brings about two distinct points: i. Lowlying energy excitations—electron-hole pairs—are absent in gapped superconductors. Owing to this, there is a unique quantum state $|N\rangle$ corresponding to a charging state with N extra electrons in the island; ii. Tunneling between the island and the lead provides a quantum-coherent transfer of a Cooper pair—two electrons—not accompanied by any dissipation and/or change of a quantum state. This provides mixing of the quantum states with different N and their superpositions. The quantum Hamiltonian describing SEB consist of two parts:

$$\begin{aligned} \widehat{H} = \sum_N E_C (N - q/e)^2 |N\rangle\langle N| + \\ \frac{E_J}{2} (|N\rangle\langle N+2| + |N\rangle\langle N-2|). \end{aligned} \tag{24}$$

Here, the first part is the Coulomb energy given by Eq. (2). Second part is Cooper-pair tunneling between the lead and the island characterized by the Josephson energy E_J. A great variety of competing Josephson qubit designs have been proposed and realized (Nazarov and Blanter, 2009). At the moment, the transmon (Koch et al., 2007) design seems to win, insensitivity to the charge noise mentioned being one of its major advantages.

Since early days of Coulomb blockade, a substantial research effort has been devoted to realization of robust metrological standard of electric current. Such device is fed by a voltage signal with frequency f and provides the current $I = \pm ef$, that is, ± 1 electrons per cycle. Early designs included single-electron turnstile, where electrons have been pulled by a bias voltage (Geerligs et al., 1990a), and single-electron pump (Pothier et al., 1992) that does not require any bias voltage. Sufficiently high currents require high frequencies and thus fast tunneling rates and relatively high conductances where co-tunneling effects result in errors in electron manipulation and decreased accuracy of the standard. Modern designs utilize superconductivity and quantum dots, and the accuracy has been improved through years to achieve metrologically relevant values (Pekola et al., 2013; Wenz et al., 2019).

We have already mentioned the use of Coulomb blockade systems for precise thermometry (Meschke et al., 2016). A very natural application of SET is its use as a sensitive electrometer: the change of induced change just by a fraction of e may change the current by order of value. A fast and efficient electrometer design has been proposed in Schoelkopf et al. (1998). The small size of SET island permits its realization on a tip of a scanning probe (Yoo et al., 1997). With these devices, one can easily image single charges and peculiarities of electric field distribution in various 2D heterostructures.

Conclusion

We reviewed here Coulomb blockade: a universal phenomenon in the field of quantum transport, that is widely manifested in man-made nanostructures at low temperatures. The phenomenon permits a closed and easy description outlined here. We explain the concepts of charge quantization and charging energy, best illustrated by Single Electron Box. The transport in Coulomb blockade regime is governed by master equation involving the tunneling rates, Single Electron Transistor being the generic example. Single Electron pump and turnstile are prototypes for applications of the phenomenon. We extend the description to incorporate the essential quantum effects that provide electron co-tunneling and weak Coulomb blockade.

References

Averin DV and Likharev KK (1986) Coulomb blockade of single-electron tunneling, and coherent oscillations in small tunnel junctions. *Journal of Low Temperature Physics* 62: 345–373. https://doi.org/10.1007/BF00683469.

Averin DV and Nazarov YV (1990) Virtual electron diffusion during quantum tunneling of the electric charge. *Physical Review Letters* 65: 2446–2449. https://doi.org/10.1103/PhysRevLett.65.2446.

Averin DV, Korotkov AN, and Nazarov YV (1991) Transport of electronhole pairs in arrays of small tunnel junctions. *Physical Review Letters* 66: 2818–2821. https://doi.org/10.1103/PhysRevLett.66.2818.

Dubois J, Jullien T, Portier F, Roche P, Cavanna A, Jin Y, Wegscheider W, Roulleau P, and Glattli DC (2013) Minimal-excitation states for electron quantum optics using levitons. *Nature* 502: 659–663. https://doi.org/10.1038/nature12713.

Fulton TA and Dolan GJ (1987) Observation of single-electron charging effects in small tunnel junctions. *Physical Review Letters* 59: 109–112. https://doi.org/10.1103/PhysRevLett.59.109.

Geerligs LJ, Anderegg VF, Holweg PAM, Mooij JE, Pothier H, Esteve D, Urbina C, and Devoret MH (1990a) Frequency-locked turnstile device for single electrons. *Physical Review Letters* 64: 2691–2694. https://doi.org/10.1103/PhysRevLett.64.2691.

Geerligs LJ, Averin DV, and Mooij JE (1990b) Observation of macroscopic quantum tunneling through the coulomb energy barrier. *Physical Review Letters* 65: 3037–3040. https://doi.org/10.1103/PhysRevLett.65.3037.

Hanna AE, Tuominen MT, and Tinkham M (1992) Observation of elastic macroscopic quantum tunneling of the charge variable. *Physical Review Letters* 68: 3228–3231. https://doi.org/10.1103/PhysRevLett.68.3228.

Iftikhar Z, Jezouin S, Anthore A, Gennser U, Parmentier FD, Cavanna A, and Pierre F (2015) Two-channel kondo effect and renormalization flow with macroscopic quantum charge states. *Nature* 526: 233–236. https://doi.org/10.1038/nature15384.

Jezouin S, Iftikhar Z, Anthore A, Parmentier FD, Gennser U, Cavanna A, Ouerghi A, Levkivskyi IP, Idrisov E, Sukhorukov EV, Glazman LI, and Pierre F (2016) Controlling charge quantization with quantum fluctuations. *Nature* 536: 58–62. https://doi.org/10.1038/nature19072.

Keeling J, Klich I, and Levitov LS (2006) Minimal excitation states of electrons in one-dimensional wires. *Physical Review Letters* 97: 116403. https://doi.org/10.1103/PhysRevLett.97.116403.

Koch J, Yu TM, Gambetta J, Houck AA, Schuster DI, Majer J, Blais A, Devoret MH, Girvin SM, and Schoelkopf RJ (2007) Charge-insensitive qubit design derived from the cooper pair box. *Physical Review A* 76: 042319. https://doi.org/10.1103/PhysRevA.76.042319.

Korshunov S (1987) Coherent and incoherent tunneling in a josephson junction with a “periodic” dissipation. *JETP Letters* 45: 342–345. URL http://jetpletters.ru/ps/1241/article_18771.shtm1.

Kulik I and Shekhter R (1975) Kinetic phenomena and charge discreteness effects in granulated media. *Journal of Experimental and Theoretical Physics* 41: 308–318. http://wwwhttp://www.jetp.ras.ru/cgi-bin/dn/e_041_02_0308.pdf.

Laakso MA, Heikkilä TT, and Nazarov YV (2010) Fully overheated singleelectron transistor. *Physical Reviews Letters* 104: 196805. https://doi.org/10.1103/PhysRevLett.104.196805.

Lafarge P, Pothier H, Williams ER, Esteve D, Urbina C, and Devoret MH (1991) Direct observation of macroscopic charge quantization. *Zeitschrift fur Physik B: Condensed Matter* 85: 327–332. https://doi.org/10.1007/BF01307627.

Lukyanov SL (2007) Notes on parafermionic qfts with boundary interaction. *Nuclear Physics B* 784: 151–201. https://doi.org/10.1016/j.nuclphysb.2007.04.034.

Matters M, Versluys JJ, and Mooij JE (1997) Electron-hole transport in capacitively coupled 1 d arrays of small tunnel junctions. *Physical Review Letters* 78: 2469–2472. https://doi.org/10.1103/PhysRevLett.78.2469.

Matveev KA (1991) Quantum fluctuations of the charge of a metal particle under the coulomb blockade conditions. *Zhurnal Eksperimental'noi i Teoreticheskoi Fiziki* 99: 1598–1606. URL http://wwwhttp://www.jetp.ras.ru/cgi-bin/dn/e_072_05_0892.pdf.

Meschke M, Kemppinen A, and Pekola JP (2016) Accurate coulomb blockade thermometry up to 60 kelvin. *Philosophical Transactions of the Royal Society A: Mathematical, Physical and Engineering Sciences* 374: 20150052. https://doi.org/10.1098/rsta.2015.0052.

Millikan RA (1913) On the elementary electrical charge and the avogadro constant. *Physics Review* 2: 109–143. https://doi.org/10.1103/PhysRev.2.109.

Nazarov YV (1999) Coulomb blockade without tunnel junctions. *Physical Review Letters* 82: 1245–1248. https://doi.org/10.1103/PhysRevLett.82.1245.

Nazarov YV and Blanter YM (2009) *Quantum Transport: Introduction to Nanoscience.* Cambridge University Press. https://doi.org/10.1017/CBO9780511626906.

Pekola JP, Saira OP, Maisi VF, Kemppinen A, Möttönen M, Pashkin YA, and Averin DV (2013) Single-electron current sources: Toward a refined definition of the ampere. *Reviews of Modern Physics* 85: 1421–1472. https://doi.org/10.1103/RevModPhys.85.1421.

Pothier H, Lafarge P, Urbina C, Esteve D, and Devoret MH (1992) Singleelectron pump based on charging effects. *Europhysics Letters (EPL)* 17: 249–254. https://doi.org/10.1209/0295-5075/17/3/011.

Schoelkopf RJ, Wahlgren P, Kozhevnikov AA, Delsing P, and Prober DE (1998) The radio-frequency single-electron transistor (rf-set): A fast and ultrasensitive electrometer. *Science* 280: 1238–1242. https://doi.org/10.1126/science.280.5367.1238.

Wendin G (2017) Quantum information processing with superconducting circuits: A review. *Reports on Progress in Physics* 80: , 106001. URL: hetps 80, ducting circuits. a review.

Wenz T, Klochan J, Hohls F, Gerster T, Kashcheyevs V, and Schumacher HW (2019) Quantum dot state initialization by control of tunneling rates. *Physical Review B* 99: 201409. https://doi.org/10.1103/PhysRevB.99.201409.

Yoo MJ, Fulton TA, Hess HF, Willett RL, Dunkleberger LN, Chichester RJ, Pfeiffer LN, and West KW (1997) Scanning single-electron transistor microscopy: Imaging individual charges. *Science* 276: 579–582. https://doi.org/10.1126/science.276.5312.579.

Conductivity, thermal

K Behnia, Ecole Supérieure de Physique et de Chimie Industrielles, Paris, France

© 2024 Elsevier Ltd. All rights reserved.

This is an update of K. Behnia, Conductivity, Thermal, Editor(s): Franco Bassani, Gerald L. Liedl, Peter Wyder, Encyclopedia of Condensed Matter Physics, Elsevier, 2005, Pages 225–229, ISBN 9780123694010, https://doi.org/10.1016/B0-12-369401-9/00723-3.

Definition 273
Thermal conductivity and thermal diffusivity 273
Kinetic theory of heat carriers 274
Thermal transport in insulating crystals 274
The case of glasses 274
Thermal conductivity of metals and the Wiedemann-Franz law 275
Superconductivity and heat transport 275
Magnetic excitations as heat carriers 276
Thermal magnetoresistivity and the Righi-Leduc effect 277
Measuring thermal conductivity 277
Further reading 277

Abstract

Mobile electrons and phonons are carriers of heat in solids. The amplitude and the temperature dependence of thermal conductivity can be understood by quantifying the concentration of such carriers, their velocity, and the distance they travel between two successive collisions. In insulators, itinerant electrons are absent, and heat propagates thanks to phonons. The latter are scattered off each other at high temperature and by defects at lower temperatures. In metals, heat can be carried by electrons, which often dominate heat conductivity thanks to their larger velocity. In superconductors, electron carriers of heat vanish to a condensate and heat is carried by phonons and thermally excited quasi-particles, which may persist down to zero temperature when the superconducting gap has nodes. Heat can also be carried by magnetic excitations, such as magnons. Analysis of thermal transport is often complicated due to the fact that there are multiple carriers and various groups of scatterers and a quantitative account requires a disentanglement of different carriers and different scattering mechanisms.

Definition

Heat travels inside solids due to a property called thermal conductivity. The magnitude of thermal conductivity is specific to each element, alloy, or compound and is defined by the equation relating the heat flow to the thermal gradient produced by this flow:

$$J_q = -\kappa \nabla T \tag{1}$$

Here, $\boldsymbol{J_q}$ and ∇T are vectors representing respectively heat current density and temperature gradient. Thermal conductivity κ is, in general, a second-rank tensor. However, when heat flows along a high-symmetry axis, the temperature gradient created is parallel to the axis and the thermal conductivity along that particular axis may be treated as a scalar. In SI units, $\boldsymbol{J_q}$ is expressed in W m^{-2} and ∇T in K m^{-1}. The SI unit of thermal conductivity is therefore W(Km)$^{-1}$.

Eq. (1) is reminiscent of Ohm's law defining the electrical conductivity as the quantity relating the electric field to current density $\boldsymbol{J} = -\sigma \nabla V$. Indeed, there are a number of analogies between the two transport properties. There is a big difference however: to conduct electric charge, a solid should host itinerant electrons. Otherwise, it would qualify as an (electric) insulator. In the world of heat conduction, such a sharp distinction between conductors and insulators does not exist. The fundamental reason behind this resides in the existence of phonons, which can carry heat even in the absence of any electronic heat conductivity.

Thermal conductivity and thermal diffusivity

Eq. (1) is relevant in the case of thermal equilibrium. In general, the exchange of heat implies a variation of temperature with time. Conservation of energy implies

$$c\frac{\partial T}{\partial t} = -\nabla \boldsymbol{J}_q \tag{2}$$

where c is the heat capacity per unit volume of the compound. Since the specific heat of various compounds is usually expressed as heat capacity per unit mass (or molar mass), it should be multiplied by the density (or the molar density) of the compound to yield the c used here. A finite $\boldsymbol{J}_q$ means that the balance of heat entering to and exiting out of a volume element is not zero and the energy surplus (or deficit) changes the local temperature.

The combination of Eqs. (1) and (2) yields the so-called equation of heat, also called the Fourier equation:

$$\frac{\partial T}{\partial t} = D\nabla^2 T \tag{3}$$

where $D = \kappa/c$ is called the thermal diffusivity. It has the dimensions of an area divided by time ($m^2 s^{-1}$ in SI units). Thermal diffusivity is thus thermal conductivity divided by specific heat.

Kinetic theory of heat carriers

Electrons and phonons are the principal carriers of heat in a solid. Phonons are the elementary excitations of a vibrating crystal. In terms of solid-state physics, it is a particle with a definite energy and wave vector. Electrons here mean itinerant electrons capable of moving from one atom to the other. In order to grasp the basic differences between these two types of carriers, it is instructive to focus on a formula derived from the kinetic theory of gases. In this picture, the thermal conductivity is expressed as

$$\kappa = 1/3cvl \tag{4}$$

where c is the specific heat per volume, v is the average velocity of the particles composing the gas, and l is the mean free path.

Phonons are bosonic quasiparticles with a specific heat displaying a T^3 temperature dependence at low temperature and then saturating to a constant value at temperatures of the order of the Debye temperature, Θ_D. The relevant velocity is the speed of sound (of the order of several kms^{-1} in a solid) and does not change much with temperature. Finally, the mean free path of phonons is limited by whatever impedes their free propagation in a crystal. At sufficiently low temperatures, nothing can scatter extended phonons of long wavelength. In this so-called "ballistic" regime, the mean free path of the phonon becomes comparable to the sample's dimensions.

Electrons are fermions. Their specific heat is a linear function of temperature in ordinary temperatures, which remain much smaller than the Fermi temperature of most metals. The relevant velocity for them is the Fermi velocity (of the order of several hundreds of kms^{-1} in common metals). Finally, even in the cleanest samples and at low temperatures, their mean free path seldom exceeds a micrometer.

Thermal transport in insulating crystals

The case of insulators is simpler as there are no electrons to conduct or to scatter, and their thermal conductivity reflects the capacity of the lattice alone to conduct heat.

The Debye temperature sets the most important energy scale in this context, Θ_D. The thermal conductivity of an insulator peaks at a temperature, which is a fraction (often one-tenth) of Θ_D. This maximum marks the border between the two regimes: while at higher temperatures it is a phonon-phonon scattering which determines the phonon mean free path, l_{ph}, at lower temperatures, collision with defects becomes the predominant limit on l_{ph}. These two regimes are considered here separately:

1. *Low temperature* (*below* $T_{peak} \sim 0.1\ \Theta_D$). At this temperature range, the T^3 specific heat dominates the temperature dependence of thermal conductivity since l_{ph} displays a weak temperature dependence. With increasing temperature, l_{ph} decreases from the maximum attained in the $T = 0$ limit. Its temperature dependence is governed by the presence of defects in the crystal which scatter phonons in various ways. The cross section of a phonon with a specific scattering center (such as a point defect, a line defect, a planar defect, or a dislocation) is a function of the phonon wavelength λ_{ph}. As the temperature rises, the dominant wavelength in the phonon population increases ($\lambda_{ph} \propto k_B T$). Therefore, the relative importance of different scattering mechanisms is shifted with the change in temperature.
2. *High temperature* (*above* $T_{peak} \sim 0.1\ \Theta_D$). The maximum is related to the inflection in the temperature dependence of C_{ph} and l_{ph}. It marks the beginning of the predominance of the phonon-phonon scattering, which leads to a sharper decrease in l_{ph}. This is a consequence of the rise in the phonon population with increasing temperature. On the other hand, the specific heat increases less rapidly and eventually saturates to a constant value. Therefore, the temperature dependence of κ is governed by $l_{ph}(T)$. The expected temperature dependence of the latter is T^{-1}. The minimum thermal conductivity at high temperature is imposed by the lattice spacing. Indeed, l_{ph} cannot become significantly lower than the latter.

The case of glasses

In amorphous solids, the mean free path of the pho-non, even at low temperatures, does not exceed a few lattice constants. Therefore, the magnitude of thermal conductivity is drastically reduced. A generic feature of glasses is the absence of a maximum in the temperature dependence of thermal conductivity. Since l_{ph} presents a weak temperature dependence, the overall behavior is governed by the variation of the specific heat. The difference of conductivities between a glass and a crystal is largely reduced at high temperatures, because of the short l_{ph} for traveling phonons in both cases. In the intermediate temperature range, the peak is often replaced with a plateau (Fig. 1).

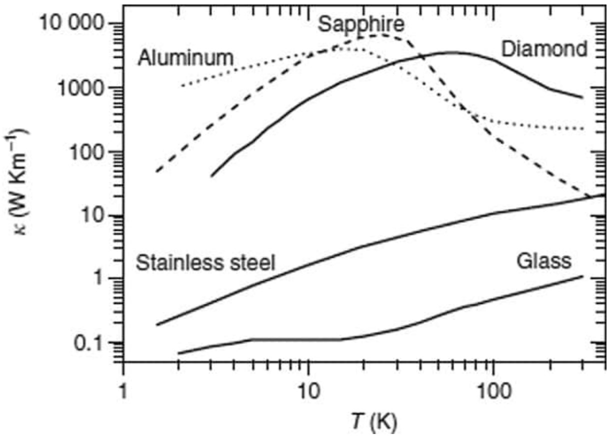

Fig. 1 Thermal conductivity of insulating and metallic solids.

Thermal conductivity of metals and the Wiedemann-Franz law

In metals, heat is carried both by phonons and electrons. Lattice conductivity in metals suffers from the presence of electrons as additional scattering centers. In the peak region of thermal conductivity (around 0.1 Θ_D), clean insulators can surpass clean metals as the best thermal conductors. In other words, the additional electronic thermal conductivity cannot compensate the loss in lattice thermal conductivity. The latter is proportional to the strength of electron-phonon coupling and introduces a T-square term to the temperature dependence of the phonon thermal conductivity.

In most cases, the predominant contribution to heat transport in a metal is of electronic origin. The application of Eq. (2) to electrons yields:

$$\kappa_{el} = 1/3 C_{el} v_F l_{el} = 1/3 C_{el} v_F^2 \tau \tag{5}$$

where τ is the scattering time. This equation has a parenthood with the classical expression for electric conductivity:

$$\sigma = \frac{ne^2\tau}{m} \tag{6}$$

with e and m representing the charge and the mass of electron, and n the carrier density. In both expressions, the conductivity is proportional to the scattering time. Thus, the ratio of the two conductivities is expected to be independent of scattering. Divided by temperature, this ratio yields the Lorentz number: $L = \kappa_{el}/\sigma T$. The Wiedemann-Franz law which establishes an intimate relationship between thermal conductivity and electric conductivity of a given metal, states that the Lorentz number is equal to a universal constant:

$$\frac{\kappa_{el}}{\sigma T} = \frac{\pi^2}{3}\left(\frac{k_B}{e}\right) = L_0 \tag{7}$$

where k_B is the Boltzmann constant and L_0 is the Sommerfeld number. Wiedemann and Franz formulated their empirical law in 1853 after measuring the conductivities of various metals at room temperature. The quantum theory of metals gave a solid foundation to this law which is expected to hold in the $T = 0$ limit irrespective of almost any particularity of any known metal. The fundamental reason behind its universality is easy to grasp. Whatever impedes the transport of charge by electrons would also affect the transport of entropy by them. The ratio of the two conductivities, therefore, does not depend on the specific electronic properties of the metal.

The argument remains rigorously valid in the absence of inelastic collisions, that is, scattering events which do not imply a transfer of energy during the scattering. Such events occur at finite temperatures when electrons are scattered by phonons and disturb the transport of heat more efficiently. Indeed, such a collision may lead to a partial loss of the electron's energy (i.e., heat) without affecting its momentum producing a thermal resistance with no counterpart in the charge channel. At high temperatures, however, the loss of energy during inelastic collisions becomes negligible compared to the thermal energy, and the validity of the Wiedemann-Franz law is more or less restored (see Fig. 2).

Superconductivity and heat transport

Many metals become superconductors below a critical temperature, T_c. The transition has drastic consequences on heat transport both by electrons and by phonons. At the onset of superconductivity, a gap opens up in the energy spectrum of the electronic spectrum and individual electrons end up in a superconducting condensate. This condensate lacks any degree of freedom in order to

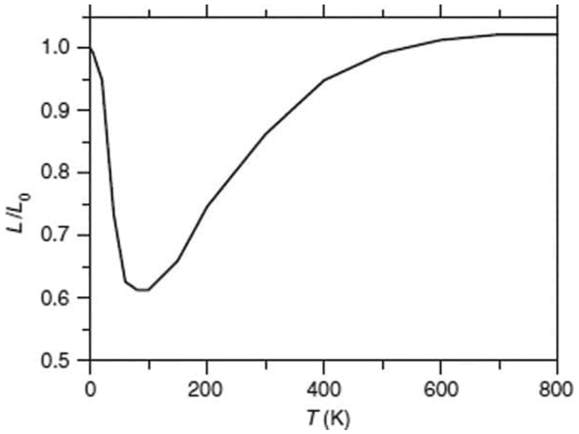

Fig. 2 The temperature dependence of the Lorentz number in a common metal (aluminum).

qualify as a carrier of entropy. Therefore, in the superconducting state, only the "normal fluid," that is, electronic excitations which happen to exist due to their thermal energy at finite temperature, can carry heat. The number of such excitations decreases exponentially with temperature and at sufficiently low temperature, they cease to play any significant role in thermal transport.

Phonon heat transport is also affected by the superconducting transition. At the onset of superconductivity in many metals, electrons are a principal source of scattering for phonons. When this is the case, the condensation of electrons leads to a sharp enhancement in the phonon mean free path and the phonon thermal conductivity. At very low temperatures, an ordinary superconductor conducts heat in a manner analogous to an insulator.

The other consequences of the superconducting transition on the thermal conductivity of electrons and phonons generate a wide variety of behaviors in real superconductors. If the electrons are the dominant heat carriers at the onset of superconductivity, then the superconducting transition is accompanied by a rapid decrease in the thermal conductivity of the system. On the other hand, if for any reason (a low carrier density, a low mean-free path, a high critical temperature, etc.) the lattice contribution happens to be significant in the normal state, the thermal conductivity can increase below T_c reflecting the enhancement of l_{ph}. The superconductor should be clean enough for this to happen, otherwise the impurity scattering of phonons is such that the disappearance of electrons would not present any significant change in phonon scattering. Thus, according to the numerous relevant parameters of each case, the superconducting transition can lead to a reduction, to an enhancement, or to no change in the thermal conductivity of the system.

The picture of heat transport in superconductors in this article has been somewhat modified by the results of the last two decades of research on unconventional superconductors. In high-T_c cuprates, the entry of the system into the superconducting state is accompanied with an upturn in thermal conductivity. It is now generally believed that part of this enhancement is due to an increase in the electronic component of thermal conductivity. While there is still no microscopic understanding of what happens, this extraordinary situation is interpreted as a signature of strong electron-electron scattering present in the normal state of the cuprates. In other words, the suppression of electrons leads to a lower number of heat carriers with a longer mean-free path in such a way that the overall result is a significant enhancement of thermal conductivity. A second feature of interest is the complex structure of the superconducting gap in unconventional superconductors. Since their gap is anisotropic with a magnitude which becomes zero along definite orientations, low-energy electronic excitations can survive down to $T = 0$. The electronic thermal conductivity is not expected to be an exponentially decreasing function of temperature. This has been confirmed by experiments probing heat transport by these "nodal" quasiparticles.

Magnetic excitations as heat carriers

In a magnetically ordered solid, a new type of heat carriers appear. The elementary excitations of a magnetic lattice are called spin waves or magnons and can transport heat in a manner analogous to phonons. Most of the considerations regarding phonons are relevant for magnon heat transport with Curie or Néel temperature replacing the Debye temperature as the relevant energy scale. A quantitative isolation of the magnon contribution to heat transport is, however, a difficult experimental task as the deconvolution of various terms in their presence is far from obvious.

Entropy carriers associated with spin degrees of freedom are also expected in metals close to a magnetic stability. Such excitations, often called spin fluctuations or paramagnons, are reported to produce a substantial enhancement of thermal conductivity in a number of exotic metals.

Thermal magnetoresistivity and the Righi-Leduc effect

A magnetic field has no direct effect on heat transport by phonons. Electronic thermal conductivity, on the other hand, is affected by a magnetic field in a manner analogous to the electric conductivity. Usually, it is diminished as the magnetic field disfavors transport by charged particles.

In type II superconductors, a magnetic field penetrates the solid in the shape of mesoscopic filaments called vortices. These superconducting vortices constitute a new type of scattering centers for heat carriers. The contribution of their own movement to heat transport is often negligible.

In the presence of a magnetic field, the electronic thermal conductivity tensor presents a nondiagonal term, κ_{xy}. The trajectory of charged carriers is skewed under the influence of the Lorentz force (or magnetically aligned scattering centers). This creates a transverse heat current, which is balanced by a transverse thermal gradient. This is the Righi-Leduc effect, sometimes dubbed the thermal Hall effect in analogy to the famous electric one.

Measuring thermal conductivity

Experimental methods to determine thermal conductivity fall into two broad groups. Steady state or “static” methods study a sample time-independent temperature profile and measure κ using Eq. (1). In contrast, non-steady-state or “dynamic” methods work with a time-dependent temperature. They often yield a quantity akin to thermal diffusivity.

Measuring the thermal conductivity of a solid implies a reliable determination of the temperature gradient produced by a heat current, and the quality of an experimental setup depends on its ability to yield accurate values of these two quantities. This proves to be more difficult than the analogous case of electrical conductivity since charge can only travel through conductors but heat can be transmitted by conductors, insulators, and even vacuum.

Further reading

Berman R (1976) *Thermal Conduction in Solids*. Oxford: Oxford University Press.
Tye RP (ed.) (1969) *Thermal Conductivity*. In: vols. I and II. London and New York: Academic Press.

Transport properties: Mass transport[☆]

R Livi, Dipartimento di Fisica e Astronomia, Università di Firenze and Sezione INFN di Firenze, Sesto Fiorentino, Italy; ISC-CNR, Sesto Fiorentino, Italy

© 2024 Elsevier Ltd. All rights reserved.

This is an update of R. Livi, Mass Transport, Editor(s): Franco Bassani, Gerald L. Liedl, Peter Wyder, Encyclopedia of Condensed Matter Physics, Elsevier, 2005, Pages 265–270, ISBN 9780123694010, https://doi.org/10.1016/B0-12-369401-9/00724-5.

Introduction 278
Transport in the presence of a gradient 279
Brownian motion 280
The Langevin approach 281
The Fokker-Planck approach 282
Conclusion 283
References 283

Abstract

This article summarizes the basic approaches historically adopted for describing transport processes and, specifically, mass transport: elementary kinetic theory, Einstein's theory of Brownian motion, Langevin stochastic equation and Fokker-Planck probabilistic approach.

Key points

- Transport by an applied gradient, Brownian motion, Langevin approach, Fokker-Planck approach.

Introduction

Transport processes concern a wide range of phenomena in hydrodynamics, thermodynamics, physical-chemistry, electric conduction, magnetohydrodynamics, etc. They typically occur in physical systems (gases, liquids or solids) made of many particles (atoms or molecules) in the presence of inhomogeneities. Such a situation can result from non-equilibrium conditions (e.g., the presence of a macroscopic gradient of density, velocity and temperature), or simply from fluctuations around an equilibrium state (Chandler, 1987; Livi and Politi, 2017).

The kinetic theory of transport phenomena provides a unified description of these apparently unlike situations. It is based on the assumption that even in non-equilibrium conditions gradients are small enough to guarantee that local equilibrium conditions still hold. In particular, the kinetic approach describes the natural tendency of the particles to transmit their properties from one region to another of the fluid by colliding with the other particles and eventually establishing global or local equilibrium conditions.

The main success of the kinetic theory is the identification of the basic mechanism underlying all the above-mentioned processes: the transport of a microscopic quantity (e.g., the mass, momentum or energy of a particle) over a distance equal to the mean free path $\bar{\ell}$ of the particles, i.e. the average free displacement of a particle after a collisions with another particle. By this definition, it is implicitly assumed that the system is a fluid, where each particle is supposed to interact with each other by collisions and propagate freely between successive collisions. Simple considerations yield the following definition

$$\bar{\ell} = \frac{1}{\sqrt{2}\sigma n}, \tag{1}$$

where n is the volumetric density of particles, which depends on the thermodynamic conditions of the system, and σ is the total cross-section of collisions between particles (e.g., for the ideal case of spheric particles of radius R, $\sigma = 4\pi R^2$). For instance, in a gas at room temperature and pressure $\bar{\ell}$ is typically

$\mathcal{O}(10^{-5})$cm, three orders of magnitude larger than the typical size of a particle, $\mathcal{O}(10^{-8})$cm. It is worth stressing that reference is made to the simple case of a homogeneous isotropic system, where $\bar{\ell}$ is the same at any point and in any direction in space.

In the following section the general case of non-equilibrium conditions are analyzed and the definitions of transport coefficients are provided. In the section "Brownian motion" the process of mass transport due to fluctuations close to equilibrium is described, by relying upon the basic example of Brownian motion.

[☆] *Change History*: July 2022. R Livi updated the chapter.

Transport in the presence of a gradient

Without prejudice of generality a system is considered where a uniform gradient of the quantity $A\left(\vec{x}\right)$ is established along the z-axis, and $A(x, y, z) = A(x', y', z) = A(z)$ for any x, x', y and y'. In particular, it is assumed that $A(z)$ is a microscopic quantity, which slowly varies at constant rate along the coordinate z of an arbitrary cartesian reference frame. Consider also a unit surface S_1 located at height z and perpendicular to the z-axis. Moving from the surface S_1 a particle will run a distance $\pm\bar{\ell}$ moving either upward or downward along the z axis, respectively. Assuming that local equilibrium is established by collisions, the particle variable will change its original value $A(z)$ into $A(z \pm \bar{\ell})$. The net transport of the quantity $A(z)$ through S_1 amounts to the number of crossings of S_1 from each side in the unit time. Consistently with the assumption of local equilibrium, the same average velocity $\bar{v}$ is attributed to all particles crossing S_1. Isotropy and homogeneity of the system imply also that "on average" $\frac{1}{3}$ of the particles move along the z-axis, half of them upward and half down-ward. Accordingly, S_1 is crossed along z in the unit time interval by $\frac{1}{6}n\bar{v}$ particles in each direction. The net amount of $A(z)$ transported through S_1 in the unit time is given by

$$\Phi(A) = \frac{1}{6}n\bar{v}[A(z-\bar{\ell}) - A(z+\bar{\ell})] \tag{2}$$

Since $\bar{\ell}$ is very small compared with the macroscopic length of the fluid, one can use the approximation $A(z \pm \bar{\ell}) \simeq A(z) \pm \bar{\ell}\frac{\partial A}{\partial z}$ and rewrite Eq. (2) as

$$\Phi(A) = -\frac{1}{3}n\bar{v}\bar{\ell}\frac{\partial A}{\partial z} \tag{3}$$

The minus sign in front of the r.h.s. of this equation indicates that A is transported in the direction opposite to the orientation of the gradient. This calculation can be performed more carefully by introducing explicitly the Maxwell distribution function of particle velocities at equilibrium (e.g., see (Livi and Politi, 2017)). Nonetheless, one recovers the same result.

The simplest case is the presence of a density gradient along the z-axis, i.e. $A(z) = n(z)$. It induces a mutual transport of particles, which diffuse through the system and

$$\Phi(n) = -\frac{1}{3}n\bar{v}\bar{\ell}\frac{\partial n}{\partial z} = D\frac{\partial n}{\partial z} \tag{4}$$

where the quantity $D = \frac{1}{3}n\bar{v}\bar{\ell}$ defines the diffusion coefficient of particles inside the fluid.

This definition can be easily extended to the case of a mixture of two different species of particles, labeled by the indices (1) and (2), which diffuse into each other. One can define the mutual diffusion coefficient

$$D_{1,2} = \frac{n_1\bar{v}_1\bar{\ell}_1 + n_2\bar{v}_2\bar{\ell}_2}{3(n_1 + n_2)} \tag{5}$$

The other cases of physical interest correspond to the situations where a gradient of velocity or temperature are present. In the former case, it is assumed that the fluid flows with constant macroscopic velocity $v(z)$ parallel to the (x, y) plane. In such a situation there is a net transport of kinetic momentum $mv(z)$ (m is the mass of a particle), yielding a strain stress $\Phi(mv(z))$ between the fluid layers laying on the (x, y) plane:

$$\Phi(mv(z)) = -\frac{1}{3}nm\bar{v}\bar{\ell}\frac{\partial v(z)}{\partial z} = \eta\frac{\partial v(z)}{\partial z} \tag{6}$$

where the quantity $\eta = \frac{1}{3}nm\bar{v}\bar{\ell}$ defines the viscosity of the fluid. By substituting Eq. (1) into the previous expression, one finds $\eta = \frac{m\bar{v}}{3\sqrt{2}\sigma}$. This implies that the viscosity of an ideal fluid is independent of its density n, that is of the pressure. This counterintuitive conclusion was first derived by J.C. Maxwell and its experimental verification sensibly contributed to establish in the scientific community a strong consensus on the "atomistic" approach of kinetic theory (Brush, 1976). It is worth stressing that such a conclusion does not hold when dealing with very dense fluids.

It remains to consider the case when $A(z)$ is the average kinetic energy of particles $\bar{\varepsilon}(z)$. At equilibrium, the energy equipartition condition yields the relation $n\bar{\varepsilon}(z) = \rho C_V T(z)$, where $\rho = m\,n$ is the mass density of particles, C_V is the specific heat at constant volume and $T(z)$ is the temperature at height z. The net flux of kinetic energy $\Phi(\bar{\varepsilon})$ can be read as the heat transported through the fluid along the z-axis:

$$\Phi(\bar{\varepsilon}) = -\frac{1}{3}\rho C_V\bar{v}\bar{\ell}\frac{\partial T(z)}{\partial z} = \kappa\frac{\partial T(z)}{\partial z} \tag{7}$$

where the quantity $\kappa = \frac{1}{3}\rho C_V\bar{v}\bar{\ell} = \frac{mC_V\bar{v}}{3\sqrt{2}\,\sigma}$ defines the heat conductivity. Also κ is found to be independent of n.

One can conclude that the transport coefficients, i.e. the diffusion constant D, the viscosity η and the heat conductivity κ, are closely related to each other and depend on a few basic properties of the particles, like their mass m, their average velocity $\bar{v}$ and their mean-free-path $\bar{\ell}$. By comparing Eqs. (6) and (7) one finds the remarkable relation

$$\frac{\kappa}{\eta} = \alpha C_V \tag{8}$$

According to the results herein reported the value of the proportionality constant is $\alpha = 1$. In real systems this constant takes different values, which depend on specific features of particles interaction (e.g., $\alpha = \frac{5}{2}$ for realistic models of monoatomic gases (Livi and Politi, 2017)). The conceptual relevance of this relation is that it concerns quantities that originate from quite different conditions of matter. In fact, on the left hand side is the ratio of two transport coefficients associated with macroscopic non-equilibrium conditions, while on the right hand side is a typically equilibrium quantity, the specific heat at constant volume. After what has been discussed in this section, this observation is far from mysterious: by assuming that even in the presence of a macroscopic gradient of physical quantities equilibrium conditions set in locally, the kinetic theory provides a unified theoretical approach for transport and equilibrium observables.

Brownian motion

The basic example of transport properties emerging from fluctuations close to equilibrium is Brownian motion (for a general overview on this topic see (Nelson, 1976)). This phenomenon had been observed by R. Brown in 1828: small pollen particles in solution with a liquid exhibited an erratic motion, whose irregularity increased with decreasing particle size (typically, 10^{-3} cm). The long scientific debate about the origin of Brownian motion lasted over almost one century and raised strong objections to the atomistic approach of the kinetic theory (see the section "Introduction"). In particular, the motion of the pollen particles could not be apparently consistent with an explanation based on collisions with the molecules of the liquid, subject to thermal fluctuations. In fact, pollen particles have exceedingly larger mass and size with respect to molecules. An easy calculation, based on orders of magnitude, yields the conclusion that the amount of velocity acquired by a pollen particle in a collision with a molecule is typically 10^{-6} m/s, so that the corresponding instantaneous displacement could not be practically observed, "a fortiori" with the optical devices available to Mr. R. Brown in 1828. The kinetic approach implies also that the number of collisions per second of the Brownian particle with liquid molecules is gigantic and random. Thermal equilibrium conditions and the isotropy of the liquid make equally probable the sign of the small velocity variations of the pollen particle. On observable time scales the effect of the very many collisions should average to zero and the pollen particle should not acquire any net displacement from its initial position in the fluid. This way of reasoning is actually wrong, as Albert Einstein argued in his theory of Brownian motion (Einstein, 1956). Einstein's methodological approach, based on the combination of simple models with basic physical principles, was very effective: he first assumed that the Brownian macroscopic particles should be considered as "big mass molecules", so that the systems composed by the Brownian particles and the solvent, where they are suspended, can be considered a mixture of two fluids at thermal equilibrium. This implies the validity of Van't Hoff law

$$P\left(\vec{x}\right) = k_B T n\left(\vec{x}\right) \tag{9}$$

where P is the osmotic pressure between the fluids, T is the equilibrium temperature of the solution, n in the volumetric density of Brownian particles (the "solute" of the binary mixture) and k_B is the Boltzmann constant ($k_B = 1.380658 \times 10^{-23}$ J K^{-1}). According to the classical kinetic theory one should not be allowed to write an equation of state like (9) for a collection of the macroscopic Brownian particles. They should be better described by the laws of dynamics, rather than by those of thermodynamics. Einstein's opposite point of view can be justified by considering that, despite their macroscopic dimension, the Brownian particles are not subject to standard macroscopic forces: they experience microscopic forces originated by thermal fluctuations of the fluid molecules and in this sense they can be assimilated in any respect to solute particles. The macroscopic nature of the Brownian particles should be recovered in the time scales associated with the collision and dissipation processes inside the fluid. Einstein guessed that Brownian motion looks random on a much larger time scale than the one needed for dissipating the energy acquired by Brownian particles through collisions with molecules. In practice, this amounts to assume that the dissipation mechanism should be described by the macroscopic Stokes' law

$$F = m\frac{dv}{dt} = -6\pi\eta R v \tag{10}$$

where F is the friction force proportional to the velocity v of the Brownian particle of radius R and η is the viscosity of the solvent. Accordingly, the energy dissipation process of Brownian particles has to occur on the time scale

$$t_d = \frac{m}{6\pi\eta R} \tag{11}$$

For $R \simeq 10^{-4}$ cm and for a standard solvent (e.g., water) one has $t_d = \mathcal{O}(10^{-7})$sec.

On a time scale much larger than t_d the Brownian particles are expected to exhibit a diffusive motion, as a consequence of the many random collisions with the solvent molecules. On the other hand, the kinetic theory associates diffusion with transport of matter in the presence of a density gradient (see section "Introduction"). Einstein then assumed that some ideal external force should be responsible of creating such a gradient along an arbitrary direction (e.g., x) yielding a flux of Brownian particles

$$J_B = D\nabla n \tag{12}$$

At a microscopic level the flux of Brownian particles J_B is defined as the product of their velocity v times their density n. For $t \gg t_d$, the velocity v is given by Eq. (10) and one can also write

$$J_B = \frac{Fn}{6\pi\eta R} \tag{13}$$

The numerator on the right hand side of this equation is the definition of the pressure gradient, which, according to Van't Hoff law (9), is proportional to the density gradient. In formulae

$$Fn = \nabla P = k_B T \nabla n \tag{14}$$

By substituting into Eq. (14) and comparing with Eq. (12) one obtains the remarkable relation

$$D = \frac{k_B T}{6\pi\eta R} \tag{15}$$

J. Perrin showed that this formula provides very good quantitative agreement with experimental data (Perrin, 1948).

In summary, Einstein's approach derives from the assumption that for $t < t_d$ it still makes sense attributing a velocity to the Brownian particle (see Eq. (10)), while for $t > t_d$ the particle is assumed to diffuse, as if it would be in the presence of an ideal density gradient (Eq. 12). It is worth stressing that the last hypothesis is purely phenomenological, since direct inspection of the movement of Brownian particles revealed its diffusive nature. Einstein's theory of Brownian motion is based on the matching between different dynamical regimes.

The Langevin approach

A mechanical approach taking explicitly into account both dynamical regimes was later proposed by P. Langevin (Livi and Politi, 2017; Van Kampen, 1985). For the first time deterministic and stochastic forces were introduced into the same equation. The deterministic component is the friction term $-\gamma \mathbf{v}$, acting on the Brownian particle: γ is the friction coefficient, which amounts to $\gamma = 6\pi\eta R$ in the Stokes regime and $\mathbf{v}$ is the three-dimensional velocity vector of the Brownian particles, whose components are denoted by v_i, $i = 1, 2, 3$. The stochastic component associated with the effect of collisions with the solvent molecules is a random, time-dependent force vector $\xi(t)$, whose components are analogously denoted by ξ_i, $i = 1, 2, 3$. Symmetry arguments indicate that each one of these components can be assumed to be independent, isotropic, uncorrelated in time (at least for $t > t_d$) and gaussian, since it results from the combination of a very large number of collisions, which can be approximately considered as independent events. Accordingly, the average of the stochastic force is null and its time-correlation function can be approximated by a Dirac delta for $t > t_d$. In formulae:

$$\langle \xi_i(t) \rangle = 0 \tag{16}$$

$$\left\langle \xi(t)_i \xi_j(t') \right\rangle = \Gamma \delta_{ij} \delta(t - t') \tag{17}$$

where the brackets $\langle\ \rangle$ indicate the statistical average, Γ is a suitable dimensional constant and δ_{ij} is a Kronecker delta. Langevin equation is a Newton equation containing the stochastic force vector ξ. For each component of the three-dimensional velocity vector it reads

$$m\frac{dv_i}{dt} = -\gamma v_i + \xi_i(t) \tag{18}$$

This equation can be formally integrated, yielding the solution

$$v_i(t) = \exp\left(-\frac{\gamma}{m}t\right)\left[v_{0i} + \int_0^t d\tau \frac{1}{m} \exp\left(\frac{\gamma}{m}\tau\right)\xi_i(\tau)\right] \tag{19}$$

where v_{0i} is the i-th component of the initial velocity. Accordingly, $v_i(t)$ is a stochastic solution which assumes properties similar to $\xi(t)$ (see Eq. (17)), namely

$$\langle v_i(t) \rangle = v_{0i} \exp\left(-\frac{\gamma}{m}t\right) \tag{20}$$

and

$$\left\langle v_i^2(t) \right\rangle = \exp\left(-\frac{2\gamma}{m}t\right)\left[v_{0i}^2 + \int_0^t d\tau \frac{1}{m^2} \exp\left(\frac{2\gamma}{m}\tau\right)\Gamma\right] \tag{21}$$

$$= \frac{\Gamma}{2m\gamma}\left[1 - \exp\left(-\frac{2\gamma}{m}t\right)\right] + v_{0i}^2 \exp\left(-\frac{2\gamma}{m}t\right) \tag{22}$$

As time t grows the average velocity vanishes exponentially with the rate $\frac{m}{\gamma}$, while the average squared velocity approaches the value

$$\lim_{t\to\infty} \left\langle v_i^2(t) \right\rangle = \frac{\Gamma}{2m\gamma} \tag{23}$$

In order to bridge this purely mechanical approach with Einstein's theory, a relation with thermodynamics has to be established. This is naturally obtained by attributing a thermal origin to the fluctuations of the stochastic force. In particular, if one assumes that the Brownian particles and the solvent are at thermal equilibrium with temperature T, the energy equipartition principle establishes that the average kinetic energy per degree of freedom in the limit of very large times is proportional to the temperature:

$$\lim_{t\to\infty} \left\langle \frac{1}{2} m v_i^2(t) \right\rangle = \frac{1}{2} k_B T \tag{24}$$

By comparison with Eq. (23) one obains the remarkable relation

$$\Gamma = 2\gamma k_B T \tag{25}$$

where the amplitude of velocity fluctuations is found to depend on the friction coefficient of the fluid, thus yielding the basic example of a fluctuation-dissipation relation (for a general approach to fluctuation-dissipation theory see (Livi and Politi, 2017; Kubo et al., 1985)).

On the other hand, this relation cannot be directly tested by experimental observations, i.e. records of the erratic trajectories of Brownian particles sampled at time intervals much larger than t_d. The very predictive content of the Langevin equation can be extracted by computing the average displacement vector **r**, whose components are related to those of **v** by the straightforward relation $r_i(t) = \int_0^t d\tau v_i(\tau)$, $i = 1, 2, 3$. The information of interest is contained in the expression of the squared average displacement $\langle r_i^2(t) \rangle$. Simple calculations yield the result

$$\left\langle r_i^2(t) \right\rangle = v_{0i}^2 t^2, \ t << \frac{m}{\gamma} \tag{26}$$

$$\left\langle r_i^2(t) \right\rangle = \frac{2k_B T}{\gamma} t, \ t >> \frac{m}{\gamma} \tag{27}$$

It is important to observe that this mechanical approach is able to account at the same time for the "ballistic" regime, expected for times smaller than the relaxation time $t_d = \frac{m}{\gamma}$, and also for the asymptotic diffusive regime. The diffusion constant is expressed by the relation

$$D = \frac{k_B T}{\gamma} \tag{28}$$

which is found to be equivalent to (15) in the Stokes friction regime, where $\gamma = 6\pi\eta R$.

The Fokker-Planck approach

The statistical content of the Langevin approach emerges explicitly from the properties attributed to the random force in Eq. (17). The statistical average $\langle \ \rangle$ can be interpreted as the result of the average over many different trajectories of the Brownian particle obtained by different realizations of the stochastic force components ξ_i in Eq. (18). By taking inspiration from Boltzmann kinetic theory (see (Huang, 1987)) one can get rid of mechanical trajectories and describe from the very beginning the evolution of Brownian particles by a suitable distribution function $f(\mathbf{x}, t)$: $f(x, t)d\mathbf{x}$ represents the probability of finding the Brownian particle at a position in between $\mathbf{x}$ and $\mathbf{x} + d\mathbf{x}$ at time t. One can introduce the transition rate $W(\mathbf{x}', \mathbf{x})$, such that $W(\mathbf{x}', \mathbf{x})d\mathbf{x}'\Delta t$ represents the probability that in the interval of time Δt the Brownian particle "jumps" from the neighborhood of $\mathbf{x}$ to $\mathbf{x}'$. In this approach any reference to instantaneous collisions with the solvent molecules is lost and one has to assume that $\Delta t \gg t_d$. As proposed by Fokker and Planck, one can write the evolution equation for $f(\boldsymbol{x}, \ t)$: as a "Master Equation", i.e. a balance equation where the variation in time of $f(\mathbf{x}, t)$ emerges as the result of two competing terms: a gain factor, due to jumps of particles from any position $\boldsymbol{x}'$ to $\mathbf{x}$, and a loss factor, due to jumps from $\mathbf{x}$ to any $\mathbf{x}'$. In formulae

$$\frac{\partial f(\mathbf{x}, t)}{\partial t} = \int_{-\infty}^{+\infty} d\mathbf{x}' [f(\mathbf{x}'', t) W(\mathbf{x}, \mathbf{x}') - f(\mathbf{x}, t) W(\mathbf{x}', \mathbf{x})] \tag{29}$$

In this equation it has been implicitly assumed that volumes are preserved in position space by the Brownian process, in particular $d\mathbf{x}' = d\mathbf{x}$. On the other hand, large displacements of the Brownian particles are highly unprobable and one can reasonably assume that the rate function $W(\mathbf{x}', \mathbf{x}) = W(\mathbf{x}'; \chi)$ is significantly different from zero only for very small values of $|\chi| = |\mathbf{x}' - \mathbf{x}|$. This allows to introduce a formal Taylor series expansion in Eq. (29) around $\chi = 0$. By considering only terms up to the second order one obtains the Fokker-Planck equation

$$\frac{\partial f(\mathbf{x}, t)}{\partial t} = -\nabla \cdot [\mu_1 f(\mathbf{x}, t)] + \frac{1}{2} \boldsymbol{\Delta} [\mu_2 f(\mathbf{x}, t)] \tag{30}$$

where

$$\mu_1 = \int_{-\infty}^{+\infty} d_\chi W(\mathbf{x}'; \chi) \chi = \left\langle \frac{\delta \mathbf{x}}{\delta t} \right\rangle = \langle \mathbf{v} \rangle \tag{31}$$

$$\mu_2 = \int_{-\infty}^{+\infty} d_\chi W(\mathbf{x}'; \chi) |\chi|^2 = \left\langle \frac{|\delta \mathbf{x}|^2}{\delta t} \right\rangle \tag{32}$$

The first term on the r.h.s. of Eq. (30) represents the contribution of viscous friction, while the second term is the diffusive contribution. Notice that vector μ_1 and scalar μ_2 are both average quantities: the former amounts to the average speed of a Brownian particles, which in general results from the balance of external forces acting on the Brownian particle with the viscous friction force produced by the solvent; the latter amounts to the average squared displacement per unit time, which, in a homogeneous isotropic medium, corresponds to the definition of the diffusion constant D. Accordingly, in the absence of external forces the viscous term can be neglected and Eq. (30) reduces to the standard form of a macroscpic diffusion equation

$$\frac{\partial f(\mathbf{x}, t)}{\partial t} = D \Delta f(\mathbf{x}, t) \tag{33}$$

The solution of this equation is

$$f(\mathbf{x},t)=\frac{1}{\sqrt{4\pi Dt}}\exp\left(\frac{|\mathbf{x}-\mathbf{x}_0|^2}{4Dt}\right)D\Delta f(\mathbf{x},t) \tag{34}$$

Here $\mathbf{x}_0$ is the initial position of the Brownian particle. The average squared displacement is given by the expression

$$\left\langle|\mathbf{x}|^2\right\rangle=\int_{-i\infty}^{+\infty}d\mathbf{x}|\mathbf{x}|^2f(\mathbf{x},\,t)=|\mathbf{x}_0|^2+6Dt \tag{35}$$

This statistical treatment of Brownian motion can be easily generalized in the presence of external forces acting on the Brownian particles. For the sake of simplicity the simple case of an elastic force acting $\mathbf{F}=-\lambda\mathbf{x}$, where λ is the elastic constant (Uhlenbeck and Ornstein, 1930), is illustrated. The mobility of Brownian particles is denoted as ν (e.g., in the Stokes regime $\nu^{-1}=6\pi\eta R$). The average viscous force is then given by $-\langle\mathbf{v}\rangle/\nu$ and it must be balanced by the elastic force, i.e. $\langle\mathbf{v}\rangle/\nu+\lambda\mathbf{x}=0$. This relation implies

$$\mu_1=\;-\lambda\nu\mathbf{x} \tag{36}$$

Since relation (35) still holds, one also obtains

$$\mu_2=\left\langle|\mathbf{x}|^2\right\rangle/t=6D \tag{37}$$

where, without prejudice of generality, one can set $\mathbf{x}_0=0$. Eq. (30) then reduces to

$$\frac{\partial f(\mathbf{x},\,t)}{\partial t}=\lambda\nu\nabla\cdot\mathbf{x}f(\mathbf{x},\,t)+3\nu k_BT\Delta f(\mathbf{x},\,t) \tag{38}$$

where the generalized Einstein's relation $D=\nu\,k_B\,T$ has been used. The solution of (38) reads

$$f(\mathbf{x},\,t)=\sqrt{\frac{\lambda}{2\pi k_BT\left(1-e^{-2\lambda\nu t}\right)}}\exp\left(-\frac{\lambda\left|\mathbf{x}-\mathbf{x}_0e^{-\lambda\nu t}\right|^2}{2k_BT\left(1-e^{-2\lambda\nu t}\right)}\right) \tag{39}$$

One can easily obtain

$$\langle\mathbf{x}\rangle=\mathbf{x}_0e^{-\lambda\nu t} \tag{40}$$

$$\left\langle|\mathbf{x}|^2\right\rangle=|\mathbf{x}_0|^2e^{-2\lambda\nu t}+\frac{k_BT}{\lambda}\left(1-e^{-2\lambda\nu t}\right) \tag{41}$$

In the limit $t\to\infty$ these relations reduce to

$$\langle\mathbf{x}\rangle=0 \tag{42}$$

$$\left\langle|\mathbf{x}|^2\right\rangle=\frac{k_BT}{\lambda} \tag{43}$$

It can be concluded that asymptotically the distribution of Brownian particles subject to an elastic force is a gaussian centered around the origin (which has been chosen as the equilibrium position of the elastic force), with variance $\frac{k_BT}{\lambda}$.

Conclusion

This manuscript contains a pedagogical overview about the basic methods employed in physics for describing mass transport in fluids, according to a historical perspective. In fact, the approach of elementary kinetic theory is first reported to provide the reader a basic intuitive understanding of transport processes, where dynamical and statistical concepts were mixed together for the first time, in order to obtain a clear definition of the phenomenological coefficients associated with diffusive processes in fluids. The understanding of Brownian motion by Einstein's theory is then illustrated as a basic contribution pointing out the role of thermodynamic equilibrium in relation with transport processes. Further mathematical achievements by Langevin stochastic equation and Fokker-Planck probabilistic equation are finally reported. By the latter formalism a short account about the problem of diffusive particles subject to an external elastic force (the so-called Ornstein-Uhlenbeck problem) is also reported.

References

Brush S (1976) *The Kind of Motion That We Call Heat*. North Holland: Yale University.
Chandler D (1987) *Introduction to Modern Statistical Mechanics*. Oxford University Press.
Einstein A (1956) *Investigations on the Theory of the Brownian Movement*. Dover: Courier Corporation.
Huang K (1987) *Statistical Mechanics*. Wiley.
Kubo R, Toda M, and Hashitsume N (1985) *Statistical Physics II*. Springer.
Livi R and Politi P (2017) *Nonequilibrium Statistical Physics*. Cambridge University Press.
Nelson E (1976) *Dynamical Theories of Brownian Motion*. Princeton University Press.
Perrin J (1948) *Les Atomes*. Gallimard.
Uhlenbeck GE and Ornstein LS (1930) *Physical Review* 36: 823.
Van Kampen NG (1985) In: Cohen EGD (ed.) *Fundamental Problems in Statistical Mechanics*. Amsterdam (Netherlands): North-Holland.

Ferroelectricity

AP Levanyuk[a], **BA Strukov**[b], **and A Cano**[c], [a]Department of Physics, University of Washington, Seattle, WA, United States; [b]Department of Physics, Lomonosov Moscow State University, Moscow, Russia; [c]Université Grenoble Alpes, CNRS, Institut Néel, Grenoble, France

© 2024 Elsevier Ltd. All rights reserved.

This is an update of A.P. Levanyuk, B.A. Strukov, Ferroelectricity, Editor(s): Franco Bassani, Gerald L. Liedl, Peter Wyder, Encyclopedia of Condensed Matter Physics, Elsevier, 2005, Pages 192–201, ISBN 9780123694010, https://doi.org/10.1016/B0-12-369401-9/00435-6.

Introduction	**284**
Probing ferroelectricity	**285**
Applications	287
Landau-Ginzburg-Devonshire framework	**287**
Applicability of the LGD theory	289
Displacive vs order-disorder limits	**290**
Dynamics	**291**
Domains, domain walls and ferroelectric textures	**292**
Ferroelectricity in liquid crystals and incommensurate ferroelectrics	**293**
Improper ferroelectricity	**293**
Multiferroics	**294**
Ferroelectricity beyond the Landau paradigm	**294**
Conclusion	**295**
References	**295**

Abstract

When the polarity of a non-centrosymmetric polar structure can be reversed one normally finds a set of additional characteristic properties, altogether designated as ferroelectricity. We outline these properties and the systems in which they are materialized with some representative examples. In particular, we delineate the standard case in which ferroelectricity is associated with a phase transition—that is, to some sort of underlying instability—and emphasize another class of ferroelectricity that is beyond this paradigm. The former can be described within the Landau theory of phase transitions and its extensions and takes place in proper ferroelectrics (e.g., $BaTiO_3$, $PbTiO_3$, $BiFeO_3$ and HfO_2), improper ferroelectrics (e.g., hexagonal manganites such as $YMnO_3$) and multiferroics (e.g., orthorhombic manganites such as $HoMnO_3$ and $TbMnO_3$). The latter, however, is beyond the Landau framework and is found in 2D van der Waals materials for example.

Key points

- Definition of ferroelectricity (from physical measurements).
- Outline of applications.
- Ferroelectricity as a structural phase transition (within the Landau-theory paradigm):
  - equilibrium states
  - dynamics
  - domains, domain walls and ferroelectric textures
  - ferroelectricity in liquid crystals and incommensurate structures
  - proper ferroelectrics, improper ferroelectrics and multiferroics.
- Ferroelectricity beyond the Landau-theory paradigm.

Introduction

Ferroelectricity refers to a set of phenomena that takes place in materials with stable polar structures whose polarity can be reversed. These materials are called ferroelectrics. Ferroelectricity is useful for a number of technological applications, including information storage. Traditionally, ferroelectrics are defined as pyroelectrics whose natural electric polarization can be switched (see e.g., Lines and Glass, 1977; Smolenskii, 1984). However, ferroelectricity is also compatible with metallicity and magnetic order. This leads to the additional categories of ferroelectric metals and multiferroics.

https://doi.org/10.1016/B978-0-323-90800-9.00164-5

In proper ferroelectrics, ferroelectricity implies a spontaneous symmetry breaking since there is always a reference non-polar structure that becomes (or would become) unstable with respect to polar distortions.[1] In many systems this happens by lowering the temperature. Such a loss of stability coincides with the transition temperature when the transition is continuous (or second order). These two points, however, are different when the transition is discontinuous (or first order). In this case, the transition point is above the undercooling limit of the non-polar state but below the overheating limit of polar one. Normally the difference between these points is small (e.g., a few degrees in the case of $BaTiO_3$) and the transition can be considered as weakly discontinuous.

The vicinity to such an instability explains not only the polarity reversal in these systems, but also their generic and multifaceted softness. The latter manifests through enhanced dielectric and piezoelectric responses, low-frequency optical vibration modes, and the appearance of ferroelectric textures such as domains and domain walls for example (that is, equivalent variants of the same ferroelectric phase and the spatial regions that separate them). In the so-called improper ferroelectrics, however, the instability is symmetry-wise different and the polar structure appears just as a by-product. Yet ferroelectrics of this type can also have interesting properties associated with the corresponding polarity, even if their inherent softness manifests differently. Furthermore, irrespective of any instability, the polarity reversal may be enabled by the weakness atomic bonding itself as in van der Waals systems, thereby defining a distinct class of genuinely different ferroelectric materials. In this article, we introduce these defining aspects of ferroelectricity in general terms.

Probing ferroelectricity

Historically, ferroelectricity has been discussed in dielectrics and defined from the electric polarization $\boldsymbol{P}$ (Lines and Glass, 1977; Smolenskii, 1984; Strukov and Levanyuk, 1998). In fact, the electric polarization $\boldsymbol{P}$ is one of the variables that formally describes the state of matter under a given set of physical conditions. Further, the equation of state (or constitutive equation) provides the relationship between these variables, which is useful in describing the properties of the corresponding system. In most ferroelectrics, the electric polarization can be associated to relatively small atomic displacements that render the corresponding structure polar[2] as illustrated in Fig. 1.

However, in traditional experiments such as the illustrated in Fig. 2, the quantity that is probed experimentally is the electric charge density instead. The so-called electric displacement $\boldsymbol{D}$ embodies such a charge density and is related to the electric polarization as $\boldsymbol{D} = \varepsilon_0\boldsymbol{E} + \boldsymbol{P}$, where ε_0 is the vacuum permittivity and $\boldsymbol{E}$ the electric field.

In the setup illustrated in Fig. 2(a), the constitutive equation $P(E)$ of the capacitor's dielectric is determined from the charge Q of the reference capacitor that is obtained via the applied voltage V ($D = Q/A$ and $E = V/d$, where A is the area of the plates and d is the plate separation). This would give the static constitutive equation if the measurement frequency is low enough. In most dielectrics P depends linearly on E up to dieletric breakdown fields [Fig. 3(a)]. In ferroelectrics, however, the form of $P(E)$ is qualitatively different [Fig. 3(b)]. Specifically, it has a nonlinear character and eventually becomes multivalued for $E = 0$ in the ferroelectric phase. Consequently, the system displays (at least) two equivalent states in which there is a "spontaneous" polarization. Then, by applying an electric field in the direction opposite to the spontaneous polarization, this polarization can be reversed if the field is higher than the

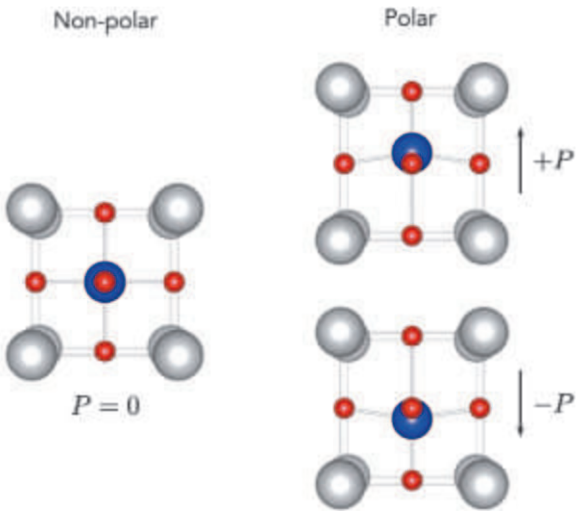

Fig. 1 Illustration of simple atomic displacements changing the symmetry of the crystal from non-polar to polar, thereby giving rise to a spontaneous polarization. For the sake of concreteness, the depicted cells correspond to the cubic → tetragonal structures of ABO_3 perovskites such as $BaTiO_3$ (A in gray, B in blue and O in red).

---

[1] The term "spontaneous symmetry breaking" is used to indicate the process in which a state becomes unstable and ends up in a less symmetric state by means of a symmetry-preserving agent such as temperature, hydrostatic pressure or chemical composition. For an illustration of this phenomenon based on a simple mechanical model see e.g., [Levanyuk, A.P., Burc M., I. and B. Okatan, M., 2020. Landau, Ginzburg, Devonshire and others. Ferroelectrics, 569(1), pp. 310–323].

[2] The crystallographic point group of a polar structure can be 1, 2, m, $mm2$, 4, $4mm$, 3, $3m$, 6, or $6mmm$, where every operation symmetry leaves more than one point unmoved (so that at least one component of vector quantities is invariant).

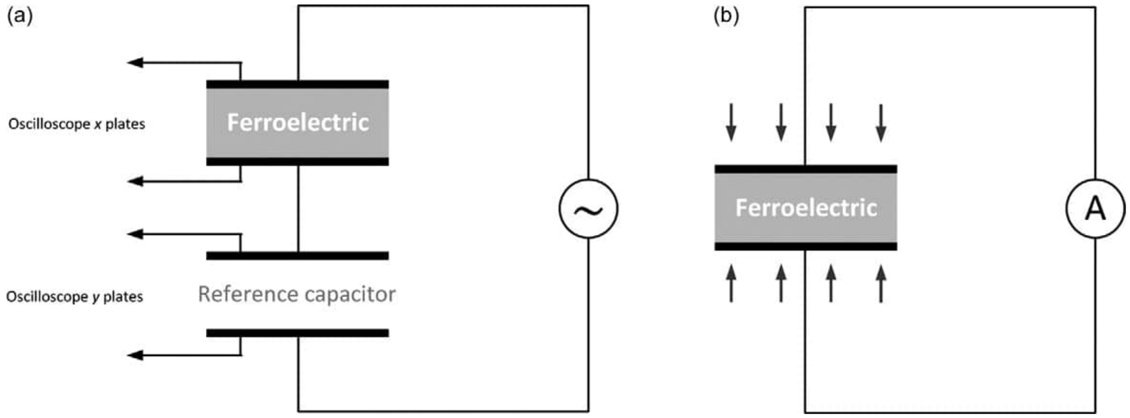

Fig. 2 The dependence of the electric polarization on the electric field can be measured with alternating voltage by means of the capacitor setup illustrated in (a). On one hand, the charge Q of the reference empty capacitor is the same as the charge of the filled capacitor. On the other hand, the y-deflection is proportional to Q while the x-deflection is proportional to the voltage on the dielectric plate. Further, the electric displacement is $D = Q/A$ with A being the area of the capacitor's plates, so that this experiment provides $D(E)$. In ferroelectrics usually $\varepsilon_0 E \ll P$ so that $D \sim P$. The change in the electric polarization, in its turn, can be measured with the setup illustrated in (b). In this case, one determines the transient currents obtained due to temperature changes (pyroelectric effect) or deformations (piezoelectric effect). The arrows indicate either heat flow or mechanical stress. The measured current then is $I = AdP/dt$.

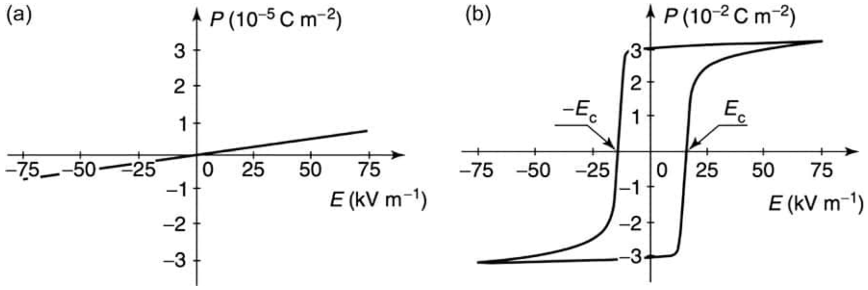

Fig. 3 Electric polarization P as a function of the electric field E for (a) a linear dielectric with $\varepsilon = 10$ and (b) the triglycine sulfate (TGS) measured at ambient temperature and frequency 0.1 Hz. The spontaneous polarization of this ferroelectric is 3.1×10^{-2}C/m^2 and the coercive field is $E_c = 15$ kV/m. From previous edition of the Encyclopedia of Condensed Matter Physics.

so-called "coercive field" [see Fig. 3(b)]. This was first observed in Rochelle salts more than 100 years ago and subsequently in other systems like potassium-dihydrogen phosphate (KDP). The oxide $BaTiO_3$, however, was the first robust-enough material in which ferroelectricity was observed in the mid-1940s and perovskites of this type still represent a testbed for ferroelectricity.

Fig. 2(b) sketches another type of canonical experiment to probe the variations of P. In this case, the setup measures transient electric currents that appear due to either a variation in temperature of the ferroelectric (pyroelectric effect) or its deformation (piezoelectric effect). In these experiments the electrodes are short-circuited. In this way, the electric field that would appear due to the spontaneous electric polarization in the ferroelectric[3] is compensated by free charges at the electrodes. This compensation is temporarily destroyed when the polarization changes due to the aforementioned perturbations and then restored via the transient currents. Thus, the measured current tracks the change in polarization and the direction of this current is linked to its orientation.

In order to have the pyroelectric effect, the structure of the system needs to be polar. Pyroelectric and piezoelectric effects, however, are not completely independent. The polarization may always change with the temperature as any characteristics of a crystal. This can happen in the absence of any deformation—i.e., in a completely clamped crystal—and also due to the thermal expansion in a free crystal. In the latter case the change in polarization can be seen as consisting of two parts: one directly associated with change in temperature, as if the crystal where clamped, and a second one due to the dependence of the polarization on the (temperature-induced) strains. The second part matches the polarization change obtained at fixed temperature when the same strains are produced by other means, and corresponds to the piezoelectric effect obtained via symmetry-preserving strains (as the thermal expansion do). However, there are also other strains that do change the symmetry of the crystal. These strains can be responsible for the piezoelectric effect even in non-polar yet non-centrosymmetric materials.

---

[3] In the hypothetical case of a free-standing ideal ferroelectric slab, homogeneously polarized, this field would be $-P/\varepsilon_0$ due to the bound charges that appear at the boundaries (recall that $-\nabla \cdot P = \rho_{\mathrm{bound}}$ where ρ_{bound} is the bound charge density). This field is the so-called depolarization field. It is opposite to the polarization and the energy associated to it represents an energy penalty that is avoided when the overall polarization is suppressed, which explains its name. In fact, to get a homogeneously polarized state as a result of phase transition with spontaneous symmetry breaking one has to eliminate this field. In theory, this is possible by means of the short-circuited ideal metallic electrodes. In practice, this field is reduced by the formation of domains—i.e., regions with opposite polarity (see below)—in most cases. The depolarizing field can also cause the diffusion of ions and the formation of charged defects.

Applications

The name “ferroelectrics” is due to the analogy between the aforementioned hysteretic behavior and that of ferromagnets. This property makes ferroelectrics similarly useful for memory and logic devices. This was proposed already in the 50s, although this type of ferroelectric devices was not suitable for commercialization due to material issues until the 90s (Auciello et al., 1998). At present new promising perspectives are discussed in this respect (Mikolajick et al., 2020, Mikolajick et al., 2021). Other applications of ferroelectrics are connected with their very large dielectric response: note the difference in scales of the P-axis in Fig. 3(a) and (b). In fact, if the electric field is low enough (in particular smaller than the coercive field), ferroelectrics behave as ordinary dielectrics but with very high dielectric constants $\varepsilon = 1 + \varepsilon_0^{-1} dP/dE$.. This enables to obtain a high capacitance in a small volume, which is exploited in commercially available capacitors. Ferroelectric ceramics based on perovskite materials such as $BaTiO_3$ and $Pb(Zr,Ti)O_3$ are commonly used in these capacitors (Lines and Glass, 1977). A high dielectric constant is also interesting for applications as gate insulators in field effect transistors. In addition, the spontaneous polarization itself can be used to retain the transistor’s state in the absence of external bias in ferroelectric field-effect transistors. In this respect, HfO_2 is currently considered as a particularly promising material. This oxide was initially introduced as a replacement of SiO_2 since it is integrable into silicon technology and displays a dielectric constant 4–6 times larger. However, the subsequent discovery of ferroelectricity in this system enlarges considerably its potential applications (Dragoman et al., 2021; Khan et al., 2020; Mikolajick et al., 2020).

The strength of both the pyroelectric and the piezoelectric effects in ferroelectrics can be much higher than in non-ferroelectric pyroelectric and piezoelectric materials due to different reasons outlined below. These features are exploited in thermal detectors, transducers, actuators and resonators (Lines and Glass, 1977; Smolenskii, 1984). The $Pb(Zr,Ti)O_3$ ceramic, in particular, has long been the most commonly used piezoelectric ceramic.

Ferroelectricity also yields specific optical properties such as second-harmonic generation that can be used to probe the properties of ferroelectric materials. Conversely, ferroelectric materials such as $LiNbO_3$ find applications thanks to these properties in nonlinear optics for example for laser frequency doubling. It becomes effective due to the so-called quasi-phase matching in a stable periodically polarized medium which can be realized in $LiNbO_3$ (Hum and Fejer, 2007). An interesting and highly non-trivial optical property of ferroelectrics and other non-centrosymmetric materials is the bulk photovoltaic effect, i.e., the generation of electric currents by light in absence of electric field and inhomogeneities (Sturman and Fridkin, 2021). Further, advances in microscopy enables to probe ferroelectricity at the atomic scale. This is particularly useful to study domains and domain walls, and thereby the local properties of ferroelectric materials that can be useful for device miniaturization. In fact, a number of ferroelectric materials can be grown with high quality by means of different deposition techniques and their ferroelectric properties can thus be engineered in heterostructures and superlattices.

Landau-Ginzburg-Devonshire framework

The electric polarization of traditional ferroelectrics has an emergent character in the sense that it can be associated to “spontaneous” changes in the structure of a reference, non-polar phase (see Fig. 1). These changes appear as a function of control parameters such as temperature or pressure in the absence of external electric field and involve relatively small atomic displacements. These displacements, however, change the symmetry of the material from non-polar to polar. This circumstance enables to describe ferroelectricity within the Landau theory of phase transitions, and thereby to describe a number of ferroelectric properties within a universal, material-independent framework (Strukov and Levanyuk, 1998). This was first put forward by Ginzburg, who identified the corresponding order parameter with the electric polarization P. A formally equivalent theory but with another background was proposed shortly after by Devonshire. Thus, when applied to ferroelectrics in this way, the Landau theory of phase transitions is called Landau-Ginzburg-Devonshire (LGD) theory.

Before illustrating the LGD theory, we first consider a conventional dielectric in the presence of an electric field $\boldsymbol{E}$. Because of the long-range nature of the Coulomb interaction, the potential energy of the dielectric depends on the overall configuration of the system beyond the dielectric itself. Bearing this in mind, it is convenient to assume that the dielectric is sandwiched between metallic plates that are connected to a charge reservoir (e.g., ideally an infinite side capacitor). Thus, the potential energy per unit volume of the dielectric as a function of the electric polarization $\boldsymbol{P}$ becomes $U = \frac{1}{2\varepsilon_0\chi}P^2 - \boldsymbol{E}\cdot\boldsymbol{P}$,[4] where χ is the electric susceptibility. The minimization of this energy with respect to $\boldsymbol{P}$ then gives the standard relationship $\boldsymbol{P} = \varepsilon_0\chi\boldsymbol{E}$ associated to Fig. 3(a). Note that, by using the potential energy to determine the polarization of equilibrium, we tacitly assume the classical limit for a system that is at zero temperature.

As we said before, the response of ferroelectrics is qualitatively different as it implies the hysteretic behavior illustrated in Fig. 3 (b). This behavior, however, can be conveniently reproduced by generalizing the above potential energy to the LGD form[5]

---

[4] The first term in the expression $U = \frac{1}{2\varepsilon_0\chi}P^2 - \boldsymbol{E}\cdot\boldsymbol{P}$ is directly associated with the dielectric while the second comes from the total electrostatic energy $\int_1 \frac{\varepsilon_0}{2}E^2 dv + \int_2 \frac{\varepsilon_0}{2}E^2 dv$. Here the first integral is carried out over the volume of the dielectric while the second one refers to the side capacitor acting as a charge reservoir. When $P = 0$ in the dielectric, then the electrostatic energy reduces to $\int_2 \frac{\varepsilon_0}{2}E^2 dv = \frac{Q^2}{2C}$ (Q is the total charge in the reservoir and C its capacitance). When $P \neq 0$, however, the charge $q = PA$ is transferred to the dielectric and therefore the electrostatic energy of the reservoir becomes $\frac{(Q-q)^2}{2C}$. The change in the electrostatic energy is therefore $\frac{(Q-q)^2}{2C} - \frac{Q^2}{2C} = -\frac{qQ}{C} + \frac{q^2}{2C} \approx -\frac{qQ}{C}$. Here $\frac{Q}{C} = V$ is the voltage difference. Since $E = VA/v_1$ and $q = PA$ in the dielectric, then the total change in electrostatic energy in energy per unit volume becomes $-EP$.

[5] For the sake of simplicity, we consider the case of a uniaxial ferroelectric in which the z direction is taken along the spontaneous polarization (so that $P = P_z$). The generalization to a multiaxial ferroelectric, in which the spontaneous polarization can point along different directions, is straightforward.

$$U = \frac{a}{2}P^2 + \frac{b}{4}P^4 - EP \tag{1}$$

whose minimization requires

$$aP + bP^3 = E. \tag{2}$$

Compared to the previous case, Eq. (1) can be seen as an energy expansion up to the next order in P as required if the $\mathcal{O}(P^2)$ term is comparatively small. The coefficient b then needs to be $b > 0$ in order to bound the energy from below. This expansion might be necessary irrespective of any ferroelectricity (i.e., for a non-linear dielectric). The emergence of ferroelectricity, however, can be described in this way by further assuming that the a coefficient in Eq. (1) vanishes and eventually changes sign from positive to negative (see Fig. 4). For $E = 0$, in particular, the solution of Eq. (2) is

$$P = \begin{cases} 0 \text{ if } a > 0 \\ \pm\sqrt{-a/b} \text{ if } a < 0 \end{cases}. \tag{3}$$

Further, the hysteretic $P(E)$ behavior shown in Fig. 3(b) is then automatically obtained as explained in Fig. 4(b) and (c).

In reality, Ginzburg and Devonshire put forth this approach to treat ferroelectric phase transitions driven by temperature. In this case, however, the equilibrium state is determined, not by the minimum of the potential energy, but by the minimum of a (non-equilibrium) free energy—i.e., the Landau free energy—whose precise meaning will be discussed below. Ginzburg and Devonshire skipped this point and directly employed a postulated free energy as we employed Eq. (1) above to successfully explain many properties of ferroelectrics. The conceptual foundations of this approach and its fundamental difficulties were pointed out at a later time as we outline below. For Ginzburg and Devonshire's purposes, however, these difficulties had no practical importance.

Thus, the original LGD theory bases on a free energy analogous to Eq. (1) where the coefficient a is assumed to vary via the temperature as $a(T) = a_0(T - T_c)$.[6] Accordingly, the electric polarization is found to increase gradually from zero in a continued fashion, describing a continuous (or second-order) paraelectric-ferroelectric transition. This is illustrated in Fig. 5(a).

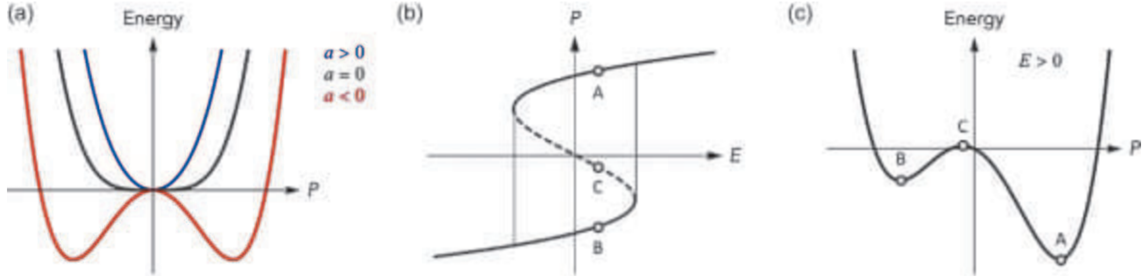

Fig. 4 (a) LGD form of the potential energy for $E = 0$. (b) Electric polarization as a function of the electric field according to Eq. (2) for $a < 0$. The solid part of the curve corresponds to solutions that, depending on the sign of the electric field, are either global or local minima of the energy while the dashed part corresponds to maxima. For $E > 0$, for example, the points A, B, and C correspond to stable, metastable and unstable states respectively as indicated in (c).

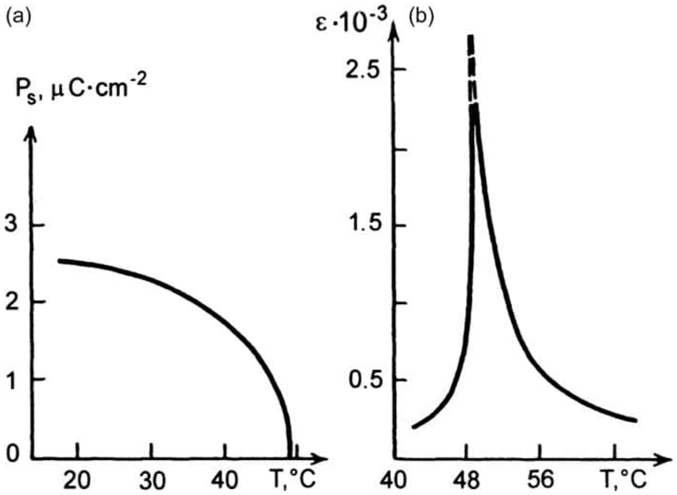

Fig. 5 Spontaneous polarization (a) and dielectric constant (b) measured as a function of temperature in triglycine sulfate (TGS). From Strukov BA, and Levanyuk AP (1998) *Ferroelectric Phenomena in Crystals*. Berlin: Springer. p. 27.

---

[6] The control parameter is typically temperature, pressure or chemical composition and the coefficients of the Landau free energy are expanded in terms of these quantities as a power series, retaining the lowest-order terms only.

The dielectric susceptibility, in its turn, is found to be $\chi = \frac{1}{\varepsilon_0}\frac{dP}{dE}\big|_{E=0} = \frac{1}{a+3bP^2}\Big|_{E=0} = \frac{1}{\zeta|a|}$ according to Eqs. (2) and (3), where $\zeta = 1$ in the paraelectric state ($P = 0$) and $\zeta = 2$ in the ferroelectric one ($P \neq 0$). Consequently, the Curie-Weiss behavior $\chi \propto |T - T_c|^{-1}$ illustrated in Fig. 5(b) is naturally reproduced within the LGD theory. Similarly, the pyroelectric coefficient becomes $\gamma = \frac{dP}{dT}\big|_{E=0} \propto |T - T_c|^{-1/2}$, which also diverges and tends to infinity near the transition point but with different scaling. Divergences of this type, however, end up into discontinuities if the spontaneous polarization changes abruptly from zero in the paraelectric phase to a finite value in the ferroelectric one.

The simplest way to reproduce a discontinuous (or first order) transition is to assume that $b < 0$ in Eq. (1) and to introduce the next higher-order term $\mathcal{O}(P^6)$ to bound the energy from below. This is in fact the case of most ferroelectrics, and in particular in the ferroelectric perovskites like $BaTiO_3$ (see Fig. 6), which is still compatible with the LGD approach if the discontinuity is relatively small. Such a discontinuity can be due to a number of different factors, but sometimes can be interpreted as due to the coupling between the electric polarization and other degrees of freedom that tacitly assumed to minimize the potential energy for a given P and therefore do not appear explicitly in Eq. (1). In those cases, a generalized LGD energy expanded not only in terms of P but also in terms of secondary variables such as strain may be invoked. The symmetry properties of these variables then determine the possible coupling terms (but obviously not their strength).

To illustrate this, let us consider the relative variation of the volume (i.e., the dilatation) u as such a secondary variable and supplement Eq. (1) with the terms $gP^2u + \frac{K}{2}u^2$. Here the first one represents the coupling term and K is the bulk modulus. The minimization of the overall potential energy with respect to the new variable implies $u = -\frac{g}{2K}P^2$. Thus, the added terms become $-\frac{g^2}{2K}P^4$ so that the actual coefficient of the eventual $\mathcal{O}(P^4)$ term reads $b - \frac{2g^2}{K}$. Consequently, if $b > 0$ but $b < \frac{2g^2}{K}$ then the transition can be interpreted as discontinuous due to the dilatation u since it would be otherwise continuous in a clamped ($u = 0$) system.

This treatment can also be generalized by considering the electric polarization as a field $P(\mathbf{r})$ rather than just a constant variable. Thus, it is possible describe states that are spatially inhomogeneous. The LGD energy then becomes a functional where the extra energy associated to a non-uniform P implies both local gradient terms and non-local interactions mediated by electric field that appears due to such a non-uniform P according to Gauss's law. By including the extra variables that describe inhomogeneous elastic strains then the non-local character of the solid-state elasticity can also be incorporated as well.

In fact, there are a number of inhomogeneous states that are relevant in relation to ferroelectricity. For example, in the aforementioned example, in which the coefficient of the $\mathcal{O}(P^4)$ term becomes negative due to the dilatation, an equilibrium two-phase state can be formed where a part of the system remains in the non-polar state while another part undergoes the polar distortion. A more important example is phase transition in a slab without electrodes with the polar axis perpendicular to the slab plane. It proves that the loss of stability of the non-polar phase occurs here not with respect to homogeneous polarization but with respect to inhomogeneous (sinusoidal) distribution of the polarization along the slab. In experiment this distribution can be observed only in special conditions (very thin slabs) because it converts into usual domain structure (see below) already in a near vicinity of the transition.

In the spirit of the Landau theory, energy expansions like Eq. (1) represent an expansion about the point at which the initial (paraelectric) state becomes unstable with respect to the corresponding order parameter (P), so that this order parameter appears "spontaneously" to minimize the energy thereby breaking the symmetry of the system (from a non-polar to a polar structure in the simplest ferroelectric case). Note that $P \propto E^{1/3}$ at $a = 0$ according to Eq. (2), so that $P/E \to \infty$ in the limit $E \to 0$ at that point. Thus, it is not surprising that in ferroelectrics $P \gg \varepsilon_0 E$, i.e., $P \approx D$.

Applicability of the LGD theory

Formally, the LGD theory can be related to a partition function in which all the internal degrees of freedom but P are integrated out, i.e., $Z(P;E) = \mathrm{tr}'\left(e^{-\hat{H}/k_B T}\right)$ where tr′ denotes such a partial integration. The LGD free energy then can be regarded as the power series expansion of $F_{\mathrm{LGD}}(P;E) = -k_B T \ln Z(P;E)$. The temperature dependence of the LGD free-energy coefficients is a natural consequence of this formal derivation. In practice, however, such a calculation is out of reach unless some approximations are

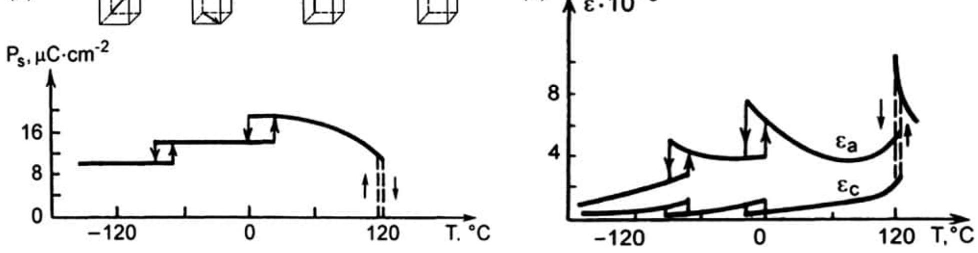

Fig. 6 Spontaneous polarization (a) and dielectric constant (b) measured as a function of temperature in $BaTiO_3$. The initial ferroelectric transition at ~120 °C is discontinuous. This transition is followed by structural transitions in which the direction of the polarization changes as indicated at the top of (a). From Strukov BA, and Levanyuk AP (1998) *Ferroelectric Phenomena in Crystals*. Berlin: Springer. p. 21.

made. These approximations justify the simple LGD power-series expansion relatively close to the transition point. However, they become invalid right at the (second-order) transition point due to the extreme specificity of this point. This is exemplified by Onsager's exact solution of the two-dimensional Ising model, which demonstrated that the behavior of this model at the transition point is fundamentally different compared to that obtained according to the Landau theory. It took several decades until this contradiction was resolved, which is considered as one of the main achievements of theoretical physics of the 20th century. Accordingly, the asymptotic behavior of various physical quantities is described in terms of "critical exponents" and there appears the notion of universality class (i.e., a group different models displaying the same critical exponents, which is eventually determined by their symmetry properties alone). Using renormalization group techniques, it was shown that the numerical value of these exponents can be calculated with reasonable accuracy.

At the same time, it was also understood that, apart from the immediate vicinity of a second-order transition, the Landau theory remains applicable in a number of realistic models. Thus, it can successfully describe many physical situations of interest. This is precisely the case of most of the conventional ferroelectrics due to some distinct features of these systems (characteristic energy scales and long-range interactions, together with the fact that in many cases the transition is discontinuous). Also, the critical behavior is extremely sensitive to disorder and defects so that the theoretical behavior expected in the ideal case is practically never observed for real ferroelectic materials. So, in practice, the LGD level of description is generally justified as a reasonable approximation.

Of more practical importance than inapplicability of the Landau theory in immediate vicinity of the instability point are inherent limitations of this theory which may hamper its consistent applications beyond this vicinity. Landau made use of a simple idea that the loss of stability is practically always with respect to a single ("critical") degree of freedom. This means that close to the instability (which coincides with the transition point for the second order transitions which this theory is about) the structural changes resulting from the stability loss can be characterized by a single variable to a good approximation (the closer the instability point the better this characterization is). In the case of proper ferroelectrics, this degree of freedom is polar by symmetry and very "soft" close to the instability point by definition. Its response to an electric field is then huge and, accordingly, dominates the total electric polarization over the contribution of the rest of polar degrees of freedom. This circumstance justifies the use of the polarization as the order parameter in the LGD theory and is the reason of its so attractive simplicity. However, it is also a reason for its limitation.

The identification of the total electric polarization with a single critical degree of freedom may become insufficient for the quantitative description of the actual structures and their properties at some distance of the instability. This has led to "extensions" of the LGD theory in which "non-critical" polar degrees of freedom, characterized via an empirical "base dielectric constant," are taken into account. This enables the qualitative explanation of experimental data in some cases. This type of extensions, however, spoils the universality of the LGD theory to become a case-by-case model (Levanyuk et al., 2016).

The shortcoming of identifying the electric polarization with the critical degree of freedom becomes most evident when the polar structure emerges in a metal such as $LiOsO_3$. In this case the polarization is screened by the free electrons, yet the polarity of the structure can still be reversed if this screening is somehow weakened as in ultrathin films. These special ferroelectrics are called ferroelectric metals (Zhou and Ariando, 2020).

The LGD approach, however, has no predictive power when it comes to material-specific quantitative questions such as the actual value of the spontaneous polarization and response functions such as the dielectric constant or, more generally, the precise chemical compositions that can host ferroelectricity. This motivates the development of complementary theoretical tools based on first principles, which have been demonstrated particularly successful in the context of ferroelectric materials (see e.g., Rabe et al., 2007). In particular, the electronic contribution to the variations of the polarization has been reformulated as a geometric quantum (Berry) phase, which is exploited in density-functional-theory calculations to compute not only the macroscopic polarization but also dielectric and piezoelectric tensors. However, the presence of defects and electrochemical effects still represents a challenge for the theoretical description of ferroelectricity in real systems.

Displacive vs order-disorder limits

More microscopically, the emergence of ferroelectricity is often regarded as either the displacive or the order-disorder limit of a structural phase transition.[7] To illustrate these two limits, let us consider a simple model of a one-dimensional crystal with two atoms per unit cell interacting via short-range potentials. Specifically, we consider intracell and intercell interactions between nearest cells only. Also, we assume that the atoms can be considered as classical particles (i.e., their masses are such that quantum effects can be neglected). This simple model is sketched in Fig. 7 (see also Strukov and Levanyuk, 1998).

---

[7] This can be additionally motivated by the characteristic energy scales that can be associated with ferroelectricity. In addition to the corresponding transition temperature T_c, some materials display another energy scale that matches the so-called atomic temperature $T_{at} \sim 10^4 - 10^5 K$ as deduced, for example, from the Curie-Weiss behavior of the electric susceptibility $\chi \sim C/|T - T_c|$ according to the Curie-Weiss constant C. The displacive limit corresponds to a situation dominated by interatomic interactions, which then provide T_{at} as a relevant energy scale. The instability behind the phase transition, and hence the corresponding value of T_c, results from the accidental cancelation of different energy contributions in this case. The order-disorder limit, in contrast, corresponds to a situation in which thermal effects play the key role with T_c as the only energy scale.

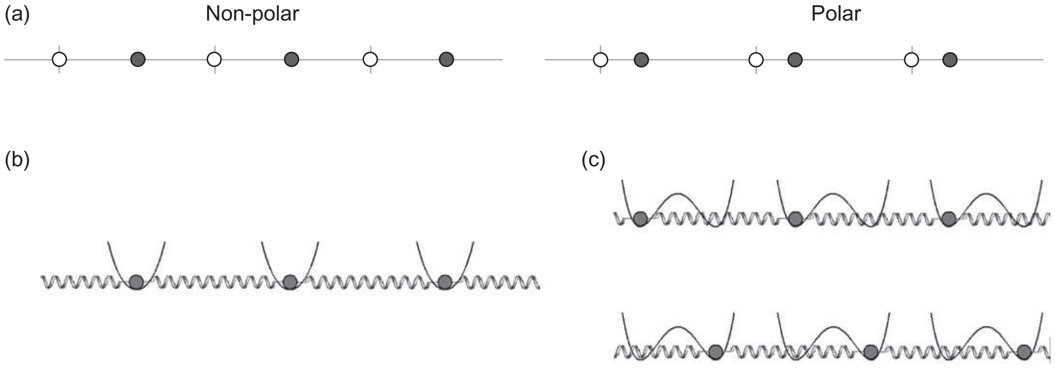

Fig. 7 (a) Sketch of a one-dimensional crystal with two atoms per unit cell undergoing a structural transition from a non-polar to a polar structure. (b) and (c) Effective model of the crystal. The balls indicate the relative displacement of the atoms in (a) while the curves represent the effective potential due to the intracell interactions and the springs model the (repulsive) intercell interactions.

In the displacive limit, the essential ingredient that produces the phase transition is the change of the intracell potential from Fig. 7(b and c). Accordingly, the particles undergo a relative displacement such that they shift from their initial centered positions either leftwards or rightwards, thereby breaking the symmetry of the crystal. The collective character of this phenomenon is enforced by the intercell interactions modeled by the springs, since they result in an energy penalty whenever the particles displace differently at different positions in the crystal.

In the order-disorder limit, in contrast, the intercell potential is always like in Fig. 7(c) and the key ingredient is the temperature.[8] At zero temperature all particles will be ordered, either leftwards or rightwards, as before. At finite temperature, however, the particles have a non-zero kinetic energy and their positions fluctuate. These fluctuations will destroy the low-temperature order toward more complex, globally disordered configurations in which the average displacement will be zero if the temperature is high enough. Effectively, this can be expected to occur when the thermal energy per particle (k_BT) becomes comparable with the change in potential energy obtained when one particle is at the "wrong" minimum of the intracell potential (i.e., comparable with intercell interactions modeled by the springs).

Note, however, that these two limits correspond to rather idealized situations. Thus, it is not surprising that real ferroelectrics may display features related to both these limits. Even for the above simple model, a mixed displacive and order-disorder behavior is to be expected if the springs are not totally rigid and/or the potential minima are not extremely narrow. In fact, at finite temperature, the order in a nominally displacive system can be expected to disappear before reaching the point at which the intracell potentials change from double- to single-well potentials due to thermal fluctuations. That is, a nominally displacive transition can be expected to become, in effect, an order-disorder one close enough the corresponding transition temperature. Similarly, at zero temperature, quantum zero-point fluctuations and/or tunneling may restore the symmetry of the system even if the intracell potentials remain double-well potentials.

Dynamics

The electric polarization in conventional ferroelectrics is directly related to collective changes in the atomic positions. In the aforementioned displacive limit, its equation of motion in the classical limit at zero temperature can be written as

$$m\frac{d^2P}{dt^2} + aP + bP^3 = E(t). \tag{4}$$

This is essentially the equation of motion of a nonlinear (anharmonic) oscillator driven by the external field. The first (inertial) term is associated with the kinetic energy of the collective motion. In the paraelectric phase, the nonlinear term can be neglected if the amplitude of the oscillations is small enough.[9] Then, the natural frequency of the oscillator is $\omega_0 = \sqrt{a/m}$ and therefore tends to zero as $a \to 0$ near the transition point. In this sense, the electric polarization is associated to a soft mode of the system.

The realistic generalization of Eq. (1) to finite temperatures, however, remains a challenge. In particular, it is necessary to describe the energy dissipation from the polarization mode to the rest of degrees of freedom of the system, which ideally represent an energy reservoir. The simplest attempt consists of introducing a dissipation term the form $\gamma \frac{dP}{dt}$.

In the order-disorder limit, in contrast, the motion is dominated by thermal activation as explained above. This situation formally matches the extreme overdamped regime ($m = 0$). The temporal processes are characterized by the relaxation time $\tau = \gamma/a$ which tends to infinity as $a \to 0$.

---

[8] Note that the model reduces to the Ising model when the potential wells are extremely narrow. In this case, the atoms can take only two positions so that their relative displacement becomes a discrete Ising variable $\pm u_0$ (rather than a continuous one).

[9] In the ferroelectric phase ($a < 0$), the non-linear term becomes essential even for small oscillations since Eq. (4) needs to be expanded about the equilibrium polarization.

In reality, this description oversimplifies the actual dynamics of P. As indicated in the previous section, the behavior of a real ferroelectric can evolve from the displacive limit to the order-disorder one as the transition temperature is approached. According to the above simplified dynamics, a soft mode should simply become overdamped sufficiently close to the transition if this is continuous. Before this happens, however, the displacive to order-disorder crossover often takes place and complicates the situation. Thus, the dynamics may remain essentially vibrational at high frequencies, but it can be expected to become relaxational at low frequencies. Experimentally, in fact, the frequency of the soft mode ceases to decrease when the transition is approached while its spectral weight, as measured in Raman experiments for example, is transferred to a low-frequency feature (i.e., the so-called central peak, see e.g., Ginzburg et al., 1980) whose integrated intensity diverges despite its width tends to zero.

Domains, domain walls and ferroelectric textures

According to Eqs. (1) and (2), there is an energy barrier for the polarization reversal from metastable to equilibrium states (see Fig. 4). This barrier formally disappears beyond a certain field $E_c^{(0)}$ that would determine the so-called thermodynamic coercive field.[10] In practice, however, the reversal is already possible at much lower fields (typically one or two orders of magnitude lower than $E_c^{(0)}$). The actual switching involves a number of processes some of which are still not well understood (Tagantsev et al., 2010). First, a nominally homogeneous polar sample can in fact contain "frozen-in" regions of opposite polarization that expand when the external field is applied. Second, the polarization can be initially reversed locally only in some regions and then these regions can grow and spread out to the entire sample (see Fig. 8). The nucleation of these regions is believed to occur at the boundaries of the sample or at volume defects, and their form is such that the corresponding depolarizing field is minimized since this field strongly contributes to the overall energy. The precise details of this "nucleation and growth" process, however, remain unclear. In particular, the estimates of both the critical dimensions and critical energy of the nucleation centers yield values that are hardly achievable by means of thermal fluctuations without the assistance of some defects or imperfections.

In any case, states with nonuniform polarization can be obtained not only during the polarization reversal but also when the system driven to the ferroelectric phase from the non-polar (paraelectric) one. The regions in which the polarization is in a uniform direction are called domains and the boundaries between these regions are dubbed domain walls. The formation of domains at phase transitions is inherent to the process of spontaneous symmetry breaking. In fact, different domains represent different possible variants of such a symmetry breaking that are energetically equivalent and they can be obtained one from another by the symmetry transformation that disappears due to the breaking.

The macroscopic structure of the domains and more microscopic details such as the structure of the domain walls—typically of a few unit cells—can be studied by means of different techniques spanning from etching and optical methods to atomic force and electron microscopy (Tagantsev et al., 2010). In general, there is an energy penalty associated with the presence of domain walls so that the formation of domains implies either a metastable state or an energy gain somewhere else compensating such a penalty. For example, if the spontaneous polarization is perpendicular to the boundary of the sample, then there will be an electric field created by the corresponding bound charges at the surface Σ since $\nabla \cdot \boldsymbol{P}|_\Sigma \neq 0$—i.e., the so-called depolarizing field. In that case, the energy of such a field can be reduced by the formation of domains despite the energy associated to the corresponding domain walls. However, if the surface bound charges are screened via the free carriers of metallic electrodes for example, then the domain-wall penalty will tend to favor the single-domain configuration. In fact, in many ferroelectrics, the application of even moderate electric field makes the crystal single domain.

The ferroelectric domain patterns can be quite diverse, especially in a multiaxial ferroelectric and even for the same crystal. However, there are some regularities, especially when it comes to the orientations of the domain walls. In conventional ferroelectrics, the domain walls tend to be such that the component of the polarization perpendicular to wall is continuous. In this way, no bound charge is generated and the domain wall remains neutral, thereby avoiding an extra electrostatic-energy penalty. Likewise, the domain walls tend to orient in such a way that the elastic energy is also minimized (which yields the so-called mechanical compatibility conditions for the polarization-induced strains). The charge-neutrality condition can be violated by creating free carriers to screen the bound charges. This leads to enhanced conductivity at the domain walls, with values that can approach metallic regimes in some cases. The domain walls then become reconfigurable two-dimensional conducting channels in otherwise insulating media, with additional properties analogous to some electronic devices (e.g., electronic switches).

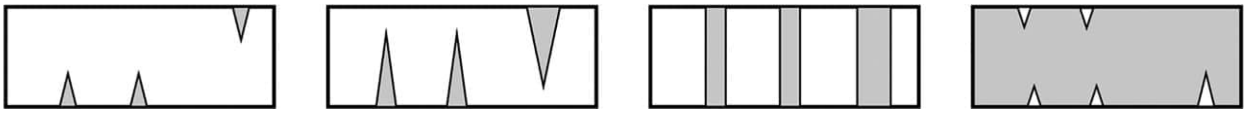

Fig. 8 Schematic representation of the polarization reversal via nucleation and growth process. The white/grey areas represent regions with opposite polarization.

---

[10] Note that thermodynamic coercive field would be associated with a process in which the polarization reversal occurs homogeneously and simultaneously across the whole ferroelectric.

In nano systems and in particular in multilayers, the interplay between depolarizing field, elastic, and gradient energy contributions can lead to complex ferroelectric textures with the electric polarization pointing in different directions. These range from the so-called flux-closure configurations to ferroelectric vortices and skyrmions, whose names announce topological properties (Das et al., 2020). Beyond that, the electric polarization in some special ferroelectrics can emerge as a by-product of another symmetry breaking and not as a primary order parameter by itself (see section "Improper ferroelectricity"). Then, if the primary order parameter displays some sort of texturing, this can be transposed to the electric polarization. The emergence of charged domain walls can be enforced in this way.

Ferroelectricity in liquid crystals and incommensurate ferroelectrics

In some liquid crystals, the so-called chiral smectics, there exists spontaneous polarization that changes its direction ("winds") if one translates along a special direction of these systems. The winding is periodic with a macroscopic pitch: 5–10 μm. The polarization can be made homogeneous by applying a relatively small electric field (Strukov and Levanyuk, 1998).

Another type of spatially inhomogeneous polarization, with changing magnitude rather than direction, is observed in some ordinary (solid) crystals. In this case, the period of the inhomogeneity just one or two orders of magnitude larger than the interatomic distance. It changes with temperature independently of the period of structural features that do not contribute to the polarization ("basic lattice"). The crystal has two independent ("incommensurate") periodicities. At some temperature, the polarization becomes homogeneous (within macroscopic domains), that is, there is a phase transition between the incommensurate and the ordinary ("commensurate") ferroelectric phase. This phase transition belongs to a special class of transitions ("lock-in transition"), which take place not only in ferroelectric but in many other systems, for example, in systems with charge density waves. In ferroelectrics, this transition is usually accompanied by a strong increase of the dielectric constant (Strukov and Levanyuk, 1998).

Improper ferroelectricity

In some materials, ferroelectricity appears not as a result of the instability with respect to P itself but as a non-linear effect arising in relation to symmetry breakings other than the non-polar to polar one (e.g., translational symmetry breaking as in all such cases reported so far, see Strukov and Levanyuk, 1998). These systems are called improper ferroelectrics and the notion of primary (Q) vs secondary (P) order parameters beyond the LGD paradigm becomes particularly helpful to describe their basic properties.

By definition, the primary order parameter Q of improper ferroelectrics has to be a multi-component quantity since the spontaneous polarization P cannot be simply proportional to it (otherwise Q and P would be equivalent from the symmetry point of view). In the simplest case, the primary order parameter is a two-component quantity $\mathbf{Q} = (Q_1, Q_2) = Q(\cos\Phi, \sin\Phi)$ and the electric polarization is $P \propto Q^n \cos(n\Phi)$ (or cos ↔ sin). Here, n is an integer that depends on the specific system under consideration ($n = 2$ in gadolinium molybdate and $n = 3$ in the hexagonal manganites for example). Such a P-Q relationship is determined by symmetry. Within the Landau theory, it can also be derived from a generalized energy expansion in terms of both Q and P under the same conditions of applicability than for standard ferroelectrics (that is, for continuous or weakly discontinuous transitions whenever critical fluctuations can be neglected). Thus, it can be understood that, while the corresponding constitutive $P(E)$ equation can lead to similar hysteresis loops as in the standard proper case, the dielectric susceptibility displays a discontinuity rather than a Curie-Weiss-like divergence.

Further, the actual domains of improper ferroelectrics are fundamentally determined by the primary order parameter and not by the spontaneous polarization alone. Likewise, the domain walls and the topological defects that can emerge in these systems are more complex objects with additional features compared to standard ferroelectrics. This facilitates the emergence of some special domain patterns with charged domain walls as illustrated in Fig. 9.

To further elaborate on this point, let us consider the particular case of the hexagonal manganites. In this case, the variable Φ appears in the Landau energy expansion via the term $gQ^6\cos(6\Phi)$ after minimization over P. Neglecting higher order terms, then the extrema of the free energy imply either $\Phi_k = k\pi/3$ or $\Phi_k = (2k+1)\pi/6$ with $k = 0, 1, \ldots 5$. Which type of solution corresponds to the minima—i.e., equilibrium states—depends on the sign of the coefficient g (which in its turn depends on the coupling to P).[11] These two sets of solutions define 6 polar states and 6 non-polar states. The 6 polar states, in their turn, correspond to 3 + 3 domains with opposite polarity. Then, unlike in proper ferroelectrics, there are now structural changes that leave the electric polarization unchanged (e.g., a translation by the unit cell of the non-polar structure, which is no more a symmetry operation of the polar phase). Consequently, there can be domain walls between different domains whose electric polarization, however, is same. Besides, the domain structure in these systems may display "topological defects" whose nature is qualitatively different compared to those that appear in proper ferroelectrics. The defects shown in Fig. 9, in particular, corresponds to 6 structural domains that meet at a singular line.

---

[11] The general phase diagram, however, can include not only the transition between the $Q = 0$ phase and one type of $Q \neq 0$ solution, but also the additional transition between different $Q \neq 0$ phases (i.e., the two phases determined by the two sets of Φ_k's).

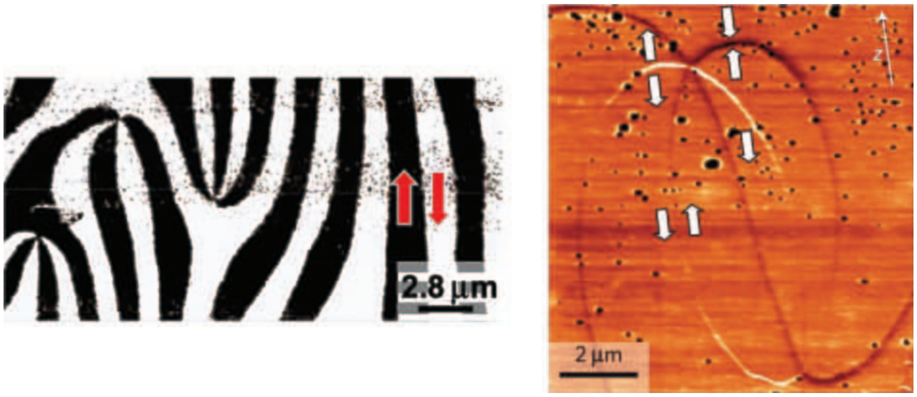

Fig. 9 Characteristic domain patterns observed in hexagonal magnanites (the arrows indicate the direction of the electric polarization). Left. Domain pattern with singular points from which there emerge six domains. The arbitrary inclination of the corresponding domain walls leads to bound charges and hence charged domain walls. Right. Conductive atomic force microscopy (c-AFM) image showing the different conductivity at the ferroelectric domain walls compared to the domains, which is linked to their charge. From Meier D, et al. (2012) Anisotropic conductance at improper ferroelectric domain walls. *Nature materials* 11(4): 284–288.

Multiferroics

The functional properties of ferroelectrics can be augmented by magnetic order like in the so-called type-I multiferroics (e.g., $BiFeO_3$ or the hexagonal manganites). In these systems ferroelectricity remains a purely structural phenomenon that emerges independently of the magnetism. However, ferroelectricity (either proper or improper) can also result from magnetic order itself and therefore be driven by spins. The systems materializing this latter possibility are called type-II multiferroics (Fiebig et al., 2016; Spaldin and Ramesh, 2019; Cano et al., 2021). The spontaneous electric polarization of type-II multiferroics is due to magneto-structural couplings. Consequently, its magnitude as well as the strength of the accompanying magnetoelectric effects depend on whether these couplings are due to relativistic effects or not. In general, the couplings trace back to either symmetric exchange interactions (e.g., Heisenberg exchange), antisymmetric exchange (Dzyaloshinskii-Moriya interaction), or both (see e.g., Bousquet and Cano, 2016). Non-centrosymmetric magnetic orders compatible with a spin-driven spontaneous polarization include the collinear *E*-type antiferromagnetic order displayed by the orthorhombic $HoMnO_3$ and the non-collinear cycloidal order observed in $TbMnO_3$. In addition, spin textures such as Néel domain walls in ferromagnets also break inversion symmetry and can locally induce an electric polarization.

Ferroelectricity beyond the Landau paradigm

As we have mentioned above, ferroelectrics are essentially pyroelectrics whose spontaneous electric polarization can be reversed due to some sort of softness of the system. We find it prudent and even compulsory to leave such a "softness" without strict definition. The reason is that, even if it can be described—case-by-case—in already known materials, it is hard to catalog and even harder to anticipate all its possible realizations.

In fact, for a century after the discovery of the first ferroelectric it was enough to associate this "softness" to the structural vicinity to another non-polar—and hence more symmetric—phase of reference. This vicinity is further the key for the success of the Landau theory-based description and classification of ferroelectrics. The reason is that it enables a description in terms of a single variable (i.e., the order parameter) with respect to which the reference (non-polar symmetric) phase losses its stability. This loss of stability is inherent in the phenomenon of the spontaneous symmetry breaking when the change of the symmetry can be achieved by any, even infinitely small, changes of atomic positions if the directions of these changes are properly defined.

More recently, however, it has been realized that this is not the only way to perceive reversible polar structures (Wu and Li, 2021). Rather than due to the vicinity to a loss of stability and the smallness of the corresponding structural changes, the softness can be effective simply due to the relative weakness of the atomic bonds themselves as in the so-called van der Waals materials. These materials can easily realize different stacking variants, either stable or metastable, some of which can be polar (see Fig. 10). Then, the polarization can be reversed by transforming one stacking into another. This generally requires a finite-distance shift in one or several directions, which however can be obtained by applying an electric field. This phenomenon was called "sliding ferroelectricity."

The classification of ferroelectrics used so far in this chapter is essentially based on the notion of order parameter and symmetry aspects as defined within the Landau theory. However, when trying to include sliding ferroelectricity within such a classification, we realize that no consistent description can be made in the spirit of the Landau theory (in particular, no order parameter can be identified). This forces us to introduce a new category and call this type of ferroelectricity non-Landau ferroelectricity.

To explain the situation, let us compare the energy profiles of the Landau and non-Landau ferroelectrics illustrated in Fig. 10. At first glance, the two profiles look the same. However, there is a very important fundamental difference between them: while the

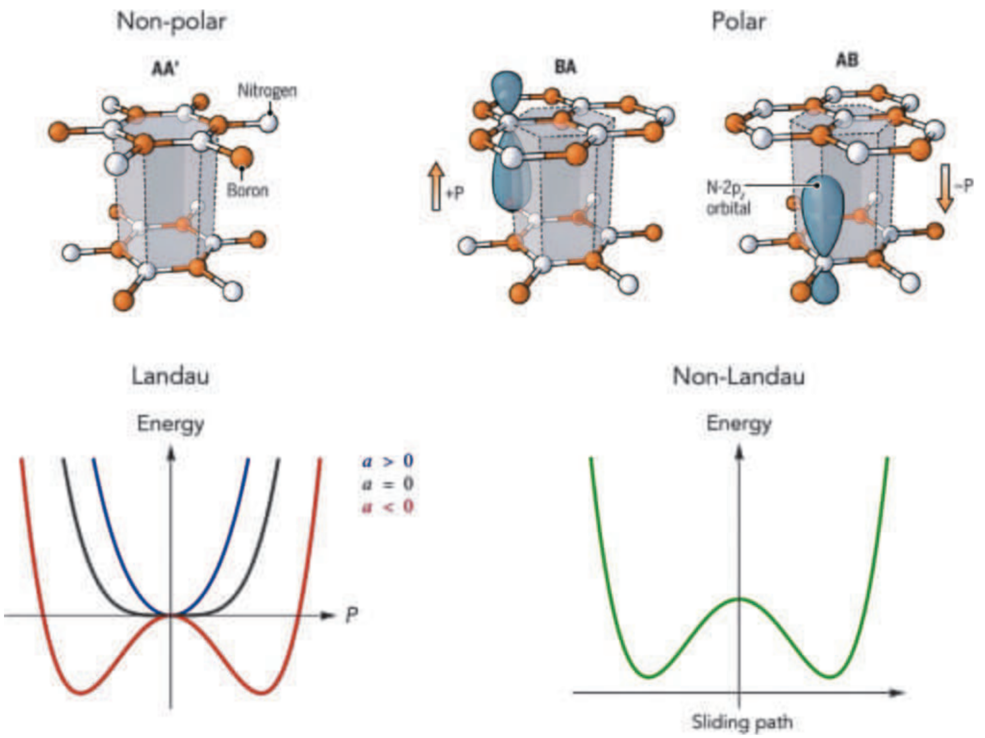

Fig. 10 Top panels: Illustration of different stackings associated to non-polar and polar structures than can be realized in non-Landau ferroelectrics like hexagonal boron nitride. The polarization in these systems can be reversed by in-plane interlayer sliding (so that the stacking changes from BA to AB or vice versa). Bottom panels: Energy landscape of Landau vs non-Landau ferroelectrics. While the former can be tuned by means of the control parameter, the latter is fixed and determined by the bondings. Adapted from Tsymbal EY (2021) Two-dimensional ferroelectricity by design. *Science* 372(6549): 1389–1390.

energy barrier and the distance between the two minima can be varied by means of the corresponding control parameter in the Landau case, they are fixed and essentially determined by the bondings in the non-Landau ferroelectric. Specifically, the point at which the barrier disappears and the distance is zero can be reached by varying the control parameter in the Landau case. This point is precisely the point at which the non-polar phase loses its stability. As emphasized above, the very existence of this point and its vicinity turns out to be fundamental for the success of the Landau-theory reasonings. The situation, however, is fundamentally different in the non-Landau case since the appearance of ferroelectricity cannot be traced back to any loss of stability. Consequently, there is no evident control parameter by means of which the energy barrier and/or the distance between the energy minima can be tuned to disappear. In this sense, the shape of the energy landscape is fixed in the non-Landau case. Of course, a theory as simple and effective as the Landau theory is highly desirable to describe these systems. At present, however, this is theory does not exist and it looks like a rather challenging problem.

Conclusion

Ferroelectricity in traditional ferroelectric materials is now a rather well understood phenomenon that can be characteristically denoted as emergent. In that case, the Landau theory of phase transitions provides a convenient starting point that can be further combined with microscopic models and *ab intio* descriptions to describe the distinct properties of ferroelectric systems. These properties promote a number of functionalities that can be supplemented with magnetic order in multiferroics and even metallicity. These multi-faceted functionalities span different length scales, from macroscopic behavior to the atomic scale, and can be engineered via the control of ferroelectric domains and domain walls as well as via the growth of heterostructures. This enables an increasing number of ferroelectricity-based applications, especially in electronics among other fields. Further, a new class of ferroelectric materials beyond the Landau paradigm has appeared recently. Ferroelectricity in these new systems does not have an immediate emergent character and thus calls for a new theoretical framework.

References

Auciello O, Scott JF, and Ramesh R (1998) The physics of ferroelectric memories. *Physics Today* 22–27.
Bousquet E and Cano A (2016) Non-collinear magnetism in multiferroic perovskites. *Journal of Physics: Condensed Matter* 28(12), 123001.
Cano A, Meier D, and Trassin M (eds.) (2021) *Multiferroics: Fundamentals and Applications*. Walter de Gruyter GmbH.
Das S, et al. (2020) A new era in ferroelectrics. *APL Materials* 8(12): 120902.

Dragoman M, et al. (2021) The Rise of Ferroelectricity at Nanoscale: Nanoelectronics is rediscovering the ferroelectricity. *IEEE Nanotechnology Magazine* 15(5): 8–19.
Fiebig M, Lottermoser T, Meier D, and Trassin M (2016) The evolution of multiferroics. *Nature Reviews Materials* 1(8): 1–14.
Ginzburg VL, Levanyuk AP, and Sobyanin AA (1980) Light scattering near phase transition points in solids. *Physics Reports* 57(3): 151–240.
Hum DS and Fejer MM (2007) Quasi-phasematching. *Comptes Rendus Physique* 8(2): 180–198.
Khan AI, Keshavarzi A, and Datta S (2020) The future of ferroelectric field-effect transistor technology. *Nature Electronics* 3(10): 588–597.
Levanyuk AP, Strukov BA, and Cano A (2016) Background dielectric permittivity: Material constant or fitting parameter? *Ferroelectrics* 503(1): 94–103.
Lines ME and Glass AM (1977) *Principles and Application of Ferroelectrics and Related Materials*. Oxford: Oxford University Press.
Mikolajick T, Schroeder U, and Slesazeck S (2020) The past, the present, and the future of ferroelectric memories. *IEEE Transactions on Electron Devices* 67(4): 1434–1443.
Mikolajick T, et al. (2021) Next generation ferroelectric materials for semiconductor process integration and their applications. *Journal of Applied Physics* 129(10): 100901.
Rabe KM, Ahn CH, and Triscone JM (2007) *Physics of Ferroelectrics, A Modern Perspective*. Berlin, Heidelberg: Springer.
Smolenskii GA (1984) *Physics of Ferroelectric Phenomena*. New York: Gordon and Breach.
Spaldin NA and Ramesh R (2019) Advances in magnetoelectric multiferroics. *Nature Materials* 18(3): 203–212.
Strukov BA and Levanyuk AP (1998) *Ferroelectric Phenomena in Crystals*. Berlin: Springer.
Sturman BI and Fridkin VM (2021) *The Photovoltaic and Photorefractive Effects in Noncentrosymmetric Materials*. Routledge.
Tagantsev A, Cross LE, and Fousek J (2010) *Domains in Ferroic Crystals and Thin Films*. New York: Springer.
Wu M and Li J (2021) Sliding ferroelectricity in 2D van der Waals materials: Related physics and future opportunities. *Proceedings of the National Academy of Sciences* 118(50): e2115703118.
Zhou WX and Ariando A (2020) Review on ferroelectric/polar metals. *Japanese Journal of Applied Physics* 59(SI): SI0802.

Planar quantum dots: Theoretical approaches

Aram Manaselyan, Vram Mughnetsyan, and Albert Kirakosyan, Department of Solid State Physics, Yerevan State University, Yerevan, Armenia

© 2024 Elsevier Ltd. All rights reserved.

Introduction 297
Confinement models and the energy spectra 298
Square well model 298
Parabolic well model 299
The effect of non-parabolicity and anisotropy of the confinement potential 300
Quantum dot in a magnetic field: Landau levels vs the Fock-Darwin states 301
Electron-electron interactions in QDs 304
Magic numbers and the Maksym-Chakraborty effect 304
Conclusion 306
Acknowledgments 306
References 306

Abstract

A brief discussion on the theoretical aspects of electron states in planar quantum dots is presented in this chapter. Some common models of electron confinement, such as rectangular and parabolic confining potentials are analyzed in detail. The deviations from the isotropy and parabolicity of the confinement are also considered in the light of the application of some well-known models such as the Woods-Saxon potential in planar quantum dot systems. Further, appearance of Fock-Darwin states in a quantum dot with parabolic confinement in a uniform magnetic field is discussed. A special attention is devoted to the electron-electron Coulomb interaction in planar quantum dots. Finally, the appearance of magic numbers and the Maksym-Chakraborty effect for Fock-Darwin states connected with the interplay of parabolic confinement and the inter-particle interactions is discussed.

Key points

- Quantum dots are fascinating objects which can have technological applications in many different fields.
- Planar quantum dots are nanosized semiconductor islands where electrons behave like 2D quasi-particles.
- Planar quantum dots are ideal systems for observation of Fock-Darwin spectrum and Landau levels.
- In quantum dots with parabolic confining potential far infrared spectrum is not affected by electron-electron interaction.
- In planar quantum dots with many electrons the ground state in a magnetic field occurs only at certain magic values of angular momentum.

Introduction

It is well known that the decrease of the geometric sizes of a specimen to the values of the order of the de Broglie wavelength of quasi-particles gives rise to the quantization of their motion in the specimen (Fröhlich, 1937) and, therefore to discrete energy levels. Quasi-particles in semiconductors have relatively large de Broglie wavelength, in particular, because of relatively small effective masses. With recent advances in crystal growth and processing techniques, it is possible to confine electrons and holes in extremely thin semiconductors with nanometer dimensions. Band gaps of semiconductors can be tuned by varying specimen sizes and when the size of the specimen decreases to the order of the electron de Broglie wavelength, the structures obtain new electronic and optical properties due to the size quantization (Guozhong, 2004). This procedure can be developed by further reducing the dimensionality of the specimen from a two-dimensional quantum well (QW) to a one-dimensional quantum well wire (QWR) and eventually to a zero-dimensional quantum dot (QD) (Davies, 1998; Harrison and Valavanis, 2016). In this context, the dimensionality refers to the number of degrees of freedom in the electron motion. The continuing reduction of dimensional features in electronic and optoelectronic devices coupled with revolutionary advances in semiconductor growth and processing technologies have opened many avenues for increasing the performance levels and functionalities of electronic and optoelectronic devices. Moreover, the advanced nanotechnologies lead to further revolutionary breakthroughs such as those exemplified by quantum dot semiconductor lasers, double barrier quantum dot diodes operating in the terahertz frequency range, single electron transistors, quantum dot solar cells and displays, etc. (Xi and King, 2012).

In this chapter the theoretical approaches of the so called planar (two-dimensional) semiconductor QDs will be described. In general, a semiconductor system can be considered as strictly two-dimensional only if the lowest two-dimensional subband is

https://doi.org/10.1016/B978-0-323-90800-9.00016-0

occupied. This is the same as the condition that the Fermi energy lies far below the second subband, or stated differently, as the condition that the thickness of the planar QD is much less than the average separation of the electrons. Similar conditions also hold for one-dimensional systems. In case of QDs the system can be considered as two dimensional if the energy separation of two neighboring discrete levels related to growth direction is much larger compared with energy separation for in-plane directions. Low-dimensional electron systems are, therefore, low dimensional only in the dynamical sense.

In section "Confinement models and the energy spectra" of this article the different models of confining potential for isotropic and anisotropic planar QDs will be described. In section "Quantum dot in a magnetic field: Landau levels vs the Fock-Darwin states" the effect of external magnetic field on energy spectra of planar QDs will be considered. Finally in section "Electron-electron interactions in QDs" the effect of electron-electron interactions will be discussed.

Confinement models and the energy spectra

Quantum dots, also popularly known as "artificial atoms" (Alivisatos, 1996; Bimberg et al., 1998; Chakraborty, 1999), in which the confining potential replaces the potential of the nucleus, are fascinating objects which can have and already have technological applications in many different fields such as memory chips, quantum computations and cryptography, room temperature quantum dot lasers (Steiner, 2004), quantum dot solar cells (Sogabe et al., 2016), bioimaging applications (Bera et al., 2010), etc. The semiconductor quantum dots are mostly semiconductor heterostructures in which a small island of narrower band-gap semiconductor (dot material) is inserted inside the matrix of wider band-gap semiconductor (barrier material). These types of quantum dots are mostly created using self-assembly growing technology (Henini, 2008).

The self-assembled quantum dots mostly have cylindrical symmetry and the size of the dot in growth direction (z-direction) is much smaller compared with planar sizes of the dot: $L_z \ll R$ or for a specimen with longitudinal sizes L_x and L_y, $L_z \ll L_x, L_y$. Due to the strong size quantization effect in the z-direction the energy difference between the first two lowest energy levels $\Delta E_\perp$ in that direction will be proportional to $\hbar^2/mL_z^2$, where m is the effective mass of the quasi-particle in the dot material. On the other hand the energy difference between neighboring states for the lateral direction $\Delta E_\parallel \sim \hbar^2/mR^2$, where R is the lateral radius of the dot. Since $L_z \ll R$, one can assume that $\Delta E_\parallel$ is much smaller than $\Delta E_\perp$, and all electrons in the QD will occupy only the ground state related to the z-direction. Therefore, one can assume with high accuracy that the particle motion in the z-direction is frozen and the system can be considered as 2D or planar.

Within the frame of the effective mass approximation the single-electron Schrödinger equation in a planar quantum dot has the form:

$$\left[-\frac{\hbar^2}{2m}\Delta + V_{\mathrm{conf}}(x,y)\right]\psi(x,y) = E\psi(x,y), \tag{1}$$

where Δ is the 2D Laplace operator and $V_{\mathrm{conf}}(x,y)$ is the confining potential of the dot. Thus one of the first steps of theoretical modeling of planar QDs is the construction of a confining potential of the dot. Here we will consider several models for the confinement.

Square well model

One of the most simple and widely used models for a confining potential of planar QDs is the square well model:

$$V_{\mathrm{conf}}(x,y) = \begin{cases} 0, & \sqrt{x^2+y^2} \le R, \\ V_0, & \sqrt{x^2+y^2} > R. \end{cases} \tag{2}$$

This model describes a disk-shaped planar QD obtained using abrupt semiconductor heterojunctions. In Eq. (2) V_0 is the height of the potential barrier, which can be determined from the band gap difference $\varDelta E_g$ between two semiconductors making the QD: $V_0 = Q_e \varDelta E_g$, where Q_e is the conduction band discontinuity fraction. For example, in GaAs/$\mathrm{Ga_{0.7}Al_{0.3}As}$ heterostructure $\varDelta E_g = 374.1$ meV, $Q_e = 0.6$ and $V_0 = 225$ meV (Adachi, 2004; Vurgaftman et al., 2001).

For a circular QD the Schrödinger equation (1) will be easier to solve in polar coordinate systems:

$$\left[-\frac{\hbar^2}{2m}\left(\frac{\partial^2}{\partial\rho^2} + \frac{1}{\rho}\frac{\partial}{\partial\rho} + \frac{1}{\rho^2}\frac{\partial^2}{\partial\varphi^2}\right) + V_{\mathrm{conf}}(\rho)\right]\psi(\rho,\varphi) = E\psi(\rho,\varphi), \tag{3}$$

where $V_{\mathrm{conf}}(\rho) = 0$ if $\rho \le R$ and $V_{\mathrm{conf}}(\rho) = V_0$ otherwise. We can search the solution of Eq. (3) in the form

$$\psi(\rho,\varphi) = \frac{C}{\sqrt{2\pi}}\exp(il\varphi)f(\rho), \tag{4}$$

where C is the normalization constant, the angular quantum number l due to the periodicity condition $\psi(\rho,\varphi+2\pi) = \psi(\rho,\varphi)$ takes the values $l = 0, \pm 1, \pm 2, \ldots$ and $f(\rho)$ is the radial wave function. By substituting Eq. (4) into Eq. (3) one can obtain an equation for the radial wave function $f(\rho)$:

$$\left[-\frac{\hbar^2}{2m}\left(\frac{d^2}{d\rho^2} + \frac{1}{\rho}\frac{d}{d\rho} - \frac{l^2}{\rho^2}\right) + V_{\mathrm{conf}}(\rho)\right]f(\rho) = Ef(\rho). \tag{5}$$

It is easy to show that the solution of Eq. (5), satisfying to conditions of continuity and finiteness of the wave function, can be expressed by the Bessel function $J_l(x)$ and the Macdonald function $K_l(x)$ (Abramowitz and Stegan, 1970):

$$f(\rho)=\begin{cases} J_l(\alpha\rho), & \rho\leq R,\\ \dfrac{J_l(\alpha R)}{K_l(\beta R)}K_l(\beta\rho), & \rho>R, \end{cases} \tag{6}$$

where $\alpha=\sqrt{2mE/\hbar^2}$ and $\beta=\sqrt{2m(V_0-E)/\hbar^2}$. Since here we are interested only with bound states in the QD, we will assume that $E<V_0$.

The energy eigenvalues of the QD can be obtained using the continuity condition of the first derivative of the radial wave function $f(\rho)$ at point $\rho=R$:

$$\left.\frac{dJ_l(\alpha\rho)}{d\rho}\right|_{\rho=R}=\frac{J_l(\alpha R)}{K_l(\beta R)}\left.\frac{dK_l(\beta\rho)}{d\rho}\right|_{\rho=R}. \tag{7}$$

By solving Eq. (7) numerically for given values of R, V_0 and l one can obtain the energy levels of the QD in the range $0\leq E\leq V_0$. For the given value of angular quantum number l the energy eigenvalues of the QD can be numbered from the lowest to the highest using the analog of the radial quantum number $n=1, 2, 3, \ldots$. Therefore each quantum state in a QD can be described using two quantum numbers n, l, i.e., $|n,l\rangle$ and the corresponding energy will be E_{nl}. It should be also noted that each state of the QD is degenerate by the sign of l and also doubly degenerate due to the spin of the electron.

In Fig. 1 the dependence of the first few energy levels of a QD with square well potential on the radius of the QD are presented for various values of the angular quantum number l. Calculations are performed for the GaAs/$\text{Ga}_{0.7}\text{Al}_{0.3}$As QD with parameters $m=0.067m_0$ (m_0 is the free-electron mass) and $V_0=225$ meV. For all values of the QD radius the ground state energy is E_{10}. With the increase of R the ground state energy decreases and tends to 0 (the bottom of the conduction band for the dot material). In the classical limit ($R\to\infty$) the distances between the neighboring energy levels tend to 0 and the continuous spectra will be obtained. For another limiting case $V_0\to\infty$ from the boundary condition at point $\rho=R$ we get $J_l(\alpha R)=0$, and an analytical expression can be obtained for the energy spectrum of the QD:

$$E_{nl}=\frac{\hbar^2\lambda_{nl}^2}{2mR^2}, \tag{8}$$

where λ_{nl} is the n-th zero of the Bessel function $J_l(x)$.

Parabolic well model

Another model of the confinement potential for the QD, widely used by many authors, is the parabolic potential well model (Chakraborty, 1999; Maksym and Chakraborty, 1990):

$$V_{\text{conf}}(\rho)=\frac{m\omega_0^2\rho^2}{2}. \tag{9}$$

This model describes a QD created by non-abrupt heterojunctions and one of the reasons for the appearance of the parabolic potential is the diffusion at the interface between the QD and the barrier materials (Barker and O'Reilly, 1999). The parameter ω_0 in Eq. (9) has the dimensionality of frequency (s^{-1}). The main advantage of this model is that it can be solved analytically. The corresponding Schrödinger equation for the QD with the confinement potential (9) coincides with the problem of 2D harmonic oscillator:

$$\left[-\frac{\hbar^2}{2m}\left(\frac{\partial^2}{\partial\rho^2}+\frac{1}{\rho}\frac{\partial}{\partial\rho}+\frac{1}{\rho^2}\frac{\partial^2}{\partial\varphi^2}\right)+\frac{m\omega_0^2\rho^2}{2}\right]\psi(\rho,\varphi)=E\psi(\rho,\varphi). \tag{10}$$

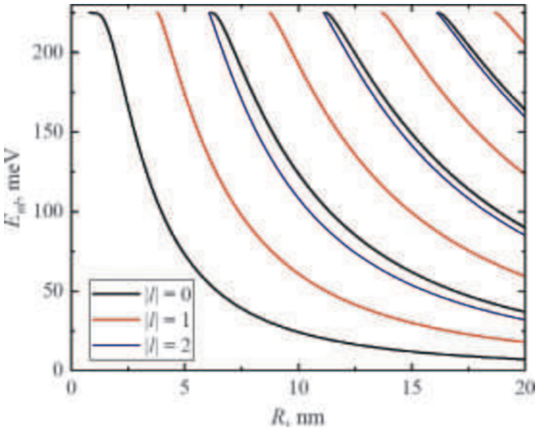

Fig. 1 First few energy levels of a planar GaAs/$\text{Ga}_{0.7}\text{Al}_{0.3}$As QD with square well confining potential vs the radius of the dot.

Due to the circular symmetry of the parabolic confinement potential we again can search the solution of Eq. (10) in the form of (4). As a result for the radial wave function we get

$$\left[-\frac{\hbar^2}{2m}\left(\frac{d^2}{d\rho^2}+\frac{1}{\rho}\frac{d}{d\rho}-\frac{l^2}{\rho^2}\right)+\frac{m\omega_0^2\rho^2}{2}\right]f(\rho)=Ef(\rho). \tag{11}$$

The solution of Eq. (11) can be found in textbooks on quantum mechanics (see e.g., Flügge, 1999). The energy eigenvalues are given by the expression

$$E_{nl}=\hbar\omega_0(2n+|l|+1),\quad n=0,1,2\ldots,\quad l=0,\pm 1,\pm 2,\ldots, \tag{12}$$

and for the corresponding wave functions we get

$$|n,l\rangle\equiv\psi_{nl}(\rho,\varphi)=\frac{1}{a}\sqrt{\frac{n!}{\pi(n+|l|)!}}\exp\left(-\frac{\rho^2}{2a^2}\right)\left(\frac{\rho}{a}\right)^{|l|}L_n^{|l|}\left(\frac{\rho^2}{a^2}\right)\exp(il\varphi), \tag{13}$$

where $a=\sqrt{\hbar/m\omega_0}$ and $L_n^l(x)$ are the Laguerre polynomials.

In Fig. 2(A) the schematic picture of the energy spectrum of a QD with parabolic confinement potential is presented. The ground state is $|n,l\rangle=|0,0\rangle$ with the energy $E_{00}=\hbar\omega_0$. All energy levels are equidistant and the separation between neighboring levels is again equal to $\hbar\omega_0$. All states except the ground state are degenerate, and the degeneracy of a state $|n,l\rangle$ is $N=2n+|l|+1$. Therefore we can state that the main parameter which describes the entire energy spectrum of parabolic QD is $\hbar\omega_0$. The question now is how to choose the correct value for it using physical parameters of the dot: radius R and the barrier height V_0. We can estimate ω_0 using, e.g., the condition $m\omega_0{}^2R^2/2=V_0/2$, which will lead to

$$\omega_0=\sqrt{\frac{V_0}{mR^2}}. \tag{14}$$

As an example in the GaAs/Ga$_{0.7}$Al$_{0.3}$As heterostructure, $m=0.067m_0$, $V_0=225$ meV and when the radius of QD $R=10$ nm we get $\hbar\omega_0\simeq 50$ meV. In Fig. 2(B) the parabolic confinement potential (solid line) and the square well potential (dashed line) are presented for GaAs/Ga$_{0.7}$Al$_{0.3}$As QD of radius 10 nm. Corresponding energy levels for a parabolic QD are also presented.

The effect of non-parabolicity and anisotropy of the confinement potential

Because of the difference of elastic constants, usually an elastic strain field arises between the QD and the surrounding material, which can lead to the breaking of the QD symmetry and hence to the modification of the band structure. For weakening of the strain and stress in such structures one should smoothen the abrupt heterojunction between the QD and the matrix. One of the efficient methods is the post-growth rapid thermal annealing (Agarwal et al., 2013) that induces interdiffusion between the heterojunction materials resulting in the disappearance of the strain field and to the smearing of QD confining potential. Such strain-free QD structures are shown to have better optical quality that makes them excellent candidates in the QD laser and photovoltaic applications (Jo et al., 2011; Wu et al., 2010). While the parabolic potential is reliable for modeling smooth and deep confining potentials, it is not appropriate for description of a finite potential with a smooth profile, especially, when one deals with an array of QDs with a non-vanishing quantum interaction. In such cases the theoretical description of electron dynamics in the QDs becomes possible owing to the application of some model potentials that are widely used in other fields of physics. One of them is the so called Woods-Saxon potential that was first introduced for modeling of the nucleons' interaction in the atomic nucleus (Woods and Saxon, 1954). The modified 2D Woods-Saxon potential which can be used to describe the confinement potential of planar QDs has the following form:

$$V_{\mathrm{conf}}(\rho)=V_0\left(1-\frac{1}{1+\exp\left(\frac{\rho-R}{\alpha}\right)}\right) \tag{15}$$

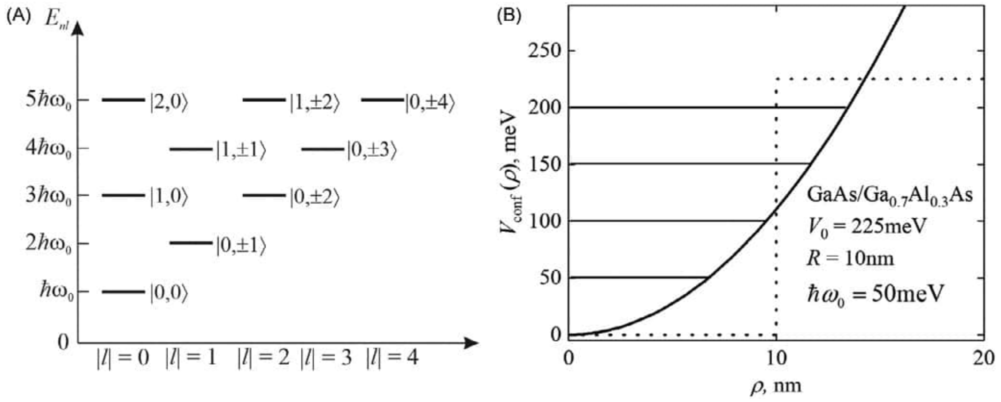

Fig. 2 (A) Schematic picture of the energy spectra with corresponding quantum states $|n,l\rangle$ of a QD with parabolic confinement potential. (B) Parabolic potential model for GaAs/Ga$_{0.7}$Al$_{0.3}$As QD of radius 10 nm with $\hbar\omega_0=50$ meV. Dashed line corresponds to the equivalent square well potential.

where ρ is the distance from the QD center, R is the QD radius, V_0 describes the "initial" (for the rectangular well without smearing) depth of the potential and α is the smearing parameter, which describes the characteristic thickness of the heterojunction. It has been shown that one can successfully fit the potential profile formed due to the interdiffusion process by an appropriate choice of the above mentioned parameters as functions of the diffusion length (Aziz Aghchegala et al., 2011; Mughnetsyan and Kirakosyan, 2008). The plot of the modified 2D Woods-Saxon potential in unites of V_0 is presented on Fig. 3(A) for different values of the smearing parameter. It is easy to see that the potential value at $\rho = R$ is the half of the "initial" potential. The rectangular potential profile, which corresponds to $\alpha \to 0$ is presented as dashed line. The dependence of the electron energies for the several lowest energy levels inside a QD on the Woods-Saxon parameter is presented on Fig. 3(B) for the QD radius $R = 10\,\text{nm}$ and the "initial" height of the potential barrier $V_0 = 228\,\text{meV}$. The energy values are calculated for the electron effective mass $m = 0.067m_0$, which corresponds to the motion in the GaAs material. As is seen from the figure the effect of smearing is comparatively strong for the energy levels in the middle of the potential well.

The anisotropy effects of a planar QD can be taken into account by a parabolic confinement potential with different ($\omega_1 \neq \omega_2$) frequencies along the x and y axes, which will model an elliptic QD:

$$V_{\text{conf}}(x, y) = \frac{m\omega_1^2 x^2}{2} + \frac{m\omega_2^2 y^2}{2}. \tag{16}$$

For this case the energy spectrum of the QD will be a sum of two 1D harmonic oscillator energies and the wave functions will be the products of two 1D harmonic oscillator eigenfunctions:

$$E_{n_1 n_2} = \hbar\omega_1\left(n_1 + \frac{1}{2}\right) + \hbar\omega_2\left(n_2 + \frac{1}{2}\right), \tag{17}$$

$$\psi_{n_1 n_2}(x, y) = C\exp\left(-\frac{x^2}{2a_1^2}\right)\exp\left(-\frac{y^2}{2a_2^2}\right)H_{n_1}\left(\frac{x}{a_1}\right)H_{n_2}\left(\frac{y}{a_2}\right), \quad n_1, n_2 = 1,2,3,\ldots, \tag{18}$$

where C is the normalization constant, $a_i = \sqrt{\hbar/m\omega_i}$ $(i = 1, 2)$ and $H_n(x)$ are the Hermite polynomials. The derivation of Eqs. (17) and (18) can be found in textbooks of quantum mechanics (see e.g., Flügge, 1999).

Quantum dot in a magnetic field: Landau levels vs the Fock-Darwin states

In this section the effect of constant uniform magnetic field on electron states in a planar QD will be discussed. Historically the electron states and the magnetic properties of free electron gas in uniform magnetic field have been studied theoretically by Landau (1930). It was demonstrated that the electron motion in a plane perpendicular to magnetic field induction vector **B** is quantized, and equidistant discrete energy levels (so called Landau levels) can be observed. Fock (1928) and Darwin (1931) have studied electron states of a 2D parabolic potential in a magnetic field. Interestingly after 60 years all of these theoretical results have been materialized and experimentally realized in quantum dots (see e.g., Chakraborty, 1999).

Let us consider a planar QD with parabolic confining potential (see Eq. (9)) in a perpendicular magnetic field. The corresponding Schrödinger equation will have the form:

$$\left[\frac{1}{2m}\left(\hat{\mathbf{p}} - \frac{e}{c}\mathbf{A}\right)^2 + \frac{1}{2}m\omega_0^2\rho^2\right]\psi(\rho, \varphi) = E\psi(\rho, \varphi), \tag{19}$$

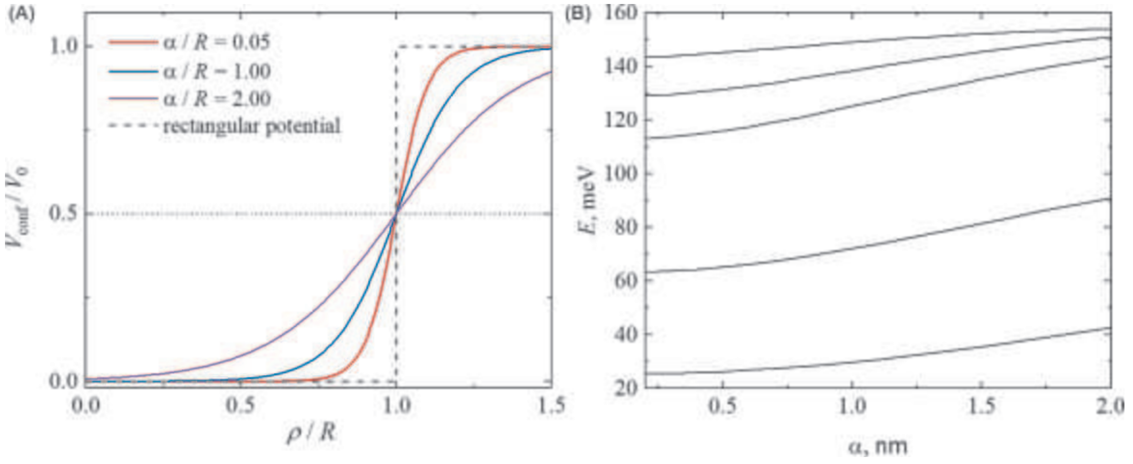

Fig. 3 (A) Woods-Saxon potential for three different values of the smearing parameter α. (B) The dependence of the energies on the parameter α for few lowest states in a planar QD with modified 2D Woods-Saxon confinement potential.

where $\widehat{\mathbf{p}}$ is the electron's momentum operator, e is the elementary charge, c is the speed of light, $\mathbf{A}$ is the magnetic field vector potential and ω_0 is the parameter of parabolic confinement potential of QD. For the vector potential we can choose the symmetric gauge $\mathbf{A} = (-By/2, Bx/2, 0)$. It is easy to see that the operator $\widehat{\mathbf{p}}$ and the vector potential $\mathbf{A}$ commute, and therefore by substituting the expression for $\mathbf{A}$ into Eq. (19) and after some manipulations we get

$$\left[-\frac{\hbar^2}{2m}\left(\frac{\partial^2}{\partial\rho^2}+\frac{1}{\rho}\frac{\partial}{\partial\rho}+\frac{1}{\rho^2}\frac{\partial^2}{\partial\varphi^2}\right)+\frac{i\hbar\omega_c}{2}\frac{\partial}{\partial\varphi}+\frac{m\omega_c^2\rho^2}{8}+\frac{m\omega_0^2\rho^2}{2}\right]\psi(\rho,\varphi)=E\psi(\rho,\varphi), \tag{20}$$

where $\omega_c = eB/mc$ is the cyclotron frequency. Since the magnetic field does not change the circular symmetry of the system we again can search the solution of Eq. (20) in a form

$$\psi(\rho,\varphi) = C\exp(il\varphi)f(\rho), \quad l = 0, \pm 1, \pm 2, \dots \tag{21}$$

By substituting Eq. (21) into Eq. (20) one can obtain an equation for the radial part of the wave function $f(\rho)$:

$$\left[-\frac{\hbar^2}{2m}\left(\frac{\partial^2}{\partial\rho^2}+\frac{1}{\rho}\frac{\partial}{\partial\rho}-\frac{l^2}{\rho^2}\right)+\frac{m\rho^2}{2}\left(\omega_0^2+\frac{1}{4}\omega_c^2\right)\right]f(\rho)=\left(E+\frac{1}{2}\hbar\omega_c l\right)f(\rho). \tag{22}$$

Eq. (22) is similar to Eq. (11) if we choose the effective frequency $\Omega = \sqrt{\omega_0^2 + \omega_c^2/4}$ and replace the energy E in Eq. (11) by $E + \hbar\omega_c l/2$. Using the solutions for the 2D harmonic oscillator, given in Eqs. (12) and (13), we can write down expressions for the energy spectrum and wave functions for parabolic QD in magnetic field:

$$E_{nl} = \hbar\Omega(2n+|l|+1)-\frac{\hbar\omega_c l}{2}, \quad n = 0,1,2\dots, \quad l = 0, \pm 1, \pm 2, \dots, \tag{23}$$

$$|n,l\rangle \equiv \psi_{nl}(\rho,\varphi) = \frac{1}{a}\sqrt{\frac{n!}{\pi(n+|l|)!}}\exp\left(-\frac{\rho^2}{2a^2}\right)\left(\frac{\rho}{a}\right)^{|l|}L_n^{|l|}\left(\frac{\rho^2}{a^2}\right)\exp(il\varphi). \tag{24}$$

In Eq. (24) the parameter $a = \sqrt{\hbar/m\Omega}$ is the effective magnetic length, which, of course, differs from the actual magnetic length $a_B = \sqrt{\hbar/m\omega_c}$.

In Fig. 4(A) the schematic picture of Fock-Darwin energy spectrum for the parabolic QD is presented. At zero magnetic field the spectrum of the 2D harmonic oscillator can be observed with $E_{nl} = \hbar\omega_0(2n+|l|+1)$. For the case of a strong magnetic field, when $a_B \ll R$ or $\omega_c \gg \omega_0$, the magnetic quantization prevails over the size quantization of the QD and the energy spectra transforms into Landau levels. The first two Landau levels with energies $\hbar\omega_c/2$ and $3\hbar\omega_c/2$ can be seen (dashed lines in Fig. 4(A)). The calculated low-energy levels of the Fock-Darwin diagram are well reproduced in the magnetotunneling experiments of QDs (Chakraborty, 1999; Schmidt, 1997). In Fig. 4(B) the gray-scale contour plot of differential conductance for a QD is presented as a function of the bias voltage and the magnetic field. Some of low-lying Fock-Darwin states and first two Landau levels are clearly visible in the figure. It is quite remarkable how the theoretical results obtained on 1930 are made visible in semiconductor quantum dots.

The effect of QD anisotropy on the Fock-Darwin spectrum has been studied by Madhav and Chakraborty (1994) and later by Avetisyan et al. (2012). Again we can choose the anisotropic confinement potential of the dot in the form of (16). The single-electron Hamiltonian in a magnetic field will have the form:

$$H = \frac{1}{2m}\left(\mathbf{p}-\frac{e}{c}\mathbf{A}\right)^2+\frac{1}{2}m\left(\omega_1^2x^2+\omega_2^2y^2\right). \tag{25}$$

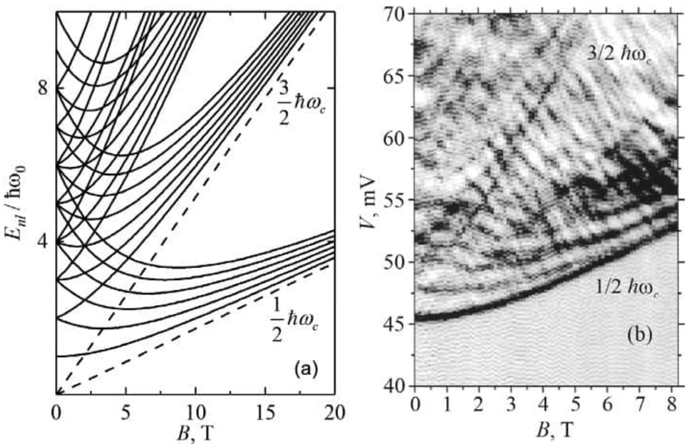

Fig. 4 (A) The Fock-Darwin spectrum for parabolic QD vs magnetic field. (B) Gray-scale plot of differential conductance for a QD as a function of magnetic field and bias voltage (Chakraborty, 1999; Schmidt, 1997). The locations of the two lowest Landau levels are also indicated.

We can introduce here the rotated coordinates and momenta q_i, $p_i\,(i=1,2)$ such that

$$\begin{aligned} x &= q_1\cos\chi - \chi_2 p_2\sin\chi, \quad y = q_2\cos\chi - \chi_2 p_1\sin\chi, \\ p_x &= p_1\cos\chi + \chi_1 q_2\sin\chi, \quad p_y = p_2\cos\chi + \chi_1 q_1\sin\chi, \end{aligned} \tag{26}$$

where

$$\chi_1 = \chi_2^{-1} = -m\left[\frac{1}{2}\left(\Omega_1^2+\Omega_2^2\right)\right]^{1/2},$$

$$\tan 2\chi = \frac{\omega_c\left[2\left(\Omega_1^2+\Omega_2^2\right)\right]^{1/2}}{\left(\Omega_1^2-\Omega_2^2\right)}, \quad \Omega_{1,2}^2 = \omega_{1,2}^2 + \frac{1}{4}\omega_c^2.$$

In terms of rotated operators the transformed Hamiltonian becomes diagonal,

$$H = \frac{1}{2m}\sum_{i=1,2}\left(\alpha_i^2 p_i^2 + m^2\beta_i^2 q_i^2\right), \tag{27}$$

where

$$\alpha_1^2 = \frac{\Omega_1^2+3\Omega_2^2+\Omega_3^2}{2\left(\Omega_1^2+\Omega_2^2\right)}, \quad \alpha_2^2 = \frac{3\Omega_1^2+\Omega_2^2-\Omega_3^2}{2\left(\Omega_1^2+\Omega_2^2\right)},$$

$$\beta_1^2 = \frac{1}{4}\left(3\Omega_1^2+\Omega_2^2+\Omega_3^2\right), \quad \beta_2^2 = \frac{1}{4}\left(\Omega_1^2+3\Omega_2^2-\Omega_3^2\right),$$

$$\Omega_3^2 = \left[\left(\Omega_1^2-\Omega_2^2\right)^2 + 2\omega_c^2\left(\Omega_1^2+\Omega_2^2\right)\right]^{1/2}.$$

Since the Hamiltonian (27) is a sum of Hamiltonians of two independent harmonic oscillators, the energy eigenvalues of an anisotropic QD in a magnetic field are obtained as

$$E_{n_1,n_2} = \left(n_1+\frac{1}{2}\right)\hbar\alpha_1\beta_1 + \left(n_2+\frac{1}{2}\right)\hbar\alpha_2\beta_2. \tag{28}$$

In Fig. 5 the energy spectrum of an anisotropic QD is presented against the magnetic field for the value $\hbar\omega_1 = 4$meV and for four different values of $\hbar\omega_2$. At zero magnetic field the system behaves like a couple of linear harmonic oscillators in the x and y directions. For large values of magnetic field induction ($\omega_c \gg \omega_1, \omega_2$) the Landau levels form as in the case of isotropic parabolic confinement. When $\omega_1 = \omega_2$ the confining potential is isotropic and parabolic, and the expression (23) can be obtained if $n_1 = n + (|l|-l)/2$ and $n_2 = n + (|l|+l)/2$. When $\omega_1 \simeq \omega_2$, the energy levels are very similar to that of the isotropic case except that the $(2n+|l|+1)$-fold degeneracy at $B=0$ is lifted due to the breaking of the circular symmetry of QD.

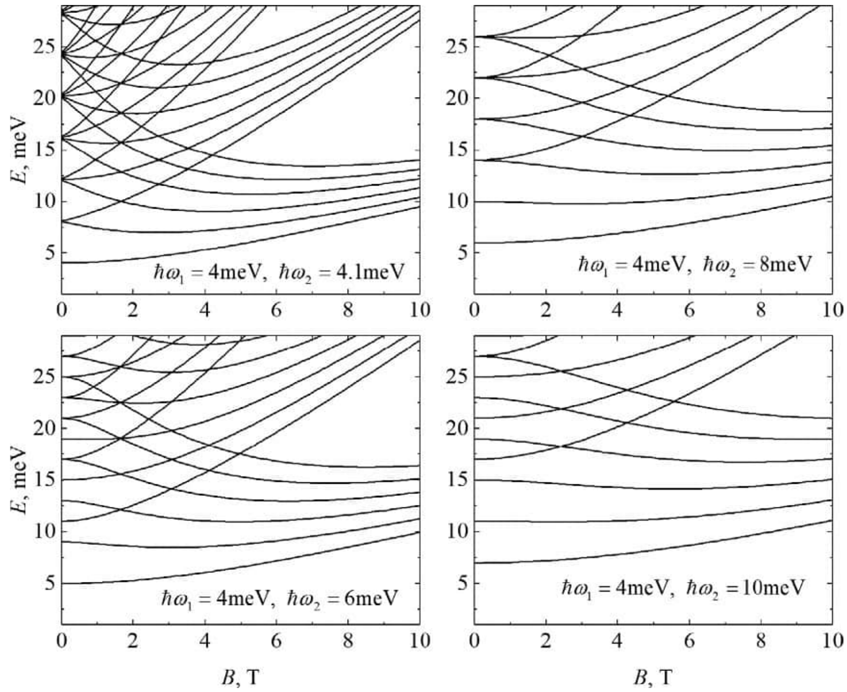

Fig. 5 Fock-Darwin spectrum of anisotropic QD for various values of confining potential parameter ω_2 for fixed value of $\hbar\omega_1 = 4$ meV.

Electron-electron interactions in QDs

Almost 60 years after the pioneering work of Fock (1928) on a single electron in a parabolic confinement potential under external magnetic field, Maksym and Chakraborty (1990) first introduced the electron-electron interaction in that system. The Hamiltonian of the interacting many-electron system in a planar QD with parabolic confinement potential in a magnetic field has the form:

$$\widehat{H} = \frac{1}{2m}\sum_{i=1}^{n_e}\left(\widehat{\mathbf{p}}_i - \frac{e}{c}\mathbf{A}_i\right)^2 + \frac{1}{2}m\omega_0^2\sum_{i=1}^{n_e}\rho_i^2 + \frac{1}{2}\sum_{i\neq j}\frac{e^2}{\varepsilon\left|\boldsymbol{\rho}_i - \boldsymbol{\rho}_j\right|}, \tag{29}$$

where n_e is the number of electrons and ε is the dielectric constant of the system. All other notations are already described in section "Quantum dot in a magnetic field: Landau levels vs the Fock-Darwin states." In the case of a QD with only few electrons, the corresponding Schrödinger equation can be solved numerically by the exact diagonalization technique using many-electron basis states of the non-interacting electrons constructed from the single-electron wave functions presented in Eq. (24). Since the wave functions (24) are the eigenfunctions of the single-electron Hamiltonian of a QD, we should calculate here only the matrix elements of the Coulomb interaction term of the Hamiltonian (29). The 2D Coulomb interaction potential of two electrons can be represented in its Fourier transformed form:

$$\begin{aligned} V(\boldsymbol{\rho}_1, \boldsymbol{\rho}_2) &= \frac{e^2}{\varepsilon|\boldsymbol{\rho}_1 - \boldsymbol{\rho}_2|} = \frac{e^2}{(2\pi)^2\varepsilon}\int\frac{2\pi}{|\mathbf{k}|}\exp\left[i\mathbf{k}(\boldsymbol{\rho}_1 - \boldsymbol{\rho}_2)\right]d\mathbf{k} \\ &= \frac{e^2}{2\pi\varepsilon}\int_0^\infty dk\int_0^{2\pi} d\varphi_k \exp\left[ik\rho_1\cos\left(\varphi_k - \varphi_1\right) - ik\rho_2\cos\left(\varphi_k - \varphi_2\right)\right]. \end{aligned} \tag{30}$$

The interaction matrix element connecting two electron states $|n_1, l_1\rangle|n_2, l_2\rangle$ and $|n_1', l_1'\rangle|n_2', l_2'\rangle$ will have the form

$$\begin{aligned} M^{n_1,l_1;n_2,l_2}_{n_1',l_1';n_2',l_2'} = \int_0^\infty \rho_1 d\rho_1\int_0^{2\pi} d\varphi_1\int_0^\infty \rho_2 d\rho_2\int_0^{2\pi} d\varphi_2 f_{n_1'l_1'}(\rho_1) f_{n_2'l_2'}(\rho_2)\exp\left[-i\left(l_1'\varphi_1 + l_2'\varphi_2\right)\right]\times \\ V(|\boldsymbol{\rho}_1 - \boldsymbol{\rho}_2|) f_{n_1l_1}(\rho_1) f_{n_2l_2}(\rho_2)\exp\left[i(l_1\varphi_1 + l_2\varphi_2)\right]. \end{aligned} \tag{31}$$

In Eq. (31) $f_{nl}(\rho)$ is the radial part of the single electron wave function taken from Eq. (24):

$$f_{nl}(\rho) = \frac{1}{a}\sqrt{\frac{n!}{\pi(n + |l|)!}}\exp\left(-\frac{\rho^2}{2a^2}\right)\left(\frac{\rho}{a}\right)^{|l|}L_n^{|l|}\left(\frac{\rho^2}{a^2}\right). \tag{32}$$

After the calculation of angular integrals the interaction matrix element will get the form:

$$M^{n_1,l_1;n_2,l_2}_{n_1',l_1';n_2',l_2'} = \frac{e^2\pi^2}{\varepsilon}\delta_{l_1+l_2,l_1'+l_2'}\int_0^\infty I_1(k)I_2(k)dk, \tag{33}$$

where

$$I_i(k) = \int_0^\infty f_{n_il_i}(\rho_i) f_{n_i'l_i'}(\rho_i) J_{|l_i - l_i'|}(k\rho_i)\rho_i d\rho_i, \quad i = 1,2.. \tag{34}$$

The presence of the Kronecker delta symbol in the expression for the interaction matrix element clearly demonstrates that the Coulomb interaction did not change the total angular momentum of the system, i.e., the latter is a conserved quantity. Therefore all states can be classified by a quantum number J which is the sum of single electrons l values. For a given value of the total angular momentum quantum number J all matrix elements can be calculated numerically and the energy spectrum of the interacting system can be obtained after numerical diagonalization of the Hamiltonian matrix created using the many-electron basis states constructed from the single-electron wave functions. The details of numerical calculations can be found in Chakraborty (1999) and Maksym and Chakraborty (1990).

Magic numbers and the Maksym-Chakraborty effect

The energy levels of three and four electron system obtained numerically by Maksym and Chakraborty (1990) for a GaAs QD with parabolic confinement potential with the parameter $\hbar\omega_0 = 4\,\text{meV}$ are shown in Fig. 6. The energy levels are plotted against the total angular momentum quantum number J for various values of the magnetic field. As can be seen in these figures, there are always two sets of broadened levels separated by a gap. In the limit of zero confinement these would be the lowest two Landau levels. The general trend is that the energies increase with J because the single-electron energies increase with l.

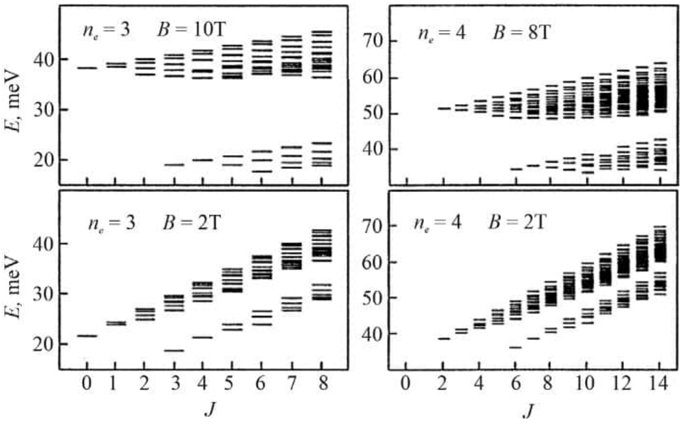

Fig. 6 Energy levels as a function of J for three and four electrons in a parabolic quantum dot (Maksym and Chakraborty, 1990).

The main difference between the low- and high-field behaviors is the ground state angular momentum. It should be noted that single-electron contribution increases linearly with J. In contrast, the interaction term decreases because electrons with higher angular momenta move in orbitals with larger radii, thereby decreasing the Coulomb energy. The net result is that the total energy as a function of J has a minimum. At low fields this minimum occurs at the lowest available J, for which all three or four electrons are placed in states with the Fock-Darwin number $N_{FD} = n + (|l| - l)/2 = 0$. For example, at $B = 2$T the ground state of a three-electron QD occurs at $J = 3$ and for the QD with four electrons at $J = 6$. The interaction, however, causes the ground state J to increase with B, and this effect is caused by the interplay of the single-electron energies and the interaction energy.

One very important result here is that the ground state of electrons in a magnetic field occurs only at certain so called magic values of angular momentum which are dependent on the number of electrons:

$$J_{\text{magic}} = \frac{1}{2}n_e(n_e - 1) + jn_e, \tag{35}$$

where j is an integer number. The ground state always occurs at one of these magic values and the competition between the interaction and the confinement determines the optimum J. To summarize, the magic numbers occur because the magnetic field compresses the wave function of the system and increases the Coulomb energy. At certain critical fields the system can reduce the energy by making a transition to a new ground state which has a larger lateral extent and a higher angular momentum. As the magnetic field is increased, we see a series of abrupt changes in the total angular momentum and the system size. The selected values of angular momentum can be explained in terms of the symmetry of the minimum of the combined confinement and interaction potential.

Surprisingly the behavior of the energy levels as a function of the magnetic field described above cannot be observed in the far-infrared (FIR) or transport spectroscopy. It means that the electron-electron interactions described above do not influence the magneto-optical spectra of the QDs at all. The experimental results demonstrate, albeit in a different situation, a variation of the original Kohn theorem (Kohn, 1961). This theorem states that, in a translationally invariant electron gas, the cyclotron resonance is unaffected by electron-electron interactions. It should be noted that the parabolic confinement potential has the unique property that the Hamiltonian can be written as:

$$H = \frac{1}{2M}\left(\mathbf{P} + \frac{Q}{c}\mathbf{A}\right)^2 + \frac{1}{2}M\omega_0^2R^2 + H_{\text{rel}}, \tag{36}$$

where $Q = en_e$, $M = mn_e$ and $\mathbf{P} = \sum_{i=1}^{n_e}\mathbf{p}_i$ are the total electron charge, mass and the center of mass momentum, respectively, and $\mathbf{R} = \sum_{i=1}^{n_e}\mathbf{r}_i/n_e$ is the center of mass coordinate of the system. The first two terms in Eq. (36) describe the motion of the center of mass and the last term is a function of only relative coordinates and includes the interaction. Here we should point out that the center of mass energy is identical to the single-electron energy E_{nl} Eq. (23) because of the fact that $e/m = Q/M$. The FIR radiation excites the center of mass, but does not affect the relative motion. This rather fundamental result for quantum dots, first reported by Maksym and Chakraborty (1990) has been called the generalized Kohn theorem or more appropriately, the Maksym-Chakraborty effect.

The interaction effects can only be probed by deliberately engineering the dots so that the center of mass and relative motions are coupled. There have been a few theoretical studies on the effect of non-parabolicity of the confinement potential and consequent coupling of the center of mass and relative motions. Deviations from the parabolic confinement potential were studied first by Gudmundsson and Gerhardts (1991). Pfannkuche and Gerhardts (1991) studied numerically the magneto-optical response to the FIR radiation of quantum dots containing two electrons. In order to study the possible deviations from the parabolic confinement, they added the non-parabolic and anisotropic terms into the confinement potential in a form:

$$U(\mathbf{r}) = \frac{1}{2} m \omega_4^2 \left(a r^4 + b x^2 y^2 \right),$$

where ω_4, a and b are constants. They concluded that even small deviations from the strictly parabolic case brings rich structure in the FIR spectra.

Conclusion

To summarize, we have presented here a brief description of the main theoretical approaches for investigation of electronic properties of semiconductor planar quantum dots. The physical conditions, for which the QDs can be considered as planar, are described. Several models of electron confinement potentials of the QDs have been considered in details. Particularly, the 2D square well model and the 2D parabolic well model are discussed. Analytical expressions for the electron energy spectrum and the wave functions are presented. The effect of non-parabolicity of confinement potential is discussed in the framework of the Woods-Saxon potential model. The models of anisotropic planar QDs are also considered using anisotropic parabolic confinement model. We have demonstrated that the planar QDs under the applied external magnetic field are ideal systems for observation of the Fock-Darwin spectrum and the Landau levels. An interesting competition between the two effects: size quantization and magnetic quantization is discussed. The effect of electron-electron interactions on the characteristics of planar QDs also has been considered. It was demonstrated that in planar QDs with many electrons the ground state in a magnetic field occurs only at certain “magic” values of the angular momentum which are dependent on the number of electrons. The magic numbers occur because the magnetic field compresses the wave function of the system and increases the Coulomb energy. Surprisingly this behavior of energy levels as a function of magnetic field cannot be observed in FIR or transport spectroscopy for planar QDs with parabolic confinement. The electron-electron interactions do not influence the magneto-optical spectra of parabolic QDs at all, because the FIR radiation excites the center of mass, but does not affect relative motion of electrons. This fundamental result for planar quantum dots has been called the generalized Kohn theorem or the Maksym-Chakraborty effect. Even small deviations from the strictly parabolic confinement case bring rich structure in the FIR spectra of QDs.

Acknowledgments

This work was supported by the Science Committee of the Ministry of Education, Science, Culture and Sport of Armenia within the frame of the research Projects No. 20TTWS-1C014, 21SCG-1C012, 21AG-1C048 and 21T-1C247.

References

Abramowitz M and Stegan IA (1970) *Handbook of Mathematical Functions: With Formulas, Graphs, and Mathematical Tables*. Dover Publications.

Adachi S (2004) *Handbook on Physical Properties of Semiconductors*. vol. 2. Kluwer Academic Publishers.

Agarwal A, Srujan M, Chakrabarti S, and Krishna S (2013) Investigation of thermal interdiffusion in InAs/In$_{0.15}$Ga$_{0.85}$As/GaAs quantum dot-in-a-well heterostructures. *Journal of Luminescence* 143: 96.

Alivisatos AP (1996) Semiconductor clusters, nanocrystals, and quantum dots. *Science* 271: 933.

Avetisyan S, Pietiläinen P, and Chakraborty T (2012) Strong enhancement of Rashba spin-orbit coupling with increasing anisotropy in the Fock-Darwin states of a quantum dot. *Physical Review B* 85: 153301.

Aziz Aghchegala VL, Mughnetsyan VN, and Kirakosyan AA (2011) Effect of interdiffusion on band structure and intersubband absorption coefficient of GaAs/GaAlAs double quantum well. *Superlattices and Microstructures* 49: 99.

Barker JA and O’Reilly EP (1999) The influence of inter-diffusion on electron states in quantum dots. *Physica E* 4: 231.

Bera D, Qian L, Tseng T-K, and Holloway PH (2010) Quantum dots and their multimodal applications: a review. *Materials* 2010(3): 2260.

Bimberg D, Grundmann M, and Ledentsov NN (1998) *Quantum Dot Heterostructures*. John Wiley & Sons.

Chakraborty T (1999) *Quantum Dots: A Survey of the Properties of Artificial Atoms*. Elsevier.

Darwin CG (1931) The diamagnetism of the free electron. *Mathematical Proceedings of the Cambridge Philosophical Society* 27: 86.

Davies JH (1998) *The Physics of Low-dimensional Semiconductors*. Cambridge University Press.

Flügge S (1999) *Practical Quantum Mechanics*. Springer.

Fock V (1928) Bemerkung zur quantelung des harmonischen oszillators im magnetfeld. *Zeitschrift für Physik* 47: 446.

Fröhlich H (1937) Die spezifische warme der elektronen kleiner metallteilchen bei tiefen temperaturen. *Physica* 4: 406.

Gudmundsson V and Gerhardts RR (1991) Self-consistent model of magnetoplasmons in quantum dots with nearly parabolic confinement potentials. *Physical Review B* 43: 12098(R).

Guozhong C (2004) *Nanostructures and Nanomaterials*. London: Imperial College Press.

Harrison P and Valavanis A (2016) *Quantum Wells, Wires and Dots*. John Wiley & Sons.

Henini M (ed.) (2008) *Handbook of Self Assembled Semiconductor Nanostructures for Novel Devices in Photonics and Electronics*. Elsevier.

Jo M, Mano T, and Sakoda K (2011) Lasing in ultra-narrow emission from GaAs quantum dots coupled with a two-dimensional layer. *Nanotechnology* 22: 335201.

Kohn W (1961) Cyclotron resonance and de Haas-van Alphen oscillations of an interacting electron gas. *Physics Review* 123: 1242.

Landau L (1930) Diamagnetism of metals. *Zeitschrift für Physik* 64: 629.

Madhav AV and Chakraborty T (1994) Electronic properties of anisotropic quantum dots in a magnetic field. *Physical Review B* 49: 8163.

Maksym PA and Chakraborty T (1990) Quantum dots in a magnetic field: Role of electron-electron interactions. *Physical Review Letters* 65: 108.

Mughnetsyan VN and Kirakosyan AA (2008) Effect of interdiffusion of In and Al atoms on excitonic states in $In_xGa_{1-x}As/Al_yGa_{1-y}As$ quantum dots. *Journal of Contemporary Physics (Armenian Academy of Sciences)* 43: 173.
Pfannkuche D and Gerhardts RR (1991) Quantum-dot helium: Effects of deviations from a parabolic confinement potential. *Physical Review B* 44: 13132(R).
Schmidt T (1997) *Dissertation*. Stuttgart: Max-Planck Institute.
Sogabe T, Shen Q, and Yamaguchi K (2016) Recent progress on quantum dot solar cells: A review. *Journal of Photonics for Energy* 6(4), 040901.
Steiner T (2004) *Semiconductor Nanostructures for Optoelectronic Applications*. Artech House.
Vurgaftman I, Meyer JR, and Ram-Mohan LR (2001) Band parameters for III–V compound semiconductors and their alloys. *Journal of Applied Physics* 89: 5815.
Woods RD and Saxon DS (1954) Diffuse surface optical model for nucleon-nuclei scattering. *Physical Review* 95(2): 577–578.
Wu J, Shao D, Dorogan VG, Li AZ, Li S, DeCuir IA, Manasreh MO, Wang ZM, Mazur YI, and Salamo GJ (2010) Intersublevel infrared photodetector with strain-free GaAs quantum dot pairs grown by high-temperature droplet epitaxy. *Nano Letters* 10(4): 1512.
Xi N and King L (2012) *Nano Optoelectronic Sensors and Devices*. Elsevier Science Press.

Quantum dots: Optical properties

V Yu Timoshenko, Faculty of Physics, Lomonosov Moscow State University, Moscow, Russia

© 2024 Elsevier Ltd. All rights reserved.

Introduction 308
Quantum confinement effect 309
Optical absorption 310
Photoluminescence 313
Effects of shells and impurities 316
Optoelectronic and biomedical applications 320
Conclusion 323
References 323

Abstract

Quantum dots (QDs) are semiconductor nanocrystals with nanometer-scale dimensions, and this results in differences in their physical properties from the properties of the corresponding bulk semiconductors. Energy states of quasiparticles (electrons, holes, excitons, phonons, etc.) in QDs are modified due to the quantum confinement effect that leads to the secondary quantization of the energy levels of those quasiparticles. The electron energy states in a QD depend strongly on its size and shape as well on impurities, defects and surface coating. The electron states in QDs determine their optical properties, such as a shift of the absorption edge to high energies, extremely bright, efficient, and size-dependent photoluminescence, which makes QDs extremely important for numerous applications in photonics, optoelectronics and biomedicine.
The chapter includes a brief introduction into the preparation methods and properties of different QDs, starting from small semiconductor nanocrystals in solid matrix discovery by Ekimov and Onushchenko in 1981, colloidal QDs, self-organized QDs in semiconductor heterostructures, and perovskite QDs. The first section describes the quantum confinement effect in QDs for different approximations, i.e., so-called "strong confinement regime" (when the Coulomb interaction between optically excited electron and hole is much weaker than the sum of their confinement energies) and "weak confinement" or "excitonic regime" (when the Coulomb interaction between the electron and hole in QDs should be considered). The next sections are devoted to the optical and luminescent properties of ODs, which are covered by the quantum confinement, defects, impurities and surface coating. The last section presents examples of the optoelectronic and biomedical applications of QDs. The main issues related to the physical background and applications of QDs as well the future of research in the field of QD optics are summarized in the conclusion.

Key points

- Spatial confinement leads to the secondary quantization of the energy states of electron, holes and excitons in quantum dots.
- Optical properties of QDs are dependent on their size, shape, impurity content, defect states and surface coating.
- Efficient radiative recombination of excitons in QDs promotes their optoelectronic applications in light emitting diodes and lasers.
- Bright photoluminescence of QDs is used for their applications as luminescent labels in bioimaging.

Introduction

Recent development of the condensed matter physics, material sciences and semiconductor technologies deals with production and investigation of semiconductor nanocrystals with physical and chemical properties, which are promising for various applications. One of the important objects in the physics of nanostructures are quasi-zero-dimensional systems or quantum dots (QDs), which usually represent semiconductor crystals with sizes in all three dimensions from units to tens of nanometers. In most cases, QDs are crystalline nanoparticles (NPs) located in some matrix having the properties of a dielectric or semiconductor with energy electronic spectra, providing potential barriers for charge carriers (electrons and holes) in the QDs.

Among the variety of QDs, there are several main types that are most often studied experimentally and theoretically and are also used in various applications. First, these are nanocrystals of semiconductors dispersed in liquids (colloidal QDs) or embedded in solid-state matrices of glasses, dielectrics or wide-band gap semiconductors, as schematically shown in Fig. 1a. When QDs are grown in a liquid or crystallized in an amorphous dielectric matrix, they usually have a spherical shape (Fig. 1a). It was in such a system, where QDs of copper chloride (CuCl) were crystallized in silicate glass and an effect of the quantum confinement for charge carriers in QDs was discovered in 1981 (Ekimov and Onushchenko, 1981).

https://doi.org/10.1016/B978-0-323-90800-9.00177-3

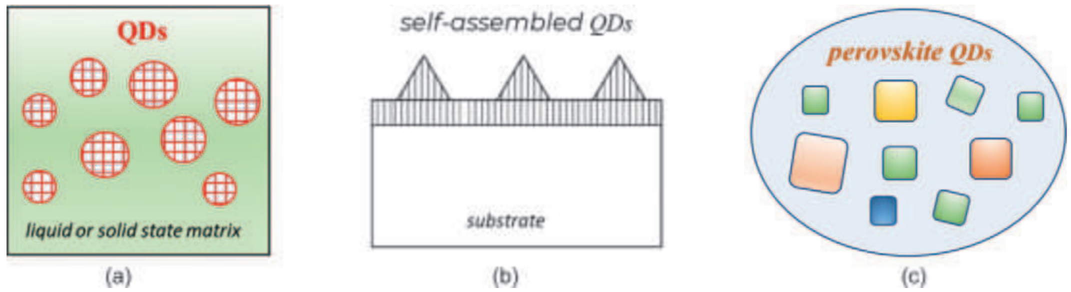

Fig. 1 Schematic images of several types of QDs: (a) colloidal or obtained by crystallization in a solid matrix, (b) self-assembled QDs on a solid substrate, and (c) Pe-QDs.

Second important type of QDs are so-called self-assembled ones, which are usually grown by molecular beam or gas-phase epitaxy (Fig. 1b). The main mechanism responsible for the self-assembling of such QDs is the Stranski–Krastanov growth, which is controlled by mechanical stress induced by mismatch between the lattice constant of the substrate and QDs (Stranski and Krastanow, 1938).

So-called perovskite QDs (Pe-QDs), which are nanocrystals of organometallic or inorganic compounds with a perovskite structure, i.e., ABX_3, where A are B cations and X is an anion. Pe-QDs are usually formed by chemical methods in solutions, are intensively studied now. Such QDs are either spherically or cubically shaped, and they are characterized by intense absorption and photoluminescence, which can be tuned in the visible and near-infrared spectral region, depending on the composition and dimensions of Pe-QDs (Zhou and Wang, 2020).

Quantum confinement effect

The quantum confinement for charge carriers influences the optical properties of semiconductor nanocrystals that becomes significant if their sizes are smaller 10–20 nm. For QDs in the so-called strong confinement mode, the wave functions of quasiparticles experience three-dimensional secondary quantization (Efros and Efros, 1982). In this case the wave functions of electrons and holes in a spherically symmetric well with a radius ***a*** and infinitely high walls have the form (Ekimov et al., 1985):

$$\Psi_{n,l,m}(r,\vartheta,\phi) = Y_{l,m}(\vartheta,\phi)\frac{\sqrt{2}}{a\sqrt{r}}\frac{J_{l+1/2}(k_{l,n}r)}{J_{l+3/2}(k_{l,n}a)} \tag{1}$$

where $Y_{l,m}$ are the normalized spherical functions, l is the momentum, m is the momentum projection to a certain direction, J_v is the Bessel function, and $k_{l,n}$ are determined by the following condition:

$$J_{l+1/2}(k_{l,n}a) = 0 \tag{2}$$

where $n=1,2,3\ldots$ is the number of the root of the Bessel function of given $l=0,1,2,\ldots$

The energy levels of electrons and holes can be expressed by the following equation:

$$E_{l,n}^{e,h} = \frac{\hbar^2\phi_{l,n}^2}{2m_{e,h}^*a^2} \tag{3}$$

where m_e^* and m_h^* are the effective masses of electrons and holes, respectively, which are assumed to be constant independently on the size of QD.

Thus, the optical forbidden gap of QD is given as follows:

$$E_g^{QD} = E_g + \frac{\hbar^2\pi^2}{2\mu a^2}\hbar\nu_{01} = \mathrm{E_g} + \frac{\hbar^2}{8\mu a^2} \tag{4}$$

where E_g and E_g^{QD} is the optical forbidden gap of the bulk semiconductor and QD, respectively, $\mu = m_e^*m_h^*/(m_e^* + m_h^*)$ is the reduced mass of the charge carriers.

Fig. 2 schematically shows the transformation of the quasi-continuous energy spectra of electron and holes in a bulk semiconductor to the discrete energy levels in the corresponding QD that is described by Eqs. (3) and (4). Note, the above mentioned analysis with Eq. (4) are valid in the case of so-called "strong confinement regime" when the Coulomb interaction between optically excited electron and hole is much weaker than the sum of their confinement energies given by Eq. (3). This regime is realized when the QD's radius is much smaller than the exciton radius, i.e., $a \ll r_{ex}\hbar\nu_{01} = \mathrm{E_g} + \frac{\hbar^2}{8\mu a^2}$ (Ekimov et al., 1985).

For the case of $a \gg r_{ex}\hbar\nu_{01} = \mathrm{E_g} + \frac{\hbar^2}{8\mu a^2}$ it is realized so-called "weak confinement" or "excitonic regime" and one should consider the Coulomb interaction between the electron and hole in QDs. It results in the following expression for the optical absorption threshold (Ekimov et al., 1985):

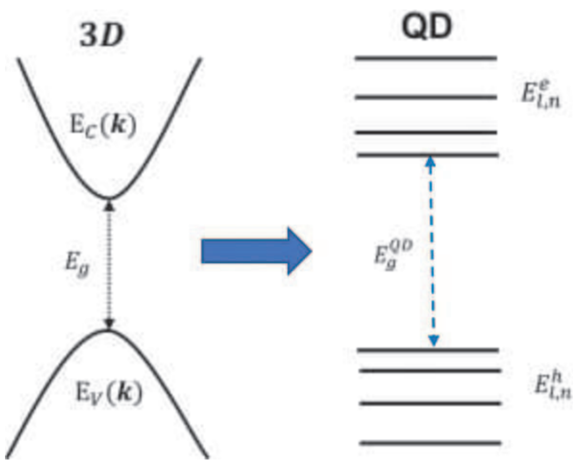

Fig. 2 Schematic of the transformation of the quasi-continuum energy dispersion curves for electrons and holes in a bulk semiconductor (3D) toward discrete energy states in a QD.

$$h\nu_0 = E_g - E_{ex} + \frac{\hbar^2\pi^2}{2Ma^2}\hbar\nu_{01} = \mathrm{E_g} + \frac{\hbar^2}{8\mu a^2} \tag{5}$$

where E_{ex} and $M = m_e^* + m_h^*$ are the binding energy (exciton Rydberg energy) and total mass of the exciton, respectively.

When the dielectric constant of a QD is larger the corresponding value of surrounding medium, the electron–hole interaction and consequently the binding energy and oscillator transition strength increase in the QD (Brus, 1984). This effect is also known as the dielectric confinement for excitons in QDs (Efros and Brus, 2021; Alivisatos, 1996). Indeed, for both colloidal QDs and those embedded in a glass or other isolating solid matrices the real part of the QD' dielectric function of in the optical range is usually larger the corresponding value of the matrix and it reduces the electric field of light due to so-called local field effect and reduces the exciton-photon coupling in the QD. Furthermore, the polarization properties of colloidal QDs as well as of their randomly oriented ensembles are determined both by the anisotropy of the local field effect and by the symmetry of the exciton states participating in the optical transitions. Therefore, the dielectric confinement changes the Coulomb interaction in an exciton in a QD and it also influences the eigen energies of electron or hole inside the QD. The latter effect can be described as an interaction between the electron (hole) with its own image charge outside of the QD (Rodina and Efros, 2016).

Optical absorption

The change in electronic states of QDs due to the quantum confinement obviously leads to a modification of their optical properties, e.g., to the high-energy shift of the absorption edge. This "blue" shift can be described by Eqs. (4) and (5) for the strong and weak confinement, respectively. The "blue" shift of the optical absorption edge in QDs crystallized in a glass matrix was unambiguously demonstrated by Ekimov and Onushchenko (1981). While it is usually difficult to obtain the absorption spectrum of a single QD in the experiment, many such QDs with some size distribution participate in the formation of the absorption spectrum.

Fig. 3 shows absorption spectra of CuCl, CuBr and CdS QDs with different mean sizes measured at low temperature. The absorption edge for all the samples exhibits a shift in high photon energy region that is well explained by the quantum confinement model. However, the spectra of CuCl and CuBr CDs consist of only two broad peaks, whose relative spectral positions cannot be described by Eqs. (4) and (5). The most relevant explanation of these tow peaks is based on considering a contribution from sub-bands of the valence bands of the corresponding semiconductors. Since the Bohr radius of an exciton in the bulk CuCl is about 0.7 nm, the corresponding QDs with sizes above 2 nm should be described by the model of weak confinement (Eq. (5)). The absence of excitonic peaks with different quantum number is explained by inhomogeneous broadening of the absorption spectrum due the size distribution of QDs (Ekimov, 1991; Efros and Brus, 2021).

For a detailed description of the optical properties of QDs, it is important to know how their electronic spectrum changes when the size of nanocrystals changes. Fig. 4 shows a transmission electron microscopy (TEM) image, schematic view of the atomic structure and optical transition diagram for an individual colloidal CdSe (Efros and Brus, 2021). However, the heterogeneous distribution of QDs in size and shape observed in the experimental samples as glasses of liquids with a QD ensemble complicates an identification of the optical transitions in the latter. Therefore, methods such as differential absorption spectroscopy, also known as the "pump-sensing" method and PL excitation spectroscopy, are used in the study of the electronic spectrum of QD. Historically, the most widely used method is the differential absorption spectroscopy (Norris et al., 1994; Norris and Bawendi, 1996). However, the photoinduced absorption complicates the interpretation of the obtained spectral features due to influences of the carrier recombination and optical gain (Klimov, 2003). The most detailed information can be provided by PL excitation spectroscopy (Ekimov, 1991).

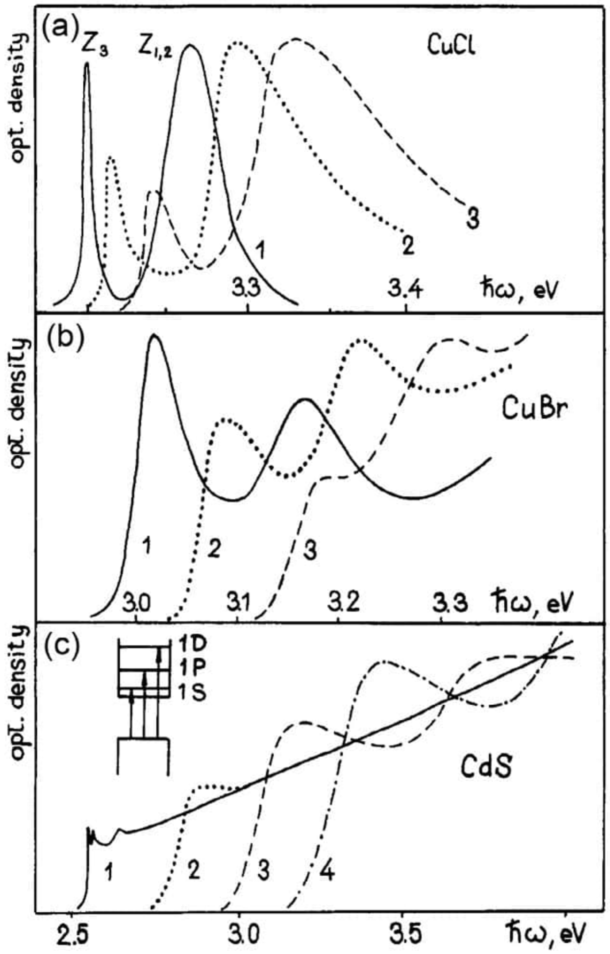

Fig. 3 Absorption spectra of different QDs in glass matrices at low temperature ($T = 4.2$ K): (a) CuCl with a = 31 nm (curve 1), 2.9 nm (curve 2), and 2.0 nm (curve 3); (b) CuBr with a = 24 nm (curve 1), 3.6 nm (curve 2), and 2.3 nm (curve 3); (c) CdS with a = 33 nm (curve 1), 2.3 nm (curve 2), 1.5 nm (curve 3), and 1.2 nm (curve 4). Reproduced with permission from Ekimov AI (1991) Optical properties of semiconductor quantum dots in glass matrix. *Physica Scripta* T39: 217–220.

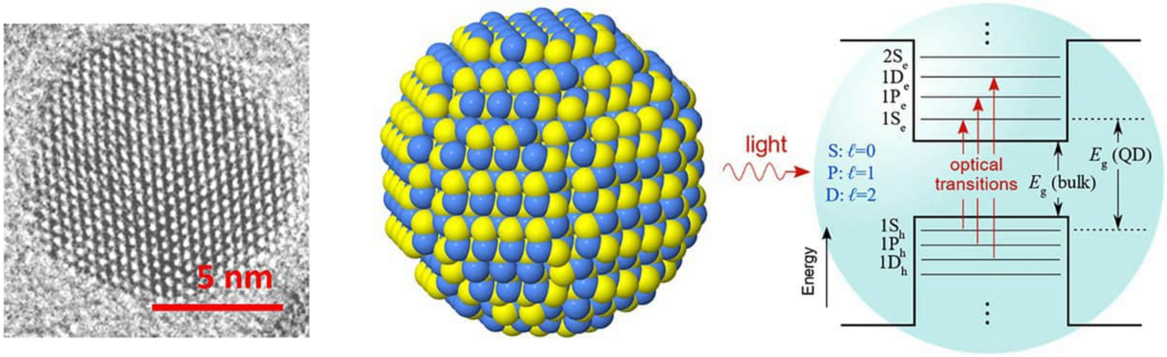

TEM image of CdSe nanocrystal   Nanocrystal atomic structure

Fig. 4 TEM image, schematic view of the atomic structure and optical transition diagram for an individual colloidal CdSe. Reproduced with permission from Efros AlL, Brus LE (2021) Nanocrystal quantum dots: From discovery to modern development. *ACS Nano* 15: 6192–6210.

Indeed, when a sample containing QDs is illuminated by light with photon energy much higher than the energy of the lower optical transition, the entire ensemble of QDs in the sample is excited. As a result, there is a wide peak (width at half the height FWHM >0.05 eV) of the PL (see Fig. 5a). At the same time, when removing the excitation spectra of PL, a narrow spectral luminescence band is selected, and the photon energy of the exciting light is scanned. As a result, the inhomogeneous broadening of the spectrum is significantly reduced (Norris and Bawendi, 1996).

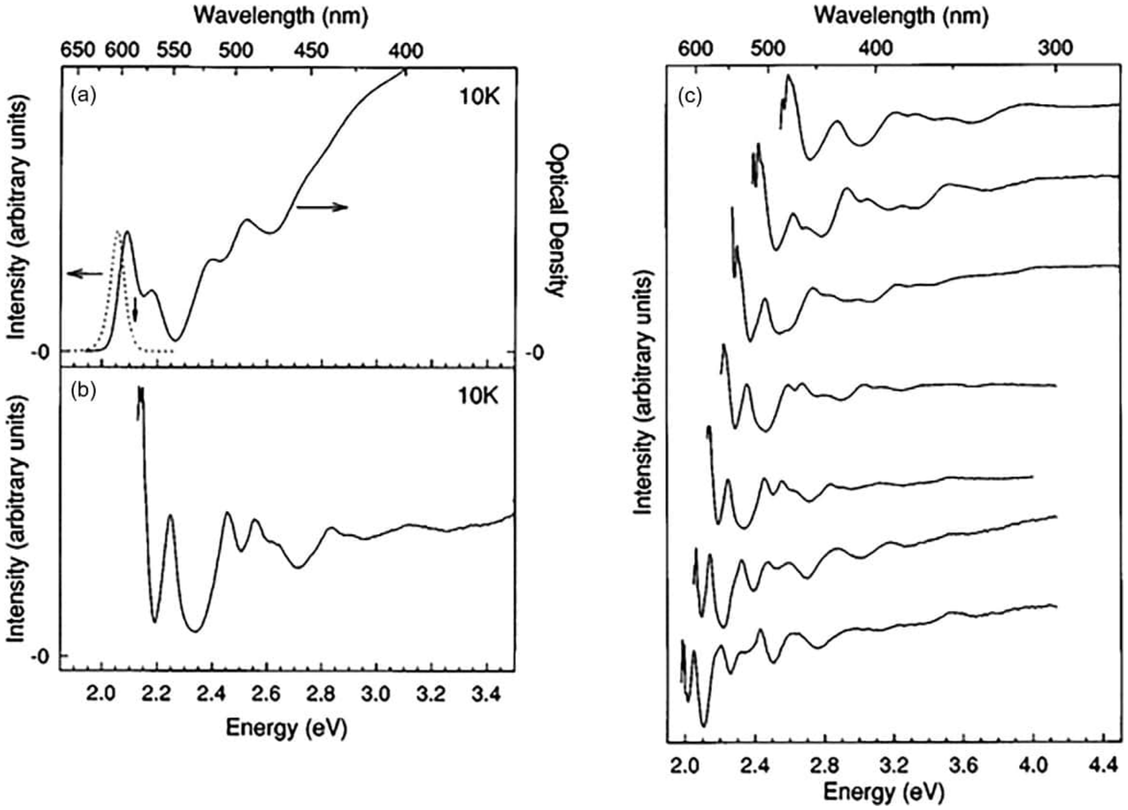

Fig. 5 (a) Absorption spectrum (solid curve) and PL (dotted curve) of CdSe QDs with an average radius of ~28 Å; (b) PL excitation spectrum of the same sample; (c) normalized PL excitation spectra for samples with seven different QD sizes in the range from ~15 to ~43 Å. All measurements at $T = 10$ K. Reproduced with permission from Norris DJ, Bawendi MG (1996) Measurement and assignment of the size-dependent optical spectrum in CdSe quantum dots. *Physical Review B* 53: 16338–16346.

As can be seen from Fig. 4, optical transitions that overlap in the absorption spectrum [Fig. 5a], become clearly resolved in the excitation spectrum of PL [Fig. 5b]. Analyzing the PL excitation spectrum of samples with different mean sizes [Fig. 5c], one can select a set of transitions in it. The dependence of the energy of the first excited states, i.e., $1S_h1S_e$, predicted by the simple effective mass model described above is approximately proportional to $1/a^2$ in a wide range of sizes as shown in Fig. 6 for CdSe QDs. However, in many cases, along with the position of the first excited state $1S_{3/2}1S_e$ it is important to know the positions of higher states, such as $2S_{3/2}1S_e$ и $1P_{3/2}1P_e$. Fig. 7 demonstrates that for the certain range of the QD radius the size dependences of the optical transitions in QDs of CuCl and CdS can be also fitted with the function proportional to $1/a^2$ in the agreement with Eqs. (4) and (5) (Efros and Brus, 2021).

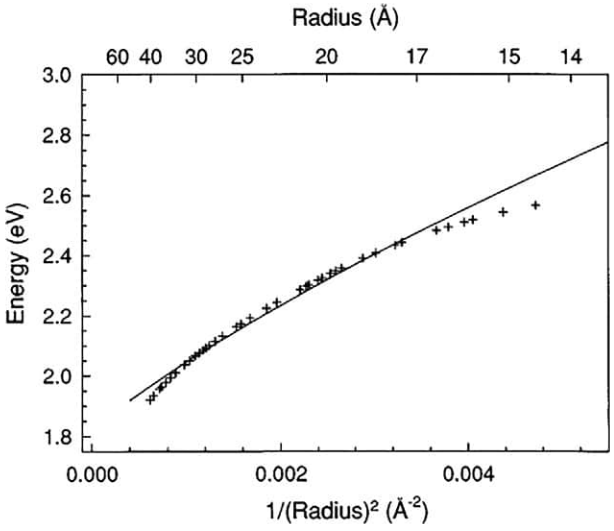

Fig. 6 Dependence of the energy of the first excited state in CdSe QDs on the square of reciprocal radius of the QDs: symbols are experimental results, solid line corresponds to the calculated values. Reproduced with permission from Norris DJ, Bawendi MG (1996) Measurement and assignment of the size-dependent optical spectrum in CdSe quantum dots. *Physical Review B* 53: 16338–16346.

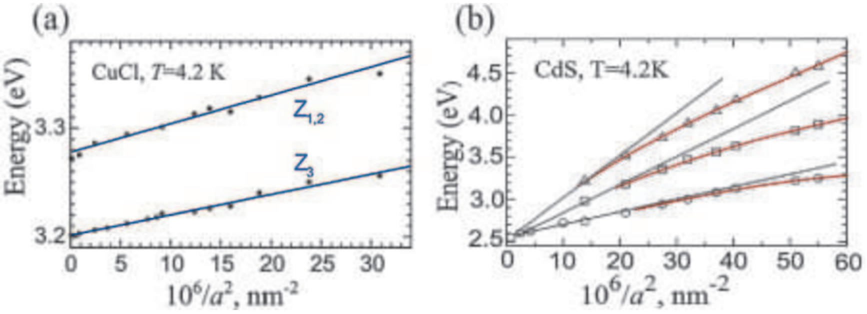

Fig. 7 (a) Dependences of the energy of the two exciton lines (Z_3 and $Z_{1,2}$) in CuCl QDs on the square of reciprocal radius. (b) Dependences of the three lowest optical transitions on the square of reciprocal radius for CdS QDs. Symbols are experimental data connected by the red lines to guide the eye. The initial slopes of the experimental dependence are shown by black straight lines. Reproduced with permission from Efros AlL, Brus LE (2021) Nanocrystal quantum dots: From discovery to modern development. *ACS Nano* 15: 6192–6210.

To accurately describe the dependence of excited states on the size of nanocrystals, it is necessary to take into account the spin-orbital interaction leading to the splitting of the valence band into subzones of heavy holes, light holes and spin-split subzones, as well as the infinite height of potential barriers, Coulomb interaction and nonparabolicity of the conduction band (Norris and Bawendi, 1996). Thus, the deviation of the theoretical curve from the experimental data at large values of the QD radius (see Figs. 6 and 7) is apparently associated with an increase in the role of the Coulomb interaction with the weakening of the confinement. While the discrepancy between theoretical and experimental data at small values of the nanocrystal size is associated either with a violation of the effective mass model, or with the finite value of the potential barrier at the boundary between QD and surrounding medium (Efros and Brus, 2021).

The heterogeneous broadening plays an important role in explaining a number of physical properties of real samples of QDs. A monotonic dependence of the position of the PL spectrum on the photon energy of exciting light was found and explained by the size distribution of QDs, taking into account the dependence of the energy of the electron and hole levels on the size of QDs and the removal of the degeneracy of the hole levels (Rodrigues et al., 1995). Due to the complex structure of the valence band of CdSe QD, the predominant absorption of the same photon can go through transitions $1P_{3/2} \rightarrow 1P_e$ or $1P^{l}_{1/2} \rightarrow 1P_e$ nanocrystals of different sizes, while exciton recombination in both cases will go through the transition $1S_e \rightarrow 1S_{3/2}$ (Ekimov et al., 1993).

Photoluminescence

The photoluminescence (PL) of QDs is their most interesting property with a number of various practical applications. Let us consider for example colloidal CdSe QDs those intensive studies were facilitated by the relative simplicity of their production and the ability to accurately control the size and shape of nanocrystals. The most common way to obtain CdSe QDs is colloidal synthesis from a solution, which results in QD suspensions of a given radius. The Bohr exciton radius in CdSe is about 5.6 nm (Efros and Brus, 2021). This means that it becomes possible to observe the quantum confinement via the "blue" shift of the PL spectrum with a decrease in the size of QDs as shown in Fig. 8. The obtained PL line is attributed to the radiative recombination of excitons in such QD. When the QD's radius changes from 1.35 to 2.4 nm it is accompanied by a shift of the maximum of PL spectrum from 510 to 610 nm [17], as can be seen from Fig. 18. For optoelectronic and biophotonic applications of QDs, a high quantum yield (QY) of the luminescence is very important. The QY value in a QD usually increases due to the spatial confinement of excitons. However, two factors, which are insignificant in the bulk crystal, may reduce the radiative recombination rate in QDs. One of them is the nonradiative recombination on surface defects. Indeed, QDs with radius of about 1–2 nm consist of about 1/3 of the atoms on their surfaces, and the radiative recombination dominates only in QDs with surfaces, which are well passivated by the corresponding chemical groups and compounds (Medenitz et al., 2005).

Because of the small volume of a QD, defects of the crystal lattice, which can exist in the bulk material, do not usually present in the former. At high optical excitation, the nonradiative Auger recombination processes are stronger in nanocrystals than in the bulk material. Under intense excitation, when the formation of more than one exciton is possible, the local concentration of electron-hole pairs in the nanocrystal, due to the geometric restriction can be very large f the order of 10^{18}–10^{20} cm^{-3}. In addition, the spatial localization leads to a break-down the quasi-momentum conservation rule, and the probability of Auger process increases (Ekimov, 1991). Another process that reduces the quantum yield of exciton PL is nonradiative recombination on surface defects. When the QD' radius $a \approx 1.5$ nm, about 1/3 of the QD' atoms are on the surface, and the radiative recombination dominates only in QDs with well passivated surfaces by the corresponding chemical groups or compounds (Efros and Brus, 2021).

The intrinsic PL of CdSe QDs with diameters from 1.7 to 6.3 nm, coated with an organic shell, was investigated in a wide temperature range from 1.3 to 300 K and the results revealed nonmonotonic temperature dependences. Fig. 9 shows an example of the temperature dependence for the spectrally integrated PL intensity of CdSe QDs with d = 4.3 nm, while similar dependences took places for all diameters of the studied QDs (de Donegá et al., 2006).

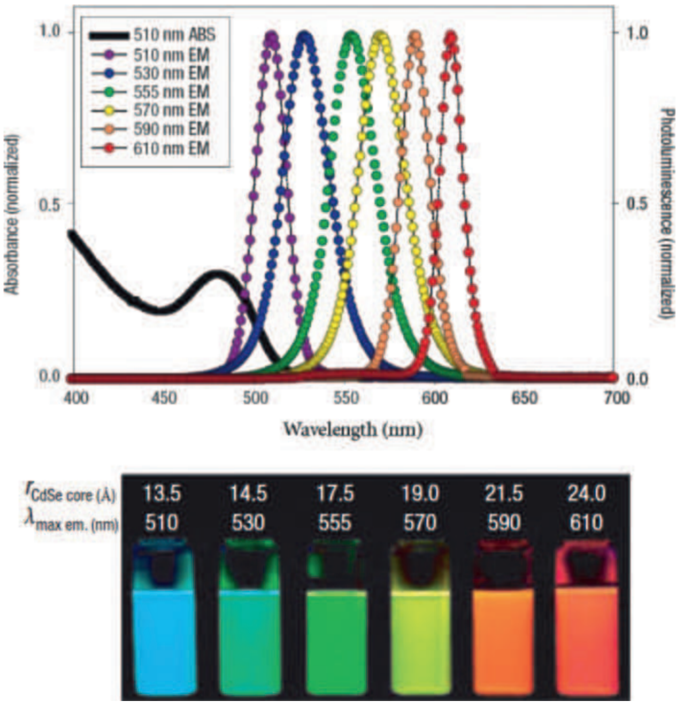

Fig. 8 Absorption (ABS) and emission (EM) spectra of CdSe QDs with different sizes indicated below in the panel nearby the corresponding PL images obtained under excitation at 365 nm. Reproduced with permission from Medenitz IL, Tetsuouyeda H, Goldman ER, Mattousi H (2005) Quantum dots bioconjugates for imaging, labelling and sensing. *Nature Materials* 4: 435–446.

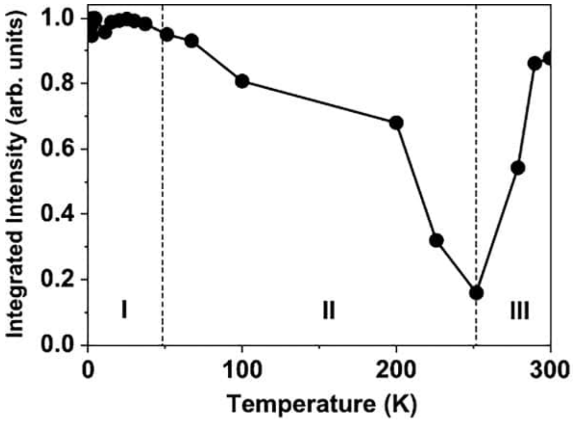

Fig. 9 Dependence of the integral PL intensity of CdSe QDs with d = 4.3 nm on temperature, where region I is the radiative mode, region II is the "attenuation" mode, and region III is the "anti-attenuation" mode. Reproduced with permission from de Donegá CM, Bode M, Meijering A (2006) Size- and temperature-dependence of exciton lifetimes in CdSe quantum dots. *Physical Review B* 74: 085320.

The temperature dependence of the exciton PL intensity of CdSe QDs can be better undesood by considering simultaneously the PL lifetimes at different temperatures. Fig. 10 shows PL transients of CdSe QDs with mean diameters of 1.7 and 4.3 nm measured at temperatures varied from 1.3 to 300 K. Fig. 11 shows dependences of the exciton PL lifetime on temperature for all studied samples. An analysis of the decay curves and integral intensities allows us to distinguish three temperature regimes of the exciton PL (de Donegá et al., 2006). The low-temperature regime (from 1.3 to 50 K) is characterized by an approximately constant QY that indicates the dominating role of the radiative recombination ("radiative regime" I in Fig. 9). At temperature 1.3 K the PL decay curves are bi-exponential for all QD sizes (Fig. 10). The fast component of the bi-exponential decay corresponds to the recombination from the bright exciton level preceding thermalization between the lower (dark exciton) and upper (bright exciton) levels. As the temperature increases, the fast component gradually disappears, while the slow component becomes faster, until the monoexponential character of the PL decay at T ~ 10 K is established. In the case of bi-exponential decay the lifetimes for the slow component are shown in Fig. 10. The PL transient curves remain monoexponential, and the rate of decay increases significantly

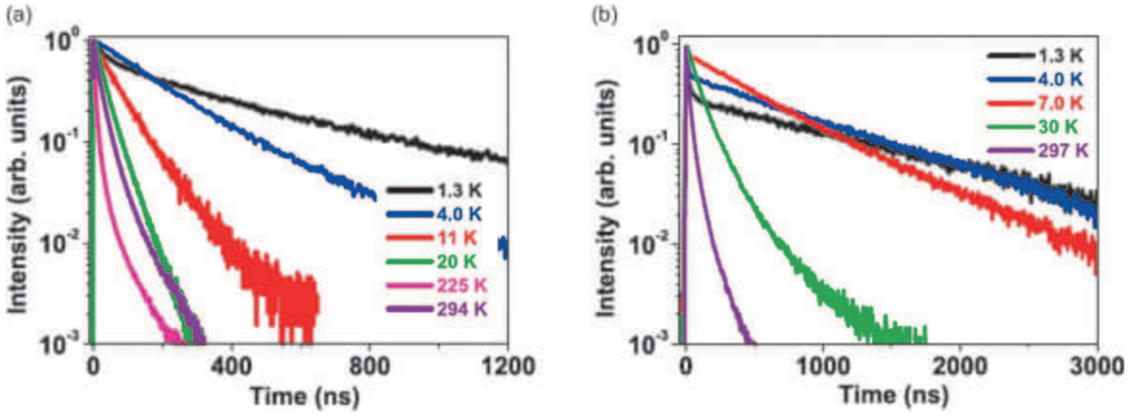

Fig. 10 PL transients of CdSe QDs with d = 4.3 nm (a) и d = 1.7 nm (b) at different temperatures indicated near the corresponding curves ($\lambda_{ex} = 406$ nm, $\lambda_{PL} = 609$ nm and 483 nm for d = 4.3 nm и 1.7 nm, respectively). Reproduced with permission from de Donegá CM, Bode M, Meijering A (2006) Size- and temperature-dependence of exciton lifetimes in CdSe quantum dots. *Physical Review B* 74: 085320.

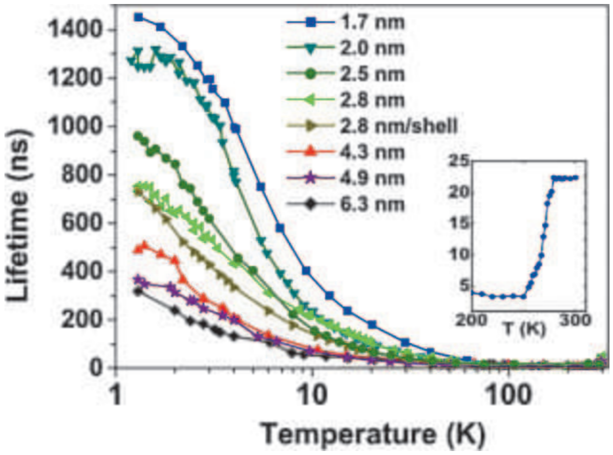

Fig. 11 Dependence of the exciton lifetimes for CdSe QDs with diameters from 1.7 to 6.3 nm. The results for the core/shell system (CdSe/ZnSe/ZnS) are also presented. The temperature scale is logarithmic. In the insert, the area is above 200 K (linear scale) for a sample with a diameter of 4.3 nm. Reproduced with permission from de Donegá CM, Bode M, Meijering A (2006) Size- and temperature-dependence of exciton lifetimes in CdSe quantum dots. *Physical Review B* 74: 085320.

with an increase in temperature to ~50 K, when the intensity of PL begins to decrease. Above 50 K, the PL decay becomes even more rapid and non-exponential, which indicates the thermal activation of electron capture on traps and non-radiative recombination ("attenuation mode" II in Fig. 9). The lifetimes determined from the exponential tails of the PL decay curves correspond to the radiative recombination of excitons and remain approximately constant at temperatures above ~50 K. It turns out that the beginning of the attenuation mode does not depend on the size of QDs or surface passivation. At temperatures above ~250 K, the intensity of PL begins to recover, while the lifetimes begin to increase, and the PL decay becomes almost monoexponential at room temperature as it was found in the experiment by de Donegá et al. (2006).

The most significant temperature and size dependence of the exciton PL in CdSe QDs is observed at temperatures below ~50 K, implying that the exciton lifetimes themselves change (Fig. 11). The dependence of the exciton lifetime on temperature in the radiative mode (mode I) can be modeled by a three-level system assuming thermal equilibrium between two radiating levels, the lower of which gives longer lifetimes (dark exciton) than the higher (bright exciton), and it can be described by the following equation (de Donegá et al., 2006):

$$\frac{1}{\tau} = \frac{1}{\tau_{dark}}\left(\frac{e^{\Delta E/KT}}{1 + e^{\Delta E/KT}}\right) + \frac{1}{\tau_{bright}}\left(\frac{1}{1 + e^{\Delta E/KT}}\right), \tag{6}$$

where τ is the measured PL lifetime, τ_{dark} and τ_{bright} are the lifetimes of dark and bright excitons, respectively, ΔE is the spitting energy between these two exciton levels. Despite its simplicity, such a model well describes the experimentally observed temperature dependence of the PL lifetime of CdSe QDs shown in Fig. 12 from the work of de Donegá et al. (2006).

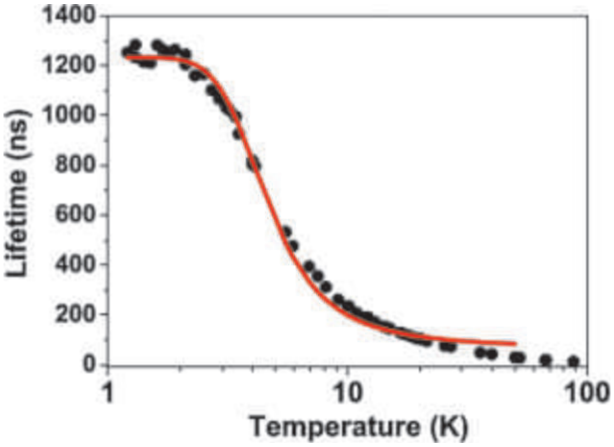

Fig. 12 Temperature dependence of the exciton lifetime of CdSe QDs with mean diameter 2 нм (black circles) and its approximation (red lines) by Eq. (6) with $\tau_{dark} = 1235$ ns, $\tau_{bright} = 40$ ns, and $\Delta E = 1.39$ meV. Reproduced with permission from de Donegá CM, Bode M, Meijering A (2006) Size- and temperature-dependence of exciton lifetimes in CdSe quantum dots. *Physical Review B* 74: 085320.

Effects of shells and impurities

Semiconductor heteronostructures, such as core/shell QDs, exhibit different optical properties depending on the spatial localization of charge carriers after photoexcitation (type I or type II), which can be controlled by changing the ratio of the diameter of the central part (core) of QD and the thickness of its shell (Chin et al., 2007). In type I QDs, electrons and holes are concentrated in the same part of the heterostructure, while in type II QDs, electrons and holes are separated in space, which leads to the formation of an indirect exciton. A consequence of the radiative recombination of an indirect exciton is a photon with an energy lower than the energy of the band gap of both the shell material and the nucleus. This makes it possible to achieve wavelengths larger than the wavelengths of single-component QDs or type I QDs (Ekimov, 1991; Ekimov et al., 1993; Klimov, 2003).

Fig. 13 shows spectra of the absorption and PL of CdTe/CdSe colloidal heteronanocrystals with a 2.6 nm diameter CdTe core and increasing shell thickness and the corresponding PL transients are shown in Fig. 14 (Chin et al., 2007). The PL spectrum and exciton lifetime are found to change dramatically during the growth of the shell of CdTe/CdSe heteronanocrystals. The maximum of PL spectra shifts from 535 nm (2.32 eV) for CdTe nuclei to 770 nm (1.61 eV) for sample E. The absorption spectra also experience redshift, but as the CdSe shell grows, the absorption spectra blur, and the oscillator strength at the emission wavelength decreases, while the exciton lifetimes become longer (Chin et al., 2007).

Increasing the CdSe shell results in an increase in the exciton lifetime and a multi-exponential decay in CdTe/CdSe QDs as shown in Fig. 14. These observations are explained by a decrease in the rate of nonradiative recombination, since it is accompanied by a significant increase in the quantum yield from 7% to 46% (Chin et al., 2007). A further increase in the thickness of the shell leads to an even greater increase in the exciton lifetime and to a transition from mono- to bi-exponential decays. The fast component of the bi-exponential decay refers to CdTe/CdSe heteronanocrystals, in which nonradiative recombination of excitons plays an essential role, while the slow component is attributed to purely radiative decay. Thus, the results obtained in this work indicate that as the thickness of the heteronanocrystal shell increases, the overlap integral of the electron and hole wave functions decreases rapidly (Chin et al., 2007).

Besides the effect of shell, the PL properties of QDs are also influenced by impurities and defect in the QD' lattice. The latter effect was observed for the copper impurities in CdSe QDs (Meulenberg et al., 2004; Tananaev et al., 2009). Fig. 15a shows PL spectra of $Cd_{1-x}Cu_xSe$ QDs compared with undoped ones (Meulenberg et al., 2004). The PL spectrum of the undoped sample consists of a narrow peak of interband recombination of excitons in CdSe QDs with a maximum at a photon energy of 2.15 eV and a wide peak in the low-energy part of the spectrum, the nature of which is associated with surface defects in CdSe. It can be seen from the figure that the introduction of copper into the QD structure leads to the quenching of the exciton PL and the appearance of an intense luminescence band in the low-energy region, which experiences a red shift with an increase in the copper content in the sample. The observed effect can be explained by the fact that the Cu_4 cluster formed when introduced into the CdSe lattice leads to the appearance of structural defects and, accordingly, deep energy levels lying lower than the energy levels of surface defects of unalloyed QDs. Charge carriers are captured at these levels. With an increase in the concentration of copper, most of the photogenerated charge carriers are captured at defect-related energy levels followed with the IR PL emission (Meulenberg et al., 2004).

An effect of the doping on both the shape and PL properties of Cd(*Cu*)Se QDs was found by Tananaev et al. (2009). The samples of Cd(*Cu*)Se QDs were obtained by introducing copper precursors as copper stearate or triphenylphosphine complex tetraiodidtetramedi $[Cu_4I_4](Ph_3P)_4$. The size of the synthesized nanocrystals varied from 2 to 5 nm and the shape for QDs synthesized with copper stearate was predominantly spherical (see Fig. 16a). According to the chemical analysis, the average copper content in Cd(*Cu*)Se QDs was varied from 0.03 to 1 at.% (Tananaev et al., 2009).

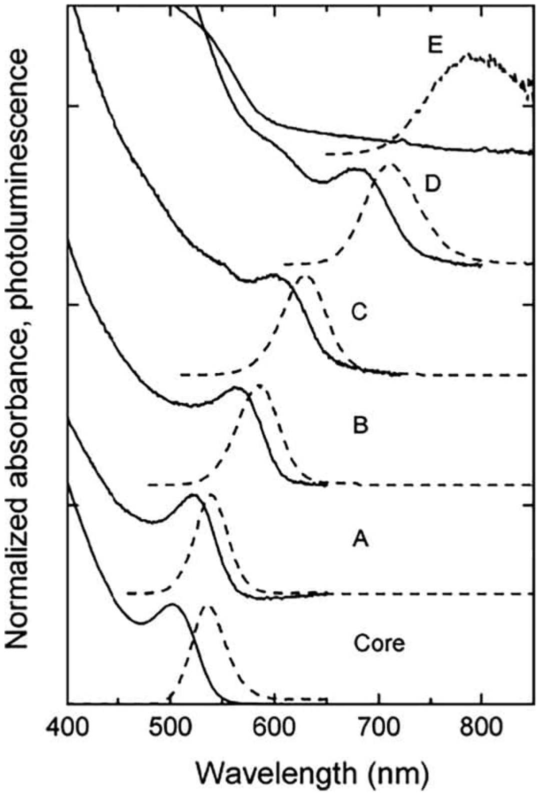

Fig. 13 Absorption spectra (solid curves) and PL (dotted curves) of CdTe/CdSe colloidal heteronanocrystals with a 2.6 nm diameter CdTe core and increasing shell thickness (corresponds to Table 1). The spectra are shifted vertically. Reproduced with permission from Chin PTK, de Donega CM, van Bavel SS, Meskers SCJ, Sommerdijk NAJM, Janssen RAJ (2007) Highly luminiscent CdTe/CdSe colloidal heteronanocrystals with temperature-dependent emission color. *Journal of the American Chemical Society* 129: 14880–14886.

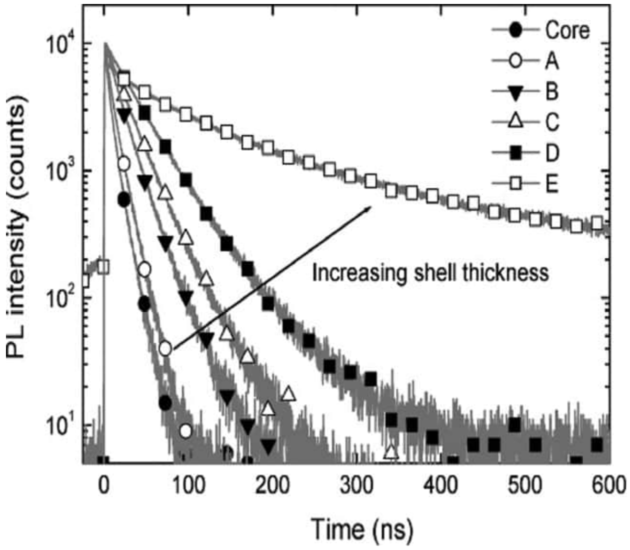

Fig. 14 PL decay transients of CdTe/CdSe colloidal heteronanocrystals with a 2.6 nm diameter CdTe core and increasing shell thickness. The decline curve of QDs CdTe used as cores is also shown. Reproduced with permission from Chin PTK, de Donega CM, van Bavel SS, Meskers SCJ, Sommerdijk NAJM, Janssen RAJ (2007) Highly luminiscent CdTe/CdSe colloidal heteronanocrystals with temperature-dependent emission color. *Journal of the American Chemical Society* 129: 14880–14886.

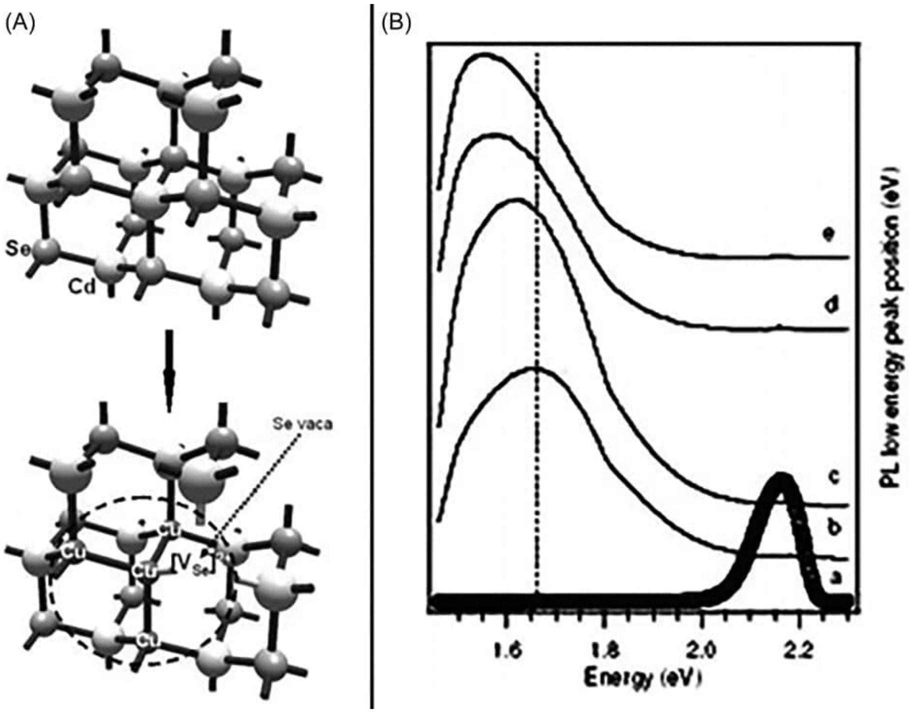

Fig. 15 (A) Scheme of the Cu_4 cluster embedded into the CdSe crystal structure; (B) Normalized PL spectra of QDs of undoped CdSe and Cd(*Cu*)Se with different copper content in at.%: 5.5 (b), 9.9 (c), 13.2 (d), and 5.2 (e). Reproduced with permission from Meulenberg RW, van Buuren T, Khanif KM, Willey TM, Strouse GF, Terminello LJ (2004) Structure and composition of Cu-doped CdSe nanocrystals using soft X-ray absorption spectroscopy. *Nano Letters* 4: 2277–2285.

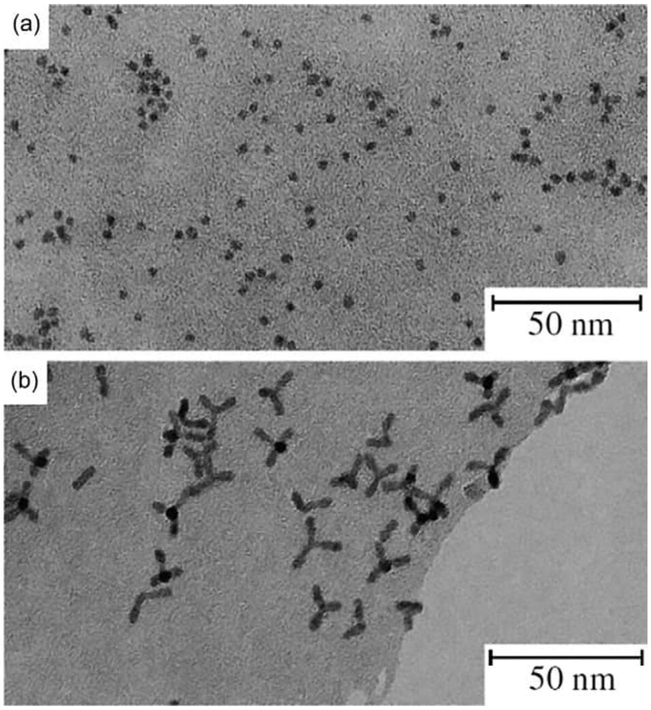

Fig. 16 (a) TEM image of Cd(*Cu*)Se QDs with mean sizes 3.4 нм synthesized by using $Cu(C_{17}H_{35}COO)_2$, and (b) TEM image of Cd(*Cu*)Se tetrapods with arm length of ~9 nm synthesized by using $[Cu_4I_4](Ph_3P)_4$. Reproduced with permission from Tananaev PN, Dorofeev SG, Dirin D, Belov D, Kuznetsova T (2009) Growth of sphere- and tetrapod-shaped Cd(Cu)Se nanocrystals from Cu(C17H35COO)2 and Cu4(PPh3)4(μ3-I)4. *Mendeleev Communications* 19: 131–132.

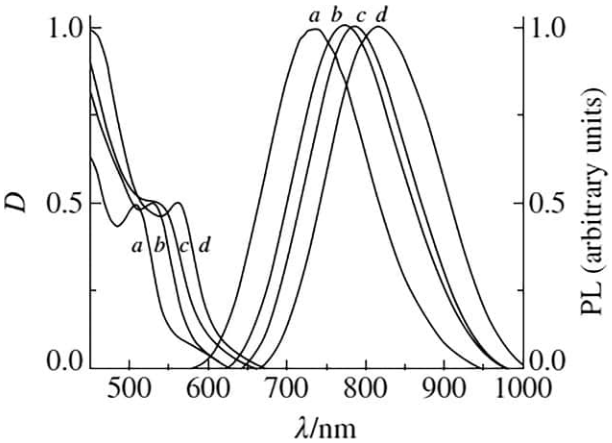

Fig. 17 Spectra of the optical density (D) and PL of Cd(*Cu*)Se QDs taken during growth at (a) 5 s, (b) 20 s, (c) 1 min and (d) 5 min that increase the size of QD' core. The samples (a) are spherical QDs, while the samples (b–d) are mostly tetrapod shaped. Reproduced with permission from Tananaev PN, Dorofeev SG, Dirin D, Belov D, Kuznetsova T (2009) Growth of sphere- and tetrapod-shaped Cd(Cu)Se nanocrystals from Cu(C17H35COO)2 and Cu4(PPh3)4(μ3-I)4. *Mendeleev Communications* 19: 131–132.

The introduction of a large amount of copper about 1% into CdSe QDs leads to a change in the shape of growing nanocrystals, i.e., from spheres they turn into tetrapods (Fig. 16b), which is an excellent illustration of the influence of impurity atoms on the growth of QDs. Thus, using [Cu4I4](Ph3P)4 clusters, it is possible to obtain Cd(*Cu*)Se QDs in the form of tetrapods. The introduction of an excessively large amount of copper leads to the quenching of the exciton luminescence and the shift of the absorption edge and PL band to the "red" spectral region as shown in Fig. 17 (Tananaev et al., 2009).

The introduction of impurity atoms into the structure of QDs makes it possible to further modify their basic properties and give them new ones rather different from those for undoped QDs that further expands their possible applications. For example, the above mentioned Cd(*Cu*)Se QDs exhibit PL bands in the near IR region (Meulenberg et al., 2004; Tananaev et al., 2009), which corresponds to the first transparency window of biotissue from ~700 to 1000 nm (Golovynskyi et al., 2018). The PL lifetime of Cd(*Cu*)Se QDs in the near-IR range was found to be about several microseconds (Tselikov et al., 2011) and it is especially useful for bioimaging applications to improve the luminescent contrast of QDs since the autofluorescence lifetime of biotissue corresponds typically to the nanosecond range (Gu et al., 2013).

Besides the above discussed compound QDs, pure silicon (Si) nanocrystals with silicon oxide or hydride shells as well as nanoparticles, which consist of Si QDs, can also emit efficient room temperature PL in the visible and near-IR spectral regions (Cullis et al., 1997; Mangolini et al., 2005; Erogbogbo et al., 2008; Park et al., 2009; Sugimoto et al., 2013; Gu et al., 2013).While Si QDs usually exhibit weaker and less stable PL than convenient A^2B^6 QDs, ligand-coated Si nanocrystals can possess a high internal QY near unity (Sangghaleh et al., 2015).

Among different physical, chemical and electro- and plasma-chemical methods of the Si nanocrystal synthesis, a method of the laser ablation of a crystalline Si target in inert gas atmosphere is used to prepare water-dispersible highly luminescent nanoparticles, which consist of Si QDs coated with silicon suboxide shells (Gongalsky et al., 2016). The bright and long-lived exciton PL at 600–900 nm and oxide shell related fast PL at 300–500 nm are detectable both in as-prepared laser-ablated films and in aqueous suspensions (Fig. 18). The near-IR band centered at 1.5 eV is explained by the radiative recombination of excitons confined in Si QD' core with diameter of 2–3 nm, while a band centered at 2.7 eV is related to the radiative transitions in the oxide shell of Si QDs (Gongalsky et al., 2016).

A remarkable property of Si QDs is relatively long PL lifetime, which is in the microsecond range and about several milliseconds at room and cryogenic temperature, respectively (Calcott et al., 1993). The long lifetimes of PL in Si QDs are explained by the spin-dependent splitting of exciton states into energetically higher singlet and lower triplet ones (Kovalev et al., 1999) that is similar to the above discussed model of "bright" and "dark" exciton in CdS QDs (de Donegá et al., 2006). The spin-dependent exciton processes in Si QDs and nanoparticles are very important for both their photonic properties (Joo et al., 2015) and biomedical applications, e.g., photosensitization of the singlet oxygen generation for the photodynamic therapy of cancer (Fomin and Timoshenko, 2020).

During last years, Pe-QDs, which represent metal-organic and inorganic lead halide perovskite nanocrystals are attracting the significant attention because of the simplicity of preparation and bright PL with QY exceeding 90% (Zhou and Wang, 2020). The PL band of Pe-QDs is narrow and it can be spectrally tunable by both halide composition, dimensionality, and quantum confinement (Fig. 19). While Pe-QDs are not stable against water and oxygen, their preparation methods are cheap, flexible and well combined with semiconductor optoelectronic technology. The excellent luminescent properties of Pe-QDs make then a promising candidate for new generation of QDs-based LEDs (Li et al., 2019) and lasers (Park et al., 2021).

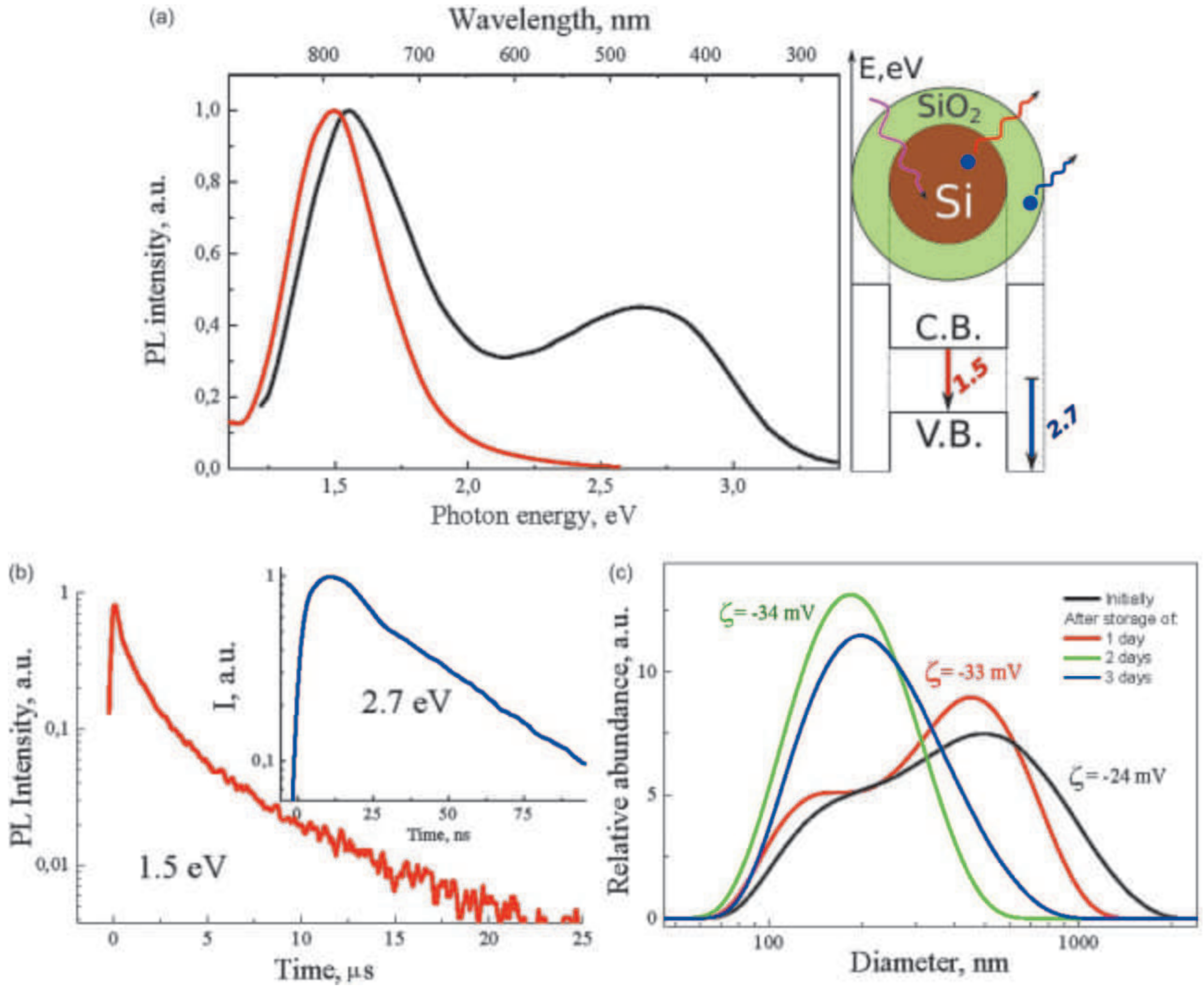

Fig. 18 (a) PL spectra of as-prepared films of Si QDs (red curve) and aqueous suspensions of Si QDs (black curve); (b) PL transients for the exciton (1.5 eV) defect-related (2.7 eV) bands; (c) Dynamic light scattering spectra from NPs composed by Si QD after different time of their storage in saline. Reproduced with permission from Gongalsky MB, Osminkina LA, Pereira A, Manankov AA, Fedorenko AA, Vasiliev AN, Solovyev VV, Kudryavtsev AA, Sentis M, Kabashin AV, Timoshenko VY (2016) Laser-synthesized oxide-passivated bright Si quantum dots for bioimaging. *Scientific Reports* 6: 24732.

Optoelectronic and biomedical applications

Specially designed QDs are characterized by PL emission with a high QY and spectral position, which can be tailored in the visible and near-IR regions, that is useful for various biophotonic applications. It is known that one of the directions of biomedical diagnostics is based on fluorescent labeling, for which organic dyes are usually used. However, the photophysical properties inherent in organic dyes, in particular, wide absorption/emission peaks and a low photobleaching threshold, limit the effectiveness of their use in long-term image formation and in the instantaneous detection of a multi-frequency signal. Therefore, QDs are of interest for biophotonics because their high PL QY, a large molar extinction coefficient (10–100 times greater than that of organic dyes), wide absorption with a narrow symmetrical (FWHM ~25–40 nm) PL peak, a large effective Stokes shift, high resistance to photobleaching and exceptionally high resistance to photo- and chemical degradation (Wu et al., 2003; Michalet et al., 2005; de Donegá et al., 2006).

Fig. 20a shows typical PL images of QD-colored living cells explaining the resistance of QDs to photobleaching and Fig. 20b shows a pseudo-color image, which corresponds to the 5-color coloration of the human epithelial cell incubated with QDs (de Donegá et al., 2006). While the PL imaging clearly demonstrates the wide biophotonic potential of QDs based on both the II–VI group compounds (Medenitz et al., 2005; Michalet et al., 2005; Kim et al., 2022) and IV-group semiconductors (Erogbogbo et al., 2008; Botsoa et al., 2008; Serdiuk et al., 2013; Gu et al., 2013; Gongalsky et al., 2016), it can be also significantly extended by using nonlinear optical bioimaging modalities as second harmonic generation and two photon excited luminescence (Kharin et al., 2019).

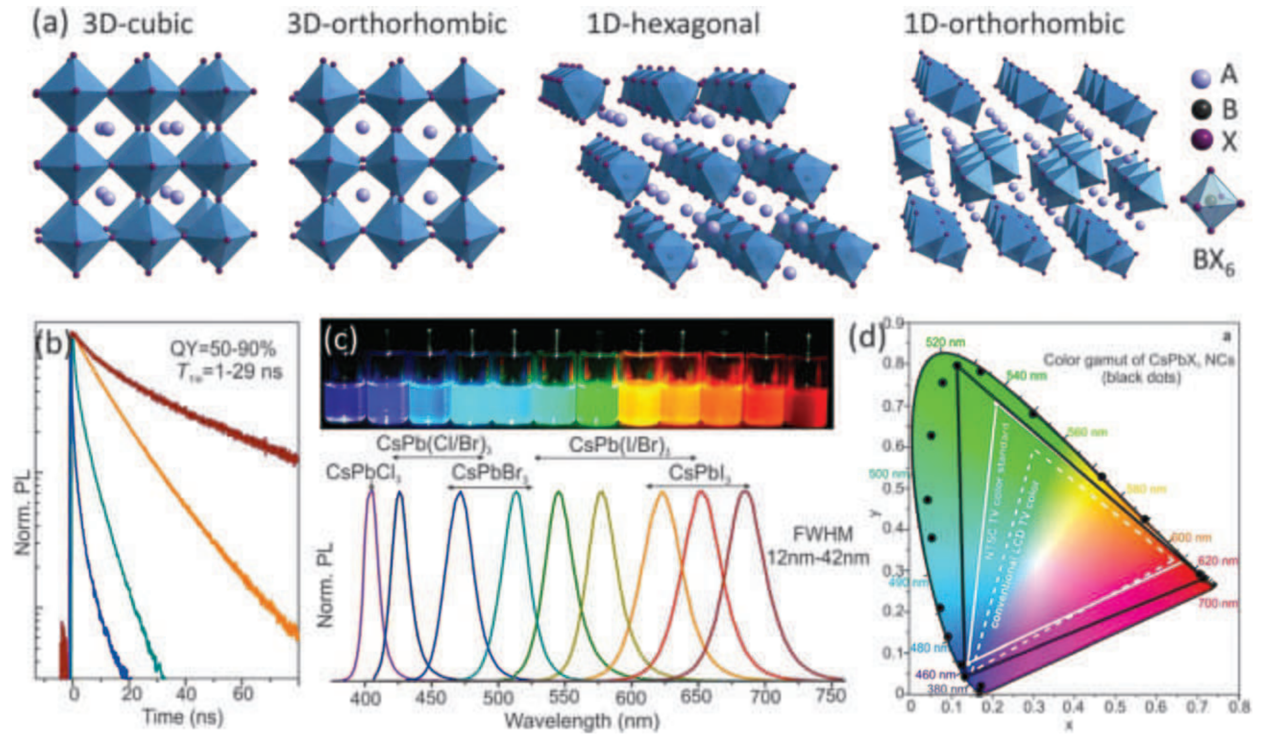

Fig. 19 (a) Basic structures of colloidal perovskite NCs. (b) Time-resolved PL decays for Pe-QDs. (c) PL spectra and corresponding photographs (under UV irradiation) of CsPbX3 QDs tuned by anions. (d) Emission from Pe-QDs (black points) compared with typical LCD TV standard (dashed triangle) and NTSC TV standard (solid triangle). Reproduced with permission from Li Y-F, Feng J, Sun H-B (2019) Perovskite quantum dots for light-emitting devices. *Nanoscale* 11: 19119–19139.

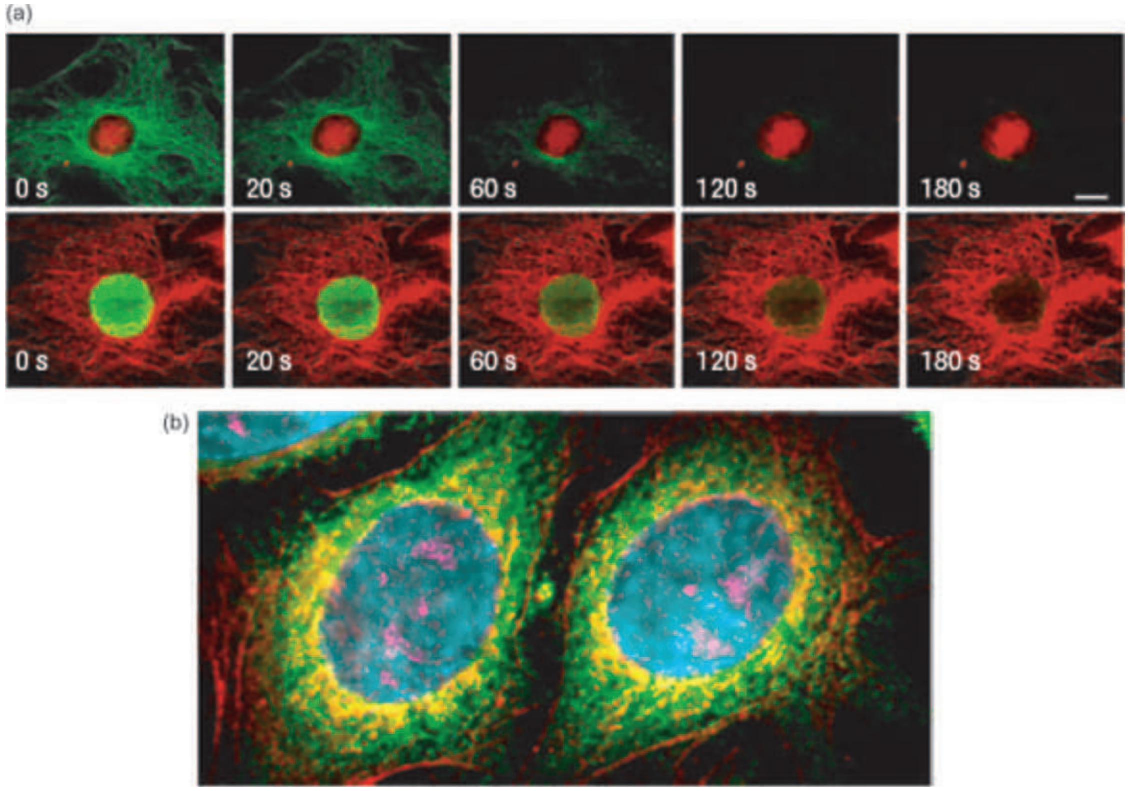

Fig. 20 (a) Top row: Nuclear antigens were labeled with QD 630–streptavidin (red), and microtubules were labeled with AlexaFluor 488 (green) simultaneously in a 3T3 cell. Bottom row: Microtubules were labeled with QD 630–streptavidin (red), and nuclear antigens were stained green with Alexa 488. Continuous exposure times in seconds are indicated (Reprinted by permission of the Nature Publishing Group). QDs as photobleaching resistant PL labels in vitro and (b) multicolored PL labeling of cells by QDs as follows: blue color corresponds to 655 nm QD marking the nucleus; yellow is related to 605 nm QD marking the Ki-67 protein; orange corresponds to 525 nm for the mitochondria; green is related to the QD marking microtubules at 565 nm; red corresponds to 705 nm of QD marking actin filaments. Reproduced with permission from de Donegá CM, Bode M, Meijering A (2006) Size- and temperature-dependence of exciton lifetimes in CdSe quantum dots. *Physical Review B* 74: 085320.

QDs prepared from pure Si (Erogbogbo et al., 2008; Gu et al., 2013; Gongalsky et al., 2016) and silicon carbide (Botsoa et al., 2008; Serdiuk et al., 2013) are attractive for bioimaging because they are significantly less toxic than the II–VI group QDs (Medenitz et al., 2005; Yildirimer et al., 2011). Moreover, Si QDs and NPs are biodegradable that results in formation of nontoxic silicic acid (Park et al., 2009).

The PL lifetime of Si QDs at room temperature is typically of the order of microseconds (Kovalev et al., 1999; Gu et al., 2013; Gongalsky et al., 2016) and it is significantly longer than the nanosecond lifetimes of autofluorescence of biomolecules in cells and tissues (Golovynskyi et al., 2018). This property of Si QDs can be utilized through the time-gated PL imaging for better discrimination of the QD′ PL from the endogenous fluorescence signal that can result in more than 100-fold contrast improvements relative to steady-state imaging (Gu et al., 2013).

Optoelectronic applications of QDs as active media for LED and electrically pumped lasers are based on high QY and temperature stability of their light-emitting properties. Fig. 21 shows a schematic image of the QD laser, which is based on the direct injection of charge carriers into QDs, as a result of which the depletion of non-basic charge carriers occurs in areas outside the QDs. Thus, the non-radiative recombination of charge carriers in these regions, mainly responsible for temperature dependence, can be suppressed (Asryan and Luryi, 2001).

Self-assembled QDs (see Fig. 1b) based on A^3B^5 semiconductors can be employed in creation of compact solid-state lasers (Liu et al., 2005, 2011). Such lasers based on multilayered structures of self-assembled InAs/GaAs QDs (Fig. 22 A) incorporated in quantum wells (QW), i.e., dot-in-a-well (DWELL) structures, together with cladding and contacting layers were epitaxially grown on c-Si substrates (Lee et al., 2012) as shown in Fig. 22b. These structures were able to emit at about 1.3 μm both in the pulsed and continuous-wave (CW) regimes at room temperature (Fig. 22c). Such NIR InAs/GaAs QD lasers being integrated on Ge/Si substrates can be used to realize the long-dreamed of integrated III-V/Si optoelectronics (Lee et al., 2012; Kwoen et al., 2019).

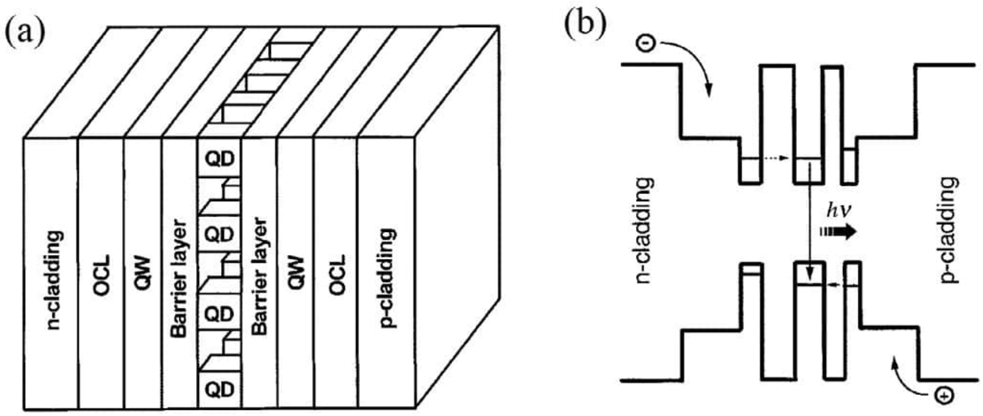

Fig. 21 Schematic view (a) and zone diagram (b) of a QD laser operating by tunnel injection. Reproduced with permission from Asryan V, Luryi S (2001) Tunneling-injection quantum-dot laser: Ultrahigh temperature stability. *IEEE Journal of Quantum Electronics* 37: 905–910.

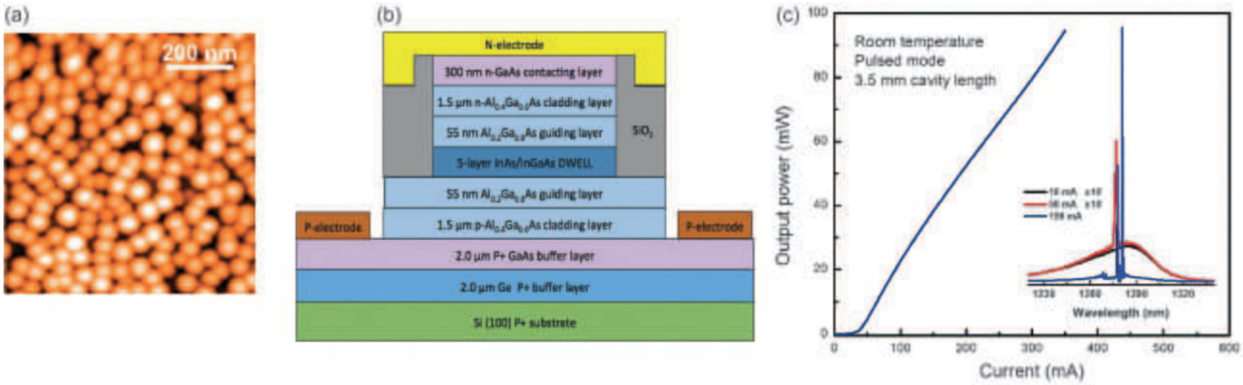

Fig. 22 (a) AFM image (1 × 1 μm^2) of InAs/GaAs QDs grown on a Ge/Si substrate. (b) Schematic image of the layer structure of an InAs/GaAs QD laser diode. (c) Light output power versus current for a QD laser under pulsed operation. Inset shows the light emission spectra of InAs/GaAs QD laser for different injection current. Reproduced with permission from Lee A, Jiang Q, Tang M, Seeds A, Liu H (2012) Continuous-wave InAs/GaAs quantum-dot laser diodes monolithically grown on Si substrate with low threshold current densities. *Optics Express* 20: 22181–22187.

The physical and chemical properties of Pe-QDs together with the simplicity of their preparation if compared to III–V QDs facilitate a wide range of applications of the former in optoelectronics (Li et al., 2019; Zhou and Wang, 2020). Chemical synthesis from liquids is usually used to form metal-organic and inorganic Pe-QDs of high crystal quality and PL QY near unity. The external quantum efficiency (EQE) of the best samples of Pe-QD LEDs has been reported to be about 10–20% (Li et al., 2019). Despite the impressive progress in Pe-QDs LEDs (Zhou and Wang, 2020; Liu et al., 2021, 2022) and lasers (Park et al., 2021) in recent years, their commercial applications remain a challenge. The efficiency and stability of Pe-QDs devices require further improvements to compete with traditional LEDs and fully organic ones.

Conclusion

Different types of QDs as semiconductor nanocrystals crystallized in a solid matrix, colloidal QDs, self-organized semiconductor nanocrystals in heterostructures, metal-organic and inorganic perovskite QDs represent examples of the zero-dimensional solid state systems with unique physical properties. The optical absorption and photoluminescence of QDs are explained by considering the quantum confinement of charge carriers (electron and holes) and electron-hole pairs (excitons) in semiconductor nanocrystals. The energy spectrum and optical properties of QDs are controlled by their chemical composition, spatially confined and localized electronic states, as well as by incorporated impurities and surface coatings. The modern chemical synthesis and semiconductor technology allow tailoring the optical properties of QDs for various applications as light-emitting structures in optoelectronics and luminescent markers in biophotonics.

References

Alivisatos AP (1996) Semiconductor clusters, nanocrystals, and quantum dots. *Science* 271: 933–937.

Asryan V and Luryi S (2001) Tunneling-injection quantum-dot laser: Ultrahigh temperature stability. *IEEE Journal of Quantum Electronics* 37: 905–910.

Botsoa J, Lysenko V, Geloen A, Marty O, Bluet JM, and Guillot G (2008) Application of 3C-SiC quantum dots for living cell imaging. *Applied Physics Letters* 92: 173902.

Brus LE (1984) Electron–electron and electron-hole interactions in small semiconductor crystallites: The size dependence of the lowest excited electronic state. *The Journal of Chemical Physics* 80: 4403–4409.

Calcott PDJ, Nash KJ, Canham LT, Kane MJ, and Brumhead D (1993) Identification of radiative transitions in highly porous silicon. *Journal of Physics. Condensed Matter* 5: L91.

Chin PTK, de Donega CM, van Bavel SS, Meskers SCJ, Sommerdijk NAJM, and Janssen RAJ (2007) Highly luminiscent CdTe/CdSe colloidal heteronanocrystals with temperature-dependent emission color. *Journal of the American Chemical Society* 129: 14880–14886.

Cullis AG, Canham LT, and Calcott PDJ (1997) The structural and luminescence properties of porous silicon. *Journal of Applied Physics* 82: 909–965.

de Donegá CM, Bode M, and Meijering A (2006) Size- and temperature-dependence of exciton lifetimes in CdSe quantum dots. *Physical Review B* 74: 085320.

Efros ALL and Brus LE (2021) Nanocrystal quantum dots: From discovery to modern development. *ACS Nano* 15: 6192–6210.

Efros ALL and Efros ⊠L (1982) Interband light absorption in semiconductor spheres. *Soviet Physics – Semiconductors* 16: 772–775.

Ekimov AI (1991) Optical properties of semiconductor quantum dots in glass matrix. *Physica Scripta* T39: 217–220.

Ekimov AI and Onushchenko AA (1981) Quantum size effects in three-dimensional microscopic semiconductor crystals. *JETP Letters* 34: 345–349.

Ekimov AI, Efros ALL, and Onushchenko AA (1985) Quantum size effects in semiconductor microcrystals. *Solid State Communications* 56: 921–924.

Ekimov AI, Hache F, Schanne-Klein MC, Ricard D, Flytzanis C, Kudryavtsev IA, Yazeva TV, Rodina AV, and Efros ALL (1993) Absorption and intensity-dependent photoluminescence measurements on CdSe quantum dots: Assignment of the first electronic transitions. *Journal of the Optical Society of America B: Optical Physics* 10: 100.

Erogbogbo F, Yong K-T, Roy I, Xu GX, Prasad PN, and Swihart MT (2008) Biocompatible luminescent silicon quantum dots for imaging of cancer cells. *ACS Nano* 2: 873–878.

Fomin VM and Timoshenko VY (2020) Spin-dependent phenomena in semiconductor micro-and nanoparticles—From fundamentals to applications. *Applied Sciences* 10: 4992.

Golovynskyi S, Golovynska I, Stepanova LI, Datsenko OI, Liu L, Qu J, and Ohulchanskyy TY (2018) Optical windows for head tissues in near-infrared and short-wave infrared regions: Approaching transcranial light applications. *Journal of Biophotonics,* e201800141.

Gongalsky MB, Osminkina LA, Pereira A, Manankov AA, Fedorenko AA, Vasiliev AN, Solovyev VV, Kudryavtsev AA, Sentis M, Kabashin AV, and Timoshenko VY (2016) Laser-synthesized oxide-passivated bright Si quantum dots for bioimaging. *Scientific Reports* 6: 24732.

Gu L, Hall DJ, Qin Z, Anglin E, Joo J, Mooney DJ, Howell SB, and Sailor MJ (2013) In vivo time-gated fluorescence imaging with biodegradable luminescent porous silicon nanoparticles. *Nature Communications* 4: 2326.

Joo J, Liu X, Kotamraju VR, Ruoslahti E, Nam Y, and Sailor MJ (2015) Gated luminescence imaging of silicon nanoparticles. *ACS Nano* 9: 6233–6241.

Kharin AY, Lysenko VV, Rogov A, Ryabchikov YV, Geloen A, Tishchenko I, Marty O, Sennikov PG, Kornev RA, Zavestovskaya IN, Kabashin AV, and Timoshenko VY (2019) Bi-modal nonlinear optical contrast from Si nanoparticles for cancer theranostics. *Advanced Optical Materials* 7: 1801728.

Kim J, Hwang DW, Jung HS, Kim KW, Pham X-H, Lee S-H, Byun JW, Kim W, Kim H-M, Hahm E, Ham K-M, Rho W-Y, Lee DS, and Jun B-H (2022) High-quantum yield alloy-typed core/shell CdSeZnS/ZnS quantum dots for bio-applications. *Journal of Nanobiotechnology* 20: 22.

Klimov VI (2003) In: Klimov VI (ed.) *Semiconductor and Metal Nanocrystals. Synthesis and Electronic and Optical Properties. Optical Science and Engineering*, 1st edn. CRC Press.

Kovalev D, Heckler H, Polisski G, and Koch F (1999) Optical properties of Si nanocrystals. *Physica Status Solidi B: Basic Solid State Physics* 215: 871–932.

Kwoen J, Jang B, Watanabe K, and Arakawa Y (2019) High-temperature continuous-wave operation of directly grown InAs/GaAs quantum dot lasers on on-axis Si (001). *Optics Express* 27: 2681–2688.

Lee A, Jiang Q, Tang M, Seeds A, and Liu H (2012) Continuous-wave InAs/GaAs quantum-dot laser diodes monolithically grown on Si substrate with low threshold current densities. *Optics Express* 20: 22181–22187.

Li Y-F, Feng J, and Sun H-B (2019) Perovskite quantum dots for light-emitting devices. *Nanoscale* 11: 19119–19139.

Liu HY, Childs DT, Badcock TJ, Groom KM, Sellers IR, Hopkinson M, Hogg RA, Robbins DJ, Mowbray DJ, and Skolnick MS (2005) High-performance three-layer 1.3-μm InAs/GaAs quantum-dot lasers with very low continuous-wave room-temperature threshold currents. *IEEE Photonics Technology Letters* 17: 1139–1141.

Liu H, Wang T, Jiang Q, Hogg R, Tutu F, Pozzi F, and Seeds A (2011) Long-wavelength InAs/GaAs quantum-dot laser diode monolithically grown on Ge substrate. *Nature Photonics* 5: 416–419.

Liu Y, Dong Y, Zhu T, Ma D, Proppe A, Chen B, Zheng C, Hou Y, Lee S, Sun B, Jung EH, Yuan F, Wang Y-K, Sagar LK, Hoogland S, de Arquer FPG, Choi M-J, Singh K, Kelley SO, Voznyy O, Lu Z-H, and Sargent EH (2021) Bright and stable light-emitting diodes based on perovskite quantum dots in perovskite matrix. *Journal of the American Chemical Society* 143: 15606–15615.

Liu Y, Li Z, Xu J, Dong Y, Chen B, Park SM, Ma D, Lee S, Huang JE, Teale S, Voznyy O, Lu Z-H, and Sargent EH (2022) Wide-bandgap perovskite quantum dots in perovskite matrix for sky-blue light-emitting diodes. *Journal of the American Chemical Society* 44(9): 4009–4016.

Mangolini L, Thimsen E, and Kortshagen U (2005) High-yield plasma synthesis of luminescent silicon nanocrystals. *Nano Letters* 5: 655–659.

Medenitz IL, Tetsuouyeda H, Goldman ER, and Mattousi H (2005) Quantum dots bioconjugates for imaging, labelling and sensing. *Nature Materials* 4: 435–446.

Meulenberg RW, van Buuren T, Khanif KM, Willey TM, Strouse GF, and Terminello LJ (2004) Structure and composition of Cu-doped CdSe nanocrystals using soft X-ray absorption spectroscopy. *Nano Letters* 4: 2277–2285.

Michalet LX, Pinaud FF, Bentolila LA, et al. (2005) Quantum dots for live cells, in vivo imaging, and diagnostics. *Science* 307: 538–544.

Norris DJ and Bawendi MG (1996) Measurement and assignment of the size-dependent optical spectrum in CdSe quantum dots. *Physical Review B* 53: 16338–16346.

Norris DJ, Sacra A, Murray CB, and Bawendi MG (1994) Measurement of the size dependent hole spectrum in CdSe quantum dots. *Physical Review Letters* 72: 2612–2615.

Park J-H, Gu L, Maltzahn GV, Ruoslahti E, Bhatia SN, and Sailor MJ (2009) Biodegradable luminescent porous silicon nanoparticles for in vivo applications. *Nature Materials* 8: 331–336.

Park Y-S, Roh J, Diroll BT, Schaller RD, and Klimov VI (2021) Colloidal quantum dot lasers. *Nature Reviews Materials* 6: 382–401.

Rodina AV and Efros ALL (2016) Effect of dielectric confinement on optical properties of colloidal nanostructures. *Journal of Experimental and Theoretical Physics* 122: 554–566.

Rodrigues PAM, Tamulatis G, Peter Yu P, and Risbud SH (1995) Size selective photoluminescence excitation spectroscopy in CdSe nanocrystals. *Solid State Communications* 94: 583–587.

Sangghaleh F, Sychugov I, Yang Z, Veinot JGC, and Linnros J (2015) Near-unity internal quantum efficiency of luminescent silicon nanocrystals with ligand passivation. *ACS Nano* 9: 7097–7104.

Serdiuk T, Lysenko V, Mognetti B, Skryshevsky V, and Géloen A (2013) Impact of cell division on intracellular uptake and nuclear targeting with fluorescent SiC-based nanoparticles. *Journal of Biophotonics* 6: 291–297.

Stranski IN and Krastanow L (1938) Zur Theorie der orientierten Ausscheidung von Ionenkristallen aufeinander. Abhandlungen der Mathematisch-Naturwissenschaftlichen Klasse IIb. *Akademie der Wissenschaften Wissenschaften* 146: 797–810.

Sugimoto H, Fujii M, Imakita K, Hayashi S, and Akamatsu K (2013) Codoping N- and P-type impurities in colloidal silicon nanocrystals: Controlling luminescence energy from below bulk band gap to visible range. *Journal of Physical Chemistry C* 117: 11850–11857.

Tananaev PN, Dorofeev SG, Dirin D, Belov D, and Kuznetsova T (2009) Growth of sphere- and tetrapod-shaped Cd(Cu)Se nanocrystals from Cu(C17H35COO)2 and Cu4(PPh3)4(μ3-I)4. *Mendeleev Communications* 19: 131–132.

Tselikov GI, Dorofeev SG, Tananaev PN, and Timoshenko VY (2011) Specific features of photoluminescence properties of copper-doped cadmium selenide quantum dots. *Semiconductors* 45: 1173–1176.

Wu X, Liu H, Liu J, Haley KN, Treadway JA, Larson JP, Ge N, Peale F, and Bruchez MP (2003) Immunofluorescent labeling of cancer marker Her2 and other cellular targets with semiconductor quantum dots. *Nature Biotechnology* 21: 41–46.

Yildirimer L, Thanh NTK, Loizidou M, and Seifalian AM (2011) Toxicological considerations of clinically applicable nanoparticles. *Nano Today* 6: 585–607.

Zhou Y and Wang Y (2020) *Perovskite Quantum Dots: Synthesis, Properties and Applications*. Springer Nature Singapore Pte Ltd.

The physics of quantum dots

Jean-Pierre Leburton, University of Illinois at Urbana-Champaign, Urbana, IL, United States

© 2024 Elsevier Ltd. All rights reserved.

Introduction **325**
Overview **326**
Planar quantum dots 326
Vertical quantum dots 326
Self-assembled quantum dots 327
Silicon nanocrystals 327
Colloidal quantum dots 328
Key issues **328**
Coulomb blockade and single electronics 328
Single electronics 328
Memory applications 329
Artificial atoms and molecules 329
Magnetic field effects 331
Artificial molecules 331
Entanglement and quantum gates 331
Optical emission from SAD's and CD's 332
Modeling and simulation 333
Conclusion **336**
References **336**

Abstract

An overview of the electronic and optical properties of the various types of quantum dots (QD) made of solid-state materials is presented. Whereas they share common physical characteristics such as small sizes and the ability to contain and manipulate few particles, QD's exhibit fundamental specificity in the manifestation of electron charge, spin, or single photon emission, each with their respective potential technological applications. In this context, five types of solid state QD's i.e. Planar QD's, Vertical QD's, Self-Assembled QD's, Silicon Nanocrystals, and Colloidal QD's are addressed with their own physical properties. Comprehensive modeling techniques suited for each type of QD are briefly mentioned.

Key points

- Types of Quantum Dots/Fabrications
- Coulomb Blockade and Single Electronics
- Artificial Atoms and Molecules/Entanglement and Quantum Gates
- Optical Emission from Self-Assembled Dots and Colloidal Dots
- Quantum Dot Modeling and Simulation

Introduction

Quantum dots (QD) are nanostructures containing few conduction band electrons or valence band holes, or both bound into excitons. These particles, of which the number ranges between a handful to a few thousand are confined into a quantum box isolated from their environment, either electrostatically or structurally, except from a small channel that controls the access of electrons to the QD. In solid state structures, mostly in semiconductors, one distinguishes among planar QDs, vertical QDs, or self-assembled QDs, depending upon their fabrication techniques and design with their sizes varying between tens to hundreds of nanometers. QDs with feature size comparable to or smaller than the particle (electrons or holes) Fermi wavelength manifest quantum mechanical properties with energy spectra similar to natural atoms. For this reason, they are often called *"artificial atoms."* In coupled QDs or "*artificial molecules*" particle (electrons or holes) behavior are governed by Coulomb and exchange interactions that can be tuned locally by design or external electric/magnetic fields. Asides from their fundamental interest in realizing tunable

https://doi.org/10.1016/B978-0-323-90800-9.00267-5

atomic and molecular entities with solid state materials at larger scale than natural atoms and molecules, QDs offer ranges of applications in *single electronics* for memory applications, *spintronics* for quantum computing, *lasers, detectors* or *single photon* sources for material characterization or quantum information processing.

Overview

Planar quantum dots

Planar (P) QDs are fabricated by patterning several Schottky metal gates above the surface of a two-dimensional electron gas (2DEG), which isolates electrostatically a few charge carriers in a small region, forming the dot. In Fig. 1 (upper left) the 2DEG is formed at the interface between an undoped GaAs and AlGaAs layer. A thin heavily doped n^+ GaAs cap layer (yellow) is grown on top of the AlGaAs to pin the Fermi level just below the conduction band edge (Meirav et al., 1990). Lateral confinement is achieved by the top metal gates (black) that consists of two slits to enable the electrons to flow from and to the 2DEG through electrostatic barriers of which the height is electrically controlled by the two metal gates. In practice, these electrostatic barriers are weak (a few meVs) and thick ($\sim$100 nm), which makes the PQD sensitive to external electric perturbation. Charge control in the PQD's is achieved by varying a back gate voltage.

Vertical quantum dots

In vertical (V) QDs, charge carriers are vertically confined between a double resonant tunneling barrier made of hetero-structure layers e.g. InGaAs/AlGaAs/GaAs, while the lateral confinement is achieved by deep mesa etching. In addition, a Schottky metal gate is wrapped around the mesa to electro statistically control the number of electrons between the two tunneling barriers (Fig. 1 upper, right) (Kouwenhoven et al., 2001). Electrical contacts are made on the top and bottom of the mesa to inject or extract electrons from the dot across the double tunneling barrier resulting in a current flowing vertically, perpendicular to the 2DEG plane. Unlike in the PQDs, the tunnel barriers determined by the conduction band offset between the heterojunction materials are high ($>$100 meV) and thin ($\sim$10 nm), but are not electrically tunable, which makes them rather insensitive to external electric perturbations. While vertical confinement is relatively strong (e.g. $\sim$10–20 nm), the VQD lateral size is similar to PQD as the diameter of the mesa (e.g. 100–200 nm). Fig. 1. (bottom) shows a scanning electron micrograph (SEM) of a typical mesa after gate deposition (Kouwenhoven et al., 2001).

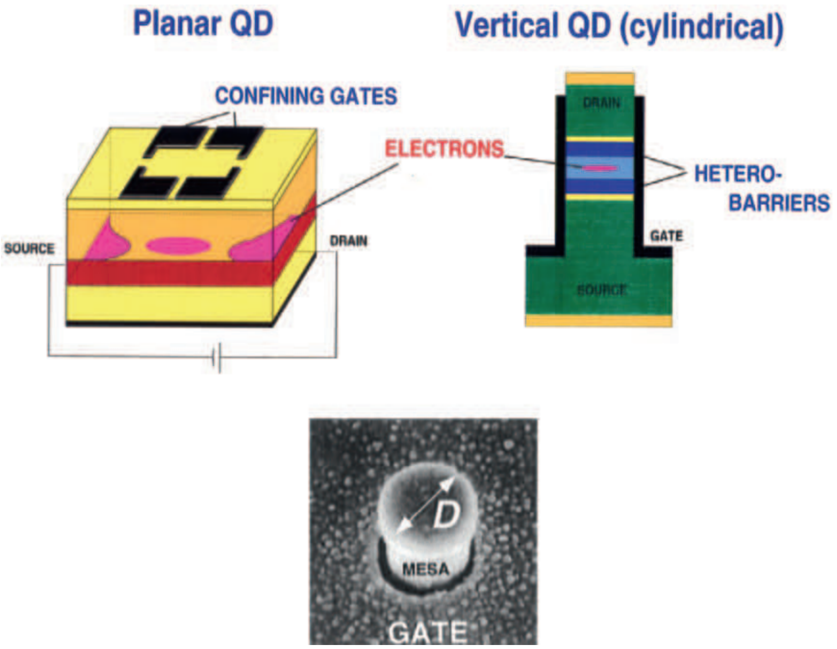

Fig. 1 (Upper left) Schematic representation of a PDQ structure with layered materials with the black areas denoting the confining metallic gates on the top surface. The 2DEG and the dot electrons show in pink, whereas the orange and dark red layered are the AlGaAs and undoped GaAs layers, respectively. (Upper right) Schematic of a VQD with the different constitutive materials; the vertical black areas on the sides are the controlling gates while the dot is represented by the light blue area sandwiched between the dark blue barriers (after Kouwenhoven et al., 2001). (Lower) SEM of a VQD pillar with a width of about 0.5 μm. (Upper) After Meirav U, Kastner MA, and Wind SJ (1990) Single-electron charging and periodic conductance resonances in GaAs nanostructures. *Physical Review Letters* 65(6): 771; (lower) after Kouwenhoven LP, Austing DG, and Tarucha S (2001) Few-electron quantum dots. *Reports on Progress in Physics* 64(6): 701.

Self-assembled quantum dots

Self-assembled (SA) QDs are tiny self-crystallized islands arising from the epitaxial growth of a small band gap/large lattice constant semiconductor e.g. InAs on a larger band gap/shorter lattice constant substrate e.g. GaAs by the so-called Stransky-Kastranov technique. During growth of the first few layers of the small gap InAs semiconductor, the strain induced by the lattice mismatch between the two materials results into randomly distributed pyramidal nanostructures on the large band gap GaAs material. When recovered by another (or the same) large band gap, these islands form lens or disk-like shaped SAQD's, often of intermediate chemical compositions. Carrier confinement in SAQDs is much stronger ($\sim$10–20 nm) in all directions than in PQDs or VQDs as a consequence of the band offsets between the strained materials, and consequently affects both the conduction and valences bands. Fig. 2A shows a 3D scanning tunneling microscope (STM) of a pyramidal InAs SAD grown on GaAs substrate with four clear facets along crystal directions indicated by their Miller indices (Marquez et al., 2001).

Silicon nanocrystals

Silicon nanocrystals (Si-nc) are nanoscale silicon (Si) crystals or Silicon-Germanium (Si-Ge) alloys embedded in a dielectric such as SiO_2. These Si-nc's with a diameter ranging between 5 and 10 nm are usually produced through self-assembling process techniques involving low-pressure chemical deposition and oxidation. Hence, their size is not limited by lithographic resolution, but due to inherent variations in in growth conditions during self-assembly, fluctuations in nc size, shape and coverage density are not

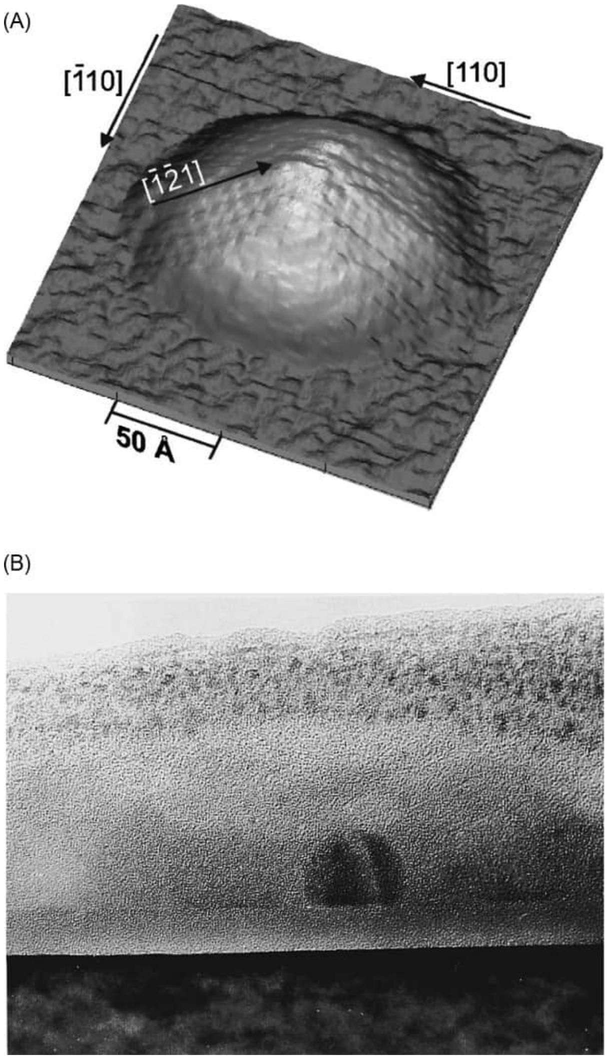

Fig. 2 (A) Three-dimensional STM image of an uncovered InAs QD grown on GaAs along the (001) direction. (B) TEM image of a Si-nc seeded in a SiO_2 dielectric grown on a silicon substrate (dark). The SiO_2 space between the Si-nc and the Si substrate forms a tunnel barrier 3 nm thick. (A) After Marquez J, Geelhaar L, and Jacobi K (2001) Atomically resolved structure of InAs quantum dots. *Applied Physics Letters* 78(16): 2309–2311; (B) After Tiwari S, Rana F, Hanafi H, Hartstein A, Crabbé EF, and Chan K (1996). A silicon nanocrystals based memory. *Applied Physics Letters* 68(10): 1377–1379.

un-common. In addition, high resolution transmission electron microscopy and X-ray analysis of Si-nc in Si/SiO_2 superlattices have revealed inhomogeneous strain ranging from 0.1% to 3.25% depending on the nc size and the process annealing temperature. The QDs are characterized by strong three-dimensional (3D) confinement of charge carriers that have provided the conditions to investigate single-electron charging effects and quantum phenomena at room temperature in Si materials with potential applications multi-bit floating gate memory. Fig. 2B shows a transmission electron micrograph (TEM) cross-section view of a Si-nc embedded in a SiO_2 and separated by 3 nm from a Si substrate (Tiwari et al., 1996).

Colloidal quantum dots

Colloidal quantum dots (CQD's) are semiconductor nanocrystals, generally III-V or II-VI compounds such as InAs, InP or PbS, PbSe or CdTe synthesized from solutions by traditional chemical or plasma processes. As their shape is controllable, but mostly spherical with diameters varying between 2 and 10 nm, their band gap is tunable which is used to select their wavelength of luminescence by recombination of the photoexcited carriers between conduction and valence bands (Kagan et al., 2016).

Key issues

Coulomb blockade and single electronics

The *Coulomb Blockade Effect* (CBE) manifests with ultra-small capacitances, when the addition of single electronic charge on a metallic island requires a discrete amount of energy to overcome the electrostatic repulsion caused by the other charges on the island. The "charging energy" is given by

$$E_C = \frac{e^2}{C} \tag{1}$$

where e is the electronic charge and C is the capacitance of the metallic island (Fig. 3 top.). The CBE was already observed with thin metallic films as early as the 1950s, and was fully explained by the so-called "orthodox theory" of Kulik and Shekhter, and Averin and Likharev in the mid 1980s (Likharev, 1999). In more recent experimental set-ups, electrons confined in a QD form an island isolated from a reservoir of charges by tunnel barriers that feed the QD with external electrons. In this configuration, the injection process is controlled by an electric gate capacitively coupled to the electronic island; electrons can then access the dot when the gate potential is large enough to overcome the repulsion of electrons in the dot. There are two conditions for the CBE to occur:

a) The tunnel barriers to access the QD should be opaque enough to prevent the electrons from leaking back and forth between the dot and the reservoir, which can be expressed mathematically by the relation $R \gg \frac{\hbar}{e^2} \sim 4\ k\Omega$, where R is the barrier resistance and the right-hand side is called the *quantum resistance*. Another way to understand this condition is to ensure that the time spent by the electron in the QD i.e. the dwell time τ, is much larger than the charging time $\Delta\tau \geq \hbar/\delta E$ where δE is the level broadening of QD electrons resulting from the interaction with the reservoir.
b) The charging energy should be much larger than the thermal energy i.e. $E_C \gg k_B T$, so that the effect wouldn't be smeared out by the noise and thermal fluctuations of the system. Fig. 3 (bottom (A)) displays a typical Coulomb staircase with the conductance peaks corresponding to the electron flow from the reservoir during the transition from N to $N + 1$ electrons in the QD, as depicted in Fig. 3 (bottom (B)) (Meirav and Foxman, 1996).

Single electronics

The ability to observe and control the CBE in QDs gave rise to the concept of "single electronics," where electronic function for applications in logic or memory are achieved by manipulating single electron charge in transistors. Among those, the single-electron transistor (SET) is a CBE-based three terminal device, where the number of electrons inside the dot and their one by one transfer from a *source* reservoir to a *drain* reservoir occurs through two tunnel junctions in series controlled by a *gate*. The SET principle of operation is similar to MOS field-effect transistor, where the active region is usually a PQD schematically depicted in Fig. 4A (Elzerman et al., 2003). Fig. 4B displays the SET channel conductance defined as $g_d = \partial I_{DS}/\partial V_{DS}$, and plotted as a function V_G, V_{DS} to exhibit the well-known two-dimensional (2D) diamond diagram illustrating the CB regime at $V_{DS} = 0$. For small V_{DS} (~150 μV) in normal operation the continuous sweeping of the gate voltage generates a succession of CBE and single-electron tunneling events in the SET, such that the drain-source current exhibits so-called *Coulomb oscillations* (CO) with a gate voltage interval between two successive tunneling event (Fig. 3) (bottom (B)) given by

$$\Delta V_G = \eta^{-1}\left\{\frac{e}{C_\Sigma} + \frac{1}{e}(\xi(N+1) - \xi(N))\right\} \tag{2}$$

with $\eta = C_G/C_\Sigma$, $C_\Sigma = C_G + C_D + C_S$, where C_G, C_S and C_D are the gate, source and drain capacitances, respectively. Here $\xi(N) = \sum_{i=1}^{N}\varepsilon_i(N) - \sum_{i=1}^{N-1}\varepsilon_i(N-1)$ where $\varepsilon_i(N)$ is the many-body energy level for the i^{th} configuration of N electrons confined under the SET gate. From Eq. (2) one defines the *quantum capacitance* of the dot as $C_Q(N) = \frac{e^2}{(\xi(N+1) - \xi(N))}$; the *addition energy* $E_a = e\eta V_G$, which is the amount of energy required to add an electron in the dot is then expressed as $E_a = e^2\left(\frac{1}{C_\Sigma} + \frac{1}{C_Q(N)}\right)$.

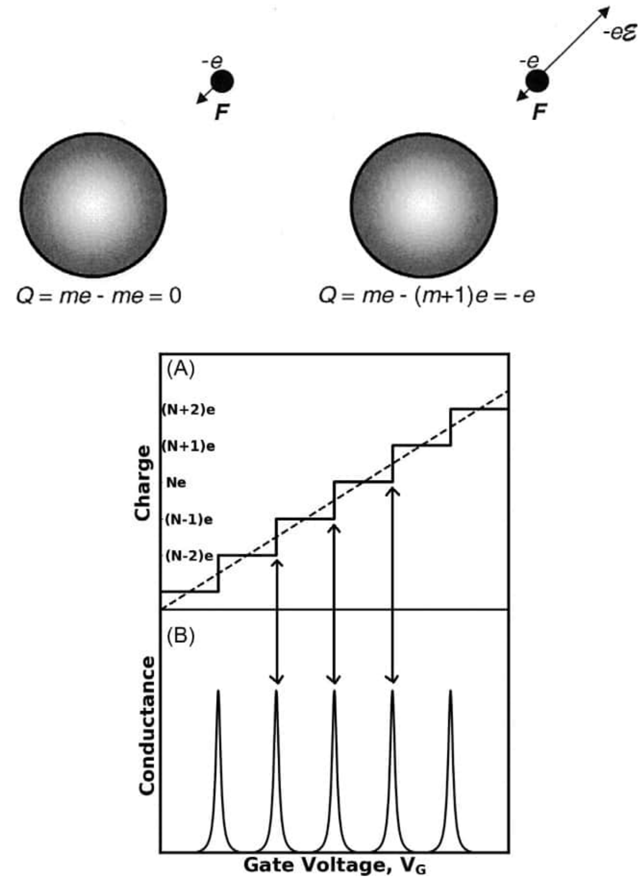

Fig. 3 (Top) Basic concept of single electron charging on a conducting island. (Left) An external force ***F*** is needed to bring an electron on the neutral island carrying m electrons. (Right) The addition of a single electron now carries an electron charge that induced a repulsive electric field *E* to any additional electrons. (Bottom) (A) Schematic of a Coulomb staircase displaying the integer multiple of the electron charge on the dot as a function the QD gate voltage V_G. If C is the QD capacitance, the stair steps arise at equidistant ΔV_G. (B) Schematic plot of the QD conductance exhibiting peaks each time a electron access the dot. (Top) After Likharev KK (1999) Single-electron devices and their applications. *Proceedings of the IEEE* 87(4): 606–632; (Bottom) after Meirav U and Foxman EB (1996) Single-electron phenomena in semiconductors. *Semiconductor Science and Technology* 11(3): 255.

Memory applications

Another example of technological application of single electronics are Si or SiGe-nc's embedded as floating gate in the dielectric of a MOSFET structure for the realization of nonvolatile memories (Fig. 5) (Tiwari et al., 1996). Here, charge carrier injection (Fig. 5B) occurs from the transistor channel through a SiO_2 tunnel barrier between the transistor channel and Si-nc's distributed in the oxide, which induces a threshold voltage shift in the transistor (Fig. 5C). Reversing the gate voltage erases the information (Fig. 5D). Asides from the interest in the subtle quantum mechanics displayed by electron and hole charge carriers in the strong confinement of Si-nc's, these nanostructures have demonstrated several attractive features such as good data retention during charge storage, write/erase endurance characteristics, and short write time compared to conventional floating gate flash memories.

Artificial atoms and molecules

In the *classical limit*, achieved when the QD size is much larger than the electron de Broglie wavelength, λ_{dB}, the individual level spacing $\Delta\varepsilon \ll E_C$, so that the second term in Eq. (2) is negligible compared to the classical charging energy e^2/C_Σ, which makes COs periodic in V_G. On the opposite, when the QD size shrinks and becomes comparable to λ_{dB}, the quantum capacitance C_Q adds a quantum mechanical contribution to the *addition energy*, so COs cease to be periodic with $\Delta V_G \approx \xi(N+1) - \xi(N)$ in the limit of small QDs. In this case, the *addition energy* E_a reflects the electronic structure of the three-dimensional confined states in the dot that can be describe with the quantum mechanical many-body Hamiltonian (Matagne and Leburton, 2004)

$$\widehat{H}_{QD} = \sum_{i=1}^{N}\left[\frac{p_i^2}{2m^*} + V(\mathbf{r}_i)\right] + \sum_{i\neq j}^{N}\frac{e^2}{\varepsilon|\boldsymbol{r}_i - \boldsymbol{r}_j|} \tag{3}$$

Here $\boldsymbol{p}_i$ and $V(\boldsymbol{r}_i)$ are the momentum and QD confining potential energy of the ith electron, respectively. Eq. (3) resembles the Hamiltonian of atoms, except for differences in the potential shape and strength defined by the QD design, the particle effective

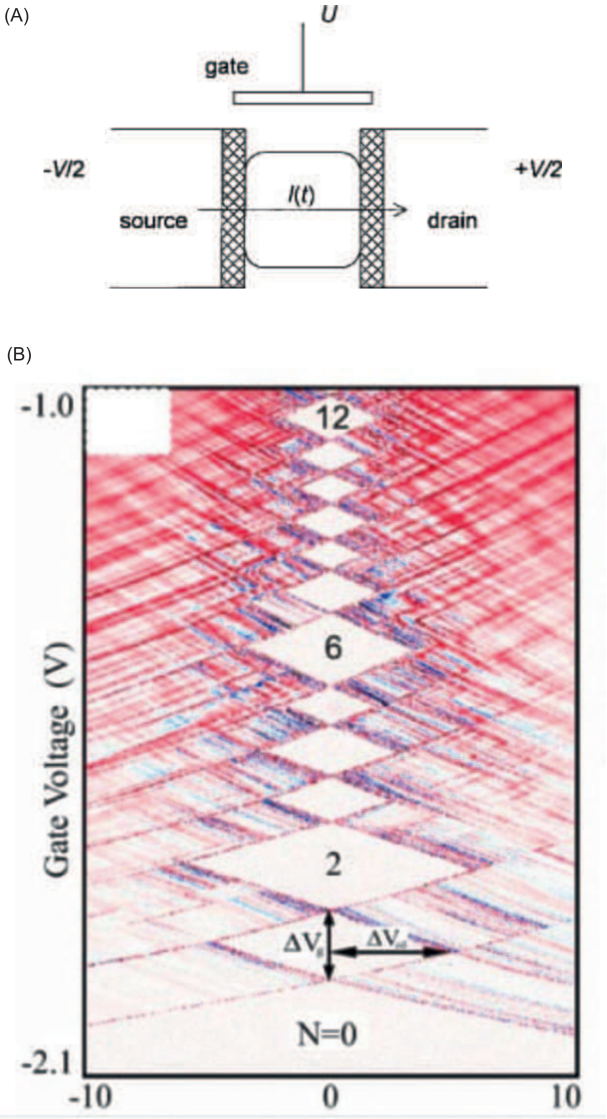

Fig. 4 (A) Schematic of a SET displaying gate, source and drain capacitances. (B) Color plot of a VQD differential conductance $\partial I/\partial V_{SD}$ in the (V_G, V_{SD}) plane for $N = 0–12$ electrons. The white Coulomb diamonds correspond to $\partial I/\partial V_{SD} \approx 0$, the red (blue) lines indicate a positive (negative) $\partial I/\partial V_{SD}$. After Kouwenhoven LP, Austing DG, and Tarucha S (2001) Few-electron quantum dots. *Reports on Progress in Physics*, 64(6): 701.

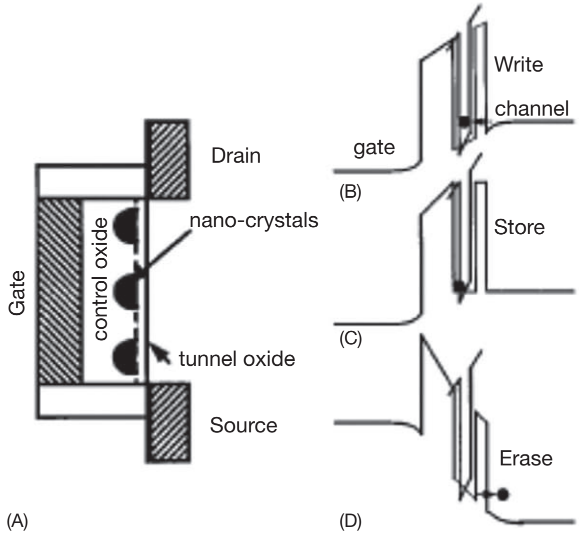
Drain
nano-crystals
Gate
control oxide
tunnel oxide
Source
(A)
Write
channel
gate
(B)
Store
(C)
Erase
(D)

Fig. 5 (A) Schematic cross section of a MOS transistor containing Si-nc's in the SiO_2 insulator, and operating a memory device. Energy band diagram illustrating the electron injection (B), storage (C) and removal from the Si-nc (D). After Tiwari S, Rana F, Hanafi H, Hartstein A, Crabbé EF, and Chan K (1996) A silicon nanocrystals based memory. *Applied Physics Letters* 68(10): 1377–1379.

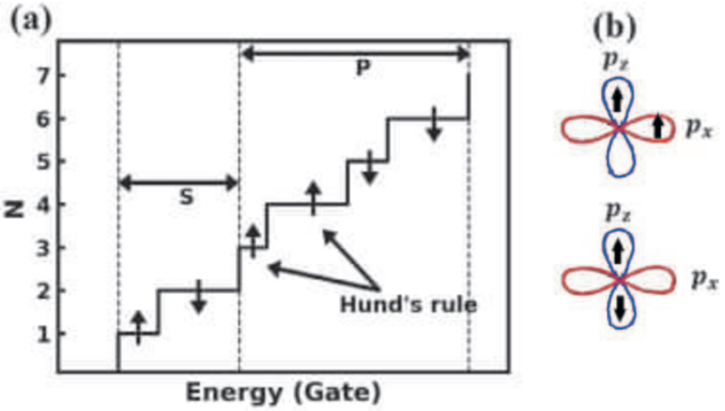

Fig. 6 (A) Schematic of a Coulomb staircase as a function of the addition energy illustrating Hund's rule with two parallel spins for the 3rd and 4th electron in the charging sequence. The two horizontal arrows indicate the occupation of the s- and p-orbitals in the dot. (B) 2D *p*-orbitals illustrating the two possible configurations of parallel (top) and anti-parallel (bottom) electron spins. After Matagne P and Leburton JP (2004) Quantum dots: Artificial atoms and molecules. In: *Encyclopedia of Nanoscience and Nanotechnology.* vol. 8, No. 177, pp. 143–177. American Scientific Publishers.

mass m^*, and dielectric constant ε of the material. Because of those resemblances, QDs are called *artificial atoms*, exhibiting similar properties as natural atoms. Among the most salient ones is the existence of *atomic shells* governed by *Hund's rules* in highly symmetric e.g. 2D cylindrical PQDs and VQDs or 3D spherical CQDs. These atomic features emerge as *magic numbers* in the addition energy spectra of the dots when a shell is completely filled with electrons. Fig. 6 illustrates these *magic numbers* at 2, 6, 12, … electrons filling successively the s-, p-, d-, … quantum states in a 2D cylindrical QD with a harmonic (r^2-dependent) confining potential. Here, the Coulomb stair case exhibits large steps for the 2^d and 6th electrons, whereas the shortest step for the 3rd electron is the manifestation of *Hund's rule*, for which the exchange energy between 2 parallel spins (3rd and 4th electrons) on different p-orbitals gives the more stable configuration (Matagne and Leburton, 2004).

Magnetic field effects

The presence of a magnetic field *B* parallel to the symmetry axis of the *artificial atoms* provides additional insight into electronic properties of the QD. Given the weakness of the electron binding energies (of the order of meV) combined with low electron effective mass m^* in materials like GaAs, relatively moderate magnetic fields of the order of 1 Tesla are sufficient to perturbed atomic-like orbitals, while the weakness of the g-factor (−0.44 in GaAs) results in a tiny Zeeman splitting. In the absence of electron-electron interaction, the atom-like spectrum of 2D cylindrical harmonic potential with proper frequency ω_0 results in the well-known Fock-Darwin states (Maksym and Chakraborty, 1990)

$$E_{n,l} = (2n + |l| + 1)\hbar\left(\omega_0^2 + \frac{\omega_c^2}{4}\right)^{\frac{1}{2}} - l\hbar\omega_0/2 \tag{4}$$

where n (= 0,1,2, …) and l (= 0, ±1, ±2, …) are the radial and the angular momentum quantum numbers, respectively, and $\omega_c = eB/m^*$ is the cyclotron frequency. Fig. 7.a displays a typical Fock-Darwin spectrum as a function of B for $\hbar\omega_0 = 3meV$ (Kouwenhoven et al., 2001). It is seen that the $B = 0$ T orbital degeneracy is lifted by positive and negative l energies with increasing B. The red-dashed line indicates the transition of the electron occupying the highest energy state to different orbital energy with increasing magnetic field.

Artificial molecules

Arrays of QDs coupled through tunnel junctions exhibit electronic properties similar to molecules, where electron states of individual dots couples to form covalent states that are delocalized over the entire arrays. These *bonding states* are lower in energy that the individual state by an amount equivalent to the binding energy of a molecule. In this context, a double QD is comparable to a *diatomic molecule*, for which the number of electrons can be varied by applying independent external voltages to the individual dots, while the quantum mechanical coupling among electrons can be tuned by varying the tunnel junction between the QD's. In the case of PQD's, vibrational motion of the *artificial molecules* can be mimicked by applying a RF voltage to the tunnel barrier. Fig. 8A shows the SEM view of a of GaAs planar double QD systems with the different gates for carrier confinement and tunnel coupling (Elzerman et al., 2003), while Fig. 8B displays the 2D potential landscape of the planar double dot obtained by self-consistent simulation. Fig. 8C depicts a schematic of the lower atomic and molecular orbitals in the case of weak coupling (2D artificial atoms) and strong coupling (artificial molecules) between the dots (Matagne and Leburton, 2004).

Entanglement and quantum gates

Semiconductor coupled QD's are promising candidates for the realization of *universal quantum logic gates*, such as a controlled-NOT gate as the building block of a solid-state *quantum computer*. In such devices, the spins of two electrons S_1 and S_2, each trapped in the

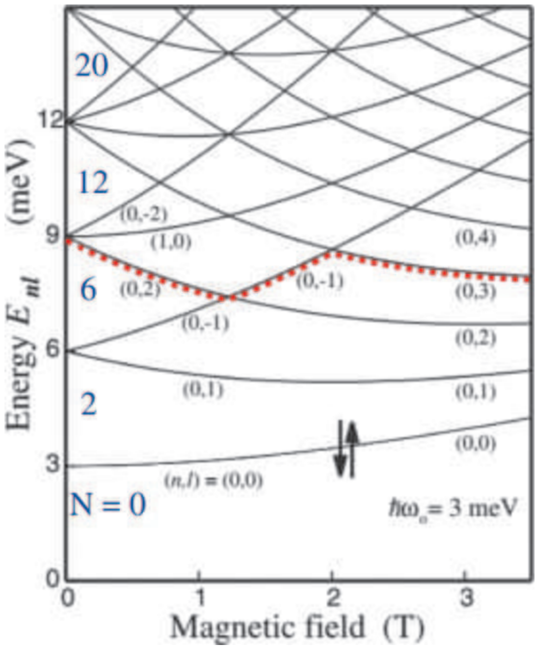

Fig. 7 Single-particle energies versus magnetic field B known as the Fock-Darwin spectrum for a particle in a parabolic potential with $\hbar\omega_0 = 3meV$. Each orbital is two-fold spin degenerate. The red-dotted line highlights the evolution of the 7th and 8th electrons as a function of ***B.*** After Kouwenhoven LP, Austing DG, and Tarucha S (2001) Few-electron quantum dots. *Reports on Progress in Physics* 64(6): 701.

individual dots of the artificial *diatomic molecules* define individual quantum bits (*qubits)* of information. Their *entanglement* is the result of the *exchange interaction J*, equivalent to the energy splitting between the lowest singlet and triplet two-electron states, modulated by the voltage applied to the tunnel junction between the two dots. This energy difference directly determines the period of Rabi oscillations, which is the so-called $\sqrt{SWAP}$ operation time required for the exchange of information between the two qubits in a QD gate. The SWAP operator U_{sw} is such as $U_{sw}\,|ij> = \,|ji>$, if $|ij>$ labels the basis states of the two spins in the S_z basis with i, $j = 0,1$ (Loss and DiVincenzo, 1998). Fig. 9 illustrates the principle of the of the spin SWAP operation through a tunnel barrier between the two QDs controlled by an external gate voltage, whereas individual spin rotations will be performed by local electron spin resonance (ESR).

Optical emission from SAD's and CD's

Because of their tiny sizes and random distribution on substrate, SAD's and CQD's pose technical interconnection challenges to individual electrical access. Moreover, unlike PQD's and VQD's, for which carrier confinement is achieved in a single band (i.e. conduction band electrons), the strong structural confinement in SAD's and CQD's involves both the conduction and valence bands. For this reason, they are optically accessible for the investigation of inter-band transitions as well as of strongly *confined excitons* by Coulomb interaction between the atomic-like electron and hole states as a function of their size, shape and strain due to lattice mismatched between the host material and the dots (Bimberg et al., 1999). The absence of continuum and the existence of well-defined electronic states makes them perfect candidates for applications in optoelectronics such as QD lasers and QD photodetectors with well-defined wavelength

$$\lambda_{ij} = \frac{hc}{E_G + E_{c_i} + E_{v_j} - E_{xc_{ij}}} \tag{5}$$

where h is the Planck constant, c is the speed of light, E_G is the material bandgap, $E_{c_i}(E_{v_j})$ is the i^{th} (j^{th}) atom-like orbital energy in the QD conduction (valence) band that can be tuned by varying the dot size, and $E_{xc_{ij}}$ is the exciton binding energy for the i,j transition. Fig. 10A shows a schematic view of lens-shape InAs/GaAs SAD structure with a contour plot of the electron ground state inside the dots (Sheng and Leburton, 2002, 2003), while Fig. 10B displays the photoluminescence spectra of a truncated pyramidal SAD exhibiting three peaks corresponding to the electron-hole transitions indicated in the panel below, and broadened by the SAD size fluctuations. Except for the first peak caused by the strong inter-band matrix element between the electron and hole ground states, the two higher peaks result from combinations of electron-holes transitions among which the most salient are represented in Fig. 10C. SAD's can also produce *single-photon* sources in which the *photon polarization* is the *qubit* of *optical quantum gates* for applications in quantum information science. However, uniformity and repeatability issues become major challenges due to atomic-size control of such tiny objects made of only few hundred atoms, for which monolayer variation causes large fluctuations in the quantum spectra. In this context, unexpected inversion of the electron-hole dipole alignment for which the heavy mass

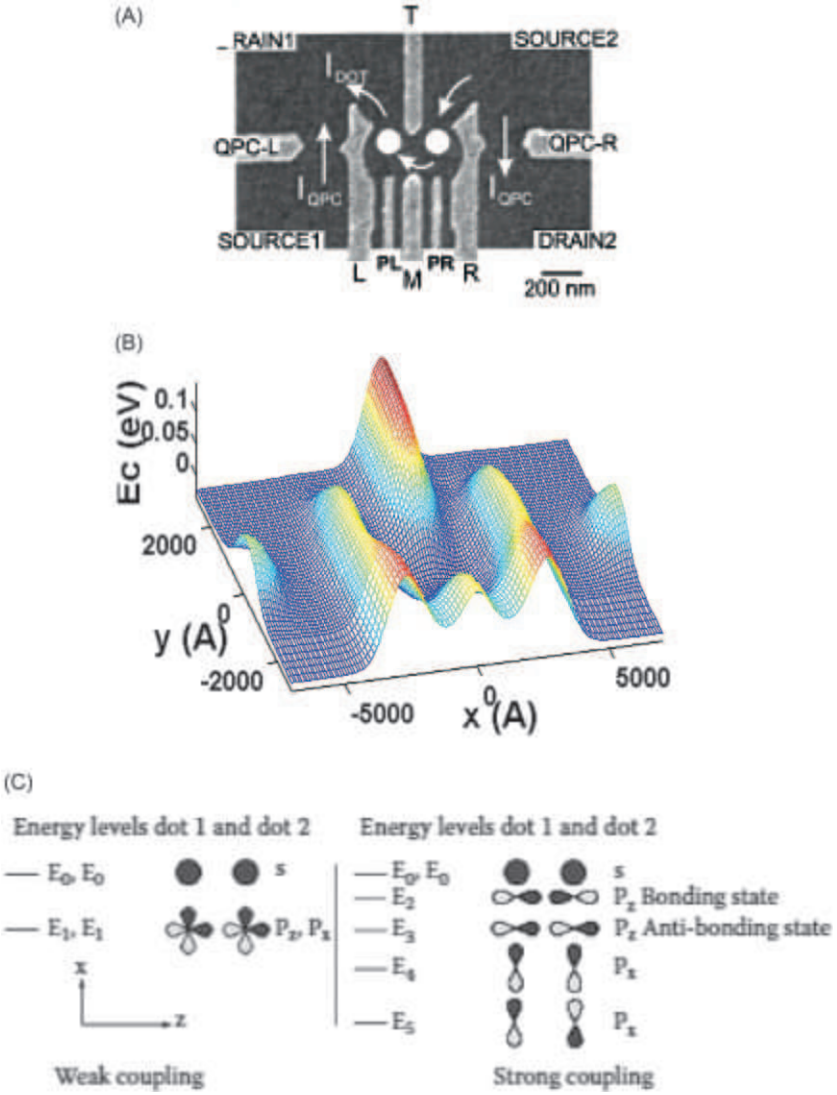

Fig. 8 (A) SEM of the top gates of a GaAs double PQD (white disks) integrated into a quantum circuit. The light gray areas show the different gates i.e. L&R gates control the left and right lateral confinement, T&M gates control the interdot electrostatic barrier, PL&PR are left and right plunger gates that control the electron number in each dot, and QPC-L and QPC-R are quantum point contacts that read the charge variation in each dot. The curved (straight) arrows show the QD (QPC) current charging (sensing) paths. (B) Corresponding electrostatic potential landscape simulated self-consistently by DFT device modeling. (C) Schematic representation of the six lower orbitals in an empty double PQD in the weak (left) and strong (right) inter dot coupling. In the former, the s-, p_x- and p_z- like orbitals are decoupled and degenerate within each dot. In the latter, the interdot interaction lifts the degeneracy of the p-states to form bonding and anti-bonding p_z-states, while the p_x-states are shifted up. The shaded area of the orbitals denotes the positive portion of the wavefunction. (A) After Elzerman JM, Hanson R, Greidanus JS, Van Beveren LW, De Franceschi S, Vandersypen LMK, Tarucha S, and Kouwenhoven LP (2003) Few-electron quantum dot circuit with integrated charge read out. *Physical Review B* 67(16): 161308; (C) after Matagne P and Leburton JP (2004). Quantum dots: Artificial atoms and molecules. In: *Encyclopedia of Nanoscience and Nanotechnology.* vol. 8, No. 177, pp. 143–177. American Scientific Publishers.

positive hole sits in the apex, while the lighter negative electron spreads at the base of the pyramidal or lens-shaped SAD may occurs as a combination of strain and atomic inter-diffusion between SAD and substrate materials. Fig. 11 illustrates the effect of Ga-In atomic inter-diffusion that pushes the electron and hole ground states toward the apex of the pyramidal SAD, with a stronger effect on the hole state that develops wings along the ridges of the pyramid in an attempt to fit best in the space of the SAD (Sheng and Leburton, 2001).

Modeling and simulation

Given the 3D non-symmetrical geometry of QD's combined with their structural confinement, as in SAD's for instance, theoretical models assuming cylindrical parabolic confinement may have limited validity. For this purpose, 3D self-consistent computational approaches, such as density functional theory (DFT), Hartree-Fock, or exact diagonalization techniques in the case of PQD's or VQD's offer more comprehensive physical insight (Leburton, 2021). For SAD's, CQD's or Si-nc's, modeling based on tight binding

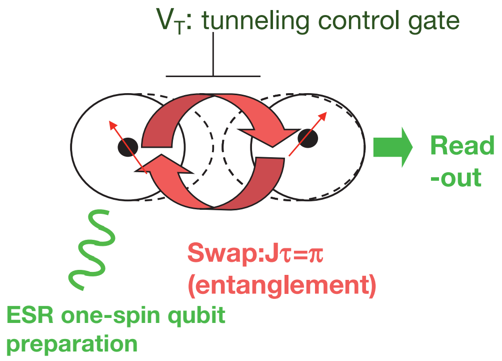

Fig. 9 Schematic of the SWAP operation between two electron spins in a double coupled QD (dashed line) achieved by electric gate control. Here, the solid circles represent the decoupled QD's, whereas the green wiggle illustrates single spin rotation by ESR.

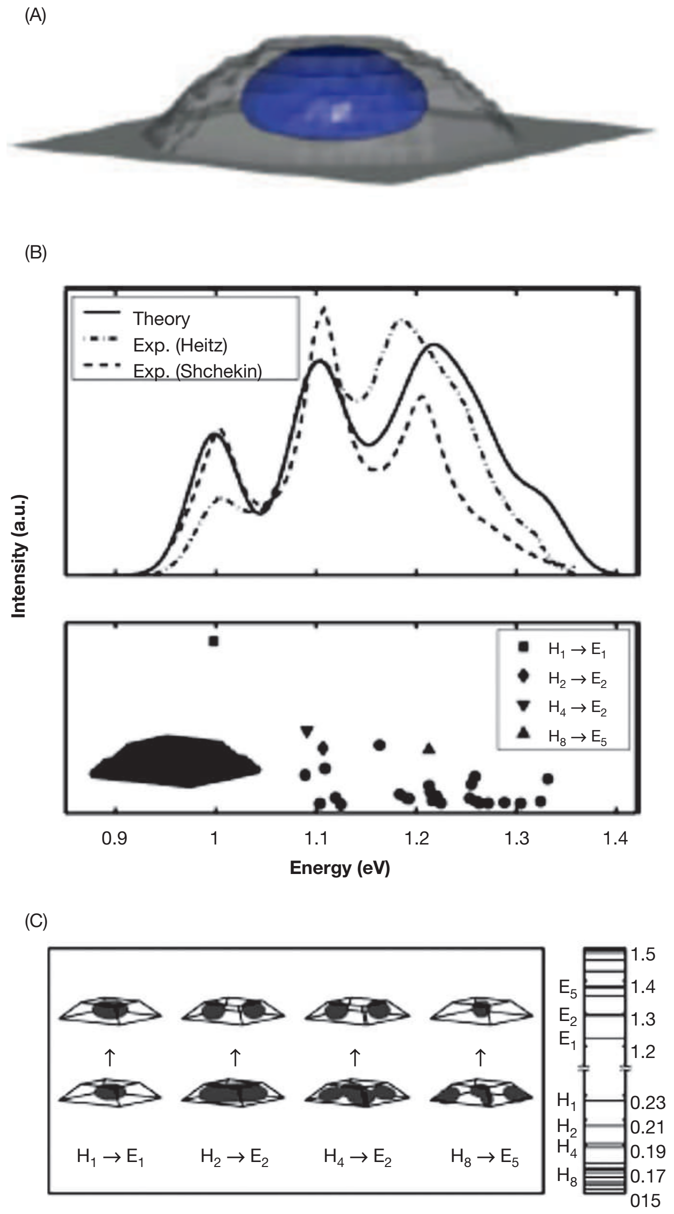

Fig. 10 (A) Schematic view of a lens-shaped InAs/GaAs SAD with 15.3 nm diameter and 3.4 nm height displaying the contour plot (blue) of the ground state probability isosurface (B) (Upper panel) Comparison between numerical simulation and experimental results of the PL spectrum of electron hole transitions for a truncated pyramidal InAs SAD with 3.6 nm height, and a 17.4 nm base length. (Lower panel) **k.p** calculated individual interband transitions. (C) (Left) Iso-surfaces of the probability density of electron and hole states involved in the interband transitions in (B). (Right) Hole and electron energy levels. (in eV). After Sheng W and Leburton JP (2002) Interband transition distributions in the optical spectra of InAs/GaAs self-assembled quantum dots. *Applied Physics Letters* 80(15): pp. 2755–2757; Sheng W and Leburton JP (2003) Electronic properties of InAs/GaAs self-assembled quantum dots: Beyond the effective mass approximation. *Physica Status Solidi B* 237(1): 394–404.

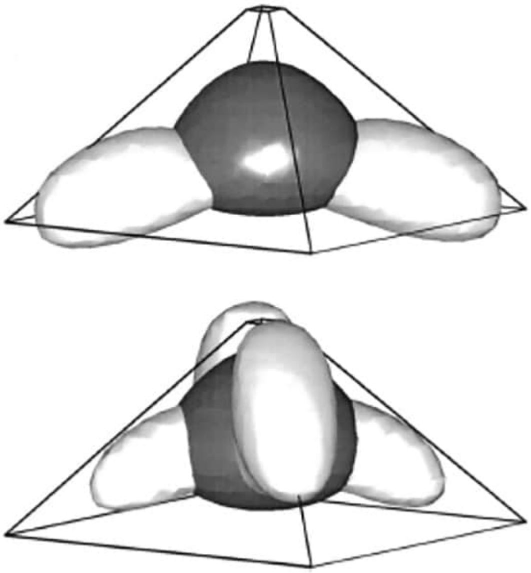

Fig. 11 Probability density isosurfaces of the electron (dark) and hole (light gray) ground sates for a pure (top) and Ga diffused (bottom) InAs/GaAs pyramidal SAD. After Sheng W and Leburton JP (2001) Electron-hole alignment in InAs/GaAs self-assembled quantum dots: Effects of chemical composition and dot shape. *Physical Review B* 63(16): 161301.

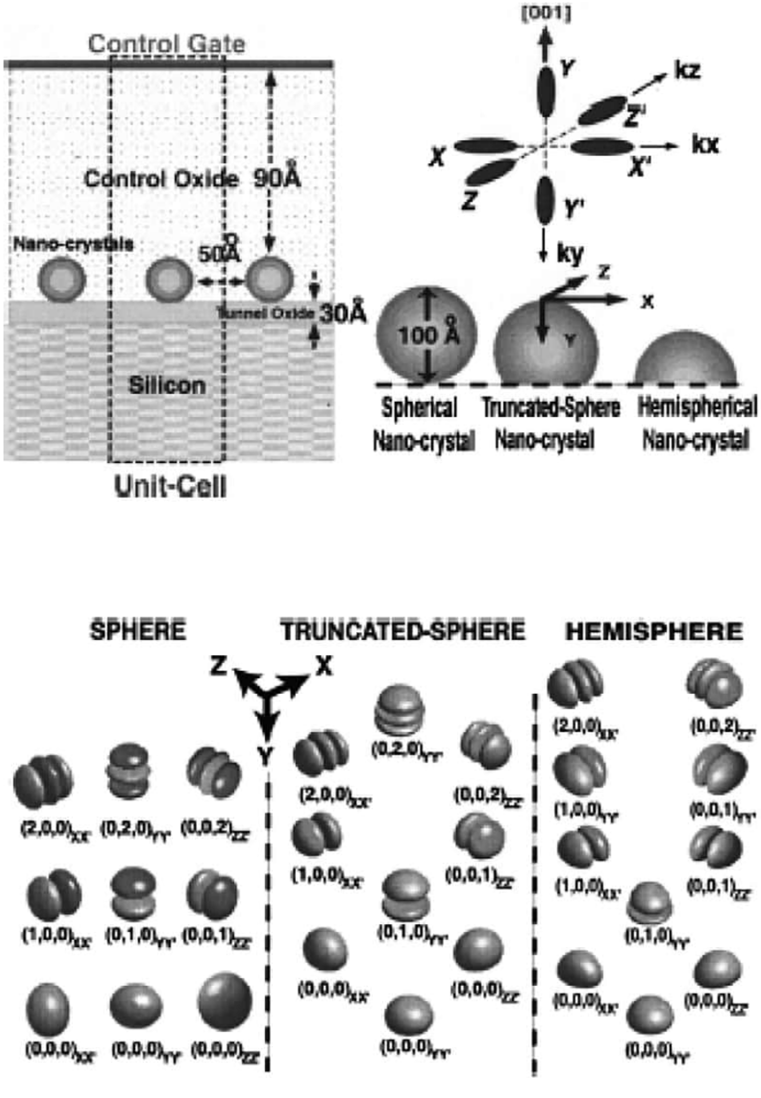
Control Gate
Control Oxide 90Å
Nano-crystals
50Å
Tunnel Oxide 30Å
Silicon
Unit-Cell
[001]
Y
kz
Z'
X
kx
X'
Z
Y'
ky
Z
X
100 Å
Y
Spherical Nano-crystal
Truncated-Sphere Nano-crystal
Hemispherical Nano-crystal
SPHERE
TRUNCATED-SPHERE
HEMISPHERE
Z
X
Y
$(2,0,0)_{XX'}$
$(0,2,0)_{YY'}$
$(0,0,2)_{ZZ'}$
$(1,0,0)_{XX'}$
$(0,1,0)_{YY'}$
$(0,0,1)_{ZZ'}$
$(0,0,0)_{XX'}$
$(0,0,0)_{YY'}$
$(0,0,0)_{ZZ'}$
$(0,2,0)_{YY'}$
$(2,0,0)_{XX'}$
$(0,0,2)_{ZZ'}$
$(1,0,0)_{XX'}$
$(0,0,1)_{ZZ'}$
$(0,1,0)_{YY'}$
$(0,0,0)_{XX'}$
$(0,0,0)_{ZZ'}$
$(0,0,0)_{YY'}$
$(2,0,0)_{XX'}$
$(0,0,2)_{ZZ'}$
$(1,0,0)_{YY'}$
$(0,0,1)_{YY'}$
$(1,0,0)_{XX'}$
$(0,0,1)_{ZZ'}$
$(0,1,0)_{YY'}$
$(0,0,0)_{XX'}$
$(0,0,0)_{ZZ'}$
$(0,0,0)_{YY'}$

Fig. 12 (Upper left) Schematic of a simulated unit cell of a metal-oxide-semiconductor with spherical Si-nc embedded in the SiO_2 insulator. (Upper right) Schematics of three different Si-nc shapes with their spatial and **k**-space orientation of the six doubly degenerate conduction band valleys. (Lower panel) Orbital ordering in the Si-nc spectra illustrated by 3D probability isosurfaces of the first nine/ten doubly degenerate wave function of a 10 nm diameter spherical Si-nc, (left column), a 7.5 nm high truncated spherical Si-nc (middle column) and a hemispherical Si-nc (right column). Energy separations between orbitals are not to scale. After Thean A and Leburton JP (2001) Geometry and strain effects on single-electron charging in silicon nano-crystals. *Journal of Applied Physics* 90(12): 6384–6390.

or **k.p** techniques are well adapted. Fig. 12 is an example of a DFT-based computational model that simulates the operation of Si-nc in a MOS transistor structure. The top left shows a unit cell of a Si-nc embedded in a SiO_2 dielectric between a control gate and a p-doped silicon substrate for a DFT-based simulation of the electronic properties of Si-nc with 3 different shapes on the right. The isosurfaces of the resulting lower electronic orbitals according to their shape and orientations are illustrated on the bottom of the figure (Thean and Leburton, 2001).

Conclusion

Often called "zero-dimensional" systems because of the absence of particle degree of freedom in 3D confinement, QD's offer a rich variety of exciting phenomena by providing the structural conditions for manipulating *single quantum objects*, such as *single electrons, single spins and single photons* at the nanoscale. Asides from solid-state physics fundamentals at play at these scales, these effects bear promises for technological exploitation in single electronics for memory applications, high efficiency lasers, quantum information processing and quantum computing with the practical realization of photon-based and spin-based quantum gates. Recently, the emergence of 2D materials like graphene and transition metal dichalcogenides is providing new ground for the study of plane or 2D QD's.

References

Bimberg D, Grundmann M, and Ledentsov NN (1999) *Quantum Dot Heterostructures*. John Wiley & Sons.

Elzerman JM, Hanson R, Greidanus JS, Van Beveren LW, De Franceschi S, Vandersypen LMK, Tarucha S, and Kouwenhoven LP (2003) Few-electron quantum dot circuit with integrated charge read out. *Physical Review B* 67(16): 161308.

Kagan CR, Lifshitz E, Sargent EH, and Talapin DV (2016) Building devices from colloidal quantum dots. *Science* 353(6302): aac5523.

Kouwenhoven LP, Austing DG, and Tarucha S (2001) Few-electron quantum dots. *Reports on Progress in Physics* 64(6): 701.

Leburton JP (2021) *Physical Models for Quantum Dots*. Singapore: Jenny Stanford.

Likharev KK (1999) Single-electron devices and their applications. *Proceedings of the IEEE* 87(4): 606–632.

Loss D and DiVincenzo DP (1998) Quantum computation with quantum dots. *Physical Review A* 57(1): 120.

Maksym PA and Chakraborty T (1990) Quantum dots in a magnetic field: Role of electron-electron interactions. *Physical Review Letters* 65(1): 108. See also Chakraborty T (1999). *Quantum Dots: A survey of the properties of artificial atoms*.

Marquez J, Geelhaar L, and Jacobi K (2001) Atomically resolved structure of InAs quantum dots. *Applied Physics Letters* 78(16): 2309–2311.

Matagne P and Leburton JP (2004) Quantum dots: Artificial atoms and molecules. In: *Encyclopedia of Nanoscience and Nanotechnology*, vol. 8, pp. 143–177. American Scientific Publishers. No. 177.

Meirav U and Foxman EB (1996) Single-electron phenomena in semiconductors. *Semiconductor Science and Technology* 11(3): 255.

Meirav U, Kastner MA, and Wind SJ (1990) Single-electron charging and periodic conductance resonances in GaAs nanostructures. *Physical Review Letters* 65(6): 771.

Sheng W and Leburton JP (2001) Electron-hole alignment in InAs/GaAs self-assembled quantum dots: Effects of chemical composition and dot shape. *Physical Review B* 63(16): 161301.

Sheng W and Leburton JP (2002) Interband transition distributions in the optical spectra of InAs/GaAs self-assembled quantum dots. *Applied Physics Letters* 80(15): 2755–2757.

Sheng W and Leburton JP (2003) Electronic properties of InAs/GaAs self-assembled quantum dots: beyond the effective mass approximation. *Physica Status Solidi B* 237(1): 394–404.

Thean A and Leburton JP (2001) Geometry and strain effects on single-electron charging in silicon nano-crystals. *Journal of Applied Physics* 90(12): 6384–6390.

Tiwari S, Rana F, Hanafi H, Hartstein A, Crabbé EF, and Chan K (1996) A silicon nanocrystals based memory. *Applied Physics Letters* 68(10): 1377–1379.

Self-organized semiconductor nanostructures (quantum dots, quantum rings and their arrays)

Euclydes Marega Jr, Instituto de Física de São Carlos, Universidade de São Paulo, São Carlos, SP, Brazil

© 2024 Elsevier Ltd. All rights reserved.

Introduction **337**
Growth of self-organized semiconductor nanostructures **338**
Molecular beam epitaxy 338
Molecular beam epitaxy growth modes 339
Self-assembled quantum rings 340
Controlling ordering on an array of quantum dots **341**
Lateral ordering of InGaAs quantum dots 342
Ordering evolution from single layer to vertically stacked QDs layers 343
Role of the indium composition 346
Low indium composition under As_2 348
Ordered self-assembled quantum ring arrays **349**
Conclusion **352**
References **352**

Abstract

A vertical stacking of quantum-dot layers at relatively high temperatures and low indium composition allows them to align laterally in uniformly sized and shaped dot chains. The quantum dots in a particular layer feel the ones underneath if the spacer layer between them is reduced to a certain extent. This kind of ordering is anisotropic due to the nature of the GaAs (001) substrate. While lithography techniques can achieve isotropic ordering, our motivation in this chapter is to show such ordering by controlling the growth parameters on GaAs without any processing. Changing different growth conditions, like substrate temperature, indium composition, background flux, and spacer layer thickness, in a systematic way allows for optimization of the growth parameters. Multilayers of InGaAs quantum dots have been grown and showed an excellent 2D ordering of quantum dots in chain-like structures. Finally, we demonstrate that with multi-stacked quantum-dot layers, the resulting GaAs surface can be used as a template to produce order in, for example, quantum rings grown on that surface.

Key points

- Self-Organization in Molecular Beam Epitaxy growth
- Mechanisms of ordering in vertically stacked quantum-dot layers
- GaAs surface templates generated by vertically stacked quantum dots
- 2D arrays of semiconductor nanostructures

Introduction

From the revolution that computing had in the 1980-ies through the diffusion of personal computers to the massive use of portable devices since the beginning of the 21st century, the search for new technologies that enhance the capacity of computing systems is increasingly necessary, facing new demands such as the development of artificial intelligence, for example. The capabilities of current computer systems are reaching their limits, and considerable potential for quantum computing to solve vastly complex problems is attracting ever greater attention and worldwide efforts to reach a new Epoch in modern civilization. In this sense, semiconductor materials, precursors of the first computational systems based on Si technology, can play again a fundamental role in developing quantum structures that can easily be incorporated into device manufacturing technologies today.

The new era of semiconductors should come with low-dimensional heterostructures (structures consisting of more than one semiconductor material with different energy band gaps) - candidates in developing quantum systems for processes and technologies that demand non-classical properties of matter. The motivations that stimulate research in this field are related to using these

https://doi.org/10.1016/B978-0-323-90800-9.00214-6

materials to study fundamental properties and to employ new devices. However, despite considerable efforts in this field, many low-dimensional systems and their properties are still somewhat ambiguous and unsettled. The current research aims to fabricate and characterize new and unexplored low dimensional systems as, for example, III-V compound semiconductors (GaAs, InAs, InGaAs, AlGaAs). Many electrical and optical applications of semiconductors can be improved by using heterostructures to assemble devices. A whole family of structures exists within heterostructures at nanoscale dimensions that allow for confinement of electrons in one, two, or three dimensions. When the carrier motion in a solid is limited within the size of the order of the exciton Bohr radius in the bulk material, one will observe the effects of size quantization. In the case of quantum structures, the electrons are confined, and the energy levels are finite as distinct from a classical continuum. With the reduction of the size of bulk material (3D) to a thin slab (2D), the confinement can be continued until the motion of the electron is restricted in all three directions (quasi-0D), producing a point-like structure, or a quantum dot (QD), where the quantum properties can be manipulated leading to novel devices.

With decreasing the crystal size, all materials properties, such as mobility and effective masses of charge carriers, refractive index, oscillator strength of radiative transitions, transport properties, optical properties, and density of electronic states, change compared to the bulk material. The density of states changes from a smooth parabola in three dimensions to a staircase in a two-dimensional system and further to a δ-function in the zero-dimensional system. Manipulating a semiconductor material's physical properties presents a new chapter in fundamental physics. Moreover, many applications of nanostructures for novel devices have been predicted, such as single-electron transistors, quantum-dot lasers, and single-photon emitters, that can be used in technologies based on the quantum properties of matter, ranging from information technology and quantum computing to environmental protection. Although semiconductor quantum structures, such as quantum dots, have many potential advantages, the applications have been limited by the challenge of their growth process.

This chapter will discuss the procedures based on Molecular Beam Epitaxy to grow highly homogeneous and ordered self-assembled arrays of III-V semiconductor QDs. Vertically stacking QDs layers at relatively high temperatures and low indium composition allows them to align laterally in uniformly sized and shaped dot chains. This is because the dots in a specific layer feel the ones underneath if the spacer layer between them is reduced to a certain extent. This kind of ordering is anisotropic due to the nature of the GaAs (001) substrate. While lithography techniques can provide isotropic ordering, the motivation is to achieve such ordering by controlling the growth parameters on GaAs without processing. This is done by choosing different growth conditions, like substrate temperature, indium composition, background flux, the composition of the material, and spacer layer thickness, in a systematic way to optimize the growth parameters. Highly ordered semiconductor nanostructures like QDs have great potential for photonic devices.

Growth of self-organized semiconductor nanostructures

The fabrication of quantum-confined nanostructures by self-assembly using Molecular Beam Epitaxy has been intensively investigated for III-V semiconductors, particularly for the InGaAs/GaAs heterostructures. Due to the nontrivial geometry, the possibility of controlling the energy levels, oscillator strength, polarizability, and magnetic properties makes self-assembled quantum dots good candidates for developing new devices. The Stranski-Krastanov growth method produces self-organized, defect-free QDs, where the nanostructure growth is driven by strain and strain relaxation. Stacking is usually used to improve the size homogeneity, quantum efficiency, and unique distribution of self-assembled nanostructures.

Molecular beam epitaxy

Molecular Beam Epitaxy (MBE) was developed in the late 1970-ies and has played a fundamental role in developing heterostructure electronics and optics. MBE can create high-quality layers with sharp interfaces and suitable thickness, composition, and doping control. In the growth procedure, the wafer is placed into an ultrahigh-vacuum (UHV) environment (typically with a base pressure of $\sim 10^{-10}$ Torr) containing an array of shuttered ovens with various materials. When these cells are heated to a specific temperature, evaporation from the liquid or solid source material produces a molecular beam that can spread across the chamber and impinge on the wafer because of the large mean free path in the UHV environment. By changing the evaporation temperature of the source material, the beam flux can be controlled. The low growth rate of 1 μm/h (~1 monolayer/s) guarantees the surface migration of the impinging species on the growing surface. The adsorbing atoms migrate across the surface and eventually incorporate with the substrate. Simple mechanical shutters placed in front of each cell are used to interrupt the beam fluxes, i. e., to start and stop the deposition. The MBE became a valuable tool in developing electronic and optical devices because of its high degree of control over material deposition. The UHV environment of MBE allows surface analysis tools, such as Reflection High-Energy Electron Diffraction (RHEED), to probe the surface properties and the growth mechanisms. Fig. 1 shows a schematic layout of a typical MBE growth chamber.

In epitaxial growth, a clean surface is necessary since contaminants from the atmosphere or other sources can easily reach a clean GaAs wafer and cause crystal defects or degrade the optical and electrical characteristics of the epitaxial layer.

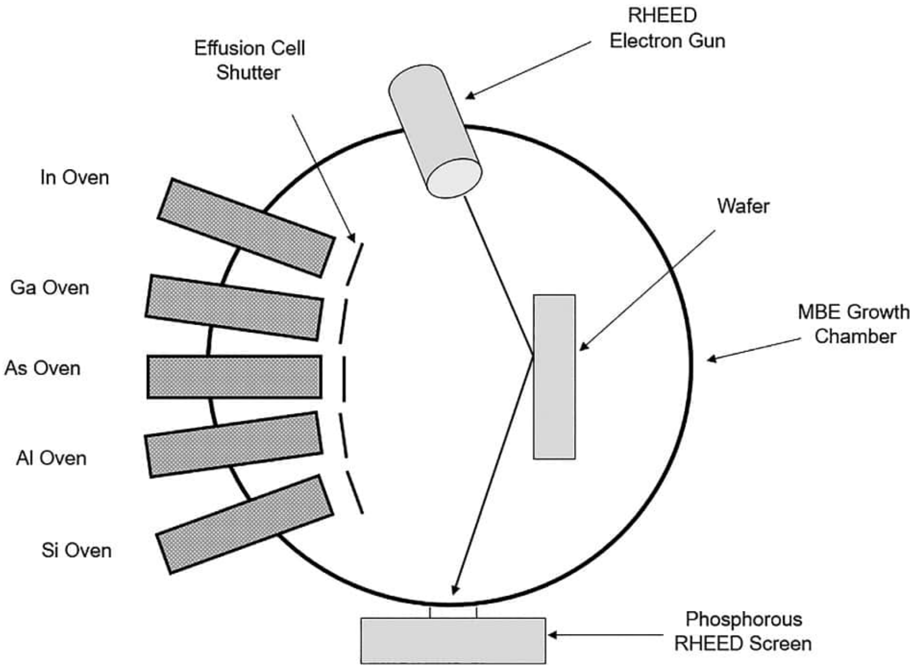

Fig. 1 Schematic layout of the MBE growth chamber.

Molecular beam epitaxy growth modes

Depending on the system's energy balance and the lattice mismatch, there are three primary growth modes: Frank-Van der Merwe, Volmer-Weber, and Stranski-Krastanov (see Fig. 2).

The interface and surface energy relationship determines the growth mode in lattice-matched systems. If the surface energy of the epilayer is γ_e, the substrate surface energy is γ_s, the energy of the interface is γ_{se}, and $\gamma_e + \gamma_{se} < \gamma_s$, then the deposited material wets the substrate surface (Bimberg et al., 1998; Shchukin and Bimberg, 1999). In this case, the growth proceeds in the Frank-van der Merwe mode. If the energy of the interface between the two materials is high, $\gamma_e + \gamma_{se} > \gamma_s$, then the growth process will develop in the Volmer–Weber mode, directly coalescing into islands to reduce the interface area by increasing the surface area. For a strained epilayer with small interface energy, the initial growth may occur layer by layer, but a thicker layer has considerable strain energy and can lower its energy by forming isolated islands in which strain is relaxed. In this case, the Stranski-Krastanov (S-K) growth mode occurs (Bimberg et al., 1998).

The thermodynamic driving force for the S-K growth mode is strain and strain relaxation. In the S-K mode (where the materials are lattice-mismatched), the growth proceeds in three stages: first, a 2D deposition, then a 2D to 3D transition, and finally, the formation of the defect-free islands (Fig. 3). In the beginning, the growth will be in a layer-by-layer mode, with the epitaxial layers starting to accommodate their lattice structure to the substrate lattice constant, forming a wetting layer. The 2D growth phase will proceed until a critical thickness. At that thickness, the strain increases, and the excess energy stored in the 2D layer reaches the energy of the 2D-3D transition barrier. In other words, the strain becomes significant for the 2D growth to continue, and any further deposition of material will force the growth to proceed in the form of 3D islands to relieve the strain (Bimberg et al., 1998; Shchukin and Bimberg, 1999).

For example, in the case of InAs growth on GaAs, the first monolayer of InAs grows to form a strained 2D layer, while 3D QDs form when the thickness of the InAs layer exceeds 1.6 monolayers (ML).

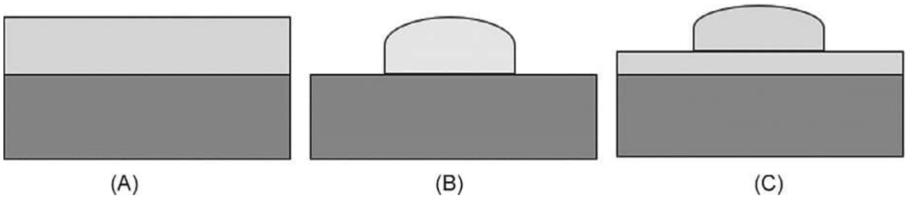

Fig. 2 Diagrams of the three possible growth modes. (A) Frank-van der Merwe, (B) Volmer-Weber, and (C) Stranski-Krastanov.

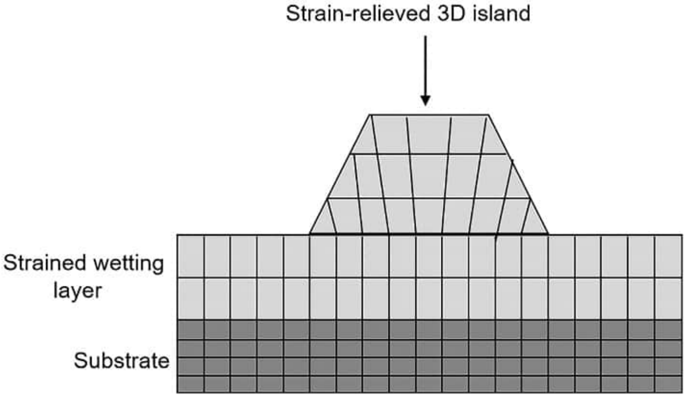

Fig. 3 Stranski-Krastanov growth mode: first material deposited onto the substrate resulting in the strained wetting layer. After a critical thickness of the 2D layer, strain is relieved by forming a 3D island.

It is well-known that a rise in the growth temperature leads to a decrease in the QD density and a corresponding increase in the QD size (Raab et al., 2002). The increased QD size and reduced QD density as a function of temperature are due to the thermally activated increase of the adatom surface diffusion length at higher substrate temperatures, which results in increased separation of the QD nucleation sites as the growth temperature increases. For a fixed indium composition and layer thickness, the size and shape of these 3D islands vary by changing the growth temperature. The growth temperature directly governs the surface diffusion length, and as a result, a higher growth temperature yields elongated QDs (Ma et al., 2001). The reason is the anisotropy of the GaAs surface due to the (2 × 4) reconstruction and a high temperature (Kley et al., 1997). The increased QD size decreases the confinement energy in the QD, raising the growth temperature.

Self-assembled quantum rings

The formation of self-assembled quantum rings can be affected by many parameters, such as diffusion, strain, and surface and interface energies. All of them can be controlled by a proper choice of growth conditions. Diffusion can be influenced by changing the growth temperature and using cracked As_2, which is more reactive than As_4 and reduces the mobility of the group III elements (Granados and Garcia, 2005; Lorke et al., 2001; Lei and Lorke, 2014). Thus, elongated islands can transform into ring-like nanostructures. A possible scenario for the ring formation is depicted in Fig. 4.

At the growth temperature of 520 °C, In atoms are very mobile on the surface, whereas the Ga atoms can diffuse little during the growth interruption (Lorke et al., 2001; Bressler-Hill et al., 1994; Llorens et al., 2018; Sanguinetti et al., 2014). As illustrated in panels (E) and (F) in Fig. 4, when atoms diffuse away from the QD, they stay fixed and do not go very far. Only then the relatively

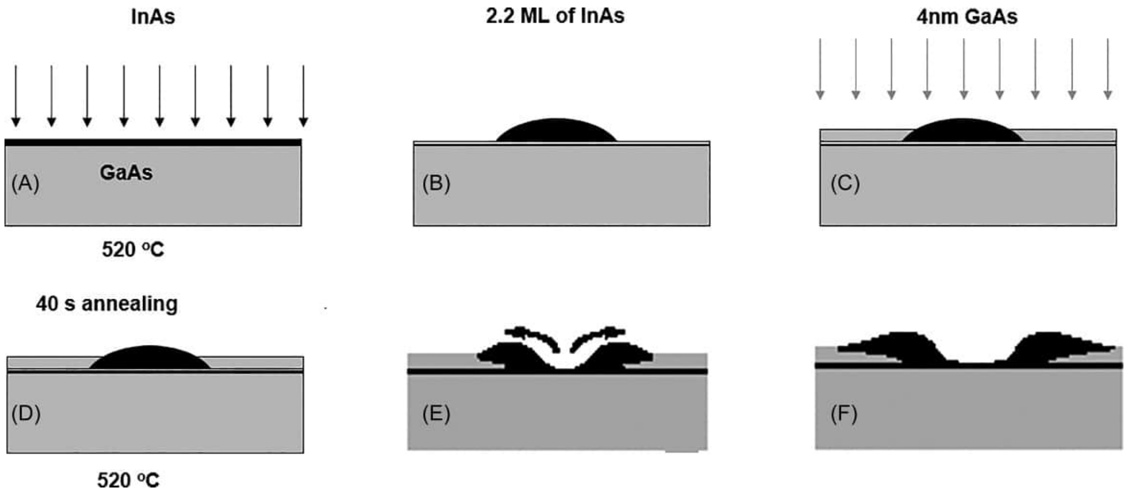

Fig. 4 Model of the diffusion-driven ring formation. (A) InAs 1ML deposition, (B) QD formation after 1.6 ML, (C) 4 nm GaAs partial capping, (D) Annealing with As flux, (E) In diffusion process, (F) QR formation. Adapted with permission from Lorke A, Luyken RJ, Garcia JM, and Petroff PM (2001) Growth and electronic properties of self-organized quantum rings. *Japanese Journal of Applied Physics* 40: 1857, https://doi.org/10.1143/JJAP.40.1857.

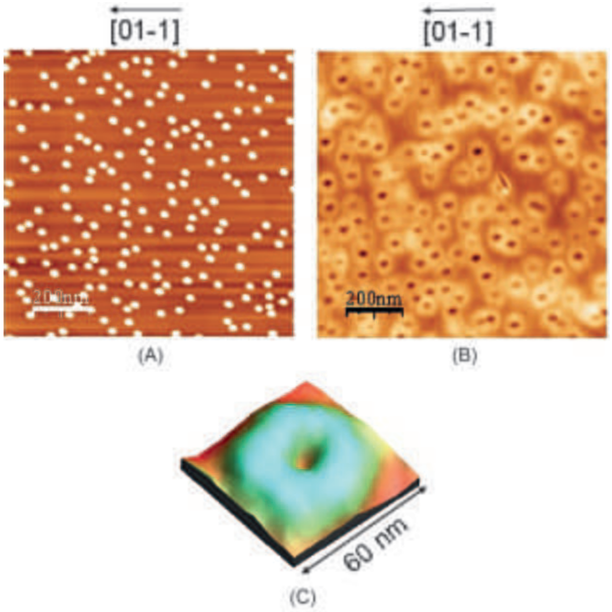

(A) (B) (C)

Fig. 5 (1 μm × 1 μm) Atomic Force Microscopy (AFM) images of (A) uncapped InAs QDs and (B) QDs after 4 nm GaAs capping layer under As_2 flux and 40s annealing. (C) 3D image reconstruction from 2D AFM showing a single quantum ring.

sharp outer edge of the rings can be obtained. This might be explained by the (InGa)As alloy formation (Granados and Garcia, 2003; Lorke et al., 2001). The model is based on kinetic considerations, namely differences in the surface diffusion rates of the indium and gallium atoms. Namely, the mobile indium atoms diffuse from the QD outwards, which allows them to avoid the original QD location (Lorke et al., 2001). The indium atoms diffuse into the surrounding GaAs crystal, forming an immobile ring-shaped InGaAs island (Lorke et al., 2001).

As shown in Fig. 4C, the relaxed InAs lattice constant at the top of the QD makes it a hostile site for the attachment of Ga atoms. Thus, the GaAs capping layer surrounds the dot like a blanket, see Fig. 4D (Lorke et al., 2001; Kegel et al., 2000; Mazur et al., 2007). Fig. 5 shows the AFM image of the formation of InGaAs QRs on a GaAs surface, as described in Fig. 4.

Controlling ordering on an array of quantum dots

The growth of the structure containing multilayers of InGaAs QDs separated by GaAs spacer layers will be referred from now to the vertical stacking of dots. The vertical stacking of QDs is important for most device applications because it allows one to increase the filling factor of QDs in a given sample and, therefore, to increase the quantum efficiency of the device. Different effects and morphologies arise depending on the thickness of the GaAs spacer layer between the vertically stacked InGaAs QDs layers and other growth factors. The strain from the InGaAs QDs layer transfers through the GaAs spacer and creates a strain filed pattern on the spacer surface, which modifies the chemical potential of surface ad-atoms (Xie et al., 2000; Tersoff et al., 1996). The minimum chemical potential on the surface corresponds to the maximum tensile strain achieved directly above the buried islands. Therefore, ad-atoms are attracted to these points as nucleation centers and QDs align vertically according to the buried islands as more layers of QDs are stacked. The strain field created by the small islands is overwhelmed by the strain field from the neighboring big islands, leading to the annihilation of small islands in the next layer. This sequence is then repeated for each successive layer, and the island spacing and size become progressively more uniform.

The vertical alignment of QDs results in size and shape uniformity throughout the layer, reducing inhomogeneous broadening in optical output (Xie et al., 2000). So far, this vertical stacking cannot provide good control over the distribution of dots (i.e., lateral ordering). Although QDs with a high indium composition can achieve better uniformity than ones with a low indium composition due to the smaller size of QDs resulting from a lower coverage, they are not subject to lateral ordering. The vertical stacking of InGaAs QDs also affects their optical properties due to the interaction of the electronic wavefunctions from different QD layers if the spacer is not thick enough. If a very thin barrier (the GaAs spacer) barely covers the first QD layer or does not cover it entirely, the QDs in the stacked layers will be strongly coupled with each other. Such an electronic coupling directly affects the optical properties of the QDs. Stacking many layers (to increase the device efficiency) becomes impossible due to the high strain accompanied by further deposition. The increased strain is relieved by the generation of defects.

In the case of a spacer thickness that is not too small and enough for QDs to feel the strain modulation, the QDs do not undergo a strong electronic coupling between them. However, a tunneling of electrons might happen. The vertical correlation in the strain transfer is still effective and leads to the vertical alignment of QDs. For relatively thick (more than 40 nm) barriers, QD layers form independently of the underlying layers' strain effect. In such structures, a random formation of QDs would be a limiting factor for device application.

Lateral ordering of InGaAs quantum dots

The vertical stacking of QDs can, under special growth conditions, result in the lateral ordering of QDs on the surface. By growing InGaAs QDs with low indium composition at a relatively high substrate temperature (540 °C) and a suitable spacer thickness (15–20 nm), the lateral ordering of InGaAs can be achieved (Mazur et al., 2003). In that work, 2 nm $In_{0.36}Ga_{0.64}As$ QDs separated by 16 nm GaAs spacers are deposited. The images of surface morphology and cross-section view of such a structure are shown in Fig. 6, revealing the QD-chain features along the [0-11] direction. The vertical correlation is due to the vertical field of strain between the stacked QDs, as discussed before, while the lateral ordering is related to the enhanced ad-atom migration length and relieving the strain field along the [0-11] direction at a high growth temperature (Mazur et al., 2003). It is also noticed in Fig. 6B that the size and shape stability is achieved after 6 to 7 layers of QDs. QDs get bigger due to stacking as the density thins down, resulting in the lateral ordering.

Layer evolution in laterally ordered InGaAs QDs was studied (Wang et al., 2004a,b) by depositing 2, 7, and 12 layers of 9 MLs $In_{0.5}Ga_{0.5}As$ spaced by 60 MLs of GaAs. The QDs start to form at 4 MLs of InGaAs deposition in the first layer, while it took 3.4 MLs to form QDs in the following layer. The strain field induced by the buried islands directs the material in the second layer to local minima of lattice mismatch; hence, it takes less time to form QDs. The QDs start to line up laterally after seven layers.

It is observed that lateral ordering is accompanied by the continuous reduction in the island density and the increase in the average island size in the subsequent layers. It has also been revealed (Wang et al., 2004a,b) that the QDs are already lined up along the [0-11] direction in the initial stage of 3.7 MLs of InGaAs deposition, which indicates that it is the nucleation rather than the ripening that is responsible for the formation of QD chains. Based on these results, favored nucleation of QDs along the chain direction is the most likely scenario for forming QD chains. This explanation requires that the strain field transferred through stacked layers of QDs has to be anisotropic. The total energy calculations of the pure migration of Ga atoms on the GaAs(001)-(2 × 4) reconstructed surface have been performed (Kley et al., 1997) and predicted an activation barrier of 1.2 eV along the As dimer rows (i.e., along the [0-11] direction) and 1.5 eV across them (i.e., along the [011] direction). This means that adatoms diffuse easier on the surface along the [0-11] direction than along the [011] direction, resulting in the elongated shape of dots in a single layer.

Furthermore, under the normal growth conditions of QDs (using As_2 flux as a background), the GaAs surface resembles a (2 × 4) surface reconstruction (Salmi et al., 1999). It is clear that the arsenic dimer rows run along the [0-11] direction and create anisotropy in the GaAs surface energy. Adatom diffusion during the formation of QDs relaxes the strain along [0-11] direction, creating an anisotropic strain field that is transferred through stacked layers. This leads to the formation of QD chains along the [0-11] direction. It is fair to say that a combination of anisotropic strain field and enhanced adatoms diffusion are the primary factors controlling the formation of vertically stacked QD chains. It is expected that the growth temperature would affect the formation of QD chains since it controls the diffusion of adatoms, as discussed above and as will be explained below in this chapter.

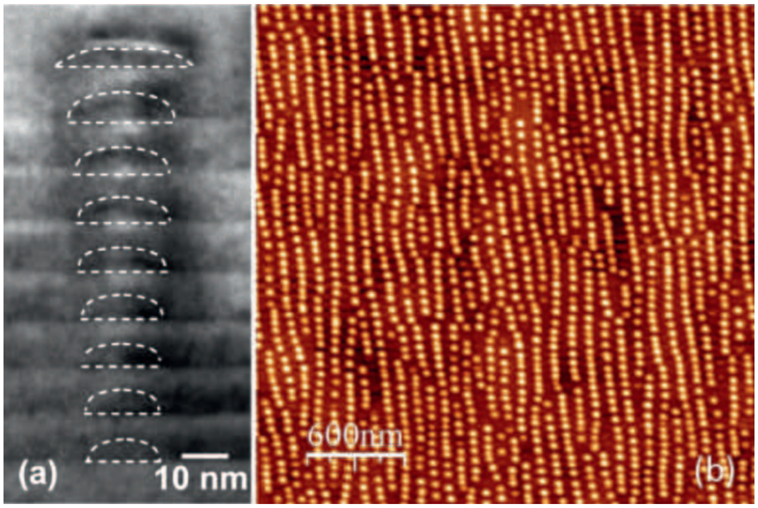

Fig. 6 (A) Dark-field cross-section TEM image of multilayered InGaAs QDs and (B) AFM image of the sample surface.

Ordering evolution from single layer to vertically stacked QDs layers

The 3 μm × 3 μm AFM images in Figs. 7 and 8 represent the morphology of an $In_{0.4}Ga_{0.6}As$ QDs surface layer for single and multilayered (16 MLs) In0.4Ga0.6As QDs, respectively. The left-hand-side images of each figure show QDs, which were grown under As_4, while the right-hand-side images ones grown under As_2. Low indium composition responds to the anisotropy of the GaAs (001) surface by forming 1D chains along the [0-11] direction. The surface anisotropy can be tuned by an intentional miscut to introduce different types of steps with different densities along the [0-11] direction. A miscut toward [0-11] (or (111)B surface) creates B-type steps, which run along the [011] direction. The B-type surface steps along [011], which are perpendicular to the [0-11] direction for GaAs (100), are characteristic of the (n11)B surfaces. For the used surfaces, (311)B and (511)B, the step size is 6 Å and 10 Å, respectively (Wang et al., 2004a, Wang et al., 2004b; Lee et al., 2002). Introducing surface steps with known densities in a

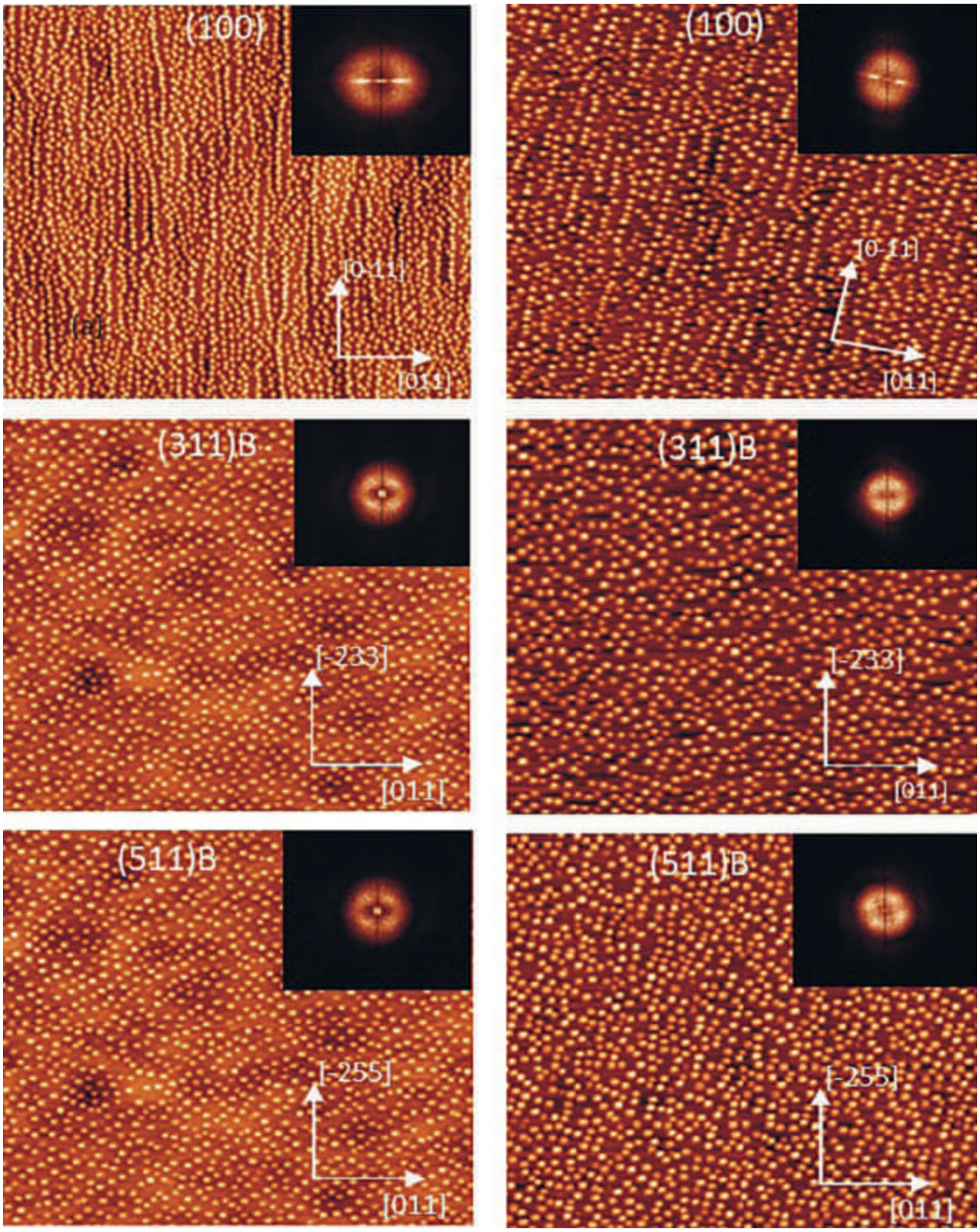

Fig. 7 (3 μm × 3 μm) AFM images of one layer of $In_{0.4}Ga_{0.6}As$ QDs grown under As_4 (left-hand-side images) and As_2 (right-hand-side images). The top right-hand-side insets of the images represent the FFT of the surfaces that shows the correlation between the QD's nearest neighbors.

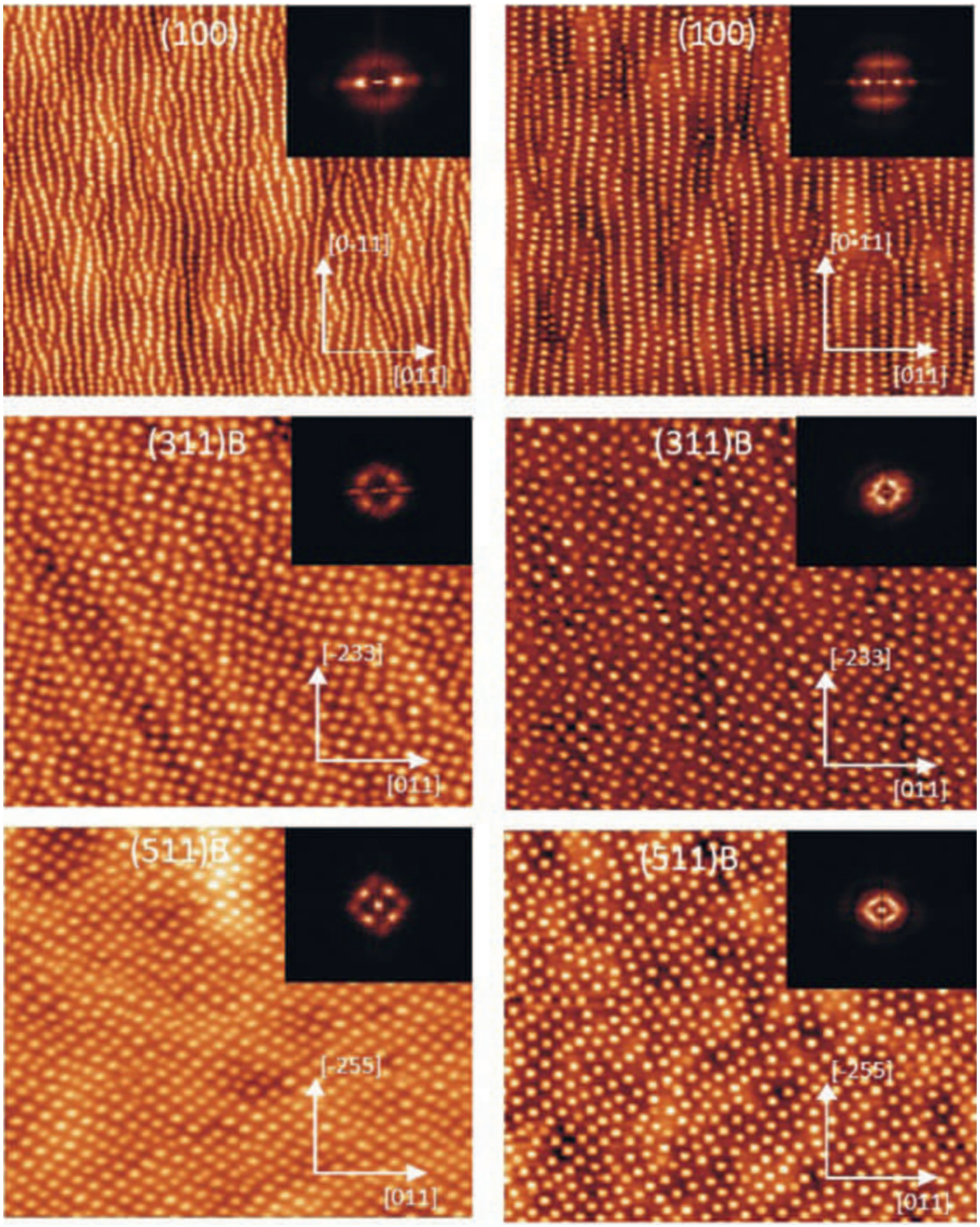

Fig. 8 (3 μm × 3 μm) AFM images of multilayered (16 layers) $In_{0.4}Ga_{0.6}As$ QDs grown under As_4 (left-hand-side images) and As_2 (right-hand-side images). The top right-hand-side insets of the images represent the FFT of the surfaces that shows the correlation between the QD's nearest neighbors.

direction perpendicular to the chains obtained in the (100) surface creates a new surface diffusion direction for the migration of adatoms. When the density of steps along the [0-11] direction in the (n11)B surfaces is comparable to the natural corrugation of the (100) 2 × 4 surface reconstruction, the 1D ordering behavior changes to a 2D ordering as observed in the (311)B and (511)B surfaces. The right-hand-side top inset in the AFM images represents the modulus of the Fast Fourier Transform (FFT) of the AFM region. The FFT shows the correlation between the QD's neighbors. For one layer QDs (Fig. 7), the ordering changes from a chain-like (1D) to a 2D diffuse square-like for the (311)B and (511)B surfaces. The ordering obtained for the multilayered structures is enhanced due to the strain transfer from the InGaAs QDs layer through the GaAs spacer that creates a strain filed pattern on the spacer surface, which leads to the modulation of the chemical potential of surface adatoms. The minimum chemical potential on the surface corresponds to the maximum tensile strain achieved directly above the buried islands. Therefore, adatoms are attracted to these points as nucleation centers, and QDs align vertically according to the buried islands as we stack more QDs layers. This cycle is repeated for each layer, and the island spacing and size become more uniform. It is important that the ordering behavior is due to surface properties combined with the growth conditions, and the stacking improves it. The usage of As_2 instead of As_4 decreases the diffusion of Ga along the [0-11] direction for (100) surface. The isotropic diffusion mechanism under As_2 can be explained by surface energy. The total energy calculations of the pure migration of Ga atoms on the GaAs (001)-(2 × 4) reconstructed surface have been performed, and they predict an activation barrier of 1.2 eV along the As dimer rows (i.e., along the [1-10] direction) and 1.5 eV across them (i.e., along the [011] direction). However, theoretical calculations have shown that the excess arsenic lowers the energy barrier for hopping in the [011] direction to a value closer to the barrier height in the [0-11] direction. In this case, the Ga atom is transformed from a one-dimensional random walker to a two-dimensional random walker. Our results reflect that As_2 has a similar effect as a very high As_4 flux but without the need for lowering the temperature and hindering diffusion. Experimentally, it has been shown that the As_2 species affect diffusion similarly to high As_4 pressure (Ripalda et al., 2003). This explanation has also been adapted as the cause of isotropic diffusion necessary for the formation of quantum rings (Kley et al., 1997).

A reduction of diffusion of the group III atoms is due to both the effect of As_2 and the surface steps for high-index surfaces. The decrease of the Ga adatoms diffusion causes a reduction in the lateral intermixing of InGaAs along the [0-11], [-233], and [-255] directions, and this increases the separation between the QDs along the above-mentioned directions. The AFM images also reveal an increase in the QDs volume (height and diameter) when using As_2. For one layer QDs, the average densities drop by 10% with the usage of As_2 from the value of 1.5×10^{10} QDs/cm^2 obtained for As_4 QDs. Compared to QDs obtained using As_4, the QDs produced with the help of As_2 are 10% bigger in height (with an average of 8 nm) and more rounded; consequently, their average size distribution has a 10% narrower width.

The effect of As_2 is more pronounced in the multilayered QD structures. As the GaAs template changes due to strain field modulation, the diffusion length increases for Ga (see above), particularly for the (100) GaAs surfaces. The multilayered QD density produced under As_4 flux is slightly lower than the average density obtained for a single layer of QDs with the help of As_4 because the obtained QDs are slightly bigger due to staking. The stacking using As_2 leads to a 20% decrease in the QDs density from 1.3×10^{10} cm^{-2} for QDs obtained with $As_{4.}$ This decrease in intensity causes an increase of 15% in height (with an average of 10 nm) for the multilayered QDs obtained under As_2 flux. Also, the average size distribution has a 15% narrower width.

The decrease in the size distribution with As_2 flux was also observed in PL measurements. Fig. 9 shows 10 K PL spectra of single and multilayer $In_{0.4}Ga_{0.6}As$ QDs grown on the (100) GaAs surfaces under (a) As_4 flux and (b) As_2 flux. The PL spectra for multilayered QDs by changing the growth environment from As_4 to As_2 reveal two significant features. First, the PL peak position is blue-shifted, and second, the FWHM is narrowed to 58 meV for the sample obtained with As_4 flux to 31 meV for the sample produced under As_2 flux. Despite the increase of the QD height from the sample (a) to the sample (b), the PL peak is blue-shifted

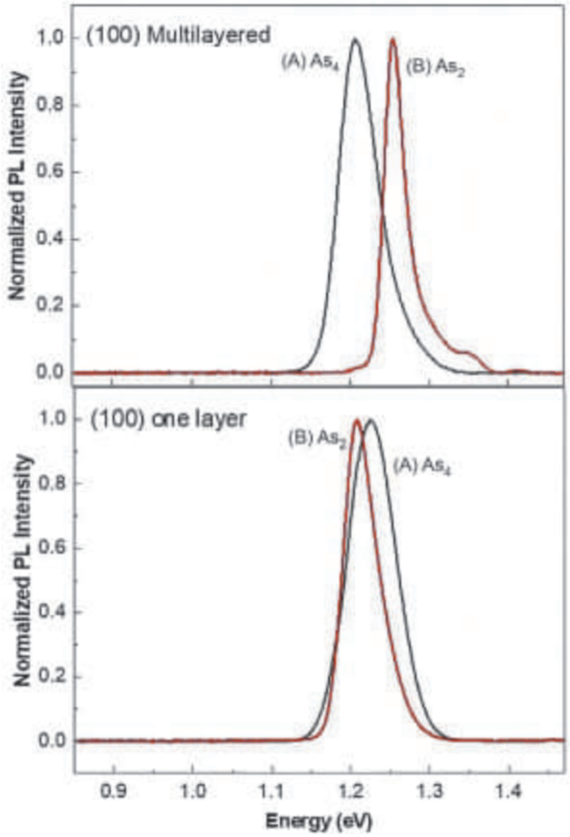

Fig. 9 PL spectra of single and multilayer (16 layers) $In_{0.4}Ga_{0.6}As$ QDs grown under (A) As_4 flux and (B) As_2 flux.

from (a) to (b). This is because QDs in the sample (a) behave more like quantum wires due to the lateral overlap between QDs along the chain direction. On the other hand, QDs in the sample (b) are well separated and behave like QDs with greater confinement resulting in a net blue shift. For a single QDs layer, the FWHM narrowing is due to the squeezing of the QD size distribution. All these results are consistent with the effect of the As_2 background.

Role of the indium composition

The indium composition is directly proportional to the strain relieved along the [0-11] direction to form anisotropic ordering. For this reason, the present section is aimed at understanding of the role of strain on lateral ordering by changing the indium composition. It is well known that increased compressive strain on the QD will hinder the migration of adatoms on the GaAs surface. This is understood because indium atoms do not diffuse as fast as Ga atoms on the GaAs surface. Also, a higher indium composition increases the strain in the InGaAs layer and makes QD formation faster. For those reasons, QDs with a higher indium composition have less response to surface anisotropy and less relief to the strain in the [0-11] direction than QDs with a lower indium composition. It is interesting to examine the effect of changing the indium composition on the vertically stacked QDs to seek the possibility of changing the anisotropic ordering. Before the growth of multi-stacked layers to observe the lateral ordering, four single-layer InGaAs QD samples were grown with different indium compositions (In%), as shown in Fig. 10. This step was needed to understand the effect of the indium composition on the shape and size of QDs in the first layer as it affects the successive ones. These samples were grown at 540 °C with different amounts of the InGaAs coverage, which was set to be around 25% above the critical thickness depending on the indium composition. For In% = 0.3, 0.4, 0.5, and 1 (i.e., InAs), the InGaAs coverage was 15, 8, 6, and 2 MLs, respectively. These samples were grown under a standard MBE growth environment (i.e., As_4 molecules as a background flux).

Table 1 summarizes the QDs' dimensions of the four samples obtained by AFM line scans. The parameters In%, h, dx, dy, T_C, and T_A refer to the indium composition, average QD height, average QD diameter along the [011] direction, critical QD diameter along the [0-11] direction, and the actual deposition, respectively. These parameters are the same in all experiments described below unless otherwise mentioned.

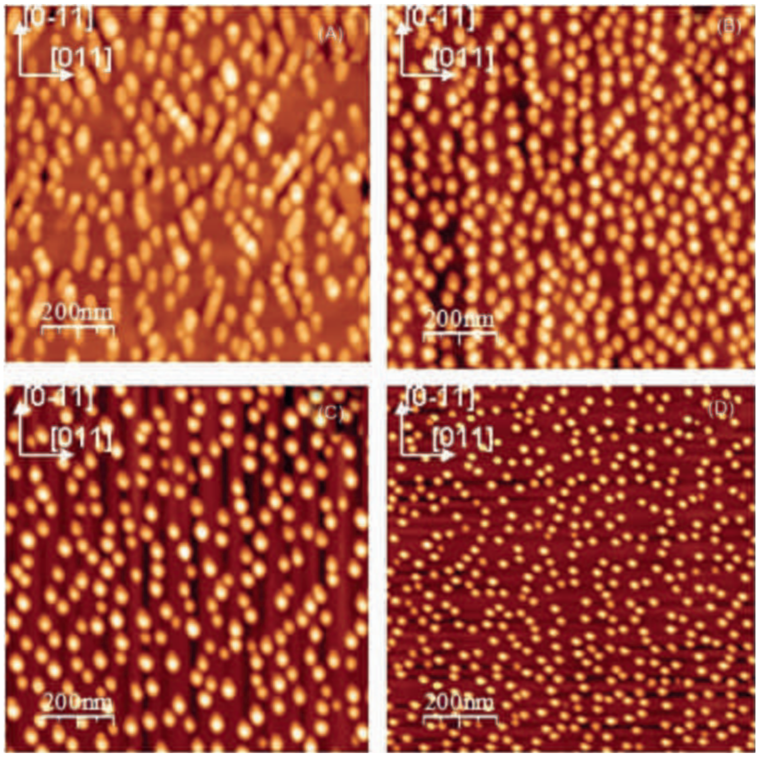

Fig. 10 AFM top views of one-layer InGaAs QDs with indium composition of (A) 0.3, (B) 0.4, (C) 0.5, and (D) 1.

Table 1 A summary of the average QD parameters for samples shown in Fig. 10.

Sample	*In%*	*h(nm)*	*dy(nm)*	*dx(nm)*	*T_C(MLs)*	*T_A(MLs)*
(a)	0.3	6.0 ± 0.7	50 ± 7	70 ± 18	12.0	15.0
(b)	0.4	7.0 ± 0.5	43 ± 6	45 ± 6	6.4	8.0
(c)	0.5	6.5 ± 0.6	38 ± 8	38 ± 8	4.8	4.8
(d)	1	5.5 ± 0.5	25 ± 5	25 ± 5	1.6	1.6

It was observed that a lower indium composition led to bigger QDs on the surface and resulted in elongated dots along the [0-11] direction due to the anisotropy of the adatom migration length in response to the (2 × 4) surface reconstruction. On the other hand, the adatom migration length and lateral intermixing after the QD formation was very low while depositing InAs QDs. In the present case, the critical thickness of InAs was 1.6 MLs, so only 0.3 MLs were deposited after that. The data in Table 1 show that QDs with a higher indium composition had smaller diameters and a more isotropic shape. To investigate the effect of stacking layers, four multilayers InGaAs QDs structures were grown at 540 °C with the same sequence of the indium composition and the amount of InGaAs deposition as the single-layer samples shown in Fig. 10.

The AFM images of the multilayer samples are shown in Fig. 11, and their corresponding dimensions are summarized in Table 2. The new parameters used in Table 2 are the average dot diameter (d) and the average spacing between the QDs' centers along the chain (y) and across chains (x), and other parameters are similar to those defined above. Comparing samples (a) through (d) reveals the effect of the indium composition on the lateral ordering of stacked QDs. In contrast, InGaAs samples with a lower indium composition responded to the anisotropy of the GaAs (001) surface by forming quantum wires along the [0-11] direction, QDs are formed at a higher indium composition due to the higher strain dominating over adatom diffusion. Although increasing the indium composition made the QDs better defined and non-overlapping along the chain, the higher indium composition also resulted in a lower density, short-chain lengths, and, eventually, no chains at all for the case of InAs. The conclusion was that increasing the indium composition reduced the diffusion and elongation of QDs along the [0-11] direction, which, in turn, affected the lateral ordering with stacked layers of QDs. The vertically stacked QDs with an indium composition higher than 0.4 were less pronounced along the chains and separated from each other as the indium composition increased. However, at the same time, that increased the strain transfer while stacking QD layers, leading to a bigger area of influence of a QD to the next layer. This led to a reduced QD density when stacked since the deposition amount was smaller and increased the chain-to-chain separation. QD chains were shorter

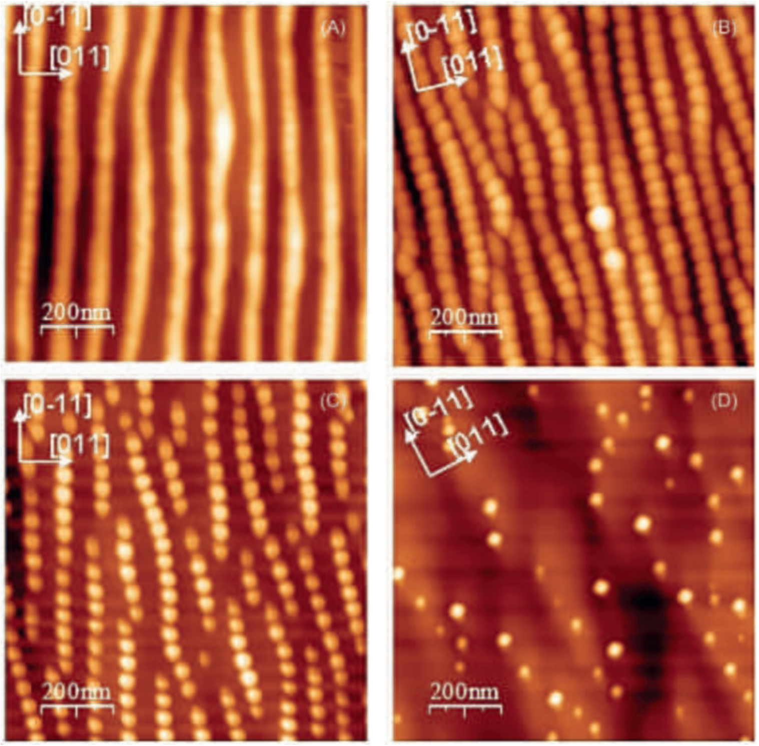

Fig. 11 AFM top views of multilayer InGaAs QDs with the indium composition of (A) 0.3, (B) 0.4, (C) 0.5, and (D) 1.

Table 2 A summary of the average QD parameters for samples shown in Fig. 11.

Sample	*In%*	*d(nm)*	*y(nm)*	*x(nm)*	*T_C(MLs)*	*T_A(MLs)*	*FFT*
(a)	0.3	65 ± 6	0	104 ± 6	12.0	15.0	1D
(b)	0.4	59 ± 6	51 ± 3	85 ± 14	6.4	8.0	1D
(c)	0.5	52 ± 8	50 ± 6	94 ± 12	4.8	4.8	1D
(d)	1	20 ± 5 49 ± 3	*	*	1.6	1.6	random

*Not applicable.

and further apart with the increased indium composition, and eventually, no ordering for the InAs QDs was observed. The next investigation was to find a way to reduce the diffusion of adatoms along the [0–11] direction but without increasing the strain.

Low indium composition under As_2

The drawback of the sample with In% = 0.3 was the presence of coalescence between QDs. The QD coalescence is due to an increased coverage (Thibado, 1999). The other three samples were grown under As_2 flux, with 30% indium composition, but with a reduced InGaAs deposition from 15 MLs to 13.5 and 12 MLs (Fig. 12). These three samples were compared to the one grown with 15 MLs deposition and shown in Fig. 11. It was observed that reducing the amount of InGaAs to 13 MLs, as in Fig. 12B, impressively resulted in a 2D lateral ordering of QDs with hexagonal geometry. The visual image was supported by the FFT of the AFM image shown in the inset of Fig. 12B. A magnification of this ordering is presented as the image Fig. 12D.

Fig. 12C showed that reducing the amount of the InGaAs deposition to 12 MLs captured the initial formation stage of QDs over the GaAs surface. However, there were two interesting observations obtained from Table 3. First, the QDs' smaller size, and second, the QDs' alignment in chains. In the areas where QDs were not yet formed, the wetting layer was wire-like corrugated along the [0-11] direction as favorable areas for QDs to nucleate. This was similar to how QDs with higher indium compositions were ordered, as seen in earlier experiments. This observation supported the earlier conclusions that smaller QDs are subject to anisotropic ordering due to low coverage. It is instructive to examine the QD ordering shown in Fig. 12D. Each QD is surrounded by the six nearest neighbors resembling a honeycomb pattern. An interesting scenario could be as follows: It is known that each QD transfers a vertical strain to the QD layer above. When two QDs are very close to each other, the profile of the transferred strain pattern overlaps with each other and only one nucleation site in the layer above from the two sites below provides a vertical ordering mechanism and reducing the QD density. As the density reduces, each QD resides at nearly the center of a circle of radius R of influence, where there are no other QDs. As a result, assuming each QD is at the center of a circle of influence, six QD circles can

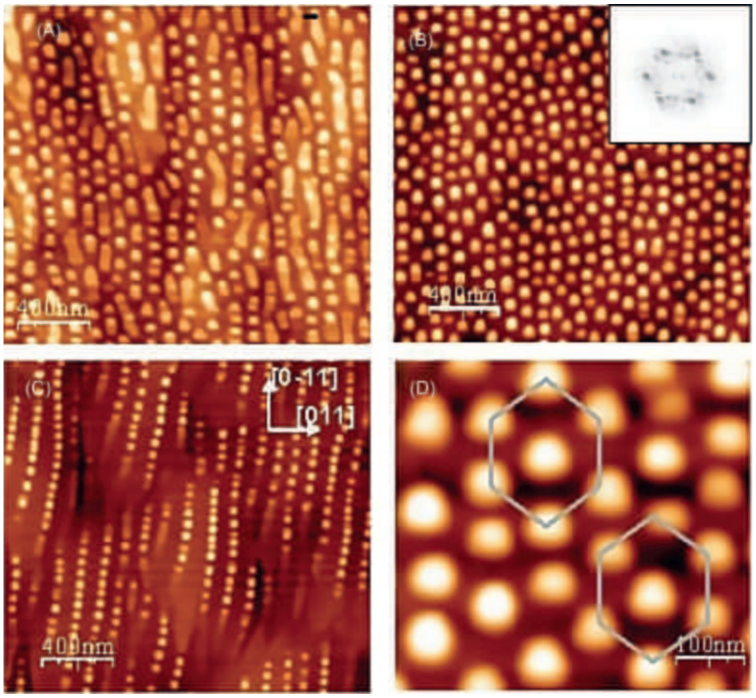

Fig. 12 AFM images of QD samples grown under As_2 flux. The amount of the InGaAs deposition is (A) 15, (B) 13, and (C) 11 MLs, (D) is a magnification of image (B).

Table 3 A summary of the average dot parameters for samples is shown in Fig. 12.

Sample	*Coverage(MLs)*	*h(nm)*	*d(nm)*
(a)	15	13.3 ± 1.6	*
(b)	13.5	12.0 ± 1.2	75 ± 9
(c)	12	10.2 ± 1.9	50 ± 5

*Not applicable.

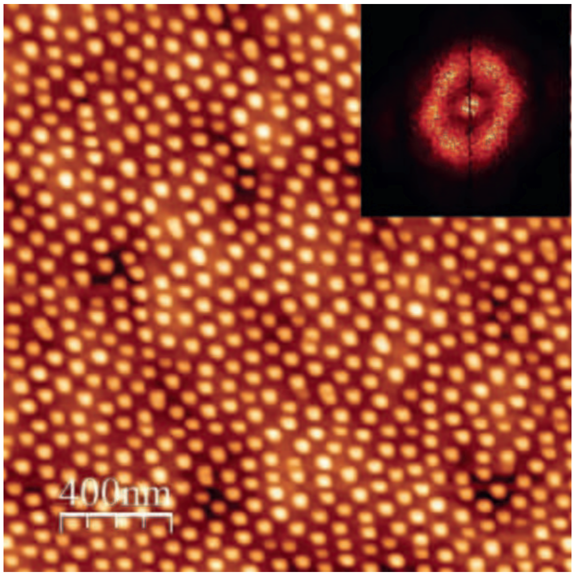

Fig. 13 AFM image of multilayer $In_{0.35}Ga_{0.65}As$ QDs grown under the As_2 flux.

neatly fit around one QD because there is no longer any favored direction of diffusion when using As_2. The final trial was to balance the indium composition and coverage. It was thought that growing QDs with In% = 0.35, for example, would result in smaller QDs than those in the case of In% = 0.3 because of a reduced deposition time. This was expected to make the size uniformity better than in the case of In% = 0.3. At the same time, the strain would be less than the case with In% = 0.4, so QDs would have more chance to be 2D ordered. Growing QDs with In% = 0.35 was then expected to make them inherit the desirable characteristics of size uniformity and 2D ordering. Multilayer $In_{0.35}Ga_{0.65}As$ QDs samples were grown under As_2 flux by depositing 11 MLs of InGaAs. The AFM scan of such a sample is displayed in Fig. 13. The size and shape uniformity was better for the sample with In% = 0.35 than in the case of In% = 0.3. At the same time, the hexagonal 2D ordering was still preserved, as shown in the FFT (inset to Fig. 13).

The growth of QDs under the As_2 environment reduced the anisotropic diffusion of Ga adatoms and made QDs well separated, and at low indium composition, dramatically reduced the strain factor and made QDs bigger in size, so that separations between QDs along and across the chain became comparable. This allowed the formation of isotropic 2D laterally ordered QDs, and, consequently, 3D ordered arrays of QDs due to the vertical correlation. At the same time, the achieved ordering reflected the uniformity of QDs, which, in turn, improved their optical properties.

Ordered self-assembled quantum ring arrays

The growth of quantum rings (QRs) was a remarkable development in the self-assembly of semiconductor nanostructures. QRs are formed with the help of the Stranski-Krastanov growth method. In this approach, a partial capping of large InAs QDs with a thin layer of GaAs results in the formation of QRs. During the annealing step at the growth temperature, a topology change occurs: the original QDs acquire a hole in their center and take on a ring-like shape, as described in Section "Growth of self-organized semiconductor nanostructures."

The growth of patterned arrays of QRs can be obtained on the GaAs(100), (311)B, and (511)B surfaces on multilayered templates of InGaAs/GaAs QDs, as described in Section "Controlling ordering on an array of quantum dots." It was observed (Wu et al., 2012; Wu and Wang, 2014), that it was possible to produce chains of QRs on the GaAs(100) surface (see Fig. 14). Individually, the QRs on the (100) surfaces were seen to have an elliptical geometry with a minimum inner radius of ~25 nm. The average radii of QRs on all three samples of ordered QRs are presented in Table 4.

These averages were calculated by taking the first derivative of the AFM height data. The places where this first derivative changes its sign corresponds to the rings' center and edges. The standard deviations are similar from sample to sample, but the average radii are larger on the high-index surfaces (311)B and (511)B. More material is typically necessary when growing dots on high-index surfaces than on the (100) surface. This is because the effective lattice constant of a high-index surface is generally larger than that of the (100) surface. Therefore, the strain due to the lattice mismatch is smaller per unit volume of material deposited than on the (100) surface. This means that QDs form later in the growth on a high-index surface than on the (100) surface, similar to the QDs shown in Figs. 7 and 8 in Section "Controlling ordering on an array of quantum dots." So, the QDs are larger, leading to larger QRs whenever partial capping is performed.

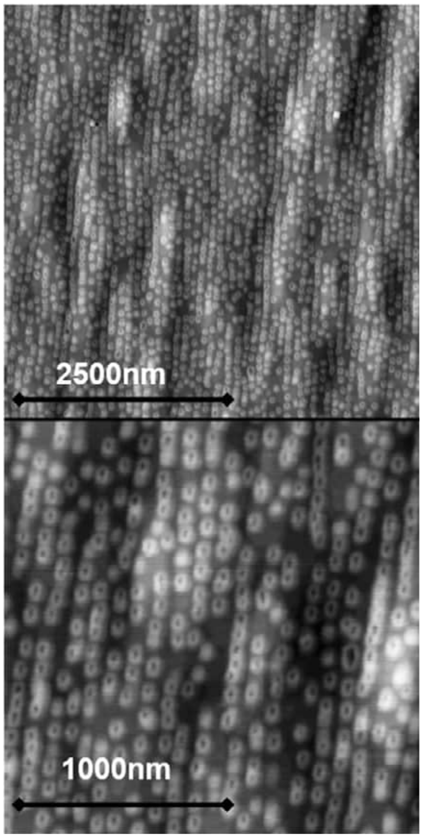

Fig. 14 AFM Topography of QR chains on the InGaAs/GaAs(100) multilayered structure.

Table 4 Average radii of ordered QRs on the GaAs(100), (311)B, and (511)B surfaces.

Surface Miller Index	*Average radius (nm)*	*Standard Deviation (nm)*	*Figure number*
(100)	26.3	8.2	14
(311)B	37.6	10.7	15
(511)B	35.2	7.5	16

The averages were calculated by analyzing the first derivative of the AFM height data.

It was supposed that the elliptical shape was because the QRs evolved out of slightly elongated QDs in the [0-11] direction. In addition, the adatom diffusion may be more favorable in the [0-11] direction. The maximum height of the QRs on (100) was about 1.4 nm, while the width (defined as the outer radius minus the inner radius), was about 25 nm. In general, it was observed that the QR chains did not persist for more than about 2 μm on QD chains. One can expect to achieve QR chains that persist for over 2 μm under the optimum growth conditions.

The AFM topography of the samples grown on the (311)B and (511)B surfaces, shown in Figs. 15 and 16, indicates very clearly defined QRs with inner diameters on the order of ~40 nm, widths of ~30 nm, and a maximum height of ~1.5 nm relative to the sample surface in between the QRs.

Moreover, these QR arrays possessed not only 1D ordering on the surface of the substrate but also 2D ordering. The QRs on both the exposed (311)B and (511)B surfaces appeared to be arranged in a 2D array, as expected.

Fig. 17 shows the 2Dl FFTs of the three samples, which is evidence that the QRs grown on them display long-range ordering.

The FFT for the (100) surface shows ordering along the horizontal axis, which indicates that they may be called QR chains. However, the FFT indicates ordering along more than one direction on the (311)B and (511)B surfaces. For example, it looks like the pattern on the (311)B surface has two axes of symmetry and that the one on the (511)B surface may have as many as four exes of symmetry. The FFT for the (511)B surface appears to have the hexagonal symmetry (as shown in Fig. 11B), and that for the (311)B surface appears to have rhombic symmetry. For this reason, it is possible to consider these arrays of QRs on the (511)B and (311)B surfaces as 2D lattices of QRs with hexagonal and orthorhombic symmetry, respectively.

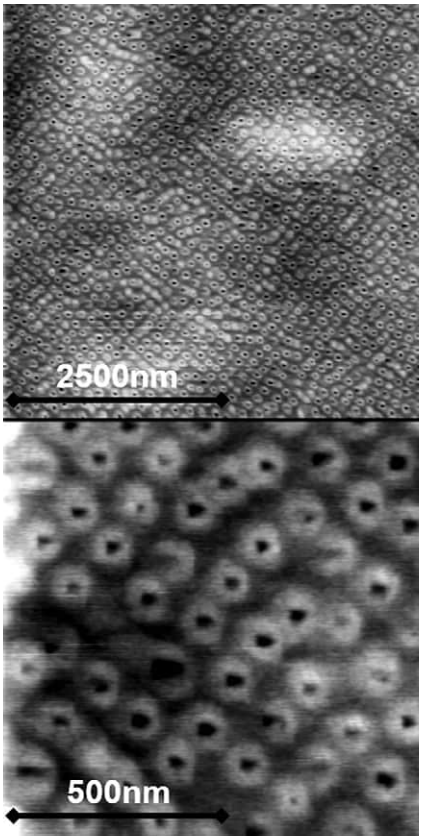

Fig. 15 AFM topography of an ordered array of QRs on the InGaAs/GaAs(311)B multilayered structure.

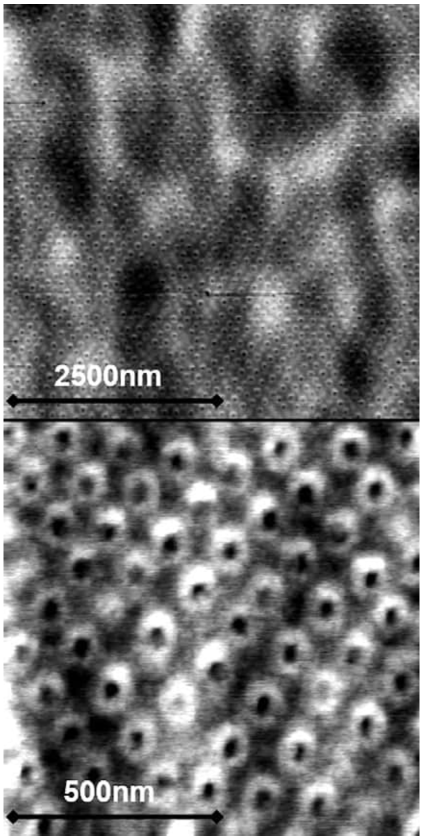

Fig. 16 AFM topography of an ordered array of QRs on the InGaAs/GaAs(511)B multilayered structure.

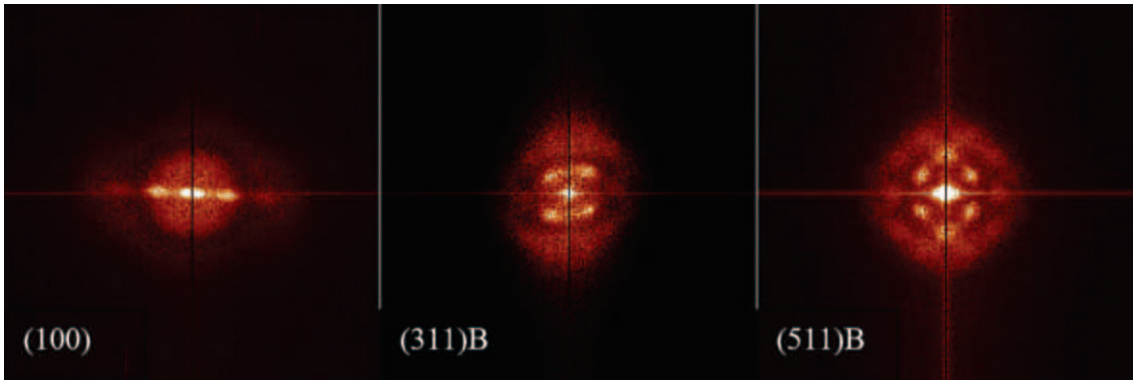

Fig. 17 Two-dimensional FFT images from the samples represented in Figs. 14–16. Notice the 2D patterns on the (311)B and (511)B surfaces and the 1D ordering on the (100) surface.

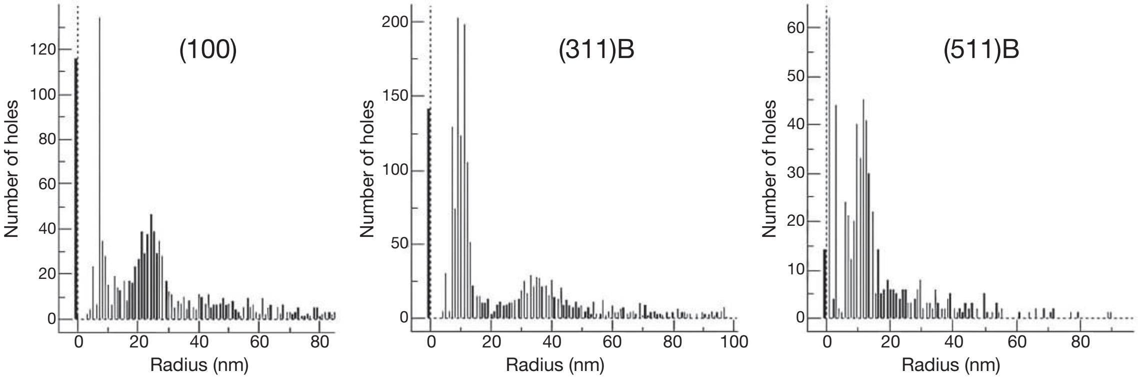

Fig. 18 Distribution of QR radii on the (100), (311)B, and (511)B surfaces.

Data showing the distribution of QR sizes are shown in Fig. 18. The average size corresponds to the values in Table 4 in all cases except the data for the (511)B surface.

In addition, one notices that the distribution data for the (311)B surface indicate a bimodal size distribution of the QRs. Interestingly, this implies the occurrence of two groups of InAs QDs on the GaAs surface prior to the partial capping that causes the above-described transition to QRs. The data for the (100) surface seem to point on this bimodality, with a small group clustered around 35 nm in the distribution.

Conclusion

In general, this chapter's main focus was exposing the underlying physics in the fabrication and characterization of self-assembled III-V compound semiconductor nanostructures. We also propose a combination of properties to control the ordering of QDs and QRs on a GaAs surface using natural surface anisotropic for (100), surface steps on high index GaAs substrates, and the Arsenic background. Ordered QDs with low indium composition on GaAs (001), (311)B, and (511)B were obtained for one and multilayered structures. We found that the ordering is due to surface properties combined with the growth conditions. The stacking only enhances the initial order provided by the surface properties and the growth conditions. We observed that using As_2 molecules as opposed to As_4 molecules as a background environment, we can modify the surface kinetics and combine this property with the diffusion of adatoms over the surface. We found that the change of the Arsenic background environment from As_4 to As_2 increases the separation of the QDs from each other without eliminating the lateral ordering and decreases their size distribution. Narrow QDs size distributions resulting from As_2 are useful for applications such as lasers and detectors and will improve their advantages.

References

Bimberg D, Grundmann M, and Lendentsov NN (1998) *Quantum dot heterostrutures*. John Wiley & Sons, ISBN: 978-0-471-97388-1.

Bressler-Hill V, Lorke A, Varma S, Petroff PM, Pond K, and Weinberg WH (1994) Initial stages of InAs epitaxy on vicinal GaAs(001)-(2×4). *Physical Review B* 50: 8479. https://doi.org/10.1103/PhysRevB.50.8479.

Granados D and Garcia JM (2003) In(Ga)As self-assembled quantum ring formation by molecular beam epitaxy. *Applied Physics Letters* 82: 2401. https://doi.org/10.1063/1.1566799.

Granados D and Garcia JM (2005) Vertical order in stacked layers of self-assembled In(Ga)As quantum rings on GaAs (001). *Applied Physics Letters* 86: 071918. https://doi.org/10.1063/1.1866228.

Kegel I, Metzger TH, Lorke A, Peisl J, Stangle J, Bauer G, Garcia JM, and Petroff PM (2000) Nanometer-scale resolution of strain and interdiffusion in self-assembled InAs/GaAs quantum dots. *Physical Review Letters* 85: 1694. https://doi.org/10.1103/PhysRevLett.85.1694.

Kley A, Ruggerone P, and Scheffler M (1997) Novel diffusion mechanism on the GaAs(001) surface: The role of adatom-dimer interaction. *Physical Review Letters* 79: 5278. https://doi.org/10.1103/PhysRevLett.79.5278.

Lee SC, Dawson LR, Malloy KJ, and Brueck SR (2002) Nanoscale limited area growth of InAs islands on GaAs(001) by molecular beam epitaxy. *Applied Physics Letters* 79: 2630. https://doi.org/10.1063/1.1436303.

Lei W and Lorke A (2014) Growth and spectroscopy of semiconductor quantum rings. In: Fomin VM (ed.) *Physics of Quantum Rings. Series: NanoSci. Technol*, pp. 27–59. Berlin - Heidelberg: Springer. ISBN: 978-3-642-39196-5, ISBN: 978-3-642-39197-2 (eBook). https://doi.org/10.1007/978-3-642-39197-2.

Llorens JM, Lopes-Oliveira V, López-Richard V, Ulloa JM, and Alén B (2018) From dot to ring: Tunable exciton topology in type-II InAs/GaAsSb quantum dots. In: Fomin VM (ed.) *Physics of Quantum Rings. Series: NanoSci. Technol*, 2nd edn, pp. 57–88. Cham: Springer International Publishing. ISBN: 978-3-319-95158-4, ISBN: 978-3-319-95159-1 (eBook). https://doi.org/10.1007/978-3-319-95159-1.

Lorke A, Luyken RJ, Garcia JM, and Petroff PM (2001) Growth and electronic properties of self-organized quantum rings. *Japanese Journal of Applied Physics* 40: 1857. https://doi.org/10.1143/JJAP.40.1857.

Ma W, et al. (2001) Shape transition of coherent three-dimensional (InGa)As islands on GaAs(100). *Applied Physics Letters* 79: 4219. https://doi.org/10.1063/1.1428107.

Mazur YI, et al. (2003) InGaAs/GaAs three-dimensionally-ordered array of quantum dots. *Applied Physics Letters* 83: 987. https://doi.org/10.1063/1.1596712.

Mazur HM, Yu I, Marega E Jr, AbuWaar ZY, and Salamo GJ (2007) Shape transformation during overgrowth of InGaAs/GaAs(001) quantum rings Appl. *Physics Letters* 91: 043103. https://doi.org/10.1063/1.2760191.

Raab A, et al. (2002) Controlling the size and density of self-assembled PbSe quantum dots by adjusting the substrate temperature and layer thickness. *Applied Physics Letters* 81: 2457. https://doi.org/10.1063/1.1509116.

Ripalda JN, Bone PA, Howe P, and Jones TS (2003) Morphological anisotropy during migration enhanced epitaxy of GaAs(001). *Surface Science* 540: L593. https://doi.org/10.1016/S0039-6028(03)00798-2.

Salmi MA, et al. (1999) Energetics and diffusion paths of gallium and arsenic adatoms on flat and stepped GaAs(001) surfaces. *Surface Science* 425: 31. https://doi.org/10.1016/S0039-6028(99)00180-6.

Sanguinetti S, Mano T, and Kuroda T (2014) Self-assembled semiconductor quantum ring complexes by droplet epitaxy: Growth and physical properties. In: Fomin VM (ed.) *Physics of Quantum Rings. Series: NanoSci. Technol*, pp. 187–228. Berlin - Heidelberg: Springer. ISBN: 978-3-642-39196-5, ISBN: 978-3-642-39197-2 (eBook). https://doi.org/10.1007/978-3-642-39197-2.

Shchukin VA and Bimberg D (1999) Spontaneous ordering of nanostructures on crystal surfaces. *Reviews of Modern Physics* 71: 1125. https://doi.org/10.1103/RevModPhys.71.1125.

Tersoff J, et al. (1996) Self-organization in growth of quantum dot superlattices. *Physical Review Letters* 76: 1675. https://doi.org/10.1103/PhysRevLett.76.1675.

Thibado P, et al. (1999) Robust optical delivery system for measuring substrate temperature during molecular beam epitaxy. *Journal of Vacuum Science and Technology B* 17: 253. https://doi.org/10.1116/1.590508.

Wang ZM, Seydmohamadi S, Lee JH, and Salamo GJ (2004a) Surface ordering of (InGa)As quantum dots controlled by GaAs substrate indexes. *Applied Physics Letters* 85: 5031. https://doi.org/10.1063/1.1823590.

Wang ZM, et al. (2004b) High anisotropy of lateral alignment in multilayered (InGa)As/GaAs(100) quantum dot structures. *Journal of Applied Physics* 96: 6908. https://doi.org/10.1063/1.1815382.

Wu J and Wang ZM (2014) Fabrication of ordered quantum rings by molecular beam epitaxy. In: Fomin VM (ed.) *Physics of Quantum Rings. Series: NanoSci. Technol*, pp. 143–159. Berlin - Heidelberg: Springer. ISBN: 978-3-642-39196-5, ISBN: 978-3-642-39197-2 (eBook). https://doi.org/10.1007/978-3-642-39197-2.

Wu J, Wang ZM, Holmes K, Marega E Jr, Zhou Z, Li H, Mazur YI, and Salamo GJ (2012) Laterally aligned quantum rings: From one-dimensional chains to two-dimensional arrays. *Applied Physics Letters* 100: 203117. https://doi.org/10.1063/1.4719519.

Xie Q, et al. (2000) Growth of vertically self-organized InGaAs quantum dots with narrow inhomogeneous broadening. *Applied Physics Letters* 76: 3082. https://doi.org/10.1063/1.126586.

Optical properties in rolled-up structures

JW Wang[a] **and LB Ma**[b], [a]School of Electronic and Information Engineering, Harbin Institute of Technology (Shenzhen), Shenzhen, China; [b]Institute for Integrative Nanosciences, Leibniz IFW Dresden, Dresden, Germany

© 2024 Elsevier Ltd. All rights reserved.

Introduction 354
Optical resonances in rolled-up tubular structures 355
Split axial modes in 3D microtube cavities 357
Rolled-up microtubes as optically active and passive devices 358
Mode responses with weak external perturbations 360
Mode splitting and non-Hermitian photonics 360
Optoplasmonic hybridization in metal/dielectric rolled-up structures 363
Spin-orbit coupling in rolled-up cavities 363
Rolled-up metamaterials 366
Conclusion 367
References 367

Abstract

Rolling-up prestrained nanomembranes combining the merits of top-down and bottom-up approaches, enables the fabrication of multilayered tubular microstructures. The great flexibilities in the tailoring of 3D morphologies and material compositions accelerate the discovery of numerous novel optical properties. For all-dielectric rolled-up microcavities, the whispering gallery mode resonances, axial optical confinements, and optical mode interactions in both weak and strong coupling regimes are discussed. These properties render the structure a great platform for studying optical spin-orbit coupling and non-Hermitian photonics. For microtubes consisting of both dielectrics and noble metals as anisotropic metamaterials, unique optical properties are discussed including optoplasmonic mode hybridization and dispersion engineering.

Key points

- Microtube structure formed by self-assembly of strained nanomembrane
- Optical resonances in rolled-up tubular structures
- Resonant mode response to weak external perturbations
- Mode splitting and non-Hermitian photonics
- Optical spin-orbit coupling in rolled-up microcavities
- Optoplasmonic hybridization
- Rolled-up metamaterials

Introduction

The “rolled-up nanotech” was developed at the beginning of the new millennium, firstly on semiconductor thin film fabricated using molecular beam epitaxy (MBE) (Schmidt and Eberl, 2001; Prinz et al., 2000). Nowadays, it is considered to be one of the most promising “origami” (a kind of talented paper folding art) technology, and usually termed “rolling origami.” Rolled-up 3D micro/nanostructures can be constructed by engineering strain gradients in the stack of 2D nanomembranes. In early works, the internal strain in nanomembranes was incorporated by exploiting the crystal lattice mismatch between two different materials such as InGaAs and GaAs. The lattice mismatch creates a differentially strained bilayer causing an up or downwards rolling.

For a typical rolling-up process, the sacrificial layer is firstly prepared on top of a substrate. Then, strained nanomembranes are deposited onto the sacrificial layer in a step-by-step manner. By etching the underneath sacrificial layer, these strained nanomembranes are released from the substrate and tend to force themselves into free-standing 3D cylinder structures to stabilize their elastic energy (see Fig. 1a). For such a self-rolling process, the nanomembrane can be bilayer or multilayer. Besides, it has been shown that a single layer of materials, e.g., silicon, can also be rolled due to the strain gradient. Over the development of more than 20 years, numerous efforts have been continuously invested in extending the compatibility of the rolling process with highly diverse nanomembrane materials, including metals, oxides, semiconductors, 2D materials, etc. (Xu et al., 2019).

The most common rolled-up 3D microstructures are tubes and helixes. For a simple bilayer case assuming the equal Young’s modules and Poisson ratios, the rolled-up tube diameter D can be estimated as follow:

https://doi.org/10.1016/B978-0-323-90800-9.00098-6

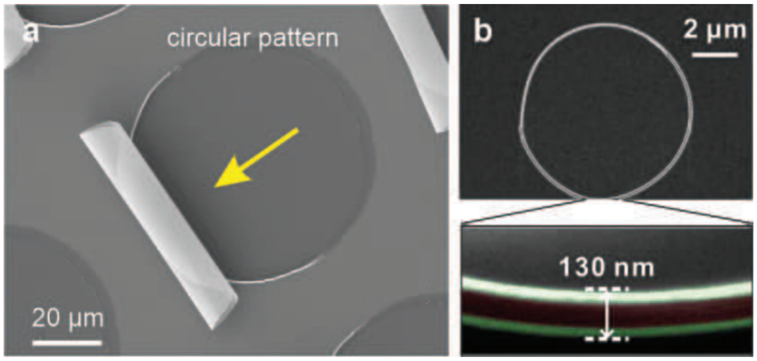

Fig. 1 (a) Top-view SEM image of a rolled-up nanomembrane with a circular nanomembrane pattern. (b) SEM image in a cross-sectional view after a focused ion beam (FIB) cut. The zoomed-in view suggests the sub-wavelength tube wall thickness. Modified with permission from (2013) *Advanced Materials* 25: 2357; Copyright © 2013 WILEY-VCH Verlag GmbH & Co. KGaA.

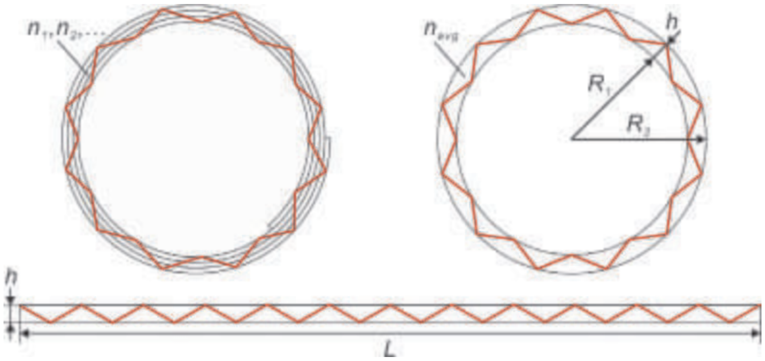

Fig. 2 Sketch of rolled-up nanomembrane and nanomembrane strip in the cross-sectional view to show the azimuthal WGM resonances, including a spiral ring (left-up), a perfect ring after approximation (right-up), and a strip expanded from a curved waveguide (bottom).

$$D = \frac{1}{3\varepsilon(1+\mu)} \frac{(d_1+d_2)^3}{d_1 d_2} \tag{1}$$

where ε is the in-plane biaxial strain between layers, μ is the Poisson ratio, d_1 and d_2 are the thickness of two membrane layers, respectively. Typically the demonstrated D is in the range of ~1–100 μm. The wall thickness depends on the thickness of the deposited nanomembrane layer and the winding number $w = L_{\mathrm{roll}}/\pi D$, where L_{roll} is the total rolling length along the rolling axis. As presented in Fig. 1b, a microtube with wall thickness down to ~130 nm can be realized.

Besides, the rolling-up process combines the advantage of both top-down (through patterning of the planar membrane geometry) and bottom-up (through strain-modulated self-assembly) strategies. The key morphology of the cylindrical structure, including the size, wall thickness, design along the axial direction, and asymmetric rolling condition can all be finely tailored. Therefore, the enabled great versatility opens up infinite potential in exploring novel optical properties and developing optical and optoelectronic applications.

Here, the following sections elaborate on the discovered optical properties of rolled-up micro/nanostructures made by different materials covering dielectrics, semiconductors, and metals. A tubular-shaped microcavity allows good light confinement through whispering gallery mode (WGM) resonance, and therefore is regarded as a powerful platform for unveiling rich physical insights, including light field manipulation in 3D space, cavity-enhanced light-matter interactions, external and internal mode couplings. Besides, the adjustable structural and material anisotropy in the rolling process results in intriguing properties such as optoplasmonic hybridization, spin-orbit coupling, and anisotropic metamaterials. All these introduced properties have been unleashing the huge potentials of miniaturized optical and optoelectronic devices, such as light sources, detectors, sensors, and waveguiding/routing elements for on-chip photonic integrated circuits (PICs), etc.

Optical resonances in rolled-up tubular structures

As one of the well-known optical resonances in microstructures, optical WGM is the exact counterpart of acoustic resonances discovered at the gallery surface of St Paul's Cathedral and systematically explained by Lord Rayleigh. In the optical regime, it describes the light trapping and propagating along the concave boundary of a dielectric structure due to total internal reflection (TIR). Optical WGM cavities in a circular or rounded shape can be roughly categorized into two types, namely solid-core ones (e.g., microspheres, microdisks, microtoroids, microbottles, and fibers) and hollow-core ones (e.g., microrings, microtubes, and microbubbles). Supposing that the tubular nanomembrane is cut and expanded into a strip with a total length of L (i.e., the circumference), light propagation within a rolled-up cavity can be considered as a similar case in an optical planar waveguide (see Fig. 2). TIR of light occurs with the incident angle $\theta <$ the critical angle θ_c. By curving the waveguide into a loop, WGM resonances can be built up by constructive interference of light traveling around the tube circumference. A longitudinal resonance condition is introduced as

$$L n_{\text{avg}} k \sin\theta = 2m\pi \tag{2}$$

where m stands for the "azimuthal" mode order in a ring form, n_{avg} accounts for the refractive index of the multilayered nanomembrane. Usually, n_{avg} can be estimated by averaging the refractive index along the multilayer wall structure. The following formula is used

$$\mathrm{n}_{avg} = \sqrt{\frac{\Sigma t_i n_i^2}{\Sigma t_i}} \tag{3}$$

where each subscript refers to an individual layer in the multilayered tube wall, and t_i is the thickness of the i$^{\text{th}}$ layer on the tube wall (with the refractive index n_i), respectively.

WGM resonances can be understood by calculations of 2D Helmholtz equation for cylindrical ring model,

$$\left[\nabla^2_{r,\varphi} + \left(n(r)\frac{\omega}{c}\right)^2\right]\Phi(r,\varphi) = 0 \tag{4}$$

where $n(r)$ is the refractive index profile along the radial direction.

The analytic solution in cylindrical coordinate is

$$\Phi(r,\varphi) = \left\{\begin{matrix} C_A J_m(n_c kr) \\ C_B J_m(n_{avg}kr) + C_C Y_m(n_{avg}kr) \\ C_D H_m^{(2)}(n_0 kr) \end{matrix}\right\} e^{\pm im\varphi} \begin{matrix} r < R_1 \\ R_1 \le r \le R_2 \\ r > R_2 \end{matrix} \tag{5}$$

where $J_m(.)$, $Y_m(.)$, and $H_m^{(2)}(.)$ are Bessel and Henkel functions, $k = \omega/c$ is free space wave vector, and m is the azimuthal mode number. The unknowns in Eq. (5) are coefficients (C_A, C_B, C_C, C_D) and the wave vector k. One can match the boundary conditions of the field and its derivative at $r = R_1$ and $r = R_2$ and get rid of the coefficients (C_A, C_B, C_C, C_D) by using a matrix method.

Due to the difference in boundary conditions, polarization degeneracy of light is lifted. And usually transverse electric (TM, $E_z = 0$) modes and transverse magnetic (TE, $H_z = 0$) modes will be separately calculated with different values of k. For TE mode ($\mathbf{E} = E_z\mathbf{z}$), we can match the boundary conditions of the field and its derivative at $r = R_1$ and $r = R_2$ and get rid of the coefficients (C_A, C_B, C_C, C_D) by using a matrix method.

For TM mode, at $r = R_1$

$$C_A J_m(n_c kR_1) - C_B J_m(n_{avg}kR_1) - C_B Y_m(n_{avg}kR_1) = 0 \text{ and } C_A J'_m(n_c kR_1) - C_B J'_m(n_{avg}kR_1) - C_B Y'_m(n_{avg}kR_1) = 0 \tag{6}$$

At $r = R_2$

$$C_B J_m(n_{avg}kR_2) + C_B Y_m(n_{avg}kR_2) - C_D H_m^{(2)}(n_0 kR_2) = 0 \text{ and } C_B J'_m(n_{avg}kR_2) + C_B Y'_m(n_{avg}kR_2) - C_D H_m^{(2)'}(n_0 kR_2) = 0. \tag{7}$$

Here the derivative notation $' = d/dr$. We can write the functions into a matrix equation and use a standard eigenvalue solver to obtain k and associated resonant energies E_m. Once the resonant energy of the interesting mode is obtained, the spectrum, 1D and 2D field profiles can be easily generated, as illustrated in Fig. 3.

For optical resonances, it is common to adopt the quality factor Q to describe the energy storing ability

$$Q = 2\pi\frac{\text{Energy stored}}{\text{Energy dissipated per cycle}} = \frac{\omega}{\Delta\omega} = \frac{\lambda_r}{\Delta\lambda_r} \tag{8}$$

where λ_r, ω_r are the resonant wavelength and frequency, and $\Delta\lambda_r$, $\Delta\omega_r$ are the corresponding linewidths.

For theoretical studies as the ideal case, the Q-factor mainly limited by the radiative loss can be calculated from

$$Q = \frac{Re\{Em\}}{2Im\{Em\}}. \tag{9}$$

In practice, the absorption, Rayleigh scattering in bulk materials, and scattering due to surface roughness all have significant contributions to the loss. The total Q factor can be written as

$$\frac{1}{\mathrm{Q_{total}}} = \frac{1}{\mathrm{Q_{rad}}} + \frac{1}{\mathrm{Q_{abs}}} + \frac{1}{\mathrm{Q_{sca}}}. \tag{10}$$

For nanomembrane microcavities, the ultra-thin cavity wall (e.g., 100–200 nm) may lead to the only observation of TE mode due to the poor confinement (low-Q) for TM mode and strong radiative loss. To support both TE and TM modes, a sufficiently thick wall (e.g., 200–300 nm for modes at visible wavelengths) is required. To this end, one can either increase the winding number w, or perform post-fabrication deposition of dielectric materials (e.g., by atomic layer deposition).

It is worth noticing that the aforesaid discussion treats the rolled-up tube as a microring with perfect rotational symmetry. There is a double degeneracy for each of the azimuthal modes with a certain polarization state, namely the clockwise (CW) and

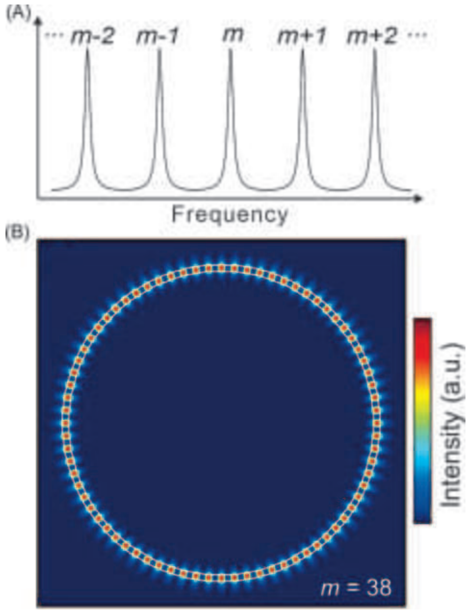

Fig. 3 (a) Schematic of a resonant spectrum covering five WGMs with different azimuthal mode number m. (b) Numerically calculated mode intensity profile at a cross-sectional view for mode with $m = 38$.

counterclockwise (CCW) modes, which can be lifted by introducing scatters and breaking the symmetry. Here, the rolling process intrinsically leads to a spiral ring with two rolling edges (i.e., one inner and one outer). Detailed discussions on mode splitting will be in section "Mode splitting and non-Hermitian photonics."

Split axial modes in 3D microtube cavities

For direct rolling of a regular nanomembrane pattern (e.g., square shape), the WGMs confined in the microtube suffer from severe substrate leakage loss due to direct contact with the substrate. It is desired to tailor the 2D membrane geometry to seek a free-standing segment so that high efficiency of light confinement and high Q factors can be obtained. Alternatively, the 2D nanomembrane can be tailored into a U-shaped design, as presented in Fig. 4a. After rolling with a predefined distance, the middle part of the patterned nanomembrane is fully rolled up while the rest two side parts continue to roll a certain distance more, leading to a self-supporting microtubular "bridge" where the middle of the rolled-up structure is separated from the substrate.

In addition to the U-shape design, the peculiar property of rolled-up nanomembrane here is that it offers an additional degree of freedom along the axial direction (i.e., z-direction) for tailoring the 3D cavity shape and manipulating the optical resonance (Strelow et al., 2012). Here the winding number $w(z)$ at the middle segment can be freely designed, leading to tailored optical confinement along the axial direction and the single azimuthal mode split into multiple axial modes.

Taking into account the tailored tube structure and its resulted optical confinement along the axial direction, the eigenmodes of a 3D microtube microcavity can be theoretically analyzed by solving the Helmholtz equation (4). Considering the cylindrical coordinates (Fig. 4b), the wave equation is expressed as follow:

$$-\frac{1}{n^2(r,\varphi,z)}\nabla^2\vec{E}(r,\varphi,z) = k^2\vec{E}(r,\varphi,z) \tag{11}$$

where k is the wavevector and n is the averaged refractive index (taking account of multilayered nanomembrane).

As the dynamic of WGM occurs mainly in the r-ϕ plane, an adiabatic approximation is applied to separate the terms of electric fields between circular and axial propagations.

Here taking the TE mode as an example, the electric field can be written as:

$$E_z(r,\varphi,z) = \Phi(r,\varphi,z)\Psi(z) \tag{12}$$

where $\Phi(r,\varphi,z)$ is the circulating term and is the axial term.

By rewriting the scalar Helmholtz equation, one has,

$$-\frac{1}{n^2(r,\varphi,z)}\nabla_{r,\varphi}{}^2\Phi(r,\varphi,z) = k^2{}_{circ}(z)\Phi(r,\varphi,z) \tag{13}$$

Where k_{circ} is the absolute value of wavevector circulating in the r-ϕ plane at a specific z. Eq. (13) can be decomposed into a scalar quasi-Schrodinger equation,

$$-\frac{1}{n^2}\frac{\partial^2}{\partial z^2}\Psi(z) + k^2{}_{circ}(z)\Psi(z) = k^2\Psi(z). \tag{14}$$

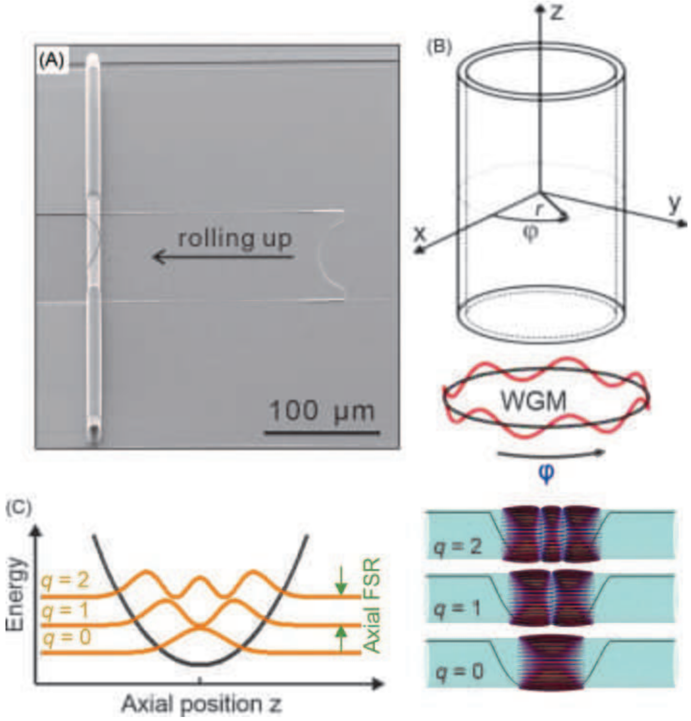

Fig. 4 (a) SEM image of a rolled-up microtube based on a U-shaped pattern design. (b) Schematic showing a 3D tubular cavity and its corresponding light WGM resonant trajectory in a cylindrical coordinate. (c) Numerically calculated mode energies upon a parabolic-shaped optical quasi-potential (upper) and the 3D mode profile (lower) for axial modes with mode numbers $q = 0$, 1, and 2. Panel (b): Modified with permission from (2019) *ACS Sensors* 4: 1476; Copyright © 2019 American Chemical Society.

The structured nanomembrane rolling length and the winding number along z-direction lead to a tailored distribution of $n(z)$ and $k_{circ}(z)$.

The Eq. (14) does not have a general solution. Notably, the equation form is highly analogous to a particle-wave in a one-dimensional potential. As an example, the middle part of a nanomembrane can be designed with a parabolic-shaped lobe (Fig. 4a). Such a parabolic quasipotential here leads to equidistant mode spacing. Fig. 4c shows the numerically and measured axial modes with almost equal mode spacing. The mechanism behind is highly similar to the bulgy structure in microbubbles for 3D optical resonances. The great flexibility of lobe design offers rich possibilities for manipulating axial modes, while the morphology of microbubbles is highly rigid and limited by the effect of surface tension.

Rolled-up microtubes as optically active and passive devices

Due to the good optical confinement, it is advantageous to incorporate a gain medium into the nanomembrane along with the rolling process so that microtubes can be easily turned into an efficient light source. Optically and electrically pumped microlasers have been demonstrated by structuring optically active quantum wells inside the multilayered nanomembrane. Other gain media, like defects in oxide, dye molecules, colloidal quantum dots, and perovskites, are all proved to be highly feasible in turning the cavity into an efficient single-mode laser or broadband light source. Fig. 5 shows the emission spectrum collected from a SiO/SiO_2 bilayer nanomembrane-based tube with a diameter of ~10 µm with a lobe design. Through optical pumping, the light emission due to natural defects in amorphous nanomembrane layers leads to coupling of photoluminescence (PL) light into multiple cavity modes with both different azimuthal and axial mode numbers. By tailoring the axial confinement, the typical Q factor can be improved from $\sim 10^2$–10^3 to $\sim 10^4$, which is attributed to the mitigated scattering and leakage loss along the axial dimension. The remaining factor preventing further pushing a higher Q factor is the intrinsic scattering loss by the two rolling edges.

Rolled-up microcavities can also work as optically passive microcavities. Probing the optical resonances can be accomplished by evanescent coupling. Tapered nanofibers (Fig. 6) and on-chip integrated waveguides (Fig. 7) serve as two main approaches for coupling with the modes. Here the light was launched from the input laser source and no intrinsic emitters are needed. By sweeping the input wavelength, resonant modes can be discerned as transmission dips.

In recent years, integrating the rolled-up microtube onto planar waveguiding devices is a significant step forward in transferring the microtube into functional integrated devices, as presented in Fig. 7. In particular, the whole process can be compatible with standard CMOS-compatible fabrications in silicon-based PICs. It is envisaged that microtubes serve as out-of-plane integrated

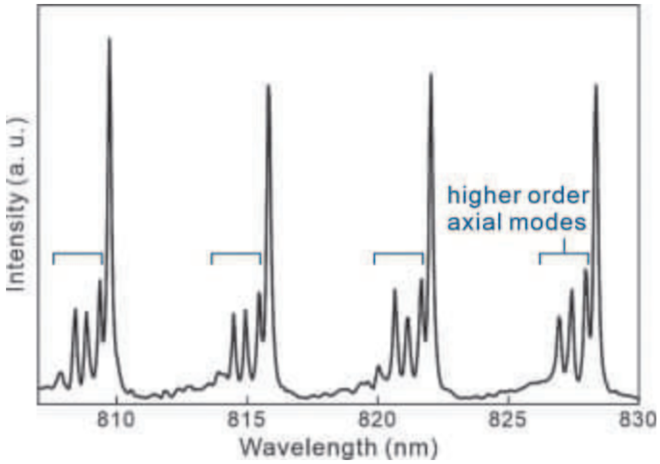

Fig. 5 Measured PL spectrum of a rolled-up microtube with higher order axial modes supported by axial confinement.

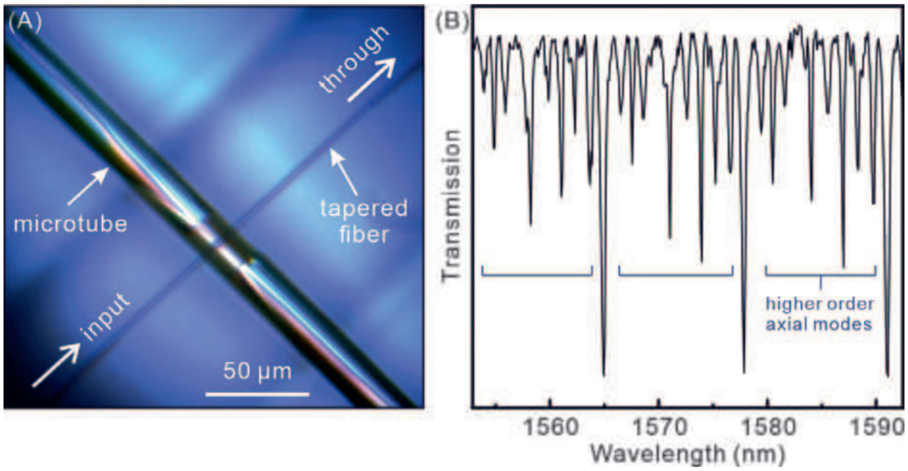

Fig. 6 (a) Optical image of a microtube cavity coupled with a tapered nanofiber. (b) Transmission spectrum measured by tapered fiber coupling with a microtube cavity. Higher order axial modes are revealed due to 3D optical confinement in the microtube cavity.

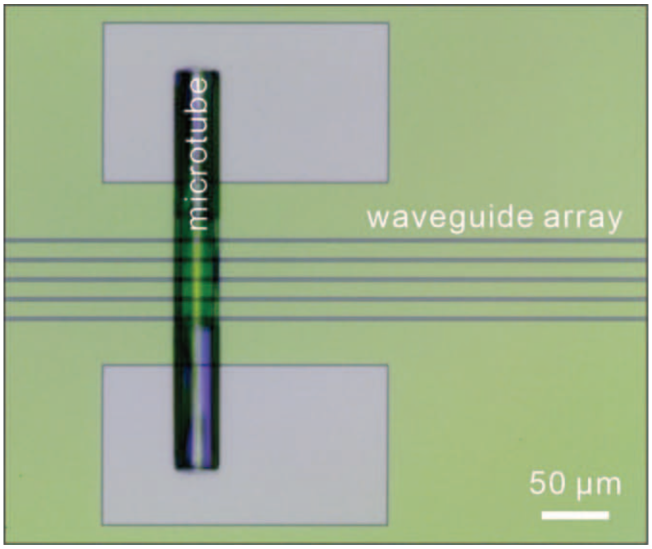

Fig. 7 Optical image showing a microtube directly integrated on top of the waveguide as a monolithic integration technology.

passive microrings as filters, switchers, and routers, or active devices like waveguide-coupled light sources. The 3D resonances in 3D tubular cavities reveal one natural advantage of simultaneous coupling with multiple independent waveguides or devices, while its studies in multiplexed and even 3D integration are in the inceptive stage.

Mode responses with weak external perturbations

For resonances confined in microstructures, evanescent fields act as a bridge between the inner and outer environments, which provide a way to tune the trapped light and sense the external perturbations. As to built-up WGMs in rolled-up microtubes, any polarizable (bio)molecules or nano-sized particles around the surface will interact with the evanescent field, and cause a slight change in the optical path length (OPL) as the product of the effective refractive index n_{eff} and the distance L. Similar to other WGM-based sensors, the change of resonance wavelength can be expressed as follow:

$$\frac{\boldsymbol{\Delta\lambda}_r}{\boldsymbol{\lambda}_r} = \frac{\boldsymbol{\Delta n}_{\text{eff}}}{\boldsymbol{n}_{\text{eff}}} + \frac{\boldsymbol{\Delta L}}{\boldsymbol{L}}. \tag{15}$$

The relative resonance mode shift can be described according to perturbation theory. It is correlated with the ratio of the interaction energy divided by the total energy:

$$\frac{\boldsymbol{\Delta\lambda}_r}{\boldsymbol{\lambda}_r} = \frac{\boldsymbol{\alpha}_{ex}|E(\boldsymbol{r}_i)|^2}{2\int \boldsymbol{\varepsilon}|E(\boldsymbol{r})|^2 \boldsymbol{dV}}, \tag{16}$$

where α_{ex} is the polarizability of the external object, r_i is the binding site and $E(r_i)$ is the local electric field at the tube surface interacting with the analyte.

Over the development of more than one decade, rolled-up optical microcavities have been widely investigated with the demonstrated capabilities of refractometer sensing, cell/microparticle detection, surface sensing, molecule dynamic binding, humidity sensing, gas sensing, etc. (Wang et al., 2019a). For two widely-known scenarios, namely detection of bulk liquid samples and absorbed molecules at the surface, two different terms of spectral sensitivity are defined:

$$S_{bulk} = \frac{\Delta\lambda}{\Delta n}; S_{surf} = \frac{\Delta\lambda}{\Delta\sigma} \tag{17}$$

where Δn is the refractive index change of the liquid sample, and $\Delta\sigma$ is the surface density of molecules homogeneously bonded to the tube surface.

Owing to the ultrathin cavity walls (~100–300 nm), strong evanescent fields at the tube surface facilitate the light-matter interactions and thus enable an ultra-sensitive detection process. For bulk liquid sensing, calibrated spectral sensitivity using a rolled-up microtube indicates a sensitivity S_{bulk} close to 1000 nm/RIU, which is roughly one order of magnitude higher than those in optical sensors with a planar design (e.g., microrings).

By virtue of the ultra-thin tube wall and intense evanescent field, rolled-up microtubes are particularly suitable for real-time detection of a surface molecular dynamic process. As an example, the dynamic evolution of nanoscale water layers on a tube surface of amorphous oxide can be probed by optical resonances (Yin et al., 2019). The interaction between absorbed molecules and the evanescent field leads to two remarkable effects (Fig. 8a). The first one is the resonant mode shift due to the increase/decrease of molecular later thickness. The estimated molecular layer thickness in such a surface sensing process can be extracted by perturbation theory, as presented in Fig. 8b. By spectrally resolving the tiny wavelength shift, the detection limit can be lower than monolayer water molecules. The second one is the resonant mode linewidth change due to the altered molecular landscape on the surface and affected scattering. Consequently, one can find out the transition point between two morphologies, planar film, and pyramid-like nanoclusters during the growth and desorption processes.

Mode splitting and non-Hermitian photonics

In addition to optical mode response upon tiny perturbations discussed in the previous section, a strong external perturbation may lead to a much higher coupling strength and very different phenomena. One well-known example is a photonic molecule consisting of two or multiple closely-packed identical optical cavities, generating prominent mode hybridization. Another example is a chain of coupled resonators, so-called coupled-resonator optical waveguides (CROWs), in which a tight-binding model can be applied for understanding the mode splitting.

For coupling in a two-mode system (Fig. 9a), this can be analyzed using a 2 × 2 Hamiltonian matrix

$$H = \begin{pmatrix} E_1 & V \\ W & E_2 \end{pmatrix} \tag{18}$$

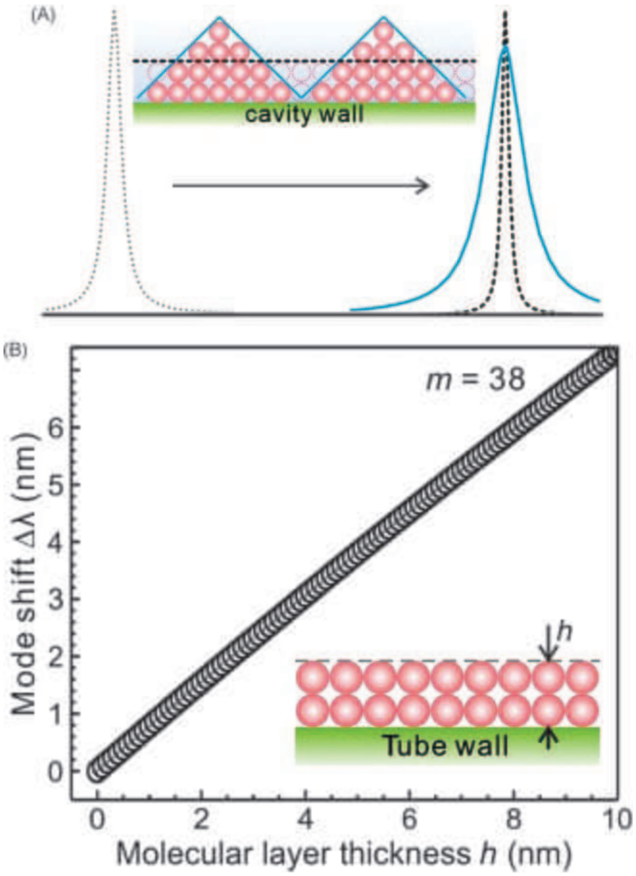

Fig. 8 (a) Schematic showing the resonance mode shift and mode broadening effects due to molecular binding. (b) Calculated mode shift as a function of molecular layer thickness using perturbation theory. Modified from Yin Y, Wang J, Wang X, Li S, Jorgensen MR, Ren J, Meng S, Ma L, Schmidt OG (2019) Water nanostructure formation on oxide probed in situ by optical resonances. Science Advances 5 (10) eaax6973. This work is licensed under a Creative Commons Attribution 4.0 International License, http://creativecommons.org/licenses/by/4.0/.

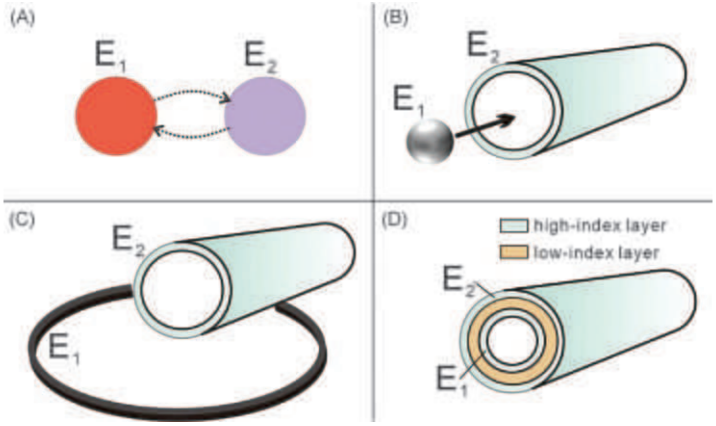

Fig. 9 Schematic of coupling in two-mode systems, including (a) a two-element photonic molecule. (b) a microtube with an embedded microsphere at the hollow core. (c) a microtube placed on top of a planar microring. (d) a microtube with two concentric high-index layers and a low-index spacing layer.

where V and W are the cross-coupling strengths. For general cases of external coupling via the continuum, $W \neq V^*$, the matrix H is non-Hermitian (Cao and Wiersig, 2015). The eigenenergies can be expressed as

$$E_{\pm} = \frac{E_1 + E_2}{2} \pm r \tag{19}$$

and

$$r = \sqrt{\frac{(E_1 - E_2)^2}{4} + VW}. \tag{20}$$

Here a simple case of internal coupling ($V = W^*$) is discussed. For the original resonant modes at two cavities that are spatially separated from each other, energy transfer is inefficient, and the eigenenergies are almost unperturbed. While the real part of original mode energies become aligned for resonant coupling $Re(E_1) = Re\,(E_2)$, one can adjust between two coupling regimes. For weak coupling $|V| < V_c$ with $V_c = |Im(E_1) - Im\,(E_2)|/2$, spectral crossing can be observed in the real part of eigenenergies. For strong coupling $|V| > V_c$, there is anticrossing for the real part of eigenenergies. As a function of the real-valued wavelength detuning parameter $\Delta = |Re(E_1) - Re\,(E_2)|$, the real part of eigenenergies come close but then repel each other. Usually, the two eigenvectors of the hybridized modes are non-degenerate. The exceptional point (EP) as a transition point between two regimes where the two or multiple eigenvalues coalesce together with their associated eigenvectors, can be reached by fine adjusting the coupling condition.

Here due to the strong evanescent field exposed outside and inside the tube wall, by transferring other WGM microcavities, it is feasible to create composite photonic molecules, e.g., microtube-microsphere (Fig. 9b), microtube-microring (Fig. 9c), and multilayered-microtube-microtube systems (Fig. 9d), etc. The coupling strength can be manipulated by adjusting the mode field overlap between two cavities. The flexibility of selectively exciting specific axial modes leads to controllable coupling strength between strong and weak coupling regimes. The interaction of strong coupling can be corroborated by the characterized spectral anticrossing.

Apart from coupled microcavities, discrete rolled-up microtubes with a deformed cavity shape are recognized as a promising platform for studying non-Hermitian photonics. The gradual increase of the radius at the cross-sectional view gives a spiral ring shape. The boundary can be defined as.

$$r(\varphi) = R\left(1 - \frac{\varepsilon}{2\pi}\varphi\right) \tag{21}$$

Where φ is the azimuthal angle that is determined by the winding number $\varphi = 2\pi w$, and the deformation parameter ε is the thickness of a single nanomembrane layer. At the starting and ending rolling positions, two nano-sized rolling edges are generated, which act like local nanoscatterers with both out-coupling of internal fields and internal coupling between CW and CCW lightwave components. For out-coupling of internal fields, the symmetry breaking turns the originally isotropic emission into deterministic bi-directional emission at two rolling edges toward the far-field (Wang et al., 2019b). The adjustable orientation (i.e., azimuthal position) of two rolling edges located at different axial positions leads to free manipulation of emission angles for multiple resonance modes. The emission can be switched between bi-directional emission and uni-directional emission regimes, which is attributed to the beating effect of CW and CCW lightwave components. The intrinsic mechanism is the de-tuned mode chirality, namely the ratio of CW and CCW lightwave components of the emission mode.

Therefore, the natural symmetry breaking in rolled-up microtubes offers a fascinating platform for studying non-Hermitian photonics. For internal coupling of CW and CCW propagating modes in a rolled-up microtube (Fig. 10), the 2 × 2 Hamiltonian matrix can be written as:

$$H = \begin{pmatrix} E_0 & 0 \\ 0 & E_0 \end{pmatrix} + \begin{pmatrix} \Gamma & A \\ B & \Gamma \end{pmatrix} \tag{22}$$

where E_0 is the original equal eigenenergy, Γ is the original scattering rate, $A(B)$ is the backscattering from the CW (CCW) to the CCW (CW) propagating mode. The strength of backscattering can be efficiently tuned by the azimuthal position of two rolling edges. Hence, the hybridization can be switched between strong and weak coupling regimes.

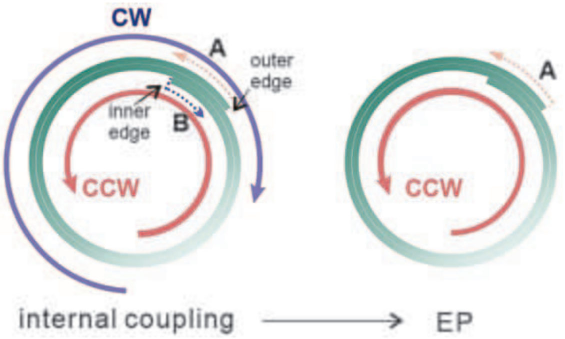

Fig. 10 Schematics showing mode internal coupling between CW and CCW components in a microtube with a spiral ring-shaped cross-section. The interaction is dependent on the two rolling edges induced unbalanced backscattering (left), and can be readily tuned to EP with a clear mode chirality (right).

For EP as a transition point between two regimes, $A = 0$ or $B = 0$, both the eigenenergies and eigenvectors collapse to a single one. Hence, $\psi_{\pm} \propto \begin{pmatrix} 1 \\ 0 \end{pmatrix}$, indicates the clear chirality of the EP. Engineering of rolling edges in either rolling process or post-fabrication modification is exploited for transforming the system to the EP, which is highly promising for cavity light-field associated applications, including unidirectional emission and chiral sensing.

Optoplasmonic hybridization in metal/dielectric rolled-up structures

Surface plasmons originate from collective electron oscillations at the interface between a noble metal (e.g., Au, Ag, Cu) surface and a dielectric under optical excitation. Surface plasmon modes, including both propagating surface plasmon polaritons (SPPs) or localized surface plasmon resonances (LSPRs), feature deep subwavelength confinement (ultra-small mode volume) and highly intense near-field effects enhancement. Typically, the huge absorption loss of metals severely reduces the Q factors of plasmonic modes. The combination of a dielectric rolled-up microtube and decorated plasmonic nanostructures lead to optoplasmonic hybridization. By combining a dielectric rolled-up microtube and decorated plasmonic nanostructures, optoplasmonic hybridization leads to compensation of metal loss by cavity-field build-up (Chen et al., 2021).

As illustrated in Fig. 11a, a simple model of a microtube (wall thickness of T) coated by a uniform metal thin film (thickness of t) is investigated by numerical simulations. For conventional hollow-core microcapillary cavities ($T/R >> 0.1$), the large T limits the mode overlapping and the hybridization effect is very weak. Due to the ultrathin cavity wall of microtube cavities ($T/R < 0.1$), the evanescent field largely facilitates the hybridization of metal nanostructures on the tube surface. The electric field of the TM-polarized mode (electric field direction perpendicular to the tube wall) is perpendicular to the metal-cavity interface, which matches the oscillation direction of the surface plasmons, resulting in the hybrid modes, stronger tunneling of lightwave out of the outer boundary suggests an intensified evanescent field (Fig. 11b and c). In contrast, TE mode results in a coupling mismatch between the cavity photons and the surface plasmons and hence suppressed lightwave tunneling at the top surface. In other words, the TE mode just experiences a "shielding" effect by the metal layer and hybridization is negligible (Fig. 11c). In practice, a straightforward and efficient mode hybridization scheme is to introduce a metal nanocap fabricated by physical vapor deposition on top of a rolled-up tube.

Another intriguing phenomenon is the hybridization between LSPRs generated from discrete metal nanostructures (e.g., particles, gaps) and WGMs in rolled-up microtubes. Due to the large mismatch of mode volumes, the coupling behavior is strongly dependent on the spatial overlapping condition. For LSPR-induced local hotspots overlapping with the antinodes of one WGM with a specific axial and azimuthal mode order, the hybridization effect is maximized. In practice, nanoparticles on the tube surface can be fabricated by localized annealing or transfer of chemically synthesized nanoparticles. A straightforward way of generating plasmonic nanogaps is to deposit a gold nanofilm onto the out rolling edge with a pre-defined orientation (Fig. 12). The rolling edge serves as a local step with the height equal to the thickness of a single nanomembrane layer (~tens of nm), hence enabling LSPRs around this nanogap and selective coupling with WGMs.

Spin-orbit coupling in rolled-up cavities

For rolled-up microtubes based on the circular nanomembrane pattern, the two sides are lifted from the substrate but the light might still be strongly trapped at the middle segment due to the relatively higher n_{eff}. In order to avoid strong leakage, the design of asymmetric cone-like optical microcavity is exploited. Interestingly, for a circular-shaped 2D nanomembrane geometry, a varied

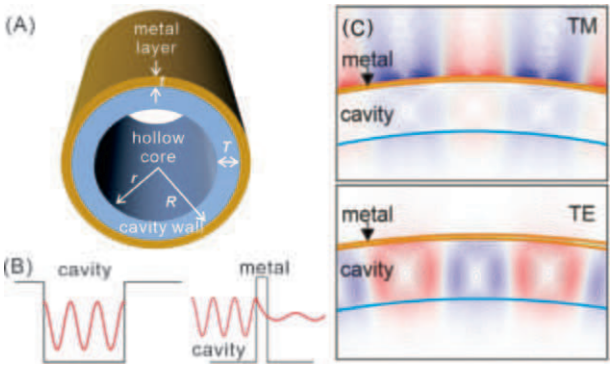

Fig. 11 (a) Schematic of a composite dielectric-metal microtube. (b) Schematic showing the original cavity mode in a pure dielectric tube and the hybridized mode with tunneling effect. (c) Simulated mode field profile showing the distinct behaviors for TM and TE modes. Modified with permission from (2017) *ACS Photonics* 4: 736; Copyright © 2017 American Chemical Society.

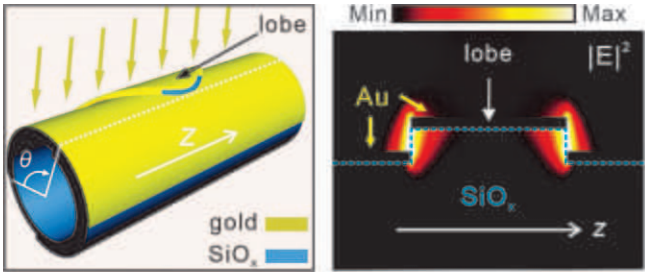

Fig. 12 A sketch of the gold thin film deposited onto a rolled-up microcavity with a nanostep due to the rolling edge (left panel) and simulated LSPRs supported by the nanogap (right panel). Modified with permission from (2016) *Physical Review Letters* 116: 253904; copyright © 2016 American Physical Society.

rolling axis during the rolling process leads to a cone-like optical microcavity. The radius of the microtube along the axial direction $R(z)$ is no longer uniform. The axial optical quasi-potential well is established around the larger-diameter-end part, so that optical resonances can be well confined at the lifted segment at the side instead of the middle segment. In particular, this symmetry breaking unleashes rich insights in photon spin-orbit coupling and generation of Berry phase (Ma et al., 2016).

Here the discussion starts with a common cylindrical ring-like microcavity, the light propagating trajectory is cyclic with a close path. The wave vector k experiences a trivial evolution when propagating along a closed loop. There is no possibility to generate the spin-orbit interactions, as optical angular momentum (OAM) along the tube axis is always orthogonal to the wave vector k (indicating the direction of the spin angular momentum (SAM)). In such a system, the optical polarization states are conserved at each resonance.

At the larger-diameter-end part of a cone-shaped tube, the variation in the number of windings leads to a resonant trajectory that slightly tilts out of the plane (Ma et al., 2016). Fermat's principle states that the trajectory light takes between two points is the trajectory that has the minimum OPL. In the larger diameter side of the tube, the variation of windings along the tube axis results in distinct thick and thin parts (with thickness T_1 and T_2, respectively). The lengths of the spiral cross sections are obtained by integrating the middle radius ($R_{\text{int}} + T_i/2$, $i = 1, 2$) of the thick part (with length L_1) and thin part (with length L_2) of the spiral tube wall. They are

$$L_1 = \int_0^{\theta_1} \left(R_{\text{int}} + \frac{T_1}{2}\right) d\theta \tag{23}$$

$$L_2 = \int_{\theta_1}^{2\pi} \left(R_{\text{int}} + \frac{T_2}{2}\right) d\theta \tag{24}$$

where θ_1 is determined by the portion in the length of the thick part ($\theta_1 = 2\pi L_1/(L_1 + L_2)$). Hence, Eqs. (23) and (24) must be solved in a self-consistent way.

Here, the trajectory of light is assumed to be within a flat plane which has a tilt angle β with respect to the horizontal plane ($\beta = 0°$) The OPL of the light trajectory can be calculated,

$$OPL = n^1_{avg} L_1(\beta) + n^2_{avg} L_2(\beta) \tag{25}$$

where $n^1{}_{avg}$ and $n^2{}_{avg}$ are the averaged refractive indices for the thick and thin part. The calculation result in Fig. 13 indicates the light should travel along a slightly inclined trajectory ($\beta \sim 2.5°$) in accordance with Fermat's principle. The tilt angle at the minimum of OPL depends on the tube geometry (i.e., the inhomogeneity of the tube wall).

Therefore, in an inhomogeneous conical ring, a tilted non-planar light trajectory is expected. The electric field vector rotates around the tube axis due to the cone shape of the microtube, generating an effective OAM along the tube axis. The tilted trajectories break the orthogonality between SAM and OAM, and enable spin-orbit coupling (Fig. 14).

The polarization state for light circulating in a cavity is determined by three factors: (i) the ordinary interference path, (ii) the spin-orbit coupling of photons, and (iii) the medium anisotropy. For an initial polarization state in terms of the Jones vector $a = \begin{pmatrix} a_+ \\ a_- \end{pmatrix}$ comprising of right $a_+ = \begin{pmatrix} a_+ \\ 0 \end{pmatrix}$ and left $a_- = \begin{pmatrix} a_- \\ 0 \end{pmatrix}$ circularly polarized basis, the final (time-invariant) polarization state can be calculated as follow:

$$a = \begin{pmatrix} a_+ \\ a_- \end{pmatrix} = \frac{1}{\sqrt{2}} exp \begin{pmatrix} -i\varphi & iC_A \\ iC_A & i\varphi \end{pmatrix} \begin{pmatrix} 1 \\ 1 \end{pmatrix} \tag{26}$$

where $\mp i\varphi$ denotes the acquired geometric phase, the non-diagonal element iC_A denotes the coupling and mutual conversion between two circular polarization components.

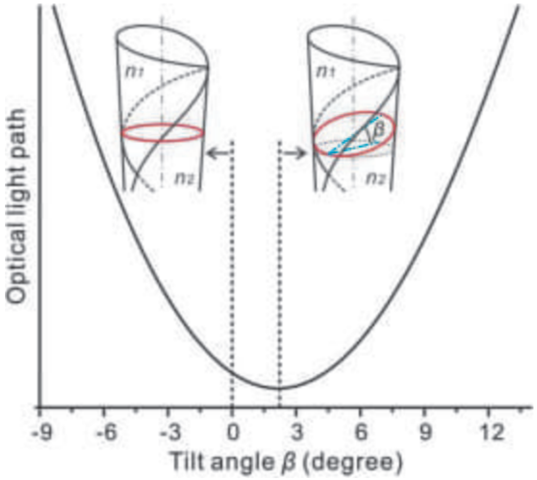

Fig. 13 Calculated OPL as a function of tilt angle β for an asymmetric microtubular cavity. Reproduced from Ma LB, Li SL, Fomin VM, Hentschel M, Gotte JB, Yin Y, Jorgensen MR, Schmidt OG (2016) Spin-orbit coupling of light in asymmetric microcavities. Nature Communications 7: 10983. This work is licensed under a Creative Commons Attribution 4.0 International License, http://creativecommons.org/licenses/by/4.0/.

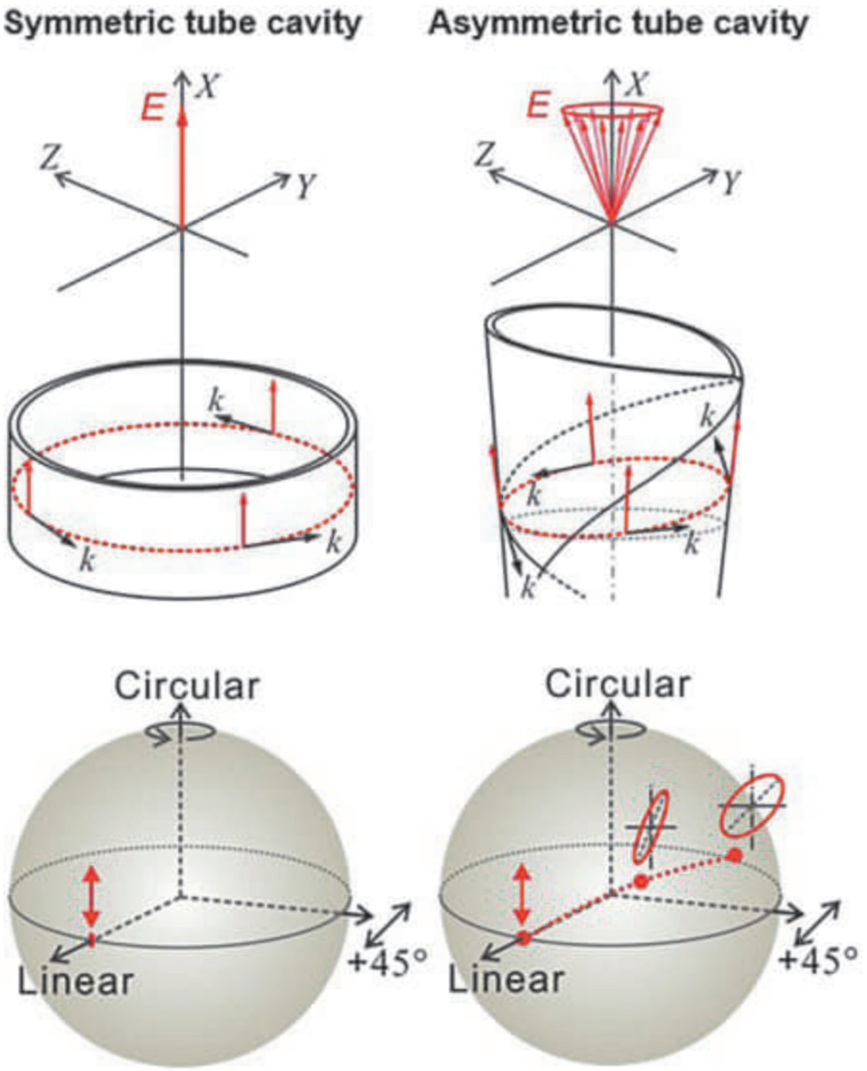

Fig. 14 Optical spin-orbit coupling in a cylindrical microring (left) and an asymmetric microtube (right), including the resonance trajectories and indicated wavevector *k* with respect to the electric field (top) and polarization evolution on the Poincare sphere (bottom). Reproduced from Reproduced from Ma LB, Li SL, Fomin VM, Hentschel M, Gotte JB, Yin Y, Jorgensen MR, Schmidt OG (2016) Spin-orbit coupling of light in asymmetric microcavities. Nature Communications 7: 10983. This work is licensed under a Creative Commons Attribution 4.0 International License, http://creativecommons.org/licenses/by/4.0/.

Here, the conversion of amplitudes between the two circular components leads to a change from a linear to an elliptical polarization, which is in contrast with the orthogonal mode pairs (TE and TM modes) in symmetric rolled-up microtubes and other WGM microcavities with rotational symmetry. Moreover, the geometric phase causes the orientation of the major axis of the polarization to tilt by an angle (equal to φ) with respect to the initial orientation.

Rolled-up metamaterials

For an anisotropic optical material, one of its components of the dielectric permittivity tensor has a different sign from the others. Two decades ago, researchers have investigated superlattices of different materials with thickness in the sub-wavelength scale for anisotropic materials that cannot be found naturally. Rolled-up nanotech serves as a unique and elegant route to generate alternating layers consisting of metal, dielectric, or semiconductors, and produce anisotropic metamaterials with tunable surface curvature.

Curved metamaterials can be readily obtained by rolling strained bilayer nanomembrane composing one layer of dielectric and one layer of metal, as illustrated in Fig. 11a. Based on the effective medium theory, the radial and tangential permittivity of the rolled-up hollow-core tubular structure can be written as:

$$\varepsilon_\theta = \frac{t_d\varepsilon_d + \mathrm{t}_m\varepsilon_m}{t_d + \mathrm{t}_m} \tag{27}$$

$$\varepsilon_r = \frac{\varepsilon_d\varepsilon_m(t_d + \mathrm{t}_m)}{t_d\varepsilon_m + \mathrm{t}_m\varepsilon_d} \tag{28}$$

where ε_d and ε_m are the permittivity of the dielectric and metal, respectively, and t_m and t_d are the ratios of thickness for metal and dielectric in a single nanomembrane bilayer ($t_m + t_d = 1$).

For TE polarization, the dispersion relation is

$$\frac{k_\theta^2}{\varepsilon_r} + \frac{k_r^2}{\varepsilon_\theta} = \frac{\omega^2}{c^2} = k^2. \tag{29}$$

For ε_θ and $\varepsilon_r > 0$, the dispersion curve is like an ellipse. While $\varepsilon_\theta < 0$ and $\varepsilon_r > 0$, it changes into a hyperbolic shape (see Fig. 15b).

The structure was implemented into the idea of creating a lens, i.e., hyperlens, which could image beyond the diffraction limit (Schwaiger et al., 2009). Due to the conservation of the angular momentum, subwavelength details can be magnified by a ratio $V = r_{outer}/r_{inner}$, where r_{outer} and r_{inner} are the outer and inner radius of the rolled-up tubular structure. Then the evanescent waves at the near-field can ve converted to propagating waves in the far-field for imaging using classical optics. Considering the dielectric layer as an optically active layer (e.g., quantum wells), the same concept has also been applied to adjusting responses of emitters, such as enhancement of Purcell factor and emission directionality.

Besides, the 3D hollow-core structure with great flexibility in dispersion engineering renders it a good candidate for metamaterial fiber optics. The hyperbolic dispersion allows waveguiding of surface plasmon polariton as a propagating mode inside the superlattice structure (Smith et al., 2010).

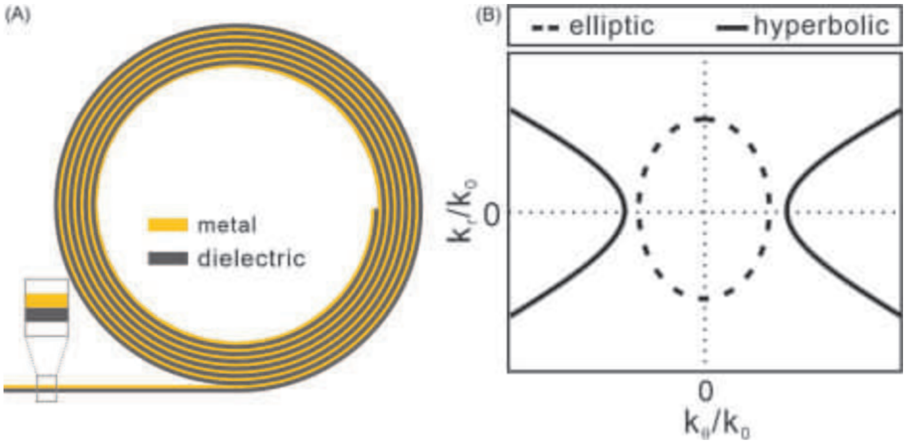

Fig. 15 (a) Schematic of rolled-up 3D radial superlattice consisting of bilayer nanomembranes. (b) The two typical dispersion relation curves.

Conclusion

In summary, we present an overview of rolled-up tubular architecture that is formed by strained nanomembranes. As a rapidly advancing nanotechnology with ~20 years of history, it stands out featuring various merits: (i) great flexibility in incorporating a plethora of materials covering dielectrics, semiconductors, and metals, (ii) feasibility of fine tailoring the scale, morphology and structural symmetry by novel 2D nanomembrane geometry design, (iii) good compatibility for on-chip standard mass-production technology on wafer levels for on-chip monolithic integration.

The unique optical properties of rolled-up nanomembrane structures have been discussed in multiple sections. The huge possibilities in microtubular structure bring fresh understanding into fundamentals like cavity QED, non-Hermitian photonics, anisotropic metamaterials, spin-orbit coupling, etc. (Fomin, 2021). Therefore, it is envisioned that the rolled-up nanomembrane-based devices and systems will bring about highly promising applications as light sources, detectors, sensors, and building blocks in on-chip photonic and optoelectronic systems.

References

Cao H and Wiersig J (2015) Dielectric microcavities: Model systems for wave chaos and non-Hermitian physics. *Reviews of Modern Physics* 87(1): 61–111.

Chen Y, Yin Y, Ma L, and Schmidt OG (2021) Recent progress on optoplasmonic whispering-gallery-mode microcavities. *Advanced Optical Materials* 9(12), 202100143.

Fomin VM (2021) *Self-rolled micro- and nanoarchitectures: effects of topology and geometry*. Berlin-Boston: De Gruyter 148.

Ma LB, Li SL, Fomin VM, Hentschel M, Gotte JB, Yin Y, Jorgensen MR, and Schmidt OG (2016) Spin-orbit coupling of light in asymmetric microcavities. *Nature Communications* 7: 10983.

Prinz VY, Seleznev VA, Gutakovsky AK, Chehovskiy AV, Preobrazhenskii VV, Putyato MA, and Gavrilova TA (2000) Free-standing and overgrown InGaAs/GaAs nanotubes, nanohelices and their arrays. *Physica E: Low-dimensional Systems and Nanostructures* 6(1): 828–831.

Schmidt OG and Eberl K (2001) Thin solid films roll up into nanotubes. *Nature* 410(6825): 168.

Schwaiger S, Broll M, Krohn A, Stemmann A, Heyn C, Stark Y, Stickler D, Heitmann D, and Mendach S (2009) Rolled-up three-dimensional metamaterials with a tunable plasma frequency in the visible regime. *Physical Review Letters* 102(16), 163903.

Smith EJ, Liu Z, Mei Y, and Schmidt OG (2010) Combined surface plasmon and classical waveguiding through metamaterial fiber design. *Nano Letters* 10(1): 1–5.

Strelow C, Schultz CM, Rehberg H, Sauer M, Welsch H, Stemmann A, Heyn C, Heitmann D, and Kipp T (2012) Light confinement and mode splitting in rolled-up semiconductor microtube bottle resonators. *Physical Review B* 85(15), 155329.

Wang J, Karnaushenko D, Medina-Sanchez M, Yin Y, Ma L, and Schmidt OG (2019a) Three-dimensional microtubular devices for lab-on-a-chip sensing applications. *ACS Sensors* 4(6): 1476–1496.

Wang J, Yin Y, Yang Y-D, Hao Q, Tang M, Wang X, Saggau CN, Karnaushenko D, Yan X, Huang Y-Z, Ma L, and Schmidt OG (2019b) Deterministic yet flexible directional light emission from spiral nanomembrane cavities. *ACS Photonics* 6(10): 2537–2544.

Xu C, Wu X, Huang G, and Mei Y (2019) Rolled-up nanotechnology: Materials issue and geometry capability. *Advanced Materials Technologies* 4(1): 1800486.

Yin Y, Wang J, Wang X, Li S, Jorgensen MR, Ren J, Meng S, Ma L, and Schmidt OG (2019) Water nanostructure formation on oxide probed in situ by optical resonances. *Science Advances* 5(10): eaax6973.

Nanostructured superconductors

Wolfgang Lang, Faculty of Physics, University of Vienna, Vienna, Austria

© 2024 Elsevier Ltd. All rights reserved.

Introduction **368**
Nanofabrication techniques **369**
Lithography and ion-beam milling 369
Electromigration 369
Templating strategies 370
Ion-induced nanostructures 370
Masked ion irradiation of thin films 371
Focused ion beam modification of thin films 372
Properties of nanopatterned superconductors **373**
Vortex pinning arrays 373
Complex pinning landscapes 374
Vortex ratchets and flux diodes 375
Guided vortex motion 376
Josephson junctions 376
Conclusion **377**
Acknowledgments **377**
References **377**

Abstract

The relevant length scales for superconductivity are of the order of nanometers. By confining the superconducting condensate to such dimensions, many physical properties change substantially, and novel phenomena emerge, which are absent in the pristine material. We discuss various methods of creating artificial nanostructures by top-down approaches in metallic and copper-oxide superconductors and their applications. Such nanostructures can be used to control magnetic flux quanta in superconductors, anchoring them to engineered defects to avoid dissipation, guiding their motion, or building artificial flux-quanta arrangements. Nanopatterned superconductors are essential for creating model systems for basic research and enable building almost dissipationless and ultrafast electronic devices and highly sensitive sensors.

Key points

- The properties of a superconductor substantially change when the superconducting condensate is confined to the nanoscale.
- Methods of nanopatterning superconductors are reviewed.
- Focused helium ion beam irradiation provides a novel technique to fabricate nanostructures in copper-oxide superconductors.
- Vortex pinning landscapes, guided vortex motion, vortex ratchets, and superconducting diodes are discussed, and their application as elements of superconducting low-dissipation electronic circuits are outlined.
- The fabrication of Josephson junctions by focused ion beam irradiation and their properties are discussed.

Introduction

Superconductivity originates from the long-range coherence of bosonic quantum particles that condense into a lower energy state and is thus called a macroscopic quantum phenomenon. One might wonder what could be the advantage of confining the superconducting condensate to the nanoscale? The answer lies in two essential characteristic lengths that characterize superconductivity. The Ginzburg-Landau coherence length ξ determines the distance over which the density of superconducting carriers can change from its peak value to zero and vice versa. The size of ξ can vary from several tens of nm in metallic superconductors down to about 1 nm in the copper-oxide superconductors with high critical temperature T_c (HTS). The other length scale is set by the London penetration depth λ which describes the decay of an external magnetic field from the edge of a superconductor toward its interior, from which it is ultimately expelled.

The ratio between these two lengths bifurcates between two types of superconductors. While so-called type-I superconductors expel a magnetic field completely (Meissner effect), the more abundant and more widely used type-II superconductors let the magnetic field enter in quantized portions of the magnetic flux $\Phi_0 = h/(2e)$, where Φ_0 is termed the flux quantum, h and e are

https://doi.org/10.1016/B978-0-323-90800-9.00014-7

Planck's constant and the elementary charge, respectively. These flux quanta in a superconductor are called fluxons or vortices; the latter name results from the fact that circular supercurrents in the surrounding material stabilize these flux quanta.

Coming back to the two characteristic lengths, it turns out that the so-called Ginzburg-Landau parameter, the ratio $\kappa = \lambda/\xi$, determines the type of a superconductor, with $\kappa \geq 1/\sqrt{2}$ leading to type-II superconductivity. Another important observation is the temperature dependence of $\xi(T) = \xi(0)(1 - T/T_c)^{-1/2}$, which implies a diverging enhancement of $\xi(T)$ from its minimal value $\xi(0)$ at $T = 0$ when T_c is approached. Ginzburg-Landau theory also predicts the same temperature dependence for $\lambda(T)$ and, thus, κ is temperature-independent near T_c.

In what follows, we will mainly discuss thin films of superconductors. In many situations, these can be considered three-dimensional (3D) materials, as long as the coherence length perpendicular to the surface is smaller than the film's thickness t_z. However, from the temperature dependence of $\xi(T)$ it is evident that close to T_c a transition to a two-dimensional (2D) behavior in very thin films might occur when $\xi(T) > t_z$.

Another issue becomes important for film thicknesses $t_z \lesssim \lambda(T)$. Then $\lambda(T)$ has to be replaced by an effective penetration depth (also called Pearl length) $\Lambda(T) = 2\lambda(T)^2/t_z$. Since $\lambda(T)$ (and $\Lambda(T)$, respectively) control the range of interactions between vortices, the relevant length scales can become macroscopic in very thin films. In any case, vortices separated by distances smaller than the (effective) penetration depth will behave as collective ensembles, occasionally termed 'vortex matter'. Note that in a magnetic field applied perpendicular to the surface of a thin superconductor, large demagnetization effects lead to a complete penetration of the magnetic flux and suppression of the Meissner screening.

Vortex physics is a fascinating and complex field of research, and only an introductory glimpse can be presented here to underpin the key issues related to nanostructured superconductors. For deeper insights, see the chapter by Brandt in this Encyclopedia and the review by Blatter et al. (1994).

Confining the superconducting condensate to the range of the length scales introduced above inevitably means that superconductors need to be structured to dimensions of a few μm and, primarily, to the nanoscale. The use of thin films and lateral nanostructuring allows one to substantially change many physical properties and create novel phenomena, absent in the pristine material. For example, the controlled manipulation of vortices by anchoring them to engineered defects, guiding their motion, or building artificial vortex matter plays a significant role. Engineered vortex systems are essential for creating model systems for basic research and enable to build almost dissipationless and ultrafast electronic devices based on vortex manipulation, the so-called fluxonics.

Taking advantage of Josephson effects in weakly-coupled superconductors requires barriers of only a few nm in width. The Josephson junction is the central building block for sensitive magnetic field sensors, rapid single flux quantum logic circuits, THz frequency generators, and, last but not least, superconducting quantum computing.

This chapter focuses on the nanostructuring of HTS that offer easy operation using cryocoolers or liquid nitrogen. However, the brittle nature and complex crystallographic structures of HTS make the fabrication of nanopatterns a problematic endeavor and call for new techniques. Many of these concepts have been developed since the first edition of this Encyclopedia. For a detailed overview of nanostructured metallic superconductors, the reader is referred to the book of Moshchalkov and Fritzsche (2011).

Nanofabrication techniques

Lithography and ion-beam milling

The standard techniques for nanopatterning of superconductor structures focus on thin-film processing. One of the most commonly used methods is photo- or electron-beam lithography, which is well known for the fabrication of semiconductor devices. After growing thin films on a suitable substrate and depositing a photoresist layer on top, the planar structures are defined by illuminating the photoresist through a mask or directly processing it with an electron-beam (e-beam) writer. While the wavelength of the light limits the former method, e-beam lithography can provide resolutions at the order of 10 nm but is a slow sequential technique.

Unfortunately, the subsequent etching processes of both photoresist and the superconductor result in significant degradation of resolution. Another issue is that etching artifacts, such as underetching below the photoresist layer, progressively limit resolution as the thickness of the superconducting film increases. Thus, patterns in metallic superconductors are generally reported with lateral structures on the order of 100 nm. For example, a vibrant application is the fabrication of single photon detectors (Gol'tsman et al., 2001) that commonly consist of few-nm thick NbN or NbTiN films patterned to long stripes, folded into meandering patterns to increase the active area (Hadfield, 2009). The above limitations are of particular importance for the reproducible fabrication of constriction-type Josephson junctions (Dayem bridges), for which a resolution of a few nanometers would be required.

For HTS, the situation is even more complicated because they are brittle and have a complex crystallographic structure. Lithographic techniques combined with etching steps have been successfully applied to create patterns with several hundred nanometers features sizes (Castellanos et al., 1997). The combination of e-beam lithography followed by argon-ion milling allowed the production of patterns with a minimum line width of 25 nm (Sochnikov et al., 2010). Since this is still too large to fabricate Josephson junctions directly, alternative fabrication methods, such as growing the thin film over a step-edge in the substrate, must been employed (Tafuri and Kirtley, 2005).

Electromigration

An elegant way to further narrow the cross-section of superconductor bridges fabricated by conventional lithography is based on electromigration. This usually undesirable process, combining a local temperature rise and a high electric field, leads to a displacement of atoms from their original crystal-lattice positions. Closed-loop controlled electromigration, however, can avoid adverse effects. With the gradual reduction of the cross-section of aluminum constrictions to $\lesssim 150$ nm^2, a geometry-induced transition from thermally-assisted phase slips to quantum phase slips has been reported (Baumans et al., 2016). Other applications of electromigration include the tuning of Nb superconducting quantum interference devices (SQUIDs) (Collienne et al., 2021) and the controlled migration of oxygen atoms in $YBa_2Cu_3O_7$ (YBCO) bridges (Marinković et al., 2020).

Templating strategies

In bottom-up fabrication methods, the nanostructures are already predefined during the growth process. Since patterning the substrate material is often less challenging, several methods have been developed that take advantage of the controlled imperfection in the substrate to introduce the desired structures into the superconductor. One example is the self-organized growth of highly ordered porous alumina, a membrane-like system consisting of triangular arrays of pores. A superconducting Nb thin film deposited directly on the alumina template with a pore spacing of 50 nm acts as a nanoscale array for vortex pinning (Vinckx et al., 2007).

Nanowires of metallic superconductors less than 10 nm in diameter and up to 1 μm in length can be fabricated by 'molecular templating' (Bezryadin et al., 2000). After a freestanding carbon nanotube is placed over a narrow and deep slit in a Si substrate, a superconductor such as MoGe is sputtered onto the entire arrangement. The resulting layer consists of the electrodes connected by the nanowire, which are all made of the same material and thus have excellent contact resistances. Subsequently, the properties of the nanowire can be further fine-tuned in a transmission electron microscope or by applying voltage pulses.

Another technique uses vicinally cut substrates with a periodic nanoscale step structure of the clean substrate surface. YBCO films grow on such substrates in a roof-tile-like arrangement of the copper-oxide layers by self-assembly. The morphology and microstructure of such vicinal films strongly depend on the miscut angle of the $SrTiO_3$ substrate and the thickness of the on-top grown YBCO (Haage et al., 1997; Pedarnig et al., 2002), $Bi_2Sr_2CaCu_2O_8$ (Durrell et al., 2000), and $Hg_{1-x}Re_xBa_2CaCu_2O_{6+\delta}$ (Re: rare earth element) (Yun et al., 2000) films. The linear arrangement of dislocations resulting from the step structure in YBCO leads to an exceptionally high critical current density. Moreover, symmetry breaking in such vicinal films also allows experimental access to out-of-plane properties of HTS, such as resistivity, Hall effect (Heine et al., 2021), photoconductivity (Markowitsch et al., 1997), and channeling of vortex strings along the *ab*-plane (Berghuis et al., 1997).

Strategies based on substrate modification are very versatile. Nanostructures can be deposited on the substrate prior to the deposition of a superconductor film to modify its structural and superconducting properties. A variety of interactions can be tailored with thickness modulation of the superconductor by insulating dots, proximity effects caused by metallic dots, or magnetic interactions with ferromagnetic dot arrays that interact with the vortex lattice in the superconductor (Martin et al., 1997).

Ion-induced nanostructures

The previously discussed patterning techniques have several disadvantages, especially when applied to HTS. First, all methods that remove material result in open side faces of the HTS, allowing the relatively mobile oxygen ions to escape from the crystallographic framework and thus lowering the oxygen content. In most cases, this leads to a degradation of the superconducting properties. On the other hand, the brittle nature of HTS limits the stability of the remaining material structures, making it challenging to achieve sub-μm resolution.

Irradiation of HTS with electrons, protons, and light or heavy ions provides an alternative route to modify the properties of HTS while leaving the surface of the material nearly intact. Before going into further details, a brief account of the limiting parameters is in order. A first consideration concerns the penetration range of irradiation. Only neutrons and high-energy ions can penetrate deeply enough into bulk materials (Weber, 2003). Irradiation with swift heavy ions produces columnar tracks of a few nm diameters in the HTS. The crystallographic structure is destroyed, and a non-superconducting amorphous channel remains (Civale, 1997). Such a columnar defect with a diameter similar to the in-plane coherence length is ideal for blocking the motion of vortices. This enhanced pinning of vortices leads to a higher critical current. These disordered arrangements of line-shaped pinning centers are not only very important for applications but have also triggered the theoretical and experimental study of novel phases of vortex matter, such as the vortex (Fisher et al., 1991) and Bose (Nelson and Vinokur, 1993) glasses.

A more subtle method of tailoring superconducting properties is to create point defects while leaving the crystallographic framework intact. They can be produced by irradiation with electrons, protons, or light ions. Point defects are imperfections at the atomic level that occur when the energy transfer from the incident particle to the crystal is on the order of the energy required to form vacancies. At energies up to a few MeV, the incident particle collides with and displaces a nucleus, eventually creating a collisional cascade that propagates through the material. The tradeoff in the choice of parameters stems from the fact that lighter particles, such as electrons, require extremely high fluence to achieve any appreciable change of the superconducting properties. In contrast, heavier particles have limited penetration depths and more significant scattering of the collisional cascades (Lang and Pedarnig, 2010).

A suitable candidate for the controlled fabrication of point defects in thin films of the most commonly used HTS, YBCO, are He^+ ions of moderate energy. The superconducting properties are tailored by displacing mainly oxygen atoms, which are more loosely bound than the other atomic species, with binding energies of 1… 2 eV for the chain atoms O1 and about 8 eV for the O2/O3 atoms in the CuO_2 planes, as shown in Fig. 1a. Their displacement creates Frenkel defects at interstitial positions (Gray et al., 2022) outlined in Fig. 1b, leading to a controllable decrease (Sefrioui et al., 2001) or complete suppression of T_c (Lang and Pedarnig, 2010), depending on the ion fluence. Since the charge transfer from the displaced atoms is still operational, Frenkel defects do not lead to a significant change in the carrier density.

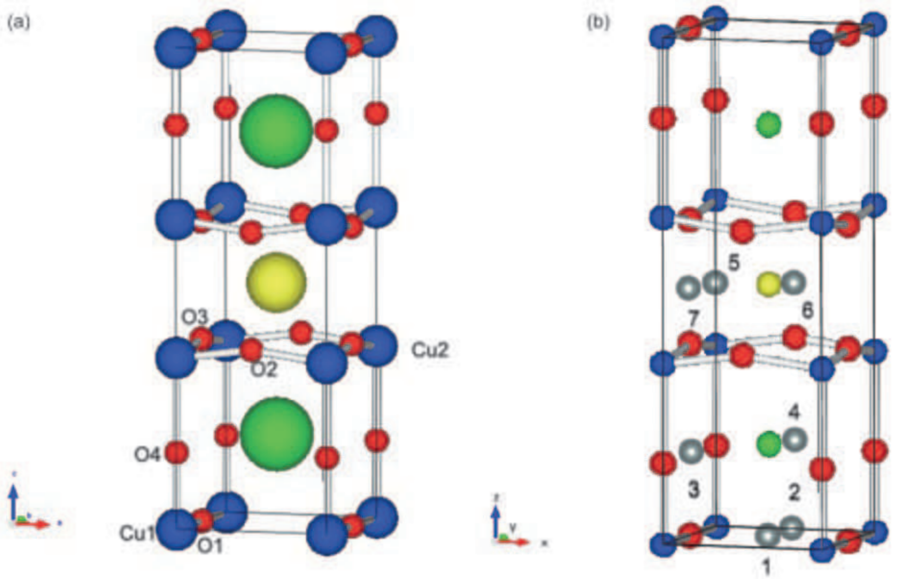

Fig. 1 (a) The crystal structure of the copper-oxide superconductor $YBa_2Cu_3O_7$. Red, blue, green, and yellow spheres correspond to oxygen, copper, barium, and yttrium. (b) The gray spheres illustrate possible interstitial sites. Figures reproduced from Gray RL, Rushton MJD, Murphy ST (2022) Molecular dynamics simulations of radiation damage in $YBa_2Cu_3O_7$. *Superconductor Science and Technology* **35**: 035010. doi:10.1088/1361-6668/ac47dc under the Creative Commons Attribution 4.0 licence.

Another process is responsible for reducing T_c: In classical superconductors with s-wave symmetry of the superconducting gap, the introduction of point defects has little effect on T_c and is even used technically to improve the critical current. In contrast, the anisotropic *d*-wave nature of the gap in HTS makes it susceptible to tiny defects that reduce not only the normal-state conductivity and carrier mobility but also T_c (Lang and Pedarnig, 2010).

However, a uniform statistical distribution of point defects is not very helpful. By focusing the ion beam before it hits the surface of the HTS film, one can create nearly cylindrical domains populated with point defects. These columnar defects (CDs) form a landscape where superconductivity is locally suppressed. Lateral modulation of ion fluence can be achieved mainly by two different methods outlined in Fig. 2.

Masked ion irradiation of thin films

An extensive array of multiple ion beams can be created by masking a wide-field collinear ion beam, which is commonly available with ion implanters, as schematically shown in Fig. 2a. An HTS film, thinner than the ion's penetration depth, is fabricated on a suitable substrate. The mask protects selected areas of the HTS film from irradiation and exposes the other sample parts to

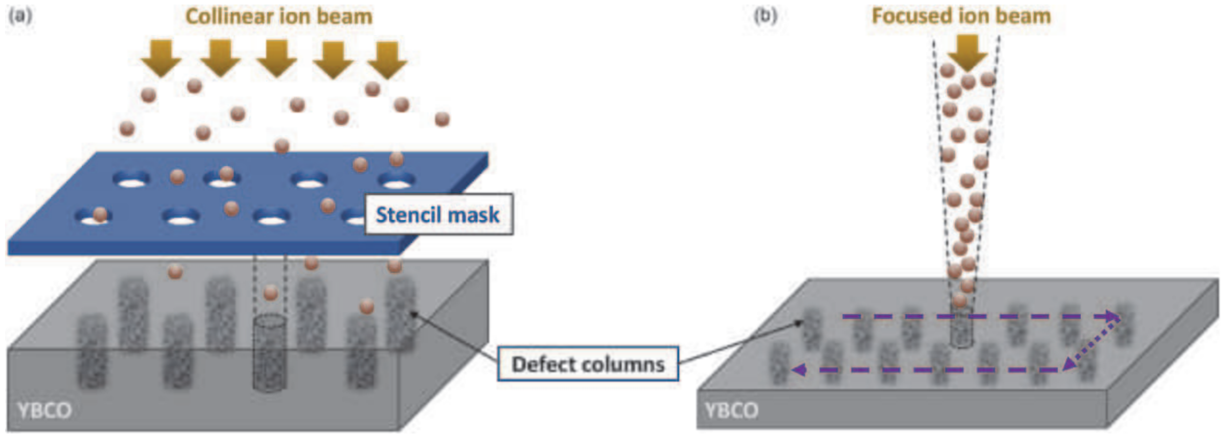

Fig. 2 Two different methods for patterning a YBCO film by He^+ ion irradiation: (a) Ion beam patterning through a stencil mask produces a large number of columnar defects in a single step. The dark areas indicate the defect-rich, non-superconducting nanocylinders. (b) Irradiation with a slightly defocused beam from a helium-ion microscope produces tailored columnar defect patterns by scanning the beam across the sample surface. Adapted from Aichner B, Mletschnig KL, Müller B, Karrer M, Dosmailov M, Pedarnig JD, Kleiner R, Koelle D, Lang W (2020) Angular magnetic-field dependence of vortex matching in pinning lattices fabricated by focused or masked helium ion beam irradiation of superconducting $YBa_2Cu_3O_{7-\delta}$ thin films. *Low Temperature Physics* 46: 331–337. https://doi.org/10.1063/10.0000863. Fiz. Nizk. Temp. 46: 402–409.

irradiation. While the former remain superconducting, the T_c of the latter is reduced or suppressed depending on the applied ion energy and fluence. Notably, the collision cascades widen due to the straggling of ion trajectories within the HTS so that the mask patterns become blurred with increasing depth. As a result, the lateral resolution is typically limited to about 10 nm, as indicated by simulations with 75 keV He^+ irradiation (Haag et al., 2014).

Different techniques were used to create the mask. Either a photoresist layer was deposited on the HTS and processed with standard UV (Kahlmann et al., 1998), e-beam, (Swiecicki et al., 2012), or focused ion beam (Katz et al., 2000) lithography, then etched and used as the mask, or a metal layer was deposited directly on the YBCO film and then patterned by ion beam milling (Kang et al., 2002). Alternatively, a Si stencil mask is fabricated and mounted at a small distance from the superconductor film (Lang et al., 2006). This method allows the mask to be reused, does not require the multiple processing steps associated with photoresist, and avoids potential surface degradation.

The main advantage of masking techniques is the parallel processing of many structures. Shortcomings are the resolution limitations resulting from the preparation of the mask, and in the case of freestanding masks, there are geometrical limitations, e.g., disconnected blocking elements are not possible.

Focused ion beam modification of thin films

In contrast to conventional focused ion beam (FIB) machines, which use Ga to ablate the material, devices for focused ion irradiation with light ions have only recently become available. The helium ion microscope (HIM) (Ward et al., 2006) combines scanning focused ion beam sources for He^+ and Ne^+ ions and imaging via secondary electron detection. The HIM consists of a gas-field ion source that emits ions from a tip containing only three atoms (the trimer), electrostatic ion optics to focus and trim the beam, and a deflection system that moves the beam across the sample stage with optional blanking (Fig. 3). Because of the high source brightness of the trimer and the short de Broglie wavelength of He^+ ions, an image resolution better than 0.5 nm and an unprecedented depth of focus can be achieved (Hlawacek and Gölzhäuser, 2016).

Using a He or Ne beam instead of the conventional Ga—FIB technique avoids contamination of the target material by Ga ions and achieves higher lateral resolution. For example, nanopores as small as 1.3 nm in diameter have been fabricated in 1 nm-thick carbon nanomembranes (Emmrich et al., 2016). As initial applications in HTS, thin barriers of insulating material, written across prepatterned YBCO microbridges with the focused ion beam, form Josephson junctions (Cybart et al., 2015), and ultradense arrays of CDs build a complex pinning landscape for vortices (Aichner et al., 2019). At the time of writing, hexagonal arrays of CDs with spacings as small as 20 nm had been fabricated in YBCO thin films (Karrer et al., 2022).

The use of He—FIB relies on the weak bonding of oxygen in HTS and cannot be employed in the same way for other superconductors. However, a focused Ne beam offers a compromise between Ga—FIB and He—FIB for direct milling of metallic

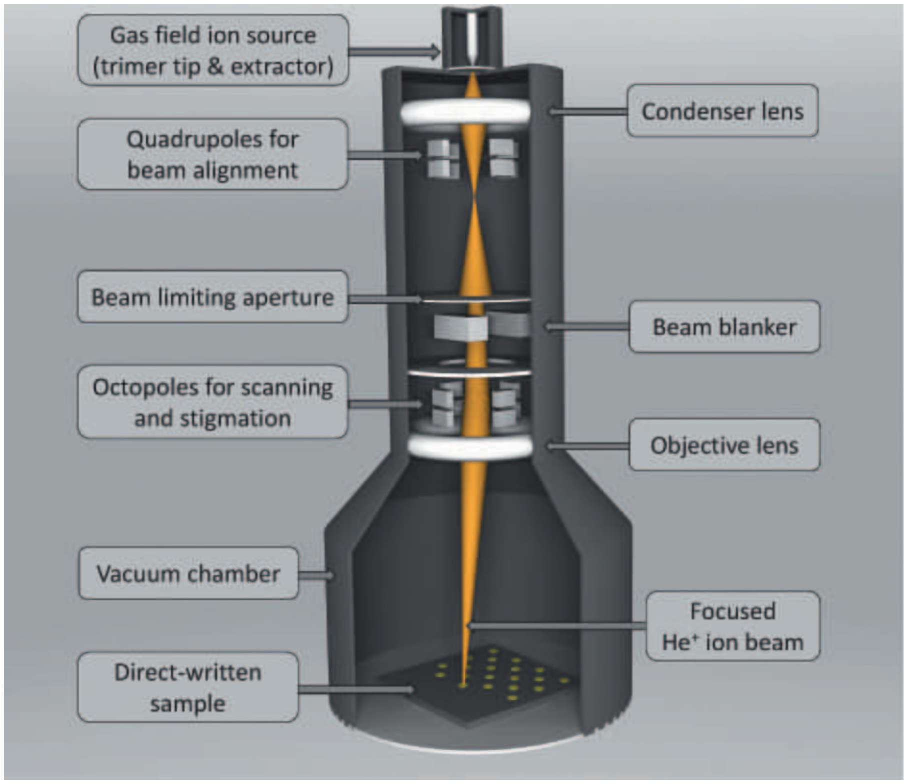

Fig. 3 Schematic drawing of the helium ion microscope used for direct-writing patterns of locally suppressed superconductivity. (Courtesy of Bernd Aichner, University of Vienna).

superconductors. This has been demonstrated, for example, for patterning constrictions in NbN films to form nanowires (Burnett et al., 2017).

Other techniques for growing superconductor nanostructures using focused electron and ion beams are discussed in the chapter by Córdoba, and the properties of superconducting microtubes and nanohelices are examined by Fomin (2020).

Properties of nanopatterned superconductors

Nanostructuring of superconductors enables selective tailoring of the superconducting condensate on length scales smaller than the London penetration depth, mainly by creating lateral structures. Such patterns allow controlled interaction of vortices, their manipulation, as well as tunneling effects between two superconducting condensates weakly coupled by a small non-superconducting interlayer. Some of these applications are described below.

Vortex pinning arrays

Lateral nanostructuring of superconducting films with regular arrays of CDs allows the creation of artificial pinning landscapes that lead to commensurability effects with the flux line lattice. This occurs at the so-called matching fields $B_k = k\Phi_0/A$, where k is an integer number of pinning sites (or a rational number of vortices) in the unit cell of the pinning array of area A. For square lattices $A = a^2$ and for hexagonal patterns $A = \sqrt{3}a^2/2$ with a the nearest neighbor spacing of the CDs.

The number of flux quanta that can be trapped inside a cylindrical hole or in a non-superconducting pinning site depends on its diameter r_p and the coherence length $\xi(T)$ of the superconductor. For anisotropic layered materials such as HTS, the in-plane coherence length $\xi_{ab}(T)$ is relevant. Once all pinning sites are filled by one flux quantum, the formation of multiquanta vortices becomes energetically favorable when r_p exceeds a certain critical radius (Buzdin, 1993). The saturation number of trapped flux quanta can be estimated by $n_S \simeq r_p/2\xi(T)$ (Buzdin and Feinberg, 1996).

A special situation arises for blind holes in a superconductor, i.e., holes that do not entirely penetrate the material. The remaining superconducting bottom layer carries the screening currents of individual vortices trapped in the blind hole. Although several flux quanta are trapped in the blind hole, individual vortices can still be made visible (Bezryadin et al., 1996).

Multiquanta vortices are a phenomenon that occurs only in nanostructured superconductors and does not exist in pure homogeneous superconductors. Conversely, when small pinning sites cannot accommodate the total flux, the excess flux is forced to enter the material via interstitial vortices. The various commensurability effects in a pinning landscape for different magnetic fields applied orthogonally to the film surface are illustrated in Fig. 4, which is based on experimental results by Lorentz microscopy of vortices in a Pb film patterned with a square array of tiny blind holes (Harada et al., 1996). For filling factors $k < 1$, the flux quanta are arranged in a superlattice with respect to the pinning array; for $k = 1$, each hole is filled with precisely one flux quantum, and for $k = 2$, the excess flux is taken up by interstitial vortices.

The commensurability effects manifest themselves in various physical parameters, such as steps in the magnetization loops and peaks in the critical current as indicators of enhanced pinning forces. Minima in the resistance versus magnetic field curves point to commensurability effects of moving vortex ensembles.

Fig. 5 shows an example of the dramatic change of the magnetization loop $M(H)$ after perforating a 60 nm-thick WGe film with a square array of holes 340 nm in diameter and 1 μm apart (Moshchalkov et al., 1996). The area of the $M(H)$ loop in the perforated film is massively increased due to the holes, which act as artificial pinning centers. Distinct cusps in the loop appear at the matching fields $B_k = k \times 2.07$ mT, indicating the trapping of multiquanta vortices. The staircase-like reduction of $M(H)$ with increasing field

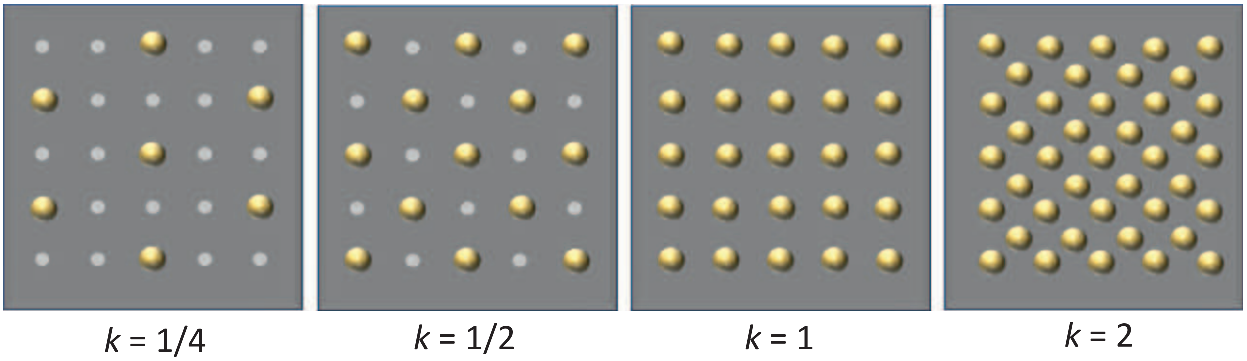

Fig. 4 Schematic representation of different commensurability patterns observed by Lorentz microscopy. Light gray circles represent holes in the superconducting film, and yellow bullets represent the magnetic flux quanta observed by a deflection of the electron beam. After Harada K, Kamimura O, Kasai H, Matsuda T, Tonomura A, Moshchalkov VV (1996) Direct observation of vortex dynamics in superconducting films with regular arrays of defects. *Science* 274: 1167–1170. https://doi.org/10.1126/science.274.5290.1167.

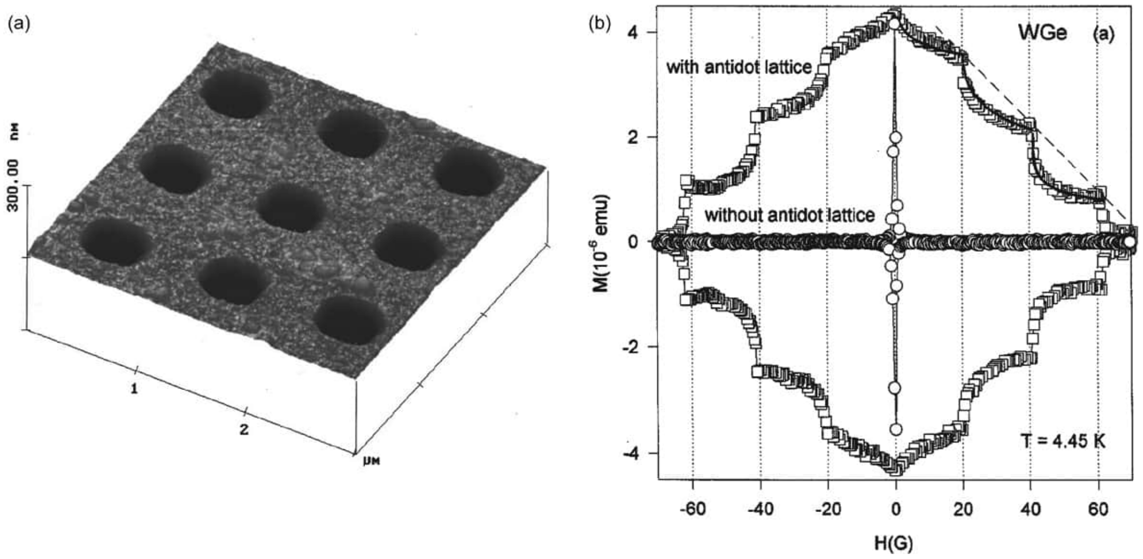

Fig. 5 (a) Atomic force microscopy image of a 60 nm-thick WGe film with a square lattice of holes (antidots) with 340 nm diameter and 1 μm spacing. (b) Magnetization loop *M*(*H*) at $T = 4.45$ K of the WGe films with and without the antidot grid. The dotted vertical lines indicate the matching fields B_k, $k = 1, 2, 3$. Figures reprinted with permission from Moshchalkov VV, Baert M, Metlushko VV, Rosseel E, Bael MJV, Temst K, Jonckheere R and Bruynseraede Y (1996) *Physical Review B* 54: 7385. Copyright 1996 by the American Physical Society.

results from the few excess vortices that appear after filling the holes with k vortices. These are initially repelled by the trapped vortices and can move in the interstitial region with higher mobility. As soon as the number of the excess vortices is large enough, they fill up the holes to $k + 1$ multiquanta vortices.

When the diameter of holes in a superconducting film is increased to a size close to their spacing, a gradual change from a pinning lattice to a multiply connected network of superconducting wires takes place. Such wire networks exhibit modulation of the critical temperature with the magnetic flux, the Little-Parks effect (Parks and Little, 1964). A further enlargement of the holes leads to the formation of disconnected superconducting islands with intriguing properties, described in detail in the chapter by Poccia.

In HTS, commensurability effects can be preferably detected by electric transport measurements, e.g., in YBCO thin films patterned with a square lattice of holes (Castellanos et al., 1997). However, the situation is more complicated because YBCO thin films have strong inherent pinning by crystallographic micro-twinning, screw dislocations, and other intrinsic defects.

The competition between pinning on these inherent defects and trapping vortices on engineered pinning sites requires that the latter be relatively dense, with a spacing of $\lesssim$300 nm. Such a resolution is hard to achieve by lithographic methods. Still, it is in reach of masked or focused ion beam modification, which can raise the magnitude of the matching fields into the range of several tesla.

A demonstration of vortex commensurability effects at high magnetic fields is shown in Fig. 6a in a YBCO film with a dense hexagonal pinning lattice with $a = 30$ nm spacing. Since a is much smaller than the Pearl length $\Lambda(0)$, peaks in the critical current caused by enhanced pinning of vortices can be observed at temperatures far below the superconducting transition. Matching effects of mobile vortices at higher temperatures can be traced as dips in the resistivity, as shown in Fig. 6b. Moreover, the preferential trapping of vortices within the CDs can be confirmed by tilting the applied magnetic field away from the axes of the CDs by an angle a, as illustrated in the inset of Fig. 6b. Then, the position of the matching dips scales with the magnetic field component parallel to the axes of the CDs. These effects prevail up to high tilt angles of $\alpha \leq 70°$ (Aichner et al., 2020).

Complex pinning landscapes

When moving from pinning lattices with hexagonal or square arrangements to more complex periodic or aperiodic tilings, numerous unusual phenomena occur. Some examples are shown in Fig. 7. Such patterns have been studied theoretically (Laguna et al., 2001; Misko et al., 2005; Reichhardt and Olson Reichhardt, 2007; Misko and Nori, 2012) and experimentally in metallic superconductors with holes (Kemmler et al., 2006; Misko et al., 2010; Bothner et al., 2014) and magnetic dots (Villegas et al., 2006; Silhanek et al., 2006; Kramer et al., 2009), like Penrose (Kemmler et al., 2006; Misko et al., 2010), honeycomb (Welp et al., 2002; Latimer et al., 2012) and Kagomé (Cuppens et al., 2011) lattices and artificial vortex ice arrangements in geometrically frustrated pinning lattices (Libál et al., 2009; Latimer et al., 2013; Xue et al., 2018).

In HTS, such studies are more challenging and could be hampered by strong intrinsic pinning. However, complex pinning structures lead to competition between the pinning forces at the CDs and the elastic energy of the vortex lattice, attempting to restore the natural hexagonal vortex configuration of a clean superconductor. For example, pinning landscapes that force the magnetic flux quanta in an ice-like flux arrangement due to a geometrically frustrated energy landscape can transition to a periodic flux distribution at higher temperatures, thawing the vortex ice (Trastoy et al., 2014).

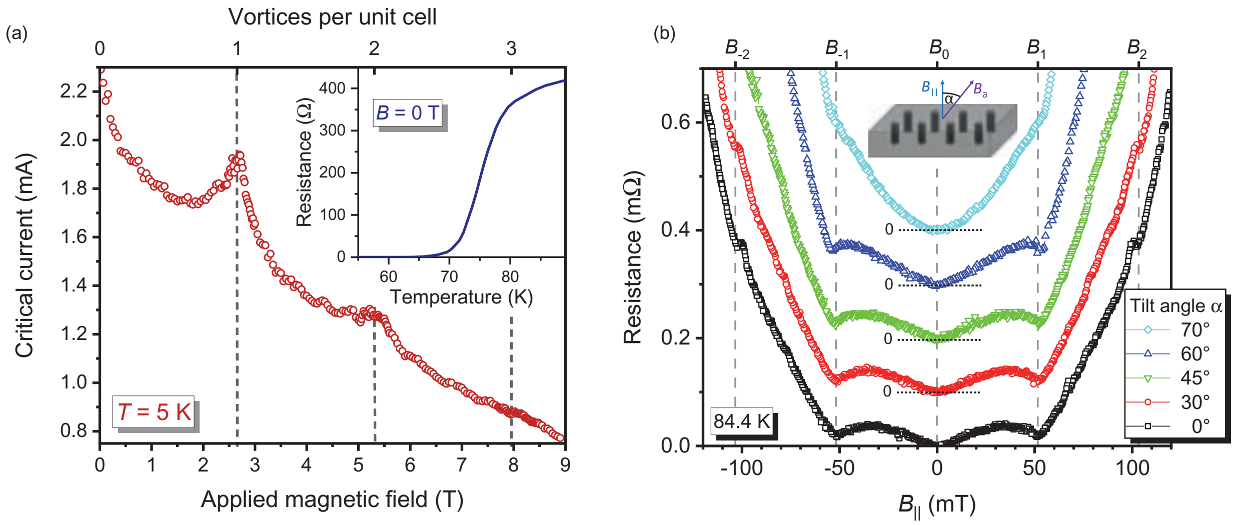

Fig. 6 Vortex commensurability effects in YBCO thin films with an array of columnar defects created by focused He^+ ion beam irradiation. (a) Critical current at 5 K as a function of the applied magnetic field of a thin YBCO film with a hexagonal pattern of columnar defects spaced 30 nm apart. At the first matching field $B_1 = 2.65$ T, a peak of the critical current is caused by strong commensurability effects. Another peak occurs when two vortices are trapped in the pins. The inset shows the superconducting transition in zero magnetic field. (b) Angular dependence of vortex matching effects in the resistance of a YBCO thin film with a square lattice of 200 nm spaced columnar defects: The resistance is plotted as a function of the applied field component along the normal of the film surface $B_{||} = B_a \cos \alpha$ for different values of α. For $\alpha > 0^\circ$, the curves are shifted by multiples of $0.1\mathrm{m}\Omega$ for better visibility. The inset shows a sketch of the experimental situation.
(a) Adapted from Backmeister L, Aichner B, Karrer M, Wurster K, Kleiner R, Goldobin E, Koelle D, Lang W (2022) Ordered Bose glass of vortices in superconducting $YBa_2Cu_3O_{7-\delta}$ thin films with a periodic pin lattice created by focused helium ion irradiation. Nanomaterials, submitted; (b) Reprinted with permission from Aichner B, Mletschnig KL, Müller B, Karrer M, Dosmailov M, Pedarnig JD, Kleiner R, Koelle D, Lang W (2020) Angular magnetic-field dependence of vortex matching in pinning lattices fabricated by focused or masked helium ion beam irradiation of superconducting $YBa_2Cu_3O_7$–δ thin films. *Low Temperature Physics* 46: 331–337. https://doi.org/10.1063/10.0000863. Fiz. Nizk. Temp. 46, 402–409.

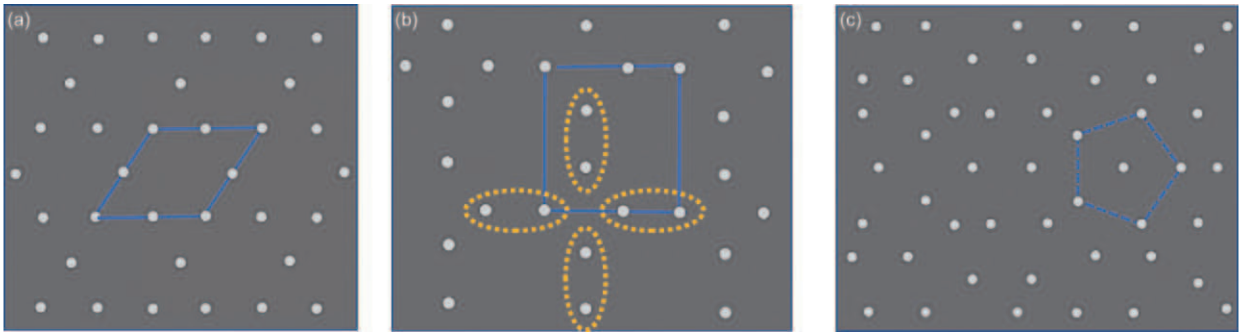

Fig. 7 Examples of complex pinning landscapes. Bright circles indicate pinning centers (holes or columnar defects), and solid blue lines the unit cell of a periodic lattice. (a) The Kagomé lattice is related to the hexagonal lattice. The latter can be recovered if one pin is added to each void's center. (b) Vortex-ice lattice: four pairs of pins (indicated by orange ellipses) meet at each vertex of a square lattice. (c) The aperiodic Penrose tiling. The dashed blue lines indicate the five-fold symmetry.

Another example of a complex pinning landscape, the quasi-Kagomé tiling, shows an unconventional commensurability effect. At elevated temperatures, all pins are occupied by vortices, and one interstitial vortex is magnetically caged in each void of the lattice. The balance between the pinning forces exerted by the CDs and the vortex caging potential can be tuned with the temperature (Aichner et al., 2019). Controlled manipulation of such magnetically confined vortices can pave the way toward fluxonic applications of HTS.

Vortex ratchets and flux diodes

By introducing spatial asymmetry into the pinning arrays, many exciting effects emerge. In general, the idea of a 'Brownian motor' refers to Brownian motion in combination with an unbiased external input signal that can induce submicron directional movement of particles (Hänggi and Marchesoni, 2009). A well-known example is the directional propagation of vortices in an appropriately structured superconductor, usually referred to as a 'vortex ratchet' or 'fluxon pump' (Wambaugh et al., 1999). It provides a flexible and well-controlled model system for studying stochastic transport processes and can operate up to THz frequencies (Hastings et al., 2003).

Vortex ratchets can be realized by various concepts, such as 2D asymmetric channel walls. They can be further extended to design 'fluxon optics' devices, concave/convex fluxon lenses that disperse/concentrate fluxons in nanodevices (Wambaugh et al., 1999). Also, asymmetric potential barriers, e.g., in the form of square arrays of triangular pinning centers (Villegas et al., 2003), double-well traps (Van de Vondel et al., 2005), or an asymmetric arrangement of symmetric traps, (Wördenweber et al., 2004; Perez de Lara et al., 2010) lead to vortex rectification effects.

Interestingly, ratchet effects are proposed in binary particle mixtures without needing an asymmetric substrate (Savel'ev and Nori, 2002). For example, in layered superconductors, such as HTS, an inclination of the magnetic field from the *c* axis leads to a mixture of pancake vortices and Josephson strings. This hybrid vortex system exhibits ratchet effects with time asymmetric drives (Cole et al., 2006).

Finally, understanding ratchet effects in different systems is an exciting topic. Studying these effects with fluxons provides a more direct and controllable experimental approach than for most other systems. Ultimately, these investigations may pave the way for cellular automata as an alternative concept (Hastings et al., 2003; Milošević et al., 2007) for performing clocked logic operations on discrete particles. Moreover, vortex ratchets are proposed (Lee et al., 1999) as an effective method for evacuating magnetic flux from superconducting devices, where inadvertently trapped flux might be detrimental to operation, such as in SQUID magnetic sensors.

A related concept is the lossless superconducting diode. This electronic device has zero resistance only for one direction of applied current and is desirable for building electronic circuits with ultra-low power consumption. It can be realized as a superconducting film patterned with a conformal array of nanoscale holes that breaks spatial inversion symmetry (Lyu et al., 2021). A conformal array is a structure resulting from the transformation of a uniform hexagonal pinning array that retains the sixfold order of the original lattice but exhibits a gradient in site density (Reichhardt et al., 2015).

Guided vortex motion

Controlled vortex motion along a predefined path can be achieved by patterning narrow channels or parallel rows of defects into a superconductor. This so-called 'guided vortex motion' results from an easy track in which vortex pinning is reduced (Dobrovolskiy et al., 2016), a row of holes (Silhanek et al., 2010), or, in HTS, the suppression of superconductivity by heavy-ion irradiation (Laviano et al., 2010). Guided vortex motion can be detected by the deflection of vortices from their trajectory imposed by the Lorentz force. This leads to a pronounced transverse voltage (Wördenweber et al., 2004) that can be distinguished from the conventional Hall effect by its even symmetry with respect to the reversal of the magnetic field. Guided vortex motion also plays an important role in experiments where vortices are accelerated to high velocities, as discussed in the chapter by Dobrovolskiy.

Josephson junctions

A ubiquitous need for nanostructuring of superconductors arises from the fabrication of Josephson junctions (JJs), where two superconducting systems are separated by an insulating or metallic barrier of a few nm thickness or by another weak coupling link. It is crucial that the Josephson weak links are stable and can be reproducibly fabricated. While for metallic superconductors, the industrial fabrication of circuits based on JJs has been established for many years (Likharev, 2012), the fabrication of JJs in HTS is much more challenging. It is still in the phase of cumulative progress.

JJs consisting exclusively of HTS materials have been produced by introducing a crystallographic fault (break junctions), by using a grain boundary between different crystallites, by growing thin HTS films over a substrate step, by narrow constrictions (Dayem bridges), or by multilayers forcing the current along the *c*-axis (Koelle et al., 1999). Here we restrict ourselves to discussing JJs in HTS produced by masked or focused ion irradiation. A general account of this subject can be found in the chapter by Tafuri.

Several attempts have been made to fabricate JJs by irradiation techniques. Initially, direct writing of narrow lines with an electron beam across a pre-patterned YBCO bridge in a scanning electron microscope resulted in somewhat unstable JJs and required high electron doses. Later, creating a weak link in YBCO bridges by implanting oxygen ions through a lithographically defined mask led to superconducting-normal-superconducting (SNS) JJs with resistively shunted junction (RSJ) properties (Tinchev, 1996; Kahlmann et al., 1998; Bergeal et al., 2005). However, the minimum width of the mask structures of about 20 nm and the inevitable straggle of ion collision cascades in the YBCO film set resolution limits and prevent fabrication of superconductor-insulator-superconductor (SIS) junctions, which would be the ultimate goal.

A similar technique, but using 200 keV Ne^+ ions allows complete penetration of the ions through the YBCO film, avoiding implantation and limiting the intended damage to the creation of point defects (Katz et al., 1998). This technique can be scaled up to integrating many JJs in a 2D series-parallel array; 15,820 (28 × 565) JJs have been demonstrated (Cybart et al., 2009).

Focused He^+ ion irradiation in a HIM took the fabrication of JJs one step further. Tunnel junctions can be directly written with the focused He-ion beam into YBCO films, as illustrated in Fig. 8. The properties of the barrier are controlled by varying the irradiation dose. With this technique, SIS junction can also be realized (Cybart et al., 2014). Scanning transmission electron analysis shows that the amorphous tracks created by 1500 He^+/nm have a lateral extension of 4 nm, while no destruction of the crystallographic structure is observed at lower fluence. Nevertheless, the devices produced with the lower doses show an explicit JJ behavior (Müller et al., 2019).

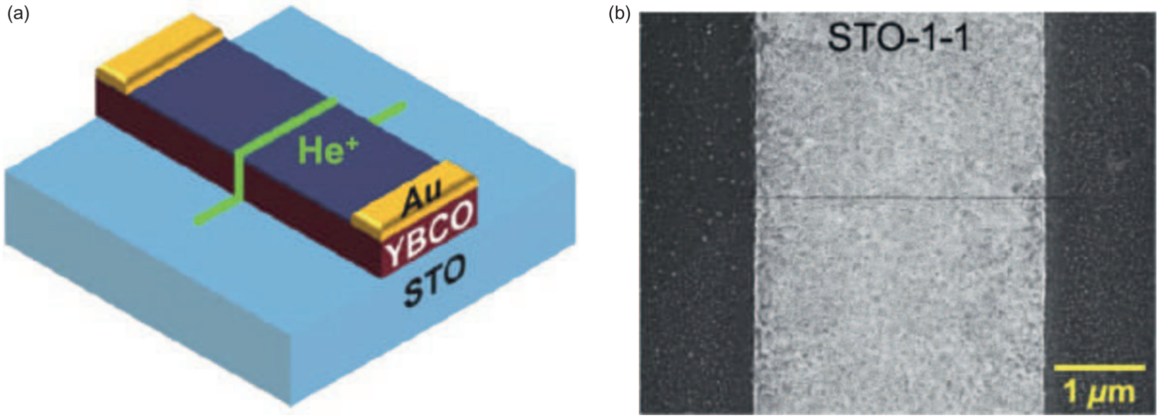

Fig. 8 (a) Schematic illustration of a Josephson junction fabricated by focused He^+ ion irradiation in a helium ion microscope. (b) Scanning electron image of the junction (visible as a thin dark line) patterned with a fluence of 600 ions/nm. Figures reprinted with permission from Müller B, Karrer M, Limberger F, Becker M, Schröppel B, Burkhardt CJ, Kleiner R, Goldobin E and Koelle D (2019) *Physical Review Applied* 11: 044082. Copyright 2019 by the American Physical Society.

The He—FIB technique can, in principle, be applied to other HTS, as demonstrated for $La_{1.84}Sr_{0.16}CuO_4$ (Gozar et al., 2017) and other superconducting materials such as MgB_2 (Kasaei et al., 2018). The versatility of directly written structures and JJs provides a tremendous advantage in fabricating superconducting quantum interference devices (Müller et al., 2019), JJ arrays (LeFebvre et al., 2019), and even more complex devices on the same substrate for various applications.

Conclusion

In this chapter, we have outlined various methods for fabricating nanostructured superconductors. While established lithographic and ion-milling techniques enable the patterning of metallic superconductors, novel techniques are required for nanoscale structures in copper-oxide superconductors. For example, focused He^+-ion beam irradiation creates columnar channels of point defects and can be used to create vortex pinning landscapes and weak links for Josephson junctions. Superconducting nanostructures are already indispensable for many applications and will bring further significant advances to superconducting electronics, from fluxonics to ultra-high sensitivity magnetometers and many others. Beyond that, the dawning age of superconducting quantum computing depends heavily on precise and reproducible nanostructured circuits on a large scale.

Acknowledgments

This work was supported by the Austrian Science Fund (FWF), grant I4865-N, and is based upon work from COST Actions CA16218 (NANOCO-HYBRI), CA19108 (Hi-SCALE), and CA19140 (FIT4NANO), supported by European Cooperation in Science and Technology (European Cooperation in Science and Technology).

References

Aichner B, Müller B, Karrer M, Misko VR, Limberger F, Mletschnig KL, Dosmailov M, Pedarnig JD, Nori F, Kleiner R, Koelle D, and Lang W (2019) Ultradense tailored vortex pinning arrays in superconducting $YBa_2Cu_3O_{7-\delta}$ thin films created by focused He ion beam irradiation for fluxonics applications. *ACS Applied Nano Materials* 2: 5108–5115. https://doi.org/10.1021/acsanm.9b01006.

Aichner B, Mletschnig KL, Müller B, Karrer M, Dosmailov M, Pedarnig JD, Kleiner R, Koelle D, and Lang W (2020) Angular magnetic-field dependence of vortex matching in pinning lattices fabricated by focused or masked helium ion beam irradiation of superconducting $YBa_2Cu_3O_{7-\delta}$ thin films. *Low Temperature Physics* 46: 331–337. https://doi.org/10.1063/10.0000863. Fiz. Nizk. Temp. 46, 402–409.

Baumans XDA, Cerbu D, Adami OA, Zharinov VS, Verellen N, Papari G, Scheerder JE, Zhang G, Moshchalkov VV, Silhanek AV, and Van de Vondel J (2016) Thermal and quantum depletion of superconductivity in narrow junctions created by controlled electromigration. *Nature Communications* 7: 10560. https://doi.org/10.1038/ncomms10560.

Bergeal N, Grison X, Lesueur J, Faini G, Aprili M, and Contour JP (2005) High-quality planar high-T_c Josephson junctions. *Applied Physics Letters* 87: 102502. https://doi.org/10.1063/1.2037206.

Berghuis P, Di Bartolomeo E, Wagner GA, and Evetts JE (1997) Intrinsic channeling of vortices along the *ab* plane in vicinal $YBa_2Cu_3O_{7-\delta}$ films. *Physical Review Letters* 79: 2332–2335. https://doi.org/10.1103/PhysRevLett.79.2332.

Bezryadin A, Ovchinnikov YN, and Pannetier B (1996) Nucleation of vortices inside open and blind microholes. *Physical Review B* 53: 8553–8560. https://doi.org/10.1103/PhysRevB.53.8553.

Bezryadin A, Lau CN, and Tinkham M (2000) Quantum suppression of superconductivity in ultrathin nanowires. *Nature* 404: 971–974. https://doi.org/10.1038/35010060.

Blatter G, Feigel'man MV, Geshkenbein VB, Larkin AI, and Vinokur VM (1994) Vortices in high-temperature superconductors. *Reviews of Modern Physics* 66: 1125–1388. https://doi.org/10.1103/RevModPhys.66.1125.

Bothner D, Seidl R, Misko VR, Kleiner R, Koelle D, and Kemmler M (2014) Unusual commensurability effects in quasiperiodic pinning arrays induced by local inhomogeneities of the pinning site density. *Superconductor Science and Technology* 27: 065002. https://doi.org/10.1088/0953-2048/27/6/065002.

Burnett J, Sagar J, Kennedy OW, Warburton PA, and Fenton JC (2017) Low-loss superconducting nanowire circuits using a neon focused ion beam. *Physical Review Applied* 8: 014039. https://doi.org/10.1103/physrevapplied.8.014039.

Buzdin AI (1993) Multiple-quanta vortices at columnar defects. *Physical Review B* 47: 11416. https://doi.org/10.1103/PhysRevB.47.11416.

Buzdin A and Feinberg D (1996) Electromagnetic pinning of vortices by nonsuperconducting defects and their influence on screening. *Physica C* 256: 303–311. https://doi.org/10.1016/0921-4534(95)00664-8.

Castellanos A, Wördenweber R, Ockenfuss G, Hart A, and Keck K (1997) Preparation of regular arrays of antidots in YBa$_2$Cu$_3$O$_7$ thin films and observation of vortex lattice matching effects. *Applied Physics Letters* 71: 962–964. https://doi.org/10.1063/1.119701.

Civale L (1997) Vortex pinning and creep in high-temperature superconductors with columnar defects. *Superconductor Science and Technology* 10: A11–A28. https://doi.org/10.1088/0953-2048/10/7a/003.

Cole D, Bending S, Savel'ev S, Grigorenko A, Tamegai T, and Nori F (2006) Ratchet without spatial asymmetry for controlling the motion of magnetic flux quanta using time-asymmetric drives. *Nature Materials* 5: 305–311. https://doi.org/10.1038/nmat1608.

Collienne S, Raes B, Keijers W, Linek J, Koelle D, Kleiner R, Kramer RBG, Van de Vondel J, and Silhanek AV (2021) Nb-based nanoscale superconducting quantum interference devices tuned by electroannealing. *Physical Review Applied* 15: 034016. https://doi.org/10.1103/physrevapplied.15.034016.

Cuppens J, Ataklti GW, Gillijns W, Van de Vondel J, Moshchalkov VV, and Silhanek AV (2011) Vortex dynamics in a superconducting film with a kagomé and a honeycomb pinning landscape. *Journal of Superconductivity and Novel Magnetism* 24: 7–11. https://doi.org/10.1007/s10948-010-0893-7.

Cybart SA, Anton SM, Wu SM, Clarke J, and Dynes RC (2009) Very large scale integration of nanopatterned YBa$_2$Cu$_3$O$_{7-\delta}$ Josephson junctions in a two-dimensional array. *Nano Letters* 9: 3581–3585. https://doi.org/10.1021/nl901785j.

Cybart SA, Cho EY, Wong TJ, Glyantsev VN, Huh JU, Yung CS, Moeckly BH, Beeman JW, Ulin-Avila E, Wu SM, and Dynes RC (2014) Large voltage modulation in magnetic field sensors from two-dimensional arrays of Y-Ba-Cu-O nano Josephson junctions. *Applied Physics Letters* 104: 062601. https://doi.org/10.1063/1.4865216.

Cybart SA, Cho EY, Wong TJ, Wehlin BH, Ma MK, Huynh C, and Dynes RC (2015) Nano Josephson superconducting tunnel junctions in YBa$_2$Cu$_3$O$_{7-\delta}$ directly patterned with a focused helium ion beam. *Nature Nanotechnology* 10: 598. https://doi.org/10.1038/nnano.2015.76.

Dobrovolskiy OV, Hanefeld M, Zörb M, Huth M, and Shklovskij VA (2016) Interplay of flux guiding and Hall effect in Nb films with nanogrooves. *Superconductor Science and Technology* 29: 065009.

Durrell JH, Gibson G, Barber ZH, Evetts JE, Rössler R, Pedarnig JD, and Bäuerle D (2000) Dependence of critical current on field angle in off-c-axis grown Bi$_2$Sr$_2$CaCu$_2$O$_8$ film. *Applied Physics Letters* 77: 1686–1688. https://doi.org/10.1063/1.1310174.

Emmrich D, Beyer A, Nadzeyka A, Bauerdick S, Meyer JC, Kotakoski J, and Golzhauser A (2016) Nanopore fabrication and characterization by helium ion microscopy. *Applied Physics Letters* 108: 163103. https://doi.org/10.1063/1.4947277.

Fisher DS, Fisher MPA, and Huse DA (1991) Thermal fluctuations, quenched disorder, phase transitions, and transport in type-II superconductors. *Physics Review* 43: 130–159. https://doi.org/10.1103/physrevb.43.130.

Fomin VM (2020) *Self-Rolled Micro- and Nanoarchitectures*. Berlin/Boston: De Gruyter. https://doi.org/10.1515/9783110575576.

Gol'tsman GN, Okunev O, Chulkova G, Lipatov A, Semenov A, Smirnov K, Voronov B, Dzardanov A, Williams C, and Sobolewski R (2001) Picosecond superconducting single-photon optical detector. *Applied Physics Letters* 79: 705–707. https://doi.org/10.1063/1.1388868.

Gozar A, Litombe NE, Hoffman JE, and Božović I (2017) Optical nanoscopy of high T_c cuprate nanoconstriction devices patterned by helium ion beams. *Nano Letters* 17: 1582–1586. https://doi.org/10.1021/acs.nanolett.6b04729.

Gray RL, Rushton MJD, and Murphy ST (2022) Molecular dynamics simulations of radiation damage in YBa$_2$Cu$_3$O$_7$. *Superconductor Science and Technology* 35: 035010. https://doi.org/10.1088/1361-6668/ac47dc.

Haag LT, Zechner G, Lang W, Dosmailov M, Bodea MA, and Pedarnig JD (2014) Strong vortex matching effects in YBCO films with periodic modulations of the superconducting order parameter fabricated by masked ion irradiation. *Physica C* 503: 75–81. https://doi.org/10.1016/j.physc.2014.03.032.

Haage T, Zegenhagen J, Li JQ, Habermeier HU, Cardona M, Warthmann JR, Forkl A, and Kronmüller H (1997) Transport properties and flux pinning by self-organization in YBa$_2$Cu$_3$O$_{7-\delta}$ films on vicinal SrTiO$_3$ (001). *Physical Review B* 56: 8404–8418. https://doi.org/10.1103/PhysRevB.56.8404.

Hadfield RH (2009) Single-photon detectors for optical quantum information applications. *Nature Photonics* 3: 696–705. https://doi.org/10.1038/nphoton.2009.230.

Hänggi P and Marchesoni F (2009) Artificial Brownian motors: Controlling transport on the nanoscale. *Reviews of Modern Physics* 81: 387–442. https://doi.org/10.1103/RevModPhys.81.387.

Harada K, Kamimura O, Kasai H, Matsuda T, Tonomura A, and Moshchalkov VV (1996) Direct observation of vortex dynamics in superconducting films with regular arrays of defects. *Science* 274: 1167–1170. https://doi.org/10.1126/science.274.5290.1167.

Hastings MB, Olson Reichhardt CJ, and Reichhardt C (2003) Ratchet cellular automata. *Physical Review Letters* 90: 247004. https://doi.org/10.1103/physrevlett.90.247004.

Heine G, Lang W, Rössler R, and Pedarnig JD (2021) Anisotropy of the in-plane and out-of-plane resistivity and the Hall effect in the normal state of vicinal-grown YBa$_2$Cu$_3$O$_{7-\delta}$ thin films. *Nanomaterials* 11: 675. https://doi.org/10.3390/nano11030675.

Hlawacek G and Golzhauser A (eds.) (2016) *Helium Ion Microscopy*. Switzerland: Springer International Publishing. https://doi.org/10.1007/978-3-319-41990-9.

Kahlmann F, Engelhardt A, Schubert J, Zander W, Buchal C, and Hollkott J (1998) Superconductor-normal-superconductor Josephson junctions fabricated by oxygen implantation into YBa$_2$Cu$_3$O$_{7-\delta}$. *Applied Physics Letters* 73: 2354–2356. https://doi.org/10.1063/1.122459.

Kang DJ, Burnell G, Lloyd SJ, Speaks RS, Peng NH, Jeynes C, Webb R, Yun JH, Moon SH, Oh B, Tarte EJ, Moore DF, and Blamire MG (2002) Realization and properties of YBa$_2$Cu$_3$O$_{7-\delta}$ Josephson junctions by metal masked ion damage technique. *Applied Physics Letters* 80: 814–816. https://doi.org/10.1063/1.1446998.

Karrer M, et al. (2022) *Personal communication*.

Kasaei L, Melbourne T, Manichev V, Feldman LC, Gustafsson T, Chen K, Xi XX, and Davidson BA (2018) MgB$_2$ Josephson junctions produced by focused helium ion beam irradiation. *AIP Advances* 8: 075020. https://doi.org/10.1063/1.5030751.

Katz AS, Sun AG, Woods SI, and Dynes RC (1998) Planar thin film YBa$_2$Cu$_3$O$_{7-\delta}$ Josephson junctions via nanolithography and ion damage. *Applied Physics Letters* 72: 2032–2034. https://doi.org/10.1063/1.121255.

Katz AS, Woods SI, and Dynes RC (2000) Transport properties of high-T_c planar Josephson junctions fabricated by nanolithography and ion implantation. *Journal of Applied Physics* 87: 2978–2983. https://doi.org/10.1063/1.372286.

Kemmler M, Gürlich C, Sterck A, Pöhler H, Neuhaus M, Siegel M, Kleiner R, and Koelle D (2006) Commensurability effects in superconducting Nb films with quasiperiodic pinning arrays. *Physical Review Letters* 97: 147003. https://doi.org/10.1103/physrevlett.97.147003.

Koelle D, Kleiner R, Ludwig F, Dantsker E, and Clarke J (1999) High-transition-temperature superconducting quantum interference devices. *Reviews of Modern Physics* 71: 631–686. https://doi.org/10.1103/revmodphys.71.631.

Kramer RBG, Silhanek AV, Van de Vondel J, Raes B, and Moshchalkov VV (2009) Symmetry-induced giant vortex state in a superconducting Pb film with a fivefold Penrose array of magnetic pinning centers. *Physical Review Letters* 103: 067007. https://doi.org/10.1103/physrevlett.103.067007.

Laguna MF, Balseiro CA, Domínguez D, and Nori F (2001) Vortex structure and dynamics in kagomé and triangular pinning potentials. *Physical Review B* 64: 104505. https://doi.org/10.1103/PhysRevB.64.104505.

Lang W and Pedarnig JD (2010) Ion Irradiation of High-Temperature Superconductors and Its Application for Nanopatterning. In: Moshchalkov VV, Wördenweber R, and Lang W (eds.) *Nanoscience and Engineering in Superconductivity*, pp. 81–104. Heidelberg: Springer. https://doi.org/10.1007/978-3-642-15137-8.

Lang W, Dineva M, Marksteiner M, Enzenhofer T, Siraj K, Peruzzi M, Pedarnig JD, Bäuerle D, Korntner R, Cekan E, Platzgummer E, and Loeschner H (2006) Ion-beam direct-structuring of high-temperature superconductors. *Microelectronic Engineering* 83: 1495–1498. https://doi.org/10.1016/j.mee.2006.01.091.

Latimer ML, Berdiyorov GR, Xiao ZL, Kwok WK, and Peeters FM (2012) Vortex interaction enhanced saturation number and caging effect in a superconducting film with a honeycomb array of nanoscale holes. *Physical Review B* 85: 012505. https://doi.org/10.1103/PhysRevB.85.012505.

Latimer ML, Berdiyorov GR, Xiao ZL, Peeters FM, and Kwok WK (2013) Realization of artificial ice systems for magnetic vortices in a superconducting MoGe thin film with patterned nanostructures. *Physical Review Letters* 111: 067001. https://doi.org/10.1103/PhysRevLett.111.067001.

Laviano F, Ghigo G, Mezzetti E, Hollmann E, and Wördenweber R (2010) Control of the vortex flow in microchannel arrays produced in YBCO films by heavy-ion lithography. *Physica C* 470: 844–847. https://doi.org/10.1016/j.physc.2010.02.052.

Lee CS, Jankó B, Derényi I, and Barabási AL (1999) Reducing vortex density in superconductors using the 'ratchet effect'. *Nature* 400: 337–340. https://doi.org/10.1038/22485.

LeFebvre JC, Cho E, Li H, Pratt K, and Cybart SA (2019) Series arrays of planar long Josephson junctions for high dynamic range magnetic flux detection. *AIP Advances* 9: 105215. https://doi.org/10.1063/1.5126035.

Libál A, Olson Reichhardt CJ, and Reichhardt C (2009) Creating artificial ice states using vortices in nanostructured superconductors. *Physical Review Letters* 102: 237004. https://doi.org/10.1103/physrevlett.102.237004.

Likharev KK (2012) Superconductor digital electronics. *Physica C* 482: 6–18. https://doi.org/10.1016/j.physc.2012.05.016.

Lyu YY, Jiang J, Wang YL, Xiao ZL, Dong S, Chen QH, Milošević MV, Wang H, Divan R, Pearson JE, Wu P, Peeters FM, and Kwok WK (2021) Superconducting diode effect via conformal-mapped nanoholes. *Nature Communications* 12: 2703. https://doi.org/10.1038/s41467-021-23077-0.

Marinković S, Fernández-Rodríguez A, Collienne S, Alvarez SB, Melinte S, Maiorov B, Rius G, Granados X, Mestres N, Palau A, and Silhanek AV (2020) Direct visualization of current-stimulated oxygen migration in $YBa_2Cu_3O_{7-\delta}$ thin films. *ACS Nano* 14: 11765–11774. https://doi.org/10.1021/acsnano.0c04492.

Markowitsch W, Stockinger C, Lang W, Bierleutgeb K, Pedarnig JD, and Bäuerle D (1997) Photoinduced enhancement of the c-axis conductivity in oxygen-deficient $YBa_2Cu_3O_{7-\delta}$ thin films. *Applied Physics Letters* 71: 1246–1248. https://doi.org/10.1063/1.119863.

Martin JI, Vélez M, Nogués J, and Schuller IK (1997) Flux pinning in a superconductor by an array of submicrometer magnetic dots. *Physical Review Letters* 79: 1929–1932. https://doi.org/10.1103/PhysRevLett.79.1929.

Milošević MV, Berdiyorov GR, and Peeters FM (2007) Fluxonic cellular automata. *Applied Physics Letters* 91: 212501. https://doi.org/10.1063/1.2813047.

Misko VR and Nori F (2012) Magnetic flux pinning in superconductors with hyperbolic-tessellation arrays of pinning sites. *Physical Review B* 85: 184506. https://doi.org/10.1103/PhysRevB.85.184506.

Misko V, Savel'ev S, and Nori F (2005) Critical currents in quasiperiodic pinning arrays: Chains and penrose lattices. *Physical Review Letters* 95: 177007. https://doi.org/10.1103/PhysRevLett.95.177007.

Misko VR, Bothner D, Kemmler M, Kleiner R, Koelle D, Peeters FM, and Nori F (2010) Enhancing the critical current in quasiperiodic pinning arrays below and above the matching magnetic flux. *Physical Review B* 82: 184512. https://doi.org/10.1103/PhysRevB.82.184512.

Moshchalkov VV and Fritzsche J (2011) *Nanostructured Superconductors.* Singapore: World Scientific. https://doi.org/10.1142/9789814343923.

Moshchalkov VV, Baert M, Metlushko VV, Rosseel E, Bael MJV, Temst K, Jonckheere R, and Bruynseraede Y (1996) Magnetization of multiple-quanta vortex lattices. *Physical Review B* 54: 7385–7393. https://doi.org/10.1103/physrevb.54.7385.

Müller B, Karrer M, Limberger F, Becker M, Schröppel B, Burkhardt CJ, Kleiner R, Goldobin E, and Koelle D (2019) Josephson junctions and SQUIDs created by focused helium-ion-beam irradiation of $YBa_2Cu_3O_7$. *Physical Review Applied* 11: 044082. https://doi.org/10.1103/PhysRevApplied.11.044082.

Nelson DR and Vinokur VM (1993) Boson localization and correlated pinning of superconducting vortex arrays. *Physical Review B* 48: 13060–13097. https://doi.org/10.1103/physrevb.48.13060.

Parks RD and Little WA (1964) Fluxoid quantization in a multiply-connected superconductor. *Physics Review* 133: A97–A103. https://doi.org/10.1103/PhysRev.133.A97.

Pedarnig JD, Rössler R, Delamare MP, Lang W, Bäuerle D, Köhler A, and Zandbergen HW (2002) Electrical properties, texture, and microstructure of vicinal $YBa_2Cu_3O_{7-\delta}$ thin films. *Applied Physics Letters* 81: 2587–2589. https://doi.org/10.1063/1.1508418.

Perez de Lara D, Alija A, Gonzalez EM, Velez M, Martin JI, and Vicent JL (2010) Vortex ratchet reversal at fractional matching fields in kagomélike array with symmetric pinning centers. *Physical Review B* 82: 174503. https://doi.org/10.1103/PhysRevB.82.174503.

Reichhardt C and Olson Reichhardt CJ (2007) Vortex molecular crystal and vortex plastic crystal states in honeycomb and kagomé pinning arrays. *Physical Review B* 76: 064523. https://doi.org/10.1103/PhysRevB.76.064523.

Reichhardt C, Ray D, and Olson Reichhardt CJ (2015) Reversible ratchet effects for vortices in conformal pinning arrays. *Physical Review B* 91: 184502. https://doi.org/10.1103/physrevb.91.184502.

Savel'ev S and Nori F (2002) Experimentally realizable devices for controlling the motion of magnetic flux quanta in anisotropic superconductors. *Nature Materials* 1: 179–184. https://doi.org/10.1038/nmat746.

Sefrioui Z, Arias D, González EM, Léon C, Santamaria J, and Vicent JL (2001) Vortex liquid entanglement in irradiated $YBa_2Cu_3O_{7-\delta}$ thin films. *Physical Review B* 63: 064503. https://doi.org/10.1103/PhysRevB.63.064503.

Silhanek AV, Gillijns W, Moshchalkov VV, Zhu BY, Moonens J, and Leunissen LHA (2006) Enhanced pinning and proliferation of matching effects in a superconducting film with a Penrose array of magnetic dots. *Applied Physics Letters* 89: 152507. https://doi.org/10.1063/1.2361172.

Silhanek AV, Van de Vondel J, and Moshchalkov VV (2010) Guided Vortex motion and Vortex ratchets in nanostructured superconductors. In: Moshchalkov VV, Wördenweber R, and Lang W (eds.) *Nanoscience and Engineering in Superconductivity*, pp. 1–24. Heidelberg: Springer. https://doi.org/10.1007/978-3-642-15137-8.

Sochnikov I, Shaulov A, Yeshurun Y, Logvenov G, and Bozovic I (2010) Large oscillations of the magnetoresistance in nanopatterned high-temperature superconducting films. *Nature Nanotechnology* 5: 516–519. https://doi.org/10.1038/nnano.2010.111.

Swiecicki I, Ulysse C, Wolf T, Bernard R, Bergeal N, Briatico J, Faini G, Lesueur J, and Villegas JE (2012) Strong field-matching effects in superconducting $YBa_2Cu_3O_{7-\delta}$ films with vortex energy landscapes engineered via masked ion irradiation. *Physical Review B* 85: 224502. https://doi.org/10.1103/physrevb.85.224502.

Tafuri F and Kirtley JR (2005) Weak links in high critical temperature superconductors. *Reports on Progress in Physics* 68: 2573–2663. https://doi.org/10.1088/0034-4885/68/11/r03.

Tinchev SS (1996) Properties of YBCO weak links prepared by local oxygen-ion induced modification. *Physica C* 256: 191–198. https://doi.org/10.1016/0921-4534(95)00615-x.

Trastoy J, Malnou M, Ulysse C, Bernard R, Bergeal N, Faini G, Lesueur J, Briatico J, and Villegas JE (2014) Freezing and thawing of artificial ice by thermal switching of geometric frustration in magnetic flux lattices. *Nature Nanotechnology* 9: 710–715. https://doi.org/10.1038/nnano.2014.158.

Van de Vondel J, Silva CCD, Zhu BY, Morelle M, and Moshchalkov VV (2005) Vortex-rectification effects in films with periodic asymmetric pinning. *Physical Review Letters* 94: 057003. https://doi.org/10.1103/PhysRevLett.94.057003.

Villegas JE, Savel'ev S, Nori F, Gonzalez EM, Anguita JV, García R, and Vicent JL (2003) A superconducting reversible rectifier that controls the motion of magnetic flux quanta. *Science* 302: 1188–1191. https://doi.org/10.1126/science.1090390.

Villegas JE, Montero MI, Li CP, and Schuller IK (2006) Correlation length of quasiperiodic vortex lattices. *Physical Review Letters* 97: 027002. https://doi.org/10.1103/physrevlett.97.027002.

Vinckx W, Vanacken J, Moshchalkov VV, Mátéfi-Tempfli S, Mátéfi-Tempfli M, Michotte S, Piraux L, and Ye X (2007) High field matching effects in superconducting Nb porous arrays catalyzed from anodic alumina templates. *Physica C* 459: 5–10. https://doi.org/10.1016/j.physc.2007.04.194.

Wambaugh JF, Reichhardt C, Olson CJ, Marchesoni F, and Nori F (1999) Superconducting fluxon pumps and lenses. *Physical Review Letters* 83: 5106–5109. https://doi.org/10.1103/physrevlett.83.5106.

Ward BW, Notte JA, and Economou NP (2006) Helium ion microscope: A new tool for nanoscale microscopy and metrology. *Journal of Vacuum Science and Technology B* 24: 2871–2874. https://doi.org/10.1116/1.2357967.

Weber HW (2003) Irradiation. In: Cardwell DA and Ginley DS (eds.) *Handbook of Superconducting Materials*. vol. 1, pp. 407–418. Bristol: IOP Publishing. https://doi.org/10.1201/9781420034202.

Welp U, Xiao ZL, Jiang JS, Vlasko-Vlasov VK, Bader SD, Crabtree GW, Liang J, Chik H, and Xu JM (2002) Superconducting transition and vortex pinning in Nb films patterned with nanoscale hole arrays. *Physical Review B* 66: 212507. https://doi.org/10.1103/physrevb.66.212507.

Wördenweber R, Dymashevski P, and Misko VR (2004) Guidance of vortices and the vortex ratchet effect in high-T_c superconducting thin films obtained by arrangement of antidots. *Physical Review B* 69: 184504. https://doi.org/10.1103/physrevb.69.184504.

Xue C, Ge JY, He A, Zharinov VS, Moshchalkov VV, Zhou YH, Silhanek AV, and Van de Vondel J (2018) Tunable artificial vortex ice in nanostructured superconductors with a frustrated kagomé lattice of paired antidots. *Physical Review B* 97: 134506. https://doi.org/10.1103/PhysRevB.97.134506.

Yun SH, Pedarnig JD, Rössler R, Bäuerle D, and Obradors X (2000) Inplane and out-of-plane resistivities of vicinal Hg-1212 thin films. *Applied Physics Letters* 77: 1369–1371. https://doi.org/10.1063/1.1289489.

Kondo effects in quantum dots: Theory

Wataru Izumida, Tohoku University, Sendai, Japan

© 2024 Elsevier Ltd. All rights reserved.

Introduction 381
Formulations for the quantum dot 382
A model of the quantum dot 382
Linear response conductance 383
Anderson model for the Kondo problem 383
Isolated quantum dot approximation 383
Non-interacting approximation 384
Kondo problem for a magnetic impurity in a metal 384
Emergence of the Kondo peak 385
Coulomb peaks to Kondo plateau 385
Conclusion 386
References 387

Abstract

Kondo effect occurs in electron transport through a quantum dot when the number of electrons in the quantum dot is odd and at low temperatures. The conductance increases due to the resonant tunneling through the Kondo peak emerging at the Fermi energy. Two Coulomb peaks gradually grow and shift to their center as the temperature decreases. Then at the lowest temperature they merge into a single plateau, the Kondo plateau. The change of conductance can be explained by the Kondo temperature which is a function of the gate voltage.

Key points

- Kondo effects take place in electron transport through a quantum dot at low temperatures
- The Kondo effect appears as conductance enhancement between the Coulomb peaks where the number of electrons in a quantum dot is odd
- The conductance shows the Kondo plateau at the absolute zero temperature
- How does the conductance change from the Coulomb peaks to the Kondo plateau when temperature decreases?
- Change of conductance is explained by the Kondo temperature
- Kondo temperature is a function of the voltage applied to a gate electrode nearby a quantum dot

Introduction

Electron transport measurement through a quantum dot is performed with left and right leads attached near the quantum dot. The schematic structure of the quantum dot for the electron transport is shown in Fig. 1.

In most cases, the electron transport through the quantum dot is forbidden because of the strong Coulomb repulsion between the electrons in the quantum dot, which is known as the Coulomb blockade.

The electrical potential in the quantum dot can be controlled by applying a voltage to a gate electrode nearby the quantum dot. When the gate voltage continuously changes, the number of electrons in the quantum dot $\langle n_\mathrm{d} \rangle$ changes by exchanging the electrons between the quantum dot and the leads. Because of the strong Coulomb repulsion, $\langle n_\mathrm{d} \rangle$ changes one by one as shown in Fig. 2A. Electrons can transport through the quantum dot only when $\langle n_\mathrm{d} \rangle$ changes. The linear response conductance as a function of the gate voltage shows peaks. The peaks reflect the change of $\langle n_\mathrm{d} \rangle$, as shown in Fig. 2. The peaks in the conductance are referred to as the Coulomb peaks.

At low temperatures the Kondo effect takes place as a strikingly remarkable effect in the electron transport through the quantum dot as was first theoretically pointed out (Glazman and Raikh, 1988; Ng and Lee, 1988; Kawabata, 1991). In the gate voltage region where there exist an odd number of electrons in the quantum dot, a local spin moment $S = 1/2$ appears in the quantum dot from an unpaired electron. The quantum dot with an odd number of electrons behaves like a magnetic impurity. The local spin moment interacts with the electrons in the left and right leads. The coupling between the local spin and the electrons in the leads becomes stronger at lower temperatures. The conductance is largely enhanced because of the strong coupling, even though the number of electrons in the quantum dot is fixed, that is, the quantum dot is in the Coulomb blockade region. This is the most typical Kondo effect in the quantum dot. The conductance plateau caused by the Kondo effect is referred to as the Kondo plateau, as shown in Fig. 2.

https://doi.org/10.1016/B978-0-323-90800-9.00049-4

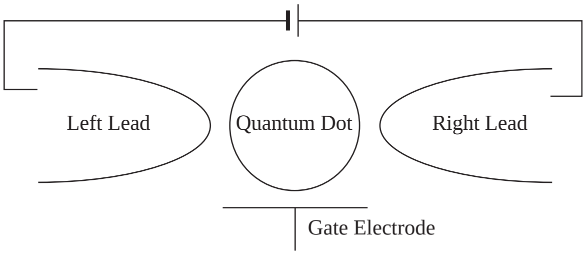

Fig. 1 Schematics of the quantum dot structure for electron transport.

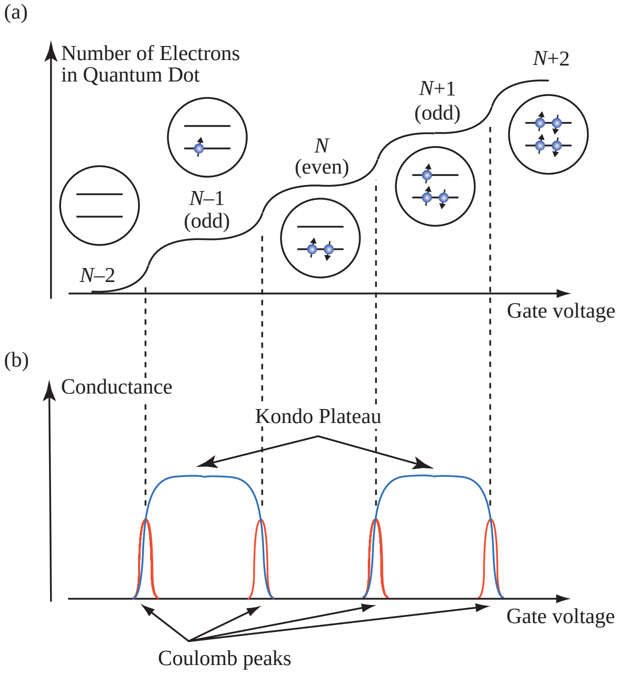

Fig. 2 (A) The number of electrons in the quantum dot as a function of the gate voltage, and schematics of electron occupation in the quantum dot in each gate voltage region. Local spin moment from an unpaired electron appears when the number of electrons is odd. (B) Linear response conductance as a function of the gate voltage. Conductance shows Coulomb peaks reflecting the change of number of electrons in the quantum dot. The Kondo effect takes place at low temperatures in the gate voltage region where the number of electrons in the quantum dot is odd. As the temperature decreases, the conductance changes from the Coulomb peaks to the Kondo plateau.

A brief introduction of the Kondo effect in the quantum dot similar to this section can be found in the book by Kondo (2012). The later part of this chapter will address how the conductance changes from the Coulomb peaks to the Kondo plateau when the temperature decreases.

This chapter is organized as follows. First, we formulate the quantum dot with the simplest model. The model can be mapped onto the Anderson model studied for the Kondo effect in a magnetic impurity in a metal. We overview the properties of the Anderson model from the viewpoint of the quantum dot. We then explain how the conductance changes from the Coulomb peaks to the Kondo plateau. In the summary, we introduce some other topics that are not discussed in the main part of this chapter.

Formulations for the quantum dot

A model of the quantum dot

Let us consider the simplest model including the Coulomb blockade and the Kondo effect for the electron transport through the quantum dot. The model contains only a single spin degenerate orbital in the quantum dot. The model is given by the following Hamiltonian,

$$H = H_{\mathrm{l}} + H_{\mathrm{d}} + H_{\mathrm{l-d}}, \tag{1}$$

$$H_\mathrm{l} = \sum_{\ell=\mathrm{L,R}} \sum_{k\sigma} \varepsilon_k c^\dagger_{\ell k\sigma} c_{\ell k\sigma}, \tag{2}$$

$$H_\mathrm{d} = \sum_{\sigma} \varepsilon_\mathrm{d} n_{\mathrm{d}\sigma} + U n_{\mathrm{d}\uparrow} n_{\mathrm{d}\downarrow}, \tag{3}$$

$$H_{\mathrm{l-d}} = \sum_{\ell=\mathrm{L,R}} \sum_{k\sigma} V_\ell d^\dagger_\sigma c_{\ell k\sigma} + \mathrm{h.c.} \tag{4}$$

H_l represents the electrons in the left ($\ell = \mathrm{L}$) and right ($\ell = \mathrm{R}$) leads. H_d represents the electrons in the quantum dot. $H_{\mathrm{l-d}}$ represents the electron tunneling between the leads and the quantum dot. $c^\dagger_{\ell k\sigma}$ is the creation operator of the electron of state k with spin $\sigma(=\uparrow,\downarrow)$ in the ℓ - lead, and ε_k is the energy for the electron of state k. $d^\dagger_\sigma$ is the creation operator of the electron in the quantum dot with spin σ. $n_{\mathrm{d}\sigma} = d^\dagger_\sigma d_\sigma$ is the number operator of the quantum dot state. The energy of the orbital in the quantum dot, ε_d, can be controlled by the gate voltage. U is the Coulomb interaction between the electrons in the quantum dot. This model covers the region in $0 \le \langle n_\mathrm{d} \rangle \le 2$, where $\langle n_\mathrm{d} \rangle = \sum_\sigma \langle n_{\mathrm{d}\sigma} \rangle$ is the expectation value of the number of electrons in the quantum dot. V_ℓ is the tunnel matrix element between the orbital in the quantum dot and the k state in the ℓ - lead, and it is assumed to be independent of k. V_ℓ can also be controlled in the setup of the quantum dot: for instance, by applying the split gate voltage between the quantum dot and the leads.

Linear response conductance

In general, the conductance for a low bias voltage between the left and right leads is expressed by the correlation function of the current $\lambda \dot{N}_\mathrm{L} - (1-\lambda)\dot{N}_\mathrm{R}$ in the linear response theory, where $\dot{N}_\ell$ is the time differentiation of the electron number in the ℓ - lead and λ is a weight. For the present single orbital model, the conductance can be expressed in the convenient expression,

$$\mathrm{G} = \frac{2e^2}{h} \alpha \int d\varepsilon \left(-\frac{\partial f}{\partial \varepsilon} \right) \pi \Gamma \rho_\mathrm{d}(\varepsilon), \tag{5}$$

where $\rho_\mathrm{d}(\varepsilon)$ is the density of states of the quantum dot per spin, $f(\varepsilon) = 1/(\mathrm{e}^{\beta(\varepsilon-\varepsilon_\mathrm{F})} + 1)$ is the Fermi distribution function, ε_F is the Fermi energy in the leads, and $\beta = 1/k_\mathrm{B}T$ is the inverse of the temperature. In the later discussion, we set $k_\mathrm{B} = 1$ and $\varepsilon_\mathrm{F} = 0$. The tunnel coupling is parameterized by the width of the energy level of the quantum dot $\Gamma = \sum_\ell \Gamma_\ell$, where $\Gamma_\ell = \pi |V_\ell|^2 \rho_\ell$ and ρ_ℓ is the density of states in the ℓ-lead. The factor in Eq. (5),

$$\alpha \equiv \frac{\Gamma_\mathrm{L}\Gamma_\mathrm{R}}{[(\Gamma_\mathrm{L} + \Gamma_\mathrm{R})/2]^2} \tag{6}$$

is caused by the asymmetry between Γ_L and Γ_R, and it has the maximum value $\alpha = 1$ for the symmetric coupling $\Gamma_\mathrm{L} = \Gamma_\mathrm{R}$.

A detailed theoretical background for this section can be found in the report by Izumida et al. (2001) and references therein. The formulation explained here was restricted to that related to the following discussion.

For the electron transport, several theoretical methods have been developed. For instance, the master equation approach treating the tunneling event semi-classically, is often utilized to explain the Coulomb blockade phenomena, as described in the book by Bruus and Flensberg (2004).

Anderson model for the Kondo problem

The model of the quantum dot is equivalent to the Anderson Hamiltonian which has been extensively studied for the Kondo problem on a magnetic impurity in a metal. The quantum dot corresponds to the magnetic impurity and the leads correspond to the metal. The equivalence of the models can be shown by the unitary transformation for the conduction electrons $s_k = (V_\mathrm{L} c_{\mathrm{L}k\sigma} + V_\mathrm{R} c_{\mathrm{R}k\sigma})/V$, where $V = \sqrt{|V_\mathrm{L}|^2 + |V_\mathrm{R}|^2}$ is the hybridization with the conduction electron states. Electronic states of the anti-symmetric combination $a_k = (V_\mathrm{L} c_{\mathrm{L}k\sigma} - V_\mathrm{R} c_{\mathrm{R}k\sigma})/V$ are disconnected to the orbital state in the quantum dot and can be discarded.

It is not easy to calculate the density of states even for such a simplified model. An analytical expression of the density of states is available for some limited cases as will be shown in this section. The detailed theoretical treatment on the Anderson model and related topics for a magnetic impurity in a metal can be found in the books by Yosida (1996), Hewson (1997), and Kondo (2012).

In the following subsections we shall consider some approximated cases, and overview the studies of the Kondo problem from the viewpoint of the Kondo effect in the quantum dot.

Isolated quantum dot approximation

Let us first consider the approximation $V_\ell = 0$, for which the quantum dot is isolated from the leads. The approximation corresponds to that is called the atomic limit in the study of the Anderson model. The density of states is given with the Dirac delta function as

$$\rho_{\mathrm{d}}(\varepsilon)=\left(1-\frac{\langle n_{\mathrm{d}}\rangle}{2}\right)\delta(\varepsilon-\varepsilon_{\mathrm{d}})+\frac{\langle n_{\mathrm{d}}\rangle}{2}\delta(\varepsilon-(\varepsilon_{\mathrm{d}}+U)), \tag{7}$$

for the non-magnetic solution $\langle n_{\mathrm{d}\uparrow}\rangle=\langle n_{\mathrm{d}\downarrow}\rangle=\langle n_{\mathrm{d}}\rangle/2$.

The number of electrons in the quantum dot changes at $\varepsilon_{\mathrm{d}}=0$ and $\varepsilon_{\mathrm{d}}+U=0$ for the solution at $T=0$. It is summarized as

$$\langle n_{\mathrm{d}}\rangle=\begin{cases}0 & \varepsilon_{\mathrm{d}}>0\\ 1 & -U<\varepsilon_{\mathrm{d}}<0\\ 2 & \varepsilon_{\mathrm{d}}<-U\end{cases} \tag{8}$$

The density of states shows peaks at $\varepsilon=\varepsilon_{\mathrm{d}}$ and $\varepsilon=\varepsilon_{\mathrm{d}}+U$. Therefore, the conductance as a function of ε_{d} has peaks at $\varepsilon_{\mathrm{d}}=0$ and $\varepsilon_{\mathrm{d}}=-U$ at which $\langle n_{\mathrm{d}}\rangle$ changes. These peaks are the Coulomb peaks. The Coulomb blockade phenomena can be captured with the approximations treating the tunnel coupling perturbatively including the master equation method.

At low temperatures, the electron transport shows a remarkable difference from the Coulomb blockade in the region of $\langle n_{\mathrm{d}}\rangle=1$. This is the main topic of this chapter. In the next subsection, we shall discuss another approximation which can be extended to describe the phenomena with the Kondo effect at low temperatures.

Non-interacting approximation

For the non-interacting case $U=0$, the problem is reduced to the single-particle problem. In this case the density of states is given by the Lorentzian function

$$\rho_{\mathrm{d}}(\varepsilon)=\frac{1}{\pi}\frac{\Gamma}{(\varepsilon-\varepsilon_{\mathrm{d}})^2+\Gamma^2}. \tag{9}$$

In this case we have the following relation between the density of states at the Fermi energy and the number of electrons in the dot at $T=0$

$$\pi\Gamma\rho_{\mathrm{d}}(0)=\sin^2\left(\frac{\pi}{2}\langle n_{\mathrm{d}}\rangle\right). \tag{10}$$

Therefore, the conductance is given by the number of electrons in the quantum dot as

$$G=\frac{2e^2}{h}\alpha\sin^2\left(\frac{\pi}{2}\langle n_{\mathrm{d}}\rangle\right). \tag{11}$$

This equation shows that the conductance has a maximum value $(2e^2/h)\alpha$ when $\langle n_{\mathrm{d}}\rangle=1$. The large conductance is due to the resonant tunneling through the energy level located at the Fermi energy $\varepsilon_{\mathrm{d}}=\varepsilon_{\mathrm{F}}$. Interestingly, the equation holds for the interacting case at low temperatures in which the system being the Fermi liquid, as described later.

Kondo problem for a magnetic impurity in a metal

As mentioned above, the Anderson model had been extensively investigated for the Kondo problem. Here we shall briefly overview these studies while focusing on the density of states.

A local spin moment appears due to the Coulomb interaction between the localized electrons. This local spin moment interacts with the conduction electrons via an exchange interaction $J=-V^2\{1/|\varepsilon_{\mathrm{d}}|+1/(\varepsilon_{\mathrm{d}}+U)\}<0$. This is the s-d model which can be deduced from the Anderson model as its effective Hamiltonian via a transformation treating the hybridization term as perturbation.

As was shown by Kondo in 1964 with the s-d model, the scattering of the conduction electrons by the local spin moment has a term $\ln T$, which increases logarithmically when the temperature T is lowered, within the second order perturbation in J. The scattering T-matrix has a contribution $\ln|\varepsilon|$ and it is connected to the local Green function G_{d} as $T=VG_{\mathrm{d}}V$. Then the logarithm corresponds to a resonance in the density of states $\rho_{\mathrm{d}}(=-\operatorname{Im}G_{\mathrm{d}}/\pi)$ at the Fermi energy at low temperatures.

The perturbation calculation in J is not valid at low temperatures since the $\ln T$ divergence. The perturbation in J, namely the perturbation in V, describes the system for high temperatures $T\gg T_K$, where T_K is known as the Kondo temperature.

At low temperatures $T\ll T_K$ the local spin strongly couples to the conduction electrons and falls into a spin singlet state. The U–perturbation theory describes the Fermi liquid properties of the system at low temperatures. The density of states near the Fermi energy is approximately expressed by Eq. (9) where the parameters are replaced by the renormalized ones: $\varepsilon_{\mathrm{d}}\to\tilde{\varepsilon}_{\mathrm{d}}\sim 0$, $\Gamma\to\tilde{\Gamma}\sim T_{\mathrm{K}}$. The density of states has a resonance peak referred to as the Kondo peak at the Fermi energy with the large value $\pi\Gamma\rho_{\mathrm{d}}(0)=1$ for $\langle n_{\mathrm{d}}\rangle=1$.

It is important for the Kondo effect in the quantum dot that Eq. (10) holds at low temperatures even for the interacting case. Then, as expressed in Eq. (11), the large value of the conductance for $\langle n_{\mathrm{d}}\rangle=1$ appears as the Kondo plateau. A natural question then is: how does the conductance change from the Coulomb peaks to the Kondo plateau as the temperature decreases?

Various approaches beyond the perturbation have been developed. The numerical renormalization group (NRG) method introduced by Wilson in 1975 successfully covers the crossover of the system state from magnetic at high temperatures to nonmagnetic at low temperatures. Later, an exact solution using the Bethe ansatz confirmed Wilson's calculation. The dynamical excitation spectra such as the density of states cannot be calculated via the Bethe ansatz. The NRG has been developed to calculate these quantities in the wide range of energy and temperature. It provides a powerful tool for the calculation of the Kondo systems. For the development of the NRG method see the review by Bulla et al. (2008).

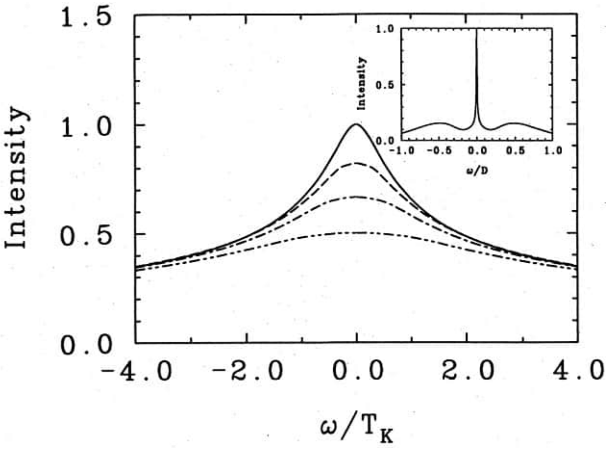

Fig. 3 Local density of states $\pi\Gamma\rho_d(\omega)$ calculated by using the NRG method. The parameters are $\Gamma = 0.03\pi$ and $U = 1.0$. The temperatures are $T/T_K = 0$ (solid line), 0.35 (dashed line), 0.7 (dot-dashed line) and 1.4 (two-dots-dashed line), where $T_K = 3.34 \times 10^{-3}$. The constant conduction band from $-D$ to D is assumed and D is chosen as the energy unit. Reproduced with permission from Shimizu Y and Sakai O (1995) Computatioonal Physics as a New Frontier in Condensed Matter Research, Study on the Excitation Spectra of the Strongly Correlated Electron Systems based on the Numerical Renormalization Group Method – Single Impurity and Infinite Dimensional Lattice Models–, 42–50. The Physical Society of Japan, 1995.). (c) 1995 The Physical Society of Japan.

We shall present the density of states calculated by the NRG in the next subsection.

Emergence of the Kondo peak

As mentioned in the previous subsection, the Kondo peak emerges when the temperature decreases. The Kondo peak plays an important role in the transport through the quantum dot. Here we shall show the density of states calculated by the NRG method.

Fig. 3 shows the calculated local density of states for the electron-hole symmetric case $\varepsilon_d + 2U = 0$ by Shimizu and Sakai (1995). This result clearly shows the expected behaviors from the discussion in the above subsections. The peaks around ε_d and $\varepsilon_d + U$ are originated from the charge excitation. The sharp and narrow peak at the Fermi energy is the Kondo peak. It is important to note that the intensity of the Kondo peak increases when the temperature decreases in the low temperatures $T < T_K$

In the next section we will show how the conductance changes from the Coulomb peaks to the Kondo plateau when the temperature decreases.

Coulomb peaks to Kondo plateau

The emergence of the Kondo peak plays a significant effect, the resonance tunneling, in the quantum dot at low temperatures. We shall discuss how the conductance changes when the temperature decreases within the NRG calculation.

Fig. 4 shows the calculated conductance as a function of energy of the orbital in the quantum dot ε_d, $G(\varepsilon_d)$, from high to low temperatures for two tunnel coupling cases. The calculation assumes the symmetric coupling i.e., $\alpha = 1$. The calculation shows the typical change of $G(\varepsilon_d)$ from the Coulomb peaks to the Kondo plateau as the temperature decreases.

When the energy of the orbital ε_d decreases, the number of electrons in the quantum dot increases as $\langle n_d \rangle \sim 0 \rightarrow 1$ at $-\varepsilon_d \sim 0$ and $\langle n_d \rangle \sim 1 \rightarrow 2$ at $-\varepsilon_d \sim U$. At high temperatures $T \sim \Gamma$, there are two Coulomb peaks reflecting the change of $\langle n_d \rangle$.

The region $0 < -\varepsilon_d < U$, in which $\langle n_d \rangle \sim 1$, is the region where the Kondo effect takes place at low temperatures. As the temperature decreases, the height of the two peaks grows. At the same time, the peak positions shift to their center. When the temperature further decreases, the conductance at the central region gradually increases. Eventually, the two peaks merge into a single plateau. This plateau is the Kondo plateau. The change of $G(\varepsilon_d)$ from the Coulomb peaks to the Kondo plateau is observed in a wider temperature range for the weaker tunnel coupling case shown in Fig. 4A.

How do we understand the change of conductance: shift of the two peaks, and their merging into the single Kondo plateau when the temperature decreases? An important point in the quantum dot is that the Kondo temperature changes when the control parameter ε_d changes. That is, the Kondo temperature is a function of ε_d. The change of conductance can be naturally understood by exploring this point. In the region between the two Coulomb peaks where $\langle n_d \rangle \sim 1$, the analytical expression of the Kondo temperature is approximately given by

$$T_K = \left(\frac{U\Gamma}{2}\right)^{1/2} \exp\left(\frac{\pi\varepsilon_d(\varepsilon_d + U)}{2U\Gamma}\right). \tag{12}$$

For a fixed ε_d, the conductance as a function of the temperature, $G(T)$, largely increases logarithmically around the Kondo temperature $0.1 < T/T_K < 10$, and then reaches to its low temperature limit value given by Eq. (11). Eq. (12) shows that $T_K(\varepsilon_d)$ has a minimum value at the electron-hole symmetric point $-\varepsilon_d = U/2$, the center of the two Coulomb peaks. $T_K(\varepsilon_d)$ exponentially

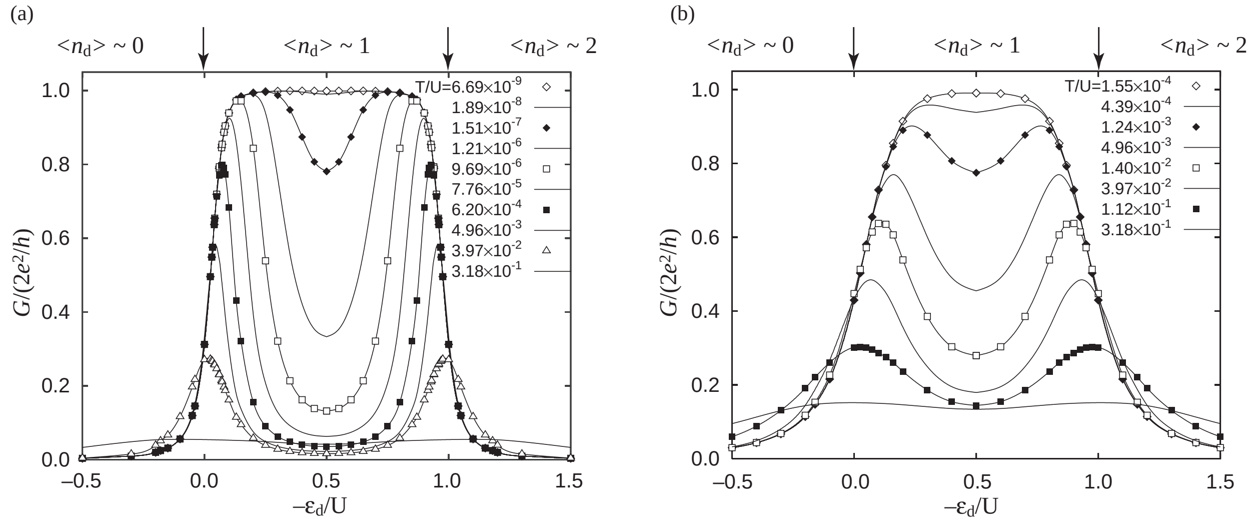

Fig. 4 Calculated conductance as a function of ε_d, $G(\varepsilon_d)$, from high to low temperatures for (A) $\Gamma/\pi U = 1.0 \times 10^{-2}$ and (B) $\Gamma/\pi U = 3.0 \times 10^{-2}$. The number of electrons in the quantum dot is $\langle n_d \rangle \sim 1$ in $0 < -\varepsilon_d < U$ where the Kondo effect takes place. At high temperatures, two Coulomb peaks are observed at $-\varepsilon_d \sim 0$ and $-\varepsilon_d \sim U$ indicated by the vertical arrows. When the temperature decreases, the two peaks grow and shift to their center, and eventually merge into a single plateau, the Kondo plateau. The change of $G(\varepsilon_d)$ is observed in a wider temperature range for the weaker coupling case in (A). The numerical data for the figures are from (Izumida et al. (2001)). Modified from Izumida W, Sakai O, and Suzuki S (2001) Kondo effect in tunneling through a quantum dot. *Journal of the Physical Society of Japan* 70(4):1045–1053.

increases when ε_d deviates from this point. Note that Eq. (12) is meaningless outside the Coulomb peaks where $\langle n_d \rangle \sim 0$ and $\langle n_d \rangle \sim 2$ since it gives a much larger value than the temperature which characterizes the low temperature behavior of the conductance.

The conductance reaches its low temperature limit from the outer sides ($-\varepsilon_d \sim 0$ and $-\varepsilon_d \sim U$) to the center ($-\varepsilon_d = U/2$) when the temperature decreases. As a result, the growth of two peaks with a shift to their center and their merging into a single plateau are observed for decreasing temperatures.

The above discussed change of conductance is in fact, observed in a wider temperature region for the weaker tunnel coupling in Fig. 4A. This is because the difference of the Kondo temperature between the center and outer is larger for the weaker tunnel coupling.

From the above discussion it is clear that a fine tuning of the tunnel coupling is required to observe the well-separated Coulomb peaks to their growth to the Kondo plateau in a moderate temperature range for the experiments. The calculations explain the experimental observations. The details of this section has been reported earlier by Izumida et al. (2001).

Conclusion

In this chapter, the Kondo effect in a quantum dot was explained for the simplest case. The Kondo effect takes place in the electron transport through a quantum dot when the number of electrons in the quantum dot is odd. As the temperature decreases the conductance increases due to the resonant tunneling through the Kondo peaks emerging at the Fermi energy in the density of states in the quantum dot. Two Coulomb peaks gradually grow and shift to their center and they eventually merge into a single Kondo plateau at the lowest temperature. This change of the conductance is explained by the Kondo temperature, which is a function of the gate voltage. Controllable parameters, which are fixed in a related bulk system, provides a variety of the phenomena of the quantum dot.

In the following we briefly introduce some topics which were not elaborated in this chapter. For other topics, see also the chapter by Yamamoto (2023). These topics could include future direction of the research on the Kondo effects in the quantum dots.

The discussions in this chapter were restricted to the linear response conductance. Electron transport away from the linear response regime can be driven by the bias voltage. Measuring the electric current I by sweeping the bias voltage V_{bias}, dI/dV_{bias} is utilized as the measurement of the electron excitation spectra such as the local density of states. In addition, the Kondo effects in the nonequilibrium have been the important and fundamental subjects after the report by Meir et al. (1993). The nonequilibrium effects have been continuously studied and are up-to-date subjects, as can be found in the discussions on construction of effective low-energy Fermi-liquid theory (Oguri and Hewson, 2018; Filippone et al., 2018) and dynamics of splitting Kondo peak (Krivenko et al., 2019). Further, shot noise measurement provides more detail information on the nonequilibrium dynamics such as the effective charge of a charge carrier in the Kondo correlation, as can be found in the review by Kobayashi and Hashisaka (2021).

Non-degeneracy of the orbitals in the quantum dot was implicitly assumed in the explanation of this chapter. If the energy levels of the orbitals are well-separated, then an up-spin and a down-spin moment make a pair to form a spin-singlet state in each orbital.

Therefore, a local spin moment from an unpaired electron in the quantum dot appears only when the number of electrons in the quantum dot is odd. Many experiments support this simplified picture. However, this is not the case when there exists degeneracy of the orbitals as observed in the quantum dots having high symmetry such as vertical quantum dots (Kouwenhoven et al., 2001) and carbon nanotube quantum dots (Laird et al., 2015). Even when the number of electrons in the quantum dot is not only odd but also even, local spin moments in the quantum dot interact with the electrons in the leads then the Kondo effects take place. The multi-orbital effects have been discussed from the early stage as reported and reviewed with the NRG calculation (Izumida et al., 1998, Izumida and Sakai, 2005), and are still being investigated (Teratani et al., 2020).

Free design and control of the quantum system by using the quantum dots hybrid system enable us to investigate more details of the Kondo effects and related phenomena; such as using the double-quantum dot and quantum dots interferometers discussed from the early period of study of the Kondo effects in quantum dots as described in the review (Izumida and Sakai, 2005). Two-impurity Kondo effect, the effect of the competition between the Kondo effect and coupling of two local spin moments, has been studied with the double-quantum dot as discussed in a review (Chang and Chen, 2009). Interference and transmission phase shift related to the Kondo effects have been discussed with the quantum dots interferometers, as hybrid structures of Aharonov-Bohm circuits and quantum dots. They have been still the current topics as described in the literature (Eto and Sakano, 2020).

Exotic Kondo effects studied in bulk systems (Cox and Zawadowski, 1999) have motivated the studies, such as the non-Fermi liquid in the two-channel Kondo effect, with hybrid quantum dot systems as proposed by Oreg and Goldhaber-Gordon (2003). For more detail on this subject see the chapter by Yamamoto (2023).

Motivated by the intensive study on the realization of the Majorana quasi-particles in semiconductor nanowires with the superconducting correlations have triggered the study of the Kondo effect in quantum dots with the superconducting correlation, as can be found in the review by Aguado (2017).

These extensive studies of the Kondo effects in quantum dots are expected to reveal new aspects on the Kondo related physics.

References

Aguado R (2017) Majorana quasiparticles in condensed matter. *La Rivista del Nuovo Cimento* 40: 523.

Bruus H and Flensberg K (2004) *Many-body Quantum Theory in Condensed matter Physics*. Oxford, England: Oxford University Press.

Bulla R, Costi TA, and Pruschke T (2008) Numerical renormalization group method for quantum impurity systems. *Reviews of Modern Physics* 80: 395.

Chang AM and Chen JC (2009) The Kondo effect in coupled-quantum dots. *Reports on Progress in Physics* 72: 096501.

Cox DL and Zawadowski A (1999) *Exotic Kondo Effect In Metals*. Taylor and Francis.

Eto M and Sakano R (2020) Fano-Kondo resonance versus Kondo plateau in an Aharonov-Bohm ring with an embedded quantum dot. *Physical Review B* 102: 245402.

Filippone M, Moca CP, Weichselbaum A, von Delft J, and Mora C (2018) At which magnetic field, exactly, does the Kondo resonance begin to split? a Fermi liquid description of the low-energy properties of the anderson model. *Physical Review B* 98: 075404.

Glazman LI and Raikh ME (1988) Resonant Kondo transparency of a barrier with quasilocal impurity states. *JETP Letters* 47: 378.

Hewson AC (1997) *The Kondo Problem to Heavy Fermions*. Cambridge: Cambridge University Press.

Izumida W and Sakai O (2005) Kondo effect in quantum dot systems –numerical renormalization group study. *Journal of the Physical Society of Japan* 74: 103.

Izumida W, Sakai O, and Shimizu Y (1998) Kondo effect in single quantum dot systems –study with numerical renormalization group method. *Journal of the Physical Society of Japan* 67: 2444.

Izumida W, Sakai O, and Suzuki S (2001) Kondo effect in tunneling through a quantum dot. *Journal of the Physical Society of Japan* 70: 1045.

Kawabata A (1991) On the electron transport through a quantum dot. *Journal of the Physical Society of Japan* 60(10): 3222.

Kobayashi K and Hashisaka M (2021) Shot noise in mesoscopic systems: From single particles to quantum liquids. *Journal of the Physical Society of Japan* 90: 102001.

Kondo J (2012) *The Physics of Dilute Magnetic Alloys*. Cambridge: Cambridge University Press.

Kouwenhoven LP, Austing DG, and Tarucha S (2001) Few-electron quantum dots. *Reports on Progress in Physics* 64(6): 701.

Krivenko I, Kleinhenz J, Cohen G, and Gull E (2019) Dynamics of Kondo voltage splitting after a quantum quench. *Physical Review B* 100: 201104.

Laird EA, Kuemmeth F, Steele GA, Grove-Rasmussen K, Nygård J, Flensberg K, and Kouwenhoven LP (2015) Quantum transport in carbon nanotubes. *Reviews of Modern Physics* 87: 703.

Meir Y, Wingreen NS, and Lee PA (1993) Low-temperature transport through a quantum dot: The Anderson model out of equilibrium. *Physical Review Letters* 70: 2601.

Ng TK and Lee PA (1988) On-site Coulomb repulsion and resonant tunneling. *Physical Review Letters* 61: 1768.

Oguri A and Hewson AC (2018) Higher-order Fermi-liquid corrections for an Anderson impurity away from half filling. *Physical Review Letters* 120: 126802.

Oreg Y and Goldhaber-Gordon D (2003) Two-channel Kondo effect in a modified single electron transistor. *Physical Review Letters* 90: 136602.

Shimizu Y and Sakai O (1995) Computatioonal Physics as a New Frontier in Condensed Matter Research. In: *Study on the Excitation Spectra of the Strongly Correlated Electron Systems based on the Numerical Renormalization Group Method – Single Impurity and Infinite Dimensional Lattice Models*, pp. 42–50. The Physical Society of Japan.

Teratani Y, Sakano R, Hata T, Arakawa T, Ferrier M, Kobayashi K, and Oguri A (2020) Field-induced SU(4) to SU(2) Kondo crossover in a half-filling nanotube dot: Spectral and finite-temperature properties. *Physical Review B* 102: 165106.

Yamamoto M (2023) Kondo effect in quantum dots: Experiment. In: Chakraborty T (ed.) *Encyclopedia of Condensed Matter Physics*, 2nd edn. Amsterdam: Elsevier Inc..

Yosida K (1996) *Theory of Magnetism*. Springer.

Kondo effects in quantum dots: Experiment

Michihisa Yamamoto, RIKEN Center for Emergent Matter Science, Wako, Japan

© 2024 Elsevier Ltd. All rights reserved.

Introduction 388
Overview 389
Transport through a Kondo-correlated quantum dot and universal scaling 389
Phase shift through a spin 1/2 Kondo-correlated quantum dot 391
Spatial extension of the Kondo cloud 392
Varieties of the Kondo effect in quantum dots 392
Non-equilibrium Kondo effect and two-particle scattering 396
Multi-channel Kondo effect 396
Kondo effect with superconductivity 397
Conclusion 397
Acknowledgments 398
References 398
Further reading 399

Abstract

We discuss the experimental research on the Kondo effect using quantum dots. Kondo-correlated quantum dots have been used to demonstrate universal scaling, scattering phase shift, spatial extension, and non-equilibrium properties of tunable Kondo systems. Varieties of the Kondo effects in quantum dots, multi-channel Kondo effect, and coupling of the Kondo state to superconductors are also discussed.

Key points

- Kondo effect for localized spin 1/2 in a quantum dot
- universal scaling
- Kondo phase shift
- spatial extension of the Kondo cloud
- orbital and SU(4) Kondo effect
- charge Kondo effect
- non-equilibrium Kondo effect and scattering between quasi-particles
- multi-channel Kondo effect
- competition between Kondo singlet and Cooper-pair singlet

Introduction

The Kondo effect is known as the screening of localized spins by surrounding conducting electrons. The history of the Kondo effect dates back to 1930s when the development of cryogenic technologies started to allow researchers to measure the electrical resistance of varieties of materials at low temperatures. It was discovered by such experiments that the resistance of metals containing impurities increases at low temperature below around 10 K. It was identified later in 1950s that this happens when a metal is doped with magnetic impurities such as cobalt. It was unexpected because the resistance of a metal should decrease until finally saturates at low temperature owing to the reduction of electron scattering by phonon. This resistance upturn remained a mystery until Jun Kondo pointed out in 1964 that it occurs due to the interaction between the localized spins and the surrounding conducting electrons (Kondo, 1964). He considered the second-order scatterings, where the localized spin can flip through intermediate states that are allowed for a short period of time according to the quantum mechanics. The behavior of the localized spin surrounded by conducting electrons at the low temperature limit was not yet understood that time. This Kondo problem was then solved in the 1980s by the development of various theoretical tools, such as the scaling analysis and numerical renormalization group calculation. The associated ground state of the system known as the Kondo ground state is the many-body singlet state (Yosida, 1966). This state is the superposition of states, in which the localized spin and one of the conducting electrons form a spin-singlet state. The formation of such a many-body singlet state is interpreted as the screening of the localized spin by the conducting electrons.

The quantum dot (QD) offers ideal platforms to study the Kondo effect and demonstrate fundamental properties of the Kondo state (Glazman and Raikh, 1988, Izumida, 2023). The number of electrons in a QD is stabilized by its charging energy. When odd

https://doi.org/10.1016/B978-0-323-90800-9.00159-1

number of electrons are confined in a QD, it contains an electron spin 1/2, which serves as a localized spin. Its coupling to the reservoirs gives rise to the Kondo effect, as the reservoir electrons screen the localized spin in the QD. In the Kondo-correlated QD, the energy levels in the QD, the coupling strength to the reservoirs, and the charging energy are all tunable by means of the gate voltages, through which the Kondo temperature is controlled. The reservoirs attached to this many-body state are used to extract the Kondo physics by the electrical transport experiment. In addition, QDs in semiconductors can be combined with varieties of mesoscopic structures, such as quantum wires, quantum interferometers, and even superconductors.

Realization of the Kondo-correlated QD in the end 1990s triggered intense studies on the tunable Kondo systems using QDs (Goldhaber-Gordon et al., 1998a, Cronenwett et al., 1998). In contrast with bulk metals containing magnetic impurities, the electrical conductance through the QD in the Kondo regime, otherwise in the Coulomb blockade regime, increases at low temperature below the Kondo temperature T_K. This enhancement of the conductance at low temperature is one of the most representative signatures of the Kondo effect in QDs. Fundamental properties and physics of the Kondo-correlated QD have then been investigated. These include universal scaling of the conductance, Fermi liquid natures, the spatial extension, and non-equilibrium properties.

Overview

The Kondo state has several fundamental properties. One is the universal scaling characterized by the scaling energy T_K, which is also known as the Kondo temperature. The physical quantities such as the resistance through a Kondo state, magnetic susceptibility, and specific heat of a Kondo system are expressed as universal functions of T/T_K, where T is the temperature. The Kondo temperature T_K defines the strength of the spin-singlet coupling.

The second is the Fermi liquid nature. The zero-energy scattering through the Kondo state is described by scattering of a single quasi-particle. Since the localized spin is screened, the spin of the incident particle is not altered by the scattering at zero temperature. Instead, the fingerprint of the spin singlet screening appears as the $\pi/2$ phase shift of the scattered particle.

The third is the spatial extension. The many-body spin entanglement around the magnetic impurity is carried by conducting electrons travelling at the Fermi velocity v_F. The many-body spin coherence thus extends by v_F times the characteristic time scale $\hbar/(k_B T_K)$ of the Kondo spin screening dynamics, where $\hbar$ is Planck constant divided by 2π and k_B is the Boltzmann constant. Owing to this spatial extension, the Kondo state is also called "Kondo cloud", as the cloud of conducting electrons that screens the localized spin. The spatial extension $\xi_K = \hbar v_F/(k_B T_K)$ can be much larger than the length scale of the Coulomb interaction, i.e., the classical charge screening length, as well as the associated length scale $\hbar v_F/J$ of the bare Kondo exchange coupling J. The Kondo cloud can thus mediate the spin entanglement between distant locations through the many-body coherence, between which the direct electronic interaction is negligible. The Kondo state is in this sense a large and fully quantum mechanical object.

We first discuss the above-mentioned fundamental properties demonstrated by the experiments using QDs. The universal scaling appears in the conductance through a Kondo-correlated QD obeying a universal function of T/T_K. Quantum interference experiments, where the Kondo-correlated QDs are embedded in electronic interferometers, are used to demonstrate the Kondo phase shift of $\pi/2$ and spatial extension of the Kondo cloud.

We then discuss various Kondo systems realized in QDs and the related physics. In QD systems, not only the spin ½ of an electron confined in the QD but also other quantum numbers of the QD give rise to the Kondo effect. The exactly solvable Kondo system also serves as a platform to study the non-equilibrium physics. Non-equilibrium Kondo states where the scattering between quasi-particles plays a significant role is discussed. Quantum phase transition can also be studied using the Kondo-correlated QDs by the multi-channel Kondo effect in which multiple channels of the reservoirs contribute to the spin screening. Finally, we consider a QD coupled to superconducting leads and discuss the competition between the Kondo singlet and the Cooper-pair singlet.

Transport through a Kondo-correlated quantum dot and universal scaling

We consider a quantum dot (QD) with the charging energy U, which contains odd number of electrons and couples with two reservoirs by tunnel-coupling energies Γ_L and Γ_R. When the orbital degeneracy is lifted at zero magnetic field, the QD contains the spin 1/2. In the Kondo physics, we consider all higher-order tunneling terms between the QD and the reservoirs. The higher-order tunneling results in the formation of the density of states around the Fermi energy of the reservoirs. This density of states is called the Kondo resonance. The width of the Kondo resonance defines the Kondo temperature and is determined by U, $\Gamma = \Gamma_L + \Gamma_R$, and the energy level ϵ_0 of the localized spin with respect to the Fermi energy:

$$k_B T_K = \frac{\sqrt{\Gamma U}}{2} \exp\left\{\frac{\pi \epsilon_0(\epsilon_0 + U)}{\Gamma U}\right\}. \tag{1}$$

Electrons can transport through this Kondo resonance for small bias between the two reservoirs at temperature lower than or comparable with T_K. When the localized spin is fully screened at the low temperature limit, the Kondo resonance is fully developed. In this "unitary limit," the transmission through the QD is described by full transmission of a single channel. Note that only one transmitting channel of the reservoirs that couples most strongly to the QD can usually mediate the Kondo resonance. The conductance at zero temperature becomes

$$G_0 = \frac{2e^2}{h} \frac{4\Gamma_L \Gamma_R}{(\Gamma_L + \Gamma_R)^2} . \tag{2}$$

This conductance reaches the quantized conductance value $2e^2/h$ for $\Gamma_L = \Gamma_R$.

At finite temperatures, the conductance is suppressed from G_0. In the strong-coupling regime defined as $T \ll T_K$, the conductance at temperature T becomes

$$G(T) = G_0 \left[1 - \left(\pi \frac{T}{T_K} \right)^2 \right] \tag{3}$$

.

This quadratic temperature dependence is characteristic of a Fermi liquid. The wide range of temperature dependence of the conductance is calculated using the numerical renormalization group method, from which the so-called empirical formula is derived as

$$G(T) = G_0 \left(\frac{{T'_K}^2}{T^2 + {T'_K}^2} \right)^s , \tag{4}$$

where $T'_K = \frac{T_K}{\sqrt{2^{1/s} - 1}}$, and $s = 0.22 \pm 0.01$ in the Kondo regime (Costi and Hewson, 1992). At high temperature $T \gg T_K$, the Kondo effect is suppressed. Eq. (4) indicates that $G(T)/G_0$ only depends on T/T_K, irrespective of the other parameters, U, Γ, and ϵ_0.

Fig. 1 shows the experimental observation of the Kondo effect in the unitary limit (van der Wiel et al., 2000). In this experiment, the linear conductance through a Kondo correlated QD was measured as a function of the gate voltage V_{gl} that directly tunes the energy level ϵ_0 and slightly affects Γ with the temperature T as a parameter. The Kondo effect occurs at the conductance valleys called Kondo valleys around $V_{gl} = -413$ mV and -375 mV, where the conductance is suppressed at relatively high temperatures but reaches almost $2e^2/h$ at low temperature. This $2e^2/h$ conductance implies $\Gamma_L \sim \Gamma_R$ from Eq. (2) and that the Kondo resonance is almost fully developed at the lowest measurement temperature. The Kondo temperature is evaluated from the temperature dependence of the conductance using the empirical formula in Eq. (4) for each gate voltage V_{gl}. While $G(T)$ depends on V_{gl}, all data points collapse onto a single curve when the conductance is plotted as a function of T/T_K. This universal scaling of the conductance on T_K is one of the most remarkable properties of the Kondo-correlated QD.

When ϵ_0 becomes close to zero, or the localized level is close to the Fermi energy, i.e., near the Coulomb peaks, the number of the electrons in the QD fluctuates and the spin is not localized. Such a regime is known as the "mixed valence regime". Although the conductance still increases with lowering the temperature in this regime, the temperature dependence becomes different from the one in the Kondo regime. In Eq. (4) , s deviates from $\sim$0.2 of the Kondo regime (Goldhaber-Gordon et al., 1998b)

The conductance through a Kondo-correlated QD also depends on the source-drain voltage V_{sd} (bias voltage between the two reservoirs) and the magnetic field B. Since the Kondo state is a quantum object of the energy scale $k_B T_K$, the large V_{sd} far exceeding $k_B T_K/e$ destroys the Kondo state. The differential conductance dI/dV_{sd} as a function of V_{sd} shows a peak at zero bias with the width of the order of $k_B T_K$. The magnetic field, on the other hand, lifts the degeneracy between the two spin states by the Zeeman energy. This also suppresses the Kondo effect. For dI/dV_{sd} as a function of V_{sd}, the zero bias peak is suppressed as B increases. At $g\mu_B B \sim 0.4 k_B T_K$, the peak starts to split into two at $\pm g\mu_B B$ by twice Zeeman energy, where g is the g-factor and μ_B is the Bohr magneton (Oguri and Hewson, 2018). These peaks also disappear for $g\mu_B B \gg k_B T_K$.

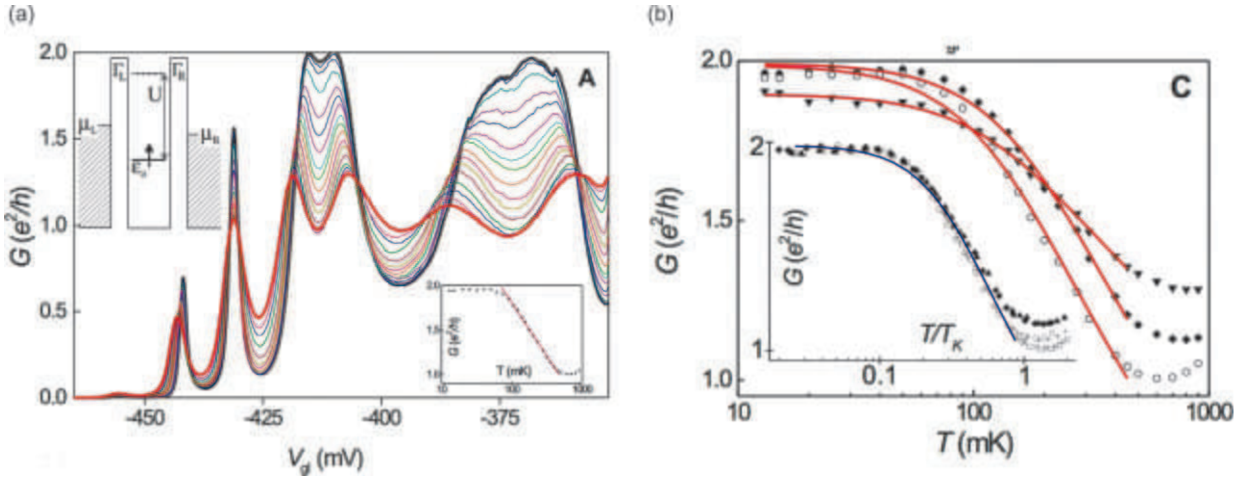

Fig. 1 The Kondo effect in the unitary limit and universal scaling. (a) Conductance through a Kondo-correlated quantum dot (QD) measured as a plunger gate voltage that shifts energy levels of the QD with temperature as a parameter. Upper inset is the schematic of the Kondo-correlated QD. Lower inset is the temperature dependence at $V_{gl} = -413$ mV. (b) Temperature dependence of the conductance as a function of the temperature for different V_{gl}. Data is fitted to the empirical formula to extract the Kondo temperature. Inset is the same data plotted as a function of T/T_K. The figure is taken from ref. van der Wiel WG. et al. (2000) The Kondo effect in the unitary limit. *Science* 289: 2105–2108.

Phase shift through a spin 1/2 Kondo-correlated quantum dot

The phase shift of a single particle scattered off a QD is generally described by the Friedel sum rule, which is valid in the Fermi liquid or single-particle scattering regime:

$$\Delta\varphi = \pi N. \tag{5}$$

Here $\Delta\varphi$ is the phase shift of the particle and N is the number of electrons in the QD. When the energy levels in the QD are swept, the phase shift generally changes by π across a resonance through which one electron is added to the QD. At resonance, where electrons can transmit through the QD, $\Delta\varphi$ differs by $\pi/2$ from the one at off-resonance.

The Kondo ground state is known as a local Fermi liquid (Nozières, 1974), where the Friedel sum rule is applicable. Since this state is the many-body singlet state, both spin-up and spin-down states of the QD are occupied by half, i.e., $N = 1/2$.This leads to the $\pi/2$ phase shift through the Kondo-correlated QD according to Eq. (5). Since the $\pi/2$ phase shift occurs in a resonant scattering in general, there appears a resonance state aligned at the Fermi energy. The formation of the Kondo resonance is thus also understood as a consequence of the spin-singlet screening and the Friedel sum rule. On the same footing, observation of the $\pi/2$ phase shift is the direct evidence of the spin screening (Gerland et al., 2000). Indeed, there is one-to-one correspondence between the conductance and the phase shift at the low temperature limit.

This $\pi/2$ phase shift appears, for instance, in the context of "anti-Kondo effect" (Kang et al., 2001). The anti-Kondo effect occurs when a Kondo correlated QD is side-coupled to a quantum wire. An electron travelling through the quantum wire interferes between the path of direct transmission and the one that experiences a round trip through the Kondo-correlated QD. In the round trip through the QD, the electron acquires the phase shift of 2 times $\pi/2$. The resulting π phase shift leads to the destructive interference with the direct path. The conductance through the quantum wire is thus suppressed in the Kondo regime. Sato et al. demonstrated this Anti-Kondo effect in such a system and showed that the result is consistent with the Kondo $\pi/2$ phase shift (Sato et al., 2005). They revealed the "Fano-Kondo" effect, where a continuous mode of the quantum wire interferes with the discrete Kondo level.

The more direct and precise measurement of the Kondo phase shift was realized by embedding a Kondo-correlated QD in one of the paths of an electronic two-path interferometer (Takada et al., 2014). The setup demonstrated in ref. (Takada et al., 2014) allows for measurement of the phase shift with precision much higher than 0.1π. In the interferometer shown in Fig. 2A, the relative phase

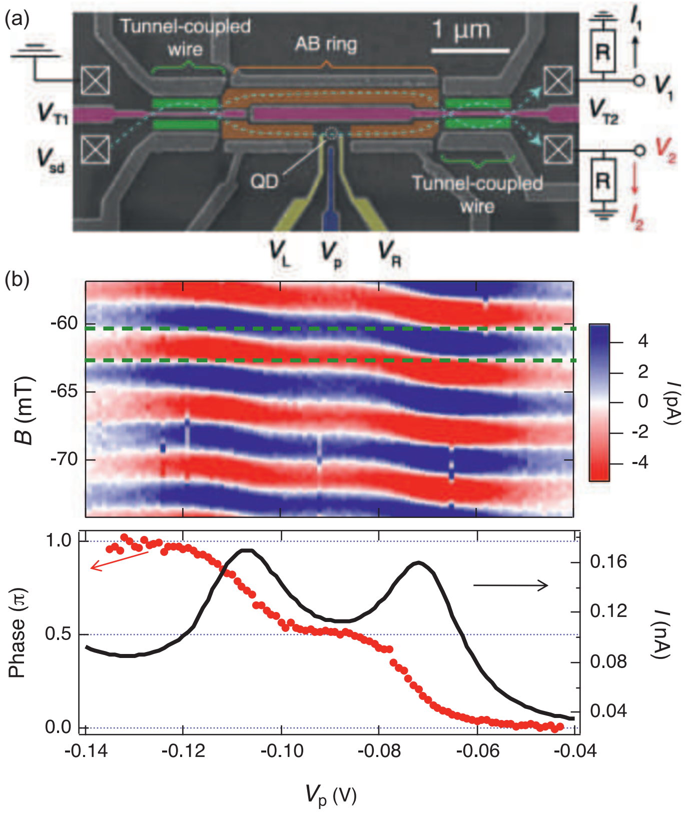

Fig. 2 Measurement of the Kondo phase shift as the proof of spin screening. (A) The quantum interferometer device used to measure the Kondo phase shift. The interferometer works as an electronic Mach-Zehnder interferometer when the tunnel-coupled wires are tuned to act as beam splitters. The Kondo-correlated quantum dot is embedded in one of the arms of the Aharonov-Bohm (AB) ring. (B) Observed AB oscillation with V_p as a parameter at $T \sim 40$mK (upper panel: oscillating component of the current I_2) and extracted phase shift across the QD plotted with the average current I_2 (lower panel). The phase plateau at $\pi/2$ appears in the Kondo valley around $V_p = -0.09$ V. $T_K \sim 50$ mK in the middle of the Kondo valley. Data is identical with the one presented in ref. Takada S et al. (2014) Transmission phase in the Kondo regime revealed in a two-path interferometer. *Physical Review Letters* 113: 126601.

between the two paths can be modulated by the perpendicular magnetic field via the Aharonov-Bohm (AB) phase. The transmission phase through the Kondo-correlated QD is measured as the phase of the AB oscillation. In Fig. 2B, the Kondo $\pi/2$ phase shift appears as a plateau in the Kondo valley for $T < T_K$. The comparison of this experimental observation with numerical renormalization group calculations also allowed for precise evaluation of the Kondo temperature.

In the mixed valence regime, where ϵ_0 becomes away from the middle of the Kondo valley and Γ/U is too large, the phase shift deviates from $\pi/2$. This is because the density of states that originates from the higher order tunneling no longer aligns with the Fermi energy and becomes away from the resonance. This phase shift in the mixed valence regime has also been experimentally confirmed (Takada et al., 2016).

Spatial extension of the Kondo cloud

The spatial extension $\xi_K = \hbar v_F/(k_B T_K)$ of the Kondo cloud is one of the most important properties of the Kondo state (Affleck, 2010). As mentioned above, the many-body spin coherence carried by the conducting electrons extends by $\xi_K = v_F/(k_B T_K)$ beyond the direct electronic and magnetic coupling distance. This cloud mediates the quantum mechanical coupling between distant spins to entangle them and plays an important role in variety of strongly correlated systems.

This spatial extension had attracted considerable attention since the infancy of the Kondo physics and numerous experiments have been attempted to detect it. Difficulty in detecting the Kondo cloud stems from the short time scale $\tau_K = \hbar/(k_B T_K)$ of the typical Kondo dynamics, $\tau_K \sim 60$ ps for $T_K = 100$ mK. One would need to measure the spin correlation between different positions within τ_K before the spins rotate, if one directly tries to detect the Kondo cloud via the spin correlation. This is a challenging task for the present technology. Alternative ways to detect the Kondo cloud have been proposed theoretically using QDs with finite size reservoirs of length L. Since ξ_K is the only length scale associated with the Kondo effect, certain physical quantity should be a universal function of L/ξ_K, similarly with the conductance being a universal function of T/T_K. In these schemes, because the energy spacing of a finite size one-dimensional reservoir of length L is $\delta\epsilon \sim \pi\hbar v_F/L$ and $\xi_K = \hbar v_F/(k_B T_K)$, L/ξ_K can be replaced with $k_B T_K/\delta\epsilon$. Therefore, one might argue that these schemes do not detect the length scale but merely compare the energy scales $k_B T_K$ and $\delta\epsilon$. However, as clearly stated in ref. 11, this conversion between the length scale and the energy scale is the essence of the coherent extension of the Kondo cloud. This conversion is possible only when the spin singlet coherence is extended over the length scale of ξ_K, which justifies the Kondo cloud detection by the L/ξ_K scaling.

Experimental observation of the Kondo cloud was realized recently in this strategy, employing a Kondo-correlated QD coupling on one side to a Fabry-Perot (FP) interferometer of variable length L, which further couples to a macroscopic reservoir (Borzenets et al., 2020). In the device shown in Fig. 3A, the QD is tuned to be more strongly coupled to the right one-dimensional reservoir that houses the FP interferometer to form a Kondo cloud there. In this setup, T_K is affected by the FP interference through modulation of the density of states of the reservoir if the Kondo cloud extends to the end of the FP interferometer. This results in oscillation of the Kondo temperature when the gate voltage V_{QPC} of one of the quantum point contacts (QPCs) is swept to change the FP interferometer length L by the order of Fermi wavelength. Using the maximum $T_{K,max}$ and minimum $T_{K,min}$ of the Kondo temperature oscillation, the modulation of the Kondo temperature is quantified by $T_{K,max}/T_{K,min}$, while the bare Kondo temperature and bare Kondo screening length without the interferometer are $T_{K,\infty} \approx (T_{K,max}/T_{K,min})^{0.5}$ and $\xi_{K,\infty} = \hbar v_F/(k_B T_{K,\infty})$, respectively. Defining the parameter $0 \le \eta \le 1$ of the density of states modulation, $T_{K,max}/T_{K,min}$ becomes a universal function of η and $L/\xi_{K,\infty}$, irrespective of other parameters. For small perturbation $\eta \ll 1$,

$$\ln(T_{K,max}/T_{K,\infty})/\eta = -\ln(L/\xi_{K,\infty}) \tag{6}$$

is simply a function of $L/\xi_{K,\infty}$. This function can be interpreted as the universal shape of the Kondo cloud.

Fig. 3B shows the universal shape of the Kondo cloud obtained in the experiment. While the FP interference was activated by three QPCs with different L, all data points collapse on a single curve, irrespective of the other parameters such as Γ, ϵ_0, and $T_{K,\infty}$. This result shows that the cloud mostly lies within ξ_K and accompanies a long tail beyond ξ_K. The absolute value of the spatial extension $\xi_K = \hbar v_F/(k_B T_K)$ was also confirmed, which is the order of several micrometers. On the other hand, the charge screening length that is comparable with the distance from the surface gate to the one-dimensional channel is the order of 200-300 nm. It confirms that the spatial extension of the spin entanglement is much larger than the length of the direct electronic or magnetic exchange interaction. This result also confirms indirectly that the time scale of the Kondo dynamics is $\tau_K = \xi_K/v_F = \hbar/(k_B T_K)$.

Varieties of the Kondo effect in quantum dots

We have discussed the standard Kondo effect occurring for a localized spin 1/2 in a QD screened by conducting electrons of reservoirs. However, the Kondo effect does not only occur for a localized spin 1/2 but also for other degenerate states. QDs serve as platforms to study varieties of the tunable Kondo effect, which are often not accessible in other systems. In this section, we describe some of the varieties, although we do not attempt to discuss all of them here.

As the first example, suppose there are two electrons confined in a QD. In the presence of a high perpendicular magnetic field B, spin triplet $S = 1$ state with 3-fold degeneracy becomes the ground state owing to the exchange interaction. Strictly saying,

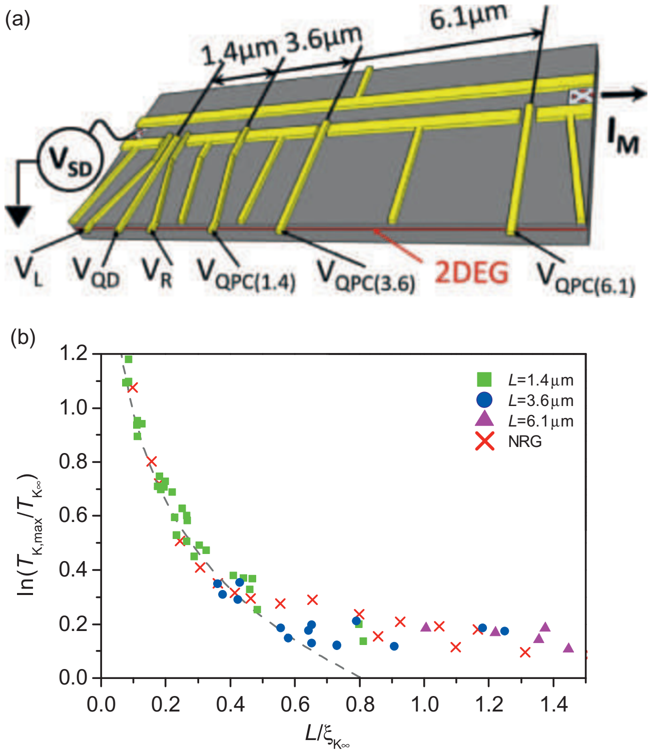

Fig. 3 Observation of the Kondo cloud. (A) Schematic of the device used for observation of the Kondo cloud. (B) Real shape of the Kondo cloud. Modulation of the Kondo temperature by V_{QPC} for the density of states modulation of ~10% is plotted as a function of $L/\xi_{K,\infty}$. The data deviate from the analytical formula of Eq. (6) (grey dashed curve) for large $L/\xi_{K,\infty}$. In this experiment, T_K was evaluated from the temperature dependence of the conductance and using the empirical formula (Eq. 4). This empirical formula is valid for the constant density of states of the reservoirs. For large $L/\xi_{K,\infty}$, the modulation of the density of states induced by the FP interference is not negligible in the energy scale of $k_B T_K$, leading to the deviation of obtained T_K from the one calculated for the constant density of states. However, numerical renormalization group calculation of the temperature dependence of the conductance and its fit to the empirical formula (red crosses) reproduce the experimental observation. Figure is taken from ref. Borzenets IV et al. (2020) Observation of the Kondo screening cloud. *Nature* 579: 210–213.

degeneracy of the $S = 1$ states is lifted by the Zeeman energy, however, they can be regarded as in degeneracy if the Zeeman splitting is smaller than the other energy scales of the system. This degenerate $S = 1$ state and coupling to the reservoirs also give rise to the Kondo effect. As mentioned, the Kondo state is usually mediated by a single channel of the reservoirs. If it is also the case, the single channel ($S = 1/2$) is not enough to fully screen $S = 1$ consisting of two electrons. This situation is called "under screening". However, the $S = 1$ state in the QD involves two orbitals owing to the antisymmetric two-body orbital wave function for the exchange of the two particles, through which two channels in the reservoirs can contribute to the spin screening. Therefore, we expect full screening of the localized $S = 1$ at zero temperature. On the other hand, the Hund's coupling suppresses the Kondo temperature. it has not been possible to observe it in QD systems owing to the small T_K.

The situation becomes different at certain B, where the spin singlet $S = 0$ and triplet $S = 1$ states become degenerate. Because $S = 0$ state can couple to all three $S = 1$ states via cotunneling (higher order tunnel coupling to the reservoirs) through vertical states, the spin screening is further promoted. The Kondo temperature T_K is enhanced and becomes even larger than that of the $S = 1/2$ Kondo effect. Fig. 4 shows the observation of the Kondo effect at the singlet-triplet degeneracy demonstrated using a rectangular vertical QD (Sasaki et al., 2000). The Kondo effect arises for $N = 6$ exactly at the transition between the spin singlet and triplet state. At the transition ($B = 0.22$ T), the Zeeman energy is much smaller than the Kondo temperature and thus the strong Kondo effect is observed in the transport experiment as enhancement of the linear conductance at low temperatures.

There are also other types of the "orbital" Kondo effect, which occurs when there are degenerate orbitals in a QD. The orbital degree of freedom or the orbital polarization can be screened by the reservoir electrons at low temperature. The orbital Kondo effect was also observed for a carbon nanotube QD that has the degenerate clockwise $|+\rangle$ and anti – clockwise $|-\rangle$ orbitals originating from the K and K′ valley of graphene (Jarillo-Herrero et al., 2005). When the magnetic field B is applied to the direction parallel to the nanotube, energy levels of the QD shift toward opposite directions between $|+\rangle$ or $|-\rangle$. At a certain B, while the spin degeneracy is lifted by the Zeeman energy, two different orbital states of the same spin, one from $|+\rangle$ and the other from $|-\rangle$, become degenerate. The purely orbital Kondo effect occurs around this degeneracy point. At $B = 0$, there is 4-fold degeneracy originating from the spin and orbital. The Kondo effect for the SU(4) symmetry (SU(4) Kondo effect) was also demonstrated (see the following section and Fig. 5).

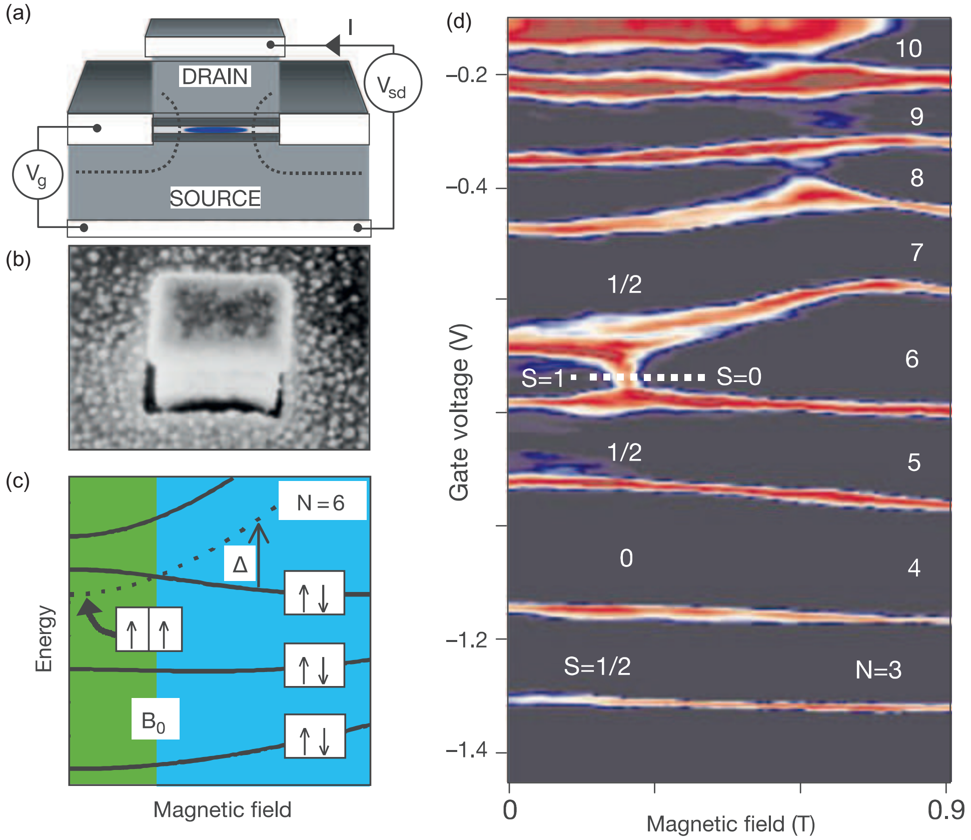

Fig. 4 The $S = 1$ Kondo effect. (A) and (B) schematic and scanning electron microscopy (SEM) image of the rectangle vertical quantum dot. (C) Schematic energy diagram of the electron state as a function of the magnetic field. (D) Observation of the $S = 1$ Kondo effect. It appears for $N = 6$ at $B = 0.22$ T as enhancement of the zero bias linear conductance (color scale) in the Coulomb blockade regime. Figure is taken from ref. Sasaki S et al. (2000) Kondo effect in an integer-spin quantum dot. *Nature* 405: 764–767 (Fig. 2).

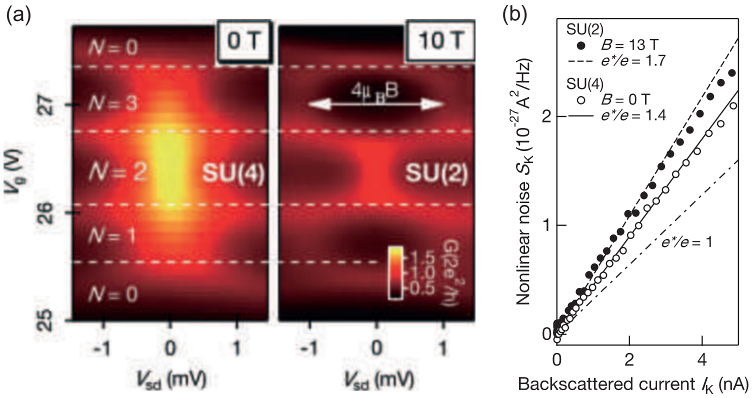

Fig. 5 SU(2) and SU(4) Kondo effect for $N = 2$ of a carbon nanotube quantum dot and effective charge evaluated from the current noise measurement. (A) SU(4) Kondo effect observed at B = 0 and SU(2) Kondo effect observed at B = 10 T. The conductance through the SU(4) Kondo state is twice as large as the one through the SU(2) Kondo state. (B) Enhanced current noise as a function of the backscattered current. The effective charge of the system is evaluated from the slope. Figure is taken from ref. Ferrier M et al. (2017) Quantum fluctuations along symmetry crossover in a Kondo-correlated quantum dot. *Physical Review Letters* 118: 196803.

The orbital effect and SU(4) Kondo effect were also demonstrated for a double quantum dot (DQD) (Keller et al., 2014). In a DQD, the pseudospin defined by the presence of the electron in either of the QDs plays a role of the orbital.

Finally, we briefly discuss the "charge" Kondo effect. The charge Kondo effect was proposed by Matveev (Matveev, 1991) before the standard spin 1/2 Kondo effect was realized for a QD. Consider a relatively large and high-density metallic island (QD), whose orbital energy spacing is much smaller than k_BT but whose charging energy U is larger than k_BT. Suppose also that the spin degree of freedom is absent owing to the application of a high magnetic field. In such a classical degenerate regime, spin and orbital degrees of freedom do not play a role. The only remaining degree of freedom is the charge, defined by the number N of electrons in the island. The charge Kondo effect is expected when the charge N state and $N + 1$ state of the electronic system are degenerate at the resonance of the $(N + 1)$th state *of the island* aligned with the chemical potential of the reservoir. The electron spin of the standard Kondo effect is replaced with the location of the $(N + 1)^{\text{th}}$ electron inside ($|\uparrow\rangle$) or outside ($|\downarrow\rangle$) the island. The misalignment from the degenerate point plays the role of the applied magnetic field. This charge Kondo effect is realized using a metallic island and reservoirs of the spin-polarized quantum Hall edge channels (see Fig. 6A) (Iftikhar et al., 2015). Although the Kondo temperature T_K is relatively low owing to small U, it is easy to control the coupling to the reservoir channels. The charge Kondo system is useful to study multi-channel Kondo effect, where the localized spin is screened by multiple channels. The multi-channel Kondo effect will be discussed in the later section.

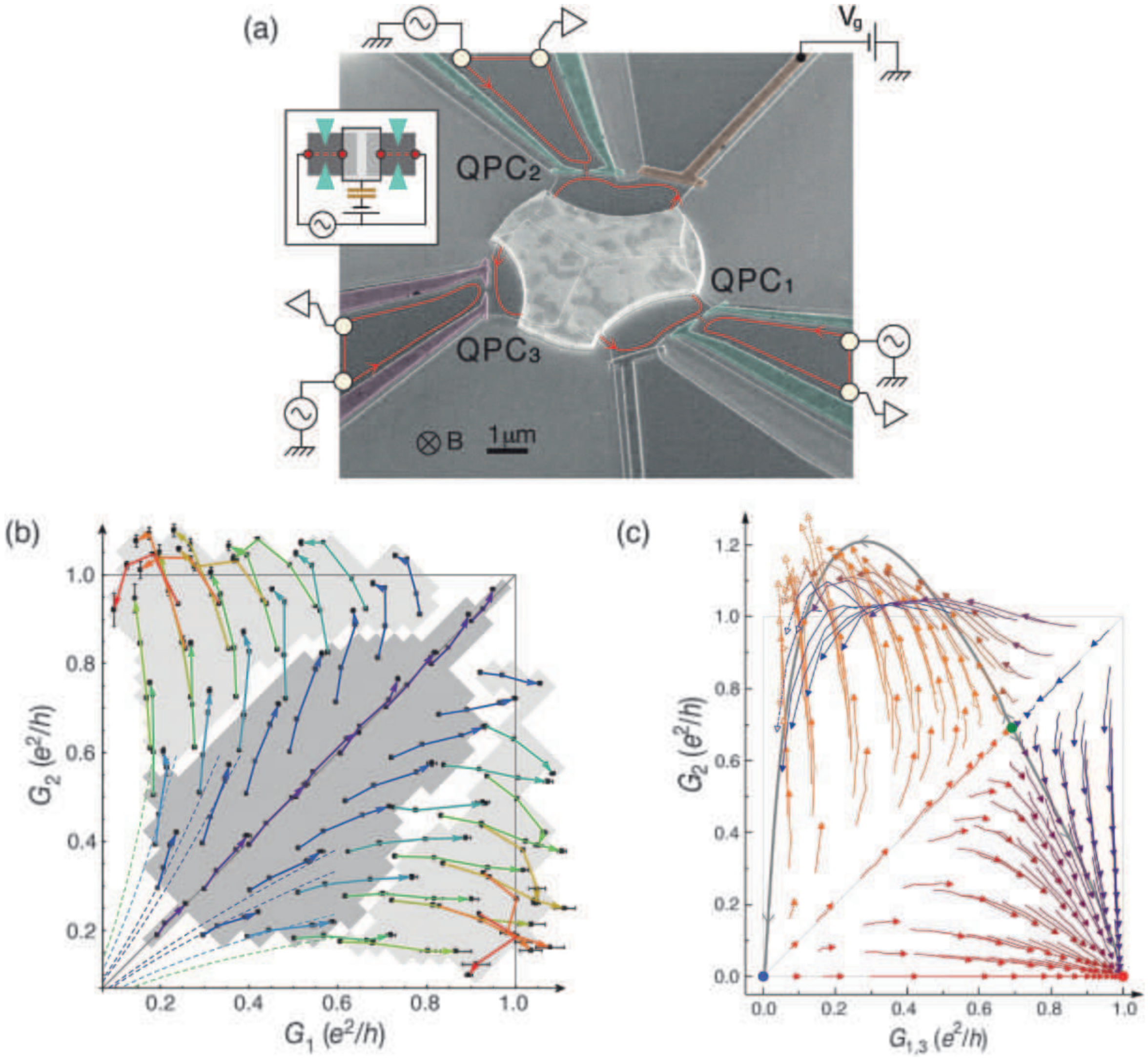

Fig. 6 Charge Kondo effect and renormalization flow of two- and three-channel Kondo effect. (A) SEM image of the device and schematic description of the measurement. Inset is the schematic for the two-channel Kondo experiment. (B) Renormalization flow of the two-channel Kondo effect. Arrows indicate change of the conductance for lowing the temperature. (C) Renormalization flow of the three-channel Kondo effect. The transmission probabilities of QPC1 and QPC3 are identical: $G_1 = G_3$. $G_{1,3} = (G_1 + G_3)/2$ and G_2 were measured while lowering the temperature. For $G_1 = G_2 = G_3$, the system approaches to the three-channel Kondo fixed point (green), otherwise, it approaches to the single channel or two-channel fixed point. Origin of the super-ballistic conductance exceeding e^2/h has not yet been understood. Figures are taken from refs. Iftikhar Z. et al. (2015) Two-channel Kondo effect and renormalization flow with macroscopic quantum charge states. *Nature* 526: 233–236 and Iftikhar Z et al. (2018) Tunable quantum criticality and super-ballistic transport in a “charge” Kondo circuit. *Science* 360: 1315–1320.

Non-equilibrium Kondo effect and two-particle scattering

The Kondo ground state is known as the local Fermi liquid, where zero-energy transport is described in a single quasi-particle picture. When a source-drain bias $V < k_B T_K/e$ is applied to the Kondo-correlated quantum dot, the system is brought into the non-equilibrium Kondo state, where the scattering between quasi-particles also plays a significant role. The two-particle scattering results in enhancement of the effective charge e^* from the electron charge e. $e^*/e = 5/3$ was predicted for the ideal SU(2) (screening of the spin 1/2) Kondo effect (Sela et al., 2006), and $e^*/e = 3/2$ was predicted for the SU(4) Kondo effect at half filling ($N = 2$). More generally, e^* for the SU(N) Kondo effect at half filling is determined by a single parameter R known as Wilson ratio (Sakano et al., 2011, Mora et al., 2009):

$$e* = \frac{1 + 9(N-1)(R-1)^2}{1 + 5(N-1)(R-1)^2}. \tag{7}$$

R characterizes the strength of the spin fluctuation and approaches to $N/(N-1)$ for the ideal Kondo regime. $(R-1)^2$ is determined by the ratio of the "renormalized" U and Γ by the Kondo effect.

The measurement of the current shot noise has widely been used to evaluate the effective charge e* of electronic systems. For the Kondo-correlated QD, influence of the two-particle scattering appears as enhancement of the current noise from the one expected for the single-particle scattering. e^* is obtained from the backscattered current I_K and resulting increase of the current noise power spectrum density S_K as $2e^* = S_K/I_K$. Here, IK is experimentally obtained as the nonlinear part of the current $I_K = I_{sd} - GV_{sd}$, where G is the linear conductance and I_{sd} is the measured total current. S_K is obtained from the measured power spectrum density S and subtracting the single-particle partition noise calculated from the transmission probability of the channel.

Fig. 5 shows the experiment on current noise through a Kondo-correlated QD (Ferrier et al., 2017). A carbon nanotube QD was employed in the experiment. Large U of the QD and resulting large T_K allows for precise evaluation of the effective charge e* at the low temperature limit. When two electrons are confined in the shell of 4-fold spin and orbital degenerate states, it is possible to tune the system between the fully screened SU(4) Kondo regime and the SU(2) Kondo regime by adjusting the magnetic field direction such that orbital energy spacing between $|+\rangle$ or $|-\rangle$ induced by the magnetic field B coincides with the spin Zeeman energy. At $B = 0$, SU(4) Kondo effect occurs owing to 6-fold degeneracy, out of which two states have zero magnetic moment. In the presence of B, the 6-fold degeneracy is lifted, but the spin-polarized and orbital-polarized states still have the same energy, giving rise to the SU(2) Kondo effect. The system therefore undergoes crossover from SU(4) to SU(2) Kondo state by the magnetic field (see Fig. 5A). As seen in Fig. 5B, the theoretically predicted effective charge e^* for the SU(2) and SU(4) Kondo effect was confirmed experimentally.

In the series of experiments, it was confirmed that up to two-particle scattering is usually enough to describe the non-equilibrium transport through the Kondo-correlated QD. However, in the presence of the magnetic field, the three-particle interaction needs to be considered (Hata et al., 2021). Suppression of the dI/dV_{sd} peak around zero bias and its splitting for $g\mu_B B > \sim 0.4 k_B T_K$ observed in experiments are theoretically reproduced by considering the three-particle interaction.

Multi-channel Kondo effect

The Kondo-correlated QDs also serve as platforms to investigate quantum phase transitions because the Kondo physics based on the Anderson impurity model provides solvable problems. In a standard Kondo-correlated QD, only a single channel of the reservoir that most strongly couples to the QD mediates the Kondo state. In certain geometries, however, it is possible to tune the coupling strengths of two or more channels to the QD and make them identical. When two channels of the reservoir are equally coupled to a QD and contribute to the screening of the localized spin, the two-channel Kondo effect occurs (Nozières and Blandin, 1980). In contrast with the standard Kondo state of a single channel, the two-channel Kondo state is known to be a non-Fermi liquid. It locates at the quantum critical point of a parameter space at the border between the two single-channel Kondo states screened by different channels.

In the single-channel Kondo effect, the localized spin $S = 1/2$ is fully screened by the reservoir spin $s = 1/2$ at zero temperature (full screening). In the two-channel Kondo effect, on the other hand, the localized spin is "over-screened". The two reservoir spins $s = 2^*1/2 = 1$ from the two channels that screen the localized spin leaves residual spin 1-1/2 = 1/2, which is further screened by the reservoir electrons. Therefore, the low-energy excitation is no longer a single quasi-particle excitation but collective excitation. Instead of the Fermi liquid's T^2 dependence of the conductance near zero temperature, $T^{0.5}$ dependence is theoretically expected. In more general, when $N(>1)$ channels are equally coupled to the localized spin 1/2, there is a residual entropy of $k_B \ln\left(2\cos\left[\frac{\pi}{N+2}\right]\right)$, which leads to the power law dependence with non-Fermi liquid scaling exponent.

The two-channel Kondo effect was demonstrated using a QD with a localized spin 1/2 connected to three reservoirs (Potok et al., 2007, Keller et al., 2015). One of the reservoirs consists of a large QD directly coupled to the Kondo-correlated QD. The orbital energy spacing of the large QD is smaller than $k_B T$ but its charging energy is larger than $k_B T$. This charging energy isolates the channel through this large QD from those of the other two reservoirs without being affected by the orbital state of the large QD. By tuning the exchange coupling J_1 between the Kondo-correlated QD and the large QD, and J_2 between the Kondo-correlated QD and the other infinite reservoirs, the system can be tuned into the two-channel Kondo regime. The two-channel Kondo regime appears in the vicinity of the quantum critical point $J_1 = J_2$ between the two single-channel Kondo states - one formed in the infinite reservoirs and the other formed in the other reservoir through the large QD. In the experiment, the temperature and source-drain voltage dependence of the conductance of the Kondo-correlated QD through the two reservoirs without the large QD is consistent with theoretical calculation for the two-channel Kondo effect. Under the application of source-drain voltage the deviation of the linear conductance from the zero-bias conductance showedV_{sd}, $\sqrt{V_{\mathrm{sd}}}$ dependence for $k_{\mathrm{B}}T \ll eV_{\mathrm{sd}}$ as expected for the two-channel Kondo effect.

The two-channel Kondo effect was also observed in a charge Kondo system (see Fig. 6) (Iftikhar et al., 2015). By tuning the transmission probability of two quantum point contacts (QPCs), one can tune the system into the two-channel Kondo regime at the quantum criticality. Because the transmission probability τ and charge-pseudospin coupling J has one-to-one correspondence, it is straightforward to achieve $J_1 = J_2$. Experiment in ref. (Iftikhar et al., 2015) revealed "renormalization flow" by measuring the linear conductance G_1 and G_2 of the two QPCs as a function of the temperature (Fig. 6B). Here, G_1 and G_2 are obtained from the conductance matrix of the system. When the temperature is lowered, the system approaches to the single-channel Kondo regime $G_1 \ll G_2 \sim e^2/h$ or $G_2 \ll G_1 \sim e^2/h$ except for $J_1 = J_2$. At $J_1 = J_2$, both G_1 and G_2 approaches to e^2/h at low temperature obeying the universal function of T/T_{K}. Here, T_{K} is determined numerically as a function of the charging energy U of the metallic island and the transmission probability τ of the two QPCs. In this charge two-channel Kondo effect, the conductance of the system through the two QPCs as well as G_1 and G_2 decays linearly with T at low temperature $T \ll T_{\mathrm{K}}$ instead of T^2. This T-linear dependence is unique for the "charge" two-channel Kondo system that has a small bandwidth (Mitchell et al., 2016).

In the charge Kondo system, three-channel Kondo effect was also demonstrated by tuning the three QPCs such that all of them have the same transmission probability (Iftikhar et al., 2018). The linear conductance G_1, G_2, and G_3 of the three QPCs were measured as functions of the temperature. The three-channel Kondo conductance $G_{1,2,3} = (G_1 + G_2 + G_3)/3$ at zero temperature is no longer e^2/h. $G_{1,2,3}$ approaches to $G_{3CK} = 2\sin^2(\pi/5)e^2/h \sim 0.7e^2/h$ at low temperature (see Fig. 6C). $|G_{1,2,3} - G_{3CK}|$ is found to be proportional to $T^{2/5}$, revealing the non-Fermi liquid scaling exponent of the three-channel charge Kondo effect.

Kondo effect with superconductivity

One of the advantages of the Kondo-correlated QD is that the Kondo state can be made coupled with various types of reservoirs such as ferromagnets, superconductors, and even topological insulators. As a typical example, we briefly discuss the experiments on Kondo-correlated QDs coupled to s-wave superconducting leads.

Consider a QD containing spin 1/2 coupled with superconducting leads. There are two competing spin-singlet couplings in the system. One is the Kondo coupling with energy $k_{\mathrm{B}}T_{\mathrm{K}}$, and the other is the Cooper pair coupling with the superconducting gap energy Δ. For $k_{\mathrm{B}}T_{\mathrm{K}} \gg \Delta$, the Kondo coupling is dominant and the localized spin in the QD is screened by forming a sub-gap spin singlet state. For $k_{\mathrm{B}}T_{\mathrm{K}} \ll \Delta$, the Kondo effect is suppressed owing to the absence of states in the superconducting gap, leaving the localized spin as a doublet state. The antiferromagnetic coupling between this spin and superconducting quasiparticles leads to formation of the Yu-Shiba-Rusinov (YSR) state. At $\Delta/(k_{\mathrm{B}}T_{\mathrm{K}}) \sim 1.1$, the first order quantum phase transition between these two states occurs.

The Kondo-correlated QD coupled with superconducting leads has been realized using carbon nanotube QDs, self-assemble InAs QDs, and InAs nanowire QDs, by depositing two superconducting leads (Buitelaar et al., 2002, Eichler et al., 2007, Buizert et al., 2007, Eichler et al., 2009, Kanai et al., 2010). In these Kondo-superconducting QD systems, both T_{K} and Δ can be tuned by means of the gate voltages and magnetic field. Zero bias linear conductance across the superconducting junction reflects the strength of the Kondo effect or the formation of the sub-gap Kondo resonance. It is suppressed for $k_{\mathrm{B}}T_{\mathrm{K}} < \Delta$ even at low temperature $T < T_{\mathrm{K}}$, while it recovers for $k_{\mathrm{B}}T$, $\Delta < k_{\mathrm{B}}T_{\mathrm{K}}$. At low enough temperature, the zero bias conductance normalized by its value for normal metal leads becomes a function of $\Delta/(k_{\mathrm{B}}T_{\mathrm{K}})$ (Buizert et al., 2007).

It is worth noting that the Kondo effect does not only compete with the superconductivity but can also enhance superconductivity. Counter-intuitively, the supercurrent through the QD junction is significantly enhanced for $k_{\mathrm{B}}T_{\mathrm{K}} > \Delta$. This is because the magnetic doublet of the QD that suppresses the supercurrent by forming a π Josephson junction is screened by the Kondo effect. This enhancement of the supercurrent by the Kondo effect has also been experimentally observed (Eichler et al., 2009; Kanai et al., 2010).

Conclusion

Quantum dots serve as platforms to study tunable Kondo effects. Fundamental properties of the Kondo effect such as the universal scaling, phase shift, spatial extension, and non-equilibrium properties have largely been revealed by experiments. Varieties of the Kondo effects, which are not easily accessible in other systems, have also been observed in QD systems.

While the multi-channel Kondo effect and competition with the Cooper-pair coupling have been investigated, phase transitions of systems consisting of Kondo states have not yet been fully understood. These include systems containing multiple magnetic impurities or multiple QDs. It is also important to understand and control dynamics of the Kondo effect. Although observation of the spatial extension $\xi_K = \hbar v_F/(k_B T_K)$ of the Kondo cloud suggests its time scale $\tau_K = \xi_K/v_F = \hbar/(k_B T_K)$, how the Kondo cloud attains its equilibrium state by certain coupling to environment has not yet been revealed.

In-situ control of quantum phase transitions and many-body dynamics of the Kondo systems using QDs may also stimulate further research toward development of novel quantum devices. For example, if one can reveal and control phase transitions and dynamics of Kondo lattice systems, it may become possible to entangle and control distant localized spins via Ruderman–Kittel–Kasuya–Yosida (RKKY) interaction mediated by overlapping Kondo clouds. The multi-channel Kondo systems also involve free Majorana fermions and parafermions, which may be used for topological quantum computation.

Further experiments using Kondo-correlated QDs may address these issues in the future.

Acknowledgments

The author acknowledges Rui Sakano for fruitful discussion and critical reading of the article.

References

Background theory

Glazman LI and Raikh ME (1988) Resonant Kondo transparency of a barrier with quasi local impurity states. *JETP Letters* 47: 452–455.

Izumida W (2023) Kondo effect in quantum dots: Theory. In: Chakraborty T (ed.) *Encyclopedia of Condensed Matter Physics*, 2nd edn Amsterdam: Elsevier Inc.

Kondo J (1964) Resistance minimum in dilute magnetic alloys. *Progress in Theoretical Physics* 32: 37–49.

Yosida K (1966) Bound state due to the s–d exchange interaction. *Physics Review* 147: 223.

The Kondo effect in quantum dots: early works

Cronenwett SM, Oosterkamp TH, and Kouwenhoven LP (1998) A tunable Kondo effect in quantum dots. *Science* 281: 540–544.

Goldhaber-Gordon D, et al. (1998a) Kondo effect in a single-electron transistor. *Nature* 391: 156–159.

Universal scaling of the Kondo effect

Costi TA and Hewson AC (1992) Resistivity cross-over for the non-degenerate Anderson model. *Philosophical Magazine B* 65: 1165. (T_K here is defined differently from the one in Equation (1). They are both defined as scaling energies and of the same order).

Goldhaber-Gordon D, et al. (1998b) From the Kondo Regime to the Mixed-Valence Regime in a Single-Electron Transistor. *Physical Review Letters* 81: 5225.

Oguri A and Hewson AC (2018) Higher-order Fermi-liquid corrections for an Anderson impurity away from half filling: Nonequilibrium transport. *Physical Review B* 97: 035435.

van der Wiel WG, et al. (2000) The Kondo effect in the unitary limit. *Science* 289: 2105–2108.

Observation of the Kondo phase shift

Gerland U, et al. (2000) Transmission phase shift of a quantum dot with kondo correlations. *Physical Review Letters* 84: 3710.

Kang K, et al. (2001) Anti-Kondo resonance in transport through a quantum wire with a side-coupled quantum dot. *Physical Review B* 63: 113304.

Nozières P (1974) A “fermi-liquid” description of the Kondo problem at low temperatures. *Journal of Low Temperature Physics* 17: 31.

Sato M, et al. (2005) Observation of the Fano-Kondo antiresonance in a quantum wire with a side-coupled quantum dot. *Physical Review Letters* 95: 066801.

Takada S, et al. (2016) Low temperature behavior of the transmission phase shift across a Kondo correlated quantum dot. *Physical Review B* 94: 081303.

Takada S, et al. (2014) Transmission phase in the Kondo regime revealed in a two-path interferometer. *Physical Review Letters* 113: 126601.

Observation of the Kondo screening cloud

Affleck I and Entin-Wohlman O (2010) The Kondo screening cloud: What it is and how to observe it. In: Aharony A (ed.) *Perspectives of Mesoscopic Physics*, pp. 1–44. World Scientific Publishing. ch. 1.

Borzenets IV, et al. (2020) Observation of the Kondo screening cloud. *Nature* 579: 210–213.

Varieties of the Kondo effect

Iftikhar Z, et al. (2015) Two-channel Kondo effect and renormalization flow with macroscopic quantum charge states. *Nature* 526: 233–236.

Jarillo-Herrero P, et al. (2005) Orbital Kondo effect in carbon nanotubes. *Nature* 434: 484–488.

Keller A, et al. (2014) Emergent SU(4) Kondo physics in a spin–charge-entangled double quantum dot. *Nature Physics* 10: 145–150.

Matveev KA (1991) Quantum fluctuations of the charge of a metal particle under the Coulomb blockade conditions. *Soviet Physics - JETP* 72: 892–899.

Sasaki S, et al. (2000) Kondo effect in an integer-spin quantum dot. *Nature* 405: 764–767.

Non-equilibrium Kondo effect

Ferrier M, et al. (2017) Quantum fluctuations along symmetry crossover in a Kondo-correlated quantum dot. *Physical Review Letters* 118: 196803.

Hata T, Teratani Y, Arakawa T, et al. (2021) Three-body correlations in nonlinear response of correlated quantum liquid. *Nature Communications* 12: 3233.

Mora C, et al. (2009) Theory of nonequilibrium transport in the SU(N) Kondo regime. *Physical Review B* 80: 155322.

Sakano R, Fujii T, and Oguri A (2011) Kondo crossover in shot noise of a single quantum dot with orbital degeneracy. *Physical Review B* 83: 075440.

Sela E, et al. (2006) Fractional shot noise in the Kondo regime. *Physical Review Letters* 97: 086601.

Multi-channel Kondo effect

Iftikhar Z, et al. (2018) Tunable quantum criticality and super-ballistic transport in a “charge” Kondo circuit. *Science* 360: 1315–1320.

Keller AJ, et al. (2015) Universal Fermi liquid crossover and quantum criticality in a mesoscopic system. *Nature* 526: 237–240.

Mitchell AK, et al. (2016) Universality and scaling in a charge two-channel Kondo device. *Physical Review Letters* 116: 157202.
Nozières P and Blandin A (1980) Kondo effect in real metals. *Journal de Physique* 41: 193–211.
Potok RM, et al. (2007) Observation of the two-channel Kondo effect. *Nature* 446: 167–171.

Kondo vs superconductor

Buitelaar MR, Nussbaumer T, and Schönenberger C (2002) Quantum dot in the Kondo regime coupled to superconductors. *Physical Review Letters* 89: 256801.
Buizert C, et al. (2007) Kondo universal scaling for a quantum dot coupled to superconducting leads. *Physical Review Letters* 99: 136806.
Eichler A, et al. (2007) Even-odd effect in Andreev transport through a carbon nanotube quantum dot. *Physical Review Letters* 99: 126602.
Eichler A, et al. (2009) Tuning the Josephson current in carbon nanotubes with the Kondo effect. *Physical Review B* 79: 161407.
Kanai Y, et al. (2010) Electrical control of Kondo effect and superconducting transport in a side-gated InAs quantum dot Josephson junction. *Physical Review B* 82: 054512.

Further reading

Hewson AC (1997) *The Kondo Problem to Heavy Fermions*. Cambridge University Press.
Kondo J (2012) *The Physics of Dilute Magnetic Alloys*. Cambridge University Press.

Spin textures in quantum dots and quantum rings☆

Wenchen Luo[a], **Shenglin Peng**[b], **and Tapash Chakraborty**[c,d], [a]School of Physics and Electronics & Hunan Key Laboratory of Nanophotonics and Devices, Central South University, Changsha, China; [b]School of Information Science and Technology, Northwest University, Xi'an, China; [c]Department of Physics, Brock University, St. Catharines, ON, Canada; [d]Department of Physics and Astronomy, University of Manitoba, Winnipeg, MB, Canada

© 2024 Elsevier Ltd. All rights reserved.

Introduction **400**
Models **401**
Index characterizing the topology of the spin texture **402**
Spin textures in quantum dots **403**
Analytical treatment for the topological charges of the spin textures 403
Control of the topological charge of the spin textures and the effect of inhomogeneous magnetic field 404
Spin textures in quantum dot helium 406
Spin textures in quantum rings **407**
Various spin textures in QRs 407
Aharonov-Bohm Period of the topological charge of the QR 410
Higher topological charge due to the impurity 411
Conclusion **412**
Acknowledgments **413**
References **413**

Abstract

The textures of the spin fields in geometrically confined systems such as, quantum dots and quantum rings are introduced in this chapter. Analogous to the topological soliton skyrmion, the topological charge of the spin fields in real space are given by the winding numbers and Pontryagin indices. The trivial and non-trivial patterns of the spin fields are discussed. Spin-orbit couplings, inhomogeneous magnetic fields, and density-related effects, such as Coulomb interaction and impurity, make the spin textures vary in style and topologically non-trivial. Different topological charges can be considered to represent information in real devices, thus the manipulation of the topological charge in the quantum dots and rings by external conditions may be useful in spintronics and information techniques.

Key points

- Spin fields are textured topologically in quantum dots and quantum rings when the spin-orbit couplings are present. The topological charge is defined by the winding number.
- Rashba and Dresselhaus spin-orbit couplings induce spin textures with topological charge +1 and −1, respectively, in quantum dots and rings.
- Inhomogeneous magnetic fields texture the spin field with different topological charges higher than ±1 and are possible to form skrymions in quantum dots.
- Coulomb interaction significantly changes the topological charge of the spin textures by deforming the density of electrons.
- The topological charge varies periodically in a quantum ring when both the Rashba and Dresselhaus spin-orbit couplings are present. The period is slightly deviated from the Aharonov-Bohm period by the width of the ring.
- A non-magnetic impurity in a quantum ring is able to promote the topological charge of the spin field to ±2.

Introduction

Topological spin textures have been extensively studied in many systems in condensed matter physics. Basically, the spin fields of electrons are textured by external magnets, spin-orbit coupling (SOC) or the electrons correlations. When the external magnetic field has a non-trivial pattern, the spin field then simply follows the magnetic field and is textured in accordance with the relations provided by the semiclassical Landau-Lifshitz-Gilbert equation. The Dzyaloshinskii-Moriya interaction microscopically induced by the SOC gives rise to spin skyrmions in helical magnets (Mühlbauer et al., 2009; Yu et al., 2010; Nagaosa and Tokura, 2013) and pseudospin skyrmions in a graphene bilayer (Côté et al., 2010, 2011). Synthetic SOCs can also be manufactured in the cold atomic

---

☆*Change History*: August 2022. Authors W Luo, S Peng, and T Chakraborty are involved in preparing the update.

https://doi.org/10.1016/B978-0-323-90800-9.00046-9

gases to texture the spin in a skyrmion-like pattern (Hu et al., 2012; Wilson et al., 2013). In the quantum Hall regime, the single-particle excitations governed by the nonlinear σ models carry topological non-trivial spin textures and the spontaneous symmetry breaking state emerged as the skyrmion or meron crystals (Ezawa, 2000).

In this chapter, we focus on the textured spin fields and their topology in confined nanostructures, e.g., quantum dots (Maksym and Chakraborty, 1990; Chakraborty, 1999; Bimberg et al., 1999; Kouwenhoven et al., 2001; Hanson et al., 2007; Kloeffel and Loss, 2013) and quantum rings (Chakraborty and Pietiläinen, 1995a; Hong-Yi Chen, 2008; Chakraborty et al., 2017, 2018; Wendler and Fomin, 1995; Lucignano et al., 2007). The topological electron states in real space induced by various effects could be important for spintronics and quantum information applications (Žutić et al., 2004; Šmejkal et al., 2018; Gomonay et al., 2017).

If there is no spin-orbit coupling, then the spin is a good quantum number. Each state of the quantum dot or quantum ring can be labeled by the spin quantum number which for simplicity is represented by the eigenvalue of the Pauli matrix σ_z. Thus, for a single-electron state, its spin field is simply polarized along the $\pm z$ axis, and the spin texture is trivial. In a many-electron case, the Coulomb interaction also commutes with σ_z and does not directly and explicitly change the spin textures. Here we restrict ourselves on the single-electron and the two-electron cases for simplicity.

To find non-trivial spin textures in a quantum dot/ring, either inhomogeneous magnetic fields or a spin-orbit coupling (Manchon et al., 2015; Ren et al., 2016) is necessary. The term of SOC (for instance Rashba SOC) in the Hamiltonian can be written as a momentum-dependent gauge. Thus the effect of the SOC can be treated as an effective momentum-dependent magnetic field. Naively, in the momentum space, the spin may be textured to a vortex-like pattern by aligning with this effective magnetic field, which in fact depends on the form of the SOC. However, if there is no confinement or magnetic field in real space, the spin texture would disappear or be as trivial as the polarized spin field. Since the Hamiltonian commutes with the momentum operator and the translational operator, $[\mathcal{H}, p_{x,\,y}] = 0$, the wave function must contain the plane wave part $e^{-i\mathbf{k}\cdot\mathbf{r}}$, where $\mathbf{k}$ is the wave vector, and the spin texture at the single electron level needs to obey the translational symmetry in real space.

Once the space is confined, say in a quantum dot/ring, $[\mathcal{H}, p_{x,\,y}] \neq 0$, the translational symmetry is naturally broken. The spin textures in the momentum space can be recovered in real space. The spin textures in quantum dot hydrogen (a single electron in a QD), quantum dot helium (two electrons in a QD) and the single-electron quantum ring (with and without an impurity) in the presence of magnetic fields will be discussed. For simplicity, only the Rashba and linear Dresselhaus SOCs (Roland, 2003) are considered. Considering that the quantum dot/ring systems can be conveniently tuned by gates, the tuning of the topological features by varying the SOCs and the external fields in these systems are also discussed.

Models

The quantum dots and quantum rings have been extensively studied both theoretically and experimentally for decades. Here we do not constrain ourselves with a specific set-up or material. The general models will be presented here that would be suitable for different materials.

The Hamiltonian is given by four parts $\mathcal{H} = \mathcal{H}_0 + \mathcal{V} + \mathcal{H}_{\mathrm{SOC}} + \mathcal{H}_{\mathrm{C}}$, where $\mathcal{H}_0$ describes the free electron, $\mathcal{V}$ is the confinement potential, $\mathcal{H}_{\mathrm{SOC}}$ contains the SOCs terms, and $\mathcal{H}_{\mathrm{C}}$ represents the Coulomb interaction. The confinement potential is different in QD and QR: $\mathcal{V}_{\mathrm{QD}} = \frac{m^*}{2}\left(\omega_x^2 x^2 + \omega_y^2 y^2\right)$ and $\mathcal{V}_{\mathrm{QR}} = \frac{m^*}{2}\omega^2 (r - R)^2$, where m^* is the effective mass of the electron. The QD could be anisotropic: the confinement frequencies $\omega_{x,y}$ in different directions are independent, while the QR is supposed to be a regular circle with radius R for simplicity. Other terms in the single-particle Hamiltonian read

$$\mathcal{H}_0 = \frac{\mathbf{P}^2}{2m^*} + \frac{\Delta}{2}\sigma_z, \tag{1}$$

$$\mathcal{H}_{\mathrm{SOC}} = g_1\left(\sigma_x P_y - \sigma_y P_x\right) + g_2\left(\sigma_y P_y - \sigma_x P_x\right), \tag{2}$$

where $\mathbf{P} = \mathbf{p} - e\mathbf{A}$ is the kinetic momentum with the vector potential $\mathbf{A}$, $\sigma_{x,y,z}$ are Pauli matrices, Δ is the Zeeman energy, and $g_{1,2}$ are the Rashba and Dresselhaus SOC strengths, respectively.

The Hamiltonian in some special cases can be solved exactly, such that the single-electron case with $g_1 = \pm g_2$ can be converted to a quantum Rabi model (Luo et al., 2019). However, the general form of the Hamiltonian may not be exactly solvable, especially when the Coulomb interaction is present. A reliable way to solve the Hamiltonian is to use the numerical exact diagonalization scheme. For simplicity, we define the unperturbed single-electron Hamiltonian,

$$H_0 = \frac{\mathbf{p}^2}{2m^*} + \frac{m^*}{2}\left(\Omega_x^2 x^2 + \Omega_y^2 y^2\right) + \frac{\Delta}{2}\sigma_z \tag{3}$$

describing a two-dimensional harmonic oscillator with the renormalized frequencies $\Omega_{x,y} = \sqrt{\omega_{x,y}^2 + \omega_c^2/4}$ and the cyclotron frequency $\omega_c = eB/m^*$. In the QR case, it is supposed that $\omega_x = \omega_y = \omega$. The confinement lengths are $R_i = \sqrt{\hbar/(m^*\omega_i)}$, while the natural lengths are $\ell_i = \sqrt{\hbar/(m^*\Omega_i)}$. The eigen-state of the harmonic oscillator with its eigen wave function $\psi_{n_x,\,n_y}(\mathbf{r})$, where $n_{x,y}$ are the quantum numbers of the oscillator, is used as the basis in the numerical exact diagonalizations.

When the QD or QR contains more than one electron, the Coulomb interaction term is,

$$\mathcal{H}_C = \frac{1}{2}\sum_{i,j,k,l}\sum_{s,s'} V_{i,j,k,l} c^{\dagger}_{i,s} c^{\dagger}_{j,s'} c_{k,s'} c_{l,s}, \tag{4}$$

where $c^{\dagger}$ is the operator of an electron, s, s' are the spin indices, and i, j, k, l stand for the collective indices, each of them contains the x, y quantum numbers of the quantum oscillator. For instance, $k = (k_x, k_y)$, $k_{x,y}$ are the quantum numbers of the oscillator in x and y directions, respectively. The Coulomb interaction matrix element $V_{i,j,k,l}$ is evaluated numerically,

$$\begin{aligned} V_{i,j,k,l} &= \frac{2}{\pi}\frac{e^2}{\varepsilon\sqrt{\ell_x \ell_y}} \prod_{\mu=x,y} (-1)^{|j_\mu - k_\mu|} \gamma(i_\mu, l_\mu)\gamma\left(j_\mu, k_\mu\right) i^{|i_\mu - l_\mu| + |j_\mu - k_\mu|} \\ &\int_{-\infty}^{\infty} dxdy \ \Phi\ (i_x, l_x, x)\ \Phi(j_x, k_x, x) \frac{\Phi(i_y, l_y, y)\Phi\left(j_y, k_y, y\right)}{\sqrt{\frac{\ell_y}{\ell_x}x^2 + \frac{\ell_x}{\ell_y}y^2}}, \end{aligned} \tag{5}$$

where ε is the dielectric constant and

$$\gamma(n, m) = \sqrt{\frac{2^{\min(n,\ m)} \min(n, m)!}{2^{\max(n,\ m)} \max(n, m)!}}, \tag{6}$$

$$\Phi(n, m, x) = x^{|n-m|} \mathrm{e}^{-\frac{1}{4}x^2} L^{|n-m|}_{\min(n,\ m)}\left(\frac{x^2}{2}\right) \tag{7}$$

with the Laguerre polynomial L. Note that the nonzero integral requires that $|i_x - l_x| + |j_x - k_x|$ and $|i_y - l_y| + |j_y - k_y|$ in the integrand are even, which also guarantees that the Coulomb interaction matrix element is real.

By diagonalizing the total Hamiltonian H, the (many-body) wave function of the studied state is obtained,

$$|\Psi\rangle = \sum_{\{j\}} d_j \left|(j_1,\ s_1), (j_2,\ s_2), \ldots (j_{N_e},\ s_{N_e})\right\rangle, \tag{8}$$

where N_e is the electron number and d_j is the coefficient of the many-particle (or a single-particle) basis obtained by the exact diagonalization. In the many-particle basis $|(j_1, s_1), (j_2, s_2), \ldots (j_{N_e}, s_{N_e})\rangle$, (j_n, s_n) are the indices for the n – th electron of the system, where j_n is the collective index containing the x, y quantum numbers of the quantum oscillator and s_n is the spin index. Then the interested spin fields σ_μ $(\mathbf{r})$ of such a state can be defined generally by

$$\begin{aligned} \sigma_\mu(\mathbf{r}) &= \sum_{\{i\},\{j\}} d_i^* d_j \sum_{k,l,s,s'} \psi^{\dagger}_{k,s}(\mathbf{r})\sigma_\mu \psi_{l,s'}(\mathbf{r}) \\ &\left\langle (i_1,\ s'_1), \ldots \left(i_{N_e},\ s'_{N_e}\right)\middle| c^{\dagger}_{k,s} c_{l,s'} \middle| (j_1,\ s_1), \ldots \left(j_{N_e},\ s_{N_e}\right)\right\rangle, \end{aligned} \tag{9}$$

and the density is given by

$$\begin{aligned} n(\mathbf{r}) &= \sum_{\{i\},\{j\}} d_i^* d_j \sum_{k,l,s} \psi^{\dagger}_{k,s}(\mathbf{r})\psi_{l,s}(\mathbf{r}) \\ &\left\langle (i_1,\ s'_1), \ldots \left(i_{N_e},\ s'_{N_e}\right)\middle| c^{\dagger}_{k,s} c_{l,s} \middle| (j_1,\ s_1), \ldots \left(j_{N_e},\ s_{N_e}\right)\right\rangle. \end{aligned} \tag{10}$$

The wave function of $\psi_{k,\ s}(\mathbf{r}) = \psi_{k_x,\ k_y,\ s}(\mathbf{r})$ is a spinor, which can be written explicitly for different spins in the basis of σ_z, $\psi_{k_x, k_y, +}(\mathbf{r}) = \psi_{k_x,\ k_y}(\mathbf{r})\ \ (1\ \ 0)^{\mathrm{T}}$ and $\psi_{k_x,\ k_y,\ -}(\mathbf{r}) = \psi_{k_x,\ k_y}(\mathbf{r})\ \ (0\ \ 1)^{\mathrm{T}}$. These quantities are observables that can be measured experimentally.

Index characterizing the topology of the spin texture

The winding number is introduced mathematically to characterize the topology of the in-plane spin fields

$$q = \frac{1}{2\pi}\oint d\phi = \frac{1}{2\pi}\oint \frac{\sigma_x(\mathbf{r})d\sigma_y(\mathbf{r}) - \sigma_y(\mathbf{r})d\sigma_x(\mathbf{r})}{\sigma_x(\mathbf{r})^2 + \sigma_y(\mathbf{r})^2}, \tag{11}$$

where ϕ $(\mathbf{r}) = \arctan[\sigma_y$ $(\mathbf{r})/\sigma_x$ $(\mathbf{r})]$. The route of the integral is a closed path around a singularity of the ϕ field. The winding number can also be written in terms of a Berry connection. Since the winding number is directly related to the topological feature of the in-plane spin field, it is therefore defined as the topological charge of the system. If the σ_z $(\mathbf{r})$ is also involved, such as for the skyrmion, the topological current is defined by $J_t(\mathbf{r}) = \overline{\boldsymbol{\sigma}}(\mathbf{r})\cdot\left(\partial_x\overline{\boldsymbol{\sigma}}(\mathbf{r}) \times \partial_y\overline{\boldsymbol{\sigma}}(\mathbf{r})\right)$, where the vector field is defined by $\overline{\boldsymbol{\sigma}}(\mathbf{r}) = \left(\sigma_x(\mathbf{r}), \sigma_y(\mathbf{r}), \sigma_z(\mathbf{r})\right)/n(\mathbf{r})$. This topological current can also be written by the Mermin-Ho relation (Han, 2017). Then the charge of the topological current is given by the Pontryagin index

$$Q = \frac{1}{4\pi}\int d^2 r J_t. \tag{12}$$

In a QD, the singularity of the ϕ field is usually located at the origin, while in a quantum ring, it is natural to define the integral route as the ring itself, i.e. the circle of $r = R$. However, when the magnetic field is varied, the electron density may not be concentrated exactly in the circle of the QR, so it would be convenient to define the winding number along the cycle with an arbitrary radius r',

$$q(r') = \frac{1}{2\pi} \oint_{r=r'} \frac{\sigma_x(\mathbf{r}) d\sigma_y(\mathbf{r}) - \sigma_y(\mathbf{r}) d\sigma_x(\mathbf{r})}{\sigma_x(\mathbf{r})^2 + \sigma_y(\mathbf{r})^2}. \tag{13}$$

Note that $q(r)$ could depend on r. As a result, the topological features of the QR are significantly different from those in QDs (Peng et al., 2021a). Moreover, the spin texture loses its relevance when the charge density is small at $|r - R| >> 0$. To eliminate the textures of the spin fields with low charge density, it would be better to define a new parameter as the reduced topological charge,

$$q' = \frac{1}{2\pi} \oint_0^{2\pi} \frac{\sigma_x(\theta) d\sigma_y(\theta) - \sigma_y(\theta) d\sigma_x(\theta)}{\sigma_x(\theta)^2 + \sigma_y(\theta)^2}, \tag{14}$$

where the spin fields are integrated on r, $\sigma_{x,\,y}(\theta) = \int_0^\infty \sigma_{x,\,y}(r,\theta) r \; dr$. It means that the texture with the highest density in the spin fields represents the most important part of its topological feature.

Spin textures in quantum dots

As stated in the last section, the winding number in Eq. (11) of the spin fields can be evaluated analytically by the given spin fields, or be computed numerically by using the data of the spin fields in real space. By performing the integral in Eq. (11), it appears that the winding number is robust against the eccentricity of the dot. This quantity is thus defined as the topological charge which is invariant in geometry deformation. In the following, the analytical treatment of the spin fields will be discussed.

Analytical treatment for the topological charges of the spin textures

Considering that the many-body Hamiltonian may not be easy to deal with, we constrain ourselves to the single-electron case in the analytical treatment. In addition, it is also difficult to solve the Hamiltonian with the arbitrary combination of the Rashba and Dresselhaus SOCs, except for the special cases $g_1 = \pm g_2$. In a straightforward way, we adopt the perturbation theory to calculate the ground state of the quantum dot. The total single-electron Hamiltonian is $\mathcal{H} = H_0 + H_p$ where the unperturbed part H_0 is given by Eq. (3), and the perturbed part is $H_p = \mathcal{H}_{L_z} + \mathcal{H}_{\mathrm{SOC}}$ with $\mathcal{H}_{L_z} = \frac{eB}{2m^*}\left(xp_y - yp_x\right)$ and $g_{1,2}$ being small. Here we choose the symmetric gauge, $\mathbf{A} = \frac{1}{2}B(-y, x, 0)$.

This decomposition of the Hamiltonian is sufficient for arbitrary magnetic field. Naively speaking, according to the simple inequality: $\frac{p_x^2}{2m^*} + \frac{m^*}{2}\left(\Omega_y^2 y^2\right) \geq \frac{\Omega_y}{2}|p_x y| > \frac{\omega_c}{2}|yp_x|$, therefore $\langle H_s \rangle > \langle \mathcal{H}_{L_z} \rangle$ for arbitrary B. On the other hand, the energy scale of H_0 is $E_0 = \hbar\Omega_x/2 + \hbar\Omega_y/2$, and the energy scale of $\mathcal{H}_{\mathrm{SOC}}$ is of the same order of $E_{\mathrm{SOC}} \sim g_{1,2}\sqrt{\hbar m^* \Omega_{x,y}}\left(1 + \frac{1}{2}\frac{\omega_c}{\Omega_{x,y}}\right) < 2g_{1,2}\sqrt{\hbar m^* \Omega_{x,y}}$. Hence, $E_{\mathrm{SOC}}/E_0 \to 0$ when the magnetic field is very large ($\Omega_{x,y} \to \infty$).

Following the standard perturbation theory, the wave function of the ground state can be calculated, so that the topological charge of the spin field defined by the winding number can be obtained (Luo and Chakraborty, 2019),

$$q = \mathtt{sgn}\left(G_{1,x}^{\pm} G_{1,y}^{\pm} - G_{2,x}^{\pm} G_{2,y}^{\pm}\right), \tag{15}$$

where

$$G_{1,(x,\,y)}^{\pm} = \frac{\left(\pm 2\hbar - eB\ell_{x,y}^2\right) g_1}{2\left(|\Delta| + \hbar\Omega_{x,y}\right)\ell_{x,y}}, \tag{16}$$

$$G_{2,(x,\,y)}^{\pm} = \frac{\left(\mp 2\hbar - eB\ell_{x,y}^2\right) g_2}{2\left(|\Delta| + \hbar\Omega_{x,y}\right)\ell_{x,y}}. \tag{17}$$

Note that ± is for different sign of Landé g factor, since the unperturbed wave functions are different. When $g > 0$, + is chosen in the formula of q, and − is chosen for $g < 0$. The topological properties of the spin field in the QD hydrogen are then clear. The winding number is robust against the ellipticity of an anisotropic dot, so it can be defined as the topological charge of the spin field.

As mentioned before, the spin can also be textured by the external inhomogeneous magnetic field (or magnetic domains (Nagase et al., 2021)). The topological properties of the spin field can be obtained without the wave function in some cases. If the magnetic field itself has a topological non-trivial pattern, it can be found that (Naseri et al., 2020),

$$\sigma_y(\mathbf{r}) B_x(\mathbf{r}) = \sigma_x(\mathbf{r}) B_y(\mathbf{r}), \tag{18}$$

which indicates that the in-plane spin textures exactly follow the texture of the in-plane magnetic fields, when the system has the symmetry, $\left[\mathcal{H}, \frac{-i}{N}\partial_\theta + \frac{\sigma_z}{2}\right]$ where N is an integer related to the winding number and θ is the angular coordinate of the plane. The winding number is then obtained by the in-plane magnetic field. If such a rotational symmetry does not exist, then a Wentzel-

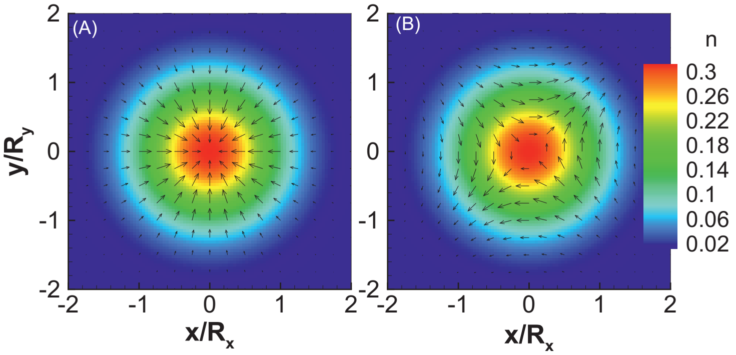

Fig. 1 The spin textures in a QD hydrogen with the size parameters $R_x = R_y = 15$ nm (the Zeeman coupling coefficient $\Delta < 0$) at $B = 0.1$ T. The parameters of the material are taken as those in InAs (Luo et al., 2019). (A) For Rashba SOC only, $\hbar g_1 = 40$ nm·meV, and (B) for Dresselhaus SOC $\hbar g_2 = 20$ nm·meV only. Hereafter, unless otherwise specified, the colors of the two-dimensional pictures represent the density of the electron, which is defined by Eq. (10), and the arrows represent the in-plane vectors $(\sigma_x(\mathbf{r}), \sigma_y(\mathbf{r}))$ where the spin fields $\sigma_{x,y}(\mathbf{r})$ are given in Eq. (9).

Kramers-Brillouin (WKB) approximation can be applied. Expand the spin fields in series of the power of a supposed small quantity $\omega_{c0} = \hbar\omega_c/E$ where E is the eigenenergy of $\mathcal{H}$ (weak magnetic field) $\sigma_j(\mathbf{r}) = \sum_{n=0}^{\infty} \omega_{c0}^n \sigma_j^{(n)}(\mathbf{r})$. Substitute it into the continuity equation and the relation between the lowest few orders of the spin fields and the magnetic fields are obtained. Hence, some properties of the spin fields can be found without explicitly solving the Schrödinger equation.

Control of the topological charge of the spin textures and the effect of inhomogeneous magnetic field

With Rashba/Dresselhaus SOC in a quantum dot hydrogen, the topological charge is apparently according to Eq. (15): $q = 1$ for the case that only Rashba SOC is present while $q = -1$ for the case that only Dresselhaus SOC exists, as shown in Fig. 1. The spin textures associated with different topological charges are described as follows: The vector $(\sigma_x(\mathbf{r}), \sigma_y(\mathbf{r}))$ of the in-plane spin rotates clockwise by $2m\pi$ if we move around the center of the dot in a clockwise direction, hence, with the winding number $+m$; If we move around the center in a clockwise direction, then the in-plane spin field rotates anticlockwise by $2m\pi$ leading to a winding number $-m$.

In fact, these spin textures are similar to those in a free two-dimensional electron gas with Rashba and Dresselhaus SOCs in momentum space. To see this point, consider the Hamiltonian $\overline{H}_{\mathrm{R}} = \mathbf{p}^2 + \sigma_x p_y - \sigma_y p_x$, which commutes with the momentum operators. Thus the momentum operators can be replaced by the wave vector of the kinetic momentum $k_{x\,y}$. To minimize the energy, the spin field in the momentum space $(\sigma_x(\mathbf{k}), \sigma_y(\mathbf{k}))$ must be anti-parallel to the vector $(k_y, -k_x)$, i.e., $(\sigma_x(\mathbf{k}), \sigma_y(\mathbf{k})) \propto (-k_y, k_x)$ which is simply a vortex with $q = 1$ having a global phase difference from the vortex of the spin field in QD in real space. If the Hamiltonian contains only the Dresselhaus SOC, $\overline{H}_{\mathrm{D}} = \mathbf{p}^2 + \sigma_y p_y - \sigma_x p_x$, then the spin field in the momentum space $(\sigma_x(\mathbf{k}), \sigma_y(\mathbf{k})) \propto (k_x, -k_y)$ has $q = -1$.

The topological charge is tunable, basically according to Eq. (15), by tuning the external parameters, when both SOCs are present. Note that the topological charge is not determined simply by the magnitudes of $|g_1|$ and $|g_2|$. The straightforward way is to tune the SOCs directly: if the magnetic field is fixed, the topological charge tends to be +1(−1) when the strength of the Rashba (Dresselhaus) SOC is dominant in the SOCs. The Rashba SOC can be simply changed by the gate (Nitta et al., 1997; Kohda et al., 2008; Ast et al., 2008; Kanai et al., 2011), while the Dresselhaus may depend more on the material itself. Nevertheless, the ratio of the Rashba SOC to the Dresselhaus SOC can be tuned in a wide range, for instance in the InAs QDs, by an in-plane magnetic field (Nowak et al., 2011).

According to Eq. (15), when both SOCs exist, tuning the magnetic field may also change the topological charge of the system. It is because the topological charge is related to the sign of the Landé g factor of the material

$$q = -\operatorname{sgn}(g), \tag{19}$$

when $\boldsymbol{B} \to \infty$ (Luo and Chakraborty, 2019). If a QD holds the topological charge of the spin field to be $q = \operatorname{sgn}(g)$ for small magnetic fields, then q must be opposite by increasing the magnetic field. Examples are shown in Fig. 2.

Although the spin fields are observable quantities and the first step in this direction has been experimentally achieved — plotting the charge density of a single electron in a QD (Camenzind et al., 2019), the textures of the spin fields, however, are not so easy to be observed thus far. An indirect measurement was proposed by measuring another observable quantity $\langle\sigma_z\rangle$ via magnetometry or optically pumped NMR measurements (Dementyev et al., 2001; Kuzma et al., 1998; Barrett et al., 1995). It is because that the topological charge may be related to the sign of $\langle\sigma_z\rangle$. Consider a QD coupled by a single spin-orbit interaction (Rashba or Dresselhaus) in a perpendicular magnetic field pointing up, the sign of $\langle\sigma_z\rangle$ is always opposite to the sign of g when the magnetic field is strong enough to polarize the whole spin field. However, the sign of $\langle\sigma_z\rangle$ of the electron may be reversed with decrease of the magnetic field when the QD is sufficiently large.

Two cases for the sign of $\langle\sigma_z\rangle$ identifying the topological charge: (i) For the negative Landé g factor material, $\langle\sigma_z\rangle > 0$ in presence of a strong magnetic field. But the Dresselhaus SOC is able to convert the sign of $\langle\sigma_z\rangle$ to negative in a weak magnetic field in a large QD; (ii) For the positive Landé g factor QD, $\langle\sigma_z\rangle < 0$ in a strong magnetic field. But the Rashba SOC is able to convert the sign of $\langle\sigma_z\rangle$

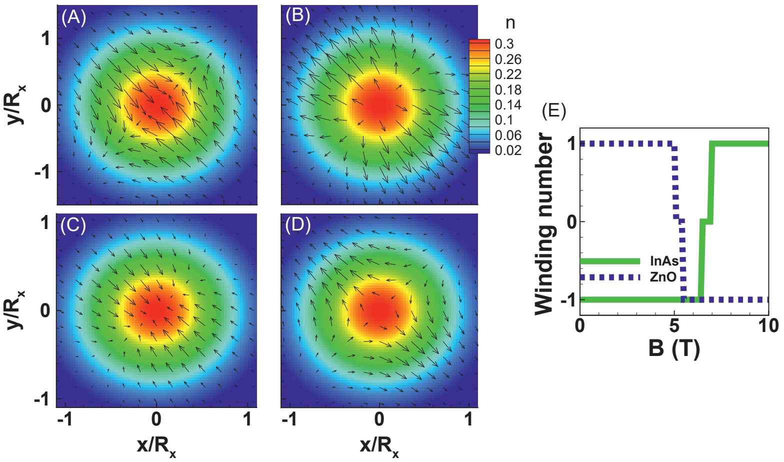

Fig. 2 The evolution of spin textures in QDs with magnetic fields in different materials. The magnetic fields are (A) B = 0.1 T, and (C) $B = 10$ T for an InAs dot, and (B) $B = 0.1$ T, (D) B = 10 T for a ZnO dot. In both dots $R_x = 15$ nm, $R_y = 14$ nm. The SOCs are $\hbar g_1 = \hbar g_2/2 = 10$ meV·nm for the InAs dot, and $\hbar g_1 = 2\hbar g_2 = 5$ meV·nm for the ZnO dot. The Landé *g* factors are negative and positive for the two materials, InAs and ZnO, respectively. (E) The winding numbers of the two cases. For the InAs QD, $q = 1$ at large magnetic field, while q = −1 for the ZnO QD, due to Eq. (19) (Luo and Chakraborty, 2019).

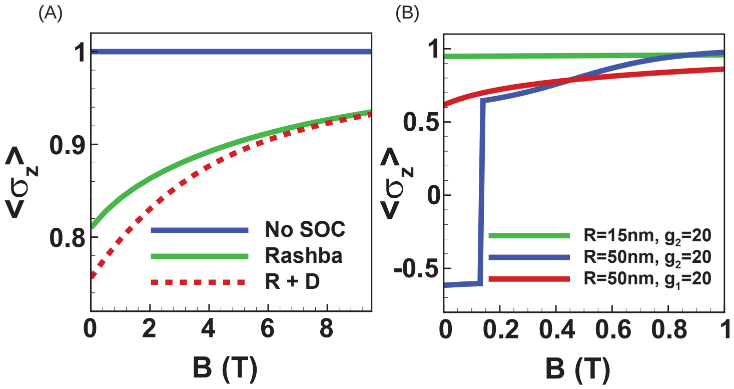

Fig. 3 The average values of the σ of the ground states in InAs QDs. (A) $\langle\sigma_z\rangle$ in a single-electron InAs QD ($R = R_x = R_y = 15$ nm) without SOC, with Rashba SOC only ($\hbar g_1 = 40$ nm·meV), and with both the two SOCs ($\hbar g_1 = 40$ nm· meV, $\hbar g_2 = 20$ nm·meV). The stronger SOCs are, the spin is more unpolarized. (B) The sign of $\langle\sigma_z\rangle$ in a large InAs dot is flipped in weak magnetic field when the Dresselhaus SOC is present for a negative Landé *g* factor material. Here g_1 and g_2 are given in units of nm·meV/ħ (Luo et al., 2019).

to positive in a weak magnetic field when the size of the QD is large enough. Since the size of the QD can be tuned by the gate, one could identify the type of SOC in the QD system by measuring if the sign of $\langle\sigma_z\rangle$ is changed or not while increasing the external magnetic field.

If both SOCs are present, the general flipping condition of $\langle\sigma_z\rangle$ can also be understood by the perturbation calculations. As a first step, compute the second-order perturbed energies $E_\pm{}^{(2)}$ based on the two unperturbed states $\psi_{0,0,+}$ and $\psi_{0,0,-}$, respectively. Then compare the two energies $E_\pm = E_\pm{}^{(0)} + E_\pm{}^{(2)} = \pm\Delta/2 + E_\pm{}^{(2)}$. The lower one determines the ground state and its spin polarization: $\langle\sigma_z\rangle > 0$ for E_+ and $\langle\sigma_z\rangle < 0$ for E_-.

For instance, we consider an InAs QD with $m^* = 0.042m_e$, and the Landé factor $g = -14$, then $E_+ < E_-$ always if only the Rashba SOC is present, which means that $\langle\sigma_z\rangle > 0$ whatever the strength of the magnetic field is. However, E_+ could be larger than E_- for a large QD if only the Dresselhaus SOC exists, which means that the ground state is with E_- and $\langle\sigma_z\rangle < 0$ in a weak magnetic field. In a strong magnetic field, the spin polarization would be forced to be parallel to the magnetic field $\langle\sigma_z\rangle > 0$ since $g < 0$. $\langle\sigma_z\rangle$ is thus flipped in a critical magnetic field. The numerical simulation also supports this phenomenon as shown in Fig. 3.

Another possible way to texture the spin is to put the quantum dot in the textured external magnetic field. The spin would be formed generally following the pattern of the magnetic field. Some examples are given in Ref. (Naseri et al., 2020). It is worth mentioning that the topological soliton, skyrmion, can be generated in a special magnetic field

$$\mathbf{B}_{sk} = B_0\left(\frac{2\kappa R_{sk}x}{r^2 + (\kappa R_{sk})^2}, \frac{2\kappa R_{sk}y}{r^2 + (\kappa R_{sk})^2}, \frac{r^2 - (\kappa R_{sk})^2}{r^2 + (\kappa R_{sk})^2}\right), \tag{20}$$

where a dimensionless parameter κ and a constant with a dimension of length R_{sk} controls the size of the skyrmion. Further numerical calculations show that the ground state is a skyrmion with topological charge $Q = -1$, as well as the first and the second excited states, as shown in Fig. 4. However, the third excited state is no longer a skyrmion.

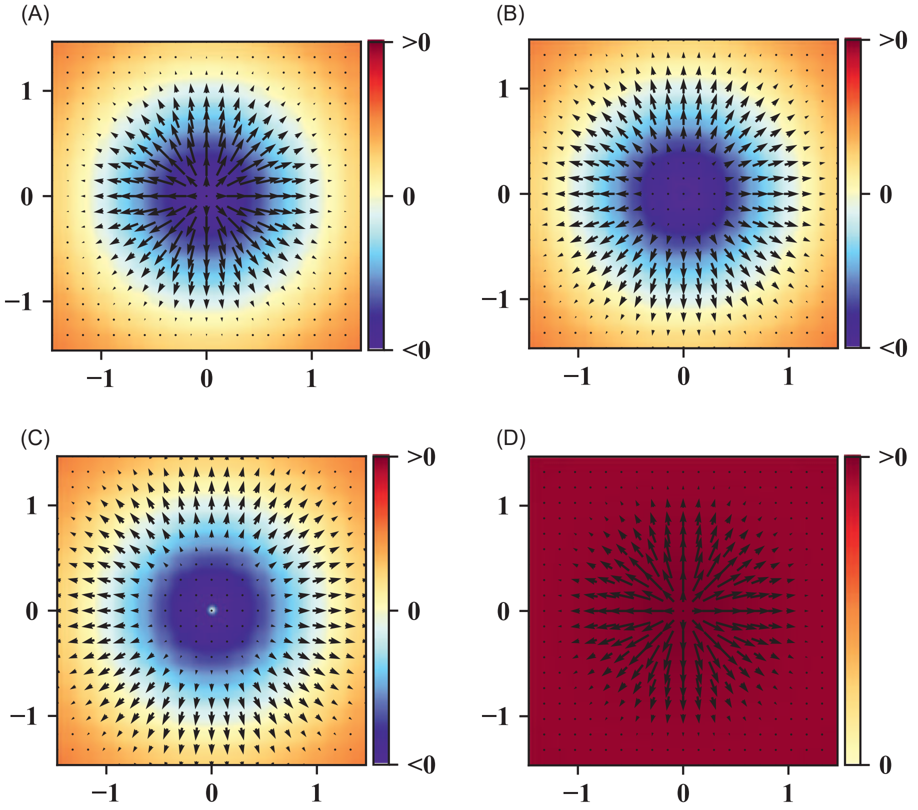

Fig. 4 In-plane spin textures presented by arrows and the colors represent $\sigma_z(\mathbf{r})$ for the magnetic field $\boldsymbol{B}_{sk}$ with the isotropic confinement $\hbar\omega_x = \hbar\omega_y = 5$ meV. In $\boldsymbol{B}_{\rm sk}$, $B_0 = 7$ T, $\kappa = 0.3$, and $R_{sk} = 1.9\,R_x = 1.9R_y$ (Naseri et al., 2020). In-plane spin textures in all the eigenstates have q = 1. Moreover, the ground-state, the first, and the second excited states have a Pontryagin index $Q = -1$ [shown in panels (A), (B), and (C), respectively]. (D) However, the third excited state has no skyrmion spin textures.

When the magnetic field has the topologically trivial pattern as $\mathbf{B} = (B_x, 0, B_z)$, the spin fields of the electron in a QD may still be topologically nontrivial. In a WKB analysis, the quantum corrections beyond the Landau-Lifshitz-Gilbert equation would generate the y component of the spin fields $\sigma_y\,(\mathbf{r}) \neq 0$ even for $B_y = 0$. An example was shown in Ref. (Naseri et al., 2020): A topologically trivial magnetic field $\mathbf{B}_m = B_0\,\left((br)^{|m|}\cos\,(m\theta),\, 0,\, 1\right)$, where b is a dimension of inverse length, is applied to an isotropic QD. The winding number of the in-plane spin field is given by $q = \pm m\text{sgn}(F_xF_y)$, where $\pm$ is taken for different eigen states and $F_{x,y}$ are the radial part of the spin fields $\sigma_{x,y}(\mathbf{r})$, respectively. Interestingly, some discontinuous magnetic fields as magnetic domains are also able to induce topological nontrivial spin textures with different topological charges for different eigenstates.

The inhomogeneous magnetic fields, whether they are continuous or discontinuous, can be realized by a modulated external magnetic field or be manufactured in some magnetic materials with different magnetic domains. Due to the extraordinary pattern, the inhomogeneous magnetic field can make the spin field in the QD hold higher topological charge, while the Rashba and linear Dresselhaus SOCs can only induce topological charge $q = \pm 1$.

Spin textures in quantum dot helium

In this subsection, we discuss how the Coulomb interaction affects the topological properties in an isotropic quantum dot helium (Luo and Chakraborty, 2019). It seems that no suitable analytical method is available in this case and we only discuss the exact diagonalization results of the spin textures and an important quantity, the z component of the angular momentum L_z characterizing the rotational symmetry of the system. The spin textures and the density profile are closely dependent and influence each other due to the existence of the Coulomb interaction. The density profile is related to $\langle L_z\rangle$, so the spin textures are related to $\langle L_z\rangle$ as well.

Note that $\langle L_z\rangle$ is quantized and evolves stepwise (akin to a first-order phase transition) by the Coulomb interaction with increase of the magnetic field if there is no SOC, and plateaus of the curve of $\langle L_z\rangle$ are discontinuous. When the SOC is present, then the curve of $\langle L_z\rangle$ still grow stepwise, but between the two plateaus the curve is no longer discontinuous, which is akin to a second-order phase transition. If only one SOC is present then the density profile looks still rotationally invariant, and the spin textures are mainly determined by the SOC, similar to those in the single-electron case.

When both the SOCs are present, overall the density profile evolves with the change of $\langle L_z\rangle$. The density has (almost) the rotational symmetry when $\langle L_z\rangle$ is (almost) an integer since L_z commutes with rotation with respect to the z axis, i.e. the density

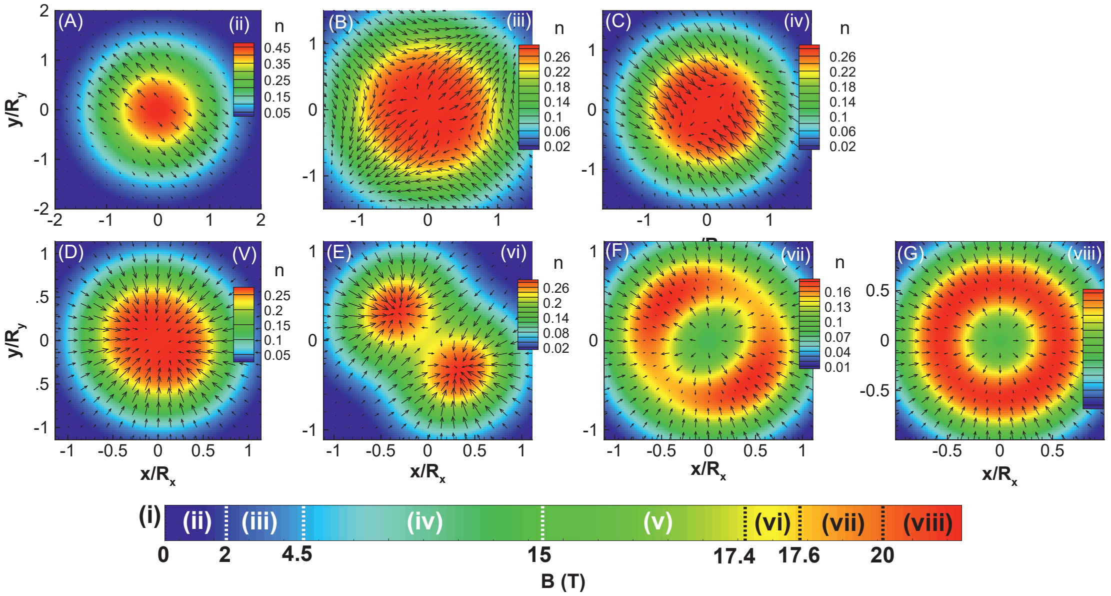

Fig. 5 Evolution of the density profiles of an InAs QD helium. The size of the QD is given by $R_x = R_y = 15$ nm. The SOCs are $\hbar g_1 = \hbar g_2 = 20$ nm·meV. The magnetic fields are gradually increased: (A) 1 T; (B) 3.7 T; (C) 6 T; (D) 12 T; (E) 17.5 T; (F) 18 T; (G) 23 T. The Roman numerals are corresponding to the states marked in panels (A) to (G) and explained in the text of Ref. (Luo and Chakraborty, 2019).

profile is a dot-shape or a ring-shape for $\langle L_z \rangle$ locating at the plateau near an integer. But the two SOCs accompanied by the Coulomb interaction make $\langle L_z \rangle$ deviate from the integer in the region between the plateaus, where the density of the electrons is stretched or split. The evolution of the density profile with increase of the magnetic field comes to a split-merge cycle, as shown in Fig. 5.

Since there may be more than one vortices appearing in the spin textures, for instance in Figs. 5B–E, a new term, the overall winding number (OWN) is introduced to characterize the topological charge of the spin fields. The OWN can be obtained in Eq. (11) by choosing the contour of the integral around the edge enclosing all the possible vortices. It can also be obtained by summing the topological charge for each vortex in the enclosed contour. It is obvious that the OWN still obeys the relation Eq. (19) when B is strong.

We note that the topological features are tunable by adding electron in the system. Consider a InAs dot with $\hbar g_1 = \hbar g_2 = 20$ meV·nm, the sign of the topological charge is altered in the QD helium by the many-body effect as shown in Fig. 6A. The ranges of the topological charge changes for the QD helium (comparing with the cases of QD hydrogen) are open when $\langle L_z \rangle$ is converted from 0 to −1 and $\langle \sigma_z \rangle$ is converted from 0 to 2. Since $\langle L_z \rangle$ is not observable in a magnetic field, the topological inversion can be traced into the region where $0 < \langle \sigma_z \rangle < 1$, which provides the clue for indirectly measuring the topological charge.

Spin textures in quantum rings

In this section the quantum ring systems with a single electron and two SOCs are discussed. The spin textures in the QRs should be very different from those in quantum dots due to the geometry differences and the existence of the magnetic flux. The windings of the spin fields in the QRs are in fact included as part of the nonadiabatic Aharonov-Anandan geometric phase (Aharonov and Anandan, 1987) and are related to the Aharonov-Casher phase (Frustaglia and Nitta, 2020). Therefore, the study of the spin textures also promotes the study of the transport issue in QR systems (Physics of Quantum Rings, 2018; Frustaglia and Richter, 2004; Peng et al., 2021b). The topology of the spin field may no longer be robust against the ellipticity of the ring, which takes new textures on the spin fields. Moreover, the quantum ring can be doped and the effect of the impurity to the spin textures will be introduced.

Various spin textures in QRs

The analytical treatment of a QR with SOCs can be simplified by considering a one-dimensional (1D) ring with zero width, when the ring is narrow. The winding number q is thus calculated by using the spin fields obtained in the 1D model. The Hamiltonian of the 1D model reads

$$H_{1\mathrm{D}} = \left[-\mathrm{i}\frac{\partial}{\partial\theta} + N + \beta_1\sigma_r(\theta) + \beta_2\sigma_\theta(-\theta) \right]^2 - \left(\beta_1^2 + \beta_2^2 + 2\beta_1\beta_2 \sin 2\theta\right) + \beta_3 N \sigma_z, \tag{21}$$

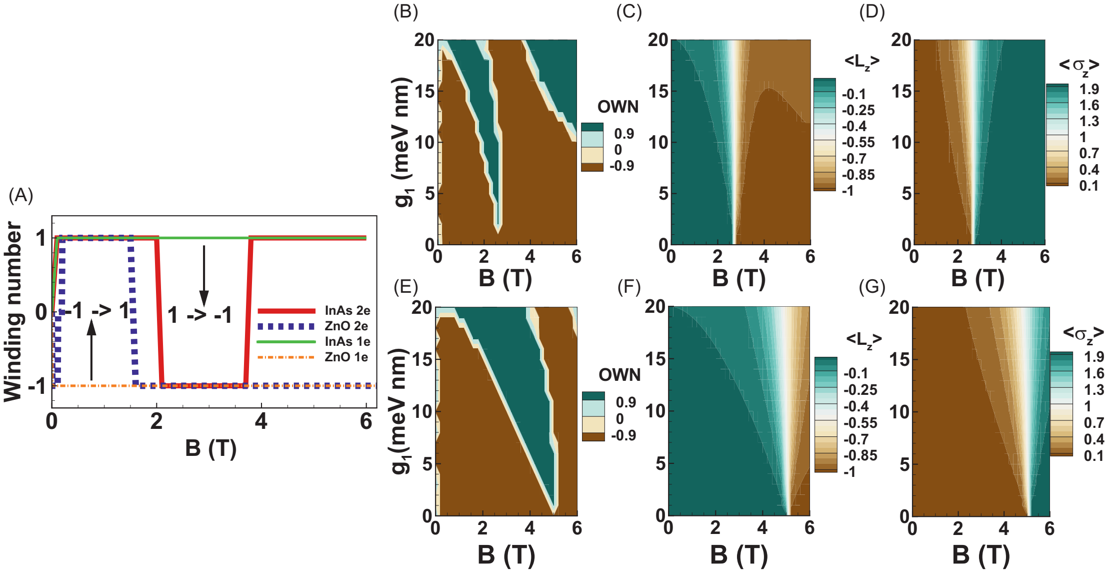

Fig. 6 (A) The overall winding number of the QDs helium: $R_{x,y} = 15$ nm, $\hbar g_{1,2} = 20$ nm·meV for the InAs dot; and $R_{x,y} = 15$ nm, $\hbar g_{1,2} = 5$ nm·meV for the ZnO dot, comparing with the OWNs of the QDs hydrogen with the same SOCs. The arrows show the OWN reversed by adding an electron. (B) The OWN, (C) $\langle L_z \rangle$, and (D) $\langle \sigma_z \rangle$ for the InAs QD helium with tuning $\hbar g_1 \in [0,20]$ meV·nm and fixed $\hbar g_2 = 20$ meV·nm. (E) In comparison, these quantities of the ground state of the two non-interacting electrons are also plotted (Luo and Chakraborty, 2019).

where $\sigma_r(\boldsymbol{\theta}) = \sigma_x \cos \boldsymbol{\theta} + \sigma_y \sin \boldsymbol{\theta}$, $\sigma_\theta(\boldsymbol{\theta}) = \sigma_y \cos \boldsymbol{\theta} - \sigma_x \sin \boldsymbol{\theta}$, $\beta_{1,2} = \frac{g_{1,2} m^* R}{\hbar}$ specify the dimensionless Rashba SOC and Dresselhaus SOC strengths, respectively, $N = \frac{eBr_0^2}{2\hbar}$ is the relative magnetic flux threading the area of the ring, and $\beta_3 = g\frac{m^*}{m_e}$ describes the dimensionless Zeeman energy.

If the magnetic field is absent, the Hamiltonian can be simplified to

$$H_{1\mathrm{D}} = \left[-i\frac{\partial}{\partial \theta} + M(\theta) \right]^2 - [M(\theta)]^2, \tag{22}$$

where $M(\theta) = A(\theta)\sigma_x + B(\theta)\sigma_y$ with $A(\theta) = \beta_1 \cos \theta + \beta_2 \sin \theta$ and $B(\theta) = A(\pi/2 - \theta)$. Therefore, A and B represent the x and y component of the effective magnetic field induced by the SOCs, respectively. Suppose that the wave function can be written by $\Psi(\theta) = f(\theta)\chi(\theta)$, where f is a scalar function and χ is a spinor function. From the Shrödinger equation $H_{1\mathrm{D}}\,\Psi = E_{1\mathrm{D}}\,\Psi$, ones obtain

$$\left(-M^2 - E_{1\mathrm{D}} \right) f - \frac{\partial^2 f}{\partial \theta^2} = 0, \tag{23}$$

$$\frac{\partial \chi}{\partial \theta} + \mathrm{i}M\chi = 0. \tag{24}$$

Eq. (23) is the well-known Mathieu equation determining the relation between the energy of the state and the magnetic field, and the density of electron $|f|^2$, which agree with the results obtained by Lía and Tamborenea (2021)). Eq. (24) determines the spin fields and the associated topological charge.

When observing the spin in the radial direction from the origin to infinity, the spin rotates as a spiral in the plane perpendicular to the *xy* plane where the electron is confined with the Rashba SOC being present. In an elliptical QR, different position in the ring has different radial length (from the origin, the center of the ellipse), so the angle between the spin orientation and the *xy* plane in different position of the ring may be different, while in a circular ring this angle is the same everywhere. For this reason, Ying et al. (Ying et al., 2016) found that in an elliptical QR with Rashba SOC, the spin fields can be textured to carry different topological charges. When the strength of the SOC increases or the ellipse ratio decreases, the spin precesses more along the ring, as shown in Fig. 7 (Ying et al., 2016).

Another way to tune the topological charge in the QR is to introduce the in-plane magnetic field (Henri Saarikoski et al., 2015; Baltanás et al., 2017; Wang et al., 2019). The spin field is textured by the Rashba SOC in a way that the spin orientation points toward or backwards to the center with rotational symmetry to the *z* axis. However, an in-plane magnetic field is able to break this symmetry to force the spin parallel to the direction of this magnetic field. Considering the continuity of the spin field as discussed in Section "Control of the topological charge of the spin textures and the effect of inhomogeneous magnetic field", the spin textures may be varied to carry different winding numbers. Some cases are shown in Fig. 8. for different Rashba SOCs and in-plane Zeeman couplings (Henri Saarikoski et al., 2015).

Tuning either the deformation of the QR or the in-plane magnetic field one can control the topology of the spin fields of the QR. Another straightforward way is to tune the SOCs directly. Sheng and Chang (Sheng and Chang, 2006) obtained analytically the

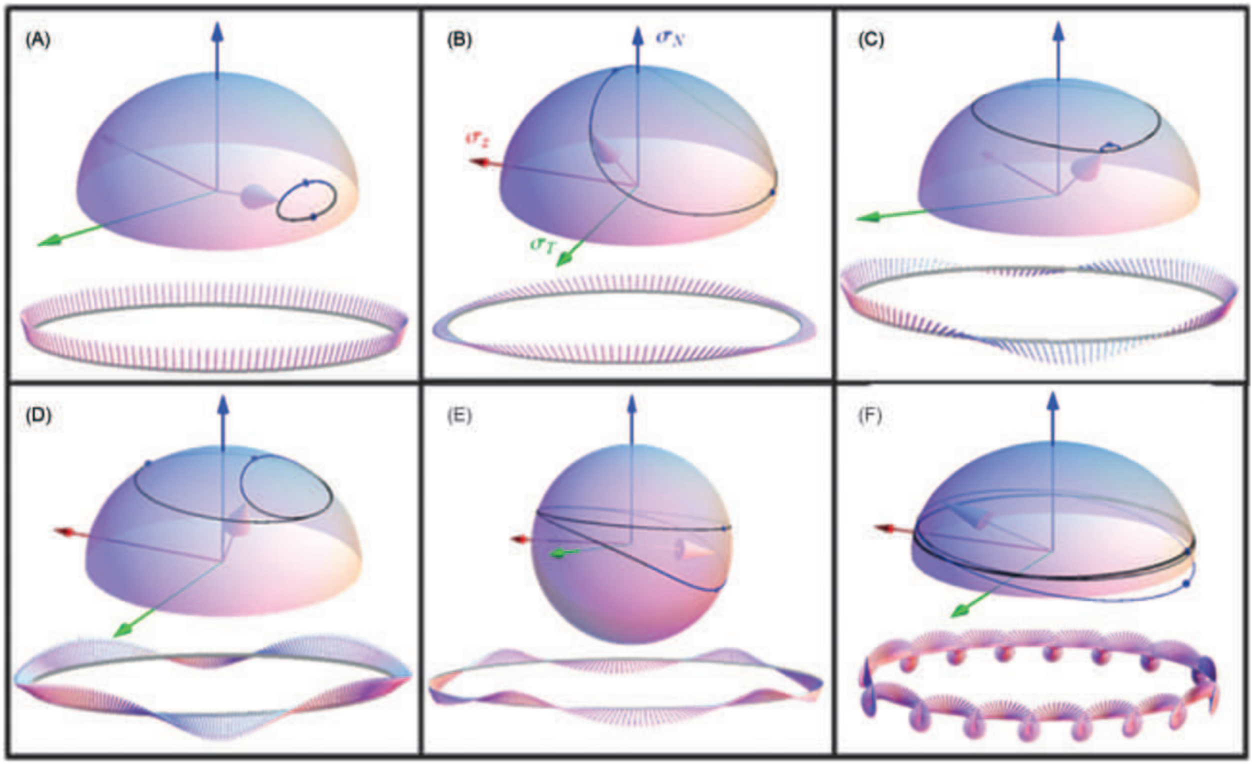

Fig. 7 The spin textures in an elliptical ring with the ratio of semi-minor axis to the semi-major axis 0.4. (A) to (F) Evolution of the spin orientation on the Bloch sphere and the spin textures in the elliptical ring with varying the Rashba SOC strengths given in Ref. (Ying et al., 2016). When the Rashba SOC is increased the winding of the spin field is also possibly increased.

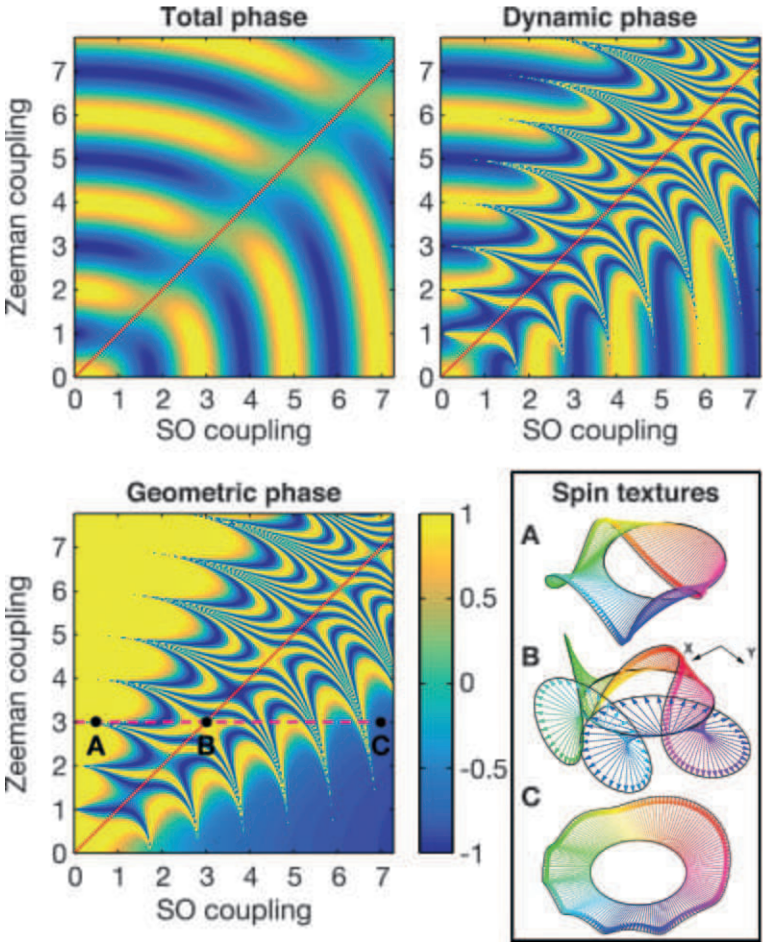

Fig. 8 Different phases are indicated for a transport problem in a QR system (Henri Saarikoski et al., 2015). Among these phases, the spin textures are closely related to the Aharonov-Anandan geometry phase. The spin textures at three selected points (cases A, B and C) are displayed in the right lower panel.

eigen states of the QR when one SOC is present in a perpendicular magnetic field. Similar to the QD, the topological charge of the QR with a single SOC is +1 (Rashba) or −1 (Dresselhaus), and the spin textures are also similar to those in Fig. 1, but only concentrated on the 1D ring (Sheng and Chang, 2006), as illustrated in Fig. 9. It would be reasonable to assume that the topological transition from $q = +1$ to −1 (or −1 to +1) could occur when both the Rashba and Dresselhaus SOCs are present. This transition will be discussed in the next subsection.

Aharonov-Bohm Period of the topological charge of the QR

Here again, the Hamiltonian with both SOCs can be solved by the perturbative theory, where the topological features of the spin fields in a QR would be very different. It has been shown that the topological transition occurs at (Peng et al., 2021a)

$$\eta = \frac{1}{2} - \frac{2\beta_3 N(N - l')}{4(N - l')^2 - 2|\beta_3 N| - 1}, \tag{25}$$

where $l' = \lfloor N + \frac{1}{2} \rfloor$, $\eta = \frac{|\beta_1|}{|\beta_1| + |\beta_2|}$, and $\lfloor \ldots \rfloor$ represents a floor function. The topological transition lines are shown in Fig. 10. It is clear that the topological charge is varied periodically when the magnetic field is increased as a result of the Aharonov-Bohm (AB) effect. The period of the topological charge is exactly identical to the AB period in the 1D model.

In a QR of finite width, numerical calculations show that the 1D model is generally correct, especially when the width is not too large. However, with the increase of the width, the spin textures in a QR gradually evolves into the case of a QD, as shown in Fig. 11. The period of the topological charge is then no longer a constant AB period but is modified a bit by the finite width. To qualitatively understand the width effect, we can use an effective radius of the ring, $R' = \int n(r, \theta) r^2 dr\ d\theta$ where $n\ (r,\ \theta)$ is the density of the electron, in the 1D model. Moreover, flipping of $\langle \sigma_z \rangle$ in a QD also exists in the QR, accordingly. Since the radius of the ring can be largely tuned, spin rotation in the radial direction is also observed in a QR, which is absent in the 1D model with zero width (Peng et al., 2021a).

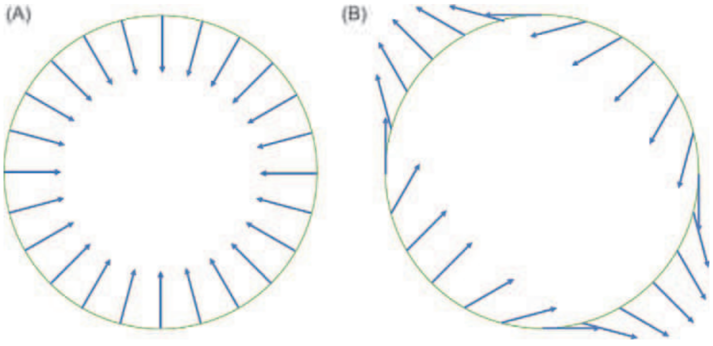

Fig. 9 The illustration of the spin textures for the 1D ring, (A) with Rashba SOC only and (B) with Dresselhaus SOC only.

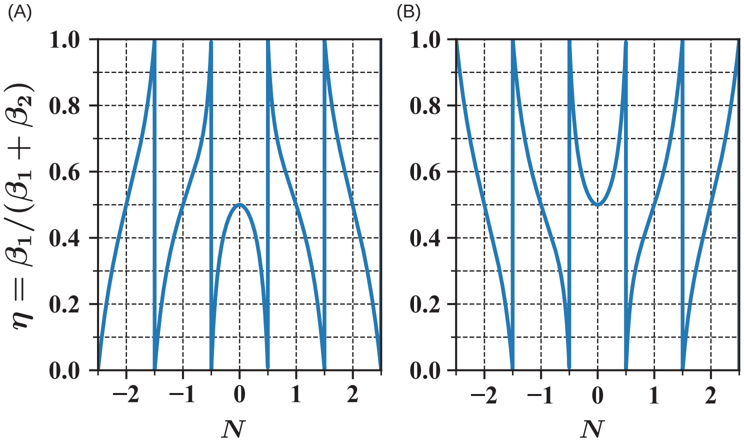

Fig. 10 The topological transition critical lines given by Eq. (25) for (A) $\beta_3 = -0.588$ and (B) $\beta_3 = 0.588$. In the regions above the critical lines the topological charge is $q = 1$, while the regions with $q = -1$ are below the critical lines (Peng et al., 2021a).

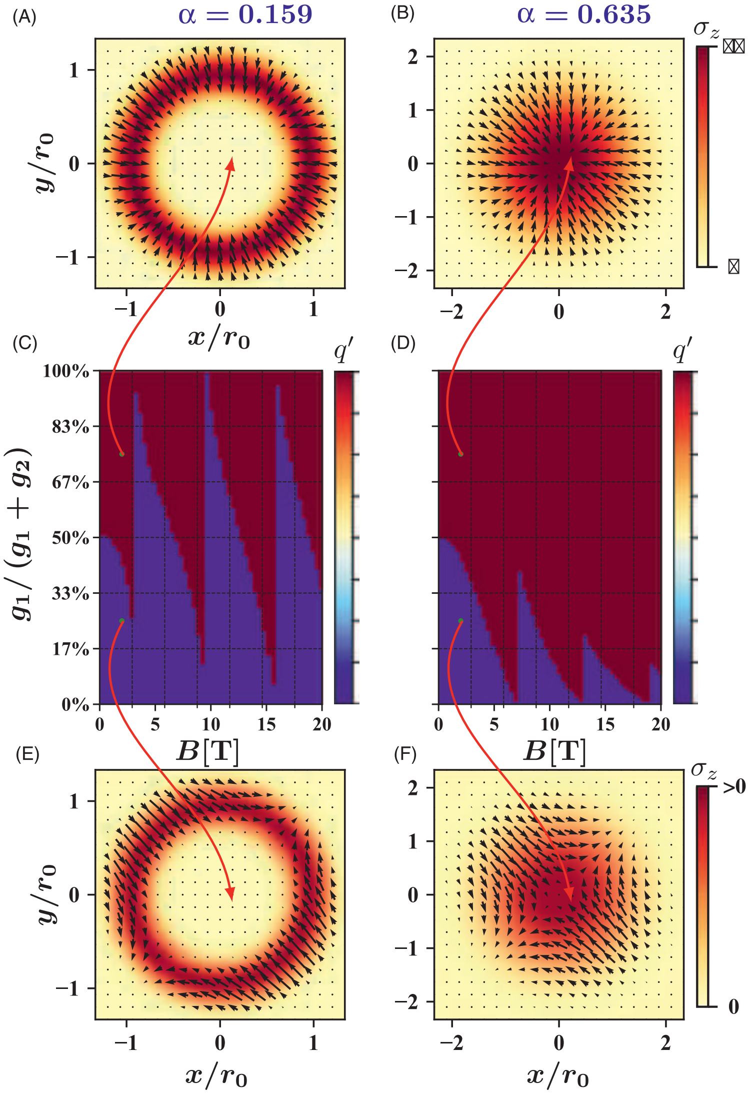

Fig. 11 The in-plane spin textures, spin density $\sigma_z\langle(\mathbf{r})\rangle$ and the topological charges q' in a narrow InAs QR [panels (A), (C), (E)], and in a wide InAs QR [panels (B), (D), (F)], respectively. $\alpha = \sqrt{\frac{\hbar}{2m^*\omega R^2}}$ describes the ratio of ring width to radius R. The system approaches the 1D model when $\alpha \rightarrow 0$. The relative magnetic flux $2N \in \mathbb{Z}$ are marked by black vertical dotted lines in (C) and (D). The period of the topological charge is no longer the constant of the AB period with increase of the magnetic field due to the width effect of the ring.

Higher topological charge due to the impurity

In a non-symmetric QR where a non-magnetic impurity is located, the density and the spin textures of the single-electron ground state jointly make a dramatic change comparing with the 1D model where the radial degree of freedom is neglected. The impurity can be treated as an external potential for which the Hamiltonian is (Chakraborty and Pietiläinen, 1995b)

$$H_I = \frac{1}{2} m^* \omega^2 R^2 \gamma e^{-\frac{(x-R)^2+y^2}{\delta^2 R^2}}, \tag{26}$$

where γ and δ are tunable dimensionless parameters characterizing the size of the impurity. Without loss of generality, the impurity is supposed to be located at $(R, 0)$. The non-magnetic impurity does not interact with the spin directly, but it does deform the density distribution of the electron. According to the theory discussed in the QD helium system in Section "Spin textures in quantum dot helium", the density modification certainly redistribute the spin textures.

In a QR, $\langle L_z \rangle$ also change stepwise by the magnetic field due to the AB effect. The ring with an impurity no longer has the rotational symmetry. As compared to the QD helium, it is also meaningful to explore $\langle L_z \rangle$ here, since the density profile would be dramatically changed when $\langle L_z \rangle$ is deviated from an integer.

Due to the fact that the density distribution of the electron may be deviated from the minimum of the ring potential, it would be better to use q' to define the topological charge of the spin fields, which eliminates the radial effect. As shown in Fig. 12, the

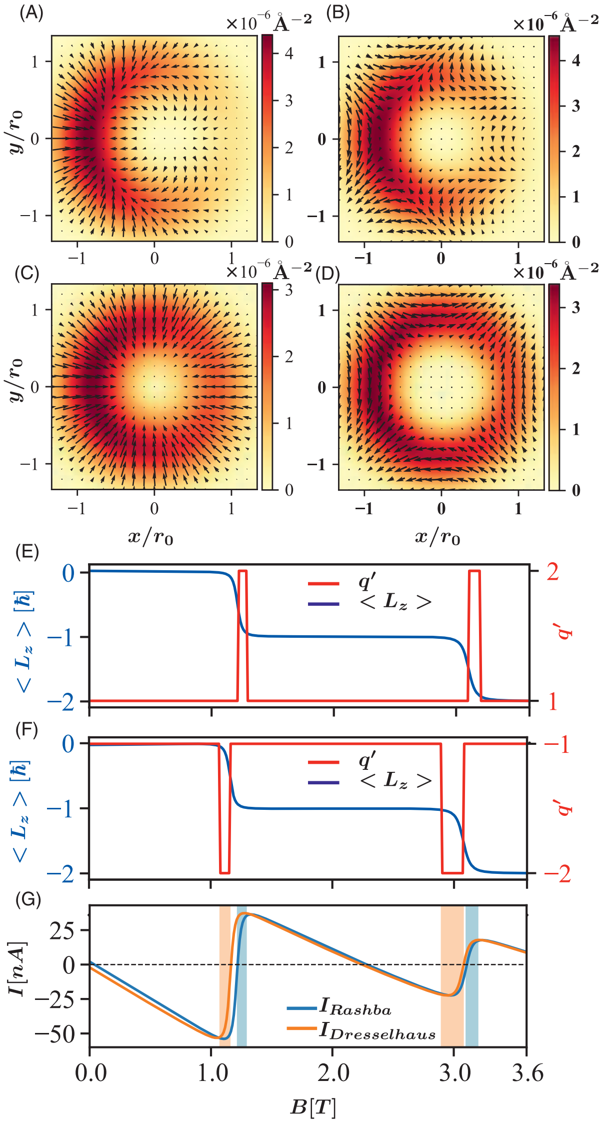

Fig. 12 The InAs QR with the radius $R = 30$ nm, the confinement $\hbar\omega = 10$ meV, includes an impurity ($\gamma = 0.02$ and $\delta = 0.3$). The in-plane spin textures of the ground state with Rashba SOC only ($\hbar g_1 = 10.0$ nm·meV) at (A) $B = 1.25$ T and (C) $B = 1.05$ T, respectively. For the cases with Dresselhaus SOC only $\hbar g_2 = 10$ nm·meV, the in-plane spin textures of the ground state at (B) $B = 3.0$ T and (D) $B = 3.5$ T, respectively. q' and $\langle L_z \rangle$ are varied in different magnetic fields, (E) with the Rashba SOC, and (F) with the Dresselhaus SOC, $q' = \pm 2$ when $\langle L_z \rangle$ varies drastically. (G) The persistent current I for (E) and (F). The yellow shadow represents higher topological charge $q' = -2$ and the blue one represents $q' = 2$.

topological charge q' can reach up to ±2 at the single-electron level by tuning the magnetic field, which indicates a great advantage over other systems in potential applications.

A simple scenario can intuitively explain why the higher topological charges appear. Suppose that the spin texture in the ring has a charge +1 for the Rashba SOC. Once an impurity is added, it forms an extra quantum dot locally, which also carries a topological charge +1. Therefore the total local topological charge of the ring can be simply obtained by the summation $q' = +1 + 1 = +2$. The same analysis is also available for the Dresselhaus SOC, where the local topological charge $q' = -1 - 1 = -2$ can be obtained.

It is worth mentioning that $q' = \pm 2$ occur only in the regions where the persistence current dramatically changes, marked as the shadowed regions in Fig. 12G For the QR with Rashba SOC, $q' = +2$ appears when the current is positive, while $q' = -2$ only appears when the current is negative for the QR with Dresselhaus SOC. According to this correspondence, the higher topological charge may be identified experimentally by measuring the current, however, in an indirect way.

Conclusion

In this chapter, we have reviewed the spin textures in quantum dots and quantum rings. The Rashba and Dresselhaus spin-orbit couplings texture the spin fields with different topological charge $q = \pm 1$ in a confined system in real space. In an inhomogeneous magnetic field which can be manufactured by the modulating external magnetic field or using magnetic domains, the different topological charge of in-plane spin fields as well as the skyrmion spin textures can be obtained. The Coulomb interaction in a quantum dot dramatically changes the density distribution associated with the spin textures of the electrons when $\langle L_z \rangle$ is biased from an integer. This phenomenon is also found in the quantum ring with a nonmagnetic impurity, where higher topological charges can be achieved. We also discuss how to observe the topological properties of the system, in which the indirect ways are proposed if the direct measurement is difficult.

Acknowledgments

This work was supported by the NSF-China under Grant No. 11804396.

References

Aharonov Y and Anandan J (1987) Phase change during a cyclic quantum evolution. *Physical Review Letters* 58: 1593. https://doi.org/10.1103/PhysRevLett.58.1593.

Ast CR, Pacilé D, Moreschini L, Falub MC, Papagno M, Kern K, Grioni M, Henk J, Ernst A, Ostanin S, and Bruno P (2008) Spin-orbit split two-dimensional electron gas with tunable Rashba and Fermi energy. *Physical Review B* 77: 081407(R). https://doi.org/10.1103/PhysRevB.77.081407.

Baltanás JP, Saarikoski H, Reynoso AA, and Frustaglia D (2017) Geometric vector potentials from nonadiabatic spin dynamics. *Physical Review B* 96: 035312. https://doi.org/10.1103/PhysRevB.96.035312.

Barrett SE, Dabbagh G, Pfeiffer LN, West KW, and Tycko R (1995) *Optically Pumped NMR Evidence for Finite-Size Skyrmions in GaAs Quantum Wells near Landau Level Filling* $v = 1$. *Physical Review Letters* 74: 5112. https://doi.org/10.1103/PhysRevLett.74.5112.

Bimberg D, Grundmann M, and Ledentsov NN (1999) *Quantum Dot Heterostructures*. Chichester: John Wiley and Sons.

Camenzind LC, Yu L, Stano P, Zimmerman AC, Gossard DL, and Zumbühl DM (2019) Spectroscopy of quantum dot orbitals with in-plane magnetic fields. *Physical Review Letters* 122: 207701. https://doi.org/10.1103/PhysRevLett.122.207701.

Chakraborty T (1999) *Quantum Dots*. Amsterdam: Elsevier.

Chakraborty T and Pietiläinen P (1995a) Electron-electron interaction and the persistent current in a quantum ring. *Physical Review B* 50(8460). https://doi.org/10.1103/PhysRevB.50.8460.

Chakraborty T and Pietiläinen P (1995b) Persistent currents in a quantum ring: Effects of impurities and interactions. *Physical Review B* 52: 1932. https://doi.org/10.1103/PhysRevB.52.1932.

Chakraborty T, Manaselyan A, and Barseghyan M (2017) Interaction-Driven Distinctive Electronic States of Artificial Atoms at the ZnO Interface. *Journal of Physics. Condensed Matter* 29: 215301. https://doi.org/10.1088/1361-648X/aa6b97.

Chakraborty T, Manaselyan A, and Berseghyan M (2018) In: Fomin VM (ed.) *Physics of Quantum Rings*. Berlin: Springer.

Côté R, Luo W, Petrov B, Barlas Y, and MacDonald AH (2010) Orbital and interlayer skyrmion crystals in bilayer graphene. *Physical Review B* 82: 245307. https://doi.org/10.1103/PhysRevB.82.245307.

Côté R, Fouquet JP, and Luo W (2011) Biased bilayer graphene as a helical quantum Hall ferromagnet. *Physical Review B* 84: 235301. https://doi.org/10.1103/PhysRevB.84.235301.

Dementyev AE, Khandelwal P, Kuzma NN, Barrett SE, Pfeiffer LN, and West KW (2001) OPNMR—A local probe of spin physics. *Solid State Communications* 119: 217. https://doi.org/10.1016/S0038-1098(01)00235-6.

Ezawa ZF (2000) *Quantum Hall Effects: Field Theoretical Approach and Related Topics*. World Scientific.

Frustaglia D and Nitta J (2020) Geometric spin phases in Aharonov-Casher interference. *Solid State Communications* 311: 113864. https://doi.org/10.1016/j.ssc.2020.113864.

Frustaglia D and Richter K (2004) Spin interference effects in ring conductors subject to Rashba coupling. *Physical Review B* 69: 235310. https://doi.org/10.1103/PhysRevB.69.235310.

Gomonay O, Jungwirth T, and Sinova J (2017) Concepts of antiferromagnetic spintronics. *Physica Status Solidi (RRL)* 11: 1700022. https://doi.org/10.1002/pssr.201700022.

Han JH (2017) *Skyrmions in Condensed Matter*. Springer International Publishing.

Hanson R, Kouwenhoven LP, Petta JR, Tarucha S, and Vandersypen LMK (2007) Spins in few-electron quantum dots. *Reviews of Modern Physics* 79: 1217. https://doi.org/10.1103/RevModPhys.79.1217.

Henri Saarikoski J, Vázquez-Lozano E, Baltanás JP, Nagasawa F, Nitta J, and Frustaglia D (2015) Topological transitions in spin interferometers. *Physical Review B* 91: 241406(R). https://doi.org/10.1103/PhysRevB.91.241406.

Hong-Yi Chen P (2008) Pietiläinen, and Tapash Chakraborty, *Some unique magnetic properties of nanoscale quantum rings subjected to a Rashba spin-orbit interaction. Physical Review B* 78: 073407. https://doi.org/10.1103/PhysRevB.78.073407.

Hu H, Ramachandhran B, Pu H, and Liu X-J (2012) Spin-orbit coupled weakly interacting Bose-Einstein condensates in harmonic traps. *Physical Review Letters* 108: 010402. https://doi.org/10.1103/PhysRevLett.108.010402.

Kanai Y, Deacon RS, Takahashi S, Oiwa A, Yoshida K, Shibata K, Hirakawa K, Tokura Y, and Tarucha S (2011) Electrically tuned spin-orbit interaction in an InAs self-assembled quantum dot. *Nature Nanotechnology* 6: 511. https://doi.org/10.1038/nnano.2011.103.

Kloeffel C and Loss D (2013) Prospects for spin-based quantum computing in quantum dots. *Annual Review of Condensed Matter Physics* 4: 51. https://doi.org/10.1146/annurev-conmatphys-030212-184248.

Kohda M, Bergsten T, and Nitta J (2008) Manipulating spin–orbit interaction in semiconductors. *Journal of the Physical Society of Japan* 77: 031008. https://doi.org/10.1143/JPSJ.77.031008.

Kouwenhoven LP, Austing DG, and Tarucha S (2001) Few-electron quantum dots. *Reports on Progress in Physics* 64: 701–736. https://doi.org/10.1088/0034-4885/64/6/201.

Kuzma NN, Khandelwal P, Barrett SE, Pfeiffer LN, and West KW (1998) Ultraslow electron spin dynamics in GaAs quantum wells probed by optically pumped NMR. *Science* 281:686. https://doi.org/10.1126/science.281.5377.686.

Lía JM and Tamborenea PI (2021) Analytical solution of narrow quantum rings with general Rashba and dresselhaus spin-orbit couplings. *Physica E* 126: 114419. https://doi.org/10.1016/j.physe.2020.114419.

Lucignano P, Giuliano D, and Tagliacozzo A (2007) Quantum rings with Rashba spin-orbit coupling: A path-integral approach. *Physical Review B* 76: 045324. https://doi.org/10.1103/PhysRevB.76.045324.

Luo W and Chakraborty T (2019) Tuning the topological features of quantum-dot hydrogen and helium by a magnetic field. *Physical Review B* 100: 085309. https://doi.org/10.1103/PhysRevB.100.085309.

Luo W, Naseri A, Sirker J, and Chakraborty T (2019) Unique spin vortices and topological charges in quantum dots with spin-orbit couplings. *Scientific Reports* 9: 672. https://doi.org/10.1038/s41598-018-35837-y.

Maksym PA and Chakraborty T (1990) Quantum dots in a magnetic field: Role of electron-electron interactions. *Physical Review Letters* 65: 108. https://doi.org/10.1103/PhysRevLett.65.108.

Manchon A, Koo HC, Nitta J, Frolov SM, and Duine RA (2015) New perspectives for Rashba spin-orbit coupling. *Nature Materials* 14: 871–882. https://doi.org/10.1038/nmat4360.

Mühlbauer S, Binz B, Jonietz F, Pfleiderer C, Rosch A, Neubauer A, Georgii R, and Böni P (2009) Skyrmion Lattice in a Chiral Magnet. *Science* 323: 915–919. https://doi.org/10.1126/science.1166767.

Nagaosa N and Tokura Y (2013) Topological properties and dynamics of magnetic skyrmions. *Nature Nanotechnology* 8: 899. https://doi.org/10.1038/nnano.2013.243.

Nagase T, So Y-G, Yasui H, Ishida T, Yoshida HK, Tanaka Y, Saitoh K, Ikarashi N, Kawaguchi Y, Kuwahara M, and Nagao M (2021) Observation of domain wall bimerons in chiral magnets. *Nature Communications* 12: 3490. https://doi.org/10.1038/s41467-021-23845-y.

Naseri A, Peng S, Luo W, and Sirker J (2020) Spin vortices and skyrmions of a single electron in inhomogeneous magnetic fields. *Physical Review B* 101: 115407. https://doi.org/10.1103/PhysRevB.101.115407.

Nitta J, Akazaki T, Takayanagi H, and Enoki T (1997) Gate Control of Spin-Orbit Interaction in an Inverted, $In_{0.53}Ga_{0.47}$**As/In**$_{0.52}Al_{0.48}$**As** Heterostructure. *Physical Review Letters* 78: 1335. https://doi.org/10.1103/PhysRevLett.78.1335.

Nowak MP, Szafran B, Peeters FM, Partoens B, and Pasek WJ (2011) Tuning of the spin-orbit interaction in a quantum dot by an in-plane magnetic field. *Physical Review B* 83: 245324. https://doi.org/10.1103/PhysRevB.83.245324.

Peng S, Ouyang F, Luo W, and Chakraborty T (2021a) Magnetic field controlled topological transitions of the spin field in quantum rings with spin orbit couplings. *Physica E* 128: 114545. https://doi.org/10.1016/j.physe.2020.114545.

Peng S, Ouyang F, Sun J, Guo A-M, Chakraborty T, and Luo W (2021b) Isotropic all-electric spin analyzer based on a quantum ring with spin-orbit couplings. *Applied Physics Letters* 118: 082402. https://doi.org/10.1063/5.0036845.

Fomin VM (ed.) (2018) *Physics of Quantum Rings*. Berlin: Springer.

Ren Y, Qiao Z, and Niu Q (2016) Topological phases in two-dimensional materials: A review. *Reports on Progress in Physics* 79: 066501. https://doi.org/10.1088/0034-4885/79/6/066501.

Roland W (2003) *Spin-Orbit Coupling Effects in Two-Dimensional Electron and Hole Systems*. Berlin: Springer.

Sheng JS and Chang K (2006) Spin states and persistent currents in mesoscopic rings: Spin-orbit interactions. *Physical Review B* 74: 235315. https://doi.org/10.1103/PhysRevB.74.235315.

Šmejkal L, Mokrousov Y, Yan B, and MacDonald AH (2018) Topological antiferromagnetic spintronics. *Nature Physics* 14: 242. https://doi.org/10.1038/s41567-018-0064-5.

Wang M, Saarikoski H, Reynoso AA, Baltanás JP, Frustaglia D, and Nitta J (2019) Geometry-assisted topological transitions in spin interferometry. *Physical Review Letters* 123: 266804. https://doi.org/10.1103/PhysRevLett.123.266804.

Wendler L and Fomin VM (1995) Possible bistability of the persistent current of two interacting electrons in a quantum ring. *Physical Review B* 51: 17814. https://doi.org/10.1103/PhysRevB.51.17814.

Wilson RM, Anderson BM, and Clark CW (2013) Meron ground state of Rashba spin-orbit-coupled dipolar bosons. *Physical Review Letters* 111: 185303. https://doi.org/10.1103/PhysRevLett.111.185303.

Ying Z-J, Gentile P, Ortix C, and Cuoco M (2016) Designing electron spin textures and spin interferometers by shape deformations. *Physical Review B* 94: 081406(R). https://doi.org/10.1103/PhysRevB.94.081406.

Yu XZ, Onose Y, Kanazawa N, Park JH, Han JH, Matsui Y, Nagaosa N, and Tokura Y (2010) Real-space observation of a two-dimensional skyrmion crystal. *Nature* 465: 901–904. https://doi.org/10.1038/nature09124.

Žutić I, Fabian J, and Das Sarma S (2004) Spintronics: Fundamentals and applications. *Reviews of Modern Physics* 76: 323. https://doi.org/10.1103/RevModPhys.76.323.

Quantum rings: Electronic properties

Luís Fernando C Pereira, Francisco AG de Lira, and Edilberto O Silva, Department of Physics, Federal University of Maranhão, São Luís, Maranhão, Brazil

© 2024 Elsevier Ltd. All rights reserved.

Introduction 415
Radial potential 416
Description of the model 417
Electronic states 419
Magnetization 420
Persistent current 422
Conclusion 422
Acknowledgments 424
References 424

Abstract

We study the model of a noninteracting spinless electron gas confined to the two-dimensional localized surface of a cone in the presence of external magnetic fields. The localized region is characterized by an annular radial potential. We write the Schrödinger equation and use the thin-layer quantization procedure to calculate the wavefunctions and the energy spectrum. In such a procedure, it arises a geometry-induced potential, which depends on both the mean and the Gaussian curvatures. Nevertheless, since we consider a ring with a mesoscopic size, the effects of the Gaussian curvature on the energy spectrum are negligible. The magnetization and the persistent current are analyzed. We observed the Aharonov–Bohm (AB) type oscillations. The finite ring width has a fundamental role in the oscillatory behavior found in physical properties as a function of the magnetic field. In general, the role of curvature is to increase the amplitude of oscillations. Nevertheless, in a system with few electrons, an adequate choice of the parameters a_1 and a_2 allows for observing the effect of the geometric potential on the physical properties.

Key points

- A particle on a curved surface experiences a potential geometric which depends on the mean and Gaussian curvatures.
- The curvature, in general, shifts the energy spectrum to higher values of energy.
- The curvature increases the amplitudes of AB-type oscillations of the magnetization and persistent current.
- A wide ring with few electrons allows for observing the effect of the geometric potential on the physical properties.

Introduction

The physics of mesoscopic systems is a remarkable field of theoretical and experimental research. There are a variety of physical phenomena observed in this regime. Among them, we mention the oscillations of the magnetoresistance in a ring as a function of the magnetic field, an interference effect that corresponds to the Aharonov–Bohm (AB) effect (Aharonov and Bohm, 1959) in the condensed matter (Washburn and Webb, 1986; Beenakker et al., 1991; Liu et al., 1993). If a ring encloses a magnetic flux Φ, it carry an equilibrium current, the so-called persistent current (Büttiker et al., 1983; Lévy et al., 1990; Mailly et al., 1993; Chakraborty and Pietiläinen, 1994). In an ideal system 1D ring, this current is periodic in the AB flux Φ with a period Φ_0, which corresponds to the flux quantum. However, in rings with finite widths, the oscillations are aperiodic due to the penetration of the magnetic field into the conducting region (Tan and Inkson, 1999). In a conducting sample through which an electric current is driven, a magnetic field normal to the direction of current flow results in two fascinating phenomena: the quantum Hall effect and the Shubnikov–de Haas oscillations (SdH) (Heinzel, 2006; Ihn, 2010). Another physical phenomenon observed in mesoscopic samples is the de Haas-van Alphen (dHvA) effect. This effect corresponds to the oscillations in the magnetization as a function of the magnetic field (Sivan and Imry, 1988; Schwarz et al., 2002; Feng and Jin, 2005; Kishigi and Hasegawa, 2021). The conductance in quantum dots shows sharp resonances as a function of the gate voltage. Between these conductance peaks, there are regions of zero conductance. This behavior is a manifestation of the Coulomb blockade, a phenomenon that arises due to the Coulomb repulsion between electrons (Kouwenhoven et al., 2001; Reimann and Manninen, 2002; Paul, 2003; Heinzel, 2006; Ihn, 2010). Mesoscopic systems also have attracted interest due to potential device applications (Kushwaha, 2001; Heinzel, 2006; Das, 2010; Ihn, 2010; Fomin, 2014). For instance, we mention the research fields of technological applications involving the optical size-dependent properties of quantum dots which leads to optimized color emission on LCD screen televisions (QLED) (Mezrag et al., 2016) and probes for

https://doi.org/10.1016/B978-0-323-90800-9.00199-2

the detection of both cancer and viral infection biomarkers (Mousavi et al., 2022; Wagner et al., 2022). Moreover, there are several current investigations on the applicability of quantum dots as a system performing a *qubit* (Zhang et al., 2018; Scarlino et al., 2022), the basic unit of information in quantum computation.

Within the past few years, there has been a growing experimental interest in fabricated conducting nanostructures with two-dimensional electron gas on a curved surface (Prinz et al., 2000, 2001). These types of structures have the potential for an enormous variety of applications as basic structures for nanomechanics, nanoelectronics, and photonics as well as in biochemistry and medical sciences (Prinz et al., 2001). Motivated by the possibility of fabricated curved electronic devices, some authors investigated electronic motion in these geometry immersed in magnetic fields and reported curvature effects in magnetotransport properties (Lorke et al., 2003; Mendach et al., 2006; Vorob'ev et al., 2007; Friedland et al., 2007). The influence of a uniform external magnetic field on electronic behavior in curved samples is spatially nonuniform because only the normal-to-surface component of the magnetic field affects the electronic movement. Interestingly, the physics of a two-dimensional electron gas (2DEG) subjected to a nonuniform magnetic was treated even in the last century and motivated the production of nonplanar 2DEG (Leadbeater et al., 1995). Theoretically, the method employed to address motion of electrons on curved surfaces follows the well-known thin-layer quantization procedure employed by da Costa (1981, 1982). Ferrari and Cuoghi (2008) extend the formalism developed by da Costa for including the effect of the magnetic field and the electric field, while Wang et al. (2014) derive the Pauli equation for a charged spin particle. The da Costa method is widely used in the literature (Bulaev et al., 2004; Furtado et al., 2007; Liang et al., 2018; Wang et al., 2017; Wang and Zong, 2016; Chang et al., 2013; Gaididei et al., 2014; Zhang and Vishwanath, 2010; Teixeira et al., 2019; Atanasov and Dandoloff, 2016; Santos et al., 2016; Schmidt, 2019; Pandey et al., 2018). An interesting result that emerges from the thin-layer quantization procedure is that a particle on a curved surface experiences a potential of purely geometric origin which depends on the mean and Gaussian curvatures, which takes into account the quantum nature of the particle. Thus, even in the absence of interactions of any nature, the particles cannot move around freely on the surface.

The aim of this work is to analyze the way how the spectrum, magnetization, and persistent current depend on the device geometry and the curvature. Quantum rings can be narrow, quasi-one-dimensional objects, or also can be wide, like a quantum dot with a small hole in the center that leads to a nontrivial topology. The electronic properties, determined by the energy spectrum, are very different in these limiting cases (Kurpas et al., 2013). We consider noninteracting spinless electron gas bound to a two-dimensional localized region in the presence of external magnetic fields. The electrons are confined on a conical curved surface. The experimental analysis of semiconductors with conical geometry can be found. For example, Cao et al. (2005) reported the growth of Si and Ge nanocones, with the controlling of the apex angles. Another experimental work involving nanocones was reported by Medvid' (2012). Making use of a new laser method, Medvid carried out the formation of nanocones on the surface of elementary semiconductors Si and Ge and semiconductor solid solutions $Si_{1-x}Ge_x/Si$ and $Cd_{1-x}Zn_xTe$. These experimental reports suit as a paradigm for the theoretical analysis of the electronic behavior in these curved devices. Although the role of the electron–electron interaction is an important topic, here this effect is neglected. The study by Chakraborty and Pietiläinen (1994) outlines how the electron–electron interaction affects magnetization in narrow and wide rings. Maksym and Chakraborty (1990) studied the role of electron–electron interactions in the eigenstates of electrons in quantum dots. Recently Pereira et al. (2019, 2021) investigate the physical implications caused by curvature effects on the magnetization and persistent currents in a quantum dot and a 2D ring containing a large number of electrons. Thus, this work focuses on analyzing the effects of curvature on magnetization and persistent current in quantum rings containing few electrons. Quantum rings with few electrons have been investigated, for example, by Lorke et al. (2000) and Lei et al. (2010). In particular, Kleemans et al. (2007) report the direct measurement of the persistent current carried by a single electron by means of magnetization experiments on self-assembled InAs/GaAs quantum rings.

The remainder of this chapter is arranged as follows: In Section "Radial potential," we present the radial potential proposed by Tan and Inkson. In this section, we also present the two rings used in the numerical analyses. We consider quantum rings of the order of 10 nm in size. This limit is of particular interest because they make it possible to study quantum rings in the true quantum limit (Lei and Lorke, 2013). In Section "Description of the model," we use the model proposed by Tan and Inkson to constrain the motion of the electrons to an annular region. By employing the thin-layer quantization procedure, we obtain the Schrödinger equation (Ferrari and Cuoghi, 2008), and solve it to find the energies and wave functions of the electrons on the two-dimensional localized curved surface. In Sections "Electronic states," "Magnetization," and "Persistent current," we present numerical results for the energy, magnetization, and persistent current, respectively. In numerical results, we assume that there is no AB flux confined to the center of the rings, that is, $\ell = 0$. We summarize our conclusions in Section "Conclusion".

Radial potential

The confinement of electrons in a limited region of the surface is described by a radial potential (Tan and Inkson, 1996), given by

$$V(r) = \frac{a_1}{r^2} + a_2 r^2 - V_0, \tag{1}$$

with $V_0 = 2\sqrt{a_1 a_2}$. This radial potential has a minimum at $r_0 = (a_1/a_2)^{1/4}$. If $r \approx r_0$, we obtain the parabolic potential model,

$$V_{par}(r) \approx \frac{\mu\omega_0^2}{2}(r - r_0)^2, \tag{2}$$

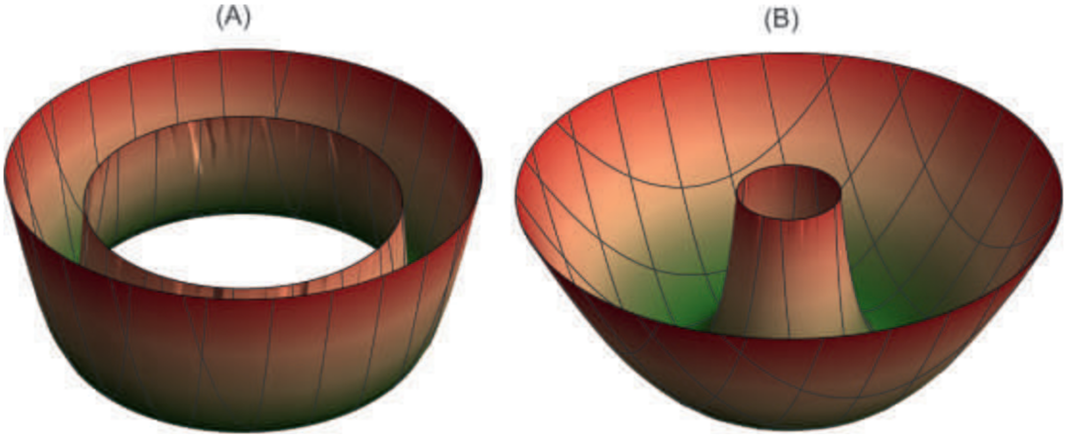

Fig. 1 In (A), the radial potential describes a narrow ring by $\hbar\omega_0 = 460$ meV, while in (B), the radial potential describes a wide ring defined by $\hbar\omega_0 = 50$ meV. The radius of both rings is $r_0 = 10$ nm.

where $\omega_0 = \sqrt{8a_2/\mu}$ characterizes the strength of the transverse confinement. Both the radius and the width of the ring can be adjusted independently by suitably choosing a_1 and a_2. Alternatively, we can use the effective radius of the ring r_0 and the characteristic frequency of the radial confinement ω_0. In particular limits, the potential (1) can describe a quantum dot, a quantum anti-dot, a two-dimensional wire, or even a 1D ring (Tan and Inkson, 1996).

Fig. 1 shows the radial potential, given by Eq. (1), for rings of different widths. In Fig. 1A, the radial potential describes a narrow ring with $r_0 = 10$ nm and $\hbar\omega_0 = 460$ meV. In Fig. 1B, the radial potential describes a wide ring with $r_0 = 10$ nm and $\hbar\omega_0 = 50$ meV. Both the samples are made of GaAs, so the electron effective mass is $\mu = 0.067\mu_e$, where μ_e is the electron mass.

Description of the model

The description of the model of a particle constrained to move on a curved surface by the action of an external potential was given by da Costa (1981). Using a thin-layer quantization procedure, it was shown that the transverse and the surface motion are exactly separable. Ferrari and Cuoghi (2008) generalized this result, and showed that using both the thin-layer quantization procedure and a proper choice of the gauge, the transverse and motion on the surface of the charged particle in the presence of external electric and magnetic fields are also decoupled. Such equations are found to be

$$i\hbar\frac{\partial}{\partial t}\chi_N = -\frac{\hbar^2}{2M}\partial_3\partial^3\chi_N + V_\lambda(q_3)\chi_N, \tag{3}$$

and

$$i\hbar\frac{\partial}{\partial t}\chi_S = \frac{1}{2\mu}\left[-\frac{\hbar^2}{\sqrt{g}}\partial_a\left(\sqrt{g}g^{ab}\partial_b\right) + \frac{ie\hbar}{\sqrt{g}}\partial_a\left(\sqrt{g}g^{ab}A_b\right) + 2ie\hbar g^{ab}A_a\partial_b + e^2g^{ab}A_aA_b + V_g + eU\right]\chi_S, \tag{4}$$

where e is the charge of the particle, μ is the effective mass and $a, b = 1, 2$. In the equation that governs the motion in the transversal direction (Eq. 3, we have just the external potential V_λ, which confines the particle on the surface (da Costa, 1981). On the other hand, in the equation that governs the dynamics on the surface (4), we have the scalar potential U and the vector potential A_i. In addition, a curvature-induced potential V_g appears in the equation that describes the dynamics on the surface, which is given by

$$V_g = -\frac{\hbar^2}{2\mu}\left(\mathcal{H}^2 - \mathcal{K}\right), \tag{5}$$

where $\mathcal{H}$ and $\mathcal{K}$ are mean and Gaussian curvatures, respectively. In our study, we are interested only in the motion on the surface without the presence of the external electric field.

Let us consider the line element in polar coordinates (Filgueiras and Moraes, 2008; Filgueiras et al., 2012),

$$ds^2 = dr^2 + \alpha^2r^2d\varphi^2, \tag{6}$$

where $r \geq 0$ and $0 \leq \varphi < 2\pi$. The α parameter defines the type of surface that the metric (6) describes. If $0 < \alpha < 1$ (deficit angle), the metric describes a conical surface while $\alpha > 1$ (proficit angle), the metric defines a saddle-like surface. If $\alpha = 1$, then we recover the flat surface. Here, we focus our analysis in the range $0 < \alpha \leq 1$. The Gaussian and the mean curvatures are given, respectively, by Carvalho et al. (2007)

$$\mathcal{K} = \left(\frac{1-\alpha}{\alpha}\right)\frac{\delta(r)}{r}, \qquad \mathcal{H} = \frac{\sqrt{1-\alpha^2}}{2\alpha r}. \tag{7}$$

The corresponding geometric potential (5) is written as

$$V_g(r) = -\frac{\hbar^2}{2\mu}\left[\frac{1-\alpha^2}{4\alpha^2 r^2} - \left(\frac{1-\alpha}{\alpha}\right)\frac{\delta(r)}{r}\right], \tag{8}$$

with μ being the electron effective mass and the $\delta(r)$ function describes a singularity at $r = 0$ region. Note that the Gaussian curvature is associated with the singularity at the cone apex.

The vector potential is chosen to be

$$\mathbf{A} = \frac{Br}{2\alpha}\hat{\varphi} + \frac{\ell\hbar}{e\alpha r}\hat{\varphi}, \tag{9}$$

where $\ell = \Phi_{AB}/\Phi_0$ is the AB flux parameter and $\Phi_0 = h/e$ is the magnetic flux quantum. The vector potential (9) implies a superposition of magnetic fields (a uniform magnetic field plus a magnetic flux tube) given by

$$\mathbf{B} = B\,\hat{\mathbf{z}} + \frac{\ell\hbar}{e\alpha r}\delta(r)\,\hat{\mathbf{z}}. \tag{10}$$

By using Eqs. (1), (8), (9), and (10) in Eq. (4), we write

$$\begin{aligned} E\chi_S(r,\varphi) = \Bigg\{ & -\frac{\hbar^2}{2\mu}\left[\frac{1}{r}\frac{\partial}{\partial r}\left(r\frac{\partial}{\partial r}\right) + \frac{1}{\alpha^2 r^2}\left(\frac{\partial}{\partial\varphi} - i\ell\right)^2\right] - \frac{\hbar^2}{2\mu}\left[\frac{ieB}{\hbar\alpha^2}\left(\frac{\partial}{\partial\varphi} - i\ell\right) + \frac{e^2B^2r^2}{4\hbar^2\alpha^2}\right] \\ & -\frac{\hbar^2}{2\mu}\left[\frac{(1-\alpha^2)}{4\alpha^2 r^2} - \left(\frac{1-\alpha}{\alpha}\right)\frac{\delta(r)}{r}\right] + \frac{a_1}{r^2} + a_2 r^2 - V_0\Bigg\}\chi_S(r,\varphi). \end{aligned} \tag{11}$$

By considering solutions of the form

$$\chi_S(r,\varphi) = e^{im\varphi}f_m(r), \text{ with } m = 0, \pm 1, \pm 2, \ldots \tag{12}$$

Eq. (11) provides us the following radial differential equation for a specific quantum number m:

$$-\frac{\hbar^2}{2\mu}\frac{1}{r}\frac{d}{dr}\left(r\frac{d}{dr}\right)f_m(r) + V_{\text{eff}}f_m(r) = E_m f_m(r), \tag{13}$$

where

$$V_{\text{eff}} = \frac{\hbar^2}{2\mu}\left(\frac{L^2}{r^2} + \frac{r^2}{4\lambda^4} - \kappa^2\right) + \frac{\hbar^2}{2\mu}\left(\frac{1-\alpha}{\alpha}\right)\frac{\delta(r)}{r} \tag{14}$$

is the induced effective potential. We define the effective angular momentum, the effective cyclotron frequency, the effective magnetic length, and a constant parameter, respectively, as

$$L = \sqrt{\left(\frac{m-\ell}{\alpha}\right)^2 + \frac{2\mu a_1}{\hbar^2} - \frac{1-\alpha^2}{4\alpha^2}}, \tag{15}$$

$$\omega = \sqrt{\left(\frac{\omega_c}{\alpha}\right)^2 + \omega_0^2}, \tag{16}$$

$$\lambda = \sqrt{\frac{\hbar}{\mu\omega}}, \tag{17}$$

$$\kappa^2 = \frac{(m-\ell)\mu\omega_c}{\hbar\alpha^2} + \frac{2\mu V_0}{\hbar^2}, \tag{18}$$

where $\omega_c = eB/\mu$ is the cyclotron frequency. It is important to emphasize that the presence of the δ function in Eq. (13), which is a short-range potential, suggests that those singular solutions should be taken into account in this approach. According to von Newman's theory of self-adjoint extensions (Reed and Simon, 1975), the necessity of inclusion of the irregular solutions of Eq. (13) stems from the fact that H (Eq. 11) is not self-adjoint for $|L| < 1$ (Andrade et al., 2012, 2013). However, as the effective angular moment (15) is larger than 1, there is no value of L belonging to the range required above. Because of this, we can ignore the δ function in the radial equation (14) and consider only the regular solution at $r = 0$. In this manner, the energy eigenvalues and wavefunctions of Eq. (11) are given by

$$E_{n,m} = \left(n + \frac{1}{2} + \frac{L}{2}\right)\hbar\omega - \frac{(m-\ell)\hbar\omega_c}{2\alpha^2} - V_0, \tag{19}$$

$$\chi_{n,m}(r,\varphi)=\frac{1}{\lambda}\sqrt{\frac{\Gamma(L+n+1)}{2^L n!\,\Gamma(L+1)^2}}e^{-\frac{r^2}{4\lambda^2}}e^{im\varphi}\left(\frac{r}{\lambda}\right)^L {}_1F_1\left(-n,1+L,\frac{r^2}{2\lambda^2}\right). \tag{20}$$

Another relevant quantity in this model is the effective radius $r_{n,m}$ of the states with quantum number m is

$$r_{n,m}=(2L)^{\frac{1}{2}}\lambda, \tag{21}$$

where L and λ are given by (15) and (17), respectively.

Electronic states

In this section, we analyze the energy spectrum of the 2D quantum ring (19). Using Eq. (19), we can see that both states with $m>0$ and $m<0$ have the same energy. This double degeneracy is due to the rotational symmetry present in the ring. The quantum states in different subbands do not have the same symmetry due to the antidot potential (Eq. 1). The separation energy between adjacent subbands is equal to $\hbar\omega_0$. All the information described above remains valid for $\alpha<1$, but now we have larger energies, except the state with $m=0$, as a consequence of the presence of the geometric potential, as can be seen by replacing $m=0$ in Eq. (19). Therefore, for a given Fermi energy E_F, the number of states with energy $E_{n,m}\leq E_F$ decreases when the α parameter decreases. For the physical phenomena that we will deal with in the next sections, the number of electrons in the system is fixed. Thus, we will observe the increase of the Fermi energy in this case. In addition, if there are a large number of electrons in the ring, the curvature also tends to increase the number of occupied subbands (Pereira et al., 2019, 2021).

In the presence of a magnetic field, Eq. (19) shows that the energy spacing between the adjacent subbands is now given by $\hbar\omega$ and it increases as the magnetic field is raised. The curvature enhances such an effect, as shown in Eq. (16). By using Eq. (19), we can show that for a specified magnetic field value, all the minimums of the subbands lie at the same state with $m=m_0$, given by

$$m_0=\frac{eBr_0^2}{2\hbar}\sqrt{1-\frac{1}{a_1}\frac{\hbar^2}{2\mu}\frac{1-\alpha^2}{4\alpha^2}}. \tag{22}$$

For $\alpha=1$, we recover the result obtained by Tan and Inkson (1996), which corresponds to the number of quantum flux threading a ring with an effective radius r_0, that is, $m_0=\Phi/\Phi_0$, where $\Phi=\pi r_0^2 B$. For a null magnetic field, all the subband minima are the $m_0=0$ state. Eq. (22) shows that the minimum of all subbands changes with the variation of the magnetic field.

The purpose of this work is to analyze the effect of curvature in narrow and wide rings. From now on, in numerical analyses, we consider the rings narrow and wide presented in Fig. 1A and B, respectively.

Fig. 2 shows the behavior of the energy levels of the narrow ring with respect to the magnetic field for some values of the α parameter. As expected, in Fig. 2A, which describes the case without curvature, the evolution of the energy levels is close to that of a 1D ring. The spectrum consists of parabolas shifted with respect to each other. In other words, the condition for periodicity of the spectrum (Avishai et al., 1993; Ihn et al., 2003)

$$E_{n,m}\left(m,\frac{\Phi}{\Phi_0}+1\right)=E_{n,m}\left(m+1,\frac{\Phi}{\Phi_0}\right) \tag{23}$$

is approximately satisfied in the magnetic field range under study. Fig. 2B and C shows the behavior of the energy levels when the parameter α takes the values 0.8 and 0.7, respectively. We can assume that the condition for the periodicity of the spectrum is still valid. On the other hand, for $\alpha=0.5$, which corresponds to Fig. 2D, we can see an evident deviation from the condition for the periodicity of the spectrum for $B>2$ Teslas. Therefore, we conclude that the curvature enhances the effect of the magnetic field at the subband minimum. Namely, in this work, the condition for periodicity of the spectrum (Eq. 23) is related to the narrow ring limit, that is, $\alpha^{-1}\omega_c\ll\omega_0$. In higher subbands, there is also a break of periodicity to lower magnetic fields since the separation energy

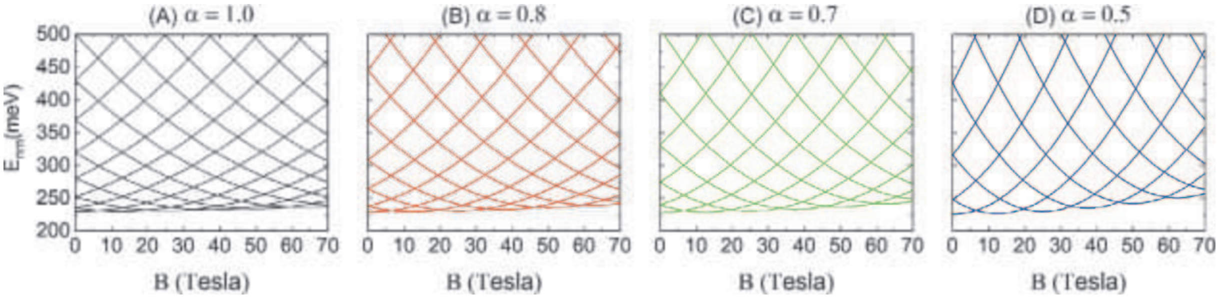

Fig. 2 The energy levels of a narrow ring, calculated without (A) and with (B–D) curvature, as a function of the magnetic field.

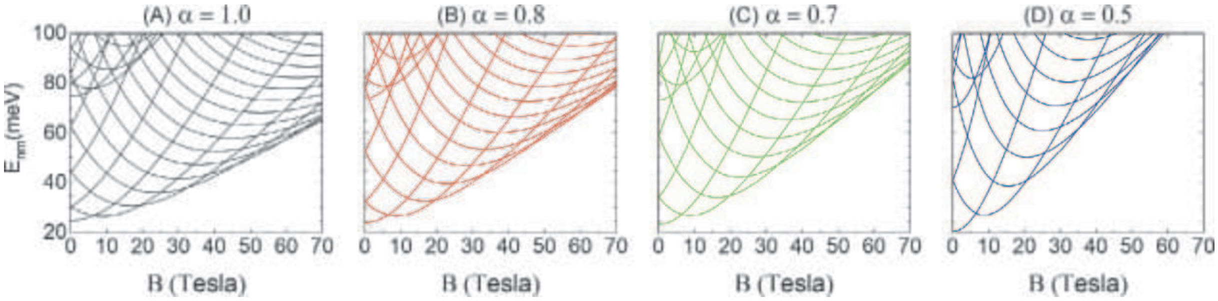

Fig. 3 The energy levels of a wide ring, calculated without (A) and with (B–D) curvature, as a function of the magnetic field.

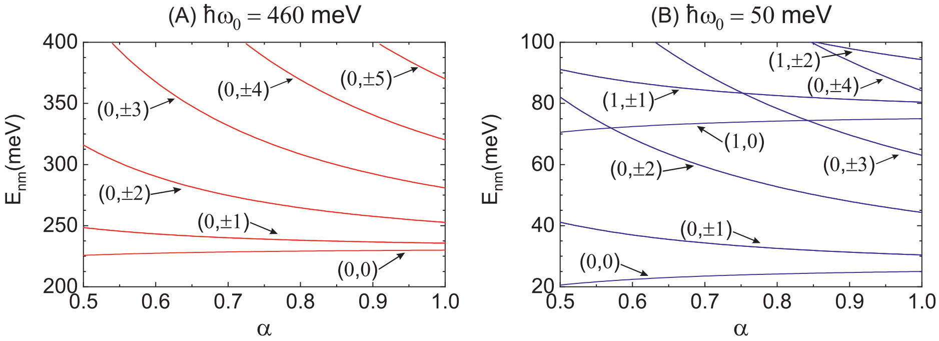

Fig. 4 The energy levels of a narrow ring (panel (A)) and wide ring (panel (B)) as a function of the α parameter for $B = 0$.

between adjacent subbands increases with the increasing magnetic field. Furthermore, we verify that the density of states decreases with increasing curvature. This result shows that the role of curvature, in general, is to shift the energy spectrum to higher values of energy.

Fig. 3, shows the behavior of the energy levels of the wide ring with respect to the magnetic field for some values of the α parameter. The energy spectrum is very different from the case of a narrow ring (see Fig. 2), which demonstrates the effect of electrostatic confinement energy $\hbar\omega_0$. In a ring with a finite width, the penetration of the uniform magnetic field into the conducting region of a ring also plays an important role (Tan and Inkson, 1996). It is clear from the discussion above that the effect of curvature is much more pronounced, as we can see in Fig. 3B–D. The behavior of energy levels is now quite complex, especially when there is more than one subband occupied. It is clear that the only effect of the geometric potential is to shift the state with $m = 0$ to lower values of energy, as shown in Fig. 4A and B, which describe, the behavior of energy levels as a function of α parameter when $B = 0$. It is interesting to note that the influence of the geometric potential is very sensitive to the geometry of the device (Pereira et al., 2021). In fact, in the limit where $r_0 = 0$, which describes a quantum dot, the state with $m = 0$ is not a physical state (Pereira et al., 2019). In the wide ring, we can see that the curvature induces energy-level crossings. This occurs because the curvature effect is more pronounced in higher states in a subband. In addition, there is the effect of the geometric potential in states with $m = 0$, as already discussed.

Magnetization

The magnetization is given by

$$M = -\frac{\partial F}{\partial B} = -\sum_{n,m} M_{n,m} f_F(E_{n,m}), \tag{24}$$

where F is the free energy, $M_{n,m} \equiv -\partial E_{n,m}/\partial B$ defines the magnetic moment, and $f_F(E_{n,m})$ is the Fermi distribution function. By using Eq. (19), the magnetic moment is written explicitly as

$$M_{n,m} = -\frac{\hbar e}{\mu \alpha^2}\left[\left(n + \frac{1}{2} + \frac{L}{2}\right)\frac{\omega_c}{\omega} - \frac{m - l}{2}\right]. \tag{25}$$

Fig. 5 presents the behavior of magnetization over a wide range of magnetic fields for the narrow ring. In Fig. 5B–D, the *dashed lines*, that correspond to the case $\alpha = 1$, allow observing the differences between the models with and without curvature. The oscillations are AB type, which arise from the states crossing in Fermi energy. In a narrow ring, not strictly 1D, the magnetization

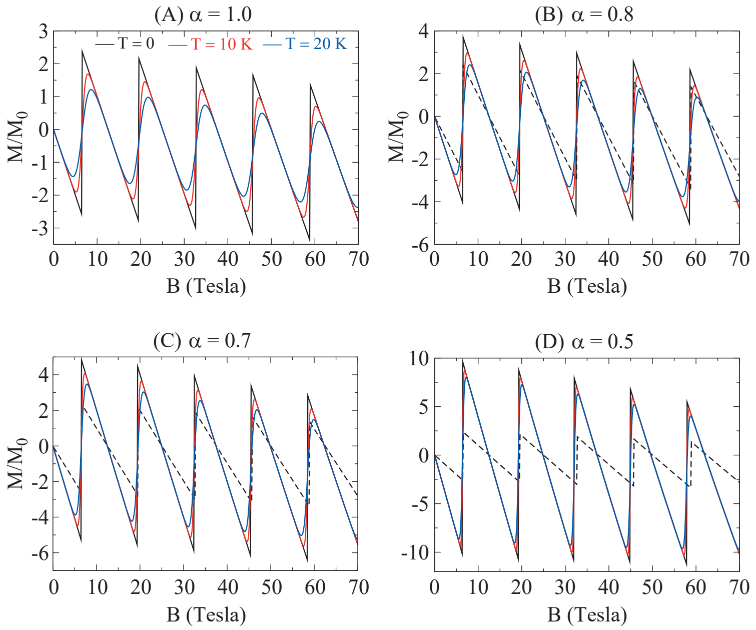

Fig. 5 Magnetization of a narrow ring, calculated without (A) and with (B–D) curvature, as a function of the magnetic field. The *dashed lines* in B–D correspond to the case without curvature $\alpha = 1.0$. Temperature removes the discontinuities of AB oscillations and decreases the oscillation amplitude.

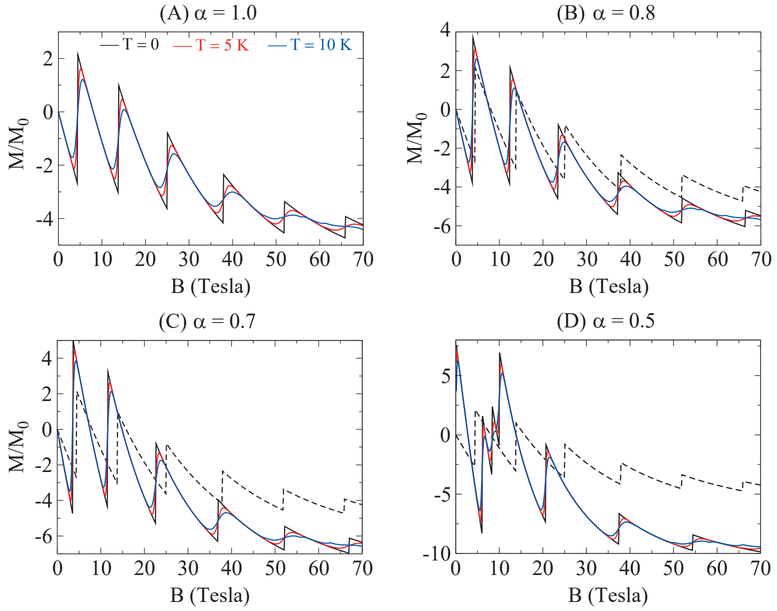

Fig. 6 Magnetization of a wide ring, calculated without (A) and with (B–D) curvature, as a function of the magnetic field. The *dashed lines* in B–D correspond to the case without curvature $\alpha = 1.0$. Temperature removes the discontinuities of AB oscillations and decreases the oscillation amplitude.

presents oscillations almost perfectly sawtoothlike. For $\alpha < 1$, Fig. 5B–D, we observe that there is an increase in the amplitude of the AB oscillations. This occurs due to an increase in the rate of change of energy levels with the magnetic field, as shown in Fig. 2B–D. The oscillations, almost sawtoothlike, are still visible. Nevertheless, for $\alpha = 0.5$, the combined effect of the magnetic field with the curvature shows a small damping of the oscillations. This result is in agreement with the one discussed in Fig. 3D, in which the effect of the magnetic field at the bottom of the first subband is quite pronounced due to the curvature. Fig. 5D also shows a smooth phase shift between the without curvature and the with curvature system.

Fig. 6 shows the behavior of the magnetization of a wide ring as a function of the magnetic field. In Fig. 6B–D, the *dashed lines*, that correspond to the case $\alpha = 1$, allow observing the differences between the models with and without curvature. As observed in Fig. 3, the energy spectrum of the wide ring is aperiodic as a function of the magnetic field. As a consequence, we can see that the amplitude of the oscillations decreases significantly as the magnetic field increases. In addition, we see a shift of the oscillations toward larger negative values when the magnetic field increases. As already reported, the curvature increases the effect of the magnetic field, as shown in Fig. 6B–D. Indeed, we can show that the magnetization tends to the value $-NM_0/\alpha^2$ when $B \to \infty$, where $M_0 = e\hbar/2\mu$ is the effective Bohr magneton. When comparing with Fig. 5, the role of confinement in the physical properties of the ring is evident. It is interesting to note the increase in the number of aperiodic oscillations at low values of the magnetic field for $\alpha = 0.5$, as we can see in Fig. 6D. Indeed, as we can discuss in Fig. 4, the effect of curvature on states is not uniform. In a curved semiconductor ring with 5 electrons, some electrons occupy a few states in the second subband, in particular, the state with $m = 0$. More electron-level crossings lead to a more complicated oscillating structure of magnetization as a function of the magnetic field as compared to the case when $\alpha > 0.5$.

In addition, Fig. 6D shows that for $\alpha = 0.5$, the magnetization presents an initial phase opposite to the cases shown in Fig. 6A–C. As shown in Fig. 3B, a crossing of degenerate levels $(0, \pm 2)$ with level $(1, 0)$ occurs at $\alpha \approx 0.63$, and the ground state configuration of the wide ring changes. Therefore, the opposing phases are not necessarily related to the even or odd number of electrons in the ring (Chakraborty and Pietiläinen, 1994). Here, opposite phases are attributed to the curvature.

The effect of temperature on the magnetization in narrow and wide rings is shown in Figs. 5 and 6, respectively. With increasing temperature, the oscillations acquire smooth behavior and decrease in magnitude. However, this effect is less pronounced when the α parameter takes on values lower. Indeed, there is an increase in energy-level spacing and, consequently, less contribution from the lower states.

Persistent current

By considering the variation of the magnetic flux confined to the hole of the ring, the persistent current is calculated using the Byers–Yang relation (Byers and Yang, 1961)

$$I_{n,m} = -\frac{\partial E_{n,m}}{\partial \Phi_{AB}} = -\frac{1}{\Phi_0}\frac{\partial E_{n,m}}{\partial \ell} \tag{26}$$

where $E_{n,m}$ is then given by Eq. (19). The total current is given by

$$I = \sum_{n,\,m} I_{n,m} f_F(E_{n,m}), \tag{27}$$

where $I_{n,m}$ is explicitly given by

$$I_{n,m} = \frac{e\omega}{4\pi\alpha^2}\left(\frac{m-\ell}{L} - \frac{\omega_c}{\omega}\right), \tag{28}$$

which is the persistent current carried by a given state $\chi_{n,m}$ of the ring.

As noted by Tan and Inkson (1999), the proportionality between the current and the magnetic moment observed in a one-dimensional ring is broken in a two-dimensional ring as a result of the penetration of the magnetic field into the conducting region of the ring. In the presence of curvature, this relation between the current and the magnetic moment is given by

$$M_{n,m} = \pi r_{n,m}^2 I_{n,m} - \frac{e\hbar}{\mu\alpha^2}\left(n + \frac{1}{2}\right)\frac{\omega_c}{\omega}. \tag{29}$$

The first term is the current in a one-dimensional ring with radius $r_{n,m}$ given by Eq. (21). The second term results from the penetration of the magnetic field into the 2D structure, being it a diamagnetic term. From this result, it is possible to show that if $\omega_c \ll \omega_0$ the persistent current and the magnetization present similar behavior.

Fig. 7 shows the persistent current in a narrow ring as a function of the magnetic field. We emphasize that the narrow ring model has a finite width, that is, it is not strictly a 1D ring. Thus, although oscillations sawtoothlike are observed, it is evident that diamagnetic term breaks the proportionality between the magnetic moment and the persistent current, as we can observe by comparing Fig. 5 with Fig. 7. In a wide ring, the effect of the magnetic field on the conducting region is more evident. Indeed, comparing Fig 6 with Fig. 8, we see that magnetization and persistent current have very different behavior.

Conclusion

In this article, we studied the electronic properties, the magnetization, and the persistent current of a 2DEG in narrow and wide rings in a conical metric and submitted to an external magnetic field. We have obtained analytically the wave functions and energy eigenvalues. It was shown that the curvature has a strong influence on the spectrum of an electron in quantum rings. This was verified by observing that the energy of the states is increased; the effects become more significant as the α parameter decreases. In particular, the size of the device, which is determined by the radius r_0 and transverse confinement ω_0, plays a crucial role in analyzing effects due to the geometric potential (see Fig. 4A and B). In other words, the influence of the mean curvature on the energies is limited by the value of the parameter a_1. This shows that the influence of the geometric potential is very sensitive to the geometry of the device. For the particular case of $r_0 = 0$, which corresponds to $a_1 = 0$, the mean curvature directly influences the behavior of the electronic states in a quantum dot (Pereira et al., 2019). These results have consequences on the occupation of the

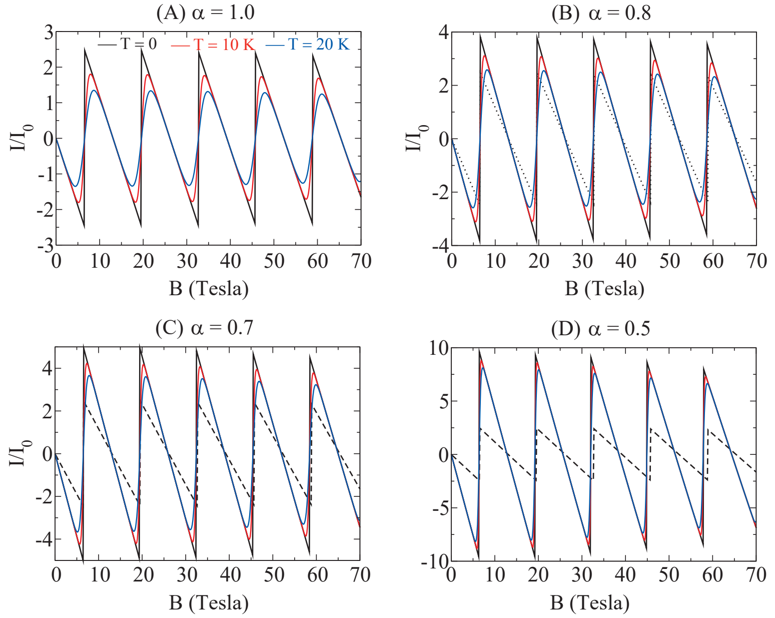

Fig. 7 Persistent current (in units of $I_0 = e\hbar/2\mu\pi r_0^2$) of a narrow ring, calculated without (A) and with (B–D) curvature, as a function of the magnetic field. The *dashed lines* in B–D correspond to the case without curvature $\alpha = 1.0$. Temperature removes the discontinuities of AB oscillations and decreases the oscillation amplitude.

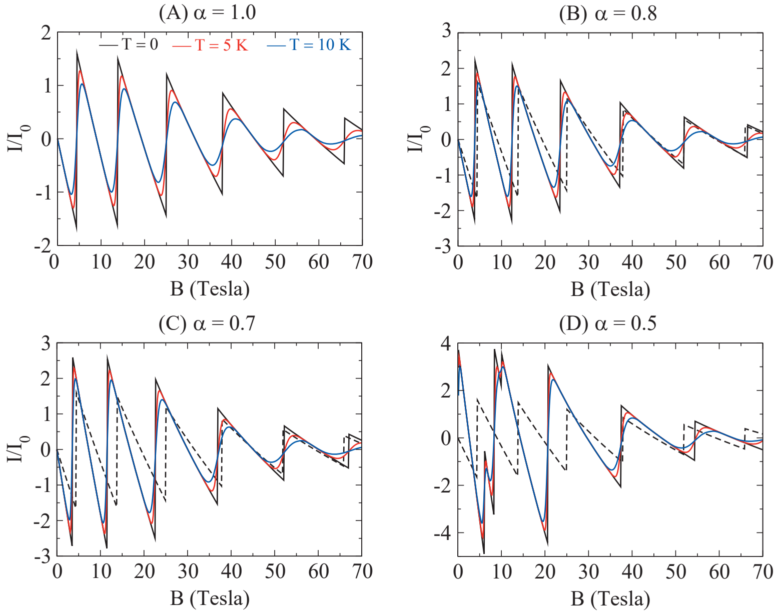

Fig. 8 Persistent current (in units of $I_0 = e\hbar/2\mu\pi r_0^2$) of a wide ring, calculated without (A) and with (B–D) curvature, as a function of the magnetic field. The *dashed lines* in B–D correspond to the case without curvature $\alpha = 1.0$. Temperature removes the discontinuities of AB oscillations and decreases the oscillation amplitude.

states in the Fermi energy, and consequently on the behavior of magnetization and persistent current. For instance, an increase in the amplitude of type-AB oscillations was noted in magnetization and persistent current. In addition, for $\alpha = 0.5$, we saw a complex pattern of AB-type oscillation in magnetization and persistent current in a wide narrow. It is evident that the low electron occupancy in quantum rings also contributes to a significant geometric potential effect on physical properties. We also investigated the effects of temperature on the physical properties of the mesoscopic ring. Figs. 5–8 showed that the amplitude of the oscillations decreases. The physical properties of mesoscopic systems are directly dependent on the temperature, which is a known result in the literature.

In the context of real physical models, the method proposed by Lorke et al. (2003) provides a possible experimental verification for the model studied in this work. In it, the authors introduced a method that allows one to lift off thin films of patterns containing a high-mobility 2DEG. Because of the flexibility of the thin film, it is then possible to transfer the heterostructure onto a cylindrical substrate and thus access the mesoscopic properties of an electron gas on a curved sample. Here, we would have a cone instead of a cylinder. This would set up a ribbon on the surface of a cone. Usual techniques could then be used to measure the persistent current. One way is to detect the magnetic field generated by the current loop by using a superconductive quantum interference device (SQUID) (Heinzel, 2006; Mailly et al., 1993).

Acknowledgments

This work was partially supported by the Brazilian agencies CAPES, CNPq, and FAPEMA. Edilberto O. Silva acknowledges CNPq Grant 307203/2019-0, FAPEMA Grants PRONEM-01852/14, and UNIVERSAL-06395/22. This study was financed in part by the Coordenação de Aperfeiçoamento de Pessoal de Nível Superior—Brasil (CAPES)—Finance Code 001.

References

Aharonov Y and Bohm D (1959) Significance of electromagnetic potentials in the quantum theory. *Physical Review* 115(3): 485. https://doi.org/10.1103/PhysRev.115.485.

Andrade FM, Silva EO, and Pereira M (2012) Physical regularization for the spin-1/2 Aharonov-Bohm problem in conical space. *Physical Review D* 85(4): 041701(R). https://doi.org/10.1103/PhysRevD.85.041701.

Andrade FM, Silva EO, and Pereira M (2013) On the spin- 1/2 Aharonov-Bohm problem in conical space: Bound states, scattering and helicity nonconservation. *Annals of Physics (New York)* 0003-4916. 339: 510–530. https://doi.org/10.1016/j.aop.2013.10.001.

Atanasov V and Dandoloff R (2016) Quantum-elastic bump on a surface. *European Journal of Physics* 38(1): 015405. https://doi.org/10.1088/0143-0807/38/1/015405.

Avishai Y, Hatsugai Y, and Kohmoto M (1993) Persistent currents and edge states in a magnetic field. *Physical Review B* 47(15): 9501.

Beenakker CWJ, van Houten H, and Staring AAM (1991) Influence of Coulomb repulsion on the Aharonov-Bohm effect in a quantum dot. *Physical Review B* 44(4): 1657–1662. https://doi.org/10.1103/PhysRevB.44.1657.

Bulaev DV, Geyler VA, and Margulis VA (2004) Effect of surface curvature on magnetic moment and persistent currents in two-dimensional quantum rings and dots. *Physical Review B* 69(19): 195313. https://doi.org/10.1103/PhysRevB.69.195313.

Büttiker M, Imry Y, and Landauer R (1983) Josephson behavior in small normal one-dimensional rings. *Physics Letters A* 0375-9601. 96(7): 365–367. https://doi.org/10.1016/0375-9601(83)90011-7. http://www.sciencedirect.com/science/article/pii/0375960183900117.

Byers N and Yang CN (1961) Theoretical considerations concerning quantized magnetic flux in superconducting cylinders. *Physical Review Letters* 7(2): 46–49. https://doi.org/10.1103/PhysRevLett.7.46.

Cao L, Laim L, Ni C, Nabet B, and Spanier JE (2005) Diamond-hexagonal semiconductor nanocones with controllable apex angle. *Journal of the American Chemical Society* 127(40): 13782–13783. https://doi.org/10.1021/ja0544814.

Carvalho AMde M, Sátiro C, and Moraes F (2007) Aharonov-Bohm-like effect for light propagating in nematics with disclinations. *Europhysics Letters* 80(4): 46002. https://doi.org/10.1209/0295-5075/80/46002.

Chakraborty T and Pietiläinen P (1994) Electron-electron interaction and the persistent current in a quantum ring. *Physical Review B* 50(12): 8460–8468. https://doi.org/10.1103/PhysRevB.50.8460.

Chang J-Y, Wu J-S, and Chang C-R (2013) Exact Hamiltonians with rashba and cubic Dresselhaus spin-orbit couplings on a curved surface. *Physical Review B* 87(17): 174413. https://doi.org/10.1103/PhysRevB.87.174413.

da Costa RCT (1981) Quantum mechanics of a constrained particle. *Physical Review A* 23(4): 1982–1987. https://doi.org/10.1103/PhysRevA.23.1982.

da Costa RCT (1982) Constraints in quantum mechanics. *Physical Review A* 25(6): 2893–2900. https://doi.org/10.1103/PhysRevA.25.2893.

Das MP (2010) Mesoscopic systems in the quantum realm: Fundamental science and applications. *Advances in Natural Sciences: Nanoscience and Nanotechnology* 1(4): 043001. https://doi.org/10.1088/2043-6262/1/4/043001.

Feng D and Jin G (2005) *Introduction to Condensed Matter Physics*. Singapore: World Scientific.

Ferrari G and Cuoghi G (2008) Schrödinger equation for a particle on a curved surface in an electric and magnetic field. *Physical Review Letters* 100(23): 230403. https://doi.org/10.1103/PhysRevLett.100.230403.

Filgueiras C and Moraes F (2008) On the quantum dynamics of a point particle in conical space. *Annals of Physics (New York)* 0003-4916. 323(12): 3150–3157. https://doi.org/10.1016/j.aop.2008.08.002.

Filgueiras C, Silva EO, and Andrade FM (2012) Nonrelativistic quantum dynamics on a cone with and without a constraining potential. *Journal of Mathematical Physics* 53(12): 122106. https://doi.org/10.1063/1.4770048.

Fomin VM (2014) *Physics of Quantum Rings*. Springer Berlin Heidelberg. https://doi.org/10.1007/978-3-642-39197-2.

Friedland K-J, Hey R, Kostial H, Riedel A, and Ploog KH (2007) Measurements of ballistic transport at nonuniform magnetic fields in cross junctions of a curved two-dimensional electron gas. *Physical Review B* 75(4): 045347. https://doi.org/10.1103/PhysRevB.75.045347.

Furtado C, Rosas A, and Azevedo S (2007) Landau quantization and curvature effects in a two-dimensional quantum dot. *EPL (Europhysics Letters)* 79(5): 57001.

Gaididei Y, Kravchuk VP, and Sheka DD (2014) Curvature effects in thin magnetic shells. *Physical Review Letters* 112(25): 257203. https://doi.org/10.1103/PhysRevLett.112.257203.

Heinzel T (2006) *Mesoscopic Electronics in Solid State Nanostructures*. Wiley. https://doi.org/10.1002/9783527618910.

Ihn T (2010) *Semiconductor nanostructures: Quantum States and Electronic Transport*. USA: Oxford University Press.

Ihn T, Fuhrer A, Sigrist M, Ensslin K, Wegscheider W, and Bichler M (2003) Quantum mechanics in quantum rings. In: Kramer B (ed.) *Advances in Solid State Physics*, pp. 139–154. Berlin, Heidelberg: Springer Berlin Heidelberg.

Kishigi K and Hasegawa Y (2021) de Haas-van Alphen oscillations near the Lifshitz transition from two electron pockets to one in the two-dimensional Dirac fermion systems. *Physical Review B* 104(8): 085412. https://doi.org/10.1103/PhysRevB.104.085412.

Kleemans NAJM, Bominaar-Silkens IMA, Fomin VM, Gladilin VN, Granados D, Taboada AG, García JM, Offermans P, Zeitler U, Christianen PCM, Maan JC, Devreese JT, and Koenraad PM (2007) Oscillatory persistent currents in self-assembled quantum rings. *Physical Review Letters* 99(14): 146808. https://doi.org/10.1103/PhysRevLett.99.146808.

Kouwenhoven LP, Austing DG, and Tarucha S (2001) Few-electron quantum dots. *Reports on Progress in Physics* 64(6): 701. http://stacks.iop.org/0034-4885/64/i=6/a=201.

Kurpas M, Zipper E, and Maśka MM (2013) Engineering of electron states and spin relaxation in quantum rings and quantum dot-ring nanostructures. *Physics of Quantum Rings*, pp. 455–479. Springer Berlin Heidelberg.

Kushwaha MS (2001) Plasmons and magnetoplasmons in semiconductor heterostructures. *Surface Science Reports* 0167-5729. 41(1): 1–416. https://doi.org/10.1016/S0167-5729(00)00007-8.

Leadbeater ML, Foden LC, Burke TM, Burroughes JH, Grimshaw MP, Ritchie DA, Wang LL, and Pepper M (1995) Electron transport in a non-uniform magnetic field. *Journal of Physics: Condensed Matter* 7(25): L307–L315. https://doi.org/10.1088/0953-8984/7/25/001.

Lei W and Lorke A (2013) Growth and spectroscopy of semiconductor quantum rings. *Physics of Quantum Rings*, pp. 27–59. Springer Berlin Heidelberg.

Lei W, Notthoff C, Lorke A, Reuter D, and Wieck AD (2010) Electronic structure of self-assembled InGaAs/GaAs quantum rings studied by capacitance-voltage spectroscopy. *Applied Physics Letters* 96(3): 033111. https://doi.org/10.1063/1.3293445.

Lévy LP, Dolan G, Dunsmuir J, and Bouchiat H (1990) Magnetization of mesoscopic copper rings: Evidence for persistent currents. *Physical Review Letters* 64(17): 2074–2077. https://doi.org/10.1103/PhysRevLett.64.2074.

Liang G-H, Wang Y-L, Lai M-Y, Liu H, Zong H-S, and Zhu S-N (2018) Pseudo-magnetic-field and effective spin-orbit interaction for a spin-1/2 particle confined to a curved surface. *Physical Review A* 98(6): 062112. https://doi.org/10.1103/PhysRevA.98.062112.

Liu J, Gao W, Ismail K, Lee K, Hong J, and Washburn S (1993) Correlations between Aharonov-Bohm effects and one-dimensional subband populations in GaAs/AlxGa1-xAs rings. *Physical Review. B, Condensed Matter* 48: 15148–15157. https://doi.org/10.1103/PhysRevB.48.15148.

Lorke A, Johannes Luyken R, Govorov AO, Kotthaus JP, Garcia JM, and Petroff PM (2000) Spectroscopy of nanoscopic semiconductor rings. *Physical Review Letters* 84(10): 2223–2226. https://doi.org/10.1103/PhysRevLett.84.2223.

Lorke A, Böhm S, and Wegscheider W (2003) Curved two-dimensional electron gases. *Superlattices and Microstructures* 0749-6036. 33(5): 347–356. https://doi.org/10.1016/j.spmi.2004.02.009. http://www.sciencedirect.com/science/article/pii/S0749603604000138. (Special issue dedicated to Professor Jorg Kotthaus on the occasion of his 60th Birthday, 29th May 2004).

Mailly D, Chapelier C, and Benoit A (1993) Experimental observation of persistent currents in GaAs-AlGaAs single loop. *Physical Review Letters* 70(13): 2020.

Maksym PA and Chakraborty T (1990) Quantum dots in a magnetic field: Role of electron-electron interactions. *Physical Review Letters* 65(1): 108–111. https://doi.org/10.1103/PhysRevLett.65.108.

Medvid' A (2012) The formation of nanocones on the surface of semiconductors by laser-induced self-assembly. *Laser Growth and Processing of Photonic Devices*, pp. 85–112. Elsevier.

Mendach S, Schumacher O, Welsch H, Heyn C, Hansen W, and Holz M (2006) Evenly curved two-dimensional electron systems in rolled-up Hall bars. *Applied Physics Letters* 88(21): 212113. https://doi.org/10.1063/1.2206135.

Mezrag F, Bouarissa N, and Boucenna M (2016) The size-dependent electronic and optical properties of InAs quantum dots. *Optik* 0030-4026. 127(3): 1167–1170. https://doi.org/10.1016/j.ijleo.2015.10.208. https://www.sciencedirect.com/science/article/pii/S0030402615015910.

Mousavi SM, Hashemi SA, Yari Kalashgrani M, Omidifar N, Lai CW, Vijayakameswara Rao N, Gholami A, and Chiang W-H (2022) The pivotal role of quantum dots-based biomarkers integrated with ultra-sensitive probes for multiplex detection of human viral infections. *Pharmaceuticals* 1424-8247. 15(7): 880. https://doi.org/10.3390/ph15070880. https://www.mdpi.com/1424-8247/15/7/880.

Pandey S, Scopigno N, Gentile P, Cuoco M, and Ortix C (2018) Topological quantum pump in serpentine-shaped semiconducting narrow channels. *Physical Review B* 97(24): 241103. https://doi.org/10.1103/PhysRevB.97.241103.

Paul DJ (2003) Nanoelectronics. *Encyclopedia of Physical Science and Technology*, pp. 285–301. Elsevier.

Pereira LFC, Andrade FM, Filgueiras C, and Silva EO (2019) Modifications of electron states, magnetization, and persistent current in a quantum dot by controlled curvature. *Annalen der Physik* 531(11): 1900254. https://doi.org/10.1002/andp.201900254.

Pereira LC, Andrade FM, Filgueiras C, and Silva EO (2021) Study of electronic properties, magnetization and persistent currents in a mesoscopic ring by controlled curvature. *Physica E: Low-Dimensional Systems and Nanostructures* 132: 114760.

Prinz VY, Seleznev VA, Gutakovsky AK, Chehovskiy AV, Preobrazhenskii VV, Putyato MA, and Gavrilova TA (2000) Free-standing and overgrown InGaAs/GaAs nanotubes, nanohelices and their arrays. *Physica E: Low-dimensional Systems and Nanostructures* 1386-9477. 6(1): 828–831. https://doi.org/10.1016/S1386-9477(99)00249-0.

Prinz VY, Grützmacher D, Beyer A, David C, Ketterer B, and Deckardt E (2001) A new technique for fabricating three-dimensional micro- and nanostructures of various shapes. *Nanotechnology* 12(4): 399. http://stacks.iop.org/0957-4484/12/i=4/a=301.

Reed M and Simon B (1975) *Methods of Modern Mathematical Physics. II. Fourier Analysis, Self-Adjointness.* New York, London: Academic Press.

Reimann SM and Manninen M (2002) Electronic structure of quantum dots. *Reviews of Modern Physics* 74(4): 1283.

Santos F, Fumeron S, Berche B, and Moraes F (2016) Geometric effects in the electronic transport of deformed nanotubes. *Nanotechnology* 27(13): 135302. https://doi.org/10.1088/0957-4484/27/13/135302.

Scarlino P, Ungerer JH, van Woerkom DJ, Mancini M, Stano P, Müller C, Landig AJ, Koski JV, Reichl C, Wegscheider W, Ihn T, Ensslin K, and Wallraff A (2022) In situ tuning of the electric-dipole strength of a double-dot charge qubit: Charge-noise protection and ultrastrong coupling. *Physical Review X* 12(3): 031004. https://doi.org/10.1103/PhysRevX.12.031004.

Schmidt AGM (2019) Exact solutions of Schrödinger equation for a charged particle on a sphere and on a cylinder in uniform electric and magnetic fields. *Physica E: Low-dimensional Systems and Nanostructures* 1386-9477. 106: 200–207. https://doi.org/10.1016/j.physe.2018.10.035.

Schwarz MP, Wilde MA, Groth S, Grundler D, Heyn C, and Heitmann D (2002) Sawtoothlike de Haas-van Alphen oscillations of a two-dimensional electron system. *Physical Review B* 65(24): 245315. https://doi.org/10.1103/PhysRevB.65.245315.

Sivan U and Imry Y (1988) de Haas-van Alphen and Aharonov-Bohm-type persistent current oscillations in singly connected quantum dots. *Physical Review Letters* 61(8): 1001–1004. https://doi.org/10.1103/PhysRevLett.61.1001.

Tan W-C and Inkson JC (1996) Electron states in a two-dimensional ring – An exactly soluble model. *Semiconductor Science and Technology* 0268-1242. 11(11): 1635. https://doi.org/10.1088/0268-1242/11/11/001.

Tan W-C and Inkson JC (1999) Magnetization, persistent currents, and their relation in quantum rings and dots. *Physical Review B* 60(8): 5626–5635. https://doi.org/10.1103/PhysRevB.60.5626.

Teixeira R, Leandro ESG, da Silva LCB, and Moraes F (2019) Schrödinger formalism for a particle constrained to a surface in R13. *Journal of Mathematical Physics* 60(2): 023502. https://doi.org/10.1063/1.5078442.

Vorob'ev AB, Friedland K-J, Kostial H, Hey R, Jahn U, Wiebicke E, Yukecheva JS, and Prinz VY (2007) Giant asymmetry of the longitudinal magnetoresistance in high-mobility two-dimensional electron gas on a cylindrical surface. *Physical Review B* 75(20): 205309. https://doi.org/10.1103/PhysRevB.75.205309.

Wagner MK, Li F, Li J, Li X-F, and Le XC (2022) Use of quantum dots in the development of assays for cancer biomarkers. *Analytical and Bioanalytical Chemistry* 397(8). https://doi.org/10.1007/s00216-010-3847-9.

Wang Y-L and Zong H-S (2016) Quantum particle confined to a thin-layer volume: Non-uniform convergence toward the curved surface. *Annals of Physics* 0003-4916. 364: 68–78. https://doi.org/10.1016/j.aop.2015.10.019.

Wang Y-L, Du L, Xu C-T, Liu X-J, and Zong H-S (2014) Pauli equation for a charged spin particle on a curved surface in an electric and magnetic field. *Physical Review A* 90(4): 042117. https://doi.org/10.1103/PhysRevA.90.042117.

Wang Y-L, Jiang H, and Zong H-S (2017) Geometric influences of a particle confined to a curved surface embedded in three-dimensional Euclidean space. *Physical Review A* 96(2): 022116. https://doi.org/10.1103/PhysRevA.96.022116.

Washburn S and Webb RA (1986) Aharonov-Bohm effect in normal metal quantum coherence and transport. *Advances in Physics* 35(4): 375–422. https://doi.org/10.1080/00018738600101921.

Zhang Y and Vishwanath A (2010) Anomalous Aharonov-Bohm conductance oscillations from topological insulator surface states. *Physical Review Letters* 105(20): 206601. https://doi.org/10.1103/PhysRevLett.105.206601.

Zhang X, Li H-O, Wang K, Cao G, Xiao M, and Guo G-P (2018) Qubits based on semiconductor quantum dots*. *Chinese Physics B* 27(2): 020305. https://doi.org/10.1088/1674-1056/27/2/020305.

Aharonov-Bohm effect in self-assembled InAs/GaAs Quantum Rings: Fabrication, formation mechanism and optical characterization[☆]

Jorge M García, Instituto de Micro y Nanotecnología, IMN-CNM, CSIC, (CEI UAM+CSIC), Isaac Newton, Madrid, Spain

© 2024 Elsevier Ltd. All rights reserved.

Introduction 426
Growth of InAs on GaAs. Wetting layer, quantum dots and quantum rings 427
Experimental details: MBE with in-situ characterization 427
Wetting layer. Presence of stress-induced melted indium 428
Quantum dots 429
Formation and optical properties of Quantum Rings 430
Quantum Ring formation mechanism: Dynamical de-wetting & diffusive alloying 432
Aharonov-Bohm effect in Quantum Rings 433
Conclusion 434
References 435

Abstract

We discuss the mechanisms of the transformation of InAs Quantum Dots into Quantum Rings (QRs) using a partial capping technique. We demonstrate the presence of a large fraction of stress-induced liquid indium that plays a fundamental role in the growth of nanostructures. The presence of liquid indium enables a de-wetting process that produces a "nano-eruption" creating Quantum Rings. A diffusive indium-gallium exchange and intermixing form alloyed InGaAs regions, what prevents further stress-induced melt. The competition between de-wetting and intermixing determines the final shape and size of these self-assembled nanostructures. Quantum Rings (QRs) are defect-free, coherent nanostructures that show an Aharonov-Bohm effect. They are excellent candidates to be used as crucial active elements for various quantum applications.

Key points

- Mechanism of Quantum Rings formation discussed
- Experimental demonstration of a stress-free indium at the surface during the deposition of InAs on GaAs(001) over a large range of substrate temperature
- Size and shape control of ensembles of Quantum Dots using partial capping technique
- Aharonov-Bohm effect demonstrated in Quantum Rings

Introduction

Semiconductor materials have contributed to the establishment of the modern current society as we know it. The majority of applications use silicon as the basic material in which the processors and devices are built. But there are many applications, mainly those in which optoelectronics are involved, in which other semiconductors based on III–V materials are crucial. These later materials are very important not only for well stablished technologies as lasers, LED, detectors, IR-detectors, concentration solar cells, power electronics; but they are expected to become the core elements for next generation of solid-state quantum computers, that could deliver the second quantum revolution in the coming decades (Dowling and Millburn, 2003; Gurioli et al., 2019). As an example, the possibility of fabrication of a single photon emitter (Michler et al., 2000) was early demonstrated. Furthermore, electrically driven and tunable plug-&-play single photon sources are being developed (Alen et al., 2019; Fuster et al., 2020).

The use of self-assembled Quantum Dot (QDs) structures fabricated on GaAs by Molecular Beam Epitaxy (MBE) and other growth techniques, is a mature technology in order to achieve this purpose. It is crucial the possibility of controlling and tuning the interaction of photons and electrons. Photonic structures provide a way of tuning the wavelength properties.

One of the most common materials systems of QDs is the use of InAs on GaAs. Since pioneering works that discovered the formation of InAs QDs in the early 1990s (Brandt et al., 1991; Leonard et al., 1993), QDs have become a central topic in nanoscience and nanotechnology. Solid pseudomorphic InAs on GaAs(001) has a −6.7% strain. This mismatch builds up a large strain energy (accumulation of stress) during the growth of InAs on GaAs, that results in the formation of self-assembled nanostructures on the surface of GaAs that help relax such elastic energy. When these lens-shaped nanostructures are capped in

---

[☆] *Change History:* August 2022. JM Garcia updated the chapter.

https://doi.org/10.1016/B978-0-323-90800-9.00032-9

an embedding GaAs matrix they confine carriers in three dimensions behaving like artificial atoms. In order to achieve accurate control of the electronic properties of these nanostructures it is required mastering the growing processes that takes place during formation and during capping. The use of techniques capable to create uniform ensembles of QDs, controlling not only the density but also their size is important.

The process of capping an ensemble of QDs is a dynamical competition between quenching its size and shape with other processes like de-wetting, segregation and alloying that drastically modify the original uncapped dots. It is possible to achieve extra control on the final confining properties by using a partial capping technique (Garcia et al., 1997). Recently, similar effects have been used to radically modify the shape of QDs to produce wetting-layer-free QDs (Löbl et al., 2019). These new QDs are excellent candidates to be used in solid-state quantum information processing devices. When the QDs are partially covered, a growth pause induces a reduction of the vertical size of the nanostructures (Garcia et al., 1998). It was early demonstrated that this growth pause allowed tuning, not only of the size, but also the shape; leading to the fabrication of Quantum Rings (QRs) (Garcia et al., 1997, 2014). Further work demonstrated that they behave like the "smallest rings of electricity" (Lorke, 2000).

The unique ring-like density of states of Quantum Rings for charge carriers, spins, plasmon and photon fields provide a rich wealth of fascinating properties and possibilities to develop strategic areas of next future technology: quantum computing based on photon and spin manipulations, photonic sources and detectors, magnetic memory, and functionalization of nanostructured metamaterials (Fomin, 2018b).

Seminal early work on other type of QRs was performed showing evidence for a flux periodic persistent current in rings made of various materials such as: copper (Lévy et al., 1990), gold (Chandrasekhar et al., 1991), GaAs-AlGaAs (Mailly et al., 1993) or AlSb/InAs/AlSb (Morpurgo et al., 1998). In all these mesoscopic structures scattering effects from fabrication defects were present inhibiting their true quantum limit behavior.

The Quantum Rings explored in this Chapter are a particular case of defect-free self-assembled nanostructures. They are fabricated by means of Molecular Beam Epitaxy. They were first developed in a pioneering work by Axel Lorke and Jorge M. García in 1997 in the group of Pierre M. Petroff in a successful collaboration that took place at the University of California Santa Barbara (UCSB), USA. During many years, the appropriate growing conditions that were used for their fabrication stayed unwillingly hindered within the secrets of the particular experimental growth reactor that was used. As a result of the research studies on the mechanism of QDs transformation into QRs that Daniel Granados performed in his PhD works at the Instituto of Micro and Nanotechnology-CSIC (in those days named Instituto of Microelectronic of Madrid), finally in 2003 the "secrets" of ring formation were unveiled. Further work focusing on the accumulated stress evolution during heteroepitaxial growth of mismatched layer, greatly contributed to the understanding of QR formation.

A few years after the report of the growth of ring-shaped nanostructures in 1997 (Garcia et al., 1997) it was demonstrated that these new types of self-assembled nanostructures were truly Quantum Rings, i.e., they were defect-free, coherent nanostructures, achieving the Heisenberg true quantum limit (Lorke, 2000; Lei and Lorke, 2014). They show characteristic and unique properties of QRs, which can be observed with the presently available magnetic fields. For example, in 2007 Kleemans et al. demonstrated by means of magnetization experiments, using a torque magnetometer, the presence of the persistent current carried by a single electron showing an Aharonov-Bohm (Aharonov and Bohm, 1959) effect. The first oscillation was observed at the magnetic field of 14 T in a sample grown with 29 layers of stacked self-assembled Quantum Rings sample, in perfect agreement with the theoretical model based on the structural properties determined by cross-sectional scanning tunneling microscopy measurements (Kleemans et al., 2007). These developments opened a vast field of research devoted to the physics of Quantum Rings (Fomin, 2014, 2018a).

There are other material systems in which defect-free self-assembled Quantum Rings have been developed, including: InAs on InP (Raz et al., 2003), the use of partial capping with AlAs (Lee and Lee, 2004), GaSb/GaAs (Kobayashi et al., 2004), droplet epitaxy (Mano et al., 2009; Heyn et al., 2011; Wu and Wang, 2014, 2018; Sanguinetti et al., 2014), GeSi ring structures from germanium dots partially capped with silicon (Cui et al., 2003).

We discuss the mechanisms of the transformation of QDs into QRs using a partial capping technique. We demonstrate the presence of a large fraction of stress-induced liquid indium that plays a fundamental role in the growth of nanostructures. The presence of liquid indium enables a de-wetting process that produces a "nano-eruption" creating nanovolcanoes, that can be truthfully called Quantum Rings. A diffusive indium-gallium exchange and intermixing form alloyed InGaAs regions, what prevents further stress-induced melt. The competition between de-wetting and intermixing determines the final shape and size of these self-assembled nanostructures. We show how to control and use these processes to taylor size and shape of nanostructures.

Growth of InAs on GaAs. Wetting layer, quantum dots and quantum rings

We review the formation of InAs nanostructures taking into account the conclusions obtained from measurements of the accumulated stress during nanostructure formation. First, we will show that during the growth of one monolayer of InAs, apparently the simplest case, the presence of liquid indium on the surface is experimentally confirmed. This understanding will later help explain the formation of Quantum Dots and Quantum Rings.

Experimental details: MBE with in-situ characterization

The MBE at IMN has several in-situ characterization techniques that make of it a unique system. It has Reflection High Energy Electron Diffraction (RHEED), Reflectance Difference (RD) and accumulated stress measurements ($\Sigma\sigma$). $\Sigma\sigma$ is acquired by measuring the radius of curvature of a thin lever-shaped sample with two laser beams impinging perpendicularly to the sample (Fig. 1).

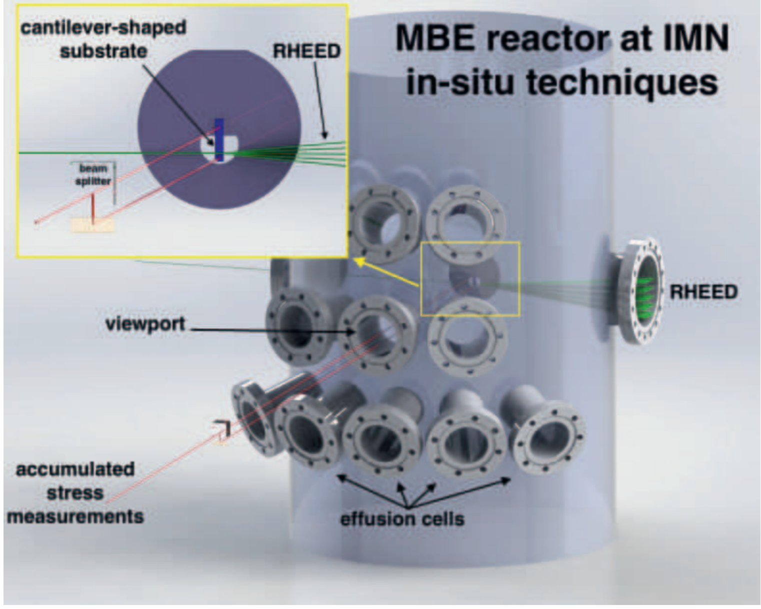
cantilever-shaped substrate
RHEED
beam splitter
MBE reactor at IMN in-situ techniques
viewport
RHEED
accumulated stress measurements
effusion cells

Fig. 1 Experimental set up for in-situ accumulated stress ($\Sigma\sigma$) measurements. A cantilever-shaped GaAs substrate is clamped in one side letting it freely bend under the accumulation of stress due to heteroepitaxial growth. Changes in $\Sigma\sigma$ are calculated using Stoney's equation by measuring the radius of curvature with two parallel laser beams. The surface reconstruction (monitored using RHEED) is used to have a precise control of the temperature of the substrate.

The sample is clamped to the sample holder in one side (see inset Fig. 1) and can freely bend induced by the accumulation of stress during the growth of mismatched materials, thanks to an opening in the substrate holder. The changes in $\Sigma\sigma$ are calculated using Stoney's equation (Freund et al., 1999; Garcia et al., 2000). A red laser beam is split into two parallel laser beams with a beam splitter. The detection of the reflected beams is made with a split photodiode or with a CCD camera. All the optics are placed outside the MBE chamber and only require an optical heated viewport placed in front of the substrate. The growth takes place on GaAs(001) samples which are cut from 100 to 150 μm-thick wafers. They are lever-shaped with the larger dimension along either [110] or $[1\bar{1}0]$ to explore the two principal crystallographic directions. During growth of InAs on GaAs, the substrate temperature is carefully calibrated and set using the RHEED patterns, since the opening in this special substrate holder makes the reading in the thermocouple completely different than when a regular holder is used.

Wetting layer. Presence of stress-induced melted indium

One of the simplest heteroepitaxial growth experiment of lattice mismatched materials is the growth of one monolayer (ML) of InAs on GaAs, commonly named wetting layer (WL). Initial stages of submonolayer InAs epitaxy on GaAs (Bressler-Hill, 1994) showed anisotropic nucleation effects, suggesting strain effects to be responsible for these observations. It is well known that 1 ML of InAs is providing not enough accumulated stress to induce a 3D roughening transition. It is commonly assumed that InAs grows lattice matched to GaAs for the first monolayer. For this reason, it commonly called wetting layer.

It was assumed (and still is nowadays) that only later during capping of this layer there was atomic segregation (Kawai et al., 1993), surface exchange between column-III atoms (Moison et al., 1989), and other processes that are responsible for the well-known problem of formation of no sharp interface which make unrealistic the assumption of abrupt potential well confinement for carriers. This is not the case, as it is demonstrated by the results of measuring the accumulated stress during growth of 1 ML of InAs on GaAs and further capping with GaAs with an Arsenic beam equivalent pressure of 2.2×10^{-6} Torr (2.93×10^{-4} Pa) at 414 °C (see Fig. 2).

The accumulated stress increases as soon as the growth of the heteroepitaxial layer begins (green trace), then, during a 30 s growth pause under arsenic, the stress stays stable (black trace), but during capping with GaAs, an unexpected further increase on the accumulated stress is observed (red trace). Isotropic results are obtained in both principal crystallographic directions [110] and $[1\bar{1}0]$, as expected from a InAs, As-terminated layer. If all the InAs were pseudomorphically incorporated into the GaAs substrate, and therefore 2D compressed, no such further increase in accumulated stress would be measured. Such behavior shines new light into the understanding of the growth on InAs on GaAs. from the ratio of the increase in $\Sigma\sigma$ during InAs deposition and during further capping, we can estimate that at this temperature only about 65% of the InAs layer is in a solid state fully stressed layer, the rest is in a fully relaxed stress-free state. So, there is a very large fraction (approx. 35%) of liquid InAs that is progressively incorporated into the GaAs matrix (see insert to Fig. 2C) during capping that induces another 1.4N/m accumulation of stress. With this technique we can also measure in-situ and in real time the segregation length (W) of InAs with subatomic precision.

The results shown in Fig. 2 demonstrate that there is a large fraction on the supplied Indium that is in a stress-free state. Based on thermodynamical calculations of Gibbs free energy (Bottomley, 2002) it can be assumed that this material is in a liquid state which has been stress-induced melted.

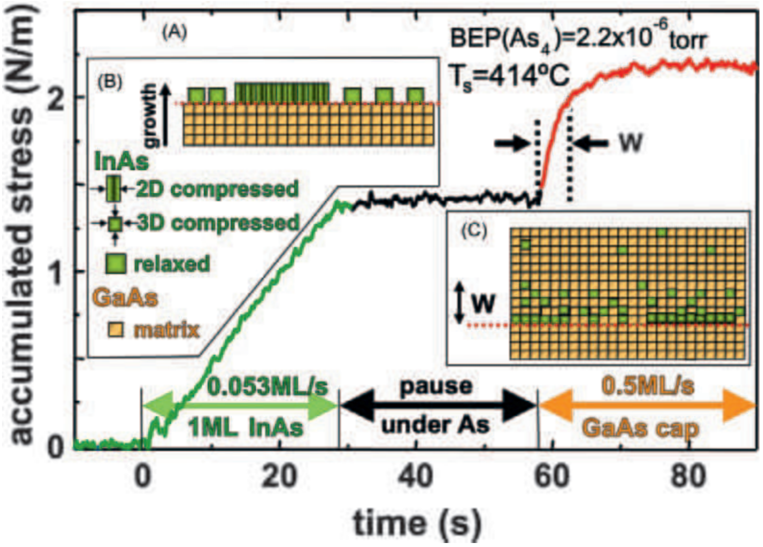

Fig. 2 (A) Measurement of accumulated stress during deposition of 1 ML of InAs (green trace), growth pause (black trace) and further capping with GaAs (red trace) on GaAs(100). (B) This insert shows a cross section scheme during deposition of InAs on GaAs. A submonolayer InAs island is fully 2D compressed but is coexisting with a large fraction of fully relaxed Indium. (C) this scheme shows a cross section of how liquid Indium is progressively incorporated pseudomorphically during capping creating a graded top interface characterized by a segregation length (W). After Garcia JM et al. (2014) 0D band gap engineering by MBE quantum rings: Fabrication and optical properties. In: Fomin, V.M., (ed.), *Physics of Quantum Rings. NanoScience and Technology*. Berlin-Heidelberg: Springer.

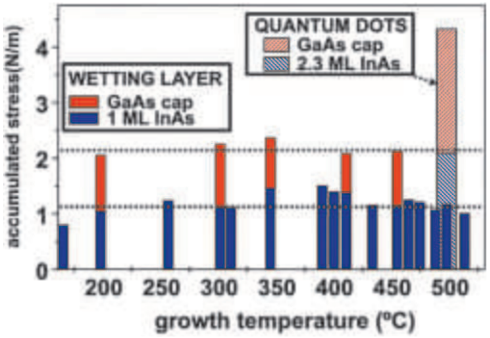

Fig. 3 Accumulated stress measurements during growth of one monolayer of InAs on GaAs at various substrate temperatures. The horizontal dotted lines are a guide to the eye showing the mean value of the measurements of 1 ML and the total increase in accumulated stress after fully covered with GaAs. It is also plotted in hatched bar graphs the accumulated stress measurements during quantum dot formation and further capping (to be discussed later in the next section). After Silveira J, Garcia JM, and Briones F (2001) Surface stress effects during MBE growth of III-V semiconductor nanostructures. *Journal of Crystal Growth* 227–228: 995–999.

This fact was theoretically predicted (Bottomley, 2000) almost at the same time that it was proved experimentally (Garcia et al., 2000). This stress-free liquid indium is present for the whole range of substrate temperatures employed in MBE growth. In this chapter, the substrate temperature during growth is expressed in degrees Celsius (°C), a unit commonly used in MBE. We have observed the same step-like behavior in the accumulation of stress during a wetting layer (1ML) growth and further cap from 170 °C to 520 °C (Silveira et al., 2001). In Fig. 3 we plot a bar graph representing the increase in $\Sigma\sigma$ during deposition of one monolayer of InAs at various temperatures (blue) which induced approximately 1.15 N/m. In some selected results we plot also the further increase of $\Sigma\sigma$ during capping (red). The total induced stress for a monolayer after capping is 2.15 N/m, close to a theoretical estimation of 1.7 N/m (Bottomley, 2002). Although a slight temperature dependance can be observed in the uncapped data, it is clear that there is always a further increase in $\Sigma\sigma$ during caping. The commonly known as wetting layer actually should be interpreted as an almost 50%:50% of wetting and "liquid" layer. There is always stress induced liquid indium during growth. This fact is key for understanding and controlling dot-to-ring re-assembly mechanisms.

Quantum dots

The fabrication of QDs that can be used for solid state device integration usually are obtained after embedding self-assembled islands into a larger band gap material, for example, InAs QD in a GaAs matrix layer. The island formation is a very fast process

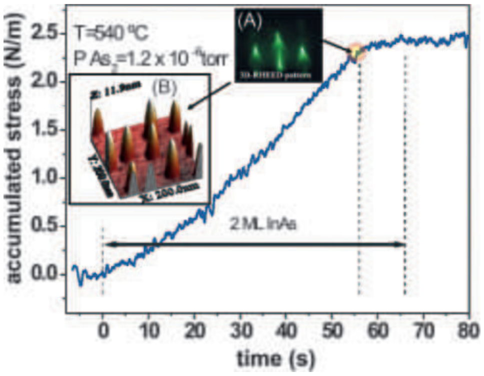

Fig. 4 Accumulated stress evolution during quantum dot (QD) formation. After deposition of 1.7 ML of InAs ($\sim t = 56$ s), the formation of 3D islands is revealed in the appearance of a characteristic 3D RHEED pattern (insert A) and revealed by AFM exploration of uncapped samples (insert B). Since the onset of the 3D RHEED pattern at $t = 56$ s till the end of InAs deposition at $t = 66$ s the increase of accumulated stress is very small.

which usually is observed clearly as an almost instantaneous appearance of a 3D RHEED pattern (see insert to Fig. 4A). At this point, if the growth is stopped and the surface characterized by ex-situ AFM, the presence of self-assembled islands is revealed as can be observed in the insert to Fig. 4B.

In spite that the evaporation of InAs is still on after the formation of pseudomorphic, crystallographically-ordered 3D islands, the measured accumulated stress increases only slightly. This observation implies a large stress-induced migration and incorporation of a large amount of stress induced melted InAs available at the base of the QD toward the tip, building up taller dots.

From the conclusion of the previous section, it important to remember that a large fraction (almost 50%) of stress-relaxed (liquid) indium is present on the GaAs interface at the onset of 3D island formation, therefore the island formation is a very complex process in which a large migration of indium (both liquid and the one which is arriving at the surface) toward the tip of the islands is expected. A very small increase in $\Sigma\sigma$ observed in Fig. 4, from $t = 56$ s to $t = 66$ s is in accordance with the stress-enhanced migration and incorporation of InAs at the tip of the dot, which is energetically favorable as the tip of these tall islands is largely relaxed (Kegel et al., 2000).

During the process of capping the islands, the same driving forces that are responsible for the formation of the islands, are present inducing a "self-disassembling" of the dots. When the dots are capped, there is an almost another 50% additional increase of $\Sigma\sigma$ (red and blue hatched bar graphs in Fig. 3), that reflects the progressive incorporation of large quantities of stress-free indium into the GaAs matrix.

All these processes are playing an important role during ring formation as will be discussed in the next section.

Formation and optical properties of Quantum Rings

We will focus on the growth of InAs QR on GaAs(100) by the partial capping technique (Garcia et al., 1997). The fabrication of self-assembled Quantum Rings (QRs) requires the use of a seed layer of self-assembled QDs.

It is crucial to use an ensemble of QD with the following properties: uniform size distribution (both vertically and in-plane), low area density ($\leq 1 \times 10^9$ QD $\times$ cm^{-2}), and with a mean value of the height of the dots larger than 7 nm. A low area density helps AFM characterization. The growth conditions for obtaining such QD ensemble (see Fig. 5A) is $T_{\text{substrate}} = 540$ °C, an As$_2$ beam equivalent pressure BEP$_{\text{As}} = 1.2 \times 10^{-6}$ Torr (1.6×10^{-4} Pa), details in reference (Granados and Garcia, 2003).

A growth pause, when the dots are partially capped, triggers the transformation of dots (Fig. 5A) into ring structures (see Fig. 5B). The dots are partially covered with 2 nm of GaAs at $T_{\text{substrate}} = 500$ °C (growth rate of 1ML/s), and then they are annealed at 500 °C for 60 s. As can be observed in the AFM profiles depicted in Fig. 6, there is a large reduction on the vertical size of the nanostructure, and an annular redistribution of material. We never obtained QRs for ensembles of QDs with vertical dimensions measured by AFM less than 7 nm. In order to achieve isotropic rings, we use a BEP of 1.5×10^{-6} Torr (2.0×10^{-4} Pa) As$_2$. It has been shown that the use of higher arsenic pressure promotes more isotopically growth along the principal direction [110] and $[1\bar{1}0]$ (Horikoshi et al., 1990). The use of As$_2$ has similar effects to employing a larger As$_4$ flux (Ogura et al., 2001).

The reduction in the vertical size observed in Fig. 6 has a strong influence in the vertical confining potential as can be observed in the low temperature photoluminescence spectra shown in Fig. 7. The transitions from the ground state E_0 can be observed at a moderately low laser pumping power of 20 mW. The emission E_0 is shifted 220 meV when an ensemble of QD (b) is compared to an ensemble of Quantum Rings (c). The WL peak can only be observed for the QR sample. The peak observed at 1.19 eV is the first excited state E_1 transition of the QDs, also observed in Fig. 8.

The possibility of fine-tuning the energy levels of quasi-0D nanostructures is a paramount tool for device design and implementation (Garcia et al., 1998).

When more excitation power is employed (Fig. 8), it is possible to observe higher excited stated both for QD (E_1, E_2, E_3, E_4, E_5) and QR (E_1). At 500 mW, a clear state filling effect can be observed in both spectra. The relaxation of carriers between transitions of

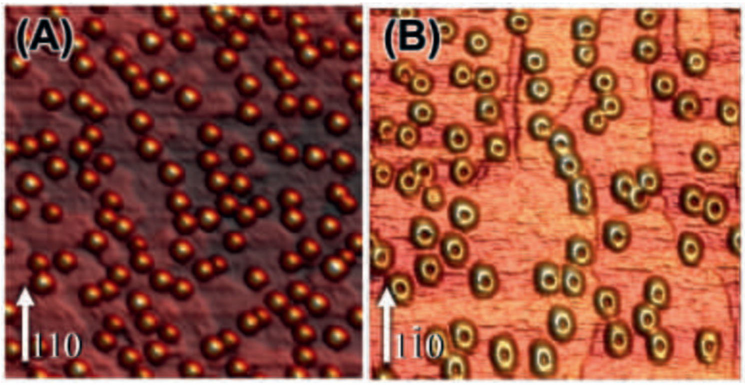

Fig. 5 $1 \times 1\ \mu m^2$ AFM image of an ensemble of optimized QD (A) to be used as a seed layer for the fabrication of self-assembled Quantum Rings shown in (B). For vertical scale see Fig. 6.

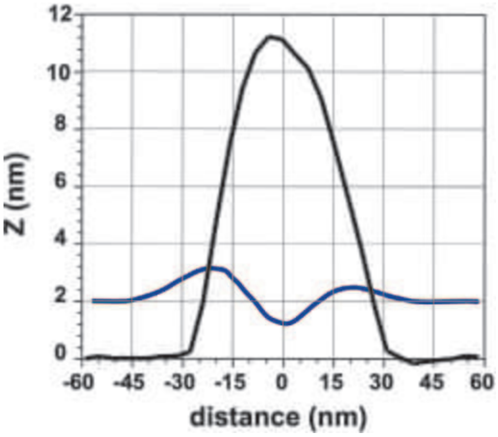

Fig. 6 AFM profiles of an uncapped QD (black) and an uncapped Quantum Ring (blue) along [$1\bar{1}0$] direction. The profile of the QR has been shifted vertically 2 nm to account for the thickness of the partial cap.

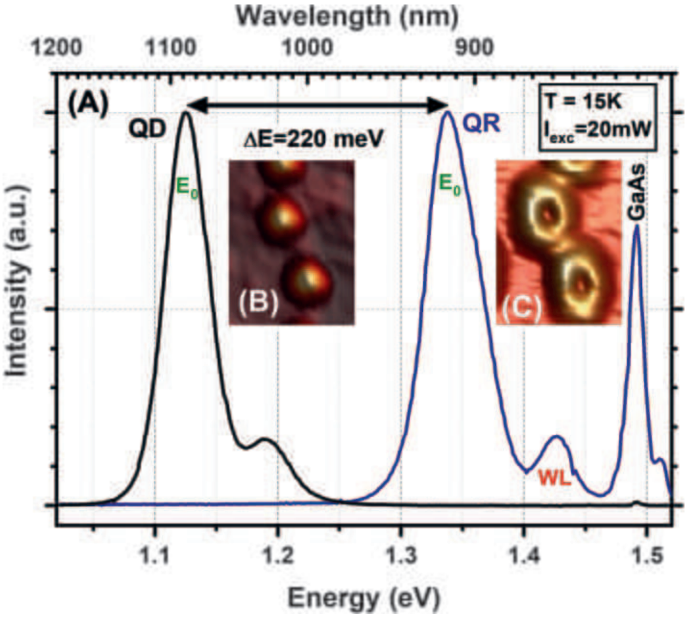

Fig. 7 (A) Photoluminescence spectra of a QD and a QR ensemble taken with a pumping power of 20 mW. The energy difference between the fundamental transition (E_0) is 220 meV, corresponding to the drastic change of shape and size from Quantum Dots (B) to Quantum Rings (C). This is a huge change in the confining potential that can be tuned on will.

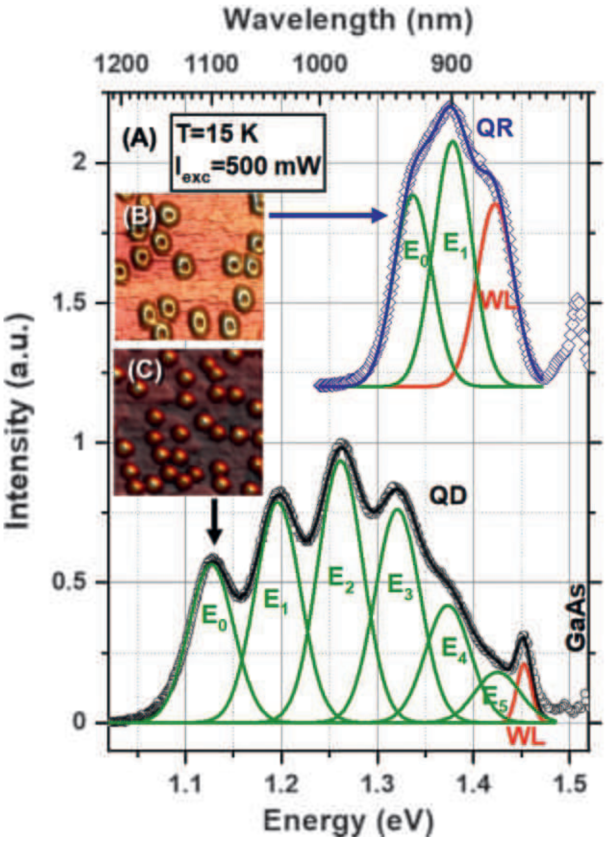

Fig. 8 (A) Low T Photoluminescence spectra of QD and QR ensembles taken with a pumping power of 500 mW. At high pumping power a state filling effect can be observed in both spectra. The experimental spectra (symbols) have been fitted with six Gaussian function (green lines) with identical FWMH. This observation reveals a high quality, highly uniform ensembles of QRs (AFM in B) and QDs (AFM in C). The transition from the wetting layer can also be observed (red line). The spectra have been normalized to its maximum value and vertically shifted for clarity.

lower states (E_0) is not fast enough to drain the photo-created carriers, so higher transitions can be observed. This observation reveals a state filling effect of a high quality, highly uniform ensemble of nanostructures. The transition from the wetting layer can also be observed (red peak contribution) in both spectra.

Quantum Ring formation mechanism: Dynamical de-wetting & diffusive alloying

A key element for the explanation of ring formation is the competition between a dynamical de-wetting process with a diffusive Ga—In diffusive intermixing. De-wetting involves the presence of liquid indium, which has been demonstrated in the previous discussion in Sections "Quantum Dots" and "Formation and optical properties of Quantum Rings." The liquification of InAs is driven by the minimization of the Gibbs free energy (Bottomley, 2002). There are theoretical results (Bottomley, 2002) showing that a biaxial epitaxial stress of InAs on GaAs(100) leads to a mixture of stress-free matter including a liquid phase of In and/or InAs. The driving force for this melting is the elastic energy (Bottomley, 2000; Garcia et al., 2000). It is expected that when QDs are partially covered, and consequently compressed, they undergo a phase transition into liquid phase and allows a de-wetting process (Lorke et al., 2002) that expels radially InAs from the QD.

Moreover, this effect has been observed (Silveira et al., 2001) to be independent of the temperature T in the 170–520 °C range. Therefore, the presence of stress-driven liquid InAs is a T independent process.

The uncapped dots are not liquid droplets (as distinct from the case of droplet epitaxy, Gurioli et al., 2019), they possess a 3D crystalline structure that is reflected in the RHEED pattern. They only become partially melted driven by the stress that the capping layer induces in the partially capped island. For taller dots this effect is more pronounced. This is the reason for using QD taller than 7 nm for self-assembling of Quantum Rings. There is a dynamical competition between de-wetting and alloying, that is why the GaAs growth rate of the capping layers plays an important role in the final size and properties of embedded QDs (Utrilla et al., 2018). The intermixing and alloying process is strongly temperature dependent. Therefore, by changing the temperature of the capping layer, we can achieve the formation of Quantum Rings or other types of nanostructures (Granados and Garcia, 2003).

Fig. 9A shows a scheme of a layer of QD that will be used for the ring formation. The materials involved are GaAs (substrate in blue, capping layer in yellow), InAs (dots in green), InGaAs QRs (in red) and arsenic vapor pressure (As, no color in Fig. 9), which is

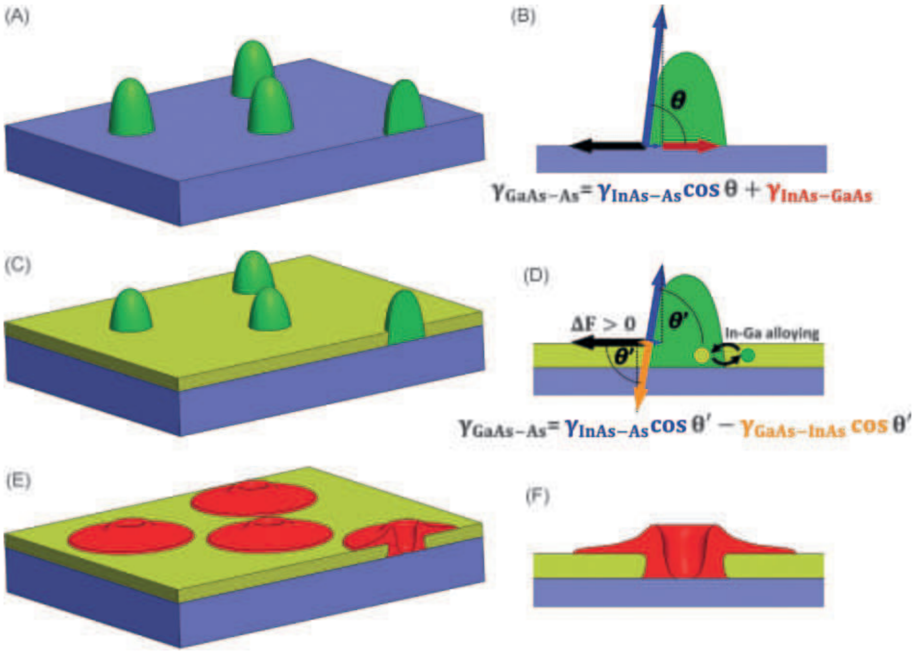
(A)
(B)
θ
$\gamma_{GaAs-As} = \gamma_{InAs-As} \cos\theta + \gamma_{InAs-GaAs}$
(C)
(D)
ΔF > 0
θ'
θ'
In-Ga alloying
$\gamma_{GaAs-As} = \gamma_{InAs-As} \cos\theta' - \gamma_{GaAs-InAs} \cos\theta'$
(E)
(F)

Fig. 9 Schematic of QR formation. (A) An ensemble of self-assembled 3D InAs islands (green) on GaAs (blue). A cross section is depicted in B) showing Young' equation of the equilibrium forces for a liquid droplet of indium. When the QDs are partially capped (yellow layer in C) and a growth pause under arsenic (As) vapor is introduced, there is an unbalance of net forces in Young's equation creating a radial force (ΔF) that pulls out the material (D). At the same time at the base of the QD there is a strong temperature-dependent intermixing and alloying between In and Ga atoms which trends to freeze the eruption of the base of the QD (D). Under the right conditions (see text) an ensemble of Quantum Rings (red) is created (E and F).

always present. The figure shows a cross section through the middle of a QD which is also shown in Fig. 9B with a simple explanation of the equilibrium forces involved for the case of an indium liquid droplet on a solid interface. The surface tensions are described by Young's equation (see Fig. 9B). The in-plane surface tension of the interface GaAs—As ($\gamma_{GaAs-As}$, black) is compensated (Fig. 9B) to the sum of the surface tension $\gamma_{InAs-GaAs}$ of the InAs-GaAs interface (red) plus the horizontal component of the surface tension of the InAs—As interface (blue), i.e., $\gamma_{InAs-As} \cos\theta$. R. Blossey and A. Lorke have suggested (Blossey and Lorke, 2002; Lorke et al., 2002) that a change in the balance of surface free energy due to the thin capping layer (see Fig. 9C and D) creates an outward pointing de-wetting force. Comparing the equation shown in Fig. 9B and D, there is an unbalance radial net force $\Delta F = \gamma_{InAs-GaAs}(1 + \cos\theta)$ (assuming that $\theta = \theta'$) responsible for the material redistribution and results in a ring-shaped structure (Fig. 9E and F).

We have to consider that there is also a simultaneous Ga—In intermixing and alloying process (Joyce et al., 1998, 2000; Garcia et al., 1997) during partial capping of the QDs (Fig. 9D). The formation of an InGaAs alloy reduces the strain energy and prevents its strain-induced melt. It is strongly T dependent (Joyce et al., 1998) and quenches the mobility of In. There is a strong alloying at the edges of the base of the QD that prevents the complete depletion of the base of the QD (Fig. 9F).

Once the material redistribution has taken place during the growth pause, these nanostructures preserve their structure during further capping, as demonstrated by cross section transmission electron microscope (TEM) (Granados et al., 2005) and cross section scanning tunneling microscope (XSTM) measurements (Offermans et al., 2005). The growth pause during partial capping enhances the formation of InGaAs alloy, and reduces concentration of large amounts on indium in some parts of the InAs islands. These two facts contribute to preservation of the Quantum Ring shape during subsequent capping.

Aharonov-Bohm effect in Quantum Rings

These new types of self-assembled nano-volcanoes clearly show a large vertical reduction in the vertical confinement, as it is demonstrated by the conclusion derived from the measurements of optical properties (shown in Figs. 7 and 8). But what makes them particularly interesting is that they truly behave as Quantum Rings, i.e., they are defect-free, coherent nanostructures, that function in the Heisenberg quantum limit showing characteristic and unique properties of rings (Lorke, 2000). In 2007 Kleemans et al. demonstrated by means of magnetization experiments, using a torque magnetometer, the presence of a persistent current carried by a single electron showing an Aharonov-Bohm (Aharonov and Bohm, 1959) effect. A sample was specifically designed and grown by MBE (Fig. 10A) and later characterized with state-of-the-art XSTM, (Fig. 10B). These data are used to create a very accurate description of the confinement potential that is used to make a theoretical model that perfectly reproduce the magnetometry measurements, taken at a temperature of 1.2 K and 4.2 K, of the first oscillation of the magnetic moment observed at a field of 14 T (Fig. 10C), also clearly observed in the inset to Fig. 10C, which displays the first derivative of the experimental magnetic moment

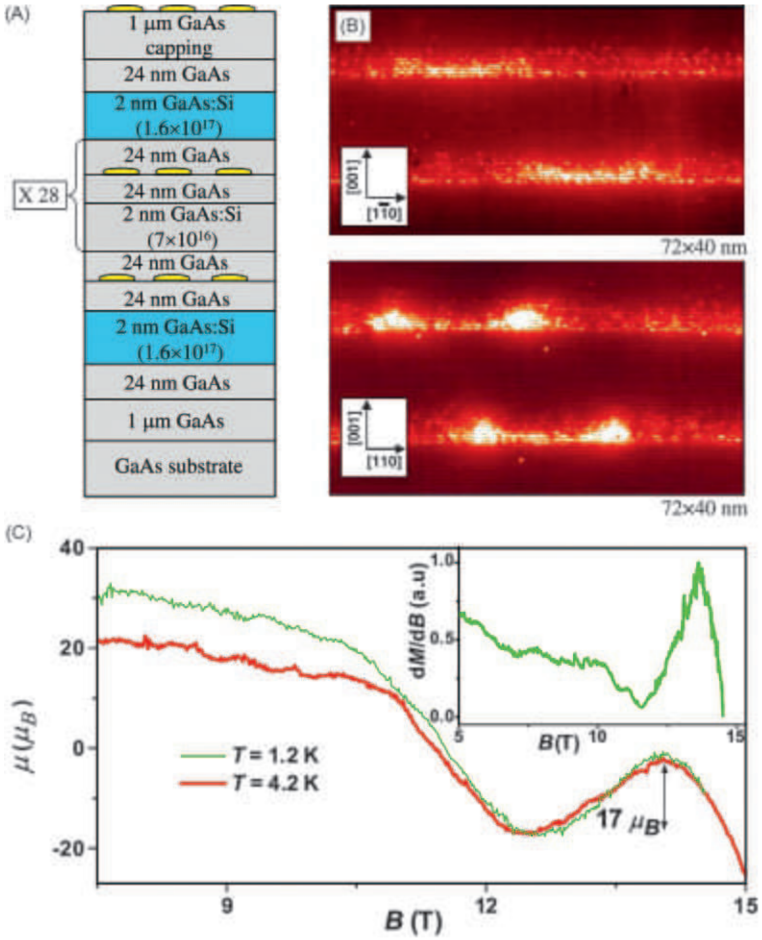

Fig. 10 (A) A test sample has been grown with 29 stacked layers of uncoupled Quantum Rings in a modulated doping structure adjusted to the density of QR to provide one electron per ring, (B) XSTM images of the cross-sections of two stacked Quantum Rings. The images have been taken along the two main principal directions. The images reveal the presence of indium (bright spots) in the center of the nanostructures, and a clear difference in the distribution of indium and the height of the rim between [110] and [1$\bar{1}$0] directions. c) Oscillation in the magnetic moment per electron, measured by torsional magnetometry at 1.2 K and at 4.2 K, after subtracting the linear background from the signal. The inset shows the first derivative of the experimental magnetic moment with respect to B at $T = 1.2$ K. Modified with permission after Kleemans NAJM et al. (2007). Oscillatory persistent currents in self-assembled quantum rings. *Physical Review Letters* 99: 146808. Copyright 2007 by the American Physical Society.

with respect to B at $T = 1.2$ K. The observed oscillation magnitude of the magnetic moment per electron is remarkably large for the topology of these nanostructures, which are singly-connected, and exhibit a pronounced shape asymmetry along [110] and [1$\bar{1}$0]. The XSTM images (Fig. 10B) show a nanoscale object which has a distribution of InAs material with no opening in the center. The InAs concentration of material resembles a "red blood cell" shape. What is outstanding is that the electron wave functions in such singly-connected material distribution are topologically identical to the electron wave functions in doubly-connected rings (Fomin, 2018b). Therefore, we can state that the electron states in self-assembled QRs are assigned to doubly-connected topology.

Conclusion

In summary, it is possible to fabricate self-assembled Quantum Rings grown by MBE by introducing a pause during the partial capping of a seed layer of QDs. We have shown that a large fraction of stress-induced melted liquid indium is present during the growth. Partial capping induces melting of InAs islands and promotes a de-wetting process that results in a nanoeruption. We describe and discuss the processes involved in their formation. The changes in shape and size lead to a drastic modification of the quantum confinement potential and enable the fabrication of Quantum Rings. We show a drastic reduction in vertical confinement revealed by a strong blue-shift in the photoluminescence spectra of highly uniform and high-quality ensembles of Quantum Rings. We demonstrate that they are defect-free coherent nanostructures that behave as Quantum Rings. Quantum Rings are very promising nanostructures with fascinating properties and possibilities to develop strategic areas of the next future quantum revolution.

Semiconductor QR-systems can be fabricated nowadays with a bottom-up approach (like self-assembly methods and vertical strain engineering) in combination with top-down techniques (like e-beam lithography and laser interferometric lithography) to provide a great complexity of ordered ring systems. In particular, single and multiple QRs, ordered arrays of QRs, complexes of QRs in combination with other nanostructures have been created recently. For example, laser emission was early demonstrated using three vertically stacked layers of QRs (Suarez et al., 2004). Some other examples of QR arrays offer superior prospects in high density magnetic memory applications as magnetic random-access memory, recording medium, and other spintronic devices (Wen et al., 2007). An alternative to MBE for the growth of nanostructures is the use of droplet epitaxy (Heyn et al., 2011; Wu and Wang, 2014, 2018; Sanguinetti et al., 2014; Gurioli et al., 2019), which provides a great engineering flexibility for fabricating various topology interesting nanostructures which can be used for the implementation of ideal quantum light sources for quantum communication and photonics-based quantum computers.

Another emerging research field is the use of QRs as promising building block for metamaterials. A possible control over the electromagnetic response in QR composite metamaterials (Linden et al., 2004) made from metals and semiconductors is an attractive goal for further investigations. QR-metamaterials can be implemented ordering laterally the rings by strain engineering of a multi-layer InGaAs quantum-dot superlattice (Wu et al., 2012a). It is also shown that two-dimensional periodically aligned QR-arrays can be fabricated on high-index GaAs(311)B and GaAs(511)B surfaces (Wu et al., 2012b) (see Chapter 00361. Self-Organized Semiconductor Nanostructures (Quantum Dots, Quantum Rings and Their Arrays) by Marega, E., Jr. in the present Encyclopedia).

Also, another exciting future trend is the development of theory and fabrication technique for the implementation of Quantum Rings with quantum point contacts, which can be used for the development of quantum information devices using semiconductor nanostructures (Diago-Cisneros and Mireles, 2003; Nagasawa et al., 2013).

The possibility of using QRs as photon sources and detectors is based on their unique optical properties associated with the excitonic Aharonov–Bohm effect. Some works (Fischer et al., 2009) have theoretically conceived a technique to completely trap and store, and later release individual photons at will, by tuning magnetic and electric fields. Application of these QRs as light capacitors or buffers is expected in the fields of photonic computing and communications technologies (Fischer et al., 2009; Borunda et al., 2008).

A very interesting future emerging field could be the experimental demonstration of a higher spin stability in Quantum Rings than in a quantum dot. The relaxation and decoherence processes take place at a time scale that is sufficiently long for spin manipulation and readout (Zipper et al., 2011). This spin stability would allow to use QRs as spin qubits.

Engineering the wave-function in type II dot-ring structures electrically offers a great possibility to modify the g factor through an external bias, and is a very interesting approach for implementation of quantum-information solid state devices. (Nowack et al., 2007). Topology driven g factor tuning in type-II quantum dots (Llorens et al., 2019) is an example of novel, topology-driven resources for functionalization in quantum electronics.

References

Aharonov Y and Bohm D (1959) Significance of electromagnetic potentials in the quantum theory. *Physical Review B* 115: 485–491. https://doi.org/10.1103/PhysRev.115.485.

Alen B, et al. (2019) Device for emitting single photons or entangled photon pairs. European Patent EP 3 361 516 B1 (filed 08/02/2017 & granted 18/12/2019). https://data.epo.org/publication-server/document?iDocId=6116444&iFormat=0.

Blossey R and Lorke A (2002) Wetting droplet instability and quantum ring formation. *Physical Review E* 65: 021603. https://doi.org/10.1103/PhysRevE.65.021603.

Borunda MF, et al. (2008) Aharonov-Casher and spin Hall effects in mesoscopic ring structures with strong spin-orbit interaction. *Physical Review B* 78: 245315. https://doi.org/10.1103/PhysRevB.78.245315.

Bottomley DJ (2000) Formation and shape of {InAs} nanoparticles on {GaAs} surfaces: Fundamental thermodynamics. *Japanese Journal of Applied Physics* 39: 4604–4608. https://doi.org/10.1143/jjap.39.4604. 7S pp.

Bottomley DJ (2002) Thermo-piezochemistry of InAs on GaAs(001). *Applied Physics Letters* 80: 4747–4749. https://doi.org/10.1063/1.1489704.

Brandt O, et al. (1991) InAs quantum dots in a single-crystal GaAs matrix. *Physical Review B* 44: 8043–8053. https://doi.org/10.1103/PhysRevB.44.8043.

Bressler-Hill V, et al. (1994) Initial stages of InAs epitaxy on vicinal GaAs(001)-(2 × 4). *Physical Review B* 50: 8479–8487. https://doi.org/10.1103/PhysRevB.50.8479.

Chandrasekhar V, et al. (1991) Magnetic response of a single, isolated gold loop. *Physical Review Letters* 67: 3578–3581. https://doi.org/10.1103/PhysRevLett.67.3578.

Cui J, et al. (2003) Self-assembled SiGe Quantum Rings grown on Si(001) by molecular beam epitaxy. *Applied Physics Letters* 83(2907): 2907–2909. https://doi.org/10.1063/1.1616992.

Diago-Cisneros L and Mireles F (2003) Quantum-ring spin interference device tuned by quantum point contacts. *Journal of Applied Physics* 114: 193706. https://doi.org/10.1063/1.4830017.

Dowling JP and Millburn GJ (2003) Quantum technology: The second quantum revolution. *Philosophical Transactions of the Royal Society A* 361: 1655–1674. https://doi.org/10.1098/rsta.2003.1227.

Fischer AM, et al. (2009) Exciton storage in a nanoscale Aharonov-Bohm ring with electric field tuning. *Physical Review Letters* 102: 096405. https://doi.org/10.1103/PhysRevLett.102.096405.

Fomin VM (ed.) (2014) *Physics of Quantum Rings*. Berlin-Heidelberg: Springer. https://doi.org/10.1007/978-3-642-39197-2.

Fomin VM (ed.) (2018a) *Physics of quantum rings*, 2nd edn Cham: Springer International Publishinghttps://doi.org/10.1007/978-3-319-95159-1.

Fomin VM (2018b) Quantum ring: A unique playground for the quantum-mechanical paradigm. In: Fomin VM (ed.) *Physics of Quantum Rings*, 2nd edn, pp. 3–32. Cham: Springer International Publishing. https://doi.org/10.1007/978-3-319-95159-1_1.

Freund LB, Floro JA, and Chason E (1999) Extensions of the Stoney formula for substrate curvature to configurations with thin substrates or large deformations. *Applied Physics Letters* 74: 1987–1989. https://doi.org/10.1063/1.123722.

Fuster D, et al. (2020) Electrically driven and tunable plug & play single photon sources. In: *3rd International Symposium on Single Photon based Quantum Technologies.* http://hdl.handle.net/10261/230620.

Garcia JM, et al. (1997) Intermixing and shape changes during the formation of InAs self-assembled quantum dots. *Applied Physics Letters* 71: 2014. https://doi.org/10.1063/1.119772.

Garcia JM, et al. (1998) Electronic states tuning of InAs self-assembled quantum dots. *Applied Physics Letters* 72(3172): 3172–3174. https://doi.org/10.1063/1.121583.

Garcia JM, Silveira J, and Briones F (2000) Strain relaxation and segregation effects during self-assembled InAs quantum dots formation on GaAs(001). *Applied Physics Letters* 77(409): 409–411. https://doi.org/10.1063/1.126992.

Garcia JM, et al. (2014) 0D band gap engineering by mbe quantum rings: Fabrication and optical properties. In: Fomin VM (ed.) *Physics of Quantum Rings*, pp. 61–82. Berlin-Heidelberg: Springer. https://doi.org/10.1007/978-3-642-39197-2_3.

Granados D and Garcia JM (2003) In(Ga)As self-assembled Quantum Ring formation by molecular beam epitaxy. *Applied Physics Letters* 82: 2401. https://doi.org/10.1063/1.1566799.

Granados D, et al. (2005) Vertical order in stacked layers of self-assembled In(Ga)As Quantum Rings on GaAs (001). *Applied Physics Letters* 86: 071918. https://doi.org/10.1063/1.1866228.

Gurioli M, et al. (2019) Droplet epitaxy of semiconductor nanostructures for quantum photonic devices. *Nature Materials* 18: 799–810. https://doi.org/10.1038/s41563-019-0355-y.

Heyn C, et al. (2011) Self-assembly of semiconductor quantum rings by local droplet etching. *Journal of Nanoelectronics and Optoelectronics* 6: 62–67. https://doi.org/10.1166/jno.2011.1134.

Horikoshi Y, et al. (1990) Growth process of III–V compound semiconductors by migration-enhanced epitaxy. *Journal of Crystal Growth* 105: 326–338. https://doi.org/10.1016/0022-0248(90)90382-U.

Joyce PB, et al. (1998) Composition of InAs quantum dots on GaAs(001): Direct evidence for (In,Ga)As alloying. *Physical Review B* 58: R15981. https://doi.org/10.1103/PhysRevB.58.R15981.

Joyce PB, et al. (2000) Effect of growth rate on the size, composition, and optical properties of InAs/GaAs quantum dots grown by molecular-beam epitaxy. *Physical Review B* 62: 10891–10895. https://doi.org/10.1103/PhysRevB.62.10891.

Kawai T, et al. (1993) Growth mechanism of (InAs)m(GaAs)n strained short-period superlattices grown by molecular beam epitaxy. *Journal of Applied Physics* 74: 7257. https://doi.org/10.1063/1.355016.

Kegel I, et al. (2000) Nanometer-scale resolution of strain and interdiffusion in self-assembled InAs/GaAs quantum dots. *Physical Review Letters* 85: 1694. https://doi.org/10.1103/PhysRevLett.85.1694.

Kleemans NAJM, et al. (2007) Oscillatory persistent currents in self-assembled quantum rings. *Physical Review Letters* 99: 146808. https://doi.org/10.1103/PhysRevLett.99.146808.

Kobayashi S, et al. (2004) Self-assembled growth of GaSb Type II quantum ring structures. *Japanese Journal of Applied Physics* 43: L662–L664. https://doi.org/10.1143/jjap.43.l662.

Lee BC and Lee CP (2004) Formation of semiconductor quantum rings using GaAs/AlAs partially capped layers. *Nanotechnology* 15(848): 848–850. https://doi.org/10.1088/0957-4484/15/7/024.

Lei W and Lorke A (2014) Growth and spectroscopy of semiconductor quantum rings. In: Fomin VM (ed.) *Physics of Quantum Rings*, pp. 27–59. Berlin-Heidelberg: Springer. https://doi.org/10.1007/978-3-642-39197-2_2.

Leonard D, et al. (1993) Direct formation of quantum-sized dots from uniform coherent islands of InGaAs on GaAs surfaces. *Applied Physics Letters* 63: 3203–3205. https://doi.org/10.1063/1.110199.

Lévy PL, et al. (1990) Magnetization of mesoscopic copper rings: Evidence for persistent currents. *Physical Review Letters* 64: 2074–2077. https://doi.org/10.1103/PhysRevLett.64.2074.

Linden S, et al. (2004) Magnetic response of metamaterials at 100 terahertz. *Science* 306: 1351. https://doi.org/10.1126/science.1105371.

Llorens JM, et al. (2019) Topology driven g-factor tuning in type-ii quantum dots. *Physical Review Applied* 11: 044011. https://doi.org/10.1103/PhysRevApplied.11.044011.

Löbl MC, et al. (2019) Excitons in InGaAs quantum dots without electron wetting layer states. *Communications on Physics* 2: 93. https://doi.org/10.1038/s42005-019-0194-9.

Lorke A (2000) The smallest rings of electricity. *Physical Review Focus* 5: 9. https://physics.aps.org/story/v5/st9.

Lorke A, et al. (2002) Morphological transformation of InyGa1 – yAs islands, fabricated by Stranski–Krastanov growth. *Materials Science and Engineering B* 88: 225–229. https://doi.org/10.1016/S0921-5107(01)00870-4.

Mailly D, Chapelier C, and Benoit A (1993) Experimental observation of persistent currents in GaAs-AlGaAs single loop. *Physical Review Letters* 70: 2020–2023. https://doi.org/10.1103/PhysRevLett.70.2020.

Mano T, et al. (2009) Self-assembly of quantum dots and rings by droplet epitaxy and their optical properties. *Journal of Nanophotonics* 3(031605): 1–18. https://doi.org/10.1117/1.3085991.

Michler P, et al. (2000) A quantum dot single-photon turnstile device. *Science* 290(5500): 2282–2285. https://doi.org/10.1126/science.290.5500.2282.

Moison J, et al. (1989) Surface segregation of third-column atoms in group III-V arsenide compounds: Ternary alloys and heterostructures. *Physical Review B* 40: 6149. https://doi.org/10.1103/PhysRevB.40.6149.

Morpurgo AF, et al. (1998) Ensemble-average spectrum of Aharonov-Bohm conductance oscillations: Evidence for spin-orbit-induced Berry's phase. *Physical Review Letters* 80: 1050–1053. https://doi.org/10.1103/PhysRevLett.80.1050.

Nagasawa F, et al. (2013) Control of the spin geometric phase in a semiconductor Quantum Ring. *Nature Communications* 4: 2526. https://doi.org/10.1038/ncomms3526.

Nowack KC, et al. (2007) Coherent control of a single electron spin with electric fields. *Science* 318(5855): 1430–1433. https://doi.org/10.1126/science.1148092.

Offermans P, et al. (2005) Atomic-scale structure of self-assembled In(Ga)As Quantum Rings in GaAs. *Applied Physics Letters* 87: 131902. https://doi.org/10.1063/1.2058212.

Ogura T, Kishimoto D, and Nishinaga T (2001) Effect of As molecular species on inter-surface diffusion in GaAs MBE for ridge structure fabrication. *Journal of Crystal Growth* 226: 179–184. https://doi.org/10.1016/S0022-0248(01)01020-X.

Raz T, Ritter D, and Bahir G (2003) Formation of InAs self-assembled Quantum Rings on InP. *Applied Physics Letters* 82: 1706. https://doi.org/10.1063/1.1560868.

Sanguinetti S, Mano T, and Kuroda T (2014) Self-assembled Semiconductor Quantum Ring Complexes by Droplet Epitaxy: Growth and Physical Properties. In: Fomin VM (ed.) *Physics of Quantum Rings*, pp. 161–196. Berlin-Heidelberg: Springer. https://doi.org/10.1007/978-3-642-39197-2_8.

Silveira J, Garcia JM, and Briones F (2001) Surface stress effects during MBE growth of III–V semiconductor nanostructures. *Journal of Crystal Growth* 227–228: 995–999. https://doi.org/10.1016/S0022-0248(01)00966-6.

Suarez F, et al. (2004) Laser devices with stacked layers of InGaAs/GaAs quantum rings. *Nanotechnology* 15: S126–S130. https://doi.org/10.1088/0957-4484/15/4/003.

Utrilla AD, et al. (2018) Size and shape tunability of self-assembled InAs/GaAs nanostructures through the capping rate. *Applied Surface Science* 444: 260–266. https://doi.org/10.1016/j.apsusc.2018.03.098.

Wen ZC, Wei HX, and Han XF (2007) Patterned nanoring magnetic tunnel junctions. *Applied Physics Letters* 91: 122511. https://doi.org/10.1063/1.2786591.

Wu J and Wang ZM (2014) Fabrication of ordered quantum rings by molecular beam epitaxy. In: Fomin VM (ed.) *Physics of Quantum Rings*, pp. 143–159. Berlin-Heidelberg: Springer. https://doi.org/10.1007/978-3-642-39197-2_7.

Wu J and Wang ZM (2018) Fabrication of ordered quantum rings by molecular beam epitaxy. In: Fomin VM (ed.) *Physics of Quantum Rings*, pp. 163–185. Berlin-Heidelberg: Springer. https://doi.org/10.1007/978-3-319-95159-1_7.

Wu J, et al. (2012a) Ordered quantum-ring chains grown on a quantum-dot superlattice template. *Journal of Nanoparticle Research* 14: 919. https://doi.org/10.1007/s11051-012-0919-0.

Wu J, et al. (2012b) Laterally aligned Quantum Rings: From one-dimensional chains to two-dimensional arrays. *Applied Physics Letters* 100: 203117. https://doi.org/10.1063/1.4719519.

Zipper E, et al. (2011) Spin relaxation in semiconductor Quantum Rings and dots – a comparative study. *Journal of Physics. Condensed Matter* 23: 115302. https://doi.org/10.1088/0953-8984/23/11/115302.

Superstripes landscape in perovskites high Tc superconductors

Gaetano Campi[a] **and Antonio Bianconi**[a,b], [a]Institute of Crystallography, CNR, Rome, Italy; [b]RICMASS Rome International Center for Materials Science, Rome, Italy

© 2024 Elsevier Ltd. All rights reserved.

Introduction **437**
Oxygen order in cuprates systems **438**
Superlattices in YBCO 438
Scale free distribution of oxygen wires in YBCO 442
Charge density waves and lattice defects **443**
LCO—Correlated disorder and phase separation in La_2CuO_{4+y} 443
Hg1201—Correlated disorder and phase separation in $HgBa_2CuO_{4+y}$ 444
Conclusion **445**
References **446**

Abstract

While a homogeneous aluminum crystal provides experimental validation of conventional *Bardeen-Cooper-Schrieffer* (BCS) superconductivity near zero temperature proposed in 1957 with a single small superconducting gap and a long range coherence length, today multiple realizations of nanoscale spatial heterogeneity have provided evidence for non-BCS multi-gap superconducting phase with high critical temperature where T_c maximum has been reached by tuning strain, dopants distribution, temperature treatments, local charge density heterogeneity, short range charge density waves, pseudo-Jahn-Teller polarons, and spin-orbit coupling. The lattice complexity controls the emergence of quantum macroscopic functionality at high-temperature. Therefore unveiling the nanoscale spatial conformations, the correlated disorder and the dynamical spatiotemporal fluctuations has been a fascinating adventure in these last years. Visualizing conformational nanoscale landscapes has been possible using advanced methodologies based on both high-precision X-ray measurements and advanced mathematical and statistical tools. Here we discuss the relations between the dynamical correlated disorder at nanoscale and the functionality in oxygen-doped perovskite superconducting materials. First, we deal with nanoscale textures of mobile interstitial oxygen; thus we show spatial correlations of oxygen ordering with short range charge density waves in perovskites high temperature superconducting compounds.

Key points

- To introduce the concept of nanoscale phase separation called superstripes
- To identify correlated disorder in doped perovskites
- To introduce complex self organization of oxygen interstitials
- To discuss scale free distribution of oxygen puddles and oxygen wires
- To introduce the superstripes landscale of short range charge density waves puddles
- To introduce synchrotron X-ray diffraction methods to unveil nanoscale complexity

Introduction

While phase separation (PS) was considered to be detrimental for conventional superconductivity in theory (Bardeen et al., 1957) it has been shown that a particular case of nanoscale phase separation called Superstripes (Bianconi et al., 1996; Bianconi et al., 1998; Bianconi, 2000; Bianconi, 2013) is the essential ingredient in the mechanism of high temperature superconductivity with different manifestations (Mazziotti et al., 2017; Mazziotti et al., 2021a,b, 2022). The heterogeneity of insulating and metallic nanoscale phases gives a two gap superconducting phase where the large and small superconducting gaps (Bianconi et al., 1998) shows a shape resonance belonging to the class of Fano resonances (Fano, 1961) driven by exchange interaction. Complexity in High Temperature Superconductors (HTS) and related materials has been unveiled by many experimental and theoretical works showing lattice fluctuations in perovskites (Thomas and Müller, 1968; Reihl et al., 1984; Glazer, 1972; Glazer, 1975; Howard and Stokes, 1998), superconductivity due to pseudo-Jahn-Teller polarons (Bianconi et al., 1996; Bednorz and Müller, 1986; Bednorz and Müller, 1988; Bednorz and Muller, 1990; Bishop et al., 1989; Keller et al., 2008; Mannhart et al., 1991; Innocenti et al., 2009; Agrestini et al., 2003; Della Longa et al., 1995), two electronic components (Müller et al., 1998; Khasanov et al., 2007) glassy phase (Deutscher and Müller, 1987) isotope effect (Weyeneth and Müller, 2020; Kochelaev et al., 2014, Bendele et al., 2017; Lanzara et al., 1999) phase separation (Muller and Benedek, 1993; Mihailovic et al., 1995; Liarokapis et al., 1996; Kaldis et al., 2012; Müller, 2000; Kremer et al., 1992; Kremer et al., 1993; Poulakis et al., 1996; Sigmund and Müller, 2012; Campi and Bianconi, 2019).

https://doi.org/10.1016/B978-0-323-90800-9.00222-5

While disorder usually suppresses the superconducting critical temperature, T_c, in conventional superconductors, the manipulation of oxygen defects in cuprate perovskites like in La_2CuO_{4+y} by thermal treatments (Fratini et al., 2010) or by X-ray photo induced effect, (Poccia et al., 2011) pumping and probing at same time the nanoscale textures has provided compelling evidence that the superconducting properties are enhanced by an optimum lattice inhomogeneity in High Temperature superconductors, HTS, with perovskites structure. The nanoscale phase separation related to the self-organization of defects has been found in $YBa_2Cu_3O_{6+y}$ (Campi et al., 2013; Ricci et al., 2013; Ricci et al., 2014; Zimmermann et al., 2003). Scanning nanoscale x ray diffraction has shown the coexistence of short range CDW puddles and oxygen rich puddles in $HgBa_2CuO_{4+y}$ tetragonal crystal with filamentary superconductivity at the interface (Campi et al., 2015; Campi and Bianconi, 2016). Interface superconductivity has been observed in several artificial perovskites superstructures (Campi and Bianconi, 2021). Recently, several theories have been proposed based on the presence in HTS of networks of nanoscale superconducting grains (Innocenti et al., 2009). The tendency toward electronic phase separation in strongly correlated multiband systems with polaronic and Fermi particles near a Mott transition is now well accepted. The Intrinsic phase separation can promote unconventional quantum phases also in chalcogenide superconductors $A_xFe_{2-y}Se_2$ (Ricci et al., 2011; Ricci et al., 2015; Ricci et al., 2020) in Sc doped $Mg_{1-x}Sc_xB_2$ (Agrestini et al., 2004; Campi et al., 2006), in cobalt oxides (Drees et al., 2014) and in nikelate perovskites, $La_{2-x}Sr_xNiO_4$, with the formation of dynamic spin and charge density wave puddles (Ricci et al., 2021; Campi et al., 2022a,b).

Oxygen order in cuprates systems

Superlattices in YBCO

The $YBa_2Cu_3O_{6+y}$ system is made of an infinite layer cuprate, $Y[Cu(2)O_2]_2$, intercalated with the defective spacer oxide $[BaO]_2$ and $Cu(1)Oi_y$ chains. The oxygen defect ions O-i_y In the chains partially fill the empty basal plane sites forming vacancies ordering in the O(1) sites. The formation of the CuO chains can be detected as satellite superstructure streaks in the X Ray Diffraction patterns of $YBa_2Cu_3O_{6+y}$. We have first studied the *tetragonal to orthorhombic phase transition* in $YBa_2Cu_3O_{6+y}$ at $y = 0.33$ with $T_c = 7$ K, probing the metamorphic phase with local oxygen concentration $y = 0.5$ observed in the range $0.33 < y < 0.62$ and called Ortho-II (v. Zimmermann et al., 2003). The diffraction patterns in the $(\boldsymbol{a}^*, \boldsymbol{b}^*)$ plane of $YBa_2Cu_3O_{6.33}$ show the diffuse streaks $q_{ortho\text{-}II}$ at $(h \pm 0.5, 0)$ due to nanoscale puddles made by O-i ordering (see Fig. 1a). The equal intensity of horizontal and vertical streaks highlighted with the black rectangles indicate a phase made of the Ortho-II puddles where the a-axis is oriented both in the vertical and horizontal direction. A Pictorial view of the basal Cu-O-i_y plane is show in Fig. 1b. Horizontal and vertical oxygen-rich metamorphic phase ($y = 0.5$), called Ortho-II, are intercalated by disordered oxygen-poor ($y < 0.33$) domains. Phase separation due to the spatial distribution of the (OII) superstructure has been visualized by scanning micro-X-ray diffraction using a 12-KeV energy and probing 1-μm thickness of the crystal surface. In Fig. 1c and d we show the color maps of the OII superstructure intensity and coherence length. The size of the Ortho-II oxygen chain puddles ranges from 3 (dark blue) to 12 nm (red) in the (a) a-axis direction. This system presents a further phase separation due to spin-up and spin-down sites, as calculated in the interfaces of the ASYNNNI system (Ceder et al., 1991). The interfaces can be generated by an exploration process in which one moves clockwise on the edges with the simple rule that to its right is always a (+) site and to its left is always a (−) site in agreement with (Najafi and Tavana, 2016).

We have studied the temperature evolution of the symmetry in the ortho-II superstructure. In Fig. 1g we show the variation of the average structure of Ortho-II puddles in the (h,k) plane of $YBa_2Cu3O_{6.33}$ measured in transmission mode. The variation of the size of the Ortho-II puddles oriented in the vertical (open squares red) and horizontal (open triangles) direction in the sample, during the warming cycle is shown in Fig. 1h. The difference between the size of vertical and horizontal Ortho-II puddles indicated by large filled (red online) dots (filled dots, blue online) in the heating (cooling) cycle shows a large value in the range $350\ K < T < 380\ K$ due to the spontaneous symmetry breaking in the fluctuation regime above 350 K. Increasing the i-O_y content, we have investigated the spatial arrangement of Ortho-VIII puddles in $YBa_2Cu_3O_{6.67}$. Upon thermal treatments we were able to switch from a first network of oxygen defect striped puddles with OVIII modulation to a second network characterized by OXVI modulation and finally to a third network with puddles of OV periodicity. We have mapped the spatial evolution of the out of plane OVIII, OXVI and OV puddle nanosize distribution via scanning micro-diffraction measurements. In Fig. 2a we show thermal evolution of the OVIII oxygen stripe superlattice profile at $\eta(a^*) = 15/H = 24$ $(30/H = 48)$ into the OV superstructure at $\eta(a^*) = 15/H = 25$ $(30/H = 50)$, passing from the incommensurate OXVI superstructure. In order to monitor the microscopic evolution of OVIII domains into OXVI and OV during the thermal manipulation, we used μXRD with a beam about 1 μm in diameter by scanning the sample over an area of $160 \times 80\ \mu m^2$. The maps of $\eta(a^*)$ and Probability Density Function (right panels) at three different temperatures during the thermal cycle where the system shows the OVIII, OV and OXVI phases are shown in Fig. 2b. We can observe the thermal cycle of the intensity, the average puddle size along a^* and along b^*. Starting from the $FWHM_{XY}$ and the h_{XY} along a^*, measured at each X–Y spatial position, we reconstructed the spatial maps of the *number of oxygen chains* (n) inside the puddles. Using the expression $n_{XY} = (1 - h_{XY})/FWHM_{XY}$, we calculate this quantity for OVIII, OXV and the annealed OV puddles (see Fig. 2c). The number of oxygen chains decreases after the thermal heating cycle from OVIII to OXVI and increases again after the cooling in the OV puddles (but remains lower than in the OVIII phase).

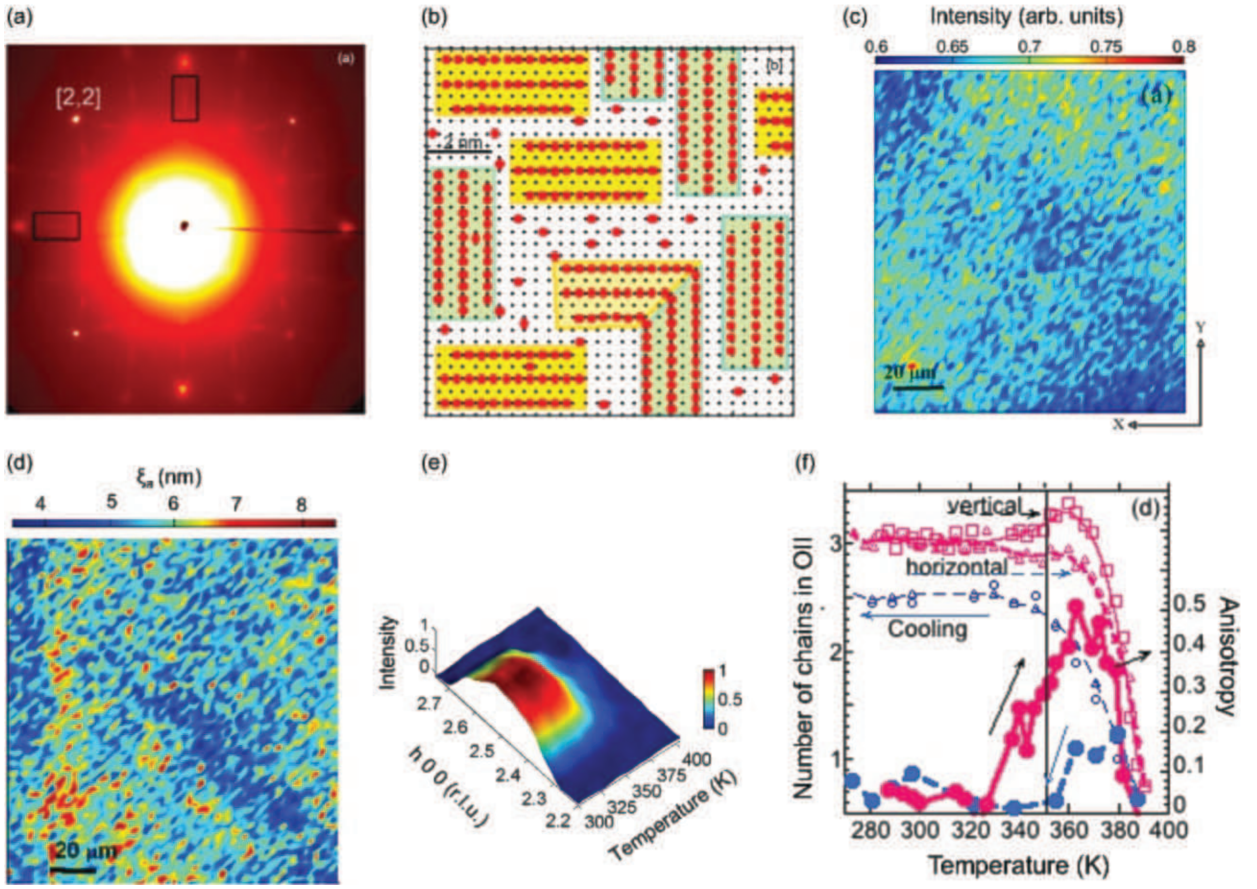

Fig. 1 (a) The diffraction pattern in the (*h*,*k*) plane of $YBa_2Cu_3O_{6.33}$ ($T_c = 7$ K) measured in transmission mode on a 100-μm-thick sample with c axis oriented in the X-ray beam direction. Here, 20-KeV photon energy and 100-μm X-ray beam size have been used. The diffuse streaks $q_{ortho-II}$ at (h ± 0.5,0) are superstructure satellites due to nanoscale puddles with Ortho-II structure made by O-i ordering after annealing at 300 K. The equal intensity of horizontal and vertical streaks highlighted with the black rectangles indicate a phase made of the Ortho-II puddles where the a-axis is oriented both in the vertical and horizontal direction. (b) Pictorial view of the basal Cu-O-i_y plane of $YBa_2Cu_3O_{6.33}$. The small black dots are the Cu(1) sites, and the large red dots are the oxygen defect ions O-i_y. Horizontal and vertical oxygen-rich metamorphic phase ($y = 0.5$) are called Ortho-II. The Ortho-II puddles are intercalated by disordered oxygen-poor ($y < 0.33$) domains. The black bar indicates 2-nm length scale. (c) OII intensity as seen by scanning micro-X-ray diffraction of a single crystal $YBa_2Cu_3O_{6.33}$ using a 12-KeV energy and probing 1-μm thickness of the crystal surface. The color map of: the OII superstructure intensity is plotted as a function of the illuminated spot position x-y in the sample surface, where x and y directions in the image correspond to the a and b crystallographic axis of the sample. The black bar indicates 20 μm length scale on the sample surface. (d) The puddle size (color) of the Ortho-II puddles is plotted as a function of the illuminated spot position xy in the sample surface. The size of the Ortho-II oxygen chain puddles ranges from 3 (dark blue) to 12 nm (red) in the (a) a-axis direction. The white bar indicates 20-μm length scale on the sample surface. (e) Temperature evolution of the $q_{ortho-II}$ satellite reflection profiles along h. The bright (red) and dark (blue) color corresponds, respectively, to the higher and lower intensities of the satellite diffraction spots. Variation of the average structure of Ortho-II puddles in the (h,k) plane of YBa2Cu3O6.33 measured in transmission mode of a 100-μm-thick sample using an X-ray beam of 20-KeV photon energy and 100-μm size. (f) The variation of the size of the Ortho-II puddles oriented in the vertical (open squares red) and horizontal (open triangles) direction in the sample, during the warming cycle. The difference between the size of vertical and horizontal Ortho-II puddles indicated by large filled (red online) dots (filled dots, blue online) in the heating (cooling) cycle shows a large value in the range $350 \text{ K} < T < 380$ K due to the spontaneous symmetry breaking in the fluctuation regime above 350 K. Reproduced from Campi G, Ricci A, Poccia N, Barba L, Arrighetti G, Burghammer M, . . . Bianconi A (2013) Scanning micro-X-ray diffraction unveils the distribution of oxygen chain nanoscale puddles in YBa2Cu3O6.33. *Physical Review B*, 87(1): 014517.

From the FWHM along c* we calculated the out of plane domain size for every spot of the scanned map. Fig. 2d shows the real space map of the out of plane domain size (along c*), before the heating (OVIII), at 390 K (OXVI) and after the cooling cycle (OV), respectively. These maps show the presence of clear intrinsic nanoscale heterogeneity in this cuprate superconductor. The OVIII probability density functions for the domain size distribution along c* is relatively sharp, and varies from 7 to 9 nm. Upon heating, the OXVI phase shows instead a very broad distribution, that spans the 1–6 nm range. After the cooling cycle, the size distribution in the OV phase sharpens again, around the decreased average value of 3 nm, therefore indicating a certain recovered order. The overall behavior indicates a sensible response of the granular network to thermal treatment.

In order to understand how the microscopic reduction of the effective hole doping affects the superconducting properties, we studied the magnetic response of our sample across the superconducting transition before and after the thermal annealing, i.e., in the OVIII and in the OV phase. Fig. 3 shows the spot-to-spot charge density (p_{XY}) as a function of the number of oxygen chains (n_{XY}), inside the OVIII, OXVI and OV puddles. The charge density has been calculated considering the difference of the superlattice

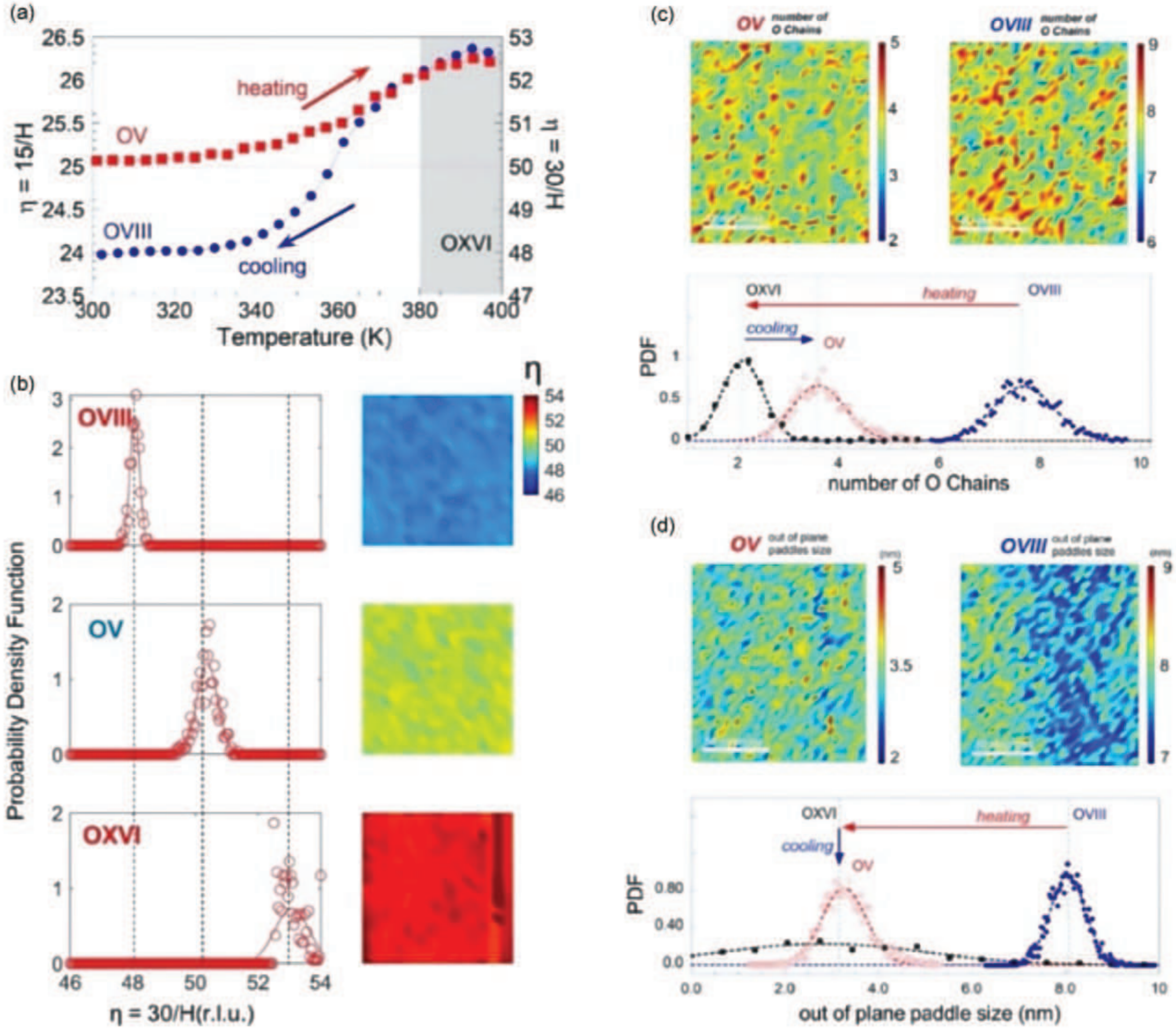

Fig. 2 (a) Thermal evolution of the OVIII oxygen stripe superlattice profile at $\eta(a^*) = 15/H = 24$ ($30/H = 48$) into the OV superstructure at $\eta(a^*) = 15/H = 25$ ($30/H = 50$), passing from the incommensurate OXVI superstructure. The temperature ranges from 300 to 400 K. The reflections of the superstructures in the $YBa_2Cu_3O_{6+y}$ crystal are measured using a large ($200 \times 200\ \mu m^2$) beam at the ELETTRA storage ring. (b) (left panels) Probability Density Function and (right panels) maps of $\eta(a^*) = 30/H$ at three different temperatures during the thermal cycle where the system shows the OVIII, OV and OXVI phases. The thermal cycle of the superlattice position along the a* crystallographic direction, (c) the intensity, (d) the average puddle size along a* and (e) along b*. (c) (upper panels) Maps and (lower panel) Probability Density Function of the number of chains in the OVIII and OV phases. (d) (upper panels) Maps and (lower panel) Probability Density Function of the out of plane puddle size in the OVIII and OV phases. Panels c, d are reproduced from Ricci A, Poccia N, Campi G, Coneri F, Barba L, Arrighetti G, . . . Bianconi A (2014) Networks of superconducting nano-puddles in 1/8 doped YBa2Cu3O6.5+y controlled by thermal manipulation. *New Journal of Physics*, 16(5): 053030.

position along a* (h_{XY}) with respect to the ortho-II (OII) phase following the relationship $p_{XY}\ h_{XY} - 0.5$, where the OII modulation corresponds to a periodicity of a filled CuO chain intercalated by one empty chain. The behavior has been fitted using an exponential model: $p_{XY} = 1 - \exp.\{-[(n_{XY} - n_0)/n_0]\}/\xi_n$. Here n_0 and ξ_n are the minimum and the maximum number of chains present in the average puddle. We studied the magnetic response of our sample across the superconducting transition before and after the thermal annealing, i.e., in the OVIII and in the OV phase, by means of the VSM option in a PPMS 6000 from Quantum Design. A first measurement is made before any annealing procedure is carried out (OVIII phase), and shows the onset temperature of the diamagnetic screening (Tc) to be about 66 K. The subsequent measurements are made upon thermal annealing at 380 K (OV phase), with increasing dwell time of 30, 60, 90 and 150 min. In all these cases Tc decreases by about 2 K.

At this iO_y content, we have investigated the spatial arrangement of Ortho-VIII puddles at different length scale using scanning micro and nano X-ray diffraction pushing the measurement of superstructure reflections down to unprecedented real space resolution of 300 nm. In particular, comparing maps obtained from measurements at different spatial scale ($1 \times 1\ \mu m^2$ vs. $300 \times 300\ nm^2$), we are able to show how the inhomogeneity appears more clearly at smaller scale, indicating such local structural inhomogeneity as an intrinsic property in these materials. The diffuse streaks shown in Fig. 4a provide direct evidence for nanoscale puddles in the basal a–b plane with Ortho-VIII modulation with a substantial disorder in the stacking of full and empty chains

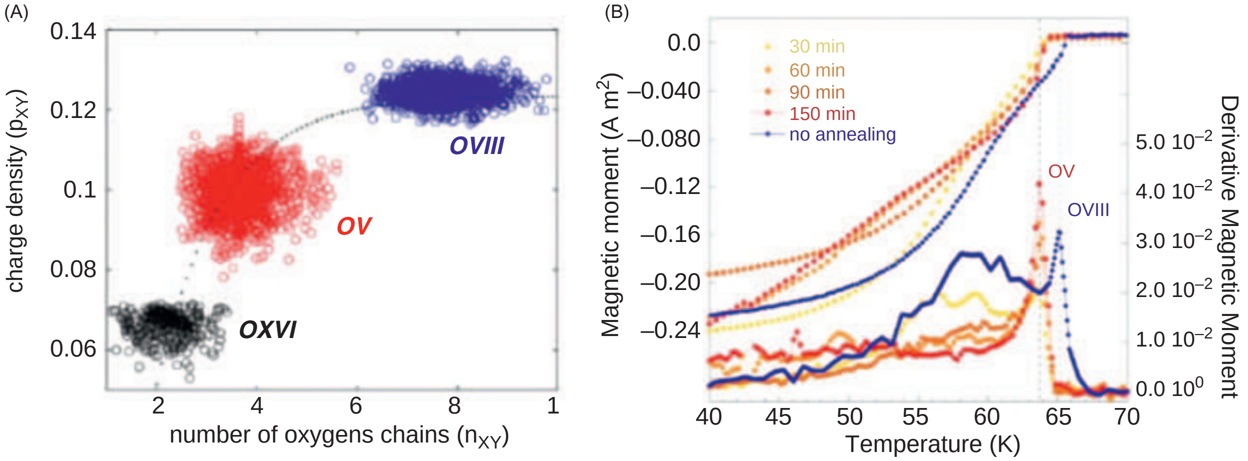

Fig. 3 (a) Charge density (hole concentration p) as a function of the number of oxygen chains, inside the OVIII, OXVI and OV puddles. The dotted curve is a fit using a model: $p = 1 - \exp.\{-[(n - n_0)/n_0]\}/\xi_n$, where n_0 and ξ_n are the minimum and the maximum number of chains present in the average puddle. (b) Left scale: zero field cooling (ZFC) diamagnetic response of YBCO upon thermal cycles in an external applied field H = 20 Oe. Blue filled circles: signal before any thermal annealing. Yellow–red squares: the magnetic moment upon sample annealing at 380 K with increasing dwell time of 30, 60, 90 and 150 min. Right scale: numerical derivative of the magnetic moment. Upon thermal cycling the onset of superconducting shielding decreases by about 2 K. Adapted from Ricci A, Poccia N, Campi G, Coneri F, Barba L, Arrighetti G, . . . Bianconi A (2014) Networks of superconducting nano-puddles in 1/8 doped YBa2Cu3O6.5+y controlled by thermal manipulation. *New Journal of Physics*, 16(5): 053030.

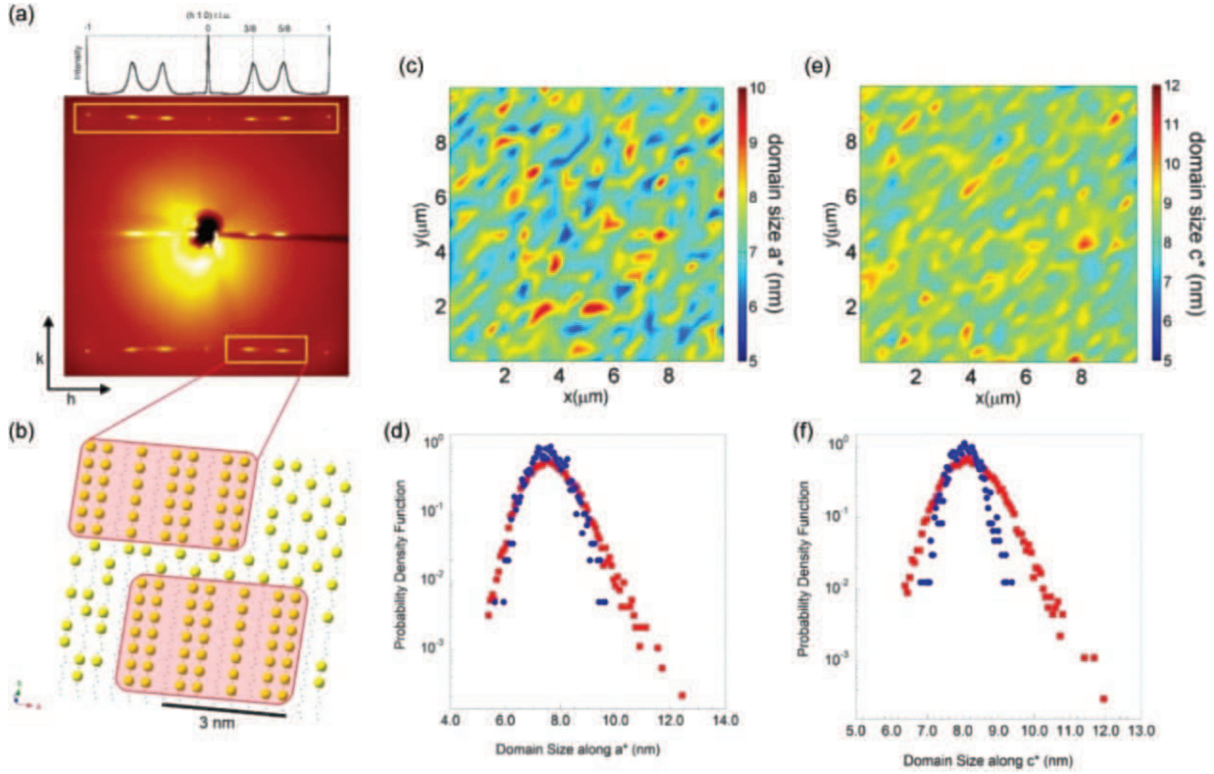

Fig. 4 (a) The X-ray diffraction pattern shows diffuse superstructure satellites at 3/8 and 5/8 positions, their profile along h is plotted. (B) Room temperature diffraction pattern collected using a transmission geometry. The CuO chains superlattice reflections $q_{\text{Ortho-VIII}}(a^*)$ 5(3/8,k,0) and $q_{\text{Ortho-VIII}}(a^*)$ 5(5/8,k,0) are highlighted in the empty yellow box. (b) Pictorial view of the basal Cu-Oi$_y$ plane of YBCO. The small gray dots are the Cu(1) sites and the large yellow dots are the oxygen ions Oi$_y$ in defective basal plane. The pictorial view of oxygen ordered metamorphic phases called Ortho-VIII, with formal oxygen content y 0.625 shown in the pink filled rectangles, are embedded in the disordered background with an oxygen content slightly larger than the average oxygen content 0.67. (c) The Ortho-VIII mapping of the domain size along a*. Here the variation is more pronounced, indeed, the intense red–yellow peaks in the two-dimensional color map represent locations in the sample with high strength of Ortho-VIII ordering, and dark blue indicates spots of disordered Ortho- VIII domains. (d) Probability density function of the domain size along a-axis obtained by the microbeam of 1 μm × 1 μm (filled circles) and the nanobeam 300 nm × 300 nm (filled squares) measurements. (e) The Ortho-VIII mapping of the domain size along c*. (f) Probability density function of the domain size along c-axis obtained by the microbeam of 1 μm × 1 μm (filled circles) and the nanobeam 300 nm × 300 nm (filled squares) measurements. Adapted from Ricci A, Poccia N, Campi G, Coneri F, Caporale AS, Innocenti D, . . . Bianconi A (2013) Multiscale distribution of oxygen puddles in 1/8 doped YBa2Cu3O6.67. *Scientific Reports* 3(1): 1–6.

along the c direction. The nanoscale size of Ortho-VIII puddles embedded in a disordered medium is shown as pictorial view in Fig. 4b representing the basal Cu-O plane of YBCO. The Ortho-VIII puddles are made of alternated 5 filled and 3 empty oxygen wires every 8 rows. The number of oxygen ions per unit in the puddles is $6.625 = 6.5 + 0.125$ that gives exactly 1/8 holes per Cu site in the Y(CuO2)2 bi-layers with Cu^{2+} ions in the chains of the basal plane. Since the average oxygen concentration is $6.67 = 6.5 + 1/6$ the hole doping in the disordered background is larger than 1/8. We reconstructed the 2D maps from the collected nXRD diffraction patterns, each one for a different spatial x–y position (a–c plane) of the sample.

Fig. 4c shows the 2D plots of the domains size variation along a crystallographic direction. The color extends from dark blue to dark red, respectively associated to 5 and 12 nm. In addition, the heterogeneous granular structure of the dopants, unveiled by the employ of a nanobeam, shows the relevance of the spatial resolution of the probe on the sample. Statistical analysis has been used to quantify the size distributions of the Ortho-VIII puddles as seen by (blue dots) scanning micro and (red squares) nano X-ray diffraction experiments. Fig. 4d shows the probability density function (PDF) of the Ortho-VIII puddles sizes along the crystallographic a-axis, observed using a beam of (blue dots) 1 μm and 300 nm of diameter. The distribution of the puddles is nearly symmetric as seen with a resolution of 1 μm while with 300 nm X-ray beam it shows a remarkable asymmetric fat tail, although the average value is comparable. Similar behavior is observed along the c direction- Fig. 4e and f show the map and the probability density function of the Ortho-VIII puddles sizes along the c crystallographic direction. The size of the puddles in the transversal direction from the CuO_2 planes is nearly symmetric while the distribution of sizes measured by the 300 nm nXRD probe, shows a remarkable fat tail. Also in this case the maps obtained by μXRD and the nXRD are in agreement for the average size of domains which is around 8 nm. The standard deviation is 0.4 nm for the 1 μm X-ray probe and 0.6 nm for the 300 nm X-ray probe.

Scale free distribution of oxygen wires in YBCO

The O-i textures from microscale to mesoscale have been studied by Scanning micro XRD measurements (SμXRD) and Scanning nano XRD measurements (SμXRD) to enhance the spatial resolution. The O-i maps measured in SμXRD and SnXRD show rich stripe-ordered O-i (yellow regions) embedded in a matrix of disordered O-i (black regions), as shown in Fig. 9a and b, respectively. In order to characterize this inhomogeneity, we have computed the Probability Density Function, PDF, of the streak intensity for both SμXRD and SnXRD. The PDF has been modeled by a power law behavior given by $PDF(I_{streak}) = C^{*}I_{streak}^{-\alpha}$. We find the critical exponent $\alpha = 2.0 \pm 0.1$ at both micron and mesoscale. I_{streak} values range from values smaller than 1 in the poor oxygen wires regions to values larger than 103 in the richer oxygen wires zones. This means that a scale-free organization of O-i is present in the sample, as already found at nanoscale in cuprates HTS. However, we observe that in the SμXRD maps the size of oxygen wires domains does not exceed the single pixel size corresponding to an area of 1×1 μm^2 given by the scanning beam size. This limitation has been overcome by enhancing the real space resolution in XRD setup using SnXRD where the beam size has been reduced to 0.1×0.3 μm^2. Indeed, in this case the submicron structural features of oxygen wire rich domains can be appreciated (see Fig. 5b).

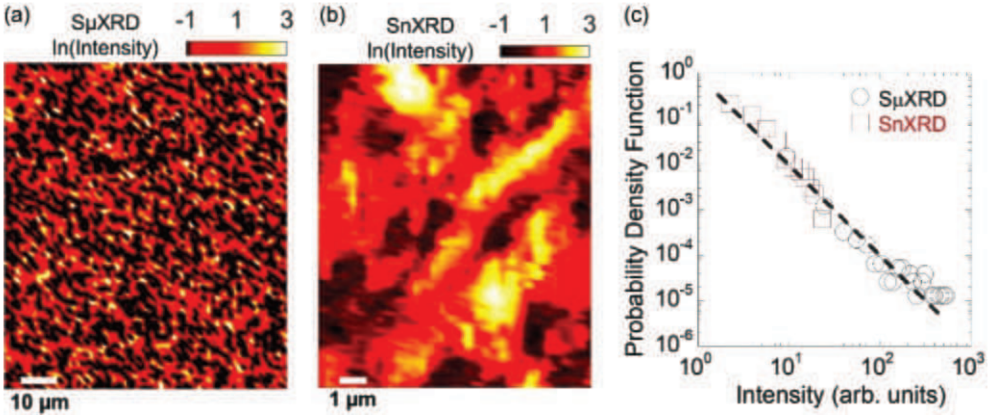

Fig. 5 (a) Logarithmic spatial map of streak intensity extracted by SμXRD with 1×1 μm^2 spatial resolution. The rich stripes-ordered O-i (yellow regions) are anticorrelated with CDW rich domains (black regions). The bar corresponds to 10 μm. (b) SnXRD spatial map measured with 0.1×0.3 μm^2 of streak intensity in logarithmic scale. Here we can appreciated the interface (red regions) between the rich stripes-ordered O-i (yellow regions) and CDW puddles (black regions). The bar corresponds to 1 μm and the size of the map corresponds to the size of the white rectangle in (a). (c) Plot of the Probability Density Function of rich stripes-ordered zones relative to the SμXRD (open squares) and SnXRD (full circles) maps in (a) and (b). Both distributions have the power law exponent $\alpha = 2$. Adapted from Campi G, Mazziotti MV, Jarlborg T, Bianconi A (2022b) Scale-free distribution of oxygen interstitial wires in optimum-doped HgBa2CuO4+ y. *Condensed Matter*, 7(4): 56.

Charge density waves and lattice defects

LCO—Correlated disorder and phase separation in La_2CuO_{4+y}

La_2CuO_{4+y} is one of the simplest perovskites, where y oxygen interstitial ions (O-i) in the rocksalt $[La_2O_{2+y}]$ are intercalated by $[CuO_2]$ layers. The high brilliance of modern synchrotron photon sources allows to detect weak satellite peaks in X Ray Diffraction measurements, which are associated with superstructures, due to oxygen interstitial O-i dopants and electronic modulations, named charge–density waves (CDW). CDWs incommensurate diffuse satellites with wave vector $q_{CDW} = 0.21b^* + 0.29c^*$, coexisting with commensurate O-i satellites displaced by $q_{O\text{-}i} = 0.25b^* + 0.5c^*$ characterized by a different staging, that is, their c^* component. Indeed, O-i and CDW have staging $c^* = 0.5$ and $c^* = 0.29$, respectively, as indicated by the white and red arrows, respectively in Fig. 6a. The commensurate O-i, with $q(b^*) = 0.25$ and $q(c^*) = 0.5$ ordering, consists of the domains ordered with periodicity of $1/q\ b^* = 4$ and $1/q\ c^* = 2$ unit cells along b and c direction, respectively, On the other hand, the incommensurate CDW, with $q\ b^* = 0.21$, with a long period about 9/42 ordering, consisting in the mixture of the 4 and 5 charge order, i.e., alternating periodicity of 4 and 5 lattice units along the b direction. The O-i and CDW ordering is schematized in Fig. 6b. We have found that these ordered domains are characterized by a strong spatial anticorrelation: oxygen-rich regions, where the system is in the over-doped metallic phase with low density of CDW, are intercalated with oxygen-poor region in the underdoped phase with high density of CDW. Fig. 6c shows the map of difference between the intensity of O-i and CDW diffraction satellites. The O-i are located in the 1/4,1/4,1/4 site, and form commensurate stripes in the La_2O_2 structure, intertwined with incommensurate lattice CDW domains (Poccia et al., 2012). Indeed, we observed micron size puddles of blue metallic oxygen-rich regions, separated by red CDW-rich zones, by a filamentary percolating interface, indicated by white space.

The different intensity of O-i and CDW superstructure measured by SμXRD is shown in Fig. 7a. A common and intriguing feature of quantum materials is that their emerging properties can be easily manipulated by weak external stimuli, such as temperature gradient, strain, and photon illumination. Due to the mobility of oxygen interstitials (O-i), our systems present structural conformational landscapes. The maps in Fig. 7b show two different O-i distributions, obtained with two different thermal treatments; the first one shows the maximum critical temperature ($T_c = 40$ K) and the second presents a macroscopic phase separation with two critical temperatures, $T_c = 16$ K and 32 K (Fratini et al., 2010). In both samples, the probability density function of O-i satellite intensity follows an exponentially truncated power–law distribution, given by.

$$P(x) = x - \alpha\ \exp(-x/x_0),$$

where α is the critical exponent and x0 is the cut-off. The critical exponent, α, results to be 2.6, both in the high-T_c (a) and low-T_c (b) conformations, indicating the fractal nature of O-i arrangement. On the other hand, the cut-off, x_0, is larger for the high-$T_c = 40$ K sample, as can be seen in Fig. 7c. This means that a larger extent of O-i satellite intensity with fractal geometry favors a higher T_c (Fratini et al., 2010).

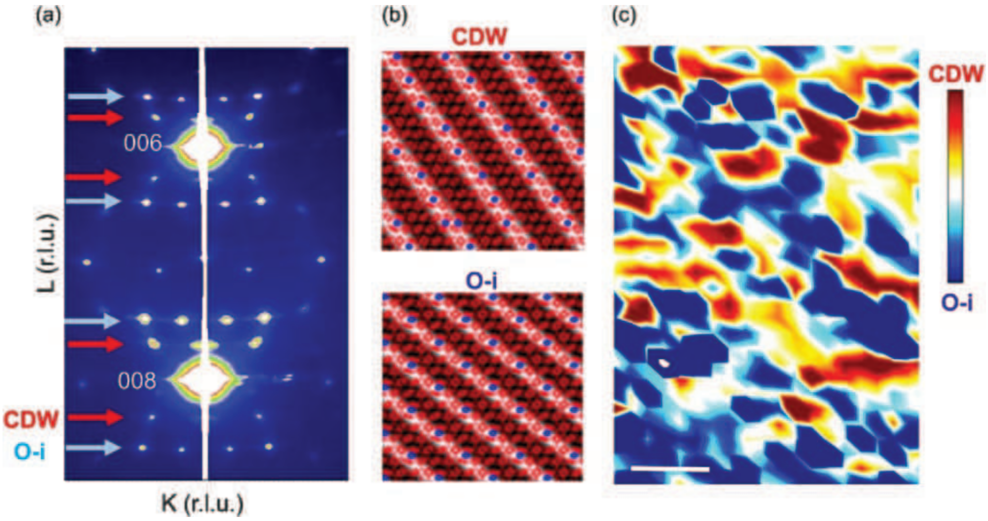

Fig. 6 (a) XRD image of b*c* plane in the reciprocal lattice of the La2CuO4.1 sample. We observed several superstructures surrounding the indicated Bragg peaks 006, and 008, due to O-i ordering and charge–density waves (CDW). The arrows indicate the O-i and CDW superlattices. (b) Lattice modulations corresponding to CDWs and O-i superstructures. (c) Map difference between the normalized intensities of both CDW and O-i satellites in La2Cu04.1. CDW puddles are dominant in red regions, while the O-i stripes are dominant in the blue zones. The lattice modulations corresponding to CDWs and O-i superstructures are depicted. The interface (white region) between CDW-rich and O-i-rich regions gives the percolating pathways where supercurrent is expected to flow. The white bars correspond to 5 μm. Panels b, c are reproduced from Campi G, Bianconi A, Joseph B, Mishra SK, Muller L, Zozulya A, ... Ricci A (2022) Nanoscale inhomogeneity of charge density waves dynamics in La2-xSrxNiO4. *Scientific Reports* 12: 15964.

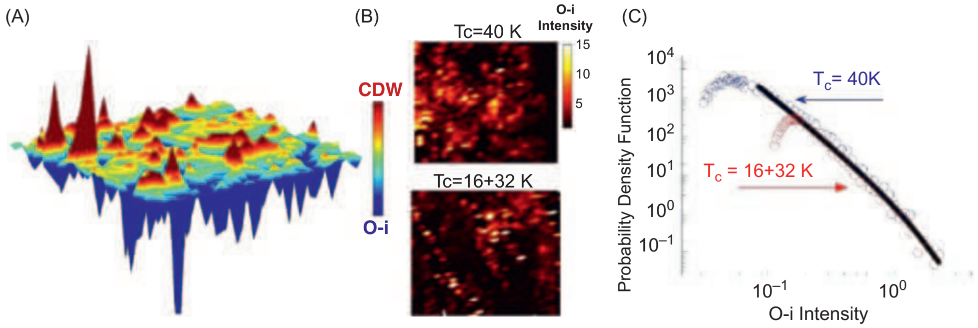

Fig. 7 (a) Map difference between the normalized intensities of both CDW and O-i satellites in La2Cu04.1. CDW puddles are dominant in red regions, while the O-i stripes are dominant in the blue zones. The interface (white region) between CDW-rich and O-i-rich regions gives the percolating pathways where supercurrent is expected to flow. The white bars correspond to 5 μm. (b) Spatial distribution of the O-i superstructure intensity for two different conformations in La$_2$Cu0$_{4.1}$ samples, with $T_c = 40$ K (upper panel) and $T_c = 16$ and 32 K phases (lower panel) in a 500 × 400 μm^2 area. The bar corresponds to 50 μm. (c) The rescaled probability distribution, $x^\chi P(x)$, of the O-i superstructure intensity for the two samples. The cut-off, x_0, increases from 8 ± 1 in the low-T_c conformation to 31 ± 2 in the high-T_c conformation. The rescaled distributions collapse on the same universal curve (black solid line). Adapted from Campi G, Bianconi A, Joseph B, Mishra SK, Muller L, Zozulya A, ... Ricci A (2022) Nanoscale inhomogeneity of charge density waves dynamics in La2-xSrxNiO4. *Scientific Reports* 12: 15964.

Hg1201—Correlated disorder and phase separation in $HgBa_2CuO_{4+y}$

$HgBa_2CuO_{4+y}$ has a single CuO_2 plane with tetragonal crystal symmetry. The oxygen interstitial ions (O-i) form atomic stripes in the spacer layer [$HgO_yBa_2O_2$] between [CuO_2] planes. We have measured the diffuse scattering associated with both CDW and oxygen interstitial arrangement in the lattice, as shown in Fig. 8a. Resolution-limited streaks connecting the Bragg peaks, due to atomic O-i stripes in the HgO_y spacer layers, have been measured in agreement with previous experiments (Izquierdo et al., 2011; Izquierdo et al., 2021).

Different charge ordering satellites have been detected, in Fig. 8 we report the analysis of the temperature and spatial distribution of the satellite with wave-vector $q_{cdw} \approx 0.23a^*$ appearing near Bragg peaks at high momentum transfer, which has been assigned to condensation of paired pseudo-Jahn Teller polarons (Bianconi et al., 1990) at the pseudo-gap temperature (Lanzara et al., 1999) forming nanoscale CDW puddles (Campi et al., 2023) called Q-balls (Mukhin, 2023). The oxygen interstitials ordering with the atomic wires formation appears below $T_{O\text{-}i} = 350$ K in Hg1201 as shown in Fig. 8. The striped charge density wave puddles made by Q-balls appear below $T_{cdw} = 240$ K (see Fig. 8b) which is close to the pseudo-gap temperature. Near different Bragg peaks we have

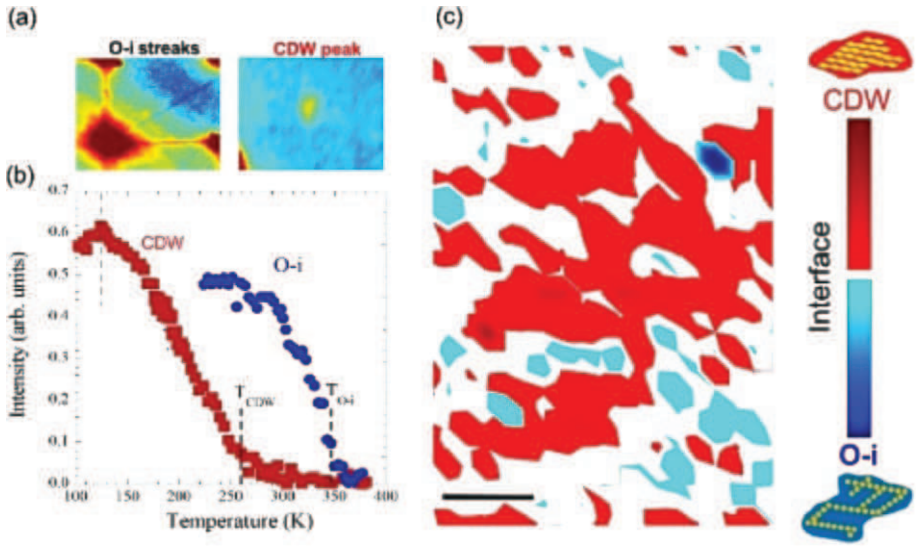

Fig. 8 (a) XRD image of a*c* plane in the reciprocal lattice of the Hg1201 sample. We observed both streaks due to O-i ordering (left panel) and diffuse satellites due to polaronic charge–density waves (right panel). (b) Temperature dependence of O-i and polaronic CDW. The onset of oxygen ordering, $T_{O\text{-}i}$, and polaronic charge ordering T_{CDW} are indicated. (c) Map difference between the normalized intensities of both polaronic short range CDW and CDW satellites puddles dominant in red regions, while the O-i stripes are dominant in the blue zones. The lattice modulations corresponding to CDWs and O-i superstructures are depicted. The interface (white region) between CDW-rich and O-i-rich regions gives the percolating pathways where supercurrent is expected to flow. The white bars correspond to 5 μm. Panel c adapted from Campi G, Bianconi A, Joseph B, Mishra SK, Muller L, Zozulya A, ... Ricci A (2022) Nanoscale inhomogeneity of charge density waves dynamics in La2-xSrxNiO4. *Scientific Reports* 12: 15964.

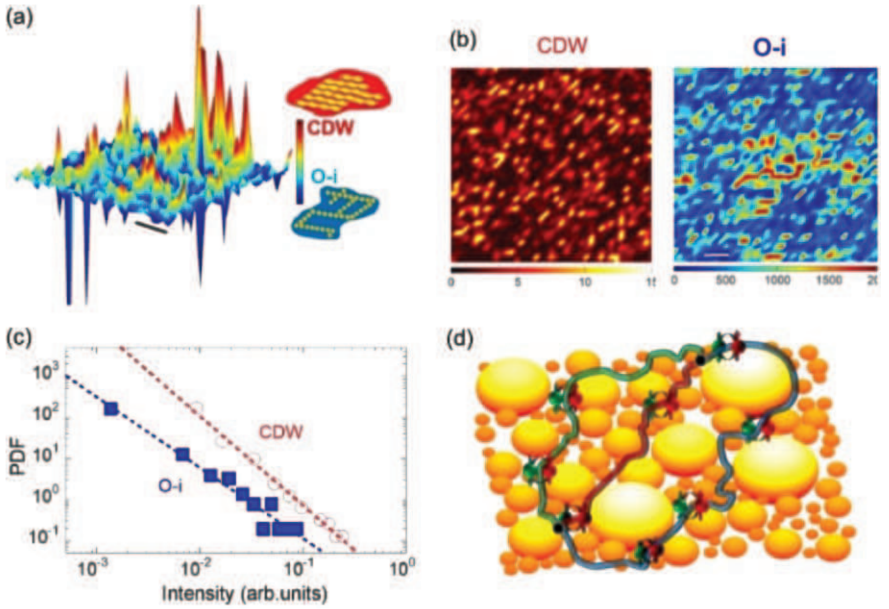

Fig. 9 (a) Map difference between the normalized intensities of both CDW and O-i satellites. CDW puddles are dominant in red regions, while the O-i stripes are dominant in the blue zones. The bar corresponds to 5 μm. (b) Color plot of the map of the (left panel) O-i streak intensity and (right panel) charge–density waves (CDW) peak in HgBa$_2$CuO$_{4.12}$ (c) Probability density function, calculated from the O-i streaks and CDW intensity map in (a,b), showing a power–law behavior. (d) Pictorial view of the free electrons liquid flowing in the interstitial space left by CDW crystalline puddles. The CDW crystalline puddles form inhomogeneous spatial patterns giving rise to a new non-Euclidean geometry in the interstitial space left by the crystals of electrons. The free electrons, which do not crystallize, form Cooper pairs flowing along paths in the interstitial space at low temperatures. Panels a, b, c are reproduced from Campi G, Bianconi A (2021) Functional nanoscale phase separation and intertwined order in quantum complex materials. *Condensed Matter* 6(4): 40. Panel d is reproduced from Campi G, Bianconi A (2016) High-temperature superconductivity in a hyperbolic geometry of complex matter from nanoscale to mesoscopic scale. *Journal of Superconductivity and Novel Magnetism* 29(3): 627–631.

found different CDW satellites with lower ordering temperature $T_{onset} = 170$ K and $q \approx 0.28a^*$ which are known to appear near the (h,k,0) Bragg peaks and have been assigned to static long range CDW. The spatial mapping shows inhomogeneity with a negative correlation between O-i order and the charge density wave puddles. The O-i atomic striped domains are phase separated from polaronic CDW (Q-balls) and long range CDW generating a percolating filamentary interface indicated by white space in Fig. 8c.

The spatial anticorrelation is well depicted in the "difference map" between CDW peaks and O-i-diffuse streaks in Fig. 9a. The poor CDW regions on the CuO$_2$ basal plane correspond to O-i-rich regions on the HgO$_y$ layers. In Fig. 9b we show the maps of the integrated intensity of CDW peak and oxygen O-i diffuse streaks, respectively, as seen by SμXRD measurements. Both O-i and CDW maps are spatially inhomogeneous, and their PDF is well modeled by a power–law behavior also in this case, as shown in Fig. 9c. The critical exponents in the two intensity distributions are 1.8 ± 0.1 and 2.2 ± 0.1 for the O-i and CDW, respectively.

Conclusion

The use of scanning micro-X-ray diffraction has provided compelling evidence for the emergence the interface space at mesoscopic scale with hyperbolic geometry favoring superconductivity in cuprate superconductors (see Fig. 9d). The hyperbolic space has recently been found to play a key role in different fields looking for the emergence of order in complex systems ranging from network theory to quantum gravity (Krioukov et al., 2012; Wu et al., 2015). The role of a spatial hyperbolic geometry in disordered media is known to be of high relevance in the design of new metamaterials showing a negative dielectric constant, as well as in the manipulation of complex light in optical metamaterials (Barthelemy et al., 2008; Bertolotti et al., 2012; Zeng et al., 2013; Esslinger et al., 2014). The hyperbolic space has recently been shown to influence critical phenomena (Mnasri et al., 2015). The search for complex materials with zero or negative dielectric constant has been one of the road maps proposed for the amplification of the superconducting critical temperature to reach room temperature superconductivity (Chu et al., 2005; Smolyaninov, 2014; Smolyaninova et al., 2014, Poddubny et al., 2012). The experiments show a hyperbolic space in the mesoscale of cuprates but it could be present also in pressurized sulfur hydride superconductors (Bianconi and Jarlborg, 2015), iron-based superconductors (Ricci et al., 2011; Ricci et al., 2015), and diborides (Campi et al., 2006) which all show local lattice fluctuations.

References

Agrestini S, Saini NL, Bianconi G, and Bianconi A (2003) The strain of CuO2 lattice: The second variable for the phase diagram of cuprate perovskites. *Journal of Physics A: Mathematical and General* 36(35): 9133.

Agrestini S, Metallo C, Filippi M, Simonelli L, Campi G, Sanipoli C, and … Bianconi A (2004) Substitution of Sc for Mg in MgB$_2$: Effects on transition temperature and Kohn anomaly. *Physical Review B* 70(13), 134514.

Bardeen J, Cooper LN, and Schrieffer JR (1957) Theory of superconductivity. *Physical Review* 108(5): 1175. (18161 citations in Jan 2023).

Barthelemy P, Bertolotti J, and Wiersma DS (2008) A Levy flight for light. *Nature* 453: 495–498. https://doi.org/10.1038/nature06948.

Bednorz JG and Müller KA (1986) Possible high T$_c$ superconductivity in the Ba−La−Cu−O system. *Zeitschrift fur Physik B: Condensed Matter* 64(2): 189–193.

Bednorz JG and Müller KA (1988) Perovskite-type oxides the new approach to high-Tc superconductivity. *Reviews of Modern Physics* 60(3): 585.

Bednorz JG and Muller KA (1990) *Earlier and Recent Aspects of Superconductivity: Lectures from the International School, Erice, Trapani, Sicily, July 4-16, 1989*. Berlin: Springer. 1990.

Bendele M, von Rohr F, Guguchia Z, Pomjakushina E, Conder K, Bianconi A, and … Keller H (2017) Evidence for strong lattice effects as revealed from huge unconventional oxygen isotope effects on the pseudogap temperature in La$_{2-x}$Sr$_x$CuO$_4$. *Physical Review B* 95(1), 014514.

Bertolotti J, van Putten EG, Blum C, Lagendijk A, Vos WL, and Mosk AP (2012) Non-invasive imaging through opaque scattering layers. *Nature* 491: 232. https://doi.org/10.1038/nature11578.

Bianconi A (2000) Superstripes. *International Journal of Modern Physics B* 14(29n31): 3289–3329.

Bianconi A (2013) Shape resonances in superstripes. *Nature Physics* 9(9): 536–537.

Bianconi A and Jarlborg T (2015) Lifshitz transitions and zero point lattice fluctuations in sulfur hydride showing near room temperature superconductivity. *Novel Superconducting Materials* 1(1). https://doi.org/10.1515/nsm-2015-0006. arXiv:1507.01093.

Bianconi A, Castrucci P, Fabrizi A, Pompa M, Flank AM, Lagarde P, and … Calestani G (1990) Earlier and recent aspects of superconductivity. *Springer Series in Solid-State Sciences* 90: 407–421.

Bianconi A, Saini NL, Lanzara A, Missori M, Rossetti T, Oyanagi H, and … Ito T (1996) Determination of the local lattice distortions in the CuO$_2$ Plane of La$_{1.85}$Sr$_{0.15}$CuO$_4$. *Physical Review Letters* 76(18): 3412.

Bianconi A, Valletta A, Perali A, and Saini NL (1998) Superconductivity of a striped phase at the atomic limit. *Physica C: Superconductivity* 296(3–4): 269–280.

Bishop AR, Martin RL, Müller KA, and Tešanović Z (1989) Superconductivity in oxides: Toward a unified picture. *Zeitschrift fur Physik B: Condensed Matter* 76: 17–24.

Campi G and Bianconi A (2016) High-temperature superconductivity in a hyperbolic geometry of complex matter from nanoscale to mesoscopic scale. *Journal of Superconductivity and Novel Magnetism* 29(3): 627–631.

Campi G and Bianconi A (2019) Evolution of complexity in out-of-equilibrium systems by time-resolved or space-resolved synchrotron radiation techniques. *Condensed Matter* 4(1): 32.

Campi G and Bianconi A (2021) Functional nanoscale phase separation and intertwined order in quantum complex materials. *Condensed Matter* 6(4): 40.

Campi G, Cappelluti E, Proffen T, Qiu X, Bozin ES, Billinge SJL, and … Bianconi A (2006) Study of temperature dependent atomic correlations in MgB$_2$. *The European Physical Journal B-Condensed Matter and Complex Systems* 52(1): 15–21.

Campi G, Ricci A, Poccia N, Barba L, Arrighetti G, Burghammer M, and … Bianconi A (2013) Scanning micro-X-ray diffraction unveils the distribution of oxygen chain nanoscale puddles in YBa$_2$Cu$_3$O$_{6.33}$. *Physical Review B* 87(1), 014517.

Campi G, Bianconi A, Poccia N, Bianconi G, Barba L, Arrighetti G, and … Ricci A (2015) Inhomogeneity of charge-density-wave order and quenched disorder in a high-Tc superconductor. *Nature* 525(7569): 359–362.

Campi G, Bianconi A, Joseph B, Mishra SK, Muller L, Zozulya A, and … Ricci A (2022a) Nanoscale inhomogeneity of charge density waves dynamics in La$_{2-x}$Sr$_x$NiO$_4$. *Scientific Reports* 12: 15964.

Campi G, Mazziotti MV, Jarlborg T, and Bianconi A (2022b) Scale-free distribution of oxygen interstitial wires in optimum-doped HgBa2CuO4+y. *Condensed Matter* 7(4): 56.

Campi G, Barba L, Zhigadlo ND, Ivanov AA, Menushenkov AP, and Bianconi A (2023) Q-Balls in the pseudogap phase of superconducting HgBa$_2$CuO$_{4+y}$. *Condensed Matter* 8(1): 15.

Ceder G, Asta M, and de Fontaine M (1991) Computation of the OI-OII-OIII phase diagram and local oxygen configurations for YBa$_2$Cu$_3$O$_z$ with z between 6.5 and 7. *Physica C: Superconductivity* 177(1–3): 106–114.

Chu CW, Chen F, Shulman J, Tsui S, Xue YY, Wen W, and Sheng P (2005) A negative dielectric constant in nano-particle materials under an electric field at very low frequencies. In: *Proceedings of SPIE 5932, Strongly Correlated Electron Materials: Physics and Nanoengineering, 59320X*. https://doi.org/10.1117/12.626267.

Della Longa S, Soldatov A, Pompa M, and Bianconi A (1995) Atomic and electronic structure probed by X-ray absorption spectroscopy: Full multiple scattering analysis with the G4XANES package. *Computational Materials Science* 4(3): 199–210.

Deutscher G and Müller KA (1987) Origin of superconductive glassy state and extrinsic critical currents in high-T c oxides. *Physical Review Letters* 59(15): 1745.

Drees Y, Li ZW, Ricci A, Rotter M, Schmidt W, Lamago D, and … Komarek AC (2014) Hour-glass magnetic excitations induced by nanoscopic phase separation in cobalt oxides. *Nature Communications* 5(1): 1–9.

Esslinger M, Vogelgesang R, Talebi N, Khunsin W, Gehring P, de Zuani S, Gompf B, and Kern K (2014) Tetradymites as natural hyperbolic materials for the near-infrared to visible. *ACS Photonics* 1(12): 1285–1289. https://doi.org/10.1021/ph500296e.

Fano U (1961) Effects of configuration interaction on intensities and phase shifts. *Physical Review* 124(6): 1866. (13340 citations in Jan 2023).

Fratini M, Poccia N, Ricci A, Campi G, Burghammer M, Aeppli G, and Bianconi A (2010) Scale-free structural organization of oxygen interstitials in La$_2$CuO$_{4+y}$. *Nature* 466(7308): 841–844.

Glazer AM (1972) *The classification of tilted octahedra in perovskites, Acta Crystallographica. Section B* 28: 3384.

Glazer AM (1975) *Simple ways of determining perovskite structures, Acta Crystallographica. Section A* 31: 756.

Howard CJ and Stokes HT (1998) *Group-theoretical analysis of octahedral tilting in perovskites, Acta Crystallographica. Section B* 54: 782.

Innocenti D, Ricci A, Poccia N, Campi G, Fratini M, and Bianconi A (2009) A model for liquid-striped liquid phase separation in liquids of anisotropic polarons. *Journal of Superconductivity and Novel Magnetism* 22: 529–533.

Izquierdo M, Megtert S, Colson D, Honkimäki V, Forget A, Raffy H, and Comès R (2011) One dimensional ordering of doping oxygen in superconductors evidenced by x-ray diffuse scattering. *Journal of Physics and Chemistry of Solids* 72: 545–548.

Izquierdo M, Freitas DC, Colson D, Garbarino G, Forget A, Raffy H, Itié J-P, Ravy S, Fertey P, and Núñez-Regueiro M (2021) Charge order and suppression of superconductivity in HgBa$_2$CuO$_{4+d}$ at high pressures. *Condensed Matter* 6: 25.

Kaldis E, Liarokapis E, and Müller KA (eds.) (2012) *High-T$_c$ Superconductivity 1996: Ten Years After The Discovery*. In: Vol. 343. Springer Science & Business Media.

Keller H, Bussmann-Holder A, and Müller KA (2008) Jahn–Teller physics and high-Tc superconductivity. *Materials Today* 11(9): 38–46.

Khasanov R, Shengelaya A, Maisuradze A, La Mattina F, Bussmann-Holder A, Keller H, and Müller KA (2007) Experimental evidence for two gaps in the high-temperature La$_{1.83}$Sr$_{0.17}$CuO$_4$ superconductor. *Physical Review Letters* 98(5): 057007.

Kochelaev BI, Müller KA, and Shengelaya A (2014) Oxygen isotope effects on T$_c$ related to polaronic superconductivity in underdoped cuprates. *Journal of Modern Physics* 5(6): 45400. https://doi.org/10.4236/jmp.2014.56057.

Kremer RK, Sigmund E, Hizhnyakov V, Hentsch F, Simon A, Müller KA, and Mehring M (1992) Percolative phase separation in La$_2$CuO$_{4+\delta}$ and La$_{2-x}$Sr$_x$CuO$_4$. *Zeitschrift fur Physik B: Condensed Matter* 86: 319–324.

Kremer RK, Hizhnyakov V, Sigmund E, Simon A, and Müller KA (1993) Electronic phase separation in La-cuprates: On the role of hole and oxygen diffusion. *Zeitschrift fur Physik B: Condensed Matter* 91: 169–174.

Krioukov D, Kitsak M, Sinkovits RS, Rideout D, Meyer D, and Boguna M (2012) Network cosmology. *Scientific Reports* 2: 793. https://doi.org/10.1038/srep00793.

Lanzara A, Zhao GM, Saini NL, Bianconi A, Conder K, Keller H, and Müller KA (1999) Oxygen-isotope shift of the charge-stripe ordering temperature in $La_{2-x}Sr_xCuO_4$ from X-ray absorption spectroscopy. *Journal of Physics: Condensed Matter* 11(48): L541.

Liarokapis E, Poulakis N, Palles D, Conder K, Kaldis E, and Müller KA (1996) Raman study of the oxygen vibrations in 123-superconductors. *Physica B: Condensed Matter* 219: 139–141.

Mannhart J, Bednorz JG, Müller KA, and Schlom DG (1991) Electric field effect on superconducting $YBa_2Cu_3O_{7-\delta}$ films. *Zeitschrift fur Physik B: Condensed Matter* 83: 307–331.

Mazziotti MV, Valletta A, Campi G, Innocenti D, Perali A, and Bianconi A (2017) Possible Fano resonance for high-Tc multi-gap superconductivity in p-Terphenyl doped by K at the Lifshitz transition. *Europhysics Letters* 118(3): 37003.

Mazziotti MV, Raimondi R, Valletta A, Campi G, and Bianconi A (2021a) Resonant multi-gap superconductivity at room temperature near a Lifshitz topological transition in sulfur hydrides. *Journal of Applied Physics* 130(17): 173904.

Mazziotti MV, Valletta A, Raimondi R, and Bianconi A (2021b) Multigap superconductivity at an unconventional Lifshitz transition in a three-dimensional Rashba heterostructure at the atomic limit. *Physical Review B* 103(2): 024523.

Mazziotti MV, Bianconi A, Raimondi R, Campi G, and Valletta A (2022) Spin–orbit coupling controlling the superconducting dome of artificial superlattices of quantum wells. *Journal of Applied Physics* 132(19): 193908.

Mihailovic D, Muller KA, Ruani G, and Kaldis E (eds.) (1995) *Anharmonic Properties of high-Tc cuprates-Proceedings of the International Workshop*. World Scientific.

Mnasri K, Jeevanesan B, and Schmalian J (2015) Critical phenomena in hyperbolic space. *Physical Review B* 92: 134423.

Mukhin S (2023) Possible manifestation of Q-Ball mechanism of high-T_c superconductivity in X-ray diffraction. *Condensed Matter* 8(1): 16. https://doi.org/10.3390/condmat8010016.

Müller KA (2000) From phase separation to stripes. *Stripes and Related Phenomena. Selected Topics in Superconductivity* Vol. 8, pp. 1–8. New York: Kluwer Academic Plenum Publishers.

Muller KA and Benedek G (eds.) (1993) *Phase Separation in Cuprate Superconductors-Proceedings of the Workshop*. World Scientific.

Müller KA, Zhao GM, Conder K, and Keller H (1998) The ratio of small polarons to free carriers in derived from susceptibility measurements. *Journal of Physics: Condensed Matter* 10(18): L291.

Najafi MN and Tavana A (2016) Universality class of the structural phase transition in the normal phase of cuprate superconductors. *Physical Review E* 94(2): 022110.

Poccia N, Fratini M, Ricci A, Campi G, Barba L, Vittorini-Orgeas A, and Bianconi A (2011) Evolution and control of oxygen order in a cuprate superconductor. *Nature Materials* 10(10): 733–736.

Poccia N, Ricci A, Campi G, Fratini M, Puri A, Di Gioacchino D, and ... Bianconi A (2012) Optimum inhomogeneity of local lattice distortions in La2CuO4+ y. *Proceedings of the National Academy of Sciences* 109(39): 15685–15690.

Poddubny AN, Rybin MV, Limonov MF, and Kivshar YS (2012) Fano interference governs wave transport in disordered systems. *Nature Communications* 3: 914. https://doi.org/10.1038/ncomms1924.

Poulakis N, Palles D, Liarokapis E, Conder K, Kaldis E, and Müller KA (1996) Phase separation and softening of the O2,3 in-phase mode in the $YBa_2Cu_3O_x$ superconductors. *Physical Review B* 53(2): R534.

Reihl B, Bednorz JG, Müller KA, Jugnet Y, Landgren G, and Morar JF (1984) Electronic structure of strontium titanate. *Physical Review B* 30(2): 803.

Ricci A, Poccia N, Campi G, Joseph B, Arrighetti G, Barba L, and ... Bianconi A (2011) Nanoscale phase separation in the iron chalcogenide superconductor $K_{0.8}Fe_{1.6}Se_2$ as seen via scanning nanofocused x-ray diffraction. *Physical Review B* 84(6): 060511.

Ricci A, Poccia N, Campi G, Coneri F, Caporale AS, Innocenti D, and Bianconi A (2013) Multiscale distribution of oxygen puddles in 1/8 doped $YBa_2Cu_3O_{6.67}$. *Scientific Reports* 3(1): 1–6.

Ricci A, Poccia N, Campi G, Coneri F, Barba L, Arrighetti G, and ... Bianconi A (2014) Networks of superconducting nano-puddles in 1/8 doped $YBa_2Cu_3O_{6.5+y}$ controlled by thermal manipulation. *New Journal of Physics* 16(5): 053030.

Ricci A, Poccia N, Joseph B, Innocenti D, Campi G, Zozulya A, and ... Saini NL (2015) Direct observation of nanoscale interface phase in the superconducting chalcogenide K x Fe 2− y Se 2 with intrinsic phase separation. *Physical Review B* 91(2): 020503.

Ricci A, Campi G, Joseph B, Poccia N, Innocenti D, Gutt C, and ... Saini NL (2020) Intermittent dynamics of antiferromagnetic phase in inhomogeneous iron-based chalcogenide superconductor. *Physical Review B* 101(2): 020508.

Ricci A, Poccia N, Campi G, Mishra S, Müller L, Joseph B, and ... Schüßler-Langeheine C (2021) Measurement of spin dynamics in a layered nickelate using X-Ray photon correlation spectroscopy: Evidence for intrinsic destabilization of incommensurate stripes at low temperatures. *Physical Review Letters* 127(5): 057001.

Sigmund E and Müller KA (eds.) (2012) *Phase Separation in Cuprate Superconductors: Proceedings of the Second International Workshop on "Phase Separation in Cuprate Superconductors" September 4–10, 1993*. Cottbus, Germany: Springer Science & Business Media.

Smolyaninov II (2014) Quantum topological transition in hyperbolic metamaterials based on high Tc superconductors. *Journal of Physics. Condensed Matter* 26: 305701. https://doi.org/10.1088/0953-8984/26/30/305701.

Smolyaninova VN, Yost B, Zander K, Osofsky MS, Kim H, Saha S, Greene RL, and Smolyaninov II (2014) Experimental demonstration of superconducting critical temperature increase in electromagnetic metamaterials. *Scientific Reports* 4: 7321. https://doi.org/10.1038/srep07321.

Thomas H and Müller KA (1968) Structural phase transitions in perovskite-type crystals. *Physical Review Letters* 21(17): 1256.

Weyeneth S and Müller KA (2020) Oxygen isotope effect in cuprates results from polaron-induced superconductivity. In: *Electron–Phonon Interaction and Lattice Dynamics in High Tc Superconductors*, pp. 173–180. World Scientific.

Wu Z, Menichetti G, Rahmede C, and Bianconi G (2015) Emergent complex network geometry. *Scientific Reports* 5: 10073. http://www.nature.com/articles/srep10073.

Zeng J, Wang X, Sun J, Pandey A, Cartwright AN, and Litchinitser NM (2013) Manipulating complex light with metamaterials. *Scientific Reports* 3: 02826. https://doi.org/10.1038/srep02826.

Zimmermann MV, Schneider JR, Frello T, Andersen NH, Madsen J, Käll M, and ... Hardy WN (2003) Oxygen-ordering superstructures in underdoped YBa2Cu3O6+x studied by hard X-ray diffraction. *Physical Review B* 68(10): 104515. https://doi.org/10.1103/PhysRevB.68.104515.

Additive nanofabrication using focused ion and electron beams[☆]

Rosa Córdoba, Institute of Molecular Science, University of Valencia, Paterna, Spain

© 2024 Elsevier Ltd. All rights reserved.

Introduction 448
Additive nano-manufacturing using FIBID and FEBID 449
Fundamentals of FIBID and FEBID 449
Materials grown with FIBID 452
Platinum 452
Tungsten 452
Copper 452
Gold 452
Cobalt 452
Niobium 454
Materials grown with FEBID 454
Single element 454
Binary compounds 455
Ternary compounds 455
Direct-writing of superconducting nanostructures 455
Planar superconducting nanostructures 455
FIBID 455
FEBID 456
3D superconducting nanostructures 457
Applications to superconducting devices 458
Planar superconducting nanostructures 458
3D superconducting nanostructures 460
Conclusion 460
Acknowledgments 461
References 461

Abstract

Focused Ion Beam Induced Deposition or Focused Electron Beam Induced Deposition are direct-write nanolithography techniques that make use of a focused beam of charged ions or electrons to pattern nanometer resolution materials at a specific location. The physical interactions between the ions or electrons and the atoms of the substrate surface and the precursor molecules delivered to the process chamber are exploited for the additive nanofabrication of different materials in all three dimensions. In this chapter, the fundamentals of the techniques are outlined, a selection of materials grown with these additive nano-manufacturing techniques are reviewed. Additionally, a special emphasis is placed on examples of direct-writing of nano-superconductors in all three dimensions and a selection of their potential applications is described.

Key points

- Direct-write nanofabrication method, fabrication and properties of 1D, 2D and 3D nano-superconductors.
- Direct-write nanolithography method.
- Properties of 1D, 2D and 3D nano-superconductors.
- Preparation of superconducting devices and circuits.

Introduction

The incessant need to manufacture more sophisticated and powerful electronic devices every day has been achieved thanks to the miniaturization of integrated circuits, being key elements in these devices. However, higher processing power on these devices implies a higher power consumption. Therefore, the fabrication and study of nanoscale materials could shed some light on

---

[☆] *Change History:* August 2022. R Córdoba prepared the update. Figs. 1-6 are updated.

https://doi.org/10.1016/B978-0-323-90800-9.00035-4

fundamental physical problems and solutions to today's limited electronics. This requires the development of a wide range of nanofabrication techniques.

In this context, Focused Ion Beam Induced Deposition (FIBID) or Focused Electron Beam Induced Deposition (FEBID) are direct-write nanolithography techniques that make use of a focused beam of charged ions (FIB) or electrons (SEM) to grow functional nanomaterials with complex shapes in all three dimensions at a specific location (Orús et al., 2020; Utke et al., 2008; van Dorp and Hagen, 2008). The best achieved resolution is 3 nm (van Kouwen et al., 2009) and the use of masks or resists is not required in contrast to more common nanofabrication techniques such as electron beam lithography (Fig. 1).

Some common applications of this FIB/SEM technology have been developed and integrated in the semiconductor industry, such as integrated circuit fabrication, photolithographic mask repair (Jonckheere et al., 2011), circuit editing (Martínez-Pérez et al., 2009), and the fabrication of very thin samples used in transmission electron microscopy (Giannuzzi and Stevie, 2005; Reyntjens and Puers, 2001).

Additive nano-manufacturing using FIBID and FEBID

Fundamentals of FIBID and FEBID

In the 1970s, FIB technology established itself as a solid approach within the nanolithography scene (Orloff and Swanson, 1978, 1975; Seliger et al., 1979; Seliger and Fleming, 1974), representing the ability to obtain, conduct, and focus a beam of charged ions at the nanometer scale for various purposes. Furthermore, the ability of SEM-induced processing for patterning was also inferred in the 1970s by the decomposition of adsorbed contaminants on a substrate leading to deposition of materials while the electron beam was scanning the substrate (Broers et al., 1976).

In the case of the FIB, as the beam is scanned over a material, several ion-matter interactions take place, such as the secondary electrons, secondary ions, sputtered atoms, backscattered ions, implanted ions, amorphized atoms, etc. These interactions result from the conservative transfer of energy and momentum from ions to atoms in the solid material (Fig. 2a). Secondary first-order electrons result from irradiation with a primary beam, while secondary second-order electrons emerge as a consequence of irradiation by backscattered ions away from the impact point of the primary beam.

In the case of the SEM, in the electron beam irradiation, high energetic electrons interact with the atoms of the material producing secondary electrons, backscattered electrons and X-ray signals (Fig. 2b). Similarly, to ion-matter interactions, secondary first-order electrons result from irradiation with a primary beam, while secondary second-order electrons emerge as a consequence of irradiation by backscattered electrons.

The generation of secondary electrons in materials is of vital importance in FIB/SEM microscopy for several reasons: (1) for the topographic contrast of the images; (2) for the material growth in FIBID and FEBID techniques.

An FIB/SEM in combination with a gaseous precursor adsorbed to the substrate surface, known as FIBID and FEBID techniques, are used to induce a partial decomposition of the precursor molecules, with subsequent material deposition at a specific location and nanoscale resolution. FIBID and FEBID processes are typically carried out on equipment that combines an FIB column with an SEM, known as FIB/SEM microscopes, and a gas injection system that is used to deliver the precursor molecules into the process chamber. Although, FIBID can also be performed on dedicated equipment known as FIB instrument and FEBID can be performed on a conventional SEM.

Specifically, for additive nano-manufacturing, FIB/SEM, FIB and SEM instruments have three main components: an ion and/or an electron column, a gas injection system and a process chamber. The column has in its upper part an ion source or electron tip, from which the ions/electrons are extracted, while in the lower part it has other elements that serve to accelerate them, focus them,

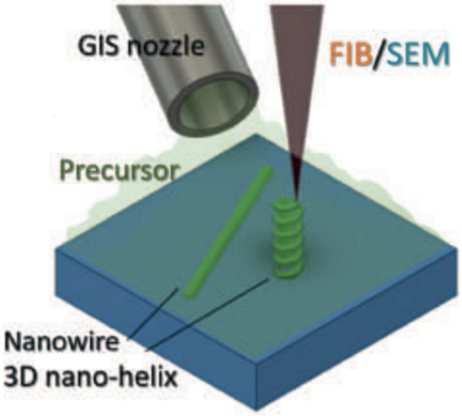

Fig. 1 Focused ion beam induced deposition or focused electron beam induced deposition. Adapted with permission of Orús et al. (2020) Focused ion beam induced processing, in *Nanofabrication*, pp. 5–1 to 5–58, IOP Publishing. Copyright © IOP Publishing Ltd. 2020.

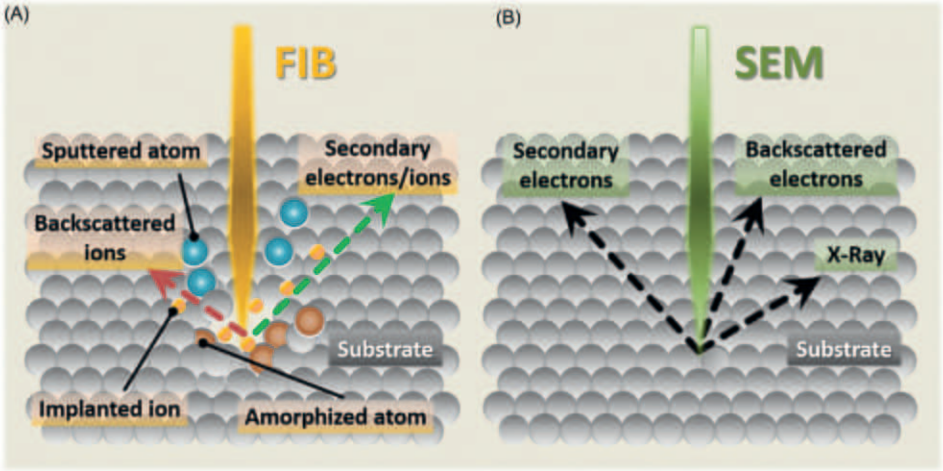

Fig. 2 (a) Sketch of the most important ion-solid matter interactions in FIB processing. (b) Sketch of the most important electron-solid matter interactions in SEM processing.

form the beam (beam diameters of <0.5 nm for SEM, of 5 nm for Ga^+ FIB and of ≈0.3 nm for He^+ FIB), and scan over a substrate surface in a controlled way. The gas injection system has a precursor reservoir and a series of elements that end in a nozzle, from where the precursor is delivered in gaseous phase to the process chamber to perform FIBID/FEBID near the focused beam incident point and the substrate surface. The process chamber is equipped with a platform that holds the substrate, several image detectors and other components to keep it under vacuum.

In general, the beam-scanned patterns in FIBID/FEBID and in FIB/FEB-induced processing are created by a series of closely spaced beam spots. The FIB/FEB remains for each spot size for a certain time (dwell time) and then moves on to the next. The pattern scan is repeated after the refresh time for a series of passes to deliver the required dose of ion/electron to the substrate surface. The beam spot has a Gaussian profile with a minimum size determined primarily by the beam current. The flexibility of the beam scanning allows one to define arbitrary shapes such as straight lines and areas, curvilinear lines and areas, polygons, etc. (Fig. 3) (Harriott, 1993).

In additive nano-manufacturing using FIB or SEM (Utke et al., 2012, 2008; Shorubalko et al., 2016; van Dorp and Hagen, 2008), FIB or FEB is scanned drawing a pre-defined pattern on a material surface, generating secondary electrons which induce the partial decomposition of precursor molecules into volatile compounds and non-volatiles. Volatile compounds are pumped out of the vacuum chamber, while non-volatile ones are deposited on the surface, creating nanomaterials in a single step (Fig. 4). FIBID or FEBID provides a working resolution range from up to hundreds of μm down to a single nm. It offers great adjustability and ease of use in terms of patterning of complex geometries at specific locations in a substrate. Its flexibility in terms of shape and its ultra-high

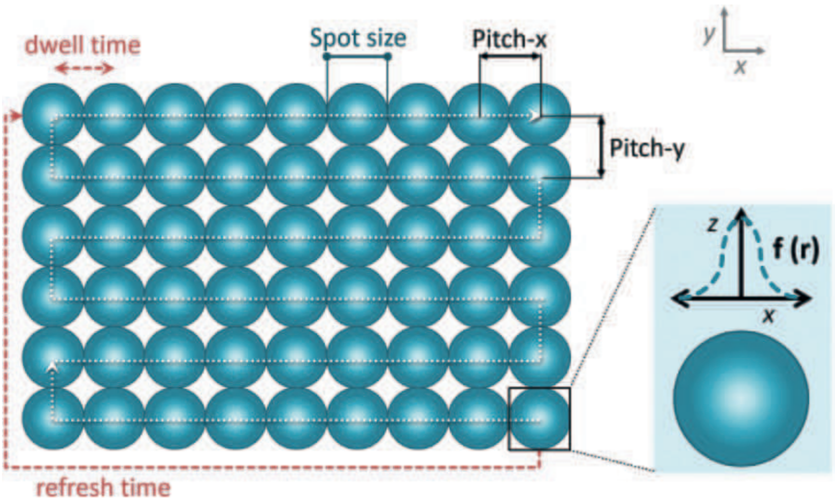

Fig. 3 Diagram of FIB/FEB scanning of a rectangular pattern. This pattern is scanned by serially exposing 54 beam spots, having a Gaussian profile, for a certain dwell time with a pitch-x and pitch-y equal to the spot size. The scanning is performed in serpentine mode. The pattern repeats for a series of passes after the refresh time.

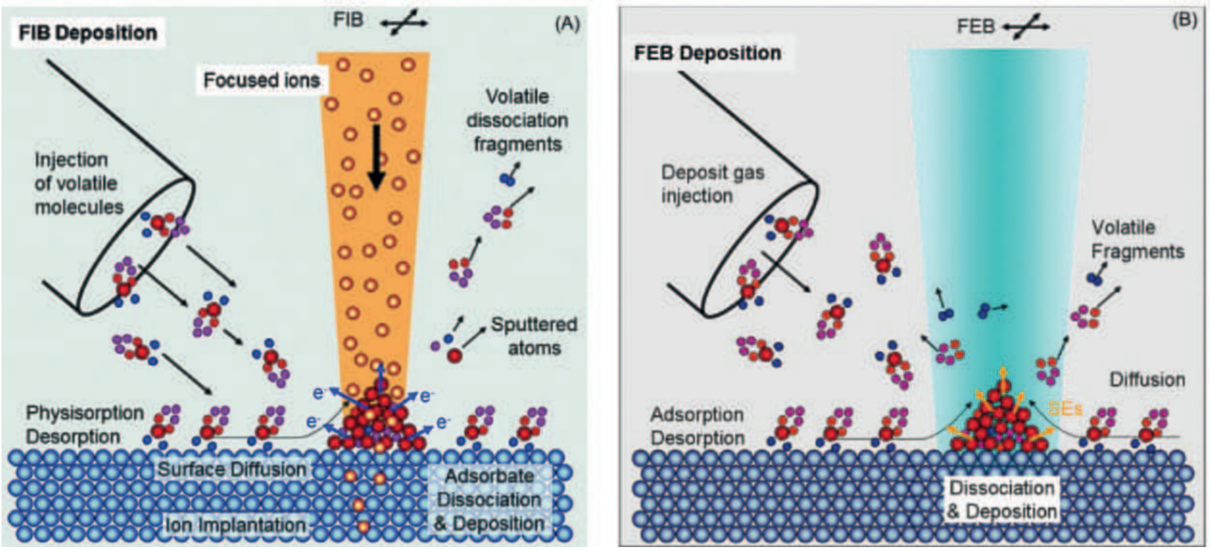

Fig. 4 (a) Principle of FIB induced deposition using a gas injection system for local deposition of 3D nanostructures by dissociating the physisorbed molecules. Gas related processes include adsorption/desorption and surface diffusion to replenish the FIB dissociated adsorbates. Note that deposition only occurs when the sputter yield is smaller than the deposition yield. (b) Physical processes involved in the principle of FEBID. Panel (A): Shorubalko, et al. (2016) Direct-write milling and deposition with noble gases, In: Hlawacek, Gölzhäuser (eds), *Helium Ion Microscopy, Nanoscience and Technology*, pp. 355–393, Cham: Springer (© Springer International Publishing 2016). With permission of Springer, Panel (B): Reprinted with permission from Utke, et al. (2008) Gas-assisted focused electron beam and ion beam processing and fabrication, *Journal of Vacuum Science & Technology, B: Microelectronics and Nanometer Structures–Processing, Measurement, and Phenomena* 26: 1197.

resolution (20–30 nm for Ga^+ FIBID, 10 nm for He^+ FIBID and 30 nm for FEBID) make it fascinating for applications that require unique and precise planar or 3D designs (Fig. 1).

The most relevant experimental parameters that govern FIBID and FEBID are listed below:

- the acceleration voltage is the potential difference used to accelerate ions/electrons along the column. In general, higher acceleration voltages produce higher resolution nanostructure growth and lower growth rate.
- the beam current is the value of the charge delivered to the substrate. Typical values of beam current are generally in the pA-nA range.
- the dwell time is the time the beam remains at each point during the scan.
- the dose is a quantification of the charge received by a material per unit area in a given period of time.
- the pitch is the distance between two consecutive points in a pattern. For areas, a different pitch can be defined for the *x*- and *y*- axis.
- the scanning strategy refers to the path of the beam within a pattern.
- the number of passes is the number of complete scans of the pattern.
- the refresh time is defined as the time required for the precursor gas molecules to replenish between passes.
- the volume per dose is the grown material volume per total charge.

Other experimental parameters, such as the ion species, the substrate material, the pattern dimensions and geometry, the gas injection nozzle position, the precursor molecule (vapor pressure, sticking coefficient to the surface, residence time, sublimation temperature), the base pressure in the vacuum chamber and during growth process, must be carefully selected for the successful additive nano-manufacturing of nano-objects.

The decomposition process of a precursor and, therefore the FIB/SEM-induced deposition rate strongly depends on several terms indicated in the following equation (Utke et al., 2008):

$$\frac{\partial n}{\partial t} = sJ\left(1 - \frac{n}{n_{ML}}\right) + D\left(\frac{\partial^2 n}{\partial r^2} + \frac{1}{r}\frac{\partial n}{\partial r}\right) - \frac{n}{\tau} - \sigma f n \qquad (1)$$

where molecule-surface adsorption, molecule-surface diffusion, molecule-surface and/or ion-stimulated desorption and molecule dissociation terms are sequentially listed. The adsorption term is governed by the flux of molecules in the vapor phase, while the desorption term is governed by the residence time of the molecules, and in the case of FIBID includes the ion–molecule energy transfer. The latter interactions depend on the velocity and mass of ions, such as interactions of the molecule with lighter ions (i.e., He^+) result in its electronic excitation, while those with heavier ions (e.g., Ne^+ and Ga^+) are mainly governed by nuclear stopping power with weak contributions from electronic excitation and heating of the molecule (Indrajith et al., 2019). The diffusion depends on the type of precursor molecules and the substrate (Utke et al., 2008). Finally, the dissociation term depends on the energy-integrated dissociation cross section (σ) and the ion/electron flux.

However, in FIBID process, the contribution of ion implantation, local heat generation, material redeposition, deposition induced by secondary second-order electrons, FIB-induced milling or sputtering must be taken into account. As an example, the use of low beam current and a short dwell time are beneficial in minimizing milling effects with respect to deposition. Thus, the growth rate of FIBID/FEBID can be defined with the following equation:

$$R = \frac{V\sigma f}{t_d} \int_0^{t_d} n \, dt - R_S \tag{2}$$

where R_S is the milling/sputtering rate caused by ion irradiation.

FIBID/FEBID occur in either an electron-limited regime, or a precursor-limited regime depending on the balance between the number of secondary electrons reaching the substrate surface and the amount of precursor molecules available at the surface for decomposition.

Since these additive nano-manufacturing techniques (Utke et al., 2012, 2008) induce partial decomposition of precursor molecules, FIBID/FEBID nanostructures commonly consist of the target element (usually a metal), carbon and oxygen (from the precursor), implanted ions (when heavy ionic species are used) and other contaminant species, which generally impair its functionality.

Materials grown with FIBID

This sub-section reviews the most significant materials grown with FIBID (Table 1). At least three different electrical conductivity regimes are reported for these materials: semiconducting, metallic, and low-temperature superconducting.

Platinum

In this regard, semiconducting and metallic Platinum-Carbon deposits were grown using $MeCpPtMe_3$ and $CpPtMe_3$ as precursors, respectively. This Pt-C material is regularly used as a protective layer against ion-induced effects in nanofabrication for cross-sectional FIB/SEM imaging and TEM sample preparation. Moreover, Pt-C nanowires are also utilized as intermediate electrical contacts for transport studies of other nano-objects.

It is found that the conductivity increases with thickness for Pt-C (Fernández-Pacheco et al., 2009a) deposits. Particularly, they behave as semiconductors below 50 nm in thickness, whereas they behave as metals for 50 nm in thickness and above (Tao et al., 1990). The metallic content of the deposits is around 33 atomic % and their microstructure consist of 5 nm size fcc phase Pt nanocrystals embedded in an amorphous carbonaceous matrix (De Teresa et al., 2009).

Despite Ga^+ FIB, the growth of Pt-C deposits has been reported using Ne^+ FIB and He^+ FIB (Wu et al., 2013). In the first case, Pt-C Ne^+ FIBID deposits behave as metals (600 μΩ cm), whereas they behave as semiconductors (180,000 μΩ cm) using He^+ FIBID. The Pt content in these deposits is around 16 atomic %.

Tungsten

Tungsten-Carbon deposits were grown using tungsten hexacarbonyl, $W(CO)_6$, as a precursor, and present a low electrical resistivity at room-temperature 200 μΩ cm (Sadki et al., 2004) and improved mechanical properties (Córdoba et al., 2017). Although the main characteristic of these nanostructures is the occurrence of superconductivity at low temperature. Planar and 3D Tungsten-Carbon nanostructures grown by FIBID are detailed explained in Sections 3.1.1 and 3.2, respectively.

Copper

Copper-based deposits were prepared using FIBID with $C_{10}H_{13}CuF_6O_2Si$ as precursor. In this respect, semiconducting and metallic deposits were obtained. It is found that its conductivity increases with ion beam current, behaving as metals. Compositional and microstructural studies in these deposits revealed a Cu content of 55 atomic % and Cu crystals embedded in an amorphous carbonaceous matrix (Della Ratta et al., 1993).

Gold

Gold-based deposits were grown using $C_7H_7F_6O_2Au$ as precursor. On this basis, semiconducting and metallic deposits were achieved. A high gold content of 75 atomic % allows obtaining metallic deposits with room temperature resistivity around 500 μΩ cm (Blauner, 1989; Shedd et al., 1986).

Cobalt

Cobalt-based deposits were fabricated using $Co_2(CO)_8$ and $Co(CO)_3NO$ as precursors, respectively. Electrical studies of these materials revealed their semiconducting and metallic behavior at room temperature. In addition, as-grown (Lapicki et al., 2002a,b) and annealed (Gazzadi et al., 2011) Co-based deposits (50 atomic % Co) behave as ferromagnetic metals with room temperature resistivity of 189 μΩ cm and 62 μΩ cm, respectively. Using He^+ FIB instead of Ga^+ FIB, high resolution and metallic Co 10 nm-wide nanowires were grown with similar room temperature resistivity values (Wu et al., 2014).

Table 1 Material, reference, precursor, ion species, composition, microstructure, electrical behavior and room-temperature resistivity of FIBID nanostructures.

Material	*References*	*Precursor*	*Ion*	*Composition (atomic %)*	*Microstructure*	*Electrical behavior*	ρ_{RT} *($\mu\Omega$ cm)*
Platinum	De Teresa et al. (2009)	$MeCpPtMe_3$	Ga^+	Pt:C:Ga:O 22:60:11:7	5–10 nm-sized nanocrystals	Metal	700
Platinum	Tao (1990)	$CpPtMe_3$	Ga^+	Pt:C:Ga:O 46:24:28:2	Amorphous	Metal	70–700
Platinum	De Teresa et al. (2009)	$MeCpPtMe_3$	Ga^+	Pt:C:Ga:O 17:72:10:-	3 nm-sized nanocrystals	Metal	800
Platinum	Wu et al. (2013)	$MeCpPtMe_3$	Ne^+	–	–	Metal	600
Platinum	Wu et al. (2013)	$MeCpPtMe_3$	He^+	–	–	Semiconductor	180,000
Gold	Blauner (1989)	$C_7H_7F_6O_2Au$	Ga^+	Au:C:Ga:O 50:35:15:0	–	Metal	500–1500
Gold	Shedd et al. (1986)	$C_7H_7F_6O_2Au$	Ga^+	Au:C:Ga:O 75:$<$5:20:$<$5	–	Metal	500–1300
Cobalt	Lapicki et al. (2002a)	$Co_2(CO)_8$	Ga^+	–	–	Metal	189
Cobalt	Gazzadi et al. (2011)	$Co(CO)_3NO$	Ga^+	Co:C:Ga:N:O 54:7:9:13:17	–	Metal	189
Cobalt	Wu et al. (2014)	$Co_2(CO)_8$	He^+	–	6 nm-sized nanocrystals	Metal	64–116
Copper	Della Ratta et al. (1993)	$C_{10}H_{13}CuF_6O_2Si$	Ga^+	Cu:C:Ga:O 55:45:0:0	20 nm-sized nanocrystals	Metal	50
Tungsten	Sadki et al. (2004)	$W(CO)_6$	Ga^+	W:C:Ga:O 40:40:20:0	Amorphous	Superconductor below 5.2 K	200
Tungsten	Córdoba Castillo (2014)	$W(CO)_6$	Ga^+	W:C:Ga:O 40:43:10:7	1–2 nm-sized nanocrystals	Superconductor below 4.2–5.1 K	275
3D Tungsten	Córdoba et al. (2018, 2019a, 2020)	$W(CO)_6$	He^+	W:C:O 72:20:8	20–30 nm-sized nanocrystals	Superconductor below 6.2–7.1 K	398
Niobium	Porrati et al. (2019)	$Nb(Nme_2)_3(N\text{-}t\text{-}Bu)$	Ga^+	Nb:C:Ga:N 29:43:15:13	15–20 nm-sized nanocrystals	Superconductor below 5.0 K	550
3D Niobium	Porrati et al. (2019)	$Nb(Nme_2)_3(N\text{-}t\text{-}Bu)$	Ga^+	–	15–20 nm-sized nanocrystals	Superconductor below 8.1 K	380

Niobium

Niobium-Carbon is other promising material grown using FIBID with $Nb(Nme_2)_3(N\text{-}t\text{-}Bu)$ as precursor It is metallic at room temperature, whereas it presents superconducting properties at low temperature (Porrati et al., 2019) (more details in Section 3.1.1 of this chapter).

Materials grown with FEBID

The applicability of FEBID is also limited to the synthesis of feasible precursors (Swiderek et al., 2018). Precursors used to induce the growth of different materials such as single elements, binary compounds and ternary compounds are briefly discussed in this section.

Single element

The most relevant materials grown with FEBID are listed below.

Platinum

Platinum-Carbon deposits grown using FEBID with $(CH_3)_3Pt(C_pCH_3)$ as precursor were the most studied material in the last decade (Botman et al., 2008; De Teresa et al., 2009). The composition and microstructure of deposits consist of 17 atomic % Pt content and 3 nm grain size of face-centered cubic Pt phase crystals embedded in an amorphous carbonaceous matrix, respectively. According to this, its electrical properties studied correspond to a semiconductor behavior.

Tungsten

Tungsten-Carbon deposits present a metal to insulator transition as a function of the W content (Huth et al., 2009). Another interesting feature of these nanostructures is the occurrence of superconductivity at low temperature (Blom et al., 2021; Sengupta et al., 2015). Planar Tungsten-Carbon superconducting deposits grown by FEBID are detailed explained in Section 3.1.2.

Cobalt

Planar metallic and magnetic Cobalt nanostructures using $Co(CO)_8$ as precursor were fabricated and characterized in the last decade (De Teresa et al., 2016; De Teresa and Córdoba, 2014; Fernández-Pacheco et al., 2009b; Serrano-Ramón et al., 2011). Additionally, the growth of high purity 3D Co nanostructures was also proved (Córdoba et al., 2010, 2016c; Fernández-Pacheco et al., 2013) extending the usage of FEBID for applications in 3D nanomagnetism and spintronics. More recently, 3D nanomagnets grown using FEBID have been key elements to study complex chiral spin states (Sanz-Hernández et al., 2020), magnetoelectrical signals (Meng et al., 2021) and complex textures in the magnetic stray field given by the effect of the curvature, torsion, chirality and magnetic coupling (Donnelly et al., 2021).

Iron

Planar magnetic Iron deposits with Fe content above 75 atomic % were grown using FEBID with $Fe(CO)_5$ (Gavagnin et al., 2014) and $Fe_2(CO)_9$ (Córdoba et al., 2012, 2016b; Lavrijsen et al., 2011) precursors. Additionally, 3D magnetic Iron pillars with purity higher than 90 atomic % were also fabricated with $Fe(CO)_5$ (Gavagnin et al., 2014) and $Fe_2(CO)_9$ (Córdoba et al., 2016c; Franken et al., 2014; Wolf et al., 2015) precursors.

Gold

Gold based deposits with Au content of up to 72 atomic % were grown using FEBID using $C_7H_{10}AuF_3O_2$ as a precursor compound (Belić et al., 2017; Koops et al., 1996).

Silver

AgO_2Me_2Bu precursor material has been utilized to direct writing silver nanostructures by FEBID. By selecting the optimized experimental conditions 75 atomic % of silver content in the structures was obtained (Höflich et al., 2017).

Ruthenium

Ruthenium based deposits with Ru content of 23 atomic % were grown using FEBID using $(\eta_3\text{-}C_3H_5)Ru(CO)_3Br$ as a precursor (Jurczyk et al., 2019).

Copper

$CuC_{16}O_6H_{26}$ precursor has been used to grow metallic structures by FEBID with copper content of 25 atomic %. A microstructural study revealed deposits consist of copper nanocrystals with sizes of up to 15 nm embedded in a carbonaceous matrix (Haverkamp et al., 2018).

Binary compounds

The possibility of preparing nanostructured binary alloys, which are crucial elements of micro- and nano-electronic devices, with a direct-write technique expands the utilization of this method for many other applications.

On the other hand, the FEBID process allows several precursors to be combined and their flux to be controlled during growth. This ability permits the tuning of the element ratio and the formation of metastable phases of different compounds, which is not feasible using conventional methods for the fabrication of binary alloys.

This is the case for a metastable Pt_2Si_3 phase of binary alloys of Pt-Si (Winhold et al., 2011). By tuning the gas flux of two precursors$(CH_3)_3CH_3C_5H_4Pt$ and $Si(SiH_3)_4$, binary alloys with specific ratios in platinum and silicon content can be fabricated using the FEBID technique. The minimum resistivity in the prepared alloys was found for a 3:2 Si:Pt ratio.

Furthermore, by adding a magnetic element such as Cobalt, Nickel or Iron to binary alloys, these alloys could include additional functionalities such as magnetism, expanding the use of this technique for applications in nano-magnetism and spintronics.

Binary compounds such as nickel oxide were synthesized by using an in situ two-step process (Córdoba et al., 2016a). As-grown Ni-C nanodeposits grown by FEBID transformed into homogeneous NiO compounds using focused electron beam irradiation under O_2 flux.

In addition, a local synthesis of fluoride compounds, such as cobalt trifluoride phase, was transformed from cobalt nanodeposits, using focused electron beam irradiation under XeF_2 flux (De Teresa et al., 2014).

Specifically, binary CoPt-C alloys consisting of amorphous CoPt nanoparticles embedded in a carbonaceous matrix can be fabricated using FEBID, by combining $C_2(CO)_8$ and $(CH_3)_3CH_3C_5H_4Pt$ precursors (Porrati et al., 2012). These nanoparticles were transformed into face centered tetragonal phase ($L1_0$) nanocrystals by post-irradiation treatment, which consists of a low-energy electron irradiation process. A transition from a superparamagnetic to a ferromagnetic state has been detected in the alloys at room temperature, allowing their magnetic state to be tuned. The as-grown samples (amorphous nanoparticles) exhibited superparamagnetic behavior evidenced by the lack of hysteresis and coercivity in Hall effect measurements, while the post-irradiated samples ($L1_0$ phase crystal) exhibited typical ferromagnetic behavior.

In the last decade, another study of binary CoSi-C FEBID alloys produced by simultaneous combination of two homonuclear precursors, $Co_2(CO)_8$ and $Si(SiH_3)_4$, was reported (Porrati et al., 2013). By modifying the precursor flux, the formation of CoSi and $CoSi_2$ nanocrystals embedded in a carbonaceous matrix was detected in the samples, which allowed the control of their electrical properties from the insulator to quasi-metallic tunneling coupling transition.

In recent years, the investigation of new and feasible heteronuclear precursors for direct-writing functional magnetic nanostructured alloys has been addressed. A first example was reported in 2015, where Porrati et al. (2015) prepared CoFe magnetic nanostructured alloys using $HFeCo_3(CO)_{12}$ as precursor. Nanowires 50 nm wide had a room temperature resistivity of 43 μΩ cm and exhibited ferromagnetic behavior. The microstructure of the prepared nanowires consisted of a bcc Co-Fe phase mixed with a spinel oxide $FeCo_2O_4$ with crystals 5 nm in diameter. More recently, specific binary Co-Si-C alloys have been grown using two new heteronuclear single-gas precursors, CoSi from $H_3SiCo(CO)_4$ and Co_2Si from $H_2Si(Co(CO)_4)_2$ (Jungwirth et al., 2021). Both Co_xSi alloys exhibited tunneling magnetoresistance at temperature near room temperature. These two works demonstrated that the use of heteronuclear precursors preserves the initial metal ratio in the prepared magnetic alloys, which encourages going further in the synthesis of more sophisticated precursors for the FEBID and FIBID technology.

Ternary compounds

The fabrication of multilayer nanostructures and even ternary compounds using a direct-writing technique such as FEBID or FIBIB could avoid the use of several serial steps typically involved in conventional lithographic preparation. Following this path, Porrati et al. (2017) reported an interesting study in which Co_2Fe/Si multilayer nanostructures were fabricated by the alternate FEBID process from $HFeCo_3(CO)_{12}$ and $Fe(CO)_5$ precursors to obtain the Co_2Fe compound and Si_5H_{12} precursor to obtain the Si layer. By using low-energy electron irradiation on the multilayers, an intermixing atomic species is induced to obtain ternary nanostructured compounds. Co_2FeSi Heusler alloy is formed for the entire multilayer for thin samples, while in thick multilayers the intermixing occurs mainly at the top of the sample.

Direct-writing of superconducting nanostructures

Planar superconducting nanostructures

FIBID

This section presents a revision of the most significant planar superconducting materials grown using FIBID (Table 2).

Tungsten-Carbon-based materials grown by FIBID using tungsten hexacarbonyl, $W(CO)_6$, as a precursor, are becoming the most studied FIBID superconductors. Thanks in large part to Sadki's discovery in 2004 (Sadki et al., 2004) that this material behaved as a superconductor below 5.1 K (its electrical resistance decreases from a finite value to zero below its superconducting critical temperature, T_C). The explanation of the huge T_C value in W-C FIBID nanostructures compared to that found for pure crystalline tungsten (15 mK) (Li et al., 2008) remains a matter of debate. Some authors (Córdoba Castillo, 2014; Li et al., 2008; Sadki et al., 2004) relate the high T_C value in nanostructures to their amorphous nature, which is enhanced by the presence of an amorphous

Table 2 Room-temperature resistivity, superconducting critical temperature, composition, and microstructure of planar superconducting FIBID nanostructures.

References	ρ_{RT} *(μΩ cm)*	T_C *(K)*	*Composition (at. %)*	*Microstructure*
Sadki et al. (2004)	200	5.2	*W:C:Ga:O* 40:40:20:0	Amorphous (XRD)
Luxmoore et al. (2007)	200	5.5	*W:C:Ga:O* 51:37:12:0	Nanocrystalline order (HRTEM)
Spoddig et al. (2007)	–	5.2	*W:C:Ga:O* 17:35:13:4	–
Li et al. (2009)	100–350	5.0–5.5	*W:C:Ga:O* 53:34:11:2	Nanocrystallite clusters (TEM)
Li et al. (2011)	330	5.0	*W:C:Ga:O* 48:30:16:6	Nanocrystallites (TEM)
Córdoba et al. (2013)	275	4.3	*W:C:Ga:O* 40:43:10:7	Nanocrystallites (TEM)
Orús et al. (2021a)	170–250	3.7–4	*W:C:O* 15:78:7	Nanocrystallites (TEM)
Porrati et al. (2019)	550	<5.0	*Nb:C:Ga:N* 29:43:15:13	Nanocrystallites (TEM)
Weirich et al. (2014)	300–600	<3.8	*Mo:C:Ga:O* 41:26:26:7	–

carbonaceous matrix (from the precursor) and implanted Ga atoms (from the FIB), which presumably amorphize the tungsten atoms. This statement is in good agreement with the high T_C value found in amorphous W-based alloys.

Another interesting feature of these nanostructures is their low electrical resistivity at room-temperature (~200 μΩ cm) that qualifies them to be used as metallic contacts at room-temperature and superconducting contacts below 5 K for electrical transport studies of nano-objects such as nanoparticles, nanowires, nanospheres, etc. and of low-dimensional materials as nano-flakes, nanoribbons, etc.

The various compositional and structural studies of W-C FIBID nanostructures already reported are in agreement with a W atomic content in the 40–50% range, a C atomic content in the 30–40% range and a Ga atomic content in the range of 10–20%, and with their amorphous or short-range order structure. An exception to these values is found in suspended bridges with enhanced mechanical properties and a W atomic content up to 70% (Córdoba et al., 2017).

The W-C FIBID material is considered as a type-II superconductor because an applied magnetic field penetrates the material in a quantized (a flux quantum) and ordered manner (lattice), forming individual superconducting vortices (Guillamón et al., 2008). A superconducting vortex consist of a circular normal core screened by a supercurrent. The circular supercurrents that surround each vortex repel each other arranging them in a triangular Abrikosov lattice. The density of the superconducting vortices in the material increases with the applied magnetic field and the value of that field at which the superconducting state is suppressed is called the upper critical magnetic field (B_{C2}). The B_{C2} in the W-C FIBID material is in the range of 7–8.5 T at 2 K (Córdoba Castillo, 2014; Dai et al., 2013; Sun et al., 2013), while extrapolated to zero temperature it is around 9.5 T (Sadki et al., 2004). Ginzburg-Landau equations predicted two characteristic lengths in a superconductor, the coherence length and the penetration depth, these determined lengths are 6.25 nm and 850 nm, respectively for the W-C FIBID material (Guillamón et al., 2009). By injecting a higher enough external electrical current into the material electrical dissipation occurs due to the unpairing of the Cooper electrons pair. The value of this electrical current is called the critical current (I_C), and the value of the critical current density (J_C) in the W-C FIBID material is in the range of 0.01–0.1 MA/cm^2 (Córdoba Castillo, 2014; Guillamón et al., 2008; Luxmoore et al., 2007; Sadki et al., 2004; Spoddig et al., 2007). Furthermore, by injecting a current into the material containing a vortex lattice results in an electrical dissipation due to vortex motion within the superconducting regions.

W-C FIBID material can be considered a remarkable system to investigate vortex-related physical phenomena in 2D and 1D structures. In the first case, this material properly follows the microscopic Bardeen–Cooper–Schrieffer (BCS) theory for superconductors (Guillamón et al., 2008). In addition, it is an excellent material to visualize the solid-liquid transition (Guillamón et al., 2009), the order-disorder transition (Guillamón et al., 2014), and the vortex creep phenomenon (Guillamón et al., 2011) in a 2D vortex lattice. In the second case, finite size effects have been investigated in narrow nanostructures (≤50 nm in diameter), which are key for their application to superconducting circuits, such as a magnetic field-driven reentrance of the superconductivity caused by vortex confinement (Córdoba et al., 2013), a vortex transfer carried by non-local motion (Córdoba et al., 2019b; Orús et al., 2021a) and an electric field-induced control of superconductivity (Orús et al., 2021b).

Other interesting materials deposited with FIBID exhibited metallic behavior at room temperature, while at low temperature they transitioned to the superconducting state. This is the case for superconducting Niobium-Carbon and Molybdenum-Carbon nanostructures grown using $Nb(Nme_2)_3(N\text{-}t\text{-}Bu)$ and $Mo(CO)_6$ as precursors respectively. In the first case, Nb-C nanostructures behave as superconductors below 5 K (Porrati et al., 2019). The compositional and structural studies revealed that this material consists of an atomic composition ratio of Nb:C:Ga:N 29:43:15:13, and a polycrystalline microstructure of fcc NbC with a crystal size of 15–20 nm. On the other hand, freestanding 3D NbC nanowires exhibit a broaden superconducting transition between 4 and 11 K. In the second case, Mo-C nanostructures behave as superconductors below 3.8 K (Weirich et al., 2014) with an atomic composition ratio of Mo:C:Ga:O 42:26:26:7.

FEBID

FEBID nanostructures typically contain a lower atomic percentage of metal than those obtained by FIBID, with a few exceptions that are beyond the scope of this chapter. In this way, those materials could be considered less suitable for applications in electronics and so on. Within this scenario, the fabrication of high-quality superconducting nanostructures using FEBID remains a challenge.

In this section, a review of the most significant planar superconducting materials grown with FEBID is presented.

There are currently only two studies of Tungsten-Carbon superconducting materials grown by FEBID using tungsten hexacarbonyl, $W(CO)_6$, as precursor (Sengupta et al., 2015; Blom et al., 2021).

In the first study, the 130 nm wide W-C nanowires behave as superconductors below 2.0 K and their upper critical magnetic field reaches up to 3.7 T. These superconducting parameters are considerably worse than those obtained with FIBID (Section 3.1.1). Although, the compositional and structural studies in W-C FEBID nanowires revealed a W atomic content of 50%, a C atomic content of 40%, and an O atomic content of 10%, and nanocrystalline structure, which are values similar to those obtained in W-C FIBID nanostructures (Sengupta et al., 2015).

In the second study, by increasing the magnitude of the electron beam current by one order (80 nA), the W-C wires 500 nm wide and with an atomic content of 38% W behave as superconductors below 4.5 K (Blom et al., 2021). The T_C value is similar to that obtained in nanowires grown with FIBID (Section 3.1.1). However, since the beam diameter increases with beam current, large beam currents prevent the fabrication of high-quality superconducting nanostructures using FEBID.

Other interesting materials deposited with FEBID exhibited metallic behavior at room temperature, while at low temperature they became superconducting. This is the case for Lead-Carbon and Molybdenum-Carbon superconducting nanostructures grown using $(CH_3CH_2)_4Pb$ and $Mo(CO)_6$ as precursors, respectively.

The 1 μm wide Pb-C structures can be tuned from insulating to metallic behavior (a room-temperature resistivity of 190 μΩ cm) and, in addition, they behave as a low-temperature superconductor with two T_C values. The first $T_C = 7.2$ K coincides with the value of bulk lead, while the second superconducting phase presents a $T_C = 6.2$–6.6 K, with an enhanced value of $B_{C2} = 10$ T. Compositional analysis revealed that this material consists of an atomic composition ratio of Pb:C:O 44:31:25 (Winhold et al., 2014).

In the case of Mo-C nanostructures grown by mixing the precursor with H_2O vapor, they exhibit superconducting behavior below ≈ 4 K. Compositional analysis revealed that this material consists of Mo:C 70:30 (Makise et al., 2014).

3D superconducting nanostructures

The exploitation of the third dimension in nano-superconductivity could represent a paradigm shift for the exploration of novel topology- and geometry-induced phenomena (Fomin, 2020, 2018), which do not arise in planar nanostructures (Rezaev et al., 2020), with potential applications in advanced sensing and quantum computing.

In the last years, FIBID is becoming an established route for the direct-writing of 3D superconducting nanoarchitectures, with resolutions down to a few tens of nanometers (Figs. 5 and 6) (Córdoba et al., 2020, 2019a, 2018). The extremely-high resolution of FIBID (Hirt et al., 2017) is the main advantage compared to direct competitors of additive manufacturing methods as two-photon lithography (Seniutinas et al., 2017) and electrodeposition (Bochmann et al., 2018).

Ga^+ FIBID has been used to grow individual 3D superconducting W-C (Li et al., 2012, 2010; Romans et al., 2010) and Nb-C wires (Porrati et al., 2019), with superconducting critical temperature and upper critical magnetic field similar to those obtained for planar nanostructures, semiconducting and insulating 3D materials (Fujii et al., 2005; Matsui et al., 2000; Morita et al., 2003; Nakai et al., 2010), as helices with aspect ratio up to 3 and diameters down to 500 nm (Wang et al., 2019); and arrays of semiconducting and insulating 3D materials (Esposito et al., 2015, 2014). Nevertheless, the resolution in this process is mainly limited by the Ga^+ beam diameter (~ 5 nm) and its high lateral scattering, preventing the growth of sub-100 nm 3D structures by Ga^+ FIBID so far.

A new Gas-FIB source based on lighter and noble-ion elements like He^+ FIB integrated in the helium ion microscope (HIM) (Scipioni et al., 2008) has been particularly successful for the growth of sub-10 nm structures (Wu et al., 2013), due to its small probe size ≈ 0.3 nm, its lower proximity effect (Maas et al., 2010) and higher sensitivity (Sidorkin et al., 2009). The HIM represents an enormous forward step for additive nanolithography method compared to Ga^+ FIBID.

He^+ FIBID has proven to be of importance in the growth of 3D superconducting nanostructures with fancy geometry, higher aspect ratio and outstanding superconducting properties ($T_c \approx 6.2$–7.1 K, $B_{c2}(0) \approx 12$–15 T), such as hollow nanocylinders (Córdoba et al., 2020, 2018) and nanohelices (Córdoba et al., 2019a).

A noteworthy example of the capabilities of 3D He^+ FIBID is the fabrication of at-will W-C 3D hollow nanocylinders with diameters down to 32 nm and with an aspect ratio of ≈ 200 (Córdoba et al., 2020, 2018) (Fig. 5). The occurrence of a hole of 6 nm in diameter at the center of the standing cylinder is the result of a balance between the milling and deposition regimes. In the particular experimental conditions, the $W(CO)_6$ precursor is decomposed and deposited over the substrate surface and over deposited material in the vicinity of the highly focused He^+ beam spot, while simultaneously is sputtered by He^+ FIB milling at the center of the beam spot, creating a hollow nanocylinder with a wall thicknesses down to 13 nm. The critical temperature of the W-C 3D hollow nanocylinder is 6.2 K, which is up to 1.5 times higher than that obtained in Ga^+ FIBID W-C nanostructures of similar dimensions. TEM-based characterization studies indicate a higher amount of W in the 3D nanostructures than those grown by Ga^+ FIBID, up to 70% of W in atomic content; and the presence of 20–30 nm-sized crystalline grains of the fcc WC_{1-x} phase, that it is close to the value of the nanowire diameter. Additionally, the determined coherence length and the penetration depth in this 3D nanostructures are 5 and 850 nm respectively.

Another remarkable example of 3D He^+ FIBID is the patterning of W-C 3D nanohelices with at-will geometries by tuning some key deposition parameters (Córdoba et al., 2019a) (Fig. 6). *Córdoba* et al. reported the smallest and more-densely-packed superconducting nanohelix ever grown so far, as small as 100 nm in diameter, and with an aspect ratio of 65. These nanohelices become superconducting at 7 K and show a large upper critical magnetic field and critical current density.

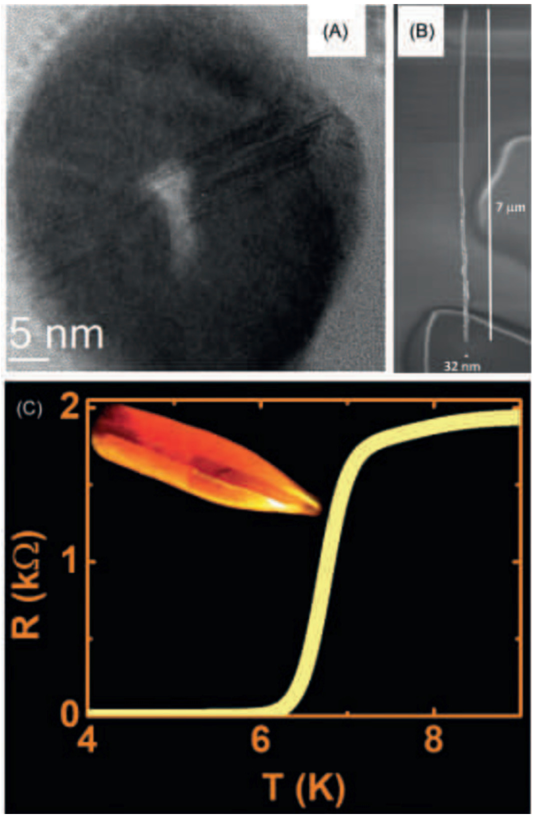

Fig. 5 Hollow crystalline W-C 3D superconducting nanocylinder grown by He^+ FIBID. (a) Cross-sectional TEM image. (b) SEM image of the standing nanocylinder. (c) High-magnification SEM image of the nanotube. Panels (a) and (b): Reproduced with permission from Córdoba et al. (2018) Vertical growth of superconducting crystalline hollow nanowires by He^+ focused ion beam induced deposition, *Nano Letters* 18: 1379–1386. https://doi.org/10.1021/acs.nanolett.7b05103. Copyright (2018) American Chemical Society. Further permission related to the figure excepted should be directed to the ACS. Panel (c): Reproduced with permission from Córdoba et al. (2020) 3D superconducting hollow nanowires with tailored diameters grown by focused He + beam direct writing. *Beilstein Journal of Nanotechnology* 11: 1198–1206. https://doi.org/10.3762/bjnano.11.104.

In addition, given its helical 3D geometry (i.e., curvature and torsion), fingerprints of vortex and phase-slip patterns determined by topologically non-trivial screening currents and confinement potentials are experimentally identified with resistance steps in their current–voltage curves and supported by numerical simulations based on the time-dependent Ginzburg-Landau equation (Fig. 6). The preparation of 3D helical nanoarchitectures could impulse the extension of vortex matter (Wördenweber, 2017) toward 3D curvilinear chiral geometries, whose experimental and theoretical investigations represent an essentially novel research direction in Abrikosov fluxonics (Dobrovolskiy, 2017).

These outstanding examples have opened a conceptually novel route for the fabrication of advanced nano-superconductors, which is unachievable with other additive manufacturing techniques, putting focused ion beam techniques at cutting-edge of the frontier of knowledge in creating 3D nano-superconductors. Although, it is fair to mention that they are still limited in ability to create a variety of 3D complex architectures and superconducting materials. Therefore, in order to exploit the potential of moving toward to three dimensions, some significant experimental challenges associated with the fabrication and characterization of complex 3D nanoscale geometries and topological configurations have to be addressed.

Applications to superconducting devices

Planar superconducting nanostructures

Basset et al. has demonstrated that planar W-C FIBID nanostructures exhibit appealing properties such as high kinetic inductance, which is an important requirement for their implementation in high-frequency superconducting circuits (Basset et al., 2019). These circuits could be very interesting to investigate mesoscopic systems where the spin degree of freedom needs to be addressed. Therefore, in this work the high performance of these hybrid *microwave resonators* with a strong non-linear response was evaluated by combining Nb thin films grown by sputtering technique with 35–75 nm-wide W-C nanowires grown with He^+ FIBID.

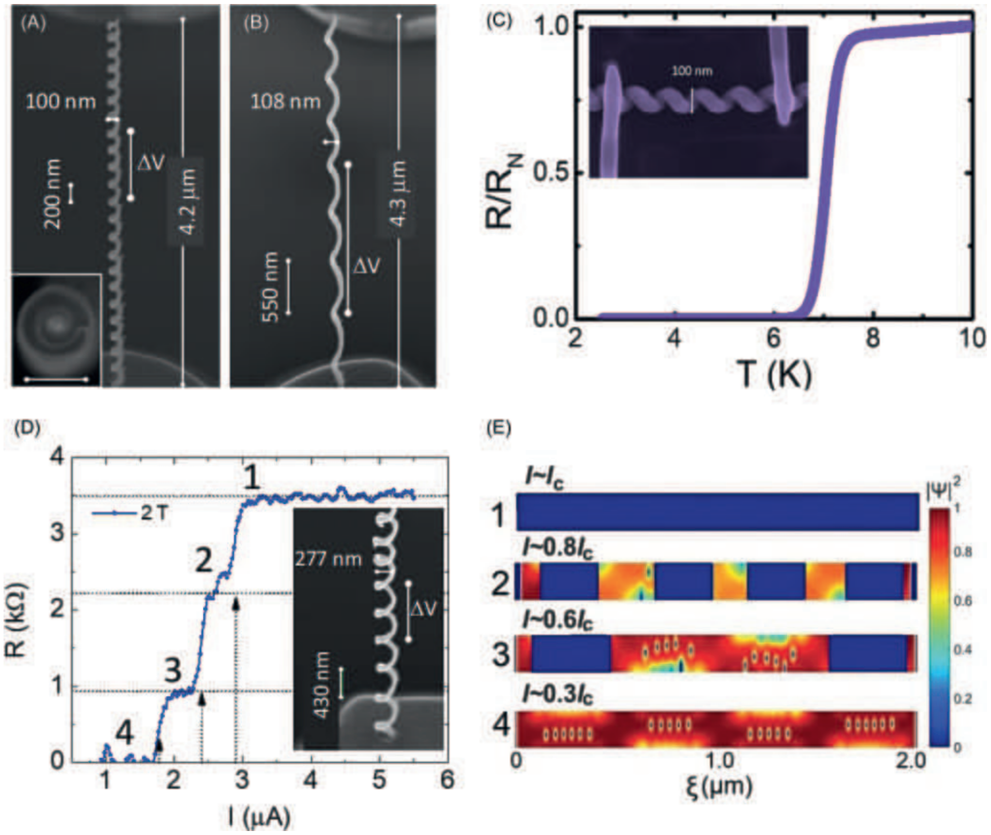

Fig. 6 3D W-C superconducting nanohelices grown by He$^+$-FIBID. (a), (b) SEM images of nanohelices of types 1 and 4 (52° tilted stage). Inset in (a) shows the top view of the nanohelix (measured bar = 100 nm). (c) Normalized resistance as a function of temperature for nanohelix of type 1. Inset shows the SEM image for the nanohelix of type 1 connected for magnetotransport measurements. (d) Experimental Resistance-Current measurement for the nanohelix of type 6. Inset shows the SEM image for this nanohelix. (e) Simulated order parameter distributions plotted over the 2D surface of the helical structure of type 6 for the magnetic field 2 T. Reproduced with permission from Córdoba et al. (2019) Three-dimensional superconducting nanohelices grown by He$^+$- focused-ion-beam direct writing, *Nano Letters* 19: 8597–8604. https://doi.org/10.1021/acs.nanolett.9b03153 Copyright (2019) American Chemical Society. Further permission related to the figure excepted should be directed to the ACS.

Remarkably, ultra-fast vortex motion was recently shown for Nb-C microwires grown with Ga$^+$ FIBID (Dobrovolskiy et al., 2020) providing an opportunity to investigate non-equilibrium superconducting systems. Furthermore, the weak vortex pinning, the critical current near the depairing current, and the fast heat removal from heated electrons allow one to consider this material as a suitable candidate for *fast single-photon detectors*.

Another recently highlighted application for W-C superconducting structures is the fabrication of *Josephson Junctions* in a single-step process using FEBID (Blom et al., 2021). Josephson coupling in these devices is revealed by the Shapiro step response for various microwave frequencies and electrical magneto-transport measurements. This approach provides an available method to fabricate highly-sensitivity detectors such as superconducting quantum interference devices (SQUIDs) and single-photon detectors at a predefined place.

Recently, *Orús* et al. presented an experimental demonstration of the modulation of the critical current in planar superconducting 45 nm-wide, 2.7 µm-long W-C FIBID nanowires using a side-gate voltage (Orús et al., 2021b). The phenomenon in which the superconductivity of a nano-superconductor can be suppressed by applying an electric field in its vicinity has already been observed in other superconducting materials (Bours et al., 2020; De Simoni et al., 2020, 2018a; Paolucci et al., 2019; Puglia et al., 2020; Rocci et al., 2021, 2020), and at the present time its microscopic explanation, which cannot be accounted for by means of the Barden-Cooper-Schrieffer theory of superconductivity only, has proven elusive and challenging and represents a matter of debate (Alegria et al., 2021; Chirolli et al., 2021; Golokolenov et al., 2021; Mercaldo et al., 2020; Puglia et al., 2022, 2021; Ritter et al., 2022, 2021; Solinas et al., 2021; Virtanen et al., 2019).

The prepared *W-C Superconducting Field Effect Transistor (S-FET)* nanodevices present comparable figures of merit to those retrieved in superconducting nanostructures (Ti, Nb, Al, V, NbN) grown using electron beam lithography. In particular, they exhibit a higher critical temperature and a lower critical gate voltage value needed to suppress superconductivity than most of the other superconductors. This modulation of the critical current is accounted for by its squeezing by the electric field within a theoretical model based on the Ginzburg–Landau equation which includes boundary conditions in the nanostructure, and adequately reproduces the experimental data.

This work provides with valuable insight in the present effervescent discussion on this puzzling phenomenon, and also presents FIBID as a powerful technique providing with enhanced patterning flexibility and not requiring the use of resists and solvents. This technique could be exploited for the fabrication of complex functional nanodevices (Paolucci et al., 2019, 2018), such as novel types of Josephson junctions (De Simoni et al., 2018b), logic gates (Lee et al., 2003), and single-photon detectors (Kadin and Johnson, 1996).

3D superconducting nanostructures

Currently, fabrication and characterization of 3D nano-superconductors remain a challenge. This is mainly due to the lack of nanofabrication techniques capable of growing these nano-superconductors with characteristic sizes in the order of magnitude of the superconducting coherence length. In this scenario, advanced lithography techniques such as those based on focused ion beams (FIB) and focused electron beams (FEB) can be utilized. Actually, 3D FIBID prototypes are adequate for investigating new concepts in the field of 3D nano-superconductivity as already mentioned in the Section 3.2 of this chapter.

In particular, nanohelix arrays can be considered *superconducting metamaterials* (Anlage, 2011) whose microwave response could be controlled by selecting the contact points of individual nanohelices for voltage-current measurements (Córdoba et al., 2019a), as detected in planar nano-superconductors (Dobrovolskiy et al., 2015). Furthermore, a fine adjustment of the shape of the nanohelices allows one to expect commensurability effects in the presence of moderate high magnetic fields (Córdoba et al., 2013; Dobrovolskiy et al., 2018) that can be considered as one more degree of freedom for the response of the 3D nano-superconductor.

Conclusion

In this chapter, we have described an advanced method for direct-writing of nanostructures in all three dimensions using focused ion and electron beams. Depending on the precursor utilized, these materials can harbor a wide range of electronic properties, from insulators to superconductors. In particular, some examples of superconducting nanostructures created by these techniques have been widely discussed, with special interest in the case of 3D nano-superconductors which can host rich and novel physical phenomena due to geometric- and topological-induced effects. These advanced nano-superconductors could be considered building blocks for applications in superconducting electronics (Makarov et al., 2022), such as magnonics, fluxonics, quantum computing, electric field-induced control of superconductivity, ultra-high sensitivity sensors and lots of others.

The future of FIBID and FEBID as a well-established additive nano-manufacturing technology largely depends on the enormous efforts in the improvement of instruments and techniques to overcome several of their current limiting factors (Hirt et al., 2017). Some of them are outlined below:

- Scalability: the reproducibility of sequential nanostructures is limited to an array size of a few tens of microns mainly due to beam proximity effects and a non-stationary state of the precursor flux (Esposito et al., 2015, 2014).
- Throughput: the throughput of FIBID and FEBID is rather limited because the process is performed only with a single beam sequentially scanning one spot after another. Direct-writing of very large areas requires high processing times and moreover, beam and precursor flux instabilities must to be addressed. The development of different ion sources, with small probe sizes and capable of providing sufficiently high current densities (Bassim et al., 2014; Smith et al., 2014) could increase the throughput of the technique and thus facilitate overcoming this critical limitation.
- Reproducibility: complete control of experimental conditions in the FIBID and FEBID processes is the only way to obtain advanced nanostructures with high reproducibility and to adjust their physical and chemical properties. The integration of a laser interferometer platform in the equipment could be considered one of the steps forward to achieve this goal (Bauerdick et al., 2013; Hentschel et al., 2020).
- Software: hybrid Monte Carlo– continuum simulations of FIBID and FEBID together with computer-aided design programs (Deinhart et al., 2021; Fowlkes et al., 2018; Keller and Huth, 2018; Skoric et al., 2020), which predict proximity effects and gas flux issues, could be adapted and improved for larger area nanofabrication.

The limiting factors mentioned above, of course, must be widely considered for the fabrication of 3D nanostructures. Particularly, the recent experimental achievements in the nanofabrication and characterization of 3D nano-superconductors together with the theoretical predictions (Section 3.2 of this chapter), surely arouse great interest in addressing more extensive studies on this subject in the coming years. For example, the ability to create chiral nanostructures enables fine tuning of the properties and place of topological states, providing an enhanced functionality for future metamaterials and devices. In this way, FIBID and FEBID could become cutting-edge additive nano-manufacturing techniques to open a conceptually novel route for the fabrication of advanced nanoarchitectures based on complex 3D geometries to allow their integration into multi-functional circuits, in highly topical fields such as sensing and electronics, what is not feasible with other additive manufacturing techniques.

We expect that this chapter encourages additional investigations in 3D nanoprinting applied to nano-superconductivity, and promotes win-win situations by addressing geometrical- and topological-induced effects in live and molecular science as well as soft and condensed matter.

Acknowledgments

The author acknowledges the financial support from the European Union via COST Action CA19140 FIT4NANO, the Spanish MICINN via Grant PID2020-117264GB-I00 funded by MCIN/AEI/10.13039/501100011033 and Excellence Unit "María de Maeztu," (CEX2019-000919-M), the Generalitat Valenciana SEJIGENT/2021/012T and "la Caixa" Foundation (ID 100010434), LCF/BQ/PR19/11700008.

References

Alegria LD, Bøttcher CGL, Saydjari AK, Pierce AT, Lee SH, Harvey SP, Vool U, and Yacoby A (2021) High-energy quasiparticle injection into mesoscopic superconductors. *Nature Nanotechnology* 16: 404–408.

Anlage SM (2011) The physics and applications of superconducting metamaterials. *Journal of Optics* 13: 024001.

Basset J, Watfa D, Aiello G, Féchant M, Morvan A, Estève J, Gabelli J, Aprili M, Weil R, Kasumov A, Bouchiat H, and Deblock R (2019) High kinetic inductance microwave resonators made by He-Beam assisted deposition of tungsten nanowires. *Applied Physics Letters* 114: 102601.

Bassim N, Scott K, and Giannuzzi LA (2014) Recent advances in focused ion beam technology and applications. *MRS Bulletin* 39: 317–325.

Bauerdick S, Bruchhaus L, Mazarov P, Nadzeyka A, Jede R, Fridmann J, Sanabia JE, Gila B, and Appleton BR (2013) Multispecies focused ion beam lithography system and its applications. *Journal of Vacuum Science & Technology, B: Microelectronics Processing and Phenomena* 31: 06F404.

Belić D, Shawrav MM, Bertagnolli E, and Wanzenboeck HD (2017) Direct writing of gold nanostructures with an electron beam: On the way to pure nanostructures by combining optimized deposition with oxygen-plasma treatment. *Beilstein Journal of Nanotechnology* 8: 2530–2543.

Blauner PG (1989) Focused ion beam fabrication of submicron gold structures. *Journal of Vacuum Science & Technology, B: Microelectronics and Nanometer Structures–Processing, Measurement, and Phenomena* 7: 609.

Blom TJ, Mechielsen TW, Fermin R, Hesselberth MBS, Aarts J, and Lahabi K (2021) Direct-write printing of josephson junctions in a scanning electron microscope. *ACS Nano* 15: 322–329.

Bochmann S, Döhler D, Trapp B, Staňo M, Fruchart O, and Bachmann J (2018) Preparation and physical properties of soft magnetic nickel-cobalt three-segmented nanowires. *Journal of Applied Physics* 124: 163907.

Botman A, Hesselberth M, and Mulders JJL (2008) Improving the conductivity of platinum-containing nano-structures created by electron-beam-induced deposition. *Microelectronic Engineering* 85: 1139–1142.

Bours L, Mercaldo MT, Cuoco M, Strambini E, and Giazotto F (2020) Unveiling mechanisms of electric field effects on superconductors by a magnetic field response. *Physical Review Research* 2: 033353.

Broers AN, Molzen WW, Cuomo JJ, and Wittels ND (1976) Electron-beam fabrication of 80-Å metal structures. *Applied Physics Letters* 29: 596–598.

Chirolli L, Cea T, and Giazotto F (2021) Impact of electrostatic fields in layered crystalline BCS superconductors. *Physical Review Research* 3: 023135.

Córdoba Castillo R (2014) *Functional Nanostructures Fabricated by Focused Electron/Ion Beam Induced Deposition*. Springer Theses Springer International Publishing.

Córdoba R, Sesé J, De Teresa JM, and Ibarra MR (2010) High-purity cobalt nanostructures grown by focused-electron-beam-induced deposition at low current. *Microelectronic Engineering* 87: 1550–1553.

Córdoba R, Lavrijsen R, Fernández-Pacheco A, Ibarra MRR, Schoenaker F, Ellis T, Barcones-Campo B, Kohlhepp JTT, Swagten HJMJM, Koopmans B, Mulders JJLJL, and De Teresa JM (2012) Giant anomalous Hall effect in Fe-based microwires grown by focused-electron-beam-induced deposition. *Journal of Physics D: Applied Physics* 45: 035001.

Córdoba R, Baturina TI, Sesé J, Yu Mironov A, De Teresa JM, Ibarra MR, Nasimov DA, Gutakovskii AK, Latyshev AV, Guillamón I, Suderow H, Vieira S, Baklanov MR, Palacios JJ, and Vinokur VM (2013) Magnetic field-induced dissipation-free state in superconducting nanostructures. *Nature Communications* 4: 1437.

Córdoba R, Barcones B, Roelfsema E, Verheijen MAA, Mulders JJLJL, Trompenaars PHFHF, and Koopmans B (2016a) Functional nickel-based deposits synthesized by focused beam induced processing. *Nanotechnology* 27: 065303.

Córdoba R, Han D-S, and Koopmans B (2016b) Manipulating the switching in modulated iron nanowires grown by focused electron beam induced deposition. *Microelectronic Engineering* 153: 60–65.

Córdoba R, Sharma N, Kölling S, Koenraad PMPM, and Koopmans B (2016c) High-purity 3D nano-objects grown by focused-electron-beam induced deposition. *Nanotechnology* 27: 355301.

Córdoba R, Lorenzoni M, Pablo-Navarro J, Magén C, Pérez-Murano F, and De Teresa JM (2017) Suspended tungsten-based nanowires with enhanced mechanical properties grown by focused ion beam induced deposition. *Nanotechnology* 28: 445301.

Córdoba R, Ibarra A, Mailly D, and De Teresa JM (2018) Vertical growth of superconducting crystalline hollow nanowires by he + focused ion beam induced deposition. *Nano Letters* 18: 1379–1386.

Córdoba R, Mailly D, Rezaev RO, Smirnova EI, Schmidt OG, Fomin VM, Zeitler U, Guillamón I, Suderow H, and De Teresa JMJM (2019a) Three-dimensional superconducting nanohelices grown by He + -focused-ion-beam direct writing. *Nano Letters* 19: 8597–8604.

Córdoba R, Orús P, Jelić ŽL, Sesé J, Ibarra MR, Guillamón I, Vieira S, Palacios JJ, Suderow H, Milosević MV, and De Teresa JM (2019b) Long-range vortex transfer in superconducting nanowires. *Scientific Reports* 9: 12386.

Córdoba R, Ibarra A, Mailly D, Guillamón I, Suderow H, and De Teresa JM (2020) 3D superconducting hollow nanowires with tailored diameters grown by focused He + beam direct writing. *Beilstein Journal of Nanotechnology* 11: 1198–1206.

Dai J, Onomitsu K, Kometani R, Krockenberger Y, Yamaguchi H, Ishihara S, and Warisawa S (2013) Superconductivity in tungsten-carbide nanowires deposited from the mixtures of $W(CO)_6$ and $C_{14}H_{10}$. *Japanese Journal of Applied Physics* 52: 075001.

De Simoni G, Paolucci F, Solinas P, Strambini E, and Giazotto F (2018a) Metallic supercurrent field-effect transistor. *Nature Nanotechnology* 13: 802–805.

De Simoni G, Strambini E, Moodera JS, Bergeret FS, and Giazotto F (2018b) Toward the absolute spin-valve effect in superconducting tunnel junctions. *Nano Letters* 18: 6369–6374.

De Simoni G, Puglia C, and Giazotto F (2020) Niobium Dayem nano-bridge Josephson gate-controlled transistors. *Applied Physics Letters* 116: 242601.

De Teresa JMJM and Córdoba R (2014) Arrays of densely packed isolated nanowires by focused beam induced deposition plus Ar + milling. *ACS Nano* 8: 3788–3795.

De Teresa JM, Córdoba R, Fernández-Pacheco A, Montero O, Strichovanec P, and Ibarra MR (2009) Origin of the difference in the resistivity of As-grown focused-ion- and focused-electron-beam-induced Pt nanodeposits. *Journal of Nanomaterials* 2009: 1–11.

De Teresa JM, Holuj P, Córdoba R, Fernández-Pacheco R, and Michalik JM (2014) Fabrication of cobalt trifluoride (CoF3) phase from metallic cobalt by XeF2-assisted focused electron beam induced processing. *Microelectronic Engineering* 125: 78–82.

De Teresa JM, Fernández-Pacheco A, Córdoba R, Serrano-Ramón L, Sangiao S, and Ibarra MR (2016) Review of magnetic nanostructures grown by focused electron beam induced deposition (FEBID). *Journal of Physics D: Applied Physics* 49(24): 243003.

Deinhart V, Kern L-M, Kirchhof JN, Juergensen S, Sturm J, Krauss E, Feichtner T, Kovalchuk S, Schneider M, Engel D, Pfau B, Hecht B, Bolotin KI, Reich S, and Höflich K (2021) The patterning toolbox FIB-o-mat: Exploiting the full potential of focused helium ions for nanofabrication. *Beilstein Journal of Nanotechnology* 12: 304–318.

Della Ratta AD, Melngailis J, and Thompson CV (1993) Focused-ion-beam-induced deposition of copper. *Journal of Vacuum Science and Technology B* 11: 2195–2199.

Dobrovolskiy OV (2017) Abrikosov fluxonics in washboard nanolandscapes. *Physica C: Superconductivity and Its Applications* 533: 80–90.

Dobrovolskiy OV, Huth M, and Shklovskij VA (2015) Alternating current-driven microwave loss modulation in a fluxonic metamaterial. *Applied Physics Letters* 107: 162603.

Dobrovolskiy OV, Bevz VM, Mikhailov MY, Yuzephovich OI, Shklovskij VA, Vovk RV, Tsindlekht MI, Sachser R, and Huth M (2018) Microwave emission from superconducting vortices in Mo/Si superlattices. *Nature Communications* 9: 4927.

Dobrovolskiy OV, Vodolazov DY, Porrati F, Sachser R, Bevz VM, Mikhailov MY, Chumak AV, and Huth M (2020) Ultra-fast vortex motion in a direct-write Nb-C superconductor. *Nature Communications* 11: 3291.

Donnelly C, Hierro-Rodríguez A, Abert C, Witte K, Skoric L, Sanz-Hernández D, Finizio S, Meng F, McVitie S, Raabe J, Suess D, Cowburn R, and Fernández-Pacheco A (2021) Complex free-space magnetic field textures induced by three-dimensional magnetic nanostructures. *Nature Nanotechnology* 17: 136–142.

Esposito M, Tasco V, Todisco F, Benedetti A, Sanvitto D, and Passaseo A (2014) Three dimensional chiral metamaterial nanospirals in the visible range by vertically compensated focused ion beam induced-deposition. *Advanced Optical Materials* 2: 154–161.

Esposito M, Tasco V, Cuscunà M, Todisco F, Benedetti A, Tarantini I, De Giorgi M, Sanvitto D, and Passaseo A (2015) Nanoscale 3D chiral plasmonic helices with circular dichroism at visible frequencies. *ACS Photonics* 2: 105–114.

Fernández-Pacheco A, De Teresa JM, Córdoba R, and Ibarra MR (2009a) Metal-insulator transition in Pt-C nanowires grown by focused-ion-beam- induced deposition. *Physical Review B: Condensed Matter and Materials Physics* 79: 1–12.

Fernández-Pacheco A, De Teresa JMM, Córdoba R, and Ibarra MRR (2009b) Magnetotransport properties of high-quality cobalt nanowires grown by focused-electron-beam-induced deposition. *Journal of Physics D: Applied Physics* 42: 055005.

Fernández-Pacheco A, Serrano-Ramón L, Michalik JM, Ibarra MR, De Teresa JM, O'Brien L, Petit D, Lee J, and Cowburn RP (2013) Three dimensional magnetic nanowires grown by focused electron-beam induced deposition. *Scientific Reports* 3: 1492.

Fomin VM (2018) *Topology-Driven Effects in Advanced Micro- and Nanoarchitectures*. Cham: Springer, 195–220.

Fomin VM (2020) *Self-Rolled Micro- and Nanoarchitectures*. Berlin-Boston: De Gruyter.

Fowlkes JD, Winkler R, Lewis BB, Fernández-Pacheco A, Skoric L, Sanz-Hernández D, Stanford MG, Mutunga E, Rack PD, and Plank H (2018) High-fidelity 3D-nanoprinting via focused electron beams: Computer-aided design (3BID). *ACS Applied Nano Materials* 1: 1028–1041.

Franken JH, Herps M, Swagten HJM, and Koopmans B (2014) Tunable chiral spin texture in magnetic domain-walls. *Scientific Reports* 4: 5.

Fujii T, Iwasaki K, Munekane M, Takeuchi T, Hasuda M, Asahata T, Kiyohara M, Kogure T, Kijima Y, and Kaito T (2005) A nanofactory by focused ion beam. *Journal of Micromechanics and Microengineering* 15: S286–S291.

Gavagnin M, Wanzenboeck HD, Shawrav MM, Belic D, Wachter S, Waid S, Stoeger-Pollach M, and Bertagnolli E (2014) Focused electron beam-induced CVD of iron: A practical guide for direct writing. *Chemical Vapor Deposition* 20: 243–250.

Gazzadi GC, Mulders JJL, Trompenaars P, Ghirri A, Rota A, Affronte M, and Frabboni S (2011) Characterization of a new cobalt precursor for focused beam deposition of magnetic nanostructures. *Microelectronic Engineering* 88: 1955–1958.

Giannuzzi LA and Stevie FA (2005) *Introduction to Focused Ion Beams*. Boston: Springer Science.

Golokolenov I, Guthrie A, Kafanov S, Pashkin YA, and Tsepelin V (2021) On the origin of the controversial electrostatic field effect in superconductors. *Nature Communications* 12: 2747.

Guillamón I, Suderow H, Vieira S, Fernández-Pacheco A, Sesé J, Córdoba R, De Teresa JM, and Ibarra MR (2008) Nanoscale superconducting properties of amorphous W-based deposits grown with a focused-ion-beam. *New Journal of Physics* 10: 93005.

Guillamón I, Suderow H, Fernández-Pacheco A, Sesé J, Córdoba R, De Teresa JM, Ibarra MR, and Vieira S (2009) Direct observation of melting in a two-dimensional superconducting vortex lattice. *Nature Physics* 5: 651–655.

Guillamón I, Suderow H, Vieira S, Sesé J, Córdoba R, De Teresa JM, and Ibarra MR (2011) Direct observation of stress accumulation and relaxation in small bundles of superconducting vortices in tungsten thin films. *Physical Review Letters* 106: 77001.

Guillamón I, Córdoba R, Sesé J, De Teresa JM, Ibarra MR, Vieira S, and Suderow H (2014) Enhancement of long-range correlations in a 2D vortex lattice by an incommensurate 1D disorder potential. *Nature Physics* 10: 851–856.

Harriott LR (1993) Digital scan model for focused ion beam induced gas etching. *Journal of Vacuum Science & Technology, B: Microelectronics and Nanometer Structures–Processing, Measurement, and Phenomena* 11: 2012.

Haverkamp C, Sarau G, Polyakov MN, Utke I, Puydinger dos Santos MV, Christiansen S, and Höflich K (2018) A novel copper precursor for electron beam induced deposition. *Beilstein Journal of Nanotechnology* 9: 1220–1227.

Hentschel M, Karst J, and Giessen H (2020) Tailored optical functionality by combining electron-beam and focused gold-ion beam lithography for solid and inverse coupled plasmonic nanostructures. *Advanced Optical Materials* 8: 2000879.

Hirt L, Reiser A, Spolenak R, and Zambelli T (2017) Additive manufacturing of metal structures at the micrometer scale. *Advanced Materials* 29: 1604211.

Höflich K, Jurczyk J, Zhang Y, Puydinger dos Santos MV, Götz M, Guerra-Nuñez C, Best JP, Kapusta C, and Utke I (2017) Direct electron beam writing of silver-based nanostructures. *ACS Applied Materials & Interfaces* 9: 24071–24077.

Huth M, Klingenberger D, Grimm C, Porrati F, and Sachser R (2009) Conductance regimes of W-based granular metals prepared by electron beam induced deposition. *New Journal of Physics* 11: 033032.

Indrajith S, Rousseau P, Huber BA, Nicolafrancesco C, Domaracka A, Grygoryeva K, Nag P, Sedmidubská B, Fedor J, and Kočišek J (2019) Decomposition of iron pentacarbonyl induced by singly and multiply charged ions and implications for focused ion beam-induced deposition. *Journal of Physical Chemistry C* 123: 10639–10645.

Jonckheere R, Bret T, Van den Heuvel D, Magana J, Gao W, and Waiblinger M (2011) Repair of natural EUV reticle defects. In: Maurer W and Abboud FE (eds.) *Photomask Technology 2011*. Bellingham: Spie-Int Soc Optical Engineering.

Jungwirth F, Porrati F, Schuck AG, Huth M, and Barth S (2021) Direct writing of cobalt silicide nanostructures using single-source precursors. *ACS Applied Materials & Interfaces* 13: 48252–48259.

Jurczyk J, Brewer CR, Hawkins OM, Polyakov MN, Kapusta C, McElwee-White L, and Utke I (2019) Focused electron beam-induced deposition and post-growth purification using the heteroleptic Ru complex $(\eta^3\text{-}C_3H_5)Ru(CO)_3Br$. *ACS Applied Materials & Interfaces* 11: 28164–28171.

Kadin AM and Johnson MW (1996) Nonequilibrium photon-induced hotspot: A new mechanism for photodetection in ultrathin metallic films. *Applied Physics Letters* 69: 3938–3940.

Keller L and Huth M (2018) Pattern generation for direct-write three-dimensional nanoscale structures via focused electron beam induced deposition. *Beilstein Journal of Nanotechnology* 9: 2581–2598.

Koops HWP, Schossler C, Kaya A, Weber M, and Amer Vacuum Soc, I.E.D.S.O.S.A (1996) Conductive dots, wires, and supertips for field electron emitters produced by electron-beam induced deposition on samples having increased temperature. In: *40th International Conference on Electron, Ion, and Photon Beam Technology and Nanofabrication (EIBPN)*, pp. 4105–4109. Atlanta, Ga: Amer Inst Physics.

Lapicki A, Ahmad E, and Suzuki T (2002a) Ion beam induced chemical vapor deposition (IBICVD) of cobalt particles. *Journal of Magnetism and Magnetic Materials* 240: 47–49.

Lapicki A, Suzuki T, Kang K, and Suzuki T (2002b) Fabrication of magnetic dot arrays by ion beam induced chemical vapor deposition (IBICVD). *IEEE Transactions on Magnetics* 38: 2589–2591.

Lavrijsen R, Córdoba R, Schoenaker FJJ, Ellis THH, Barcones B, Kohlhepp JTT, Swagten HJMJM, Koopmans B, De Teresa JMM, Magén C, Ibarra MRR, Trompenaars P, and Mulders JJLJL (2011) Fe:O:C grown by focused-electron-beam-induced deposition: Magnetic and electric properties. *Nanotechnology* 22: 25302.

Lee S-B, Hutchinson GD, Williams DA, Hasko DG, and Ahmed H (2003) Superconducting nanotransistor based digital logic gates. *Nanotechnology* 14: 188–191.

Li W, Fenton JC, Wang Y, McComb DW, and Warburton PA (2008) Tunability of the superconductivity of tungsten films grown by focused-ion-beam direct writing. *Journal of Applied Physics* 104: 093913.

Li W, Fenton JC, and Warburton PA (2009) Focused-ion-beam direct-writing of ultra-thin superconducting tungsten composite films. In: *IEEE Transactions on Applied Superconductivity* 2819–2822.

Li W, Gu C, and Warburton PA (2010) Superconductivity of freestanding tungsten nanofeatures grown by focused-ion-beam. *Journal of Nanoscience and Nanotechnology* 10: 7436–7438.

Li W, Fenton JC, Gu C, and Warburton PA (2011) Superconductivity of ultra-fine tungsten nanowires grown by focused-ion-beam direct-writing. *Microelectronic Engineering* 88: 2636–2638.

Li W, Fenton JC, Cui A, Wang H, Wang Y, Gu C, McComb DW, and Warburton PA (2012) Felling of individual freestanding nanoobjects using focused-ion-beam milling for investigations of structural and transport properties. *Nanotechnology* 23: 105301.

Luxmoore IJ, Ross IM, Cullis AG, Fry PW, Orr J, Buckle PD, and Jefferson JH (2007) Low temperature electrical characterisation of tungsten nano-wires fabricated by electron and ion beam induced chemical vapour deposition. *Thin Solid Films* 515: 6791–6797.

Maas D, van Veldhoven E, Chen P, Sidorkin V, Salemink H, van der Drift E, and Alkemade P (2010) Nanofabrication with a helium ion microscope. In: Raymond CJ (ed.) *Metrology, Inspection, and Process Control for Microlithography Xxiv*, p. 763814. SPIE.

Makarov D, Volkov OM, Kákay A, Pylypovskyi OV, Budinská B, and Dobrovolskiy OV (2022) New dimension in magnetism and superconductivity: 3D and curvilinear nanoarchitectures. *Advanced Materials* 34: 2101758.

Makise K, Mitsuishi K, Shimojo M, and Shinozaki B (2014) Microstructural analysis and transport properties of MoO and MoC nanostructures prepared by focused electron beam-induced deposition. *Scientific Reports* 4: 5740.

Martínez-Pérez MJ, Sesé J, Córdoba R, Luis F, Drung D, Schurig T, and Schuring T (2009) Circuit edit of superconducting microcircuits. *Superconductor Science and Technology* 22: 125020.

Matsui S, Kaito T, Fujita J, Komuro M, Kanda K, and Haruyama Y (2000) Three-dimensional nanostructure fabrication by focused-ion-beam chemical vapor deposition. In: *Papers from the 44th International Conference on Electron, Ion, and Photon Beam Technology and Nanofabrication. AVS, Rancho Mirage, California, (USA)*, 3181–3184.

Meng F, Donnelly C, Abert C, Skoric L, Holmes S, Xiao Z, Liao J-W, Newton PJ, Barnes CHW, Sanz-Hernández D, Hierro-Rodriguez A, Suess D, Cowburn RP, and Fernández-Pacheco A (2021) Non-planar geometrical effects on the magnetoelectrical signal in a three-dimensional nanomagnetic circuit. *ACS Nano* 15(4): 6765–6773.

Mercaldo MT, Solinas P, Giazotto F, and Cuoco M (2020) Electrically tunable superconductivity through surface orbital polarization. *Physical Review Applied* 14: 034041.

Morita T, Kometani R, Watanabe K, Kanda K, Haruyama Y, Hoshino T, Kondo K, Kaito T, Ichihashi T, Fujita J, Ishida M, Ochiai Y, Tajima T, and Matsui S (2003) Free-space-wiring fabrication in nano-space by focused-ion-beam chemical vapor deposition. *Journal of Vacuum Science & Technology, B: Microelectronics and Nanometer Structures–Processing, Measurement, and Phenomena* 21: 2737.

Nakai Y, Kang Y, Okada M, Haruyama Y, Kanda K, Ichihashi T, and Matsui S (2010) Mechanical characteristics of nanosprings fabricated by focused-ion-beam chemical vapor deposition using ferrocene source gas. *Japanese Journal of Applied Physics* 49: 06GH07.

Orloff JH and Swanson LW (1975) Study of a field-ionization source for microprobe applications. *Journal of Vacuum Science and Technology* 12: 1209–1213.

Orloff J and Swanson LW (1978) Fine-focus ion beams with field ionization. *Journal of Vacuum Science and Technology* 15: 845–848.

Orús P, Córdoba R, and De Teresa JM (2020) Focused ion beam induced processing. In: *Nanofabrication*, pp. 5-1–5-58. IOP Publishing.

Orús P, Córdoba R, Hlawacek G, and De Teresa JM (2021a) Superconducting properties of in-plane W-C nanowires grown by He + focused ion beam induced deposition. *Nanotechnology* 32: 085301.

Orús P, Fomin VM, De Teresa JM, and Córdoba R (2021b) Critical current modulation induced by an electric field in superconducting tungsten-carbon nanowires. *Scientific Reports* 11: 17698.

Paolucci F, De Simoni G, Strambini E, Solinas P, and Giazotto F (2018) Ultra-efficient superconducting dayem bridge field-effect transistor. *Nano Letters* 18: 4195–4199.

Paolucci F, Vischi F, De Simoni G, Guarcello C, Solinas P, and Giazotto F (2019) Field-effect controllable metallic josephson interferometer. *Nano Letters* 19: 6263–6269.

Porrati F, Begun E, Winhold M, Schwalb CH, Sachser R, Frangakis AS, and Huth M (2012) Room temperature L1 0 phase transformation in binary CoPt nanostructures prepared by focused-electron-beam-induced deposition. *Nanotechnology* 23: 185702.

Porrati F, Kämpken B, Terfort A, and Huth M (2013) Fabrication and electrical transport properties of binary Co-Si nanostructures prepared by focused electron beam-induced deposition. *Journal of Applied Physics* 113: 53707.

Porrati F, Pohlit M, Müller J, Barth S, Biegger F, Gspan C, Plank H, and Huth M (2015) Direct writing of CoFe alloy nanostructures by focused electron beam induced deposition from a heteronuclear precursor. *Nanotechnology* 26: 475701.

Porrati F, Sachser R, Gazzadi GC, Frabboni S, Terfort A, and Huth M (2017) Alloy multilayers and ternary nanostructures by direct-write approach. *Nanotechnology* 28: 415302.

Porrati F, Barth S, Sachser R, Dobrovolskiy OV, Seybert A, Frangakis AS, and Huth M (2019) Crystalline niobium carbide superconducting nanowires prepared by focused ion beam direct writing. *ACS Nano* 13: 6287–6296.

Puglia C, De Simoni G, and Giazotto F (2020) Electrostatic control of phase slips in Ti josephson nanotransistors. *Physical Review Applied* 13: 054026.

Puglia C, De Simoni G, and Giazotto F (2021) Gate control of superconductivity in mesoscopic all-metallic devices. *Materials (Basel)* 14: 1243.

Puglia C, De Simoni G, and Giazotto F (2022) Phase slips dynamics in gated Ti and V all-metallic supercurrent nano-transistors. *Journal of Physics D: Applied Physics* 55: 055301.

Reyntjens S and Puers R (2001) A review of focused ion beam applications in microsystem technology. *Journal of Micromechanics and Microengineering* 11: 287–300.

Rezaev RO, Smirnova EI, Schmidt OG, and Fomin VM (2020) Topological transitions in superconductor nanomembranes under a strong transport current. *Communications on Physics* 3: 144.

Ritter MF, Fuhrer A, Haxell DZ, Hart S, Gumann P, Riel H, and Nichele F (2021) A superconducting switch actuated by injection of high-energy electrons. *Nature Communications* 12: 1266.

Ritter MF, Crescini N, Haxell DZ, Hinderling M, Riel H, Bruder C, Fuhrer A, and Nichele F (2022) Out-of-equilibrium phonons in gated superconducting switches. *Nature Electronics* 5: 71–77.

Rocci M, De Simoni G, Puglia C, Esposti DD, Strambini E, Zannier V, Sorba L, and Giazotto F (2020) Gate-controlled suspended titanium nanobridge supercurrent transistor. *ACS Nano* 14: 12621–12628.

Rocci M, Suri D, Kamra A, Gilvânia Vilela G, Takamura Y, Nemes NM, Martinez JL, Hernandez MG, and Moodera JS (2021) Large enhancement of critical current in superconducting devices by gate voltage. *Nano Letters* 21: 216–221.

Romans EJ, Osley EJ, Young L, Warburton PA, and Li W (2010) Three-dimensional nanoscale superconducting quantum interference device pickup loops. *Applied Physics Letters* 97: 222506.

Sadki ES, Ooi S, and Hirata K (2004) Focused-ion-beam-induced deposition of superconducting nanowires. *Applied Physics Letters* 85: 6206–6208.

Sanz-Hernández D, Hierro-Rodriguez A, Donnelly C, Pablo-Navarro J, Sorrentino A, Pereiro E, Magén C, McVitie S, de Teresa JM, Ferrer S, Fischer P, and Fernández-Pacheco A (2020) Artificial double-helix for geometrical control of magnetic chirality. *ACS Nano* 14(7): 8084–8092.

Scipioni L, Stern LA, Notte J, Sijbrandij S, and Griffin B (2008) Helium ion microscope. *Advanced Materials and Processes* 166: 27.

Seliger RL and Fleming WP (1974) Focused ion beams in microfabrication. *Journal of Applied Physics* 45: 1416–1422.

Seliger RL, Ward JW, Wang V, and Kubena RL (1979) A high-intensity scanning ion probe with submicrometer spot size. *Applied Physics Letters* 34: 310–312.

Sengupta S, Li C, Baumier C, Kasumov A, Guéron S, Bouchiat H, and Fortuna F (2015) Superconducting nanowires by electron-beam-induced deposition. *Applied Physics Letters* 106: 042601.

Seniutinas G, Balčytis A, Reklaitis I, Chen F, Davis J, David C, and Juodkazis S (2017) Tipping solutions: Emerging 3D nano-fabrication/ -imaging technologies. *Nanophotonics* 6: 385307.

Serrano-Ramón L, Córdoba R, Rodríguez LALA, Magén C, Snoeck E, Gatel C, Serrano I, Ibarra MRMR, and De Teresa JMJM (2011) Ultrasmall functional ferromagnetic nanostructures grown by focused electron-beam-induced deposition. *ACS Nano* 5: 7781–7787.

Shedd GM, Lezec H, Dubner AD, and Melngailis J (1986) Focused ion beam induced deposition of gold. *Applied Physics Letters* 49: 1584–1586.

Shorubalko I, Pillatsch L, and Utke I (2016) *Direct–Write Milling and Deposition with Noble Gases*. Cham: Springer355–393.

Sidorkin V, van Veldhoven E, van der Drift E, Alkemade P, Salemink H, and Maas D (2009) Sub-10-nm nanolithography with a scanning helium beam. *Journal of Vacuum Science & Technology, B: Microelectronics and Nanometer Structures–Processing, Measurement, and Phenomena* 27: L18.

Skoric L, Sanz-Hernández D, Meng F, Donnelly C, Merino-Aceituno S, and Fernández-Pacheco A (2020) Layer-by-layer growth of complex-shaped three-dimensional nanostructures with focused electron beams. *Nano Letters* 20: 184–191.

Smith NS, Notte JA, and Steele AV (2014) Advances in source technology for focused ion beam instruments. *MRS Bulletin* 39: 329–335.

Solinas P, Amoretti A, and Giazotto F (2021) Sauter-Schwinger effect in a Bardeen-Cooper-Schrieffer superconductor. *Physical Review Letters* 126: 117001.

Spoddig D, Schindler K, Roediger P, Barzola-Quiquia J, Fritsch K, Mulders H, and Esquinazi P (2007) Transport properties and growth parameters of PdC and WC nanowires prepared in a dual-beam microscope. *Nanotechnology* 18: 495202.

Sun Y, Wang J, Zhao W, Tian M, Singh M, and Chan MHW (2013) Voltage-current properties of superconducting amorphous tungsten nanostrips. *Scientific Reports* 3: 1–7.

Swiderek P, Marbach H, and Hagen CW (2018) Chemistry for electron-induced nanofabrication. *Beilstein Journal of Nanotechnology* 9: 1317–1320.

Tao T (1990) Focused ion beam induced deposition of platinum. *Journal of Vacuum Science & Technology, B: Microelectronics and Nanometer Structures–Processing, Measurement, and Phenomena* 8: 1826.

Tao T, Ro J, Melngailis J, Xue Z, and Kaesz HD (1990) Focused ion beam induced deposition of platinum. *Journal of Vacuum Science & Technology, B: Microelectronics Processing and Phenomena* 8: 1826–1829.

Utke I, Hoffmann P, and Melngailis J (2008) Gas-assisted focused electron beam and ion beam processing and fabrication. *Journal of Vacuum Science & Technology, B: Microelectronics and Nanometer Structures–Processing, Measurement, and Phenomena* 26: 1197.

Utke I, Moshkalev S, and Russell P (2012) *Nanofabrication Using Focused Ion and Electron Beams, Oxford Series on Nanomanufacturing*. Oxford University Press.

van Dorp WF and Hagen CW (2008) A critical literature review of focused electron beam induced deposition. *Journal of Applied Physics* 104: 81301.

van Kouwen L, Botman A, and Hagen CW (2009) Focused electron-beam-induced deposition of 3 nm dots in a scanning electron microscope. *Nano Letters* 9: 2149–2152.

Virtanen P, Braggio A, and Giazotto F (2019) Superconducting size effect in thin films under electric field: Mean-field self-consistent model. *Physical Review B* 100: 224506.

Wang M, Salut R, Suarez MA, Martin N, and Grosjean T (2019) Chiroptical transmission through a plasmonic helical traveling-wave nanoantenna, towards on-tip chiroptical probes. *Optics Letters* 44: 4861.

Weirich PM, Schwalb CH, Winhold M, and Huth M (2014) Superconductivity in the system MoxCyGazOδ prepared by focused ion beam induced deposition. *Journal of Applied Physics* 115: 174315.

Winhold M, Schwalb CH, Porrati F, Sachser R, Frangakis AS, Kämpken B, Terfort A, Auner N, and Huth M (2011) Binary Pt–Si nanostructures prepared by focused electron-beam-induced deposition. *ACS Nano* 5: 9675–9681.

Winhold M, Weirich PM, Schwalb CH, and Huth M (2014) Superconductivity and metallic behavior in PbxCyOδ structures prepared by focused electron beam induced deposition. *Applied Physics Letters* 105: 162603.

Wolf D, Rodriguez LA, Béché A, Javon E, Serrano L, Magen C, Gatel C, Lubk A, Lichte H, Bals S, Van Tendeloo G, Fernández-Pacheco A, De Teresa JM, and Snoeck E (2015) 3D magnetic induction maps of nanoscale materials revealed by electron holographic tomography. *Chemistry of Materials* 27: 6771–6778.

Wördenweber R (2017) *Superconductors at the Nanoscale*. De Gruyter.

Wu HM, Stern LA, Chen JH, Huth M, Schwalb CH, Winhold M, Porrati F, Gonzalez CM, Timilsina R, and Rack PD (2013) Synthesis of nanowires via helium and neon focused ion beam induced deposition with the gas field ion microscope. *Nanotechnology* 24(17): 175302.

Wu H, Stern LA, Xia D, Ferranti D, Thompson B, Klein KL, Gonzalez CM, and Rack PD (2014) Focused helium ion beam deposited low resistivity cobalt metal lines with 10 nm resolution: Implications for advanced circuit editing. *Journal of Materials Science: Materials in Electronics* 25: 587–595.

Microstucture and macrostructure[☆]

Gregory S Rohrer, Department of Materials Science and Engineering, Carnegie Mellon University, Pittsburgh, PA, United States

© 2024 Elsevier Ltd. All rights reserved.

This is an update of G.S. Rohrer, Micro- and Macrostructures, Editor(s): Franco Bassani, Gerald L. Liedl, Peter Wyder, Encyclopedia of Condensed Matter Physics, Elsevier, 2005, Pages 403–415, ISBN 9780123694010, https://doi.org/10.1016/B0-12-369401-9/00694-X.

Introduction **465**
Single phase microstructures **466**
Single phase microstructures by sintering 466
Single phase microstructures by crystallization 470
Grain boundaries in single phase microstructures 472
Duplex microstructures **474**
Duplex microstructures formed by consolidation 474
Duplex microstructures by solidification 475
Duplex microstructures by transformation in the solid phase 478
Conclusion **480**
References **480**

Abstract

Inhomogeneities in the orientation, composition, and configuration of the atomic structure of a solid collectively make up what is referred to as the internal structure or microstructure. The term macrostructure is sometimes used to refer to the largest components of the internal structure. In this article, the microstructures of inorganic materials are surveyed, identifying important components of each type of microstructure. Throughout, attention is given to the mechanisms by which microstructures form during materials processing.

Key points

- Microstructures are defined by the shapes, sizes, and orientations of the individual crystals contained within the macrostructure, as well as the configuration of grain boundaries and interfaces that connect them.
- The microstructure is inherited from the materials processing conditions and very different microstructures are formed by sintering, solidification, vapor deposition, recrystallization, and phase transformation.
- The energies of the grain boundaries and interfaces within the microstructure provide the driving force for microstructure evolution during thermal processing.

Introduction

A crystalline solid is made up of indistinguishable groups of atoms positioned at the sites of a Bravais lattice. If the atomic structure is approximately uniform in both orientation and composition throughout the solid, the material is referred to as a single crystal. When the atomic structure is not uniform, it is known as a polycrystal. In this second and more common instance, the irregularities in the orientation, composition, and configuration of the atomic structure collectively make up what is referred to as the internal structure or microstructure. The term macrostructure is sometimes used to refer to the largest components of the internal structure. Within this article, all components of the internal structure will be referred to as the microstructure.

Polycrystals can be thought of as aggregates of much smaller crystals joined together by a network of internal interfaces, as illustrated schematically in Fig. 1. Within the aggregate, the individual crystals are referred to as grains. The interface that separates two grains of the same composition, but different lattice orientation, is called a grain boundary and the interface that separates two grains with different compositions is called a phase boundary. The granular nature of polycrystalline matter has been recognized since at least 1775 when Grignon sketched grains observed on the surface of a piece of fractured wrought iron. This first recorded observation points to an important feature of the interfaces within the microstructure: they are frequently points of internal weakness along which failure, by fracture or corrosion, propagates through the interfacial network. During the last century, microstructural studies have flourished amid the realization that many of the macroscopic properties of polycrystalline solids are

---

[☆] *Change History:* March 2023. All changes made by Gregory S. Rohrer. Figures 16, 17, and 28 were updated. Sections Grain boundaries in single phase microstructures and Duplex microstructures by transformation in the solid phase were updated.

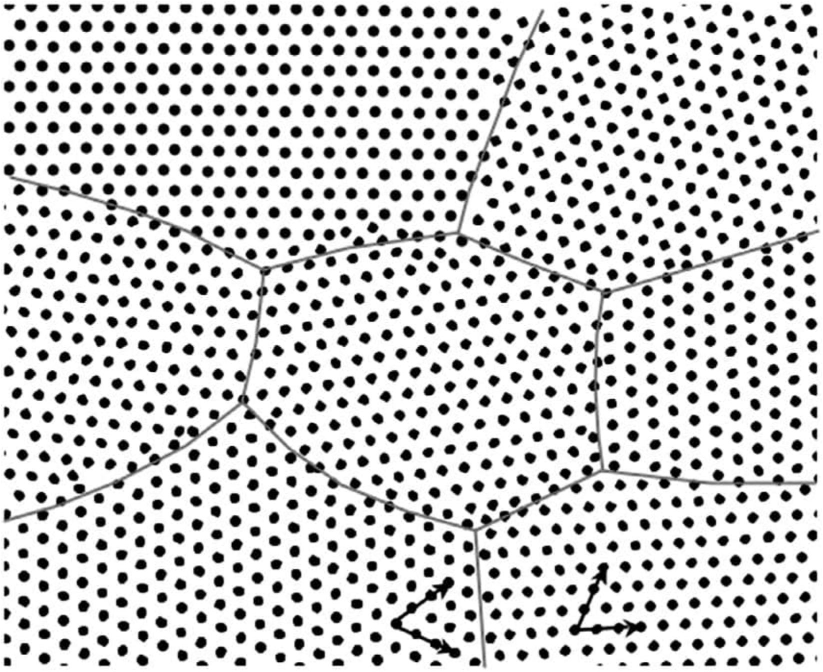

Fig. 1 Schematic illustration of a polycrystalline solid, with black dots representing points on the lattice and gray lines denoting boundaries between grains with different orientations.

strongly influenced by the internal structure. While these studies established the solid foundation of knowledge that will be reviewed in this article, it should also be recognized that there are many unresolved questions about microstructural genesis and the microstructure-property link that continue to be actively researched. In general terms, one can say that polycrystalline microstructures result from crystal nucleation, growth, and capillarity driven morphological changes that lead to a reduction in the interfacial energy. In this article, the basic principles behind these processes will be described and examples of prototypical microstructures will be presented. The article will focus on dense, inorganic, polycrystalline microstructures that occur in man-made materials. Single phase microstructures are discussed first and multiphased structures are described in the second section.

Single phase microstructures

The term single phase polycrystal is used to describe an aggregate of crystals that is uniform in its atomic structure and composition. Throughout a single-phase microstructure, it is only the orientation of the Bravias lattice within the individual grains that differs. The defining elements of the microstructure are the distribution of crystal sizes, the distribution of crystal shapes, the distribution of crystal orientations, and the types of grain boundaries between the crystals. Single phase microstructures can be formed by sintering a solid powder, by crystallizing a precursing liquid, gaseous, or amorphous phase, or by recrystallizing a deformed precursor. Microstructures resulting from each of these states are described briefly below.

Single phase microstructures by sintering

The excess free energy per unit area of a grain boundary (γ) can be thought of as the energy to create equal areas of the two free surfaces on either side of the boundary, minus a binding energy associated with the formation of bonds across the interface as the surfaces are joined. Therefore, if there is bonding across the interface, it is energetically preferable to replace two free surfaces with a grain boundary of the same area. This is the driving force for the process of sintering, in which individual crystalline particles change shape and bond with one another to form a dense polycrystal. Further heating after complete densification leads to grain growth, an increase in the average grain size. This too is a capillarity driven process, because as the average grain size increases, the total grain boundary area (and its associated energy) decreases. If the grain boundary energy and mobility are not too anisotropic, then an equiaxed microstructure develops. In other words, each grain has approximately the same dimensions in all directions. An equiaxed microstructure is illustrated in Fig. 2.

The shapes of the grains are determined in part by the relative rates at which the crystal grows in different directions (a kinetic effect), and in part by the requirement that the interfacial forces balance at their points of intersection (an equilibrium effect). The equilibrium equation for the point where three interfaces meet is known as the Herring condition (Herring, 1953):

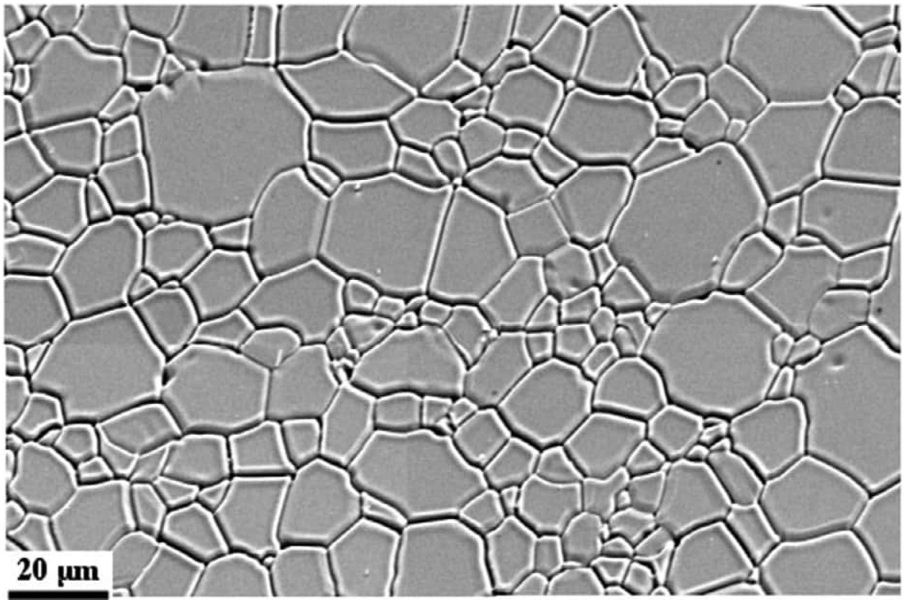

Fig. 2 Montage of scanning electron microscope (SEM) images of spinel, $MgAl_2O_4$. The contrast at the grain boundaries results from thermal grooving.

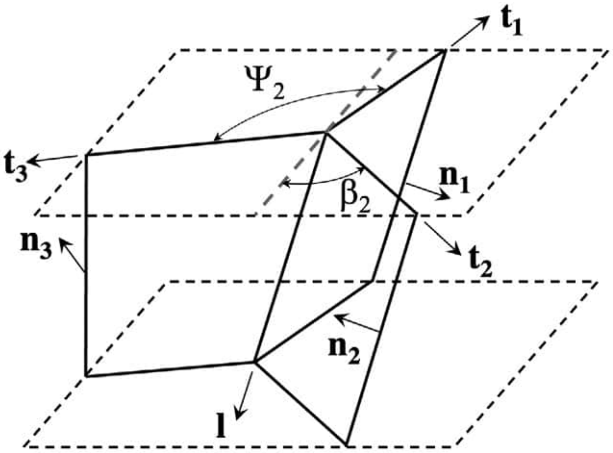

Fig. 3 Schematic of the triple line (**l**) along which three interfaces meet, defining the terms in the Herring equation.

$$\sum_{i=1\ to\ 3} \gamma_i \hat{t}_i + \frac{\partial \gamma_i}{\partial \beta_i} \hat{n}_i = 0$$

The terms in this expression are described in Fig. 3. Under the condition that the energy does not depend on orientation, this reduces to the more familiar Young equation,

$$\frac{\gamma_1}{\sin \Psi_1} = \frac{\gamma_2}{\sin \Psi_2} = \frac{\gamma_3}{\sin \Psi_3}$$

where the Ψ_i are the dihedral angles in Fig. 3. If the energies of all the interfaces are assumed to be equal, then the dihedral angles are 120°. If this is the case, then dihedral angles at quadrajunctions where four triple lines intersect must be 109.5°. To meet these conditions and fill space, some curvature must be introduced in the boundaries and this creates a driving force for motion. If the grain boundary energies are isotropic, boundaries move toward their center of curvature to reduce their total area. The situation was considered in two-dimensions by von Neumann and Mullins (Mullins, 1956), who showed that if equilibrium dihedral angles are to be maintained in an isotropic structure, then grains with more than six sides will always grow and grains with fewer than six sides will shrink (see Fig. 4). While the problem is not easily solved in three dimensions, it is currently thought that grains with 13 or fewer faces shrink while those with 14 or more grow. Recent three-dimensional studies suggest that the number of grain sides does not provide a reliable prediction of whether a grain will grow or shrink (Bhattacharya et al., 2019). In a variety of studies, the average number of faces per grain has been measured to be between 12 and 14. A sketch of a typical grain is shown in Fig. 5.

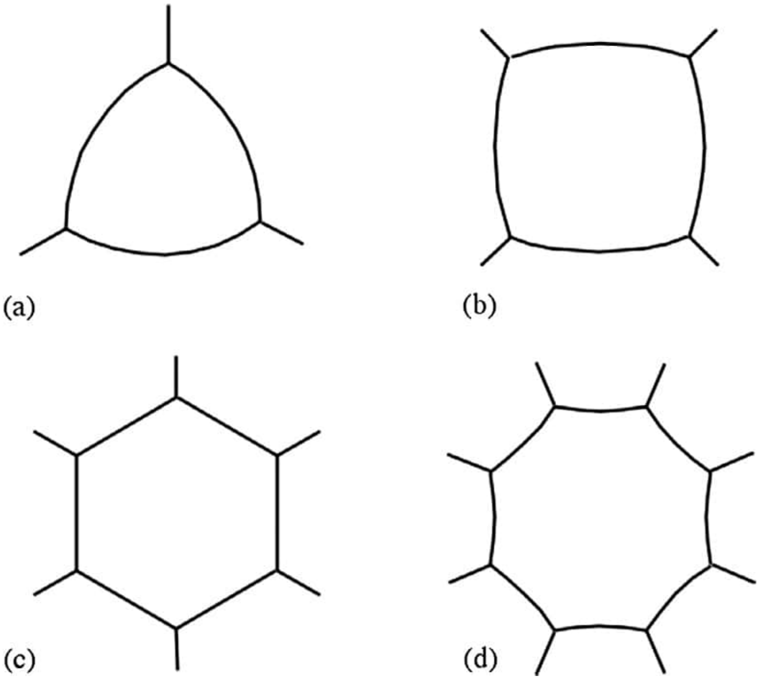

Fig. 4 Schematic showing the configurations of boundaries in a two dimensional system under the assumption that the grain boundary energy is isotropic. In this case, the boundaries must always meet with 120° dihedral angles. This means that if a grain has fewer than six sides, the boundaries are convex and will move inward (a and b), if it has exactly six sides there is no curvature and the boundaries are stationary (c) and if it has more than six sides (d) the boundaries are concave and move outward.

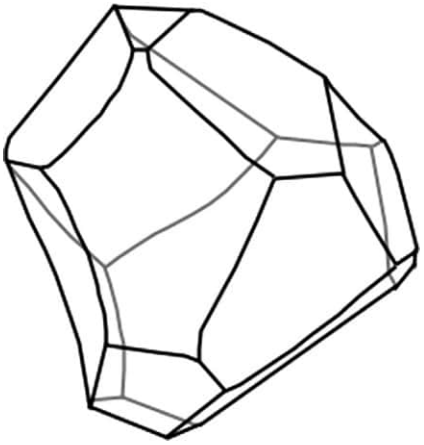

Fig. 5 A schematic showing the three dimensional shape of a grain within a polycrystal. The black lines are edges on the front of the grain and the gray lines are edges on the back of the grain.

Kinetic grain growth theories generally predict that the average grain size increases with the square root of time (t) so that the average radius, <r>, is:

$$\langle r \rangle = (Kt)^n$$

Where K is a positive constant and n, the grain growth exponent, is ideally equal to 1/2. Furthermore, after the effects of the initial grain size distribution have disappeared, there is a steady state distribution of grain sizes that is scale invariant. The form of the distribution, originally derived by Hillert (Hillert, 1965), has a maximum grain size that is about 3/2 times the average size:

$$P_H(\rho) = (2e)^3 \frac{3\rho}{(2-\rho)^5} exp\left[-6/(2-\rho)\right]$$

In this equation, $\rho = r/r^*$, where r^* is the critical radius; grains smaller than r^* shrink while grains larger than r^* grow. The distribution is plotted in Fig. 6. In practice, observed grain growth exponents are usually less than 1/2, the maximum grain size

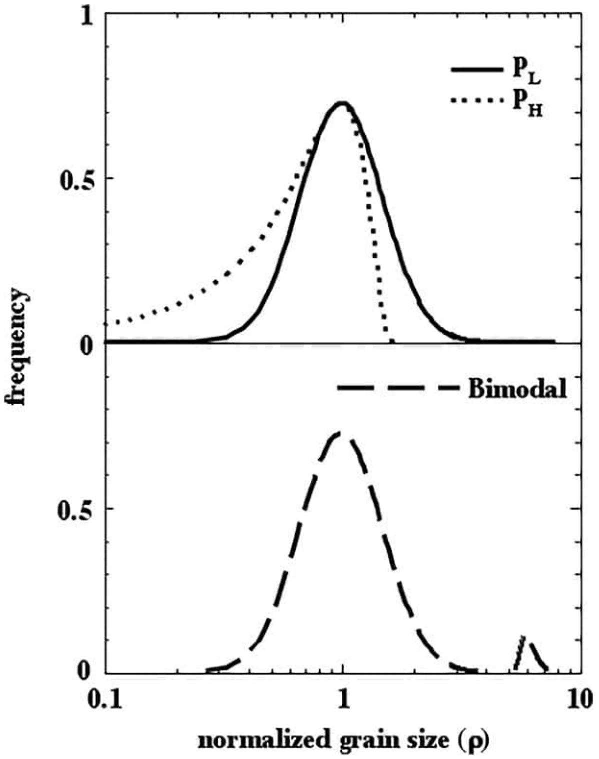

Fig. 6 Grain size distributions. The most commonly observed distribution of grain sizes is lognormal (P_L) while the theory of capillary driven grain growth predicts a different distribution (P_H). A schematic of a bimodal distribution is shown in the lower part of the figure.

greatly exceeds 3/2 times the average, and the distribution of grain sizes is most frequently reported to be lognormal, where the number of grains with dimensionless size ρ is:

$$P_L(\rho) = \frac{1}{\sqrt{2\pi\sigma}} \frac{1}{\rho r^*} exp\left[-(\ln \rho)^2/2\sigma^2\right]$$

In this expression, σ is the width of the distribution. Microstructures that exhibit unimodal and roughly lognormal distributions of grain sizes are usually called normal. However, in some cases the distribution of grain sizes is bimodal (see Fig. 6 for comparison to normal distributions) and such distributions are said to be the result of abnormal growth. An example of a microstructure with an abnormal distribution of grain sizes is illustrated in Fig. 7.

When the anisotropy in the grain boundary energy and mobility is large, the grains adopt distinct shapes and are frequently bounded by flat interfaces, indicating that the orientation corresponds to a cusp or singularity in the function that describes the

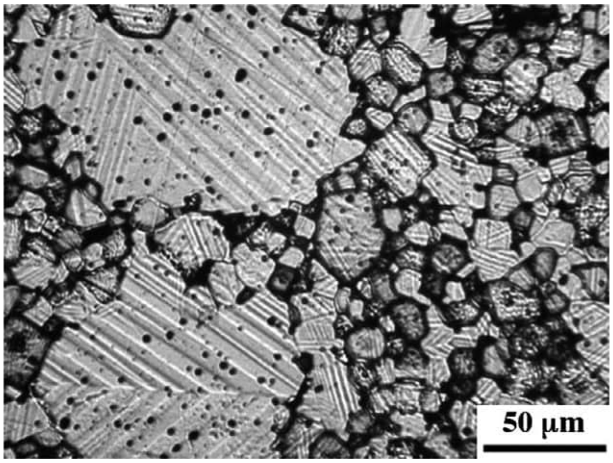

Fig. 7 Visible light micrograph showing the microstructure of a polycrystalline $BaTiO_3$ specimen. Parts of two grains on the left are much larger than the cluster of average grains on the right. The regular patterns within each grain are twin plates that formed by a martinsitic transformation during cooling.

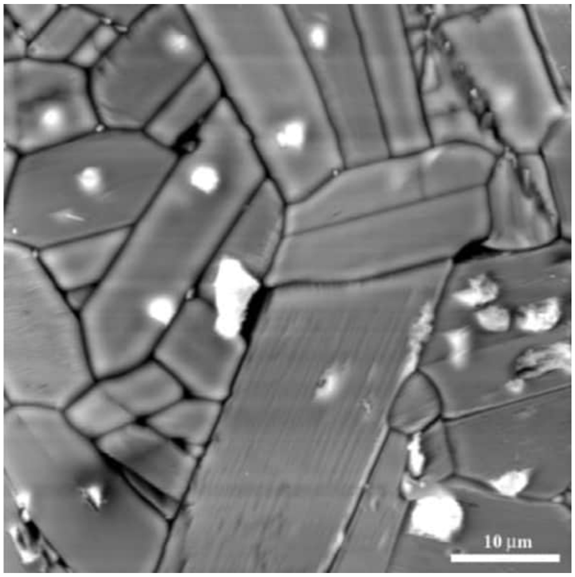

Fig. 8 Atomic force microscope image of polycrystalline $Sr_2Nb_2O_7$. The orthorhombic material has platy grains elongated along the **a** and **c** axes.

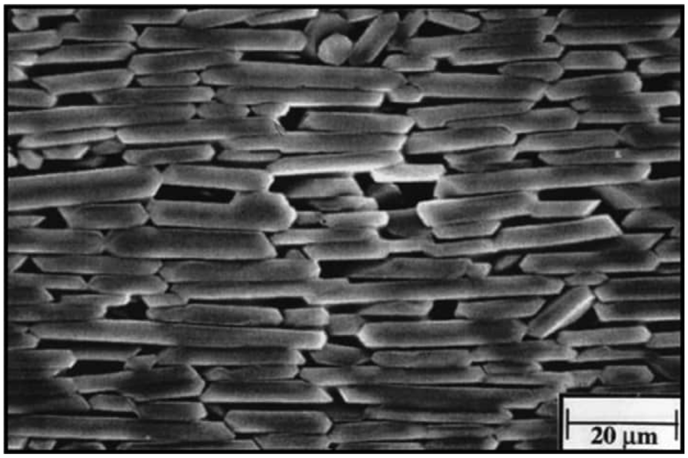

Fig. 9 SEM micrograph of a tabular alumina microstructure formed by templated grain growth. The short dimension of the crystal is oriented along the [0001] axis. Micrograph courtesy of Gary L. Messing and Matthew M. Seabaugh, Department of Materials Science and Engineering, Pennsylvania State University.

orientation dependence of the grain boundary energy. For example, the microstructure in Fig. 8 shows a section through randomly oriented plate-like grains. Depending on the processing, the shapes may also exhibit preferred orientation or texture, as illustrated in Fig. 9. In this case, the [0001] axes of the rhombohedral lattice of Al_2O_3 are oriented in the vertical direction. The general phenomena of nonrandom distributions of crystal orientations with respect to the external reference frame, as illustrated in Fig. 9, is referred to as texture.

Single phase microstructures by crystallization

When a microstructure forms by crystallization from a liquid, gas, or amorphous matrix, crystal nucleation requires the formation of an interface between the crystalline and noncrystalline phase. Assuming the interface energy (γ_s) is isotropic and that the change in free energy per volume upon crystallization is ΔG_v, then the free energy change for the formation of a nucleus with radius r is given by

$$\Delta G(r) = 4\pi r^2 \gamma_s - \frac{4}{3}\pi r^3 \Delta G_V$$

As illustrated in Fig. 10, the change in the free energy as a function r is initially positive. Only after a critical size is reached will further growth stabilize the crystal. Thus, there is an energy barrier, ΔG^*, that inhibits homogeneous nucleation. If a heterogeneous surface is present (for example, the mold walls of a casting system or a substrate in a vapor deposition system), and there almost always is,

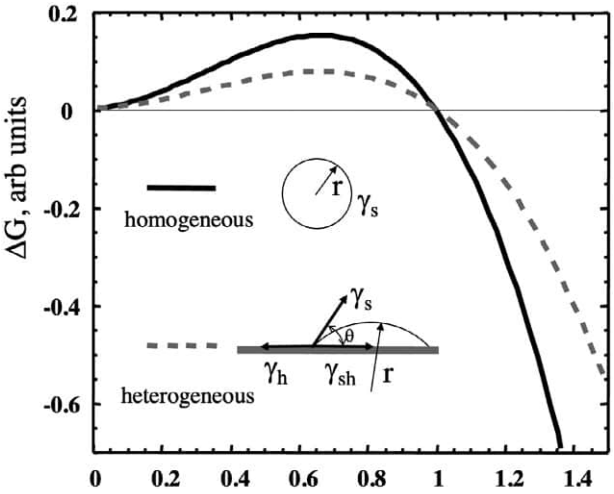

Fig. 10 Plot of the free energy change as a function of nucleus radius. The change is initially positive. Additional growth reduces the energy only beyond a critical size. For heterogeneous nucleation, the barrier is lower.

then we must consider not only the creation of the surface dividing the nucleus from the surrounding liquid or gas, but also the elimination of the heterogeneous surface and the creation of the interface between the nucleus and the heterogeneous surface. Using the Young equation, the relationship between the various interface energies can be expressed as a contact angle, θ, in the following way:

$$cos\theta = \frac{(\gamma_h - \gamma_{sh})}{\gamma_s}$$

The terms in the equation above are defined in the Fig. 10, assuming the crystallization of a spherical cap on the heterogeneous surface. With this parameter, the free energy change for heterogeneous nucleation can be written in a form similar to that for homogeneous nucleation:

$$\Delta G(r) = \left[4\pi r^2 \gamma_s - \frac{4}{3}\pi r^3 \Delta G_V\right] S(\theta)$$

Where the shape factor is $S(\theta) = (2 + \cos\theta)(1-\cos\theta)^2/4$. Because this term is always less than unity, the free energy change for heterogenous nucleation is always less than that for homogeneous nucleation. Thus, crystal formation always initiates from a heterogeneity and most frequently from the walls of the container or a deliberately introduced substrate. This leads to so-called columnar microstructures, such as those illustrated in Figs. 11 and 12. The microstructure in Fig. 11 results from nucleation and growth from the walls of a mold in a casting and the microstructure in 12 results from the deposition of a vapor on a substrate. It should be recognized that heterogeneous nucleation can be initiated in a more or less uniform manner by introducing a finely dispersed heterogeneity and this can lead to a equiaxed microstructure. Uniform heterogeneous nucleation can also occur when a material is recrystallized from a deformed matrix.

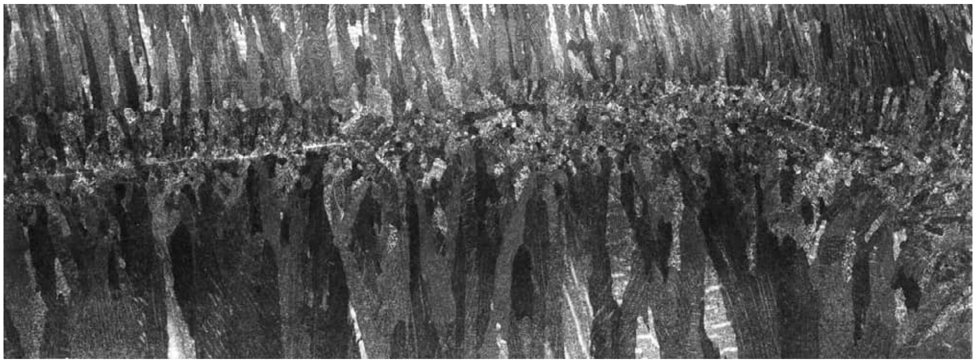

Fig. 11 Section through a cylindrical casting. The elongated grains nucleated on the mold walls (top and bottom of the micrograph) and grew toward the center. Micrograph courtesy of H.P. Paxton, Department of Materials Science and Engineering, Carnegie Mellon University.

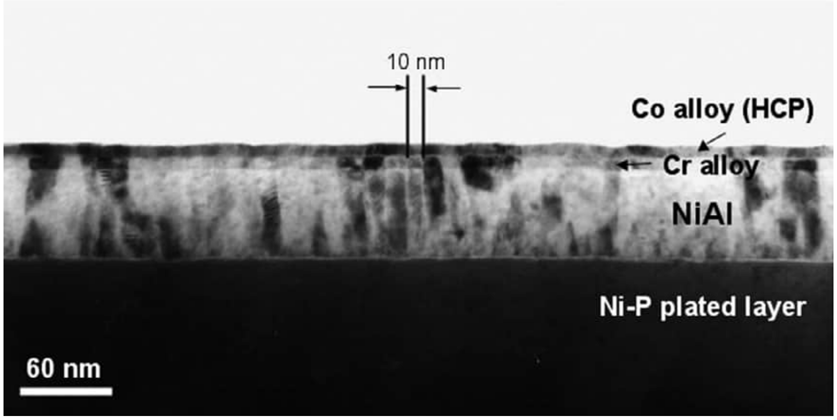

Fig. 12 Columnar thin film multilayer microstructure. The NiAl grains nucleated on the Ni-P layer and the columnar structure is maintained through the Co and Cr layers. Micrograph courtesy of David E. Laughlin, Department of Materials Science and Engineering, Carnegie Mellon University.

Grain boundaries in single phase microstructures

The complexity of the grain boundary networks within polycrystals arises from the number of crystallographic degrees of freedom. Three parameters are required to describe the lattice misorientation between two crystals and two additional parameters are required to describe the orientation of the grain boundary plane. The number of distinguishable boundary types in this five-dimensional parameter space is large. For example, in a cubic material, if the five parameters are measured with 5° of resolution, then there are 5×10^4 distinguishable types of grain boundaries (Rohrer et al., 2004). In general, the distribution of grain boundary surface area is not uniform over the five parameters. Textures have been measured both in the space of lattice misorientations and grain boundary orientations. For example, Fig. 13 shows the distribution of lattice misorientations in WC, showing that boundaries with a 30° misorientation about [0001] and a 90° misorientation about occur with a higher and random frequency. These data are plotted without regard for the particular boundary plane. In Fig. 14, the distribution of grain boundary plane area is shown for the two highly populated misorientations identified in Fig. 13. These data demonstrate that hexagonal WC has a preference for grain boundary planes terminated on $\{0001\}$ and $\{10\bar{1}0\}$ surfaces (Kim et al., 2008).

The origin of texture in the space of grain boundary types depends on the origin of the microstructure. In the case that the microstructure results from normal grain growth, grain boundary texture results from the anisotropy of the grain boundary energy. It has been reported that in many materials, low energy grain boundaries are observed more frequently than higher energy grain boundaries. Three-dimensional microstructure data (obtained by serial sectioning or x-ray microscopy) can be used to determine the anisotropy of the grain boundary energy as a function of all five grain boundary parameters. The process involves measuring the geometry and crystallography of all of the triple lines in the microstructure and finding the optimized set of energies that satisfy the Herring equation (Shen et al., 2019). In addition to the grain boundary energy, it is also possible to measure the grain boundary curvature and the grain boundary velocity as a function of all five grain boundary parameters. While curvature and velocity are linearly related in bicrystals, no similar relation has been found in polycrystals (Bhattacharya et al., 2021). The mechanisms that cause grain boundary texture in microstructures formed by transformation or recrystallization are still being explored.

In cubic close packed metals, twins commonly form during recrystallization. In general, a twin is any grain boundary with a mirror in the grain boundary plane. In cubic close packed metals, the most common twin is a grain boundary with a misorientation

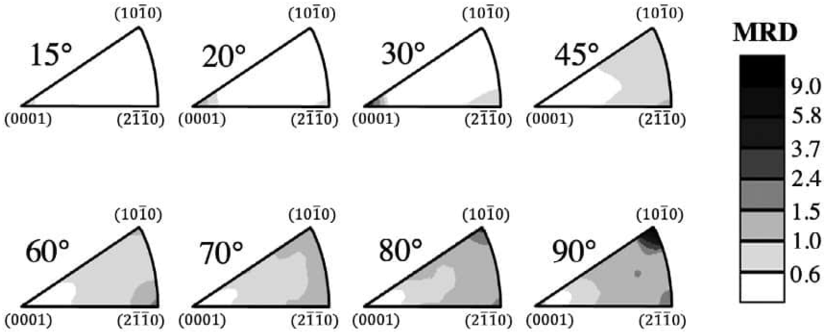

Fig. 13 The grain boundary character distribution in WC, plotted in axis-angle space. The entire range of distinguishable misorienation axes in the hexagonal system is represented in each triangle, and the individual triangles represent different rotations about these axes. The units are in multiples of a random distribution (MRD).

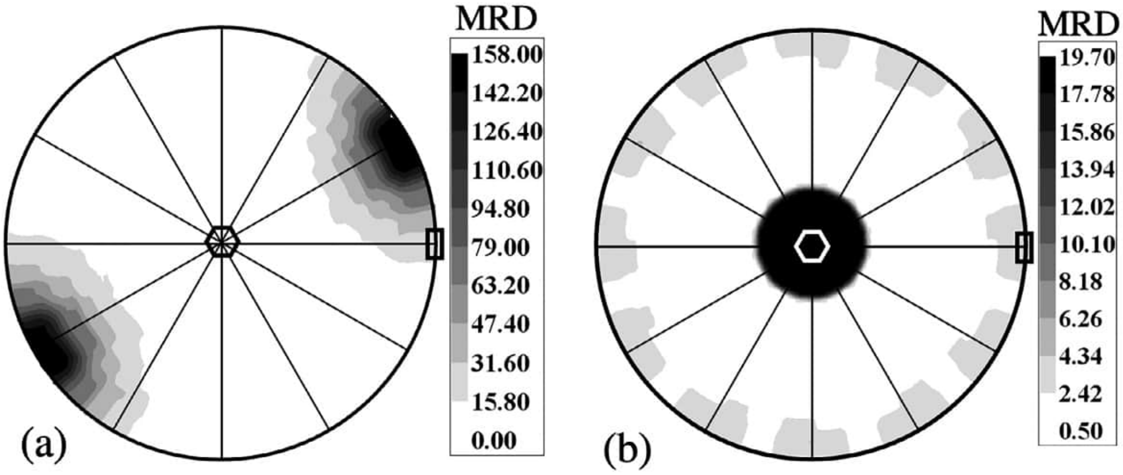

Fig. 14 The distribution of grain boundary planes at two specific misorientations: (a) for 90° rotations about the axis and (b) 30° about the [0001] axis. The hexagon marks to position of the [0001] axis and the rectangle the position of the [1000] axis. The positions of the peaks indicate that for both types of grain boundaries, the pure twist configuration is preferred.

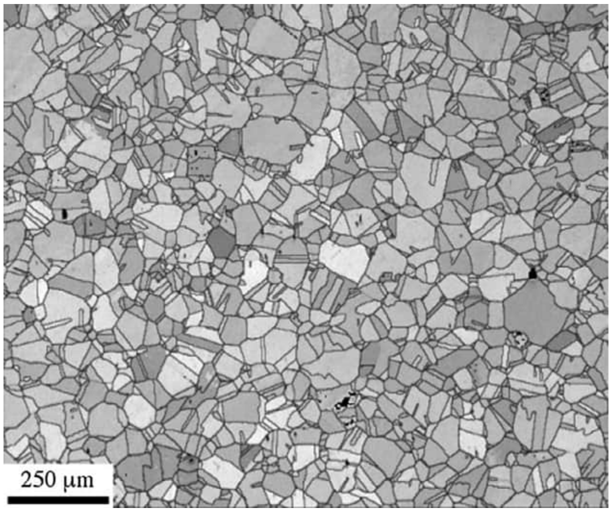

Fig. 15 Image quality electron backscattered pattern map of alpha brass. The black lines indicate the positions of grain boundaries. The straight boundaries are twins. Micrograph courtesy of Valerie Randle, University of Wales, Swansea.

of 60° about [111] on the (111) plane. An example of a highly twined alpha brass microstructure is illustrated in Fig. 15. In lower symmetry materials, if the crystal structure has only small deviations from the ideal cubic structure, then mosaic twinning in common. A twinned WO_3 microstructure is illustrated in Fig. 16. The crystal structure deviates slightly from the ideal cubic perovskite structure and the primary domains have misorientations of ≈90° around the [100] axis and are on {110} grain boundary planes, where the indices refer to the cubic perovskite structure.

Grain boundaries are often classified according to their inverse lattice coincidence number (Σ), where a low Σ number signifies high coincidence. It has been common in the literature to assume that grain boundaries with a low Σ have a low energy. However, there is no evidence to suggest that this is true. In fact, the largest surveys of grain boundary energies conducted by atomistic modeling and by experiment indicate no relationship between the inverse coincidence number and energy, as illustrated in Fig. 17 (Ratanaphan et al., 2015). The data in Fig. 17 illustrate that grain boundaries with the same value of Σ can have a wide range of energies and that some low energy grain boundaries have large values of Σ.

It has been found that certain properties of cubic close packed materials are improved by increasing the fraction of Σ3 boundaries. Because of crystallographic constraints at grain boundary triple lines, this also increases the fraction of Σ9 and Σ27 boundaries; the three grain boundary types are collectively referred to as $\Sigma 3^n$ boundaries. The process referred to as grain boundary engineering, which usually involves repeated cycles of mild deformation followed by recrystallization, has been used to increase the fraction of $\Sigma 3^n$ boundaries in cubic close packed materials with low to medium stacking fault energies such as Cu, Ni, and Pb.

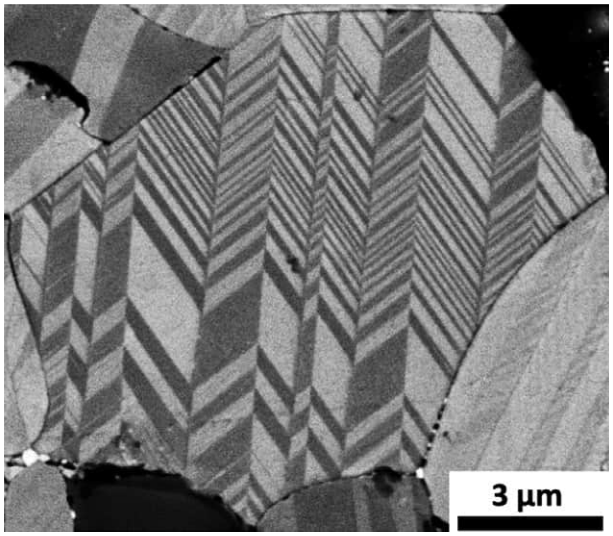

Fig. 16 Backscatter electron contrast image of γ-WO$_3$. The contrast results from domains formed when the crystal transformed from a higher symmetry phase to a lower symmetry phase during cooling.

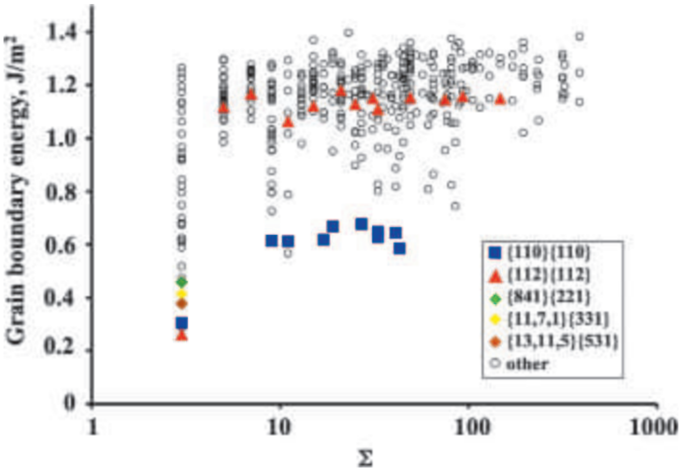

Fig. 17 Energies of 408 grain boundaries in Fe calculated by the embedded atom method and plotted as a function of their inverse coincidence (Σ number).

The micrograph in Fig. 15, discussed above, shows an example of a grain boundary engineered microstructure in which approximately 45% of the boundaries are of the type $\Sigma 3^n$. As these boundaries increase in concentration, they break up percolating clusters of general boundaries that are more susceptible to failure.

Duplex microstructures

Duplex microstructures contain two distinct phases, which are materials that can be distinguished by their structure or composition. In principle, a microstructure may contain many different phases, but the discussion here is limited to the case of two phases. The defining elements of the two-phase microstructure are the same as in the single-phase microstructure, only it is also necessary characterize the configuration of the two phases and the volume fractions. As in the single-phase microstructures, the configuration is determined both by equilibrium phenomena and kinetic phenomena. Because of the added complexity, there are a wider range of possibilities. Selected cases are discussed in the following sections.

Duplex microstructures formed by consolidation

The most direct method to create a duplex microstructure is to physically mix the two phases and then consolidate the mixture by sintering. The degree to which the two phases wet each other strongly influences the configuration. Referring once again to the

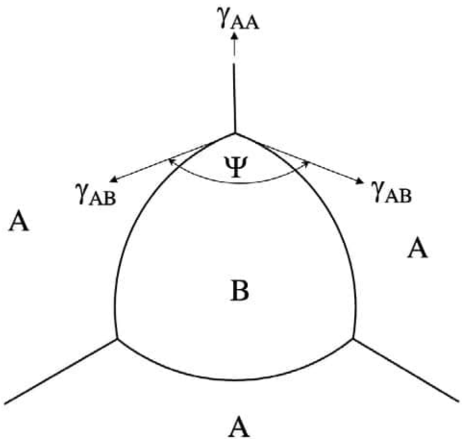

Fig. 18 Schematic of the interfacial equilibrium at the point where phase B meets three grains of phase A. The dihedral angle, Ψ, is a measure the relative interfacial energies.

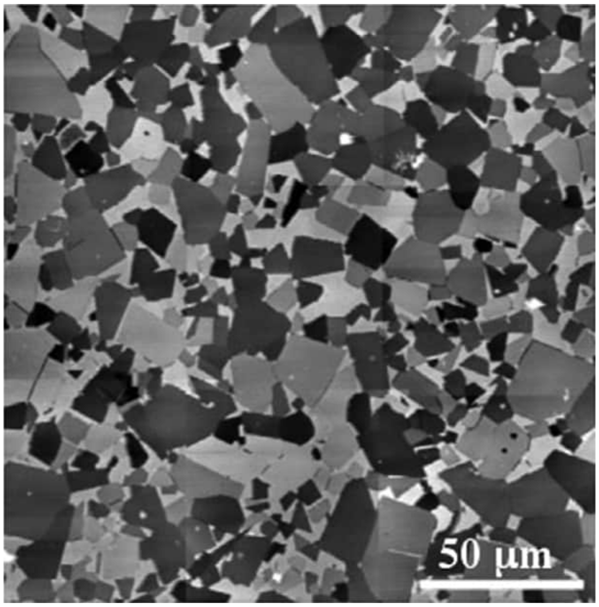

Fig. 19 Montage of topographic AFM images of a WC/Co surface. The surface was etched in such a way that the WC crystals were attacked preferentially, and they appear as the darker contrast. The Co matrix has the lightest contrast.

Young equation, the equilibrium geometry at the points where the phases meet is a function of the interfacial energies. If we label the phases A and B, and assume that their interface energies are isotropic, then the dihedral angle between the two AB interfaces (see Fig. 18) is given by:

$$\cos(\Psi) = \gamma_{AA}/2\gamma_{AB}$$

Note that when $2\gamma_{AB} \ll \gamma_{AA}$, the dihedral angle goes to zero and in this case the two phases completely wet each other. As γ_{AB} approached γ_{AA}, the two phases become increasing non-wetting and the dihedral angle increases toward 180°. Two examples are shown in Figs. 19 and 20. In Fig. 19, Co, which is liquid at the processing temperature, completely wets the angular WC crystals. In this case, the WC crystals occupy 90% of the volume and form an interconnected, skeletal network. The aluminum oxide - tanatalum oxide mixture in Fig. 20 provides an example of a non-wetting combination. The dark grains are the Al-rich phase which poorly wets the Ta_2O_5 boundaries.

Duplex microstructures by solidification

When microstructures form by the solidification of a homogeneous liquid, the phases are not as uniformly dispersed as when formed by a physical mixture followed by consolidation. Interestingly, well defined patterns can develop under these conditions.

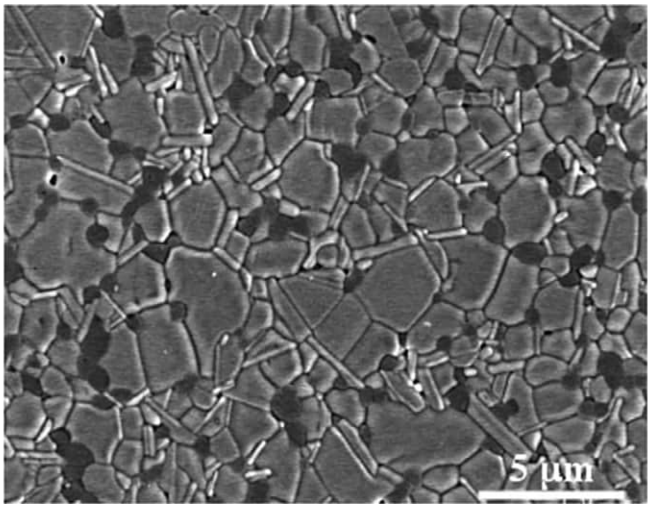

Fig. 20 SEM image of Ta_2O_5 doped with 3 wt% Al_2O_3 and 1.5 wt% La_2O_3. The dark grains are Al-rich and the anisotropic grains are a La-rich phase. Micrograph courtesy of Suxing Wu, Helen M. Chan, and Martin P. Harmer, Department of Materials Science and Engineering, Lehigh University.

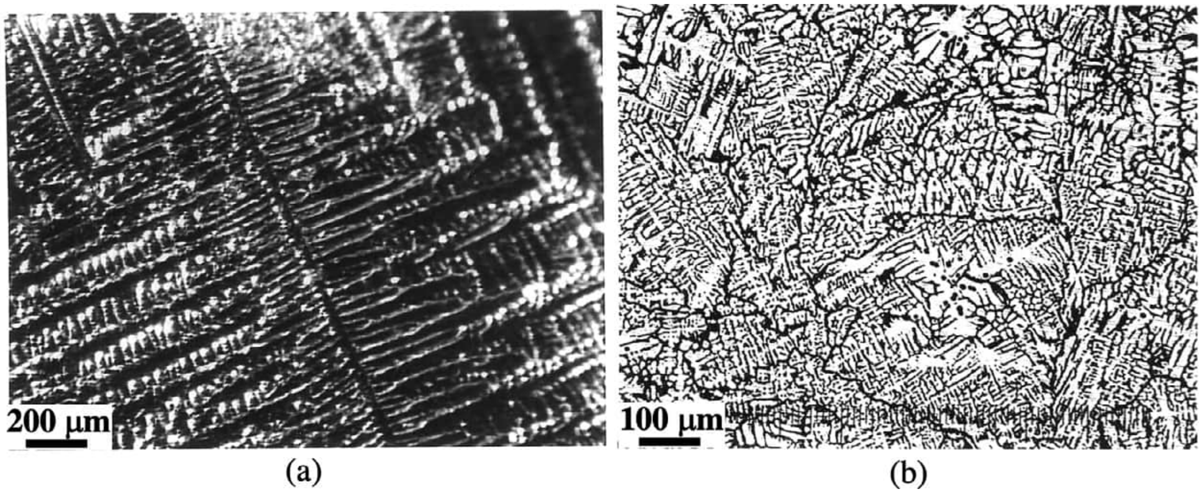

(a) (b)

Fig. 21 (a) A dendrite observed on the surface an Al-4.5 wt% Cu casting. (b) A section through the same casting, illustrating the appearance of random sections through the network of Al dendrites. The dark contrast is the Cu rich phase.

When a single phase liquid is crystallized in a two phase region where a solid and liquid phase coexist, one of the most common morphological patterns to develop is the dendrite, or branched structure, as illustrated by the microstructures in Figs. 21 and 22. It should be noted that while dendrites can also form during the solidification of a pure material into a supercooled liquid, this situation is far less common than that of the binary alloy. For the single-phase case, one can imagine that protrusions in the growth front can be stabilized if the liquid is supercooled and the latent heat of crystallization is extracted through the solid. In this case, heat is removed more efficiently from the tip of the protrusion that juts out into the supercooled fluid than it is from the valleys between protrusions.

To describe the mechanism by which dendrites form in a binary alloy, consider the simple binary eutectic phase diagram illustrated in Fig. 23. For an alloy with composition C at a temperature less than T_L, there is a range of temperature where the solid and liquid coexist, but with different compositions. The solid alloy α has composition C_α and always contains less B than the liquid, with composition C_L. In fact, one can say that the solid is always relatively more pure than the liquid from which it crystallizes. This means that as the crystal grows, the liquid at the interface is relatively enriched in B and that the enriched liquid freezes at a lower temperature, specified by the liquidus line in Fig. 23. Therefore, a protrusion in the interface can be stabilized because it juts into a relatively more pure liquid (see Fig. 24). In the valleys between protrusions, on the other hand, the liquid rich in B is trapped between opposing growth fronts. Thus, the growth front at the tip of the protrusion is in contact with a liquid that freezes at a higher temperature than the liquid in the valleys between the protrusions. This causes the tip to grow faster than the lateral surfaces and the result is cellular or, more commonly, a dendritic morphology.

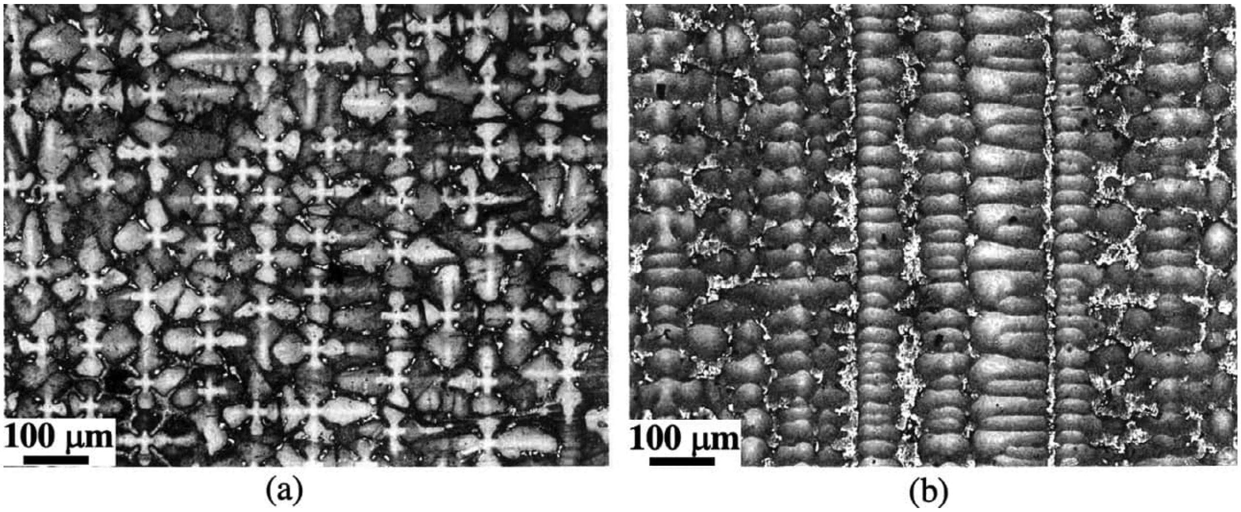

Fig. 22 (a) transverse and (b) lateral sections through a directionally solidified Ni alloy. The transverse section shows the shape of the primary dendrite while the lateral section shows the arm spacing.

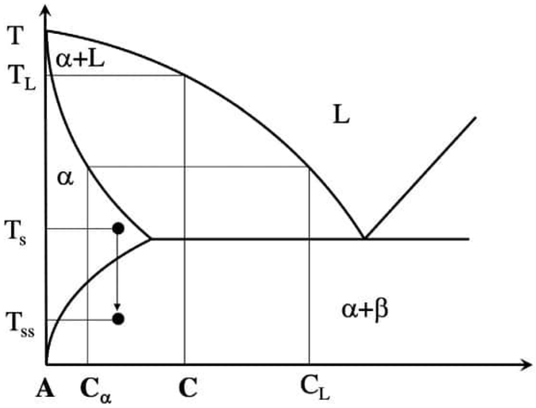

Fig. 23 Schematic binary alloy phase diagram.

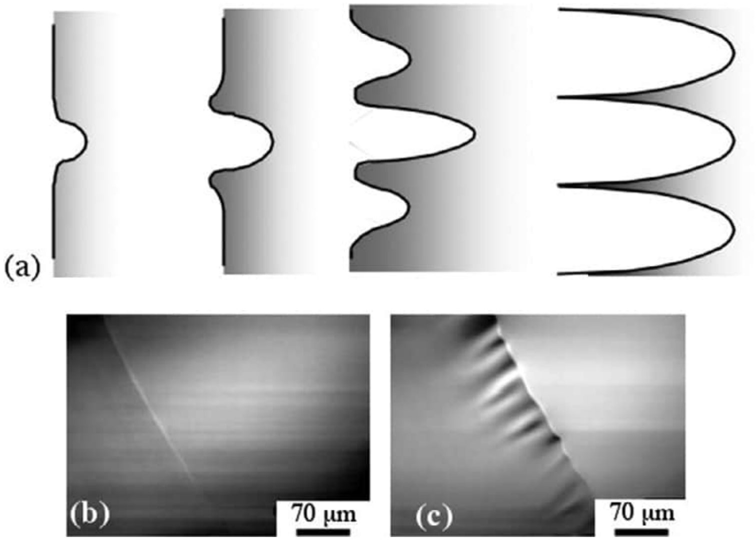

Fig. 24 (a) Schematic of interface instability by constitutional supercooling. As solute is rejected from the solidifying crystal, it accumulates in the valleys between the dendritic protrusions (the solute concentration is indicated by the shading). Since the relatively more pure liquid at the ends of the protrusions freezes at a higher temperature, these portions of the solid grow faster. (b and c) In situ laser confocal microscope image of a solidification front in Fe-Co-Ni alloy at 1597 °C. (b) the front is planar (c) a few seconds later, an instability develops. Micrograph courtesy of Chanjoon Paek and Sridhar Seetharaman, Department of Materials Science and Engineering, Carnegie Mellon University.

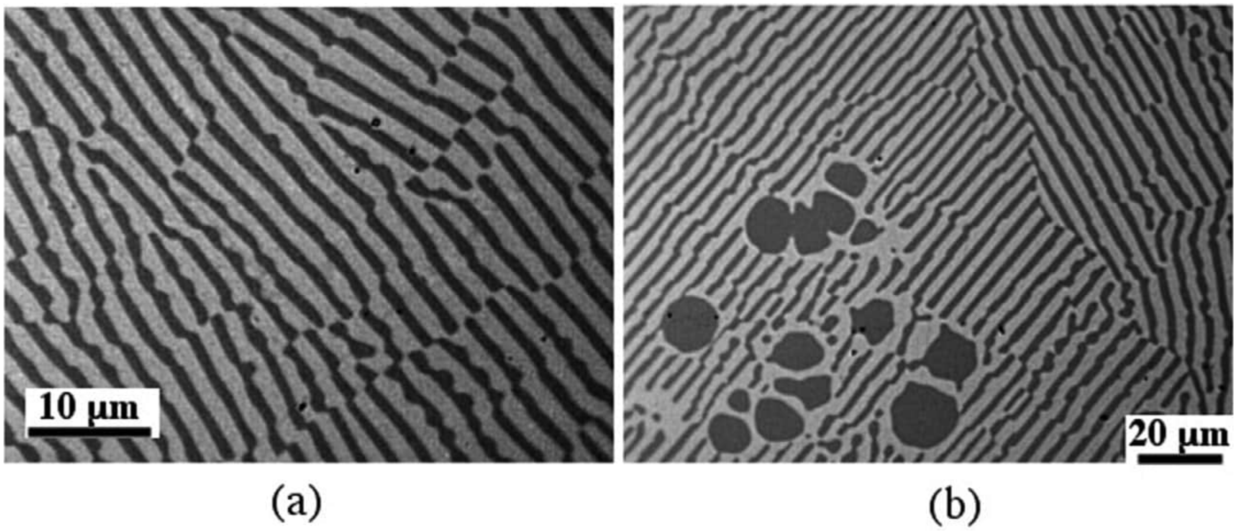

Fig. 25 Light microscope images of the microstructure of directionally solidified (a) CoO-ZrO_2 and (b) NiO-ZrO_2 eutectic microstructures. The darker phase is ZrO_2 and the lighter phase is CoO in (a) and NiO in (b). Micrographs courtesy of Nasim Alem and Vinayak P. Dravid, Department of Materials Science and Engineering, Northwestern University.

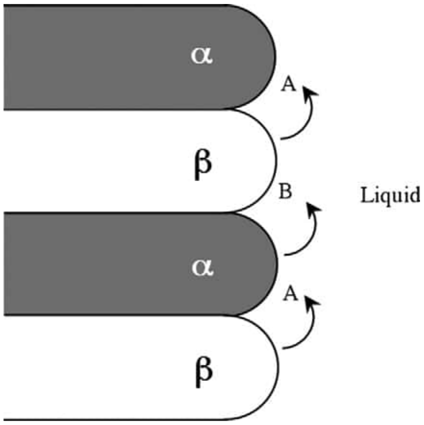

Fig. 26 Schematic of the growth of a lamellar microstructure maintaining a nearly planar growth front.

When the remaining liquid cools to the temperature T_E, two solid phases (α and β) crystallize directly from the liquid. This most frequently results in a lamellar microstructure, such as those shown in Fig. 25, where the two phases have alternating bands of dark and light contrast. Because both solids are in equilibrium with the same liquid, but themselves have very different compositions, they must simultaneously reject solute to feed the growth of the other phase. In other words, as a layer of the α phase grows, it must reject solute (B) laterally to supply neighboring lamella of the β phase. As the β phase crystallizes, it rejects A, which sustains the growth of the α phase. This cooperative process, schematically illustrated in Fig. 26, stabilizes a nearly planar growth front.

In most solidification processes, cooling will take the materials through a region of solid-liquid coexistence, in which a dendritic structure will grow. When the remaining liquid reaches the eutectic temperature, it will solidify in a lamellar microstructure, leading to a mixed microstructure. In general, this situation is not an equilibrium configuration. Annealing at a temperature just below the eutectic will cause the compositional concentration gradients to homogenize and the morphologies of the crystals to spheroidize and become more equiaxed.

Duplex microstructures by transformation in the solid phase

Duplex microstuctures can also form by transformation in the solid phase. As an example, consider the rapid cooling of α on the phase diagram in Fig. 23, from T_s to T_{ss}. At T_{ss}, the supersaturated a phase will decompose to α + β, and this will happen entirely in the solid state. As with solidification, the characteristics of the microstructure that develop are determined by the nucleation and growth of the phase. The free energy change during the nucleation process is similar to that for heterogeneous nucleation, except that an additional term must be added to account for the volumetric strain energy associated with any expansion or contraction that might accompany the transformation. The disposition and shape of this phase depends on the structural relationship between the parent and child phases, features preexisting in the microstructure that serve as heterogeneous nucleation sites, the degree of supersaturation during the nucleation and growth of the phase, and the mechanism of the transformation. Because of all of these parameters, there are a wide range of possible microstructures that can form and only a few of characteristic examples are described in the remainder of this article.

Precipitation from a supersaturated solid solution requires the long range diffusion of solute to the site of growth. For this reason, the distribution of a precipitated phase will depend in the degree of undercooling or supersaturation. When large, the driving force for the precipitation reaction is amplified and atomic mobility is limited. This leads of a uniform distribution of very small precipitates. For example, the microstructure in Fig. 27 shows cuboidal γ' precipitates in a $Ni_{70}Cr_{20}Al_{10}$ superalloy. In this case, the structure of precipitating phase differs little from that of the parent phase, so there is an orientation relationship between the two. In cases where the kinetics for transport are higher and the supersaturation is not as large, precipitates will nucleate at heterogeneities such as grain boundaries.

The formation of lamellar microstructures from the solidification of a eutectic has already been described. In the case of the eutectoid reaction, where a single solid phase decomposes to two new solid phases, the microstructure that is formed is similar to that formed by the eutectic reaction, but the lamellar phase typically nucleates and grows from the grain boundaries. Similar microstructures can also be generated by the cellular transformation from a supersaturated solid solution.

There are also solid to solid transformations that do not require long range diffusion and these processes also lead to distinct microstructures. In the massive transformation, a single phase decomposes to one or more phases that have the same composition, but different crystal structures. Because it is not necessary to alter the composition, the interface can move very rapidly. The massive transformation frequently nucleates at grain boundaries and the rapid interface motion leaves an irregularly shaped precipitate.

Martensitic transformations are diffusionless processes by which a material changes crystal structure without requiring any of the atoms to change position by more than a lattice spacing. Typically, the parent and child structure are related by a shear deformation process. In the resulting microstructure, lens shaped precipitates grow quickly to the size of the grains of the parent phase, creating the characteristic microstructure, such as the one illustrated in Fig. 28. The fully martensitic microstructure in Fig. 28 formed by quenching a steel from the high temperature austenitic phase field. The polygonal austenite grains are replaced by a refined structure of smaller plate shaped grains that form to accommodate the shape change associated with the transformation. It has been shown that the interface between the precipitate and the parent phase can move at velocities approaching the speed of sound.

Microstructures formed by martensitic transformations are common in alloys used as structural materials. For example, in ferrous alloys, the face centered cubic to body centered cubic (bcc) transition is often martensitic and in titanium alloys the bcc to hexagonal close packed (hcp) transition is also often martensitic. In microstructures that results from martensitic transformations, there are common orientation relationships between the phases that align the closest packed layer of the parent phase with the closest packed layer of the child phase. For example, in titanium alloys, the {110} planes of the high temperature bcc phase are aligned with the {0001} planes of the low temperature hcp phase.

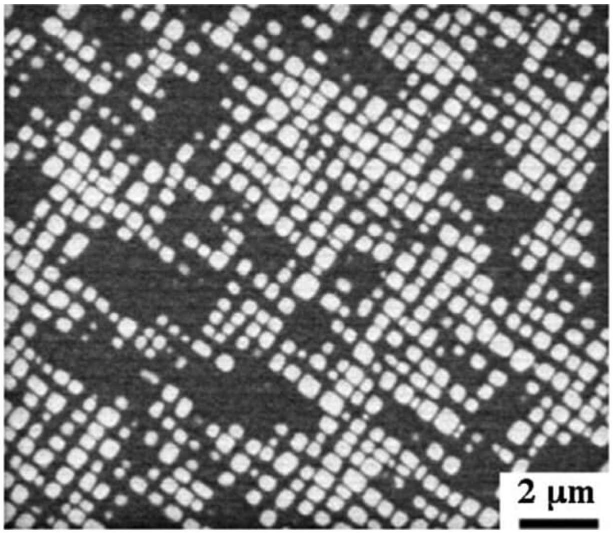

Fig. 27 Focused Ion Beam microscope image of cuboidal γ' precipitates in a $Ni_{70}Cr_{20}Al_{10}$ superalloy. Micrograph courtesy of Dr. Michael Uchic, Wright Patterson Air Force Base, and Marc De Graef, Department of Materials Science and Engineering, Carnegie Mellon University.

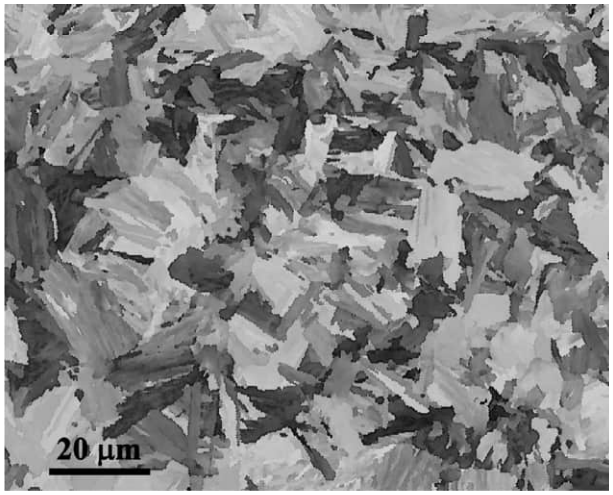

Fig. 28 EBSD map of a fully martensitic steel formed by quenching.

Conclusion

The shapes, orientations, and arrangements of crystals within polycrystalline solids vary widely and define what we call microstructure. The single feature that has the strongest influence on the microstructure is the processing route. Inorganic solids can be formed by solidification, the sintering of powders, vapor deposition, recrystallization, or phase transformation and each path leads to a distinct microstructure. The energies of the interfaces between the crystals have an excess energy and during thermal annealing, this excess energy provides a driving force for the microstructure to evolve in a way that reduced the total interface energy.

References

Bhattacharya A, Shen YF, Hefferan CM, Li SF, Lind J, Suter RM, and Rohrer GS (2019) Three-dimensional observations of grain volume changes during annealing of polycrystalline Ni. *Acta Materialia* 167: 40–50.

Bhattacharya A, Shen YF, Hefferan CM, Li SF, Lind J, Suter RM, Krill CE, and Rohrer GS (2021) Grain boundary velocity and curvature are not correlated in Ni polycrystals. *Science* 374: 189–193.

Herring C (1953) The use of classical macroscopic concepts in surface energy problems. In: Gomer R and Smith CS (eds.) *Structure and Properties of Solid Surfaces; Proceedings of a Conference Arranged by the National Research Council and held in September, 1952, in Lake Geneva, Wisconsin, USA., Chicago, University of Chicago Press, Chicago*, 5–81.

Hillert M (1965) On theory of normal and abnormal grain growth. *Acta Metallurgica* 13: 227–238.

Kim CS, Massa TR, and Rohrer GS (2008) Interface character distributions in WC-Co composites. *Journal of the American Ceramic Society* 91: 996–1001.

Mullins WW (1956) 2-Dimensional motion of idealized grain boundaries. *Journal of Applied Physics* 27: 900–904.

Ratanaphan S, Olmsted DL, Bulatov VV, Holm EA, Rollett AD, and Rohrer GS (2015) Grain boundary energies in body-centered cubic metals. *Acta Materialia* 88: 346–354.

Rohrer G, Saylor D, El Dasher B, Adams B, Rollett A, and Wynblatt P (2004) The distribution of internal interfaces in polycrystals. *Zeitschrift für Metallkunde* 95: 197–214.

Shen YF, Zhong XT, Liu H, Suter RM, Morawiec A, and Rohrer GS (2019) Determining grain boundary energies from triple junction geometries without discretizing the five-parameter space. *Acta Materialia* 166: 126–134.

Structures: Orientation texture[☆]

Stuart I Wright[a] **and Ralf Hielscher**[b], [a]EDAX, St George, UT, United States; [b]Fakultät für Mathematik, Technische Universität Chemnitz, Chemnitz, Germany

© 2024 Elsevier Ltd. All rights reserved.

This is an update of S.I. Wright, Orientation Texture, Editor(s): Franco Bassani, Gerald L. Liedl, Peter Wyder, Encyclopedia of Condensed Matter Physics, Elsevier, 2005, Pages 221–233, ISBN 9780123694010, https://doi.org/10.1016/B0-12-369401-9/00696-3.

Introduction **482**
Crystallographic orientation **483**
Orientation descriptions 483
Symmetry 484
Graphical descriptions 485
Texture measurement techniques **487**
X-ray diffraction 487
Electron backscatter diffraction 488
Mathematical constructs **489**
Basic equations 489
ODF estimation from individual orientations 489
ODF estimation from diffraction pole figure measurements 491
Harmonic method 491
WIMV method 492
MTEX method 493
Examples **493**
Thin films 493
Rolled sheet 493
Other texture related entities **495**
Misorientation 495
Microtexture 496
Materials properties and modelling **496**
Tensor averaging 496
Modelling 497
Conclusion **498**
Acknowledgments **498**
References **498**

Abstract

Orientation texture describes the distribution of crystallographic orientations of the constituent grains in polycrystalline materials. Crystallographic orientation describes the orientation of the crystal lattice with respect to a sample reference frame. Texture evolves during materials processing and is often the governing factor in the degree of anisotropy exhibited in the physical properties of crystalline materials. Texture is typically measured using X-Ray or neutron diffraction pole figures or individual orientation measurements obtained by electron backscatter diffraction. Various statistical treatments have been developed to analyze the texture data – the key element being the orientation distribution function or ODF.

Key points

- Show the link between crystallographic texture and anisotropy in materials properties.
- Provide the framework for describing crystallographic orientation both mathematically and graphically.
- Introduce the methods used for both collecting and statistically analyzing orientation data.
- Give some examples of texture analysis in polycrystalline materials.

[☆] *Change History*: July 2022. SI Wright updated text and figures.

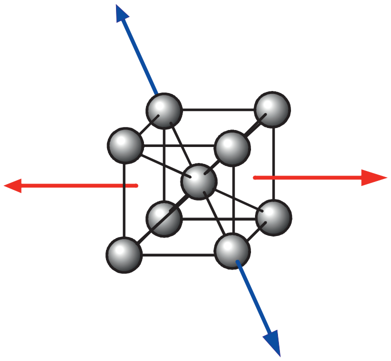

Fig. 1 Schematic of elastic moduli measured for stresses applied along the <111> (body diagonal) and ⟨100⟩ (normal to the cube faces) crystal directions in a body centered cubic crystal.

Introduction

Many single crystals exhibit properties that vary with direction (anisotropy). For example, consider the elastic modulus of a copper single crystal illustrated schematically in Fig. 1. The elastic modulus measured for an applied uniaxial tensile stress parallel to the ⟨111⟩ crystal direction (i.e. the body diagonal) is nearly three times larger than the modulus measured with a stress axis parallel to ⟨100⟩ (i.e. normal to the cube faces).

Most materials are not single crystals; but polycrystals. To first order, a given property that varies with direction, such as the elastic modulus, can be approximated for a polycrystal by averaging the property for each constituent crystal. For example, if the elastic stiffness of a single crystal is represented as a fourth order tensor – C_{ijkl} then one approximation of the average elastic stiffness tensor ($\overline{C}_{ijkl}$) for the polycrystal is given as follows:

$$\overline{C}_{ijkl} = \frac{1}{V}\sum_{n=1}^{N} v(\mathbf{g}^n) g_{ip}^n g_{jq}^n g_{kr}^n g_{ls}^n C_{pqrs} \quad (1)$$

Where V is the total volume of the polycrystal, $\mathbf{g}^n$ is the orientation of the nth grain in the polycrystal and $v(\mathbf{g}^n)$ is the volume of the grain. N and V are the total number and volume of grain respectively. ${g_{ip}}^n$ are the components of $\mathbf{g}^n$ assuming it is given in matrix form.

If a polycrystal is composed of grains where the crystal lattices are all in similar orientations (as shown schematically in the right-hand side of Fig. 2 where grains of different color have different orientation) then the properties of the polycrystal would mimic the inherent anisotropy of the constituent crystals. If the grains were all oriented randomly (as shown schematically in the left-hand side of Fig. 2 where grains of similar color have similar orientation) then the properties of the polycrystal would not reflect the anisotropy of the constituent crystals, but would instead be isotropic (i.e. the properties would not vary with direction.).

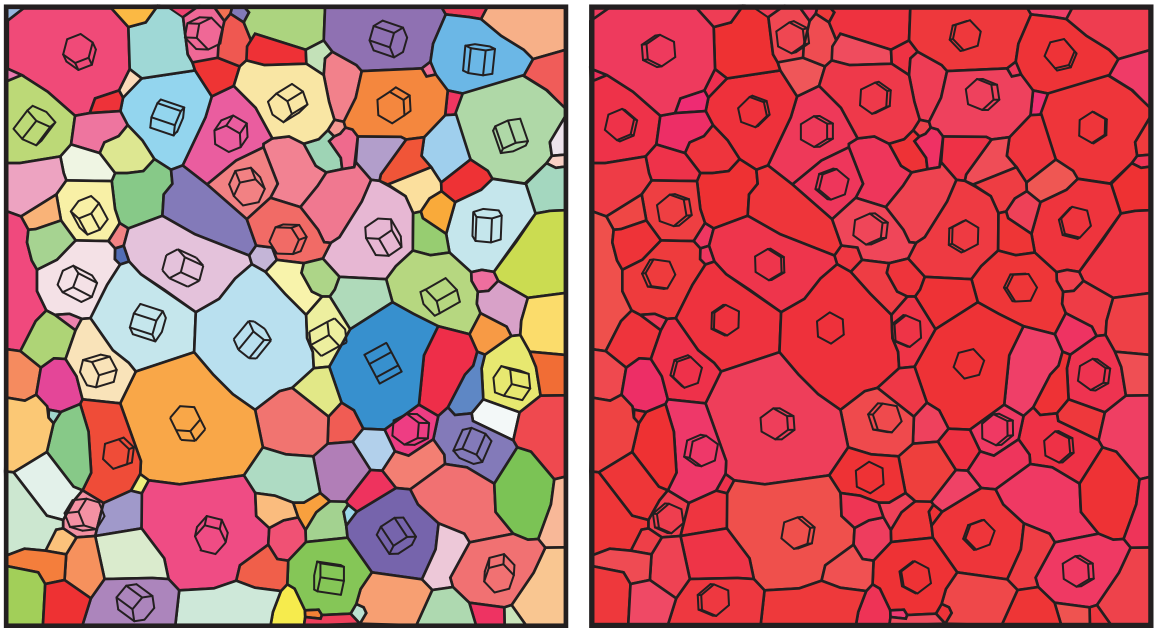

Fig. 2 Schematic of a polycrystal with a strong texture and a polycrystal with a random texture.

Real polycrystals may vary between these two extremes depending on the processing route used to form the material. The terms preferred orientation, crystallographic texture, orientation texture or simply texture are used to describe the statistical distribution of grain orientations (Dillamore and Roberts, 1965; Bunge, 1982.) In addition to texture, the terms lattice preferred orientation (LPO) or fabric are also used within the geological community (Wenk, 1985, 2003). In fact, the term grain generally describes a domain where the orientation of the crystal lattice is the same or at least very nearly the same. A grain boundary is then an interface between two crystal lattices of different orientation.

As nearly all materials forming processes produced textured materials, the characterization of texture is an important element to understanding the relationship between microstructure and properties as well as the evolution of microstructure during processing. This article reviews the definition of crystallographic orientation and graphical representations of orientations, techniques for the measurement of texture, the mathematical formalism used in processing texture data, and a few examples of texture analysis.

Crystallographic orientation

Orientation descriptions

In order to describe a crystallographic orientation, two coordinate systems must be defined: one for the sample, referred to as $\mathbf{X}^S$ and one for the crystallite, $\mathbf{X}^C$. The choice of sample axes is somewhat arbitrary, however, the choice usually follows the sample shape or processing used to form the sample. For example, consider a coupon obtained from rolled sheet and the orientation of the crystal lattice within each its constituent grains as shown in Fig. 3. It is common to assign $X_1{}^S$ to the rolling direction, $X_2{}^S$ to the transverse direction and $X_3{}^S$ to the sample normal direction. The coordinate system for the crystallite generally follows that traditionally used in defining the unit cell, i.e. $X_1{}^C$ is assigned to the [100] crystal direction, $X_2{}^C$ to [010] and $X_3{}^C$ to [001]. Both coordinate systems are right-handed coordinate systems. While the assignment of the reference frame to a cubic crystal, as given here, is straightforward, the assignment is less straightforward for other crystal systems such as hexagonal. Nonetheless, a coordinate system can be assigned, e.g. for a hexagonal crystal one convention is $X_1^C \| [2\bar{1}\bar{1}0], X_2^C \| [01\bar{1}0]$ and $X_3{}^C \| [0001]$.

There are many ways to describe the orientation of a crystal with respect to the coordinate system of a sample. The most common is the (*hkl*)[*uvw*] notation (sometimes referred to as metallurgical notation) where (*hkl*) are the Miller indices of the plane perpendicular to the sample normal (generally $X_3{}^S$) and [*uvw*] describes the crystal direction parallel to $X_1{}^S$. However, as integers are used, this description is not as convenient for describing any arbitrary orientation. In texture analysis, a common way to describe the orientation of the crystal lattice with respect to a sample reference frame is to use three Euler angles. In this case, the Euler angles describe three successive rotations that bring the sample reference frame into coincidence with the crystal reference frame as shown in Fig. 4.

The various descriptions are equivalent and can be converted from one description to another as shown in Fig. 5.

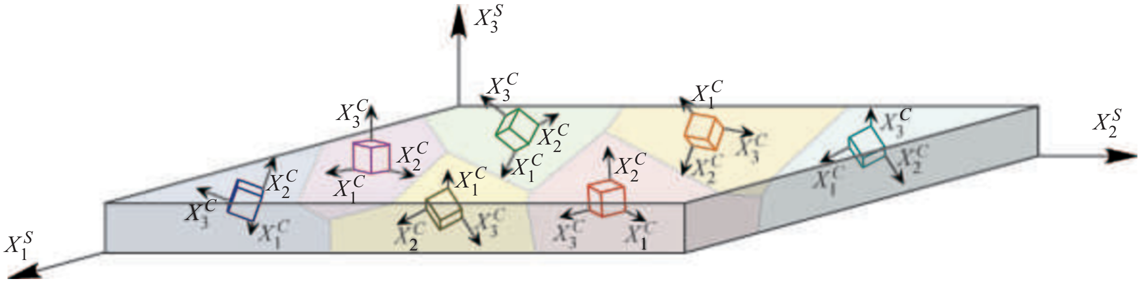

Fig. 3 Schematic of the coordinate system fixed to the sample, $\mathbf{X}^S$ and the coordinate system fixed to individual crystals, $\mathbf{X}^C$.

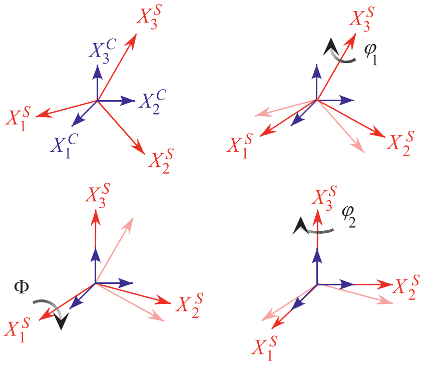

Fig. 4 Schematic showing the definition of the three Euler angles, φ_1, Φ, φ_2.

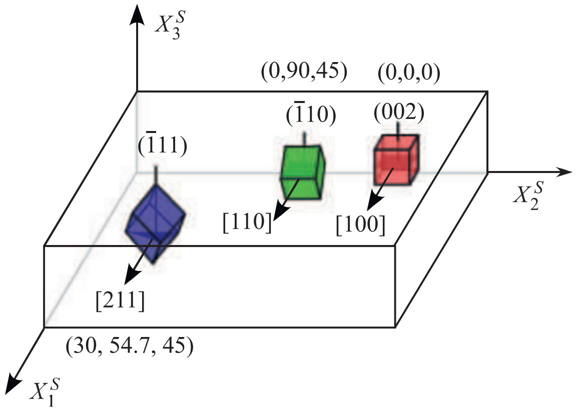

Fig. 5 Two equivalent descriptions of crystallographic orientation: Euler angles and standard plane normal and crystal direction notation (i.e. (*hkl*)[*uvw*]).

A matrix, **g**, can also be used to describe the orientation. It can be derived from the Euler angles according to:

$$\begin{bmatrix} \cos\phi_1\cos\phi_2 - \sin\phi_1\sin\phi_2\cos\Phi & \sin\phi_1\cos\phi_2 + \cos\phi_1\sin\phi_2\cos\Phi & \sin\phi_2\sin\Phi \\ -\cos\phi_1\sin\phi_2 - \sin\phi_1\cos\phi_2\cos\Phi & -\sin\phi_1\sin\phi_2 + \cos\phi_1\cos\phi_2\cos\Phi & \cos\phi_2\sin\Phi \\ \sin\phi_1\sin\Phi & -\cos\phi_1\sin\Phi & \cos\Phi \end{bmatrix} \tag{2}$$

The matrix representation is particularly useful for describing orientation in computer algorithms. Other representations that lend themselves well to implementation in the computer are Rodrigues Vectors and Quaternions (Morawiec, 2003). These are more compact representations than the matrix form but, as with matrices, they allow for easy numerical manipulation.

The rotation of the sample reference frame into coincidence with the crystal reference frame is termed a passive rotation. Conversely, rotating the crystal reference frame into coincidence with the sample reference frame is termed an active rotation.

Symmetry

The three Euler angles form a bounded space: $0 \le \phi_1 < 2\pi,\ 0 \le \Phi < \pi,\ 0 \le \phi_2 < 2\pi$. As most crystals exhibit some degree of symmetry, for any given crystallographic orientation, there exist other symmetrically equivalent orientations. For example, consider a material with cubic crystal symmetry. There are 24 symmetry elements for a cube: the four-fold rotations about axes normal to the faces of the cube (i.e., 90° rotations about the $\langle 001\rangle$ crystal directions) the two-fold rotations about the face diagonals (180° rotations about $\langle 110\rangle$) and the three-fold rotations about the body diagonals (120° about $\langle 111\rangle$). Thus, for any orientation of a cubic crystal there are 24 equivalent orientations within Euler space. A space can be defined within Euler space containing only asymmetric orientations. An example is shown for cubic symmetry in Fig. 6. This subspace is termed the asymmetric domain or the fundamental zone. However, it is important to note that the fundamental zone is not the same for each crystal symmetry (Morawiec, 2003).

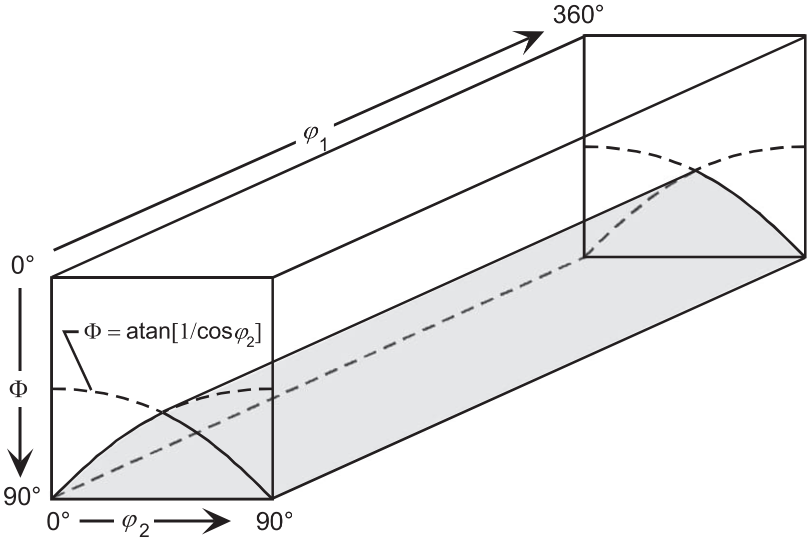

Fig. 6 The asymmetric domain for cubic crystal symmetry.

Since texture is a statistical distribution of orientations, another type of symmetry must also be considered, namely sample symmetry. Sample symmetry arises from the symmetry inherent to the forming process. Consider for example the rolling of sheet metals. This forming operation has orthotropic symmetry. For a rolled cubic material, the four orientations shown in Fig. 7 would appear with the same statistical frequency in the microstructure. Thus, the term statistical symmetry is a more accurate description.

If the matrix notation is used, then the symmetry operations can be applied as follows:

$$\mathbf{g}^e = \mathbf{L}_i\mathbf{g}\mathbf{R}_j \tag{3}$$

Where $\mathbf{g}^e$ denotes an equivalent orientation, $\mathbf{L}_i$ is one of the crystal symmetry elements and $\mathbf{R}_j$ is one of the statistical symmetry elements. Because of the form of this relation, the crystal symmetry is sometimes referred to as left-handed symmetry and the statistical symmetry as right-handed.

Graphical descriptions

Pole figures provide a graphical representation of orientation. A pole figure is a two-dimensional graphical representation of orientation showing the orientation of a selected plane normal (a pole) with respect to the sample reference frame. The pole is a vector in three-dimensional space. If one imagines a hemisphere surrounding a crystal unit cell, then a pole would intersect the hemisphere at some location in three-dimensional space. The intersection location can be projected into a two-dimensional plot using a variety of projection schemes. An example of a pole figure is shown in Fig. 8, this pole figure shows the (0001) and $(10\bar{1}0)$ poles for a hexagonal crystal, note that there is only one pole for the (0001) plane and 3 for the $(10\bar{1}0)$ plane. The additional poles in the $(10\bar{1}0)$ case arise from crystal symmetry. In the pole figures, poles from the negative hemisphere are shown in gray. Fig. 9 shows three common "projection schemes" found in the literature (the equal angle is not a projection in the strictest sense; but, rather, a mapping of the polar angle).

A complement to the pole figure is the inverse pole figure. An inverse pole figure shows the location of a sample direction relative to the crystal reference system. For pole figures the plane of interest is selected, whereas in inverse pole figures the sample direction of interest is selected. It is bit more intuitive to think of an inverse pole figure as showing which plane normal in the crystal is parallel to the selected sample direction. Fig. 10 shows an example. In this case, it shows the poles aligned with the sample normal ($X_3{}^S$) for three different orientations as well as the poles aligned with the $X_1{}^S$ sample direction. Because of crystal symmetry, the full circle need not be displayed, only the asymmetric portion of it.

While pole figures and inverse pole figures are useful representations of orientations, they provide only a partial description of orientation. For example, consider the (0001) pole figure shown in Fig. 8. While the orientation of the (0001) pole is known, the rotation of the crystal about this pole is unknown. A second pole figure (such as the $(10\bar{1}0)$) is needed to completely fix the orientation. When the orientations of many crystallites are displayed, the use of multiple pole figures is quite limited. In this case, it is more productive to show the orientations in constant angle sections of Euler space. Fig. 11 shows 30,000 discrete orientations from rolled copper in a portion of Euler space along with the corresponding (111) pole figure.

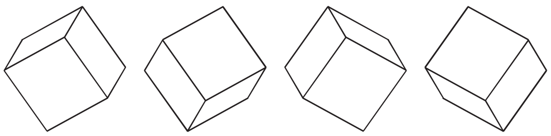

Fig. 7 Four equivalent orientations for orthotropic sample symmetry.

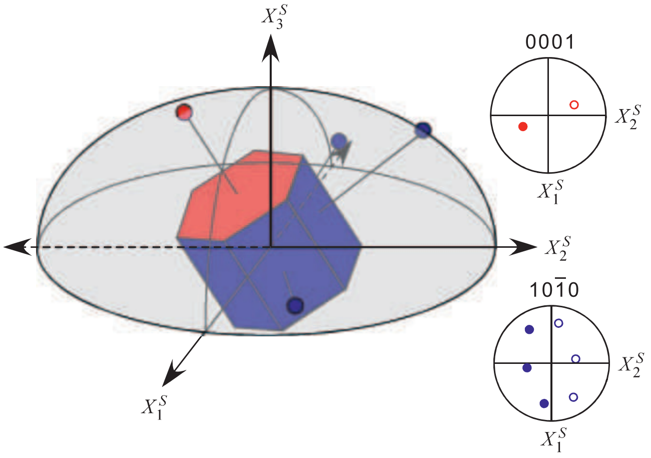

Fig. 8 Schematic showing the orientation of a hexagonal crystal and the corresponding (0001) pole figure.

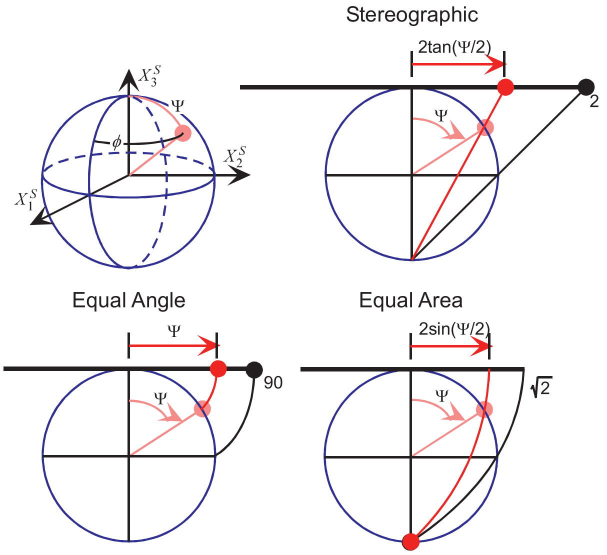
Stereographic
2tan(Ψ/2)
X_3^S
Ψ
φ
X_2^S
X_1^S
2
Equal Angle
Ψ
90
Equal Area
2sin(Ψ/2)
√2

Fig. 9 Stereographic, Equal Angle and Equal Area pole figure projections.

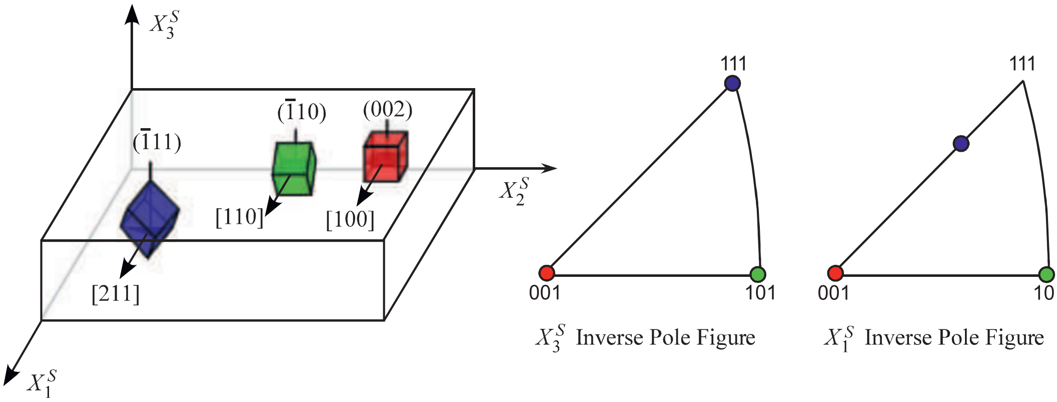
X_3^S
X_2^S
X_1^S
$(\bar{1}11)$
$(\bar{1}10)$
(002)
[211]
[110]
[100]
111
001
101
X_3^S Inverse Pole Figure
111
001
101
X_1^S Inverse Pole Figure

Fig. 10 Schematic showing the representation of orientation in inverse pole figures.

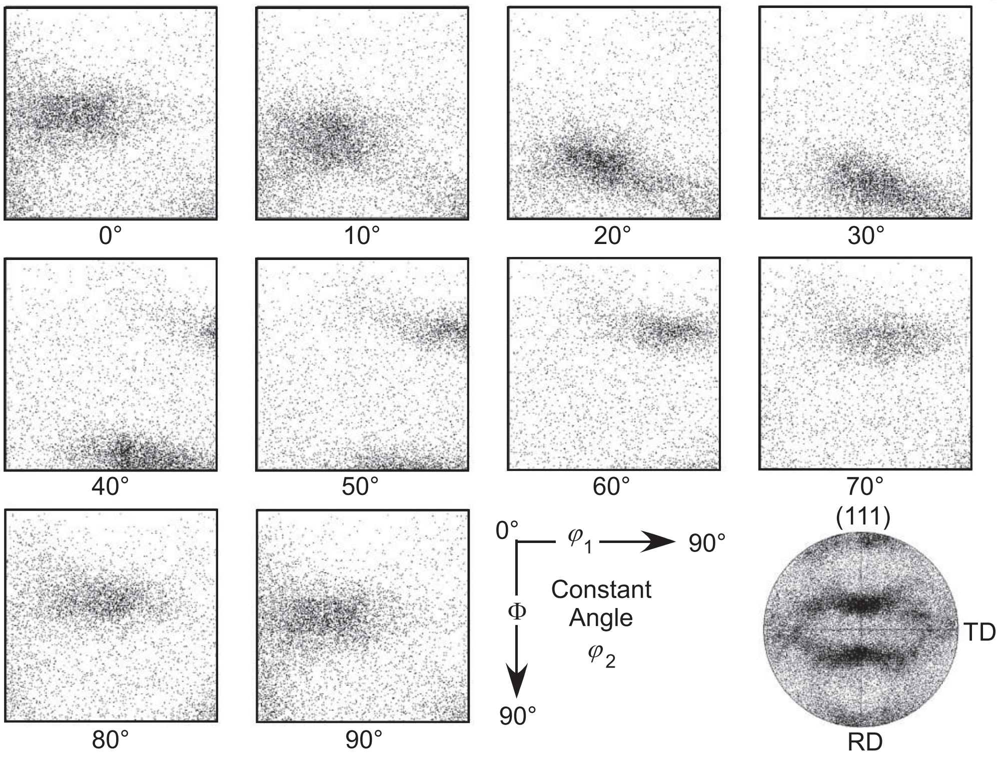

Fig. 11 Plot of 30,000 discrete orientations from rolled copper in constant angle sections through Euler Space accompanied by a (111) pole figure of the same data.

Texture measurement techniques

X-ray diffraction

There are essentially two ways of measuring textures, measuring pole figures or measuring the orientations of individual grains. Until recently most textures have been measured using pole figures obtained by X-Ray or neutron diffraction. The governing equation for a pole figure is Bragg's law.

$$\lambda = 2d_{hkl}\sin\theta \tag{4}$$

where λ is the wavelength of the X-Rays, d_{hkl} is the interplanar spacing of pole figure to be measured (recall that the pole is the normal to a (*hkl*) plane) and θ is the Bragg angle as shown in Fig. 12.

In a pole figure measurement, a sample is placed in a goniometry so that the sample can be rotated while under the X-ray beam. For each rotation (in both Ψ and ϕ), the signal from those grains satisfying Bragg's law is measured as shown in Fig. 13. An intensity value is measured at successive tilts (Ψ) and rotations (ϕ) of the sample.

This is typically done for a series of pole figures. For example, for a base-centered cubic material, the (110), (200) and (112) pole figures are typically measured. A similar approach is employed for neutron diffraction. The major difference is that X-ray pole figures are typically measured in a reflective mode whereas neutron diffraction is done in transmission. Thus, neutron measurements have the advantage of providing a volumetric measure of texture, whereas the signal for x-rays comes from the surface of the sample. Various corrections must be applied to the pole figures to account for defocusing and absorption effects.

An alternative to pole figure measurement is the use of High-Energy X-Ray Diffraction Microscopy (HEDM) to non-destructively measure individual crystallites in the volume of sample (Pokharel, 2018). This approach has also been adapted to work in the laboratory setting using diffraction contrast crystallography (Holzner et al., 2016).

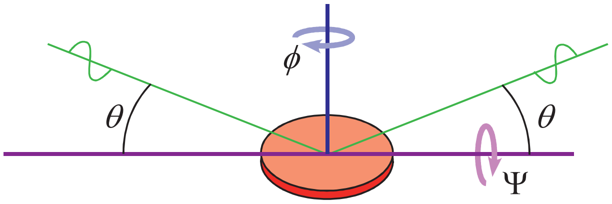

Fig. 12 Diagram showing the pole figure measurement geometry.

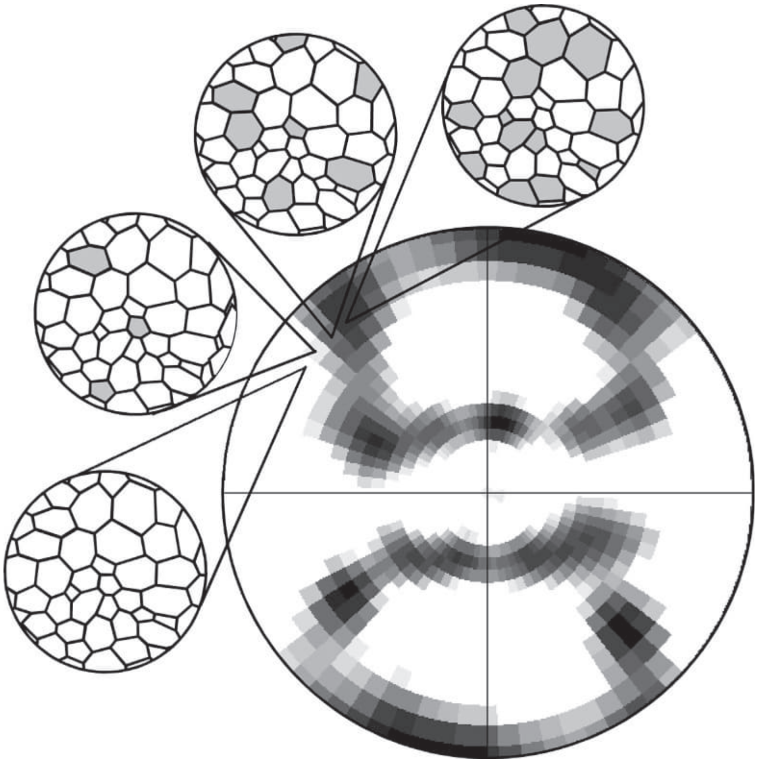

Fig. 13 Schematic showing grains satisfying the Bragg condition for successive 5° rotations about the sample normal (ϕ).

Electron backscatter diffraction

In the last three decades, the automation of electron backscatter diffraction (EBSD) in the scanning electron microscope (SEM) has made it practical to measure textures using the orientations of individual grains.

In EBSD, a highly tilted sample (~70°) is placed in the SEM as shown in Fig. 14. When a stationary electron beam impinges on a grain in the sample, a diffraction pattern is generated. The pattern is a function of the orientation of the lattice within the diffracting volume. As the electron beam is moved from grain to grain the diffraction pattern changes.

The pattern is imaged on a phosphor screen and transmitted to a computer using a high-gain camera. The orientation of the lattice in the diffracting volume can be derived from the pattern. This can be done automatically in the computer. The computer also controls the location of the beam on the sample. Typically, the beam is stepped across the sample to form a regular scan grid as shown in Fig. 15. An orientation measurement is made at each point in the grid. This process is fully automated and current rates exceed 5000 measurement points per second.

Despite the rapid measurement provided by automation, EBSD does not generally sample as many grains as the conventional X-Ray pole figure technique. However, EBSD has the advantage of spatially specific measurements of orientations allowing not only the distribution of orientations to be characterized, but misorientations and local texture gradients as well. If the texture is the sole focus of the EBSD analysis it is prudent to measure larger areas with a coarser step size so as to sample as many grain orientations as possible.

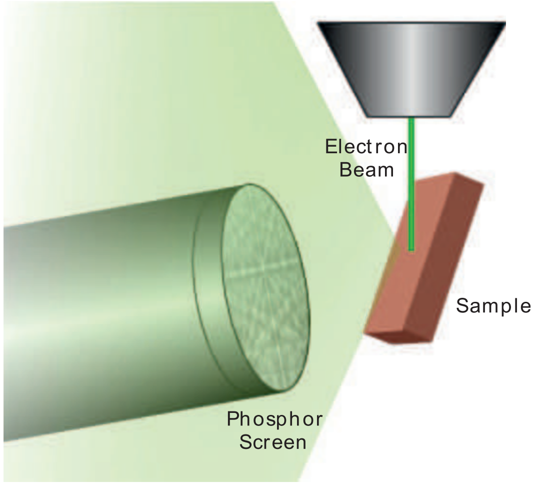

Fig. 14 Schematic of electron backscatter diffraction.

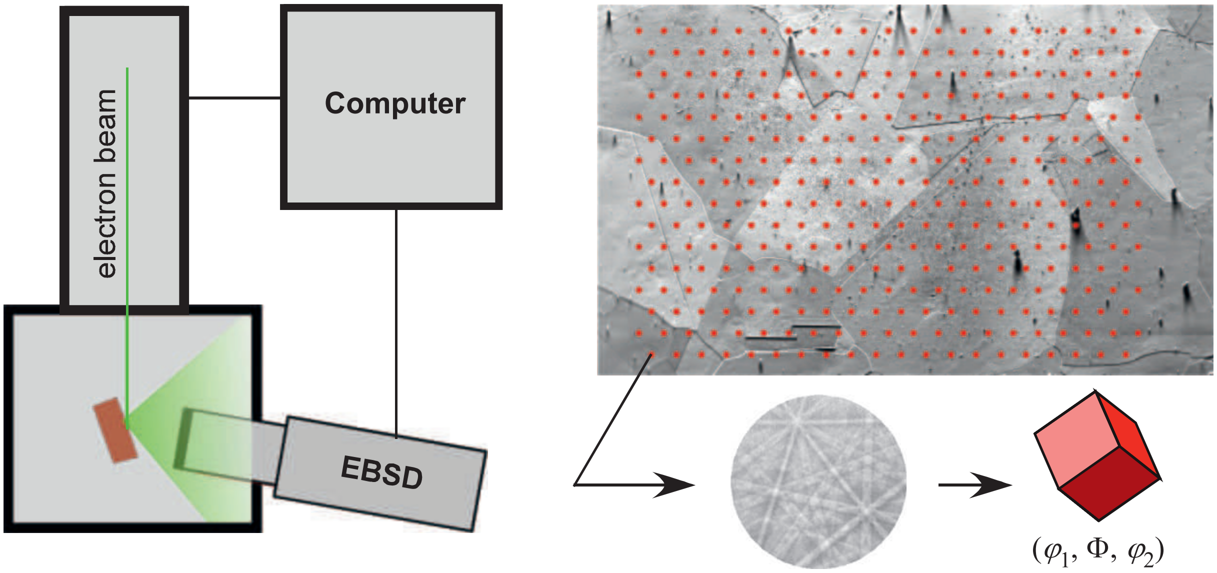

Fig. 15 Schematic of automated electron backscatter diffraction.

Rauch and Véron (2005) and Rauch et al. (2008) have automated orientation determination from electron diffraction spot patterns in the TEM to the state where this technique is now practical for texture measurements. Precession is used to acquire spot patterns with nearly double the number of spots as would appear in conventional selected area electron diffraction patterns. This allows rapid and reliable measurements of individual orientations on a scan grid similar to the EBSD approach but using template matching for orientation determination. However, given the limited area typically sampled in a TEM foil, the technique can be used to measure textures only in nanostructured materials.

Mathematical constructs

Basic equations

The basis of texture analysis is the orientation distribution function or ODF. The ODF is a probability density function describing the probability of finding a grain with an orientation,g, within a given angular distance, Δg, of a specified orientation, g_o, in a polycrystal; or, alternatively, the volume fraction of material oriented within Δg of g_o. These two descriptions are related through the following equation.

$$\frac{\Delta V_{(g_0+\Delta g)}}{V} = \oint_{g\in(g_0+\Delta g)} f(g)dg \tag{5}$$

Where the quantity to the left side of the equation is the volume fraction of material oriented within Δg of g_o and the function $f(g)$ inside the integral is the ODF. It should be noted that the following condition must be met for a density function:

$$\oint f(g)dg = 1 \tag{6}$$

where the integration is carried out over all of orientation space. The ODF gives the probability of finding a grain in a polycrystal with a specific orientation. If, for example, $f(g)$ is 3 then the chance of finding a grain with orientation, g, would be 3 times greater than that expected in a polycrystal with a random distribution of orientations. An ODF

$$f(g) = \sum_{l=0}^{\infty}\sum_{m=-l}^{l}\sum_{n=-l}^{l} C_l^{mn} T_l^{mn}(g) \tag{7}$$

may be represented as a sum of generalized spherical harmonics $T_l^{mn}(g)$ weighted by the so called C-coefficients C_l^{mn}. This representation is especially useful for the computation of mean tensorial properties as discussed in a subsequent section as for the computation of pole figures. While the direct computation of the sum in Eq. (7) is numerically challenging and is generally performed up to a maximum rank of $l = 34$, recent algorithms, which make use of fast Fourier techniques allow for the evaluation of the series expansion up to degree 200 reducing truncation errors (Potts et al., 2009; Hielscher, 2015). Kalidindi et al. (2009) have demonstrated that the fast Fourier techniques can be used in alternate series expansion schemes to estimate the ODF.

A pole figure can be derived through integration of the ODF along a specific path in orientation space according to

$$P_{\mathbf{h}}(\mathbf{y}) = \frac{1}{2\pi}\int_{\mathbf{h}||\mathbf{y}} f(g)d\chi \tag{8}$$

Where $P_{\mathbf{h}}(\mathbf{y})$ is the pole figure, $\mathbf{h}$ represents the (hkl) of the pole figure (a vector in the crystal reference frame), $\mathbf{y}$ is a vector in the pole figure (i.e. a vector in the sample reference frame represented by the rotation and tilt angles, ϕ and Ψ introduced previously). The integration is carried out along the path, χ, where $\mathbf{h}$ and $\mathbf{y}$ are coincident. With the C-coefficients C_l^{mn} from Eq. (7) the pole figures may be represented as sum of spherical harmonics, $k_l^n(\mathbf{y})$:

$$P_{\mathbf{h}_i}(\mathbf{y}) = \sum_{l=0}^{\infty}\frac{4\pi}{2l+1}\sum_{m=-l}^{l}\sum_{n=-l}^{l} C_l^{mn} k_l^{*m}(\mathbf{h}_i) k_l^n(\mathbf{y}) \tag{9}$$

ODF estimation from individual orientations

The objective of texture analysis is to process the pole figures or the individual orientation measurements to determine the ODF. It is easiest to conceptualize the ODF determination using the individual orientation measurements. Consider a set of orientation measurements, where the orientations can be described as points on a number line as shown schematically in Fig. 16. If the line is partitioned into a finite set of bins, then the number of orientations in each box can be counted and a histogram constructed as shown. A curve can then be fit to the histogram. The resulting curve is essentially the ODF.

It should be noted that the distribution of orientations shown schematically in Fig. 16 could be described using other distributions as shown in Fig. 17 depending on the size of the bins used to form the histogram. The choice is somewhat arbitrary; however, tensor properties, like elastic anisotropy or piezoelectricity, rely only on a low order description of texture and, hence, are not so sensitive to choice of bin size.

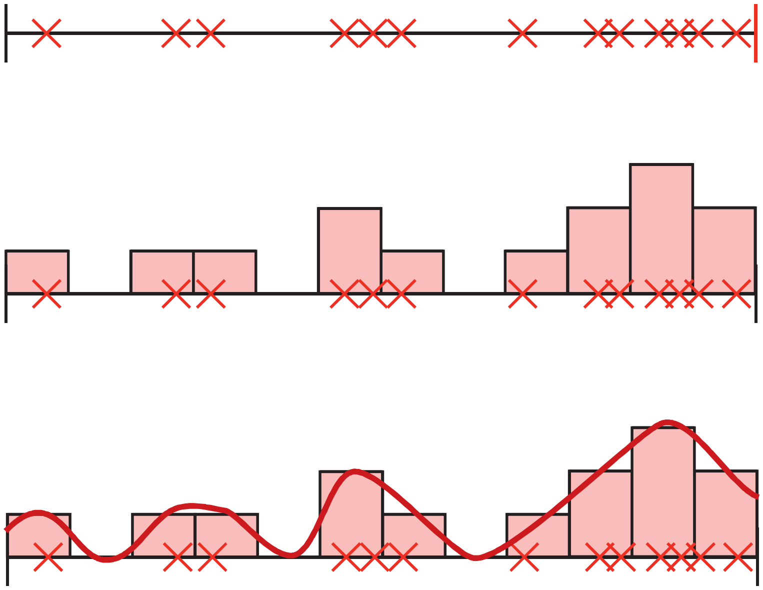

Fig. 16 A schematic of the determination of the ODF from individual orientation measurements.

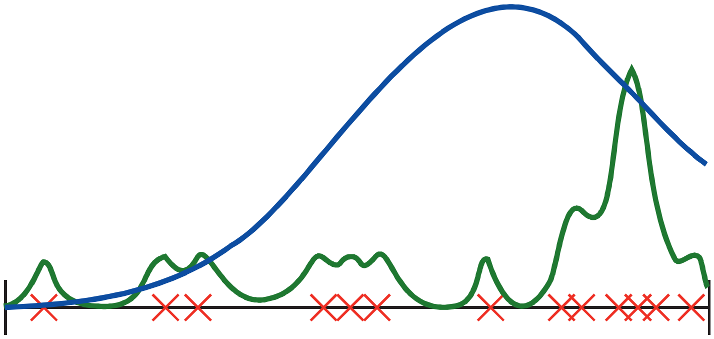

Fig. 17 Schematic showing lower and higher order descriptions of the texture shown in Fig. 16.

A second approach to determining the ODF from individual orientations is to estimate its *C*-coefficients according to the formula:

$$C_l^{mn} = \frac{2l+1}{N} \sum_{i=1}^{N} KT_l^{mn}(g_i) \tag{10}$$

where g_i represents one orientation from a set containing N individual orientation measurements. K is a smoothing factor. If single orientation measurements are made where only one measurement per grain is recorded then a weighting factor proportional to the grain area must also be introduced.

When estimating the ODF from individual measurements it is important that enough measurements are collected to ensure statistical reliability no matter the approach used to calculate the ODF (Hielscher, 2013; Wright et al., 2007). While scans with a fine step size are helpful for reconstructing the microstructure they may not be well suited for characterizing the texture of a sample. Fig. 18 shows an example from the cross-section of an aluminum bar. Two EBSD scans were measured, both containing approximately 1 million individual orientation measurements but collected at different magnifications in the microscope. The scan in Fig. 18A is excellent for reconstructing the microstructure but only samples a handful of grains whereas Fig. 18B does not give as good of a reconstruction of the microstructure it provides a very good measurement of the texture with over 29,000 grain orientations sampled. In both cases the orientation maps are constructed to show the crystal direction aligned with sample normal according to the stereographic triangle color legend – this color mapping scheme is used for all subsequent orientation maps. Note the lack of symmetry in the horizontal direction in the pole figures in Fig. 18 corresponds to the texture gradient visible in the corresponding orientation map of the sample. The left edge of the scan is near the surface of the bar.

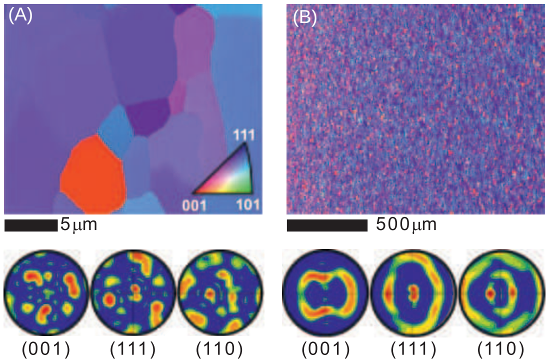

Fig. 18 Orientation map (showing the crystal direction aligned with the normal direction of the sample) reconstructed from two EBSD datasets on the cross-section of an aluminum bar along with pole figures calculated from the EBSD data using the harmonic method. (A) 1.02 million point dataset at a high magnification (B) 1.06 million point dataset collected at a low magnification.

ODF estimation from diffraction pole figure measurements

Unlike textures measured using individual orientations, it is important to note that there is no one-to-one relationship between measured pole figure data and ODFs. The ambiguity has two major reasons. First the limited number of pole figures available from X-ray measurements. This is illustrated in Figs. 19 and 20 which display 8 pole figures for two entirely different ODFs, 6 of which are completely identical.

The second source of ambiguity is the fact that in the integral equation (7) the odd order *C*-coefficients are mapped to zero and, hence, cannot be reconstructed from diffraction pole figures without additional assumptions. The effect of this ambiguity is illustrated in Fig. 21 which displays two radially symmetric ODFs with all pole figures being identical. Usually, the ODF with its peak at the component is considered to be the true ODF and the peaks at distance of 180° from the preferred orientation in the second ODF are referred to as ghosts (Matthies, 1980).

While there are multiple methods of performing the data reduction from the pole figures, three have emerged as the most common: the Harmonic, the WIMV and the MTEX methods. The WIMV (an acronym formed from the names of the originators of the technique) is essentially a binning method as outlined previously whereas the Harmonic method uses a series expansion approach, converting the orientation measurements directly to an ODF.

Harmonic method

The historically first method for reconstructing ODFs from diffraction pole figures was the series expansion using a set of harmonic functions developed independently by Bunge (1965) and Roe (1965). The harmonic method utilizes Eq. (9) to compute the C-coefficients C_l^{mn} of the ODF from the pole figure intensities by solving a set of systems of linear equations. These systems are well posed up to a maximum series expansion, *l*, which depends on the crystal symmetry and the number of pole figures measured. Since

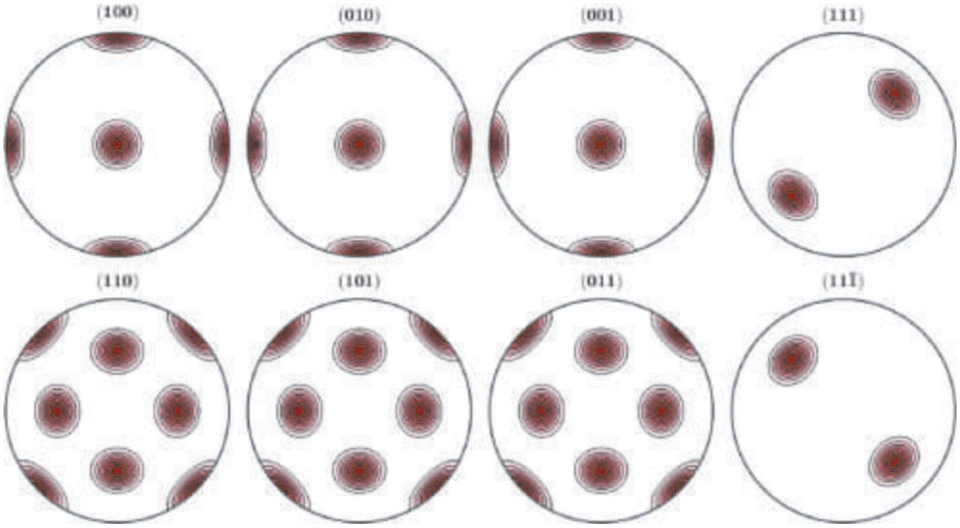

Fig. 19 Pole figures of an ODF from a material with orthorhombic crystal symmetry with preferred orientations at (0,90,0), (90,0,0) and (90,90,270) Euler angles.

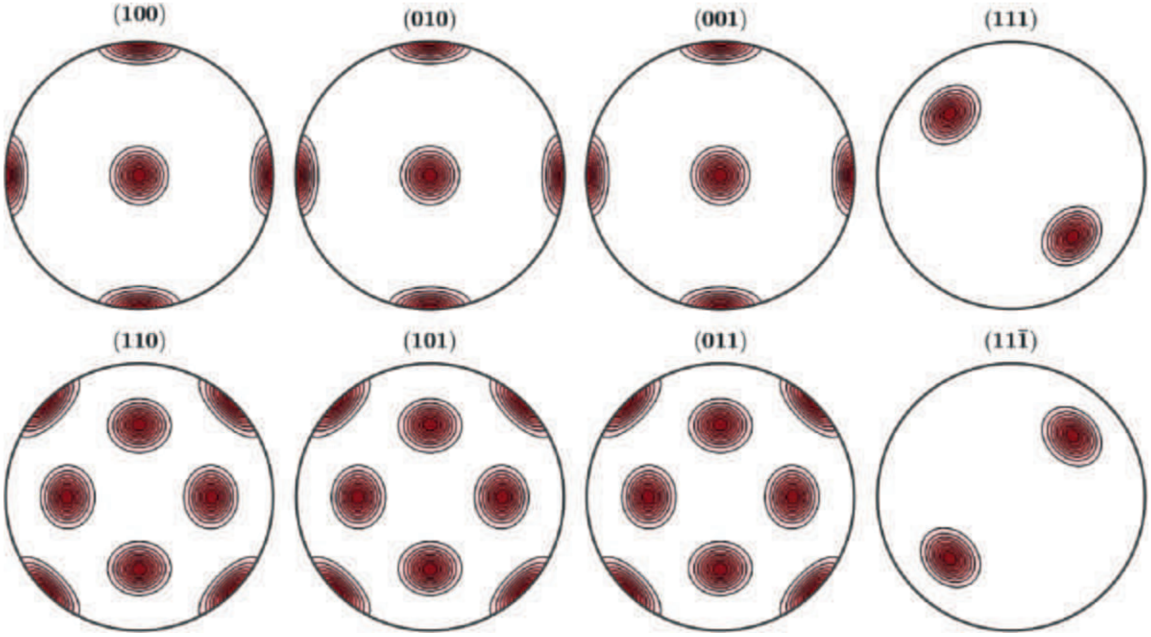

Fig. 20 Pole figures of an ODF from a material with orthorhombic crystal symmetry with preferred orientations at (0,0,0), (90,90,0) and (180,90,90) Euler angles.

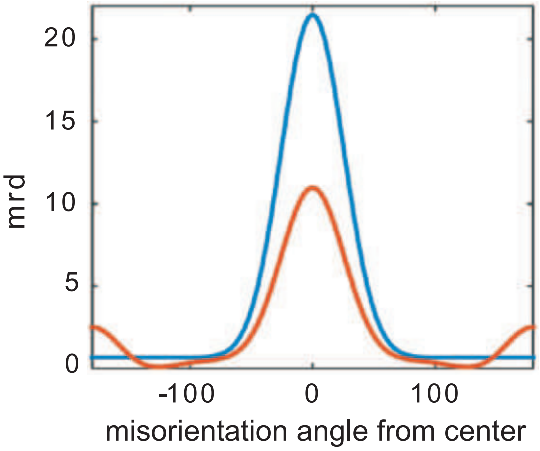

Fig. 21 Two triclinic radially symmetric ODFs which have the same even order C-coefficients and, hence, exactly the same pole figures. The small peak at 180° of the blue ODF is usually referred to as ghost effect.

the maximum harmonic degree, l, is generally quite low, sharp ODFs reconstructed by the harmonic method typically suffer from truncation errors. As mentioned previously this is not a major concern when dealing with physical properties as those depend only on the lower order C-coefficients, e.g., for characterizing elastic anisotropy arising from texture, the harmonic series need only be expanded out to $l = 4$. Another drawback of this approach stems from the fact that in diffraction pole figures all odd order C-coefficients C_l^{mn} are zero and, hence, the odd order C-coefficients of the reconstructed ODF are zero as well. This might result in negative values in the reconstructed ODF which are not allowed for density functions and makes ghost correction impossible.

WIMV method

The WIMV-method was initially described in Matthies and Vinel (1982) and later refined by Lutterotti et al. (1997). In contrast to the harmonic method it is based on a discretization of the orientation space into boxes resulting in a piecewise constant ODF. The relation between the ODF values at these boxes and the pole figure intensities can be expressed as a large system of linear equations which is solved iteratively. The iterative solver is designed to allow only positive values for the ODF, which is a big advantage over the harmonic method. One of the challenges of this technique is the ambiguity of Euler space at $\Phi = 0°$. At $\Phi = 0$, ϕ_1 and ϕ_2 are not fully defined but rather governed by $\phi_1 + \phi_2$ equals a constant. The volume of the bins vary as a function of Φ, bins centered on

$\Phi = 2.5°$ have a volume of 0.044 rad cubed and bins centered on $\Phi = 87.5°$ have a volume of 0.999 assuming 5° x 5° x 5° bins. In contrast to WIMV, the refinements embodied in eWIMV (Lutterotti et al., 1999) applies some subsequent smoothing to the reconstructed ODF to hide the initial piecewise constant nature.

MTEX method

The MTEX method was first described by Hielscher and Schaeben (2008) and can be seen as a synthesis of the harmonic and the WIMV methods. The MTEX method relies on a discretization of the ODF by bell shaped functions

$$f(g) = \sum_{k=1}^{K} c_k \phi(g_k g) \tag{11}$$

which is similar to the WIMV method as it is based on a discrete grid g_k in the orientation space. Though, the g_k do not need to form a regular grid but are usually placed to represent equal volume in the orientation space. On the other hand, the discretization (11) directly translates into a representation of the ODF in terms of generalized spherical harmonics:

$$f(g) = \sum_{l=0}^{\infty} \widehat{\phi}(l) \sum_{m=-l}^{l} \sum_{n=-l}^{l} T_l^{mn}(g) \sum_{k=1}^{K} c_k T_l^{mn}(g_k) \tag{12}$$

The MTEX method uses representation (11) to ensure the non-negativity of the ODF and representation (12) to link the ODF with the pole figures by equation (9). The transition between representation (11) and (12) is done via a fast Fourier transform in orientation space. The coefficients c_k are computed from the pole figure intensities by iteratively solving a system of linear equations.

Examples

Thin films

Thin films are typically characterized by the alignment of a particular crystallographic axis with the sample normal. Fig. 22A shows a (111) pole figure for an aluminum thin film. The axisymmetric character of this material is sometimes called a (111) fiber texture. Some thin film properties (such as the mean time to failure in microelectronic devices) have been correlated to the sharpness of the fiber texture. An axisymmetric texture can be more simply analyzed by a pole plot as shown in Fig. 22B. The pole plot is essentially a slice through the pole figure as shown. For more accurate results, the pole plot can be improved by averaging azimuthally.

While the pole plot is helpful for analyzing thin film textures, calculating the pole figures to verify that the texture is truly axisymmetric is always recommended. For example, in a copper thin film, a (111) fiber texture is expected. However, other fibers may also be present. The axisymmetric nature of the texture can be confirmed using a pole figure and the presence of other fibers discovered using an inverse pole figure as shown in Fig. 23.

Rolled sheet

One of the most studied materials using texture analysis is rolled aluminum sheet for beverage cans. The texture of this material must be as well controlled as possible in order to produce stock well suited for the deep drawing of cans. A typical (111) pole figure for rolled aluminum is shown in Fig. 24.

The bulk of the orientations typically lie within a "fiber" in Euler space as shown in Fig. 25. In order to simplify the analysis of rolled face-centered cubic (fcc) materials such as aluminum, components associated with key locations along this fiber have been identified. These key components are shown in Euler space and in a (111) pole figure.

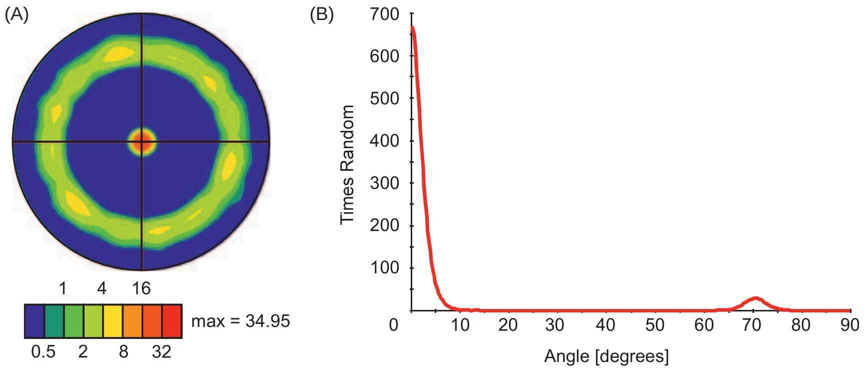

Fig. 22 (A) (111) Pole figure and (B) corresponding pole plot from an aluminum thin film.

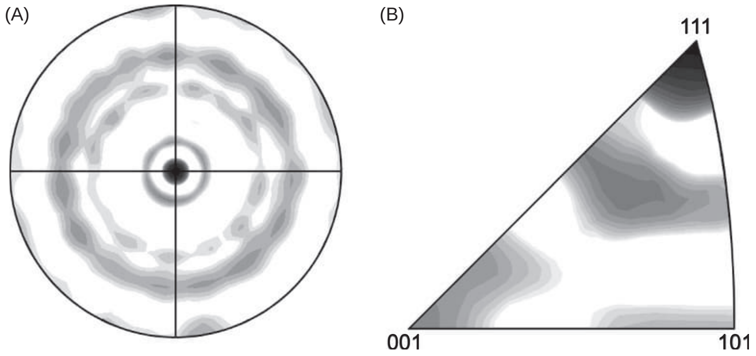

Fig. 23 (A) (111) Pole figure and (B) an inverse pole figure for a copper thin film.

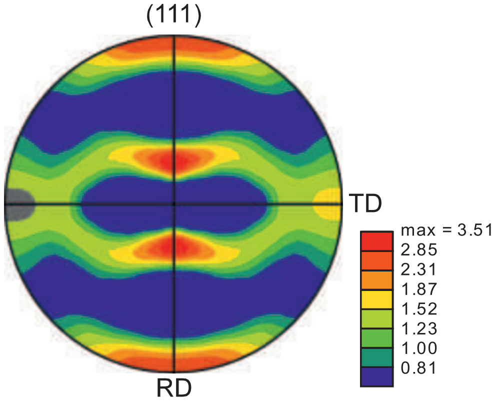

Fig. 24 (111) Pole figure calculated using the harmonic method on individual orientation measurements obtained using EBSD on rolled aluminum. Orthotropic sample symmetry was enforced in the calculations.

(A)

Name	Indices	(φ_1,Φ,φ_2)
▲copper	{112}<11$\bar{1}$>	90°, 35°, 45°
●S3	{123}<63$\bar{4}$>	59°, 37°, 63°
◆brass	{110}<$\bar{1}$12>	35°, 45°, 0°
■Goss	{110}<001>	0°, 45°, 0°

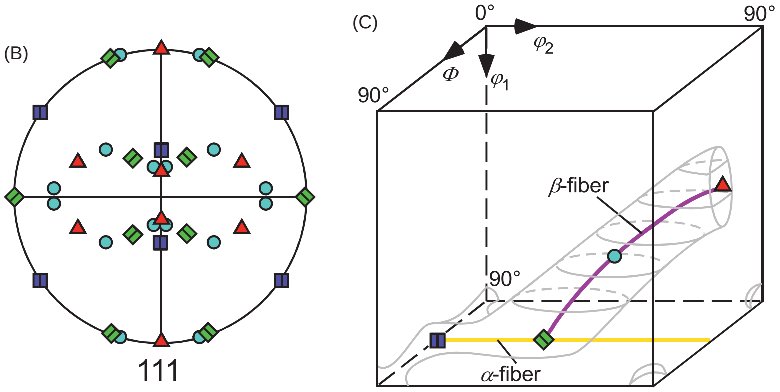

Fig. 25 (A) Table ideal components for face-centered cubic rolling textures. (B) location of ideal texture components in (A) shown in a (111) pole figure. (C) texture fibers shown in Euler angle space.

An FCC rolling texture can then be simply characterized by the intensities of these ideal components. This approach has been successfully used in refining the thermomechanical processes of rolled aluminum to achieve textures that optimize the deep-drawing performance of beverage can stock. Different fibers or texture components are used in rolled steel (Kocks et al., 1998) or in rolled hexagonal materials (Tenckhoff, 1988).

Fig. 26 shows the evolution of texture in a cold-rolled interstitial free steel. Note that the initial texture is relatively random but increases in both intensity but also in reflecting the orthotropic symmetry of the rolling process with increasing reduction.

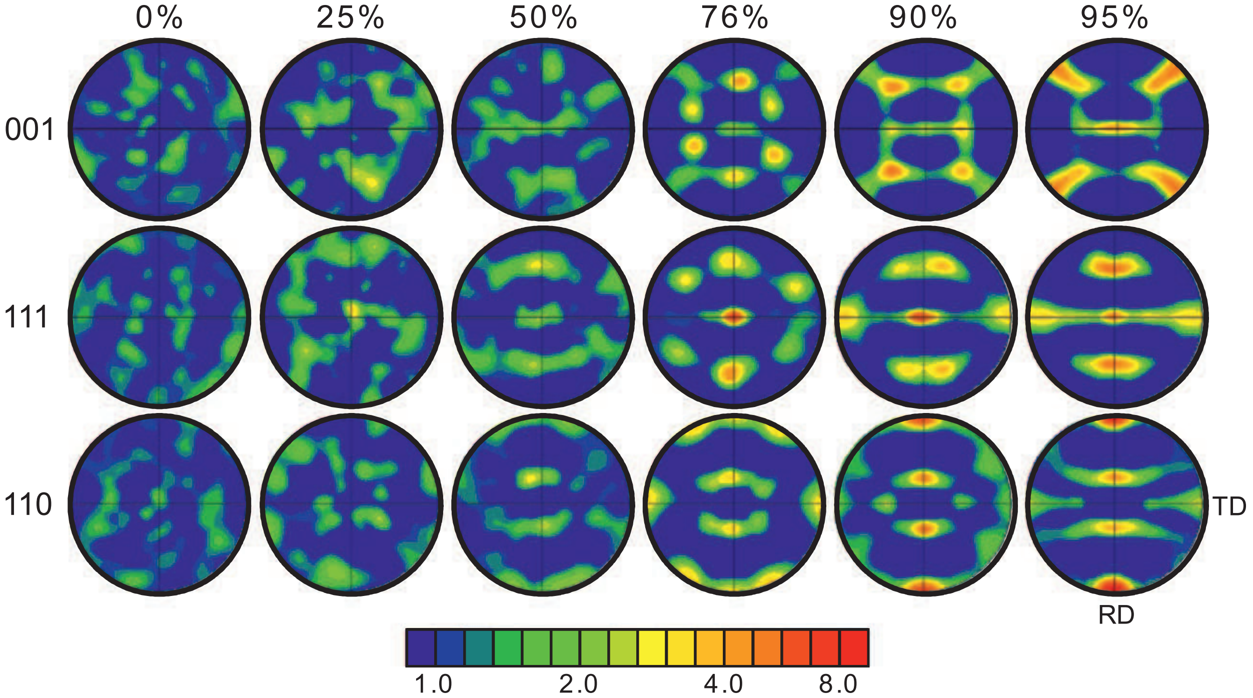

Fig. 26 Pole figures for successive cold-rolling reductions of an interstitial-free steel as measured by EBSD and analyzed using the harmonic method. The intensities are given in multiples for a random distribution.

Other texture related entities

Misorientation

To this point, the orientation of a crystal has been described relative to the sample coordinate system. However, the orientation of one crystal could also be described relative to the coordinate system associated with a neighboring crystal. Such a description is more often denoted a misorientation (or alternatively a disorientation or orientation difference). While misorientations can be described similar to orientations, i.e. in terms of Euler angles or matrices, it is usually more convenient to describe them in terms of an axis-angle pair. For two crystals in any two orientations, it is always possible to find a common axis around which one crystal can be rotated until it is in coincidence with the other. The misorientation can thus be described as a rotation about the common axis. As with orientation, crystal symmetry plays a role in the description of misorientations. For example, for a crystal with cubic symmetry there are 24 symmetrically equivalent orientations. Thus, for a misorientation between two cubic crystals, there are 576 (24×24) symmetrically equivalent misorientations. This is realized in axis-angle space as essentially 24 axes of rotation, each of with a specific angle of rotation associated with it and 24 different permutations of the indices describing the axes. Generally, the misorientation from the symmetrically equivalent set of misorientations of minimum angle of rotation is used to and is called the disorientation. In the same manner as ODFs, Misorientation Distribution Functions (MDFs) may also be calculated. However, point specific measurements are needed so EBSD is generally used to acquire the misorientation data for MDF calculations.

Fig. 27 shows an example for a bend-specimen of titanium (primarily the hexagonal close packed α phase). The material accommodates strain through twinning. Four types of twins are expected, two tensile types and two compressive types. There is a good mix of the tensile twin described by a 94.8° rotation about the $\langle\bar{1}2\bar{1}0\rangle$ crystal direction as well as the compression twin of 64.3° rotation about $\langle\bar{1}100\rangle$ accompanied by a few 34.8° rotation about $\langle\bar{1}100\rangle$ twins. However, the 57.0° rotation about $\langle\bar{1}2\bar{1}0\rangle$ compression twins were not observed. The balance between these different twins can be quantified using the MDF. The MDF shown in Fig. 27B is shown for axis-angle space, where the constant sections are for successive disorientation angles and the sections are given in the stereographic unit triangle for hexagonal crystal symmetry. While, in this case, the twins were known, in a material where the twins were unknown, the MDF could be utilized to identify the most important boundary types. This methodology can also be used, for example, to find specific boundaries susceptible and/or resistant to damage, or boundaries prone to grain boundary sliding.

The terms grain boundary texture and mesotexture are sometimes used to describe the texture associated with misorientation at grain boundaries. When 3D data is acquired via EBSD and serial sectioning or HEDM then the link between misorientation and the orientation of the boundary plane can be characterized through five dimensional distribution function analysis (Rohrer and Randle, 2009).

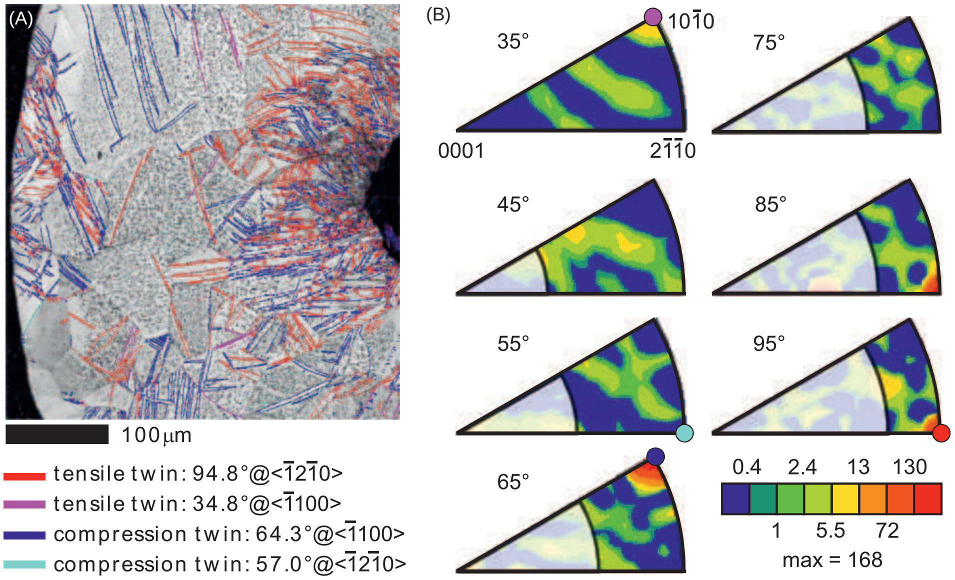

Fig. 27 (A) EBSD pattern quality map for an α titanium bend sample overlaid with tensile and compression twins. (B) Misorientation distribution function for boundaries greater than 15° with the tensile and compression twins highlighted. The non-faded portions correspond to the asymmetric domain for hexagonal symmetry in axis-angle space that show the asymmetric domain.

Microtexture

As a material deforms, the orientations of individual grains rotate due to slip of specific crystallographic planes in the material. Orientation gradients will form within grains and may also fragment into subgrains. The local variation in orientation within individual grains is often termed microtexture. In general, the ODF based analysis is not employed in analyzing microtextures but rather the study of local disorientations is used (Wright et al., 2011). Fig. 28 shows an example from an in-situ tensile test of a medium carbon steel sample. EBSD measurements on the surface were performed as the sample was held in tension at increasing levels of strain. For each EBSD scan, the spread in the orientation within the individual grains was tracked. As the strain increases, the spread in orientation also increases (Wright et al., 2016). The variation in orientation is also visible in the orientation map as evidenced by the subtle changes in color within the individual grains.

Materials properties and modelling

Tensor averaging

One way to capture the anisotropic materials properties is through the use of tensors as shown in Nye's classic text on the subject (1957). When individual orientation measurements collected on a regular grid are used to characterize the texture of a polycrystal

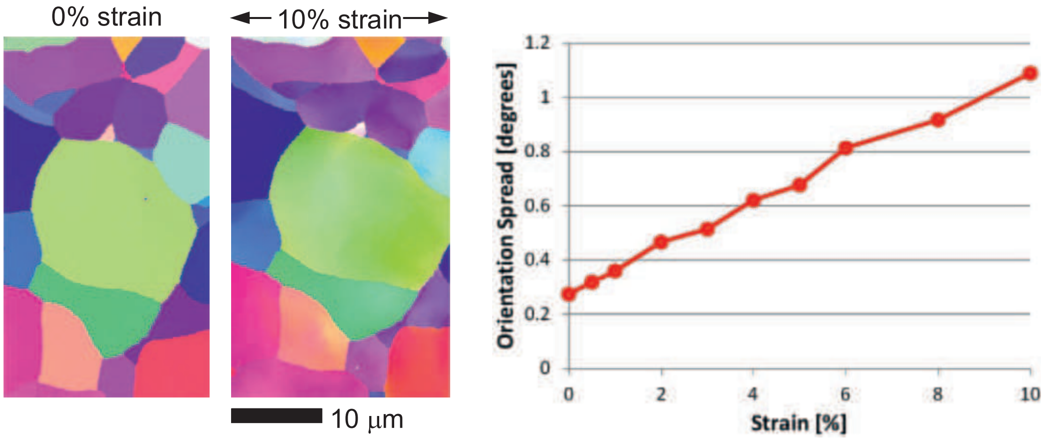

Fig. 28 Orientation maps reconstructed from in-situ EBSD measurement on a tensile steel sample prior to the tensile test and at 10% strain. Corresponding plot of orientation spread as a function of strain.

(as is the case for EBSD measurements) then if the property tensor for the single crystal is known the upper or Voigt bound for the polycrystal property tensor can be determined as shown for a fourth rank tensor in Eq. (1). In this case, each orientation is simply weighted by 1. The lower or Reuss bound can be determined similarly but employing the inverse of the property tensor. For example, for elastic anisotropy the stiffnesses (C_{ijkl}) are used to calculate the Voigt bound and the compliances (S_{ijkl}) are used to calculate the Reuss bound as shown in Eq. (13).

$$\overline{S}_{ijkl} = \frac{1}{N}\sum_{n=1}^{N} g^n_{ip}g^n_{jq}g^n_{kr}g^n_{ls}S_{pqrs} \tag{13}$$

Fig. 29 shows an example for a 95% cold-rolled interstitial free steel. In this figure, Young's modulus at several points in the microstructure (a region from the data used to construct the textures shown in Fig. 27) is shown and as well as the bulk average as calculated from the texture. The average Young's modulus is the average of the Voigt and Reuss bounds for the sample (Fig. 29).

Bunge (1982) has also shown that if the C_l^{mn}-coefficients of the harmonic series expansion are determined, then these can also be used to estimate a given property tensor for a bulk materials in conjunction with the single crystal property tensor. It should be noted that the rank of the C_l^{mn}-coefficients used in the estimation would be on the same order as the rank of the tensor. For example, for elastic stiffnesses the rank of the tensor is four and thus, only C_l^{mn}-coefficients up to a rank of $l = 4$ are used in the calculation. While we have used the example of elastic stiffness here, the same principles can be applied to other properties which lend themselves to the tensorial representation. Average property tensors of any order can be computed as demonstrated by Mainprice et al. (2011) using fast algorithms. For example, Mainprice et al. (2014) have computed the average anisotropic piezoelectric property tensor from texture data which is a third rank tensor.

Several authors have proposed methodologies to derive a representative set of weighted individual orientations from an ODF (Eisenlohr and Roters, 2008; Toth and Van Houtte, 1992; Kocks et al., 1990; Melchior and Delannay, 2006). Such methods can be applied to an ODF calculated using any approach. The representative set of orientations and their weights can then be used in the manner shown in Eq. (1) to calculate a bulk polycrystal property tensor.

Modelling

This section is not intended to provide comprehensive coverage of the wealth of models that have been developed to simulate the evolution of texture during deformation; but, rather provide a brief introduction to this field of research.

Two basic approaches are the Sachs (1929) and Taylor (1938) models. In the Sachs model each grain in the polycrystal is assumed to experience the same amount of stress whereas in the Taylor model each grain is assumed to undergo the same amount of strain. Furthermore, in the Sachs model the strain is achieved through slip on a single slip system; whereas for the Taylor model deformation is accommodated through slip on multiple slip systems. In the Sachs model equilibrium is satisfied at the grain boundaries but the compatibility conditions are not which leads to gaps and overlaps between the grains. The converse is true in the Taylor model – the compatibility conditions are met between the grains but the equilibrium at grain boundaries is not. The Taylor model is well suited for large strains where it is unlikely any single grain will deviate much from the average.

In terms of texture evolution, it is important to recall that slip produces grain rotation. Thus, effective modelling of the slip enables the evolution of texture to be predicted. Adaptations of these models and other more sophisticated models have been developed since these early models such as the relaxed constraints Taylor model, the self-consistent model (Kröner, 1961; Budiansky and Wu, 1962; Molinari et al., 1987) and the viscoplastic model (Asaro and Needleman, 1985). One adaptation is to

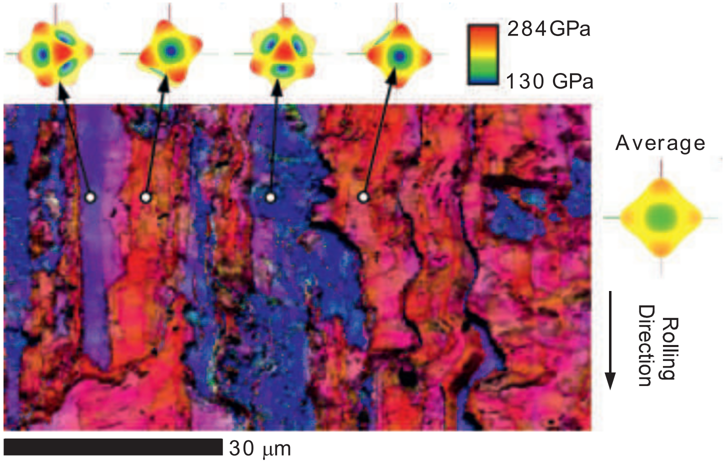

Fig. 29 Map reconstructed from a subset of the EBSD data obtained on the 95% cold-rolled steel sample shown in Fig. 26. The color in the map shows the crystal direction aligned with the normal direction, the gray scale reflects the relative quality of the EBSD pattern at each point in the scan. Schematics of Young's modulus at selected locations in the microstructure are shown along with the Voigt-Reuss average for the full dataset.

essentially embed a polycrystal plasticity model into each individual element of a Finite-Element Model (Beaudoin et al., 1994; Van Houtte et al., 2005; Roters et al., 2010). This then allows some of the limitations of these models to be overcome and applied to the simulation of polycrystals in complex geometries with heterogeneous boundary conditions and in three dimensions. Other adaptations include the treatment of materials which deform not only by slip but also by mechanical twinning (Beyerlein and Tomé, 2010) and also more complexity in the treatment of strain hardening on the slip systems (Rollett and Kocks, 1993).

Another area of modelling is that of recrystallization and grain growth. A good overview of the subject is given by Rollett (1997). Important areas of research include the balance between oriented nucleation versus oriented growth and the role grain boundaries play in these processes, both in terms of the orientation of the boundary planes as well as the misorientations between neighboring grains (Rollett, 2013).

Conclusion

Texture analysis focuses on the distribution of lattice orientations of the constituent grains in polycrystalline materials. Texture is typically measured using X-Ray or neutron diffraction pole figures or individual orientation measurements obtained by electron backscatter diffraction or high energy X-Ray diffraction. Various mathematical methods have been developed to reduce the texture data to the core orientation distribution function in three-dimensional orientation space. Analysis of the ODF through various data can provide understanding on the governing mechanisms in the evolution of the microstructure during thermo-mechanical processing. It can also be used predict anisotropy in the physical properties of crystalline materials.

Acknowledgments

Matthew Nowell of EDAX and Seiichi Suzuki of TSL Solutions are gratefully acknowledged for providing EBSD datasets used in constructing several of the figures.

References

Asaro RJ and Needleman A (1985) Overview no. 42 Texture development and strain hardening in rate dependent polycrystals. *Acta Metallurgica et Materialia* 31: 1951–1976.
Beaudoin AJ, Dawson PR, Mathur KK, Kocks UF, and Korzekwa DA (1994) Application of polycrystal plasticity to sheet forming. *Computer Methods in Applied Mechanics and Engineering* 117: 49–70.
Beyerlein IJ and Tomé CN (2010) A probabilistic twin nucleation model for HCP polycrystalline metals. *Proceedings of the Royal Society A: Mathematical, Physical and Engineering Sciences* 466: 2517–2544.
Budiansky B and Wu TT (1962) Theoretical prediction of plastic strains of polycrystals. In: Proceedings of the 4th U.S. National Congress on Applied Mechanics, pp. 1175–1185. New York: American Society of Mechanical Engineers.
Bunge HJ (1965) Zur Darstellung Allgemeiner Texturen. *International Journal of Materials Research* 56: 872–874.
Bunge HJ (1982) *Texture Analysis in Materials Science: Mathematical Methods*. London: Butterworths.
Dillamore IL and Roberts WT (1965) Preferred orientation in wrought and annealed metals. *Metallurgical Reviews* 10: 271–380.
Eisenlohr P and Roters F (2008) Selecting a set of discrete orientations for accurate texture reconstruction. *Computational Materials Science* 42: 670–678.
Hielscher R (2013) Kernel Density Estimation on the rotation group and its application to crystallographic texture analysis. *Journal of Multivariate Analysis* 119: 119–143.
Hielscher R (2015) MTEX 4.0 - A texture calculation toolbox. mtex-toolbox.github.io.
Hielscher R and Schaeben H (2008) A novel pole figure inversion method: Specification of the MTEX algorithm. *Journal of Applied Crystallography* 41: 1024–1037.
Holzner C, Lavery L, Bale H, Merkle A, McDonald S, Withers P, Zhang Y, Juul Jensen D, Kimura M, Lyckegaard A, Reischig P, and Lauridsen EM (2016) Diffraction contrast tomography in the laboratory – Applications and future directions. *Microscopy Today* 24: 34–43.
Kalidindi SR, Knezevic M, Niezgoda S, and Shaffer J (2009) Representation of the orientation distribution function and computation of first-order elastic properties closures using discrete Fourier transforms. *Acta Materialia* 57: 3916–3923.
Kocks UF, Kallend JS, and Biondo AC (1990) Accurate representations of general textures by a set of weighted grains. *Textures and Microstructures* 14-18: 199–204.
Kocks UF, Tomé CN, and Wenk HR (1998) *Texture and Anisotropy: Preferred Orientations in Polycrystals and their Effect on Materials Properties*. Cambridge: Cambridge University Press.
Kröner E (1961) Zur plastichen Verformung des Vielkristalls. *Acta Materialia* 9: 155–161.
Lutterotti L, Matthies S, Wenk HR, Schultz AS, and Richardson JW Jr. (1997) Combined texture and structure analysis of deformed limestone from time-of-flight neutron diffraction spectra. *Journal of Applied Physics* 81: 594–600.
Lutterotti L, Matthies S, and Wenk HR (1999) In: Sen-Gupta S (ed.) *MAUD: A friendly Java program for material analysis using diffraction*. Commission on Powder Diffraction Newsletter 21, pp. 14–15. International Union of Crystallography.
Mainprice D, Hielscher R, Schaeben H, Prior DJ, Rutter EH, and Tatham DJ (2011) Calculating anisotropic physical properties from texture data using the MTEX open source package. *Geological Society - Special Publications* 360: 175–192.
Mainprice D, Bachmann F, Hielscher R, Schaeben H, and Lloyd GE (2014) Calculating anisotropic piezoelectric properties from texture data using the MTEX open source package. *Geological Society - Special Publications* 409: 223–249.
Matthies S (1980) Demonstration of the ghost effect in the presentation of the orientation distribution of texturized materials. *Physica Status Solidi B: Basic Solid State Physics* 97: 547–556.
Matthies S and Vinel GW (1982) On the reproduction of the orientation distribution function of texturized samples from reduced pole figures using the conception of a conditional ghost correction. *Physica Status Solidi B: Basic Solid State Physics* 112: K111–K114.
Melchior MA and Delannay L (2006) A texture discretization technique adapted to polycrystalline aggregates with non-uniform grain size. *Computational Materials Science* 37: 557–564.
Molinari A, Canova GR, and Ahzi S (1987) A self consistent approach of the large deformation polycrystal viscoplasticity. *Acta Metallurgica et Materialia* 35: 2983–2994.

Morawiec A (2003) *Orientations and Rotations*. Berlin Heidelberg: Springer-Verlag.

Nye JF (1957) *Physical Properties of Crystals: Their Representation by Tensors and Matrices*. Oxford: Oxford University Press.

Pokharel R (2018) Overview of High-Energy X-Ray Diffraction Microscopy (HEDM) for Mesoscale Material Characterization in Three-Dimensions. In: Lookman T, Eidenbenz S, Alexander F, and Barnes C (eds.) *Materials Discovery and Design*. *Springer Series in Materials Science*, vol. 280. Cham: Springer.

Potts D, Prestin J, and Vollrath A (2009) A Fast algorithm for nonequispaced Fourier transforms on the rotation group. *Numerical Algorithms* 52: 355–384.

Rauch EF and Véron M (2005) Coupled microstructural observations and local texture measurements with an automated crystallographic orientation mapping tool attached to a TEM. *Materialwissenschaft und Werkstofftechnik* 36: 552–556.

Rauch EF, Véron M, Portillo J, Bultreys D, Maniette Y, and Nicolopoulos S (2008) Automatic crystal orientation and phase in TEM by precession diffraction. *Microscopy and Analysis* 93: S5–S8.

Roe RJ (1965) Description of crystallite orientation in polycrystalline materials. III. General solution to pole figure inversion. *Journal of Applied Physics* 36: 2024–2031.

Rohrer GS and Randle V (2009) In: Schwartz AJ, Kumar M, Adams BL, and Field DP (eds.) *Measurement of the Five-Parameter Grain Boundary Distribution from Planar Sections*, pp. 215–229. New York: Springer.

Rollett AD (1997) Overview of modeling and simulation of recrystallization. *Progress in Materials Science* 43: 79–99.

Rollett AD (2013) Implementation of anisotropic grain boundary properties in mesoscopic simulations. In: Molodov DA (ed.) *Microstructural Design of Advanced Engineering Materials*, pp. 161–186. Weinheim: Germany, Wiley VCH Verlag.

Rollett AD and Kocks UF (1993) A review of the stages of work hardening. *Solid State Phenomena* 35-36: 1–18.

Roters F, Eisenlohr P, Hantcherli L, Tjahjanto DD, Bieler TR, and Raabe D (2010) Overview of constitutive laws, kinematics, homogenization and multiscale methods in crystal plasticity finite-element modeling: Theory, experiments, applications. *Acta Materialia* 58: 1152–1211.

Sachs G (1929) Zur Ableitung einer Fliessbedingun. In: *Mitteilungen der deutschen Materialprüfungsanstalten*, pp. 98–102. Berlin Heidelberg: Springer-Verlag.

Taylor GI (1938) Plastic strain in metals. *Journal of the Institute of Metals* 62: 307–324.

Tenckhoff E (1988) *Deformation Mechanisms, Texture and Anisotropy in Zirconium and Zircaloy*. Philadelphia: ASTM.

Toth LS and Van Houtte P (1992) Discretization techniques for orientation distribution functions. *Textures and Microstructures* 19: 229–244.

Van Houtte P, Li S, Seefeldt M, and Delannay L (2005) Deformation texture prediction: from the Taylor model to the advanced Lamel model. *International Journal of Plasticity* 21: 589–624.

Wenk HR (1985) *Preferred Orientation in Deformed Metals and Rocks: An Introduction to Modern Texture Analysis*. Orlando: Academic Press.

Wenk HR (2003) Texture and anisotropy. In: Karato S and Wenk H-R (eds.) *Plastic Deformation of Minerals and Rocks, Reviews in Mineralogy and Geochemistry*. vol. 51, pp. 291–321. Berlin, Boston: De Gruyter.

Wright SI, Nowell MM, and Bingert JF (2007) A comparison of textures measured using x-ray and electron backscatter diffraction. *Metallurgical and Materials Transactions A: Physical Metallurgy and Materials Science* 38: 1845–1855.

Wright SI, Nowell MM, and Field DP (2011) A review of strain analysis using electron backscatter diffraction. *Microscopy and Microanalysis* 17: 316–329.

Wright SI, Suzuki S, and Nowell MM (2016) In situ EBSD observations of the evolution in crystallographic orientation with deformation. *JOM* 68: 2730–2736.

Nanostructures, Electronic Structure of

JR Chelikowsky, University of Texas at Austin, Austin, TX, USA

© 2005 Elsevier Ltd. All rights reserved.

This is an update of J.R. Chelikowsky, Nanostructures, Electronic Structure of, Editor(s): Franco Bassani, Gerald L. Liedl, Peter Wyder, Encyclopedia of Condensed Matter Physics, Elsevier, 2005, Pages 51–58, ISBN 9780123694010, https://doi.org/10.1016/B0-12-369401-9/00468-X.

Introduction 500
Theory for the Electronic Structure at the Nanoscale 502
Approximations to the Electronic Structure Problem 503
The Kohn–Sham Equation 504
Computational Approaches for Nanostructures 505
Calculated Electronic Levels in Nanostructures 506
Further Reading 508

Nomenclature

a	box size (m)
$\mathbf{e}$	electron charge (C)
E	energy (J)
E_{c}	correlation energy (J)
E_{gap}	optical gap (J)
E_n	energy eigenvalue (J)
E_{x}	exchange energy (J)
$\mathscr{E}_x$	exchange energy density (J m^{-3})
$\mathbf{G}$	reciprocal lattice vector (m^{-1})
h	grid spacing (m)
H	Hamiltonian operator (J)
H^{KS}	Kohn–Sham Hamiltonian (J)
$\hbar$	Planck's constant (J s)
$\mathbf{k}$	wave vector (m^{-1})
m	electron mass (kg)
$\mathscr{M}$	nuclear mass (kg)
$\mathbf{p}$	momentum (kg m s^{-1})
r	electronic position (m)
$\mathbf{R}$	dot radius (m)
R	nuclear position (m)
$\mathscr{R}$	lattice vector (m)
t	time (s)
V_{H}	Hatree potential (J)
V_{p}	ionic pseudopotential (J)
V_{p}	pseudopotential (J)
V_{xc}	exchange–correlation potential (J)
$\mathbf{x}$	particle position (m)
Z	atomic number
$\boldsymbol{\rho}$	electronic charge density (Cm^{-3})
$\boldsymbol{\varphi}$	electronic orbital
$\boldsymbol{\Phi}_j$	localized orbital
$\boldsymbol{\Psi}$	wave function

Introduction

At the atomic scale, electronic states are typically characterized by discrete energy levels that are often separated by electron volts; the spatial distribution of these states is highly localized. In contrast, electronic states in crystalline matter are typically characterized by energy bands: the energy states form a quasicontinuous spectrum with delocalized spatial distributions. At the nanoscale, the distribution of energy states resides between these limits. This evolution of energy levels from an atom to large clusters to "quantum dots" is illustrated in Figure 1. A large cluster in this scheme may possess hundreds or thousands of atoms. When its surface is

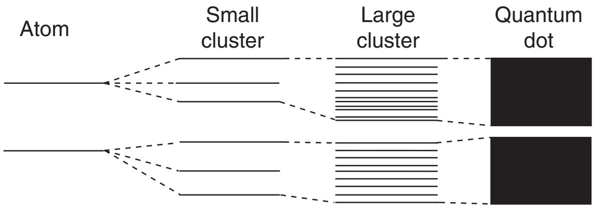

Figure 1 Schematic energy levels for an atom, a cluster, and a quantum dot.

electronically passivated, such large clusters are called quantum dots. While the energy spacing between electronic levels in a quantum dot is not quasicontinuous, it is usually too small to be measured. For example, the spacing may be much smaller than the thermal energy associated with a vibrational mode.

Understanding the evolution of the electronic structure of matter at the nanoscale is a challenging task. Matter at this length scale is not especially amenable to techniques based on atomic or macroscopic descriptions, as the spatial and energetic distribution of electron states are quite disparate. Methods for calculating the electronic properties of these systems usually start from either the atomic or molecular limit or from the solid-state limit. Atomic or molecular methods are often not equipped to handle the large number of atoms or electrons in nanoscale materials whereas solid-state methods often require translational symmetry, which is not present for confined systems. Moreover, the electronic interactions and spatial extent of wave functions at the nanoscale can be remarkably different than either the atomic or macroscopic limit.

An electron confined within a one-dimensional box of size a is considerd. The lowest energy level of this system is given in elementary textbooks as

$$E = \frac{\pi^2 \hbar^2}{2ma^2} \qquad [1]$$

where $\hbar$ is the Planck constant divided by 2π, and m is the mass of the particle, for example, the mass of an electron. If the size of the box is reduced, then E increases.

This phenomenon, that is, the energy level spacing increasing with reduced dimensionality, is called quantum confinement. Quantum confinement can be readily understood from the Heisenberg uncertainty principle. The uncertainty principle states that the uncertainty in momentum and position must be such that the product exceeds $\hbar/2$:

$$\Delta p \cdot \Delta x \geq \frac{\hbar}{2} \qquad [2]$$

where Δp is the uncertainty in the momentum and Δx is the uncertainty in the position of the electron. Consider the energy of a free electron with momentum p:

$$E = \frac{p^2}{2m} \qquad [3]$$

Since the uncertainty in the momentum cannot exceed the momentum itself, one can write $p > \Delta p$. As such, one has the following inequality:

$$E > \frac{\hbar^2}{8ma^2} \qquad [4]$$

If one tries to localize the position of an electron by reducing the box size, its energy must increase and diverge as the confining region vanishes.

Although this very simple picture of quantum confinement is given for one dimension, it is also true for an electron confined in three dimensions. For example, if a particle is confined within a sphere whose radius is R, one might expect an energy level to vary with the radius according to

$$E(R) = E_\infty + \frac{\alpha}{R^2} \qquad [5]$$

where α is a constant and E_∞ is the energy as $R \to \infty$. Suppose one considers an optical gap, E_{gap}, as the difference between the high filled and lowest empty states for a system confined in a sphere of size R. In the simplest description of the gap, one might expect E_{gap} to scale as

$$E_{\text{gap}}(R) = E_{\text{gap}} + \frac{\beta}{R^2} \qquad [6]$$

where β is a constant.

Quantum confinement has been observed experimentally for nanostructures such as quantum dots of Si and CdSe. In Figure 2, a quantum dot of hydrogenated silicon is illustrated. The interior of the dot consists of silicon atoms in the bulk diamond structure; the surface of the dot is hydrogenated. Hydrogen removes any dangling bonds on the surface. As such, all the atoms in the system should be fully coordinated and should not contribute to the electronic properties of the quantum dot. Typically, a quantum dot is a

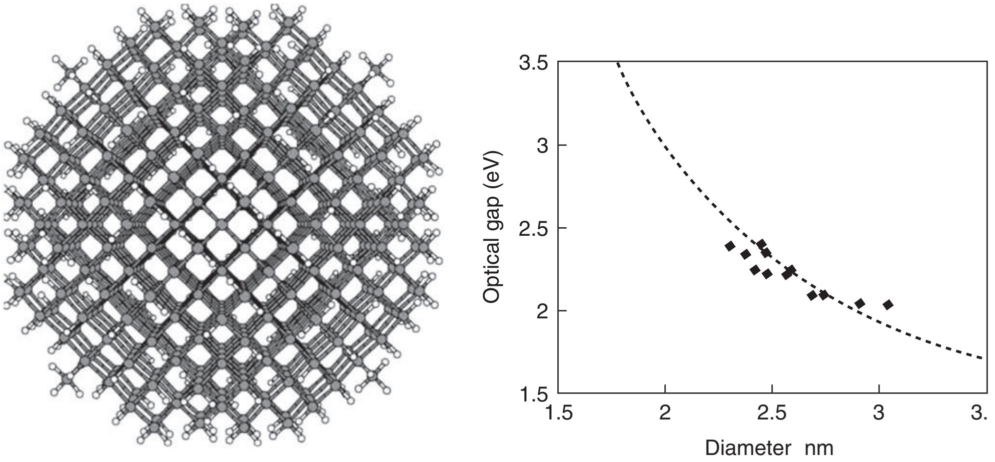

Figure 2 Ball and stick model for a quantum dot of hydrogenated silicon (left). The gray balls represent the silicon atoms, the white balls represent the hydrogens. Also shown is the corresponding optical absorption. Note the increase in gap size from the known bulk gap of silicon, which is 1.1 eV.

few nanometers to tens of nanometers in size. The smallest dots contain hundreds of atoms whereas large dots may contain hundreds of thousands of atoms.

Also illustrated in Figure 2 is the corresponding optical gap as a function of the dot size. The quantum dot gap with this size range is approximately twice the gap of crystalline silicon; silicon exhibits weak optical absorption near 1.1 eV. The absorption is weak owing to the nature of the gap in silicon. It is an indirect gap because the optical excitation couples an electron with a hole of different crystalline momentum or wave vector. Conservation of crystal momentum would require the electron and hole to have the same momentum. As such, this process can only occur by the participation of the quantized vibrational modes of the lattice or phonons, which provide the required momentum to satisfy the conservation rules. Unlike a two-body process (electron and hole), a three-body process (electron, hole, and phonon) results in a very weak interaction between light and matter.

In finite systems, crystal momentum is not well defined, owing to the lack of translation symmetry. As the system approaches nanoscale sizes, the nature of an indirect gap or direct gap becomes moot. Consequently, the optical absorption becomes stronger in quantum dots and the size of the gap increases owing to quantum confinement. An approximate fit of eqn [6] is consistent with the experimental data shown in Figure 2. This example shows the striking effect of size on the electronic structure of nanostructures, that is, silicon at this length scale is transformed from an optical inactive material to an optically active one.

Theory for the Electronic Structure at the Nanoscale

Quantum mechanical laws that describe the behavior of matter at the nanoscale were discovered in the first part of the twentieth century. Using these laws, it is possible to predict the electronic structure of matter from the atomic- to nano- to the macroscale, at least in principle. While it is relatively easy to write down the equations for interacting atoms, that is, interacting nuclei and electrons, obtaining a solution to the problem that is sufficiently accurate to make predictions is a formidable task.

Consider N nuclei of charge Z_n at positions $\{\boldsymbol{R}_n\}$ for $n=1, \ldots, N$ and M electrons at positions $\{\boldsymbol{r}_i\}$ for $i=1, \ldots, M$. This is shown schematically in Figure 3. The quantum mechanical equation for this system in its simplest form can be written as

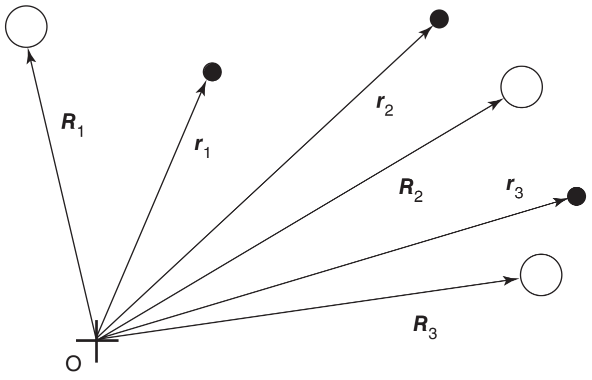

Figure 3 Simplified picture of electrons and nuclei in matter.

$$\mathscr{H}(\boldsymbol{R}_1,\boldsymbol{R}_2,\boldsymbol{R}_3,\ldots;\boldsymbol{r}_1,\boldsymbol{r}_2,\boldsymbol{r}_3\ldots)=\sum_{n=1}^{N}\frac{-\hbar^2\nabla_n^2}{2\mathscr{M}_n}+\frac{1}{2}\sum_{n,\,m=1,\,n\neq m}^{N}\frac{Z_nZ_me^2}{|\boldsymbol{R}_n-\boldsymbol{R}_m|}-\sum_{i=1}^{M}\frac{-\hbar^2\nabla_i^2}{2m}-\sum_{n=1}^{N}\sum_{i=1}^{M}\frac{Z_ne^2}{|\boldsymbol{R}_n-\boldsymbol{r}_j|}+\frac{1}{2}\sum_{i,\,j=1,\,i\neq j}^{M}\frac{e^2}{|\boldsymbol{r}_i-\boldsymbol{r}_j|} \quad [7]$$

$\mathscr{M}_n$is the mass of the nucleus. This expression omits some terms such as those involving relativistic interactions, but captures the essential features for nanoscale matter.

Using the Hamiltonian in eqn [7], the quantum mechanical equation known as the Schrödinger equation for the electronic structure of the system can be written as:

$$\mathscr{H}(\boldsymbol{R}_1,\boldsymbol{R}_2,\boldsymbol{R}_3,\ \ldots;\boldsymbol{r}_1,\boldsymbol{r}_2,\boldsymbol{r}_3\ldots)\times\Psi(\boldsymbol{R}_1,\boldsymbol{R}_2,\boldsymbol{R}_3,\ \ldots;\boldsymbol{r}_1,\boldsymbol{r}_2,\boldsymbol{r}_3\ldots)=E\Psi(\boldsymbol{R}_1,\boldsymbol{R}_2,\boldsymbol{R}_3,\ \ldots;\boldsymbol{r}_1,\boldsymbol{r}_2,\boldsymbol{r}_3\ldots) \quad [8]$$

where E is the total electronic energy of the system and Ψ is the many-body wave function.

Soon after the discovery of the Schrödinger equation, it was recognized that this equation provided the means of solving for the electronic and nuclear degrees of freedom. Using the variational principle which states that an approximate wave function will always have a less favorable energy than the true ground-state energy, one had an equation and a method to test the solution. One can estimate the energy from

$$E=\frac{\int\Psi^*\mathscr{H}\Psi\mathrm{d}^3R_1\mathrm{d}^3R_2\mathrm{d}^3R_3\ldots\mathrm{d}^3r_1\mathrm{d}^3r_2\mathrm{d}^3r_3\ldots}{\int\Psi^*\Psi\mathrm{d}^3R_1\mathrm{d}^3R_2\mathrm{d}^3R_3\ldots\mathrm{d}^3r_1\mathrm{d}^3r_2\mathrm{d}^3r_3\ldots} \quad [9]$$

However, a solution of eqn [8] for anything more complex than a few particles becomes problematic even with the most powerful computers. Obtaining an approximate solution for systems with many atoms is difficult, but considerable progress has been made since the advent of reliable computers.

Approximations to the Electronic Structure Problem

A number of highly successful approximations have been made to solve for both the ground-state and excited-state energies of matter. These approximations are constructed to remove as many unimportant degrees of freedom from the system as possible.

For example, one common approximation is to separate the nuclear and electronic degrees of freedom. Since the nuclei are considerably more massive than the electrons, the electrons will respond instantaneously to any changes in the nuclear coordinates. This approximation is called the Born–Oppenheimer or adiabatic approximation. It allows one to treat the nuclear coordinates as classical parameters. For most condensed matter systems, this assumption is highly accurate.

Another highly useful approximation is the pseudopotential approximation. The pseudopotential model of a solid has led the way in providing a workable model for computing the electronic properties of materials. Using pseudopotentials, it is possible to predict accurately the properties of complex nanosystems such as quantum dots with hundreds, if not thousands of atoms. The pseudopotential model treats matter as a "sea of valence electrons" moving in a background of ion cores (Figure 4). The ion cores are composed of nuclei and inert inner electrons. Within this model, many of the complexities of an all-electron calculation are avoided. Since only the valence electrons are considered, a group IV solid such as C with six electrons is no more difficult than Pb with 82 electrons as both elements have four valence electrons.

Pseudopotential calculations center on replicating the wave function in the spatial region from the core, that is, within the chemically active bonding region. The smoothly varying pseudo-wave-function is taken to be identical to the all-electron wave function in the bonding regions.

A third approximation is based on the density-functional theory. Methods for understanding the electronic structure of matter based on a knowledge of the charge density have existed since the late 1920s. For example, the Thomas–Fermi description of atoms was based on a knowledge of the electronic density. This theory was one of the first attempts at a quantitative theory for the electronic structure of atoms.

Most contemporary treatments of the density-functional theory begin by considering a free electron gas of uniform charge density. The justification for this starting point comes from the observation that simple metals, such as aluminum and sodium have properties that appear to resemble those of a free electron gas. In the mid 1960s, Hohenberg, Kohn, and Sham published a classic set of papers on the density-functional theory. Their work justified the replacement of the many-body wave function by one-electron orbitals based on the electronic charge density.

A key aspect of their work is the local density approximation. Within this approximation, one can express the exchange energy as

$$E_{\mathrm{x}}[\rho(\boldsymbol{r})]=\int\rho(\boldsymbol{r})\mathscr{E}_{\mathrm{x}}[\rho(\boldsymbol{r})]\mathrm{d}^3r \quad [10]$$

where $\mathscr{E}_{\mathrm{x}}[\rho]$ is the exchange energy per particle of uniform gas at a density of ρ. Within this framework, the true exchange potential is replaced by a potential determined from the functional derivative of $E_{\mathrm{x}}[\rho]$:

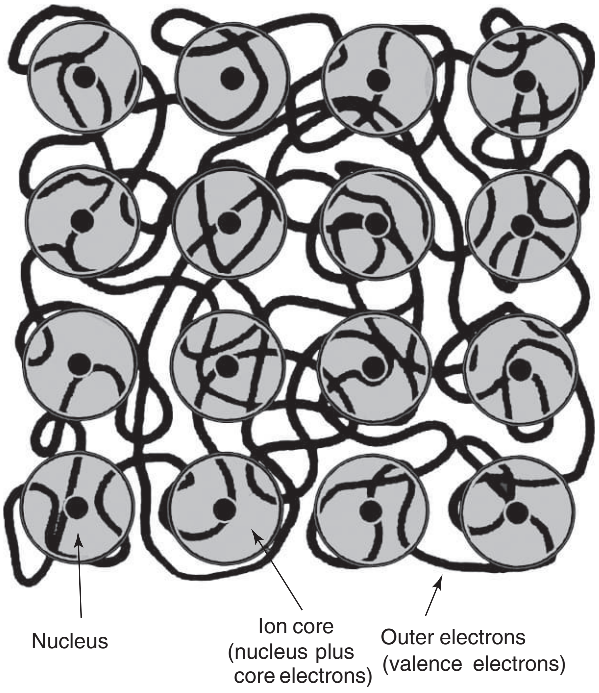

Figure 4 Schematic of the pseudopotential model of condensed matter.

$$V_{\mathrm{x}}[\rho] = \frac{\delta E_{\mathrm{x}}[\rho]}{\delta \rho} \qquad [11]$$

One serious issue is the determination of the exchange energy per particle, $\mathscr{E}_{\mathrm{x}}$, or the corresponding exchange potential, V_{x}. The exact expression for either of these quantities is unknown, save for special cases. If one assumes the exchange energy to be given by the Hartree–Fock expression for the exchange energy of the free electron gas, then one can write

$$E_{\mathrm{x}}[\rho] = -\frac{3e^2}{4\pi}\left(3\pi^2\right)^{1/3}\int [\rho(\boldsymbol{r})]^{4/3}\mathrm{d}^3 r \qquad [12]$$

and taking the functional derivative, one obtains

$$V_{\mathrm{x}}[\rho] = -\frac{e^2}{\pi}\left(3\pi^2\rho(\boldsymbol{r})\right)^{1/3} \qquad [13]$$

In contemporary theories, numerical studies have been performed on uniform electron gases resulting in local density expressions of the form: $V_{\mathrm{xc}}[\rho(\boldsymbol{r})] = V_{\mathrm{x}}[\rho(\boldsymbol{r})] + V_{\mathrm{c}}[\rho(\boldsymbol{r})]$, where V_{c} represents contributions to the total energy beyond the Hartree–Fock limit. It is also possible to describe the role of spin explicitly by considering the charge density for up and down spins: $\rho = \rho_{\uparrow} + \rho_{\downarrow}$. This approximation is called the local spin density approximation.

The Kohn–Sham Equation

The work of Kohn and Sham resulted in a workable framework for the electronic structure problem. Specifically, the Kohn–Sham equation for the electronic structure of matter is given by

$$\left(\frac{-\hbar^2\nabla^2}{2m} + V_{\mathrm{p}}^{\mathrm{ion}}(\boldsymbol{r}) + V_{\mathrm{H}}(\boldsymbol{r}) + V_{\mathrm{xc}}[\rho(\boldsymbol{r})]\right) \times \varphi_i(\boldsymbol{r}) = E_i\varphi_i(\boldsymbol{r}) \qquad [14]$$

$V_{\mathrm{p}}^{\mathrm{ion}}$ is the ion core pseudopotential, V_{H} is the Hartree or Coulomb potential, and V_{xc} is the exchange–correlation potential. The Hartree potential is obtained from

$$\nabla^2 V_{\mathrm{H}}(\boldsymbol{r}) = -4\pi e\rho(\boldsymbol{r}) \qquad [15]$$

where the charge density is given by

$$\rho(\boldsymbol{r}) = -e\sum_{i,\,\mathrm{occup}} |\varphi_i(\boldsymbol{r})|^2 \qquad [16]$$

The summation is over occupied states. When pseudopotentials are employed, these states correspond to the valence states of the system.

The Kohn–Sham equation is solved self-consistently. An approximate charge is assumed to estimate the exchange–correlation potential and to determine the Hartree potential from eqn [15]. These estimated potentials are inserted in the Kohn–Sham equation. Once the Kohn–Sham equation is solved, a new output charge density is determined from eqn [16]. The output charge density is used to estimate new exchange–correlation and Hartree potentials. The process is repeated until the input and output charge densities or potentials are identical to within some prescribed tolerance.

Given a solution of the Kohn–Sham equation, the total energy, E_{T}, can be computed from

$$E_{\mathrm{T}} = \sum_i^M E_i - 1/2\int \rho(\boldsymbol{r})V_{\mathrm{H}}(\boldsymbol{r})\mathrm{d}^3 r + \int \rho(\boldsymbol{r})(E_{\mathrm{xc}}[\rho(\boldsymbol{r})] - V_{\mathrm{xc}}[\rho(r)]\mathrm{d}^3 r \qquad [17]$$

where E_{xc} is a generalization of eqn [10], that is, the correlation energy density is included. The electronic energy as determined from E_{T} must be added to the ion–ion interactions to obtain the structural energies. This is a straightforward calculation for confined systems.

Owing to its ease of implementation and overall accuracy, the local density approximation is a popular choice for describing the electronic structure of matter. It is relatively easy to implement and surprisingly accurate. Recent developments have included the so-called generalized gradient corrections to the local density approximation. The generalized gradient approximation often yields accurate cohesive energies.

Computational Approaches for Nanostructures

Several methods exist for determining the electronic structure of nanostructures. These methods are often based on choosing a basis set for the electronic wave functions and directly solving the Kohn–Sham equation. For example, the wave functions can be expanded as

$$\boldsymbol{\Psi}_n(\boldsymbol{r}) = \sum_{jk} a_{j,k}(n)\Phi_j(\boldsymbol{r} - \boldsymbol{R}_k) \qquad [18]$$

where the sum is over (j, k). These indices label the atomic positions, given by $\boldsymbol{R}_{\mathrm{k}}$, and a local orbital, Φ_{j}, associated with an $(s, p, d, \ldots)$ state. The local orbitals, Φj, can be taken to be atomic orbitals, Gaussians, exponentials, and so on. With the form of eqn [18] as the basis, the eigenvalue problem takes the form of the matrix equation:

$$\mathbb{H}^{\mathrm{KS}}\boldsymbol{\Psi}_n = E_n \mathbb{S}\boldsymbol{\Psi}_n \qquad [19]$$

where the Hamiltonian matrix elements,$H^{\mathrm{ks}}_{\mathrm{lm}}$, are given by

$$H^{\mathrm{ks}}_{\mathrm{lm}} = \sum_{jk,\,j'k'} a^*_{j,k}(l)a_{j',k'}(m)\int \Phi^*_j(\boldsymbol{r} - \boldsymbol{R}_k) \times H^{\mathrm{ks}}\Phi_{j'}(\boldsymbol{r} - \boldsymbol{R}_{k'})\mathrm{d}^3 r \qquad [20]$$

and the overlap matrix elements, S_{lm}, is given by

$$S_{\mathrm{lm}} = \sum_{jk,\,j'k'} a^*_{j,k}(l)a_{j'k'}(m)\int \Phi^*_j(\boldsymbol{r} - \boldsymbol{R}_k)\times\Phi_{j'}(\boldsymbol{r} - \boldsymbol{R}_{k'})\mathrm{d}^3 r \qquad [21]$$

The Kohn–Sham Hamiltonian is given as in eqn [14]:

$$H^{\mathrm{KS}} = \frac{-\hbar^2\nabla^2}{2m} + V^{\mathrm{ion}}_{\mathrm{p}}(\boldsymbol{r}) + V_{\mathrm{H}}(\boldsymbol{r}) + V_{\mathrm{xc}}[\rho(\boldsymbol{r})] \qquad [22]$$

The matrix elements can be computed directly if H^{KS} is specified. Otherwise, the matrix elements can be fit to experiment. Once the matrix elements are specified, the eigenvalue and eigenfunctions can be found using standard matrix operation packages.

Methods using local orbitals can be very efficient for nanostructures. If the local orbital expansion is restricted to a small number of orbitals, the size of the matrix in eqn [19] can be quite tractable.

Another option is to use a plane wave basis instead of a localized basis, such as a set of Gaussian orbitals. In the case of a plane wave basis, pseudopotentials play a crucial role. The pseudopotential can be expanded using a rapidly converging set of plane waves. Likewise, no cusps are present in the wave functions allowing a much smaller set of plane waves than would be sufficient to converge the all-electron wave function. The plane wave basis can be written as

$$\Psi_{n,\boldsymbol{k}'}(\boldsymbol{r}) = \sum_{G} a_G(n) \exp(i(\boldsymbol{k} + \boldsymbol{G})\cdot\boldsymbol{r}) \qquad [23]$$

$\boldsymbol{k}$ is a wave vector as for a Bloch state in a crystal and $\boldsymbol{G}$ is a reciprocal lattice vector. The reciprocal lattice vectors are defined by the size and shape of the crystalline unit cell. They are defined such that

$$\exp(\mathrm{i}\boldsymbol{G}\cdot\mathcal{R}) = 1 \qquad [24]$$

where $\mathcal{R}$is a lattice vector.

A plane wave basis is a well-known and utilized instrument for calculating the electronic structure of crystalline matter. Methods based on a plane wave basis can be implemented for localized systems such as a quantum dot by retaining an artificial periodic system, for example, by placing the system of interest in a large unit cell, or supercell. Provided the cell size is sufficiently large, the solution of the problem results in the electronic structure of the isolated quantum dot. This method is very easy to implement and has been employed for systems of several thousand atoms. A significant complication concerns charged systems. In this case, the supercell is not neutral and the net charge on the system diverges. Compensating background charges are sometimes used to overcome this problem.

It is also possible to solve the Kohn–Sham equations without the use of an explicit basis. One approach is to solve the eigenvalue problem in real space where a grid serves the role of a basis. The real space method is highly advantageous over the plane wave method in a number of respects. Real space methods do not require supercells, and as a consequence, can be employed to examine charged systems without adding compensating backgrounds.

Real space methods for nanostructures are often based on a three-dimensional cubic grid. The Kohn–sham equation can be discretized via a higher-order finite differencing procedure over the grid to yield

$$\begin{aligned} &-\frac{\hbar^2}{2m}\left[\sum_{n_1=-M}^{M} C_{n_1}\psi_n(x_i + n_1 h, y_j, z_k) + \sum_{n_2=-M}^{M} C_{n_2}\psi_n(x_i, y_j + n_2 h, z_k) + \sum_{n_3=-M}^{M} C_{n_3}\psi_n(x_i, y_j z_k + n_3 h)\right] \\ &+ [V_{\mathrm{ion}}(x_i, y_j, z_k) + V_{\mathrm{H}}(x_i, y_j, z_k) + V_{\mathrm{xc}}(x_i, y_j, z_k)]\psi_n(x_i, y_j, z_k) = E_n\psi_n(x_i, y_j, z_k) \end{aligned} \qquad [25]$$

where h is the grid spacing, $C(n_1, n_2, n_3)$ are coefficients for the finite difference, the summation is over M neighboring grid points, for example, if M=1, then standard finite differencing is used.

Real space methods can be utilized without a uniformly spaced cubic grid, but such implementations are more complicated, especially when used to compute interatomic forces. A uniformly spaced grid within a three dimensional is frequently used for nanostructures. Simple boundary conditions are employed, such as outside a spherical domain, the wave functions are constrained to zero. Special data structures are used to discard these points and keep only those having a nonzero value for the wave function. Iterative diagonalization methods, which can be made very efficient for sparse grids, are easy to implement for real space problems.

Calculated Electronic Levels in Nanostructures

Solutions of the Kohn–Sham equation can be used to describe the electronic structure of a variety of nanostructures such as nanowires, nanotubes, or quantum dots. In the case of nanowires or nanotubes, the structure is localized in two dimensions and often periodic in the third. In this case, Bloch wave functions can be used for the periodic structure. For quantum dots, supercells or localized domains can be utilized along with plane waves or grid methods.

In Figure 5, the evolution of energy levels are illustrated for GaAs quantum dots. The stoichiometry of the dots are $(\mathrm{GaAs})_n\mathrm{H}^*_m$. The H^*_m notation refers to fictitious hydrogen-like atoms used to passivate any dangling or partially occupied bonds. In this example, the structure of the dots is taken to be that of a fragment of the GaAs crystal. For small dots such as $(\mathrm{GaAs})_2\mathrm{H}^*_6$, the energy levels are well separated and the gap between filled and empty states is of the order of ~6 eV. Technically, this gap cannot be compared to the observed gap as these energy levels do not correspond to those created by an electron–hole pair. The Kohn–Sham eigenvalues have meaning only in solving for the total energy as in eqn [17]. However, more realistic approaches to excited state properties have validated the use of Kohn–Sham eigenvalues as a qualitative or, in some cases, a semiquantitative method of determining the optical gap.

As a function of cluster size, the size of the gap between empty and filled states decreases as the size of the cluster increases. This is illustrated in Figure 6 where the gap size is plotted versus the cube root of the number of GaAs units present. The cube root should

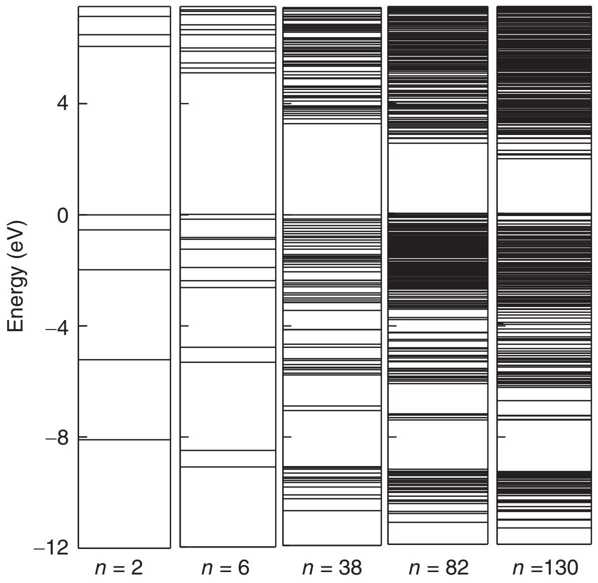

Figure 5 Energy levels of $(\mathrm{GaAs})_n\mathrm{H}^*_\mathrm{m}$ quantum dots. The number of GaAs units is indicated in the figure. The highest occupied level is taken as the zero energy reference.

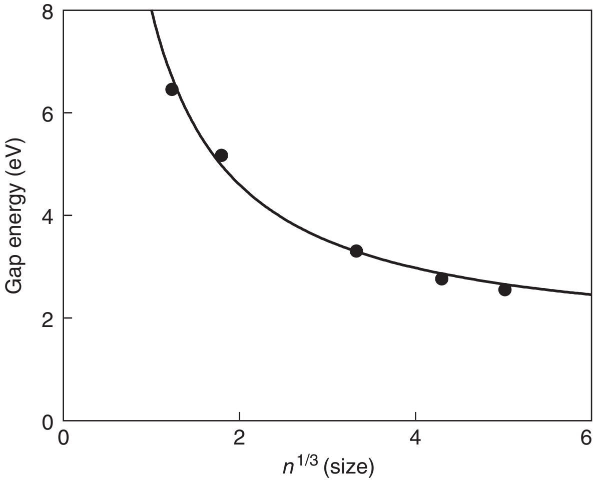

Figure 6 The energy gap in quantum dots of $(\mathrm{GaAs})_n\mathrm{H}^*_m$ vs. the size of the dot. The size of the dot is estimated by the cube root of the number of GaAs units in the dot. The curve is after eqn [6] with a scaling of R^{-1}, see text.

scale with the diameter of the quantum dot, provided a large number of atoms are present. The general trend of the gap with the size of the dot is consistent with eqn [6] with one notable exception. The scaling is not consistent with R^{-2} behavior, which would only be expected for a particle contained by an infinite well. Owing to the finite size of the quantum well in real systems, the scaling obtained from accurate calculations yields gaps that scale closer to R^{-1} as indicated in Figure 6.

A notable feature of the energy level spacings is the distribution of these states as a function of the dot size. For large systems, the distribution of the eigenvalues should approach the crystalline state. In Figure 7, the crystalline density of states is compared, that is, the number of states per unit energy, to the number of eigenvalues per unit of time for a large dot. The structure in the density of states can be attributed to the topology of energy bands. When the energy band is flat, that is, the derivative of the energy with respect to the wave function vanishes, the density of states possesses an identifiable structure. As a function of size, one would expect large clusters to possess similar structural features. The number of atoms in a dot required to reproduce bulk features of the density of states can be assessed through the direct calculation of the eigenvalue spectrum. In Figure 7, a comparison between the crystal and dot density of states for the dot, $(\mathrm{GaAs})_{342}\mathrm{H}^*_{192}$ is illustrated. The distribution of eigenvalue states matches the bulk density of states very well with one notable exception. Some states are associated with the fictitious hydrogens; these states have been removed from Figure 7. More complex nanostructures can be examined using similar approaches.

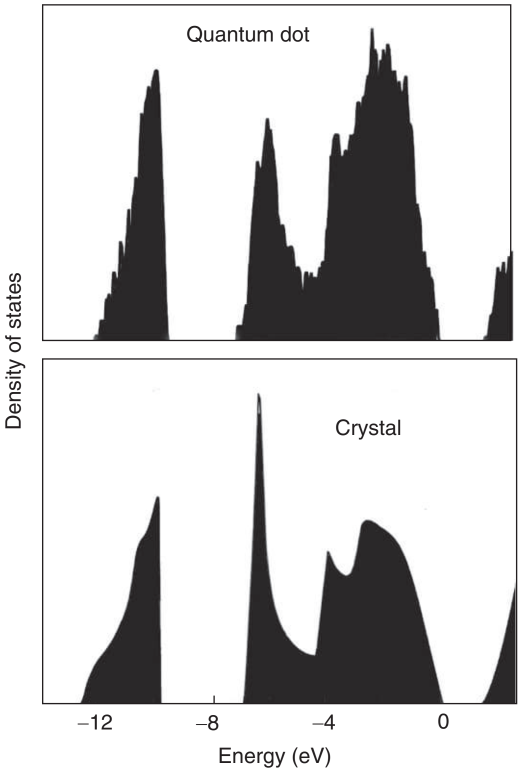

Figure 7 Densities of states for crystal gallium arsenide (bottom) and the eigenvalue distribution for $(\mathrm{GaAs})_{342}\mathrm{H}^{*}_{192}$ quantum dot (top). Extrinsic contributions have been removed from the plot.

Further Reading

Alivisatos AP (1996) Semiconductor clusters, nanocrystals and quantum dots. *Science* 271: 933.

Beck TL (2000) Real-space mesh techniques in density functional theory. *Review of Modern Physics* 72: 1041.

Brus LE (1983) A simple model for the ionization potential, electron affinity and aqueous redox potentials of small semiconductor crystallites. *Journal of Chemical Physics* 79: 5566.

Chelikowsky JR (2000) The pseudopotential-density functional method applied to nanostructures. *Journal of Physics D* 33: R33.

Chelikowsky JR and Louie SG (eds.) (1996) *Quantum Theory of Real Materials*. Boston: Kluwer Press.

Cohen ML and Chelikowsky JR (1989) *Electronic Structure and Optical Properties of Semiconductors*, 2nd edn. New York: Springer.

Fong CY (1998) *Topics in Computational Materials Science*. River Edge: World Scientific.

Furukawa S and Miyasato T (1988) Quantum size effects on the optical band gap of microcrystalline SiH. *Physical Review* 38: 5726.

Harrison WA (1999) *Elementary Electronic Structure*. River Edge: World Scientific.

Hohenberg P and Kohn W (1964) Inhomogeneous electron gas. *Physics Review* 136: B864.

Hummel R (1984) *Electronic Properties of Materials*. New York: Springer.

Kittel C (1996) *Introduction to Solid State Physics*, 7th edn. New York: Wiley.

Kohn W and Sham L (1965) Self-consistent equations including exchange and correlation effects. *Physics Review* 140: A1133.

Yu P and Cardona M (1996) *Fundamentals of Semiconductors*. New York: Springer.

THz light and manipulations of matter

M Basini and V Unikandanunni, Department of Physics, Stockholm University, Stockholm, Sweden

© 2024 Elsevier Ltd. All rights reserved.

Introduction **509**
Perspective: From optical to THz control over matter **510**
THz sources **510**
Weak THz sources 510
Strong THz sources 511
THz light-matter interaction and experimental tools **512**
Equilibrium 512
Out-of-equilibrium 512
THz control over matter **513**
Resonant control 513
Control over lattice 513
Control over magnetism 514
Control over superconductivity 514
Non-resonant control 515
Control over magnetism 515
Control of electron dynamics 515
Phase transitions and hidden orders driven (resonantly and non-resonantly) by THz light 516
Conclusion **516**
References **517**

Abstract

Terahertz (THz)-based science is growing rapidly thanks to its unique capability to investigate, excite and master degree of freedom in matter. In contrast to the existing thermal excitation mechanisms, which rely on high energy excitations, terahertz radiation, in resonance with low-energy excitations and quasiparticles, offers a non-thermal excitation pathway that is able to selectively populate excited states. In less than 10 years, scientists have made outstanding progresses in terahertz-based science and are now able to excite and control structural, electronic and spin dynamics that ultimately may result in phase transitions. Intriguingly, a terahertz-driven out-of-equilibrium configuration can reveal hidden states of matter, inaccessible in the static configuration.

Key points

- To guide the reader in the understanding of the unique capability of THz radiation to study and control degree of freedom in matter
- To describe the main sources for THz generation
- To describe equilibrium and out of equilibrium states in the THz range
- To describe resonant and non-resonant THz control of matter
- To describe actual example of THz-driven phase transitions
- To present a future outlook for the field of THz light and manipulation of matter

Introduction

Electromagnetic waves have provided extremely versatile stimuli for probing and exciting different degree of freedom in matter. Each time that the development of suitable sources and detectors have accessed new regions of the electromagnetic spectrum, its capability to manipulate degrees of freedom in matter has been exploited. In the same spirit, recent technological advances in the THz spectral range (defined here as approximately 0.1 THz to 30 THz) allowed for unexplored pathway to control matter. Importantly, THz waves are nonionizing and nonthermal. These unique characteristics make them suitable for identifying, probing and controlling a variety of material properties. In contrast to optical radiation (photon energy of the order of eV) predominantly interacts with valence electrons, THz radiation (photon energy of the order of meV) allows direct access to numerous low-energy excitations in condensed matter. The THz region encompasses a range of phenomena, including lattice vibrations, intraband transitions in semiconductors, spin waves, and internal excitations of bound electron-hole and electron-electron pairs. In addition

https://doi.org/10.1016/B978-0-323-90800-9.00184-0

to a resonant coupling to such excitation, the strong THz fields now available also permit non-resonant control of magnetization and electron dynamics.

This chapter guides the reader through the wide field of *THz light and manipulation of matter*.

Section "Perspective: From optical to THz control over matter" start by giving a perspective overview of *optical* vs *THz* control over matter, focusing on the difference in the involved excitation mechanisms. This paragraph provides a reading key to interpret the fast-developing THz science in comparison to the well-established methods that make use of optical light.

Section "THz sources" describes the main sources of THz radiation available up to now, discerning between *weak* and *strong THz sources*.

Section "THz light-matter interaction and experimental tools" discusses the fundamental interaction mechanisms of THz radiation with matter. Particularly useful is to distinguish between the study of material properties at *equilibrium* and *out of equilibrium*. More attention will be given to this last aspect, being more related to the chapter topic.

In the same spirit, *section "THz control over matter"* concentrates on the capability of strong THz radiation to manipulate and control different degrees of freedom in condensed matter. Some fascinating examples of *resonant* and *non-resonant control* over the lattice, spin and electronic degree of freedom will be presented. It will be will point out how, in some cases, the delicate balance between different degrees of freedom brings the system on the edge of stability between different phases and the THz light drives highly nonlinear collective responses that may result in electronic or structural phase transitions and, intriguingly, can reveal hidden orders.

Perspective: From optical to THz control over matter

The energy of an optical photon (eV) is at least one order of magnitude higher than the energy scale of the main collective excitations in condensed matter systems. When dealing with optical excitation of matter, the extra energy results in highly incoherent dynamics, less control and unwanted temperature increase. In contrast, THz light (meV), being in resonance with them, allows for direct coupling to relevant low-lying excitations such as electron plasmas in metals, superconducting gaps, vibrational modes of the crystal lattice and magnetic excitations.

Given the possibility to target a certain resonance, the THz excitation path is mainly a mode-selective process that is inherently non-thermal in nature (i.e., it can be described as a redistribution of quasiparticle populations on a particular mode, in contrast to a thermal effect which equally distribute energy among all quasiparticles) (De la Torre et al., 2021).

Non-thermality and mode-selectivity have important consequences on the description of excitation pathway:

(i) First, it is possible to overcome the simplified models that neglects nonthermal effects resulting from ultrafast light-matter coupling. It is indeed true that in many correlated systems, the notion of thermality, breaks down on ultrashort (femtosecond) to intermediate (subpicosecond) timescales (Abdurazakov et al., 2018)

In this sense, by means of ultrafast experiment triggered by THz radiation, it is possible to access processes dominated by dynamics that cannot be described by a hot electronic subsystem that thermalizes back to equilibrium through heat exchange with the cold crystalline lattice (phonons), i.e., modeled by the two-temperature models, (Anisimov et al., 1974) or microscopic three-temperature generalizations (Koopmans et al., 2010).

(ii) Second, it is possible to investigate the cooperation of electrons and nuclei in dynamics that may occur beyond the Born-Oppenheimer approximation. More in general, one can overcome the assumption that the mutual couplings between degrees of freedom are not modified by the excitation. Indeed, whereas an electromagnetic wave in the optical range interact predominantly with electronic states and exert forces on the nuclei only indirectly, an electromagnetic wave in the THz range can drive electric-dipole active vibrational modes by exerting forces directly on the charged nuclei. As a consequence of the nuclear excitation, the electron-phonon coupling is modified and, in some cases, emergent electronic properties result from the excitation of the nuclear degree of freedom. This is a research line that goes beyond the Born Oppenheimer approximation, as it treats the electronic and nuclear degrees of freedom no more as separate systems. As we are going to discuss in the next chapter, the research field is strongly active, with ongoing exciting experiments which go hand by hand with theory (Johonson, 2022; Basini et al., 2022a,b,c; Appleby et al., 2022; Rodríguez et al., 2022).

THz sources

Terahertz sources showing high stability and covering a broad spectral range are nowadays produced in wide range of new technologies. The following paragraphs provide a list of the most common source available for generation of *weak* and *strong* terahertz radiation.

Weak THz sources

Photoconductive Antennas. To generate THz radiation by means of photoconductive antennas (PCA), a highly resistive direct semiconductor thin film with two electric contact pads is excited by an optical pulsed laser with pulse width < 1 ps and photon energy larger than the semiconductor energy gap (Bacon et al., 2021). Each photon absorbed by the film creates a free electron in the conduction band and a hole in the valence band. The pair becomes then electrical conducting until the carriers are recombined, generating photons in the THz range. A PCA can be used as THz transmitter as well as THz receiver. In case of a *transmitter*, the excited carriers are accelerated by a voltage V connected on the electrical contacts resulting in a short broadband electromagnetic pulse. A number of semiconductor crystals are used for the sources: Si, GaAs, InAs, InP, and ZnTe. PCA sources can emit THz radiation in the bandwidth 0.1–4 THz (Katzenellenbogen and Grischkowsky, 1991), with an average radiation power of up to 40 μW (Zhao et al., 2022). In case of a THz *receiver*, an amplifier is connected on the electrical contacts and the excited carriers are accelerated by the electric field component of the incident terahertz leading to a voltage signal across the antenna gap.

Quantum cascade Lasers (QCL). QCLs are electrically pumped semiconductor lasers (Wen and Ban, 2021; Sirtori et al., 2013). Their operation mechanism exploits transitions in cascaded quantum well structures to generate terahertz radiation between 2 THz to and 5 THz. QCL emission frequency is determined by the size and width of the quantum wells and is independent of the materials used. The name quantum cascade laser is due to the number of emitted THz photon for each electron that goes through the quantum well (typically around 100, as the number of periods in the laser).

The limitation of QCL is in low operation temperature needed, i.e., the highest operation temperature realized to date is 250 K in pulse mode (Khalatpour et al., 2021).

Strong THz sources

Optical rectification. The main class of strong THz sources makes use of optical rectification of intense laser pulses in nonlinear media (Hoffmann and Fülöp, 2011), commonly DSTMS (Vicario et al., 2015), OH1 (Vicario et al., 2015), DAST (Schneider et al., 2006) and BNA (Shalaby et al., 2016) crystals. Optical rectification is a second-order nonlinear optical process, a special case of difference-frequency generation (DFG), where the spectral components from an optical laser pulse with duration sub-100 fs are mixed, generating a spectral component in the THz range. The conversion efficiency is limited by the phase mismatch between the driving laser, which propagates faster, and the generated THz pulse, which propagates slower. By tilting the wavefront of the driving laser, the phase velocity of the generated pulse can be equal to that of the driving pulse, enabling a huge increase in the generated field (Salén et al., 2019).

It is worth mentioning that the spectra of the generated THz is broad, covering a range of 0.5 THz–6 THz. Anyway, a narrowband could be preferred, for example if one needs to selectively access a particular excitation. In this case, (i) by changing the modulation period of the laser pump (Vicario et al., 2020), or (ii) by difference-frequency mixing of two linearly chirped near-infrared pulses in an organic nonlinear crystal (Liu et al., 2017), a frequency-tunable narrowband and intense THz field can be generated.

Spintronic emitters. Spintronic emitters consist of multilayer heterostructures of ferromagnetic and nonmagnetic layers, usually heavy metal (Papaioannou and Beigang, 2021). They generate THz radiation by means of a physical mechanism called inverse spin Hall effect (Kampfrath et al., 2013a). Seifert et al., 2017 explored the up-scaling capabilities of metallic spintronic stacks in order to achieve intense THz sources.

Plasma based. Femtosecond-laser-induced plasma formation in gaseous and solid foil media is also a source of THz radiation. After the laser excitation, hot electrons are "blown" away from the foil leaving behind a strong electrostatic potential. This potential ionizes atoms, and the dynamics of an induced plasma leads to strong THz transients. Nowadays, electric field amplitude of 10 MV/cm can be reached, even if theoretical modeling shows that it is possible to achieve values up to 100 MV/cm (V/Å) (Sun et al., 2022; Herzer et al., 2018).

Radiation from charged particles. When a charged particle moving with a constant velocity traverses an interface, an electromagnetic field in the THz range can be generated, known as transition radiation (Ginzburg and Tsytovich, 1979). In particular, the transition radiation from relativistic electron bunches passing through a metallic foil is used able to generate THz radiation, with electric filed amplitude of the order of tens of MV/cm with a cutoff frequency limited by the inverse bunch duration. Given that electron bunches with kinetic energy of the order of GeV are needed to produce 10 MV/cm THz pulses, the availability of strong THz sources based on transition radiation is very limited. Only a few national laboratories in the world operate such sources (Salén et al., 2019).

Synchrotrons and free electron lasers. Synchrotron radiation (SR) is the type of radiation emitted by relativistic charged particles in an external magnetic field. The origin of SR lies in classical electrodynamics: whenever a charged particle is accelerated, the surrounding electric field distribution is distorted. Then, a fraction of the field detaches from the particle and constitutes a waveform of separate photons. Synchrotron are able to produce field strength of the order of 0.1 MV/cm.

In order to increase the pulse energy of synchrotron radiation, electron bunch deflected by aa periodic magnetic field can be used (Mak et al., 2019). The emitted energy becomes N times larger compared to that from a bending magnet, where N is the number of oscillations performed by the bunch. Electric field amplitude of around 5 MV/cm can be achieved. Given that the bandwidth of the emitted THz is inversely proportional to the number of undulator periods, this type of sources generates very narrow bandwidth, which can be a limit for certain applications.

Recently, a new class of strong-field single-cycle sources based on the idea to enable constructive interference between broadband light waveforms emitted by different bunches has recently been proposed and studied theoretically (Tanaka, 2015; Kida et al., 2016; Goryashko, 2017).

THz light-matter interaction and experimental tools

Terahertz light has proven to be a fine tool to *probe* and *control* quasi-particles and collective excitations in solids, to drive phase transitions and associated changes in material properties (Koshihara et al., 2022; Irizawa et al., 2021; Salén et al., 2019; Dhillon et al., 2017; Nicolatti and Cavallei, 2016; Ferguson and Zhang, 2022). Weak terahertz sources are mainly used to study equilibrium states by means of spectroscopy methods (Neu and Schmuttenmaer, 2018; Lee, 2009). However, owing to recent developments in high-power sources, scientists have started to abandon the role of pure observers and are now exploiting intense THz radiation to engineer transient states of matter. Strong terahertz sources enable the study of out-of-equilibrium states by means of pump-probe techniques, able to resolve in time the evolution of the system after excitation.

To develop strategies for THz excitation and control of matter, it is helpful to consider the basic interaction mechanisms between THz light and matter. When a THz wave interacts with matter, the oscillating electric ($\boldsymbol{E}$) and magnetic components ($\boldsymbol{B}$) of the electromagnetic radiation exert a force on the ions and the electrons of charge q, in the Lorentz form of $\boldsymbol{F} = q\boldsymbol{E} + q\boldsymbol{v} \times \boldsymbol{B}$, where v is the velocity of the charged particle. The Coulomb term, proportional to E, induces an electric-dipole density (polarization) P, which is accompanied by an electrical current density dP/dt. At the large THz electric field amplitudes considered here, the relationship between P and E can become extremely nonlinear. The Lorentz force arising from the THz magnetic field B is usually neglected in equation, as it is smaller than the Coulomb force by a factor of v/c (where c is the speed of light in vacuum). However, as explained in details in paragraph 4, the magnetic field can exert a significant torque on magnetic dipole moments. The torque moment has the form of $\boldsymbol{\tau} = \boldsymbol{\mu} \times \boldsymbol{B}$ and act on any magnetic-dipole moment $\boldsymbol{\mu}$ in the solid (which is not parallel or antiparallel to B), such as the one carried by the electron spins.

Equilibrium

At equilibrium, THz radiation is an efficient tool to probe low-energy excitations with the unique capability to explore the material properties which have been inaccessible until recently. The result obtained experimentally correlates well with theoretical study showing that terahertz spectroscopy provides resonant access to the motions of free electrons, the vibrations of crystal lattices and the precessions of spins. In comparison with optical spectroscopy which requires spectrometers to resolve the response of the system, THz spectroscopy allows to characterize the complete electric field of a THz pulse, to yield full phase and amplitude information of the material response directly in time domain. The complex dielectric function of a sample in the beam path can thus be determined directly (Fattinger and Grischkowsky, 1989) without having to rely on Kramers-Kronig relations.

From the complex dielectric function in the THz range at equilibrium, it is possible to reveal the presence of dipole active phonons, magnons, and electronic plasma resonance. Particularly relevant is the study of the complex conductivity to identify a superconductive state. In this case, large increase in carrier mobility, accompanied by the opening of a gap in the real part of the optical conductivity is expected, whereas the imaginary part diverges at low frequencies due to the inductive nature of the response of superconducting carriers (Zimmermann et al., 1991).

Out-of-equilibrium

The emergence of collective order in matter is among the most fundamental and intriguing phenomena in physics. As explained in paragraph 1, THz radiation allows for a dynamical control and creation of novel ordered states of matter that goes beyond the simple melting of thermal states by laser-induced heating. In this sense, one has to consider non-thermality as a resource to exert control over materials on ultrashort timescales in a flexible and reversible manner. Fig. 1 (De la Torre et al., 2021) shows an illustration of the nonthermal pathways triggered by laser excitation as a function of growing excitation strength. The system coordinates, such as an electronic order parameter or a lattice displacement are displayed on the x-axis, the potential (o the free energy landscape) is displayed on the y-axes.

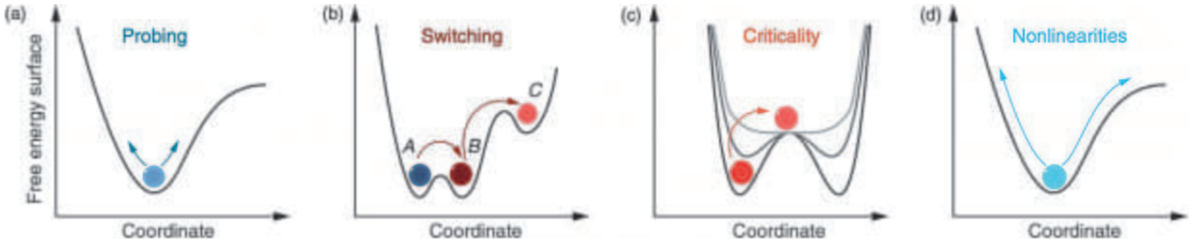

Fig. 1 Illustration of nonthermal pathways triggered by laser excitation. All panels show a potential or free energy landscape as a function of a system coordinate, such as an electronic order parameter or a lattice displacement. (a) Weak excitations around a stable minimum (ground state) permit one to probe collective modes and their mutual couplings. (b) With a short, more intense laser pulse, one can switch between degenerate ground states (A and B) or drive the material to a nonthermal, metastable excited state C. (c) Nonequilibrium critical behavior can be induced by a short, even more intense excitation that transiently modifies the free energy landscape itself. (d) With a strong excitation, the system can also be driven into anharmonic regimes with deviations from parabolic behavior, which allows one to probe nonlinear effects and change effective couplings in the material. (De la Torre et al., 2021).

Another class of nonthermal phenomena (not shown here) are those that occur for the duration of the laser pulse, where the microscopic degrees of freedom are strongly coupled to the amplitude, frequency, and polarization of the light field, in some cases forming dressed states that can be described by Floquet theory (Sono et al., 2022; De la Torre et al., 2021; Uchida et al., 2016).

In this sense, THz provides a unique strategy to investigate emergent phenomena with no equilibrium counterpart.

In order to study the out-of-equilibrium stated described above, time-resolved techniques, such as pump-probe, are needed. In a pump-probe experiment, an ultrashort pump pulse of laser light triggers a process, and another ultrashort pulse interacts with the system and measures the transient change in the material response after a well-defined time delay. The dynamics induced by a THz pump pulse (usually in the picosecond timescale) are often monitored using a femtosecond probe pulses in almost any region of the electromagnetic spectrum (X-ray, ultraviolet, visible, infrared, or THz) thus accessing changes in the structural, electronic, or optical properties of the excited material. It is worth citing that within the study of out-of-equilibrium phenomena, the development of pump-probe techniques recently achieved the possibility to isolate responses which are purely nonlinear. To this aim, inspired by nuclear magnetic resonance spectroscopy, experimental works that make use of a double (or more) pump scheme. The ultimate nonlinear THz experiments rely on 2D-THz spectroscopy, which has the potential to observe the nonlinear response, typically to all orders. In such experiments, both pump and probe processes act in the THz regime, and the experiment measures the nonlinear component of the system response to the applied THz fields (Lu et al., 2018; Elsaesser et al., 2019).

THz control over matter

This paragraph provides an overview of how the electric and magnetic fields of intense THz transients can be used to control matter. An unprecedented degree of control over material functionality on the femtosecond timescale ($1 \text{ fs} = 10^{-15}$ s) will be discussed.

The electric and magnetic field amplitudes of existing strong THz radiation can exceed 1 MV cm^{-1} and 0.33 T, respectively. When such a pulse is incident on matter, it interacts with various degrees of freedom, and it offers a versatile way to control crystal lattice vibration, spins precession and electrons acceleration and excitation.

Some of the examples of THz control presented below take advantage of resonant coupling to some material degrees of freedom, thus allowing for coherent accumulation of the energy deposited by the driving THz field in a selected mode. In addition to such resonant manipulation, high-field THz sources allow a non-resonant control, as they can accelerate electrons to very high energies over just half a cycle of their driving field.

Resonant control

The energy of THz photons matches the fine energy structure of phonons, magnons in antiferromagnets and electron vibrations (i.e., cooper pair in superconductors) thus allowing for a specific target and control on such excitations.

Control over lattice

The control of coherent lattice vibrations (i.e., phonons) is crucial to promote and tune several properties of matter. As will be shown later, the control of phonon frequencies and amplitudes allows the tuning of structural distortions, switching of ferroelectric and ferroelastic properties and in some cases, generation of a local magnetic field.

Traditionally, coherent lattice excitation by short light pulses has been obtained by optical femtosecond pulses in Raman scattering techniques (Zeiger and Dresselhaus, 1992; Merlin, 1997; Yan et al., 1985) where the coherent phonon modes are excited by scattering of the radiation via an intermediate electronic energy level. The vibration symmetry that can be controlled by Raman scattering is even, and the mechanism is not very efficient due to the non-resonant process and to the energy dissipation in electronic transitions. On the other hand, infrared (IR)-active phonons (i.e., odd symmetry) can be excited directly by means of a resonant THz field. The mechanism is extremely efficient and can lead to coherent atomic motions whose amplitude exceed the 10% of the unit cell dimension (Salén et al., 2019; Kozina et al., 2019; Nicolatti and Cavallei, 2016). When infrared (IR)-active vibrational modes are driven to large amplitudes, nonlinear coupling between infrared- and Raman-active modes can occur. There exist two distinct pathways: (1) the so-called nonlinear phononics effect of phononic rectification, alternatively called *ionic Raman scattering (IRS)* (Maradudin and Wallis, 1970; Wallis and Maradudin, 1971; Humphreys, 1972), in which the coupling occurs via the anharmonic lattice potential (Juraschek and Maehrlein, 2018; Nicolatti and Cavallei, 2016; Först et al., 2011b), and (2) the *infrared-resonant Raman scattering* (IRRS) (Khalsa et al., 2021). This last mechanism is governed by the nonlinear lattice polarizability, via a Raman-scattering mechanism mediated by the displacements of IR phonons. Both contributions exert a unidirectional force on the Raman coordinates and can lead to a change of crystalline symmetry, giving rise to opportunities for ultrafast control of functional properties of crystalline materials linked to symmetry.

A resonant drive of the lattice may also permit control of electronic properties such as conductivity. Of particular interest are many of the perovskite-type crystals with central ions having only partially filled d orbitals form complex correlated electronic phases. Phonons in these crystals have been resonantly excited with midinfrared ultrashort pulses, and in some cases, dramatic transient changes in the electrical conductivity have been observed as a result of coupling between the lattice and electronic degrees of freedom (Salén et al., 2019; Koshihara et al., 2022). Also, the topological properties of topological semimetals can be manipulated through lattice distortions. It was demonstrated that the THz light excitation of lattice displacements alters considerably the electronic structure of these materials, generating an interlayer strain with less lattice damage than uniaxial straining. It is worth to note that the possibility of an ultrafast manipulation of the topological properties of such materials opens the intriguing possibility to develop a topological switch in the THz frequency range (Sie and Lindenberg, 2019).

Control over magnetism

The magnetic degree of freedom (i.e., spin orientation and spin dynamics) of a material can be controlled by the magnetic field of an external THz transient by means of the so-called *Zeeman interaction*. An external transient magnetic field B can indeed exert a torque on the magnetic moments present in the material and causes a spin precession along its axis. In ferromagnets, collective spin modes typically exhibit frequencies lower than 100 GHz, in contrast to antiferromagnets whose resonant modes can easily reach the THz range. THz spin control of antiferromagnets indeed rely on the enhanced spin-light coupling at magnetic resonances, such as spin waves (magnons). Direct excitation has the advantage of minimal excess heat deposition, but is on the other hand very challenging due to the low magnetic-field strengths of currently realizable THz sources.

A prototype antiferromagnet where resonant magnon excitation has been achieved, is NiO (Kampfrath et al., 2011). Due to the relatively long lifetime of the spin wave (tens of ps), control of the dynamics was possible over an extended time window. Importantly, it was possible to switch off the spin precession almost entirely by using the torque of a second THz magnetic pulse arriving precisely 6.5 oscillation cycles after the first. An exciting future goal would be the use of arbitrary THz pulse sequences or pulse-shaping for nonlinear spin control.

Besides spin waves in antiferromangnets, THz radiation recently allowed the first direct experimental evidence of an intrinsic inertial spin dynamics in the form of nutation of the magnetization vector in a ferromagnet, i.e., intrinsic oscillations of the axis during precession, which occurs at frequency of approximately 0.5 THz (Neeraj et al., 2021). The terahertz magnetic field acts here as a driving periodic force, to which the magnetization responds, revealing the presence of underlying resonance (nutation) THz superimposed on the purely off-resonant, forced response of lower amplitude (precession induced by the torque).

Importantly, the temporal evolution of the nutation after THz excitation revealed that its resonance frequency is intimately related to the magnetocrystalline anisotropy (Unikandanunni et al., 2022a).

Finally, a new interesting possibility for controlling magnetism is offered by multiferroics materials, where the coexistence of electric and magnetic order result in the presence of electromagnon, a mixture of phonons and magnons that exhibit both electric and magnetic dipole moments. A resonant electric field in the THz range can couple to such the electric dipole which, in turn, modify the magnetic structure of multiferroic. In this case, the spin motion is indirectly driven by the electric field, and the delay between THz pump and sample response corresponds exactly to half of a single oscillation cycle. Remarkably, the efficiency of the driving mechanism was more than an order of magnitude larger than that expected for spin precession driven directly by the magnetic-field component of the THz pulse (Kubacka et al., 2014; Pimenov et al., 2006), revealing the great potential of multiferroic materials for this kind of application.

Phonomagnetism and magnetophononics. Spin-lattice interaction makes it possible to use phonons as the intermediary between the laser pulse and the magnetic order. In this sense, resonant phonon excitation can be used to coherently manipulate macroscopic magnetic states (Juraschek et al., 2020). For example, THz activated spin-lattice interactions causes the generation of magnetization in antiferromagnets (Disa et al., 2020; Baier et al., 2016) or a magnetization switching in ferromagnets (Afanasiev et al., 2021; Li et al., 2013). In antiferromagnets, is also possible to excite a spin precession (magnons) driving a circular dynamic in the lattice. The lattice rotation causes a breaking of time-reversal invariance and mimics the application of a magnetic field (Nova et al., 2017). On the other hand, it is true that, if driven coherently in a circular path, a phonon may itself carry a magnetic moment (Juraschek and Spaldin, 2019). Juraschek and Spaldin, 2019, the first experimental evidence of a phonon-associated magnetic moment was revealed by a circularly polarized THz electric field in a non-magnetic material (Basini et al., 2022a). This mechanism, named as dynamical multiferroicity (Juraschek et al., 2017) underlines the THz capability to reveal hidden orders in matter.

In all the above-mentioned studies, the transfer of energy is directed from phonons to magnons. The dual mechanisms, in which the transfer of energy is directed from magnons to phonons, is also possible. Anyway, photon-magnon coupling tends to be weaker than photon-phonon coupling, and photon-to-magnon-to-phonon system would require a more efficient coupling mechanism between the different quasiparticles (Jurashek and Narang, 2021). This is the case of the prototype antiferromagnetic compound cobalt fluoride (CoF_2), where a THz-driven efficient coupling between magnons and phonons was recently demonstrated (Mashkovich et al., 2021). The material hosts a magnon that couples its spin precession to the magnetic field of the THz light and in turn generates coherent structural oscillations corresponding to a Raman active phonon mode through a previously unknown energy-transfer mechanism and with unprecedented efficiency. The Raman mode is again coupled to the electron orbits and the magnetization of the bulk material.

Control over superconductivity

We now turn to electronic degrees of freedom. Because electrons have a much larger charge-to-mass ratio than ions, they are expected to exhibit a more pronounced nonlinear response to strong THz pulses (see also next chapter). Resonant THz control has been applied to the weakly bound electronic states of superconducting condensates, the so-called Cooper pairs, which are characterized by typical binding energies in the single-THz range (∼10 meV). Selective breaking of these pairs by intense THz transients was possible in the classical BCS superconductor NbN (Matsunaga and Shimano, 2012) where the quenching of the superconductive state was observed. Moreover, Cuprate superconductors support so-called *Josephson plasmons*, that is, wavelike excitations of the Cooper-pair density oscillating at a frequency of several THz. Such a plasmon can also be resonantly driven by a strong THz wave, resulting in highly nonlinear dynamics. Another remarkable result achieved upon THz driving is the observation of radiation-enhanced superconductivity (Beck et al., 2013; Mankowsky et al., 2014, 2017). As it will be shown in the paragraph dedicated to THz-driven phase transition (4.C), THz allows not only to tune, but also to induce superconductive properties (Fausti et al., 2011; Mitrano et al., 2016).

Non-resonant control

In addition to the resonant excitation of coherent phonons and magnons, high-intensity THz pulses can also manipulate matter by depositing significant amount of energy into non-resonant degrees of freedom (Kampfrath et al., 2013b). This can be done either through the magnetic field component of the THz pulse or through the electric field component. In this section, we demonstrate the non-resonant control of magnetization and electron dynamics using THz electric/magnetic fields with a few examples.

Control over magnetism

Coherent magnetization dynamics. Magnetic field component of THz pulse can exert Zeeman torque on the magnetization of ferromagnetic materials driving coherent precessional dynamics (Vicario et al., 2013). This dynamics is accurately described by the Landau-Lifshitz equation. For small deviation of magnetization from equilibrium, Landau-Lifshitz equation has the following analytic solution: $M(t) = \gamma \sin\theta \int H_{THz}(t)dt$ where M is the magnetization, H_{THz} is the THz magnetic field, θ is the angle between M and H_{THz}, and γ is the gyromagnetic ratio. From the equation it is clear that the exerted torque is maximum when M and H_{THz} are perpendicular to each other and zero when they are parallel (Bonetti et al., 2016). Coherent magnetization precession driven by the torque exerted by THz magnetic field has been suggested as a potential mechanism for ultrafast, non-thermal magnetization switching (Polley et al., 2018; Hudl et al., 2019).

Incoherent ultrafast demagnetization. In addition to the THz magnetic field-driven coherent precessional dynamics, the THz electric field can also trigger an ultrafast, incoherent demagnetization process. During this process, the material's magnetization is partially quenched within the duration of the pump pulse. In some cases, it is followed by the non-resonant excitation of the ferromagnetic resonance (FMR) on slower nanosecond timescales. The process of ultrafast demagnetization is caused by the energy deposited by THz pump to the non-resonant electronic degrees of freedom and is identical to the optically-driven ultrafast demagnetization (Chekhov et al., 2021). In orientations where both coherent and incoherent processes can occur, incoherent demagnetization dominates at high THz fields due to its quadratic dependence on the electric field amplitude.

Magnetization switching. Ultrafast, non-thermal magnetization switching using intense THz magnetic fields has been challenging due to the weak interaction between the THz magnetic field and the sample magnetization. In addition, for metallic ferromagnets, the incoherent electronic heating caused by THz electric fields can result in irreversible changes in the material (Shalaby et al., 2018). However, there are ways to overcome these challenges and achieve ultrafast, non-thermal magnetization switching. One approach is to enhance the THz magnetic field while minimizing the electric field, which can be done using metamaterial structures (Polley et al., 2018). Another approach is to isolate the THz magnetic field from the electric field by using azimuthal THz fields with spatially-isolated magnetic fields (Sánchez-Tejerina et al., 2022). Both of these methods can enhance the Zeeman interaction and reduce incoherent heating, enabling ultrafast, non-thermal magnetization switching.

Control of electron dynamics

Intense THz pulse with peak electric field of the scale of MV/cm can accelerate electrons to kinetic energies as high as a few eVs. The work done by the THz electric field on an electron of charge *e* and effective mass *m** within an optical half cycle is estimated by the pondermotive energy U_p expressed as,

$$U_p = \frac{e^2 E_{max}^2}{4m^* \omega^2}$$

where E_{max} is the peak electric field amplitude and $\omega/2\pi$ is the central frequency of the THz pulse. For example, an electric field of peak strength 1 MV/cm and central frequency of 1 THz can accelerate free electrons in vacuum to an energy of approximately 3 eV within a radiation half-cycle. Such an acceleration of electrons in material medium can in some cases even result in processes such as impact ionization and field emission of electrons. Here, we provide a few examples of non-resonant control of electron dynamics using THz electric fields possessing large pondermotive energy.

High-field carrier generation. Intense THz electric fields can generate charge carriers in semiconductors through two mechanisms: impact ionization and interband tunneling. In impact ionization, conduction electrons are accelerated by the THz electric field, leading to the excitation of valence electrons to higher conduction states through inelastic scattering. This process results in an avalanche of free electrons and an increase in the free-carrier density. For example, in the narrow-band gap semiconductor InSb, the free-carrier density increased by 700% following THz electric field excitation at an amplitude of 100 kV/cm (Hoffmann et al., 2009). The second mechanism, interband tunneling, involves the promotion of valence electrons to the conduction band through quantum-mechanical tunneling in the presence of an intense THz electric field. The rate of tunneling is greatly influenced by the rate at which decoherence occurs between valence and conduction band states, which is influenced by the lattice temperature. This results in a temperature-dependent carrier generation, unlike impact ionization, which is not directly affected by temperature (Kuehn et al., 2010a). In addition to these incoherent carrier generation mechanisms, intense THz electric fields can also cause coherent ballistic transport of electrons along the conduction band (Kuehn et al., 2010b; Houver et al., 2019).

Field emission. Intense THz electric fields can drive ultrafast emission of electrons through the tilting of the vacuum potential, allowing for the tunneling of electrons from the surface to the vacuum (Lange et al., 2020). Field-driven electron emission is preferred when the dimensionless Keldysh parameter γ_k is significantly smaller than one (Keldysh, 1965). This parameter is defined as $\gamma_k = \omega\sqrt{2m\phi}/eE_{loc}$, where $\omega/2\pi$ is the central frequency of the THz pulse, E_{loc} is the local electric field amplitude, ϕ is the work function of the metal, and e, m are, respectively, the charge and the mass of the electron. From the expression for Keldysh parameter it is evident that field emission is likely to occur when THz fields have high electric field strength and low frequency, or in other words, when they possess a large pondermotive energy. In most observed cases of THz electric field-driven electron emission, a local field enhancement is required to push γ_k into field emission regime. This is achieved through the use of engineered metasurfaces, metallic nanotips or nanometer-scale surface inhomogeneities (Li and Jones, 2016; Unikandanunni et al., 2022b).

Franz-Keldysh effect. Intense THz electric fields can induce ultrafast changes in the conduction/valence bands of a semiconductor. These induced changes include absorption below the band edge, oscillatory behavior of the absorption above the band edge, and an absorption edge blue-shifted by U_p of the driving electric field. This *terahertz-dressed electronic state* can non-linearly interact with near bandgap optical probe (frequency, Ω_{NIR}) to emit optical sidebands of frequency $\Omega_{NIR} \pm 2n\omega_{THz}$ (Nordstrom et al., 1997).

The Franz-Keldysh effect can be divided into two regimes: the static Franz-Keldysh effect and the dynamical Franz-Keldysh effect. The static Franz-Keldysh effect occurs when the pondermotive energy of the electric field is larger in magnitude compared to the photon energy. In this case, the conduction and valence bands are can adiabatically follow the applied low frequency THz field. The dynamical Franz-Keldysh effect, on the other hand, is characterized by a pondermotive energy that is comparable to the photon energy. In this case, the conduction and valence bands are unable to adiabatically follow the applied high-frequency THz field (Novelli et al., 2013).

Phase transitions and hidden orders driven (resonantly and non-resonantly) by THz light

Strong THz excitation lead to the observation of a broad variety of dynamical phenomena ending in a phase transition or revealing orders that are hidden in the static configuration at equilibrium (Koshihara et al., 2022; Aeppli et al., 2020). Compared with other phase transition schemes, light illumination has great advantages, such as its non-contact nature and easy tunability.

In THz-driven phase transition, the dynamics of the ground state or its mode-selective excitation, become accessible and act as a fuse for:

Structural phase transitions. An orthorhombic-to-monoclinic and centrosymmetric phase induced by strong THz pulses was observed in a Weyl semimetal (i.e., tungsten ditelluride) (Sie and Lindenberg, 2019).

Insulator-to-metal phase transition. Resonant THz-excitation of a phonon mode in a magnetoresistive manganite drives a non-equilibrium transition from a stable insulating phase to a metastable metallic phase (Rini et al., 2007; Iwai, 2012). Non-resonant THz-driven, insulator-to-metal transition was also shown in vanadium dioxide (Li et al., 2012; Gray et al., 2018).

Magnetic phase transition. Melting (Baldini et al., 2018), driving (Först et al., 2011a) or switching (Stupakiewicz et al., 2021) of magnetic order can be driven by THz radiation. Even more fascinating are recent evidence of THz-driven antiferromagnetic-to-ferromagnetic phase transition (Disa et al., 2020) and THz-driven dynamical multiferroicity (Basini et al., arXiv), this last occurring in a nonmagnetic and paraelectric material, i.e., $SrTiO_3$.

Ferroelectric Phase transition. It is possible to use terahertz fields to drive the ions into a new the positions that drive the crystal into a metastable ferroelectric phase, that do not exist in the phase diagram of the material and that can persist for many hours (Nova et al., 2019; Li et al., 2019; Subedi, 2017).

Superconductive phase transition. Light in the high THz range can be used to dynamically perturbed the non-superconducting phase in cuprates, allowing for the emergence of a transient superconducting state at temperatures where the non-superconductive phase is the ground state of the system (Fausti et al., 2011; Mitrano et al., 2016). It is worth to note that, excitation in the visible range has already been used in the past to enhance, superconductivity (Nieva et al., 1992). However, the enhancement could be achieved only after the relaxation of hot incoherent carriers back to the ground state and was not triggered directly by the light field.

Topological Phase transition. The possibility to develop of an ultrafast manipulation of the different phases of a topological material was recently studied, only theoretically (Zhou et al., 2021).

Conclusion

In this chapter, we discussed on THz light-matter coupling as promising approach for the creation and control of material properties on an ultrafast timescale. These advances rely on an unprecedented range of optical excitations to probe and excite different degree of freedom. THz can indeed induce thermally inaccessible states which may lead to phase transitions, being a promising route to achieving nonequilibrium new functionality. By means of THz light, we are now able to create metastable states, but we are still far from mastering them. A better understanding on the coupling to the other environmental degrees of freedom and on the role of dissipation channels, is needed. The final aim would be a clever use of the energy dissipation processes with respect to the material functionality.

As more laboratories with strong terahertz sources will develop, the already active research field is expected to expand quickly. In this framework, theoretical and computational work plays a crucial role in the fundamental understanding and description of these emerging phenomena, allowing for prediction of new physical mechanisms and materials in which to find them (Juraschek et al., 2021, 2020; Vega et al., 2020; Fechner et al., 2018; Gu and Rondinelli, 2018). Finally, given the multidisciplinary skills needed in this field, a common language and concepts still need to be developed with the goal of unifying themes and contextualize THz control within the new field of ultrafast science.

References

Abdurazakov O, Nevola D, Rustagi A, Freericks JK, Dougherty DB, and Kemper AF (2018) Nonequilibrium electron dynamics in pump-probe spectroscopy: Role of excited phonon populations. *Physical Review B* 98: 245110.

Aeppli G, Balatsky AV, Rønnow HM, and Spaldin NA (2020) Hidden, entangled and resonating order. *Nature Reviews Materials* 5: 477–479.

Afanasiev D, et al. (2021) Ultrafast control of magnetic interactions via light-driven phonons. *Nature Materials* 20: 607.

Anisimov SI, Kapeliovich BL, and Perelman TL (1974) Electron emission from metal surface exposed to ultrashort laser pulses. *Soviet Physics - JETP* 39: 375–377.

Appleby M, Barlow K, Basini M, Benfatto L, Boeije Y, Burnett A, Chen LX, Collet E, Dürr HA, Fleming G, Girija AV, Hassan MT, Hedayat H, Iwai S, Johansson JO, Johnson SL, Katsumi K, Kim P, McCusker JK, Phelps R, Rost JM, Sutcliffe E, Wagner J, Weinstein J, and Zerdane S (2022) Optical excitation processes: General discussion. *Faraday Discussions* 237: 80.

Bacon DR, Madéo J, and Dani KM (2021) Photoconductive emitters for pulsed terahertz generation. *Journal of Optics* 23: 064001.

Baier S, Hohenleutner M, Kampfrath T, Zvezdin AK, Kimel AV, Huber R, and Mikhaylovskiy RV (2016) Nonlinear spin control by terahertz-driven anisotropy fields. *Nature Photonics* 10(11).

Baldini E, et al. (2018) Lattice-mediated magnetic order melting in TbMnO3. *Physical Review B* 97: 125149.

Basini M, Pancaldi M, Wehinger B, Udina M, Tadano T, Hoffmann MC, Balatsky AV, and Bonetti S (2022a) Terahertz electric-field driven dynamical multiferroicity in SrTiO3. *arXiv*. 2210.01690.

Basini M, Benfatto L, Boeije Y, Bronsch W, Chen LX, Collet E, Girija AV, Hedayat H, Ishizaka K, Iwai S, Johansson JO, Johnson JO, Katsumi K, Koshihara S, Rost JM, Rostami H, Stähler J, and Udina M (2022b) Material science: Ultrafast transformation, electron-phonon coupling, multi-scale aspects: General discussion. *Faraday Discussions* 237: 80.

Basini M, Benfatto L, Collet E, Girija AV, Huitric G, Iwai S, Johansson JO, Johnson SL, Koshihara S, Mikhaylovskiy RV, Rost JM, Rostami H, and Sutcliffe E (2022c) THz and laser field excitation processes: General discussion. *Faraday Discussions* 237: 80.

Beck M, Rousseau I, Klammer M, et al. (2013) Transient increase of the energy gap of superconducting NbN thin films excited by resonant narrow-band Terahertz pulses. *Physical Review Letters* 110: 267003.

Bonetti S, et al. (2016) THz-driven ultrafast spin-lattice scattering in amorphous metallic ferromagnets. *Physical Review Letters* 117(8): 087205.

Chekhov AL, et al. (2021) Ultrafast demagnetization of iron induced by optical versus terahertz pulses. *Physical Review X* 11(4): 041055.

De la Torre A, Kennes DM, Claassen M, Gerber S, McIver JW, and Sentef MA (2021) Colloquium: Nonthermal pathways to ultrafast control in quantum materials. *Reviews of Modern Physics* 93: 041002.

Dhillon SS, Vitiello MS, Linfield MS, et al. (2017) The 2017 terahertz science and technology roadmap. *Journal of Physics D: Applied Physics* 50: 043001.

Disa S, Fechner M, Nova TF, Liu B, Först M, Prabhakaran D, Radaelli PG, and Cavalleri A (2020) Polarizing an antiferromagnet by optical engineering of the crystal field. *Nature Physics* 16: 937.

Elsaesser T, Reimann K, and Woerner M (2019) *Concepts and Applications of Nonlinear Terahertz Spectroscopy—iopscience.iop.org.*

Fattinger C and Grischkowsky D (1989) Terahertz beams. *Applied Physics Letters* 54: 490–492.

Fausti, et al. (2011) Light-induced superconductivity in a stripe-ordered cuprate. *Science* 331: 14.

Fechner M, Sukhov A, Chotorlishvili L, Kenel C, Berakdar J, and Spaldin NA (2018) Magnetophononics: Ultrafast spin control through the lattice. *Physical Review Materials* 2: 064401.

Ferguson B and Zhang XC (2022) Materials for terahertz science and technology. *Nature Materials* 1.

Först M, et al. (2011a) Driving magnetic order in a manganite by ultrafast lattice excitation. *Physical Review B* 84: 241104.

Först M, Manzoni C, Kaiser S, Tomioka Y, Tokura Y, Merlin R, and Cavalleri A (2011b) Nonlinear phononics as an ultrafast route to lattice control. *Nature Physics* 7: 854–856.

Ginzburg V and Tsytovich V (1979) Several problems of the theory of transition radiation and transition scattering. *Physics Reports* 49(1): 1–89.

Goryashko VA (2017) Quasi-half-cycle pulses of light from a tapered undulator. *Physical Review Accelerators and Beams* 20(8): 080703.

Gray AX, et al. (2018) Ultrafast terahertz field control of electronic and structural interactions in vanadium dioxide. *Physical Review B* 98: 045104.

Gu M and Rondinelli JM (2018) Nonlinear phononic control and emergent magnetism in Mott insulating titanates. *Physical Review B* 98: 024102.

Herzer S, Woldegeorgis A, Polz J, Reinhard A, Almassarani M, Beleites B, Ronneberger F, Grossl R, Paulus G, Hübner U, May T, and Gopal A (2018) 2S Herzer et al An investigation on THz yield from laser-produced solid density plasmas at relativistic laser intensities. *New Journal of Physics* 20: 063019.

Hoffmann MC and Fülöp JA (2011) Intense ultrashort terahertz pulses: Generation and applications. *Journal of Physics D: Applied Physics* 44(8): 83001.

Hoffmann MC, et al. (2009) Impact ionization in InSb probed by terahertz pump—terahertz probe spectroscopy. *Physical Review B* 79(16): 161201.

Houver S, et al. (2019) 2D THz spectroscopic investigation of ballistic conduction-band electron dynamics in InSb. *Optics Express* 27(8): 10854–10865.

Hudl M, et al. (2019) Nonlinear magnetization dynamics driven by strong terahertz fields. *Physical Review Letters* 123(19): 197204.

Humphreys LB (1972) Ionic Raman effect. III. First- and second-order ionic raman effects. *Physical Review B* 6: 3886.

Irizawa A, Lupi S, and Marcelli A (2021) Terahertz as a frontier area for science and technology. *Condensed Matter* 6: 23.

Iwai S (2012) Photoinduced phase transitions in α-, θ-, and κ-type ET salts: ultrafast melting of the electronic ordering. *Crystals* 2(2): 590–617.

Johonson SL (2022) Spiers memorial lecture: From optical to THz control of materials. *Faraday Discussions* 2022(237): 9–26.

Juraschek DM and Spaldin NA (2019) Orbital magnetic moments of phonons. *Physical Review Materials* 3(6): 064405. 73.

Juraschek DM, Fechner M, Balatsky AV, and Spaldin NA (2017) Dynamical multiferroicity. *Physical Review Materials* 1(1): 014401.

Juraschek DM, Narang P, and Spaldin NA (2020) Phono-magnetic analogs to opto-magnetic effects. *Physical Review Research* 2(4): 043035.

Juraschek DM, Wang DS, and Narang P (2021) Sum-frequency excitation of coherent magnons. *Physical Review B* 103: 094407.

Jurashek DM and Narang P (2021) Magnetic control in the terahertz. *Science* 374(6575): 1.

Juraschek DM and Maehrlein SF (2018) Sum-frequency ionic Raman scattering. *Physical Review B* 97(17): 174302.

Kampfrath T, et al. (2011) Coherent terahertz control of antiferromagnetic spin waves. *Nature Photonics* 5: 31–34.

Kampfrath T, Battiato M, Maldonado P, et al. (2013a) Terahertz spin current pulses controlled by magnetic heterostructures. *Nature Nanotechnology* 8: 256.

Kampfrath T, Koichiro T, and Nelson KA (2013b) Resonant and nonresonant control over matter and light by intense terahertz transients. *Nature Photonics* 7(9): 680–690.

Katzenellenbogen N and Grischkowsky D (1991) Efficient generation of 380 fsec pulses of THz radiation by ultrafast laser pulse excitation of a biased metal semiconductor interface. *Applied Physics Letters* 58(3): 222–224.

Keldysh LV (1965) Ionization in the field of a strong electromagnetic wave. *Soviet Physics—JETP* 20(5): 1307–1314.

Khalatpour A, Paulsen AK, Deimert C, Wasilewski ZR, and Hu Q (2021) High-power portable terahertz laser systems. *Nature Photonics* 15.

Khalsa G, Benedek NA, and Moses J (2021) Ultrafast control of material optical properties via the infrared resonant Raman effect. *Physical Review X* 11: 021067.

Kida Y, Kinjo R, and Tanaka Y (2016) Synthesizing high-order harmonics to generate a sub-cycle pulse in free-electron lasers. *Applied Physics Letters* 109(15): 151107.

Koopmans B, Malinowski G, Dalla Longa F, Steiauf D, Fähnle M, Roth T, Cinchetti M, and Aeschlimann M (2010) Explaining the paradoxical diversity of ultrafast laser-induced demagnetization. *Nature Materials* 9: 259–265.

Koshihara S, Ishikawa T, Okimoto Y, Onda K, Fukaya R, Hada M, Hayashi Y, Ishihara S, and Luty T (2022) Challenges for developing photo-induced phase transition (PIPT) systems: From classical (incoherent) to quantum (coherent) control of PIPT dynamics. *Physics Reports* 942: 1–61.

Kozina M, Fechner M, Marsik P, van Driel T, Glownia JM, Bernhard C, Radovic M, Zhu D, Bonetti S, Staub U, and Hoffmann MC (2019) Terahertz-driven phonon upconversion in SrTiO3. *Nature Physics* 15: 387–392.

Kubacka T, Johnson JA, Hoffmann MC, et al. (2014) Large-amplitude spin dynamics driven by a THz pulse in resonance with an electromagnon. *Science* 343: 21.

Kuehn W, et al. (2010a) Coherent ballistic motion of electrons in a periodic potential. *Physical Review Letters* 104(14): 146602.

Kuehn W, et al. (2010b) Terahertz-induced interband tunneling of electrons in GaAs. *Physical Review B* 82(7): 075204.

Lange SL, et al. (2020) Ultrafast THz-driven electron emission from metal metasurfaces. *Journal of Applied Physics* 128(7): 070901.

Lee YS (2009) *Terahertz Spectroscopy of Condensed Matter, Principles of Terahertz Science and Technology*. Springer.

Li S and Jones RR (2016) High-energy electron emission from metallic nano-tips driven by intense single-cycle terahertz pulses. *Nature Communications* 7(1): 1–7.

Li M, et al. (2012) Terahertz-field-induced insulator-to-metal transition in vanadium dioxide metamaterial. *Nature* 34(5): 487.

Li T, et al. (2013) Femtosecond switching of magnetism via strongly correlated spin–charge quantum excitations. *Nature* 496: 69–73.

Li X, et al. (2019) Terahertz field–induced ferroelectricity in quantum paraelectric Srtio3. *Science* 364(6445): 1079–1082.

Liu B, Bromberger H, Cartella A, Gebert T, Först M, and Cavalleri A (2017) Generation of narrowband, high-intensity, carrier-envelope phase-stable pulses tunable between 4 And 18 Thz. *Optics Letters* 42.

Lu J, Li X, Zhang Y, Hwang HY, Ofori-Okai BK, Nelson KA, Neu J, and Schmuttenmaer CA (2018) Tutorial: An introduction to terahertz time domain spectroscopy (THz-TDS). *Journal of Applied Physics* 124: , 231101. Two-Dimensional Spectroscopy at Terahertz Frequencies, Top Curr Chem (Z) 376:6.

Mak G, Shamuilov P, Salén D, Dunning J, Hebling Y, Kida R, Kinjo BWJ, McNeil T, Tanaka N, Thompson Z, Tibai G, and Tóth VG (2019) Attosecond single-cycle undulator light: A review. *Reports on Progress in Physics* 82(2): 025901.

Mankowsky R, Subedi A, Först M, et al. (2014) Nonlinear lattice dynamics as a basis for enhanced superconductivity in $YBa_2 Cu_3 O_{6.5}$. *Nature (London)* 516: 71.

Mankowsky R, Fechner M, Först M, et al. (2017) Optically induced lattice deformations, electronic structure changes, and enhanced superconductivity in $YBa_2 Cu_3 O_{6.48}$. *Structural Dynamics* 4: 044007.

Maradudin AA and Wallis RF (1970) Ionic Raman effect. I. Scattering by localized vibration modes. *Physical Review B* 2: 4294.

Mashkovich EA, Grishunin KA, Dubrovin RM, Zvezdin AK, Pisarev RV, and Kimel AV (2021) Terahertz light–driven coupling of antiferromagnetic spins to lattice. *Science* 374(6575): 1608–1611.

Matsunaga R and Shimano R (2012) Nonequilibrium BCS state dynamics induced by intense terahertz pulses in a superconducting NbN film. *Physical Review Letters* 109: 187002.

Merlin R (1997) Generating coherent THz phonons with light pulses. *Solid State Communications* 102(2–3): 207–220.

Mitrano M, et al. (2016) Possible light-induced superconductivity in K3C60 at high temperature. *Nature* 530: 461–464.

Neeraj K, Awari N, Kovalev S, et al. (2021) Inertial spin dynamics in ferromagnets. *Nature Physics* 17: 245–250.

Neu J and Schmuttenmaer CA (2018) Tutorial: An introduction to terahertz time-domain spectroscopy (THz-TDS). *Journal of Applied Physics* 124(23): 231101.

Nicolatti D and Cavallei A (2016) Nonlinear light–matter interaction at terahertz frequencies. *Advances in Optics and Photonics* 8: 3.

Nieva G, et al. (1992) *Applied Physics Letters* 60: 2159.

Nordstrom KB, et al. (1997) Observation of dynamical franz-keldysh effect. *Physica Status Solidi B* 204(1): 52–54.

Nova TF, Cartella A, Cantaluppi A, Först M, Bossini D, Mikhaylovskiy RV, Kimel AV, Merlin R, and Cavalleri A (2017) An effective magnetic field from optically driven phonons. *Nature Physics* 132–136.

Nova TF, Disa AS, Fechner M, and Cavalleri A (2019) Metastable ferroelectricity in optically strained SrTiO3. *Science* 364(6445): 1075–1079.

Novelli F, et al. (2013) Mixed regime of light-matter interaction revealed by phase sensitive measurements of the dynamical Franz-Keldysh effect. *Scientific Reports* 3(1): 1–5.

Papaioannou ET and Beigang R (2021) *Nanophotonics* 10(4): 1243–1257.

Pimenov A, Mukhin AA, Ivanov VY, Travkin VD, Balbashov AM, and Loidl A (2006) Possible evidence for electro- magnons in multiferroic manganites. *Nature Physics* 2: 97.

Polley D, et al. (2018) THz-driven demagnetization with perpendicular magnetic anisotropy: Towards ultrafast ballistic switching. *Journal of Physics D: Applied Physics* 51(8), 084001.

Rini M, et al. (2007) Control of the electronic phase of a manganite by mode-selective vibrational excitation. *Nature* 449: 72–74.

Rodríguez MA, Basini M, Benfatto L, Boeije Y, Burghardt I, Burnett A, Chen L, Collet E, Cowin R, Eremin I, Fleming G, Girija AV, Ishida K, Iwai S, Johansson JO, Johnson SL, Katsumi K, McCusker J, Odin C, Puviani M, Rost JM, Rostami H, Udina M, and Weinstein J (2022) Theory of out of equilibrium light-induced phenomena: General discussion. *Faraday Discussions* 237: 80.

Salén P, Basini M, Bonetti S, Hebling J, Krasilnikov M, Nikitin MY, Shamuilov G, Tibai Z, Zhaunerchyk V, and Goryashko V (2019) Matter manipulation with extreme terahertz light: Progress in the enabling THz technology. *Physics Reports* 836–837: 1–74.

Sánchez-Tejerina L, et al. (2022) All-optical non-linear chiral ultrafast magnetization dynamics driven by circularly polarized magnetic fields. *arXiv.* preprint arXiv:2206.12238.

Schneider A, Neis M, Stillhart M, Ruiz B, Khan RUA, and Günter P (2006) *Journal of the Optical Society of America B* 23(9): 1822–1835.

Seifert T, Jaiswal S, Sajadi M, et al. (2017) Ultrabroadband singlecycle terahertz pulses with peak fields of 300 kV/cm from a metallic spintronic emitter. *Applied Physics Letters* 110: 252402.

Shalaby M, Vicario C, Thirupugalmani K, Brahadeeswaran S, and Hauri CP (2016) *Optics Letters* 41(8): 1777–1780.

Shalaby M, et al. (2018) Coherent and incoherent ultrafast magnetization dynamics in 3 d ferromagnets driven by extreme terahertz fields. *Physical Review B* 98(1): 014405.

Sie EJ and Lindenberg AM (2019) An ultrafast symmetry switch in a Weyl semimetal. *Nature* 565: 61–66.

Sirtori C, Barbieri S, and Colombelli R (2013) *Nature Photonics* 7: 691–701.

Sono N, et al. (2022) Phonon-dressed states in an organic Mott insulator. *Communications on Physics* 5: 72.

Stupakiewicz, et al. (2021) Ultrafast phononic switching of magnetization. *Nature Physics* 17: 489–492.

Subedi A (2017) Midinfrared-light-induced ferroelectricity in oxide paraelectrics via nonlinear phononics. *Physical Review B* 95: 134113.

Sun W, Wang X, and Zhang Y (2022) Terahertz generation from laser-induced plasma. *Opto-Electronic Science* 1(8): 220003-1.

Tanaka T (2015) Proposal to generate an isolated monocycle X-ray pulse by counteracting the slippage effect in free-electron lasers. *Physical Review Letters* 114(4): 044801.

Uchida K, et al. (2016) Subcycle optical response caused by a terahertz dressed state with phase-locked wave functions. *Physical Review Letters* 117: 277402.

Unikandanunni V, Medapalli R, Asa M, Albisetti E, Petti D, Bertacco R, Fullerton EE, and Bonetti S (2022a) Inertial spin dynamics in epitaxial cobalt films. *Physical Review Letters* 129: 237201.

Unikandanunni V, et al. (2022b) Ultrafast electron dynamics in platinum and gold thin films driven by optical and terahertz fields. *Applied Physics Letters* 120(2): 021601.

Vega MR, et al. (2020) Phonon-mediated dimensional crossover in bilayer CrI3. *Physical Review B* 102: 081117(R).

Vicario C, et al. (2013) Off-resonant magnetization dynamics phase-locked to an intense phase-stable terahertz transient. *Nature Photonics* 7(9): 720–723.

Vicario C, Jazbinsek M, Ovchinnikov AV, Chefonov OV, Ashitkov SI, Agranat MB, and Hauri CP (2015) *Optics Express* 23(4): 4573–4580.

Vicario C, Trisorio A, Allenspach S, Ruegg C, and Giorgianni F (2020) Narrow-band and tunable intense terahertz pulses for mode-selective coherent phonon excitation. *Applied Physics Letters* 117: 101101.

Wallis RF and Maradudin AA (1971) Ionic Raman effect. II. The first-order ionic Raman effect. *Phys. Rev. B* 3: 2063.

Wen B and Ban D (2021) *Progress in Quantum Electronics* 80: 100363.

Yan Y-X, Gamble EB, and Nelson KA (1985) Impulsive stimulated scattering: General importance in femtosecond laser pulse interactions with matter, and spectroscopic applications. *The Journal of Chemical Physics* 83(11): 5391–5399.

Zeiger HJ and Dresselhaus MS (1992) Theory for displacive excitation of coherent phonons. *Physical Review B* 45: 768–778.

Zhao G, Schouten RN, Van Der Valk N, Wenckebach WT, and Planken PCM (2022) Design and performance of a THz emission and detection setup based on a semi-insulating GaAs emitter. *The Review of Scientific Instruments* 73(4): 1715–1719.

Zhou J, Xu H, Shi H, and Li J (2021) Terahertz driven reversible topological phase transition of monolayer transition metal dichalcogenides. *Advancement of Science* 8: 2003832.

Zimmermann W, et al. (1991) Optical conductivity of BCS superconductors with arbitrary purity. *Physica C* 183: 99–104.

The importance of full-scale experiments for the study of seismic metamaterials

Stéphane Brûlé[a], **Stefan Enoch**[a], **and Sébastien Guenneau**[b], [a]Aix-Marseille Université, CNRS, Centrale Marseille, Institut Fresnel, Marseille, France; [b]The Blackett Laboratory, Department of Physics, Imperial College, London, United Kingdom

© 2024 Elsevier Ltd. All rights reserved.

Introduction 519
Seismic wave amplification and seismic site effects 520
Elasticity hypothesis for soils and analog approaches 521
Real case study of a full-scale structured ground 521
Defining a periodic soil model 521
1D soil model for Rayleigh waves 522
2D soil model for shear waves 523
Emergence of seismic metamaterial in earthquake engineering 523
Main classification of seismic metamaterial 524
In situ measurement: The key solution for understanding complex phenomena involved with seismic metamaterials 524
Reminder of the assumptions of the propagation medium: Superficial soil 524
Interest of Green's functions for elastodynamics in the case of structured soil 524
Extracting information 525
Conclusion 526
References 527
Further reading 528

Abstract

This chapter shows how full-scale experiments have contributed to the development of seismic metamaterials. The link between theoretical seismic cloaking and vibrational energy capture is presented. These theoretical concepts were borrowed from transformation optics and applied to geosciences and towards construction thanks to experiments carried out in full scale in summer 2012. The current nomenclature of seismic metamaterials has grown up and allowed for the emergence of the concept of meta-cities and auxetic materials for buildings.

Key points

- Emergence of seismic metamaterial.
- New concepts and challenges in soil dynamics and earthquake engineering.
- Perspectives for smart cities.

Introduction

In Civil Engineering, the high density of shallow and deep foundation or ground reinforcement techniques for buildings (Fig. 1), have led wave physicists to believe in a significant interaction of these buried structures mainly with surface Rayleigh waves propagating in low velocity soil (Fig. 2). As it transpires in Fig. 1, foundations for buildings can be modeled as periodic structures for which it has long been known that so-called stop bands can exist. Stop bands ("band gaps") underpin notably the physics of semiconductors. However, stop bands are also associated with intervals of frequencies for which waves are disallowed to propagate in a periodic medium (John, 1987; Yablonovitch, 1987; Markos and Soukoulis, 2008; Craster and Guenneau, 2013; Deymier, 2013). Applied to the building foundations in Fig. 1, the concept of elastic stop bands allows physicists to predict that surface ground vibrations of certain frequency ranges would be reflected, and this might be a way to protect the building erected atop these foundations from surface Rayleigh and Love waves. However, elastic waves originating from a source located underneath these foundations would still be able to hit the building since these foundations present a periodicity in the horizontal plane only. It is then tempting to draw analogies with the theory of metasurfaces and gratings in optics. On the other hand, a periodic structure in all three directions of space such as that proposed in John (1987) and Yablonovitch (1987) to control electromagnetic waves, may reflect elastic waves for all polarizations coming for all directions. It seems however unlikely that modern civil engineering techniques can structure the soil in all three directions proceeding for instance as is done with 3D printing technology.

https://doi.org/10.1016/B978-0-323-90800-9.00266-3

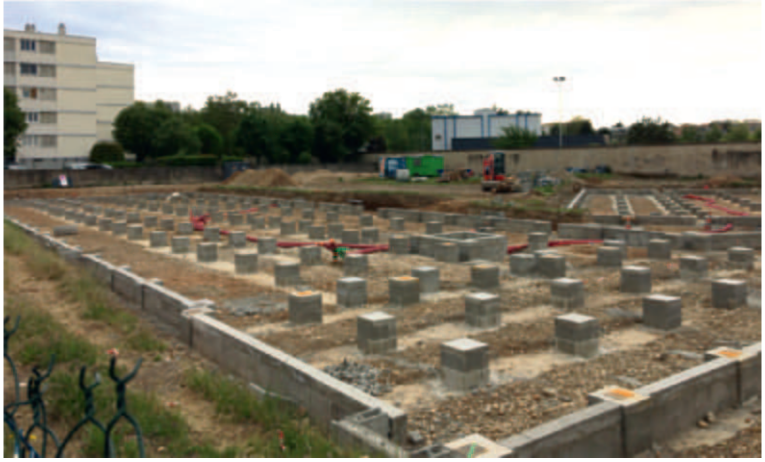

Fig. 1 illustration of a real case of a large scale metasurface consisting of shallow square foundations arranged in a 2D periodic square mesh (Courtesy of S. Brûlé).

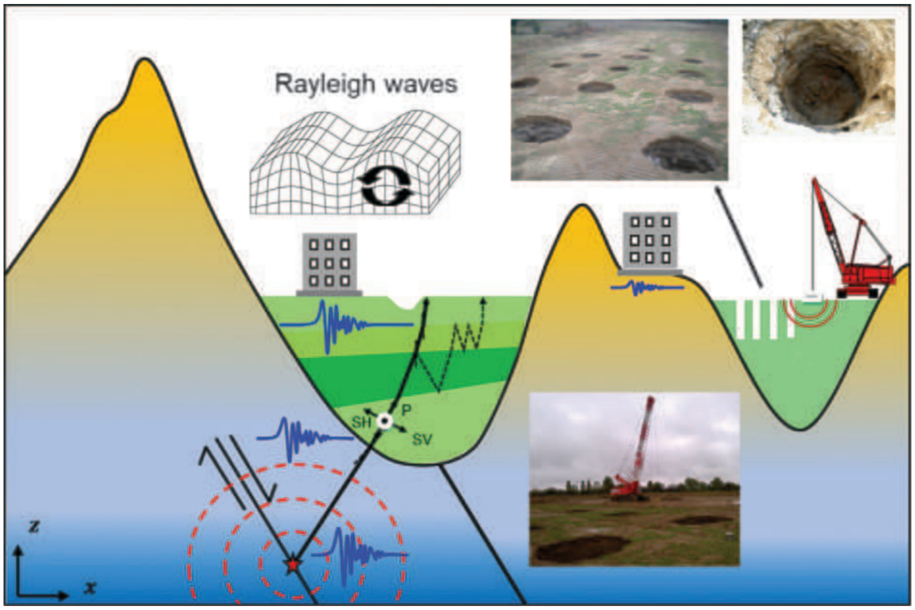

Fig. 2 Illustration (cross-sectional view in the $x - z$ plane) of the principle of seismic site effect (left) and seismic testing device (right) with photos of the periodically structured soil made of a 7×7 m grid of 2 m diameter self-stable holes in Saint-Priest near the French city of Lyon. The large scale experiment conducted in Summer 2012 is a proof of concept for a seismic flat lens via negative refraction of surface Rayleigh waves (Brûlé et al., 2017). P, S_H, and S_V waves are respectively, pressure, horizontal shear and vertical shear waves.

In §1, we recall the essential assumptions about earthquake engineering and soil dynamics, enabling us to draw an analogy with electromagnetism (§2); §3 illustrates the existence of large-scale structured media in urban areas, and §4 shows soil models for wave propagation in structured soils; §5 and 6 review the reasons for the emergence of seismic metamaterials and their classification. §7 reminds us of the importance of measuring on real, full-scale models and §8 opens the discussion on emergent topics.

Seismic wave amplification and seismic site effects

In earthquake engineering, the trapping of seismic waves in natural u-shaped basin filled with very soft sediments remains a major issue. The 1985 and 2017 earthquakes in Mexico City were devastating since this city was erected on a former drought lake (Bard and Bouchon, 1985; Bard et al., 1988; AFPS, 2018). Basically, we are looking for kinematic site effects, i.e. the amplification of the seismic signal in "soft" soils located a few tens of meters deep below the earth's surface. These amplifications, if they are not well anticipated due to insufficient knowledge of the geology, can seriously damage the buildings resting on the surface. The velocity of seismic waves is low in these soft soils. For example, the shear wave velocity V_s may be less than 300 $m \cdot s^{-1}$ even 100 $m \cdot s^{-1}$.

Shear waves (S-waves) are of particular interest in earthquake engineering because they contribute to the rocking motion of buildings, and concrete structures are sensitive to bending and shearing. However, Rayleigh waves (R waves), propagating in sedimentary basins filled with soft soils, are of real interest because the ground motion associated with R waves also has a horizontal component. In this article, we discuss more specifically the case of R waves.

In soil dynamics, the design is necessarily conservative because the goal is the safety of people during earthquakes. It is worth noting that the design of the deep foundations is often carried out in pseudo-static conditions. Thus, frequency effects are not highlighted in the same way as with a seismic metamaterial approach. The interest of the metamaterial approach lies in the description of additional complex wave phenomena in structured soils: filtering, polarization, etc.

Elasticity hypothesis for soils and analog approaches

For shear strain ranging γ from 10^{-6} to 10^{-4}, the constitutive law for soil is elasticity (Brûlé, 2023). Once we have explained the properties of poorly consolidated soils, it is easier to explain that much stiffer inclusions (steel, concrete, wood, etc.) or voids in the soil can interact with seismic waves. Young's modulus of concrete is 1000 times greater than that of soil. These two conditions allow us to seek analogies with other areas of physics.

The seemingly disconnected concepts of photonic crystals (John, 1987; Yablonovitch, 1987) and metamaterials (Smith et al., 2004; Anantha Ramakrishna and Grzegorczyk, 2008) belong to the nano-scale world and electromagnetism. Typically, photonic crystals and metamaterials refer to periodic arrangements of elements with size comparable or much smaller than the considered wavelength (typically hundreds of nanometers for optical wavelength) that acquire effective properties of materials with unusual properties or applications such as negative optical index for a flat convergent lens (Veselago, 1968) with subwavelength resolution (Pendry, 2000), or highly anisotropic materials such as hyperbolic metamaterials or invisibility cloaking devices (Pendry et al., 2006). It might come as a surprise that one can mitigate surface Rayleigh waves in geophysics in a way like what physicists do for surface electromagnetic waves in optics and plasmonics.

It is this story that we want to tell in this chapter. Indeed, researchers in photonics who have made research advances in electromagnetic metamaterials and plasmonics have created a pathway for an enhanced control of unwanted ground vibrations induced by urban traffic, human activities, and seismic waves.

Amazingly, some experiments on extraordinary transmission of light through nanoholes in metals (Ebbesen et al., 1998) and even on broadband cloaking of spoof plasmon polaritons on metal surfaces structured with TiO_2 at the nanoscale (Renger et al., 2010) can be translated to the realm of seismic metamaterials at the meter scale (Brûlé et al., 2014, 2017). We point out that drawing analogies between surface Rayleigh waves in geophysics and spoof plasmon polariton in plasmonics makes it possible to envision seismic cloaks and carpets at the decameter and kilometer scales. Research advances in photonics and plasmonics in the past 20 years might lead to a paradigm shift in earthquake engineering in the near future. However, we are not quite there yet. Much remains to be done to overcome theoretical and practical obstacles, among which is the highly heterogeneous nature of soil, as can be inferred from the photos in Fig. 2 (MetaMAT's 10th webinar S2—https://www.youtube.com/watch?v=HkikTHPEAqY).

Real case study of a full-scale structured ground

One wonders whether there are any real cases of structured ground. Large-scale 2D structures have been shown to exist in urban environments (Brûlé, 2023). This is one of the interesting aspects of research in seismic metamaterials i.e., to identify existing structures and to study how they interact with elastic waves in light of the theory of locally resonant metamaterials. Here, the phenomenon of stop bands can occur at ultra-low frequencies, and this allows one to mitigate elastic waves of very large wavelength compared to the periodicity of the structure. This is the case of underground quarries exploited with a periodic geometry of cavities and pillars, which also interests us (Fig. 3a and b).

Moreover, urban soils are already so structured by underground installations (metro, trains, sewers, etc.) that, in some cases, the soil has been heavily substituted. We can no longer speak of wave propagation in homogeneous soil. This real ground should be considered when modeling wave propagation.

Defining a periodic soil model

There are several ways of describing wave propagation in a periodic medium consisting of soft soil with rigid elements. Here we illustrate the plane-wave case for S and R waves passing through an artificial device. We propose a mass and spring 1D model and a 2D diffraction model for R and S waves respectively.

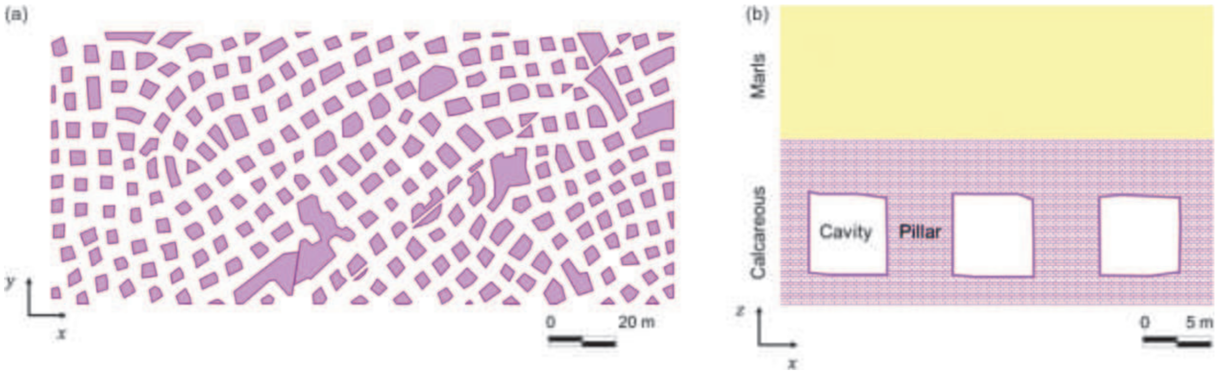

Fig. 3 Top view of an underground quarry near Paris (France) (a). Cross section of the quarry (b).

1D soil model for Rayleigh waves

Fig. 4 simply illustrates the interaction of shallow square inclusions buried in the soil, with a Rayleigh wave. The ground motion at the surface can have been modified by the propagation of the waves in a new equivalent medium made of soil and inclusions and described by equivalent properties (equivalent density ρ_{eq}, equivalent shear modulus G_{eq}). In very soft soil, we can also describe the wave-matter interaction by the frequency effects obtained by modeling the inclusions and the ground as a diatomic chain (Fig. 5). This canonical example illustrates the complexity of wave phenomena involved in surface soils.

By examining the motion of three-square foundations submitted to a monochromatic Rayleigh wave, we note that the area of interest for observing relative motion corresponds to a spacing $a < \lambda_R$. Footings distant from λ_R vibrate in phase. In Fig. 4, for boxes e to h, the shear wave velocity $V_s = 200$ m/s leads to a wavelength of the order of 18 m, for a frequency of 15 Hz. We are interested in the relative motion between the foundations. The three footings shown are 1 m wide and the spacing is $a = 4$ m. For models with masses and springs, the challenge lies in the relevance of horizontal stiffnesses.

This example illustrates the complexity of wave phenomena involved in surface soils. For this case we have illustrated what is called the modification of the kinematic effect. Of course, in the case of a building, it is also necessary to consider the interaction of the foundations with the structure which is itself a periodic structure most often.

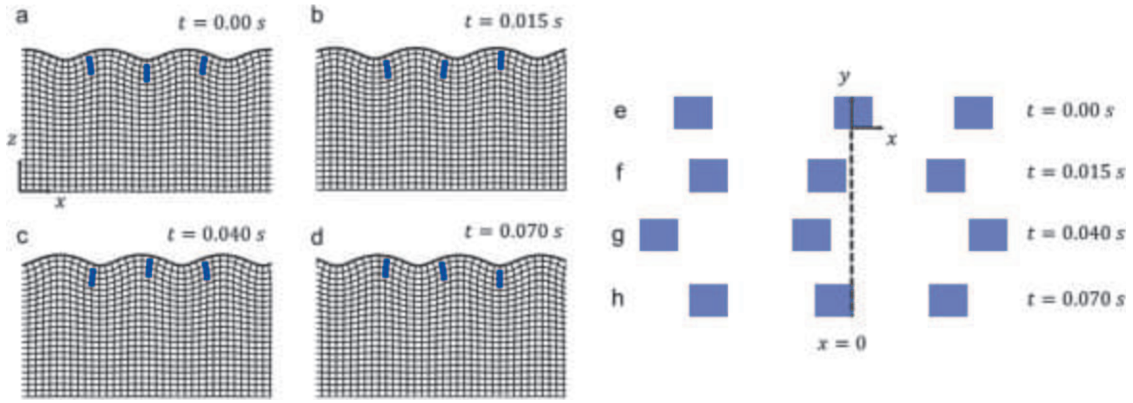

Fig. 4 Illustration of the depth of influence of Rayleigh waves on the soil motion $u(x, z)$ for inclusion of length p (boxes a to d correspond to four representative time-steps). Here the ratio Rayleigh wavelength over p, $\lambda_R/p = 5.7$ and the Poisson ratio $\nu = 0.45$. Top view of differential horizontal motion $u(x, z = 0)$ of three square inclusions spaced by $a = 5$ m. Here $\lambda_R/a = 4.7$ and $\nu = 0.33$ (boxes e to h correspond to the four time-steps of boxes a to b in left panel).

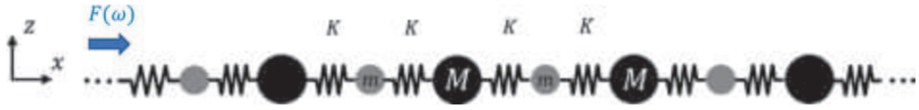

Fig. 5 1D diatomic model (masses m for foundation and M for soil). Horizontal stiffness is $K = K_x$. The parameter a is the spacing between two masses M or m. $F(\omega)$ is the harmonic force applied at one end of the model.

2D soil model for shear waves

For the case of shear waves S arriving at the surface with an angle i with the vertical axis z (Fig. 6a), it is the apparent velocities v_{app} and wavelengths λ_{app} that will concern the foundations for the study of horizontal motion (Fig. 6b). The most advanced case study is indeed the performance of a full-scale Fresnel lens (Fig. 6c).

Emergence of seismic metamaterial in earthquake engineering

Léon Brillouin (1946) emphasized that "All waves behave in a similar way, whether they are longitudinal or transverse, elastic or electric" (Brillouin, 1946). On the basis of this sentence, there are two paradigm shifts that have influenced the emergence of seismic metamaterials (Brûlé, 2023). The first one is conceptual and concerns the mechanical system studied (soil, buried foundations, buildings) with acceptance of the richness of its vibratory identity. The second one coincides with the idea that measuring signals experimentally illustrate the diversity of wave phenomena (Brûlé et al., 2014, 2017).

The first paradigm shift is based on a more in-depth study of diffraction phenomena at the scale of elementary objects, including metric size, and on taking into account the individual (local resonances) and group properties of all these objects considered as free oscillators or damped oscillators located on the surface or inside the ground. The use of diffraction is realistic because the superficial soils, few tens or even hundreds of meters thick, offer low shear wave velocity, less than 800 $\text{m} \cdot \text{s}^{-1}$. Due to these speed ranges and the identified frequency content (a few Hz), the seismic wavelengths are from a few tens to hundreds of meters, i.e., of the same order of magnitude as the characteristic lengths of surface structures.

The second paradigm shift lies in the search for the specific modal signatures of all these objects (structured soils, foundations, etc.), which requires the implementation of specific material means in the field (seismic sensors, sensor density, etc.) and also analysis tools to extract the data of interest. The transposition of the principles of periodic media to materials as specific as terrestrial materials requires rigorous definition of the validity conditions (Brûlé, 2023). In particular, these conditions are the strain range of the soil making possible the justification of an elastic behavior and a thick and homogeneous sedimentary site to limit the reflection effects of the underlying geological layers of contrasted impedance. The interpretation of the measurements is carried out from the perspective of the physical phenomena expected in periodic media. The seismic lenses tested (Brûlé et al., 2014, 2017) are explored as phononic crystals and metamaterials. By the effects observed, we point out the diffraction including Bragg reflection and double image of the source as a result of the negative refraction of a flat lens. However, a metamaterial is defined as an artificial composite material made from the assembly of resonators of smaller dimensions, whose wavelength at resonance is much larger than their physical dimension. These possibilities of local resonances are verified for Helmholtz resonators or very soft soils with rigid inclusions. On a macroscopic scale, a metamaterial is likely to exhibit properties that are not found in nature, such as negative refractive index. In addition to these early interpretations, there is an analysis of the modification of the polarization of surface waves. This new reading of the data opens the discussion on other descriptions of phenomena such as the existence of local resonances of rigid elements placed in a soil, and no longer of empty cylinders, as well as on static or dynamic homogenization approaches, dynamic anisotropy, transformational optics, surface resonators, etc. The modification of the signal by the fact of a structured soil and surface resonators are the link with Civil Engineering and the soil-structure interaction practiced in Earthquake Engineering. Research subjects converge in seismology and on the effects of secondary sources generated by surface buildings.

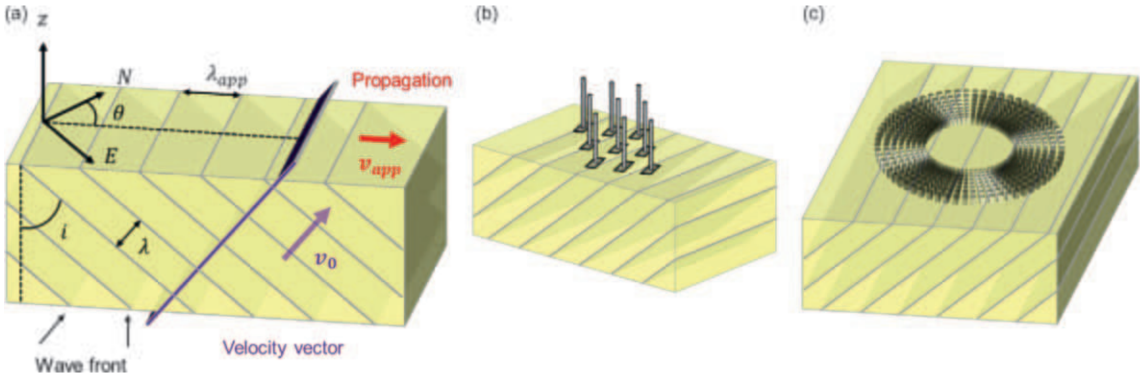

Fig. 6 (a) Block diagram representing the propagation of a monochromatic S plane wave in a homogeneous medium with an incidence angle i with respect to the vertical z-axis. (b) Illustration of the phase difference for each element of a set of shallow foundations. (c) Application to the case of the Fresnel cloak consisting of many elements within a ring surrounding a protected area.

Main classification of seismic metamaterial

We can affirm that after a decade, three types of seismic metamaterials (Fig. 7) have emerged in scientific publications (Brûlé et al., 2020): "Seismic Soil-Metamaterials" (SSM), "Buried Mass-Resonators" (BMR) and "Above-Surface Resonators" (ASR). A few authors have suggested an intermediate concept between pure seismic isolators and devices located at foundation level. The device is then designed with the metamaterials tools (Casablanca et al., 2018; Xiang et al., 2012; Brun et al., 2011). There are good prospects for SSM because the process is capable of producing large quantities of elements in the soil, and ASR, especially if their effects can be coupled. In parallel, new possibilities to dissipate the seismic energy in the superstructures themselves are emerging thanks to the contributions of auxetic materials (Ungureanu et al., 2015; D'Alessandro et al., 2018). Let us further stress that SSM and ASR need not be periodic structures, e.g., the concept of graded metamaterials whereby the elementary cells can vary smoothly spatially (thus generating an almost periodic structure), first applied to the rainbow trapping effect for light (Tsakmakidis et al., 2007) has led to the concept of seismic rainbow to convert surface Rayleigh waves in harmless downward propagating shear volume waves: In Palermo et al. (2016), a seismic rainbow that falls in the category of SSM consists of spatially graded vertical subwavelength resonators, whereas its ASR counterpart consists of trees of varying height in Colombi et al. (2016).

In situ measurement: The key solution for understanding complex phenomena involved with seismic metamaterials

Reminder of the assumptions of the propagation medium: Superficial soil

Seismic waves propagate in a 3D elastodynamic medium. The seismicity is moderate, and we are in the far field, i.e., not close to an active fault zone. As the measurements are made in sedimentary basins, the sediments can be under consolidated and with a high-water content due to the presence of the water table at a shallow depth. For experiments, sources and sensors are located at the surface. Only the dynamic response recorded at the surface interests us. The soil is assumed to behave elastically under seismic disturbance.

The real soils are not homogeneous most of the time but stratified. However, the impedance contrasts between two successive soils are not high enough to create a powerful reflector at low depth. In fact, such a reflector would alter the signal collected at the surface due to a first arrival of a reflected wave mixing with the direct signal. The magnitude of seismic ambient noise can be high but the artificial source generates a much higher energy. For the demonstration, the source used is a punch ponder of 17 t, falling 20 m. The technology is the dynamic compaction for ground densification of 5–10 m thick soils. Clearly it is an impact source at the Earth's surface. This allows us to continue the discussion on Green's functions.

Interest of Green's functions for elastodynamics in the case of structured soil

The Green's function $G_{nk}(\boldsymbol{x}, t; \boldsymbol{x}', t')$ equates to the displacement response $u_n(\boldsymbol{x}, t)$ of an elastic medium to a unit delta function force δ:

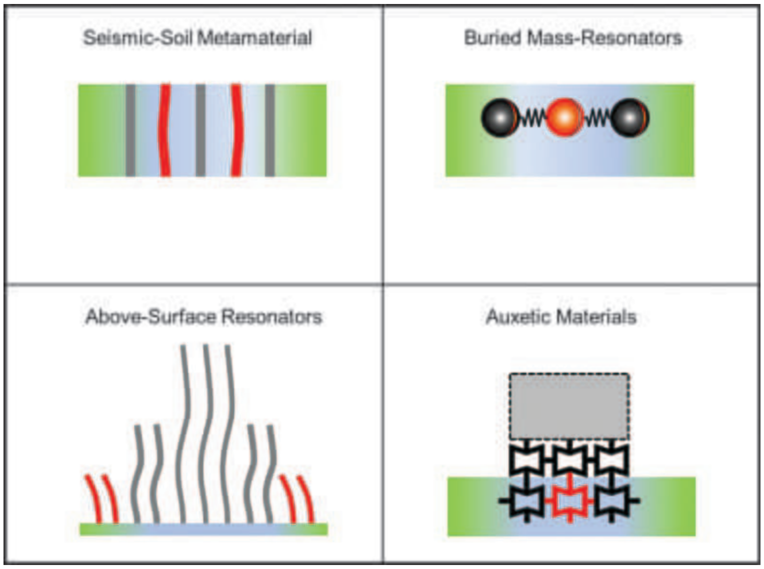

Fig. 7 Categories of seismic metamaterials as first proposed in Brûlé et al. (2020). Seismic-Soil Metamaterial in the upper left panel may consist for instance of boreholes (Brûlé et al., 2014) or concrete columns. Buried Mass-Resonators in the upper right panel have been proposed in Finocchio et al. (2014), with a further chiral twist in Achaoui et al. (2016), and are reminiscent of the diatomic chain in Fig. 5. Above-Surface Resonators in the lower left panel may consist of forest of trees (Colombi et al., 2016) or buildings (Guéguen et al., 2000; Housner, 1957; Wirgin and Bard, 1996). Auxetic Materials in the lower right panel are described by a negative Poisson ratio (Milton, 2002) and have been proposed as smart foundations in Ungureanu et al. (2015).

$$F(\boldsymbol{x}, t) = \delta(\boldsymbol{x} - \boldsymbol{x}')\delta(t - t')\boldsymbol{e}_k \tag{1}$$

in the $\boldsymbol{e}_k$ direction at location x' and time t'. In the case of homogeneous isotropic elastic medium with Lamé parameters λ and μ, this implies:

$$G_{nk}(\boldsymbol{x}, t; \boldsymbol{x}', t') = u_n(\boldsymbol{x}, t) \tag{2}$$

where $u_n(\boldsymbol{x}, t)$ satisfies the Navier equation:

$$\rho \frac{\partial^2}{\partial t^2} u_n(\boldsymbol{x}, t) = (\lambda + 2\mu)\nabla(\nabla . u_n(\boldsymbol{x}, t)) + \mu \nabla^2 u_n(\boldsymbol{x}, t) + \boldsymbol{F}(\boldsymbol{x}, t) \tag{3}$$

The assumption of a homogeneous isotropic elastic medium implies the P and S waves velocities in the medium are uniform:

$$v_p = \sqrt{\frac{\lambda + 2\mu}{\rho}} \tag{4}$$

$$v_p = \sqrt{\frac{\mu}{\rho}} \tag{5}$$

In general, P and S wave velocities are not constant throughout a true elastic medium, in which case the Green's function $G_{nk}(\boldsymbol{x}, t; \boldsymbol{x}', t')$ is not determined by an analytic solution to Eq. (3). Therefore we prefer direct measurement on full-scale devices, with 3D sensors.

In terms of the transfer function, Green's function is the spatial and temporal impulse response of the system defined by the wave equation. This is the signal that a perfect sensor would register, in any propagation medium, if the source were a pulse $\delta(\boldsymbol{x} - \boldsymbol{x}')\delta(t - t')$.

By definition, δ contains all frequencies. G_{nk} has the particularity of containing all the information related to propagation. If we know G_{nk}, we can know the structure of the medium. Whether earthquake, explosion or vibrating truck, dynamic compaction, the signal recorded by the receivers always contains the signature of the source. It then becomes difficult to determine which part of the signal corresponds respectively to the source and to the medium. Only precise knowledge of the source (frequency band, amplitude) can allow one, by a convolution operation, to go back to G_{nk}. In natural medium, this knowledge is always limited and G_{nk} can only be approximated.

For the case of structured soils with vertical elements (holes, inclusions), we build another type of anisotropic medium. We hope the natural soil is as thick and homogeneous as possible. Through measurement, we obtain experimental Green's functions in an anisotropic medium, approximate because the real impact is not a Dirac function, but a Ricker-like function (Fig. 8) in time series. It is noted here that the dynamic compaction, on compressible granular soils, causes a signal focused around 9.5 Hz. About two thirds of the energy emitted on impact propagate as Rayleigh waves.

Extracting information

Several ways of valuing complex signals measured on the surface have been developed (Brûlé, 2023). We retain the approaches in total energies integrating all the time steps over the duration of the recording and energy snapshots for each time step. The transfer functions, ideal for studying frequency effects, obtained for two configurations are also used. First, the functions calculated between

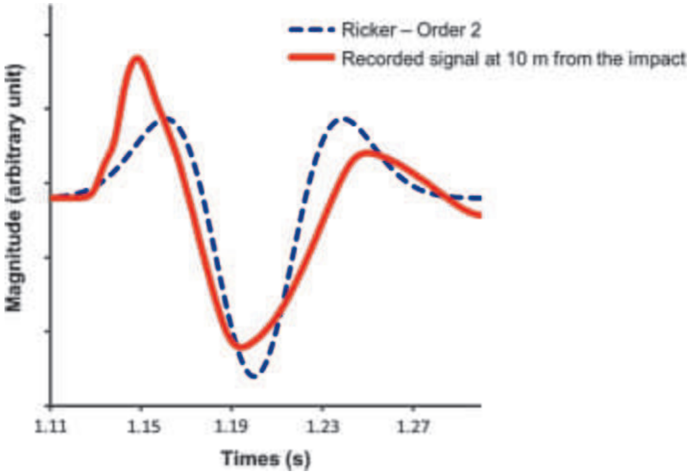

Fig. 8 Signal measured along x by a sensor located at 10 m from the point of impact on the ground of the 17 t compaction mass (red solid line) and in dotted blue line, the theoretical function representing a Ricker function of order 2.

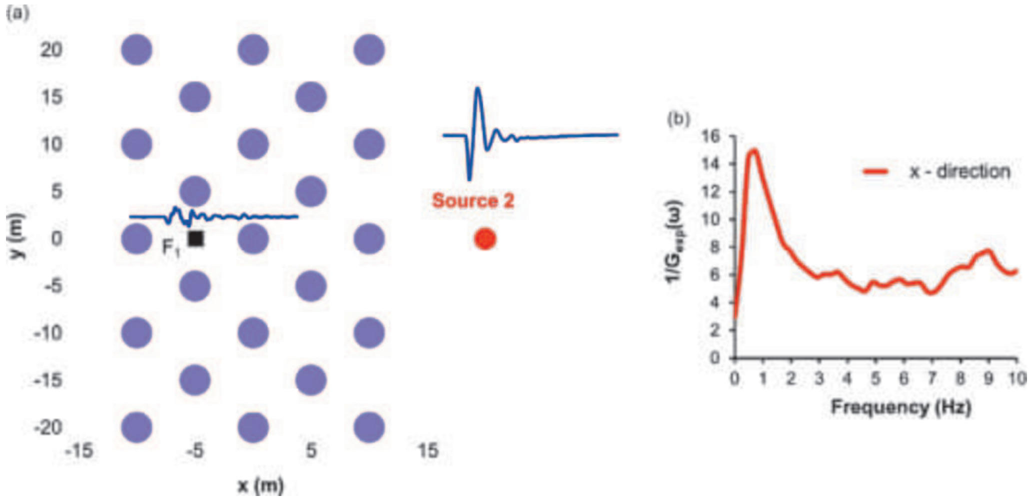

Fig. 9 (a) Top schematic view of the full-scale experiment of Saint-Priest (2012), see also photos in Fig. 2. Purple disks are cylindrical vertical holes (5 m in depth) and black square is the sensor located at the surface. Red disk is the impact point source. Blue solid lines are accelerograms in time series (*x* component). (b) The graph represents the inverse of the Green's function according to *x* for the sensor F_1 located in the grid of holes.

two points located at the same place, before and after inclusions in the ground, then the functions calculated between two distant points, also before and after inclusions. As mentioned previously, we also have the case of approximate and experimental Green functions for the case of impact sources. Thus Fig. 9a shows the signal along *x*-axis recorded at 5 m from the source (and assimilated to the source) and the signal along *x*-axis recorded in the network of holes (sensor F_1). One can notice the rapid energy decrease over a short distance (25 m). In Fig. 9b, we can see the experimental Green's function along *x*-axis (Boué and Paul, 2020). To better highlight the frequency content of this function, we have chosen to represent its inverse $1/G_x$. We see that this function reflects de-amplification at low frequency below 2 Hz and between 7 and 10 Hz.

$$\frac{v_x(\omega)}{s_x(\omega)} = G_x(\omega) \tag{6}$$

Between the hollow cylinders, the energy can be channeled too (Brûlé and Guenneau, 2021).

Conclusion

This chapter on seismic metamaterials highlights the reality of the interaction of buried structures with short seismic wavelengths (tens to hundreds of meters). We have shown that it is possible in principle to achieve a significant control of seismic waves (intensity and frequency content) in artificially structured soils. Seismic metamaterials could be complementary to the existing passive systems used in earthquake engineering. Finally, we note that seismic metamaterials can be classified as in Fig. 7, and notably some of them can be found in nature as forest of trees (Colombi et al., 2016). It is actually possible to show a complete correspondence for Love waves propagating in forests of trees and spoof plasmon polaritons propagating at structured metal surfaces (Maurel et al., 2018). We believe that seismic metamaterials based on analogies with photonic crystals might offer some interesting perspectives in earthquake protection and energy harvesting (Guenneau et al., 2018; Brûlé and Guenneau, 2021).

However, there is more to seismic metamaterials. These are based on analogies with electromagnetic metamaterials which is a research area at the interface between different disciplines. Electromagnetic metamaterials encompass notably the field of transformation optics that got started with the seminal paper (Pendry et al., 2006). Transformation optics essentially develops a theory of graded metamaterials that are anisotropic, based on Maxwell's equations that behave nicely under geometric transforms. Indeed, starting from a reference medium that is isotropic and homogeneous (typically vacuum in optics, what amounts to a homogeneous soil in geophysics), it is possible to locally distort the virtual electromagnetic space to detour wave trajectories at will: as an illustrative example, space geodesics that are straight lines in flat space, are curved lines in a non-Euclidean space such as the surface of the sphere, and everyone has experienced that shortest trajectories are no longer straight lines when traveling long distances on airplanes. However, one does not need to resort to non-Euclidean spaces to distort geodesics: it is enough for that to make a coordinate change in a flat space that maps a disk onto a ring to create a hole in the flat space (literally by blowing up a point). This bold proposal of Pendry and coworkers was first met with gentle skepticism in 2006, but this exclusion zone created by the invisibility cloak was rapidly validated experimentally for microwaves at 8.5 GHz in a follow up article of (Pendry et al., 2006). Using the similar formalism, it is possible to design some invisibility cloaks for different types of waves, even for governing equations which are not transformation invariant, such as the elasticity equations. In Xu et al. (2015), a metamaterial cloak 20 cm in diameter designed at the Institut Fresnel in 2006 to control linear surface water waves (Farhat et al., 2008), is shown to also work for

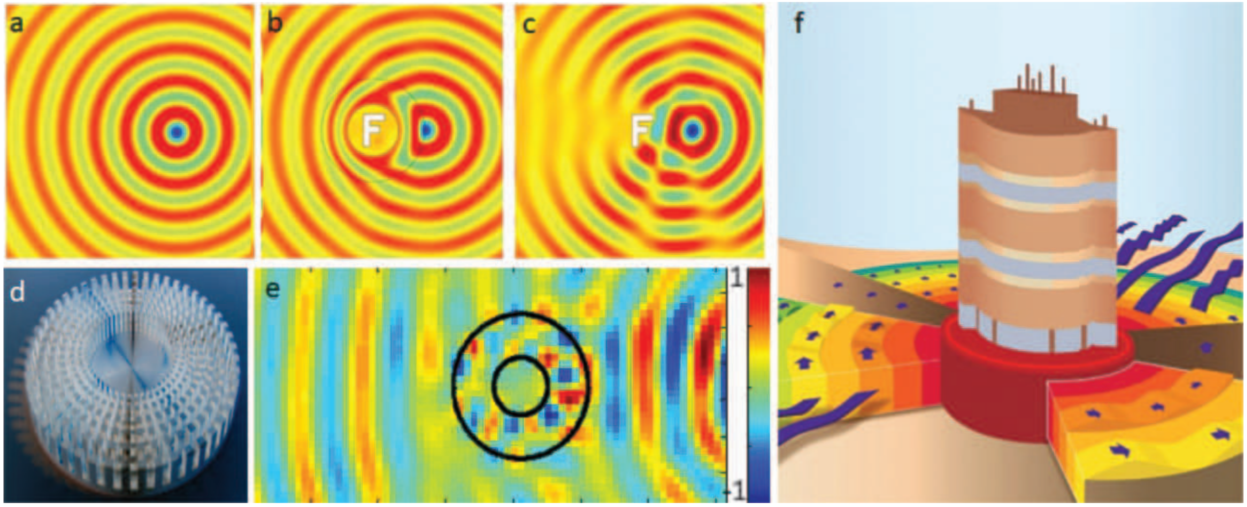

Fig. 10 Concept of invisibility cloak for surface (Rayleigh) seismic waves: (a) Point force in a thin homogeneous isotropic elastic plate generating a concentric flexural wave; (b) Same as (a) when the point force is located in the neighborhood of an invisibility cloak (consisting of a spatially varying anisotropic medium) that hides a clamped F-shaped obstacle; (c) Same as (b) when the cloak is removed; (d) Photo of a multi-physics Fresnel cloak designed for acoustic waves, water waves and electromagnetic waves (Farhat et al., 2008; Xu et al., 2015), see also Fig. 6c for its seismic counterpart; (e) Experimental demonstration of microwave cloaking (credit: Redha Abdeddaim and Elodie Georget, Institut Fresnel); (f) CNRS infography for a seismic cloak based upon (a–e).

airborne acoustic waves and microwaves (in one light polarization) in the same range of wavelengths: indeed, in a cylindrical configuration the same Helmholtz equation can be used for all three types of waves, and the transformed medium parameters are achieved using some homogenization approach based on perforated media, that is simply underpinned by geometrical considerations. The three types of perforated media correspond in Xu et al. (2015) to the metamaterial shown in Fig. 10d, that is either perforating a free air-liquid interface (for surface water waves), or perforating air (in the sense that the pillars constituting the metamaterial are rigid inclusions for airborne acoustic waves and infinite conducting inclusions for the transverse magnetic polarization at GHz frequencies). Mathematically, one supplies the Helmholtz equation with Neumann boundary conditions on the perforations. Clearly, the cloak works as expected in Fig. 10e, since the wavefield is almost unperturbed outside of the cloak and is vanishing inside the exclusion zone. This is achieved through the required artificial anisotropy of the effective medium within the ring that finely approximates the transformed medium parameters. This experimental validation for broadband cloaking for microwaves (between 3 and 7 GHz) confirmed similar experiments for water waves (between 8 and 15 Hz (Farhat et al., 2008)) and for airborne sound waves (between 4 and 8 kHz) by the group of Nicholas Fang at Massachusetts Institute of Technology in 2013. The same geometry allows for the control of flexural waves in thin elastic plates as theoretically and numerically shown in Mohamed et al. (2009) and experimentally demonstrated in Stenger et al. (2012). We propose to scale up the Fresnel cloak to design a seismic cloak for surface Rayleigh waves that would consist of same arrangement of concrete pillars buried in soil, as depicted in Fig. 10f. Transformation elasticity and homogenization theory predict similar effect of wave control. Fig. 10 summarizes our strategy for the design of such a seismic cloak based on analogies with optics.

We hope we have convinced the reader of this Chapter that the field of seismic metamaterials is worth investigating and we hope that new proposals will emerge from cross-disciplinary collaborations in condensed matter theory, wave physics and civil engineering.

References

Achaoui Y, Ungureanu B, Enoch S, Brûlé S, and Guenneau S (2016) Seismic waves damping with arrays of inertial resonators. *Extreme Mechanics Letters* 8: 30–38.

AFPS (2018) *Report of the Post-seismic Mission on the Mexico earthquake of September 19th, 2017, French Association of Earthquake Engineering.*

Anantha Ramakrishna S and Grzegorczyk TM (2008) *Physics and Applications of Negative Refractive Index Materials.* CRC Press/SPIE Press.

Bard PY and Bouchon M (1985) The two-dimensional resonance of sediment-filled valleys. *Bulletin of the Seismological Society of America* 75(2): 519–541.

Bard P-Y, Campillo M, Chávez-Garcia FJ, and Sánchez-Sesma FJ (1988) The Mexico earthquake of September 19, 1985—A theoretical investigation of large-and small-scale amplification effects in the Mexico City Valley. *Earthquake Spectra* 4(3): 609–633.

Boué P and Paul A (2020) Imagerie sismique par corrélation de bruit ambiant: Du laboratoire à l'échelle globale. *Reflets de la Physique* 64: 12–16.

Brillouin L (1946) *Wave Propagation in Periodic Structures.* McGraw-Hill Book Company Inc.

Brûlé S (2023) *Propagation of Seismic Waves in Artificially Structured Surface Soils. Theoretical and Experimental Approach. The Seismic Metamaterials.* PhD Thesis, Aix Marseille University.

Brûlé S and Guenneau S (2021) Past, present and future of seismic metamaterials: Experiments on soil dynamics, cloaking, large scale analogue computer and space–time modulations. *Comptes Rendus Physique* 21(7–8): 767–785.

Brûlé S, Javelaud EH, Enoch S, and Guenneau S (2014) Experiments on seismic meta-materials: Molding surface waves. *Physical Review Letters* 112: 133901.

Brûlé S, Javelaud EH, Enoch S, and Guenneau S (2017) Flat lens effect on seismic waves propagation in the subsoil. *Scientific Reports* 7(1): 18066.

Brûlé S, Enoch S, and Guenneau S (2020) Emergence of seismic metamaterials: Current state and future perspective. *Physics Letters A* 384(1): 126034.

Brun M, Giaccu GF, Movchan AB, and Movchan NV (2011) Asymptotics of eigenfrequencies in the dynamic response of elongated multi-structures. *Proceedings of the Royal Society of London A* 468(2138): 378–394.
Casablanca O, Ventura G, Garescì F, Azzerboni B, Chiaia B, Chiappini M, and Finocchio G (2018) Seismic isolation of buildings using composite foundations based on metamaterials. *Journal of Applied Physics* 123: 174903.
Colombi A, et al. (2016) A seismic metamaterial: The resonant metawedge. *Scientific Reports* 6(1): 27717. https://doi.org/10.1038/srep27717.
Colombi A, Roux P, Guenneau S, Gueguen P, and Craster V (2016) Forests as a natural seismic metamaterial: Rayleigh wave bandgaps induced by local resonances. *Scientific Reports* 6: 19238.
Craster R and Guenneau S (2013) *Acoustic Metamaterials: Negative Refraction, Imaging, Lensing and Cloaking.* Springer Verlag.
D'Alessandro L, Zega V, Ardito R, and Corigliano A (2018) 3D auxetic single material periodic structure with ultra-wide tunable bandgap. *Scientific Reports* 8: 2262.
Deymier P (2013) *Acoustic Metamaterials and Photonic Crystals.* Springer Verlag.
Ebbesen TW, Lezec HJ, Ghaemi HF, Thio T, and Wolff P (1998) Extraordinary optical transmission through sub-wavelength hole arrays. *Nature* 391: 667–669.
Farhat M, et al. (2008) Broadband cylindrical acoustic cloak for linear surface waves in a fluid. *Physical Review Letters* 101(13). https://doi.org/10.1103/PhysRevLett.101.134501.
Finocchio G, Casablanca O, Ricciardi G, Alibrandi U, Garesci F, Chiappini M, and Azzerboni B (2014) Seismic metamaterials based on isochronous mechanical oscillators. *Applied Physics Letters* 104: 191903.
Guéguen P, Bard PY, and Semblat JF (2000) From soil-structure interaction to site-city interaction. In: *12th World Conference on Earthquake Engineering, Auckland, New-Zealand.*
Guenneau S, Enoch S, Colombi A, Roux P, and Brûlé S (2018) Métamatériaux pour la protection sismique. *Photoniques* 90: 37–40.
Housner GW (1957) Interaction of building and ground during an earthquake. *Bulletin of the Seismological Society of America* 47: 179–186.
John S (1987) Strong localization of photons in certain disordered dielectric superlattices. *Physical Review Letters* 58: 2486–2489.
Markos P and Soukoulis CM (2008) *Wave Propagation: From Electrons to Photonic Crystals and Left-Handed Materials.* Princeton University Press.
Maurel A, Marigo JJ, Pham KK, and Guenneau S (2018) Conversion of Love waves in a forest of trees. *Physical Review B* 98(13): 134311.
Milton GW (2002) *Theory of Composites.* Cambridge University Press.
Mohamed F, et al. (2009) Ultrabroadband elastic cloaking in thin plates. *Physical Review Letters* 103: 024301. https://doi.org/10.1103/PhysRevLett.103.024301.
Palermo A, et al. (2016) Engineered metabarrier as shield from seismic surface waves. *Scientific Reports* 6(1): 39356. https://doi.org/10.1038/srep39356.
Pendry JB (2000) Negative refraction makes a perfect lens. *Physical Review Letters* 85: 3966–3969.
Pendry JB, Schurig S, and Smith DR (2006) Controlling electromagnetic fields. *Science* 312: 1780–1782.
Renger J, Kadic M, Dupont G, Aćimović S, Guenneau S, Quidant S, and Enoch S (2010) Hidden progress: Broadband plasmonic invisibility. *Optics Express* 18: 15757.
Smith DR, Pendry JB, and Wiltshire MCK (2004) Metamaterials and negative refractive index. *Science* 305: 788–792.
Stenger N, et al. (2012) Experiments on elastic cloaking in thin plates. *Physical Review Letters* 108: 014301. https://doi.org/10.1103/PhysRevLett.108.014301.
Tsakmakidis K, et al. (2007) Trapped rainbow storage of light in metamaterials. *Nature* 450: 397–401. https://doi.org/10.1038/nature06285.
Ungureanu B, et al. (2015) Auxetic-like metamaterials as novel earthquake protections. *EPJ Applied Metamaterials* 2: 17. https://doi.org/10.1051/epjam/2016001.
Ungureanu B, Achaoui Y, Enoch S, Brûlé S, and Guenneau S (2015) Auxetic-like metamaterials as novel earthquake protections. *EPJ Applied Metamaterials* 2: 17.
Veselago VG (1968) The electrodynamics of substances with simultaneously negative values of ε and μ. *Soviet Physics Uspekhi* 10: 509–514.
Wirgin A and Bard PY (1996) Effects of buildings on the duration and amplitude of ground motion in Mexico City. *Bulletin of the Seismological Society of America* 86(3): 914–920.
Xiang HJ, Shi ZF, Wang SJ, and Mo YL (2012) Periodic materials-based vibration attenuation in layered foundations: Experimental validation. *Smart Materials and Structures* 21: 112003.
Xu J, Jiang X, Fang N, Georget E, Abdeddaim R, Geffrin JM, Farhat M, Sabouroux P, Enoch S, and Guenneau S (2015) Molding acoustic, electromagnetic and water waves with a single cloak. *Scientific Reports* 5: 10678.
Yablonovitch E (1987) Inhibited spontaneous emission in solid-state physics and electronics. *Physical Review Letters* 58: 2059.

Further reading

Seismic Defence Structures (2018) *Seismic Defence Structures* WO 2018/073412 Al.
Brûlé S, Enoch S and Guenneau S (2021) *Métamatériaux acoustiques, électromagnétiques et sismiques pour les ondes du nanomètre au mètre.* E1042 v1. Techniques de l'Ingénieur.

Relevant websites

http://www.cfms-sols.org/sites/default/files/Actes/1447-1449.pdf—Comité français de mécanique des sols. Vers les métamatériaux sismiques.
http://events.femto-st.fr/GdR-META/—GdR META.
http://www.cnrs.fr—Centre national de la recherche scientifique.
http://www.univ-amu.fr—Aix Marseille Université.
http://www.centrale-marseille.fr—École centrale de Marseille.
http://www.fresnel.fr—Institut Fresnel.
http://www.imperial.ac.uk—CNRS-Imperial "Abraham de Moivre" International Research Laboratory.
http://www.isterre.fr—ISTerre—Institut des sciences de la Terre.
http://www.femto-st.fr—Femto-sciences et technologie.
http://www.icfo.eu—ICFO.
http://www.kit.edu—Karlsruher Institut für Technologie.
http://mecanique.univ-lille1.fr—IEMN—Université Lille 1.
http://www.institut-langevin.espci.fr—Institut Langevin.
http://www.msc.univ-paris-diderot.fr—Laboratoire matière et systèmes complexes.

Quantum devices of reduced dimensionality☆

M Grundmann, Universität Leipzig, Leipzig, Germany

© 2024 Elsevier Ltd. All rights reserved.

This is an update of M. Grundmann, Quantum Devices of Reduced Dimensionality, Editor(s): Franco Bassani, Gerald L. Liedl, Peter Wyder, Encyclopedia of Condensed Matter Physics, Elsevier, 2005, Pages 17–22, ISBN 9780123694010, https://doi.org/10.1016/B0-12-369401-9/00500-3.

Introduction **529**
Quantum mechanical effects 530
Quantization in potential wells 530
Two-dimensional carrier gases 530
Quantum wires 531
Quantum dots 531
Josephson junctions 532
Conclusion **532**
References **533**

Abstract

Reduced size in one, two or three (all) dimensions leads to quantum effects when the length scale comes into the range of the de Broglie matter wavelength. Among these effects are size quantization and the associated sublevels and changes in the density of states, tunneling and interference effects, single electron effects, as well as coherence and entanglement.

Key points

- Quantum mechanical confinement in 1, 2 and 3 dimensions.
- The effects of tunneling, coherence and entanglement.
- Connecting physical effects and device functionality.
- Improving device performance and new device principles.

Introduction

A "quantum device" could be defined as a device whose functionality or principle of operation depends essentially on quantum mechanical effects. However, this definition somehow seems too vague. For example, a chair obtains its holding power from the quantum mechanical overlap of the wave functions of its constituents or a toaster relies on quantum mechanical scattering processes for converting electrical current and power into heat. Therefore a "quantum device" shall be defined here more rigorously as a "device that intentionally employs or harnesses quantum mechanical effects for its operation." This article is limited to condensed matter devices, thus completely (but intentionally) bypassing the "natural" use of quantum mechanics in living organisms.

A large number of devices already function based on the control of quantum mechanical interactions or effects. Prominent examples are the LASER (light amplification by stimulated emission of radiation) and the SQUID (superconducting quantum interference device). A possibly larger number awaits its commercialization or even their invention. This section discusses, in particular, quantum devices with "reduced dimensionality." These shall be understood as devices that rely on structures that confine charge carriers in one, two, or all three dimensions. Such systems are called quantum films or wells, quantum wires, and quantum boxes or dots, respectively. Given the typical de Broglie wavelength of electrons in semiconductors, typical sizes of such structures are in the 1–10 nm range. It is noted that currently (2022) the smallest feature size in mass-market consumer electronics is below 10 nm. Over the years, the predicted miniaturization limits have hit many marks which have been overcome by ingenuity. Clearly though the granularity of matter limits the miniaturization of individual devices at the atomic level or the lattice constant of solids (about 0.5 nm). Therefore, quantum and statistical effects seem unavoidable even in mainstream microelectronics.

The natural enemies of quantum devices are dephasing events such as scattering of an otherwise coherently evolving quantum state, increasing temperature, either due to higher scattering rate or the modification of thermodynamic distribution functions, and increasing structural size, mostly leading to a transition to classical behavior.

☆*Change History*: September 2022. M Grundmann updated Tables 1 and 2.

Quantum mechanical effects

The quantum effects that are used in quantum devices are sorted by increasing order of complexity and decreasing order of fundamental understanding and employment in devices:

1. single particle effects,
2. Pauli's exclusion principle,
3. quantization of electronic states in confining potentials,
4. tunneling effect,
5. spatial and temporal coherence of the wave function,
6. spin,
7. quantum liquids, and
8. entanglement.

Examples for the use of these effects in condensed matter devices is discussed below. The list, however, may not be exhaustive as eventually any quantum mechanical effect, for example, the quantization of other degrees of freedom or still unexplored effects, may be used in devices.

Quantization in potential wells

Quantum devices of reduced dimensionality depend some way or another on the presence of potential wells that limit the motion of charge carriers in *c* dimensions compared to bulk material. The motion can be limited in one dimension within a quantum film or well (QW), in two dimensions within a quantum wire (QWR), or in all three dimensions within a quantum dot (QD) or box. These structures can be combined to double or multiple structures or even periodic arrays (Table 1).

The confining potential can arise from applied spatially modulated electric potentials or the effect of band offsets in heterostructures or a combination of both. The quantization depends on the size, shape, and barrier height of the confining potential. By controlling the barrier height between confinement structures the degree of quantum mechanical coupling can be varied.

The simplest picture arises from the particle in a rectangular box with side lengths L_x, L_y, and L_z and infinite barriers. The quantization energy is given by

$$E = \frac{\pi^2 \hbar^2}{2m} \left(\frac{n_x^2}{L_x^2} + \frac{n_y^2}{L_y^2} + \frac{n_z^2}{L_z^2} \right)$$

with m being the effective mass of the particle (here taken as isotropic) and the n_i being the quantum numbers ($n_i \geq 1$).

If the confining potential is harmonic, the energy levels are equidistant.

$$E = (d/2 + n)\hbar\omega$$

$d = 3\text{-}n$ shall be the dimension of the confinement potential with n being the number of unconfined dimensions (see Table 1). For a parabolic confinement potential, the generalized Kohn's theorem applies, which states that the resonance energies of many electrons in the dot are the same as for a single electron and that dipole radiation interacts only with the center of mass motion of the electrons.

Since self-assembled nanostructures often involve strained systems, the confining potential depends on the local strain and the resulting piezoelectric field which both may be spatially strongly inhomogeneous.

The finite barrier height limits the number and the localization energy of confined states. In quantum dots, there is a critical minimum size for which at least one state is confined. Quantum dots smaller than the critical size do not exhibit any confined states, as opposed to quantum wells that always exhibit at least one localized and quantized state.

Two-dimensional carrier gases

A particularly important confined electron system is the two-dimensional electron gas (2DEG). Such a gas can develop in a quantum well. However, a single interface between two semiconductors of different bandgaps is sufficient to cause the creation of a 2DEG. If modulation doping, that is spatially inhomogeneous doping, is used, a high carrier concentration can be achieved in the 2DEG without the dopant atoms being located in or close to the 2DEG. In this way, impurity scattering is avoided and a high

Table 1 Structures with two-, one-, and zero-dimensional confinement.

Confinement of motion to n *dimensions*	*Name*	*Combination of two*	*Periodic structure*
2	Quantum well	Double quantum well	Superlattice
1	Quantum wire	Quantum wire pair	Quantum wire array
0	Quantum dot	Quantum dot molecule	Quantum dot chain/array

mobility is achieved. For GaAs/AlGaAs structures the mobility record (2004) stands at 3.1×10^7 Vs cm^{-2} low temperatures. Thus, 2DEG and its manipulation are the basis for many quantum devices, in particular exhibiting magneto-transport effects. In a high electron mobility transistor (HEMT), the transport in a 2DEG is used as channel conductivity in a field effect transistor. HEMTs display high transconductance and low noise figure and are used for many high-frequency applications such as satellite receivers. In order to maximize the carrier confinement, pseudomorphic quantum wells, for example, InGaAs/AlGaAs on GaAs, are used. The highest performance is achieved with InGaAs/InAlAs quantum wells on InP substrate. In order to transfer this technology to (larger and cheaper) GaAs substrates, a metamorphic, dislocated buffer is grown, and such a device is called MHEMT. Similar strategies apply to SiGe/Si HEMTs.

Magnetotransport effects in 2DEGs at low temperature have been studied in detail. In the integral quantum Hall effect (IQHE) the conductivity of the 2DEG exhibits extended plateaus for a range of magnetic fields with a well-defined conductivity value σ_{xy} that takes integer multiples of e^2h^{-1}, the (inverse) von-Klitzing constant (von Klitzing et al., 1980). This quantum mechanical value is found to be independent from details of the sample (within reasonable spread) such as doping, layer thickness, and growth method. The IQHE can be used for fabrication of a standard for the resistance and the unit "Ohm" (Bachmair et al., 2003). The precision of the QHE normal is two orders of magnitude better than the realization of the ohm in the old SI system. For this purpose, parallel and serial circuits of QHE resistors can also be used and an AC measurement technique can be devised.

It is to be noted that more complicated phenomena, the fractional quantum Hall effect, are observed and discovered in such quantum liquids at even more extreme conditions (very low temperatures and high magnetic fields).

Quantum wells are also very successfully used as active mediums in semiconductor laser diodes. Charge carriers are captured efficiently from the barrier material (high bandgap) into a quantum well or multiple quantum wells (low bandgap). Due to their small thickness, a high-density carrier gas is easily achieved and inversion is reached quickly. The finite density of states at the sub-band edges provides a favorable gain spectrum. This leads ultimately to low lasing threshold current density of $\sim$40 A cm^{-2} (Grundmann, 1999). Their combination with high-finesse optical cavities using high-reflectivity dielectric layer packages (Bragg mirrors) leads to vertical surface emitting lasers (VCSEL) and tests the use of quantum electrodynamic (QED) effects (e.g., the modification of spontaneous emission lifetime—Purcell effect).

Quantum wires

Many device applications have been envisioned for quantum wires. Since they are positioned in terms of reduced dimensionality between quantum wells and quantum dots, for some properties the ultimate solution is quantum dots. Since quantum dots can be fabricated in a self-assembled manner, they have made some of the quantum wire devices and approaches obsolete.

However, quasi-one-dimensional conduction poses interesting physics (e.g., reduced scattering and Luttinger liquids). Quantum wires can be used also as channels in transistors. In order to draw a sufficient current, many wires may have to be used in parallel. Due to the one-dimensional k-space, carrier scattering is reduced and thus a higher mobility should be possible. Recent progress in the self-assembled fabrication of quantum wire nanowhiskers or nanorods/nanopillars and heterostructures incorporated in them makes them seem attractive for a variety of applications including LEDs, lasers, and sensors.

Quantum dots

Quantum dots confine carriers in all three spatial dimensions. These are therefore sometimes termed "artificial atoms." The embedding into a solid-state matrix makes them more readily accessible to manipulation with electrodes, currents, fields, etc. than atoms in a trap. However, this comes at the price of stronger (compared to ions in a trap) coupling to external degrees of freedom, such as charge fluctuations and thermal bath.

The primary effect of quantum confinement is to create singular density of states at the quantized levels. The energetic broadening for a single quantum dot is typically small at low temperature (μeV range). With increasing temperature, additional dephasing mechanisms can increase the homogeneous broadening to the 10 meV range. An ensemble of quantum dots exhibits inhomogeneous broadening because the individual nanostructures are not exactly identical with respect to size, shape, and possibly chemical composition. The ultimate type of quantum dot is a single lattice defect, often termed "color center," NV (nitrogen-vacancy) centers in diamond being a prominent example. Devices based on single dots have been envisioned, realized, and investigated for storage of single electrons, emission of single or entangled photons, and quantum information processing.

The storage of single electrons is comparably straightforward. The capture of a single electron causes a second electron to need a larger energy to be on the dot due to Coulomb repulsion. While for typical shallow donors in semiconductors this effect is so strong that only the neutral state (with one electron) is localized, the Coulomb interaction energy in self-assembled quantum dots is typically in the range of 20 meV. At sufficiently low temperature for a given potential landscape, a second electron cannot enter the dot (Coulomb blockade) and the dot charge is fixed to an integer number of electrons, possibly one or zero. The storage of single electrons has been successfully demonstrated at low temperatures. Efforts are underway to maintain the effects up to liquid nitrogen temperature. The dots are typically built into a transistor structure to make a single electron transistor (SET). Here the gate electrode contains the quantum dot close to the channel. Due to electrostatic interaction the source-drain channel only becomes conductive after a sufficient source-drain voltage larger than the voltage related to the Coulomb energy has been applied. Conversely, in a single-electron memory, the conductance of the SET can be used to test whether a single electron is located on the quantum dot or not. By periodically modulating the applied bias voltages in a suitable manner with a frequency f, a single electron can be transferred by tunneling onto and off the dot from source to drain for each cycle. Such a device is called turnstile device and can be used to define a current normal via $I = f\,e$.

Quantum dots can be used in what is called a "photon gun." In such a device, a trigger impulse causes the reliable emission of a single photon. This is a nonclassical form of light which cannot be produced from dimming a conventional source. In classical light the time difference between photons follows Poisson statistics while a photon gun is supposed to create a periodic stream of single photons. With such photons, higher data rates for quantum cryptographic transmissions can be realized. Upon trigger the pulse carriers are injected into the quantum dot. Emission on the single exciton line occurs only once for each trigger with little time delay between trigger and emission.

The emission of entangled photons is possible if the cascade relaxation from biexciton to exciton and exciton to empty quantum dot is used. If the single exciton state is degenerate with respect to the two in-plane polarization directions, the photons are entangled and can be used for quantum cryptographic information transmission schemes. The polarization degeneracy calls for quantum dots with certain geometrical symmetry as strain, piezoelectric fields, and geometric asymmetries contribute to the lifting of the degeneracy. The two emitted photons have different energies unless the biexciton binding energy is zero. This is generally possible and depends on the size and shape of the quantum dot.

Several schemes have been devised to use quantum dots in quantum computing schemes. The spin degree of freedom seems a good candidate for quantum computational operations due to its long dephasing time of up to several milliseconds. Many of the current experiments involve optical sampling of the quantum information with polarized light and suitable pulses. NV centers are an example of quantum dots for which the spin state can be coherently manipulated even at room temperature. Electronic means are easier to integrate for access the quantum dots, making electrical readout of quantum information an active field. This has been accomplished for NV centers but also for quantum dots defined with in-plane gates, but for the latter only at very low temperatures. Using clever combinations of the Coulomb blockade mechanisms and external bias, the occupation and the spin orientation of a single electron can be tested electronically at low temperatures. Quantum computing schemes based on cellular automata (QCA) have been proposed extensively to realize quantum computational algorithms. QCA rely on arrays of quantum dots that interact to allow for switching of their polarization state.

Quantum dots can be used as active-gain medium in semiconductor diode lasers, which record small transparency current densities due to the fairly small volume for carrier inversion. Till date, reasonable laser performance has been obtained by using only self-assembled quantum dots. The discrete density of states leads, in an ideal situation, to very large T_0 values (small temperature-dependence of the threshold current) and zero alpha-factor (also termed line width enhancement factor). Realistically, the T_0 values have been found to be large (close to infinity) only up to 150–200 K; for higher temperatures the T_0 values are not particularly advantageous compared to conventional quantum well lasers because of loss of carriers from the quantum dots due to thermal excitations or the Auger effect. Small α-factors have been realized, also leading to a reduction of current filamentation and a homogeneous optical near field. These properties allow for improved high-power lasers.

Typically, lasing is designed to occur on the ground state of the quantum dots since this results in the lowest threshold (below $10\ \mathrm{A\ cm^{-2}}$) for laser diodes. Excited states provide higher gain and can be made to contribute to the lasing process simultaneously with the ground state. By intentionally increasing the width of the inhomogeneous broadening, for example, by growing vertically stacked dots with slightly different geometrical properties, the gain spectrum can be made very broad. Such gain medium would allow for wide tunability.

The management of strain and chemical composition allows to create 1300 and 1550 nm emission, important for datacom and telecom applications, respectively, on GaAs substrate. In particular, the use of metamorphic buffers has been successful recently. Quantum dot lasers are found to have a strongly improved radiation hardness compared to quantum well lasers.

Josephson junctions

A Josephson junction is made up from two superconductors sandwiching a thin non-superconducting layer such that electrons can tunnel through the barrier. The coherence of the wave function in the superconductor leads to DC or AC currents. The DC Josephson current is proportional to the phase difference between the two superconductors. The frequency f of the AC Josephson current is proportional to the voltage V applied across the junction, $f = 2eV\ h^{-1}$. This allows for a voltage normal based on a frequency. A Josephson junction standard can realize a voltage with an accuracy of 10^{-10}. For a standard in the volt regime several thousand junctions are put in series. A superconducting loop with two Josephson junctions in either arm is very sensitive (10^{-14} T) to the magnetic flux enclosed (SQUID, superconducting quantum interference device).

Conclusion

Devices relying on quantum effects have a broad spectrum of applications (Table 2). Generally, it is difficult to achieve operation at ambient temperatures. Great progress has been made in the field of metrology where quantum devices will become standards that can be easily reproduced, at least in a laboratory environment. Room temperature operation has been achieved, for example, for quantum dot lasers with the preservation of several advantages from the quantum nature of the gain medium.

Table 2 Quantum devices, the effects they are based on, and applications.

Device	*Quantum effect*	*Performance/Use*
High electron mobility transistor	2D confinement	High-speed, low-noise amplifier, low-threshold laser
Quantum well laser	2D confinement	Low threshold
Quantum dot laser	0D confinement	Low threshold, small α
Quantum Hall effect	Quantum liquid	Resistance standard
Electron turnstile	Tunneling, single electrons	Current standard
Photon gun	Single-particle effect	Quantum cryptography
Quantum cellular automata	0D confinement, coherence	Quantum computing
Quantum dot, color centers	Entanglement, coherence	Quantum computing, quantum cryptography, quantum sensing
Josephson junction	Coherence of wave function	Voltage standard
SQUID	Coherence of wave function	Sensitive magnetometer

References

Bachmair H, Göbel EO, Hein G, Melcher J, and Schumacher B (2003) The von Klitzing resistance standard. *Physica E* 20: 14.

Grundmann M (1999) The present status of quantum dot lasers. *Physica E* 5: 167.

von Klitzing K, Dorda G, and Pepper M (1980) New method for high-accuracy determination of the fine-structure constant based on quantized hall resistance. *Physical Review Letters* 45: 494.

Thermoelectric energy conversion devices

H Julian Goldsmid, School of Physics, University of New South Wales, Sydney, NSW, Australia

© 2024 Elsevier Ltd. All rights reserved.

This is an update of J.W. Sharp, Thermoelectric and Energy Conversion Devices, Editor(s): Franco Bassani, Gerald L. Liedl, Peter Wyder, Encyclopedia of Condensed Matter Physics, Elsevier, 2005, Pages 173–180, ISBN 9780123694010, https://doi.org/10.1016/B0-12-369401-9/00507-6.

Introduction 534
The thermoelectric figure of merit 535
Optimizing the Seebeck coefficient 536
Semiconductor thermoelements 536
Reducing the lattice conductivity 537
Thermoelectric materials 537
A limit on the figure of merit 538
Thermoelectric modules 538
Conclusion 538
Acknowledgments 539
References 539

Abstract

Thermocouples have long been used for the measurement of temperature, but they can also be used as heat engines for the generation of electrical power and for heat pumping or refrigeration. However, their efficiency as generators and their coefficient of performance as heat pumps fall well short of the ideal limits. This is because the reversible thermoelectric effects are always accompanied by the irreversible phenomena of electrical resistance and thermal conduction. It is shown that the performance of thermoelectric energy convertors can be expressed in terms of a quantity known as the figure of merit. The figure of merit is highest for semiconductors that have a low lattice thermal conductivity, a high carrier mobility and a high density of electronic states. The figure of merit is high in both p-type and n-type bismuth telluride, though there is still plenty of room for improvement. It is explained that the electronic parameters can be optimized for a given thermoelectric material. Also, various means of reducing the phonon conductivity are discussed. These include the use of solid solutions rather than simple elements and compounds and the reduction of the grain size to enhance boundary scattering. Mention is made of PGEC materials that combine phonon transport in glass with electron transport in crystals. There is also the possibility of improving the figure of merit by making use of nanostructures. However, it is also argued that the performance of thermoelectric energy convertors is unlikely to exceed about 40% of that of an ideal thermodynamic machine.

Key points

- The thermoelectric effects.
- Energy conversion and efficiency.
- Heat conduction in solids.
- Electrical resistance.
- The power factor.
- Scattering of electrons and phonons.
- Thermoelectric materials.
- Thermoelectric modules.

Introduction

The discovery of thermoelectricity is usually attributed to Thomas Seebeck and Jean Peltier and the two main effects are named after them. When the junction between two different electrical conductors is heated, an electromotive force is developed. This is the Seebeck effect. Similarly, when an electric current is passed through such a junction, Peltier heating or cooling is observed. Despite the thermoelectric effects appearing at the interface between two conductors, the Seebeck and Peltier coefficients are essentially bulk properties. Absolute values for these coefficients in a given material can, in principle, be defined by supposing that it is joined to a superconductor, all superconductors having zero Peltier and Seebeck coefficients.

https://doi.org/10.1016/B978-0-323-90800-9.00195-5

It was shown by Kelvin that the Seebeck coefficient, α, is related to the Peltier coefficient, π, by the expression $\pi = \alpha T$. This is of practical significance since the Seebeck coefficient is much easier to measure than the Peltier coefficient. Thus, even when a thermocouple is used as a heat pump or refrigerator, its performance can be expressed in terms of the Seebeck coefficient.

When there is both a flow of current and a temperature gradient in a single material, a third thermoelectric effect is apparent. This reversible heating or cooling is related to the Seebeck and Peltier effects and is known as the Thomson effect. It can be used in the extrapolation of the Seebeck and Peltier coefficients to elevated temperatures.

The thermoelectric effects can be exploited in the generation of electricity from heat and in heat pumping or refrigeration. The effects are reversible, but they are always accompanied by the irreversible effects of electrical resistance and heat conduction. This means that the efficiency of a thermoelectric generator is usually much smaller than that of an ideal heat engine Likewise, the coefficient of performance (COP) of a thermoelectric heat pump is limited by the irreversible effects. The need for materials with large thermoelectric coefficients and small electrical resistivity and thermal conductivity has long been realized (Altenkirch, 1911), but suitable thermocouples did not become available until the 1950s.

A thermoelectric energy convertor usually consists of a number of thermocouples connected thermally in parallel and electrically in series. Each thermocouple has a positive and negative branch. The dimensions of the branches are selected so as to minimize the combined effects of electrical resistance and heat conduction.

Let us suppose that the temperature difference between the hot and cold junctions is small compared with the absolute temperature; $\Delta T/T \ll 1$. Then the efficiency, η, is given by

$$\eta \simeq \frac{\Delta T}{T}\left(\frac{M-1}{M+1}\right) \tag{1}$$

and the coefficient of performance, ϕ, is given by

$$\phi = \frac{T}{\Delta T}\left(\frac{M-1}{M+1}\right) \tag{2}$$

In these equations the quantity M is equal to $(1+ZT)^{1/2}$ where Z is known as the thermoelectric figure of merit (Ioffe et al., 1957).

The thermoelectric figure of merit

The figure of merit of a thermocouple is given by the expression

$$Z = \frac{\left(\alpha_p - \alpha_n\right)^2}{\left\{\left(\lambda_p \rho_p\right)^{1/2} + \left(\lambda_n \rho_n\right)^{1/2}\right\}^2} \tag{3}$$

where λ represents the thermal conductivity and ρ represents the electrical resistivity. The subscripts p and n indicate the positive and negative branches respectively. It is assumed that the relative dimensions of the branches have been optimized.

It is common practice to make use of a figure of merit for a single material, that is either the positive or negative branch. This quantity is equal to $\alpha^2/\lambda\rho$ and will be denoted by the symbol z. Usually the thermocouple figure of merit, Z, is close to the average of the figures of merit z_{p} and z_{n} for the two branches. More often than not, one encounters the dimensionless figure of merit, ZT, rather than Z, and recently, a method that uses Peltier cooling was developed for measuring the dimensionless figure-of-merit of a semiconductor using semiconductor-metal thermocouples (Bhattacharya et al., 2022).

The product $\lambda\rho$ has its smallest value for metallic conductors but unfortunately the Seebeck coefficient is then also small. Much larger Seebeck coefficients are to be found for semiconductors but then the product $\lambda\rho$ also becomes larger. This is because the conduction of heat by the lattice vibrations is dominant in such materials. In general, one can optimize the figure of merit for a semiconductor by changing the carrier concentration using donor or acceptor impurities.

The effect of changing the carrier concentration can be described in terms of the position of the Fermi level within the energy bands. The Fermi level is the energy at which the probability of a state being occupied is ½. The thermoelectric coefficients depend on the energy difference between the Fermi level and the edge of the appropriate band. The valence band contains the so-called positive holes while the conduction band contains the negative carriers, the electrons. It is preferable for the energy gap between the conduction and valence bands to be large enough for only one type of carrier to contribute significantly to the transport processes. When both types of carriers are present they act in opposition to one another. For a p-type or positive thermoelectric material the Fermi level lies in or near the valence band and for an n-type or negative material it lies close to the conduction band.

The contribution of the carriers in a particular band depends on their concentration and on their mean free path. Both these quantities in turn are related to the effective mass of the carriers. A large effective mass is beneficial in that it implies a large density-of-states, but it also means that the scattering of the carriers is stronger. Actually, there is more than one effective mass. Thus, there is a density-of-states mass and an inertial mass. The two are related to one another but it is possible to find a low inertial mass combined with a high density-of-states mass in a multi-valley semiconductor. In such a material the band edge is located, not at the center of wave-vector space, but at multiple points that satisfy the crystal symmetry.

A good thermoelectric material combines a high density-of-states mass, m^*, with a high mobility, μ. It is also necessary for the lattice thermal conductivity, λ_L, to be as small as possible. In the search for thermoelectric materials, we look for a high value of $(\mu/\lambda_L)(m^*/m)^{3/2}$ where m is the mass of a free electron. It is common practice (Chasmar and Stratton, 1959) to combine these properties in a parameter β that is defined by the equation

$$\beta = \left(\frac{k}{e}\right)^2 \frac{\sigma_0 T}{\lambda_L} \tag{4}$$

where

$$\sigma_0 = 2e\mu\left(\frac{2\pi m^* kT}{h^2}\right)^{3/2}. \tag{5}$$

Of course, besides selecting a material with a high value of β it is also necessary to optimize the carrier concentration.

Optimizing the Seebeck coefficient

Let us discuss the effect of changing the Fermi energy when there is only one type of carrier, say positive holes. The Seebeck coefficient will become larger as the Fermi level moves away from the valence band edge into the energy gap. On the other hand, this will lead to a decrease in the carrier concentration. To obtain a high figure of merit it is desirable that the quantity α^2/ρ, known as the power factor, should be large. This usually means that the Fermi level should lie close to the band edge and the Seebeck coefficient is then of the order of ±200 μV/K. However, we must also take into account the effect of the electronic thermal conductivity, which will generally not be negligible compared with the lattice contribution. This means that the optimum Seebeck coefficient will be greater than that which yields the highest power factor.

In Fig. 1 we show the variation of zT with Seebeck coefficient for materials with different values of $(zT)_{\max}$ (Goldsmid, 2017). In fact, values of $(zT)_{\max}$ for the best present-day thermoelectric materials do not exceed 3 so the optimum Seebeck coefficient is never more than about ±300 μV/K.

Semiconductor thermoelements

The Seebeck effect has long been used for the measurement of temperature. For that purpose, at least one of the branches of the thermocouple is a metal or metallic alloy. However, by the middle of the twentieth century it was realised that worthwhile figures of merit could only be achieved using semiconductors. The question, then, was how to find a semiconductor with a large value of β.

A major contribution was made by Ioffe and Ioffe (Ioffe and Ioffe, 1954) who carried out a systematic study of the lattice thermal conductivity of non-metallic crystals. They showed that in any given series of elements or compounds the lattice conductivity fell with increasing mean atomic weight. This idea is exemplified by the compound PbTe which was one of the first materials to be used

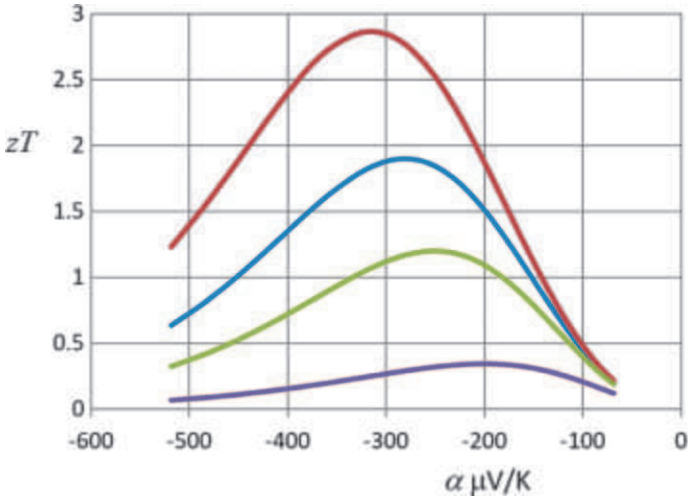

Fig. 1 Plots of zT against Seebeck coefficient for various values of $(zT)_{\max}$. The graphs are for n-type material but would be identical for p-type material apart from the sign of the Seebeck coefficient. Reproduced with permission from Ref. Goldsmid HJ (2017) *The Physics of Thermoelectric Energy Generation.* IOP Publishing: Bristol.

in practical thermoelectric generators. Likewise, the compound Bi_2Te_3 was the first material to be used in thermoelecric refrigerators that could yield worthwhile depressions of temperature through the Peltier effect (Goldsmid and Douglas, 1954). A simple theory relating the lattice conductivity to the mean atomic weight has been developed by Keyes (Keyes, 1959).

Since its introduction in the mid-1990s bismuth telluride and its alloys have remained the most widely used thermoelectric materials. Bismuth telluride in both its p-type and n-type forms has a value for the product $\mu(m^*/m)^{3/2}$ that is higher than for almost any other semiconductor. Not surprisingly, in view of its high mean atomic weight, the lattice thermal conductivity is also exceptionally low. There are, however, some features of bismuth telluride that are unfavorable. The energy gap is no more than 0.13 eV which means that it is difficult to avoid the influence of minority carriers. This problem becomes more severe as the temperature is raised so bismuth telluride becomes unsuitable for generation and refrigeration at elevated temperatures. Also, the structure is such that the compound forms crystals that are weakly bonded in the trigonal direction, a factor that must be borne in mind when designing thermoelectric modules.

The figure of merit of both p-type and n-type bismuth telluride is highest for current flow perpendicular to the trigonal axis, that is parallel to the basal planes. It is not necessary that the material be in the form of a single crystal. Polycrystalline sintered material is mechanically stronger than single crystals and can be preferentially aligned if produced by extrusion or hot pressing (Airapetyants and Efimova, 1958).

Reducing the lattice conductivity

Ioffe and his colleagues (Ioffe et al., 1956) showed that the figure of merit of any particular element or compound can be improved by forming a solid solution or alloy. Thus, the lattice conductivity of bismuth telluride can be reduced by forming a solid solution with antimony telluride or bismuth selenide. Likewise, lead telluride can be improved by alloying with lead selenide. Perhaps surprisingly, the formation of a solid solution does not necessarily affect the mobility of the charge carriers provided that the long-range order is maintained.

Of particular interest are the alloys of silicon and germanium. Silicon is one of the few semiconductors that has a product $\mu(m^*/m)^{3/2}$ that is substantially superior to that of bismuth telluride. However, the lattice conductivity of silicon is exceptionally high, being comparable with the total thermal conductivity of most metals. The value of β for silicon is, therefore, not very large but this quantity becomes more promising for silicon-germanium alloys and, in fact, these are worthwhile generator materials.

It is well known that the lattice conductivity of a crystal can be reduced by making the grain size smaller but this is usually thought of as a low-temperature phenomenon (Blakemore, 1985). However, boundary scattering can also be observed at high temperatures. It is likely to be most noticable for solid solutions in which most of the heat is carried by low-frequency phonons. Boundary scattering has been observed at ordinary temperatures for silicon-germanium alloys.

The lattice conductivity of bismuth telluride is of the order of 1 W/m K and similar values are found for some other crystalline materials but substantially lower values are expected for glasses. Slack introduced the useful concept of a PGEC that is a phonon-glass electron-crystal. It has been shown that promising thermoelecric properties can be found among crystals that have large unit cells containing loosely bound atoms.

Thermoelectric materials

In spite of the fact that bismuth telluride and its alloys have been in use as thermoelectric materials for more than half a century, they are still the basis of most thermoelectric refrigerators. They have also been used in generators at moderately high temperatures, but their small energy gap is a severe disadvantage for most generator applications. There are, however, several other materials that have attracted interest in the field of thermoelectric energy conversion.

One of the earliest materials to be studied was the semi-metal, bismuth. Although it has a negative energy gap (that is an overlap of the conduction and valence bands) the transport properties are dominated by the electrons, and it was used as a negative thermoelement with bismuth telluride as the positive branch in the earliest thermoelectric refrigerator.

It has been found that certain alloys of bismuth and antimony have a positive energy gap, and are marginally superior to bismuth telluride at low temperatures (Yim and Amith, 1972). The electrons in bismuth and Bi—Sb alloys have a high mobility and, therefore, exhibit large magneto- thermoelectric effects (Horst and Williams, 1980). These include not only longitudinal changes in the thermoelectric parameters but also transverse effects. The transverse equivalents of the Seebeck and Peltier effects are the Nernst and Ettingshausen effects. They have an advantage over the longitudinal effects in that they allow independent control of the electrical and thermal resistance in perpendicular directions.

Compounds and alloys based on lead telluride have a larger energy gap than bismuth telluride, 0.3 eV compared with 0.13 eV, and have long been used in thermoelectric generators. The so-called TAGS materials are alloys of $AgSbTe_2$ with GeTe. They are closely related to PbTe although they do not have the rock salt structure. They have values for z_pT in excess of unity at temperatures greater than about 600 K (Skrabek and Trimmer, 1994). A related compound that exhibits the largest value of zT at present is SnSe. At ordinary temperatures it has a distorted rock salt structure that changes to the undistorted form above 800 K. SnSe is remarkable in that zT is as high as 2.62 at 923 K (Zhao et al., 2014). The main reason for this exceptional value is a lattice conductivity of only 0.23 W/m K.

Silicon-germanium alloys have already been mentioned and have come into their own at high temperatures. In fact, one might have expected them to be even better since electrons in *pure* silicon have a value for $\mu(m^*/m)^{3/2}$ about four times greater than in bismuth telluride. However, for thermoelectric applications one needs to add donor impurities to such a level that ionized-impurity scattering has substantially reduced the mobility. It has been suggested that the scattering of electrons would not be as strong if the impurities were present as ionized nanoparticles rather than as ionized atoms (Bahk et al., 2011).

Several compounds have been studied with the aim of achieving low lattice conductivities. One group that has been extensively studied is the skutterudites. The unit cell of a skutterudite is relatively open with spaces that can be occupied by loosely bound atoms that are very effective scatterers of phonons. The skutterudites form a large family of compounds, and several members have zT values of the order of unity at elevated temperature (Nolas et al., 2001). The clathrates are another family with open structures and a low lattice conductivity. It is not too difficult to find materials with zT of the order of unity above room temperature so one needs to take other factors into account in selecting generator materials. For example, various oxides have reasonably good figures of merit and have the advantage of stability. $SrTiO_3$ is an n-type material with a rather low electron mobility but it makes up for this with a high density-of-states effective mass, with zT of about 0.4 at 973 K (Zhilun et al., 2016). By way of contrast there are also organic thermoelectrics with mechanical flexibility (Zhang et al., 2014).

Recent studies have been devoted to nanostructured thermoelectric materials. The band structure is modified if the grain size is reduced to the order of the interatomic spacing in at least one direction. This could lead to an improvement in the power factor as well as a reduction in the lattice thermal conductivity. In practice it has proved to be difficult to achieve an improvement in the electronic properties for any nanostructure but there is good evidence for a reduction in the lattice conductivity (Venkatasubramanian et al., 2001).

A limit on the figure of merit

In principle there is no upper limit to the figure of merit. However, as the quantity β becomes larger the optimum Fermi level moves away from the edge of the valence or conduction band. The carrier concentration then falls rapidly. This means that zT rises only slowly with increasing β. The problem is that the Seebeck coefficient varies linearly with the Fermi energy whereas the carrier concentration displays an exponential dependence. It is not unreasonable to expect that we shall find materials that combine a glass-like phonon conductivity with a mobility-effective mass product that is close to that of electrons in pure silicon. This combination of properties would give a value of about 4 for zT at the optimum carrier concentration. However, any further improvement would be difficult to achieve.

We know that β is equal to about 0.4 for alloys of bismuth telluride with zT then equal to 1. A rise of β to about 3.2 would enable zT to climb to 4 but a further doubling of β would only allow zT to reach 5. If zT were equal to 5 the parameter M in Eqs. 1 and 2 would become close to 2.4 and $(M-1)/(M+1)$ would be about 0.4. In other words, we do not expect the efficiency of thermoelectric generators or the COP of thermoelectric heat pumps to exceed about 40% of their ideal values.

Thermoelectric modules

In principle one can obtain any amount of cooling power or generate any amount of electricity using a single thermocouple. However, this would entail inconveniently large electric currents and small voltages. Thus, most thermoelectric devices incorporate a multiplicity of thermocouples in the form of modules. A thermoelectric module consists of a number of thermoelements connected electrically in series and thermally in parallel. In theory each thermoelement can be of any length or cross-section area but it is obviously economical to make the volume as small as possible. However, when the thermoelements are very small the performance can be impaired by electrical contact resistance and by heat transfer other than through the thermoelectric material. There is a significant reduction in the temperature depression that can be achieved by a thermoelectric cooler if the thermoelements are much less than 1 mm in length.

Although most practical thermoelectric modules comprise a single stage one also encounters multi-stage devices. For example, a multi-stage thermoelectric refrigerator can be used to reach a temperature that is lower than that which can be achieved with a single stage. Also, thermoelectric generators become more efficient as the temperature difference between the heat source and the heat sink becomes larger and this may be realized by using a cascade. It is sometimes worthwhile to use graded thermoelements in which the thermoelectric properties are matched to the local temperature.

Conclusion

Thermoelectric generators and refrigerators are now recognized as practical energy conversion devices. They have no moving parts and can be adapted to handle very large or very small amounts of power. However, the reversible thermoelectric effects are always accompanied by irreversible Joule heating and heat conduction. This means that their efficiency is much smaller than that of an ideal thermodynamic machine. Their performance depends on the so-called figure of merit which is proportional to the square of the Seebeck coefficient and inversely proportional to the electrical resistivity and the thermal conductivity of the materials that form the positive and negative branches. The best thermoelectric materials at ordinary temperatures are alloys based on the compound bismuth telluride, Bi_2Te_3. Materials that can be used at higher temperatures include alloys based on lead telluride and silicon-germanium alloys. It is expected that the figure of merit will improve as a more favorable combination of the mobility and effective mass is found and as the lattice conductivity becomes smaller, but the efficiency and COP are unlikely to exceed 40% of their ideal values.

Acknowledgments

The author wishes to thank Sriparna Bhattacharya and Herbert Behlow from Clemson University for help with the final editing of this article.

References

Airapetyants SV and Efimova BA (1958) *Soviet Physics. Technical Physics* 3: 1632.

Altenkirch E (1911) *Physikalishce Zeitschrift* 12: 920.

Bahk JH, Bian Z, Zebarjadi M, Santhanam P, Ram R, and Shakouri A (2011) *Applied Physics Letters* 99: 072118.

Bhattacharya S, Behlow H, Rancu I, Rao AM, and Goldsmid HJ (2022) *Journal of Applied Physics* 132: 175106.

Blakemore JS (1985) *Solid State Physics*, 2nd edn, p. 137. Cambridge University Press.

Chasmar RP and Stratton R (1959) *Journal of Electronics* 7: 52.

Goldsmid HJ (2017) *The Physics of Thermoelectric Energy Generation*. Bristol, UK: IOP Publishing.

Goldsmid HJ and Douglas RW (1954) *British Journal of Applied Physics* 5: 386.

Horst RB and Williams LR (1980) *Proceedings of the Third International Conference on Thermoelectrics, Arlington, Texas, IEEE, New York*, p. 183.

Ioffe AV and Ioffe AF (1954) *Doklady Akademii Nauk SSSR* 97: 821.

Ioffe AF, Airepetyants SV, Ioffe AV, Kolomoets NV, and Stil'bans LS (1956) *Doklady Akademii Nauk SSSR* 106: 981.

Ioffe AF, Stil'bans LS, Iordanishvili EK, and Stavitskaya TS (1957) *Semiconductor Thermoelements and Thermoelectric Cooling*. Revised and supplemented by Prof. AF Ioffe for the English edition. Translated by A Gelbtuch. Edited by HJ Goldsmid. Infosearch, London.

Keyes RW (1959) *Physics Review* 115: 564.

Nolas GS, Sharp J, and Goldsmid HJ (2001) *Thermoelectrics: Basic Principles and New Materials Developments*, p. 177. Berlin: Springer.

Skrabek EA and Trimmer DS (1994) In: Rowe DM (ed.) *CRC Handbook of Thermoelectrics*, p. 267. Boca Raton: CRC Press.

Venkatasubramanian R, Silvola E, Colpitts T, and O'Quinn B (2001) *Nature* 413: 597.

Yim WM and Amith A (1972) *Solid State Electronics* 15: 1141.

Zhang Q, Sun Y, Xu W, and Zhu D (2014) *Advanced Materials* 26: 6829.

Zhao LD, Lo SH, Zhang Y, Sun H, Tan G, Uher C, Wolverton C, Dravid VP, and Kanatzidis MG (2014) *Nature* 508(373): 177.

Zhilun L, Zhang H, Lei W, Sinclair DC, and Reaney IM (2016) *Chemistry of Materials* 28(3): 925–993.

Geometry matters: Gamete transport using magnetic microrobots

David Castellanos Robles[a,*], **Farzin Akbar**[a,*], **and Mariana Medina-Sánchez**[a,b], [a]Micro- and NanoBiomedical Engineering Group (MNBE), Institute for Integrative Nanosciences, Leibniz Institute for Solid State and Materials Research (IFW), Dresden, Germany; [b]Chair of Micro- and NanoSystems, Center for Molecular Bioengineering (B CUBE), Dresden University of Technology, Dresden, Germany

© 2024 Elsevier Ltd. All rights reserved.

Introduction 540
Physical principles of microrobots motion at low Reynolds numbers 541
Optimization of microrobots efficiency 541
Chemical microrobots 542
Tubular microrobots 542
Janus microrobots 542
Biohybrid microrobots 542
Physically-driven microrobots 542
Helical microrobots 543
Cilia-based microrobots 543
Alternative geometries 544
Optimization of microrobot biocompatibility and their immunological response 544
Gamete/zygote transport 545
Transportation of sperm cells 545
Transportation of egg/zygote cells 546
Navigating reproductive system barriers 547
Conclusion 548
Acknowledgments 548
References 548

Abstract

Medical microrobots are tiny devices designed to perform diagnostic and/or therapy non-invasively, targeting molecules and cells at their scale. However, they should be designed based on their function and cargo transport requirements. These features are directly related to the microrobots geometry, which varies depending on the size, cargo compliance, adopted locomotion strategy, and their working environment. Geometry also affects the immunological response and the microrobots interaction with their surroundings. Here we discuss the influence of a proper microrobot design and material selection when envisioning a biomedical application, giving a particular focus to the optimization of gametes/zygotes microrobotic transport for in-vivo assisted reproduction.

Key points

Highlight the importance of a proper microrobot design and material selection according to the intended medical application

- Evaluate how the geometry influences the efficiency of cargo transport and release, in the case of gametes (sperm and oocytes) and early embryos
- Analyze the different reported microrobots designs for an optimal motion in viscoelastic fluids, against flow, and in contact to rough surfaces, when employing external magnetic fields
- Identify the impact of the microrobot geometry on the immunological response

Introduction

Since it was conceived by Richard Feynman in his "There's plenty of room at the bottom" lecture in 1959, micro/nanodevices have been devised for many high impact applications in electronics, electromechanics, analytical chemistry, and biotechnology, as well as medical microrobotics (Feynman, 1960). Microrobots are microscopic structures that convert the input energy (e.g. chemical, electrical) into mechanical motion. Microrobots can be divided into three categories based on their mode of operation: chemical, biohybrid, and physical (Medina-Sánchez and Schmidt, 2017). Chemically actuated microrobots can propel themselves by the fuel

---

[*] Equal contribution.

https://doi.org/10.1016/B978-0-323-90800-9.00231-6

energy from a catalyst (platinum, silver, palladium, etc.) on microrobots reacting with liquid medium (hydrogen peroxide, organic compounds, etc.) (Gao et al., 2011; Golestanian et al., 2005; Mei et al., 2011; Paxton et al., 2004). Such toxic fuels cannot be used in medical or biological applications. Therefore, for in vivo biomedical uses, physiological fluids such as glucose, urea should be developed for the microrobot actuation (Sun et al., 2019, 2019). Biohybrid microrobots can be constructed by motile organisms such as bacteria and muscle or sperm cells with a synthetic component (Lin et al., 2022; Schwarz et al., 2017; Yang et al., 2019). They can be steered by the organisms themselves, as they move, sense and respond to biochemicals, acidity or magnetic fields. However, considering in vivo conditions, the abundance of sticky proteins may pose a big threat to the motility of biohybrid microrobots, and the motion directionality should be improved for biomedical applications as well as multifunctionality. On the other hand, physical actuation methods have been devised by various external fields such as optical, acoustic, and magnetic methods. For example, the optical method was utilized to steer phototactic bacteria and algae, but the light is poorly transparent to biological tissues. Ultrasound has not been extensively utilized for steering microrobots due to its poor reliability and reversibility but it is a method that indeed would be compatible with various imaging modalities and suitable for in vivo applications. Magnetic control holds the most significant promise because magnetic force can have efficient and fast response time as well as safe penetration to biological environments. In addition, regarding the safety, a static magnetic field under 8 T is not considered dangerous for human medical use (Schenck, 2000). To date, a variety of magnetic robots have been pursued toward the biological applications such as magnetic hyperthermia (B. Wang et al., 2018), targeted drug delivery (Schmidt et al., 2020), and minimally invasive surgery (Srivastava et al., 2016).

Physical principles of microrobots motion at low Reynolds numbers

Due to their small size, the microrobots operate in the low Reynolds numbers regime where the viscous forces dominate inertial forces. To produce a net motion in the low Reynolds number regime, microrobots must undergo a specific nonreciprocal motion. In order to design efficient microrobots, it is crucial to investigate the factors that impact their efficiency. The two main factors that influence the microrobot motion are the environment in which they operate and the microrobot geometry. Environmental factors include temperature, fluid viscosity, flow velocity, and fuel concentration. The ultimate geometry design has also proven to have an influence on the microrobot-cell interaction which could lead to an undesired immunological reaction. Finally, a selection of materials and coating is also included, being important for their final implementation in real biological environments.

To improve the efficiency of the microrobots, it is important to focus on their geometry design since the environment in which they operate is often beyond our control. By optimizing the shape and structure of the microrobots, one can enhance their performance and efficiency at achieving the intended tasks. The smart designed geometry of the microrobots provides them with different efficient modes of operation such as rolling or twisting (Bozuyuk et al., 2021; Schwarz et al., 2020; Xu et al., 2019).

The motion of the microrobots is determined by the Stokes' law which is derived from the Navier-Stokes equation for low Reynolds numbers as follows. For a simple spherical microrobot with a radius of 'r'. The Stoke' law is as follows:

$$F = 6\pi r\eta v \tag{1}$$

Where 'F' is the drag force on the microrobot, 'η' is the fluid viscosity, and 'v' is the microrobot velocity. This law suggests that the drag force of the microrobot is proportional to the viscosity of the solution, suggesting that the velocity decreases with increasing viscosity. The parametric design in the Stokes' law is the radius of the microrobot. One way to design efficient microrobots is by using the Stokes law to calculate the drag force on the microrobots with identical radii. The drag coefficient also plays an important role for the efficient design of the microrobots. It is a dimensionless quantity that describes the resistance experienced by a microrobot as it moves through the surrounding liquid. The drag coefficient can be influenced by geometric factors such as the shape and size of the microrobot. It has been reported that the drag coefficient first sharply decreases as the ration of length to radius of the microrobot increases (Li et al., 2015). This is followed by a slight increase of the drag coefficient for higher length to radius ratios. The drag coefficient can be obtained from the following equation:

$$\mathrm{C_d} = \frac{\frac{4\xi^2}{\mathrm{Re}}}{(\ln \xi' + \alpha)} \tag{2}$$

Where $\xi = L/R_{max}$, $\xi' = L/R_m$, with R_m defined as the radius in the middle cross-section of a microrobot, and α is microrobot shape dependent coefficient (Li et al., 2015). By measuring the velocity of the microrobots and calculating the drag coefficient, one can optimize the design to minimize the drag force on the microrobots and develop microrobots with efficient modes of operation.

Optimization of microrobots efficiency

An efficient and viable form of motion is desired from the microrobots for practical applications. In addition to theoretical analysis, one can use numerical simulations and conduction of experiments to enhance the microrobots efficiency. This allows for a more comprehensive and practical assessment of the microrobot's performance and can lead to the development of more efficient microrobots. There have been multiple studies that combine the theoretical, numerical, and experimental approaches to tune the shape and design more advanced microrobots which will be discussed further in this chapter. Furthermore, the size of a microrobot also plays an important role in its efficiency. Small microrobots motion are governed by the viscous forces whereas the inertial forces limit the velocity of larger microrobots. This effect was investigated in a work by Dkhil et al. using analytical and numerical methods. An optimal radius of 20 μm was found for a magnetic spherical microrobots operating in water (Dkhil et al., 2014).

Chemical microrobots

The catalytic microrobots are a sub-category of chemical microrobots, where the release of gas bubbles on the surface of the microrobots cause them to recoil and propel forward. These microrobots have been developed in three general forms of rod structures, tubular, and spherical shapes. They require different geometry improvement techniques to become more efficient.

Tubular microrobots

Bimetalic nanorods were among the first microrobots that showed the catalytic decomposition of hydrogenperoxide as a means of propulsion (Wang et al., 2006), these nanorods were later enhanced to form tubular microrobots with the vision of integrated battery and electronics (Mei et al., 2011). Further development resulted into cone shaped microrobots (Wrede et al., 2021) with increased velocities and propulsion forces (Li et al., 2014). The hydrodynamic of bubble growth in the microrobots were studied by Li et al. and a theory model was used for experimental results validation (Li et al., 2014). According to Mitrovic (Mitrovic, 1997), the asymmetry of the bubble creates a pressure difference known as a Laplace pressure. This pressure propels the bubbles along the inner wall of the tube. In a conical geometry, the asymmetry of the shape leads to the formation of a capillary force, leading to the movement of the generated bubble to the larger opening of the semi-conical microrobot (Fomin et al., 2014). It has been reported in an analytical study that when the aspect ratio ξ (Eq. 2) is held constant, the drag coefficient decreases with an increasing semi-cone angle which in turn leads to higher velocities (Li et al., 2015).

Janus microrobots

Named after the Roman god with two faces, the Janus microrobots have a two-material structure and are propelled by the catalytic reaction between the catalytic surface and the surrounding electrolyte. Since only half of a spherical Janus microrobot is coated with a catalytic layer, the bubbles are generated on this half only, which in turn propel the microrobot in a single direction. One way to enhance the speed of Janus microrobots has been reported to increase the surface roughness. The higher surface area of the rough surface leads to a higher rate of catalytic reaction which in turn leads to higher velocities (Jurado-Sánchez et al., 2015). Another approach to increase the efficiency of such spherical microrobots is to change their geometry to develop hollow spherical structures that demonstrate high relative velocities of 125 body lengths/s (Wu et al., 2012).

Biohybrid microrobots

An alternative approach to utilizing entirely synthetic microrobots, is to exploit motile biological microorganisms. In this approach the biological microorganisms are typically steered by an external stimulus to reach the desired target. Felfoul et al. used a swarm of inherently magnetotactic bacteria loaded with drug to treat tumor cells. The swarms were guided toward the tumor cells via magnetic fields (Felfoul et al., 2016). In the case of nonmagnetic organisms, polymeric caps that fit the organisms were coated with magnetic materials. It has been shown that microorganisms such as sperm cells bond to such caps. This allows the steering of such biohybrid microrobots via the magnetic field (Magdanz et al., 2013). To unload the cap from microorganisms such as sperms, Xu et al. designed a specific "tetrapod" cap that opens when the biohybrid microrobot is pushed against the target causing the sperm to release (Xu et al., 2018). To steer multiple sperm cells rather than one to increase the fertilization efficiency in assisted fertilization applications, several approaches have been proposed. Xu et al. developed a train cap to carry multiple sperm cells (Xu et al., 2020a). In another work from the same group, the sperms were immobilized on a microflake based on hyaluronic acid, and were subsequently released after reaching the target (Xu et al., 2020b). In a recent work by Rajabasadi et al., a special kind of temperature sensitive cap with multiple entries were developed to carry multiple sperms. By controlling the temperature the cap would expand and cause the release of sperms in the targeted area (Rajabasadi et al., 2022).

Physically-driven microrobots

One of the most common ways a microrobot is propelled is via magnetic fields. By making the microrobots from magnetic materials, they are responsive to magnetic field and can be moved via magnetic field gradients or other forms of magnetic fields such as a rotating magnetic field. The movement of a microrobot in a magnetic field gradient was shown in one of the earliest reports of microrobots where winged shape ellipsoids with a main symmetry axis along the long axis were designed allowing a magnetization along this axis. Furthermore, it was reported that the winged shape design decreases the side-ways drift due to the increased liquid drag along the axis perpendicular to the main axis (Yesin et al., 2005). Due to the challenges associated with the creation of a magnetic field gradient, other microrobots with alternative clever geometric designs were fabricated to move in other forms of magnetic fields such as rotating fields.

Helical microrobots

One of the most common shapes for magnetic microrobots is the helical microstructure. These microstructures resemble a corkscrew and can propel forward in viscous environments by rotating. These microrobots mimic the corkscrew movement of some bacteria such as *E.* coli. Their geometry Optimization has been studied by Johan et al. and it was found that a low number of turns of 1 to 1.5 demonstrate a better performance compared to the helices with higher number of windings. Furthermore, it was found that a triangular cross section for the helices demonstrate a higher propulsion velocity (Fig. 1A) (Quispe et al., 2019). Using COMSOL, FEM Simulations were used in this work to investigate and compute the propulsion force where it was found that the fluidic force on the microrobots follows the same trend as the microrobot velocity (Quispe et al., 2019).

On the other hand, a biomimetic approach can be beneficial for designing the microrobots since it allows the utilization of features of biological systems that have been optimized through evolution. It has been reported that in the flagellated bacteria, the mechanical coupling between the body and the flagella, plays an important role in the bacteria swimming behavior. To investigate this effect, Huang et al. (Huang et al., 2017) fabricated tubular magnetic microrobots that are connected to thin flexible artificial flagella structures (Fig. 1B). It was found that flexible flagella tail would introduce a wobbling effect on the body that causes a precession. When the helical trajectory of the microrobot body possesses identical chirality as the tail, the overall velocity of the microrobot increases.

Cilia-based microrobots

Another type of biomimetic microrobots, are the ones that mimic the cilia propulsion of microorganisms. In a work by Kim et al. (Kim et al., 2016) the cilia structures are implemented with thin hair like polymeric structures coated with Ni-Ti that allows the propulsion and steering of the microrobot (Fig. 1C). Geometry of such synthetic cilia in the form of their arrangement and beating can affect the net flow in low Reynolds numbers. The cilia arrangement has been studied by Sitti et al. (Dong et al., 2020) by computational fluid dynamics simulations and experiments. It was found that antiplectic metachronal waves could enhance the fluid flows in the low Reynolds numbers via the synthetic cilia (Dong et al., 2020).

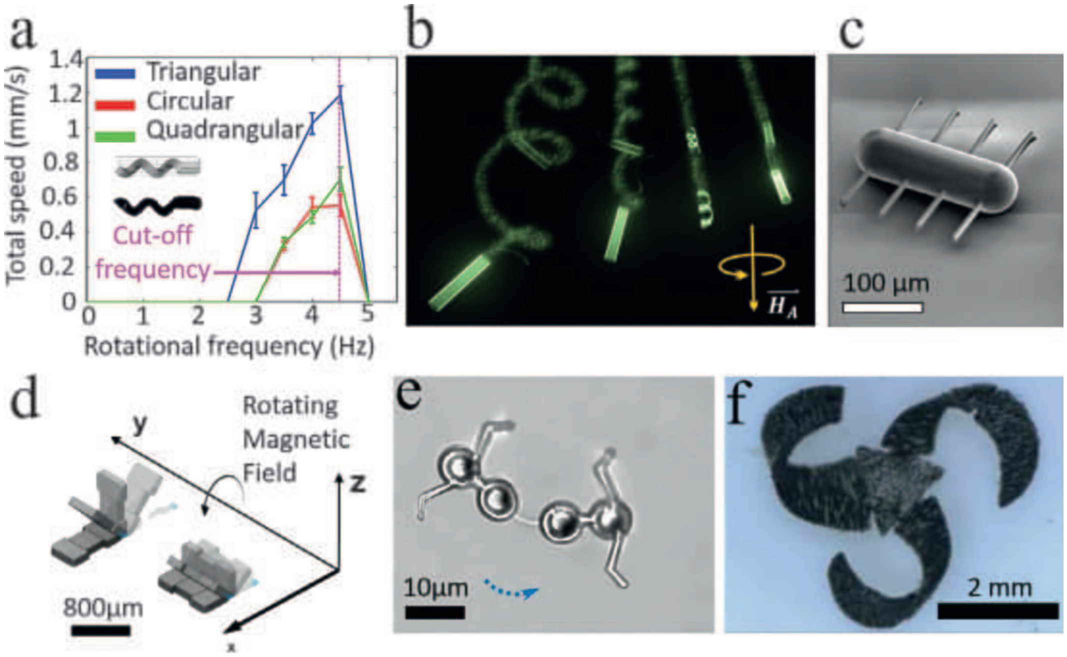

Fig. 1 Different geometries of magnetically driven microrobots. (A) helical magnetic microrobots based on three different cross sections showing a velocity enhancement in the case of triangular cross section. (B) coupling of flexible tails to the tubular and helical soft microrobots as a means of performance optimization. (C) a biomimetic ciliary magnetic microrobot (Kim et al., 2016) (D) a rectangular rolling magnetic microrobot (Bi et al., 2018) (E) a microrobot consisting of Janus particles linked with soft and rigid polymeric microstructures performing a lizard like walk in an oscillating magnetic field (Hu et al., 2021). (F) a fan shape flexible magnetic robot with 3D magnetization. (A) Reproduced from Quispe JE, Oulmas A, and Regnier S (2019) Geometry optimization of helical swimming at low Reynolds number. *Proc. MARSS 2019 4th Int. Conf. Manip. Autom. Robot. Small Scales.* https://doi.org/10.1109/MARSS.2019.8860937, with the permission of IEEE; (B) Reproduced from Huang HW, Chao Q, Sakar MS, and Nelson BJ (2017) Optimization of tail geometry for the propulsion of soft microrobots. *IEEE Robotics and Automation Letters* 2: 727–732. https://doi.org/10.1109/LRA.2017.2651167, with the permission of IEEE; (F) Reproduced from Xu T, Zhang J, Salehizadeh M, Onaizah O, and Diller E (2019a). Millimeter-scale flexible robots with programmable three-dimensional magnetization and motions. *Science robotics* 4, with the permission of IEEE.

Alternative geometries

Recently other geometries of microrobots that are propelled via magnetic fields were investigated. Among them, are microrobots that roll on the surface via rotational magnetic fields. Examples of these microrobots geometries are spiral microrobots (Schwarz et al., 2020), and rod like microrobots (Fig. 1D) (Bi et al., 2018) that rotate and roll on a surface to propel.

More complex magnetic robots were developed by combining magnetic Janus particles with soft and rigid 3D printed microstructures that act as appendages of the microrobots (Fig. 1E) (Hu et al., 2021). Another new design that has gained interest in the magnetic robotic researchers community 3d magnetization of soft magnetic structures (Goudu et al., 2020). Such soft magnetic robots can undergo complex shape changes when subjected to a magnetic field (Fig. 1F) (Xu et al., 2019a). This shape change is dependent on their magnetization during the fabrication process. Such new alternative designs add complexity to the motion and function of magnetically actuated robots and enables them to perform more intricate tasks.

Understanding the geometric factors that lead to designing more efficient microrobots for specific applications is of extreme importance. By taking the type of the microrobot into account, one can design the microrobot with geometric parameters that enable them with efficient and effective modes of operations such as twisting, rolling, and beating at high velocities and forces.

The optimization of the design and geometry of microrobots has had a huge effect on their speed and efficiency. In order for the microrobots to function properly in the body, biocompatibility and immunological reactions should also be considered. Additionally, is worth-noting that other physical propulsion methods like the ones employing ultrasound or light should be taken into account according to the intended functionality and operation environment.

Optimization of microrobot biocompatibility and their immunological response

Geometry of medical microrobots also play in important role when referring to potential immunoreactions. Our immunological system protects us from foreign pathogens and synthetic materials can affect the function of the envisioned medical devices. This phenomenon is often observed when introducing implants in the body, or for example when using nanomedicines and more recently medical microrobots. All these devices or external biological entities can trigger the activation of macrophages which can hinder the performance of such medical devices in vivo. Various strategies to overcome these hurdles have been suggested, mainly oriented to the use of specific materials and coatings. For example, cell-camouflage coatings have been employed, enzymatic and polymeric layers have been also shown to improve the circulation time of nanomedicines and some of the reported medical microrobots. More recently, other materials like zwitterionic polymers have shown to avoid their detection by macrophages over 90 h.

The morphology or geometry of the microrobots is also a key parameter to be optimized to minimize the physical interactions with cells of the immune system. Yasa et al. recently investigated the interplay between geometry and coatings of such microrobots on the immunological response (Yasa et al., 2020), they studied different variations of helical microrobot designs and put them in contact to mouse macrophages and splenocytes, freshly retrieved from mouse spleens. They found that these cells recognize these microrobots and trigger an immune response which depends on the helix turn number, with the same size, material properties and surface chemistry. These findings suggest that the microrobot geometry optimization is crucial not only to achieve optimal locomotion in physiological relevant environments but also to avoid the undesired triggering of the immune system.

Untethered small-scale robots have significant potential in broad areas, such as targeted drug delivery, (Chen et al., 2017; Mostaghaci et al., 2017; Park et al., 2017; Wang et al., 2018a) tissue engineering (Nawroth et al., 2012), minimally invasive surgery (Hines et al., 2017; Nelson et al., 2010; Ricotti et al., 2017; Sitti, 2009, 2018; Sitti et al., 2015; Wu et al., 2018), sensing and diagnosis (Chałupniak et al., 2015), by functioning in dynamic interaction with their local environment (Ceylan et al., 2019; Wang et al., 2018b). In comparison with the thermal (Le et al., 2019; Liu et al., 2012; Maeda et al., 2007), optical (Huang et al., 2015a) and electrical methods (Tan et al., 2015), the utilization of magnetic field (Abbott et al., 2009; Ceylan et al., 2019; Diller et al., 2014; Hu et al., 2018; Kim et al., 2018; Ren et al., 2019; Wang et al., 2018c; Xu et al., 2019a) is particularly promising to control the mobility and function of the robots by virtue of its ease of use, fast response time as well as safe penetration to biological environment. Compared to rigid magnetic small-scale robots, soft materials enable robots to have unique advantages regarding the flexibility and shape-changing ability. Rigid magnetic robots lack the ability to form a time-varying shape deformations since their internal structure of the body is fully confined by the homogeneous distribution of magnetic moments of the particles (Kim et al., 2013; Medina-Sánchez et al., 2016; Servant et al., 2015). Hence, these robots are limited to perform simple translational and rotational motions to reach target regions. To overcome such limitations, soft robots with programmed magnetization profile, which enables shape deformations with high spatial resolutions have been developed to achieve complex locomotion modes and functions (Abbott et al., 2009; Diller et al., 2014; Hu et al., 2018; Kim et al., 2018; Ren et al., 2019; Xu et al., 2019b).

However, magnetic soft robots developed so far are limited to define their potential aspects in biomedical applications since they are made of non-degradable polymer materials with embedded magnetic microparticles which are mostly non-biocompatible, such as NdFeB (Hu et al., 2018) and $BaFe_{12}O_{19}$ (Diller and Sitti, 2014) and cobalt magnets (Cui et al., 2019). To date, polymer materials used to build the backbone of the soft milli-robots(Goudu et al., 2020) including polyvinyl alcohol (PVA) (Zrínyi et al., 1998), Irogran PS455-203(Schmauch et al., 2017), a thermoplastic polyurethane (TPU) (Mishra et al., 2016), PDMS (Huang et al., 2015b), PEGDA (Kim et al., 2011) and Ecoflex 00-10 (Hu et al., 2018) have been demonstrated to exhibit good interaction with the magnetic filler particles and allow shape changing upon interaction with the external magnetic fields. Despite the enormous recent development in the field, such polymer materials are non-biodegradable, and not suitable to be used in biomedical applications. Hence, it is utmost importance to develop soft, biodegradable and implantable small-scale robots with properties that can fulfill the requirements of potential biomedical applications as the safety issues are becoming prominent and major concern in the field. Biodegradable materials such as CELLINK gelatin methacrylate (GelMA), collagen, silk, alginate or calcium carbonate provide sufficient mechanical support to the microrobot body. The Young's modulus of these biodegradable materials is in the order of kPa. Thus, they are very soft and adapt to the changes in the biological environment during movement toward the targeted location inside the human body. The flexibility and the shape changing ability of the robots allow them to actively pass through the biological barriers to access hard-to-reach anatomical locations in a minimally invasive manner. They also induce versatile shape deformations and undergo multimodal locomotion depending on the mechanical properties of the geometrical design, magnetization of the magnetic material, magnetization profile inside the robot body, applied external magnetic field, and the viscosity of the biological fluid. The tuning of these properties to achieve highly flexible structures at the microscale becomes challenging since it requires precise predictions of finite deformations according to the desired medical application at a clinical level. Application of magnetic fields to the fabricated robots induces magnetic torques, which creates the internal deformation of the robots due to internal magnetization profile of the robots.

Gamete/zygote transport

Microrobots, in general, are envisioned as carriers that transport various types of cargo within the organism to specific sites, improving the efficiency of the delivery process. The optimal geometry of the microrobot depends specifically on the characteristics of the cargo, the site in the body where transport and release are to be accomplished, and the specific demands of the medical procedure to be performed. The transport of gamete cells has recently attracted the attention of microrobot researchers for its application in assisted fertilization.

Gametes are reproductive cells that include sperm cells in males and egg cells in females. During fertilization, the sperm fuses with the egg cell that results in the formation of a zygote cell. Transportation of zygotes and egg cells is fundamentally different from that of sperm cells. The former are cells of several tens of micrometers that are essentially immotile and spherical, while sperm cells are motile, elongated cells whose length is barely longer than 10 μm. In general, sperm transport is more efficient when more cells can be transported, whereas zygotes and egg cells tend to be less abundant and require to be transported individually or in small numbers. Sperms, in addition, tend to be more resistant to changes in temperature and pH for moderate periods of time, whereas zygotes and egg cells are highly sensitive cells. Because of these differences, two different microrobot design strategies need to be considered which is discussed below.

Transportation of sperm cells

In the case of sperm cells, we have demonstrated the guidance and transport of motile and immotile sperm by microcarriers actuated by weak external magnetic fields, in vitro, employing biological-relevant fluids. The design of these microrobots were made to assist sperm cells in two male infertility scenarios: when sperm count is low but sperm are motile (oligospermia), or when sperm motility is low (asthenospermia). For the first scenario, designs such as cylindrical, streamlined caps, and caps with different inner cavities, have been developed (Magdanz et al., 2013; Xu et al., 2020a; Striggow et al., 2020) (Fig. 2). In case of low motility,

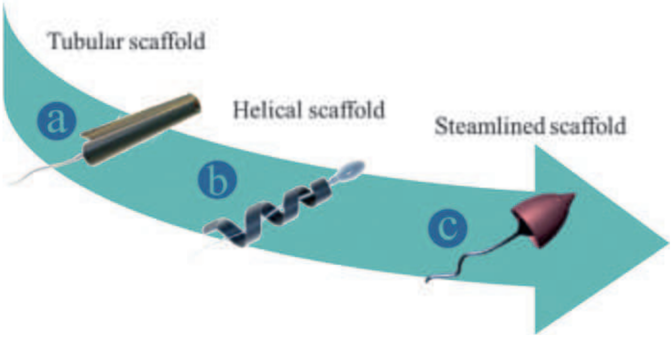

Fig. 2 Hybrid micromotors which consisted on a scaffold for sperm cells: (A) Tubular scaffold with semi-conical shape, (B) chiral scaffold with a helix-shaped design, and (C) streamlined scaffolds designed after hydrodynamic considerations for enhanced motion. (A) Reproduced from Magdanz V, Sanchez S, and Schmidt OG (2013) Development of a sperm-flagella driven micro-bio-robot. *Advanced Materials* 25: 6581–6588. https://doi.org/10.1002/adma.201302544, with the permission of John Wiley & Sons – Books. (B) Reproduced from Medina-Sánchez M, Schwarz L, Meyer AK, Hebenstreit F, and Schmidt OG (2016) Cellular cargo delivery: Toward assisted fertilization by sperm-carrying micromotors. *Nano Letters* 16: 555–561. https://doi.org/10.1021/acs.nanolett.5b04221, with the permission of American Chemical Society. (C) Reproduced from Xu H, Medina-Sánchez M, Maitz MF, Werner C, and Schmidt OG (2020a) Sperm micromotors for cargo delivery through flowing blood. *ACS Nano* 14: 2982–2993. https://doi.org/10.1021/acsnano.9b07851, with the permission of American Chemical Society.

magnetic microhelices have been suggested as artificial flagellum which move by means of a rotating magnetic field (Medina-Sánchez et al., 2016). In both scenarios, the transport of multiple sperm cells is crucial to increase the chances of fertilization. For that, we have evaluated different approaches: first clustering individual spermbots by employing magnetic fields, and second using protein-hyaluronic acid based microflakes which capture mature sperm (motile or immotile) (Xu et al., 2020a; Xu et al., 2020b). The last approach involves the function of in-situ sperm selection and preparation for further fertilization as it is made of hyaluronic acid which is used to select mature sperm with intact DNA. And more recently, we have shown that using 4D printed microcaps we can transport multiple sperm cells, capacitate them in situ and release hyaluronidase, an enzyme that digest the cumulus complex that surround the oocyte, to facilitate the journey of sperm and facilitate the sperm-oocyte interaction (Rajabasadi et al., 2022).

Transportation of egg/zygote cells

Likewise, for zygotes and egg cells, the first demonstration was made by Schwarz et al. using specially designed spiral microrobots to secure zygotes and egg cells inside (Fig. 3A) (Schwarz et al., 2020). The spiral microrobots are driven by rotational magnetic fields. The magnetized spiral microrobot rotates along its longitudinal axis to align its magnetic dipole moment with the external rotating magnetic field, that causes the continuous rotation of the spiral microrobot. The rotation of the spiral produces a net displacement that leads to the continuous propulsion of the microrobot. The possibility of aligning the rotation of the magnetic field in any direction in space and its frequency of rotation gives precise control over the movement of the microrobot. These microrobots have the advantage of being driven by rotating magnetic fields, which have been shown to generate more uniform motion than oscillatory or gradient fields (Liu et al., 2022). By rotating the microrobot in the vicinity of a zygote or egg cell, it is possible to capture them, and by continuing the rotation in the same direction the microrobot is propelled carrying the cell; the release is performed by rotating the microrobot in the opposite direction. The mechanism of securing the zygotes and egg cells allows, theoretically, to capture and transport of a small number of cells, although it is highly dependent on the dexterity of the user and can generate stress on the cells due to the friction they suffer in the process. Similarly, the transported zygotes and egg cells are in direct contact with the surrounding media, allowing a direct exchange of nutrients to the cells, but leaving the cells exposed to contaminants and fluid resistance. Additionally, this structure is rigid, which provides mechanical protection to the transported cells, although it may restrict the development of the zygotes.

A particularly interesting geometry for the untethered transport of individual zygotes and egg cells is the microgrippers (Nauber et al., 2023). A gripper is a particularly versatile mechanism because it allows the grasping, transport, and release of microobjects. Its structure consists of a series of flexible fingers that self-actuate in response to a stimulus. The ability of the fingers to self-fold into shape is the key to grasping microobjects. The versatility of a microgripper is based on its ability to switch between different process steps (grasp, transport, and release) at convenience, allowing it to rectify failed attempts, adapt to unforeseen situations, and be reused in different processes. The miniaturization of these mechanisms represents a series of challenges that have opened a new area of research around them, with several strategies available to activate them, however, most of them require a tethered transmission of electrical energy: electrothermal, piezoelectric, and electromagnetic actuation (Yang and Xu, 2017). In the case of untethered microgrippers, strategies based on transformable soft materials that respond to different stimuli, such as temperature, pH, or external magnetic fields, have been reported (Yin et al., 2019). Using changes in temperature and pH to actuate a microgripper in the

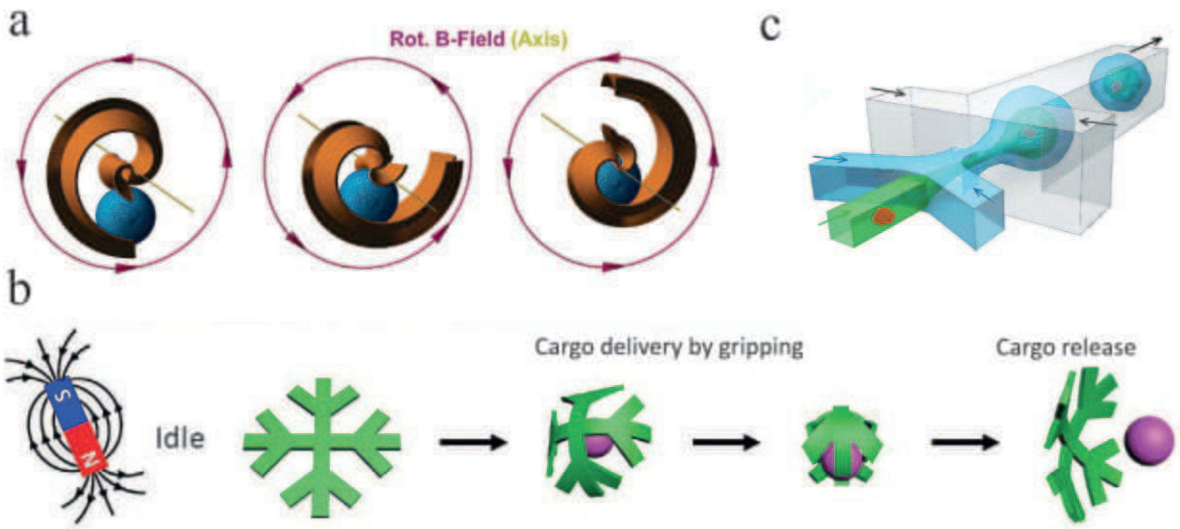

Fig. 3 (A) Spiral microrobot which demonstrated the cargo, transport, and release of zygotes (Schwarz et al., 2020). (B) Magnetic untethered gripper for microcargo grasping, transport and release (Goudu et al., 2020). (C) Microfluidic fabrication of cell-laden microcapsules with a liquid core and a soft shell. Reproduced from Xu J, Shamul JG, Staten NA, White AM, Jiang B, and He X (2021) Bioinspired 3D culture in nanoliter hyaluronic acid-rich core-shell hydrogel microcapsules isolates highly pluripotent human iPSCs. *Small* 17. https://doi.org/10.1002/smll.202102219, with the permission of John Wiley & Sons - Books.

body is complicated by the tendency of the metabolism to self-regulate and maintain homeostatic equilibrium. If this balance is disturbed, adverse reactions can occur, and the immune system can be activated. Magnetic microgrippers can be manipulated autonomously in three-dimensional space utilizing harmless external magnetic fields, allowing them to be stirred in an untethered fashion (Fig. 3B). Control over the magnitude and direction of the magnetic fields can regulate the actuation speed and applied force of the gripper, however, this control is indirect and can be optimized as including tactile sensors in these untethered microdevices remains a challenge (Liu et al., 2022). Magnetic grippers have been shown to gently manipulate biological matter and their shape and conformation can be modified according to the needs of different procedures (Jia et al., 2019). All these features make magnetic microgrippers a suitable alternative for transporting immobile cells such as zygotes and egg cells. The ability of the fingers to unfold gradually and the compatibility of the process with soft materials is optimal to allow the development of a zygote, as it can adapt to the constant increase in size, but can lead to complications of the process if the load is unintentionally released. The distance between the closed fingers of a microgripper could be beneficial for the direct transport of fluids and nutrients to the cells, however, the lack of insulation exposes the cargo to external stresses and contamination during transport. Microgrippers require precise 3D maneuverability to coordinate the gripping and delivery processes, which is difficult to achieve in complex biological environments and even more so with little or no visibility. Further studies are needed to improve the controllable motion of magnetic microgrippers, as most reports focus on their responsiveness to grip and release.

Alternatively, we propose the encapsulation of zygotes and egg cells in compartments within microrobots of arbitrary geometry. Microcapsules with a liquid core and a solid shell can be fabricated, for example, using droplet microfluidics (Fig. 3C) (Xu et al., 2021; Hennequin et al., 2009). The core could be a medium with the proper conditions to allow cell development and the shell could contain pores that allow outward molecular exchange. The shell of a microcapsule provides structural stability and support for the other components, which could include a magnetic coating or magnetic particles embedded in the structure itself. The magnetic material added to the microcapsule generates a net magnetic dipole moment. By placing this microcapsule under rotating magnetic fields, the dipole moment tends to align to the field vector, generating a magnetic torque that propels the microcapsule to tumble over the surface. The ability to control the direction of the magnetic field vector on the horizontal axis allows control of the direction of motion of the microcapsule (Yang and Zhang, 2021). The method of fabrication of these microcapsules would require considerable optimization to incorporate the sensitive zygotes and egg cells without damaging them, but once fabricated they would form a stable system optimized for the cells. The use of soft, biocompatible materials for the shell would be ideal to allow gentle interactions between the microcapsule and the environment, as well as allow zygotes to develop. The size of the capsule could be easily adapted to the number of cells desired to be encapsulated. Encapsulation of the cells would protect them from external contaminants and stresses that could be generated during transport, although it represents a challenge for the delivery of the cells to the desired site. Mechanisms of controlled degradation or fragmentation of the shell must be foreseen and optimized so as not to damage the cells in the process.

Navigating reproductive system barriers

Of equal importance is the optimization of the way in which the microrobots navigate through the various biological barriers that are found in the reproductive system. First and foremost, the microrobots must enter the reproductive system, typically through the vagina, and navigate the cervix and uterus. Navigation through these organs would be difficult due to their large size and the continuous but changing flow they are subjected to. Micromotors should be able to swim against these flows, even as the texture and volume of the fluids change. These fluids have high viscosities and may be composed of biological matter similar in size to the microrobots, such as cells and pieces of tissue, so hydrodynamic considerations must be considered to minimize the pressure exerted on the microrobot and to reduce the drag forces of the fluid. It has been shown that streamlined microrobots minimize the static pressure exerted on the microrobot, resulting in improved motility in complex media (Striggow et al., 2020; Xu et al., 2020a). A final treatment should avoid if possible the microrobot navigation through the aforementioned reproductive organs as cannulas can be used to introduce the micromotors close to the site of interest.

Depending on the treatment, some procedures would require passage through the fallopian tubes, which are a narrow and tortuous structure covered by a layer of mucus that would greatly complicate the hydrodynamic movement of the micromotors. A cannula cannot pass through this organ. In this case, mechanisms such as rolling or tumbling should be more efficient by using nearby surfaces for propulsion compared to swimming methods. These therapies should be synchronized with ovulation, when the mucosal layer thins and changes its acidity, facilitating sperm survival. In addition, contractions in the fallopian tubes are essential for sperm to navigate upward in them, and for micromotors to take advantage of these movements, they must have a resilient structure that can withstand the stress caused by these movements while being soft enough not to cause damage to the surrounding tissue. Soft biomaterials such as hydrogels are envisioned as excellent building materials for medical micromotors due to their excellent mechanical properties, resilience, biocompatibility, and ease of functionalization for the transport of molecules.

For sperm transport, the microrobots must be able to penetrate the cluster of cumulus cells and the zona pellucida surrounding the oocyte, which is normally achieved by the enzymatic dissolution of hyaluronic acid, and then open the intercellular spaces, which are mechanically enlarged until the sperm can reach the oocyte. For this, the micromotors should be loaded with hyaluronidase and designed to release it when near the oocyte, and the movement of the micromotor should exert enough pressure in the right direction to help penetrate the cumulus and zona pellucida. Hydrogels, in turn, are capable of absorbing large amounts of polar molecules due to their high-water content. On the other hand, the spiral motion has demonstrated excellent control over directional actuation and the combination of rotational and translational motion should maximize the mechanical stress applied to the barriers.

Navigation through biological matter is typically hampered by the stickiness of surfaces to which micromotors tend to adhere. In addition to optimized motion strategies and protocols, the surfaces of microrobots should be designed to minimize interactions, e.g. by pattern design or chemical functionalization of the surfaces.

Conclusion

The medical microrobots are envisioned to enable various applications such as drug delivery, microsurgery, therapy, diagnostics, and assisted fertilization. To realize such a vision, it is necessary to optimize and improve the efficiency of microrobots in terms of their speed, maneuverability, biodegradability, and biocompatibility. Since geometry can affect the efficiency of microrobots, the design and material selection play an important role in their optimization. The optimal geometry of the microrobot depends on the cargo requirements (e.g. biological cells) and the environmental properties such as viscosity and flow velocity. Three main types of microrobots have been investigated by the research community. First, the chemical microrobots, which typically use available ambient fuel to generate gas bubbles that in turn propel the microrobot. Second, the biohybrid microrobots that utilize motile microorganisms coupled with synthetic magnetic microcaps or other magnetic microstructures that allow them to be guided by external magnetic fields. The third type is the physical microrobots, which are typically driven and controlled by external magnetic fields. This kind of microrobot is of great interest for medical treatments because of its fast response and the ability of magnetic fields to safely penetrate the body and control the magnetic microrobots in deep tissues. Increasingly, microrobot researchers are turning their attention to assisted fertilization using magnetic microrobots. To accomplish this, various microrobots have been designed to transfer gametes such as sperm, and zygotes. These designs include microspirals, microgrippers, and microcapsules. Finally, to achieve in vivo assisted fertilization or embryo cargo-release using microrobots, they must navigate through the female reproductive tract. This poses additional challenges for the microrobots. For this scenario, they should be composed of soft biomaterials, capable of a high degree of internal and external functionalization, and able to deliver drugs and molecules beneficial to the medical procedure.

A smart design of such microrobots would allow them to perform multiple actuation modes such as rotational and tumbling motion. This equips the microrobots with better performance with regard to perturbances in in-vivo conditions such as fluid flows caused by hear beats, and peristaltic motions in the body.

In our opinion, many of the challenges of microrobots should be addressed by other established technologies in combination with the microrobot. This includes the delivery of the microrobot by smart catheters with capabilities to sense the environment and even help track the microrobots. Externally, the tracking methods and the magnetic field generators should be coordinated and algorithms should be implemented for enhanced navigation that is capable of learning and adapting to the obstacles.

Furthermore, to transfer these technologies to preclinical studies, initial studies of some of the spermbots have been performed in microfluidic channels containing ex-vivo oviduct fluid. We have also reported the successful tracking of magnetically driven microrobots in phantoms, ex vivo, and in living mice with high spatial and temporal resolution using infrared, photoacoustic, and high-frequency ultrasound imaging, making the first steps toward their application in living mice. However, in vitro fertilization using these microcarriers has not yet been demonstrated. Among the remaining challenges are: increasing the number of transported sperms, separating the sperm-carrying micromotors from the free-floating sperm, and finally the stability when moving from one environment to another (e.g., from one chamber to another, or from a petri dish to an ex-vivo or in-vivo organ).

In conclusion, the functions of the microrobots should be limited to the minimum to reduce the possibility of failures and to place most of the functions on external components that do not have such limitations in terms of the size and complexity of their structures as the micromotors do. This trade-off between maximizing the capabilities of the micromotor and delegating capabilities to other systems is complementary, since delegating tasks to other systems allows the micromotor to perform its tasks with greater dexterity and can also provide greater versatility in the treatment.

Acknowledgments

This work is part of the project that has received funding from the European Research Council (ERC) under the European Union's Horizon 2020 research and innovation program (Grant agreement nos. 853609). We would also like to acknowledge the fruitful discussions on biodegradable materials for medical microrobots with Dr. Sandhya Goudu.

References

Abbott JJ, Peyer KE, Lagomarsino MC, Zhang L, Dong L, Kaliakatsos IK, and Nelson BJ (2009) How should microrobots swim? *International Journal of Robotics Research* 28: 1434–1447. https://doi.org/10.1177/0278364909341658.

Bi C, Guix M, Johnson BV, Jing W, and Cappelleri DJ (2018) Design of microscale magnetic tumbling robots for locomotion in multiple environments and complex terrains. *Micromachines* 9: 1–17. https://doi.org/10.3390/mi9020068.

Bozuyuk U, Alapan Y, Aghakhani A, Yunusa M, and Sitti M (2021) Shape anisotropy-governed locomotion of surface microrollers on vessel-like microtopographies against physiological flows. *Proceedings of the National Academy of Sciences of the United States of America* 118: 1–10. https://doi.org/10.1073/pnas.2022090118.

Ceylan H, Yasa IC, Yasa O, Tabak AF, Giltinan J, and Sitti M (2019) 3D-printed biodegradable microswimmer for theranostic cargo delivery and release. *ACS Nano* 13: 3353–3362. https://doi.org/10.1021/acsnano.8b09233.

Chałupniak A, Morales-Narváez E, and Merkoçi A (2015) Micro and nanomotors in diagnostics. *Advanced Drug Delivery Reviews* 95: 104–116. https://doi.org/10.1016/j.addr.2015.09.004.

Chen XZ, Hoop M, Mushtaq F, Siringil E, Hu C, Nelson BJ, and Pané S (2017) Recent developments in magnetically driven micro- and nanorobots. *Applied Materials Today* 9: 37–48. https://doi.org/10.1016/j.apmt.2017.04.006.

Cui J, Huang TY, Luo Z, Testa P, Gu H, Chen XZ, Nelson BJ, and Heyderman LJ (2019) Nanomagnetic encoding of shape-morphing micromachines. *Nature* 575: 164–168. https://doi.org/10.1038/s41586-019-1713-2.

Diller E and Sitti M (2014) Three-dimensional programmable assembly by untethered magnetic robotic micro-grippers. *Advanced Functional Materials* 24: 4397–4404. https://doi.org/10.1002/adfm.201400275.

Diller E, Zhuang J, Zhan Lum G, Edwards MR, and Sitti M (2014) Continuously distributed magnetization profile for millimeter-scale elastomeric undulatory swimming. *Applied Physics Letters* 104. https://doi.org/10.1063/1.4874306.

Dkhil M, Bolopion A, Régnier S, and Gauthier M (2014) Optimization of the size of a magnetic microrobot for high throughput handling of micro-objects. *IEEE/ASME International Conference on Advanced Intelligent Mechatronics, AIM*: 372–377. https://doi.org/10.1109/AIM.2014.6878107.

Dong X, Lum GZ, Hu W, Zhang R, Ren Z, Onck PR, and Sitti M (2020) Bioinspired cilia arrays with programmable nonreciprocal motion and metachronal coordination. *Science Advances* 6. https://doi.org/10.1126/SCIADV.ABC9323.

Felfoul O, Mohammadi M, Taherkhani S, De Lanauze D, Zhong Xu Y, Loghin D, Essa S, Jancik S, Houle D, Lafleur M, Gaboury L, Tabrizian M, Kaou N, Atkin M, Vuong T, Batist G, Beauchemin N, Radzioch D, and Martel S (2016) Magneto-aerotactic bacteria deliver drug-containing nanoliposomes to tumour hypoxic regions. *Nature Nanotechnology* 11: 941–947. https://doi.org/10.1038/nnano.2016.137.

Feynman R (1960) There's plenty of room at the bottom. *Engineering and Science* 23: 22–36. https://doi.org/10.1201/9780429500459.

Fomin VM, Hippler M, Magdanz V, Soler L, Sanchez S, and Schmidt OG (2014) Propulsion mechanism of catalytic microjet engines. *IEEE Transactions on Robotics* 30: 40–48. https://doi.org/10.1109/TRO.2013.2283929.

Gao W, Sattayasamitsathit S, Orozco J, and Wang J (2011) Highly efficient catalytic microengines: Template electrosynthesis of polyaniline/platinum microtubes. *Journal of the American Chemical Society* 133: 11862–11864. https://doi.org/10.1021/ja203773g.

Golestanian R, Liverpool TB, and Ajdari A (2005) Propulsion of a molecular machine by asymmetric distribution of reaction products. *Physical Review Letters* 94. https://doi.org/10.1103/PhysRevLett.94.220801.

Goudu SR, Yasa IC, Hu X, Ceylan H, Hu W, and Sitti M (2020) Biodegradable untethered magnetic hydrogel milli-grippers. *Advanced Functional Materials* 30. https://doi.org/10.1002/adfm.202004975.

Hennequin Y, Pannacci N, De Torres CP, Tetradis-Meris G, Chapuliot S, Bouchaud E, and Tabeling P (2009) Synthesizing microcapsules with controlled geometrical and mechanical properties with microfluidic double emulsion technology. *Langmuir* 25: 7857–7861. https://doi.org/10.1021/la9004449.

Hines L, Petersen K, Lum GZ, and Sitti M (2017) Soft Actuators for Small-Scale Robotics. *Advanced Materials* 29. https://doi.org/10.1002/adma.201603483.

Hu W, Lum GZ, Mastrangeli M, and Sitti M (2018) Small-scale soft-bodied robot with multimodal locomotion. *Nature* 554: 81–85. 5547690. https://doi.org/10.1038/nature25443.

Hu X, Yasa IC, Ren Z, Goudu SR, and Ceylan H (2021) Magnetic soft micromachines made of linked microactuator networks. *Science Advances* 7(23): 1–10.

Huang C, Lv JA, Tian X, Wang Y, Yu Y, and Liu J (2015a) Miniaturized swimming soft robot with complex movement actuated and controlled by remote light signals. *Scientific Reports* 5: 1–8. https://doi.org/10.1038/srep17414.

Huang S, Pessot G, Cremer P, Weeber R, Holm C, Nowak J, Odenbach S, Menzel AM, and Auernhammer GK (2015b) Buckling of paramagnetic chains in soft gels. *Soft Matter* 12: 228–237. https://doi.org/10.1039/c5sm01814e.

Huang HW, Chao Q, Sakar MS, and Nelson BJ (2017) Optimization of tail geometry for the propulsion of soft microrobots. *IEEE Robotics and Automation Letters* 2: 727–732. https://doi.org/10.1109/LRA.2017.2651167.

Jia H, Mailand E, Zhou J, Huang Z, Dietler G, Kolinski JM, Wang X, and Sakar MS (2019) Universal soft robotic microgripper. *Small* 15: 1–8. https://doi.org/10.1002/smll.201803870.

Jurado-Sánchez B, Sattayasamitsathit S, Gao W, Santos L, Fedorak Y, Singh VV, Orozco J, Galarnyk M, and Wang J (2015) Self-propelled activated carbon janus micromotors for efficient water purification. *Small* 11: 499–506. https://doi.org/10.1002/smll.201402215.

Kim J, Chung SE, Choi SE, Lee H, Kim J, and Kwon S (2011) Programming magnetic anisotropy in polymeric microactuators. *Nature Materials* 10(10): 747–752. https://doi.org/10.1038/nmat3090.

Kim S, Qiu F, Kim S, Ghanbari A, Moon C, Zhang L, Nelson BJ, and Choi H (2013) Fabrication and characterization of magnetic microrobots for three-dimensional cell culture and targeted transportation. *Advanced Materials* 25: 5863–5868. https://doi.org/10.1002/adma.201301484.

Kim S, Lee S, Lee J, Nelson BJ, Zhang L, and Choi H (2016) Fabrication and manipulation of ciliary microrobots with non-reciprocal magnetic actuation. *Scientific Reports* 6: 30713. https://doi.org/10.1038/srep30713.

Kim Y, Yuk H, Zhao R, Chester SA, and Zhao X (2018) Printing ferromagnetic domains for untethered fast-transforming soft materials. *Nature* 558: 274–279. https://doi.org/10.1038/s41586-018-0185-0.

Le X, Lu W, Zhang J, and Chen T (2019) Recent progress in biomimetic anisotropic hydrogel actuators. *Advancement of Science* 6: 1–14. https://doi.org/10.1002/advs.201801584.

Li L, Wang J, Li T, Song W, and Zhang G (2014) Hydrodynamics and propulsion mechanism of self-propelled catalytic micromotors: Model and experiment. *Soft Matter* 10: 7511–7518. https://doi.org/10.1039/c4sm01070a.

Li L, Wang J, Li T, Song W, and Zhang G (2015) A unified model of drag force for bubble-propelled catalytic micro/nano-motors with different geometries in low Reynolds number flows. *Journal of Applied Physics* 117. https://doi.org/10.1063/1.4915114.

Lin Z, Jiang T, and Shang J (2022) The emerging technology of biohybrid micro-robots: A review. *Bio-Design and Manufacturing*. https://doi.org/10.1007/s42242-021-00135-6.

Liu Y, Takafuji M, Ihara H, Zhu M, Yang M, Gu K, and Guo W (2012) Programmable responsive shaping behavior induced by visible multi-dimensional gradients of magnetic nanoparticles. *Soft Matter* 8: 3295–3299. https://doi.org/10.1039/C2SM07206H.

Liu D, Guo R, Wang B, Hu J, and Lu Y (2022) Magnetic micro/nanorobots: A new age in biomedicines. *Advanced Intelligent Systems* 4: 2200208. https://doi.org/10.1002/aisy.202200208.

Maeda S, Hara Y, Sakai T, Yoshida R, and Hashimoto S (2007) Self-walking gel. *Advanced Materials* 19: 3480–3484. https://doi.org/10.1002/adma.200700625.

Magdanz V, Sanchez S, and Schmidt OG (2013) Development of a sperm-flagella driven micro-bio-robot. *Advanced Materials* 25: 6581–6588. https://doi.org/10.1002/adma.201302544.

Medina-Sánchez M and Schmidt OG (2017) Medical microbots need better imaging and control. *Nature* 545: 406–408. https://doi.org/10.1038/545406a.

Medina-Sánchez M, Schwarz L, Meyer AK, Hebenstreit F, and Schmidt OG (2016) Cellular cargo delivery: Toward assisted fertilization by sperm-carrying micromotors. *Nano Letters* 16: 555–561. https://doi.org/10.1021/acs.nanolett.5b04221.

Mei Y, Solovev AA, Sanchez S, and Schmidt OG (2011) Rolled-up nanotech on polymers: From basic perception to self-propelled catalytic microengines. *Chemical Society Reviews* 40: 2109. https://doi.org/10.1039/c0cs00078g.

Mishra SR, Dickey MD, Velev OD, and Tracy JB (2016) Selective and directional actuation of elastomer films using chained magnetic nanoparticles. *Nanoscale* 8: 1309–1313. https://doi.org/10.1039/c5nr07410j.

Mitrovic J (1997) Formation of a liquid jet after detachment of a vapour bubble. *International Journal of Heat and Mass Transfer* 40: 4309–4317. https://doi.org/10.1016/S0017-9310(97)00085-9.

Mostaghaci B, Yasa O, Zhuang J, and Sitti M (2017) Bioadhesive bacterial microswimmers for targeted drug delivery in the urinary and gastrointestinal tracts. *Advancement of Science* 4: 1–9. https://doi.org/10.1002/advs.201700058.

Nauber R, Goudu SR, Goeckenjan M, Bornhäuser M, and Ribeiro C (2023) Medical microrobots in reproductive medicine from the bench to the clinic. *Nature Communications* 14(1): 728.

Nawroth JC, Lee H, Feinberg AW, Ripplinger CM, McCain ML, Grosberg A, Dabiri JO, and Parker KK (2012) A tissue-engineered jellyfish with biomimetic propulsion. *Nature Biotechnology* 30(8): 792–797. https://doi.org/10.1038/nbt.2269.

Nelson BJ, Kaliakatsos IK, and Abbott JJ (2010) Microrobots for minimally invasive medicine. *Annual Review of Biomedical Engineering* 12: 55–85. https://doi.org/10.1146/annurev-bioeng-010510-103409.

Park BW, Zhuang J, Yasa O, and Sitti M (2017) Multifunctional bacteria-driven microswimmers for targeted active drug delivery. *ACS Nano* 11: 8910–8923. https://doi.org/10.1021/acsnano.7b03207.

Paxton WF, Kistler KC, Olmeda CC, Sen A, St. Angelo SK, Cao Y, Mallouk TE, Lammert PE, and Crespi VH (2004) Catalytic nanomotors: Autonomous movement of striped nanorods. *Journal of the American Chemical Society* 126: 13424–13431. https://doi.org/10.1021/ja047697z.

Quispe JE, Oulmas A, and Regnier S (2019) Geometry optimization of helical swimming at low Reynolds number. In: *Proc. MARSS 2019 4th Int. Conf. Manip. Autom. Robot. Small Scales*. https://doi.org/10.1109/MARSS.2019.8860937.

Rajabasadi F, Moreno S, Fichna K, Aziz A, Appelhans D, Schmidt OG, and Medina-Sánchez M (2022) Multifunctional 4D-printed sperm-hybrid microcarriers for assisted reproduction. *Advanced Materials*. 2204257. https://doi.org/10.1002/adma.202204257.

Ren Z, Hu W, Dong X, and Sitti M (2019) Multi-functional soft-bodied jellyfish-like swimming. *Nature Communications* 10(1): 1–12. https://doi.org/10.1038/s41467-019-10549-7.

Ricotti L, Trimmer B, Feinberg AW, Raman R, Parker KK, Bashir R, Sitti M, Martel S, Dario P, and Menciassi A (2017) Biohybrid actuators for robotics: A review of devices actuated by living cells. *Science robotics* 2: 1–18. https://doi.org/10.1126/scirobotics.aaq0495.

Schenck JF (2000) Safety of strong, static magnetic fields. *Journal of Magnetic Resonance Imaging* 12: 2–19. https://doi.org/10.1002/1522-2586(200007)12:1<2::AID-JMRI2>3.0.CO;2-V.

Schmauch MM, Mishra SR, Evans BA, Velev OD, and Tracy JB (2017) Chained iron microparticles for directionally controlled actuation of soft robots. *ACS Applied Materials & Interfaces* 9: 11895–11901. https://doi.org/10.1021/acsami.7b01209.

Schmidt CK, Medina-Sánchez M, Edmondson RJ, and Schmidt OG (2020) Engineering microrobots for targeted cancer therapies from a medical perspective. *Nature Communications* 11: 1–18. https://doi.org/10.1038/s41467-020-19322-7.

Schwarz L, Medina-Sánchez M, and Schmidt OG (2017) Hybrid biomicromotors. *Applied Physics Reviews* 4: 031301. https://doi.org/10.1063/1.4993441.

Schwarz L, Karnaushenko DD, Hebenstreit F, Naumann R, Schmidt OG, and Medina-Sánchez M (2020) A rotating spiral micromotor for noninvasive zygote transfer. *Advancement of Science* 7: 1–14. https://doi.org/10.1002/advs.202000843.

Servant A, Qiu F, Mazza M, Kostarelos K, Nelson BJ, Servant A, Mazza M, Kostarelos Nanomedicine Lab, K, Kostarelos K, Qiu F, and Nelson BJ (2015) Controlled in vivo swimming of a swarm of bacteria-like microrobotic flagella. *Advanced Materials* 27: 2981–2988. https://doi.org/10.1002/ADMA.201404444.

Sitti M (2009) Miniature devices: Voyage of the microrobots. *Nature* 458: 1121–1122. https://doi.org/10.1038/4581121a.

Sitti M (2018) Miniature soft robots — road to the clinic. *Nature Reviews Materials* 36(3): 74–75. https://doi.org/10.1038/s41578-018-0001-3.

Sitti M, Ceylan H, Hu W, Giltinan J, Turan M, Yim S, and Diller E (2015) Biomedical applications of untethered mobile milli/microrobots. *Proceedings of the IEEE* 103: 205–224. https://doi.org/10.1109/JPROC.2014.2385105.

Srivastava SK, Medina-Sánchez M, Koch B, and Schmidt OG (2016) Medibots: Dual-action biogenic microdaggers for single-cell surgery and drug release. *Advanced Materials* 28: 832–837. https://doi.org/10.1002/adma.201504327.

Striggow F, Medina-Sánchez M, Auernhammer GK, Magdanz V, Friedrich BM, and Schmidt OG (2020) Sperm-driven micromotors moving in oviduct fluid and viscoelastic media. *Small* 16. https://doi.org/10.1002/smll.202000213.

Sun J, Mathesh M, Li W, and Wilson DA (2019) Enzyme-powered nanomotors with controlled size for biomedical applications. *ACS Nano* 13: 10191–10200. https://doi.org/10.1021/acsnano.9b03358.

Tan Y, Wu R, Li H, Ren W, Du J, Xu S, and Wang J (2015) Electric field-induced gradient strength in nanocomposite hydrogel through gradient crosslinking of clay. *Journal of Materials Chemistry B* 3: 4426–4430. https://doi.org/10.1039/c5tb00506j.

Tottori S, Zhang L, Qiu F, Krawczyk KK, Franco-Obregõn A, and Nelson BJ (2012) Magnetic helical micromachines: Fabrication, controlled swimming, and cargo transport. *Advanced Materials* 24: 811–816. https://doi.org/10.1002/adma.201103818.

Wang Y, Hernandez RM, Bartlett DJ, Bingham JM, Kline TR, Sen A, and Mallouk TE (2006) Bipolar electrochemical mechanism for the propulsion of catalytic nanomotors in hydrogen peroxide solutions. *Langmuir* 22: 10451–10456. https://doi.org/10.1021/la0615950.

Wang B, Chan KF, Yu J, Wang Q, Yang L, Chiu PWY, and Zhang L (2018) Reconfigurable swarms of ferromagnetic colloids for enhanced local hyperthermia. *Advanced Functional Materials* 28: 1705701. https://doi.org/10.1002/adfm.201705701.

Wang X, Hu C, Schurz L, De Marco C, Chen X, Pané S, and Nelson BJ (2018a) Surface-chemistry-mediated control of individual magnetic helical microswimmers in a swarm. *ACS Nano* 12: 6210–6217. https://doi.org/10.1021/acsnano.8b02907.

Wang X, Qin X-H, Hu C, Terzopoulou A, Chen X-Z, Huang T-Y, Maniura-Weber K, Pané S, Nelson BJ, Wang X, Hu C, Terzopoulou A, Chen X, Huang T, Pané S, Nelson BJ, Qin X, and Maniura-Weber K (2018b) 3D printed enzymatically biodegradable soft helical microswimmers. *Advanced Functional Materials* 28: 1804107. https://doi.org/10.1002/ADFM.201804107.

Wrede P, Medina-sánchez M, Fomin VM, and Schmidt OG (2021) Switching propulsion mechanisms of tubular catalytic micromotors. *Small*. https://doi.org/10.1002/smll.202006449.

Wu Y, Wu Z, Lin X, He Q, and Li J (2012) Autonomous movement of controllable assembled Janus capsule motors. *ACS Nano* 6: 10910–10916. https://doi.org/10.1021/nn304335x.

Wu Z, Troll J, Jeong HH, Wei Q, Stang M, Ziemssen F, Wang Z, Dong M, Schnichels S, Qiu T, and Fischer P (2018) A swarm of slippery micropropellers penetrates the vitreous body of the eye. *Science Advances* 4: 1–11. https://doi.org/10.1126/sciadv.aat4388.

Xu H, Medina-Sánchez M, Magdanz V, Schwarz L, Hebenstreit F, and Schmidt OG (2018) Sperm-hybrid micromotor for targeted drug delivery. *ACS Nano* 12: 327–337. https://doi.org/10.1021/acsnano.7b06398.

Xu T, Yu J, Vong CI, Wang B, Wu X, and Zhang L (2019) Dynamic morphology and swimming properties of rotating miniature swimmers with soft tails. *IEEE/ASME Transactions on Mechatronics* 24: 924–934. https://doi.org/10.1109/TMECH.2019.2912404.

Xu T, Zhang J, Salehizadeh M, Onaizah O, and Diller E (2019a) Millimeter-scale flexible robots with programmable three-dimensional magnetization and motions. *Science robotics*: 4.

Xu H, Medina-Sánchez M, Maitz MF, Werner C, and Schmidt OG (2020a) Sperm micromotors for cargo delivery through flowing blood. *ACS Nano* 14: 2982–2993. https://doi.org/10.1021/acsnano.9b07851.

Xu H, Medina-Sánchez M, and Schmidt OG (2020b) Magnetic micromotors for multiple motile sperm cells capture, transport, and enzymatic release. *Angewandte Chemie, International Edition* 59: 15029–15037. https://doi.org/10.1002/anie.202005657.

Xu J, Shamul JG, Staten NA, White AM, Jiang B, and He X (2021) Bioinspired 3D culture in nanoliter hyaluronic acid-rich core-shell hydrogel microcapsules isolates highly pluripotent human iPSCs. *Small* 17. https://doi.org/10.1002/smll.202102219.

Yang S and Xu Q (2017) A review on actuation and sensing techniques for MEMS-based microgrippers. *Journal of Micro-Bio Robotics* 13: 1–14. https://doi.org/10.1007/s12213-017-0098-2.

Yang L and Zhang L (2021) Motion control in magnetic microrobotics: From individual and multiple robots to swarms. *Annual Review of Control, Robotics, and Autonomous Systems* 4: 1–26. https://doi.org/10.1146/annurev-control-032720-104318.

Yang J, Zhang C, Wang XD, Wang WX, Xi N, and Liu LQ (2019) Development of micro- and nanorobotics: A review. *Science China Technological Sciences*. https://doi.org/10.1007/s11431-018-9339-8.

Yasa IC, Ceylan H, Bozuyuk U, Wild AM, and Sitti M (2020) Elucidating the interaction dynamics between microswimmer body and immune system for medical microrobots. *Science robotics* 5: 1–14. https://doi.org/10.1126/scirobotics.aaz3867.

Yesin KB, Exner P, Vollmers K, and Nelson BJ (2005) Design and control of in-vivo magnetic microrobots. *Medical Image Computing and Computer Assisted Intervention* 8: 819–826. https://doi.org/10.1007/11566465_101.

Yin C, Wei F, Zhan Z, Zheng J, Yao L, Yang W, and Li M (2019) Untethered microgripper-the dexterous hand at microscale. *Biomedical Microdevices* 21. https://doi.org/10.1007/s10544-019-0430-9.

Zrínyi M, Barsi L, and Büki A (1998) Deformation of ferrogels induced by nonuniform magnetic fields. *The Journal of Chemical Physics* 104: 8750. https://doi.org/10.1063/1.471564.

Memory devices—Non-volatile memories[☆]

Elena Gnani and Giorgio Baccarani, Department of Electrical Electronic and Information Engineering (DEI), and Advanced Research Center on Electronic Systems E. de Castro (ARCES), University of Bologna, Bologna, Italy

© 2024 Elsevier Ltd. All rights reserved.

This is an update of G. Baccarani, E. Gnani, Memory Devices, Nonvolatile, Editor(s): Franco Bassani, Gerald L. Liedl, Peter Wyder, Encyclopedia of Condensed Matter Physics, Elsevier, 2005, pp. 324–337, ISBN 9780123694010, https://doi.org/10.1016/B0-12-369401-9/01167-0.

Introduction **552**
Non-volatile memory classification **553**
Read-only memory **554**
Electrically programmable read only-memory **555**
Electrically erasable and programmable read-only memory **556**
Flash EEPROM **558**
Flash array architecture 558
Reliability of flash memories 560
Multi-bit memory storage 562
Charge-trap flash (CTF) 562
Three-dimensional flash memories 562
Non-volatile random-access memories **564**
Magnetic RAM (MRAM) 564
Ferroelectric RAM (FRAM) 567
Phase-change memories (PCM) 570
Resistive RAM (RRAM) 571
In-memory computing **573**
Conclusion **574**
References **575**

Abstract

In this entry, the most important non-volatile memories used for a wide variety of applications are presented, with detailed information on their structural and functional properties. The first part addresses charge-based memories, including read-only memories, electrically programmable read-only memories, electrically erasable and programmable read-only memories, and flash memories. In a broad sense, all them can be considered non-volatile read-only memories, meaning that reading the stored information can be performed in a relatively short time, but programming and erasing require much longer times, if at all possible. The second part of the presentation encompasses non-volatile memories which exhibit similar read/write (R/W) access times, and can thus be regarded as random-access memories to all effects. More specifically, we illustrate magnetic memories, ferroelectric memories, phase-change memories and resistive memories, and discuss their future market perspectives.

Key points

- Non-volatile memory classification
- Charge-base memories
- Resistance-based memories
- In-memory computing

Introduction

The key attribute of non-volatile memory devices is their ability to retain the stored information for several years both under ON and OFF power conditions. Owing to this property, they have found widespread use in a variety of professional systems as well as consumer products. Professional systems include computers, phone exchanges, measurement setups, robotic and control systems,

---

[☆] *Change History:* May 2023. E Gnani and G Baccarani updated table, and Figs. 9, 11, 20, 21, 24, and 28.

https://doi.org/10.1016/B978-0-323-90800-9.00236-5

automotive and medical electronics systems. Commodities and consumer products encompass smart phones, personal digital assistants (PDAs), digital video recorders, still cameras, digital TV (DTV), set top boxes, GPS-based navigation systems, toys, radio-frequency identification devices (RFIDs) and smart cards.

The stand-alone non-volatile memory market, largely dominated by flash memories, has become a sizeable fraction of the whole memory market. Therefore, dedicated technological processes have been developed to optimize their performance. The divergence of flash technology from the CMOS process, however, prevents their application as embedded memories in systems on chip. The harmonization of the two technological processes was attempted at the expense of a reduced areal density, increased number of processing steps and fabrication cost.

Non-volatile random-access memories (NV-RAM) have been investigated for a long time, but have become successful or promising products only recently. Their compatibility with the back-end CMOS process, as well as many functional improvements, make them attractive for embedded applications in systems-on-chip, or even in advanced microprocessors.

This entry is organized as follows: Section "Non-volatile memory classification" introduces the classification of non-volatile memories and illustrates their general features. Sections "Read-only memory," "Electrically programmable read only-memory" and "Electrically erasable and programmable read-only memory" are devoted to read-only memories (ROM), electrically programmable read-only memories (EPROMS) and electrically erasable and programmable read-only memories (EEPROMS). Section "Flash EEPROM" addresses NOR and NAND-type flash memories, and is composed by five subsections devoted to: (i) flash array architectures; (ii) reliability issues; (iii) charge trap memories; (iv) multi-bit storage and, (v) three-dimensional NAND flash memories. Section "Non-volatile random-access memories" treats NV-RAMs, and contains four subsections devoted to: (i) magnetic memories (MRAM); (ii) ferroelectric memories (FRAM); (iii) phase-change memories (PCM) and, (iv) resistive memories (RRAM). Section "In-memory computing" introduces the fascinating theme referred to as "in-memory computing" (IMC). Section "Conclusion" is a summary of this entry and provides indications for future trends.

Non-volatile memory classification

Non-volatile semiconductor memories are usually classified according to their functional properties with respect to the programming and erasing operations, as shown in the flow chart depicted in Fig. 1.

Non-volatile memories can be functionally classified in two broad classes: read-only memories (NV-ROM) and read/write memories (NV-RAM). The former memories allow a relatively fast reading, but a much slower data writing into the cell, or no writing on field. The latter memories, instead, exhibit very similar and short R/W random access times, and are thus classified as non-volatile random-access memories.

Read-only memories (ROMs) are programmed at the mask level during the fabrication process by suitably interconnecting logic gates able to generate appropriate logic functions of the input data. Therefore, the reading operation is carried out by a logic computation of combinational logic circuits, which can be manufactured by a standard CMOS process. ROMs, however, suffer a lack of flexibility, which dramatically restricts their application area.

Electrically programmable read-only memories (EPROMs) are based instead on a different physical principle, and store information by controlling the threshold voltage of a special MOSFET structure with two overlapping gates, the lower of which is electrically floating. Injecting electrons into the floating gate changes the conduction threshold of the cell. A low threshold voltage

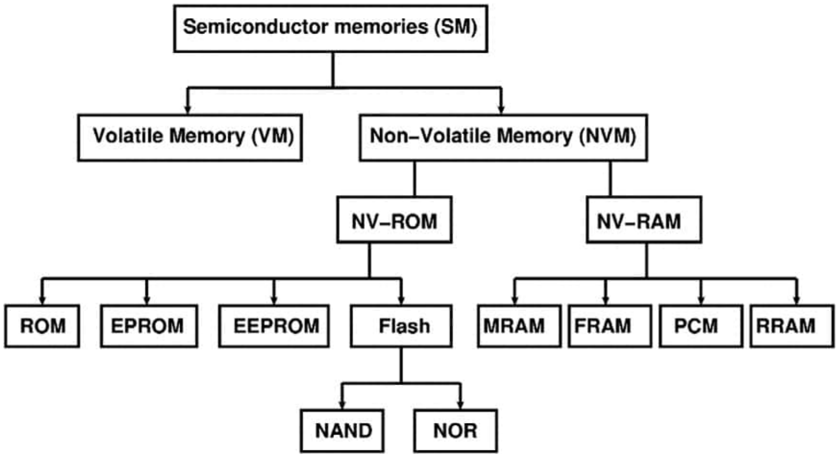

Fig. 1 Non-volatile memory classification according to functional criteria.

characterizes a conductive cell, and is associated with a logical "1," while a high threshold voltage represents a logical "0." The natural threshold of a virgin cell is low since the floating gate is electrically neutral; hence, it automatically stores a logical "1." Writing (or programming) the cell, by which its content is turned into a logical "0," means injecting electrons into the floating gate.

EPROMs can be electrically programmed on field and be optically erased by exposing the cell array to ultra-violet (uv) light. Erasing the memory, however, requires a long exposure of the cell array (~30 min) so that electrons confined within the floating gate can be emitted by photoelectric effect. This requires a special package with a quartz cover transparent to uv light. Quite often EPROMs are encapsulated within a standard package and used as one-time programmable ROMs (PROMs).

Electrically erasable and programmable read-only memories (EEPROMs) can be electrically programmed and erased on field, which makes them more flexible than EPROMs. A selection transistor, however, is required within the cell in addition to the EEPROM device. For a given silicon area, the increased cell size implies a smaller capacity and a higher cost per bit.

Flash EEPROMs (or simply flash) combine instead the EPROM's cell size with the EEPROM's flexibility and are thus largely preferred in a wide variety of applications, already mentioned in the Introduction. In flash memories, all cells of a sector are erased in parallel, which justifies their "flash" name, and re-programmed afterwards. On the other hand, reading a full page of data can be performed very quickly, which makes the long erasure time (several tenths of a second) acceptable at the system level.

NV-RAMs exploit different physical principles encompassing magnetic memories, ferroelectric memories, phase-change memories and resistive memories. With the exception of FRAMs, the above memories exhibit a state-dependent resistance value at the output, and are often referred to as "memristors."

MRAMs rely on the resistance change of a magnetic tunnel junction (MTJ), where one of the two ferromagnetic metal electrodes has a pinned magnetic polarization and the other one has a free magnetic polarization, which represents the stored data bit. If the two polarizations are parallel, a low MTJ resistance is found. If they are antiparallel, a high resistance is detected.

FRAMs exploit the hysteretic behavior of ferroelectric materials, where electrical dipoles can be oriented in two opposite directions. Data bits are stored within a ferroelectric capacitor, and are detected by cycling the applied capacitor voltage and checking if a switch of electrical polarization has occurred.

PCMs are based on the property of chalcogenide materials to switch from a microcrystalline to an amorphous phase and back under the influence of thermal processes generated by appropriate current pulses. The data bit is thus the chalcogenide phase, detected by a resistance change.

Finally, RRAMs are based on the conductive properties of metal-insulator-metal (MIM) two-terminal devices, which exhibit a hysteretic current-voltage relationship. The low-resistance state is due to the migration of metal ions or oxygen vacancies into the insulator, forming a filamentary conductive path across the oxide. The return to the high-resistance state is achieved by breaking the filamentary metal with the application of a higher positive voltage or by applying a negative voltage, which pushes the oxygen vacancies to the top electrode interface and removes them from the oxide.

Read-only memory

Read-only memories behave functionally as encoders, for they associate an M-bit output word, which is the memory content, to an N-bit input word representing a physical address. The ROM output can always be expressed as a sum of products of the input bits. Therefore, the reading process occurs in two steps: first, a decoder, which generates the minterms of the N input bits raises high one of the 2^N word lines; next, an encoder generates the output word by OR-ing the minterms from the selection of the physical address. The output word is thus computed by activating a combinational logic circuit; hence, the content of the memory is defined at the mask level during the fabrication process, and no programming changes are possible afterwards.

In view of their functional task, the decoder is often called the AND plane and the encoder is referred to as the OR plane of the ROM. However, the logic gates used to generate both the OR and the AND planes are often NOR gates because of speed considerations. NAND gates can sometimes be used for small ROMs with some density advantage, but are unpractical for a number of input bits in excess of 4 to 8.

Fig. 2a illustrates the typical structure of the AND plane for the simple case of a two-bit structure. The p-channel MOSFETs with grounded gate act as pull-up transistors of pseudo n-MOS logic gates. Alternatively, the load gate may be connected to the clock phase Φ. When $\Phi = 0$ the bit lines are precharged high. When $\Phi = V_{DD}$ the bit lines enter a high-impedance state and can be conditionally discharged to ground if a conducting path is activated by the n-channel MOSFETs connected in a NOR configuration. Indicating with A and B the input bits and with A' and B' their complements, the output nodes of the AND plane, referred to as WL_n, ($n = 1, \ldots 4$) turn out to be

$$\begin{aligned} WL_1 &= (A' + B')' = AB \\ WL_2 &= (A' + B)' = AB' \\ WL_3 &= (A + B')' = A'B \\ WL_4 &= (A + B)' = A'B' \end{aligned}$$

where De Morgan's theorem has been applied. Thus, the minterms of the two input bits are generated by NOR operations.

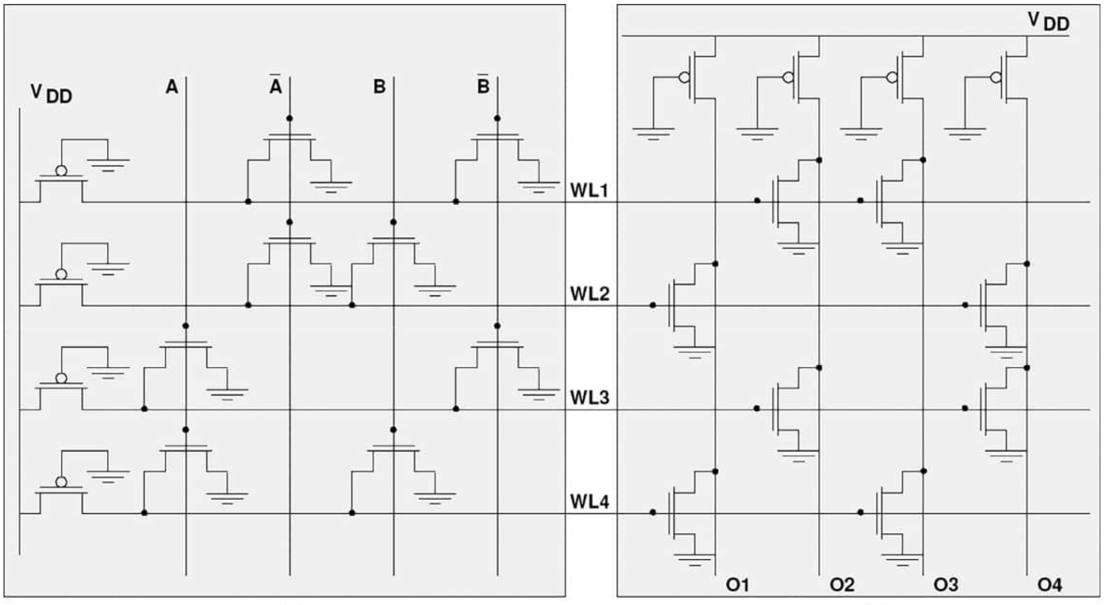

(a) (b)

Fig. 2 NOR-based implementation of a ROM; (a) AND plane; (b) OR plane.

The OR plane, again implemented by NOR gates possibly followed by inverters, is shown in Fig. 2b. The latter realizes the following Boolean equations

$$
\begin{aligned}
O_1 &= WL_1 + WL_3 = (WL_2 + WL_4)' \\
O_2 &= WL_2 + WL_4 = (WL_1 + WL_3)' \\
O_3 &= WL_2 + WL_3 = (WL_1 + WL_4)' \\
O_4 &= WL_1 + WL_4 = (WL_2 + WL_3)'
\end{aligned}
$$

The truth table implemented by the ROM shown in Fig. 2 is represented below.

A	B	WL_1	WL_2	WL_3	WL_4	O_1	O_2	O_3	O_4
0	0	0	0	0	1	0	1	0	1
0	1	0	0	1	0	1	0	1	0
1	0	0	1	0	0	0	1	1	0
1	1	1	0	0	0	1	0	0	1

A similar procedure can be followed using a NAND implementation of the above Boolean equations.

Electrically programmable read only-memory

Electrically programmable read-only memories rely on a cell structure with two overlapping gates, as shown in Fig. 3. The lower gate is fully surrounded by silicon dioxide and is thus electrically floating. The upper gate is instead accessible and is referred to as control gate. Due to the need of two polycrystalline silicon layers and a relatively high gate oxide thickness, EPROM fabrication is not fully compatible with the standard CMOS technology.

Electrons traveling from source to drain under large gate and drain voltages can possibly achieve an energy exceeding the Si-SiO_2 potential barrier, which is about 3.1 eV. If such an electron undergoes a re-directing collision with a final momentum normal to the silicon surface, can overcome the potential barrier and be injected into the oxide conduction band. If the floating-gate voltage V_{FG} exceeds the drain voltage V_D, the field in the oxide will favor electron injection into the floating gate, where it becomes trapped. As more and more electrons are injected and trapped into the floating gate, its potential V_{FG} is lowered and the threshold voltage of the control gate V_{TC} increases.

The basic relationship connecting the floating-gate voltage V_{FG} with the charge injected into the floating gate Q_{inj} and the cell voltages is.

$$V_{FG} = \alpha_G V_{CG} + \alpha_S V_S + \alpha_D V_D + \alpha_B (V_B + \Phi_{MS}) + Q_{inj}/C_T$$

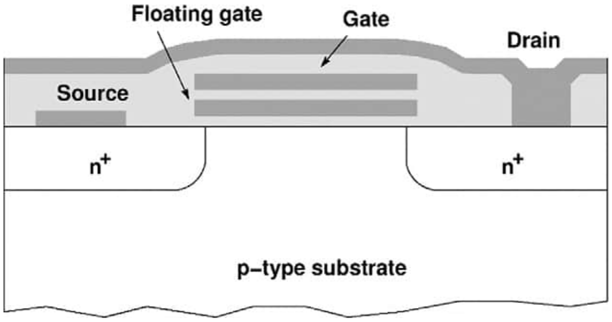

Fig. 3 Cross section of a floating-gate EPROM cell.

where V_{CG} is the control-gate voltage, V_S is the source voltage, V_D is the drain voltage, V_B is the bulk voltage and Φ_{MS} is the work function difference between the heavily doped n^+ polycrystalline silicon gate and the underlying *p*-doped silicon substrate. Also, α_G, α_S, α_D, α_B, are coupling coefficients expressed by the ratios of the gate, source, drain and bulk capacitances C_{GG}, C_{GS}, C_{GD} and C_{GB} with respect to the total capacitance of the floating gate $C_T = C_{GG} + C_{GS} + C_{GD} + C_{GB}$. The above equation shows that V_{FG} is a linear combination of the external voltages, with weighting factors given by the coupling coefficients, and that a negative charge Q_{inj} lowers the floating-gate voltage. When V_{FG} equals the threshold voltage for current conduction within the EPROM cell V_{TF}, the control-gate threshold voltage V_{TC} reads.

$$V_{TC} = (1/\alpha_G)\, V_{TF} - (\alpha_S/\alpha_G)\, V_S - (\alpha_D/\alpha_G)\, V_D - (\alpha_B/\alpha_G)\, (V_B + \Phi_{MS}) - Q_{inj}/C_{GG}$$

It may be seen from the above equation that the threshold voltage experienced by the control gate increases if electrons are injected into the floating gate. Strictly speaking, the gate-source, gate-drain and gate-bulk capacitances are non-linear; thus, the coupling factors are bias dependent. Quite often, however, such factors may be treated as constants. Furthermore, if $V_S = V_D = V_B = 0$, the above equation may be simplified to give.

$$V_{TC} = (1/\alpha_G)\, V_{TF} - (\alpha_B/\alpha_G)\, \Phi_{MS} - Q_{inj}/C_{GG}$$

Channel hot-electron (CHE) injection requires large gate and drain voltages to be applied to the EPROM cell, with the former higher than the latter. Thus, a large current is flowing in the channel while programming, with substantial power dissipation. This process is rather inefficient, since only a small fraction of electrons moving from source to drain is indeed injected into the floating gate, and the required time to program the cell may be as large as a few hundred microseconds. After being injected into the floating gate, electrons dissipate their excess kinetic energy by emitting phonons, and become permanently trapped within a deep (3.1 eV) potential well.

As already pointed out, native cells are conductive when the control-gate voltage is at the high level; hence, they are naturally programmed with a logical "1." Charge injection shifts the threshold voltage above the supply voltage V_{DD}, and the cell exhibits an off state when read out. Thus, the high-voltage threshold indicates a logical "0."

The former success of floating-gate EPROMs was largely due to the small cell size and the resulting high bit capacity, as well as to their on-field programmability. Erasing the content of the memory, however, can only occur by exposing the device to uv light for quite some time. This need requires a special package with a quartz cover transparent to uv light. Electrons absorbing a high-energy photon by photoelectric effect can reach an energy exceeding the Si-SiO_2 potential barrier and be ejected either into the control gate or into the silicon substrate.

The cell array organization is shown in Fig. 4. The memory cell only contains a floating-gate device with its source connected to ground, its drain connected to the bit line and its control gate connected to the word line. The source regions are shared by two neighboring cells in the same column, and so are the drain diffusions.

When the cell is addressed, the word line is raised high, and the bit line is set by the sense amplifier at a smaller voltage (about 1 V). If a substantial current flows along the bit line, the sense amplifier detects a logical "1." Otherwise, a logical "0" is revealed.

Electrically erasable and programmable read-only memory

Electrically erasable and programmable read-only memories provide a further improvement over the functionality of EPROMs by allowing the information to be electrically written and erased at the bit level. Their basic cell differs from the EPROM one in that the floating gate extends over the drain region, where a small oxide area is thinned down to a few nm to allow for electron tunneling into and out of the floating gate. This device, called FLOTOX, is shown in Fig. 5.

The physical mechanism used to program and erase the EEPROM cell is electron tunneling across the thin oxide region between floating gate and drain. In order to let electrons tunnel into the floating gate, the control gate must be biased at a large positive voltage around 15 V, while drain is kept at zero voltage.

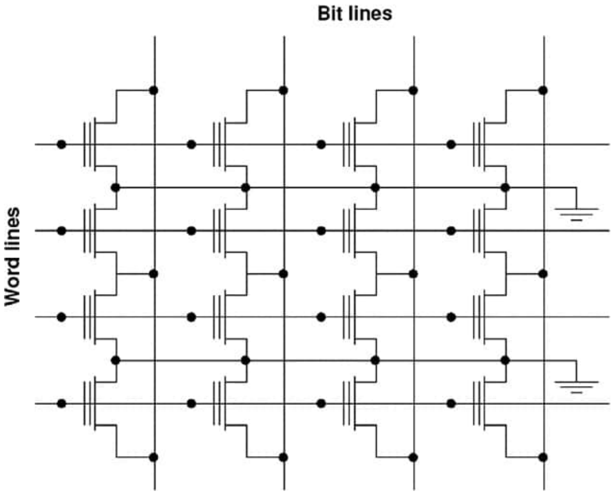

Fig. 4 EPROM cell array organization.

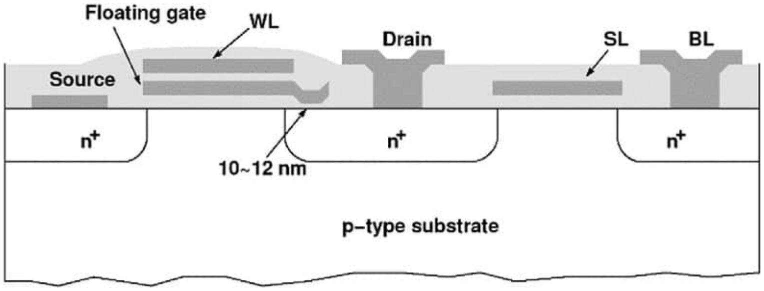

Fig. 5 Schematic cross section of a floating-gate EEPROM (FLOTOX) cell.

Likewise, cell erasing is carried out by applying a large negative voltage to the control gate, while keeping the drain at zero or positive voltage. So doing, a large oxide field close to 10 MV/cm is applied to the tunnel oxide for both programming and erasing processes, albeit with opposite directions. The large field shapes the energy barrier to become triangular and reduces the tunneling distance. Fowler-Nordheim tunneling then occurs and either fills or depletes the floating gate of the formerly injected charge, thus raising the threshold voltage above V_{DD} or lowering it down below zero.

The poor threshold voltage control of an erased device, however, requires that the basic memory cell contain an additional MOSFET, referred to as selection transistor, connected in series with the FLOTOX device, as shown in Figs. 5 and 6. The drain of the selection transistor is connected to the bit line BL, its gate is connected to the select line SL and the control gate of the FLOTOX device

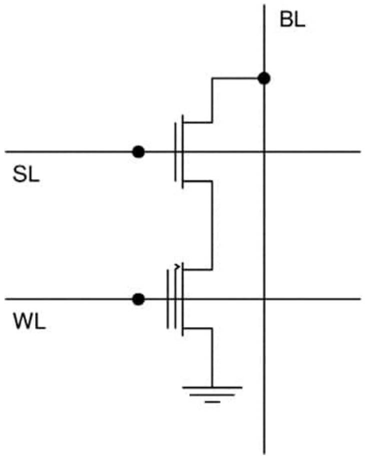

Fig. 6 Circuit schematics of the EEPROM cell.

is connected to the word line WL. When the cell is not addressed, the select line SL is at zero voltage, which ensures that no leakage current flows even when the floating-gate device has a negative threshold voltage.

When the memory cell is addressed, both the word line WL and the select line SL are raised to V_{DD}, thus allowing current to flow across the cell if its threshold voltage is low. Otherwise, no current flows, and the sense amplifier detects a logical "0." In order to program the EEPROM cell, the word line is raised to the large positive voltage V_{pp} with the select line at V_{DD}, while keeping the bit line at ground potential. The V_{PP} voltage is chosen such that electron tunneling into the floating gate can occur. The bit line of unselected cells is left floating, to prevent their undesired programming. When the cell is erased, the word line is negatively biased, generating the appropriate voltage drop across the tunnel oxide. The drain of the cell is often raised high, to reduce the negative gate voltage value. To do so, the bit line is biased at V_{DD} while keeping the select line positively biased. Due to the small tunneling currents, several hundred microseconds may be required to complete an erasure cycle.

As opposed to CHE injection, tunneling is an energetically efficient process, as the electron flow is directly charging, or discharging, the floating gate. Repeated electron tunneling across the thin oxide, however, is responsible for reliability problems due to electron trapping within the oxide itself. This aging process deteriorates the oxide integrity, resulting in data retention problems and limited cell endurance.

Flash EEPROM

Flash EEPROMs are electrically erasable and programmable read-only memories. The basic flash cell is structurally similar to the EPROM's, which is essentially a MOSFET with two overlapping gates. The flash array exhibits either a NOR-type, for faster random-access, or a NAND-type organization, when high capacity and lower cost per bit are the main design goals. As opposed to full-featured EEPROMs, the selection transistor is no longer required within the basic cell structure, to the advantage of memory density. However, flash erasing can only be carried out collectively at the sector (or block) level by electron tunneling into the source from the floating gate. The typical block size is 64–256 kB in NOR flash and 16–512 kB in NAND flash chips.

An electron micrograph of a NOR flash is shown in Fig. 7. This cross section is cut along the bit line, which contacts the cell drains by vertical tungsten plugs. The tungsten silicide word line is perpendicular to the cross section and appears in the micrograph as the light rectangular area overlapping the control gate of the cell. The polycrystalline silicon gates are self-aligned; the drain regions are shared by two neighbor mirrored cells, and so are the ground-connected sources. The lateral cell extension, measured between source and drain mid-axes, is roughly 500 nm in this technology.

Cell programming is carried out by CHE injection in NOR-flash and by electron tunneling in NAND-flash array organizations. Erasing is done by electron tunneling in both architectures. In the NOR case, the erasing process is always followed by a cell-by-cell programming, with a concurrent monitoring of the threshold voltage value. In NAND-flash, instead, the negative threshold voltages resulting from the erasing process are required for memory functionality. Programming is thus performed only for "0" storing cells.

Flash array architecture

As already stated, the cell array of flash memories can be organized according to either a NOR or a NAND architecture. The former organization has a shorter random-access time, but the latter is much denser and, thus, cheaper. NOR flashes are thus required whenever a small amount of data, such as software codes, must be quickly accessed. NAND flashes, on the other hand, can read and

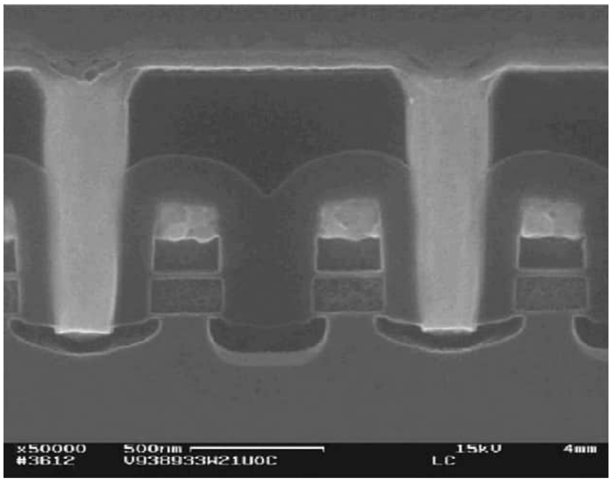

Fig. 7 Scanning electron micrograph of the ETOX flash cell in 0.18 μm technology. Courtesy of ST Microelectronics.

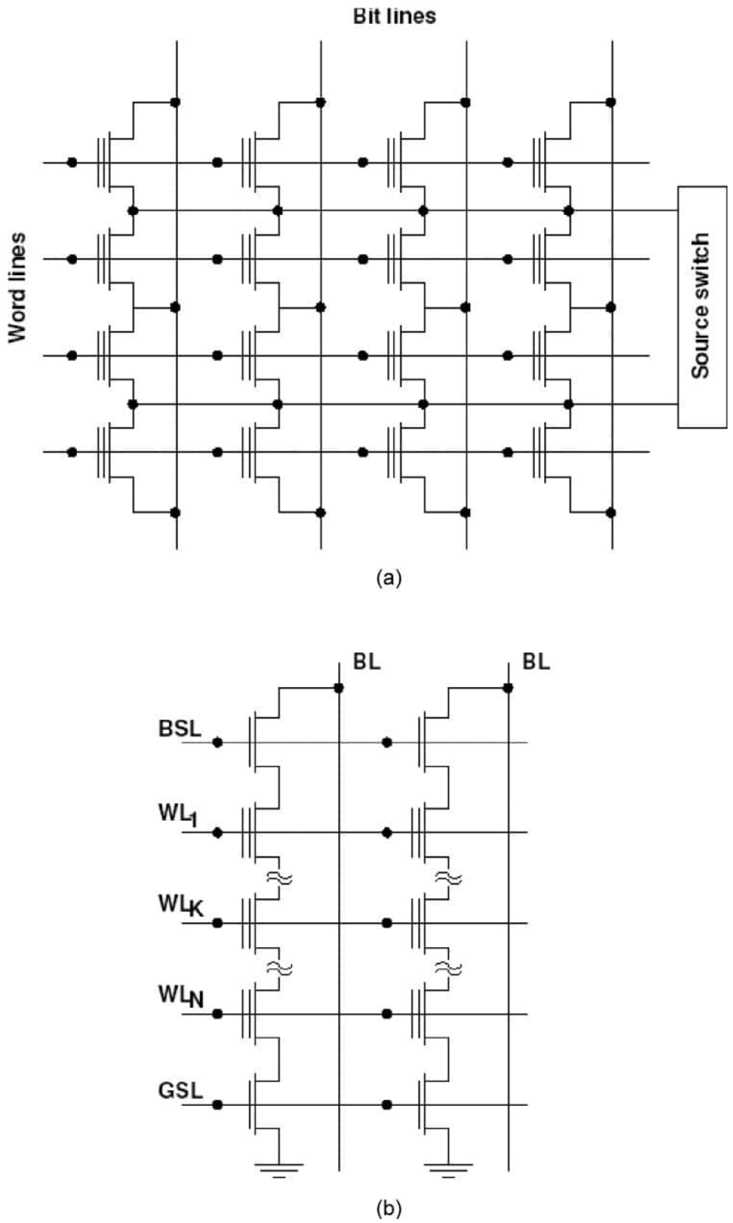

Fig. 8 Flash EEPROM cell array organization; (a) NOR architecture; (b) NAND architecture.

transfer one full data page with only one random access. Hence, they are especially used when massive amount of data must be read out and transferred with the lowest possible latency to the central memory. To date, the NAND architecture is covering a much larger fraction of the flash memory market.

The array organization of the NOR flash is shown in Fig. 8a. Cells within the same row share the word line, while cells within the same column share the bit line. Successive cells along the column are mirrored, so that one common source line is shared by two cell rows. Also, the drain diffusion is shared by two adjacent cells, to the advantage of cell size and number of contacts to the bit line. The common-source lines of a sector are shorted and kept at ground potential during a read cycle, but are raised to a positive voltage when an erasing operation takes place for the whole array sector. Because of the common source configuration of the flash cells during a read, this cell array organization is referred to as a NOR architecture.

Cell programming by CHE injection requires a supply voltage $V_{PP} \approx 10\text{–}12$ V to be applied to the control gate and a drain voltage $V_{DS} \approx 5$ V. A special circuit called "charge pump" is used to generate the high voltage internally.

Flash erasing requires a control-gate voltage $V_{CG} \approx -12$ V, and a source voltage $V_S \approx 5$ V, while keeping the drain floating. So doing, the oxide field becomes large enough to reduce the tunneling distance down to a few nm. The negative voltage is again generated on chip by a charge pump. The use of negative voltages requires a triple-well CMOS technology, with the external *p*-well biased at the most negative voltage to prevent shorting of the *p*-*n* junctions with the *n*-layer biased at negative voltages.

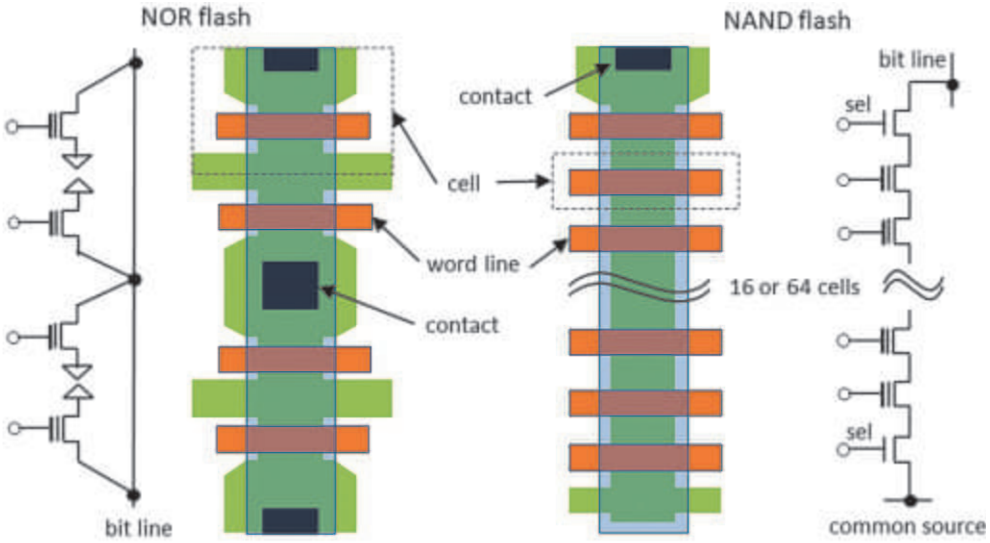

Fig. 9 Typical layout of a few NOR flash and NAND flash cells (Veendrick, 2017).

The NAND array organization is illustrated in Fig. 8b. A large number of cells, typically 16 to 64, are connected in series, which allows for a compact layout and a higher density within the array due to the unique bit line contact per string and the absence of the common source lines within the array. Hence, a reduced word-line pitch becomes possible, leading to a cell size of $4F^2$, as shown in Fig. 9.

Two select transistors are present at the top and bottom of the flash column, to prevent an undesired leakage current in standby conditions. The upper select transistor connects the cell string to the bit line and the lower one to ground.

The word lines are normally biased at the supply voltage V_{DD} so that all transistors are normally on. A read operation is carried out by raising the two select lines and lowering the word line down to 0 V. In this configuration, the unaddressed cells act as pass gates regardless of their actual threshold, which is typically much smaller than V_{DD}. If the addressed cell has a negative threshold, a bit line current is detected by the sense amplifier, and a logical "1" is identified. In the opposite case, no current flows on the bit line, and a logical "0" is read out.

Reading a current through a series of several cells and two select transistors is, however, a slow operation: the random-access time is in fact of the order of 20 µs. On the other hand, due to the inherent parallelism of the memory array, one full page of data corresponding to one word line is read out in parallel. Hence, the sequential access time is typically around 20 ns/bit, and the corresponding data rate is very large (Veendrick, 2017).

While programming a cell, the control gate is driven to a large positive voltage $V_{PP} \approx 15$ V, and the corresponding bit line is kept at 0 V. This ground potential is transferred to the source and drain of the addressed cell via the select transistors and the series of flash cells, with a negligible voltage drop due to the small tunneling currents flowing into the floating gate. The remaining bit lines must be kept at V_{DD} and the unselected word lines at a voltage $V_m \approx 10$ V, large enough to ensure a good pass-gate function irrespective of the cell threshold voltage, yet sufficiently small to prevent electron tunneling into the floating gate of the unselected cells.

This approach limits program disturbances of the unselected cells on the same word line.

To erase a sector, electrons are injected from the floating gates to their respective channels, again by Fowler-Nordheim tunneling. This process is carried out by turning on the select transistors, applying a large negative voltage to the word lines (up to −20 V) while keeping the bit lines at zero voltage. Compared with the NOR architecture, the erase operation is much faster since it does not require the successive program to "0" to be performed.

In NAND flash architectures, the required oxide field to ensure Fowler-Nordheim tunneling to erase one full block of cells is only due to the negative voltage applied to the control gates. This requires a large negative voltage generated on chip, making the charge pump less efficient. On the other hand, electron tunneling does not involve high currents, which prevents the overload of the charge pump despite the large number of cells erased in parallel.

Reliability of flash memories

Flash memories can undergo multiple program and erase cycles; hence, reliability problems are rather severe. The endurance of a flash cell is the property of experiencing multiple write and erase operations without affecting the memory performance. Connected with endurance is data retention, i.e., the property of maintaining the written data unaltered for a long time with or without any power supply.

Flash memories must typically ensure a data retention of 10 years. Hence, leakage currents must be very small even under the influence of external voltages. This implies that the gate oxide and the inter-poly dielectric must behave as ideal insulators. Therefore, the gate oxide is relatively thick (≈8–10 nm) compared with the typical gate oxide thickness of standard CMOS transistors designed for logic. The inter-poly dielectric, called ONO, is made by a silicon nitride (Si_3N_4) layer sandwiched between two SiO_2 layers, with a total thickness of 12–14 nm.

When a NOR flash is programmed, all cells connected to the same word line are indeed subject to a large positive gate voltage around 12 V. Hence, some electrons can possibly tunnel into the floating gate from the channel, if the cell is in its conductive state, or into the control gate from the floating gate if the cell is in the off state. In the former case, the gate disturbance tends to convert a logical "1" into a logical "0" while, in the latter, the opposite occurs. Likewise, all cells connected to the same bit line experience a relatively large drain voltage around 5 V and, due the low gate voltage, electron tunneling can occur from the floating gate into the drain. In this case, the disturbance generated by cell programming tends to convert a logical "0" into a logical "1."

A read disturbance additionally occurs when a cell is read, despite the relatively smaller gate and drain voltages. The drain voltage heats up electrons traveling from source to drain of the addressed cell. Hence, some hot-electrons from the tail of the energy distribution can be occasionally injected into the floating gate in this case too. Due to the unlimited number of read operations, the drain disturbance must be carefully controlled. In order to prevent this effect, drain is usually kept by the sense circuitry at a voltage of the order of 1 V, well below the energy threshold for hot-electron injection. The cumulative effects of gate and drain disturbance during write and read operations can affect the integrity of the stored information within flash cells and reduce data retention below 10 years. Therefore, parity bits for error detection and correction become necessary to improve the memory reliability.

The large oxide fields needed for electron tunneling may be responsible for a degradation of the gate oxide. Charge loss in flash memories can be caused by (i) defects in the gate oxide; (ii) defects in the inter-poly dielectric and, (iii) mobile ion contamination.

The charge trapped in the tunneling oxide and the related aging effects limit the flash endurance, as the high threshold voltage of cells storing a logical "0" tends to decrease and the low threshold voltage of cells storing a logical "1" tends to increase, when the number of erasing cycles progresses, as shown in Fig. 10. The closing window between the high and low threshold voltages sets an upper limit to the maximum number of erasing cycles, which is typically about 10^5 (Bez et al., 2003). An even distribution of the erased blocks improves the memory lifetime. An appropriate control circuitry changes the physical allocation of re-written blocks to ensure such an even distribution.

The degradation of the gate oxide typically occurs due to electron trapping during the write and erase cycles. This degradation may be responsible for premature oxide breakdown or low-voltage leakage, referred to as "stress-induced leakage current" (SILC). The latter is an anomalously large current flowing across the gate oxide in a small, but significant, number of cells. SILC is due to the percolation of electrons through a string of defects located within the oxide. The percentage of cells affected by SILC is a strong function of the gate oxide thickness. Therefore, the latter cannot be scaled below 8 nm. Similar considerations apply to the inter-poly dielectric, which has a lower limit of about 12 nm. The non-scalability of the gate oxide and inter-poly dielectric, in turn, does not allow the programming and erasing voltages to be lowered, in sharp contrast with CMOS voltage scaling. Besides, the generation of large programming and erasing voltages by means of charge pumps operating at a small supply voltage is a rather inefficient process.

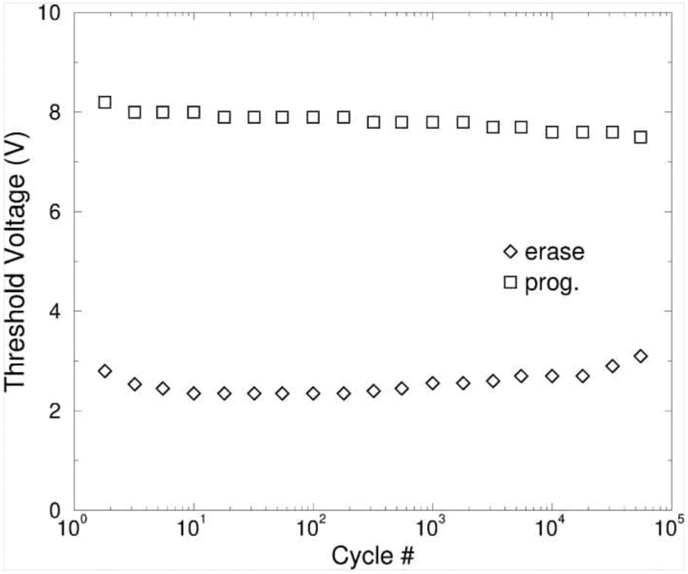

Fig. 10 Aging effect on the threshold voltage of flash EEPROM cells.

The SILC problem is mitigated by the provision of a redundant number of rows within the flash array. If information loss is detected in one or more cells of a row, the word line address is internally reconfigured to access one of the additional rows. With this approach, the memory functionality is re-established with a small increment of the overall chip area.

Multi-bit memory storage

The capacity of a flash EEPROM can be increased by storing two or three bits per cell, if four to eight different threshold voltages, rather than two, can be accommodated within the cell. For reliable operation, it is requested that the standard deviation associated with the statistical distribution of the threshold voltages be much smaller than the average separation between their central values. This may be accomplished with a tighter control of the injected charge into the floating gate, and with a more sophisticated reading procedure. More specifically, the threshold voltage must be monitored when programming, while the number and duration of writing pulses is controlled by a suitable logic.

The reading procedure requires a number of steps involving successive comparisons of the output current with reference currents made available by suitably pre-programmed dummy cells. So doing, the memory capacity is increased by a factor of 2 or 3 for a given array size, at the expense of a degraded access time and reduced data retention and endurance.

Charge-trap flash (CTF)

Two evolutionary approaches were pursued to mitigate the flash reliability problems by a change of the cell structure: the nanocrystal cell and the charge-trap flash (CTF) cell. In the first approach, a large number of silicon nanocrystals embedded within the gate oxide replace the floating gate. Programming and erasing are still carried out by electron tunneling across the gate insulator. The advantage of nanocrystals is twofold: first, if a leaky percolation path exists, only one nanocrystal can be affected and not the entire floating gate; next, the gate dielectric could be made much thinner, with a substantial advantage for the scaling properties of the cell. Besides, electron tunneling across a thin gate insulator is known to produce less oxide defects. The nanocrystal approach, however, was unable to generate sufficient trapping states to differentiate the high and low device threshold voltages, and is no longer pursued.

The second approach, first referred to as Silicon-Oxide-Nitride-Oxide-Silicon (SONOS) and, ultimately, Charge Trap Flash (CTF), is based on the use of an ONO gate dielectric, where the nitride layer replaces the floating gate. Electrons injected into the oxide are captured and permanently trapped within the intermediate nitride layer, raising the threshold voltage of the cell. By reversing the applied voltages, holes are injected into the nitride layer, compensating the negative charge and lowering the cell threshold. CTFs have two distinct advantages over the standard flash cell: first, a localized oxide defect, which could totally deplete the floating gate by SILC, has a little impact, as electrons are trapped in deep nitride centers and are not mobile. Next, the interaction between floating gates in adjacent cells becomes more and more important as the device dimensions are scaled down and packed more densely, possibly leading to erroneous readings of the cell content. CTF cells are instead nearly immune to such interactions and promise a more reliable operation at the lowest dimensional cell sizes.

Three-dimensional flash memories

The increasing problems related with planar flash scaling below 20 nm has triggered the development of a novel three-dimensional (3D) NAND flash architecture based on vertically oriented cylindrical gate-all-around charge trap cells, represented in Fig. 11. Such an architecture is referred to as V-NAND. The use of the third dimension, combined with multi-bit storage, makes it possible to further improve the bit density with relaxed lithography rules, reaching record capacities up to 8 Tb on chip (Micron, 2020).

The fabrication of V-NAND flash memories relies on a very complex process technology. Its detailed description, which is beyond the scope of this entry, can be found in (Veendrick, 2017). In essence, the starting point is the deposition of a large number (over 100) of alternating oxide (≈6 nm) and nitride (≈32 nm) layers. Then, vertical cylindrical holes, with 100 nm diameter, are opened by anisotropic etch, and successive layers of blocking oxide, trapping nitride, gate oxide and polysilicon channels are deposited on the lateral hole walls by the atomic-layer deposition (ALD) technique. Next, vertical trenches are opened, crossing laterally and vertically the whole structure. Horizontal nitride layers are dissolved by wet etch penetrating through the trenches, and replaced with tungsten, again deposited by ALD, forming the control gates of the individual cells. W is then removed from the trenches, in order to isolate the control gates of different layers and a dielectric is deposited on the trench walls. Trenches are subsequently filled with W again, to provide a distributed low-resistance ground connection.

Fig. 12 is an electron micrograph of the final 3D V-NAND flash structure. Vertical light plugs crossing the whole structure are the W-filled trenches, which extend in the third dimension not shown in this image. In this view, vertical cell strings appear between successive trenches, and the two light spots on the sides of each cell represent the W control gates cut along their diameters. The cell inner part appears in dark color.

In this technology, the cell height is controlled by the thickness uniformity of the nitride layers (≈32 nm). The equivalent cell width, measured by the inner circumference of the tunnel oxide, turns out to be about 200 nm, with a cell form factor $W/L \approx 6$, as opposed to a gate width of 14 nm with $W/L \approx 1$ for advanced planar technologies. Therefore, the cell physical dimensions are much more relaxed for the V-NAND flash, and the amount of stored charge is accordingly increased. This makes it possible to store 4 bits

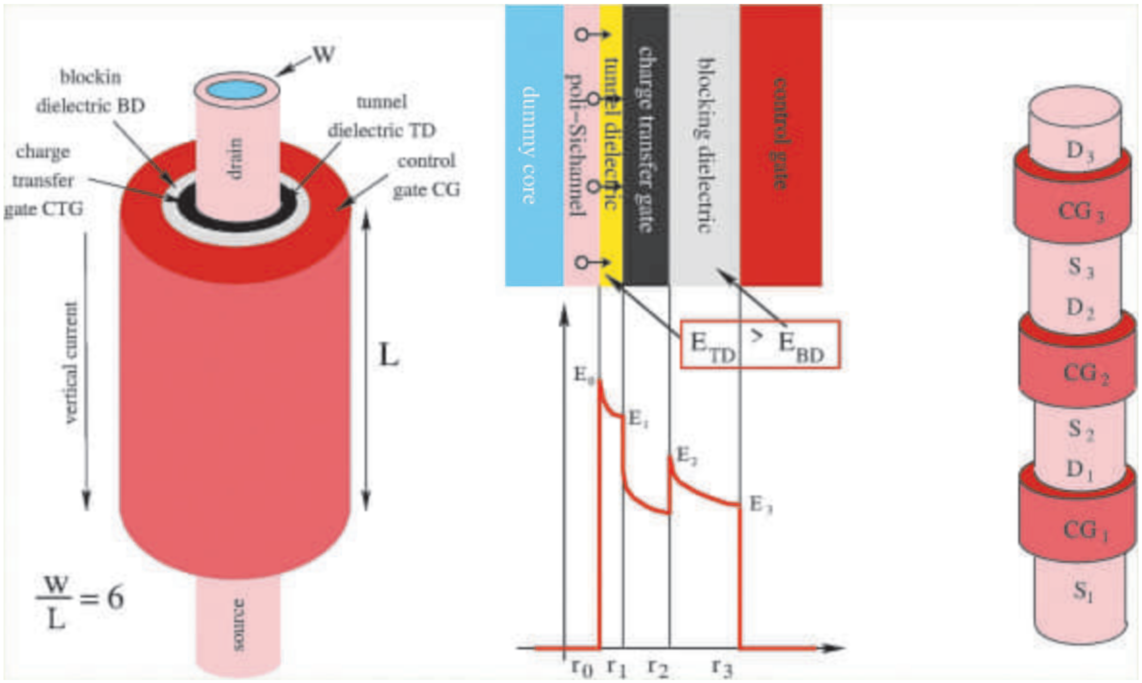
blockin
dielectric BD
W
tunnel
dielectric TD
charge
transfer
gate CTG
control
gate CG
drain
vertical current
L
$\frac{W}{L} = 6$
source
dummy core
poli–Sichannel
tunnel dielectric
charge transfer gate
blocking dielectric
control gate
$E_{TD} > E_{BD}$
E_0
E_1
E_2
E_3
r_0
r_1
r_2
r_3
D_3
CG_3
S_3
D_2
CG_2
S_2
D_1
CG_1
S_1

Fig. 11 Cylindrical gate-all-around CTF cells for V-NAND architectures (Veendrick, 2017).

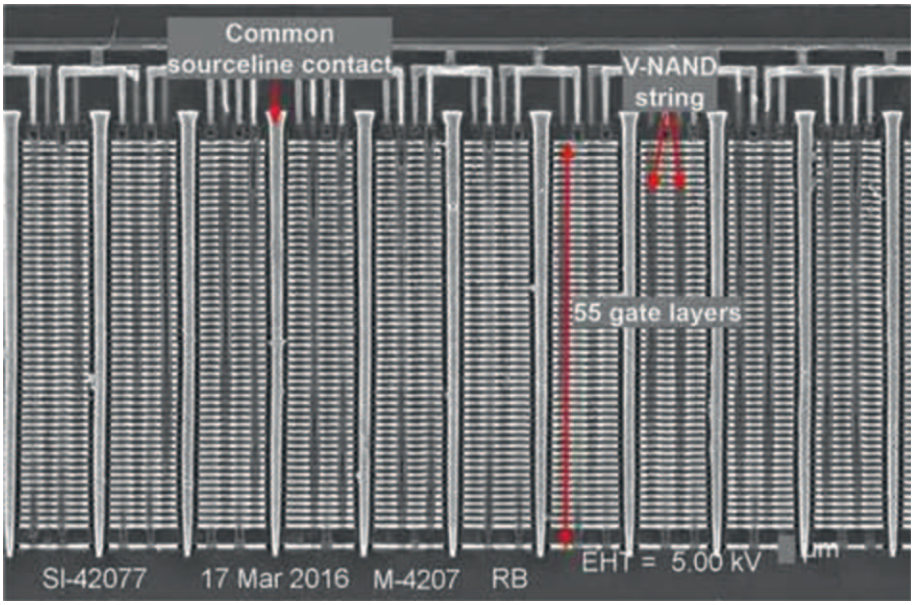
Common
sourceline contact
V-NAND
string
55 gate layers
SI-42077
17 Mar 2016
M-4207
RB
EHT = 5.00 kV
μm

Fig. 12 Electron micrograph of a 3D V-NAND flash memory (TechInsights via EE Times https://www.eetimes.com/first-look-at-samsungs-48l-3d-v-nand-flash/2/).

per cell. An additional consideration is that, within a circular structure, the radial field is inversely proportional to the radius, meaning that the field is smaller in the blocking dielectric than within the tunnel oxide. This makes it possible to reduce the programming voltage from 20 to 25 V down to 15–18 V (Veendrick, 2017).

3D V-NAND flash memories are having a great market success and are now the workhorse for a wide variety of applications requiring high capacity, small cost per bit, and high data rate. To date, V-NAND flash chips containing up to 176 cell layers, 8 Tb capacity, and a data rate of 1600 MT/s are being produced (Micron, 2020). Also, solid-state disk drives with up to 16 TB capacity have become available on the market.

Non-volatile random-access memories

In addition to the read-only memories illustrated in the previous sections, which presently dominate the non-volatile memory market, different device concepts have emerged. Some of them, such as Magnetic RAMs (MRAM) and Ferroelectric RAMs (FRAM), have been around since many years, but only recently have become competitive products. These memories are based on the properties of ferromagnetic or ferroelectric materials, which exhibit a hysteretic M-H and P-E relationships, respectively. Here M is the magnetic moment and H the magnetic field; P is the electric polarization and E the electric field. MRAMs, while not being competitive in density and cost with DRAMs, have lower access times, an excellent radiation hardness, and are non-volatile. As such, they have mainly been used for military and space applications.

FRAMs are based on the properties of ferroelectric materials (Perovskite crystals, such as $Pb(Zr,Ti)O_3$, shortly referred to as PZT) containing electrical dipoles oriented in either one of two opposite directions. The resulting polarization can be switched by the application of an electric field opposed to the dipole orientation. Hence, the two polarization states can be used to store one bit of information. PZT is a contaminating material requiring special precautions in the fabrication process. The recent discovery of a ferroelectric phase of HfO_2, well established as a high-k material in CMOS and memory technologies, has further improved the commercial perspectives of FRAMs. To date, ferroelectric RAMs based on 1T-1C cells are being manufactured and are very appealing because of the simplicity of the basic cell, which promises a small size and a high density, as well as easier write operations with respect to flash memories.

A third development line is based on the use of chalcogenide materials, i.e., an alloy of Ge, Sb and Te (GST), which undergoes a phase change when heated up to high temperatures. More specifically, if a polycrystalline GST alloy is heated up to the melting temperature (about 650 °C) turns into an amorphous state when it cools down. On the other hand, if an amorphous material is heated up to 500 °C, it turns back into a polycrystalline state. The final state is indefinitely conserved at room temperature; hence, these materials can provide a non-volatile memory function. Due to the large resistance change associated with a phase change, it is straightforward to read the stored information by a simple current measurement.

Finally, resistive memories (RRAM) are intensely investigated due to the cell simplicity and the possibility to realize cross-point memory architectures with minimal area consumption. A resistive memory is essentially a metal-insulator-metal (MIM) two-terminal device where a filamentary path is initially created by soft electrical breakdown induced by the application of a positive voltage to the top electrode. The large concentration of oxygen vacancies or metallic ions injected from the top electrode are then driven by field-induced migration and diffusion into the insulator, where a conductive filament is formed, leading to a low-resistance state. The application of a negative voltage pushes instead those defects toward the upper electrode, re-establishing a high resistance state.

It should be noticed that MRAMs, PCMs and RRAMs are all resistive memories, despite their different physical mechanism, as the cell state is represented by a low/high resistance value. All of them can thus be classified as "memristors." As opposed to charge-based memories, memristors offer the opportunity to treat resistances as input or output values of a computation, leading to a new computing paradigm with increased logical flexibility. This property can be exploited by an emerging discipline called "in-memory computing." See, e.g., (Ielmini and Pedretti, 2020).

Magnetic RAM (MRAM)

Magnetic memories are based on the properties of ferromagnetic materials, such as iron (Fe), cobalt (Co) and nickel (Ni), which exhibit a non-linear hysteretic M-H relationship, as shown in Fig. 13. The residual magnetization of the above materials after the field return to zero is due to the alignment of the electron spin, which is conserved at room temperature.

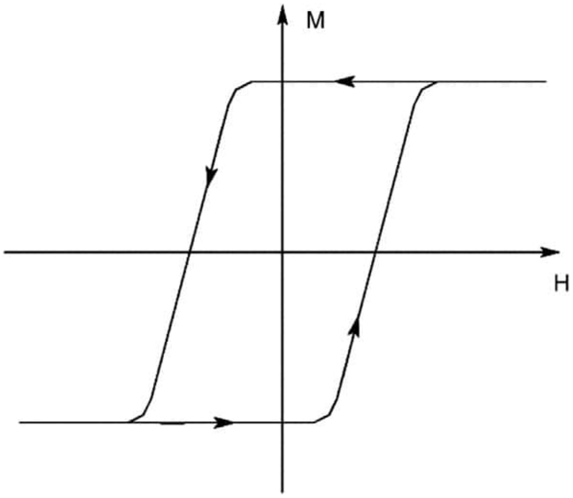

Fig. 13 Magnetic moment against magnetic field in typical ferromagnetic materials.

Magnetic core memories were used in early mainframe computers, where a matrix of current carrying wires was used to program magnetic rings referred to as nuclei. Subsequent memory devices kept storing the information on magnetic elements, but the sensing scheme became entirely different, being based on the magnetoresistance (MR) effect, namely, a resistance change of a thin metallic layer due to the presence of a magnetic field. Magnetoresistance, however, is a small effect, with resistance changes of the order of 1%.

More interesting from this standpoint was the giant magneto-resistance effect, which occurs when a thin metal layer, typically Cu, is sandwiched between two magnetic films consisting of NiFe. Normally, a ferromagnetic material can be polarized at random directions. If, however, the magnetic film is narrower than the magnetic domain width, the film exhibits only two polarization states. This makes the switching threshold well defined.

When the magnetic moments are parallel, the "up" electrons do not scatter, and only the "down" electrons scatter at the interface with the magnetic materials. When the magnetic moments in the two films are in opposition, instead, both type of electrons scatter and a significant resistance increase, which can be as large as 15%, typically occurs. The effect according to which electrons with long mean-free paths travel with low resistance when the magnetic materials have parallel alignments is called "spin valve" and the discipline which investigates the spin-related material properties is called "Spintronics."

Several different configurations of magnetic films have been proposed for data storage in MRAMs. These include: (i) the anisotropic MRAM; (ii) the Spin-Valve MRAM; (iii) the pseudo-spin valve (PSV) MRAM; (iv) the Magnetic Tunnel Junction (MTJ) and, ultimately, (v) the Spin Transfer Torque (STT) MTJ. The last cell configuration promises to become competitive with SRAMs due to its specific properties. In what follows, the MTJ MRAM cell will be first discussed, as the STT MTJ is just a simplified version of it, which improves in memory density and power consumption.

A schematic view of the MTJ memory cell is shown in Fig. 14. The MTJ contains a thin insulating layer sandwiched by two magnetic films. In the most recent implementations, the insulating layer is typically made by thin film ($\approx$1 nm) of crystalline MgO, and the two magnetic films are made by a CoFeB alloy. The upper magnetic layer, called free layer (FL), is used to store one bit of information according to its polarization. The lower magnetic layer, called pinned layer (PL), has instead a fixed magnetization due to the presence of an underlying antiferromagnetic layer made by PtMn or by IrMn. When the magnetic moments of the two magnetic layers are parallel, the cell resistance is low, and a logical "1" is associated with the state of the cell. When magnetic layers' polarizations are antiparallel, the cell resistance is higher, and a logical "0" is associated with the state of the cell. Additional metallic films can be added at the top and bottom of the MTJ to improve its properties.

The MTJ is located at the intersection of two conductors (word and bit lines) whose orientations are parallel and perpendicular to the magnetization vector. For a write operation, orthogonal current pulses I_x and I_y generate longitudinal and transverse magnetic fields H_y and H_x, respectively, whose vector sum switches the magnetic moment in the free magnetic layer.

The use of two perpendicular components of the magnetic field lowers the switching threshold of the cell, as shown in Fig. 15. This figure plots in the H_x-H_y plane the locus of the magnetic-field components at which the MTJ cell undergoes a switching. The asteroid shape of the curve indicates that, combining suitable values of H_x and H_y, allows much smaller magnetic fields (and reduced currents) to be used to the advantage of the stability of the pinned-layer polarization. The same plot indicates that the normal component of the magnetic field (easy axis field) switches the cell at a smaller field than the longitudinal component (hard axis field). The required writing currents, however, are very large and increase as the diameter of the MTJ pillar is scaled down (Apalkov, 2013).

In order to sense the cell resistance, the isolation transistor is turned on, enabling a vertical current flow across the insulating layer of the MTJ. The current is sensed by a suitable circuitry, which generates the appropriate logic level.

Non-volatility, fast switching ($\approx$5 ns) and radiation hardness are the most important merits of MTJ MRAMs. On the other hand, the MTJ cell size is very large ($\approx$20–30 F^2) and the high switching currents lead to a high-power consumption. Therefore, MTJ-based memories are mainly used for military and aerospace applications. An additional problem is that the cell resistance change decreases as the operating temperature is increased, possibly leading to information loss.

The basic STT-MTJ memory cell, represented in Fig. 16, is a simplified version of the magnetic tunnel junction. The word line and the bypass line are no longer required due to the different writing scheme, so that the cell can be aligned to the drain of the

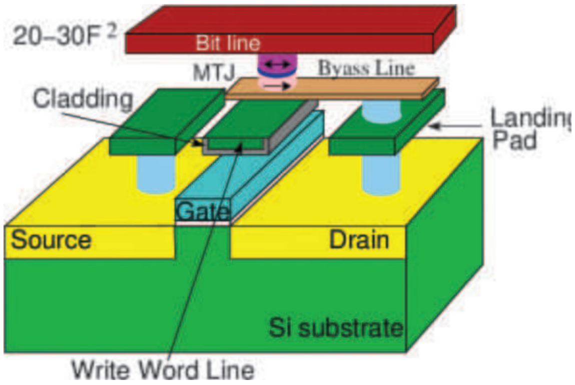

Fig. 14 Schematic view of the MTJ memory cell (Apalkov, 2013).

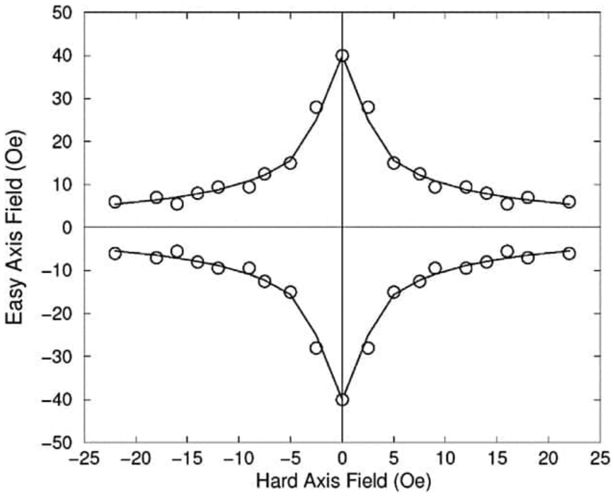

Fig. 15 Switching threshold locus of the MTJ memory cell (Asteroid curve).

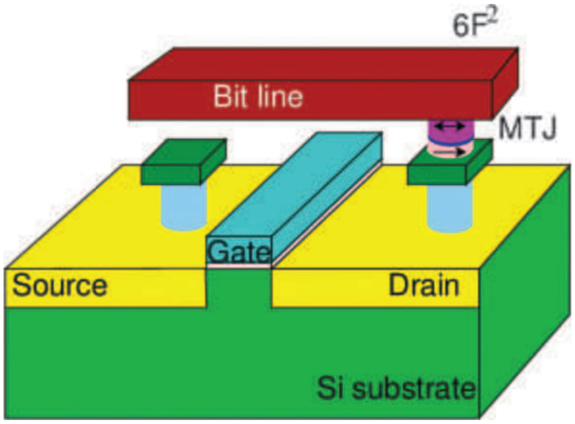

Fig. 16 Schematic view of the magnetic tunnel junction (MTJ) memory cell (Apalkov, 2013).

isolation-transistor. The cell size is thus reduced to about 6–8 F^2 so long as the MTJ pillar diameter can be scaled according to the minimum feature size of the implementation technology. This is no longer true for advanced technology nodes, due to the lower limit of the MTJ optimal size.

The spin-transfer torque (STT) effect is the magnetization switching in the free layer when a spin-polarized current is forced across the MTJ. The passing current causes the free layer magnetization to switch to an alignment that is either parallel or antiparallel to the pinned layer, depending on the current flow direction. This mechanism was theoretically predicted in 1996 and experimentally demonstrated in 2004 (Huai et al., 2004).

The STT MTJ cell design strives for the optimization of three main parameters: (i) low writing current; (ii) high tunneling magnetoresistance (TMR) and, (iii) good thermal stability. Here TMR is defined as $(R_{ap} - R_p)/R_p$ with R_{ap} and R_p the antiparallel and parallel MTJ resistances, respectively. Slight modifications of the basic cell structure have been thoroughly investigated, including perpendicular anisotropy, material selection and thicknesses of the free layer and the tunneling oxide. Quite often the improvement of one of the above parameters is detrimental to one (or both) of the remaining two. Besides, the optimization must account for the specific technology node. Critical aspects are temperature stability, which could possibly put at risk the MRAM non-volatility, and process uniformity, due to the extremely small MgO insulator thickness, which is only about 1 nm. The STT memory cell endurance is about 10^6 write cycles, a good figure for most applications, but no longer unlimited, due to the relatively large writing currents and the related tunneling-oxide aging process (Lee et al., 2018).

The memory organization is schematically shown in Fig. 17 (Lin et al., 2009). The horizontal word lines are connected to the gate of the access transistors. The select and bit lines are instead extended vertically and are normally set at zero voltage. When a cell is addressed, the word line and the select line are raised high and a current flows across the bit line. The sense amplifier, not shown in the figure, compares such a current with the average current experienced by two MTJs with parallel and antiparallel magnetic

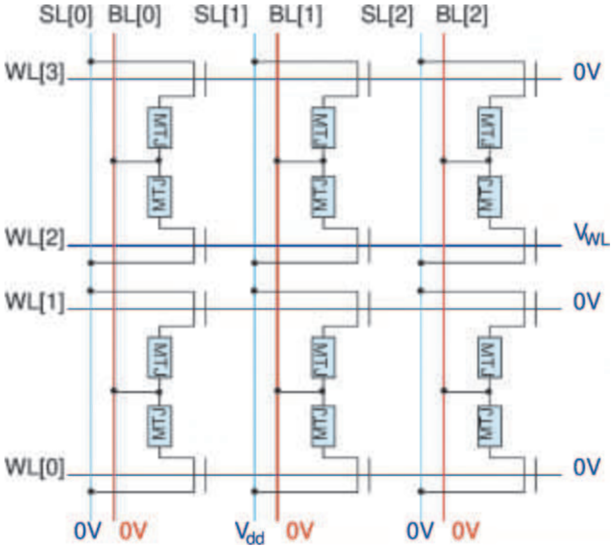

Fig. 17 Cell array organization of an STT MTJ memory (Lin et al., 2009).

moments. The current mismatch is translated into a logical signal at the output. The use of twin cells to generate the reference current has the advantage to track the resistance change with temperature.

A twin cell organization, where information is always stored in two MTJ cells with opposite states, could further improve the read reliability by doubling the current difference to be detected. This read reliability improvement, however, is achieved at the expense of doubling the array area.

Embedded STT MRAMs operating in the industrial temperature range between −40 and 125 °C were successfully incorporated in a 28-nm technology and are being used for microcontroller units (MCU) and Internet of Things (IoT) applications (Lee et al., 2018).

A recent study, based on an MRAM model validated experimentally from the measurement of one million samples, has predicted a performance of the STT MTJ memory, projected to the incoming 5 nm technology node, summarized by the following figures. Read and write access times equal to 3.1 and 6.2 ns, respectively, writing current density $J_{sw} = 5.5\ MA/cm^2$ with a pillar diameter equal to 38 nm, and a breakdown voltage of 0.99 V (Sakhare et al., 2020). Based on the above figures, the authors predict STT MRAM to become a possible candidate for last-level caches in advanced microprocessors at the 5 nm technology node.

An alternative to the STT MTJ is the Spin-Orbit Torque (SOT) MTJ with perpendicular magnetic anisotropy, where the switching current flows within a metal layer adjacent to the FL of a top-pinned (upside down) MTJ. The SOT effect was discovered in 2011 (Miron et al., 2011), and its advantages are sub-nanosecond switching and better endurance than STT MTJ. Forcing a relatively large writing current through the thin MgO layer leads to oxide degradation with adverse effects on memory endurance. Instead, decoupling the write-current from the read-current paths has beneficial effects, which become extremely important in the cache application perspective. A record switching time of 0.210 ns and endurance $>10^{11}$ cycles has been demonstrated (Garello et al., 2019). SOT MTJ memories are still in an early development stage. Their fundamental properties, however, promise exciting opportunities for high-performance innovative products.

Ferroelectric RAM (FRAM)

Ferroelectric materials exhibit a hysteretic *P-E* relationship, shown in Fig. 18, which can be used to fabricate non-volatile memories, referred to as FRAMs. The information is stored within the ferroelectric insulator of a capacitor in the form of an upward or a downward polarization. If a positive voltage is applied to the capacitor with an upward polarization, no change occurs in the compensating charge, and a small voltage shift is observed in the external circuit. If the polarization is downward, instead, the biased domains switch, causing a compensating charge to flow in the capacitor and the external circuit, and changing the capacitor voltage by a greater amount.

This means that the stored information can only be read by erasing the content of the memory, which must then be restored to its previous state. The conventional FRAM cells contain either two transistors and two capacitors (2T-2C), or one transistor and one capacitor (1T-1C). In the former case, the two capacitors are always biased with opposite polarizations, so that a differential reading can be carried out. Due to the obvious advantages of the 1T-1C memory cell in terms of area efficiency, only this cell will be treated in what follows. As shown in Fig. 19, the 1T-1C cell looks like the DRAM one. The FE capacitor is connected between the transistor source and the plate line (PL) which, in this case, is not at a fixed potential.

A logical "0" can be written in the cell by setting the bit line to zero, raising the word line and the plate line to V_{DD} and, after the ferroelectric material switches to a negative polarization, lowering the word line and, subsequently, the plate line down to ground. The remnant polarization will be at the lower intersection point with the vertical axis marked with 0 in Fig. 18. Writing a logical "1"

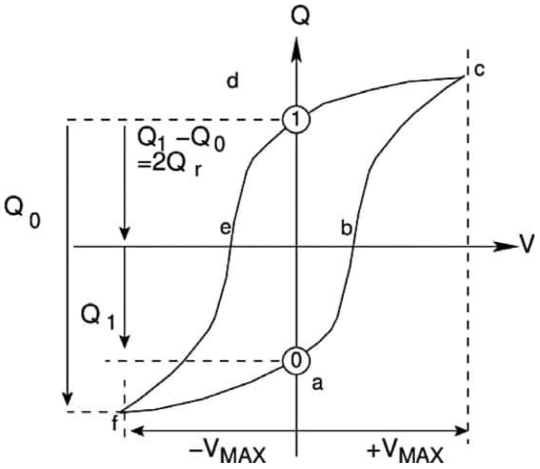

Fig. 18 Plot of the electric polarization vs. electric field for a ferroelectric material (Koike et al., 1996)

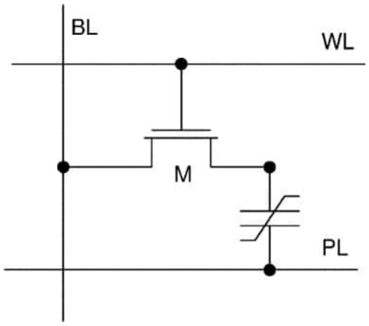

Fig. 19 Circuit schematic of the 1T-1C cell of a ferroelectric memory.

can be done instead by setting the plate line to zero, raising the word line and the bit line to V_{DD} and, after the positive polarization of the ferroelectric material, lowering the word line and, slightly later, the bit line. In this case, the remnant capacitor polarization is at the upper intersection point marked with 1 in Fig. 18. In standby conditions, the gate, drain, and plate are kept at zero voltage. The cell polarization is thus indefinitely conserved. Fig. 20 is an electron micrograph showing: (a) a peripheral memory region, (b) the FRAM region and, (c) the FE cell structure (Jung et al., 2008).

Reading is accomplished by turning the word line on while setting the bit line at 0 V in a high impedance state and cycling the plate line from 0 to V_{DD}. For a cell in the "0" state, there will be a minimal voltage change on the bit line, since the capacitor does not

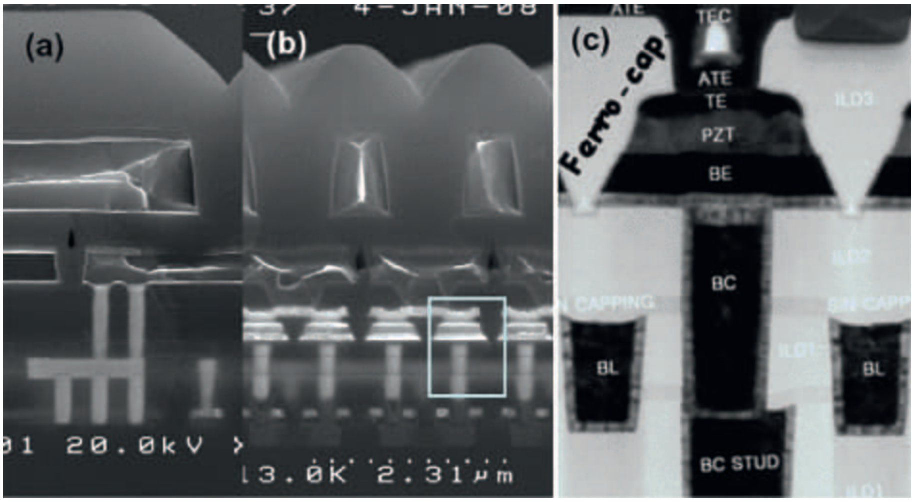

Fig. 20 Electron micrograph showing: (a) Peripheral circuit region; (b) FRAM cell region; (c) FRAM capacitor. From Jung DJ et al. (2008) An endurance-free ferroelectric random access memory as a non-volatile RAM. Symposium on VLSI Technology Digest of Technical Papers, pp. 102–103.

switch its polarization. For a cell in the "1" state, there will be a much larger voltage change on the bit line since the capacitor switches its polarization and the compensating charge flows in the bit line. A voltage change at the sense amplifier input is compared with a reference voltage suitably set at an intermediate value between the expected low and high voltage levels. This switch from "1" to "0" requires a flip back of the capacitor to restore the previous state before the word line is turned off.

The use of a ferroelectric dummy cell to generate the reference voltage has the potential advantage of tracking the variations of the ferroelectric storage capacitors. However, the dummy cell would be switched many more times than the storage cells, thus generating a reliability problem due to fatigue; besides, being the dummy cell far away from the storage cells, additional factors, such as uniformity of the ferroelectric material and temperature dependence of the *P-E* relationship, may come into play.

A disadvantage of the R/W scheme illustrated above is due to the large plate line resistance and capacitance. PL switching is thus time consuming, and the resulting access time is about three times higher than the corresponding access time of a DRAM fabricated with a comparable technology. A different R/W scheme was thus proposed, which does not require the PL to switch (Koike et al., 1996). In this scheme, the plate line is permanently kept at $V_{DD}/2$ and only the word and bit lines are switched. This scheme requires a low coercive voltage material, like $SrBi_2Ta_2O_9$ (SBT), as the writing voltage applied to the FE capacitor is halved if the supply voltage is kept constant. On the other hand, the high-impedance sensing node may lose charge in standby due to junction leakage, leading to an unwanted switching from the "1" to a "0" state. Another read technique, called bit-line driven scheme (Hirano et al., 1997), keeps the plate line at zero voltage during a read operation, but requires PL switching for data restoration and cell writing. Hence, the access time is reduced, but the cycle time is still rather large.

A clever FRAM cell-array organization, called chain FRAM (CFRAM), is shown in Fig. 21 (Takashima and Kunishima, 1998). This scheme is formed by a chain of 8 cells, each of which is made by a parallel connection of a FE capacitor and a transistor. The plate line is connected to the common source of two central transistors and is biased at $V_{DD}/2$. Two block selection transistors (BST) connect the cell chain to the bit line. Under standby conditions, the BSTs are off and the word lines are high, thus shorting the FE capacitors, which keep their own polarization with no charge loss. When a cell is addressed, the corresponding word line is driven low and the selection transistor on the same side of the addressed cell is turned on. At the same time, the bit line is set at zero voltage. The addressed cell capacitor is thus subject to a half-V_{DD} voltage and, depending on its polarization, can inject a current in the bit line detected by the sense amplifier.

The present scheme overcomes the two major problems of the conventional 1T-1C cell array organization. First, the cell size can be made as small as $4F^2$ with stacked capacitors as for DRAMs. Next, all FE capacitors are short-circuited by the corresponding transistors. Hence, junction leakage does not affect the cell state, and refresh is no longer required. Moreover, it achieves fast non-driven half-V_{DD} cell-plate operation, and reduces the bit-line capacitance to about one-quarter of the conventional one. Finally, random access is possible. A practical implementation of the chain FRAM led to the development of a 128 Mb memory chip with a 1.6 GB/s double-data rate (Shiga et al., 2010).

The FRAM read access time is of the order of 70 ns, quite comparable with that of early DRAMs, but considerably slower than the access time of state-of-the-art DRAMs, which is currently around 14 ns. The write access time is around 100 ns, i.e., much faster than the write operation of a flash memory, Likewise, the write endurance of the FRAM, which ranges between 10^8 and 10^{12} cycles depending on the ferroelectric material, is much better than the endurance of commercial flash memories.

The recent discovery of an orthorhombic HfO_2 phase with ferroelectric properties made it possible to develop ferroelectric FETs (FeFET), as shown in Fig. 22, where an FE layer is integrated in the gate stack (Dünkel et al., 2017). This device, fabricated with a 22 nm SOI technology, can embody by itself a simple 1T memory cell with the conventional gate, source and drain connections to the word, plate and bit lines, respectively, and is fully compatible with the 22 nm SOI CMOS technology for logic. The reported

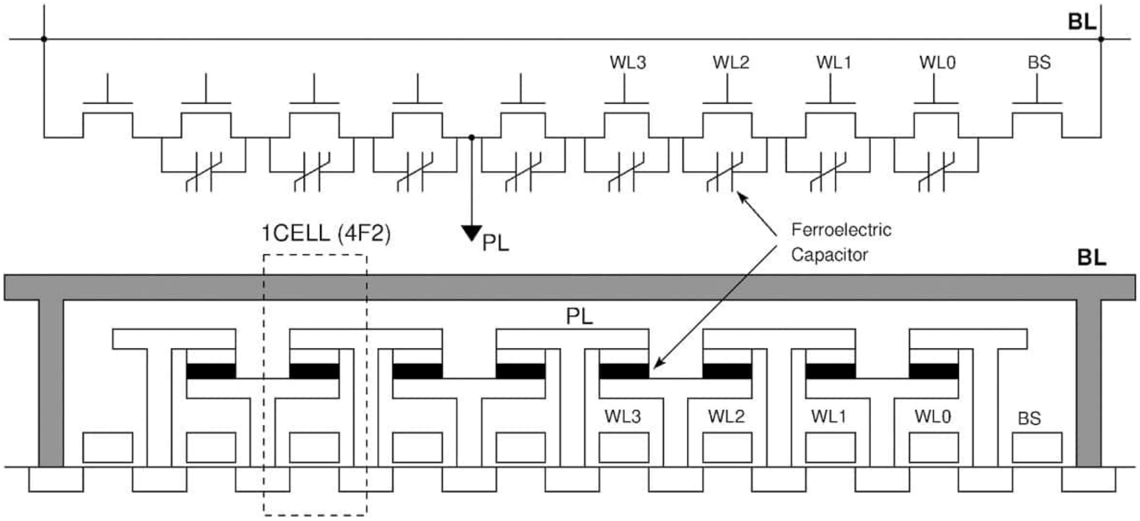

Fig. 21 FRAM cell array organization (Takashima and Kunishima, 1998).

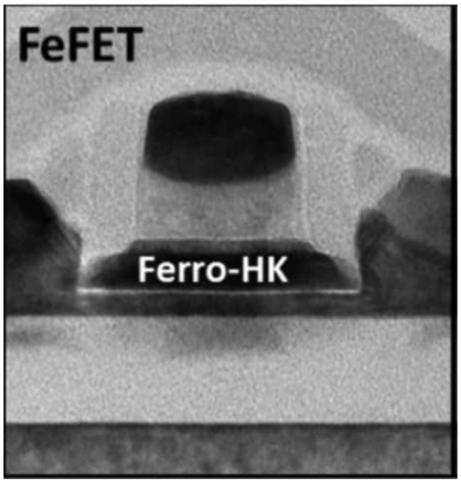

Fig. 22 Cross section of a ferroelectric FET fabricated in a 22 nm SOI technology (Dünkel et al., 2017).

endurance was only 10^5 cycles, but performance improvements are expected in the near future. Therefore, the FeFET is a candidate for the development of low-cost high-performance embedded non-volatile memories.

Phase-change memories (PCM)

Phase-change memories (PCMs) are based on peculiar properties of chalcogenide materials, i.e., compounds often based on germanium, antimony and tellurium, namely, $Ge_2Sb_2Te_5$ (GST), which is the most frequently-used material for PCMs. Different compounds are often used for optical applications in CDs, DVDs, and Blu-Ray disks. Memory switching in these materials is primarily a thermal process, which involves a phase transformation from a polycrystalline to an amorphous state, and vice versa, under the influence of a heat source. When the heating process stops, the material retains its new state, thus exhibiting memory. In practice, this transformation is obtained by passing a constant current pulse through the sample for an appropriate time. The resistance change between the two states is about 2–3 orders of magnitude, so that reading can easily be accomplished by low-bias non-destructive detection of the cell resistance.

A schematic cross section of two PCM cells is shown in Fig. 23. The cell core is basically given by a crystalline GST layer located between a vertical resistive heater and a horizontal metal line (bit line). The vertical resistor is connected to the emitter of a p-n-p bipolar transistor, the base of which is connected to the word line. In a process variant, the access transistor can be a MOSFET, rather than a BJT.

In order to let a phase change occur, the GST layer is heated by a current pulse by Joule effect. An intense, but relatively short, current pulse raising the local GST temperature up to the melting point of about 650 °C, followed by fast cooling, turns the polycrystalline material into an amorphous high resistance state within a mushroom-like volume above the heater (reset). A longer, but less intense, current pulse heating the material up to about 500 °C turns it to a polycrystalline, low resistance state (set). The

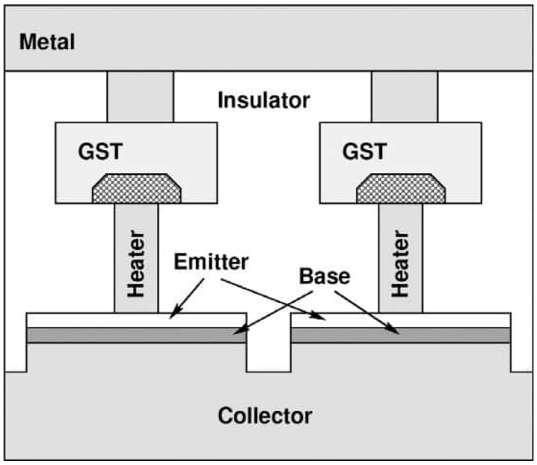

Fig. 23 Schematic cross section of two PCM cells.

current levels and the time duration of the current pulses depend on the thermal capacity of the GST layer. Hence, scaling down the GST volume is a primary objective of PCM design to reduce random access time and energy consumption.

An obvious concern of this technology is the thermal cross talk between adjacent cells. In principle, the local heating of the GST layer up to the melting temperature during a reset could spread around heat and, possibly, set a neighbor cell. Thermal simulations, however, seem to indicate that this is not the case, and that no appreciable thermal crosstalk would in fact occur down to the lowest technology nodes of the ITRS. This is mainly due to the linear scalability of the reset current with the contact area for a given cell geometry. If all physical dimensions of the cell are scaled down by a common factor κ, instead, one would expect the set and reset resistances, as well as the thermal resistance, to increase by the same factor κ, and the programming currents to decrease by κ at constant voltage.

The advantages of PCM memories are manifold. First, the additional processing steps required to deposit the GST layer and delineate the cell geometry can be performed in the back end of the fabrication process, and do not interfere with the front-end CMOS technology.

Compared with flash memories, PCMs exhibit a much lower random access time, low set and reset voltages, and fulfill the 10-year retention requirement. In addition, memory endurance can be made as high as $\approx 10^{12}$ S/R cycles with an appropriate cell design and with a Sb-rich chalcogenide material (Kim et al., 2016).

Combined with a two-terminal ovonic threshold switch (OTS) device, resistive memories like PCMs can be arranged in a cross-point architecture, which provides the highest possible density with a cell size equal to $4F^2$ (Kau et al., 2009). Fig. 24a shows an electron micrograph of the PCM cell with the OTS selection device. Fig. 24b represents a cross-point array architecture sandwiched between the M2 and M3 metal layers (Karpov et al., 2010). Also, multi-layer 3D memories can be manufactured with this technology.

Stand-alone PCMs were produced as of year 2008. The latest product is Intel's Optane M15 solid-state drive, referred to as X-point (Le Gallo and Sebastian, 2020). The chip fabrication technology has not been disclosed, but is widely supposed to be a PCM-OTS. Optane, announced in year 2018 and distributed in 2019, is based on 128 Gb 3D memory chips. The disk drive maximum capacity is 64 GB; the read and write latencies are 6.75 and 12 μs, respectively, and the sequential R/W rates are 2000 and 900 MB/s. Its maximum throughput is still lower than that delivered by high-end NAND flash SSDs with high queue depths, but the write random access time is considerably shorter due to the simpler writing scheme of PCM memories.

The scalability of the PCM cell, the elimination of the large voltages required by flash memories, the reduced set and reset times and the addressability of every single cell make the PCM memory technology an interesting candidate for low-voltage, high-density, low-cost, future-generation products.

Resistive RAM (RRAM)

The physical structure of the resistive memory cell is a metal-insulator-metal (MIM) device with a top electrode (TE), a bottom electrode (BE) and a metallic oxide in between. The initial low-voltage resistance is thus very high, due to the presence of the insulating layer. This is the high-resistance state of the cell, corresponding to a logical "0." The application of a positive voltage to the TE can start a soft breakdown, generation of defects such as oxygen vacancies, and a migration of metallic ions through the insulator. A conductive filament is thus formed that crosses the oxide and reaches the BE and a low-resistance state is eventually obtained, corresponding to a logical "1." The reset operation is carried out by the application of a negative voltage, which pushes those oxygen vacancies toward the upper electrode, re-establishing a high resistance state. This kind of cells is called "bipolar." As an alternative, some cells are reset by the application of a higher positive voltage, due to the breaking of the conductive filament, which behaves in this case as a fuse.

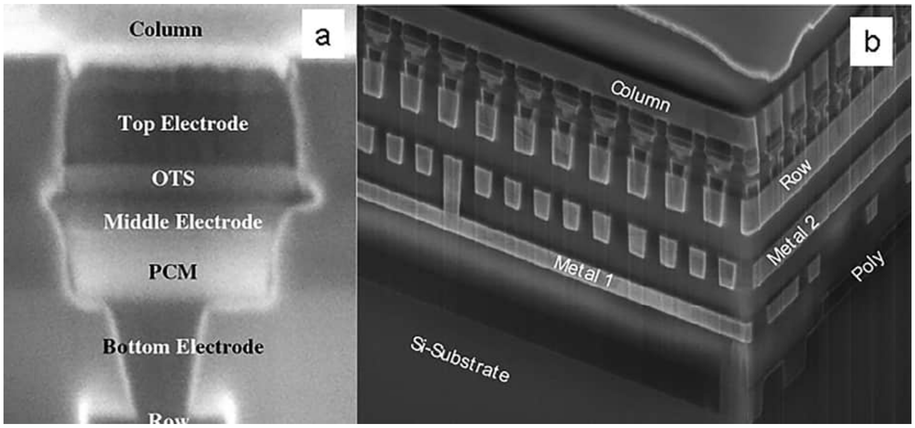

Fig. 24 (a) Scanning Electron Micrograph of a PCM cell with a chalcogenide selector device; (b) PCM cross-point array sandwiched between M2 and M3 metal layers (Karpov et al., 2010).

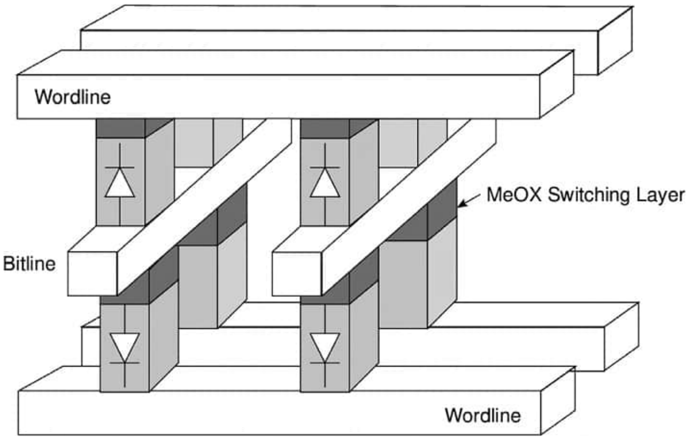

Fig. 25 RRAM stacked cross-point architecture (Liu et al., 2014).

The resistive cell may, or may not, be accompanied by a selection device connected in series with it. In the latter case, however, sneak currents severely limit the array size. For larger memory blocks, an access device is required. In order to maintain the minimum size of $4F^2$, and the related area efficiency, a diode-like two-terminal device must be chosen, even if a three-terminal FET could improve the reading uniformity of the addressed cells. Another motivation to exclude transistors is that a multi-layer cross-point architecture can be fabricated in the back end of the process. Fig. 25 shows a sketch of a two-layer structure, with the bit lines shared by the upper and lower layers and separate word lines at the top and bottom of the structure. Fig. 26 shows a practical implementation of the two-layer concept in a 32 Gb RRAM (Liu et al., 2014).

Resistive memories are scalable and CMOS-compatible, and their fabrication technology has been integrated into foundry processes. Open research problems for these devices are still a better understanding of their set/reset physical mechanisms and reliability issues.

The array organization is a cross-point scheme with resistive cells connected at the crossing between vertical bit lines and horizontal word-lines. Actually, the function of horizontal lines differs from that of standard word lines, as the access device is a two-terminal diode and is not driven by the word line. The read operation is illustrated in Fig. 27 (Liu et al., 2014). For a read operation, the selected bit lines and the unselected word lines are biased at the same voltage V_{read}, while the selected word lines and unselected BLs are biased at the unselected BL voltage $V_{UB} < V_{read}$. The selected cells, denoted with S in Fig. 27, are biased between the V_{read} and V_{UB} voltage levels and conduct some current. With this biasing scheme, the half-selected cells on the selected BLs (F cells) and the half-selected cells on the selected WL (H cells) are nominally biased at 0 V. The unselected cells (U cells) are reverse biased between V_{read} and V_{UB}, and they conduct a small current due to the reverse biased access diodes and the low bias level. The H and F cells are targeted to have zero bias but, due to parasitic resistance in a large array, a voltage offset from the power supply grid and the circuitry can create a nonzero bias across those cells.

The program operation is performed by driving the selected BLs to the V_{WR} voltage and the selected WL at zero voltage (Fig. 28). The unselected cells are reverse biased between the unselected word line voltage V_{UX} and the unselected bit line voltage V_{UB}. The half selected cells connected to the selected BL and those connected to the selected WL are forward biased below the disturb level and conduct current along the selected BL or the selected WL. These currents cause a voltage drop, which reduces the write voltage across the selected cell.

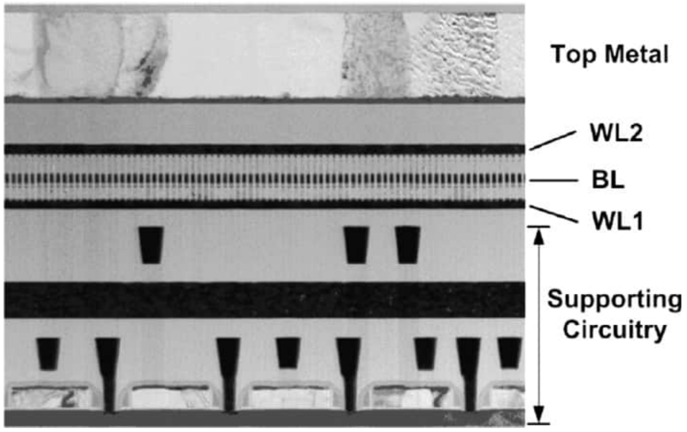

Fig. 26 Resistive memory cross-section showing two layers of RRAM cells above the supporting circuitry (Liu et al., 2014).

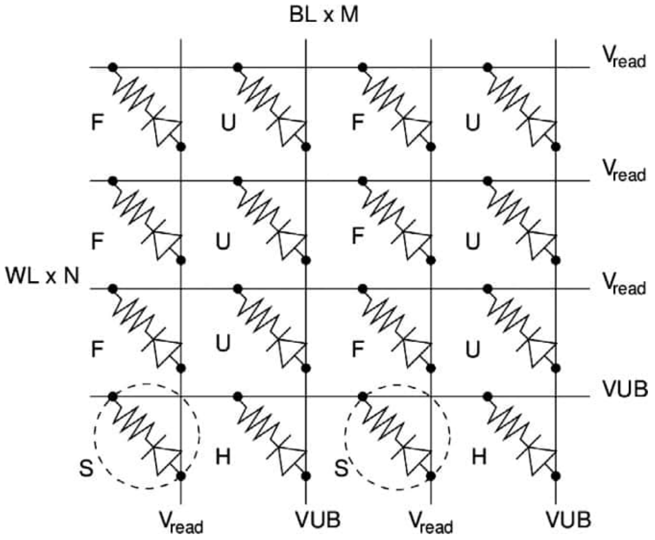

Fig. 27 Reading scheme of a resistive RAM (Liu et al., 2014).

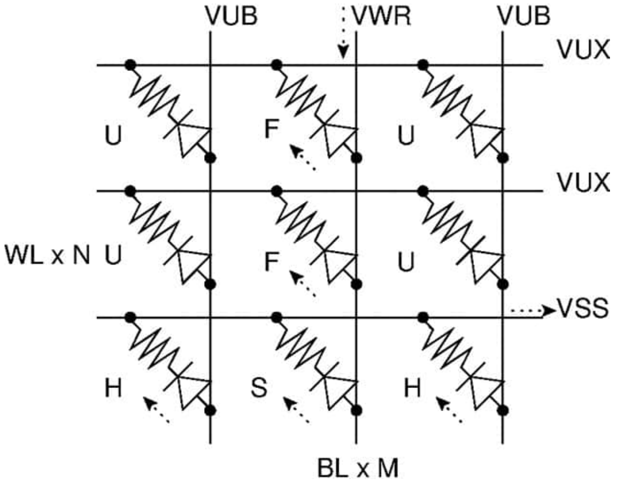

Fig. 28 Writing scheme of a resistive RAM (Liu et al., 2014).

A compensation scheme is implemented to account for the above parasitic effects. In essence, the sense amplifier samples the leakage currents in the bit lines before the write pulse is asserted, and generates the compensation currents to be injected into the bit lines. The WL pulse amplitude is then established according to the required programming target voltage. Without this compensation scheme, the program pulse could fail to switch the cell as desired (Liu et al., 2014).

In-memory computing

The large computational burden required by the management of big data and artificial intelligence (AI) problems, such as the control of autonomous systems, poses serious challenges to the traditional Von Neumann computer architecture. Data transfer from memory to CPU and back represents a well-known bottleneck, which degrades latency and additionally consumes thousand times more energy than that strictly required for the computation itself. The concept of transferring computation into memory, rather than doing the opposite, has thus emerged. An entirely new discipline, referred to as "In-Memory Computing" (IMC), investigates possible approaches to the above problem, identifying innovative solutions and new avenues to system development.

In principle, IMC can be performed using either charge driven memories, like SRAM, DRAM and NOR flash, or resistive memories, such as RRAM, PCM, and MRAM (Sebastian et al., 2020). Resistive memories, however, offer the opportunity to consider resistance values as input or output data of a given operation, which extends the flexibility of traditional logic functions by introducing implication (IMP) (Borghetti et al., 2010) and threshold logic function (Ielmini and Wong, 2018). A new computing paradigm is thus introduced. An additional advantage of RRAMs and PCMs is the opportunity to arrange cell arrays in a cross-point configuration, minimizing the overall area occupation.

Detailed investigations were carried out on the entire architecture, including crossbar and CMOS controller, required for data-intensive parallel addition (Nguyen et al., 2017). This study led to the conclusion that the IMC parallel adder improves area and energy consumption by at least two orders of magnitude, compared with a multicore parallel adder.

Both digital and analog computations are possible with a suitable supporting circuitry. Analog computation takes advantage from the natural addition of currents injected into the same node (Kirchhoff current law) and the natural multiplication expressed by Ohm's low, namely, $I = GV$, where I is the current, G is the conductance of the memory cell and V the applied voltage. Matrix-vector multiplication can thus be obtained if the memory array || G || stores the matrix data and || V || represents the input vector. The resulting output currents are thus

$$I_j = \Sigma_{\mathrm{k}} G_{jk} V_k.$$

This computation can be carried out by a matrix of conductances connected between horizontal lines at the voltage V_k and vertical lines connected to the inputs of operational amplifiers with a constant feedback resistance. Different array architectures can be used to solve linear systems and regression problems (Ielmini and Pedretti, 2020).

As is well known, analog computing is affected by noise and by the limited accuracy of the conductance matrix entries. Therefore, the obtained results can be converted to digital form and sent to a digital solver running an iterative solution algorithm. Due to the excellent accuracy of the first-order solution, very few iterations suffice to reach convergence (Le Gallo et al., 2018).

Conclusion

In this Encyclopedia entry, non-volatile random-access memories are presented, with special emphasis on cell structure, array organization, R/W and erase approaches and applications. The stand-alone non-volatile memory market is presently dominated by 3D flash memories in NAND configuration, which exhibit record density and capacity, low cost per bit, high data rate and long retention time. Possible drawbacks are the dedicated process technology, which makes them unsuitable for embedded applications in systems-on-chip, a moderate endurance and a poor random access time. It should be noticed that floating-gate cells, which have been the flash workhorse for a long time, are no longer used in 3D memories to the advantage of charge trap cells in vertical-configuration flash memories.

Several memory types, based on different physical principles, have been deeply investigated, leading to the development of more or less successful products. Among them, magnetic RAMs, which exhibit the best radiation hardness, high endurance and short switching time, were mainly used in the past for military and space applications. The later development of the STT MTJ memory has considerably improved some weaknesses of early magnetic RAMs, including cell area, high switching currents and compatibility with back-end CMOS process. To date, the most advanced STT MRAMs are expected to compete with static RAMs for last-level cache applications at the 5 nm technology node (Sakhare et al., 2020).

Ferroelectric RAMs have been developed since the mid-nineties. Their potential advantages are fast switching time, long endurance, and relatively small 1T-1C cell area (comparable with that of DRAM cells). Clever array topologies and reading procedures were conceived to improve the access time. The recent discovery of a FE phase of HfO_2 made it possible to develop ferroelectric FETs at the 22 nm technology node by directly incorporating the FE HfO_2 in the gate stack (Dünkel et al., 2017). With this approach, the FE cell is reduced to just one transistor fully compatible with the CMOS process. Dense memories can thus be expected to be developed for embedded applications by exploiting such a new type of cell.

Among the relatively new non-volatile memory types, the phase change memory is one of the most successful. Strong points of this memory type are retention time, endurance and moderate random access time for read and write processes (70–100 ns). Compatibility with the back-end CMOS process makes the PCM RAM especially suitable for embedded applications in systems-on-chip.

Stand-alone PCM memories were developed in the last decade, leading to the Octane M15 solid-state drive, which exhibits a capacity ranging between 16 and 64 MB, sequential R/W up to 2000 and 900 MB/s, respectively, and R/W random latencies up to 6.75 and 12 µs. The specific materials used for the memory cell and the access transistor of the 3D X-Point™ chip were never disclosed, but it is widely believed that these materials are two different types of chalcogenide, along the lines of previous papers (Kau et al., 2009). The chip capacity is 128 Gbit and the array organization is known to be a two-level cross-point. This product represents an additional memory level in the computer memory hierarchy, which complements DRAMs with its non-volatility and improves the responsiveness of computers with a traditional flash-based SSD.

Further developments to compete with vertical flash memories in capacity appear to be unlikely, due to a possible PCM limitation in the number of stacked layers. Likewise, the hope to replace DRAMs with a "universal" PCM memory, turned out to be unsuccessful. State-of-the-art SDRAMs exhibit a latency around 14 ns, well below the R/W access time of PCMs.

Resistive memories are in an advanced development phase, but the set/reset mechanisms are not fully understood. An important achievement has been the successful fabrication of a 32 Gb test chip (Liu et al., 2014). No information is provided on the specific cell materials and selection device. The block size is much increased with respect to previous RRAM implementations by a careful control of sneak currents. As for other resistive RAMs, stand-alone implementations are unlikely to become competitive with vertical flash memories. On the other hand, smaller-capacity embedded RRAMs can possibly be incorporated in systems-on-chip due to their compatibility with the back-end CMOS process. Finally, they are the subject of many investigations for IMC, due to the cell simplicity and the small area occupation of the cross-point architecture.

References

Apalkov D (2013) Spin-transfer torque magnetic random-access memory (STT-MRAM). *ACM Journal on Emerging Technologies in Computing Systems* 9-2: 1–35.

Bez R, et al. (2003) Introduction to flash memory. *Proceedings of the IEEE* 91-4: 489–502.

Borghetti J, et al. (2010) 'Memristive' switches enable 'stateful' logic operations via material implication. *Nature* 464: 873–876.

Dünkel S, et al. (2017) A FeFET based super-low-power ultra-fast embedded NVM technology for 22nm FDSOI and beyond. In: *IEEE IEDM Tech. Dig.*, pp. 485–488.

Garello K, et al. (2019) Spin-Orbit Torque MRAM for ultrafast embedded memories: From fundamentals to large scale technology integration. In: *IEEE 11th International Memory Workshop (IMW)*.

Hirano H, et al. (1997) 2-V/100-ns 1T/1C nonvolatile ferroelectric memory architecture with bitline-driven read scheme and nonrelaxation reference cell. *IEEE Journal of Solid-State Circuits* 32-5: 649–654.

Huai Y, et al. (2004) Observation of spin-transfer switching in deep submicron-sized and low-resistance magnetic tunnel junctions. *Applied Physics Letters* 84-16: 3118.

Ielmini D and Pedretti G (2020) Device and circuit architectures for in-memory computing. *Advanced Intelligent Systems* 2020: 2000040.

Ielmini D and Wong H-SP (2018) In-memory computing with resistive switching devices. *Nature Electronics* 1: 333–343.

Jung DJ, et al. (2008) An endurance-free ferroelectric random access memory as a non-volatile RAM. In: *Symposium on VLSI Technology Digest of Technical Papers*, pp. 102–103.

Karpov I, et al. (2010) Phase change memory with chalcogenide selector (PCMS): Characteristic behaviors, physical models and key material properties. In: *Mater. Res. Soc. Symp. Proc., 1250 © 2010 Materials Research Society*.

Kau DC, et al. (2009) A stackable cross point phase change memory. In: *IEEE IEDM Tech. Dig., 27-1-12009*, pp. 617–620.

Kim W, et al. (2016) ALD-based confined PCM with a metallic liner toward unlimited endurance. In: *IEEE IEDM Tech. Dig.*, pp. 83–86.

Koike H, et al. (1996) A 60-ns I-Mb nonvolatile ferroelectric memory with a nondriven cell plate line write/read scheme. *IEEE Journal of Solid State Circuits* 31(11): 1625–1634.

Le Gallo M and Sebastian A (2020) An overview of phase-change memory device physics. *Journal of Physics D: Applied Physics* 53-213002: 1361–1388.

Le Gallo M, et al. (2018) Mixed-precision in-memory computing. Nature. *Electronics* 1-4: 246–253.

Lee YK, et al. (2018) Embedded STT-MRAM in 28-nm FDSOI logic process for industrial MCU/IoT application. In: *Symposium on VLSI Technology - Digest of Technical Papers*, pp. 181–182.

Lin CJ, et al. (2009) 45nm low power CMOS logic compatible embedded STT MRAM utilizing a reverse-connection 1T/1MTJ cell. In: *IEEE IEDM Tech. Dig*, pp. 11.6.1–11.6.4.

Liu TY, et al. (2014) A 130.7-mm 2-layer 32-Gb ReRAM memory device in 24-nm technology. *IEEE Journal of Solid-State Circuits* 49–1: 140–153.

Micron (2020) *Micron Transitions to Next-Generations 3D NAND-Replacement Technology*. White Paper.

Miron IM, et al. (2011) Perpendicular switching of a single ferromagnetic layer induced by in-plane current injection. *Nature* 476: 189–193.

Nguyen HAD, et al. (2017) On the implementation of computation-in-memory parallel adder. *IEEE Transactions on Very Large Scale Integration (VLSI) Systems* 25–8: 2206–2219.

Sakhare S, et al. (2020) JSW of 5.5 MA/cm2 and RA of 5.2-$\Omega \cdot \mu$m2 STT-MRAM technology for LLC application. *IEEE Transactions on Electron Devices* 67-9: 3618–3625.

Sebastian A, et al. (2020) Memory devices and applications for in-memory computing. *Nature Nanotechnology*. https://doi.org/10.1038/s41565-020-0655-z.

Shiga H, et al. (2010) A 1.6 GB/s DDR2 128 Mb chain FeRAM with scalable octal bitline and sensing schemes. *IEEE Journal of Solid-State Circuits* 45-1: 142–152.

Takashima D and Kunishima I (1998) High-density chain ferroelectric random access memory (chain FRAM). *IEEE Journal of Solid-State Circuits* 33-5: 787–792.

Veendrick HJM (2017) *Nanometer CMOS ICs, From Basics to Asics*, 2nd edn. Heeze, The Netherlands: Springer.

Memory devices – Volatile memories

Elena Gnani and Giorgio Baccarani, Department of Electrical Electronic and Information Engineering (DEI), and Advanced Research Center on Electronic Systems E. de Castro (ARCES), University of Bologna, Bologna, Italy

© 2024 Elsevier Ltd. All rights reserved.

This is an update of G. Baccarani, E. Gnani, Memory Devices, Nonvolatile, Editor(s): Franco Bassani, Gerald L. Liedl, Peter Wyder, Encyclopedia of Condensed Matter Physics, Elsevier, 2005, Pages 324–337, ISBN 9780123694010, https://doi.org/10.1016/B0-12-369401-9/01167-0.

Introduction 576
Memory classification 577
Volatile memories 578
Static random-access memory 578
Cell array organization 580
Cell reading and writing 580
Sense amplifier 581
SRAM applications 581
Dynamic random-access memory 581
DRAM cell array organization 583
DRAM sense amplifier 585
DRAM architecture 585
Asynchronous DRAM 586
Synchronous DRAM 587
Rambus DRAM 587
Graphics applications 588
Capacitorless DRAM cell 588
General considerations on volatile memories 589
Content-addressable memory 590
Conclusion 591
References 591

Abstract

In this Encyclopedia entry, volatile random-access memories used for a wide variety of applications are presented. More specifically, the structural and functional properties of static and dynamic RAMs, including cell topologies, cell array organizations, reading and writing procedures, reliability issues and typical applications are illustrated with a detail compatible with the allowed entry size. Content addressable memories are also treated in the final part of this entry. Conclusions and future trends complete the presentation.

Key points

- Volatile memory classification
- Static random-access memory
- Dynamic random-access memory
- Asynchronous and synchronous RAMs
- Content addressable memory

Introduction

Modern computer architectures rely on a hierarchy of memories, which differ in access times and density. The higher speed is typically achieved at the expense of a larger cell area, smaller memory capacity and, thus, higher cost per bit. At the upper levels of the hierarchy, we find registers, which are deeply rooted within the logic circuits of the processor, and three levels of cache memory. Caches typically employ static random-access memories (SRAMs) based on six transistors per cell. At the next level, the computer central memory uses dynamic random-access memories (DRAMs) based on cells comprising only one capacitor and one transistor. At the lower levels of the hierarchy, one finds several mass-memory devices, namely: solid-state drives or magnetic disks, optical disks, and flash memory cards. Magnetic tapes are used to archive large amount of data to be seldom retrieved. As opposed to static and dynamic RAMs, which are volatile memories, mass-memory devices are non-volatile, i.e., they retain the stored information upon power loss or shutdown. This is an essential requisite, which allows information to be safely stored and retrieved whenever necessary.

Memory devices have found widespread use not just within computers and smart phones, but also in a variety of professional systems, such as telecommunication networks and phone exchanges, robotic and control systems, automotive and medical electronics systems, as well as commodities and consumer products, including personal digital assistants (PDAs), digital video recorders and still cameras, digital TV (DTV), set top boxes, GPS-based navigation systems, toys, and smart cards. Despite this wide variety of applications, which require a different throughput, latency and power consumption, and the related diversification of the memory market, we shall concentrate in what follows on unifying factors, such as basic physical principles, and general architectural features, which allow us to treat this subject within the constraints of a tutorial presentation.

This treatment specifically addresses semiconductor memories (mass memory devices based on magnetic and optical storage are discussed elsewhere within the Encyclopedia) and is split in two parts: part I is devoted to volatile memories, which are at the highest levels of the hierarchy in view of their excellent performance and unlimited endurance; part II is devoted instead to non-volatile memories, which are being used when the non-volatility is an essential requisite of the application.

The classification of semiconductor memories is presented in the next section. Section "Volatile memories" discusses the general features of volatile memories and defines the most important performance-qualifying parameters. Reliability issues related with soft error rates are also mentioned. Section "Static random-access memory" provides detailed descriptions on structural and functional SRAM properties, including basic cell topologies, cell array organization, sense amplifier structure and typical applications related with access time, power consumption and reliability issues. Section "Dynamic random-access memory" is devoted to the structural and functional DRAM properties. It contains the description of the one-transistor, one-capacitor memory cell, the organization of the cell array, the structure and operation of the sense amplifier and the fundamental DRAM architectures, namely: asynchronous, synchronous, RAMBUS and Video RAM (V-RAM). A short description of the capacitorless DRAM cell is finally provided. Section "Content-addressable memory" illustrates the 10-transistor cell structure. Next, the operation of associative memories, as well as their basic application as tag memory of set-associative caches is briefly outlined. Concluding remarks and future trends about volatile memories and their main applications areas are made in Section "Conclusion".

Memory classification

Semiconductor memories can be classified according to both structural and functional criteria. Following the latter approach, they are split first into volatile and non-volatile memories, as indicated in Fig. 1. As pointed out in the Introduction, volatile memories do not retain the stored information if the power supply is turned off, while non-volatile memories do retain the stored information in the above conditions. Also, volatile memories can be written and read on field in very short times. Non-volatile memories, instead, can only be read on field in short times, whereas repeated programming and erasing operations may not be possible or, if possible, typically require much longer times. Different physical approaches are used to store information in the above memories.

Most volatile memories are randomly accessed and are thus referred to as random-access memories (RAM). Sequential memories, where bits are written and read sequentially, are only used for specific applications, being outperformed by RAMs both in terms of speed and power consumption.

Content-addressable memories (CAM) are functionally and structurally different from RAMs. In the latter memories, every single bit, byte, or word can be accessed from the knowledge of its physical address. CAMs are instead addressed by an associative search using a data word as input and provide an address as-a-result of this search.

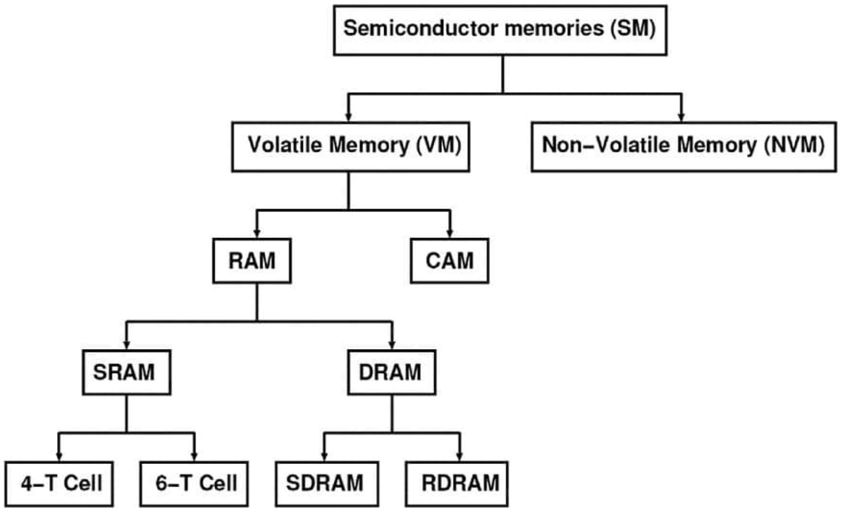

Fig. 1 Semiconductor volatile memory classification according to functional criteria.

Volatile memories store the information either statically (SRAM) or dynamically (DRAM). In the former case, the storing mechanism is based on a regenerative circuit characterized by two stable states. In the latter case, information is stored as a charge on a capacitor.

Static RAMs use a basic cell containing either six or four transistors per cell. The former type of cell is obviously larger, but is compatible with the standard CMOS technology, and is typically used for fast embedded memories employed in first, second and third-level caches. The latter type requires a thin-film transistor (TFT) technology not compatible with the standard CMOS process. It provides a higher density and was preferred in the past for large, stand-alone third-level caches outside the processor chip. To date, device miniaturization makes it possible to integrate third-level caches on chip, with huge performance advantages in terms of speed and power consumption.

Dynamic RAMs may be characterized by different architectures. In the past, DRAMs used to be only asynchronous, and could start a memory cycle whenever three external commands referred to as row-address strobe (RAS), column-address strobe (CAS) and write enable (WE) were successively asserted. More recently, the need to improve the cycle time and the throughput of DRAMs has suggested more sophisticated architectures, which operate synchronously under the control of the system clock. The synchronous DRAM (SDRAM) is the most widely used memory architecture. A variant of the SRAM is the Rambus DRAM (RDRAM), by which a careful design of the memory board allows for very large clock frequencies.

Volatile memories

The most important parameter characterizing the memory performance is the access time, i.e., the time elapsed between a read request and the availability of the requested word. The cycle time is instead the minimum time between two successive read requests; its inverse is the memory throughput. The access time of embedded SRAMs may vary from one to several ns, depending on the memory size and the resulting capacitances of the word and bit lines. Therefore, these memories are used at the highest levels of the hierarchy within advanced computers, PCs, and smart phones.

DRAMs feature the smallest bit size and are typically used for the computer central memory. To date, a central memory of 8–16 GBs is common practice for desktop, portable PCs and cell phones. Servers or mainframes typically employ several hundred GB of central memory; hence, the one-transistor DRAM cell is by far the most-largely produced semiconductor device in modern Industry. Under the assumption of an average main memory of one GB and a worldwide production of 100 million computers/year, and even more cell phones, it turns out that $\approx 10^{18}$ DRAM cells are manufactured every year. The access time of DRAMs is of the order of 40 to 60 ns. Therefore, accessing data stored within the central memory of a computer requires several tens of clock cycles for a modern processor.

Volatile memories can suffer data loss due to soft errors, which are caused by the interaction of energetic nuclear particles, such as α, β and cosmic rays, with the silicon substrate. These events may occur due to the radioactive decay of some impurity atoms contained within the package material and/or the metal layers of the memory chip. Alternatively, as for cosmic rays, these energetic particles may come from the outside space and occasionally hit the memory device. A charged energetic particle penetrating through a semiconductor substrate generates many electron-hole pairs, which are then separated by the electric field within the device active region. These carriers can possibly compensate the charge stored within a cell capacitor and modify its state. Even static memories are not immune to soft errors, for an energetic particle impinging onto a bi-stable circuit can upset it and change its state. In both cases, a soft error would occur.

In-order-to ensure the full reliability of the system, several strategies are pursued. At the device level, the geometry of the active region is designed in such a way as to drain excess carriers generated by the energetic particle by reverse-biased p-n junctions, so that the charge stored with-in a cell capacitor can hardly suffer a substantial change; also, the word bits are not stored at consecutive physical locations, so that at most one bit of a word can be changed due to the occurrence of a soft error. At the system level, a few more parity bits are stored together with a 32- or 64-bit word. When a word is retrieved from the memory, the examination of the parity bits makes it possible to detect the occurrence of one or more soft errors and correct the wrong bit.

Static random-access memory

The simplest bistable circuit is obtained by cross-connecting two CMOS inverters M1-M2 and M3-M4, as shown in Fig. 2. Clearly, such a circuit can be biased in either one of two states, characterized by $V_{o1} = 0$, $V_{o2} = V_{DD}$ or $V_{o1} = V_{DD}$, $V_{o2} = 0$, respectively. By associating the logical value "0" to the former, and the logical value "1" to the latter bias condition, we store one bit of information within such a circuit. So long as the power supply is on, this cell will indefinitely preserve the stored information. Hence, the definition of static memory.

In-order-to access the information, however, two more devices M5 and M6 are needed within the cell, as shown in the same figure. These devices act as pass transistors, which isolate the cell if the word line is low or connect the cell to the bit lines if the word line is high. Hence, the total number of transistors per cell is six. The bit lines, which are shared by all cells within the same column, provide the read-out information to the sense amplifier, i.e., the circuit which generates a logical output data from a slight unbalance of the bit lines.

In four-transistor memory cells, the pull-up MOSFETs M2, M4, are replaced by either passive resistors, as shown in Fig. 3, or thin-film transistors (TFTs) made by polycrystalline silicon. In both cases, pull-up devices are laid out on top of the n-type transistors, with an area saving of about 30%. In the former case, the resistance R must be very large, since the stand-by current

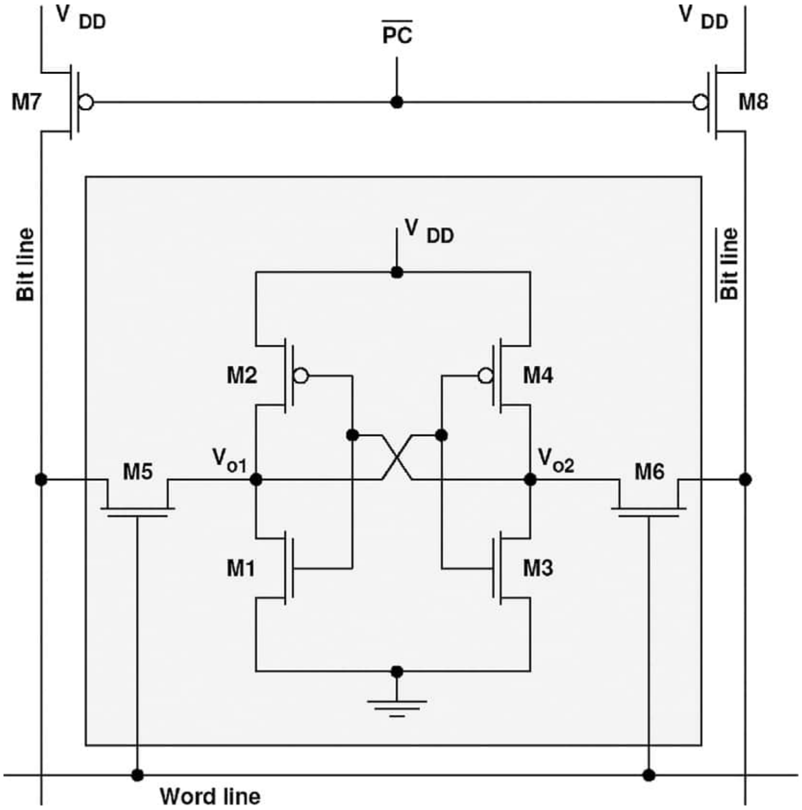
V DD
V DD
$\overline{PC}$
M7
M8
Bit line
$\overline{\text{Bit line}}$
V DD
M2
M4
V_{o1}
V_{o2}
M5
M6
M1
M3
Word line

Fig. 2 The six-transistor CMOS SRAM cell.

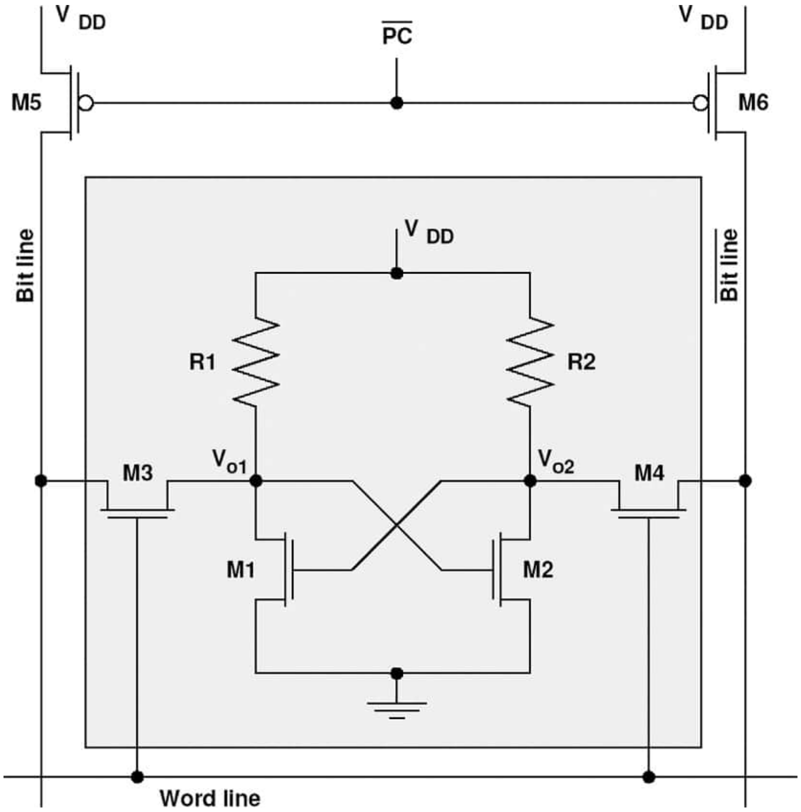
V DD
V DD
$\overline{PC}$
M5
M6
Bit line
$\overline{\text{Bit line}}$
V DD
R1
R2
V_{o1}
V_{o2}
M3
M4
M1
M2
Word line

Fig. 3 The four-transistor CMOS SRAM cell.

consumption of the cell is given by V_{DD}/R. The resistance value is thus defined according to the need of supplying the minimum current to preserve the high voltage of the node. In practice, $R \approx 1–10\ G\Omega$, which can be achieved using a second layer of a lightly doped polycrystalline silicon film. The use of TFTs as pull-up devices reduces the leakage current by nearly two orders of magnitude with respect to the passive resistor cell and improves the current drive capability of the pull-up devices in the on-state.

This improvement can be achieved at the expense of a more complex technology, involving an additional masking step, and the deposition of an undoped polycrystalline silicon film. It was thus used only for stand-alone memories, which are now seldom used.

Cell array organization

The cell array of an SRAM is schematically organized as indicated in Fig. 4. A row decoder receives at the input the row address of the required word and raises the corresponding word line high. Hence, all cells pertaining to the above row become connected to their respective bit lines.

The output multiplexer acts as a column decoder, and selects the appropriate bit, byte, or word. The corresponding bit lines are then connected to the sense amplifier(s), which detect the stored information within the selected cells. If the depth of the column decoder is too large, it may be worth interposing one sense amplifier between a first partial column decoder, acting on the bit lines which carry analog signals, and a second column decoder acting on the digital outputs of the sense amplifiers. Clearly, reducing the number of sense amplifiers is an advantage from the standpoint of power consumption but, on the other hand, interposing too many pass transistors between the bit lines and the inputs of the sense amp could be detrimental to the accuracy of the readings.

It should be noticed that, if the row decoder receives a K-bit address and the column decoder gets an L-bit address, the array contains 2^K rows and 2^L columns. Thus, a total number of 2^N cells is present within the array, with $N = K + L$. The number of selected outputs m depends on the memory organization: if the SRAM is fully decoded, $m = 1$. In this case, one single bit is read from, or written into, the array. Alternatively, m can be either 8 (byte decoding), 16 (half-word decoding) 32 (word decoding) or 64 (double-word decoding).

Cell reading and writing

A reading cycle proceeds as follows: (i) the bit lines, pre-charged at V_{DD}, are turned to a high impedance state; (ii) The word line is raised, thus connecting the cells within the addressed row to the bit lines; (iii) The pull-down transistors of the addressed cells discharge one of the two bit lines, while leaving the other at V_{DD}; (iv) The selected bit lines are connected to the sense amps via the

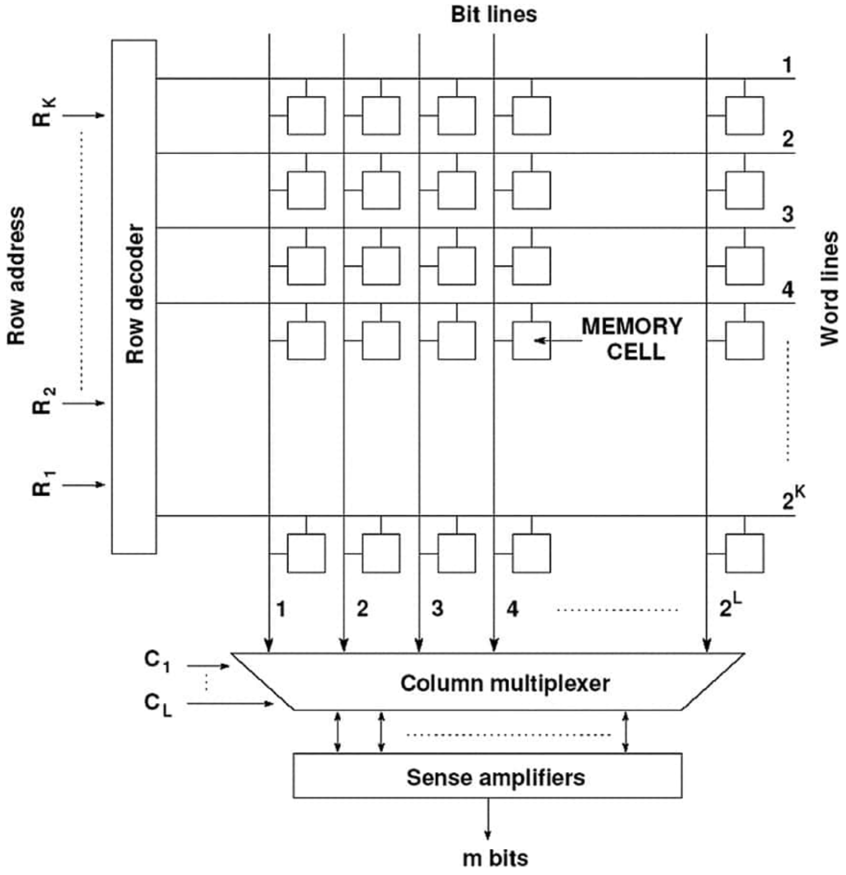

Fig. 4 SRAM cell array organization.

column decoder; (v) The sense amps read the content of the addressed cells and make the bit information available to the output circuitry; (vi) The row and column decoders are reset; (vii) The bit lines are reset to V_{DD}.

Likewise, a writing cycle proceeds as follows: (i) The row and column decoders are activated, thus connecting the addressed cell to the respective bit lines and the latter to the output circuitry; (ii) One of the two bit lines connected to the cell is discharged to zero; (iii) The bit line connected to ground either confirms the status of the cell or upsets the cell in order to make it biased according to the desired input; (iv) The row and column decoders are reset; (v) The bit lines are pre-charged to V_{DD}. The timing of the above operation sequence is controlled by internally generated signals.

Sense amplifier

For static memories, the sense amplifier is often the standard one-stage CMOS differential amplifier with single-ended output, as shown in Fig. 5A. The function of the sense amp is in this case that of allowing for a quick reading of the differential signal on the bit lines, so that the discharging process can be stopped as soon as possible, to the advantage of speed and power consumption. One major drawback of this simple scheme is that the differential-pair M1, M2 operate in the triode region, as the bit lines are pre-charged to V_{DD}, leading to a severe degradation of the voltage gain.

A better solution is provided by a two-stage circuit scheme, where a differential level shifter, shown in Fig. 5B, is interposed between the bit lines and the voltage amplifier. The positive feedback of this circuit increases its differential voltage gain. Most important, the appropriate DC bias of the differential pair optimizes the amplifier gain, resulting in an excellent performance of the sense amp.

SRAM applications

In the past, when the available technology did not allow a huge number of transistors to be integrated on chip, stand-alone SRAMs were fabricated for the second level (L2) cache of Intel microprocessors.

Subsequently, device miniaturization made it possible to integrate L1, L2 and even L3 caches on chip as embedded memories, taking advantage from the SRAM compatibility with CMOS logic, with great performance and power consumption advantages at the system level. To date, cache memory is the dominant application of embedded six-transistor SRAMs for advanced microprocessors to be used in a wide variety of applications, from mobile to high performance servers. On the other hand, the market share of stand-alone SRAMs can be estimated to be less than 1% of the whole memory market.

In view of the above, the four-transistor memory cell with polycrystalline pull-up resistors or thin-film transistors has been practically abandoned due to the diminishing returns of its increased fabrication complexity, and to the difficulty to control the leakage current of pull-up resistors when the memory capacity becomes very large.

Dynamic random-access memory

Early DRAM cells were made by three transistors. The first proposal of a one-transistor, one capacitor (1T-1C) dynamic RAM cell was made by R.H. Dennard in 1966, who subsequently filed the US Patent no. 3,387,286 entitled "Field-Effect Transistor Memory," dated June 4, 1968 (Dennard, 1968). His basic idea was that cell information could be dynamically stored as a charge on a capacitor, as indicated in Fig. 6. Here again the MOSFET acts as a pass transistor, which can either isolate the cell or connect it to the bit line. The inner node voltage V_c may be set either at the supply voltage V_{DD} or at the ground voltage 0. In-order-to charge the cell capacitor

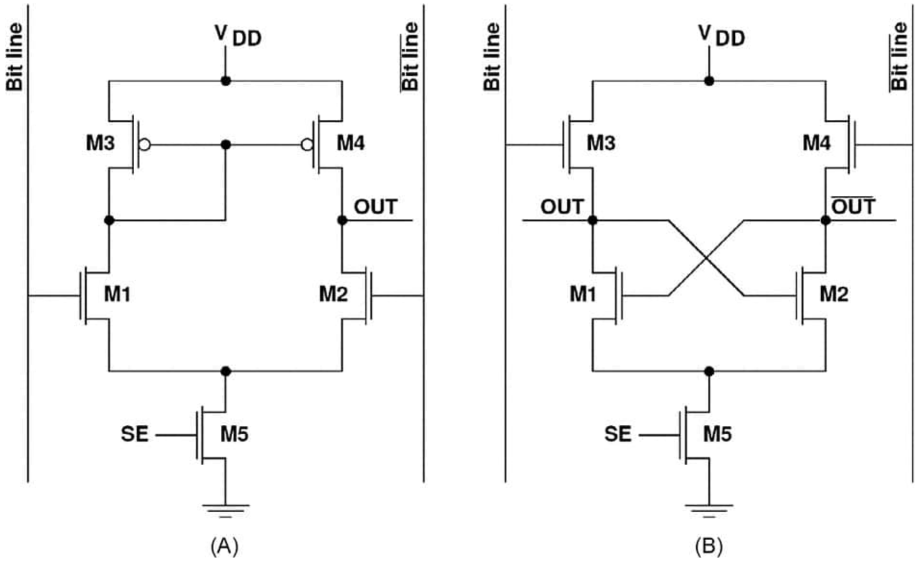

Fig. 5 SRAM sense amplifier; (A) Voltage amplifier; (B) Level shifter.

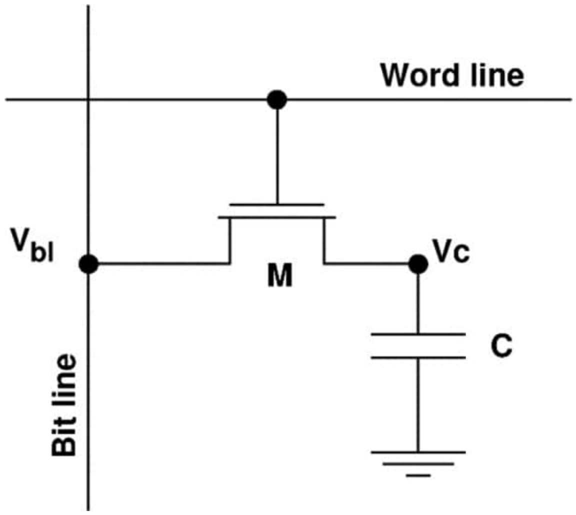

Fig. 6 One-transistor one-capacitor DRAM cell.

to V_{DD}, the word line must be driven to a higher supply voltage V_{PP} generated on chip. A disadvantage of this storage scheme is that, due to the transistor leakage current, the charge is not indefinitely conserved within the capacitor but, rather, leaks out in a time of the order of a several tens or a few hundred milliseconds. The limited DRAM retention time requires the information to be refreshed some tens or hundred times per second; hence, the definition of dynamic memory.

The cell capacitance must be as large as possible to ensure a long retention time as well as a safer reading of the stored information. At the same time, it must occupy a small silicon area, to allow for a large density and a small cost per bit. These conflicting requirements were pursued in the 1990s with either a trench or a stacked cell. In the former case, the capacitor was placed in a deep trench engraved within the silicon substrate by reactive ion-etching. The trench surface was thermally oxidized and filled with polycrystalline silicon electrically connected to the MOSFET source. This solution has been abandoned in recent years due to the extreme form factor required by the need to generate large capacitances with decreasing diameters values.

The stacked cell, shown in Fig. 7, aims to deploy a large capacitance (about 30 fF) by extending the surface of the upper electrode in an extended structure overlapping the word line (Koyanagi et al., 1978). This solution was subsequently improved by Taguchi et al. (1993) with a double-fin structure, usually made by electrically insulated polycrystalline silicon, and surrounded by the second electrode representing the capacitor plate. An added advantage of the stacked cell is that high-k dielectrics, such as ZrO_2 and/or Al_2O_3, can be used as insulating layers, maximizing the total capacitance for a given occupation area.

Fig. 8 shows an electron micrograph of the stacked-capacitor cell (Taguchi et al., 1993). The double-fin structure, in light color as the silicide layer overlapping the transistor gate, represents the first electrode of the cell capacitor surrounded by a thin dielectric and a dark polysilicon plate. The transistor gate is connected to the word line by vertical W plugs shown in the upper part of the micrograph. The cell connection to the bit line is not shown in this cross section. More recently, the stacked cell has been

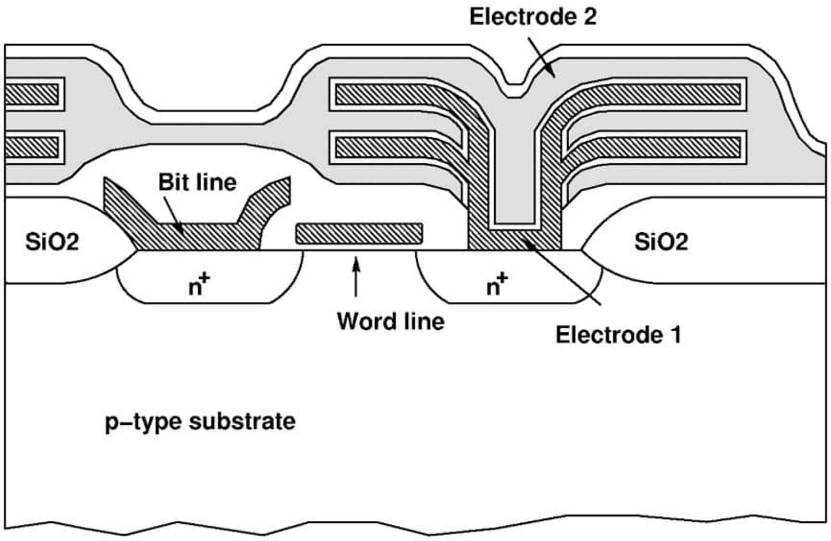

Fig. 7 Schematic view of a stacked DRAM cell.

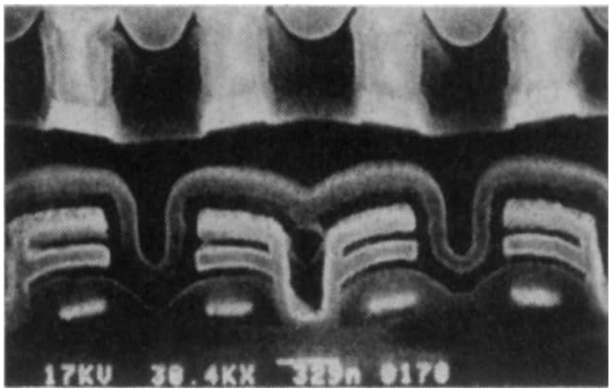

Fig. 8 Electron micrographs of a stacked DRAM cell (Taguchi et al., 1993).

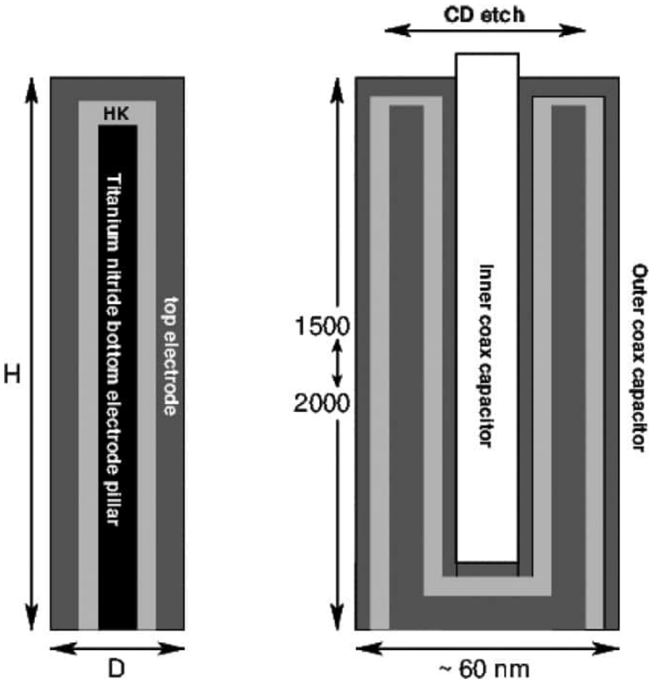

Fig. 9 DRAM capacitor structures. (Left) Pillar structure; (Right) Crown structure.

manufactured as a cylindrical pillar resembling a coaxial cable, or as a crown, as shown schematically in Fig. 9 (Left) and (Right), respectively. At the 25 nm technology node, the required capacitance value could be scaled to 17 fF, which can more easily be achieved with the crown structure comprising two capacitors connected in parallel.

On the other hand, the crown structure cannot be laterally reduced below a certain limit, thus preventing a full scaling of the cell. The pillar structure is thus used in advanced technologies, with an increased aspect ratio H/D about equal to 100 to achieve the required capacitance value at the 20 nm node. With such a capacitor structure, the DRAM cell can approach the minimum size of $4F^2$, with F the minimum feature size (half pitch) of the implementation technology. Fig. 10 is an electron micrograph showing a DRAM structure with vertical stacked capacitors (James, 2010).

DRAM cell array organization

The DRAM cell array may be organized as indicated in Fig. 11. The bit line is split in two identical segments connected to the sense amplifier, which allows for a differential reading of the stored information and halves the bit-line capacitance for a given column size. The bit-line folding makes it easier to match the layout of the sense amp onto the wider pitch of the two half columns and allows for an easy placement of the column decoders.

The bit lines are initially precharged at $V_{DD}/2$ by turning on transistor EQ and are then kept in a high impedance state. As for SRAMs, the row decoder addresses a row of cells and turns the corresponding pass transistors on, thus connecting the cell capacitors to their respective bit lines.

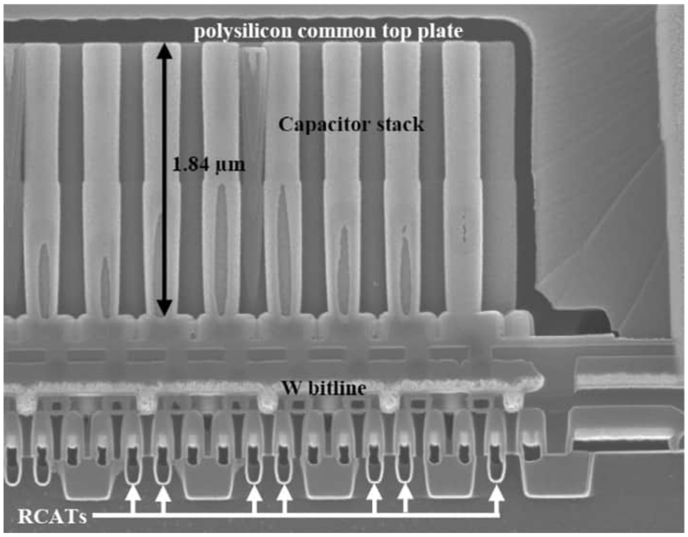
polysilicon common top plate
Capacitor stack
1.84 µm
W bitline
RCATs

Fig. 10 Electron micrograph of a stacked-capacitor DRAM structure (Samsung 90-nm).

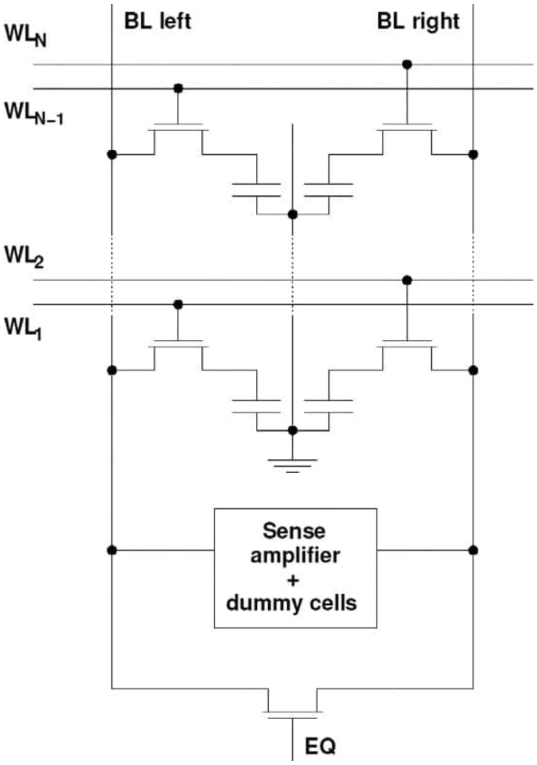
WL$_N$
BL left
BL right
WL$_{N-1}$
WL$_2$
WL$_1$
Sense amplifier + dummy cells
EQ

Fig. 11 Folded bit-line organization of the DRAM cell array.

Due to the large capacitance ratio between the parasitic bit line and the cell capacitances C_{bl} and C_c, respectively, the bit-line voltage is only slightly affected. More specifically, the voltage change ΔV_{bl} of the bit line connected to the cell equals.

$$V_{bl} = [C_c/(C_{bl} + C_c)]\,(V_c - V_{DD}/2)$$

where V_c is the cell voltage, which may be either 0 or V_{DD}. If the ratio $C_c/C_{bl} \approx 0.1$ the voltage change ΔV_{bl} is only about one hundred mV. Due to an unavoidable offset of the sense amp, the cell capacitance must be as large as possible, while being dimensionally small to allow for a high bit density.

It is clear from the previous expression that the bit line voltage increases with respect to $V_{DD}/2$ if the cell voltage $V_c = V_{DD}$ and decreases if $V_c = 0$. The second input of the sense amp is connected to a reference voltage generated by a dummy cell precharged at $V_{DD}/2$, as the bit lines. Therefore, the properties of the sense amp must be the following: (i) It must detect and amplify a small voltage difference between the two bit lines, eventually generating logic levels; (ii) Upon reading, it must refresh the content of the cell by re-establishing the original value of the charge stored within the capacitor.

DRAM sense amplifier

The schematic of the DRAM sense amp is reported in Fig. 12 (Rabaey, 1996). Here M1-M4 form a regenerative, bi-stable circuit connected to ground via M5 and to V_{DD} via M6. An additional pass transistor M7 may either connect or isolate the two bit-lines, thus enabling their pre-charge at $V_{DD}/2$. Two dummy cells are located on the opposite sides of the sense amp and their capacitor is pre-charged at $V_{DD}/2$ by a straight connection to the bit lines. The function of the dummy cells is that of balancing the bit lines by letting them undergo the same transient conditions before readout.

At the start of a reading, SE is low, keeping M5 and M6 off; the bit lines are precharged at $V_{DD}/2$ and left in a high-impedance state. Thus, the cross-coupled transistors M1-M4 are self-biased on their respective thresholds, and the voltages V_3 and V_4 set at $V_{DD}/2 - V_{Tn}$ and $V_{DD}/2 + |V_{Tp}|$, respectively, V_{Tn} and V_{Tp} being the threshold voltages of the n- and p-channel MOSFETs, respectively.

The reading sequence is the following: (i) The word line of the addressed cell is activated, thus connecting its capacitor to the corresponding bit line, and so is the word line connected to the dummy cell on the opposite side of the addressed cell; (ii) SE is gradually raised high, allowing the sense amp to unbalance and reach its final state; (iii) The sense amps are read out via a column multiplexer; (iv) The word lines are reset to their low value; (v) The signal SE is switched low, thus turning off M5 and M6; (vi) The bit lines are shorted by raising the signal EQ, which drives them and the dummy-cell capacitors to $V_{DD}/2$; (vii) M7 is turned off by lowering EQ and leaving the bit lines in a high-impedance state. So doing, the initial reading conditions of the sense amp are reset.

It may be worth pointing out that, following the gradual raise of SE in step (ii), M5 and M6 turn on lowering V3 and raising V4. The cross-coupled transistors M1-M4 turn on and unbalance the sense amp according to the initial voltage mismatch. If the initial bit-line voltage $V_{bl(left)} > V_{DD}/2$, which reflects the content of a logic "1" in the addressed cell, the transient drives it to V_{DD} while the right bit-line voltage $V_{bl(right)}$ goes to zero. The opposite situation occurs if $V_{bl(left)} < V_{DD}/2$, which reflects the content of a logic "0" within the same cell. Thus, reading the addressed cell restores the original voltage within the cell capacitor, which makes the reading non-destructive. Also, if the two bit-line capacitances are equal, pre-charge to $V_{DD}/2$ is simply achieved with no additional power consumption by connecting them via M7.

DRAM architecture

The block diagram of a DRAM bank is shown in Fig. 13. The block splitting in two parts is meant to reduce the bit-line capacitances. The row addresses are delivered to the row decoders, which activate one word line. All cells associated with that word line are thus connected to their respective bit lines, which become slightly unbalanced. The column addresses set the column decoder (actually, a simple multiplexer) and select the requested bytes or words, by connecting the corresponding bit lines to their respective sense

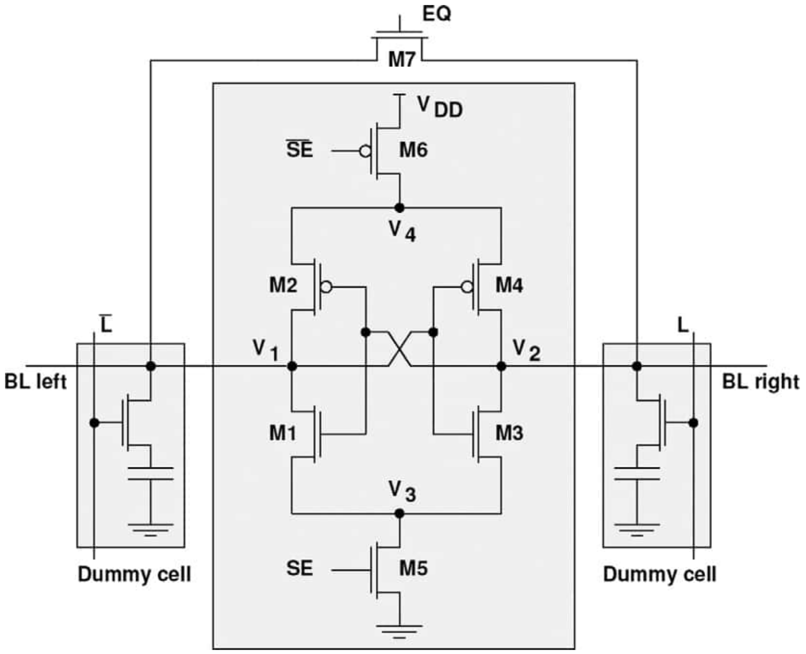

Fig. 12 Schematic of the DRAM sense amplifier.

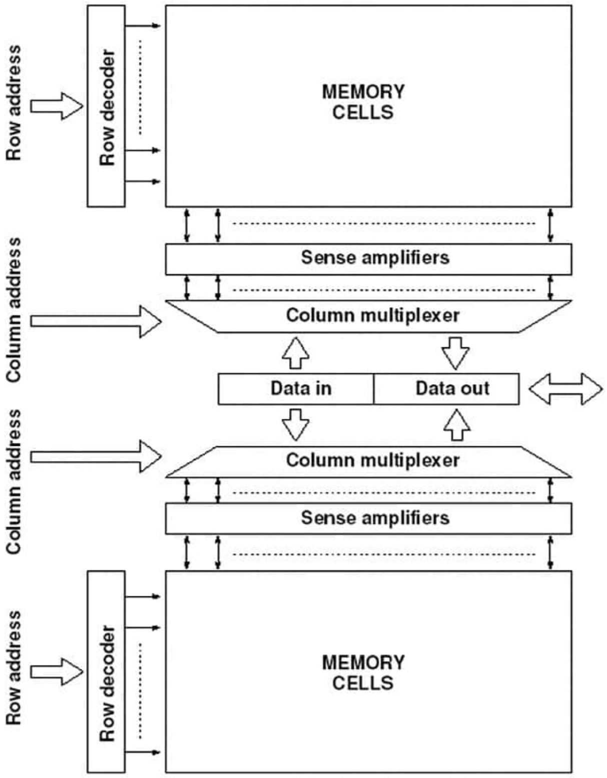

Fig. 13 DRAM bank architecture.

amps. The logic levels generated by the sense amps are delivered to the output registers. Multiple column readings can be performed in sequence for any given row address, which improves the DRAM data rate. The above structure may be mirrored and replicated as many times as needed. The size of a DRAM bank is defined according to conflicting constraints: increasing the cell array size makes the layout more compact for a given DRAM capacity, but deteriorates the access time and, ultimately, the reading integrity, due to the larger word- and bit-line capacitances. In-order-to save package pins, a multiplexed addressing scheme, where the row and column addresses are presented in sequence to the same bus, is typically used. In this addressing scheme, two main control signals, namely, the row-address strobe (RAS) and the column address strobe (CAS) must be provided to the DRAM. Another control signal (WE) indicates if the intended operation is a read or a write.

Asynchronous DRAM

Basic DRAMs operate asynchronously under the control of external commands. The timing diagram of a read operation is shown in Fig. 14 (IBM, 1996), where the control signals RAS, CAS and WE are shown in complementary form, here denoted as RAS′, CAS′ and WE′, respectively. The RAS′ signal is switched low only after valid row address bits are present at the DRAM input buffer. In turn, the CAS′ signal goes low only when valid column address bits and a valid WE signal are set to their respective values. The time t_{CAS} is the minimum time that CAS′ must be kept low to generate valid output data; likewise, the time t_{RAS} is the minimum time that RAS′ must be kept low to generate valid output data; finally, the cycle time t_{cycle} is the minimum time needed between two successive RAS′ commands.

Improved asynchronous architectures, referred to as Fast Page Mode (FPM) and Extended Data Out (EDO) Mode, were developed since the early 1990s. An FPM DRAM makes it possible to access data located within the same row with a unique RAS command followed by multiple CAS signals, so long as all addressed words reside in the same row. Besides, the column address is latched, rather than being set up, at the falling edge of the CAS′ signal. So doing, a reduced page cycle is obtained compared with conventional DRAMs (Veendrick, 2017).

The EDO DRAM differs from the FPM DRAM in that an additional register holds the output data. This makes it possible to start the next reading cycle before the previous one is completed. The cycle time is thus reduced, with some speed improvement over FPM DRAMs (Veendrick, 2017).

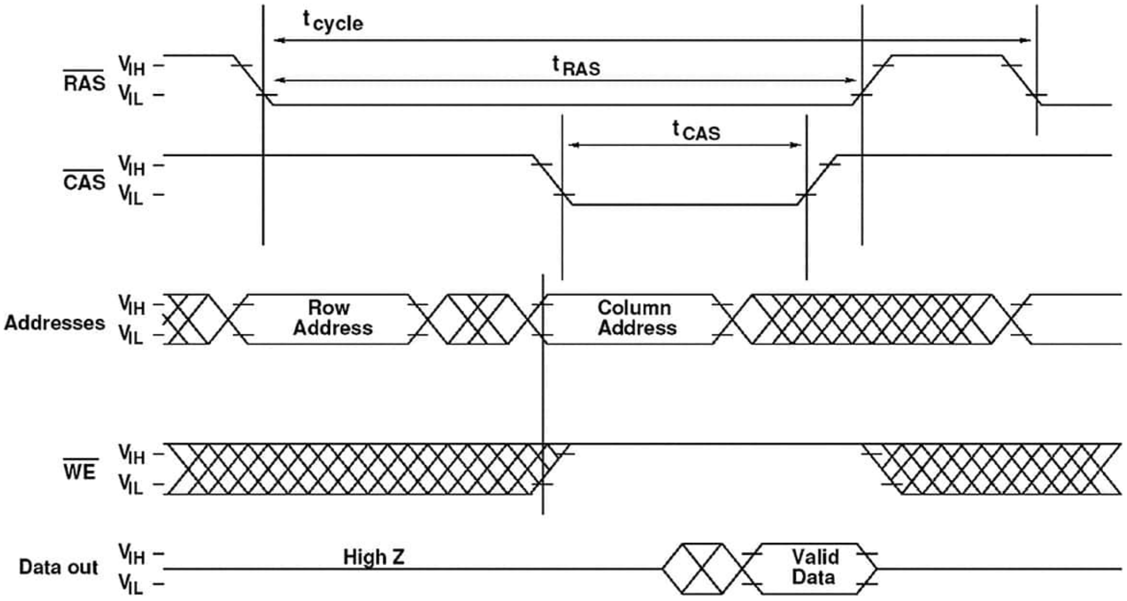

Fig. 14 Timing diagram of the DRAM input signals.

Synchronous DRAM

Synchronous DRAMs are driven by the system clock and are thus referred to as SDRAMs. Synchronous operation has several advantages: most notably, the possibility of a pipelined DRAM architecture with concurrent row and column addressing, and high-speed I/O operations. Taking advantage from the inherent parallelism of the memory core, this architecture improves the DRAM data rate, which is the most important performance parameter, while leaving its latency scarcely affected. Due to the hierarchical memory organization in modern computers, entire data blocks are in fact retrieved from the central memory when a block miss occurs at a higher level of the hierarchy. To date, the SDRAM data rate may be as large as 3.2 Gb/s/pin. This comes at the penalty of extra latches and buffers, as well as high-speed circuitry to support the I/O interface (Veendrick, 2017).

Basic SDRAM commands are chip select (CS), row address strobe (RAS), column address strobe (CAS), write enable (WE), data mask (DM) and data strobe (DQS). All of them are latched to the rising edge of the system clock. The CS signal is used to let the chip know that the incoming commands over the bus are intended for it. RAS, CAS and WE retain the usual meanings of row- and column-address strobe and write enable. DM masks the input data to unselected cells during a write; DQS is instead a bidirectional edge-aligned data strobe which toggles at the same time as the output data. This is made possible by a delay locked loop (DLL) which shifts the output data aligning DQ (I/O pins) and DQS. The bus width is most often 64-bit wide.

Basic SDRAM operations are activate (ACT), read (RD) or write (WR) followed by pre-charge. SDRAM operation can be configured for CAS latency and burst length by setting the 12 bits of the load mode register (LMR). The burst length determines the amount of data transferred in consecutive cycles between the memory controller and the memory after applying one start address. The typical delay between the RAS and CAS signals is two clock cycles, and the CAS latency is again two clock cycles; thus, the access time is four clock cycles. The SDRAM cycle time t_{cycle} depends in this case on the bus width and the burst length (Veendrick, 2017).

Several generations of SDRAMs were successively offered to the market: Double Data Rate (DDR) 1, 2, 3 and 4, with progressively decreased supply voltages and improved data rate. The key concept of DDR SDRAMs is that both the falling and rising edge of the clock are used to double the data throughput. DDR2 operates at 400–800 MHz bus rates with a supply voltage $V_{DD} = 1.8$ V. DDR3 operates with bus rates of 800–1600 MHz at $V_{DD} = 1.5$ V. The doubling of the bus rate in DDR3 is achieved by prefetching 8 rather than 4 words. So doing, a total of 8 words are accessed in parallel for a read or write operation. In DDR4, the connection between CPU and Memory is not done using a bus but, rather, point-to-point direct channels. This simplified connection puts an additional burden on the memory controller, which must operate reliably at very high frequency maintaining the signal integrity. To do this, impedance matching is required to prevent signal reflections (Veendrick, 2017).

Rambus DRAM

The direct Rumbus DRAM (RDRAM) architecture is based on a system approach, which maximizes the data rate on the memory board by carefully synchronizing data, addresses and commands with the clock signal (Crisp, 1997). The key elements of this technology are the following: (i) a 16-bit wide, 800 MHz channel; (ii) an on-board interface that lets the memory controller talk to the RDRAM and, (iii) an in-line memory module called RIMM.

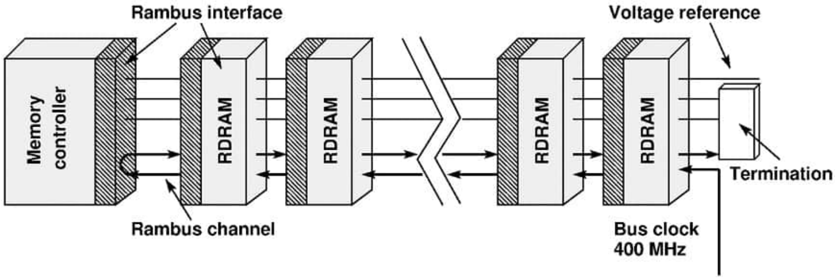

Fig. 15 Direct Rambus DRAM architecture.

A Rambus channel includes a controller and a variable number of RDRAM chips connected via a linear common bus. As shown in Fig. 15, the controller is located at one end, and the RDRAMs are distributed along the bus, which is terminated at the opposite end with the characteristic impedance of the lines connected to the high-voltage level. Therefore, the bus driver operates in the open-drain configuration. The 400 MHz clock signal is generated at this same end; it propagates along a bus line connecting the clock generator to the controller and turns back to the terminating end of the bus line. All commands, addresses and data moving from the controller to the RDRAM chips and back are synchronized on the edges of the clock which propagates in the same direction. So doing, clock skew is minimized.

The channel uses 18 data pins, two of which for error correction code (ECC), cycling at 800 Mb/s per pin to provide a bandwidth of 1600 MB/s. This is achieved by latching data on both the rising and the falling edges of the clock signal. The RDRAM has a pipelined micro-architecture, which fully supports concurrent RAS and CAS operation, as well as read/write buffering. Also, it provides 16 bytes every 10 ns on the internal bus. The Rambus interface transforms the 10 ns internal bus into an external, two-byte wide, 1.25 ns external bus.

All signal wires have an equal loading and fan-out and are routed parallel to each other on the top trace of a PCB with a ground plane located underneath. The addition of more RDRAM chips linearly increases the load and the delay, but leaves the phase relationships of the clock, data, addresses and commands unaltered. Also, the memory granularity is simply given by the memory capacity of one chip.

Graphics applications

Graphics applications require extremely high bandwidths, being characterized by high speed and wide I/O buses. Video RAMs (VRAM) and Synchronous Graphics RAMs (SGRAM) are specifically designed for such applications and are widely used in graphical signal processors (GSP) for PC video cards. Most VRAMs are a dual-ported version of a DRAM, meaning that the display is reading its image from the video RAM, while the processor is writing a new image into it. One access port is used to constantly refresh the display and the other is used to change the data to be displayed in the next frame. A bandwidth doubling and faster video performance is thus obtained, with reduced CPU strain. The VRAM acts as a buffer between the processor and the display monitor and is often called frame buffer.

SGRAM architectures are similar to SDRAM's, while being optimized for color graphics applications. More specifically, SGRAMs support block write and write-per-bit functions. These features are made possible by special registers used to store the color data associated with large areas of a single color. Write per-bit allows the masking of certain inputs during write operations; hence, only some memory locations are written rather than the whole frame, resulting in faster and more efficient read and write operations (Veendrick, 2017).

Capacitorless DRAM cell

Several capacitorless DRAM cells have been proposed, which take advantage from the floating body effect of silicon-on-insulator (SOI) technology (Yoshida and Tanaka, 2006; Okhonin et al., 2008). Besides reducing the cell area and fabrication complexity due to the elimination of the stacked capacitor, the added advantage is the full compatibility with the SOI CMOS process, which makes these memories suitable for embedded implementations in systems-on-chip.

The information is typically stored as a hole charge within the isolated body of a partially depleted (PD) SOI transistor, which lowers its threshold voltage and makes it more conductive, as shown in Fig. 16. The hole charge is inserted into the transistor body either by Impact Ionization (II) at large drain voltages or by a negative gate voltage pulse which enables Gate-Induced Drain Leakage (GIDL) under positive drain voltage. The latter approach is preferable from the standpoint of power consumption. Electrons from the body valence band tunnel into the positively biased drain, leaving behind several holes within the transistor body. This corresponds to the write 1 command. Holes can be removed from the transistor body by a drain negative pulse, which makes the body-drain junction forward biased. Holes are thus injected into the drain, so that the transistor body becomes fully depleted, and the threshold voltage is raised. This represents the write 0 command. The Read operation can simply be carried out by sensing the source current at low drain bias (typically 0.2 V).

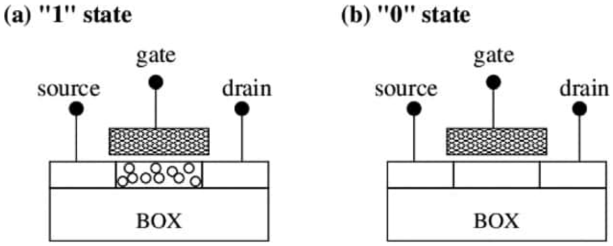

Fig. 16 Schematic of a capacitorless DRAM cell.

Retention times are shown to be acceptable under standby conditions ($V_{GS} = -1$ V, $V_{DS} = 0$ V), despite the small capacitance value of the floating body. As opposed to standard DRAM cells, however, a write disturb can affect the 0 content of unselected cells connected to the addressed word line, when a large negative pulse is applied to it for a write 1 operation. Likewise, a write 0 command using a negative drain pulse can affect the unselected cells connected to the addressed bit line.

Readout is carried out at small drain voltages and is non-destructive but, at the same time, does not refresh the cell content. Therefore, memory refresh does not occur automatically by starting a read cycle word line after word line, as for standard DRAMs, but requires the cell content to be read and rewritten location after location. Capacitorless DRAMs are compatible with the SOI technology and can be easily integrated in systems on chip fabricated in that technology. For the time being, only embedded memories with limited capacities have been produced.

General considerations on volatile memories

Stand-alone SRAMs exhibit a performance advantage over DRAMs by a factor of about 4, partially due to different design goals of the two memory types. The former memories are in fact designed with the aim to optimize performance, while the latter ones are designed for high density and, thus, low cost per bit. As a result, the sizes of SRAM and DRAM cells are about 100–150 F^2 and 4–6 F^2, respectively. Multiplexing the row and column addresses to reduce the pin number, and the consequential need to assert the RAS and CAS signals in sequence, shows that the cycle time was sacrificed to the cost target.

On the other hand, DRAM designers managed to improve the data rate by accessing a full page without requiring a new reading cycle to start. A page is given by all cells sharing the same word line and can be as large as one or more kilobit. The simultaneous readout of a full page makes the data rate as large as one or more Gbit/s in the most advanced page-mode designs. Therefore, the market share of standalone memories is dominated by DRAMs, while SRAMs cover only about 1% of the whole memory market.

DRAM chips only use 2–4 metal layers, as opposed to the 10 metal layers of advanced microprocessors. Besides, the stacked capacitor cell requires additional processing steps which are not compatible with the state-of-the-art CMOS technology. A consequence of such a specialized DRAM technology is that embedded DRAMs in systems on chip require a much larger planar capacitor, which increases the cell size by a factor of 6 to 8. The area efficiency of stand-alone DRAMs is thus largely lost in embedded applications. Nevertheless, embedded DRAMs have been used for high-performance systems-on-chip requiring a relatively small memory capacity, such as graphics and multimedia applications (Yamazaki. et al., 1999).

Embedded memories for high performance applications, such as cache memories, are predominantly SRAMs. Fig. 17 shows Intel's Nehalem microarchitecture chip comprising four i7 cores. It appears that the shared L3 SRAM area occupation is about one third of the whole chip, while the four L2 SRAMs are recognizable as the regular layout areas in the lower right or left sides of every core processor (Thomadakis, 2011).

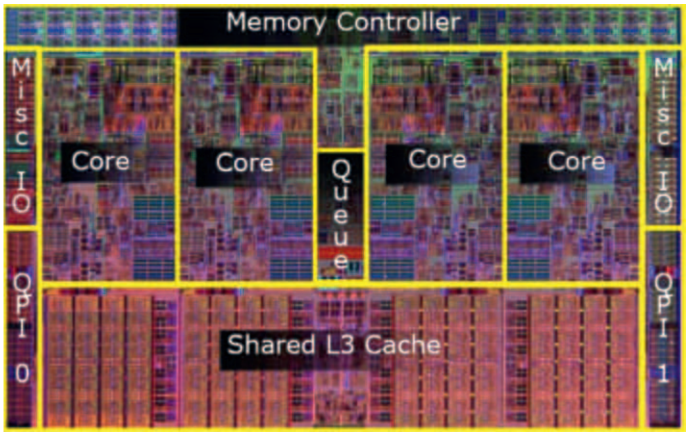

Fig. 17 Intel's Nehalem architecture comprising four i7 cores and a large shared L3 cache.

Content-addressable memory

Modern computer architectures rely on a hierarchy of memories comprising three levels of cache in addition to the central memory. This complex organization is due to the design consideration that smaller memories are faster, and to the locality principle, according to which programs tend to reuse either data which have already been used in previous cycles (temporal locality) or data sets stored next to the used data (spatial locality).

At the first level of the hierarchy, we typically find an instruction and a data cache with a typical capacity of 16–64 KB, and a data rate of one instruction/data per cycle if a hit occurs. The second-level caches are larger, around a few MB, and relatively slower. Third-level caches are typically shared by the on-chip cores and their capacity may be several hundred MB. The area occupation of the third level cache is a very substantial fraction of the whole microprocessor chip.

Cache memories are classified according to the criteria by which the central memory is mapped onto it. In a fully associative cache, data blocks can be stored anywhere within the cache, as opposed to direct-mapped memories, where the block address uniquely defines its location. In most cases, cache memories are n-way set associative; this means that the cache memory is split in several sets each containing n blocks: the block address uniquely defines the set where it must be stored, but the location of the block inside the set (way) is free.

In any case, a tag memory containing a list of the block addresses stored within the cache is needed. When a new instruction or a new data is requested by the processor, an associative search must be performed on the tag memory to find out if the block containing that instruction or data is stored within the cache and, in case it is, in what location. As opposed to standard memories, the input of the tag memory is a data word, and its output is the local block address within the cache. The tag memory is therefore a content addressable memory (CAM). The basic cell of a CAM, shown in Fig. 18, contains 10 transistors.

The information bit is stored within a static latch made by the two cross-coupled inverters I1 and I2. Two pass transistors M1 and M2, driven by the write line (WL), connect the input data D and its complement D′ to the latch outputs, thus writing the input bit to be stored. As shown in the figure, two couples of pass transistors M3-M4, M5-M6, driven by the input data D and D′ and by the latch outputs connect to ground a pre-charged match line (ML). If the stored bit is opposite to the input data, either one of the two couples of pass transistors is on discharging the match line. Otherwise, the match line remains biased at V_{DD}. The former case indicates that no match occurs between the input and the stored data; the latter indicates the opposite condition.

The above cells are organized within an array, and all the cells of a column, sharing the same write line and the same match line, contain the address of one memory block. If any one of the above cells does not match its input bit, it drives the match line to ground, indicating that no match occurs between the input word and the stored address. If none of the columns matches the input word, this means that a block miss is occurring; all the match lines are at ground potential and a NOR gate rises the block-miss signal high. If, on the other hand, all input bits of a column match their respective bits stored within the cells, the match line remains high. This is an indication that the requested block is stored within the cache, and the high match line indicates the internal address of the block within the cache memory. In this case a hit signal is released.

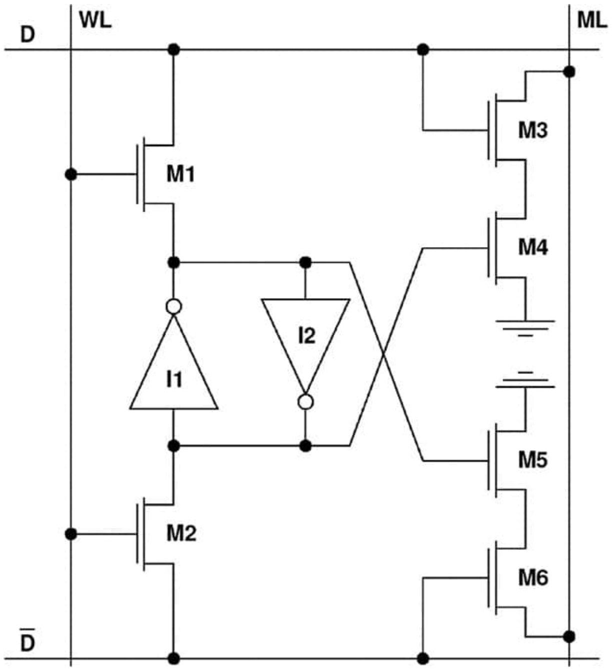

Fig. 18 The 10-transistor CAM cell.

Conclusion

In this Encyclopedia entry, volatile random-access memories are presented, with special attention to static and dynamic RAMs. Cell topologies, array organizations, reading and writing procedures, reliability issues and typical applications are illustrated. Their performance properties, including access time, data rate, area efficiency and power consumption are discussed with some detail, specifying the different application-specific architectures. Content addressable memories are also treated in the final part of this entry.

The stand-alone memory market is and will be dominated by DRAMs in the foreseeable future, due to their area efficiency, unlimited endurance, low cost per bit and high data rate, which has grown to fulfil the requirements of high-performance processors, despite the relatively large DRAM access time compared with the cycle time of the internal clock. To compensate this mismatch, every access to the central memory is going to transfer a full page, both for writing and for reading after a block miss of the L3 cache.

As far as embedded memories are concerned, SRAMs are the typical high-performance solution. For less demanding and lower cost applications, different kinds of memories are being used. Due to the limited DRAM suitability, these memories are in most cases non-volatile and compatible with logic technologies with a small additional number of processing steps in the back end of the chip fabrication. Among them, phase-change memories, to be discussed in the next entry of this memory presentation, are often used for systems on chip.

As the supply voltage of advanced microprocessors was scaled down to 0.7 V, however, SRAMs turned out to be affected by two major weaknesses: (i) an increased leakage current, due to threshold voltage scaling and, (ii) a deterioration of the noise margins, which led to more complex cell architectures with additional devices and/or to the use of external assist circuits. The former point is detrimental to power consumption, which must be contained due to the limited heat extraction capability from chips and to the need to save power in mobile applications. The latter point affects the SRAM read reliability and its solution leads to an increased chip size and fabrication cost.

The advent of the FinFET (tri-gate) device architecture for logic at the 22 nm technology node and below, has added additional constraints to the SRAM design, due to the fixed FET effective width $W_{eff} = 2H + W$, with H the fin height and W its physical width at the top, uniquely defined by the fabrication technology. High-performance SRAMs use one single Fin-FET for the pull-up devices M2 and M4 (see Fig. 2), two parallel FinFETs for each of the pass transistors M5 and M6 and two or three parallel FinFETs for the pull-down devices M1 and M3. These constraints are detrimental to the cell size, which can become as large as 150 F^2.

According to a recent study, Spin Transfer Torque (STT) magnetic RAMs could possibly replace SRAMs as the last level cache (LLC) in microprocessors at the 5 nm technology node (Sakhare et al., 2020). This could be a major technology shift, as the number of transistors in LLCs is a large fraction of their total number, which amounts to a few billion.

References

Crisp R (1997) Direct Rambus Technology: The New Main Memory Standard. *IEEE Micro* 17–28.

Dennard RH (1968) *Field Effect Transistor Memory, USP-3387286, June 4, 1968.*

IBM (1996) Understanding DRAM Operation. *Application Note* 12–96.

James D (2010) Recent innovations in DRAM manufacturing. *IEEE/SEMI Advanced Semiconductor Manufacturing Conference (ASMC)* 265-269: .

Koyanagi M, et al. (1978) Novel high-density stacked capacitor CMOS RAM. *Technical Digest - International Electron Devices Meeting* 348–351.

Okhonin S, et al. (2008) A capacitor-less 1T-DRAM cell. *IEEE Electron Device Letters* 29-7: 85–87.

Rabaey JM (1996) *Digital Integrated Circuits - A Design Perspective*. Prentice Hall Inc.

Sakhare S, et al. (2020) JSW of 5.5 MA/cm^2 and RA of 5.2-$\Omega\cdot\mu$m^2 STT-MRAM Technology for LLC Application. *IEEE Transactions on Electron Devices* 67-9: 3618–3625.

Taguchi M, et al. (1993) A 40 ns 64 Mb DRAM with 64-b parallel data bus architecture. *IEEE Journal of Solid-State Circuits* 26-11: 1493–1497.

Thomadakis ME (2011) The architecture of the Nehalem processor and Nehalem-EP SMP platforms. *JFE Technical Report.*

Veendrick HJM (2017) *Nanometer CMOS ICs, From Basics to Asics*, 2nd edn Heeze, The Netherlands: Springer.

Yamazaki A, et al. (1999) A 5.3-GB/s embedded SDRAM core with slight-boost scheme. *IEEE Journal of Solid-State Circuits* 34(5): 661–669.

Yoshida E and Tanaka T (2006) A capacitorless 1T-DRAM technology using gate-induced drain-leakage (GIDL) current for low-power and high-speed embedded memory. *IEEE Transactions on Electron Devices* 53-4: 692–697.

Residual stress and strain evaluation across the scales

Alexander M Korsunsky, Trinity College, Oxford, United Kingdom

© 2024 Elsevier Ltd. All rights reserved.

Introduction 592
Eigenstrain theory 593
Stress and strain multi-scaling 593
Statistical considerations 594
'*Live*' vs *residual* strains and stresses 594
Digital image correlation (DIC) 595
Experimental techniques 596
Material removal method illustration: FIB-DIC 596
Diffraction 598
'Rich' tomography of strain and stress 599
Influence of residual stress on structural integrity 599
Conclusion 599
References 600

Abstract

Residual stresses and strains are introduced through *nuclei of strain* (elastostatics 'charges') and, in the case of continuous distributions, *eigenstrains* ('frozen-in' permanent inelastic strains). The problem of eigenstrain is introduced using a form of the complementary energy functional for the problem of elastostatics in the presence of eigenstrain. The direct and inverse problems of eigenstrain are introduced then, and the approaches to solving them are presented. The means of experimental evaluation of stress and strain are critically reviewed. The challenge of 3D reconstruction of a sample's internal residual deformation state is considered in the context of stress/strain tomography. Residual stress and strain effects on structural integrity are briefly reviewed.

Key points

- To introduce the concept of residual stresses and strains in complex hierarchically structured materials
- To identify eigenstrain as the source of residual stress
- To introduce eigenstrain theory of residual stresses along with the direct and inverse problems of eigenstrain
- To introduce the continuum mechanical theoretical (variational) framework for residual stress analysis
- To introduce the statistical and multi-scale nature of residually stressed and strained states
- To introduce key experimental approaches to residual stress evaluation
- To discuss the Focused Ion Beam – Digital Image Correlation (FIB-DIC) technique
- To introduce synchrotron X-ray diffraction methods for residual stress analysis
- To introduce the concept of 3D strain analysis by diffraction strain tomography

Introduction

Residual stresses represent internal forces that persist inside solid objects upon the removal of all external mechanical loads and constraints. The very nature of this definition implies the presence of some internal source(s) of residual deformation that gives rise to residual stresses. To identify these sources, it is instructive to consider the additivity of strain expressed by the simple formula

$$\varepsilon^{tot} = e + \varepsilon^{*}. \tag{1}$$

Here the total strain is additively decomposed into elastic strain denoted e and inelastic part denoted ε^* that is often termed *eigenstrain* in the literature (Mura, 1982; Korsunsky, 2017). *Eigenstrain* represents *material memory* of inelastic deformation that may be induced by plastic flow, phase transformation, spatially inhomogeneous thermal expansion, and imaginary cutting and gluing exercises (Hills et al., 1996). The total strain ε^{tot} must satisfy Saint-Venant's compatibility equations to preserve material continuity, while the elastic strain via the generalized Hooke's law is linked to the stresses that must satisfy equilibrium conditions.

https://doi.org/10.1016/B978-0-323-90800-9.00215-8

Eigenstrain theory

The problem of residual stress determination from a known *eigenstrain* distribution – the *direct problem* of *eigenstrain* (Korsunsky, 2017) – is simple and can be readily solved using analytical or numerical approaches, e.g., by imposing *eigenstrain* as pseudo-thermal strain distributed within the volume of consideration. Examples of *eigenstrain* acting as a source of residual stress can be drawn from the solutions in the theory of elasticity (Love, 1944; Eshelby, 1957). Further examples of nuclei of strain (term used by Mindlin and Cheng, 1950) can be derived for more complex situations e.g., related to problems in the theory of fracture (Korsunsky, 2017, 1995; Hills et al., 1996).

In most practically relevant problems, however, the underlying distribution of eigenstrain that gives rise to the residual stress distribution is unknown. This gives rise to the *inverse problem* of *eigenstrain*, namely, its determination from partially evaluated distribution of residual stress, residual elastic strain (also referred to as r.e.s.) denoting the elastic strain e that is present within an unloaded solid object complying simultaneously with the compatibility and equilibrium equations. The inverse problem of *eigenstrain* is a hard problem in the sense that it is implicit and can be ill-posed in terms of non-uniqueness of solution and limited extent of input data for *eigenstrain* reconstruction.

A number of methodologies have been proposed for the solution of the inverse problem of *eigenstrain*. The most straightforward approach involves the representation of *eigenstrain* distribution as a weighted sum of basis functions that may be globally defined on the entire domain of consideration or locally, e.g., in the form of element-based or radial basis functions related to specific locations within the sample. Using this representation, the residual stresses can be obtained as a linear sum of basis solutions of the direct problem of *eigenstrain* with the same weights. Optimal matching of the linear sum representation to the observations e.g., by minimizing the sum of squared mismatch values with respect to the unknown coefficients via non-iterative inversion of the linear system of equations (Korsunsky, 2017). Further refinement of the approach can be derived using variational calculus, e.g., using the complementary energy functional in the form (Wang et al., 2022):

$$\Pi\left(\sigma_{ij}, \varepsilon_{ij}^{*}\right) = \int_{V} B\left(\sigma_{ij}\right)\mathrm{d}V - \int_{S_u} \sigma_{ij} n_j \overline{u_i}\mathrm{d}S + \int_{V} \sigma_{ij}\varepsilon_{ij}^{*}\mathrm{d}V. \tag{2}$$

Here the boundary displacement $\overline{u_i}$ is known on the part of the boundary S_u of the material volume V, and $B(\sigma_{ij})$ is the complementary energy defined by its relation to the elastic strain ε_{ij}^{e},

$$\frac{\mathrm{d}B\left(\sigma_{ij}\right)}{\mathrm{d}\sigma_{ij}} = \varepsilon_{ij}^{e}. \tag{3}$$

Thus, if the inelastic strain (eigenstrain) ε_{ij}^{*} is known throughout the body, then the residual stress distribution σ_{ij} is found to deliver a stationary value to the variation of the above functional $\delta\Pi$, thus providing the solution to the *direct problem of eigenstrain*. If the eigenstrain ε_{ij}^{*} is unknown, the above formulation can be modified to account for a region of known stress, and the eigenstrain determined, providing the solution to the *inverse problem of eigenstrain*.

A key aspect of residual stress state is that the distributions must be self-equilibrating in terms of force and moment balance. Importantly, this requirement applies not only to the entire volume of the object being considered, but also to any subset of it that can be obtained by real or imaginary sectioning. Sub-volumes of material must experience self-equilibrating surface tractions that are found at its surfaces during imaginary sectioning. This thought experiment immediately leads to the realization that residual stresses possess hierarchical nature and can be thought of at different scales depending on the choice of imaginary section dimensions.

Stress and strain multi-scaling

To aid the appreciation of the hierarchy of internal stresses, classifications related to scale have been introduced (Davidenkov, 1950; Hauk, 1997). This is concisely expressed in the additive scale-related decomposition that can be applied to both stresses and strains:

$$\sigma = \sigma^{I} + \sigma^{II} + \sigma^{III}, \varepsilon = \varepsilon^{I} + \varepsilon^{II} + \varepsilon^{III}. \tag{4}$$

Type I stresses and strains are associated with the overall geometry of an engineering component or sample, typically varying smoothly on the scales from millimeters to meters and greater. A key aspect of Type I stresses (and strains) is the assumption that material can be thought of as continuum with uniform or slowly varying properties. In contrast, Type II stresses and strains manifest themselves at the scale of typical microstructural elements of metallic and ceramic polycrystals, i.e., grains that possess distinct lattice orientation and associated orientation-dependent elastic and plastic properties (anisotropy). Type II stress and strain components represent grain-average deviation (addition) to Type I macroscopic continuum base line (Fig. 1B). Type III stresses and strains represent the additional deviation from Type I+II values associated with intragranular crystal lattice defects that can be discerned on the scale from hundreds down to single nanometers. A rational physical explanation for the emergence of these distinct scales has been proposed (Korsunsky and Salimon, 2018) in relation to the prevalence of distinct sets of equations of mathematical physics at each recognizable scale that determine the deformation behavior and its suitable description.

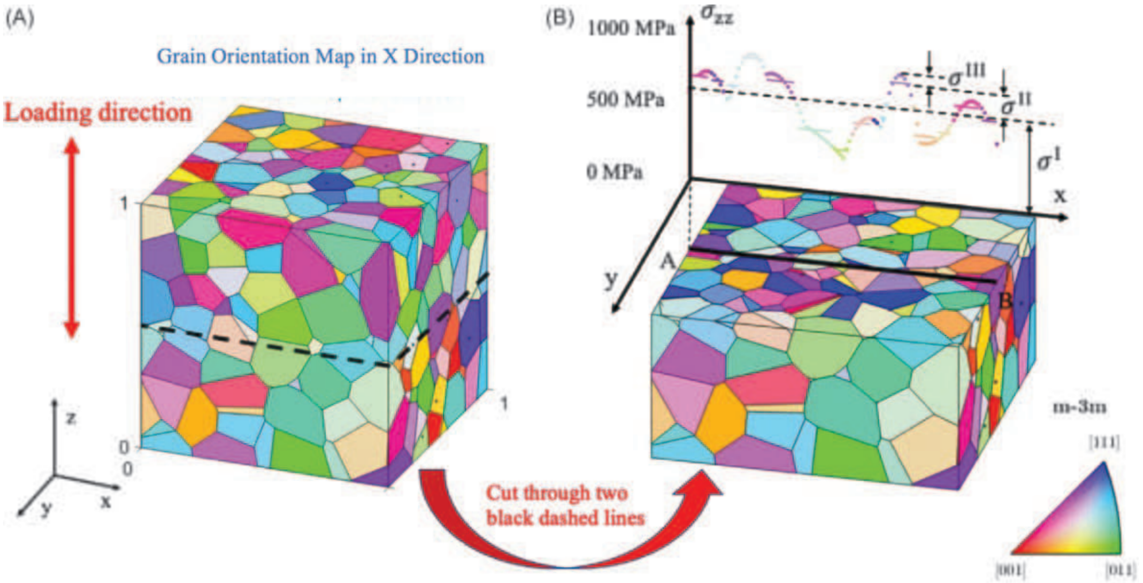

Fig. 1 (A) The microstructure of a metallic alloy representative volume element (RVE), with (B) superimposed line profile of a residual stress component variation obtained by crystal plasticity finite element modelling (CPFEM). Reproduced with permission from Chen JW, Wang Z, and Korsunsky AM (2022) Multiscale stress and strain statistics in the deformation of polycrystalline alloys. *International Journal of Plasticity* 152: 103260.

Statistical considerations

It is further possible to consider the problem of internal stresses and strains within the framework of multi-scale statistics description. To aid discussion, we borrow the illustration in Fig. 1 from (Chen et al., 2022) that shows a line profile of a particular component of (residual) stress obtained from crystal plasticity finite element model (CPFEM) that has received extensive validation against experimental methods of residual stress evaluation (discussed later here). Viewed at the finest (nanometric) scale of discretization and evaluation, the line profile of residual stress represents a one-dimensional signal that contains high and low frequency components. The application of a low pass filter to this profile returns a representation of the stress variation that is smoothed to a chosen extent (length scale) that can be chosen e.g., to obtain Type I contribution. The application of an intermediate pass filter similarly returns Type I+II sum, so that Type II stress profile can be obtained as the difference. Finally, the subtraction of the Type I+II sum from the original distribution returns Type III contribution.

The above discussion paves the way to further spectral analysis of stress contributions at different length scales as a function of the spatial period of variation. To illustrate the idea, the left panel in Fig. 2 shows a line profile of a stress component along with the right panel containing an annotated *periodogram*, i.e., a power spectral density plot. For convenience of analysis, the RVE was chosen to extend from −0.5 to 0.5 consistently with the accepted convention in spectral signal analysis. Since the modelling approach used in the CPFE simulation of Fig. 1 did not contain explicit description of intragranular defects (strain nuclei), the profile was enhanced with random variation at this scale, as can be seen in Fig. 2A. Spectral analysis illustrated in Fig. 2B allows three ranges to be identified. Namely, at length scales exceeding 0.25 units (approximately twice the linear grain size) the periodogram appears appreciably flat and corresponds to Type I residual stress variation at the longer (super-granular) length scale. The range between 0.1 and 0.25 units shows a transition that covers the intermediate scale that corresponds to Type II (inter-granular) length scale. Finally, in the range below 0.1 units the periodogram shows further increase in magnitude toward the maximum observed for the smallest dimensions and corresponds to the Type III (intra-granular) length scale.

The approach outlined in the paragraph above sets the basis for a range of further possible generalizations. For example, the highly successful Krylov-Bogolyubov method of approximations for oscillating mechanical systems has not been applied, to the best of our knowledge, to two- or three-dimensional distributions of strains and stresses in deformable solids. To a large extent this can be explained by the experiment impediments to obtaining sufficiently reliable and detailed 2D and 3D maps of these complex multi-component quantities, in contrast with the ready availability of 1D signal data. However, in recent decades significant advances were made using experimental techniques based on strain relief (mechanical milling and sectioning) and high-resolution strain mapping that employ focused X-ray and electron beams.

'*Live*' vs *residual* strains and stresses

Before embarking on the more in-depth discussion of experimental techniques for strain measurement and stress evaluation, it is important to establish a distinction between strains that are observed to evolve 'live' from initial to current state, on the one hand,

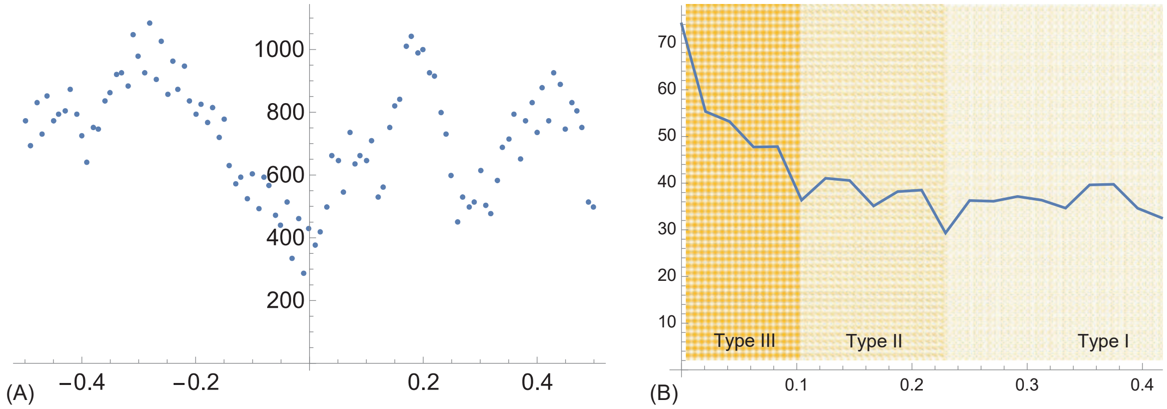

Fig. 2 (A) Line profile from Fig. 1B modified to introduce short range stresses reflecting intragranular variation, and (B) "periodogram" of the distribution with the Type I, II and III ranges indicated.

and strains that persist within an object or sample as a consequence of processing that was not or could not be observed; in other words, when a 'reference state' is not known.

The concepts of 'reference state' and 'current state' are generally important and worth dwelling on here. In traditional continuum solid mechanics, as the material is considered to be homogeneous and structure-free, it is natural to assume that the reference state corresponds to the situation when there is neither elastic nor inelastic strain present in it, and all subsequent deformation can be measured in relation to that state. In many cases when small deformations are considered, it is convenient and suitable to use Lagrangian description that follows individual material 'particles'.[1] Tracking the field of displacements of these particles throughout the deformation from the reference to the current state furnishes complete information sufficient to compute the strain field. This task is most conveniently accomplished using Digital Image Correlation (DIC) (Paine, 1986) for 2D mapping of surfaces (or 2D projections for non-flat samples), or Digital Volume Correlation (DVC) (Baimpas et al., 2012) for 3D mapping when non-destructive volumetric imaging can be obtained using X-ray, optical, or other tomography techniques. A noteworthy demonstration of 2D mapping of 3D displacements at sample surface using height-sensitive Digital Image Correlation (hDIC) employing image stacking optical microscopy is presented in Uzun and Korsunsky (2019). Numerous examples can also be found in the literature illustrating DVC deformation mapping in 3D (Baimpas et al., 2012).

Digital image correlation (DIC)

DIC and/or DVC mapping of displacements thus provides a general solution to the problem of 'live' strain evaluation. It can be accomplished using digital imaging techniques at any resolution sought (subject to resolution attainability). Note that the total strain field thus obtained does not provide decomposition into elastic and inelastic parts according to Eq. (1). Since the former is required to evaluate the stress field, there remains the need to employ some means of separating the elastic strain.

Further challenges arise when the reference state cannot be registered prior to deformation, precluding the possibility of displacement tracking. Indirect approaches have been proposed that monitor some aspect of material physical response to external excitation to deduce the local residual stress state via its coupling to, e.g., magnetic permeability, birefringence, spectroscopic signature (Raman), hardness, etc. While these techniques provide useful guidance, they are often qualitative, sensitive to hydrostatic stress rather than specific components, and restrictive in terms of materials classes (ferromagnetic steels, transparent polymers), and will not be considered further here.

A general quantitative approach to residual stress evaluation involves minimally disturbing material removal associated with the creation of new surfaces and unloading (reduction of tractions), sometimes incorrectly referred to as 'strain relaxation' – this implies inelastic deformation, whereas in fact the assumption is made of only elastic *strain relief* taking place. As a consequence, at least some material volumes undergo partial or complete unloading back toward the strain-free reference state, allowing the current state to be reconstructed via numerical analysis.

The following sections are devoted to the techniques for quantitative experimental evaluation of residual strain and stress tensors. These form two principal classes, namely, the partially destructive material removal and strain relief methods, and the diffraction methods.

---

[1] It is worth noting that this principle, however, requires the installation (or, at least, identification) of embedded 'markers' and thus contradicts the assumption of featureless continuum.

Experimental techniques

The experimental evaluation of residual stress must be understood precisely. In practice, it is not possible to *measure* stress because of its definition as internal force component acting on a chosen imaginary cross-sectional area. At best, the force may be assessed, but in practice most of the time it is the deformation parameters (displacements and strains) that are measured, while stress is deduced. This is aided by the universality of the Hooke's law that can be understood to act both ways: stress is expressed as the sum of products of material stiffnesses by the corresponding components of elastic strain; and conversely, elastic strains can be thought as those obtained from partitioning in Eq. (1) that are related to the stresses via Hooke's law. Thus, the determination of elastic strains is tantamount to indirect stress evaluation because of the necessary further step of Hooke's law application that carries unavoidable additional uncertainties.

As noted above, a particular difficulty in residual stress evaluation through elastic strain measurement is that the reference state is no longer accessible by the time the sample is provided – otherwise it would be possible to trace the evolution of elastic strains throughout the processes that led to the residually stressed current state. However, such is the complexity of such processes as casting, rolling, hot forging, machining etc. that are known to give rise to residual stresses that it is practically not possible to equip the object with spatially distributed markers for strain monitoring. Furthermore, in all of these processes strain arises as a combination of elastic and inelastic parts, presenting the additional challenge of their separation according to Eq. (1) for the purpose of stress evaluation.

The paradigm of residual stress evaluation illustrated in Fig. 3 is based on material removal (severing the material connections that transmit internal stress) accompanied by monitoring and quantifying the induced strain relief (Lunt and Korsunsky, 2015). These examples are drawn from microscopic studies (note the scale bars) but represent the geometries commonly used at the macro-scale, also illustrating the scalability of this class of approaches. The two crucial aspects here concern the availability of the means of precise minimally disturbing milling and strain evaluation at the appropriate resolution. In the case of macroscopic analysis, high speed milling, drilling and electric discharge machining are used in combination with strain gages, touch probe or optical profilometry (Schajer, 1992; Prime, 2001). At the micro- to nano-scales, experiments are performed within the vacuum chamber of a Focused Ion Beam – Scanning Electron Microscope (FIB-SEM) instrument, with ion particles used for material removal and electrons for surface imaging.

Material removal method illustration: FIB-DIC

We dwell here in particular on the discussion of the micro-ring-core FIB-SEM method (Fig. 3C) (Korsunsky et al., 2008) that provides a convenient illustration of the key aspects of material removal and relief methods. In this method, the severing of the

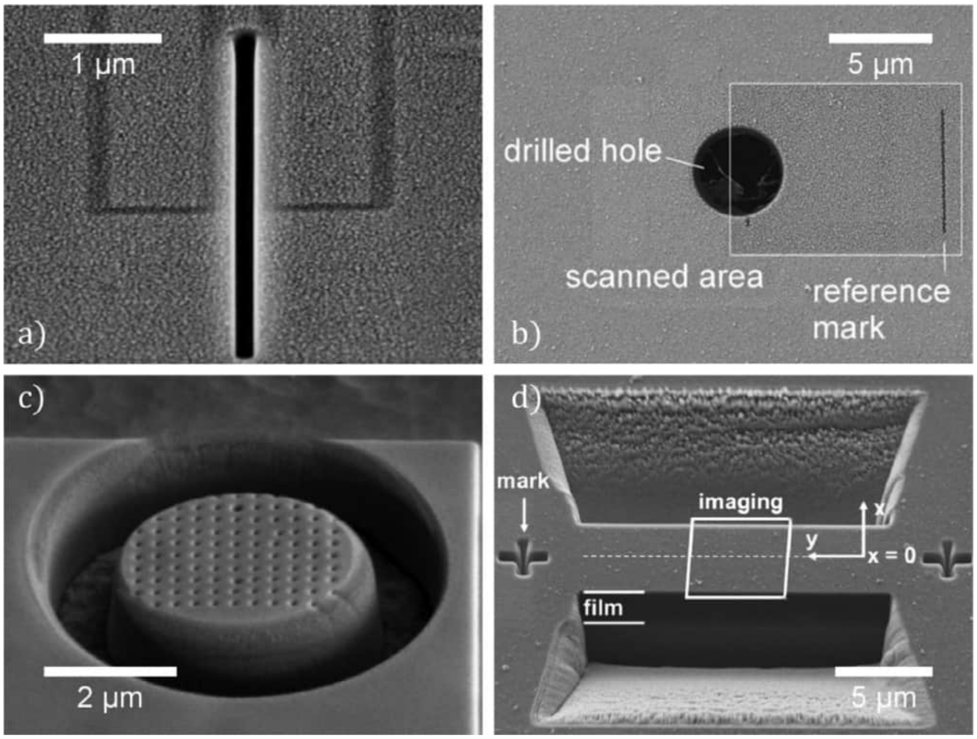

Fig. 3 A gallery of material removal and strain relief geometries: (A) Slitting, (B) Blind hole drilling, (C) Ring-core milling, (D) H-bar geometry. Reproduced with permission from Lunt AJG and Korsunsky AM (2015) A review of micro-scale focused ion beam milling and digital image correlation analysis for residual stress evaluation and error estimation. *Surface and Coating Technology* 283: 373–388.

connections between the central micropillar and the surrounding material leads to progressive unloading from the prior residual stress as the cut deepens. When the circular ‘trench’ depth becomes equal to the central pillar diameter, surface relief becomes complete (Salvati et al., 2019). The method thus represents the embodiment of the principle of strain relief back to the reference state. The strain change that is registered at the micropillar top surface due to milling represents the opposite of the local residual elastic strain that was present in the residually stressed sample. In accordance with the aforementioned scale-dependent definition of strain and stress, the micropillar diameter sets the scale for averaging, so that a single value of each strain and stress component should be assigned to the entire volume to avoid ambiguity. The smallest reported diametral dimension of the micro-pillar used in the FIB-DIC micro-ring-core method was smaller than one micron (Salvati et al., 2019). It should be known that the macroscopic equivalent known as the ring-core method has been known since 1950s and more recently described in detail by Keil (1992).

Exhaustive reviews of the experimental procedure and data analysis and interpretation for the FIB-DIC micro-ring-core method were provided by Lunt (Lunt and Korsunsky, 2015). Salvati et al. (2016a, b) considered the effects of material elastic anisotropy on the strain relief and incorporated this in the procedure for residual stress evaluation. This important advance opens up the path toward probing local grain scale effects in metallic and ceramic materials with clearly defined crystalline grains of specific orientation that can be determined, e.g., using back-scattered electron diffraction (EBSD).

Depth profiling of residual stress using the FIB-DIC micro-ring-core method has pushed the limit of the spatial resolution toward the nano-scale, with the smallest reported resolution step being as small as 50 nm (Salvati et al., 2019). This has been accomplished using multiple core diameters and employing eigenstrain-based analysis.

The micro-scale nature of the FIB-DIC micro-ring-core method allowed performing studies that reveal the multi-scale and statistical nature of residual stress states in polycrystalline materials. Everaerts et al. (2018) carried out the evaluation of residual stress in a laser shock peened sample with the average grain size of 6 μm. Fig. 4 illustrates the alloy microstructure (Fig. 4A) along with FIB-DIC data obtained using 5 μm and 10 μm diameter micro-ring-core milling (Fig. 4B). Fig. 4C shows the comparison with the measurements carried out about a decade earlier using an alternative technique of synchrotron X-ray diffraction (see discussion below). There is a significant disagreement (Fig. 4B) between the two sets of results that could be incorrectly attributed to residual stress modification (relaxation). However, once the core diameter was increased to 10 μm, much better match is obtained between these independent methods. The difference between the results obtained from FIB-DIC micro-ring-core must be attributed to the

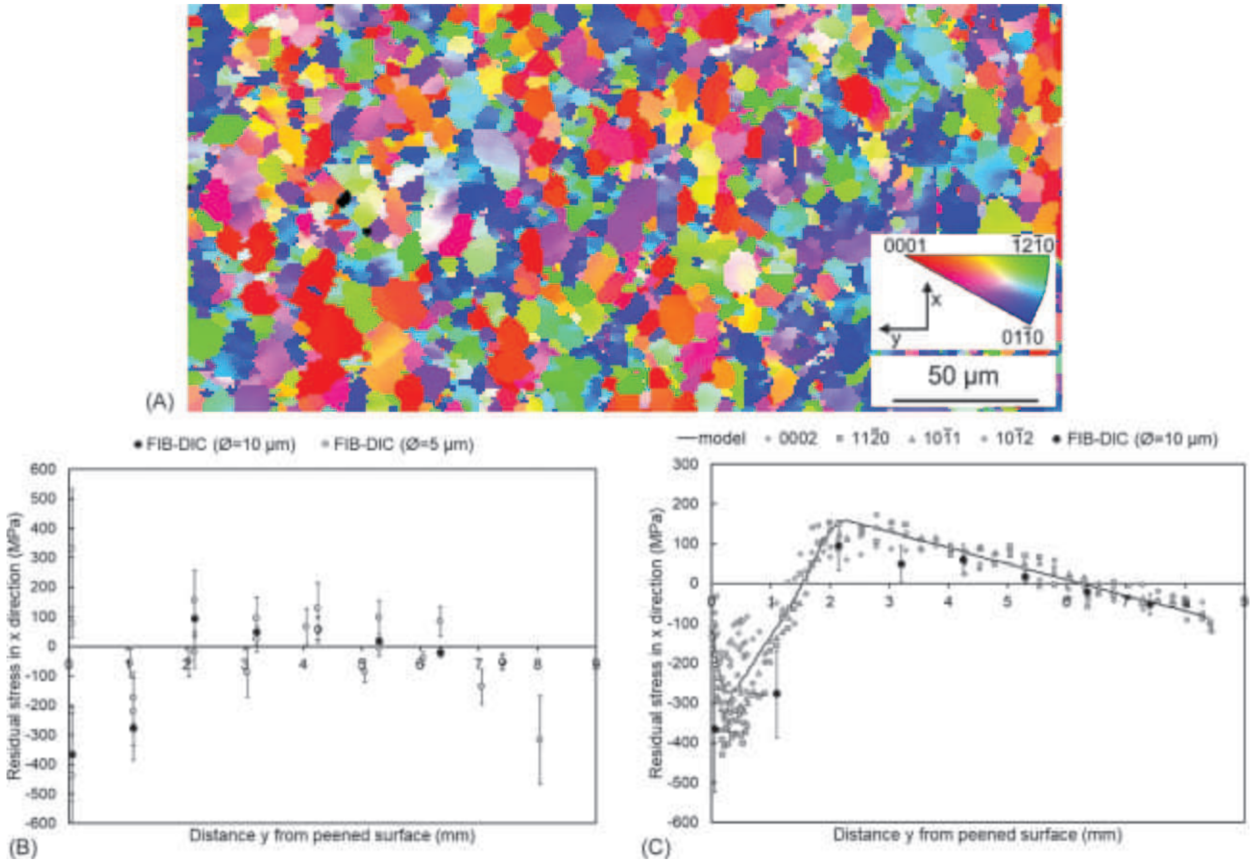

Fig. 4 (A) EBSD map of Ti-6Al-4V alloy bar. (B) Results of FIB-DIC evaluation of residual stress using ring-core diameters of 5 μm and 10 μm. (C) Comparison of 10 μm ring-core FIB-DIC results with synchrotron XRD profiling of residual stress. Reproduced with permission from Everaerts J, Song X, Nagarajan B, Korsunsky AM (2018) Evaluation of macro-and microscopic residual stresses in laser shock-peened titanium alloy by FIB-DIC ring-core milling with different core diameters. *Surface and Coating Technology* 349: 719–724.

scale dependence of residual stress: 5 μm diameter core measurements contain information about both Type I and Type II contributions to the residual stress, while 10 μm appears to provide sufficient averaging similar to that achieved using large scattering volume used in the synchrotron X-ray experiment (Korsunsky et al., 2006a) to reveal pure Type I stress contribution.

The results obtained in this study motivated a further investigation (Salvati and Korsunsky, 2017) aimed at revealing the statistical multi-scale nature of residual stress states within metallic polycrystals. An aluminum alloy polycrystal sample in a form of bar was subjected to plastic bending to create a controlled distribution of residual stresses of Type I, II and III. The macroscopic stress-strain curve of the material was collected and used to calibrate the continuum description of the plastic flow that was incorporated into a finite element model of the bending process. The model was validated through comparison with the observation of sample bending and matching the residual bending curvature. In addition, crystal plasticity finite element modelling (CP-FEM) was carried out that provided numerical prediction of local residual stresses (Type I + II). FIB-SEM evaluation of residual stress was carried out to obtain experimental values of Type I + II + III stresses.

Comparison between the modelling and experimental data obtained demonstrated that the microscopic (Type II + III) residual stresses possess significant statistical variation that obeys a Gaussian distribution with the width that is comparable in magnitude with the local Type I stress value. It is important to note that this statistical variation represents the physical nature of the complex internal stress state within the material and should not be confused with random measurement error or scatter.

Diffraction

Crystalline materials are distinguished by the presence of a regular internal lattice composed of repeated pattern (unit cell) that fills the space in a repeated manner and is characterized by a long-range order with specific dimensional periods depending on the chosen direction. The fact that lattice periods for metallic and ceramic materials typically lie in the range 1-10 Å was discovered by Laue and *co*-workers when they successfully conducted first polychromatic X-ray diffraction experiments to reveal crystal symmetries and formulated the relationship between the radiation wavelength, interplanar lattice spacings and scattering angles. This was subsequently expressed by Braggs in the form of the simple equation

$$2d\sin\theta = \lambda, \tag{5}$$

where θ is half of the scattering angle 2θ. The above expression signifies that the interaction of material with any penetrating radiation of a suitable wavelength provides a means of precise measurement of lattice spacing and its change. For example, if monochromatic radiation with a precisely set wavelength is used, then the following relationship between lattice spacing change δd and angle change $d\theta$ can be obtained:

$$\delta d\sin\theta + d\cos\theta\delta\theta = 0. \tag{6}$$

If the lattice parameter change is induced by elastic strain, then it can be expressed from the above equation as

$$\varepsilon^{el} = \frac{\delta d}{d} = -\cot\theta\delta\theta. \tag{7}$$

The application of Bragg's law to the problems in the mechanics of materials provides a means of elastic strain evaluation by monitoring the variation of scattering angle 2θ as a function of applied or residual stress. Beams of electrons or X-rays commonly employed for this purpose are often monochromated to fix the radiation wavelength and collimated to define the interaction volume within which the measurement is performed.

The advantage of the above method is that it does not require the introduction of markers nor material milling, and thus can be classed as truly non-destructive. Furthermore, inelastic deformation such as crystal slip is associated with lattice plane gliding and not dilatation (change of spacing), so diffraction provides a means of separating the total strain into the elastic (measured) part and inelastic part. Due to the geometrically precise nature of beam-materials interaction, the strain component (direction) determined in this way is precisely defined, allowing in principle the complete elastic strain tensor to be determined. As specific lattice reflections are employed, the method also allows distinguishing between different crystallographic and thermodynamic phases.

A major challenge in applying the diffraction method to residual elastic strain determination is the need for the reference state information, namely, the unstrained lattice parameter value d to be used in Eq. (7). This requirement is often dealt with by grinding the material into fine powder effectively making use of the approach mentioned above: relieving surface tractions on small particles to allow their internal stresses to reduce to zero. Scattering from untextured powders provide azimuthally symmetric scattering of incident beam into a family of Debye-Scherrer cones with half-angles of 2θ. In contrast, textured polycrystals often display strong variation of intensity around the azimuthal angle along with a weak variation in the scattering angles since elastic strains in crystalline materials typically do not exceed 1%.

However, elastic strain is not the only nor the principal source of lattice parameter variation, since compositional variations also induce significant changes in the lattice parameters and are widely reported in welds, castings, etc. As a means of avoiding the need to determine the unstrained lattice parameter, the so-called $\sin^2\psi$ method is often employed (Romano-Brandt et al., 2020).

An important aspect of diffraction-based strain evaluation concerns the use of white (polychromatic) X-ray beams that produce scattering patterns consisting of discrete peaks. These patterns (sometimes referred to as *Lauegrams*) contain information about crystal lattice orientation (rotation) and distortion (strain). Recent decades have seen progressive use of X-ray beams focused into tight spots of a few microns and down to 100 nm or smaller. This allows probing intragranular strains and stresses corresponding to the Type I + II + III sum of components, opening the way to further development of the multi-scale statistical description of these complex distributions of deformation parameters. A key advantage of micro-beam Laue diffraction concerns the ability to obtain information from severely deformed material volumes compared, e.g., with electron diffraction analysis used in EBSD (see below). Important advancements in *Lauegram* evaluation have been achieved by applying DIC to their interpretation that allows higher precision detection of grain rotations and small strains (Petit et al., 2015).

Electron Back-Scattered Diffraction (EBSD) is a well-established electron microscopy technique employed for surface mapping of the sample grain structure and micro-texture evaluation. This is achieved by the analysis of the so-called Kikuchi bands formed by the scattering of conically divergent secondary electron beams originated under sample surface. The detection of small changes in the Kikuchi patterns using DIC analysis to determine elastic strains has become known as HR-EBSD (Wilkinson et al., 2006). Plastic strains cause deterioration of Kikuchi pattern quality that allows qualitative mapping of inelastic deformation but places a limit on elastic strain evaluation due to the loss of fitting accuracy.

An important aspect of EBSD is the possibility of combining it with FIB serial sectioning to obtain three-dimensional maps of grain orientation. This tomographic method provides a resolution of one of the central problems of materials science, namely, 3D visualization of grain structure down to the nanometer level. In principle, this approach can be used for 3D strain evaluation using HR-EBSD, with the following two caveats. Firstly, the act of material FIB removal causes stress re-equilibration and strain redistribution that must be taken into account, e.g., using eigenstrain analysis. Secondly, the process of ion milling may itself introduce additional eigenstrain sources of residual stress and residual elastic strain (Salvati et al., 2016a, b). One of the challenges in implementing this approach lies in the difficulty of identifying or producing a sample with known micro- to nano-scale residual stress-strain state that can be used for validation.

'Rich' tomography of strain and stress

One of the most challenging tasks in residual stress analysis concerns non-destructive evaluation of 3D strain distribution at desired resolution and with adequate statistical reliability. This is most likely achieved using diffraction methods combined with tomographic reconstruction techniques.

Initial feasibility study of strain reconstruction tomography (Korsunsky et al., 2006a,b) made use of the algebraic reconstruction technique applied to strain component aligned with the axis of rotation. This principle later became referred to as the rotational invariance of the scattering pattern. The choice of the axial scattering component allows the reduction of the complex tensor tomography problem to that of a scalar. A subsequent study (Korsunsky et al., 2011) provided demonstration that the strain value determined from the scattering pattern from a pencil-shaped gage volume illuminated by the incident beam equates to the mean of the strain distribution within it. With appropriate data pre-processing this permits determination of the strain distribution within the entire sample cross section which was validated by comparison with numerical deformation modelling.

Collectively, the family of 'rich' tomography techniques can be defined as the reconstruction of three-dimensional fields that take vector, tensor or function (distribution) values. In recent years this has been applied to the analysis of Small Angle X-ray Scattering (SAXS) data to determine fibrillar orientation within polymers and biological tissues.

Influence of residual stress on structural integrity

A range of studies reported in the literature considered the influence of residual stress on structural integrity (Bouchard, 2001). It is often stated that compressive residual stress inhibits the formation of cracks and their growth that leads to component failure, while tensile stress promotes crack formation and reduces safe life. In practice, more detailed and precise consideration of the modes of loading, damage and failure is required for successful residual stress engineering – tailoring material processing to control residual stress for maximum structural integrity under given service conditions.

Structural integrity can be understood as the fracture resistance and load-bearing limit under monotonic, cyclic or long-term loading. Material capacity to withstand external loading depends not merely on the mean (Type I) stress within it, but also on the local peak values representing Type I + II + III applied stresses in combination with residual stresses at appropriate scales.

The approach to residual stress and strain analysis presented above suggests that in the same way as these physical quantities display statistical character and depend on the scale of consideration, so must their limiting values that appear in the criteria for damage initiation and growth or failure. In other words, the presented multi-scale analysis of stresses and strains necessitates scale-dependent structural integrity approach. This methodology is in the early stages of development in such important areas as structural composites, energy storage devices etc., and is expected to undergo a period of active advancement in the coming decade.

Conclusion

The present treatment began with aspects of theoretical description of the multi-scale, statistical distributions of internal stresses and strains within engineering materials and components, particularly using the concept of *eigenstrain*. This was necessitated by the fact that this theoretical framework is indispensable for correct evaluation of residual stress independently of the chosen experimental approach. Furthermore, statistical description must be employed in a manner that preserves consistency across different scales (Krylov and Bogolyubov, 1937).

A crucial aspect of a valid residual stress state within a sample is that it must comply with volumetric relationships (equations of equilibrium) and surface conditions (traction-free). Accordingly, there has been progression toward residual stress evaluation using eigenstrain-based description that involves the entire object and ensures compliance with the constraints of materials mechanics. It has been shown that the incorporation of eigenstrain confers advantages in the use of established approaches, such as the contour method and residual stress depth profiling using incremental drilling, or FIB-DIC micro-ring core milling.

The presented summary of experimental techniques of residual stress evaluation covered the two principal classes, namely, material removal and diffraction-based methods. State-of-the-art review was followed by the discussion of new and developing approaches, such as 'rich' tomography of strain.

References

Baimpas N, Xie MY, Song X, Hofmann F, Abbey B, Marrow J, Mostafavi M, Mi J, and Korsunsky AM (2012) Rich tomography techniques for the analysis of microstructure and deformation. In: *International Conference on Experimental Mechanics (ACOME), Vietnam*.

Bouchard PJ (2001) Residual stresses in lifetime and structural integrity assessment. In: *Encyclopedia of Materials: Science and Technology*, pp. 8134–8142. Elsevier.

Chen JW, Wang Z, and Korsunsky AM (2022) Multiscale stress and strain statistics in the deformation of polycrystalline alloys. *International Journal of Plasticity* 152: 103260.

Eshelby JD (1957) The determination of the elastic field of an ellipsoidal inclusion, and related problems. *Proceedings of the Royal Society of London* A241: 376–396.

Everaerts J, Song X, Nagarajan B, and Korsunsky AM (2018) Evaluation of macro-and microscopic residual stresses in laser shock-peened titanium alloy by FIB-DIC ring-core milling with different core diameters. *Surface and Coating Technology* 349: 719–724.

Hauk V (1997) *Structural and Residual Stress Analysis by Non-destructive Methods*. Amsterdam: Elsevier.

Hills DA, Kelly PA, Dai DN, and Korsunsky AM (1996) *Solution of Crack Problems - The Distributed Dislocation Technique*. Dordrecht: Springer.

Keil S (1992) Experimental determination of residual stresses with the ring-core method and an on-line measurement system. *Experimental Techniques* 16(50): 17–24.

Korsunsky AM (1995) Fundamental eigenstrain solutions for axisymmetric crack problems. *Journal of the Mechanics and Physics of Solids* 43(8): 1221–1241.

Korsunsky AM (2017) *A Teaching Essay on Residual Stresses and Eigenstrains*. Oxford: Elsevier.

Korsunsky AM and Salimon AI (2018) On the paradigm of hierarchically structured materials, in conjunction with the virtual special issue on functional materials. *Materials & Design* 158: 1–4.

Korsunsky AM, Liu J, Laundy D, Golshan M, and Kim K (2006a) Residual elastic strain due to laser shock peening: Synchrotron diffraction measurement. *Journal of Strain Analysis for Engineering Design* 41: 113–120.

Korsunsky AM, Vorster WJJ, Zhang SY, Dini D, Latham D, and Golshan M (2006b) The principle of strain reconstruction tomography: Determination of quench strain distribution from diffraction measurements. *Acta Materialia* 54(8): 2101–2108.

Korsunsky AM, Sebastiani M, and Bamporad E (2008) Focused ion beam ring drilling for residual stress evaluation. *Materials Letters* 63(22): 1961–1963.

Korsunsky AM, Baimpas N, Song X, Belnoue J, Hofmann F, and Abbey B (2011) Strain tomography of polycrystalline zirconia dental prostheses by synchrotron X-ray diffraction. *Acta Materialia* 59(6): 2501–2513.

Krylov NM and Bogolyubov NN (1937) *Introduction to non-linear mechanics* (in Russian). Kiev: Izdatel'stvo AN SSSR.

Love AEH (1944) *A Treatise on the Mathematical Theory of Elasticity*, 4th edn. New York: Dover.

Lunt AJG and Korsunsky AM (2015) A review of micro-scale focused ion beam milling and digital image correlation analysis for residual stress evaluation and error estimation. *Surface and Coating Technology* 283: 373–388.

Mindlin RD and Cheng DH (1950) Nuclei of strain in the semi-infinite solid. *Journal of Applied Physics* 21: 926.

Mura T (1982) *Micromechanics of Defects in Solids*. Dordrecht: Kluwer.

Davidenkov NN (1950) On the measurement of residual stresses. *Industrial laboratory/Materials diagnostics* 16(2): 188.

Paine SH (1986) An evaluation of errors in automated digital image correlation. *Canadian Journal of Remote Sensing* 12(2).

Petit J, Castelnau O, Bornert M, Zhang FG, Hofmann F, Korsunsky AM, Faurie D, Le Bourlot C, Micha JS, Robach O, and Ulrich O (2015) Laue-DIC: a new method for improved stress field measurements at the micrometer scale. *Journal of Synchrotron Radiation* 22(4): 980–994.

Prime MB (2001) Cross-sectional mapping of residual stresses by measuring the surface contour after a cut. *Journal of Engineering Materials and Technology* 123: 162–168.

Romano-Brandt L, Salvati E, Le Bourhis E, Moxham T, Dolbnya IP, and Korsunsky AM (2020) Nano-scale residual stress depth profiling in Cu/W nano-multilayers as a function of magnetron sputtering pressure. *Surface and Coating Technology* 381: 125–142.

Salvati E and Korsunsky AM (2017) An analysis of macro-and micro-scale residual stresses of Type I, II and III using FIB-DIC micro-ring-core milling and crystal plasticity FE modelling. *International Journal of Plasticity* 98: 123–138.

Salvati E, Sui T, and Korsunsky AM (2016a) Uncertainty quantification of residual stress evaluation by the FIB–DIC ring-core method due to elastic anisotropy effects. *International Journal of Solids and Structures* 87: 61–69.

Salvati E, Sui T, Lunt AJG, and Korsunsky AM (2016b) The effect of eigenstrain induced by ion beam damage on the apparent strain relief in FIB-DIC residual stress evaluation. *Materials & Design* 92: 649–658.

Salvati E, Romano-Brandt L, Mughal MZ, Sebastiani M, and Korsunsky AM (2019) Generalised residual stress depth profiling at the nanoscale using focused ion beam milling. *Journal of the Mechanics and Physics of Solids* 125: 488–501.

Schajer GS (1992) Non-uniform residual stress measurements by the hole drilling method. *Strain* 28(1): 19–22.

Uzun F and Korsunsky AM (2019) The height Digital Image Correlation (hDIC) technique for the identification of triaxial surface deformations. *International Journal of Mechanical Sciences* 159: 417–423.

Wang JL, Zhang JB, Chen Z, and He L (2022) Hellinger–Reissner variational principle for a class of specified stress problems. *International Journal of Nonlinear Sciences and Numerical Simulation*. https://doi.org/10.1515/ijnsns-2021-0039.

Wilkinson AJ, Meaden G, and Dingley DJ (2006) High-resolution elastic strain measurement from electron backscatter diffraction patterns: New levels of sensitivity. *Ultramicroscopy* 106(4–5): 307–313.

Terahertz nondestructive evaluation of additively manufactured and multilayered structures

Alexander T Clark, Jessy Nemati, Christopher Bolton, Nickolas Warholak, Jimmie Adriazola, Ian Gatley, Samuel Gatley, and John F Federici, Department of Physics, New Jersey Institute of Technology, Newark, NJ, United States

© 2024 Elsevier Ltd. All rights reserved.

Introduction **602**
Terahertz nondestructive evaluation 602
Additive manufacturing—Plastics and ceramics 602
THz NDE of multilayer paint stacks 603
Additive manufacturing **603**
THz spectral characterization of materials 604
Additively manufactured THz optical components 604
THz NDE of additively manufactured components 605
THz NDE of infill structures 607
THz imaging of defects 607
Effect of 3D printing parameters on FDM printed components 608
Refractive effects 610
THz computed tomography of additively manufactured components 610
Birefringence 614
Multilayer paint stacks **618**
Terahertz NDE of multilayer paints 618
Terahertz NDE of paint corrosion 620
Accelerated corrosion protocols 621
Results 622
Conclusion **626**
Acknowledgments **627**
References **627**

Abstract

A major barrier in the adaptation of additive manufacturing into the realm of accepted manufacturing technologies is the requirement for rapid and standardized approaches for qualification of materials and processes. Terahertz nondestructive evaluation techniques could play a major role in the creation of a standardized qualification process for additively manufactured components. This chapter showcases the current use of terahertz nondestructive evaluation on two emerging material applications: additively manufactured components and multilayer paint stacks.

Key points

- Terahertz nondestructive evaluation techniques could play a major role in the creation of a standardized qualification process for additively manufactured components.
- The current use of terahertz nondestructive evaluation on two emerging material applications are showcased: additively manufactured components and multilayer paint stacks.
- As new materials for additive manufacturing are developed and new printing techniques are created, standardized approaches for rapid qualification of these materials and processes will be required.
- Owing to refractive effects, terahertz nondestructive evaluation is best suited to planar structures. Examples include the material characterization and thickness measurements of multilayer paint stacks.
- Based on the accelerated corrosion studies using salt-fog exposure and humidity cycling, a 5.6% change in the reflectivity from the metallic layer indicates significant chemical corrosion of the multilayer paint coating prior to any visible evidence of a blister on the coating surface. Further chemical corrosion (and commensurate decrease in terahertz reflectivity) leads to detachment of the coating from the substrate.
- The major driving force behind the development of additively manufactured terahertz and microwave components is the development of next-generation wireless communication systems.

https://doi.org/10.1016/B978-0-323-90800-9.00112-8

- Various terahertz quasi-optical devices including GRIN lenses, topological waveplates, phase plates, polarization splitters, q-plates, and stepped-refractive-index lenses have been fabricated by 3D printing.
- Terahertz imaging can detect defects in additively manufactured structures which could significantly impact their functionality.
- Terahertz computed tomography of additively manufactured parts has many of the same analysis capabilities as X-ray computed tomography: detection of internal voids and defects, measure internal and external geometry, and ability to compare printed parts to their computer-aided design.
- Corrections to terahertz computed tomography analysis to account for Gaussian beam propagation as well as refractive effects have been demonstrated.

Introduction

Terahertz nondestructive evaluation

Terahertz (THz) radiation refers to the range of electromagnetic waves between the microwave and infrared from 0.1 to 10 THz and wavelengths of 3 mm–30 μm (Wang and Zhang, 2004). Technology related to the creation, manipulation, and implementation of these waves within the "THz gap" is still relatively new and not widely utilized. Since THz waves are nondestructive and do not carry enough energy per quantum to ionize the atoms or molecules that are exposed to them, THz radiation offers many benefits over other traditional material evaluation techniques. These frequencies can be used for spectroscopy, imaging, and structural evaluation. There are many ways to generate and detect THz waves. THz systems can employ either continuous wave or pulsed wave configurations. The most common continuous wave systems use photomixing for tunable narrowband generation while pulse-based systems generate a broadband pulse using biased photoconducting antennas (PCA) (Mittleman, 2003).

Nondestructive evaluation (NDE) methods test and inspect various aspects and characteristics of materials, components, and full systems without permanent damage. NDE is extremely useful in various fields of research and industry because it can save time and money by allowing for rapid, successive, and significant assessment without sacrificing the object being inspected. Valuable or rare samples can be spared where other evaluation techniques might damage them (Sathishkumar et al., 2020).

This chapter describes the use of THz spectroscopy and imaging for NDE on two emerging material applications: additively manufactured components and multilayer paint stacks. For the first application, NDE of fused deposition modeling (FDM) printed plastics and nanoparticle jetted ceramics are emphasized. For the second application, NDE is used to determine both the frequency-dependent permittivity and thicknesses of individual paint layers, while also evaluating corrosion which is hidden below the outer paint surface.

Additive manufacturing—Plastics and ceramics

The terms additive manufacturing (AM) and three-dimensional (3D) printing can generally be used interchangeably: they encompass all the processes that create objects or structures by adding material as opposed to removing it in subtractive manufacturing. There are currently seven common types of additive manufacturing: material extrusion, sheet lamination, vat polymerization, powder bed fusion, material jetting, binder jetting, and direct energy deposition (Alfattni, 2022). The specific process chosen depends on the application's needs. Despite its popularity and promise, AM is currently being held back from becoming a mainstream manufacturing technique by the lack of standards for quality assurance and qualification of the AM parts. Many industries have expressed concern about this lack of standardization, and The National Institute of Standards and Technology (NIST) reports that there are presently no additive manufactured materials or processes that have been specifically qualified for aerospace or critical defense applications (Moylan, n.d.).

In 2021, the United States Department of Defense (DoD) released an updated version of an AM roadmap, originally created in 2016 with *America Makes*, outlining the current objectives of AM and the barriers that must be overcome. Specifically, this roadmap lays out the steps needed to mature the technology of AM in order both for the DoD to fully adopt and utilize this technology, and to allow applications in the public sector. In this current strategy, the DoD identifies the number one barrier to moving AM into the realm of accepted manufacturing technologies as "rapid and standardized approaches for qualification of materials and processes, and certification of AM parts." Yet, as stated in the original DoD roadmap, additive manufacturing has the ability to become cheaper, faster, and more reliable than most current manufacturing techniques (Fielding et al., 2021). The development of THz NDE techniques for these AM parts can play a major role in the full adoption of this technology through the creation of a standardized qualification process (Joint Defense Manufacturing Council, 2021).

The term "qualification" refers to the fulfillment of requirements in the original design: for example, the final product must satisfy dimension constraints, and a major concern with additively manufactured parts is post-printing material shrinkage. An application example that requires strict dimensional constraints is dental crowns, where research has been performed on creating low shrinkage ratio materials; but even those optimized AM materials show signs of shrinkage of over 2% (Zhao et al., 2021).

In a wide variety of applications, for a product to be functional, evaluation and qualification of its final dimensions is crucial. AM parts frequently have structural defects and internal voids caused by the printing process that are not seen under inspection because the part is not transparent to visible light; but in such circumstances, THz NDE can allow defect detection through non-contact imaging.

THz spectroscopy can also characterize the electromagnetic properties of AM structures and has been proven to be a reliable means for optical property characterization (Yasuda and Hosako, 2008; Yilmaz and Akan, 2020; Waddie et al., 2020; Ruan and Chan, 2019). Recently, there have been advances in using FDM printers to print microwave and THz-based passive optical components including waveplates, phase plates, antennas, and lenses (Rohrbach et al., 2021; Zhang et al., 2017; Siemion et al., 2020). AM ceramic structures have been designed for applications in capacitors, filters, dielectric resonator antennas, and 5G devices (Goulas et al., 2020; Morales et al., 2021). The accuracy, reproducibility, and electromagnetic response of such AM structures will likely depend on the structures' printing parameters, and so the ability to tune properties such as refractive index, attenuation coefficient, birefringence, and relative permittivity will be important. Utilization of THz NDE for printed optical components and their material characteristics will be discussed later in this chapter.

Terahertz NDE is well-suited for the characterization of planar structures, where refractive effects due to curved surfaces are minimized. Moreover, using broad-banded terahertz pulses with time durations in the few picoseconds range results in high spatial resolution in the direction of the pulse propagation (a typical resolution is about 10 μm, which is much smaller than the wavelength of the terahertz radiation). In the transverse direction, the spatial resolution of freely propagating terahertz radiation is limited by Gaussian beam propagation and diffraction to several electromagnetic wavelengths.

THz computed tomography (CT) can be used to create 3D reconstructions of a structure being imaged. Like traditional X-ray CT, THz CT has been implemented for NDE internal structure observation; previous research includes the comparison and evaluation of various reconstruction algorithms using THz CT (Recur et al., 2011). But to date, little research has been done utilizing THz CT on 3D printed structures, although various correction algorithms have been created to correct for refraction losses and Fresnel reflection boundary effects observed when utilizing THz for CT (Abraham et al., 2010; Mukherjee et al., 2013). If implemented, THz CT of AM structures could be useful in rapid prototyping, failure analysis, and material characterization.

THz NDE of multilayer paint stacks

An important example of THz NDE of planar structures is the study of multilayer paint systems. Terahertz waves can penetrate many non-conductive materials, enabling a contactless testing method. In such studies, terahertz time-domain reflection measurements are sometimes referred to as terahertz pulse imaging (TPI). In its simplest form, the THz-TD transmitter emits a near-single cycle electromagnetic pulse with a bandwidth from ~0.1 to 3 THz. This extremely wide bandwidth pulse is focused on the coating, and echo pulses are generated from each interface (air-layer, layer-layer, layer-substrate). The terahertz radiation penetrates the whole coating stack and samples the properties of each layer provided that the layer is not metallic. By analyzing the reflected THz pulse, one can reconstruct the thicknesses as well as the permittivity ε and permeability μ of each paint layer. Equivalently, one can characterize the properties of each layer through its complex refractive index $\tilde{n} = \sqrt{\varepsilon\mu/\varepsilon_o\mu_o}$ where $\varepsilon/\varepsilon_o$ and μ/μ_o are the permittivity and magnetic permeability of the paint layer relative to a vacuum.

Over the last 15 years, terahertz nondestructive evaluation and imaging has found application to various multilayer coating structures (paints and ceramic coatings) for several industries including aerospace and automotive (Krimi et al., 2016; Krimi et al., 2017; Catapano et al., 2017; Bohn and Petkie, 2013; Su et al., 2014; Ellrich et al., 2020; Stoik et al., 2008; Yasuda et al., 2007; Su et al., 2014). More specifically, it has been used as a method for the testing of dried paint layers on automotive vehicles for quality control as well as determining the thickness of the paint layers (Takeshi Yasui et al., 2005; Yasuda et al., 2006; Federici, 2012; Yasuda et al., 2007; Su et al., 2014; Krimi et al., 2016). As pointed out by Krimi et al. (2017) materials for coatings and substrates are continuously improved requiring concomitant improvements in quality control and thickness monitoring technologies. Examples of substrate innovations over standard metals include carbon fiber-reinforced polymers and glass fiber-reinforced polymers. In many cases, the substrate materials are highly reflective, thus requiring that terahertz NDE be performed in a reflective mode. Terahertz techniques are effective not only for measuring the frequency-dependent permittivity and thicknesses of the various layers but also for detecting the presence of defects.

Additive manufacturing

This section mainly focuses on the use of FDM printing and nanoparticle jetting for AM, but all AM follows a general order-of-procedures to 3D print an object. First, a 3D model of the structure is created using Computer-Aided Design (CAD) software. The model is then transferred to slicing software, where the different structural parameters are chosen. The structure's infill, layer heights, size, orientation, and other parameters can be altered. The slicing software then converts the model into a programming language called G-code which commands the printer to print the model (Evans, 2012) in a hands-off process to complete the part. Once an object or sample has been printed, THz NDE can be employed.

The major driving force behind the development of additively manufactured terahertz and microwave components is the development of next-generation wireless communication systems (Federici et al., 2016; Federici et al., 2013; Federici and Moeller, 2010). Since these additively manufactured components are designed specifically to focus, split, and otherwise manipulate terahertz radiation, it is critical to characterize the refractive index, attenuation, and birefringence of the component materials in the terahertz frequency range. Aside from terahertz optical components, THz NDE is important for material characterization of additively manufactured materials—such as polymers, ceramics, and composites. Using THz NDE, images of the structure can be taken, optical properties of the materials can be characterized, defects in the structures can be discovered, 3D computed tomography models can be created, residual stresses in the structures can be mapped, etc. Generally speaking, the end goal is to qualify the additively manufactured part—does it function (physical dimensions, mechanical stress, porosity, etc.)—as designed?

THz spectral characterization of materials

THz NDE has the capability to characterize different optical properties of materials. Analysis of the THz waves can be implemented in the time-domain, for example, by measuring the time delay of a waveform or in the frequency domain via the Fourier transform of the time versus THz electric field measurements (Mittleman, 2003). By taking the discrete Fourier transform (DFT) of measured voltages, using a Fast Fourier Transform (FFT) algorithm, the time domain data can be represented in the frequency domain for analysis. Using frequency domain data, the complex refractive index, transmission coefficient, attenuation coefficient, relative permittivity, and birefringence of THz transparent materials can all be measured. For calculation of the complex refractive index of a material, while considering the sample's thickness, three THz waveforms are required: an averaged sample waveform, a reference waveform, and a background waveform. The reference waveform usually consists of the measured time-domain waveform with either the sample removed (for a transmission geometry) or the sample replaced by a perfect mirror (for a reflection geometry). The background waveform corresponds to a measured offset in the time-domain waveform which is recorded when the THz beam is blocked. Subtracting the background waveform from the sample waveform removes the offset.

The time-domain waveform data is converted to the frequency domain via a Fourier transform to calculate both the real and imaginary parts of the refractive index as a function of frequency. The phase angles as a function of frequency are calculated for both the averaged sample and reference waveforms and are used to calculate the frequency-dependent real refractive index $n_r(v)$ using the relationship

$$n_r(v) = 1 + \frac{c_o \Delta\phi(v)}{2\pi L v} \tag{1}$$

where c_o is the speed of light, $\Delta\phi(v)$ is the frequency-dependent phase difference between the sample and reference waveforms, L is the thickness of the sample measured, and v is the frequency. Once the frequency-dependent real refractive index is calculated, it is possible to select a specific frequency at which to compare the real refractive indices.

Since most non-conductive plastic samples are relatively transparent in the THz frequency range, the imaginary refractive index is small compared to the real refractive index. The measured amplitude of the transmitted THz Fourier transform can be corrected for Fresnel reflection losses at the air-sample and sample-air interfaces (Prabhu, 2018). Using the real refractive index to correct for losses at the boundary, the imaginary refractive index can be calculated using

$$n_i(v) = \frac{c_o}{2\pi v L} \ln\left(\frac{|E_R(v)|}{|E_S(v)|} t_{12} t_{21}\right) \tag{2}$$

where $|E_R(v)|$ and where $|E_S(v)|$ represent the magnitudes of the DFT of the electric field measurements of the reference and sample waveforms, respectively. The Fresnel transmission coefficients at normal incidence between air and the sample and the sample and air are represented by t_{12} and t_{21} and are calculated using

$$t_{12}(v) = 2/(1 + n_r(v)) \tag{3}$$

and

$$t_{21}(v) = 2n_r(v)/(n_r(v) + 1). \tag{4}$$

The attenuation coefficient can be calculated using the resulting corrected imaginary refractive index by

$$\alpha = 2\pi v n_i / c_o. \tag{5}$$

The frequency-dependent refractive indices and attenuation coefficients for many common 3D printable plastics have been previously characterized (Castro-Camus et al., 2020; Clark et al., 2021).

Additively manufactured THz optical components

Using the THz spectral measurements in combination with AM, recent studies have shown that it is possible to create operable microwave and THz optical components. One of the technical applications driving the push to develop low-cost terahertz and sub-terahertz components is the shift of wireless communications from the currently used few GHz bands to higher carrier

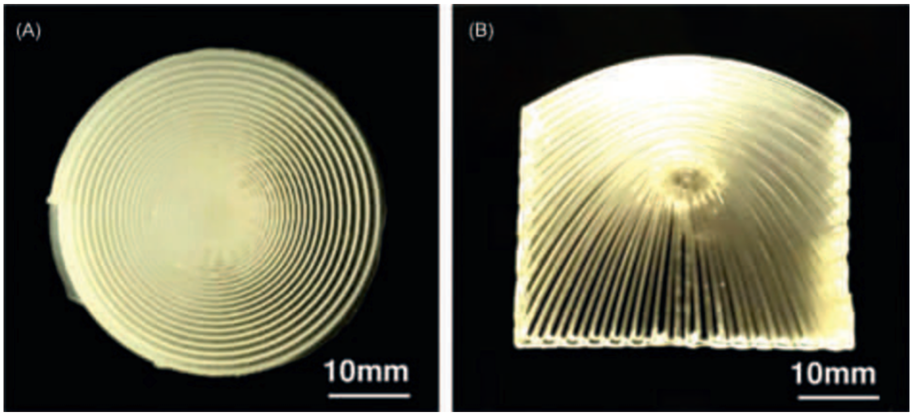

Fig. 1 Examples of 3D printed terahertz components. (a) A Gradient-Refractive-Index (GRIN) lens (b) topological waveplate. From Castro-Camus E, Koch M and Hernandez-Serrano AI (2020) Additive manufacture of photonic components for the terahertz band. *Journal of Applied Physics* **127**: 210901.

frequencies in the several hundreds of GHz band (Federici et al., 2016; Federici et al., 2013; Federici and Moeller, 2010). Several research teams have succeeded in creating various THz quasi-optical devices fabricated by 3D printing. Fig. 1 shows examples of a 3D printed gradient-index (GRIN) lens as well as a topological waveplate. Because the resulting refractive index and birefringence of these materials could be measured using THz NDE, it was possible to tailor these lenses for specific applications (Castro-Camus et al., 2020). As another example, Fig. 2 shows experimental nylon polyamide (PA6) diffractive lenses and their resulting irradiance measured at the plane of the lens—another successful implementation of using FDM for the creating of THz-based optical components (Furlan et al., 2016). Many other THz optical components (including phase plates (Rohrbach et al., 2021), polarization splitters, q-plates, and stepped-refractive-index lenses (Serrano, 2018)) have also been created using AM for the terahertz frequency range.

The AM fabrication process of terahertz optical components presently suffers several limitations. Currently, there are only a limited number of materials that are usable within FDM 3D printers, and even fewer whose transparency is within a usable range (Castro-Camus et al., 2020). For example, polylactic acid (PLA) is a common 3D printed plastic, but unfortunately, it exhibits a high absorption in the terahertz frequency range. Consequently, unless the material is very thin, it will not transmit sufficient terahertz radiation to be functional. Some of the currently used polymers for the manufacturing of terahertz optical components include high-density polyethylene (HDPE), polypropylene, polystyrene, TOPAS (also known as cyclic olefin copolymer (COC)). Most of these polymers exhibit relatively minimal attenuation, but also have refractive indices close to 1.5. A consequence of this similarity of refractive indices is that certain optical components, such as photonic crystals with large bandgaps (where a significant refractive index contrast is required), are very challenging to print.

Another limitation of current economically viable FDM 3D printers is their relatively poor resolution. Since the resolution of these printers is still relatively coarse, the resulting printed optical components must operate within the low range of a few hundred gigahertz, the low end of the THz band. Other types of AM such as stereolithography (SLA) resin printers can produce higher resolution prints, but generally they are much more expensive, and the compositions of the materials may be proprietary. Yet, as FMD technology progresses and evolves, more polymers will be adapted, and the resolution will improve, allowing for increased quality in optical component fabrication (Castro-Camus et al., 2020).

THz NDE of additively manufactured components

In this section, several THz NDE modalities for characterizing additively manufactured components are described. The modalities focus on key aspects of component specification:

- THz for infill structures—Internal infill structure and infill percentage are major considerations for the structural and mechanical strength of 3D printed components.
- THz imaging for defect detection—Defects in the 3D printed structures could significantly impact their functionality. Simple examples include cracks/ voids in the printed structure or regions of high mechanical stress.
- Effect of print parameters on THz properties—3D printing parameters can have an effect on the resulting optical properties of the final printed structure. The ability to fine-tune the optical properties of these structures including refractive index, attenuation coefficient, and birefringence is crucial to the design and fabrication of various optical components.
- THz CT—A complete 3D image of an AM part could enable a detailed comparison of design versus printed dimensions, structural defects, etc. THz CT of AM parts has many of the same analysis capabilities as X-ray CT: detection of internal voids and defects, measure internal and external geometry, and ability to compare printed parts to their CAD design. However, THz CT

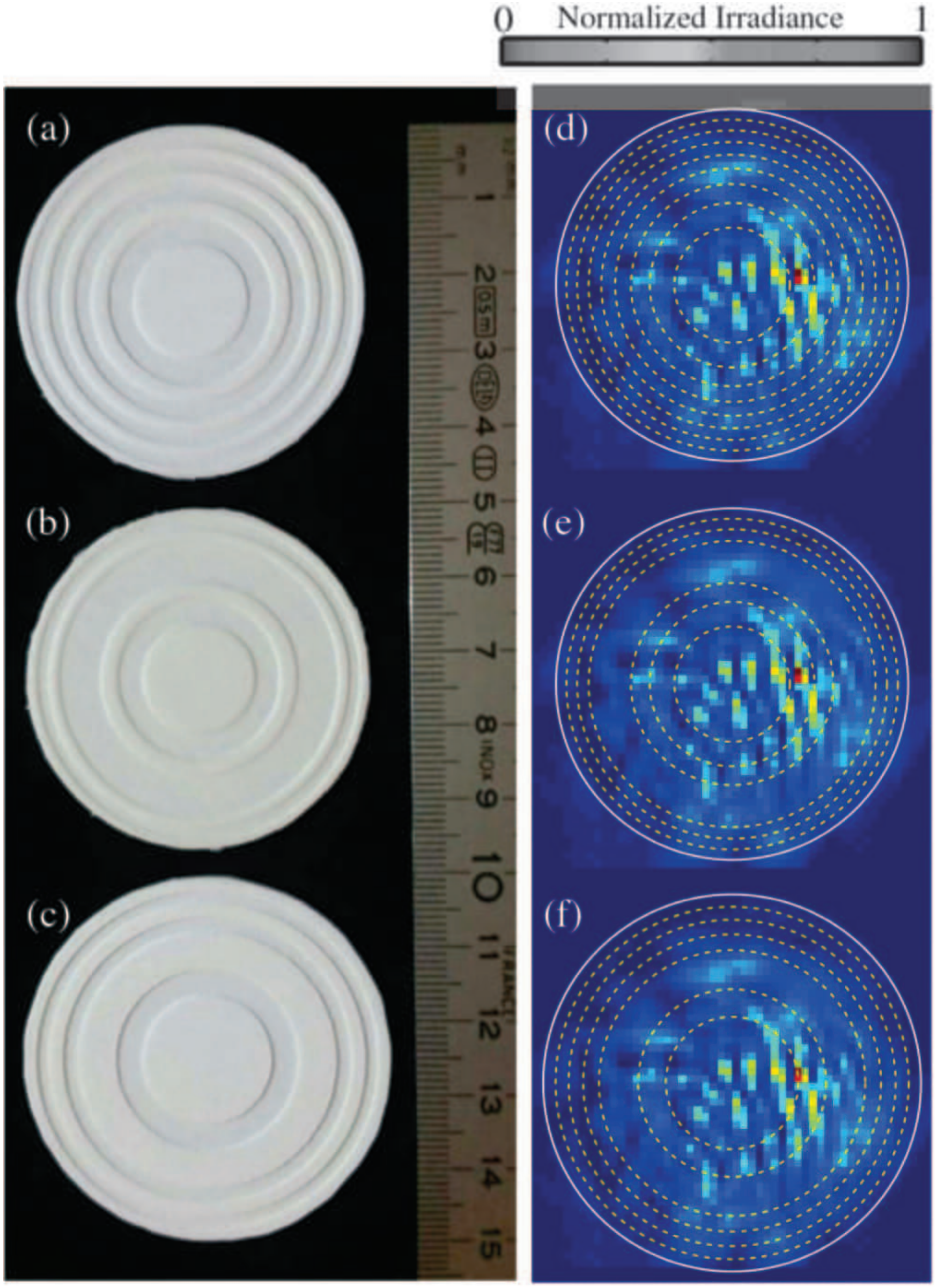

Fig. 2 Examples of 3D printed THz diffractive lenses. (a) Fresnel, (b) fractal, and (c) Fibonacci models. The corresponding maps of THz irradiance measured at the plane of the lens are shown in the second column of images. Reprinted with permission from Furlan WD, Ferrando V, Monsoriu JA, Zagrajek P, Czerwińska E and Szustakowski M (2016) 3D printed diffractive terahertz lenses. *Optics Letters* **41**: 1748–1751.© The Optical Society.

exhibits some challenges as well as advantages when compared to X-ray CT. Challenges include correcting for refraction of THz rays, Gaussian beam profiles, and more limited spatial resolution. However, THz enables an additional modality which X-Ray CT does not: visualization of stress/strain in the printed part through the photoelastic effect.

- THz birefringence—Clearly, characterizing the birefringence of additively manufactured materials is an important parameter for 3D printed terahertz components. The birefringence, typically manifested through a photoelastic effect—can be either intrinsic due to residual internal stress within the material or induced via an externally applied stress. For some components, such as additively manufactured lenses, one would typically require minimal birefringence. For other components such as those whose functionality is dependent upon the phase delay of propagating terahertz waves, the ability to fabricate structures with a controllable birefringence might be important.

THz NDE of infill structures

Key structural and mechanical strength considerations of 3D printed structures are the internal infill structure and infill percentage. Terahertz time-domain imaging of 3D printed infill structures (Busboom et al., 2021) shows that THz NDE can be used to visualize the infill structures. Useful imaging modalities include both transmitted power in a frequency band as well as pulse time-of-flight measurements. Transmission measurements are easier to implement, but are limited if the material is too thick (ABS which was used in (Busboom et al., 2021) to fabricate the structures exhibits a large absorption in the terahertz range) or the infill structure is too complex. Reflection measurements are useful to determine which grid direction is printed first enabling a clearing visualization of the infill structure. While these results are interesting, the samples under study were oriented such that the walls of the infill were always perpendicular to the propagating terahertz beam direction. An arbitrary orientation of the infill structure relative to the beam direction would require a computed tomography modality to render a 3D image of the infill structure.

THz imaging of defects

As an example of defect imaging, NDE of ceramic samples is presented (Clark et al., 2021) in this section. The samples were fabricated using an XJet Carmel 1400 nanoparticle jet printer. Nanoparticle jetting is a proprietary printing technology developed by XJet, which falls under the category of binder jetting additive manufacturing. ZrO_2 nanoparticles are suspended in a polymer binder and carrier agent to form an ink. As multiple print nozzles deposit layers of the ZrO_2 dispersion on top of one another, as well as support structure material, the carrier agent is evaporated and the layers are dried using heat lamps and hot air dryers. The support material is dissolved from the print by submerging the structure in water. After a period of drying in a desiccating chamber, the samples are ready for sintering. Processing above 1200 °C is required to convert the mixture of monoclinic and tetragonal phases into a mixture of tetragonal and cubic phases and join the individual ZrO_2 particles into a dense ceramic structure. Voids form as the polymer binder decomposes, where the size, shape, and distribution of these defects depend upon the maximum firing temperature. The samples used in this example were all printed with identical printing parameters, but experienced different maximum firing temperatures varying from 750 °C to 1450 °C in increments of 100 °C. The samples were 50 mm^2, 2–3 mm thick, with printed layer thicknesses of 10 μm, and a jetting resolution of roughly 20 μm.

The relative permittivity of the extruded ceramics was measured by mounting the samples to an XY gantry away from the focal point of the lens. This was done to create a larger spot size interacting with the samples in a transmission configuration. The samples are measured between 60 GHz and 3 THz using the T-ray 5000 system using an average of 2000 acquired THz waveforms. Valid data is extracted between 110 GHz and 550 GHz due to the low signal-to-noise ratio. To show and verify that this data is accurate and repeatable, the samples are also measured between 75 GHz and 110 GHz using a free-space focused beam system.

The data in Fig. 3 from the free-space system matches the T-ray 5000 data very well, confirming that these are accurate measurements. This data confirms that as a product of increased firing temperature, the relative permittivity increases, while not

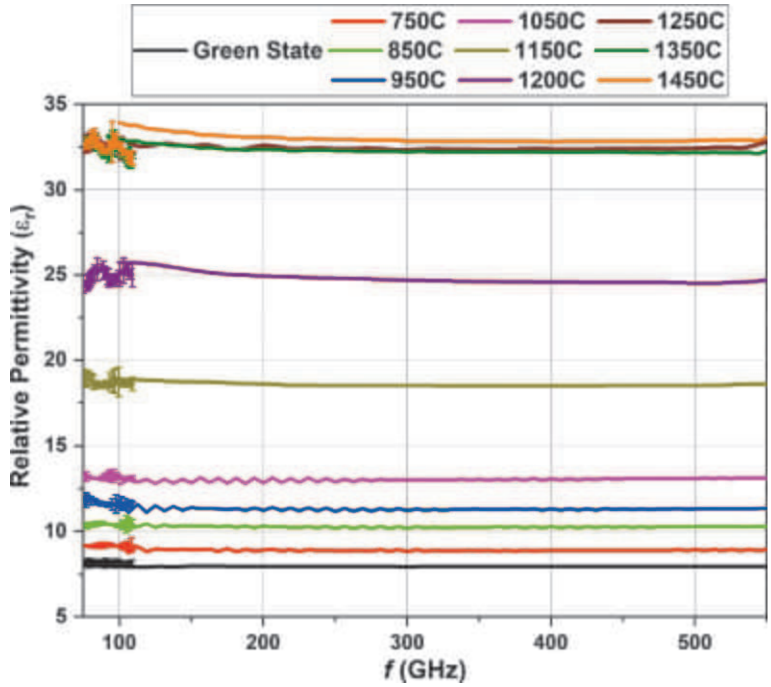

Fig. 3 Relative permittivity of the various sintered ceramic samples at different sintering temperatures showing data between 75 GHz and 550 GHz provided by Paul Parsons. "Green State" refers to an un-sintered sample. From Clark AT (2022) *Nondestructive Evaluation of 3D Printed, Extruded and Natural Polymer Structures using Terahertz Spectroscopy and Imaging*. Ph.D. Doctoral Dissertation, New Jersey Institute of Technology.

varying over a relatively large frequency range. At temperatures above 1200 °C, where the structure conversion takes place, the relative permittivity reached a value where the increase between samples decreased dramatically, almost to zero.

Small location-dependent variations in the relative permittivity were observed when the THz beam was focused over a small spot size on the sample. Images were taken by raster scanning the samples in a transmission configuration to investigate these variations. The contrast of the images shows the variations in the dielectric constant of the material at each pixel. As the particles begin to sinter, and voids begin to disappear with increasing temperature, all the samples show clear isotropic volume reduction. The samples decrease in volume from 1% up to 18% at the highest sintering temperature of 1450 °C. There are also numerous horizontal striations seen in all the samples. An alignment issue with the XJet printer, verified by Xjet staff, was the cause of these striations, resulting in a major flaw throughout each of the prints. The flaws shown in Fig. 4, a consequence of misaligned print heads, are effectively an inhomogeneity in the dispersion of the ZrO_2 particles.

In the 1450 °C sample, a dark wavy horizontal feature about one-third of the way down is visible, marked by the white arrow. This is a crack that runs throughout the entire length of the sample. A combination of material shrinkage and inhomogeneous particle density caused by the misaligned print heads is to blame. More importantly, this crack is not fully visible under visual inspection. With post THz imaging, only then the full extent of the crack was observed. This is a clear and successful application of using THz NDE for both electromagnetic property characterization as well as the detection of defects within AM ceramic structures.

Effect of 3D printing parameters on FDM printed components

When printing optical components such as the GRIN lens or diffractive lenses shown in Figs. 1 and 2, it is important to know if the printing parameters will have any effect on the resulting optical properties of the final structure. When any structure is printed, there are multiple different parameters that are either automatically chosen by the slicing software or manually picked by the user. The ability to fine-tune the optical properties of these structures including refractive index, attenuation coefficient, and birefringence will rest on detailed knowledge of such dependencies (Alfattni, 2022). Commonly altered printing parameters include the printer's nozzle size, the layer height within the print, or a print's orientation. For example, if the refractive index of a 3D printed terahertz lens varies with printing parameters, then the focal length of the lens would be dependent on printing parameters. Likewise, if the attenuation depended on printing parameters, then the throughput transmission of the lens would be dependent on the printing parameters as well. Similarly, if the refractive index, attenuation coefficient, or birefringence of a printed THz waveguide were to vary due to printing parameters, then the device performance (e.g. propagation speed of guided terahertz, numerical aperture of the waveguide, loss per unit length of the waveguide) would all be dependent on the various printing parameters.

Refractive index, attenuation coefficient, and level of birefringence have been measured for a set of 3D printed samples printed with various printing parameters (Clark et al., 2021). The samples were rectangular blocks of various clear filaments printed using a commercial 3D printer. Changes in the optical properties of these printed structures are observed and compared. The THz optical properties of the materials studied here have previously been demonstrated to be frequency-dependent. Optical property changes have been isolated at 500 GHz. At this frequency, there is a good signal-to-noise ratio and lack of interference oscillations in the measured data.

Table 1 shows the variation based on changing the print orientation of the structure. The print orientation dictates whether the rectangular block sample was printed either laying down (horizontal) or up on edge (vertical). By changing the print orientation, the planes in which individual layers are printed are altered. There is a clear correlation between print orientation and change in refractive index: an average increase of 1.9% in the real refractive index at 500 GHz when the samples are printed horizontally compared to vertically. Three of the four measurable attenuation coefficients have increases greater than the calculated uncertainty.

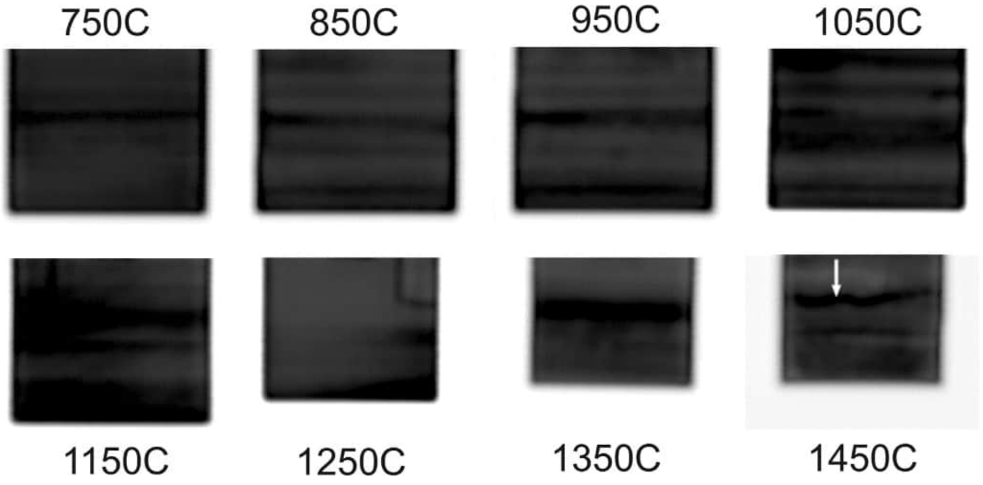

Fig. 4 Raster scan images of the dielectric constants of varying sintering temperature ZrO_2 samples. Horizontal striations seen throughout are a result of print head misalignment during the printing process. A crack in the 1450 °C is indicated by the white arrow. From Clark AT (2022) *Nondestructive Evaluation of 3D Printed, Extruded and Natural Polymer Structures using Terahertz Spectroscopy and Imaging.* Ph.D. Doctoral Dissertation, New Jersey Institute of Technology.

Table 1 Real refractive indices and attenuation coefficients of samples at 500 GHz based on variation in print orientation (Clark et al., 2021).

Filament Material	*Print Orientation*	*Real Refractive Index (n)*	*Attenuation Coefficient (cm^{-1})*
PLA	Horizontal	1.654	4.429
	Vertical	1.604	5.092
Nylon	Horizontal	1.749	4.015
	Vertical	1.741	4.099
PC	Horizontal	1.649	1.944
	Vertical	1.623	2.444
CPE	Horizontal	1.683	3.343
	Vertical	1.650	3.191
PP	Horizontal	1.492	N/A
	Vertical	1.457	N/A

Note: Standard printing parameters of a 0.4 mm nozzle and 0.2 mm layer heights were used. Uncertainties in the real refractive index: $2\sigma = \pm 0.010$ and attenuation coefficient: $2\sigma = \pm 0.025$.

From Clark AT, Federici JF and Gatley I (2021) Effect of 3D printing parameters on the refractive index, attenuation coefficient, and birefringence of plastics in terahertz range. *Advances in Materials Science and Engineering* **2021**: 8276378.

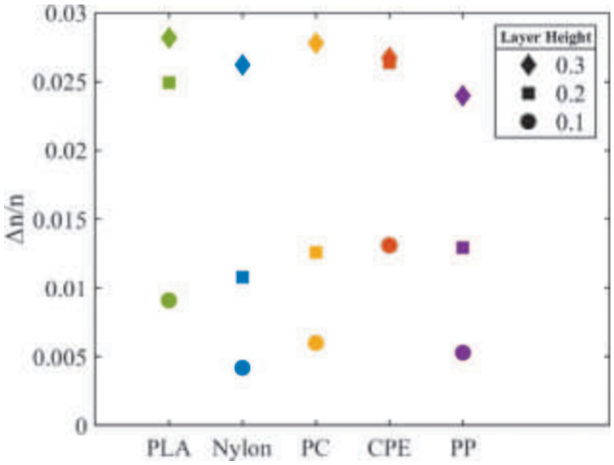

Fig. 5 Level of birefringence ($\frac{\Delta n}{n}$) measured at 250 GHz in vertically printed samples using a 0.4 mm nozzle and standard printing parameters with variation of print layer height. From Clark AT, Federici JF and Gatley I (2021) Effect of 3D printing parameters on the refractive index, attenuation coefficient, and birefringence of plastics in terahertz range. *Advances in Materials Science and Engineering* **2021**: 8276378.

The samples were cut and their cross sections were viewed using a light optical microscope but no air gaps within the prints were discovered. It is plausible that the surface texture differences between the horizontal and vertical samples might cause these correlations. In a vertically printed sample, the THz beam is interacting with a repeating structure surface layer with features of similar size to its wavelength. Previously reported, increasing the surface roughness of various samples measured in the THz range has increased the uncertainty of thickness measurements as well as increased the measured values of real refractive indices (Burger et al., 2021; Fukuchi et al., 2013). Changes in the refractive index and attenuation coefficient based on a change in nozzle size and layer height were also measured and are shown in Clark et al. (2021).

Using the same samples, the birefringence dependent on varying printing parameters was also measured. Vertically printed samples show birefringence levels above the experimental uncertainty and are shown in Fig. 5. As the layer height of the samples increases, the birefringence present in the sample also increases. This trend is seen in every filament material. Additional stresses may be induced into the material as it is rapidly heated and cooled from printing temperature back to room temperature during the FDM 3D printing process. These large thermal fluctuations combined with forced extrusion could create a birefringence within the final structure as the layers are deposited on top of one another. Increasing in nozzle size from 0.4 mm to 0.8 mm causes an average of 125% decrease in birefringence, shown in (Clark et al., 2021). One possible explanation for this decrease is that with the larger nozzle size each layer of the sample is printed faster and, since each layer is printed faster, there is less elapsed time for that layer to cool. With shorter time between layers, there will be a decrease in the introduction of residual stresses into the material due to thermal differences between those layers. As shown in the slower printing 0.4 mm nozzle samples, thermal differences between layers will create a larger measurable birefringence than the faster printing 0.8 mm nozzle layers (Clark et al., 2021). These measurements showcase another application of THz NDE; the ability to measure and track changes to important optical characteristics of AM structures.

Refractive effects

THz radiation will undergo refraction when entering a sample at any angle other than normal incidence. This refraction leads to a redirection of the beam that needs to be accounted for in image reconstruction. This shortcoming can be mitigated in some cases using an index matching material. This material, typically a fluid, can be used to surround the sample, and be shaped in such a way as to create boundaries of normal incidence that couple the THz radiation into the sample by minimizing refraction and reflection of the beam as it interacts with the sample.

A simple example is provided by the study of insects embedded in ancient amber. Samples of Dominican amber (in which ancient termites are sometimes encased) typically have an irregular rounded shape. In order to remove most of the topological refractive effects, the round sample of amber is suspended in a cubical container filled with a liquid of similar refractive index to the amber, such as mineral oil. Under a perfect refractive index match, the surface topology of the sample will vanish because there will be no reflections from the surface of the sample, allowing inclusions within the sample to be studied free from distortions. Fig. 6 shows a measurement using a closely matched refractive index fluid to minimize the refractive effects caused by the amber matrix. Alternative methods of refractive correction algorithms are discussed in the next section.

THz computed tomography of additively manufactured components

The approach of 3D image reconstruction using computed tomography (CT) is illustrated using the parallel ray configuration of Fig. 7 to image a slice of an object. The line scans, which are a collection of measurements along parallel ray paths, are called projection measurements. The measured quantity can be transmission, absorption, time-of-flight, refractive index, or some other electromagnetic quantity. A projection measurement is a set of line integrals that represent the interaction between the incident radiation and the medium represented by a 2D function $f(x,y)$ that it interacts with and transmits through along one axis of measurement. Projection measurements are performed at multiple rotation angles θ. These projection measurements are the primary source of data for the tomographic reconstruction of the 2D slice through the object. Full 3D reconstruction is achieved by translating the object perpendicular to the page and acquiring data for each 2D slice.

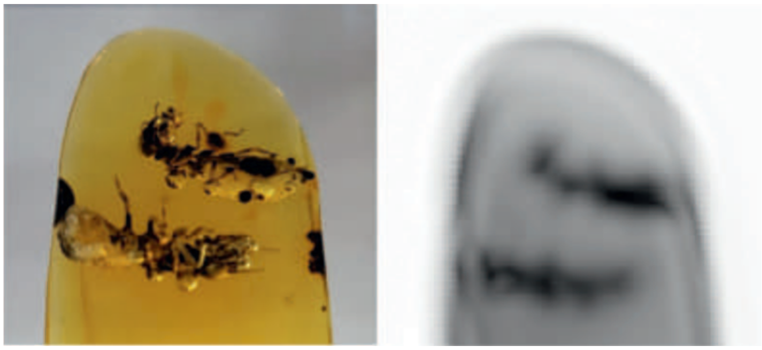

Fig. 6 (Left) Dominican amber sample. (Right) 0.5–2 THz frequency range integration image of the amber sample submerged in Fisher Scientific pure mineral oil, a closely matched refractive index fluid, to reduce refractive effects (Clark, 2022).

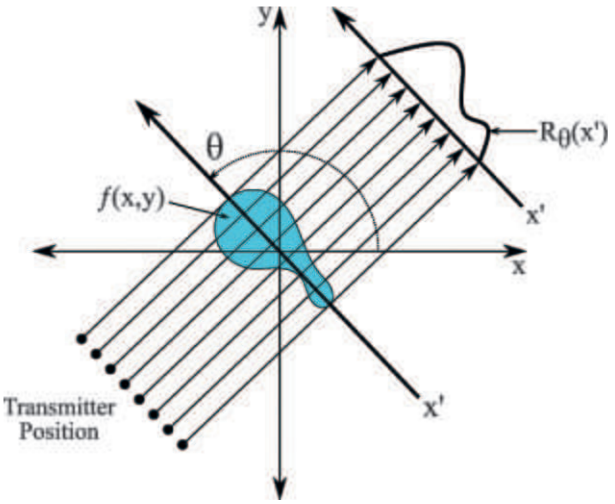

Fig. 7 Illustration of a parallel beam projection measurement where $f(x,y)$ is the two-dimensional (2D) function representing the sample and $R_\theta(x')$ is the resulting projection measured at angle θ (Clark, 2022).

A Radon transformation is a linear operator used to take a known function ƒ in a 2D coordinate plane and represent it in what is known as the projection domain. A projection of an object can be represented by the sum of several sine waves. At each measured z value (see Fig. 7), a set of projections from discrete angles is then formed into a 2D representation of the object in the projection domain known as a sinogram (Taubmann et al., 2018). A sinogram is a stack of projection measurements that can be used to construct a tomographic image of the structure that was scanned.

Converting the sinogram measurements to a reconstructed tomographic image is an inverse problem. The sinogram measurements are used in various reconstruction methods such as the standard filtered back-projection (FBP) algorithm, iterative techniques such as the algebraic reconstruction technique (ART), or an even faster simultaneous algebraic reconstruction technique (SART) to create 2D tomographic images (Dhawan, 2003; Recur et al., 2011). Iterative reconstruction methods generally result in more accurate reconstructions but require much more computational power and time. The tomographic images, or "slices", are top-down views of the selected plane through the object scanned. By stacking these individual tomographic images and utilizing reconstruction software, it is possible to create a 3D reconstruction of the structure based on the chosen optical property or waveform attribute that was measured.

Despite the commonality of approach between X-Ray and THz CT, there are some major distinctions in applying computed tomography in the two different spectral regions. X-ray CT is much simpler than THz CT because X-Ray radiation travels through the target material in almost straight lines without much refraction, but THz waves are susceptible to refraction and loss of signal from boundaries: specifically, due to refraction at boundaries, reconstructed THz–CT images exhibit enhanced attenuation at the boundaries and also a distortion of the boundary shapes. Examples of the boundary effect can be seen in many papers on THz CT imaging (Ferguson et al., 2002; Mittleman et al., 1997; Zhang, 2003; Wang and Zhang, 2004; Chan et al., 2007). When elementary back-projection of filtered-projections (BFP) image reconstruction is utilized, only in the case of a low refractive index contrast material (Li et al., 2012; Kim et al., 2012; Lee et al., 2012; Nishina et al., 2012) can the refractive and reflective effects be ignored in the image reconstruction. Refraction of THz radiation by materials—unless the material is immersed in an index matching material—is therefore an inevitable aspect of THz CT.

Perraud et al. (2016) used THz CT to inspect 3D printed components for biomedical implants (PEEK) as well as for aviation components (polyamide). Their CT reconstruction algorithm accounts for a THz Gaussian beam profile. They observe that the finite beam size effect convoluted with the geometric effects (that is, the deflection of the THz beam by the refraction) distorts the reconstructed images and leads to a "systematic over-evaluation of the measured external dimensions and underestimation of the internal ones."..."After interaction with the object, [the] refraction effect of the THz beam makes it difficult to properly identify the amplitude since an important part of the signal is lost out of the detector. Moreover, each interface and nonparallel surfaces accentuate refraction losses and explain the discrepancies obtained for internal diameter measurements."

A small number of papers have studied the refraction/ boundary artifacts phenomenon and have tried to remove the prominent boundary effect phenomena by different methodologies. Abraham et al. (2010) introduce a multi-peak averaging method to eliminate boundary effects due to refraction losses of the THz beam inside the material. In applying this technique to 3D THz-CT images of a Teflon (refractive index 1.37) cylinder with a hole on it, the effect of the boundaries is reduced, but the boundaries are still visibility enhanced in the reconstructed image.

Using a completely different methodology, (Mukherjee et al., 2013) showed that by correcting for the two most dominant phenomena (i.e. steering of the THz beam and Fresnel reflection) prior to image reconstruction using filtered backpropagation, the boundary effect can be essentially eliminated. If the shape and refractive index of a 'standardized' object were known a-priori, then in principle the effects of Fresnel reflection and refraction would be removed from CT projection data prior to applying filtered backpropagation to reconstruct the image. Because the desired shape and materials of 3D printed structures are known a priori, it is possible to correct for the refraction effects of terahertz beam propagation.

More advanced image reconstruction methodologies are better suited to address the refraction effects of terahertz beam propagation. As an example, consider a more complicated structure such as the "C" shaped structure in Fig. 8 in which direction of a THz ray changes several times as it propagates through the structure. The BFP image reconstruction approach is not valid since the individual rays are not straight lines. The refraction from additional material boundaries in the ray's path might result from complicated surface geometries, printing infills less than 100% (i.e., not a solid object), or from the use of different materials and consequently different refractive indices in the printed structure. Clearly, for more complicated structure, another method such as Algebraic Reconstruction Techniques (ART), Landweber iteration, or SART (Dhawan et al., 2008; Dhawan, 2003; Tepe et al., 2017; Posodeder et al., 2022) rather than filtered backpropagation is required to reconstruct THz CT images.

As illustrated in Fig. 8, an ART reconstructive grid is defined with each pixel corresponding to a spatial location of the object to be imaged. Optical properties (e.g., absorption or refractive index) of the material are associated with each pixel location. If one propagates an X-ray through the structure (i.e., no refraction for Ray A), the ray sum p_i in the projection data can be expressed as

$$p_i = \sum_{j=1}^{N} w_{i,j} f_j \tag{6}$$

where $i = 1, \ldots, M$ and M is the number of projection rays. The weighting function $w_{i,\,j}$ represents the contribution from each pixel to the ray sum. The representation of Eq. (6) yields M equations for the N unknown pixel values. Conceptually, the pixel values are determined by comparing the measured projection ray values to those calculated from Eq. (6) and minimizing the error. For each iteration to minimize the error, the difference between the computed ray and measured projection ray sums is calculated and then distributed among the pixels in a weighted manner prior to the next iteration.

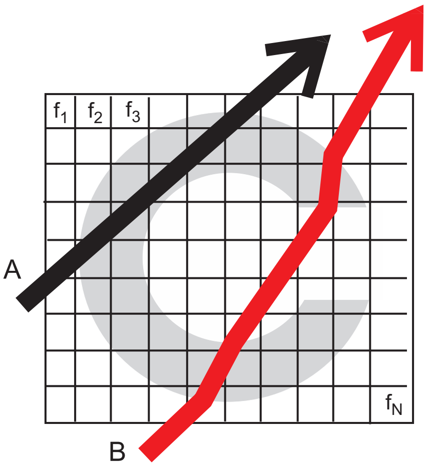

Fig. 8 Reconstruction grid with two rays which would define path sums for ART for rays passing through the "C" shaped structure. Ray A (black) illustrates ray propagation through the structure with no refraction present (e.g., X-Ray) and while Ray B (red) illustrates propagation with refraction present (e.g., THz).

In the generalized implementation of ART, the iterative process is initiated by pre-assigning values for each pixel. However, one can take advantage of the fact that for 3D printed components, the design values for the geometry and material properties of the 3D printed components are known a priori. Hence, the initial values for each pixel can be determined from the 3D design files for the component. Furthermore, one can integrate geometric ray tracing of the rays through the reconstruction grid to account for changes in the direction of an individual ray due to refraction as it propagates through the structure. Essentially, one needs to iteratively update both the ray paths and the optical properties of the pixels to reconstruct the THz CT image. Note that with this ART approach, multiple changes in the direction of a propagating ray due to refraction can easily be included as well as Fresnel reflection losses from boundaries. There is no longer the requirement, as is routinely assumed in conventional THz CT, that the THz rays propagate as straight lines through the test object.

Fig. 9 compares using three different reconstruction methods including back-projection of filtered-projections (BFP), simultaneous algebraic reconstruction technique (SART) reconstruction, and an ordered subsets expectation maximization (OSEM) method. These different reconstruction methods were used to create reconstructions of a white foam parallelepiped with two

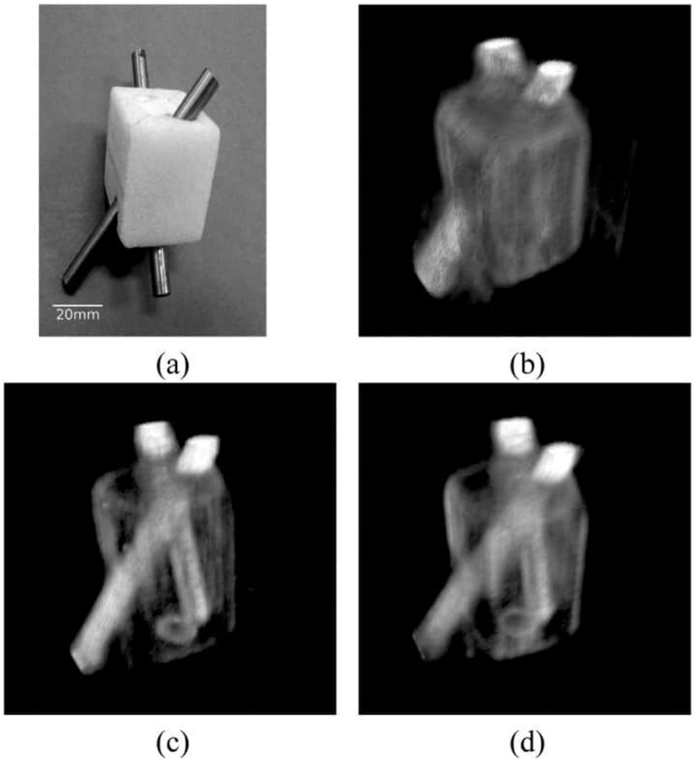

Fig. 9 Successful 3D CT reconstruction using THz NDE (240 GHz frequency) showcasing the differences between three different reconstruction methods. The object is a 30 mm cube size white foam parallelepiped with two oblique metallic bars (6 mm diameter). (a) Photograph of the 3D sample (b) BFP reconstruction (c) SART reconstruction (d) OSEM reconstruction. Reprinted with permission from Recur B, Younus A, Salort S, Mounaix P, Chassagne B, Desbarats P, Caumes JP and Abraham E (2011) Investigation on reconstruction methods applied to 3D terahertz computed tomography. *Optics Express* **19**: 5105–5117. © The Optical Society.

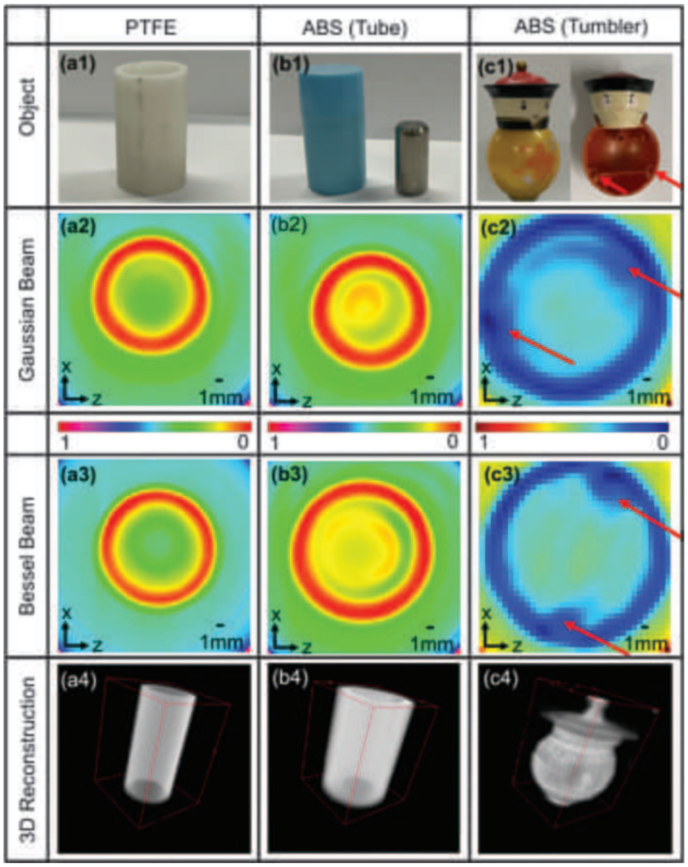

Fig. 10 3D CT reconstructions using THz NDE showcasing the use of Gaussian and Bessel beams for tomogram creation. Reprinted with permission from Wang D, Ning R, Li G, Zhao J, Wang Y and Rong L (2022) 3d image reconstruction of terahertz computed tomography at sparse angles by total variation minimization. *Applied Optics* **61**: B1–B7. © The Optical Society.

metal bars throughout. Different types of reconstruction methods are created to reduce or eliminate artifacts in the reconstructions. For example, BFP suffers largely from terahertz beam refraction that needs to be accounted for using corrective algorithms. This experiment was performed to show the ability in visualizing the internal structure of the foam nondestructively, while also showcasing the first application of SART and OSEM to THz CT (Recur et al., 2011). Fig. 10 shows THz CT being used on two different polymer tubes and a polymer tumbler. This figure is comparing the difference between using a Gaussian and Bessel beam for BFP reconstruction. It is shown that in these tomograms the Bessel beam reduces the effects of refraction at the boundaries allowing for a closer reconstruction to the original sample (Wang et al., 2022).

The accuracy to which complex shapes can be resolved using ART techniques is shown in Fig. 11 (Posodeder et al., 2022). Using the design geometry as an a priori guess as to the shape and refractive index properties of the 3D printed structure, geometric optics (i.e., Snell's law) is used to propagate the terahertz radiation through the 'guess' reconstructed structure in order to mathematically correct for refractive effects. Based on a minimization of the error in comparing the measured and reconstructed image, the initial guess as to the shape and refractive index properties of the object are updated for the next iteration in the optimization algorithm. The L1 regularization algorithm, which assumes that large parts of the sample consist of air, produces a reconstructed image whose wall thicknesses most closely match the physical sample.

Another limitation in THz CT compared to X-ray CT is its spatial resolution. Since the wavelength of terahertz radiation (300 μm at 1 THz) is much larger than the wavelength of X-rays, the spatial resolution of X-rays can be significantly better due to diffractive effects. As an example, Ref. (Markl et al., 2017) compared the performance of X-ray and THz CT on pharmaceutical solid dosage forms. Two dosage forms were fabricated by FDM; a single compartment structure with a nominal shell thickness of 0.7 mm and a two-compartment structure with each shell 1.4 mm thick. A key challenge in additively manufactured pharmaceutical dosage forms is the quality control of each single dosage unit. Their results show that X-ray CT provides very detailed information about the microstructure and defects in the 3D print. However, due to the long acquisition and reconstruction times of X-ray CT images, it is not feasible to perform quality control on every printed dosage form. While terahertz imaging, due to its rapid acquisition of depth profiles, could enable quality control of a much larger number of samples, there is insufficient spatial resolution in the terahertz images to extract the essential information about the microstructure.

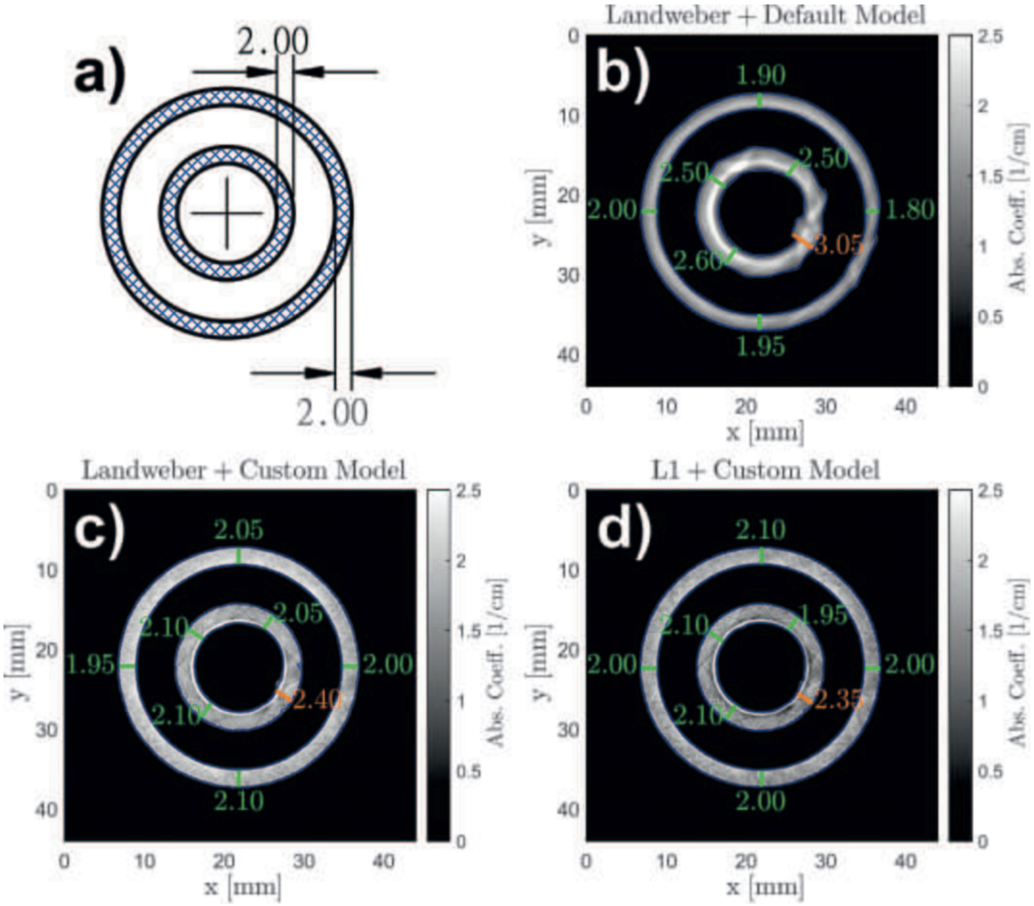

Fig. 11 Results of a 2D THz CT reconstruction of a 3D printed polypropylene double tube sample. (A) The nominal design structure including the thicknesses of the tube wall. Three different image reconstructions of the sample using (B) Landweber iteration plus a default model as implemented in (Fosodeder et al., 2021). No refractive corrections are included (c) Landweber iteration with refraction corrections and (d) L1 regularization with refractive corrections. The last reconstruction gives the most accurate wall thicknesses. Reprinted with permission from Posodeder P, Frank SV and Rankl C (2022) Highly accurate THz-CT including refraction effects. *Optics Express* **30**: 3684–3699. © The Optical Society.

Despite the limited spatial resolution of THz CT compared to X-ray CT, there are complementary approaches one might use to offset the limited spatial resolution of terahertz imaging. For the present example, in which the microstructure and porosity are critical to the functionality of the dosage form, one might be able to employ an index matching fluid to fill in open pores. Introduction of the index matching fluid would reduce the scattering from the porous material enabling a quantitative evaluation of the microstructure and porosity (Naftaly et al., 2020).

Birefringence

It is well-known that stress-induced birefringence occurs in many transparent materials when load is applied (Hecht, 2017). Consequently, the stress-induced birefringence enables photoelasticity measurements to experimentally visualize stress analysis in transparent material (Dally, 1978). In a stress-less experiment with an isotropic (non-birefringent) material placed between two polarizers whose transmission axes are orthogonal, the light which passes through the first polarizing filter maintains its polarization as it propagates through the isotropic material; therefore no light emerges from the second crossed polarizer. However, if the material experiences either applied stress or intrinsic stress, the induced birefringence rotates the plane of polarization of light propagating through the material resulting in some transmission through the second crossed polarizing filter.

The advantage of using terahertz radiation rather than visible radiation for birefringence measurements is that terahertz radiation can be used to probe non-metallic materials which are opaque to visible light. Example materials include plastics, ceramics, as well as composite materials. Several experimental configurations of terahertz birefringence instrumentation have been demonstrated including a very simple measurement in which the arrival times of terahertz pulses with various polarization orientations are measured (Clark et al., 2021). From the difference in pulse arrival times for various polarization orientations, the magnitude and direction of sample birefringence may be calculated.

A cross-polarizer experimental geometry as introduced by Kang et al. (2021) enabled precise birefringence measurements in the terahertz frequency range. Fig. 12 illustrates the relative orientations of the polarizers as well as the relative orientation of the fast

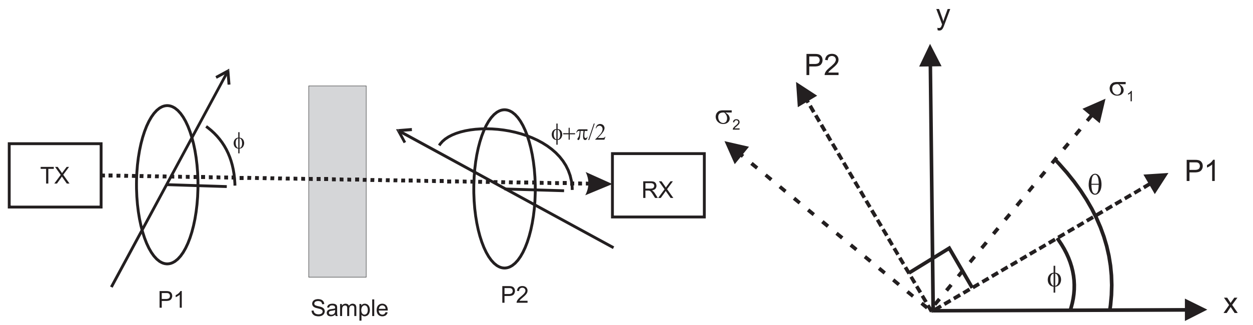

Fig. 12 Experimental configuration for measurement of birefringence in a transmission mode. (a) relative positions of the transmitter/polarizer P1 module, birefringent sample, and receiver/polarizer P2 module. (b) orientation of transmission axes of polarizers P1 and P2, relative to the laboratory horizontal x-axis. The terahertz pulse is propagating into the page. The fast σ_1 and slow σ_2 axes of the birefringent material are assumed to be orthogonal.

and slow refractive index axes of the sample. Rather than analyzing the polarization properties of the transmitted terahertz waves in Fig. 12 using a Jones Matrix approach (as was performed in Kang et al., 2021), here an alternative method is used which is more amenable to the time-domain.

For simplicity, it is assumed that the sample can be treated as a uniaxial birefringent material in which the principle stress axes are perpendicular to the propagation direction of the terahertz waves. The electric field after transmission through polarizer P1 in Fig. 12 can be expressed as

$$E_{TX} = E_{inc}(t)(\hat{x}\cos\phi + \hat{y}\sin\phi) \tag{7}$$

where ϕ is the angle between the horizontal x-axis and the transmission axis of polarizer P1. As the terahertz pulse enters the sample, the vector components of the electric field are written in terms of the basis vectors of the fast (lower refractive index) and slow (higher refractive index) of the material with the fast axis oriented at an angle θ with respect to the horizontal x-axis:

$$\hat{x} = \hat{\sigma}_1\cos\theta - \hat{\sigma}_2\sin\theta \tag{8}$$

$$\hat{y} = \hat{\sigma}_1\sin\theta + \hat{\sigma}_2\cos\theta \tag{9}$$

The electric field just as it enters the sample, using Eqs. (7–9), can be expressed as

$$E_{s\_in}(t) = E_{inc}(t)\tau_{as}[\hat{\sigma}_1(\cos\phi\cos\theta + \sin\phi\sin\theta) + \hat{\sigma}_2(\sin\phi\cos\theta - \cos\phi\sin\theta)] \tag{10}$$

where τ_{as} is the transmission coefficient in propagating from air into the material. Since the electric field is expressed in terms of the basis for the fast and slow axes, the additional time delay for propagation through the sample and back into the air can be expressed as

$$E_{s\_out}(t) = \tau_{as}\tau_{sa}[\hat{\sigma}_1 E_{inc}(t + \Delta t_{\sigma_1})(\cos\phi\cos\theta + \sin\phi\sin\theta) + \hat{\sigma}_2 E_{inc}(t + \Delta t_{\sigma_2})(\sin\phi\cos\theta - \cos\phi\sin\theta)] \tag{11}$$

where the propagation times for the two principal axes in the material are given by $\Delta t_{\sigma_1} = n_{\sigma_1}L/c_o$ and $\Delta t_{\sigma_2} = n_{\sigma_2}L/c_o$. The product $\tau_{as}\tau_{sa}$ accounts for any losses in transmission due to reflection of a portion of the terahertz pulse at the air-sample interfaces.

After propagating the terahertz pulse through the sample, one translates Eq. (11) back into the laboratory x-y frame using

$$\hat{\sigma}_1 = \hat{x}\cos\theta + \hat{y}\sin\theta \tag{12}$$

$$\hat{\sigma}_2 = -\hat{x}\sin\theta + \hat{y}\cos\theta. \tag{13}$$

Finally, the resulting electric field through the polarizer P2 is calculated by taking the dot product with the transmission axis polarization of P2 given by $\hat{P}2 = -\hat{x}\sin\phi + \hat{y}\cos\phi$. After rearranging terms, the final electric field detected by the receiver can be expressed as

$$E_{RX}(t) = \tau_{as}\tau_{sa}[E_{inc}(t + \Delta t_{\sigma_1}) - E_{inc}(t + \Delta t_{\sigma_2})]\left(\sin\theta\cos\theta\left(\cos^2\phi - \sin^2\phi\right) + \sin\phi\cos\phi\left(\sin^2\theta - \cos^2\theta\right)\right) \tag{14}$$

As a quick check, when there is no birefringence, then $\Delta t_{\sigma_1} = \Delta t_{\sigma_2}$ and the detected electric field vanishes. Likewise, if $\theta = \phi$ then the polarizers P1 and P2 are along the principal stress and birefringence axes yielding no detectable electric field since for this orientation of the sample relative to the polarizers, the birefringence does not rotate the polarization of the incident terahertz pulse.

The next step is to evaluate the difference in the two time-shifted electric fields $E_{inc}(t + \Delta t_{\sigma_1}) - E_{inc}(t + \Delta t_{\sigma_2})$. To facilitate the calculation, Fourier transforms as defined below will be utilized

$$f(\nu) = \int_{-\infty}^{\infty} f(t)\,e^{-i2\pi\nu t}dt \tag{15}$$

$$f(t) = \int_{-\infty}^{\infty} f(v)\, e^{i2\pi v t} dv. \tag{16}$$

If one assumes that the refractive indices along the principle stress directions are constant as a function of frequency, the Fourier transform of the time-shifted incident electric field may be evaluated as

$$E_{\sigma_1}(v) = \int_{-\infty}^{\infty} E_{inc}(t + \Delta t_{\sigma_1})\, e^{-i2\pi v t} dt = E_{inc}(v) e^{i2\pi v\, \Delta t_{\sigma_1}}. \tag{17}$$

This result is expected because, in the frequency domain, the time delay is manifested as a simple multiplication by a phase factor. Using Eq. (17), the difference in the time-shifted electric fields of Eq. (14) can be evaluated as

$$E_{inc}(t + \Delta t_{\sigma_1}) - E_{inc}(t + \Delta t_{\sigma_2}) = \int_{-\infty}^{\infty} \left(E_{\sigma_1}(v) - E_{\sigma_2}(v)\right) e^{i2\pi v t} dv. \tag{18}$$

Factoring out the average phase shift on the right-hand side of the equation gives

$$E_{inc}(t + \Delta t_{\sigma_1}) - E_{inc}(t + \Delta t_{\sigma_2}) = \int_{-\infty}^{\infty} E_{inc}(v) e^{i2\pi v\left(\Delta t_{\sigma_2} + \Delta t_{\sigma_1}\right)/2} \left(e^{i2\pi v\left(\Delta t_{\sigma_1} - \Delta t_{\sigma_2}\right)/2} - e^{-i2\pi v\left(\Delta t_{\sigma_1} - \Delta t_{\sigma_2}\right)/2}\right) e^{i2\pi v t} dv \tag{19}$$

$$= -\int_{-\infty}^{\infty} 2iE_{inc}(v) e^{i2\pi v\left(\Delta t_{\sigma_2} + \Delta t_{\sigma_1}\right)/2} \sin(\pi v\, \Delta n\, L/c_o)\, e^{i2\pi v t} dv. \tag{20}$$

where the birefringence $\Delta n = (n_{\sigma_2} - n_{\sigma_1})L/c_o$. In the limit that the birefringence is small such that $\pi v\, \Delta n L/c_o \ll 1$, the sine function can be approximated such that

$$E_{inc}(t + \Delta t_{\sigma_1}) - E_{inc}(t + \Delta t_{\sigma_2}) \simeq -2\pi i \frac{L\,\Delta n}{c_o} \int_{-\infty}^{\infty} v E_{inc}(v) e^{i2\pi v\left(\Delta t_{\sigma_2} + \Delta t_{\sigma_1}\right)/2} e^{i2\pi v t} dv \tag{21}$$

$$\simeq -\frac{\Delta n\, L}{c_o} \frac{d}{dt}\left[E_{inc}\left(t + \frac{\Delta t_{\sigma_2} + \Delta t_{\sigma_1}}{2}\right)\right] = \frac{\Delta n\, L}{c_o} \lim_{\Delta t_0 \to 0} \left[\frac{E_{inc}\left(t + \frac{\Delta t_{\sigma_2} + \Delta t_{\sigma_1}}{2}\right) - E_{inc}\left(t + \Delta t_0 + \frac{\Delta t_{\sigma_2} + \Delta t_{\sigma_1}}{2}\right)}{\Delta t_0}\right] \tag{22}$$

where on the right-hand side of Eq. (22) the time derivative of the incident electric field pulse is approximated as a finite difference. This equation justifies the following model for the difference in the time-delayed incident pulses

$$E_{inc}(t + \Delta t_{\sigma_1}) - E_{inc}(t + \Delta t_{\sigma_2}) \simeq \Delta n\, A\, E_{diff}(t) \tag{23}$$

where Δn is the material birefringence, $E_{diff}(t) = E_{inc}(t + (\Delta t_{\sigma_2} + \Delta t_{\sigma_1})/2) - E_{inc}(t + \Delta t_0 + (\Delta t_{\sigma_2} + \Delta t_{\sigma_1})/2)$, and $A = L/c_o\Delta t_o$ is a scaling factor. The differential electric field pulse E_{diff} can be generated mathematically by subtracting the incident electric field waveform shifted in time by Δt_o, from the incident waveform. For simplicity, a value of $\Delta t_o = 0.1$ ps is used which is the time interval in the terahertz waveforms digitized by the T-Ray 5000 system.

Combining Eqs. (14) and (23) gives the detected terahertz time-domain waveform as

$$E_{RX}(t) = \tau_{as}\tau_{sa}\left[\Delta n\, A\, E_{diff}(t)\right]\left(\sin\theta\cos\theta\left(\cos^2\phi - \sin^2\phi\right) + \sin\phi\cos\phi\left(\sin^2\theta - \cos^2\theta\right)\right). \tag{24}$$

The goal of the terahertz birefringence measurement is to measure the detected terahertz waveform at two different values of ϕ to determine uniquely the birefringence magnitude Δn and the stress principle stress direction θ of the material. Evaluating the measured time-domain waveform for the polarizer P1 making angles of $\phi = 0^{o}$ and $\phi = 45^{o}$ with respect to the x-axis (polarizer P2 is orthogonal to P1 for both values of ϕ) gives two equations for the measured waveforms

$$E_0(t) = \tau_{as}\tau_{sa}\left[\Delta n\, A\, E_{diff}(t)\right](\sin\theta\cos\theta), \tag{25}$$

$$E_{45}(t) = \tau_{as}\tau_{sa}\left[\Delta n\, A\, E_{diff}(t)\right]\left(\sin^2\theta - \cos^2\theta\right)/2. \tag{26}$$

By extracting the pulse amplitudes of the waveforms denoted by E_0 and E_{45}, the stress direction

$$\frac{E_o}{E_{45}} = \frac{2\sin\theta\cos\theta}{\sin^2\theta - \cos^2\theta} = -\tan 2\theta \tag{27}$$

may be calculated by dividing Eqs. (25) and (26). This is the same result as derived by Kang et al. (2021).

The magnitude of the birefringence can be determined by measuring the amplitudes of the waveforms denoted by E_0, E_{45}, and $\tau_{as}\tau_{sa}E_{diff}$. Eqs. (25) and (26) may be squared and added to yield

$$\Delta n = \frac{2c_o\Delta t_o}{L}\sqrt{\left(\frac{E_o}{\tau_{as}\tau_{sa}E_{diff}}\right)^2 + \left(\frac{E_{45}}{\tau_{as}\tau_{sa}E_{diff}}\right)^2}. \tag{28}$$

Note that the denominator of Eq. (28) takes into account the reflective losses of the incident electric field pulse as it propagates through the air-sample interfaces. An added benefit in measuring the time shifts Δt_{σ_1} and Δt_{σ_2} referenced to no sample in the terahertz beam path enables one to normalize out the thickness from Eq. (28). In this case the average of the time shifts may be written as

$$\frac{\Delta t_{\sigma_1}+\Delta t_{\sigma_2}}{2}=\frac{L}{c_o}\left(\left(\frac{n_{\sigma_1}+n_{\sigma_2}}{2}\right)-1\right)=\frac{L}{c_o}\left(n_{average}-1\right). \tag{29}$$

Dividing Eq. (28) by Eq. (29) gives the relative birefringence as

$$\frac{\Delta n}{n_{average}-1}=2\frac{\Delta t_o}{(\Delta t_{\sigma_1}+\Delta t_{\sigma_2})/2}\sqrt{\left(\frac{E_o}{\tau_{as}\tau_{sa}E_{diff}}\right)^2+\left(\frac{E_{45}}{\tau_{as}\tau_{sa}E_{diff}}\right)^2}. \tag{30}$$

Evaluation of Eq. (30) requires measurement of the amplitudes and arrival times of the three waveforms denoted by E_o, E_{45}, and $\tau_{as}\tau_{sa}E_{diff}$.

Extraction of the stress direction from Eq. (27) and the relative birefringence from Eq. (30) requires measurement of 4 THz pulse waveforms. The time-domain waveforms through the sample with polarizers P1 and P2 oriented orthogonally as illustrated in Fig. 12 with $\phi = 0^o$ and $\phi = 45^o$ correspond to E_o and E_{45}. The measured waveform through the sample with P1 and P2 oriented parallel to each other corresponds to $\tau_{as}\tau_{sa}E_{inc}(t+(\Delta t_{\sigma_2}+\Delta t_{\sigma_1})/2)$. The waveform $\tau_{as}\tau_{sa}E_{diff}$ is calculated by shifting the waveform by one time slot (corresponding to 0.1 ps for the Terametrix T-Ray 5000 system) and subtracting the shifted waveform from the unshifted waveform. The last required waveform is one with the sample removed which essentially measures $E_{inc}(t)$. The time delay of the waveform with the sample present compared to the sample removed effectively measures $(\Delta t_{\sigma_2}+\Delta t_{\sigma_1})/2$.

The amplitudes of the measured waveforms are calculated using a deconvolution calculation. The amplitudes and arrival times for the E_o and E_{45} waveforms are mathematically determined by a deconvolution process using Matlab software with $\tau_{as}\tau_{sa}E_{diff}$ as the reference pulse for the deconvolution. The deconvolution is performed using Fourier transforms

$$E_{deconv}(t)=A_o\, ifft\left(fft(E(t))/fft\left(E_{ref}(t)\right)\left(\exp\left(-(2\pi\nu t_w)^2/2\right)\right)\right) \tag{31}$$

where$E_{ref}(t)$ denotes a reference waveform. The parameter $t_w = 4$ ps represents a smoothing time window. The normalization constant A_o is chosen such that the amplitude of a deconvoluted waveform with itself (i.e., $E(t)=E_{ref}(t)$) is unity. Once the deconvoluted waveform is calculated, the amplitude A and arrival time t_a of the deconvoluted pulse is determined by fitting the peak of the waveform to a Gaussian shape $G(A,t_a,c)=A\exp\left(-((t-t_a)/c)^2\right.$. Typically, the best fit is performed on data only within ±0.7 ps of the deconvoluted waveform peak. The arrival time $(\Delta t_{\sigma_2}+\Delta t_{\sigma_1})/2$ is calculated by deconvolving the waveform $\tau_{as}\tau_{sa}E_{inc}$ with $E_{inc}(t)$ as the reference.

As an example, a 10 mm sheet of extruded high-density polyethylene (HDPE) is characterized. Fig. 13 shows experimental measurements of the birefringence from a small piece of extruded HDPE. Fig. 13a shows the measured received electric field amplitude as a function of angle of rotation φ for the orthogonal polarizers. Note that the theoretical fit to the experimental data is very good. The images of Fig. 13b and c show 2D mages of the local direction of the intrinsic stress in the sample as well as the measured normalized birefringence given by $\Delta n/(n_{avg}-1)$ where Δn is the difference in refractive index along the two principle stress directions, and n_{avg} is the average refractive index of the material.

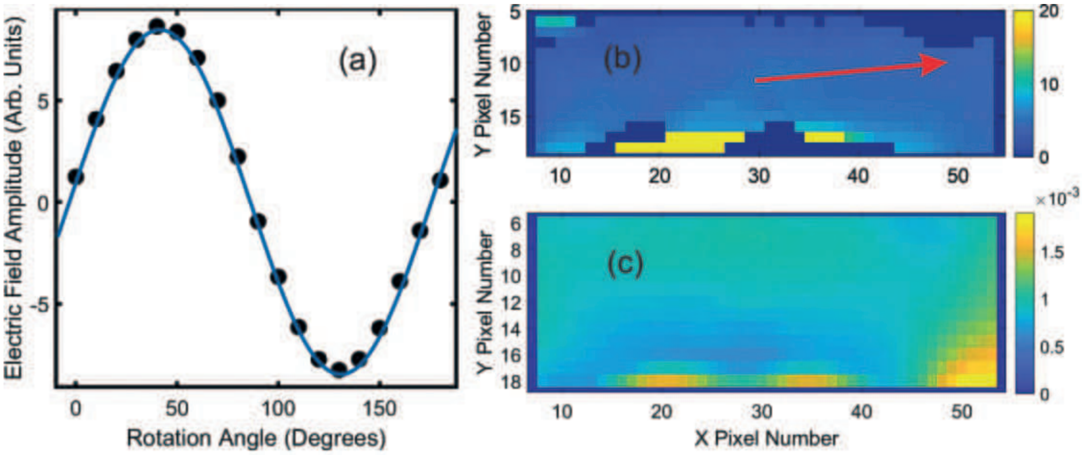

Fig. 13 (a) at a fixed point in the sample, measurement of the amplitude of the received electric field amplitude as a function of angle of rotation φ for the orthogonal polarizers. The theoretical line is from Eq. (14). (b) extracted stress angle in units of degrees from Eq. (27) and (c) normalized birefringence from Eq. (30).

Multilayer paint stacks

Terahertz NDE of multilayer paints

The analysis geometry is illustrated in Fig. 14a for an $N = 3$ layer paint stack. The terahertz pulse is incidence from air onto N dielectric layers before encountering a metallic substrate. Each layer is characterized by a thickness d_j and complex refractive index $\tilde{n}_j$. There are three basic approaches to analyzing the THz reflectivity data. The first approach is to deconvolve the reflected terahertz waveform with a reference waveform which is acquired by reflection from a perfect metal. The peaks in the deconvolved waveform represent reflections from the various material boundaries in the multilayer stack. Application of this approach is discussed in more detail in Section "Results".

A second approach is to convert the time-domain THz waveform to the frequency domain through a Fourier transform. Analysis and extraction of the layer thicknesses and their refractive indices (both real part and imaginary part) are performed by fitting the measured reflectivity spectra to a theoretical model of multiple reflections through a multi-layer stack of layers. This method can be effective for relatively thick layers. However, as the layers become thinner, the reflected THz waveforms significantly overlap in time.

As described in van Mechelen et al. (2014), a stratified sample structure such as a paint layer stack, is difficult to analyze in the frequency domain since the reflectivity $R(\omega)$ has multiple internal reflections from the various layer boundaries. Moreover, in order to extract the refractive index by fitting the experimentally measured reflectivity to a model of the reflectivity, one would typically assume that the refractive index was real (i.e., no absorption due to the imaginary refractive index) and frequency independent. While modeling of the refractive index as primarily real and frequency independent reduces the number of fitting parameters to the experimental data, it was not a realistic description of the paint layers.

A superior method of analyzing stratified paint stack structures is to use realistic models for the frequency-dependent complex refractive index as well as fitting the theoretical model to the measured experimental data in the time-domain (van Mechelen et al., 2014; Krimi et al., 2016) rather than the frequency domain. The main benefit of the time-domain fitting is the stratified dispersive model which parameterizes each layer with a small number of fitting parameters enabling simultaneous extraction of the individual electromagnetic material parameters in multilayer structures. For application to multilayer paint structures, many dielectrics such as the polymers used in paint obey a Debye dielectric relaxation model. For this model, the frequency (ω) dependent index of refraction of the layer j material is given by

$$\tilde{n}_j(\omega) = \left(\varepsilon_j^\infty + \frac{\varepsilon_j^s - \varepsilon_j^\infty}{1 + i\omega\tau_j}\right)^{1/2} \tag{32}$$

where ε_j^∞ is the permittivity at the high-frequency limit, ε_j^s is the static, low-frequency permittivity, and τ_j is the characteristic relaxation time of the jth paint layer. The real part of the refractive index controls the time delay of the THz pulse or equivalently the speed of the THz pulse through the material. The imaginary part of the refractive index is responsible for the absorption of the THz pulse as it propagates through a layer.

As summarized by Krimi et al. (2017), the typical analysis process involves three steps: calibration, mathematical modeling of the terahertz propagation through the multilayer structure, and optimization. In the calibration step, a reference waveform is measured by replacing the paint stack layer with a flat metallic mirror. Since the front surface of the mirror cannot be placed in exactly the same plane as the front surface of the paint stack, the analysis incorporates an overall time delay ξ between the time-domain reference and reflected pulses. The calibration step may also include terahertz measurements of individual layers of each material to extract their complex refractive indices and Debye model fitting parameters.

The modeling step mathematically propagates an input terahertz pulse waveform through the multilayer stack to calculate the resulting reflected waveform. The mathematical modeling can be typically performed first by Fourier transforming the input

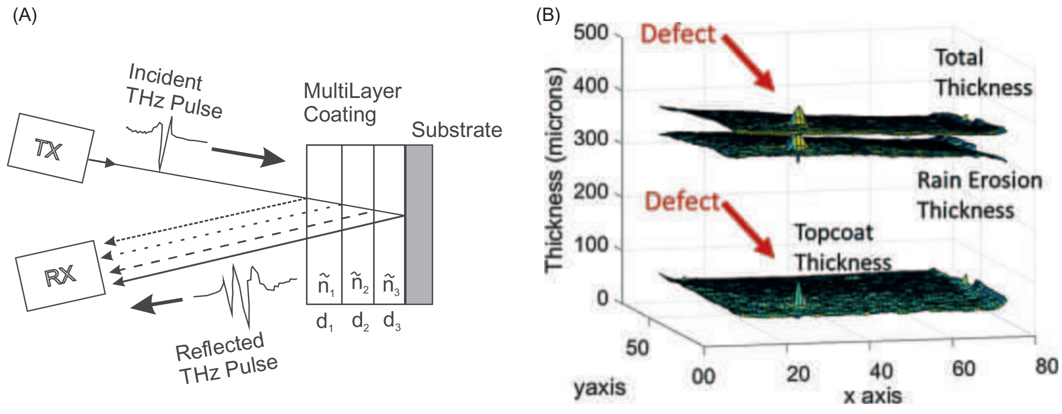

Fig. 14 (a) Illustration of terahertz reflection from multilayer paint coating. The transmitter and receiver are indicated by TX and RX, respectively. Each layer is parameterized by its thickness d_i and its complex refractive index $\tilde{n}_i$. After the incident pulse waveform interacts with the paint stack, the reflected THz waveform is measured. (b) A reconstructed 3D thickness image of a two-layer sample. The presence of a defect in the coating is indicated by the red arrows.

time-domain waveform into the frequency domain. The input waveform is then propagated through the multilayer stack by an optical transfer matrix method. As an example, a Debye dielectric relaxation model can be assumed for each non-metallic paint layer. The $j = 0$ layer is assumed to be air with $n_o = 1$. The parameter N represents the number of dielectric layers such that the metal substrate is the $N + 1$ layer. In the metal substrate, various models can be used to model the metal. One option is to use a Drude model for metal for which

$$\tilde{n}_{N+1}(\omega) = \left(\frac{\varepsilon^{\infty}_{N+1}}{\varepsilon_o} - i \frac{\sigma_o}{\varepsilon_o \omega} \frac{1}{(1 + i\omega\tau_{N+1})} \right)^{1/2} \tag{33}$$

where σ_o is the substrate's static conductivity, and ε_o denotes the vacuum electric permittivity. If the dielectric layers and metallic layer are characterized as part of the calibration step, then the Debye parameters ε_j^{∞}, ε_j^{s}, and τ_j as well as the metallic layer parameters, $\varepsilon^{\infty}_{N+1}$, σ_o, and τ_{N+1} are known for each layer. Alternatively, they could also be determined in the optimization step.

Given the functional form for the complex refractive indices and layer thicknesses, an incident pulse is propagated through the multilayer coating/substrate combination. One approach is to use an optical transfer matrix approach (Saleh and Teich, 1991). At each interface, it is assumed that the incident electromagnetic wave interacts at near normal incidence so that using Fresnel coefficients, the matrix representing the boundary is given by

$$P_{j.j+1}(\omega) = \frac{1}{2n_{j+1}} \begin{pmatrix} \tilde{n}_{j+1} + \tilde{n}_j & \tilde{n}_{j+1} - \tilde{n}_j \\ \tilde{n}_{j+1} - \tilde{n}_j & \tilde{n}_{j+1} + \tilde{n}_j \end{pmatrix}. \tag{34}$$

After propagating through an interface between adjacent layers, the transmitted light propagates through the thickness d_j of each layer. As the wave propagates through each layer, it experiences a frequency-dependent phase shift and is expressed through the diagonal matrix

$$D_j(\omega) = \begin{pmatrix} e^{-i\omega d_j \tilde{n}_j / c_o} & 0 \\ 0 & e^{i\omega d_j \tilde{n}_j / c_o} \end{pmatrix} \tag{35}$$

where d_j is the thickness of each optical layer, and c_o is the speed of light in a vacuum. In order to calculate the total effect, these matrices are cascaded layer by layer through the product

$$M(\omega) = \prod_{j=0}^{N} D_j P_{j,j+1} = \begin{pmatrix} M_{11} & M_{12} \\ M_{21} & M_{22} \end{pmatrix}. \tag{36}$$

The matrix Eq. (36) is known as the optical transfer matrix and completely characterizes the transmission and reflection in the multi-layered system. The reflectivity from the paint stack is calculated using the optical transfer matrix from

$$R(\omega) = \frac{M_{21}(\omega)}{M_{11}(\omega)}. \tag{37}$$

Lastly, there is an optimization step in which the thicknesses of the various layers are optimized in order to minimize the error between the measured time-domain reflected waveform and the waveform predicted by the mathematical modeling. The time-domain reflected electric field from an N-layer paint coating may be expressed as

$$E_R(t) = \mathcal{F}^{-1}\left[e^{-2\pi i \xi} R(\omega) \mathcal{F}[E_I(t)] \right] \tag{38}$$

where $\mathcal{F}[E_I(t)]$ is the Fourier transform of the incident Terahertz pulse. The analysis incorporates an overall time-delay ξ between the time-domain reference and reflected pulses. If the Debye model parameters for each layer have not been determined in the calibration step, they could be determined in the optimization step. Multiplying the Fourier Transform of the incident electric field by the reflectivity Eq. (37) and the overall phase shift effectively accounts for the propagation of the THz pulse through the various layers of the paint layer stack. The inverse Fourier transform converts the frequency-domain back into a time-domain pulse. The time-domain reflected pulse depends on the refractive indices and thicknesses of each paint layer, the reflectivity of the metallic substrate, and the overall time delay ξ.

Extraction of best-fit parameters is accomplished using a minimization algorithm to optimize the fitting parameters by minimizing the difference in the measured terahertz waveform compared to the waveform generated from Eq. (38) with the fitting parameters. As an example, a least-squares fitting process could be used as outlined below. To this end, let m be the number of fitting parameters. For example, with a two-layer model there are 2 paint layer thicknesses, there are 6 Debye parameters for the paint layers, 3 Drude parameters for the metal substrate, and an overall time delay for a total of $m = 12$ parameters. The measured data $E_{data}(t)$ is defined over some time window $[0, T]$. While the maximum value of $T = 160$ ps could be used since the Tray 5000 THz instrumentation used in this project records a 160 ps window of data, the time window is restricted to a 65 ps window centered on the main structure of the terahertz pulse (Fig. 15). The computational problem can be expressed as minimizing the squares of the error between the measured and fitted time-domain data. More precisely,

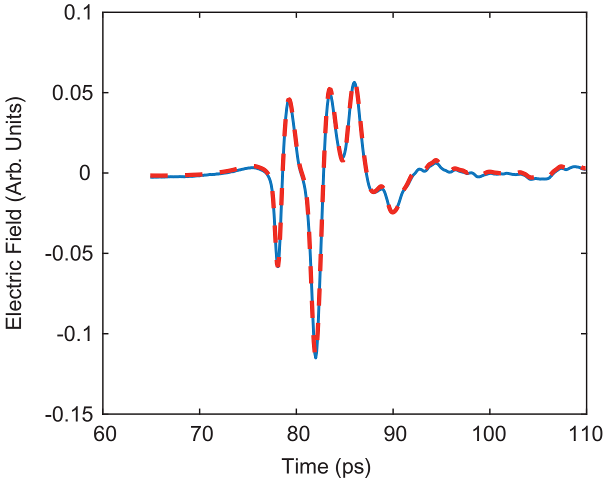

Fig. 15 Comparison of experimental reflected terahertz waveform (blue) to theoretical fit (red) using a two layer model.

$$\min_{\vec{P}\in\mathbb{R}^m} Error = \min_{\vec{P}\in\mathbb{R}^m}\left[\frac{1}{2}\left\|E_{data}(t) - E_R\left(\vec{P},t\right)\right\|^2_{L^2([0,T])}\right] \tag{39}$$

where $\vec{P}$ is a vector storing the m fitting parameters, and the fitting parameters must be part of a physically realizable parameter space (for example the thicknesses must be positive values). The norm defining the error is given by

$$\|\ .\ \|_{L^2([0,T])} = \left(\int_0^T |\ .\ |^2 dt\right)^{1/2}, \tag{40}$$

and $E_R\left(\vec{P},t\right)$ is the parameter-dependent electric field computed in the frequency domain and mapped back to the time-domain through Eq. (38). The norm of the difference $E_{data}(t) - E_R\left(\vec{P},t\right)$ measures the misfit, over the time-domain $[0,T]$, between the experimentally obtained data and the reflected electric field. The integration required by the norm is computed numerically via the trapezoidal rule.

As an example of the quality of the fit, Fig. 15 shows the experimentally measured and fitted electric field for a two-layer paint stack consisting of a UV topcoat, rain erosion layer, and metallic substrate (assumed to be a perfect metal). This data represents one pixel on a 2D painted sample. By recording the terahertz reflected waveforms on a pixel-by-pixel basis, refractive index and layer thickness maps similar to those in Fig. 14b may be extracted from the terahertz imaging data.

In adapting the terahertz pulsed imaging technique to real-time evaluation of paints, attention must be given to rapid processing of the images and reducing the computational time of the minimization algorithm. Krimi et al. (2017) have shown that utilizing Rouard's method (Krimi et al., 2016) rather than an optical transfer matrix approach enables one to reduce the computational time by a factor of 1.7 and the graphics processing unit (GPU) allocated memory by a factor of about 2.3. The methodology of (Krimi et al., 2017) utilizes a genetic algorithm optimization rather than a least squares optimization to provide best-fit parameters. This approach enables resolution of individual layer thicknesses of typically 7 μm with an absolute accuracy of less than 1 μm. Terahertz nondestructive monitoring of automobile multilayer paints has in fact been implemented on a limited scale in industrial automobile factories (https://das-nano.com/success-story/volkswagen/).

Terahertz NDE of paint corrosion

While terahertz pulse imaging has been adapted for industrial quality control measurements of paint layer thicknesses, another application of the methodology is detection of underlying corrosion of multilayer structures. To a large extent, the same terahertz instrumentation and methodology which was developed to assess the fabrication of multilayer structures can be used to assess the structure's degradation due to corrosion. An early example is the characterization of corrosion under Space Shuttle tiles which used the same instrumentation which was developed to inspect sprayed-on foam insulation (Anastasi et al., 2007).

Several studies demonstrating the feasibility of corrosion detection by terahertz imaging have been reported. As an example, one study (Tu et al., 2021) created buried corrosion layers by painting over rusted areas to create a 'hidden' corrosion defect. By comparing the terahertz pulse shape where no rust was present compared to a rusted area under the paint, it was readily observable that the terahertz pulse shape was significantly changed by the presence of rust. Changes in terahertz pulse shape were also present for which adjacent paint layers separated and also when the coating became detached from the substrate (some reports refer to the detachment of the coating from the substrate as 'blistering'). The change in pulse shape due to delamination of different coating layers can be easily understood due to the presence of additional material boundaries which partially reflect the propagating terahertz radiation as well as additional time delays between pulse peaks as the spatial separation between layers increases (Dong et al., 2017).

Using a similar sample fabrication method, (Fuse et al., 2012) tested the viability of rust detection hidden under epoxy using carbon steel plates as substrates. Rusted areas on the substrate were created by placing a few drops of salt solution on its surface. After wiping off the residual solution, epoxy resin was used to cover the substrate surface. Terahertz reflection measurements showed that the rust strongly attenuates the terahertz radiation compared to uncorroded metal enabling sufficient contrast in terahertz pulsed imaging reflection measurements to detect the presence of the buried rust.

In a follow-up paper (Fuse et al., 2016), the technique was extended to higher terahertz frequencies using a quantum cascade laser (QCL) as the terahertz source and a terahertz camera for detection. Samples were exposed to a coastal environment for 27 months. The buried substrate surface corrosion resulted in an increase in surface roughness which increased the scattering, resulting in a concomitant decrease in the terahertz reflectivity. In comparing the QCL detection system to the THz TDS system, the QCL system was more effective in detecting early onset of corrosion since the rust resulting from γ-FeO(OH) exhibits absorption peaks at around 6.6 THz and 9.3 THz whose tails spectrally overlap the frequency range of the QCL. The authors report that the absorption coefficient for 2.5 THz waves (QCL) is about 40 times higher as compared to the ~0.3 THz waves which are employed in THz-TDS thereby enabling detection using the QCL system of even small amounts of corrosion with corresponding relatively weak terahertz absorption.

In developing terahertz nondestructive evaluation to evaluate the degradation of multilayer paint stacks with aging, it is important to consider what aspects of the paint layer properties that are probed by terahertz waves might change with coating degradation. Clearly, if the dielectric paint layers are degraded, this might be manifested either in changing layer thicknesses or in the Debye model permittivity. In addition, chemical corrosion of a metallic substrate or layer, as discussed above, creates a rough surface that increasingly scatters terahertz radiation with corrosion. Changes in these parameters will alter not only the amplitudes but also the timings of the reflected pulses from each layer in the paint stack resulting in a change in the overall reflected THz-TD waveform as well as the deconvoluted waveform.

The reflectivity of a rough metallic surface can be modeled using the Beckmann and Spizzichino model (Beckmann and Spizzichino, 1987; Cacciari and Siano, 2017). Using this model, the mean power (i.e., square amplitude of electric field) in the specular reflected direction may be written as

$$P_s = e^{-g}\left(1 + \frac{\tau_L\sqrt{\pi}}{2D}\sum_{m=1}^{\infty}\frac{g^m}{m!\sqrt{m}}\right) \tag{41}$$

where

$$\sqrt{g} = 4\pi\frac{R_q v}{c_o}, \tag{42}$$

D is the terahertz beam spot size, R_q is the standard deviation of the normally distributed heights of the rough surface, τ_L is the correlation distance, c_o is the speed of light in a vacuum, and v is the terahertz frequency. When $R_q = 0$, corresponding to a flat metallic surface with no surface roughness, Eq. (41) reduces to unity indicating perfect reflection from a flat metal surface. When the surface roughness is present, the power in the specular reflected direction is reduced with increasing roughness since the rough surface scatters some of the terahertz power into non-specular directions. In the limit of small roughness $g \ll 1$, the power P_s can be shown to approximately depend quadratically on the terahertz frequency

$$P_s \simeq 1 - \left(\frac{4\pi R_q v}{c_o}\right)^2\left(1 - \frac{\tau_L\sqrt{\pi}}{2D}\right). \tag{43}$$

If the terahertz source is a broad-banded pulse source, such as with terahertz time-domain spectroscopy, the spot size D of the focused pulse depends on the terahertz frequency. Assuming a terahertz Gaussian beam with initial diameter D_f which is focused to a spot size D using a lens of focal length f, the spot size at the focus can be approximated as $D = c_o f/\pi D_f v$. In this case, the power P_s becomes

$$P_s \simeq 1 - \left(\frac{4\pi R_q v}{c_o}\right)^2\left(1 - \frac{\tau_L\pi^{3/2}D_f v}{2c_o f}\right). \tag{44}$$

Accelerated corrosion protocols

Many of the published studies of terahertz nondestructive evaluation of buried corrosion layers, such as those cited above, did not follow any established protocol for accelerated corrosion testing of samples. Their emphasis was to establish the prospect of terahertz NDE of buried corrosion. In the rest of this section, terahertz NDE of multilayer paint samples is described in which the samples were exposed to an accelerated corrosion test method (Dante, 2019). The samples are periodically removed from the accelerated corrosion chamber to characterize the corroded samples using terahertz NDE.

The accelerated corrosion methodology combines cycling of dry and wet environmental conditions with 'aggressive'—meaning higher salt concentration and higher acidity (pH < 5)—salt-fog solutions. For the work presented in this section, the accelerated corrosion test method of Dante (2019) was adopted. The core components of the corrosion solution are seawater as detailed in Table 2. As described by Dante, nitrate is added because all coastal sites from which they acquired chemical samples showed nitrate. Moreover, the nitrate solution is realistic since it is also an important oxidizer in atmospheric chemistry. The low pH is the result of sea salt aerosols (around 1 μm) exhibiting pH values of approximately 3. Due to the low pH in the solution, the saltwater solution is only applied via fog for 6 h twice a week. Subsequent to fog exposure, the relative humidity is cycled for either 3 or 4 days until the next salt fog exposure. The relative humidity cycling is performed at 40 °C; the samples spend 2 h at 90% RH 3 h at 65% RH and 1 h at 40% RH. This cycle repeats until the next fog exposure with a total of two fog exposures in a 1 week period.

The multilayer paint samples, illustrated in Fig. 17a consisted of an aluminum substrate, primer layer (approximately 0.7 mils thick), conductive layer (approximately 1.1 mils thick), a second primer layer, rain erosion layer (approximately 10 mils), and an ultraviolet blocking topcoat layer (approximately 1.7 mils). The tested coupons (roughly 3 in. by 3 in.), were cut from larger painted panels. These cuts made the edges of the samples vulnerable to the solution seeping in through the side of the sample as opposed to through the topcoat layer, so the edges of the samples were covered with waterproof tape.

On a weekly basis, just prior to exposure in the salt fog chamber, the multilayer paint samples are removed from the humidity chamber for THz-TD testing. Prior to testing, the samples are rinsed with deionized water and blown dry with air to remove any surface build-up of salt deposits. The surface salt deposits are removed so that their presence on the surface does not lead to any artifacts in the terahertz waveform due to scattering from the deposits. Experiments have shown that the subsequent 6 h exposure to salt fog will fully saturate the coating for the next humidity cycle. To eliminate potential contribution of water absorbed into the paint layers to the measured terahertz waveform, prior to terahertz characterization the samples are dried in a constant flow of 50 °C dry air for 1 h. Time-domain waveforms and images were acquired using a Terametrix T-Ray 5000 THz time-domain system.

Results

By measuring the amplitude of the reflected terahertz radiation within a fixed frequency band, one can easily generate images of the corrosion progression as shown in Fig. 16. The frequency-dependent reflectivity is calculated by dividing the reflected frequency-dependent magnitude by the frequency spectrum of a reference pulse which was reflected from a flat metal plate. The average reflectance within a specific frequency band is then calculated for each pixel. The upper left image is recorded from the sample prior to any accelerated corrosion. The darker gray lines near the boundary of the sample represent the edges of the tape on the samples. Note that prior to accelerated corrosion (upper left image) that the reflectivity of the sample is very uniform across the sample. As the sample undergoes accelerated corrosion, the reflectivity decreases near the corners and edges of the sample where the salt-fog is able (a) to penetrate through gaps in the tape or (b) effectively collect under the tape near the sample edges.

In addition to the time-domain analysis described above in which the permittivity of each layer is assumed to obey a Debye relaxation model (Eq. 32), the reflected terahertz waveform may also be analyzed using a deconvoluted pulse approach. In its simplest form, the deconvoluted pulses represent the partial reflection of terahertz radiation from each boundary in the multilayer paint stack. The deconvolution analysis enables one to determine the amplitude as well as the arrival time from each partial reflection. The advantage of this simplified approach compared to the time-domain analysis in Section "Terahertz NDE of multilayer paints" is that one does not need to assume any particular functional form (i.e., Debye relaxation model) for the paint layer permittivity.

A typical terahertz time-domain reflected waveform from an undegraded sample and the corresponding deconvoluted waveform which is calculated using the Tray 5000 software is shown in Fig. 17b. The deconvolution algorithm uses a reference waveform which is acquired by replacing the sample with a flat metallic plate. The deconvolution waveform shows four main peaks. Peak 1 is the front reflection from the air-top coat boundary. Peak 2 is the reflection from the top coat/rain erosion boundary. Peak 3 is a reflection from the aluminum substrate. Peak 4 is due to multiple reflections between the front surface of the coating and the aluminum substrate. The refractive index of the rain erosion layer is similar to that of the thin primer layer such that there is no observable reflection from the rain erosion/primer boundary.

A simple analytical method to determine if the multilayer paint stack is changing with corrosion is to analyze the arrival times and amplitudes of the deconvoluted pulses. For this analysis method, assumptions of particular models for the dielectric layers (i.e., Debye) nor metallic substrate (e.g., Drude) are not required. As an example, the time delay between the deconvolved pulse 2 and 1 is a measure of the optical path length (i.e., real refractive index multiplied by the thickness) of the topcoat layer while the time delay

Table 2 Composition of modified sea salt solution for corrosion testing.

Modified Sea Salt Solution with Nitrate Ions	
NaCl	22.26 g L^{-1}
$MgCl_2 \bullet 6H_2O$	11.10 g L^{-1}
Na_2SO_4	4.00 g L^{-1}
$NaNO_3$	3.27 g L^{-1}
HCl (1 N)	(1 mL)

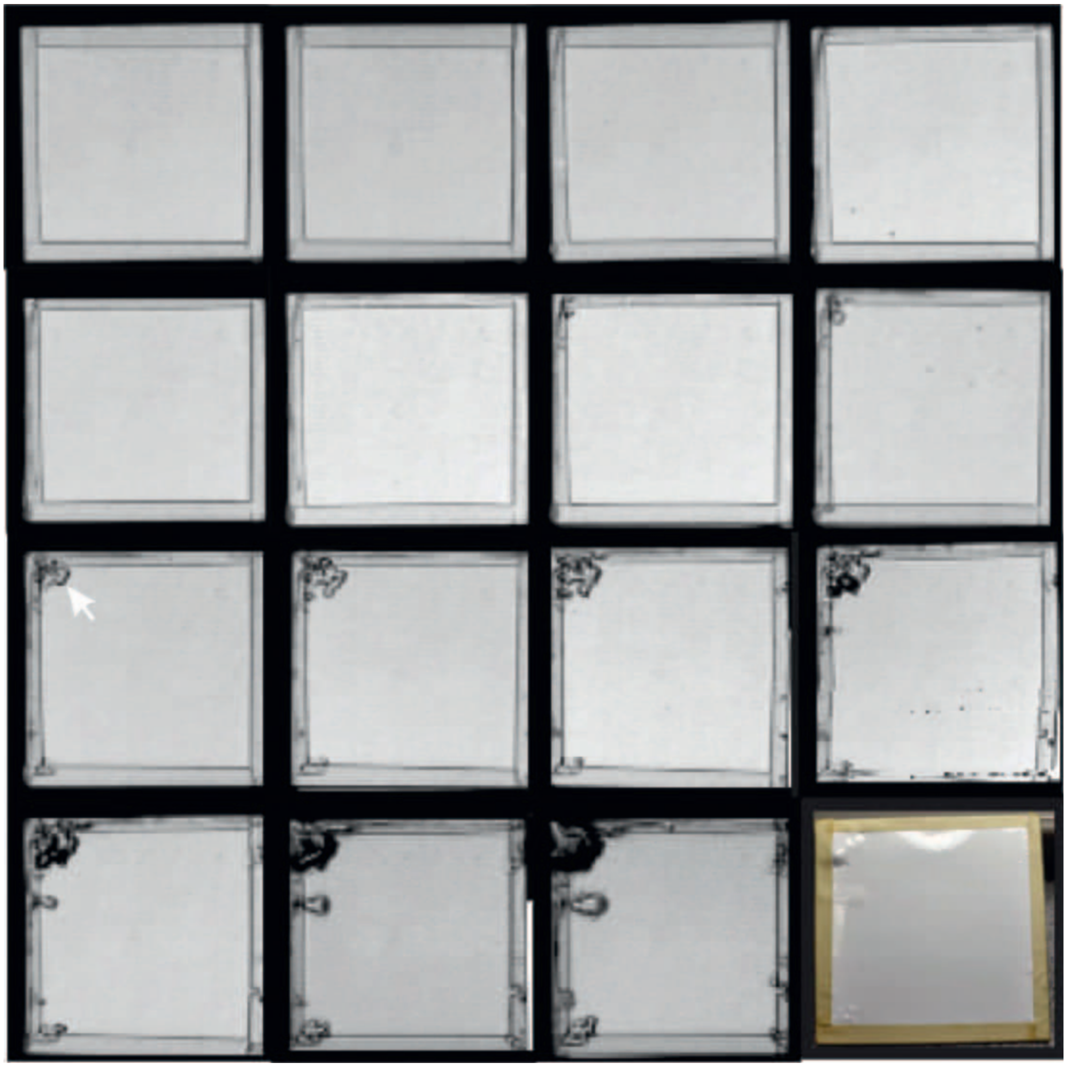

Fig. 16 Time sequence of terahertz images taken at weekly intervals during accelerated aging. The images correspond to the average measured reflectivity of the terahertz waveform in the 0.5–1 THz range. Top left image was acquired prior to aging. The presence of tape on the edges of the sample is evident in the images as well as the onset of corrosion from the edges of the sample.

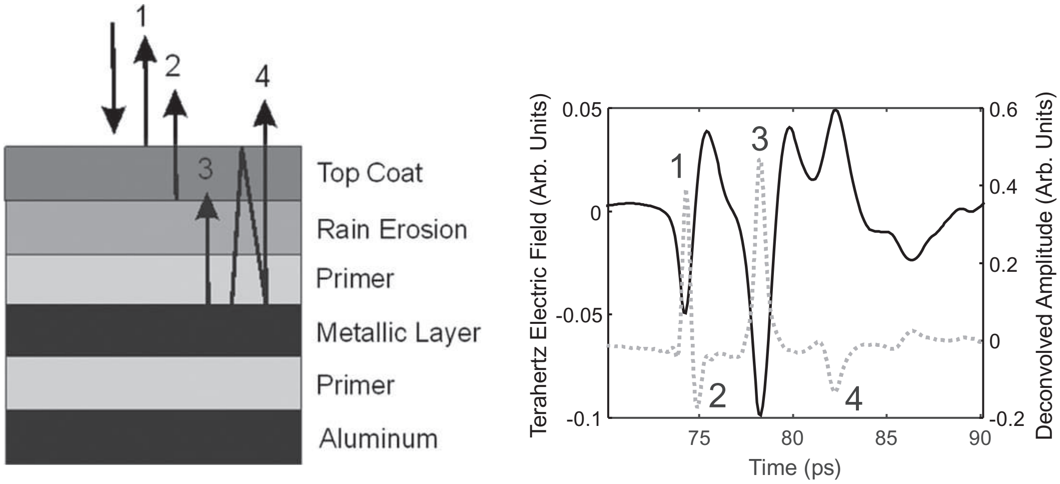

Fig. 17 (a) Schematic of multilayer paint samples. (b) Typical reflected terahertz waveform (solid black, left axis) and deconvoluted waveform (dashed gray, right axis) from center pixel location of the sample. Main peaks of the deconvolved waveform are labeled from 1 to 4.

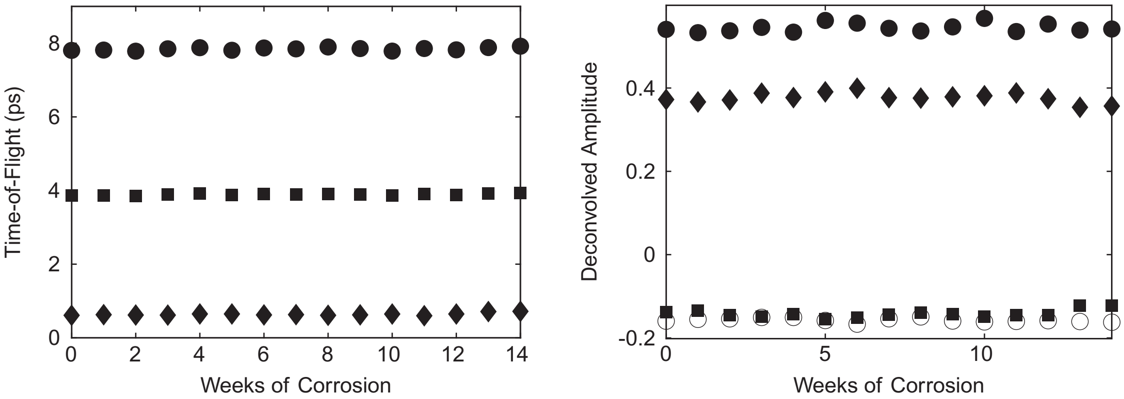

Fig. 18 (a) Measured time-of-flight between pulses 2 and 1 (diamond), 3 and 1 (square), and 4 and 1 (circle) as a function of number of weeks of corrosion. (b) Deconvolved amplitudes of pulses 1 (diamond), 2 (square), 3 (circle), and 4 (open circle) as a function of weeks of corrosion. Data is taken from a pixel at the center of the sample.

between pulse 3 and 2 is a measure of the optical path length of the rain erosion layer. Fig. 18a shows the measured time of flight between the various pulses as measured from the center of the sample. Note that the pulse time-of-flight relative to the front reflection from the center of the paint layer stack does not significantly change during the corrosion process. Likewise, the amplitudes of the various deconvoluted pulses (Fig. 18b) show essentially no change with accelerated corrosion. This suggests that the salt-fog corrosion degradation through the coating is a very slow process compared to corrosion through edges of the sample. Even after 14 weeks of degradation, the 'shine' of the topcoat layer as measured by visible light illumination is still present. Consequently, one may conclude that for the accelerated corrosion protocol used in this study, the Debye permittivity function and thicknesses of the dielectric layers are not degraded.

This result is consistent with the functioning of the UV-rain erosion layers. These layers are hydrophobic and tend to repulse the acidic salt fog. However, at the edges of the sample, the acidic salt fog is in contact with the metallic substrate under the paint layers. Consequently, the corrosion of the metallic layer through the edges of the sample is a much faster process than the comparably slow degradation through the UV-rain erosion layers.

The progress of the corrosion from the edges of the sample under the tape and inward towards the center of the sample is evidenced by the changing reflectance with increasing weeks of corrosion. The mechanism by which the reflectivity decreases is twofold: For the first step, the corrosion leads to an increase in roughness of the aluminum substrate which more efficiently scatters incident terahertz radiation. The second mechanism is a 'bulging' or 'blistering' of the multilayer paint stack as the corrosion continues and the paint layer stack detaches from the substrate. As shown in the visible image of the sample (bottom right panel of Fig. 16) after 14 weeks of corrosion, the chemical corrosion lifts the paint stack from the sample. Moreover, visible images of the edges of the sample confirm the failure of the primer layer and detachment of the rain erosion layer from the substrate surface.

After the edges of the sample corrode, the multilayer paint stack detaches from the substrate as shown by the visible images in Fig. 19. The topcoat appears white with a shiny finish. The thickest layer is the rain erosion layer which appears black in visible light. Visual inspection shows that for the triangular section of Fig. 19b for which the rain erosion layer (black in color) has completely detached from the substrate, the primer layers have failed: there are locations where no primer is still attached to the rain erosion layer. In other areas, the primer still remains attached to the rain erosion layer, but the bottom primer/metallic layers are no longer intact. Probing of the detached area with an ohmmeter indicates no electrical conductivity meaning that the metallic layer between the two primer layers has been rendered highly resistive.

By analyzing the arrival times and amplitudes of the deconvolved waveforms, one can observe the progression of the corrosion in time. Fig. 20 shows the measured amplitude of the deconvoluted pulse amplitudes as measured at the point indicated by the white arrow in Fig. 16. Prior to 7 weeks of degradation, the amplitudes of the pulses are essentially unchanged. However, in week 8 begins a reduction in the magnitude of all four pulses indicating the progression of corrosion to that point on the sample.

It is interesting to note that while the deconvoluted amplitudes show evidence of corrosion at 8 weeks, the time-of-flight measurements do not show any significant change until 12 weeks. The unchanging time-of-flight values indicate that the multilayer stack from the top coat/rain erosion layer/primer layer/metallic layer remains intact during the early stages of corrosion. Examination of the deconvoluted pulses suggests that the four peaks of Fig. 17b remain at fixed relative positions even as the substrate roughens during corrosion. In this scenario, the detachment of the paint layer primarily occurs at the primer/ substrate boundary.

While Fig. 16 clearly shows the progression of corrosion under the multilayer paint stack with aging, the regions of reduced terahertz reflectivity very closely follow regions of bulging which are readily apparent in the visible images. Does terahertz NDE reveal the presence of corrosion before the effects of the corrosion are visibly apparent on the surface? To answer this question, one needs to separate the two contrast mechanisms for detection of corrosion: (a) increased surface roughness of the metal due to chemical corrosion (b) followed by bulging of the surface due to detachment of the multilayer paint stack from the substrate. The roughening of the metallic layer precedes and ultimately causes the detachment of the multilayer paint stack from the substrate.

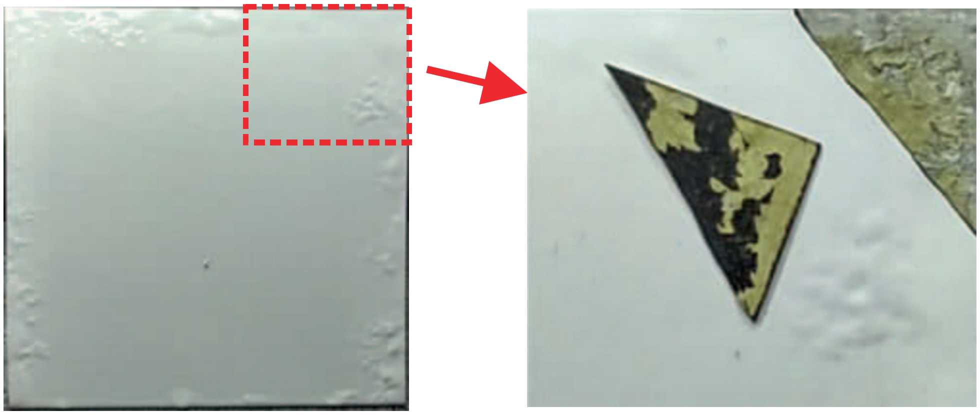

Fig. 19 Visible images of a corroded sample after 15 weeks. (a) top view of the corroded sample. (b) close up of the same sample with detached portion of coating cut away.

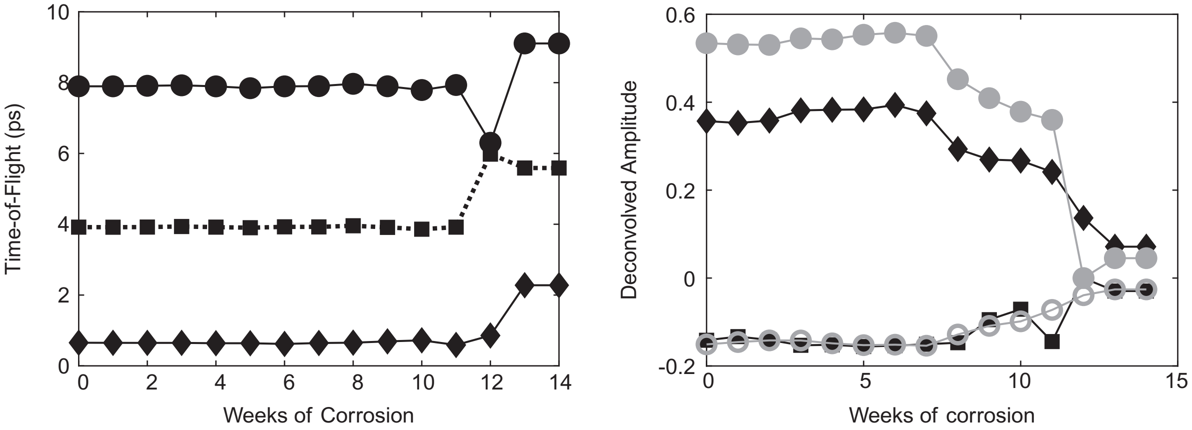

Fig. 20 Measured (a) pulse time-of-flight and (b) deconvolved amplitude at pixel (x = 15, y = 13). This pixel is denote by the white arrow. Notation for symbols is the same as Fig. 18.

The bulging leads to a reduction in the detected reflected terahertz power since the tilt of the bulging surface directs some terahertz power away from the terahertz receiver.

The topology (and bulging) of the front surface of the paint stack can be extracted from the terahertz data by plotting the arrival time of the deconvolved pulse from the front surface reflection (i.e., air-top coat boundary) of the paint stack. The local height of the bulge can be calculated by measuring the time difference of pulse Δt reflected from a region of the sample where no bulge is present and a location where the bulge is present. The height of the bulge is simply given by $c_o \Delta t/2$.

Fig. 21a shows a higher resolution (0.2 mm pixel size) reflectivity image of a small portion of the sample after 15 weeks of corrosion. A horizontal slice of data, as indicated by the black line, is analyzed to extract the surface height and Peak 3 amplitude. The dashed line in Fig. 21b indicates the location where the surface height begins to increase indicating the edge of the bulging blister as the pixel position moves from right to left towards the bulging paint surface. At larger pixel positions (~72–80), the bulging is proceeded by a reduction in the peak 3 amplitude as a result of increased surface roughness due to corrosion. A measurable reduction with accelerated corrosion in the amplitude of the 3rd deconvolved pulse from the metallic layer may be an early indicator that the entire stack will soon detach from the substrate creating a bulge (i.e., blister) on the surface.

Regions of increased substrate roughness due to corrosion may also be visualized using polarized light reflection. Monte Carlo modeling of terahertz propagation and reflection from rough surfaces (Xie et al., 2022) show that roughening of the metallic surface leads to a randomization of the polarization direction of the reflected radiation. As an example, (Xie et al., 2022) shows significant cross-polarization scattering for radiation with a terahertz wavelength of 0.3 mm when the RMS surface roughness R_s becomes 0.5 mm and the correlation length τ decreases to 5 mm. The T-Ray 5000 transmitter and receiver modules are polarization sensitive. Cross-polarization images are acquired by orienting the polarization axes of the transmitter and receiver modules so that they are orthogonal. With this cross-polarization orientation, only reflected radiation that has been scattered into the cross-polarization orientation will be detected. Fig. 22 highlights areas of the sample which surround the bulge in the paint layers. The area immediately surrounding the bulge represents regions of the metallic layer which has been roughened by corrosion.

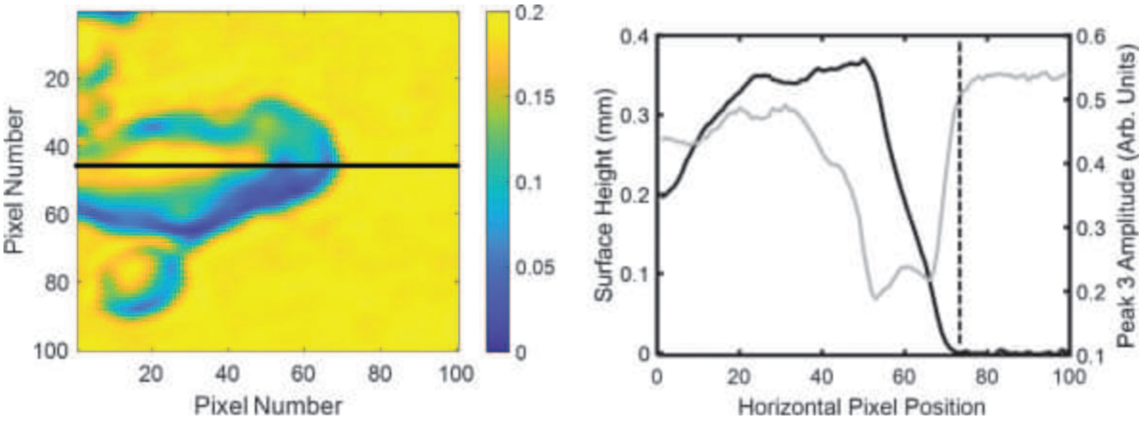

Fig. 21 (a) High resolution Terahertz reflectivity image (arbitrary units) in the 0.5–1 THz frequency band of a 20 mm by 20 mm section of sample showing a bulging blister on the paint layer surface. (b) The surface height and peak 3 amplitude as measured along a horizontal slice as indicated by the black horizontal line in (a). The dashed line indicates the location where the surface height begins to increase indicating the edge of the bulging blister. At higher pixel positions, the bulging is preceded by a reduction in the peak 3 amplitude as a result of increased surface roughness due to corrosion.

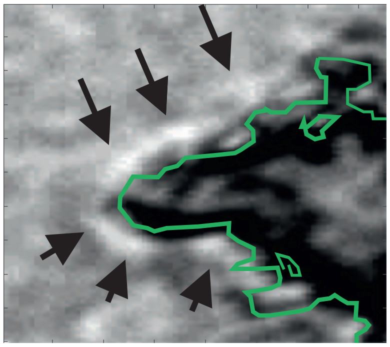

Fig. 22 Cross polarization image (0.2 mm pixel size) measuring total power (unnormalized) in 0.5–1 THz band. Green outline indicates boundary—as determined by the time arrival of the front surface reflection (pulse 1) from the paint layer stack—that is bulging at least 30 μm. Brighter portions of the image surrounding edge of bulge (indicated by black arrows) indicate regions of enhanced scattering due to surface roughness from corrosion.

Conclusion

In its current strategy, the DoD defines the number one barrier to moving AM into the realm of accepted manufacturing technologies as "rapid and standardized approaches for qualification of materials and processes, and certification of AM parts." Terahertz nondestructive evaluation techniques could play a major role in the creation of a standardized qualification process for additively manufactured components. This chapter has showcased the current use of THz NDE on two emerging material applications: additively manufactured components and multilayer paint stacks. For the first application, NDE of fused deposition modeling (FDM) printed plastics and nanoparticle jetted ceramics were emphasized. These examples represent an initial utilization of this technology for AM. As new materials for AM are developed and new printing techniques are created, the requirement to standardize approaches for rapid qualification of materials and processes will be unchanged. THz NDE can and should be applied to aid in the maturing process of this technology, whether it is using it for defect detection, creating full 3D reconstructions, or measuring a material's electromagnetic properties as just a few prime examples.

Aside from terahertz optical components, THz NDE of additively manufactured components can detect defects in the 3D printed structures which could significantly impact their functionality. Simple examples include cracks/voids in the printed structure and regions of high mechanical stress. A complete 3D image of an AM part could enable detailed comparison of design versus printed dimensions, structural defects, etc. THz CT of AM parts has many of the same analysis capabilities as X-ray CT: detection of internal voids and defects, measure internal and external geometry, and ability to compare printed parts to their CAD design. A significant challenge to the implementation of THz CT is refraction of the THz rays by the sample. Corrections to THz CT analysis to account for Gaussian beam propagation as well as refractive effects (using SART, ART, etc.) have been demonstrated.

Owing to refractive effects, THz NDE is best suited to planar structures. Examples include the material characterization and thickness measurements of multilayer paint stacks. Adapting THz NDE to corrosion detection shows that the methodology has sufficient sensitivity for early detection of failures due to corrosion in multilayer paint structures. Based on the accelerated corrosion studies using salt-fog exposure and humidity cycling, a 5.6% change in the reflectivity from the metallic layer indicates significant chemical corrosion of the multilayer paint coating prior to any visible evidence of a blister on the coating surface. Further chemical corrosion (and commensurate decrease in terahertz reflectivity) leads to detachment of the coating from the substrate.

The major driving force behind the development of additively manufactured terahertz and microwave components is the development of next-generation wireless communication systems. Some of the currently used polymers for the manufacturing of terahertz optical components include high-density polyethylene (HDPE), polypropylene, polystyrene, and TOPAS. Most of these polymers exhibit relatively minimal attenuation, but also have refractive indices close to 1.5. Several research teams have succeeded in creating by 3D printing various THz quasi-optical devices including GRIN lenses, topological waveplates, phase plates, polarization splitters, q-plates, and stepped-refractive-index lenses.

Acknowledgments

The authors gratefully thank P. Parsons and M. Mirotznik for the ceramic samples and microwave measurements described in this chapter. The amber samples used in this study were provided by P. Barden. The authors gratefully acknowledge the support of the Strategic Environmental Research and Development Program (SERDP) and US Army Combat Capabilities Development Command (CCDC) Armaments Center, Picatinny Arsenal.

References

Abraham E, Younus A, Aguerre C, Desbarats P, and Mounaix P (2010) Refraction losses in terahertz computed tomography. *Optics Communications* 283: 2050–2055.

Alfattni R (2022) Comprehensive Study on Materials used in Different Types of Additive Manufacturing and their Applications. *International Journal of Mathematical, Engineering and Management Sciences* 7: 92–114.

Anastasi RF, Madaras EI, Seebo JP, Smith SW, Lomness JK, Hintze PE, Kammerer CC, Winfree WP, and Russell RW (2007) Terahertz NDE Application for Corrosion Detection and Evaluation under Shuttle Tiles. *Proceedings of SPIE* 6531: 65310W.

Beckmann P and Spizzichino A (1987) *The Scattering of Electromagnetic Waves from Rough Surfaces.* Norwood, Artech House.

Bohn M and Petkie D (2013) Terahertz applications in the aerospace industry. In: Saeedkia D (ed.) *Handbook of Terahertz Technology for Imaging, Sensing, and Communications.* Philadelphia: Woodhead Publishing.

Burger R, Frisch J, Hübner M, Goldammer M, Peters O, Rönneberg E, and Wu D (2021) Thz-tds reflection measurement of coating thicknesses at non-perpendicular incidence: Experiment and simulation. *Sensors* 21: 3473.

Busboom I, Nguyen TT, Christmann S, Feige VKS, Haehnel H, and Tibken B (2021) Terahertz Imaging of 3D Print Infill Structures. In: *15th European Conference on Antennas and Propagation*, EuCAP 2021.

Cacciari I and Siano S (2017) Use of THz Reflectometry for Roughness Estimations of Archeological Metal Surfaces. *Journal of Infrared, Millimeter, and Terahertz Waves* 38: 503–517.

Castro-Camus E, Koch M, and Hernandez-Serrano AI (2020) Additive manufacture of photonic components for the terahertz band. *Journal of Applied Physics* 127: 210901.

Catapano I, Soldovieri F, Mazzola L, and Toscano C (2017) THz Imaging as a Method to Detect Defects of Aeronautical Coatings. *Journal of Infrared, Millimeter, and Terahertz Waves* 38: 1264–1277.

Chan WL, Deibel J, and Mittleman DM (2007) Imaging with terahertz radiation. *Reports on Progress in Physics* 70: 1325–1379.

Clark AT (2022) *Nondestructive Evaluation of 3D Printed, Extruded and Natural Polymer Structures using Terahertz Spectroscopy and Imaging.* Ph.D. Doctoral Dissertation, New Jersey Institute of Technology.

Clark AT, Federici JF, and Gatley I (2021) Effect of 3D Printing Parameters on the Refractive Index, Attenuation Coefficient, and Birefringence of Plastics in Terahertz Range. *Advances in Materials Science and Engineering* 2021: 8276378.

Dally JW (1978) *Experimental Stress Analysis*, 3rd edn. McGraw-Hill.

Dante JF (2019) *Cyclic Corrosion and Failure Mechanisms.* Available: https://www.serdp-estcp.org/Tools-and-Training/Webinar-Series/04-25-2019/Webinar-88-Slides.

Dhawan AP (2003) *Medical Image Analysis.* Hoboken, NJ: John Wiley & Sons.

Dhawan AP, Huang HK, and Dim D-S (2008) *Principles and Advanced Methods in Medical Imaging and Image Analysis.* New Jersey: World Scientific.

Dong J, Locquet A, and Citrin DS (2017) Terahertz quantitative nondestructive evaluation of failure modes in polymer-coated steel. *IEEE Journal on Selected Topics in Quantum Electronics* 23.

Ellrich F, Bauer M, Schreiner N, Keil A, Pfeiffer T, Klier J, Weber S, Jonuscheit J, Friederich F, and Molter D (2020) Terahertz Quality Inspection for Automotive and Aviation Industries. *Journal of Infrared, Millimeter, and Terahertz Waves* 41: 470–489.

Evans B (2012) *Practical 3D Printers: The Science and Art of 3D Printing.* Netherlands: Apress.

Federici JF (2012) Review of Moisture and Liquid Detection and Mapping using Terahertz Spectroscopy and Imaging. *IEEE Transactions on Terahertz Science and Technology* 33: 97–126.

Federici J and Moeller L (2010) Review of terahertz and subterahertz wireless communications. *Journal of Applied Physics* 107: 111101.

Federici J, Moeller L, and Su K (2013) Terahertz communication. In: Saeedkia D (ed.) *Handbook of Terahertz Technology for Imaging, Sensing, and Communications.* Cambridge: Woodhead Publishing.

Federici JF, Ma J, and Moeller L (2016) Review of Weather Impact on Outdoor Terahertz Wireless Communication Links. *Nano Communication Networks* 10: 13–26.

Ferguson B, Wang S, Gray D, Abbott D, and Zhang X-C (2002) Towards functional 3D T-ray imaging. *Physics in Medicine and Biology* 47: 3735–3742.

Fielding J, Davis A, Bouffard B, Kinsella M, Delgado T, Wilczynski J, Marchese K, and Wing I (2021) *Final Report - Department of Defense Additive Manufacturing Roadmap.* Washington, DC: Department of Defense. Available: https://www.americamakes.us/wp-content/uploads/2021/10/Final-Report-DoDRoadmapping-FINAL120216.pdf.

Fosodeder P, Hubmer S, Ploier A, Ramlau R, van Frank S, and Rankl C (2021) Phase-contrast THz-CT for non-destructive testing. *Optics Express* 29: 15711–15723.

Fukuchi T, Fuse N, Mizuno M, and Fukunaga K (2013) THz measurement of refractive index and thickness of ceramic coating on a metal substrate. In: *Pacific Rim Conference on Lasers and Electro-Optics, CLEO - Technical Digest.*

Furlan WD, Ferrando V, Monsoriu JA, Zagrajek P, Czerwińska E, and Szustakowski M (2016) 3D printed diffractive terahertz lenses. *Optics Letters* 41: 1748–1751.

Fuse N, Fukuchi T, Takahashi T, Mizuno M, and Fukunaga K (2012) Evaluation of applicability of noncontact analysis methods to detect rust regions in coated steel plates. *IEEE Transactions on Terahertz Science and Technology* 2: 242–249.

Fuse N, Fukuchi T, Mizuno M, and Fukunaga K (2016) High-speed underfilm corrosion imaging using a terahertz camera. *Electronics and Communications in Japan* 99: 86–92.

Goulas A, Chi-Tangyie G, Wang D, Zhang S, Ketharam A, Vaidhyanathan B, Reaney IM, Cadman DA, Whittow WG, Vardaxoglou JYC, and Engstrøm DS (2020) Microstructure and microwave dielectric properties of 3D printed low loss $Bi_2Mo_2O_9$ ceramics for LTCC applications. *Applied Materials Today* 21: 100862.

Hecht E (2017) *Optics*, 5th edn. Pearson Education Limited.

Joint Defense Manufacturing Council (2021) *Department of Defense Additive Manufacturing Strategy*. Washington, DC: Office of the Under Secretary of Defense for Research and Engineering. Available: https://www.cto.mil/wp-content/uploads/2021/01/dod-additive-manufacturing-strategy.pdf.

Kang K, Du Y, Wang S, An Li L, Wang Z, and Li C (2021) Full-field stress measuring method based on terahertz time-domain spectroscopy. *Optics Express* 29: 40205–40213.

Kim H, Kim KW, Park J, Han JK, and Son JH (2012) Terahertz tomographic imaging of topical drugs. In: *2012 Conference on Lasers and Electro-Optics, CLEO*.

Krimi S, Klier J, Jonuscheit J, Von Freymann G, Urbansky R, and Beigang R (2016) Highly accurate thickness measurement of multi-layered automotive paints using terahertz technology. *Applied Physics Letters* 109: 021105.

Krimi S, Torosyan G, and Beigang R (2017) Advanced GPU-Based Terahertz Approach for In-Line Multilayer Thickness Measurements. *IEEE Journal of Selected Topics in Quantum Electronics* 23.

Lee AWM, Kao TY, Burghoff D, Hu Q, and Reno JL (2012) Terahertz tomography using quantum-cascade lasers. *Optics Letters* 37: 217–219.

Li Q, Li YD, Ding SH, and Wang Q (2012) Terahertz computed tomography using a continuous-wave gas laser. *Journal of Infrared, Millimeter, and Terahertz Waves* 33: 548–558.

Markl D, Zeitler JA, Rasch C, Michaelsen MH, Müllertz A, Rantanen J, Rades T, and Bøtker J (2017) Analysis of 3D prints by X-ray computed microtomography and terahertz pulsed imaging. *Pharmaceutical Research* 34: 1037–1052.

Mittleman D (2003) *Sensing With Terahertz Radiation*. Springer.

Mittleman DM, Hunsche S, Boivin L, and Nuss MC (1997) T-ray tomography. *Optics Letters* 22: 904–906.

Morales CD, Morlaas C, Chabory A, Pascaud R, Grzeskowiak M, and Mazingue G (2021) 3D-printed ceramics with engineered anisotropy for dielectric resonator antenna applications. *Electronics Letters* 57: 679–681.

Moylan, S. (n.d.) *Qualification for Additive Manufacturing Materials, Processes, and Parts*. Gaithersburg, MD: NIST. Available: https://www.nist.gov/programs-projects/qualification-additive-manufacturing-materials-processes-and-parts.

Mukherjee S, Federici J, Lopes P, and Cabral M (2013) Elimination of fresnel reflection boundary effects and beam steering in pulsed terahertz computed tomography. *Journal of Infrared, Millimeter, and Terahertz Waves* 34: 539–555.

Naftaly M, Tikhomirov I, Hou P, and Markl D (2020) Measuring open porosity of porous materials using thz-tds and an index-matching medium. *Sensors (Switzerland)* 20.

Nishina S, Takeuchi K, Shinohara M, Imamura M, Shibata M, Hashimoto Y, and Watanabe F (2012) Novel nondestructive imaging analysis for catalyst washcoat loading and DPF soot distribution using terahertz wave computed tomography. *SAE International Journal of Fuels and Lubricants* 5: 343–351.

Perraud JB, Obaton AF, Bou-Sleiman J, Recur B, Balacey H, Darracq F, Guillet JP, and Mounaix P (2016) Terahertz imaging and tomography as efficient instruments for testing polymer additive manufacturing objects. *Applied Optics* 55: 3462–3467.

Posodeder P, Frank SV, and Rankl C (2022) Highly accurate THz-CT including refraction effects. *Optics Express* 30: 3684–3699.

Prabhu SS (2018) Terahertz Spectroscopy: Advances and Applications. In: *Molecular and Laser Spectroscopy: Advances and Applications*. Elsevier.

Recur B, Younus A, Salort S, Mounaix P, Chassagne B, Desbarats P, Caumes JP, and Abraham E (2011) Investigation on reconstruction methods applied to 3D terahertz computed tomography. *Optics Express* 19: 5105–5117.

Rohrbach D, Kang BJ, and Feurer T (2021) 3D-printed THz wave- and phaseplates. *Optics Express* 29: 27160–27170.

Ruan X and Chan CH (2019) Terahertz free-space dielectric property measurements using time- and frequency-domain setups. *International Journal of RF and Microwave Computer-Aided Engineering* 29.

Saleh BEA and Teich MC (1991) *Fundamentals of Photonics*. New York: John Wiley & Sons.

Sathishkumar N, Udayakumar ASM, Vincent B, and Kumar VA (2020) Study and analysis of 3D printed FDM components by non-destructive testing techniques. *International Journal of Research and Review* 5: 6.

Serrano AIH (2018) *Terahertz Quasi-Optical Devices Fabricated by 3D Printing*. PhD, León, Guanajuato, México.

Siemion A, Melaniuk A, Zagrajek P, Komorowski P, Walczakowski M, Surma M, Sobotka P, Ducin I, and Czerwinska E (2020) THz diffractive lens manufactured using 3D printer working for 0.6 THz. In: *2020 23rd International Microwave and Radar Conference, MIKON 2020*, pp. 225–228.

Stoik CD, Bohn MJ, and Blackshire JL (2008) Nondestructive evaluation of aircraft composites using transmissive terahertz time domain spectroscopy. *Optics Express* 16: 17039–17051.

Su K, Shen Y, and Zeitler JA (2014) Terahertz Sensor for Non-Contact Thickness and Quality Measurement of Automobile Paints of Varying Complexity. *IEEE Transactions on Terahertz Science and Technology* 4: 432–439.

Takeshi Yasui TY, Sawanaka KI, and Araki T (2005) Terahertz paintmeter for noncontact monitoring of thickness and drying progress in paint film. *Applied Optics* 44: 6849–6856.

Taubmann O, Berger M, Bögel M, Xia Y, Balda M, and Maier A (2018) Computed tomography. In: Maier A, Steidl S, Christlein V, and Hornegger J (eds.) *Medical Imaging Systems: An Introductory Guide*. Cham: Springer.

Tepe J, Schuster T, and Littau B (2017) A modified algebraic reconstruction technique taking refraction into account with an application in terahertz tomography. *Inverse Problems in Science and Engineering* 25: 1448–1473.

Tu W, Zhong S, Luo M, and Zhang Q (2021) Non-destructive evaluation of hidden defects beneath the multilayer organic protective coatings based on terahertz technology. *Frontiers in Physics* 9: 676851.

van Mechelen JLM, Kuzmenko AB, and Merbold H (2014) Stratified dispersive model for material characterization using terahertz time-domain spectroscopy. *Optics Letters* 39: 3853–3856.

Waddie AJ, Schemmel PJ, Chalk C, Isern L, Nicholls JR, and Moore AJ (2020) Terahertz optical thickness and birefringence measurement for thermal barrier coating defect location. *Optics Express* 28: 31535–31552.

Wang S and Zhang X-C (2004) Pulsed terahertz tomography. *Journal of Physics D: Applied Physics* 37: R1–R36.

Wang D, Ning R, Li G, Zhao J, Wang Y, and Rong L (2022) 3d image reconstruction of terahertz computed tomography at sparse angles by total variation minimization. *Applied Optics* 61: B1–B7.

Xie P, Guan K, He D, Yi H, Dou J, and Zhong Z (2022) Terahertz Wave Propagation Characteristics on Rough Surfaces Based on Full-Wave Simulations. *Radio Science* 57. e2021RS007385.

Yasuda H and Hosako I (2008) Measurement of terahertz refractive index of metal with terahertz time-domain spectroscopy. *Japanese Journal of Applied Physics* 47: 1632–1634.

Yasuda T, Yasui T, Araki T, and Abraham E (2006) Real-time two-dimensional terahertz tomography of moving objects. *Optics Communications* 267: 128–136.

Yasuda T, Iwata T, Araki T, and Yasui T (2007) Improvement of minimum paint film thickness for THz paint meters by multiple-regression analysis. *Applied Optics* 46: 7518–7526.

Yilmaz T and Akan OB (2020) Attenuation constant measurements of clear glass samples at the low terahertz band. *Electronics Letters* 56: 1423–1425.

Zhang X-C (2003) Three-dimensional terahertz wave imaging. *Philosophical Transactions of the Royal Society A* 362: 283–299.

Zhang B, Chen W, Wu Y, Ding K, and Li R (2017) Review of 3D printed millimeter-wave and terahertz passive devices. *International Journal of Antennas and Propagation* 2017: 1297931.

Zhao M, Geng Y, Fan S, Yao X, Zhu M, and Zhang Y (2021) 3D-printed strong hybrid materials with low shrinkage for dental restoration. *Composites Science and Technology* 213: 108902.

Excitons in nanoscale semiconductor structures

Alexander L Efros, Center for Computational Material Science, Naval Research Laboratory, Washington, DC, United States

© 2024 Elsevier Ltd. All rights reserved.

Introduction	629
Spatial confinement of carriers in nanoscale semiconductor structures	632
Optical properties of spherical nanocrystals	632
Optical properties of anisotropic semiconductor nanostructures	637
Effect of dielectric confinement on electron-hole energy spectra	637
Two dimensional excitons in nanoplatelets	638
One dimensional excitons in nanorods and nanowires	639
Photoluminescence of excitons in nanoscale semiconductor structures	640
Conclusion	642
Acknowledgments	642
References	642

Abstract

We discuss the electronic and optical properties of various semiconductor nanostructures: nanocrystals, nanorods, nanowires and nanoplatelets. The modification of the shapes of these structures leads to very different energy spectra and different densities of carrier states. We show that the optical properties of all these structures are controlled by excitons. Optical properties are also strongly affected by the large difference in dielectric constants of the semiconductor and the matrix in which the nanostructures are embedded. This phenomenon leads to the dielectric confinement effect that increases the energies of the electron and hole confined levels and, due to the small dielectric constant of the matrix, increases the exciton binding energy by up to 0.5 eV in the thinnest nanoplatelets. In the end, we discuss the exciton fine structures created by electron-hole spin-spin exchange interaction enhanced by the spatial confinement of carriers in nanoscale semiconductors. This fine structure, consisting of the dark (optically passive) and bright (optical active) exciton sublevels, strongly affects photoluminescence and polarization properties in various nanostructures.

Glossary

Exciton Electron-hole pair bound by Coulomb attraction.

Semiconductor Extended solid with a non-conductive gap in the band structure.

Nanocrystal (NC) A large molecule in which the core atoms are organized in the crystal structure of the corresponding bulk compound.

Quantum size effect Energy increase of an electrical carrier due to confinement in a small crystal volume.

Nanocrystal characterized by a 3D confinement potential for carriers resulting in a discrete energy spectrum **Nanorod (NR)** Semiconductor nanocrystal that has strongly elongated ellipsoidal shape.

Nanoplatelet (NPL) Semiconductor nanocrystal, that has shape of two dimensional large size flakes.

Key points

- Four basic nanoscale semiconductor structures are introduced: spherical nanocrystals, nanorods, nanoplatelets and nanowires.
- Spatial confinement of carriers and the density of states in these four basic structures is discussed.
- Size dependence of the optical properties of spherical nanocrystals is considered.
- Effect of dielectric confinement on electron-hole energy spectra in anisotropic semiconductor nanostructures is discussed.
- Two-dimensional excitons control optical properties of nanoplatelets.
- One-dimensional excitons control optical properties of nanorods and nanowires.
- The exciton fine structure created by the electron-hole exchange interaction enhanced by spatial confinement explains the photoluminescence properties of nanostructures.

https://doi.org/10.1016/B978-0-323-90800-9.00171-2

Introduction

There are four basic chemically synthesized, nano-scale semiconductor structures: spherical nanocrystals (NCs), nanorods (NRs), nanoplatelets (NPLs), and nanowires. Transition electron microscopy (TEM) images of these nanostructures are shown in Fig. 1. The TEM image of a bare CdSe NC and its atomistic structure in Fig. 1A show that the nanocrystal is just a big molecule with its atoms organized in a bulk crystal structure (see Fig. 1B). Current technology allows us to vary the size of these NCs in a controlled manner from 1 to 100 nm. Semiconductor NCs are the most heavily studied of the nano-scale semiconductors. The size dependence of NC optical properties was discovered independently in two different materials: in semiconductor-doped glasses by Ekimov and Onushchenko (1981) and in aqueous solutions by Brus (1983). After more than 40 years of research, we have a solid theoretical basis that allows us to understand most of the electronic, optical, and transport properties of NCs.

Current technology allows for the growth of strongly elongated NCs that have ellipsoidal shape; so called NRs. The TEM image of the CdSe NRs grown by Peng et al. (2000), is shown in Fig. 1D. Even more unexpectedly, current technology allows for the growth of NCs that have the shape of freestanding, two-dimensional semiconductor sheets, in which thickness can be changed from 2 to 7 monolayers. These nanostructures are called nanoplatelets (NPLs) and a TEM image of three monolayer thick CdSe NPLs is shown in Fig. 1C (Ithurria et al., 2011). Nanometer thick crystals that can be several millimeters long are grown today. They are called nanowires, and a TEM image of $CsPbBr_3$ nanowires is shown in Fig. 1E (Folie et al., 2020).

Scientists have grown various modification of these four basic structures. Today, they are typically complex core-multishell heterostructures, often with chemically functionalized surfaces. These were created to satisfy specific engineered properties, that can include the frequency of light emission, ability to transfer photoexcited electrons, suppression of nonradiative recombination,

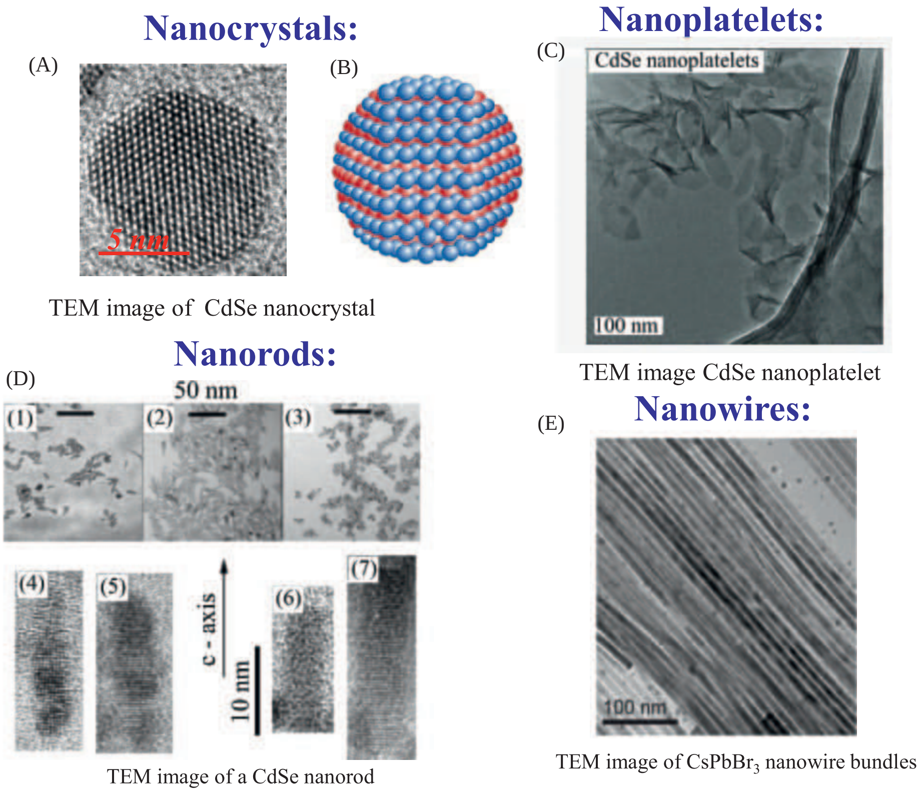

Fig. 1 Transmission electron microscopy (TEM) images of four basic nanostructures. A—TEM image of 5 nm radius spherical CdSe nanocrystal (NC). B—atomistic structure of 5 nm radius CdSe NC. C—TEM image of three monolayers thick CdSe NPLs. D—TEM images of different samples of NRs. (1)–(3) Low resolution of TEM images of the three samples with different sizes and aspect ratio; (4)–(6) High resolution TEM images of four nanorods. E—TEM image of 10 nm diameter nanowire bundles, showing alignment, length, and monodispersity of nanowires. Panels A and B are reproduced with permission from Efros AL and Brus LE (2021) Nanocrystal quantum dots: From discovery to modern development. *ACS Nano* 15: 6192–6210. Copyright 2021 American Chemical Society, Panel C: Modified with permit Ithurria S, Tessier MD, Mahler B, Lobo RPSM, Dubertret B, Efros AL (2011) Colloidal nanoplatelets with two-dimensional electronic structure. *Nature Materials* 10: 936–941 (Copyright 2011 Springer Nature). Panel D: From Efros AL and Brus LE (2021) Nanocrystal quantum dots: From discovery to modern development. *ACS Nano* 15: 6192–6210 (Copyright 2021 American Chemical Society). Adapted with permission from Peng X, Manna L, Yang W, Wickham J, Scher E, Kadavanich A, Alivisatos AP (2000) Shape control of CdSe nanocrystals. *Nature* 404: 59–61 (Copyright 2000 Springer Nature). Panel E: Reproduced with permission from Folie BD, Tan JA, Huang J, Sercel PC, Delor M, Lai M, Lyons JL, Bernstein N, Efros AL, Yang P, Ginsberg NS (2020) Effect of anisotropic confinement on electronic structure and dynamics of band edge excitons in inorganic perovskite nanowires. *The Journal of Physical Chemistry A* 124(9): 1867–1876 (Copyright 2020 American Chemical Society).

shortening of the radiative decay time, doping, and/or specific solubility in various environments. The most important of these modifications are the core/shell heterostructures that prevent optically excited carriers from escaping to the nanostructure surface and increase the photoluminescence (PL) quantum yield (Hines and Guyot-Sionnest, 1996).

Recent advances in the fabrication, physical understanding, and application of chemically synthesized nanoscale semiconductors, such as spherical NCs, NRs, NPLs and nanowires, have been driven by intense interest in their unusual and potentially useful electronic and optical properties. A wide class of semiconductors, such as covalent Si and Ge, III-V group compounds such as GaAs, InAs, GaP, InP; II-VI group compounds, such as CdSe, CdS, CdTe, ZnSe, PbS, PbSe, HgTe; I-VII group compounds such as CuCl, CuBr, AgBr semiconductors, and perovskites can be prepared today in nanoscale form (Efros and Brus, 2021). Size- and shape-controlled tunability of their electronic, optical, and transport properties (see Fig. 2, that shows size-tunable absorption and PL of CdSe NC, Efros et al., 1996, where the spectral colors reflect the color of emission line) combined with the ability to chemically and physically manipulate these "free-standing" nanostructures with nanometer precision, open exciting new opportunities for the development of novel functional materials with a wide range of applications. Such materials allow "bottom up" chemical approaches for assembly.

Nanoscale semiconductors can be positioned and assembled into two-dimensional and three-dimensional artificial super "crystals," custom-designed nanocrystal "molecules," and functional nanocrystal-biomolecular conjugates. Thus, multiple applications of their fundamental properties to real-world devices is closer than ever. Research into nanocrystals has been already translated into the production of commercial devices. In May 2011, the company Nanosys announced a product called the Quantum Dot Enhancement Film 6. This is a thin layer of nanocrystal quantum dots (QDs) that convert the blue light of a GaN light-emitting diode into bright colors which can be used in liquid-crystal displays. Around the same time, Samsung announced the creation of a 4-inch quantum-dot-based color display, with higher definition and lower power consumption than commercial liquid- crystal displays. Today, the production of quantum dot TVs is a $3 billion business for the Samsung corporation.

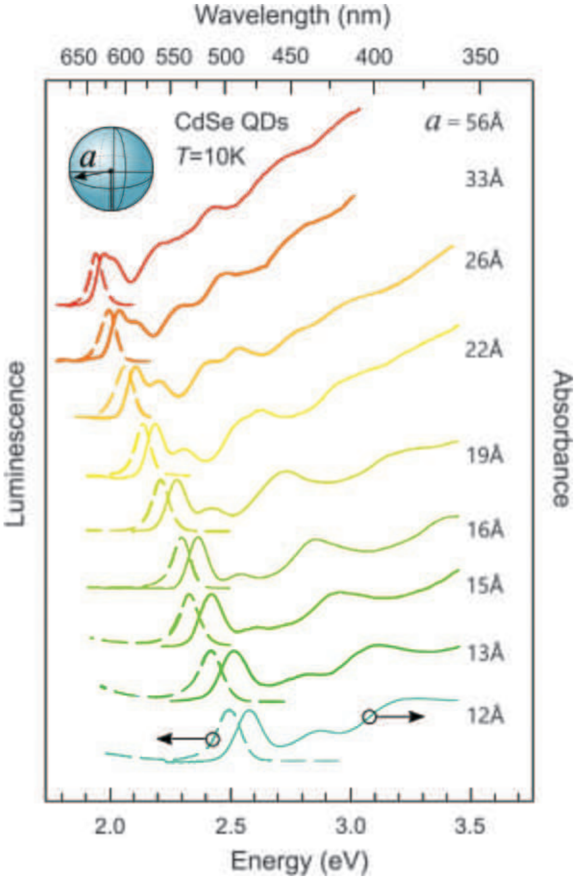

Fig. 2 Low temperature absorption spectra and photoluminescence of CdSe NCs with sizes varying from 12 to 56 Å grown in aqueous solutions. Color of absorption lines shows the real color of emission of the corresponding sample. Adapted with permission from Efros AL, Rosen M, Kuno M, Nirmal M, Norris DJ, Bawendi MG (1996) Band edge exciton in quantum dots of semiconductor with a degenerate valence band: Dark and bright exciton states. *Physical Review B* 54: 4843–4856 (Copyright 1996 American Physical Society).

Spatial confinement of carriers in nanoscale semiconductor structures

The significant blue shift of band-edge optical transitions, and the corresponding increase of the optical energy gap up to 1 eV, which is seen in CdSe NCs with decreasing NC size (shown in Fig. 2) is connected with the spatial confinement of carriers. This increase of the optical gap is even larger in lead chalcogenide NCs and CdSe nanoplatelets and nanorods (Efros and Brus, 2021). The spatial confinement of the carriers depends on the geometry of the nanoscale semiconductor structures. In a parabolic band approximation, each electron and hole state in spherical NCs is characterized by angular momentum, *l*. The energy of the corresponding confinement levels in this zero-dimensional structures (0D): (Efros and Efros, 1982)

$$E_{e,h}^{0D}(l,n) = \frac{\hbar^2 \varphi_{l,n}^2}{2m_{e,h}a^2} \tag{1}$$

is inversely proportional to the effective mass of electrons, m_e, and holes, m_h, and the square of the NC radius a. $\varphi_{l,n}$ are n-th, the roots of the spherical Bessel function of index $l(l = 0,1,2,..)$. The lowest roots are: $\varphi_{0,1} = \pi$, $\varphi_{1,1} \approx 4.49$, $\varphi_{2,1} \approx 5.76$ and $\varphi_{0,2} = 2\pi$. Adopting the notation from atomic physics, the levels with angular momentum 0, 1, and 2… are called S, P, and D.

The electronic properties of NPLs are very similar to those of semiconductor quantum wells. The motion of carriers in the NPL plane is almost free, but they are strongly confined in the perpendicular direction. This confinement type leads to the formation of numerous two-dimensional (2D) electron and hole subbands, the bottom of which is described as

$$E_{e,h}^{2D}(N) = \frac{\hbar^2 \pi^2 N^2}{2m_{e,h}L^2}, \tag{2}$$

where L is the thickness of the NPL, and N is the subband number $(N = 1,2,3\ldots)$..

In nanowires, carrier motion is free along the nanowire axis and is strongly confined in the perpendicular directions. This confinement type leads to the formation of numerous one-dimensional (1D) electron and hole subbands. In cylindrical-shape nanowires, the bottom of such 1D subbands are described as:

$$E_{e,h}^{1D}(l_z,n) = \frac{\hbar^2 \varphi_{l_z,n}^2}{2m_{e,h}\rho^2}, \tag{3}$$

where ρ is the nanowire radius, and $\varphi_{l_z,\,n}$ are the n-th roots of Bessel functions of integer index $l_z : J_{l_z}(\varphi_{l_z}) = 0 (l_z = 0, \pm 1, \pm 2, ..)$. The lowest roots are: $\varphi_{0,1} \approx 2.40$, $\varphi_{1,1} \approx 3.83$, $\varphi_{2,1} \approx 5.14$ and $\varphi_{0,2} \approx 5.52$. Adopting the notation from atomic physics, the levels with angular momentum 0, 1, and 2… are called Σ, Π, and Δ (Shabaev and Efros, 2004).

All nanoscale semiconductor structures are low dimension structures—for which carrier spectra are usually characterized by the density of states;

$$\rho(\varepsilon) = \sum\nolimits_{\varepsilon-\Delta\varepsilon}^{\varepsilon+\Delta\varepsilon} N_i, \tag{4}$$

which is the number of states, N_i, in the small energy interval Δε. In 3D, 2D, and 1D structures, where carriers have the opportunity to move freely in at least one dimension, the density of states is quasi-continuous as you can see in Fig. 3. For structures with different dimensionality, D, the density of states can be written as

$$\rho(\varepsilon) \sim \left(\varepsilon - E^D\right)^{(D-2)/2}, \tag{5}$$

where E^D is the bottom of the corresponding subband.

One can see from Eq. (5) that in bulk, $D = 3$, the density of states is proportional $\sim \sqrt{\varepsilon}$. In NPLs and quantum wells, the density of states has the form of a sum of steps starting at the positions of quantum-confined levels described in Eq. (2) (see Fig. 3B). In one-dimensional structures like nanowires, $D = 1$. the density of states consists of sharp, asymmetric peaks (see Fig. 3C). This occurs because although motion across the wire is strongly quantized, there is a continuous contribution to the density of states that is associated with the free motion of carriers along the wire. Finally, in zero-dimensional systems (0D) like NC quantum dots, the density of states consists of sharp, discrete lines for each level of size quantization (see Fig. 3D).

Dimensionally, NRs are between zero-dimensional and one-dimensional systems. The motion of carriers across the NR is strongly quantized, but there is only weak confinement along the NR axis. The density of states contains bunches of discrete states, separated by energies determined by strong confinement across the nanorod. The structure of levels inside the bunch is determined by slow motion along the NR axes (see Fig. 3E).

Optical properties of spherical nanocrystals

The optical properties of nanoscale semiconductors are controlled by excitons, because in nanostructures one can never separate an electron and a hole photoexcited optically or injected electrically at such large distances that they do not affect each other. The effect of electron-hole Coulomb interaction on the optical spectra depends on the ratio of electron and hole confined energies, and the

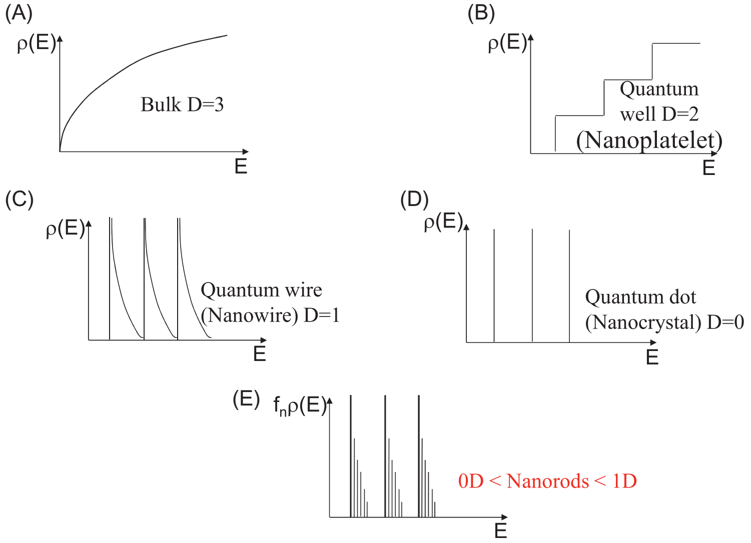

Fig. 3 Density of states in various nanostructures: A—bulk 3D semiconductors; B—2D quantum wells, nanoplatelets; C—1D quantum wires, nanowires; D—0D quantum dots, nanocrystals; E—between 0D and 1D structure, nanorods.

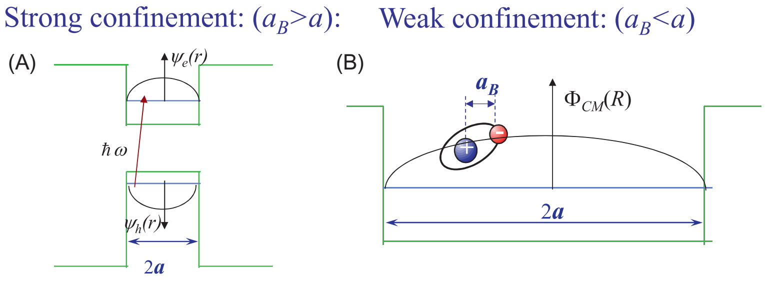

Fig. 4 Schematic image of the wave function of an exciton confined in NCs with radius *a*. A—strong confinement regime. B—weak confinement regime.

strength of the electron-hole Coulomb interaction. The different geometrical shapes of nanoscale semiconductor structures strongly affect this ratio. In this chapter we don't consider physics of excitons in epitaxial quantum dots and rings, graphene and TMD (transition metal dioxide) layers. The discussion of their optical properties one can find in "Excitons in crystals" Chapter of ECMP 2^{nd} edition.

In spherical NCs, the relationships between the confined energy and strength of Coulomb interaction can be characterized by the ratio of the exciton Bohr radius, a_B, to the NC radius a (Efros and Efros, 1982). A strong confinement regime (when the confined energy is larger than the Coulomb energy) exists if the NC radius is smaller than the exciton Bohr radius. The optical properties of such nanocrystals are determined by transitions between electron and hole quantum size levels. As a result, the absorption spectra of NCs in this limit can be written as: (Efros and Efros, 1982; Brus, 1984; Ekimov and Onushchenko, 1984)

$$\hbar\omega_{l,n} = E_g + E_e(l,n) + E_h(l,n) - 1.8\frac{e^2}{\varepsilon_s a}, \tag{6}$$

where ε_s is the semiconductor dielectric constant. The last term considers the electron-hole Coulomb attraction, which is calculated perturbatively. The selection rules for optically allowed transitions between electron and hole confinement levels in the strongly confined limit are controlled by the square of the overlap integral $\left|\int d^3r\psi_e\left(\vec{r}\right)\psi_h\left(\vec{r}\right)\right|^2$ between electron $\psi_e\left(\vec{r}\right)$ and hole $\psi_h\left(\vec{r}\right)$ wave functions (see Fig. 4A). In the parabolic band approximation, the electron and hole wave functions are identical, and due to orthogonality conditions, transitions are allowed only between levels with the same quantum levels: from $1S_h$ to $1S_e$ or from $1P_h$ to $1P_e$ levels, etc. The radiative decay rate $1/\tau$ in this limit is also proportional to the overlap integral $1/\tau = 1/\tau_0\left|\int d^3r\psi_e\left(\vec{r}\right)\psi_h\left(\vec{r}\right)\right|^2$, where the decay time factor τ_0 is on the order of several nanoseconds in various semiconductors (Efros and Brus, 2021).

In the opposite case of a weak confinement regime (that is realized when the exciton Bohr radius (a_B) is much smaller than the NC radius ($a >> a_B$)) the exciton binding energy is larger than the confinement energy. The optical properties in this case are determined by the spectra of confined excitons. Excitons move in a NC as hydrogen atoms move in a box (see Fig. 4B).

The size dependence of the blue shift of the lowest exciton levels is described by the "particle-in-a-box" equation that can be found in any handbook on quantum mechanics. Assuming that the NC has a spherical shape and is surrounded by infinitely high potential barriers, this gives the following expression for the size dependence of the exciton lines (Ekimov and Onushchenko, 1981; Efros and Efros, 1982):

$$\hbar\omega = E_g - E_{ex} + \frac{\hbar^2\pi^2}{2Ma^2}, \tag{7}$$

where E_g and E_{ex} are the bulk energy gap and exciton binding energy, and M is the effective mass of the exciton center of mass motion. The wave function of the confined exciton in this limit can be written as $\Psi\left(\vec{r}_e, \vec{r}_h\right) = \phi_{ex}\left(\vec{r}\right)\Phi_{CM}\left(\vec{R}\right)$, where $\phi_{ex}\left(\vec{r}\right)$ is the wave function that describe relative motion of electron and hole within exciton, and $\Phi_{CM}\left(\vec{R}\right)$ is the wave function of the exciton confined in NCs. The radiative decay rate in this case is also proportional to the overlap integral and can be written as (Efros and Efros, 1982):

$$\frac{1}{\tau} = \frac{1}{\tau_0}\left|\int d^3r\,\Psi\left(\vec{r},\vec{r}\right)\right|^2 = \frac{\varphi_{ex}^2(0)}{\tau_0}\left|\int d^3R\,\Phi_{CM}\left(\vec{R}\right)\right|^2 \sim \frac{1}{\tau_0}\frac{a^3}{a_{ex}^3} \tag{8}$$

One can see from Eq. (8) that the ground exciton state is characterized by a giant oscillator transition strength, proportional to the cube of the NC radius, and connected with coherent exciton motion throughout the entire nanocrystal volume. This could lead to a significant shortening of the radiative decay time.

The optical spectra of excitons can be also described analytically as the range of sizes: $\frac{\varepsilon_s\hbar^2}{m_e e^2} \gg a \gg \frac{\varepsilon_s\hbar^2}{m_h e^2}$ which can be realized in semiconductors where the effective mass of holes is much larger than the effective mass of electrons ($m_{,h} >> m_e$). In this size regime, which is called intermediate confinement, the hole moves in an adiabatic static potential created by the fast motion of the strongly confined electron at the NC center (Efros and Efros, 1982; Ekimov et al., 1986). A summary of the size-dependent optical spectra for these three above-mentioned regimes in different semiconductor NCs was reported by Ekimov et al. (1985).

Let us start from the weak confinement regime. In CuCl, the bulk exciton radius is 0.7 nm, and the weak confinement regime holds in all studied NCs. Fig. 5A shows the low temperature absorption spectra of CuCl NCs measured in three different glass

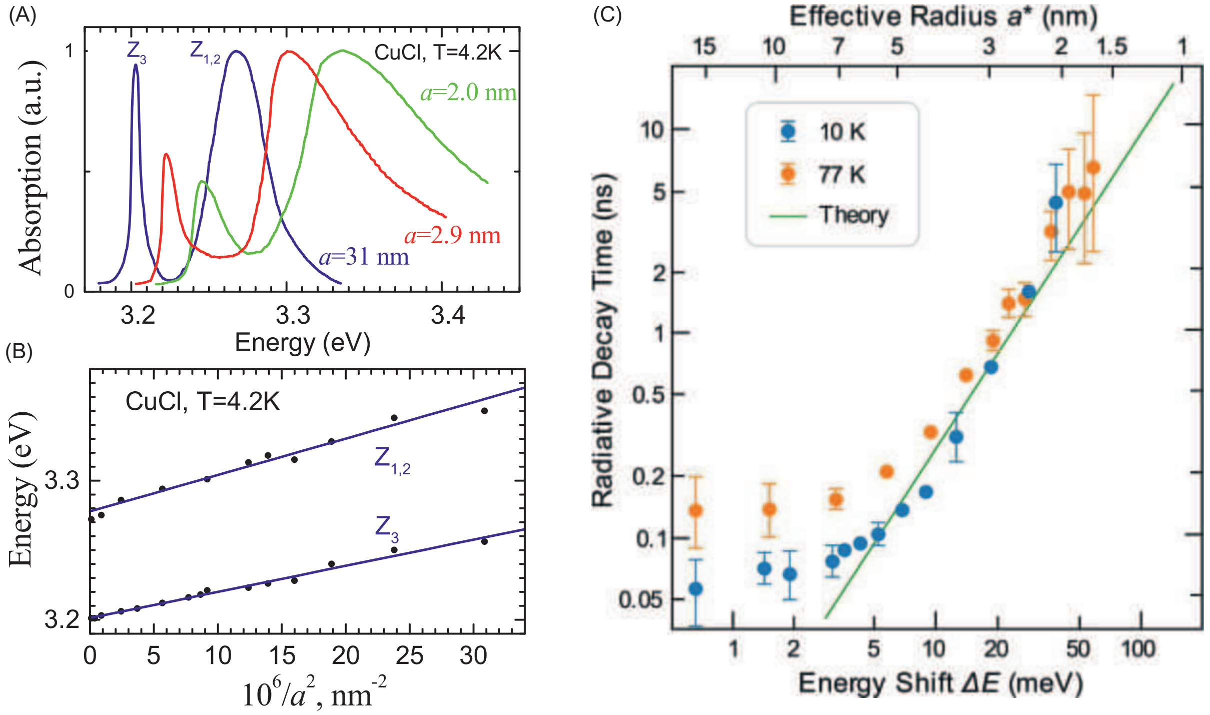

Fig. 5 Size dependent absorption spectra and photoluminescence decay times of CuCl NCs. A—absorption spectra of 2, 2.9 and 31 nm radius CuCl NCs. B—the energy dependence of the two exciton lines (Z_3 and $Z_{1,\ 2}$) on CuCl NC radius, *a*. C—energy dependent radiative decay time of CuCl NCs measured at 10 and 77 K. Panel A: Reproduced with permission from Efros AL and Brus LE (2021) Nanocrystal quantum dots: From discovery to modern development. *ACS Nano* 15: 6192–6210. Copyright of 2021 American Chemical Society. Adapted with permission from Ekimov AI, Efros AL, Onushchenko AA (1985) Quantum size effect in semiconductor microcrystals, *Solid State Communications* 56: 921–924. Copyright 1985 Elsevier. Panel B: Reproduced with permit from Efros AL and Brus LE (2021) Nanocrystal quantum dots: From discovery to modern development *ACS Nano* 15: 6192–6210. Copyright of 2022 American Chemical Society. Adapted from Ekimov AI, Onushchenko AA (1981) Quantum size effect in three-dimensional microscopic semiconductor crystals. *JETP Letters* 34: 345–349. Copyright 1981 Russian Academy of Science. Panel C: Reproduced with permission from Itoh T, Fumiya M, Ikehara T, Gourdon C (1990) Size-dependent radiative decay time of confined excitons in CuCl microcrystals. *Solid State Communications* 73: 271–274. Copyright 1990 Elsevier.

samples with average NC radius $a = 2.0, 2.9$, and 31 nm (Ekimov and Onushchenko, 1981). All spectra exhibit two exciton lines connected with the two valence band subbands (Z_3 and $Z_{1,2}$) of CuCl. The absorption spectra of the largest 31 nm radius NCs are nearly identical to those of the bulk and both exciton lines blueshift as NC size decreases (Efros and Brus, 2021). The shift of both exciton lines plotted as a function of the inverse square of the NC radius is shown in Fig. 5B. The size dependence of the shift is linear in this scale, and for all investigated sizes is very well described by Eq. (7) (Ekimov and Onushchenko, 1981).

The ground exciton state in CuCl NCs indeed shows the giant oscillator transition strength. The giant oscillator transition strength proportional to the ratio a^3/a_{ex}^3 (see Eq. (8)) brings the radiative decay times of these NC (shown in Fig. 5C) to the sub-nanosecond range at low temperatures (Itoh et al., 1990). The solid line in Fig. 5C shows that radiative decay times are scaled as $1/a^3$ with increasing NC radius a. Recently, the sub-nanosecond radiative decay times connected with giant oscillator transition strengths of confined excitons were also measured in large perovskite NCs (Becker et al., 2018).

Detailed investigations of strong confinement regime have been conducted in CdS and CdSe NCs, where $a_B = 28$ Å and $a_B = 56$ Å, respectively. Fig. 6A shows the low-temperature absorption spectra of CdS NCs measured in four different glass samples with average NC radius $a = 1.2, 1.5, 2.3$, and 33 nm (Ekimov and Onushchenko, 1984). The red curve shows the absorption spectra of very large 33 nm radius NCs. These spectra are nearly identical to the absorption spectra of bulk CdS, and have a bulk energy gap equal to 2.5 eV. The fine structure at the band edge is created by the three excitons connected with the three valence subbands of this material. It is seen that a decrease in NC size leads to a strong shift of the absorption edge to higher energy, and is accompanied by the oscillations of interband absorption magnitude. The energy gap increases dramatically: up to 0.8 eV in the smallest NCs.

The experimental size dependence of the band edge (empty circles) and spectral positions of oscillations maxima (empty triangles and squares) measured in CdS NCs at liquid helium temperatures is connected with the size-dependent optical transitions described by Eq. (6) (shown in the cartoon in Fig. 6B). This size dependence is plotted as a function of the inverse square of the NC radius in Fig. 6C. The red lines going through these data are plotted as a guide to the eye. The dependence should be almost linear in $1/a^2$ scale in the parabolic approximation, according to Eq. (6). The deviations from linear dependence seen in Fig. 6C are connected

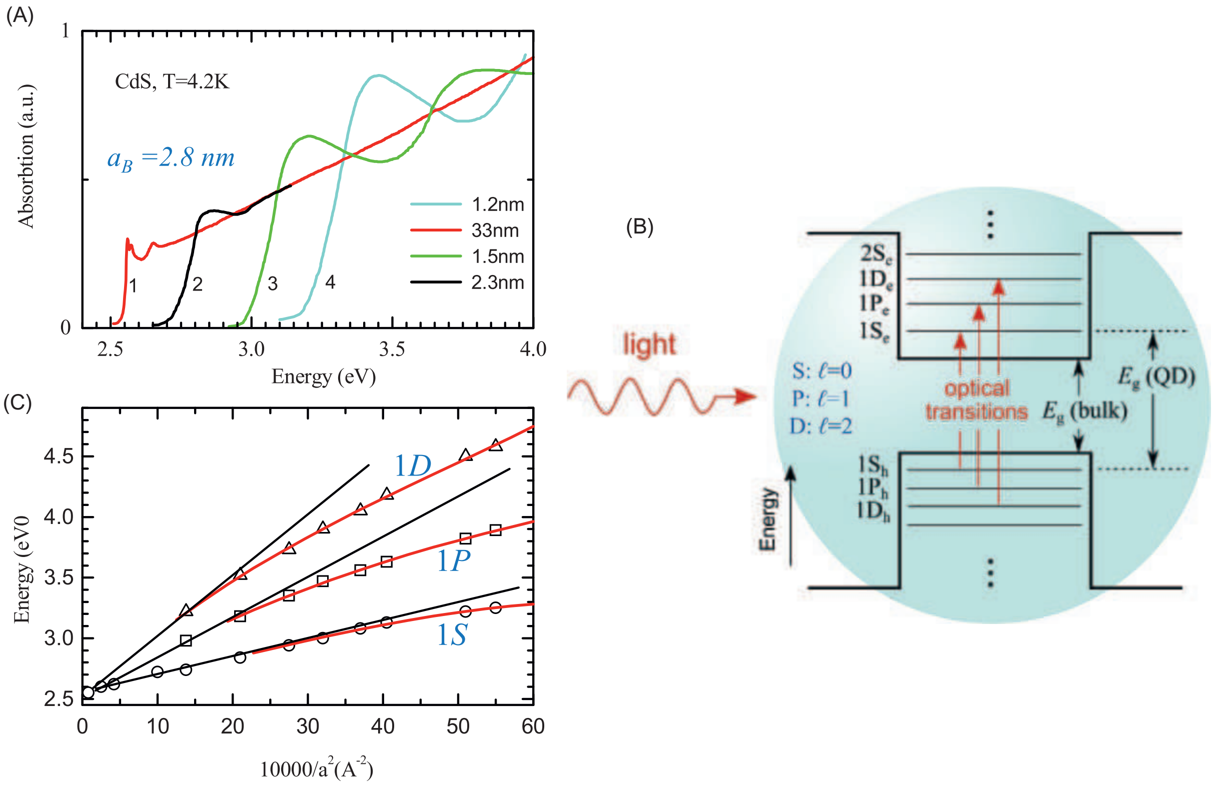

Fig. 6 Size dependent absorption spectra of CdS NC and schematic diagram of optically allowed optical transitions. A—low temperature absorption spectra of 1.2, 1.5, 2.3 and 33 nm radius CdS NCs. B—the cartoon shows schematically the structure of lowest electron and hole levels in NCs. Here we adopted the level notation from atomic physics: S, P, and D for the level with angular momentum 0, 1, and 2. The arrows show the allowed transitions between these levels allowed by optical selection rules. C—the energy dependence of the three lowest optical transitions on CdS NC radius. Symbols are experimental data connected by the read lines to guide the eye. The initial slops of the experimental dependence are shown by black straight lines. Panel A: Reproduced with permission from Efros AL and Brus LE (2021) Nanocrystal quantum dots: From discovery to modern development. *ACS Nano* 15: 6192–6210. Copyright 2021 American Chemical Society. Adapted with permission from Ekimov AI, Efros AL, Onushchenko AA (1985) Quantum size effect in semiconductor microcrystals. *Solid State Communications* 56: 921–924. Copyright 1985 Elsevier. Panel B: Reproduced with permission from Efros AL and Brus LE (2021) Nanocrystal quantum dots: From discovery to modern development *ACS Nano* 15: 6192–6210. Copyright 2021 American Chemical Society. Panel D: Adapted with permission from Ekimov AI, Onushchenko AA (1984) Size quantization of the electron energy spectrum in semiconductor microcrystals. *JETP Letters* 40: 1136–1139, Copyright 1984 Russian Academy of Science.

with the nonparabolicity of the electron energy spectra. The initial slopes of the curves that describe the absorption spectra in very large NCs (black straight lines) are in a very good agreement with Eq. (6), if one uses an electron effective mass $m_e = 0.2\ m_0$ for bulk CdS, where m_0 is the free electron mass. Only electron levels are resolved in the absorption spectra. The 15% dispersion of CdS NC sizes in the samples studied in Ekimov and Onushchenko (1984) was too large to resolve the hole level structures. The spacing between hole levels is too small due to the very large hole effective mass of CdS, and dispersion completely washes this structure out.

It took 9 more years for the structure of the hole levels in CdSe NCs to be revealed, which occurred when Ekimov et al. (1993) was able to narrow the size-distribution of these NCs to 5%. Fig. 7A shows the absorption spectrum and its second derivative for CdSe NCs with mean radii 3.8, 2.6, and 2.1 nm (Ekimov et al., 1993). This observed level structure, however, cannot be described within the parabolic-band model even qualitatively, because the valence band of CdSe consists of 6 subbands, which changes both the level structure and optical selection rules. The appropriate theory, which accounts for the multiband structure of the valence band, was developed by Grigoryan et al. (1990a,b). The complete description of absorption spectra in Ekimov et al. (1993) is also required to take into account the non-parabolicity of the electron spectra. Fig. 7B shows the size dependence of the lowest electron and hole levels calculated within the 6-band effective mass model, plotted as a function of the inverse square of the NC radius. The red and blue arrows in Fig. 7B show the optically allowed transitions to the 1S and 1P electron levels. One can see that there are no selection rules connected with the main quantum number, and transitions to the lowest electron S and P levels are allowed from many hole levels having S and P angular symmetry.

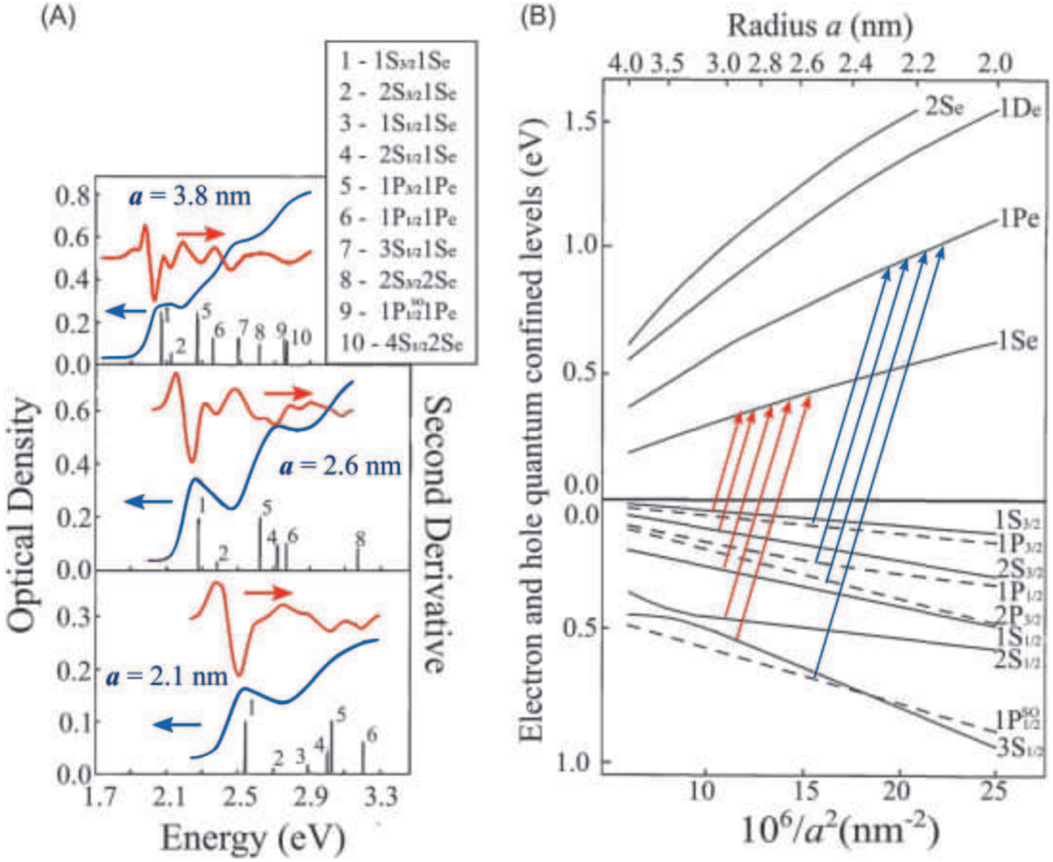

Fig. 7 Size dependent absorption spectra of CdSe NCs. A—the absorption spectrum and its second derivation for CdSe nanocrystals with mean radii 3.8, 2.6, and 2.1 nm. B—the size dependence of the lowest electron and hole levels of CdSe NCs calculated within the 6-band effective mass model. The red and blue arrows show the optically allowed transitions to the 1S and 1P electron levels. The calculated position of allowed transitions and their relative intensities are indicated by the vertical lines in panel A. The insert table identifies these transitions. Panel A: Reproduced with permission from Efros AL and Brus LE (2021) Nanocrystal quantum dots: From discovery to modern development. *ACS Nano* 15: 6192–6210, Copyright 2021 American Chemical Society. Adapted with permission from Ekimov AI, Hache F, Shanne-Klein MC, Ricard, D, Flitzanis C, Kudriavtsev IA, Rodina AV, Efros AL (1993) Absorption and intensity-dependent photoluminescence measurements on CdSe quantum dots: Assignment of the first electronic transitions. *Journal of the Optical Society of America B* 10: 100–107. Copyright 1993 The Optical Society. Panel B: Reproduced with permission from Efros AL and Brus LE (2021) Nanocrystal quantum dots: From discovery to modern development *ACS Nano* 15: 6192–6210. Copyright 2022 American Chemical Society. Adapted with permission from Ekimov AI, Hache F, Shanne-Klein MC, Ricard D, Flitzanis C, Kudriavtsev IA, Rodina AV, Efros AL (1993) Absorption and intensity-dependent photoluminescence measurements on CdSe quantum dots: Assignment of the first electronic transitions. *Journal of the Optical Society of America B* 10: 100–107. Copyright 1993 The Optical Society.

Optical properties of anisotropic semiconductor nanostructures

After the first 20 years of research (20 years ago), the electronic and optical properties of spherical NCs were very well understood (Efros and Brus, 2021). Even the first report on NC shape control and the growth of NRs by Peng et al. (2000) has showed, however, that NR optical properties differ significantly from those of spherical NCs. An even more dramatic change of these properties was reported for NPLs grown 8 years later by Ithurria and Dubertret (2008). For example, even the first grown NRs and NPLs showed high PL quantum yields (Peng et al., 2000; Bouet et al., 2013; Ithurria et al., 2011). Nonradiative Auger recombination is suppressed (Htoon et al., 2003a,b; She et al., 2014; Kunneman et al., 2013) and consequently, NRs and NPLs show low-threshold stimulated emission (Kazes et al., 2002; Htoon et al., 2003a,b; She et al., 2014; Grim et al., 2014). NR photoluminescence is nearly 100% linear polarized (Hu et al., 2001; Shabaev and Efros, 2004). Photoluminescence of NPLs show very narrow PL linewidths and sub-nanosecond decay times (Tessier et al., 2012; Biadala et al., 2014).

The exciting optical properties of NRs and NPLs clearly indicate that they will be important building blocks in future nanotechnology and may replace spherical NCs in biological labeling, lasing applications, and solar energy harvesting applications. So what is the source of the improved properties of NRs and NPLs, and how can we control them? I will show below that most of these improved optical properties are related to the spectra of one-dimensional excitons in NRs and two-dimensional excitons in NPLs that control the PL of these anisotropic structures.

The strong anisotropy of the nanostructure shape leads to the spatial confinement anisotropy of the electron and hole energy spectra (which is discussed above) and anisotropy of dielectric confinement. Both of these effects play an important role in exciton creation and exciton properties, and allow for independent control of NR and NPL optical properties. The effect of spatial confinement anisotropy was discussed above, so let us consider the effect of dielectric confinement connected with small dielectric constant of the media surrounding the nanostructures.

Effect of dielectric confinement on electron-hole energy spectra

Now let us discuss how the difference in dielectric constant of semiconductors and their surrounding media affect the electron-hole spectra in anisotropic nanoscale semiconductor structures such as NRs, NPLs, or nanowires. The charge near the surface that separates two media with different dielectric constants creates media polarization. For a flat surface, this polarization can be described by an image charge positioned at some distance from the surface, and whose value is proportional to the difference in dielectric constants. This image charge creates a force acting on the original charge—the so-called "mirror force." If the dielectric constant of the external media is smaller than the dielectric constant of internal media, the "mirror force" is repulsive. This leads also to a repulsive potential that pushes the electron away from the surface (see Fig. 8A).

In nano-scale semiconductors surrounded by media with a smaller dielectric constant, this repulsive potential increases the energy of the electron and hole quantum size levels. In the diagram, shown in Fig. 6B the dashed line shows the quantum size level in the absence of the dielectric confinement effect. The repulsive electrostatic potential connected with the mirror force decreases the depth of the quantum well, and increases the energy of the quantum size level.

Now let us consider the effect of dielectric confinement on the electron-hole Coulomb interaction. Although electrons and holes are confined in NRs, NPLs or nanowires, the electric field of their charge distribution is not confined within the rod, and penetrates into the surrounding medium as it is shown in Fig. 8C. The dielectric constant of this medium is significantly smaller than in the semiconductor. This enhances significantly the "e-h" Coulomb interaction.

This effect is practically non-existent in NCs, because electron and hole charge distributions are almost identical in spherical NCs, and they compensate each other at each point of the NC. The NC retains its local neutrality even after exciton creation (see Fig. 8B). If there is no charge in the NC, there is no electric field outside of the nanocrystal. This is not the case for NRs, NPLs and nanowires and the electron-hole interaction at a distance larger than their thickness is characterized by the external (small) dielectric constant, $\varepsilon_{m^{\cdot}}$.

The enhanced "e-h" Coulomb interaction in all these nanostructures can be written in the following form,

$$U\left(\vec{r}_e, \vec{r}_h\right) = -\frac{e^2}{\varepsilon_s\left|\vec{r}_e - \vec{r}_h\right|} - eV_s\left(\vec{r}_e, \vec{r}_h\right) + \frac{e}{2}V_s\left(\vec{r}_e, \vec{r}_e\right) + \frac{e}{2}V_s\left(\vec{r}_e, \vec{r}_e\right), \tag{9}$$

where the first term is the direct "e-h" interaction in the semiconductor, the second term is the "e-h" Coulomb interaction mediated by the difference in dielectric constants of a semiconductor and the surrounding media, and the last two terms are the self-interaction of electrons and holes, each with its own image, which take mirror forces into account.

The enhancement of the Coulomb interaction in thin semiconductor films was first calculated by Ritova (1967). Later, her results were independently reproduced by Keldysh (1979) who gave the following analytical expression which describes this interaction:

$$V(\boldsymbol{\rho}, z_e, z_h) = -\frac{4\pi e^2}{\varepsilon_s}\int \frac{d^2k}{(2\pi)^2} e^{2ik\boldsymbol{\rho}} \frac{ch\left[|\boldsymbol{k}|\left(\frac{d}{2} - z_e\right) + \boldsymbol{\eta}\right] ch\left[|\boldsymbol{k}|\left(\frac{d}{2} - z_h\right) + \boldsymbol{\eta}\right]}{|\boldsymbol{k}| sh[|\boldsymbol{k}| + 2\eta]} \tag{10}$$

where $\boldsymbol{\rho} = (\boldsymbol{x}_e - \boldsymbol{x}_h) + (y_e - y_h)$ is the distance between an electron and a hole in the film plane, z_e and z_h are the electron and hole coordinates in the direction perpendicular to the film plane, d is the film thickness and $\eta = 0.5\, ln\ [(\varepsilon_s + \varepsilon_m)/(\varepsilon_s - \varepsilon_m)]$.

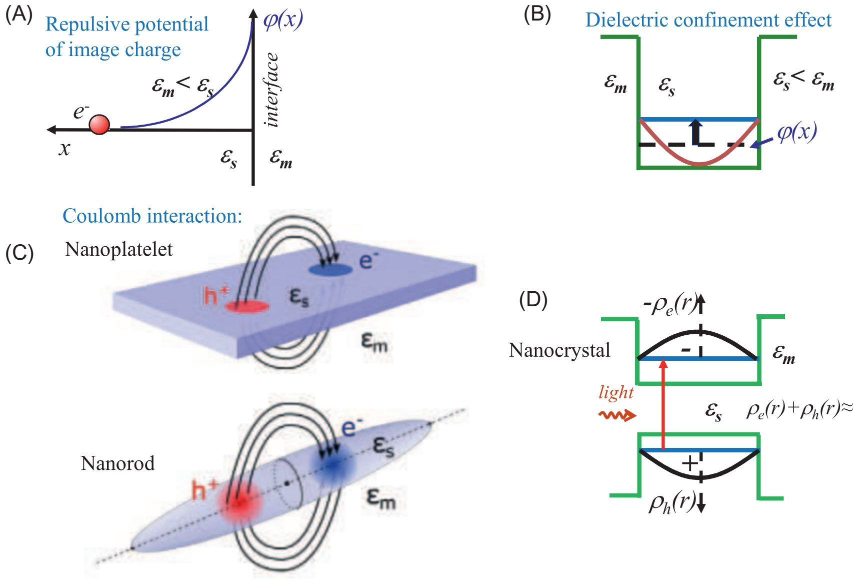

Fig. 8 Effect of difference of dielectric constant and surrounding media. A—Potential created by the image charge pushes an electron from the surface. B—Cartoon that shows that the mirror force potential in a semiconductor nanostructure embedded in media with a small dielectric constant, resulting in the shift of the carrier-confined level to a higher energy—this is the dielectric confinement effect. C—The enhancement of the Coulomb interaction due to penetration of the electric field of carriers confined in nanoplatelets and nanorods in the surrounding media. D—Absence of the Coulomb enhancement in spherical NCs due to local compensation of electron and hole charges at each point in the NC. Reproduced with permission from Efros AL and Brus LE (2021) Nanocrystal quantum dots: From discovery to modern development *ACS Nano* 15: 6192–6210. Copyright 2021 American Chemical Society.

When the distance between the electron and hole is smaller than the film thickness d, the Keldish-Ritova Coulomb potential describes the three-dimensional attraction between the electron and hole $-e^2/\varepsilon_s r$, with dielectric constant of semiconductors, where $r = \sqrt{\rho^2 + |z_e - z_h|^2}$. At the largest distances when $\rho > > (\varepsilon_s/\varepsilon_m)d$ it has the form of a 2D Coulomb interaction—$-e^2/\varepsilon_m \rho$ with the smaller dielectric constant of surrounding media, ε_m. At intermediate distances, $d < < \rho < < (\varepsilon_s/\varepsilon_m)d$, the attractive Coulomb potential has a weak logarithmic dependence on the distance $\sim \ln[(\varepsilon_s/\varepsilon_m)(d/\rho)]$, that provides a slow transition from one law to the other.

The self-interaction potentials for electrons $\frac{e}{2}V_s\left(\vec{r}_e, \vec{r}_e\right)$ and holes $\frac{e}{2}V_s\left(\vec{r}_h, \vec{r}_h\right)$ in films can be obtained from the electron-hole Coulomb potential described by Eq. (10) (Botao et al., 2020):

$$\frac{e}{2}V_s(z,z) = -\frac{1}{2}\left[V(\boldsymbol{\rho}, z_e, z_h) + \frac{e^2}{\varepsilon_s|\vec{r}_e - \vec{r}_h|}\right]_{\vec{r}_e \to \vec{r}_h} \tag{11}$$

In addition to films, the analytical form of enhanced electron-hole Coulomb interaction was found for bodies with high symmetry such as: balls, ellipsoids and cylinders, see, for example, Batygin and Toptygin (1965), and Smythe (1950) correspondingly. The corresponding expressions were used for calculations of the exciton spectra in NCs by Grigoryan et al. (1990a,b) and CdSe (Shabaev and Efros, 2004) and PbSe (Bartnik et al., 2010) NRs by and CdSe (Benchamekh et al., 2014) and CsPbBr$_3$ (Gramlich et al., 2021) NPLs.

Two dimensional excitons in nanoplatelets

Let us discuss the optical properties of NPLs. Fig. 9A shows the TEM images of CdSe NPLs reported in Ithurria and Dubertret (2008). You can see that the lateral size of these structures is on the order of 10–20 nms. The well-defined thicknesses of these NPLs vary in a controlled manner, from 2 to 10 monolayers. This was shown using transmission electron microscopy and optical spectroscopy.

Fig. 9B shows the absorption and the emission spectra of CdSe NPLs with four different thicknesses (Ithurria et al., 2011). The number of CdSe monolayers for these samples is shown here: 5, 4, 3 and 2. You see that the two absorption lines shift to blue by nearly 1.2 eV from that of the bulk energy gap of CdSe (equal to 1.8 eV). These NPLs have electronic properties of quantum wells. The absorption spectra display two well- resolved transitions that correspond to the electron-heavy hole transition (lowest energy) and to the electron-light hole transition (highest energy).

You see in Fig. 9B that the full width half maximum of each emission spectrum is <35meV, and there is practically no Stokes shift for the three thickest NPLs. The small width of the band edge NPL absorption line clearly shows that this width is not connected with fluctuations of the NPL thickness, as the NPLs are atomically flat. A Stokes shift of 70 meV is observed only for the thinnest CdSe NPLs, which is only two monolayers thick. This suggests that the uniformity of NPLs begins to drop in the 12-angstrom-thick structures.

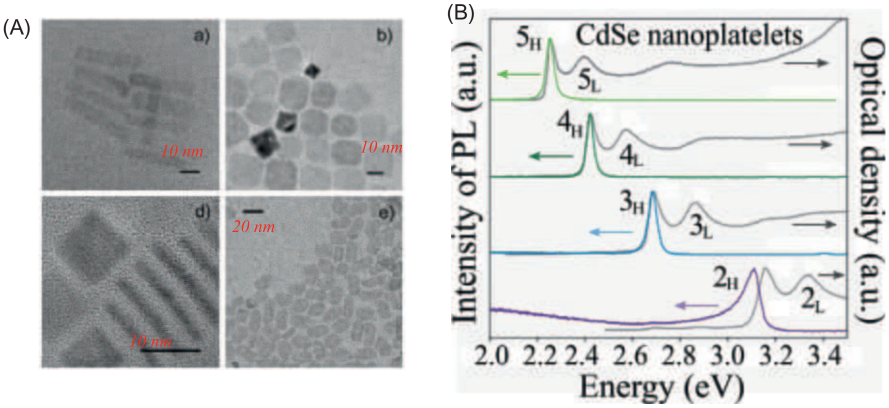

Fig. 9 Transmission electron microscopy (TEM), absorption and photoluminescence of CdSe NPLs. A—TEM images of CdSe NPLs. B—Absorption spectra and photoluminescence measured in two-, three-, four-, and five-monolayer-thick nanoplatelets. Panel A: Reproduced with permission from Ithurria S, Dubertret B (2008) Quasi 2D colloidal CdSe platelets with thicknesses controlled at the atomic level. *Journal of the American Chemical Society* 130: 16504–16505 (Copyright 2008 AMERICAN Chemical Society). Panel B: Modified with permission from Ithurria S, Tessier MD, Mahler B, Lobo RPSM, Dubertret B, Efros AL (2011) Colloidal nanoplatelets with two-dimensional electronic structure. *Nature Materials* 10: 936–941 (Copyright 2011 Springer Nature).

How can we describe the absorption spectra of CdSe NPLs? The procedure used is similar to the one applied to the description of the optical properties of quantum wells, with a difference resulting from the small dielectric constant of the surrounding NPL dielectric constant matrix. First, one needs to calculate the optical transition energy between the lowest electron and hole quantum confined levels equal to

$$E_g + E_e^{2D}(1) + E_h^{2D}(1) = E_g + \frac{\hbar^2\pi^2}{2m_eL^2} + \frac{\hbar^2\pi^2}{2m_hL^2}, \tag{12}$$

where the energy of the electron and hole 2D subbands calculated in parabolic band approximation is described in Eq. (2). Eq. (2) does not consider, however, the self-interaction of electrons and holes with their own image, that shifts the quantum confined levels to higher energy (see Fig. 8B). These self-interaction energies for the lowest level of electrons, Σ_e, heavy holes, Σ_{hh}, and light holes, Σ_{lh}, can be calculated in first order perturbation theory, and they are equal to each other in the parabolic band approximation. The calculated dependence of these energies on NPL thickness is shown in Fig. 10A (Botao et al., 2020). The small difference of these energies that can be seen in the narrowest NPLs is connected with taking into account the nonparabolicity of the electron and hole energy spectra in CdSe. The self-interaction energy of Σ_{lh}, as you can see from this Fig. 10A, is larger than the others, because the light hole on average is closer to the NPL surface. As a result, for the total energy of the optical transition between the lowest electron and the heavyhole sublevels and between the electron and light-hole sublevels, the effective energy gaps can be written as:

$$E^{2D}_{g,e-hh;e-lh}(1) = E_g + \frac{\hbar^2\pi^2}{2m_eL^2} + \frac{\hbar^2\pi^2}{2m_{hh;lh}L^2} + \Sigma_e + \Sigma_{hh;lh}, \tag{13}$$

where m_{hh} and m_{lh} are the heavy hole and light hole effective masses, respectively. The calculated size dependence of the energy gap between non- interacting electrons and heavy holes is shown in Fig. 10B from Benchamekh et al. (2014). This energy gap could be measured in STM experiments as was shown by Botao et al. (2020).

As discussed above the electron-hole Coulomb interaction is significantly enhanced due to the small dielectric constant of the matrix surrounding NPLs. The thickness dependence of the binding energies of optically active S—exciton states calculated in CdSe NPL are shown in Fig. 10C (Benchamekh et al., 2014). One can see that the binding energy of the 2D exciton, E^{2D}_{ex} in a 1 nm thick NPL could be as large as 250 meV (Benchamekh et al., 2014). The optical gap of CdSe NPLs can be found as:

$$\hbar\omega_{NP} = E^{2D}_{g,e-hh}(1) - E^{2D}_{ex} \tag{14}$$

where $E^{2D}_{g,\,e-hh}(1)$ is defined in Eq. (13). The calculated size dependence of the optical gap in CdSe NPLs is shown in Fig. 10B by the red line, together with experimental measurements of this gap in different NPL samples. The comparison shows an excellent agreement between theory an experiment (Benchamekh et al., 2014).

One dimensional excitons in nanorods and nanowires

The optical properties of NRs and nanowires are controlled by the spectra of the one-dimensional excitons. Due to the very large binding energy of the 1D excitons, enhanced by the small dielectric constant of the matrix, the optical gap of these structures is significantly smaller than the effective gap for free carriers measured in STM experiments. The difference from NPLs is that the energy

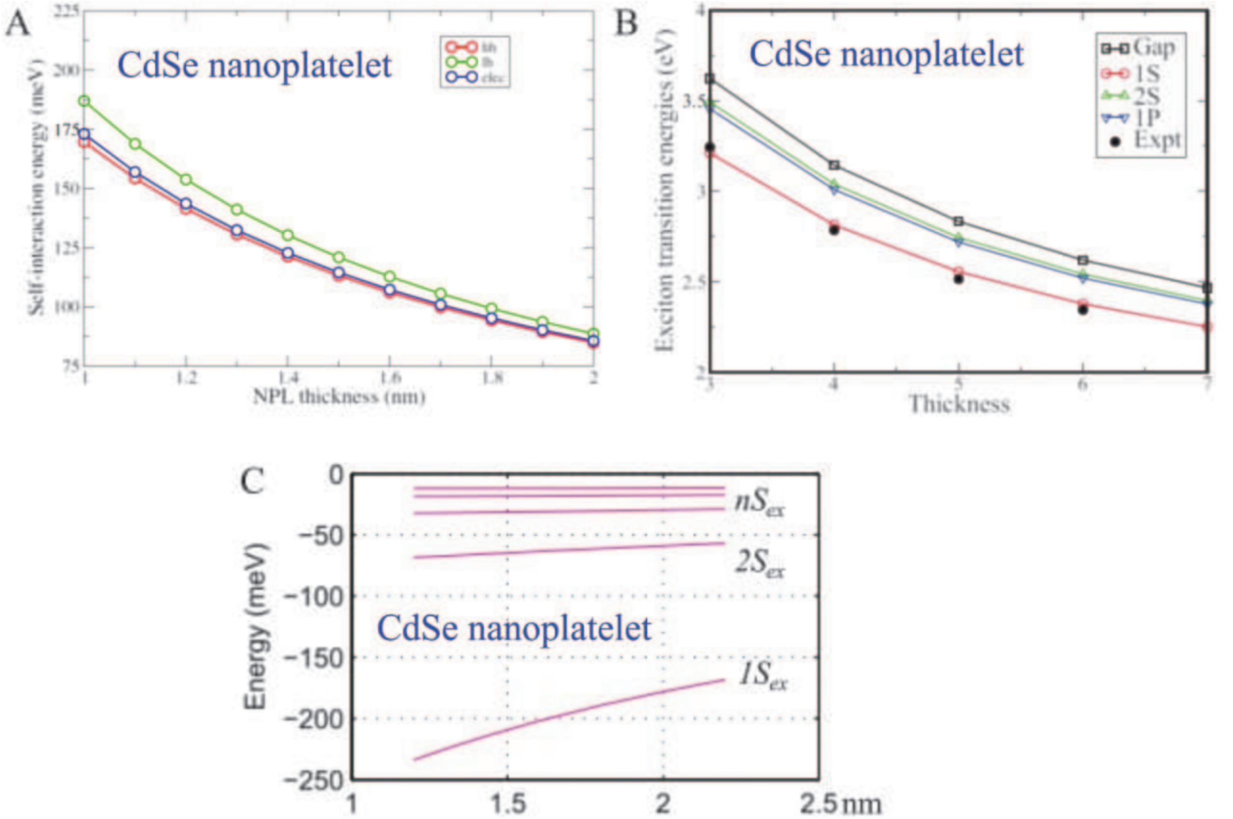

Fig. 10 Effect of dielectric confinement on the electron and hole self-interaction and exciton binding energy in NPLs. A—The thickness dependence of self-interaction energies in CdSe NPLs for lowest levels of electrons, heavy holes and light holes. B—The thickness dependence of the free carrier energy gap, 1S exciton optical energy and 1S and 1P optical transition energies in CdSe NPLs. The experimental data of the optical energy gap measurement are shown by black filled circles. C—The thickness dependence of the binding energies of the $1S_{ex}$ ground and higher nS_{ex} optically allowed exciton states used in the calculation of optical transition energies in Benchamekh et al. (2014). Panel A: Reproduced with permission from Ji Botao, Eran Rabani, Alexander L Efros, Roman Vaxenburg, Or Ashkenazi, Doron Azulay, Uri Banin, Oded Millo (2020) Dielectric confinement and excitonic effects in two-dimensional nanoplatelets. *ACS Nano* 14: 8257–8265 (Copyright 2020 American Chemical Society). Panel B: Reproduced with permission from Benchamekh R, Gippius NA, Even J, Nestoklon MO, Jancu J-M, Ithurria S, Dubertret B, Efros AL, Voisin P (2014) Tight-binding calculations of image-charge effects in colloidal nanoscale platelets of CdSe. *Physical Review B* 89: 035307 (Copyright 2014 American Physical Society).

of electron and hole sublevels in NRs and nanowires are described by Eq. (3) instead of Eq. (2). The full analyses of experimental data conducted in CdSe NRs by Katz et al. (2002) and PbSe NRs by Bartnik et al. (2010), that takes into account the complex band structures and nonparabolicity of these semiconductors and dielectric confinement effects show very good agreement between theory and experiment for both materials (see Shabaev and Efros, 2004 and Bartnik et al., 2010, respectively).

It is interesting to note that one dimensional excitons control also optical properties of monoatomic carbon chains. This system represents ultimate nano-wires where a carbon chain behaves as a direct gap semiconductor and shows narrow exciton and trion resonances in low-temperature photoluminescence spectra (Kutrovskaya et al., 2020, 2021).

Photoluminescence of excitons in nanoscale semiconductor structures

Exciton photoluminescence (PL) in nanostructures is controlled by their fine structure, created by the exchange interaction between electron and hole spins. The electron-hole exchange interaction splits the spin degenerate ground exciton state into an optically allowed (bright) and optically forbidden (dark) exciton sublevels (Efros et al., 1996). In practically all bulk semiconductors and all existing semiconductor heterostructures, the ground exciton state is an optically passive "dark" exciton. The direct optical excitation of this state by a single photon, or its direct photon emission, is forbidden due to the parallel alignment of the electron and hole spin states caused by the ferromagnetic character of the electron–hole exchange interaction. Only exciton states with antiparallel alignment of electron and hole spins ("bright" exciton states) can be excited directly by a photon and directly emit a photon. The only known exception to this rule was reported recently by Becker et al. (2018), in which it was proposed that 10–15 nm size lead-halide perovskite NCs have a bright ground exciton state.

In bulk semiconductors, (Knox, 1963) epitaxial quantum wells, (Kusrayev et al., 1997) and quantum dots, (Bayer et al., 2002; Smoleński et al., 2012; Korkusinski and Hawrylak, 2013) the dark-bright exciton splitting is usually smaller than the thermal energy, even at helium temperature. This results in equal populations of all band-edge exciton levels and a decrease of the total radiative recombination rate of these semiconductors and semiconductor structures by the ratio of the number of bright-emitting exciton states to the total number of the band-edge exciton states. This is not the case, however, for small-size colloidal NCs, NRs, and NPLs, in which the strong spatial confinement leads to dark–bright exciton splitting on the order dozens of meVs (Nirmal et al., 1995; Efros et al., 1996; Chamarro et al., 1996; Korkusinski et al., 2010; Shabaev and Efros, 2004; Biadala et al., 2014) and the slow radiative recombination of the dark exciton affects the PL, even at room temperature. The absolute majority of investigations of the exciton fine structure were conducted in CdSe NCs. That is why we will mainly focus on the band edge excitons in the heavily studied CdSe NCs and only briefly will discuss exciton fine structure in NRs, and NPLs and other materials.

The optically passive dark exciton was discovered by Bawendi et al. (1990) when the resonance excitation of the PL line of 3.2 nm diameter CdSe NCs showed a significant Stokes shift of the PL and microsecond decay time at helium temperatures. These data were later explained within the dark/bright exciton model, which explained also the magnetic field dependence of the PL fine structure observed under resonant excitation (Nirmal et al., 1995; Efros et al., 1996). The starting point of the model is the assumption of a spherical NC symmetry. In spherically symmetric CdSe NCs (meaning spherical-shaped NCs with a cubic lattice structure), the electron ground 1Se level is doubly degenerate with respect to its spin projection, $s_z = \pm 1/2$, and the hole ground $1S_{3/2}$ level is fourfold degenerate with respect to projections $M = 3/2$, $1/2$, $-1/2$, and $-3/2$ of its total angular momentum, F ($F = 3/2$) (Efros and Rodina, 1989; Ekimov et al., 1993). As a result, the absorption band edge and the PL of these NCs is determined by the $8 = 2 \times 4$ optical exciton transitions between these lowest electron and hole levels. The electron –hole exchange interaction splits the eightfold degenerate exciton state in spherical NCs into a ground optically passive (dark) fivefold degenerate state with a total momentum $\mathcal{F} = 2$ and an upper optically active threefold degenerate state with $\mathcal{F} = 1$. The short- and long-range contributions to this splitting $4\eta_{1S_{3/2}1S_e}{}^{SR}$ and $4\eta_{1S_{3/2}1S_e}{}^{LR}$ as it is shown in Fig. 11 (Sercel and Efros, 2018). Both contributions to the *e-h* exchange interactions are inversely proportional to the NC volume $\sim 1/a^3$, and could be as large as dozens of meVs.

In addition, the spherical symmetry of NCs can be broken by the internal hexagonal crystal field in semiconductors with wurtzite structure (such as CdSe) and the nonspherical, ellipsoidal shape of NCs. These two effects split $M = \pm 3/2$ and $\pm 1/2$ into so-called "heavy" and "light" hole sublevels. The splitting is described by Efros et al. (1996) as $(\Delta/2)\ [5/4 - M^2]$, where the total splitting $\Delta = \Delta_{\text{int}} + \Delta_{\text{sh}}$ is the sum of the splitting caused by the hexagonal field, Δ_{int}, and by the NC shape, Δ_{sh}. The anisotropy finally leads to five band-edge exciton states, $\mathcal{F}_z = \pm 2$, $\pm 1^{L,\ U}$, $0^{L,\ U}$ with different projections, $\mathcal{F}_z = M + s_z$, on the hexagonal c-axis of the NC. The complete theory of exciton fine structure that valid for II-VI and III-V compound NCs was developed by Sercel and Efros (2018) and was applied to CdSe NCs. A schematic structure of the exciton sublevel is shown in Fig. 11.

Detailed investigations of the exciton fine structure were conducted for CdSe NRs by Shabaev and Efros (2004). These calculations also explain the linear polarization of PL observed in these nanostructures. The fine structure and polarization properties of the excitons were described theoretically for $CsPbBr_3$ NCs in Sercel et al. (2019). Recently, a huge (up to 35 meV) dark-bright exciton splitting was measured in $CsPbBr_3$ NPs, and quantitively described using a multiband effective mass theory of electron-hole exchange interaction in Gramlich et al. (2021).

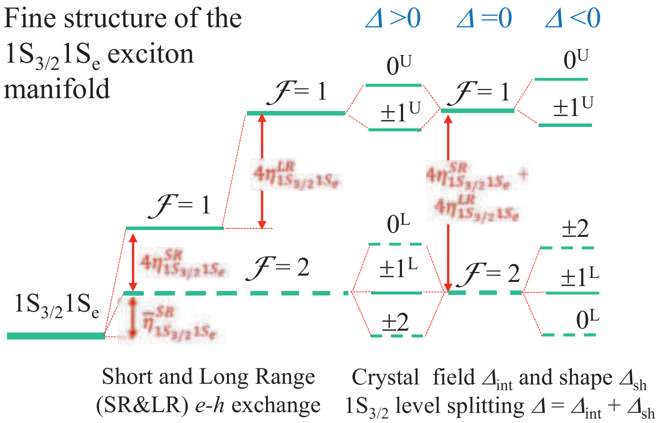
Fine structure of the $1S_{3/2}1S_e$ exciton manifold
$\Delta > 0$
$\Delta = 0$
$\Delta < 0$
0^U
$\mathcal{F} = 1$
$\pm 1^U$
$\mathcal{F} = 1$
0^U
$\pm 1^U$
$4\eta^{LR}_{1S_{3/2}1S_e}$
$4\eta^{SR}_{1S_{3/2}1S_e} + 4\eta^{LR}_{1S_{3/2}1S_e}$
$\mathcal{F} = 1$
0^L
± 2
$4\eta^{SR}_{1S_{3/2}1S_e}$
$\mathcal{F} = 2$
$\pm 1^L$
$\mathcal{F} = 2$
$\pm 1^L$
$1S_{3/2}1S_e$
$\bar{\eta}^{SR}_{1S_{3/2}1S_e}$
± 2
0^L
Short and Long Range (SR&LR) *e-h* exchange
Crystal field Δ_{int} and shape Δ_{sh} $1S_{3/2}$ level splitting $\Delta = \Delta_{\text{int}} + \Delta_{\text{sh}}$

Fig. 11 The schematic diagram of the exciton fine structure in CdSe NCs. The diagram shows how the eightfold degenerate $1S_{3/2}1S_e$ exciton in spherical NCs is split by short- and longrange exchange interaction into the optically passive (dark) exciton state with total momentum 2 (shown by dashed line) and a optically active (bright) exciton state with total momentum 1 (shown by solid line). The crystal field and shape asymmetry further split the eightfold exciton into 5 exciton sublevels and activate the lowest exciton state $\pm 1^L$ with angular momentum projection on the hexagonal axis ± 1. Reproduced with permission from Sercel PC, Efros AL (2018) Band-edge exciton in CdSe and other II–VI and III–V compound semiconductor nanocrystals—revisited. *Nano Letters* 18: 4061–4068 Copyright 2018 American Chemical Society.

Conclusion

All nanoscale semiconductor structures are building blocks for novel bottom-up composite materials, that is why their research and development continues with strong momentum. This is a true interdisciplinary field, at the mutual junction of chemistry, physics, and materials science. The tunability of their optical properties controlled by excitons is, so far, the main application of these structures. The field is not yet mature, and hundreds of scientists and engineers are working on improving synthesis, novel structures, and prototype devices.

In addition to the previously mentioned production of quantum dot TVs based on InP NCs, systematic and persistent synthetic efforts have also created nearly perfect photoluminescence properties in CdSe based core/shell NCs, with quantum yields of 80–95% at room temperature (see Zhou et al., 2017). The use of II-VI alloy compositions has lowered the Cd content in some structures to an acceptable level for commercial use. CdSe based NCs are used in some TVs and displays, in addition to the InP NCs. Within the past 2 years, Osram has begun to use CdSe-based luminescent NCs in GaN LED chips for area (i.e., ceiling) lighting, creating white light of variable designed properties. The success of these efforts depends largely on the continued chemical progress in NC quality and assembly processing, which have shown significant progress in the past decade.

Acknowledgments

The author would like to thank J. Lyons for valuable comments, and M. Swift and R. Vaxenburg for assistance with manuscript preparation. Al. L. Efros acknowledges support of the Office of Naval Research through the Naval Research Laboratory's Basic Research Program.

References

Bartnik AC, Efros AL, Koh W-K, Murray CB, and Wise FW (2010) Electronic states and optical properties of PbSe nanorods and nanowires. *Physical Review B* 82: 195313.

Batygin VV and Toptygin IN (1965) *Problems in Electrodynamics*. London&New York: Academic Press.

Bawendi MG, Wilson WL, Rothberg L, Carroll PJ, Juju TM, Steigerwald ML, and Brus LE (1990) Electronic structure and photoexcited-carrier dynamics in nanometer-size CdSe clusters. *Physical Review Letters* 1990(65): 1623–1626.

Bayer M, Ortner G, Stern O, Kuther A, Gorbunov AA, Forchel A, Hawrylak P, Fafard S, Hinzer K, Reinecke TL, Walck SN, Reithmaier JP, Klopf F, and Schäfer F (2002) Fine structure of neutral and charged excitons in self-assembled In(Ga)As/(Al)GaAs quantum dots. *Physical Review B* 65: 195315.

Becker MA, Vaxenburg R, Nedelcu G, Sercel PC, Shabaev A, Mehl MJ, Michopoulos JG, Lambrakos SG, Bernstein N, Lyons JL, Stöferle T, Mahrt RF, Norris DJ, Kovalenko MV, Rainò G, and Efros AL (2018) Bright Triplet Excitons in caesium lead halide perovskites. *Nature* 553: 189–193.

Benchamekh R, Gippius NA, Even J, Nestoklon MO, Jancu J-M, Ithurria S, Dubertret B, Efros AL, and Voisin P (2014) Tight-binding calculations of image-charge effects in colloidal nanoscale platelets of CdSe. *Physical Review B* 89: 035307.

Biadala L, Liu F, Tessier MD, Yakovlev DR, Dubertret B, and Bayer M (2014) Recombination dynamics of band edge excitons in quasi-two-dimensional CdSe nanoplatelets. *Nano Letters* 14(3): 1134–1139.

Botao J, Rabani E, Efros AL, Vaxenburg R, Ashkenazi O, Azulay D, Banin U, and Millo O (2020) Dielectric confinement and excitonic effects in two-dimensional nanoplatelets. *ACS Nano* 14: 8257–8265.

Bouet C, Tessier MD, Ithurria S, Mahler B, Nadal B, and Dubertret B (2013) Flat colloidal semiconductor nanoplatelets. *Chemistry of Materials* 25(8): 1262–1271.

Brus LE (1983) A simple model for the ionization potential, electron affinity, and aqueous redox potentials of small semiconductor crystallites. *The Journal of Chemical Physics* 79: 5566–5571.

Brus LE (1984) Electron-electron and electron-hole interactions in small semiconductor crystallites: The size dependence of the lowest excited electronic state. *The Journal of Chemical Physics* 80: 4403–4409.

Chamarro M, Dib M, Gourdon C, Lavallard P, Lublinskaya O, and Ekimov AI (1996) Electronic structure of O-D exciton ground state in CdSe nanocrystals. *MRS Online Proceedings Library* 452: 341–346.

Efros AL and Brus LE (2021) Nanocrystal quantum dots: From discovery to modern development. *ACS Nano* 15: 6192–6210.

Efros AL and Efros AL (1982) Interband absorption of light in semiconductor sphere. *Soviet Physics – Semiconductors* 16: 772–775.

Efros AL and Rodina AV (1989) Confined excitons, trions, biexcitons in semiconductor microcrystals. *Solid State Communications* 72: 645–648.

Efros AL, Rosen M, Kuno M, Nirmal M, Norris DJ, and Bawendi MG (1996) Band edge exciton in quantum dots of semiconductor with a degenerate valence band: Dark and bright exciton states. *Physical Review B* 54: 4843–4856.

Ekimov AI and Onushchenko AA (1981) Quantum size effect in three-dimensional microscopic semiconductor crystals. *JETP Letters* 34: 345–349.

Ekimov AI and Onushchenko AA (1984) Size quantization of the electron energy spectrum in semiconductor microcrystals. *JETP Letters* 40: 1136–1139.

Ekimov AI, Efros AL, and Onushchenko AA (1985) Quantum size effect in semiconductor microcrystals. *Solid State Communications* 56: 921–924.

Ekimov AI, Onushchenco AA, and Efros AL (1986) Quantization of the energy spectrum of holes in the adiabatic potential of the electron. *JETP Letters* 43: 376–380.

Ekimov AI, Hache F, Shanne-Klein MC, Ricard D, Flitzanis C, Kudriavtsev IA, Rodina AV, and Efros AL (1993) Absorption and intensity-dependent photoluminescence measurements on CdSe quantum dots: Assignment of the first electronic transitions. *Journal of the Optical Society of America B* 10: 100–107.

Folie BD, Tan JA, Huang J, Sercel PC, Delor M, Lai M, Lyons JL, Bernstein N, Efros AL, Yang P, and Ginsberg NS (2020) Effect of anisotropic confinement on electronic structure and dynamics of band edge excitons in inorganic perovskite nanowires. *The Journal of Physical Chemistry. A* 124(9): 1867–1876.

Gramlich M, Swift MW, Lampe C, Lyons JL, Döblinger M, Efros AL, Sercel PC, and Urban AS (2021) Dark and bright excitons in halide perovskite nanoplatelets. *Advancement of Science* 2021: 2103013.

Grigoryan GB, Kazaryan EM, Efros AL, and Yazeva TV (1990a) Quantized holes and the absorption edge in spherical semiconductor microcrystals with a complex valence band structure. *Soviet Physics - Solid State* 32: 1031–1035.

Grigoryan GB, Rodina AV, and Efros AL (1990b) Excitons and biexcitons in quantum-confined semiconductor microcrystals embedded in dielectric glass matrix. *Soviet Physics - Solid State* 32(4): 2037.

Grim JQ, Christodoulou S, Di Stasio F, Krahne R, Cingolani R, Manna L, and Moreels I (2014) Continuous-wave biexciton lasing at room temperature using solution-processed quantum wells. *Nature Nanotechnology* 9: 891–895.

Hines MA and Guyot-Sionnest P (1996) Synthesis and characterization of strongly luminescing ZnS-capped CdSe nanocrystals. *The Journal of Physical Chemistry* 100: 468–471.

Htoon H, Hollingworth JA, Malko AV, Dickerson R, and Klimov VI (2003a) Light amplification in semiconductor nanocrystals: Quantum rods versus quantum dots. *Applied Physics Letters* 82: 4476–4778.

Htoon H, Hollingsworth JA, Dickerson R, and Klimov VI (2003b) Effect of zero- to one-dimensional transformation on multiparticle auger recombination in semiconductor quantum rods. *Physical Review Letters* 91: 227401.

Hu JT, Li LS, Yang WD, Manna L, Wang LW, and Alivisatos AP (2001) Linearly polarized emission from colloidal semiconductor quantum rods. *Science* 292: 2060–2063.

Ithurria S and Dubertret B (2008) Quasi 2D colloidal CdSe platelets with thicknesses controlled at the atomic level. *Journal of the American Chemical Society* 130: 16504–16505.

Ithurria S, Tessier MD, Mahler B, Lobo RPSM, Dubertret B, and Efros AL (2011) Colloidal nanoplatelets with two-dimensional electronic structure. *Nature Materials* 10: 936–941.

Itoh T, Fumiya M, Ikehara T, and Gourdon C (1990) Size-dependent radiative decay time of confined excitons in CuCl microcrystals. *Solid State Communications* 73: 271–274.

Katz D, Wizansky T, Millo O, Rothenber E, Mokari T, and Banin U (2002) Size-dependent tunneling and optical spectroscopy of CdSe quantum rods. *Physical Review Letters* 89: 086801.

Kazes M, Lewis DY, Ebenstein Y, Mokari T, and Banin U (2002) Lasing from semiconductor quantum rods in a cylindrical microcavity. *Advanced Materials* 4: 317–321.

Keldysh LV (1979) Coulomb interaction in thin semiconductor and semimetal films. *JETP Letters* 29: 658–660.

Knox RS (1963) *Theory of Excitons*. New York: Academic Press.

Korkusinski M and Hawrylak P (2013) Atomistic theory of emission from dark excitons in self-assembled quantum dots. *Physical Review B* 87: 115310.

Korkusinski M, Voznyy O, and Hawrylak P (2010) Fine structure and size dependence of exciton and biexciton optical spectra in CdSe nanocrystals. *Physical Review B* 82: 245304.

Kunneman LT, Tessier MD, Heuclin H, Dubertret B, Aulin YV, Grozema FC, Schins JM, and Siebbeles LDA (2013) Bimolecular auger recombination of electron–hole pairs in two-dimensional CdSe and CdSe/CdZnS core/shell nanoplatelets. *Journal of Physical Chemistry Letters* 4(21): 3574–3578.

Kusrayev YG, Zakharchenya BP, Karczewski G, Wojtowicz T, and Kossut J (1997) Fine structure of exciton levels in quantum wells. *Solid State Communications* 104: 465–468.

Kutrovskaya S, Osipov A, Baryshev V, Zasedatelev A, Samyshkin V, Demirchyan S, Pulci O, Grassano D, Gontrani L, Hartmann RR, Portnoi ME, Kucherik A, Lagoudakis P, and Kavokin A (2020) Excitonic fine structure in emission of linear carbon chains. *Nano Letters* 20: 6502–6509.

Kutrovskaya S, Demirchyan S, Osipov A, Baryshev S, Zasedatelev A, Lagoudakis P, and Kavokin A (2021) Exciton radiative lifetime in a monoatomic carbon chain. *New Journal of Physics* 23: 033007.

Nirmal MD, Norris J, Kuno M, Bawendi MG, Efros AL, and Rosen M (1995) Observation of the “Dark Exciton” in CdSe quantum dots. *Physical Review Letters* 75: 3728–3731.

Peng X, Manna L, Yang W, Wickham J, Scher E, Kadavanich A, and Alivisatos AP (2000) Shape control of CdSe nanocrystals. *Nature* 404: 59–61.

Ritova NC (1967) *Screened Potential of a Point Charge in a Thin Film*. Vestnik of Moskow University.30–36. Translated to English in: arXiv e-prints 2019, No. 00976. https://arxiv.org/abs/1806.00976.

Sercel PC and Efros AL (2018) Band-edge exciton in CdSe and other II–VI and III–V compound semiconductor nanocrystals—revisited. *Nano Letters* 18: 4061–4068.

Sercel PC, Lyons JL, Bernstein N, and Efros AL (2019) Quasicubic model for metal halide perovskite nanocrystals. *The Journal of Chemical Physics* 151: 234106.

Shabaev A and Efros AL (2004) 1D exciton spectroscopy of semiconductor nanorods. *Nano Letters* 4: 1821–1825.

She I, Fedin I, Dolzhnikov DS, Demortière A, Schaller RD, Pelton M, and Talapin DV (2014) Low-threshold stimulated emission using colloidal quantum wells. *Nano Letters* 14: 2772–2779.

Smoleński T, Kazimierczuk T, Goryca M, Jakubczyk T, Kłopotowski Ł, Cywiński Ł, Wojnar P, Golnik A, and Kossacki P (2012) In-plane radiative recombination channel of a dark exciton in self-assembled quantum dots. *Physical Review B* 86: 241305.

Smythe WR (1950) *Static and Dynamic Electricity*. New York: McGraw-Hill.

Tessier MD, Javaux C, Maksimovic I, Loriette V, and Dubertret B (2012) Spectroscopy of single CdSe nanoplatelets. *ACS Nano* 6(8): 6751–6758.

Zhou J, Zhu M, Meng R, Qin H, and Peng X (2017) Ideal CdSe/CdS Core/Shell nanocrystals enabled by entropic ligands and their core size-, shell thickness-, and ligand-dependent photoluminescence properties. *Journal of the American Chemical Society* 139: 16556–16567.

Bose-Einstein Condensation of Excitons in a bulk semiconductor

Kosuke Yoshioka, Photon Science Center, School of Engineering, The University of Tokyo, Tokyo, Japan

© 2024 Elsevier Ltd. All rights reserved.

Introduction	644
Excitons in cuprous oxide	644
Early experiments	645
Collision-induced loss	646
Excitonic Lyman spectroscopy	647
Experiments at sub-Kelvin temperatures	648
Conclusion	650
References	651

Abstract

The search for Bose-Einstein condensation of long-lived excitons decoupled from the radiation field in bulk semiconductor cuprous oxide is presented. The condensate, which was not confirmed for about 60 years since its theoretical prediction, has been finally observed experimentally. This was achieved by developing a method for the quantitative evaluation of the density and temperature of dark excitons, as well as the cooling to the 100 mK region that proved necessary because of the density-dependent loss. Notably, the discovered exciton condensate exhibits features that have not yet been elucidated, and it is a genuinely new physical system that may exhibit the characteristics of non-equilibrium open systems of quantum many-body Bose particles.

Key points

- Elucidation of the properties of long-lived exciton states in bulk semiconductor Cu_2O.
- Summary of historical aspects of the search for exciton BEC in Cu_2O.
- Explanation of the need for cooling to sub-Kelvin temperatures.
- Summary of the recent discovery of exciton BEC using mid-infrared absorption imaging.

Introduction

The photoexcitation of a semiconductor crystal creates excitons. Excitons are hydrogen-like quasiparticles comprising an electron in the conduction band and a hole in the valence band. Excitons often have short lifetimes due to radiative recombination, but in carefully selected systems, radiative recombination is prohibited or weakly allowed, resulting in relatively long lifetimes. Such exciton systems decoupled from the radiation field are purely matter-like physical systems generated in solids and closely resemble positronium atoms. An exciton comprises a pair of fermions. Therefore, an ensemble that reaches quasi-thermal equilibrium is expected to exhibit Bose-Einstein condensation (BEC) under low-temperature and high-density conditions (Blatt et al., 1962). However, since excitons are elementary excitations in the many-body electron system of semiconductors, there is a limit to treating excitons as composite bosons. Therefore, the appearance of the BEC state itself is not apparent. It is also unknown whether the BEC behaves as a quantum fluid when generated. This problem also encompasses fundamental issues, such as understanding the mass of quasiparticles and how we should quantify the spontaneous breaking of gauge symmetry, which is considered essential also in the BCS theory of superconductivity. Therefore, the experimental observation of spontaneous BEC formation of excitons in bulk semiconductors has been regarded as a holy grail in many research fields, such as solid-state spectroscopy and nonequilibrium quantum statistical mechanics. Here, we will introduce the history of the attempts to realize exciton BECs, which took several twists and turns, mainly from an experimental standpoint.

Excitons in cuprous oxide

The exciton system in bulk cuprous oxide (Cu_2O) is a representative example of a Wannier-Mott exciton, and the discovery of the famous hydrogen-like absorption spectrum was made in Cu_2O (Hayashi and Katsuki, 1950, 1952; Gross and Karryev, 1952a, 1952b). The search for exciton BECs in Cu_2O is only possible because of the rich and solid physics established by many researchers in the past. In the direct-gap semiconductor Cu_2O, the lowest energy conduction band derives from the 4s orbital of Cu, and the highest energy valence band derives from the 3d orbital of Cu (Elliott, 1961). Therefore, 1*s* excitons are optically forbidden (parity

https://doi.org/10.1016/B978-0-323-90800-9.00190-6

forbidden) and have very long radiative recombination lifetimes. In addition, these bands have no orbital degeneracy, and the exciton has a simple electronic structure. The 1*s* exciton state is fourfold degenerate, taking the spin degrees of freedom into account. Because of the exchange interactions between electrons and holes, it splits into a triple degenerate orthoexciton and a non-degenerate paraexciton (the energy splitting is 12 meV). Because the exciton binding energy is large (151 meV for the 1*s* paraexciton), 1*s* excitons are stable. The considerable electron-hole exchange interaction prevents the formation of exciton molecules that require spin recombination. In addition, because Cu_2O is a direct-gap semiconductor, no electron-hole droplets are produced, implying that excitons can be maintained at high densities and low temperatures.

In the case of the 1*s* orthoexciton state, the optical transition from the crystal ground state to the exciton state is dipole-forbidden, but electric quadrupole transitions are allowed. The lifetime is about 3 ns at 2 K. By contrast, the 1*s* paraexciton state is composed of pure spin triplets; therefore, the optical transition to the ground state of the crystal is completely forbidden. Hence, the lifetime is extremely long. For example, the lifetime of 1*s* paraexcitons in a high-purity natural single crystal has been reported to be in the microsecond range (Mysyrowicz et al., 1979). Therefore, both the 1*s* ortho- and paraexciton systems can reach thermal equilibrium with the lattice system within their lifetimes. This means that a sufficiently low-temperature exciton system can be prepared by cooling the crystal. For this reason, the 1*s* exciton system in Cu_2O has attracted much attention as the most promising candidate for realizing exciton BECs.

Early experiments

The critical density n_c of the BEC transition in a 3-dimensional ideal Bose particle system as a function of temperature T is

$$n_c = 2.612\left(\frac{m_{1s}k_B T}{2\pi\hbar^2}\right)^{\frac{3}{2}}.$$

Substituting the effective mass of the exciton $m_{1s} = 2.6m_0$ (Brandt et al., 2007, m_0 is the electron mass at rest) into this expression, the BEC transition density is $n_c = 8 \times 10^{16}\ \mathrm{cm}^{-3}$ at a superfluid liquid helium temperature of $T = 2$ K. A high-density excitation with a pulsed laser can be employed to prepare 1*s* excitons of this density. Exciton BEC is expected to occur if we wait for the exciton system to cool through interaction with the 2 K lattice. This naive consideration suggests that experimental confirmation of exciton BEC in Cu_2O is feasible.

The analysis of the spectral shape of the LO-phonon-assisted luminescence is conventionally used to experimentally evaluate the thermal distribution function of the translational motion of 1*s* excitons. In early experiments, nanosecond laser pulses were used to generate high-density electrons and holes near the crystal surface by band-to-band excitation, and subsequent time-resolved emission measurements were performed. Researchers reported many important phenomena, such as the observation of a change in the distribution function from the classical Maxwellian to the quantum degenerate Bose-Einstein distribution; a "quantum saturation" (Snoke et al., 1987) phenomenon in which 1*s* orthoexcitons stay just before the BEC phase boundary; and a peculiar thermal distribution suggestive of the BEC of 1*s* paraexcitons (Fig. 1, Snoke et al., 1990a, 1990b).

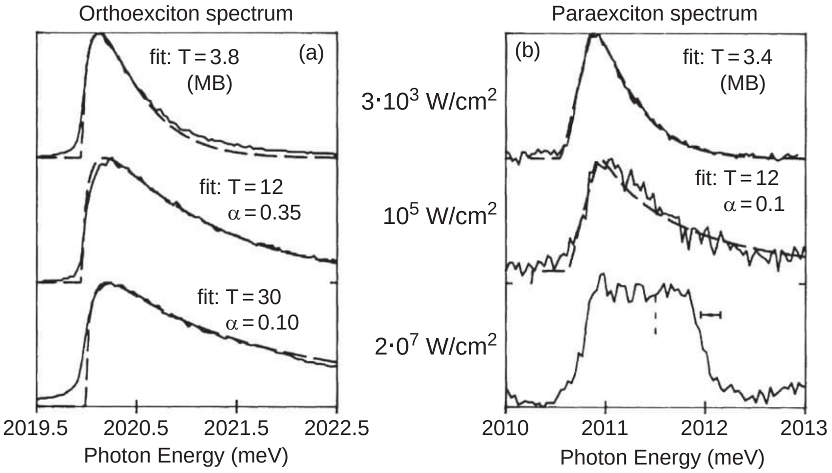

Fig. 1 Typical LO-phonon-assisted luminescence spectra of 1*s* orthoexcitons (left) and 1*s* paraexcitons (right) that suggest the generation of quantum degenerate gas of 1*s* excitons. The time-resolved luminescence spectra were recorded under a 10-ns, near-surface pulsed excitation at 2 K. Both exciton species can be fitted well with the Bose-Einstein distribution function, which allowed authors to evaluate the density and the temperature of the gasses. When 1*s* paraexcitons satisfied the BEC criterion, a "bump" structure appeared. From Snoke DW, Wolfe JP, Mysyrowicz A (1990a) Evidence for Bose-Einstein condensation of a two-component exciton gas. *Physical Review Letters* **64**: 2543–2546.

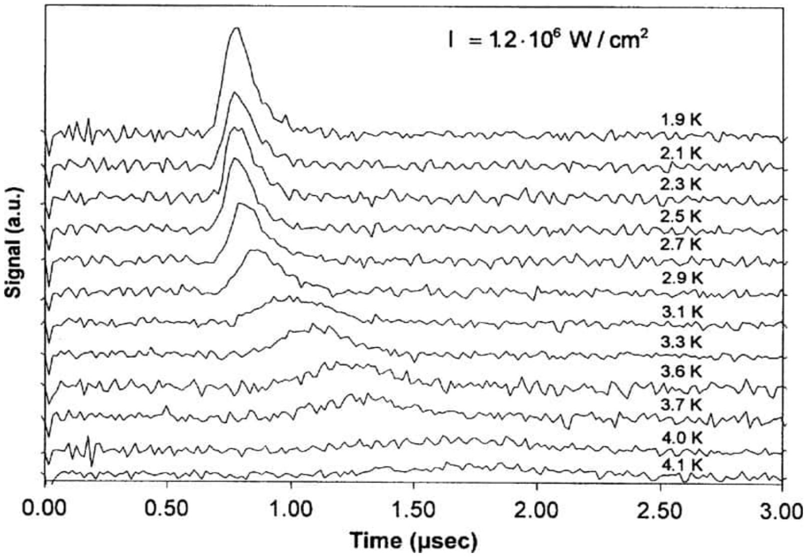

Fig. 2 Time-resolved photovoltaic signal under a 10-ns laser pulse irradiation at 532 nm. Initially, high-density excitons were generated near the surface, which was 3.56 mm away from the electrodes. Since the photovoltaic signal originates from excitons that dissociate because of a built-in voltage near the electrodes, the time-resolved signal reflects the propagation of the excitons across the 3.56-mm thickness of the Cu_2O crystal. A sudden change from diffusive to ballistic propagation appeared when the lattice temperature decreased. Similar behavior was confirmed when the excitation intensity was increased at a constant lattice temperature. The ballistic propagation velocity was nearly equal to the longitudinal sound velocity of the crystal. From Fortin E, Fafard S, Mysyrowicz A (1993) Exciton transport in Cu_2O: Evidence for excitonic superfluidity? *Physical Review Letters* **70**: 3951–3954.

In addition, time-resolved observations of exciton-mediated currents under similar experimental conditions revealed ballistic propagation signals that suggested exciton superfluidity (Fig. 2, Fortin et al., 1993). Although a conclusion was seemingly reached regarding the observation of BEC of excitons, questions still remained. For example, the emission of paraexcitons is extremely weak, which raised concerns about the reliability of the lineshape analyzes. In addition, the ground-state component with zero kinetic energy was absent from the luminescence spectrum. In particular, the lack of quantitativeness of the exciton density was fatal to the evidence for BECs.

The ballistic photovoltaic signals discussed above are remarkable. Nevertheless, quantitative information on exciton density and temperature is lacking. Therefore, it is still unknown whether this phenomenon is correlated with exciton BECs. Another explanation for this propagation is the so-called phonon wind phenomenon (Kopelevich et al., 1996), which is unrelated to quantum condensation. Thus, theuantitative evaluation of 1*s* excitons, particularly the density, became an important aspect of elucidating the mechanism underlying many of the interesting phenomena mentioned previously.

Collision-induced loss

For 1*s* orthoexcitons, a relatively bright emission signal can be obtained. Through careful experiments, researchers determined the number of 1*s* orthoexcitons created in a crystal from the light intensity by evaluating the quantum efficiency of the detection system (O'Hara et al., 1999). They found that the gas is orders of magnitude more dilute than the exciton density that can be evaluated from shape analyses of the emission spectrum. The decrease in density is due to a density-dependent nonradiative recombination process, wherein one of the excitons disappears in the two-body collisions between excitons. The two-body process accelerates the other exciton that survives. The effective lifetime of the exciton τ_{eff} is then

$$1/\tau_{\text{eff}} = An$$

(A is the two-body scattering coefficient and n is the exciton density). They found that the collision coefficient is extremely large, i.e., approximately $A = 10^{-16}\ \text{cm}^3/\text{ns}$. They also showed that the spectral shape of the quantum degenerate Bose-Einstein distribution is actually the result of a superposition of classical distributions such that the temperature and density are high near the surface and low inside the crystal (O'Hara and Wolfe, 2000). The experimentally observed temperature corresponding to the Bose-Einstein distribution was considerably higher than the lattice temperature, supporting the scenario. Thus, researchers revealed that the 1*s* orthoexcitons remain classical by quantitatively evaluating the exciton density (Fig. 3).

The physical mechanism of the aforementioned two-body scattering-induced loss is currently unknown. A similar process called the exciton Auger process is well-established, although the theoretical scattering coefficient is orders of magnitude smaller than the actual one (Kavoulakis and Baym, 1996; Kavoulakis and Mysyrowicz, 2000).

With the possibility of quantum degeneracy of 1*s* orthoexcitons denied, researchers focused on quantifying the density of 1*s* paraexcitons and the magnitude of the two-body loss rate. However, the intensity of the LO-phonon-assisted luminescence of the

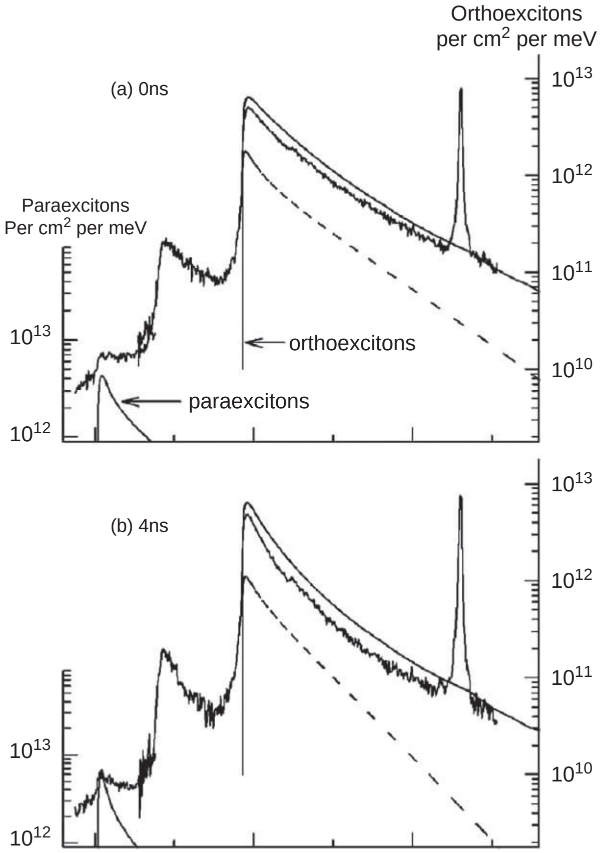

Fig. 3 Simulated LO-phonon-assisted luminescence spectrum of 1*s* orthoexcitons assuming spatially inhomogeneous Maxwell-Boltzmann distributions (solid curves). Dashed curves are Bose-Einstein distribution functions, intentionally displaced vertically. Both curves well explain the experimental luminescence spectra, but the simulated ones provide a better fit, particularly on the high-energy side of the spectra. From O'Hara KE and Wolfe JP (2000) Relaxation kinetics of excitons in cuprous oxide. *Physical Review B* **62**: 12909–12922.

1*s* paraexciton state is about three orders of magnitude weaker than that of orthoexcitons. Therefore, the quantitative evaluation of 1*s* paraexcitons through luminescence experiments is nearly impossible.

Excitonic Lyman spectroscopy

Researchers began to develop an alternative spectroscopic method to detect the density and temperature of 1*s* paraexcitons quantitatively. In principle, excitons in the 1*s* state can be excited to the p-series excited states with higher principal quantum numbers, i.e., 2*p*, 3*p*, 4*p*, etc., because of the hydrogen-like energy structure (Nikitine, 1984). These transitions, called excitonic Lyman transitions, are strongly electric dipole allowed. The transitions change the relative motion of an electron and a hole; therefore, they are spin-independent and function for both ortho- and paraexcitons. Therefore, relatively dilute excitons can be detected with high sensitivity. Furthermore, because of central-cell corrections, the effective mass of the 1*s* exciton is heavier than that of other exciton states. Therefore, the energy distribution of the translational motion of the 1*s* excitons is reflected in the spectrum of excitonic Lyman transitions. Several research groups succeeded in detecting the 1*s*-2*p* transitions located in the mid-infrared wavelength range in the early 2000s (Kuwata-Gonokami et al., 2004; Jörger et al., 2005; Fishman et al., 2006).

Under the quantitative evaluation of the paraexciton density using the 1*s*-2*p* transition with a resonance at 128 meV (wavelength of 9.6 μm), experiments were performed to evaluate the two-body scattering-induced loss coefficient and its temperature dependence. It was found that the two-body loss coefficient for the 1*s* paraexciton is as large as that for the 1*s* orthoexcitons reported in O'Hara et al. (1999), which is about $A = 10^{-16}$ cm^3/ns, and that the coefficient is independent of temperature (Yoshioka et al., 2010). The result means that even if the BEC critical density of 10^{17} cm^{-3} at 2 K is realized, the effective lifetime is only 0.1 ns instead of being in the microsecond range. Considering that the cooling time of 1*s* paraexcitons because of the exciton-phonon interaction with the lattice is several nanoseconds, the exciton temperature remains much higher than 2 K. Furthermore, the high excitation powers required to compensate for the collisional annihilation and maintain a high density, as well as the resultant heat generation in the crystal, render the realization of BECs at 2 K impossible (Fig. 4).

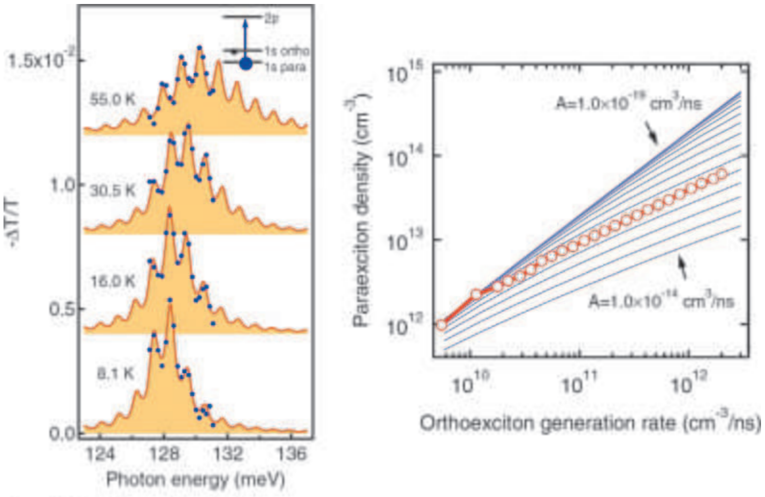

From (Yoshioka et al., 2010)

Fig. 4 (left) Typical 1*s*-2p induced absorption spectrum of paraexcitons in the quasi-steady-state, measured under a quasi-continuous-wave excitation. 1*s* orthoexcitons were generated via the phonon-assisted absorption process, and subsequently, the orthoexcitons were spontaneously converted into 1*s* paraexcitons. The 1*s*-2*p* transition resonance is located in the mid-infrared wavelength region. A tunable carbon dioxide laser was used because the oscillation wavelengths accidentally coincided with the resonance. The spectrum reflects the thermal distribution of 1*s* paraexcitons, and one can measure the absolute paraexciton density from the spectral area. The oscillatory structure originates from the Fabry-Perot interference effect of the 220-μm thick natural single crystal used in the experiment. (right) Measured paraexciton density as a function of the generation rate of orthoexcitons. The paraexciton density shows a sublinear dependence when the density is well below the BEC transition density at 2 K, implying that the nonlinear loss process is efficient. The solid curves are simulated results in which the two-body collision loss coefficient *A* is considered an adjustable parameter. From Yoshioka K, Ideguchi T, Mysyrowicz A, Kuwata-Gonokami M (2010) Quantum inelastic collisions between paraexcitons in Cu_2O. *Physical Review B* **82**: 041201(R).

Experiments at sub-Kelvin temperatures

To achieve BECs, the frequency of scattering-induced losses must be reduced. Because the mechanism of the density-dependent exciton loss and methods of controlling it are unknown, the only way to satisfy the BEC criterion is to lower the exciton temperature and set the BEC critical density to a lower value. Several research groups initiated experiments to cool semiconductor crystals to sub-Kelvin temperatures to satisfy the BEC criteria. Because it is expected to take more than several nanoseconds for an exciton gas to attain thermal equilibrium with the lattice below 2 K, the 1*s* paraexciton state is the only option.

It is well-established that 1*s* paraexcitons diffuse ballistically on the millimeter scale within their lifetime at low temperatures (Trauernicht et al., 1984; Trauernicht and Wolfe, 1986). The rapid diffusion can be avoided by forming a three-dimensional trap by applying inhomogeneous stress via a Hertzian contact (Trauernicht et al., 1983; Trauernicht et al., 1986; Snoke and Negoita, 2000; Naka and Nagasawa, 2002, 2004, 2005; Sandfort et al., 2011). The trap acts as a harmonic potential for excitons at low temperatures, and the number of excitons N_c required for the BEC transition in the trap is

$$N_c = 1.2\left(\frac{k_B T}{\hbar\overline{\omega}}\right)^3,$$

where $\overline{\omega}$ is the geometric mean of the trap frequencies. The critical number is proportional to the cube of the temperature. Therefore, it is feasible to satisfy the BEC condition by a quasi-steady-state excitation using a continuous-wave laser and accumulating long-lived paraexcitons, even with the limited cooling capacity of a refrigerator.

In 2011, a BEC transition of trapped 1*s* paraexcitons at an exciton temperature of 800 mK was reported by using a ^{3}He refrigerator to cool a Cu_2O crystal to 354 mK (Yoshioka et al., 2011). The BEC critical density at 800 mK is $n_c = 1.9 \times 10^{16}$ cm^{-3}, and the corresponding number of exciton is $N_c = 7.6 \times 10^8$. The experiment observed the spatially resolved luminescence spectrum of thermal paraexciton components because the direct recombination process is weakly allowed under a finite strain field. When the BEC criterion was met, a threshold-like rise of exciton components with high kinetic energies was found. This phenomenon is a "relaxation explosion" associated with the BEC transition. In this case, the condensate is unstable. In a harmonic potential, macroscopic occupation of the ground state wavefunction results in high-density excitons, followed by the aforementioned frequent two-body collision-induced loss process. The relaxation process was originally introduced to the BEC of atomic hydrogen in a magnetic trap, which decays rapidly because of enhanced inelastic two-body collisions induced by the density increase associated with the condensate formation (Fig. 5).

To achieve stable condensates, the BEC transition density must be further reduced; i.e., the exciton temperature must be lowered. Two research groups in Japan and Germany performed experiments using dilution refrigerators (Stolz et al., 2012; Yoshioka et al., 2013; Morita et al., 2019). 1*s* paraexcitons are cooled via the emission of LA phonons. However, the exciton temperature cannot be

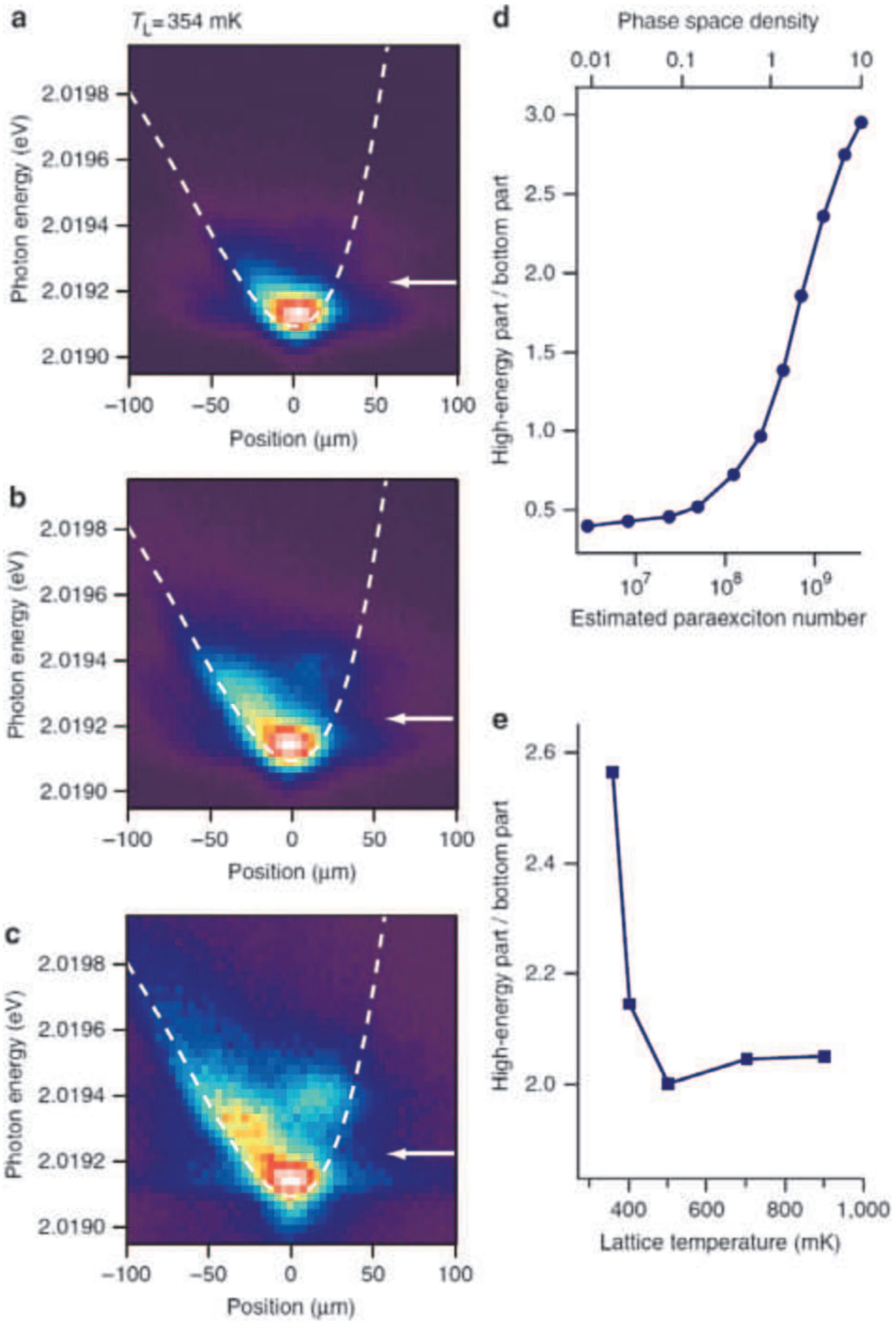

Fig. 5 Relaxation explosion of 1*s* paraexcitons accumulated in a strain-induced trap potential. When the number of paraexcitons is below the critical number, the spatially resolved luminescence spectrum suggests that the gas is in a quasi-equilibrium state with an exciton temperature of 800 mK. A hot exciton component appeared in a threshold-like manner when the number of excitons exceeded the critical number for BEC. The sudden increase of the hot component also occurred by decreasing the lattice temperature while maintaining the trapped number of paraexcitons constant. From Yoshioka K, Chae E, Kuwata-Gonokami M (2011) Transition to a Bose–Einstein condensate and relaxation explosion of excitons at sub-Kelvin temperatures. *Nature Communications* **2**: 328.

reduced below 1 K, irrespective of the crystal temperature. This limitation originates from the dispersion relations of LA phonons and paraexcitons and the conservation law of energy and momentum. However, the crystal symmetry is reduced under a finite strain field, and the interaction between 1*s* paraexcitons and TA phonons is activated. The sound velocity of the TA phonon is slower than that of the LA phonon, and the activation of the additional cooling channel results in an unprecedentedly low exciton temperature of 100 mK (Yoshioka et al., 2013) (Fig. 6).

Following being cooled to the 100 mK temperature region, the 1*s* paraexciton exhibits a very low interaction rate with phonons. Therefore, the motion of the para exciton approaches that of a ballistic one with little scattering. In fact, high diffusion coefficients

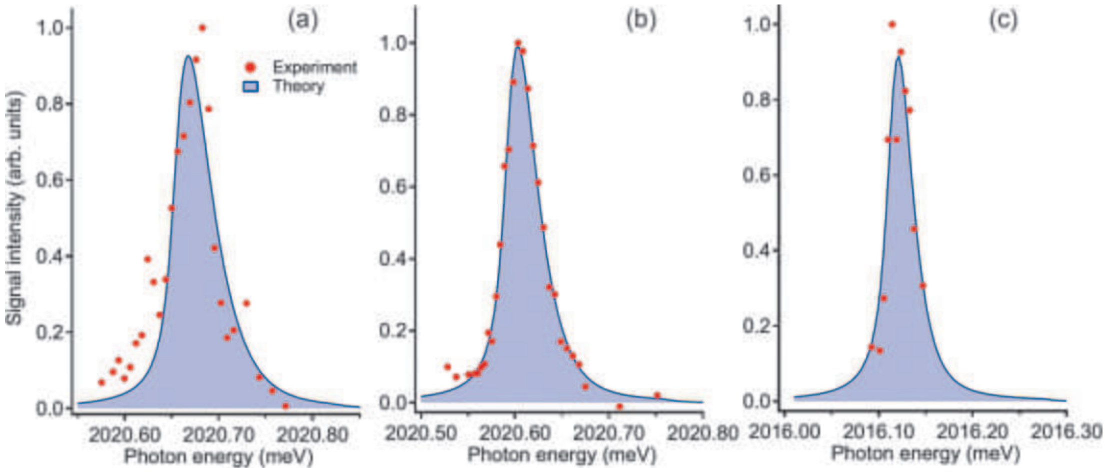

Fig. 6 Applied stress dependence of the luminescence spectrum of 1*s* paraexcitons in a strain-induced trap potential. The lattice temperature was 40 mK, and the excitation power was maintained as low as 4 nW to preclude heating effects and find the lowest possible exciton temperature. When the stress was increased from (a) 1.0 kbar to (c) 2.7 kbar, the paraexciton temperature dropped from 207 ± 33 mK to 97 ± 33 mK. This is the lowest exciton temperature achieved to date in bulk semiconductors. The stress dependence demonstrates that the cooling channel via transverse acoustic phonons is activated in strain-induced trap potentials. From Yoshioka K, Morita Y, Fukuoka K, Kuwata-Gonokami M (2013) Generation of ultracold paraexcitons in cuprous oxide: A path toward a stable Bose-Einstein condensate. *Physical Review B* **88**: 041201(R).

and mobilities, which have never been observed in bulk semiconductors previously, are observed in time- and space-resolved luminescence measurements (Morita et al., 2019). This means that a clean system is prepared in which the spatial distribution of the ensemble is defined by the designed strain-induced trapping potential and exciton-exciton interactions, almost unaffected by scattering from phonons, lattice defects, and impurity sites in the crystal. In high-density conditions, however, the two-body collision-induced loss process can accelerate paraexcitons, and therefore, continuous cooling by the cold phonon bath should play an essential role in the global behavior of the exciton ensemble.

In bulk semiconductors, both quantum degenerate exciton states at such a low temperature and condensates cannot be detected by conventional luminescence measurements. This is because the exciton momentum is extremely small, such that excitons cannot supply the photon momentum in the radiative recombination process. Instead, mid-infrared absorption imaging of excitons using the 1*s*-2p transition of paraexcitons (Yoshioka and Kuwata-Gonokami, 2015) has been applied to dilution refrigerator experiments, and a threshold-like appearance of condensates at the bottom of a trap was finally observed at a peak density on the order of 10^{15} cm^{-3} (Morita et al., 2022).

Morita et al. (2022) have shown that the spatial spread of the condensate in the ground state of the trap broadens as the number of excitons in the condensate increases. This behavior can be described based on the Gross-Pitaevskii equation, as in the case of weakly interacting dilute atomic gasses. The elastic scattering length between 1*s* paraexcitons was extracted based on this expanding behavior. The results were consistent with the theoretical scattering length evaluated by quantum Monte Carlo calculations (Shumway and Ceperley, 2001). In this manner, the conventional understanding of condensates can describe some phenomena, whereas other behaviors cannot be understood. The best example is the small condensate fraction. The maximum condensate fraction is only 1.6%, although the interparticle interaction is significantly weaker than in liquid helium. This feature cannot be explained in the framework of conventional theories and may correspond to the characteristics of quantum condensates in nonequilibrium open systems (Fig. 7).

Conclusion

The observation of spontaneous BEC of excitons in bulk semiconductors has proved that purely matter-like quasiparticles, decoupled from the radiation field, form a macroscopic quantum state. Consequently, the research field of many-body and low-temperature exciton systems has entered a new stage. This type of BECs constitutes a new state beyond the framework of conventional theories and is expected to provide an opportunity to profoundly deepen our understanding of the physics of the spontaneous formation of quantum coherence under various dissipation channels in the environment of a solid. Furthermore, the quasi-equilibrium state of the exciton system is formed by contact with a thermal bath, that is a cold phonon system, rather than by elastic scattering between excitons; therefore, it is also important as one of the physical systems that exhibit the interaction-free phase transitions envisioned by Einstein. Elucidating the following phenomena will be the key to a detailed description of this physical system and will help promote further research in this field:

- Observation of the dynamics of condensate formation through the time-resolved absorption imaging of trapped paraexcitons.
- Evaluation of the second-order spatial coherence.

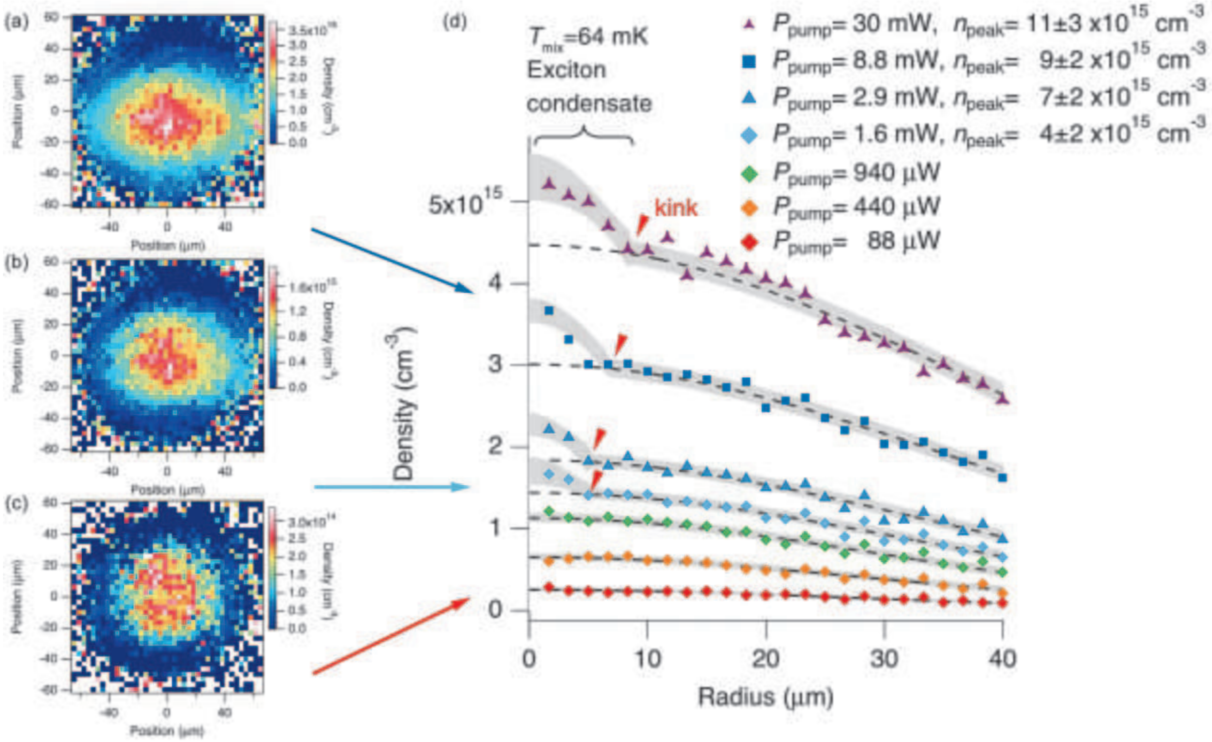

Fig. 7 Visualization of a Bose-Einstein condensate of 1*s* paraexcitons in a strain-induced trap potential using the mid-infrared absorption imaging technique. Macroscopic occupation at the trap bottom was found, and its density exceeded the BEC critical density at the measured exciton temperature of 170 mK. The spatial spread of the condensate increases through the exciton-exciton elastic interactions, which can be described by the Gross-Pitaevskii equation similarly to weakly-interacting cold atomic gasses. However, the small maximum condensate fraction of 1.6% is a newly discovered and unexplained phenomenon. From Morita Y, Yoshioka K, Kuwata-Gonokami M (2022) Observation of Bose-Einstein condensates of excitons in a bulk semiconductor. *Nature Communications* **13**: 5388.

- Elucidation of the behavior of condensate fractions at low exciton temperatures.
- Measurements of the conversion rate from 1*s* orthoexcitons produced by laser excitation to 1*s* paraexcitons in the 100 mK temperature region.
- Elucidation of the physical mechanism of two-body collision-induced exciton loss and the development of control methods.
- Development of a method for growing single crystals of Cu_2O with high purity. The density of lattice defects is generally considered to limit the paraexciton lifetime because the radiative lifetime is considerably longer than the actual lifetime of around one microsecond. In addition, if impurities or defect sites are involved in the exciton-exciton collision-induced losses, the high-purity crystals may dramatically simplify exciton BEC experiments.
- Evaluation of the relevance of condensation phenomena observed in two-dimensional physical systems, particularly long-lived exciton systems in coupled quantum wells that are weakly coupled with the radiation field and cavity exciton-polaritons that are strongly coupled to the radiation field.

References

Blatt JM, Böer KW, and Brandt W (1962) Bose-einstein condensation of excitons. *Physics Review* 126: 1691–1692.
Brandt J, Fröhlich D, Sandfort C, Bayer M, Stolz H, and Naka N (2007) Ultranarrow optical absorption and two-phonon excitation spectroscopy of Cu_2O paraexcitons in a high magnetic field. *Physical Review Letters* 99: 217403.
Elliott RJ (1961) Symmetry of excitons in Cu_2O. *Physics Review* 124: 340–345.
Fishman DA, Revcolevschi A, and van Loosdrecht PHM (2006) Exciton dynamics in cuprous oxide. *Physica Status Solidi C* 3: 2469–2472.
Fortin E, Fafard S, and Mysyrowicz A (1993) Exciton transport in Cu_2O: Evidence for excitonic superfluidity? *Physical Review Letters* 70: 3951–3954.
Gross EF and Karryev IA (1952a) Light absorption by cuprous oxide crystal in infrared and visible spectrum. *Doklady Akademii Nauk SSSR* 84: 261–266.
Gross EF and Karryev IA (1952b) Exciton optical spectrum. *Doklady Akademii Nauk SSSR* 84: 471–474.
Hayashi M and Katsuki K (1950) Absorption spectrum of cuprous oxide. *Journal of the Physical Society of Japan* 5: 380–381.
Hayashi M and Katsuki K (1952) Hydrogen-like absorption spectrum of cuprous oxide. *Journal of the Physical Society of Japan* 7: 599–603.
Jörger M, Fleck T, Klingshirn C, and von Baltz R (2005) Midinfrared properties of cuprous oxide: High-order lattice vibrations and intraexcitonic transitions of the 1*s* paraexciton. *Physical Review B* 71: 235210.
Kavoulakis GM and Baym G (1996) Auger decay of degenerate and Bose-condensed excitons in Cu_2O. *Physical Review B* 54: 16625–16636.
Kavoulakis GM and Mysyrowicz A (2000) Auger decay, spin exchange, and their connection to Bose-Einstein condensation of excitons in Cu_2O. *Physical Review B* 61: 16619–16622.
Kopelevich GA, Gippius NA, and Tikhodeev SG (1996) Exciton transport in Cu_2O: Nonequilibrium phonons instead of bose condensation. *Solid State Communications* 99: 93–97.

Kuwata-Gonokami M, Kubouchi M, Shimano R, and Mysyrowicz A (2004) Time-resolved Excitonic Lyman Spectroscopy of Cu_2O. *Journal of the Physical Society of Japan* 73: 1065–1069.

Morita Y, Suzuki H, Yoshioka K, and Kuwata-Gonokami M (2019) Observation of ultrahigh mobility excitons in a strain field by space- and time-resolved spectroscopy at subkelvin temperatures. *Physical Review B* 100: 035206.

Morita Y, Yoshioka K, and Kuwata-Gonokami M (2022) Observation of Bose-Einstein condensates of excitons in a bulk semiconductor. *Nature Communications* 13: 5388.

Mysyrowicz A, Hulin D, and Antonetti A (1979) Long exciton lifetime in Cu_2O. *Physical Review Letters* 43: 1123–1126.

Naka N and Nagasawa N (2002) Two-photon diagnostics of stress-induced exciton traps and loading of 1*s*-yellow excitons in Cu_2O. *Physical Review B* 65: 075209.

Naka N and Nagasawa N (2004) Two-photon tomography of strain-induced potential wells of excitons in Cu_2O. *Physical Review B* 70: 155205.

Naka N and Nagasawa N (2005) Bosonic stimulation of cold excitons in a harmonic potential trap in Cu_2O. *Journal of Luminescence* 112: 11–16.

Nikitine S (1984) On the possibility of observation and the intensity of (nn') and (nn) transitions between exciton states in Cu_2O. *Journal of Physics and Chemistry of Solids* 45: 949–954.

O'Hara KE and Wolfe JP (2000) Relaxation kinetics of excitons in cuprous oxide. *Physical Review B* 62: 12909–12922.

O'Hara KE, Suilleabhain LO, and Wolfe JP (1999) Strong nonradiative recombination of excitons in Cu_2O and its impact on Bose-Einstein statistics. *Physical Review B* 60: 10565–10568.

Sandfort C, Brandt J, Finke C, Fröhlich D, Bayer M, Stolz H, and Naka N (2011) Paraexcitons of Cu_2O confined by a strain trap and high magnetic fields. *Physical Review B* 84: 165215.

Shumway J and Ceperley DM (2001) Quantum Monte Carlo treatment of elastic exciton-exciton scattering. *Physical Review B* 63: 165209.

Snoke DW and Negoita V (2000) Pushing the Auger limit: Kinetics of excitons in traps in Cu_2O. *Physical Review B* 61: 2904–2910.

Snoke D, Wolfe JP, and Mysyrowicz A (1987) Quantum saturation of a Bose gas: Excitons in Cu_2O. *Physical Review Letters* 59: 827–830.

Snoke DW, Wolfe JP, and Mysyrowicz A (1990a) Evidence for Bose-Einstein condensation of a two-component exciton gas. *Physical Review Letters* 64: 2543–2546.

Snoke DW, Wolfe JP, and Mysyrowicz A (1990b) Evidence for Bose-Einstein condensation of excitons in Cu_2O. *Physical Review B* 41: 11171–11184.

Stolz H, Schwartz R, Kieseling F, Som S, Kaupsch M, Sobkowiak S, Semkat D, Naka N, Koch T, and Fehske H (2012) Condensation of excitons in Cu_2O at ultracold temperatures: Experiment and theory. *New Journal of Physics* 14: 105007.

Trauernicht DP and Wolfe JP (1986) Drift and diffusion of paraexcitons in Cu_2O: Deformation-potential scattering in the low-temperature regime. *Physical Review B* 33: 8506–8521.

Trauernicht DP, Mysyrowicz A, and Wolfe JP (1983) Strain confinement and thermodynamics of free excitons in a direct-gap semiconductor. *Physical Review B* 28: 3590–3592.

Trauernicht DP, Wolfe JP, and Mysyrowicz A (1984) Highly mobile paraexcitons in cuprous oxide. *Physical Review Letters* 52: 855–858.

Trauernicht DP, Wolfe JP, and Mysyrowicz A (1986) Thermodynamics of strain-confined paraexcitons in Cu_2O. *Physical Review B* 34: 2561–2575.

Yoshioka K and Kuwata-Gonokami M (2015) Absorption imaging of trapped 1*s* paraexcitons in bulk Cu_2O. *Physical Review B* 91: 195207.

Yoshioka K, Ideguchi T, Mysyrowicz A, and Kuwata-Gonokami M (2010) Quantum inelastic collisions between paraexcitons in Cu_2O. *Physical Review B* 82: 041201(R).

Yoshioka K, Chae E, and Kuwata-Gonokami M (2011) Transition to a Bose–Einstein condensate and relaxation explosion of excitons at sub-Kelvin temperatures. *Nature Communications* 2: 328.

Yoshioka K, Morita Y, Fukuoka K, and Kuwata-Gonokami M (2013) Generation of ultracold paraexcitons in cuprous oxide: A path toward a stable Bose-Einstein condensate. *Physical Review B* 88: 041201(R).

Nonlocal optical response of nanostructures☆

Hajime Ishihara[a,b] **and Kikuo Cho**[c], [a]Department of Materials Engineering Science, Osaka University, Osaka, Japan; [b]Center for Quantum Information and Quantum Biology, Osaka University, Osaka, Japan; [c]Emeritus of Osaka University, Kobe, Japan

© 2024 Elsevier Ltd. All rights reserved.

This is an update of K. Cho, Nanostructures, Optical Properties of, Editor(s): Franco Bassani, Gerald L. Liedl, Peter Wyder, Encyclopedia of Condensed Matter Physics, Elsevier, 2005, Pages 58–64, ISBN 9780123694010, https://doi.org/10.1016/B0-12-369401-9/00602-1.

Introduction **654**
Scheme of microscopic response **655**
Cavity effect **657**
Nonlocal scheme in terms of cavity green function 657
EM Green function of cavity polariton 658
Examples of observed phenomena **659**
Nonlocality-enhanced electric quadrupole transition 659
Radiative correction of nondipole-type excited states 662
Ultrafast radiative decay overcoming thermal dephasing at room temperature 663
Conclusion **663**
References **664**
Further reading **664**

Abstract

The characteristic aspect of the optical properties of nanostructures is described with an emphasis on the size and shape dependence of optical responses, in contrast to that of macroscopic systems. The microscopic treatment for the theoretical description of such systems is outlined, which requires nonlocal relationship between light field and induced polarization, allowing one to treat the regime beyond long wavelength approximation (LWA). The radiative shift and width, which are system-specific, are shown to play an important role in nanostructures. The effect of microcavity is also discussed in terms of renormalized radiation Green function, which allows for a systematic description within the microscopic nonlocal scheme. Examples of the experimental observation reflecting characteristics of optical responses of nanostructures, in particular, for the beyond-LWA regime are shown.

Key points

- One of the remarkable aspects of nanostructures is the explicit dependence of optical response on the size, shape, and internal structure due to quantum mechanically confined electronic systems.
- The nonlocal response is the key concept to providing a good overview and technical ease based on the first-principles formulation of light-matter interaction in nanostructures.
- The microscopic nonlocal response theory provides self-consistent solutions containing the radiative corrections (shift and width) with dependence on the size, shape, and internal structure.
- The mode structure modification of the electromagnetic field of the cavity effect can be included in the microscopic nonlocal theory through the electromagnetic Green function of the background and/or environmental medium.
- Typical phenomena characterized by the nonlocal response, where the spatial variation in the electric field is remarkable, have been observed as a large optical nonlinearity and an ultra-fast response of non-dipole type excited states in various types of experiments.

Nomenclature

$X_{\mu\nu}$	Another expansion coefficient of induced polarization
ε_b	Background dielectric constant
ξ, η	Cartesian coordinates
$J(r, \omega)$	Current density at position r with frequency ω

☆*Change History*: April 2015. H Ishihara added the section "Examples of Observed Phenomena", and "References". January 2022. H. Ishihara added some descriptions and references in the section "Examples of Observed Phenomena".

$\boldsymbol{\varepsilon}_0$:	Dielectric constant of vacuum
$\widehat{\boldsymbol{P}}(\boldsymbol{r})$	Electric dipole density operator
$E(r, \boldsymbol{\omega})$	Electric field at position $\boldsymbol{r}$ with frequency ω
$E_{\mathbf{b}}$	Electric field induced by the scattering of an incident field from background dielectric alone
$\boldsymbol{E}_{\nu}{}'$	Energy eigenvalue including the screening effect of the background dielectrics
$\boldsymbol{E}_{\boldsymbol{\nu}}$	Energy of the ν-th eigenstate of matter, $\nu = 0$ for the ground state
$\boldsymbol{F}_{\boldsymbol{\mu\nu}}$	Expansion coefficient of induced polarization
$\mathrm{G}_{\mathbf{b}}$	Green function describing the propagation of EM field in the presence of background dielectric
$\mathrm{G}_{\mathbf{cp}}$	Green function describing the propagation of EM field of cavity polariton
$\boldsymbol{\Theta}$	Heaviside function to describe the size and shape of background dielectric
$\boldsymbol{\chi}^{(1)}$	Linear polarizability
$P_{\mathbf{NL}}$	Nonlinear part of induced polarization
$\boldsymbol{\chi}_{\mathbf{b}}$	Polarizability of background dielectric
$P(r, \boldsymbol{\omega})$	Polarization at position $\boldsymbol{r}$ with frequency ω
$\mathscr{A}^{(\mathrm{b})}$	Radiative interaction energy between the components of induced polarization via the EM field of background dielectric
$\mathscr{A}_{\mu 0,0\nu}(\omega)$	Radiative interaction energy between the matter citations $(0 \rightarrow \mu)$ and $(0 \rightarrow \nu)$ via the EM field of frequency ω
$P_{\mathbf{res}}$	Resonant part of induced polarization
$E^{(\mathbf{0})}$	Solution of homogeneous differential equation, usually an incident field inducing polarization
$A(r, \boldsymbol{\omega})$	Vector potential at position $\boldsymbol{r}$ with frequency ω
DBR	Distributed Bragg reflector
EM	Electromagnetic
G	Green function describing the propagation of EM field
LWA	Long wavelength approximation
$\boldsymbol{q}$	Wave number of light in vacuum $(=\omega/c)$
QED	Quantum electrodynamics
Q-value	Quality factor of a resonance, i.e., resonant frequency divided by resonance width
QW	Quantum well
RWA	Rotating wave approximation
S	Coefficient matrix of the linear equation to determine X

Introduction

The reason for the optical properties of nanostructures to attract special attention is the explicit dependence of optical response on the size, shape and internal structure of a matter, which leads to an additional possibility of controlling materials for various applicational purposes. In view of the importance of the coherence of matter excitations in the description of the optical processes in nanostructures, which has been neglected in the traditional theory for bulk systems, it is worth having a separate item for this subject.

Optical properties of matter is the consequence of the interaction between matter and light (oscillating EM field), which depends sensitively on the space-time structure of the EM field and the induced polarization of the matter. The factors to determine this dependence are the frequency or pulse structure, polarization, and propagation direction of light, and the amplitudes of the induced polarization of matter with various resonance frequencies corresponding to the quantum mechanical level structure of the matter.

The light-matter interaction is fully described by the equations of motion for the dynamical variables of light and matter. As such variables, a usual choice is electric field $\boldsymbol{E}(\boldsymbol{r}, t)$ and polarization $\boldsymbol{P}(\boldsymbol{r}, t)$, but there is another choice, i.e., vector potential of light $\boldsymbol{A}(\boldsymbol{r}, t)$ and current density of matter $\boldsymbol{J}(\boldsymbol{r}, t)$. The latter is slightly more general, because current density may include magnetic one (proportional to the rotation of magnetization). If we neglect this contribution, $\boldsymbol{J}(\boldsymbol{r}, t)$ and $\boldsymbol{P}(\boldsymbol{r}, t)$ are simply related as $\boldsymbol{J} = \partial \boldsymbol{P}/\partial t$, which applies to most cases of optical response of matter.

The scheme of equations of motion for $\boldsymbol{A}$ and $\boldsymbol{J}$ (or $\boldsymbol{E}$ and $\boldsymbol{P}$) is common to quantum electrodynamics (QED) with quantized EM field and the semiclassical treatments in terms of classical EM field. The difference is whether the vector potential is treated as operator or not. This difference does not always lead to a difference in calculated physical quantities. In QED, photons of each mode are described as a statistical ensemble, while in semiclassical picture EM field of each mode is represented by a complex amplitude corresponding to an average value of photon ensemble. The QED description is absolutely necessary when the physical quantity is related with some details of photon ensemble, or when the optical processes involve the contribution of non-commutative relation of photon creation and annihilation operators. Typical examples will be the squeezed light or various multi-time correlation functions. However, there are many other quantities which can be correctly calculated semi classically i.e., those depending just on the average photon number and phase (of each mode) arising from the optical processes without involving non-commutative terms of photon operators. Examples are the light intensities arising from the linear and nonlinear processes without involving same photon modes in the elementary steps of light-matter interaction.

Another important aspect in optical processes is the microscopic spatial structure in $\boldsymbol{E}(\boldsymbol{r}, t)$ and $\boldsymbol{P}(\boldsymbol{r}, t)$. This has been neglected in macroscopic response theories, and also in QED treating atoms and molecules. In such a treatment, the $\boldsymbol{r}$-dependence of EM field is assumed to be always much weaker than that of induced polarization, so that the latter is represented by its zero-th moment, i.e., the electric dipole moment of the transition,

$$\int \mathrm{d}\boldsymbol{r}\left\langle \mu|\widehat{\boldsymbol{P}}(\boldsymbol{r})|\nu\right\rangle \tag{1}$$

where μ, ν are the quantum numbers of matter eigenstates. In other words, all the optical transitions are approximated as point-like electric dipoles with various eigenfrequencies and amplitudes in the long wavelength approximation (LWA) for EM field.

Nanostructures have attracted attention because of the size quantized energy levels of matter. The microscopic spatial structure of induced polarization is exactly the counterpart of the energy quantization, so that it is quite consistent to consider these aspects simultaneously in the description of optical response in nanostructures. Every quantum state has its own resonant frequency and the characteristic spatial structure in its induced polarization, which depend sensitively on the size and shape of matter. Though this applies in principle also to atomic and macroscopic systems, it is only in nanostructures that we can easily observe the size- and shape-dependence of optical responses.

Optical properties of matter are usually described in terms of linear and nonlinear polarizabilities (electric susceptibility, or more simply, susceptibility). In macroscopic systems, they are considered to be intensive quantities, i.e., independent of the size and/or shape of matter, which can be derived by the so-called Lorentz oscillator model based on classical mechanics (forced oscillation of harmonic oscillator with damping) under LWA. However, a quantum mechanical calculation of polarizabilities without the use of LWA gives an expression in terms of the energy eigenvalues $\{E_\nu\}$ and the matrix elements of dipole density operator, a different result from Lorentz model. For example, the linear susceptibility at absolute zero Kelvin is given, in units of ε_0, as

$$\chi^{(1)}_{\xi\eta}\left(\boldsymbol{r},\boldsymbol{r}',\omega\right) = \sum_{\nu}\left\{\frac{<0\left|\widehat{P}_\xi(\boldsymbol{r})\right|\nu><\nu\left|\widehat{P}_\eta(\boldsymbol{r}')\right|0>}{E_\nu - E_0 - \hbar\omega - i0^+} + \frac{<0\left|\widehat{P}_\eta(\boldsymbol{r}')\right|\nu><\nu\left|\widehat{P}_\xi(\boldsymbol{r})\right|0>}{E_\nu - E_0 + \hbar\omega + i0^+}\right\} \tag{2}$$

where $\nu = 0$ stands for the ground state. The positive infinitesimal (0^+) represents the adiabatic switching of light-matter interaction. When the nonradiative damping of matter excitations needs to be considered, the $\{0^+\}$'s are replaced with the self-energies of the excitations caused by nonradiative scattering, and are often approximated by a phenomenological parameter.

This polarizability, as well as higher order ones, is not an intensive quantity, but a position dependent integral kernel with various resonances appearing as poles of frequency dependent functions. It depends on the size and shape of matter through the resonant frequencies $(E_\nu - E_0)/\hbar$ and the coupling matrix elements of transitions, which is most conspicuously seen in the range of nano-meters. One of the fundamental problems is the evolution of polarizabilities from size-dependent to size-independent regimes, which is due to the size dependence of (i) the contribution of single quantum states and (ii) the intervals of neighboring quantum states. In the case of nonlinear polarizabilities, the size dependence is deeply related with the so-called cancellation problem.

The dependence of the resonance frequencies, i.e., absorption and/or emission peaks, on the system size and shape is due to the boundary condition for the wave function of each excited state extending coherently over the whole structure. This is understood from an analogy of a particle of mass M confined in a one-dimensional well of size d. The boundary condition restricts the form of its wave function to $\sin(kx)$ and the energy eigenvalue $E = \hbar^2k^2/2M$, with the size-quantized wave number $k = \text{integer} \times \pi/d$.

This allows us to design the optical properties of matter for various aims. Together with the technical development of nano-size fabrication, it has encouraged the studies of applicational aspects of nanostructures. At the same time, this has opened a new phase of fundamental character of matter, in particular of nanostructured materials, where the coherence of matter states plays an essential role. Due to the coherence of the excited state of matter maintained over whole nanostructure, a full quantum mechanical treatment of polarizabilities is required. In other words, the microscopic character of EM field and induced polarization need to be thoroughly considered, which inevitably leads to the nonlocal polarizability. (See the item "Polarizability".)

The nonlocal nature of optical response in microscopic theory means that the cause (EM field) and the result (polarization) may occur at microscopically different spatial points, as far as the points are within the extension of the relevant wave functions. The nonlocality of response is a common feature to all excitations of wave-like character, such as sound, light, and the quantum mechanical excitations described by wave functions.

It may look a complication that polarizabilities become position dependent integral kernels, in comparison with their constant values in macroscopic approach. It is not simply the case, however, because the fact that they are in general separable kernels allows us to rewrite (Maxwell) integral equations into simultaneous polynomial equations, which is certainly easier to handle. In this sense, nonlocal response is a key method to provide a good overview and technical ease, based on the first-principles formulation of light-matter interaction.

Scheme of microscopic response

For a given initial condition of light and matter, the optical response is obtained in the following way. We write the polarization induced by EM field and the EM field produced by polarization, and solve them simultaneously. For nanostructures, it is necessary to do this in terms of the microscopic polarizabilities and without the use of LWA. In view of the importance of resonant processes in nanostructures, which reflect the size and shape dependence sensitively, it is essential to solve the equations self-consistently (simultaneously).

The two sets of equations to be solved, in the case of, e.g., linear response, are

$$P_\xi(\boldsymbol{r},\omega) = \varepsilon_0 \int \mathrm{d}\boldsymbol{r}' \chi^{(1)}_{\xi\eta}(\boldsymbol{r},\boldsymbol{r}';\omega) E_\eta(\boldsymbol{r}';\omega), \tag{3}$$

and

$$E_\xi(\boldsymbol{r},\omega) = E^{(0)}_\xi(\boldsymbol{r},\omega) + \sum_\eta \int \mathrm{d}\boldsymbol{r}'\, G_{\xi\eta}(\boldsymbol{r},\boldsymbol{r}';\omega) P_\eta(\boldsymbol{r}';\omega). \tag{4}$$

The latter equation is the solution of the Maxwell equations for a given source polarization $\boldsymbol{P}(\boldsymbol{r},\omega)$ in terms of the radiation Green function $\mathbf{G}(\boldsymbol{r},\boldsymbol{r}';\omega)$ of vacuum EM field

$$\mathbf{G}(\boldsymbol{r},\boldsymbol{r}';\omega) = \frac{4\pi}{V}\sum_{\boldsymbol{k}\sigma} \widehat{\boldsymbol{e}}_\sigma(\boldsymbol{k}) \frac{\mathrm{e}^{\mathrm{i}\boldsymbol{k}\cdot(\mathrm{r}-\mathrm{r}')}}{k^2 - (q+\mathrm{i}\delta)^2} \widehat{\boldsymbol{e}}_\sigma(\boldsymbol{k}) \tag{5}$$

where $q = \omega/c$ and $\widehat{\boldsymbol{e}}_\sigma(\boldsymbol{k})\,(\sigma = 1, 2)$ are two mutually orthogonal unit vectors perpendicular to $\boldsymbol{k}$, and V $(\rightarrow\infty)$ is the quantization volume. This Green function describes the propagation of light in vacuum. The initial condition of light (incident light, for example) is represented by $E^{(0)}_\xi(\boldsymbol{r},\omega)$, and that of matter (usually, the ground state) is included in the susceptibilities. For nonlinear response, we need to add the terms of nonlinear polarizations to the right hand side of Eq. (3). The equations are a closed set for a given frequency ω in the case of linear response, but they are not in nonlinear cases.

The set of integral Eqs. (3) and (4) can be put into a set of simultaneous linear equations for the variables $X_{\mu0}(\omega) = g_\mu(\omega)F_{\mu0}(\omega)$ and $X_{0\mu}(\omega) = h_\mu(\omega)F_{0\mu}(\omega)$, where

$$\begin{aligned} g_\mu(\omega) &= \frac{1}{E_\mu - E_0 - \omega - i0^+}, \\ h_\mu(\omega) &= \frac{1}{E_\mu - E_0 + \omega + i0^+}, \end{aligned} \tag{6}$$

$$F_{\mu\nu}(\omega) = \int \mathrm{d}\boldsymbol{r}\, \boldsymbol{E}(\boldsymbol{r},\omega)\cdot\left\langle \mu|\widehat{\boldsymbol{P}}(\boldsymbol{r})|\nu\right\rangle. \tag{7}$$

The solution of such equations gives the polarization $\boldsymbol{P}$ as

$$\boldsymbol{P}(\boldsymbol{r},\omega) = \sum_\nu \left[X_{0\nu}\left\langle \nu|\widehat{\boldsymbol{P}}(\boldsymbol{r})|0\right\rangle + X_{\nu0}\left\langle 0|\widehat{\boldsymbol{P}}(\boldsymbol{r})|\nu\right\rangle\right]. \tag{8}$$

The simplest version of the linear equations to determine $\{X\}$ is the one in rotating wave approximation (RWA) and is given as

$$F^{(0)}_{\mu0}(\omega) = \sum_\nu \left[(E_\nu - E_0 - \hbar\omega - \mathrm{i}0^+)\delta_{\mu\nu} + \mathscr{A}_{\mu0,0\nu}(\omega)\right]X_{\nu0}(\omega), \tag{9}$$

where

$$F^{(0)}_{\mu0}(\omega) = \int \mathrm{d}\boldsymbol{r}\, \boldsymbol{E}^{(0)}(\boldsymbol{r},\omega)\cdot\left\langle \mu|\widehat{\boldsymbol{P}}(\boldsymbol{r})|0\right\rangle \tag{10}$$

is a known factor for a given incident light, and the radiative correction $\mathscr{A}$ is defined as

$$\mathscr{A}_{\mu0,0\nu}(\omega) = -\int \mathrm{d}\boldsymbol{r} \int \mathrm{d}\boldsymbol{r}' < \mu|\widehat{\boldsymbol{P}}(\boldsymbol{r})|0 > \cdot\, \mathbf{G}(\boldsymbol{r},\boldsymbol{r}',\omega)\cdot < 0|\widehat{\boldsymbol{P}}(\boldsymbol{r}')|\nu >. \tag{11}$$

This is a complex quantity representing the interaction energy between two induced dipole densities $< 0|\widehat{\boldsymbol{P}}(\boldsymbol{r})|\mu >$ and $< 0|\widehat{\boldsymbol{P}}(\boldsymbol{r})|\nu >$ via the EM field of frequency ω. The real and imaginary parts of a diagonal term ($\mu = \nu$) represent the shift and width, respectively, of the matter transition energy $E_\mu - E_0$. The off-diagonal elements $A_{\mu0,0\nu}$ represent the radiative interaction among different matter excitations, giving additional contribution to the radiative shift and width.

The solution of Eq. (9) determines the polarization via Eq. (8) (without the terms $X_{0\nu}$ because of RWA), which further determines the induced field via Eq. (4). In this way, the optical response is determined uniquely from the set of simultaneous linear equations. In the case of nonlinear response, Eq. (3) contains nonlinear terms of factors $F_{\mu\nu}(\omega)$ for various μ, ν and ω, and in this case the equations to be solved are a set of simultaneous polynomial equations of order N, where N is the order of non-linearity in consideration.

In this way of solution, there is obviously no requirement of the boundary conditions for EM field at the surface/interface of matter. This is because the boundary conditions (of matter system) are already taken into account in the expression of polarizability, so that there is no need of boundary conditions for EM field any more. Additional boundary condition (ABC) is neither required when the matter excitations contain the effect of spatial dispersion. In fact, this way of solution is a method developed from an ABC-free formalism to solve confined exciton problems without using ABC.

It should be stressed that the condition det $|\,\mathbf{S}\,| = 0$, where $\mathbf{S} = (E_\nu - E_0 - \hbar\omega)\mathbf{1} + \mathscr{A}$, for the existence of non-trivial solution of Eq. (9) in the absence of external field (i.e., $F^{(0)} = 0$), is exactly the resonance condition for X in the presence of the external field. The modes satisfying this condition are the eigenmodes of the coupled light-matter system. They are self-sustaining modes in the sense that they consist of finite amplitudes of $\boldsymbol{E}$ and $\boldsymbol{P}$ in the absence of external excitation. Thus we understand that the resonance in optical spectra appears at the frequency of self-sustaining mode, i.e., matter excitation energy corrected by radiative shift and broadening. When there is translational symmetry in the matter system, the matrix $\mathbf{S}$ is diagonal with respect to the corresponding wave number, so that $\det|\mathbf{S}| = 0$ holds for each wave number separately, giving dispersion relation $\omega = \omega(k)$. This is a most general dispersion equation for interacting light-matter systems.

The factor $X_{\nu 0}$ contains an energy denominator which diverges at a matter excitation energy $E_\nu - E_0$, while the factor $X_{\nu 0}$ itself is enhanced, not at $E_\nu - E_0$, but at the energy corrected by radiative shift. One of the peculiar points of nanostructures is that the intervals of matter excitation energies and the radiative corrections, which are both sensitive to the size and shape of matter, are comparable in magnitude. Thus the proper treatment of radiative shift is essential in obtaining correct results of optical responses. An example of the size dependence of (complex) eigenmode energies with the radiative shift $\mathrm{Re}[\mathscr{A}]$ and width $\mathrm{Im}[\mathscr{A}]$ is shown in Fig. 1 for an exciton weakly confined in a dielectric sphere. The large resonant variation at a certain size for each mode is due to the radiative correction $\mathscr{A}$, which shows the central importance of this quantity in the calculation of response spectrum.

In a macroscopic response theory, a resonance is ascribed to that of susceptibility, i.e., the resonance with a matter excitation energy. However, in the microscopic treatment, the resonance is ascribed to the resonant enhancement of internal electric field. Thus the self-consistent treatment of response is seen to lead to a rather different picture of resonance.

Cavity effect

Nonlocal scheme in terms of cavity green function

Induced polarization consists of various frequency components corresponding to the transitions among quantized levels of matter. For a given frequency of incident light, some of them are resonant and others are non-resonant. Since the number of transitions is infinite in general, it is not feasible to consider all the transitions in the above set of Eq. (9). To neglect all the non-resonant components is permissible only for optically thin systems, such as gases of atoms and molecules. For solids (and liquids, too),

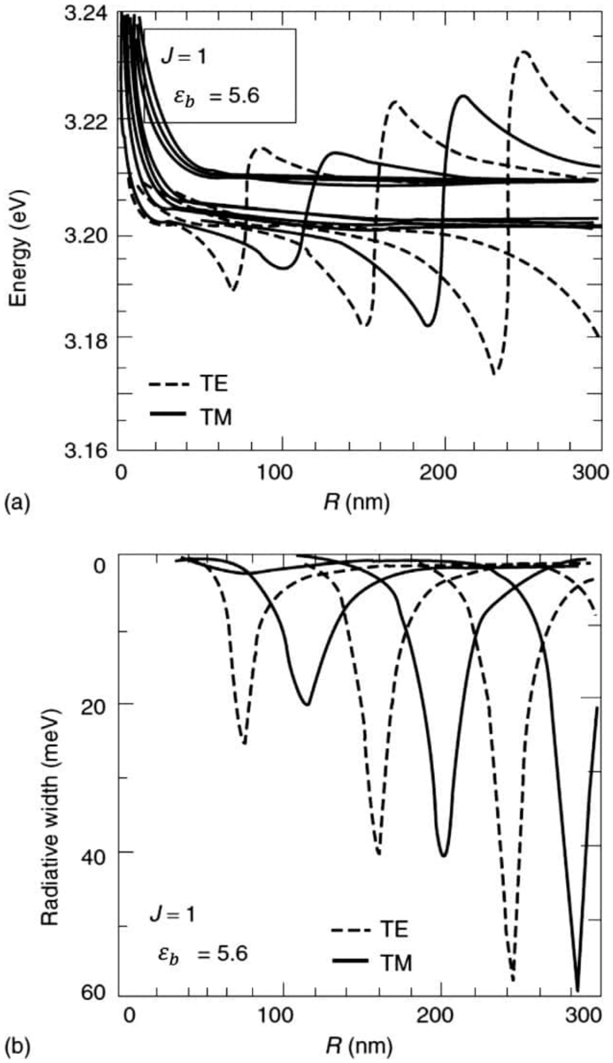

Fig. 1 (i) Real and (ii) imaginary parts of the eigenmode energies of an exciton in a sphere with a background dielectric constant of $\varepsilon_b = 5.6$. The material parameters correspond to those of the Z_3 exciton in CuCl. Each curve is specified by the total angular momentum J, its projection, the TE or TM mode character, and the radial quantum number for the exciton state.

however, we have to consider the effect of non-resonant (but infinitely many) components in dealing with the motions of resonant components. For appropriate configurations, these components produces "cavity modes" of EM field, which have completely different frequency spectrum and spatial structure from those of vacuum modes. The interaction of cavity modes and resonant matter transitions offers very interesting problems of cavity QED, remarkable enhancement effects and various typical situations showing the mechanism of light-matter interaction in a simplified manner.

A well-known recipe dealing with this kind of situation is to regard all the non-resonant components as an effective background medium of a given shape and size with electric susceptibility χ_b (background polarizability). Then, the Maxwell equation to determine electric field $\boldsymbol{E}(\boldsymbol{r}, \omega)$ is written as

$$\nabla \times \nabla \times \boldsymbol{E} - q^2 \varepsilon_0 [1 + \chi_b \Theta(\boldsymbol{r})] \boldsymbol{E} = q^2 \boldsymbol{P}_{\rm res} \tag{12}$$

where $\boldsymbol{P}_{\rm res}$ is the resonant part of polarization. Defining the EM Green function $\mathbf{G}_b(\boldsymbol{r}, \boldsymbol{r}'; \omega)$ of the background medium as

$$\nabla \times \nabla \times \mathbf{G}_b - q^2 \varepsilon_0 [1 + \chi_b \Theta(\boldsymbol{r})] \mathbf{G}_b = q^2 \delta(\boldsymbol{r} - \boldsymbol{r}'), \tag{13}$$

where $\Theta(\boldsymbol{r}) = 1$ or 0 for $\boldsymbol{r}$ inside or outside the background medium, respectively, we can derive the solution of Eq. (12) as

$$\boldsymbol{E}(\boldsymbol{r}, \omega) = \boldsymbol{E}_b(\boldsymbol{r}, \omega) + \int \mathrm{d}\boldsymbol{r}' \, \mathbf{G}_b(\boldsymbol{r}, \boldsymbol{r}'; \omega) \cdot \boldsymbol{P}_{\rm res}(\boldsymbol{r}'; \omega),$$

where $\boldsymbol{E}_b$ is the field due to the background polarization alone. This field is equivalent to that of (4), expressed differently in terms of the Green function $\mathbf{G}_b$.

In a nanostructure, resonant polarization of interest will consist of a few frequency components, and is written in the form of Eq. (8) with $\nu = 1, 2, \ldots$, s. The equations to determine the X's are Eq. (9) for $\nu = 1, 2, \ldots$, s, but the parameters in the equations should be changed as follows. [A] The excitation energies $\{E_\nu - E_0\}$ contain the interaction energy of induced polarizations, which are affected by the presence of background dielectrics. This "screening" effect can be divided into bulk type and surface/interface type contributions. The former is the screened Coulomb interaction by the factor $1/\varepsilon_b$, where $\varepsilon_b = 1 + \chi_b$, and the latter is the image potential effect for the interaction among the components of induced charge density. [B] The evaluation of radiative interaction $\mathscr{A}$ should be made in terms of $\mathbf{G}_b$ instead of $\mathbf{G}$. In terms of the modified excitation energies $\{E_\nu^{'} - E_0\}$ and radiative correction $\mathscr{A}^{(b)}$, we solve Eq. (9) for $\nu = 1, 2, \ldots$, s to obtain the (modified) expansion coefficients X, which uniquely determine the response field and induced polarization.

A typical effect of cavity on the optical response of matter is the modification of mode structure of EM field and the characteristic spatial pattern of each mode. Through this change in EM field, the coupling with matter excitations can be strongly affected, and their resonant frequencies and widths are modified rather strongly. In optical response, there appear the resonant contribution of both cavity modes and matter excitations in general, where we can distinguish two regimes, namely, the case where cavity mode has much smaller Q-value than that of matter excitation and the case where their Q-values are comparable. In the former case, only the effect on the matter excitation is appreciable as an increase in its width, while, in the latter, there occur new coupled modes through the mixing of the cavity mode and matter excitation.

The two regimes mentioned above can be described by the single scheme of the microscopic response in a cavity. The condition for the existence of non-trivial solution of the modified equations for $\{X_{\nu 0}\}$ in the absence of external field leads to the eigenmodes of the matter in a cavity. The fact that this solution covers two different regimes can be seen from the structure of the eigenmode equation. The Green function $\mathbf{G}_b$ has poles at the energies of cavity modes, so that the radiative correction $\mathscr{A}$ has the same poles with the strength determined by the coupling with matter excitations. Thus, the eigenvalue equation

$$\det \left| \left(E_\nu' - E_0 - \hbar\omega \right) \mathbf{1} + \mathscr{A}^{(b)} \right| = 0 \tag{15}$$

provides the complex roots for the coupled cavity modes and matter excitations. Depending on the coupling strength in $\mathscr{A}^{(b)}$ and the imaginary parts of cavity modes contained in $\mathbf{G}_b$, two regimes appear as mentioned in the previous paragraph.

EM Green function of cavity polariton

A typical example of matter in a cavity is a quantum well in a DBR (Distributed Bragg Reflector). In this case, the coupled modes are called cavity polaritons, and it is a very popular subject to study the nonlinear response of cavity polaritons, such as pump-probe spectroscopy, four wave mixing, parametric amplification, and so on. In these optical processes, probe beams are sent from outside the cavity, and the result of nonlinear process inside the cavity is observed as external light coming out of the cavity. A standard treatment of these processes is the so-called quasi-mode coupling scheme, where the cavity mode is assumed to be completely confined in the cavity, i.e., to have infinitely large Q-value. The well-defined cavity mode allows a simple and rigorous treatment of the light-matter coupling at various nonlinear levels, and the resulting signal light is calculated by assuming the coupling of ($Q = \infty$) cavity mode and the photon modes outside the cavity. The coupling strength is assumed to be such that it reproduces the radiative width of the cavity polaritons. This is used rather often, but it is a kind of make shift approach. This cannot be justified in a rigorous sense, because the problem of boundary conditions at the cavity surfaces cannot be translated into that of interaction between spatially separated modes of EM field.

An alternative way to handle such a problem rigorously is to use the Green function of cavity polariton, which is defined by renormalizing exciton linear polarization as well as background polarization comprising the cavity mode into the definition of EM field causing the nonlinear optical interaction. The equation to define this Green function $\mathbf{G}_{\text{cp}}$ has a similar form as Eq. (13). The only difference is that it additionally contains on the left hand side a term representing the linear polarization due to exciton.

$$\nabla \times \nabla \times \boldsymbol{E} - q^2\varepsilon_0[1 + \chi_{\text{b}}\Theta(\boldsymbol{r})]\boldsymbol{E} + \varepsilon_0 \int \mathrm{d}\boldsymbol{r}'\chi_{\text{x}}^{(1)}(\boldsymbol{r}, \boldsymbol{r}'; \omega)\boldsymbol{E}(\boldsymbol{r}') = q^2\boldsymbol{P}_{\text{NL}} \tag{16}$$

Keeping the nonlocal character of $\chi_{\text{x}}^{(1)}$, one can solve this integro-differential equation, and obtain the analytical form of $\mathbf{G}_{\text{cp}}$ in terms of $\mathbf{G}_{\text{b}}$ alone. Since $\mathbf{G}_{\text{b}}$ is obtained in a simple form for a QW in a DBR cavity, $\mathbf{G}_{\text{cp}}$ can be used as a practical tool. Considering that $\mathbf{G}_{\text{cp}}$ describes the propagation of EM field both inside and outside the cavity according to the detailed construction of the cavity, we understand the merit of this Green function to calculate the signal field outside the cavity caused by the nonlinear interaction in the cavity.

The EM field produced by the nonlinear polarization is given as

$$\boldsymbol{E}(\boldsymbol{r}, \omega) = \boldsymbol{E}_{\text{cp}}(\boldsymbol{r}, \omega) + \int \mathrm{d}\boldsymbol{r}\, \mathbf{G}_{\text{cp}}(\boldsymbol{r}, \boldsymbol{r}', \omega)\cdot\boldsymbol{P}_{\text{NL}}(\boldsymbol{r}', \omega). \tag{17}$$

The main issue in this formalism is to give the explicit form of $\boldsymbol{P}_{\text{NL}}$ according to the problem in question. The nonlinear polarization contains several components of EM field, so that we need to require self-consistency conditions based on the above solution. It is noteworthy that the Green function for cavity polariton is obtained in a closed form through the use of nonlocal form of exciton linear polarizability. The use of local approximation for this polarizability leads to a Bethe-Salpeter type equation, which is much complicated to solve. Thus, the nonlocal description makes the solution much easier than the local one. This is another example to recommend the use of nonlocal way of description.

Examples of observed phenomena

The typical phenomena characterized by the microscopic description of the optical response remarkably emerge under the conditions beyond LWA scheme, where the spatial variation in the electric field becomes obvious. Thus, studying these phenomena under non-LWA conditions is helpful for understanding some essential elements of the optical response of nanostructures.

Nonlocality-enhanced electric quadrupole transition

At the resonance condition for X in Eq. (9) in the presence of an external field, induced polarizations are enhanced along with the internal field associated with the same spatial patterns of the polarizations. Because the nonlinear component of the polarization depends on the internal field, the signal intensity of the nonlinear response shows sensitive size and shape dependence under resonance conditions. This type of resonant enhancement has been observed for thin layered structures of high-quality GaAs crystals (Ishihara et al., 2002). In this experiment, the thickness dependence of four-wave mixing, which is a type of third-order nonlinear response, was studied, and a remarkable enhancement in the signal was observed for a particular thickness region around 100 nm (Fig. 2). The theoretical analysis based on microscopic nonlocal theory revealed that the enhanced response was caused by the polarization with a quadrupole-type spatial pattern that is optically forbidden under typical LWA conditions. This observation demonstrates the significant role of the microscopic nonlocality in the optical response of nanostructures.

In the macroscopic description based on the LWA, only the transition associated with the dipole-type polarization strongly contributes to the optical response. In reality, however, the nanoscale spatial structure of the field plays a significant role depending on the sample structure and the resonance condition; thus, the conventional selection rule does not necessarily hold true. The abovementioned observation in GaAs thin layers is a typical example. Such a breakdown also appears for single molecules when they couple with the highly localized electric field arising from elementary excitations such as surface plasmons. The collective oscillation of free electrons in metallic media is known as plasmons. In particular, in the presence of metallic nanostructures such as nanoscale gaps, the plasmons can be excited by incident light, and the associated electric field is a strongly localized and enhanced, which is called localized surface plasmon-polaritons. If the molecules interact with such strongly inhomogeneous electric field, optically forbidden transitions easily occur because the strong spatial structure of the field does not follow the selection rule of LWA regime. An experimental demonstration of this phenomenon has been reported for single-walled carbon nanotubes (SWCNTs) lying in nanogaps between gold nanoblocks (Takase et al., 2013). By using the resonant Raman scattering, an optically forbidden electronic transition for a single carbon nanotube has been observed, where the associated polarization has a quadrupole-type spatial pattern in the cross section of the SWCNT of approximately 1 nm in diameter. The theoretical verification has been made by nonlocal theory to properly treat the spatial relationship between the electric field and the induced polarizations in the SWCNT, which elucidates significant signal intensity from the optically forbidden transition (Fig. 3).

The scanning type of microscopy associated with photo-excitation is a promising technique to observe the optically forbidden transitions of single nanostructures. Among such techniques, photo-induced force microscopy (PiFM) is considered a powerful method (Rajapaksa et al., 2010). PiFM uses a probe of atomic force microscopy (AFM) coated with a metal and detects the photo-induced force between the sample and the probe tip irradiated with light. The electric field in the vicinity of the sample and the probe is strongly enhanced by the localized surface plasmon resonance, and the induced force is strengthened. As this method

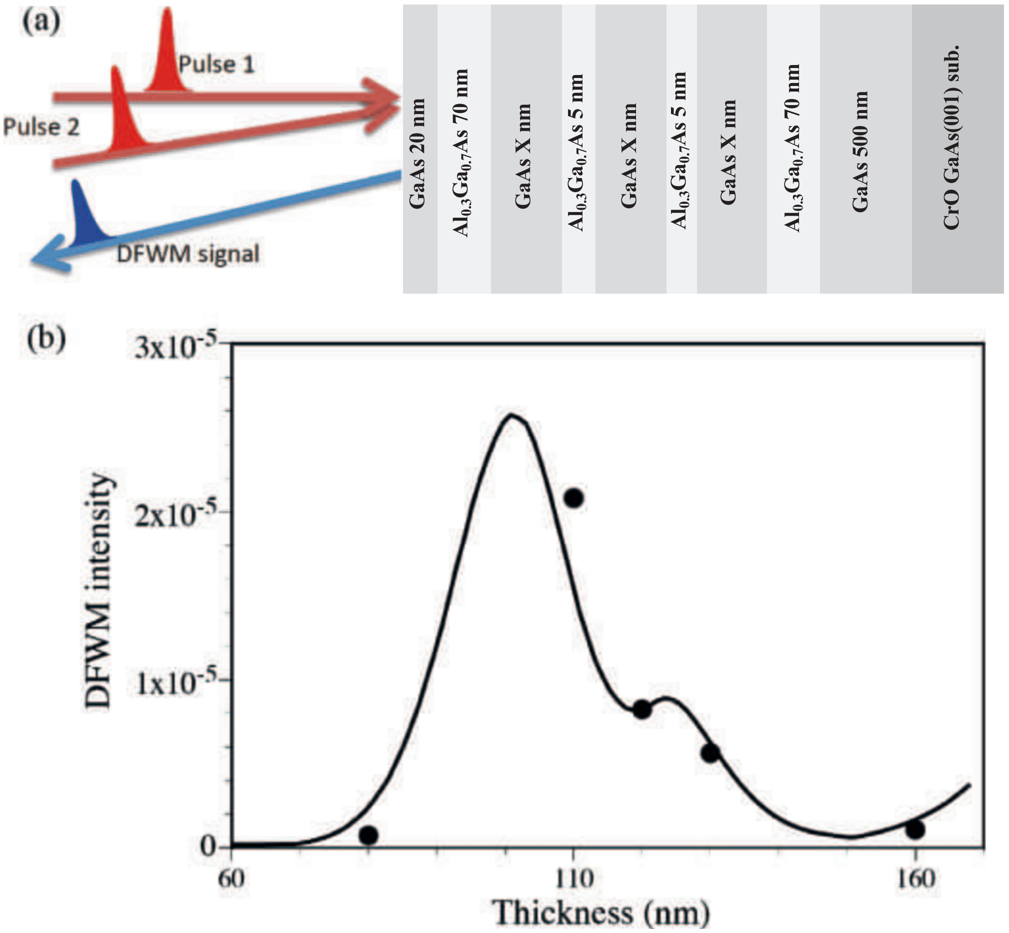

Fig. 2 (a) Schematic picture of the layered sample structure, incident pulses, and degenerate four-wave mixing (DFWM) signal. (b) The thickness (X in the picture of (a)) dependence of the peak value of the DFWM intensity. Closed circles are measured values in arbitrary units. The solid line shows the calculated values normalized by the incident probe intensity. The assumed damping constant is 0.03 meV. Modified after Ishihara H, Cho K, Akiyama K, Tomita N, Nomura Y and Isu T (2002) Large four-wave mixing of spatially extended excitonic states in thin gaas layers. *Physical Review Letters* **89**(1): 017402.

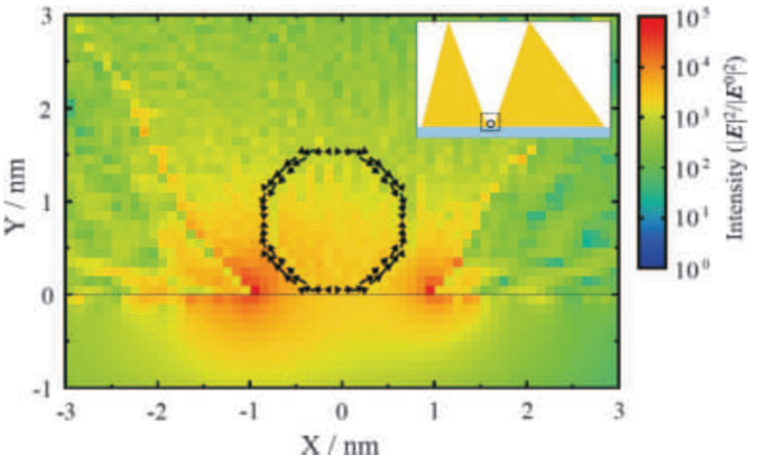

Fig. 3 Cross-sectional view of the calculated intensity of the electric field under resonant excitation conditions of the exciton with quadrupole-type polarization of an SWCNT lying between gold nanoblocks. The calculated quadrupole polarization is indicated by the black arrows. The grids show the cell size in the calculation by the discrete dipole approximation (DDA). The inset shows the overall view of the gold nanoblocks and SWCNT. Modified after Takase M, Ajiki H, Mizumoto Y, Komeda K, Nara M, Nabika H, Yasuda S, Ishihara H and Murakoshi K (2013) Selection-rule breakdown in plasmon-induced electronic excitation of an isolated single-walled carbon nanotube. *Nature Photonics* **7**(7): 550–554.

does not require the detection of the scattered or propagated fields, it possesses a high potential of molecular scale resolution. Recently, a scheme of high-resolution PiFM has been developed based on the heterodyne frequency modulation method in an ultrahigh vacuum (Yamanishi et al., 2017) to remove the photothermal oscillations. Presuming the potential of this technique, the observation of the spatial polarization patterns of the optical forbidden transitions in the nanostructures have been theoretically demonstrated (Yamane et al., 2020), as shown in Fig. 4. This effect can be considered a typical example to observe the non-LWA aspect of the optical response in nanostructures.

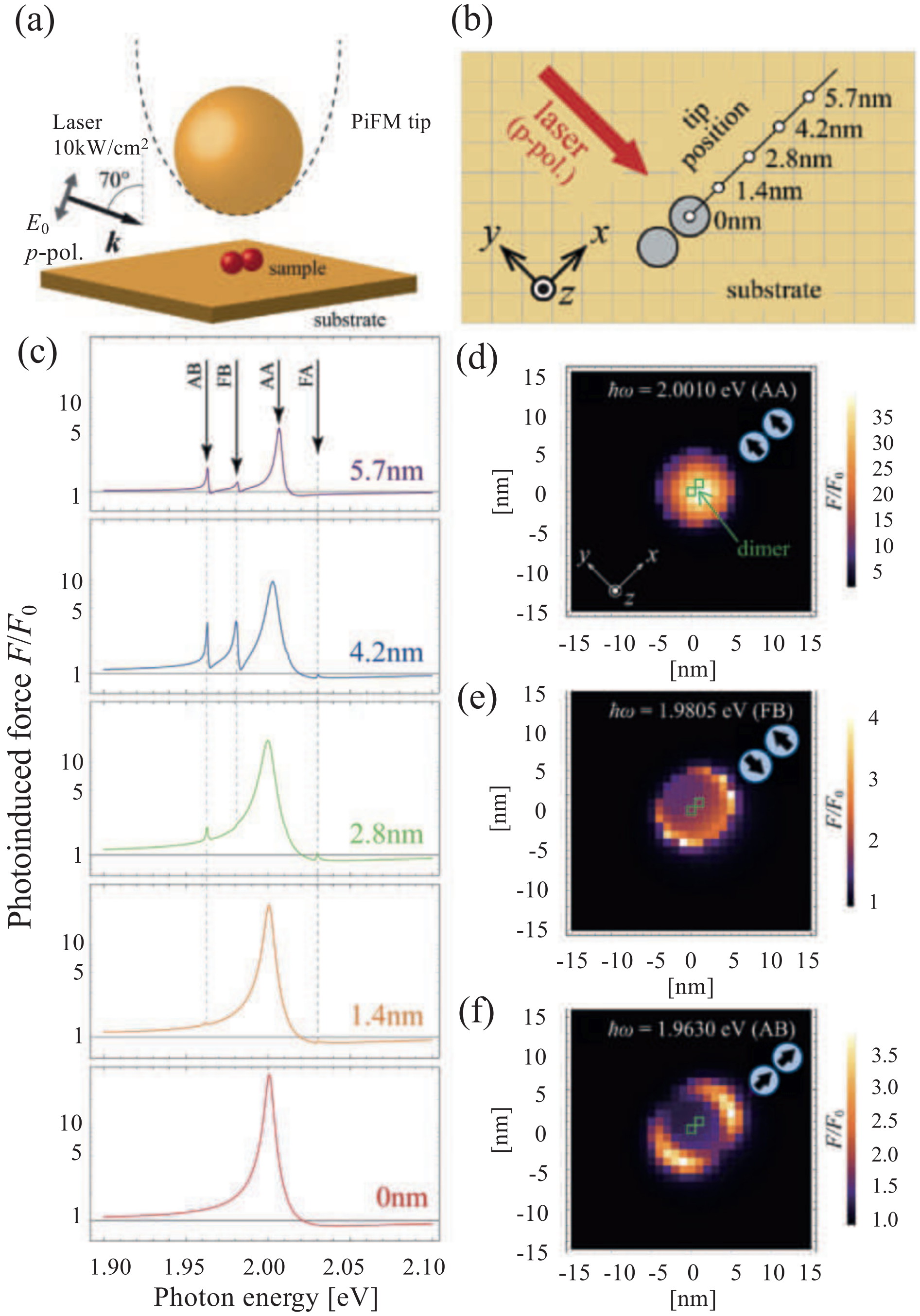

Fig. 4 (a) Schematic of the PiFM model. The metal-coated tip is modeled as a gold sphere. (b) Schematic illustration of the dimer on the gold substrate with the tip position. The grid on the substrate represents the cells in the DDA calculation. The center of the tip is represented by the white dots. (c) Photo-induced force spectra. The lines represent the dimer states, and each tip position in (b) is shown. As the tip moves away from the dimer, the peak corresponding to the allowed anti-bonding (AA) state becomes smaller, whereas the peaks corresponding to the allowed bonding (AB) and the forbidden bonding (FB) states appear strongly in the range of 2.8–4.2 nm. Also, the forbidden anti-bonding (FA) state appears in the same range. (d), (e), and (f) depict the PiFM images of the dimer for the AA, FB, and AB states, respectively (For the polarization patterns of AA, FB, and AB, see, insets of (d), (e) and (f), respectively.). The PiFM images are normalized by the force when the tip is just on the substrate (F_0). The dimer is represented by the green squares. Modified after Yamane H, Yamanishi J, Yokoshi N, Sugawara Y and Ishihara H (2020) Theoretical analysis of optically selective imaging in photoinduced force microscopy. *Optics Express* **28**(23): 34787–34803.

Radiative correction of nondipole-type excited states

As explained in Section "Scheme of microscopic response", det $|\mathbf{S}| = 0$ provides the complex eigenenergies $\{\hbar\Omega_\lambda\}$ of the coupled light-matter system. Generally, $\hbar\Omega_\lambda$ includes the radiative correction, namely, the real part of $\hbar\Omega_\lambda$ corresponds to the eigenenergy of the λ state including the shift from the original bare excited level, and the imaginary part corresponds to its radiative decay rate. One of characteristic phenomena that microscopic response theory predicts is the large radiative correction of nondipole-type excited states appearing beyond the LWA regime. If the wavefunctions of dipole-type excited states coherently extend over the entire volume of the sample within the LWA regime, the light-matter interaction volume and the radiative correction are proportional to the sample volume. However, if the sample size becomes comparable to the wavelength of the external light in a medium, this size-linear enhancement is saturated owing to the spatial variation in the light field in reality. On the other hand, beyond the LWA regime, the higher-order (nondipole-type) states strongly couple with light if the sample size allows the phase of their polarization waves to match the light wave in a medium. Thus, the light-matter interaction volume itself is not limited by the light wavelength, and the higher-order states (including the optically forbidden one in the LWA) attain maximum coupling at a particular size one after the other, leading to a large light-matter interaction volume. This situation was theoretically predicted, as seen in Fig. 1.

Because the respective components of polarization $X_{\nu 0}$ are resonantly enhanced at $Re[\hbar\Omega_\lambda]$ in the presence of the external field, a corresponding radiative shift can be observed in the spectra of the light scattering, photoluminescence, and so on. As an example, in Ref. Syouji et al. (2004), nondegenerate two-photon excitation scattering was employed to observe light-matter coupled modes, where both of the incident two beams are far from resonance with the one-photon excitation energy. (It should be noted that the resonance structures of $X_{\nu 0}$ do not correctly appear in the one-photon spectrum such as the reflectance or transmittance because of the interference between the scattered light and the external light.) When the sum energy of the photons from the two lasers resonates with the excitation energy of the light-matter coupled state, $\hbar\Omega_\lambda$, resonant scattering occurs. This experiment was done by using CuCl thin films and validated the characteristic size dependence of the radiative shift predicted in Fig. 1, where the shift drastically decreases and increases depending on the phase relation between the induced polarization and the light. In Ref. Syouji et al. (2004), a level interchange due to a large radiative shift was demonstrated, where the lowest state in the original bare level scheme overtakes the upper levels one by one as the thickness increases. In other nonlinear spectroscopy, four-wave mixing is also an effective method to observe the light-matter coupled states. Information about $\{\hbar\Omega_\lambda\}$ can be clearly obtained because the spectrum reflects $\mathrm{Re}[X_\lambda]$ well (Fig. 5) (Ichimiya et al., 2009). The luminescence spectra also directly reflect the light-matter coupled levels (Phuong et al., 2012). Typically, luminescence occurs from the excited states around the lowest one after reaching quasi-equilibrium. However, the spectra observed in Phuong et al. (2012) are different from the usual ones; the peak structures corresponding to the light-matter coupled states clearly appear, even for higher-order states with non-dipole type polarization patterns because those excited states emit light before their dephasing process owing to their large radiative decay rate, as explained below.

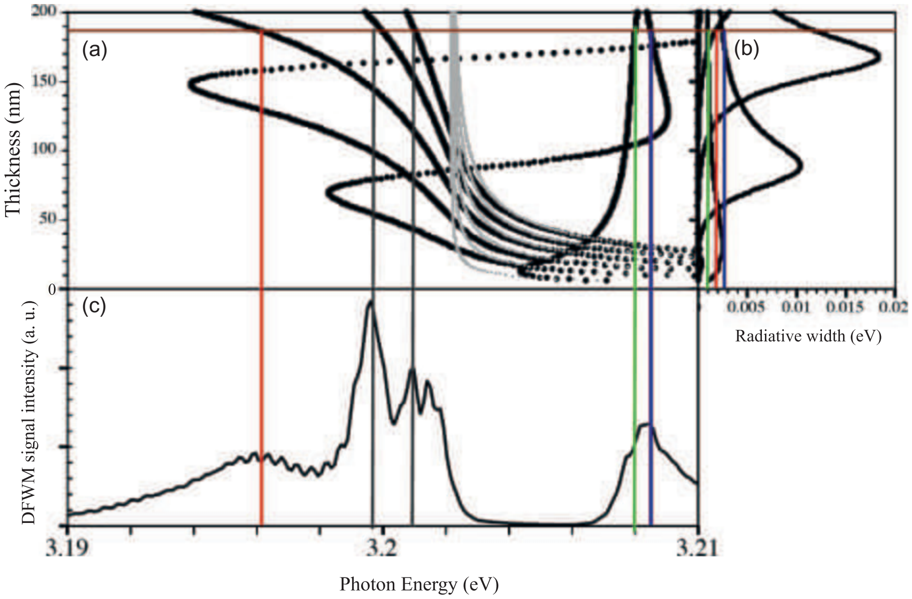

Fig. 5 (a) Gray lines: Calculated eigenenergies of bare excitons confined in a CuCl thin film. Black lines: Calculated real parts of the eigenenergies of the light-exciton coupled mode. (b) Calculated imaginary parts (radiative widths) of the eigenenergies of the light-exciton coupled mode. (c) Observed spectrum of the DFWM intensity. Vertical lines show the eigenergies of the light-exciton coupled mode for the 187-nm-thick film.

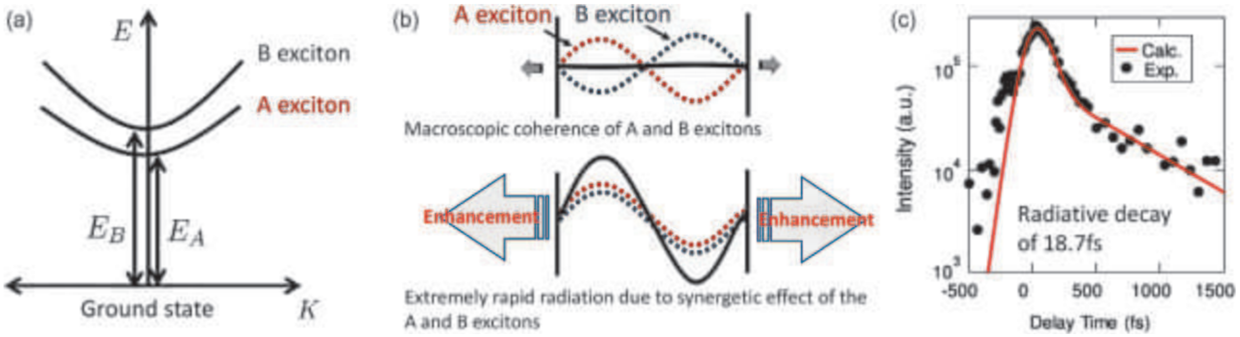

Fig. 6 (a) Schematic illustration of the double component excitons in ZnO. (b) Schematics of the radiative coupling of the A and B exctions. The bright modes formed by the multipoles of A and B excitons show a cooperative emission that becomes faster than the thermal dephasing at room temperature. (c) Experimentally observed fast radiative decay in the order of 10 fs. The solid red lines represent the fitting curves by a double-exponential function convoluted using the excitation laser profile. Modified after Kinoshita T, Matsuda T, Takahashi T, Ichimiya M, Ashida M, Furukawa Y, Nakayama M and Ishihara H (2019) Synergetic enhancement of light-matter interaction by nonlocality and band degeneracy in zno thin films. *Physical Review Letters* **122**(15): 157401.

Ultrafast radiative decay overcoming thermal dephasing at room temperature

Another characteristic manifestation of enhanced light-matter coupling beyond the LWA regime is ultrafast radiative decay reflecting the large $\mathrm{Im}[\hbar\Omega_\lambda]$. As explained above, the radiative correction is proportional to the sample volume in the LWA regime; therefore, the radiative decay rate exhibits a size-linear enhancement. This effect is known as "one-photon super radiance (giant oscillator strength)." On the other hand, beyond the LWA regime, the radiative decay rate exhibits a different type of size dependence, which is not simply the size-linear type but that overlapped with resonance behavior (as seen in Fig. 1), and exceptionally fast radiative decay occurs. This type of super radiance has been demonstrated in Ref. Phuong et al. (2012) for a CuCl thin film with a thickness of a few of hundred nanometers, where some modes exhibited radiative decay within approximately 100 fs. If we aim for further optimized conditions, we can realize significantly faster radiative decay reaching an order of 10 fs decay time. Such a decay time is shorter than the typical dephasing time of the excited states of solids at room temperature (Becker et al., 1988). Thus, in this scenario, the photoluminescence is completed before the thermal disturbance occurs, namely, a thermal-free optical response would be possible. A similar type of fast radiative decay has been observed in experiments for ZnO thin films (Kinoshita et al., 2019). The ZnO excitons have a multi-component nature arising from the nearly degenerate valence bands. The excitons related to the transitions from the topmost and the second valence bands are labeled A and B excitons, respectively. Because of the synergetic enhancement of the light-matter interaction due to these two exciton branches, the radiative decay time becomes shorter than a couple of tens of fs as observed by the transient grating spectroscopy, as depicted in Fig. 6.

Finally, it is useful to address how the super radiance regime is logically connected with the radiative decay scheme for the bulk regime. It is known that the radiative decay rate of light-matter coupled states (polaritons) in the bulk regime is inversely proportional to the sample size, which is opposite to that for the super radiance regime because the decay in the bulk regime is described as the escape of polariton wavepackets from the sample surfaces. In the super radiance regime, the apparent propagation speed v_p of the light-matter coupled mode with the strongest coupling for each thickness can be defined (see Ref. Bamba and Ishihara, 2009 for details). At the crossover size between the super radiance regime and the bulk regime, v_p reaches the group velocity $c/2n_{bg}$ of a polariton, where n_{bg} is the refractive index of the background medium. Then, beyond this condition, the photon created by electron-hole recombination cannot go outside of the film without reabsorption when its propagation speed is beyond the group velocity. This explains how we can understand the crossover between the size regimes described with the super radiance scheme and that described with the polariton scheme. This crossover behavior has been experimentally observed by Takahata et al. through the absorption measurement of carefully prepared Cu_2O tapered thin films (Takahata et al., 2018). Around the resonance regions of the blue and violet excitons, the systematic thickness dependence of the eigenenergies of the radiatively coupled excitons is investigated and the crossover from the super radiance and the polariton regimes is confirmed.

Conclusion

One characteristic aspect of the optical response of nanostructures is the explicit dependence on the size, shape, and internal structure of matter. These characteristics arise owing to the confined excited states whose eigen energies are quantized and the wave functions demonstrate various spatial structures depending on the boundary conditions. The optical response of nanostructures is also strongly modified by the dielectric structures of the background and/or environmental medium. This chapter has discussed the scheme to address these features with a single theoretical framework and illustrated some typical examples of phenomena observed in various experiments.

The nonlocal response is the key concept to providing a good overview of the optical response of nanostructures based on the first-principles formulation of light-matter interaction. To address the microscopic nonlocal response, we describe the susceptibility as a function of two positions using the system's wave functions extended coherently over the entire sample. By coupling the constitutive equations described with the non-local susceptibility and the microscopic Maxwell equation, the self-consistent optical response can be obtained. Solutions include radiative correction (energy shift and width corresponding to the inverse of the lifetime). The radiative width is a more generalized measure of the strength of the light-matter interaction than the oscillator strength that has been used conventionally under the long-wavelength approximation. This framework can be applied not only to the linear response but also to the nonlinear response by providing nonlinear susceptibility.

The strong modification of the mode of the EM field owing to the spatial dielectric structures of the background and/or environmental medium can be reflected through the EM Green function in the Maxwell equation. The cavity effect from the low-Q to the high-Q cases can be treated by this method. Depending on the Q-value, the mode structure of the EM field and the characteristic spatial pattern of each mode are modified. Through this change in the EM field, the coupling with matter excitations can be strongly affected, and their resonant frequencies and widths are strongly modified.

The effects characterized by the nonlocal response, namely the effects where the interplay between the spatial structures of matter wave functions and those of EM fields plays an essential role, have been observed in various experiments. Typical examples are the large nonlinear response of the electric quadrupole transition of semiconductor thin films, and the Raman scattering by the resonant excitation of the optically forbidden states of single-walled carbon nanotubes lying near metallic nanogaps sustaining localized surface plasmons. Another remarkable manifestation of the non-local response is the ultrafast response at a single fs level caused by the exciton-light coupling beyond the LWA scheme.

As demonstrated in experiments, the microscopic nonlocal theory is not only significant for rigorous descriptions of nanostructure optical responses but also crucial for revealing unconventional optical effects beyond the dipole approximation of matter systems and long-wavelength approximations of the field. Namely, paying attention to the full spatial degrees of freedom of the EM field and the matter wave functions in nanostructures paves a new avenue for exploring the potential of nanostructures as functional materials and for designing novel devices.

References

Bamba M and Ishihara H (2009) Crossover of exciton-photon coupled modes in a finite system. *Physical Review B* 80(12): 125319.

Becker P, Fragnito H, Cruz CB, Fork R, Cunningham J, Henry J, and Shank C (1988) Femtosecond photon echoes from band-to-band transitions in gaas. *Physical Review Letters* 61(14): 1647.

Ichimiya M, Ashida M, Yasuda H, Ishihara H, and Itoh T (2009) Observation of superradiance by nonlocal wave coupling of light and excitons in cucl thin films. *Physical Review Letters* 103(25): 257401.

Ishihara H, Cho K, Akiyama K, Tomita N, Nomura Y, and Isu T (2002) Large four-wave mixing of spatially extended excitonic states in thin gaas layers. *Physical Review Letters* 89(1): 017402.

Kinoshita T, Matsuda T, Takahashi T, Ichimiya M, Ashida M, Furukawa Y, Nakayama M, and Ishihara H (2019) Synergetic enhancement of light-matter interaction by nonlocality and band degeneracy in zno thin films. *Physical Review Letters* 122(15): 157401.

Phuong L, Ichimiya M, Ishihara H, and Ashida M (2012) Multiple light-coupling modes of confined excitons observable in photoluminescence spectra of high-quality cucl thin films. *Physical Review B* 86(23): 235449.

Rajapaksa I, Uenal K, and Wickramasinghe HK (2010) Image force microscopy of molecular resonance: A microscope principle. *Applied Physics Letters* 97(7): 073121.

Syouji A, Zhang B, Segawa Y, Kishimoto J, Ishihara H, and Cho K (2004) Interchange of the quantum states of confined excitons caused by radiative corrections in cucl films. *Physical Review Letters* 92(25): 257401.

Takahata M, Tanaka K, and Naka N (2018) Superradiance-to-polariton crossover of wannier excitons with multiple resonances. *Physical Review Letters* 121(17): 173604.

Takase M, Ajiki H, Mizumoto Y, Komeda K, Nara M, Nabika H, Yasuda S, Ishihara H, and Murakoshi K (2013) Selection-rule breakdown in plasmon-induced electronic excitation of an isolated single-walled carbon nanotube. *Nature Photonics* 7(7): 550–554.

Yamane H, Yamanishi J, Yokoshi N, Sugawara Y, and Ishihara H (2020) Theoretical analysis of optically selective imaging in photoinduced force microscopy. *Optics Express* 28(23): 34787–34803.

Yamanishi J, Naitoh Y, Li Y, and Sugawara Y (2017) Heterodyne technique in photoinduced force microscopy with photothermal effect. *Applied Physics Letters* 110(12): 123102.

Further reading

Gaponenko SV (1998) *Optical Properties of Semiconductor Nanocrystals*. Cambridge: Cambridge University Press.

Cho K (2003) *Optical Response of Nanostructures: Microscopic Nonlocal Theory*. Heidelberg, New York: Springer Verlag.

Takagahara T (ed.) (2003) *Quantum Coherence, Correlation and Decoherence in Semiconductor Nanostructures*. Amsterdam: Academic Press.

Keller O (1996) Local fields in the electrodynamics of mesoscopic media. *Physics Reports* 268: Elsevier.

Stahl A and Balslev I (1987) *Electrodynamics of Semiconductor Band Edge*. Springer.

Pekar SI and Kocherga OD (1983) *Crystal Optics and Additional Light Waves*. Benjamin/Cummings.

Halevi P (ed.) (1992) *Spatial Dispersion in Solids and Plasmas*, p. 339. Elsevier.

Optical properties of dielectrics and semiconductors

EL Ivchenko, Ioffe Institute, Russian Academy of Sciences, St. Petersburg, Russia

© 2024 Elsevier Ltd. All rights reserved.

Introduction **666**
Electromagnetic waves in solids **666**
Complex dielectric function 667
Optical reflection and transmission **668**
Thin films 668
Optical absorption **668**
Interband absorption 668
Intraband absorption 669
The tensor nature of the permittivity **669**
Birefringence 670
Magneto- and electro-optical effects 671
Piezospectroscopy 671
Natural optical activity 671
Metamaterials 672
Coulomb interaction effects **672**
Fine structure of exciton levels 673
Optical properties of two-dimensional systems 673
Polaritons 674
  Phonon polaritons 674
  Exciton polaritons 675
  Polaritons in quantum microcavities 676
Resonant photonic crystals 676
Photoluminescence **677**
Color centers 677
Optical orientation of electron spins 678
  Spin photoexcitation 678
  Electron spin kinetics 678
  Photoluminescence polarized by the optical orientation 678
  Magnetic field influence 678
  Spin and valley optical orientation in transition metal dichalcogenides 679
Magnetic circular polarization of exciton photoluminescence 679
Purcell effect 679
Single-photon sources 679
Two-photon entanglement 679
Nonlinear optics **680**
Pump-probe spectroscopy 681
  Spin Faraday and Kerr rotation 681
  Pump-probe micro-spectroscopy 681
Conclusion **681**
Acknowledgments **682**
References **682**
Further reading **682**

Abstract

In this chapter we review basic features of semiconductors and dielectrics from the perspective of optical and infrared properties. We consider Maxwell's macroscopic equations and the propagation of electromagnetic waves in solids. The constitutive material relation is described by the dielectric tensor which is a function of light frequency and may also depend on the external or internal parameters leading to birefringence, magneto- and electro-optical effects, piezospectroscopy and the spatial dispersion, e.g., natural optical activity. The linear optics is focused on the light reflection, transmission and absorption as the standard methods of noninvasive characterization of materials. An important attention is attracted to the excitonic effects in semiconductors, semiconductor structures and molecular crystals, as well as to the fine structure of exciton levels. Mixing of a photon and a quasi-particle excitation is shown to result in formation of hybrid excitations, polaritons. We outline the well-established optical materials such as dielectrics activated by impurities and novel solids such as

https://doi.org/10.1016/B978-0-323-90800-9.00009-3

metamaterials, resonant microcavities and photonic crystals. The chapter also touches upon the polarized photoluminescence spectroscopy. The nonlinear optics is represented by second harmonic generation and pump-probe spectroscopy. Novel trends are illustrated by single-photon sources and two-photon entanglement.

Key points

The basic optical properties of semiconductors and dielectrics are the main theme of this chapter.

- Maxwell's macroscopic equations and the propagation of electromagnetic waves in solids
- Dielectric tensor, complex dielectric function
- Light reflection and transmission
- Light absorption, direct and indirect transitions
- The tensor nature of the permittivity
- Coulomb interaction effects, excitons, fine structure of exciton levels, Sommerfeld factor
- Phonon and exciton polaritons
- Quantum microcavities, metamaterials, photonic crystals
- Polarized photoluminescence, optical orientation of electron spins, magnetic circular polarization of photoluminescence
- Color centers, laser materials
- Single-photon sources, two-photon entanglement
- Nonlinear optics, second harmonic generation, pump-probe spectroscopy, spin Faraday and Kerr rotation

Introduction

The chapter addresses basic features of semiconductors and dielectrics from the perspective of optical and infrared properties. These solids differ from metals by existence of the electron band gap E_g. Without doping and defects and at low temperature they have absolutely empty conduction bands above completely filled valence bands and are insulators contradistinguished from metals by their vanishing direct-current conductivity at low temperature. In most textbooks, the insulating/metallic behavior is explained by means of the band structure theory, focusing on the position of the Fermi level of the given material: either in a bandgap (dielectrics and semiconductors), or within a band (metals).

The dielectrics are characterized by wide band gaps and narrow allowed electron bands, whereas wide allowed and narrow forbidden bands are typical for semiconductors. Strictly speaking, there is no well-defined division between these substances, but nevertheless, for most cases, it is possible. The examples of typical semiconductors are Ge, Si, Te, GaAs and other A_3B_5 compounds, CdTe and other A_2B_6 compounds, MoS_2 and other transition metal dichalcogenides. The well-known examples of dielectrics include quartz, corundum (Al_2O_3), BN ($E_g \approx 6$ eV), NaCl ($E_g \approx 9$ eV), EuF_2, anthracene, solid C_{60} (fullerite).

Optical spectroscopy suggests noninvasive studies of solid state materials, bulk crystals and disordered solids as well as low-dimensional structures. Various optical spectroscopic techniques provide investigation of light reflection, transmission, absorption, luminescence, light scattering, nonlinear optics. Each of these fields examines the different mechanisms of the light-matter interaction. In particular, the field of light scattering includes elastic, or Rayleigh, and inelastic (free-carrier, Brillouin and Raman) scattering processes. In its turn the Raman scattering can involve participation of optical phonons, plasmons, spin-flip and intersubband electronic excitations, surface or interface vibrations etc. The nonlinear optics comprises nonlinear absorption (e.g., the two-photon absorption), four-wave mixing, optical harmonic generation etc. The study of photocurrent generation, a nonlinear effect of the second order, reveals combined optical and transport properties. A full review of all these phenomena lies beyond the present chapter. Here we mostly focus on the linear optical phenomena, light propagation, reflection, absorption and luminescence. An outlook to some light-scattering and nonlinear optical issues is given in this chapter as well.

It should be noted that Guizzetti and Patrini (2023) and the present chapter provide two levels of presentation. In the former, the optical properties are described, basing mostly on classical arguments, for homogeneous, isotropic and non-magnetic materials. The latter presents a more in-depth description and needs the knowledge of quantum mechanics and band theory of solids.

Electromagnetic waves in solids

The propagation of electromagnetic waves in solids is described by Maxwell's macroscopic equations

$$\begin{gathered}\operatorname{curl} \boldsymbol{H} = \frac{\partial \boldsymbol{D}}{\partial t},\ \operatorname{curl} \boldsymbol{E} = -\frac{\partial \boldsymbol{B}}{\partial t},\\ \operatorname{div} \boldsymbol{D} = 0,\ \operatorname{div} \boldsymbol{B} = 0,\end{gathered} \tag{1}$$

which relate four fields: the electric field vector $\boldsymbol{E}$, the electric displacement $\boldsymbol{D}$, the magnetic field strength $\boldsymbol{H}$ and the magnetic induction field, or the magnetic flux density, $\boldsymbol{B}$. In order to apply the Maxwell's equations, it is necessary to specify two additional relations between these fields. In SI, the electric permittivity and magnetic permeability in vacuum are fundamental physical constants: $\mu_0 = 4\pi \times 10^{-7}$ Hm^{-1}, $\varepsilon_0 = (\mu_0 c^2)^{-1}$, where c is the speed of light in vacuum. Here we mostly use the form of constitutive relations where the magnetic induction $\boldsymbol{B}$ coincides with $\mu_0 \boldsymbol{H}$ and the electric field $\boldsymbol{E}$ and the electric displacement $\boldsymbol{D}$ are connected by the dielectric tensor. This form of the material equations is possible as soon as the electromagnetic field frequency is nonzero. However, in Section "Metamaterials" while discussing the directional energy flux of an electromagnetic wave (Poynting vector) we use a more general description.

An electric field of the plane monochromatic light wave propagating in a homogeneous medium is a linear combination of the complex conjugate exponential functions

$$\boldsymbol{E}(t, \boldsymbol{r}) = \boldsymbol{E}(\omega, \boldsymbol{q})\mathrm{e}^{-\mathrm{i}\omega t + \mathrm{i}\boldsymbol{q}\boldsymbol{r}} + \boldsymbol{E}^*(\omega, \boldsymbol{q})\mathrm{e}^{\mathrm{i}\omega t - \mathrm{i}\boldsymbol{q}\boldsymbol{r}},$$

where ω and $\boldsymbol{q}$ are the light frequency and wave vector, $\boldsymbol{E}(\omega, \boldsymbol{q})$ is the complex electric field amplitude. For the plane waves, the material equation reads

$$D_\alpha(\omega, \boldsymbol{q}) = \varepsilon_0 \varepsilon_{\alpha\beta}(\omega, \boldsymbol{q}) E_\beta(\omega, \boldsymbol{q}), \tag{2}$$

where $\varepsilon_{\alpha\beta}$ is the relative permittivity tensor or the dielectric tensor. The Onsager symmetry relations impose the following constraint on the dielectric tensor

$$\varepsilon_{\alpha\beta}(\omega, \boldsymbol{q}) = \varepsilon_{\beta\alpha}(\omega, -\boldsymbol{q}). \tag{3}$$

It should be noted that the macroscopic description of fields in solids is valid as soon as the light wavelength $\lambda = 2\pi/q$ exceeds the microscopic dimension of the crystal unit cell. In the transparency frequency region, i.e., in the absence of absorption, the dielectric tensor is a Hermitian matrix, $\varepsilon_{\alpha\beta}(\omega, \boldsymbol{q}) = \varepsilon_{\beta\alpha}{}^*(\omega, \boldsymbol{q})$. The frequency dependence of $\varepsilon_{\alpha\beta}$ means that the displacement $\boldsymbol{D}(t)$ is determined by the electric field $\boldsymbol{E}(t')$ not only at the same time $t' = t$ but also at previous instances $t' < t$. In the same way, the $\boldsymbol{q}$-dependence of the dielectric tensor, or the spatial dispersion, implies a nonlocal response in real space, such that $\boldsymbol{D}(t, \boldsymbol{r})$ depends on $\boldsymbol{E}(t', \boldsymbol{r}')$ in some region around the point $\boldsymbol{r}$.

The dielectric tensor may also depend on the external or internal parameters, namely, the strain tensor components u_{ij}, the static electric field $\boldsymbol{E}^{(0)}$ or magnetic field $\boldsymbol{B}^{(0)}$, the static magnetization $\boldsymbol{M}$ etc. Consequently, in this case the transposition in Eq. (3) should be accompanied by the time inversion T of these parameters, $Tu_{ij} = u_{ij}$, $T\boldsymbol{E}^{(0)} = \boldsymbol{E}^{(0)}$, $T\boldsymbol{B}^{(0)} = -\boldsymbol{B}^{(0)}$, $T\boldsymbol{M} = -\boldsymbol{M}$ in the argument of the dielectric tensor.

It is worth mentioning that sometimes, instead of the dielectric tensor, one uses the electric susceptibility $\boldsymbol{\chi}$ which connects the induced electric polarization density of the medium $\boldsymbol{P}$ with the electric field $\boldsymbol{E}$

$$P_\alpha = \varepsilon_0 \chi_{\alpha\beta} E_\beta. \tag{4}$$

The two tensors are connected by $\varepsilon_{\alpha\beta} = \varepsilon_0(\delta_{\alpha\beta} + \chi_{\alpha\beta})$. Note also that, on some occasions, the introduction of the optical conductivity tensor $\sigma_{\alpha\beta}(\omega) = -\mathrm{i}\omega\varepsilon_0[\varepsilon_{\alpha\beta}(\omega) - \delta_{\alpha\beta}]$, instead of $\varepsilon_{\alpha\beta}$, makes more sense. This tensor relates the electric current density $\boldsymbol{j} = -\mathrm{i}\omega\boldsymbol{P}$ with the vector $\boldsymbol{E}$

$$j_\alpha = \sigma_{\alpha\beta} E_\beta. \tag{5}$$

In crystals of cubic symmetry and in the absence of the spatial dispersion the dielectric tensor is isotropic and reduces to a scalar dielectric function $\varepsilon(\omega)$.

Complex dielectric function

The dielectric function $\varepsilon(\omega)$ is a complex function of the real frequency ω. Its real and imaginary parts, ε' and ε'', obey the Kramers–Kronig relationship

$$\begin{aligned} \varepsilon'(\omega) - 1 &= \frac{1}{\pi}\mathcal{P}\int_{-\infty}^{\infty} \frac{\varepsilon''(\Omega)}{\Omega - \omega} d\Omega, \\ \varepsilon''(\omega) &= -\frac{1}{\pi}\mathcal{P}\int_{-\infty}^{\infty} \frac{\varepsilon'(\Omega) - 1}{\Omega - \omega} d\Omega, \end{aligned} \tag{6}$$

where $\mathcal{P}$ denotes the Cauchy principal value.

In a solid with the dielectric function $\varepsilon(\omega)$, the dispersion equation relating $\boldsymbol{q}$ with ω has the form

$$\left(\frac{cq}{\omega}\right)^2 = \varepsilon(\omega) \tag{7}$$

and, therefore, the wave vector is given as $q(\omega) = (\omega/c)\overline{n}(\omega)$. Here we introduced the complex index of refraction

$$\bar{n} = \sqrt{\varepsilon} = n + \mathrm{i}\kappa.$$

The parameters n and κ are called the refractive index and extinction coefficient, respectively. The equations relating real and imaginary parts of ε and $\bar{n}$ are $\varepsilon' = n^2 - \kappa^2$ and $\varepsilon'' = 2n\kappa$.

A plane light wave propagating in the homogeneous media with the extinction coefficient κ exhibits the attenuation. The Beer–Lambert–Bouguer law relates the attenuation of light intensity $I \propto |\boldsymbol{E}(\omega, z)|^2$ to the extinction coefficient of the bulk material through which the light is traveling along the z axis: $I(z) = I(0)\mathrm{e}^{-\alpha z}$, where the absorption coefficient $\alpha = 2\omega\kappa/c = \omega\varepsilon''/cn$.

Optical reflection and transmission

Let a plane electromagnetic wave be incident on a plane boundary between two solids with the complex refractive indices $\bar{n}_1$ and $\bar{n}_2$. The amplitude reflection and transmission coefficients, r and t respectively, are described by the Fresnel equations. At normal incidence from the medium 1 into the medium 2 they read

$$r = \frac{\bar{n}_1 - \bar{n}_2}{\bar{n}_1 + \bar{n}_2}, \quad t = \frac{2\bar{n}_1}{\bar{n}_1 + \bar{n}_2}. \tag{8}$$

For real $\bar{n}_{1,2}$ the light wave exhibits a phase shift of 180° when the reflectance takes place in a medium of lower refractive index than the adjoining medium, and zero if $n_1 > n_2$. The reflectance R (the intensities ratio) is the squared absolute value of r.

The reflection under oblique incidence from vacuum to the material with the refractive index $\bar{n}$ is characterized by the complex amplitude reflection coefficients

$$\begin{aligned} r_s &= \frac{\cos\theta_t - \bar{n}\cos\theta_i}{\cos\theta_t + \bar{n}\cos\theta_i}, \\ r_p &= -\frac{\cos\theta_i - \bar{n}\cos\theta_t}{\cos\theta_i + \bar{n}\cos\theta_t}, \end{aligned} \tag{9}$$

where the indices s and p indicate the light polarization, respectively perpendicular and parallel to the plane of incidence, θ_i is the incidence angle (real) and the refractive angle is defined by $\theta_t = \sqrt{1 - \sin^2\theta_i/\bar{n}^2}$. The negative sign in the second Eq. (9) is due to the choice of the direction of the p-polarized reflected light. If the medium of refraction is transparent, $\bar{n} = n$, the refractive angle θ_t is real and connected with θ_i by the Snell's law $\sin\theta_i = n \sin\theta_t$. In this case the reflectivity of p-polarized light vanishes at Brewster's angle $\theta_{\mathrm{Br}} = \arctan n$.

The spectroscopic ellipsometry technique allows to measure the ratio $\rho = r_p/r_s$ known as the ellipsometric function and presented in the form $\rho = \mathrm{e}^{i\Delta}\tan\Psi$, where $\tan\Psi$ is the amplitude ratio and Δ is the phase shift upon reflection. For real values of ε the phase shift takes two values $\Delta = 0$ and 180°.

Thin films

Let us consider a thin film coated on a thick substrate. Then the light components reflected at the top and bottom surfaces of the film interfere with each other. In general, the phase shift ϕ between the two components can take any value. The special cases are $\phi = 2N\pi$ and $\phi = (2N+1)\pi$, where N is an integer. In the former case it is said that the beams interfere constructively and in the latter destructively. By adjusting the film parameters one can achieve the antireflection which is more or less complete cancellation of the reflected components.

An opposite effect of a high reflectance can be obtained from a distributed Bragg reflector which is a stack of thin quarter-wave dielectric layers of alternate high and low indices n_1 and n_2. The layer thicknesses a_1, a_2 satisfy the conditions

$$n_1 \frac{\varpi}{c} a_1 = n_2 \frac{\varpi}{c} a_2 = \frac{\pi}{2},$$

where ϖ is the frequency chosen to be in the center of the enhanced reflection spectral region.

Optical absorption

The absorption spectrum spans a wide energy range extending from the above- or near-bandgap energies to the low energy transitions involving free carriers and optical phonons.

Interband absorption

The simplest form of absorption may be a direct transition from the valence to the conduction band. The optical excitation of one electron from the valence band v to the conduction band c leads to a generation of an extra electron with the wave vector $\boldsymbol{k}_c$ in the conduction band, leaving an empty state with the wave vector $\boldsymbol{k}_\upsilon$ in the valence band. The vertical transitions between the electronic bands υ and c occur for $\boldsymbol{k}_c = \boldsymbol{k}_\upsilon = \boldsymbol{k}$ and obey the energy conservation law

$$\varepsilon_{c\boldsymbol{k}} - \varepsilon_{\upsilon\boldsymbol{k}} = \hbar\omega,$$

where $\hbar\omega$ is the excitation photon energy.

For the direct optical transitions one has

$$\varepsilon'' = \frac{cn}{\omega}\alpha = \frac{4\pi^2 e^2}{\omega^2 V}\sum_{n'n\boldsymbol{k}} |\boldsymbol{e}\boldsymbol{v}_{n'n}(\boldsymbol{k})|^2 (f_{n'\boldsymbol{k}} - f_{n\boldsymbol{k}})\,\delta(\varepsilon_{n'\boldsymbol{k}} - \varepsilon_{n\boldsymbol{k}} - \hbar\omega), \tag{10}$$

where V is the sample volume, e is the electron charge, the indices n', n enumerate the electron bands, $\boldsymbol{v}_{n'n}(\boldsymbol{k})$ is the matrix element of the velocity operator between the Bloch states n', $\boldsymbol{k}$ and n, $\boldsymbol{k}$, $\varepsilon_{n\boldsymbol{k}}$ is the electron energy dispersion in the n-th band, and $f_{n\boldsymbol{k}}$ is the electron distribution function. For the allowed band-to-band transitions $\upsilon \to c$ in direct-gap semiconductors Eq. (10) may be written down as

$$\varepsilon'' = C\left(\frac{ep_{c\upsilon}}{\hbar\omega m_0}\right)^2 \sqrt{\mu_{c\upsilon}^3 (\hbar\omega - E_g)}, \tag{11}$$

where C is the dimensionless coefficient and m_0 is the electron mass in vacuum, $p_{c\upsilon}$ is the interband matrix element of the momentum operator, $\mu_{c\upsilon}$ is the electron-hole reduced effective mass. Clearly, the absorption coefficient follows the interband density of states.

In indirect-gap semiconductors, the energy maximum in the valence and minimum in the conduction band do not occur at the same wave vector. In this case near-bandgap absorption takes place due to the indirect optical transitions provided by simultaneous scattering by phonons or static defects. For the non-phonon indirect transitions the absorption coefficient increases with frequency as the square of the energy difference $\hbar\omega - E_g$. For indirect transitions with the participation of lattice phonons the momentum conservation law reads $\boldsymbol{k}_c = \boldsymbol{k}_\upsilon \pm \boldsymbol{k}_{\text{phon}}$, and the absorption coefficient is proportional to $(\hbar\omega - E_g \pm \hbar\omega_{\text{phon}})^2$, where $\boldsymbol{k}_{\text{phon}}$, ω_{phon} are the phonon wave vector and frequency, the sign ± corresponds to the absorption and emission of the phonon. Fig. 1 presents the electronic indirect band structure in bulk MoS_2 and direct band structure in monolayer MoS_2 (Yazyev and Kis, 2015).

The absorption far below E_g can arise due to the transitions involving free carriers, defects, donors or acceptors or deep centers, as well as phonons. It can also be related to surface energy states within the band gap. This is particularly the case in topological insulators. A topological insulator is an electronic material that has a band gap in its interior like an ordinary insulator but possesses conducting states on its edge or surface. In the topological band theory, the role of the Gaussian curvature and the Euler characteristic of a topological space is played by the Berry curvature and the Z_2 topological invariant. Two insulators are equivalent if they can be transformed one into the other by slowly changing the Hamiltonian without gap closure, their topological invariants coincide. Let us consider a spatial interface between two insulators with different topological invariants (two materials or a material neighboring vacuum). Somewhere along the normal to the interface the energy gap has to vanish, because otherwise the two phases would be equivalent. The gapless states are surface states (or edge states in two-dimensional systems) that are topologically protected and exhibit conducting properties. The light absorption appears due to optical transitions between the surface states and between the surface and bulk states of the conduction or valence bands.

Intraband absorption

Considering free-carrier intraband absorption in the Drude model, we can start from the classical equation for a free motion of conduction electrons in the ac electric field of the electromagnetic wave

$$\dot{\boldsymbol{v}}(t) + \frac{\boldsymbol{v}(t)}{\tau_p} = \frac{e}{m^*}\boldsymbol{E}(t), \tag{12}$$

where $\boldsymbol{v}$ is the mean electron velocity, m^* and τ_p are the electron effective mass and the momentum relaxation time. The amplitudes of the electric current density and the electric field are related by

$$\boldsymbol{j}(\omega) = eN\boldsymbol{v}(\omega) = \sigma(\omega)\boldsymbol{E}(\omega),$$

where $\sigma(\omega) = \sigma(0)/(1 - i\omega\tau_p)$ is the ac conductivity (or the contribution of free carriers to the optical conductivity), $\sigma(0) = e^2 N\tau_p/m^*$ is the dc conductivity and N is the electron density. The absorption coefficient is given by

$$\alpha = \frac{4\pi}{cn}\operatorname{Re}\{\sigma(\omega)\} = \frac{4\pi\sigma(0)}{cn\left(1 + \omega^2\tau_p^2\right)}. \tag{13}$$

The tensor nature of the permittivity

The tensorial character of the permittivity is manifest in anisotropic structures or in crystals of cubic symmetry if they are subjected to external forces or the spatial dispersion is taken into consideration.

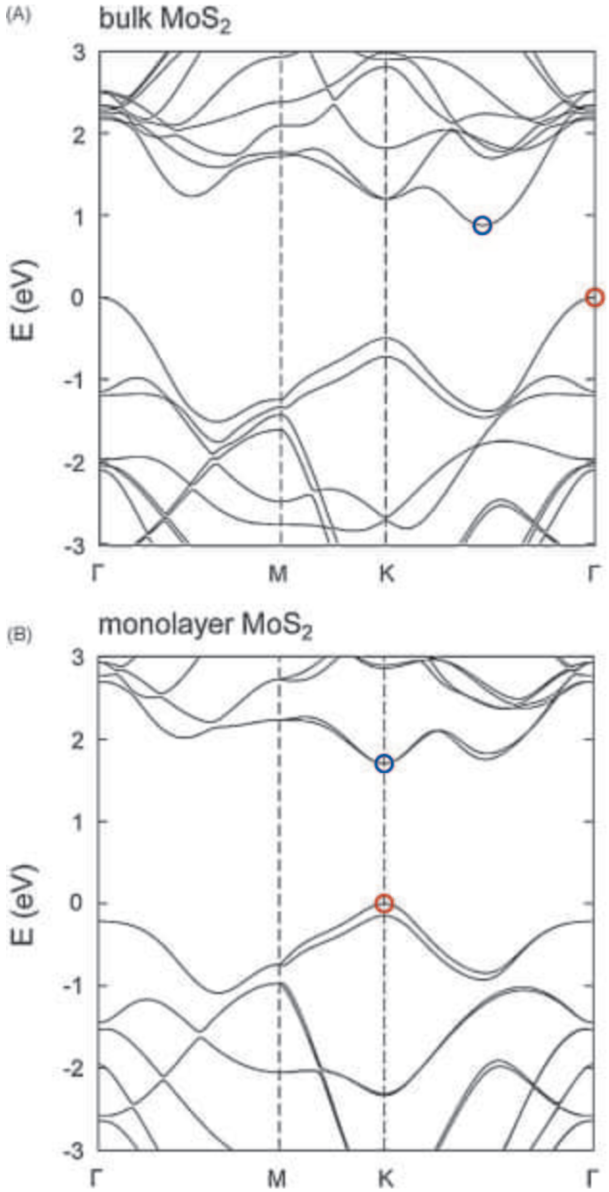

Fig. 1 Schematics of indirect- and direct-gap electron band structure of transition metal dichalcogenides (TMDC). (a) Bulk material. The valence band top, red circle, lies at the center of the Brillouin zone (Γ point) and conduction band bottom, blue circle, is located between Γ and K points. (b) TMDC monolayer. The valence band maximum and conduction band minimum lie at the same point K (vortex of the hexagon Brillouin zone). Reproduced by permission Yazyev OV and Kis A (2015) MoS_2 and semiconductors in the flatland. *Materials Today* 18: 20–30.

Birefringence

Anisotropic crystals are very different from the isotropic media: in an anisotropic medium a refractive index depends on the polarization and propagation direction of light. First, we consider non-magnetic crystals unaffected by external forces and ignore the spatial dispersion. Then the dielectric tensor $\varepsilon_{\alpha\beta}(\omega)$ is symmetric and, therefore, there is a Cartesian coordinate frame with the axes 1, 2, 3 where this tensor becomes diagonal with the components ε_{11}, ε_{22} and ε_{33}. If all three components are different, the crystal is called biaxial.

In a uniaxial material the two principal components coincide, e.g. $\varepsilon_{11} = \varepsilon_{22} = \varepsilon_{\perp}$, and differ from the third component $\varepsilon_{33} \equiv \varepsilon_{\parallel}$. The two fundamental light waves propagating in a particular direction are linearly polarized and have, except for $\boldsymbol{q} \parallel 3$, different refractive indices. One of them, called ordinary or transverse-electric (TE), is polarized perpendicularly to the optical axis (the axis 3) and the vector $\boldsymbol{q}$ and governed by the refractive index $\bar{n}_o = \sqrt{\varepsilon_{\perp}}$. The electric field in the other mode, extraordinary or transverse-magnetic (TM), is polarized in the plane formed by the wave vector and optical axis. For the light propagating in any direction perpendicular to the optical axis, the refractive index of the extraordinary wave $\bar{n}_e$ equals $\sqrt{\varepsilon_{\parallel}}$. If at the initial point the electric field vector of the light makes 45° with the optical axis, its polarization oscillates as a function of the propagation coordinate changing from linear to circular at the quarter-wave distance and to orthogonal linear at the half-wave distance. Birefringent materials, e.g. quartz SiO_2, calcite $CaCO_3$ or even plastics, are used to construct quarter- and half-wave plates, the former converts the linear polarization into circular polarization and the latter rotates the linear polarization direction by 90°.

Magneto- and electro-optical effects

Confining ourselves to the second-order magneto-optic effects, the dielectric tensor can be expanded in the components of the external static magnetic field $\boldsymbol{B}^{(0)}$

$$\varepsilon_{\alpha\beta}\left(\omega, \boldsymbol{B}^{(0)}\right) = \varepsilon_{\alpha\beta} + f_{\alpha\beta}B_{\eta}^{(0)} + Q_{\alpha\beta\eta\xi}B_{\eta}^{(0)}B_{\xi}^{(0)}. \tag{14}$$

It follows from the Onsager relation that, in non-magnetic media invariant under time reversal, the tensor $\boldsymbol{f}$ is antisymmetric and the tensor $\boldsymbol{Q}$ is symmetric with respect to permutation of the indices α and β..

The tensor f describes the Faraday effect of the optical rotation produced in a beam of linearly polarized light traversing a medium along the lines of force of an external magnetic field. This tensor also describes the circular dichroism and magneto-optical Kerr effect observed in reflection. The tensor $\boldsymbol{Q}$ describes the Voigt effect (or Cotton-Mouton effect) and contributes to a magnetic-field induced birefringence which can be observed when the light propagates perpendicularly to the applied magnetic field.

The expansion of the dielectric tensor in powers of the magnetic field is valid in the optical regions far enough from the exciton resonances. Otherwise, one has to take into account the excitonic effects and terms of higher order in $\boldsymbol{B}^{(0)}$ in Eq. (14) become important.

In ferromagnets and antiferromagnets, it is reasonable to reveal the role of the magnetic subsystems and express a change in $\varepsilon_{\alpha\beta}$ as a function of the internal parameters of the magnetic ordering. In a two-sublattice antiferromagnet one can write down

$$\begin{aligned}
\varepsilon^{a}_{\alpha\beta}(\omega, \boldsymbol{L}, \boldsymbol{M}) &= f^{\mathrm{L}}_{\alpha\beta\nu}L_{\nu} + f^{\mathrm{M}}_{\alpha\beta\nu}M_{\nu},\\
\varepsilon^{s}_{\alpha\beta}(\omega, \boldsymbol{L}, \boldsymbol{M}) &= \varepsilon_{\alpha\beta}(\omega) + Q^{\mathrm{LL}}_{\alpha\beta\nu\xi}L_{\nu}L_{\xi} + Q^{\mathrm{LM}}_{\alpha\beta\nu\xi}L_{\nu}M_{\xi} + Q^{\mathrm{MM}}_{\alpha\beta\nu\xi}M_{\nu}M_{\xi}.
\end{aligned}$$

Here ε^{a} and ε^{s} are the symmetric and antisymmetric parts of the dielectric tensor, the antiferromagnetic vector $\boldsymbol{L}$ is the difference of magnetizations of the two sublattices, $\boldsymbol{M}_1$ and $\boldsymbol{M}_2$, and $\boldsymbol{M}$ is the magnetic polarization $\boldsymbol{M}_1 + \boldsymbol{M}_2$ induced by the external magnetic field.

Electro-optics includes the Pockels and the Kerr effects which are, respectively, a linear and quadratic change in the refractive index of a material in response to an applied electric field. The former is allowed in crystals of the piezoelectric symmetry class only. In particular, for the electric field $\boldsymbol{E}^{(0)}$ applied along the [001] axis of a zinc-blende-structure crystal and the light propagating along this axis, the Pockels effect induces a difference between the refractive indices of rays polarized along the [110] and $[1\bar{1}0]$ directions. The Pockels effect is the basis of the operation of Pockels cells.

Piezospectroscopy

The piezo-optical birefringence is described by the phenomenological equation

$$\delta\chi_{\alpha\beta} = P_{\alpha\beta ij}u_{ij}$$

relating a susceptibility change and the strain tensor u_{ij}. The components $P_{\alpha\beta ij} = \partial\chi_{\alpha\beta}/\partial u_{ij}$ are called the elasto-optical coefficients.

The elasto-optical tensor also describes the light scattering by acoustic phonons. In this case the components u_{ij} are considered as time-dependent strain fluctuations produced by lattice vibrations and causing fluctuations of the susceptibility. As a result, the lattice vibrations produce in the medium a transient optical superlattice which causes the Brillouin scattering of light. In a piezoelectric, $\delta\chi_{\alpha\beta}$ includes, in addition to the deformation contribution, also an electro-optical term $P^{E}{}_{\alpha\beta ij}\mathcal{E}_k$, where $P^{E}{}_{\alpha\beta k} = (\partial\chi_{\alpha\beta}/\partial\mathcal{E}_k)_{u_{ij}=0}$ is the electro-optical tensor and $\mathcal{E}$ is the electric field induced by acoustic vibrations.

Natural optical activity

If the spatial dispersion is weak, the tensor $\varepsilon_{\alpha\beta}$ may be expanded in powers of the wave vector $\boldsymbol{q}$. Retaining the zeroth- and first-order terms we have

$$\varepsilon_{\alpha\beta}(\omega, \boldsymbol{q}) = \varepsilon_{\alpha\beta}(\omega) + \mathrm{i}\gamma_{\alpha\beta\eta}(\omega)q_{n}. \tag{15}$$

In the coordinate representation the connection between $\boldsymbol{D}$ and $\boldsymbol{E}$ converts to

$$D_{\alpha} = \varepsilon_0\left[\varepsilon_{\alpha\beta}(\omega)E_{\beta} + \gamma_{\alpha\beta\eta}(\omega)\frac{\partial E_{\beta}}{\partial x_{\eta}}\right].$$

Applying the Onsager relation we get the antisymmetric condition

$$\gamma_{\alpha\beta\eta}(\omega) = -\gamma_{\beta\alpha\eta}(\omega).$$

In the absence of dissipation, there is an additional restriction $\gamma^*\alpha_{\beta\eta}(\omega) = -\gamma_{\beta\alpha\eta}(\omega)$ and the third-rank tensor γ becomes real. Media allowing nonzero components of the tensor $\gamma_{\alpha\beta\eta}$ are said to have natural optical activity or natural gyrotropy, in contrast to the artificially induced gyrotropy in the Faraday effect.

The well-known naturally gyrotropic materials are crystal quartz and tellurium. Their point-group symmetry is D_3, the nonzero γ tensor components are $\gamma_{xyz} = -\gamma_{yxz}$ and $\gamma_{xzy} = -\gamma_{zxy} = \gamma_{zyx} = -\gamma_{yzx}$. Similarly to the Faraday effect, a linearly polarized light propagating along the trigonal axis $C_3 \parallel z$ exhibits a rotation of the linear polarization governed by the real part of the component γ_{xyz} and ellipticity due the imaginary part of this component. Both quartz and tellurium have enantiomorphic pairs of space groups $D_3{}^4$ and $D_3{}^6$. The two modifications differ in sign of the tensor $\gamma_{\alpha\beta\eta}$ and, therefore, in the direction of polarization rotation.

Linear-$\boldsymbol{q}$ terms in the expansion (15) can appear due to the external influence of the static electric field (electro-gyration), strain (piezo-gyration) and magnetic field (magneto-spatial dispersion, or birefringence due to magnetic-field induced spatial dispersion).

It is important to stress the difference between the natural gyration and the Faraday gyration. In the former case the rotation angle of the light wave reflected from the bottom interface and propagating backwards decreases. In contrast, in the latter case, for the same beam of light reflected back and forth through the medium, its rotation increases each time.

Metamaterials

Electromagnetic metamaterials may be defined as a class of artificial media where the unit cell or elementary building block is small as compared to the light wavelength. More generally, a metamaterial is any material engineered to have a property that is not found in nature. We consider here negative-index metamaterials whose refractive index for an electromagnetic wave has a negative value over a certain frequency range. For this purpose it is more convenient to use the description of Maxwell's equations with two material equations. The medium is assumed to be isotropic and characterized by the relations

$$\boldsymbol{D} = \varepsilon_0 \varepsilon_p \boldsymbol{E}, \quad \boldsymbol{B} = \mu_0 \mu_p \boldsymbol{H}. \tag{16}$$

Here ε_p and μ_p are the relative electric permittivity and magnetic permeability taken to be real and frequency independent. In the description with $\boldsymbol{B} = \mu_0 \boldsymbol{H}$ instead of the second Eq. (16) they are interconnected with the relative dielectric constant by $\varepsilon = \varepsilon_p \mu_p$. The waves are propagating for a positive pair of ε_p and μ_p as well if they are both negative.

By the definition, the phase velocity $\boldsymbol{v}_{\mathrm{ph}}$ of the electromagnetic wave is directed along the wave vector $\boldsymbol{q}$, while its group velocity $\boldsymbol{v}_{\mathrm{gr}}$ complies with the direction of the Poynting vector $\boldsymbol{S}$. The latter is expressed by the fields $\boldsymbol{E}$ and $\boldsymbol{H}$ as follows

$$\boldsymbol{S} = \boldsymbol{E} \times \boldsymbol{H} = \frac{\boldsymbol{E} \times \boldsymbol{B}}{\mu_0 \mu_p}. \tag{17}$$

For a plane wave one has

$$\boldsymbol{S} = \frac{2\boldsymbol{q}}{\omega \mu_0 \mu_p} |\boldsymbol{E}(\omega, \boldsymbol{q})|^2. \tag{18}$$

We see that, for positive values of ε_p, μ_p, the directions of $\boldsymbol{v}_{\mathrm{ph}}$ and $\boldsymbol{v}_{\mathrm{gr}}$ coincide. For negative ε_p and μ_p, the two velocities are antiparallel. This means, for example, that if the energy flux of an electromagnetic wave is directed along the z axis, the wave vector of this wave equals $q = n\omega/c$ with the negative refractive index $n = -\sqrt{\varepsilon}$. Media with negative permittivity and permeability form one class of metamaterials.

Another class of negatively refracting materials are resonant chiral structures, e.g., gyrotropic (chiral) media filled with resonant electric dipoles. Negative refraction has also been demonstrated in hyperbolic metamaterials which are uniaxial solids with either $\varepsilon_\parallel < 0$ and $\varepsilon_\perp > 0$ or $\varepsilon_\parallel > 0$ and $\varepsilon_\perp < 0$.

Coulomb interaction effects

In Section "Intraband absorption" we followed the single-particle Bloch scheme describing the independent motion of charge-carrying electrons and holes. The allowance for the electron-hole Coulomb interaction substantially modifies the near-band-edge absorption.

Similarly to a hydrogen atom, an electron and a hole in semiconductors form bound states, the Wannier–Mott excitons, with the excitation energy below the band gap, and the interband light absorption spectrum consists of a series of discrete levels of bound exciton states below the band gap E_g and a continuum due to unbound but correlated electron-hole pairs above the band edge. As a result the absorption edge becomes red-shifted by the ground-state exciton binding energy.

The wave function of the Wannier-Mott exciton can be decomposed into the states of noninteracting electron-hole pairs as follows

$$\Psi^{\mathrm{exc}} = \sum_{s\boldsymbol{k}_e,\, m\boldsymbol{k}_h} C_{s\boldsymbol{k}_e, m\boldsymbol{k}_h} |s\boldsymbol{k}_e,\, m\boldsymbol{k}_h\rangle. \tag{19}$$

Here s, m are the indices identifying the conduction- and valence-band spin branches, $\boldsymbol{k}_{e,h}$ is the electron or hole wave vector, $|s\boldsymbol{k}_e,\, m\boldsymbol{k}_h\rangle$ is the excited state of the crystal in which only one conduction-band state $|s\boldsymbol{k}_e\rangle$ is occupied and only one valence state $\widehat{\mathcal{K}}|m\boldsymbol{k}_h\rangle$ is empty. Here $\widehat{\mathcal{K}}$ is the time inversion operator $-\mathrm{i}\sigma_y\mathcal{K}_0$, σ_y the second spin Pauli matrix and $\mathcal{K}_0$ the complex conjugation operation. By the envelope wave function of the exciton in the real-space representation, or the $\boldsymbol{r}$-representation, one understands the function obtained by inverse Fourier transform

$$\varphi^{\mathrm{exc}}_{sm}(\boldsymbol{r}_e,\, \boldsymbol{r}_h) = \sum_{\boldsymbol{k}_e\boldsymbol{k}_h} \mathrm{e}^{\mathrm{i}(\boldsymbol{k}_e\cdot\boldsymbol{r}_e+\boldsymbol{k}_h\cdot\boldsymbol{r}_h)} C_{s\boldsymbol{k}_e,m\boldsymbol{k}_h}. \tag{20}$$

For the simple (parabolic and isotropic) conduction and valence bands, the envelope functions are hydrogen-like. For example, the ground-state exciton, or 1 s-exciton, is described by the envelope

$$\varphi^{\mathrm{exc}}_{1s}(\boldsymbol{r}_e,\, \boldsymbol{r}_h) = \frac{\mathrm{e}^{\mathrm{i}\boldsymbol{K}\cdot\boldsymbol{R}}}{\sqrt{V}}\varphi_{1s}(\boldsymbol{r}), \quad \varphi_{1s}(\boldsymbol{r}) = \frac{\mathrm{e}^{-r/a_{\mathrm{B}}}}{\sqrt{\pi a_{\mathrm{B}}^3}}. \tag{21}$$

Here we use the notation V for the crystal volume, $\boldsymbol{R}$ for the exciton center of mass $(m_e\boldsymbol{r}_e + m_h\boldsymbol{r}_h)/(m_e + m_h)$, $m_{e,\,h}$ for the electron or hole effective masses, $\boldsymbol{K}$ for the exciton translational wave vector, r for $|\boldsymbol{r}_e - \boldsymbol{r}_h|$, and a_{B} for the exciton Bohr radius $\varepsilon\hbar^2/(\mu_{cv}e^2)$.

The excitation energy of exciton state with the principal quantum number $n = 1, 2, \ldots$ is $E = E_g - R_{\mathrm{exc}}/n^2 + \hbar^2K^2/2M$, where M is the exciton translational mass $m_e + m_h$, and R_{exc} is ground-state 1 s-exciton binding energy, or exciton Rydberg, given by $(\mu_{cv}/m_0)\varepsilon^{-2}R_\infty$, $R_\infty = 13.6$ eV is the Rydberg energy constant, ε is the dielectric function at the frequency $\Omega \sim R_{\mathrm{exc}}/\hbar \ll E_g/\hbar$.

For the above-gap electron-hole excitations, a residual effect of the Coulomb mutual attraction of an electron and a hole gives rise to a correlation of their positions in space and an enhanced wave function overlap. This enhances the optical transition matrix elements compared to the negligible electron-hole interaction and affects the spectral shape of the continuum absorption spectrum at $\hbar\omega > E_g$. The ratio of the absorption coefficients above the band edge with and without the Coulomb interaction is called the Sommerfeld factor or the Coulomb enhancement factor. In a three-dimensional (3D) semiconductor, due to this factor the absorption coefficient changes the square-root dependence (11) to a constant absorption closely above the bandgap. In a two-dimensional (2D) system, the bare band-to-band step absorption spectrum is multiplied by the 2D Sommerfeld factor which equals 2 at the gap edge and unity far above the gap. In both 3D crystals and 2D semiconductors, III-V and II-VI based quantum wells, the changes in the absorption spectrum are seen in the range of a few exciton Rydberg energies.

In dielectrics, e.g. ionic and molecular crystals, the photoexcited electron and hole are tightly bound to each other within the same unit cell or nearest-neighbor unit cells and form the Frenkel excitons. Due to the dipole-dipole interaction, intra-cell excitation is transferred to other cells and propagates in the crystal. The optical spectra of Frenkel excitons in molecular crystals with more than one equivalent molecular entity in the unit cell reveal the so-called Davydov splitting. A notable example of excitons of the intermediate type are charge-transfer excitons. All types of excitons possess a common property: the free exciton is an electron excitation which involves correlated motion of electrons and holes, does not carry current, but does carry energy.

Fine structure of exciton levels

If allowance is made for free-carrier spin, then the ground state $n = 1$ of an exciton is degenerate, even in the case of simple bands. For direct-gap Γ-point excitons, the ground-state degeneracy is equal to the product of the conduction- and valence-band degeneracies at $\boldsymbol{k} = 0$. The wave functions of the ground state transform according to the representation $D_{\mathrm{exc}} = \Gamma_e \times \Gamma_h$, where the representations Γ_e and Γ_h characterize the symmetry of electron and hole states at the extremum point. The representation D_{exc} is reducible and may be decomposed into irreducible representations of the point group of the bulk or nanostructure material. The electron-hole exchange interaction partially removes the degeneracy and splits the 1 s-exciton level into states transforming according to the irreducible representations.

For illustration, let us consider a pair of the conduction band Γ_6 and the heavy-hole valence band Γ_6 in a zinc-blende-based quantum well structure of the D_{2d} symmetry. In accordance with the multiplication law $\Gamma_6 \times \Gamma_6 = \Gamma_1 + \Gamma_2 + \Gamma_5$ we obtain that the heavy-hole exciton level 1 s is split into a doubly degenerate state Γ_5 active in the polarization perpendicular to the C_2 axis and two dipole-forbidden singlet levels Γ_1 and Γ_2.

Optical properties of two-dimensional systems

The Bouguer law is unadapted to two-dimensional structures. In this case the absorption property is conveniently described by the absorptance A defined as a ratio of the absorbed radiant flux to the incident flux. For a 2D graphene flake lying on the substrate with the refractive index n the absorptance takes the form

$$A = f\frac{\pi e^2}{\hbar c},$$

where $f = 4/(n + 1)^2$. For a free-standing flake where $f = 1$ the absorptance has a universal value of the fine structure constant $e_2/(\hbar c)$ times π. The calculation shows that, with allowance for the electron-electron Coulomb interaction, the coefficient A is renormalized by a factor $1 + \mathcal{D}g$, where the interaction strength parameter $g = e^2/(n^2/\hbar\upsilon_0)$, υ_0 is the so-called Fermi velocity, and $\mathcal{D} = (19 - 6\pi)/12 \approx 0.0125$. Thus, in graphene the Coulomb renormalization is negligible.

In bulk semiconductors an exciton polariton is formed by a 3D exciton and a 3D photon, see the next section. Nanostructures of different dimensionalities allow one to study coupling between 3D photons and 2D, 1D or 0D excitons. The coupling between a 3D photon and a 2D exciton is realized in a quantum well (QW) structure. The coefficient of amplitude reflection and transmission of light from a single QW is given by

$$r_{QW} = \frac{\mathrm{i}\Gamma_0}{\omega_0 - \omega - \mathrm{i}(\Gamma_0 + \Gamma)}, \tag{22}$$

where ω_0, Γ_0 and Γ are the exciton resonance frequency, radiative and nonradiative decay rates. The meaning of these parameters can be conveniently interpreted in terms of the time-resolved experiment: after a short-pulse photoexcitation of the exciton the time variation of its wave function is described by the factor $\exp[-(\mathrm{i}\omega_0 + \Gamma + \Gamma_0)t]$. The parameter Γ_0 enters both the numerator and denominator and can be thought of as the exciton oscillator strength. The amplitude transmission coefficient is related to the reflection coefficient by $t_{QW} = 1 + r_{QW}$ which leads to the QW absorptance

$$A = 1 - |r_{QW}|^2 - |t_{QW}|^2 = \frac{2\Gamma_0\Gamma}{(\omega_0 - \omega)^2 + (\Gamma_0 + \Gamma)^2}.$$

The reduced dimensionality of nanostructures gives rise to an increased charge carrier interaction leading to high exciton binding energies. The quantum confinement of electron and hole wave functions enhances the exciton oscillator strength and supports the existence of exciton complexes such as biexcitons and trions. Biexciton is a positronium-molecule-like four-body system of two electrons and two holes. There are both the negatively and positively charged trions, X^- and X^+, composed of two electrons and one hole or two holes and one electron, respectively. The complexes, called originally "excitonic molecule" and "excitonic ion," are analogous, respectively, to a hydrogen molecule H_2 and to an ion H^- or ionized molecule H_2^+.

The trions can be optically excited in the systems containing resident charge carriers. In the reflection spectra they are observed as an additional resonant contour below the exciton resonance. In such two-pole reflection spectrum, the amplitude reflection coefficient near the trion resonance is also described by Eq. (22) where ω_0 and Γ_0 are replaced by the trion resonance frequency $\omega^{\mathrm{tr}}{}_0$ and the radiative damping rate $\Gamma^{\mathrm{tr}}{}_0$, the latter being proportional to the density of resident carriers. With the increasing density, the enhancement in the trion oscillator strength $\Gamma^{\mathrm{tr}}{}_0$ is accompanied by a decrease in the exciton oscillator strength Γ_0.

The biexciton binding energy $\varepsilon_{\mathrm{bi}}$ is defined as the difference between the biexciton excitation energy $\hbar\omega^{\mathrm{bi}}{}_0$ and two ground-state exciton energies $2\hbar\omega_0$. Biexciton forms mainly through the following three mechanisms: (i) two-photon absorption, (ii) -exciton-exciton binding in condensed exciton environment, and (iii) resonant excitation from a single exciton.

Polaritons

The optical properties of bulk solids are strongly modified in the vicinity of the resonance frequency of the quasi-particle excitation such as optical phonon or exciton. A photon and a quasi-particle mix in the dispersion-crossover region, losing their identity in a combined quasi-particle called the polariton, phonon polariton or exciton polariton, satisfying the dispersion Eq. (7).

Phonon polaritons

We start from the optical spectroscopy of optical phonon polaritons and consider a crystal lattice of cubic symmetry with two distinct atoms per unit cell. In such a material the optical phonons are infrared-active and the dielectric function has the Lorentz type of dispersion

$$\varepsilon(\omega) = \varepsilon^\infty + \frac{(\varepsilon^0 - \varepsilon^\infty)\omega_T^2}{\omega_T^2 - \omega^2 - \mathrm{i}\omega\Gamma}, \tag{23}$$

where ε^0 and ε^∞ are static and high frequency dielectric constants, ω_T is the resonant frequency of the transverse optical phonon, or the TO phonon, and Γ is the phonon decay rate. Note that the existence of a bandgap in an insulator is confirmed by the optical transparency below this bandgap, except in the lower energy region where the absorption is due to lattice vibrations because in realistic materials $\Gamma \neq 0$ and the imaginary part of the dielectric function is nonzero.

Neglecting the decay, we can rewrite Eq. (23) as

$$\varepsilon(\omega) = \varepsilon^\infty \frac{\omega_L^2 - \omega^2}{\omega_T^2 - \omega^2}, \tag{24}$$

where the longitudinal phonon frequency ω_L is given by Lyddane–Sachs–Teller relation

$$\frac{\omega_L^2}{\omega_T^2} = \frac{\varepsilon^0}{\varepsilon^\infty}.$$

Physically, polaritons can be conveniently considered in terms of an effective two-oscillator model. Particularly, in a phonon polariton, the uncoupled photonic and phononic oscillators are characterized by the same wave vector $\boldsymbol{q}$ and the bare-particle eigen

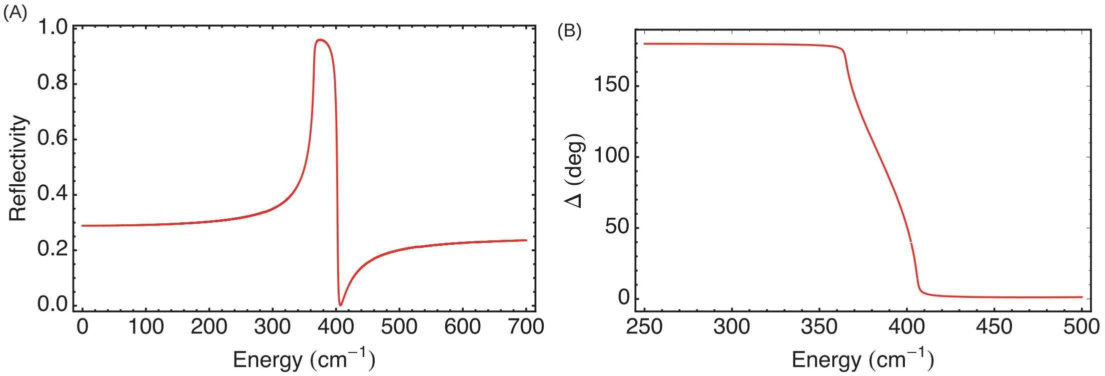

Fig. 2 Optical properties of a GaP crystal in the infrared region. (A) Normal-incidence reflectivity calculated for the following set of parameters: $\varepsilon^{\infty} = 9.08$, $\omega_T = 364.81$ cm^{-1}, $\omega_L = 402.33$ cm^{-1}, $\Gamma = 1.61$ cm^{-1}. (B) Ellipsometric phase shift Δ at 70° angle of incidence versus photon energy. The parameters are taken from Samarasingha and Zollner, 2021.

frequencies ω_T and $\omega_{\rm phot} = cq/\sqrt{\varepsilon^{\infty}}$. The coupling is governed by the value of the phonon longitudinal-transverse splitting, $\omega_{\rm LT} = \omega_L - \omega_T$. The two-oscillatory analogy is clearly seen in a rewritten version of Eqs. (7) and (24)

$$\left(\omega^2 - \omega^2_{\rm phot}\right)\left(\omega^2 - \omega_T^2\right) = \omega^2\left(\omega_L^2 - \omega_T^2\right).$$

In the general consideration, the numerator and denominator in Eq. (24) contain the terms $-i\omega\Gamma_L$ and $-i\omega\Gamma_T$ with different decay rates Γ_T and Γ_L.

Fig. 2 shows the infrared reflection spectrum of a GaP bulk crystal under normal incidence and the phase shift Δ as a function of photon energy calculated at the incidence angle 70°.

Since in the interval $\omega_T < \omega < \omega_L$ (the so-called Reststrahlen region) the dielectric function (24) is negative and, therefore, the refractive index $\overline{n}$ is imaginary, the reflectance $R = 1$. Moreover, at the frequency $\omega = \sqrt{(\varepsilon^{\infty}-1)/(\varepsilon^{0}-1)}\omega_T < \omega_T$ the refractive index $\overline{n}$ equals to unity and the reflection vanishes, $R = 0$. With increasing frequency above ω_L, the reflectivity saturates and is determined by the high-frequency refractive index $n = \sqrt{\varepsilon^{\infty}}$. Evidently, with allowance for the phonon decay rate Γ the reflection spectra are smoothed.

Exciton polaritons

For excitons, the longitudinal-transverse splitting ω_{LT} is small as compared with the resonance frequency ω_0 and the dielectric function in the vicinity of ω_0 can be reduced to

$$\varepsilon(\omega, \boldsymbol{q}) = \varepsilon_b\left(1 + \frac{\omega_{LT}}{\omega_0(q) - \omega - i\Gamma}\right).$$

Here ε_b is the background dielectric constant, and as compared with Eq. (23) we take into account the spatial dispersion, namely, the dependence of the exciton resonance frequency on the wave vector: $\omega_0(q) = \omega_0 + (\hbar q^2/2M)$. The consequence is that the dispersion Eq. (7) becomes a second-order algebraic equation for q^2 with two solutions, photon-like and exciton-like polaritons. For the calculation of the reflectivity, the Maxwell boundary conditions must be supplemented with an additional boundary condition. The theory of exciton polaritons is applicable to both the Wannier–Mott and Frenkel excitons. However, the exciton wave function and fine structure of excitonic levels are certainly treated quite differently in these two models.

For the Wannier–Mott exciton wave function (21), the longitudinal-transverse splitting is given by

$$\omega_{LT} = \frac{4\pi}{\hbar\varepsilon_b}\left(\frac{ep_{cv}}{\omega_0 m_0}\right)^2 \varphi^2_{1s}(0). \tag{25}$$

where $\varphi_{1s}(0) = (\pi a^3{}_B)^{-1/2}$ is the probability amplitude that the electron and the hole are found on the same site which is nonvanishing only for the *s*-like states. This equation is true if the interband matrix element of the momentum operator p_{cv} taken between the conduction and valence bands at the extremum point is nonzero. By contrast, in Cu_2O crystals the interband matrix elements vanish at the extremum point and depend linearly on the electron wave vector $\boldsymbol{k}$. In this case the exciton oscillator strength of the *s*-excitons vanishes and optically active are the *p*-excitons. This explains why, in Cu_2O, the exciton absorption peaks start from the principal number $n = 2$. In the same way, the two-photon optical transitions are forbidden for the *s*-excitons and allowed for *p*-shell excitons if the matrix element p_{cv} is nonzero at the extremum point and the *s*-excitons are optically active in one-photon absorption. Fig. 3 shows the one-photon absorption spectrum of the *p*-excitons obtained from the transmission experiments, revealing a large number of lines (Kazimierczuk et al., 2014). To take a closer look at the high-energy part, the spectrum is zoomed with increasing resolution.

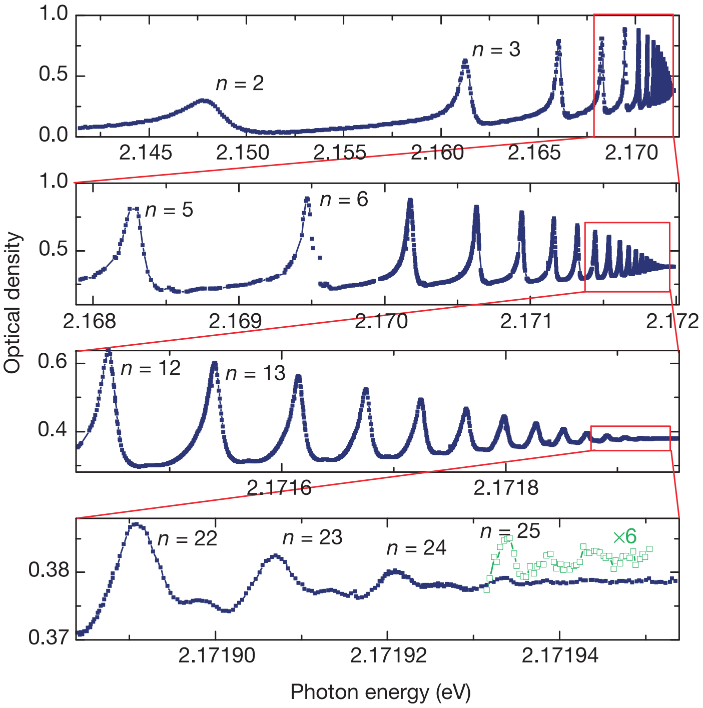

Fig. 3 High-resolution absorption spectra of yellow *P* excitons in bulk Cu_2O. Spectra are measured with a single-frequency laser on a natural sample of thickness 34 mm at 1.2 K. Reproduced by permission Kazimierczuk T, Fröhlich D, Scheel S et al. (2014) Giant Rydberg excitons in the copper oxide Cu_2O. *Nature* 514: 343–347, doi: 10.1038/nature13832.

Polaritons in quantum microcavities

The modern technology allows one to reduce the dimensionality of photonic quantum states. Particularly, a 2D photon is realized in a planar optical microcavity which is a multilayer heterostructure consisting of an active layer sandwiched between left-hand and right-hand distributed Bragg reflectors. If one or few QWs are embedded inside the active layer, the structure is called the quantum microcavity. The cavity exciton-polariton is a generalization of the concept of exciton polariton in a bulk material and can be also modeled by a pair of two coupled classical oscillators, one representing a 2D photon mode and another representing a 2D exciton in the QW. In the simplest case of a single QW placed inside the active layer, the eigen-frequencies $\omega_\pm$ of two 2D exciton-polariton modes are two solutions of the equation

$$\left[\omega - \varpi\left(\boldsymbol{q}_\parallel\right) + \mathrm{i}\bar{\gamma}\right](\omega - \omega_0 + i\Gamma) = V^2. \tag{26}$$

Here $\boldsymbol{q}_\parallel$ is the in-plane wave vector, ω_0 and Γ are the exciton resonance frequency and nonradiative damping rate, $\varpi(q_\parallel) = \sqrt{\tilde{\omega}^2 + \left(cq_\parallel/n_b\right)^2}$, ϖ and $\bar{\gamma}$ are the resonance frequency and damping rate of the photon mode, $n^2{}_b = \varepsilon_b$ is the dielectric constant of the active layer, the coupling parameter V determines the so-called Rabi splitting 2 V. In the strong-coupling regime, $(\Gamma - \bar{\gamma})^2 < (2V)^2$, the two eigen-frequencies of Eq. (26) reveal themselves as two dips in the reflection spectra and peaks in the transmission or absorption spectra.

Resonant photonic crystals

Photonic crystals are media with the dielectric constant periodically varying in space with a period allowing for the Bragg diffraction of light in the visible or infrared range. In this context, a simplest example of a photonic (one-, two-, or three-dimensional) crystal is a periodic structure consisting of two materials with different refractive indices, like a distributed Bragg reflector. Natural opal gemstones and artificial opals represent 3D photonic crystals. Similarly to X-ray diffraction in conventional crystals, the photonic crystals allow for diffraction for optical wavelengths.

Of particular interest are periodic structures, in which the dielectric response of one of the structural blocks as a function of frequency has a pole at a certain resonance frequency ω_0. They form a special class of resonant photonic crystals. In these systems, normal light waves are polaritons. The resonant Bragg structure is a special kind of multiple QWs with the period d satisfying the condition

$$q(\omega_0) = \frac{\pi}{d} \quad \text{or} \quad d = \frac{\lambda(\omega_0)}{2},$$

where $q(\omega) = \omega n_b/c$ and $\lambda(\omega_0) = 2\pi c/\omega_0 n_b$ are the light wavevector and wavelength at the exciton resonant frequency, $n_b = \sqrt{\varepsilon_b}$. Evolution of the reflection spectrum of the resonant Bragg structure with the QW number N demonstrates a transition from the superradiative regime, $N \ll \sqrt{\omega_0/\Gamma_0}$, to the photonic-crystal regime, $\sqrt{\omega_0/\Gamma_0} \ll N$. In the former regime, the reflectance is given by Eq. (26) where Γ_0 is simply replaced by $N\Gamma_0$. In the latter regime, the structure shows itself as a true photonic crystal with a stop-band of the width $2\sqrt{2\Gamma_0\omega_0/\pi}$.

Photoluminescence

Photoluminescence is the emission of radiation induced by the optical excitation of a sample by using an external source of light. The conventional photoluminescence spectroscopy is based on measurements of secondary-emission spectrum at fixed parameters of the primary radiation. In this set-up the measured spectrum is mainly determined by the oscillator strength and occupancy of the radiative states. In its turn, the occupancy is controlled by the lifetime and energy relaxation processes of charge carriers and excitons. In another technique, known as photoluminescence excitation spectroscopy, the spectrometer is set to detect emission of a fixed photon energy from the sample. The intensity of this emission is recorded as a function of the excitation photon energy. Photoluminescence excitation spectra give information about the absorption spectrum above the fundamental edge, rather than about the lifetimes of excited states.

In particular cases of resonant optical excitation a secondary-emission process can be considered both as the photoluminescence and light scattering. On the other hand, as in light scattering the spectrum of the secondary radiation is tied to the initial light frequency and shifts with shifting this frequency. On the other hand, the same process has features of the photoluminescence because it can be described in terms of a two-step process with a real intermediate state. On this basis, sometimes the general term "resonant secondary emission" is used. In most cases, however, the difference between the two phenomena can be justified. Indeed, in light scattering defined in the traditional way the excited states of a system are virtual, whereas in conventional photoluminescence the emission of the secondary photon is usually preceded by multiple transitions of the system between different real excited states.

Color centers

Insulating crystals with point defects of a lattice (impurity atoms or ions, vacancies etc.) represent a special class of optical materials. The defects introduce additional energy levels lying between the conduction-band bottom and valence-band top, so that lower-energy photons are allowed to participate in absorption processes. Crystal defects can form color centers and allow for both the spontaneous and stimulated emission of light at new wavelengths. In alkali halides, a color center formed by an electron trapped in an anion vacancy is called the F center. Alternatively, completely transparent crystals and glasses exhibit pronounced colors by doping with ions often called activators.

The photoluminescence (or fluorescence) of defects in an insulating solid, e.g. F center in an alkali halide, is characterized by the Stokes shift which means that the fluorescence emission occurs at a longer wavelength than the incident light. The explanation is given in the configuration coordinate model. Once excited, the electron trapped by the vacancy causes significant displacements of nearby atoms to their new equilibrium positions (lattice relaxation). From this "relaxed excited state," the electron returns to the ground state emitting a photon. The peak of the emission band is displaced from that of the absorption band by the Stokes shift, both bands being described by Gaussian-like shape. In the model both the optical excitation and radiative recombination follow the Franck–Condon principle which, classically, states that an electronic transition is most likely to occur without changes in the positions of nuclei in the surrounding environment.

The ruby laser was the first with which laser radiation was generated at a wavelength of 694.3 nm. It uses a solid medium of crystalline aluminum oxide Al_2O_3 containing chromium ions which replace Al atoms. When light is incident on the Cr^{3+} ion, an electron is raised from its ground state $^4A_2$ to its excited states $^4T_2$ and $^4T_1$ lying roughly at 2.2 eV and 3.0 eV above the ground state, respectively. These states decay non-radiatively by phonon emission until the electron reaches its lowest excited metastable state ^2E which on a transition to $^4A_2$ ground state emits the laser radiation. Historically, the second laser material was uranium-doped calcium fluoride U^{3+}:CaF, and then the neodymium-doped calcium-tungstate ($CaWO_4$) laser was made emitting on the now-standard 1.06 - μm transition.

Point defects in glasses are atomic size deviations of the short range order (intrinsic defects) and the isolated impurity atoms or ions in the glass network (impurity defects). In an ideal structure of glass, the lattice is defined as solid network, in which each atom has the same short range order. For example, in the fused silica glass network (SiO_2) each silicon atom is tetrahedrally surrounded by four oxygen atoms and each oxygen atom is surrounded by two silicon atoms. In this optical glass, the broad transparent transmission range covers the complete visible spectrum and extends far into the infrared and ultraviolet regions where electronic and vibronic absorption takes place. The existence of point defects usually manifests as changes of spectroscopic properties in the transparency region. Mainly all glass-based lasers act on electronic transitions between impurity defect (activator) levels.

Optical orientation of electron spins

Since the pioneer work by Lampel (1968) the optical orientation of free-carrier spins in semiconductors has become an effective method, contactless and nondestructive, for investigations of semiconductor band structure and kinetic parameters. The essence of the method is to analyze the photoluminescence polarization as a function of the polarization of the initial light. We first formulate the basics of optical orientation of free-carrier spins. For simplicity we assume that the light propagates along the normal z to the sample surface and the luminescence is registered in the backscattering geometry. We use also the following notations: $P^0{}_c$ for the degree of circular polarization of the initial light, $n_\pm$ for the densities of electrons with the spin up and down with respect to the z direction, n for the total electron density $n_+ + n_-$, $g_\pm$ for the partial photogeneration rates, g for the total electron generation rate $g_+ + g_-$, S_z for the total electron spin polarization $(n_+ - n_-)/2$, and p for the degree of the spin polarization $(n_+ - n_-)/(n_+ + n_-)$.

Spin photoexcitation

Under optical interband excitation by circularly polarized light, the angular momentum component of σ_+ (or σ_-) photons is transferred to the spin of free carriers. The spin polarization of the photogenerated electrons depends on the selection rules for the interband transitions. The initial degree of spin polarization, $p_0 = (g_+ - g_-)/(g_+ + g_-)$, is proportional to the degree of circular polarization of the initial light: $p_0 = \kappa P_c{}^0$. The coefficient κ depends on the selection rules: for the interband transitions $\Gamma_8 \to \Gamma_6$ in the bulk GaAs-type semiconductors $\kappa = -1/2$, while for the optical transitions from the heavy-hole valence subband in a GaAs-based quantum well structure $\kappa = -1$.

Electron spin kinetics

The rate equations for the densities n_+ and n_- have the form

$$\begin{aligned} \frac{dn}{dt} + \frac{n_+}{\tau_0} + \frac{1}{2\tau_s}(n_+ - n_-) &= g_+, \\ \frac{dn_-}{dt} + \frac{n_-}{\tau_0} + \frac{1}{2\tau_s}(n_- - n_+) &= g_-. \end{aligned} \tag{27}$$

Here τ_0 is the lifetime of photoelectrons in the conduction band and τ_s is the spin relaxation time. Under steady-state excitation, the solution of the above rate equations reads $n = g\tau_0$ and $p = (T/\tau_0)p_0$, where T is the lifetime of optically oriented spins defined by $T^{-1} = \tau_0^{-1} + \tau_s^{-1}$. If the photoelectron lifetime τ_0 is not too long as compared to the spin relaxation time τ_s, then the photoelectrons retain spin polarization (at least partially).

Photoluminescence polarized by the optical orientation

Due to the same selection rules for interband optical transitions, the radiative recombination of spin-polarized photocarriers gives rise to a (partial) circular polarization of the photoluminescence $P_c = \kappa p$. This equation is valid for recombination with unpolarized holes which takes place in bulk GaAs, where the hole spin relaxation is very fast. In quantum well structures, the holes also can retain their spin polarization. If the both electron and hole degrees of spin polarization, p_e and p_h, are nonzero, the circular polarization (in a GaAs quantum well) is given by a more complicated equation

$$P_c = \frac{p_h - p_e}{1 - p_c p_h}.$$

Magnetic field influence

The transverse magnetic field, $\boldsymbol{B}^{(0)} \perp z$, leads to depolarization of the photoluminescence. The rate equation for the spin polarization $\boldsymbol{S}$ in the transverse magnetic field can be written down in the form

$$\frac{\boldsymbol{S}}{T} + \boldsymbol{S} \times \boldsymbol{\Omega}_L = \boldsymbol{G}_s, \tag{28}$$

where $\boldsymbol{\Omega}_L = g_e \mu_B \boldsymbol{B}^{(0)}/\hbar$ is the Larmor frequency, g_e is the electron's effective g factor, and $\boldsymbol{G}_s$ is the spin generation rate.

Let $\boldsymbol{B}^{(0)} \parallel x$, then under the normal incidence, $\boldsymbol{G}_s \parallel z$, one has

$$S_z\left(B^{(0)}\right) = \frac{S_z(0)}{1 + (\Omega_L T)^2}, \; S_y\left(B^{(0)}\right) = -\frac{\Omega_L T}{1 + (\Omega_L T)^2} S_z(0), \; S_x = 0,$$

where $S_z(0)$ is the spin polarization at zero magnetic field. One can see that in the transverse magnetic field the average electron spin is rotated around $\boldsymbol{B}^{(0)}$ and depolarized. This is the so-called Hanle effect. By measuring the photoluminescence intensity and analyzing its circular polarization in the transverse magnetic field, one can extract the characteristic time parameters τ_0 and τ_s.

Similarly to free carriers, exciton spins (or angular momenta) can be optically oriented as well by circularly polarized light. The circular polarization of the exciton photoluminescence is governed by the exciton lifetime and spin relaxation time.

Spin and valley optical orientation in transition metal dichalcogenides

In a monolayer of transition metal dichalcogenides, e.g. MoS_2, the spin orientation is accompanied by the valley polarization which is an inherent property of their band structure. In these atomically thin direct-gap materials, the conduction- and valence-band extrema are located not at the center of the two-dimensional hexagonal Brillouin zone, but rather at its vertices K_+ and K_-. Due to the spin-orbit interaction, the spin sublevels in the conduction and valence bands are remarkably split even at the extremum points with the opposite signs of the splitting in the $K_\pm$ valleys. As a result, under optical excitation by circularly polarized light near the band edge E_g the spin-polarized photocarriers and excitons are generated either in the K_+ valley or in the K_- valley depending on the sign of circular polarization, σ_+ or σ_-.

Magnetic circular polarization of exciton photoluminescence

The exchange interaction leading to the splitting of excitonic levels leaves some sublevels degenerate. In an external magnetic field, an additional modification of the exciton spectrum occurs, in particular, the remaining degeneracy of the exciton states is removed (Zeeman effect). Each of the split, optically active states emits circularly or elliptically polarized light in the direction of the magnetic field. In majority of situations, the exciton luminescence bandwidth exceeds the exchange and Zeeman splitting of exciton levels, due to the inhomogeneous broadening of the exciton's resonance frequency. This situation takes place when excitons are localized on deep levels in bulk crystals, composition fluctuations in solid solutions, fluctuations of the width of quantum wells, interfaces of a type II superlattice, and also in the case of size quantum effects for excitons in quantum dots or colloid nanocrystals allowing for the dispersion of their size and shape within the illuminated spot. This spectrally hidden fine structure manifests itself in the magnetic circular polarization of luminescence and in the dependence of the luminescence intensity on the magnetic field. The polarization appears due to a thermal selective population of split exciton spin levels. The optical spin orientation discussed in the previous section is most clearly observed under conditions, where the spin relaxation time τ_s is longer than the lifetime τ_0. In contrast to the optical orientation, the magnetic circular polarization of luminescence is high in the opposite case, $\tau_s < \tau_0$, when the populations of the Zeeman sublevels are quasi-equilibrium.

Purcell effect

The Purcell effect in the broad sense is the enhancement of a quantum system's spontaneous emission rate by its environment. For a point light source inserted into a photon resonant cavity, the effect is described by the Purcell factor f defined as the ratio between lifetimes of spontaneous emission in the infinite homogeneous medium filled with the cavity material and in a system with the cavity. Under the optimal conditions, where the resonance frequency of the emitter ω_0 is tuned to the cavity photon frequency ω_c and the emitter is placed in the field antinode, the Purcell factor is given by

$$f = \frac{3Q\lambda^3}{4\pi^2 V},$$

where V is the volume of the resonator, Q is the quality factor, $\lambda \equiv \lambda_0$ is the light wavelength in vacuum if the cavity is empty and $\lambda = \lambda_0/n$ if the cavity is filled with a substance with the refractive index n.

Single-photon sources

Single-photon emitters are non-classical light sources. The promising types are atom-like solid-state single-photon emitters including fluorescent atomic defects (in diamond, SiC, Nd-doped $Y_3Al_5O_{12}$ garnet, Y_2SiO_5, ZnO, BN), semiconductor quantum dots and nanocrystals (InAs, GaN, core/shell CdSe/ZnS), localized excitons in two-dimensional materials (WSe_2, $MoSe_2$ monolayers) and carbon nanotubes. If the sample contains plenty of isolated light sources, e.g., quantum dots, at low enough density they can be isolated to be used as a single-photon emitter.

One of the most important characteristics of light sources is the second order correlation function $g^{(2)}(\tau)$, which can be measured in the Hanbury-Brown-Twiss experiment. Here τ is the photon pair separation time. If a two-level quantum system emits a photon at a time t, it is impossible for it to emit another one immediately after that, because it is necessarily in the ground state. The next photon can only be emitted after a waiting time. In an ideal single-photon source, the function $g^{(2)}(\tau)$ vanishes at $\tau \to 0$ (the photon antibunching effect) and is described by $1 - \exp\,[-t(\Gamma + W)\tau]$, where Γ is the electron-hole recombination rate and W is the effective generation rate of the quantum system.

Two-photon entanglement

Quantum entanglement is a physical phenomenon that occurs when, in two or more particles, the quantum state of each particle cannot be described independently of the state of the others, including even when the particles are separated by a large distance. The simplest example of an entangled photon pair is the quantum-mechanical state

$$\Psi = \frac{1}{\sqrt{2}}\left(|\hbar\omega_1,\sigma_+\rangle|\hbar\omega_2,\sigma_-\rangle + |\hbar\omega_1,\sigma_-\rangle|\hbar\omega_2,\sigma_+\rangle\right), \tag{29}$$

where $|\hbar\omega_j, \sigma_\pm\rangle$ is a single photon state of the energy $\hbar\omega_j$ ($j = 1, 2$) and right- or left-hand circular polarization. Note that these photons can propagate in arbitrary relative directions.

Entangled photons on demand can be generated in the biexciton-exciton radiative cascade in a single semiconductor quantum dot. In the biexciton ground state, two electrons or two holes form spin singlet states. Starting from this ground state, one of the electrons recombines with a hole and emits a σ_+ or σ_- photon. Then the second electron of the opposite spin recombines with the second hole of the opposite spin, and, due to the selection rules, a photon of opposite polarization is emitted. Because of the interparticle interaction, the biexcitonic ground state has an energy $\hbar\omega_{\text{bi}}$ different by few meV from the doubled energy $2\hbar\omega_0$ of excitonic ground state. Therefore, the first emitted photon 1 and the second emitted photon 2 have different energies $\hbar\omega_1$ and $\hbar\omega_2$.

If instead of circular polarization the linear polarization is analyzed, the state (29) can be written down in an equivalent form as $(\hbar\omega_1, X\rangle|\hbar\omega_2, X\rangle + |\hbar\omega_1 Y|\hbar\omega_2, Y\rangle)/\sqrt{2}$ in which case the entangled photons are collinearly polarized in the x or y directions.

Nonlinear optics

Many nonlinear effects can be phenomenologically described by expanding the electric polarization in powers of the light-wave electric field $\boldsymbol{P} = \boldsymbol{P}^{(1)} + \boldsymbol{P}^{(2)} + \boldsymbol{P}^{(3)} + \ldots$ The first term describes the conventional linear response (4). The second and third terms represent the nonlinear responses of the second and third orders

$$\begin{gathered}
P_\alpha^{(2)}(\boldsymbol{r},t) = \varepsilon_0\chi^{(2)}_{\alpha\beta\gamma}(\omega_1,\omega_2)E_\beta(\omega_1,\boldsymbol{k}_1)E_\gamma(\omega_2,\boldsymbol{k}_2)\exp\left[\mathrm{i}(\boldsymbol{k}_1+\boldsymbol{k}_2)\cdot\boldsymbol{r} - \mathrm{i}(\omega_1+\omega_2)t\right],\\
P_\alpha^{(3)}(\boldsymbol{r},t) = \varepsilon_0\chi^{(2)}_{\alpha\beta\gamma\delta}(\omega_1,\omega_2,\omega_3)E_\beta(\omega_1,\boldsymbol{k}_1)E_\gamma(\omega_2,\boldsymbol{k}_2)E_\delta(\omega_3,\boldsymbol{k}_3)\\
\times\exp\left[\mathrm{i}(\boldsymbol{k}_1+\boldsymbol{k}_2+\boldsymbol{k}_3)\cdot\boldsymbol{r} - \mathrm{i}(\omega_1+\omega_2+\omega_3)t\right].
\end{gathered} \tag{30}$$

Here ω_j is the frequency, $\boldsymbol{k}_j$ the wave vector, $\boldsymbol{E}(\omega_j, \boldsymbol{k}_j)$ the amplitude of the j-th constituent of the electromagnetic field. For single crystals or short-period SLs, $\boldsymbol{r}$ is the 3D radius-vector while, in QW structures, $\boldsymbol{r}$ is a vector with the components x, y, z_l, where z_l is the position of the l-th well, for instance, the coordinate of its center (the choice of point z_l within a well is arbitrary if its width is small compared with the light wavelength). The frequencies in Eq. (30) may assume both positive and negative values, the corresponding amplitudes being related through

$$\boldsymbol{E}(-\omega,\ -\boldsymbol{k}) = E^*(\omega,\boldsymbol{k}).$$

For the sake of simplicity, we neglect in Eq. (30) the spatial dispersion of the susceptibility, i.e., the dependence of $\chi^{(n)}$ on $\boldsymbol{k}_1$, $\boldsymbol{k}_2$, $\boldsymbol{k}_3$.

The second-order susceptibility $\chi^{(2)}$ describes the generation of optical harmonics at the sum or difference frequency, in particular, at $\omega_1 = \omega_2$, second-harmonic generation. The dc photogalvanic current $\boldsymbol{j}$ is obtained from $\chi^{(2)}$ in the limit $\omega_2 \to -\omega_1$.

Fig. 4 shows the intensity of the second harmonic generation (SHG) observed in the magnetoelectric antiferromagnet CuB_2O_4 (Mund et al., 2020). The exciting laser light is polarized along the z axis, the electric field of the second harmonic $E^{2\omega} \parallel x$, the external magnetic field $\boldsymbol{B}^{(0)}$ is directed either along or against the x axis. The difference $|E^{2\omega}(\boldsymbol{B}^{(0)})|^2 - |E^{2\omega}(-\boldsymbol{B}^{(0)})|^2$ demonstrates the nonlinear nonreciprocity effect described by the product $B_x{}^{(0)}T_x|E_z{}^{\omega}|^4$, where $\boldsymbol{T}$ is the toroidal vector expressed via the antiferromagnetic vector $\boldsymbol{L}$ as $\boldsymbol{T} = \hat{e}_x L_y + \hat{e}_y L_x$.

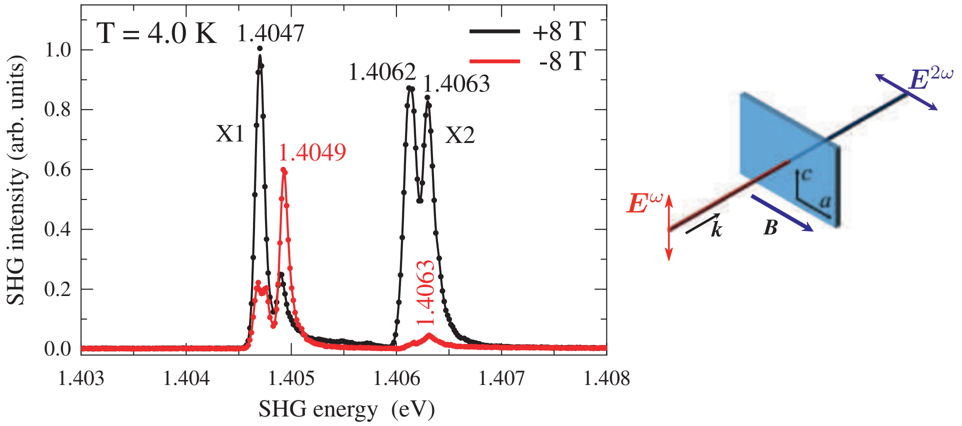

Fig. 4 Second harmonic generation spectra measured in CuB_2O_4, at T = 4 K for opposite magnetic fields demonstrates a strong spectral nonreciprocity reaching almost 100% at some lines, e.g., at 1.4062 eV line. The right-hand part shows geometry of the experiment. Reproduced by permission Mund J, Yakovlev DR, Poddubny AN et al. (2020) Toroidal nonreciprocity of optical second harmonic generation. *Phys. Rev. B* 103: 180410.

The third-order susceptibility $\chi^{(3)}$ describes a variety of phenomena, namely, third-harmonic generation (at $\omega_1 = \omega_2 = \omega_3$), two-photon absorption of a monochromatic light wave (two of the three values of ω_j coincide, the third one differs from them in sign, e.g., $\omega_2 = \omega_3 = -\omega_1$) or two monochromatic waves (two of the three frequencies differ in sign and do not coincide with the third one, e.g., $\omega_2 = -\omega_3 \neq \pm\omega_1$), a photoinduced change in the absorption or reflection of a probe beam linear in pump-beam intensity (photoabsorption or photoreflection), photoinduced gyrotropy or birefringence, four-wave mixing of three light waves ω_j, $\boldsymbol{k}_j$ ($j = 1, 2, 3$) accompanied by generation of a new harmonic at the frequency $\omega_1 + \omega_2 - \omega_3$ and the wave vector $\boldsymbol{k}_1 + \boldsymbol{k}_2 - \boldsymbol{k}_3$. Degenerate four-wave mixing is a particular case of the latter process, where two beams with the coinciding frequencies and different propagation directions, $\boldsymbol{k}_1 \neq \boldsymbol{k}_2$, interact and induce a new spatial harmonic $2\boldsymbol{k}_1 - \boldsymbol{k}_2$ or $2\boldsymbol{k}_2 - \boldsymbol{k}_1$.

Pump-probe spectroscopy

In a widely-used two-pulse optical excitation of a solid, the first pulse (pump) stimulates the system from its equilibrium state. The excited state exhibits a time scale of picosecond or femtosecond for relaxation dynamics. Then a probe (second laser pulse) examines the system at varying temporal delays in the excited state. This nonlinear optical method of study of excited state dynamics is termed as pump-probe spectroscopy. The technique is applicable to different classes of solids, semiconductors and dielectrics, ferro- and antiferromagnetics, ferroelectrics and multiferroics as well as the nanomaterials such as quantum wells, nanowires, nanotubes, quantum dots, graphene etc. First we describe this technique applied to study spin or magnetization dynamics.

Spin Faraday and Kerr rotation

At present the optical orientation of electron spins described in Section "Optical orientation of electron spins" is mostly studied in the polarized pump-probe measurements. A first short intense pulse of circularly polarized light generates the nonequilibrium spin-oriented electrons and holes and creates a macroscopic spin polarization. In accordance to Section "Magnetic field influence", in a constant transverse magnetic field, $\boldsymbol{B}^{(0)}$, applied to the sample, the macroscopic polarization starts to precess around the field direction with the Larmor frequency (the so-called spin quantum beats). The spin can also precess in time at zero magnetic field due to the splitting of spin sublevels governed by the Dresselhaus bulk and Rashba structural inversion asymmetries. The optically created polarization, its precession and transport can be probed by short pulses of linearly polarized light via rotation of their polarization plane after the propagation through the photoexcited medium (spin Faraday effect) or reflection from this medium (spin Kerr effect). The probe pulses of linearly polarized light show a remarkable sensitivity to the practically instant population of electron spin sublevels.

The pump-probe spin-dependent rotation techniques are especially useful for manipulation and measurement of electron spin polarization in singly charged quantum dots due to a very long coherence time of resident-electron spins.

The spin Faraday or Kerr rotation is so sensitive that it allows to monitor equilibrium randomly-varying spin fluctuations by means of the linearly polarized continuous wave probe without any pump ray. This kind of spin noise technique is especially well suited to study slow spin relaxation in semiconductor nanostructures.

Pump-probe micro-spectroscopy

An important type of the technique is the pump-probe micro-spectroscopy which combines the near-diffraction-limited spatial resolution with femtosecond temporal resolution. The pump-probe microscope is capable of exciting a sample in one location and probing the pump-induced change in another location, e.g. a change in absorption or spin Kerr rotation. It enables direct imaging of transport phenomena such as free carrier charge and spin diffusion, exciton migration and plasmon propagation in solids. At close-to-zero delay, the probe pulse is affected only within the area of the pump excitation. At longer delay times, changes in the pump-probe signal extend, due to the transportation, far from the excitation spot.

Conclusion

The analysis of optical properties of semiconductors and dielectrics reveals our understanding of the light-matter interaction. In the present chapter we have considered the propagation of electromagnetic waves in solids as described by Maxwell's macroscopic equations and the dielectric tensor. The latter is a function of light frequency and may also depend on the external or internal parameters leading to birefringence, magneto- and electro-optical effects, piezospectroscopy and the spatial dispersion, in particular, natural optical activity. The optical reflection, transmission and absorption are the standard methods of noninvasive characterization of materials. An important attention is attracted to the excitonic effects in semiconductors and semiconductor nanostructures (Wannier–Mott excitons) and molecular crystals (Frenkel excitons), fine structure of exciton levels. Mixing of a photon and a quasi-particle excitation results in formation of hybrid excitations, e.g., optical-phonon and exciton polaritons. We have outlined the well-established optical materials, such as dielectrics activated by impurities, e.g., active species in solid lasers and novel materials, metamaterials, resonant microcavities and photonic crystals. The secondary light emission is presented by polarized photoluminescence spectroscopy due to optical orientation of free-carrier spins. The nonlinear optics is represented by second harmonic generation and pump-probe spectroscopy. Novel trends are illustrated by single-photon sources and two-photon entanglement.

Acknowledgments

This work was financially supported by the Russian Science Foundation, grant 19-12-00051. The author thanks M.M. Glazov, L.E. Golub, M.O. Nestoklon, A.N. Poddubny and S.A. Tarasenko for stimulating discussions.

References

Guizzetti G and Patrini M (2023) *Optical properties of materials. Chapter NNN in ECM*. 2nd edn.: Elsevier.

Kazimierczuk T, Fröhlich D, Scheel S, Stolz H, and Bayer M (2014) Giant Rydberg excitons in the copper oxide Cu_2O. *Nature* 514: 343–346.

Lampel G (1968) Nuclear dynamic polarization by optical electronic saturation and optical pumping in semiconductors. *Physical Review Letters* 20: 491.

Mund J, Yakovlev DR, Poddubny AN, Dubrovin RM, Bayer M, and Pisarev RV (2020) Toroidal nonreciprocity of optical second harmonic generation. *Physical Review B* 103: 180410.

Samarasingha NS and Zollner S (2021) Temperature dependence of the optical phonon reflection band in GaP. *Journal of Vacuum Science and Technology B* 39: 052201.

Yazyev OV and Kis A (2015) MoS_2 and semiconductors in the flatland. *Materials Today* 18: 20–30.

Further reading

Elliott RJ (1957) Intensity of optical absorption by exciton. *Physics Review* 108: 1384–1389.

Smolenskii GA, Pisarev RV, and Sinii IG (1975) Birefringence of light in magnetically ordered crystals. *Soviet Physics Uspekhi* 18: 410.

Rashba EI and Sturge MD (eds.) (1982) Excitons. Series. *Modern Problems in Condensed Matter Sciences*. In: Agranovich VM and Maradudin AA (eds.) (1982) vol. 2. Amsterdam, New York: North-Holland Publishing Co.

Landau LD and Lifshits EM (1984) *Electrodynamics of Continuous Media*. Oxford: Pergamon Press.

Yu PY and Cardona M (1996) *Fundamentals of Semiconductors*. Berlin: Springer.

Khitrova G, Gibbs HM, Jahnke F, Kira M, and Koch SW (1999) Nonlinear optics of normal-mode-coupling semiconductor microcavities. *Reviews of Modern Physics* 71: 1591.

Miniscalco WJ (2001) Optical and electronic properties of rare earth ions in glasses. In: Digonnet MJF (ed.) *Rare-Earth-Doped Fiber Lasers and Amplifers, Revised and Expanded*, 2nd edn. CRC Press.

Chambouleyron I and Martinez JM (2002) Optical properties of dielectric and semiconductor thin films. *Ch. 12 in Handbook of Thin Films*, vol. 3, 593–622.

Toyozawa Y (2003) *Optical Processes in Solids*. Cambridge: Cambridge University Press.

Ivchenko EL (2005) *Optical Spectroscopy of Semiconductor Nanostructures*. Harrow, UK: Alpha Science International.

Veselago V, Braginsky L, Shklover V, and Hafner C (2006) Negative refractive index materials. *Journal of Computational and Theoretical Nanoscience* 3: 1–30.

Agranovich VM (2009) *Excitations in Organic Solids*. Oxford: Oxford University Press.

Poddubny AN, Iorsh I, Belov P, and Kivshar Y (2013) Hyperbolic metamaterials. *Nature Photonics* 7: 958.

Aharonovich I, Englund D, and Toth M (2015) Solid-state single-photon emitters. *Nature Photonics* 10: 631–641.

Armstrong E and O'Dwyer C (2015) Artificial opal photonic crystals and inverse opal structures – fundamentals and applications from optics to energy storage. *Journal of Materials Chemistry C* 3: 6109–6143.

Castelletto S and Boretti A (2019) Silicon carbide color centers for quantum applications. *Journal of Physics: Photonics* 2: 022001.

Polarizability and its generalization☆

Kikuo Cho, Emeritus of Osaka University, Kobe, Japan

© 2024 Elsevier Ltd. All rights reserved.

This is an update of K. Cho, Polarizabilities, Reference Module in Materials Science and Materials Engineering, Elsevier, 2016, ISBN 9780128035818, https://doi.org/10.1016/B978-0-12-803581-8.01172-3.

Traditional aspects 683
Macroscopic polarizability 684
Microscopic polarizability 684
Microscopic nonlocal response 685
Determination of microscopic response 685
Polariton dispersion equation 686
Oscillator strength and its size dependence 686
Different definitions of polarizability 687
Cancellation problem in nonlinear polarizabilities 688
Generalization of polarizability 688
Single susceptibility for three different polarizations 688
Basics of single susceptibility theory 688
Derivation of macroscopic susceptibility 690
Phenomenology of chiral polarization 692
Comparison of different single susceptibility theories 692
Conclusion 692
References 693

Abstract

Traditional and newly developed aspects of polarizability are described from the viewpoint of micro and macroscopic responses, local and non-local behavior, and their roles in electromagnetic (EM) responses. A generalization of polarizability is given as a single susceptibility covering electric, magnetic and chiral polarizations for isolated charged particles in transversal and longitudinal external EM fields. It gives the first-principles expression of chiral susceptibility, absent in the literature. The argument is based on the minimal coupling Lagrangian for charged particles in an EM field, and the response is guaranteed to be gauge invariant.

Abbreviations

ABC	Additional boundary condition
ChC	Chiral constitutive
DBF	Drude-Born-Fedorov
EEM	Emergent electromagnetic
EM	Electromagnetic
LT	Longitudinal-transverse
LWA	Long wavelength approximation
QED	Quantum electrodynamics
QW	Quantum well

Traditional aspects

Electromagnetic (EM) field in the presence of a matter is described by the Maxwell equations with source terms of charge and current densities. The current density consists of $\partial \boldsymbol{P}/\partial t$ and $\nabla \times \boldsymbol{M}$, where $\boldsymbol{P}$ and $\boldsymbol{M}$ are electric and magnetic polarization, respectively. In the usual definition of polarizability only $\boldsymbol{P}$ is considered as the induced change of matter. In this section we follow this line of argument, and a more general one is given in Sec"Generalization of polarizability".

☆*Change History*: October 2022. K Cho updated some part of section Generalization of polarizability.

The induced charge and current densities in the Maxwell equations should be determined from the self-consistent motions of matter and EM field. Today this can be done with quantum mechanics and a computer if necessary. Historically, a phenomenology has been used with the Maxwell equations, where constant value is assigned to the polarizability of each part of material as a parameter. It describes the induced polarization as a function of incident EM field, which allows to find the solution in each part of material with a same polarizability. Then, these solutions are connected with one another via the so-called Maxwell boundary conditions, i.e., the continuity of the normal or tangential components of EM field across a surface/interface (Jackson, 1998). This determines the response of matter to an incident EM field uniquely. Another naming "electric susceptibility" is also used for polarizability.

Polarizability can be calculated quantum mechanically by evaluating the induced polarization from Trace $\left\{\rho_M \widehat{\boldsymbol{P}}\right\}$ in the presence of incident EM field, where ρ_M is the density matrix of the matter and $\widehat{\boldsymbol{P}}$ the polarization (or dipole density) operator. The result is called constitutive equation, which gives $\widehat{\boldsymbol{P}}$ as a power series expansion of EM field. Solving the Maxwell and constitutive equations simultaneously, we obtain the solution on a higher theoretical level than phenomenology.

Macroscopic polarizability

In macroscopic (local) theory of optical response, the polarizability relates a source electric field $\boldsymbol{E}(\boldsymbol{r},\omega)$ with the induced polarization $\boldsymbol{P}(\boldsymbol{r},\omega)$ of a matter as

$$\begin{aligned} P_\xi(\mathbf{r},\ \omega) &= \varepsilon_0 \sum_\eta \overline{\chi}^{(1)}_{\xi,\eta}(\omega) E_\eta(\mathbf{r},\ \omega) \\ &+ \varepsilon_0 \sum_\eta \sum_\zeta \overline{\chi}^{(2)}_{\xi,\eta,\zeta}(\omega',\ \omega'') E_\eta(\mathbf{r},\ \omega') E_\zeta(\mathbf{r},\ \omega'')\big|_{\omega'+\omega''=\omega} \\ &+ \cdots \end{aligned} \tag{1}$$

where $\boldsymbol{r}$ and ω are position and frequency, respectively, (ξ,η) stand for the Cartesian coordinates, ε_0 the dielectric constant of vacuum, and $\overline{\chi}^{(N)}$ the polarizability of the N-th order nonlinear process. The coefficients $\left\{\overline{\chi}^{(N)}\right\}$ are tensor quantities because they give relationships between different vectors. $N = 1$ corresponds to linear process, and $N = 2,\ 3$, etc. to the nonlinear ones of the second-, third-order etc., respectively. This equation is called local in the sense that $\boldsymbol{P}$ and $\boldsymbol{E}$ at the same position are related. This should be contrasted with the microscopic nonlocal polarizability to be mentioned later.

These polarizabilities are allowed to have dependence, not on position, but on frequencies, within the framework of macroscopic response. A typical model with the frequency dependence is the so-called Lorentz oscillator model, which regards matter as an assembly of charged oscillators. Using a model of 'damped harmonic oscillator in a vibrating force' of classical mechanics, one can derive a simple expression of the frequency dependence of, e.g., linear polarizability as

$$\overline{\chi}^{(1)}(\omega) = \frac{N_0 Q^2}{M} \frac{1}{\omega_0^2 - \omega^2 - i\gamma\omega}, \tag{2}$$

where N_0, Q, M, ω_0, γ are the number density, charge, mass, resonant frequency, and the damping parameter, respectively, of the oscillators. Appropriate choice of these parameters for a given material allows us to describe the ω-dependence of response spectrum. The ω-dependence of $\overline{\chi}^{(1)}(\omega)$ is, apart from the parameter values, essentially same as the quantum mechanical result, as shown below. For a given material, there can be many different types of oscillators with different parameters.

The frequency ω_0 corresponds to the excitation energy (divided by ħ) of the matter, so that there are infinitely many of them in general. For an optical process near a resonance, it is often the case that this particular one is treated as a Lorentz oscillator explicitly and all the others as a frequency independent background medium. Thus the $\overline{\chi}^{(1)}$ to be used in such a treatment is the resonant term (2) plus a constant background polarizability χ_b. The idea of introducing background medium is a kind of "wisdom" to circumvent the tedious complexity arising from the infinite number of freedom.

Microscopic polarizability

Polarizabilities can be calculated quantum mechanically by evaluating the induced polarization as a functional of source electric field via a time dependent perturbation calculation with respect to the matter-EM field interaction. If one does it properly, we obtain microscopic constitutive equation, i.e., a nonlocal relationship between $\boldsymbol{P}$ and $\boldsymbol{E}$ as

$$\begin{aligned} P_\xi(\mathbf{r},\omega) &= \varepsilon_0 \sum_\eta \int \mathrm{d}\boldsymbol{r}' \chi^{(1)}_{\xi,\,\eta}(\boldsymbol{r},\boldsymbol{r}',\omega) E_\eta(\boldsymbol{r}',\omega) \\ &+\varepsilon_0 \sum_\eta \sum_\zeta \int \mathrm{d}\boldsymbol{r}' \int \mathrm{d}\boldsymbol{r}'' \chi^{(2)}_{\xi,\,\eta,\,\zeta}(\boldsymbol{r},\boldsymbol{r}',\boldsymbol{r},'' ;\omega,' ,\omega,'') E_\eta(\boldsymbol{r}',\omega,') E_\eta(\boldsymbol{r},'' ,\omega,'')\Bigg|_{\omega' + \omega''=\omega} \\ &+\cdots. \end{aligned} \tag{3}$$

The integral kernels $\chi^{(1)}$ and $\chi^{(\mathrm{n})}$ $(\mathrm{n} = 2,3,\ldots)$ are the nonlocal polarizabilities of the linear and the n-th order nonlinear processes, respectively. The quantum mechanical expressions of, for example, the linear susceptibility at absolute zero Kelvin is given as (D'Andrea and Del Sole, 1982)

$$\chi^{(1)}_{\xi,\,\eta}(\boldsymbol{r},\boldsymbol{r}',\omega) = \sum_v \left\{ \frac{< 0\left|\widehat{P}_\xi(\boldsymbol{r})\right|v >< v\left|\widehat{P}_\eta(\boldsymbol{r}')\right|0 >}{E_v - E_0 - \hbar\omega - i\gamma} + \frac{< 0\left|\widehat{P}_\eta(\boldsymbol{r}')\right|v >< v\left|\widehat{P}_\xi(\boldsymbol{r})\right|0 >}{E_v - E_0 + \hbar\omega + i\gamma} \right\}, \tag{4}$$

where ν runs over all the excited states of the matter from the ground state $|0>$. The parameter γ is, for idealized systems, a positive infinitesimal (0^+) representing the adiabatic switching of light-matter interaction, and for realistic systems, it is the self-energy of the excitation $E_\nu - E_0$, caused by nonradiative scattering, and is often approximated as a ω-independent phenomenological parameter. The effect of radiative damping appears automatically on solving the coupled equations for $\boldsymbol{E}$ and $\boldsymbol{P}$, as shown later. Therefore it should not be included in γ to avoid double counting of the interaction. The introduction of the background polarizability can be done similarly as before.

Microscopic nonlocal response

The nonlocal relationship between the polarization and electric field in the above expression is due to the coherence of the relevant wave functions and also to the intension to consider the spatial structure microscopically down to the subatomic scale. Macroscopic response theory is derived from microscopic one via long wavelength approximation (LWA), and therefore its local character is meant, not on microscopic, but on macroscopic scale.

Nonlocality becomes important when we consider resonant EM response, since the resonant condition picks up a particular excited state with an enhanced amplitude. This leads to the dominance of the polarization structure due to this particular excitation. Therefore, the validity condition of LWA in this situation is that the resonant wavelength is much larger than the spatial extension of the polarization pattern. Atomic excitations are the examples of valid LWA, so that an excitation is safely described by excitation energy and transition dipole moment, which is the first moment of transition dipole density. Namely, the nonlocal polarizability (4) can be reduced to a local one (2) through the replacement

$$\hbar\omega_0 \to E_{\nu 0}, \quad \frac{Q^2}{M} \to \frac{2E_{\nu 0}}{\hbar}|M_{\nu 0}|^2 \tag{5}$$

where $M_{\nu 0}$ is the electric dipole moment of the transition with the excitation energy $E_{\nu 0}$.

The typical example of invalid LWA is the problem of additional boundary condition (ABC) for polariton, because the spatial extension of polariton can never be smaller than resonant wavelength. The ABC problem of polariton has a long history of conflicting arguments since its proposal (Pekar, 1957), because it was regarded as a problem of macroscopic EM response. The right answer was found when this problem is of a microscopic EM response, i.e., one needs to solve Maxwell equation with the polarizability explicitly containing material boundary. This way of solution was shown to be feasible because of the separable nature of polarizability in general (D'Andrea and Del Sole, 1982; Zeyher et al., 1972), which can further be extended to ABC-free theory of polariton, and finally, to a more general scheme of nonlocal EM response theory (Cho, 2003). The main stage of the nonlocal response theory is the nanostructured materials, which show the EM response dependent on the size, shape and internal structure of samples. This is a reflection of their size quantized energy levels and the corresponding spatial structure of excited states.

The main difference between the macroscopic and microscopic response theories lies in whether or not the boundary condition for EM field is required. The reason why it is required in the macroscopic theory is that a medium is defined by position-independent polarizabilities surrounded by surfaces/interfaces, so that the boundary problem exists, not for materials, but for EM field. In the case of microscopic response, on the other hand, the information about sample boundary is included in polarizability so that there is no need of boundary problem for EM field at the surface/interface of a sample.

Determination of microscopic response

The solution for microscopic EM response is obtained by solving Maxwell and microscopic constitutive equations simultaneously. From the Maxwell equation with polarization as a source term, the electric field produced by the polarization can be written as (Cho, 2003)

$$E_\xi(\boldsymbol{r},\omega) = E_{0,\xi}(\boldsymbol{r},\omega) + \sum_\eta \int \mathrm{d}\boldsymbol{r}' G_{\xi,\eta}(\boldsymbol{r},\boldsymbol{r}',\omega) P_\eta(\boldsymbol{r}',\omega) \tag{6}$$

where $\boldsymbol{E}_0$ is an incident field, and $G_{\xi,\eta}(\boldsymbol{r},\boldsymbol{r}',\omega)$ is the (ξ,η)-tensor component of the radiation Green's function of vacuum, which satisfies the differential equation

$$\left(\nabla \times \nabla \times + \frac{\omega^2}{c^2}\right)\mathbf{G}(\boldsymbol{r},\boldsymbol{r}',\omega) = \mathbf{1}\,\delta(\boldsymbol{r}-\boldsymbol{r}'). \tag{7}$$

The self-consistent solution of the EM field and the induced polarization is obtained by solving (3) and (6) simultaneously. For this purpose one introduces the new variables

$$F_{\mu\nu}(\omega) = \int \mathrm{d}\boldsymbol{r}\,\boldsymbol{E}(\boldsymbol{r},\,\omega)\cdot < \mu|\widehat{\boldsymbol{P}}(\boldsymbol{r})|\nu > . \tag{8}$$

The induced polarization $\boldsymbol{P}$ is written as a polynomial series of these variables, which together with (6) gives $\boldsymbol{E}$ also in a polynomial series of these $\{F\}$'s. Substituting the latter into (8), one obtains a set of polynomial equations to determine $\{F\}$'s. For a given order of optical process, linear or N-th order nonlinear one, the solution of these simultaneous polynomial equations determines the response for a given incident field $\boldsymbol{E}_0$.

For linear process, one has a set of linear equations for $\{F\}$'s. The condition for the existence of nontrivial solution in the absence of incident field $\boldsymbol{E}_0$ is given as the vanishing of the determinant of the coefficient matrix $\det|\mathbf{S}| = 0$. This is the equation for the eigenmode of the light-matter coupled system. In the rotating wave approximation, where only the first term on the right hand side of (4) is retained, we have

$$S_{\mu\nu} = \left(E_\mu - \hbar\omega\right)\delta_{\mu\nu} + \mathcal{A}_{\mu0,0\nu}(\omega). \tag{9}$$

The quantity $\mathcal{A}_{\mu0,0\nu}(\omega)$ represents the interaction energy between the induced polarization components via transverse EM field (vacuum photons) with frequency ω as

$$\mathcal{A}_{\mu0,\,0\nu}(\omega) = -\int d\mathbf{r}\int d\mathbf{r}' < \mu|\widehat{\boldsymbol{P}}(\mathbf{r})|0 > \cdot\mathbf{G}(\mathbf{r},\mathbf{r}',\omega)\cdot < 0|\widehat{\boldsymbol{P}}(\mathbf{r})|\nu > , \tag{10}$$

which is a complex quantity. Since the eigenmode of the coupled system gives the resonant structure in optical spectrum, the real and imaginary parts of $\mathcal{A}_{\mu0,0\nu}(\omega)$ represent of the radiative shift and width of the matter excitation energy with frequency dependence. In this sense, a matter is an assembly of oscillating dipole densities with finite spatial extension and radiative shift and width, which can be defined precisely on a quantum mechanical basis. In atomic systems, this radiative correction is very small, but in nanoscale systems and in the bulk, this correction can be comparable to or even exceeds the level spacing of matter. For example, the difference between the dispersion curves of an exciton and polariton is just the radiative shift defined above. More examples of the radiative correction in nonlocal situations can be found in Sections 4 and 5 of Cho, (2003) (Ishihara and Cho, 2023).

Polariton dispersion equation

Polarizability plays an essential role to determine the eigenmodes of light-matter coupled systems. Among various examples of such an eigenmode, let us take the case of an exciton in a three-dimensional crystal. The eigenmode of the coupled light-matter system is an exciton-polariton, whose dispersion equation is obtained from the coupled linear equations

$$0 = \boldsymbol{k}\times\boldsymbol{k}\times\boldsymbol{E}(\boldsymbol{k},\,\omega) + \frac{\omega^2}{c^2}\left(1+\chi_{\mathrm{B}}^{(1)}\right)\boldsymbol{E}(\boldsymbol{k},\,\omega). \tag{11}$$

If symmetry allows pure T modes, this leads to the polariton dispersion equation $1+\chi_{\mathrm{B}}^{(1)} = (ck/\omega)^2$.

A more general equation for matter excitation coupled with EM field is the eigenmode equation $\det|\mathbf{S}| = 0$ mentioned in connection with (9). This requests the finite amplitudes of matter polarization and response field in the absence of external excitation, which may appropriately be called 'self-sustaining mode'. This applies not only to polaritons but also to any matter excitation with radiative correction. Furthermore, it can be extended to X-ray scattering, since the Umklapp effect can easily be included through the Fourier components of the induced microscopic polarization. This can be used for the X ray propagation in a crystal in the dynamical scattering regime (Batterman and Cole, 1964). The generalized dispersion equation has the form

$$0 = \det\left|\left\{|\boldsymbol{k}+\boldsymbol{g}|^2 - q^2\right\}\delta_{i,j}\delta_{\boldsymbol{g},\boldsymbol{g}'} - q^2\widehat{\boldsymbol{e}}_i(\boldsymbol{k}+\boldsymbol{g})\cdot\chi_{\mathrm{A}}^{(1)}\cdot\widehat{\boldsymbol{e}}_j\left(\boldsymbol{k}+\boldsymbol{g}'\right)\right|, \tag{12}$$

where $q=\omega/c$, $\{\boldsymbol{g}\}$ reciprocal lattice vectors, and $\{\widehat{\boldsymbol{e}}_i(\boldsymbol{k}+\boldsymbol{g});\, i=1,\,2\}$ are the mutually orthogonal unit vectors perpendicular to $\boldsymbol{k}+\boldsymbol{g}$. The polarizability $\chi_{\mathrm{A}}^{(1)}$ is the $\{\boldsymbol{k}+\boldsymbol{g},\boldsymbol{k}+\boldsymbol{g}'\}$ Fourier components of the polarizability of the scheme [A] mentioned before, which can contain all the resonances of the crystal.

If one neglects the matrix elements with suffices of finite reciprocal lattice vectors in (12), the reduced equation can be shown to be equivalent to the general dispersion equation obtained from (11), which allows the LT mixed mode polaritons.

From the fact that the generalized dispersion Eq. (12) contains the effect of both resonance and Bragg scattering, it can be used in diverse situations such as polaritons, X-ray dynamical scattering, and photonic crystal (Inoue and Ohtaka, 2004) in extended frameworks.

Oscillator strength and its size dependence

There is a quantity closely related with polarizability, namely, oscillator strength, which characterizes the coupling strength of a matter excitation with EM field. It is defined as

$$f_{\nu0} = \frac{2mE_{\nu0}}{\hbar^2 e^2}|M_{\nu0}|^2\cos^2\theta \tag{13}$$

where θ is the angle between the transition dipole moment vector and light polarization direction. This factor is proportional to the numerator of the resonant polarizability in (2), as shown in (5). This is a useful concept within LWA. In nanoscale systems, there can be a quantum state extending over the whole sample region, which may exhibits size linear enhancement of its oscillator strength. As sample size approaches the wavelength of resonant light from below, this size enhancement tends to saturate. This enhancement is not reflected on the linear polarizability, because induced (linear or nonlinear) polarization is defined as the induced dipole moment per volume. Following this definition, however, it has an effect on nonlinear polarizability. For example, $\chi^{(3)}$ for macroscopic response can exhibits size-linear enhancement, which is of course valid only in LWA.

Beyond the size region of LWA, oscillator strength is no more an appropriate measure of the coupling strength. As a more general measure, one can use the radiative width of each excitation, i.e., the imaginary part of $A_{\nu 0,\, 0\nu}$ defined in (10). This quantity can be used irrespective of LWA. Since it is proportional to $|M_{\nu 0}|^2$, i.e., to oscillator strength, in LWA, it can be used more generally than oscillator strength. The size dependence of radiative width is very sensitive to the spatial structure of size quantized excitations. Following the size evolution of a given excitation, one can observe, not only the size-linear enhancement in LWA regime, but also size-resonant enhancement beyond LWA. For each type of excitations, there is a characteristic size where the coupling with EM field becomes maximal. Examples for excitons in a slab cab be found in Chapter 00176 (Ishihara and Cho, 2023).

If the coupling with EM field becomes very large as, e.g., in a resonant Bragg reflector consisting of regular arrays of quantum wells (QW's) with electronic resonances, where the resonant light satisfies the Bragg condition, it is no more appropriate to neglect the frequency dependence of radiative correction, (10). In this situation, the coupling of light-matter system is so strong that it is no more valid to regard its eigenmode as a matter oscillator corrected with radiative shift and width. In the above example, there is formation of photonic bands with a gap mode branch by increasing the number of QW's (Ikawa and Cho, 2002).

Different definitions of polarizability

The definition of polarizability depends on what the polarizing field is. When a light is incident on an isolated matter, the light polarizes the matter, and the induced oscillating polarization emits EM field with the same frequency, and this EM field polarizes the matter further, and so on. Even if a polarizing field is purely transverse (T), the induced polarization can generally contain both longitudinal (L) and T components. Both of them act as the course term in the Maxwell equations, leading to the Maxwell field with both T and L components. Since the L component of the Maxwell field is caused by the induced charge density, the interaction of this L field with the matter polarization is a part of the Coulomb interaction among the charged particles, i.e., the Coulomb interaction among the induced charge densities $H_{\text{cc.}}$ Electron-hole exchange interaction can also be rewritten in such a form. The LT splitting of polarization waves in a crystal may be expressed as a part of matter excitation energy, but it could also be ascribed to the interaction energy of a polarization wave with induced depolarization field.

There are two points of view about the treatment of H_{cc}, i.e., as a part of [A] matter Hamiltonian, or [B] the interaction between matter and external field (Cho, 1999). For each viewpoint, there is a suitable set of 'matter Hamiltonian, external EM field, the interaction between them, and polarizability'. Namely, H_{A} should contain the full Coulomb interaction, while H_{cc}, a part of the Coulomb interaction, should be excluded from H_{B}, i.e., $H_{\text{B}} = H_{\text{A}} - H_{\text{cc}}$. The fields inducing the polarization should be chosen as the full Maxwell field $\boldsymbol{E}$ in scheme [B], while it is only the T component of $\boldsymbol{E}$ in scheme [A]. The linear polarizability in each case is given in the same form as (4), but the energy eigenvalues and the matrix elements of polarization operator are different because of the difference in the matter Hamiltonian. One can show the equivalence of these two points of view, at least for linear response. Depending on the problem to be considered, one can choose either of them with proper consideration of the matter Hamiltonian to be used.

As a simple example, let us consider the electronic excitations in a crystal, i.e., the case where wave vector is a good quantum number. Neglecting the effect of finite reciprocal wave vectors (Umklapp processes), we can treat $\chi^{(1)}$ as a function of $\boldsymbol{r} - \boldsymbol{r}'$ alone. Its Fourier transform $\chi^{(1)}(\boldsymbol{k}, \omega)$ has a different relationship, depending on the scheme [A] and [B], with dielectric function defined as $\boldsymbol{D}(\boldsymbol{k}, \omega) = \varepsilon_0 \varepsilon(\boldsymbol{k}, \omega) \boldsymbol{E}(\boldsymbol{k}, \omega)$. From $\nabla \cdot \boldsymbol{D} = 0$ and $\boldsymbol{P} = \varepsilon_0 \chi_{\text{A}}^{(1)} \boldsymbol{E}^{(\text{T})} = \varepsilon_0 \chi_{\text{B}}^{(1)} \boldsymbol{E}$, one can derive

$$\varepsilon = 1 + \chi_{\text{B}}^{(1)}, \tag{14}$$

and

$$\chi_{\text{B}}^{(1)} = \chi_{\text{A}}^{(1)} + \chi_{\text{A}}^{(1)} \cdot \frac{\boldsymbol{k}\boldsymbol{k}}{k^2} \cdot \chi_{\text{B}}^{(1)}. \tag{15}$$

The excitation energies of the matter Hamiltonian appear as the poles of $\chi^{(1)}$. Therefore all the matter excitation energies of both T and L characters in the scheme [A] appear as the poles of $\chi_{\text{A}}^{(1)}$. The matter Hamiltonian in the scheme [B] does not contain H_{cc}, so that its T and L levels are degenerate. The interaction with the external L field lifts the degeneracy and gives an additional energy to the L state alone, which finally leads to the same resonant positions of the T and L levels of the light-matter coupled system. This situation in the scheme [B] is reflected in the above relationship, namely, the L mode excitations appear as the zeros of the dielectric function $\varepsilon = 1 + \chi_{\text{B}}^{(1)}$, and the T mode excitations as the poles of $\chi_{\text{B}}^{(1)}$.

The above relationship between $\chi_{\text{A}}^{(1)}$ and $\chi_{\text{B}}^{(1)}$ can be generalized to the case without translational symmetry. If we denote the $(\boldsymbol{k}, \boldsymbol{k}')$-Fourier components of the linear polarizabilities as $\chi_{\text{A}}^{(1)}(\boldsymbol{k}, \boldsymbol{k}'; \omega)$ and $\chi_{\text{B}}^{(1)}(\boldsymbol{k}, \boldsymbol{k}'; \omega)$, respectively, their relationship is generally given as

$$\chi_{\text{B}}^{(1)}(\boldsymbol{k}, \boldsymbol{k}') = \chi_{\text{A}}^{(1)}(\boldsymbol{k}, \boldsymbol{k}') + \frac{1}{2\pi^2} \int \mathrm{d}\boldsymbol{q} \chi_{\text{A}}^{(1)}(\boldsymbol{k}, \boldsymbol{q}) \cdot \frac{\boldsymbol{q}\boldsymbol{q}}{q^2} \cdot \chi_{\text{B}}^{(1)}(\boldsymbol{q}, \boldsymbol{k}'), \tag{16}$$

with the omission of the common variable ω.

Cancellation problem in nonlinear polarizabilities

For the calculation of polarizabilities in (3), we use the time dependent perturbation theory with lightmatter interaction

$$H_{\mathrm{int}} = -\int \mathrm{d}\boldsymbol{r}\,\widehat{\boldsymbol{P}}(\boldsymbol{r})\cdot\boldsymbol{E}(\boldsymbol{r}, t) \tag{17}$$

as the perturbation Hamiltonian. The n-th order nonlinear polarizability is expressed as the n-fold time integral of the n-fold commutator of polarization operators in interaction representation. For the explicit calculation, one expands the n-fold commutator into the sum of various products of the polarization operators, and carry out the time integrations. When one sums up these integrated terms, there occurs partial or total cancellation among them for n larger than or equal to 2. A typical example is the polarization made of pure Bosons such as harmonic oscillators. In this case, the innermost commutator of two polarization operators in the interaction representation at different times becomes a c-number, so that its commutator with another operator turns out to be zero. This means that all the nonlinear polarizabilities should be zero for this model. However, each of the contributions from the expanded terms of the n-fold commutator is generally nonvanishing, which means that the complete cancellation occurs in summing up these expanded terms. For general cases of light-matter interaction, matter excitations are not pure Bosons, and there is interaction among them, which leads to finite nonlinear polarizability. But there always exists a partial cancellation in summing up the expanded terms.

This feature is important when one considers the size enhancement of nonlinear polarizabilities for a nanoscale matter. As we mentioned above, this enhancement tends to saturate as sample size grows to be comparable to the resonant wavelength. However, each of the expanded terms of the n-fold commutator is kept enhanced also beyond LWA. The saturation occurs only through the cancellation among such terms. This means that beyond LWA the leading order terms are cancelled out, leaving the next order terms as a finite contribution (Cho, 2003). Therefore, it is essential to make a very careful treatment of cancellation in the calculation of nonlinear polarizabilities. Otherwise, one would be left with a large error in their values.

Generalization of polarizability

Single susceptibility for three different polarizations

Polarizability is a quantity describing one particular aspect of EM response of matter, i.e. the electric polarization. Though it is in many cases a central importance, there are other type of EM responses, such as magnetic and chiral polarizations. In most cases, they are treated separately as if they are independent from one another. However, they obviously cannot be independent, if we consider the number of freedom of the cause (EM field) and the result (matter polarization) in general. Actually it is three for both of them, i.e., for any choice of EM variables from $\boldsymbol{E}$, $\boldsymbol{B}$, $\boldsymbol{A}$, ϕ there are only three independent components, and the use of current density $\boldsymbol{J}$ is general enough for the induced change of matter. The linear relation between 2 three-component vectors is represented by a 3×3 tensor. Since current density contains electric and magnetic polarizations as $\boldsymbol{J} = \partial\boldsymbol{P}/\partial t + \nabla \times \boldsymbol{M}$, the 3×3 tensor should contain electric and magnetic susceptibilities, and, furthermore, chiral susceptibility in lower symmetry case where electric and magnetic polarizations are mixed.

This argument is closely related with EM response theory with minimal number of variables. This should apply to any level of response theories from quantum electrodynamics (QED) to micro- and macro- scopic semiclassical theories. These levels of response theories are mutually related via certain approximations, and form a single hierarchy with the rigorous QED at the top. In the hierarchy, macroscopic semiclassical theory is peculiar in the sense that it appeared in early days before quantum mechanics and relativity theory were born. Because of this historical background, there have been various ways of arguments based on empirical knowledge, making its logical position in the hierarchy difficult to see. After the first edition of this chapter, the author developed a first-principles scheme for the derivation of macroscopic Maxwell equations (Cho, 2010, 2018). The logical step from micro- to macroscopic theory is the application of LWA to the general form of microscopic constitutive equation. The resulting expression of the macroscopic single susceptibility is shown to be rewritten reversibly into separate forms of electric, magnetic and chiral susceptibilities. This includes the quantum mechanical expression of chiral susceptibility, which is absent in the literature.

In the following, we give some details of the formulation how to prepare the base of minimal number of necessary variables for general case of EM response, which was developed in Cho (2018).

Basics of single susceptibility theory

The formulation is based on the minimal coupling Lagrangian for interacting system of charged particles and EM field as

$$\mathcal{L} = \sum_{\ell} \frac{1}{2} m v_\ell^2 + \int \mathrm{d}\boldsymbol{r}\{-\rho\phi + \boldsymbol{J}\cdot\boldsymbol{A}\} + \frac{\varepsilon_0}{2}\int \mathrm{d}\boldsymbol{r}\left\{\left(\frac{\partial \boldsymbol{A}}{\partial t} + \nabla\phi\right)^2 - c^2(\nabla \times \boldsymbol{A})^2)\right\}. \tag{18}$$

where ℓ is particle index, ρ charge density, and ϕ, $\boldsymbol{A}$ scalar and vector potential, respectively. As a general framework of EM response, we consider an isolated system of charged particles interacting with an external EM field with transverse (T) and longitudinal (L) components. The external EM field is a fixed quantity playing the role of source field inducing current density.

The number of variables for EM field in this Lagrangian is redundant, because the least necessary number of its components is three, while vector and scalar potentials provide four. In order to reduce the number of variables, we carry out a variable transformation to eliminate scalar potential by using the Lagrange equation for ϕ, i.e., Gauss law. This does not change the Lagrange equations of all the other variables because the generalized velocity for ϕ is missing in $\mathcal{L}$ (Cohen-Tannoudji et al., 1989). The transformed Lagrangian turns out to be a sum of gauge independent term $\mathcal{L}'$ and gauge dependent term $\mathcal{L}''$, as

$$\mathcal{L}' = \sum_{\ell} \frac{1}{2} m_\ell v_\ell^2 - U_{\mathrm{Ct}} + \int d\boldsymbol{r}\, \boldsymbol{J}_{\mathrm{T}} \cdot \boldsymbol{A}_{\mathrm{T}} + \frac{\varepsilon_0}{2} \int d\boldsymbol{r} \left\{ \left(\frac{\partial \boldsymbol{A}_{\mathrm{T}}}{\partial t} \right)^2 - (\nabla \times \boldsymbol{A}_{\mathrm{T}})^2 \right\} \tag{19}$$

$$\mathcal{L}'' = -\frac{d}{dt} \int d\boldsymbol{r}\, \boldsymbol{P}_{\mathrm{L}} \cdot \boldsymbol{A}_{\mathrm{L}} \tag{20}$$

where U_{Ct} is the Coulomb potential among all the internal and external charged particles, obtained from the self-energy of longitudinal electric field by the help of Gauss law $\nabla \cdot \boldsymbol{E}_{\mathrm{L}} = \rho/\varepsilon_0$. The suffices T and L are for the transverse and longitudinal components, respectively, and $\boldsymbol{J}_{\mathrm{L}} = \partial \boldsymbol{P}_{\mathrm{L}}/\partial t$ is noted. $\boldsymbol{J}_{\mathrm{T}}$ in the third term can be written as $\boldsymbol{J}$, since the additional contribution of $\boldsymbol{J}_{\mathrm{L}}$ vanishes. Being the total time derivative, $\mathcal{L}''$ does not contribute to the least action principle, and can be dropped. The remaining Lagrangian $\mathcal{L}'$ is that of Coulomb gauge. This means that the Lagrangian in arbitrary gauge can always be replaced by that of Coulomb gauge. It should be noted that this result is obtained, not by choosing a gauge, but by using a more general rule of the least action principle.

The part of U_{Ct} representing the interaction between external and internal charges can be rewritten as 'the interaction of external L field $\boldsymbol{E}_{\mathrm{extL}}$ with the polarization $\boldsymbol{P}$ due to internal charge density ρ' ($-\nabla \phi_{\mathrm{ext}} = \boldsymbol{E}_{\mathrm{extL}}, \nabla \cdot \boldsymbol{P} = -\rho$), or 'the potential energy of ρ in the external potential ϕ_{ext}'. The remaining part, U_{C}, represents the Coulomb interaction among internal charges alone. The T field $\boldsymbol{A}_{\mathrm{T}}$ consists of the sum of external and internal (induced) components.

From $\mathcal{L}'$ we get Hamiltonian via standard procedure, which is appropriate for dealing with nonrelativistic systems of spinless particles in an EM field. In order to extend the range of problems to spin related ones, we add spin Zeeman interaction

$$\mathcal{H}_{\mathrm{SZ}} = -\int d\boldsymbol{r} \boldsymbol{M}_{\mathrm{s}}(\boldsymbol{r}) \cdot \boldsymbol{B}(\boldsymbol{r}) = -\int d\boldsymbol{r} \boldsymbol{J}_{\mathrm{s}}(\boldsymbol{r}) \cdot \boldsymbol{A}(\boldsymbol{r}), \tag{21}$$

and spin-orbit interaction

$$\mathcal{H}_{\mathrm{SO}} = \sum_{\ell} \frac{e_\ell \hbar}{4 m_\ell^2 c^2} \boldsymbol{p}_\ell \cdot (\boldsymbol{\sigma}_\ell \times \boldsymbol{E}_{\mathrm{L}}). \tag{22}$$

They are derived from Dirac equation for relativistic particles under the assumption of weakly relativistic condition (An additional remark about the relativistic correction will be made at the end of this section.). Note that $\mathcal{H}_{\mathrm{sZ}}$ has the same form as the interaction between orbital current density and vector potential. This allows us to combine the spin and orbital parts into the total current density operator, as shown below. Altogether, the Hamiltonian becomes $\mathcal{H}_{\mathrm{sc}} + \mathcal{H}_{\mathrm{EM}}$, where

$$\mathcal{H}_{\mathrm{sc}} = \sum_{\ell} \frac{1}{2m_\ell} \{\boldsymbol{p}_\ell - e_\ell \boldsymbol{A}_{\mathrm{T}}(\boldsymbol{r}_\ell)\}^2 + U_{\mathrm{C}} - \int d\boldsymbol{r}\, \boldsymbol{P}(\boldsymbol{r}) \cdot \boldsymbol{E}_{\mathrm{extL}}(\boldsymbol{r}) + \mathcal{H}_{\mathrm{sZ}} + \mathcal{H}_{\mathrm{SO}}, \tag{23}$$

$$\mathcal{H}_{\mathrm{EM}} = \frac{1}{2} \int d\boldsymbol{r} \left\{ \varepsilon_0 \left(\frac{\partial \boldsymbol{A}_{\mathrm{T}}}{\partial t} \right)^2 + \frac{1}{\mu_0} (\nabla \times \boldsymbol{A}_{\mathrm{T}})^2 \right\}. \tag{24}$$

where $m_\ell, e_\ell, \boldsymbol{r}_\ell, \boldsymbol{p}_\ell$ are the mass, charge, coordinate, and momentum, respectively, of the ℓ-th particle. Index ℓ is restricted to the internal particles alone. The vector potential $\boldsymbol{A}_{\mathrm{T}}$ consists of internal and external (applied) components. This Hamiltonian provides a starting point for general class of problems about the EM response of interacting charged particles (neutral as a whole) and EM field. Polarizability and/or susceptibility appears in the semiclassical theory, where EM field is treated classically. This means that each mode of EM field, specified by frequency, polarization and propagation direction, is described by two dynamical variables, phase and amplitude (in contrast with the ensemble of photon states in QED). Thus, the theory of EM response is to determine the phases and amplitudes of EM field and induced current density of matter for a given initial condition (Though we stay in semiclassical regime, it is worth noting that this Hamiltonian can be used for QED in weakly relativistic condition just by quantizing $\boldsymbol{A}_{\mathrm{T}}$.).

As a standard example, we calculate linear susceptibility of matter at zero Kelvin for an incident EM field with T and L components. Solving Schrödinger (Pauli) equation $i\hbar(\partial\Psi/\partial t) = H_{\mathrm{sc}}\Psi$, we have Ψ in the lowest order perturbation, and this allows us to calculate the expectation value of current density as $\langle \boldsymbol{J} \rangle(t) = \langle \Psi(t) | \boldsymbol{J} | \Psi(t) \rangle$. Its Fourier transform gives $\langle \boldsymbol{J} \rangle(\omega)$.

Separating $\mathcal{H}_{\mathrm{sc}}$ into matter part $\mathcal{H}_{\mathrm{m}}$ and linear and quadratic interaction terms $\mathcal{H}_{\mathrm{int1}} + \mathcal{H}_{\mathrm{int22}}$, we have

$$\mathcal{H}_{\mathrm{m}} = \sum_{\ell} \frac{1}{2m_\ell} \boldsymbol{p}_\ell^2 + U_{\mathrm{C}} + \mathcal{H}_{\mathrm{SO}}, \tag{25}$$

$$\mathcal{H}_{\text{int}\,1} = -\int \mathrm{d}\boldsymbol{r}\,\boldsymbol{I}(\boldsymbol{r})\cdot\boldsymbol{A}_{\mathrm{T}}(\boldsymbol{r},t) - \int \mathrm{d}\boldsymbol{r}\,\boldsymbol{P}_{\mathrm{L}}(\boldsymbol{r})\cdot\boldsymbol{E}_{\mathrm{extL}}(\boldsymbol{r},t), \tag{26}$$

$$\mathcal{H}_{\text{int}\,2} = \frac{1}{2}\int \mathrm{d}\boldsymbol{r}\,\widehat{N}(\boldsymbol{r})\boldsymbol{A}_{\mathrm{T}}(\boldsymbol{r})^2, \tag{27}$$

where

$$\widehat{N}(\boldsymbol{r}) = \sum_{\ell}\left(e_\ell^2/m_\ell\right)\delta(\boldsymbol{r}_\ell - \boldsymbol{r}), \tag{28}$$

$$\boldsymbol{I}(\boldsymbol{r}) = \boldsymbol{J}_0(\boldsymbol{r}) + \nabla\times\boldsymbol{M}_{\mathrm{s}}(\boldsymbol{r}), \tag{29}$$

$$\boldsymbol{J}_0(\boldsymbol{r}) = \sum_{\ell}\frac{e_\ell}{2m_\ell}\{\boldsymbol{p}_\ell\delta(\boldsymbol{r}_\ell - \boldsymbol{r}) + \delta(\boldsymbol{r}_\ell - \boldsymbol{r})\boldsymbol{p}_\ell\}, \tag{30}$$

$$\boldsymbol{M}_{\mathrm{s}}(\boldsymbol{r}) = \sum_{\ell}\frac{e_\ell\hbar}{m_\ell}\boldsymbol{\sigma}_\ell\delta(\boldsymbol{r}_\ell - \boldsymbol{r}). \tag{31}$$

The quadratic term $\mathcal{H}_{\text{int2}}$ is neglected for the argument of linear susceptibility. The total current density operator is $\boldsymbol{I}_{\mathrm{t}} = \boldsymbol{I} - \widehat{N}(\boldsymbol{r})\boldsymbol{A}_{\mathrm{T}}$. Taking the ω Fourier component of the expectation value of $\langle\Psi(t)|\boldsymbol{I}_{\mathrm{t}}|\Psi(t)\rangle$, we obtain the induced current density as a linear functional of $\boldsymbol{A}_{\mathrm{T}}$ and $\boldsymbol{E}_{\mathrm{extL}}$.

$$\bar{\boldsymbol{I}}_{\mathrm{t}}(\boldsymbol{r},\omega) = \int \mathrm{d}\boldsymbol{r}'\chi_{\mathrm{cd}}(\boldsymbol{r},\boldsymbol{r}',\omega)\cdot\boldsymbol{A}_{\mathrm{T}}(\boldsymbol{r}',\omega) + \int \mathrm{d}\boldsymbol{r}'\chi_{\mathrm{EL}}(\boldsymbol{r},\boldsymbol{r}',\omega)\cdot\boldsymbol{E}_{\mathrm{extL}}(\boldsymbol{r},\boldsymbol{r}',\omega), \tag{32}$$

where χ_{cd} and χ_{EL} are the microscopic susceptibilities with respect to the source fields $\boldsymbol{A}_{\mathrm{T}}$ and $\boldsymbol{E}_{\mathrm{extL}}$, respectively. Their quantum mechanical expressions are given as

$$\chi_{\mathrm{cd}}(\boldsymbol{r},\boldsymbol{r}',\omega) = -\left\langle 0|\widehat{N}(\boldsymbol{r})|0\right\rangle + \sum\left[g_v(\omega)\boldsymbol{I}_{0v}(\boldsymbol{r})\boldsymbol{I}_{v0}(\boldsymbol{r}') + h_v(\omega)\boldsymbol{I}_{v0}(\boldsymbol{r})\boldsymbol{I}_{0v}(\boldsymbol{r}')\right], \tag{33}$$

$$\chi_{\mathrm{EL}}(\boldsymbol{r},\boldsymbol{r}',\omega) = \sum_{v}\left[g_v(\omega)\boldsymbol{I}_{0v}(\boldsymbol{r})(\boldsymbol{P}_{\mathrm{L}})_{v0}(\boldsymbol{r}') + h_v(\omega)\boldsymbol{I}_{v0}(\boldsymbol{r})(\boldsymbol{P}_{\mathrm{L}})_{0v}(\boldsymbol{r}')\right] \tag{34}$$

$$g_v(\omega) = 1/(E_{v0} - \hbar\omega - i0^+), h_v(\omega) = 1/(E_{v0} + \hbar\omega * i0^+), \tag{35}$$

where $\mathcal{H}_m \mid v\rangle = E_v \mid v\rangle$ and $E_{v0} = E_v - E_0$. By the help of the identity $\boldsymbol{I}_{\mathrm{L}} = \partial\boldsymbol{P}_{\mathrm{L}}/\partial t$, which leads to $\langle\mu|\boldsymbol{P}_{\mathrm{L}}|v\rangle = -i(\hbar/E_{\mu v})\langle\mu|\boldsymbol{I}_{\mathrm{L}}|zv\rangle$, χ_{EL} can be rewritten, in terms of current density matrix elements, as

$$\chi_{\mathrm{EL}}(\boldsymbol{r},\boldsymbol{r}',\omega) = -\frac{i}{\omega}\sum_{v}\left[\bar{g}_v(\omega)\boldsymbol{I}_{0v}(\boldsymbol{r})\boldsymbol{I}_{v0}^{(\mathrm{L})}(\boldsymbol{r}') + \bar{h}_v(\omega)\boldsymbol{I}_{v0}(\boldsymbol{r})\boldsymbol{I}_{0v}^{(\mathrm{L})}(\boldsymbol{r}')\right] \tag{36}$$

where $\overline{g}_v(\omega) = g_v(\omega) - 1/E_{v0}$ and $\overline{h}_v(\omega) = h_v(\omega) - 1/E_{v0}$.

Both of the susceptibilities describe the nonlocal response, i.e., current density can be induced at positions different from those of incident field. The spatial extension of this nonlocality is determined by that of the relevant matter excited states given by $|0\rangle$ and $|v\rangle$. If this spatial extension is comparable to or larger than the wavelength of the EM field resonant to this excitation, we cannot use LWA. In that case, we have to calculate the EM response via proper consideration of nonlocality. Thereby, the separable character of the susceptibilities as integral kernel allow us to rewrite integral equations into simultaneous linear equations, which in many cases allows successful treatments beyond LWA (Cho, 2003).

Problems of our interest are resonant EM responses, where incident EM field is resonant with some excitations of matter. The contributions of resonant and off-resonant matter excitations to the susceptibility are treated differently. There are generally infinite number of off-resonant states, and their total contribution to induced current density would show mild dependence on spatial and ω variation in contrast to that of resonant states. Then, the contribution of off-resonant states to susceptibility may be replaced by some background constant without ω and spatial dependence, which alone can be treated as macroscopic response. It is the spatial extension of resonant states which determines whether the total response may be treated as macro- or microscopic response.

Derivation of macroscopic susceptibility

In order to carry out LWA in the microscopic constitutive equation, we make Fourier expansion of the corresponding current density matrix elements and keep the lower order terms of wave number components, which, together with the Maxwell equations in $\boldsymbol{k}$ representation, provides the fundamental equations of macroscopic response theory. For systems which allow LWA, this is the model-independent, logically acceptable way to derive macroscopic theory.

In this way, we can have a macroscopic EM response theory belonging to the lowest rank of the hierarchy of EM response theories, which consists of [a] relativistic QED and [b] weakly-relativistic QED, [c] semiclassical microscopic theory, and [d] semiclassical macroscopic theory, related through well-defined approximations. In the past arguments, the logical step from [c] to [d] was not quite clear, because of model dependent arguments and of the absence of examination of validity condition. Typical example is the ABC problem mentioned in Section "Microscopic nonlocal response", which was first proposed for [d], but the right answer was found from [c].

Before showing the detailed form of LWA averaged susceptibility, it may be useful to consider the rewriting of the non-resonant term $\sim \left\langle 0|\widehat{N}(\boldsymbol{r})|0\right\rangle$ in χ_{cd}. This term is the ground state charge density. Because of the weighting factor e_ℓ^2/m_ℓ, electrons dominate over heavier nuclei. In X-ray diffraction, it plays an essential role with its $\boldsymbol{r}$-dependence reflecting the positions of nuclei of the matter. As averaged uniform charge density in LWA, it contributes to plasma frequency. For macroscopic EM response, we rewrite this term, to the lowest order $O(k^0)$, as

$$\left\langle 0|\widehat{N}(\boldsymbol{r})|0\right\rangle = \left\langle 0\left|\left[\boldsymbol{J}_{\boldsymbol{k}}^{(\xi)}, P_{-\boldsymbol{k}}^{(\eta)}\right]\right|0\right\rangle. \tag{37}$$

Further rewriting via $\langle\mu|\boldsymbol{P}_{\boldsymbol{k}}|\nu\rangle = (-i/\omega_{\mu\nu})\langle\mu|\boldsymbol{J}_{\boldsymbol{k}}|\nu\rangle$ allows to renormalize it into the form of resonant terms with g, h replaced by $\overline{g}$,$\overline{h}$. With this approximation, we have a neat expression of the macroscopic constitutive equation for general T and L source field

$$\bar{\boldsymbol{I}}_{\text{t}}(\boldsymbol{k},\omega) = \chi_{\text{em}}(\boldsymbol{k},\omega)\cdot\left\{\boldsymbol{A}_{\text{T}}(\boldsymbol{k},\omega) - \frac{i}{\omega}\boldsymbol{E}_{\text{extL}}(\boldsymbol{k},\omega)\right\}, \tag{38}$$

where

$$\chi_{\text{em}}(\boldsymbol{k},\, \omega) = V\sum_{\nu}\left[\overline{g}_\nu(\omega)\boldsymbol{I}_{0\nu}(\boldsymbol{k})\boldsymbol{I}_{\nu 0}(\,-\boldsymbol{k}) + \overline{h}_\nu(\omega)\boldsymbol{I}_{\nu 0}(\boldsymbol{k})\boldsymbol{I}_{0\nu}(\,-\boldsymbol{k})\right]. \tag{39}$$

The $\boldsymbol{k}$ Fourier component of matrix element is given as a power series of $\boldsymbol{k}$ as

$$\tilde{\boldsymbol{I}}_{\mu\nu}(\boldsymbol{k}) = \frac{\exp\left(\,-i\boldsymbol{k}\cdot\bar{\boldsymbol{r}}\right)}{V}\left[\bar{\boldsymbol{J}}_{\mu\nu} - i\boldsymbol{k}\cdot\bar{\mathbf{Q}}_{\mu\nu}^{(\text{e2})} + i\boldsymbol{k}\times\bar{\boldsymbol{M}}_{\mu\nu} + \cdots\right], \tag{40}$$

in terms of the electric dipole (E1), electric quadrupole (E2) and magnetic dipole (M1) moments of transition matrix elements. V is the volume to define $\boldsymbol{k}$ via periodic boundary condition, and $\bar{\boldsymbol{r}}$ is the center coordinate to define moments for each transition $|0\rangle \leftrightarrow |\nu\rangle$. The zero-th order moment of $\boldsymbol{J}_0$ is the E1 moment

$$\bar{\boldsymbol{J}}_{\mu\nu} = \int \mathrm{d}\boldsymbol{r}\,\langle\mu|\boldsymbol{J}_0(\boldsymbol{r})|\nu\rangle, \tag{41}$$

The $O(k^1)$ moment of $\boldsymbol{J}_0$ is the sum of the E2 moment $\overline{\boldsymbol{Q}}_{\mu\nu}^{(\text{e2})}$ defined by

$$\boldsymbol{k}\cdot\bar{\boldsymbol{Q}}_{\mu\nu}^{(\text{e2})} = \sum_\ell \frac{e_\ell}{2m_\ell}\int \mathrm{d}\boldsymbol{r}[\langle\mu|(\boldsymbol{r}_\ell - \bar{\boldsymbol{r}})\boldsymbol{k}\cdot\boldsymbol{p}_\ell\delta(\boldsymbol{r}_\ell - \bar{\boldsymbol{r}}) + \delta(\boldsymbol{r}_\ell - \bar{\boldsymbol{r}})(\boldsymbol{r}_\ell - \bar{\boldsymbol{r}})\boldsymbol{k}\cdot\boldsymbol{p}_\ell|\nu\rangle] \tag{42}$$

and the orbital M1 moment

$$\bar{\boldsymbol{M}}_{\mu\nu}^{(\text{orb})} = \sum_\ell \frac{e_\ell}{2m_\ell}\int \mathrm{d}\boldsymbol{r}[\langle\mu|\boldsymbol{L}_\ell(\bar{\boldsymbol{r}})\delta(\boldsymbol{r}_\ell - \bar{\boldsymbol{r}}) + \delta(\boldsymbol{r}_\ell - \bar{\boldsymbol{r}})\boldsymbol{L}_\ell(\bar{\boldsymbol{r}})|\nu\rangle] \tag{43}$$

where $\boldsymbol{L}_\ell(\bar{\boldsymbol{r}}) = (\boldsymbol{r}_\ell - \bar{\boldsymbol{r}}) \times \boldsymbol{p}_\ell$. The total M1 moment $\overline{\boldsymbol{M}}_{\mu\nu}$ in (40) is the sum of the orbital M1 moment and the spin M1 moment $\langle\mu|\boldsymbol{M}_{\text{s}}(\boldsymbol{r})|\nu\rangle$.

The macroscopic susceptibility χ_{em} includes all the effects of electric, magnetic, and chiral polarizations, i.e., $O(k^0)$ terms represent the E1 transition, $O(k^1)$ terms the mixed (E1-E2) and (E1-M1) transitions, and $O(k^2)$ terms the E2 and M1 transitions. It is remarkable that a single susceptibility describes all these polarization effects. Furthermore, this constitutive equation can be reversibly rewritten into the four equations of ($\boldsymbol{E}$ and $\boldsymbol{B}$) induced (electric and magnetic) polarizations. For that purpose, we note the relation $\boldsymbol{I} = \partial\boldsymbol{P}/\partial t + \nabla \times \boldsymbol{M}$, which holds as both operators and expectation values. If we write the new constitutive equations as $\boldsymbol{P} = \chi_{\text{eE}}\boldsymbol{E} + \chi_{\text{eB}}\boldsymbol{B}$ and $\boldsymbol{M} = \chi_{\text{mE}}\boldsymbol{E} + \chi_{\text{mB}}\boldsymbol{B}$, the new susceptibilities are given as

$$\begin{aligned}\chi_{\text{eE}} = \frac{1}{\omega^2 V}\sum_\nu \Big[&\bar{g}_\nu\left(\bar{\boldsymbol{J}}_{0\nu} + i\boldsymbol{k}\cdot\bar{\mathbf{Q}}_{0\nu}^{(\text{e2})}\right)\left(\bar{\boldsymbol{J}}_{\nu 0} - i\boldsymbol{k}\cdot\bar{\mathbf{Q}}_{\nu 0}^{(\text{e2})}\right)\\ &+\bar{h}_\nu\left(\bar{\boldsymbol{J}}_{\nu 0} + i\boldsymbol{k}\cdot\bar{\mathbf{Q}}_{\nu 0}^{(\text{e2})}\right)\left(\bar{\boldsymbol{J}}_{0\nu} - i\boldsymbol{k}\cdot\bar{\mathbf{Q}}_{0\nu}^{(\text{e2})}\right)\Big],\end{aligned} \tag{44}$$

$$\chi_{\text{eB}} = \frac{-i}{\omega V}\sum_\nu\left[\bar{g}_\nu\left(\bar{\boldsymbol{J}}_{0\nu} + i\boldsymbol{k}\cdot\bar{\mathbf{Q}}_{0\nu}^{(\text{e2})}\right)\bar{\boldsymbol{M}}_{\nu 0} + \bar{h}_\nu\left(\bar{\boldsymbol{J}}_{\nu 0} + i\boldsymbol{k}\cdot\bar{\mathbf{Q}}_{\nu 0}^{(\text{e2})}\right)\bar{\boldsymbol{M}}_{0\nu}\right], \tag{45}$$

$$\chi_{\text{mB}} = \frac{1}{V}\sum_\nu\left[\overline{g}_\nu\overline{\boldsymbol{M}}_{0\nu}\overline{\boldsymbol{M}}_{\nu 0} + \overline{h}_\nu\overline{\boldsymbol{M}}_{\nu 0}\overline{\boldsymbol{M}}_{0\nu}\right], \tag{46}$$

$$\chi_{\text{mE}} = \frac{i}{\omega V}\sum_\nu\left[\bar{g}_\nu\bar{\boldsymbol{M}}_{0\nu}\left(\bar{\boldsymbol{J}}_{\nu 0} - i\boldsymbol{k}\cdot\bar{\mathbf{Q}}_{\nu 0}^{(\text{e2})}\right) + \bar{h}_\nu\bar{\boldsymbol{M}}_{\nu 0}\left(\bar{\boldsymbol{J}}_{0\nu} - i\boldsymbol{k}\cdot\bar{\mathbf{Q}}_{0\nu}^{(\text{e2})}\right)\right]. \tag{47}$$

χ_{eE} and χ_{mM} are usual electric polarizability and magnetic susceptibility, respectively. The rewriting of (38) into the two equations relating ($\boldsymbol{P}$, $\boldsymbol{M}$) with ($\boldsymbol{E}$, $\boldsymbol{B}$) does not break the single susceptibility nature of the theory, because the rewriting is reversible. In this sense, these four equations may still be called single susceptibility scheme.

Phenomenology of chiral polarization

The terms χ_{eB} and χ_{mE} represent cross polarizations, i.e., $\boldsymbol{E}$-induced $\boldsymbol{P}$ and $\boldsymbol{B}$-induced $\boldsymbol{M}$. They are the microscopic expressions of chiral susceptibilities. Materials with chiral symmetry have the excited states of mixed E1 and M1 transitions, which contribute to the finite values of χ_{eB} and χ_{mE}.

The EM response of chiral systems has traditionally been treated via Drude-Born-Fedorov constitutive equations (Band, 2006)

$$\boldsymbol{D} = \varepsilon(\boldsymbol{E} + \beta\nabla\times\boldsymbol{E}),\quad \boldsymbol{B} = \mu(\boldsymbol{H} + \beta\nabla\times\boldsymbol{H}). \tag{48}$$

This is a phenomenology for uniform, isotropic chiral systems (Lakhtakia, 2000). It was derived, not by quantum mechanical calculation, but from symmetry consideration (Drude, 1912; Born, 1933; Fedorov, 1959a, 1959b). A contrasting phenomenology can be made from the result of the previous subsection. We rewrite the r.h.s. of $\boldsymbol{D} = \varepsilon_0\boldsymbol{E} + \boldsymbol{P},\ \boldsymbol{H} = (1/\mu_0)\boldsymbol{B} - \boldsymbol{M}$ in terms of $\boldsymbol{E}$ and $\boldsymbol{B}$ as

$$\boldsymbol{D} = \varepsilon\boldsymbol{E} + i\xi\boldsymbol{B},\quad \boldsymbol{H} = (1/\mu)\boldsymbol{B} + i\eta\boldsymbol{E}. \tag{49}$$

where the coefficients ε, ξ, μ, η are given as

$$\varepsilon = \varepsilon_0 + \chi_{eE},\quad \mu = 1/\mu_0 - \chi_{mB},\quad \xi = \chi_{eB},\quad \eta = -\chi_{mE}. \tag{50}$$

Regarding them as macroscopic parameters, we have another phenomenological form of chiral constitutive equations, which we denote here ChC equations. The parameters describing chiral effect in these equations are β and (ξ,η).

Though the two sets of macroscopic equations might look rather similar, they are quite different. The normal mode dispersion is given as

$$\frac{ck}{\omega} = \pm\frac{\sqrt{\varepsilon\mu}}{1\pm(\beta\omega/c)\sqrt{\varepsilon\mu}} \tag{51}$$

for DBS equations, and

$$\frac{ck}{\omega} = \pm\frac{2\varepsilon\mu}{\Lambda\pm\sqrt{\Lambda^2+4\varepsilon\mu}} \tag{52}$$

for ChC equations, where $\Lambda = \mu(\xi+\eta)$. The expression in the square root determines the range of real branch, to which β does not contribute in DBF case, but (ξ,η) do in ChC case. This is also connected with the clear distinction about the absence and occurrence of linear crossing in the resonant region of dispersion curves in left-handed medium (Cho, 2018). These results indicate the preference of ChC to DBF equations as phenomenology.

Comparison of different single susceptibility theories

The present scheme of single susceptibility theory uses the three components of current density as the minimal necessary variables. Another choice is possible, and actually an example was shown by Landau and Lifshitz (1963). What they chose for this purpose is "generalized polarization $\boldsymbol{P}^{(LL)}$ containing $\boldsymbol{M}$" through the definition $\partial\boldsymbol{P}^{(LL)}/\partial t = \boldsymbol{J}$. The third possibility in this connection is "generalized magnetization $\boldsymbol{M}^{(A)}$ containing $\boldsymbol{P}$", defined by $\nabla\times\boldsymbol{M}^{(A)} = \boldsymbol{J}$ (Chipouline et al., 2012). But the lack of L component in $\boldsymbol{M}^{(A)}$ does not allow the comparison with the other two cases. In order to make proper comparison, we need to restrict their difference only in T components, while keeping a common L component. The appropriate choice is (a) $\{\boldsymbol{P}_{\mathrm{T}}^{(LL)},\boldsymbol{J}_{\mathrm{L}}\}$, (b) $\{\boldsymbol{M}_{\mathrm{T}}^{(A)},\boldsymbol{J}_{\mathrm{L}}\}$, and (c) $\{\boldsymbol{J}_{\mathrm{T}},\boldsymbol{J}_{\mathrm{L}}\}$. Though the case (a) is the first proposal as a single susceptibility theory, the corresponding susceptibility was not worked out thoroughly. It is only in case (c) that the full quantum mechanical form of susceptibility is derived. Knowing this result, we can easily derive the susceptibilities of (a) and (b). From the definition of $\boldsymbol{P}^{(LL)}$ and $\boldsymbol{M}^{(A)}$, we can write their T components as

$$\boldsymbol{P}_{\mathrm{T}}^{(LL)} = (i/\omega)\boldsymbol{J}_{\mathrm{T}},\quad \boldsymbol{M}_{\mathrm{T}}^{(A)} = \left(i/k^2\right)\boldsymbol{k}\times\boldsymbol{J}_{\mathrm{T}} \tag{53}$$

Substituting the constitutive equation of (c) in the $\boldsymbol{J}_{\mathrm{T}}$ on the r.h.s., we get $\boldsymbol{P}_{\mathrm{T}}^{(LL)}$ and $\boldsymbol{M}_{\mathrm{T}}^{(A)}$ as functions of source EM field, namely their constitutive equations. In this sense, we can formulate different single susceptibility theories with any one of these variables (Cho, 2018). However, the use of unfamiliar physical quantity, $\boldsymbol{P}_{\mathrm{T}}^{(LL)}$ or $\boldsymbol{M}_{\mathrm{T}}^{(A)}$, would need a particular motivation, while the use of $\boldsymbol{J}_{\mathrm{T}}$ is a standard procedure.

Conclusion

The main part of the revision is made in Section "Generalization of polarizability" to strengthen the base of semiclassical EM response theory with respect to (i) the choice of minimal necessary number of the variables for description, combined with (ii) the natural consequence of gauge invariant single susceptibility theory. It is stressed that the quantum mechanical form of chiral susceptibility is given in model-independent manner by this formulation, of which consequence is discussed in the macroscopic form of ChC vs. DBF equations. Altogether, the content of this chapter provides a sound basis of EM response theory for a very general class of problems.

The next stage of this theory will be its application to various problems. In Cho (2003) many examples are discussed about the size and shape dependent optical responses of semiconductor samples. One of the nice aspects of these treatment is the possibility of size dependent analysis beyond LWA, which extends the credibility of arguments. On the other hand, there are many different types of materials with corresponding properties and EM responses. Spectroscopy and transport are standard categories of EM response, and optical manipulation for nanoscale materials is a new branch (Ishihara, 2021). Another new area of this topic may be the emergent EM (EEM) theory, which seems to require certain extension of EM response theory for less simple matter systems having, e.g., permanent electric and/or magnetic polarizations.

The starting equations of EEM and the single susceptibility theories are very similar, i.e., the Schrödinger equation in a EM field with relativistic correction terms (spin-orbit interaction, spin Zeeman term, etc.), called Pauli equation, for charged particles. A new aspect with EEM is that it has two types of gauge symmetry, the standard U(1) symmetry and spin related SU(2) symmetry. The latter arises from the inclusion of spin-orbit interaction. However, in the fundamental papers of the field (Nagaosa and Tokura, 2012; Frölich and Studer, 1993; Leurs et al., 2008), there seems to be a controversial points about the form of this term and whether or not the SU(2) symmetry exists.

In the calculation of relativistic correction terms from Dirac equation, one assumes that the rest energy (mc^2) is much larger than all of the kinetic energy of charged particle, the EM field energy, and the interaction energy of particle and EM field. If we do it properly, we need a revision of the spin-orbit interaction in (22) by the replacements $\boldsymbol{p} \rightarrow \boldsymbol{p} - e\boldsymbol{A}$ and $\boldsymbol{E}_{\mathrm{L}} \rightarrow \boldsymbol{E}$.

Relativistic correction affects, not only the motion of charged particles, but also the source terms of Maxwell equation. An obvious example is spin Zeeman term, which contributes as spin dependent current density $\nabla \times \boldsymbol{M}_{\mathrm{s}}$ The spin-orbit term mentioned above could also have a similar effect. However, these effects on the source term of Maxwell equations are not considered in both of EEM and single susceptibility theory.

One possible future problem for the single susceptibility theory would be the comparison with EEM theory and the effect of revised $\mathcal{H}_{\mathrm{SO}}$ on the source terms of Maxwell equations. In view of the same starting (Pauli) equation for both theories, it is desirable to clarify where and how their difference appears.

References

Band YB (2006) *Light and Matter*. New York: John Wiley & Sons.

Batterman BW and Cole H (1964) Dynamic Diffration of X rays by Perfect Crystals. *Reviews of Modern Physics* 36: 681–717.

Born M (1933) *Optik*. Heidelberg: Springer.

Chipouline A, Simovski K, and Tretyakov S (2012) Basics of averaging the Maxwell equations. *Metamaterials* 6: 77–120.

Cho K (1999) Mechanisms of LT Splitting of Polarization Waves: A Link between electron-hole Exchange Interaction and Depolarization Shift. *Journal of the Physical Society of Japan* 68: 683–691.

Cho K (2003) *Optical Response of Nanostructures: Microscopic Nonlocal Theory*. Heidelberg: Springer.

Cho K (2010) *Reconstruction of Macroscopic Maxwell Equations: A Single Susceptibility Theory*, 1st edn. Heidelberg: Springer.

Cho K (2018) *Reconstruction of Macroscopic Maxwell Equations: A Single Susceptibility Theory*, 2nd edn. Heidelberg: Springer.

Cohen-Tannoudji C, Dupont-Roc CJ, and Grynberg G (1989) *Photons and Atoms: Introduction to Quantum Electrodynamics*. New York: Wiley. pp. 84–85.

D'Andrea A and Del Sole R (1982) Wannier-Mott excitons in semi-infinite crystals: Wave functions and normal incidence reflectivity. *Physics Review* B25: 3714–3730.

Drude P (1912) *Lehrbuch der Optik*. Leipzig: Hirtzel.

Fedorov FI (1959a) On the theory of optical activity in crystals. I. The law of conservation of energy and the optical activity tensors. *Optics and Spectroscopy* 6: 49–53.

Fedorov FI (1959b) On the theory of optical activity in crystals. II. Crystals of cubic symmetry and plane classes of central symmetry. *Optics and Spectroscopy* 6: 237–240.

Frölich J and Studer UM (1993) Gauge invariance and current algebra in nonrelativistic many-body theory. *Reviews of Modern Physics* 65: 733–802.

Ikawa T and Cho K (2002) Structure Dependence of Radiation-Matter Interaction in Arrays of Resonant Units. *Journal of the Physical Society of Japan* 71: 1381–1392.

Inoue K and Ohtaka K (2004) *Photonic Crystals: Physics, Fabrication, and Applications*. Tokyo: Springer.

Ishihara H (2021) Optical Manipulation of nanoscale materials by linear and nonlinear resonant optical responses. *Advances in Physics: X* 6(1): 1885991. https://doi.org/10.1080/23746149.2021.1885991.

Ishihara H and Cho K (2023) Chapter 00176: Optical Response of Nanostructures. In: *Encyclopedia of Condensed Matter Physics*. Oxford: Elsevier.

Jackson JD (1998) *Classical Electrodynamics*, 3rd edn. New York: J. Wiley & Sons.

Lakhtakia A (2000) In: Singh ON and Lakhtakia A (eds.) *Electrmagnetic Fields in Unconventional Materials and Structres*, p. 123. New York: Wiley Interscience.

Landau LL and Lifshitz EM (1963) *Electrodynamics of Continuous Media*. Oxford: Pergamon Press. pp. 337–342.

Leurs BWA, Nazario Z, Santiago DI, and Zaanan Z (2008) Non-Abelian hydrodynamics and the flow of spin in spin-orbit coupled substances. *Annals of Physics* 323: 907–945.

Nagaosa N and Tokura Y (2012) Emergent Electromagnetism in Solids. *Physica Scripta* T146: 014020(1-15).

Pekar SI (1957) The theory of electromagnetic waves in a crystal in which excitons are produced. *Zhurnal Eksperimental'noi i Teoreticheskoi Fiziki* 33: 1022–1036. [Sov. Phys. JETP 6, 785-796(1958)].

Zeyher R, Birman JL, and Brenig W (1972) Spatial dispersion effects in resonant polariton scattering I. Additional boundary condition for polarization field. *Physics Review* B6: 3613–4616.

Ultrafast spectroscopy of correlated materials

D Bossini[a] **and AV Kimel**[b], [a]Department of Physics and Center for Applied Photonics, University of Konstanz, Konstanz, Germany; [b]Institute for Molecules and Materials, Radboud University, Nijmegen, The Netherlands

© 2024 Elsevier Ltd. All rights reserved.

Introduction 694
Methods 695
Single-color pump-probe spectroscopy 696
Broadband pump-probe spectroscopy 697
Time-domain THZ spectroscopy 697
Other time-domain techniques 697
Ultrafast magnetism 697
Ultrafast dynamics in ferromagnets 697
Ultrafast dynamics in ferrimagnets 698
Ultrafast dynamics in antiferromagnets 699
Ultrafast dynamics in ferroelectrics 700
Ultrafast dynamics in magnetoelectrics and multiferroics 700
Ultrafast phono-magnetism 701
Ultrafast charge dynamics in superconductors and Mott insulators 701
Theoretical and computational approaches in ultrafast dynamics of correlated materials 702
Conclusion 702
Acknowledgments 702
References 702

Abstract

Correlated materials display macroscopic properties arising from short-range electronic interactions. Dynamics of the lattice, electrons and spins faster than the time required to reach thermodynamical equilibrium can be photo-induced, manipulated and detected. Despite the remarkable progress in understanding the equilibrium physics of correlated materials, this approach has succeeded in disclosing a plethora of novel phenomena. After the illumination, the relaxation toward equilibrium via non-equilibrium states takes place on the femtosecond and picosecond timescales. During this process, correlated materials display macroscopic properties not-observable in the thermodynamic phase diagram. This research field discloses even the potential to implement the photo-induced manipulations of the macroscopic electronic and magnetic properties of correlated materials in applications, such as information technology.

Key points

- Introducing the unique possibilities provided by ultrafast spectroscopic methods, concerning correlated materials.
- Comprehensive description of the ultrafast optical techniques, able to induce and track electronic, lattice and spin dynamics with femtosecond time-resolution.
- Summary of the milestone experimental achievements reported in the literature so far for a few specific material classes, namely magnetic materials, ferroelectrics, magnetoelectrics and multiferroics, magnetoelastic media, high-Tc superconductors and Mott insulators.
- Brief description of the theoretical and computational methods relevant for correlated materials.
- Outlook of the possible developments of the research field of correlated materials.

Introduction

Correlated materials are solids, in which short-range classical and/or quantum mechanical interactions between electrons result in cooperative macroscopic phenomena and order. Examples of such ordered states of matter are ferromagnetism, ferrimagnetism, antiferromagnetism, ferroelectricity, multiferroicity, superconductivity. Despite the quantum mechanical origin, a substantial progress in understanding the physics of correlated materials was achieved using the laws of thermodynamics and classical mechanics, by introducing the concept of order parameter (Landau and Lifshitz, 1984). Thermodynamics appeared to be very helpful in understanding ground states of correlated materials. In particular, different macroscopic phases and phase transitions can be observed, as external parameters (temperature, pressure, magnetic and electric fields, strain) are adiabatically varied. These

https://doi.org/10.1016/B978-0-323-90800-9.00064-0

observations can be explained in terms of the laws of thermodynamics, as the concept of thermodynamic equilibrium properly applies (Landau and Lifshitz, 1980).

As a consequence of the invention and the development of femtosecond lasers, condensed matter physicists have obtained the fastest ever stimulus—bursts of electromagnetic fields with durations down to a few femtoseconds and, more recently, even hundreds of attoseconds. These stimuli are able to excite media on a timescale much faster than the characteristic times of spin-spin, spin-lattice, electron lattice and even electron-electron interaction in solids (Shah, 1996). Dynamical processes on a timescale shorter than the time required to reach thermodynamic equilibrium (i.e., sub-100 ps) are conventionally called *ultrafast* (Giannetti et al., 2016). Femtosecond laser pulses can directly excite specific electronic or phononic transitions. Electronic, lattice and spin resonances can be driven by ultrashort laser pulses via the process of stimulated Raman scattering (Shen and Bloembergen, 1965; Pershan et al., 1965; Pershan, 1963; Shen, 2003). Moreover, femtosecond laser excitation can generate nearly single cycle THz pulses, ultrashort pulses of charge (Smith et al., 1989) or spin-currents (Battiato et al., 2010; Lichtenstein et al., 2011). In the simplest case, relying on absorption of femtosecond laser pulses, the latter can be used as an ultrafast heater. All the mentioned (sub)-picosecond stimuli bring matter into a strongly non-equilibrium state, for which the conventional description of correlated materials in terms of thermodynamics is no longer valid. More particularly, these stunningly short stimuli can:

- inducing phase transitions and activating functionalities, expressed by the different regions of the phase diagram, at an unprecedented speed;
- create new non-equilibrium states, not present in the thermodynamic phase diagrams, and initiate phenomena in these states, which cannot be accessed via equilibrium spectroscopies;
- select and drive the non-equilibrium excitation and relaxation channels, by addressing specific transitions to induce or to detect;
- induce coherent collective electronic, phononic and magnetic modes, while avoiding an increase of entropy. The interaction between a coherent mode, which typically implies dynamics of the order parameter, and the other degrees of freedom can then be accessed.

A particular group of correlated materials, so-called *strongly correlated materials*, exhibits peculiar electronic properties, such as high-temperature superconductivity, charge- or spin-density-wave and the metal-insulator transition (Giannetti et al., 2016). These compounds are generally described by means of the Hubbard model, or more sophisticated versions of it, as they are elusive of the band-theory. The reason is that electronic correlations and interactions play a major role in shaping both the electronic ground- and the excited-states, while band-theory presents a single-electron description of solids.

Among all types of correlated materials, non-equilibrium states triggered by femtosecond laser pulses are most actively studied in media with long-range magnetic order, i.e., ferro-, ferri- and antiferromagnetic materials. Here we are going to provide: (i) a description of the experimental methods in ultrafast spectroscopy of correlated materials, providing a few examples of remarkable observations allowed by these methods; (ii) a general overview of the experimental and theoretical milestones achieved in ultrafast magnetism; (iii) a brief description of ultrafast phenomena in different classes of correlated materials.

Methods

The cornerstone of ultrafast spectroscopic approaches is the *pump-probe* technique, which is based on the idea of exciting the medium by means of an intense pulsed laser beam (the *pump*) and detecting the dynamical evolution of macroscopic observables in the material, as a result the interaction between the sample and another beam (the *probe*). This simple concept can be realized in a wide variety of schemes, aimed at detecting different macroscopic quantities of a given medium, as discussed in the following. Fig. 1 shows how different implementations of the detection in the pump-probe schemes allows to selectively monitor the ultrafast dynamics of different degrees of freedom in solids.

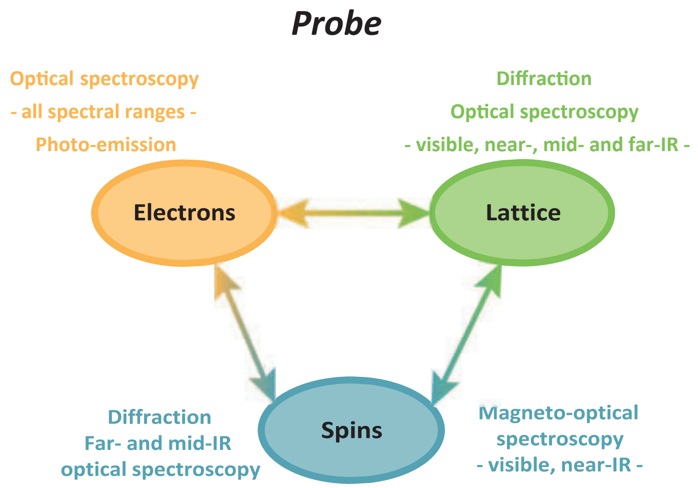

Fig. 1 Methods enabling the detection of the dynamics of different reservoirs of energy.

As for the pump, we define three distinct experimental regimes:

- *Weak perturbation*. The pump excites non-thermally quasiparticles, without qualitative changes of the general properties of the system, i.e., the medium remains in the original phase and no major changes of the shape of the thermodynamic potential occur. The concept of *effective temperature* is introduced to describe the quasi-equilibrium state of various reservoirs of energy (electrons, lattice, spins) in the medium. This state is portrayed as in equilibrium albeit with increased temperature, in comparison with the state prior to the photoexcitation.
- *Strong perturbation*. The pump beam drives the system so far from equilibrium, that a transition to either a different region of the thermodynamical phase diagram or even to a phase not accessible at all via adiabatic transformations is induced. The strong perturbation regime is vastly explored aiming at manipulating the macroscopic electronic (metal-insulator transition, superconductivity, charge-density wave), lattice (structural phase transitions) and magnetic (reversal of the order parameter, magnetic phase transitions) on the ultrafast timescale made available by the duration of the laser pulses.
- *Coherent macroscopic dynamics of the order parameters*. Coherent oscillations of order parameters (electronic, magnetic, vibrational) can be induced by an impulsive excitation. The lowest order coupling between high-frequency light waves and low-frequency coherent modes is mediated by Raman processes. Therefore the cross-section, selection rules and time-scale of the oscillatory signals (both frequency and lifetime) can be inferred from the Raman spectrum of the material.

State-of-the-art ultrafast spectroscopic experiments enable to investigate the optical properties in a gigantic spectral regime, spanning the THz—X-rays range, in combination with temporal resolutions entering even the attoseconds scale.

Single-color pump-probe spectroscopy

Table-top femtosecond laser sources combined with the lock-in detection (or an equivalent digital version of it) enable to monitor the transient changes of the optical properties, i.e., reflectivity or transmissivity, with a signal-to-noise ratio as high as 10^{-8} (Giannetti et al., 2016). The typical repetition rate of the source is in the kHz regime, although MHz amplified laser systems are already available. Fast digitizers allow even single-pulse measurements. The addition of waveplates and polarizing optics, such as a Wollaston prism, before the detector enables both the measurement of additional quantities (i.e., rotation and ellipticity of the probe polarization) and an increased sensitivity, as the intensity fluctuations of the light source are canceled. This scheme, called balanced detection, is vastly employed for experiments in magnetic materials, as magneto-optical effects allow to track the pump-induced ultrafast spin dynamics via the detection of the rotation and ellipticity of the polarization of the probe beam.

The most common laser sources employed rely on Titanium sapphire (Ti:Sa) as active medium. Consequently the laser pulses have central photon energy of 1.55 eV. In the introduction we discussed already the advantages provided by the tunability of the photon energy, which is achieved by means of non-linear optical interactions. The simplest approach is to generate harmonics of the fundamental frequency of the laser relying on non-linear crystals. A more sophisticated approach, allowing to cover the visible, near infrared and near ultra-violet spectral range (0.5–3.5 eV) consists in employing optical parametric amplifiers (OPA). These devices allow to tune almost continuously the photon energy of a beam in the aforementioned range. Considering the goal of driving and investigating ever faster processes, it is worth to mentioned that the non-collinear scheme of an OPA (NOPA) grants a superior time resolution, as laser pulses with few optical cycles can be synthesized, which means durations comparable to, or even lower than, 10 fs throughout the tunability spectral range can be achieved. The beams generated by an OPA can be further employed for non-linear optical interactions, so that ultrashort laser pulses in the mid-IR spectral range (photon energy below 0.20 eV) can be generated. This particular energy regime is relevant in order to explore the resonant drive of lattice and magnetic collective modes.

A further extension of the pump-probe scheme consists in multi-pulses technique, in which more than one beam induce a desired state in the material, whose dynamics is then monitored by means of the probe beam. An example is the destruction pump-probe technique, based on the idea that the first (*destruction*) beam quenches a long-range order (i.e., the charge-density-wave) and, in so doing, induces a high symmetry state (Yusupov et al., 2010). From this state a conventional pump-probe experiment is performed, so that the dynamics of the order parameter can be accessed even at any time-instant during the destruction-induced symmetry-breaking process. Another example, which is gaining massive popularity, is the two-dimensional spectroscopy (Nardin, 2015; Cundiff and Mukamel, 2013; Stone et al., 2009; Purz et al., 2021). This scheme allows a direct disentanglement of linear and non-linear contribution to the time-resolved signal, which unravels the possible coupling between several photo-induced modes. We note that the experimental approach typically employed to achieve the coherent control of the amplitude of coherent lattice, charge and magnetic modes, requires two excitation beams as well.

Non-linear optical method are able to track the ultrafast dynamics of the ferroelectric, ferromagnetic and antiferromagnetic order parameter. More specifically, the photon-energy of the probe beam is tuned to be resonant with an electronic transition of the material, so that resonant second harmonic generation can take place. The intensity of this non-linear signal is then detected (Duong et al., 2004). In the case of the ferroelectric polarization, the measurement of SHG is an indirect probe of the dynamic polarization. Conveniently the second harmonic method can be implemented table-top. However, whether the nonlinear optical signal provides reliable informations concerning the dynamics of the ferroelectric polarization is still subject of intense debate. On the other hand, it is paramount to mention, that in the case of magnetic materials, the SHG signal contains multiple different contributions, so that a direct interpretation of SHG dynamics in terms of pure spin dynamics is likely to lead to misinterpretations of the physical processes under investigation (Duong et al., 2004; Huber et al., 2015).

All the approaches discussed so far provides spectroscopic information in rather limited spectral range for each measurements, as the laser beams are *single-color*. A broader spectroscopic response of the material is obtained in consecutive measurements by tuning the photon-energy of the beams with (N)OPAs (Cerullo and Silvestri, 2003; Brida et al., 2009; Manzoni and Cerullo, 2016).

Broadband pump-probe spectroscopy

This approach aims at a time-dependent reconstruction of the frequency-dependent dielectric function. Focusing amplified ($E > 0.5$ μJ/pulse) femtosecond laser pulses in transparent non-linear crystals, it is possible to generate a broadband pulse, so called *supercontinuum*, via self-phase modulation. The width of the supercontinuum ranges from 450 to 1300 nm. Alternatively, the supercontinuum can be generated also with low-energy ($E < 100$ nJ/pulse, i.e., non-amplified) by means of a photonic-crystal fibers.

The intrinsic advantage of this approach, which justifies the increased technical complexity of the experiments, clearly lies in the simultaneous measurement of the spectral dependence of the optical response, in a very broad range. This is a way more robust and solid starting point for the development of effective nonequilibrium models for the dielectric function than single-color measurements (Conte et al., 2012; Giannetti et al., 2016).

Technically this approach can be extended to the time-resolved measurement of the spectral-dependent magneto-optical response of a magnetic material. However, this is far from trivial. Implementing the balanced detection on multichannel detectors requires to disperse the two polarization components of the supercontinuum probe beam in exactly the same way on two different detectors. This is the main reason why this approach has been barely pursued so far.

Time-domain THZ spectroscopy

The THz spectral range is typically defined as the frequency interval from 0.1 THz (0.4 meV = 4 K) to 5 THz (20 meV = 220 K). Several nonlinear crystals can be employed to generate radiation in this range, by means of optical rectification, for instance ZnTe, GaSe, $LiNbO_3$ (Kozina et al., 2019; Hudl et al., 2019; Bonetti et al., 2016) and even organic compounds (Unikandanunni et al., 2022; Polley et al., 2018; Brunner et al., 2008; Puc et al., 2019). The electric field produced in this way enters the MV/cm regime. The THz pulses are detected by means of electro-optical sampling: the radiation is sent onto a detection crystal inducing birefringence, which is transferred into the ellipticity of a near-infrared probe beam. This detection scheme allows to detect experimentally both the amplitude and phase of the electromagnetic field throughout its entire spectrum, without relying on the Kramers-Kronig transformation.

THz-pulses can be employed to monitor the optically-induced changes in the optical properties of materials in the THz region, once combined with a visible or near-infrared pump beam. It is worth to mention, that THz pulses have been already successfully employed in multi-pulses schemes, such as the 2D-spectroscopy.

Other time-domain techniques

The concept of the pump-probe scheme can be extended to the following techniques:

- *Time-resolved photoemission*. The pump beam induces dynamics in the material, while the probe beam triggers the photoemission process. The probe photon energy must exceed the work function, thus typically UV photons are necessary. Kinematic constraints require the extreme ultraviolet spectral range, which can be achieved via high-harmonic generation, in order to access the entire Brillouin zone. This method is extremely powerful, as it allows to reconstruct the non-equilibrium band structure of a given medium (Giannetti et al., 2016; Zonno et al., 2021). However, it is also rather limited in terms of material choice, as mostly thin high-quality metallic layers, which have to be prepared in-situ are employed. Semiconductors and dielectrics can be hardly investigated in this scheme.
- *Time-resolved electron and X-ray diffraction, imaging and spectroscopy*. The THz/mid-IR/near-IR/visible/pump beam is combined with an ultrashort X-ray (or electronic) probe beam. In the case of X-rays, this approach has been recently becoming more popular because of the possibility of performing element specific detection at the edges of various elements (Fe, Co, Ni, Cu, Gd, Tb, etc.) using the femtosecond flashes of light from advanced beamlines at synchrotrons and free electron laser (Schmising et al., 2014; Pfau et al., 2012; Kubacka et al., 2014; Johnson et al., 2011; Grübel et al., 2016; Dornes et al., 2019). As far as electrons are concerned, femtosecond electron pulses are generated via photoemission from a cathode.

Ultrafast magnetism

Ultrafast dynamics in ferromagnets

The goal of understanding the response of ferromagnets to femtosecond laser pulses opened up the whole field of ultrafast magnetism in 1996 (Beaurepaire et al., 1996). It was shown that femtosecond laser excitation of metallic Ni causes an ultrafast collapse of the magnetic order (i.e., demagnetization) of the ferromagnet on a timescale of 2 ps. The authors described their data in terms of thermodynamic three-temperature (3T) model, modeling the medium as three reservoirs of energy representing free electrons, ordered spins and lattice, respectively (Agranat et al., 1984). Assuming that femtosecond laser pulses transfer their energy predominantly to the free electrons, thermodynamics predicts that such a transfer will be followed by heat transfer from electrons to the lattice and from the lattice to spins, on the time-scale of electron lattice relaxation (≈1–2 ps) and spin-lattice relaxation (10–100 ps), respectively. Increasing the spin temperature results in a quench of the spin order, which can experimentally be observed as demagnetization. Experiments demonstrated that the excitation of electrons with femtosecond laser pulses discloses a previously unexplored channel of heat transfer between the electrons and spins on a timescale of 2 ps. The original observations were followed by a plethora of experimental, computational and theoretical studies of ultrafast demagnetization in ferromagnetic metals, semiconductors and dielectrics. Interestingly, the 3T-model proposed in the very first paper, is still one of main means to describe ultrafast magnetic phenomena in ferromagnetic media. One of the main consequences of the model is that the efficiency of the ultrafast demagnetization depends only on the amount of heat deposited into free carriers, but not on the way of deposition. For instance, ultrashort pulses in THz, infrared and visible spectral range seem to cause similar demagnetization despite the photon energy changes by three order of magnitude (Bonetti et al., 2016; Mashkovich et al., 2020; Shalaby et al., 2016; Chekhov et al., 2021). Ultrafast demagnetization can also be triggered by picosecond-long pulses of charge current.

The attempt to understand the ultrafast demagnetization in metallic multilayers led to interesting developments in spintronics. In particular, it was realized that the ultrafast demagnetization of Fe in Fe/Au bilayer launches super diffusive spin transport into the Au-layer, which results in magnetizing gold (Battiato et al., 2010). Such a spin transport is concomitant by an efficient THz emission due to the spin Hall effect in Au. Substituting Au (Lichtenstein et al., 2011; Battiato et al., 2010) with Pt, Ta and other heavy metals enhances the THz emission (Seifert et al., 2016; Kampfrath et al., 2013). Although in pure ferromagnets ultrafast laser excitation results only in a partial loss of the spin order, in FePt and Co/Pt multilayers repetitive excitation with a sequence of femtosecond pulses of circularly polarized light can lead to magnetization reversal (Lambert et al., 2014). A more conventional approach to the magnetization reversal was explored in ferromagnets using magnetic field pulses with the duration of $\leq$100 ps (Schumacher, 2005; Back et al., 1998, 1999; Acremann et al., 2000, 2001; Gerrits et al., 2002; Stamm et al., 2005; Tudosa et al., 2004). If the magnitude of the magnetization is conserved, by applying the external magnetic field perpendicular to the magnetization results in the strongest torque applied to the spins. If the field is applied only during half a period of the precession, the magnetization is reversed (Back et al., 1999).

Ultrafast dynamics in ferrimagnets

One of the first experiments on ultrafast demagnetization of ferrimagnets showed that femtosecond laser excitation results in a much more dramatic effect. The excitation of ferrimagnetic GdFeCo alloy with a single 40 fs-circularly polarized laser pulse resulted in magnetization reversal, such that the final state was deterministically defined by the helicity of light (Stanciu et al., 2007). The physical picture of this phenomenon is summarized as it follows: femtosecond laser pulses heat free electrons and thus launches the ultrafast demagnetization of antiferromagnetically coupled Gd and FeCo sublattices, respectively. While the demagnetization of FeCo sublattices occurs on a time of 1 ps, the demagnetization of Gd takes much longer. Due to cooling of the electrons via electron-phonon interaction, the process of demagnetization is exhausted at about 2 ps leaving the spin system in a strongly nonequilibrium state. In fact, in this state the FeCo sublattice is nearly demagnetized, while the Gd sublattice is only slightly affected. A relaxation from this state driven by the exchange spin-spin interaction is accompanied by the magnetization reversal resulting in ultrafast writing of magnetic bits. It was shown that the effect is observed only for intensities above a certain threshold, which allows to bring the sublattices far enough from the equilibrium. Using circularly polarized light and relying on magnetic circular dichroism in the ferrimagnet, right and left-handed circularly polarized beams are absorbed differently, so that the process of the magnetization reversal becomes helicity-dependent. The helicity dependence is observed only in a narrow range of intensities (Khorsand et al., 2012). For intensities above this range the magnetization becomes helicity independent and every pulse triggers magnetization reversal (Ostler et al., 2012). It was demonstrated that the bits can be written with a spatial resolution down to 40 nm. Moreover the writing does not necessarily require femtosecond laser pulses, as the process can be activated with the help of picosecond pulses of charges (Yang et al., 2017) or spin currents (Hees et al., 2020) as well. Magnetization reversal induced by femtosecond laser pulses was demonstrated in a broad class of ferrimagnets in the vicinity of their compensation temperature, at which the magnetizations of the antiferromagnetically coupled sublattices are equal and thus cancel each other out (Mangin et al., 2014; Kimel, 2014). The ultimate frequency of repetitive all-optical magnetization reversal in ferrimagnets was studied in Wang et al. (2021). In GdFeCo, for instance, it is shown that although magnetic writing launched by the first pulse is completed after 100 ps, a reliable rewriting of the bit by the second shot requires a delay between the shots of at least 300 ps. In the half-metallic Heusler ferrimagnet $Mn_2Ru_{0.9}Ga$ the reliable rewriting by the second pulse was reported for delays as short as 10 ps (Banerjee et al., 2021).

Interestingly, ferrimagnets facilitate mechanisms allowing to write magnetic domains with the help of femtosecond laser pulses without relying on heat. In particular, using Co-doped yttrium iron garnet (YIG:Co) it was shown that light can effectively control the magnetic anisotropy in the material by means of an active pumping of a $d-d$ electronic transition in the Co^{2+} ions in the tetrahedral and octahedral crystallographic positions, respectively (Stupakiewicz et al., 2017, 2019). The interplay between cubic magneto-crystalline and uniaxial photo-induced anisotropy results in magnetization dynamics, displaying a heavily damped precessional reversal of the order parameter between different metastable states along the cube diagonals. While the unperturbed Co-doped garnet has four axes of magnetic anisotropy, ultrafast laser pumping creates non-equilibrium population of excited states in Co^{2+} ions and thus hardens/softens different axes depending on the polarization of light. Hence using linearly polarized femtosecond laser pulses it is possible to write and read magnetic domains (bits) in such an iron garnet, without relying on the optical excitation of free electrons. A write-read event was accompanied by an unprecedentedly low heat load (5 aJ when normalized to a $(10\ \text{nm})^3$ bit) and could be repeated at a rate of 20 GHz (Szerenos et al., 2019), where the latter is practically defined by the frequency of spin resonance in this compound.

Ultrafast dynamics in antiferromagnets

As the frequency of the spin resonance in antiferromagnets can be 1000 time higher than in ferromagnets (Kittel and Kittel, 1951), it can be expected that the reorientation of spins occurs up to a 1000 times faster. Moreover, the minima of the thermodynamic potential in antiferromagnets have equivalent energies, entropies and angular momenta, i.e., writing bits by rotating antiferromagnetic spins does not imply an irreversible transfer of energy or angular momentum between the lattice and the spins. Hence almost from the early days of ultrafast magnetism antiferromagnets have been considered as a promising playground in the quest for the fastest and the least dissipative data storage.

The first experimental studies of spin dynamics triggered in antiferromagnets by femtosecond laser pulses were focused on the class of weak ferromagnets (Kimel et al., 2002). Due to the Dzyaloshinskii-Moriya interaction, antiferromagnetically coupled spins are slightly canted from the purely antiparallel orientation. The canting results in a small magnetization, which greatly simplifies experimental studies of antiferromagnetic materials. In particular, it allows the manipulation of spin structures with the help of relatively small magnetic fields. The detection of antiferromagnetically coupled spins is carried on via the magneto-optical Faraday effect, similarly to ferro- and ferrimagnetic materials. A particular attention in this research was given to rare-earth orthoferrites. These systems host several magnetic phases and exhibit spin reorientation phase transitions induced by temperature, strain and/or magnetic field. Launching such a spin-reorientation phase transition in $TmFeO_3$ via ultrafast heating with the help of femtosecond laser pulses, it was shown that spins in antiferromagnets can be reoriented at the record breaking speed and potentially facilitate writing of magnetic bits at THz rates (Kimel et al., 2004). Recently, it was shown that the very same phase transition can be initiated without heating, but by pumping an electronic $f-f$ transition in Tm^{3+} ions with the help of intense, nearly single-cycle THz pulses (Baierl et al., 2016; Schlauderer et al., 2019).

FeRh is another example of intensively studied antiferromagnet. Heating this antiferromagnet above 350 K triggers a counter-intuitive phase transition to a ferromagnetic state. These magnetic changes are accompanied by lattice expansion. Whether this is a magnetic phase transition, which results in structural changes, or whether the structural phase transition is accompanied by magnetic changes, has been a daunting question for several decades (Kittel, 1960; Tu et al., 1969; McKinnon et al., 1970; Mryasov, 2005). It was believed that performing time-resolved measurements of spin and lattice dynamics induced by femtosecond heating, the dilemma could be solved (Ju et al., 2004; Thiele et al., 2004; Bergman et al., 2006; Radu et al., 2010). However, it is still a subject of intense debates.

Also antiferromagnets with fully compensated magnetic sublattices have been receiving increasingly high attention over the last decades. Intuitively it may be assumed that the lack of magnetization in the ground state makes these materials not responsive to a magnetic field less intense than 1 T. Nevertheless, the situation is profoundly different, if the field rapidly varies in time. Already 40 years ago it was theoretically predicted that dynamics of spin in antiferromagnets can also be launched by a relatively small external magnetic field, if the latter is not constant (Zvezdin, 1979; Ivanov et al., 1985; Zvezdin and Mukhin, 1981; Andreev and Marchenko, 1980). Kampfrath et al. (2010) showed that a linear coupling of the THz magnetic field to the sublattice-magnetizations triggers coherent spin oscillations, at the frequency of antiferromagnetic resonance in NiO. Similar coherent spin oscillations could also be excited via a nonlinear coupling mechanism of light to spins (Satoh et al., 2010). In both cases, the role of a driving force is played by the time derivative of the effective magnetic field $\partial H/\partial t$. The observation of the coherent spin oscillations in the antiferromagnet was achieved by measuring the magneto-optical Faraday effect. Although for unperturbed compensated antiferromagnets both the magnetization and the magneto-optical Faraday effect vanish, a signal emerges due to the excitation of coherent spin oscillations at the frequency of the antiferromagnetic resonance.

In antiferromagnets, it is possible to generate coherent spin waves near the very edges of the Brillouin zone, by means of sub-10 fs laser pulses (Bossini et al., 2016, 2019; Bossini and Rasing, 2017). The interplay between spins and lattice in antiferromagnets seems to play the central role in the formation of antiferromagnetic domains. Understanding the role of the lattice in spin dynamics in antiferromagnets can appear to be crucial for the development of antiferromagnetic data storage. In the very recent years, several counter-intuitive experimental observations further fueled interest into magnetoelasticity (Bossini et al., 2021b), piezomagnetism and phonomagnetism.

Although several computational and theoretical studies have already claimed the possibility of record fast writing of antiferromagnetic bits using ultrashort stimuli such as THz magnetic field pulses, femtosecond spin (photo)currents and even femtosecond laser pulses, none of the experimental time-resolved studies of spin dynamics in antiferromagnets has demonstrated the writing of bits at a picosecond timescale (Wienholdt et al., 2012; Chirac et al., 2020; Dannegger et al., 2021). Moreover, the majority of the experimental reports of spin dynamics in antiferromagnets showed merely a harmonic response, which suggests only a small perturbation of the spins in the vicinity of the equilibrium state. At the same time, Olejník et al. (2018) showed that excitation of antiferromagnetic CuMnAs in a multidomain state with GHz or THz pulses can switch the magnet between multiple stable states. Reversible optical switching of antiferromagnetic domains in $TbMnO_3$ was reported in Manz et al. (2016). However, none of these papers reported about the actual dynamics of the switching. Very recently, employing ultrafast pumping of Tm^{3+} ions in antiferromagnetic $TmFeO_3$ with the help of intense THz pulses, it was possible to drive spin dynamics in this antiferromagnet into an anharmonic regime. In particular, the triggered dynamics even acquired characteristic features showing that in a part of the sample the spins were navigated over a potential barrier (Schlauderer et al., 2019). However, ultrafast writing of antiferromagnetic bits has not yet been demonstrated, calling for either stronger stimuli for antiferromagnetic spins or more efficient mechanisms for antiferromagnetic switching.

Aiming at applications in terms of data storage, the ability to convert ultrafast spin dynamics into a charge-signal must be developed. This milestone would allow an integration of this novel technological paradigm with nowadays available CMOS technology. Correlated antiferromagnets provide also a promising platform in this sense. It has been known since long that spins and charges are intrinsically coupled in the ground state of several antiferromagnetic semiconductors (Ferrer-Roca et al., 2000). More precisely the energy of the bandgap has a magnetic contribution, quadratic to the antiferromagnetic order parameter (Bossini et al., 2020; Güntherodt et al., 1971). While early attempts to exploit this property in dynamics have already been reported (Deltenre et al., 2021; Subkhangulov et al., 2014; Bossini et al., 2021a; Formisano et al., 2020), it has been realized that this coupling is not specific of a few peculiar materials. Actually it has been demonstrated that any correlated antiferromagnet, i.e., an antiferromagnet that can be described in the framework of the Mott-Hubbard theory, displays the coupling between band-gap and magnetic order (Hafez-Torbati et al., 2021).

Ultrafast dynamics in ferroelectrics

The traditional method to manipulate the ferroelectric polarization relies on static or pulsed electric fields. The mechanism responsible for the reversal of the polarization in this case is the nucleation and growth of oppositely polarized domains. Consequently the speed of switching with this approach is inherently limited to hundreds of picoseconds (Mankowsky et al., 2017).

A possible route to ultrafast coherent dynamics and even reversal of the polarization in ferroelectric consists in driving the soft-mode (Fahy and Merlin, 1994). This particular phonon possesses the same symmetry of the order parameter and, as the name suggests, it softens at the critical temperature. THz pulses have been employed in multiple ferroelectrics to resonantly excite the phonon mode. The corresponding ionic motion has been tracked by means of X-rays scattering (Grübel et al., 2016). A quantitative estimation of the modulation of the polarization gave a 8% value. Simulations predict the same approach to be able to induce even a reversal of the ferroelectric polarization, provided that the electric field of the THz pulses reaches the MV/cm regime, which is possible with nowadays sources (Kimel et al., 2020, Grübel et al., 2016).

Alternatively it has been predicted that the impulsive stimulated Raman scattering excitation of the ferroelectric mode should enable the ultrafast reversal of the polarization (Fahy and Merlin, 1994). This method successfully resulted in generating coherent and strongly anharmonic dynamics of the ferroelectric mode, but no switching (Brennan and Nelson, 1997).

Recently the nonlinear phononics approach has been explored in $LiNbO_3$ (Mankowsky et al., 2017). The excitation of the ferroelectric soft mode could be achieved indirectly, by exciting a vibrational mode in mid-infrared spectral range, which is anharmonically coupled to the soft mode. The authors tracked the dynamics of the order parameter by means of time-resolved second harmonic generation (SHG). The experimental results were interpreted in terms of a femtosecond switching of the ferroelectric polarization, although the claimed switched state was not stable (Mankowsky et al., 2017). This work is indeed interesting and controversial, as the theoretical model of the switching of the polarization employed by the authors has been questioned (Mertelj and Kabanov, 2019).

Ultrafast dynamics in magnetoelectrics and multiferroics

The coexistence of the ferroelectric polarization and of the magnetic ordering in the same structure has potential for the realization of storage devices, provided that the two orders can be optically coupled on the ultrafast timescale.

Two main material classes have been explored: composite (or artificial) multiferroics and natural magnetoelectric multiferroics.

The former are 1-, 2-, or 3D heterostructures, which combine the coupled magnetically ordered and ferroelectric constituents. It is thus appealing to use such structures, in which the order parameter in one of the layers is sensitive to photoexcitation, while another order parameter is controlled via associated strain changes. For instance, ferroelectrics allow the generation of large-amplitude strains due to the femtosecond photoexcitation, because of piezoelectricity. An example of an experimental demonstration of this concept was realized on a $Ba_{0.1}Sr_{0.9}TiO_3$ (BSTO)/$La_{0.7}$ $Ca_{0.3}$ MnO_3 (LCMO) heterostructure: the laser-induced demagnetization results in strain via magnetostriction. Such strain induces dynamics of the electric polarization, tracked via transient SHG (Sheu et al., 2014).

Natural multiferroics have been hitherto not extensively investigated, especially as far as the optical modification of the magnetoelectric coupling is concerned. Often these materials have been regarded as conventional magnetic materials. However, the presence of the magnetoelectric coupling allows unique and peculiar excitations. For instance, relying on the impulsive stimulated Raman scattering mechanism, collective coherent lattice and spin modes have been triggered in the multiferroic $GdFeO_3$ (Sheu et al., 2018). Different detection schemes have been employed to monitor the lattice and spin dynamics. More specifically, time-resolved SHG provided access to the lattice dynamics. On the other hand, the optical transmissivity enabled the measurement of the magnon dynamics. This result is peculiar and remarkable: in a conventional magnetic material, spin dynamics can be detected via magneto-optical effects only, as the optical properties are not coupled to spins. Differently, in a multiferroic the magnetoelectric coupling provides an additional contribution to the optical response, which is proportional to the magnetization. This concept has been demonstrated in a very neat way in $GdFeO_3$ (Sheu et al., 2018).

Another peculiar phenomenon in multiferroics is the electromagnon: this is an electric-dipole active spin excitations directly connected to the magnetoelectric coupling. In a time-resolved experiment, THz laser pulses have been shown to resonantly drive this transition in $TbMnO_3$ (Kubacka et al., 2014). The consequence of the photo-excitation for the magnetic systems have been detected via resonant X-ray diffraction. This excitation mechanism, relying on the electric field of light, generates a modulation of the magnetic signal one order of magnitude bigger than the canonical magnetic-field induced spin precession (Kubacka et al., 2014).

Finally we would like to mention two works reporting photo-induced phase transitions in magnetoelectric materials. The relevance of these experiments lies in the phase diagram of the materials investigated, as the transition from a non-magnetoelectric to a magnetoelectric phase is optically induced. Nearinfrared laser pulses induce a picosecond magnetic phase transition in CuO, which was tracked by means of resonant X-ray diffraction. A phase transition from the collinear (non-magnetoelectric) to the spiral (magnetoelectric) antiferromagnetic phase is reported on the picosecond timescale. The transition shows a rich and complex dynamics, which was resolved in details as it takes place on the picosecond time-scale (Johnson et al., 2011). Another example is CuB_2O_4, whose phase diagram exhibits also two magnetic phases, one of which magnetoelectric. In this material, high-energy magnons can be resonantly induced by means of near-infrared laser pulses, because of an hybridized electronic and magnonic transition, the so-called exciton-magnon. The resonant drive of high-frequency and short-life-time spin excitations perturbs the magnetic ground state so strongly, that the phase transition was observed in less than 1 ps (Bossini et al., 2018). The magnetoelectric phase can be unambiguously detected with pure optical methods, as the magnetoelectric coupling enables new optical phenomena proportional to the magnetic ordering (Toyoda et al., 2016, 2015). From the theoretical side, it was predicted- that a time-dependent electric polarization can induce a magnetization, even in materials lacking a longrange magnetic order. This effect has been called dynamical multiferroicity (Juraschek et al., 2017).

Ultrafast phono-magnetism

In this section we would like to highlight a more general concept of coupling lattice dynamics to the motion of a macroscopic order parameter. The coupling of the lattice, in either the form of phonons or strain waves, to spins in magnetic (ferro-, ferri-magnets and antiferromagnets) media induces femtosecond coherent and incoherent spin dynamics, even beyond the linear regime. A first example concerns antiferromagnets in multi-domain states: magneto-elastic interactions mediated by the walls can couple different magnon modes in different domains, on the ultrafast timescale (Bossini et al., 2021b; Gomonay and Bossini, 2021).

The material class of rare-earth doped yttrium iron garnet displays also a remarkable magnetoelastic coupling, which can be exploited to trigger ultrafast spin dynamics. For instance, time-resolved magneto-optical imaging was employed to detect photo-induced magnetoelastic waves in Lu-doped yttrium iron garnet. The processing of the data allowed to reconstruct the dynamics of the dispersion of both the spin and elastic waves (Hashimoto et al., 2017, 2018). Moreover, the optically induced strain allowed to manipulate the frequency of the magnetic resonance in a 17 nm-thick crystal of Bismuth-doped yttrium iron garnet. This approach resulted in a 20% increase of the resonance frequency, attained via a manipulation of the magnetoelastic coupling due to the optically-triggered strain waves (Soumah et al., 2021).

Strain waves can also be generated optically heating a metallic layers deposited on the back of the sample of interest. This layer works as a transducer. The illumination induces a femtosecond expansion, which results in the generation of a strain wave. This approach has been demonstrated to be able to trigger coherent precession of the magnetization is ferromagnetic semiconductors (Scherbakov et al., 2010) and metals (Jäger et al., 2015).

The resonant pumping of phonons, with the proper frequency and symmetry, can result in the generation of coherent magnons (Nova et al., 2016). This effect consists in essence in Raman scattering of the phonon fields on magnons, with the very same phenomenology of the canonical inelastic light scattering on magnons (Juraschek et al., 2020). Recently, it was demonstrated that resonant pumping of longitudinal optical phonons results in the switching of the magnetization in iron garnets (Stupakiewicz et al., 2021) and control of the domain texture in antiferromagnets (Stremoukhov et al., 2022).

Ultrafast charge dynamics in superconductors and Mott insulators

The electronic non-equilibrium properties of charge-transfer insulators, Mott-insulators and, specifically, high-Tc superconductors have been massively investigated. Considering that extensive reviews on this topic have been already published, we limit ourselves to a short list of the main experimental findings:

- *Insulator-to-metal transition*. A plethora of reports revealed that the photo-excitation of some transition metal oxides (manganites (Rini et al., 2007), vanadates iron oxides (Pashkin et al., 2011)) can lead to metallicity on the (sub)-picosecond timescale (Giannetti et al., 2016). The prototypical system for this transition is VO_2: below the critical temperature $T_c = 340$ K, this material is in an insulating phase. At ambient temperature, the photo-excitation with visible and near-IR pulses results in a sudden (shorter than 1 < ps) change of the electronic properties: the conductivity increases massively, implying that the highly photo-excitepd VO_2 reaches a metallic state immediately after photoexcitation (Giannetti et al., 2016).
- *Optical modification of the superconductivity*. Two main milestones have been achieved in cuprates superconductors (Giannetti et al., 2016). A time and spectrally-resolved investigation in the visible and near infrared spectral ranges revealed the relaxation processes, following the optical excitation of a high-Tc superconductors. The combination of this challenging experiment with a differential extended Drude-Lorentz model of the transient reflectivity, allowed to identify spin excitations as the main bosonic interaction channel with electrons. As thus, this experiment strongly suggests the nature of the bosonic-glue of the Cooper pairs

to be magnetic in origin (Conte et al., 2012). Another milestone in the physics of high-Tc superconductivity is the demonstrated light-induced superconductivity in a material with *striped* charge order. The emergence of this peculiar macroscopic charge arrangement suppresses the superconductivity. Mid-infrared laser pulses destroy the striped-order, allowing a transient superconducting state to appear and to be detected by optical means (Fausti et al., 2011).

- *Coherent dynamics of the superconducting amplitude modes*. The amplitude mode of the superconductor corresponds to the oscillation of the order parameter $\eta(t)$ at the double frequency of the superconducting gap $2\Delta_{sc}/\hbar$ (Giannetti et al., 2016). We recall that the order parameter of a superconductor is the expectation value of the number of Cooper pairs, typically expressed in terms of the destruction $(\hat{c})$ and construction $(\hat{c}^{\dagger})$ operators of Cooper pairs, i.e., $\eta = \langle \hat{c}^{\dagger}\hat{c} \rangle$. The intrinsic oscillation frequency is derived from the microscopic BCS theory and it implies that the collective mode has gained mass. This is similar to the Higgs mechanism in the standard model, that is why the amplitude mode is often referred to as Higgs mode in superconductors. This mode was photo-induced and detected in terms of oscillations of the band-gap by means of time-resolved photoemission spectroscopy and optical spectroscopy (Matsunaga et al., 2014).

Theoretical and computational approaches in ultrafast dynamics of correlated materials

As any other emerging area of physics driven by experiments, ultrafast spectroscopy of correlated materials challenges current theories. At the same time, the need for intuitive models stimulates the search for approximations and/or postulates that would still allow to describe the dynamics in terms of intuitive classical mechanics and equilibrium thermodynamics. In this respect, the 2- and 3-temperature models are among the main theoretical tools allowing to interpret ultrafast dynamics in superconducting and magnetic materials, respectively. For instance, most of theoretical studies of the ultrafast demagnetization of metals either aim at a physical interpretation of the electron-spin interaction postulated in the 3-temperature model or employ the 3-temperature model in atomistic or macromagnetic simulations of ultrafast laser-induced spin dynamics.

Time-dependent density functional theory (TDDFT), which extends density functional theory into the time domain, is a formally exact method for describing ultrafast spins- and charge-dynamics under the influence of an external field. The technique does not require any empirical parameters, it is fully ab initio, and it is not only linear but also includes all nonlinear processes naturally as part of the simulation.

Dynamical Mean-Field Theory (DMFT) is seen as one of the most appealing approaches to describe ultrafast dynamics in strongly correlated materials (Mott insulators, superconductors). DMFT is a non-perturbative, yet computationally affordable method that can be used either to solve simple models (Hubbard and related models) or it can be combined with density-functional theory to describe accurately actual solids. It can treat different interactions (electron-electron, electron-phonon) and aspects of the electronic structure of a material without assuming any hierarchy of energy scales.

Conclusion

During the whole history of ultrafast phenomena in correlated materials, the progress in the field was mainly driven by experimental observations and boosted by the development of new experimental techniques. Further development of techniques in THz, XUV and X-ray spectral ranges will allow to improve the sensitivity of the measurements. In this way, THz, visible, XUV and X-ray magneto-optics will provide four complementary views on the same ultrafast phenomenon. It is expected that obtaining the complete experimental information will stimulate further close collaboration between theory and experiments, aimed at the formulation of new approximations and conceptually novel theoretical approaches to describe ultrafast magnetism. The interpretation of ultrafast transient states can also benefit from the on-going rapid developments of theoretical and computational methods for multiscale modeling of non-equilibrium dynamics of essentially quantum systems. It is also expected that in the coming years, the continuously increasing demand for ever faster information processing will significantly fuel the fundamental interest into ultrafast dynamics of charge, orbital and spin degrees of freedom. These developments will naturally stimulate proposals of novel devices that are capable to process and store information at THz rates.

Acknowledgments

This work was supported by the Deutsche Forschungsgemeinschaft through the COST Action MAGNETOFON (grant number CA17123, STSM number CA17123-44749). D.B. acknowledges support from the Deutsche Forschungsgemeinschaft (DFG) program BO 5074/1-1. AVK acknowledges the Netherlands Organization for Scientific Research (NWO).

References

Acremann Y, Back CH, Buess M, Portmann O, Vaterlaus A, Pescia D, and Melchior H (2000) Imaging precessional motion of the magnetization vector. *Science* 290(5491): 492–495.
Acremann Y, Buess M, Back CH, Dumm M, Bayreuther G, and Pescia D (2001) Ultrafast generation of magnetic fields in a Schottky diode. *Nature* 414(6859): 51–54.
Agranat MB, Ashitkov SI, Granovskii AB, and Rukman G (1984) *JETP* 59: 804.

Back CH, Weller D, Heidmann J, Mauri D, Guarisco D, Garwin EL, and Siegmann HC (1998) Magnetization reversal in ultrashort magnetic field pulses. *Physical Review Letters* 81(15): 3251–3254.

Andreev AF and Marchenko VI (1980) Symmetry and the macroscopic dynamics of magnetic materials. *Soviet Physics Uspekhi* 23(1): 21–34.

Back CH, Allenspach R, Weber W, Parkin SSP, Weller D, Garwin EL, and Siegmann HC (1999) Minimum field strength in precessional magnetization reversal. *Science* 285(5429): 864–867.

Baierl S, Hohenleutner M, Kampfrath T, Zvezdin AK, Kimel AV, Huber R, and Mikhaylovskiy RV (2016) Nonlinear spin control by terahertz-driven anisotropy fields. *Nature Photonics* 10: 715–718.

Banerjee C, Rode K, Atcheson G, Lenne S, Stamenov P, Coey JMD, and Besbas J (2021) Ultrafast double pulse all-optical reswitching of a ferrimagnet. *Physical Review Letters* 126(17), 177202.

Battiato M, Carva K, and Oppeneer PM (2010) Super diffusive spin transport as a mechanism of ultrafast demagnetization. *Physical Review Letters* 105(2), 027203.

Beaurepaire E, Merle J-C, Daunois A, and Bigot J-Y (1996) Ultrafast spin dynamics in ferromagnetic nickel. *Physical Review Letters* 76(22): 4250–4253.

Bergman B, Ju G, Hohlfeld J, Veerdonk RJMVD, Kim J-Y, Wu X, Weller D, and Koopmans B (2006) Identifying growth mechanisms for laser-induced magnetization in FeRh. *Physical Review B* 73(6), 060407.

Bonetti S, Hoffmann MC, Sher MJ, Chen Z, Yang SH, Samant MG, Parkin SSP, and Dürr HA (2016) THz-driven ultrafast spin-lattice scattering in amorphous metallic ferromagnets. *Physical Review Letters.*

Bossini D and Rasing T (2017) Femtosecond optomagnetism in dielectric antiferromagnets. *Physica Scripta* 92(2), 024002.

Bossini D, Conte SD, Hashimoto Y, Secchi A, Pisarev RV, Rasing T, Cerullo G, and Kimel AV (2016) Macrospin dynamics in antiferromagnets triggered by sub20 femtosecond injection of nanomagnons. *Nature Communications* 7: 10645.

Bossini D, Konishi K, Toyoda S, Arima T, Yumoto J, and Kuwata-Gonokami M (2018) Femtosecond activation of magnetoelectricity. *Nature Physics* 14: 370–374.

Bossini D, Conte SD, Cerullo G, Gomonay O, Pisarev RV, Borovsak M, Mihailovic D, Sinova J, Mentink JH, Rasing T, and Kimel AV (2019) Laser-driven quantum magnonics and terahertz dynamics of the order parameter in antiferromagnets. *Physical Review B* 100(2), 024428.

Bossini D, Terschanski M, Mertens F, Springholz G, Bonanni A, Uhrig GS, and Cinchetti M (2020) Exchange-mediated magnetic blue-shift of the band-gap energy in the antiferromagnetic semiconductor MnTe. *New Journal of Physics* 22(8), 083029.

Bossini D, Conte SD, Terschanski M, Springholz G, Bonanni A, Deltenre K, Anders F, Uhrig GS, Cerullo G, and Cinchetti M (2021a) Femtosecond phononic coupling to both spins and charges in a room-temperature antiferromagnetic semiconductor. *Physical Review B* 104(22), 224424.

Bossini D, Pancaldi M, Soumah L, Basini M, Mertens F, Cinchetti M, Satoh T, Gomonay O, and Bonetti S (2021b) Ultrafast amplification and nonlinear magnetoelastic coupling of coherent magnon modes in an antiferromagnet. *Physical Review Letters* 127(7), 077202.

Brennan CJ and Nelson KA (1997) Direct time-resolved measurement of anharmonic lattice vibrations in ferroelectric crystals. *The Journal of Chemical Physics* 107(22): 9691–9694.

Brida D, Manzoni C, Cirmi G, Marangoni M, Bonora S, Villoresi P, Silvestri SD, and Cerullo G (2009) Few-optical-cycle pulses tunable from the visible to the mid-infrared by optical parametric amplifiers. *Journal of Optics* 12(1), 013001.

Brunner FDJ, Kwon O-P, Kwon S-J, Jazbinajek M, Schneider A, and Ganter P (2008) A hydrogen-bonded organic nonlinear optical crystal for high-efficiency terahertz generation and detection. *Optics Express* 16(21): 16496.

Cerullo G and Silvestri SD (2003) Ultrafast optical parametric amplifiers. *Review of Scientific Instruments* 74(1): 1.

Chekhov AL, Behovits Y, Heitz JJF, Denker C, Reiss DA, Wolf M, Weinelt M, Brouwer PW, Münzenberg M, and Kampfrath T (2021) Ultrafast demagnetization of iron induced by optical versus terahertz pulses. *Physical Review X* 11(4), 041055.

Chirac T, Chauleau J-Y, Thibaudeau P, Gomonay O, and Viret M (2020) Ultrafast antiferromagnetic switching in NiO induced by spin transfer torques. *Physical Review B* 102(13), 134415.

Conte SD, Giannetti C, Coslovich G, Cilento F, Bossini D, Abebaw T, Banfi F, Ferrini G, Eisaki H, Greven M, Damascelli A, Marel DVD, and Parmigiani F (2012) Disentangling the electronic and phononic glue in a high-Tc superconductor. 335(6076): 1600–1603.

Cundiff ST and Mukamel S (2013) Optical multidimensional coherent spectroscopy. *Physics Today* 66(7): 44–49.

Dannegger T, Berritta M, Carva K, Selzer S, Ritzmann U, Oppeneer PM, and Nowak U (2021) Ultrafast coherent all-optical switching of an antiferromagnet with the inverse Faraday effect. *Physical Review B* 104(6): L060413.

Deltenre K, Bossini D, Anders FB, and Uhrig GS (2021) Lattice-driven femtosecond magnon dynamics in α-MnTe. *Physical Review B* 104(18), 184419.

Dornes C, Acremann Y, Savoini M, Kubli M, Neugebauer MJ, Abreu E, Huber L, Lantz G, Vaz CAF, Lemke H, Bothschafter EM, Porer M, Esposito V, Rettig L, Buzzi M, Alberca A, Windsor YW, Beaud P, Staub U, Zhu D, Song S, Glownia JM, and Johnson SL (2019) The ultrafast Einstein-de Haas effect. *Nature* 565(7738): 209–212.

Duong NP, Satoh T, and Fiebig M (2004) Ultrafast manipulation of antiferromagnetism of NiO. *Physical Review Letters* 93(11), 117402.

Fahy and Merlin (1994) Reversal of ferroelectric domains by ultrashort optical pulses. *Physical Review Letters* 73(8): 1122–1125.

Fausti D, Tobey RI, Dean N, Kaiser S, Dienst A, Hoffmann MC, Pyon S, Takayama T, Takagi H, and Cavalleri A (2011) Light-induced superconductivity in a stripe-ordered cuprate. *Science* 331(6014): 189–191.

Ferrer-Roca C, Segura A, Reig C, and Munoz V (2000) Temperature and pressure dependence of the optical absorption in hexagonal MnTe. *Physical Review B* 61(20): 13679–13686.

Formisano F, Medapalli R, Xiao Y, Ren H, Fullerton EE, and Kimel AV (2020) Femtosecond magneto-optics of EuO. *Journal of Magnetism and Magnetic Materials* 502: 166479.

Gerrits T, Berg HAMVD, Hohlfeld J, Bär L, and Rasing T (2002) Ultrafast precessional magnetization reversal by picosecond magnetic field pulse shaping. *Nature* 418(6897): 509–512.

Giannetti C, Capone M, Fausti D, Fabrizio M, Parmigiani F, and Mihailovic D (2016) Ultrafast optical spectroscopy of strongly correlated materials and hightemperature superconductors: A non-equilibrium approach. *Advances in Physics* 65(2): 58–238.

Gomonay O and Bossini D (2021) Linear and nonlinear spin dynamics in multidomain magnetoelastic antiferromagnets. *Journal of Physics D: Applied Physics* 54: 374004.

Grübel S, Johnson JA, Beaud P, Dornes C, Ferrer A, Haborets V, Huber L, Huber T, Kohutych A, Kubacka T, Kubli M, Mariager SO, Rittmann J, Saari JI, Vysochanskii Y, Ingold G, and Johnson SL (2016) Ultrafast X-ray diffraction of a ferroelectric soft mode driven by broadband terahertz pulses. *arXiv*. 1602.05435v1.

Güntherodt G, Wachter P, and Imboden DM (1971) Energy level scheme and the effect of magnetic order on the optical transitions in europium chalcogenides. *Physik der Kondensierten Materie* 12(4): 292–310.

Hafez-Torbati M, Bossini D, Anders FB, and Uhrig GS (2021) Magnetic blue shift of Mott gaps enhanced by double exchange. *Physical Review Research* 3(4), 043232.

Hashimoto Y, Daimon S, Iguchi R, Oikawa Y, Shen K, Sato K, Bossini D, Tabuchi Y, Satoh T, Hillebrands B, Bauer GEW, Johansen TH, Kirilyuk A, Rasing T, and Saitoh E (2017) All-optical observation and reconstruction of spin wave dispersion. *Nature Communications* 8: 15859.

Hashimoto Y, Bossini D, Johansen TH, Saitoh E, Kirilyuk A, and Rasing T (2018) Frequency and wavenumber selective excitation of spin waves through coherent energy transfer from elastic waves. *Physical Review B* 97(14), 140404.

Hees YLWV, Meugheuvel PVD, Koopmans B, and Lavrijsen R (2020) Deterministic all-optical magnetization writing facilitated by non-local transfer of spin angular momentum. *Nature Communications* 11(1): 3835.

Huber L, Ferrer A, Kubacka T, Huber T, Dornes C, Sato T, Ogawa K, Tono K, Katayama T, Inubushi Y, Yabashi M, Tanaka Y, Beaud P, Fiebig M, Scagnoli V, Staub U, and Johnson SL (2015) Coherent acoustic perturbation of second harmonic generation in NiO. *Physical Review B* 92(9), 094304.

Hudl M, da Aquino M, Pancaldi M, Yang S-H, Samant MG, Parkin SSP, Dürr HA, Serpico C, Hoffmann MC, and Bonetti S (2019) Nonlinear magnetization dynamics driven by strong terahertz fields. *Physical Review Letters* 123(19), 197204.

Ivanov BA, Bar'yakhtar VG, Ivanov BA, and Chetkin MV (1985) Dynamics of domain walls in weak ferromagnets. *Uspekhi Fizicheskih Nauk* 146(7): 417.

Jäger JV, Scherbakov AV, Glavin BA, Salasyuk AS, Campion RP, Rushforth AW, Yakovlev DR, Akimov AV, and Bayer M (2015) Resonant driving of magnetization precession in a ferromagnetic layer by coherent monochromatic phonons. *Physical Review B* 92(2), 020404.

Johnson SL, Souza RAD, Staub U, Beaud P, Möhr-Vorobeva E, Ingold G, Caviezel A, Scagnoli V, Schlotter WF, Turner JJ, Krupin O, Lee W-S, Chuang Y-D, Patthey L, Moore RG, Lu D, Yi M, Kirchmann PS, Trigo M, Denes P, Doering D, Hussain Z, Shen Z-X, Prabhakaran D, and Boothroyd AT (2011) Femtosecond dynamics of the collinear-to-spiral antiferromagnetic phase transition in Cuo. *Physical Review Letters* 108(3), 037203.

Ju G, Hohlfeld J, Bergman B, Veerdonk RJMVD, Mryasov ON, Kim J-Y, Wu X, Weller D, and Koopmans B (2004) Ultrafast generation of ferromagnetic order via a laser-induced phase transformation in FeRh thin films. *Physical Review Letters* 93(19), 197403.

Juraschek DM, Fechner M, Balatsky AV, and Spaldin NA (2017) Dynamical multiferroicity. *Physical Review Materials* 1(1), 014401.

Juraschek DM, Narang P, and Spaldin NA (2020) Phono-magnetic analogs to opto-magnetic effects. *Physical Review Research* 2(4), 043035.

Kampfrath T, Sell A, Klatt G, Pashkin A, Mährlein S, Dekorsy T, Wolf M, Fiebig M, Leitenstorfer A, and Huber R (2010) Coherent terahertz control of antiferromagnetic spin waves. *Nature Photonics* 5(1): 31–34.

Kampfrath T, Battiato M, Maldonado P, Eilers G, Nötzold J, Mährlein S, Zbarsky V, Freimuth F, Mokrousov Y, Blügel S, Wolf M, Radu I, Oppeneer PM, and Münzenberg M (2013) Terahertz spin current pulses controlled by magnetic heterostructures. *Nature Nanotechnology* 8(4): 256–260.

Khorsand AR, Savoini M, Kirilyuk A, Kimel AV, Tsukamoto A, Itoh A, and Rasing T (2012) Role of magnetic circular dichroism in all-optical magnetic recording. *Physical Review Letters* 108(12), 127205.

Kimel AV (2014) All-optical switching: Three rules of design. *Nature Materials* 13(3): 225–226.

Kimel AV, Pisarev RV, Hohlfeld J, and Rasing T (2002) Ultrafast quenching of the antiferromagnetic order in FeBO$_3$: Direct optical probing of the phonon magnon coupling. *Physical Review Letters* 89(28): 287401.

Kimel AV, Kirilyuk A, Tsvetkov A, Pisarev RV, and Rasing T (2004) Laser induced ultrafast spin reorientation in the antiferromagnet TmFeO3. *Nature* 429(6994): 850–853.

Kimel A, Kalashnikova A, Pogrebna A, and Zvezdin A (2020) Fundamentals and perspectives of ultrafast photoferroic recording. *Physics Reports* 852: 1–46.

Kittel C (1960) Model of exchange-inversion magnetization. *Physical Review* 120(2): 335–342.

Kittel C and Kittel C (1951) Theory of antiferromagnetic resonance. *Physical Review* 82(4): 565.

Kozina M, Fechner M, Marsik P, Driel TV, Glownia JM, Bernhard C, Radovic M, Zhu D, Bonetti S, Staub U, and Hoffmann MC (2019) Terahertz-driven phonon upconversion in SrTiO3. *Nature Physics* 15(4): 387–392.

Kubacka T, Johnson JA, Hoffmann MC, Hoffmann MC, Vicario C, Jong SD, Beaud P, Grübel S, Huang S-W, Huber L, Patthey L, Chuang YD, Turner JJ, Dakovski GL, Lee WS, Minitti MP, Schlotter W, Moore RG, Hauri CP, Koohpayeh SM, Scagnoli V, Ingold G, Johnson SL, and Staub U (2014) Large-amplitude spin dynamics driven by a THz pulse in resonance with an electromagnon. *Science* 343(6177): 1333–1336.

Lambert C-H, Mangin S, Varaprasad BSDCS, Takahashi YK, Hehn M, Cinchetti M, Malinowski G, Hono K, Fainman Y, Aeschlimann M, and Fullerton EE (2014) All-optical control of ferromagnetic thin films and nanostructures. *Science* 345(6202): 1337–1340.

Landau LD and Lifshitz EM (1980) *Statistical Physics, Part 1, Vol. 5 of Course of Theoretical Physics*. Oxford: Butterworth-Heinemann.

Landau LD and Lifshitz EM (1984) *Electrodynamics of Continuous Media, Course of Theoretical Physics*. Pergamon-Press, New York.

Lichtenstein AI, Melnikov A, Razdolski I, Wehling TO, Papaioannou ET, Roddatis V, Fumagalli P, Aktsipetrov O, and Bovensiepen U (2011) Ultrafast transport of laser-excited spin-polarized carriers in Au/Fe/MgO(001). *Physical Review Letters* 107(7), 076601.

Mangin S, Gottwald M, Lambert C-H, Steil D, UhlírÅ V, Pang L, Hehn M, Alebrand S, Cinchetti M, Malinowski G, Fainman Y, Aeschlimann M, and Fullerton EE (2014) Engineered materials for all-optical helicity-dependent magnetic switching. *Nature Materials* 13(3): 286–292.

Mankowsky R, Hoegen AV, Först M, and Cavalleri A (2017) Ultrafast reversal of the ferroelectric polarization. *Physical Review Letters* 118(19): 197601.

Manz S, Matsubara M, Lottermoser T, Büchi J, Iyama A, Kimura T, Meier D, and Fiebig M (2016) Reversible optical switching of antiferromagnetism in TbMnO3. *Nature Photonics* 10: 653–656.

Manzoni C and Cerullo G (2016) Design criteria for ultrafast optical parametric amplifiers. *Journal of Optics* 18((10), 103501.

Mashkovich EA, Grishunin KA, Munekata H, and Kimel AV (2020) Ultrafast demagnetization of ferromagnetic semiconductor InMnAs by dual terahertz and infrared excitations. *Applied Physics Letters* 117(12), 122406.

Matsunaga R, Tsuji N, Fujita H, Sugioka A, Makise K, Uzawa Y, Terai H, Wang Z, Aoki H, and Shimano R (2014) Light-induced collective pseudospin precession resonating with Higgs mode in a superconductor. *Science* 345(6201): 1145–1149.

McKinnon JB, Melville D, and Lee EW (1970) The antiferromagnetic ferromagnetic transition in iron-rhodium alloys. *Journal of Physics C: Solid State Physics* 3(1S): S46–S58.

Mertelj T and Kabanov VV (2019) Comment on “Ultrafast reversal of the ferroelectric polarization” *Physical Review Letters* 123(12), 129701.

Mryasov ON (2005) Magnetic interactions and phase transformations in FeM, Mâ = â(Pt, Rh) ordered alloys. *Phase Transitions* 78(1–3): 197–208.

Nardin G (2015) Multidimensional coherent optical spectroscopy of semiconductor nanostructures: A review. *Semiconductor Science and Technology* 31(2), 023001.

Nova TF, Cartella A, Cantaluppi A, Först M, Bossini D, Mikhaylovskiy RV, Kimel AV, Merlin R, and Cavalleri A (2016) An effective magnetic field from optically driven phonons. *Nature Physics* 13(2): 132–136.

Olejník K, Seifert T, Kaspar Z, Novák V, Wadley P, Campion RP, Baumgartner M, Gambardella P, Nemec P, Wunderlich J, Sinova J, Kuzel P, Müller M, Kampfrath T, and Jungwirth T (2018) Terahertz electrical writing speed in an antiferromagnetic memory. *Science Advances* 4(3): eaar3566.

Ostler TA, Barker J, Evans RFL, Chantrell RW, Atxitia U, Chubykalo-Fesenko O, Kirilyuk A, Moussaoui SE, Guyader LL, Heyderman LJ, Mengotti E, Nolting F, Tsukamoto A, Itoh A, Ivanov BA, Kalashnikova AM, Afanasiev D, Ivanov BA, Kalashnikova A, Vahaplar K, Mentink J, Kirilyuk A, Rasing T, and Kimel AV (2012) Ultrafast heating as a sufficient stimulus for magnetization reversal in a ferrimagnet. *Nature Communications* 3: 666.

Pashkin A, Kübler C, Ehrke H, Lopez R, Halabica A, Haglund RF, Huber R, and Leitenstorfer A (2011) Ultrafast insulator-metal phase transition in VO$_2$ studied by multiterahertz spectroscopy. *Physical Review B* 83(19), 195120.

Pershan PS (1963) Nonlinear optical properties of solids: Energy considerations. *Physical Review* 130(3): 919–929. URL http://link.aps.org/doi/10.1103/PhysRev.130.919.

Pershan P, Ziel JVD, Malmstrom L, Ziel JPVD, Pershan PS, and Malmstrom LD (1965) Optically-induced magnetization resulting from the inverse faraday effect. *Physical Review Letters* 15(5): 190–193. URL http://link.aps.org/doi/10.1103/PhysRevLett.15.190.

Pfau B, Schaffert S, Schaffert S, Müller L, Gutt C, Al-Shemmary A, Büttner F, Delaunay R, Düsterer S, Flewett S, Frömter R, Geilhufe J, Guehrs E, Günther CM, Hawaldar R, Hille M, Jaouen N, Kobs A, Li K, Mohanty J, Redlin H, Schlotter WF, Stickler D, Treusch R, Vodungbo B, Klaüi M, Oepen HP, Lüning J, Grübel G, and Eisebitt S (2012) Ultrafast optical demagnetization manipulates nanoscale spin structure in domain walls. *Nature Communications* 3: 1100.

Polley D, Pancaldi M, Hudl M, Vavassori P, Urazhdin S, and Bonetti S (2018) THz-driven demagnetization with perpendicular magnetic anisotropy: Towards ultrafast ballistic switching. *Journal of Physics D: Applied Physics* 51(8), 084001.

Puc U, Bach T, Michel V, Zgonik M, Medrano C, and Jazbinsek M (2019) DSTMS-based ultra broadband terahertz time-domain spectroscopy. In: *2019 Conference on Lasers and Electro-Optics Europe & European Quantum Electronics Conference, OSA Technical Digest (Optica Publishing Group, 2019) p. paper cc_1_3.*

Purz TL, Martin EW, Rivera P, Holtzmann WG, Xu X, and Cundiff ST (2021) Coherent exciton-exciton interactions and exciton dynamics in a MoSe2/WSe2 heterostructure. *Physical Review B* 104(24): L241302.

Radu I, Stamm C, Pontius N, Kachel T, Ramm P, Thiele JU, Dürr HA, and Back CH (2010) Laser-induced generation and quenching of magnetization on FeRh studied with time-resolved X-ray magnetic circular dichroism. *Physical Review B* 81(10), 104415.

Rini M, Tobey R, Dean N, Itatani J, Tomioka Y, Tokura Y, Schoenlein RW, and Cavalleri A (2007) Control of the electronic phase of a manganite by mode selective vibrational excitation. *Nature* 449(7158): 72–74.

Satoh T, Cho S-J, Iida R, Shimura T, Kuroda K, Ueda H, Ueda Y, Ivanov BA, Nori F, and Fiebig M (2010) Spin oscillations in antiferromagnetic NiO triggered by circularly polarized light. *Physical Review Letters* 105(7), 077402.

Scherbakov AV, Salasyuk AS, Akimov AV, Liu X, Bombeck M, Brüggemann C, Yakovlev DR, Sapega VF, Furdyna JK, and Bayer M (2010) Coherent magnetization precession in ferromagnetic (Ga,Mn)As induced by picosecond acoustic pulses. *Physical Review Letters* 105(11), 117204.

Schlauderer S, Lange C, Baierl S, Ebnet T, Schmid CP, Valovcin DC, Zvezdin AK, Kimel AV, Mikhaylovskiy RV, and Huber R (2019) Temporal and spectral fingerprints of ultrafast all-coherent spin switching. *Nature* 569(7756): 383–387.

Schmising CVK, Lüning J, Pfau B, Schneider M, Günther CM, Giovannella M, Perron J, Vodungbo B, Müller L, Capotondi F, Pedersoli E, Mahne N, and Eisebitt S (2014) Imaging ultrafast demagnetization dynamics after a spatially localized optical excitation. *Physical Review Letters* 112(21), 217203 URL http://link.aps.org/doi/10.1103/PhysRevLett.112.217203.

Schumacher HW (2005) Ultrafast bit addressing in a magnetic memory matrix. *Journal of Applied Physics* 98(3), 033910.

Seifert T, Jaiswal S, Martens U, Hannegan J, Braun L, Maldonado P, Freimuth F, Kronenberg A, Henrizi J, Radu I, Beaurepaire E, Mokrousov Y, Oppeneer PM, Jourdan M, Jakob G, Turchinovich D, Hayden LM, Wolf M, Münzenberg M, Kläui M, and Kampfrath T (2016) Efficient metallic spintronic emitters of ultrabroadband terahertz radiation. *Nature Photonics* 10(7): 483–488.

Shah J (1996) *Ultrafast Spectroscopy of Semiconductors and Semiconductor Nanostructures, Solid-State Sciences*. Heidelberg: Springer.

Shalaby M, Vicario C, and Hauri CP (2016) Low frequency terahertz-induced demagnetization in ferromagnetic nickel. *Applied Physics Letters* 108: 182903.

Shen YR (2003) *The Principles of Nonlinear Optics*. Hoboken, New Jersey: Wiley-Interscience.

Shen YR and Bloembergen N (1965) Theory of stimulated brillouin and Raman scattering. *Physical Review* 137(6A): A1787–A1805.

Sheu YM, Trugman SA, Yan L, Jia QX, Taylor AJ, and Prasankumar RP (2014) Using ultrashort optical pulses to couple ferroelectric and ferromagnetic order in an oxide heterostructure. *Nature Communications* 5: 6832.

Sheu YM, Ogawa N, Tokunaga Y, Chan HC, and Tokura Y (2018) Selective probe of coherent polar phonon and quasiferromagnetic resonance modes in multiferroic GdFeO3. *Physical Review B* 98(10), 100301.

Smith FW, Le HQ, Diadiuk V, Hollis MA, Calawa AR, Gupta S, Frankel M, Dykaar DR, Mourou GA, and Hsiang TY (1989) Picosecond GaAsâ based photoconductive optoelectronic detectors. *Applied Physics Letters* 54(10): 890–892.

Soumah L, Bossini D, Anane A, and Bonetti S (2021) Optical frequency upconversion of the ferromagnetic resonance in an ultrathin garnet mediated by magnetoelastic coupling. *Physical Review Letters* 127(7), 077203.

Stamm C, Tudosa I, Siegmann HC, Stöhr J, Dobin AY, Woltersdorf G, Heinrich B, and Vaterlaus A (2005) Dissipation of spin angular momentum in magnetic switching. *Physical Review Letters* 94(19), 197603.

Stanciu CD, Hansteen F, Kimel AV, Kirilyuk A, Tsukamoto A, Itoh A, and Rasing T (2007) All-optical magnetic recording with circularly polarized light. *Physical Review Letters* 99(4), 047601.

Stone KW, Gundogdu K, Turner DB, Li X, Cundiff ST, and Nelson KA (2009) Two-quantum 2D FT electronic spectroscopy of biexcitons in GaAs quantum wells. *Science* 324(5931): 1169–1173.

Stremoukhov P, Carl SD, Safin A, Nikitov S, and Kirilyuk A (2022) Phononic manipulation of antiferromagnetic domains in NiO. *New Journal of Physics* 24(2), 023009.

Stupakiewicz A, Szerenos K, Afanasiev D, Kirilyuk A, and Kimel AV (2017) Ultrafast nonthermal photo-magnetic recording in a transparent medium. *Nature* 542: 71.

Stupakiewicz A, Szerenos K, Davydova MD, Zvezdin KA, Zvezdin AK, Kirilyuk A, and Kimel AV (2019) Selection rules for all-optical magnetic recording in iron garnet. *Nature Communications* 10(1): 612.

Stupakiewicz A, Davies CS, Szerenos K, Afanasiev D, Rabinovich KS, Boris AV, Caviglia A, Kimel AV, and Kirilyuk A (2021) Ultrafast phononic switching of magnetization. *Nature Physics* 17: 489–492.

Subkhangulov RR, Henriques AB, Rappl PHO, Abramof E, Rasing T, and Kimel AV (2014) All-optical manipulation and probing of the d-f exchange interaction in EuTe. *Scientific Reports* 4(1): 4368.

Szerenos K, Kimel A, Maziewski A, Kirilyuk A, and Stupakiewicz A (2019) Fundamental limits on the repetition rate of photomagnetic recording. *Physical Review Applied* 12(4), 044057.

Thiele J-U, Buess M, and Back CH (2004) Spin dynamics of the antiferromagnetic-to-ferromagnetic phase transition in FeRh on a subpicosecond time scale. *Applied Physics Letters* 85(14): 2857–2859.

Toyoda S, Abe N, Kimura S, Matsuda YH, Nomura T, Ikeda A, Takeyama S, and Arima T (2015) One-way transparency of light in multiferroic CuB_2O_4. *Physical Review Letters* 115(26), 267207.

Toyoda S, Abe N, and Arima T (2016) Gigantic directional asymmetry of luminescence in multiferroic CuB_2O_4. *Physical Review B* 93(20), 201109.

Tu P, Heeger AJ, Kouvel JS, and Comly JB (1969) Mechanism for the first order magnetic transition in the FeRh system. *Journal of Applied Physics* 40(3): 1368–1369.

Tudosa I, Stamm C, Kashuba AB, King F, Siegmann HC, Stöhr J, Ju G, Lu B, and Weller D (2004) The ultimate speed of magnetic switching in granular recording media. *Nature* 428(6985): 831–833.

Unikandanunni V, Rigoni F, Hoffmann MC, Vavassori P, Urazhdin S, and Bonetti S (2022) Ultrafast electron dynamics in platinum and gold thin films driven by optical and terahertz fields. *Applied Physics Letters* 120(2), 021601.

Wang S, Wei C, Feng Y, Cao H, Li W, Cao Y, Guan B-O, Tsukamoto A, Kirilyuk A, Kimel AV, and Li X (2021) Dual-shot dynamics and ultimate frequency of all-optical magnetic recording on GdFeCo. *Light, Science & Applications* 10(1): 8.

Wienholdt S, Hinzke D, and Nowak U (2012) THz switching of antiferromagnets and ferrimagnets. *Physical Review Letters* 108(24), 247207.

Yang Y, Wilson RB, Gorchon J, Lambert C-H, Salahuddin S, and Bokor J (2017) Ultrafast magnetization reversal by picosecond electrical pulses. *Science Advances* 3(11), e1603117.

Yusupov R, Mertelj T, Kabanov VV, Brazovskii S, Kusar P, Chu J-H, Fisher IR, and Mihailovic D (2010) Coherent dynamics of macroscopic electronic order through a symmetry breaking transition. *Nature Physics* 6(9): 681–684.

Zonno M, Boschini F, and Damascelli A (2021) Time-resolved ARPES on cuprates: Tracking the low-energy electrodynamics in the time domain. *Journal of Electron Spectroscopy and Related Phenomena* 251: 147091.

Zvezdin AK (1979) Dynamics of domain-walls in weak ferromagnets. *JETP Letters* 29(10): 553–557.

Zvezdin AK and Mukhin A (1981) Novel nonlinear dynamical effects in antiferromagnets. *Bulletin of the Lebedev Physics Institute* 12: 10–15.

Excitons in crystals

Fabrice P Laussy[a,b] **and Alexey Kavokin**[c,b,d], [a]Faculty of Science and Engineering, University of Wolverhampton, Wolverhampton, United Kingdom; [b]Russian Quantum Center, Skolkovo, Moscow Region, Russia; [c]International Center for Polaritonics, School of Science, Westlake University, Hangzhou, Zhejiang Province, China; [d]Moscow Institute of Physics and Technology, Institutskiy Pereulok, Dolgoprudny, Moscow Oblast, Russia

© 2024 Elsevier Ltd. All rights reserved.

This is an update of B.P. Zakharchenya, S.A. Permogorov, Excitons in Crystals, Editor(s): Franco Bassani, Gerald L. Liedl, Peter Wyder, Encyclopedia of Condensed Matter Physics, Elsevier, 2005, Pages 171–179, ISBN 9780123694010, https://doi.org/10.1016/B0-12-369401-9/01147-5.

Introduction **707**
Historical background: Frankel & Wannier-Mott excitons 707
The existence of excitons 707
Overview of excitonic physics **709**
Theory of excitons 709
Excitons in various materials 711
Spin structure 712
Optical properties of solids 713
Exciton-polaritons 713
Excitons interactions 714
Multiexcitons 715
Excitons in heterostructures 715
Quantum wells, wires and rings excitons 716
Quantum Dots excitons 716
Direct and indirect excitons 718
Key issues and trending topics **718**
Rydberg excitons 718
Excitons in quantum Hall bilayers 719
Excitonic matter 719
Exciton BEC and superfluids 720
Emerging trends and future directions **722**
Moiré excitons 722
Topological excitons, insulators and superconductors 722
Excitonic devices 723
Conclusion **724**
References **724**

Abstract

Excitons are elementary electrical excitations of crystals. They are bound states of negatively charged electrons and positively charged holes, which makes them neutral composite bosons. They can exist in either tight- (Frenkel) or weak- (Wannier) binding conditions. The most important property of excitons is to be created by photon absorption and to emit photons when they annihilate. This makes optical methods most appropriate for their studies. They constitute driven-dissipative quantum systems characterized by a rich variety of optical, spin, transport and transfer phenomena. They are important for both fundamental and applied aspects of condensed-matter physics.

Key points

- The concept of exciton is central to condensed-matter physics.
- Excitons are among the oldest quasi-particles identified and studied, both theoretically and experimentally.
- Excitons are involved in a broad and varied range of effects, mainly optical ones but not exclusively.
- Excitons are expected to undergo a rich set of quantum phases, from Bose-Einstein condensation to superfluidity passing by quantum crystals, Mott insulators and other nontrivial topological phases.
- Excitons remain complex objects even at the two-particle level, whose properties, role, description and sometimes even existence remain hotly debated.
- There is an increasingly thriving activity on excitons thanks to technological progresses and the emergence of new materials.
- There are rich prospects for unique future applications based on excitons, such as stretchable screens.

https://doi.org/10.1016/B978-0-323-90800-9.00163-3

Introduction

Historical background: Frankel & Wannier-Mott excitons

The concept—and name—of exciton comes from the soviet theorist Frenkel (1931), starting with his theory for the excitation of atomic states when they are part of a lattice. Excitations in the form of motion or vibrations (sound or heat waves) were already established, by Debye, Tamm, Born and others. Frenkel—who incidentally also named their quantum version as "phonons"—considered instead the case of neutral electronic excitation, that is to say, in raising in energy the quantum state of a single atom in an otherwise frozen (non-vibrating) crystal. The localization of such an excitation does not correspond to a stationary state of the crystal and it is instead diluted over all the atoms in the form of what Frenkel first termed an "excitation wave." The excited state is then shared by other atoms of the crystal, propagating in this way energy yet with no transfer of charge, as well as momentum yet with no transfer of mass. These running exciton states are the proper stationary states of the static crystal. Such a Frenkel exciton thus describes the situation of an excitation that is not associated with a particular atom, but is travelling from one to another, yet remaining in itself of a size or extent commensurable with the atom. This corresponds to a tight-binding case. Frenkel arrived to the conclusion that the absorption spectrum of a crystal, when not affecting its vibrational state, yields single lines that correspond one-to-one to the absorption lines of an isolated atom of the crystal. This surprising result (at the time) explained why the absorption spectra of solid bodies, which at ordinary temperatures are continuous, break down at low temperatures into spectral lines, as is the case for gases. Such paradoxical observations had indeed been made with the rare earth and iodine spectra, while at higher temperatures, vibrational motion blur this excitonic structure into a continuum. The quantization of such waves and their group packets have been interpreted by Frenkel as giving rise to a particle whose motion is characterized by a wavefunction similar to that of an electron, with a momentum $\mathbf{p}$ and kinetic energy $p^2/(2\,m^*)$ where m^* is an effective mass. Frenkel named this particle an exciton. A record is found for instance in his 1959 textbook "Introduction to the Theory of Metals" where he writes *"This originating state somewhere does not stay in the place where it was formed but moves uniformly along this or that row of atoms as some particle which I call "an exciton" ("an excitation quantum")."* Frenkel thus developed a theory of light scattering in crystals that was an analog to Schrödinger's theory of the Compton effect (scattering of light by a free electron), the electron wave being replaced in his case by his excitation wave. In dielectrics, this also explains why there is no photoconductivity despite the fact that two charges are created in the band model. Pekar reported an interjection during a seminar where this puzzle was being entertained, where Frenkel, after asking why the same phenomenon was not a mystery in gases, simply advised to *"consider a dielectric as a compressed gas."* This is the foundation of exciton physics. In Frenkel (1931)'s own visionary words: *"the development of the theory sketched above in the quantitative direction* [. . .] *does not present any difficulty, for this calculation can be easily reduced to the corresponding calculation for an isolated atom or molecule."* This fact that characteristics and fingerprints of isolated atoms can survive when the atoms themselves dissolve into an object of an altogether different nature—a solid with a band structure—is an embodiment of the basic idea of *quasi-particles,* the tenet of condensed-matter physics. This similarly allows an electron in the conduction band as well as its absence in the valence band (the "electron-hole," or "hole" for short) to be treated as negative and positive particles, respectively. This is discussed in more details by La Rocca (2022) in this volume. Beyond the formulation of the exciton as a quasi-particle, Frenkel also analyzed excitons' interactions with the environment, localization and their optical characteristics. Frenkel (1936) later generalized critically his previous results in order to account for arguments from Peierls (1932) regarding weak excitations, producing what he called "small" excitons, which are now known as *Frenkel excitons.* Since they exist predominantly in molecular (organic) crystals, they are also called "molecular excitons." Several molecules enter the elementary cell of such crystals, and any of them may be optically excited. The other regime, also anticipated by Frenkel who called them "megaexcitons," occurs in semiconductors, for instance, in copper peroxide, a popular material of practically all the semiconductor experiments of the 1930s, as well as in the other major classes of semiconductors: germanium, gallium arsenide and the like. Wannier (1937) made a general theory for excitons in the Bloch band continuum, and recognized the case where *"the electron does not escape its hole,"* thus producing no current, despite the fact that the bound electron and hole could be considerably separated in space. They, however, remain correlated, maintaining in particular a well-defined wavevector for their joint propagation. Such large-radii excitons are now known as *Wannier excitons,* and constitute the bulk of excitonic physics in optoelectronics, cf. Fig. 1A. While it is Wannier who derived the Schrödinger equation for the Hydrogen atom for such excitons, it is Mott (1938) who painted the explicit picture for them of an electron and hole bound to each others by the Coulomb interaction in a medium with dielectric constant ε and migrating around their center-of-mass. This remains, by far, the predominant description of excitons. For this reason, such excitons are also known as *Wannier-Mott excitons.* While his name did not remain attached to excitons, Peierls was also one of the fathers of their conception.

The existence of excitons

Frenkel's seminal idea was first received reservedly by the authorities of the time, in particular by Pauli who deemed it to be outright "falsch" (hence not trivial, was Frenkel's rebuttal). There remained controversy for a while until it became apparent, with Slater and Shockley (1936)'s analysis, that the result was robust to alternative theoretical treatments. The existence of isolated spectral lines, in particular, was drawing attention, since the band-theory of solids precisely dissolves the isolated quantized levels of atoms into continuous bands, so their resurgence was suspicious. Interestingly, modern onlookers of such lines have also raised doubts as to their systematic connection to actual excitons in the system. Kira et al. (1998), for instance, regard this question as a many-body problem of Coulomb-interacting fermionic electrons and holes, which, instead of making transitions between sets of excitons, involve polarization fields. The quantum-mechanical luminescence equations of the electron-hole system happen to produce excitonic resonances, either in absorption or luminescence, even when there is no exciton population in the model. This understanding insists on the difference between the excitonic *polarization* and the excitonic *population.* The former is a complex-valued correlator that probes the transitions permitted by the system, is a coherent quantity subject to dephasing and is

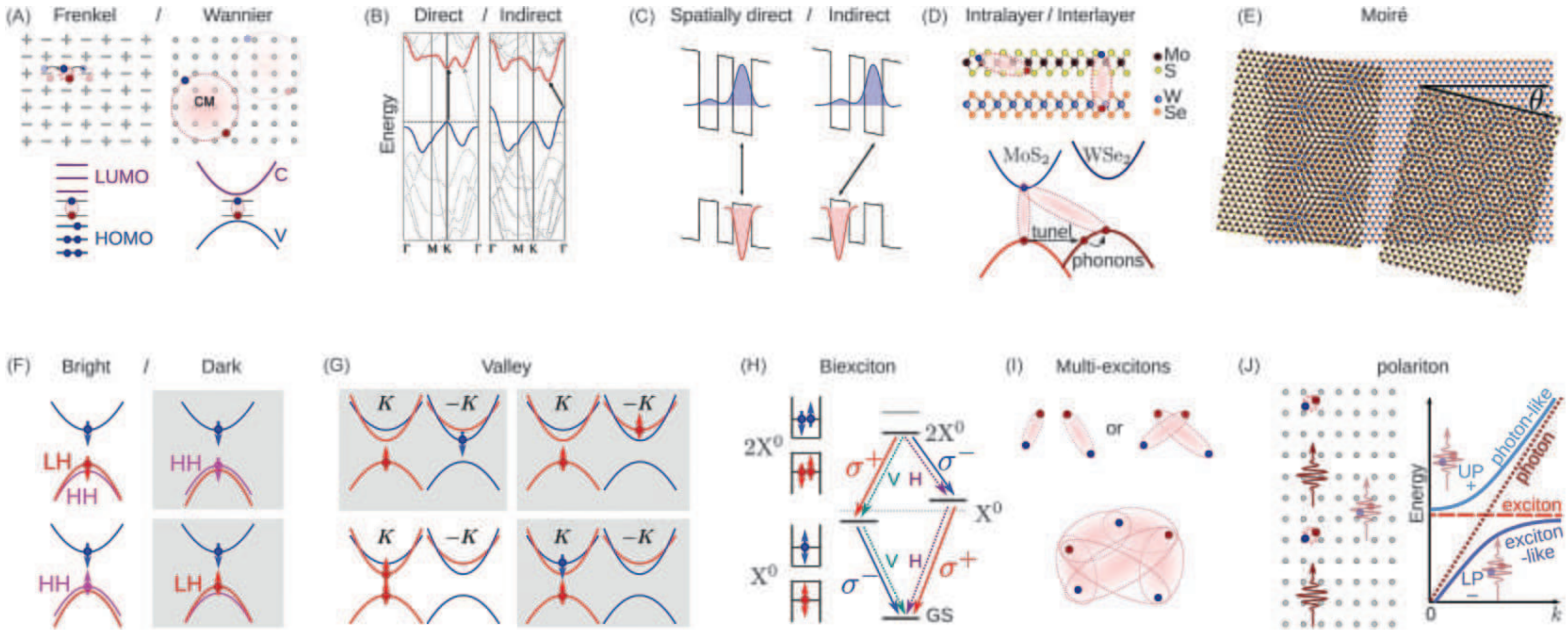

Fig. 1 Basic concepts of excitons: (A) **Frenkel and Wannier excitons,** attached to one site of the crystal or involving widely separated sites, which translates in the energy diagrams as occupying Highest Occupied (HOMO) and Lowest Unoccupied (LUMO) Molecular Orbitals in one case and living in the band structure in the other. As a result, these two types of excitons are of small and large spatial extension, respectively. Both are, however, delocalized throughout the entire crystal (represented as ghostly images), (B) **Direct and indirect excitons** from negligible or large exchanged momentum in the interband transitions, allowing or preventing an optical process (emission or absorption). Here the character of the transition changes from direct in a MoS$_2$ monolayer (left) to indirect in its bulk, (C) **Spatially direct and indirect excitons** in coupled QWs. The horizontal axis is the growth direction and the energy levels can be biased by an electric field, with electron (up, blue) and hole (red, bottom) wavefunctions localized in one or the other QW, resulting in single-well excitons or, in contrast, little-overlapping wavefunctions excitons with strong dipole moment and long lifetimes, (D) **Intra and Interlayer excitons** in bilayers of 2D-material TMDs (e.g., MoS$_2$ and WSe$_2$) implement similar ideas than traditional heterostructures in new generations of materials, (E) **Moire excitons** occur in 2D-heterostructures for various twisting angles θ between the two sheets, resulting in potentials of varying lengths and geometries. This new degree of freedom is one of the peculiarities of the new 2D materials, (F) **Bright and Dark excitons** are those which, for various reasons, can and cannot couple to light, respectively. A typical factor is conservation of angular momentum, ruled by the spin of the particles, with only spin ± 1 excitons recombining (or being created) with a transfer of angular momentum to (from) the photon. This is ruled by the spin of the light-hole (LH) and heavy-hole (HH) bands, (G) **Valley excitons** arise in so-called valleys in the bandgap, which are minima that occur elsewhere than at the zero-momentum (Γ) point, typically at the $\pm \boldsymbol{K}$ points on the border of the Brillouin zone.
In addition to their spin (red, spin-up; blue, spin-down), electron-hole pairing from different valleys results in momentum-forbidden transitions, leading to more bright/dark configurations (dark shaded in gray). Filling up the bands with more electrons and holes leads to charged valley excitons. (H) **Biexcitons** are the bound states of two electrons and two holes, or two excitons. A biexciton in a QD is sketched with its cascade toward the ground state leading to polarization-entangled photons, which can be hindered by the fine-structure splitting between excitonic states, (I) **Multiexcitons** represent the complicated problem of the identity and description of multiple excitons. Even at the two-exciton level, the indistinguishability of electrons and holes make the formulation in terms of excitons ill-defined. In the presence of even more excitons, charged multi-excitons, trions, quatrons, etc., provide convenient mental pictures which may, however, require independent treatment, (J) **Exciton-polaritons** occur from the strong-coupling between excitons and, e.g., photons, leading to the disappearance of these states as they Rabi oscillate from one type to the other, to give rise to quantum superpositions of a mixed new quasiparticle, in-phase (UP) and out-of-phase (LP) and with new energies which result in a characteristic anticrossing.

not ruled by thermodynamics, while the latter is a real-valued quantity referring to real states (or quasi-particles), subject to relaxation dynamics, equilibrium (if given enough time) and phase transitions. Chatterjee et al. (2004) also find that a plasma of unbound electrons and holes emits at the exciton resonances. Such distinctions are important when it comes to seeking new phases of matter, such as Bose condensation, of particles that may in fact not even be present in the system. The persistence of excitonic lines in a variety of scenarios make the determination of the actual origin a tricky one, with the possibility that the parameter range in which true exciton populations exist is in fact limited despite their ubiquitous manifestation. This conclusion has been amply debated (with as yet no consensual resolution), for instance by Deveaud et al. (2005), although dedicated experimental investigations, such as those by Hägele et al. (1999), tend to confirm that the excitonic problem is indeed more complicated than a bound electron-hole pair popping up and recombining. It could, instead, be explained by much-less intuitive Coulomb-correlation contributions to the photon-assisted recombination of free electron-hole pairs. Kaindl et al. (2003) have sought alternative signatures than spectral lines to evidence the presence of real excitons, including "quasi-particle spectroscopy," which consists in probing transitions between their Coulombic internal exciton levels, prominently between their 1s and 2p states, which typically falls in the THz range for direct-gap semiconductors. They concluded to a coexistence of excitons with electron-hole pairs but with an ultrafast (quasi-instantaneous) excitonic formation at lower temperatures. Hägele et al. (1999) proposed to measure the electron-hole exchange energy which, when the exciton is bound in the state ψ, is proportional to its electron and hole overlap $|\psi(0)|^2$. This can be obtained from the quantum beating of spin since the exchange energy, when it is present, turns the linear dependence of its frequency on an applied magnetic field into a parabolic one (due to a correction to the Zeeman splitting). They concluded that a dominant population of excitons is present only under stringent experimental conditions. Progress from material science, providing more robust excitons, is helping to bring back an unanimous recognition of excitons. In TMDC materials for instance, excitons are believed by Steinhoff et al. (2017) to prevail over electron-hole plasma even up to room temperature, through balancing processes of a fission-fusion type between the two types.

Another hotly debated problem with excitons is whether they qualify, or even exist, as bosons. The commutator of the annihilation and creation operators of excitons is not 1 but deviates from this bosonic limit by an order na_B^D in D dimensions, giving hope of behaving as good bosons at low enough densities. The composite nature of excitons, however, combined to their large size and delocalized character has been hailed as voiding their validity as interacting bosons already at the two-particle level. Since electrons and holes cannot be attributed to any single exciton, one should deal directly with a fermionic four-particle complex dominated by the Pauli exclusion principle. Illustratively, the interaction of any electron with any hole is part of the exciton-exciton scattering when these particles are assumed to belong to different excitons, but are also constitutive of the excitons themselves when belonging to the same exciton, in which case they should be ignored since they have already been taken into account to bind the exciton in the first place (Fig. 1I). Combescot and Betbeder-Matibet (2002), in particular, argue that purely fermionic contributions are of the same order as Coulomb contributions and, more importantly, forbid an effective Hamiltonian, since two-exciton interactions involve all other excitons. This is because Pauli exclusion is intrinsically a N-body effect, which precludes an exact description with a standard two-body interactions, even with some inclusions of the exchange terms. They observed, for instance, that such an ad hoc procedure produces a non-Hermitian Hamiltonian. They conclude that the conventional "bosonization"—which consists in mapping the original fermion problem into one of elementary bosons so as to apply known and familiar techniques—are erroneous and should not be used, but replaced by a many-body theory of "cobosons" (for composite bosons), such as that exposed by Combescot et al. (2008). The extent to which the composite nature of excitons affects the dynamics of several excitons remains a problem of active research.

Overview of excitonic physics

Theory of excitons

Excitons are primarily a theoretical concept: a useful physical picture to capture the essence of a phenomenon which, in its full complexity, fails to adhere exactly to any but a complete, so-called "ab-initio" or "first-principle," brute force calculation of the Schrödinger equation for the full system with no phenomenological parameters. Although ab initio methods are better suited for ground states calculations (with density functional theory), they can also compute elementary excitations in a self-consistent way and derive optical response. A so-called GW (G is for "Green function" and W refers to screening of the Coulomb interaction) approximation combined to the Bethe-Salpeter equation (describing bound states in quantum field theory, so particularly suitable for excitons), or GW-BSE approach, has proved particularly accurate to reproduce experiments in great details. In such cases, one needs not speak of excitons but focus on the calculated observables and compare them to experiments. The agreement in some cases can be extremely good. Even such approaches remain however limited by computational resources and need to make some approximations, that have to be both understood and controlled. Various models thus derive various excitons in different limits. Frenkel and Wannier excitons are obtained in this way from the same underlying theory but using different basis functions. They both start with the Born-Oppenheimer approximation, that decouples the electrons and ions dynamics so that Schrödinger's equation can now focus on the electronic wavefunction $\phi(\mathrm{r}_1, \mathrm{r}_2, \cdots)$ alone, i.e., for the joint probability amplitude to find the $N \gg 1$ electrons in the crystal at positions r_i. If the crystal is assumed static (frozen atoms), the Hamiltonian retains electrons' kinetic energies $-\frac{\hbar^2}{2m}\sum_i \nabla_i^2$ (m the electron mass and ∇_i acting on the ith variable of ϕ), the electron-crystal Coulomb interaction $-\frac{1}{4\pi\varepsilon}\sum_i\sum_n Ze^2/|\mathbf{X}_n - \mathbf{r}_i|$ and electron-electron interactions $\frac{1}{2}\,\frac{1}{4\pi\varepsilon}\sum_i\sum_{j\neq i} e^2/|\mathbf{r}_i - \mathbf{r}_j|$, with Z the number of charges of each atomic site, e the electron charge, $\mathbf{X}_n$ the positions of the atoms, that define the crystal and ε the dielectric constant. Since each electron interacts with every atom of the crystal and with every other electron, the problem, although simply formulated, is extremely complicated. The next popular step is the one-electron approximation that breaks ϕ into a product $\phi(\mathbf{r}_1, \mathbf{r}_2, \cdots) = A\varphi_1(\mathbf{r}_1)\varphi_2(\mathbf{r}_2)\cdots$ with A the antisymmetry operator that changes signs whenever two electrons are permuted, to enforce their Fermi-statistics. This factorization makes the electrons uncorrelated, which is clearly an oversimplification, but correlations are recovered by linear superpositions of such states that serve as basis functions, and which have been introduced in this form to decide on an explicit form. Two popular choices—tight-binding and Bloch functions—lead to the two main types of excitons: Frenkel and Wannier. With tight-binding functions, the electron remains localized to its atom, as is the case in organic solids where there is weak overlap between lattice sites due to small intersite interactions. Bloch functions, on the other hand, have the periodicity of the crystal built-in as $\varphi_j(\mathbf{r}_j) \equiv u_{\mathbf{k}_j}(\mathbf{r}_j)\exp(i\mathbf{k}_j \cdot \mathbf{r}_j)$, introducing a momentum $\mathbf{k}_j$ as a label of states and with $u_{\mathbf{k}_j}(\mathbf{r}_j + \mathbf{R}) = u_{k_j}(\mathbf{r}_j)$ for any vector $\mathbf{R}$ connecting two sites of the crystal. They thus delocalize the electron in the solid thanks to the band structure. In both pictures—bound and propagating electrons—the exciton that arises from exciting one electron from any one site, is propagating (i.e., is delocalized), like the Bloch electron. Frenkel and Wannier excitons are thus two limiting models of the same theory, cf. Fig. 1A. The Wannier model is typically valid for low-lying exciton states in semiconductors and crystals with a large dielectric constant. It breaks down for small-radius excitons because first-order corrections are large and hard to calculate, and also because small distances mean a large spread in momentum and thus sensibility to the non-parabolic band structures. A beautiful feature of the Wannier treatment is the natural emergence of Schrödinger's equation for the hydrogen atom for the electron-hole pair. From this, follows straightforwardly the energy of an exciton in a semiconductor crystal as $E_X(\mathbf{k}) = E_{\text{gap}} - R_y + \frac{\hbar k^2}{2m^*} + \cdots$ where E_{gap} is the bandgap energy, and R_y is the binding energy. The latter is known from the hydrogen atom as the Rydberg energy $R_y \equiv \frac{e^4\mu_0}{2\varepsilon^2\hbar^2}$ with $\mu_0 \equiv m_e m_h/(m_e + m_h)$ the reduced mass computed from the electron m_e and hole m_h effective masses. These masses correspond to a quadratic fit to the dispersion relation of the exciton as given by band theory, and can be negatives. This connection to atomic physics is a central manifestation of excitons in crystals, as shown in Fig. 2. The excitonic Bohr radius is also obtained from the atomic theory as $a_{\mathrm{B}} = \frac{\varepsilon\hbar^2}{\mu_0 e^2}$. Therefore, one can relate the size of the exciton, as estimated by its Bohr radius, to its binding energy as $R_y = \frac{e^2}{2\varepsilon a_{\mathrm{B}}}$, i.e., chiefly through the dielectric constant ε, that can vary a lot from one dielectric to the other. The dielectric constant, also called "relative permittivity," quantifies the polarizability of a dielectric and how this affects the Coulomb force between two point charges in the medium as compared to the vacuum. This is frequency dependent, due to retardation effects (the polarization of a material does not follow instantaneously variations of an electric field). This results in phase shifts that make the dielectric constant complex-valued. The short-range interaction is governed by the low frequency limit of the dielectric constant, while the long-range interaction is ruled by its high (optical) frequencies. Since the Coulomb potential is central to the electron-hole interaction, the features of the dielectric constant impact directly the structure of the exciton. For instance, the dielectric constant is typically large in semiconductors, resulting in important screening of the interaction and thus a weak binding energy, or, in turn, large excitons. Frenkel and Wannier excitons therefore typically occur in small and large dielectric constant materials, respectively, although this admits exceptions. Dimensionality is another crucial factor for the dielectric constant and thus also for the exciton. First Rytova (1967) and Stern (1967), independently, (later, also Keldysh (1979) and others) derived the screened Coulomb potential in two-dimensional structures, featuring a logarithmic shape at short distances and a hyperbolic shape at long distances.

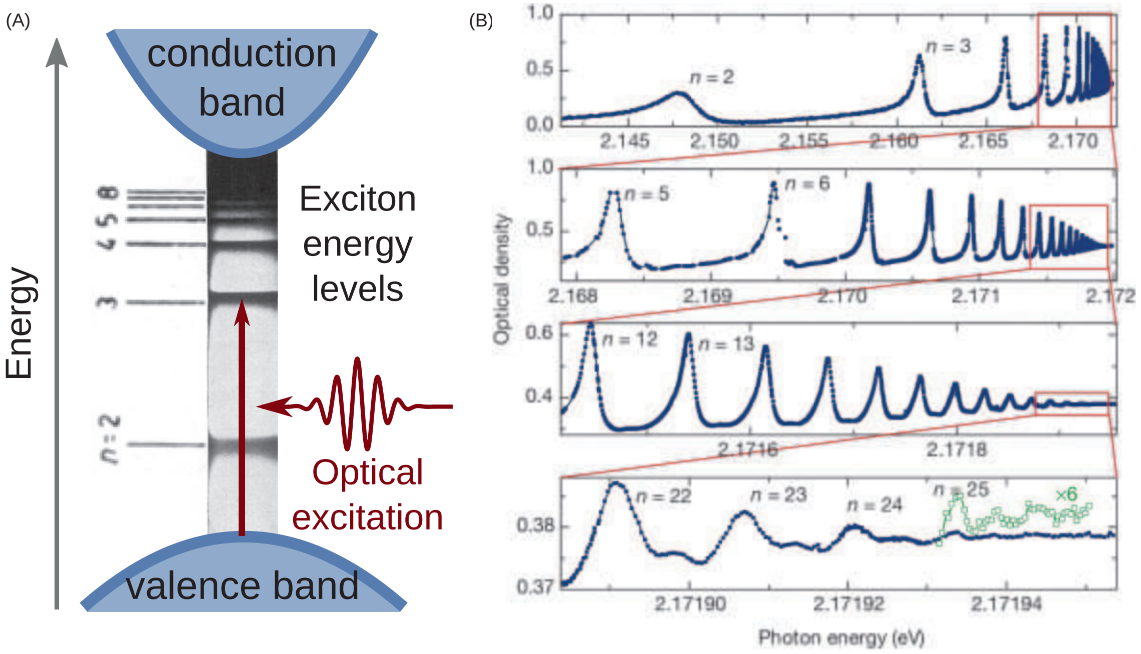

Fig. 2 Optical excitation of an exciton in the semiconductor cuprous oxide: the spectral lines are observed in the bandgap due to the negative (binding) energy of the excitonic states. In (A), as first observed by Gross (1956) (up to $n = 8$) and in (B), as best observed by the Manfred Bayer group (Kazimierczuk et al., 2014) with very-high (Rydberg) exciton states (up to $n = 25$). The same material, Cu_2O, shows the impressive progress of technology in the course of a half-century. (A) From Gross EF (1956) Optical spectrum of excitons in the crystal lattice. *Il Nuovo Cimento* 3:672, https://doi.org/10.1007/BF02746069. Panel (B) is reproduced with permission from Kazimierczuk T, Fröhlich D, Scheel S, Stolz H, and Bayer M (2014) Giant Rydberg excitons in the copper oxide CU_2O. *Nature* 514:343.

In one-dimension, one can encounter large-radius excitons with large binding energies, i.e., of a mixed Frankel–Wannier character, due to the shape of the Coulomb potential in such a case (large dielectric constant but small screening). Another potential of note was introduced by Haken (1956), to describe the electron-hole interaction screening in an oscillating lattice, which occurs with phonon vibrations. This results in a distance-dependent dielectric function. In all cases, the binding energy also quantifies the exciton's stability with temperature, up to $T \approx R_y/k_B$ (through Boltzmann constant). The hydrogenic theory also provides a suitable framework to study excitonic responses to applied external fields, in particular through perturbation methods. Understood as huge atoms, one can indeed account for a wealth of properties of excitons that are well-known from atomic physics, such as their easy ionization (with relatively weak electric field as compared to hydrogen), or, before this happens, the Stark effect (shift of the spectral lines under an applied electric field) that is observed with hundreds of volts only, or the diamagnetic effect, Zeeman splitting, Landau levels, etc. Most of these observations have been made in the early years of the field, mainly by Gross (1962) and coworkers (in particular, Zakharchenya) in the wake of their observation of the spectral structure. Littlewood (2022) provides a more detailed exposition of the theory of excitons in this volume.

Excitons in various materials

Excitons appear in solids of various types: in molecular, ionic (particularly the alkali halides), and semiconductor crystals, and in complicated organic compounds. Excitons are too-short lived in most metals to be observable but they occur in superconductors. They have also been observed in some liquids, and even in living matter, where their migration is believed to be an important mechanism of energy transport for photochemical reactions such as photosynthesis. At a more basic level, exciton generation, diffusion, and annihilation are known to be involved in the efficiency of photovoltaic solar cells, although processes there are typically too complex to be described in these terms. It is definitely in crystals that excitons are currently the best understood and the most actively studied. Common properties are found in all cases which can be seen as those defining the exciton (such as the hydrogenoid spectrum $-R_y/n^2$ for Wannier excitons). Still, the details of each solid make their corresponding excitons be sui generis objects. We now give a broad overview of how various materials give rise to various excitons (cf. Fig. 3).

One crystal of choice for excitons is the one in which their first compelling observation was made, namely, cuprous oxide, Cu_2O. This is one of the main oxide of copper (the other being cupric oxide CuO) through the process $4Cu + O_2+ \rightarrow 2Cu_2O$. This red (sometimes yellowish) semiconductor remains to this day—surprisingly, in its natural form even better than when

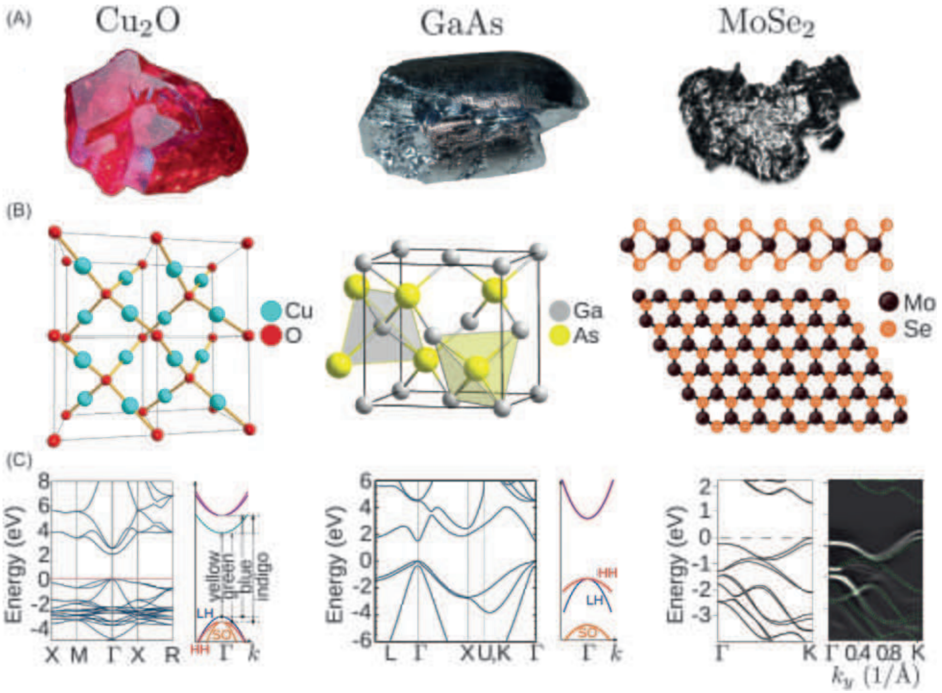

Fig. 3 Emblematic materials hosting excitons: Cu_2O, GaAs and $MoSe_2$, with comparisons of (A) the bulk crystals (an exfoliated foil for $MoSe_2$), (B) the crystal structures (a mono-layer as seen from the side and from the top for $MoSe_2$) and (C) the band structures. For Cu_2O (after Meyer et al. (2013)) and GaAs (after Richard et al. (2004)), the full calculated bandgap is shown along with the parabolic approximation around the Γ point. For a monolayer of $MoSe_2$, the experimental band structure is superimposed by Zhang et al. (2014a) to the theoretical prediction, showing a stronger direct bandgap than is calculated. Panels (C) are adapted with permissions from Meyer BK, Polity A, Reppin D, Becker M, Hering P, Kramm B, Klar R, Sander T, Reindl C, Heiliger C, Heinemann M, Müller C, and Ronning C (2013) The Physics of Copper Oxide (Cu_2O). Academic Press, chapter 6. https://doi.org/10.1016/B978-0-12-396489-2.00006-0 and Zhang Y, Chang T-R, Zhou B, Cui Y-T, Yan H, Liu Z, Schmitt F, Lee J, Moore R, Chen Y, Lin H, Jeng H-T, Mo S-K, Hussain Z, Bansil A, and Shen Z-X (2014) Direct observation of the transition from indirect to direct bandgap in atomically thin epitaxial $MoSe_2$. *Nature Nanotechnology* 9:111.

synthesized—the best one to host the cleanest and finest excitonic states, as illustrated in Fig. 2. The highest valence and lowest conduction bands stem from the copper atoms in the 3d and 4 s orbitals, respectively. The exciton formed by the corresponding electron and hole provides the so-called "yellow series" with energies around 2.1 eV. The 1 s state has a binding energy of order 150 meV. This lowest exciton state in Cu_2O is optically forbidden but becomes activated under a strong magnetic field and has been resolved in this way by Brandt et al. (2007) as an essentially perfect Lorentzian with a linewidth as small as 80neV, making it the narrowest bulk exciton resonance ever observed.

Excitons have also been extensively studied in III—V semiconductors. Gallium Arsenide (GaAs) is the prototypical conventional semiconductor for exciton physics. Semiconductors with a large dielectric constant have only weakly bound excitons, which can be observed only at cryogenic temperatures. In GaAs, the binding energy of excitons is 4 meV, so they ionize much before room temperature. In contrast, in GaN, the exciton binding energy is as large as 28 meV, which makes this wide bandgap semiconductor material suitable for exciton studies at room temperature. In silicon and germanium, the mass is not as isotropic as in other semiconductors and the band structure is more complex, requiring heavy calculations to derive the experimentally observed binding energies. II-VI materials, such as ZnO, ZnTe and CdSe, feature much higher excitons with binding energy in the range from 50 to 200 meV, so they are stable at room temperature, but such structures come with their own limitations, such as a higher disorder. II-VI semiconductor alloys containing magnetic ions such as Mn^{2+} offer a convenient playground for studies of magneto-excitons and exciton magnetic polarons. Such materials are typically characterized by giant Zeeman splitting of exciton states that would be described by effective exciton g-factors of the order of 50.

Graphene—a single layer of carbon atoms arranged in a two-dimensional honeycomb lattice—pioneered a new era of 2D crystals. Graphene's dispersion relation becomes linear and its electrons thus behave as Dirac (massless) particles, with conduction and valence bands that touch on the edges of the Brillouin zone, thus making graphene a semimetal (or gapless semiconductor). For this reason, its excitonic features, while existing, are not compelling. Rolled-up version of graphene—carbon nanotubes—can be either metallic or semiconducting depending on how they are rolled. Even when completely metallic, and thus expected to be even less excitonic than graphene, the strong 1D screening can reduce interactions sufficiently so that metallic excitons have been observed in nanotubes by Wang et al. (2007). Semiconductor nanotubes, on the other hand, sustain a rich variety of excitons, characterized by large oscillator strengths. In lower dimension, another allotrope (structural-variation) of carbon—the so-called carbyne—is strongly believed to exist in the form of a linear carbon chain of the type $(-C \equiv C-)_\infty$. Partial chains of this type stabilized at their ends, known as polyynes, are well established and have been shown by Kutrovskaya et al. (2020) to exhibit sharp excitonic features at low temperatures. In the wake of graphene, material physics developed other similar two-dimensional crystals that are semiconductors, such as hexagonal boron nitride (hBN, known as "white graphene"), molybdenum disulfide (MoS_2), 2D tungsten disulfide (WS_2), tungsten diselenide (WSe_2), molybdenum diselenide ($MoSe_2$) and many other dichalcogenides and layered oxides. Their excitonic properties are particularly important since 2D crystals are more stable when they are insulators or semiconductors. Transition metal dichalcogenides (TMDs or TMDCs) are those with the chemical formula MX_2 with M an atom from the transition metal family, in particular Mo (Molybdenum) or W (Tungsten), while X is a chalcogen, i.e., an atom from the group 16 of the periodic table, which is that of oxygen, but, for TMD, with X = S (Sulfur), SE (Selenium) or Te (Tellurium). While bulk versions of these materials are indirect bandgap semiconductors, atomically thin layers acquire a direct bandgap in the near-infrared and visible regions, so of great interest for opto-electronics. This is shown from calculations reported by Splendiani et al. (2010) in Fig. 1B and was established with spectroscopy by Mak et al. (2010). These materials also have exceptionally strong electron-hole Coulomb interactions, with record-value binding energy on the order of several hundreds of meV, thanks again to the reduced screening of the Coulomb interaction in 2D, that also manifests in its excited or charged states. This makes their exciton stable at room temperature. While they are of the Wannier type, their huge binding energy is more characteristic of Frenkel excitons. They also have energy-degenerate band edges at the $\pm K$ points, at the corners of the Brillouin zone, resulting in several extrema of the band structure, known as "valleys," whose occupation result in *"valley excitons"* (cf. Fig. 1G), which differ substantially from excitons in conventional semiconductors whose bandgap is at the center of the Brillouin zone (Γ point). To start with, they come with a large variety of bright and dark configurations, especially when also combining valleys with the electron and hole spins. Optical transitions come with new selection rules, with each circular polarization coupling to one valley (+K to σ^+ and −K to σ^-) allowing to easily address each valley by polarization. A strong spin-orbit interaction produces spin splitting of several hundred meV in the valence band and of a few meV only in the conduction band. Valley excitons also behave differently under applied external fields and present great technological prospects. The lowest energy bright valley exciton (known as the "A exciton"), is accompanied by an higher-energy, shorter-lifetime version (the "B exciton"), with the hole residing in the higher energy spin-split valence band, and that decays non-radiatively to the A exciton. There is also a rich collection of charged excitons from the various possible combinations in the valley and split-bands. These valley excitons additionally feature a strong fine-structure due to the exchange interactions between the valleys. While their characterization is complicated, there are also more tools to do so, e.g., polarization-resolved pump-probe and spectral hole-burning measurements.

Spin structure

The exciton spin state is given by the spin of its constituents: electrons and holes. Being fermions, electrons and holes have semi-integer spins that add up to integer numbers, so that excitons should be bosons according to the spin-statistics theorem. The spin projections of electrons and holes onto the crystal axis are not necessarily $+\frac{1}{2}$ and $-\frac{1}{2}$. As an example, in Zincblende (two interpenetrating face-centered-cubic lattices) semiconductors such as GaAs or CdTe, the valence band is two-fold degenerate with branches characterized by spin (strictly speaking, an effective spin comprising also the angular momentum) projections of $\pm\frac{3}{2}$, referred to as heavy holes, and $\pm\frac{1}{2}$, referred to as light holes. In quantum wells, the degeneracy of the valence band is lifted, and the lowest-energy exciton state is formed by a heavy hole and an electron. Heavy-hole excitons are characterized by four possible spin projections on the structure axis: −2, −1, +1 and +2. Momentum selection rules only enable exciton states with ± 1 spin projections to emit or absorb photons, which are known as *bright excitons,* cf. Fig. 1F. In contrast, ± 2 excitons cannot be directly excited by light and they cannot recombine by emitting a single photon. These optically inactive excitons are thus referred to as *dark excitons.* They play an important albeit implicit role, by interacting with optically active or bright excitons. Spin-orbit interactions for excitons are prominent for the understanding of their optical properties. They stem from two origins: (1) spin orbit interactions for the constituent electrons and holes, such as Eliot-Yaffet, Dyakonov-Perel' and Bir-Aronov-Pikus mechanisms and (2) short- and long-range exchange interactions, which result in the specific fine structure of exciton energy spectra. The longitudinal-transverse (LT) splitting—which is the splitting between exciton resonances in the absorption spectra of light polarized parallel and perpendicular to the in-plane component of the exciton wavevector, in-plane of the quantum well—is caused by the long-range electron-hole exchange interaction. LT-splitting is at the origin of the Maialle-Sham mechanism of spin relaxation for excitons (published by Maialle et al. (1993)), that is similar to the Dyakonov-Perel' spin relaxation mechanism for electrons.

Optical properties of solids

The most important properties of the most common type of excitons arise from their link to light absorption (creating excitons) and emission (when excitons recombine), thus connecting electrical excitations inside the crystal to photons outside, cf. Fig. 3A. This admits exceptions as excitons can also be formed by electrical injection of electrons and holes, e.g., as implemented by Schneider et al. (2013) to realize an electrically pumped exciton-polariton laser. Nevertheless, excitons play a predominant role in the optical properties of solids. Optical methods are also the most appropriate to study them. The most common form of characterization of excitons is found in the absorption and reflection spectra of insulating crystals. The case of semiconductors is particularly important, due to their rich physics and technological importance. Another successful method for characterizing the excited states of excitons is to create them with photons of energy greater than that of the energy gap and to measure the far-infrared absorption due to direct transitions between excitonic levels. A third experimental technique is to detect the luminescence emitted when the photo-produced exciton recombines. The system can also be probed by two-photon excitation, in which case, not the ground state 1s but the excited 2p couples to light. This allows, among other things, to measure the excitonic energy spectrum and thus to get an estimate of the binding energy. In regions of no absorption, the semi-classical theory of radiation conveniently describes the optical response due to excitons through the dielectric constant of the crystal. In regions of absorption, the quasi-particle picture is favored. In semiconductors with a small binding energy, excitons are the main mechanism of light emission and absorption, although at low temperature only, since at higher temperature, they are not bound anymore and form a plasma of electrons and holes instead. At low-enough temperature, the hydrogen-like spectrum of absorption is observed just below the band gap, which is itself easily identified as an edge in the absorption spectrum. Optical properties are strongly dependent on dimensionality. In bulk, the exciton absorption lines are asymmetric with a characteristic Fano lineshape, described by Toyozawa (1958), which is typical whenever a discrete state (here the exciton) interacts or interferes with a continuum (here optical phonons). The total energy of the exciton is determined by the band-gap energy, the binding energy and the kinetic energy due to its center-of-mass motion. Photoluminescence (PL) can provide information on all these aspects, allowing in particular to extract the distribution of excitons velocity. In 2D, in the absence of excitonic effects, direct band to-band transitions exhibit a step function spectrum that echoes the energy-independent density of states, but in the presence of excitons, the sharp hydrogenoid resonances are observed on top of this structure. In many instances, excitons can also be controlled optically through the quantum coherent phenomenon of Rabi oscillations, i.e., the hermitian cycling that alternates stimulated emission by the exciton of a photon and the reverse absorption of the photon by the exciton. Controlled pulses thus allow to prepare the exciton in a deterministic quantum state, such as a full exciton or a quantum superposition with its ground state. In fact, such coherent light-matter processes are inherent to excitons and give rise to a whole chapter of excitonic physics: polaritonics.

Exciton-polaritons

Just like a self-consistent theory of the electron demands the electromagnetic field (for gage invariance) and thus its interaction with light, a theory of the exciton cannot dispense from the electromagnetic field. Hopfield (1958) pointed out that the semiclassical description of light absorption by excitons is not "completely satisfactory," in contrast to absorption due to interband transitions for instance, because of strong photon-exciton coupling phenomena. These were referred to as "light-excitons" in the soviet literature but Hopfield christened them "polaritons" instead, as a general phenomenon of coupling light with a polarization field, that is not limited to excitons (e.g., optical phonons also provide a polarization field for light). This polaritonic effect implies that in bulk semiconductors, excitons actually impede luminescence and radiation, by trapping light into cyclic (Rabi) oscillations with the excitons (Fig. 1J), which breaks only at the surface so that in an infinite crystal, excitons are non-radiative. Similarly, light is not absorbed by excitons but converted into exciton-polaritons, so that true absorption is the result of other mechanisms, such as exciton-phonon scattering, in the absence of which light would be reflected or transmitted. Quantum mechanics also makes the exciton-photon coupling relevant even in absence of photons. In particular, the polariton vacuum is not the crystal vacuum. At the heart of such polaritonic effects lies the one-to-one coupling of the modes (electromagnetic and excitonic), so that in a system of reduced dimensionality, luminescence is indeed dominated by free excitons, as shown by Weisbuch et al. (1981). This results from a Wigner-Weisskopf dissipation of one exciton to a continuum of photon modes. To restore strong coupling, one must embed the lower-dimensional crystal in a microcavity that also reduces the dimensionality for photons. This gives rise to cavity-polaritons, that are half-light/half-matter quasi-particles combining the electronic properties of the exciton (strong interactions, large mass, . . .) and the ultrafast ones of the photon (high coherence, small mass. . .). This new brand of quasi-particles has been revealed in optical experiments by Weisbuch et al. (1992) in two dimensions, by Tartakovskii et al. (1998) in one dimension and by Yoshie et al. (2004) and Reithmaier et al. (2004) in zero dimension. Unlike bulk polaritons—that are tricky to monitor, let alone controlled, due to their dynamics being buried inside the material until they reach its borders—cavity polaritons can be conveniently and continuously monitored thanks to the leakage of the photon from the cavity. A typical degree of freedom in such systems is the exciton/photon fraction of the polaritons, quantified by the Hopfield coefficients that act as a probability amplitude for the quantum superposition between the photon and the exciton. This can be tuned by matching the dispersions of the two modes, so that the excitation can be smoothly changed from one extreme (exciton) to the other (photon) passing by equal superpositions. Even at resonance, where the admixture is half-light, half-matter, different excitation schemes can yield exciton-like or photon-like polariton dynamics in dissipative systems. This results in qualitative differences of their luminescence from a coupled-oscillator model, that otherwise simply links the splitting of the lines to the Rabi coupling, as discussed by Laussy et al. (2008). Thanks to their even more strongly driven-dissipative character, polaritons have rapidly grown from an annex of exciton physics to rapidly expanding and independent research fields, which are overviewed by Kavokin et al. (2017) and discussed in more details in this volume by Litinskaya (2022).

Excitons interactions

Excitons interactions concern the problem of an exciton in presence of other particles or quasi-particles, either other excitons, in which case one deals with self-interactions, or with other types, such as photons (as discussed previously), electrons, holes, phonons, plasmons, etc. Excitons can also interact with (scatter off) defects. Each interaction constitutes a field of research on its own. The basic picture of quasi-particles allows one to embrace the main ideas at a glance.

The exciton-phonon interaction is both important and enlightening as a particular case. It involves the exciton in the more basic problem of electron-phonon coupling, which can itself be described by a variety of models. Prominent electron-phonon Hamiltonians include the Fröhlich and the Holstein Hamiltonians. Exciton-phonon scattering amplitudes can be computed from them with Fermi's golden rule applied to the corresponding exciton-phonon matrix elements. Physically, the presence of an exciton modifies the charge configuration within the crystal by shifting the equilibrium positions of the lattice ions, which gives rise to a coupling between excitons and lattice phonons. Depending on the type of phonons, the interaction can be short range (acoustic phonons) or long range (optical phonons). When such interactions are very strong, and when the hole and electron are greatly separated, they may polarize the lattice individually, the result being a polaron bound to a hole-polaron (the polaron itself being the particle that arises from strong electron-phonon coupling). The "*exciton-polaron*," on the other hand, refers to strong electron-exciton coupling. Strong phonon-exciton coupling can also cause self-trapping, whereby small-radius excitons are clouded by phonons which impede their ability to move. Phonons are affecting a broad range, if not all of the excitonic behaviors, including their energy, oscillator strength, lifetime, coherence, relaxation dynamics, diffusion, luminescence and spectral shapes. In all cases, this can be identified by a temperature dependence. Phonons also open a new (so-called non-radiative) decay channel, which increases with temperature and also causes broadening of the spectral lines. The other way around, phonons are also required to bind an exciton from a pre-existing free hole and free electron, to conserve energy and momentum. They also couple bright and dark excitons. Ab initio Bethe-Salpeter calculations by Marini (2008) in two-limiting cases of weak (in bulk silicon) and strong (in hexagonal Boron nitride) exciton-phonon coupling reproduced accurately the thermal properties of these systems, and found that phonons cause substantial changes even at zero temperatures, such as renormalization (weakening) of their binding energy. Joint incoherent contributions—with independent interactions from the electron and hole of the exciton with the lattice vibration, dominant at weak coupling—and coherent ones—affecting the exciton as a whole and in particular contributing to its buildup at stronger coupling—were identified. Also, a microscopic mechanism for bright and dark excitons transitions was found, based on a transfer of optical strength between energetically-close excitons. Overall, such successful simulations of the excitons-phonons interactions show both their variety and importance in realistic systems, even at low temperatures. Other approaches, for instance based on a master equation formalism, have similarly captured counter-intuitive results and qualitative departures of excitons from atomic systems due to their solid-state environment and coupling to phonons, such as McCutcheon and Nazir (2013)'s finding of an increased quantum coherence due to thermalization of the dressed states.

If there is one basic problem for which the hydrogen body of knowledge brought little insights when applied to its excitonic version, this is the fundamental one of exciton self-interactions. The similarity of the masses of all particles is a first departure from the hydrogen atom. The delocalization of the exciton throughout the crystal, i.e., involving all electrons and holes, is another crucial difference that makes two excitons intrinsically overlapping even when neglecting their interactions, which is the existential problem of cobosons previously discussed. For 1s excitons, since they are electrically neutral, their Coulomb interaction is small, even though largely separated excitons can experience a van der Waals interaction. Exciton interactions become notable when the two excitons get in close proximity to each other. In this case, exchange interactions of the constituent electron and hole become dominant while the direct Coulomb interaction remains small. The exchange interaction is due to the antisymmetry of the fermionic wavefunction, that tends to push particles apart, as opposed to bosonic symmetry that produces an attraction. The simplest, because the most familiar, and for this reason also the most popular treatment of exciton-exciton interactions is through their bosonization, in which case they are assumed to be structureless (ideal) bosons. Although this procedure, introduced by Hanamura (1974) and others, is still of unclear accuracy or even validity, it appears to provide satisfying result to account for a wealth of experimental results. These include a blueshift of the exciton energy with increasing excitation, a saturation of the oscillator strength as well as collisional broadening, or homogeneous increase of the linewidth. Ciuti et al. (1998) computed scattering strengths (in 2D as befits quantum wells) taking into account the exchange terms, which are the dominant ones. Besides, they differ qualitatively from the direct Coulomb term, being maximum ($\approx 6E_\mathrm{B}a_\mathrm{B}^2/S$ with S the surface area) for no-exchanged momentum while the Coulomb interaction vanishes in this case. Spin also plays an important role in exciton interactions, with possible scatterings into dark states. Depending on the relative spin, both attraction and repulsion between excitons are possible. Excitons with different spins are distinguishable and thus the dominant exchange terms do not apply to them. In this case, another strong channel of scattering involves the bound state known as biexciton, which we discuss next. While the problem of exciton interactions in its full generality remains a complex area of hotly disputed research, basic consequences such as bound states have gained wide recognition.

Multiexcitons

When several excitons bind together, they form a multiexciton (cf. Fig. 1I). The most popular multiexciton is the biexciton, the quasiparticle composed of two electrons and two holes and that constitutes the solid counterpart of a molecule (Fig. 1H). This complex may be stable thanks to the dipole-dipole attraction of two excitons polarized in opposite directions. The spin structure of the constituent electrons and holes is thus essential in this formation. Usually, only singlet states formed by excitons with opposite spins are stable. This imposes a polarization selection rule: biexcitons cannot be directly optically excited by a circularly polarized light as it would only generate excitons with parallel spins that repel each other because of the exchange interaction. In contrast, biexcitons can be excited by a linearly polarized light capable of generating excitons with opposite spins. As the excitation of each biexciton requires two photons, the probability of their generation increases quadratically with the intensity of pumping light, which is a typical signature of their formation. The two-photon excitation energy should be lower than that of two unbound excitons due to their binding energy and spin interactions (higher if these turn out, for structural reasons, to exceed two-excitons energy). Other complexes exist. Trions consist of positively or negatively charged excitons composed by two holes and one electron or two electrons and one hole, respectively. They can be excited in doped semiconductor structures containing residual electrons or holes: an optically excited electron-hole pair binds itself to a residual carrier giving rise to the trion formation. Trion binding energies in bulk semiconductors are usually very small because of the little effective mass imbalance between electrons and holes. In quantum confined structures, such as quantum wells, wires and dots, trions gain a sizeable binding energy and oscillator strength. They can be observed as distinct low-energy satellites to excitonic peaks in absorption or photoluminescence spectra. Quatrons are exotic four-particle complexes with an electric charge of $\pm 2e$ that can occur in a variety of contexts, typically as a doubly charged exciton in a quantum dot. As an example of a particular specie of quatrons, the *Suris tetron* appears at intermediate concentration ranges in the two-dimensional electron-gas between the exciton-trion dominated regime at lower densities and the Fermi-sea at higher ones, with the binding of a hole to a trion, as identified by Koudinov et al. (2014). They can also be understood as trions repulsing the electron gas.

Excitons in heterostructures

Excitons are even more important in systems of reduced dimensionality. These are possible thanks to the concept of heterostructure, that arose from the idea of forming an artificial lattice by alternating layers of two (or more) materials. Initially, this was to improve mechanical properties but the idea proved to be even more fruitful for electronic properties. In the limiting cases of a few layers, such "superlattices" result in a quantum confinement of the carriers and thus, in the case of semiconductors, of the excitons. This opens fascinating chapters of exciton physics in systems of reduced dimensionality, from 2D-excitons in Quantum Wells (QWs) to completely frozen excitons in Quantum Dots (QDs), passing by 1D-excitons in Quantum Wires. For a long time, such semiconductor heterostructures were mainly obtained by epitaxial growth. A more recent but increasingly popular type of heterostructures is that assembled by stacking layers of different 2D crystals. These are known as van der Waals heterostructures, due to the weak interaction between different layers (as opposed to the strong covalent bonds within each 2D layer). This major and fruitful development allowed by a breakthrough in the material physics of semiconductor 2D crystals, revisits the discipline as a whole by allowing an hitherto impossible atomic-level accuracy in the design of crystals, with no constrains from lattice mismatch at the interface. At the crudest level, depositing two flakes of such crystals realizes, by viscoelastic stamping, such an heterostructure. More complex structures are possible, in particular tri-layers, with a large-bandgap material interposed between two active monolayers to further control the recombination rate and dipole moment. Reduced dimensionalities bring a wealth of consequences on the physics of the respective excitons, starting with their density of states. Another immediate and illustrative consequence is the quantum confined Stark effect: applying an electric field perpendicularly to the direction of the exciton confinement does not result in its ionization, as is the case in bulk, since the heterostructure provides a safeguarding confining potential, but modifies instead greatly the exciton's energy and oscillator strength. This increases drastically the radiative lifetime and produces giant Stark shifts of the photoluminescence lines. This is due to the electron and hole being pushed in opposite directions by the electric field and thus reducing the overlap of their respective wavefunctions, which quantifies their recombination rate. Similarly to bulk excitons, quantum wire and quantum well excitons feature an energy continuum at the end of their quantized energy spectrum, due to their possible motion through the crystal. QDs are particular in that, by confining all the degrees of freedom, they effectively turn the exciton into a two-level system. Excitons are more relevant in optical QDs, since other types of quantum dots, formed by electrostatic gates, are better described in terms of uncorrelated electronic charges. The physics of excitons in various dimensions is different enough as to be treated independently, which we do in the next sections.

Quantum wells, wires and rings excitons

Excitons emit photons within a radiative zone defined by the conservation of the in-plane or in-wire wavevector between the exciton and the photon, which is defined by a light-cone. Excitons with a larger momentum and thus outside of the light-cone, can be scattered there, by defects, phonons or other excitons, and thus act as a long-lived (non-radiative) reservoir. They also typically act as a background dynamical and spatial potential for the bright excitons. The radiative decay inside the light-cone is very fast, as shown by Deveaud et al. (1991). This led to a thriving field of ultrafast optics in the form of time-resolved photoluminescence. The radiative lifetime is determined by the exciton oscillator strength, and should produce a Lorentzian line (from its exponential decay in time). Other possible decay channels, in particular non-radiative, broaden but otherwise maintain this shape for the spectral line, in which case one speaks of homogeneous broadening. Pure dephasing enters in this category. Other processes can cause an inhomogeneous broadening that results from the emission of excitons of different frequencies, as is typically the case in presence of disorder due to fluctuations of energies in the crystal. This produces, instead, Gaussian lineshapes. Bright trions have different recombination rules than excitons regarding their momentum, since trion recombination leaves the third particle (electron or hole) in the crystal which can absorb the momentum leftover. This process, that still decays exponentially with increasing momentum, produces a characteristic low-energy tail in the trion spectrum.

An auxiliary between 1D and 0D confinement of the exciton can be found with so-called quantum rings (QRs), which close the loop of a wire so as to realize a unique geometry, specific to the solid-state. This makes them appealing for a wide range of problems related to rotational symmetry, discussed by Fomin (2014). QRs attracted special attention in the context of the fundamental problem of the geometric phase, also known as the Berry phase. They are particularly suited for the so-called Aharonov-Bohm effect that describes the geometric phase of a charged particle that goes both ways in a ring bathed in a magnetic field and that interferes with itself when completing the loop. Observable effects from a vector potential that produces no magnetic field are one of the most uncanny features of quantum mechanics and a spectacular manifestation of gage theory. Excitons are neutral and the effect, first demonstrated with a charged exciton in a ring by Bayer et al. (2003), was thought to be too small for uncharged excitons, which indeed did not evidence it. However, the underlying electron and hole's geometric phases do result in a rich phenomenology for their wavefunction, that does produce an excitonic (also called optical) Aharonov-Bohm effect. This was first noted by Chaplik (1995) as peculiar properties of excitons confined in rings, with a theoretical dependence of their binding energy, effective mass and dispersion on a perpendicularly applied magnetic field. Those have been observed under an applied magnetic flux, first by Ribeiro et al. (2004) as oscillations in PL observables, in so-called type II QDs where the electron is bound by the dot but the hole repelled so as to produce a ring geometry (unlike in type I where both carriers are bound inside the dot), and then, in actual rings, as an oscillator strength periodically changing in time also detected in photoluminescence, by Teodoro et al. (2010).

Quantum Dots excitons

Quantum Dots (QDs) are the ultimate confining crystallite, trapping particles in all three dimensions in systems with sizes ranging from sub-nanometers to small fractions of micrometers and made up from a few thousands only to millions of atomic nuclei. The first quantum dots were reported by Ekimov and Onushchenko (1981) who synthesized nanocrystals of copper chloride in glass, and observed a shift of their excitonic spectral line as a function of the heat-treatment to prepare the crystals, which they interpreted as an effect of size quantization. This was confirmed by Éfros and Éfros (1982) who described the nanocrystallite as a spherical box of varying radius for both one dot and an inhomogeneous ensemble. They also considered various limits of the size, leading to a separate confinement of the electron and hole or of the exciton as a whole. Éfros (2022) provides a detailed account of excitons in nanocrystals in this volume. Several ways have since been found to produce a broad family of QDs. For instance, molecular beam epitaxy can deposit a thin layer of, say, InAs on a GaAs substrate. The strain caused by the lattice constants mismatch lead to the spontaneous and self-assembled formation of little islands of various sizes and shapes depending on the growth conditions. By tailoring the shape, size and composition of the QD, one can tune the excitonic energy spectrum, its interaction energies, Coulomb energies, kinetic energies, electron-hole separations, oscillator strengths, etc. Typically, single QDs from an assembly each present a unique excitation spectrum. If dealing with such a group at large, the specificities of each individual are blurred in the averaging which results in broad emission spectra. Techniques have been developed to isolate single QDs, such as single-dot spectroscopy. This makes QDs rich laboratories to control and study electronic excitations. Such investigations led to describe them as "artificial atoms," in particular for their adherence to the basic atomistic rules of thumb, namely, the "aufbau" (filling-up of successive shells), and Hund's rule (occupying different orbitals of the same energy singly, before alternating spins). These account for how successive excitations get distributed in the energy levels of a QD, as shown in Fig. 4A. When the system fills up with excitons—which is the case under optical excitation—one can in this way witness the successive formation of excitonic atoms

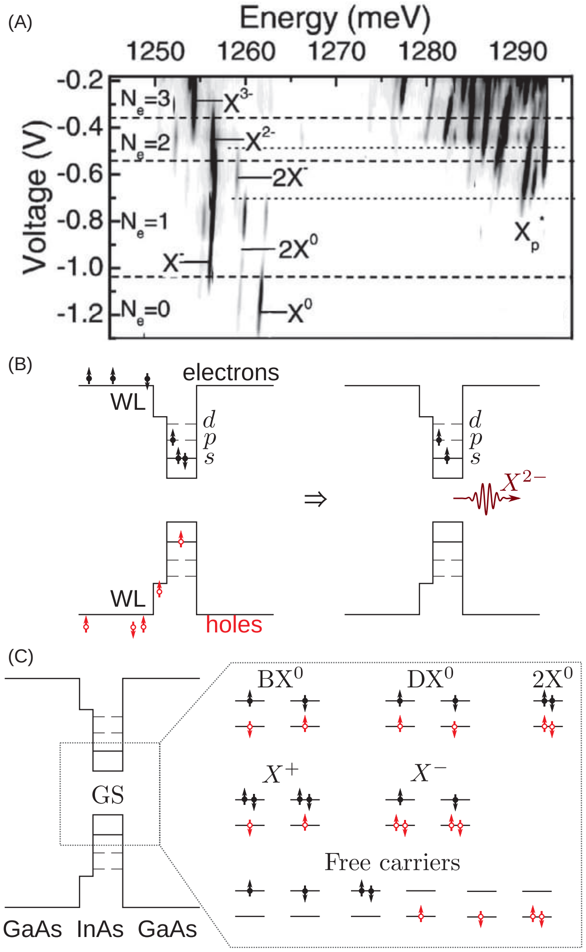

Fig. 4 (A) Charging of multi-exciton states in a single InGaAs Quantum Dot, by Finley et al. (2001). The discrete spectral lines result from excitonic recombinations of states with a well-defined number of electrons and holes, such as X^0 (exciton), $2X^0$ (biexciton), X^{n-} (exciton with *n* electrons). The charging is here by lowering the applied voltage, which reduces the electrostatic potential of the QD to allow increasing numbers of electrons to tunnel inside (with corresponding thresholds indicated by the dashed horizontal lines), thus not allowing X^{n+} states with *n* holes, which are also possible in other configurations. The X_p^* lines at higher energies originate from *p*-shell transitions. (B) Example of a recombination responsible for the X^{2-} line: while the exciton recombines in the *s*-shell, it involves electrons in the *p* shells, (C) In the *s*-shell alone, in addition to the Ground State (GS), there are 15 possible configurations of excited states, with neutral Bright (BX^0), Dark (DX^0) and bi- ($2X^0$) excitons along with their charged $X^{\pm}$ versions or isolated electrons and holes. Panel (A) is reproduced with permission from Finley JJ, Fry PW, Ashmore AD, Lemaître A, Tartakovskii AL, Oulton R, Mowbray DJ, Skolnick MS, Hopkinson M, Buckle PD, and Maksym PA (2001) Observation of multicharged excitons and biexcitons in a single InGaAs quantum dot. *Physical Review B* 63:161305(R).

similar to hydrogen (a single exciton in the *s* shell), helium (two excitons in the s-shell or s^2 in atomic notations), lithium (two excitons in the s-shell, one in the p shell, s^2p), beryllium (s^2p^2), boron (s^2p^3) and carbon (s^2p^4), as described and reported by Hawrylak (1999) and Bayer et al. (2000). When the system fills up with single electrons (or holes)—which is the case under gating or by doping—the single exciton remains the fundamental excitation but gets charged with subsequent excitations and one thus encounters trions $X^{1\pm}$, quatrons $X^{2\pm}$ and higher-still excited states $X^{k\pm}$ with, in the case of Warburton et al. (2000), k up to 5 when completing the *p* shell. These are referred to collectively as "excitonic complexes" or "multiexcitons." The respective lines can be identified by a series of signatures, including the order in which they appear and disappear as the QD fills up according to Hund's rules, the dependence of their intensity on excitation power, e.g., quadratic for biexcitons, their polarization, that is ruled by their spin composition and still other tricks, such as the lack of a fine-structure for the X^{1-} charged exciton that voids its exchange interaction or its large extent in gate voltage. Circular polarizations originate from exciton recombinations while linear polarizations from their quantum superpositions, which can be caused by a fine structure splitting. On the other hand, their distribution in energy indicates, e.g., whether electron-hole attraction or electron-electron repulsion dominates in the multi-exciton configuration, which can change depending on the lateral spatial extension of the electron and hole wavefunction, as shown by Finley et al. (2001) (cf. Fig. 4). Quantum Dots thus represent flexible artificial atoms, whose properties, although reminiscent of real atoms, can greatly vary in both qualitative and quantitative ways. For instance, the number of *p* and higher (*d*, etc.) shells thus becomes restricted to 2 in case of in-plane confinement for QD with cylindrical symmetry, as opposed to 3, 5, etc., for real (3D) atoms. There is also typically an asymmetry of QDs formed by interface fluctuations, which results in elongated shapes which further lift the degeneracy of these states, resulting in a fine-structure splitting between them with polarized emission (those grown by colloidal chemistry, on the other hand, have a much greater spherical symmetry). Quantum dots are nowadays highly controlled both experimentally and theoretically. The fine-structure of their excitons is particularly well understood, with Bayer et al. (2002) taking into account spin interactions, such as the exchange Coulomb interaction, as well as hyperfine interactions with the nuclear spin from host atoms in the lattice, and the Zeeman interaction with an applied magnetic field. Rabi oscillations of QDs excitons have been first observed by Stievater et al. (2001) and demonstrated the validity of single excitons to realize the quantum optical physics of atoms, with π-optical pulse that revert their state, i.e., preparing the exciton in the one-particle state or, if already present, returning the system to the crystal vacuum by stimulated emission. The Rabi flopping could later be observed by Ramsay et al. (2010) for over 14 π-pulses with a dephasing due to LA phonons and with a renormalization of the Rabi frequency attributed to fluctuations in the phonon bath, making the effect a solid-state analogue of the QED Lamb-shift for the hydrogen atom in vacuum. Related quantum optical milestones, such as the Mollow triplet of resonance fluorescence—where the exciton forms a quantum superposition with the laser photons to produce a ladder of equally-spaced dressed states—have also been unambiguously reported, for instance by Flagg et al. (2009).

Direct and indirect excitons

Heterostructures allow to design complex arrangements of the confining potentials which permit to design sophisticated trapping for the electrons and holes, giving rise to new types of excitons, for instance by separating spatially their electron and hole. One can thereby grow two QWs (a so-called double QW) side to side and apply an electric field normal to their plane, forcing the electron in one well and the hole in the other (cf. Fig. 1C). Their binding across the barrier that separates the two wells leads to a spatially *"Indirect Exciton,"* denoted as IX. Same-well excitons are still possible and become known, in contrast, as spatially *Direct Excitons* (DX). The qualification of "spatial" is added if there is the need to distinguish from excitons in direct and indirect bandgap materials, where the separation is in momentum instead of in real space, and with the same consequence of decoupling the excitons from direct photon recombination/excitation, requiring, e.g., phonons to assist in the process (Fig. 1B). Recombination of IX is also possible, by tunnelling through the barrier, but is strongly reduced as compared to the DX one, as indeed the wavefunctions are spatially separated and their overlap becomes much smaller. This increases considerably their lifetime, by several orders of magnitudes in GaAs structures which can thus span over ns to tens of μs as compared to few ps only for direct excitons. Another advantage of IX is their strong-dipole moment ed aligned perpendicularly to the QW, with d the distance between the electron and hole layers (for this reason, they are also called "dipolar excitons"). Applying an electric field perpendicular to the QW plane results in an IX energy shift, known as the quantum confined Stark effect, and varying this field in space allows to create highly-tunable potential landscapes, of various shapes and extent, that can be static or dynamic. A diamond-shaped trap, for instance, allows to create a parabolic potential, which collects excitons and trap them at the center. One can thus apply a force through an electric field for these otherwise neutral particles, through a gradient of the field that turns into a gradient of energy shifts for the indirect excitons. Strong dipole moments also result in dipolar interactions that are stronger than the exchange interaction of direct excitons, and also of a long-range character $\propto 1/r^3$ at large separations. Their repulsive character of oriented electric dipoles make them more stable against bound states or condensed phases. Indeed, the dipole polarization of excitons is not random but is imposed by the structure geometry and dipole-dipole repulsion prevents the formation of biexcitons. The same idea also applies to excitons in van der Waals heterostructures, as demonstrated by Rivera et al. (2018) (cf. Fig. 1D), with the advantage of a much enlarged space of parameters and with better control of the crystals. In that case, although the concepts and consequences are the same, one commonly speaks of *"interlayer exciton"* (ILX) instead of indirect ones. Besides, in addition of being spatially indirect, ILX can also be momentum-indirect, with the electron located in the K valley while the hole is located at the T point, as shown by Kunstmann et al. (2018). Quantum dots, as artificial atoms, can in a similar way be designed to form quantum dot molecules (QDMs), for instance by stacking two quantum dots on top of each other, as done by Schedelbeck et al. (1997). The exciton can now be formed by having its electron in one QD and its hole in the other, also producing an indirect exciton which, in a QD, becomes a solid-state counterpart of the H_2^+ hydrogen molecule with one electron orbiting two protons, with the formation of bonding and antibonding states from the coherent excitonic wavefunction delocalized over the two QDs. The photoluminescence of QDM is markedly different from its single (atomic) QD counterpart: in addition to single lines indicating the multi-excitonic states, a rich phenomenology of crossing and anticrossing patterns emerge, involving states with much larger electric field dependencies thereby producing lines with very different slopes in the PL spectra as a function of the applied electric field. These are due to the strong Stark shift enabled by indirect excitons. The coupling of excitons and biexcitons, both inter and intra QDs, give rise to a characteristic X patterns, studied by Stinaff et al. (2006) and Scheibner et al. (2007), that are observed when the initial and final states undergo level resonances at similar electric fields.

Key issues and trending topics

Rydberg excitons

Rydberg atoms are atoms whose outermost electron is excited in a quantum state $|nlm\rangle$ with a high principal quantum number n. Since the effective size of the atom grows with n as $\frac{1}{2}a_{\mathrm{B}}(3n^2-l(l+1))$, Rydberg atoms are huge atoms with a correspondingly large dipole moment and thus a strong response to external fields as well as strong interactions. This makes them valuable for a wealth of applications, such as their minute control in quantum optical experiments (leading to the 2012 Nobel prize, for "measuring and manipulation of individual quantum systems"). For the Rydberg exciton counterpart, a large binding energy is required, so that high values of n can be reached. From thermal dissociation alone, since the binding energy of the n shell scales like n^{-2}, the highest possible n is of the order of $\sqrt{\frac{E_B}{k_B T}}$ which is about 6 for GaAs while it is close to 30 for Cu_2O, which is the material where Rydberg excitons are currently flourishing. Bringing excitons into a Rydberg state, as demonstrated by Kazimierczuk et al. (2014) and shown in Fig. 2, is another compelling demonstration of their status of solid-state atoms. Low-level Wannier excitons being already large, their Rydberg version becomes gigantic, extending to Bohr radii as large as several micrometers, that is to say, over billions of sites of the lattice, for what remains a two-particle wavefunction. Despite stressing the excitonic picture of a bound state inside its host crystal to the limit, observations adhere remarkably well to relatively simple theoretical modellings. For instance, deviations from a pure Coulomb potential (such as is caused by the screening from inner electrons) can be taken into account through a so-called quantum defect δ that renormalizes the hydrogenoid spectrum as $E_n = -R_y/(n - \delta)^2$. Rydberg excitons allow a detailed study of fundamental atomic effects, in particular of scaling properties: not only the size of the state but other characteristic properties scale with power-law dependencies on the principal quantum number, as studied in details by Heckötter et al. (2017). These include the binding energy (like n^{-2}), the linewidth and the oscillator strength (n^{-3}), leading to ultra-sharp resonances, and still other observables, such as the van der Waals interactions, scaling as n^{11} and thus producing a huge nonlinear absorption, referred to as Rydberg blockade, as per the blockade mechanism whereby the presence of one excited state prohibits the excitation of other states by direct repulsion. Furthermore, although of mesoscopic sizes and in a highly excited state, Rydberg excitons are believed to retain their quantum coherence, as was discussed by Grünwald et al. (2016). Rydberg excitons are therefore currently at one forefront of research into quantum-optical and exotic condensed-matter effects and could enjoy in the solid state the same fruitful path as their vacuum counterparts in a breadth of applications.

Excitons in quantum Hall bilayers

An exotic breed of excitons consists in pairing, not an electron with a hole, but two electrons, in so-called electron bilayers, that are similar to the coupled QWs used for IX but such that both wells have conduction electrons and using a magnetic field instead of an electric one. This allows to bring the physics of Landau levels: the quantization of the electron cyclotron orbits under the applied magnetic field produces equally-spaced energy levels (the Landau levels) which are degenerate with a number of electrons per level proportional to the strength of the magnetic field. Each layer in isolation at half-filling of the lowest Landau level, constitutes a compressible Fermi liquid that behaves as a nonquantized Hall phase. Their pairing gives rise to new physics. Similarly to missing electrons in the valence band being treated as hole quasi-particles, an empty state for the Landau levels becomes an anti-particle with opposite charge. The fraction of occupied Landau levels, known as the filling factor, is tunable with the magnetic field. It is, in particular, possible to equate the number of electrons and holes, in which case one gets a counterpart of the standard "optical excitons." Since such Landau levels are at the heart of the quantum Hall effect, the structures hosting such excitons are known as quantum Hall bilayers and the reliance on the magnetic field also brands their excitations as *magneto-excitons*. An immediate obvious advantage of the bilayer electrons, is that the excitons they form are stable: they do not recombine. They can therefore reach a true equilibrium with no race for thermalization against their finite lifetime, which is the main limitation for exciton thermodynamics.

Excitonic matter

Once one recognizes that the excitonic picture of an effective hydrogen-like quasi-particle wandering freely within the crystal is valid, or at least useful, the next step is to keep on pushing the analogy and inquire whether condensed phases of excitons are possible, even though these would arise from quasi-particles of a more fundamental condensed system in the first place. The meta-analogy will be complete when one reaches the exciton state of excitonic matter itself. Interestingly, such questions have been entertained from the earliest days of excitonic physics, but remain among the most trendy and fundamental ones to this day. We now survey the most popular excitonic phases, starting with classical ones. The simplest is the gaseous phase, in the most extreme case of which excitons are assumed to be independent from each others, which, if at all possible, is to be sought at low densities. By sending laser pulses on a crystal and making snapshot of its luminescence (from exciton recombination) at different intervals, it has been possible to evidence clearly the drift of an exciton gas, accordingly to the kinetic theory of (normal) gases, in particular with the correct distribution of their velocities, with a temperature given by the lattice and a very large diffusion coefficient as mandated by the low exciton mass. Low-density excitons therefore qualify as a gas of particles confined inside the solid. Their mobility is considerably higher than even other solid-state particles, like electrons. Excitons have been shown by Tamor and Wolfe (1980) to drift under applied strain at speeds exceeding several hundred meters per seconds (as opposed to a few millimeters per seconds for an electron) over distances of several millimeters (cf. Fig. 5A). The strain is applied mechanically and causes a change of the bandgap, in turn resulting in a force applied to the exciton, which can be tracked by photoluminescence. To evolve from the dilute gas picture of excitons to more strongly correlated phases, one can simply increase the optical power to create more excitons. Doing so, one should not reach densities so high that excitons ionize into an electron and hole plasma, a process known as the Mott (1968) transition. Indeed distinct from a condensed phase of excitons, electron-hole liquids have long been known to exist but they arise when excitons themselves have been destroyed, or ionized, and thus, although interesting for their own sake, do not count as excitonic matter. A proper excitonic liquid can still be formed by the strong repulsive dipolar interaction between indirect excitons.

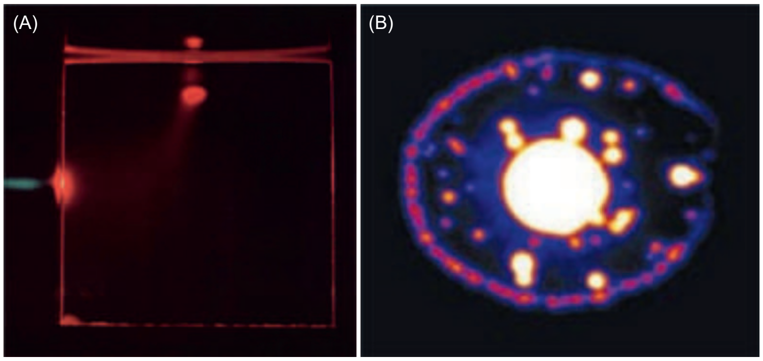

Fig. 5 Two phases of excitonic matter: (A) drift of an exciton gas in Cu_2O, photographed by Trauernicht, Wolfe and Mysyrowicz (1984), showing how excitons created by a green laser (left) drift and recombine (red glow) in the minimum of a potential stress induced by pressure exerted on top of the 3D crystal, (B) At higher densities, indirect-excitons in 2D quantum wells, imaged by Butov et al. (2002) in-plane of the well, exhibit an unanticipated ring structure that is fragmented in a highly-ordered way. The laser that drives the system is in the central bright spot, or "inner ring." The localized bright spots, which unlike the other rings do not follow the laser but remain fixed, are believed to be excitons trapped by defects. These images show how the excitonic picture, compelling in its gaseous phase, displays complex and original phenomenologies beyond expectations in its condensed phase. Panel (A) is reproduced with the permission from Wolfe JP and Mysyrowicz A (1984) Excitonic matter. *Scientific American* 250:98 and (B) from Butov LV, Gossard AC, and Chemla DS (2002) Macroscopically ordered state in an exciton system. *Nature* 418:751.

This is a regime of strong correlations, albeit believed to be of a classical character since it occurs with a negligible overlap of the excitonic wavefunctions. This phase is observed to behave thermodynamically, appearing abruptly below a critical temperature and above a critical density, and, when it is formed, to extend gradually to cover the full sample but with a low diffusivity. It also has a low conductance and its lineshape in PL is Gaussian and narrowing with increasing densities, like a liquid which is strongly correlated at short distances and as opposed to an uncorrelated gas which has a low energy tail characteristic of a fluctuating volume around the excitons. Its coexistence with another phase that matches an electron-hole plasma, reported by Stern et al. (2014), gives a picture of excitonic droplets. In between these droplets, it is believed that one finds a rarefied excitonic gas. After the gaseous and liquid phases, comes the crystalline phase. One has been predicted by Suris (2016) based on a calculated lower free energy for a triangular lattice than for the gaseous state, but in 2D and with long-range repulsive interactions, which is, however, the case for IX. Exciton interactions differing in the two phases, the desublimation (gas to crystal transformation) is predicted to yield strong qualitative signatures, with a clamping of two lines of photoluminescence as the excitonic crystal grows. At higher densities, when the system undergoes its Mott transition, a BCS-like mechanism for excitons has also been theorized by Keldysh and Kopaev (1965), that would also lead to a solid phase. In indirect bandgap semimetals, i.e., with a gap in momentum rather than energy, a spatial symmetry breaking (as opposed to $U(1)$ symmetry breaking in a superconductor) should exhibit perfect conductivity yet with no Meissner effect (expulsion of magnetic field), which has been described as an excitonic solid, the "excitonium," being also an analogy of a Wigner crystal but for excitons rather than electrons. In all these cases, there is the question whether the phase is classical, with their strong correlations and ordering being alike to solids, or, given the nature of the quasi-particles undergoing the transition, quantum. What constitutes specifically or genuinely quantum effects in such excitonic phases is still highly debated, as is overviewed in the next section.

Exciton BEC and superfluids

Macroscopic quantum phases realized by the solid state and exhibiting exotic effects are not disputed, thanks to their broad range of compelling manifestations. These include superconductivity, superfluidity and Bose-Einstein condensation. Whether quasi-particles themselves can directly undergo such quantum transitions is much more open to debate. Superconductivity gives rise to Cooper pairs, for instance, but whether the superconducting phase itself can be understood as a Bose–Einstein condensate (BEC) of Cooper pairs is not widely agreed upon. The relevance, accuracy or even correctness of such an understanding as applied to any type of quasi-particles leads to many discussions in the literature. Excitons have been among the most hotly disputed quasi-particles to take part in such arguments. This is despite the fact that their delocalized nature throughout the entire lattice makes them intrinsically ideal to exhibit long-range order quantum coherence. While such macroscopic coherence for a single excitation is typically not expected despite being foundational to the theoretical picture, it can in fact be observed as was demonstrated by Dubin et al. (2006) with a single-exciton state—as compared to a dense gas—exhibiting fringes and so coherence at both ends (10 μm apart) of a conjugated polymer chain (that behaves like a quantum wire). Nevertheless, the most basic picture of quantum coherence relies on the coherent teaming of a large assembly of bosons. The Bose statistics of excitons, as well as their diluted hydrogen-like gaseous structure at densities $n \lessapprox 1/a_B^D$ in a D-dimensional system, thus make them prime candidates for the phenomenon of Bose condensation. Moskalenko (1962) and Blatt et al. (1962) had considered them as strong contenders much before the first experimental BEC demonstration, which was with cold rubidium atoms in 1995. Such a Bose condensation can be understood as a condensation in momentum space where, consequently, the system becomes delocalized in space into a macroscopic wavefunction, as opposed to exciton droplets, which are classical condensates in real space. The small effective mass and large Bohr radius of excitons make their critical temperature for 2D BEC $T_c = 2\pi\hbar^2 n/(mk_B)$ a few K for densities of the order of 10×10^{10} cm^{-2}, i.e., well within reach. Strictly speaking, in 2D, not BEC but a related phase transition—the Berenziski-Kosterlitz-Thouless (BKT) one—describes coherence, which cannot be of infinite extent as it is destroyed by fluctuations, but decays slowly (as a power-law) instead. This is however for ideal systems while a real sample, in addition to be of finite dimensions, presents spatial fluctuations that act as local potentials in which 2D condensation becomes possible. This can be understood most simply by assuming a single potential that quantizes at least the lowest energy levels, or elaborately by considering the density of states of a disordered system that smooths out the 2D ideal case of an abrupt jump, into a 3D-looking one with a smooth vanishing of the state density. Besides, given that excitons have a large spatial extension, the picture of pointless bosons eventually breaks down at large enough densities and their underlying structure becomes significant, in which case an electron-hole Cooper pairing should occur instead, as hypothesized by Keldysh and Kozlov (1968). In any case, despite favorable conditions from basic estimates, there are many difficulties to achieve exciton condensation. Unlike atoms, the exciton temperature is not directly accessible by direct cooling, only that of the lattice is and excitons are created with vastly larger temperatures, especially at the high densities required for their condensation. Their short radiative lifetime also makes it difficult to reach an equilibrium before excitons have recombined. The ground state of Cu_2O being optically inactive, it was hoped to circumvent this difficulty, but excitonic Auger processes (two-exciton collision annihilating one and transferring excess energy to the other) turned out to have a detrimental density/temperature contribution. To avoid coherence induced by the driving laser and let the system spontaneously form coherence through a spontaneous symmetry breaking, one should also seek signatures under non-resonant excitation, ideally, an electric one. A difficulty in such a case where all types of excitons are allowed, is that dark indirect excitons have typically slightly lower energy than the bright ones, due to the exchange interaction, and so the ground state of the exciton fluid should be dark, thus not directly optically observable, as indeed reported by Cohen et al. (2016). Not least is that even if the phase is actually realized, its unambiguous identification is problematic since a realm of alternative unrelated phenomena can produce a similar phenomenology, e.g., the Peierls phase—a spontaneous crystal distortion driven by the electron-phonon interaction and unrelated to excitons—for Bose condensation or the phonon wind—a drift force imparted by non-equilibrium phonons that push the excitons—pausing for superfluidity of particles with an already high mobility. Indirect excitons overcome several of the main limitations, with an increased lifetime and stronger interactions, added to the relaxation of their momentum conservation perpendicular to the plane that couples them to a continuum and thus speeds up their relaxation as opposed to the one-to-one coupling in bulk. This allows them to reach less than a tenth of the theoretical critical temperature within their lifetime. There are various ways to study the macroscopic quantum coherence of such excitons. To excite them non-resonantly, one can either create an excitonic population with a pulse and let it relax in time, or use continuous excitation but observe them farther apart from the laser spot after they drifted or have been transported there, and cooled down to lattice temperature. In the second scheme, an unexpected ring-structure, centered around the laser spot, with no emission in between, has been observed by Butov et al. (2002) (cf. Fig. 5B) and Snoke et al. (2002). While not apparent in Fig. 5B where the intensity gets saturated by the laser, Butov et al. (2002) actually resolves two kinds of rings: an internal one, which is remote from the laser-excitation spot by a distance comparable with the exciton diffusion length, in addition to the external ring, whose radius grows with increasing pumping power or decreasing applied voltage. This external ring can thus be sent to distances commensurable with the millimeter, away from the excitation spot, validating it as a macroscopic effect. It also exhibits a macroscopic pattern formation, consisting of periodically-spaced exciton bright spots referred to as a "macroscopically ordered exciton state." This structure is pinned to the excitation laser beam and moves coherently with it if the beam is displaced. The whole structure of rings and spots collapses with increasing temperature into a Gaussian spot around the laser while the macroscopic ordering of bright spots appears below a critical temperature. The interpretation of this phenomenology is as follows: at high-enough density, excitons are freely moving particles, with strong dipolar interactions allowing them to screen potential fluctuations from the sample. Excitons that are moving too fast are beyond the light cone of possible radiative emission and thus do not emit photons. As they cool down, their individual kinetic energy lowers and they become radiative. The interplay of this with the potential landscape of the laser spot explains the inner ring. The outer ring, on the other hand, has been explained by Butov et al. (2004) and Rapaport et al. (2004) as exciton generation at the interface of the electron-rich (n) and hole-rich (p) regions. More intriguing is the periodic ordering displayed by the excitons in the external ring observed by Butov's group. The periodic pattern has been attributed by Levitov et al. (2005) to a Turing-type of instability as applied to a Bose gas undergoing stimulated scattering. This not only identifies the phenomenon as quantum, unlike the rings and bright spots which can be understood classically, but also shows how exciton condensation exhibits original and unforeseen phenomena not found in any other system. The coherence of these excitons, as well as those from the bright localized spot, was established by High et al. (2012) both through the classic measurement of their first-order correlation function $g^{(1)}(\Delta r)$ as well as from the build-up of polarization, both furthermore occurring together. The degree of coherence is larger on the edges of the spots, suggesting that the ideal density for condensation is not the highest one. The coherence length extends over several microns, so order of magnitudes more than for the classical exciton gas. Such dislocations and their ordering are reminiscent of vortices in superfluids and superconducting phases, and indeed phase dislocations have also been evidenced. However, their connection to the ring itself as opposed to isolated vortices, suggests a more complex and original structure of the excitonic condensate than had been theorized. Shift-interferometry experiments that allow to discriminate between various types of phase dislocations have been used by Leonard et al. (2021) to further support Bose condensation of indirect excitons by evidencing a flow of excitonic matter waves from localized bright spots, producing a moiré effect consistent with the observations. In other structures, similar quantum phases have been claimed. In quantum Hall bilayers, for instance, where lifetime is not an issue and critical densities for condensation can be fine-tuned, the possible tunnelling of an electron hoping from one layer to the other signals a collective state of excitons, in the form of an ultra-sharp peak in the tunnelling rate for a critical separation between the layers, as was reported by Spielman et al. (2000). Such a peak can be explained as a pairing of electrons and holes in an excitonic, i.e., correlated fashion. Another dramatic observation by Kellogg et al. (2004) is the collapse of the Hall voltage when excitons are formed, as their electrical neutrality does not result in a flow of charge in the structure even though electrons and "holes" (that are also electrons) in both layers are in motion. In absence of their correlations (due to unmatched filling factors or distances between the layers beyond the critical one), two opposite Hall voltage cancel together but exist in each layer. In presence of such correlations, no voltage at all is present. This proves a correlated excitonic motion, as opposed to one of uncorrelated electrons and holes that cancels on average. The same effect was reported with indirect excitons in GaAs by Nandi et al. (2012) where it was described as a perfect Coulomb drag with a flow in on layer correlating a counter-flow in the other thanks to the condensation, and a similar phenomenology was also found with van der Waals semiconductors ($MoSe_2$-WSe_2), where a hBN barrier was used to suppress radiative recombination from interlayer excitons in the two TMD layers. The observation of a critical threshold for electroluminescence depending only on the exciton density and with a large and narrow peak of its intensity for equal electron and hole densities, also supports an excitonic BEC, from coherent and correlated pairing of the excitons from a condensed phase. While 2D systems have been the focus for the search of excitonic condensation since the early attempts in Cu_2O, it has also been claimed in the 3D indirect bandgap semimetal $TiSe_2$ by Kogar et al. (2017) with a dedicated momentum-resolved electron energy-loss spectroscopy technique. That allowed them to probe the collective excitations and evidence the Goldstone mode of the excitonic condensate (exciton sound) that thus distinguishes the BEC phase from the Peierls one by exhibiting electronic as opposed to phononic modes. In all these cases, while the evidence is very strong, it still awaits consensual and unambiguous recognition that a BEC of excitons is, not only present, but to which extent, with which characteristics and with what relationships to related quantum phases. The complications of a finite lifetime in a disordered environment have furthermore been theoretically anticipated by Glazov and Suris (2018) to bring other and more surprising conceptual departures from equilibrium systems, such as requiring a finite temperature below which BEC becomes impossible, in contrast to the usual picture that the lower the temperature, the better. Excitonic condensates are thus clearly complicated objects as compared to their atomic counterparts, in a way that the single exciton is not. Although it does not transport neither charge nor mass, exciton superfluidity is another appealing quantum phase. The spectrum of elementary excitations of the excitonic BEC is expected to be linear and thus to adhere to the Landau criterion for superfluidity, by opening a gap for the possible excitations of the system, that is thus resilient to small perturbations, although other models regard the excitonic BEC as insulating.

Emerging trends and future directions

Moiré excitons

A twist made possible with the emerging van der Waals structures is to play with their angular crystallographic alignment, namely, to rotate one plane on top of the other (cf. Fig. 1E), something not possible with conventional crystal growth. This produces moiré patterns that in turn produce periodic and large-scale potentials, i.e., superlattices, with a characteristic wavelength that can range from a few to hundred nanometers. The excitons trapped in these particular landscapes give rise to a new brand of excitons: the moiré excitons, e.g., as reported by Seyler et al. (2019) in $MoSe_2/WSe_2$ heterobi-layers. Inter-layer excitons are highly sensitive to such an angle, with strong variations of their PL emission, due to electron and holes at different K points having a finite momentum. This makes the corresponding excitons dark with zero momentum but becoming radiative if their exciton has the opposite momentum. This can be set by the angle, which controls the intervalley momentum separation between layers. Moiré excitons also exhibit spatially modulated selection rules for optical transitions with excitons localized at different sites of the moiré lattice and in different valleys emitting different polarizations. Short-range moiré lattices, on the other hand, produce minibands with folding of intra- and inter-layer excitonic bands, resulting in an hybridization between the intra- and interlayer excitons. This was reported by Alexeev et al. (2019) with holes from MoSe2 binding to a twist-dependent superposition of electron states in the adjacent layers. The moiré potentials can be sufficiently strong to further quantize the trapped excitons, leading to antibunching (time separation) of their photon emission. The variety of phenomena ruled by the angle between the layer is so considerable that a new field of "twistronics" has emerged.

Topological excitons, insulators and superconductors

While BEC and superfluidity have been, and remain, greatly discussed for excitons over several decades, more exotic quantum phases have emerged recently or are gaining increasing attention, especially when linked to the recent developments brought in condensed-matter physics by topology. A central topological phase is the Mott-insulator, describing a crystal that should be a metal according to conventional band theory but which, due to strong Coulomb interactions, behaves as an insulator instead. The simplest model to account for this physics is given by the Bose-Hubbard Hamiltonian, that rules the interplay between on-site interactions of bosons in a lattice and the energy tunnelling between adjacent sites. Such a phase has been already demonstrated with ultracold atoms, and was recently realized with dipolar excitons, in both triangular-lattice of moiré excitons in van der Waals structures (by Tang et al., 2020) and square lattices nano-patterned by metallic electrodes deposited on GaAs bilayers (by Lagoin et al., 2022). The Mott insulator phase consists of a distribution of the excitons to occupy each lattice site with a fixed and identical number of particles. Such non-fluctuating particle numbers are typical of strongly quantum correlated phases, as they break the normally-distributed fluctuations of most classical systems. In the GaAs case, for instance, two Mott phases with one and two excitons per site, all in the same Wannier state, have been evidenced through spectral observations echoing in the PL the ordering of excitons in the lattice. Another insulating phase, this time directly attributed to excitons—the excitonic insulator—arises when the exciton's binding energy competes with the bandgap and is thus particularly relevant in semimetals. This phase is now believed to have been observed by Jia et al. (2022) for the first time, in WTe_2, and to account for another paradigmatic topological phase but for electrons, the quantum spin Hall effect, that locks their momentum to their spin and thus constrains their motion on the edge of the sample in one direction only (preventing back scattering at zero magnetic field). It has also been linked to exciton condensation by Sun et al. (2022). Realizing and controlling such topological phases is important for prospects of harnessing quantum coherent effects, including condensation, superfluidity and superconductivity, as well as for building quantum simulators, that implement in a physical platform a model Hamiltonian that is too awkward to be described theoretically or computationally, but that can be simulated by observing the actual system. This could target topical systems such as high-T_c and d-wave superconductors in other platforms, supersolids, Luttinger liquids, Kitaev models, generalized Kane-Mele model with a topological flat band, interaction-driven Haldane insulator, quantum magnets, Majorana modes, etc. An advantage of excitons as compared to electronic systems, such as graphene, is that optical recombination allows a convenient and precise observation of the underlying physics. Even when excitons themselves do not play the predominant role in such quantum phases, they can be crucial auxiliaries to aid or witness other quasi-particles into their quantum transition, such as for the formation of Wigner crystals (crystal of electrons) where excitons feel the periodic potential from the electrons, that undergo a typical scattering (Umklapp) producing a telltale signature in the form of a resonance. This approach has been exploited by Smoleński et al. (2021).

Among the most topical effects, superconductivity, at first sight, appears to be not relevant for excitons since they are neutral particles. A trion, however, is not, and conventional charge-transport is thus possible in this way, as demonstrated by Sanvitto et al. (2001), while their Bose condensation in a superfluid regime would result in their superconductivity, which was first suggested by Lozovik and Yudson (1976). Indeed, excitonic BEC in bilayers allows a net flow of charge intra-layers while still producing no net electric flow inter-layers if they are of the same magnitude but opposite directions, a mechanism that can be interpreted as "counterflow superconductivity." Related mechanisms are important for superconductivity of paired electrons, for instance in graphene, but put more emphasis on the underlying constituents than on the excitonic quasi-particle as a whole. Less forthright for exciton superconductivity is a proposal from Ginzburg (1968) and taken-up by Bardeen (1978) himself, the historical figure who understood how phonons mediate superconductivity by pairing electrons into Cooper pairs. Together with Allender et al. (1973), Bardeen considers a bilayer structure, where phonons are to be substituted by excitons, the so-called "exciton mechanism" (of Ginzburg). In Bardeen–Cooper–Schrieffer (BCS) theory, the critical temperature is of the type $k_{\mathrm{B}}T_c = \Theta_e^{-1/g}$ with Θ the Debye energy (cutoff energy for a maximum phonon energy) and $g = \mathcal{N}(0)V$ the product of $\mathcal{N}(0)$ the electron density at the Fermi level and V the electron-phonon interaction, which result in the low-temperatures observed in conventional superconductors. One can thus raise T_c by increasing Θ and/or g, which remains marginal with phonons. Substituting for excitonic values, that can produce a much stronger electron-electron attraction even if the retardation effect characteristic of BCS superconductivity is reduced. Taking both competing effects into account, one finds $\Theta/k_{\mathrm{B}} \approx 10^3$–$10^4$ K and $g \approx \frac{1}{5}$–$\frac{1}{2}$ resulting in critical temperatures of several hundred Kelvin, which pioneered the quest for high-temperature superconductors. At still another level of the same idea, one can mediate Cooper pairing not with excitons which, just as phonon in BCS, are virtual excitations mediating the interaction, but with real excitons present in the system as a condensate, in which case their virtual excitations become those mediating the interaction. Since forming an exciton BEC is difficult, this can be eased by involving polaritons in a microcavity, as proposed by Laussy et al. (2010) or driving the excitonic BEC with a laser, thereby realizing a light-induced superconductivity mediated by excitons, which has also been predicted to possibly reach room temperature. While such effects have not yet been observed, related strongly-correlated quantum phases mediated by light, such as ferromagnetism of excitons, have indeed been realized by Wang et al. (2022) with moiré excitons exhibiting a characteristic hysteresis loop in their magnetic response.

Excitonic devices

Excitonic devices already exist. They will probably invade the market as both technology and theoretical understanding progress and the transition from proof-of-principle demonstrations to a working superior excitonic technology will be achieved. In zero-dimension, quantum dot excitons already power some of the best quantum light sources, both at the single-photon level and for LED or laser applications. For the display industry, they offer high color purity and ultra-high resolution from thin screens, with also excellent brightness and a large color gamut, including perfect black. For lasing, excitons in colloidal quantum dots—that already provide efficient photoluminescence over a wider spectrum than their epitaxial counterpart—have also demonstrated with Dang et al. (2012) single-exciton gain, allowing to implement highly-efficient, low-threshold full-color lasers. For quantum applications, multiplexed (i.e., synchronized) QDs have, among other services, already allowed to claim quantum supremacy in boson sampling. All these feasts follow from the highly-tunable excitonic properties in artificial atoms that can be molded at will in a thriving material physics. The QD exciton that behaves like a two-level system becomes, in quantum mechanical terms, a qubit, i.e., the fundamental unit of quantum information processing which can sustain superpositions of states and nonlocal entanglement, needed for quantum information processing. Coupled excitons in a single QD have been used in this way by Li et al. (2003) to build a two-qubit gate. In a paradigmatic which-way recombination, the biexciton's decay to its ground state through a radiative cascade passing by one or the other exciton, leads to entanglement of the emitted photons, as shown by Akopian et al. (2006). By quantum-correlating deterministically hundreds of photons—so-called cluster states, able to power universal quantum computation—the interplay of dark excitons with the biexciton through a precise timing by optical pulses allowed Schwartz et al. (2016) to entangle the polarization in a stream of emitted photons. The spin-degree of freedom is useful for that purpose, thanks to its long coherence time, due to a weak interaction with the environment, yet with a great ease of direct control with optical pulses. This allowed Kroutvar et al. (2004) to implement optically fully-programmable spin memories. In two-dimensions, there is the prospect of taking advantage of exciton propagation, and thereby to implement more powerful functionalities. This, however, comes at the price of being more difficult to master and only proof-of-principle demonstrations of 2D excitonic devices, including some with similar functionalities as those above (light-source, memory storage, etc.), have been demonstrated. Transport applications start with the exciton conveyors, such as those implemented by Winbow et al. (2011) and Peng et al. (2022), that literally transport excitons on an electrostatic carpet powered by surface acoustic waves, whose amplitude and speed are directly controlled through the applied voltage and AC frequency, respectively. A near-field piezoelectric field periodically modulates the exciton energy to drag them over distances an order of magnitude greater than by diffusion alone, that is already very large. This could develop into a new kind of excito-phononic circuits. A technological grail is the transistor, whose electronic implementation comes with the drawback of high energy consumption and heat dissipation. Purely photonic transistors lack the nonlinearities inherent to the device. Excitons thus appear an ideal compromise to realize an opto-electronic transistor, also interfacing the two basic tenets of technology: electronics (control) and optics (communication). Excitonic transistors as well as their combination in a circuit, have been demonstrated by High et al. (2008) to effectuate such a conversion of photons into excitons that flow through the device before their ultimate reconversion into photons. The principle of an excitonic transistor is, similarly to its electronic FET model, to control via an applied voltage the flow of excitons through two terminals conditioned to the state of a third one. A transistor acting as a switch (as opposed to as an amplifier, the other typical function of a transistor) was demonstrated, with a control of the flux of excitons in the source electrode by a gate voltage. At the heart of the mechanism, an applied electric field creates an energy barrier or trap for IX and therefore can suppress or enable exciton diffusion. From the optical side, the exciton recombination rate can thus be controlled with an applied electromagnetic field. Three such excitonic transistors have also been coupled to share a common electrode, thereby realizing an excitonic circuit, with one application implemented to directionally switch the exciton flux. At this time, 2D excitonic transistors are not functional enough to power a substituting technology. The binding energies of the materials where they have been implemented require cryogenic cooling, and their performances do not yet compete with even decades-old electronics. While quantum devices would be worth running at cryogenic temperatures, classical devices should certainly operate at room temperature to rival those already existing, in which case strongly-bound excitons such as those provided by van der Waals structures are required. Emerging materials could, indeed, push forward excitons as strong contenders to replace electronics. These also reinforce the role of the excitons over the electrons and holes in conventional semiconductor devices, due to their strong binding, oscillator strengths and Coulomb interactions, so that new generations of excitonic LEDs, junctions, electrically controllable routers and transistors become possible, operating with currents as low as nanoamps. In the case of the transistor, room-temperature operation with a transport of excitons over five micrometers distance, has already been demonstrated by Unuchek et al. (2018). In addition to that, the rich valley-physics opens new functionalities, such as the control of light handedness that allowed Zhang et al. (2014b) to implement flexible chiral optoelectronics. These rapid developments open the route, not only toward an excitonic computer, but also entirely new types of devices such as transparent and stretchable screens.

Conclusion

Excitons have been part of condensed-matter physics since its early days and they remain at the forefront of its most active, fruitful and promising developments. They have retained throughout their history a mixed nature of being a compelling quasi-particle and a dubious one to truly or rigorously account for the complexity of condensed matter systems. In both cases, they are central, in one form of another, to a vast and varied range of phenomena. Even as they get tentatively discarded from even their excitonic resonances, they re-appear in the most unexpected places, such as metals. Excitons will likely remain unavoidable mental pictures, forever introduced as electron-hole pair bound states, and as technological applications—possibly room-temperature superconducting excitonic quantum devices—develop from ideas based on their conception, they will continue to occupy a central position in condensed-matter physics.

References

Akopian N, Lindner NH, Poem E, Berlatzky Y, Avron J, Gershoni D, Gerardot BD, and Petroff PM (2006) Entangled photon pairs from semiconductor quantum dots. *Physical Review Letters* 96: 130501. https://doi.org/10.1103/PhysRevLett. 96.130501.

Alexeev EM, Ruiz-Tijerina DA, Danovich M, Hamer MJ, Terry DJ, Nayak PK, Ahn S, Pak S, Lee J, Sohn JL, Molas MR, Koperski M, Watanabe K, Taniguchi T, Novoselov KS, Gorbachev RV, Shin HS, and Fal’ko, V. I. and Tartakovskii, A. I. (2019) Resonantly hybridized excitons in moiré superlattices in van der Waals heterostructures. *Nature* 567: 81. https://doi.org/10.1038/s41586-019-0986-9.

Allender D, Bray J, and Bardeen J (1973) Model for an exciton mechanism of superconductivity. *Physical Review B* 7: 1020. https://doi.org/10.1103/PhysRevB.7.1020.

Bardeen J (1978) Excitonic superconductivity? *Journal of the Less-Common Metals* 62: 447. https://doi.org/10.1016/0022-5088(78)90058-9.

Bayer M, Stern O, Hawrylak P, Fafard S, and Forchel A (2000) Hidden symmetries in the energy levels of excitonic ‘artificial atoms. *Nature* 405: 923. https://doi.org/10.1038/35016020.

Bayer M, Ortner G, Stern O, Kuther A, Gorbunov AA, Forchel A, Hawrylak P, Fafard S, Hinzer K, Rei-necke TL, Walck SN, Reithmaier JP, Klopf F, and Schäfer F (2002) Fine structure of neutral and charged excitons in self-assembled In(Ga)As/(Al)GaAs quantum dots. *Physical Review B* 65. https://doi.org/10.1103/PhysRevB.65.195315. 195315.

Bayer M, Korkusinski M, Hawrylak P, Gutbrod T, Michel M, and Forchel A (2003) Optical detection of the Aharonov-Bohm effect on a charged particle in a nanoscale quantum ring. *Physical Review Letters* 90: 186801. https://doi.org/10.1103/PhysRevLett.90.186801.

Blatt JM, Böer KW, and Brandt W (1962) Bose–Einstein condensation of excitons. *Physics Review* 126: 1691. https://doi.org/10.1103/PhysRev,126.1691.

Brandt J, Fröhlich D, Sandfort C, Bayer M, Stolz H, and Naka N (2007) Ultranarrow optical absorption and two-phonon excitation spectroscopy of Cu$_2$O paraexcitons in a high magnetic field. *Physical Review Letters* 99: 217403. https://doi.org/10.1103/PhysRevLett.99.217403.

Butov LV, Gossard AC, and Chemla DS (2002) Macroscopically ordered state in an exciton system. *Nature* 418: 751. https://doi.org/10.1038/nature00943.

Butov LV, Levitov LS, Mintsev AV, Simons BD, Gossard AC, and Chemla DS (2004) Formation mechanism and low-temperature instability of exciton rings. *Physical Review Letters* 92: 117404. https://doi.org/10.1103/PhysRevLett.92.117404.

Chaplik AV (1995) Magnetoexcitons in quantum rings and in antidots. *JETP Letters* 62: 900. http://jetpletters.ru/ps/1222/article_18474.pdf.

Chatterjee S, Ell C, Mosor S, Khitrova G, Gibbs HM, Hoyer W, Kira M, Koch SW, Prineas JP, and Stolz H (2004) Excitonic photoluminescence in semiconductor quantum wells: Plasma versus excitons. *Physical Review Letters* 92: 067402. https://doi.org/10.1103/PhysRevLett.92.067402.

Ciuti C, Savona V, Piermarocchi C, Quattropani A, and Schwendimann P (1998) Role of the exchange of carriers in elastic exciton-exciton scattering in quantum wells. *Physical Review B* 58: 7926. https://doi.org/10.1103/PhysRevB.58.7926.

Cohen K, Shilo Y, West K, Pfeiffer L, and Rapaport R (2016) Dark high density dipolar liquid of excitons. *Nano Letters* 16: 3726. https://doi.org/10.1021/acs.nanolett.6b01061.

Combescot M and Betbeder-Matibet O (2002) The effective bosonic hamiltonian for excitons reconsidered. *Europhysics Letters* 58: 87. https://doi.org/10.1209/epl/i2002-00609-3.

Combescot M, Betbeder-Matibet O, and Dubin F (2008) The many-body physics of composite bosons. *Physics Reports* 463: 215. https://doi.org/10.1016/j.physrep.2007.11.003.

Dang C, Lee J, Breen C, Steckel JS, Coe-Sullivan S, and Nurmikko A (2012) Red, green and blue lasing enabled by single-exciton gain in colloidal quantum dot films. *Nature Nanotechnology* 7: 335. https://doi.org/10.1038/nnano.2012.61.

Deveaud B, Clérot F, Roy N, Satzke K, Sermage B, and Katzern DS (1991) Enhanced radiative recombination of free excitons in GaAs quantum wells. *Physical Review Letters* 67: 2355. https://doi.org/10.1103/PhysRevLett.67.2355.

Deveaud B, Kappei L, Berney J, Morier-Genoud F, Portella-Oberli MT, Szczytko J, and Piermarocchi C (2005) Excitonic effects in the luminescence of quantum wells. *Chemical Physics* 318: 104. https://doi.org/10.1016/j.chemphys.2005.06.045.

Dubin F, Melet R, Barisien T, Grousson R, Legrand L, Schott M, and Voliotis V (2006) Macroscopic coherence of a single exciton state in an organic quantum wire. *Nature Physics* 2: 32. https://doi.org/10.1038/nphysl96.

Éfros AL (2022) Excitons in nanoscale semiconductor structures. In: *Encyclopedia of Condensed Matter Physics*, 2nd edn.

Éfros AL and Éfros AL (1982) Interband absorption of light in a semiconductor sphere. *Soviet Physics: Semiconductors* 16: 772.

Ekimov AI and Onushchenko AA (1981) Quantum size effect in three-dimensional microscopic semiconductor crystals. *JETP Letters* 34: 345. http://jetpletters.ru/ps/1517/article_23187.pdf.

Finley JJ, Fry PW, Ashmore AD, Lemaître A, Tartakovskii AL, Oulton R, Mowbray DJ, Skolnick MS, Hopkinson M, Buckle PD, and Maksym PA (2001) Observation of multicharged excitons and biexcitons in a single InGaAs quantum dot. *Physical Review B* 63: 161305(R). https://doi.org/10.1103/PhysRevB.63.161305.

Flagg EB, Muller A, Robertson JW, Founta S, Deppe DG, Xiao M, Ma W, Salamo GJ, and Shih CK (2009) Resonantly driven coherent oscillations in a solid-state quantum emitter. *Nature Physics* 5: 203. https://doi.org/10.1038/nphysll84.

Fomin VM (ed.) (2014) *Physics of Quantum Rings*. Berlin, Heidelberg: Springer.

Frenkel J (1931) On the transformation of light into heat in solids. II. *Physics Review* 37: 1276. https://doi.org/10.1103/PhysRev.37.1276.

Frenkel YI (1936) On the absorption of light and the trapping of electrons and positive holes in crystalline dielectrics. *Physikalische Zeitschrift der Sowjetunion* 9: 158. https://doi.org/10.3367/UFNr.0093.196711c. 0408.

Ginzburg VL (1968) The problem of high temperature superconductivity. *Contemporary Physics* 9: 355. https://doi.org/10.1080/00107516808220090.

Glazov MM and Suris RA (2018) Exciton condensation in a two-dimensional system with disorder. *Journal of Experimental and Theoretical Physics* 126: 833. https://doi.org/10.1134/S1063776118060092.

Gross EF (1956) Optical spectrum of excitons in the crystal lattice. *Il Nuovo Cimento* 3: 672. https://doi.org/10.1007/BF02746069.

Gross EF (1962) Excitons and their motion in crystal lattices. *Soviet Physics Uspekhi* 5: 195. https://doi.org/10.1070/PU1962v005n02ABEH003407.

Grünwald P, Assmann M, Heckötter J, Fröhlich D, Bayer M, Stolz H, and Scheel S (2016) Signatures of quantum coherences in Rydberg excitons. *Physical Review Letters* 117. https://doi.org/10.1103/PhysRevLett.117.133003. 133003.

Hägele D, Hübner J, Rühle W, and Oestreich M (1999) When do excitons really exist? *Physica B* 272: 328. https://doi.org/10.1016/S0921-4526 (99)00384-1.

Haken H (1956) Zur Quantentheorie des Mehrelektronensystems im schwingenden Gitter. F. *Zeitschrift für Physik* 146: 527. https://doi.org/10.1007/BF01333179.

Hanamura E (1974) Theory of many Wannier excitons. I. *Journal of the Physical Society of Japan* 37: 1545. https://doi.org/10.1143/JPSJ.37.1545.

Hawrylak P (1999) Excitonic artificial atoms: Engineering optical properties of quantum dots. *Physical Review B* 60: 5597. https://doi.org/10.1103/PhysRevB.60.5597.

Heckötter J, Freitag M, Fröhlich D, Assmann M, Bayer M, Semina MA, and Glazov MM (2017) Scaling laws of Rydberg excitons. *Physical Review B* 96: 125142. https://doi.org/10.1103/PhysRevB.96.125142.

High AA, Katerin E, Novitskaya AE, Butov LV, Hanson M, and Gossard AC (2008) Control of exciton fluxes in an excitonic integrated circuit. *Science* 321: 5885. https://doi.org/10.1126/science.1157845.

High AA, Leonard JR, Hammack AT, Fogler MM, Butov LV, Kavokin AV, Campman KL, and Gossard AC (2012) Spontaneous coherence in a cold exciton gas. *Nature* 483: 584. https://doi.org/10.1038/naturel0903.

Hopfield JJ (1958) Theory of the contribution of excitons to the complex dielectric constant of crystals. *Physics Review* 112: 1555. https://doi.org/10.1103/PhysRev.H2.1555.

Jia Y, Wang R, Chiu C-L, Song Z, Jäck GYB, Lei S, Klemenz S, Cevaflos FA, Onyszczak M, Fishchenk N, Liu X, Farahi G, Xie F, Xu Y, Watanabe K, Taniguchi T, Bernevig BA, Cava RJ, Schoop LM, Yazdani A, and Wu S (2022) Evidence for a monolayer excitonic insulator. *Nature Physics* 18: 87. https://doi.org/10.1038/s41567-021-01422-w.

Kaindl RA, Carnahan MA, Hägele D, Lövenich R, and Chemla DS (2003) Ultrafast terahertz probes of transient conducting and insulating phases in an electron-hole gas. *Nature* 423: 734. https://doi.org/10.1038/nature01676.

Kavokin A, Baumberg JJ, Malpuech G, and Laussy FP (2017) *Microcavities*, 2nd edn. Oxford University Press.

Kazimierczuk T, Fröhlich D, Scheel S, Stolz H, and Bayer M (2014) Giant Rydberg excitons in the copper oxide Cu$_2$O. *Nature* 514: 343. https://doi.org/10.1038/naturel3832.

Keldysh LV (1979) Coulomb interaction in thin semiconductor and semimetal films. *JETP Letters* 29: 716. http://jetpletters.ru/ps/1458/article_22207.shtml.

Keldysh LV and Kopaev YV (1965) Possible instability of the semimetallic state toward coulomb interaction. *Soviet Physics - Solid State* 6: 2219.

Keldysh LV and Kozlov AN (1968) Collective properties of excitons in semiconductors. *Journal of Experimental and Theoretical Physics* 27: 521.

Kellogg M, Eisenstein J, Pfeiffer L, and West K (2004) Vanishing Hall resistance at high magnetic field in a double-layer two-dimensional electron system. *Physical Review Letters* 93: 036801. https://doi.org/10.1103/PhysRevLett.93.036801.

Kira M, Jahnke F, and Koch SW (1998) Microscopic theory of excitonic signatures in semiconductor photoluminescence. *Physical Review Letters* 81: 3263. https://doi.org/10.1103/PhysRevLett.81.3263.

Kogar A, Rak MS, Vig S, Husain AA, Flicker F, Joe YI, Venema L, MacDougall GJ, Chiang TC, Fradkin E, van Wezel J, and Abbamonte P (2017) Signatures of exciton condensation in a transition metal dichalcogenide. *Science* 358: 1314. https://doi.org/10.1126/science. aam6432.

Koudinov A, Kehl C, Rodina A, Geurts J, Wolverson D, and Karczewski G (2014) Suris tetrons: Possible spectroscopic evidence for four-particle optical excitations of a two-dimensional electron gas. *Physical Review Letters* 112: 147402. https://doi.org/10.1103/PhysRevLett.112.147402.

Kroutvar M, Ducommun Y, Heiss D, Bichler M, Schuh D, Abstreiter G, and Finley JJ (2004) Optically programmable electron spin memory using semiconductor quantum dots. *Nature* 432: 81. https://doi.org/10.1038/nature03008.

Kunstmann J, Mooshammer F, Nagler R, Chaves A, Stein F, Paradiso N, Plechinger G, Strunk C, Schüller C, Seifert G, Reichman DR, and Korn T (2018) Momentum-space indirect interlayer excitons in transition-metal dichalcogenide van der Waals heterostructures. *Nature Physics* 14: 801. https://doi.org/10.1038/s41567-018-0123-y.

Kutrovskaya S, Osipov A, Baryshev S, Zasedatelev A, Samyshkin V, Demirchyan S, Pulci O, Grassano D, Gontrani L, Hartmann RR, Portnoi ME, Kucherik A, Lagoudakis PG, and Kavokin A (2020) Excitonic fine structure in emission of linear carbon chains. *Nano Letters* 9: 6502. https://doi.org/10.1021/acs. nanolett. 0c02244.

La Rocca G (2022) Electrons and holes. In: *Encyclopedia of Condensed Matter Physics*, 2nd edn.

Lagoin C, Suffit S, Baldwin K, Pfeiffer L, and Dubin F (2022) Mott insulator of strongly interacting two-dimensional semiconductor excitons. *Nature Physics* 18: 149. https://doi.org/10.1038/s41567-021-01440-8.

Laussy FR, del Valle E, and Tejedor C (2008) Strong coupling of quantum dots in microcavities. *Physical Review Letters* 101: 083601. https://doi.org/10.1103/PhysRevLett.101.083601.

Laussy FP, Kavokin AV, and Shelykh IA (2010) Exciton-polariton mediated superconductivity. *Physical Review Letters* 104: 106402. https://doi.org/10.1103/PhysRevLett.104.106402.

Leonard JR, Hu L, High AA, Hammack AT, Wu C, Butov LV, Campman KL, and Gossard AC (2021) Moiré pattern of interference dislocations in condensate of indirect excitons. *Nature Communications* 12: 1175. https://doi.org/10.1038/s41467-021-21353-7.

Levitov LS, Simons BD, and Butov LV (2005) Pattern formation as a signature of quantum degeneracy in a cold exciton system. *Physical Review Letters* 94: 176404. https://doi.org/10.1103/PhysRevLett.94.176404.

Li X, Wu Y, Steel D, Gammon D, Stievater TH, Katzer DS, Park D, Piermarocchi C, and Sham LJ (2003) An all-optical quantum gate in a semiconductor quantum dot. *Science* 301: 809. https://doi.org/10.1126/science.1083800.

Litinskaya M (2022) Polaritons. In: *Encyclopedia of Condensed Matter Physics*, 2nd edn.

Littlewood PB (2022) Excitons: Theory. In: *Encyclopedia of Condensed Matter Physics*, 2nd edn.

Lozovik YE and Yudson V (1976) A new mechanism for superconductivity: pairing between spatially separated electrons and holes. *Journal of Experimental and Theoretical Physics* 44: 389.

Maialle MZ, Andrada de Silva EA, and Sham LJ (1993) Exciton spin dynamics in quantum wells. *Physical Review B* 47: 15776. https://doi.org/10.1103/PhysRevB.47.15776.

Mak KF, Lee C, Hone J, Shan J, and Heinz TF (2010) Atomically thin MoS$_2$: A new direct-gap semiconductor. *Physical Review Letters* 105: 136805. https://doi.org/10.1103/PhysRevLett.105.136805.

Marini A (2008) *Ab Initio* finite-temperature excitons. *Physical Review Letters* 101. https://doi.org/10.1103/PhysRevLett.101.106405. 106405.

McCutcheon DS and Nazir A (2013) Model of the optical emission of a driven semiconductor quantum dot: Phonon-enhanced coherent scattering and off-resonant sideband narrowing. *Physical Review Letters* 110. https://doi.org/10.1103/PhysRevLett.110.217401. 217401.

Meyer BK, Polity A, Reppin D, Becker M, Hering P, Kramm B, Klar R, Sander T, Reindl C, Heiliger C, Heinemann M, Müller C, and Ronning C (2013) *The Physics of Copper Oxide (Cu$_2$O)*. Academic Press. chapter 6.

Moskalenko S (1962) Reversible optico-hydrodynamic phenomena in a non ideal exciton gas. *Soviet Physics - Solid State* 4: 199.

Mott NF (1938) On the absorption of light by crystals. *Proceedings of the Royal Society A* 167: 384. https://doi.org/10.1098/rspa.1938.0137.

Mott NF (1968) Metal-insulator transition. *Reviews of Modern Physics* 40: 677. https://doi.org/10.1103/RevModPhys.40.677.

Nandi D, Finck ADK, Eisenstein JP, Pfeiffer LN, and West KW (2012) Exciton condensation and perfect Coulomb drag. *Nature* 488: 481. https://doi.org/10.1038/naturell302.

Peierls R (1932) Zur Theorie der Absorptionsspektren fester Körper. *Annalen der Physik* 405: 905. https://doi.org/10.1002/andp.19324050803.

Peng R, Ripin A, Ye Y, Zhu J, Wu C, Lee S, Li H, Taniguchi T, Watanabe K, Cao T, Xu X, and Li M (2022) Long-range transport of 2d excitons with acoustic waves. *Nature Communications* 13: 1334. https://doi.org/10.1038/s41467-022-29042-9.

Ramsay AJ, Gopal AV, Gauger EM, Nazir A, Lovett BW, Fox AM, and Skolnick MS (2010) Damping of exciton Rabi rotations by acoustic phonons in optically excited InGaAs/GaAs quantum dots. *Physical Review Letters* 104: 017402. https://doi.org/10.1103/PhysRevLett.104.017402.

Rapaport R, Chen G, Snoke D, Simon SH, Pfeiffer L, West K, Liu Y, and Denev S (2004) Charge separation of dense two-dimensional electron-hole gases: Mechanism for exciton ring pattern formation. *Physical Review Letters* 92: 117405. https://doi.org/10.1103/PhysRevLett.92.117405.

Reithmaier JP, Sek G, Löftier A, Hofmann C, Kuhn S, Reitzenstein S, Keldysh LV, Kulakovskii VD, Rei-necker TL, and Forchel A (2004) Strong coupling in a single quantum dot-semiconductor microcavity system. *Nature* 432: 197. SST1 https://doi.org/10.1038/nature02969.

Ribeiro E, Govorov AO, Carvalho W, and Medeiros-Ribeiro G (2004) Aharonov-Bohm signature for neutral polarized excitons in type-II quantum dot ensembles. *Physical Review Letters* 92: 126402. https://doi.org/10.1103/PhysRevLett.92.126402.

Richard S, Aniel F, and Fishman G (2004) Energy-band structure of Ge, Si, and GaAs: A thirty-band k · p method. *Physical Review B* 70: 237204. https://doi.org/10.1103/PhysRevB.70.235204.

Rivera P, Yu H, Seyler KL, Wilson NP, Yao W, and Xu X (2018) Interlayer valley excitons in heterobilayers of transition metal dichalcogenides. *Nature Nanotechnology* 1: 1004. https://doi.org/10.1038/s41565-018-0193-0.

Rytova NS (1967) The screened potential of a point charge in a thin film. *Moscow University Physics Bulletin* 22: 18. http://vmu.phys.msu.ru/abstract/1967/3/1967-3-030/.

Sanvitto D, Pulizzi F, Shields AJ, Christianen PCM, Holmes SN, Simmons MY, Ritchie DA, Maan JC, and Pepper M (2001) Observation of charge transport by negatively charged excitons. *Science* 294: 837. https://doi.org/10.1126/science.1064847.

Schedelbeck G, Wegscheider W, Bichler M, and Abstre-iter G (1997) Coupled quantum dots fabricated by cleaved edge overgrowth: From artificial atoms to molecules. *Science* 278: 1792. https://doi.org/10.1126/science.278.5344.1792.

Scheibner M, Schmidt T, Worschech L, Forchel A, Bacher G, Passow T, and Hommel D (2007) Superradiance of quantum dots. *Nature Physics* 3: 106. https://doi.org/10.1038/nphys494.

Schneider C, Rahimi-Iman A, Kim NY, Fischer J, Savenko IG, Amthor M, Lermer M, Wolf A, Worschech L, Kulakovskii VD, Shelykh IA, Kamp M, Reitzenstein S, Forchel A, Yamamoto Y, and Höfling S (2013) An electrically pumped polariton laser. *Nature* 497: 348. https://doi.org/10.1038/naturel2036.

Schwartz I, Cogane D, Schmidgall R, Don Y, Gantz L, Kenneth O, Lindner NH, and Gershoni D (2016) Deterministic generation of a cluster state of entangled photons. *Science* 354: 434. https://doi.org/10.1126/science. aah 4758.

Seyler KL, Rivera P, Yu H, Wilson NP, Ray EL, Mandrus DG, Yan J, Yao W, and Xu X (2019) Signatures of moiré-trapped valley excitons in MoSe2/WSe2 heterobilayers. *Nature* 567: 66. https://doi.org/10.1038/s41586-019-0957-l.

Slater JC and Shockley W (1936) Optical absorption by the alkali halides. *Physics Review* 50: 705. https://doi.org/10.1103/PhysRev.50.705.

Smoleński T, Dolgirev PE, Kuhlenkamp C, Popert A, Shimazaki Y, Back P, Lu X, Kroner M, Watanabe K, Taniguchi T, Esterlis I, Demler E, and Ĭmamoğlu A (2021) Signatures of Wigner crystal of electrons in a mono-layer semiconductor. *Nature* 595: 53. https://doi.org/10.1038/s41586-021-03590-4.

Snoke D, Denev S, Liu Y, Pfeiffer L, and West K (2002) Long-range transport in excitonic dark states in coupled quantum wells. *Nature* 418: 754. https://doi.org/10.1038/nature00940.

Spielman IB, Eisenstein JP, Pfeiffer LN, and West KW (2000) Resonantly enhanced tunneling in a double layer quantum Hall ferromagnet. *Physical Review Letters* 84: 5808. https://doi.org/10.1103/PhysRevLett.84.5808.

Splendiani A, Sun L, Zhang Y, Li T, Kim J, Chim C-Y, Galli G, and Wang F (2010) Emerging photoluminescence in monolayer MoS$_2$. *Nano Letters* 10: 1271. https://doi.org/10.1021/nl903868w.

Steinhoff A, Florian M, Rösner M, Schönhoff G, Wehling TO, and Jahnke F (2017) Exciton fission in monolayer transition metal dichalcogenide semiconductors. *Nature Communications* 8: 1166. https://doi.org/10.1038/s41467-017-01298-6.

Stern F (1967) Polarizability of a two-dimensional electron gas. *Physical Review Letters* 18: 546. https://doi.org/10.1103/PhysRevLett.18.546.

Stern M, Umansky V, and Bar-Joseph I (2014) Exciton liquid in coupled quantum wells. *Science* 343: 6166. https://doi.org/10.1126/science.1243409.

Stievater TFl, Li X, Steel DG, Gammon D, Katzer DS, Park D, Piermarocchi C, and Sham LJ (2001) Rabi oscillations of excitons in single quantum dots. *Physical Review Letters* 87: 133603. https://doi.org/10.1103/PhysRevLett.87.133603.

Stinaff EA, Scheibner M, Bracker AS, Ponomarev IV, Korenev VL, Ware ME, Doty MF, Reinecke TL, and Gammon D (2006) Optical signatures of coupled quantum dots. *Science* 311: 636. https://doi.org/10.1126/science.1121189.

Sun B, Zhao W, Palomaki T, Fei Z, Runburg E, Malinowski R, Fluang X, Cenker J, Cui Y-T, Chu J-FL, Xu X, Ataei SS, Varsano D, Palummo M, Molinari E, Rontani M, and Cobden DFl (2022) Evidence for equilibrium exciton condensation in monolayer WTe_2. *Nature Physics* 18: 94. https://doi.org/10.1038/s41567-021-01427-.

Suris RA (2016) Gas-crystal phase transition in a 2d dipolar exciton system. *Journal of Experimental and Theoretical Physics* 122: 602. https://doi.org/10.1134/S1063776116030110.

Tamor MA and Wolfe JP (1980) Drift and diffusion of free excitons in Si. *Physical Review Letters* 44: 1703. https://doi.org/10.1103/PhysRevLett.44.1703111.

Tang Y, Li L, Li T, Xu Y, Liu S, Barmak K, Watanabe K, Taniguchi T, MacDonald AH, Shan J, and Mak KF (2020) Simulation of Hubbard model physics in WSe_2/WS_2 moiré superlattices. *Nature* 579: 353. https://doi.org/10.1038/s41586-020-2085-3.

Tartakovskii AL, Kulakovskii VD, Forchel A, and Reithmaier JP (1998) Exciton-photon coupling in photonic wires. *Physical Review B* 57: R6807(R). https://doi.org/10.1103/PhysRevB.57.R6807.

Teodoro MD, Campo VL, Lopez-Richard V, Marega E Jr., Marques GE, Gobato YG, Iikawa F, Brasil MJSP, AbuWaar ZY, Dorogan VG, Yu I, Mazur MB, and Salamo GJ (2010) Aharonov-Bohm interference in neutral excitons: Effects of built-in electric fields. *Physical Review Letters* 104: 086401. https://doi.org/10.1103/PhysRevLett.104.086401.

Toyozawa Y (1958) Theory of line-shapes of the exciton absorption bands. *Progress of Theoretical Physics* 20: 53. https://doi.org/10.1143/PTP.20.53.

Unuchek D, Ciarrocchi A, Avsar A, Watanabe K, Taniguchi T, and Kis A (2018) Room-temperature electrical control of exciton flux in a van der Waals heterostructure. *Nature* 560: 340. https://doi.org/10.1038/s41586-018-0357-y.

Wang F, Cho DJ, Kessler B, Deslippe J, Schuck PJ, Louie SG, Zettl A, Heinz TF, and Shen YR (2007) Observation of excitons in one-dimensional metallic single-walled carbon nanotubes. *Physical Review Letters* 99: 227401. https://doi.org/10.1103/PhysRevLett.99.227401.

Wang X, Xiao C, Park H, Zhu J, Wang C, Taniguchi T, Watanabe K, Yan J, Xiao D, Gamelin DR, Yao W, and Xu X (2022) Light-induced ferromagnetism in moiré superlattices. *Nature* 604: 468. https://doi.org/10.1038/s41586-022-04472-z.

Wannier GH (1937) The structure of electronic excitation levels in insulating crystals. *Physics Review* 52: 191. https://doi.org/10.1103/PhysRev.52.191.

Warburton RJ, Schäflein C, Haft D, Bickel F, Lorke A, Karrai K, Garcia JM, Schoenfeld W, and Petroff PM (2000) Optical emission from a charge-tunable quantum ring. *Nature* 405: 926. https://doi.org/10.1038/35016030.

Weisbuch C, Miller R, Dingle R, Gossard AC, and Wiegman W (1981) Intrinsic radiative recombination from quantum states in GaAs- $A1_{x}$ Ga_{1-x} as multi-quantum well structures. *Solid State Communications* 37: 219. https://doi.org/10.1016/0038-1098(81)91017-6.

Weisbuch C, Nishioka M, Ishikawa A, and Arakawa Y (1992) Observation of the coupled exciton-photon mode splitting in a semiconductor quantum microcavity. *Physical Review Letters* 69: 3314. https://doi.org/10.1103/PhysRevLett.69.3314.

Winbow AG, Leonard JR, Remeika M, Kuznetsova YY, High AA, Hammack AT, Butov LV, Wilkes J, Guenther AA, Ivanov AL, Hanson M, and Gossard AC (2011) Electrostatic conveyer for excitons. *Physical Review Letters* 106: 196806. https://doi.org/10.1103/PhysRevLett.106.196806.

Wolfe JP and Mysyrowicz A (1984) Excitonic matter. *Scientific American* 250: 98. https://doi.org/10.1038/scientificamerican0384-98.

Yoshie T, Scherer A, Heindrickson J, Khitrova G, Gibbs HM, Rupper G, Ell C, Shchekin OB, and Deppe DG (2004) Vacuum Rabi splitting with a single quantum dot in a photonic crystal nanocavity. *Nature* 432: 200. https://doi.org/10.1038/nature03119.

Zhang Y, Chang T-R, Zhou B, Cui Y-T, Yan H, Liu Z, Schmitt F, Lee J, Moore R, Chen Y, Lin H, Jeng H-T, Mo S-K, Hussain Z, Bansil A, and Shen Z-X (2014a) Direct observation of the transition from indirect to direct bandgap in atomically thin epitaxial $MoSe_2$. *Nature Nanotechnology* 9: 111. https://doi.org/10.1038/nnano.2013.277.

Zhang YJ, Oka T, Suzuki R, Ye JT, and Iwasa Y (2014b) Electrically switchable chiral light-emitting transistor. *Science* 344: 725. https://doi.org/10.1126/science.1251329.

Optical properties of surface enhanced Raman scattering[☆]

G Mattei[a] **and SN Aqida**[b], [a]CNR, Istituto dei Sistemi Complessi, Rome, Italy; [b]Automotive Engineering Centre, Universiti Malaysia Pahang, Pekan, Pahang, Malaysia

© 2024 Elsevier Ltd. All rights reserved.

This is an update of G. Mattei, Optical Properties of Surface Layers Enhanced Raman Scattering, Editor(s): Franco Bassani, Gerald L. Liedl, Peter Wyder, Encyclopedia of Condensed Matter Physics, Elsevier, 2005, Pages 191–200, ISBN 9780123694010, https://doi.org/10.1016/B0-12-369401-9/00604-5.

Introduction 728
The origin of the enhancement of Raman intensities 728
Flat metal surface: Raman enhancement and surface selection rules 729
Electromagnetic enhancement due to surface plasmons and surface electromagnetic waves: Flat and roughed surfaces 730
Electromagnetic enhancement due to metal particles 733
Surface-enhanced Raman scattering 735
Conclusion 738
References 738
Further reading 738

Abstract

This article elaborates on surface-enhanced Raman scattering (SERS) technique, increase of Raman scattering due to various factors namely; chemical effect, charge transfer, resonance, electromagnetic field amplification. The electromagnetic enhancement mechanism is caused by the electric field from the surface, surface plasmons excitation and surface electromagnetic waves. SERS technique increased the Raman intensity by factors up to 10^{15} using recent hybrid substrate materials such as graphene-based 2D and 3D nanostructures of silver and gold.

Key points

- The effects of electromagnetic (e.m.) amplification on Raman scattering.
- Electromagnetic enhancement for flat and rough surface, metal particles and clusters.
- Nanostructures in surface-enhanced Raman scattering.

Introduction

The subject of this article is the description of the properties of metal surfaces and metal particles that are sources of strong enhancement of the intensity of the scattered Raman light from molecules and thin films, which are in contact with them or in their close vicinity in the nanoscale range. First, the origin of the enhancement of the Raman intensity is discussed showing that the main source of the effect is the amplification of the electromagnetic (e.m.) field at the interface of two media (e.g., metal/dielectric), when surface e.m. waves and/or surface or localized plasmons are excited. The cases of flat and corrugated metal surfaces, single metal particles, and metal clusters are discussed. The last section is devoted to the illustration of the surface-enhanced Raman scattering (SERS), commonly characterized by enhancement of the Raman intensity of 4–8 orders of magnitude, and originated from metal (e.g., Au, Ag, Cu) surfaces which are rough on nanoscale (10–100 nm) and from metal nanoparticles and nanoclusters. Not all the subjects are treated in detail since some of them are presented exhaustively in other articles of this encyclopedia.

The origin of the enhancement of Raman intensities

As it is well known, Raman scattering is a nonlinear process (e.g., two photons and one quantum of vibration are involved) which is characterized by a very low cross-section, σ (in m^2), defined by the relation: $P_{SC} = \sigma I_{in}$, where P_{SC} is the power (in W) of the scattered light and I_{in} is the intensity of the exciting light (in Wm^{-2}). For the normal Raman scattering, the cross-section (average value $\approx 10^{-33}$ m^2) is nine orders of magnitude smaller than that of the infrared absorption process and this prevents the detection of a very small amount of material as it is necessary, for example, in surface science. To achieve the surface sensitivity (detection limit of a fraction of the monolayer), some enhancement in the process is necessary. Two mechanisms are possible sources of this

---

[☆] Change History: March 2022. S.N. Aqida updated abstract; add keypoints and summary, expanded text with additional review materials; updated list of reference; updated History.

https://doi.org/10.1016/B978-0-323-90800-9.00056-1

enhancement. The first one is related to the cross-section itself. In some systems, molecules as well as crystals and films, at special frequencies σ present a resonant behavior due to the direct absorption of the incident photons by suitable electronic levels coupled with vibrational states. In this condition, that is, resonant Raman scattering, the intensity of the scattered light can be enhanced up to six orders of magnitude. In some cases, chemisorption on metal is accompanied by the formation of new electronic levels in the visible range for the adsorbate/metal system, allowing the resonant Raman scattering to occur. Of course, this resonant process (average enhancement factor 100), often indicated as "chemical effect," is strongly dependent on the frequency of the exciting light and is specific to the excited system. The second source of Raman intensity amplification is related to the enhancement of the local electric field seen by the excited medium (e.g., adsorbed molecules on a metal surface or on a small metal particle). Indeed I_{in} being proportional to the square of the electric field amplitude of the excitation light, an increase of this amplitude by a factor 10^2 implies an enhancement of the Raman intensity by a factor 10^4, for example. This enhancement mechanism of the Raman intensity, called "electromagnetic effect," is somehow independent of the excited system and presents some specificity that allows one to discriminate it from the "chemical effect." Of course, in some cases, both effects can contribute to the total Raman enhancement. The following sections illustrate the e.m. effect through the use of system models, namely various metal surfaces. Undoubtedly, the properties of the surface itself play an important role in the Raman enhancement. Among them, the surface shape and size, and also the frequency-dependent dielectric function of the metal, have to be considered.

Flat metal surface: Raman enhancement and surface selection rules

Consider the case of molecules adsorbed (or in the near proximity) on a flat metal mirror where an e.m. wave, impinging on with an angle of incidence θ, is reflected (Fig. 1) (Mattei, 2005).

The molecules see a local electric field at surface, E^{su}, that is due to the coherent superposition of the electric fields E^{i} and E^{r} of the incident and the reflected e.m. waves. Considering the two polarizations, s (TE) and p (TM), one has, for the x, y, and z components of the local field,

$$E_x^{\mathrm{su}} = E_{s,0}^{\mathrm{i}}(1 + r_s)$$
$$E_y^{\mathrm{su}} = E_{p,0}^{\mathrm{i}}\left(1 - r_p\right)\cos(\theta)$$
$$E_z^{\mathrm{su}} = E_{p,0}^{\mathrm{i}}\left(1 + r_p\right)\sin(\theta)$$

where $E_{s,\,0}^{\mathrm{i}}$ and $E_{p,\,0}^{\mathrm{i}}$ are the components of the incident electric field of s (TE) and p (TM) polarization, and r_s and r_p are the Fresnel coefficients, being:

$$r_s = \left[\cos(\theta) - \left(\varepsilon - \sin^2(\theta)\right)^{1/2}\right] / \left[\cos(\theta) + \left(\varepsilon - \sin^2(\theta)\right)^{1/2}\right]$$

$$r_p = \left[\varepsilon\cos(\theta) - \left(\varepsilon - \sin^2(\theta)\right)^{1/2}\right] / \left[\varepsilon\cos(\theta) + \left(\varepsilon - \sin^2(\theta)\right)^{1/2}\right]$$

It is to be noted that the dielectric function $\varepsilon(\omega)$ is a complex function of the frequency ω (here the dependence on the wave vector of the light is neglected). In the case of metals, the real part $\mathrm{Re}[\varepsilon(\omega)]$ can be strongly negative below the plasma frequency ω_{p} and almost zero around ω_{p}. It is easy to demonstrate that when $|\varepsilon|$ is very large, $r_s \to -1$ and $r_p \to +1$; it is just the opposite in the limit of very small $|\varepsilon|$, $r_s \to +1$ and $r_p \to -1$.

In the light scattering process, the local electric field $E^{\mathrm{su}}(\omega_{\mathrm{ex}})$ induces on the molecules at the surface a dipole moment $\boldsymbol{\mu}$, given by: $\boldsymbol{\mu}(\omega_{\mathrm{sc}}) = \alpha E^{\mathrm{su}}(\omega_{\mathrm{ex}})$, $\widehat{\alpha}$, the polarizability of the molecules being a tensor of the second rank. The frequencies ω_{ex} and ω_{sc} are those of the incident and scattered light, respectively. $|\omega_{\mathrm{ex}} - \omega_{\mathrm{sc}}| = \omega_{\mathrm{vibr}}$ is the frequency of the normal vibrational mode of the molecule involved in the scattering process. The scattered light, collected along a direction θ' far away from the surface, is then the superimposition of the light emitted directly in this direction together with the scattered light directed toward the metal surface

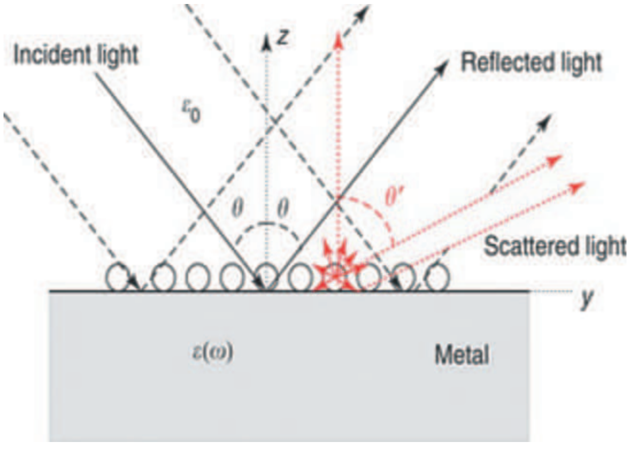

Fig. 1 Scheme of the Raman scattering of molecules (circles) adsorbed on the flat interface between a dielectric and a metal. Reproduced from Mattei G. (2005) Optical properties of surface layers enhanced Raman scattering. In: Bassani F., Liedl G.L., Wyder P. (eds.) *Encyclopedia of Condensed Matter Physics.* Elsevier.

and then reflected in the same direction (Fig. 1). Hence, the intensity of the scattered light, that is proportional to the square of the amplitude of the scattered electric field, will be affected by two surface contributions due to the reflection of the incident and of the scattered light as well. From the above expressions, the Raman intensities for the possible polarization (*s* and/or *p*) of the incident and scattered light can be obtained:

$$I_{\mathrm{ss}} \propto \omega_{\mathrm{sc}}^4 \left|\alpha_{xx}(1+r_s)(1-r_s')\right|^2$$

$$I_{\mathrm{ps}} \propto \omega_{\mathrm{sc}}^4 \left|\alpha_{xy}(1-r_p)(1+r_s')\cos(\theta)+\alpha_{zy}(1+r_p)(1+r_s')\sin(\theta')\right|^2$$

$$I_{\mathrm{sp}} \propto \omega_{\mathrm{sc}}^4 \left|\alpha_{yx}\left(1+r_s\right)\left(1-r_p'\right)\cos(\theta')+\alpha_{zx}(1+r_s)\left(1+r_p'\right)\sin(\theta')\right|^2$$

$$I_{\mathrm{pp}} \propto \omega_{\mathrm{sc}}^4 \left|\left[\alpha_{\mathrm{yy}}(1-r_p)\cos(\theta)+\alpha_{\mathrm{yz}}(1+r_p)\sin(\theta)\right]\left(1-r_p'\right)\cos(\theta')+\left[\alpha_{\mathrm{zy}}(1-r_p)\cos(\theta)+\alpha_{\mathrm{zz}}(1+r_p)\sin(\theta)\right]\left(1+r_p'\right)\sin(\theta')\right|^2$$

In these equations, all the quantities including the Raman polarizability components are referred to the frame of axis indicated in the figure with *z* along the metal surface normal. The primes indicate those quantities that are to be evaluated at the frequency and angle of the scattered light. It is clear that the observed scattered intensity depends in a quite complex way on the chosen scattering geometry (through the angles, the polarizations, and the Fresnel coefficients), the optical properties of the metal (through its frequency-dependent dielectric function), the symmetry of the molecular vibration, and the orientation of the molecule with respect to the surface (through the α_{ij} components of the polarizability). These relations determine the surface selection rules that control the Raman scattering of molecules adsorbed or posed on a flat metal surface. According to these selection rules, the Raman spectra can be very different from those of free molecules: the relative band intensities can be altered, some band can be strongly attenuated, others can be enhanced with respect to the free molecules. Even the dependence on the scattering frequency of the Raman intensity for single modes can deviate significantly from the ω^4 rule typical of the Raman scattering of free molecules. Finally, it is easy to verify that the maximum expected enhancement of the Raman intensity for any mode is 16 but for real systems, this value is seldom obtained, while enhancement values around 6–10 can be usually measured on flat metal mirrors.

Electromagnetic enhancement due to surface plasmons and surface electromagnetic waves: Flat and roughed surfaces

As it is well known, at the vacuum/metal interface, surface collective charge modes, named surface plasmons (sp), polaritons do exist. They are evanescent waves produced by the oscillations of the surface charges, and propagate along the interface with a real wave vector *K*, given by

$$K=(\omega/c)\sqrt{\varepsilon_0\varepsilon/(\varepsilon_0+\varepsilon)}$$

In this equation, which represents the sp. dispersion curve (ω vs K), ε_0 and ε are the dielectric function of the dielectric (e.g., the air) and of the metal, respectively. No radiation is emitted from the surface in the two semispaces. The electric field that can be very intense at the surface, decays exponentially with the distance from the interface. Indeed, the components of the wave vector perpendicular to the surface are basically purely imaginary being: $K_\perp = \mathrm{i}(\omega/c)\left|\varepsilon_\mathrm{i}^2/(\varepsilon_0+\varepsilon)\right|^{1/2}$, where ε_i is equal to ε_0 in the dielectric medium and to ε in the metal, respectively.

The sp. condition of existence and their dispersion curve are illustrated in Fig. 2, where for simplicity the metal dielectric function, ε, has been approximated with that of a free electron gas, namely: $\varepsilon = 1-(\omega_\mathrm{p}/\omega)^2$. In the figure, "reduced" adimensional quantities have been used for frequency, ω/ω_p, and surface wave vector, cK/ω_p.

It is clear from the comparison of the frequency dependences of the dielectric function and of the sp. dispersion that sp. do exist only for $\omega < \omega_\mathrm{p}$, where the bulk modes cannot propagate in the metal, being $\varepsilon < 0$. For large K values, the sp. polaritons dispersion curve tends to frequency $\omega_\mathrm{p}/(1-\varepsilon_0)^{1/2}$ for which it is $\varepsilon = -\varepsilon_0$. Since the sp. are not radiative modes, they cannot be directly excited

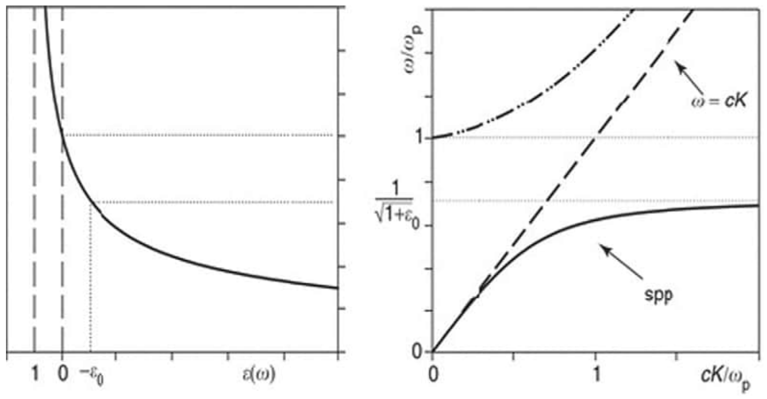

Fig. 2 On the left, dielectric function vs reduced frequency, ω/ω_p, (ω_p is the plasma frequency) for a metal in the free electron gas approximation; on the right, surface plasmon polaritons (spp) dispersion curve for the metal/dielectric interface. *K* is the real wave vector parallel with the surface. The dashed straight line represents the photon dispersion in vacuum. Reproduced from Mattei G. (2005) Optical properties of surface layers enhanced Raman scattering. In: Bassani F., Liedl G.L., Wyder P. (eds.) *Encyclopedia of Condensed Matter Physics.* Elsevier.

by light propagating in one of the two media. Indeed, for a given frequency ω, the component parallel to the surface, $k_{||}$ of the light wave vector will be always smaller than the corresponding component, K, of the sp. wave vector. As a matter of fact, it is always $k_{\|} = (\omega/c)\varepsilon_0^{1/2} \sin \theta_i < (\omega/c)\varepsilon_0^{1/2} < K$, where θ_i is the angle of incidence of the light on the metal surface.

Hence, the conditions for the energy and wave vector conservation cannot be simultaneously satisfied. Nevertheless, sp. excitation by light can be obtained in special conditions, namely: by grating coupling and in attenuated total reflection (ATR) geometry.

When a metal surface is sinusoidally modulated with a period d to form a grating, if the amplitude of the modulation is small compared with the wavelength of light, there is a modification of the light wave vector parallel to the surface, $k_{||}$, into $K_n = (k_{\|} + 2\pi n/d)$ with $n = 0, \pm 1, \pm 2$, etc. It is then possible that, for suitable value of θ and n, the coupling condition, $K_n = K$, be satisfied, allowing the sp. excitation by light radiation (Fig. 3).

Wood anomalies in gratings, experimentally well known since the beginning of the twentieth century, can be attributed to this effect. Besides, sp. can have their wave vector modified by a surface modulation and become radiative waves. On this basis, it is clear that a rough metal surface can allow to some extent the excitation of sp. waves by light and their radiative emission.

Another way to excite sp. is the use of a prism in total reflection condition to generate surface e.m. evanescent waves that can couple with the spp. modes. The ATR in the so-called "Otto configuration" is illustrated in Fig. 4a, where a prism (dielectric constant ε_p) is separated by a thin layer of thickness d and dielectric constant $\varepsilon_0 < \varepsilon_p$ from a metal surface S. If a light beam strikes the interface prism/interlayer at an angle of incidence θ_i greater than the critical angle $\theta_c = \arcsin (\varepsilon_0/\varepsilon_p)^{1/2}$, total reflection occurs: no light is transmitted in the ε_0 medium. At the interface, an evanescent e.m. wave is produced with real wave vector parallel to the surface $k_{\|} = (\omega/c)\varepsilon_p^{1/2} \sin \theta_i > (\omega/c)\varepsilon_0^{1/2}$ and perpendicular wave vector component purely imaginary in

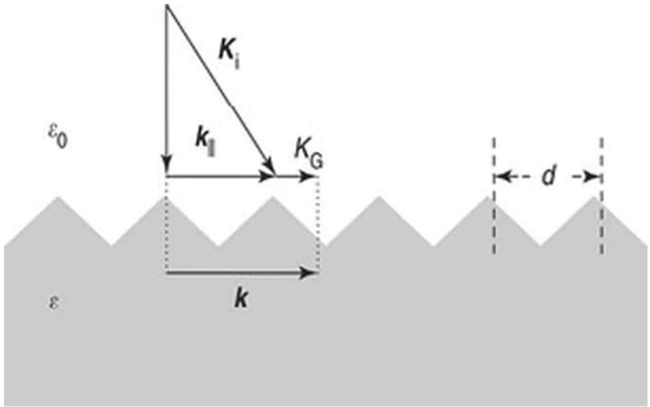

Fig. 3 Scheme of the spp. excitation of a metal grating of period *d* by incident light of wave vector K_i. $K_G = (2\pi n/d)$ is the surface wave vector due to the grating. $K_{\|}$ are the surface wave vectors parallel to the surface of the incident light and of the spp. excitations. Reproduced from Mattei G. (2005) Optical properties of surface layers enhanced Raman scattering. In: Bassani F., Liedl G.L., Wyder P. (eds.) *Encyclopedia of Condensed Matter Physics.* Elsevier.

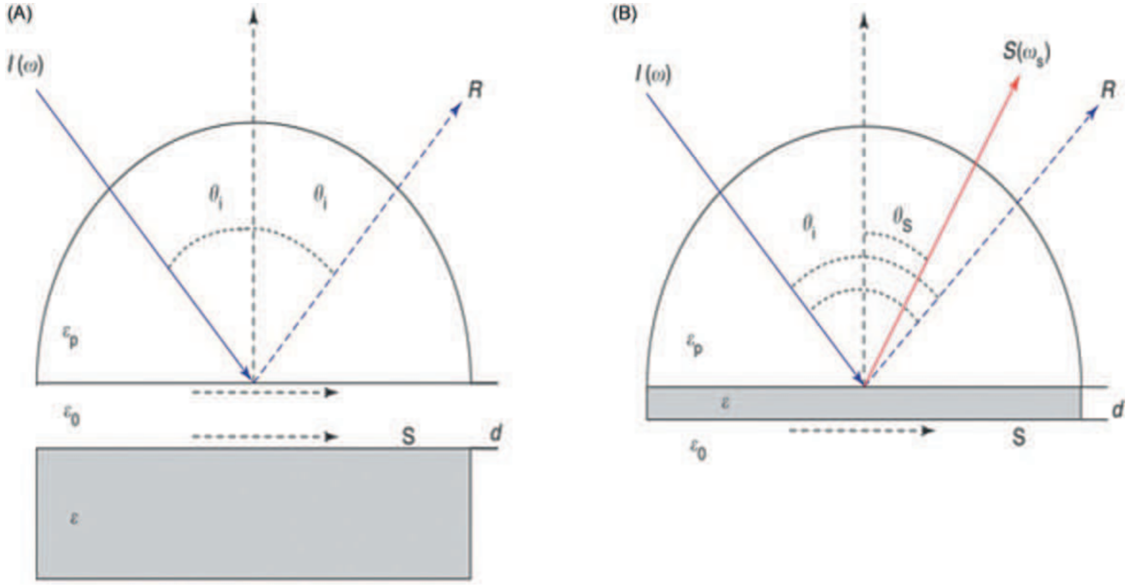

Fig. 4 ATR geometries: (a) Otto configuration, (b) Kretschmann configuration: I, R and S represent the incident, the reflected, and the scattered beams, respectively; *d* is the thickness of the interlayer between prism and metal (a) or of the metal film (b). Reproduced from Mattei G. (2005) Optical properties of surface layers enhanced Raman scattering. In: Bassani F., Liedl G.L., Wyder P. (eds.) *Encyclopedia of Condensed Matter Physics.* Elsevier.

the ε_0 media. The amplitude of the electric field decays rapidly in the interlayer, but, if the thickness d is of the order of the wavelength, the surface e.m. waves can interact with the sp. evanescent waves generated at the interface metal/interlayer when the wave vector ($k_{\parallel} = k$) and the frequency ($\omega_{\text{light}} = \omega_{\text{spp}}$) conservation laws are satisfied. When this resonant coupling occurs, the intensity of the reflected beam, R, is attenuated or "frustrated" allowing the detection of sp. modes.

Since both the Snell's law (i.e., the conservation of the parallel component of the wave vector at the interface) and the dispersion relation of sp. are symmetrical with respect to ε_0 and ε, it is possible to interchange the role of these two media with respect to the prism. This is shown in Fig. 4b where the ATR in the so-called "Kretschmann configuration" is illustrated. The thickness d of the thin metal film must be sufficiently small to allow enough energy to reach the metal/dielectric interface. Again, attenuation of the intensity of the reflected light as a function of the frequency and of the angle of incidence allows the detection of sp. waves.

Calculated angular dependence of the reflectivity at 530 nm as a function of the angle of incidence in the Kretschmann configuration (prism ($\varepsilon_p = 2.1$), metal film ($\varepsilon = \varepsilon' + \varepsilon'' = -17.35 + i0.56$), air ($\varepsilon_0 = 1$)) are presented in Fig. 5a for different values of d. The minimum of the reflectivity, corresponding to the excitation of the sp. at the interface metal/air, is deepest for an optimal film thickness. Note that the angle and the angular width of this minimum depend on the thickness, because in the case of thin film the sp. modes of the two interfaces fill each other, and influence and modify the corresponding dispersion curves depending on the distance d between the interfaces.

An important consequence of the excitation of the sp. waves by ATR is that the intensity of the electric field at the metal/dielectric (metal/air, in this case) interface can be significantly larger than that of the incident e.m. wave. As an example, in Fig. 5b, the field intensity enhancement, namely the ratio between the intensity of the electric field at the metal/air interface and the one of the incident wave at the prism/metal interface, is reported as a function of the angle of incidence, for the case of Fig. 5a. As it is clear, in the optimal condition, an enhancement of two orders of magnitude can be achieved. As a consequence, enhanced Raman scattering from molecules adsorbed on the metal/air interface can be excited in this configuration. Considering that the scattered light can be also converted in sp. excitations and, through the ATR system, into light emitted in the prism at a suitable angle, a final enhancement of about four orders of magnitude can be obtained. Indeed, in the literature, several experimental evidences of enhanced Raman scattering using ATR configuration, with the enhancement factor ranging from a few tens to ten thousand, have been reported. For example, studies by enhanced Raman spectroscopy of metal/liquid interfaces and Langmuir–Blodget layers on smooth Ag surfaces have been reported. Using Langmuir–Blodgett technique, modifying sizes and shapes of nanoparticles shapes into nanostars, nanorods and nanospheres produced optimal performance that tuning plasmonic coupling (Tahghighi et al., 2020; Tim et al., 2022).

Besides, a combination of ATR spp. excitation and near-field Raman spectroscopy has been used to scan, with high sensitivity, the species present on the electrode surfaces.

Finally, for completeness, it is important to note that the conversion of traveling e.m. waves into surface evanescent e.m. waves can be used to enhance Raman scattering intensity at the interface between two dielectric media, when the exciting light strikes the interface from the denser medium in total reflection condition. As a matter of fact, the Raman scattering excited in a total reflection condition has been used for studying adsorbates, films, and even the surface phonon-polaritons dispersion at the interface between a prism and a transparent crystal.

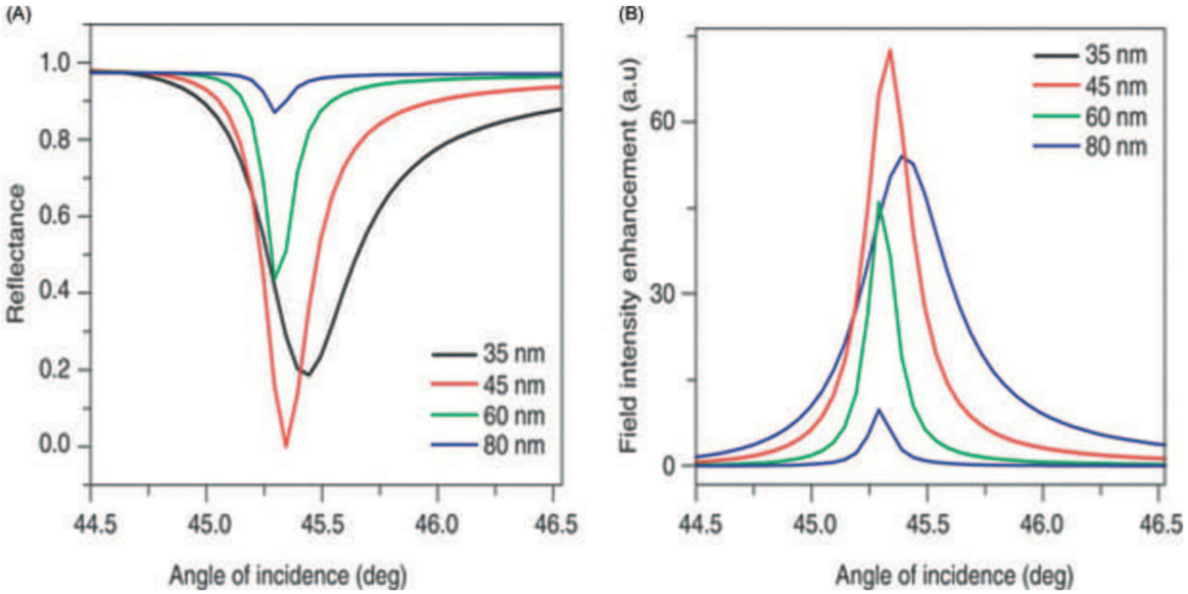

Fig. 5 ATR in the Kretschmann configuration, wavelength 530 nm. (a) Angular dependence of the reflectivity in the prism for various Ag film thicknesses. (b) Angular dependence of the electric field intensity at the air/metal interface for various Ag film thicknesses. Reproduced from Mattei G. (2005) Optical properties of surface layers enhanced Raman scattering. In: Bassani F., Liedl G.L., Wyder P. (eds.) *Encyclopedia of Condensed Matter Physics.* Elsevier.

Electromagnetic enhancement due to metal particles

The following case is considered first, that is, the case of single isolated metal sphere of radius R, small with respect to the light wavelength λ: that is, R'' λ ("Rayleigh limit" or "electrostatic approximation"). If such a sphere, of dielectric function $\varepsilon(\omega)$ and embedded in a medium of dielectric function ε_0, is irradiated by an e.m. wave with electric field amplitude E_i polarized in the z direction (see scheme in Fig. 6), a dipole moment $p = gR^3E_\mathrm{i}$ is generated inside the sphere. The potential, V, outside the sphere, due to the incident electric field and the electric dipole p, expressed in spherical coordinates (r, θ, φ), is

$$V(r,\ \theta) = E_\mathrm{i}\left(r - gR^3/r^2\right)\cos(\theta)$$

where $g = (\varepsilon - \varepsilon_0)/(\varepsilon + 2\varepsilon_0)$. The radial, E_n, and tangential, E_t, components of the electric field at the surface of the sphere can be obtained in a standard way from the potential. The intensity of the two electric components, averaged over all the solid angle, are proportional to

$$\overline{E}_n^2 \propto |1 + 2g|^2$$
$$\overline{E}_\mathrm{t}^2 \propto 2|1 - g|^2$$

Because of the resonant denominator in g, when it is $\mathrm{Re}[\varepsilon(\omega)] = -2\varepsilon_0$ (condition of excitation of localized sp. of the metal sphere) and the $\mathrm{Im}[\varepsilon(\omega)]$ is small (as in the case of coinage metals), the electric field intensity at the surface of the metal particle can be much larger that of the incoming radiation.

Let the light scattering process be considered now, assuming that the molecules are adsorbed on the spherical metal particle with the z-axis of the molecule-fixed coordinate frame along the normal to the surface. The average Raman intensity can be simply considered as dependent on the average intensity of the incident and scattered fields. The metal particle enhances not only the incident electric field on the molecule, but also the Raman scattered field. It acts as an antenna, through the dipole induced in it by the molecular dipole, which amplifies the scattered light intensity. Considering the polarizability tensor of the molecule, three kinds of vibrations can be distinguished. The α_{zz}-type modes require a radial field, E_n, to be excited and produce an induced dipole with only a radial component. Hence, the average intensity due to only the radial electric field will contribute twice to the detected Raman intensity: once in excitation and once again in emission. Similar considerations can be made for the other two kinds of modes, $\alpha_{xx}, \alpha_{yy}, \alpha_{xy}$ (only tangential components), and $\alpha_{xz}\alpha_{yz}$,(mixture of tangential and radial components).

The intensity of enhanced Raman spectra of these kinds of modes will therefore depend on the frequency through the following functions:

$$\alpha_{zz}\ -\text{type}$$
$$\overline{E}_n^2\overline{E}'^2_n \propto |1 + 2g|^2|1 + 2g'|^2$$
$$\alpha_{zz}, \alpha_{yy}, \alpha_{xy},\ -\text{type}$$
$$\overline{E}_n^2\overline{E}'^2_n \propto |1 - g|^2|1 - g'|^2$$
$$\alpha_{xy}, \alpha_{yz},\ -\text{type}$$
$$\frac{1}{2}\left(\overline{E}_n^2\overline{E}'^2_t + \overline{E}_t^2\overline{E}'^2_n\right)$$
$$\propto \left[|1 + 2g|^2|1 - g'|^2 + |1 - g'|^2|1 + 2g'|^2\right]$$

where the prime indicates quantities to be evaluated at the frequency of the scattered light. In Fig. 7 the dependence on the frequency of these functions is presented for a fictitious free-electron metal particle. For simplicity, it has been considered that ε_0 and $g = g'$.

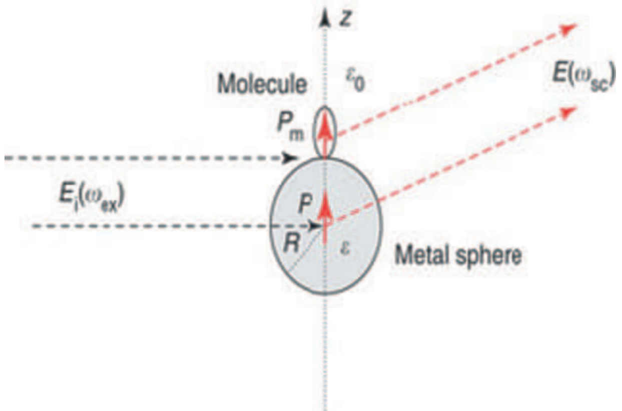

Fig. 6 Scheme of the Raman scattering from a molecule adsorbed on a metal spherical particle of radius R. E_i and E indicate the electric field of the incident and of the scattered light, respectively; p_m and p are the electric dipole induced in the molecule and in the metal particle, respectively. Reproduced from Mattei G. (2005) Optical properties of surface layers enhanced Raman scattering. In: Bassani F., Liedl G.L., Wyder P. (eds.) *Encyclopedia of Condensed Matter Physics.* Elsevier.

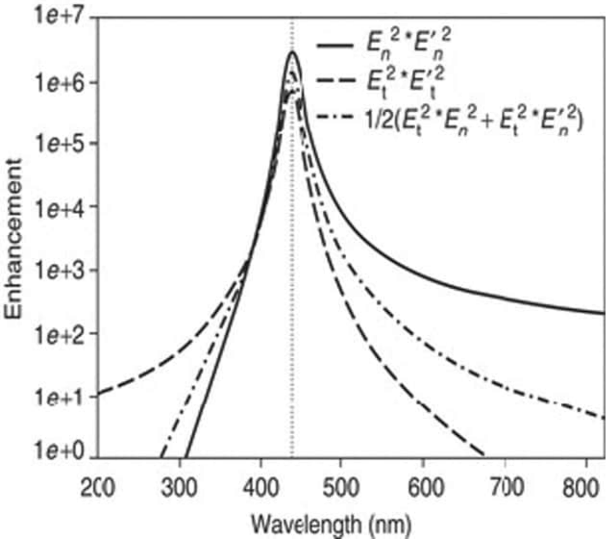

Fig. 7 Wavelength dependence of the enhancement factors for the three kinds of molecular modes for a molecule adsorbed on a metal particle of radius R in the Rayleigh limit (R' wavelength of the exciting light). Reproduced from Mattei G. (2005) Optical properties of surface layers enhanced Raman scattering. In: Bassani F., Liedl G.L., Wyder P. (eds.) *Encyclopedia of Condensed Matter Physics.* Elsevier.

As expected, all three functions have a sharp maximum (corresponding enhancement factor 10^6) at a wavelength for which Re $[\varepsilon(\omega)] = -2$. Besides, at longer wavelengths, the α_{zz}-type modes dominate in the Raman spectrum, whereas at lower wavelengths all the modes are almost equally enhanced. It is clear that the number and the relative intensity of the bands present in the enhanced Raman spectrum can vary significantly with the frequency of the excitation light. Indeed, often very rich spectra can be measured with the distribution of the intensity that apparently violates the surface selection rules.

The model discussed above, although quite simple, provides the main features associated with the enhanced Raman scattering of molecule adsorbates on small metal particles. A more realistic model must include the effects of the particle shape and size distribution.

As the particle size increases beyond the Rayleigh regime, the used electrostatic approximation is not longer valid. The computer-intensive Lorenz–Mie or electrodynamics formalism, which accurately accounts for the effects due to the phase retardation and the quadrupole and higher order poles, must be used to obtain an exact solution. Also the conversion of the near-field electric field due to the molecule through the metal particle acting as an antenna into far-field radiation must be then taken into account. Generally, as a consequence, the intensity enhancement of the Raman scattered radiation can be significantly reduced.

Considering the shape effect, in the case of an isolated spheroid of eccentricity b/a (a and b being the length of the short and the long principal axis, respectively), in presence of an external electric field (due to an e.m. wave) oriented along the b-axis, it can be demonstrated that the Raman enhancement is always larger for the more aspherical particles. In the limiting case of $(b/a) \to \infty$, the calculated enhancement at the tip positions can be of some order of magnitude larger than for the case of spherical particles ("lightning rod effect").

Finally, to treat the case of interacting metal particles and of metal clusters that are also of great practical relevance, various model systems have been considered, for example, two interacting metal spherical particles ("bispheres"), aggregates of metal spheres, set of parallel metal cylinders of variable diameter and interdistance, etc. The calculation of the optical properties of these systems and of the effects on the Raman scattering is generally quite complex and can include retardation effects and high-order multipoles. The general result is that the interaction between two plasmon-resonant nanoparticles leads to additional resonances (at longer wavelengths) for the coupled system. Besides, the electric field in the gap between the particles or around the contact region (for two contacting particles) can be much strong in other places near the particles and stronger than in any place around an isolated particle. Hence, the Raman enhancement can be much larger than for isolated metal nanoparticles. Indeed, enhancement value as large as 10^8–10^9 has been predicted for such metal systems.

It has been recognized early that small-particle composites, or disordered clusters present in metal colloidal solution, as well as some rough metal surface have a fractal character. Studies have been developed to relate the enhancement of the local electric fields in these systems with their fractal dimension. An interesting example is illustrated in Fig. 8, where the calculated dependence on the wavelength, λ, of the local electric field enhancement factor for three systems made by 500 metal spherical nanoparticles ($d''\lambda$) is presented.

In the case of a gas of spherical particles (RGP curve), the characteristic sharp feature due to the excitation of the sp. in isolated spheres is clearly observed below 400 nm. The absence of other features above that wavelength indicates a very lithe interaction among the particles. For the ordered particle aggregate (CPSP curve), the single-particle excitation is attenuated and the enhancement increases in the long-wavelength region of the spectrum as a result of the mutual particle interactions. Clearly, the largest enhancement in the local field, up to 10^3 times the one of isolated particle, is predicted for the fractal system (CCA curve). On this basis, huge enhancement factors for the intensity of Raman scattering from molecules on fractal systems can be expected.

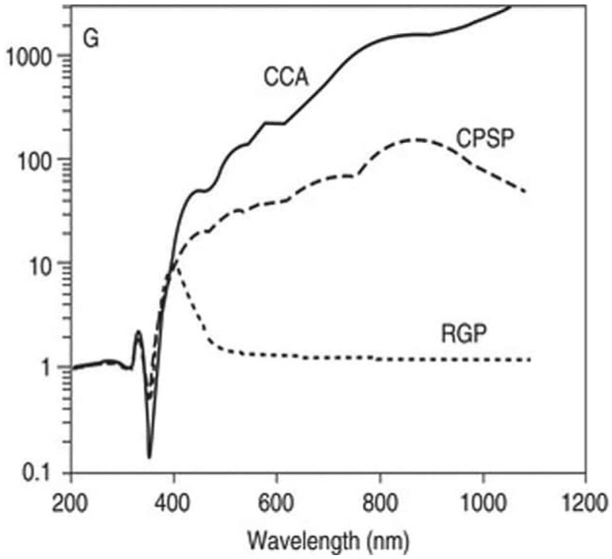

Fig. 8 Wavelength dependence of the averaged local field intensity for a gas of spherical particles (RGP), a close-packed crystal of spherical particles (CPSP), and a fractal aggregate (CCA). Reprinted from Shalaev V.M. Electromagnetic properties of small-particles composites. *Physics Reports* 272: 61–137, Copyright (1996), with permission from Elsevier.

Surface-enhanced Raman scattering

SERS was discovered, although not recognized as such, by M Fleishman and co-workers in 1974. They observed an intense Raman signal from pyridine adsorbed onto a roughened silver electrode surface from an aqueous solution. They attributed, erroneously, the observed enhancement of the Raman signal to an increase of the surface area due to the roughening process. In 1977, the nature of this enhancement was attributed by D L Jeanmair and R V Van Duyne, and independently by M G Albert and J A Creighton to a new phenomenon related with the increase of the effective Raman cross section of adsorbates on some rough metal surfaces. Since then, many studies and works have being carried out to understand the fundamental aspects as well as to exploit all the applicative potentialities related with SERS. A wide variety of metal substrates have been found to exhibit SERS: electrochemically roughened electrodes, chemically etched surfaces, colloids (especially aggregated colloids), island films, particles grafted on silanized glasses, regular particle arrays, hybrid, etc. The dominant metals in SERS are the coinage (Cu, Au, Ag) and alkali (Li, Na, K) metals. Moreover, although with lower enhancement, transition metals (e.g., Pt, Ru, Rh, Pd, Fe, Co, Ni and their alloys) have also been used. Generally, the observed enhancement ranges from 10^4 up to 10^8 in standard SERS measurements. The largest enhancement occurs for surfaces which are rough on the nanoscale (10–100 nm).

Advances in nanofabrication transpired different types of SERS substrates, such as Ag nanospheres, nanorods and nanostars (López-Lorente, 2021; Tahghighi et al., 2020), hexagonal nanopatterns (Chakraborty et al., 2021), dimple nanostructures/ nano-bowls (Li et al., 2021; Yang et al., 2022), 3D hybrids nanostructures (Mehrvar et al., 2017), (Geng et al., 2021) that produced high-density hot spots, leading to a strong Raman signal. Specifically in solar cells panel application, hybrid nanostructures substrate resulted in ultra-high electromagnetic field enhancement where Ag nanoparticles decorated silicon double nanocones (Si-DNCs) array could produce 22 times stronger SERS signal than crystalline Si (Mehrvar et al., 2017). This is also achievable in the deposition of Ag nanoparticles on Au-coated surface textured monocrystalline Si solar cell substrates. Thicker Au coating on textured Si increases Raman intensity between 1400 and 1800 cm^{-1} wavenumber due to the chemical enhancement of Rhodamine 6G (R6g) molecular charge transfer, as shown in Fig. 9 (Li et al., 2020).

In Lofrumento et al. (2015), for molecules adsorbed on the surface of a metal nanoparticle, the Raman signal can be enhanced by factors as high as 10^{15} caused by combined effects of strong local field and direct chemical interactions.

Composite SERS substrate combines graphene-based with noble metallic nanostructure (nanoparticles, nanoshells, nanowires, nanodots and nanoporous films) (Zhao et al., 2015; Li et al., 2015; Ding et al., 2015).

Graphene oxide (GO) has excellent electronics and structural properties and has been used as a substrate for enhancing Raman scattering of adsorbed analyte molecules. GO-based SERS decorated with noble metallic nanoparticles allow combination of electromagnetic mechanism and chemical mechanism effects (Li et al., 2015).

Enhanced SERS activities are also found in GO nanosheet-silver nanoparticles composites and gold nanoparticles on graphene sheets hybrids (Ding et al., 2015; Lee et al., 2014). Furthermore, developing 3D hybrid substrates has created more hot spots in nanoparticle–nanoparticle junctions which can be comprised of different sizes and geometry such as nanosphere and nanooctahedra. (Kaushik et al., 2022). Dimple nanostructures enhanced the absorption of incident light and generated multiple hotspots that occurred in nano-tips gaps (at the top of the structure) of less than 10 nm which significantly amplify Raman signals (Li et al., 2021; Yang et al., 2022).

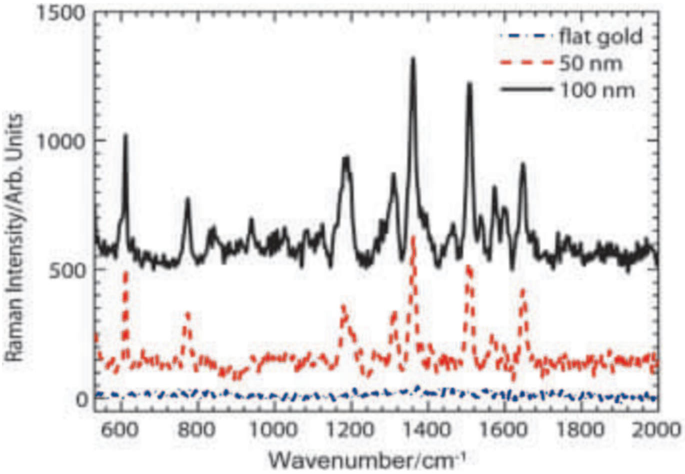

Fig. 9 SERS spectrum of R6G on the (50 nm and 100 nm) gold-coated flat bulk silicon and surface textured monocrystalline silicon solar cell substrates. Reprinted from Li R., Lei J., Zhou Y., Li H. Hybrid 3D SERS substrate for Raman spectroscopy. *Chemical Physics Letters* 754: 137733, Copyright (2020), with permission from Elsevier.

Semiconductors such as TiO_2 and ZnO have been used as SERS-active substrates, (reviewed by Zhao et al., 2015). In fact, TiN nanorods can produce electromagnetic field enhancements similar to those of gold nanostructure (Zhao et al., 2015).

The main observed features of SERS spectra are the followings: (1) the intensities of the bands generally fall off with increasing vibrational frequency (e.g., C-H stretching vibrations are relatively weak, overtones and combination bands are seldom observed), (2) selection rules are relaxed, even forbidden Raman modes can be detected, (3) the spectra tend to be completely depolarized, (4) excitation profiles differ from the dependence on the fourth power of the frequency, ω_{in}^4, typical of nonresonant Raman scattering, and (5) although the enhancement is mainly concentrated on the first layer of adsorbates, often the effect can extend to a quite long range (up to tens of nanometers).

As suggested before, two mechanisms must be considered to explain SERS, namely the e.m. and the chemical effects. Previous sections describe the foundation of the e.m. effect of the SERS, since the behavior and the properties of metal substrates and particles that sustain the SERS effect can be described using the models presented there. First of all, the dominance of the coinage metals arises from the optical properties of these metals as indicated for Ag in Fig. 10.

Indeed, the resonance condition with the sp. (e.g., $\text{Re}[\varepsilon(\omega)] = -2\varepsilon_0$) is satisfied at visible frequency generally used for Raman spectroscopy. Besides, the imaginary part of the dielectric function, $\text{Im}[\varepsilon(\omega)]$, which is related with losses in the material, is very small at the resonance frequency, thus allowing strong enhancement of the local electric field on the rough surface and colloidal particle made with these metals.

The e.m. model explains many of the experimental features of SERS listed above, including the order of magnitude of the observed enhancement of the Raman intensities. For example, in feature (1), the need to have simultaneously the frequency of the incident and of the scattered light as close as possible to the resonance frequency implies a more effective enhancement for the vibrations with lower Raman shift. The modification of the Raman selection rules as well as the deviation from the ω_{in}^4 dependence of the Raman intensity for SERS are also suggested from the model. The dipole decay law with the distance explains the long-range effect of the SERS enhancement often observed. Finally, the observed depolarization can be easily explained considering that a SERS-active surface is a collection of roughness features of different sizes and shapes into which the molecules adsorb in a variety of orientations and the occurrence of multiple scattering.

Although the e.m. model is able to explain most of the experimental SERS features, some observations strongly support the existence of a second mechanism of Raman enhancement of adsorbates on metal, namely the "chemical effect." Synonyms found in literature for chemical effect in SERS are charge-transfer excitations, short-range effects, atomic-scale roughness, SERS-active sites, adatoms, and energy-transfer excitations. Some SERS measurements indicate a dependence of the observed signal on the special studied adsorbates that cannot be explained by an e.m. effect. For example, the SERS spectra of CO and N_2 molecules that exhibit near identical polarizability differ from a factor 200, hard to explain invoking only the e.m. enhancement. A second evidence supporting the chemical effect is the potential dependence of SERS measured in electrochemical experiments. When the potential is scanned at a fixed laser frequency, or the laser frequency is scanned at a fixed potential, broad resonances are observed.

A simple Raman resonance mechanism can provide the explanation of this chemical effect. It is not unusual that the highest occupied molecular orbital (HOMO) and the lowest unoccupied molecular orbital (LUMO) of the adsorbate, which arise from the chemisorption, are symmetrically positioned in energy with respect to the Fermi level of the metal, as indicated in Fig. 11.

Since for molecules normally studied by SERS the LUMO is typically in the ultraviolet, the charge transfer excitations (either from the metal to the molecule or vice versa) can occur at about half the energy of the intrinsic intramolecular excitations, namely in the visible region of the spectrum.

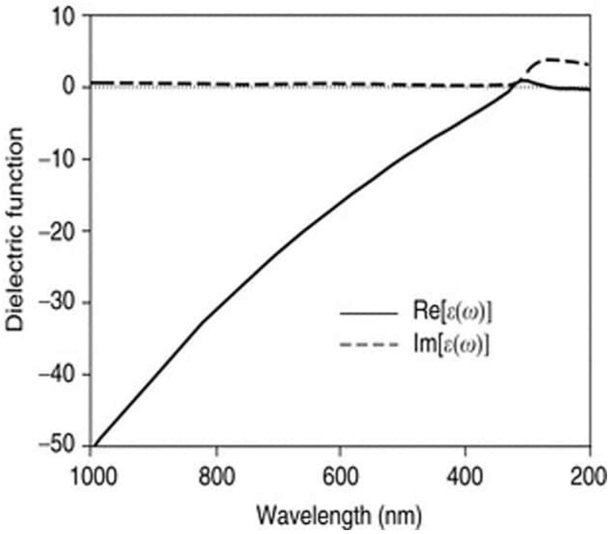

Fig. 10 Experimental dielectric function, ε(ω), of a silver film. The combined contributions of the free electron and interband transitions cause Re[ε(ω)] of Ag to approach 0 in the visible range even though the free electron plasma frequency is in the ultraviolet. In the same range Im[ε(ω)] is quite small. Reproduced from Mattei G. (2005) Optical properties of surface layers enhanced Raman scattering. In: Bassani F., Liedl G.L., Wyder P. (eds.) *Encyclopedia of Condensed Matter Physics.* Elsevier.

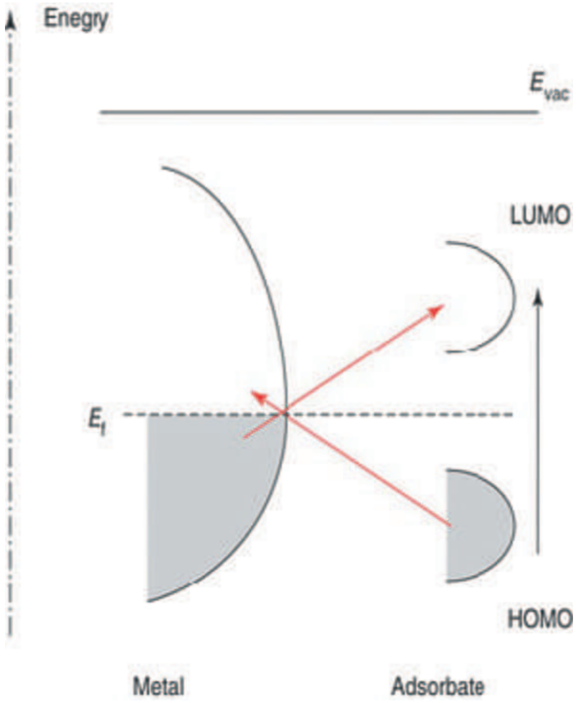

Fig. 11 Typical energy level diagram for a molecule adsorbed on a metal surface. Possible charge transfer excitations are shown. Reproduced from Mattei G. (2005) Optical properties of surface layers enhanced Raman scattering. In: Bassani F., Liedl G.L., Wyder P. (eds.) *Encyclopedia of Condensed Matter Physics.* Elsevier.

In recent years, the advent of new very sensitive Raman instrumentation with high spatial resolution, for example, micro-Raman and near-field systems, allowed the selective observation of single particles by SERS. Those experiments demonstrated that SERS from adsorbed species on metal particles show huge enhancement, around 10^{12}–10^{15}, allowing the detection of the Raman signal from a single molecule and opening new fields of applications. Theoretically, the Raman signal of molecule can be enhanced up to a 10^{13} factor for a potential single molecule detection (Giovannozzi et al., 2014). In the case of experiments performed on aggregate clusters of colloidal particles, their fractal nature has been invoked to explain the observed enhancement whereas in the case of single particles (in the dimension range of 100–500 nm), the multiplicative effect of resonance Raman enhancement of the molecule and surface enhancement at the metal surface has been considered the main source of the effect. Besides, not all the particles showed an efficient enhancement but only a few called "hot spots" did so. In most cases there is a time dependence of the intensity of every Raman band, which is called “blinking.” Finally, this huge Raman enhancement can be reconciled with the more commonly observed value (10^6–10^8) for SERS considering the particles population averaging that occurs in conventional experiments (macro-Raman). These last findings have attracted considerable attention from both basic and practical viewpoints. Indeed, a detailed understanding of the mechanisms operating to generate such a huge local Raman enhancement is not achieved yet and, hence, represents a very interesting area for study. Potential applications are, for example, in analytical chemistry as an ultrasensitive detection technique and in the development of micro-instrumentation, by combining scanning near-field microscopy with SERS.

Conclusion

The factors for Raman scattering enhancement are described. The amplification of electromagnetic field was discussed on flat and roughed surface, metal particles, and metal clusters. In SERS technique, electromagnetic and chemical effect have been discussed involving dominant metals (gold, silver and copper), alkali and transition metals at nanoscale surface conditions. Recent researches have developed significant hybrid substrate, and 3D nanostructures to amplify Raman signals for specific applications.

References

Chakraborty S, Awasthi V, Goel R, and Dubey SK (2021) Numerical design of SERS-active substrate for analyte detection using gold-hexagonal patterns. *Vibrational Spectroscopy* 117: 103312.
Ding G, Xie S, Liu Y, Wang L, and Xu F (2015) Graphene oxide-silver nanocomposite as SERS substrate for dye detection: Effects of silver loading amount and composite dosage. *Applied Surface Science* 345: 310–318.
Geng X, Wu C, Liu S, Han Y, Song L, and Zhang Y (2021) Fabrication optimization and application of 3D hybrid SERS substrates. *RSC Advances* 11: 31400–31407.
Giovannozzi AM, Rolle F, Sega M, Abete MC, Marchis D, and Rossi AM (2014) Rapid and sensitive detection of melamine in milk with gold nanoparticles by Surface Enhanced Raman Scattering. *Food Chemistry* 159: 250–256.
Kaushik V, Kagdada HL, Singh DK, and Pathak S (2022) Enhancement of SERS effect in Graphene-Silver hybrids. *Applied Surface Science* 574: 151724.
Lee JU, Lee W, Yoon SS, Kim J, and Byun JH (2014) Site-selective immobilization of gold nanoparticles on grapheme sheets and its electrochemical properties. *Applied Surface Science* 315: 73–80.
Li JJ, An HQ, Zhu J, and Zhao JW (2015) Improve the surface enhanced Raman scattering of gold nanorods decorated graphene oxide: the effect of CTAB on the electronic transition. *Applied Surface Science* 347: 856–860.
Li Y, Feng L, Li J, Li X, Chen J, Wang L, Qi D, Liu X, and Shi G (2021) Fabrication of an insect-like compound-eye SERS substrate with 3D Ag nano-bowls and its application in optical sensor. *Sensors and Actuators B: Chemical* 330: 129357.
Li R, Lei J, Zhou Y, and Li H (2020) Hybrid 3D SERS substrate for Raman spectroscopy. *Chemical Physics Letters* 754: 137733.
Lofrumento C, Platania E, Ricci M, Mulana C, Becucci M, and Castellucci EM (2015) The SERS spectra of alizarin and its ionized species: The contribution of the molecular resonance to the spectral enhancement. *Journal of Molecular Structure* 1090: 98–106.
López-Lorente AI (2021) Recent developments on gold nanostructures for surface enhanced Raman spectroscopy: Particle shape, substrates and analytical applications. A review. *Analytica Chimica Acta* 1168: 338474.
Mattei G (2005) In: Bassani F, Liedl GL, and Wyder P (eds.) *Optical properties of surface layers enhanced Raman scattering*. Encyclopedia of Condensed Matter Physics: Elsevier.
Mehrvar L, Sadeghipari M, Tavassoli SH, Mohajerzadeh S, and Fathipour M (2017) Optical and surface enhanced Raman scattering properties of Ag modified silicon double nanocone array. *Scientific Reports* 7: 12106.
Tahghighi M, Janner D, and Ignés-Mullol J (2020) Optimizing gold nanoparticle size and shape for the fabrication of SERS substrates by means of the Langmuir–Blodgett technique. *Nanomaterials* 10: 2264.
Tim B, Błaszkiewicz P, Nowicka AB, and Kotkowiak M (2022) Optimizing SERS performance through aggregation of gold nanorods in Langmuir-Blodgett films. *Applied Surface Science* 573: 151518.
Yang J-Y, Park S-G, Jung S, Byeon E-Y, Kim D-G, Jung HS, Kim HJ, and Lee S (2022) SERS substrates based on self-organized dimple nanostructures on polyethylene naphthalate films produced via oxygen ion beam sputtering. *Applied Surface Science* 572: 151452.
Zhao J, Lin J, Wei H, Li X, Zhang W, Zhao G, Bu J, and Chen Y (2015) Surface enhanced Raman scattering substrates based on titanium nitride nanorods. *Optical Materials* 47: 219–224.

Further reading

Agranovich VM and Mills DL (1982) Surface polaritons electromagnetic waves at surfaces and interfaces. In: Agranovich VM and Maradudin AA (eds.) *Modern Problem in Condensed Matter Sciences*. vol. I. Elsevier. North-Holland, Amsterdam.
Campion A and Kambhampati P (1998) Surface-enhanced Raman scattering. *Chemical Society Reviews* 27: 241–250.
Cardona M and Güntherodot G (eds.) (1984) *Light Scattering in Solids IV*, pp. 289–418. Berlin: Springer.
Chang RK and Furtak TE (1982) *Surface enhanced Raman scattering*. New York: Plenum.
Kneipp K, Kneipp H, Itzkan I, Dasari RR, and Feld MS (1999) Ultrasensitive chemical analysis by Raman spectroscopy. *Chemical Reviews* 99: 2957–2975.
Kneipp K, Kneipp H, Itzkan I, Dasari RR, and Feld MS (2002) Nonlinear Raman probe of single molecules attached to colloidal silver and gold clusters. In: Shalaev VM (ed.) *Optical Properties of Nanostructured Random Media*. vol. 82. Berlin: Springer.
Kneipp K, Kneipp H, Itzkan I, Dasari RR, and Feld MS (2002) Surface-enhanced Raman scattering and biophysics. *Journal of Physics. Condensed Matter* 14: R597–R624.
Laserna J (1996) *Modern Technique in Raman Spectroscopy*. Chichester: Wiley.
Malekpour H and Balandin AA (2018) Raman-based technique for measuring thermal conductivity of graphene and related materials. *Journal of Raman Spectroscopy* 49: 106–120.
Moskovits M (1985) Surface enhanced Raman spectroscopy. *Reviews of Modern Physics* 57: 783–826.
Otto A (1984) Surface-enhanced Raman scattering ‘classical’ and ‘chemical’ origins. In: Cardona M and Güntherodot G (eds.) *Light Scattering in Solids IV*. Berlin: Springer.
Otto A, Mrozek J, Grabhorn H, and Akemann W (1992) Surface-enhanced Raman scattering. *Journal of Physics. Condensed Matter* 4: 1143–1212.
Sánchez-Gil JA, Garcia-Ramos JV, and Méndez ER (2000) Microstructures in rough metal surfaces electromagnetic mechanism in surface-enhanced Raman spectroscopy. In: Moreno F and Gonzáles F (eds.) *Light Scattering from Microstructures. Lecture Notes in Physics*. vol. 534. Berlin: Springer.
Shalaev VM (1996) Electromagnetic properties of small-particles composites. *Physics Reports* 272: 61–137.

Photonic Bandgap Materials, Electronic States of

M Agio and LC Andreani, Università degli Studi di Pavia, Pavia, Italy

© 2005 Elsevier Ltd. All rights reserved.

This is an update of M. Agio, L.C. Andreani, Photonic Bandgap Materials, Electronic States of, Editor(s): Franco Bassani, Gerald L. Liedl, Peter Wyder, Encyclopedia of Condensed Matter Physics, Elsevier, 2005, Pages 286–294, ISBN 9780123694010, https://doi.org/10.1016/B0-12-369401-9/00464-2.

Introduction 739
Photonic Band Structure: General Properties 739
Theoretical Methods 740
Three-Dimensional Photonic Crystals 741
Two-Dimensional Photonic Crystals 743
Photonic Crystal Slabs 743
Defect States 744
Measuring the Photonic Band Structure 746
Further Reading 747

Introduction

Photonic crystals are materials whose dielectric function is periodic in one, two, or three spatial dimensions (1D, 2D, 3D). The propagation properties of photons in periodic media are analogous to those of electrons in crystalline solids, as covered by several sections of the encyclopedia. Translational invariance leads to the validity of the Bloch theorem (called Floquet theorem in optics) and to the formation of allowed and forbidden frequency regions. The allowed states of the electromagnetic field are organized into "photonic bands," in analogy to electron bands in periodic solids. A frequency window for which light cannot propagate is named a "photonic gap" and periodic dielectric media are often called "photonic bandgap materials."

The concept of a 1D periodic dielectric medium has been a familiar one in optics, where it is known as a distributed Bragg reflector (or dielectric mirror) with well-defined stop bands. However, a stop band (or photonic gap) in 1D forbids propagation of light only in a limited angular cone. The field of photonic crystals is considered to have started in 1987 with seminal papers dealing with the control of spontaneous emission and with light localization in three dimensions. Indeed, the presence of a full photonic bandgap in 3D leads to the suppression of vacuum fluctuations of the electromagnetic field and, therefore, to the inhibition of spontaneous emission of a light source at frequencies within the bandgap. Moreover, the presence of disorder may lead to a weak localization of light at frequencies close to a band edge. Photonic crystals are now of great interest for basic physical properties related to the control of light propagation, radiation–matter interaction and quantum electrodynamic effects, localization and microcavities, nonlinear properties as well as for applications to optoelectronic and photonic devices such as lasers, optical fibers, filters, dispersion compensators, and integrated optical interconnects.

The article starts with the general properties of the photonic band structure and discusses the main theoretical approaches for calculating photonic bands and optical properties. Then photonic bands in three and two dimensions as well as photonic crystals embedded in planar waveguides (also known as photonic crystal slabs) are described. Defect states in photonic crystals are then considered. This section concludes with a few remarks about methods for measuring the photonic band dispersion.

Photonic Band Structure: General Properties

Maxwell equations for the electromagnetic field in matter with neither free charges nor currents can be cast into a second-order equation for the harmonic components of the electric field

$$\nabla \times \nabla \times \boldsymbol{E}(\boldsymbol{r}) = \left(\frac{\omega^2}{c^2}\right)\varepsilon(\boldsymbol{r})\boldsymbol{E}(\boldsymbol{r}) \qquad [1]$$

or of the magnetic field

$$\nabla \times \left[\frac{1}{\varepsilon(\boldsymbol{r})}\nabla \times \boldsymbol{H}(\boldsymbol{r})\right] = \frac{\omega^2}{c^2}\boldsymbol{H}(\boldsymbol{r}) \qquad [2]$$

Here, nonmagnetic media $(\mu(\boldsymbol{r}) = 1)$ are assumed. The first equation should be combined with the divergence equation $\nabla\cdot\varepsilon(\boldsymbol{r})\boldsymbol{E}(\boldsymbol{r}) = 0$, while the second one requires $\nabla\cdot\boldsymbol{H}(\boldsymbol{r}) = 0$. The equation for the magnetic field is normally taken as the starting point for photonic band structure computations for two reasons. First, it has the form of an eigenvalue problem $\boldsymbol{\Theta}\boldsymbol{H}(\boldsymbol{r}) = (\omega^2/c^2)\boldsymbol{H}(\mathbf{r})$, with $\boldsymbol{\Theta}$ being a Hermitian operator. Second, the divergence equation for the magnetic field does not contain the dielectric function and is easier to implement. Working with a Hermitian eigenvalue problem is convenient from a computational point of view and has strong analogies with the matrix formulation of quantum mechanics.

The basic electromagnetic equations have a very useful property of "scale invariance." If $\boldsymbol{H}(\boldsymbol{r})$ is a solution at frequency ω corresponding to the dielectric constant $\varepsilon(\boldsymbol{r})$, then the scaled system with dielectric constant $\varepsilon'(\boldsymbol{r}) = \varepsilon(\boldsymbol{r}/s)$ has a solution $\boldsymbol{H}'(\boldsymbol{r}) = \boldsymbol{H}(\boldsymbol{r}/s)$ with frequency $\omega' = s\omega$. Reducing the length scale of the system by a factor s leads to eigenfrequencies that are multiplied by the same factor. Thus, there is no fundamental length scale for the photonic problem (unlike for electrons in solids, for which the Bohr radius is the natural unit of length).

A periodic dielectric medium (in 3D, say) is invariant under translations by vectors $\boldsymbol{R} = n_1\boldsymbol{a}_1+n_2\boldsymbol{a}_2+n_3\boldsymbol{a}_3$ $(n_1,n_2,n_3\in Z)$, where $\boldsymbol{a}_1$, $\boldsymbol{a}_2$, and $\boldsymbol{a}_3$ are primitive vectors and the set of all $\boldsymbol{R}$'s forms a "Bravais lattice." The dielectric constant satisfies the relation

$$\varepsilon(\boldsymbol{r}+\boldsymbol{R}) = \varepsilon(\boldsymbol{r}) \qquad [3]$$

and the magnetic field has the form implied by the Bloch–Floquet theorem:

$$\boldsymbol{H}_{nk}(\boldsymbol{r}+\boldsymbol{R}) = \mathrm{e}^{\mathrm{i}\boldsymbol{k}\cdot\boldsymbol{r}}\boldsymbol{H}_{nk}(\boldsymbol{r}) \qquad [4]$$

where $\boldsymbol{k}$is the Bloch vector (which may be restricted to the first Brillouin zone or Wigner–Seitz cell of the reciprocal lattice) and n is a discrete band index. The frequency eigenvalues have the form $\omega = \omega_n(k)$ and the set of all frequencies for $\boldsymbol{k}$ spanning the first Brillouin zone is called a photonic band. In addition to translational invariance leading to Bloch vector conservation, discrete rotational symmetries of the lattice may also be used to analyze the photonic bands, again in close similarity to the electronic problem. The density of states (DOS) is defined as

$$N(\omega) = \sum_n \int_{\mathrm{BZ}} \delta(\omega-\omega_n(\boldsymbol{k}))\mathrm{d}^3\boldsymbol{k} \qquad [5]$$

and is strongly modified as compared to the photonic DOS in vacuum or in a homogeneous medium, which increases with the square of the frequency.

Theoretical Methods

The most common method for calculating photonic band structures consists of expanding the magnetic field on a basis of plane waves that satisfy the Bloch theorem and the divergence equation:

$$\boldsymbol{H}_{nk}(\boldsymbol{r}) = \sum_{\mathrm{G},\lambda} c_n(\boldsymbol{k}+\mathbf{G},\lambda)\hat{\varepsilon}(\boldsymbol{k}+\mathbf{G},\lambda)\mathrm{e}^{\mathrm{i}(\boldsymbol{k}+\mathrm{G})\cdot\boldsymbol{r}} \qquad [6]$$

where G are reciprocal lattice vectors and $\hat{\varepsilon}(\boldsymbol{k}+\mathbf{G},\lambda)$, $\lambda = 1, 2$ are unit and mutually orthogonal polarization vectors perpendicular to $\boldsymbol{k}+\boldsymbol{G}$. The second-order eqn [2] is transformed into the matrix equation

$$\sum_{G'\lambda'} \boldsymbol{H}_{G\lambda,G'\lambda'} c_n(\boldsymbol{k}+\mathbf{G}',\lambda') = \frac{\omega^2}{c^2} c_n(\boldsymbol{k}+\mathbf{G},\lambda) \qquad [7]$$

where

$$\boldsymbol{H}_{G\lambda,G'\lambda'} = |\boldsymbol{k}+\mathbf{G}||\boldsymbol{k}+\mathbf{G}'| \times \varepsilon^{-1}(\mathbf{G},\mathbf{G}') \begin{bmatrix} \hat{\varepsilon}_2.\hat{\varepsilon}_2' & -\hat{\varepsilon}_2.\hat{\varepsilon}_1' \\ -\hat{\varepsilon}_1.\hat{\varepsilon}_2' & \hat{\varepsilon}_1.\hat{\varepsilon}_1' \end{bmatrix} \qquad [8]$$

and $\varepsilon^{-1}(\boldsymbol{G},\boldsymbol{G}') \equiv \varepsilon^{-1}(\boldsymbol{G}-\boldsymbol{G}')$ is the Fourier transform of $\varepsilon^{-1}(\boldsymbol{r})$. Numerically, the linear eigenvalue problem is solved by retaining a finite number of reciprocal lattice vectors and using standard matrix diagonalization routines or more efficient methods based on fast Fourier transforms and iterative eigensolvers. The accuracy of the method depends on the number of plane waves in the basis and on their ability to reproduce the spatial variations of the magnetic field in the periodic structure and Maxwell boundary conditions when dielectric discontinuities are present. It turns out that convergence of the method is substantially improved when $\varepsilon^{-1}(\boldsymbol{G},\boldsymbol{G}')$ is obtained by first calculating $\varepsilon(\boldsymbol{G},\boldsymbol{G}') \equiv \varepsilon(\boldsymbol{G}-\boldsymbol{G}')$ as the Fourier transform of $\varepsilon(\boldsymbol{r})$ and inverting the resulting matrix numerically. Still, convergence of the method should always be checked and it may become problematic in special situations (e.g., high dielectric discontinuities and/or complex bases in the unit cell with close-packing dielectric spheres).

Just like plane-wave expansion, other techniques for photonic band structure calculations are borrowed from corresponding methods for the electronic problem. For example, in the case of spherical (for 3D) or circular bases (for 2D), the Korringa–Kohn–Rostoker method based on expanding the Green function in the basis of symmetry-adapted functions satisfying appropriate boundary conditions can be applied. This method has the advantage that it can easily incorporate frequency dispersion of the dielectric function (thus it can be used, for example, for photonic crystals containing metallic components), but it can be applied easily only to structures with bases of special symmetry.

The calculation of photonic bands assumes ideal structures, that is, infinitely extended in space and without imperfections. On the other hand, real samples are always finite and carry a certain degree of imperfection. Furthermore, there are quantities such as the transmission and reflection coefficients that manifest the existence of photonic bandgaps and are relatively easy to obtain experimentally. Among the numerical methods that are able to compute transmission and reflection, the most widely used are the transfer matrix, the scattering matrix, and the finite-difference time-domain method.

The transfer matrix method works in real space. The Maxwell curl equations are discretized on a mesh of subcells, so that the field propagation in the structure is defined by a nearest-neighbor interaction. The matrix of the resulting linear system of equations is called a “transfer matrix,” as it transfers the fields from a subcell to another. Since the interaction is limited to the first neighbors, the matrix is sparse. Propagation across the whole structure is obtained by multiplication of sparse matrices. Once the transfer matrix is obtained, the calculation of transmission and reflection is straightforward. It is worth mentioning that when the system is periodic, the eigenvalues of the transfer matrix of a single unit cell yield an alternative method for computing the photonic band structure. This is especially useful when dealing with dispersive media.

The scattering matrix method is more suitable for the study of photonic crystal slabs (see description below). It computes reflection, transmission, and diffraction coefficients for propagation along a direction perpendicular or parallel to the waveguide plane. Maxwell equations are first solved in each layer by plane wave expansion. Then, using the scattering matrix (S), instead of the transfer matrix, boundary conditions are imposed at each interface. The S-matrix connects the ingoing amplitudes to the outgoing amplitudes. The scattering matrix $S(0,N)$ of the whole structure is constructed starting from the scattering matrix of the first interface $S(0,1)$, by applying the recursion formula $S(0,l)->S(0,l+1)$. The S-matrix yields better numerical stability than the transfer matrix.

When working with more complex systems, with imperfections or explicitly designed defects, a more flexible numerical approach is required. This is fulfilled by the finite-difference time-domain (FDTD) method. The derivatives in the Maxwell curl equations

$$\nabla \times \boldsymbol{E} = -\frac{1}{c}\frac{\partial \boldsymbol{B}}{\partial t}, \nabla \times \boldsymbol{H} = +\frac{1}{c}\varepsilon(\boldsymbol{r})\frac{\partial \boldsymbol{E}}{\partial t} \qquad [9]$$

are discretized by central finite differences, both in space and time. The electromagnetic field is thus defined on two meshes in space and time, one for the ***E*** field and one for the ***H*** field. These meshes are interlaced in order to have each ***E*** field position surrounded by nearest neighbor ***H*** field positions and vice versa. The equations are recast in the so-called “Yee algorithm,” which is illustrated here for a two-dimensional case:

$$\boldsymbol{E}_x|^{n+1/2}_{i,j+1/2} = \boldsymbol{E}_x|^{n-1/2}_{i,j+1/2} + \frac{c\Delta t}{\varepsilon_{i,j+1/2}\Delta y}\left(H_z|^{n}_{i,j+1} - \boldsymbol{H}_z|^{n}_{i,j}\right) \qquad [10]$$

$$\boldsymbol{E}_y|^{n+1/2}_{i+1/2,j} = \boldsymbol{E}_y|^{n-1/2}_{i+1/2,j} - \frac{c\Delta t}{\varepsilon_{i+1/2,j}\Delta x}\left(H_z|^{n}_{i+1,j} - \boldsymbol{H}_z|^{n}_{i,j}\right) \qquad [11]$$

$$\boldsymbol{H}_z|^{n+1}_{i,j} = \boldsymbol{H}_z|^{n}_{i,j} - \frac{c\Delta t}{\Delta x}\left(E_y|^{n+1/2}_{i+1/2,j} - \boldsymbol{E}_y|^{n+1/2}_{i-1/2,j}\right) + \frac{c\Delta t}{\Delta y}\left(E_x|^{n+1/2}_{i,j+1/2} - \boldsymbol{E}_x|^{n+1/2}_{i,j-1/2}\right) \qquad [12]$$

Looping on i, j (space), and n (time) simulates the propagation of the electromagnetic field through the structure. Once the Yee algorithm has been implemented, the discretization of the dielectric constant $\varepsilon(r)$ is the only step that needs to be adapted to the specific simulation. This is a great advantage of FDTD with respect to the transfer matrix method. A Gaussian pulse is sent along a chosen direction, while detection lines collect the incident and outgoing power. The transmission coefficient is simply the ratio of outgoing to incident power. The reflection coefficient can be obtained in a similar manner. When the system is periodic, it is also possible to obtain the band structure from an FDTD simulation. Specific implementations of the FDTD method have been developed to treat media with strong frequency dispersion, such as metallic or metallo-dielectric systems.

Three-Dimensional Photonic Crystals

The first photonic structure that has been shown to possess a complete bandgap in three dimensions is the diamond lattice of dielectric spheres in air or air spheres in a dielectric material. The photonic gap opens provided the dielectric constant is large enough and it exists in a wide range of filling factors. Another simple 3D structure with a complete bandgap is the f.c.c. lattice of air spheres in a dielectric material: this is often called the “inverse opal” structure. An example of photonic bands and DOS for this structure is shown in Figure 1. The frequencies are given in dimensionless units $\omega a/(2\pi c) \equiv a/\lambda$, where a is the lattice constant, and as such they are invariant under a scale transformation. A full bandgap forms between the eighth and ninth bands with a relative width $\Delta\omega_g/\omega_g \approx 4\%$. On the other hand, no gap is formed between lower-lying bands, but a pseudogap with low photonic DOS occurs around $a/\lambda = 0.52$: a degeneracy between the second and the third bands at the W point and along the XU line prevents a gap from opening.

The inverse opal is derived from the (direct) opal structure, that is, an f.c.c. lattice of dielectric spheres in air: indeed, the opal is a natural gem consisting of a close-packed lattice of silica spheres with an f.c.c. arrangement. Artificial opals can be obtained by self-assembling of spheres in a colloidal solution. The voids are then filled with a high-index material (Si or TiO_2) and the template is subsequently removed to obtain the inverse structure. This procedure allows one, in principle, to realize a photonic crystal with a complete bandgap in the optical region. In real systems, however, a small amount of disorder is always present: the gap shown in Figure 1 is not very robust as it is relatively narrow and is formed between higher-lying bands, which are very sensitive to disorder.

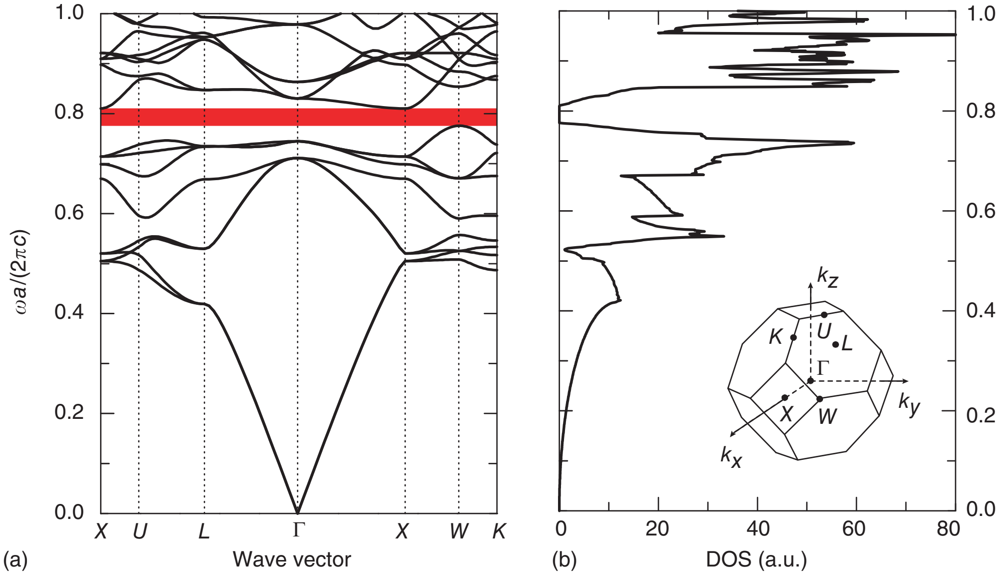

Figure 1 (a) Photonic bands and (b) DOS for an f.c.c. structure of close-packing air spheres in a dielectric material with $\varepsilon = 12$. The shaded area in (a) denotes the photonic gap. Inset: Brillouin zone and symmetry points of the f.c.c. lattice.

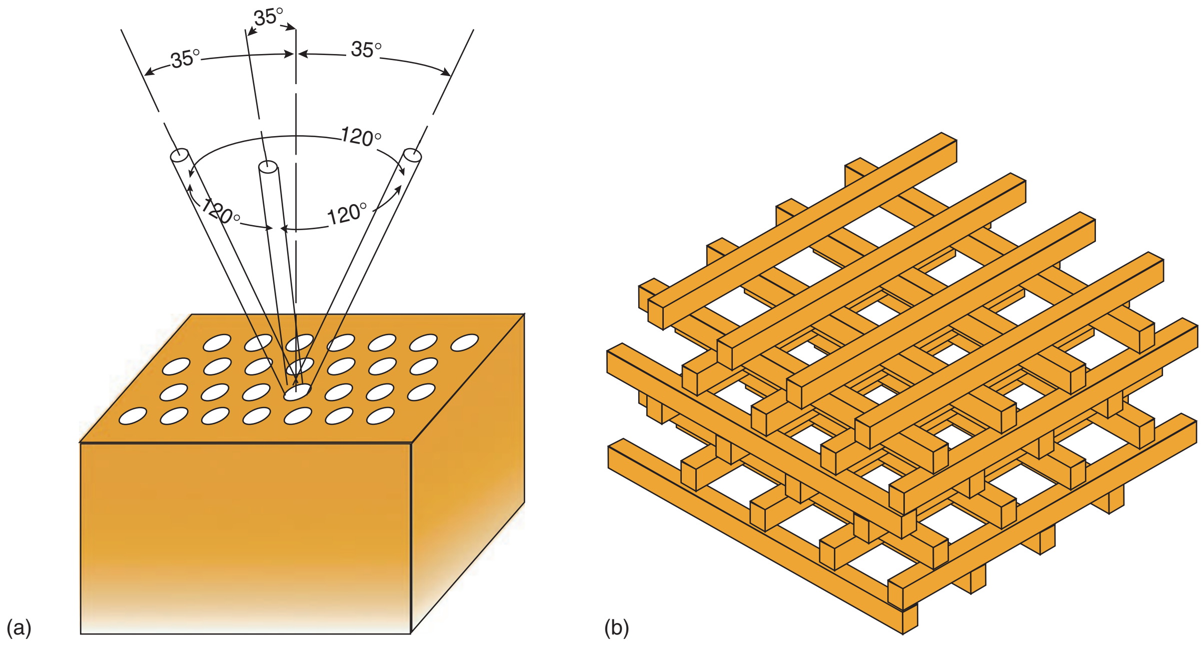

Figure 2 Schematic plots of the Yablonovite (a) and woodpile (b) photonic structures.

Many other structures possessing a complete photonic gap in three dimensions have been studied. Two of them are shown in Figure 2. The structure in Figure 2a, called the "Yablonovite" (from the name of its proponent, E Yablonovitch) is obtained by drilling three sets of cylindrical holes with a triangular pattern, at 35.26° from the surface normal and at 120° with respect to each other. It represents a distortion of the diamond structure of air spheres in a dielectric material, where the surface is a (1 1 1) plane of the crystal and the holes correspond to [1 1 0] open channels of the diamond structure. The Yablonovite can be realized, in principle, at infrared and optical wavelengths by deep lithography. The structure in Figure 2b, often called "woodpile," is obtained by stacking four alternate layers of dielectric rods: starting from a first layer, the second layer is rotated by 90° with respect to the first, and the third layer is shifted by $a/2$ (a is the lattice constant) with respect to the first one. The woodpile structure can be realized by a series of stacking steps. The fabrication procedures of Yablonovite and of woodpile are examples of "top-down" and "bottom-up" approaches, respectively.

Two-Dimensional Photonic Crystals

2D photonic crystals have a dielectric constant that is periodic in a plane (xy) and homogeneous in the third (z) direction. The most interesting situation is when light propagates in the xy plane, that is, for a vertical wave vector $\boldsymbol{k}_z = 0$. The system is invariant under specular reflection with respect to the mirror plane xy; thus the electromagnetic eigenmodes can be classified as even or odd with respect to this mirror symmetry. Even states have nonvanishing field components (E_x, E_y, H_z) and are called H- (or TE-) polarized modes, while odd states have nonzero field components (H_x, H_y, E_z) and are called E- (or TM-) polarized. Unlike in the 3D case, there is a strong polarization dependence of the photonic bands.

Most 2D structures that have been studied are based on a square or on a hexagonal Bravais lattice. In general, the most favorable situation for a complete photonic gap is to have a structure with the highest possible rotational symmetry: this helps in achieving an overlap between bandgaps along different directions of the Brillouin zone. The square Bravais lattice has a fourfold symmetry axis, while the hexagonal lattice has a sixfold rotational axis that is the maximum possible symmetry for periodic Bravais lattices. Higher rotational symmetries are possible for nonperiodic structures, such as quasicrystals.

Figure 3 shows two examples of 2D photonic bands in structures with a full bandgap for all directions and polarizations, namely the triangular lattice of air holes in a dielectric medium (Figure 3a) and the graphite or honeycomb lattice of dielectric pillars in air (Figure 3b). Both structures are based on the 2D hexagonal Bravais lattice. The triangular lattice of holes has a large gap between the first and the second H-band and a smaller gap between the second and the third E-band, which overlap in the region shown by a dashed area in Figure 3a. For the assumed value of the dielectric constant ($\varepsilon = 12$), the H-gap is found to open for hole radii $r/a > 0.16$, while the E-gap opens only for hole radii $r/a > 0.4$; therefore, a polarization-independent gap exists only for relatively high values of the air fraction. The graphite lattice of pillars, instead, has two complete bandgaps between higher-lying bands. Notice that the graphite lattice of pillars supports a large gap between the second and third E-bands, which however does not overlap any H-gap.

As a general rule, structures with a connected dielectric lattice (like that of Figure 3a) tend to have larger gaps for H-polarization, while structures with disconnected dielectric pillars (like that of Figure 3b) tend to support larger E-gaps. This criterion, which can be traced back to Maxwell boundary conditions for the nonvanishing field components, is generally followed for both square and hexagonal Bravais lattices. The overlap of H- and E-gaps is a stronger condition that occurs only in a few cases, those shown in Figure 3 being the most common examples. In real systems, the complete gap shown in Figure 3a is easier to realize, because it is lower in frequency and less sensitive to disorder. For technological applications, a polarization-sensitive gap is often sufficient and the commonly used structure is the triangular lattice of air holes for smaller air fractions than shown in Figure 3a, in order to reduce radiation losses.

2D photonic structures can be defined by a top-down procedure based on lithography and etching. The prototype of a 2D photonic crystal is macroporous silicon, which is obtained by wet etching of Si in an electrochemical cell. It should be remembered that the photonic bands such as those shown in Figure 3, refer only to propagation in the xy plane: in a system that can be considered as homogeneous in the z-direction, the bands retain an out-of-plane dispersion and light is free to propagate in the vertical direction. This mechanism is exploited in a new class of optical fibers, which are known as holey- or photonic crystal fibers.

Photonic Crystal Slabs

In order to achieve a better control of light propagation, a 2D photonic structure can be embedded in a planar (slab) dielectric waveguide, thereby realizing a “photonic crystal slab.” A few possible structures are shown in Figure 4. The theoretically simplest system is the “air bridge” (Figure 4a), which consists of a self-standing patterned dielectric membrane surrounded by air. The air bridge has the highest refractive index contrast between the core and the cladding. Figure 4b exemplifies the silicon-on-insulator (SOI) structure, consisting of an air/Si/SiO_2 waveguide in which only the Si layer is patterned. A system with a weak refractive index contrast is shown in Figure 4c, and it can be realized with GaAs/AlGaAs or with InP/InGaAsP waveguides: both the core and the cladding need to be patterned in order to maintain the guiding properties of the slab. The fabrication of photonic crystal slabs requires epitaxial growth, lithography, and dry (reactive-ion) etching steps.

Photonic crystal slabs are characterized by the light-line issue. Only photonic modes that lie below the light dispersion of the cladding material(s) in the $k - \omega$ plane are truly guided and stationary, while modes that lie above the cladding light line(s) are radiative and only quasi-guided. For a specified value of the in-plane wave vector, the truly guided modes lie in a frequency region of the discrete spectrum, while quasi-guided modes lie in the region of the continuous spectrum and appear as resonances: their line width can be related to an imaginary part of the mode frequency.

An example of mode dispersion in a photonic crystal slab is shown in Figure 5 and it refers to an air bridge patterned with a triangular lattice of holes. Figure 5a shows the real part of the frequency dispersion in the Γ–K direction. The cladding light line (dotted line in the figure) separates the regions of guided and quasi-guided modes. The planar waveguide is monomode up to a frequency $\omega a/(2\pi c) \cong 0.61$, where a second-order mode appears. $\mathrm{Re}(\omega)$ is generally larger than for the ideal 2D case due to a vertical confinement in the slab waveguide: this effect is particularly pronounced for a strong index-contrast slab. Figure 5b displays the calculated reflectance of a plane wave incident on the surface of the slab, for increasing values of the angle of incidence. Spectral structures appear in reflectance spectra, which mark the excitation of photonic modes and whose evolution as a function of the incidence angle corresponds to the $\omega(k)$ dispersion of Figure 5a: the wave vector parallel to the surface is conserved and it equals $k = (\omega/c)\sin\theta$ (modulo a reciprocal lattice vector). Figure 5c shows the imaginary part of the frequency of quasi-guided modes

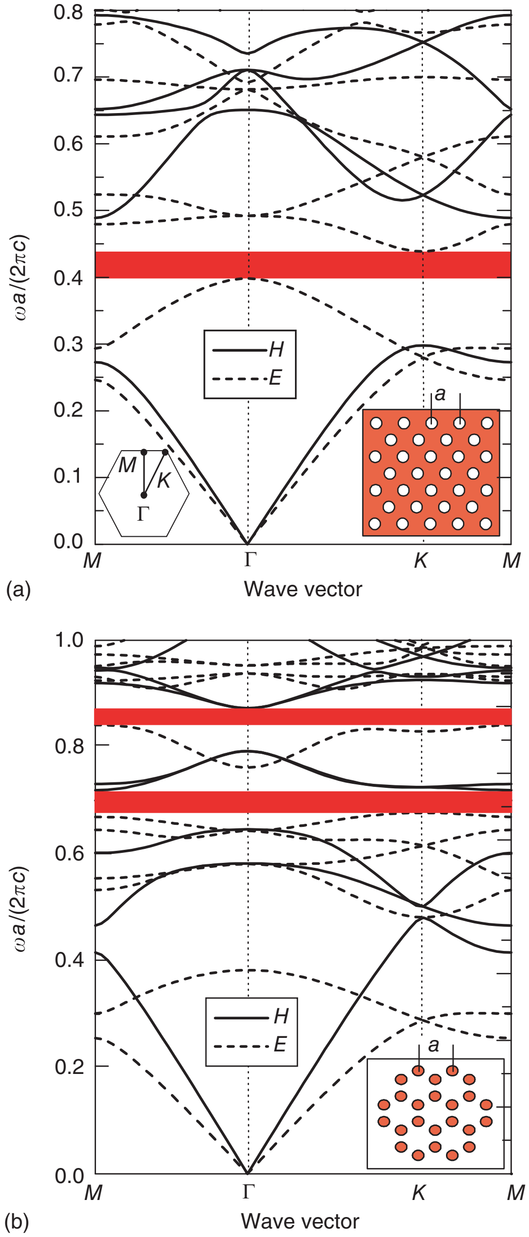

Figure 3 Photonic bands of (a) a triangular lattice of air holes with radius $r/a = 0.45$ in a dielectric material and (b) a graphite lattice of dielectric pillars with radius $r/a = 0.18$ in air. The dielectric material has $\varepsilon = 12$ in both cases. Solid (dashed) lines represent *H*- (*E*-) polarized modes: they are even (odd) with respect to a horizontal mirror plane. The shaded areas denote the photonic gaps. Insets: structures and 2D Brillouin zone.

plotted as a function of the real part. The imaginary part depends strongly on the mode index and on the wave vector, and it vanishes when the real part of the dispersion crosses the light line and goes into the guided mode region. It can be seen that an increasing imaginary part in Figure 5c corresponds to an increasing line width of the reflectance structure in Figure 5b.

The imaginary part of the mode frequency leads to an imaginary part of the wave vector through the relation $\mathrm{Im}(k) = \mathrm{Im}(\omega)/v_g$, where $v_g = d\omega/dk$ is the group velocity. Physically, a propagating quasi-guided mode in an ideal photonic crystal slab is subject to intrinsic radiative losses due to diffraction out of the 2D plane. In real systems, extrinsic diffraction losses related to fabrication aspects (insufficient hole depth, nonvertical profile, roughness of the sidewalls) are present for both guided and quasi-guided modes.

Defect States

It is well known in the electronic structure theory that localized defects introduce impurity states in the gap. An analogous phenomenon takes place in photonic crystals. A common example is a planar defect in a 1D photonic crystal, which is known as

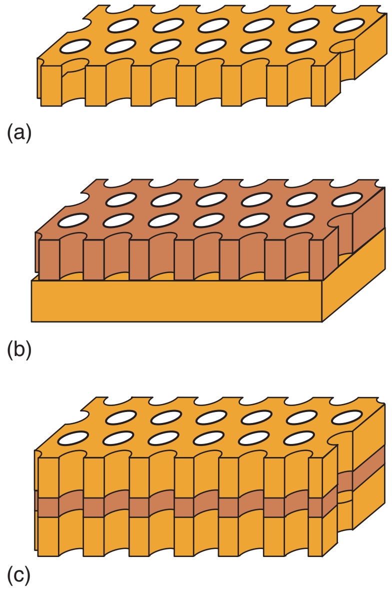

Figure 4 Schematic plots of photonic crystal slabs: (a) air bridge, or self-standing membrane, (b) SOI, where only the Si core layer is patterned, and (b) AlGaAs/GaAs/AlGaAs, where all layers are patterned.

a planar (or Fabry–Pérot) microcavity. Linear and point defects in photonic crystals of higher dimensionality also give rise to defect modes within the photonic bandgap. The simplest kinds of defects can be treated with the methods introduced for bulk photonic crystals, provided the defect is repeated with supercell periodicity.

An example of photonic bands for a line defect, or channel waveguide in a photonic crystal slab is shown in Figure 6. The structure consists of a single missing row of holes in the Γ–K direction of the triangular lattice (see inset). The defect modes are found outside the projections of the 2D bands onto the Γ–K direction, which are denoted by shaded regions. The defect mode that falls below the photonic gap of the triangular lattice is called "index-guided," because it is laterally confined by the dielectric discontinuity between the channel region and the surrounding photonic crystal. The modes that exist only within the bandgap of the 2D lattice are called "gap-guided" and are laterally confined by the photonic gap, that is, by the lack of electromagnetic eigenmodes in the surrounding material. Both index- and gap-guided modes can be seen in Figure 6. Notice that the defect modes

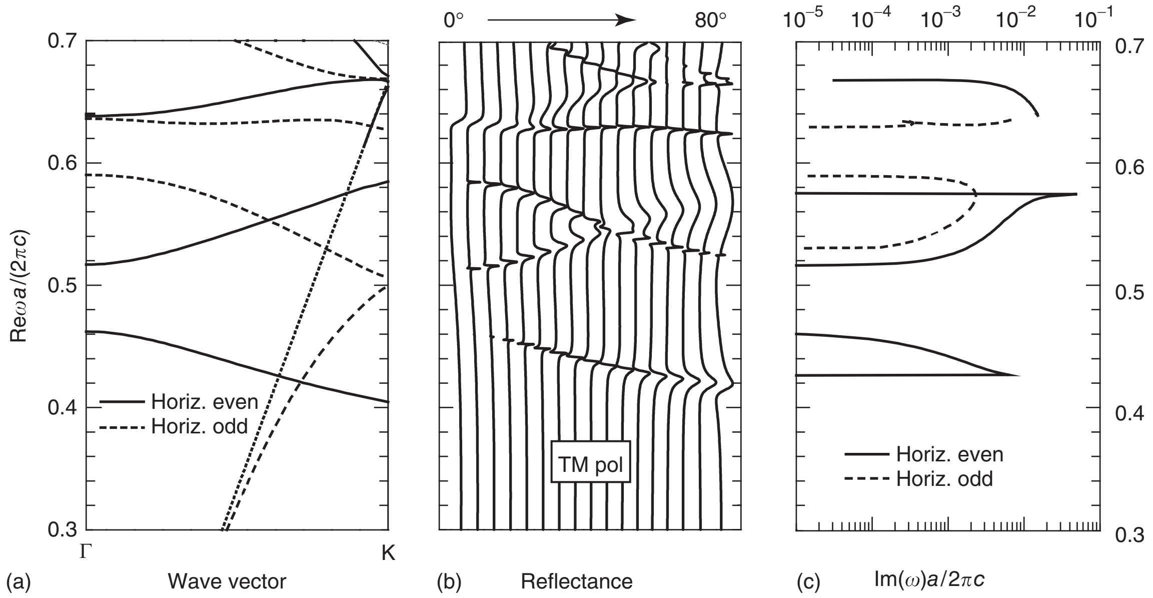

Figure 5 (a) Real part of the frequency; (b) specular reflectance from the surface at angles of incidence from 0° to 80° in steps of 5°; and (c) imaginary part of the frequency for a photonic crystal slab with a triangular lattice of air holes of radius $r/a = 0.3$ patterned in a membrane with core thickness $d/a = 0.3$ and dielectric constant $\varepsilon = 12$. All curves calculated for TM polarized (even) modes with respect to the plane of incidence along the Γ–K orientation. Solid (dashed) lines in (a) and (c) correspond to even (odd) modes with respect to a horizontal symmetry plane. The dotted line in (a) represents the dispersion of light in air.

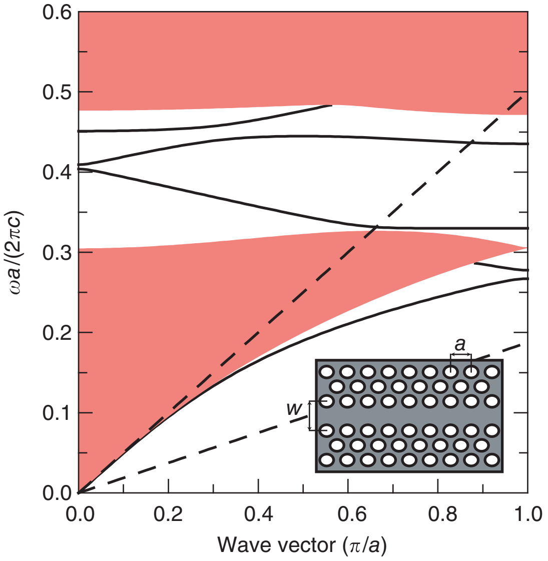

Figure 6 Dispersion of defect modes of a linear waveguide in a membrane with thickness $d/a = 0.3$ and dielectric constant $\varepsilon = 12$. The structure is shown in the inset and the holes in the triangular lattice have a radius $r/a = 0.36$. Only horizontally even and vertically odd modes are shown. The shaded regions correspond to the projected bands of the periodic lattice and the dashed lines denote the light dispersion in the dielectric material and in air.

can be either guided or quasi-guided, according to their frequency with respect to the cladding light line. Truly guided defect modes allow, in principle, for straight propagation without losses.

The linear defect structure in a photonic crystal lends itself to the realization of ultra-compact waveguides with sharp bends, which cannot be obtained with conventional dielectric waveguides based on total internal reflection. Figure 7 shows an example of wave propagation through a 120° bend in the triangular lattice of holes – the electromagnetic pulse is guided through the bend by the existence of a photonic gap in 2D. The FDTD method is particularly useful to model this kind of structures.

Measuring the Photonic Band Structure

In conclusion, a few experimental methods for measuring the photonic band structure are mentioned. The frequency window of a photonic bandgap can be obtained by transmission (or reflection) measurements. The conceptually simplest method for obtaining the photonic band dispersion in the direction of light propagation is to measure the phase delay $\varphi(\omega)$ of an electromagnetic wave through the photonic crystal: if d is the thickness of the sample, the wave vector at any given frequency can be obtained from the relation $\varphi(\omega) = k(\omega)d$. This method has been applied by means of phase-sensitive measurements, first in the microwave spectral region and later in the near infrared and visible regions. The band dispersion in the direction of light propagation can also be obtained by analyzing Fabry–Pérot fringes in reflection or transmission through a sample of finite size. The photonic dispersion in two or three dimensions can also be derived by measuring the beam propagation (i.e., the refraction) of a light beam impinging on the photonic crystal at nonnormal incidence. The 2D band dispersion above the light line in photonic crystal slabs can be obtained

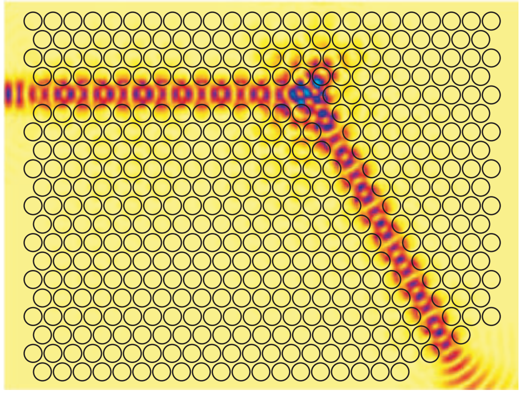

Figure 7 Electric field profile for an electromagnetic wave propagating through a 120° bend designed in a triangular lattice of air holes (FDTD calculation in two dimensions). The modulus of the field is represented in a linear scale.

by variable-angle reflectance measurements from the crystal surface. The principle is apparent from Figure 5b: the spectral position of a resonant structure in reflectance yields both the frequency and the parallel wave vector of a photonic mode. The same variable-angle reflectance technique can be applied to 2D and 3D photonic crystals, and in this case, it leads to the dispersion of photonic bands in a plane parallel to the crystal surface. Finally, the photonic dispersion can also be obtained by angle-resolved luminescence measurements in the far field: this is the photonic analog of angle-resolved photoemission spectroscopy for electronic systems.

Further Reading

Bowden CM and Zheltikov AM (eds.) (2002) *Nonlinear photonic crystals*, *Feature Issue, Journal of the Optical Society of America B* 19: 1961–2296.
Busch K, Lölkes S, Wehrspohn RB, and Föll H (eds.) (2004) *Photonic crystalsadvances in design, fabrication, and characterization*. Weinheim: Wiley-VCH.
Joannopoulos JD, Meade RD, and Winn JN (1995) *Photonic Crystals – Molding the Flow of Light*. Princeton NJ: Princeton University Press.
John S (1987) Strong localization of photons in certain disordered dielectric superlattices. *Physical Review Letters* 58: 2486–2489.
Johnson SG and Joannopoulos JD (2001) *Photonic CrystalsThe Road from Theory to Practice*. Boston: Kluwer Academic Publishers.
Krauss TF and Baba T (eds.) (2002) *Photonic crystal structures and applications*, *Feature Section, IEEE Journal of Quantum Electronics* 38: 724–963.
Rarity J and Weisbuch C (eds.) (1996) In: *Microcavities and Photonic Band GapsPhysics and Applications*, vol. 324. Dordrecht: Kluwer Academic NATO ASI Series E.
Sakoda K (2001) *Optical Properties of Photonic Crystals*, vol. 80. Berlin: Springer Springer Series in Optical Sciences.
Sigalas MM, Ho KM, Soukoulis CM, Biswas R, and Tuttle G (1999) Photonic crystals. In: Webster J (ed.) *Wiley Encyclopedia of Electrical and Electronics Engineering*, vol. 16, pp. 345–359. New York: Wiley.
Slusher RE and Eggleton BJ (eds.) (2003) *Nonlinear Photonic Crystals*, vol. 10. Berlin: Springer Springer Series in Photonics.
Soukoulis CM (2001) Photonic band gap materials. In: Fouque JP (ed.) *Diffuse Waves in Complex Media*, pp. 93–107. Dordrecht: Kluwer.
Soukoulis CM (ed.) (2001) *Photonic Crystals and Light Localization in the 21st Century*, vol. C563. Dordrecht: Kluwer NATO Science Series.
Yablonovitch E (1987) Inhibited spontaneous emission in solid-state physics and electronics. *Physical Review Letters* 58: 2059–2062.

Integrated Circuits

M Van Rossum, IMEC, Leuven, Belgium

© 2005 Elsevier Ltd. All rights reserved.

This is an update of M. Van Rossum, Integrated Circuits, Editor(s): Franco Bassani, Gerald L. Liedl, Peter Wyder, Encyclopedia of Condensed Matter Physics, Elsevier, 2005, Pages 394–403, ISBN 9780123694010, https://doi.org/10.1016/B0-12-369401-9/00503-9.

Introduction 748
IC Materials 748
IC Technology 749
Device Fabrication 749
The transistor well 749
The gate insulator 750
Gate, source, and drain 750
Contacts 750
Interconnects 750
Packaging 752
Processing Techniques 753
Photolithography 753
Dry Etching 754
Deposition Techniques 754
PVD 754
CVD 754
Epitaxy 754
Physics of Integrated Circuits 754
Integration Density: Moore's Law 754
Speed and Power 755
Applications 755
Memories 755
Random-access memory (RAM) 755
Read-only memory (ROM) 755
Microprocessors and Custom ICs 756
Microprocessors 756
Custom ICs 756
Further Reading 756

Introduction

The performance of a complex electronic circuit usually scales with the number of its components. In the early days of electronics, circuits were bulky assemblies of vacuum valves (invented by Lee de Forest in 1906), resistors, and capacitors fixed on a metal frame, and connected with soldered copper wires. The invention of the transistor by Bardeen, Brattain, and Shockley in 1947 already contained the seed of further circuit miniaturization, but it would take more than 10 years before this potential was fully recognized. In 1959, Jack Kilby from Texas Instruments and Robert Noyce from Fairchild independently filed patents for an electronic circuit whose components were fabricated on a single piece of semiconductor material (germanium for Kilby and silicon for Noyce). Kilby's circuit measured 0.2×0.8 inches and had 12 components, connected together with tiny gold wires. To quote his own words, "what we didn't realize then was that the integrated circuit would reduce the cost of electronic functions by a factor of a million to one, nothing had ever done that for anything before." Today, integrated circuits (ICs) may contain tens of millions of transistors per square centimeter. Jack Kilby received the Nobel prize for his invention in 2000 (Figure 1).

IC Materials

The vast majority of ICs are fabricated on single crystal silicon. Although not the best semiconductor material, silicon is still unrivaled thanks to its crystalline perfection, its excellent combination of electrical and thermomechanical properties, as well as the outstanding quality of its natural oxide, SiO_2. For some low-cost applications where data speed is not an issue, polycrystalline silicon films deposited on glass can also be used. The most recent IC technology is silicon-on-insulator (SOI), which consists of a thin monocrystalline silicon film, isolated from the bulk silicon substrate by an intercalated SiO_2 layer.

Over the years, other substrate materials have found a role in niche technologies, targeting applications for which silicon is not the optimal choice. The most important IC technology after silicon is based on III–V compound semiconductors. Prominent among

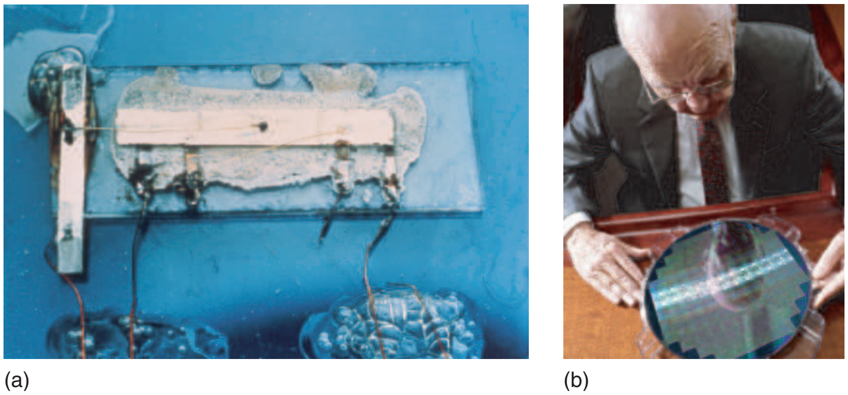
(a) (b)

Figure 1 (a) The first integrated circuit. (b) Jack Kilby contemplating a 300 mm silicon wafer with state-of-the-art ICs. (Courtesy of Texas Instruments.)

them is gallium arsenide (GaAs), which is a better semiconductor than silicon although less robust from a manufacturing point of view. Due to its high electron mobility and high bulk resistivity, it is the substrate of choice for high-frequency circuits. As a direct bandgap material, gallium arsenide is also an efficient light emitter and therefore well suited for optoelectronic devices, a domain where silicon cannot compete since its own bandgap is indirect. GaAs can be combined with indium, phosphorous, or antimony to tune the band structure for specific applications. Indium phosphide (InP), another III–V compound, is a convenient substrate for many epitaxial films made from ternary or even quaternary III–V alloys. A new player in this area is gallium nitride (GaN), well-suited for power electronics and optoelectronics. GaN is not available as a bulk substrate and must be grown on sapphire or silicon carbide (SiC). Together with SiC and diamond, it belongs to a special class of wide bandgap semiconductors, which are fit for high-voltage device fabrication. However, their present materials quality is lagging far behind silicon and the commercial future of these technologies is still unclear.

IC substrates are usually produced as circular wafers, a few hundred micrometers in thickness, cut from as-grown cylindrical ingots of various diameters. Silicon wafers are commercially available with diameters up to 300 mm, whereas other semiconductor substrates are significantly smaller. Silicon ICs can be classified into two groups based on the type of transistors they contain. Bipolar circuits use bipolar junction transistors as their principle elements. Metal oxide semiconductor ICs contain mainly *n*- and *p*-type metal-oxide semiconductor field-effect transistor (MOSFET) as their active components and are the dominant technology for logic circuits (i.e., processors and memories, also called digital circuits). Today, the most common architecture for digital electronics is complementary MOS (CMOS), which uses a combination of a *p*-MOSFET and *n*-MOSFET as its basic device to minimize the power consumption during switching.

IC Technology

The making of an IC typically proceeds through three standard stages: (1) fabricating individual devices, (2) wiring the devices together to form the circuit, and (3) encapsulating the IC in a package. The full sequence of the fabrication steps required to produce a complete circuit is called the process flow. Different IC technologies therefore require different process flows. In the following, the focus will be on CMOS technology because of its dominant position in the IC market.

Device Fabrication

Starting from a clean substrate, the first stage of IC fabrication – commonly called front-end process – is to form individual devices. The devices are produced through several levels of patterning, each level consisting of a well-defined combination of photolithography, deposition and etching steps. For a MOSFET, the typical front-end sequence is the following:

1. doping and isolation of the transistor wells and junctions
2. growth of the gate insulator
3. patterning of the gate electrode
4. formation of the metal contacts

In total, a CMOS process may require several hundred individual steps. The most important ones are outlined below.

The transistor well

The well is the region of the substrate containing the transistor body. Since current must pass through the device, the well must be doped to provide charge carriers (electrons or holes). After the device area has been delineated by photolithography and isolated from its surroundings by thin grooves (so-called shallow trenches), etched into the substrate and filled with a dielectric material, dopants are introduced into the well region. For *n*-type MOSFETs, the well must be *p*-doped whereas *p*-MOSFETs need *n*-doped wells. In the early days of MOS technology, diffusion of impurities from a gaseous or solid-state source was the standard doping technique. However, with present deep-submicron device dimensions, this method has been replaced by ion implantation, which offers far better flexibility, precision and depth control. Ions of boron (for *p*-type), phosphorous or arsenic (for *n*-type) are accelerated by an electric field and gain a kinetic energy of a few tens of kiloelectronvolts, allowing them to penetrate some hundred nanometers into the substrate. Several implantation steps are usually required to reach the desired dopant profile. The as-implanted region has high electrical resistance due to the radiation-induced lattice damage, which can range from isolated point defects to complete amorphization. The high defect density prevents the dopants from occupying substitutional lattice sites, thereby leaving them electrically inactive. In order to activate the dopants, damage must be removed by a high-temperature annealing step (typically between 800 and 1000°C). This can be done in a conventional furnace, but a short thermal pulse produced by halogen lamps (the so-called rapid thermal process or RTP) is often preferred in order to minimize the motion of the implanted species during annealing.

The gate insulator

The thinnest feature of the transistor is the gate insulator, which consists of a few nm of silicon dioxide (SiO_2) deposited directly on top of the transistor well. The gate oxide is formed by thermal oxidation of the silicon surface, which involves heating the substrate above 900°C in an oxygen atmosphere (dry oxidation) or a mixture of oxygen and water (wet oxidation). Trace amounts of other gases are often added to improve the electrical quality of the oxide. Both the temperature gradients and the gas flow pattern in the furnace must be accurately controlled to obtain a very thin and uniform oxide. Short thermal pulses produced by rapid thermal processing can also be used. Although the as-grown oxide layer is structurally amorphous, the high quality of its chemical bonds with the silicon surface limits the density of interface defects to very low levels (less than $10^{10}\,cm^{-2}$). The quality of the gate oxide and of the Si/SiO_2 interface is a crucial factor to ensure the good electrical behavior of the MOSFET. However, there are now indications that further shrinking of the devices will push SiO_2 toward its application limit. For very thin oxides, direct carrier tunneling through the gate insulator produces a sizable current leakage and unwanted power dissipation. This problem can, in principle, be overcome by introducing "high-*k* insulators," that is, gate dielectrics with a higher polarizability than SiO_2. These materials would allow the physical thickness of the insulator to increase (thereby keeping tunneling currents at an acceptable level), while maintaining a strong capacitive coupling between the gate and the channel. At this time, refractory metal oxides such as HfO_2 as well as some ferroelectrics are potential candidates for replacing silicon dioxide in future ICs.

Gate, source, and drain

The gate electrode sits on top of the oxide and regulates the current inside the transistor channel. It is made of doped polycrystalline silicon (usually designated as "poly"), which is a reasonably good conductor and can be patterned into very narrow lines. Today, the most advanced commercial transistors have a physical gate length of ~50 nm. Since the gate is the narrowest feature on any IC, its formation involves the most demanding steps of the front-end process flow. First, a blanket layer of poly is deposited by chemical vapor deposition (CVD), after which the gate fingers are defined by a lithography step and patterned by dry etching. In order to achieve the right threshold voltage for the transistor, the poly-gate on the NMOS is *n*-doped whereas on PMOS it is *p*-doped. Both doping steps are performed by ion implantation and annealing. In a MOSFET, the current input and output electrodes are called source and drain. They are defined by local implantation of complementary doping species (*n* for *p*-well and *p* for *n*-well) very close to the surface, thereby forming shallow *p*–*n* or *n*–*p* junctions, depending on the transistor type. Fine-tuning of the junction profiles requires additional implantation steps followed by annealing.

Contacts

Metals are needed for electrical contacts to the three device electrodes. The contact material must exhibit low electrical resistance and be chemically compatible with silicon in order to avoid interface degradation over time. For many years, metal silicides have been used extensively on the source and the drain: first titanium disilicide ($TiSi_2$), and more recently cobalt disilicide ($CoSi_2$) and nickel monosilicide (NiSi). The silicide layers are formed by solid-state reaction of a deposited metal film with the underlying silicon; therefore, it is important that the reaction should not consume too much silicon. In the same way, a polycrystalline silicide layer or polycide is formed on top of the poly in order to contact the gate electrode and to reduce the gate series resistance (Figures 2 and 3).

Interconnects

Connecting the individual transistors is an essential step in the production of an IC. The process flow needed for interconnect fabrication is called the back-end sequence. Since the early days of IC technology, aluminum-based alloys have been used as the interconnect metal. This choice was dictated by the low resistivity of aluminum, its high ductility, easy etching behavior, and good coverage of nonplanar geometries. The latter property is particularly important, since complex ICs normally require many levels of wiring stacked on top of each other, giving rise to a multilayer structure called the multilevel interconnect scheme. To improve the electrical reliability of the wires, particularly with respect to electromigration, aluminum–silicon and aluminum–silicon–copper alloys are preferred over pure aluminum. However, in the late nineties the series resistance of aluminum-based lines became a bottleneck for circuit performance. After more than 30 years of use, the aluminum wires were finally abandoned in favor of a copper-based metallization scheme. Copper conducts about 60% better than aluminum, but patterning it into submicron wires is difficult because traditional plasma etch techniques do not work on copper. A novel process called "damascene" had to be

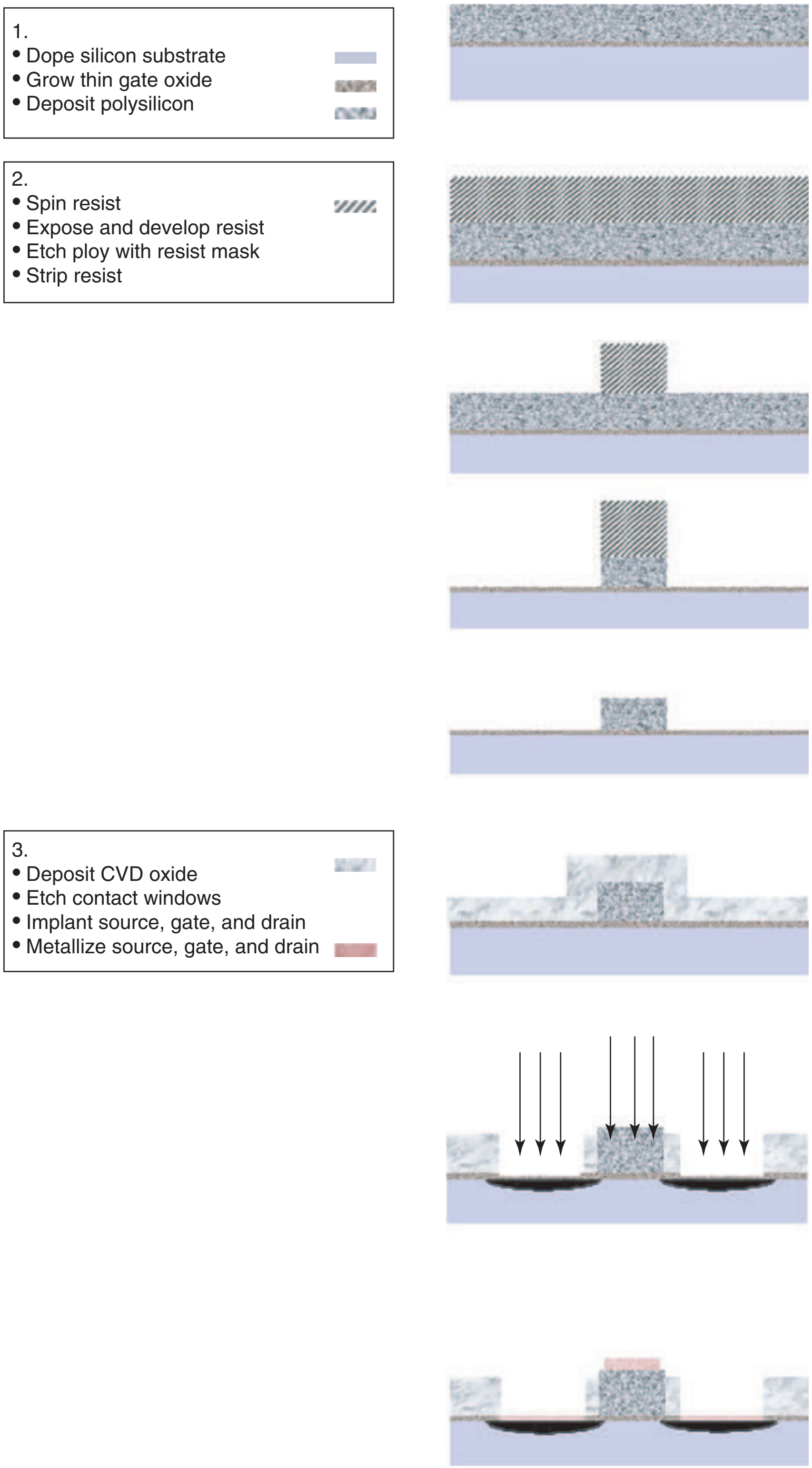
1.
• Dope silicon substrate
• Grow thin gate oxide
• Deposit polysilicon
2.
• Spin resist
• Expose and develop resist
• Etch ploy with resist mask
• Strip resist
3.
• Deposit CVD oxide
• Etch contact windows
• Implant source, gate, and drain
• Metallize source, gate, and drain

Figure 2 Schematic process flow for an MOS transistor.

introduced, due to its similarity with the well-known metal inlaid technique that goes back to the Middle Ages. Following this process, the conductor wires are embedded in a dielectric film deposited on the silicon substrate or on a previous interconnect layer. Copper lines are formed by electroplating the metal inside preformed trenches, which have been etched into the dielectric. The formation of a multilevel damascene scheme requires special polishing techniques (called chemical mechanical polishing or CMP) to planarize each interconnect layer by removing the excess metal outside the trenches (Figure 4).

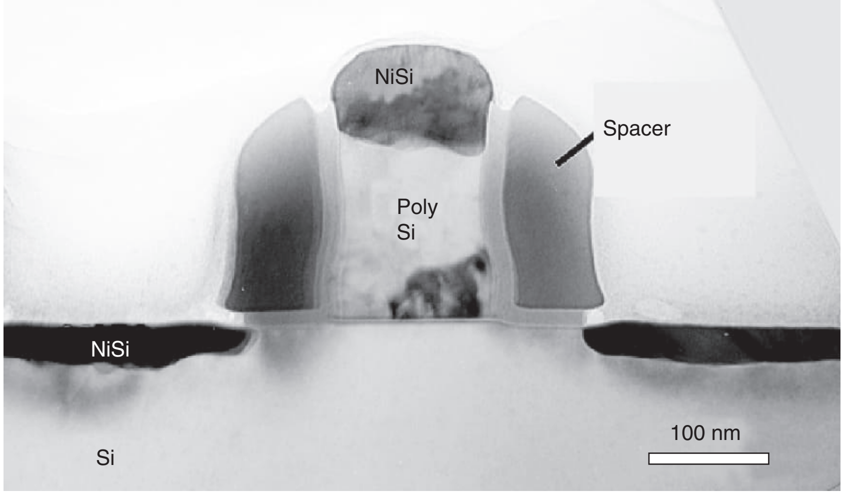

Figure 3 Cross-sectional scanning electron microscopy picture of an integrated MOS transistor. (Courtesy of IMEC.)

Packaging

Packaging the IC serves a twofold purpose: to protect the chip against mechanical damage and corrosion, and to provide electrical connections with the outside circuitry. An IC package consists of a sealed box which is either from ceramic material (for hermetic sealing) or from a plastic mold (for low-cost packaging). Metallic pins are attached to the base plate of the package, to be inserted in the printed circuit board. After completing the back-end process, the backside of the chip is fixed to the package base plate using a

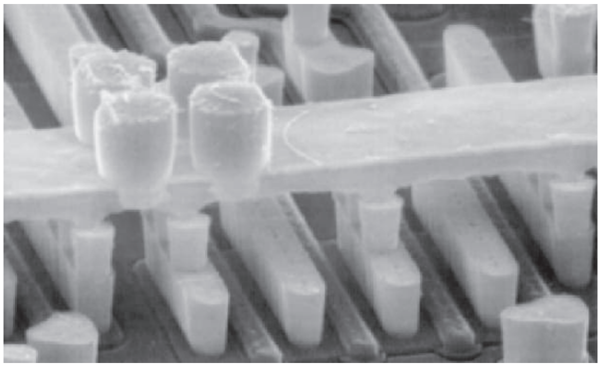
(a)

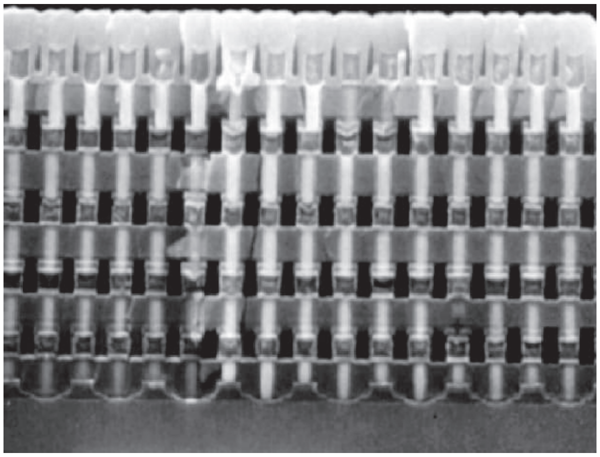
(b)

Figure 4 (a) Top view, and (b) cross section picture of a multilevel interconnect structure. (Courtesy of IMEC.)

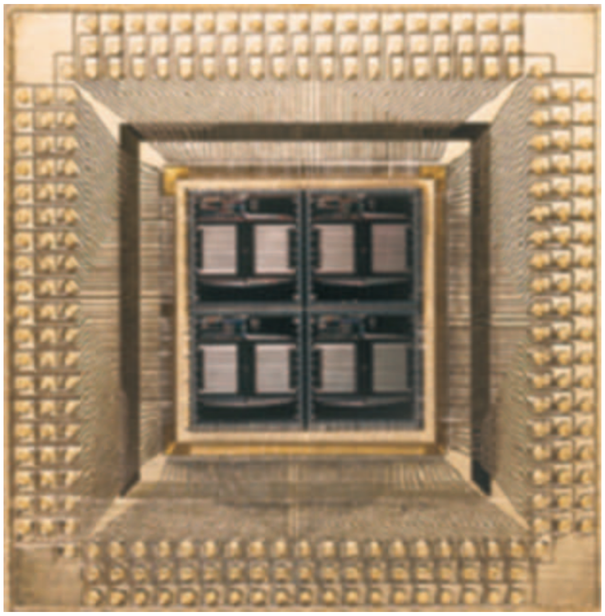

Figure 5 IC in package. (Courtesy of IMEC.)

conductive paste or metal solder. Next, the bonding pads of the chip are connected to the package pins. The most common technique is wire bonding: thin aluminum or gold wires are thermally bonded to the IC pads and to the pins, sometimes with the help of ultrasonic vibrations. Wire bonding is cheap and reliable, but cannot handle the increasing density of bonding pads in the most recent IC generations. Flip-chip bonding is now an increasingly popular alternative. Microscopic solder balls are first deposited on the IC bonding pads. The chip is then positioned face down to the package base plate, so that the solder balls can be attached directly to the pin pads. Since this method does not use wires, it offers both higher connection density and better reliability than the traditional bonding schemes. After wiring, the upper lid of the package is sealed or molded to the base plate for final encapsulation (Figure 5).

Processing Techniques

Photolithography

Photolithography uses a beam of photons to transfer a pattern written on an optical mask to the substrate surface. In a complex IC process, a wafer will go through the photolithographic step in the order of 20–30 times. Photolithography is, therefore, the key technology of IC fabrication and an essential driver behind the miniaturization trend commonly known as Moore's law. It was introduced almost simultaneously with the invention of the IC in 1959, but in the meantime, the minimum dimensions on the masks have decreased by several orders of magnitude, forcing continuous improvement in lithography tools and processes.

A standard lithography sequence involves a large number of steps. The wafer is initially cleaned and heated to remove any moisture from its surface. After deposition of an adhesion promotor, a liquid polymer called photoresist is spun on the surface while the wafer is kept rotating at high speed. After a thermal bake-out, the substrate is introduced in an optical projection tool called stepper/scanner. A light beam passing through the mask is focused on the wafer through a reduction lens system to produce the desired image in the photoresist. In order to achieve high resolution, only a small portion of the mask is imaged once, but the small image field is repeated over the surface of the wafer by a combination of stepping and scanning operations. During exposure, the photoresist material undergoes some light-triggered chemical reactions, which cause the illuminated regions to be either more or less acidic. If they become more acidic, the material is called a positive photoresist, while in the reverse case it is a negative photoresist. The resist is then developed in an alkali solution such as sodium hydroxide (NaOH), which removes either the exposed (positive photoresist) or the unexposed (negative photoresist) polymer. After development, the wafer is finally "hardbaked" at high temperature in order to solidify the remaining photoresist. The resist can then be used as a patterning mask for etching, deposition or implantation. After patterning, the resist is stripped from the wafer with appropriate solvents.

The optical resolution of the lithography system is the main factor determining the smallest device size that can be fabricated at any time. The ability to form a clear image of a very small feature is limited by the wavelength of the light and the ability of the lens system to capture enough diffraction orders of the illuminated mask. Although theoretically the Rayleigh diffraction limit determines the maximal achievable resolution, in practice, it is possible to use special (but costly) tricks called resolution enhancement techniques that improve resolution beyond the Rayleigh limit by a factor of 2 or more. Current state-of-the-art photolithography tools use deep ultraviolet light (DUV) with wavelengths of 248 and 193 nm, allowing feature sizes below 100 nm to be printed with good yield. Extreme ultraviolet (EUV) systems using 13 nm radiation are presently under development for introduction by the end of this decade. Because such short wavelength radiation cannot be diffracted by lens systems or absorbed by bulk masks, the EUV technology will require a transition from diffractive to fully reflective optics.

Dry Etching

The aim of the etching process is to remove material from the IC surface in the areas left uncovered after photoresist development. For most patterning steps, dry (plasma) etching is now the standard procedure, while "wet" etching using liquid chemicals is still used to clean wafers. The main advantage of dry etching is its ability to achieve sharp etch profiles with nearly vertical sidewalls. This creates features with a high aspect ratio, as required by the relentless miniaturization of the circuit elements. A hot plasma formed by RF excitation of a neutral gas species is directed on the wafer by a static electric field. The radicals in the gas react with the substrate material to form volatile byproducts which are either evacuated from the etch chamber or deposited on the chamber walls. The mixture normally consists of a hydrogenated hydrocarbon diluted in an inert gas. However, the gas composition depends on the material to be etched, and will be different for silicon, metals or SiO_2. The strength of the DC field also plays a role in the etch process. A strong field increases the kinetic energy of the ions, and therefore enhances the amount of physical etching, which depends on mechanical sputtering. On the other hand, low-energy ions will act essentially by chemical etching, which proceeds through surface reactions resulting in smoother patterns. In this way, the etching mechanism can be tuned to optimize the shape of the patterned structures.

Deposition Techniques

PVD

In standard silicon processing, physical vapor deposition (PVD) uses target sputtering rather than target evaporation because of its better step coverage. For aluminum interconnect layers, plasma-induced sputtering is the most convenient technique. The sputtered metal lands on the wafer surface where it forms a thin metal film, which can be further etched into wires. The film thickness is proportional to the width of the conductor lines, and usually lies in the range of a few hundred nanometers. Plasma sputtering can also be employed to deposit nonmetallic layers, especially insulators, although for the latter, CVD is the preferred method.

CVD

Chemical vapor deposition is a process by which a thin film is deposited on a substrate by chemical reaction in a gas at an elevated temperature. If required, the reaction temperature can be lower by using plasma-enhanced CVD (PECVD). Over the years, CVD has become very popular due to its versatility, speed of deposition, and excellent step coverage. CVD can be used for metal, semiconductor, and insulating films. The structure of the deposited film can be monocrystalline, polycrystalline, or amorphous. The lattice structure depends primarily on the substrate, the reaction rate, and the temperature. Selective deposition is also possible, by choosing precursor gases that react preferentially with specific surfaces. CVD is the preferred method to deposit polycrystalline silicon, as well as various types of oxide films used for isolation of the interconnect layers. These interlayer dielectrics are grown by CVD at low pressure (LPCVD). Thin metallic layers such as titanium nitride (TiN), which are used as seed layers for copper electroplating or as a seal between the interlayer dielectrics, are also deposited by CVD.

Epitaxy

Epitaxy is a process by which a deposited film is forced into a high degree of crystallographic alignment with the substrate lattice. Several epitaxy techniques are now available, such as molecular beam epitaxy (MBE), epitaxial CVD, or atomic layer epitaxy (ALE). In all cases, the deposition process must be slow enough to allow the atoms to rearrange themselves on the surface according to the lattice orientation of the substrate. Contamination of the surface by impurities must be kept minimal, since it will disturb the epitaxial alignment. Epitaxial layers are now widely used in IC technology and the number of applications is still growing. In the early days, the epitaxy process was limited to deposition of silicon on silicon (homoepitaxy). Today, an increasing number of devices require thin film hetero-epitaxy, for example, growing a binary alloy such as silicon–germanium (SiGe) epitaxially on the silicon wafer. For layers with high Ge concentration, the epitaxy is made difficult by the lattice mismatch between the substrate and the thin film. However, using appropriate techniques, the epitaxial layer can be grown pseudomorphically, meaning that the distance between the film atoms will adapt itself spontaneously to the bond length of the substrate material.

Physics of Integrated Circuits

Integration Density: Moore's Law

Moore's original statement, made in 1965, was modestly presented as an educated guess at the expected development of ICs over the next ten years. Or, to put it in his own words: "With unit cost falling as the number of components per circuit rises, by 1975 economics may dictate squeezing as many as 65.000 components on a single silicon chip" (see Further Reading Section). Almost four decades later, unit cost is still falling with the number of components, and as long as this favorable trend persists, the "law" will remain firmly in place. The continuation of Moore's law is made possible by the relentless shrinking of the MOSFET dimensions. Now, spanning more than two orders of magnitude, the downscaling of the MOSFET is a truly unique occurrence in the history of technology. The physical base for this miniaturization is a set of scaling rules defined some years after Moore's initial paper.

In essence, the scaling algorithms tell us that the transistor performance (mainly its gate delay time and overall power dissipation) will improve with decreasing dimensions, provided the rules are properly applied. However, a point has been reached where the presence of nonscaling quantities such as the thermal voltage kT/q and the semiconductor bandgap (together with some others) can no longer be neglected. These nonscaling parameters are giving rise to so-called "short-channel" effects, such as threshold voltage shifts and many others, which tend to degrade the transistor switching speed and lower its power efficiency. These disturbing effects can be acted upon with specific counter-measures, partly technological and partly design-related. Up to now, device engineers have been remarkably successful in alleviating the negative impact of short-channel effects. However, it appears increasingly difficult to define a universal approach similar to the early scaling laws, and a certain amount of specialization in the circuit technologies (such as distinguishing between high-speed and low-power applications) is becoming unavoidable.

Speed and Power

Power and speed issues are strongly linked by the scaling rules. The width, length, and gate oxide thickness all scale roughly equally by a common factor. Therefore, the primary effect of the device scaling is to reduce all the capacitances, which provides a proportional decrease in power consumption and RC delays. However, not all the vertical dimensions of the circuit scale down by the same factor. In particular, the thickness of the interconnect lines cannot change as fast due to fundamental technology limitations. This increases the fringe capacitance from the metal side to the substrate, as well as the capacitance between adjacent line segments. Compounding this problem, the decreasing wire width raises the series resistance of the lines. As a result, RC delays in the lines tend to become more important with respect to transistor delays. This can be counteracted by optimizing the interconnect layout, and by introducing low-*k* dielectrics as the insulating layers between the copper wires.

The scaling rules also impact on the power consumption of the IC. There are two main sources of power dissipation: dynamic switching power due to the charging and discharging circuit capacitances, and static dissipation from leakage currents. When CMOS devices switch, the output is either charged up to the transistor bias voltage, or discharged down to the ground. The power dissipated during switching is therefore proportional to the switching speed and to the capacitive load. Decreasing the clock frequency of the circuit is, therefore, an efficient way to lower the dynamic power consumption.

Static power dissipation is linked with two types of leakage currents: reverse-bias diode leakage on the transistor drains, and subthreshold leakage through the channel when the transistor is turned off. Diode leakage must be tackled through process optimization, mainly by improving the quality of the junctions. Subthreshold current is a more complex issue. The process parameter that predominantly affects its value is the threshold voltage, since reducing the latter exponentially increases the subthreshold current. Static power dissipation can, however, be reduced by shrinking the transistor size, and by lowering the supply voltage.

Applications

Most ICs belong to one of three main categories: memories, microprocessors, and custom ICs.

Memories

Random-access memory (RAM)

A type of computer memory that can be accessed randomly; that is, any byte of memory can be accessed without disturbing the other bytes. RAM is the most common type of memory found in computers and other information processing devices. There are two basic types of RAM: dynamic RAM (DRAM) and static RAM (SRAM). Both are volatile memories, meaning that they lose their contents when the electrical power is turned off. RAM circuits are organized in cells, with each cell storing a binary 1 or 0. DRAM cells are very simple, consisting basically of one transistor and one capacitor for charge storage. Because this capacitor leaks, a DRAM needs to be refreshed thousands of times per second. This makes DRAM relatively slow and power-hungry. However, due to the small cell size, DRAM is best-suited for high-density storage (Figure 6). SRAMs are more complex, with 4–6 transistors per cell, providing a stable storage, which does not need to be refreshed. SRAM is very fast and power-efficient, but the complexity of its cell makes it much more expensive than DRAM. Due to its high cost, SRAM is used mainly as a memory cache.

Read-only memory (ROM)

Computers almost always contain a read-only memory that holds instructions to boot the operating system and perform diagnostics. ROM is nonvolatile, that is, it does not need electrical power to keep its data stored. Like RAM, ROM memories are random-access, but they cannot change their content during the computer operation. However, some types of ROM allow changing the content by special procedures. The most common ones are erasable programmable read-only memory (EPROM), electrically erasable programmable read-only memory (EEPROM) and FLASH EEPROM. FLASH (not an acronym) memories, which store the information bits in a second transistor gate called the floating gate, have become increasingly popular in recent years. They can be erased and reprogrammed in blocks instead of one byte at a time, which is faster and less power consuming than other EEPROMs. PCs have their basic input-output system (BIOS) stored on a flash memory chip so that it can easily be updated if necessary. Flash memory is also very common in communication appliances and portable devices such as cellular phones and smartcards.

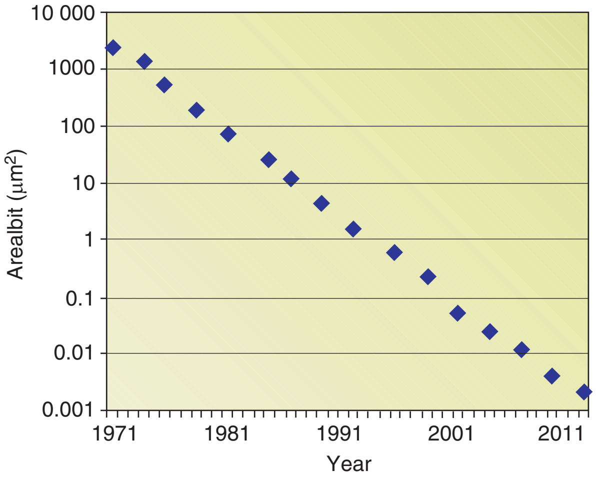

Figure 6 Moore's law in action: evolution of the chip area / bit for a standard DRAM memory cell.

Microprocessors and Custom ICs

Microprocessors

Also called central processing unit (CPU), microprocessors are ICs that can execute instructions by running a software program. Although computer microprocessors have become a benchmark for the IC industry, they only represent a small part (~2% in unit sales) of the total CPU market. By far, the largest, by number, are the embedded microprocessors (also called microcontrollers), which can be found in many consumer products, ranging from toys to automobiles.

Custom ICs

In contrast to standard memories and microprocessors, custom ICs are specially designed for specific product applications. The main types are:

- *Application-specific ICs (ASICs)*. They are meant to achieve optimal performance in terms of speed and/or power consumption. ASICs are custom-designed for a specific application, either full custom (meaning that the design is made from scratch) or starting from standard cells or gate arrays, where the designers can take advantage of pre-existing blocks.
- *Field-programmable chips*. These are special chips that can be reconfigured by the customer. The most popular ones are field-programmable gate arrays (FPGAs). Their circuits are diced into regular arrays, which can be disconnected by blowing microscopic fuses. In this way, the desired functionality is "burned into" the IC. This process is reversible, meaning that the original connections can be restored and a new pattern burned. Although FPGAs are usually slower and less power-efficient than ASICs, they have become very popular due to their flexibility and ease of programming.
- *Analog/RF ICs*. Even if digital signal processing today represents the largest market for the semiconductor industry, there is also a wide variety of ICs handling analog and high-frequency signals. Some chips process both digital and analog information and are called mixed-mode ICs. Typical applications are amplifiers, mixers, multiplexers, and analog-to-digital converters. Wireless communication devices make heavy use of these components, which can be found in every cellular phone set.

Further Reading

Moore GE (1965) Cramming more components onto integrated circuits. *Electronics* 38(8): 114–117.
Sze SM and Chang CY (1996) *ULSI Technology*. New York: Mc Graw-Hill.
Turley J (2003) *The Essential Guide to Semiconductors*. Upper Saddle River: Prentice-Hall.
Wolf S and Tauber RN (2000) *Silicon Processing for the VLSI ERA*, 2nd edn. Sunset Beach: Lattice Press.

Semiconductor Devices

T Takahashi, University of Tokyo, Tokyo, Japan

© 2005 Elsevier Ltd. All rights reserved.

This is an update of T. Takahashi, Semiconductor Devices, Editor(s): Franco Bassani, Gerald L. Liedl, Peter Wyder, Encyclopedia of Condensed Matter Physics, Elsevier, 2005, Pages 264–273, ISBN 9780123694010, https://doi.org/10.1016/B0-12-369401-9/00497-6.

Introduction 757
Junction Diodes 757
Bipolar Transistors 758
Field Effect Transistors 759
Memories 762
Photodetectors and Photodiodes 763
Solar Cells 765
Light Emitting Diodes 766
Laser Diodes 766
Wide Bandgap Materials 768
Further Reading 769

Introduction

Semiconductor devices are key devices in modern electronics, and are roughly categorized into electronic devices and optical devices. The main applications as electronic devices are junction diodes, transistors, and memories, which are widely used in large-scale integrated circuits (LSI), as well as power devices such as thyristors and so on. As optical devices, light emitting diodes (LEDs), laser diodes (LDs), and photo detectors (PDs) are utilized in optical display and communication systems, while solar cells are important for energy conservation. In the following sections, the basic principles of these devices are described.

Junction Diodes

A junction of *p*-type and *n*-type semiconductors makes a diode structure as shown in Figure 1. Electrons or holes are the majority carriers in the *n*-type or *p*-type semiconductor, respectively. In the thermal equilibrium condition, the electrons in the *n*-type region near the *p*–*n* junction interface diffuse toward the *p*-type region because of the concentration gradient, and the holes in the *p*-type region diffuse vice versa. Then a depletion region or a space charge region, where no free carriers exist, appears. If one assumes an ideal *p*–*n* junction, which is very abrupt and the depletion completely occurs as shown in Figure 2, the built-in potential V_{bi} that appears across the junction is given by

$$V_{\mathrm{bi}} = \frac{1}{2} E_{\mathrm{m}} (x_{\mathrm{p}} + x_{\mathrm{p}})$$

where

$$E_{\mathrm{m}} = \frac{qN_{\mathrm{A}} x_p}{\varepsilon_{\mathrm{s}}} = \frac{qN_{\mathrm{D}} x_n}{\varepsilon_{\mathrm{s}}}$$

and the depletion region width W is given by

$$W = \sqrt{\frac{2\varepsilon_{\mathrm{s}}}{q} \left(\frac{N_{\mathrm{A}} + N_{\mathrm{D}}}{N_{\mathrm{A}} N_{\mathrm{D}}} \right) V_{\mathrm{bi}}}$$

(here, q is the unit charge and ε_{s} is the dielectric constant).

When a positive bias V is applied to the *p*-type region with respect to the *n*-type region, the holes in the *p*-type region easily move into the *n*-type region, and the electrons in the *n*-type region move in the opposite direction. Thus a large current flows across the junction. Such a bias condition is called a forward bias. When, on the other hand, the bias condition is inversed, which is called a reverse bias, the majority carriers are not able to move at all. Then the total current density J flowing across the junction is given by $J = J_{\mathrm{s}}(e^{qV/kT} - 1)$, where J_{s} is the saturation current density, k is the Boltzmann constant and T is the temperature. Therefore, the diode has asymmetric current–voltage characteristics against the bias voltage V as shown in Figure 3, and the diode device achieves a rectification property for alternating currents. This rectification effect in the *p*–*n* junction is very important in most semiconductor devices because it can control the current flow by blocking undesirable current leakage. In the real *p*–*n* junction diode, however, a voltage breakdown occurs at a high reverse bias, which gives the reverse bias tolerance of the diode, also shown in Figure 3.

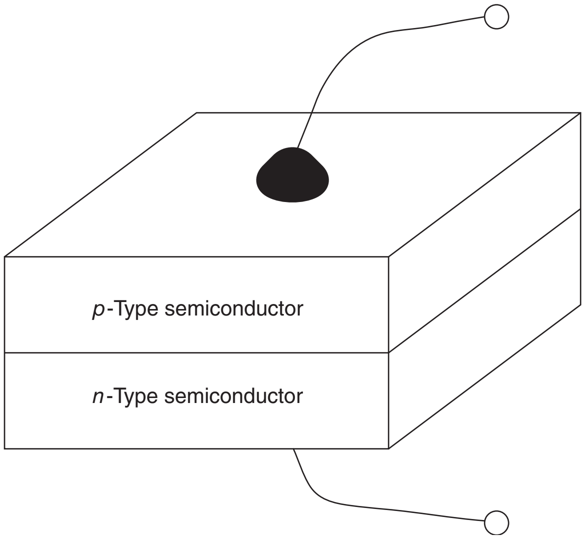

Figure 1 A schematic illustration of a *p–n* junction diode.

Bipolar Transistors

The bipolar transistor which was invented by a research group at Bell Laboratories in 1947 has become one of the most important semiconductor devices today. It consists of two *p–n* junctions, that is, *p–n–p* or *n–p–n* structures as shown in Figure 4. These three regions are called emitter, base, and collector. In the symbols of the *p–n–p* and *n–p–n* transistors, the arrow indicates the direction of current flow under normal operating conditions, where forward and reverse biases are applied to the emitter–base and collector–base junctions, respectively. The specific features in the bipolar transistor are the very thin base and the highly doped emitter. The latter brings a high injection of carriers into the base region, where the injected carriers becomes the minority, while those carriers pass through the base region into the collector with a very small recombination rate owing to the former feature. Therefore, the collector current I_C can be represented by the emitter current I_E as $I_C = \alpha I_E$, where α is slightly less than 1. In general, a forward bias V_{EB} is applied to the emitter–base junction, but the collector–base bias V_{CB} is in a reverse bias condition. Since the collector junction is highly and reversely biased, the power amplification against the input power to the emitter junction is achieved. In the following discussion, the *p–n–p* transistor is considered but an appropriate change of polarities makes the results applicable to the *n–p–n* transistor. The basic model for the bipolar transistor is the Ebers–Moll model, in which the transistor is represented by two diodes connected face to face and two current sources. A circuit diagram in the Ebers–Moll model for the *p–n–p* transistor is illustrated in Figure 5. In this model, a current I_R flowing through the collector–base diode determines a current value from the current source in the emitter side, and a current I_F through the emitter–base diode determines a current from the current source in the collector side. Here, amplitudes of current gain α_R and α_F that are barely less than 1.

There are three configurations of the bipolar transistors as shown in Figure 6. In the common-base configuration, where the base lead is used as a common terminal for input and output, a signal is inputted to the emitter–base junction that is forwardly biased, while a load resistance is connected to a side of the reversely biased collector–base junction to extract an output signal. The common-base configuration is suited for a low input impedance circuit. According to the Ebers–Moll model, the collector current I_C is given by $-\alpha_F I_F$ because I_R is almost zero. In this configuration, therefore, only voltage amplification is obtained without current amplification. On the other hand, the common-emitter configuration, in which the emitter lead is used as a common terminal, is most widely used, and the current amplification as well as the voltage amplification is achieved because the collector current I_C is given by $I_C = \alpha_F I_B/(1-\alpha_F)$ and the collector–base junction is still reversely biased. On the contrary, the common-collector configuration gives only a current gain without the voltage amplification, which is useful as an impedance converter. The typical output characteristics for the bipolar transistor in the common-base and common-emitter configurations are illustrated in Figure 7.

Since a current density strongly depends on the *p–n* junction cross section, and a switching speed is determined by the base region thickness in the bipolar device, they can easily be improved by using a large junction cross section and a thin base region, respectively. Therefore, bipolar devices are also suited for high speed and/or power devices. The three *p–n* junctions in series, such as *p–n–p–n* or *n–p–n–p* structures, are used in three- or four-terminal devices, in which bistable operations with low-power dissipation is possible. These devices are called thyristors and are applicable in high-current, high-voltage, or high-power switching devices.

One may change one or all the lead materials in the bipolar devices in order to be different from others as shown in Figure 8; such devices are called heterobipolar devices. In heterobipolar devices, many performances are well improved. For instance, (1) high-emitter efficiency owing to the blockade of the hole injection (the minority carrier injection for the emitter) from the base into the emitter by the high barrier in the valence band, (2) low-voltage drop at the emitter–base junction, and (3) high-frequency response owing to a high-current gain and low-base resistance because heavy doping in the base region is possible without degrading emitter efficiency.

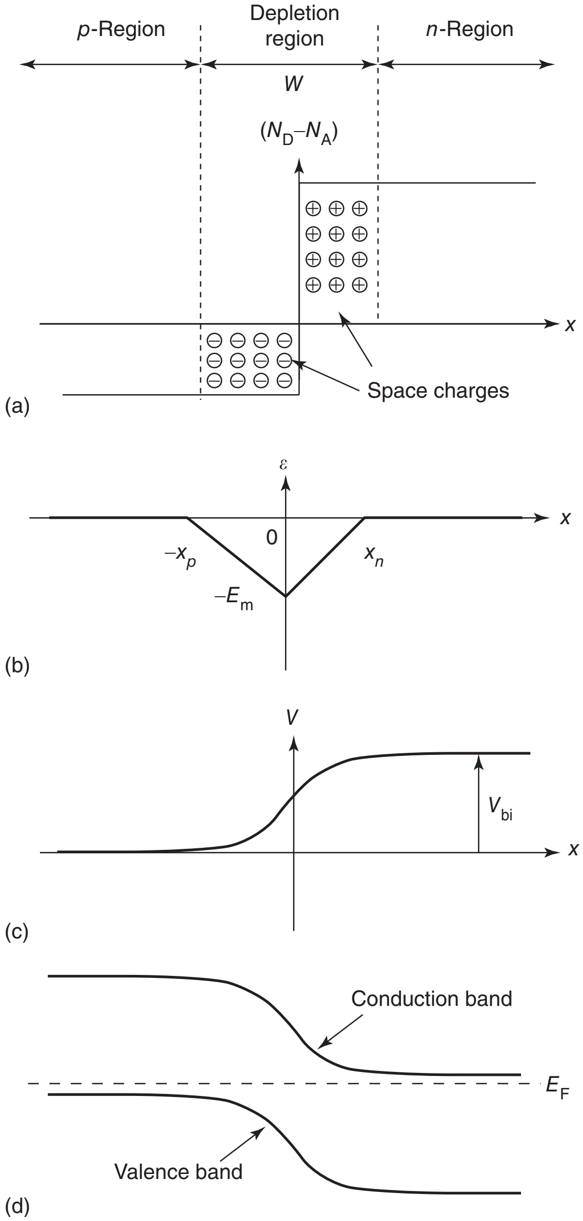

Figure 2 (a) Space charge distribution, (b) electric field distribution, (c) potential variation, and (d) energy band diagram of an ideal *p*–*n* junction in thermal equilibrium condition.

Field Effect Transistors

Similar to the bipolar transistor, a field effect transistor (FET) has three terminals, called source, gate, and drain. There are some variations of FET structures as illustrated in Figure 9. In the junction FET(JFET), which was the first proposed of all FET devices, the gate bias voltage varies the depletion region width at the *p*–*n* junction under the gate to control a channel conductance. In the metal–semiconductor FET (MESFET), a Schottky junction is formed between a gate metal and a channel semiconductor, and the depletion width is varied by the gate voltage. On the other hand, a metal-insulator-semiconductor (MIS) structure, in which an insulator film is inserted under the gate electrode to prevent current leakage between the gate and the channel, is suited for FET devices. Especially, silicon dioxide is widely used as an insulator in silicon FETs, which are called metal-oxide–semiconductor FET (MOSFET). In contrast to the bipolar transistor in which both positive and negative charges play important roles, only unipolar charges flow in the FET channel. Thus the FET is classified into either an *n*-channel or a *p*-channel FET. It is also possible to categorize MOSFET by the conductivity at zero gate bias into a normally-off type or a normally-on type as shown in Figure 10. If the channel conductance is very low at the zero gate bias and a positive bias to the gate is required to form a conductive *n*-channel, this type is called the normally-off (or enhancement) *n*-channel MOSFET. The MOSFET, in which the *n*-channel is sufficiently conductive even

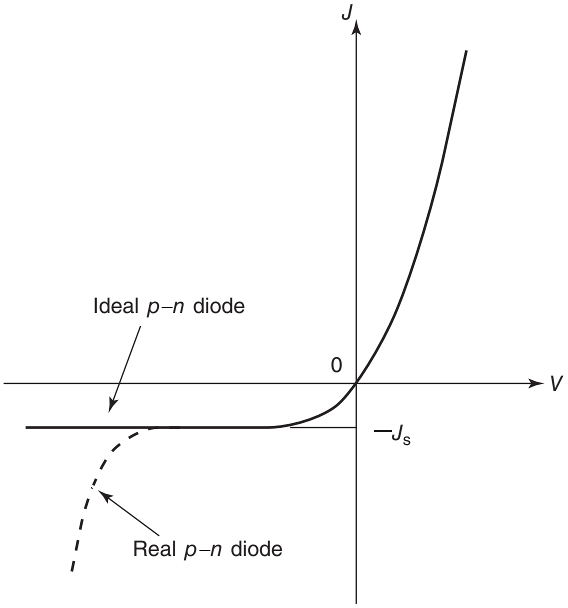

Figure 3 Current voltage characteristics in the p–n junction diode.

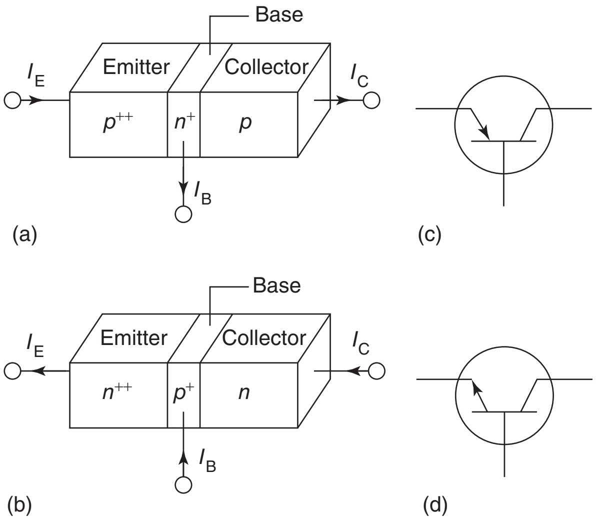
Base
Emitter
Collector
I_E
I_C
p^{++}
n^+
p
I_B
(a)
(c)
Base
Emitter
Collector
I_E
I_C
n^{++}
p^+
n
I_B
(b)
(d)

Figure 4 Schematic illustrations of (a) p–n–p, (b) n–p–n bipolar transistors and their symbols (c–d).

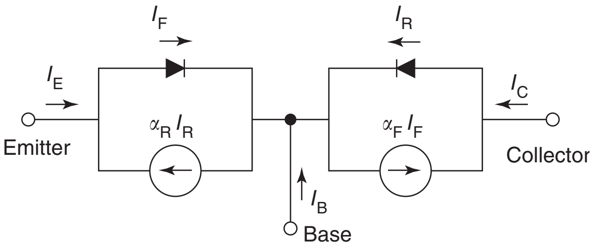
I_F
I_R
I_E
I_C
Emitter
$\alpha_R I_R$
$\alpha_F I_F$
Collector
I_B
Base

Figure 5 A circuit diagram of the Ebers–Moll model of the p–n–p bipolar transistor.

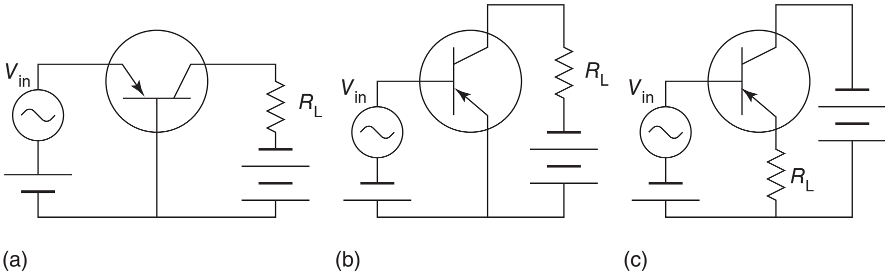

Figure 6 Configurations of the bipolar transistors; (a) common-base configuration, (b) common-emitter configuration, and (c) common-collector configuration.

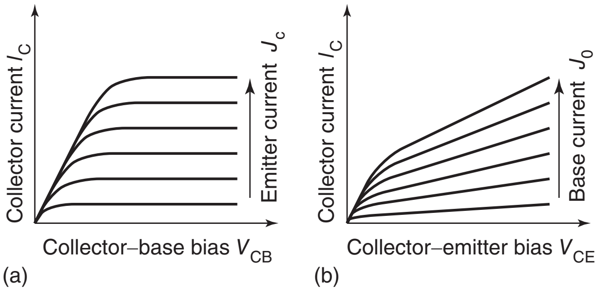

Figure 7 Typical output characteristics for the bipolar transistor in the (a) common-base, and (b) common-emitter configurations.

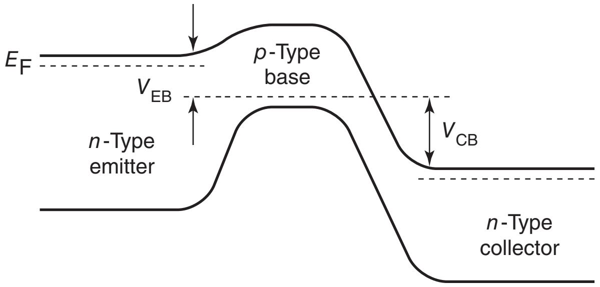

Figure 8 A schematic of the *n–p–n* heterobipolar transistor.

at the zero gate bias and one has to apply a negative bias to the gate to reduce the channel conductance by depleting the channel carriers, is the normally-on (or depletion) *n*-channel MOSFET. Similarly, there are the normally-off (enhancement) and normally-on (depletion) *p*-channel MOSFETs.

Now, a complementary use of the *p*-channel and *n*-channel MOSs in series, for instance, the normally-on *p*-channel and the normally-off *n*-channel MOSs, forms a complimentary MOS (CMOS) configuration as shown in Figure 11. In the CMOS, a low-input voltage (typically, $V_{low}=0\,V$) keeps the *n*-channel enhancement MOS (normally-off) in the "off-state" (highly resistive) and the *p*-channel depletion MOS (normally-on) in the "on-state" (highly conductive). Therefore, an output is equal to the high source voltage. In contrast, a high input (typically, $V_{high}=5\,V$) turns the *n*-channel MOS into an "on" state and the *p*-channel MOS into an "off" state, and therefore, the output becomes low level. Thus an inverter operation is realized by the CMOS configuration. In addition, a steady current passing through both the *n*-channel and *p*-channel MOSs can be sufficiently suppressed and the passing current only flows at the switching period, resulting in a very low power consumption in the circuits. Moreover, since the FET suits a planar configuration, CMOS transistors are mostly used in an integrated circuit (IC) or LSI.

By using compound semiconductor hetero-structures and a modulation doping technique, a high electron mobility transistor (HEMT) was realized as shown in Figure 12. The potential confinement of electrons at the heterointerface gives rise to a two-dimensional electron gas (2DEG). In the 2DEG system, the electron scattering probability is reduced because the states that the electrons can occupy are limited. In addition, the modulation doping also reduces the electron scattering rate by impurities because of a spatial separation between the conducting electrons and the impurities. Owing to these two effects, very high electron mobility is achieved in the HEMT device. Consequently, the HEMT device is practically used in high-speed applications.

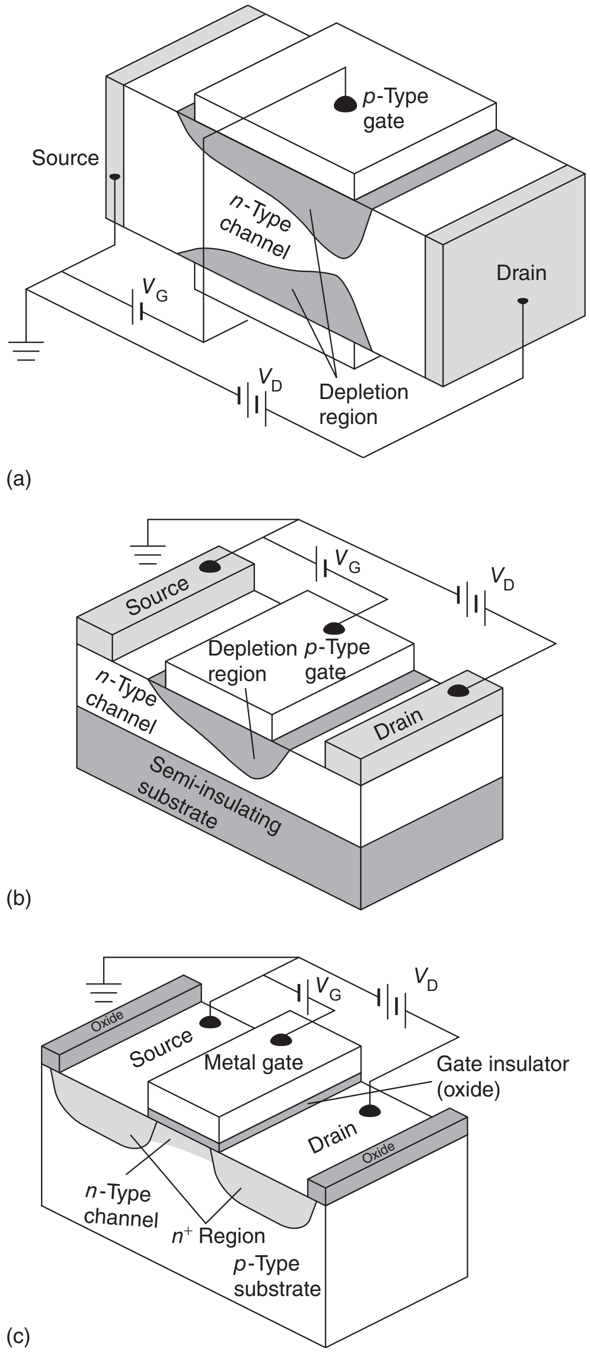
Source
p-Type
gate
n-Type
channel
V_G
V_D
Depletion
region
Drain
(a)
Source
V_G
V_D
Depletion
region
p-Type
gate
n-Type
channel
Drain
Semi-insulating
substrate
(b)
Oxide
Source
V_G
V_D
Metal gate
Gate insulator
(oxide)
Drain
Oxide
n-Type
channel
n^+ Region
p-Type
substrate
(c)

Figure 9 Some variations of the FETs; (a) a JFET, (b) a MESFET, and (c) a MISFET. In the case of using an Si dioxide film as an insulator, the FET is specially called a MOSFET.

Memories

Another key device for the LSI circuits is a memory device. A conventional memory cell needs capacitors, in which data are stored as charges, and the memory devices can be categorized into volatile and nonvolatile types. The volatile memory allows a very high access rate though it consumes a large quantity of power for keeping data, a typical device of which is a dynamic random access memory (DRAM). The DRAM, therefore, is suited for main memories in the LSI circuits. In order to integrate a lot of DRAMs in the LSIs, a deep-trench structure is used for keeping capacitance sufficiently large. In the nonvolatile one, on the other hand, the access time is relatively long but data can be kept without power consumption; typical devices are floating gate RAM (FRAM) and static RAM (SRAM), which are applied to mobile telephones, for instance.

In most of the cases, the memory is fabricated by the compatible process of CMOS technologies. To access the memory, charging or discharging the capacitor is done for writing or reading, respectively, through the transistor connected to an addressing line.

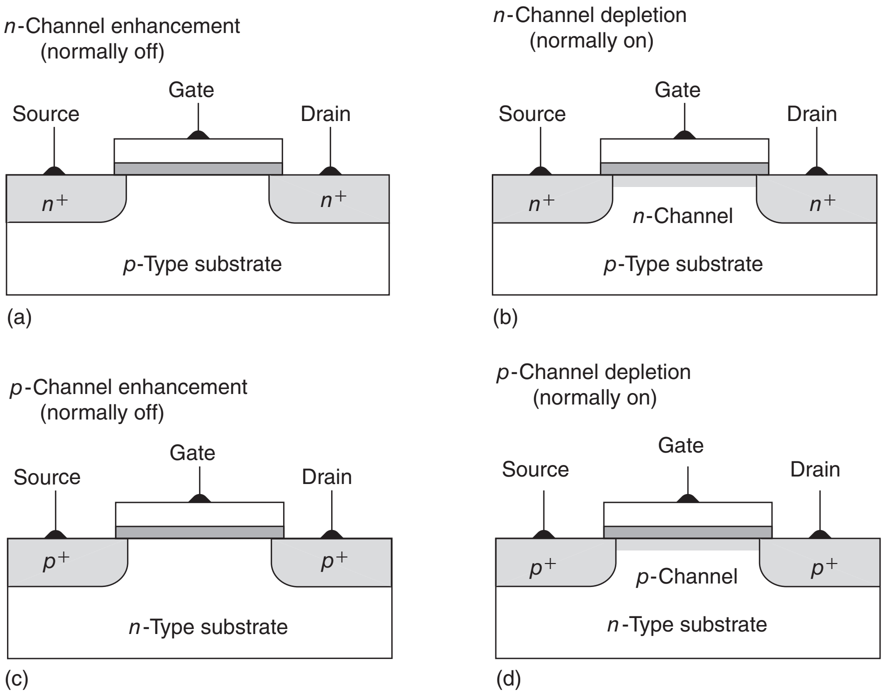
n-Channel enhancement
(normally off)
Gate
Source
Drain
n+
n+
p-Type substrate
(a)
n-Channel depletion
(normally on)
Gate
Source
Drain
n+
n-Channel
n+
p-Type substrate
(b)
p-Channel enhancement
(normally off)
Gate
Source
Drain
p+
p+
n-Type substrate
(c)
p-Channel depletion
(normally on)
Gate
Source
Drain
p+
p-Channel
p+
n-Type substrate
(d)

Figure 10 Four basic types of MOSFETs at zero gate voltage.

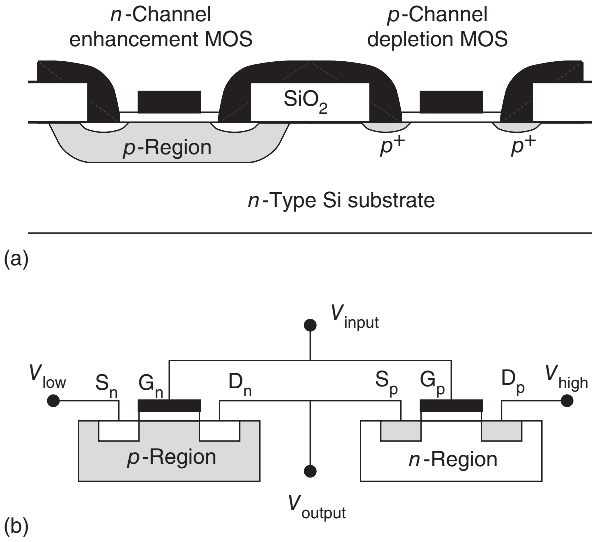
n-Channel
enhancement MOS
p-Channel
depletion MOS
SiO2
p-Region
p+
p+
n-Type Si substrate
(a)
Vinput
Vlow
Sn
Gn
Dn
Sp
Gp
Dp
Vhigh
p-Region
n-Region
Voutput
(b)

Figure 11 (a) A schematic of the CMOS structure, and (b) its equivalent electrical scheme.

Figure 13 shows a one-bit memory cell in the simplest DRAM. For writing, the transistor channel is opened by an appropriate bias applied to the addressing line with a high bias applied to the data line, and subsequently the capacitor C_s is charged. For reading, on the contrary, the transistor channel is also opened and a voltage appearing in the data line is detected. If the capacitor has been charged, a certain value of voltage appears, while no voltage appears when no charge has been stored in the capacitor. These two states correspond to "1" and "0" as one bit in the binary logic.

Photodetectors and Photodiodes

Semiconductor photodetectors can detect optical signals through electronic processes. Light incident on a semiconductor excites electrons from the valence band to the conduction band, if the photon energy of the incident light exceeds a semiconductor bandgap energy, and, then, a current or a voltage is generated in the semiconductor. Thus, the photodetector acts as a current source or a voltage source under the light illumination.

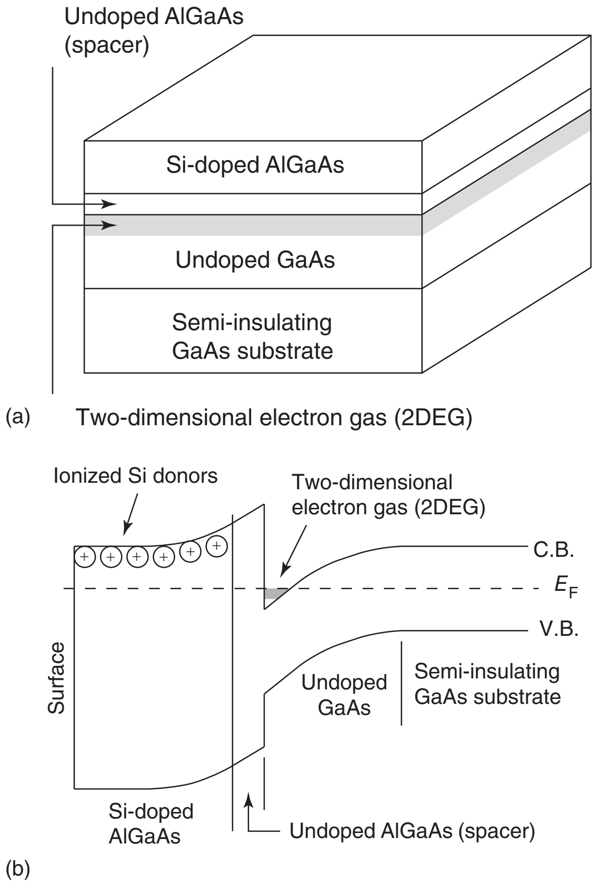
Undoped AlGaAs
(spacer)
Si-doped AlGaAs
Undoped GaAs
Semi-insulating
GaAs substrate
(a)
Two-dimensional electron gas (2DEG)
Ionized Si donors
Two-dimensional
electron gas (2DEG)
C.B.
E_F
V.B.
Surface
Undoped
GaAs
Semi-insulating
GaAs substrate
Si-doped
AlGaAs
Undoped AlGaAs (spacer)
(b)

Figure 12 (a) A device structure, and (b) an energy band diagram of the HEMT realized by using the semiconductor heterostructures.

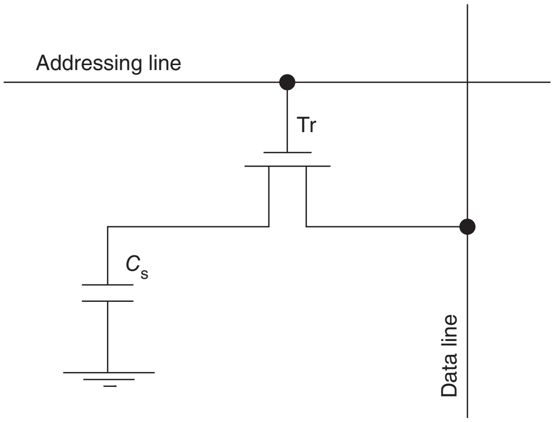
Addressing line
Tr
C_s
Data line

Figure 13 A schematic of a one-bit memory cell in the simplest DRAM.

Generally, photodiodes consist of *p*–*n* or *p*–*i*–*n* (*i* means an intrinsic layer) structures. An electric field, existing at the depletion region around the *p*–*n* interface or the intrinsic region, is very important to separate photogenerated electron–hole pairs. The thin depletion region leads to a high-speed operation but low quantum efficiency (a ratio of the generated electron–hole pairs to the incident photons), while the thick one leads to the opposite. The basic operation mode of the *p*–*i*–*n* photodiode is illustrated in Figure 14. When the reversal bias applied to the *p*–*i*–*n* structure enhances a separation rate of the photogenerated electron–hole pairs, a high-speed operation is possible even if the depletion region is thick enough to achieve a high quantum efficiency. Especially, when a very high electric field is applied in the thick intrinsic region, secondary ionization occurs and thus the number of electrons and holes dramatically increases, resulting in quite high efficiency, which is called an avalanche photodiode (APD).

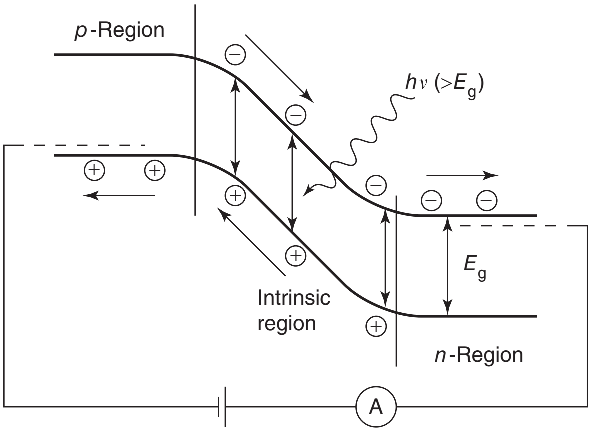

Figure 14 Basic operation mode of the *p–i–n* photodiode.

The detectable wavelength range of the photodiode is an important parameter. The long-wavelength cutoff is determined by the bandgap of the semiconductor material used in the photodiode because of the lower photon energy light, which means that a wavelength, longer than the bandgap cannot be absorbed in the semiconductor. On the other hand, the absorption coefficient for a short-wavelength light is quite high, so such a light is absorbed very near the surface. Since, the carrier recombination occurs very frequently via the surface states, most of the photocarriers recombine without either being collected in the *p–n* junction or contributing to the current. This limits the short-wavelength cutoff in photodiodes.

Solar Cells

A similar *p–n* diode structure in the photodiode can be used as a solar cell, which works as an electricity source. In particular, a detectable wavelength range in the solar cell is well optimized to fit the spectrum of sunlight. The photocarriers generated in the *p–n* diode are extracted as a current source, while photovoltage appears between the *p*- and *n*-type semiconductor ends due to the photocarrier separation. A current–voltage curve in the *p–n* diode changes under the light illumination as shown in Figure 15. The property of the solar cell is characterized by three important parameters; the short-circuit current I_{SC}, the open-circuit voltage V_{OC},

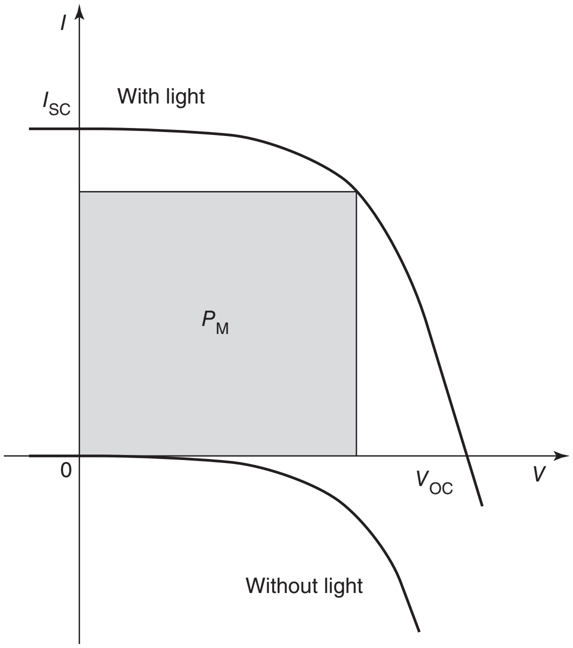

Figure 15 Typical current–voltage characteristics in the *p–n* solar cell with or without the light illumination.

and the maximum power rectangle P_M. High I_{SC} and V_{OC}, resulting in large P_M, are desirable. Since the photoabsorption spectrum of Si material matches the incident sunlight spectrum to some extent, Si is one of the best materials for solar cells. Si solar cells have already been used as alternative energy resources in both high- and low-power applications.

Light Emitting Diodes

When the electron–hole pair disappears by recombination, it should convert its energy to other constituents because of the energy conservation law. In direct transition semiconductors such as GaAs, photons whose energy corresponds to the recombination energy are emitted, while phonons are emitted, in most cases, in indirect transition semiconductors, and the semiconductor materials are heated. Especially where electrons and holes are intentionally injected from electrodes, a current–light conversion is achieved in the direct transition semiconductors. The *p–n* or *p–i–n* diode structures are suited for devices similar to photo detectors, and they are called LEDs. The electrons supplied from the *n*-type region and the holes from the *p*-type region recombine near the *p–n* interface or in the intrinsic region with light emission as illustrated in Figure 16. Since most electrons and holes distribute at the conduction and valence band edges, respectively, the emitted photon energy is almost equal to the bandgap energy. Therefore, the wavelength of the emitted light can be selected by an appropriate choice of the semiconductor materials. Especially by using compound semiconductors, the wavelength of the LED can be tuned in a wide range, for instance, from orange to near-infrared through red wavelengths by $A1_xGa_{1-x}As$ or $GaAs_{1-x}P_x$ materials with various mole fraction x. Very recently, green or blue LEDs were achieved by GaN-related materials. As a result, semiconductor LEDs can realize full color display devices.

Laser Diodes

In LEDs, the light is emitted through a spontaneous recombination process of the electron–hole pairs. On the other hand, the electron–hole recombination is stimulated if there exists a light whose photon energy is same as the recombination energy. This stimulated recombination process plays an important role in lasers. Since the basic structure of the semiconductor laser is almost same as that of the LED, semiconductor lasers are often called laser diodes (LDs). The difference between LDs and LEDs is that the LDs have a cavity for lasing as shown in Figure 17. In the cavity, the light travels back and forth and is amplified by the stimulated emission. It is assumed that an incident plane wave to the cavity is $E_{in} = E_0 e^{j(\omega t - kx)}$, reflectances for input and output mirrors are R_1 and R_2, transmittances for the input and output mirrors are T_1 $(=1-R_1)$ and T_2 $(=1-R_2)$, respectively, and a parameter representing a change in both amplitude and phase for one way in the cavity is γ. Then the total output E_{out} is given by

$$\begin{aligned} E_{out} &= E_{in}T_1T_2e^{-\gamma L} + E_{in}T_1T_2R_1R_2e^{-3\gamma L} + E_{in}T_1T_2R_1^2R_2^2e^{-5\gamma L} + \cdots \\ &= E_{in}T_1T_2e^{-\gamma L}(1 + R_1R_2e^{-2\gamma L} + R_1^2R_2^2e^{-4\gamma L} + \cdots) \\ &= E_{in}T_1T_2e^{-\gamma L}\frac{1}{1-R_1R_2e^{-2\gamma L}} \end{aligned}$$

If $1-R_1R_2e^{-2\gamma L} = 0$ is satisfied, a finite output is obtained even when $E_{in}=0$, and this is the oscillation condition for lasers. Now, γ can be rewritten as $\gamma = i2\pi\bar{n}/\lambda_0 + (\alpha_{in} - g)/2$ where $\lambda_0, \bar{n}, \alpha_{in}$, and g are the wavelength in vacuum, the refractive index, the cavity internal loss, and the optical gain in the cavity, respectively. Therefore, one can introduce the following equations from the amplitude and phase condition for lasing:

$$R_1R_2\exp[(g-\alpha_{in})L] = 1-2i(2\pi\bar{n}/\lambda_0)L = i2m\pi \ (m = 1, 2, 3, \ldots)$$

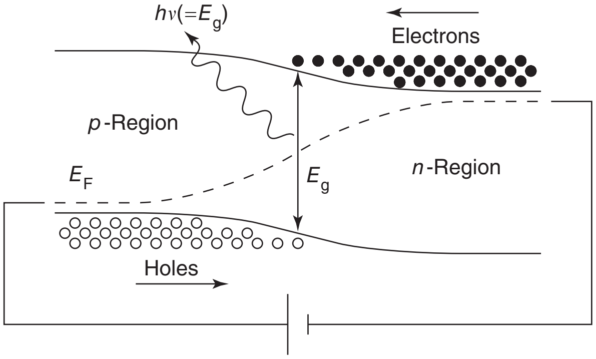

Figure 16 Electron and hole injections through *n*-type and *p*-type regions, respectively, in the LED. The emitted photon energy is almost equal to the bandgap energy.

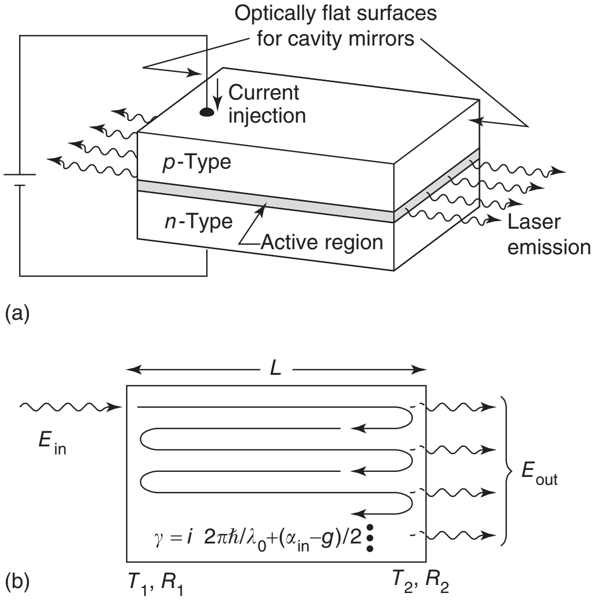
Optically flat surfaces
for cavity mirrors
Current
injection
p-Type
n-Type
Active region
Laser
emission
(a)
L
E_{in}
E_{out}
$\gamma = i\ 2\pi\hbar/\lambda_0+(\alpha_{in}-g)/2$
(b)
T_1, R_1
T_2, R_2

Figure 17 (a) A schematic of the LD where a laser cavity is added to the LED structure to achieve the laser oscillation, and (b) a model of light traveling in the laser cavity.

From the former equation, the threshold gain for lasing is given as $g = \alpha_{in} + (1/L)\ln R_1R_2$, and the longitudinal mode of lasing light wavelength is given as $\lambda = 2L/m$ from the latter one. Consequently, if the amplifying gain owing to the carrier injection from outside is high enough to exceed the cavity losses (summation of internal loss and mirror loss), a laser emission occurs, that is, some threshold current is needed to achieve the laser emission. Above the threshold, the laser output power strongly increases as an increase of the injected current, as schematically illustrated in Figure 18. Since, on the other hand, the lasing wavelength is determined by the cavity length, the emitted light from the LDs is very coherent, very monochromatic, and highly directional, similar to other lasers such as solid-state lasers and gas lasers. The greatest advantage in LDs is their compactness in size. In order to

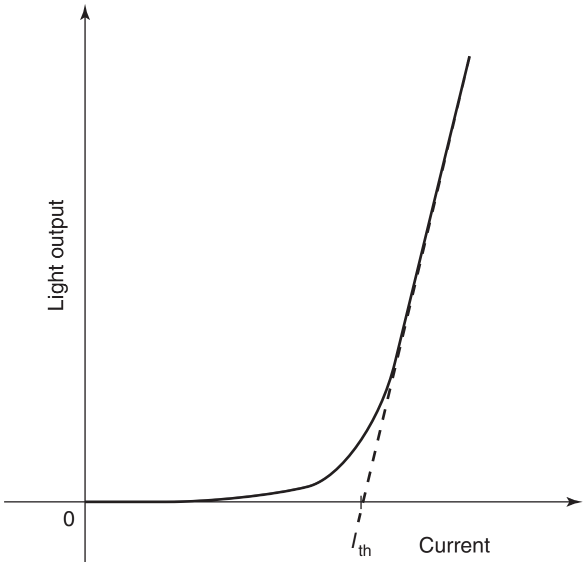

Figure 18 Typical current–light characteristics in the LD.

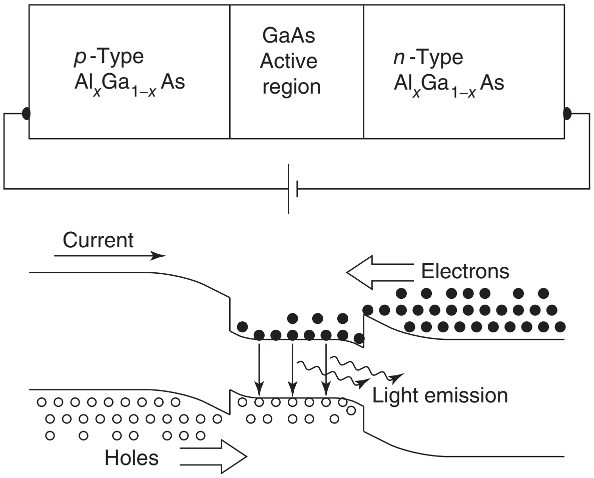

Figure 19 A double heterostructure to confine the carriers in the active region efficiently.

confine the carriers in the active region where a stimulated recombination occurs, double heterostructures are widely used as shown in Figure 19. The active region, in which the bandgap is tuned to be a desirable photon energy, is sandwiched by the barrier regions which have wider bandgaps than the active region and are oppositely doped to inject electrons and holes separately. Such active and barrier regions also act as core and clad regions for a waveguide structure, respectively, owing to the difference in refractive index. As a result, the traveling light wave and the injected carriers are effectively confined in the active region, which contributes to the high emission efficiency in the LDs.

When electrons are confined in very fine quantum well (QW) heterostructures, a 2DEG is formed similar to the HEMT device. As illustrated in Figure 20, the electron density of states in the 2DEG system looks like a staircase, so the electron distribution in the 2DEG is more concentrated near the band edge than that in the three-dimensional free electron system, which well raises the current–light conversion efficiency in the QW. As a result, many improvements in the laser characteristics, such as low threshold current, high modulation frequency, and narrow spectrum line width, are realized. In addition, by adopting lower-dimensional electron systems in quantum wires (QWI) and quantum dots (QD), more improvements are expected owing to their sharper density of states, as illustrated in Figure 20.

Wide Bandgap Materials

For semiconductor devices such as Si, Ge, GaAs, InP and their compounds have widely been used since the invention of the bipolar transistor. Their bandgaps are 1–2 eV, resulting in most of the applications for optic devices being limited in the yellow, red, and

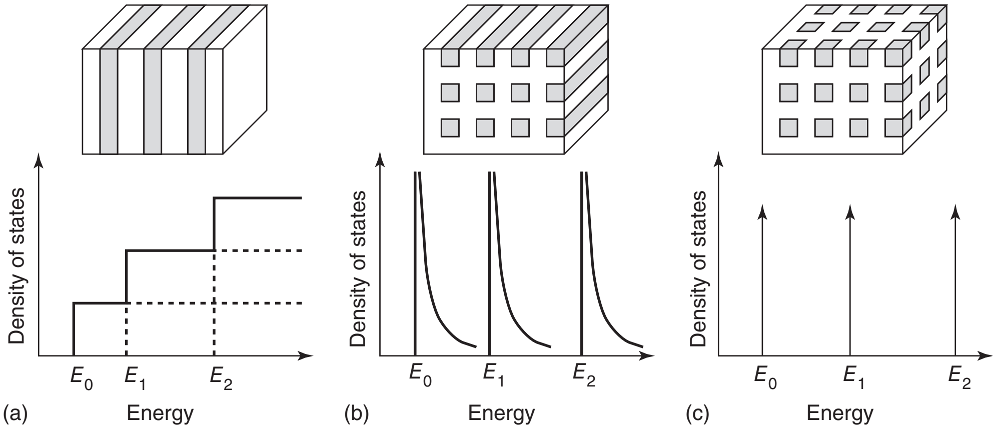

Figure 20 Schematics of the electron density of states in (a) two-dimensional, (b) one-dimensional, and (c) zero-dimensional electron gas systems in the QW, QWI, and the QD, respectively.

infrared regions. However, according to the recent progress in crystal growth, it has been possible to fabricate the $\mathrm{A1}_x\mathrm{Ga}_{1-x}\mathrm{N}$ materials that have a wide bandgap, over 3 eV. By using them, green or blue light emission is realized. In addition, wide-gap materials have high voltage tolerance compared with the narrow-gap materials such that high electric fields can be applied to accelerate electrons, which brings about a possibility for very high-speed operations. Therefore, $\mathrm{A1}_x\mathrm{Ga}_{1-x}\mathrm{N}$ materials are very hopeful for electronic devices as well.

Further Reading

Sze SM (1981) *Physics of Semiconductor Devices*, 2nd edn. Wiley.
Yariv A (1997) *Optical Electronics*, 5th edn. Oxford: Oxford University Press.

Semiconductor Lasers

M-C Amann, Technische Universität Munchen, Garching, Germany

© 2005 Elsevier Ltd. All rights reserved.

This is an update of M.-C. Amann, Semiconductor Lasers, Editor(s): Franco Bassani, Gerald L. Liedl, Peter Wyder, Encyclopedia of Condensed Matter Physics, Elsevier, 2005, Pages 281–289, ISBN 9780123694010, https://doi.org/10.1016/B0-12-369401-9/00502-7.

Introduction 771
Population Inversion and Gain in Semiconductors 771
Semiconductor Heterostructures 772
Semiconductor Heterostructure Material Systems 773
Stripe Laser Diodes 773
Waveguiding in Laser Diodes, Effective Refractive Index, and Confinement Factor 774
Output Power versus Current Characteristic 775
Emission Spectrum and Beam Properties 775
Dynamic Properties and Noise 776
Single-Frequency Semiconductor Lasers 777
Vertical-Cavity Surface-Emitting Semiconductor Lasers 779
Further Reading 780

Nomenclature

a_0	lattice constant (nm)
c	vacuum speed of light (cm s^{-1})
d	thickness of active region (μm)
D	diameter of circular active region in VCSEL (μm)
e	elementary charge (As)
E_c	conduction band edge energy (eV)
E_{Fc}	quasi-Fermi level in conduction band (eV)
E_{Fv}	quasi-Fermi level in valence band (eV)
E_g	bandgap energy (eV)
E_V	valence band edge energy (eV)
f	frequency (Hz)
g	optical material gain (cm^{-1})
h	Planck's constant (VAs^2)
H	modulation response
I	current (mA)
I_{th}	laser threshold current (mA)
k	wave vector (cm^{-1})
k_0	free-space wave vector $k_0=2\pi/\lambda$ (cm^{-1})
k_B	wave vector at Bragg wavelength (cm^{-1})
L	laser length (μm)
L_B	length of Bragg grating (μm)
$n=n'+jn''$	complex refractive index
n_{eff}	effective refractive index of a waveguide mode $n_{eff}=\beta/k_0$
n_g	group refractive index
n_{sp}	spontaneous emission coefficient (typically 1–2)
N	carrier density (cm^{-3})
N_c	effective density of states in conduction band (cm^{-3})
N_{th}	carrier density at laser threshold (cm^{-3})
N_v	effective density of states in valence band (cm^{-3})
P	optical power (mW)
R	recombination rate (cm^{-3} s^{-1}), mirror reflectivity (dimensionless)
RIN	relative intensity noise (dB Hz^{-1})
S	photon density (cm^{-3})
SMSR	side-mode suppression ratio (dB)
V_a	active region volume (cm^3)
v_g	group velocity (cm s^{-1})

$\boldsymbol{w}$	stripe width (μm)
$\boldsymbol{W}$	full width at half maximum (FWHM) (μm) of laser near-field
$\boldsymbol{\alpha}$	optical loss coefficient (cm^{-1})
$\boldsymbol{\alpha}_{\mathbf{H}}$	Henry's line width enhancement factor
$\boldsymbol{\alpha}_{\mathbf{i}}$	intrinsic optical loss (cm^{-1})
$\boldsymbol{\alpha}_{\mathbf{m}}$	mirror loss (cm^{-1})
$\boldsymbol{\alpha}_{\mathbf{tot}}$	total optical loss $\alpha_{\mathrm{tot}}=\alpha_{\mathrm{i}}+\alpha_{\mathrm{m}}$ (cm^{-1})
$\boldsymbol{\beta}$	propagation constant (cm^{-1})
$\boldsymbol{\Gamma}$	confinement factor of an optical mode
$\boldsymbol{\Delta E}_{\mathbf{F}}$	difference of quasi-Fermi levels, E_{Fc}–E_{Fv} (eV)
$\boldsymbol{\Delta\Phi}$	FWHM of laser far-field (rad,^{O})
$\boldsymbol{\kappa}$	coupling coefficient of Bragg grating (cm^{-1})
$\boldsymbol{\Lambda}$	(Bragg) grating period (nm)
$\boldsymbol{\lambda}$	wavelength (μm)
$\boldsymbol{\lambda}_{\mathbf{B}}$	Bragg wavelength (μm)
$\boldsymbol{\nu}$	frequency (Hz)
$\boldsymbol{\tau}_{\mathbf{d}}$	differential carrier lifetime (s)
$\boldsymbol{\tau}_{\mathbf{on}}$	turn-on delay time (s)
$\boldsymbol{\tau}_{\mathbf{s}}$	photon lifetime (s)
$\boldsymbol{\omega}$	circular frequency (s^{-1})
$\boldsymbol{\omega}_{\mathbf{d}}$	damping circular frequency (s^{-1})
$\boldsymbol{\omega}_{\mathbf{r}}$	relaxation circular frequency (s^{-1})

Introduction

Even though more than four decades have passed since the first demonstration of lasing in semiconductors, the pace of development of new and further improved semiconductor lasers continues to be rather high. Judging by their economic impact, semiconductor lasers can be considered today as the most important type of laser. From the beginning, the development of semiconductor lasers has been closely connected with the progress of semiconductor technology and device physics. Hence, the invention of semiconductor heterostructures as well as the straightforward implementation of quantum effects together with improved epitaxial techniques have had a decisive impact on the evolution of these lasers. Besides the physical background and the various device concepts, a proper treatment of semiconductor lasers has to particularly include a description of the relevant materials and their fabrication technology.

After a brief review of the conditions for laser action in semiconductors, this article gives an overview of the most relevant semiconductor materials and material systems. Besides the materials, it is also shown that the various choices among the various laser structures makes this laser class well suited for a vast number of applications. The stationary, dynamic, and spectral characteristics of state-of-the-art semiconductor lasers are presented in the next section and a brief discussion on single-frequency and vertical-cavity surface-emitting semiconductor lasers completes this article.

Population Inversion and Gain in Semiconductors

A fundamental concept in laser physics is to achieve population inversion between two discrete states in a nonequilibrium physical system, so that the stimulated emission can overcome absorption and losses yielding a net optical gain. In a semiconductor, however, the energy states for electrons and holes are continuously distributed within energy bands that are separated by forbidden bands as schematically shown in Figure 1 for a direct semiconductor, where the width of the forbidden band is denoted as bandgap energy E_{g}. The population of these bands is governed by the Fermi distribution characterized by the Fermi level at which the population probability equals 0.5. A population inversion can be achieved by heavily pumping the semiconductor via a current injection. As shown in Figure 1, the nonequilibrium electron and hole distributions can be described by two equilibrium Fermi distributions with two Fermi levels E_{Fc} and E_{Fv} for the conduction and valence bands, respectively. This is possible due to the fast relaxation of the carriers within the bands, hence, E_{Fc} and E_{Fv} are named quasi-Fermi levels. In 1961, Bernard and Duraffourg derived the condition for population inversion in semiconductors essentially stating that the energy difference $\Delta E_{\mathrm{F}} = E_{\mathrm{Fc}} - E_{\mathrm{Fv}}$ needs to exceed the bandgap energy, and the photon energy $\hbar\omega$ is between ΔE_{F} and E_{g}:

$$\delta E_{\mathrm{F}} > \hbar\omega \geq E_{\mathrm{g}}$$

The Bernard and Duraffourg condition requires that the population of at least one band is degenerate, that is, the carrier density exceeds the effective density of states N_{c} and N_{V} of the conduction and/or the valence band, respectively. This means that the semiconductors are operated in the high-injection regime, since N_{c} and N_{V} are rather large. In GaAs, for instance, at room temperature, $N_{\mathrm{c}} \cong 4 \times 10^{17}\ \mathrm{cm}^{-3}$ and $N_{\mathrm{v}} \cong 8 \times 10^{18}\ \mathrm{cm}^{-3}$. Normally, undoped active regions are applied, so that the electron and hole densities are equal causing the conduction band to become degenerate. While, in principle, population inversion is

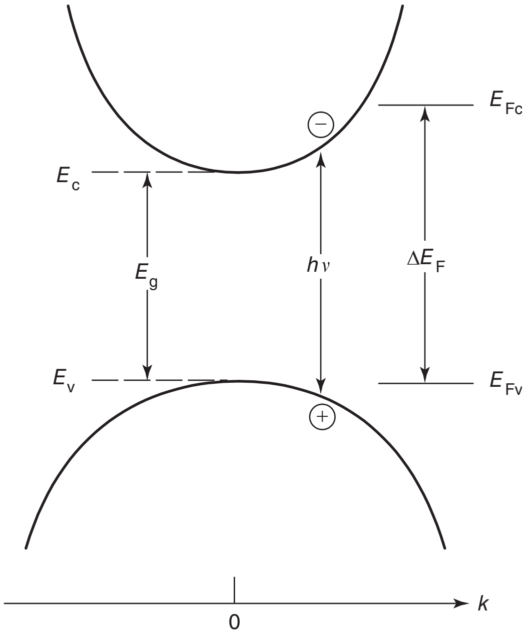

Figure 1 Schematic diagram of energy bands and quasi-Fermi levels of an inverted semiconductor illustrating the Bernard and Duraffourg condition.

possible in direct and indirect semiconductors, a sufficient gain to overcome internal absorption losses can hardly be achieved in indirect semiconductors.

For injection levels exceeding the threshold as defined by the Bernard and Duraffourg condition, an optical gain due to stimulated emission by the inverted band occupation occurs. The injection level at which this gain exactly compensates the material losses, such as free-carrier absorption or scattering losses, is defined as the transparency threshold. At even higher injection, the increasing gain may also compensate the mirror losses of an optical cavity enabling laser operation. It should be noted that inverted semiconductors may provide very large optical gain g up to the order of 1000 cm^{-1}, exceeding that of any other optical gain medium.

Semiconductor Heterostructures

Laser operation in homojunction semiconductors is difficult to achieve because of the high current densities required to achieve optical gain. For low-threshold operation, it is therefore necessary to reduce the volume of the active region in which the injection occurs and to exclude optical absorption in the surrounding semiconductor regions. This goal can most effectively be achieved by applying semiconductor heterostructures, in which semiconductors with different bandgap energy are combined. The most effective among them is the so-called "double heterostructure," in which the active region is completely embedded into p- and n-doped semiconductors with a larger bandgap energy as shown schematically in Figure 2. The double heterostructure provides two essential features relevant for laser operation:

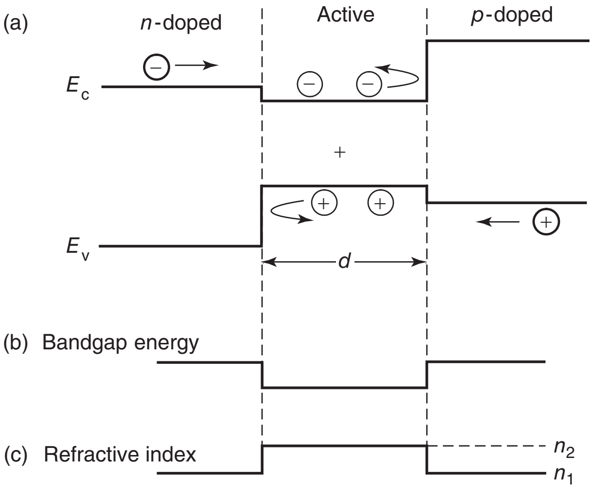

Figure 2 Schematic illustration of (a) semiconductor double heterostructure, (b) spatial profiles of bandgap energy, and (c) refractive index.

1. *Carrier confinement*. This almost completely concentrates electrons and holes within the active region even for active regions having thickness in the nm-regime.
2. *Optical confinement*. This yields optical waveguiding, establishing a slab waveguide with the active region as core because of the smaller refractive indices of the higher bandgap energy semiconductors sandwiching the active region.

Compared to the carrier confinement, the optical confinement as measured by the optical confinement factor

$$\Gamma = \frac{\text{mode power carried in active layer (region)}}{\text{total mode power}}$$

is not as complete for small dimensions, and the optimal radiation-matter interaction in the active region occurs where Γ/d is maximal. Depending on the material constants, accordingly, active region thicknesses are usually $\sim$100 nm.

Further, an improved optical gain performance shows the quantum-well (QW) structures, in which the active region thickness is reduced to below the de Broglie wavelength ($\sim$30 nm). In QWs, the quantization of the electronic states along the normal layer results in a two-dimensional (2D) electron (and hole) gas with a modified density of states that makes the inversion population possible for smaller injection levels. The density of states in the valence band can additionally be modified by introducing elastic strain that lifts the degeneracy of light and heavy valence bands, so that only one of the two valence bands needs to be inverted yielding still smaller thresholds. Extending the quantization to the other two dimensions, one obtains quantum wire and quantum dot structures, corresponding to one-dimensional (1D) and zero-dimensional (0D) electron (hole) systems with distinct threshold reduction. In case of the quantum dot, atom-like discrete states appear to make this kind of gain medium rather similar to atomic laser media. In general, reducing the dimensionality of the carrier systems results in reduced thresholds and smaller temperature dependence of the optical gain. Because of the significant advantages achieved with double heterostructures, all modern laser diodes normally comprise a QW double heterostructure.

Semiconductor Heterostructure Material Systems

The benefits of the semiconductor heterostructure can be exploited only if the composite crystal exhibits a high crystalline quality. This generally requires that all constituents of the heterostructure have the same lattice constant a_0, while the difference in bandgap energy should be large (several hundred meV). The lattice-matching requirement strongly limits the possible semiconductor combinations because semiconductor heterostructures are almost entirely grown on binary substrates. This is because binary substrates, such as GaAs or InP, are unambigous chemical compounds in contrast to, for example, $\mathrm{In}_x\mathrm{Ga}_{1-x}\mathrm{As}$ and typically provide more than an order of magnitude of better thermal conductivity than ternary (or quaternary) compounds because of the nonoccurance of alloy scattering of the phonons.

Lattice-matched double heterostructures, therefore, consist of ternary and quaternary (or even quinternary) compounds grown on binary substrates. The lattice-matching condition can be found from Vegard's law which states that the lattice constant of a compound can be calculated as a linear interpolation between the constituting binaries. For a quaternary compound $\mathrm{A}_x\mathrm{B}_{1-x}\mathrm{C}_y\mathrm{D}_{1-y}$, where A and B, and C and D each share the same sublattice, the lattice constant is

$$a_0\left(\mathrm{A}_x\mathrm{B}_{1-x}\mathrm{C}_y\mathrm{D}_{1-y}\right) = xya_0(\mathrm{AC})+x(1-y)a_0(\mathrm{AD})+(1-x)ya_0(\mathrm{BC})+(1-x)\times(1-y)a_0(\mathrm{BD})$$

On the other hand, the bandgap energy of a compound shows a more complicated and nonlinear dependence on composition. As a consequence, with a proper choice of semiconductor materials, rather large bandgap energy differences can be achieved with lattice-matched compounds making numerous heterostructure combinations possible. Semiconductor lasers are nowadays made from numerous III–V and other compound semiconductors covering the entire visible as well as the infrared regime up to $\sim$100 μm wavelength.

Stripe Laser Diodes

A schematic drawing of the basic stripe-geometry semiconductor laser structures is depicted in Figure 3. All of them comprise a transverse (vertical, x-axis) double heterostructure to define the vertical extension of the laser-active area with a pn-junction at or in the active layer. A laser current is fed via stripe contacts on the top and bottom of the laser chips. Three basic types of lasers can be distinguished: gain-guided (GG), index-guided (IG), and quasi-index-guided (QIG) laser structures, where the guiding relates to the in-plane (lateral) waveguiding along the y-axis. While the transverse waveguiding (x-axis) is accomplished by index guiding via the double heterostructure, the lateral waveguiding may either be done (1) simply by the lateral gain profile in the active layer (GG), (2) similar to the transverse direction by a lateral double heterostructure (IG), or (3) by a partial lateral replacement of part of the structure by a lower index material without attaching the active layer (QIG). While the GG lasers require the lowest technological effort and generally show an excellent long-term stability because of the nonmodified active layer, the IG lasers exhibit the smallest thresholds and optimum laser performance; however, the lateral removal of part of the active layer may worsen the reliability. Often a reasonable compromise are the QIG lasers that, in all aspects, show the behavior in between the other two structures. An optical feedback is provided by the cleaved end-facets of the laser chips, which for typical refractive indices of the semiconductors (2.5–3.5)

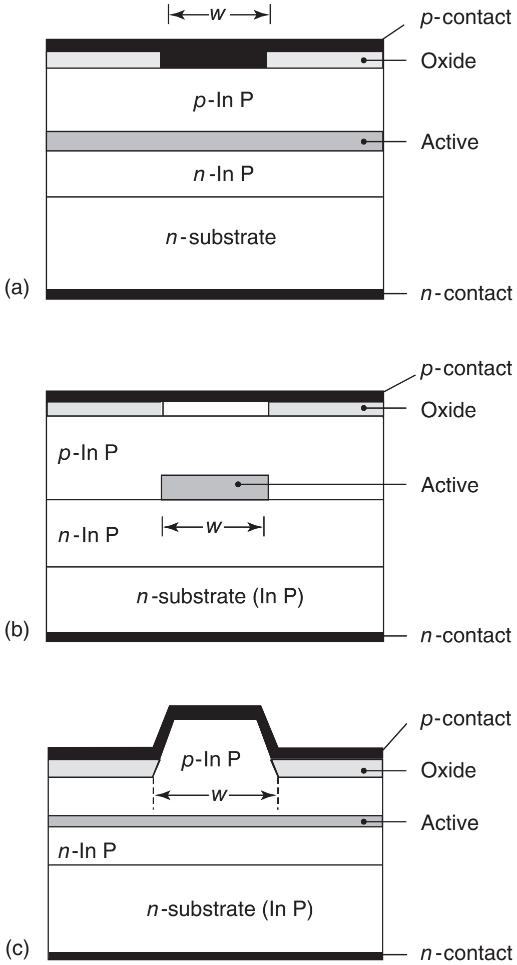
w
p-contact
Oxide
p-In P
Active
n-In P
n-substrate
(a)
n-contact
p-contact
Oxide
p-In P
Active
n-In P
w
n-substrate (In P)
(b)
n-contact
p-contact
p-In P
Oxide
w
Active
n-In P
n-substrate (In P)
(c)
n-contact

Figure 3 The three different lateral waveguiding types (a) Gain-guiding (GG), (b) index-guiding (IG), and (c) quasi-index-guiding (QIG).

show a reflectivity ~30% against air. Due to the large gain of the semiconductor laser, this comparatively small mirror reflectivity can be compensated for by laser lengths of the order of several hundred micrometers.

Waveguiding in Laser Diodes, Effective Refractive Index, and Confinement Factor

The transverse double heterostructure represents an optical slab waveguide with the schematic index profile shown in Figure 2c. Depending on the active layer (core) thickness d and the index profile, this slab may carry one or more guided transverse electric (TE) and transverse magnetic (TM) modes, respectively. For a sufficiently thin active layer,

$$d < \frac{\lambda}{2\sqrt{n_2^2 - n_1^2}}$$

only the fundamental TE- and TM-modes are guided, which is normally aimed for.

The optical gain which the modes acquire, that is, the mode gain g_m, is the product of the active region material gain g and the optical confinement factor Γ for the particular mode. For a given slab waveguide, the (fundamental) TE-mode exhibits a larger confinement than the (fundamental) TM-mode. Also, the facet reflectivity shows a certain polarization dependence favoring the TE-modes as well. As a consequence, semiconductor lasers normally operate in the fundamental transverse TE-mode. In a good approximation, the confinement factor for the fundamental TE-mode is

$$\Gamma \cong \left[1 + \left(\frac{d_0}{d}\right)^2\right]^{-1} \quad \text{with} \quad d_0 = \frac{\lambda}{2\pi}\sqrt{\frac{2}{n_2^2 - n_1^2}}$$

A further mode property is the effective refractive index n_{eff}, that describes the mode propagation along the waveguide in analogy with a plane wave in a homogeneous medium, with the refractive index equal to n_{eff}. The effective refractive index, which is the ratio of the propagation constant β and the free-space wave number k_0, is between n_1 and n_2.

Considering complex refractive indices $n = n' + jn''$, where the imaginary part is related to the material gain (or loss) g as $n'' = g/2k_0$, it is obvious that the gain in the active region leading to the mode gain produces a slightly complex propagation constant and a complex effective refractive index with imaginary part equal to $n'' = \Gamma g/2k_0$.

Besides transverse profiles of the real part of n, those of the imaginary part of n may also produce optical waveguiding. This explains why the lateral gain profile constitutes a waveguide for laser radiation in the GG lasers. For common gain values, however, the GG mechanism is much smaller than IG, with the consequence that the maximum stripe width w for lateral single-mode operation is much larger in the GG lasers than in their IG counterparts.

Output Power versus Current Characteristic

A representative plot of an optical output power versus current characteristic for a semiconductor laser is shown in Figure 4, together with the principal current-dependent carrier density in the active region. Relevant parameters of this characteristic are threshold current I_{th}, output power P, and differential quantum efficiency η_{d}. The threshold current is related to the active region volume V_{a} and the spontaneous recombination rate R at lasing threshold carrier density N_{th}

$$I_{\mathrm{th}} = eV_{\mathrm{a}}(N_{\mathrm{th}})$$

where e is the elementary charge. The active region gain $g(N_{\mathrm{th}})$ at injection level N_{th} yields a mode gain that equals the total losses α_{tot} comprising internal losses (e.g., absorption and scattering) α_{i} and the mirror losses α_{m}:

$$\Gamma \mathrm{g} = \alpha_{\mathrm{i}} + \alpha_{\mathrm{m}} \quad \text{with the mirror losses}$$

$$\alpha_{\mathrm{m}} = \frac{1}{2L} \ln \frac{1}{R_1 R_2}$$

where L is the laser length, and R_1 and R_2 are the front facet mirror reflectivities. For a symmetric laser with $R_1 = R_2 = R$, the optical output power per facet (above threshold) is

$$P(I) = \frac{h\nu}{2e} \frac{\alpha_{\mathrm{m}}}{\alpha_{\mathrm{tot}}} (I - I_{\mathrm{th}})$$

and the differential quantum efficiency reads

$$\eta_{\mathrm{d}} = \frac{\mathrm{d}P/h\nu}{\mathrm{d}I/e} = \frac{\ln 1/R}{2\alpha_{\mathrm{tot}} L}$$

Emission Spectrum and Beam Properties

With state-of-the-art semiconductor technology, it is possible for most emission wavelengths to fabricate narrow-stripe laser waveguides that carry only one transverse and one lateral mode each. Even though the length of semiconductor cavities (typically

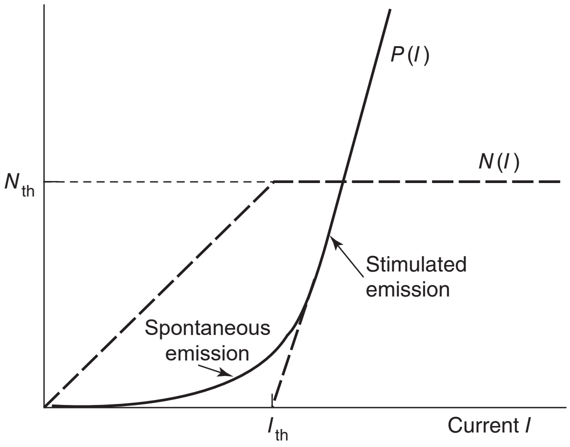

Figure 4 Schematic profile of optical output power P and carrier density in active region N vs. current in a semiconductor laser.

0.1–1 mm) is orders of magnitude smaller than that of most other laser types, the length-(effective)-refractive-index-product is still of the order of several thousand wavelengths. Therefore, the longitudinal mode spacing

$$\Delta\lambda = \frac{\lambda^2}{2n_\mathrm{g}L}\,(n_\mathrm{g} : \text{group (effective) index})$$

is very small against the spectral width of the active region gain characteristic, which in terms of energy is of the order of the thermal energy ($k_\mathrm{B}T$). As a consequence, the mode gains of the modes near the gain peak are only slightly different, so that the usual Fabry–Perot-type semiconductor lasers generally emit in many longitudinal modes. The purity of the spectrum can be described by the side-mode suppression ratio (SMSR) that measures the ratio of the dominant mode to the next strongest one. Given the mode gain difference Δg_m between the two strongest modes, the SMSR of a symmetric semiconductor laser (R_1=R_2), under stationary conditions, is proportional to the power in the dominant mode P according to

$$\mathrm{SMSR} = \frac{2P\Delta g}{h\nu n_\mathrm{sp} v_g \alpha_\mathrm{tot}\alpha_\mathrm{m}}$$

where n_sp is the spontaneous emission coefficient (typically 2), that is specific for semiconductor lasers taking into account the incomplete inversion of the bands, and v_g is the group velocity. Truly single-mode lasers, that is, single-frequency lasers, show an SMSR>30 dB, that is, three orders of magnitude, requiring a Δg of 0.01–0.1 cm^{-1}, which generally cannot be accomplished solely by the spectrally dependent active region gain. Single-frequency laser diodes, therefore, need additional wavelength selective elements such as Bragg reflectors as shown below.

An important spectral parameter, particularly for single-frequency semiconductor lasers, is the spectral line width of the mode(s). As with other lasers, the line width is obtained by the Schawlow–Townes formula; however, due to the gain-phase coupling in semiconductor lasers, the Schawlow–Townes formula must be completed yielding the so-called "Schawlow–Townes–Henry line width formula"

$$\Delta\nu = \frac{h\nu v_\mathrm{g}^2 \alpha_\mathrm{tot}\alpha_\mathrm{m} n_\mathrm{sp}}{8\pi P}\left(1+\alpha_\mathrm{H}^2\right)$$

where α_H is Henry's line width enhancement factor describing the gain-phase coupling accompanying carrier density changes in the active region which has the form

$$\alpha_\mathrm{H} = -2k_0\frac{\partial n'/\partial N}{\partial g/\partial N}$$

The physical origin for nonzero α_H is the nonsymmetric gain versus wavelength characteristic of semiconductor gain media. While the gain-wavelength characteristics of most other laser materials are symmetric, the asymmetry in semiconductors yields nonvanishing changes of the refractive index at the gain maximum, that is, at the laser wavelength, during the occurence of gain changes, for instance, during relaxation oscillations or after each spontaneous emission event into the lasing mode(s). It should be noted that α_H is significantly smaller for QW lasers, particularly for strained QW lasers, than for bulk lasers. In case of the recently developed quantum dot lasers, α_H approaches zero because of the almost completely symmetric atom-like gain-wavelength characteristic.

The radiation beam of normal laser-diodes is transversely single-mode and nearly diffraction limited. In this case, the near-field and far-field widths depend on each other as

$$\Delta\Phi = \arctan\left(\frac{2\lambda}{\pi W}\right)$$

where $\Delta\Phi$ and W are the full width at half maximum (FWHM) of the far-field and near-field angles, respectively. Because of the narrow stripe widths of transversely single-mode semiconductor lasers (typically 0.5–3 μm at 1–2 μm emission wavelength), the diffraction-limited far-field width is of the order of several tens of degrees, in contrast to most other laser types.

Dynamic Properties and Noise

The dynamic properties of laser diodes are relevant for their use as a direct current-modulated light source in high-speed data transmission applications. Thereby, the two limiting cases of a linear response at a small-signal modulation and a nonlinear response at a large-signal (generally pulse) modulation are of great interest.

Modulating the laser around average current I and average output power P per facet, respectively, the small-signal modulation response $H(\omega)$ can be described by the transfer function of a damped second-order low-pass filter

$$H(\omega) = \frac{1}{1-(\omega/\omega_\mathrm{r})^2+j(\omega/\omega_\mathrm{d})}$$

where the relaxation and damping circular frequencies ω_r and ω_d are given as

$$\omega_{\mathrm{r}} = \frac{1}{\tau_{\mathrm{s}}}\sqrt{\frac{2a\Gamma}{v_{\mathrm{g}}\alpha_{\mathrm{m}}\alpha_{\mathrm{tot}}h\nu V_{\mathrm{a}}}P} \quad \text{and} \quad \omega_{\mathrm{d}} = \frac{\tau_{\mathrm{s}}}{\gamma}\omega_{\mathrm{r}}^2$$

respectively. Here, the linear gain parameter $a = \partial g/\partial N$ and the photon lifetime in the cavity $\tau_{\mathrm{s}} = (v_{\mathrm{g}}\alpha_{\mathrm{tot}})^{-1}$ appear, and γ is

$$\gamma = \frac{aS}{\alpha_{\mathrm{tot}}} + \frac{\tau_{\mathrm{s}}}{\tau_{\mathrm{d}}} + \frac{n_{\mathrm{sp}}\Gamma}{V_{\mathrm{a}}S}$$

with τ_{d} being the differential carrier lifetime in the active region determined by the total spontaneous emission rate and nonradiative recombination processes (typically several nanoseconds). S is the photon density in the active region corresponding to output power P

$$S = \frac{2\Gamma}{v_{\mathrm{g}}\alpha_{\mathrm{m}}h\nu V_{\mathrm{a}}}P$$

With an increase in the laser current or output power, respectively, the relaxation frequency as well as the damping frequency increases. The absolute value of the modulation response versus frequency f is shown in Figure 5 for a typical 1.55 μm wavelength InGaAsP laser in comparison with an LED made from the same semiconductor material. It is usual to measure $|H(\omega)|$ in decibels, that is, $10\log|H(\omega)|$. The characteristic 3-dB bandwidth is only slightly larger than the relaxation resonance, so that the latter can be used as a reasonable measure for the modulation bandwidth.

The large-signal pulse modulation can be described by rather accurate approximations for the turn-on delay τ_{on}

$$\tau_{\mathrm{on}} \cong \tau_{\mathrm{d}}\frac{I_{\mathrm{on}}-I_{\mathrm{off}}}{I_{\mathrm{on}}-I_{\mathrm{th}}} \text{ for } I_{\mathrm{off}} < I_{\mathrm{th}} < I_{\mathrm{on}} : \text{off–state below threshold}$$

$$\tau_{\mathrm{on}} \cong \frac{\sqrt{2}}{\omega_{\mathrm{r}}}\ln\frac{P_{\mathrm{on}}}{P_{\mathrm{off}}} \text{ for } I_{\mathrm{th}} < I_{\mathrm{off}} < I_{\mathrm{on}} : \text{off–state above threshold}$$

where switching occurs from $P_{\mathrm{off}}(I_{\mathrm{off}})$ to $P_{\mathrm{on}}(I_{\mathrm{on}})$. While for lasers biased below threshold, the τ_{on} delay is of the order of the comparatively long differential carrier lifetime τ_{d}, τ_{on} delays ~0.1 ns can be obtained with an above-threshold bias.

Besides the phase noise that determines the modal line width, an intensity noise occurs in semiconductor lasers. This is usually described in terms of the relative intensity noise (RIN)

$$\mathrm{RIN}\left(\text{in dB Hz}^{-1}\right) = \frac{1}{\Delta f}\log\left(\frac{\Delta P}{P}\right)^2$$

where ΔP denotes the power fluctuations of the laser output within bandwidth Δf. The RIN shows a frequency dependence similar to the modulation response with typical low frequency values ~135 dB Hz^{-1}.

Single-Frequency Semiconductor Lasers

Semiconductor lasers can be made single-frequency lasers by introducing additional wavelength-selective elements into the laser cavity that select only one of the longitudinal modes. This is commonly accomplished with Bragg gratings monolithically integrated into the laser structure. As shown in Figure 6, the gratings may either replace the laser mirrors and are therefore put at one or both laser facets (distributed Bragg reflector (DBR) laser with a longitudinal integration of grating) or may homogeneously be collocated with the active region over the entire laser length (distributed feedback (DFB) laser with a transverse integration of grating). To avoid interference with the end facet reflection, antireflection coatings are normally applied onto those facets of DBR lasers where the gratings provide the feedback. In DFB lasers, therefore, both facets need an antireflection coating to suppress these interferences.

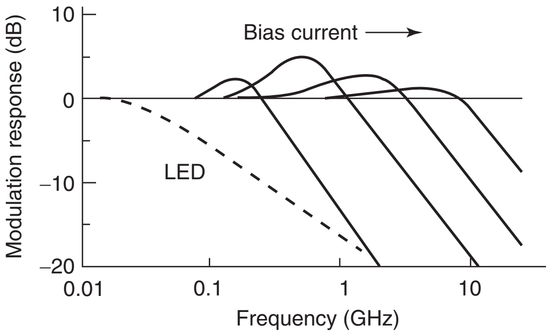

Figure 5 Absolute value $|H(f)|$ of the modulation response of a laser diode.

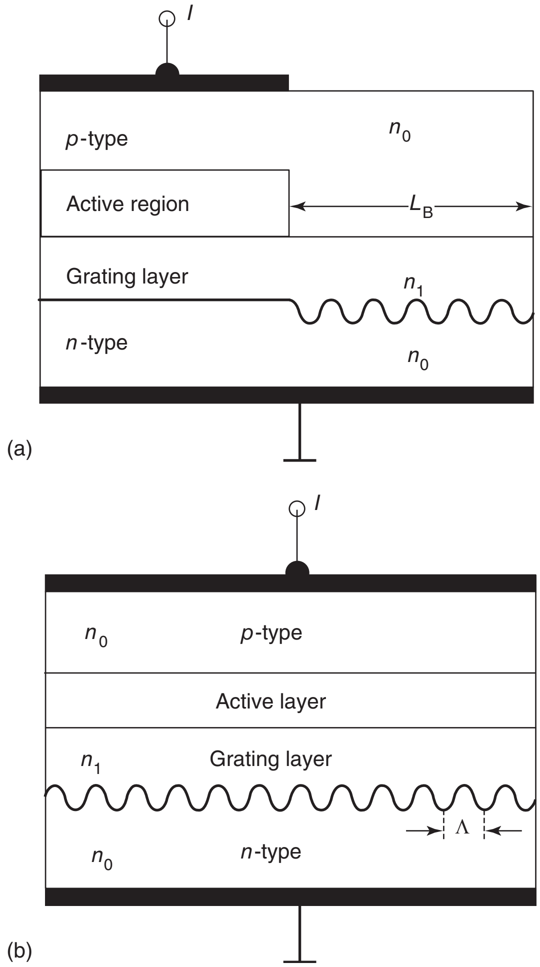

Figure 6 (a) DBR (longitudinal integration), and (b) DFB (transverse integration) single-frequency semiconductor laser structures.

The Bragg gratings are made by periodic thickness variations of a grating layer sandwiched between layers of different refractive indices, so that the thickness variations result in effective refractive index variations Δn_{eff} of the same periodicity. In the DBR laser, the Bragg grating introduces a wavelength-dependent mirror loss with a minimum loss or maximum reflectivity at the (free-space) Bragg wavelength

$$\lambda_{\mathrm{B}} = 2n_{\mathrm{eff}}\Lambda$$

where Λ is the grating period, (Figure 6b). In the interesting regime around the Bragg wavelength, the wavelength-dependent reflectivity can be calculated by the coupled-mode theory yielding

$$R(\lambda) = \left|\frac{\kappa \sinh(sL_{\mathrm{B}})}{\mathrm{j}\Delta\beta\sinh(sL_{\mathrm{B}})+s\cosh(sL_{\mathrm{B}})}\right|^2$$

where κ, the coupling coefficient of the grating describing the strength of the grating feedback has the form

$$\kappa = \frac{k_0\Delta n_{\mathrm{eff}}}{4}$$

and $\Delta\beta$ is the deviation of the wave vector $k_0 n_{\mathrm{eff}}$ from the wave vector at the Bragg wavelength k_{B} and is thus a measure of the difference $\Delta\lambda=\lambda-\lambda_{\mathrm{B}}$

$$\Delta\beta = k_0 n_{\mathrm{eff}} - k_{\mathrm{B}} \cong -\frac{2\pi n_{\mathrm{eff}}}{\lambda_{\mathrm{B}}^2}\Delta\lambda$$

L_{B} is the grating length, and $s = \sqrt{\kappa^2-\delta\beta^2}$. At the Bragg wavelength, the reflectivity is maximal and is given by

$$R(\lambda_{\mathrm{B}}) = \tanh^2(\kappa L_{\mathrm{B}})$$

For most DBR semiconductor lasers, it is possible to achieve κL_B-products of the order 1 or more and thus to realize reasonable reflectivities exceeding even the facet reflectivity of the semiconductor–air interface in the Fabry–Perot semiconductor lasers. However, the relative spectral position of the Bragg wavelength and the longitudinal mode spectrum is not controlled well in DBR lasers, particularly, if a wide operation temperature range is considered with resulting relative shifts of both against each other. The wavelength control and stability is much better in the DFB lasers because the longitudinal DFB laser modes are intrinsically related to the Bragg wavelength, and the grating and the active region are spatially not separated, so that any index changes in the active region or the grating layer may not change this relationship. As a consequence, DFB lasers have become commercial single-frequency lasers, while more sophisticated DBR devices have gained importance in the area of wavelength-tunable semiconductor lasers. Properly designed DFB lasers show excellent single-frequency performance with SMSR well exceeding 30 dB.

Vertical-Cavity Surface-Emitting Semiconductor Lasers

Vertical-cavity surface-emitting lasers (VCSELs) are relatively new semiconductor lasers in which the laser cavity is not along the wafer plane but vertical to it. Consequently, the length of the gain region along which the optical gain compensates internal and mirror losses is drastically reduced to the thickness of the active region (e.g., 50 nm) instead of its length (e.g., 500 μm). Because of the large optical gains achievable with semiconductors, it is possible to realize a sufficient gain along a gain path length of only 5–50 nm for the compensation of the losses of high-reflective mirrors. A schematic illustration of the basic VCSEL geometry is shown in Figure 7. Top and bottom mirrors of the VCSEL consist of several ten quarter-wavelength semiconductor layer pairs with alternating refractive index that can precisely be fabricated with molecular beam epitaxy (MBE) or metal-organic vapor-phase epitaxy (MOVPE).

The cavity length of VCSELs is of the order of the wavelength and thus orders of magnitude shorter than that of the edge-emitting lasers. Accordingly, the laser performance shows substantial differences, such as a longitudinal single-mode operation or the onset of quantization effects of the optical field.

Using thin QW active layers, the thickness d of the active region can be made much thinner than a quarter wavelength in the semiconductor, that is, $\lambda/4n$, so that by placing the active region in a maximum of the field intensity $|E|^2$ as shown in Figure 7, the gain is twice as large for the long active regions in edge-emitting layers, where the gain works on the averaged field intensity, including nodes of $|E|^2$ as well. The threshold condition for this design, therefore, reads (note the factor of 2)

$$2dg = \alpha_i L_{\text{eff}} + \frac{1}{2}\ln\frac{1}{R_1 R_2}$$

where the effective cavity length L_{eff} is the vertical extension of the standing wave within the $1/e$-decay on both ends. Due to the ultra-small d, the mirror reflectivities need to be near unity, typically >99%. This can be achieved by DBRs made of alternating (and conductive) semiconductor layers of different composition yielding different refractive indices. Mathematically, the peak reflectivity of such a DBR at the Bragg wavelength is expressed as

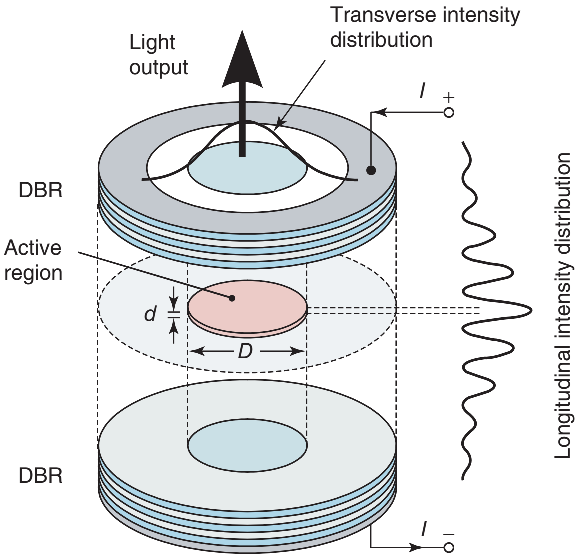
Light output
Transverse intensity distribution
I +
DBR
Active region
d
D
Longitudinal intensity distribution
DBR
I −

Figure 7 Schematical illustration of principal vertical-cavity surface-emitting laser (VCSEL) structure.

$$R = \left[\frac{1-(n_0/n_2)(n_2/n_1)^{2N}}{1+(n_0/n_2)(n_2/n_1)^{2N}}\right]^2$$

where N is the number of layer pairs in the DBR, n_0 and n_2 are the refractive indices of the medium outside the VCSEL (e.g., air: $n_0=1$) and the inner semiconductor region respectively, and n_1 is the refractive index of the second semiconductor in the DBR. With refractive index differences up to 5–10% in usual semiconductor material systems (GaAlAs/GaAs, InGaAlAs/InP), several ten-layer pairs give reflectivities of the order 99.5–99.9% against air. With these high reflectivities, the laser threshold can be achieved with reasonable active region gains ~500–1000 cm^{-1}. Up to now, room-temperature continuous-wave VCSELs have successfully been demonstrated for the wavelength ranges 850–1000 nm in Ga(In)AlAs/GaAs, 1.2–1.3 μm in GaInNAs/GaAs, and 1.3–2.0 μm in AlGaInAs/InP.

The lateral diameter of the active region can be kept small enough to favor single transverse-mode operations and is typically ~3–10 μm. As a consequence of the small active region volume, the threshold currents of VCSELs are rather small, typically <1 mA, even though the threshold current density might be quite large to obtain the required large threshold gain. Another consequence of the small active region is that the output power of a VCSEL is accordingly small, typically of the order of a few milliwatts, which is, however, sufficient for the vast majority of applications in communications, measurements, and sensing.

Further Reading

Casey HC and Panish MB (1978) *Heterostructure Lasers – Part AFundamental Principles*, 1st edn. New York: Academic Press.
Casey HC and Panish MB (1978) *Heterostructure Lasers – Part BMaterials and Operating Characteristics*, 1st edn. New York: Academic Press.
Chuang SL (1995) *Physics of Optoelectronic Devices*, 1st edn. Chichester: Wiley.
Coldren LA and Corzine SW (1995) *Diode Lasers and Photonic Integrated Circuits*, 1st edn. Chichester: Wiley.
Kapon E (1999) *Semiconductor Lasers IFundamentals*, 1st edn. San Diego: Academic Press.
Kapon E (1999) *Semiconductor Lasers IIMaterials and Structures*, 1st edn. San Diego: Academic Press.
Li H and Iga K (2002) *Vertical-Cavity Surface-Emitting Laser Devices*, 1st edn. Berlin: Springer.
Morthier G and Vankwikelberge P (1997) *Handbook of Distributed Feedback Laser Diodes*, 1st edn. Norwood: Artech House.
Petermann K (1988) *Laser Diode Modulation and Noise*, 1st edn. Dordrecht: Kluwer Academic Publishers.
Zory PS (1993) *Quantum Well Lasers*, 1st edn. Boston: Academic Press.

Transistors

Y Hirayama, NTT Basic Research Laboratories, Kanagawa, Japan

© 2005 Elsevier Ltd. All rights reserved.

This is an update of Y. Hirayama, Transistors, Editor(s): Franco Bassani, Gerald L. Liedl, Peter Wyder, Encyclopedia of Condensed Matter Physics, Elsevier, 2005, Pages 214–222, ISBN 9780123694010, https://doi.org/10.1016/B0-12-369401-9/00499-X.

Introduction 781
Bipolar and Hetero-Bipolar Transistors 781
Field Effect Transistors: MISFET, MESFET, and HEMT 783
Backgated Structures 787
In-Plane-Gate Transistor 787
Single–Electron Transistor 788
Further Reading 790

Introduction

A transistor is a three-terminal device, where the voltage or current applied to one terminal controls the current flow between the other two terminals. Transistors are designed to have current or voltage gain, which means a drivability of multistep transistor circuits. Submicron lithography and self-alignment have been used to improve the high-frequency operation of transistors. Transistors are key devices in cutting-edge semiconductor integrated circuits.

There are mainly two types of transistors, bipolar and field effect transistors. Transistors have been made on many systems, mainly semiconductor systems, including Si, SiGe, and III–V semiconductors. Since this encyclopedia concerns condensed matter physics, the basic principles of transistor operation and the fundamental performance of transistors, with emphasis on III–V semiconductor transistors, are discussed. Although the basic principles can be applied to many different systems, detailed discussions of transistor structures, transistor materials, processing, and circuit designs are omitted due to space constraints. (See "Further reading" section for details.)

Transistors, that is, three-terminal control devices, are important not only for electrical applications but also for physics studies. Several transistor devices often used in the study of transport physics at low temperatures are also discussed in the second half of this article.

Bipolar and Hetero-Bipolar Transistors

The principal operation of the (hetero) bipolar transistor is schematically shown in Figure 1. Although a bipolar transistor with *n*-type emitter, *p*-type base, and *n*-type collector (*n*–*p*–*n* transistor) is assumed in this figure, similar parameters are applicable to a *p*–*n*–*p* transistor. In the bipolar transistor, the most important factor determining transistor operation is current gain, that is, the ratio between J_C and J_B, where J_C and J_B are corrector current and base current, respectively. When this ratio becomes larger than unity, the transistor has a gain. The current injected from the emitter passes through the base and reaches the collector. When the diffusion constant of electrons in the *p*-type base is small or the base layer is thick, the probability of electron transmission to the collector decreases. Some amount of the base current also diffuses to the emitter. Calculating all these factors results in the current gain h_{fe} determined by the emitter injection efficiency:

$$h_{fe} = \frac{n_E}{p_B}\frac{v_e}{v_h}\frac{N_{CB}}{N_{CE}}\frac{N_{VB}}{N_{VE}}\exp\left(\frac{\Delta E_g}{KT}\right) \qquad [1]$$

where n_E and p_B are, respectively, the emitter and base doping concentration, v_e (v_h) is electron (hole) effective velocity toward the collector (toward the emitter) at the corrector-side (emitter-side) base edge, and, N_{CB} and N_{CE} (N_{VB} and N_{VE}) are densities of states in the conduction (valence) band for base and emitter, respectively. $\Delta E_g = E_{ge} – E_{gb}$ is the bandgap difference between emitter and base semiconductors.

For a thick emitter, v_h is determined by $v_h = D_h/L_E$, where D_h is the hole diffusivity in the emitter region and $L_E = \sqrt{D_h \tau_E}$ is the diffusion length. τ_E is the recombination lifetime in the emitter region. In the case of the thin base with $W_B < L_B$, v_e is represented as

$$v_e = D_n/(L_B \sinh(W_B/L_B)) = D_n/W_B$$

where D_n, L_B, and W_B are the electron diffusivity in the base region, electron diffusion length in the base, and the base thickness, respectively. In this situation,

$$h_{fe} = \frac{n_E}{p_B}\frac{L_E}{W_B}\frac{D_n}{D_h}\frac{N_{CB}}{N_{CE}}\frac{N_{VB}}{N_{VE}}\exp\left(\frac{\Delta E_g}{kT}\right) \qquad [2]$$

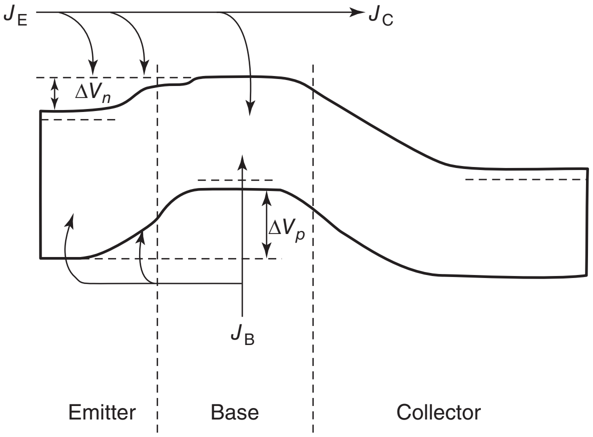

Figure 1 Schematic band diagram of a HBT with graded emitter-base junction. The schematic current flow, which determines the transistor operation, is also shown.

In the case of a homojunction bipolar transistor, such as an Si bipolar transistor, $\Delta E_g = 0$, and h_{fe} is mainly determined by $n_E/p_B/W_B$. In order to maintain a suitable high value of h_{fe}, n_E/p_B ~100–1000 is typically chosen. The hole density of the base, p_B, usually becomes 10^{17}–10^{18} cm^{-3} for the emitter electron density, n_E, of 10^{20}–10^{21} cm^{-3}. The current gain also increases with decreasing base layer thickness. However, the base resistance increases with decreasing p_B and W_B, so that there is a limitation to how far these parameters can be decreased in actual transistors. Si bipolar transistors are widely used in high-speed semiconductor circuits, owing to the many improvements in techniques for forming the emitter and base junctions, in isolation methods, and in the degree of self-alignment between the different device regions. Silicon is an indirect bandgap semiconductor and has a long recombination lifetime, so that the situation $W_B < L_B$ and a low-base resistance can be achieved even for a small p_B. However, direct bandgap semiconductors, such as GaAs, have a short recombination time, and the high n_E/p_B ratio necessary for the high-current gain is not possible. Therefore, it is difficult to build high-performance homojunction bipolar transistors from III–V semiconductors.

When heterojunctions are used, $\exp(\Delta E_g/kT)$ makes the most important contribution to h_{fe}. Improved transistor performance is expected by combining silicon-based transistors and Si/SiGe heterojunction systems. Furthermore, the large bandgap difference in III–V semiconductors enables one to use direct bandgap semiconductors in heterobipolar transistors (HBTs). This is because the term $\exp(\Delta E_g/kT)$ sufficiently compensates for the small n_E/p_B, and a thin base layer with high-carrier density becomes available. HBTs using many kinds of III–V semiconductor materials have been demonstrated.

At an abrupt heterojunction between different semiconductors, there is a discontinuity in the energy of the conduction-band minima and valence-band maxima. An energy barrier in the conduction band at the emitter–base junction tends to retard the flow of electrons from the emitter to the base. To avoid the barrier in the conduction band, a graded-alloy composition at the emitter–base junction has been used as shown in Figure 1. However, it is noteworthy that the barrier at the emitter–base junction is advantageous for high-speed operation because of the higher-energy electron injection from the emitter to the base. Therefore, an optimal design of the graded junction is necessary in actual HBTs.

For HBTs, many kinds of heterostructures have been studied. Figure 2 shows a comparison of the breakdown electric field of HBTs composed of Si/SiGe, InGaP/GaAs, InP/InGaAs, and GaN/InGaN material systems. The breakdown electric field of nitride-based HBTs is much higher than those reported for HBTs composed of other material systems. Therefore, GaN-based HBTs have recently received much attention as candidates for high-power and high-speed devices in the future. Here, the typical structures and characteristics of HBTs are discussed using GaN-based HBTs as examples. Figure 3 illustrates the schematic structure of the GaN/InGaN HBTs. In this peculiar device, the graded region is formed between the base and collector to reduce electron

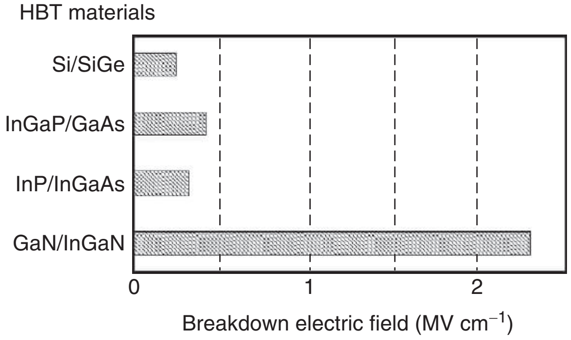

Figure 2 Comparison of breakdown electric field of HBTs composed of various material systems.

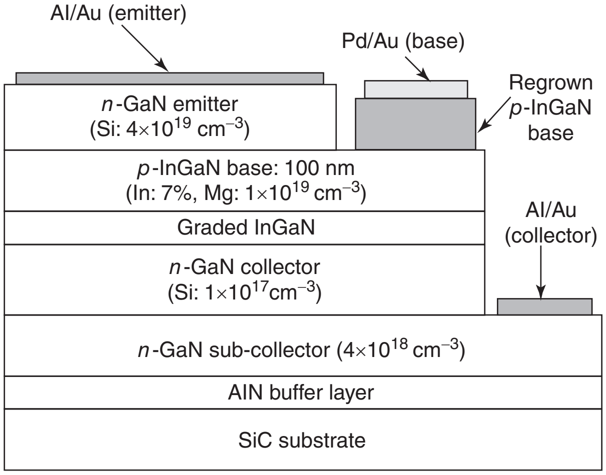

Figure 3 GaN/InGaN HBT structure with a regrown *p*-InGaN extrinsic base layer.

scattering at the collector barrier, because the same bandgap material (GaN) is used for both the emitter and corrector. A regrowth InGaN base contact is adopted to decrease the series resistance of the base. Actually, how to make a good contact to a thin base layer is a very important issue for HBTs with a thin base layer, and efforts to resolve this issue are underway for many heterostructure HBTs. The common emitter current–voltage characteristics of GaN/InGaN HBT with a 50 μm×30 μm emitter area are shown in Figure 4. The maximum collector gain exceeds 2000 in this device. Although this current gain is still less than the maximum gain of 5000 for Si/SiGe systems and 50000 for InP-based systems, the current gain for GaN-based systems has increased almost two orders of magnitude from the year 2000.

Field Effect Transistors: MISFET, MESFET, and HEMT

Bipolar transistors use both majority and minority carriers in semiconductors. There is, however, another type of transistor, where only the majority carriers are used and their density is controlled by an electric field effect. This type of transistor is called a field effect transistor (FET) and is widely used in many semiconductor systems. Several types of FETs are schematically shown in Figure 5. Metal–insulator–controlled semiconductor FETs (MISFETs) are shown in Figure 5a. When a positive bias is applied to the gate, conductive electrons start accumulating at the semiconductor–insulator interface. Due to the confinement by the electric field, the accumulated electrons have a two-dimensional (2D) nature. The threshold voltage, V_{th}, where electrons start accumulating, is determined by the semiconductor properties and interface characteristics. The density of accumulated charge, Q, is proportional to the gate bias and is represented as

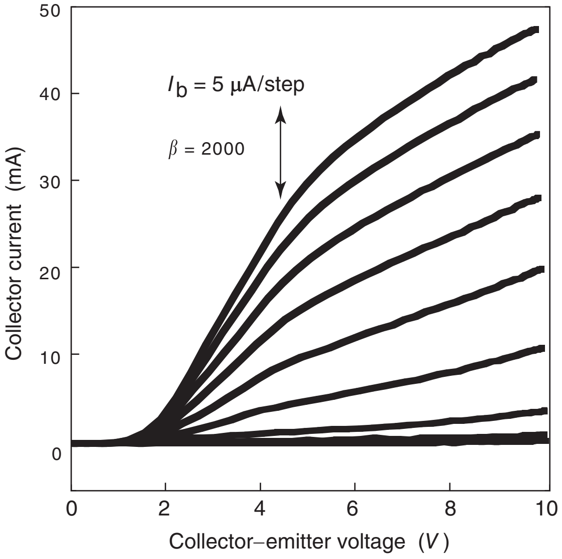

Figure 4 Common-emitter current–voltage characteristics of a GaN/InGaN HBT at room temperature. Base current is 5 μA/step.

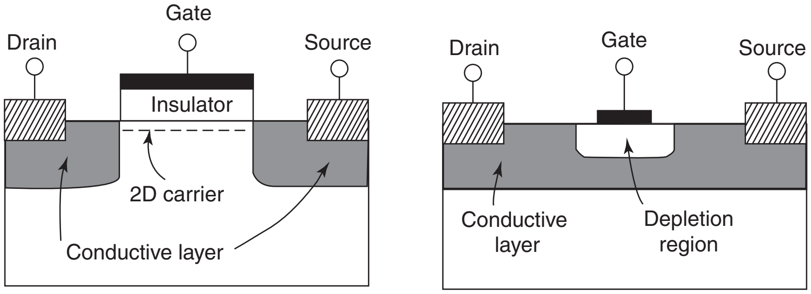

(a) MISFET (MOSFET) (b) MESFET

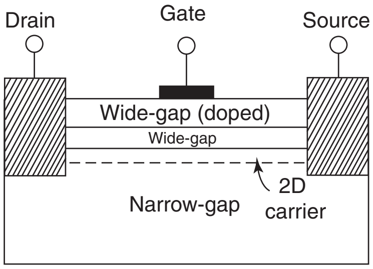

(c) HEMT (MODFET)

Figure 5 Schematic diagrams of field effect transistors (FETs). (a) MISFET (MOSFET), (b) MESFET, and (c) HEMT (MODFET).

$$Q = ne = C_g(V_g - V_{th}) \qquad [3]$$

where n, e, and C_g are the area density of electrons, electron charge, and capacitance of the gate insulator, respectively. When the bias is applied between the source and drain (V_d), the drain current (I_d) is determined by the carrier density (n) and the mobility of the carrier (μ). In the case of small V_d, where carrier density is constant over the whole device,

$$I_d = \frac{Z}{L}\mu n e V_d \qquad [4]$$

where Z and L are the channel width and length of the MISFET. In the case of the MISFET, ne is expressed by eqn [3], then

$$I_d = \frac{Z}{L}\mu C_g(V_g - V_{th})V_d \qquad [5]$$

With increasing V_d, the carrier density near the drain edge decreases and finally becomes zero (pinch-off) at around $V_d = V_g - V_{th}$. Further increasing V_d results in an almost constant drain current independent of V_d, because a balance is achieved between the pinch-off of the carrier and the high electric field concentrating in the pinch-off region. Therefore, I_dV_d characteristics of MISFETs, schematically shown in Figure 6, are separated into linear and saturated regions. The drain current in the saturated region, I_{ds}, is approximately expressed as

$$I_{ds} = \alpha\frac{Z}{L}\mu C_g(V_g - V_{th})^2 \qquad [6]$$

where α is a constant close to unity.

In the case of Si, silicon dioxide (SiO_2) is used as the gate insulator. Therefore, the FET is normally called metal-oxide–semiconductor FETs (MOSFETs). It is also possible to accumulate conductive holes by applying negative bias to the gate. Combining n-type (electron transport) MOSFETs and p-type (hole transport) MOSFETs results in complementary MOSFET devices (CMOS devices). The Si MOSFET and CMOS devices are the most important devices in the very large scale integrated circuits used in microprocessors and semiconductor memories.

In MISFET devices, some other combinations of insulators and semiconductor materials are also possible. A good example is the InP MISFET, where electrons can accumulate at the interface between the InP and insulator, such as Al_2O_3. However, the conductive carriers cannot be accumulated at the interface when the density of states of the interface defects is very large, as is the case at insulator–GaAs interface.

To avoid a direct and uncontrollable leakage current between the drain and source, n-type (p-type) MISFETs are fabricated on p-type (n-type) or semi-insulating materials. For the purpose of distinguishing these two types of MISFETs, the former is called an inversion-type MISFET and the latter an accumulation-type MISFET. For both types, the gate-induced carriers need to contact the

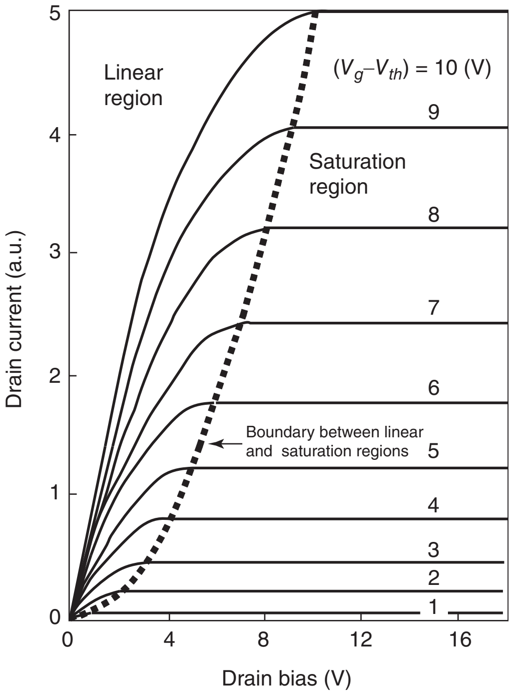

Figure 6 Schematic drain current-drain bias characteristics of a MISFET (MOSFET). Actual value of the drain current depends on device parameters and carrier mobility.

source- and drain-conductive regions (doped regions) so that an overlap between source- (drain-) conductive regions and gate is essential for the FET operation. The self-alignment process allows one to make such an overlap without increasing the capacitance between the gate and source (drain).

Another type of FET is the metal–semiconductor FET (MESFET). Figure 5b is a schematic diagram of a MESFET. In this device, conductive carriers are supplied from the 3D doping layer, and the number of conductive carriers is controlled by a depletion region spreading from the Schottky metal gate. The conductive layer thickness is determined by subtracting the depletion region thickness (W_d) from the total thickness of the doping layer. For the *n*-type conducting channel,

$$W_d = \sqrt{\frac{2\varepsilon(V_{bi}-V_g)}{eN_d}} \qquad [7]$$

where V_{bi}, ε, and, N_d are the built-in potential of the Schottky gate, dielectric constant of semiconductor, and donor density of the doping layer, respectively. The area density of the conductive carrier can be easily estimated from the conductive layer thickness, and the drain current is determined by eqn [4] in small V_d regions. Forming the conductive layer involves several techniques, such as ion-implantation and epitaxial growth.

Finally, there is the high-electron-mobility transistor (HEMT) which is shown in Figure 5c. The HEMT utilizes conductive carriers accumulated at the hetero-interface between wide- and narrow-gap semiconductors. A triangular-shaped confinement potential at the interface defines the conductive carrier in a thin 2D channel. Modulation doping, that is, doping in the wide-gap semiconductor and conductive carriers at the interface, enables one to separate conductive carriers from dopant impurities, which results in a strong suppression of impurity scattering. Therefore, HEMTs are also called modulation-doped FETs (MODFETs). The density of the 2D electron system is controlled by the gate bias and the I_dV_d characteristics are roughly represented by eqns [3]–[6]. The most widely studied HEMT devices are based on the AlGaAs/GaAs system; however, many different material combinations, such as InAlAs/InGaAs and AlGaN/GaN systems, have been developed recently.

High-frequency FETs are key devices in recent optical communications technology, where they enable the practical use of 40 Gbit s^{-1}. Figure 7 summarizes current gain cut-off frequencies (f_T's) for various kinds of FETs. Among them, InP-based HEMTs, where a conductive two-dimensional electron gas (2DEG) channel is formed in the InAlAs/InGaAs heterostructures lattice-matched with InP substrate, have achieved record f_T's for a wide range of gate lengths (L_g's) by many research groups. The effective saturation velocity of InAlAs/InGaAs HEMTs is 2.7×10^7 cm s^{-1}, ~1.3 times higher than that of GaAs-based HEMTs. Moreover, higher electron mobility and sheet-carrier density of the 2DEG at the InAlAs/InGaAs hetero-interface reduce channel and parasitic charging times, and make possible the effective use of higher saturation velocity. The current record f_T for a discrete device is beyond 400 GHz.

Integrated circuits (ICs) based on InP have been developed with the aim of achieving a 100 Gbit s^{-1} class communications technology. The schematic structure of such an IC is shown in Figure 8. A 0.1 μm-gate InAlAs/InGaAs HEMT is integrated with

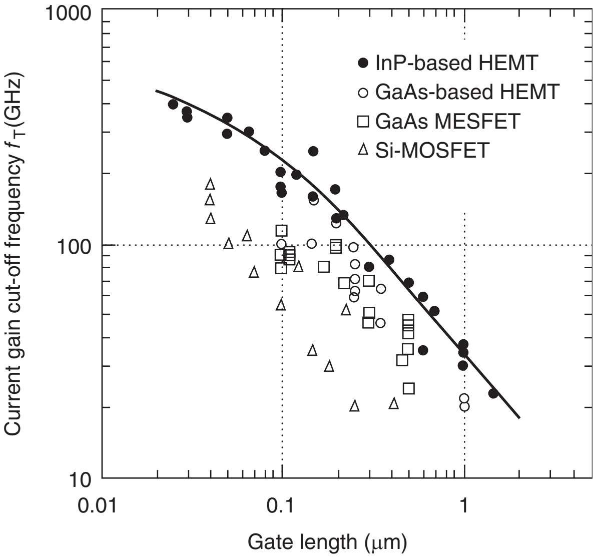

Figure 7 Current gain cut-off frequencies for various kinds of FETs.

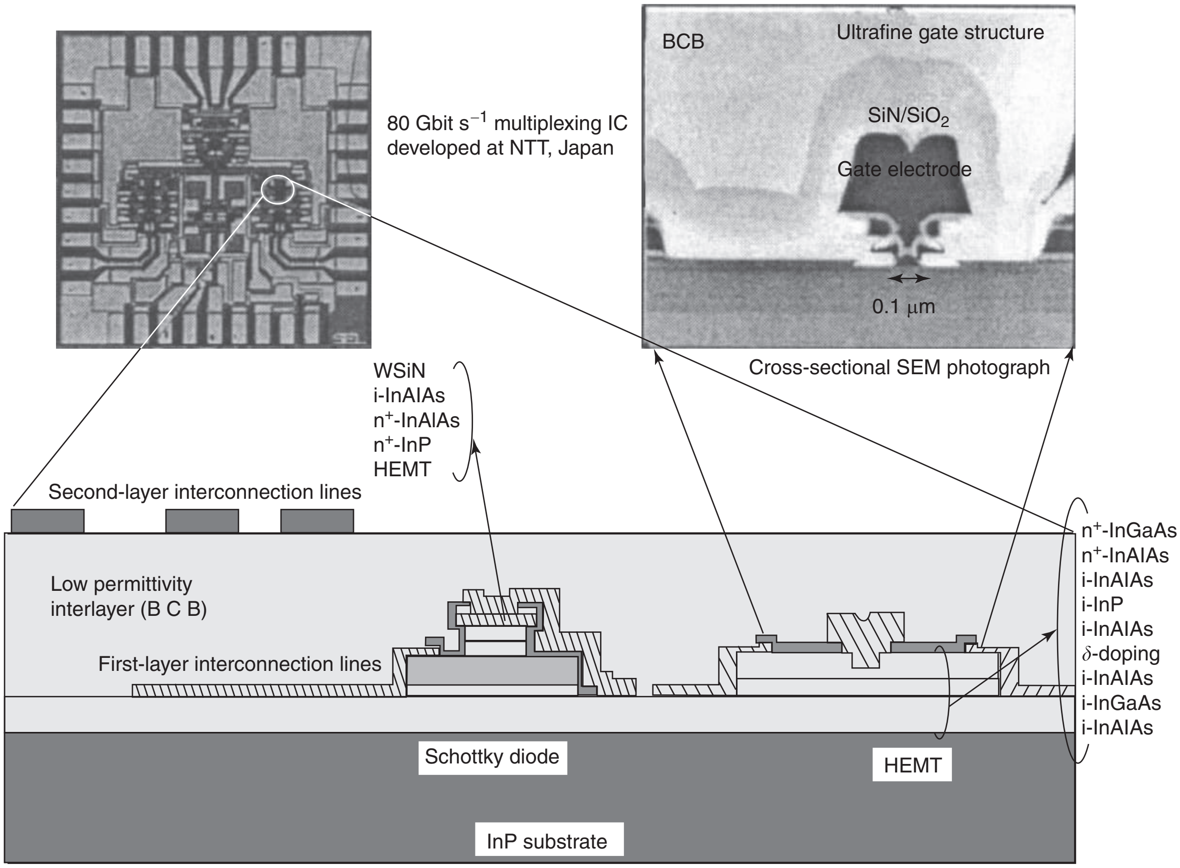
80 Gbit s^{-1} multiplexing IC developed at NTT, Japan
BCB
Ultrafine gate structure
SiN/SiO$_2$
Gate electrode
0.1 μm
Cross-sectional SEM photograph
WSiN
i-InAlAs
n$^+$-InAlAs
n$^+$-InP
HEMT
Second-layer interconnection lines
Low permittivity interlayer (B C B)
First-layer interconnection lines
Schottky diode
HEMT
InP substrate
n$^+$-InGaAs
n$^+$-InAlAs
i-InAlAs
i-InP
i-InAlAs
δ-doping
i-InAlAs
i-InGaAs
i-InAlAs

Figure 8 Schematic diagram of an InP-based HEMT IC.

InAlAs Schottky diodes, metal resistors, and metal-insulator-metal (MIM) capacitors in this example. The mushroom-shaped gate improves transistor performance.

Modulation-doped HEMT structures are important not only as cutting-edge room-temperature devices but also as key devices for studies of low-temperature physics. The 2D electron system at the AlGaAs/GaAs interface has the highest mobility at low temperatures, and has been very important in quantum Hall effect research. Mobility up to $10^7\,\mathrm{cm}^2\,\mathrm{V}^{-1}\,\mathrm{s}^{-1}$ has been obtained in several laboratories in the USA, Europe, and Japan. The mobility is still limited by background impurities; therefore, it can be improved by increasing electron density. Recently, Bell Laboratories used a sophisticated MBE technique and two-side modulation-doping, and achieved mobility of around $3\times10^7\,\mathrm{cm}^2\,\mathrm{V}^{-1}\,\mathrm{s}^{-1}$.

Backgated Structures

The backgated structure, where carrier density is modulated from the back side by a voltage applied to the backgate, is also attractive. Although the gate capacitance limits high-frequency applications, the density control from the back side enables one to use the free surface for many kinds of structures. When fine structures are formed on the surface side, the structure behaves as a density-tunable mesoscopic system.

An example of a backgated heterostructure is shown in Figure 9. In this example, the 2D electron system accumulates at the hetero-interface between AlGaAs and GaAs. Conductive electrons are supplied from the ohmic contacts as in Si MOSFETs. The threshold voltage of the 2D electron accumulation is determined by the balance between surface charge and backgate bias. In case of the GaAs, the surface charge is frozen at low temperatures and the surface Fermi level is not pinned at the midgap. These features help in accumulating 2D electron systems with a small threshold voltage at low temperatures. Once the 2D electron system is accumulated at the hetero-interface, its density can be precisely controlled by the backgate bias, that is, an electric field applied between the 2D electrons and the backgate.

In-Plane-Gate Transistor

Transistors, that is, three-terminal devices, have been applied to confine electron systems to low dimensions, such as one and zero dimensions. When a pair of split Schottky gates is formed on a semiconductor heterostructure, such as AlGaAs/GaAs, the 2D electron system under the gates is depleted by a negative gate bias applied to the Schottky gates (see Figure 10a). The small distance between the two gates results in a narrow electron channel, which shows clear 1D features at low temperatures. Quantized conductance characteristics have been observed for such narrow and ballistic 1D channels, which are called quantum point contacts.

A unique transistor structure, called the in-plane-gate transistor, is formed by separating a 2D electron system into three parts using insulated lines as shown in Figure 10b. These insulating lines are made by trench etching or ion implantation. When a negative bias is applied to two side gates against the center region, the depletion region spreads from the insulating lines and a 1D channel is formed in the center channel. As shown in Figure 10c, quantized conductance characteristics have been reported, reflecting the successful formation of such a channel. Although the in-plane-gate FET is limited to a 1D system from the operation principle, three-terminal structures are made without Schottky gates. Therefore, the in-plane-gate FET is beneficial for many narrow-gap semiconductors, where the formation of a good Schottky gate is difficult.

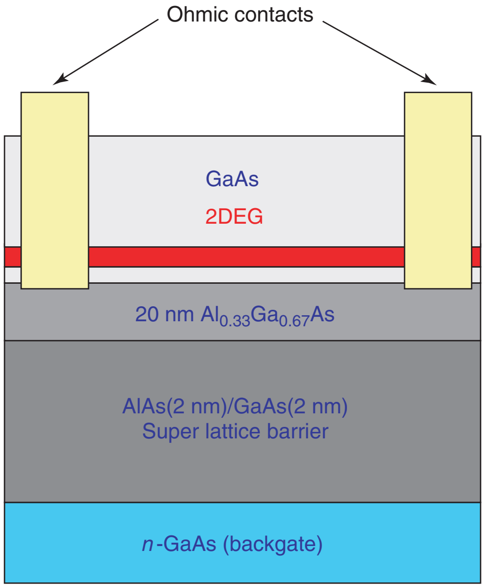

Figure 9 Example of a backgated heterostructure.

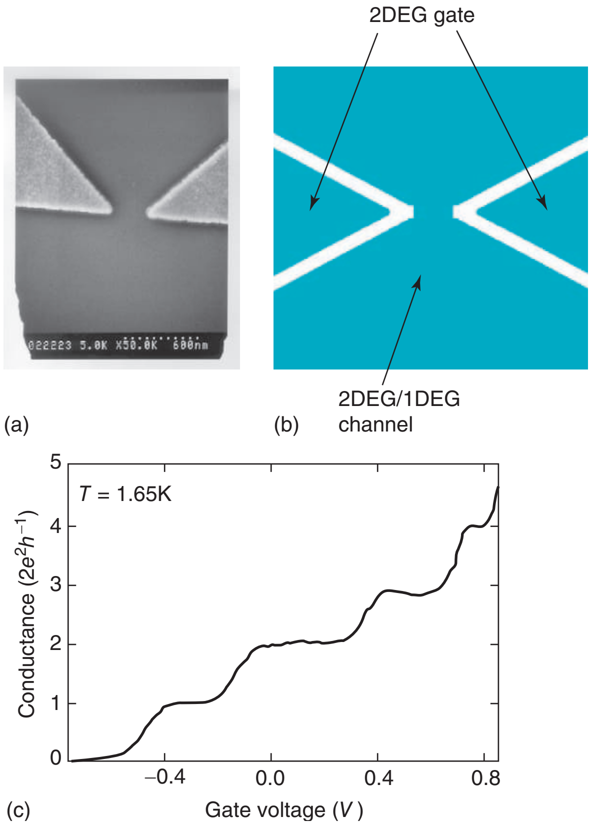

Figure 10 Quantum point contacts (QPCs) fabricated by the FET technique. (a) Split Shcottky gate QPC, (b) in-plane-gate QPC, and (c) typical characteristics of an in-plane-gate QPC fabricated on InSb quantum-well structure.

Single–Electron Transistor

In FETs, the number of carriers in the channel is determined by the gate bias through capacitance coupling. By combining FETs and nanotechnologies, it becomes possible to realize the structure schematically shown in Figure 11a. There is a small channel, like a quantum dot, which is separated from the source and drain by two barriers. The barrier height is set high enough to protect normal current flow, but low enough to permit tunneling coupling between the quantum dot and source (drain). The charge in the quantum dot increases linearly with the gate bias as represented by $Q = C_g V_g + Q_0$, where Q is the charge in the quantum dot, C_g gate

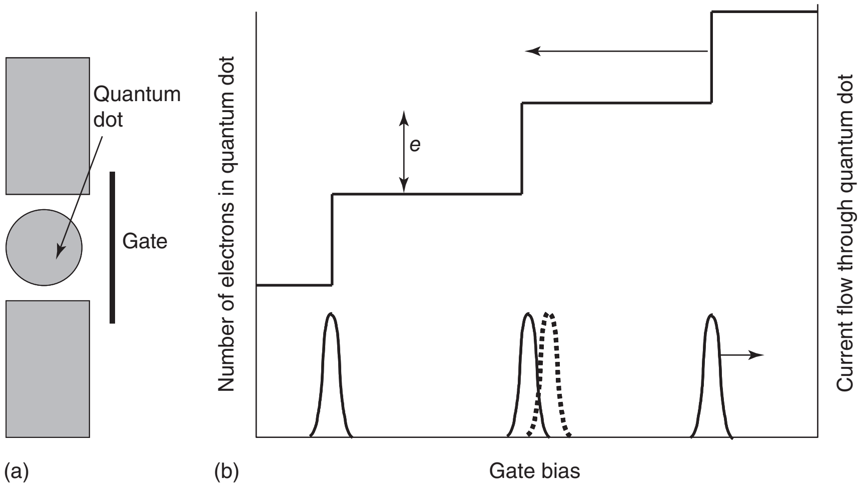
Quantum
dot
Gate
(a)
Number of electrons in quantum dot
e
Current flow through quantum dot
(b)
Gate bias

Figure 11 (a) Schematic diagram and (b) schematic operation principle of an SET. The position of the conductive peak is extremely sensitive to the charge balance in the circumstances schematically shown by the dotted lines.

capacitance, V_g gate bias, and Q_0 the background charge determined by the balance of the quantum dot in the system. When electrons accumulate in the quantum dot, Q should be an integer multiple of e, the charge of a single electron. This discrete nature of the charge is not important for a large system, but becomes essential for a small system such as the quantum dot, where $\Delta V_g = e/C_g$ becomes larger than the thermal broadening, kT/e. This situation is fully satisfied for the small quantum-dot system at low temperatures, and such three-terminal structures are called single-electron transistors (SETs).

A schematic diagram of an SET operation is shown in Figure 11. According to the increase in the gate bias, the charge in the quantum dot increases along a step function Ne (N: integer). A current flow, that is, electron flow, should be accompanied by a change of the number of electrons in the quantum dot. Therefore, the current flow is limited only in the condition where N can change with $\Delta N = 1$. On the other hand, the current flow is blocked when N is constant (Coulomb blockade).

Some SET characteristics are shown in Figure 12. The quantum dot has a circular disk shape in this example. The interval of current peaks determined by $\Delta V_g = e/C_g$ decreases with increasing bias. This is because an increase in the disk size with gate bias results in increased gate capacitance. In addition to the classical charging effect, quantum effects, such as the formation of zero-dimensional energy states, become important in small quantum dots. The zero-dimensional energy levels are represented by the diagram in Figure 12b for the parabolic confinement, which is a good approximation of the disk-shaped quantum dot. Here, hω_0 represents the zero-dimensional energy-level separation arising from the parabolic confinement. The zero-dimensional energy levels degenerate at zero magnetic field, where $\omega_c = 0$. Each energy level can include two electrons with different spins. Therefore, ΔV_g increases for $N = 2, 6, 12, \ldots$ where the zero-dimensional energy separation should be compensated by the gate bias in addition to e/C_g. Such periodic features have actually been observed as shown in Figure 12a for a circular quantum dot. This periodic feature comes from the same principle as the periodic table of real atoms, so that these SETs are sometimes called semiconductor artificial atoms.

At low temperatures, the conductive peak becomes sharp as experimentally shown in Figure 12a. Furthermore, the peak position shifts when the charge situation around the quantum dot is slightly modified as schematically shown in Figure 11b. Therefore, the conductance change in an SET operates as a very sensitive electrometer. Recently, the single electron motion in semiconductor nanostructures was detected by using the SET-based highly sensitive electrometer.

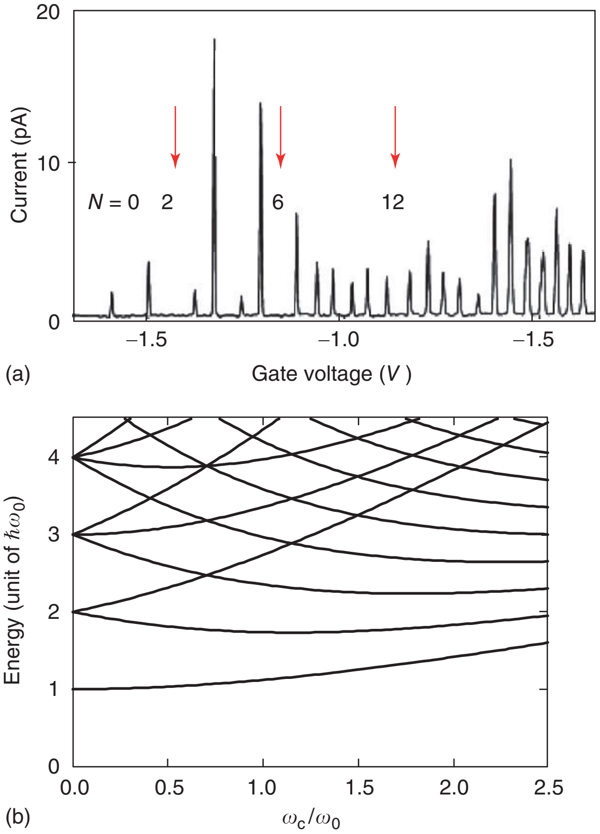

Figure 12 (a) Current vs. gate voltage characteristics experimentally observed for the disk-shaped SET. The current peak interval becomes wider for N (the number of electrons in the quantum dot) of 2, 6, 12, . . ., as shown by arrows. Such characteristics are explained by the zero-dimensional energy levels formed in the circular quantum dot and shown in (b). This energy diagram is calculated for a parabolic confinement potential, $V = m\omega_0^2(x^2+y^2)/2$. h$\omega_c$ is the cyclotron energy separation in the perpendicular magnetic field.

Further Reading

Adir Bar-Lev CWJ (1984) *Semiconductors and Electronic Devices*, 2nd edn. New Jersey: Prentice-Hall.

Beenakker and van Houten H (1991) Quantum transport in semiconductor nanostructures. In: Ehrenreich H and Turnbull D (eds.) *Solid State Physics*, vol. 44, p. 1. New York: Academic Press.

Enoki T, Sano E, and Ishibashi T (2001) Prospects of inp-based ic technologies for 100-Gbit/s-class lightwave communications systems. *International Journal of High Speed Electronics and Systems* 11: 137.

Fujisawa T, Austing DG, Tokura Y, Hirayama Y, and Tarucha S (2003) Electrical pulse measurement, inelastic relaxation, and non-equilibrium transport in a quantum dot. *Journal of Physics: Condensed Matter* 15: R1395. (topic review).

Kiehl RA and Sollner TCLG (1994) *High Speed Heterostructure Devices, Semiconductors and Semimetals*, vol. 41. New York: Academic Press.

Kouwenhoven LP, Markus CM, McEuen PL, Tarucha S, Westervelt RM, *et al.* (1997) Electron transport in quantum dots. In: Sohn LL, Kouwenhoven LP, and Schoen G (eds.) *Mesoscopic Electron Transport*, NATO ASI Series. Dordrecht: Kluwer Academic.

Kroemer H (1982) Heterojunction bipolar transistors and integrated circuits. *Proceedings of the IEEE*, 13.

Makimoto T, Kumakura K, and Kobayashi N (2002) *International Workshop on Nitride Semiconductors (IWN2002)*, p. 379, Aachen.

Mishra UK, Parikh P, and Wu Yi-Feng M (2002) AlGaN/GaN HEMTs – an overview of device operation and applications. *Proceedings of the IEEE* 90: 1022.

Reed P (ed.) (1992) *Nanostructured Systems, Semiconductors and Semimetals*, vol. 35. New York: Academic Press.

Roblin and Rohdin H (2002) *High-Speed Heterostructure DevicesFrom Device Concepts to Circuit Modeling*. Cambridge: Cambridge University Press.

Sze SM (ed.) (1990) *High-Speed Semiconductor Devices*. New York: Wiley.

Sze SM (2002) *Semiconductor DevicesPhysics and Technology*, 2nd edn. New York: Wiley.

Tarucha S, Austing DG, Sasaki S, Kouwenhoven LP, Reimann S, Koskinen M, and Manninen M (2001) Electronic states in circular and ellipsoidally deformed quantum dots. In: Yao T (ed.) *Physics and Applications of Semiconductor Quantum Structurech. 9*, pp. 194–216. Bristol: IOP Publishing.

Taur Y and Ning TH (1998) *Fundamentals of Modern VLSI Devices*. Cambridge: Cambridge University Press.

Uyemura JP (2001) *Introduction to VLSI, Circuits and Systems*. New York: Wiley.

Silicon, History of

F Seitz, Rockefeller University, New York, NY, USA
NG Einspruch, University of Miami, Coral Gables, FL, USA

© 2005 Elsevier Ltd. All rights reserved.

This is an update of F. Seitz, N.G. Einspruch, Silicon, History of, Editor(s): Franco Bassani, Gerald L. Liedl, Peter Wyder, Encyclopedia of Condensed Matter Physics, Elsevier, 2005, Pages 368–378, ISBN 9780123694010, https://doi.org/10.1016/B0-12-369401-9/00483-6.

In 1781, Henry Cavendish discovered that water is not a primary chemical element, as had been believed for millennia, but a compound formed by the combination of hydrogen and oxygen. This discovery provided Antoine Laurent Lavoisier with insight concerning the true nature of the elements and stimulated him to undertake extensive experimental investigations in a search to identify as many elements as possible. His views were formalized in 1789 by the publication of a two-volume treatise (Figure 1) that provided the platform for the evolution of modern chemistry.

In his search for new elements, Lavoisier commonly attempted to reduce with hydrogen what were presumably compounds of the elements, a procedure that was particularly successful with the heavy metal oxides. In the course of this work, he decided that the mineral quartz was probably the oxide of an interesting element, but failed in his attempts to reduce it. A quarter of a century later, the distinguished Swedish chemist Joens Berzelius (Figure 2) finally achieved that goal. The newfound element ranked as an oddity. While it had some of the characteristics of a metal, such as a somewhat shiny metallic luster and the ability to conduct electricity, its conductivity was poor compared to that of silver and copper and decreased rather than increased as the temperature was lowered.

Since no immediate use was found for it, early samples of silicon were in the main assigned an honored place within exhibits of the chemical elements. However, the situation with respect to silicon changed radically during the last quarter of the nineteenth century, by which time professional chemists, well-trained in scientific methods, were in charge of research and development in fields such as metallurgy, ceramics, enamels, pigments, and dyes, replacing the ancient breed of investigators who had depended with some degree of success upon tradition, hunches, and mysticism. There was, for example, much interest at this time in the study of the magnetic properties of iron and its alloys that were being used in electric generators, motors, and transformers for many power-handling applications. Systematic research disclosed the existence of a family of iron–silicon alloys whose magnetic properties were much better than those of pure iron for many purposes. Moreover, relatively modest additions of silicon to some forms of steel could confer superior properties in matters such as toughness. In any event, silicon had finally become a very useful element in technical application and was beginning to be produced commercially at a level of ~98% purity.

During this same period, two other developments that were to influence the use of silicon in fields of technology occurred. First, a young German physicist, Dr. Ferdinand Braun (Figure 3), decided to extend prior research carried out earlier by Michael Faraday on the electrical properties of materials that were neither good insulators nor good electrical conductors. His target group included some ionic crystal, such as salts that permit ionic conductivity, and what are now called semiconductors, which were found eventually to conduct electronically. Both types of substance are distinguished by the fact that their electrical conductivity decreases toward zero at sufficiently low temperatures. Working with specimens of semiconductors, particularly with heavy metal sulfides, Braun discovered crystal rectification in 1874, that is, asymmetrical flow of current in a crystalline specimen for a given voltage when applied in opposite directions. In the course of his investigations, he demonstrated that it was a surface effect, Ohm's law connecting the current and field strength being valid in the bulk of the specimen.

The second significant development was Heinrich Hertz's production of electromagnetic radiation in the meter and shorter range of wavelength with hand-fabricated condensers, inductance, and antennae. This generated widespread interest in the possibility of long-range transmission and reception of such waves, a goal that was led in a very dynamic way by Guglielmo Marconi.

Initially, the propagation of an electromagnetic wave was detected by means of an ingenious device known as the coherer, invented in 1890 by the French physicist Edouard Branly. The coherer contained a bundle of metallic needles that aligned parallel to one another when an electromagnetic wave passed through the needles, thereby altering the collective electrical conductivity of the bundle.

Apparently, at some time toward the end of the 1890s, the prolific Canadian inventor Reginald A Fessenden (Figure 4) discovered that one can hear the electromagnetic pulses with earphones of the type used in telephones, provided one rectifies the electric current produced by the signals so that the resulting pulse contains frequencies in the audible range to which the earphones could respond. He invented a rectifier consisting of a wire dipped in an electrolytic solution. Soon after, a brilliant young Indian physicist, Sir Jagadish Chandra Bose (Figure 5), who was studying at Cambridge University when Hertz published his research and had done much to improve the coherer, patented the use of crystalline lead sulfide (the mineral galena), a rectifying semiconductor of the type discovered by Braun, as a replacement for the electrolytic device. This represented a very significant milestone in the development of solid-state electronics. Incidentally, Marconi was greatly assisted in his work by a very competent group of electrical engineers of the Italian Navy, who kept abreast of most technical developments in the field. He presumably used a semiconductor rectifier in his first successful transatlantic transmission in 1901.

In 1900 the American Telephone and Telegraph Company (AT&T) served only local communities because of limitations in the distance over which copper wire would transmit voice messages without amplification. The principal city was New York. The management of the company soon decided, however, that it should develop a national network in order to provide more uniform, consolidated service throughout the country. As a result, AT&T began to assemble an excellent technical staff to assist in determining the best route to follow. The range of possibilities included use of a wireless system. Dr. G W Pickard (Figure 6), a member of the

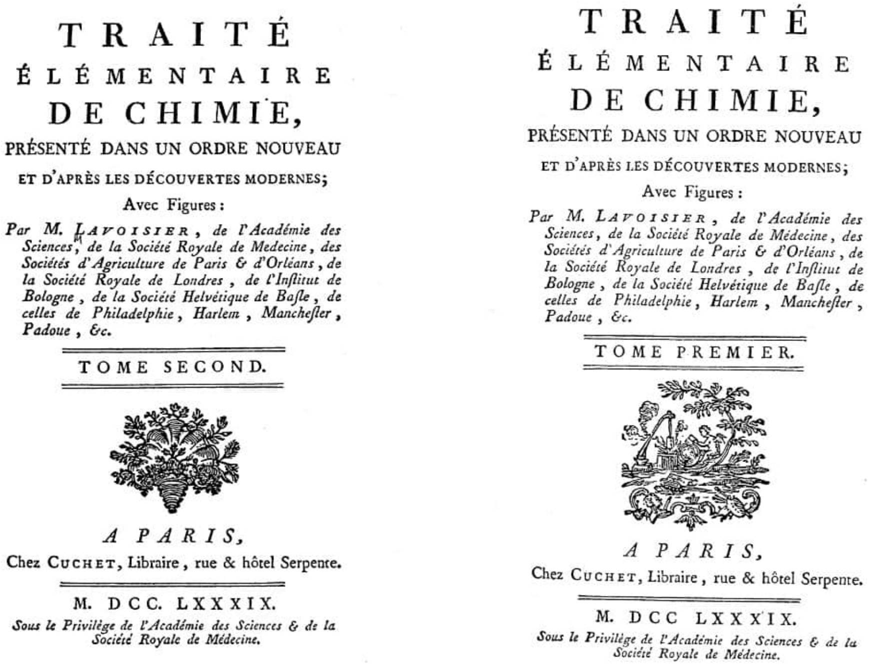

TRAITÉ
ÉLÉMENTAIRE
DE CHIMIE,
PRÉSENTÉ DANS UN ORDRE NOUVEAU
ET D'APRÈS LES DÉCOUVERTES MODERNES;
Avec Figures:
Par M. Lavoisier, de l'Académie des
Sciences, de la Société Royale de Medecine, des
Sociétés d'Agriculture de Paris & d'Orléans, de
la Société Royale de Londres, de l'Inſtitut de
Bologne, de la Société Helvétique de Baſle, de
celles de Philadelphie, Harlem, Mancheſter,
Padoue, &c.
TOME SECOND.

A PARIS,
Chez Cuchet, Libraire, rue & hôtel Serpente.
M. DCC. LXXXIX.
Sous le Privilège de l'Académie des Sciences & de la
Société Royale de Médecine.

TRAITÉ
ÉLÉMENTAIRE
DE CHIMIE,
PRÉSENTÉ DANS UN ORDRE NOUVEAU
ET D'APRÈS LES DÉCOUVERTES MODERNES;
Avec Figures:
Par M. Lavoisier, de l'Académie des
Sciences, de la Société Royale de Médecine, des
Sociétés d'Agriculture de Paris & d'Orléans, de
la Société Royale de Londres, de l'Inſtitut de
Bologne, de la Société Helvétique de Baſle, de
celles de Philadelphie, Harlem, Mancheſter,
Padoue, &c.
TOME PREMIER.

A PARIS,
Chez Cuchet, Libraire, rue & hôtel Serpente.
M. DCC LXXXIX.
Sous le Privilège de l'Académie des Sciences & de la
Société Royale de Médecine.

Figure 1 Lavoisier's two-volume treatise on chemistry that opened the doorway to modern chemistry. It was published in 1789. (Courtesy of the library of the American Philosophical Society.)

Figure 2 The Swedish chemist Joens J Berzelius, who isolated elemental silicon in 1823. (Courtesy of the Deutsches Museum, Munich.)

technical staff who had become interested in the possibility of employing wireless communication, decided to see if there was a crystalline rectifier that was superior to galena. It is reported that he investigated more than a thousand compounds. In any case, carefully selected crystals of the commercially available grade of silicon turned out to have the best properties of all the specimens included in his search. The management of AT&T permitted him to set up an independent company to market the silicon rectifiers he developed.

Figure 3 Ferdinand K Braun who discovered rectification in semiconductors in 1874, soon after completing his doctorate. He became one of the foremost leaders in the field of radio technology during his time. He demonstrated the important role that resonant circuits can play in long-distance transmission. He shared a Nobel Prize with Marconi in 1909. (Courtesy of the Tuesday Morning Club of Tübingen, the library of the University of Tübingen.)

In the meantime, many scientists began to study the properties of the electron beams (cathode rays) that could be produced in a vacuum from a negatively charged electrode. One of the investigators, John A Fleming, showed that a device containing such an electron source and a positively charged collecting electrode could serve as a rectifier. Subsequently, Dr. Lee De Forest demonstrated that one could add a third electrode to Fleming's rectifier and use it to modulate the magnitude of the collected current. With appropriate feedback, De Forest's triode could be used as the basis for creating an electronic amplifier or an oscillator. Since vacuum technology was fairly primitive at the time, the early versions of the two devices behaved in an unpredictable manner and were generally treated as interesting curiosities.

However, the technical staffs of AT&T and the General Electric Company, as well as scientists and engineers in other countries, recognized the importance of the principles involved in De Forest's invention and began to improve both vacuum tube diodes and triodes. By 1915, the telephone system established by AT&T, which incorporated greatly improved vacuum tube relay-amplifiers, was able to span the continent. By the end of World War I, essentially the entire field of electronics was in the hands of vacuum tube experts. Semiconductors were almost forgotten, although inexpensive cuprous oxide and selenium rectifiers were widely used to rectify ordinary fifty- or sixty-cycle current for special purposes, such as providing rectified current to vacuum-tube filaments. As amusement, individuals in their early teens commonly made simple, inexpensive crystal-detector radio receivers that enabled them to listen to local broadcasting stations using earphones. Galena was generally used as a rectifier in such sets. Many older boys entered the world of vacuum tube technology when they could afford to acquire such tubes.

Fortunately, semiconductors were not completely forgotten since they display two important characteristic properties: they do not need a specially designed cathode and associated energy source since some conduction electrons become free at ambient temperatures; as such, semiconductors could be fabricated into monolithic devices whose useful lifetime was not determined by burn-out or other factors that influence vacuum tubes. In continuous operation at full power, a typical vacuum tube has a lifetime of $\sim$1000 h. To overcome this major limitation, a number of individuals attempted to develop a triode analog of the De Forest tube

Reginald A. Fessenden

Figure 4 Reginald A Fessenden, the prolific Canadian inventor who invented amplitude modulation (AM) radio, introduced rectification and the heterodyne principle which made it possible to alter the frequencies of electromagnetic waves. He was also responsible for the first two-way wireless transmission across the Atlantic Ocean on a steady basis and for the invention of sonar. (Courtesy of the Fessenden collection of the Archives of the State of North Carolina in Raleigh, North Carolina.)

using semiconductors prior to World War II. Some inventors succeeded in obtaining conceptual design patents for proposed devices, but none were actually "reduced to practice."

One of the individuals who took this issue very seriously in the 1920s was Dr. Mervin J Kelly (Figure 7), who was then in charge of the production of vacuum tubes at the Western Electric Company, the manufacturing arm of AT&T. He was thoroughly conscious of the limitations of vacuum tubes and was captivated by the thought of replacing, or at least complementing, them by semiconductor devices. He decided that if he were ever made Head of the Bell Telephone Laboratories, he would establish a team to explore semiconductor-based technology fully. He became head of the Laboratories in the mid-1930s and, in keeping with his plans, hired Dr. William S Shockley, a doctoral graduate of the Massachusetts Institute of Technology, to join forces with Dr. Walter H Brattain, who was already at the Laboratories, in characterizing the properties of various semiconductors. While they made a preliminary study of cuprous oxide, they were diverted to other problems as World War II approached. Kelly's plan was forced to await the end of the war.

Research and development in the field of radar was a major activity among scientists and engineers during World War II. Although many significant investigations were carried out earlier, the first microsecond pulsed radar was developed in 1932 by an ingenious engineer, Dr. Hans E Hollmann, who used it to study the reflections of electromagnetic waves from the ionosphere in the upper atmosphere of the Arctic region – the layers that make transmission of radio waves in the kilohertz and lower megahertz region of the radio spectrum possible over long distances on the curved earth. He observed the reflected pulses on an oscilloscope with a synchronized time sweep and found that he could pick up features of the landscape such as mountain ranges. The German Navy used this knowledge to produce its first radar system soon thereafter. It operated with wavelengths in the vicinity of 2.4 m. Dr. Robert Page achieved the first comparable development in the US at the Naval Research Laboratory in 1939, delays in funding having retarded research that was initiated in the 1920s.

It should be added that Hollmann so distrusted Hitler and his plans for world conquest that he discontinued all research that might be employed in offensive warfare and focused on medical applications of electronics. While making the shift, however, he wrote a two-volume treatise in the field of high-frequency electronics that was by far the most advanced work of its kind when it

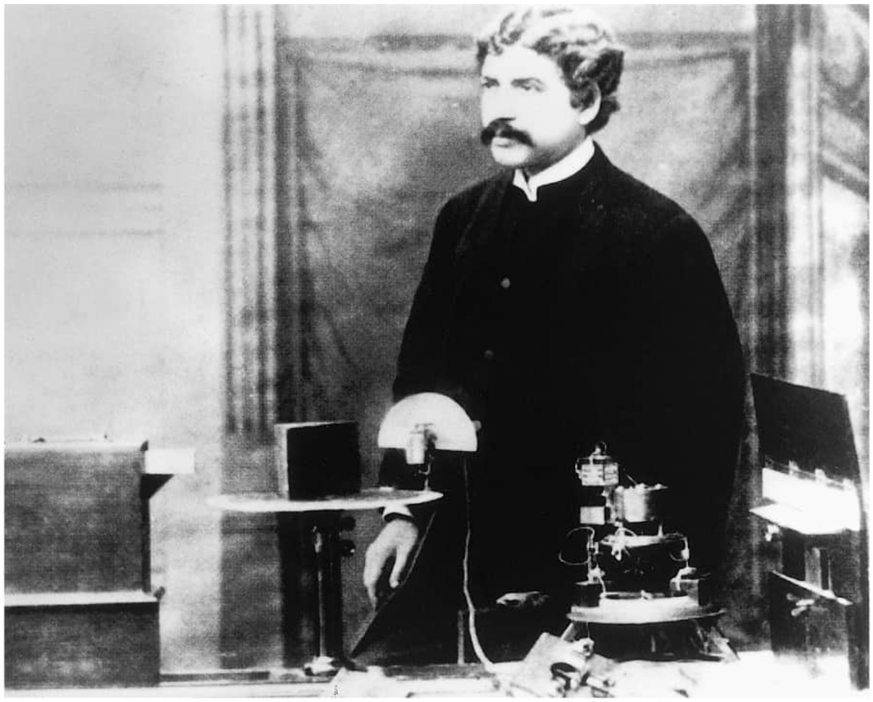

Figure 5 Jagadish C Bose who was at Cambridge University in England when Hertz published his papers on the generation of electromagnetic waves. Bose immediately began research in the centimeter and millimeter range of wavelengths. He invented many items of apparatus that were later re-invented in the 1930s, during the early days of microwave radar. He was the first person to employ a semiconductor (galena) as a rectifier. (Courtesy of the Jagadish Chandra Bose Research Institute, Calcutta, India.)

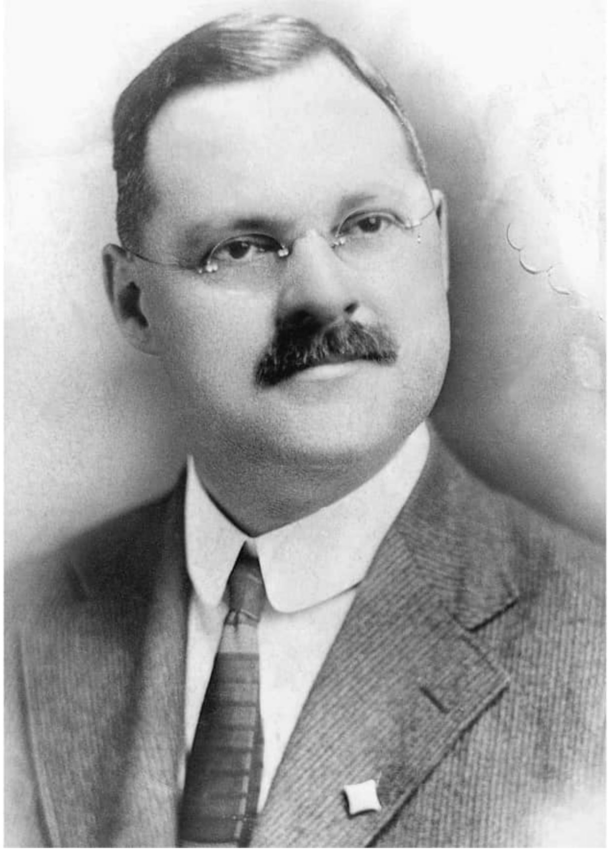

Figure 6 G W Pickard who, in 1905 while working for AT&T, made a thorough search among available semiconductors to find the best rectifier. He concluded that silicon was the preferred choice and began marketing units that contained good specimens. (Courtesy of the Center for the History of Electrical Engineering of the Institute of Electrical and Electronics Engineers, Rutgers University.)

Figure 7 Dr. Mervin J Kelly who was in charge of the production of vacuum tubes at The Western Electric Company, the manufacturing arm of AT&T, in the 1920s. (Courtesy of the Emilio Segre Visual Archives of the American Institute of Physics. Photo by Werner Wolff.)

appeared in 1936. At the end of the war, he migrated to the US at the invitation of the government and became an expert consultant to industry during the early development of transistor technology.

In the meanwhile, the British, French, and Russians were pursuing the development of radar for their own military needs. In addition to carrying on research in the meter range that was to be used in the long-range perimeter defense of their island, the British were eager to increase the resolution of radar images and decrease the size and weight of equipment for airborne and other critical uses. To achieve this purpose, they extended their research to the decimeter and centimeter range of wavelengths. Consequently, a young English engineer, Denis M Robinson (Figure 8), who had been employed in servicing British television transmitters, which had broadcast programs several times a week until 1939, found himself seconded to a secret laboratory in Scotland by The Telecommunications Research Establishment (TRE), the agency that was guiding radar development in Britain. He was instructed to produce a radar system that could operate at a wavelength of 10 cm.

The means to generate and transmit such radiation was already available. Devising appropriate equipment to process and display the return signal, however, presented a problem. What Robinson needed most was a nonlinear device, or "mixer," that had the capability of converting the reflected return signal to a frequency that could be handled by available amplifiers and the auxiliary equipment involved in display. There was no available vacuum tube, such as a rectifier, that could serve as a mixer in the low centimeter range. Developing one during wartime would take valuable time with an uncertain outcome. He went to a University library nearby and found Hans Hollmann's two-volume treatise mentioned above. This treatise asserted that crystal rectifiers could be useful as rectifying detectors in the centimeter range of wavelengths. Robinson remembered the use of galena from his teen years and decided to team up with Dr. H W B Skinner, previously at the University of Bristol and later also at TRE. The latter was much more familiar with the so-called solid-state devices than Robinson was. After some deliberate investigations, Skinner ascertained that selectively chosen specimens of silicon, available in its somewhat variable impure metallurgical form, would provide the answer to their immediate problem of fabricating a mixer. It is interesting to note that Dr. R S Ohl, working in the field of microwave research at the Bell Telephone Laboratories in close cooperation with Dr. G C Southworth, had recently come to the same conclusion in a search for a suitable detector, thereby reaffirming the conclusion reached by his former colleague, Dr. G W Pickard, some thirty years earlier at the start of wireless communication.

When the government of France fell before the advancing German army in May of 1940, a high-level group of French scientists and engineers had been involved in research on a very advanced form of microwave generator known as the cavity magnetron. It operated at wavelengths in the vicinity of 16 cm. At one of the last possible moments, Maurice Ponte, one of the leaders of the French group, flew their working model to England, where it added significantly to the development of the magnetron being carried on there. The French, it turned out, had not yet faced up to the problem of searching for the best heterodyne mixer in that wavelength range and marveled in their turn at the effectiveness of the silicon diodes that the British were using.

Figure 8 Denis M Robinson who decided early in WWII, and after reading the treatise on microwave technology written by Hans Hollmann, to search for a semiconductor that could serve as a suitable heterodyne mixer in the 10 cm range of wavelengths. He joined forces with HWB Skinner who determined that commercially available silicon would serve their immediate purpose adequately. (Courtesy of the book *Five Years at the Radiation Laboratory* (Massachusetts Institute of Technology, 1946). Reprinted by IEEE in International Microwave Symposium, 1991.)

Once France had fallen and Britain was isolated from any immediate help from the continent, Winston Churchill decided that he must form the closest possible relationship with the US, which was still formally neutral but was preparing to become fully armed. As a positive step, Churchill offered to share with the US all secret technical research with which Britain was involved, including its developments in radar. President Franklin D Roosevelt readily agreed to the plan and established an Office of Scientific Research and Development within the Executive branch of the government.

In further keeping with Churchill's suggestion, Roosevelt selected two highly respected scientists to head the office, namely James B Conant and Vannevar Bush, the former from Harvard and the latter from the Massachusetts Institute of Technology (MIT). One of their first steps was to create the Radiation Laboratory, a radar research and development center, at MIT, to supplement on a large scale what the British had already been developing, with particular focus on applications in the microwave region. Dr. Lee A DuBridge, an already distinguished younger scientist-administrator, was selected to be the director; he would remain so throughout the war. The laboratory was rapidly staffed by a highly selective group of scientists and engineers, many from the top ranks of university faculties.

Most of the staff of the Radiation Laboratory were not familiar with semiconductors other than in a very peripheral way, such as the crystal radio sets of their early teen years. To them, the British-made silicon rectifier-mixers that were used for frequency conversion of the returning radar signals were both a curiosity and an abomination because of the great variability of the metallurgical-grade silicon used as starting material. Many on the staff felt that they should take the time to develop vacuum tube rectifiers that would operate in the microwave region.

Fortunately, DuBridge was familiar with research on crystalline solids and called on one of the authors of this article (FS) to see if a way to salvage the situation could be found. An excellent physical chemist, Dr. C Marcus Olson (Figure 9), in the Pigments Department of the DuPont Corporation near Wilmington, Delaware, found that he could produce a form of silicon that was uniformly pure to several parts in one hundred thousand by reacting purified silicon chloride with comparably pure metallic zinc. When this form of the element was properly treated with controlled additions of other elements that influenced its electrical conductivity, it could be used to produce highly satisfactory silicon diodes on a mass-production basis (Figure 10). Moreover, DuPont was prepared to manufacture the purer grade of silicon in practical quantities.

Once this point was reached, the Radiation Laboratory added a semiconductor section under the leadership of Dr. Henry C Torrey. It followed progress in industrial production and administered an extended research program, including research on diodes made from the semiconductor germanium, the sister-element to silicon, which found very special uses in situations in which the rectifier experienced high reverse voltages. Both semiconductors permitted conductivity by both negative and positive carriers depending upon the addition of small controlled quantities of foreign elements, known as "dopants." The positive carriers ("holes") were associated with a dearth of electrons in what normally are fully occupied shells or bands of electron states in silicon. The empty

Figure 9 Dr. CM Olson (center), on the staff of the Pigments Department of the DuPont Company. During the early part of World War II he developed a procedure for producing elemental silicon that was sufficiently pure to permit routine mass production of silicon diodes. (Courtesy of CM Olson.)

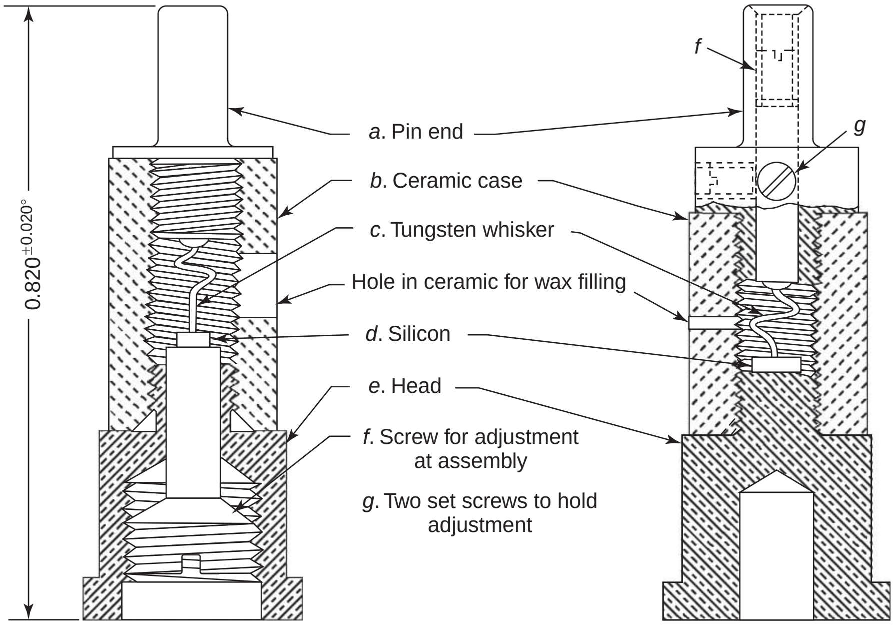
0.820±0.020°
f
g
a. Pin end
b. Ceramic case
c. Tungsten whisker
Hole in ceramic for wax filling
d. Silicon
e. Head
f. Screw for adjustment at assembly
g. Two set screws to hold adjustment

(a) Sylvania

(b) Western electric

Figure 10 Two typical silicon rectifiers of the World War II period. The tip of the pointed tungsten catwhisker rests on the silicon chip. (Courtesy of archives of the Radiation Laboratory of The Massachusetts Institute of Technology. From the book *Crystal Rectifiers* by HC Torrey and CA Whitmer in the series published by the Radiation Laboratory of the Massachusetts Institute of Technology at the end of World War II under contract with the US Government.)

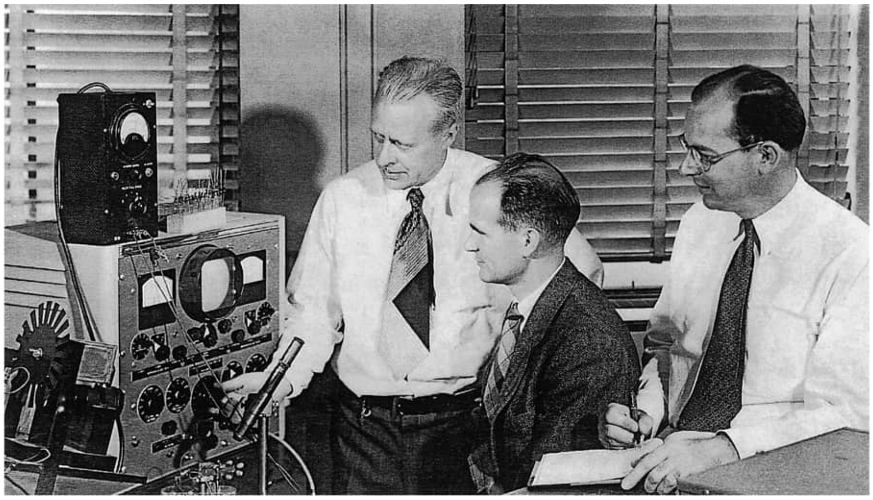

Figure 11 John Bardeen, William S Shockley, and Walter H Brattain (right to left) who developed the first transistors at the Bell Telephone Laboratories. The three shared a Nobel Prize for their discoveries. (Courtesy of Professor Lillian H Hoddeson and Lucent Technologies Bell Laboratories.)

states are equivalent to bubbles in a fluid, which will move opposite to the direction of any applied forces that cause acceleration of the fluid. The two types of conductors were designated *n*-type (negative) and *p*-type (positive), respectively.

When World War II ended, Dr. Kelly returned to the secret pursuit of a semiconductor triode armed with an increased staff and the extensive new knowledge of semiconductors gained during the war. Shockley was appointed head of the group and had the good fortune to attract John Bardeen, a highly experienced engineer-physicist who possessed strong background knowledge in solid-state science, as part of the team. Brattain who knew Bardeen well joined him in a remarkably productive working partnership (Figure 11).

As a first step, Shockley attempted to develop what later became known as the field-effect transistor in which the density of carriers in the bulk semiconductor is altered by application of an electric field transverse to the direction of current. He failed to achieve the desired effect and turned to other matters, leaving his colleagues to carry on. Bardeen suspected that the failure was a result of a temperature-related shift in surface charge that compensated the applied field within the bulk of the semiconductor. He and Brattain demonstrated this by repeating the experiment at temperatures sufficiently low so that the surface charges would be frozen. Much later, means of stabilizing the surface charge at normal operating temperatures were found and the resulting "field effect transistor" became an important member of the transistor family.

While extending this research in December of 1947, Bardeen and Brattain invented, partly by chance, what became known as the "point-contact transistor." It was the first truly amplifying semiconductor triode. Shockley returned to research in this field at this point and invented what became known as the "discrete *p*–*n* junction transistor." The principles involved in its operation were to play a major role in the development of electronics during the next decade.

In the course of events, one of the members of the Laboratories developed a method for purifying germanium to a very high level that was particularly applicable to that element. As a consequence, Shockley mandated that all research on transistors under his direction be carried out with crystals of germanium. A courtly strong-minded Texan on the staff, Dr. Gordon K Teal (Figure 12), aware of the superior chemical and physical properties of silicon from wartime research, began to produce single crystals of it surreptitiously in his laboratory. Teal shifted his activity to Texas Instruments Incorporated, in Dallas, Texas, in 1953 when that company obtained a license from AT&T to produce transistors. The company gave him a warm welcome in his pursuit of the work on silicon. Methods were soon found to purify silicon to parts per billion and to improve crystal perfection, which Teal knew to be very important. The element became the mainstay of production of transistors, particularly when the beneficial characteristics of its relatively stable oxide were fully appreciated. Nevertheless, much research continued to be carried out with germanium. In fact, discrete transistors made of silicon or germanium were manufactured throughout much of the 1950s.

The invention of the integrated circuit by Jack Kilby (Figure 13) in 1958, led to previously unforeseen increases in circuit complexity, eventually at very low cost – a process requiring a good part of a decade. It was not clear at first whether such circuits, which permitted the creation and interlinking of vast arrays of transistors on a single silicon chip, would find uses other than in military applications where a premium price might be acceptable. By the mid-1960s, however, the most farsighted manufacturers began to express optimism. For example, in 1964 Patrick E Haggerty, the President of Texas Instruments, published a paper in the Proceedings of the Institute of Electrical and Electronics Engineers in which he stated that if the remaining problems of large-scale production were resolved in an economical manner, one could expect devices based on the use of integrated circuits to become "pervasive" in human affairs, creating a revolution in such matters as information processing, communications, and controls. A year later Dr. Gordon E Moore, then at Fairchild Semiconductor and later a founder of Intel, had the foresight and courage to predict that the cost of integrated circuits would soon go through a period in which the cost per transistor would be halved about every eighteen

Figure 12 Gordon K Teal who successfully pursued the development of monocrystalline silicon-based transistors, first at the Bell Telephone Laboratories and then at Texas Instruments. (Courtesy of The American Institute of Physics Emilio Segre Visual Archives.)

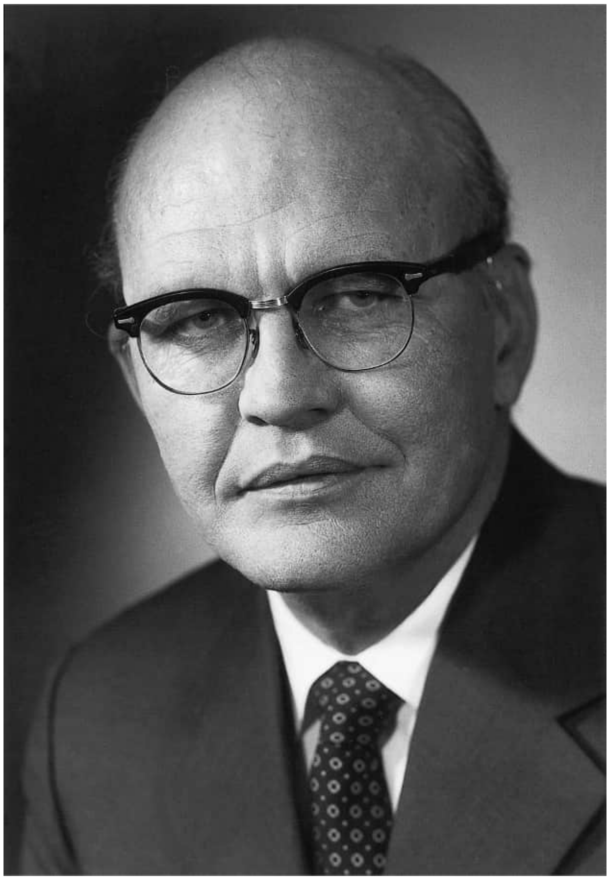

Figure 13 J S Kilby who invented the integrated circuit and received a Nobel Prize for it. (Courtesy of Kilby JS.)

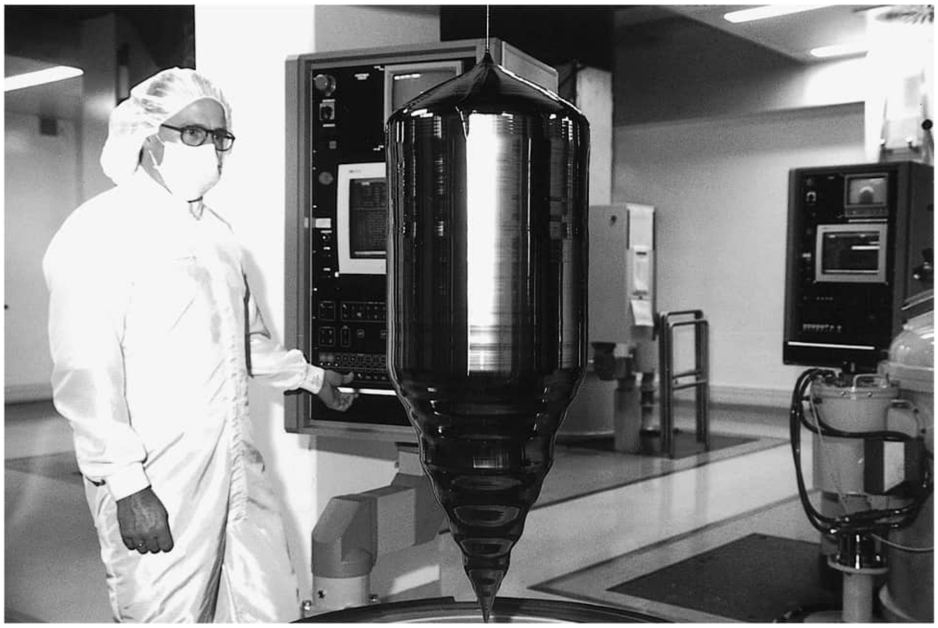

Figure 14 A single crystal ingot of silicon having a diameter of 300 mm. Such an ingot is sliced horizontally into circular wafers whose surfaces become the site of integrated circuits. (Courtesy of H Fusstetter of Wacker and Siltronics AE.)

months, accelerating their use. Widespread applications of the device finally reached Moore's expansive stage by the end of the 1960s, along with the rapid growth in sophistication of the technology associated with design of operating systems and applications software, the linchpins of the computer era. The end of the evolution of this field is not yet in sight. All evidence suggests that silicon will continue to play an unending role in electronics (Figure 14).

Further Reading

Seitz F and Einspruh NG (1998) *The Electronic Genie*. Urbana, ILL: University of Illinois Press.

Local field effects

A-M Leventi-Peetz[a], **EE Krasovskii**[b,c,d], **V Silkin**[b,c,d], **and W Schattke**[b,e], [a]Federal Office for Information Security (BSI), Bonn, Germany; [b]Donostia International Physics Center DIPC, P. Manuel de Lardizabal 4, San Sebastián, Spain; [c]Departamento de Polímeros y Materiales Avanzados: Física, Química y Tecnología, Universidad del Pais Vasco/Euskal Herriko Unibertsitatea, Donostia-San Sebastián, Spain; [d]IKERBASQUE, Basque Foundation for Science, Bilbao, Spain; [e]Institut für Theoretische Physik und Astrophysik der Christian-Albrechts-Universität, Leibnizstraße 15, Kiel, Germany

© 2024 Elsevier Ltd. All rights reserved.

This is an update of W. Schattke, Local Field Effects, Editor(s): Franco Bassani, Gerald L. Liedl, Peter Wyder, Encyclopedia of Condensed Matter Physics, Elsevier, 2005, Pages 145–151, ISBN 9780123694010, https://doi.org/10.1016/B0-12-369401-9/00428-9.

Introduction 802
Induced field 803
Macroscopic fields 804
Dielectric response 806
Exchange and correlation 807
Photoemission from layered crystals 807
Nonlocal dielectric response 808
Further application 809
Conclusion 810
Acknowledgments 811
References 811

Abstract

The dielectric response of matter as described by Maxwell's equations incorporates on the microscopic level the properties of the material which subsequently has to be suitably averaged to be accessible to macroscopic observation. So-called local fields appear on an intermediate level which instead of the pure applied field constitute more close relation to the observable quantities and give rise to partly essential local field corrections to the results obtained from the bare applied field alone. In this chapter detailed examples are shown considering local field effects from optical bulk spectroscopy over photoemission in layered crystals to surface sensitive non-local response effects.

Introduction

If a dielectric material is exposed to an electric field, a dipole moment is established which is detected by the force the field exerts on it. It is a common experience to have felt the attraction acted by a charged external body as by a comb on one's hair. Such materials show induced polarization in an external electric field usually observed as surface charges disregarding the microscopic details of the interior. However, the field acts in the interior of the whole dielectric body and induces the polarization therein through the polarizability of the atomic constituents of the body, see Fig. 1 for a sketch of such polarization in a solid.

The well-known textbook Lorentz-Lorenz construction of the so-called local field is applied, which explicitly takes into account the presence of an induced field adding to the external field and being self-consistently determined at every point. In course of time, the Lorentz-Lorenz construction has been set on an ab initio fundament by considering the total many-body system, which also led to the quantitative determination by well-accepted definite rules though the whole problem cannot be solved in a closed manner.

From a macroscopic point of view, say, considering length dimensions in centimeters, the polarization is continuously spread over space, discontinuities arising at the edges of bounded bodies only. The total dipole moment causes a resulting induced field which adds to the external field usually screening it, i.e., reducing it within the material. Of course, the sources for the induced fields may be inhomogeneously distributed and arbitrarily macroscopically shaped. For example, a spherical solid dielectric body introduced between the plates of a condenser expels the initially homogeneous field from the interior by creating dipole charges on the surface of the sphere opposite to the condenser plates. This general macroscopic situation has its origin on an atomic scale that finally gives rise to what is called "local field effects."

From a microscopic point of view, atomic polarization constitutes the source of macroscopic polarization. The atomic polarization is localized being attached to the electronic cloud around the nuclei and showing a global distribution of the dipole moments reflecting the positions of the nuclei. The variability of local charge density created on an atomic scale relates to the notion of local fields. Thus, the local field considered here arises from the electric response of atomically structured material to an external field. It can be viewed as an induced granular field, which in the special case of a crystalline solid is structured by the details of the potential within the unit cell being periodically repeated. Such a local field occurs in insulators, as well as in semiconductors and metals (Slater, 1967). Crystallinity is a widely understood origin for the existence of local structure in the response fields, though the general atomic consistence of matter gives rise to local response fields also. However, the former are much easier to be dealt with than classifying or calculating, for example, amorphous or gaseous material.

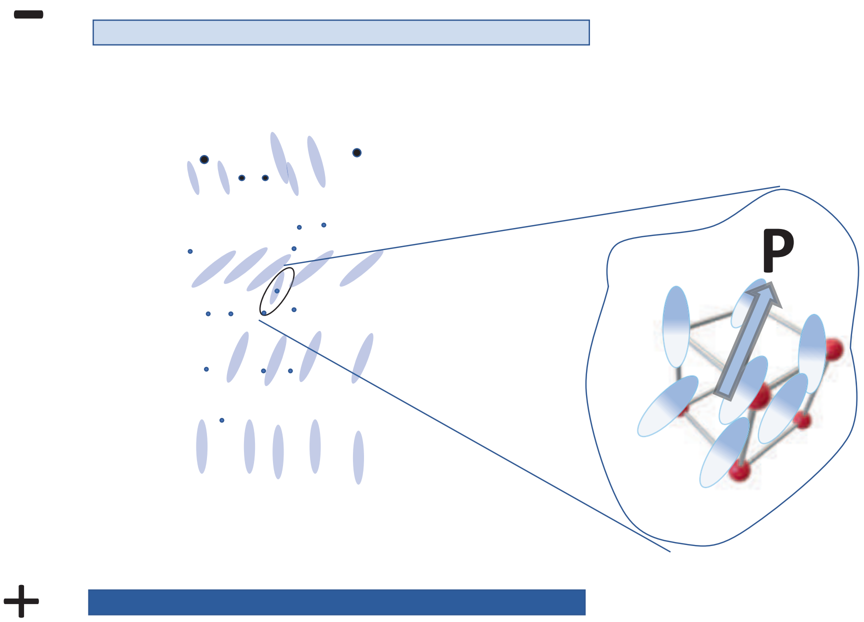

Fig. 1 Local field that originates from the bare homogeneous electric field between two condenser plates by the sketched induced polarization *P* in molecular matter.

The above interpretation is not to be confused with the notion of local field as applied to a theoretical extension of the random phase approximation (RPA), which is a very common and basic approximation in the calculation of dielectric properties of general condensed matter. This also traces back to the roots of the Lorentz local field, though the emphasis does not lie on the granularity and geometric structure but on the many-body influences which affect even homogeneous systems.

$$\varepsilon_M = 1 + \frac{\alpha/\varepsilon_0}{1 - \alpha/3\varepsilon_0}. \tag{1}$$

The first achievement along both lines may be seen in the Lorentz-Lorenz formula for the macroscopic dielectric constant ε_M in terms of atomic polarizability per unit volume α with vacuum permittivity ε_0 (SI units used).

In Section "Induced field" the dielectric response in the frame of Maxwell's equations is described. The transition from microscopic to macroscopic quantities follows in Section "Macroscopic fields." The general notion of the dielectric function within the dielectric response is set in Section "Dielectric response" which is specified according to the influence of exchange and correlation on optical spectroscopy in Section "Exchange and correlation." The appearance of local field effects in photoemission from layered crystals constitutes Section "Photoemission from layered crystals". Section "Nonlocal dielectric response" is devoted to extending the local response to the nonlocal case followed by a few remarks to further topics in connection with local fields in Section "Further application" and a concluding Section "Conclusion".

Induced field

For the theory of dielectrics, Maxwell's equations of electrostatics constitute the framework

$$\mathrm{div}\boldsymbol{D} = \varrho, \mathrm{rot}\boldsymbol{E} = 0 \tag{2}$$

to be supplemented by the appropriate material's equation, specifically

$$\boldsymbol{D} = \varepsilon\varepsilon_0\boldsymbol{E} \tag{3}$$

for a linear relation between the so-called dielectric displacement $\boldsymbol{D}$ and the electric field $\boldsymbol{E}$ with dielectric constant or relative permittivity ε of the medium. The charge density ϱ refers only to the sources of the external field $\boldsymbol{E}_{ext}$ which can be written as $div\varepsilon_0\boldsymbol{E}_{ext} = \varrho$. One usually splits off the electric field from $\boldsymbol{D}$ by defining the polarization $\boldsymbol{P}$, i.e., the dipole moment per unit volume, and the external field from the microscopic field by defining the induced field $\boldsymbol{E}_{ind}$

$$\boldsymbol{D} = \varepsilon_0\boldsymbol{E} + \boldsymbol{P}, \boldsymbol{E} = \boldsymbol{E}_{ext} + \boldsymbol{E}_{ind}. \tag{4}$$

Inserting Eq. (4) in Eq. (2) yields

$$div\varepsilon_0\boldsymbol{E}_{ind} = -div\boldsymbol{P} = \varrho_{ind}. \tag{5}$$

This identifies –div $\boldsymbol{P}$ as the source of the induced field associating with the induced polarization charge ϱ_{ind}, an analogue of the external charge, which is a rather trivial statement from the atomic point of view.

In principle, the electrostatic relations have to be complemented in order to deal with optics. The topic of local field effects, however, allows a reduction to the discussion of the longitudinal case, i.e., to the above equations of electrostatics, decoupling it from the transverse fields introduced by the time-dependent electromagnetic field. The approximation is valid as long as the length scale of the induced field is small compared to the optical wavelength. Transverse components are of course nonzero and need the full dielectric tensor which may be anisotropic. But the simplification occurs because the self-consistent generation of the total electric field from the applied external field (see Section "Macroscopic fields") derives this approximation solely from the longitudinal field, for which Maxwell's electrostatic equations are already sufficient.

The above simple relationship is, however, a compact abbreviation of the most general linear relation which should be written as

$$D_i(\mathbf{r}t) = \sum_j \int_{-\infty}^{+\infty} dt' \int d^3\mathbf{r}' \varepsilon_{ij}(\mathbf{r}, t; \mathbf{r}', t')\varepsilon_0 E_j(\mathbf{r}'t') \tag{6}$$

where the indices refer to the Cartesian axes of a tensor relation through ε_{ij}, the time integration sums up contributions of the electric field at various times to the dielectric displacement, and the space integration does similarly with respect to position. In physical terms, the tensor character relates an electric field in a certain direction to the displacement in any other direction with a specific factor, for example, as an anisotropic material would imply. The time integration takes into account a delay in the effect of the electric field on, for example, the polarization, which for a causal relation obviously implies zero ε for $t' > t$. Switching on a field or, in terms of Fourier transforms, an incident optical wave which as an oscillating process, excites an oscillating polarization with a weight depending on the frequency, this is the standard case of optical spectroscopy. The dependence on position in space, is the interesting quantity in view of the effects considered here. An electric field at a specific position in principle can excite polarizations everywhere and all contributions are summed up by the integral. The above quantity ε is usually called the microscopic dielectric constant, and "constant" is often replaced by "function" to stress the functional dependence on its variables.

Macroscopic fields

Measurements as, for example, in classical optical spectroscopy with wavelengths orders of magnitude larger than atomic distances may not resolve the atomic structure of matter, and therefore deal with spatially averaged quantities instead of the microscopic fields considered above. The averaging follows from space integration or from the zeroth Fourier component when expressing the field equations by Fourier transforms as conveniently done. Dealing with the example of a crystalline solid, the periodic repetition of the unit cell imposes this symmetry also on all observable quantities as fields, densities, coefficients of linear relations in position, space, etc., as long as the external fields are homogeneous. Then, the periodicity allows a representation of the total field by a Fourier series

$$\boldsymbol{E}(\boldsymbol{r}) = \sum_G e^{iG\cdot r}\boldsymbol{E}_G \tag{7}$$

omitting the time or respective frequency dependence in the notation. The vectors $\boldsymbol{G}$ (bold face not used here at index positions) constitute the reciprocal lattice of the crystal. A nonhomogeneous external field may vary on a macroscopic scale, then $\boldsymbol{E}_G$ will also depend on $\boldsymbol{r}$. However, the length scales of this field as well as those of the additional variations of the induced fields are large. In which case, all considerations still apply locally within ranges limited by that length scale. After the Fourier transformation the linear relation (3) reads:

$$\boldsymbol{D}_G = \sum_{G'} \hat{\varepsilon}_{GG'}\boldsymbol{E}_{G'} \tag{8}$$

where the hat is used to indicate a tensor instead of writing the Cartesian indices explicitly. If a homogeneous electric field is applied to an infinitely extended crystal, then the displacement field is constant everywhere and thus possesses only a zeroth Fourier component which is given by a suitable distribution (e.g., charged condenser plates) of its sources, the external charges. Inversion of Eq. (8) then yields

$$\boldsymbol{E}_G = \left(\varepsilon^{-1}\right)_{G0}\boldsymbol{D}_0 \tag{9}$$

the Fourier components of the microscopic field, i.e., local field which, in principle may spatially fluctuate on all length scales within the periodicity cell. Taking only the zeroth component of Eq. (9), one obtains the observable averaged electric field $\boldsymbol{E}_0$ and can write the material's equation as

$$\boldsymbol{D}_0 = \frac{1}{\left(\varepsilon^{-1}\right)_{00}}\boldsymbol{E}_0 \tag{10}$$

This linear relation between averaged quantities constitutes what is called the local field effect, specifically a macroscopic permittivity ε_M which is the reciprocal of the (0,0) element of the inverse microscopic dielectric function matrix $\varepsilon_{GG'}$

$$\varepsilon_M = \frac{1}{\left(\varepsilon^{-1}\right)_{00}} \tag{11}$$

and applies to homogeneous external fields.

Furthermore, it also covers the case that the field additionally depends on **q** within the Brillouin zone describing larger length scales than the lattice length. Then also ε carries this additional dependence, (see Section "Dielectric response"). As indicated before, the derivation of Eq. (11) is valid for the longitudinal response to longitudinal fields, so the hat was omitted because it is a scalar quantity. The transverse average fields are related following a similar reasoning. The general tensor can be written as $\widehat{\varepsilon}_M$ consisting of the bare ε and an added longitudinal correction which originates from the polarization by the Coulomb interaction.

$$\hat{\varepsilon}_M = \hat{\varepsilon}_{00} - \sum_{GG'(\neq 0)} \hat{\varepsilon}_{0G} \left(\hat{\varepsilon}_r^{LL}\right)^{-1}_{GG'} \hat{\varepsilon}_{G'0}. \tag{12}$$

The quantity $\widehat{\varepsilon}_r^{LL}$ is the microscopic dielectric constant matrix in reciprocal space restricted (subscript r) to the subspace of nonzero reciprocal lattice vectors. Only the longitudinal component of the tensor is involved which is denoted by the upper index, i.e., the tensor can be written as the product of the dyad $(\boldsymbol{q} + \mathbf{G})/ \parallel \boldsymbol{q} + \mathbf{G} \parallel \otimes (\boldsymbol{q} + \mathbf{G}')/||\boldsymbol{q} + \mathbf{G}'||$ with a scalar $\varepsilon^{LL}_{GG'}$. Taking the longitudinal component of Eq. (12), algebraic manipulations lead back to Eq. (11), $\varepsilon_M^{LL} = 1/((\varepsilon^{LL})^{-1})_{00}$, with inversion of the whole unrestricted matrix. This generalization refers to the local field effect of optical and related spectra valid as long as the wavelength $\lambda = 2\pi/ \parallel \boldsymbol{q} \parallel$ is much larger than the length scale of the atomic structure (Mochan and Barrera, 1985).

A main access to the structure of solids is used with optical spectroscopy (Ehrenreich, 1965). Below some examples are shown that make the general importance of local fields in a solid visible in those optical spectra.

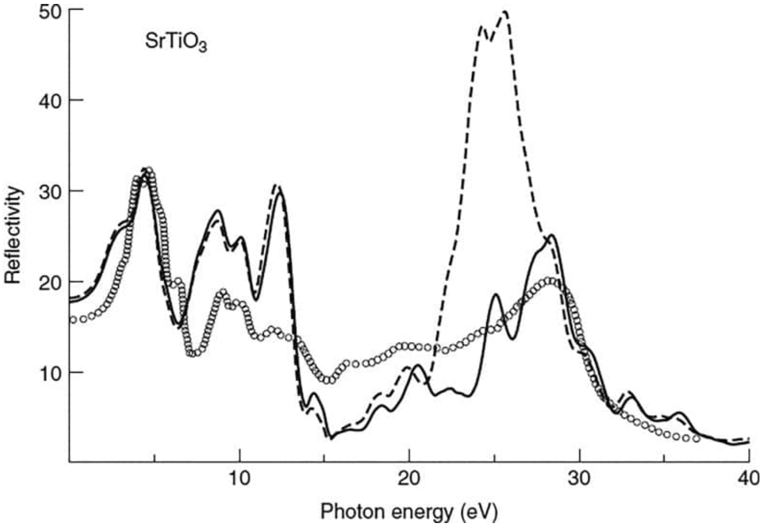

Fig. 2 Calculated reflectivity of SrTiO$_3$, with local field effects included (solid) and neglected (dashed) compared to experiment (circles).

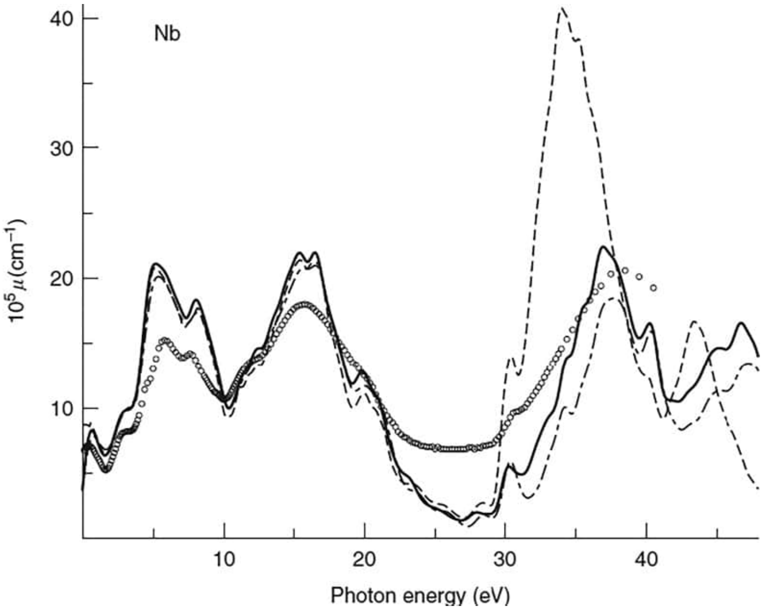

Fig. 3 Calculated absorption coefficient of Nb, with local field effects included (dotdash) and neglected (dashed) compared to experiment (circles); solid line includes XC corrections neglected otherwise.

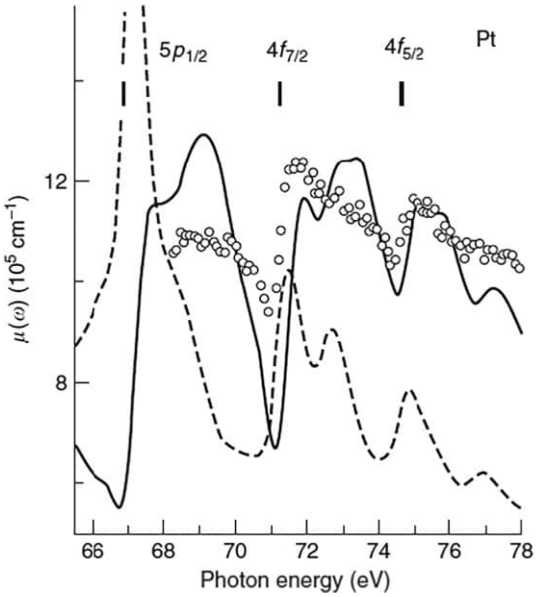

Fig. 4 Theoretical absorption coefficient of Pt including local field effects (solid) compared with experiment (absorption: circles, XPS energy levels: |), and neglecting local field effects (dashed) (Krasoskii and Schattke, 2001).

Figs. 2 and 3 compare with experiment the optical spectra of $SrTiO_3$ and Nb calculated up to the vacuum ultraviolet with or without the local field effect (Krasovskii and Schattke, 1999). The importance of the local field effect in describing the experimental result is striking. To discuss these effects in simple terms, e.g. the disappearance of the huge peak at 25 eV in Fig. 2, a lucid picture is absent, as a matrix inversion is involved. The comparison of theory with experiment shows agreement with respect to the relative positions of maxima and minima, whereas the strength of the variation is smoothed by experimental broadening not considered in the theoretical calculation. It should be noted that the theoretical curves are obtained ab initio with the density-functional theory, and broadening from additional many-body corrections might also occur. Occasionally the connection with the local polarization is obvious in the spectra as shown in Fig. 4 for Pt.

A steep slope marks the onset of absorption from the localized semicore levels, $5p_{1/2}$, $4f_{7/2}$, $4f_{5/2}$, in both experiment and theory. Specifically, the $5p_{1/2}$ peak and also the relative intensities need local field effects to be included to explain the exponent. Both $4f$ peaks are considerably enhanced by the accompanying high atomic polarization of the medium. This proves its origin from local field effects, even though the overall shape of a spectrum may hide such a connection, as it often happens at low-energy excitations of valence states.

Dielectric response

Maxwell's theory describes the field from its source, i.e., the total charge. Conversely, the total field forces the positional adjustment of the charges through the laws of quantum mechanics, which is condensed into the dielectric constant ε. Once the bare response to a small test field is known through ε, the numerical evaluation of charge and field from Eqs. (2) and (10) is straightforward by using a suitable mathematical solution. Thus, one has to determine quantitatively the dielectric function. As already stated, the RPA is the basic approximation for calculating these properties ab initio with generally sufficient accuracy. The quantum mechanical change of the density $\delta\varrho$ induced as a response to a change of the field $\delta\boldsymbol{E}$ is obtained from first-order perturbation expansion with respect to the latter. The total field must be treated here as a perturbation. Eq. (2) is used in Fourier space, $i(\boldsymbol{q}+\boldsymbol{G})\cdot\delta\boldsymbol{D}(\boldsymbol{q}+\boldsymbol{G}) = \delta\varrho(\boldsymbol{q}+\boldsymbol{G})$, and the field in Eq. (3) is replaced by its associated potential, $\delta\boldsymbol{E}(\boldsymbol{q}+\boldsymbol{G}) = -i(\boldsymbol{q}+\boldsymbol{G})\delta\phi(\boldsymbol{q}+\boldsymbol{G})$. Then, the induced charge is given by the difference between total charge $\delta\varrho_{tot} = \varepsilon_0 \mid \boldsymbol{q}+\boldsymbol{G} \mid^2 \delta\phi$ and external charge $\delta\varrho$ with the result

$$\sum_{G'} (\boldsymbol{q}+\boldsymbol{G})\cdot\left(\hat{1}\delta_{G,G'} - \hat{\varepsilon}_{G,G'}(\boldsymbol{q}\omega)\right)\cdot(\boldsymbol{q}+\boldsymbol{G}')\delta\phi(\boldsymbol{q}+\boldsymbol{G}') = \delta\varrho_{ind}(\boldsymbol{q}+\boldsymbol{G})/\varepsilon_0. \tag{13}$$

This has to be compared with the expression obtained for the induced charge from the perturbation expansion, which finally leads to

$$\varepsilon^{LL}_{G,G'}(\boldsymbol{q}\omega) = \delta_{G,G'} + \frac{e^2}{2\pi^2\varepsilon_0 \,\|\boldsymbol{q}+\boldsymbol{G}\|\|\boldsymbol{q}+\boldsymbol{G}'\|}\sum_{\lambda\lambda'}\int_{BZ} d^3\boldsymbol{k}\,\frac{\langle \boldsymbol{k}+\boldsymbol{q}\lambda'|e^{i(\boldsymbol{q}+\boldsymbol{G}')\mathbf{r}}|\boldsymbol{k}\lambda\rangle\langle \boldsymbol{k}\lambda|e^{-i(\boldsymbol{q}+\boldsymbol{G})\mathbf{r}}|\boldsymbol{k}+\boldsymbol{q}\lambda'\rangle}{E_{\lambda'}(\boldsymbol{k}+\boldsymbol{q}) - E_{\lambda}(\boldsymbol{k}) - \hbar\omega - i\hbar\eta}. \tag{14}$$

Here, a single matrix element of the dielectric function for reciprocal lattice vectors **G** and **G**′ is represented by a sum over occupied λ and unoccupied λ' states and an integral over an elementary cell (Brillouin zone) of the reciprocal lattice in an expression which, of course, reminds of the quantum mechanical perturbation theory. It contains the denominator for the energy difference between the ground and the excited states of the system including the photon energy $\hbar\omega$, and the numerator with the matrix elements for a transition between both states caused by the phase factor of the Fourier decomposition of the perturbing potential. The wave vector $\boldsymbol{q}$ which is confined to the first Brillouin zone appears only once as an independent variable of ε which is diagonal with respect to it. Owing to translational symmetry, charge and field can differ in total momentum only by reciprocal lattice vectors. One observes again that only longitudinal fields are involved in this electrostatic treatment and consequently only longitudinal components $\varepsilon^{LL'}$ of the dielectric tensor

$$\varepsilon^{LL}_{G,G'}(\boldsymbol{q},\omega) = \frac{(\boldsymbol{q}+\mathbf{G})}{\|\boldsymbol{q}+\mathbf{G}\|}\cdot\hat{\varepsilon}_{G,G'}(\boldsymbol{q},\omega)\cdot\frac{(\boldsymbol{q}+\mathbf{G}')}{\|\boldsymbol{q}+\mathbf{G}'\|} \tag{15}$$

are accessed. They constitute, nevertheless, the dominant contributions in the domain of optics and related fields.

Exchange and correlation

As mentioned before, the notion of local field effects can also be applied to the many-body extensions of RPA. A treatment of the many-body corrections goes beyond perturbational approximations such as the RPA and the microscopic details change. Various partial summations of the perturbational series and additional decoupling mechanisms are to be applied. In this contribution here, a more detailed description is not tried because of its complexity. For simplicity, the main work is usually directed toward homogeneous systems though special quantitative calculations also exist for solids. In Fig. 3, such corrections for considering exchange and correlation (XC) which go beyond RPA are shown. The observed influence is rather small compared to the usual local field effects. The comparison of ab initio calculations with experimental spectra still leaves many questions open and the importance of many-body corrections depends on the details of the considered system and is an active field of present research.

Here, one development may be mentioned that is related to layered materials which are known for their special two-dimensional behavior and their respective correlation enhancement. The pump-probe excitation spectroscopy of transition metal dichalcogenide monolayers show local field structures of excitonic origin at a few electron volts. The local field is ascribed there to the polarization of an exciton population, e.g., in a $MoSe_2$ monolayer (Katsch et al., 2020; Rodek et al., 2021). Local field effects are observed in layered materials also at higher energies as described in more detail in the subsequent section.

Photoemission from layered crystals

In this section, $TiSe_2$ is chosen as a typical representative of the layered transition-metal dichalcogenides. Exciting a solid by a photon of frequency ω, the emitted photocurrent in an angle-resolved experiment is generally written as

$$\boldsymbol{j}(\boldsymbol{R},E) = \frac{e^2}{16m^2c^2}\,\frac{e\hbar}{2\pi m}\lim_{R\to R'}(\nabla_R-\nabla_{R'})\left\langle \boldsymbol{R}\middle| G^r(E+\omega)\hat{O}_0\hat{G}(E)\hat{O}_0^{\dagger}G^a(E+\omega)\middle|\boldsymbol{R}'\right\rangle \tag{16}$$

in the one-step model (Caroli et al., 1973) denoting the photoemission process as a unique transition from the electron's initial bound state to a propagating outgoing state (Schattke and Van Hove, 2003). The latter can be identified by a low energy electron diffraction (LEED) state. The excitation operator is

$$\hat{O}_0 = \hat{\boldsymbol{p}}\cdot\boldsymbol{A}_0(\hat{\boldsymbol{r}}) + \boldsymbol{A}_0(\hat{\boldsymbol{r}})\cdot\hat{\boldsymbol{p}} \tag{17}$$

in the dipole approximation with the vector potential A_0 suitably screened, e.g., according to the lines discussed above to obtain A^{scr} (Leventi-Peetz et al., 1995), viz.

$$\boldsymbol{A}^{scr}(\boldsymbol{r},\omega) = \sum_G e^{i\mathbf{G}\cdot\boldsymbol{r}}\left(\hat{\varepsilon}^{LL}\right)^{-1}{}_{G,0}(0;\omega)\boldsymbol{A}_0(0,\omega) \tag{18}$$

simplifying for photons of long wavelengths up to energies ω of the vacuum ultraviolet. The Fourier-transformed incident vector potential, $A_0(0,\omega)$ has thus only the zero wave vector. The dielectric matrix function is calculated in RPA with subsequent inversion accounting for the local fields. The layered structure of $TiSe_2$ shows the strong local field effect for normal emission perpendicular to the layers and the surface, as it is plotted in Fig. 5.

This figure shows a peak dispersing between 0 and 3 eV binding energy in the theoretical emission spectra which noticeably coincides with the dispersion of a band between Γ and A in the same range of binding energies, see Fig. 5A. This agreement is also found in the measured spectra. The band consists of Se p_z orbitals in a bonding state, binding neighboring $TiSe_2$ layers. The wavefunction modulus of this bound state has highest amplitude all along the z direction, i.e., the normal emission direction. The latter defines the outgoing state, which couples to the initial state via $\hat{\boldsymbol{p}}\cdot\boldsymbol{A}_0$, where the momentum operator is associated with the outgoing electron. Thus, normal emission picks up the surface perpendicular component of the photon amplitude, in our case of the 45° incidence of p-polarized light, i.e., polarized parallel to the plane of incident ray and surface normal. Constructive interference between both states may happen if their phases match. Imagine one of the plane waves is mainly composing the outgoing LEED state and a direct transition occurs from initial to final state with momentum conservation. Then a constructive

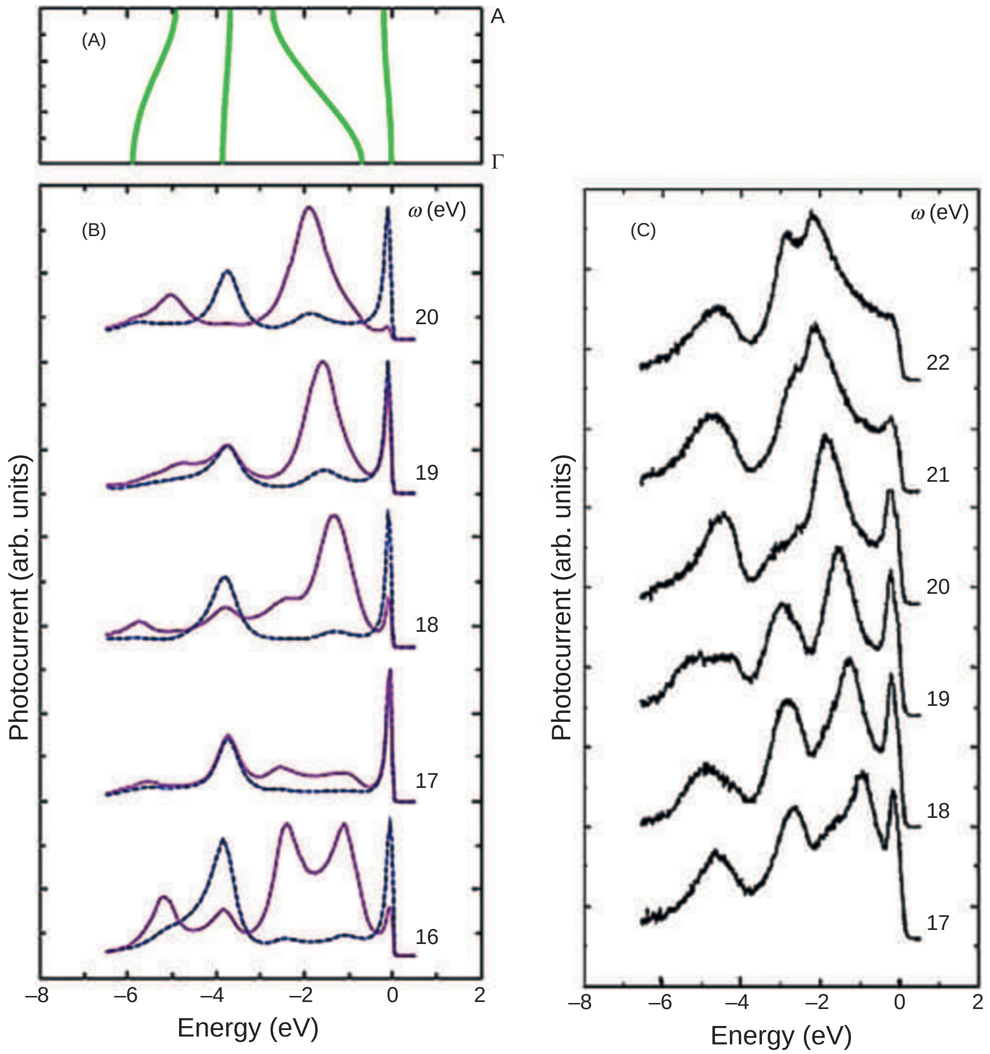

Fig. 5 $TiSe_2$ photoemission: (A) band structure for momentum direction ΓA perpendicular to the surface layer plane, (B) calculated, and (C) measured photocurrent for normal emission with photon incidence angle of 45° toward the surface normal and photon energies as labelled at the curves. Solid lines in (B) include the screening of the photon field by the solid, whereas broken lines show the unscreened case (Bödicker et al., 1996).

phase match, if it occurs at one point, will be independent of the momentum over the whole Γ – A Brillouin zone. The binding energy of the peak will shift with photon energy, whereas its intensity remains almost constant.

The above is a rough illustration how to understand the peak in Fig. 5 that is most significantly dispersing. As an important fact the photon energy lies close to the plasma frequency of 17 eV where ε approaches zero and its inverse becomes large. As a consequence one expects enhanced local fields A^{scr} from Eq. (18) leading to an enhanced spectroscopic response.

For completeness, the interpretation of the other peaks is added. They originate mainly from the high density of states which appears at the high symmetry points Γ and A where the slope of an emitting band vanishes, and from the flat bands appearing at 0 and 4 eV binding energy. The latter are connected with layer-parallel orbitals.

Angle resolved photoemission spectroscopy (ARPES) reflects the local fields themselves as they cause specific photoexcitations, but also depends sensitively on the nonlocal multipole plasmon generation. Their main effects are observed near the plasma frequency and can attain an order of magnitude change.

Nonlocal dielectric response

The term nonlocal response can be taken literally as a far reaching effect of a local perturbation. The local field effects stem from considerations under the restriction of smoothly varying external fields on a macroscopic scale, i.e., long wavelengths ($q = 2\pi/\lambda \approx 0$). This condition is relaxed here. However, both effects interfere in the experiment and one has to be discerning in its interpretation. A change of the field at one site can result in changes of the dielectric displacement at very distant sites, which, of course, is also contained in the general dependence of Eq. (6). As this dependence of the field on the charges is provided by a nonlocal long range relation, Coulomb's law, each local internal polarization by the field causes induced fields and hence, dielectric displacement everywhere. This holds in the static as well as in the dynamic case where the plasmon excitation is a very prominent long-range feature.

This rather general theoretical effect (Forstmann and Gerhardts, 1986) will not be easily detected in measurements on homogeneous systems, it becomes visible by local perturbations as, for example, a surface imposes (Feibelman, 1982). There the surface may be the source for plasmon waves which travel into the bulk and modulate the field. In addition, even below the plasmon frequency multipole surface plasmons enhance the frequency-dependent nonlocal response. The theoretical treatment, essentially governed by Eq. (6), can be based on Eq. (13) with the potential representing the full self-consistent field (SCF) in time-dependent local density approximation (LDA)

$$\delta\varphi_{\mathrm{SCF}} = \varphi_{\mathrm{ext}} + \delta\varphi + \delta V_{XC}. \tag{19}$$

Self-consistency is imposed by coupling the self-consistent potential $\delta\phi_{SCF}$ to the induced charge density as before in RPA, see Eq. (13), with Poisson's equation through $-\Delta\delta\phi = \delta\varrho_{ind}/\varepsilon_0$, and by using the exchange-correlation potential in LDA through $\delta V_{XC} = V_{XC}{}'(\varrho_0)\delta\varrho_{ind}$ (Liebsch, 1997). Because of the surface, translational symmetry is broken in one direction and calculation is restricted to real space in that direction utilizing an iterative process based on self-consistency. The centroid $d_\perp(\omega)$ of the charge density is suitable to characterize the surface response, i.e., it yields the position of the electromagnetically effective surface by its real part and the absorbed power by its imaginary part. For a jellium model, it shows a resonance at ~0.8 of the plasma frequency. The combined effect of local fields and nonlocal response shows a rather complex behavior as seen in Fig. 6.

The excitation from an external field localized just below the surface extends into the bulk with a penetration depth increasing with frequency and attains long-range behavior first at the surface plasma frequency ($\hbar\omega = 6.7$eV) and above the bulk ($\hbar\omega = 9.2$eV) plasma frequency. Closely around the surface, a dipole charge distribution establishes, which is replaced by a complex multipole behavior above the bulk plasma frequency. The granularity in the depth dependence reflects local field effects. Typical implications of the effect of the nonlocal fields at the surface on the photoemission intensity are illustrated in Fig. 7.

Further application

In addition to traditional optical spectroscopy, the reflection anisotropy/difference spectroscopy (RAS/RDS) offers surface-sensitive optical tools for access to details of the electromagnetic response. Local field effects are of importance not only in optical and related

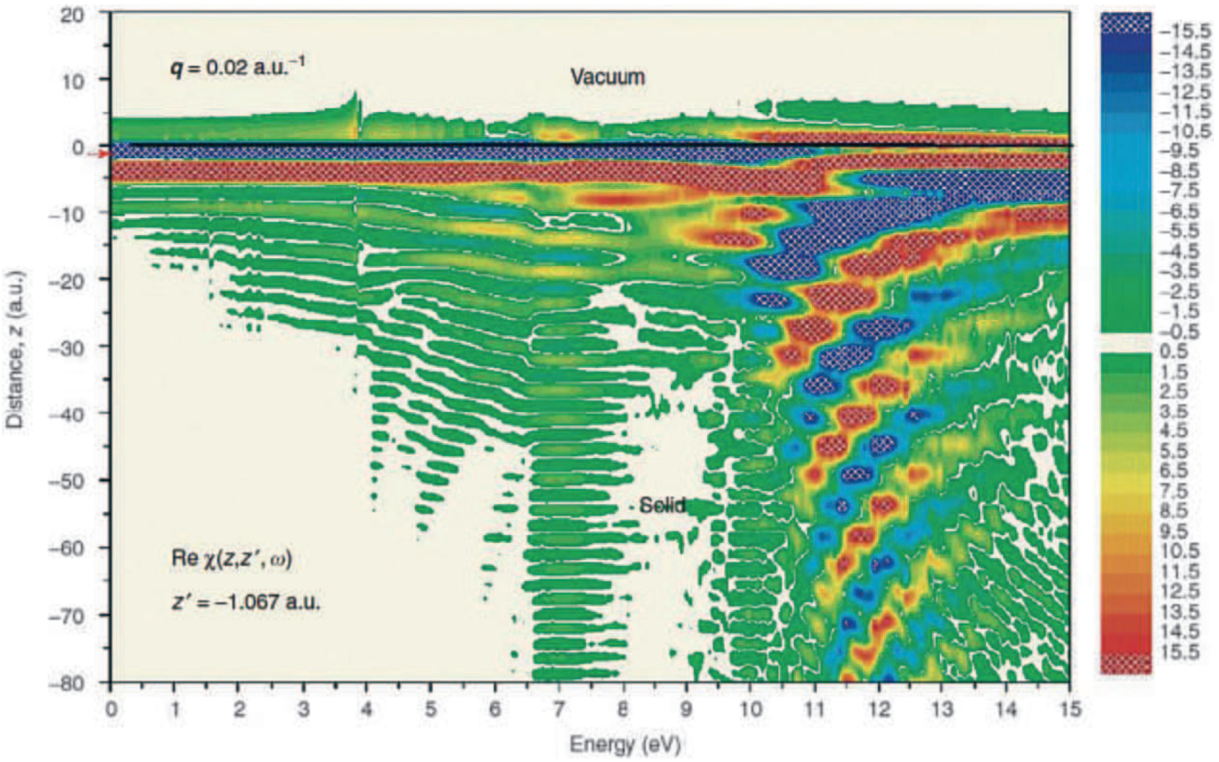

Fig. 6 Susceptibility of Ag (111) slab, i.e., charge density at varying depth z from the surface at $z = 0$ as response to a local excitation potential at z' with lateral wave vector $\boldsymbol{q}$, plotted vs excitation frequency, model potential used for bulk (Silkin et al., 2004).

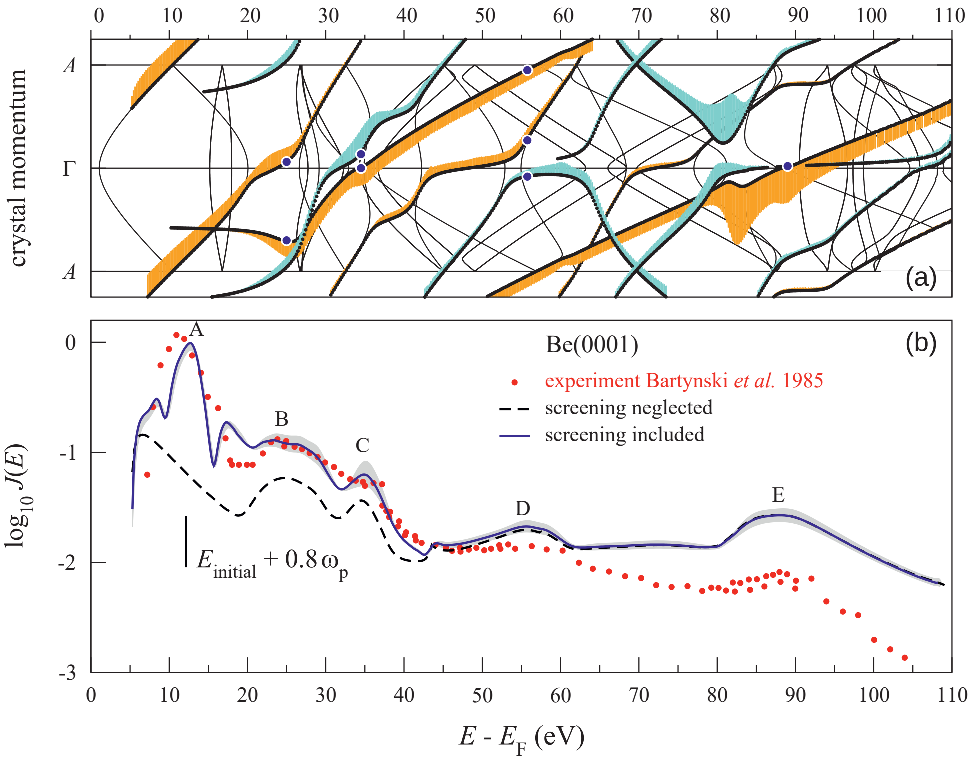

Fig. 7 Band structure analysis of the photoemission from the surface state at $\bar{\Gamma}$ on Be(0001) according to Krasovskii et al. (2010) (a) Complex band structure of Be(0001) along the $A\Gamma A$ interval: thick lines show Bloch waves that contribute to LEED states. Vertical extent of the shading is proportional to the modulus (not squared) of the contribution to the matrix element from the individual partial wave. Circles indicate $k_\perp$ vectors of the Bloch waves at the maxima B–E. Thin lines are the bulk band structure in the $A\Gamma A$ interval. (b) Experimental semilogarithmic intensity profile log10 J(ω) (circles) of the $\bar{\Gamma}$ surface state emission according to Bartynski et al. (1985) compared to the theory with (solid line) and without screening (dashed).

spectroscopy but they strongly affect also electron spectroscopy as, for example, electron losses (EELS) or photoexcited electrons of ARUPS, as shown above. The loss function of EELS

$$S(\boldsymbol{q}, \omega) = -Im \frac{1}{\varepsilon_M(\boldsymbol{q}, \omega)} \tag{20}$$

measures the macroscopic ε_M. The development of photonics toward the nanoscale regime opened the door to the details of the position dependence of electromagnetic response. For example, small metallic particles close to a molecule on a surface may produce surface enhanced Raman scattering (SERS) of that molecule by many orders of magnitude, because the field considerably increases in this geometrical configuration. At sufficiently small scales, nonlocal effects will become important such that the full dielectric function will be needed for theoretical considerations there also. Many interesting developments are affected by local fields or affect the visibility of local fields. Such considerations as e.g. nonlinear optics or composite materials go beyond the present contribution and deserve a presentation itself.

Conclusion

The term "Local Field Effects" has been related to its frequently used applications in order to describe effects of macroscopic fields induced in the microscopic electrical response on the atomic scale. The generalization of the Lorentz-Lorenz formula associates the dielectric displacement from the external charges with the microscopic field by a linear relationship that includes the polarization induced by the presence of matter. The procedure links microscopically the external charges to the vacuum electrostatic field according to Maxwell's equation and takes into account its influence on the atomic material by quantum mechanical laws. This is a self-consistent loop connecting the total electric field with its vacuum sources, external as well as polarization charges: the field that is produced by charges produces parts of them itself. In simple terms: external charge ⇒ external field ⇒ total charge ⇔ total field.

The relationship denoted by a dielectric function is considered here as linear, leaving e.g. nonlinear optics out of scope. Nevertheless, the linear case is fundamental and important. Thus, one has to include the linear polarization fields in basic investigations of condensed matter as in optical or in electron photoemission spectroscopies in order to get reasonable agreement with observation as shown in this contribution.

Acknowledgments

The author W.S. is indebted to the Deutsche Forschungsgemeinschaft for the support under FOR 353.

References

Bartynski RA, Jensen E, Gustafsson T, and Plummer EW (1985) Angle-resolved photoemission investigation of the electronic structure of Be: Surface states. *Physical Review B* 32: 1921–1926.

Bödicker A, Leventi-Peetz A, and Schattke W (1996) Photoemission and photon screening in layered crystals. *The Journal of Electron Spectroscopy and Related Phenomena* 78: 481–484.

Caroli C, Lederer-Rozenblatt D, Roulet B, and Saint-James D (1973) Inelastic effects in photoemission: Microscopic formulation and qualitative discussion. *Physical Review B* 8: 4552–4569.

Ehrenreich H (1965) *The Optical Properties of Solids*. New York: Academic.

Feibelman PJ (1982) Surface electromagnetic fields. *Progress in Surface Science* 12: 287407.

Forstmann F and Gerhardts RR (1986) *Metal Optics Near the Plasma Frequency. Springer Tracts in Modern Physics*. vol. 109. Berlin: Springer-Verlag.

Katsch F, Selig M, and Knorr A (2020) Theory of coherent pump-probe spectroscopy in monolayer transition metal dichalcogenides. *2D Mater* 7: 015021.

Krasoskii EE and Schattke W (2001) Semirelativistic technique for $\mathbf{k}\cdot\mathbf{p}$ calcuations: Optical properties of Pd and Pt. *Physical Review B* 63: 235112–235121.

Krasovskii EE and Schattke W (1999) Local field effects in optical excitations of semicore electrons. *Physical Review B: Condensed Matter and Materials Physics* 60: R16 251–R16 254.

Krasovskii EE, Silkin VM, Nazarov VU, Echenique PM, and Chulkov EV (2010) Dielectric screening and band-structure effects in low-energy photoemission. *Physical Review B* 82: 125102–125106.

Leventi-Peetz A, Krasovskii EE, and Schattke W (1995) Dielectric function and local-field effects of TiSe2. *Physical Review B* 51: 17965–17971.

Liebsch A (1997) *Electronic Excitations at Metal Surfaces*. New York: Plenum.

Mochan WL and Barrera RG (1985) Electromagnetic response of systems with spatial fluctuations. *Physical Review B* 32: 49844988.

Rodek A, Hahn T, Kasprzak J, Kazimierczuk T, Nogajewski K, Polczynska KE, Watanabe K, Taniguchi T, Kuhn T, Machnikowski P, Potemski M, Wigger D, and Kossacki P (2021) Local field effects in ultrafast lightmatter interaction measured by pump-probe spectroscopy of monolayer MoSe2. *Nanophotonics* 10: 27172728.

Schattke W and Van Hove MA (2003) *Solid-State Photoemission and Related Methods*. Weinheim: Wiley-VCH.

Silkin VM, García-Lekue A, Pitarke JM, Chulkov EV, Zaremba E, and Echenique PM (2004) Novel low-energy collective excitation at metal surfaces. *Europhysics Letters* 66: 260.

Slater JC (1967) *Insulators, Semiconductors, and Metals*. New York: McGraw-Hill.

Dielectric function☆

Jan Petzelt and Ivan Rychetský, Institute of Physics, Czech Academy of Sciences, Prague, Czech Republic

© 2024 Elsevier Ltd. All rights reserved.

This is an update of J. Petzelt, I. Rychetský, Dielectric Function, Editor(s): Franco Bassani, Gerald L. Liedl, Peter Wyder, Encyclopedia of Condensed Matter Physics, Elsevier, 2005, Pages 426–429, ISBN 9780123694010, https://doi.org/10.1016/B0-12-369401-9/00427-7.

Introduction 812
Definition and general properties of the dielectric susceptibility and permittivity 812
Kramers-Kronig relations 813
Sum rule 814
Fluctuation – Dissipation theorem 814
Polaritons 814
Physical mechanisms and models of dielectric dispersion 814
Dielectric response of homogeneous materials 815
Effective dielectric function of inhomogeneous materials 816
Conclusion 817
Acknowledgments 817
References 817

Abstract

After definition and discussion of the symmetry and basic properties of the linear complex dielectric susceptibility and permittivity tensors in crystals, their main possible types of frequency dispersions up to the visible range are described. Then various material types with pronounced dielectric properties (ferroelectrics, relaxors, dielectric – conductor composites) are briefly discussed.

Key points

- Definition and general properties of the linear complex dielectric function;
- Kramers-Kronig dispersion relations and sum rules;
- Fluctuation – dissipation theorem;
- Polaritons and their relation to the dielectric function;
- Models of the dielectric dispersion;
- Dielectric response of homogeneous materials;
- Effective dielectric response of inhomogeneous materials and effective medium approximation.

Introduction

In this chapter we introduce the linear dielectric response of solids and briefly summarize its main functional and symmetry properties. The main discussion is devoted to the frequency dependence of the long-wavelength ($\mathbf{k} = 0$) complex dielectric permittivity and its modeling up to the infrared - visible range due to the polar phonons and free charges and at the lower-frequency range due to the charged localized defects, polar nanoregions and structural disorder. The effective dielectric response of inhomogeneous materials is discussed within the effective medium approximation with a focus to giant permittivity phenomena.

Definition and general properties of the dielectric susceptibility and permittivity

Electromagnetic field in a condensed matter medium is described by Maxwell equations containing charge densities $\rho(\mathbf{r},t)$ and currents of electrons and ions in the medium. Dependence of charge density on the macroscopic electric field (averaged over local field variations due to the discrete atomic structure) constitutes a material relation characteristic for the material. The charge density

---

☆*Change History*: July 2022. J Petzelt and I Rychetsky prepared the update.

can be expressed by means of the dipole moment vector per unit volume (polarization) **P** or by the electrical displacement vector **D** (Fröhlich, 1958):

$$\rho = -div\mathbf{P}, \mathbf{D} = \varepsilon_0\mathbf{E} + \mathbf{P} = \varepsilon_0(\chi + 1)\mathbf{E},$$

where ε_0 is the permittivity of vacuum and χ is the linear dielectric susceptibility tensor. Applying generally spatial and time dependent electric field $\mathbf{E}(\mathbf{r}, t)$, the polarization vector in the linear approximation is (Fröhlich, 1958)

$$P_i(\mathbf{r}, t) = \varepsilon_0 \int_{-\infty}^{t} dt' \int d\mathbf{r}' \chi_{ij}(\mathbf{r} - \mathbf{r}', t - t') E_j(\mathbf{r}', t')$$

and may depend on the spatial surrounding (non-local response) and history of **E** (for causality reasons only on previous times). Assuming space and time homogeneity, the dependences are only on the differences $\boldsymbol{R} = \mathbf{r} - \mathbf{r}'$ and $\tau = t - t'$. Defining the time and spatial Fourier transform of the field $E_i(\omega, \mathbf{k}) = \int_{-\infty}^{\infty} dt \int d\mathbf{r}\, E_i(\mathbf{r}, t) e^{i(\omega t - \mathbf{kr})}$, the Fourier components (i.e. plane waves) of polarization and electric displacement are $P_i(\omega, \mathbf{k}) = \varepsilon_0 \chi_{ij}(\omega, \mathbf{k}) E_j(\omega, \mathbf{k})$ and $D_i(\omega, \mathbf{k}) = \varepsilon_0\ \varepsilon_{ij}(\omega, \mathbf{k}) E_j(\omega, \mathbf{k})$, where the linear dielectric function (relative dielectric permittivity or dielectric constant) $\varepsilon_{ij}(\omega, \mathbf{k}) = \delta_{ij} + \chi_{ij}(\omega, \mathbf{k})$ and susceptibility $\chi_{ij}(\omega, \mathbf{k})$ are complex functions of the real **k**-vector and angular frequency ω:

$$\varepsilon_{ij}(\omega, \mathbf{k}) = \delta_{ij} + \int_0^{\infty} d\tau \int d\mathbf{R}\ \chi_{ij}(\mathbf{R}, \tau) e^{i(\omega\tau - \mathbf{kR})}.$$

The dielectric function describes the linear relation between **D** and the macroscopic electric field **E**.

The frequency and **k**-vector can be mathematically considered as complex quantities. Since the fields are real, the dielectric function in non-magnetic materials (magnetic susceptibility is zero) fulfills the relation $\varepsilon_{ij}(\mathbf{k}, \omega) = \varepsilon_{ij}(-\mathbf{k}^*, -\omega^*)^*$ or, for real ω and $\mathbf{k}$, $\varepsilon_{ij}(\mathbf{k}, \omega) = \varepsilon_{ij}(-\mathbf{k}, -\omega)^*$. In non-gyrotropic (i.e. without optical activity) media, where $\varepsilon_{ij}(\omega, \mathbf{k}) = \varepsilon_{ij}(\omega, -\mathbf{k})$, the dielectric function tensor is symmetric $\varepsilon_{ij}(\omega, \mathbf{k}) = \varepsilon_{ji}(\omega, \mathbf{k})$. If the wave vectors obeys the constraint $ak = \pi a/\lambda << 1$, where a is of the order of the characteristic system inhomogeneities (in crystals the interatomic distances), the dielectric function can be expanded in ak:

$$\varepsilon_{ij}(\omega, k) = \varepsilon_{ij}(\omega) + O\left((ak)^2\right) \approx \varepsilon_{ij}(\omega).$$

Neglecting the second term on the right-hand side we assume that the response is local so that we neglect the spatial dispersion effects. Then only the frequency dependence has to be considered:

$$\varepsilon_{ij}(\omega) = \delta_{ij} + \int_0^{\infty} d\tau\ \chi_{ij}(\tau) e^{i\omega\tau}.$$

In most cases of practical interest for macroscopically homogeneous media this approximation is well justified (Landau and Lifshitz, 1960) and we shall limit our further discussion to this case.

The complex dielectric function (complex permittivity) has the real and imaginary part, $\varepsilon_{ij}(\omega) = \varepsilon_{ij}^{'}(\omega) + i\varepsilon_{ij}^{''}(\omega)$, which are even and odd functions of real ω, respectively:

$$\varepsilon_{ij}'(\omega) = \varepsilon_{ij}'(-\omega), \varepsilon_{ij}''(\omega) = -\varepsilon_{ij}''(-\omega).$$

It is a symmetric second-rank tensor which in crystals along the principle optical axes reduces to complex scalar properties (Nye, 1985). Further we shall discuss only these properties.

In the case of capacitor, the real part of the dielectric function describes its capacity and the imaginary part determines the rate of losses of the radiation energy which is (Landau and Lifshitz, 1960)

$$Q = \frac{1}{2}\varepsilon_0 |E(\omega)|^2 \omega \varepsilon''(\omega).$$

In the case of electromagnetic waves, the real part describes the change of the wavelength compared to that in vacuum ($\lambda \propto 1/\sqrt{\varepsilon'}$) and the imaginary part its absorption (attenuation).

Instead of the dielectric function, the AC electric conductivity tensor $\varepsilon_{ij}(\omega) = i\sigma_{ij}(\omega)/\varepsilon_0\omega$ can be equivalently used. Along the principal axes of the dielectric tensor in non-magnetic media, where the magnetic permeability $\mu = 1$, also the complex index of refraction $\widehat{n}(\omega) = \sqrt{\varepsilon(\omega)} = n(\omega) + i\kappa(\omega)$ is frequently used to describe the dielectric response at optical frequencies. Here n is the real refractive index and κ index of absorption (characterizing the wave attenuation factor within one wavelength).

Kramers-Kronig relations

The causality principle provides analyticity of $\varepsilon_{ij}(\omega)$ in the upper complex half-plane (in the lower half-plane $\varepsilon_{ij}(\omega)$ has singularities, mostly simple poles) and results in Kramers-Kronig dispersion relations (Landau and Lifshitz, 1960):

$$\varepsilon_{ij}'(\omega) - \delta_{ij} = \frac{2}{\pi} \mathrm{P} \int_0^{+\infty} \frac{x\varepsilon_{ij}''(x)}{x^2 - \omega^2} dx$$

$$\varepsilon''_{ij}(\omega) - \frac{\sigma_{ij}(0)}{\varepsilon_0\omega} = -\frac{2\omega}{\pi}\mathrm{P}\int\limits_{0}^{+\infty}\frac{\varepsilon'_{ij}(x) - \delta_{ij}}{x^2 - \omega^2}dx.$$

Checking the validity of Kramers-Kronig relations is an important issue for experimentalists measuring independently the real and imaginary part of the dielectric response even in somewhat limited frequency range (Milton et al., 1997).

Sum rule

Finite charges in the medium of interest result in so called sum rule for the oscillator strengths (*f*-sum rule) (Landau and Lifshitz, 1960):

$$\int_0^{\infty}\omega\varepsilon''_{ij}(\omega)d\omega = \delta_{ij}\frac{\pi}{2}\omega_p^2,\, \omega_p^2 = \frac{Ne^2}{m\varepsilon_0}$$

$$\int_0^{\infty}\varepsilon'_{ij}(\omega)d\omega = \delta_{ij} - \frac{2\pi^2}{\varepsilon_0}\sigma_{ij}(0).$$

where N is the density of charges e and m their mass (assuming for simplicity only one type of charges of uniform density). These sum rules are of practical importance when discussing temperature or pressure dependences of the dielectric function which undergoes pronounced changes (e. g. metal-insulator and superconductive phase transitions), since the total charge in the system is conserved.

Fluctuation – Dissipation theorem

Dielectric function is closely related to thermal fluctuations of the polarization characterized by the autocorrelation function $\langle\delta P_i(t)\delta P_j(0)\rangle$, the Fourier component of which

$$S_{ij}(\omega) = \int\limits_{-\infty}^{+\infty}\langle\delta P_i(t)\delta P_j(0)\rangle e^{i\omega t}dt$$

is called the spectral density function. This function is proportional to dynamic structure factor measured in inelastic neutron scattering experiments and to inelastic light scattering (Raman and Brillouin) cross section. The fluctuation - dissipation theorem (Kubo, 1957) relates this function to dielectric losses:

$$\varepsilon_0\varepsilon''_{ij}(\omega) = \frac{1}{2\hbar}\left(1 - e^{-\hbar\omega/kT}\right)S_{ij}(\omega) \approx \frac{\omega}{2kT}S_{ij}(\omega),$$

where the last approximation is valid in the classical high-temperature limit $kT >> \hbar\omega$.

Polaritons

Dielectric function $\varepsilon(\omega, \mathbf{k})$ describes the dielectric response to the plane-wave electric field $E(\omega, \mathbf{k})e^{-i(\omega t - \mathbf{kr})}$, which can be in principle realized for arbitrary values of ω, $\mathbf{k}$ by using appropriate external electric charges and currents. When we limit ourselves to propagating electromagnetic waves in macroscopically homogeneous media, the values ω, $\mathbf{k}$ become mutually dependent. E.g., for transverse waves $\mathbf{E}\perp\mathbf{k}$, which propagate along the optical axes, $k(\omega)^2 = \frac{\omega^2}{c^2}\varepsilon(\omega)$. Such waves, whose propagation in characterized by a complex wave vector, characterize mixed electromagnetic and lattice vibrational (phonon) or electron excitations called polaritons (Hopfield, 1958; Barker and Loudon, 1972). Knowing the complex dielectric function, the polariton dispersion branches are fully determined.

Physical mechanisms and models of dielectric dispersion

Dielectric function provides direct and important information about the polarization mechanisms in the medium. In all systems the dominant dispersion and absorption mechanism in the high-frequency optic range (visible and/or ultraviolet) is caused by electronic excitations (transitions from populated to empty electron levels). Since these transitions involve the whole Brillouin zone, there are no simple phenomenological models used for the description of this dispersion. Instead, microscopic calculations based on the known or calculated electron band structure are usually used and compared with experiment.

In the infrared range, the dominating dispersion and absorption mechanism in dielectrics is due to lattice vibrations (one-phonon absorption). Only polar phonons connected with the long-wavelengths dipole-moment fluctuations in the $\mathbf{E}$ direction, i.e. transverse phonons whose eigenvectors have polar vector symmetry, are infrared active. Their dielectric response can be well described by that of classical damped harmonic oscillators. Assuming s infrared active (i.e. polar) phonon modes, the dielectric function in approximation which neglects the mutual coupling among the oscillators is a simple sum of individual oscillator responses (Barker Jr., 1975):

$$\varepsilon(\omega) = \varepsilon(\infty) + \sum_{j=1}^{s} \frac{\omega_{pj}^2}{\omega_{TOj}^2 - \omega^2 - i\gamma_{TOj}\omega}$$

where $\varepsilon(\infty)$, ω_{pj}^2, ω_{TOj}, γ_{TOj} is the high-frequency (optic) permittivity due to electronic transitions, oscillator strength (square of the mode plasma frequency), square root of the force constant and damping of the j-th transverse optical phonon mode, respectively. A more general function frequently used particularly for fitting the experimental infrared reflectivity, is so-called factorized form of the dielectric function (product of generalized oscillators) (Lowndess, 1970):

$$\varepsilon(\omega) = \varepsilon(\infty) \prod_{j=1}^{s} \frac{\omega_{LOj}^2 - \omega^2 - i\gamma_{LOj}\omega}{\omega_{TOj}^2 - \omega^2 - i\gamma_{TOj}\omega},$$

where the frequencies and dampings of longitudinal optical phonons are introduced explicitly. All the parameters are real positive numbers. For nonzero damping, the transverse and longitudinal eigenfrequencies correspond to complex poles and zeros of the dielectric function, respectively. Only in the limit of small dampings the eigenfrequencies approach the corresponding ω_{TO} and ω_{LO} frequencies. In the static limit $\omega = 0$, the factorized dielectric function yields the generalized Lyddane-Sachs-Teller relation. It shows that high values of the static permittivity can be reached particularly by low ω_{TO} frequencies. This is the case of displacive ferroelectrics, where the Curie—Weiss divergence $\varepsilon = C/(T - T_C)$ is achieved by softening of the soft phonon mode $\omega_{TO}{}^2(soft) \propto T - T_C$ (Cochran law) (Cochran, 1960).

In highly conducting materials (metals) the lattice response is screened by free charges (electrons) and their absorption dominates up to the infrared range. It can be usually well described by the simple Drude response (Ziman, 1972):

$$\varepsilon(\omega) = \varepsilon(\infty) - \frac{\omega_p^2}{\omega(\omega + i\gamma)}.$$

It is the response of a damped harmonic oscillator for zero force constant. The zero of this dielectric function is called screened plasma frequency (plasmon eigenfrequency) and characterizes longitudinal oscillations of the free carrier plasma density. Notice that unlike the case of oscillators, contribution of the Drude term to the static permittivity is negative.

Below the lattice absorption range no polarization (absorption) mechanism exists in an ideal non-piezoelectric dielectric crystal. In piezoelectric crystals the coupling between polar optic and acoustic waves activates the acoustic waves in a finite sample, which provides additional dielectric resonances, typically in the MHz frequency range, whose frequencies are, however, sample size and shape dependent (Gonzalez et al., 2016).

However, structural disorder and strong lattice anharmonicities or all kinds of movable charged defects usually induce further dispersion in the microwave and lower frequency range. Such dispersion is as a rule of relaxation type, the simplest model being the Debye relaxation (Jonscher, 1999):

$$\varepsilon(\omega) - \varepsilon(\infty) = \frac{\omega_p^2}{\omega_0^2 - i\gamma\omega} = \frac{\Delta\varepsilon}{1 - i\tau\omega}$$

where $\tau = \gamma/\omega_0^2$, $\Delta\varepsilon = \omega_p^2/\omega_0^2$ are relaxation time and dielectric strength, respectively. It is seen that in the low-frequency range $\omega \leq 1/\tau$ this function approaches that of the oscillator with frequency ω_0 and damping γ. If the oscillator is overdamped (pure imaginary eigenfrequency for $\gamma \geq 2\omega_0$), the dielectric losses are peaked approximately at $\omega_0{}^2/\gamma$ like the Debye relaxation. This frequency characterizes the dynamics of the defects or hopping frequency of the localized charges. In more complex cases, distribution of Debye relaxations has to be used to fit the broad-band dielectric spectra. In these cases, frequently appearing e.g. in polymers, much effort was exerted to study the universal dispersion laws which rule the tails of the broad loss peaks. However, till now no generally accepted picture has been achieved.

The simplest model which yields the Debye dispersion in solids is hopping of charges over a potential barrier E_a much higher than the thermal energy kT. If the charges do not interact, its temperature dependence is described by the Arrhenius law $\tau = \tau_\infty \exp(E_a/kT)$. If the charges interact, the effective barrier for hopping increases on cooling and the temperature law is usually modified either to phenomenological Vogel-Fulcher law $\tau = \tau_\infty \exp(E_a/k(T - T_g))$ or to critical slowing-down $\tau \propto 1/(T - T_C)$. Here T_g is the glass transition (freezing) temperature (Berthier and Biroli, 2011) and T_C the critical temperature (connected e.g. with an order-disorder ferroelectric transition (Kamba, 2021)) where the relaxation time tends to infinity. In the latter case the systems tend to order below T_C and the relaxation gradually vanishes. In the former case the long-range order is prohibited by some frustration due to the structural disorder so that the disorder remains frozen down to low temperatures (glass phase (Berthier and Biroli, 2011) and relaxor ferroelectrics (Bokov, 2012)) and becomes non-ergodic.

Dielectric response of homogeneous materials

The static permittivity (dielectric constant) of homogeneous solids may acquire values reaching from ~2 up to the order of 10^6. Materials from both ends of this broad spectrum are required for contemporary microelectronic applications: low-permittivity materials (Grill et al., 2014) like organosilicate films for advanced on-chip interconnects and high-permittivity materials as energy storing capacitors, tunable ferroelectric films and low-loss ceramics for microwave passive elements in communication systems. As discussed above, the permittivity value is determined by several usually positive contributions in the dielectric spectra. In low-permittivity materials both electronic and vibrational contributions are very weak, which is typical for weak bonding among non-polar molecules in organic substances. In high-permittivity dielectric materials for energy storage applications (Yang et al., 2019; Zou et al., 2019) mostly the vibrational contribution of strong low-frequency polar modes dominates, since the electronic contribution ε_∞ is always relatively small due to high frequencies of the electronic transitions. Also, the order-disorder ferroelectrics may reach high permittivity values close to T_C, but these are usually of no practical use because of strong temperature dependences of ε' and high losses. The most perspective high-permittivity materials are relaxor ferroelectrics (special type of structurally disordered ferroelectrics), where only a short-range polar ordering is reached and the dominant dielectric dispersion is due to the high-frequency dynamics of the polar nano-clusters. In doped semiconducting materials, the permittivity may also acquire giant values at low frequencies (so called giant or colossal permittivity materials (Lunkenheimer et al., 2010; Petzelt et al., 2012)), but, due to the high losses, this effect is so far not much used in applications.

Effective dielectric function of inhomogeneous materials

In the case of macroscopically or mesoscopically inhomogeneous media (e.g. nanocomposites, ceramics and films with granular structure) the standard experimental techniques cannot determine the bulk dielectric functions of individual constituents, but only so-called effective dielectric function. Historically, most frequently this function was modeled by using various equivalent schemes of parallel and series combinations of capacitors and resistors. The disadvantage of this approach is that the physical interpretation of individual capacitors and resistors is not always clear and, moreover, they are assumed to be frequency independent, which usually limits their use to relatively low frequencies (below the MHz range). Instead of this, the effective dielectric function can be more realistically determined using so-called effective medium approximation (EMA) (Bergman and Stroud, 1992; McLachlan et al., 2000), if the probing electric field is homogeneous on the scale of inhomogeneities and the boundaries between homogeneous regions are sharp. Within this approximation, the effective dielectric function still must obey the Kramers-Kronig relation and sum rules. EMA is justified as long as the wavelengths of the probing wave are much larger than the individual homogeneous parts and, in the case of absorbing components, also the local penetration lengths (skin depth) should be much larger than the sizes of all the homogeneous parts. Examples of inhomogeneous materials for which the EMA can be used could be ceramics and all kinds of micro- and nano-composites with the grain sizes of the order of μm or less. In slightly conducting systems also the grain boundaries as well as the interface layers between the electrodes and sample may play an important role, which are known to be source of the Maxwell-Wagner relaxation phenomena (McLachlan et al., 2000) at low frequencies. In ceramics, the inhomogeneity is usually just due to the grain anisotropy in the case of non-cubic grain structures, or due to different properties (mainly conductivity) of grain bulk and grain boundaries. The case of uniaxial grain anisotropy is equivalent to a composite of isotropic components, whose dielectric functions are equal to the principal dielectric functions of the anisotropic grains.

The most used EMA model, so called Bruggeman model for a two-component composite (Bruggeman, 1935), consists of two types of spherical particles with dielectric functions $\varepsilon_1(\omega)$, $\varepsilon_2(\omega)$ and volume fractions x, 1-x, respectively, embedded into the effective medium. In this case the effective dielectric function $\varepsilon_{\mathrm{eff}}(\omega)$ is given by

$$x\frac{\varepsilon_1-\varepsilon_{eff}}{\varepsilon_1+2\varepsilon_{eff}}+(1-x)\frac{\varepsilon_2-\varepsilon_{eff}}{\varepsilon_2+2\varepsilon_{eff}}=0.$$

In a general treatment within EMA, so called Bergman approach (Bergman, 1978), the effective response of any two-component composite with dielectric functions ε_1 and ε_2 of volume fractions x_1 and x_2 ($x_2 = 1$-x_1) respectively, can be separated into three additive parts:

$$\varepsilon=V_1\varepsilon_1+V_2\varepsilon_2+\int_0^1 v_{12}(n)\frac{\varepsilon_1\varepsilon_2}{(1-n)\varepsilon_2+n\varepsilon_1}dn$$

with

$$V_1+V_2+\int_0^1 v_{12}(n)dn=1$$

and

$$V_1+\int_0^1(1-n)v_{12}(n)dn=x_1,\quad V_2+\int_0^1 nv_{12}(n)dn=x_2$$

The first two terms on the right-hand side describe the responses of pure components just weighted by factors $0\le V_1\le x_1$ and $0\le V_2\le x_2$. This part does not depend on the depolarizing field and corresponds therefore to the volume parts (clusters) which are macroscopically percolated in the direction of probing E. $v_{12}(n)dn$ represents the clusters characterized by the depolarization factor n, $0 < n < 1$. $v_{12}(n)$ function, so called spectral function, characterizes the shape, topology and interactions of individual homogeneous components. All acceptable dielectric mixing formulas correspond to a particular choice of V_1, V_2 and $v_{12}(n)$.

If the difference between complex responses of both components is pronounced, particularly strong changes in $\varepsilon_{\text{eff}}(\omega)$ appear near the percolation threshold (Nan et al., 2010) of the higher-response component, which in the Bruggeman EMA model appears for $x = 1/3$. In ceramics and films the percolation threshold of the bulk grain properties cannot be reached (if each grain is separated from its neighbors by the grain boundary with different dielectric properties) and therefore the effective dielectric spectra of high-permittivity or semiconducting materials are often strongly influenced by the grain boundaries. For instance, combining semiconducting grains with insulating boundaries can lead to effective giant permittivities (up to $\sim 10^6$) with strong dielectric relaxations at low or medium frequencies (Petzelt et al., 2013; Rychetsky et al., 2020), which are absent in the response of both bulk components.

Conclusion

After introducing the linear complex dielectric response and its basic properties, the main permittivity contributions to it and their frequency dependences up to the infrared range and their modeling are discussed. It is shown that the largest permittivity contributions in homogeneous materials are due to soft phonon modes and/or critical relaxations near the ferroelectric phase transitions, whereas the largest contributions in inhomogeneous materials are usually due to conductivity inhomogeneities, which are the main sources of giant permittivity phenomena.

Acknowledgments

The research has been supported by the Czech Science Foundation (Project LA 20-20326L) and by Operational Programme Research, Development and Education (financed by European Structural and Investment Funds and by the Czech Ministry of Education, Youth and Sports), Project No. SOLID21 – CZ.02.1.01/0.0/0.0/16_019/0000760. It is based on our previous chapter (Petzelt and Rychetský, 2005).

References

Barker AS Jr. (1975) Long-wavelength soft modes, central peaks, and the Lyddane-Sachs-Teller relation. *Physical Review B* 12: 4071–4084.

Barker AS Jr. and Loudon R (1972) Response functions in the theory of Raman scattering by vibrational and polariton modes in dielectric crystals. *Reviews of Modern Physics* 44: 18–47.

Bergman DJ (1978) The dielectric constant of a composite material—A problem in classical physics. *Physics Reports* 43: 377–407.

Bergman DJ and Stroud D (1992) Physical properties of macroscopically inhomogeneous media. *Solid State Physics* 46: 147–269.

Berthier L and Biroli G (2011) Theoretical perspective on the glass transition and amorphous materials. *Reviews of Modern Physics* 83: 587–645.

Bokov AA and Ye Z-G (2012) Dielectric relaxation in relaxor ferroelectrics. *Journal of Advanced Dielectrics* 2: 1241010-1/24.

Bruggeman DAG (1935) Berechnung verschiedener physikalischer Konstanten von heterogenen Substanzen. I. Dielektrizitätskonstanten und Leitfähigkeiten der Mischkörper aus isotropen Substanzen. *Annalen der Physik* 416: 636–664.

Cochran W (1960) Crystal stability and the theory of ferroelectricity. *Advances in Physics* 9: 387–423.

Fröhlich H (1958) *Theory of Dielectrics: Dielectric Constant and Dielectric Loss*, 2nd edn *Monographs on the Physics & Chemistry of Materials*2nd edn, Oxford at the Clarendon Press.

Gonzalez AM, Garcia A, Benavente-Peces C, and Pardo L (2016) Revisiting the characterization of the losses in piezoelectric materials from impedance spectroscopy at resonance. *Materials* 9(72): 1–18.

Grill A, Gates SM, Ryan TE, Nguyen SV, and Priyadarshini D (2014) Progress in the development and understanding of advanced low k and ultralow k dielectrics for very large-scale integrated interconnects—State of the art. *Applied Physics Reviews* 1: 011306-1/17.

Hopfield JJ (1958) Theory of the contribution of excitons to the complex dielectric constant of crystals. *Physics Review* 112: 1555–1567.

Jonscher AK (1999) Dielectric relaxation in solids. *Journal of Physics D: Applied Physics* 32: R57–R70.

Kamba S (2021) Soft-mode spectroscopy of ferroelectrics and multiferroics: A review. *APL Materials* 9: 020704-1/22.

Kubo R (1957) Statistical-mechanical theory of irreversible processes. I. General theory and simple applications to magnetic and conduction problems. *Journal of the Physical Society of Japan* 12: 570–586.

Landau LD and Lifshitz EM (1960) *Electrodynamics of Continuous Media*. Oxford: Pergamon.

Lowndess RP (1970) Influence of lattice anharmonicity on the longitudinal optic modes of cubic ionic solids. *Physical Review B* 1: 2754–2763.

Lunkenheimer P, Krohns S, Riegg S, Ebbinghaus SG, Reller A, and Loidl A (2010) Colossal dielectric constants in transition-metal oxides. *The European Physical Journal Special Topics* 180: 61–89.

McLachlan DS, Hwang J-H, and Mason TO (2000) Evaluating dielectric impedance spectra using effective media theories. *Journal of Electroceramics* 5: 37–51.

Milton GW, Eyre DJ, and Mantese JV (1997) Finite frequency range Kramers Kronig relations: Bounds on the dispersion. *Physical Review Letters* 97: 3062–3065.

Nan C-W, Shen Y, and Ma J (2010) Physical properties of composites near percolation. *Annual Review of Materials Research* 40: 131–151.

Nye JF (1985) *Physical Properties of Crystals. Their Representation by Tensors and Matrices*, New edn Oxford: Clarendon Press.

Petzelt J and Rychetský I (2005) Dielectric function. In: Bassani F, Liedl GL, and Wyder P (eds.) *Encyclopedia of Condensed Matter Physics*, 426–429.

Petzelt J, Rychetsky I, and Nuzhnyy D (2012) Dynamic ferroelectric–like softening due to the conduction in disordered and inhomogeneous systems: Giant permittivity phenomena. *Ferroelectrics* 426: 171–193.

Petzelt J, Nuzhnyy D, Bovtun V, Savinov M, Kempa M, and Rychetsky I (2013) Broadband dielectric and conductivity spectroscopy of inhomogeneous and composites conductors. *Physica Status Solidi A* 210: 2259–2271.

Rychetsky I, Nuzhnyy D, and Petzelt J (2020) Giant permittivity effects from the core–shell structure modeling of the dielectric spectra. *Ferroelectrics* 569: 9–20.

Yang L, Kong X, Li F, Hao H, Cheng Z, Liu H, Li J-F, and Zhang S (2019) Perovskite lead-free dielectrics for energy storage applications. *Progress in Materials Science* 102: 72–108.

Ziman JF (1972) *Principles of the Theory of Solids*, 2nd edn Cambridge University press.

Zou K, Dan Y, Xu H, Zhanh Q, Lu Y, Huang H, and He Y (2019) Recent advances in lead-free dielectric materials for energy storage. *Materials Research Bulletin* 113: 190–201.

Mechanical properties: Fatigue

D Klenam[a], F McBagonluri[b], and W Soboyejo[c], [a]Academic Development Unit & School of Chemical and Metallurgical Engineering, University of the Witwatersrand, Johannesburg, South Africa; [b]Department of Mechanical Engineering, Academic City University College, Accra, Ghana; [c]Department of Mechanical Engineering, Worcester Polytechnic Institute, Worcester, MA, United States

© 2024 Elsevier Ltd. All rights reserved.

This is an update of F. McBagonluri, W. Soboyejo, Mechanical Properties: Fatigue, Editor(s): Franco Bassani, Gerald L. Liedl, Peter Wyder, Encyclopedia of Condensed Matter Physics, Elsevier, 2005, Pages 291–298, ISBN 9780123694010, https://doi.org/10.1016/B0-12-369401-9/00573-8

Introduction 819
Mechanisms of fatigue 820
Fatigue crack initiation 820
Fatigue crack propagation 820
Empirical approaches 820
Stress-based 820
Strain-based 821
Variable-amplitude fatigue 821
LEFM approaches 822
Fundamentals of fracture mechanics 822
Fracture mechanics and fatigue 823
Fatigue crack growth laws 823
Paris' model 824
Forman's model 824
Walker's model 824
Multiparameter law 824
Elber's model (crack-closure model) 824
Fatigue fracture modes 824
The short crack problem 825
Applications of data science and machine learning to fatigue 825
Overview of fatigue of complex concentrated alloys 828
Overview of fatigue of additively manufactured metals/alloys 832
Conclusion 834
Acknowledgments 834
References 834

Abstract

This chapter discusses the fatigue behavior and mechanisms of materials. It provides an overview of the various empirical, linear elastic fracture mechanics (LEFM) and data-science approaches to estimating fatigue properties of materials. The empirical approaches are stress- and strain-based, and variable-amplitude. The LEFM approaches are by the crack growth rates and fracture mechanics models. The concept of short and long crack problems are briefly highlighted. The chapter identifies current application of data science based machine learning (ML) models use to predict fatigue behavior. The ML techniques are supervised, unsupervised and reinforcement learning. The fatigue behavior of the emerging field of complex concentrated alloys are also discussed with implications for future research directions highlighted.

Key points

- Stress-based and strain-based approaches are the empirical methods for estimating fatigue behavior of mechanical components.
- Stress-life (S–N) approach is used for components with fatigue life exceeding $\sim 10^3$ cycles, while assuming only elastic strains in the loaded component with no plastic strains included. The method is quantitative with significant computational errors.

- Strain-based approach assumes the strain range to provide the overarching mechanisms that controls fatigue. The plastic strains are used to quantify the structural response to fatigue.
- The rate of crack growth occurs when the crack-tip stress intensity factor, K, exceeds the fracture toughness of the material under the linear elastic fracture mechanics framework.
- Machine learning based neural networks and support vector machines are used to model fatigue behavior with input variables being mean stresses and environmental factors. Data are categorized as training and testing datasets. The training datasets are experimental data mined from literature and used to teach the model, whereas the test data is mainly for validation of the model.
- Three distinct fatigue behavior for complex concentrated alloys (CCAs) based on crystal structure and microstructural features are observed. The low fatigue resistance of face centered cubic CCAs is attributed to the competing effects of initiated cracks resulting from multiple slips systems and annealing/deformation twins.
- For the BCC CCAs, fatigue cracks are initiated at the grain boundaries which then propagates through the grains for body centered cubic CCA due to their limited slip systems.
- There is pronounced phase transformation in the vicinity of the crack tip associated with metastable CCAs with associated work hardening, which induce crack tip blunting.
- The fatigue and fracture mechanisms of multi-phase CCAs with mostly eutectic and non-eutectic structure shows crack initiations at the phase boundaries and persistent slip bands (PSBs). The crack propagation paths are straight or branched depending on the microstructural features.
- Conventional long crack growth models overestimate fatigue behavior of additively manufactured components, whereas the short crack models are more ideal with crack sizes of ∼100 mm applicable for defect-based fatigue estimation criterion.

Introduction

Fatigue is a deleterious damage mechanism that occurs in advanced engineering structural components subjected to alternating loadings (Suresh, 1985, 1998). Fatigue damage is driven by initiation and propagation stages (Laird and Smith, 1962). Different types of fatigue mechanisms have been identified in structural components, based primarily on loading conditions and prevailing loading environment. Most of these fatigue mechanisms manifest as fretting, dwell, thermomechanical, and multi-axial (Suresh, 1998).

The result of fatigue failures is high casualty numbers and major financial losses. In fact, over 80% of mechanical failures in engineering structures and components are attributed to fatigue failures (Soboyejo, 1988). Attempts to eliminate or reduce the incidence of fatigue failures have been the principal driving force behind the tremendous amount of research investments into the investigation of the initiation and propagation stages of fatigue (Soboyejo, 1988).

Research in fatigue began over a century and a half ago following a series of industrial and railway accidents and the desire to reduce incidence of such failures (Klenam et al., 2022). Much of the research was driven by the desire to understand the premature failures of components subjected to cyclic loading conditions at stress levels that were substantially below the pertinent design loads under monotonic loading.

The first systematic study of fatigue failures is usually attributed to the German engineer, A Wöhler (1858–1871) (Wohler, 1855, 1870). In his preliminary studies, Wöhler concluded that when subject to cyclic loading conditions, the strengths of steel railway axles were lower than their static strengths. Thus, the fatigue life was determined by the load range and not by the maximum load, as previously suggested (Wohler, 1855, 1870).

Ewing and Rosenhain, and Ewing and Humphrey conducted the first mechanistic studies of fatigue (Ewing and Humfrey, 1903; Ewing and Rosenhain, 1900). In their studies conducted on Swedish iron, they identified the stages of fatigue crack initiation and propagation. In a series of investigations, they inferred, from published optical micrographs of the surfaces of cyclically damaged specimens, that slip bands developed in the grains of polycrystalline materials subjected to alternating loads. They inferred that these slip bands increased with fatigue deformation, leading ultimately to crack formation (Ewing and Humfrey, 1903; Ewing and Rosenhain, 1900).

Empirical models for characterizing fatigue damage evolution were developed by many researchers over the years to provide tools for the modeling of fatigue behavior. For instance, Basquin developed stress-based laws to characterize stress-life (S–N) curves of metals (Basquin, 1910). He showed that a log-log plot of stress versus cycles exhibited a linear relationship over a large range of stresses.

Coffin and Manson, working independently in the early 1950s, noted that plastic strains were primarily responsible for cyclic damage (Coffin, 1954; Manson, 1953). They proposed an empirical relationship between the number of load reversals to fatigue failure and the plastic strain amplitude. This formulation, known also as the Coffin-Manson relationship, is the most widely used approach for strain-based characterization of fatigue damage. Coffin and Manson also found that the plastic strain-life data can be linearized on a log-log scale. These relationships were combined to relate total strain range to life-to-failure. This relationship is called the strain-life relation. In the strain-life approach, the transition fatigue life represents the life at which the elastic and plastic strain ranges are equivalent.

The mathematical framework for the quantitative modeling of fatigue failure came later and was primarily driven early by the stress analyzes work of Inglis (Inglis, 1913) and later by the energy concepts of Griffith (Griffith, 1921). This was followed by the work of Irwin (Irwin, 1957). Irwin showed that the amplitude of the stress singularity ahead of a crack could be expressed in terms of the stress intensity factor, K. This formulation was developed based on the representation of the crack-tip stresses by the stress functions proposed originally by Westergaard (1939), and the elasticity solutions of Love (1888, 1901).

Paris and co-workers observed that the increment of fatigue crack advance per stress cycle, da/dN, can be related to the range of the stress intensity factor, ΔK, under constant amplitude cyclic loading (Paris and Erdogan, 1963). This observation set the stage for the direct application of linear elastic fracture mechanics to fatigue problems. In this approach, fatigue damage is characterized by fatigue cracks under conditions of small-scale plastic deformation at the crack tip (Paris and Erdogan, 1963). When gross plasticity occurs at the crack tip, the problem is one amenable to elastic-plastic or plastic analysis.

Elber provided further insights into the application of linear elastic fracture mechanics (LEFM) to fatigue (Elber, 1970). In studies of fatigue crack growth that were conducted by him as a graduate student in Australia, he noted that fatigue cracks could remain closed, even under cyclic tensile loads. He showed that the effective value of ΔK given by (Eqs. 1 and 2) controls the fatigue crack growth rate, da/dN. Note that K_{cl} and K_{op} are the respective crack-closure and crack-opening stress intensity factors.

$$\mathit{\Delta} K_{\text{eff}} = K\text{cl}_{\max} \tag{1}$$

$$\mathit{\Delta} K_{\text{eff}} = K\text{op}_{\max} \tag{2}$$

Further progress in fatigue investigations led to the breakdown of the similitude concept, in which cracked components in different dimensions were assumed to exhibit the same amount of crack growth, when subjected to the same far-field stress intensity factor range, ΔK. Following the pioneering work of Pearson, small cracks were found to exhibit anomalous crack growth behavior, with relatively fast growth rates occurring at ΔK level below the long crack fatigue threshold (Pearson, 1975).

Mechanisms of fatigue

Fatigue crack initiation

In most engineering structures and components, regions of high stress concentration are preferred crack initiation sites. The formation of microcracks around notches, scratches, inclusions, and along or across grain boundaries represent the onset of fatigue damage evolution. In metallic structures, microcracking is often driven by slip processes. Ewing and Humfrey referred to these slip bands as persistent slip bands (PSBs) (Ewing and Humfrey, 1903), in reference to the fact that these bands were restored after electropolishing and then re-fatiguing. Fatigue crack initiation can occur by any one of the following identified processes (Soboyejo, 1988; Suresh, 1998):

1. From regions of localized strain hardening or softening resulting from slip step accumulation occurring at the surfaces of structures subjected to high plane strain amplitudes.
2. Formation of intrusions and extrusions on the surfaces of engineering structures resulting from sequential slip at the intersection of slip planes (Cottrell and Hull, 1957; Soboyejo, 1988).
3. Microcrack formation along crystallographic planes of maximum shear stress by mode II mechanisms (Forsyth and Ryder, 1960).
4. The coalescence of microcracks to form macrocracks, which are amenable to LEFM characterization (Forsyth and Ryder, 1960).

Fatigue crack propagation

Fatigue crack propagation generally occurs in two stages, namely stage I and II. In stage I, crack propagation rate is characterized by low stress intensity factors (Forsyth and Ryder, 1960). The crack growth behavior at this stage is associated with a threshold stress intensity value, ΔK_{th}, below which fatigue crack growth is negligible. Fatigue crack growth in the threshold is affected by stress ratio, frequency of loading, and prevailing environmental conditions (Suresh, 1985, 1998).

Stage II fatigue crack growth is characterized by high ΔK and long crack lengths. In this region, crack growth rates are extremely high and most fatigue life is usually expended prior to this stage. On a plot of log da/dN versus log ΔK, the stage II region is linear (Fig. 1). The Paris-Erdogan formulation is generally used to characterize fatigue crack growth within this regime. In variable-amplitude loading, the Forman and Walker fatigue crack propagation models are used (Dowling, 1990; Forman, 1972).

Empirical approaches

Stress-based

The stress-life method, based on Wohler's S–N diagram, was the first quantitative approach. The stress-life approach is used in applications where the applied stress is essentially within the elastic range, and the material has a long cyclic life.

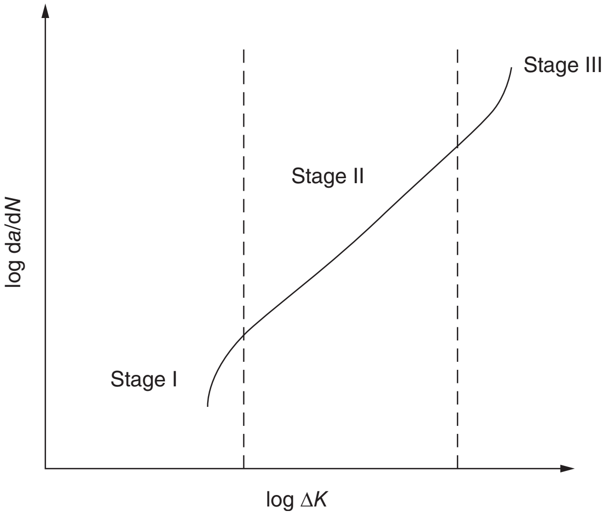

Fig. 1 Schematics of the three distinct regimes of fatigue crack propagation.

In general, the stress-life approach is used in situations where the fatigue life is more than 10^3 cycles. In addition, the stress-life approach excludes the true stress-strain behavior and assumes that only elastic strains are effective within the loaded structure. This assumption introduces significant computational errors, since plastic strains resulting from plastic deformation are a recognized crack initiation protocol. Thus, computational results using the stress-life approach are only informative when the degree of plastic straining is negligible, as in high cycle fatigue (HCF), where plastic strains are relatively small (Dowling, 1990).

Stress-life data are usually represented by S–N curves, in which the stress range or stress amplitudes are plotted against the log of the number of cycles to failure, N. The S–N data for body-centered cubic materials generally exhibit an endurance limit, that is, a stress below which the specimens appear to have infinite life. In the case of face-centered cubic and hexagonal-closed-packed metals, a fatigue limit is often defined as a stress corresponding to a specified fatigue life, for example, 10^7 cycles.

Strain-based

The strain-life method is one of the two classes of empirical approaches for the characterization of fatigue life in structural components. The other approach is the stress-life approach that was discussed in the preceding section. The strain-life model is based on the observation that in many structural components, the response of the material in critical locations, such as notches, is strain or deformation dependent.

Thus, the principal assumption for calculating fatigue life of a component under constant amplitude cyclic loading is that the strain range, $\Delta\varepsilon$, controls fatigue life. In the strain-life approach, the plastic strain is used directly to quantify the structural response to fatigue. However, in the stress-life approach, the plastic strain is not accounted for. The strain-based approach stipulates that at long fatigue lives, beyond the transition life, N_t, the elastic strain dominates the fatigue life, while the plastic strain is negligible with increasing life. In this case, fatigue strength (σ_f'/E) dominates fatigue.

In the case of short fatigue lives, the plastic strain is dominant and fatigue ductility (ε_f') is the controlling fatigue parameter. In general, most engineering structures are designed such that the nominal loads remain elastic. However, due to stress concentrations around notches, localized plasticity is often encountered in engineering structures and components.

One key attribute of the strain-life approach is that it disregards the presence of precracks. Fatigue life prediction using the strain-life approach requires the following essential inputs: (1) cyclic stress-strain response and strain-life data, (2) stress-strain history obtained from critical locations such as notches, (3) damage counting techniques such as cycle counting, (4) mean stress effect models, and (5) damage summation techniques such as Miner's rule (Dowling, 1990). In the strain-life approach (see Fig. 2), the relationship between the total strain amplitude and the number of load reversals to failure is given as

$$\frac{\Delta\varepsilon}{2} = \frac{\sigma_f'}{E}\left(2N_f\right)^b + \varepsilon_f'\left(2N_f\right)^c \tag{3}$$

where ε_f' is the fatigue ductility, c is the fatigue ductility exponent, σ_f' is the fatigue strength coefficient, $\Delta\varepsilon$ is the strain amplitude range, $2N_f$ is the number of load reversals to failure, and b is the Basquin's exponent.

Variable-amplitude fatigue

Under service conditions, most engineering structures and components are exposed to a host of load spectra. For instance, an aircraft under turbulent conditions may be exposed to unique load spectra, compared to the conditions that are inherent to normal operating scenarios. It is, therefore, important to design for a wide range of loading conditions that can occur under unintended and uncontrollable service conditions.

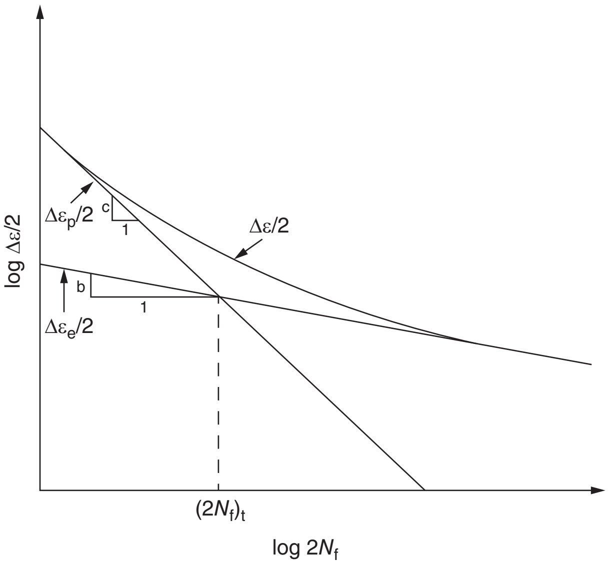

Fig. 2 Schematics of the plot of elastic and plastic strain amplitude vs. life showing total strain amplitude.

The extensive literature on fatigue crack growth shows that experimental test data often differ considerably from predictions of crack growth under variable-amplitude loading conditions (Dowling, 1990; Suresh, 1998). Under constant-amplitude loading, the crack growth increment, Δa, is dependent only on the present crack size and the applied load. However, under variable-amplitude loading, the increment of fatigue crack growth is also dependent on the preceding cyclic loading history. In most cases, the interactions that occur under variable-amplitude loading adversely affect the fatigue lives of engineering components and structures (Suresh, 1998).

LEFM approaches

Fundamentals of fracture mechanics

The concept of linear elastic fractures has been applied to the design of engineering structures for nearly five decades. LEFM assumes that the material is isotropic and linearly elastic. Based on these assumptions, the stress field near the crack tip is often calculated using the theory of elasticity (Love, 1888, 1901) and Westergaard stress function (Westergaard, 1939). Within the framework of LEFM, crack growth occurs when the crack-tip stress intensity factor, K, exceeds the material fracture toughness, K_{IC} (Irwin, 1957). LEFM formulations are usually derived for either the plane stress or plane strain conditions associated with the three basic modes of loadings on a cracked body, namely, crack opening, sliding, and tearing (Irwin, 1957; Suresh, 1998).

The formulation of LEFM assumes that under applied loading conditions, crack tips produce a $1/\sqrt{r}$ singularity. The stress fields near a crack tip of an isotropic linear elastic material can be expressed as a product of $1/\sqrt{r}$ and a function of θ with a scaling factor K (Dowling, 1990; Hertzberg, 1996; Soboyejo, 2002). The stress intensity factor plane strain formulations for mode I stress fields in Cartesian coordinates are given in Eq. 4.

$$\begin{Bmatrix} \sigma_{xx} \\ \sigma_{yy} \\ \sigma_{zz} \end{Bmatrix} = \frac{K_I}{\sqrt{2\pi r}} \cos\frac{\theta}{2} \begin{bmatrix} 1 - \sin\frac{\theta}{2}\sin\frac{3\theta}{2} \\ 1 + \sin\frac{\theta}{2}\sin\frac{3\theta}{2} \\ \sin\frac{\theta}{2}\cos\frac{3\theta}{2} \end{bmatrix} \tag{4}$$

In practical applications, the magnitude of the maximum stress near the crack tip and whether it exceeds the fracture toughness of a given material is usually of interest to design engineers. Hence, the stress intensity factor, K, which is a function of the loading and geometry, is expressed in terms of the "applied stresses," σ at a location expressed in polar coordinate by $r \to 0$ and $\theta = 0$ (where r and q are cylindrical coordinates of a point with respect to a crack tip). The solution of crack problems using the fracture toughness approach requires: (1) the determination of the crack geometry, (2) the calculation of the stress intensity factor, K, (3) the determination of the fracture toughness, K_C of the material (usually obtained from a material handbook), and (4) ensuring that the failure criteria $K \geq K_C$ is satisfied.

Fracture mechanics and fatigue

Paris and co-workers proposed that the increment of fatigue crack advance per stress cycle, da/dN, could be related to the range of the stress intensity factor, ΔK, under constant-amplitude cyclic loading (Paris and Erdogan, 1963). They formulated the relationship given by Eq. (5).

$$\frac{da}{dN} = f(\Delta K, K_{\max}()) \tag{5}$$

where

$$\Delta K = K\Delta\sqrt{\pi a}^{m}\ \mathrm{min}_{\max} \tag{6}$$

where $K_{\max}$ and $K_{\min}$ are the maximum and minimum stress intensity factors, respectively.

Paris and Erdogan, in their subsequent work, established that the fatigue crack advance per stress cycle could be related to the stress intensity range as follows:

$$\frac{da}{dN} = C(\Delta K)^{m} \tag{7}$$

where C and m are material constants.

In practical applications, two independent fracture mechanics parameters are required to characterize the state of stress at the evolving crack tip. A combination of any two of the following can be used: $K_{\max}$, $K_{\min}$, ΔK, and R.

Using Eq. (3) and assuming a constant Y, both sides of Eq. (7) can be integrated:

$$\int_{a_0}^{a_f} \frac{da}{a^{m/2}} = CY^{m}(\Delta\sigma)^{m}\pi^{m/2}\int_{0}^{N_f} dN \tag{8}$$

For $m > 2$:

$$N_f = \frac{2}{(m-2)CY^{m}(\Delta\sigma)^{m}\pi^{m/2}}\left[\frac{1}{(a_0)^{(m-2)/2}} - \frac{1}{(a_f)^{(m-2)/2}}\right] \tag{9}$$

For $m = 2$:

$$N_f = \frac{1}{CY^{2}(\Delta\sigma)^{2}\pi}\, ln\, \frac{a_f}{a_0} \tag{10}$$

The constants C and m are material parameters that are usually determined experimentally. Typically, m values are in the range of 2–4 for most metals. For intermetallics, m is generally between 6 and 20. However, for ceramics, m can be as high as 100. For cases where Y depends on crack length, the above integrations are usually performed numerically. It is also important to note that the crack growth rate in the Paris regime is weakly sensitive to load ratio and is driven by ΔK (Soboyejo, 1988, 2002; Suresh, 1998).

The initial crack, a_0, can be determined using non-destructive die penetrants inspection, ultrasonics, or X-ray techniques. If no cracks are detected, one can assume a crack length to be at the resolution of the detection system. The critical crack length can be determined from the failure criterion when $KC_{\max}$.

Fatigue crack growth laws

Numerous fatigue propagation (see Fig. 1) models have been developed to characterize fatigue damage evolution in engineering materials. However, none of these models capture all aspects of the mechanisms of fatigue crack propagation. For instance, the extent of crack growth over a range of stress levels cannot be determined a priori from these models. However, these models do highlight the processes associated with the crack-tip opening during crack propagation.

Forsyth and Ryder proposed that fatigue crack extensions were the result of sporadic bursts of brittle and ductile fracture and that the contribution of each mechanism to crack propagation was a function of the ductility of the pertinent material (Forsyth and Ryder, 1960). They also proposed that cracking occurs by necking, which obstructs the material until void coalescence occurs. These voids are usually created during forward cycling.

Fatigue crack propagation models include models by Paris and Erdogan (1963), Forman (1972), Walker and Elber (1970), Newman and Elber (1988). The application of these models to practical engineering situations depends on the material type and loading conditions. Paris-Erdogan and Forman's models are used for constant-amplitude loading (Forman, 1972; Paris and Erdogan, 1963), while Walker and Elber models are used for variable-amplitude loading (Elber, 1970; Newman and Elber, 1988). These variable-amplitude loading models incorporate crack-growth retardation or acceleration, and threshold effects.

Paris' model

In the mid-DK regime, the law shows that the crack advance per stress cycle is related to the stress intensity range (Eq. 11).

$$\frac{da}{dN} = A(\Delta K)^{m} \tag{11}$$

where A and m are material constants determined experimentally.

Forman's model

The Forman's equation is a form of the Paris' law that takes the effect of the applied stress ratio into consideration. It provides an empirical model for fatigue life estimation with mean stress effects as shown Eq. (12).

$$\frac{da}{dN} = \frac{c(\Delta K)^{n}}{K_{f}(1 - R) - \Delta K} \tag{12}$$

where c is a pre-exponential constant, n is the power law exponent, K_{f} is a material constant, R is the stress ratio, and ΔK is the stress intensity factor range.

Walker's model

The Walker's equation also accounts for stress ratio effects. The Walker and Forman's relationships are equivalent to Paris' law when $R = 0$, and the crack growth rate depends solely on the ΔK (Eq. 13).

$$\frac{da}{dN} = c[Km^{n}{}_{\max} \tag{13}$$

where $K_{\max}$ is the maximum stress intensity factor, R is the stress ratio, c is a pre-exponential constant, m is the power-law exponent, and n is a material constant.

Multiparameter law

The multiparameter law proposes a fatigue life prediction approach using the combined effect of multiple variables on fatigue crack growth (Bhalerao et al., 2003). The formulation is based on the multiple regression analysis and involves the representation of crack growth rate, $\mathrm{d}a/\mathrm{d}N$, as a multiple variable statistical expression. Examples of such variables include stress intensity factor range, ΔK, crack-closure stress intensity factor, K_{cl}, and stress ratio, R.

Elber's model (crack-closure model)

Elber formulated a crack-closure technique by modifying Paris' equation to include the dependence of the crack growth rate on the stress ratio (Elber, 1970; Newman and Elber, 1988). According to Elber, the plastic zone evolves around the crack tip, when the yield stress of the material is exceeded. Subsequently, a wake of plastically deformed material is developed and is encapsulated by the surrounding elastic medium as the crack grows. When the loaded component is being unloaded, the plastically deformed material causes crack surfaces to contact at zero tensile loads.

Elber concluded that crack closure retards fatigue crack growth rate by reducing the stress intensity range, ΔK. He introduced the effective stress intensity range, ΔK_{eff}, for use in Paris' law Eq. (14), with the modified Paris' law given in Eq. (16).

$$\Delta K_{\mathrm{eff}} = K\mathrm{op}\Delta_{\max} \tag{14}$$

where

$$U = \frac{\Delta K_{\mathrm{eff}}}{\Delta K} \tag{15}$$

$$\frac{da}{dN} = D[\Delta K_{\mathrm{eff}}]^{P} \tag{16}$$

where $K_{\max}$ is the maximum stress intensity, K_{op} is the stress intensity at which the crack opens, U is the so-called Elber closure ratio, and D is a pre-exponential constant.

Fatigue fracture modes

The surface morphologies of fatigue cracks are classified as follows:

- *Transgranular cleavage*. This occurs along defined planes in crystal structures. Cleavage formation is the result of high stress along the three axes where significant deformation occurs at low temperatures. Cleavage morphology is characterized by cleavage steps, feather markings, herringbone structure, and microtwins. Such morphologies are often observed in the near-threshold region (Shen et al., 2004a, 2004b; Soboyejo et al., 2004).

- *Fatigue striations*. These occur generally in the mid-ΔK and high-ΔK regimes. In general, the striation spacings correspond to the crack growth rate under HCF conditions (Fine and Ritchie, 1979; Mercer et al., 1999, 2000, 2003; Pelloux, 1970; Sinha et al., 2000; Soboyejo et al., 1995; Suresh and Ritchie, 1982). However, under low cycle fatigue (LCF) conditions striations are sometimes not definable and hence cannot be correlated with crack growth rates.
- *Combined striations and static fracture modes*. At high-ΔK levels, a combination of fatigue striations and static fracture modes is observed, with the incidence of static modes increasing with increasing ΔK. The static modes often include secondary cracks and ductile dimples that are akin to those observed under monotonic loading (Mercer et al., 2001; Pelloux, 1970; Ritchie and Knott, 1973).

The short crack problem

Studies of fatigue behavior of short cracks (Fig. 3) have attracted considerable attention since the total fatigue life of many components may be dominated by the short crack regime (Lou et al., 2001; Mercer et al., 2001; Ritchie and Lankford, 1986; Shrotriya et al., 2002; Sinha et al., 2000; Soboyejo et al., 1995; Suresh and Ritchie, 1983). These studies have altered the fatigue limit concept, from a damage limit to a critical propagation limit.

As a result of the successful application of the concepts of LEFM to the growth of long cracks, significant attempts have been made to apply similar methods to modeling the behavior of short cracks. The extent of localized plasticity, however, violates the assumptions of LEFM. This so-called short crack problem was first observed by Pearson (1975). It has been attributed to the synergistic interactions between the effects of microstructure and localized plasticity.

A classification scheme for short cracks was proposed by Ritchie and Lankford by comparing their lengths to appropriate plasticity and microstructural length scales. For instance, mechanically small cracks have lengths that are comparable to their estimated plastic zone sizes; microstructurally short cracks are those that have lengths comparable to the microstructural dimensions of the pertinent continua. Physically, short cracks refer to those cracks that have dimension of $\leqslant 1$ mm.

Three common phenomena have been advanced to explain why small/short cracks can grow at higher growth rates than long cracks. These include: (1) limited crack-closure effects when the small crack has little or no wake ("physically small"), (2) inhomogeneous sampling of the microstructure when the cracks are smaller than relevant microstructural dimensions ("microstructurally small"), and (3) similarity between small crack lengths and the plastic zone size.

Applications of data science and machine learning to fatigue

There are four paradigms for materials development and the estimation of mechanical properties such as those associated with fatigue, as shown in Fig. 4. This section focuses on the emerging applications of data science to fatigue. This includes predictive analytics, materials information, and relationship mining.

There is increasing application of data science and machine learning in studying fatigue in structural and functional metals and alloys. This includes quantitative approaches based on statistical methods where constitutive models are fitted to large data sets

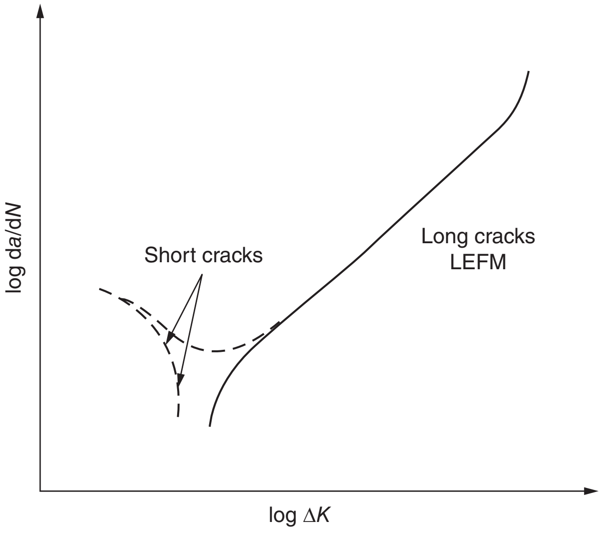

Fig. 3 Schematic of typical fatigue crack growth behavior of short and long cracks.

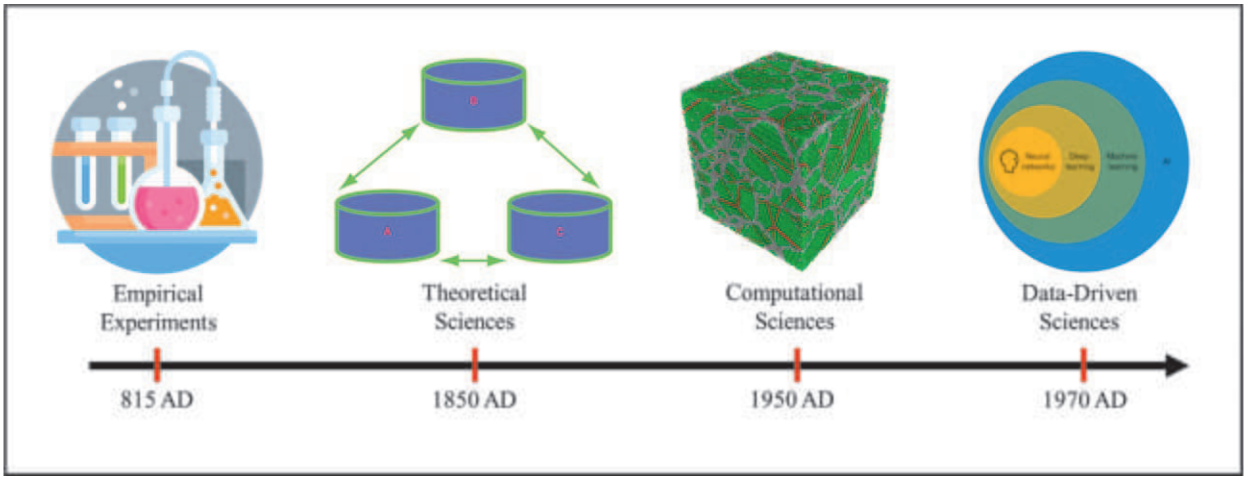
Empirical Experiments
Theoretical Sciences
Computational Sciences
Data-Driven Sciences
815 AD
1850 AD
1950 AD
1970 AD

Fig. 4 Four paradigm for material development and mechanical property estimation.

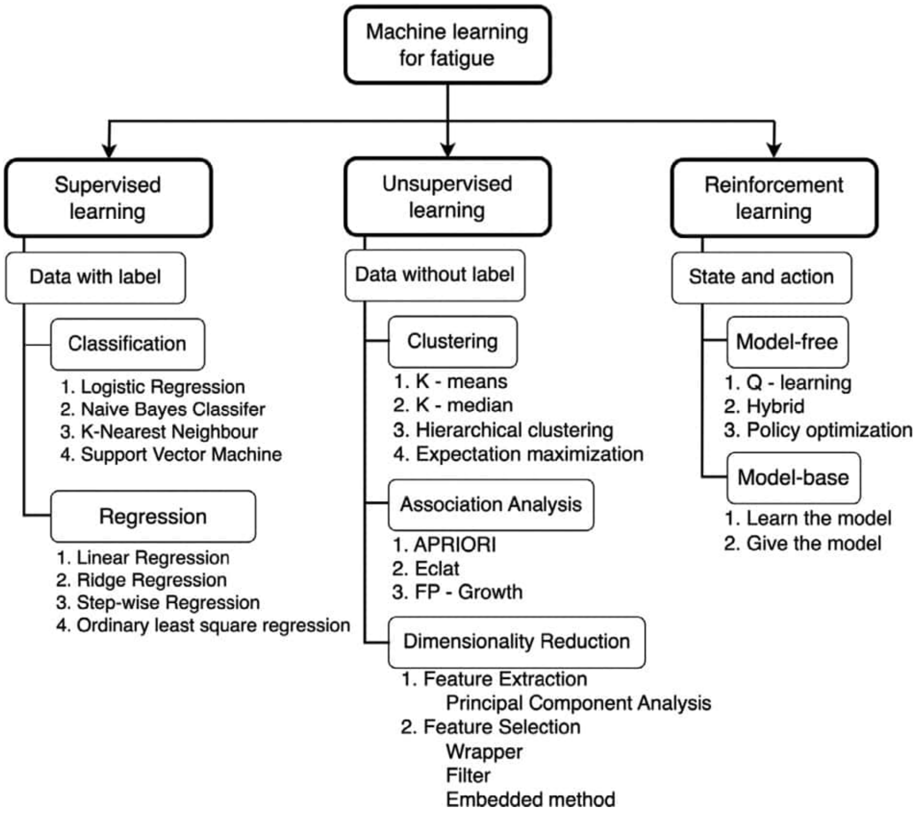
Machine learning for fatigue
Supervised learning
Unsupervised learning
Reinforcement learning
Data with label
Classification
1. Logistic Regression
2. Naive Bayes Classifer
3. K-Nearest Neighbour
4. Support Vector Machine
Regression
1. Linear Regression
2. Ridge Regression
3. Step-wise Regression
4. Ordinary least square regression
Data without label
Clustering
1. K - means
2. K - median
3. Hierarchical clustering
4. Expectation maximization
Association Analysis
1. APRIORI
2. Eclat
3. FP - Growth
Dimensionality Reduction
1. Feature Extraction
Principal Component Analysis
2. Feature Selection
Wrapper
Filter
Embedded method
State and action
Model-free
1. Q - learning
2. Hybrid
3. Policy optimization
Model-base
1. Learn the model
2. Give the model

Fig. 5 Schematic representation of machine learning approaches used to estimate fatigue of materials.

(Stinville et al., 2022). Thus, data science and machine learning provide the platform to make decisions and/or predictions through gleaning insight from data. With ~5000 years of metallurgical history and data on composition-structure-property-performance history, combined with increasing computational infrastructure, compositions and mechanical properties are easily predictable.

Machine learning approaches are being used to determine fatigue behavior of materials. These include the applications of Supervised, Unsupervised and Reinforcement Learning, as shown in Fig. 5. Supervised Learning (SL) uses historical data to make predictive analyzes. This is done by relying on the concept of learning from the past trends to predict the future. Supervised Learning is based primarily on data with labels, and is often considered to be a mature machine learning technique. It is used widely in materials science and engineering for the prediction of mechanical properties.

The two main SL approaches are regression, which is in the domain of continuous target variable, and classification under the categorical target variable data label. Therefore, SL is generally referred to as “data with label”. Unsupervised learning (UL) is an

Table 1 Typical machine and deep learning approaches for mechanical property estimation.

ML/DL Technique	*Characteristics/Behavior modeled*	*Mechanical Property Assessed*
Linear and polynomial regression	Relation between input and output parameters	Young's modulus (Yang et al., 2019), yield and tensile strength (Zhao et al., 2021).
Random forest (RF)	Decision trees	Young's Modulus (Yang et al., 2019; Zhao et al., 2021), Toughness (Lei et al., 2019; Yamasaki et al., 2021)
Support vector machine (SVM)	High-dimensional data space	Strength (Zhao et al., 2021), Hardness, Optimized structural topology (Wei et al., 2018), fatigue
Neural networks (NNs)—feedforward	Use neurons and hidden layers with one directional flow of information	Strength (Wang et al., 2019; Zhao et al., 2021), Toughness (Lei et al., 2019; Yamasaki et al., 2021), Hardness (Ravinder et al., 2020), Hyperelastic and plastic behavior (Huang et al., 2020; Yang et al., 2020)
Neural network—recurrent	Connected neurons using historical data in hidden layers for sequential flow of data	Fracture behavior in polycrystals (Liu et al., 2020) (Alipour et al., 2021)
Neural network—convoluted	Data assessment at hierarchical levels—voxel- or pixel-based dataset	Strain-stress field prediction, elastic properties of composites, modulus of unidirectional composites, strength of additively manufactured metallic components, fatigue crack propagation in polycrystalline alloys (Niu and Srivastava, 2022).
Generative adversarial networks	Two component neural network trained to generate trends in data per training dataset	Modulus distribution based on inverse elasticity problems, strain-stress fields in composites, composite design, structural topology optimization, design of architecture materials
Gaussian process regression and Bayesian learning	Input parameters treated as random variables to estimate the probability distribution. This is used to predict and quantify uncertainty	Modulus (Yang et al., 2019), strength and design of recoverable metamaterials and super compressible
Graph neural networks (GNN)	Uses non-Euclidean data for node, link, and graph classification	Hardness prediction and for the design of architecture materials

exploratory analyzes technique that is used to find hidden correlations (extract information from data without labels). In materials science and engineering, this can be within the composition—processing—structure—property relationships of alloys which are not evident in small datasets. Reinforcement learning (RL) is a process of decision making that relies on through trial-and-error interactions based on the sets of instruction in a dynamic environment. Thus, the learning agent perceive and interpret the environment, take actions, and then learn through the process in a trial-and-error manner (Kaelbling et al., 1996). Most RL are based on state and action focusing on either a model-base or model-free approaches. Typical ML processes used for estimating mechanical properties, i.e., fatigue life of mechanical components is summarized in Table 1.

The physics-guided modeling of fatigue is based on the random fatigue-limit model. This model should satisfy two conditions based on the fatigue life and applied stress (strain). These are: (i) the standard deviation of fatigue life of mechanical components decreases with increasing applied strain (stress) and (ii) the curvatures of typical fatigue curves are indicative of the incorporation of the fatigue limit in the statistical model (Chen and Liu, 2021a, 2021b). The curve is asymptotic near the fatigue limit, except for cases where there are no fatigue limits for the alloy. Considering "N" as fatigue life and "s" as stress level, then the fatigue life can be estimated using Eq. (17) (Gan et al., 2021). This is slight modification of Basquin's explicit regression model establishing the relationship between fatigue life and stress levels. The drawback of typical explicit regression models is the few parameters needed to estimate the fatigue behavior. Due to the small parameters used, functional relationship between fatigue life and applied loads are underestimated. This has stimulated the recent application of machine learning models (Chen and Liu, 2021a). Through machine learning models, additional parameters such as the notch factor, tensile and yield strengths can be included for best-fit prediction.

$$log\left(N\right) = \beta_0 + \beta_1\, log\left(s - \gamma\right) + \varepsilon, s > \gamma \tag{17}$$

where β_0 *and* β_1 are coefficient of fatigue curve, γ is the fatigue limit of the specimen and the error term is ε.

Machine learning techniques that are based on neural networks have been used to model fatigue behavior (Gan et al., 2021; Huang et al., 2006, 2011). The approach uses input variables such as mean stresses and environmental factors. Machine learning algorithms are data intensive. Two categories of data are used: training and testing datasets. The training datasets are experimental data that are used to teach the model or algorithms or network. This is to extract the required features that are relevant to the problem that is being solved through a deterministic process. This is for the optimization of the hyper-parameter, which reduces the possibility of under- and over-estimation (Chen and Liu, 2021a, 2021b; Choi et al., 2021; Gan et al., 2021; Kamble et al., 2020; Luo et al., 2021). The testing data is used to check the generalized capability of model or algorithm or network to ensure the right trends, insights, and desired predictions. This is to reduce the margin of error associated with underestimation or overestimation.

The prediction of fatigue crack growth is critical for the estimation of the residual lives of mechanical components, and also for engineering failure analyzes (Klenam et al., 2022). Supervised ML-based regression models that are used to estimate crack growth rates in the Stage II and Stage III regimes include Ridge regression, K-nearest neighbor regression and polynomial regression (Kamble et al., 2020). The input parameters used for the model were ΔK and frequency of loading. The models are trained using experimental datasets. The application of polynomial and Ridge regression enables multiple features to be correlated. Hence, simple linear regression will result in overestimation of the crack growth rates.

The K-NN model is based on similarity measure. It has been used to estimate the average numerical target of the nearest neighbor. The main drawback of the K-NN is when there are more than two distinct types of variables, i.e., numerical, and categorical variables. Similarly, the accuracy of the model is dependent on pre-processing and selection of the training data, and the choice of the hyper parameter associated with the model. The hyper parameter, α, determines how best the data will be fitted to the experimental value. For fatigue crack growth rate, α is ~0.5. The K-NN provided the best accuracy for crack growth rate in Regimes II and III.

ML-based neural networks have been used to estimate fatigue lives of engineering components (Gan et al., 2021; Huang et al., 2006, 2011). Neural networks with single-hidden layer are ideal for estimating the remaining fatigue lives of mechanical components within a multi-step loading approach (Huang et al., 2006, 2011). The extreme learning machine (ELM) is widely used for this purpose, as it randomizes the assignment of hidden parameters. There is no multivariate optimization process, which increases the training speed. Also, the ELM does not have any local minima associated with output error. The instability of output performance of residual life estimation of component leads to development of an enhanced ELM, which is a Kernel-Extreme Learning Machine (KELM) (Gan et al., 2021; Huang et al., 2006, 2011, 2012). The inadequacies associated with the randomization of parameters in ELM are not associated with the KELM approach, which provides the best generalization that has been used in widely (Huang et al., 2006, 2011, 2012). The KELM approach applied to over 169 experimental results was based on the implementation model given in Fig. 6. The auto-learning attribute of most KELM models makes them ideal and adaptable for estimating residual fatigue life of components with different permutation of loading conditions and material classes (Gan et al., 2021).

The data-driven approaches present more mechanistic understanding of contributions of intrinsic mechanical properties and parameters in the Basquin's empirical model for estimating fatigue life of components. The plot of experimental fatigue data for various metallic materials showed very low fatigue efficiency (normalized fatigue strength as percentage of yield or tensile strengths) (Omar and El-Awady, 2022; Stinville et al., 2022). Thus, fatigue strength of metallic materials does not necessarily increase with increasing yield or tensile strength. Failures have been observed as low as 25% of yield strength for high strength dilute and concentrated metallic alloys, as shown for some alloys in Fig. 7 (Stinville et al., 2022).

This shows the relationship between the yield strength and intensity of slip localization. Data science and ML approaches augment empirical stress- and strain-based approaches which are time-consuming and expensive.

The support vector machine (SVM) is an optimization algorithm based on supervised ML (Bao et al., 2021). It uses the structural risk minimization principle to predict the fatigue life of mechanical components. When this method is applied for regression, it becomes the support vector regression (SVR). An overview of the fatigue life prediction process based on SVM is given in Fig. 8 (Bao et al., 2021).

Overview of fatigue of complex concentrated alloys

Complex concentrated alloys (CCAs) are multiple principal elements with compositions in near equal amounts. This paradigm shift in alloy design was pioneered in Cantor et al. (2004) and Yeh et al. (2004) with other naming conventions being high entropy alloys

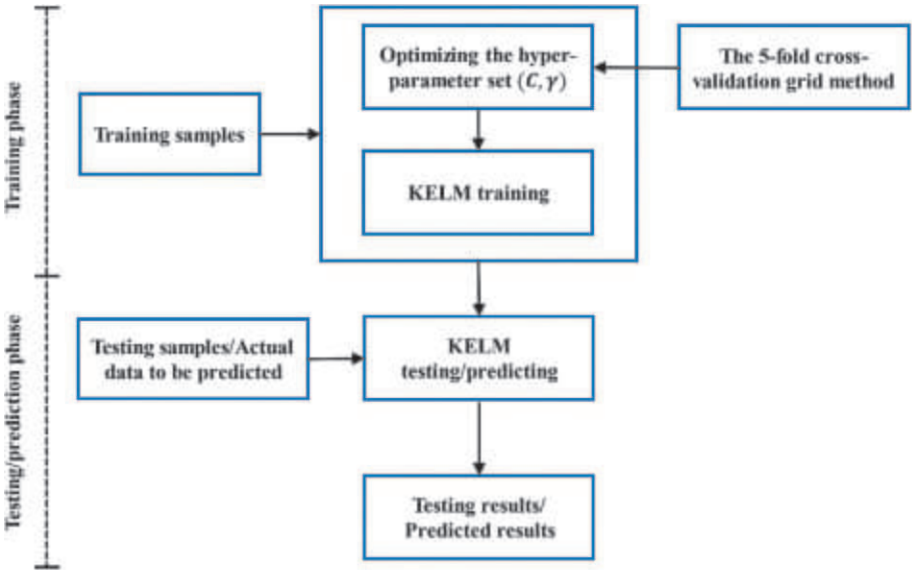
Training phase
Training samples
Optimizing the hyper-parameter set (C, γ)
The 5-fold cross-validation grid method
KELM training
Testing/prediction phase
Testing samples/Actual data to be predicted
KELM testing/predicting
Testing results/ Predicted results

Fig. 6 Typical KELM implementation model used for estimating remaining fatigue life of a component (Gan et al., 2021). From Gan L, Zhao X, Wu H, Zhong Z (2021) Estimation of remaining fatigue life under two-step loading based on kernel-extreme learning machine. *International Journal of Fatigue* **148**.

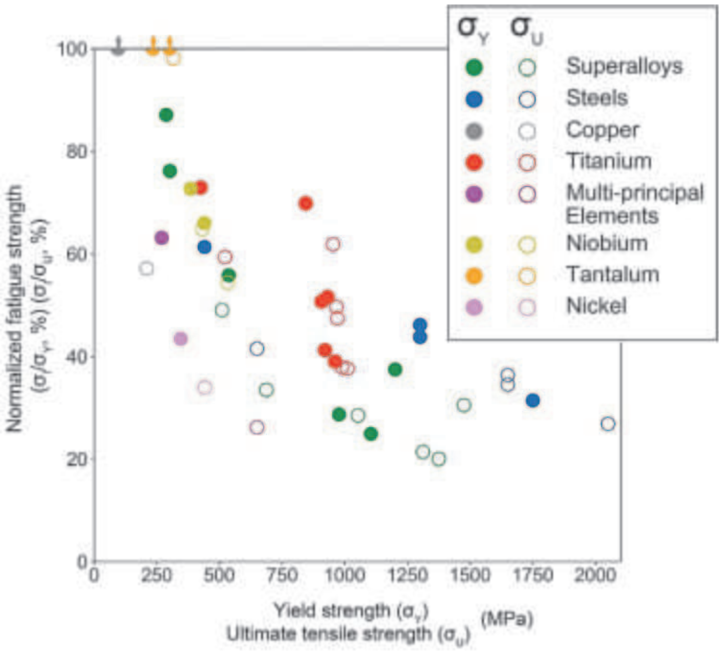

Fig. 7 Relationship between fatigue strength and tensile properties of dilute and concentrated metallic alloys where solid dots and open circles are fracture strength expressed as a percent of the yield strength and tensile strength. [Fatigue tests were performed at very high fatigue regime at a frequency of 20 kHz, to ∼10^9 cycles in a tension-compression mode and at $R = -1.0$. Emphasis was on alloys with minute extrinsic defects and deformed by slip] (Stinville et al., 2022). From Stinville JC, Charpagne MA, Cervellon A, Hemery S, Wang F, Callahan PG, Valle V (2022) On the origins of fatigue strength in crystalline metallic materials. *Science* 1071: 1065–1071.

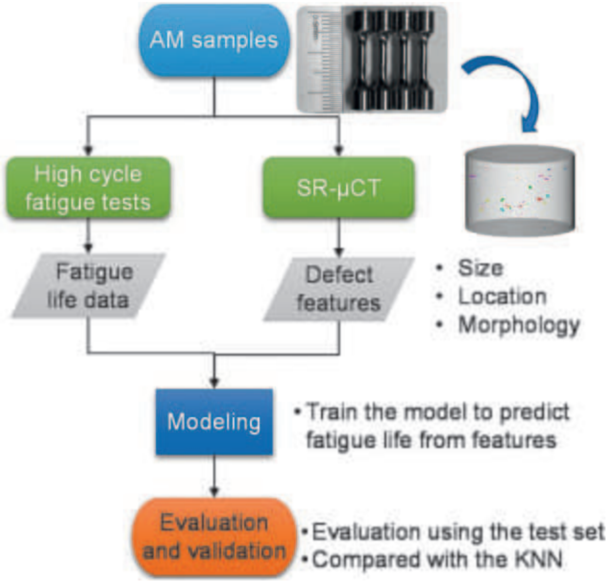
AM samples
High cycle fatigue tests
SR-μCT
Fatigue life data
Defect features
• Size
• Location
• Morphology
Modeling
• Train the model to predict fatigue life from features
Evaluation and validation
• Evaluation using the test set
• Compared with the KNN

Fig. 8 Typical support vector machine representation for fatigue life prediction (Bao et al., 2021). From Bao H, Wu S, Wu Z, Kang G, Peng X, Withers PJ (2021) A machine-learning fatigue life prediction approach of additively manufactured metals. *Engineering Fracture Mechanics* **242**. https://doi.org/10.1016/j.engfracmech.2020.107508.

(HEAs) and medium entropy alloys (MEAs) (Fig. 9). Composition ranges are at the central regions of the phase diagrams of the constituent elements. While the initial hypothesis focused on equiatomic compositions, there are deviations resulting in non-equiatomic and interstitial based CCAs (Akinbami et al., 2022; Klenam et al., 2022b, 2022c, 2022d, 2022e). These alloys extend the frontiers for alloy design beyond the conventional dilute alloying concentrations with potentially superior mechanical, physical and chemical properties (Klenam et al., 2022d).

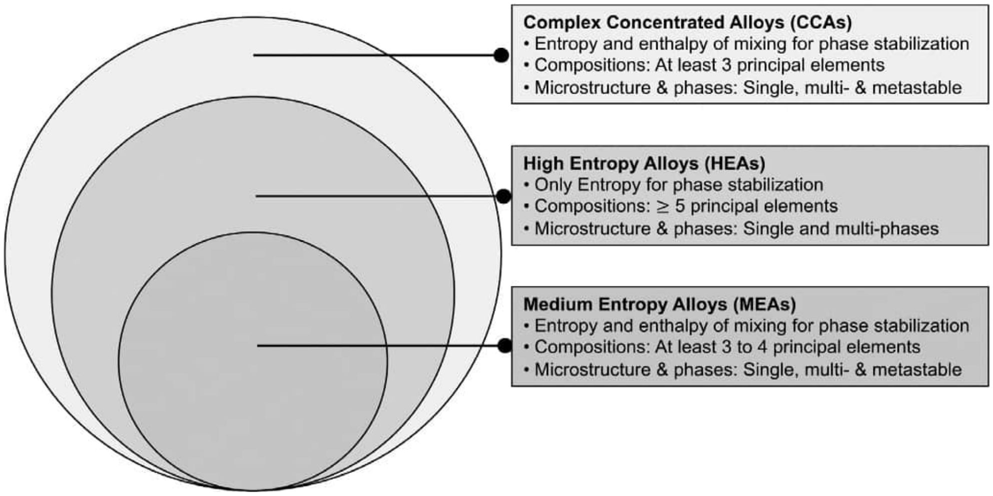
Complex Concentrated Alloys (CCAs)
• Entropy and enthalpy of mixing for phase stabilization
• Compositions: At least 3 principal elements
• Microstructure & phases: Single, multi- & metastable
High Entropy Alloys (HEAs)
• Only Entropy for phase stabilization
• Compositions: ≥ 5 principal elements
• Microstructure & phases: Single and multi-phases
Medium Entropy Alloys (MEAs)
• Entropy and enthalpy of mixing for phase stabilization
• Compositions: At least 3 to 4 principal elements
• Microstructure & phases: Single, multi- & metastable

Fig. 9 Schematic diagram showing the classes of complex concentrated alloys based on compositions.

Based on the crystal system and phase classification, the four classes are single phase face centered cubic (FCC), single phase body centered cubic (BCC), metastable and multi-phase CCAs/HEAs (Li et al., 2020). The single-phase FCC alloys have great ductility but poor strength, whereas the single-phase BCC alloys have high strength but poor ductility. This is mainly due to the strength-ductility trade-off associated with conventional metallic materials.

The domain of metastable and multiple phases show promise to solving the strength-ductility trade-offs. This has been attributed to deformation mechanisms associated with hierarchical and gradient microstructures with multiple and metastable phases. This induces simultaneous improvements in strengthening and toughening. Beyond strengthening mechanisms, such as solid solution, interstitials, dislocation, precipitation, grain size and back stress strengthening, other microstructural features such as microbands, nanotwinning or nanoprecipitates are great contributing factors to superior mechanical properties.

As a burgeoning field, there are few studies on fatigue behavior of CCAs. These studies have been done using standardized empirical approaches and some computational techniques based on knowledge-based and probabilistic physics-guided machine learning. The single-phase FCC-based alloys have the lowest fatigue strength due to the inherently low strength as shown in Fig. 10 (Li et al., 2020). These are comparable to Cu -, Mg - and some low strength steel alloys. Alloys with multi-phase microstructures had relatively high fatigue strength, whereas alloys with metastable phases outperformed most of the high-end conventional steels and Ti-based alloys. A typical example is the Fe—Mn—Co—Cr—Si—Cu alloy (Fig. 10). The fatigue strength is about 36% of the ultimate tensile strength (~1200 MPa). These fatigue behaviors are attributed to the microstructural features associated with the various crystal structures.

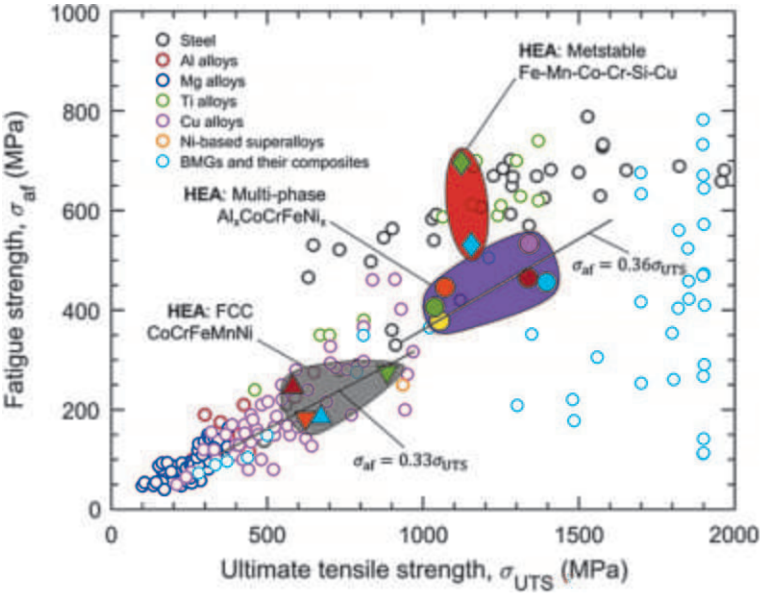

Fig. 10 Relationship between ultimate tensile strength and fatigue strength between some conventional alloys and the four classes of CCAs based on crystal structure and phases (Li et al., 2020). From Li W, Chen S, Liaw PK (2020) Discovery and design of fatigue-resistant high-entropy alloys. *Scripta Materialia* **187**: 68–75.

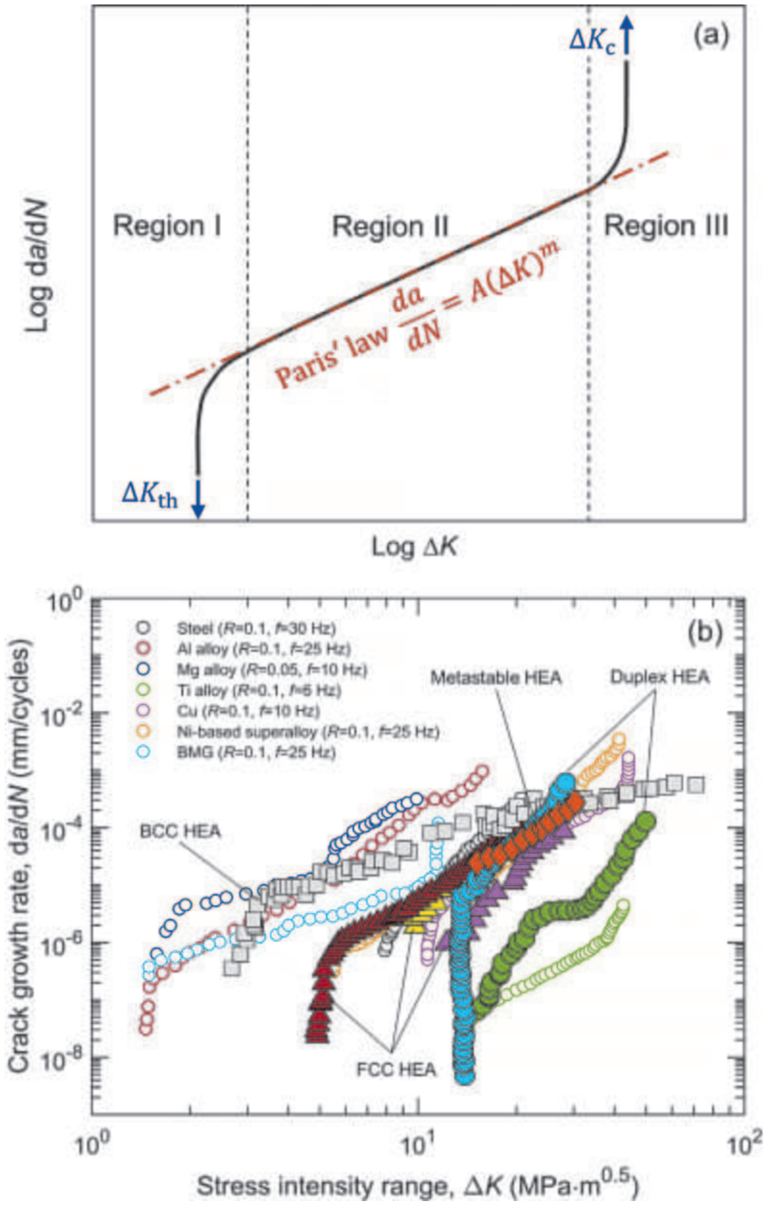

Fig. 11 Typical crack growth rate as a function of stress intensity factor where (a) schematic representation of the three regions and (b) fatigue crack growth rate of various conventional and CCAs (Li et al., 2020). From Li W, Chen S, Liaw PK (2020) Discovery and design of fatigue-resistant high-entropy alloys. *Scripta Materialia* **187**: 68–75.

The application of fatigue crack growth rate on CCAs have been studied within the three regions following the linear elastic fracture mechanic approach (Fig. 11). The CCAs with single phase FCC and BCC had the lowest fatigue crack growth rates. The complexities associated with metastable and multi-phase (duplex) CCAs lead to high fatigue crack growth rates (Fig. 11b). The mechanisms promoting these mechanical behaviors are further discussed.

The fatigue and fracture mechanisms based on the crystal structure and phase classifications (Fig. 12) (Li et al., 2020). There are intrinsic microstructural characteristics such as slip localization on the fatigue behavior of structural metals as shown in Fig. 12. The fatigue and fracture mechanisms are driven by cracks initiating along the planar slips and at twin boundaries for FCC-based CCAs (Fig. 12a). When there is initiation of cracks at multiple slips, a zig zag crack path is observed (schematically shown in Fig. 12a).

Generally, the low fatigue resistance of FCC CCAs is attributed to the competing effects of initiated cracks resulting from multiple slips systems and annealing/deformation twins. These were observed for Cantor alloy and its derivatives: CrCoFeMnNi, CrCoFeNi, $CrCoFeNiMo_{0.2}$. A linear dependence of fatigue strength on slip amplitude has been observed for various conventional alloys and FCC-based CCAs/HEAs. For the BCC CCAs, fatigue cracks are initiated at the grain boundaries which then propagates through the grains. Due to the limited slip systems in BCC materials, the mechanism is simple. In BCC HfnbTaTiZr, intergranular cracks nucleated at grain boundaries and then propagates in a transgranular manner. Thus, BCC alloys generally have low stress threshold (fatigue limit) and high fatigue crack growth rates.

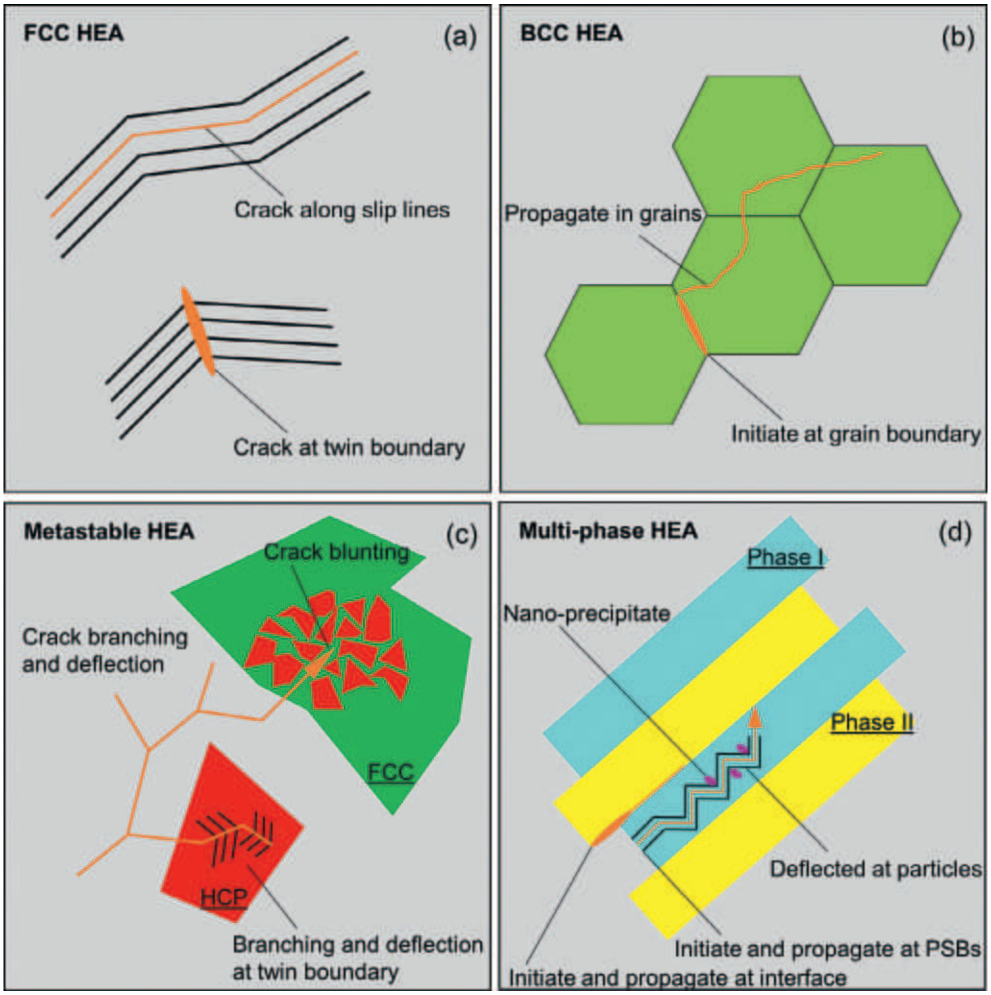
FCC HEA
(a)
Crack along slip lines
Crack at twin boundary
BCC HEA
(b)
Propagate in grains
Initiate at grain boundary
Metastable HEA
(c)
Crack blunting
Crack branching
and deflection
FCC
HCP
Branching and deflection
at twin boundary
Multi-phase HEA
(d)
Phase I
Nano-precipitate
Phase II
Deflected at particles
Initiate and propagate at PSBs
Initiate and propagate at interface

Fig. 12 Fatigue and fracture mechanisms associated with different crystal structures of CCAs/HEAs showing (a) FCC-based, (b) BCC-based, (c) Metastable and (d) multi-phase (Li et al., 2020). From Li W, Chen S, Liaw PK (2020) Discovery and design of fatigue-resistant high-entropy alloys. *Scripta Materialia* **187**: 68–75.

In the case of metastable CCAs, the phase transformation from FCC to HCP is pronounced in the vicinity of the crack tip. This is associated with work hardening, which is critical for crack tip blunting. Within the fracture-process zone, the dynamic phase transformation promotes crack branching and deflection. In the HCP phase, there are deformation and mechanical twins formed contributing to arresting, branching and deflection of cracks during the crack initiation and propagation stages. This directs propagating cracks towards twin boundaries. Thus, the metastable phases lead to deceleration and retardation of cracks propagation, resulting in relatively high fatigue resistance.

The fatigue and fracture mechanisms of multi-phase CCAs with mostly eutectic and non-eutectic structure shows crack initiations at the phase boundaries and persistent slip bands (PSBs) (Liu et al., 2019a, 2019b; Shukla et al., 2018; Tang et al., 2015). The crack propagation trajectories along the phase interfaces are either straight or branched depending on the microstructures. Generally, the crack propagations along PSBs follows a zig-zag pattern attributed to the intersection of multiple slip systems(Liu et al., 2019a, 2019b; Shukla et al., 2018; Tang et al., 2015). If nano-sized precipitates are observed in the microstructure and along the path of propagating fatigue cracks, there is crack deflection at these precipitates. The complex microstructural features of multi-phase CCAs activate tortuous crack propagation behavior, contributing to the overall fatigue resistance. These mechanisms are schematically shown in Fig. 11d.

Overview of fatigue of additively manufactured metals/alloys

Additive manufactured (AM) or 3D printed components are being used under complex load-bearing applications in the automotive, aerospace, and biomedical industries (Kermavnar et al., 2021; Klenam et al., 2022a; Stavropoulos and Foteinopoulos, 2018; Thomas and Gilbert, 2014). However, the challenge with 3D printed mechanical components are the intrinsic defects such as lack of

Table 2 Defects, causes and characteristics features associated with additively manufactured components (Sanaei and Fatemi, 2021).

Types of defects	*Causes/sources*	*Characteristic features*
Keyholing	Excessive energy	Keyholes not properly closed
Gas porosity		Gas entrapment
Unmelted powder	Insufficient energy	Incomplete melting of powders
Lack of fusion		Non-sintered patches
Oxides particles	Oxygen contents	Oxygen entrapment
Surface roughness	Layer-by-layer deposition and feedstock	Partial melting of feedstocks
Balling phenomenon	Lack of wetting of solid particles	Material discontinuity
Secondary phases	Recurrent heating and cooling with complex phase transformation	–
Small cracks	Residual stresses	–
Bead-up	Solidification of melt as droplet lines	

From Sanaei N, Fatemi A (2021) Defects in additive manufactured metals and their effect on fatigue performance: A state-of-the-art review. *Progress in Materials Science* **117**: 100724.

fusion and gas porosities and extrinsic defects adversely affecting mechanical properties, acting as sites for crack initiation under monotonic and cyclic loading (Barroqueiro et al., 2019; Hashemi et al., 2022; Sanaei and Fatemi, 2021).

Fatigue behavior of mechanical components are sensitive to defects. These defects are intrinsic in AM parts resulting from the starting materials which are mainly powder or wire. The other factors are the layer-by-layer material deposition with associated localized heating and cooling cycles leading to differential solidification and lack of fusion. The main defects associated with 3D printed mechanical components, causes and distinguishing features (Table 2) (Sanaei and Fatemi, 2021). Postprocessing of AM parts are applied to eliminate these defects with considerable success. The challenge with postprocessing of near-net shape manufacturing techniques is the serious cost implications.

Fracture mechanics-based techniques have been used for defect-based fatigue life estimation of 3D printed mechanical components. Multiscale and multistage computational models have also been incorporated in some of these estimations (Nyshadham et al., 2019; Panchal et al., 2013). The fracture mechanics approach included defect characteristics such as size, shape, location, geometry, microstructural dependent crack growth properties and the loading information (monotonic or cyclic). In cases where there are large defects, extreme value statistics (EVS) was used to estimate the maximum or critical defect size allowable in a large volume to induce fatigue failure. This was then used to correlate the fatigue performance of mechanical components produced using the powder bed fusion AM parts.

In a 3D printed Ti6Al4V alloy, conventional long crack growth models were overestimating. Thus, short crack models with crack sizes on the scale of 100 μm were applicable for AM components considering the defect-based fatigue estimation criterion. Small cracks have lengths comparable to features at the microstructural scale. Mechanically, the length is comparable to the local plasticity scale and physically are in the order of 0.1–1 mm (Sanaei and Fatemi, 2021). For the nominal stress intensify factor, fatigue crack growth rates of short cracks are statistically significant and much higher than for the long cracks, which significantly affect the fatigue life prediction results. Short cracks can grow in Mode II, which is shear as well as mixed mode, which is critical for extracting relevant fatigue crack growth behavior other than for long cracks, which are mostly Mode I. Surface and internal defects that are critical factors that affect additively manufactured components are presented in Table 3.

Semi-empirical, phenomenological and fracture mechanics-based models are used to evaluate fatigue behavior of various classes of alloys. A typical approach is correlate the fatigue strength to the area of critical defect and the hardness (Eq. 18). Stress intensity factor and fatigue life have been estimated using micro-CT scan of defects and fractography of AM components (Eqs. 19 and 20).

$$\sigma_f = \frac{C(HV + 120)}{(\sqrt{area})^{\frac{1}{6}}} \tag{18}$$

$$\Delta K = Y\Delta\sigma\sqrt{\pi\sqrt{area}} \tag{19}$$

$$\frac{da}{dN} = C\left[\left(\frac{1-f_N}{1-R}\right)\Delta K\right]^n\left(1-\frac{\Delta K_{th}}{\Delta K}\right)^p \tag{20}$$

where: σ_f is fatigue limit, C is a constant based on fracture mechanics based on the critical defects, HV is the Vickers hardness and Y = 0.65 and 0.5 for surface and internal defects.

Generally, intrinsic, and extrinsic defects, coupled with heterogeneous microstructures affect the fatigue performance of AM components considerably. These lead to scatter in fatigue life data. Hence, thorough characterization is needed to prevent under- or over-estimation of the fatigue lifetimes.

Table 3 Internal defects in AM components and their characteristics on fatigue behavior of various metallic components.

Alloy	*AM Method*	*Defect Categories*	*Features and Observation*
Ti–6Al–4V	SLM	Internal defects (double conical defects), gas porosity, pores, and unmelted zones	• Significant effects of the internal defects on poor fatigue performance (Gong et al., 2012). • Fatigue failure due to crack initiation at the internal defect (gas porosity) site, irrespective of applied load (Wycisk et al., 2015). • Reducing porosity improved fatigue strength of the AM component, comparable to wrought processed Ti–6Al–4V (Leuders et al., 2013). • Small defects (notches and micro-pore) lead to failure sites at earlier stages of nucleation (Brenne et al., 2013). • Fatigue crack initiation sites were at the unmelted zones near the surface with high stress concentration (Chastand et al., 2016).
	EBM	Voids, pores, entrapment of gasses	• Improved fatigue strength after hot isostatic pressing (HIP) postprocessing due to internal pores and voids (Hrabe et al., 2017). • Pores affect fatigue strength significantly, while acting as crack propagation sites(de Formanoir et al., 2016; Shui et al., 2017). • Significant deviation from optimum process parameters leading to large defects and inferior fatigue properties (Gong et al., 2015).
AISI 316L SS	SLM	Pores	• Crack growth rate and high cycle fatigue (HCF) performance were not affected by the pores due to the ductility of the alloy (Riemer et al., 2014).
Hastelloy X		Cracks, pores	• Excellent fatigue properties due to optimized process parameters and HIPing (Wang, 2012).
AlSi10Mg		Pores	• Great fatigue properties irrespective of defects and imperfections (Brandl et al., 2012).
17-4 SS		Caves, crevices, pores, unmelted regions	• High thermal stress cracking resulting in porosity with adverse effect on fatigue properties (Yadollahi et al., 2017). • Unmelted regions acted as site for fatigue crack nucleation with adverse effect on fatigue strength (Gu et al., 2013).

From Sanaei N, Fatemi A (2021) Defects in additive manufactured metals and their effect on fatigue performance: A state-of-the-art review. *Progress in Materials Science* **117**: 100724.

Conclusion

The study of fatigue in mechanical components spans over a century and a half of effort and is still an ongoing process. A basic understanding of fatigue damage stages currently finds applications in various fields such as biomedical, aerospace, and automotive. With the development of new materials and manufacturing processes, the quest to develop mechanistically based life prediction protocols is intense. The short crack problem, which defies the conventional LEFM approach to fatigue modeling, needs further research to develop models that include short crack effects. Recent advances in MEMS technology will provide nano- and microscopic damage information required to develop constitutive-based life prediction protocols. Furthermore, the fatigue of CCAs is affected by microstructural features and phases. The metastable and multi-phase alloys show superior fatigue properties compared to the single-phase FCC and BCC. For AM components, the variableness of defects, heterogenous microstructure, scatter in fatigue data and uncertainties are significant. Hence, the development of defect-free models relating fatigue with microstructural features requires further work. Semi-empirical, phenomenological, and ML-based models are applicable for industrial applications and able to optimally assess the nature of defects. However, the application of ML (supervised and unsupervised learning) and multiscale models a rational and strategic approach. This will reduce the overall cost and time taken for empirical approaches to fatigue testing.

Acknowledgments

The authors are grateful to Bruce Fenton and Dale Wilson of the Federal Aviation Authority (FAA) and Dr. Carmen Huber of the National Science Foundation (NSF) for their support and encouragement of this work. Appreciation is also extended to the Worcester Polytechnic Institute (WPI) for the Global Fellowship that was awarded to Desmond Klenam.

References

Akinbami O, Mohlala L, Klenam DEP, van der Merwe J, and Bodunrin M (2022) The status of high entropy alloys studies in Africa: An overview. *Key Engineering Materials* 917: 41–53.
Alipour M, Esatyana E, Sakhaee-Pour A, Sadooni FN, and Al-Kuwari HA (2021) Characterizing fracture toughness using machine learning. *Journal of Petroleum Science and Engineering* 200: 108202.
Bao H, Wu S, Wu Z, Kang G, Peng X, and Withers PJ (2021) A machine-learning fatigue life prediction approach of additively manufactured metals. *Engineering Fracture Mechanics* 242. https://doi.org/10.1016/j.engfracmech.2020.107508.

Barroqueiro B, Andrade-Campos A, Valente RAF, and Neto V (2019) Metal additive manufacturing cycle in aerospace industry: A comprehensive review. *Journal of Manufacturing and Materials Processing* 3: 1–21.

Basquin OH (1910) The exponential law of endurance test. In: *Proceedings of American Society for Testing and Materials*, pp. 625–630. Philadelphiapp: American Society for Testing Materials.

Bhalerao K, Shen W, Soboyejo ABO, and Soboyejo WO (2003) A probabilistic multiparameter framework for the modeling of fatigue crack growth in concrete. *Cement and Concrete Composites* 25: 607–615.

Brandl E, Heckenberger U, Holzinger V, and Buchbinder D (2012) Additive manufactured $AlSi_{10}Mg$ samples using Selective Laser Melting (SLM): Microstructure, high cycle fatigue, and fracture behavior. *Materials and Design* 34: 159–169.

Brenne F, Niendorf T, and Maier HJ (2013) Additively manufactured cellular structures: Impact of microstructure and local strains on the monotonic and cyclic behavior under uniaxial and bending load. *Journal of Materials Processing Technology* 213: 1558–1564.

Cantor B, Chang ITH, Knight P, and Vincent AJB (2004) Microstructural development in equiatomic multicomponent alloys. *Materials Science and Engineering A* 375–377: 213–218.

Chastand V, Tezenas A, Cadoret Y, Quaegebeur P, Maia W, and Charkaluk E (2016) Fatigue characterization of titanium Ti-6Al-4V samples produced by additive manufacturing. *Procedia Structural Integrity* 2: 3168–3176.

Chen J and Liu Y (2021a) Probabilistic physics-guided machine learning for fatigue data analysis. *Expert Systems with Applications* 168: 114316.

Chen J and Liu Y (2021b) Fatigue property prediction of additively manufactured Ti-6Al-4V using probabilistic physics-guided learning. *Additive Manufacturing* 39: 101876.

Choi J, Quagliato L, Lee S, Shin J, and Kim N (2021) Multiaxial fatigue life prediction of polychloroprene rubber (CR) reinforced with tungsten nano-particles based on semi-empirical and machine learning models. *International Journal of Fatigue* 145: 106136.

Coffin LF (1954) A study of the effect of cyclic thermal stresses on ductile metal. *Transactions of the American Society of Mechanical Engineers* 76: 931–950.

Cottrell AH and Hull D (1957) Extrusion and intrusion by cyclic slip in copper. *Proceedings of the Royal Society of London* A242: 211–213.

de Formanoir C, Michotte S, Rigo O, Germain L, and Godet S (2016) Electron beam melted Ti-6Al-4V: Microstructure, texture and mechanical behavior of the as-built and heat-treated material. *Materials Science and Engineering A* 652: 105–119.

Dowling NE (1990) *Mechanical Behaviour of Materials—Engineering Methods for Deformation, Fracture and Fatigue*, 2nd ed. Upper Saddle River: Prentice-Hall.

Elber W (1970) Fatigue crack closure under cyclic tension. *Engineering Fracture Mechanics* 2: 37–45.

Ewing JA and Humfrey JCW (1903) The fracture of metals under repeated alternations of stress. *Philosophical Transactions of the Royal Society of London* 200: 241–250.

Ewing JA and Rosenhain W (1900) Experiments in micro-metallurgy—effects of strain—preliminary notice. *Philosophical Transactions of the Royal Society of London* 65: 85–90.

Fine ME and Ritchie RO (1979) Fatigue-crack initiation and near-threshold crack growth. In: *Fatigue and Microstructure*, pp. 245–278. Springer.

Forman RG (1972) Study of fatigue crack initiation from flaws using fracture mechanics theory. *Engineering Fracture Mechanics* 4: 333–345.

Forsyth PJE and Ryder DA (1960) Fatigue fracture. *Aircraft Engineering* 32: 96–99.

Gan L, Zhao X, Wu H, and Zhong Z (2021) Estimation of remaining fatigue life under two-step loading based on kernel-extreme learning machine. *International Journal of Fatigue* 148: 106190.

Gong H, Rafi K, Starr T, and Stucker B (2012) Effect of defects on fatigue tests of as-build Ti-6Al-4V parts fabricated by selective laser melting. In: *International Solid Freeform Fabrication Symposium University of Texas at Austin*.

Gong H, Rafi K, Gu H, Janaki Ram GD, Starr T, and Stucker B (2015) Influence of defects on mechanical properties of Ti-6Al-4V components produced by selective laser melting and electron beam melting. *Materials and Design* 86: 545–554.

Griffith AA (1921) The phenomena of rupture and flow in solids. *Philosophical Transactions of the Royal Society* 45: 251–266.

Gu H, Gong H, Pal D, Rafi K, Starr T, and Stucker B (2013) Influences of energy density on porosity and microstructure of selective laser melted 17–4PH stainless steel. In: *International Solid Freeform Fabrication Symposium*.

Hashemi SM, Parvizi S, Baghbanijavid H, Tan ATL, Nematollahi M, Ramazani A, Fang NX, and Elahinia M (2022) Computational modelling of process–structure–property–performance relationships in metal additive manufacturing: A review. *International Materials Reviews* 67: 1–46.

Hertzberg IRW (1996) *Deformation and Fracture Mechanics of Engineering Materials*, 4th edn. New York: John Wiley & Sons.

Hrabe N, Gnäupel-Herold T, and Quinn T (2017) Fatigue properties of a titanium alloy (Ti–6Al–4V) fabricated via electron beam melting (EBM): Effects of internal defects and residual stress. *International Journal of Fatigue* 94: 202–210.

Huang GB, Zhu QY, and Siew CK (2006) Extreme learning machine: Theory and applications. *Neurocomputing* 70: 489–501.

Huang GB, Wang DH, and Lan Y (2011) Extreme learning machines: A survey. *International Journal of Machine Learning and Cybernetics* 2: 107–122.

Huang GB, Zhou H, Ding X, and Zhang R (2012) Extreme learning machine for regression and multiclass classification. *IEEE Transactions on Systems, Man, and Cybernetics, Part B: Cybernetics* 42: 513–529.

Huang D, Fuhg JN, Weißenfels C, and Wriggers P (2020) A machine learning based plasticity model using proper orthogonal decomposition. *Computer Methods in Applied Mechanics and Engineering* 365: 113008.

Inglis CE (1913) Stresses in a plate due to the presence of cracks and sharp corners. *Transactions of the Royal Institution of Naval Architects* 55: 219–241.

Irwin GR (1957) Analysis of stresses and strains near the end of a crack traversing a plate. *Journal of Applied Mechanics* 24: 361–364.

Kaelbling LP, Littman ML, and Moore AW (1996) Reinforcement learning: A survey. *Journal of Artificial Intelligence Research* 4: 237–285.

Kamble RG, Raykar NR, and Jadhav DN (2020) Machine learning approach to predict fatigue crack growth. *Materials Today: Proceedings* 38: 2506–2511.

Kermavnar T, Shannon A, and O'Sullivan LW (2021) The application of additive manufacturing/3D printing in ergonomic aspects of product design: A systematic review. *Applied Ergonomics* 97: 103528.

Klenam DEP, Chown LH, Papo MJ, and Cornish LA (2022) Steels for rail axles—An overview. *Critical Reviews in Solid State and Materials Sciences*. https://doi.org/10.1080/10408436.2022.2137462.

Klenam DEP, Bamisaye OS, Williams IE, van der Merwe JW, and Bodunrin MO (2022a) Global perspective and African outlook on additive manufacturing research—An overview. *Manufacturing Review* 9: 1–38. https://doi.org/10.1051/mfreview/2022033.

Klenam DEP, Egowan G, Bodunrin MO, van der Merwe JW, Rahbar N, and Soboyejo WO (2022b) Complex concentrated alloys: A cornucopia of possible structural and functional applications. In: *Reference Module in Materials Science and Materials Engineering*. Elsevier. https://doi.org/10.1016/B978-0-12-822944-6.00056-6.

Klenam DEP, Rahbar N, and Soboyejo WO (2022c) Critical review of limitations of equiatomic composition alloying strategy of complex concentrated alloys. In: *Reference Module in Materials Science and Materials Engineering*. Elsevier. https://doi.org/10.1016/B978-0-12-822944-6.00055-4.

Klenam DEP, Rahbar N, and Soboyejo WO (2022d) Mechanical properties of complex concentrated alloys: Implications for structural integrity. In: *Reference Module in Materials Science and Materials Engineering*. Elsevier. https://doi.org/10.1016/B978-0-12-822944-6.00047-5.

Klenam DEP, Rahbar N, and Soboyejo WO (2022e) Critical review of factors hindering scalability of complex concentrated alloys. In: *Reference Module in Materials Science and Materials Engineering*. Elsevier. https://doi.org/10.1016/B978-0-12-822944-6.00051-7.

Laird C and Smith GC (1962) Crack propagation in high stress fatigue. *Philosophical Magazine* 7: 847–857.

Lei X, Liu C, Du Z, Zhang W, and Guo X (2019) Machine learning-driven real-time topology optimization under moving morphable component-based framework. *Journal of Applied Mechanics, Transactions ASME* 86: 1–9.

Leuders S, Thöne M, Riemer A, Niendorf T, Tröster T, Richard HA, and Maier HJ (2013) On the mechanical behaviour of titanium alloy TiAl6V4 manufactured by selective laser melting: Fatigue resistance and crack growth performance. *International Journal of Fatigue* 48: 300–307.

Li W, Chen S, and Liaw PK (2020) Discovery and design of fatigue-resistant high-entropy alloys. *Scripta Materialia* 187: 68–75.

Liu K, Gwalani B, Komarasamy M, Shukla S, Wang T, and Mishra RS (2019a) Effect of nano-sized precipitates on the fatigue property of a lamellar structured high entropy alloy. *Materials Science and Engineering A* 760: 225–230.

Liu K, Komarasamy M, Gwalani B, Shukla S, and Mishra RS (2019b) Fatigue behavior of ultrafine grained triplex $Al_{0.3}$CoCrFeNi high entropy alloy. *Scripta Materialia* 158: 116–120.

Liu X, Athanasiou CE, Padture NP, Sheldon BW, and Gao H (2020) A machine learning approach to fracture mechanics problems. *Acta Materialia* 190: 105–112.

Lou J, Mercer C, and Soboyejo WO (2001) An investigation of the effects of temperature on fatigue crack growth in a cast lamellar Ti-45Al-2Mn-2Nb + 0.8 vol% TiB_2 alloy. *Materials Science and Engineering A* 319–321: 618–624.

Love AEH (1888) The small free vibrations and deformation of a thin elastic shell. *Philosophical Transactions of the Royal Society of London* 179: 491–546.

Love AEH (1901) The integration o f the equations o f propagation o f electric waves. *Philosophical Transactions of the Royal Society of London* 197: 1–45.

Luo YW, Zhang B, Feng X, Song ZM, Qi XB, Li CP, Chen GF, and Zhang GP (2021) Pore-affected fatigue life scattering and prediction of additively manufactured Inconel 718: An investigation based on miniature specimen testing and machine learning approach. *Materials Science and Engineering A* 802: 140693.

Manson SS (1953) *Behaviour of Materials Under Conditions of Thermal Stress*. National Advisory Committee for Aeronautics.

Mercer C, Soboyejo ABO, and Soboyejo WO (1999) Micromechanisms of fatigue crack growth in a forged Inconel 718 nickel-based superalloy. *Materials Science and Engineering A* 270: 308–322.

Mercer C, Lou J, and Soboyejo WO (2000) An investigation of fatigue crack growth in a cast lamellar Ti-48Al-2Cr-2Nb alloy. *Materials Science and Engineering A* 284: 235–245.

Mercer C, Lou J, Allameh SM, and Soboyejo WO (2001) Effects of temperature on the fatigue crack growth behavior of cast gamma-based titanium aluminides. *Metallurgical and Materials Transactions A, Physical Metallurgy and Materials Science* 32: 2781–2794.

Mercer C, Shademan S, and Soboyejo WO (2003) An investigation of the micromechanisms of fatigue crack growth in structural gas turbine engine alloys. *Journal of Materials Science* 38: 291–305.

Newman JC and Elber W (1988) *Mechanics of Fatigue Crack Closure, Mechanics of Fatigue Crack Closure*. ASTM International.

Niu S and Srivastava V (2022) Simulation trained CNN for accurate embedded crack length, location, and orientation prediction from ultrasound measurements. *International Journal of Solids and Structures* 242: 111521.

Nyshadham C, Rupp M, Bekker B, Shapeev Av, Mueller T, Rosenbrock CW, Csányi G, Wingate DW, and Hart GLW (2019) Machine-learned multi-system surrogate models for materials prediction. *NPJ Computational Materials* 5: 51.

Omar MM and El-Awady JA (2022) Foreseeing metal failure from its inception. *Science* 1979(377): 3–5.

Panchal JH, Kalidindi SR, and McDowell DL (2013) Key computational modeling issues in Integrated Computational Materials Engineering. *CAD Computer Aided Design* 45: 4–25.

Paris P and Erdogan F (1963) A critical analysis of crack propagation laws. *Journal of Basic Engineering* 85: 528–533.

Pearson S (1975) Initiation of fatigue cracks in commercial aluminium alloys and the subsequent propagation of very short cracks. *Engineering Fracture Mechanics* 7: 235–347.

Pelloux RMN (1970) Crack extension by alternating shear. *Engineering Fracture Mechanics* 1: 679–704.

Ravinder R, Sridhara KH, Bishnoi S, Grover HS, Bauchy M, Jayadeva KH, and Krishnan NMA (2020) Deep learning aided rational design of oxide glasses. *Materials Horizons* 7: 1819–1827.

Riemer A, Leuders S, Thöne M, Richard HA, Tröster T, and Niendorf T (2014) On the fatigue crack growth behavior in 316L stainless steel manufactured by selective laser melting. *Engineering Fracture Mechanics* 120: 15–25.

Ritchie RO and Knott JF (1973) Mechanisms of fatigue crack growth in low alloy steel. *Acta Metallurgica* 21: 639–648.

Ritchie RO and Lankford J (1986) Small fatigue cracks: A statement of the problem and potential solutions. *Materials Science and Engineering* 84: 11–16.

Sanaei N and Fatemi A (2021) Defects in additive manufactured metals and their effect on fatigue performance: A state-of-the-art review. *Progress in Materials Science* 117: 100724.

Shen W, Soboyejo ABO, and Soboyejo WO (2004a) Microstructural effects on fatigue and dwell-fatigue crack growth in/Ti-6Al-$_2$Sn-$_4$Zr-$_2$Mo-$_{0.1}$Si. *Metallurgical and Materials Transactions A* 35A: 163–187.

Shen W, Soboyejo WO, and Soboyejo ABO (2004b) An investigation on fatigue and dwell-fatigue crack growth in Ti-6Al-$_2$Sn-$_4$Zr-$_2$Mo-$_{0.1}$Si. *Mechanics of Materials* 36: 117–140.

Shrotriya P, Mercer C, and Soboyejo WO (2002) Contact fatigue of biomedical materials. In: Blom AF (ed.) *Proceedings of the 8th International Fatigue Congress, Cradley Heath, England*, pp. 2093–2104.

Shui X, Yamanaka K, Mori M, Nagata Y, Kurita K, and Chiba A (2017) Effects of post-processing on cyclic fatigue response of a titanium alloy additively manufactured by electron beam melting. *Materials Science and Engineering A* 680: 239–248.

Shukla S, Wang T, Cotton S, and Mishra RS (2018) Hierarchical microstructure for improved fatigue properties in a eutectic high entropy alloy. *Scripta Materialia* 156: 105–109.

Sinha V, Mercer C, and Soboyejo WO (2000) An investigation of short and long fatigue crack growth behavior of Ti-6Al-4V. *Materials Science and Engineering A* 287: 30–42.

Soboyejo WO (1988) *The Propagation of Defects Under Fatigue Loading*. University of Cambridge.

Soboyejo WO (2002) *Mechanical Properties of Engineered Materials*. New York: Marcel Dekker, Inc.

Soboyejo WO, Aswath PB, and Mercer C (1995) Mechanisms of fatigue crack growth in Ti-48Al at ambient and elevated temperature. *Scripta Metallurgica et Materiala* 33: 1169–1176.

Soboyejo WO, Shen W, and Srivatsan TS (2004) An investigation of fatigue crack nucleation and growth in a Ti-6Al-4V/TiB in situ composite. *Mechanics of Materials* 36: 141–159.

Stavropoulos P and Foteinopoulos P (2018) Modelling of additive manufacturing processes: A review and classification. *Manufacturing Review* 5: 1–26.

Stinville JC, Charpagne MA, Cervellon A, Hemery S, Wang F, Callahan PG, and Valle V (2022) On the origins of fatigue strength in crystalline metallic materials. *Science* 1071: 1065–1071.

Suresh S (1985) Fatigue crack deflection and fracture surface contact: Micromechanical models. *Metallurgical Transactions A* 16: 249–260.

Suresh S (1998) *Fatigue of Materials*, 2nd edn. Cambridge, UK: Cambridge University Press.

Suresh S and Ritchie RO (1982) Mechanistic dissimilarities between environmentally influenced fatigue-crack propagation at near-threshold and higher growth rates in lower strength steels. *Metal Science* 16: 529–538.

Suresh S and Ritchie RO (1983) On the influence of environment on the load ratio dependence of fatigue thresholds in pressure vessel steel. *Engineering Fracture Mechanics* 18: 785–800.

Tang Z, Yuan T, Tsai CW, Yeh JW, Lundin CD, and Liaw PK (2015) Fatigue behavior of a wrought $Al_{0.5}$CoCrCuFeNi two-phase high-entropy alloy. *Acta Materialia* 99: 247–258.

Thomas DS and Gilbert SW (2014) *Costs and Cost Effectiveness of Additive Manufacturing*. Special Publication (NIST SP), Gaithersburg, MD: National Institute of Standards and Technology. https://doi.org/10.6028/NIST.SP.1176.

Wang F (2012) Mechanical property study on rapid additive layer manufacture Hastelloy® X alloy by selective laser melting technology. *International Journal of Advanced Manufacturing Technology* 58: 545–551.

Wang C, Fu H, Jiang L, Xue D, and Xie J (2019) A property-oriented design strategy for high performance copper alloys via machine learning. *NPJ Computational Materials* 5: 1–8.

Wei H, Zhao S, Rong Q, and Bao H (2018) Predicting the effective thermal conductivities of composite materials and porous media by machine learning methods. *International Journal of Heat and Mass Transfer* 127: 908–916.

Westergaard HM (1939) Bearing pressures and cracks. *Journal of Applied Mechanics* 49: A49–A53.

Wohler A (1855) Theorie rechteckiger eiserner Bruckenbalken mit Gittetwanden und mit Blechwanden. *Zeitschrift fur Bauwesen* 5: 121–166.

Wohler A (1870) Uber die Festigkeitsversuche mit Eisen und Stahl. *Zeitschrift fur Bauwesen* 20: 73–106.

Wycisk E, Siddique S, Herzog D, Walther F, and Emmelmann C (2015) Fatigue performance of laser additive manufactured Ti–6Al–$_4$V in very high cycle fatigue regime up to 10^9 cycles. *Frontiers in Materials* 2: 72.

Yadollahi A, Shamsaei N, Thompson SM, Elwany A, and Bian L (2017) Effects of building orientation and heat treatment on fatigue behavior of selective laser melted 17-4 PH stainless steel. *International Journal of Fatigue* 94: 218–235.

Yamasaki S, Yaji K, and Fujita K (2021) Data-driven topology design using a deep generative model. *Structural and Multidisciplinary Optimization* 64: 1401–1420.

Yang K, Xu X, Yang B, Cook B, Ramos H, Krishnan NMA, Smedskjaer MM, Hoover C, and Bauchy M (2019) Predicting the young's modulus of silicate glasses using high-throughput molecular dynamics simulations and machine learning. *Scientific Reports* 9: 1–11.

Yang H, Qiu H, Xiang Q, Tang S, and Guo X (2020) Exploring elastoplastic constitutive law of microstructured materials through artificial neural network—A mechanistic-Based data-Driven approach. *Journal of Applied Mechanics, Transactions ASME* 87. 091005-1–091005-9.

Yeh JW, Chen SK, Lin SJ, Gan JY, Chin TS, Shun TT, Tsau CH, and Chang SY (2004) Nanostructured high-entropy alloys with multiple principal elements: Novel alloy design concepts and outcomes. *Advanced Engineering Materials* 6: 299–303.

Zhao Q, Yang H, Liu J, Zhou H, Wang H, and Yang W (2021) Machine learning-assisted discovery of strong and conductive Cu alloys: Data mining from discarded experiments and physical features. *Materials and Design* 197: 109248.

Mechanical Properties: Elastic Behavior

K Bowman, Purdue University, West Lafayette, IN, USA

© 2005 Elsevier Ltd. All rights reserved.

This is an update of K. Bowman, Mechanical Properties: Elastic Behavior, Editor(s): Franco Bassani, Gerald L. Liedl, Peter Wyder, Encyclopedia of Condensed Matter Physics, Elsevier, 2005, Pages 286–291, ISBN 9780123694010, https://doi.org/10.1016/B0-12-369401-9/00568-4.

Introduction **838**
Defining Elastic Constant **838**
Isotropic Materials 838
Anisotropy 840
Measuring Elastic Constants **841**
The Fundamental Nature of Elastic Constants **842**
Extremes of Elasticity: Hyperelasticity **842**
Further Reading **843**

Introduction

When we say that something is elastic we usually think that it is something that springs back to its original shape after we stretch, bend, twist, or compress it. The elastic properties of materials are those that govern the change in shape and the tendency of the material to return the bonds between atoms or molecules back to their original condition. Of course, we can exceed the level at which the material can completely recover its original shape resulting in permanent deformation (plastic deformation) or fracture. Even if plastic deformation or fracture intercedes, the shape change that the material which is elastic has undergone will reverse, returning the material back to its unstretched state.

The model for the elastic response of materials most commonly used is that of a spring. The response of a spring is well known for a linear relationship between force and displacement even to relatively large extensions or strains. When we apply this model to solid materials the mechanical response is approximately linear to very small strain levels. Although this nearly linear response may have been known for quite a long period in man's history, it was not until the seventeenth century that Robert Hooke defined the essential relation showing the proportionality between a tensile stress and the resulting tensile strain. That the changes in shape in all dimensions held similarly near linear responses became understood subsequently through the work of Thomas Young, S D Poisson, and others. Figure 1 shows the linear relationships between normal stress, σ (force divided by the cross-sectional area perpendicular to it) and normal strain, ε (the displacement normalized to the length over which it is measured).

By the twentieth century, it became apparent that the simple relations developed to describe elastic properties could vary with the direction of loading in single crystals, oriented polycrystals, and oriented molecules. This directionality is often called anisotropic elasticity. If a material does not possess this directional variation in properties, it is called isotropic. With isotropic elasticity, only two of the material properties called elastic constants are necessary to fully describe the elastic response of a material. More recently, researchers have increasingly probed the larger strain response of materials that can be decidedly nonlinear. Many biomaterials demonstrate this extended range of elasticity that is often called hyperelasticity.

Defining Elastic Constant

Isotropic Materials

Elastic constants are the constants describing mechanical response of a material when it is elastic. The isotropic elastic constants for some common materials are given in Table 1. If the engineering approximation that this mechanical response is linear is made, one can define a set of constants that relate any applied stress to the corresponding strain. When the material can also safely be treated as isotropic, the number of independent elastic constants required to completely describe the elastic response of a material is two. Any further elastic constants can then be defined in terms of the other two.

For a simple tension or compression test, the easiest elastic constant to define is Young's modulus, E. Young's modulus is the elastic constant defined as the proportionality constant between stress and strain:

$$E = \frac{\sigma}{\varepsilon} \qquad [1]$$

Young's modulus has the same units as stress, which is normally expressed in terms of pascals (Pa), equivalent to newtons per square meter, or pounds per square inch (psi). Strain is, of course, a dimensionless proportionality between a change in length and an original length. The Young's modulus is the slope of the linear elastic response for a number of materials as shown in Figure 1.

Another elastic constant that can be obtained in a tension or compression test wherein the strain along the loading direction and orthogonal to it is called Poisson's ratio, ν. Poisson's ratio is the ratio between width or diameter strain, ε_1, of a tension or

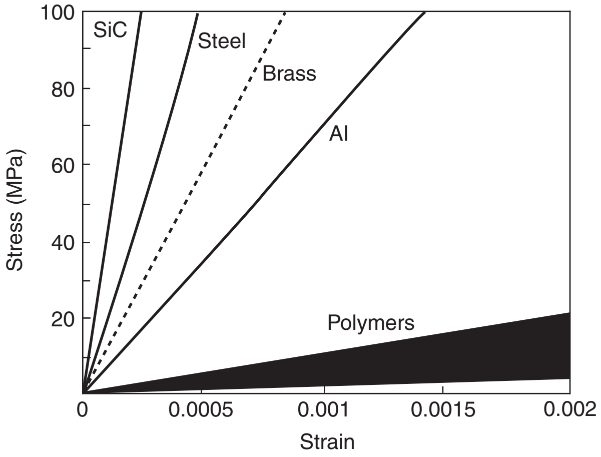

Figure 1 The stress vs. strain behavior for a number of materials measured from tensile loading experiments on commercial materials. The elastic constant called Young's modulus is the slope of each of these curves. (Adapted from Bowman KJ (2004) *An Introduction to Mechanical Behavior of Materials*. Wiley; © Wiley. This material is used by permission of John Wiley and Sons, Inc.)

Table 1 Approximate elastic properties of various materials (and dilute alloys) at room temperature

Material	Young's modulus, E (GPa)	Shear modulus, μ (GPa)	Poisson's ratio, ν
Aluminum and aluminum alloys	69–72	24–26	0.35
Copper and copper alloys	125–135	47–50	0.34
Irons and steels	205–215	80–84	0.29
Stainless steels	190–200	75–78	0.33
Titanium and titanium alloys	115	42–44	0.32
Aluminum oxide	380–390	155–165	0.25
Silicon carbide	440–460	195–200	0.14
Glass	70–90	28–32	0.27
Polyethylene (PE)	0.2–2	[a]	0.4
Polymethylmethacrylate (PMMA)	2–3	[a]	0.4
Polystyrene (PS)	2–4	[a]	0.35
Bone[b]	5–30	3–8	0.25–0.5
Tendon[b]	0.8–1.5		

[a] These values are typically about one-third of Young's modulus.

[b] Bone and tendon are not only strongly anisotropic, but the stiffness also varies with type, position, and moisture content.

Adapted from Bowman KJ (2004) *An Introduction to Mechanical Behavior of Materials*. Wiley; © Wiley. This material is used by permission of John Wiley and Sons, Inc.

compression specimen and the strain along the tension or compression axis, ε_3. This dimensionless proportionality constant can be written as

$$\nu = \frac{-\varepsilon_1}{\varepsilon_3} \qquad [2]$$

So far, the possibility of stresses occurring in multiple directions have not been considered. To do so, one needs to extend the idea of assigning a coordinate system to the stress state as shown in Figure 2a. If such a multiaxial loading condition is considered, the relations between a set of normal stresses and the corresponding strains as given by Hooke's law can be written as

$$\begin{aligned} \varepsilon_1 &= \frac{\sigma_1 - \nu(\sigma_2+\sigma_3)}{E} \\ \varepsilon_2 &= \frac{\sigma_2 - \nu(\sigma_1+\sigma_3)}{E} \\ \varepsilon_3 &= \frac{\sigma_3 - \nu(\sigma_2+\sigma_1)}{E} \end{aligned} \qquad [3]$$

This relation enables a set of normal stresses to be translated into corresponding strains using just the Young's modulus and Poisson's ratio.

A type of stress called a shear stress, τ, can also be defined which can produce a shear strain, γ. For shear stresses, the force is applied across the area and it results in a shearing of the material. Just as for normal stresses, shear loading can result in a mechanical response that is elastic and nearly linear, but the shape change is called a shear strain as shown in Figure 2b. The specific case in

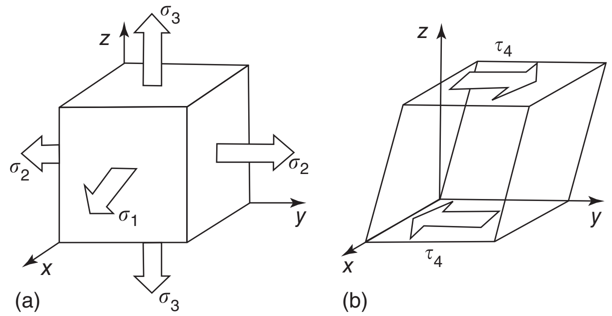

Figure 2 (a) Normal stresses referenced to an orthogonal coordinate system (b) shear stresses and resulting distortion called shear strain.

Figure 2b shows τ_4, which consists of a shear displacement in the *y*-direction on the *z*-face and in the negative *y*-direction on the negative *z*-face. To have a stable distortion, a similar pair of forces would need to be applied on the *y*-faces to cancel the rotational moment imposed by τ_4. The elastic constant that describes the linear relation between τ and γ is called the shear modulus, μ. So, one can write

$$\mu = \frac{\tau}{\gamma} \tag{4}$$

For isotropic materials, the relation between these three elastic constants is

$$E = 2\mu(1+v) \tag{5}$$

Values for all three elastic constants are given for a number of materials at room temperature in Table 1. The values are given as ranges to represent variations expected from alloying.

Because elastic constants are related to bonding, they generally scale with melting temperature and the type of bonding. The strength and the type of bond determines the relationship between an applied force and changes in the distance between atoms. The spacing between atoms or molecules in a material that is not under stress comes about from a balance between attractive and repulsive forces that prevent the atoms or molecules from getting too close, and attractive forces that bring the atoms together. The sum of these two opposite forces is called the interatomic potential. Application of a stress to the material changes the balance point. Because the relationship between force and displacement is nearly linear, the elastic properties of materials can be described using linear relationships. As materials increase in temperature, they undergo increased thermal vibration that leads to thermal expansion. This increase in lattice constants also leads to a reduction in elastic constants with increasing temperature as indicated by Figure 3.

Anisotropy

When a material is anisotropic, the elastic constants vary with the direction along which the material is mechanically loaded. Even single-crystal materials have significant elastic anisotropies such that, the Young's modulus in one-crystal direction can be much

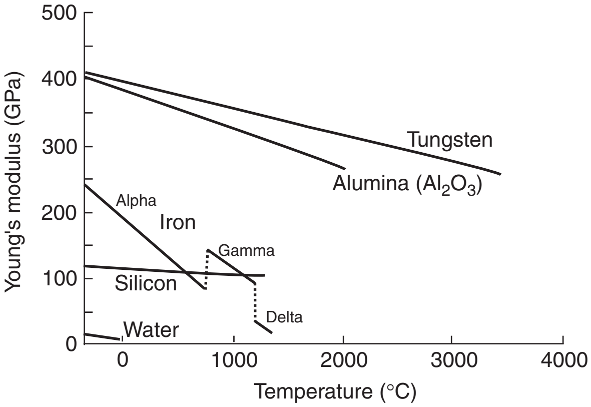

Figure 3 The dependence of Young's modulus on temperature for a number of materials. The curve for iron shows the values of Young's modulus for the three phases found in iron as a function of temperature. (Adapted from Bowman KJ (2003) *An Introduction to Mechanical Behavior of Materials*. Wiley; © Wiley. This material is used by permission of John Wiley and Sons, Inc.)

different from that along another crystal direction. For example, in copper, elastically stretching the crystals along the cube axes of its unit cell requires one third as much stress as along the body-diagonal of the unit cell to produce the same strain. In iron single-crystals, the ratio between the smallest and largest Young's moduli is over two.

Because many engineering applications use materials that are comprised of many crystals or polycrystalline, the impact of directional processing (rolling, vapor deposition, extrusion, etc.) on producing elastic anisotropy was only recognized fairly recently. Developing ways to describe the relationship between oriented polycrystalline materials and the intrinsic single crystal properties has been an important area of research. Many newer applications of materials, including single crystals of superalloys used at high temperatures in jet turbines and the single crystals used in silicon computer chips, employ materials that have strongly anisotropic elastic properties.

Fiber-reinforced polymer composite materials posses directional properties that correspond to the arrangement of the fibers, which are normally stiffer than the polymer matrix material. Although models for fiber composite materials have existed for many years, their predictive capacity is often limited. The effects of the interfacial bonding, fiber arrangement and size scales, and their influence on anisotropic elasticity are not particularly well understood.

The importance of including elastic anisotropy in predictions of performance has also entered in evaluation of elastic constants of natural composite materials such as bone. Like nearly all natural materials, directional growth processes lead to elastic anisotropy. This elastic anisotropy depends on the type of bone, location on the bone, and the age of the bone. All three of these factors affect the ratio between the collagen and mineral contents of bone. The elastic properties and corresponding anisotropy have been increasingly recognized in the increasing fragility of bone with age and bone diseases, such as osteoporosis.

Defective growth patterns that occur in osteoporosis, bone diseases such as cancer or Paget's disease, can lead to bones with reduced elastic properties and strength. The mineral crystal content of bones is critical to maintaining stiff and strong bones. Bone mineral density (BMD) is measured to evaluate the condition of bone in aging patients, and provides a very potent indicator of decreasing elasticity and greater likelihood of bone fracture. One of the recently recognized limitations of bone density measurements is that it does not take into account the detailed structure of the bone mineral content, which can strongly affect the elastic properties of the bone. The morphology and preferred orientation of the bone mineral content results in strong elastic anisotropy such that the Young's modulus of a bone along its length can be nearly twice that in the radial direction. This anisotropy also plays a role in the lifetime of joint replacements. Many knee and hip replacements are principally constructed of metals or ceramics that have much higher elastic stiffnesses and lower degrees of anisotropy than does bone (see Table 1). The mismatch in elastic properties can lead to failure of the hip replacement.

Specification or the anisotropic elastic constants are usually facilitated through writing tensor relations between stress and strain. When the elastic constants are specified such that individual stresses are reported in terms of strains, the coefficients are called stiffnesses, c_{ij}, such that

$$\sigma_i = c_{ij}\varepsilon_j \qquad [6]$$

In eqn [6] the strain term on the right-hand side is the sum of all possible values of j.

When the elastic constants are written such that the individual strains are reported in terms of stresses, the coefficients are called compliances, s_{ij} such that

$$\varepsilon_i = s_{ij}\sigma_j \qquad [7]$$

In eqn [7], the stress term on the right-hand side is the sum of all possible values of j. The Young's modulus is the inverse of the compliance since a single applied stress can be related to the strain in the same direction, for example, for a stress applied in the x-direction.

$$\varepsilon_1 = s_{11}\sigma_1$$

Measuring Elastic Constants

For isotropic materials, direct measurements of elastic constants as shown in Figure 1 is an effective approach to evaluate elastic constants such as Young's modulus and Poisson's ratio. Using tension and compression tests to measure anisotropic elastic constants requires testing of multiple specimens at a number of orientations. Easier approaches use other characteristics of the material that are related to elastic properties.

Probably, the easiest approach for measuring the anisotropic elastic constants of materials is to use measurements of sound velocity in a material. By transmitting ultrasound pulses and measuring the time it takes for the pulse to propagate through the material, a quick and easy assessment of the elastic properties can often be made. When waves are propagated through a material, they interact with the mass of the atoms and the strength of the bonds between the atoms. The number of independent elastic constants required to fully describe the elasticity of materials is directly related to the symmetry of the crystals. For cubic crystals, three independent elastic constants are required to describe the elastic constants. For crystals and bulk materials with orthogonal symmetry (such that the character of the materials can be described by an orthogonal coordinate system), at least nine independent elastic constants must be determined.

Two types of waves are readily propagated through the bulk of materials, normal waves and shear waves. When normal waves are propagated through a material in the *x*-direction, the velocity is related to the normal stiffness as

$$v_1 = \sqrt{c_{11}/\rho} \qquad [8]$$

where ρ is the density and c_{11} is the normal stiffness. The normal stiffness c_{11} relates a stress to a strain in the same direction when the material is constrained such that, all other strains are held to zero.

For shear waves the velocity is related to the shear stiffness by the relation

$$v_4 = \sqrt{c_{44}/\rho} \qquad [9]$$

A recent development has been finding the anisotropic elastic constants using the resonant frequencies of crystals. The technique can be accomplished on a single specimen by oscillating the sample over a wide range of frequencies and finding the resonant values.

Increasing interest in nanoscale materials has led to the development of techniques to evaluate the elastic constants of thin films and particles of materials on size scales approaching a nanometer. Carbon nanotubes, which are derived from research on carbon C_{60} or "bucky balls," consist of several hundreds of carbon atoms and have diameters in the order of 1 nm. Many early predictions of their elastic properties overpredicted the Young's modulus. The planar structure of graphite leads to a very high Young's modulus within the planes of 1000 GPa and a Young's modulus across the planes that is more than a hundred times lower. The elastic constants of carbon nanotubes are also strongly anisotropic with values along the tube axis of several hundred GPa and values in the radial direction of less than 10 GPa.

Similar challenges in assessing the elastic properties are apparent in thin films as nanoindentation and scanning microscopy processes usually produce load versus displacement relations that are nonlinear due to loading geometry. When the loading behavior is modeled, it is often difficult to directly compare the elastic constants recovered to those for bulk materials. This can lead to scientists erroneously deciding that the thin film possesses an elastic behavior different from what is observed in the bulk. Thin film effects and other scaling impacts on elastic properties should always be evaluated carefully.

The Fundamental Nature of Elastic Constants

The details of the relationship between bonding and the elastic properties of materials has become more interesting as measurement techniques have improved and computer modeling has become more sophisticated. It has long been understood that elastic constants decrease almost monotonically as materials undergo greater thermal vibration at higher temperatures (see Figure 3). Once the melting temperature is reached the material loses its ability to support a load and the elastic constants fall to zero.

The balance between attractive forces and repulsive forces is often modeled with relatively simple expressions that can fail to accurately predict thermal expansion and elasticity and their temperature dependences. Although the approximate temperature dependence shown in Figure 3 is useful for engineering calculations, in careful measurements, the elastic constants change rapidly as phase transformations are approached. It is apparent that the thermodynamic changes that occur at a phase transformation are signaled by strongly nonlinear changes in properties as the phase transformations are approached. The effects of alloying elements on elastic properties in solid solutions have also been shown to depend on the electronic structures of the materials, relative atomic radii, and other details of the components.

Many of the most advanced models for elastic response rely on constructing computer models that simulate the atomic arrangement in the material with assigned bonds between each of the atoms. Then virtual experiments can be conducted on a computer to simulate either the direct elastic response or the response of the lattice to wave propagation.

Extremes of Elasticity: Hyperelasticity

Materials with more than one type of fundamental bond, for example, ceramic and polymeric glasses, and materials tested under conditions at which they can sustain very high stress levels without failure, can become decidedly nonlinear in their response. Understanding this nonlinearity and its effects of material performance has resulted in the study of what is called hyperelasticity. Hyperelastic responses are particularly observable in compressive loading with superposed hydrostatic stresses and complex localized stress states such as plane strain fracture and indentation loading. Many models for mechanical processes that rely on assumptions of linear elasticity may require substantial modification to describe the effects of hyperelasticity.

Further Reading

Badawi F and Villain P (2003) Stress and elastic-constant analysis by X-ray diffraction in thin films. *Journal of Applied Crystallography* 36: 869–879.

Betschart AA (1998) Soliton numbers. In: Pomeranz Y (ed.) 3rd edn., *Optical Soliton Pulses in Fibers*, 3rd edn., vol. 2, pp. 91–130. London: Academic Press.

Buehler MJ, Abraham FF, and Gao J (2003) Hyperelasticity governs dynamic fracture at a critical length scale. *Nature* 426: 141–146.

Grigoras S, Gusev AA, Santos S, and Suter UW (2002) Evaluation of the elastic constants of nanoparticles from atomistic simulations. *Polymer* 43: 489–494.

Hartley CS (2003) Single crystal elastic moduli of disordered cubic alloys. *Acta Materialia* 51: 1373–1391.

Hurley DC, Shen K, and Jennett NM (2003) Atomic force acoustic microscopy methods to determine thin-film elastic properties. *Journal of Applied Physics* 94: 2347–2354.

Liu X, Wang X, and Niebur GL (2003) Effects of damage on the orthotropic material symmetry of bovine tibial trabecular bone. *Journal of Biomechanics* 36: 1753–1759.

Rhee M, Stolken JS, Bulatov VV, de la Rubia TD, Zbib HM, et al. (2001) Dislocation stress fields for dynamic codes using anisotropic elasticitymethodology and analysis. *Materials Science and Engineering* A309–310: 288–293.

Roeder RK, Sproul MM, and Turner CH (2003) Hydroxyapatite whiskers provide improved mechanical properties in reinforced polymer composites. *Journal of Biomedical Materials Research* 67A: 801–812.

Vijay A and Verma TS (2000) Analysis of temperature dependence of elastic constants and bulk modulus for ionic solids. *Physica B* 291: 373–378.

Zysset PK (2003) A review of morphology–elasticity relationships in human trabecular boneTheories and experiments. *Journal of Biomechanics* 36: 1469–1485.

Mechanical Properties: Plastic Behavior

G Gottstein, M Goerdeler, and GVSS Prasad, Institut für Metallkunde und Metallphysik, Aachen, Germany

© 2005 Elsevier Ltd. All rights reserved.

This is an update of G. Gottstein, M. Goerdeler, G.V.S.S. Prasad, Mechanical Properties: Plastic Behavior, Editor(s): Franco Bassani, Gerald L. Liedl, Peter Wyder, Encyclopedia of Condensed Matter Physics, Elsevier, 2005, Pages 298–305, ISBN 9780123694010, https://doi.org/10.1016/B0-12-369401-9/00569-6.

Deformation Fundamentals 844
Crystallographic Slip 844
Twinning 846
Deformation Microstructure 847
Hardening Behavior 847
Texture 848
Softening: Recovery and Recrystallization 848
Modeling 850
Applications 851
Further Reading 852

Nomenclature

b	Burgers vector
F	external force
G	shear modulus
K	Peach–Koehler force (scalar)
K	Peach–Koehler force (vector)
l	instantaneous length of the specimen
l_0	original length of the specimen
M	Taylor factor
q	instantaneous cross section of the specimen
q_0	initial cross section of the specimen
s	dislocation line vector
S	dislocation structure
T	temperature
T_m	melting point
V_i	volume fraction of the cell interiors
V_w	volume fraction of the cell walls
α	geometric constant
γ	shear strain
Δl	change in length of the specimen
ε	strain
$\dot{\varepsilon}$	strain rate
ν	average velocity of a dislocation
ρ	dislocation density
ρ_m	mobile dislocation density
σ	stress
σ_i	flow stress in the cell interiors
σ_w	flow stress in the cell walls
τ	shear stress

Deformation Fundamentals

Crystallographic Slip

Metals are crystalline except for very special conditions. Metals and alloys generally crystallize in a face-centered cubic (f.c.c.), body-centered cubic (b.c.c.), and hexagonal close-packed (h.c.p.) crystal structure. There is unambiguous evidence that metals retain their crystal structure during plastic deformation. This conservation principle of crystal plasticity has serious consequences for the deformation process and material properties. In a noncrystalline material, a macroscopic shape change can be accommodated on an

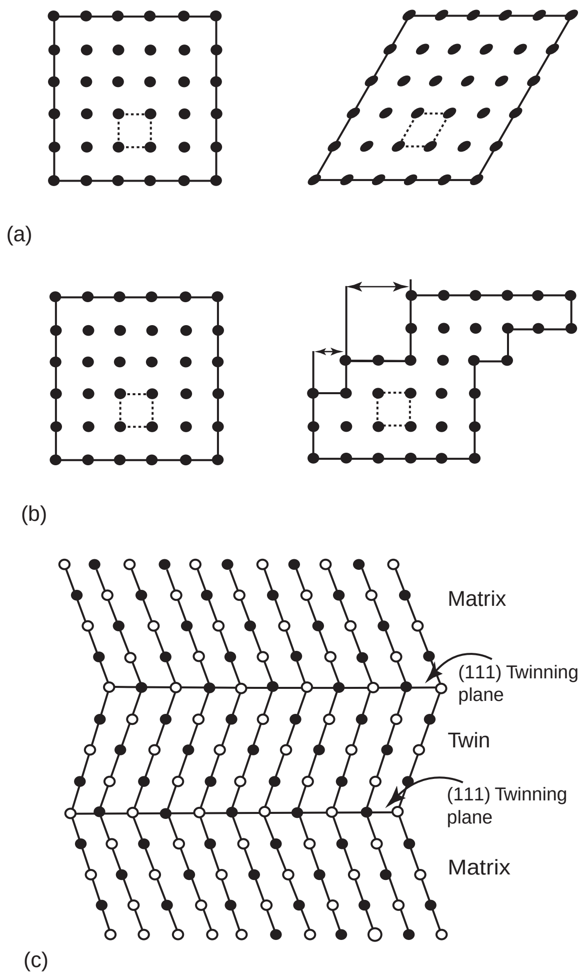

Figure 1 Plastic deformation of crystals (dotted lines=unit cell): (a) with change of crystal structure; (b) by crystallographic glide; and (c) by deformation twinning.

atomistic level by a respective atomic rearrangement. If a macroscopic deformation of a crystal is also copied on an atomistic level, the crystal structure would change (Figure 1a); this is however contrary to observation. The crystal structure can be conserved, if the shape change on an atomistic level is accommodated by a displacement along crystallographic planes in multiples of translation vectors of the crystal lattice (Figure 1b). This phenomenon is referred to as crystallographic glide (or crystallographic slip). As a result, crystal plasticity proceeds by a structure conserving simple shear deformation. In principle, there are an infinite number of planes and translation vectors to accomplish an imposed shape change. Due to energetic reasons, crystallographic glide is confined only to a few crystallographic planes (slip planes) and directions (slip directions), normally the most densely packed planes and directions in a crystal. A slip plane and a slip direction constitute a slip system and the most prominent slip systems of the three major crystal structures of metals are given in Table 1. The mechanism of crystallographic glide is related to the motion of crystal dislocations. The glide plane of a dislocation and the direction of its Burgers vector correspond to the slip plane and slip direction, respectively. On an atomistic level, therefore, plastic deformation of a metal requires the generation and motion of crystal dislocations.

Table 1a Slip systems of the major metallic crystal structures

Crystal structure	*Slip plane*	*Slip direction*	*Number of nonparallel planes*	*Slip directions per plane*	*Number of slip systems*
f.c.c.	$\{1\,1\,1\}$	$\langle 1\bar{1}0\rangle$	4	3	12=(4×3)
	$\{1\,1\,0\}$	$\langle \bar{1}11\rangle$	6	2	12=(6×2)
b.c.c.	$\{1\,1\,2\}$	$\langle 11\bar{1}\rangle$	12	1	12=(12×1)
	$\{1\,2\,3\}$	$\langle 11\bar{1}\rangle$	24	1	24=(24×1)
	$\{0\,0\,0\,1\}$	$\langle 11\bar{2}0\rangle$	1	3	3=(1×3)
h.c.p.	$\{10\bar{1}0\}$	$\langle 11\bar{2}0\rangle$	3	1	3=(3×1)
	$\{10\bar{1}1\}$	$\langle 11\bar{2}0\rangle$	6	1	6=(6×1)

Table 1b Twinning systems of the major metallic crystal structures

Crystal structure	*Twinning plane*	*Shear direction*	*Displacement plane*	*Displacement plane*
f.c.c.	{1 1 1}	⟨112⟩	⟨110⟩	Ag, Cu
b.c.c.	{1 1 2}	⟨111⟩	⟨110⟩	α-Fe
h.c.p.		⟨10–11⟩		Cd, Zn

Dislocations are crystal defects and, therefore, cause a distortion of the atomic arrangement, which manifests itself into a long-range stress field. Via their stress field, dislocations interact with each other. This constitutes a glide resistance, which is macroscopically felt as a yield stress and eventually causes immobilization of moving dislocations. The traveling distance (slip length) of a moving dislocation is normally much smaller than the macroscopic dimension of the deformed body; therefore, dislocations are stored in the crystal and the dislocation density grows with progressing deformation which in turn increases dislocation interaction and thus the flow stress. The relation between flow stress σ and dislocation density ρ can be represented by the Taylor equation

$$\sigma = \alpha M G \boldsymbol{b} \sqrt{\rho} \tag{1}$$

where the dislocation density $\rho(\mathrm{m}^{-2})$ is defined as the total dislocation line length per unit volume – typically $10^{10}\mathrm{m}^{-2}$ for annealed and $10^{16}\mathrm{m}^{-2}$ for heavily deformed metals, $\boldsymbol{b}$ is the Burgers vector (slip vector), G is the shear modulus, and M is the Taylor factor which relates the applied stress to the shear stress in the glide system and depends on crystallographic texture (see below). Typically, $M{\sim}3$, and the geometrical constant $\alpha{\sim}0.5$.

Any change in the glide resistance of the moving dislocations will affect the flow stress. This is the reason for work hardening (increasing dislocation density), other strengthening mechanisms (grain size, solute atoms, particles, precipitates, etc.), and softening by recovery and recrystallization (decreasing dislocation density). It is important to note that the macroscopic deformation behavior can be related to the microscopic properties of the crystal dislocations. The force $\boldsymbol{K}$ on a dislocation due to a stress σ applied to a crystal is given by the Peach–Koehler equation

$$\boldsymbol{K} = \sigma \boldsymbol{b} \times \boldsymbol{s} \tag{2a}$$

or the magnitude of the force K in the slip system due to the resolved shear stress τ

$$K = \tau \boldsymbol{b} \tag{2b}$$

The imposed strain rate is reflected by the dislocation velocity through the Orowan equation

$$\dot{\varepsilon} = \rho_m \boldsymbol{b} v \tag{3}$$

where ρ_m is the density of the mobile dislocations moving with an average velocity v. The velocity, of course, depends on the applied stress σ. One can imagine the dislocations as rigid rods, moving with velocity v due to a force K, and this process is experienced macroscopically as a plastic deformation with strain rate $\dot{\varepsilon}$ at a flow stress σ.

Twinning

While crystallographic glide by dislocation slip is the dominating deformation mechanism in metals, deformation twinning is also observed to accommodate a plastic strain, particularly at low temperatures in metals and many intermetallics. A deformation twin has an atomic arrangement that is the mirror image of the parent crystal. Due to the mirror symmetry, the crystallographic structure is conserved, but the crystal has a different shape (Figure 1c). The generation of a twin corresponds to a simple shear deformation by a displacement parallel to the twinning plane (mirror plane). In contrast to the dislocation glide, the shear strain γ is constant for a given crystal structure, for example, $\gamma = \sqrt{2}/2$ for cubic crystals. Twinning plane and displacement direction constitute a twin system in analogy to a slip system (Table 1).

Since for a given shear strain, the atomic displacement increases with growing distance from the twinning plane (Figure 1c), twins are usually thin, and their formation requires high stresses which are available only at low temperatures because the material strength increases with decreasing temperature. Deformation twinning is liable to occur if the flow stress is high and the twin boundary energy (approximately half of the stacking fault energy (SFE)) is low. The f.c.c. metals and alloys with low SFE undergo deformation twinning, such as silver at room temperature or copper at liquid nitrogen temperature. As the SFE decreases upon alloying, most alloys are prone to twinning during low-temperature deformation, for example, copper alloys, such as α brass (Cu–Zn) where twinning constitutes the major low-temperature deformation mechanism. Deformation twinning is most prominent in materials where dislocation slip cannot fully accommodate the imposed strain, for example, in h.c.p. metals and alloys with $c/a > 1.63$ owing to their low number of crystallographic slip systems. For an arbitrary deformation, a crystal needs to activate five independent slip systems to satisfy the five independent elements of the strain tensor. (A slip system of a set is independent, if its deformation cannot be accomplished by the other systems of the set.)

In h.c.p. metals with $c/a{>}1.63$ (e.g., zinc), there is only slip on the basal plane and therefore, there are only two independent slip systems. This is sufficient to deform single crystals to very large strains. However, the individual grains of a polycrystal have to deform compatibly with the adjacent grains to avoid occurrence of holes or overlap. This can be accomplished only if the individual grains can undergo an arbitrary shape change at their boundaries, for which five independent slip systems are required. Therefore, polycrystals of zinc, for example, have to activate mechanical twinning for deformation. Owing to the high stresses and the less perfect adaptation to the shape change of neighboring grains in a polycrystal by twinning, the strain to fracture is smaller than in material deforming only by dislocation slip. Also, due to crystallographic effects, h.c.p. metals and alloys with $1.63{\leq}c/a{\leq}1.73$ cannot deform to a large degree by twinning, since twinning ceases to comply with the imposed shape change due to crystal reorientation and the fact that only one sense of twinning shear is crystallographically possible (the opposite shear $-\gamma$ does not generate a twin orientation). This is the reason why polycrystalline h.c.p. magnesium ($c/a = 1.63$) and its alloys are not ductile at ambient temperature. Note that hexagonal metals such as titanium, beryllium, or zirconium are very ductile even at low temperatures since their ratio $c/a{<}1.63$, which favors nonbasal slip and thus, provides sufficient independent slip systems.

Deformation Microstructure

When gliding dislocations become immobile, they are stored in the crystal. The spatial distribution of these stored dislocations can occur at random or in distinct patterns. Most metals and alloys reveal nonstatistical dislocation distributions. Typically, dislocations arrange in cellular patterns, that is, in high dislocation density (cell) walls, which enclose volumes (cells) of considerably lower dislocation densities. For most commercial cold forming processes – such as rolling, the cellular arrangements are superimposed by deformation inhomogeneities, which typically have a band-like shape and can assume macroscopic dimensions to be recognized by the bare eye. In rolled materials, besides microscopic microbands, which appear like distinctly framed elongated dislocation cells under the microscope, there are two major types of deformation inhomogeneities namely, deformation bands and shear bands which can best be recognized in micrographs of the lateral surface. Deformation bands are elongated microstructural features that extend parallel to the rolling direction and that gradually accommodate a large misorientation to the matrix. Shear bands are deformation inhomogeneities, which extend under an angle of 30–35° to the rolling direction. Copper-type shear bands comprise clusters of elongated cells, which are confined to grain dimensions. In contrast, brass-type shear bands have (macroscopic) dimensions comparable to the sample thickness. Their internal structure is composed of very small granular features, typically globular grains of nanometer size. The origin and structure of shear bands are far from being understood, but they are generally assumed to be due to local softening (like texture softening) or enforced macroscopic shear in case of obstructed dislocation glide. Brass-type shear bands occur typically in alloys with low SFE (e.g., alpha brass). Copper-type shear bands are formed during cold rolling of f.c.c. metals and alloys with higher SFE.

Hardening Behavior

The mechanical properties of a material are typically measured in a uniaxial tension test, where the force is recorded to elongate a cylindrical specimen at constant speed. The force F divided by the initial cross section q_0 defines the engineering stress, and the length change Δl divided by the original length l_0 defines the engineering strain. If force and elongation are normalized by the instantaneous cross section q or length of the specimen l, they are referred to as true stress and true strain, respectively. The hardening curve is the dependence of the true stress on true strain. The true stress at a given strain is called the flow stress.

The storage of dislocations during deformation leads to an increased glide resistance for moving dislocations which is experienced as an increased flow stress with increasing strain (Figure 2a). The rise of stress σ with strain ε, is referred to as strain hardening or work hardening, and the slope of the hardening curve $d\sigma/d\varepsilon$ is the work-hardening coefficient or hardening rate. It is conventionally measured in uniaxial tension or compression tests. While the hardening curves of different materials or at deformation conditions vary considerably, there is a characteristic shape of the engineering stress–strain curve, namely after yielding a curve with a single maximum, although the strength level and hardening rate can be very different.

Of particular interest for forming processes is the hardening behavior for large strain deformation, for example, sheet rolling. A typical true stress–strain behavior for large strain deformation exhibits, after yielding, some transient with high but decreasing hardening rate until a low but constant rate is attained (Figure 2b), that is, the stress increases linearly with strain, and eventually a steady state (constant flow stress) is attained. Correspondingly, the large strain-hardening curve exhibits five distinct stages:

1. Right after yielding, transition to athermal hardening (observed only in single crystals oriented for single slip);
2. Athermal hardening with constant high hardening rate $d\sigma/d\varepsilon{\approx}G/30$ (extended range only in single crystals at low temperatures);
3. Dynamic recovery range, hardening rate decreasing linearly with stress;
4. Large strain hardening with constant low hardening rate; and
5. Transition to steady state or unstable microstructure, usually not attained during cold deformation.

The important stages of the flow curves of commercial metals and alloys for industrial forming processes are stages 3 and 4. Their extent and level depends on material composition and processing and, thus, is history dependent! The hardening behavior reflects the glide resistance of the moving dislocations and, therefore, depends on the dislocation structure S, which is strongly dependent on processing history, that is, at strain rate $\dot{\varepsilon}$ and temperature T:

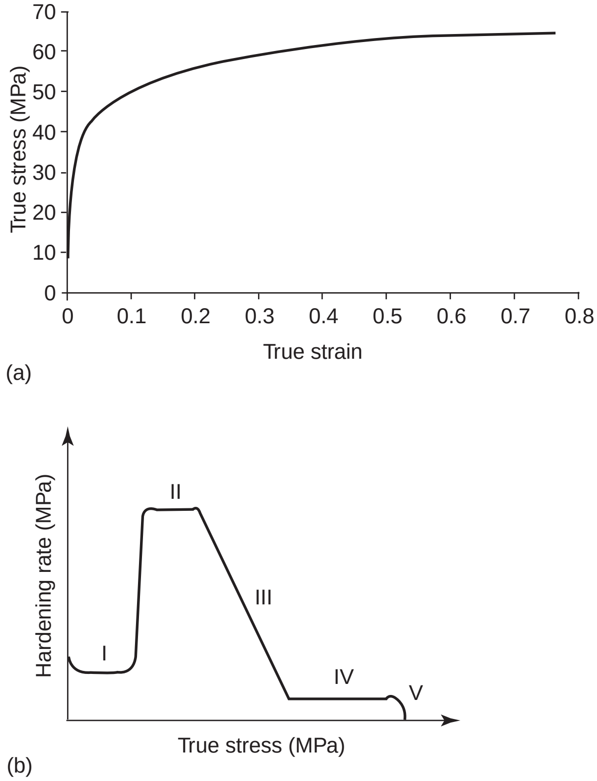

Figure 2 (a) True stress–true strain curve of an Al–1%Mn alloy (AA3103), measured at 300°C and a constant true strain rate of 0.1 s^{-1}; (b) $d\sigma/d\varepsilon$ vs. σ.

$$\sigma = \sigma(\dot{\varepsilon}, T, S) \qquad [4]$$

For this particular reason, the macroscopic strain is not a state parameter and, therefore, a prediction of flow stress as an empirical function of strain $\sigma(\varepsilon)$ is physically wrong although, due to simplicity, it has been a longstanding engineering practice.

Texture

A simple shear deformation is always accompanied by a rigid-body rotation, because the displacement gradient tensor is not symmetrical. Since plastic deformation in metallic materials proceeds by simple shear mechanisms (dislocation glide, mechanical twinning), the grains in a polycrystal change their crystallographic orientation during deformation – except for a few orientations which are stable under the imposed deformation conditions – and rotate toward the stable orientations. For a given forming process, such as rolling, wire drawing, or extrusion typical orientation distributions, that is, crystallographic textures develop, depending on deformation mechanism. An orientation distribution is most adequately represented in orientation space, where each orientation is represented by one point. The orientation distribution after large strain deformation is confined to a small volume in orientation space. For instance, the rolling texture of f.c.c. materials appears like a tube in orientation space (Figure 3) and can essentially be understood as consisting of only a few (ideal) orientations with some scatter. Crystallographic textures cause anisotropic mechanical properties, which make themselves felt during thermomechanical processing, metal forming, and in-service behavior.

Softening: Recovery and Recrystallization

During plastic deformation, dislocations are introduced to accommodate the imposed shape change. Dislocations, however, are crystal defects which are not stable in thermodynamic equilibrium; thus, the crystal strives to remove them. At low temperatures, the dislocation arrangement is in mechanical equilibrium and, therefore, stable. At elevated temperatures, however, thermally activated processes destabilize the dislocation structure and substantially change or even remove the deformation-induced microstructure which drastically affects microstructure, texture, and mechanical properties (Figure 4). There are two major restoration processes: recovery and recrystallization. They are termed static processes if they occur subsequent to deformation during annealing, or are referred to as dynamic recovery and dynamic recrystallization if they proceed during deformation. Dynamic recovery is also strain

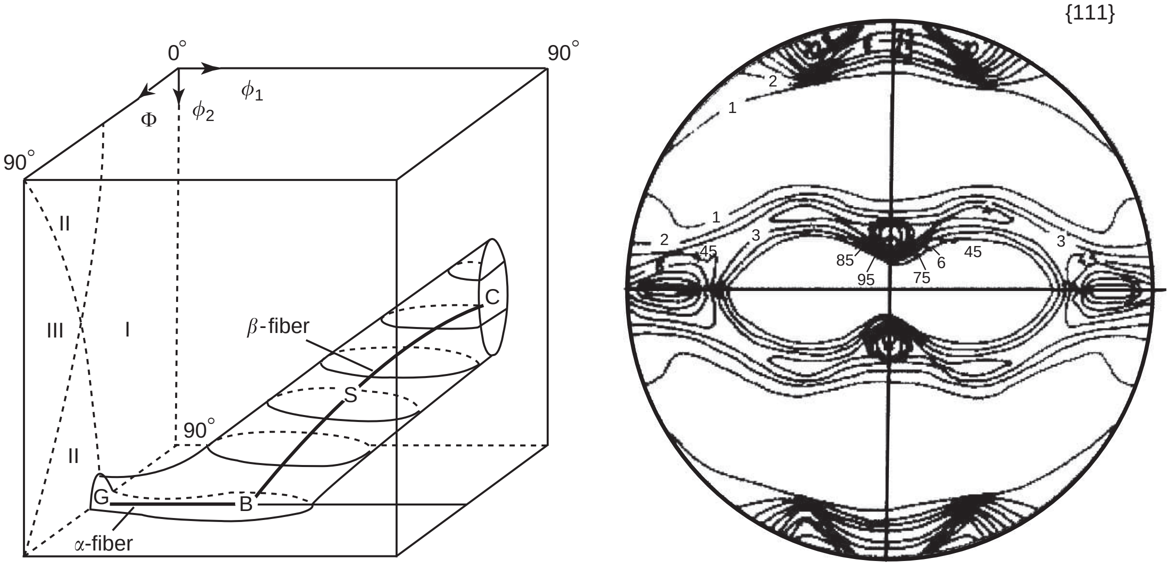

Figure 3 Rolling texture of pure copper: three-dimensional representation in orientation (Euler) space, {1 1 1} polefigure.

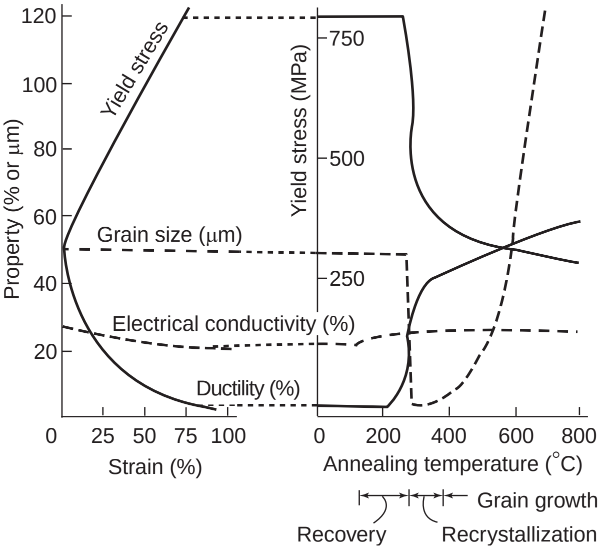

Figure 4 The effect of cold forming and annealing on the properties of a Cu–35%Zn alloy.

induced and is, therefore, an integral part of the strain-hardening process at any temperature. Dynamic recrystallization is an important phenomenon during hot working (see below) and liable to occur for $T>0.5T_\mathrm{m}$ (T_m – melting temperature). While recovery essentially consists of a dislocation rearrangement in the as-deformed structure, a completely new microstructure is formed atom by atom during recrystallization. Recrystallization proceeds by nucleation of virtually dislocation-free grains, which grow at the expense of the deformed matrix. The moving grain boundaries of the expanding nuclei are capable of absorbing the deformation-induced dislocations so that finally an almost dislocation-free granular structure is generated. Typical dislocation densities of recrystallized polycrystals are $10^{10}\,\mathrm{m}^{-2}$ compared to up to $10^{16}\,\mathrm{m}^{-2}$ for heavily deformed materials.

Recovery and recrystallization have different kinetics and different impact on properties. Invariably either process causes a softening of the material, and fully recovered and fully recrystallized materials have comparable yield stresses. The texture development is very different, however. The deformation texture is essentially retained during recovery or slightly increased in sharpness. During recrystallization, a completely new and different texture is generated. The recrystallization texture can be very sharp, like the cube texture in rolled and annealed aluminum, which gives rise to strong anisotropy during subsequent forming of the sheet. Typically, specific types of deformation textures, as shown in Figure 3 for rolling, transform to specific recrystallization textures in f.c.c. and b.c.c. materials. However, small changes in chemical composition or processing history can totally alter the recrystallization texture, even if the deformation texture appears unchanged. Advanced codes for recrystallization structure and

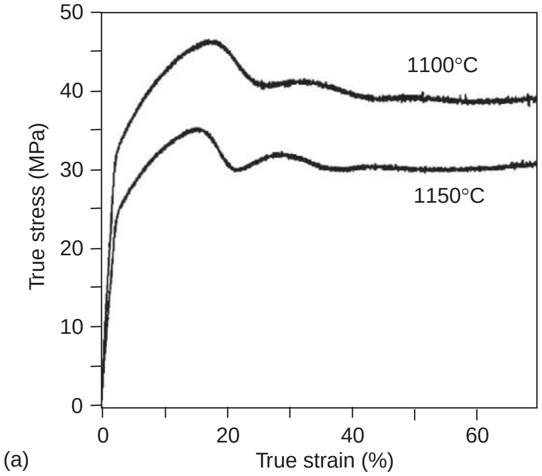

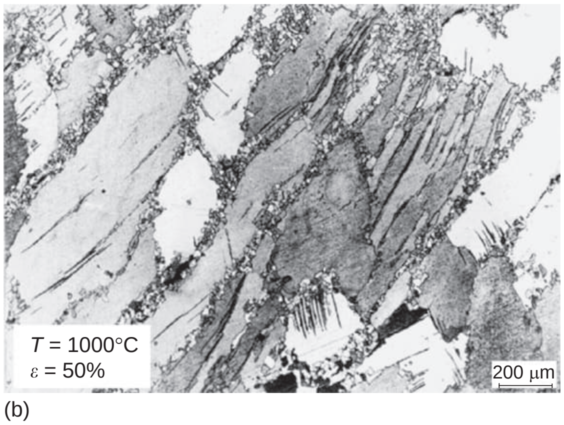

Figure 5 (a) Stress–strain curves of dynamically recrystallizing material (alloy 800 H); (b) the first recrystallized grains form predominantly at grain boundaries (necklace structure in Ni_3Al).

texture prediction with high spatial and temporal resolution (e.g., cellular automata or Monte Carlo simulation approaches) are now available which can be interfaced to FEM or superimposed to real deformation microstructures to account for spatial variation of the microstructure.

At temperatures above $0.5T_m$, recrystallization can also occur concurrently with deformation. This is referred to as dynamic recrystallization and makes itself felt by either a single-peak or multiple-peak flow stress behavior. A typical flow curve of a dynamically recrystallizing material and its associated microstructure are shown in Figure 5. Dynamic recrystallization typically occurs during the hot working of low SFE materials. Important examples are austenitic steels and copper alloys. It limits the flow stress and therefore, keeps hot working forces low and at the same time, it improves ductility (strain to fracture). The dynamically recrystallized grain size depends only on the flow stress and thus can be controlled by the strain rate and deformation temperature.

Modeling

For engineering practice, the mechanical behavior of materials must be known (e.g., the hardening curve). Most commonly, it is measured and fit to empirical functions. These functions, however, do not have any predictive power and cannot be used beyond the tested limits. For predictions of mechanical properties with the change of materials chemistry or processing conditions, microstructural models have to be used, since microstructure defines the state variables of materials properties.

Advanced work-hardening models are based on the dislocation theory. These models can either be statistical dislocation density-based models or dislocation dynamic models (Figure 6a). Statistical models follow a common scheme, namely, the formulation of a structure evolution equation ($d\rho/d\varepsilon$) and a kinetic equation of state ($\sigma = f(\rho, T, \dot{\varepsilon})$) to relate the structure with the glide resistance. These relations are formulated as differential equations and hence can account for the transient microstructure evolution. The total change of dislocation density $d\rho$ in a strain increment $d\varepsilon$ reflects the structure evolution due to production of dislocations $d\rho^+$ and dynamic recovery (e.g., annihilation, dipole formation, lock formation) $d\rho^-$:

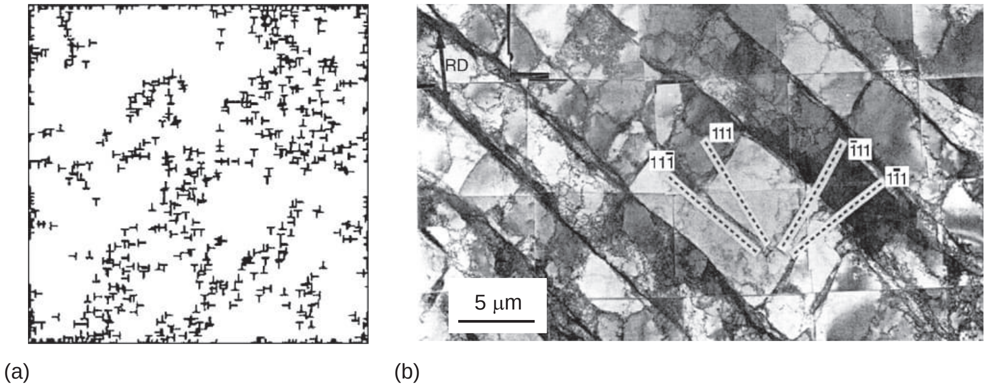

(a) (b)

Figure 6 Deformation microstructure: (a) generated by two-dimensional dislocation dynamics; (b) observed in pure aluminum, cold rolled to a strain of 0.1. (Modified from Liu *et al.* (1998) Effect of grain orientation on deformation structure in cold rolled polycrystalline aluminum. *Acta Materialia* 46: 5819–5838, with permission from Elsevier.)

$$\mathrm{d}\rho = \mathrm{d}\rho^{+} - \mathrm{d}\rho^{-} = (f_1 - f_2)\mathrm{d}\varepsilon \qquad [5]$$

The functions f_1 and f_2 have to be determined from the dislocation theory. They depend on the particular processes considered, and their actual values vary with the dislocation structure. The major problem is a proper incorporation of dislocation patterning in the theory. It is a common conception that the dislocations are arranged in a cell structure (Figure 6b), but different approaches have been proposed for the dominant stress and strain rate controlling processes. Due to the nonhomogeneous dislocation distribution, the flow stress will be a volume (V) weighted average of the flow stress in cell walls σ_w and cell interiors σ_i

$$\sigma = \sigma_\mathrm{w} V_\mathrm{w} + \sigma_\mathrm{i} V_\mathrm{i} \qquad [6]$$

In a dislocation dynamics model, the dislocations are modeled as line defects in a continuum and represented by their stress field. Since the continuum theory of dislocations is well established, the equations of motion can be formulated and the dislocation arrangement can be calculated from eqns [2] and [3]. However, the fundamental approach and the applicability to arbitrary deformation conditions have to be paid for by a substantial investment in computer power and computation time.

Owing to the long-range stress fields and the self-interaction of curved dislocations in three-dimensional dislocation dynamics, the problem becomes intractable for today's and tomorrow's high-power computers. Simulations with two-dimensional geometry are possible and have been performed but can only be applied to problems of two-dimensional geometry such as thin films. For bulk deformation, two-dimensional dislocation dynamics are of limited use.

Applications

Plasticity is the main prerequisite for metal forming, for example, rolling, forging, wire drawing, to produce semi-finished products and for the final shaping of parts, for example, by sheet forming. The excellent formability of metals is one of the reasons for their extensive industrial use. During the classical processing route of a metallic part, from the liquid state to the finished product, the material undergoes multiple deformation and heat treatment cycles. For example, consider the fabrication of an aluminum (or steel) can from a sheet (Figure 7).

After casting and homogenization the material is hot rolled, cold rolled, and annealed before the final part is produced from the sheet by deep drawing. While the material undergoes a shape change and experiences work hardening during rolling, it softens

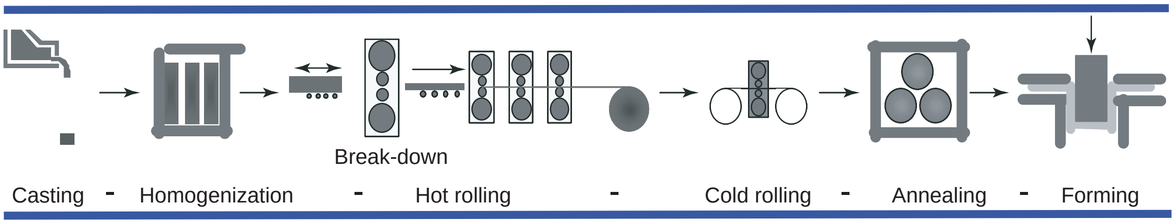

Figure 7 Production chain for sheet-forming process.

during interstand times and during back annealing. Since the microstructure changes during each processing step and as the microstructure determines the properties of the final part, processing has to be fine-tuned to meet terminal material specifications. These processes and the respective microstructural evolution can now be simulated by advanced computer codes.

Further Reading

Backofen WA (1972) *Deformation Processing*. Reading: Addison-Wesley.
Cottrell AH (1961) *Dislocations and Plastic Flow in Crystals*. Oxford: Clarendon.
Courtney H (1999) *Mechanical Behavior of Materials*, 1st edn. Singapore: McGraw-Hill.
George ED (1988) *Mechanical Metallurgy*. London: McGraw-Hill.
Gottstein G (2004) *Physical Foundations of Materials Science*. Berlin: Springer.
Honeycombe RWK (1984) *The Plastic Deformation of Metals*, 2nd edn. London: Edward Arnold.
John PH and Jens L (1968) *Theory of Dislocations*. New York: McGraw-Hill.
Kocks UF, Argon AS, and Ashby MF (1975) Thermodynamics and kinetics of slip. *Progress in Materials Science*, vol. 19. Oxford: Pergamon.
Kocks UF and Mecking H (2003) Physics and phenomenology of strain hardeningthe FCC case. *Progress in Materials Science* 48: 171–273.
Meyers MA and Chawla KK (1998) *Mechanical Behavior of Materials*. NJ: Prentice-Hall.
Nabarro FRN (ed.) (1979) *Dislocations in Solids*. Amsterdam: North-Holland.
Reed-Hill RE (1973) *Physical Metallurgy Principles*, 2nd edn. New York: Van Nostrand.

Mechanical Properties: Strengthening Mechanisms in Metals

AC Lund and CA Schuh, Massachusetts Institute of Technology, Cambridge, MA, USA

© 2005 Elsevier Ltd. All rights reserved.

This is an update of A.C. Lund, C.A. Schuh, Mechanical Properties: Strengthening Mechanisms in Metals, Editor(s): Franco Bassani, Gerald L. Liedl, Peter Wyder, Encyclopedia of Condensed Matter Physics, Elsevier, 2005, Pages 306–311, ISBN 9780123694010, https://doi.org/10.1016/B0-12-369401-9/00576-3.

Introduction 853
Low-Temperature Dislocation-Based Strengthening Mechanisms 853
Work Hardening 854
Solid Solution Strengthening 855
Particle Strengthening 855
Grain-Boundary Strengthening 857
Low-Temperature Continuum-Level Strengthening 857
Limitations of Strengthening Mechanisms due to Thermal Activation 858
Bulk Diffusion Effects 858
Intercrystalline Diffusion Effects 859
Further Reading 859

Nomenclature

b	Burger's vector magnitude (length)
c	concentration of solute (atomic fraction)
d	grain size (length)
L	spacing between obstacles (length)
r	average particle radius (length)
T_m	melting temperature (K)
v_f	volume fraction of particles
α	dimensionless constant for work hardening
β	dimensionless constant for solid solution strengthening
γ	dimensionless constant for particle strengthening
$\Delta\tau$	additional strength increment (force/area)
κ	constant for grain-boundary strengthening (length$^{1/2}$)
λ	interparticle spacing (length)
μ	shear modulus (force/area)
ρ	dislocation density (length^{-2})
σ	stress (force/area)

Introduction

The strength of metallic materials depends in considerable detail upon the structure at many length scales, from the fundamental atomic interactions at $\sim 10^{-10}$ m to interaction among macroscopic structural components as large as $\sim 10^{-3}$ m. The mechanisms responsible for strengthening metals have been the subject of considerable study for many decades, and are relatively well understood for traditional microstructural length scales. At low temperatures, the strength of crystalline metals is in large part governed by the interaction of dislocations with one another and with other features of the microstructure. Therefore, the main focus of this article is on these interactions, and the general scaling laws that relate these microscopic processes with macroscopic measurements of strength. In metals with microstructural components large enough to be regarded as continua, additional strength can be derived by sharing of the applied load between phases, which is discussed briefly. Finally, the limitations of these various strengthening mechanisms are discussed for cases where the temperature is high or the characteristic microstructural length scale is very fine.

Low-Temperature Dislocation-Based Strengthening Mechanisms

In crystalline metals, strength and other mechanical properties are governed by the prevalence and mobility of defects in the crystal structure. At low temperatures (i.e., below about one-third of the melting point), the most important defects in this regard are dislocations, which can be regarded as the "carriers" of plastic strain. Hence, the primary goal of most forms of metal strengthening is to regulate the movement of dislocations, which is generally accomplished through the introduction of obstacles. The four main strengthening mechanisms at ambient temperature, that is, work hardening, solid solution strengthening, particle hardening, and grain-boundary strengthening, are all variations upon this theme. Each of these mechanisms has been studied and modeled in considerable detail, and the reader is referred to the "Further reading" section for more exhaustive discussions. Here these concepts are explored within the framework of a relatively general scaling law that predicts the shear strength increment $\Delta\tau$ gained by incorporating obstacles of spacing L in the structure:

$$\delta\tau \propto \frac{1}{\mathrm{L}} \qquad [1]$$

This additional stress is required to allow dislocations to bypass the obstacles, and the proportionality constant depends in large part upon whether dislocations can cut through the obstacles ("soft" obstacles), or must bypass them by bowing ("hard" obstacles).

In what follows, how eqn [1] applies for the important mechanisms listed above is discussed broadly, assuming pure metals or dilute alloys, and neglecting details such as the crystallography of defects or the underlying crystal structure of the base metal. Furthermore, the homogeneous nucleation of dislocations is not considered to contribute to strength, since most engineering metals and alloys already contain an appreciable density of dislocations ($\sim 10^{10}$–$10^{14}\,\mathrm{m}^{-2}$) prior to plastic flow.

Work Hardening

The principle underlying work hardening is that plastic flow induces structural changes which make subsequent plastic flow ever more difficult; the more it is deformed, the stronger a metal becomes. During plastic flow of a polycrystalline metal, work is dissipated by the motion and interaction of dislocations. Strain energy is stored through a net increase in dislocation line length through processes such as bowing around various obstacles and pinning points, and the sequential emission of new dislocations from, for example, Frank–Read sources.

As dislocations entangle, they can form sessile kinks or jogs which act as pinning points along the dislocation line, such that the obstacle spacing L is proportional to $\rho^{-1/2}$, with ρ the dislocation density. When this scaling is introduced into eqn [1], it yields the classical parabolic-hardening law used widely for polycrystalline metals:

$$\delta\tau = \alpha\mu b\sqrt{\rho} \qquad [2]$$

where the constants α, μ, and b have now been introduced. In this formulation μ is the shear modulus, b is the magnitude of the Burger's vector, and α is a temperature-dependent proportionality constant ~0.2–1 in the athermal limit.

Equation [2] has been experimentally validated for many metals; an example of data compiled for copper is shown in Figure 1. Perhaps counter-intuitively, the nature of the dislocation distribution does not affect the general relevance of eqn [2]. For example, in some materials dislocations self-assemble into inhomogeneous spatial configurations. In such cases, it is possible to parametrize, for example, the average dislocation cell size, and use it to produce additional scaling laws; these ultimately reduce to either eqn [2] or other very similar relationships.

Although eqn [2] is surprisingly general in its applicability, it is important to note that $\Delta\tau$ from work hardening is fundamentally limited by the maximum value of ρ that can be sustained in a given metal. With large amounts of plastic strain, the dislocation

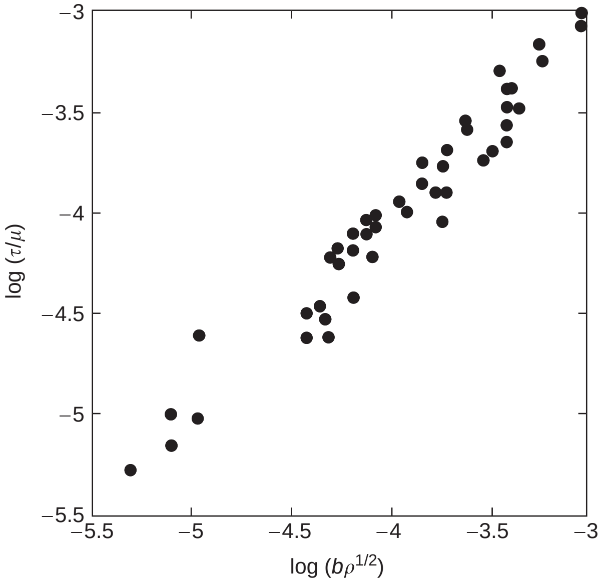

Figure 1 Data relating the shear strength of copper (normalized by the shear modulus μ) to the square root of dislocation density (normalized by the Burger's vector magnitude). The dislocation density has been obtained by chemical etching and optical microscopy on planar cross sections. (Data from Mecking H and Kocks UF (1981) Kinetics of flow and strain hardening. *Acta Metallurgica* 29: 1865–1875.)

density can increase by orders of magnitude before saturating at a temperature- and material-dependent value as high as $10^{16}\,\mathrm{m}^{-2}$. This saturation is a consequence of "dynamic recovery," wherein the production of new dislocation line length is offset by annihilation processes which become more active with increasing dislocation density. Nonetheless, strain hardening can increase a metal's strength by orders of magnitude compared with the stress required to move an isolated dislocation.

A topic of current research interest is the effect of nonuniform deformation on strain-hardening behavior, in which plastic strain gradients are necessitated by the test or microstructural geometry. Plastic strain gradients require the presence of "geometrically necessary" dislocations to accommodate them, so it has been speculated that higher total dislocation densities will result whenever such gradients exist. These effects become increasingly important at fine length scales, for example, in very small specimens or thin films, nanoindentation experiments, or for metals with fine scale microstructural features; in these cases, the strain gradients resulting from nonuniform deformation are steeper owing to the reduced dimensionality. In general, strain gradient effects are believed to occur in metals at length scales below ~100 μm.

Solid Solution Strengthening

For pure metals, the addition of a low concentration of a second component in solution can provide soft barriers to the motion of dislocations through the crystal. Solutes interact with dislocations through two main effects. First, solute atoms change the local values of elastic constants, which in turn change the line energy of a dislocation. Solute atoms which stiffen the matrix repel dislocations, while those which make the matrix more compliant attract them. Second, solute atoms added to a pure metal create distortions in the crystalline lattice, and the associated stress fields can interact with dislocations; again the interaction can be either attractive or repulsive, depending upon the size mismatch of the solute atoms with respect to the matrix and their position with respect to the dislocation core. Whether the solutes repel or attract dislocations, the net result is strengthening, as additional stress is required to force a dislocation to approach or depart, respectively, the vicinity of a solute atom.

Within a slip plane, the density of solute atoms is given by their concentration, c, and the spacing between solutes goes as $b\times c^{-1/2}$. Therefore, eqn [1] takes a parabolic form with respect to concentration:

$$\delta\tau = \beta\mu b\frac{\sqrt{c}}{b} \qquad [3]$$

where the proportionality constant β depends upon how strongly the solute atoms interact with dislocations. In the case of substitutional alloying additions, the stress field around solute atoms is approximately spherical, which leads to rather mild interactions and values of β much less than unity. For some crystal symmetries, the strain field associated with an interstitial solute can be nonspherical, providing much harder obstacles to dislocation motion, and values of β near unity. A common important example in this regard is the interstitial sites in a body-centered cubic lattice, where the distortion accompanying a solute is tetragonal. Models are available to predict β with reasonable accuracy in each of these cases. Figure 2 shows some classical data sets for substitutional and interstitial alloying, where the parabolic form of eqn [3] is validated and the relative strengths of the two obstacle types are apparent.

Particle Strengthening

In the same vein as solid solution atoms, fine dispersed particles can also serve as dislocation pinning points. When second-phase particles are present by virtue of nucleation and growth processes, the metal is said to be "precipitation strengthened," whereas the extrinsic incorporation of fine particles is generally referred to as "dispersion strengthening." In the simplest case these particles can be assumed to be "hard" obstacles to dislocation motion, and their strengthening effect is based upon the spacing of the particles, L. Unlike solute atoms or dislocation locks, particles have finite sizes that can be of similar order to the interparticle spacing, λ.

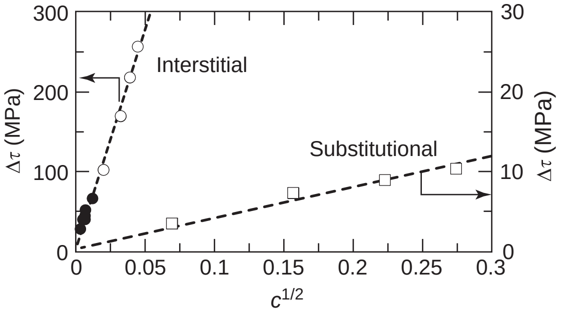

Figure 2 Classic examples of the concentration dependence of the solid solution strength increment $\Delta\tau$. Solutes with symmetric strain fields such as the substitutional case of Cu dissolved in Al (□) generally have a modest strengthening effect, while asymmetric strain fields associated with, for example, interstitial C in Fe (●) or N in Nb (○) produce more significant strengthening. (Data are from Wert CA (1950) *Journal of Metals* 188: 1242–1244, Evans PRV (1962) *Journal of the Less-Common Metals* 4: 78–91, and Koppenaal TJ and Fine ME (1962) *Transactions of the Metallurgical Society of AIME* 224: 347–353.)

Therefore, the effective obstacle spacing is given by $L \approx (\lambda - 2r)$, where r is the average radius of the particles. For small particles, the spacing of obstacles in the slip plane of a dislocation goes roughly as $v_f^{1/2} r^{-1}$, so the familiar parabolic strengthening law is recovered using eqn [1]:

$$\delta\tau = \gamma \mu b \frac{\sqrt{v_f}}{r} \tag{4}$$

The proportionality constant γ is close to unity for hard particles, for example, for dispersed ceramic particulates or very large precipitated particles in a metallic matrix.

In many cases the particulate obstacles are, at least in principle, capable of being sheared by the passage of a dislocation. In these cases, the obstacles are said to be "soft," and the energy penalty associated with shearing them is the source of strengthening. Some notable examples by which such soft obstacles can promote strengthening are as follows:

1. Coherent particles with a lattice parameter mismatch to the matrix phase create strain fields that interact with dislocations in a manner similar to that described above for solid solution strengthening.
2. The shearing of particles creates additional interfacial area and thereby increases the total interfacial energy of the system.
3. In "order strengthening," an incident dislocation creates an antiphase boundary (with an attendant interfacial energy term) in a chemically ordered particle.
4. The difference in elastic modulus between particle and matrix changes the dislocation energy as it traverses the particle, providing an obstacle to either its entrance or exit from the particle.

All of these "soft" obstacle strengthening mechanisms, as well as some more obscure ones, tend to obey the scaling law of eqn [4], with different scaling parameters γ that can also be functions of the particle size r. However, it should be noted that some derivations for case (2) can yield a linear volume fraction dependence.

Apart from the volume fraction dependence of particle strengthening described in detail above, the absolute magnitude of the average particle dimension also has a measurable impact on the strength required to pass a dislocation. Larger average particle sizes promote strengthening by creating "harder" obstacles, because a passing dislocation must traverse a larger area of precipitate, requiring more energy via mechanisms (2) and (3) above, while the stress field of a coherent particle also increases with size and enhances strength via mechanism (1). However, a larger average particle size necessitates a proportionally wider interparticle spacing if their volume fraction is held constant; this effect leads to a weakening via eqn [1]. Therefore, for a constant v_f, increasing the average particle size gives rise to a "cutting-to-bowing" transition, with the material strength first increasing and then decreasing with average particle size. These two regimes correspond to shearing of soft obstacles for small particle sizes (cutting), and pinning of dislocations at hard obstacles for larger particle sizes (bowing). An example of such a transition is shown for the technologically relevant nickel–aluminum system in Figure 3, in which the particles are precipitates of the Ni_3Al phase.

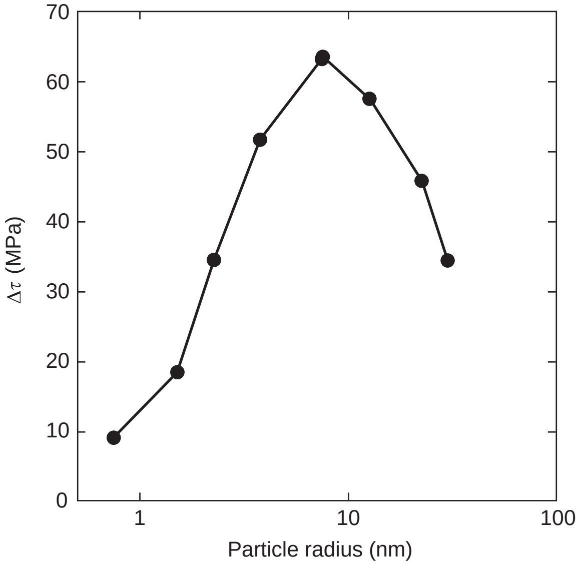

Figure 3 The strengthening of Ni due to the presence of a constant volume fraction dispersion of fine Ni_3Al precipitates with a given average radius. Over the range of radii <10 nm, increasing the precipitate size promotes strengthening, but beyond this range causes weakening. These regimes correspond to the "cutting" and "bowing" mechanisms, respectively. (Data from Brown LM and Ham RK (1971) Dislocation–particle interactions. In: Kelly A and Nicholson RB (eds.) *Strengthening Methods in Crystals*, pp. 12–135. London: Applied Science Publishers.)

Grain-Boundary Strengthening

Because the adjacent crystals at a grain boundary have a misorientation between both the slip plane traces and the slip directions, dislocations cannot, in general, transmit through grain boundaries without an additional increment of applied strain energy. For more extreme misorientations, the stress required for transmission can be higher than that required to activate a new dislocation source in the adjacent grain. In either case, dislocations on a common slip plane in the first grain tend to pile up at the grain boundary, until the stress at the head of the pileup becomes large enough to activate slip in the second grain. In this manner, grain boundaries present very "hard" obstacles to dislocation motion, but they are not point obstacles in the same vein as solute atoms or particles. Therefore, the scaling law of eqn [1] does not simply apply to the case of boundary strengthening, although a similar parabolic hardening law does emerge from analysis of the slip transmission problem:

$$\delta\tau = \kappa\frac{1}{\sqrt{d}} \qquad [5]$$

where d is the average grain size of the metal and κ is a material-specific constant with units of $(\text{length})^{1/2}$; eqn [5] is commonly referred to as the Hall–Petch relationship.

In Figure 4 the hardness, which is linearly proportional to strength, is plotted for pure Ni as a function of the reciprocal square root of grain size. The data from multiple authors indicate that the strength increases linearly with $d^{-1/2}$, and eqn [5] holds over orders of magnitude in grain size, from hundreds of microns in standard engineering materials down into the increasingly important nanocrystalline regime. As evidenced by the conformity of the data from various authors working on different specimens, eqn [5] is quite robust. Potentially complicating issues such as distributions of grain size or grain-boundary misorientation tend to be subsidiary to the scaling law of eqn [5], and are subsumed in the constant κ. Far stronger variations are observed from one material to another, most particularly depending on the number of slip systems available.

A current topic of particular interest in the area of grain-boundary strengthening is the validity of the Hall–Petch relationship at grain sizes in the nanometer range, where extreme strength has been reported. However, at a grain size of zero, the Hall–Petch relationship would predict an unphysical infinite strength, so it has been widely speculated that eqn [5] will break down at nanometer length scales. Recent experimental and computational work has supported this speculation, including the experimental data for nickel shown in Figure 4 below ~12 nm. This breakdown is associated with the activation of deformation mechanisms normally associated with high temperature, as will be discussed in more detail in a later section.

Low-Temperature Continuum-Level Strengthening

On a coarser structural scale, it is possible to strengthen a base metal by adding a second phase that can bear a disproportionate fraction of the load. This is often desirable when the base metal has properties critical to the application, such as low density, high

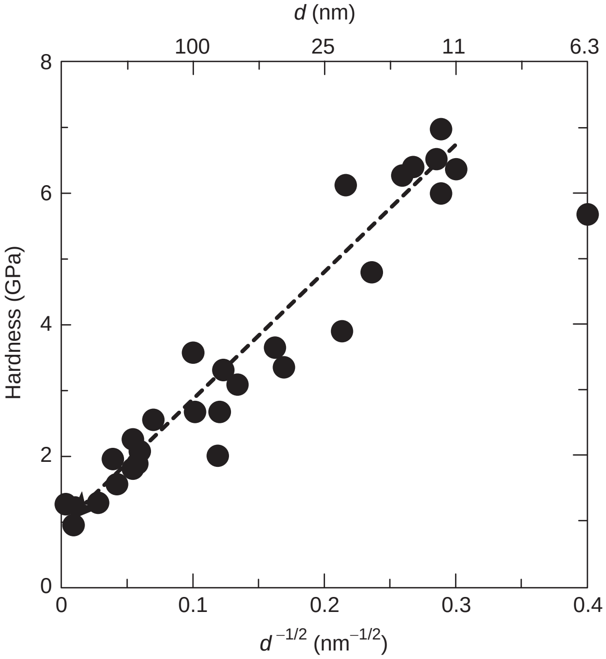

Figure 4 A typical "Hall–Petch" plot showing the hardness (which is proportional to the yield stress) of nickel as a function of the reciprocal square-root grain size, *d*. (Data are collected in Schuh CA *et al.* (2002) *Scripta Materialia* 46: 735–740, from various other sources.)

ductility, conductivity, or corrosion resistance, but lacks sufficient mechanical strength. The concept of load sharing is the basis of many technological structural materials from reinforced concrete to advanced polymeric composites. In the area of metallurgy, load sharing operates in microstructures with second phases formed *in situ*, such as steels containing coarse iron carbide or martensite phases, as well as in metal–matrix composites such as SiC-reinforced aluminum.

The load-sharing mechanism arises completely due to mismatch between the mechanical properties of the constituent phases, and, from a mechanistic perspective, can be regarded as independent of microscale mechanisms; dislocation interactions with coarse second phases are less important than the global transfer of load that results from such interactions. Accordingly, continuum mechanical approaches are generally used to derive the strengthening effect from load transfer. If the two phases or components of the microstructure are initially deformed only elastically, then the only variable controlling the strength of the dual-phase structure is the fraction of the applied stress that is carried by each. The total applied stress σ partitions such that the average stress carried by each phase (σ_1 and σ_2 for phase "1" and "2," respectively) obeys

$$\sigma = \sigma_1(1-v_f)+\sigma_2 v_f \qquad [6]$$

where v_f is the volume fraction of phase 2. Although this rule is generally true for any dual-phase structure when the stresses are averaged over the volume of the material, eqn [6] is not always useful to predict, for example, yield strength. This is because the local values of stress may be significantly concentrated, leading to local yielding in one of the phases. Despite this limitation, eqn [6] illustrates the basic principle of load transfer, where a stronger phase can relieve the stress borne by the weaker, giving a strength intermediate between the two components. Accurate predictions of yield and fracture strengths for dual-phase materials are dependent on the details of the composite geometry, for which a vast literature exists. The reader is referred to the "Further reading" section for more detailed treatments of specific cases.

Limitations of Strengthening Mechanisms due to Thermal Activation

The strengthening mechanisms described above can all be understood on an athermal basis, and are best applied in the limit where diffusional rearrangement of matter is slow. When dislocation motion and diffusion have similar timescales, for example, at high temperatures, the above scaling laws no longer strictly apply. In these cases, new physics are required to accurately predict the strength and rheology of metals. Although it is beyond the scope of this article to treat diffusive deformation mechanisms in detail, it is important to appreciate the limitations on the mechanisms described above for cases in which (1) bulk diffusion and (2) interfacial or grain-boundary diffusion are active at the deformation temperature.

Bulk Diffusion Effects

For many of the strengthening mechanisms described above, the motion of dislocations (particularly those of edge character) is considered to be restricted to a plane. However, the climb of edge dislocations out of their slip plane can occur by the absorption or emission of vacancies at the dislocation core. In many cases, this enables an additional means for obstacle bypass, albeit one that is rate-limited by the diffusive flow of vacancies to (or from) the dislocation core. The supply of vacancies needed to enable dislocation climb can flow either through the bulk, which generally requires temperatures above about two-thirds of the melting temperature, T_m, or along the core of the dislocation itself, which can be significant at somewhat lower temperatures above about $T_m/3$.

For solid-solution strengthened materials, diffusion can also lead to mobility of the obstacles themselves. In cases where there is an attractive interaction between solute atoms and dislocations, there is a tendency for these features to move in tandem. For example, at temperatures where the solute mobility is high, the motion of dislocations becomes a viscous process as the solute atoms follow the moving dislocation. At somewhat lower temperatures, the phenomenon known as "strain-aging" can occur, whereby plastic deformation initially detaches dislocations from solute pinning points, but extended time or thermal exposure can allow solutes to redistribute and again pin the dislocations. For substitutional solid solutions, the solute can be regarded as essentially immobile at temperatures below approximately $T_m/2$, while for interstitial solid solutions this limit can be considerably lower, down even to ambient temperature.

In multiphase microstructures, high temperatures or long durations can also lead to evolution of the size and spacing of precipitated obstacles. During this so-called "coarsening" process, the volume fraction of precipitate phase remains constant while the average precipitate size increases linearly with the cube root of time. As described above, a limited amount of such particle growth can be beneficial, but the maximum strength associated with the cutting-to-bowing transition generally occurs at very fine precipitate sizes, such that microstructural coarsening usually leads to weakening. This issue is sometimes suppressed in practice through the addition of slow diffusing elements that decelerate coarsening. Finally, coarsening is not usually an issue for dispersion-strengthened materials, which employ particles with low solubility and/or diffusivity in the matrix.

Intercrystalline Diffusion Effects

Additional time-dependent deformation mechanisms are associated with the diffusive rearrangement of atoms in intercrystalline regions such as grain and phase boundaries or triple junctions. For example, it is possible for strain to be accommodated solely by the diffusional flow of atoms along grain boundaries, from interfaces under net compression to those in net tension. For fine microstructures, grains can even become mobile relative to one another through the operation of viscous "grain-boundary sliding" and stress-induced grain rotations. Although these mechanisms do not directly influence all of the dislocation-based strengthening mechanisms described earlier, they can negate the expected scaling laws set forth above when they operate at a lower stress level than the athermal mechanisms. For example, the Hall–Petch scaling law that describes grain-boundary strengthening is known to fail at high temperatures, where finer grains actually promote weakening due to the dominance of diffusive deformation mechanisms. For these reasons it is common to develop coarse microstructures or even single crystals for high-temperature structural metals. Continuum-level load sharing can also be frustrated by interfacial diffusion and sliding between phases in a composite structure, increasing the fraction of load borne by the weaker matrix phase.

Because interfaces tend to have excess free volume, they also represent "short-circuit" diffusion paths that are more easily activated, and therefore intercrystalline diffusion can become significant at even lower temperatures than bulk diffusion. Additionally, since the net amount of matter that can be transported along interfaces scales with the interface density, these processes are also accelerated in microstructures of fine scale. For example, it is presumed that the high density of crystalline interfaces in nanocrystalline materials leads to diffusional deformation mechanisms even at room temperature, again leading to the breakdown of the Hall–Petch boundary strengthening law.

Further Reading

Courtney TH (2000) *Mechanical Behavior of Materials*, 2nd edn. New York: McGraw-Hill.

Hirth JP and Lothe J (1982) *Theory of Dislocations*, 2nd edn. Malabar, FL: Krieger Publishing Company.

Kocks UF and Mecking H (2003) Physics and phenomenology of strain hardeningthe FCC case. *Progress in Materials Science* 48: 171–273.

Martin JW (1980) *Micromechanisms in Particle-Hardened Alloys.* Cambridge: Cambridge University Press.

Mura T (1987) *Micromechanics of Defects in Solids*, 2nd edn. Dordrecht, The Netherlands: Martinus Nijhoff Publishers.

Nembach E (2000) Order strengtheningrecent developments with special reference to aluminum–lithium alloys. *Progress in Materials Science* 45: 275–338.

This page intentionally left blank

Encyclopedia of Condensed Matter Physics

Second Edition

EDITOR-IN-CHIEF:

Tapash Chakraborty
University of Manitoba, Winnipeg, Manitoba, Canada

SECTION EDITORS:

Ana M. Sanchez
Department of Physics, University of Warwick, Coventry, United Kingdom

Hideo Aoki
Department of Physics, University of Tokyo, Tokyo, Japan

Robert H. Blick
Center for Hybrid Nanostructures, University of Hamburg & DESY, Hamburg, Germany

Roberto Raimondi
Mathematics and Physics Department, Roma Tre University, Rome, Italy

Rudolf A. Roemer
Department of Physics, University of Warwick, Coventry, United Kingdom

Vladimir Mihajlovic Fomin
Leibniz Institute for Solid State and Materials Research (IFW), Dresden, Germany

Volume ISBN
ISBN 978-0-443-21825-5
9 780443 218255

Set ISBN
ISBN 978-0-323-90800-9
9 780323 908009

ELSEVIER

ACADEMIC PRESS
An imprint of Elsevier
elsevier.com/books-and-journals

ENCYCLOPEDIA OF CONDENSED MATTER PHYSICS

SECOND EDITION

This page intentionally left blank

ENCYCLOPEDIA OF CONDENSED MATTER PHYSICS

SECOND EDITION

EDITOR-IN-CHIEF

Tapash Chakraborty[*]

Professor, Tier-I Canada Research Chair, University of Manitoba, Winnipeg, MB, Canada

VOLUME 4

ELSEVIER

---

[*] Retired.

Elsevier
Radarweg 29, PO Box 211, 1000 AE Amsterdam, Netherlands
The Boulevard, Langford Lane, Kidlington, Oxford OX5 1GB, United Kingdom
50 Hampshire Street, 5th Floor, Cambridge MA 02139, United States

Copyright © 2024 Elsevier Ltd. All rights reserved

No part of this publication may be reproduced or transmitted in any form or by any means, electronic or mechanical, including photocopying, recording, or any information storage and retrieval system, without permission in writing from the publisher. Details on how to seek permission, further information about the Publisher's permissions policies and our arrangements with organizations such as the Copyright Clearance Center and the Copyright Licensing Agency, can be found at our website: www.elsevier.com/permissions.

This book and the individual contributions contained in it are protected under copyright by the Publisher (other than as may be noted herein).

Notices
Knowledge and best practice in this field are constantly changing. As new research and experience broaden our understanding, changes in research methods, professional practices, or medical treatment may become necessary.

Practitioners and researchers may always rely on their own experience and knowledge in evaluating and using any information, methods, compounds, or experiments described herein. In using such information or methods they should be mindful of their own safety and the safety of others, including parties for whom they have a professional responsibility.

To the fullest extent of the law, neither the Publisher nor the authors, contributors, or editors, assume any liability for any injury and/or damage to persons or property as a matter of products liability, negligence or otherwise, or from any use or operation of any methods, products, instructions, or ideas contained in the material herein.

Library of Congress Cataloging-in-Publication Data
A catalog record for this book is available from the Library of Congress

British Library Cataloguing-in-Publication Data
A catalogue record for this book is available from the British Library

ISBN 978-0-32-390800-9

For information on all publications visit our website at http://store.elsevier.com

ELSEVIER Book Aid International
Working together to grow libraries in developing countries
www.elsevier.com • www.bookaid.org

Publisher: Oliver Walter
Acquisitions Editor: Oliver Walter
Content Project Manager: Naman Negi
Associate Content Project Manager: Nandhini Mahendran
Designer: Mark Rogers

EDITOR-IN-CHIEF BIOGRAPHY

Tapash Chakraborty is a retired professor of physics from the University of Manitoba, Canada, where he was also the Canada Research Chair in Nanoscale Physics (2003–17). His research focus has been on many-body theories of various quantum materials, such as nuclear matter, helium liquids, and electron-hole liquids, that he studied under the tutelage of late Professor Manfred Ristig, at the University of Köln (1979–81). Just a year after the discovery of the fractional quantum Hall effect, he (working with his coworkers) demonstrated that electron–electron interactions could actually lead to quantum Hall states with nontrivial spin configurations, and that the low-lying excitations could be described as "spin-reversed quasiparticles." This prediction motivated much experimental work from laboratories around the world, as a result of which the concept of spin-reversed quasi-particles was established.

Similarly, his work on the quantum Hall states in double layer systems has received much attention from the community. Furthermore, Dr. Chakraborty (working with Dr. P. Maksym and others) made pioneering contributions to the many-electron theory of quantum dots. Dr. Chakraborty has also contributed to the theory of electronic properties of various nanoscale systems, such as spin-orbit coupled quantum dots, quantum rings, and single- and double-layer graphene (primarily with Dr. V. Apalkov). He has authored many books and reviews: the book with Dr. Pietiläinen on the quantum Hall effect and the single-authored book on quantum dots have become standard references in their respective fields.

This page intentionally left blank

EDITORIAL ADVISORY BOARD

Ana M. Sanchez
Department of Physics, University of Warwick, Coventry, United Kingdom

Hideo Aoki
Department of Physics, University of Tokyo, Tokyo, Japan

Robert H. Blick
Center for Hybrid Nanostructures, University of Hamburg & DESY, Hamburg, Germany

Roberto Raimondi
Mathematics and Physics Department, Roma Tre University, Rome, Italy

Rudolf A. Roemer
Department of Physics, University of Warwick, Coventry, United Kingdom

Vladimir Mihajlovic Fomin
Leibniz Institute for Solid State and Materials Research (IFW), Dresden, Germany

This page intentionally left blank

INTRODUCTION

> Electrons in orbits contained by the quantum,
> And atoms conjoined by the dipolar force,
> Gravity balanced by pressure
> And flap of a wing.
> Here, I remember the angles and curves,
> Calculus, I learned it all –
> Each bird bit and moon fracture
> Fixed by the symmetries,
> Airborne and airless, aloft.
>
> – Alan Lightman: *Song of Two Worlds*

Condensed matter physics (CMP) is the largest discipline in physics, involving a wide variety of interesting concepts and challenges. To quote Leggett (1992), CMP embraces topics "as diverse as traditional solid-state physics, neutron stars and the physics of biological matter." He further added that, by a liberal definition "just about all of physics outside atomic, nuclear and particle physics and cosmology" fall in this vast enterprise[1]. One of the primary goals of CMP is to explore the fundamental properties of matter—solids, liquids or gasses—comprising a large number of *interacting* constituent particles (Laughlin and Pines, 2000). The quantum-mechanical nature of these many-body systems makes condensed-matter highly nontrivial, sometimes counterintuitive and even astonishing. Superconductivity and the fractional quantum Hall effect (FQHE) naturally fall within that category. In fact, for the past four decades, the quantum Hall effects (QHEs) have been the epitome of elegant CMP (von Klitzing et al., 2020). Our fundamental system of units has been redefined following the discovery of the QHE when the "von Klitzing constant" $R_K = 25,\ 812.8074593045\ \Omega$ came into being (von Klitzing, 2019; Nawrocki, 2019). Observation of the QHE in graphene[2] was crucial in determining the Dirac nature of charge carriers there (see for example, Jiang et al., 2007).

Another effect that outwardly resembles the QHE but is conceptually quite different is the FQHE, which is a quintessential manifestation of electron correlations governed by the Coulomb interaction (Störmer, 1992; Eisenstein and Stormer, 1990). To explain this fascinating effect, Laughlin (1983) introduced his eponymous wave function that not only provided the foundation for understanding the effect but also triggered a new wave of ideas with impact far beyond the realm of CMP[3]. Who would have imagined that a large collection of interacting electrons confined on a plane in a perpendicular magnetic field would result in elementary excitations (quasiholes and quasiparticles) (Chakraborty and Pietiläinen, 1988, 1995; Halperin, 1983; Clark and Maksym, 1989) carrying fractional electron charge and obeying the exotic exchange statistics of anyons (Halperin, 1984; Arovas et al., 1984)? These quasiparticles and quasiholes of the Laughlin state still remain an enigma (Laughlin, 1984; Chakraborty, 1985; Morf and Halperin, 1986). Fractional statistics is a truly path-breaking concept in CMP that was introduced by Leinaas and Myrheim (1977), and has been recently confirmed experimentally (Bartolomei et al., 2020; Nakamura et al., 2020).

Much of the history of CMP can be viewed as a series of paradigm shifts[4]. The field evolved rapidly through frequent ground-breaking discoveries that challenged existing paradigms and opened up new applications, and this evolution is expected to continue (Leggett, 2018; Cohen, 2008). For example, our current understanding of

the FQHE required deep mathematical analysis and a wide range of experimental exploration, which revealed a treasure trove of unique phenomena that are yet to be fully understood or explained. Other studies of electron correlations in low spatial dimensions have ushered in many groundbreaking notions, such as Pfaffian states, Majorana fermions in condensed matter, Chern insulators, and topological quantum materials that promise a fault tolerant means to perform quantum computation. The presence of incompressible FQHE states in monolayer graphene (Apalkov and Chakraborty, 2006), bilayer graphene (Apalkov and Chakraborty, 2010, 2011), and double-layer graphene (Liu et al., 2019) has demonstrated the robustness of the effect, and provides invaluable insight into the nature of this effect.

---

[1] Interestingly, some similarities do exist between the mathematical frameworks that describe low-temperature CMP and early-universe cosmology. See Kibble and Srivastava (2013).

[2] An isolated single layer of graphite consisting of carbon atoms bonded together in a hexagonal structure. See, e.g., Abergel et al. (2010).

[3] For example, an important aspect of Laughlin's theory is its seamless concinnity of classical plasma physics and the planar electron gas that has inspired others to use a similar approach to quark-gluon plasma (Lu, 2022).

[4] A detailed exposition of the meaning and examples of "paradigm shifts" (Kuhn-type) can be found in Leggett (2018).

The dynamics of an electron in a periodic potential subjected to a perpendicular magnetic field has been an intriguing problem for more than half a century (Obermair and Wannier, 1976; Osadchy and Avron, 2001)[5]. Within the nearest neighbor tight-binding description of the periodic potential the electron energy spectrum is described by the Harper equation (Harper, 1955). Numerical solution of this equation (Hofstadter, 1976) has revealed that the applied field splits the Bloch bands into subbands and gaps. As the field is varied, the splitting of band continues indefinitely, leading to bands within bands within bands. When plotted as a function of the magnetic flux per lattice cell, the energy spectrum depicts a *fractal* pattern (a self-similar pattern that repeats at every scale) and is known in the literature as Hofstadter's butterfly because of the resemblance of the pattern to butterflies[6]. Observation of the butterfly spectra in real systems is an arduous task. For example, in ordinary crystalline lattices, the required magnetic field to see the butterflies exceeds 1000 Tesla, which is far beyond the reach of present-day technology. Graphene seems to be the ideal system in the quest of those fractal butterflies (Weiss, 2013). It is interesting to note that a mathematical solution of the Harper equation, in contrast to the numerical solution mentioned above, remained a challenging problem (the so-called Ten Martini Problem) for mathematicians until it was solved (Avila and Jitomirskaya, 2006) in 2006.

Magnetism has been known to mankind since ancient times, and it remains a major topic in CMP. The road to understanding magnetism has been long and tortuous. At various times in history, magnets were claimed to have the healing power to cure a myriad of ailments that included epilepsy, arthritis, gout, and baldness. Magnets were the prime ingredients for the "elixir of life" by Paracelsus (1493–1541). Then there was the healing process of "animal magnetism" proposed by Franz Anton Mesmer (1734–1815) (mesmerism)[7], which was famously mocked in Mozart's *Così fan tutte* (Steptoe, 1986). Our current understanding of magnetism is deeply rooted in quantum mechanics as Van Vleck explained (Van Vleck, 1978): "Quantum mechanics is the key to understand magnetism. When one enters the first room with this key there are unexpected rooms beyond, but it is always the master key that unlocks each door." For centuries, the magnetism of certain rocks and metallic iron was only used for the practical purposes of direction finding, particularly navigation with a compass. Motors, generators, and electrical distribution networks appeared only in the 19th century after the discovery of the deep connection between electricity and magnetism. Magnetic order is a collective phenomenon akin to superconductivity and superfluidity that involves a very large number of particles. The rich variety of magnetically ordered states in solids, not only ferromagnetism but also antiferromagnetism, ferrimagnetism, and a range of noncollinear structures, was confirmed only in the middle of the 20th century, with the availability of neutron beams in research reactors. A range of new magnetic materials are taking their place as active layers in thin film sensors and memory devices (Baltz et al., 2018). Besides information storage (Blundell, 2001), important technical applications include magnetic resonance imaging (MRI) and the use of magnetic nanoparticles in medicine.

Many outstanding discoveries in magnetism and magnetic materials have resulted in rapid advances in information storage technology. Over the last two decades spintronics has emerged as an important field of research both from the point of view of fundamental science and advanced technological applications (Yamaguchi et al., 2021; Pinarbasi and Kent, 2022). The giant magnetoresistance (GMR) effect, the spin Hall effect, and the spin galvanic effects are typical examples of developments in the field. Spintronics aims at understanding how the spin degree of freedom of the electrical carriers can be controlled in order to obtain devices with new functionalities and better performance. This endeavor often combines concepts from different aspects of condensed matter systems, giving the topic a fascinating interdisciplinary flavor. Spintronic phenomena are now being studied in an impressive range of different materials ranging from metals to half-metals to semiconductors, graphene and other two-dimensional systems such as transition metal dichalcogenides.

---

[5] For a recent review on butterflies in graphene, see for example Chakraborty and Apalkov (2015).

[6] However, as one of the authors of this Encyclopedia has (somewhat humorously) pointed out, this butterfly has Lebesgue measure zero, that is, it cannot fly!.

[7] A wonderful account of the use of magnetism in medicine since ancient times can be found in Mourino (1991).

The GMR effect and the related tunnel magnetoresistance effect (TMR) found their first commercial use in magnetic field sensors for hard-disk read-heads, before broadening their field of application to include magnetic sensors for the automobile industry, solid-state compasses, biosensors, and nonvolatile magnetic memory (Hartmann, 2000). The ability to manipulate the magnetic state of ferromagnetic structures led to initial developments in spintronics, where the spin direction was controlled by externally applied magnetic fields. However, the push for downscaling and faster timescales has prompted research advances in the past decade where the manipulation of magnetic configurations is achieved by local electric currents (the spin torque effect) (Brataas et al., 2012; Locatelli et al., 2014). In recent years, various novel concepts, such as chiral spintronics, skyrmionic spin textures, and magnetic domain walls in spintronics, have been actively pursued. The rate of progress in spintronics is truly astounding (Editorial, 2022).

In the past century, superconductivity has raised many theoretical challenges and triggered numerous technical developments. Discovered in mercury in 1911, this unique phenomenon occurs when the electrical resistance of many metals and alloys drops to zero when cooled below about 4 K, the temperature of liquid helium. More significantly, the material expels magnetic flux and becomes perfectly diamagnetic. Superconductivity has been adopted or evaluated for a wide range of technical applications (Rogalla and Kes, 2012). These include electric power generation, electric power transmission, high-speed maglev transportation, and ultra-strong magnetic field generation in high-resolution MRI and other nuclear magnetic resonance (NMR) systems. Interestingly, it took almost 50 years after the original discovery for the phenomena to be explained by the BCS theory (Tinkham, 2004) of reciprocal-space electron pairing, via the electron–phonon interaction. This electron–phonon mediated superconductivity became known as “conventional superconductivity” after the discovery of “high-temperature superconductivity” (Müller and Bednorz, 1987) at liquid nitrogen temperatures in tetragonal copper oxides in 1986. This threw open a new challenge to explain the properties of strongly correlated *anisotropic* electronic systems. Further new classes of superconductors that remain to be properly understood include the iron-based pnictides discovered in 2008 (Hosono et al., 2018). Recently, a two-dimensional superlattice made from a twisted bilayer of “magic angle” graphene was found to exhibit unconventional superconductivity (Cao et al., 2018), driven by electron–electron interactions.

The phenomenon of spontaneous symmetry breaking (SSB) is ubiquitous in physics, and plays a fundamental role in CMP, particle physics, and even in cosmology. A classic illustration of SSB being Heisenberg’s 1928 paper on ferromagnetism (Heisenberg, 1928). It is responsible for various collective modes, such as the famous Nambu-Goldstone (NG) and Higgs modes. Named by Baker and Glashow (Baker and Glashow, 1962), SSB corresponds to the case where the ground or lowest-energy state does not have the symmetry of the underlying dynamics. Instead, multiple degenerate ground states are available and the symmetry breaking is *spontaneous* because it is not clear, a priori, which one of those ground states will be chosen. In this well-trodden territory a simple analogy of this abstruse concept given by A. Salam is illuminating (CERN, 1977): “Imagine a banquet where guests sit at round tables. A bird’s eye view of the scene presents total symmetry, with serviettes alternating with people around each table. A person could equally well take a serviette from his right or from his left. The symmetry is spontaneously broken when one guest decides to pick up from his left and everyone else follows suit.” Over the years, development of the concept of SSB has taken a circuitous route (Gaudenzi, 2022): “from the land of particle physics to the physics of many bodies (solids and nuclei), from there to the province of superconductivity, and from the latter back to particle physics ... .” SSB’s significance extends beyond the physics of the Higgs boson to the study of low-energy phenomena such as superconductivity, superfluidity, magnetism, and others. Historically, the particle physics community has been guided by this exploration in their quest to understand and discover particles like the Higgs boson. More to the point, when a continuous symmetry is spontaneously broken, a gapless mode, the NG mode, appears which governs the low-energy behavior of the system. As an example, in a solid, the acoustic phonon is the NG mode associated with translational symmetry breaking and determines the behavior of the specific heat at low temperature (the Debye T^3 law). Recently, signatures of Higgs and Goldstone modes have been proposed to exist in a perovskite oxide (Marthinsen et al., 2018), in other crystalline structures (Vallone, 2019), and also in various other quantum systems (Léonard et al., 2017). On a lighter note, it is the symmetry breaking that is claimed to have prevented the fabled donkey (Weintraub, 2012) in the parable by Jean Buridan (1300–50) from dying of starvation (Fubini, 1974).

Common to the theoretical descriptions of these phenomena across CMP and high-energy physics is Quantum field theory (QFT). QFT was originally developed to describe the fundamental processes in high-energy physics, but has now become a valuable tool to address problems across physics, in particular, in CMP (Fradkin, 2013; see also, Mustafa, 2023), statistical physics, modern quantum chemistry, and even in

pure mathematics (Folland, 2008). Advances in our understanding of strongly correlated electron systems in CMP such as high-temperature superconductivity and the FQHE have been aided by the QFT. It has facilitated the treatment of spontaneous symmetry broken states, such as superfluids. Interestingly, many of the conceptual developments in CMP have, in return, had a reciprocal impact in QFT. A spectacular example being Nambu's work in dynamical symmetry breaking (Weinberg, 1986; Nambu, 2009) in particle physics, based on the BCS theory of superconductivity.

A glass is a noncrystalline solid obtained by quenching a liquid. It has a liquid-like structure, but a transition from liquid to solid behavior occurs on cooling. It may have one of a continuum of possible ground states that exhibit frozen-in liquid-like disorder. The term "spin glass" was coined by B.R. Coles (Mydosh, 1993) in 1970 for a diluted magnetic material with frozen-in paramagnetic-like spin disorder where the magnetic moments interact with randomly varying positive or negative exchange interactions leading to a multitude of possible ground states with different, random orientations of the spins. As in a normal glass, the energy barriers between the continuum of metastable states prevent it from ever reaching equilibrium. This phase of condensed matter has been an important and productive area of research. Spin-glass models are conceptually simple, but embody sophisticated physics. These models have become a paradigm for the solution of complex optimization problems (Mézard, 2022): much like the undulating flight patterns of starlings around the skies over Rome (Parisi, 2023). After cooling from the paramagnetic phase, the spin glass remains out of equilibrium, and it slowly evolves. This aging phenomenon corresponds to the growth of a "spin-glass order" parameter, whose correlation length can be measured (Joh et al., 1999). A cooling temperature step during aging causes a partial "rejuvenation," while the "memory" of previous aging is stored and can be retrieved (Refregier et al., 1987; Bouchaud et al., 2001). Many glassy materials present aging, and rejuvenation and memory effects can be found in other cases, but they are usually less pronounced. Numerical simulations of these phenomena are under active investigation using custom-built computers (Baity-Jesi et al., 2023; Vincent, 2023). A general understanding of glassy systems, to which spin glasses bring some special insight, is being pursued. It was realized decades ago that the physics of spin glasses has deep connections with the behavior of complex biological systems. In fact, spin-glass type states in neural network models offer interesting insights into states of high and low brain activity, as observed in mammals (Recio and Torres, 2016). These analogies are potentially useful for applications in fields such as robotics and artificial intelligence (AI) (Andriuschenko et al., 2022).

One of the most spectacular phenomena in CMP, discovered in the last century, was Bose-Einstein condensation (BEC). This macroscopic quantum phenomenon had its genesis in the work of Satyendra Nath Bose (Bose, 1924; Blanpied, 1972; Tomczyk, 2022) (whose name is forever associated with bosons), and has fascinated physicists for decades, ever since the first observation of this exotic state of matter in an ultracold gas of rubidium atoms (Georgescu, 2020). Among the advances made in this field, we highlight only a few: simulation of correlated electron states, such as the FQHE state and a bosonic analog of the Laughlin state, and the famous BEC-BCS crossover from a BEC to a BCS superfluid of weakly bound Cooper pairs, as the interparticle interaction strength is varied. Noteworthy is the recent measurement of the dynamic structure factor in an ultracold Fermi gas of lithium-6 atoms in the "unitary" limit, where a linear phonon mode for low momentum transfer can be clearly discerned (Biss et al., 2022). Perhaps such a method might one day shed light on the Laughlin quasiparticle gap and the collective modes that are still largely unresolved (Chakraborty and Pietiläinen, 1988, 1995; Halperin, 1983; Clark and Maksym, 1989).

Liquid helium, ^{4}He, and the less common isotope ^{3}He are unique quantum systems (Volovik, 2009). They remain liquid even at absolute zero temperature, a direct manifestation of Heisenberg's uncertainty principle and zero-point energy. The light mass of helium atoms and their weak interatomic attraction leads to a substantial zero-point kinetic energy and the system remains in the liquid state at ambient pressure. Solidification occurs when a pressure of about 25 MPa is applied. The different quantum statistics of the two helium isotopes (^{4}He is a boson while ^{3}He is a fermion) are responsible for the different physical characteristics of the two systems. Microscopic approaches to understand the ground state and low-energy excitations of the liquid state have occupied researchers for many decades (see for example, Ristig and Clark, 1976; Lam et al., 1977). These highly correlated quantum fluids have been established as systems where the efficacies of different many-body theories can be tested (Kallio and Smith, 1977; Lantto et al., 1977). These systems have been described as Ariadne's thread in this Encyclopedia, where the strongly interacting constituent particles are treated by a variety of ingenious theoretical and experimental approaches. Interestingly, liquid helium has been proposed to be a medium to design multiexcitation detectors to probe *dark matter* (Schutz and Zurek, 2016) in the keV mass limit. Although this looks far afield from CMP, the interface between CMP and high-energy particle physics could inspire new horizons in CMP, as discussed earlier.

CMP also has an enormous impact on our daily lives with unceasing technological innovation stemming directly from the advances in CMP research. It is also closely associated with the progress of our understanding of materials science and mechanical, chemical, and electrical engineering that deals with properties of novel materials and devices. As some authors have very aptly pointed out (Chaikin and Lubensky, 1995): The use and understanding of matter in its condensed (liquid or solid) state have gone hand in hand with the advances of civilization and technology since the first use of primitive tools. So important has the control of condensed matter been to man that prehistoric ages—the Stone Age, the Bronze Age, the Iron Age—are named after the material dominating the technology of the time. In fact, modern civilization is entirely dependent on our deep understanding and practical use of materials, old and new: Steel, glass, and concrete have shaped our modern living with comfort, health, longevity, and material wealth. All around us, from a tiny paper clip to giant skyscrapers, from jet planes to modern medicines, and the ubiquitous plastics that are integrated into nearly all aspects of human life, are testaments to our control over the myriad behavior of materials (Miodownik, 2014). Today, a large number of materials are designed by using principles of quantum mechanics (Freeman, 2002).

The Silicon chip that launched the information age is a great example of the effect of CMP on our daily lives. The scaling of transistors down to the nanometer range has enabled them to be embedded in greater numbers in the all-pervasive electronic devices that have transformed every facet of life all around the world. The transition from room-size to pocket-size computers with ever increasing computational power and memory, that occurred in only a few decades, epitomizes the unrelenting progress made in this direction. Advances in nanoscale research have opened the door to exploration of the natural world at the ultra-small scale (Chakraborty, 2022), with the potential to shape our future world.

Quantum dots (QDs), the quasi-zero-dimensional electron systems, are one of the most extensively studied nanostructures in the past three decades. They represent the ultimate reduction in dimensionality of a semiconductor device. Here the electrons are confined (either electrostatically or structurally) in all three directions and occupy spectrally sharp energy levels similar to those found in atoms (Chakraborty, 1999), hence the popular moniker *artificial atoms* (Maksym and Chakraborty, 1990). QDs and other similar nanostructures (Chakraborty, 2003) offer a rich variety of fundamental phenomena that result from manipulation of single electrons (single electronics) or single spins at the nanoscale. The study of interacting electrons in a QD requires large-scale numerical computations involving matrices of dimensions in the millions ("monster matrices") (Chakraborty and Pietiläinen, 2005; Pietiläinen and Chakraborty, 2006). QDs are also thought to have vast potential for future technological applications. One prominent example being quantum cryptography where the QDs are used in single photon emitters (Nowak et al., 2014), and in single photon detectors (Shields et al., 2000). Quantum cryptography, in turn, forms the basis of the *quantum Internet* (Liao et al., 2018). Other applications include lasers, and spintronics in quantum computing, entertainment industry (Bourzac, 2013), and even in biology (Bruchez and Holz, 2007).

Research in recent years has increasingly revealed that quantum phenomena are also ubiquitous in the natural world (Ball, 2011). They govern how birds are able to navigate around the globe using Earth's magnetic field or how plants use photosynthesis to harvest sunlight for conversion to chemical energy. All depend on subtle quantum effects that are now coming to light, thereby ushering the topic of quantum biology into CMP. Deoxyribonucleic acid (DNA), the molecule responsible for storage of genetic information in the cells of all living organism, is entrusted with the task of preserving, copying, and transmitting information that are necessary for living beings to grow and function. It is often referred to as the body's hereditary material as DNA is replicated and transmitted from parents to their offspring. This "molecule of life" was discovered in 1869 by Friedrich Miescher in Tübingen, Germany, who called it "nuclein," as it was isolated from the nucleus of white blood cells (Dahm, 2005; Thess et al., 2021). It took more than eighty years from that momentous event, to discover that DNA has a right-handed double-helix structure with appropriate base pairing (Watson and Crick, 1953; Klug, 2004). That discovery was so important that it has been compared with the discovery of the atomic nucleus in physics (Frank-Khamenetskii, 1997). Understanding the structure of the atom heralded quantum physics, while understanding of the structure of DNA brought forth the field of molecular biology.

DNA has several remarkable properties that make this molecule a prime candidate for nano-electronic materials (Chakraborty, 2007). These include molecular recognition and the ability to self-assemble via the complementarity of the base sequences on the two strands, which means that DNA can be integrated error-free in current semiconductor technology. DNA can also detect information about its own integrity that can trigger its eventual repair mechanism. All these properties are perfectly suitable for developing nanoscale electronics involving DNA

(Taniguchi and Kawai, 2006). Despite the promise of harnessing biology to realize integrated molecular electronics remains fascinating, much work remains to be done to make it a reality (Braun and Keren, 2004).

Protein molecules play a vital role in all living organisms. They are described as Nature's robots (Tanford and Reynolds, 2001) because for every imaginable task required in a living organism, and for every step of that task, there is a protein designed to carry it out. These proteins are even programmed to know when to turn on or off. Just as the twenty-six letters in the alphabet can spell out hundreds of thousands of words, there are twenty different naturally occurring amino acids that can be combined into many more different proteins than there are atoms in the known universe! Protein's biological function is determined by its unique and native three-dimensional structures that are characteristic of individual proteins (Gomes and Faísca, 2019; Echenique, 2007). The question of how proteins fold to their unique, compact, and highly organized functional states has remained an enduring challenge ("The protein-folding problem") (Chan and Dill, 1993; Dill and MacCallum, 2012; Wolynes and Eaton, 1999). Recently, there has been a tremendous development in this area of research. In November 2020, an AI program called AlphaFold, designed to tackle the problem of protein folding, predicted the three-dimensional structures of almost every protein known to science—about 200 millions in all (Jumper et al., 2021). AlphaFold uses a machine learning methodology to bring together information from preexisting knowledge of protein structures, and other geometric and physical constraints to predict protein structures. While this has been heralded a watershed moment in structural biology (Perrakis and Sixma, 2021), there are many key questions that AlphaFold cannot address yet. These include aspects of protein behavior that cannot be understood from a static structure, such as how proteins respond to their environment or how intrinsically disordered proteins actually are organized. Some authors (Nasser et al., 2021) have likened it to solving a crime story: while AlphaFold presents a snapshot in time, the question about how we get there remains unanswered. Biological systems have developed elaborate mechanisms to ensure that proteins fold correctly, or otherwise, they are detected and degraded before any serious harm can result to the host organism. However, protein misfolding does happen and that misfolding in the cell is linked to an array of diseases, including cancers, cardiovascular disease, type II diabetes, and numerous neurodegenerative diseases, such as Alzheimer's, Parkinson's, and Huntington's disease. NMR spectroscopy has been an important technique to study protein folding where valuable insights are gained into many aspects of the folding process (Jane Dyson and Wright, 1996).

In this Encyclopedia, we strive to present a taste of all the developments in CMP described above (and much more), written by experts in the field. We are keenly aware that many important and interesting topics are not covered here. However, that is not for want of trying. As some authors had rightly pointed out (Hoddeson, 1992): The field is huge and varied and lacks the unifying features beloved of historians, neither a single hypothesis or set of basic equations underpin the field, as in quantum mechanics or relativity theory, nor a single spectacular and fundamental discovery such as uranium fission for nuclear technology or the structure of DNA for molecular biology. CMP owes what unity it has simply to a common concern with solid and liquid materials. This encompasses such a large range of theories and methods that the field resembles a confederation of interest groups rather than a single entity. Clearly, the task of collecting everything in one place is a monumental endeavor, but we do hope that our compilation of a large number of chapters in this five-volume work, covering a broad range of in-depth descriptions of varied phenomena in CMP will be a treasured source of facts and ideas for the community.

It is undeniably true that there would have been no Encyclopedia without the extraordinary contributions of the large number of authors whose valuable time and efforts brought this project to fruition. My sincere thanks to all of them. I also wish to extend my deep appreciation to the staff at Elsevier for their skillful handling of this huge project. The cover image was created by Hong-Yi Chen from National Taiwan Normal University. The image below was created by Elisabetta Collini, one of the authors. My deepest appreciation to them for taking the time to do this work. Finally, my sincere thanks to the Section editors, Vladimir Fomin, Ana Sanchez, Roberto Raimondi, Hideo Aoki, Rudolf Römer, and Robert Blick for the effort they all expended, that has contributed to the success of this venture. Special thanks go to Vladimir Fomin and Ana Sanchez for securing a large share of the chapters and for their enduring help in providing valuable advice and support to bring the project to fruition. Thanks are also due to many of my friends and colleagues, in particular, Michael Coey, Jürg Fröhlich, Sinéad Griffin, Peter Maksym, Eric Vincent, and Jakob Yngvason for their careful and critical reading of the introduction.

Tapash Chakraborty
St. Catharines
Ontario, Canada

References

Abergel DSL, Apalkov V, Berashevich J, Ziegler K, and Chakraborty T (2010) Properties of graphene: A theoretical perspective. *Advances in Physics* 59: 261. https://doi.org/10.1080/00018732.2010.487978.

Andriuschenko P, Kapitan D, and Kapitan V (2022) A new look at the spin glass problem from a deep learning perspective. *Entropy* 24: 697. https://doi.org/10.3390/e24050697.

Apalkov VM and Chakraborty T (2006) Fractional quantum Hall states of Dirac electrons in graphene. *Physical Review Letters* 97: 126801. https://doi.org/10.1103/PhysRevLett.97.126801.

Apalkov VM and Chakraborty T (2010) Controllable driven phase transitions in fractional quantum Hall states in bilayer graphene. *Physical Review Letters* 105: 036801. https://doi.org/10.1103/PhysRevLett.105.036801.

Apalkov VM and Chakraborty T (2011) Stable pfaffian state in bilayer graphene. *Physical Review Letters* 107: 186803. https://doi.org/10.1103/PhysRevLett.107.186803.

Arovas D, Schrieffer JR, and Wilczek F (1984) Fractional statistics and the quantum Hall effect. *Physical Review Letters* 53: 722. https://doi.org/10.1103/PhysRevLett.53.722.

Avila A and Jitomirskaya S (2006) Solving the ten martini problem. *Lecture Notes in Physics* 690: 5. https://doi.org/10.1007/3-540-34273-7_2.

Baity-Jesi M, et al. (2023) Memory and rejuvenation effects in spin glasses are governed by more than one length scale. *Nature Physics* 19: 978–985. https://doi.org/10.1038/s41567-023-02014-6.

Baker M and Glashow SL (1962) Spontaneous breakdown of elementary particle symmetries. *Physics Review* 128: 2462. https://doi.org/10.1103/PhysRev.128.2462.

Ball P (2011) Physics of life: The dawn of quantum biology. *Nature* 474: 272. https://doi.org/10.1038/474272a.

Baltz V, et al. (2018) Antiferromagnetic spintronics. *Reviews of Modern Physics* 90: 015005. https://doi.org/10.1103/RevModPhys.90.015005.

Bartolomei H, et al. (2020) Fractional statistics in anyon collisions. *Science* 368: 173. https://doi.org/10.1126/science.aaz5601.

Biss H, et al. (2022) Excitation spectrum and superfluid gap of an ultracold Fermi gas. *Physical Review Letters* 128: 100401. https://doi.org/10.1103/PhysRevLett.128.100401.

Blanpied WA (1972) Satyendranath Bose: Co-founder of quantum statistics. *American Journal of Physics* 40: 1212. https://doi.org/10.1119/1.1986805.

Blundell S (2001) *Magnetism in Condensed Matter*. New York: Oxford U.P.

Bose SN (1924) Plancks gesetz und lichtquantenhypothese. *Zeitschrift für Physik* 26: 178. https://doi.org/10.1007/BF01327326.

Bouchaud J-P, Dupuis V, Hammann J, and Vincent E (2001) Separation of time and length scales in spin glasses: Temperature as a microscope. *Physical Review B* 65: 024439. https://doi.org/10.1103/PhysRevB.65.024439.

Bourzac K (2013) Quantum dots go on display. *Nature* 493: 283. https://doi.org/10.1038/493283a.

Brataas A, Kent AD, and Ono H (2012) Current-induced torques in magnetic materials. *Nature Materials* 11: 372. https://doi.org/10.1038/nmat3311.

Braun E and Keren K (2004) From DNA to transistors. *Advances in Physics* 53: 441. https://doi.org/10.1080/00018730412331294688.

Bruchez MP and Holz CZ (2007) *Quantum Dots: Applications in Biology*. New Jersey: Humana Press. https://doi.org/10.1385/1597453692.

Cao Y, et al. (2018) Unconventional superconductivity in magic-angle graphene superlattices. *Nature* 556: 43. https://doi.org/10.1038/nature26160.

CERN. (1977) Gauge theories with the lid, partially, off. *CERN Courier* 17: 271. https://cds.cern.ch/record/1730245/files/vol17-issue9-p271-e.pdf.

Chaikin PM and Lubensky TC (1995) *Principles of Condensed Matter Physics*. Cambridge University Press. https://doi.org/10.1017/CBO9780511813467.

Chakraborty T (1985) Elementary excitations in the fractional quantum Hall effect. *Physical Review B* 31: 4026. https://doi.org/10.1103/PhysRevB.31.4026.

Chakraborty T (1999) *Quantum Dots: A Survey of the Properties of Artificial Atoms*. Amsterdam: North-Holland. https://doi.org/10.1016/B978-0-444-50258-2.X5000-7.

Chakraborty T (2003) Nanoscopic quantum rings: A new perspective. *Advances in Solid State Physics* 43: 79. https://doi.org/10.1007/978-3-540-44838-9_6.

Chakraborty T (ed.) (2007) *Charge Migration in DNA*. Springer. https://doi.org/10.1007/978-3-540-72494-0.

Chakraborty T (2022) *Nanoscale Quantum Materials: Musings on the Ultra-Small World*. CRC Press. https://doi.org/10.1201/9781003090908.

Chakraborty T and Apalkov VM (2015) Fractal butterflies of Dirac fermions in monolayer and bilayer graphene. *IET Circuits, Devices and Systems* 9: 19. https://doi.org/10.1049/iet-cds.2014.0275.

Chakraborty T and Pietiläinen P (1988) *The Fractional Quantum Hall Effect*. Springer Verlag. https://doi.org/10.1007/978-3-642-97101-3.

Chakraborty T and Pietiläinen P (1995) *The Quantum Hall Effects*, 2nd. Springer. https://doi.org/10.1007/978-3-642-79319-6.

Chakraborty T and Pietiläinen P (2005) Optical signatures of spin-orbit interaction effects in a parabolic quantum dot. *Physical Review Letters* 95: 136603. https://doi.org/10.1103/PhysRevLett.95.136603.

Chan HS and Dill KA (1993) The protein folding problem. *Physics Today* 46: 24. https://doi.org/10.1063/1.881371.

Clark R and Maksym P (1989) Fractional quantum Hall effect in a spin. *Physics World* 2: 39. https://doi.org/10.1088/2058-7058/2/9/23.

Cohen ML (2008) Fifty years of condensed matter physics. *Physical Review Letters* 101: 250001. https://doi.org/10.1103/PhysRevLett.101.250001.

Dahm R (2005) Friedrich miescher and the discovery of DNA. *Developmental Biology* 278: 274. https://doi.org/10.1016/j.ydbio.2004.11.028.

Dill KA and MacCallum JL (2012) The protein-folding problem, 50 years on. *Science* 338: 1042. https://doi.org/10.1126/science.1219021.

Echenique P (2007) Introduction to protein folding for physicists. *Contemporary Physics* 48: 81. https://doi.org/10.1080/00107510701520843.

Editorial (2022) New horizons in spintronics. Nature Materials 21: 1. https://doi.org/10.1038/s41563-021-01184-z.

Eisenstein JP and Stormer HL (1990) The fractional quantum Hall effect. *Science* 248: 1510. https://doi.org/10.1126/science.248.4962.1510.

Folland GB (2008) *Quantum Field Theory: A tourist guide for Mathematicians*. American Mathematical Society. https://doi.org/10.1090/surv/149.

Fradkin E (2013) *Field Theories of Condensed Matter Physics*. Cambridge University Press. https://doi.org/10.1017/CBO9781139015509.

Frank-Khamenetskii MD (1997) *Unraveling DNA: The Most Important Molecule of life*. Basic Books.

Freeman AJ (2002) Materials by design and the exciting role of quantum computation/simulation. *Journal of Computational and Applied Mathematics* 149: 27. https://doi.org/10.1016/S0377-0427(02)00519-8.

Fubini S (1974) Present trends in particle physics. In: *Proc. Intl. Conf. on High Energy Physics*. Didcot, England: Rutherford Laboratory. https://cds.cern.ch/record/417271/files/CM-P00060491.pdf.

Gaudenzi R (2022) *Historical Roots of Spontaneous Symmetry Breaking: Steps Towards an Analogy*. Springer. https://doi.org/10.1007/978-3-030-99895-0.

Georgescu I (2020) 25 Years of BEC. *Nature Reviews Physics* 2: 396. https://doi.org/10.1038/s42254-020-0211-7.

Gomes CM and Faísca PFN (2019) *Protein Folding: An Introduction*. Springer. https://doi.org/10.1007/978-3-319-00882-0_1.

Halperin BI (1983) Theory of the quantized Hall conductance. *Helvetica Physica Acta* 56: 75. https://doi.org/10.5169/seals-115362.

Halperin BI (1984) Statistics of quasiparticles and the hierarchy of fractional quantized Hall states. *Physical Review Letters* 52: 1583. https://doi.org/10.1103/PhysRevLett.52.1583.

Harper PG (1955) Single band motion of conduction electrons in a uniform magnetic field. *Proceedings of the Physical Society. Section A* 68: 874. https://doi.org/10.1088/0370-1298/68/10/304.

Hartmann U (2000) *Magnetic Multilayers and Giant Magnetoresistance: Fundamentals and Industrial Applications*. Berlin: Springer Verlag. https://doi.org/10.1007/978-3-662-04121-5.

Heisenberg W (1928) Zur theorie des ferromagnetismus. *Zeitschrift für Physik* 49: 619. https://doi.org/10.1007/BF01328601.

Hoddeson L (1992) *Out of the Crystal Maze: Chapters From the History of Solid-State Physics*. N.Y.: Oxford University Press.

Hofstadter D (1976) Energy levels and wave functions of Bloch electrons in rational and irrational magnetic fields. *Physical Review B* 14: 2239. https://doi.org/10.1103/PhysRevB.14.2239.

Hosono H, et al. (2018) Recent advances in iron-based superconductors toward applications. *Materials Today* 21: 278. https://doi.org/10.1016/j.mattod.2017.09.006.

Jane Dyson H and Wright PE (1996) Insights into protein folding from NMR. *Annual Review of Physical Chemistry* 47: 369. https://doi.org/10.1146/annurev.physchem.47.1.369.

Jiang Z, et al. (2007) Quantum Hall effect in graphene. *Solid State Communications* 143: 14. https://doi.org/10.1016/j.ssc.2007.02.046.

Joh YG, Orbach R, Wood JJ, Hammann J, and Vincent E (1999) Extraction of the spin glass correlation length. *Physical Review Letters* 82: 438. https://doi.org/10.1103/PhysRevLett.82.438.

Jumper J, et al. (2021) Highly accurate protein structure prediction with alphafold. *Nature* 596: 583. https://doi.org/10.1038/s41586-021-03819-2.

Kallio A and Smith RA (1977) How simple can HNC be and still be right? *Physics Letters B* 68: 315. https://doi.org/10.1016/0370-2693(77)90483-X.

Kibble T and Srivastava A (2013) Condensed matter analogues of cosmology. *Journal of Physics. Condensed Matter* 25: 400301. https://doi.org/10.1088/0953-8984/25/40/400301.

Klug A (2004) The discovery of the DNA double helix. *Journal of Molecular Biology* 335: 3. https://doi.org/10.1016/j.jmb.2003.11.015.

Lam PM, Clark JW, and Ristig ML (1977) Density matrix and momentum distribution of helium liquids and nuclear matter. *Physical Review B* 16: 222. https://doi.org/10.1103/PhysRevB.16.222.

Lantto LJ, Jackson AD, and Siemens PJ (1977) HNC variational calculations of boson matter. *Physics Letters B* 68: 311. https://doi.org/10.1016/0370-2693(77)90482-8.

Laughlin RB (1983) Anomalous quantum Hall effect: An incompressible quantum fluid with fractionally charged excitations. *Physical Review Letters* 50: 1395. https://doi.org/10.1103/PhysRevLett.50.1395.

Laughlin RB (1984) Primitive and composite ground states in the fractional quantum Hall effect. *Surface Science* 142: 163. https://doi.org/10.1016/0039-6028(84)90301-7.

Laughlin RB and Pines D (2000) The theory of everything. *Proceedings of the National Academy of Sciences of the United States of America* 97: 28. https://doi.org/10.1073/pnas.97.1.28.

Leggett A (1992) On the nature of research in condensed-state physics. *Foundations of Physics* 22: 221. https://doi.org/10.1007/BF01893613.

Leggett A (2018) Reflections on the past, present and future of condensed matter physics. *Science Bulletin* 63: 1019. https://doi.org/10.1016/j.scib.2018.07.004.

Leinaas JM and Myrheim J (1977) On the theory of identical particles. *Il Nuovo Cimento B* 37: 1. https://doi.org/10.1007/BF02727953.

Léonard J, et al. (2017) Monitoring and manipulating higgs and goldstone modes in a supersolid quantum gas. *Science* 358: 1415. https://doi.org/10.1126/science.aan2608.

Liao S-K, et al. (2018) Satellite-relayed intercontinental quantum network. *Physical Review Letters* 120: 030501. https://doi.org/10.1103/PhysRevLett.120.030501.

Liu X, Hao Z, Watanabe K, Taniguchi T, Halperin BI, and Kim P (2019) Interlayer fractional quantum Hall effect in a coupled graphene double layer. *Nature Physics* 15: 893. https://doi.org/10.1038/s41567-019-0546-0.

Locatelli N, Cros V, and Grollier J (2014) Spin-torque building blocks. *Nature Materials* 13: 11. https://doi.org/10.1038/nmat3823.

Lu W (2022) Quark-gluon plasma and nucleons à la Laughlin. *International Journal of Geometric Methods in Modern Physics* 19: 2250061. https://doi.org/10.1142/S021988782250061X.

Maksym P and Chakraborty T (1990) Quantum dots in a magnetic field: Role of electron-electron interactions. *Physical Review Letters* 65: 108. https://doi.org/10.1103/PhysRevLett.65.108.

Marthinsen A, et al. (2018) Goldstone-like phonon modes in a (111)-strained perovskite. *Physical Review Materials* 2: 014404. https://doi.org/10.1103/PhysRevMaterials.2.014404.

Mézard M (2022) Spin glasses and optimization in complex systems. *Europhysics News* 53: 15. https://doi.org/10.1051/epn/2022105.

Miodownik M (2014) *Stuff Matters: Exploring the Marvelous Materials That Shape Our Man-Made World*. N.Y.: Houghton Mifflin Harcourt.

Morf R and Halperin BI (1986) Monte Carlo evaluation of trial wave functions for the fractional quantized Hall effect: Disk geometry. *Physical Review B* 33: 2221. https://doi.org/10.1103/PhysRevB.33.2221.

Mourino MR (1991) From thales to lauterbur, or from the loadstone to MR imaging: Magnetism and medicine. *Radiology* 180: 593. https://doi.org/10.1148/radiology.180.3.1871268.

Müller KA and Bednorz JG (1987) The discovery of a class of high-temperature superconductors. *Science* 237: 1133. https://doi.org/10.1126/science.237.4819.1133

Mustafa MG (2023) An introduction to thermal field theory and some of its application. *The European Physical Journal Special Topics* 232: 1369–1457. https://doi.org/10.1140/epjs/s11734-023-00868-8.

Mydosh JA (1993) *Spin Glasses: An Experimental Introduction*. CRC Press.

Nakamura J, et al. (2020) Direct observation of anyonic braiding statistics. *Nature Physics* 16: 931. https://doi.org/10.1038/s41567-020-1019-1.

Nambu Y (2009) Nobel lecture: Spontaneous symmetry breaking in particle physics: A case of cross fertilization. *Reviews of Modern Physics* 81: 1015. https://doi.org/10.1103/RevModPhys.81.1015.

Nasser R, Dignon GL, Razban RM, and Dill KA (2021) The protein folding problem: The role of theory. *Journal of Molecular Biology* 433: 167126. https://doi.org/10.1016/j.jmb.2021.167126.

Nawrocki W (2019) *Introduction to Quantum Metrology*, 2nd. Springer. https://doi.org/10.1007/978-3-030-19677-6.

Nowak AL, et al. (2014) Deterministic and electrically tunable bright single-photon source. *Nature Communications* 5: 3240. https://doi.org/10.1038/ncomms4240.

Obermair GM and Wannier GH (1976) Bloch electrons in magnetic fields: Rationality, irrationality, degeneracy. *Physica Status Solidi (B)* 76: 217. https://doi.org/10.1002/pssb.2220760122.

Osadchy D and Avron JE (2001) Hofstadter butterfly as quantum phase diagram. *Journal of Mathematical Physics* 42: 5665. https://doi.org/10.1063/1.1412464.

Parisi G (2023) *In a Flight of Starlings: The Wonders of Complex Systems*. Penguin Press.

Perrakis A and Sixma TK (2021) Ai revolutions in biology. *EMBO Reports* 22: e54046. https://doi.org/10.15252/embr.202154046.

Pietiläinen P and Chakraborty T (2006) Energy levels and magneto-optical transitions in parabolic quantum dots with spin-orbit coupling. *Physical Review B* 73: 155315. https://doi.org/10.1103/PhysRevB.73.155315.

Pinarbasi M and Kent AD (2022) Perspectives on spintronics technology: Giant magnetoresistance to spin transfer torque magnetic random access memory. *APL Materials* 10: 020901. https://doi.org/10.1063/5.0075945.

Recio I and Torres JJ (2016) Emergence of low noise frustrated states in E/I balanced neural networks. *Neural Networks* 84: 91. https://doi.org/10.1016/j.neunet.2016.08.010.

Refregier P, Vincent E, Hammann J, and Ocio M (1987) Ageing phenomena in a spin-glass: Effect of temperature changes below Tg. *Journal of Physics (France)* 48: 1533. https://doi.org/10.1051/jphys:019870048090153300.

Ristig ML and Clark JW (1976) Density matrix of quantum fluids. *Physical Review B* 14: 2875. https://doi.org/10.1103/PhysRevB.14.2875.

Rogalla H and Kes PH (2012) *100 Years of Superconductivity*. Boca Raton: Taylor & Francis Group. https://doi.org/10.1201/b11312.

Schutz K and Zurek KM (2016) Detectability of light dark matter with superfluid helium. *Physical Review Letters* 117: 121302. https://doi.org/10.1103/PhysRevLett.117.121302.

Shields AJ, et al. (2000) Detection of single photons using a field-effect transistor gated by a layer of quantum dots. *Applied Physics Letters* 103: 3673. https://doi.org/10.1063/1.126745.

Steptoe A (1986) Mozart, mesmer and 'cosi fan tutte'. *Musics and Letters* 67: 248. https://doi.org/10.1093/ml/67.3.248.

Störmer HL (1992) Two-dimensional electron correlation in high magnetic fields. *Physica B: Condensed Matter* 177: 401. https://doi.org/10.1016/0921-4526(92)90138-I.

Tanford C and Reynolds J (2001) *Nature's Robots: A History of Proteins*. Oxford University Press.

Taniguchi M and Kawai T (2006) Dna electronics. *Physica E: Low-dimensional Systems and Nanostructures* 33: 1. https://doi.org/10.1016/j.physe.2006.01.005.

Thess A, et al. (2021) Historic nucleic acids isolated by Friedrich Miescher contain RNA beside DNA. *Biological Chemistry* 402: 1179. https://doi.org/10.1515/hsz-2021-0226.

Tinkham M (2004) *Introduction to Superconductivity*. N.Y.: Dover.

Tomczyk H (2022) Did Einstein predict Bose-Einstein condensation? *Studies in History and Philosophy of Science* 93: 30. https://doi.org/10.1016/j.shpsa.2022.02.014.

Vallone M (2019) Higgs and goldstone modes in crystalline solids. *Physica Status Solidi* 257: 1900443. https://doi.org/10.1002/pssb.201900443.

Van Vleck JH (1978) Quantum mechanics—The key to understanding magnetism. *Reviews of Modern Physics* 50: 181. https://doi.org/10.1103/RevModPhys.50.181.

Vincent E (2023) Rejuvenated but remembering. *Nature Physics* 19: 926–927. https://doi.org/10.1038/s41567-023-02097-1.

Volovik GE (2009) *The Universe in a Helium Droplet*. Oxford University Press. https://doi.org/10.1093/acprof:oso/9780199564842.001.0001.

von Klitzing K (2019) Essay: Quantum Hall effect and the new international system of units. *Physical Review Letters* 122: 200001. https://doi.org/10.1103/PhysRevLett.122.200001.

von Klitzing K, Chakraborty T, Kim P, Madhavan V, Dai X, McIver J, Tokura Y, Savary L, Smirnova D, Rey AM, Felser C, Gooth J, and Qi X (2020) 40 years of the quantum Hall effect. *Nature Reviews Physics* 2: 397. https://doi.org/10.1038/s42254-020-0209-1.

Watson JD and Crick FHC (1953) Molecular structure of nucleic acids. *Nature* 171: 737. https://doi.org/10.1038/171737a0.

Weinberg S (1986) Superconductivity for particular theorists. *Progress of Theoretical Physics Supplement* 86: 43. https://doi.org/10.1143/PTPS.86.43.

Weintraub R (2012) What can we learn from Buridan's ass? *Canadian Journal of Philosophy* 42: 281. https://doi.org/10.1353/cjp.2012.0013.

Weiss D (2013) The butterfly emerges. *Nature Physics* 9: 395. https://doi.org/10.1038/nphys2680.

Wolynes PG and Eaton WA (1999) The physics of protein folding. *Physics World* 12: 39. https://doi.org/10.1088/2058-7058/12/9/24.

Yamaguchi A, Hirohata A, and Stadler BJH (2021) *Nanomagnetic Materials: Fabrication, Characterization and Application*. Elsevier. (Chapter 5). https://doi.org/10.1016/C2018-0-05445-6.

This page intentionally left blank

LIST OF CONTRIBUTORS FOR VOLUME 4

Betony Adams
Quantum Research Group, University of KwaZulu-Natal, Durban, South Africa; National Institute for Theoretical and Computational Sciences, Stellenbosch, South Africa; The Guy Foundation, Dorset, United Kingdom

Antonio Agnesi
Dipartimento di Ingegneria Industriale e dell'Informazione, Università degli Studi di Pavia, Pavia, Italy

D Alesini
Laboratori Nazionali di Frascati (L.N.F) of Istituto Nazionale di fisica Nucleare (I.N.F.N), Frascati, Roma, Italy

Y Ando
National Institute of Advanced Industrial Science and Technology, Tsukuba, Japan

SN Aqida
Ahmad Universiti Malaysia Pahang, Pekan, Malaysia

M Baldus
Max-Planck-Institute for Biophysical Chemistry, Göttingen, Germany

A Bansil
Northeastern University, Boston, MA, United States

B Barbiellini
LUT University, Lappeenranta, Finland; Northeastern University, Boston, MA, United States

Albert P Bartók
Warwick Centre for Predictive Modelling, School of Engineering and Department of Physics, University of Warwick, Coventry, West Midlands, United Kingdom

M Baruscotti
Università degli Studi di Milano, Milan, Italy

E Bauer
Arizona State University, Tempe, AZ, United States

Marco Bellini
Istituto Nazionale di Ottica (CNR-INO), Florence, Italy; LENS and Department of Physics & Astronomy, University of Firenze, Florence, Italy

W Biberacher
Walther-Meissner-Institut, Garching, Germany

Tomasz Blachowicz
Institute of Physics—Center for Science and Education, Silesian University of Technology, Gliwice, Poland

P Böni
Physik-Department E21, Technische Universität München, Garching, Germany

A Bosak
ESRF, The European Synchrotron, Grenoble, France

RA Broglia
Universitá degli Studi di Milano, Milan, Italy

NB Brookes
ESRF, The European Synchrotron, Grenoble, France

Davide Cassi
Dipartimento di Scienze matematiche, fisiche e informatiche, Università di Parma, Parma, Italy

Bikas K Chakrabarti
Saha Institute of Nuclear Physics, Kolkata, India

Gervais Chapuis
École Polytechnique Fédérale de Lausanne, Institute of Physics, Lausanne, Switzerland

P Chiaradia
Università di Roma, Rome, Italy

Oliver J Clark
Helmholtz-Zentrum Berlin für Materialien und Energie, Berlin, Germany; School of Physics and Astronomy, Monash University, Clayton, VIC, Australia

Elisabetta Collini
Department of Chemical Sciences, University of Padova, Padova, Italy; Padua Quantum Technologies Research Center, Padova, Italy

I Cristiani
Università di Pavia, Pavia, Italy

Paola De Padova
Consiglio Nazionale delle Ricerche-ISM, Roma, Italy; Istituto Nazionale di Fisica Nucleare-Laboratori Nazionali di Frascati—INFN-LNF, Frascati, Italy

V Degiorgio
Università di Pavia, Pavia, Italy

R Del Sole
Università di Roma, Rome, Italy

Artur Erbe
Department of Nanoelectronics, Helmholtz-Zentrum Dresden-Rossendorf, Institute of Ion Beam Physics and Materials Research, Dresden, Germany

Mehmet Erbudak
Solid State Physics, ETHZ, Zürich, Switzerland

Patrícia FN Faísca
Departamento de Física and BioISI – Biosystems and Integrative Sciences Institute, Faculdade de Ciências, Universidade de Lisboa, Lisboa, Portugal

Rosario Fazio
The Abdus Salam *International Centre for Theoretical Physics, Trieste, Italy*

M Ferrario
Laboratori Nazionali di Frascati (L.N.F) of Istituto Nazionale di fisica Nucleare (I.N.F.N), Frascati, Roma, Italy

F Forstmann
Freie Universität Berlin, Berlin, Germany

MD Frank-Kamenetskii
Boston University, Boston, MA, United States

P Galloni
Casaccia Research Center, ENEA, Rome, Italy

Si Gao
College of Material Science and Engineering, Nanjing Tech University, Nanjing, China

Rosario A Gerhardt
Georgia Institute of Technology, Atlanta, GA, United States

J Gimsa
University of Rostock, Rostock, Germany

Thilo Glatzel
Department of Physics, University of Basel, Basel, Switzerland

R Harada
University of Tsukuba, Tsukuba, Japan

JB Hartwig
ESRF, Grenoble, France

J Härtwig
ESRF, Grenoble, France

LL Hench
Imperial College, London, UK

JL Herek
FOM Institute for Atomic and Molecular Physics, Amsterdam, The Netherlands

Jurgen M Honig
Department of Chemistry, Purdue University, West Lafayette, IN, United States

CE Hughes
Max-Planck-Institute for Biophysical Chemistry, Göttingen, Germany

Y Inagaki
University of Tsukuba, Tsukuba, Japan

SE Jackson
University of Cambridge, Cambridge, UK

JR Jones
Imperial College, London, UK

Anjam Khursheed
Department of Electrical and Computer Engineering, National University of Singapore, Singapore, Singapore

M Kogan
University of Michigan, Ann Arbor, MI, United States

Florian F Krause
Institute of Solid State Physics, University of Bremen, Bremen, Germany

M Krisch
ESRF, The European Synchrotron, Grenoble, France

Neill Lambert
Theoretical Quantum Physics Laboratory, Cluster for Pioneering Research, RIKEN, Wakoshi, Saitama, Japan

Guy Le Lay
Aix Marseille Université, CNRS, PIIM UMR 7345, Marseille, France

David R Leadley
Department of Physics, University of Warwick, Coventry, United Kingdom

C Luchinat
University of Florence, Florence, Italy

FT Mahi
Trinity College Dublin, Dublin, Ireland

Wei Mao
National Laboratory of Solid State Microstructures, Jiangsu Key Laboratory of Artificial Functional Materials, College of Engineering and Applied Sciences and Collaborative Innovation Center of Advanced Microstructures, Nanjing University, Nanjing, China

G Margaritondo
Ecole Polytechnique Fédérale de Lausanne, (EPFL), Lausanne, Switzerland

C Marino
Casaccia Research Center, ENEA, Rome, Italy

S Maslov
Brookhaven National Laboratory, Upton, NY, USA

C Merla
Casaccia Research Center, ENEA, Rome, Italy

Ernst Meyer
Department of Physics, University of Basel, Basel, Switzerland

T Miyake
National Institute of Advanced Industrial Science and Technology, Tsukuba, Japan

A Moroni
Università degli Studi di Milano, Milan, Italy

Sudip Mukherjee
Barasat Government College, Kolkata, India; Saha Institute of Nuclear Physics, Kolkata, India

Knut Müller-Caspary
Department of Chemistry and Centre for NanoScience, Ludwig-Maximilians-Universität München, Munich, Germany

G Timothy Noe II
National High Magnetic Field Laboratory, Pulsed-Field Facility, Los Alamos National Laboratory, Los Alamos, New Mexico, United States

Franco Nori
Theoretical Quantum Physics Laboratory, Cluster for Pioneering Research, RIKEN, Wakoshi, Saitama, Japan; Center for Quantum Computing, RIKEN, Wakoshi, Saitama, Japan; Department of Physics, The University of Michigan, Ann Arbor, MI, United States

G Parigi
University of Florence, Florence, Italy

Juan MR Parrondo
Departamento de Estructura de la Materia, Física Térmica y Electrónica and GISC, Universidad Complutense de Madrid, Madrid, Spain

Rémy Pawlak
Department of Physics, University of Basel, Basel, Switzerland

Stephen J Pennycook
Department of Materials Science and Engineering, University of Tennessee, Knoxville, TN, United States; School of Physical Sciences and CAS Key Laboratory of Vacuum Sciences, University of Chinese Academy of Sciences, Beijing, China

John H Perepezko
Department of Materials Science and Engineering, University of Wisconsin-Madison, Madison, WI, United States

Paolo Perfetti
Consiglio Nazionale delle Ricerche-ISM, Roma, Italy

Giuseppe Pesce
Physics Department "E. Pancini", University of Naples "Federico II", Naples, Italy

Francesco Petruccione
Quantum Research Group, University of KwaZulu-Natal, Durban, South Africa; National Institute for Theoretical and Computational Sciences, Stellenbosch, South Africa; School of Data Science and Computational Thinking and Department of Physics, Stellenbosch University, Stellenbosch, South Africa

Roberto Piazza
Department of Chemistry, Materials Science and Chemical Engineering, Politecnico di Milano, Milano, Italy

G Piccitto
Università di Catania, Catania, Italy

A Pifferi
CNR—Institute of Crystallography, Rome, Italy

Oliver Rader
Helmholtz-Zentrum Berlin für Materialien und Energie, Berlin, Germany

Giancarlo Reali
Dipartimento di Ingegneria Industriale e dell'Informazione, Università degli Studi di Pavia, Pavia, Italy

Giulia Rusciano
Department of Physics E. Pancini, University of Naples "Federico II", Napoli, Italy

ChJ Sahle
ESRF, The European Synchrotron, Grenoble, France

Jaime Sánchez-Barriga
Helmholtz-Zentrum Berlin für Materialien und Energie, Berlin, Germany; IMDEA Nanoscience, Madrid, Spain

J Sanderson
Mary Lyon Centre, MRC Harwell, Harwell Campus, Oxfordshire, United Kingdom

Peter Schaaf
TU Ilmenau, Institute of Materials Science and Engineering, Chair Materials for Electrical Engineering and Electronics, Ilmenau, Germany

F Sette
ESRF, The European Synchrotron, Grenoble, France

Y Shigeta
University of Tsukuba, Tsukuba, Japan

John Singleton
National High Magnetic Field Laboratory, Pulsed-Field Facility, Los Alamos National Laboratory, Los Alamos, New Mexico, United States; University of Oxford Department of Physics, The Clarendon Laboratory, Oxford, United Kingdom

K Sneppen
Niels Bohr Institutet, Copenhagen, Denmark

MJ Solomon
University of Michigan, Ann Arbor, MI, United States

Wolfgang Sturhahn
Division of Geological and Planetary Sciences, California Institute of Technology, Pasadena, CA, United States

Ping-Heng Tan
State Key Laboratory of Superlattices and Microstructures, Institute of Semiconductors, Chinese Academy of Sciences, Beijing, China

G Thiel
Darmstadt University of Technology, Darmstadt, Germany

G Tiana
Universitá degli Studi di Milano, Milan, Italy

A Variola
Sezione di Roma1 of Istituto Nazionale di Fisica Nucleare (I.N.F.N), c/o Dipartimento di Fisica, Edificio, G. Marconi, Roma, RM, Italy

Dimitri D Vvedensky
The Blackett Laboratory, Imperial College London, London, United Kingdom

Peng Wang
Department of Physics, University of Warwick, Coventry, United Kingdom

Xin Zhang
State Key Laboratory of Superlattices and Microstructures, Institute of Semiconductors, Chinese Academy of Sciences, Beijing, China

Liqi Zhou
National Laboratory of Solid State Microstructures, Jiangsu Key Laboratory of Artificial Functional Materials, College of Engineering and Applied Sciences and Collaborative Innovation Center of Advanced Microstructures, Nanjing University, Nanjing, China

Anastasia Zhuravelva
School of Molecular and Cellular Biology, Faculty of Biological Sciences & Astbury Centre for Structural Molecular Biology, University of Leeds, Leeds, United Kingdom

Dmitry Zyabkin
TU Ilmenau, Institute of Materials Science and Engineering, Chair Materials for Electrical Engineering and Electronics, Ilmenau, Germany

CONTENTS OF VOLUME 4

Low-energy electron microscopy 1
E Bauer

Mössbauer spectroscopy 15
Peter Schaaf and Dmitry Zyabkin

Photoelectron spectromicroscopy 29
G Margaritondo

Scanning electron microscopy 36
Anjam Khursheed

Scanning probe microscopy 51
Ernst Meyer, Rémy Pawlak, and Thilo Glatzel

Microscopy: Transmission electron microscopy 63
Stephen J Pennycook

Electron ptychography 71
Wei Mao, Liqi Zhou, Si Gao, and Peng Wang

Momentum-resolved scanning transmission electron microscopy 95
Knut Müller-Caspary and Florian F Krause

Confocal optical sectioning microscopy 109
J Sanderson, MJ Solomon, and M Kogan

Cyclotron resonance in metals, with a focus on quasiparticle scattering rates 115
John Singleton

Cyclotron resonance: Semiconductors 132
G Timothy Noe II, David R Leadley, and John Singleton

Scattering, inelastic: Electron 150
Dimitri D Vvedensky and Mehmet Erbudak

Raman spectroscopy: Nanostructures 160
Xin Zhang and Ping-Heng Tan

Scattering Techniques, Compton 173
B Barbiellini and A Bansil

Scattering: Inelastic Scattering Technique—Brillouin 187
Tomasz Blachowicz

Scattering, inelastic: X-ray (methods and applications) 194
ChJ Sahle, A Bosak, NB Brookes, M Krisch, and F Sette

Nuclear resonant scattering 205
Wolfgang Sturhahn

Scattering, Rayleigh 215
Roberto Piazza

Shubnikov–de Haas and de Haas–van Alphen Techniques 228
W Biberacher

Core photoemission from graphene to silicene 237
Paola De Padova, Paolo Perfetti, and Guy Le Lay

Harmonic generation frequency conversion 246
Marco Bellini

Valence photoemission 257
G Margaritondo

Spectroscopy: Impedance spectroscopy and mobility spectra 266
Rosario A Gerhardt

Plasmon-enhanced Raman spectroscopy: Principles and applications 300
Giulia Rusciano

Optical tweezers: Theory and practice 317
Giuseppe Pesce

Angle-resolved photoemission of topological materials 334
Jaime Sánchez-Barriga, Oliver J Clark, and Oliver Rader

Metals and Metallic Alloys, Optical Properties of 370
F Forstmann

Nonlinear Optics 382
V Degiorgio and I Cristiani

Surfaces, Optical Properties of 392
R Del Sole and P Chiaradia

X-Ray Topography 399
JB Hartwig, J Härtwig, and SN Aqida

Laser radiation sources 408
Antonio Agnesi and Giancarlo Reali

Synchrotron radiation 425
G Margaritondo

Radiation sources: X-ray sources 433
A Pifferi

Neutron sources 443
P Böni

Electron and positron sources 460
D Alesini, M Ferrario, and A Variola

The fundamental laws of thermodynamics; Role of surroundings in heat and work transfer 475
Jurgen M Honig

Irreversible thermodynamics as applied to basic electron transport theory in solids 487
Jurgen M Honig

Thermodynamics: Phase transformations 497
John H Perepezko

Incommensurate phases 509
Gervais Chapuis

Thermodynamics of information 522
Juan MR Parrondo

Quantum annealing and computation 536
Bikas K Chakrabarti and Sudip Mukherjee

Molecular dynamics calculations: Machine learning 543
Albert P Bartók

Materials informatics with machine learning 553
T Miyake and Y Ando

Classical statistical mechanics 559
Davide Cassi

Statistical mechanics: Quantum 571
Rosario Fazio and G Piccitto

Quantum biology: An overview 577
Neill Lambert and Franco Nori

Fundamental aspects of quantum biology 584
Elisabetta Collini

Nature's novel materials: A review of quantum biology 593
Betony Adams and Francesco Petruccione

Physics of protein folding 605
Patrícia FN Faísca

How protein fold: Insights from nuclear magnetic resonance spectroscopy 619
Anastasia Zhuravelva

Solid-State NMR Structural Studies of Proteins 636
CE Hughes and M Baldus

Protein Folding, Engineering of 644
SE Jackson

Protein Folding and Aggregation 651
RA Broglia and G Tiana

Protein Folding and Evolution 656
R Harada, Y Inagaki, and Y Shigeta

DNA and RNA, biophysical aspects 663
MD Frank-Kamenetskii

DNA and RNA, electronic and electric properties 675
Artur Erbe

Genetic Algorithms for Biological Systems 684
K Sneppen and S Maslov

Ion Transport in Biological Membranes 690
M Baruscotti, G Thiel, and A Moroni

Electric and Magnetic Fields in Cells and Tissues 699
J Gimsa

Biological Effects of Electromagnetic Fields 709
C Marino, P Galloni, and C Merla

Metalloproteins, Structural Determination of 718
C Luchinat and G Parigi

Photosynthesis, Physics of 731
JL Herek and FT Mahi

Biomedical Materials 739
JR Jones and LL Hench

This page intentionally left blank

Low-energy electron microscopy[☆]

E Bauer, Arizona State University, Tempe, AZ, United States

© 2024 Elsevier Ltd. All rights reserved.

This is an update of E. Bauer, Low-Energy Electron Microscopy, Editor(s): Franco Bassani, Gerald L. Liedl, Peter Wyder, Encyclopedia of Condensed Matter Physics, Elsevier, 2005, Pages 161–172, ISBN 9780123694010, https://doi.org/10.1016/B0-12-369401-9/00583-0.

Introduction	**1**
Electron–specimen interaction	**2**
Instrumentation	**4**
Applications	**6**
Clean surfaces	6
Chemisorption, chemical reactions and oxidation	7
Thin film growth	7
Band structure analysis	10
Spin-polarized LEEM	12
Conclusion	**14**
References	**14**

Abstract

This chapter describes Low energy electron microscopy (LEEM) and several other imaging, diffraction and spectroscopy methods, which can be combined with LEEM in the same instrument, and illustrates their application in condensed matter physics by a number of examples. After a discussion of the fundamental electron-solid interactions on which these methods are based an overview over the instrumentation needed for them is presented. The application examples include studies of clean surface, chemical reactions on surfaces, oxidation, growth and structure of thin films without and with gas/substrate reaction, electronic structure determination on the sub-micron scale and applications in thin film magnetism.

Key points

- Imaging with low energy electrons
- Study of surface and thin film phenomena
- Thin film magnetism

Introduction

Modern surface science, thin film science, and in particular, nanoscience needs characterization methods with high lateral resolution. The most prominent of these methods are scanning probe methods such as scanning tunneling microscopy and atomic force microscopy that probe the topmost layer of a surface with atomic resolution. Scanning imaging is slow. For the study of dynamic processes real time imaging is needed, frequently also a somewhat larger and somewhat tunable probing depth. This is provided by elastic reflection of slow electrons that has been used for many years in low-energy electron diffraction (LEED) in the structure analysis of the top several layers of crystals. Similar to the diffracted fast electrons in conventional transmission electron microscopy (TEM), diffracted low-energy electrons can also be used for imaging in low-energy electron microscopy (LEEM) though not with the high lateral resolution that scanning probe microscopy and transmission electron microscopy provide. Essential features of LEEM are not so much the tunable sampling depth but the well-defined wavelength, the high sensitivity to surface topography, and the spin-dependent interaction of slow electrons with magnetic materials that allows imaging of the magnetization distribution on surfaces and in thin films in spin-polarized LEEM (SPLEEM).

Understanding the image formation in LEEM and SPLEEM requires an understanding of the electron–specimen interaction and of the electron optics needed to form an image with the reflected electrons. This chapter describes briefly electron–specimen interaction, image formation, instrumentation and illustrates the application of LEEM and SPLEEM with a number of examples. Examples are also given for imaging with photoelectrons, both in real and in reciprocal space, which is frequently used together with

---

[☆] *Change History*: August 2022. E Bauer updated all sections. All figures are either modified (Figs. 1–4, 6, 8, 16) or new (Figs. 5, 7, 9–15, 17). Old figures (6, 9, 11–15) have been eliminated.

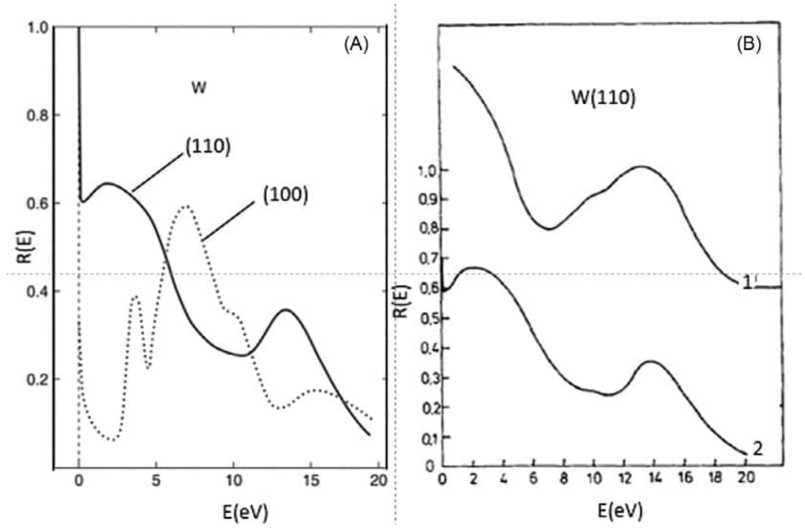

Fig. 1 (a) Specular reflectivity of two W surfaces for slow electrons. (b) Electron reflection coefficient from a tungsten (110) surface, (1) without, (2) with surface barrier. (a): Adapted from Bauer E. (1994) Low-energy electron microscopy. *Reports on Progress in Physics* 57: 895–938. With permission from IOP Publishing Limited. (b): Adapted from Herlt H.-J., et al. (1991) *Solid State Communications* 38: 973–976. With permission from Pergamon Press Ltd.

LEEM in the same instrument. More detailed information can be found in a book (Bauer, 2014), book chapters (Bauer, 2019; Tromp, 2019) and review papers cited in them.

Electron–specimen interaction

Electrons are scattered in matter elastically and inelastically. Elastic scattering in the backward direction determines the number of electrons available for imaging. Contrary to the fast electrons used in TEM, which are nearly completely scattered in the forward direction, low-energy electrons are also strongly scattered in the backward direction. This is illustrated in Fig. 1a for 180° scattering at normal incidence from two surfaces of a W single crystal. In single crystals, the backscattered electrons are focused by diffraction into narrow beams whose intensity is determined by diffraction, that is, by the periodicity of the crystal, and by the scattering potential of its constituents. The different periodicity normal to the two surfaces shown in Fig. 1a causes the strong difference in reflected intensity and is one of the major contrast mechanisms in LEEM, called diffraction contrast. Different periodicity causes different electronic band structure, which is reflected in the energy dependence of the intensity (Fig. 1b), taking damping by inelastic scattering and the surface barrier into account. Other diffracted beams selected by an aperture may also be used for imaging. They give information on the lateral periodicity of the surface. When the specimen is not a single crystal with a low index surface but more complex (e.g., vicinal surface or polycrystalline) imaging is always possible with aperture-selected beams, though experimentally more tedious. Because there are no diffracted beams in amorphous specimens, LEEM is possible only upon defocus and in very special cases such as via magnetic contrast. For all these reasons, LEEM and SPLEEM are mainly used for the study of specimens with strong preferred crystal orientation, which allows image acquisition at video rates and therefore the study of the dynamics of surface processes.

The wave nature of the electron, which is a basic requirement for diffraction, can also be used in other ways to produce image contrast. Optical path differences of the electrons reflected from the terraces adjoining a surface step produce phase contrast that can be made visible by lens aberrations and/or defocusing. This so-called step contrast is illustrated in Fig. 2a to make the monoatomic steps on a Mo(110) surface clearly visible. Another contrast mechanism that rests on the wave nature of the electron is the so-called quantum size contrast. In a thin film with parallel boundaries and thickness *t*, standing electron waves can form whenever $n\lambda/2 + \phi = t$, where λ is the wavelength and ϕ represents the phase shift at the boundaries. This causes reflectivity differences between regions with different thicknesses as illustrated in Fig. 2b, similar to the interference phenomena in thin films in light optics. The energy ($E \sim \lambda^{-2}$) dependence of the reflectivity (Fig. 2c) can also be described in a simple band structure model as shown for Cu films on W(110) (Altman et al., 1998). At very low energies local field variations caused by surface potential differences or surface roughness produce work function contrast and topographic contrast, respectively. These contrast mechanisms are most pronounced when the electrons are reflected immediately in front of the surface, that is, when the instrument is operated in the mirror mode (mirror electron microscopy (MEM)). MEM does not require crystalline surfaces and, thus, is widely applicable.

In SPLEEM magnetic contrast is obtained making use of the different reflectivity for electrons with spin polarization **P** parallel or antiparallel to the magnetization **M** in the near surface region as illustrated in Fig. 3a and b. In the difference images (Fig. 3a and b) the structural features of the surface are eliminated, resulting in a contrast, which is proportional to the magnetization. Similarly, with **P** perpendicular to **M** the difference image (Fig. 3d) shows the magnetization in the domain wall between the domains seen in Fig. 3c.

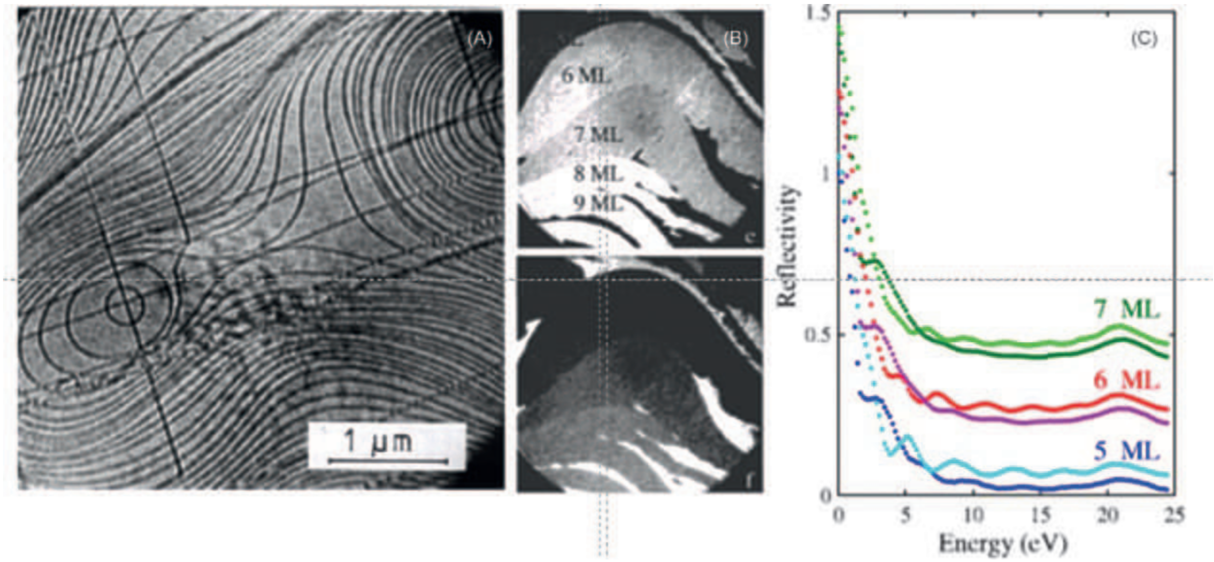

Fig. 2 (a) Monatomic steps on a Mo(110) surface. Sublimation and glide steps are visible, electron energy 14 eV. (b) Quantum size contrast in a Fe layer on a W(110) surface. The film thickness varies from terrace to terrace as indicated in the top image taken with 11.0 eV electrons. A comparison with the bottom image, taken with 16.4 eV electrons, illustrates the dependence of the contrast upon thickness and energy. (c) Spin-dependent energy dependence of the reflectivity of 5, 6 and 7 monolayer thick Fe films on W(110). (a): Reproduced from Telieps W., Bauer E. (1985) An analytical reflection and emission UHV electron microscope. *Ultramicroscopy* 17: 57–66. With permission from Elsevier. (b): Reproduced with permission from Zdyb R., Bauer E. (2002) Spin dependent quantum size effects in the electron reflectivity of ultrathin ferromagnetic crystals. *Surface Review Letters* 9: 1485–1491. With permission from World Scientific. (c): Adapted from Zdyb R., Bauer E. (2013) Spin-resolved inelastic mean free path of slow electrons in Fe. *Journal of Physics: Condensed Matter* 25: 272201-1-4. With permission from IOP Publishing.

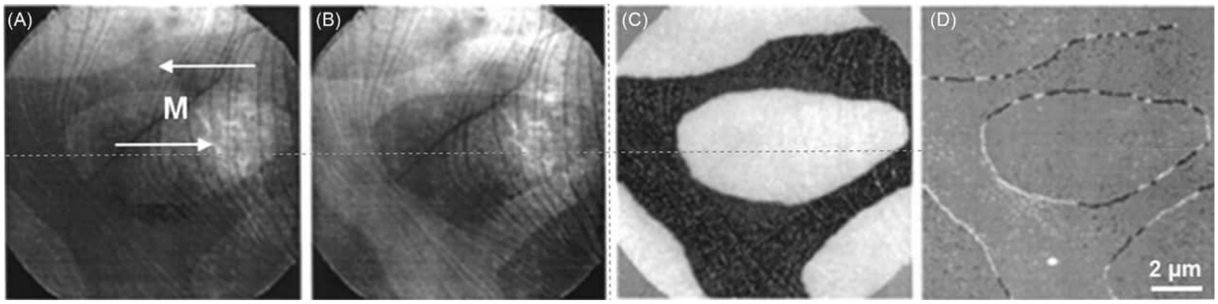

Fig. 3 Imaging of the magnetization distribution in a thin Co layer on a W(110) surface with SPLEEM. Images (a) and (b) are taken with opposite direction of the polarization **P** parallel to ± **M**. Their difference image (c) eliminates the structural features and the detector defect and shows only the magnetic domains while the difference image taken with **P** $\perp \pm$ **M** (d) shows the domain walls (electron energy 2 eV). Reproduced from Bauer E., et al. (1996) LEEM studies of the microstructure and magnetic domain structure of ultrathin films. *Journal of Magnetism and Magnetic Materials* 156: 1–6, with permission from Elsevier.

Before turning to the influence of inelastic scattering on LEEM, one important difference between the scattering of fast and slow electrons has to be mentioned. While the scattering of fast electrons by atoms can be described to a good approximation by the first Born approximation, which predicts increasing scattering strength with increasing nuclear charge Z, this is not true any longer for the backscattering of slow electrons. The backscattering cross section does not vary monotonically with increasing Z or energy E. Atoms with small Z may backscatter in certain energy ranges much more than atoms with large Z. For example, at about 50 eV Al and Si backscatter much stronger than W. Therefore, there is no analog in LEEM to the Z contrast in transmission electron microscopy (TEM).

Inelastic scattering of the electrons determines the sampling depth of LEEM unless elastic backscattering is very strong and inelastic scattering weak. Inelastic scattering involving small energy losses, such as excitation of lattice vibrations or spin waves in magnetic specimens, is not eliminated from the image by the energy-dispersive elements of present LEEM/SPLEEM instruments and thus does not limit the sampling depth. The sampling depth is limited by energy losses of say more than 0.5–1 eV, to give a rough limit. These electrons do not contribute to the image formation. In electron spectroscopy, the sampling depth is normally defined by the inelastic mean free path λ_i that takes into account all losses ranging from single electron excitation to collective electron (plasmon) excitation to inner shell ionization. Its energy dependence is usually described by a universal curve, which is a good approximation for many materials at energies above about 50 eV but breaks down in the energy range mainly used in LEEM ($\leqslant$20 eV). Here, the energy loss mechanisms are strongly material-dependent. For example, in noble metals such as Au, λ_i may be as large as several nanometers whereas in graphene (Geelen et al., 2019) and in 3*d* metals such as Fe (Zdyb and Bauer, 2013), it is only a few tenths of a nanometer. Surface and depth sensitivities are thus strongly material-dependent.

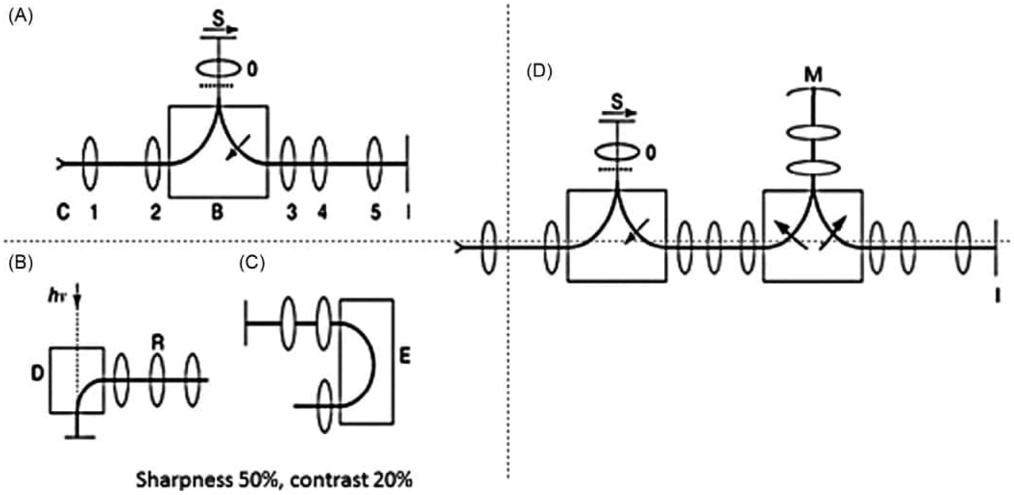

Fig. 4 Schematic of a LEEM instrument. (a) Basic instrument setup, (b) illumination system of a SPLEEM instrument, (c) imaging system for a spectroscopic instrument ("SPELEEM") and (d) aberration-corrected LEEM ("ACLEEM"). For explanation see text. The locations of the first image and diffraction planes are indicated in (a) by an arrow and dotted line, respectively.

Instrumentation

Because of the high surface sensitivity of low-energy electrons, the instruments using them require ultrahigh vacuum (UHV) and surface cleaning facilities. For electron-optical reasons, the electrons are decelerated from high energy as they approach the specimen. This is done in a so-called cathode lens whose light-optical analog is the immersion lens. In order to be able to observe the image of the surface, the illumination beam has to be separated from the imaging beam by a beam separator. This leads to a system configuration as schematically shown in Fig. 4a. Lens 1 produces a demagnified image of the electron source (cathode C)—or more precisely of the "crossover" in front of C—which is imaged by lens 2 into the back focal plane of the objective lens O. In the objective lens—which also includes the specimen S—the electrons are decelerated from the high initial energy, typically 10–20 keV, to the desired low energy, which is determined by the potential difference between cathode C and specimen S. After reflection from the surface, the electrons are accelerated again to high energy. The objective lens produces the diffraction pattern of the specimen in its back focal plane and a first intermediate image in the middle of the beam separator B. The subsequent lenses produce further intermediate images and lens 4 allows switching between imaging the specimen and its diffraction pattern, which is imaged by lens 5 into the image plane I. The brightness of the image is enhanced by a pair of channel plate multipliers so that it is high enough on the final fluorescent screen to be recorded with a CCD camera with short image acquisition times. The electron lenses are, in general, magnetic lenses but electrostatic lenses are used too. The magnetic beam separator B is designed so as to minimize the unidirectional focusing by its magnetic field. Not shown in Fig. 4a are the deflection elements needed for beam alignment, the stigmators for correction of the astigmatism of the electron-optical components, and the apertures needed for confining the angular acceptance of the system and for selecting the specimen area contributing to the LEED pattern. The first aperture, the so-called contrast aperture, is placed in the intermediate image of the diffraction pattern produced by lens 3, the second one either in the first intermediate image of the specimen in the beam separator or into the symmetric position in the illumination beam. Various beam separators are used with deflection angles ranging from 16° to 90°.

The heart of the microscope is the objective (cathode) lens because it determines the resolution and transmission of the microscope. Cathode lenses have much larger chromatic and spherical aberrations than the lenses used in TEM. Therefore, the acceptance angle α has to be strongly limited by the "contrast aperture" in the diffraction pattern. While in TEM the contrast aperture may accept many diffracted beams, which allows one to reach resolutions in the 0.1 nm range, in LEEM only one diffracted beam, usually the (00)-beam, and its immediate environment can be used for optimum resolution. The best resolution achieved without aberration correction is about 4 nm, using a field emission cathode that has a narrow energy distribution and, thus, minimizes the chromatic aberration, which is dominant at low energies. Most instruments use magnetic cathode lenses because of their somewhat lower aberrations and higher transmission. Resolution can be increased somewhat by monochromatizing the illumination beam but significant resolution improvement requires aberration correction, which is possible with an electron mirror M. Insertion of this mirror requires transfer of the first image into a second beam separator and decelerating/accelerating optics (Fig. 4d). Calculations for mirror correctors predict resolutions of about 1 nm and somewhat less (Tromp et al., 2010; Schramm et al., 2012). In the laboratory about 1.5 nm has been achieved while commercial instruments such as the one shown in Fig. 5b claim resolutions of

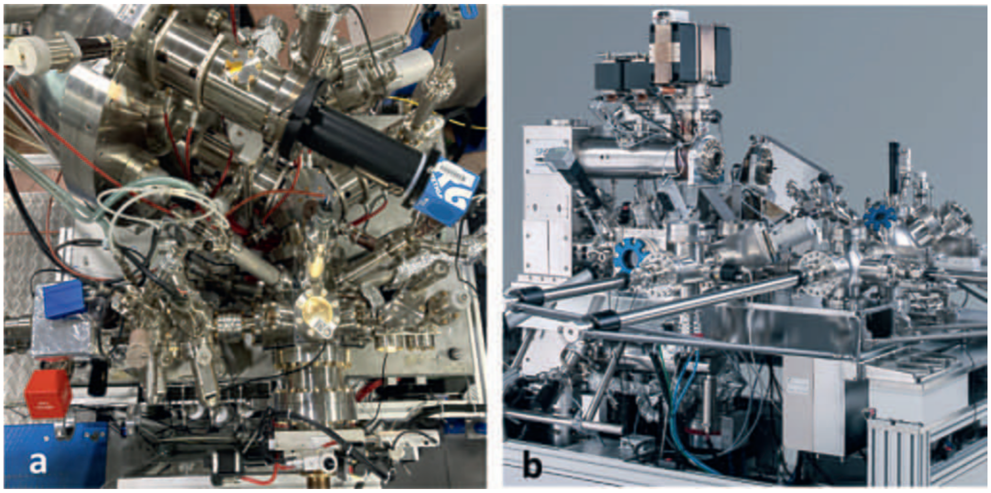

Fig. 5 Commercial LEEM instruments. (a) A SPELEEM with horizontal electron optics, 60° beam separator and energy filter (upper left), top view (ELMITEC, courtesy Mentes T. O.). (b) An ACLEEM with vertical electron optics, 90° beam separator and aberration corrector (hidden below support system), side view (courtesy SPECS Surface Nano Analysis GmbH). The instruments have attachments for sample transfer and preparation, evaporators, gas and light sources allowing in-situ studies of surface processes at pressures from 10^{-10} to 10^{-5} mbar.

better than 2 nm. The routine resolutions of 10 nm in uncorrected instruments (Fig. 5a) are largely determined by the stability of the specimen and by local charging, not by the electron optics.

Extensions of the basic LEEM instrument shown schematically in Fig. 4a are the SPLEEM instrument and the LEEM instrument equipped with an imaging energy filter (Fig. 4c), called spectroscopic photo-emission and low-energy electron microscope (SPELEEM) because it allows also spectroscopic photoemission microscopy and spectroscopy. SPLEEM requires a different illumination system schematically shown in Fig. 4b. The electron source is now not a field emitter or a LaB_6 cathode as used in LEEM but a GaAs(100) single crystal surface which has been exposed to Cs and an electronegative gas, usually O_2, so that the lowest point of the conduction band of GaAs is slightly above the vacuum level. This surface is illuminated with circular polarized light from a laser with an energy hν corresponding to the direct bandgap of GaAs so that electrons excited from the top of the valence band into the bottom of the conduction band can be emitted. Due to optical selection rules, up to 50% of the photoemitted electrons are spin-polarized with their spin perpendicular to the surface. With strained multilayer superlattice photocathodes a spin-polarization of 100% is theoretically possible, in practice 90% has been achieved. Changing the helicity of the light from right to left circular polarization inverts the spin direction, characterized by the polarization vector **P**. When a magnetic surface with local magnetization **M** is illuminated with these electrons, then the reflected intensity not only depends upon the topography and crystal structure, but also upon **P·M.** The difference image between two images taken with opposite directions of **P** eliminates all nonmagnetic contrast and shows only the distribution of **M**. In order to determine the direction of **M** completely, **P** must not only be inverted but adjustable in any direction. This is achieved with the 90° electrostatic/magnetic deflector D and a spin rotator lens R. Pure electrostatic deflection leaves **P** unchanged; in pure magnetic deflection, **P** rotates along with the direction of the beam, and mixed deflection allows one to cover all **P** directions between these two directions, that is within the plane of the drawing of Fig. 4b. The rotator lens allows **P** rotation around the beam direction, which is out of this plane so that all directions are accessible. Alternately, **P** rotation in any desired direction can be achieved with a Wien filter (Yasue et al., 2014). Usually the direction normal to the specimen surface and two preferred directions in it are selected. Fig. 3 illustrates the application of these possibilities.

In the SPELEEM, the imaging column is modified by inserting an energy filter and adding additional lenses at its output. In the example shown in Fig. 4c, the energy filter is a 180° electrostatic analyzer in which the electrons are retarded to a fraction of the input energy and reaccelerated at its output to the input energy again. Energy selection is made by a slit in the dispersive plane at the exit of the energy filter. By choosing the excitation of the pre-filter lenses 4 and 5 and of a lens in the filter, either the energy-filtered image or the diffraction pattern can be obtained with the lenses behind the filter. These can also be used to image the dispersive plane and thus to do electron spectroscopy from small specimen regions selected by the field-limiting aperture. An energy resolution of about 0.2 eV can be obtained without much loss of intensity in LEEM and LEED. The advantage of energy filtering in LEEM and LEED is the elimination of secondary electrons, which can cause a strong background in specimens with large electronic band gaps. The main application of the energy filter is however in X-ray photon-excited secondary electron emission microscopy, usually called XPEEM, in which the filter allows selection of a small energy window in the wide secondary electron energy distribution and thus improves the resolution. A second application is in XPEEM with photoelectrons from inner shells characteristic for the specimen composition. Fig. 5a shows the presently most widespread SPELEEM.

Applications

Clean surfaces

Because of its importance in microelectronics, Si is the material that has been studied most extensively. The discovery in 1985 that the "reconstruction" of the Si(111) surface with bulk periodicity into one with sevenfold periodicity at about 1100 K, the Si(111)-(1 × 1) → Si(111)-(7 × 7) transition, is a first-order phase transition, demonstrated the power of LEEM. It also clearly showed the limitations of laterally averaging studies because surfaces with the same LEED pattern produced completely different LEEM images as shown in Fig. 6. The transition between the two surface terminations and the diffusion processes involved have been subject of many LEEM studies.

The most important Si surface in semiconductor industry is the (100) surface. It has p(1 × 2) and p(2 × 1) reconstruction alternating between terraces separated by monolayer steps whose direction-dependent roughness changes simultaneously as illustrated in Fig. 7a. Extensive work on Si(111) and Si(100) surfaces has not only brought a detailed understanding of these surfaces but has contributed immensely to the understanding of processes on clean surfaces such as surface diffusion, adatom density, two-dimensional nucleation, step dynamics, and stability. Images of the Si(100) surface (Fig. 7), taken with illumination tilted in one of the p(2 × 1) directions to produce contrast, illustrate some of these processes: (b) isotropic monolayer by monolayer sublimation starting from hole nuclei, (c) anisotropic growth during Si deposition caused by step anisotropy and

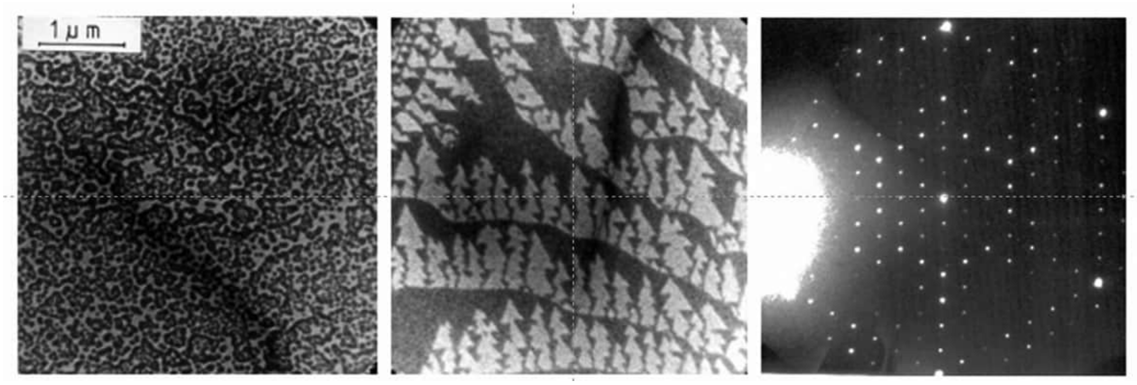

Fig. 6 Coexistence of (7 × 7) regions (bright) and (1 × 1) regions (dark) on a quenched Si(111) surface. The surface in (a) was annealed for a long time at 1150 K, that in (b) was quenched directly from 1450 K (electron energy 11 eV). (c) LEED pattern of the two surfaces. The bright region on the left side is caused by secondary electrons. Reproduced from Bauer E. (1990) Low-energy electron microscopy. In: King D.A., Woodruff D.P. (eds.) *Chemistry and Physics of Solid Surfaces VIII*, pp. 46–65. Berlin: Springer. With permission from Springer Nature.

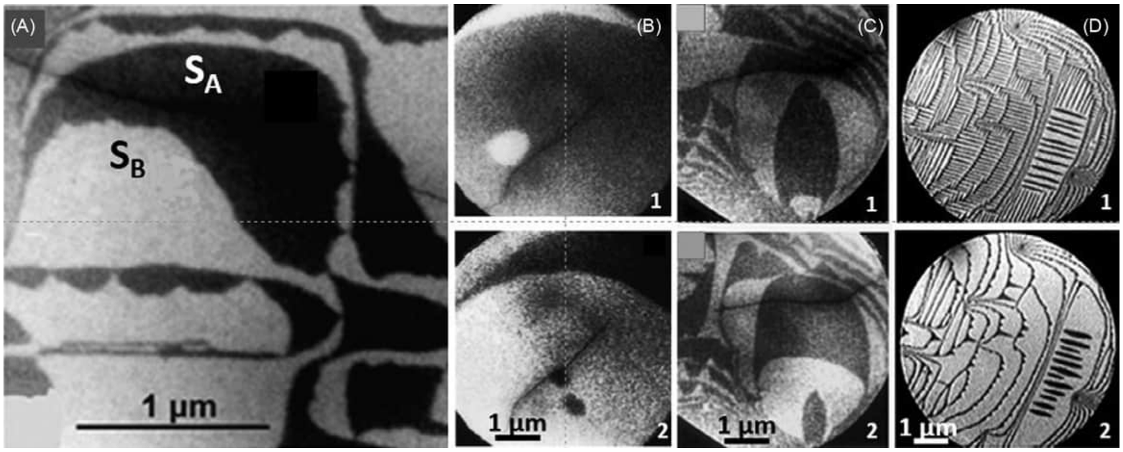

Fig. 7 LEEM images of the Si(100) surface. (a) Monolayer terrace and step structure. (b)–(d) Video frames of surface processes: (b) sublimation at about 1200 K, (c) growth at about 800 K, (d) step proliferation due to B segregation in B-doped Si. 1 and 2 show different stages of these processes. Adapted with permission (a): From Bauer E., Telieps E. (1988) Emission and low energy reflection electron microscopy. In: Howie A., Valdre U. (eds.) *Surface and Interface Characterization by Electron Optical Methods, NATO ASI Series B: Physics*, vol. 191, pp. 195–233. New York: Plenum Press; (b): From Bauer E. (1992) Low-energy electron microscopy of surface processes. *Applied Surface Science* 60/61: 350–358, Elsevier; (c): From Swiech W., Bauer E. (1991) The growth of Si on Si(100): A video-LEEM study. *Surface Science* 255: 219–228, Elsevier; (d): From Bauer E. (1999) Multi-method surface analysis in the 10 nm range. In Furukawa Y., Mori Y., Kataoka T. (eds.) *Precision Science and Technology of Perfect Surfaces*, pp. 75–762. Tokyo: The Japan Society for Precision Engineering. With permission of the respective publishers.

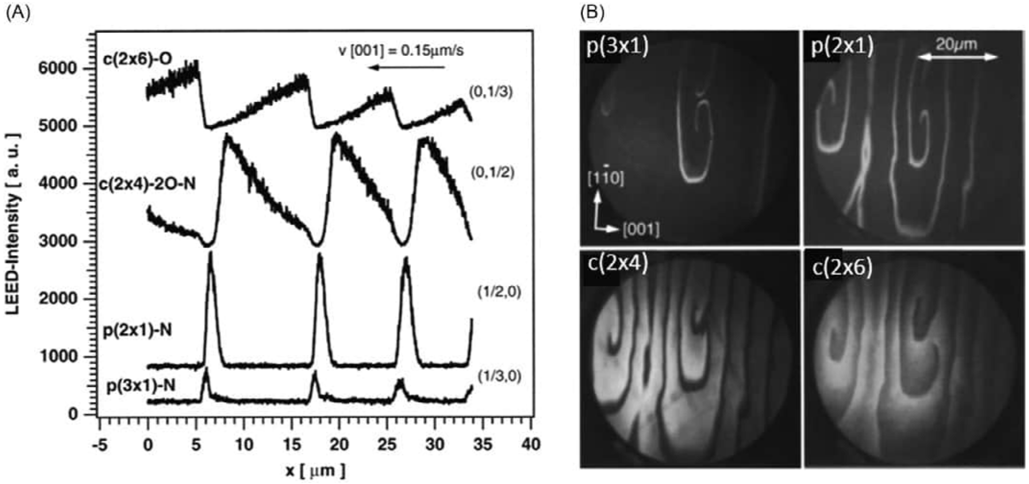

Fig. 8 LEEM images of the oscillatory reaction of adsorbed NO and H_2 on a Rh(110) surface taken with diffracted beams from different ordered phases that form locally during reaction. Reproduced from Schmidt Th., et al. (2000) In situ imaging of structural changes in a chemical wave with low-energy electron microscopy: The system Rh(110)/NO + H_2. *Chemical Physics Letters* 318: 549–554, with permission from Elsevier.

(d) unidirectional growth during B segregation from heavily B doped Si caused by disappearing S_A step energy (for details see Hannon et al., 1998). Segregation of bulk impurities to clean metal surfaces can cause much stronger surface changes. Examples are S and C in transition metals.

Chemisorption, chemical reactions and oxidation

The fast image acquisition time of LEEM images combined with diffraction over a wide temperature range makes LEEM very powerful for the study of surface processes such as chemisorption and surface reactions up to pressures in the middle 10^{-5} mbar range. As an example Fig. 8 shows the use of LEEM and LEED in the study of the catalytic reaction $NO + H_2 \rightarrow N_2 + H_2O$ on the Rh(110) surface under conditions in which the reaction oscillates. In this experiment, the LEEM chamber is used as a continuous flow reactor in the 10^{-7}–10^{-6} mbar range. Starting at defects chemical waves propagate across the surface causing different surface compositions along the propagation direction with characteristic LEED patterns corresponding to pure N, mixed N + O and pure O coverage. Fig. 8a shows the time dependence of the intensity of the characteristic LEED spots, converted into a distance scale via the known pulse velocity. Selecting a small surface region with an aperture and imaging with these diffracted beams allows following the chemical composition of the wave in real space (Fig. 8b).

Oxidation at low temperatures usually leads to a poorly ordered or amorphous layer for which LEEM is not well suited. Annealing causes crystallization and breakup of the layer into many small oxide crystals whose number decreases while their size increases with increasing temperature, a process for which dark field imaging with characteristic LEED spots is well suited. An example is the NIAl(110) surface oxidized at 325 °C. Images were taken with diffracted beams of the substrate and of the two oxide domains, which form on this surface after annealing up to the decomposition temperature of 1015 °C (McCarty, 2001). LEEM imaging is not only possible at room temperature after annealing but also during oxidation at high temperature. Fig. 9 illustrates this with real time images of the oxidation of the NiAl (110) surface at 955 °C in about 1×10^{-7} mbar O_2. The antiphase boundaries are quite mobile at the high temperature and are attributed to relaxation of the strain between the alumina island and the substrate. The first crystal nucleates at a step, a second one with many antiphase boundaries grows along a step.

Another example of the example of LEEM combined with selected area LEED is the oxidation of the Ru(0001) surface at elevated temperature at which RuO_2 crystals with complex shapes and several epitaxial orientations grow with increasing temperature (Flege and Grinter, 2018 and references therein).

Thin film growth

The study of the growth of thin films and their structural/chemical changes with temperature and environment is one of the main applications of LEEM. Thin films can be grown by a variety of methods. An example is graphene, the most studied thin film. It can be grown by decomposition of hydrocarbons which is possible on many surfaces or by decomposition of the near surface regions of SiC. In the former method large areas with constant thickness can be produced, in the latter this is in general not the case as shown in Fig. 10a. The pronounced energy-dependent intensity variations in the image indicate strong reflectivity differences whose cause can be determined by selected area I(V) measurements (Fig. 10b): the quantum size oscillations in the direct energy gap below about 5 eV show that these differences are due to thickness differences.

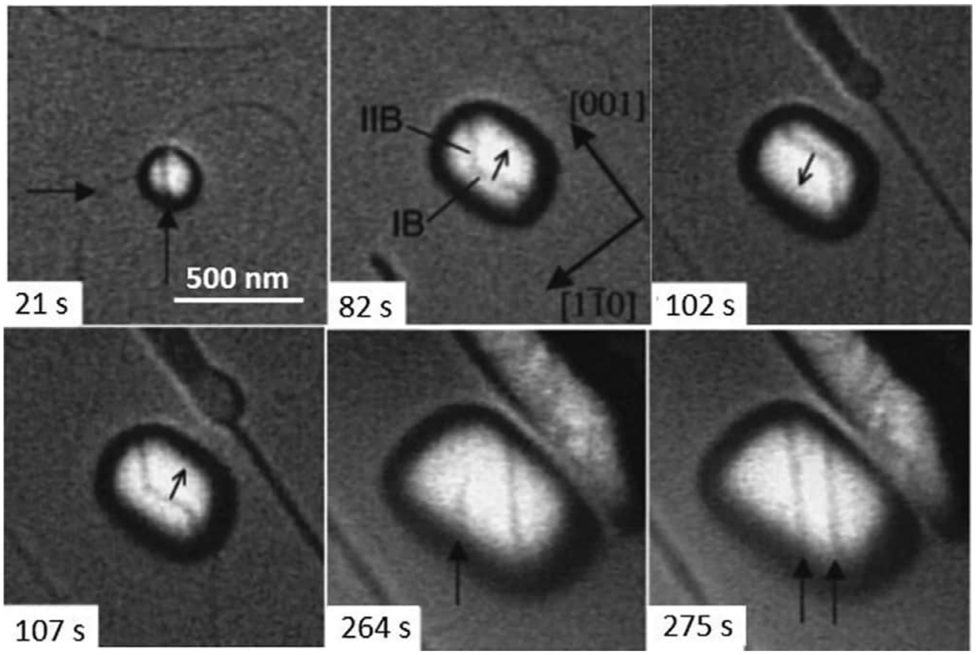

Fig. 9 Alumina island growth on the NiAl(110) surface during oxidation at 955 °C. The lines within the crystals are antiphase boundaries. Adapted from McCarty et al. (2006). Translation-related domain boundaries form to relieve strain in a thin alumina film on NiAl (110). *Applied Physics Letters* 88: 141902-1-3. With permission from The American Institute of Physics.

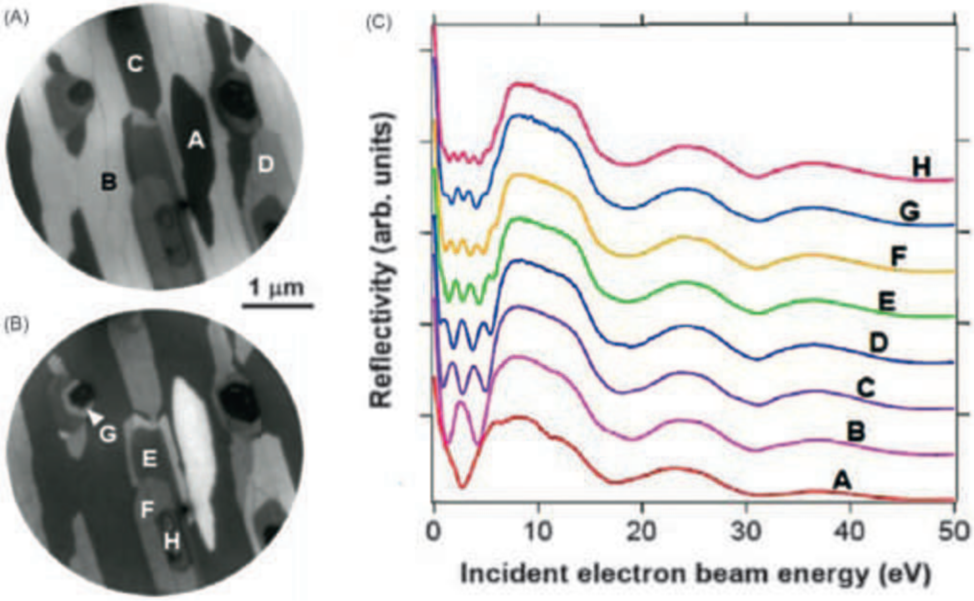

Fig. 10 Graphene multilayer grown on SiC(0001) by annealing at 1450 °C. LEEM images taken at (a) 2.5 eV and (b) 4.5 eV. (c) shows the LEEM I(V) curves from the areas marked in (a) and (b). Adapted from Hibino H., et al. (2008) Thickness determination of graphene layers formed on SiC using low-energy electron microscopy. *e-Journal of Surface Science and Nanotechnology* 6107–110. With permission from The Japan Society of Vacuum and Surface Science.

Monolayer and bilayer graphene films have been studied extensively because of their unusual electronic structure (linear band dispersion, Dirac cone) and their possible application in microelectronics. The contact with the substrate has a mayor influence on the properties of these layers and can be reduced significantly by inserting atoms or molecules between the layer and the substrate (intercalation). This is illustrated in the images and I(V) curves in Fig. 11. Exposure of a graphene monolayer on Pt to CO causes a dramatic decrease of reflectivity at 1.5 eV and in the I(V) curve due to the decoupling of graphene from the substrate by CO intercalation. The ability to intercalate molecules has let to studies of catalysis under cover (Fu and Bao, 2017).

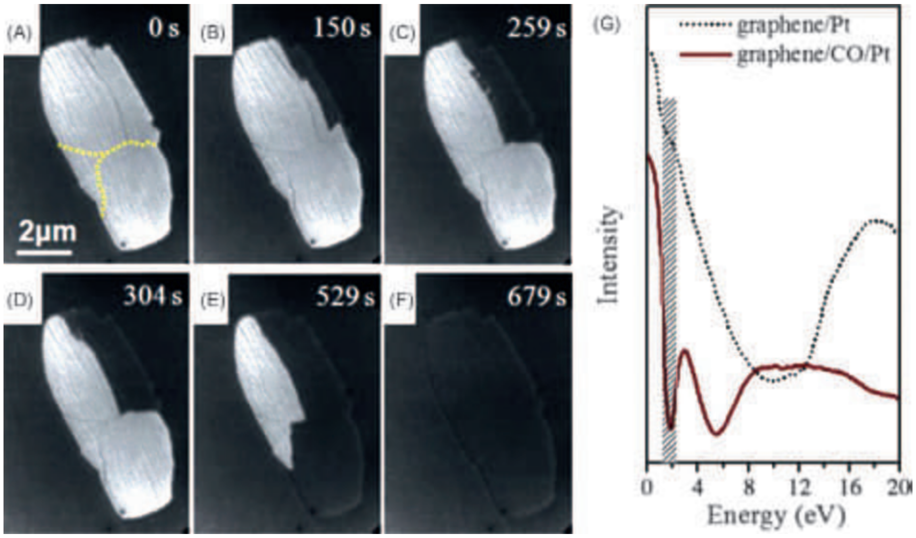

Fig. 11 Intercalation of a graphene monolayer island on Pt(111) exposed to 1 × 10^{-6} mbar CO at room temperature. (a)–(f) LEEM movie frames at increasing exposure time. Electron energy 1.8 eV. (g) LEEM I(V) curves of graphene before exposure and after saturation. Reproduced from Mu R., et al. (2012) Visualizing chemical reactions confined under graphene. *Angewandte Chemie International Edition* 51: 4856–4859. With permission from Wiley-VCH.

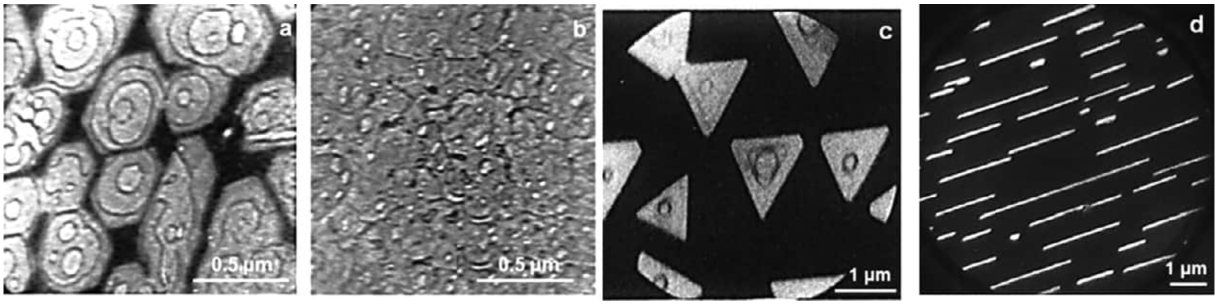

Fig. 12 Video frames of the growth of Pb on Si single crystal surfaces near room temperature. (a) and (b) Si(111), (c) Si(100), (d) Si(755). Except in (b) three-dimensional crystals grow directly on a Pb wetting layer while in (b) growth occurs on a chemisorbed Au layer in quasi-layer-by-layer mode. Thickness in monolayers, electron energy in eV: (a), (b) 5, 8, (c) 12, 6.2, (d) 6.6, 7.1. Adapted from: (a) and (b): Schmidt Th., Bauer E. (2000) Interfactant-mediated quasi-Frank–van der Merwe growth of Pb on Si(111). *Physical Review B* 62: 15815-18825. (c): Li L., et al. (1994) Surface morphology of Pb overlayers grown on Si(100)-(2 × 1). *Physical Review B* 50: 10834–10842. (d) Jalochowski M., Bauer E. (2001) Growth of metallic nanowires on anisotropic Si substrates: Pb on vicinal Si(001), Si(755), Si(533), and Si(110). *Surface Science* 480: 109–117. With permission of the respective publishers.

Thin films are grown in general in situ by deposition of the film material on single crystal surfaces provided that the material does not dissociate during evaporation/sublimation. The growth mode and structure of the film depends on substrate temperature, orientation, surface treatment, deposition rate, angle of incidence of the vapor beam and background pressure and is frequently monitored with video image acquisition. The video frames in Fig. 12 of the growth of Pb films at similar rates in the 10^{-10} mbar range on various Si surfaces illustrate some of these dependences. In (a) and (c) Pb was deposited on the clean surface, first forming a Pb wetting layer. On top of it isolated three-dimensional Pb crystals with (111) orientation nucleate and grow, initially (e.g., in (c)) by supply from extremely mobile Pb atoms adsorbed on the wetting layer, later (e.g., in (a)) predominantly directly from the incident vapor. The dominant lateral supply of atoms at large island distance (c) and the slower diffusion on top of the islands causes rim formation and concave islands. On the vicinal Si surface (d) Pb crystals nucleate at the Au-decorated steps and the fast supply of the atoms from the wetting layer on the terrace causes fast growth along the steps and normal to the surface. Three-dimensional growth can be suppressed by depositing first a layer that strongly interacts with Si and Pb ("interfactant"), which causes quasi-layer-by-layer growth as illustrated in (b). This type of film growth occurs also in film-substrate systems with very small misfit at least up to several monolayers and has been studied extensively with LEEM.

While monatomic films can be grown from one source most compound films require reactive growth on the substrate, either from volatile compound sources as for example used in compound semiconductor growth or in the presence of reactive gases. In situ growth of III–V and II–VI compounds is generally avoided because of system contamination but the growth of oxide films at pressures up the 10^{-5} mbar range poses no problems. The growth of rare earth oxide films, some of which are important in catalysis, is an example and illustrated for the case of praseodymium oxide in Fig. 13. Crystals nucleate at steps and step bunches and grow

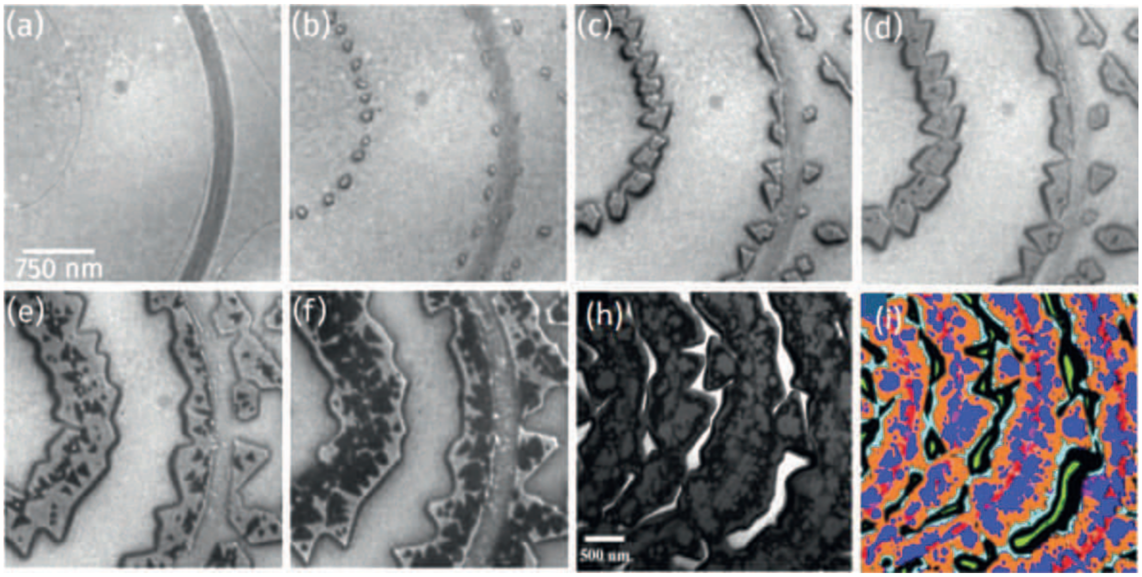

Fig. 13 Growth of praseodymium oxide films on Ru(0001) by deposition of Pr in about 7 × 10^{-7} mbar O_2 at 760 °C. (a) clean Ru(0001) surface, after (b) 9 s, (c) 59 s, (d) 75 s, (e) 160 s, (f) 250 s and (g) very long deposition. (h) phase composition map. (a)–(f): Adapted from Höcker J., et al. (2017) Growth and structure of ultrathin praseodymium oxide layers on ruthenium(0001). *Physical Chemistry Chemical Physics* 19: 3480–3485. (g) and (h): Adapted from Flege J.I., et al. (2017) Nanoscale analysis of the oxidation state and surface termination of praseodymium oxide ultrathin films on ruthenium(0001). *Ultramicroscopy* 183: 61–66. With permission from Royal Society of Chemistry and Elsevier, respectively.

lateral and vertical in triangular islands, which form with increasing coverage bands along the steps, separated by oxygen-covered substrate regions. At large thickness their topography becomes very complex. The comparison of LEEM image pixel-by-pixel I(V) measurements with calculated I(V) curves and data from similar oxides reveal a considerable structural heterogeneity across the bands attributed to oxygen content variations.

In the case of rare earth oxide growth on Ru or Ir surfaces substrate material is not part of the layer. In the growth of other compound films the substrate supplies one of the film components, the other coming from the gas phase or from impurities in the substrate. Examples are the growth of Si nitride films by nitriding the Si surface with active nitrogen or ammonia and carbide films by segregation from carbon-doped metals.

Sometimes reactive film growth is unintentional, a case being the growth of Fe nanowire films on ZnS(100) with the goal of spin injection into ZnS. In the first study about 1 nm thick Fe films were deposited at 200 °C and annealed at 400 °C. This produced two types of nanowires, previously identified as Fe by transmission electron microscopy, diffraction and energy-dispersive spectroscopy. An in situ SPELEEM study of the growth of these wires, using all the characterization modes available in this instrument at a synchrotron light source (Fig. 14), however, showed that one type of the wires had reacted with the substrate. This was achieved by combining LEEM with selected area LEED, X-ray photoemission microscopy (XPEEM), selected area XPS and X-ray magnetic circular dichroism PEEM (XMCDPEEM). While the LEED pattern of crystal A can be attributed to the substrate and to Fe covered with an adsorbate, that of crystal B could not be identified. The local XPS spectra show that the adsorbate on A is S and that crystal B is not Fe but a Fe-S compound. This allowed interpretation of the weak spots in the LEED pattern of crystal B as one of several $Fe_{1-x}S_x$ compounds, two of which are magnetic. XMCDPEEM (not shown here) limited their number to these two sulfides, which have different Curie temperatures. Measurement of the temperate dependence of the magnetic contrast finally lead to the identification of crystal B as Fe_3S_4 (greigite). This example shows that LEEM and LEED sometimes need to be combined with spectroscopic and magnetic imaging for complete sample characterization.

Band structure analysis

The band structure of the unoccupied states of solids is generally determined by inverse photoelectron spectroscopy. As already discussed at the beginning, the energy dependence of the LEEM intensity depends strongly on the band structure $E(\mathbf{k})$. Therefore measurement of the intensity of elastically reflected beam allows to measure $E(\mathbf{k})$. This was done first using the quantum well oscillations at normal incidence on epitaxial (110)-oriented Fe films with well-defined thickness shown in Fig. 2c. The extrema of the quantum well conditions define the $k_\perp$ values for a given energy E. Analysis of the data obtained with spin-polarized electrons gave the data points shown in Fig. 15a. This method has been used successfully also for other materials such as MgO, epitaxially grown on a Fe(100) surface (Wu et al., 2006) but gives only $E(\mathbf{k})$ for $\mathbf{k}$ normal to the surface. It is limited to thin films exhibiting constant thickness regions large enough for selection them in LEEM with an aperture.

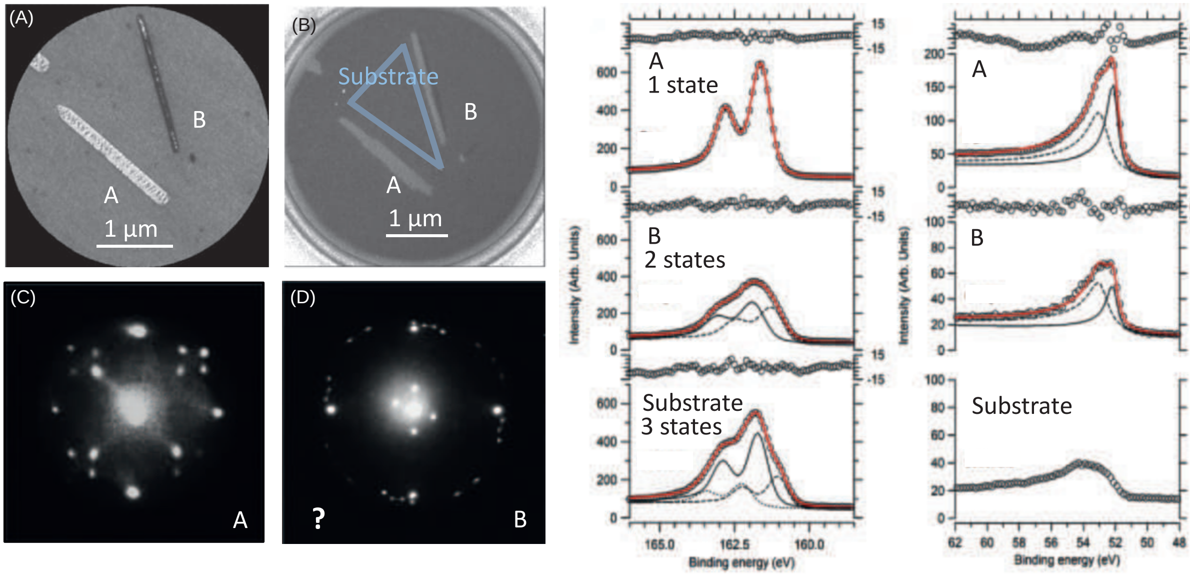

Fig. 14 Reactive growth of Fe on ZnS(100). (a) LEEM image, (c and d) LEED patterns from crystals A and B, (b) XPEEM image with area called "substrate" in the XPS spectra on the right side marked. The S (left) and Fe (right) spectra of the crystals A and B were obtained by setting an aperture in the XPEEM images. Adapted from Bauer E., et al. (2014) Fe_3S_4 (greigite) formation by vapor–solid reaction. *Journal of Materials Chemistry A* 2: 1903–1913. With permission from the Royal Society of Chemistry.

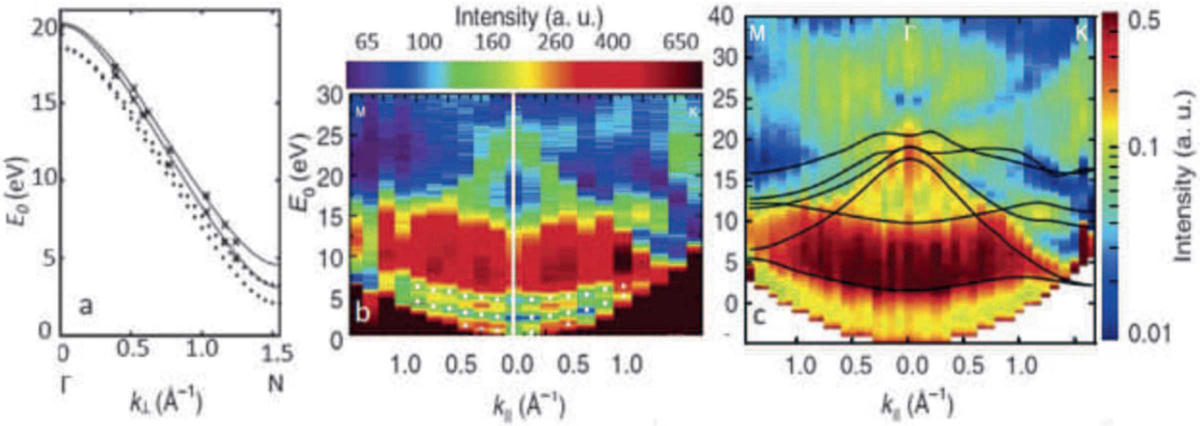

Fig. 15 Determination of the unoccupied state band structure from the specular reflectivity. (a) Spin-resolved band structure of Co along the ΓNdirection using epitaxial Co(0001) films; normal incidence ($k_\perp$). Crosses and solid lines from experiment, dotted lines theory. (b) Reflectivity of trilayer graphene as function of $k_{//}$, E_0. (c) Reflectivity of graphite as function of $k_{//}$, E_0 and its relation to the theoretical band structure (black lines). (a): Reproduced from Zdyb R., Bauer E. (2002) Spin-resolved unoccupied electronic band structure from quantum size oscillations in the reflectivity of slow electrons from ultrathin ferromagnetic crystals. *Physical Review Letters* 88: 166403-1-4. (b): Adapted from Jobst J., et al. (2015) Nanoscale measurements of the unoccupied band dispersion in few-layer graphene. *Nature Communications* 6: 8926-1-6. (c): Adapted from Jobst J., et al. (2016) Quantifying electronic band interactions in van der Waals materials using angle-resolved reflected-electron spectroscopy. *Nature Communications* 7: 13621-1-6. With permission from (a) American Physical Society, (b) and (c) Nature Publishing Group.

Band structure information for non-normal **k** can be obtained by measurements of the intensity of specular reflected electrons as a function of $k_{//}$ and E in selected $\mathbf{k}_{//}$ directions (angle-resolved reflected-electron spectroscopy (ARRES)). This is shown in Fig. 15b for graphene grown on SiC(0001). The data are from three monolayer thick regions (marked C in Fig. 10a), whose I(V) curves have three quantum size minima (Fig. 10b) corresponding to quantum well states. At energies between about 6 and 15 eV the reflectivity is high due to the large band gap of graphene in this energy range. The images are taken for discrete E, $k_{//}$ values, evident in the square pixels, for two $\mathbf{k}_{//}$ directions, ΓM and ΓK. The correlation between these plots, which are representative for the density of unoccupied states, and the band structure is better visible in Fig. 15c, in which the data are taken in smaller E, $k_{//}$ steps and with a higher dynamic range and compared with the calculated band structure. Detailed explanation of the measured data requires calculations taking the energy-dependent damping by inelastic scattering and boundary effects into account as it was done in the comparison between experiment and theory in Fig. 1 for **k** normal to the surface.

The band structure of occupied states is usually determined with angle-resolved photo-electron spectroscopy (ARPES) without spatial resolution. SEPLEEM allows band structure studies with 1 μm resolution as already shown in early work (Schmidt et al., 1998). This is important in the study of heterogeneous systems. Such a system is graphene (GR) on Ni(111) grown by chemical vapor deposition at high temperatures. Upon cooling to room temperature Ni carbide forms via carbon segregation from Ni as illustrated in Fig. 16. The LEEM images (a, c, d), taken with the beams marked in the LEED pattern (b), indicate two large area graphene phases I (EG), II (RG) and a high density of small (≤250 nm) irregular shaped patches III in phase II. Selected XPEEM images, taken at energies around the C 1 s level in the manner as in Fig. 14, show that the patches III (RGC) are carbide. Measurements of E(k) with photoelectrons around the K points show Dirac cones for all three phases with different positions and shapes, indicating different interaction with the Ni substrate. The dark field XPEEM images taken with K point electrons show that the Dirac point of phase III is close to the Fermi level, indicating decoupling from Ni. Together with the local XPS spectrum the decoupling is attributed to local Ni carbide formation. Phases I and II are strongly coupled to Ni though somewhat different as seen in position and shape of the Dirac cone.

Spin-polarized LEEM

SPLEEM has found many applications in thin film physics largely motivated by the importance of ultrathin films in spintronics. SPLEEM has lead to the understanding of the magnetic domain structure and domain wall structure in films ranging from monolayer to thick films. Of pure scientific interest has been the co-called spin reorientation transition with increasing thickness or temperature, mostly between in-plane and out-of-plane. For more practical importance is the interlayer exchange coupling between ferromagnetic layers through a nonmagnetic layer. This depends upon interlayer material and thickness and the spins are either parallel or antiparallel in the ferromagnetic layers. Fig. 17 shows a more complex case, a Co/Au/Co sandwich. The bottom Co layer has strong in-plane magnetization with large domains and small out-of-plane magnetized regions. Three Co monolayers on top of the Au layer enhance the out-of-plane component of the magnetization while simultaneously strongly reduces its in-plane component. Adding four more monolayers Co produces pure but complex in-plane magnetization consisting of a parallel and a 90° rotated component. This so-called biquadratic exchange coupling is caused usually by roughness but occurs also in perfect layer systems. In tri-layer systems the coupling is dominated by quantum size effects because of the different wavelength of spin-up and spin-down electrons. For example in the Co/Au/Co system the [1 – 10] component of the top layer is antiferromagnetic coupled when the Au interlayer is only five monolayers thick instead of the ferromagnetic coupling seen in Fig. 17. SPLEEM is ideally suited for this kind of studies.

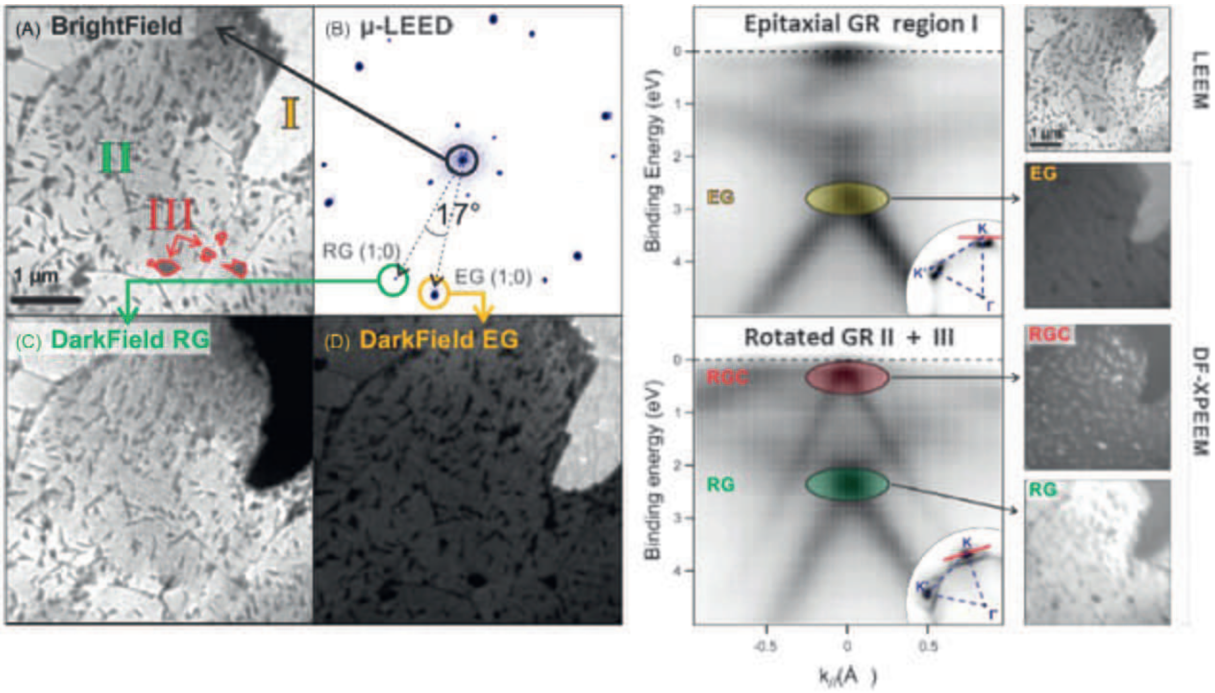

Fig. 16 Graphene on Ni(111). Left: LEED pattern and LEEM images taken with the (00) and diffracted beam shown in (b). Right: Photoelectron E(k) spectra taken with photoelectrons in a plane through the K point normal to the Γ-K direction, indicated in the photoelectron diffraction patterns (insets). Far right: Darkfield XPEEM images taken with electrons at the Dirac points as marked by arrows. Adapted from Africh et al. (2016) Switchable graphene-substrate coupling through formation/dissolution of an intercalated Ni-carbide layer. *Scientific Reports* 6: 19734-1-8. With permission from Nature Portfolio.

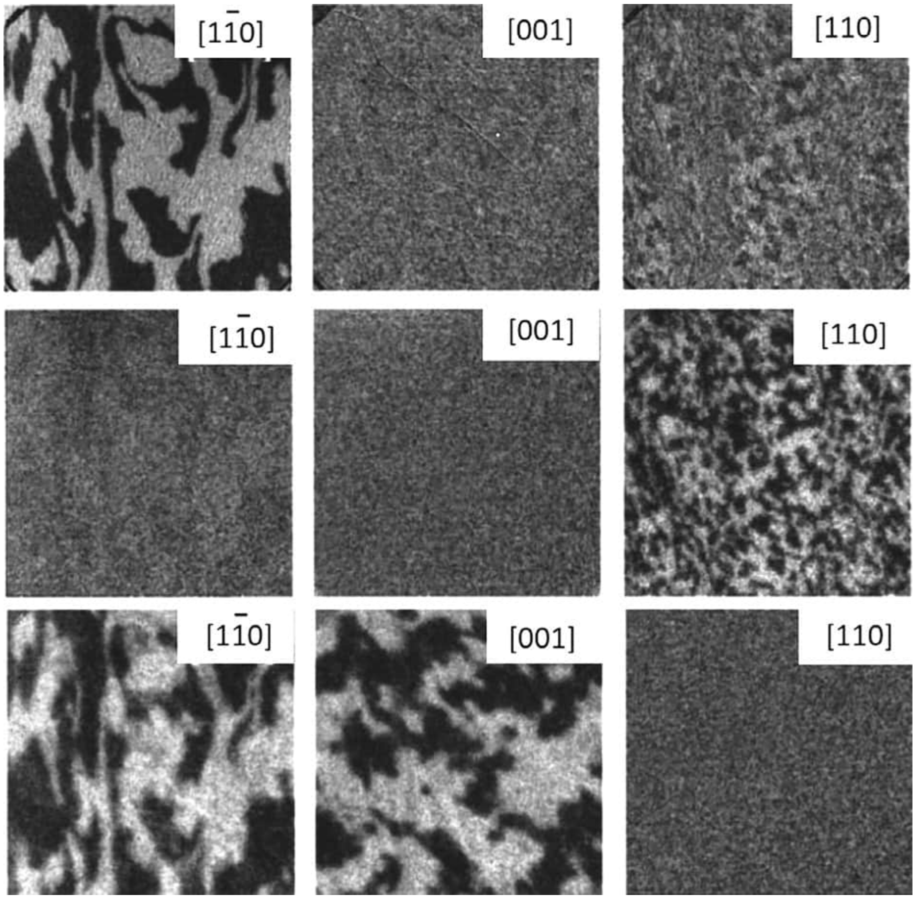

Fig. 17 SPLEEM images of the interlayer coupling between Co layers through a 6 monolayer (ML) thick Au film grown on a W(110) surface. The spin direction of the incident beam is along the two high symmetry in-plane directions and along the surface normal ([110]). Top: 7 ML Co, center: 3 ML Co on 6 ML Au on 7 ML Co, bottom: 7 ML Co on 6 ML Au on 7 ML Co. The images of the Au-covered Co layer are nearly identical to those in the top row. Adapted from Duden T., Bauer E. (1999) Biquadratic exchange in ferromagnetic/nonferromagnetic sandwiches: A spin-polarized low-energy electron microscopy study. *Physical Review B* 59: 474–479. With permission of the American Physical Society.

An emerging field in SPLEEM studies is skyrmion physics, which is not only of fundamental interest but also motivated by the drive for higher and higher bit density in magnetic storage devices. Skyrmions may be considered as magnetic nanobubbles and may be suitable for bubble memories provided that they are stable at room temperature without an external applied field and can be fabricated in reproducible manner. The first goal can be achieved with suitable thin film structures as shown in Fig. 18. A double layer consisting of 2.5 ML Fe and 2 ML Ni is out-of-plane magnetized with **M** pointing in opposite directions forming stripe domains with constant chirality domain walls. Application of a sufficiently high magnetic field **B** normal to the surface eliminates the domains with opposite **M**. Within a narrow **B** range the stripes break up into skyrmions (Fig. 18b and c). The field necessary for skyrmion formation is provided by the magnetic field of a thick Ni layer with perpendicular magnetization through a Cu layer (interlayer exchange coupling, Fig. 18a). All layers are grown in situ in the SPLEEM instrument and are epitaxial. Small skyrmions with a narrow size and shape distribution as shown in Fig. 18 form only in a limited Cu thickness range (8.5 ML). With increasing thickness (decreasing **B**) the size and size/shape distribution increases significantly (Lo Conte et al., 2020). The color wheel presentation of the SPLEEM image in Fig. 18d and e shows the direction of the spins in a skyrmion, Fig. 18f the three-dimensional spin structure. Finer details require better resolution, which is expected from aberration corrected SPLEEM instruments (Yu et al., 2020).

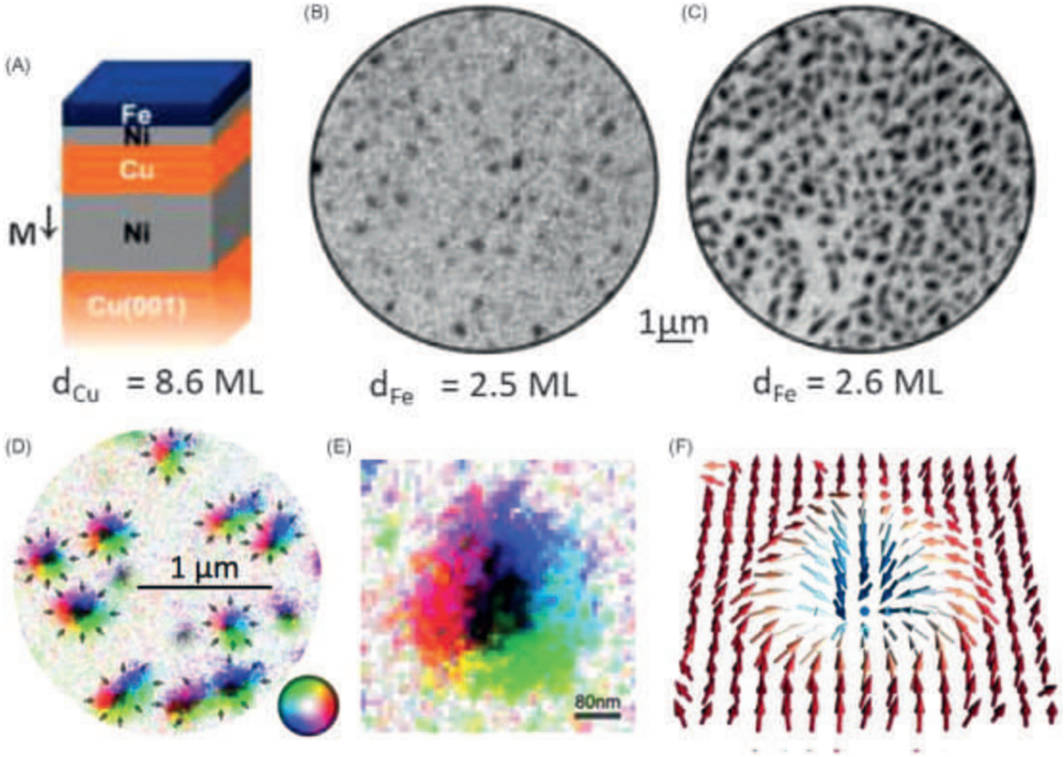

Fig. 18 Skyrmions. (a) Layer structure in which the skyrmions shown in the SPLEEM images (b), (c) form; (d), (e) Color wheel presentation of the spin distribution in the images. (f) Three-dimensional spin distribution. Adapted from Chen G., et al. (2015) Room temperature skyrmion ground state stabilized through interlayer exchange coupling. *Applied Physics Letters* 106: 242404-1-5. With permission from the American Institute of Physics.

Conclusion

LEEM is only one of many methods for the study of materials possible in a LEEM instrument. Only some of them have been discussed here. LEED and I(V) analysis are standard, so is mirror electron microscopy (MEM), thermionic emission microscopy and UV radiation-excited photo emission electron microscopy. Standard methods in LEEM instruments with an energy analyzer at synchrotron radiation sources are various modes of XPEEM, X-ray magnetic imaging, selected area XPS and ARPES. Laterally resolved ARPES has developed into a separate field, momentum microscopy (Tusche et al., 2015, 2020). It does not require a beam separator but can be done simpler in a PEEM instrument with an energy filter and for magnetic imaging with a spin selector.

References

Altman MS, Chung WF, and Liu CH (1998) LEEM phase contrast. *Surface Review and Letters* 5: 1129–1141.
Bauer E (2014) *Surface Microscopy With Low Energy Electrons*. New York: Springer.
Bauer E (2019) LEEM, SPLEEM and SPELEEM. In: Hawkes PW and Spence JCH (eds.) *Springer Handbook of Microscopy*, pp. 487–563. Springer Nature Switzerland.
Flege JI and Grinter DC (2018) In situ studies of oxide nucleation, growth, and transformation using slow electrons. *Progress in Surface Science* 93: 21–45.
Fu Q and Bao X (2017) Surface chemistry and catalysis confined under two-dimensional materials. *Chemical Society Reviews* 46: 1842–1874.
Geelen D, et al. (2019) Nonuniversal transverse electron mean free path through few-layer graphene. *Physical Review Letters* 123: 086802-1–5.
Hannon JB, et al. (1998) LEEM measurements of step energies at the (001) surface of heavily boron-doped silicon. *Surface Review and Letters* 5: 1159–1165.
Lo Conte R, et al. (2020) Tuning the properties of zero-field room temperature ferromagnetic skyrmions by interlayer exchange coupling. *Nano Letters* 20: 4739–4747.
McCarty KF (2001) Imaging the crystallization and growth of oxide domains on the NiAl(110) surface. *Surface Science* 474: L165–L172.
Schmidt T, et al. (1998) SPELEEM: Combining LEEM and spectroscopic imaging. *Surface Review and Letters* 5: 1287–1296.
Schramm SM, et al. (2012) A contrast transfer function approach for image calculations in standard and aberration-corrected LEEM and PEEM. *Ultramicroscopy* 115: 88–108.
Tromp RM (2019) Spectroscopy in the low energy electron microscope. In: Hawkes PW and Spence JCH (eds.) *Springer Handbook of Microscopy*, pp. 565–604. Springer Nature Switzerland.
Tromp RM, et al. (2010) A new aberration-corrected, energy-filtered LEEM/PEEM instrument. I. Principles and design. *Ultramicroscopy* 10: 852–861.
Tusche C, Krasyuk A, and Kirschner J (2015) Spin resolved bandstructure imaging with a high resolution momentum microscope. *Ultramicroscopy* 159: 520–529.
Tusche C, Chen Y-J, Plucinski L, and Schneider CM (2020) From photoemission microscopy to an "all-in-one" photoemission experiment. *e-Journal of Surface Science and Nanotechnology* 18: 48–56.
Wu YZ, Schmid AK, and Qiu ZQ (2006) Spin-dependent quantum interference from epitaxial MgO thin films on Fe(001). *Physical Review Letters* 97: 217205-1- 217205-4.
Yasue T, et al. (2014) Novel multipole Wien filter as three-dimensional spin manipulator. *Review of Scientific Instruments* 85: 043701-1-6.
Yu L, et al. (2020) Aberration corrected spin polarized low energy electron microscope. *Ultramicroscopy* 216: 113017-1-7.
Zdyb R and Bauer E (2013) Spin-resolved inelastic mean free path of slow electrons in Fe. *Journal of Physics: Condensed Matter* 25: 27220-1—4.

Mössbauer spectroscopy☆

Peter Schaaf and Dmitry Zyabkin, TU Ilmenau, Institute of Materials Science and Engineering, Chair Materials for Electrical Engineering and Electronics, Ilmenau, Germany

© 2024 Elsevier Ltd. All rights reserved.

This is an update of P. Schaaf, Mössbauer Spectroscopy, Editor(s): Franco Bassani, Gerald L. Liedl, Peter Wyder, Encyclopedia of Condensed Matter Physics, Elsevier, 2005, Pages 20–31, ISBN 9780123694010, https://doi.org/10.1016/B0-12-369401-9/01152-9.

Introduction 16
The nucleus and nuclear radiation 16
From the effect to spectroscopy 18
Internal conversion 20
Hyperfine interactions 21
Isomer shift 21
Quadrupole splitting 22
Magnetic splitting 22
Mixed hyperfine interaction 22
Angular dependence of absorption and emission 24
Synchrotron based methods 24
eMS - Emission Mössbauer spectroscopy 24
Applications 25
Phase analysis 26
Site determination 26
Magnetic orientation Mössbauer spectroscopy 27
Conclusion 27
References 27

Abstract

The current chapter provides the reader with a general introduction of Mössbauer effect following by its unique utilization, which became known as Mössbauer spectroscopy. Mössbauer spectroscopy is based on the recoilless emission and following resonant absorption of gamma radiation by atomic nuclei and has been at the scientific forefront of physics, chemistry, biology, mineralogy for more than 60 years. Soon after the discovery of the Mössbauer effect, it became obvious that this effect can be used to study various properties of materials on a microscopic scale via hyperfine interactions with an unprecedented resolution. This was the beginning of a new analytical tool - Mössbauer spectroscopy. Today, it has developed into a standard analytical technique used in many laboratories and big research facilities. The current chapter provides the reader with a general introduction, explains the underlying hyperfine interactions and gives examples of the possible application of the method.

Nomenclature, Symbols, Units

a, a_A	Isotopic abundance
aA	Atomic density (1/cm^3)
B	Magnetic field (T)
c, c_0	Speed of light (m/s)
d_A	Absorber thickness (m)
E	Electric field (V/m)
e	Elementary charge (A s)
E_0	Transition Energy (eV)
E_n, E_g, E_e	Energy levels of states, excited, ground state (eV)
f	Area fraction
fD, fA	Debye-Waller factor
g, g_N	Landé factor

☆*Change History*: November 2022. P Schaaf and D Zyabkin updated this chapter. Tables are intact. A new section about Emission Moessbauer Spectroscopy was added, this section includes 1 new figure. List of references has undergone an update, from the recommended literature, to literature based on which the authors wrote the chapter. In the second revision of it several figures were updated to fit the updated style of the encyclopedia, namely figures: 1,2,4,5,6,10,12,13.

https://doi.org/10.1016/B978-0-323-90800-9.00137-2

h, $\hbar$	Planck constant (J s, eV s)
I	Spin, nuclear spin
I, I_0,$I(v)$, $I(E)$	Intensity (counts)
m	Magnetic quantum number
M	Mass, atomic mass
p	Momentum ($\vec{p} = \hbar\vec{k}$)
R, R_e, R_g	Nuclear radius (m)
t_A	Effective thickness ($t_A = \sigma_0 f_A N_A d_A a_A$)
V	Electric potential (V)
v	Velocity (m/s)
V_{zz}	Field gradient (V/m^2)
Z	Atomic number
α	Conversion coefficient
Γ	Line width (FWHM) (eV, mm/s)
γ	Photon, radiation
δ	Isomer shift, shift (eV, mm/s)
η	Asymmetry parameter
θ	Angle
λ	Wavelength ($\nu \cdot \lambda = c$)
ν, ω	Frequency ($\omega = 2\pi\nu$)
σ, σ_0	Cross section, maximum cross section (barn)
τ_n	Life time (s)
Ψ	Wavefunction

Introduction

The discovery of the recoilless nuclear resonance emission and absorption in solids has recently celebrated its 60th anniversary. Although the resonance absorption of gamma rays by nuclei is analogous to the well-known optical phenomenon of resonance fluorescence and the underlying physics of the phonon theory of the lattice (Debye) and its quantum mechanical theory (Dirac, Lamb) had been well known before and nuclear resonance absorption had already been predicted in 1929, it was only in 1957 that Rudolf L. Mößbauer discovered this phenomenon during his doctoral studies (Mössbauer, 1958a, b). So it took a long time to combine nuclear physics with solid state physics and to transfer absorption and emission resonances from the electron shell to the nucleus. This recoilless nuclear resonance absorption was named after R. L. Mößbauer, who was awarded the Nobel Prize in 1961, and has been known as the *Mössbauer Effect* since then. This effect is an easy way to eliminate the recoil energy loss that occurs during the emission and absorption of photons. Consequently, γ-lines of the highest possible sharpness could be obtained and applied. Soon after the discovery of the Mössbauer effect, it became obvious that this effect can be used to study various properties of materials on a microscopic scale via hyperfine interactions with an unprecedented resolution. This was the beginning of a new analytical tool - Mössbauer spectroscopy. Today, it has developed into a standard analytical technique in many laboratories (Frauenfelder, 1962).

It is the purpose of this article to first give a short introduction to the basic physical processes and the hyperfine interactions, to sketch the typical experimental setup, and then to show how this can be applied as a unique analytical tool to many problems in solid state physics. For more details and further reading, we refer to the bibliography, where the physical principles and applications of the Mössbauer effect and Mössbauer spectroscopy are described in great detail in a series of textbooks (Wertheim, 1964; Murad and Cashion, 2004; Greenwood and Gibb, 1971; May, 2012). Regarding the most recent developments of the method, the current original literature has to be searched, for a recent review is still missing. Nonetheless, there are several interesting directions taken for the future applications, such as significantly improved signal processing, and combining the focusing polycapillary with Mössbauer spectroscopy. The latter allows one to perform unique investigation of tiny samples in the anvil cell, especially if such approach is combined with on-line studies (Abrecht et al., 2015; Novak et al., 2019; Kočiščák et al., 2022; Zyabkin et al., 2020). Furthermore, the ongoing new developments with respect to the synchrotron-based methods (e.g. Nuclear Resonance Scattering) deserve a separate article.

The nucleus and nuclear radiation

When either an atom or a nucleus undergoes a transition from an excited state (E_e) to a lower or the ground state (E_g), a quantum of electromagnetic radiation (a photon) is emitted. This photon, in turn, can induce the opposite transition in an atom or nucleus of the same kind. This principle of resonant emission and absorption is sketched in Fig. 1.

If a nucleus in an excited state with a mean lifetime of τ_N (e.g. $\tau_N = 141$ ns for ^{57}Fe) emits γ-radiation, the energy distribution $I(E)$ follows the Breit-Wigner law (Lorentzian):

$$I(E) = I_0 \cdot \frac{(\Gamma/2)^2}{(E - E_0)^2 + (\Gamma/2)^2} \tag{1}$$

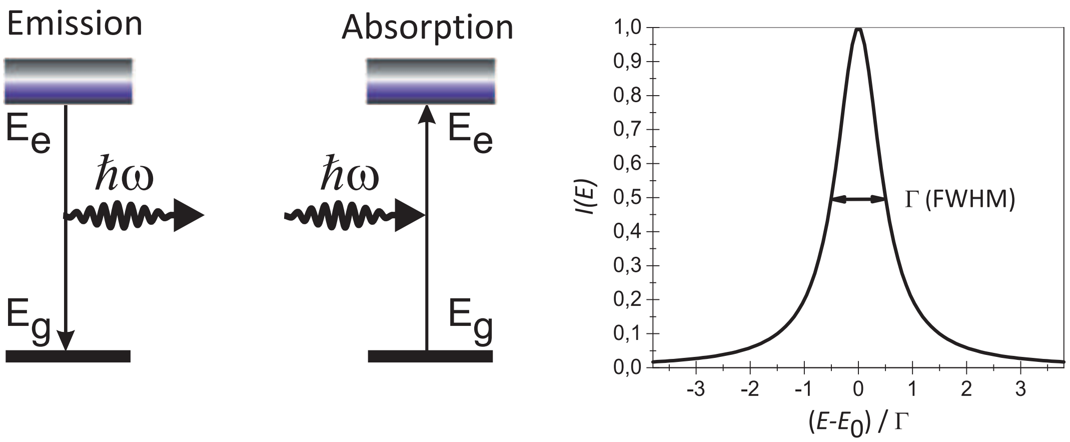

Fig. 1 Schematic view of resonant emission and absorption. States with a finite lifetime are spread in energy according to the Heisenberg uncertainty principle, as indicated for the excited levels. This gives rise to a Lorentzian shape in the energy distribution of the corresponding emission (absorption) line.

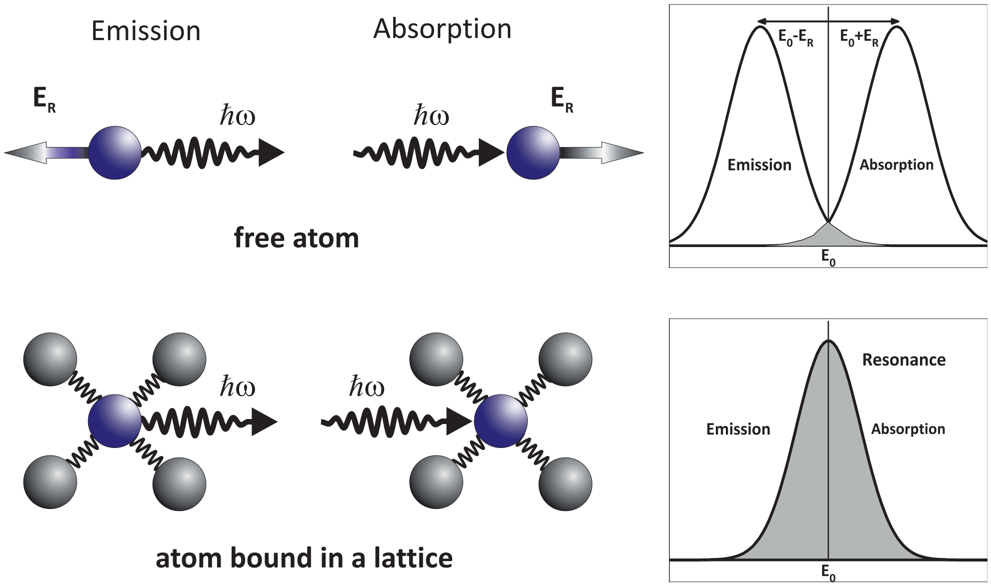

Fig. 2 Principles of emission and absorption with and without recoil. In the upper part a free atom involves a free atom involves recoil for emission and absorption. If the atom and thus the nucleus is bound in a lattice, the recoil is transferred to the whole lattice if the springs are tight enough. The shaded area represents the probability for resonance absorption.

where E_0 is the transition energy ($E_0 = E_e - E_g$) and $\Gamma = \hbar/\tau_N$ is the resonance width (FWHM) ($E_0 = 14.401$ keV, $\Gamma = 4.7 \times 10^{-9}$ eV for ^{57}Fe). The momentum of the γ quantum is $\vec{p} = \hbar\vec{k}$.

Momentum conservation for the emission process causes the energy available for the emission process to be shared by the emitted quantum and the recoiling atom or nucleus. A free atom of mass M emitting a γ-quantum will experience a recoil with the energy $E_r = p_\gamma^2/2M$, which is generally much larger than the natural line width Γ ($E_r = 2 \times 10^{-3}$ eV is much higher than $\Gamma = 4.7 \times 10^{-9}$ eV for ^{57}Fe).

As the same is true for the absorption process also the absorption energy is increased by the recoil energy of the absorbing nucleus. Thus, the energy shifts by the recoiling nuclei are big enough to preclude resonance absorption of the emitted photon by other nuclei. This is sketched in Fig. 2 for the free atom. The shifts lead to an only very small overlap of the emission and absorption Lorentzians and thus a very low probability of resonance, illustrated in Fig. 2 by the shaded area.

If the nucleus is bound in a solid and the springs in Fig. 2 are strong enough, i.e. the atoms are bound rigidly, the recoil goes to the whole lattice, and the recoiled mass M is drastically increased ($M \rightarrow 10^{16}\,M$). Thus, the recoil energy E_R becomes negligibly small. Since the lattice does not consist of rigid springs, in other words the phonon system (the spring) is a quantized system, there is a certain probability that lattice vibrations (phonons) will be excited and the recoil of the atom is transferred to phonons. On the other hand, there is also a high probability that no phonons will be excited and the whole solid takes the recoil. Thus, in a solid for a certain fraction of nuclei, the emission and in an equivalent manner the absorption, occurs without recoil energy loss. The chance that the emission takes place without inducing any phonons is called, in analogy to X-ray diffraction, the Debye-Waller factor,

$f_D = \exp(-k^2 < x^2 >)$, when $\vec{k}$ is the wave vector of the photon and $< x^2 >$ the mean square displacement of the nuclei (atom). This factor – sometimes more accurately called Lamb-Mössbauer factor – depends on the temperature T, the energy of the γ-quantum $k = E_0/(\hbar c)$, and the Debye temperature Θ_D (representing the stiffness of the lattice springs) of the solid:

$$f_D(T) = \exp\left(-\frac{3\hbar^2 k^2}{4Mk_B\Theta_D}\left[1 + 4\left(\frac{T}{\Theta_D}\right)^2 \int_0^{\Theta_D/T} \frac{y}{\exp(y) - 1} dy\right]\right). \tag{2}$$

The fraction of recoilless emission or absorption is $f_D = 0.76$ for ^{57}Fe in α-Fe with $\Theta_D = 470$ K at room temperature and thus allows fast measurement of the nuclear resonance, the Mössbauer effect. For the sake of completeness, it should be mentioned that the Debye Waller factors can be different in different crystallographic directions, causing the Goldanski-Karyagin effect, which leads to an anisotropy in the observed line intensities (Melzer, 1981).

Another decisive factor for the feasibility and speed of the measurements is the cross-section of the absorption. It determines the probability of a photon with matching energy to be absorbed by the corresponding nucleus. This cross-section σ is given, together with the maximum cross-section σ_0, as a Lorentzian by

$$\sigma = \sigma_0 \cdot \frac{\left(\frac{\Gamma}{2}\right)^2}{(E - E_0)^2 + \left(\frac{\Gamma}{2}\right)^2} \tag{3}$$

The maximum cross-section can be determined from the nuclear spin number I in the excited and ground state, the photon wavelength λ, and the internal conversion coefficient α via

$$\sigma_0 = \frac{\lambda^2}{2\pi} \cdot \frac{2I_e + 1}{2I_g + 1} \frac{1}{1 + \alpha}. \tag{4}$$

The internal conversion coefficient α represents the ratio of the number of γ quanta interacting upon emission with the electron shell and thus leads to the emission of conversion electrons and conversion X-rays to the number of γ quanta with undisturbed emission, i.e. the resulting probability of the γ emission is $\frac{1}{1+\alpha}$.

In order to obtain the γ quanta, one has to populate the excited state; in other words, we need a source for the Mössbauer radiation. This is normally achieved easily via parent isotopes, which then decay to the corresponding nucleus in the excited state. Such a source is illustrated in Fig. 3, where the decay scheme of the ^{57}Co source for ^{57}Fe Mössbauer spectroscopy is shown. The ^{57}Co isotope decays via electron capture to the excited state of ^{57}Fe. The half-life of ^{57}Co is about 272 days, so that with such a source one can easily measure for a couple of years. The parent isotopes are normally produced by nuclear reactions (neutron, deuterons, protons) in reactors or in accelerators and are commercially available. In addition, the radioactive isotopes are embedded into an appropriate matrix - normally chosen to be a cubic nonmagnetic material - in order to achieve a high Debye-Waller factor and a single line source. Embedding in magnetic material can give multi-line and polarized sources for certain applications. ^{57}Co is mostly embedded into the fcc Rh metal as the source for Fe Mössbauer spectroscopy.

From the effect to spectroscopy

In the case of recoil-less emission and absorption, one observes extremely sharp γ lines, the so-called *Mössbauer lines.* The width of these lines is often much smaller than the line shifts caused by interactions between the emitting or absorbing nuclei and their environment in the solid. For this reason, the Mössbauer effect is very suitable for resolving and measuring hyperfine interactions via a Doppler modulation of the γ energy by moving the source and the absorber relative to each other with velocity v.

$$E(v) = E_0 \cdot \left(1 + \frac{v}{c}\right) \tag{5}$$

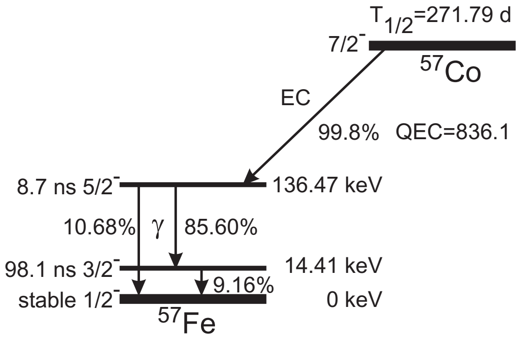

Fig. 3 Schematic view of the ^{57}Co source for ^{57}Fe Mössbauer spectroscopy. The energy levels, spins, probabilities, and lifetimes are indicated.

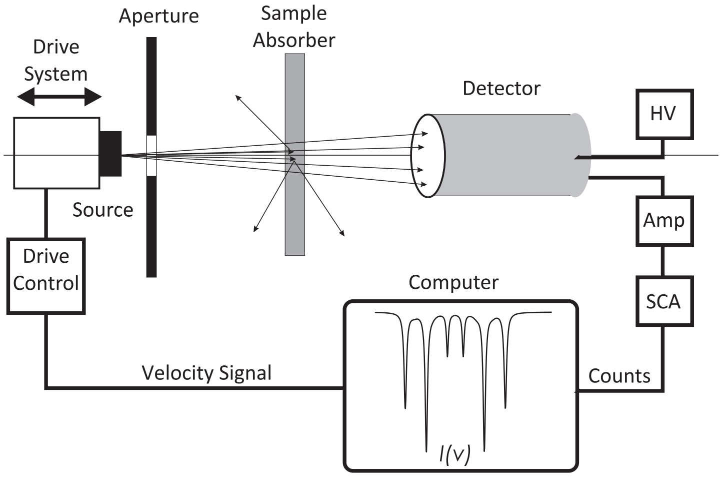

Fig. 4 Schematic view of the setup for measuring a Mössbauer spectrum in transmission geometry. The source is moved in a controlled way and the photons are detected in a detector (HV-high voltage), whose signals are amplified (Amp). The single channel analyzer (SCA) selects only those signals corresponding to the desired Mössbauer transition. These counts are stored in the computer for the respective drive velocities.

Usually, the source is moved and the velocities required for ^{57}Fe lie in the range of 10 mm/s, which can easily be produced and controlled in the lab.

Another Doppler effect is caused by the thermal vibrations in the lattice. The atoms and nuclei in source and absorber have a finite temperature, have thermal energy and are thus vibrating. As we have seen before, the movement causes a shift in energy, but the thermal velocities are isotropic and thus the positive and negative velocities cancel each other, leading to only a small broadening of the spectral lines. Nevertheless, there are also relativistic effects, which are causing a net shift of the energies with the temperatures, which is called *second order Doppler shift* (SOD).

$$\delta_{SOD} = \frac{\overline{v}^2}{2c^2}E_0 \tag{6}$$

The standard geometry of Mössbauer spectroscopy is the transmission geometry (TMS - transmission Mössbauer spectroscopy), which is shown schematically in Fig. 4.

The sample is irradiated from the source and the absorption is measured with a detector behind the sample. The source is moved by a drive system (constant acceleration, sinusoidal or constant velocity) and the emitted and Doppler-modulated photons are heading through an aperture toward a detector. Only those quanta are counted that have the involved transition energy E_0. Gas filled proportional counters or solid state detectors are most widely used for that purpose. For the measurement, the sample is placed in between source and detector and absorbs photons at certain energies represented by a certain source velocity. Of course, this absorption is again followed by emission, but it is directed to the detector any more, but emitted more or less homogeneously into the full 4π solid angle (and additionally diminished by the internal conversion process). This way, one obtains a velocity-correlated intensity spectrum $I(v)$, which then contains all the information from the Mössbauer effect. These Mössbauer spectra are stored in a multichannel scaler. Sometimes, source or absorber (sample) are put into a cryostat, an oven, or a magnetic field, etc. in order to measure temperature-dependent effects or the effects of certain physical situations. If the sample is too thick, then there is no count rate left behind it and multiple absorption and emission processes can influence the spectra. If the sample is too thin, there are not enough nuclei for the absorption process, and not enough statistics for analysis is available (there is always non-resonant background). To be concise, one has to solve the full Hamiltonian (transmission integral) to find the absorption spectrum ($I(E) \sim I(v)$). Nevertheless, one can derive an analytical solution for the transmission integral (i.e. the folding of the emission, absorption and re-emission over the sample), if the absorber can be treated as a thin absorber. The effective thickness of the absorber (sample) t_A is given by

$$t_A = \sigma_0 f_A N_A d_A a_A, \tag{7}$$

with the maximum cross section σ_0, the recoilless fraction (Debye-Waller-factor) f_A, the atomic density N_A, the absorber thickness d_A, and the abundance of the Mössbauer isotope a_A. For ^{57}Fe at room temperature we have the following values: $\sigma_0 = 256.6 \cdot 10^{-20}$ cm^2, $f_A \approx 0.75$, $N_A = 8.476 \cdot 10^{22}$atoms/cm^3, $a_A = 2.19\%$. The effective thickness should have values of $t_a \approx 1$, allowing fast measurements with the thin absorber approximation still valid. Then we have the simple folding of the emission and the absorption spectra (with their respective energy eigenvalues E_i or v_i), resulting in a Lorentzian line again.

$$I(v) = I_0 - I_{abs}\frac{\Gamma^2}{(E - E_0)^2 + \Gamma^2} \tag{8}$$

In this thin absorber approximation this results in the double line width (more general by the sum of source and absorber line width: $\Gamma = (\Gamma_S + \Gamma_A)$.

If the absorber becomes thicker, the lines become somewhat broader due to multiple re-emission and absorption effects and for thick samples one has to solve the full transmission integral.

A calibration of the Mössbauer spectrometer is carried out by measuring standard materials with well known properties. For Fe, calibration is usually performed using a 10–25 μm α-Fe foil at room temperature (α-Fe: $B_{hf} = 33$ T or 10.6245 mm/s). All isomer shifts are normally related to the center of the α-Fe spectrum at room temperature. The spectra are fitted according to a least squares routine by superimposing Lorentzian lines in simple cases or by more sophisticated theories for complicated samples.

If a sample consists of several sites or phases, the relative area of the corresponding set of Lorentzians gives the atomic fraction of the Mössbauer spy isotope in the site or phase. To calculate the real fraction, this area has to be corrected by the Debye-Waller factor. The latter is hardly known, so it has to be determined experimentally. As a simplification, it is often assumed that all subspectra and all phases have the same Debye-Waller factors f_D and neglecting (most of the times) smaller errors caused by that. Thus, the phase fraction can be identified with the relative fractions (areas) of the phases in the Mössbauer spectrum (Gonser, 1981).

The isotopes most frequently used for Mössbauer spectroscopy are (listed according to their importance): ^{57}Fe, ^{119}Sn, ^{151} Eu, ^{121}Sb, ^{125}Te, ^{197}Au, ^{129}I, ^{155}Gd, ^{161}Dy, and some others. Their properties are summarized in Table 1.

Internal conversion

The effect of internal conversion plays an important role in Mössbauer spectroscopy. It is most important for lower mass numbers and becomes negligible for very heavy atoms. For a certain fraction of nuclei, the emitted photon does not leave the atom, but spends its energy for kicking off an electron from the shell - a conversion electron. As a result of internal conversion, conversion electrons, and subsequently a cascade of Auger electrons and conversion X-rays are emitted. They too can be used for the measurements, since they contain the same information as the originally absorbed (emitted) photon. This internal conversion is shown in Fig. 5.

If the electrons originating from the internal conversion process are detected for the Mössbauer measurement, this is called CEMS ≡ Conversion Electron Mössbauer Spectroscopy. Because the electrons cannot penetrate detector windows the samples have

Table 1 Properties of the most frequently used Mössbauer isotopes.

Isotope	a *[%]*	E_0 *[keV]*	τ_N *[ns]*	I_e	I_g	σ_0 *[10^{-20} cm^2]*	*2Γ [mm/s]*	E_r *[10^{-3} eV]*
^{57}Fe	2.19	14.41300	98.1	3/2	1/2	256.6	0.1940	1.957
^{57}Fe	2.19	136.4743	8.7	5/2	1/2	4.300	0.2304	175.4
^{119}Sn	8.58	23.871	17.75	3/2	1/2	140.3	0.6456	2.571
^{151}Eu	47.82	21.64	9.7	7/2	5/2	11.42	1.303	1.665
^{125}Te	6.99	35.46	1.48	3/2	1/2	26.56	5.212	5.401
^{121}Sb	57.25	37.15	3.5	7/2	5/2	19.70	2.104	6.124
^{129}I	–	27.77	16.8	5/2	7/2	40.32	0.5863	3.210
^{197}Au	100	77.35	1.90	1/2	3/2	3.857	1.861	16.31
^{161}Dy	18.88	25.65	28.1	5/2	5/2	95.34	0.3795	2.194
^{161}Dy	18.88	43.84	920	7/2	5/2	28.29	0.006782	6.410
^{161}Dy	18.88	74.57	3.35	3/2	5/2	6.755	1.095	18.55

a - natural isotopic abundance, E_0 - transition energy, τ_N - half lifetime, I_e and I_g - nuclear spin quantum number of excited and ground state, σ_0 - maximum resonance cross section, Γ - natural line width (FWHM), E_r - recoil energy of a free atom.

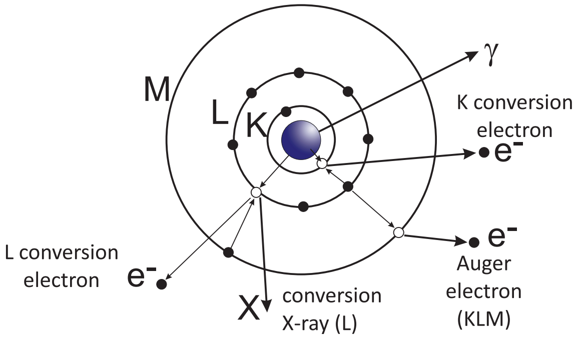

Fig. 5 The internal conversion process during emission of γ-radiation. Instead of the photons also conversion electrons can be emitted leading to a cascade of Auger electrons and conversion x-rays.

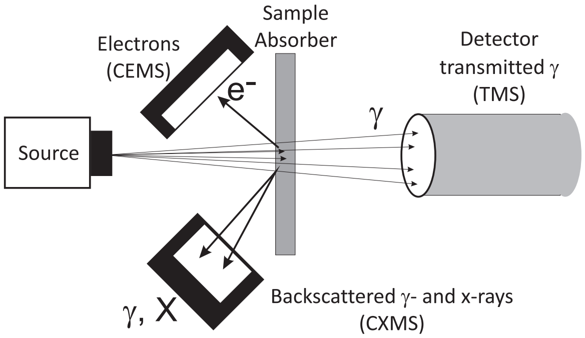

Fig. 6 Mössbauer measurements in backscattering geometry leading to CEMS and CXMS. In combination with TMS this is resulting in STRMS.

to be mounted inside an appropriate detection system. Depending on the material and the electron energies, the electrons can only escape from the sample surface within 10–500 nm. Therefore, CEMS is especially suited for the investigation of surfaces and thin films (up to a depth of some 100 nm for Fe-Mössbauer spectroscopy) and even able to measure the properties of a monolayer (Schatz et al., 1996).

Also the conversion X-rays or re-emitted γ radiation can be used to measure the Mössbauer effect in the samples under investigation. This method is named CXMS ≡ Conversion X-ray Mössbauer Spectroscopy. The X-rays can penetrate about 10–30 µm of most metals and thus the information depth of CXMS is in this order. For such backscattering measurements as visualized in Fig. 6 in reasonable times, special detectors with large solid angles have been developed.

Based on the different information depths of the different modifications of Mössbauer spectroscopy, it is especially interesting to measure these different radiations simultaneously. Simultaneous measurements achieve a discrete depth profile of the measured samples. The arrangement for the simultaneous measurement of all three modifications was named STRMS ≡ Simultaneous Triple Radiation Mössbauer Spectroscopy. It should be noted again that the sampling range in the case of iron-based materials for the CEMS measurements is about 150 nm, while for CXMS it is 10–20 µm and TMS scans the whole sample (Gonser, 1975).

Hyperfine interactions

Hyperfine interactions are based on effects caused by the interplay between the atomic nucleus and its electronic environment. As early as in 1924, Wolfgang Pauli interpreted the hyperfine structure of atomic spectral lines by the magnetic coupling between the nucleus and its electronic shell and also predicted properties of the Zeeman and Paschen-Back splittings in the presence of a nuclear magnetic moment. So the hyperfine interactions were merely an extension of the fine structure and observed in the atomic spectra with increasing resolution of the experiments in atomic physics.

The high energy resolution of the Mössbauer effect (as well as that of other nuclear methods like nuclear magnetic resonance or perturbed angular correlation) allows the direct observation of the hyperfine interactions, i.e. the change of the energy levels due to electric or magnetic fields acting at the Mössbauer nucleus. These interactions are mainly the electric monopole interaction, the electric quadrupole interaction and the magnetic dipole interaction.

Isomer shift

The electric monopole interaction is the interaction of the nuclear charge *Ze* with the electron density at the nucleus with finite size. It leads to a difference in the energy states in source (S) and absorber (A), when comparing to a point nucleus (infinite small):

$$E_S = E_0 + \frac{2}{5}\pi Z e^2 |\Psi_S(0)|^2 \quad \left[R_e^2 - R_g^2\right] \tag{9}$$

$$E_A = E_0 + \frac{2}{5}\pi Z e^2 |\Psi|_A(0)|^2 \quad \left[R_e^2 - R_g^2\right] \tag{10}$$

Here, *R* is the radius of the nucleus in the appropriate state (g - ground state, e - excited state) and Ψ the electron wave function. $e|\Psi(0)|^2$ then gives the electron density at the nucleus. These shifts of the levels (equivalent to the isotope effect in atomic physics) leads to the isomer shift δ as sketched in Fig. 7:

$$\delta = E_A - E_S = \frac{2}{5}\pi Z e^2 \left[|\Psi_A(0)|^2 - |\Psi_S(0)|^2\right] \quad \left[R_e^2 - R_g^2\right]. \tag{11}$$

Thus the lines for materials with different electron densities at the nucleus are shifted by δ with respect to the undisturbed center. Thus, charge densities in the materials can be calculated from this isomer shift.

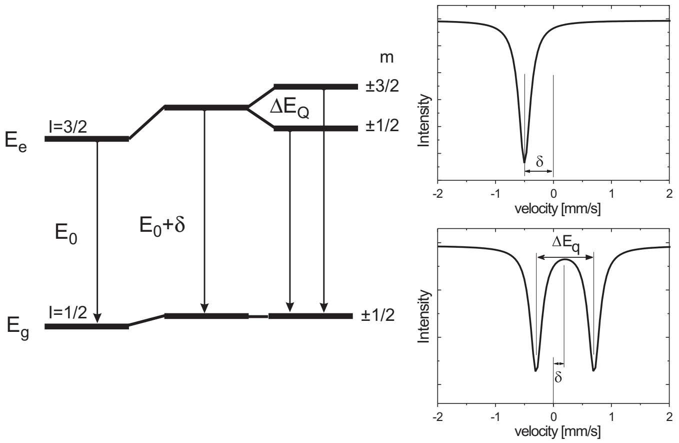

Fig. 7 Electric monopole and quadrupole interaction cause a shift and a splitting of the nuclear levels, and accordingly shift and split the lines in the Mössbauer spectrum.

Quadrupole splitting

An electric quadrupole moment of the nucleus eQ, i.e. a non-spherical shape of the nucleus, interacts with an electric field gradient (EFG) acting at the nucleus, which leads to a splitting of the energy levels, as displayed in Fig. 7. Diagonalizing the EFG tensor $V_{ij} = \frac{\partial^2}{\partial r_i \partial r_j} V$ (V = electrical potential) with $|V_{zz}| \geq |V_{yy}| \geq |V_{xx}|$ and $V_{xx} + V_{yy} + V_{zz} = 0$, the asymmetry parameter η is given by:

$$\eta = \frac{V_{xx} - V_{yy}}{V_{zz}} \tag{12}$$

and the energy eigenvalue for a state with spin I and magnetic quantum number m_I is:

$$E_q(m_I) = \frac{eQV_{zz}}{4I(2I-1)} \left[3m_I^2 - I(I+1)\right] \sqrt{1 + \frac{1}{3}\eta^2}. \tag{13}$$

For ^{57}Fe with $I_g = 1/2$ and $I_e = 3/2$, only the excited state splits and the quadrupole splitting ΔE_q is:

$$\Delta E_q = E_q(m_I = 3/2) - E_q(m_I = 1/2) = \frac{1}{2} eQV_{zz} \sqrt{1 + \frac{1}{3}\eta^2} \tag{14}$$

This leads to a doublet in the Mössbauer spectrum, where the splitting, i.e. the distance between the two lines, determines the magnitude of the quadrupole interaction and thus the field gradient. Consequently, charge distributions of atomic arrangements or defect structures can be deducted. Lattices with cubic symmetry and without any defects always result in single lines, because, due to the symmetry, no EFG can be present.

Magnetic splitting

The magnetic moment μ of the nucleus interacts with a magnetic field B acting at the nucleus (Nuclear Zeeman Effect). This interaction gives rise to the splitting of the otherwise degenerated states. The state with spin I splits into $2I + 1$ magnetic substates with the eigenvalues:

$$E_m = -\frac{\mu B m_I}{I} = -g_N \mu_N B m_I, \tag{15}$$

where the magnetic quantum number m_I can have the values $m_I = I, I - 1, \ldots, -(I - 1), -I$. The magnetic moment μ is given by the Bohr magneton μ_N and the Landé factor g_N by:

$$\mu = g_N \mu_N I. \tag{16}$$

Based on the selection rule for absorption (emission) of dipole radiation $\Delta m = 0, \pm 1$, only six transitions are allowed, and they represent the significant Zeeman sextet structure in the Mössbauer spectra of magnetic materials, as demonstrated in Fig. 8.

Mixed hyperfine interaction

If the magnetic dipole interaction and electric quadrupole interaction act together, the eigenvalues cannot be determined as easily as for each interaction alone. Normally, perturbation methods are applied. As the magnetic interaction is usually much stronger, first

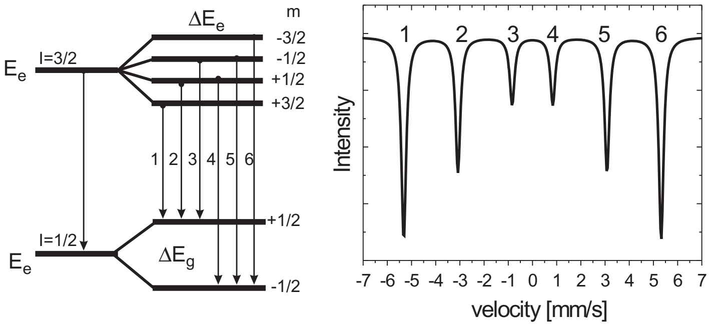
ΔE$_e$
m
-3/2
-1/2
+1/2
+3/2
E$_e$
I=3/2
1 2 3 4 5 6
+1/2
I=1/2
E$_e$
ΔE$_g$
-1/2
1 2 3 4 5 6
Intensity
-7 -6 -5 -4 -3 -2 -1 0 1 2 3 4 5 6 7
velocity [mm/s]

Fig. 8 Magnetic dipole interaction causes a splitting of the nuclear levels, and accordingly leads to the typical Zeeman sextet in the Mössbauer spectrum.

the eigenvalues are determined for this magnetic interaction and the electric interaction is treated as a perturbation. For the energy states in a first order perturbation calculation one finds:

$$E_m = -g_N \mu_N B m_I + (-1)^{|m_I|+\frac{1}{2}} \cdot \frac{1}{4} \cdot eQV_{zz} \cdot \frac{1}{2}\left(3\cos^2\theta - 1 + \eta \sin^2\theta \cos 2\phi\right), \tag{17}$$

where θ and ϕ are the angles between the direction of the magnetic field B and the principal axis of the EFG component V_{zz}. For ^{57}Fe we have:

$$E_q = \frac{1}{8} eQV_{zz}\left(3\cos^2\theta - 1 + \eta \sin^2\theta \cos 2\phi\right). \tag{18}$$

Now the line positions for the general case can be given by Eq. (19).

$$\begin{aligned} L_1 &= \delta - g_1 \mu_N B + E_q \\ L_2 &= \delta - g_2 \mu_N B - E_q \\ L_3 &= \delta - g_3 \mu_N B - E_q \\ L_4 &= \delta + g_3 \mu_N B - E_q \\ L_5 &= \delta + g_2 \mu_N B - E_q \\ L_6 &= \delta + g_1 \mu_N B + E_q. \end{aligned} \tag{19}$$

The g-factors g_i result from the Landé-factors of the ground state g_g and the excited state g_e:

$$\begin{aligned} g_1 &= \frac{1}{2} \cdot \left(3|g_e| + g_g\right) \\ g_2 &= \frac{1}{2} \cdot \left(|g_e| + g_g\right) \\ g_3 &= \frac{1}{2} \cdot \left(|g_e| - g_g\right). \end{aligned} \tag{20}$$

The resulting shift of the energy levels and the shift of the inner 4 lines in the spectrum with respect to the our lines 1 and 6 is sketched in Fig. 9.

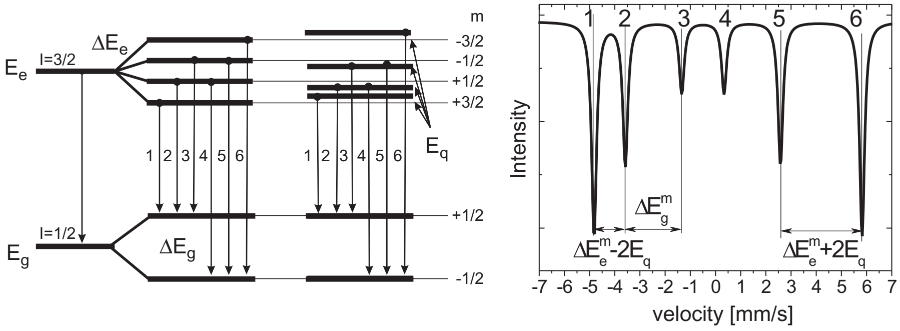
m
-3/2
-1/2
+1/2
+3/2
ΔE$_e$
E$_e$
I=3/2
1 2 3 4 5 6
1 2 3 4 5 6
E$_q$
+1/2
I=1/2
E$_g$
ΔE$_g$
-1/2
1 2 3 4 5 6
Intensity
ΔE^m_g
ΔE^m_e-2E$_q$
ΔE^m_e+2E$_q$
-7 -6 -5 -4 -3 -2 -1 0 1 2 3 4 5 6 7
velocity [mm/s]

Fig. 9 Mixed hyperfine interaction: magnetic dipole interaction causes a Zeeman splitting of the nuclear levels and an additional smaller electric quadrupole interaction shifts the split lines, which is also visible in the Mössbauer spectrum.

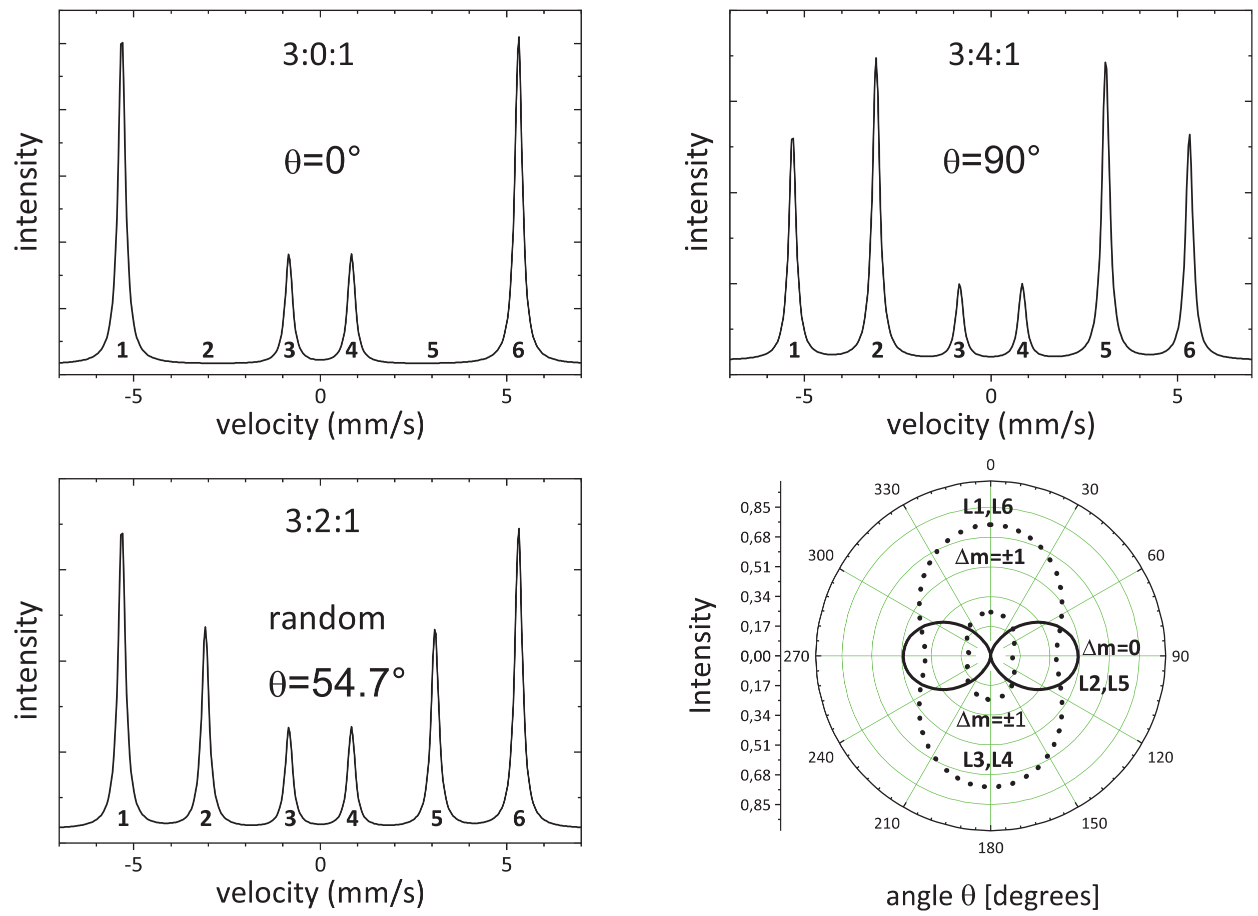

Fig. 10 Angular characteristics of the dipole radiation: the angle θ is formed by the k vector of the γ radiation and the spin direction of the nucleus (i.e. the magnetization direction). The shown emission Mössbauer spectra illustrate some important cases.

Angular dependence of absorption and emission

The relative line intensities I_i for a sextet depend on the angle $\theta = \angle\left(\vec{k}, \vec{I}\right)$ between the propagation direction $\vec{k}$ of the γ-radiation and the direction of the spin (magnetization) $\vec{I}$, as shown in Fig. 10.

For $\theta = 90°$ the intensity ratio is $I_1 : I_2 : I_3 = 3 : 4 : 1$, whereas for $\theta = 0°$ the lines 2 and 5 disappear and the ratio is $I_1 : I_2 : I_3 = 3 : 0 : 1$. If the directions of magnetization are randomly (isotropic) distributed $\left(\overline{\theta} = 54.7°\right)$, the ratios are $I_1 : I_2 : I_3 = 3 : 2 : 1$.

This can be used to determine the magnetization orientation in the sample. Mössbauer polarimetry and Magnetic Orientation Mössbauer spectroscopy (MOMS) have evolved as specialized methods for this purpose.

Synchrotron based methods

The improvement of recent synchrotron facilities and the development of new channel-cut monochromators with superior resolution allowed the transformation from the classical Mössbauer spectroscopy in the energy domain into the time domain of nuclear resonance scattering (NRS). Many methods and applications have evolved here, found its application in various structural dynamic studies on a ps-μs timescale. These studies include but not limited to rotation motion and jump diffusion, electronic and magnetic structure of disordered micro- and nano-structures, often under severe pressure and temperature conditions. Unfortunately, here this comprehensive subject cannot be treated and additional information about the method should be obtained elsewhere (Schlage and Röhlsberger, 2013; Röhlsberger, 2004).

eMS - Emission Mössbauer spectroscopy

In contrast to the traditional transmission arrangement (TMS) described in Section "From the effect to spectroscopy", there exists an alternative approach called Emission Mössbauer Spectroscopy (eMS), where the sample under the scope acts as the source, while we deal with the stable absorber. The emergence of eMS has broadened significantly the scope of physics available to Mössbauer spectroscopy. All the other basic principles remain unchanged, except that now one can choose what to move: either the stable

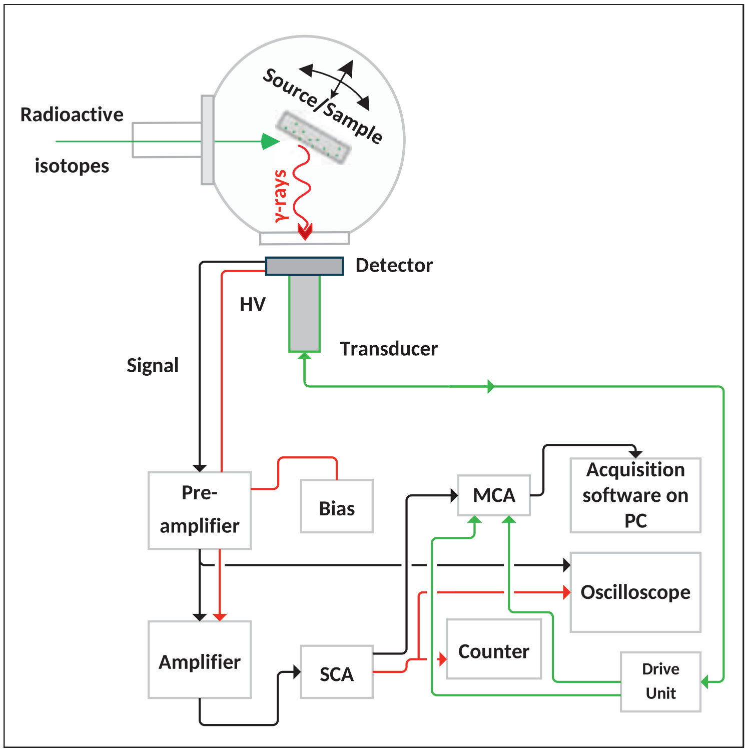

Fig. 11 Schematic representation of the setup for measuring a Mössbauer spectrum in emission geometry while implanting on-line. The setup consists of the implantation chamber with a mounted sample (source), and a stable-isotope detector installed on a transducer. The signal on the detector is firstly amplified (pre- and amplifier), then single channel analyzer (SCA) facilities in selection of a desired energy range, after this the resulting data is synchronized with transducer's velocity in multichannel analyzer (MCA), which outputs the resulted spectrum. Based on authors previous Elsevier article Zyabkin DV, Vetter U., Linderhof FMA, Gunnlaugsson HP, Schaaf P (2020) eMIL: Advanced emission Mössbauer spectrometer for measurements in versatile conditions. *Nuclear Instruments and Methods in Physics Research A* 968: 163973.

absorber or the radioactive sample. Frequently, the desired parent isotope is introduced into the sample by ion implantation, less frequently by electrochemical deposition. In the case of implantation, there are off-line (longlived) and on-line (shortlived) experiments. In the first scenario, activity produced elsewhere is mass-separated and implanted at low energies, while the second approach is carried out at on-line radioactive beam facilities, such as ISOLDE/CERN (Weyer, 2000).

The latter is performed depending on the specific lifetime, where measurements may take place simultaneously with implantation. Implantation of radioactive isotopes induces radiation damage in solids, and the final location of the implanted probes may be of big concern. This is especially the case for heavy ions ($\geqslant$10 keV), when annealing is prohibited and damage cascades of displaced host atoms are formed, thus boosting the local defect density (e.g. interstitials, vacancy clusters). The standard experimental arrangement during emission experiments is depicted schematically in Fig. 11. If the fluence is $>10^{13}$cm^2, and a certain threshold of defects density is exceeded, a formation of local amorphous areas takes place. From a standpoint when no annealing is possible, introduction of probes by electrochemical deposition and following diffusion-annealing could be beneficial, although the surface usually behaves as the sink for the defects and the concentration of the probes (dopant) via this approach is high. In studies at temperatures where the damage is mostly annealed, probe's location is determined by the dynamic equilibrium forces. Controlling the implantation energy, it becomes feasible to perform depth selective studies of the local structure, to follow the rapid local dynamic phenomena on the atomic scale, collective excitation, diffusion, properties of electronic and magnetic structure in both semiconductor and metal physics. There is a growing interest toward possible application in chemistry experiments. Furthermore, employing ion-implantation allows providing a truly dilute concentration (3×10^{12} ions/cm^2), thus neither perturbing the local environment nor forming precipitates. Besides, various isotopes decay differently and the impact of it varies from the relocation of implanted atoms into interstitial sites to perturbation of the electronic configuration around the probe. The limiting factor for eMS lies in the confined number of radioactive isotopes available and the information, which is not possible to obtain by eMS, hence other hyperfine interaction methods should be looked at.

Applications

One of the first applications of the Mössbauer effect was the proof of the gravitational red shift. Due to its extremely high energy resolution, Mössbauer spectroscopy was able to verify the tiny energy shift of $\delta_{grav.} = \frac{gd}{c^2} E_0$, which a γ quantum experiences when it falls only d = 20 m in earth's gravity g.

Phase analysis

One of the standard applications of Mössbauer spectroscopy is the accurate phase analysis (Stevens and Shenoy, 1982; Mashlan et al., 2003). One of the first examples was the determination of the amount of retained austenite in heat-treated steels. Here, Mössbauer spectroscopy is superior to any other method (e.g. XRD) with respect to its detection limit ($< 1\%$) and accuracy ($< 1\%$). In addition, by using Mössbauer spectroscopy the question of the interstitial arrangements of carbon and nitrogen in the retained austenite could be solved and it also allows an accurate calculation of the carbon or nitrogen content.

Another famous application of Mössbauer spectroscopy is the determination of Fe^{2+}/Fe^{3+} ratios in bio-matter, minerals and other oxides for medical, archeological or industrial applications (Long and Stevens, 1986; Long and Grandjean, 1996). Currently, the first Mössbauer spectrometer is doing this even on the surface of Mars.

The excellent resolution of the hyperfine interactions also allows the determination of the magnetic properties of materials, which is especially useful in alloys, magnetic and amorphous materials. Due to the short lifetime of the nuclear states, all dynamic effects occurring in this time regime influence the Mössbauer spectra in shape and line width. This fact has been used to study diffusion and hopping mechanisms, relaxation, superparamagnetism, nanocrystalline materials, effects by rf-fields, and other time dependent effects. More recent developments also deal with Mössbauer diffraction or the production of X-ray lasers.

Site determination

The ability of Mössbauer spectroscopy for determining and quantifying different sites in a phase is demonstrated by a simple example, the iron nitride γ'-Fe_4N.

This material has an anti-perovskite structure Pm3m, which is presented in Fig. 12. The iron forms an fcc structure and the nitrogen is located in the center of the unit cubes in an ordered manner. There are two crystallographic iron sites, Fe-I at the corners of the cube and Fe-II at the face centers, both sites having 12 iron nearest neighbors at the same distance. The Fe-I site has no nitrogen nearest neighbor (0 nn N), whereas the Fe-II sites have exactly two nitrogen nearest neighbors (2 nn N).

In contrast to these two crystallographic sites, the Mössbauer spectrum of this material, as shown in Fig. 13, has to be fitted with three subspectra corresponding to three different arrangements for the iron. The hyperfine fields are 34 T for the Fe-I sites and 21.6 T for the Fe-II sites. The difference in the two different Fe-II sites has to be explained by the magnetism of the material, which is invisible for X-ray diffraction.

The hyperfine parameters and the subspectral abundances are summarized in Table 2.

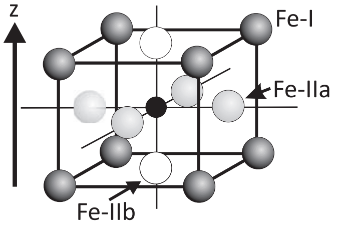

Fig. 12 Crystallographic structure of the cubic γ'-Fe_4N with site assignment explained in the text.

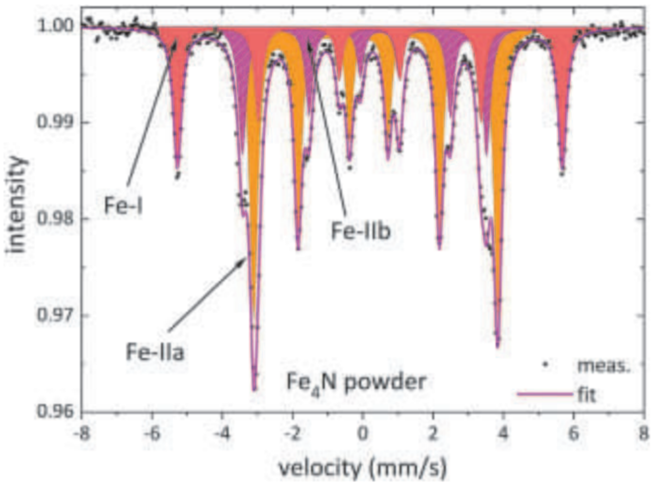

Fig. 13 Mössbauer spectrum at room temperature in transmission geometry of Fe_4N powder. The spectrum is fitted by superimposing 3 Lorentzian sextets, corresponding to 3 different atomic Fe sites in the material as explained in the text.

Table 2 Hyperfine parameters as measured for Fe_4N powder at room temperature.

Site	*IS* δ *[mm/s]*	*QS* E_q *[mm/s]*	*BHF* B_{hf} *[T]*	*LW* Γ *[mm/s]*	*RA* f *[%]*
Fe-I	0.19(2)	0.00(1)	34.0(2)	0.28(1)	25.0(13)
Fe-IIa	0.27(2)	0.10(1)	21.6(2)	0.28(1)	51.9(09)
Fe-IIb	0.26(2)	−0.22(1)	21.6(2)	0.28(1)	23.1(21)

IS - isomer shift, QS - quadrupole splitting, BHF - hyperfine field, LW - line width, RA - relative area.

The fcc material is ferromagnetic with a Curie temperature of $T_C = 767$ K, i.e. well above the measurement temperature, which in this case is room temperature in this case. The magnetic easy axis is the (100) direction, which is indicated by the z-axis in Fig. 12. There is no electric field gradient for the Fe-I site, but one for the Fe-II site having nitrogen neighbors. Thus, we have to distinguish two cases for the Fe-II site: for sire Fe-IIa, the main component V_{zz} is collinear with the hyperfine field B_{hf}, i.e. $\theta = 0°$. For the site Fe-IIb, EFG and z-axis are perpendicular, i.e. $\theta = 90°$. For both cases, the asymmetry parameter is $\eta = 0$ and V_{zz} is identical. From Eq. (17), we see that we achieve E_q with opposite signs and its value is twice as large for the Fe-IIa site as for the Fe-IIb site. This exactly matches the experimental findings in Table 2.

The subspectra areas should behave like Fe-I:Fe-IIa:Fe-IIb = 1:2:1, because 25% of the iron atoms are located at the corners, and Fe-IIa:Fe-IIb = 50%:25% because four Fe-atoms at the face centers have $\theta = 0$ and only two have $\theta = 90°$. This theory is nicely reflected in the experimental results. This example demonstrates the ability and power of Mössbauer spectroscopy in site determination.

Magnetic orientation Mössbauer spectroscopy

For Mössbauer polarimetry, magnetic fields and multi-line Mössbauer sources (e.g. ^{57}Co in Fe gives 6 lines from the source and when measuring Fe with 6 absorption lines, this results in a spectrum of 36 lines) are used to polarize the quanta from the source and thus obtain information about the magnetic domain orientations in magnetic samples. On the other hand, with a proper modification of the traditional Mössbauer technique, with a method called Magnetic Orientation Mössbauer Spectroscopy (MOMS), one is also able to determine the spin distribution in sample. An important advantage of this MOMS technique in comparison to e.g. the Magneto-Optical Kerr Effect technique (MOKE) is the absence of any external magnetic field during the measurements, which may change actual magnetization and spin distribution. Thus, it is also a magnetically non-destructive method.

In standard geometry, the photon beam is incident along the normal direction of the sample. For the MOMS experiments the specimen normal is tilted by various angles α away from the incident γ-beam and then the spectra are measured subsequently after different sample rotations around their normal. This way, the spin distribution can be obtained by fitting the intensity ratio $I_2(\varphi)/I_3(\varphi)$ of the second and the third sextet lines as a function of the various tilt and rotation angles, yielding a 'picture' of the spin distribution in the sample.

Conclusion

In summary, it should have become obvious that Mössbauer spectroscopy is a very powerful method, which has proven its suitability for many problems in solid state and materials physics, chemistry, geology, archeology, environmental and space physics, and even relativistics. Mössbauer spectroscopy is based on nuclear physics, solid state physics and hyperfine interactions. It gives a microscopic image of the Mössbauer spy isotope and its immediate surroundings, which makes the method very powerful to study properties, short range order and dynamic effects in many interesting materials. It is still under development and not used as widely as it should be. This may be due to the fact that 'suppliers' (Mössbauer spectroscopists) and 'customers' (scientists with questions) do not know enough of each other. Especially the new developments of its synchrotron-based branch seem to lead to another push in its applications. Mössbauer spectroscopy should be seen as a powerful analytical tool, which can significantly contribute to answer many open questions for many materials. So ask your questions to a Mössbauer spectroscopist.

References

Abrecht DG, Schwantes JM, Kukkadapu RK, McDonald BS, Eiden GC, and Sweet LE (2015) Real-time noise reduction for Mössbauer spectroscopy through online implementation of a modified Kalman filter. *Nuclear Instruments and Methods in Physics Research A* 773: 66–71. https://doi.org/10.1016/j.nima.2014.10.053.

Frauenfelder H (1962) *The Mössbauer Effect: A Review, with a Collection of Reprints*. WA Benjamin.

Gonser U (1975) *From a Strange Effect to Mössbauer Spectroscopy*. Berlin, Heidelberg: Springer Berlin Heidelberg.

Gonser U (1981) *Mössbauer Spectroscopy II: The Exotic Side of the Method*. Berlin, Heidelberg: Springer Berlin Heidelberg.

Greenwood NN and Gibb TC (1971) *Mössbauer Spectroscopy*. Netherlands, Dordrecht: Springer.

Kočiščák J, Novák P, Chmelíčková H, and Procházka V (2022) Properties of focusing polycapillary utilized in ^{57}Fe Mössbauer spectroscopy. *Measurement* 192: 110842. https://doi.org/10.1016/j.measurement.2022.110842.

Long GJ and Grandjean F (eds.) (1996) *Surface and Thin Film Analysis by Mössbauer Spectroscopy and Related Techniques*. US, Boston, MA: Springer.

Long GJ and Stevens JG (eds.) (1986) *The Dozen Uniquenesses of the Mössbauer Effect*. US, Boston, MA: Springer.

Mashlan M, Miglierini M, and Schaaf P (eds.) (2003) *Mössbauer Effect in Iron-Based Nanocrystalline Alloys*. Netherlands, Dordrecht: Springer.

May L (2012) *An Introduction to Mössbauer Spectroscopy*. Springer Science & Business Media.

Melzer K (1981) *Grundlagen und Anwendungen der Mössbauerspek-troskopie: Von D. Barb, Bukarest, Editura Academiel Republicii Socialiste Romania, Berlin*. vol. 21, Akademie-Verlag468. 1980.

Mössbauer RL (1958a) Kernresonanzabsorption von Gammastrahlung in Ir^{191}. *Naturwissenschaften* 45: 538.

Mössbauer RL (1958b) Kernresonanzfluoreszenz von Gammastrahlung in Ir^{191}. *Zeitschrift für Physik* 151.

Murad E and Cashion J (2004) *Theory and Characteristics of the Mössbauer Effect*. US, Boston, MA: Springer.

Novak P, Prochazka V, Stejskal A, Kopp J, and Pechousek J (2019) Pulse length and amplitude filtration of gamma radiation detection, utilization in the ^{57}Fe Mössbauer spectroscopy. *Nuclear Instruments and Methods in Physics Research A* 940: 152–155. https://doi.org/10.1016/j.nima.2019.06.012.

Röhlsberger R (2004) *Nuclear Condensed Matter Physics with Synchrotron Radiation—Basic Principles, Methodology and Applications*. Springer Publishers.

Schatz G, Weidinger A, and Gardner J (1996) *Nuclear Condensed Matter Physics: Nuclear Methods and Applications*. Wiley.

Schlage K and Röhlsberger R (2013) Nuclear resonant scattering of synchrotron radiation: Applications in magnetism of layered structures. *Journal of Electron Spectroscopy and Related Phenomena* 189: 187–195. https://doi.org/10.1016/j.elspec.2013.02.005.

Stevens J and Shenoy G (1982) Mössbauer spectroscopy and its chemical applications. *Analytical Chemistry* 54: 202A.

Wertheim GK (1964) *Mössbauer Effect: Principles and Applications*. Academic Press.

Weyer G (2000) Mössbauer spectroscopy at ISOLDE. *Hyperfine Interactions* 129: 371–390.

Zyabkin DV, Vetter U, Linderhof FM, Gunnlaugsson HP, and Schaaf P (2020) eMIL: Advanced emission Mössbauer spectrometer for measurements in versatile conditions. *Nuclear Instruments and Methods in Physics Research A* 968: 163973. https://doi.org/10.1016/j.nima.2020.163973.

Photoelectron spectromicroscopy[☆]

G Margaritondo, Ecole Polytechnique Fédérale de Lausanne, (EPFL), Lausanne, Switzerland

© 2024 Elsevier Ltd. All rights reserved.

This is an update of G. Margaritondo, Photoelectron Spectromicroscopy, Editor(s): Franco Bassani, Gerald L. Liedl, Peter Wyder, Encyclopedia of Condensed Matter Physics, Elsevier, 2005, Pages 272–279, ISBN 9780123694010, https://doi.org/10.1016/B0-12-369401-9/00587-8.

Spectromicroscopy 29
The development of photoelectron spectromicroscopy 30
Two approaches to photoelectron spectromicroscopy 30
Practical implementation: Photon-focusing approach 31
Focusing mirrors 31
Schwarzschild objectives 32
Fresnel zone plates 32
Refractive lenses and compound refractive lenses 32
Practical implementation: Electron-optics approach 33
Selected examples and performances 33
Resolution and sensitivity 34
Recent developments 35
Conclusion 35
Further reading 35

Abstract

Spectromicroscopy is a class of experimental techniques that combine spectroscopic performances with high spatial resolution. One important member of this class is photoelectron spectromicroscopy, which is based on the spectroscopic techniques exploiting the photoelectric effect. Two different approaches are discussed here: photon-focusing spectromicroscopy and electron-optics photoelectron spectromicroscopy. The discussion includes a few selected examples, an analysis of relevant performances and a short presentation of the current developments.

Key points

- Photoelectron spectromicroscopy
- Photon-focusing approach
- X-ray lenses: Fresnel zone plates, Schwarzschild objectives, Kirkpatrick-Baez mirrors, compound refractive lenses
- Electron-optics approach
- Photoelectron emission microscope (PEEM)
- Partial yield
- Resolution and sensitivity
- Ultrabright storage ring synchrotron sources
- Free electron lasers

Spectromicroscopy

The term "spectromicroscopy" broadly applies to all spectroscopic techniques implemented with high spatial resolution. The discussion here is focused on a leading example: spectromicroscopy techniques based on the photoelectric effect.

Besides photoemission spectroscopy, other important types of spectromicroscopy are (1) electron energy loss spectroscopy, which can be performed with high spatial and energy resolution providing local information on the electronic and chemical composition and bounding in the material; (2) Auger spectromicroscopy, a surface-specific analytical technique, using a focused electron beam to combine high lateral and depth resolution; (3) X-ray-excited fluorescence spectromicroscopy ("fluorescence microprobe"), a powerful and relatively straightforward technique for microchemical analysis, and (4) near-field vibrational spectromicroscopy, which beats the Abbe diffraction limits of far-field microscopy by exploiting evanescent waves.

[☆] *Change History*: September 2022. G Margaritondo updated all sections. Figs. 1 was updated The original Fig. 2 was eliminated The original Figs. 3 and 4 were replaced and updated by Figs. 2 and 3. Fig. 5 was replaced and updated by Fig. 4, Fig. 7 was replaced and updated by Fig. 6 Fig. 8 was replaced and updated by Fig. 7, Fig. 9 was eliminated. Fig. 8 is new.

The development of photoelectron spectromicroscopy

Photoelectron spectroscopy, a technique based on the photoelectric effect, emerged in the late 1960s as a leading probe of the electronic structure in condensed matter systems. The progress in the experimental tools progressively eliminated its historical limitations of this technique, enhancing its impact and expanding its domains of application. The development of photoelectron spectromicroscopy was a major component of this evolution.

Until the late 1980s, photoemission experiments were performed with almost no lateral resolution—whereas the natural surface sensitivity of the photoelectron emission process automatically provided atomic scale resolution in the direction perpendicular to the emitting surface. Technical problems, primarily related to the low signal level, forced the photoemission experiments to probe a sample area not smaller than $1 \times 1\ \text{cm}^2$—or even larger. This was a severe limitation in the study of laterally inhomogeneous systems and processes.

In 1988–89, the first examples of photoemission experiment with high lateral resolution were presented (see, e.g., Fig. 1), opening up new opportunities for the field of photoemission techniques. Lateral resolution could be achieved thanks to the use of high-brightness synchrotron radiation sources such as the undulators—which enhanced the signal-to-noise ratio. In the subsequent years, photoemission spectromicroscopy in different forms expanded becoming a leading subdomain of photoelectron spectroscopy.

One important aspect of this evolution was the impact on the life sciences. Without lateral resolution, photoelectron spectroscopy had been almost useless in biology, biophysics, and the medical research. Spatial dimensions such as the size of cells and cell components determine, in fact, the minimum spatial resolution required to provide meaningful information in these domains. Before the late 1980s, photoelectron spectroscopy was, as mentioned, very far from such resolution levels.

After the advent of photoelectron spectromicroscopy, photoemission-based probes became instead quite important in biology and medical research. They provided, in fact, very valuable microchemical information without requiring extensive sample preparation and the consequent risk of artifacts. However, photoelectron spectromicroscopy requires ultrahigh vacuum and this constitutes a limitation in biological applications.

Two approaches to photoelectron spectromicroscopy

There exist basically two approaches to achieve lateral resolution in a photoemission technique (Fig. 2). In the first case, the primary photon beam is focused into a small sample area and photoelectrons are produced only from that region. This approach is used in two complementary data-taking procedures.

In the first case (Fig. 2a), the photon beam is kept in a constant position on the sample surface and photoemission spectra are taken from that small spot. In the second case (Fig. 2b), the focused beam is scanned on the sample surface (or, more practically, the sample is scanned with respect to the beam) while photoelectrons are collected for a constant set of parameters—in particular a fixed energy. This gives two-dimensional photoemission intensity "images."

Consider (Fig. 3) the case in which the focused spot is scanned while the collected photoelectron energy corresponds to photoelectrons excited from a core level of a given element. The photoemission intensity roughly corresponds to the concentration of that element. Therefore, the "images" are two-dimensional maps of the chemical composition at a microscopic scale.

Furthermore, a core-level energy changes slightly depending on the oxidation state of the element. Therefore, by fine-tuning the collected photoelectron energy one can obtain chemical maps of a given element in different chemical environments. Since photoelectron spectromicroscopy has the high surface sensitivity typical of nearly all photoemission experiments, such chemical

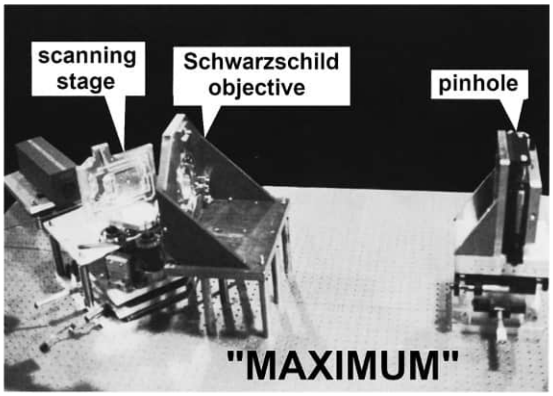

Fig. 1 "MAXIMUM," one of the first photoelectron spectromicroscopy instruments, realized at the University of Wisconsin Synchrotron Radiation Center by a team led by Franco Cerrina (see Margaritondo G., Cerrina F. (1990) Overview of soft-X-ray photoemission spectromicroscopy. *Nuclear Instruments and Methods* A291: 26–35).

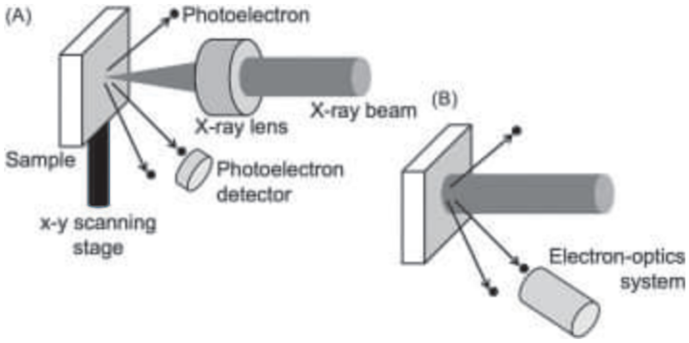

Fig. 2 The two implementation modes of photoelectron spectromicroscopy: in (a) the lateral resolution is achieved by focusing the X-ray photon beam. In (b) the resolution is produced by an electron lens system.

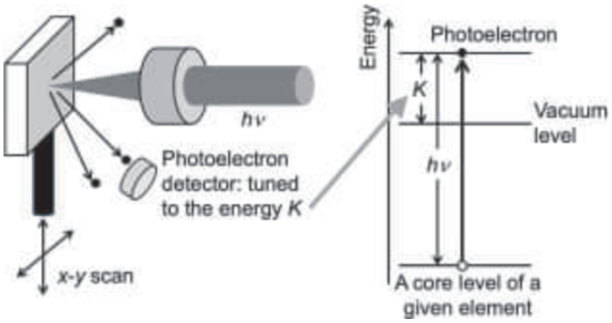
Energy
Photoelectron
K
hν
Vacuum level
hν
Photoelectron detector: tuned to the energy K
x-y scan
A core level of a given element

Fig. 3 Chemical microanalysis with the photon-focusing mode of photoelectron spectromicroscopy. The photoelectron detector is tuned to a kinetic energy *K* corresponding to the photoelectron emission from a core level of a given chemical element. This energy is above the vacuum level, which is the minimum energy to leave the sample. The corresponding photoemission intensity map reveals the presence and spatial distribution of the element.

maps correspond to the region near the sample surface—and provide extremely valuable information on surface processes including catalysis, corrosion and passivation.

The second approach to photoelectron spectromicroscopy (Fig. 2b) does not require focusing the photon beam. Lateral resolution is achieved instead by processing the emitted photoelectrons with an electron–optical system similar to an electron microscope.

Several years of practical experience demonstrated that the two approaches have advantages and disadvantages with respect to each other. In essence, they are largely complementary.

Practical implementation: Photon-focusing approach

Focusing photon beams is a major technical problem. The photons must have sufficient energy to enable electrons inside the solid to overcome the surface energy barrier and become photoelectrons. The photon energy falls in the ultraviolet range or above.

Furthermore, the energy of the photons must be sufficient to extract photoelectrons from the core levels of relevant chemical elements. The corresponding photon energies range from the vacuum ultraviolet to the X-rays.

Focusing is a relatively easy task only in a small portion of this spectral range, corresponding to its lowest photon energies (a few eV). For higher photon energies, it is a very difficult task.

There are three main reasons: (1) solid materials absorb photons in a large portion of the vacuum ultraviolet and soft-X-ray ranges, making it impossible to use transmission optical devices similar to optical lenses. (2) Hard X-rays can travel through solid materials, but the refractive index is very close to that of vacuum ($n \approx 1$), drastically limiting the effectiveness of refractive focusing devices. (3) The reflection of X-rays is extremely weak except for near-grazing incidence, and this tendency becomes stronger when the wavelength decreases. This limits the effectiveness of focusing by reflection except at extreme grazing incidence.

Effective technical solutions for these problems have been conceived and implemented. Fig. 4 shows a series of widely used X-ray-focusing devices suitable for several spectral domains.

Focusing mirrors

Mirrors can provide X-ray focusing as long as the angle of incidence is close to grazing incidence. This, however, complicates the fabrication processes and makes them quite expensive. The surface profile must, in fact, meet stringent requirements over a large area.

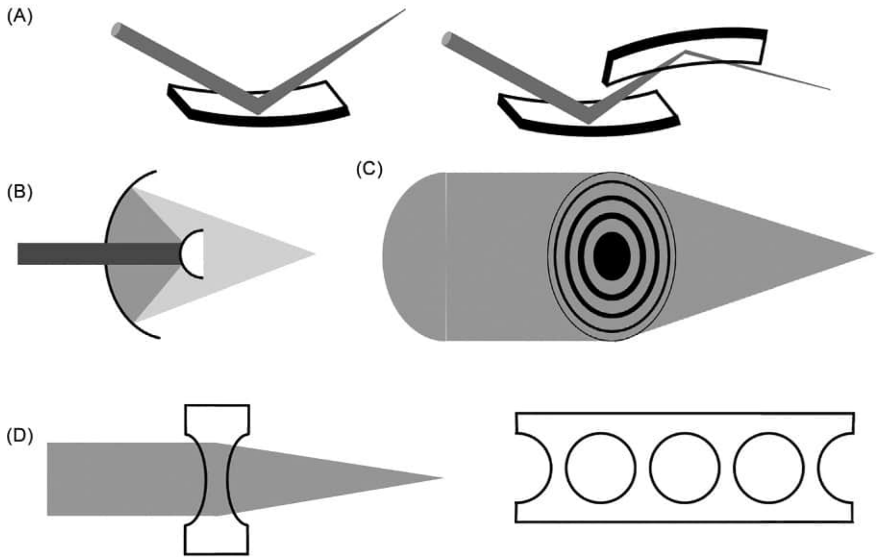

Fig. 4 Different X-ray focusing devices. (a) A single cylindrical, grazing-incidence mirror (left) focuses only in one direction, whereas (right) a combination of two such mirrors (Kirkpatrick–Baez lens) provides bidirectional focusing. (b) A Schwarzschild objective is formed by a convex spherical lens and a concave spherical lens, with nongrazing-incidence reflection enhanced by multilayer coatings. (c) A Fresnel zone plate (FZP). (d) (Left) a single biconcave refractive lens for hard-X-rays, and (right) a compound refractive lens (CRL).

The focusing surface can be toroidal, parabolic, or spherical (with some degree of aberration). Machining such surfaces with the required accuracy is technically difficult. It is also possible to use cylindrical surfaces that are easier to fabricate (e.g., by bending the mirror), but focus only in one direction. Bidirectional focusing requires, therefore, a pair of mirrors combined together in a "Kirkpatrick–Baez" device (Fig. 4a, right).

Schwarzschild objectives

These devices (Fig. 4b) focus visible light as well as X-rays, and this facilitates the alignment of the optical system. The lens is the combination of two reflecting spherical surfaces. Note that the reflection is not at grazing incidence, and this could sharply limit the throughput.

The problem can be solved by a suitable multilayer coating that enhances the reflection. The corresponding technology is, however, quite complicated. Furthermore, these lenses can only work in a limited spectral range that is typically located at photon energies below 100 eV. Even with these limitations, the Schwarzschild objectives did play a significant role in the development of photoelectron spectromicroscopy.

Fresnel zone plates

The Fresnel zone plates (FZPs) are widely used as focusing devices in different spectral ranges. As schematically illustrated in Fig. 4c, the working principle is based on the interference of rays passing through a series of alternating transmitting and blocking circular zones. The blocking zones are supported by a very thin substrate that allows a reasonable transmission of the X-ray beam.

The main difficulty in fabricating FZPs for X-rays is caused by the size of the zones. Their radial thickness decreases from the center to the periphery of the plate. Furthermore, the size decreases as the wavelength decreases. For X-ray wavelengths, the outermost-zone size is of the order of hundreds of angstroms. Therefore, the fabrication process requires sophisticated—and expensive—electron-beam lithography techniques. These problems notwithstanding, FZPs are now extensively used in X-ray microscopy and spectromicroscopy.

Refractive lenses and compound refractive lenses

For hard X-rays, the difficulties related to the limited transmission become progressively less important as the wavelength decreases—and it is possible to use refractive lenses. There exist, however, a significant difference between the refractive lenses for visible light and those for X-rays. The refractive index for X-rays is smaller in a material than in vacuum, whereas the contrary is true for visible light. An X-ray focusing lens, therefore, is not biconvex but biconcave (Fig. 4d).

As already mentioned, the refractive index differences between a material and vacuum are extremely limited. As a consequence, the focal length of a single biconcave refractive lens would be unreasonably large. The solution is provided by a series of lenses in the form of spherical cavities created inside a block—as also shown in Fig. 4d, right. Such a device is known as a "compound refractive lens" or CRL.

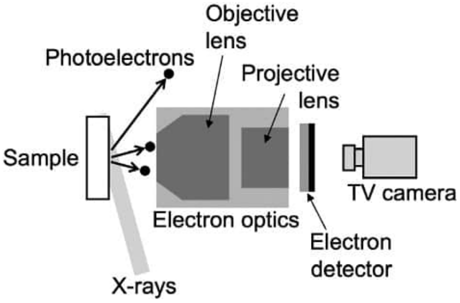

Fig. 5 Schematic experimental setup of a photoelectron emission microscope (PEEM) for the second mode of photoelectron spectromicroscopy.

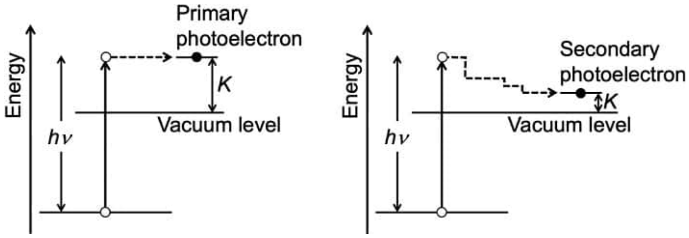

Fig. 6 Left: primary photoelectrons are emitted with an energy *K* (above the vacuum level) corresponding to the initial energy in the solid plus the photon energy, without losses. Right: a secondary photoelectron loses part of its energy, typically through multiple losses, while traveling through the sample and before leaving it. The partial yield (PY) mode of photoelectron spectroscopy and spectromicroscopy is based on the detection of secondary photoelectrons.

Practical implementation: Electron-optics approach

Fig. 5 shows a typical electron-optics system for the implementation of this second approach to photoelectron spectromicroscopy. The standard name for this type of instrument is "photoelectron emission microscope" (PEEM).

Without photon focusing, it becomes easier to perform photoemission techniques that require changing the photon energy, which influences the focusing mechanisms. The most frequent way to use a PEEM is to perform "partial yield" (PY) measurements with high lateral resolution. A PY experiment is implemented by taking the intensity of the "secondary" photoelectrons as a function of the photon energy—see Fig. 6.

The secondary photoelectrons are the low-kinetic-energy electrons emitted from the sample after a loss of energy with respect to the of their excitation energy (the sum of the initial energy in the sample plus the photon energy). Such losses are typically due to multistep phenomena. The yield of secondary photoelectrons is proportional to the number of absorbed photons. Therefore, a PY curve closely resembles the plot of the X-ray absorption spectrum as a function of the photon energy.

Note, however, that the PY technique is surface sensitive—although the surface sensitivity is not as high as for other photoemission techniques due to the low kinetic energy of the detected secondary photoelectrons. Therefore, a PY curve primarily reflects the absorption coefficient of the region near the surface rather than that of the bulk.

With a PEEM, PY curves can be taken from small sample areas. This is a very powerful way to explore the local elemental composition and other chemical properties. An X-ray absorption spectrum is dominated by the absorption threshold of the component elements in the specimen and reveals their presence and chemical status. This approach is particularly convenient when local chemical information must be rapidly obtained.

The technique is typically implemented by first taking overall images corresponding to the partial-yield intensity emitted from different sample areas with a fixed photon energy (or with a "white" photon beam). Such images reveal the overall micromorphology of the specimen. Then, specific areas are selected for a more detailed analysis and PY spectra are taken from them.

PEEM is not limited to the detection of secondary electrons. By selecting the detected electron energies to coincide with specific primary photoelectrons, one can in fact implement very interesting experiments yielding sophisticated information.

Selected examples and performances

Fig. 7 shows an early example of photoelectron spectromicroscopy in the photon-focusing mode. The spectra illustrate a core level (Ge3d) of a Ge film on a semiconducting GaSe substrate.

This particular system has been considered as a typical example of interface in which no chemical reaction takes place. On the contrary, spectra taken in different areas of the interface show clear differences, even in the presence of noise, providing evidence for local chemical reactions that were not visible in a photoemission spectrum without spatial resolution. Therefore, without lateral resolution photoelectron, spectroscopy can be misleading.

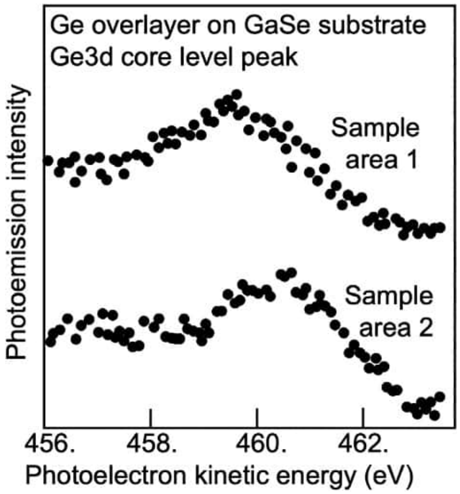

Fig. 7 An example of photon-focusing photoelectron spectromicroscopy result. Two spectra taken at two different spots of a thin Ge overlayer on a GaSe substrate reveal different Ge3d core-level peaks—putting in evidence totally unexpected local chemical reactions. Experimental data extracted from Almeida J., Vobornik I., Berger H., Kiskinova M., Kolmakov A., et al. (1997) Spectromicroscopic evidence of Ge-GaSe chemical reactions: Not a Schottky system. *Physical Review B* 55: 4899.

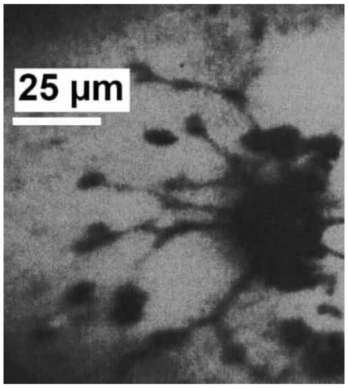

Fig. 8 One of the first applications of electron-optics photoelectron spectromicroscopy to biological specimens. The PEEM image shows a mice neuron culture. Experimantal data extracted from De Stasio G., Hardcastle S., Koranda S.F., Tonner B.P., Mercanti D., Ciotti M.T., Perfetti P., Margaritondo G. (1993) Photoemission spectromicroscopy of neurons. *Physical Review* E47: 2117.

Fig. 8 shows an example of electron-optics photoelectron spectromicroscopy obtained with a PEEM operating in the PY mode. Note that the experiment concerns a biological sample: the PEEM technique is in fact particularly suited for studies in the life sciences and in medical research.

Resolution and sensitivity

The most relevant performances for photoelectron spectromicroscopy are the spatial resolution and the sensitivity to trace elements. Concerning lateral resolution, for both approaches to photoelectron spectromicroscopy it is necessary to distinguish between the "system" (optical or electron–optical) resolution and the practical level that can be obtained while performing real experiments.

The final resolution is, in fact, also limited by practical factors such as the signal level. Consider for example the comparison between the resolution delivered by an electron optics system used as an electron microscope and the corresponding resolution when the system is used for PEEM. In the first case, the lateral resolution reached long ago the nanometer level. But the spectromicroscopy resolution is worse because of the need for a reasonable signal-to-noise ratio.

Likewise, X-ray focusing devices can deliver in principle excellent resolution levels, but the practical resolution in spectromicroscopy is more limited. Consider for example a Fresnel zone plate: its optical resolution depends on the size of the outermost zone and can reach the nanometer level. However, the spectromicroscopy resolution although at the nanometer level, is typically limited to several nanometers.

Note that, the practical lateral resolution in a spectromicroscopy experiment is the result of a compromise between conflicting requirements. For example, lateral resolution can be reduced in order to achieve the required energy resolution while keeping the signal-to-noise ratio at a reasonable level. Achieving a sensible compromise is essential for a good use of spectromicroscopy, and cannot be handled with automated procedures.

Chemical sensitivity is an important point for spectromicroscopy. In a normal photoemission experiment without lateral resolution, the minimum detectable relative atomic concentration is 0.01–0.001. This is, of course, the local concentration in the near-surface region probed by photoemission. If the minority species is concentrated in that region, the equivalent relative concentration limit for the entire specimen is much lower.

Spectromicroscopy analyzes areas much smaller than $\approx 1\ \text{mm}^2$. If the minority species is not homogeneously distributed, by focusing on high-concentration areas the equivalent detectable concentration limit can be significantly lowered.

Recent developments

Photoelectron spectromicroscopy has become a standard technique for microchemical analysis. Spectacular performance improvements have been achieved in recent years. The primary factor has been the boost in the quality of the X-ray sources.

Several storage rings used as synchrotron radiation sources have been recently modified adopting new magnet lattices. This enabled them to reach the "diffraction limit" for most or all of their emission spectrum. The corresponding increases in brightness and coherence are by orders of magnitude. This progress directly translates into better performances in spectromicroscopy.

Also spectacular has been the impact of the X-ray free electron lasers. These devices are still rare but their number is expanding. And their performances are truly exceptional: a peak brightness exceeding that of storage rings by several orders of magnitude and a pulse duration of femtoseconds or less.

This opens the door to the analysis of many important phenomena in the same time scale. Therefore, photoelectron spectromicroscopy is becoming a fast time-resolved technique with an outstanding potential for new applications in many different disciplines.

Conclusion

By combining spatial resolution with spectroscopy analytical capability, the different types of spectromicroscopy techniques became very powerful instruments for materials sciences and biomedical research. This is particularly true for photoelectron spectromicroscopy in its different modes of implementation within their two main classes—photon focusing and electron optics. The applications are now further expanded by the advent of new and very advancer X-ray sources such as the free electron lasers and ultrabright storage rings.

Further reading

Ade H (ed.) (1997) *Spectromicroscopy With VUV Photons and X-rays*. Amsterdam: Elsevier.

Bauer E (2001) Photoelectron spectromicroscopy: Present and future. *Journal of Electron Spectroscopy* 114: 975–987.

Gilbert B, Andres R, Perfetti P, Margaritond G, Rempfer G, and Gelsomina DS (2000) Charging phenomena in X-PEEM imaging and spectroscopy. *Ultramicroscopy* 83: 123.

Gilbert B, Margaritondo G, Mercanti D, Casalbore P, and De Stasio G (2001) Synchrotron spectromicroscopy in medicine and biology. *J. Alloys Compounds* 328(2001): 8.

Gilbert P (2014) *Photoemission Spectromicroscopy for the Biomineralogist*. Boca Raton: CRC Press.

Gunther S, Kaulich B, Gregoratti L, and Kiskinova M (2002) Photoelectron microscopy and applications in surface and materials science. *Progress in Surface Science* 70: 187–260.

Gunther S, Kolmakov A, Kovac J, and Kiskinova M (1998) Artefact formation in scanning photoelectron emission microscopy. *Ultramicroscopy* 74: 35–51.

Kinoshita T (2002) Application and future of photoelectron spectromicroscopy. *Journal of Electron Spectroscopy* 124: 175–194.

Margaritondo G and Cerrina F (1990) Overview of soft-X-ray photoemission spectromicroscopy. *Nuclear Instruments and Methods* A291: 26–35.

Margaritondo G (1995) The information content of photoemission spectroscopy and spectromicroscopy. *Surface Review and Letters* 2: 305–313.

Margaritondo G (1999) Photoelectron microscopy and its applications to semiconductor science. *Japanese Journal of Applied Physics* 38: 8.

Margaritondo G (2010) Photoelectron spectromicroscopy and spectronanoscopy at synchrotrons: growing impact on life sciences and materials science. *Journal of Electron Spectroscopy* 178–179: 273.

Margaritondo G and De Stasio G (1997) Photoelectron spectromicroscopy with synchrotron radiation: Applications to neurobiology. In: Ade H (ed.) *Spectromicroscopy With VUV Photons and X-rays*, pp. 137–147. Amsterdam: Elsevier.

Margaritondo G and Ge DS (1997) Synchrotron spectromicroscopy for the life sciences: general considerations and special procedures. *International Journal of Imaging Systems and Technology* 8: 188–203.

Thieme J, Schmahl G, Rudolph D, and Umbach E (eds.) (1998) *X-ray Microscopy and Spectromicroscopy: Status Report From the Fifth International Conference, Wurzburg, August 19–23, 1996*. Heidelberg: Springer.

Vaz CAF, Kleibert A, and El Kazzi M (2020) *Nanoscale XPEEM Spectromicroscopy*. Boca Raton: CRC Press.

Scanning electron microscopy[☆]

Anjam Khursheed, Department of Electrical and Computer Engineering, National University of Singapore, Singapore, Singapore

© 2024 Elsevier Ltd. All rights reserved.

This is an update of S.J. Pennycook, Transmission Electron Microscopy, Editor(s): Franco Bassani, Gerald L. Liedl, Peter Wyder, Encyclopedia of Condensed Matter Physics, Elsevier, 2005, Pages 240–247, ISBN 9780123694010, https://doi.org/10.1016/B0-12-369401-9/00582-9.

Introduction 36
SEM basic principles 37
Electron optical figures of merit 40
Conclusion 49
Acknowledgments 49
Conflict of Interest 49
References 49

Abstract

The scanning electron microscope is widely used in condensed matter physics research for providing nano-scale topographic images of material surfaces. This chapter introduces the subject of scanning electron microscopy, mostly in terms of describing the basic principles behind how the scanning electron microscope (SEM) instrument functions and its main figures of merit, such as image resolution and signal-to-noise. The chapter emphasizes how the overall performance of a scanning electron microscope is critically dependent on a variety of different factors, such as the quality of its electron source, the low aberration design of its objective lens, and primary beam-specimen interaction effects.

Introduction

The scanning electron microscope (SEM) is an indispensable research and development tool in the subject of condensed matter physics. It is the most widely used instrument for examining the surface topography and morphology of bulk materials on the nanoscale. It is capable of routinely obtaining an image resolution of 1–2 nm on a variety of different materials, a factor of around 200 times better than the spatial resolution of conventional optical microscopes.

In the category of electron microscopes, the SEM is smaller, cheaper, and more accessible than a transmission electron microscope (TEM) or a scanning transmission electron microscope (STEM). Its specimens require much less preparation and its images are much easier to interpret. These advantages come from the fact that it functions by detecting reflected/scattered electrons from bulk specimens rather than relying on an electron beam propagating through a thin specimen (nm thick), as is the case with transmission electron microscopes. These advantages come at the price of its overall image resolution being around an order of magnitude poorer than those that can be obtained by a TEM or a STEM. In general, however, the SEM plays a complementary role to transmission electron microscopes. It provides information on a sample's surface and its composition, while a TEM or STEM acquires information on the inner structure of the sample, such as crystal structure.

Several companion analytical tools have been developed for the SEM that transform it into a powerful material analysis tool, taking it beyond a purely topographical imaging mode of operation. The energy dispersive X-ray (EDX) spectroscopy technique for instance, is used in the SEM to capture atomic transitions that emit characteristic X-rays, enabling it to carry out quantitative material analysis. The electron backscatter diffraction technique (EBSD) inside the SEM is routinely used to provide a material's crystal structure, orientation, phase, and strain information. SEMs have also been developed to operate with a gaseous environment inside the specimen chamber, which provides the option of using wet samples and uncoated non-metallic samples. These SEMs are known as environmental SEMs (ESEMs). There have also been many other advances, such as the inclusion of a gun monochromator unit to lower the primary beam energy spread, further improving the electron optics of SEMs. However, the focus of this chapter will be mainly to describe the basic principles upon which a SEM functions, give its main figures of merit, provide some sample high resolution experimental images, and highlight some promising avenues for future development.

The development of the SEM instrument took place approximately between the years 1925–65, shortly after which the first commercial SEM was launched (McMullan, 1995), and since then, the instrument has undergone many technological improvements (Khursheed, 2011; Goldstein et al., 2017; Brodusch et al., 2018). In particular, over the last few decades, the technique of low voltage scanning electron microscopy (LVSEM) has overcome many traditional limitations. The LVSEM technique has been able to reduce the energy with which the primary electron beam strikes the specimen while at the same time keeping its probe size small by taking advantage of various electron optical innovations, and thereby greatly improving its overall image resolution capability. LVSEMs also have higher signal yields, a smaller beam/specimen interaction volume, greater surface information, and are able to

---

[☆] *Change History:* November 2022. A Khursheed updated this chapter.

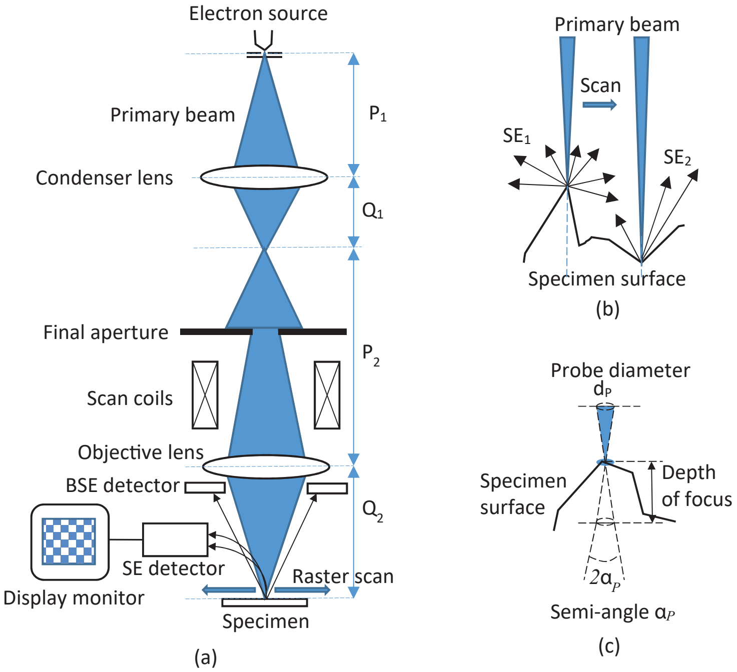

Fig. 1 Schematic drawing of how a scanning electron microscope (SEM) functions. (a) Electron optics of the primary electron beam column. (b) Emission of secondary electrons (SEs) from the specimen surface. (c) Primary beam probe depth of focus.

minimize charging effects while inspecting non-conductive specimens. This chapter will describe the SEM instrument mainly in terms of its transformation into the LVSEM.

SEM basic principles

The SEM functions by raster scanning a focused beam of electrons over the surface of a bulk specimen, as shown in Fig. 1a. The beam of electrons, usually referred to as the primary beam, is generated and accelerated to energies from 0.5 to 30 keV inside an electron source unit located at the top of the SEM. The electron source is rotationally symmetric and is designed to emit a round shaped primary beam. The primary beam is emitted with an effective source diameter, energy spread and brightness, and is then subsequently demagnified and focused by a series of electron optical lenses in order to produce a primary electron beam probe of nano-size dimensions that is scanned over the specimen surface.

The number of electron optical lenses required in the column depends on the effective source diameter of the electron source. Fig. 1a depicts two demagnifying lenses, a condenser lens placed just below the electron source, and an objective lens placed just above the specimen. This configuration is widely used for the Schottky electron source (SE), which emits electrons by using the principle of thermal field emission (Bronsgeest, 2014). The amount of demagnification applied to the primary electron beam, M_B, can be estimated by using simple first-order optics principles using the focal spot distances P_1, Q_1, P_2, and Q_2 shown in Fig. 1a. The demagnification factor M_B is given by $(Q_1/P_1).(Q_2/P_2)$. It can also be obtained in terms of the initial source semi-angle α_S ratio with the final beam probe semi-angle α_P, by α_S/α_P. The source spot size needs to be demagnified by a factor of only 5–15 for the Schottky electron source, but for conventional heated tungsten wire electron sources (TE), demagnification factors can range up to 10,000 (Oatley, 1975).

A final circular aperture filters out wide-angle electrons in the primary beam before it enters the objective lens, and a scan unit, usually consisting of magnetic coils, performs the deflection action of raster scanning the primary beam over the specimen surface. The purpose of filtering out wide-angle electrons in the primary beam is to reduce objective lens aberration effects, ensuring that the primary beam electrons striking the specimen have low semi-angles (down to a few millirad) and that they travel close to the objective lens rotational axis of symmetry (within tens of microns). The rotational axis of symmetry of all electron lenses in the SEM is often simply referred to as the SEM's optical axis.

On striking the specimen, the primary beam generates scattered electrons that leave the specimen surface over a wide range of angles and energies. The low energy scattered electrons, known as the secondary electrons (SEs), are attracted on to an electron detector located away to one side of the axis, below the objective lens. The SE energy range is usually defined from 0 to 50 eV, where the upper limit is an arbitrary number having no physical importance. The number of SEs captured by the SE detector is strongly modulated by the specimen's surface topography, as shown in Fig. 1b, which is then translated into image brightness variations on a display monitor. The SE detector signal is amplified and synchronized to the scan deflector unit, so that each scanned point on the specimen corresponds to a single point in the SE display image.

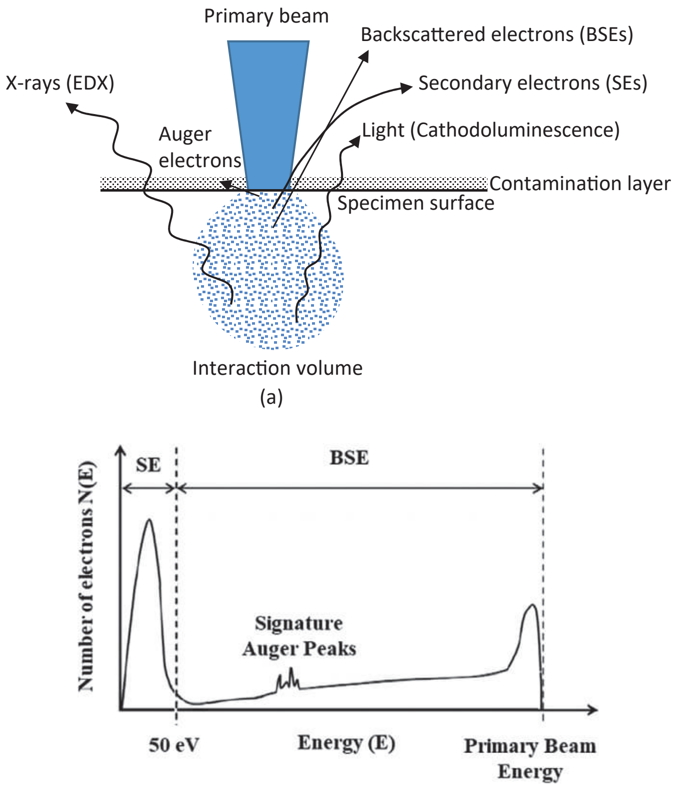

(a)

(b)

Fig. 2 Electron primary beam-specimen scattering characteristics. (a) Interaction volume and the electron/photons leaving the specimen surface. (b) Energy distribution of the scattered electrons leaving the specimen surface.

The size of the primary beam focused on to the specimen surface, the probe diameter, d_P, depends not only on the overall demagnification of beam, M_B, but also on the objective lens aberrations. The probe diameter d_P is an important parameter limiting the final SE image resolution, and together with the final semi-angle α_P, it also determines the image depth-of-focus, the specimen depth over which points in the SEM image still appear to be in focus, as illustrated in the schematic diagram shown in Fig. 1c. SEM images have the desirable feature of having a relatively large depth of focus compared to optical microscopes, an advantage which comes from them having relatively small final semi-angles (in the several milli-rad range).

After the primary beam strikes the specimen surface, it loses energy by undergoing a series of multiple collisions inside the specimen, which are largely confined to a balloon shaped region known as the interaction volume, as shown in Fig. 2a. The complex set of events that take place inside the interaction volume generate a cascade of electrons and photons, some of which are able to leave the specimen surface. The lower energy scattered electrons that escape from the specimen surface, the SEs, typically come from nanometer size depths, while the higher energy scattered electrons, the backscattered electrons (BSEs), are typically generated from depths that range from tens to hundreds of nanometers. Since the number of emitted BSEs rises with specimen atomic number, a BSE detector is commonly placed under the objective lens in order to obtain a material contrast image. The BSE image is only capable of providing a map of qualitative material/density changes, and its image resolution is in general significantly poorer than the one provided by the SE image. For these reasons, the BSE image is usually used together with the SE image in order to provide extra material information about the specimen.

Although Auger electrons are generated from even shallower depths inside the specimen than the SEs, they are generally masked by the presence of a nanometer thick hydrocarbon contamination layer. This contamination layer comes from the interaction of the primary beam with the specimen surface and residual gas molecules inside the high vacuum (HV) specimen chamber (10^{-6}–10^{-5} Torr). In practice, the only detectable Auger electrons inside a SEM specimen chamber are those that are generated from within the contamination layer (carbon peak). At micron depths below the specimen surface, characteristic X-rays created from atomic transitions are emitted, and they are used by the energy dispersive X-ray (EDX) spectroscopy technique to perform quantitative material analysis, most commonly used to identify the different types of materials present in the sample. At even lower depths, photons emitted in the 200–800 nm wavelength range are used by the Cathodoluminescence technique in order to provide information about trace elements contained in mineral samples or capture the presence of mechanically induced defects in crystals.

The scattered electrons emitted from the specimen surface have a wide range of energies, as shown in Fig. 2b. The lower part of the distribution is dominated by the SE energy distribution, whose peak typically lies in the 1–2 eV range. In the higher part of the scattered electron energy distribution, there is the BSE peak. Elastically scattered BSEs, known as low loss BSEs, make up the upper part of the electron energy spectrum close to the primary beam energy. Since low loss BSEs emanate from nanometer size depths

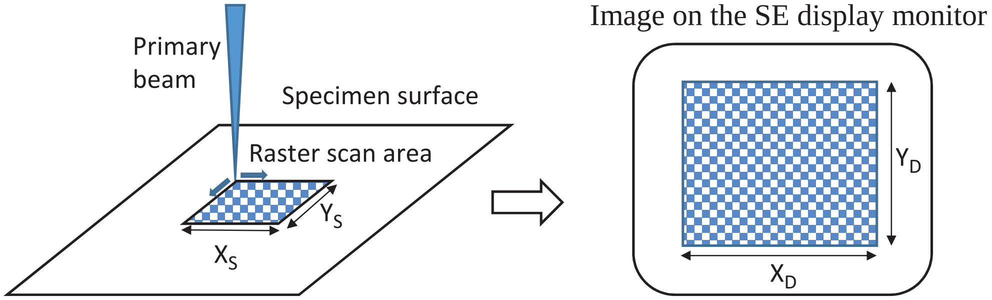

Fig. 3 Schematic drawing of raster scan area on the specimen and its corresponding image on the SE signal monitor display.

inside the specimen, they can be used to provide a way of improving the BSE image resolution (Luo and Khursheed, 2007). Detection of low loss BSEs in some SEM columns is achieved by placing high pass energy filters placed in front of the BSE detector.

It is important to note that the SEM does not function like a conventional optical microscope, where a transparent specimen is illuminated by a collimated light beam, and where the subsequent transmitted/scattered light propagating along an optical axis is then magnified into an image by a series of projection lenses. The TEM functions in this way, but not the SEM. Instead of projecting and magnifying a transmitted electron beam into an image, the SEM demagnifies an electron beam coming from an electron source into a nanosize probe which is raster scanned over the surface of the specimen, and its final image is formed from reflected/scattered electrons that leave the specimen. Unlike the parallel action of a TEM, where points from a region of the specimen are simultaneously projected and focused into a set of corresponding points in a final image, an SEM image is formed one point at a time, in a sequential way, similar to how the early generation of cathode ray tubes formed their images, or how an image is formed on a radar screen. In fact, historically, both cathode ray tubes and the invention of radar greatly influenced the way the SEM was invented and subsequently developed (Smith, 1997).

Fig. 3 shows the area of scan on the specimen's surface created by electronic deflection of the primary beam and its corresponding image displayed on the SE monitor. The field of view is given by the area scanned on the specimen surface, (X_S, Y_S), while the image magnification M_I is given by the ratio of the image size displayed on the SE monitor, (X_D, Y_D), to the scan area size on the specimen, X_D/X_S or Y_D/Y_S. It is important not to confuse the electronic image magnification M_I, with the primary beam spot demagnification factor, M_B. The magnification displayed on the monitor screen refers to the electronic image magnification M_I, while the primary beam demagnification factor is not usually given explicitly. A relative indication of its value can be inferred by a "spot size parameter" on the condenser lens settings.

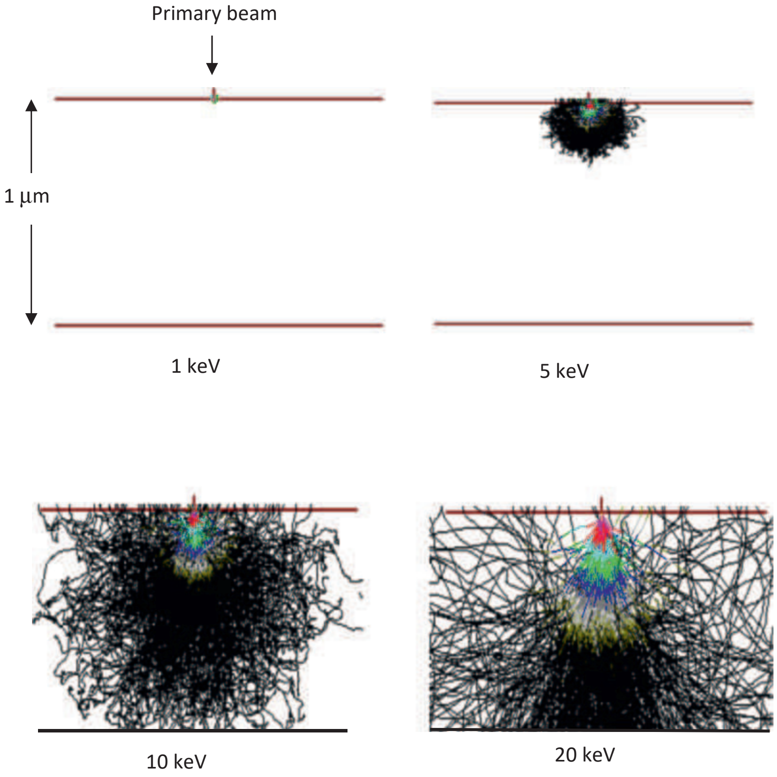

Fig. 4 Monte Carlo simulation of primary electrons striking a silicon sample at energies 1, 5, 10, and 20 keV.

The best achievable image resolution of an SEM is limited by a variety of different factors. Apart from electron optical demagnification/focusing considerations, there are also primary beam-specimen interaction effects. An illustration of how primary beam-specimen interaction effects can limit the spatial resolution of an SEM is shown in Fig. 4, which depicts Monte Carlo simulation results of a primary beam scattering inside a silicon specimen at different primary beam landing energies. The scattering region, approximately equivalent to the interaction volume, effectively generates areas of SE/BSE emission on the surface of the specimen. The size of these emission areas can easily exceed the focused primary beam probe size, and therefore limit SEM image resolution. The Monte Carlo simulations shown in Fig. 4 predict that at a landing energy of 1 keV, the interaction volume is tens of nanometers wide. At 5 keV, the interaction volume is predicted to span hundreds of nanometers. Beyond 10 keV, the simulated interaction volume reaches micron dimensions. Historically, due to poor electron optical performance at low primary beam voltages (<5 kV), the first generation of SEMs were usually operated with primary beam energies in the 5–30 keV range. The simulations shown in Fig. 4 help explain why the first generation of SEMs could only achieve image resolutions in the submicron to micron range.

As already mentioned, significant improvements to SEM image resolution were made when it became possible to lower the landing energy of the primary beam to landing energies of 1 keV or lower, without significantly enlarging the primary beam probe size. Most modern SEMs today function in this way, in the low voltage SEM mode of operation (LVSEM). LVSEM relies on technological advances made in the production of electron detectors, and improvements made in the design of electron sources and objective lenses.

Another advantage of LVSEMs is that they can minimize primary beam induced charging effects while observing non-conductive specimens. The first generation of SEMs needed to sputter non-conductive specimens with a nanometer thick layer of gold or carbon in order to suppress the charging effect. Other advantages of LVSEM over conventional SEMs include them having higher signal yields and that they provide a greater amount of surface information. It is now possible for SEMs to operate with nanometer image resolution on a wide variety of different specimens. LVSEMs are finding an increasing number of applications in subjects such as biology and chemistry which involve observing organic samples directly.

When inspecting a specimen by an SEM, it is important to strike the right balance between acquiring adequate signal-to-noise and minimizing the effects of surface contamination. The main source of noise in the output image comes from shot noise in the primary beam, which for a sufficiently large number of detected electrons has an approximate normal distribution. In most modern SEMs, tens of pA primary beam current in tens of seconds image acquisition time can in principle provide adequate signal-to-noise ratios, but in practice, whether the final captured image is acceptable or not depends on the rate at which the specimen surface carbon contamination layer builds-up.

Contamination on the surface of a specimen is most severe when acquiring high resolution images. This is because high resolution imaging requires small fields of view, which for the same primary beam current and scan rate, leads to larger current densities being present at the specimen surface, and this creates conditions for a greater rate of contamination build-up. The compensating action of adjusting down the primary beam current or total acquisition time when capturing high resolution images partially helps avert this problem, but it can only be done within the constraints of obtaining an adequate output signal-to-noise ratio. For this reason, beam induced contamination is one of the main parameters that limit the ultimate image resolution of SEMs.

The other main beam-specimen interaction parameter limiting image resolution is the interaction volume. Although the interaction volume is made much smaller by operating in LVSEM mode, its finite size also plays an important role in limiting how good the image resolution in an SEM can be. The image resolution limiting role played both by beam induced contamination and the interaction volume helps explain why the same type of electron optical aberration correctors that have worked well for transmission electron microscopes (STEM/TEM) have not worked well for the SEM. Transmission electron microscopes form their output images from a primary electron beam that travels through a thin specimen, in which beam-specimen interaction effects played a relatively minor role compared to electron optical aberrations. In the SEM however, since the image is formed from reflected/scattered electrons that leave the surface of a bulk specimen, beam-specimen interaction effects are much larger, and are comparable in size or greater than the primary beam probe size. Although electron optical aberration correction techniques in the SEM can in principle reduce the primary beam probe to have sub-nanometer diameters, in practice, beam-specimen interactions cause the image resolution limit to be well over a nanometer. There are also inaccuracies caused by mechanical vibrations and electromagnetic interference. At a landing energy of 100 eV, the image resolution of an aberration corrected SEM was found experimentally to be around 2 nm on a test sample having gold particles on a carbon substrate, despite its probe diameter being predicted to be less than 1 nm (Cheng et al., 2019).

On non-conductive samples, there is also the local charging effect. Although LVSEMs are able to achieve an overall global charge balance on a variety of different non-conductive specimens, local charging inevitably occurs over nanometer distances on the specimen surface, and it can distort and deflect the primary beam probe, which in turn can degrade the overall achievable image resolution. This effect causes well known image distortions and resolution limitations in the context of using Critical Dimension (CD) SEM measurements on semiconductor specimens (Arat et al., 2019).

Electron optical figures of merit

The performance of an SEM is critically dependent on the type of electron source being used. The column optics is adjusted so that the projected size of the source on the specimen is small. The energy spread of electrons emitted from the electron source limits the resolution of the SEM at low voltages, and the final image quality depends upon how much current the gun can provide. There have been two types of thermionic sources, and two types of field emission sources used in commercially available SEMs so far.

In the category of thermionic electron sources, there is the tungsten hairpin wire source and the lanthanum hexaboride crystal (LaB_6) source. Both these electron sources form a real crossover point between the cathode and anode. They do this by employing an extra electrode placed between the cathode and anode and biasing it more negatively than the cathode. A current is passed through the cathode and heats it to high temperatures so that electrons are emitted from the cathode surface. The electric field strength at the cathode surface is relatively low, and a negative space-charge cloud region consisting of slower moving emitted electrons forms in front of the cathode. The emission current settles to an equilibrium value limited by the formation of the space-charge cloud.

Field emission sources function by applying a high electric field between an anode electrode and a finely pointed cathode. The radius of curvature of the cathode tip can be as low as 100 nm and the electric field strength can be several V/nm. Electrons leave the cathode tip via quantum tunneling and do not form a real crossover, instead, they form a "virtual source," which is found by projecting back the emitted rays from the anode plane. The virtual source position typically lies several nanometers behind the cathode electrode tip and ranges from a few to tens of nanometers in diameter. The Schottky electron source supplements its quantum tunneling action with some degree of cathode heating. Cold field emission (CFE) cathodes function at room temperature.

The brightness of an electron gun, β, is an important parameter that characterizes how much current it can provide. The brightness β is defined by

$$\beta = \frac{J}{\pi\alpha^2} \tag{1}$$

where J is the current density and α is the beam semi-angle at the cathode. For a given SEM column, the brightness has a constant value along the primary beam path. The current density at the cathode usually falls off sharply with increasing α. Since the brightness of a gun rises approximately linearly with the anode voltage (primary beam voltage V_p), it is sometimes quoted as the "reduced brightness," β_R, where $\beta_R = \beta/V_p$.

The conservation of brightness along the optical axis provides a means for estimating the primary beam probe current at the specimen surface. If at the specimen, there is a projected source diameter of d_0 and semi-angle of α_0, the primary beam probe current, I_p, is given by

$$I_P = \frac{\pi^2}{4}\beta d_0^2\alpha_0^2 \tag{2}$$

The available probe current is directly proportional to the gun brightness. From this expression, it is clear that high probe currents cannot be obtained with small probe diameters (required for high resolution) and that a compromise between the two must be found. A minimum requirement on the probe current comes from inherent signal-to-noise limitations in the SEM detection/display system.

Each SEM electron source type varies in accordance with the amount of current it can produce, its effective projected size, its intrinsic energy spread, the stability of its emitted current, and its lifetime. Table 1 presents some typical values of these parameters. It should be noted that the values in Table 1 are only approximate, and that some of them depend on the primary beam voltage, such as brightness.

Although the traditional thermionic tungsten hairpin source has the lowest brightness and highest energy spread of all SEM electron sources types, it is reliable, relatively inexpensive, and well understood. For many SEM applications where high brightness and high spatial resolution is not required, and where stable high currents are needed, the thermionic tungsten filament may be used without loss of performance, and may, in fact, be the best choice. The LaB_6 source offers better performance than the tungsten hairpin filament, but it comes at the price of needing to provide a better vacuum level and is more complicated to install and maintain. In practice, the tungsten hairpin filament is much more widely used.

In the category of field emission electron sources, the tungsten cold field emission source has the highest brightness and lowest energy spread, but it faces many difficult technical challenges and is the least reliable of all electron sources for the SEM. It typically requires extreme UHV (XUHV) conditions in order to operate, and its cathode needs to be regularly joule-heated (flashed) every few hours in order to restore degradation of emission caused by the steady build-up of carbon contamination on the cathode tip surface. It also has the highest current instability of all SEM electron source types. For these reasons, although the Schottky electron source is worse from an electron optical performance point of view than tungsten cold field emission sources, it is the most widely used type of field emission source in SEMs.

Fig. 5 shows the kind of magnetic objective lens design that has been widely used in conventional SEM columns. The magnetic objective lens axis is rotationally symmetric, and its axis of symmetry defines the central optical axis for the primary electron beam. A current carrying coil energizes a magnetic circuit made of soft magnetic material, typically an alloy of iron, and a magnetic gap in

Table 1 Electron source performance comparison.

Source	*Brightness (A/cm^2 sr)*	*Lifetime (hours)*	*Source size*	*Energy spread ΔE (eV)*	*Current stability*	*Vacuum pressure (Pa)*
Tungsten hairpin thermionic source	2×10^4 to 2×10^5	40–100	20–50 μm	1–3	1%	$<10^{-3}$
LaB_6 thermionic source	10^6	200–1000	5–20 μm	0.5–2	1%	$<10^{-5}$
Schottky field emission source	10^7–10^8	>1000	15–30 nm	0.5	2%	$<10^{-7}$
Tungsten Cold field emission source	10^8–10^9	>1000	< 5 nm	0.2–0.3	5%	$<10^{-8}$

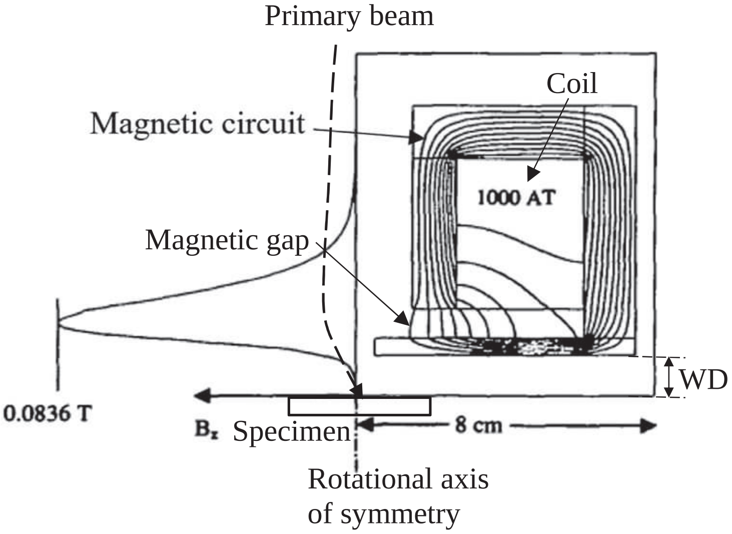

Fig. 5 Simulated on-axis magnetic field distribution $B_Z(z)$ and flux distribution of a conventional Cambridge S100 SEM magnetic objective lens design.

the circuit creates the axial magnetic field region that focuses the primary electron beam on to the specimen. Fig. 5 shows the simulated flux lines of the Cambridge S100 objective lens design for a coil excitation of 1000 AT and its associated axial field distribution. The axial field peak field strength is 0.0836 Tesla, capable of focusing a 20 keV primary beam to a point 5 mm below the lower lens pole-piece. The focusing action, illustrated schematically in Fig. 5, comes from the radial variation in objective lens magnetic field intensity. The magnetic field intensity is a minimum on the axis, and it increases in strength radially out toward the pole-pieces. This field distribution causes electrons in the primary beam to rotate about the axis and exerts a radial force on them, pushing them toward the axis. The strength of the radial force increases with off-axis distance, applying a stronger force on the wider angle electrons and a weaker force on the near axis electrons.

The Cambridge S100 objective lens shown in Fig. 5 is an example of a "below-the-lens" design. The specimen in these types of objective lenses is placed in a field free region under the lens assembly. The distance from the specimen to the lens lower pole-piece is known as the working distance (WD), and is similar to the working distance between specimen and objective lens in conventional optical microscopes. Just as in optical microscopes, short focal lengths are required when operating in high magnification mode, which in turn, necessitates the use of short working distances. In practice, SEM columns that use below-the-lens objective lens designs achieve their highest image resolution by setting the working distance to its minimum possible value. Most conventional SEMs have an operational working distance range of around 3–30 mm.

Fig. 6 shows the kind of column lens design used in conventional tungsten hairpin filament SEMs. It consists of two magnetic condenser lenses and a magnetic objective lens. This is different to the Schottky electron source single condenser lens column design shown in Fig. 1a. An extra condenser lens in the case of the conventional tungsten hairpin filament SEM column is required, since the beam crossover size formed inside tungsten hairpin filaments is typically a thousand times bigger than Schottky electron source virtual source sizes.

In addition to limitations in electron optical performance that come from the electron source, objective lens aberrations also play a critical role. In order to keep the aberrations of the objective lens down to an acceptable level, a final aperture is used to filter out the wider angle electrons in the primary electron beam. The final aperture is usually positioned just above the objective lens, and its diameter is selected to keep the semi-angles of electrons reaching the specimen to be typically less than 5 mrad. Fig. 7 shows the kind of lens aberration effects that enlarge the primary beam probe size. They are similar to the kind of aberration effects that exist in optical microscopes.

Spherical aberration is caused by the objective lens over-focusing the wider angle electrons in the primary beam, as shown in Fig. 7a. They travel further off-axis than the narrower angle ones and experience a stronger focusing action acting on them, producing a spherical aberration spot radius r_{SP} which is proportional to the cube of the final semi-angle as follows,

$$r_{SP} = C_S(\alpha_P)^3 \tag{3}$$

where the constant C_S is defined to be the spherical aberration coefficient.

Chromatic aberration comes from the inherent energy spread of electrons in the primary beam. Higher energy primary beam electrons focus at focal points further down the axis than the lower energy primary beam electrons, as shown in Fig. 7b. The change in focal point position along the axis, Δz, varies linearly with relative energy spread, $\Delta E/E$, as follows,

$$\Delta z = C_C(\Delta E/E) \tag{4}$$

where the constant C_C is the chromatic aberration coefficient. In field free focusing regions, the chromatic aberration spot radius, r_{chr}, is given in terms of the final semi-angle α_P by, $r_{chr} = \Delta z\ \alpha_P$.

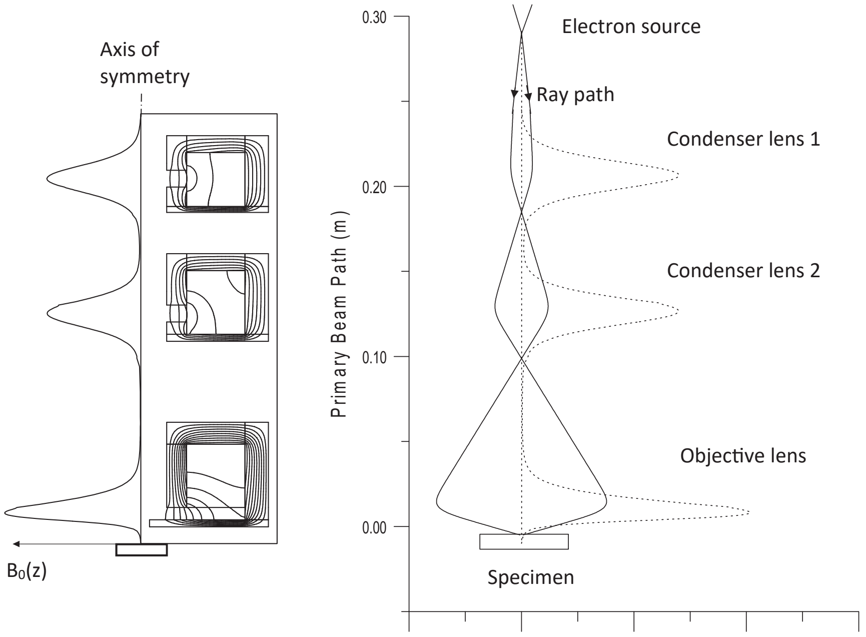

(a) (b)

Fig. 6 Simulated ray tracing of the primary electron beam through a column having two magnetic condenser lenses and a S100 objective lens. (a) Axial field distribution. (b) Ray tracing of the primary beam, where the radial coordinate is exaggerated for reasons of scale.

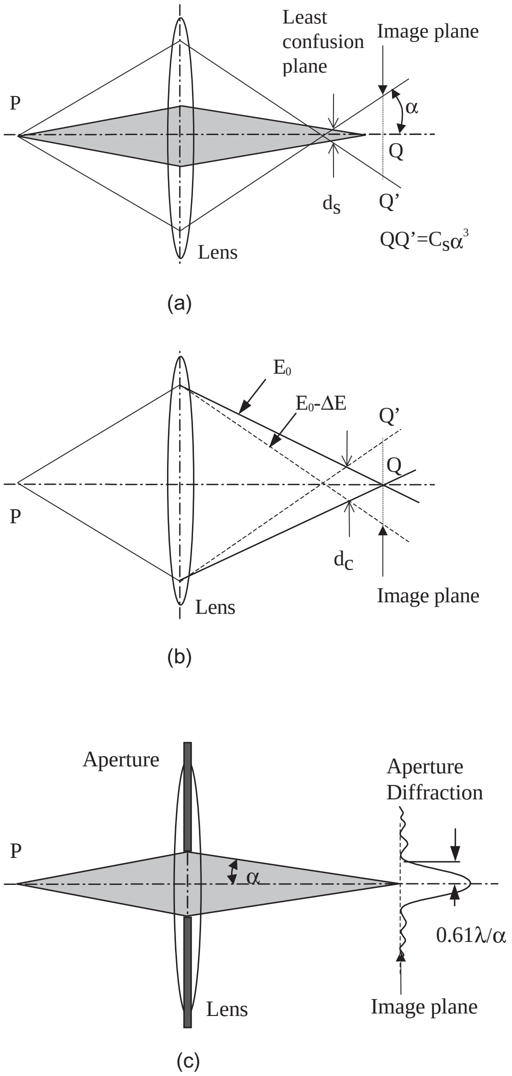
Least confusion plane
Image plane
P
α
Q
d_S
Q'
Lens
$QQ'=C_S\alpha^3$
E_0
E_0-ΔE
Q'
Q
P
d_C
Image plane
Lens
Aperture
Aperture Diffraction
P
α
$0.61\lambda/\alpha$
Lens
Image plane

(a)

(b)

(c)

Fig. 7 Schematic drawing illustrating primary electron beam on-axis focusing aberrations. (a) Spherical. (b) Chromatic. (c) Diffraction.

An aperture diffraction aberration spot is also produced at the plane of the specimen. This diffraction effect comes from the intrinsic wave nature of the electrons in the primary beam. As in light optics, the diameter of the diffraction aberration spot produced by a round aperture is 0.61 λ/α_P, where λ is the De Broglie wavelength and α_P is the final semi-angle. The diffraction spot size is taken from the first zero point of a zero order Bessel function radial diffraction distribution, as shown in Fig. 7c. The De Broglie wavelength of an electron beam in an SEM is related to the primary beam voltage V_P by, $\lambda = 1.226/\sqrt{V_P}$, where the primary beam voltage is measured in volts and the wavelength is measured in nanometers. Using this formula, the wavelengths for a beam of electrons at 1 and 25 keV are 38.7 pm and 7.74 pm respectively. Although this wavelength is several orders of magnitude smaller than it is for say a visible light beam, the relatively small final semi-angles used in an SEM, in the mrad range, increases the diffraction spot diameter of the primary beam probe to nanometer sizes, making it comparable in size to the spot diameters produced by spherical and chromatic aberration.

A convenient way of estimating the spatial resolution of a SEM column design is to use the Barth-Kruit root-power-sum formula (Barth and Kruit, 1996), which approximates it to be equivalent to the final probe diameter containing 50% of the primary beam current. This formula has been found to agree well with the more exact wave optical approach, and is widely used to calculate the spatial resolution of an electron objective lens. It uses the electron source parameters of energy spread ΔE, source brightness β, objective lens on-axis spherical aberration coefficient C_S, chromatic aberration coefficient C_C, primary beam current I, landing energy E, beam wavelength λ, and beam final semi-angle α_P. The Barth-Kruit root-power-sum formula for the probe diameter d_P is given by,

$$d_p^2 = \left[\left(d_{sp}^2 + d_{df}^2\right)^{\frac{1.3}{4}} + d_G^{1.3}\right]^{\frac{2}{1.3}} + d_{chr}^2 \tag{5}$$

where, $d_{sp} = \left(\frac{1}{2}\right)^{5/2} C_s \alpha_p^3$

$$d_G = \left(\frac{2}{\pi}\right)\left(\frac{I}{\beta}\right)^{1/2}\frac{1}{\alpha_p}$$

$$d_{chr} = 0.34 C_c \frac{\Delta E}{E}\alpha_p$$

$$d_{df} = 0.54\frac{\lambda}{\alpha_p}$$

Aberration coefficients for objective lenses can be found directly from numerical ray tracing methods, or indirectly by a perturbation method that uses the axial field distribution (Khursheed, 1999). For the Cambridge S100 objective lens shown in Fig. 5 operating in LVSEM conditions, where the lens strength is adjusted to focus a 1 keV beam on to a specimen located at a working distance of 5 mm, the focal length, f, and aberration coefficients, C_S and C_C were simulated by numerical ray tracing to be, $f = 15.69$ mm, $C_S = 30.6$ mm, and $C_C = 13.29$ mm (Khursheed, 2011). Fig. 8 uses these optical parameters to plot the corresponding probe diameter/probe current dependence using the Barth-Kruit formula (Eq. 5) for both thermionic tungsten hairpin filament (TE) and Schottky (SE) electron sources. The TE source here is assumed to have a brightness of 2×10^4 Acm^{-2} sr^{-1} and an energy spread of 2 eV, while the SE source is assumed to have a brightness of 10^7 Acm^{-2} sr^{-1} and an energy spread of 0.5 eV. For every probe current value, the final aperture radius is varied in order to obtain the optimal semi-angle which minimizes the probe diameter.

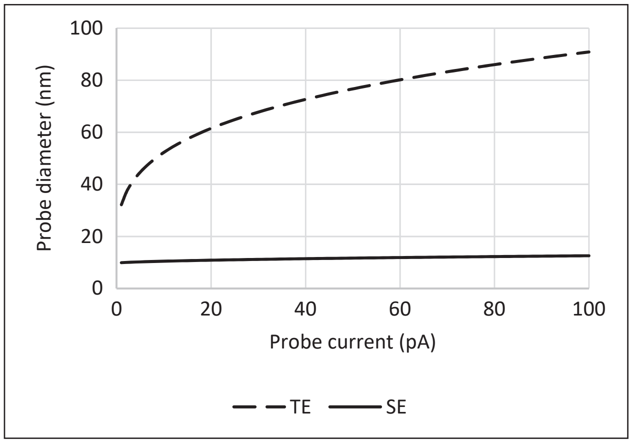

Fig. 8 Simulation of the probe diameter/current dependence of a conventional Cambridge S100 SEM objective lens design using thermionic tungsten hairpin filament (TE) and Schottky (SE) electron sources. The working distance is set to 5 mm for a primary beam energy of 1 keV, and the simulated focusing on-axis aberrations are, $f = 15.69$ mm, $C_S = 30.6$ mm, and $C_C = 13.29$ mm. The TE source is assumed to have a brightness of 2×10^4 Acm^{-2} sr^{-1} and an energy spread of 2 eV, while the SE source is assumed to have a brightness of 10^7 Acm^{-2} sr^{-1} and an energy spread of 0.5 eV.

The simulated probe current-diameter performance shown in Fig. 8 illustrates why the early generation of SEMs, which used a thermionic tungsten hairpin filament combined with a below-the-lens objective lens design, were seldom operated in LVSEM mode. At a primary beam energy of 1 keV, the simulated TE source S100 objective lens simulated probe diameter varies from 50 to 90 nm over the probe current range of 10–100 pA, while the probe diameter of the SE emission source for the same operating conditions stays around 10 nm. The better simulated performance for the SE electron source comes from it having a much higher brightness and lower energy spread than the TE electron source. The image resolution of SEMs that use TE sources is mostly probe current limited when operated in LVSEM mode, while the image resolution of field emission SEMs is generally objective lens aberration limited.

Figs. 9b–d presents schematic diagrams of various LVSEM objective lens design improvements that have been made over the last few decades. Unlike the conventional below-the-lens objective lens layout, shown in Figs. 5 and 9a, they function by either immersing the specimen in a magnetic field, shown in Fig. 9b, or by applying a strong decelerating electric field above the specimen, shown in Fig. 9c, or by combining a decelerating electric field with a magnetic immersion field, shown in Fig. 9d. These objective lens design improvements are known as LVSEM "in-lens" designs since they involve placing the specimen inside objective lens electric/magnetic focusing fields. Another important difference is that since the specimen is now placed inside a lens field distribution, the emitted SEs travel back up through the objective lens bore and are detected either inside the lens assembly or above it (Figs. 9b–d). In conventional objective lens designs, SEs are always detected below the lens assembly (Figs. 5 and 9a).

The LVSEM layout depicted in Fig. 9b uses the magnetic field created around a single conical shaped pole-piece to define a sharply varying field distribution under which the specimen is placed. This kind of lens is sometimes referred to as single-pole lens since its primary beam focusing field is created around only one pole-piece. It is also known as a semi-in-lens design, in order to distinguish it from the kind of full magnetic immersion lens designs used in TEMs, in which the specimen is inserted into a small magnetic gap region between two pole-pieces.

Fig. 10 shows the simulated flux lines of a typical single-pole magnetic semi-in-lens objective lens design. A sharply varying axial magnetic field is projected down into the region immediately below the inner conical pole-piece. The specimen needs to be positioned close to the pole-piece tip with a working distance of only a few millimeters (1–3 mm), so that the primary beam can be

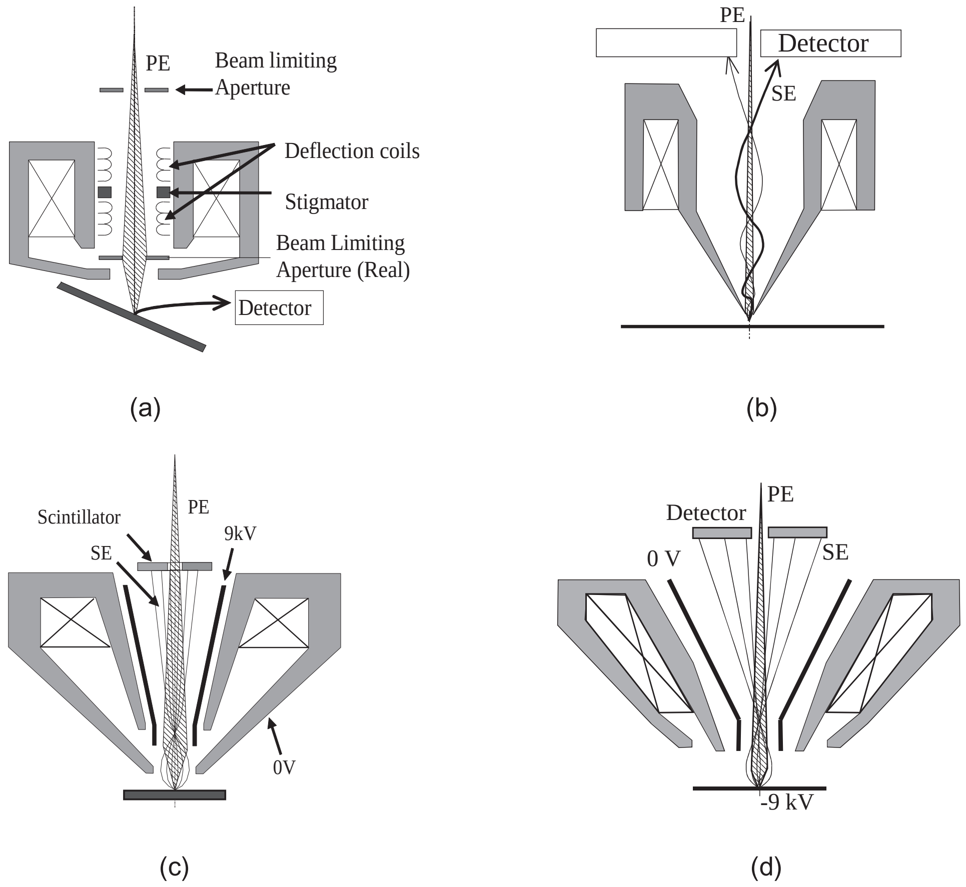

Fig. 9 Different types of objective lens designs used for the SEM. (a) Conventional lens where specimen is placed in a field-free region below the objective lens pole-pieces. (b) Magnetic semi-in lens where the specimen is immersed in a magnetic field region below the lens pole-pieces. (c) Retarding field design using a booster electrode (9 kV) combined with a conventional magnetic objective lens. (d) Retarding field design using negative specimen bias (−9 kV) combined with a magnetic semi-in-lens.

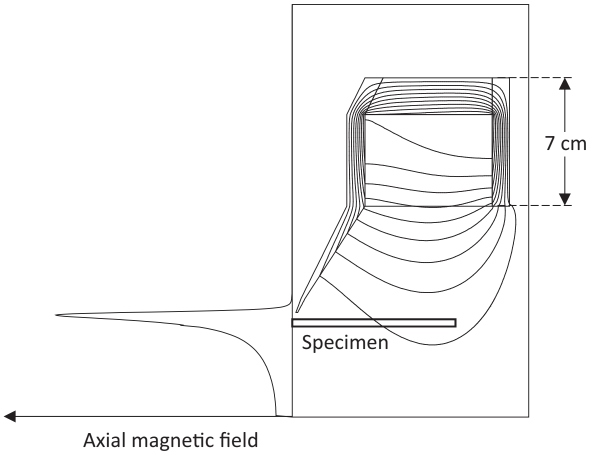

Fig. 10 Simulated flux lines of a single-pole magnetic semi-in-lens objective lens design.

focused on to the specimen with millimeter size focal lengths. This type of objective lens design was reported over three decades ago. For a single pole-piece with an outer slope angle of 45° having an overall pole diameter of 5 mm and a bore diameter of 3 mm, set to focus a 1 keV primary beam on to a specimen located at a working distance of 2.5 mm, its on-axis focusing aberrations were simulated to be $f = 1.8$ mm, $C_S = 1.5$ mm, and $C_C = 1.3$ mm (Shao and Lin, 1989). These lens aberration coefficients are around an order of magnitude smaller than the on-axis aberrations of conventional below-the-lens designs for the same operating conditions.

In the case of the LVSEM design shown in Fig. 9c, a booster electrode (9 kV) keeps the primary beam energy high as it travels down the column (10 keV), and a 0 V specimen retards the beam to have a landing energy of 1 keV. The primary beam is slowed down sharply just before it strikes the specimen, over a distance of only a few millimeters. Since the primary beam travels through most of the magnetic focusing field region at a high energy and is slowed down only in the tail end part of its distribution, the lens on-axis aberrations and focal length are considerably smaller than the case where there is no retarding field. An LVSEM column using the kind of layout shown in Fig. 9c, decelerating a 10 keV primary beam energy down to a landing energy of 1 keV, was reported to have lower on-axis aberrations than corresponding magnetic objective lens designs for LVSEM applications. Frosien et al. for instance, presented a retarding field objective lens design having a C_S less than 3 mm and C_C around 1 mm for a landing energy of 1 keV, in which the specimen was not immersed in a strong magnetic field (Frosien et al., 1995). Unlike most LVSEM columns using magnetic semi-in-lens designs, their objective lens design had the advantage of being able to image magnetic specimens.

From an electron optical point of view, the lowest focusing aberrations are produced by an LVSEM objective lens design that uses a combination of both a magnetic immersion field and a decelerating electric retarding field, such as the lens design shown in Fig. 9d. In this case, a 10 keV primary beam travels down a 0 V column, and is retarded to have a landing energy of 1 keV on a specimen that is biased to −9 kV. This lens design achieves the same strong retarding field electric field action as the retarding field design shown in Fig. 9c, but has the desirable feature of not having to use a booster electrode in the column. At the same time, the specimen is placed in a semi-in-lens magnetic field distribution.

Fig. 11 shows simulated field distributions of a mixed field semi-in-lens LVSEM design based on the one reported by Beck et al. (1995). This lens design uses a 9 kV booster electrode to create a retarding electric field while at the same time is immersing the specimen in a magnetic field. The magnetic field projects down from a large radial gap in the magnetic circuit, as shown in Fig. 11c. Fig. 11b shows the axial electric potential distribution of its decelerating electric field. This type of deceleration action, as well as the semi-in-lens magnetic immersion field distribution, significantly lowers the on-axis aberrations of the objective lens. Beck et al. reported simulated focusing on-axis aberration parameters of $f = 4.24$ mm, $Cs = 0.77$ mm, $Cc = 0.62$ mm for a 10 keV primary beam retarded down to a landing energy of 1 keV at a working distance of 5 mm (Beck et al., 1995).

Fig. 12 presents the probe diameter vs probe current dependence using the Barth-Kruit formula of the three main objective lens designs discussed so far operating with a Schottky electron source at a landing energy of 1 keV. Simulated on-axis aberration parameters are used for the conventional S100 design operating at a working distance of 5 mm, the single-pole magnetic semi-in-lens design operating at a working distance of 2.5 mm, and the mixed field semi-in-lens design operating at a working distance of 5 mm. The results support the general point that the image resolution of FE SEMs for LVSEM applications is mainly aberration limited, and not probe current limited like TE source SEMs (see Fig. 8). The probe diameter for the lens designs shown in Fig. 12 does not change significantly with primary beam current. The probe diameter of the mixed field semi-in-lens design is around a factor of five times smaller than the probe diameter of the conventional S100 objective lens, and about 1 nm smaller than the magnetic semi-in-lens design.

Fig. 13 shows the kind of probe diameter/probe current improvement that can be expected by using a CFE source in combination with semi-in-lens LVSEM designs. The CFE source mixed field semi-in-lens design is predicted to have a probe diameter of around half the probe diameter of a SE source magnetic semi-in-lens column design, a factor of improvement which becomes better with increasing probe current. The predicted probe diameter for the CFE source mixed field semi-in-lens design in the 1–100 pA range lies

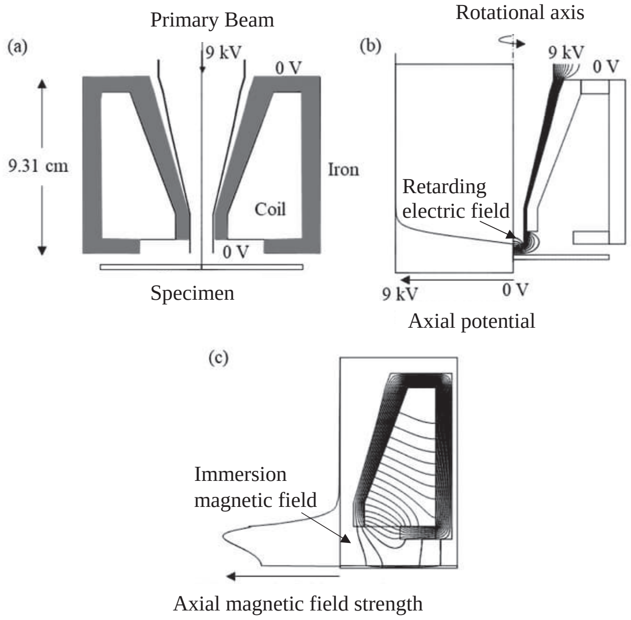
(a)
Primary Beam
9 kV
0 V
9.31 cm
Iron
Coil
0 V
Specimen
(b)
Rotational axis
9 kV
0 V
Retarding
electric field
9 kV
0 V
Axial potential
(c)
Immersion
magnetic field
Axial magnetic field strength

Fig. 11 Simulated field distributions of a LVSEM mixed field semi-in-lens objective lens design based upon the one proposed by Beck et al. (1995). (a) Electrode/excitation coil layout. (b) Retarding electric field distribution. (c) Immersion magnetic field distribution.

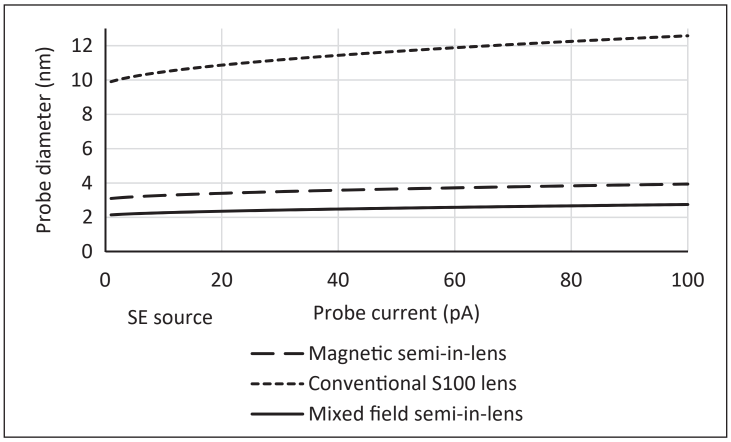

Fig. 12 Simulated probe diameter/probe current dependence for different types of objective lens designs using a SE source operating at a landing energy of 1 keV. The simulated on-axis parameters are, $f = 15.69$ mm, $C_S = 30.6$ mm, and $C_C = 13.29$ mm for a working distance of 5 mm of the S100 lens design, $f = 1.8$ mm, $C_S = 1.5$ mm, and $C_C = 1.3$ mm for a working distance of 2.5 mm of a magnetic semi-in-lens design, and $f = 4.24$ mm, $C_S = 0.77$ mm, and $C_C = 0.62$ mm for a working distance of 5 mm for a mixed field semi-in-lens design. The SE source is assumed to have a brightness of 10^7 Acm^{-2} sr^{-1} and an energy spread of 0.5 eV.

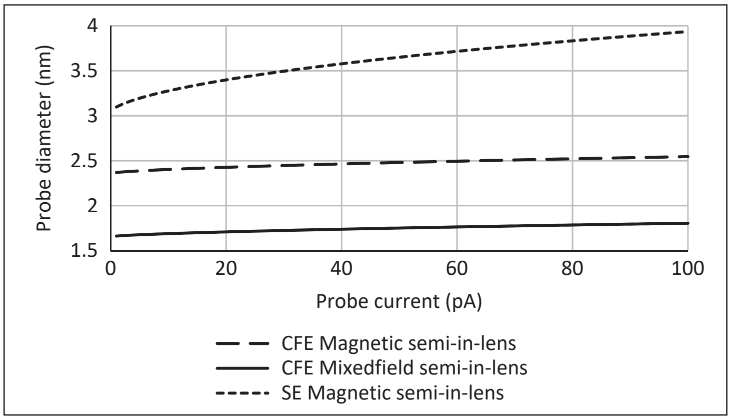

Fig. 13 Simulated probe diameter/current dependence of different LVSEM in-lens designs. The simulated on-axis aberration parameters are $f = 1.8$ mm, $Cs = 1.5$ mm, $Cc = 1.3$ mm for a working distance of 2.5 mm for a magnetic semi-in-lens design, and $f = 4.24$ mm, $Cs = 0.77$ mm, $Cc = 0.62$ mm for a working distance of 5 mm of a mixed field semi-in-lens design. The SE source is assumed to have a brightness of 10^7 Acm^{-2} sr^{-1} and an energy spread of 0.5 eV, and the CFE source is assumed to have a brightness of 10^8 Acm^{-2} sr^{-1} and an energy spread of 0.3 eV.

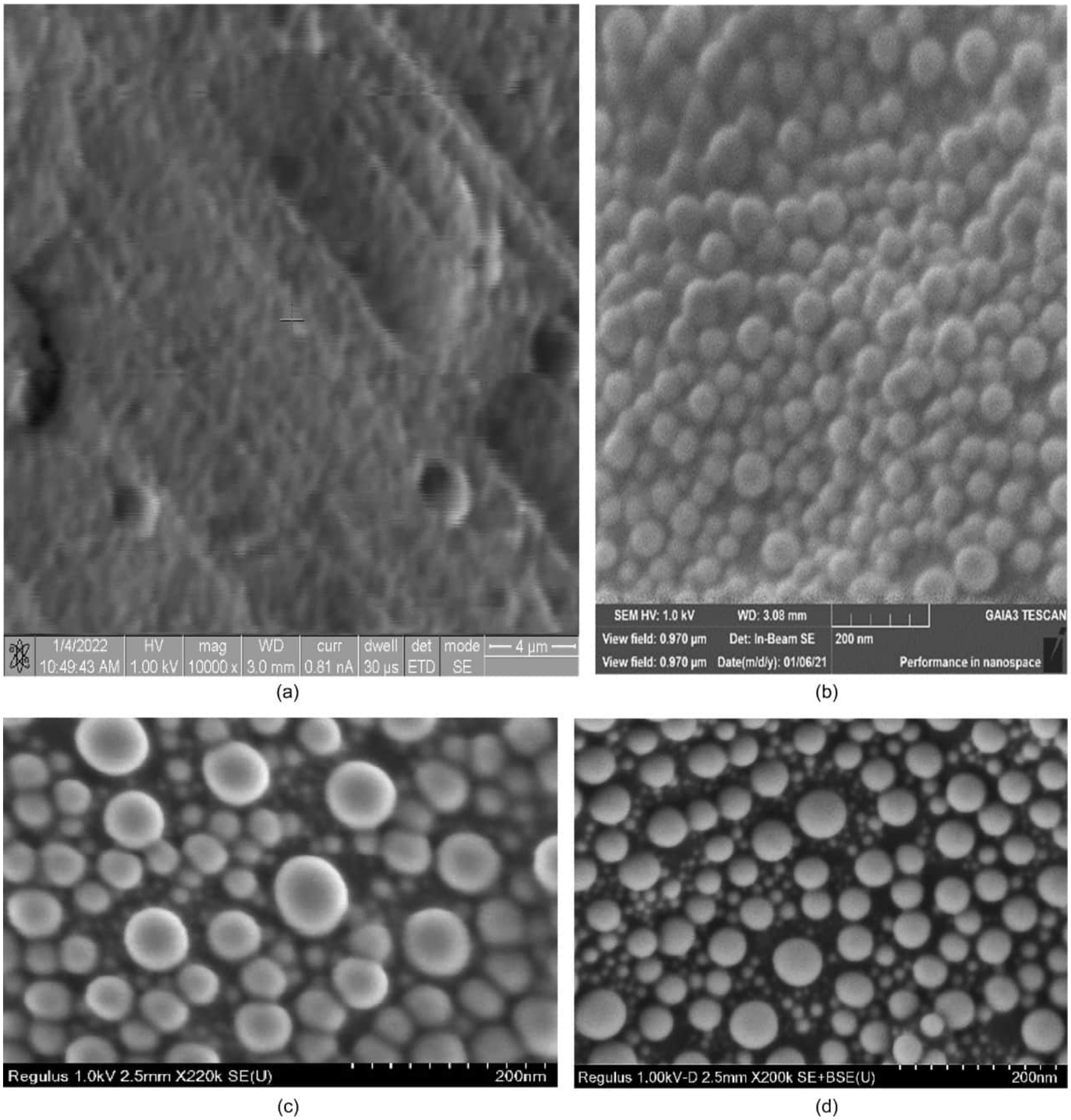
1/4/2022
10:49:43 AM
HV
1.00 kV
mag
10000 x
WD
3.0 mm
curr
0.81 nA
dwell
30 μs
det
ETD
mode
SE
4 μm
SEM HV: 1.0 kV
WD: 3.08 mm
GAIA3 TESCAN
View field: 0.970 μm
Det: In-Beam SE
200 nm
View field: 0.970 μm
Date(m/d/y): 01/06/21
Performance in nanospace
Regulus 1.0kV 2.5mm X220k SE(U)
200nm
Regulus 1.00kV-D 2.5mm X200k SE+BSE(U)
200nm

(a) (b)

(c) (d)

Fig. 14 Comparison of experimental images from different SEM designs taken at a landing energy of 1 keV of a tin balls-on-carbon calibration specimen. The diameter of the tin balls ranges from a few nanometers to around 60 nm. (a) Image from a conventional thermionic tungsten hairpin source below-the-lens SEM design operating at a working distance of 3 mm. The image magnification is 10,000 and was obtained from a dual beam FEI Quanta 200 3D FIB-SEM. (b) Image from a Schottky electron source magnetic semi-in lens SEM operating at a working distance of 3.08 mm. The image was obtained from a Tescan Gaia3 FIB-SEM. (c) Image from a cold field emission electron source magnetic semi-in-lens SEM operating at a working distance of 2.5 mm and image magnification of 220,000. The image was obtained from a Hitachi Regulus 8230 SEM. (d) A cold field emission electron source semi-in-lens SEM operating in retarding field mode with a working distance of 2.5 mm and image magnification of 200,000. A 3 keV primary beam was used with a—2 kV specimen bias. The image was obtained from a Hitachi Regulus 8230 SEM.

well below 2 nm. In practice, LVSEMs rarely achieve an image resolution of better than 2 nm at a landing energy of 1 keV. This limitation comes mainly from environmental disturbances such as mechanical vibrations and electromagnetic interference, as well as beam-specimen interaction effects.

Fig. 14 shows experimental images from different SEM columns, each having a different electron source/objective lens combination. A calibration specimen consisting of tin balls-on-carbon was used, where the diameter of the tin balls ranged from a few nanometers to around 60 nm. Details about each SEM column design and the operating conditions used are given in the figure caption. These experimental images generally confirm the probe diameter/probe current simulation predictions shown in

Figs. 8, 12, and 13. The tin balls are not visible in the image provided by the conventional thermionic tungsten hairpin source shown in Fig. 14a, which uses a below-the-lens objective lens design. In order to focus this image, broader topographical features on the specimen were used. The next best image resolution is provided by the Schottky source magnetic semi-in-lens column design, shown in Fig. 14b. The bigger size tin balls are visible in this image. A further improvement is obtained by the CFE source magnetic semi-in-lens SEM column image shown in Fig. 14c, in which some of the smaller tin balls become visible. However, the best image, shown in Fig. 14d, is obtained by the CFE magnetic semi-in-lens SEM column operating in retarding field mode (mixed field semi-in-lens). Small nano-size tin balls are clearly visible in this image.

Conclusion

This chapter has summarized SEM basic principles, presented its main figures of merit, and provided an illustration of its high resolution experimental images. The chapter has highlighted instrument developments mainly in the context of low voltage scanning electron microscopy (LVSEM). Looking ahead, there are several other future promising lines of development.

Aberration corrected SEMs might prove useful for some specialized ultra-low voltage/high current applications, but are unlikely to become new general purpose SEMs. This is because SEM image resolution limitations are mainly set by specimen-beam interaction effects, such as the size of the interaction volume and beam induced contamination. These effects already limit the best achievable LVSEM image resolution to lie somewhere between 1 and 2 nm for most bulk specimens, so further reduction of the projected primary electron beam probe size into the sub-nanometer range is unlikely to provide image resolution improvement.

Further work on making cold field-emission (CFE) sources more reliable and easier to use is another promising line of development. Research is presently being carried out on the possibility of using different CFE cathodes, apart from the conventional tungsten one. However, none of them are as yet in a form that can be reliably used in commercial SEMs. Another area of SEM development receiving attention is the challenge of miniaturizing SEM columns, especially for the purpose of making large multi-column LVSEM arrays that can inspect semiconductor wafer specimens. Multi-beam SEM designs have proven to be feasible, where an array of beamlets are created from a single source. However, they have a relatively small overall field of view, typically in the sub-millimeter range, and the optics of each beamlet cannot be individually tuned. The next stage of development will be to make a LVSEM column array that can provide parallel inspection of a large specimen, where each column has its own separate source with individually tunable electron optics.

Another promising area of SEM development is to explore ways of reducing beam induced contamination. Beam induced contamination effects limit both LVSEM ultimate image resolution and image signal-to-noise. Specimen preparation methods borrowed from UHV electron spectroscopy chambers might prove useful, such as pre-cleaning the specimen by low energy ion bombardment or applying UV irradiation.

Finally, there is the possibility of using electron energy spectroscopy techniques inside the SEM. At present, LVSEM lacks a companion material science tool. This is because EDX only functions well for primary beam landing energies of 6 keV or higher, and the landing energies inside LVSEM systems, of 2 keV or less, are not high enough to generate the necessary atomic transitions that emit characteristic X-rays. In principle, energy spectroscopy of SEs and BSEs has the potential for developing new material analysis tools for LVSEM, acquiring material information in a manner similar to Auger electron spectroscopy (AES) or reflection electron energy loss spectroscopy (REELS). The success of this approach will also most likely depend on how effectively beam induced contamination effects can be reduced.

Acknowledgments

The author would like to acknowledge the help of Dr. Zheng Minrui, a Research Fellow at the National University of Singapore, for carrying out the research work to obtain the SEM experimental images presented in this chapter.

Conflict of Interest

The author declares that there is no conflict of interest.

References

Arat KT, Klimpel T, and Hagen CW (2019) Model improvements to simulate charging in scanning electron microscope. *Journal of Micro/Nanolithography, MEMS and MOEMS* 18(4): 044003.
Barth JE and Kruit P (1996) Addition of different contributions to the charged particle probe size. *Optik* 101(3): 101–109.
Beck S, Plies E, and Schiebel B (1995) Low voltage probe forming columns for electrons. *Nuclear Instruments and Methods in Physics Research A* 363: 31–42.
Brodusch N, Demers H, and Gauvin R (2018) *Field Emission Scanning Electron Microscope, New Perspectives for Materials Characterization.* Springer Publisher.
Bronsgeest M (2014) *Physics of Schottky Electron Sources, Theory and Optimum Operation.* Jenny Stanford Publishing.

Cheng ZH, Dohi H, Hayashi S, Hirose K, and Kazumi H (2019) Application of aberration corrected low voltage SEM for metrology. In: *Proc. SPIE 10959, Metrology, Inspection, and Process Control for Microlithography XXXIII, 1095922.*

Frosien J, Lanio S, and Feuerbaum HP (1995) High precision electron optical system for absolute and CD-measurements on large substrates. *Nuclear Instruments and Methods in Physics Research A* 363: 25–30.

Goldstein JI, Newbury DE, Michael JR, Ritchie NWM, Scott JHJ, and Joy DC (2017) *Scanning Electron Microscopy and X-Ray Microanalysis*. Springer.

Khursheed A (1999) *The Finite Element Method in Charged Particle Optics*. Kluwer Academic Publishers.

Khursheed A (2011) *Scanning Electron Microscope Optics and Spectrometers*. World Scientific Publishers 29.

Luo T and Khursheed A (2007) Imaging with surface sensitive backscattered electrons. *Journal of Vacuum Science and Technology B* 25(6). https://doi.org/10.1116/1.2781523.

McMullan D (1995) Scanning electron microscopy 1928-1965. *Scanning* 17(3): 175–185.

Oatley CW (1975) The tungsten filament gun in the scanning electron microscope. *Journal of Physics E: Scientific Instruments* 8: 1037.

Shao Z and Lin PSD (1989) High resolution low-voltage electron optical system for very large specimens. *Review of Scientific Instruments* 60(11): 3434–3441.

Smith KCA (1997) Charles Oatley: Pioneer of scanning electron microscopy. In: Rodenburg JM (ed.) *Electron Microscopy and Microanalysis*. CRC Press.

Scanning probe microscopy

Ernst Meyer, Rémy Pawlak, and Thilo Glatzel, Department of Physics, University of Basel, Basel, Switzerland

© 2024 Elsevier Ltd. All rights reserved.

This is an update of J. Gomez-Herrero, R. Reifenberger, Scanning Probe Microscopy, Editor(s): Franco Bassani, Gerald L. Liedl, Peter Wyder, Encyclopedia of Condensed Matter Physics, Elsevier, 2005, Pages 172-182, ISBN 9780123694010, https://doi.org/10.1016/B0-12-369401-9/00585-4.

Introduction 51
Principles of SPM 52
Scanning and Control 52
Scanning tunneling microscopy 52
Atomic force microscopy 53
Other SPMs 59
Conclusion 61
References 61

Abstract

Scanning probe microscopy (SPM) is based upon a probing tip, which is scanned across surfaces. The interactions between tip and sample are used to regulate the distance and acquire maps of topography with high lateral resolution. In addition, local information about a variety of physical and chemical properties can be gained. The most common methods of SPM are discussed, including scanning tunneling microscopy (STM) and atomic force microscopy (AFM).

Key points

- Main components of SPM are introduced, including probing tips, piezoelectric scanners, feedbacks, and operation modes
- Introduction to scanning tunneling microscopy (STM) with discussion of tunneling effect and main operation modes
- Atomic force microscopy from noncontact to contact
- Other scanning probe microscopes

Introduction

Scanning probe microscopy (SPM) is a real-spacing imaging technique, where a needle-type tip is approached and raster scanned across a surface. The microscope can be operated in different environments, such as ambient atmosphere, ultrahigh vacuum, or liquids. In addition, the external variables of temperature or pressure can be adapted to the needs of the experiment. The highest resolution, which was achieved with scanning tunneling microscopy (STM) as well as with atomic force microscopy (AFM), is atomic resolution, where individual atoms can be resolved. Impressive results were achieved with CO-terminated tips by AFM, where submolecular resolution was observed on planar molecules or nanoribbons. In addition to the imaging possibilities, SPM offers additional modes, which can give further insights into the physical or chemical properties of the surfaces. For example, it is possible to determine local mechanical properties, such as elasticity, adhesion, or friction by some adaptions of AFM. SPMs can also be used to characterize electronic properties of surfaces by the use of current vs. voltage curves, which gives information about the local density of states (LDOS). Alternatively, conductive AFM can be used to measure the local conductivity. Kelvin probe force microscopy (KPFM) can give information about the dipolar character of molecules or can determine the local contact potential difference (CPD). If a magnetic tip is used, information about the magnetic structure can be gained.

The chapter will give an overview about the basic components of SPM, which are the probing tip, scanning units, controllers, and vibration isolation. The methods of STM and AFM will be discussed in more detail because these are the most common SPMs. A collection of other SPMs, such as scanning nearfield optical microscopy (SNOM), scanning nearfield acoustic microscopy (SNAM), scanning ion conductance microscopy (SICM), photo-induced force microscopy (PIFM), STM with inverse Photoemission (STMiP), tip Enhanced Raman Scattering (TERS), electrochemical STM (ECSTM), scanning thermal microscopy (SThM), scanning noise microscopy (SNM), scanning potentiometry microscopy (SPotM), scanning capacitance microscopy (SCM), scanning spreading resistance microscopy (SSRM), Tera-Hertz STM (THz STM), or electron spin resonance STM (ESR-STM), will end the chapter.

Principles of SPM

Scanning and Control

All scanning probe microscopes (SPMs) need a scanning unit to move the probing tip across the surface. Tube scanners consist of a piezo-ceramic tube, which has four outer electrodes and one inner electrode. Typically, scan voltages $\pm V_x$ are applied to two outer electrodes and $\pm V_y$ to the other two electrodes. The output of the feedback loop, called z-signal V_z, is applied to the inner electrode. Tube scanners are very compact and have a relatively high resonance frequency. The length extension Δl in z-direction is given by

$$\Delta l = \frac{d_{31} l V_z}{h},$$

where l is the length of the tube, V_z is the voltage applied to the inner electrode, and h is the wall thickness of the tube. The lateral displacement Δx is given by

$$\Delta x = \frac{2\sqrt{2} d_{31} l^2 V_x}{\pi D h},$$

where $-V_x$ and $+V_x$ are voltages applied to opposite side electrodes and D is the average diameter of the tube (Chen, 2007; Yang and Huang, 1998). A typical piezo tube with a wall thickness $h = 1$ mm, length $l = 30$ mm, diameter $D = 2.2$ mm, and a transversal piezoelectric constant $d_{31} = 1.8$Å/V would give a length extension of ±4.5 μm and a maximum lateral deflection $\Delta x = \pm 35$ μm, when a voltage of ±250 V is applied. Operation at 4K will result in a reduction of scan range by a factor five.

Piezoelectric tube scanners have a number of deviations from this linear dependence. The most disturbing effect of piezoelectric materials is hysteresis and creep. Forward and backward scan can show significant deviations of the order of 10%. It is most pronounced for the large extensions in the micron range. It is of less importance for high-resolution scans in the nm range.

If hysteresis has to be avoided, a closed-loop scanner can be used, where the position is measured with a capacitive or optical sensor. Closed-loop sensors have high accuracy for metrological applications, but have a limited signal-to-noise ratio, which becomes problematic for high-resolution scans. The mass of closed-loop scanners is usually larger, which also gives some limitations for high speed imaging. The calibration of scanners can be done with suitable calibration structures, which are imaged by STM or AFM mode. Very often, the atomic lattice of surfaces, such as graphite, Au(111), or Si(111)7 × 7, are used for calibration of the scanner. The z-direction is calibrated by imaging of mono atomic steps or microfabricated structures of defined height.

As mentioned before, the z-direction is regulated by a feedback loop (cf. Fig. 1). For STM, the difference between the actual tunneling current and the setpoint current is used to adjust the z-position. This error signal is to be minimized by the controller. In most cases, relatively simple PI controllers are used, where a signal proportional to the error signal (P) and an integrated part (I) is fed to the high voltage amplifier and then to the z-piezo. Values for the proportional gain and integral gain have to be optimized. A simple procedure is to increase the P-gain until oscillations are observed. Then, the P-gain is reduced to 2/3. The integral gain is then increased until first signs of oscillations occur. The gain of the whole feedback loop depends on the tip conditions; thus, it is rather common to optimize the feedback conditions before every experiment. Another concern is the nonlinear dependence of the feedback signal vs. distance. In STM, the logarithm of the tunneling current is an efficient way to linearize across a large distance range. Generally, SPM input signals have a limited range, where a stable operation of the feedback can be achieved. Tip crashes can lead to drastic changes of the feedback characteristics. An automatized tip saver, which retracts the tip at some threshold value, is a valuable tool to minimize tip crashes.

Scanning tunneling microscopy

STM was introduced by Binnig et al. (1982, 1983), where atomic resolution was observed on the surface of Si(111)7x7. The microscope is based on the scanning of a probing tip across the surface. A tunneling current of the order of few pA to nA flows

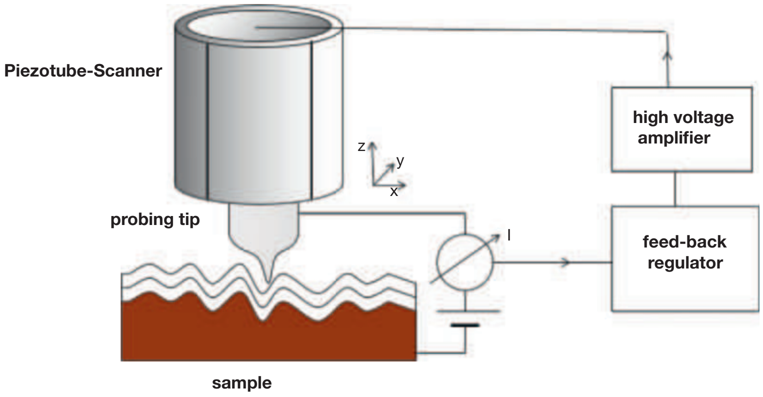

Fig. 1 Scheme of a scanning tunneling microscope. The tunneling tip is mounted to the piezoelectric tube scanner. The tunneling current between tip and sample is used as input signal for the feedback loop. The distance between tip and sample is regulated by keeping the current constant to a preset value. Raster scans in x- and y-directions give an image of the surface.

between the probing tip and the sample. This tunneling current depends exponentially on distance, which gives an excellent input parameter for the feedback loop to control the distance between tip and sample during scanning. Typical separations are of the order of 1 nm, but depend on the exact parameters of bias voltage, set point current, and electronic properties of tip and sample. If the feedback loop is on, lines of constant tunneling current are acquired, which correspond to a height information, sometimes called topography. However, one has to keep in mind that the profiles of constant tunneling current can be affected by local variations of the conductivity of the sample. For example, if several materials are present, the height information can be determined by topography as well as variations of the local electronic structure. The tunneling current is of quantum-mechanical nature, where the wave function decays exponentially across the vacuum barrier. According to Frenkel (1930), the tunneling current, I, is an exponential function of the distance, z, between the metallic electrodes:

$$I(z) = f(V)\exp(-A\sqrt{\Phi}z),$$

where V is the bias voltage, Φ is the work function of the metal, and $A = 1.025\text{Å}^{-1}\text{eV}^{-1/2}$. With a typical work function of 4.5 eV, one gets an increase of the tunneling current by a factor of 10 by reducing the distance by 1Å. Therefore, the tunneling current is an extremely sensitive input signal to regulate the distance between tip and sample. Since it needs a current flow, it is mostly limited to metallic or highly doped semiconductor surfaces. Atomic resolution was achieved on a large variety of metallic surfaces, such as Au, Ag, Cu, Pt, Ir, Cr, Ni, or Fe. Suitable preparation under ultrahigh vacuum conditions is needed to image theses surfaces. Corrugation heights of some tenths of pm can be observed on closed-packed surfaces. In addition, reconstructions, such as the herringbone reconstruction on Au(111), can be observed (cf. Fig. 2). Highly doped semiconductors can be imaged, of which the most famous example is the Si(111)7 × 7 reconstruction. Other examples are GaAs, where gallium and arsenic atoms can be distinguished by application of different voltage polarity (Feenstra et al., 1987).

The ability to measure currents in the sub-pA range widened the applications of STM to thin insulating films, where the current decays partially in the insulating film. On top of these insulating films, organic molecules were deposited and high resolution imaging became possible. It is found that the differential conductance dI/dV curves show peaks at the highest occupied molecular orbital (HOMO) and at the lowest unoccupied molecular orbital (LUMO). If the bias voltage is selected on the HOMO or LUMO peaks, one can image molecular orbitals, which are in excellent agreement with theoretical calculations. Therefore, the deposition of the molecules on insulators decouples the molecules from the metal and gives the opportunity to image undisturbed molecular orbitals. The method works best with planar molecules, such as pentacene, deposited on a few layers of NaCl (Repp et al., 2005).

Atomic force microscopy

AFM is based upon the measurement of the deflection of a cantilever-type spring, which gives the opportunity to measure the force between probing tip and sample (cf. Fig. 3). Typical dimensions of cantilevers are a width of some tens of μm, a length of 100–500 μm and a thickness of 0.1 to 10 μm. This results in spring constants in the range of 0.01–100 N/m. Soft springs with $k_N < 1$ N/m are used for contact force microscopy, where the static deflections are used for force measurements. Harder spring constants $k_N > 10$ N/m are used for noncontact force microscopy or tapping mode AFM, which helps to avoid the jump to contact.

The spring constant of a cantilever with a rectangular cross section is given by

$$k_N = \frac{Ewt^3}{4l^3}, \tag{1}$$

where w is the width, l is the length, t is the thickness of the cantilever, and E is the Young's modulus of the material. The width and length are relatively well-known from the fabrication process or by optical microscopy. Cantilevers can also be characterized by the measurement of the resonance frequency (free cantilever) of the first flexural mode:

$$f_1 = \frac{1.875^2}{l}t\sqrt{\frac{E}{12\rho}}. \tag{2}$$

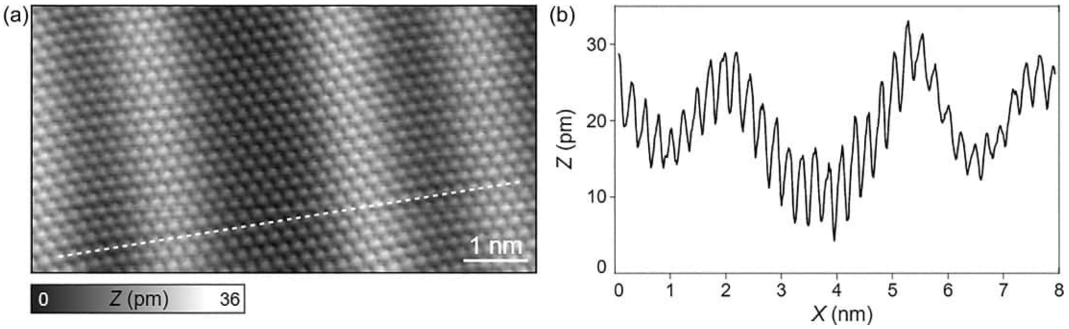

Fig. 2 (A) STM measurement on Au(111), where the atomic structure is observed with a corrugation of about 10 pm. In addition, the herringbone 22 $\times\sqrt{3}$ reconstruction can be observed. Bright areas correspond to dislocation lines, which separate areas of hcp stacking and fcc stacking. (B) Profile of the STM topography along the line as indicated in (A).

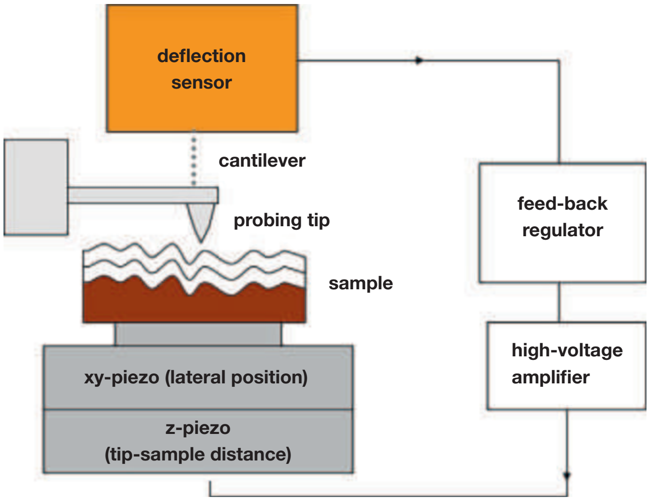

Fig. 3 Scheme of an atomic force microscope. The probing tip is attached to the cantilever, where forces between tip and sample lead to deflections of the cantilever-type spring. The distance is regulated with the deflection signal from the cantilever, which corresponds to profiles of constant interaction force.

Table 1 Examples of silicon cantilevers with spring constant and first flexural resonance frequency

Length (μm)	*Width (μm)*	*Thickness (μm)*	*k_N (N/m)*	*f_1 (kHz)*
125	32	4	44	352
225	38	7	48	190
450	53	2	0.2	13.6

The thickness is most difficult to be determined with reasonable accuracy. Either electron microscopy can be used or the resonance frequency of the first flexural mode, f_1, is determined, which gives an accurate estimate of the thickness:

$$t = \frac{2\sqrt{12}\pi}{1.875^2}\sqrt{\frac{\rho}{E}}f_1 l^2, \tag{3}$$

where ρ is the mass density (ρ=2330 kg/m^3 and $E = 1.69\ 10^{11}$ N/m^2 for silicon).

To give an example, the length of a particular cantilever is $l = 450$ μm and width is $w = 53$ μm. From manufacturing data, one might expect a thickness of 1 μm, which would give a theoretical value $f_1 = 6.793$ kHz. However, one observes a resonance frequency of 10.3 kHz. Therefore, the corrected thickness is t = 1.5 μm as given by Eq. 3. Accordingly, the spring constant changes from $k_N = 0.02$ N/m to $k_{N,corr} = 0.09$ N/m. Thus, the correction of the thickness is important, at least for soft cantilevers with thicknesses of only a few μm. Further examples are shown in Table 1.

Noncontact atomic force microscopy (nc-AFM): For nc-AFM, the shift of resonance frequency Δf_1 is used to determine the force or force gradient between tip apex and surface. For small amplitudes $A < 1$Å, the force gradient $\frac{\partial F}{\partial z}$ is given by

$$\frac{\partial F}{\partial z} = -2k_N\frac{\Delta f}{f}. \tag{4}$$

For larger amplitudes, one has to integrate over the oscillation period. An accurate inversion formula is elaborated in the paper by Sader and Jarvis (2004). In this case, the forces can be determined for arbitrary amplitudes A. In the large amplitude case $A > 100$Å, one observes a dependence of the frequency shift with amplitude, which is proportional to $A^{-3/2}$. Therefore, it makes sense to introduce a reduced frequency shift

$$\gamma_{freq} = \frac{\Delta f}{f}k_N A^{3/2}, \tag{5}$$

which is useful for comparing results recorded with different experimental parameters (Giessibl and Bielefeldt, 2000). Approximately, one can say that constant γ_{frequ} corresponds to constant interaction forces independent of the amplitude A or in the limit of short range forces of constant distance between tip and sample. Actually, it is quite common to calibrate the amplitude by keeping γ_{frequ} constant for various amplitudes and to determine the motion of the piezo under the assumption of constant separation between tip apex and sample.

Experimentally, there are a number of possibilities to measure the deflection of the cantilever-type spring. The most common method is the optical beam deflection method, where a laser beam is reflected of the backside of the cantilever (cf. Fig. 4).

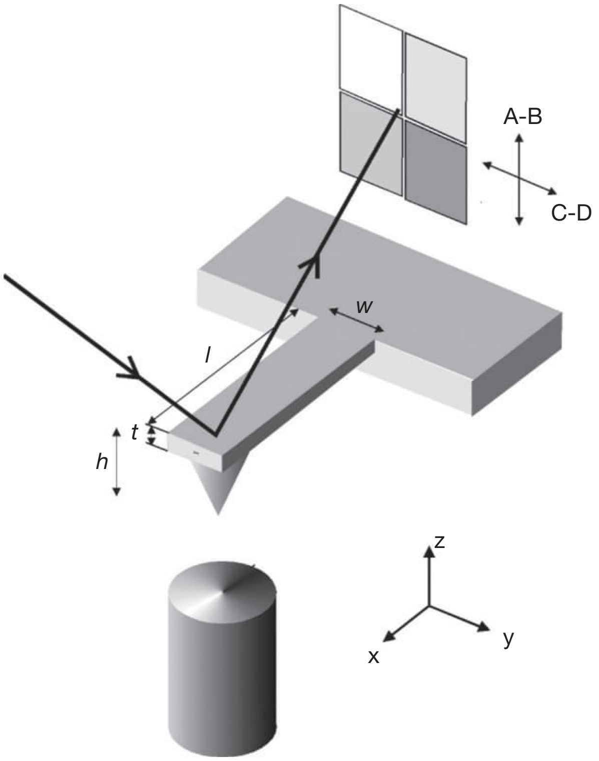

Fig. 4 Beam-deflection AFM: A laser beam is used to measure the deflections of the cantilever. The position of the reflected beam on the 4-quadrant photodiode gives information about normal and lateral forces.

The position of the reflected beam is measured with a 4-quadrant photodiode. The difference signal between upper and lower half is proportional to the flexural deflection of the cantilever. The difference between left and right side is related to the torsional deflection of the cantilever, which is then related to lateral forces. Alternative deflection sensors are optical interferometry, where fiber optics is combined with the cantilever. The deflection sensors can be also integrated by a suitable microfabrication process. For example, the piezoresistance of cantilevers can be used as sensor. Other methods involve the measurement of the capacitance or piezoelectricity. At low temperature, tuning forks, as used in quartz watches, are combined with probing tips. The resonance frequency can be measured from the piezoelectric signal. Q-factors of 10,000 to 30,000 were achieved with this setup. A relatively large spring constant of 1800 N/m and resonance frequency in the range of 20 kHz are used (Giessibl, 2003).

An example of nc-AFM imaging of a NaCl(001) surface is shown in Fig. 5, where every other ion is observed. In most cases, the brighter dots correspond to the chlorine ions, but contrast can be reversed by the change of the probing tip. Typical corrugations heights are in the range of 40–50 pm. For controlling the z-distance, the cantilever is excited at its resonance frequency by using a phase locked loop (PLL) or just a frequency demodulator (Fig. 6). By adjusting the excitation voltage also the oscillation amplitude is kept constant. The excitation corresponds to the dissipated energy in one oscillation cycle while the frequency shift is proportional to the conservative forces as discussed above.

Typical force vs. distance curves show an attractive part, which is related to van der Waals forces and electrostatic forces and a repulsive part due to Pauli repulsion forces. In between these regimes, chemical forces due to the interaction between the apex of the probing tip and the sample surface atoms have to be considered (Guggisberg et al., 2000). The earliest examples of atomic

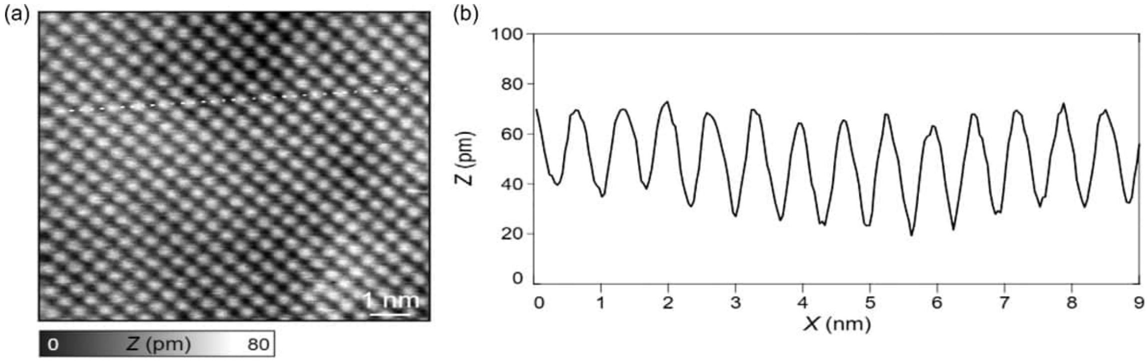

Fig. 5 (A) Constant frequency shift image of NaCl(001) surface. (B) Profile of the topography as indicated in (A). The corrugation is 40–50 pm.

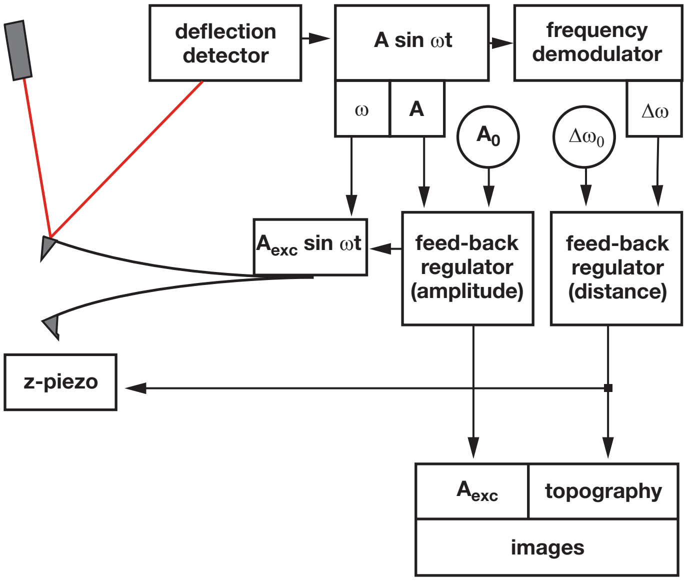

Fig. 6 Scheme of noncontact AFM (nc-AFM).

resolution were acquired on graphite surfaces, where carbon rings were observed. Later, the Si(111)7 × 7 was observed, where the main contrast was related to the adatom layer, but also rest atoms were resolved under optimum conditions. Atomic resolution on insulators, such as NaCl(001) is nowadays standard and shows the added value of AFM. A major improvement was to functionalize the probing tip with a CO-molecule, where submolecular resolution was achieved on a number of organic molecules or nanowires (Gross et al., 2009). The main advantage of a CO-terminated tip is its inertness, which gives the opportunity to enter the repulsive force regime. This has demonstrated the highest lateral resolution of chemical structure of molecules. Metallic tips are more reactive and often a bond is formed between tip and sample atoms at close separations, which leads to instabilities and nonreversible surface or tip damage.

In comparison to high-resolution STM, high-resolution AFM is not sensitive to the electronic structure and mostly represents topographic information. Simulation programs assume that the CO molecule senses the ionic repulsion forces, which gives profiles of total charge density. The observed contrast can be affected by the deformations of the CO molecule, which behaves like a small pendulum, which leads to image distortions with some enlargement of intramolecular atom separations (Hapala et al., 2014). Nc-AFM imaging has the highest lateral resolution. In combination with the CO-terminated tips, it has become one of the most efficient ways to observe the structure of molecules on surfaces. It is mostly restricted to planar molecules, but in some cases 3D arrangement was investigated by imaging at different heights (Kawai et al., 2020; Pawlak et al., 2020). An example of the 3,6,14,17-tetrabromodibenzo[a,c]-dibenzo[5,6:7,8]quinoxalino-[2,3-i]-phenazine (TBQP) molecule is shown in Fig. 7, where bromine atoms, visible as bright dots, are still attached to the molecule (Pawlak et al., 2021).

Tapping mode force microscopy: In contrast to noncontact force microscopy, where the frequency shift of the cantilever is measured, tapping mode force microscopy uses the amplitude of oscillation at fixed frequency. Typically, oscillation amplitudes of 2–10 nm are excited close to the resonance frequency. Then the interaction with samples can lead to a shift of the resonance curve, which either increases or decreases the amplitudes. Usually, one assumes that an attractive interaction leads to a decrease of the resonance frequency. Depending on the position of the excitation frequency, the amplitude will be reduced or increased. The amplitude can also be reduced due to an intermittent contact during each cycle, which also motivated the term tapping mode force microscopy.

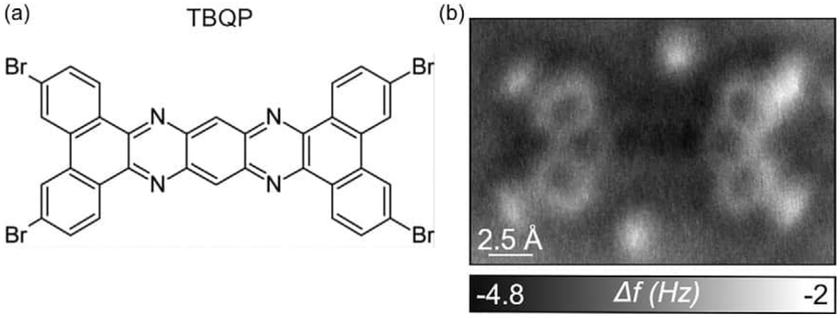

Fig. 7 (A) The chemical structure of 3,6,14,17-tetrabromodibenzo[a,c]-dibenzo[5,6:7,8]quinoxalino-[2,3-i]-phenazine (TBQP) molecule. (B) Nc-afm imaging of a TBQP molecule with a CO-terminated tip.

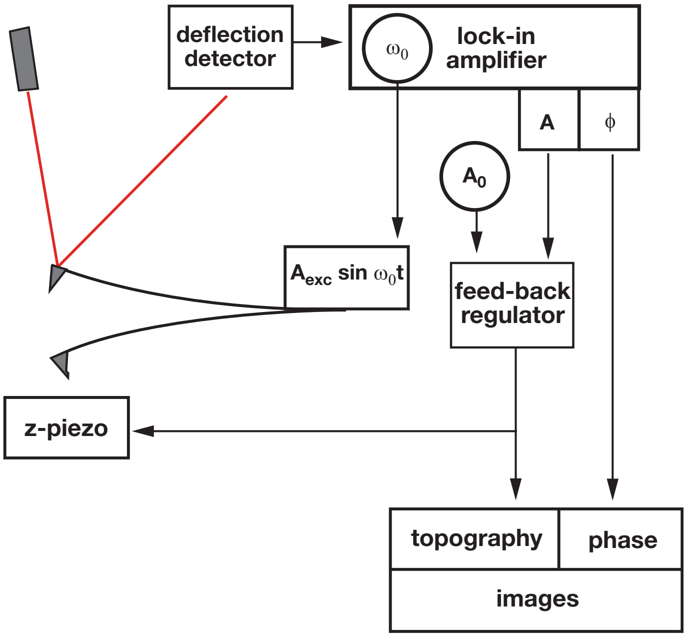

Fig. 8 Scheme of the tapping mode AFM.

Thus, the method is not very quantitative, but is a reliable tool to image surfaces. In comparison to contact mode, the lateral forces are reduced. A relatively large amplitude is needed to overcome capillary forces by the restoring force of the cantilever. Tapping mode force microscopy works quite well on biological material with a resolution in the nm range. It was also shown that the tip does not tap the surface (noncontact regime), if relatively small oscillation amplitudes and small changes in the setpoint are selected. The operation in liquids is not trivial, because many oscillation modes of the liquid cell are observed, which are not so easy to distinguish from the resonance frequency of the cantilever. The main criterium is the distance dependence of the cantilever resonance. Alternatively, photothermal excitation of the cantilever can be used, where a modulated laser beam is reflected off the cantilever, heating the cantilever in a periodic manner. The photothermal excitation, which gives a much cleaner spectrum, makes it much easier to find the resonance of the cantilever in liquids (Fig. 8).

Phase imaging: If the cantilever is operated at fixed frequency, one can measure the phase shift between the excitation signal and the cantilever oscillation. Phase images can be acquired on heterogeneous surfaces, which can show strong material contrast. The interpretation of the phase images is not completely clarified. If the oscillation is sinusoidal, one can relate the phase shift to energy dissipation. If the wave-form is distorted due to contact formation, the interpretation is more complex. There are also attempts to relate the phase shift to physical properties, such as elasticity or viscosity, which is to some extend possible for relatively soft materials, where nonlinear effects are not dominant.

Pulsed force mode: The pulsed force mode is a nonresonant intermittent contact mode, where the sample is modulated. The response of the cantilever is acquired with fast data acquisition, where a full force vs. distance curve is visible, including snap to repulsive contact and pull-out of the contact. When the maximum adhesion peak is reached, the cantilever jumps out of contact and free oscillations of the cantilever are visible. Each approach and retraction cycle can be analyzed, where the stiffness of the contact, the maximum normal force, and the maximum adhesive force can be determined. In combination with a suitable elasticity model, it is possible to determine the local elasticity of polymeric samples or biological material. The method works well in liquids and gives some quantitative values about elasticity and adhesion.

High-speed AFM: The scan speed of AFM can be increased by increasing the resonance frequency of the cantilever. Microcantilevers are fabricated, which are reduced in dimensions compared to conventional AFM: A length of 5–10 μm is combined with a width of a few μm. The corresponding resonance frequency is in the range of 1–10 MHz. The mechanical relaxation time

$$\tau = \frac{Q}{\pi f_1} \tag{6}$$

is given by the Q-factor of the cantilever and the resonance frequency of the first flexural mode. With $f_1 = 1$ MHz and Q = 2 (typical Q-factor in liquids), one gets 0.6 μs, which allows to operate the feed-back loop in the 100–500 kHz range. The benchmark of high-speed AFM is the number of frames per seconds (fps). Some tens of fps were achieved with microcantilevers and optimized scanners. Examples of imaging of the motion of biomolecules in liquid environment were reported. For example, the motion of an individual myosin protein walking along an actin filament was observed by high-speed AFM (Ando, 2012).

Bimodal AFM: In addition to the oscillation of the first flexural mode, one can also oscillate higher modes, such as the second flexural mode or the first torsional oscillation mode (Kawai et al., 2009, 2010b). In bimodal AFM, the microscope is operated with constant frequency shift of the first flexural mode and the second flexural mode is oscillated with smaller amplitude. In this case, the second mode is shown to be proportional to the force gradient, whereas the first mode is related to an average of the normal force, as described by the Sader–Jarvis method. Alternatively, the first flexural mode is combined with torsional oscillation mode. It is found that the shift of the torsional resonance frequency gives higher resolution than normal nc-AFM. To first approximation, the torsional signal is related to the lateral force gradient.

Kelvin probe force microscopy (KPFM): It is based on AFM in tapping or noncontact mode, where the applied voltage is varied and electrostatic forces are measured separately (Sadewasser and Glatzel, 2011; Sadewasser and Glatzel, 2018; Glatzel et al., 2022). While in electrostatic force microscopy (EFM), the electrostatic forces are measured qualitatively, in KPFM, a DC bias voltage is applied between tip and sample to compensate the electrostatic forces. KPFM was first developed by Nonnenmacher et al. (1991) and allows to image surface electronic properties, namely, the contact potential difference (CPD). The name "Kelvin probe force microscope" originates from the macroscopic method developed by Lord Kelvin in 1898 using a vibrating parallel plate capacitor arrangement, where a voltage applied to one vibrating plate is controlled such that no current is induced by the vibration (Kelvin, 1898). The reduction of this exact principle to the microscopic scale, however, results in a poor sensitivity, since the size of the capacitor plates is too small to generate a sufficient current. Therefore, in KPFM, the electrostatic force is measured instead and a DC bias voltage corresponding to the CPD is applied to the sample (or the tip) in such a way that the electrostatic forces between tip and sample are minimized. Thus the CPD or at atomic and molecular scale also called local CPD (LCPD) can be measured with high spatial and energy sensitivity (Bocquet et al., 2008; Enevoldsen et al., 2008; Kawai et al., 2010a).

The electrostatic force is typically described by a capacitor model with a voltage-independent capacitance, which contains all information on the geometrical details (Hudlet et al., 1998). It quadratically depends on the applied voltage and is measured by force vs. bias voltage curves. The frequency shift signal in nc-AFM follows a parabolic shape depending on the position above the sample and has a maximum exactly at the point where the average electrostatic forces are zero. In many cases this assumption is sufficient and by introducing an AC (V_{AC}) and DC (V_{DC}) voltage component and the CPD (V_{CPD}), the electrostatic force can be described by

$$F_{el} = \frac{1}{2}\frac{\partial C}{\partial z}V^2 = F_0 + F_\omega + F_{2\omega}, \tag{7}$$

where

$$F_0 = \frac{\partial C}{\partial z}\left[\frac{1}{2}(V_{DC} - V_{CPD})^2 + \frac{V_{AC}^2}{4}\right], \tag{8}$$

$$F_\omega = \frac{\partial C}{\partial z}(V_{DC} - V_{CPD})V_{AC}\sin(\omega t), \tag{9}$$

$$F_{2\omega} = -\frac{\partial C}{\partial z}\frac{V_{AC}^2}{4}\cos(2\omega t). \tag{10}$$

The 0-component induces a static bending of the cantilever and is similarly as the 2ω-component proportional to the square of the applied AC voltage and the distance dependent capacitance gradient. The ω-component is directly proportional to AC voltage, the capacitance gradient, and the difference between applied DC voltage and CPD. Typically in KPFM setups, this ω-component or its gradient is detected and minimized by applying a DC voltage compensating the CPD and resulting ideally in $F_\omega = 0$. A limitation of this description is the fact that not in all cases the capacitance is independent of the applied voltage, especially in the case of semiconducting surfaces (Polak and Wijngaarden, 2016; Glatzel et al., 2022).

Two main modes of detecting and compensating the electrostatic forces separately from the other forces are the amplitude (AM) and frequency (FM) modulated techniques. Both offer not only certain benefits but also drawbacks that have to be taken into account and are described in several publications (Krok et al., 2004; Glatzel et al., 2003), the most recent overview and thorough comparison was given by Axt et al. (2018).

As an example, a measurement of hybrid organic–inorganic lead halide perovskite surface prepared for the application in solar cells is shown in Fig. 9. To avoid contamination and degradation of the film, the sample was prepared, transferred, and analyzed under inert gas N_2 atmosphere. A Flex-AFM system from Nanosurf was used in tapping mode with a nominal amplitude of 3 nm and a feedback setpoint of 80%. The used cantilever was a PtIr-coated cantilever from Nanosensors (PPP-NCLR) with a resonance frequency of $f_1 = 158$ kHz. For KPFM, the AM mode at the second resonance of the cantilever $f_2 = 985$ kHz was applied with an AC bias voltage of 500 mV applied together with the compensation voltage to the sample. The overview image with a size of 4×4 μm^2 shows the polycrystalline character of the surface. The simultaneously measured CPD shows variations of up to 100 mV induced by different facet orientations, chemical composition, and grain boundaries. These variations become more apparent in the magnified measurement below showing clearly the variations between the grains which will finally impact the properties of the resulting solar cell devices. With an appropriate calibration of the work function of the cantilever, absolute work function values can be extracted.

Friction force microscopy (FFM): It is operated in repulsive contact, where the deflections in normal direction (normal force) and the deflections in lateral direction (lateral force) are measured. If the beam deflection method is used to measure the deflections, the torsional signal is directly related to the lateral forces. To convert the deflections into forces, one needs the torsional spring constant, which is given by

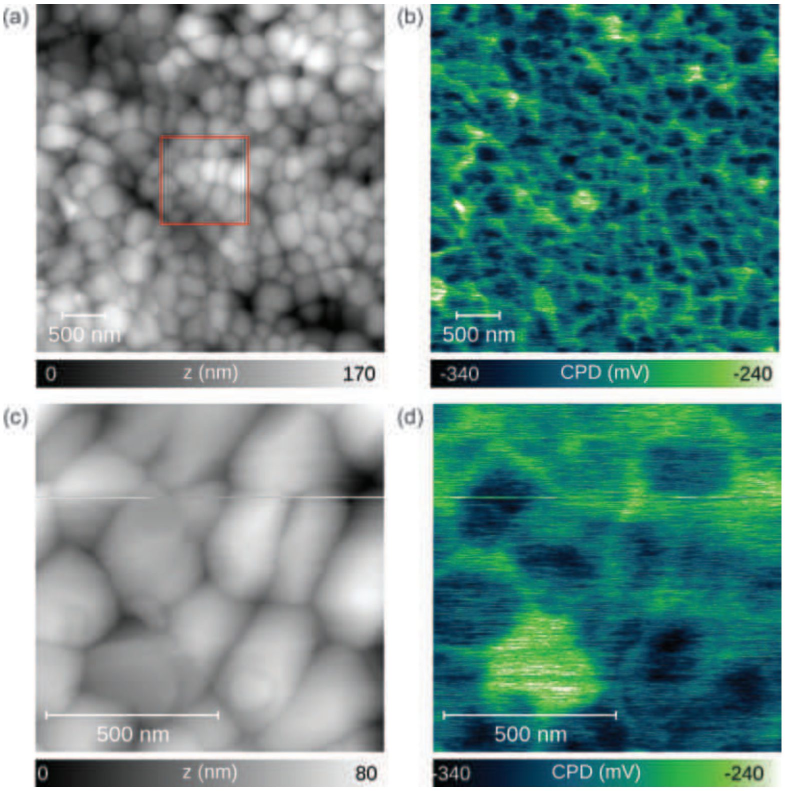

Fig. 9 Topography z (A and C) and contact potential difference CPD (B and D) of a perovskite surface measured by tapping mode AFM in a glove box with nitrogen gas and in AM-KPFM mode. C and D are a magnification of the area indicated with a *red box* in A.

$$k_T = \frac{Gwt^3}{3h^2 l}, \tag{11}$$

where G is the shear modulus of the cantilever material.

Dissipation force microscopy: In order to keep the oscillation amplitude A constant during nc-AFM operation, one has to apply an excitation voltage A_{exc} to a dither piezo. The free cantilever has some internal damping, which gives the reference value $A_{exc,0}$. If the tip is approached to the surface, one can determine the energy loss per second due to dissipative interactions by equation:

$$P_{tip} = \frac{1}{2}\frac{kA^2\omega}{Q_0}\left(\frac{A_{exc}}{A_{exc,0}} - 1\right), \tag{12}$$

where k is the spring constant, Q_0 is the Q-factor of the free cantilever, and ω is the resonance frequency in rad/sec. Typical dissipation power is on the order of 10^{-15}W, which can be related to atom reordering on the tip or sample on the time scale of the oscillation period, which then gives dissipation due to hysteresis, where in downward and upward motions of the tip, different atomic structure is encountered. It is also very common to indicate the power loss in energy loss per cycle, which is found to be in the range of meV up to eV per cycle (Yildiz et al., 2019).

Magnetic force microscopy (MFM): In magnetic force microscopy, a ferromagnetic tip is attached to the cantilever, either by evaporation of materials, such as Co, or by glueing a small piece of a ferromagnet, such as cobalt samarium. Then domain walls on ferromagnetic samples can be observed by operation in noncontact mode. The forces due to magnetic interactions are relatively small and the separation between tip and sample has to be kept large in order not to alter the domain structure by the probing tip.

Other SPMs

Other members of the SPM family are described in this section. All SPMs have a probing tip, which can be rather different from the standard metallic tips of STM (cf. Fig. 10).

The *scanning nearfield optical microscopy (SNOM)* uses a glass fiber, which is coated with a metallic film. Then, light is coupled into the fiber. The evanescent light interacts with nanometer-sized objects on the surface, which changes the far field intensity, which is detected by a suitable detector.

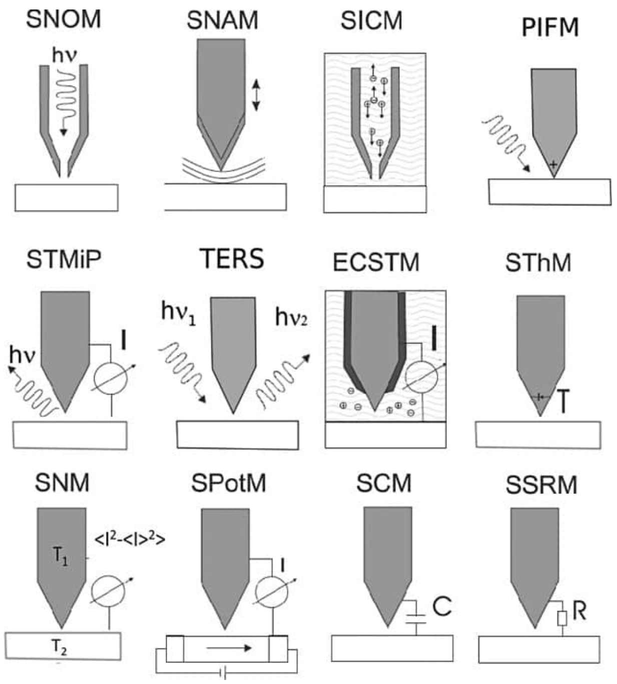

Fig. 10 A collection of scanning probe microscopes as described in the main text.

Scanning nearfield acoustic microscopy (SNAM) excites an acoustic wave with a piezoelectric transducer. Hydrodynamic losses lead to a damping of the SNAM signal when the sensor is approached to the surface.

Scanning ion conductance microscopy (SICM) uses a micropipette immersed in an electrolyte and measures the ion current. If approached to the surface, the cross-section of ion path is reduced and the conductance is reduced (Lipson and Hersam, 2013).

Photo-induced force microscopy (PIFM): Light illumination of the probing tip in close proximity to the samples leads to photo-induced polarizability. If modulated at the resonance of a cantilever, one can detect photoinduced forces. The change of the wavelength gives information about the absorption characteristics of the material, which is a way to identify components of heterogeneous surfaces.

STM with inverse Photoemission (STMiP) or scanning tunneling induced luminescence microscopy (STlM): Injection of electrons into metallic films leads to the emission of surface plasmons. If molecules are decoupled from the metallic substrate by a thin insulating film, it becomes possible to inject electrons into the molecules and to observe electroluminescence. Apart from the luminescence line, one can also observe vibrational modes, where the spectrum is in good agreement with Raman spectra (Doppagne et al., 2017).

Tip-Enhanced Raman Scattering (TERS): The metallic tip apex in vicinity to a metallic substrate gives a strong enhancement of the electromagnetic field. By matching the resonance of the nanocavity plasmon to molecular vibrations, it becomes possible to increase the Raman sensitivity. Single porphyrin molecules can be imaged with submolecular resolution. Molecular vibrations are suitable to get a fingerprint to identify subgroups of a molecule (Zhang et al., 2013).

Electrochemical STM (ECSTM) and scanning electrochemical microscopy (SECM): The probing tip is immersed in an electrolyte. By suitable isolation, the ionic current can be reduced and the tunneling current is measurable (ECSTM) (Wittstock et al., 2007) or it is directly detected and electroactive ions or molecules in the solution are imaged with spatial resolution (SECM) (Sun et al., 2007; Martin et al., 2014). The sample can be modified in the electrochemical cell.

Scanning thermal microscopy (SThM) uses a miniaturized thermal sensor at the apex of the probing tip. Local temperature inhomogeneities due to heat sources, such as electrical currents in wires, can be observed. If heated periodically, one can get information about the thermal conductivity as well as the thermal diffusivity. If a wire is heated periodically with a frequency f, one can get information about the Joule heating as well as the Peltier component by the measurement of f and $2f$ components (Menges et al., 2016).

Scanning noise microscopy (SNM) measures the mean square noise current in an STM. It can be shown that this is Johnson noise, which depends on temperature. If the tip is heated, a thermovoltage builds up, which then can be used to map different materials on the surface. It is also found that the current noise doubles from single- to double-charge transfer in a junction between superconductive tip and superconductive sample (Bastiaans et al., 2019).

Scanning potentiometry microscopy (SPotM): A voltage is applied across the sample, which can be used to investigate the electrical potential landscape of wires or assemblies of nanoparticles. Defects in nanowires or percolation paths in nanoparticle assemblies can be observed by this method.

Scanning capacitance microscopy (SCM) measures the capacitance between the tip and sample. If stray capacitances are sufficiently reduced, the method is very well suited for the characterization of semiconductor surfaces, where the depletion layer leads to a reduction of the capacitance. Maps of dopant concentrations can be deduced from these measurements (Williams, 1999).

Scanning spreading resistance microscopy (SSRM) measures the current between a conductive cantilever and a semiconductive surface. The current is limited by the spreading resistance, which can be related to dopant concentration of the sample. Therefore, maps of dopant concentrations can be recorded, if the sensor is calibrated with a suitable sample, where defined impurity concentrations are observed (Eyben et al., 2002).

THz STM uses a THz laser pulse in combination with STM, where the THz pulse adds an additional electrical field to the junction, which can open the current flow through molecular orbitals, such as LUMO or HOMO. Time resolution in the sub-ps becomes possible, which gives the opportunity to observe ultrafast dynamics of molecules (Cocker et al., 2013).

Electron spin resonance STM (ESR-STM) is a combination of an RF-field and spin polarized STM, where the magnetoresistance is measured at the electron spin resonance (Baumann et al., 2015). At different static B-fields, the resonance condition is related to the Zeeman energy splitting. Small z-excursions of the magnetic adsorbate atom in the inhomogeneous field of the magnetic tip lead to the B_1 variation, which is necessary to induce electron spin resonance.

Conclusion

SPM is a versatile type of microscopy, which can be operated in almost any environment from liquids to vapors or vacuum. STM is an excellent microscope for atomic resolution in combination with LDOS mapping. AFM is widely used for imaging on the nanometer scale in combination with mechanical properties, such as elasticity, adhesion, or friction or electrical properties, for example, work function, capacitance, or local conductivity. The option of nc-AFM imaging with CO-terminated tips gives submolecular resolution of planar molecules. In terms of resolution, SPM has reached the atomic scale with STM and nc-AFM. In addition, many physical and chemical properties can be characterized on the nanometer scale. To determine the chemical composition on the nanometer scale seems still a goal for the future. Techniques like NMR, photoemission, or mass spectroscopy are not easy to be combined with SPM.

References

Ando T (2012) High speed atomic force microscopy coming of age. *Nanotechnology* 23(6): 062001. https://doi.org/10.1088/0957-4484/23/6/062001.

Axt A, Hermes IM, Bergmann VW, Tausendpfund N, and Weber SAL (2018) Know your full potential: Quantitative Kelvin probe force microscopy on nanoscale electrical devices. *Beilstein Journal of Nanotechnology* 9: 1809–1819.

Bastiaans KM, Cho D, Chatzopoulos D, Leeuwenhoek M, Koks C, and Allan MP (2019) Imaging doubled shot noise in a Josephson scanning tunneling microscope. *Physical Review B* 100(10): 104506. https://doi.org/10.1103/PhysRevB.100.104506. 2469-9950, 2469-9969.

Baumann S, Paul W, Choi T, Lutz CP, Ardavan A, and Heinrich AJ (2015) Electron paramagnetic resonance of individual atoms on a surface. *Science* 350(6259): 417–420. https://doi.org/10.1126/science.aac8703. 0036-8075, 1095-9203.

Binnig G, Rohrer H, Gerber Ch, and Weibel E (1982) Tunneling through a controllable vacuum gap. *Applied Physics Letters* 40(2): 178–180. https://doi.org/10.1063/1.92999.

Binnig G, Rohrer H, Gerber Ch, and Weibel E (1983) 7 × 7 reconstruction on Si(111) resolved in real space. *Physical Review Letters* 50: 120–123. https://doi.org/10.1103/PhysRevLett.50.120.

Bocquet F, Nony L, Loppacher Ch, and Glatzel Th (2008) Analytical approach to the local contact potential difference on (001) ionic surfaces: Implications for Kelvin probe force microscopy. *Physical Review B* 78: 035410.

Chen CJ (2007) *Introduction to Scanning Tunneling Microscopy.* Oxford, New York: Oxford University Press. https://doi.org/10.1093/acprof:oso/9780199211500.001.0001.

Cocker TL, Jelic V, Gupta M, Molesky SJ, Burgess JAJ, Reyes GDL, Titova LV, Tsui YY, Freeman MR, and Hegmann FA (2013) An ultrafast terahertz scanning tunnelling microscope. *Nature Photonics* 1749-4893. 7(8): 620–625. https://doi.org/10.1038/nphoton.2013.151.

Doppagne B, Chong MC, Lorchat E, Berciaud S, Romeo M, Bulou H, Boeglin A, Scheurer F, and Schull G (2017) Vibronic spectroscopy with submolecular resolution from STM-induced electroluminescence. *Physical Review Letters* 118: 127401. https://doi.org/10.1103/PhysRevLett.118.127401.

Enevoldsen GH, Glatzel T, Christensen MC, Lauritsen JV, and Besenbacher F (2008) Atomic scale Kelvin probe force microscopy studies of the surface potential variations on the TiO_2(110) surface. *Physical Review Letters* 100: 236104.

Eyben P, Xu M, Duhayon N, Clarysse T, Callewaert S, and Vandervorst W (2002) Scanning spreading resistance microscopy and spectroscopy for routine and quantitative two-dimensional carrier profiling. *Journal of Vacuum Science and Technology B* 1071-1023. 20(1): 471–478. https://doi.org/10.1116/1.1424280 (6th International Workshop on Fabrication, Characterization, and Modelling of Ultra-Shallow Doping Profiles in Semiconductors, NAPA VALLE, CALIFORNIA, APR 22-26, 2001).

Feenstra RM, Tersoff J, and Fein AP (1987) Atom-selective imaging of the GaAs(110) surface. *Physical Review Letters* 58: 1192. https://doi.org/10.1103/PhysRevLett.58.1192.

Frenkel J (1930) On the electrical resistance of contacts between solid conductors. *Physics Review* 36: 1604–1618. https://doi.org/10.1103/PhysRev.36.1604.

Giessibl FJ (2003) Advances in atomic force microscopy. *Reviews of Modern Physics* 75: 949–983. https://doi.org/10.1103/RevModPhys.75.949.

Giessibl FJ and Bielefeldt H (2000) Physical interpretation of frequency modulation atomic force microscopy. *Physical Review B* 61: 9968–9971. https://doi.org/10.1103/PhysRevB.61.9968.

Glatzel T, Sadewasser S, and Lux-Steiner MCh (2003) Amplitude or frequency modulation-detection in Kelvin probe force microscopy. *Applied Surface Science* 210(84): 84–89.

Glatzel T, Gysin U, and Meyer E (2022) Kelvin probe force microscopy for material characterization. *Microscopy* 71(Supplement_1): i165–i173. https://doi.org/10.1093/jmicro/dfab040.

Gross L, Mohn F, Moll N, Liljeroth P, and Meyer G (2009) The chemical structure of a molecule resolved by atomic force microscopy. *Science* 325: 1110. https://doi.org/10.1126/science.1176210.

Guggisberg M, Bammerlin M, Loppacher Ch, Pfeiffer O, Abdurixit A, Barwich V, Bennewitz R, Baratoff A, Meyer E, and Güntherodt H-J (2000) Separation of interactions by noncontact force microscopy. *Physical Review B* 61(16): 11151.

Hapala P, Kichin G, Wagner C, Tautz FS, Temirov R, and Jelínek P (2014) Mechanism of high-resolution STM/AFM imaging with functionalized tips. *Physical Review B* 90: 085421. https://doi.org/10.1103/PhysRevB.90.085421.

Hudlet S, Jean MS, Guthmann C, and Berger J (1998) Evaluation of the capacitive force between an atomic force microscopy tip and a metallic surface. *The European Physical Journal B* 2: 5.

Kawai S, Glatzel T, Koch S, Such B, Baratoff A, and Meyer E (2009) Systematic achievement of improved atomic-scale contrast via bimodal dynamic force microscopy. *Physical Review Letters* 103: 220801. https://doi.org/10.1103/PhysRevLett.103.220801.

Kawai S, Glatzel T, Hug H-J, and Meyer E (2010a) Atomic contact potential variations of Si(111)-7 x 7 analyzed by Kelvin probe force microscopy. *Nanotechnology* 21(24): 245704.

Kawai S, Glatzel T, Koch S, Such B, Baratoff A, and Meyer E (2010b) Ultrasensitive detection of lateral atomic-scale interactions on graphite (0001) via bimodal dynamic force measurements. *Physical Review B* 81(8): 085420. https://doi.org/10.1103/PhysRevB.81.085420. 1098-0121, 1550-235X.

Kawai S, Krejčí O, Nishiuchi T, Sahara K, Kodama T, Pawlak R, Meyer E, Kubo T, and Foster A (2020) Three-dimensional graphene nanoribbons as a framework for molecular assembly and local probe chemistry. *Science Advances* 28: eaay8913. https://doi.org/10.1126/sciadv.aay8913.

Kelvin L (1898) Contact electricity of metals. *Philosophical Magazine* 46: 82.

Krok F, Kolodziej JJ, Such B, Czuba P, Struski P, Piatkowski P, and Szymonski M (2004) Dynamic force microscopy and Kelvin probe force microscopy of KBr film on InSb(001) surface at submonolayer coverage. *Surface Science* 566(Part 1): 63–67.

Lipson AL and Hersam MC (2013) Conductive scanning probe characterization and nanopatterning of electronic and energy materials. *Journal of Physical Chemistry C* 1932-7447. 117(16): 7953–7963. https://doi.org/10.1021/jp312594s.

Martin CJ, Bozic-Weber B, Constable EC, Glatzel T, Housecroft CE, and Wright IA (2014) Development of scanning electrochemical microscopy (SECM) techniques for the optimization of dye sensitized solar cells. *Electrochimica Acta* 0013-4686. 119: 86–91. https://doi.org/10.1016/j.electacta.2013.11.172.

Menges F, Mensch P, Schmid H, Riel H, Stemmer A, and Gotsmann B (2016) Temperature mapping of operating nanoscale devices by scanning probe thermometry. *Nature Communications* 2041-1723. 7(1): 10874. https://doi.org/10.1038/ncomms10874.

Nonnenmacher M, O'Boyle MP, and Wickramasinghe HK (1991) Kelvin probe force microscopy. *Applied Physics Letters* 58(25): 2921.

Pawlak R, Drechsel C, D'Astolfo P, Kisiel M, Meyer E, and Cerda JI (2020) Quantitative determination of atomic buckling of silicene by atomic force microscopy. *Proceedings of the National Academy of Sciences* 117: 228–237. https://doi.org/10.1073/pnas.191348911.

Pawlak R, Liu X, Ninova S, D'Astolfo P, Drechsel C, Liu J-C, Häner R, Decurtins S, Aschauer U, Liu S-X, and Meyer E (2021) On-surface synthesis of nitrogen-doped kagome graphene. *Angewandte Chemie International Edition* 60(15): 8370–8375. https://doi.org/10.1002/anie.202016469. 1433-7851, 1521-3773.

Polak L and Wijngaarden RJ (2016) Two competing interpretations of Kelvin probe force microscopy on semiconductors put to test. *Physical Review B* 2469-9969. 93(19): 195320. https://doi.org/10.1103/physrevb.93.195320.

Repp J, Meyer G, Stojković SM, Gourdon A, and Joachim C (2005) Molecules on insulating films: Scanning-tunneling microscopy imaging of individual molecular orbitals. *Physical Review Letters* 94: 026803. https://doi.org/10.1103/PhysRevLett.94.026803.

Sader JE and Jarvis SP (2004) Accurate formulas for interaction force and energy in frequency modulation force spectroscopy. *Applied Physics Letters* 0003-6951. 84(10): 1801–1803. https://doi.org/10.1063/1.1667267.

Sadewasser S and Glatzel T (2018) *Kelvin Probe Force Microscopy - From Single Charge Detection to Device Characterization*. Springer International Publishing. https://doi.org/10.1007/978-3-319-75687-5.

Sadewasser S and Glatzel Th (2011) Kelvin Probe Force Microscopy Measuring and Compensating Electrostatic Forces. *Springer Series in Surface Sciences.* Springer-Verlag Berlin Heidelberg.

Sun P, Laforge FO, and Mirkin MV (2007) Scanning electrochemical microscopy in the 21st century. *Physical Chemistry Chemical Physics* 1463-9076. 9(7): 802–823. https://doi.org/10.1039/B612259K.

Williams CC (1999) Two-dimensional dopant profiling by scanning capacitance microscopy. *Annual Review of Materials Science* 29(1): 471. https://doi.org/10.1146/annurev.matsci.29.1.471.

Wittstock G, Burchardt M, Pust SE, Shen Y, and Zhao C (2007) Scanning electrochemical microscopy for direct imaging of reaction rates. *Angewandte Chemie International Edition* 1521-3773. 46(10): 1584–1617. https://doi.org/10.1002/anie.200602750.

Yang S and Huang W (1998) Three-dimensional displacements of a piezoelectric tube scanner. *Review of Scientific Instruments* 0034-6748. 69(1): 226–229. https://doi.org/10.1063/1.1148500.

Yildiz D, Kisiel M, Gysin U, et al. (2019) Mechanical dissipation via image potential states on a topological insulator surface. *Nature Materials* 18: 1201–1206. https://doi.org/10.1038/s41563-019-0492-3.

Zhang R, Zhang Y, Dong ZC, Jiang S, Zhang C, Chen LG, Zhang L, Liao Y, Aizpurua J, Luo Y, Yang JL, and Hou JG (2013) Chemical mapping of a single molecule by plasmon-enhanced Raman scattering. *Nature* 1476-4687. 498(7452): 82–86. https://doi.org/10.1038/nature12151.

Microscopy: Transmission electron microscopy

Stephen J Pennycook, Department of Materials Science and Engineering, University of Tennessee, Knoxville, TN, United States; School of Physical Sciences and CAS Key Laboratory of Vacuum Sciences, University of Chinese Academy of Sciences, Beijing, China

© 2024 Elsevier Ltd. All rights reserved.

Introduction 63
Electron optics of the microscope: STEM vs. TEM, reciprocity 64
Principles of image formation 65
Coherent imaging 65
Incoherent imaging 67
The TEM as a nano-laboratory 69
Future directions 69
Conclusion 70
References 70

Abstract

The basic principles of operation of the two complementary modes of transmission electron microscopy, fixed beam and scanning, are described and related through the reciprocity principle. The nature of image contrast in both is described, both coherent and incoherent imaging modes, and their resolution limits, highlighting recent advances in the correction of lens aberrations. Finally, recent developments including so-called four-dimensional imaging using pixelated detectors and the new imaging modes they make possible are introduced.

Key points

- Image formation in Transmission Electron Microscopy (TEM) and Scanning Transmission Electron Microscopy (STEM); reciprocity.
- Resolution and contrast, contrast transfer function.
- Coherent and incoherent imaging.
- Phase contrast and *Z*-contrast.
- Future directions.

Introduction

The distinguishing feature of transmission electron microscopy (TEM) is its ability to form images of atomic arrangements at localized regions within materials. It provides a view of the microstructure, that is, the variations in structure from one region to another, and the interfaces between them. TEM plays a critical role whenever macroscopic properties are controlled or influenced by defects or interfaces, for example, in the development of advanced structural materials with their complex microstructure of second phases, or electronic materials, which rely on the exquisite control of interfaces and multilayers. X-ray or neutron diffraction can determine the average structure of complex materials very precisely, but in a material comprised of an intimate array of different phases the average structure may be irrelevant. As condensed matter physics moves toward the study of ever more complex materials, and at the same time interest in nanoscale physics, two-dimensional materials and devices is increasing, TEM or its scanning counterpart STEM, is finding a rapidly increasing role in basic condensed matter physics research.

The unique role of the TEM arises because electrons are charged particles, and therefore, unlike X-rays or neutrons, are able to be accelerated and focused into atomic dimensions by electromagnetic fields. The scattered beams can be collected by a lens and refocused to form a true real space image in the manner of an optical microscope, where each point in the image corresponds to a specific point in the object. Electrons also interact much more strongly with matter and electron diffraction can be performed on materials of nanometer lateral dimensions (Hawkes and Spence, 2019; van Tendeloo et al., 2012). For accelerating voltages of 100–1000 kV, the electron wavelength ranges from 0.004–0.001 nm, orders of magnitude lower than atomic spacings in materials. It would therefore appear relatively trivial to form atomic resolution images of materials. However, it is only very recently that atomic resolution imaging could be said to be at all trivial. The major limitation was realized early in the history of the microscope to be the high inherent aberrations of a round magnetic lens. Until recently, spherical aberration has been the dominant aberration, which leads to a ray deviation of $C_s\alpha^3$, where α is the semiangle of the objective lens. With electron lenses, C_s is of the same order as the focal length. This has meant that only very small apertures could be used, and since microscope resolution is given by $0.61\ \lambda/\sin\alpha$, where λ is wavelength, the best resolution would be limited by diffraction to $\sim 50\lambda$.

https://doi.org/10.1016/B978-0-323-90800-9.00194-3

It took roughly 50 years from the development of the first transmission electron microscopes in the 1930s to achieve sufficient electrical and mechanical stability to allow imaging of crystal lattices at 0.2–0.3 nm resolution in the 1980s. Over the next 20 years, resolution improved incrementally to 0.1–0.2 nm. In the last 20 years or so it has finally proved successful to compensate for the dominant lens aberrations using a series of non-round magnetic lenses, thanks to the development of solid-state devices, specifically the computer, and charge-coupled-device (CCD) detectors. The gain in resolution over the last few years is comparable to that seen in the previous few decades. Sub-Ångstrom resolution has indeed become almost trivial, and materials are revealing their atomic-scale secrets like never before. The pace of materials physics has hugely increased as a result.

Aberration-correction brings more than just resolution; better resolution brings increased sensitivity, and the imaging of single atoms within materials and on their surfaces, together with their spectroscopic identification by electron energy loss spectroscopy (EELS) is also practically routine. Furthermore, entirely new modes of microscopy have appeared. Most promising is the development of so-called 4D STEM, where the probe still rasters a 2D region of specimen, but the detectors are replaced by a pixelated detector to record the entire 2D diffraction pattern at each probe position, a 4D data set. This allows the detector configurations to be determined after the scan, which can then be analyzed in multiple ways to produce complementary image modes and even map electric and magnetic fields at the atomic scale.

Electron optics of the microscope: STEM vs. TEM, reciprocity

Fig. 1(a) shows a schematic ray diagram for conventional TEM (Williams and Carter, 2009; Carter and Williams, 2016). The specimen is illuminated through a condenser aperture, and transmitted electrons are gathered by the objective lens and recombined into an image. Historically, the size of the condenser aperture was always been chosen to be as small as practically possible to provide a close approximation to parallel illumination. Such is required for diffraction contrast imaging, when only one diffracted beam is passed through the objective aperture. With parallel illumination crystal defects such as dislocations, precipitates and interfaces are observable, and many details of their atomic structure can be obtained indirectly by detailed analysis of image contrast (for example, lattice shifts across an interface, the intrinsic or extrinsic nature of stacking faults, coherency strains of precipitates, Burgers vectors of dislocations). Nearly parallel illumination provides a long coherence length in the specimen, approximately λ/β, where β is the illumination semiangle. For small β many lattice spacings are illuminated in phase, an example of coherent imaging. If the objective aperture α is opened up to include several diffracted beams, the conventional TEM lattice-imaging mode is obtained, often known as high-resolution electron microscopy (HREM), another example of coherent imaging.

In scanning transmission electron microscopy (STEM) the electron beam is focused to a small probe and scanned across the specimen (Pennycook and Nellist, 2011). Fig. 1(b) shows the ray diagram; detectors are used to pick up a signal which is used to form an image pixel by pixel as the probe is scanned. The STEM allows complete flexibility in choice of detector, and multiple detectors are normally used giving complementary information. For example, an annular dark field (ADF) detector collects electrons scattered out of the beam and gives an image of mass thickness, that is, a signal that increases with increasing scattering cross section and specimen thickness; a hole appears dark. A bright field (BF) signal can also be detected using an on-axis detector (holes appear

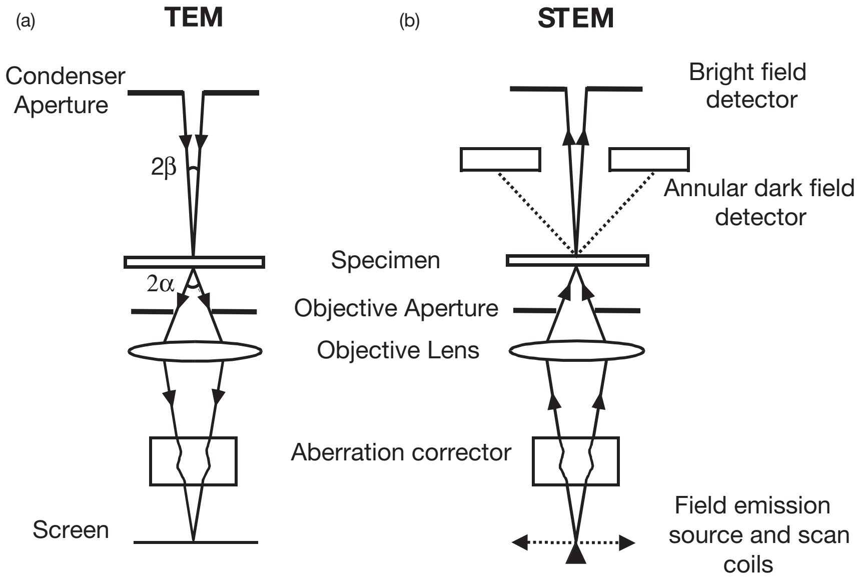

Fig. 1 Ray diagrams for (a) the TEM and (b) the STEM, showing the reciprocal nature of the optical pathways. The TEM image is obtained in parallel, the STEM image pixel by pixel by scanning the probe. The STEM also provides simultaneous annular dark field (ADF) imaging. Actual microscopes have several additional lenses and the beam limiting aperture positions may differ.

bright). If the bright field detector subtends a small angle β at the specimen, then it is clear from comparing the two ray diagrams in Fig. 1 that the only difference in the optics of the two forms of microscope is the direction of the electron beam. The major source of image contrast is elastic scattering, for which only the scattering angle is important—not the direction of propagation (an example of time-reversal symmetry in physics). This is one example of the principle of reciprocity, where interchange of source and detector leads to the same image, and explains why images formed in bright-field STEM may show identical contrast behavior to those in TEM. If the bright field detector aperture is small, these images are coherent images exactly equivalent to bright field TEM images.

Reciprocity applies even if aberration correctors are added to both columns. In TEM the corrector is placed after the specimen to correct the objective lens aberrations, while in STEM it is placed before the specimen, the purpose being again to correct the aberrations of the objective lens (now used as a probe-forming lens). Fig. 1 makes clear that for the same set of aberration parameters and equivalent angles before and after the specimen, the same images are to be expected, and this is seen experimentally. However, reciprocity does not mean the images will have the same signal to noise ratio. Before aberration correction the angle β necessary to ensure good coherent imaging conditions was so small that the STEM image used only a small fraction of the electrons passing through the specimen. This resulted in noisy images and unnecessary specimen irradiation. With aberration correction, not only can the objective aperture α be made much larger, but β can also be increased and STEM bright-field imaging becomes a useful practical possibility.

The primary motivation for the STEM has been its ability to detect signals other than the bright field image, in particular, the ADF image. Based on the concept of a coherence width in the specimen, if the angle β is sufficiently large, the coherence width in the specimen is below the typical atomic spacings in materials. Although the third dimension along the beam direction must also be considered, the ADF image does represent a good approximation to incoherent imaging. An incoherent image gives a simple relationship between the object and image, as in a camera, and is easier to interpret than a coherent image which can show contrast reversals (atoms may be light or dark). The very different characteristics of coherent and incoherent imaging will be discussed in the next section.

One of the advantages of STEM is that it allows for microanalysis, with the same probe as used for imaging, using one or more additional signals generated as the beam passes through the specimen. Perhaps the most important of these is inelastic scattering, which allows elemental identification from inner shell excitations. Furthermore, the fine structure at the absorption edges carries information about the electronic structure of the excited atom. EELS is equivalent to X-ray absorption spectroscopy, but is available with the spatial resolution of the probe (Egerton, 2011). In the so-called spectrum-imaging mode, one complete spectrum is recorded for each pixel in the image. Similar information can be obtained on a TEM using an imaging filter, which produces 2D images corresponding to particular energy losses. A set of such images at different energy losses is somewhat equivalent to a spectrum image on the STEM. However, reciprocity does not apply to inelastic scattering and there are important differences between TEM and STEM: in the TEM the inelastically scattered electrons must be focused by the image-forming lens which leads to problems with chromatic aberration, whereas in the STEM there are no imaging lenses after the specimen. Although chromatic aberration correctors have been developed this greatly increases the cost and complexity of a microscope.

Energy Dispersive X-ray Spectroscopy, known as EDX or EDS, collects x-rays emitted as the atom relaxes into its ground state following inner shell excitation, and the x-ray energy is again characteristic of the element. The peak resolution is much lower than for EELS, but the peaks lie on a lower background. The major problem is the low efficiency of collection. X-rays are emitted over 4π steradians and only a small fraction can be collected by the detector, whereas the corresponding core loss electrons are forward peaked and a high fraction can be collected for EELS. Recently, much larger collection angles have become feasible, and even multiple detectors have been used, so that atomic resolution EDX mapping is now feasible. Other possible imaging signals include the secondary electrons for imaging surfaces and visible photons (cathodoluminescence) for mapping optical properties.

As mentioned above, microdiffraction, or more recently nanodiffraction patterns can be recorded with an imaging detector in STEM, a so-called pixelated detector. This is very useful for identifying minority phases within bulk materials or new phases not possible to synthesize in large volumes, and also for quantitative measurements of charge modulation. For long wavelength modulations electron diffraction is much more sensitive than X-ray diffraction because of the cancelation of the scattering due to the electrons and nucleus; electron scattering sees the imbalance of charge, whereas X-ray scattering sees the total electron density and is less sensitive to small changes.

For much of the history of electron microscopy it was not possible to have high-resolution STEM and TEM imaging in a single machine. In recent years however great advances have been made in instrument design, and it is now perfectly feasible to purchase microscopes that will give good performance in both modes of operation, often simply at the push of a button. It is also possible today to purchase an instrument with two aberration-correctors, one before the specimen to correct the probe and one after the specimen to provide parallel-detection phase contrast imaging, although some compromises need to be made. Generally, two machines are preferable to one combined instrument, but at higher cost.

Principles of image formation

Coherent imaging

With parallel illumination, a crystal aligned near a zone axis will generate a set of diffracted beams leaving the sample at specific angles, as depicted in Fig. 2(a). The objective lens brings these beams to a focus in its back focal plane to form the diffraction pattern. In diffraction contrast imaging, one diffracted beam is passed through a small objective aperture and the resulting image represents a

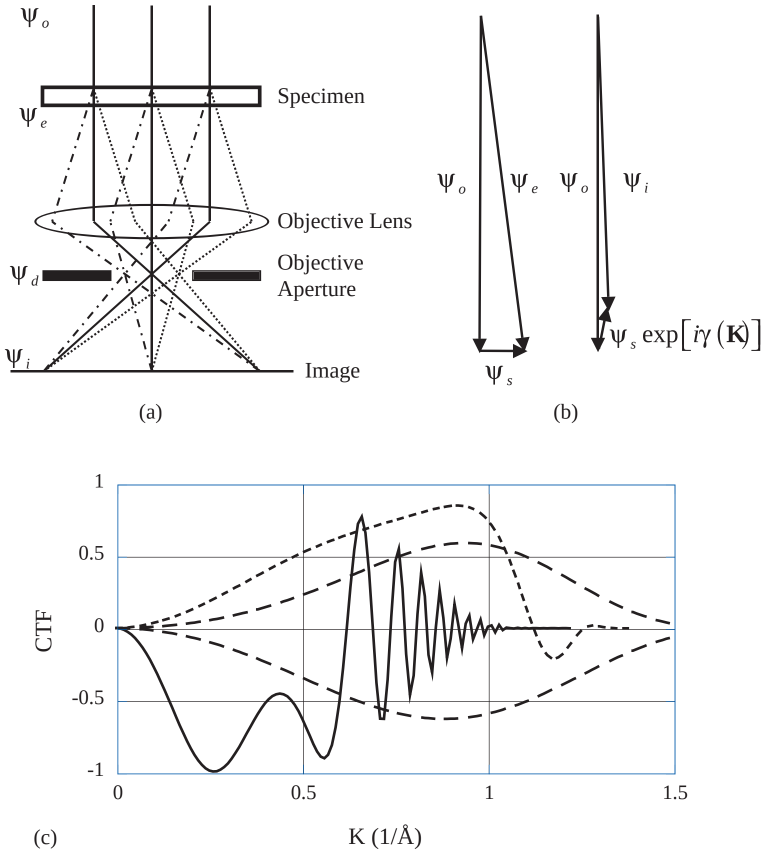

Fig. 2 (a) Ray diagram for coherent phase contrast imaging of a crystal. Diffracted beams emerge from the specimen at specific angles and are brought to a focus in the back focal plane of the objective lens. They are recombined in the image plane. Imaging is therefore two consecutive Fourier transforms. (b) Vector diagram for a weak phase object showing the incident beam, a small scattered beam with $\pi/2$ phase change and the resultant transmitted beam. Lens aberrations are used to rotate the phase of the scattered beam an additional $\pi/2$ to create amplitude contrast from the phase changes. (c) Contrast transfer functions for an uncorrected 300 kV microscope, solid line, ($C_S = 0.6$ mm, $\Delta f = -45$ nm, energy spread 2 nm typical for a Schottky field emission source), a corrected 300 kV microscope, dotted line, ($C_S = -37$ μm. $C_5 = 100$ mm, $\Delta f = 5$ nm, energy spread 1 nm typical for a cold field emission source), and a 200 kV microscope with full correction of all 5th order aberrations, dashed line, ($C_S = 23$ μm. $C_5 = -2$ mm, $C_7 = 100$ mm, energy spread 1 nm). The upper trace is for $\Delta f = 1$ nm giving white atom contrast in a thin specimen, the lower one is for $\Delta f = -2$ nm giving black atoms.

map showing the distribution of diffracted intensity from the specimen. The crystal lattice is unresolved, but the image is useful for studying defects and interfaces. To resolve the crystal lattice itself the objective aperture is opened up to include more than one diffracted beam. Now each point in the image receives contributions from multiple diffracted beams that interfere to generate image contrast, which depends on their relative phases. The principles of coherent phase contrast lattice imaging are best illustrated for the idealized case of a thin sample where multiple scattering can be ignored. The incident electron wave function takes the form of a plane wave Ψ_o which interacts with the electrostatic potential of the specimen $\phi(\boldsymbol{r})$ (ignoring magnetic fields). Here, lower case letters refer to three-dimensional variables while upper case variables refer to the two transverse dimensions normal to the direction of beam propagation, z, for example, the position vector $\boldsymbol{r} = (\boldsymbol{R}, z)$, and the electron wave vector $\boldsymbol{k} = (\boldsymbol{K}, k)$. Assuming an incident beam of unit amplitude, a thin specimen acts as a weak phase grating, refracting the incident beam but not changing its amplitude: the exit face wave function is given by

$$\Psi_e(\boldsymbol{R}) = \exp\{-i\sigma\phi(\boldsymbol{R})\} \approx 1 - i\sigma\phi(\boldsymbol{R})$$

where $\sigma = 2\pi m e\lambda/h^2$ is the interaction constant and $\phi(\boldsymbol{R}) = \int \phi(\boldsymbol{r})dz$ is the projected potential (Reimer, 1997; De Graef, 2009; Kirkland, 2010; Spence, 2013). Phase changes in the exit wave therefore map the projected potential of the specimen. These phase changes can be represented vectorially by generation of a scattered wave $\psi_s(\boldsymbol{R}) = -i\sigma\phi(\boldsymbol{R})$ which is oriented at $\pi/2$ to the incident wave, as shown in Fig. 2(b). Entering the objective lens, the diffracted amplitude ψ_d is just the Fourier transform of the exit face wave function

$$\psi_d(\boldsymbol{K}) = \delta(0) - i\sigma\phi(\boldsymbol{K})$$

where the delta function at $\boldsymbol{K} = 0$ is the unscattered beam. For a crystal aligned to a zone axis the diffraction pattern consists of a set of sharp diffracted beams at specific directions ($\boldsymbol{K}$ vectors). With a pure phase object, none of the individual diffracted beam intensities show an image. To form an image of ψ_s, the diffracted beams must be passed through the objective lens and interfered with the unscattered beam. As shown in Fig. 2(b), the phase of the scattered beams should ideally be rotated an additional $\pi/2$ to convert the phase changes to perfect amplitude contrast. In this ideal case the image amplitude would become $\psi_i(\boldsymbol{R}) = 1 \pm \sigma\phi(\boldsymbol{R})$ and the intensity $I(\boldsymbol{R}) = \psi_i(\boldsymbol{R})^2 = 1 \pm 2\sigma\phi(\boldsymbol{R})$. In practice, the most convenient source of additional phase changes are the lens aberrations themselves, in particular, defocus. The phase change introduced by the objective lens is referred to as the transfer function phase factor $\exp[i\gamma(\boldsymbol{K})]$ where

$$\gamma(K) = \pi\left(\Delta f\lambda K^2 + \frac{1}{2}C_3\lambda^3K^4 + \frac{1}{3}C_5\lambda^5K^6\right)$$

if only the rotationally symmetric aberrations are included so that $K = |\boldsymbol{K}|$. Here Δf is defocus, C_3 is the third order spherical aberration coefficient, usually referred to simply as C_s before aberration-correction became viable, with typical values of the order of 1 mm. In a microscope corrected for third-order aberrations, the fifth order spherical aberration coefficient C_5 takes over as the limiting aberration. Today, aberrations up to and including fifth order are often corrected. The diffraction amplitude transmitted by the lens becomes

$$\psi_d(\boldsymbol{K}) = \delta(0) - i\sigma\phi(\boldsymbol{K})\exp[i\gamma(\boldsymbol{K})],$$

and for small phase changes the intensity becomes

$$I(\boldsymbol{R}) = 1 - 2\sigma\phi(\boldsymbol{R}) \otimes f(\sin\gamma(\boldsymbol{K})).$$

The phase changes $\phi(\boldsymbol{K})$ contribute to the image with a contrast given by $\sin\gamma(\boldsymbol{K})$, which is therefore referred to as the phase contrast transfer function, and the image is given by a convolution of the projected potential with the Fourier transform of $\sin\gamma(\boldsymbol{K})$.

The different aberrations depend on spatial frequencies to different powers and can therefore only be approximately balanced over a finite range. Fig. 2(c) shows examples for some uncorrected and aberration-corrected microscopes. Note phase contrast imaging provides no contrast at zero spatial frequency because there is negligible additional phase change from lens aberrations. An uncorrected microscope shows rapid contrast oscillations at high spatial frequencies where the C_sK^4term increases very rapidly; such oscillations are largely avoided in the corrected microscopes. The substantial drop in contrast at high spatial frequencies is due primarily to the finite energy spread of the beam. In this regard the cold field emission source is preferable to the Schottky thermal source. One characteristic of phase contrast is immediately apparent. The defocus phase factor is used to balance the dominant term in spherical aberration, but changes sign either side of Gaussian focus. In many cases it is possible to reverse the image contrast on changing the focus (see Fig. 2(c)) and atoms may look black or white in a phase contrast image. This can also happen if the specimen becomes thicker and additional relative phase changes occur between the diffracted beams due to dynamical diffraction (multiple scattering). The exit face wave function no longer relates simply to projected potential and becomes increasingly non-local. The general expression for the image intensity is

$$I(\boldsymbol{R}) = |\psi_e(\boldsymbol{R}) \otimes P(\boldsymbol{R})|^2,$$

the square of a convolution of the exit face wave function with the point response function of the objective lens. The point response function is just the Fourier transform of the transfer function phase factor,

$$P(\boldsymbol{R}) = \int A(\boldsymbol{K})e^{2\pi i\boldsymbol{K}\cdot\boldsymbol{R}}e^{i\gamma(\boldsymbol{K})}d\boldsymbol{K}$$

where $A(\boldsymbol{K}) = 1$ over the range of the objective aperture. Because the image is given by a square of the convolution, sum and difference spatial frequencies can appear, and for these reasons image simulations are normally required to relate a phase contrast image to an object.

Incoherent imaging

Incoherent imaging provides a simple relationship between the object and image

$$I(\boldsymbol{R}) = O(\boldsymbol{R}) \otimes |P(\boldsymbol{R})|^2,$$

where the object $O(\boldsymbol{R})$ is simply blurred by the resolution function of the imaging device. Strictly this applies only when each point on the object emits independently of its neighbors so that there are no permanent phase relationships between them and no persistent interference can occur. The coherence length of the sun on earth is about 0.02 mm, so that observation on a larger length scale is effectively incoherent. This is the kind of imaging familiar from the camera, for example, where changing focus merely blurs the image but does not invert the contrast. It also applies to optical microscopy if a large aperture condenser lens is used to give effectively incoherent illumination, as first analyzed by Rayleigh (1896).

In the STEM, $|P(\boldsymbol{R})|^2$ is the intensity profile of the probe (see Fig. 1(b)). Not every image takes the form of a simple convolution, as seen already for the case of the small axial detector. The requirement for an incoherent image is that all of the scattering (or other generated signal) be collected by the detector. In the case of inelastic scattering or X-ray emission it is relatively simple to collect all of the signal, or at least a representative fraction of it. In the case of elastically scattered electrons it is not so obvious, because collecting all of the transmitted electrons will give no image contrast; the specimen does not absorb any electrons, it only scatters them, and detection of those scattered electrons is therefore necessary to generate an image.

One way to form an incoherent image is to detect all of the scattering. Then the detected signal is *insensitive* to any interference that may be occurring among different scattered beams. Interference rearranges intensity but the total scattering is constant, by conservation of energy. The annular detector provides a close approximation to incoherent imaging because it can be arranged to average over a large number of diffracted beams. The inner detector angle should also be large to avoid being dominated by a few low order beams around the inner hole. In practice, the image still shows strong incoherent characteristics even if the inner angle is just larger than the objective aperture angle, which is a mode that gives efficient dark field imaging of single atoms and was the original motivation for the introduction of the detector by Crewe et al. (1970).

High angle scattering comes from the sharpest part of the atomic potential, the nucleus, and its intensity is approximately proportional to the square of atomic number (Z). An annular detector with a large hole therefore gives an image showing strong *Z*-contrast, also referred to as a high-angle annular dark field (HAADF) image. A sufficiently small probe provides an atomic-resolution Z-contrast image in which atomic columns are seen bright (consistent with it being a dark field image) and their relative contrast is dependent on their projected mean square atomic number. The atomic-resolution contrast again comes from the interference of diffracted beams, except that no phase plates are necessary to create the intensity. The total intensity on the detector rises and falls as the probe scans the lattice because of interference between the diffracted beams reaching the detector, as shown in Fig. 3(a). Each beam takes the form of a disc the size of the objective aperture (the incident beam in STEM). Interference occurs wherever the discs overlap and there are two or more different pathways that can interfere. The conditions for optimum defocus are that the entire area of overlap shows the strongest possible interference as the probe scans. This is quite different from the conditions for optimum phase contrast with a (small) bright field detector, and for the example depicted, the bright field detector covers no overlaps and will show no image.

Smaller spacings will give diffraction discs further apart with smaller regions of overlap and lower maximum contrast. The incoherent transfer function is therefore a slowly decreasing function of spatial frequency, and is obtained from the Fourier transform of the image intensity,

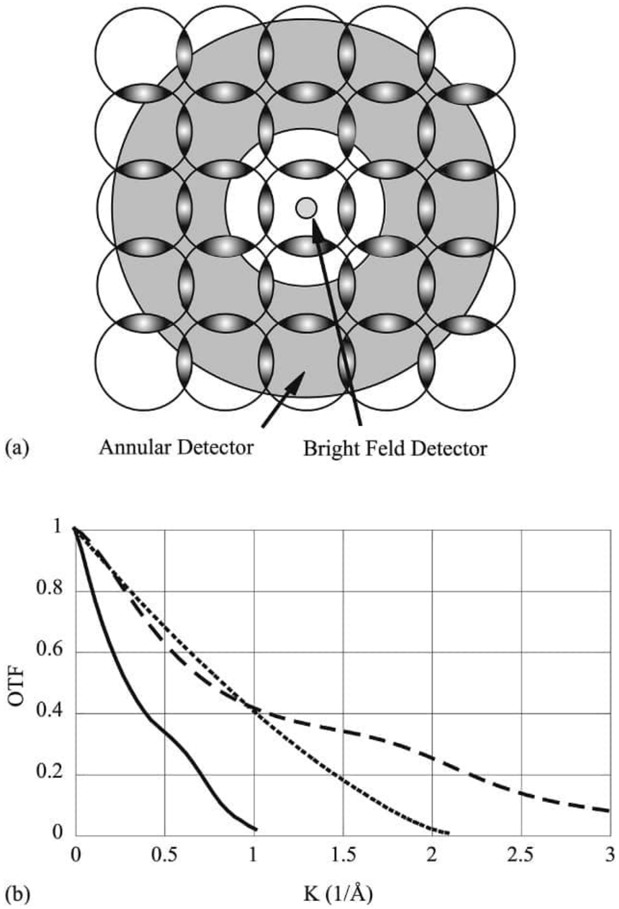

Fig. 3 (a) Schematic showing overlapping diffraction discs on the STEM annular detector. The regions of overlap show interference as the probe scans leading to an atomic resolution image. Note for the spacings depicted the bright field detector covers no overlaps and shows no image. (b) Incoherent object transfer functions for an uncorrected 300 kV STEM, solid line, (conditions correspond to those in Fig. 2 except $\Delta f = -34$ nm), a corrected 300 kV STEM, dotted line, (as Fig. 2 except $\Delta f = 2$ nm), a 200 kV STEM with correction up to 5th order, dashed line, (as Fig. 2 except $\Delta f = 0$ nm).

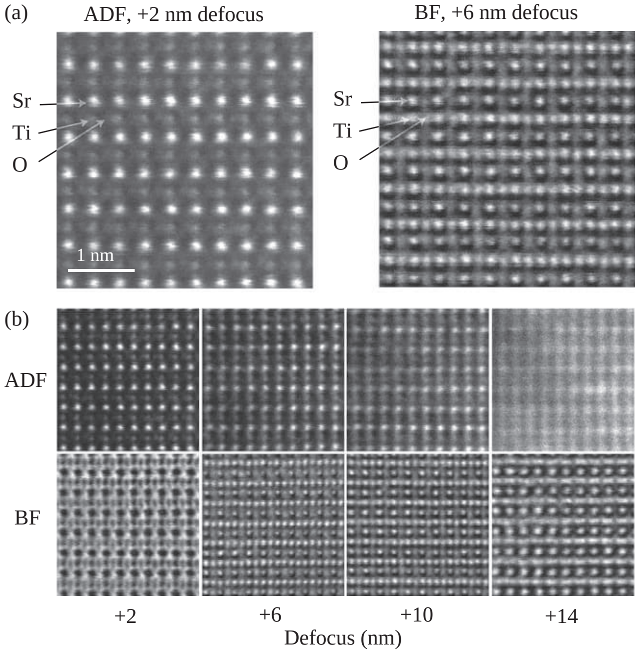

Fig. 4 Comparison of incoherent and coherent imaging of $SrTiO_3$ in the $\langle 110 \rangle$ projection in a 300 kV aberration-corrected STEM (a VG Microscopes HB603U with Nion aberration corrector, conditions as in Figs. 2 and 3). A defocus series was taken using ADF and coherent BF detectors simultaneously. (a) the ADF image shows good *Z*-contrast, with O barely visible, while the phase contrast BF image shows the O columns with high contrast. (b) a through focal series with 4 nm defocus steps from the position of optimum ADF defocus showing how the incoherent ADF image contrast slowly blurs while the phase contrast image shows many different forms of contrast. Images are raw data and show some instabilities. Courtesy of M. F. Chisholm, A. R. Lupini and A. Borisevich.

$$I(\boldsymbol{K}) = O(\boldsymbol{K}) \cdot |P(\boldsymbol{K})|^2.$$

The transfer function is just the Fourier transform of the probe intensity, and is referred to as a modulation transfer function or object transfer function $|P(\boldsymbol{K})|^2$. Generally this remains a positive function even as defocus is varied so inverted contrast is not observed. Fig. 3(b) shows incoherent transfer functions corresponding to the coherent contrast transfer functions of Fig. 2(c).

Fig. 4 compares aberration-corrected coherent and incoherent images of $SrTiO_3$ in the $\langle 110 \rangle$ projection, obtained simultaneously in an aberration-corrected STEM. There is one optimum focus for the *Z*-contrast image, where the Sr column is brightest and the TiO column less bright. A small peak is present at the oxygen column position but is difficult to detect above the noise because of its low *Z*. In the phase contrast image, a good image of the oxygen columns is obtained at a defocus of +6 nm, but other images are seen at other defocus values.

The TEM as a nano-laboratory

The TEM is a very versatile instrument and is more like a nano-laboratory than an optical instrument, with a large array of imaging and spectroscopic methods available to probe materials at the atomic scale. Imaging modes are available for electric and magnetic fields (4D STEM, Lorentz imaging, Foucault imaging, holography, Ophus, 2019), and movies have been taken of flux line motion in superconductors. Many applications desire measurements under conditions other than the high vacuum, room temperature environment that is standard for TEM; phase transformations can be observed with a heating holder; studies of catalysis benefit from imaging in an active gas environment; many condensed matter physics investigations require low temperatures; nanowires can be observed while being stretched with simultaneous measurement of conductance. *In-situ* and *operando* microscopy also benefit from aberration correction because it is possible to maintain resolution with a larger gap between the objective lens pole pieces, allowing more room for liquid/gas cells (Ross, 2016) and other devices such as a cathodoluminescence detection system.

Future directions

The achievement of aberration-correction in TEM is likely to be seen as one of the most significant events in the history of the microscope. Aberration-correction substantially improves vision at the atomic scale, through better resolution and better contrast, for the first time giving useful sensitivity to single atoms within materials and on their surfaces. Equal improvements apply to

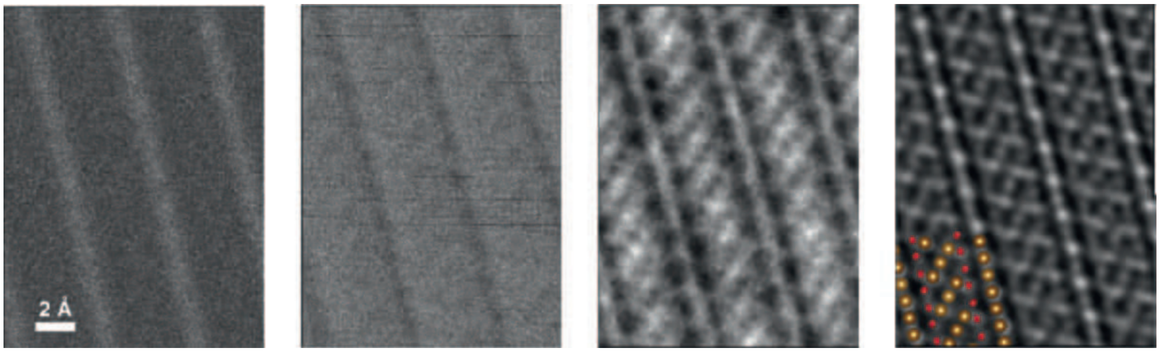

Fig. 5 Comparison of various modes available with 4D STEM, using a low electron dose. From left to right, ADF, BF, iCOM and ptychography. Courtesy C. Gao, C. Hofer and T. J. Pennycook.

spectroscopy. These developments have brought a new level of insight into the physics of interfaces, defects and nanostructures, issues relevant to the majority of materials and devices of a technological world.

A TEM image presents a two-dimensional projection of a 3D specimen. Stereo techniques have been used to obtain information on the third dimension, and recently, full 3D tomography has been demonstrated at atomic resolution from a series of images taken over a range of sample tilts. 4D STEM is allowing multiple image modes to be obtained from a single data set including HAADF, annular bright and dark field (ABF and ADF), ptychography, differential phase contrast (DPC), integrated DPC (iDPC) and integrated center of mass (iCoM) imaging (Lazić et al., 2016). Such modes not only allow electric fields and charge densities to be quantitatively extracted, they are significantly more efficient than conventional ADF or BF, allowing images to be formed at lower doses. Fig. 5 shows an image of $SrTiO_3$ taken at a low dose where the ADF and BF images are showing reduced resolution due to the high noise, while the ptychography and iCOM images still retain excellent quality.

Conclusion

The basic imaging modes of the fixed beam TEM and the STEM have been described in relation to each other, the former providing a coherent phase contrast image and the latter both a coherent and also an incoherent image, depending on the geometry of the detector used. Simultaneous coherent and incoherent images are available in STEM, and with a pixelated detector the geometry can be selected after recording the 4D data set, giving huge flexibility. Most 4D pixelated detectors are presently rather slow, but this is a rapidly evolving area and great progress can be anticipated. The STEM also allows simultaneous imaging and analysis through EELS and EDX. *In-situ* or *operando* imaging is usually more efficient in the fixed beam TEM, but the additional imaging and analysis modes available in STEM can be advantageous. The major advances in atomic scale imaging and analysis due to aberration correction are having a significant impact on the fundamental, atomic-scale understanding of materials properties, and synergistic development of new materials through a combination of synthesis/processing, transmission electron microscopy and theoretical calculations is an increasingly productive pathway.

References

Carter CB and Williams DB (2016) *Transmission Electron Microscopy: Diffraction, Imaging, and Spectrometry*. Switzerland: Springer.
Crewe AV, Wall J, and Langmore J (1970) Visibility of single atoms. *Science* 168: 1338–1340.
De Graef M (2009) *Introduction to Conventional Transmission Electron Microscopy*. Cambridge: Cambridge University Press.
Egerton RF (2011) *Electron Energy-Loss Spectroscopy in the Electron Microscope*, 3rd edn. Boston: Springer.
Hawkes PW and Spence JCH (2019) *Handbook of Microscopy*. Switzerland: Springer Nature.
Kirkland EJ (2010) *Advanced Computing in Electron Microscopy*, 2nd edn. Boston: Springer.
Lazić I, Bosch EGT, and Lazar S (2016) Phase contrast STEM for thin samples: Integrated differential phase contrast. *Ultramicroscopy* 160: 265–280.
Ophus C (2019) Four-dimensional scanning transmission electron microscopy (4D-STEM): From scanning nanodiffraction to ptychography and beyond. *Microscopy and Analysis* 25: 563–582.
Pennycook SJ and Nellist PD (eds.) (2011) *Scanning Transmission Electron Microscopy*. New York: Springer.
Rayleigh L (1896) On the theory of optical images with special reference to the microscope. *Philosophical Magazine* 42: 167–195.
Reimer L (1997) *Transmission Electron Microscopy*, 4th edn. Berlin: Springer-Verlag.
Ross F (ed.) (2016) *Liquid Cell Electron Microscopy (Advances in Microscopy and Microanalysis)*. Cambridge: Cambridge University Press.
Spence JCH (2013) *High Resolution Electron Microscopy*, 4th edn. Oxford: Oxford University Press.
van Tendeloo G, van Dyke D, and Pennycook SJ (eds.) (2012) *Handbook of Nanoscopy*. Weinheim: Wiley-VCH.
Williams DB and Carter CB (2009) *Transmission Electron Microscopy*, 2nd edn. Boston: Springer.

Electron ptychography

Wei Mao[a], **Liqi Zhou**[a], **Si Gao**[b], **and Peng Wang**[c], [a]National Laboratory of Solid State Microstructures, Jiangsu Key Laboratory of Artificial Functional Materials, College of Engineering and Applied Sciences and Collaborative Innovation Center of Advanced Microstructures, Nanjing University, Nanjing, China; [b]College of Material Science and Engineering, Nanjing Tech University, Nanjing, China; [c]Department of Physics, University of Warwick, Coventry, United Kingdom

© 2024 Elsevier Ltd. All rights reserved.

Introduction 71
Ptychography algorithms 73
Direct methods 74
Single side band (SSB) 74
Wigner distribution deconvolution (WDD) 74
Iterative algorithms 76
Ptychographic iterative engine 78
Difference map (DM) 79
Optical configuration 80
Focused and defocused probe ptychography 81
Fourier ptychography 81
Recent applications 83
Recent advances in technical development 85
Multiple states 86
Probe position errors 87
Multiple scattering 88
Low-frequency information transfer 88
Conclusion: Multidimensional ptychography 88
References 91

Abstract

Over the past decade, the developments of electron ptychography have revolutionized electron microscopy in the characterization of the atomic structure of matter. Ptychography is a computational imaging technique that has no limits imposed by lens aberrations, thereby offering a spatial resolution well beyond the traditional numerical-aperture-limited resolution with the added benefit of quantitatively accessing and solving the phase of the electron waves. In this review, we summarize the most commonly used ptychographic algorithms and optical configurations, and highlight the recent applications and latest advanced developments. We further discuss the future of multidimensional electron ptychography in combination with other microscopic capabilities, heralding a new era in the characterization of engineered and biological materials.

Key points

- An introduction of electron ptychography and its history (Section "Introduction");
- An overview of associated algorithms (Section "Ptychography algorithms") and optical configurations (Section "Optical configuration");
- The latest applications (Section "Recent applications") and technological advancements (Section "Recent advances in technical development") based on newly developed ultra-fast detectors;
- The challenges and future perspectives (Section "Conclusion: Multidimensional ptychography").

Introduction

To understand how detailed structures at the scale of one billionth of a meter can control the macroscopic properties of condensed matter such as semiconductors, complex oxides (Muller et al., 2008), metals, and biological samples, scientists use transmission electron microscopes (TEMs), which are best known for their ability to form images at the highest resolution of any instrument. Currently, the state-of-the-art aberration-corrected TEM and scanning TEM (STEM) (Muller et al., 2008; Jia et al., 2008; Batson et al., 2002) can produce images with a resolution ranging from a few angstroms (10^{-10} m) to sub-angstrom.

https://doi.org/10.1016/B978-0-323-90800-9.00245-6

For short-wavelength microscopes, especially electron microscopes, high-quality lenses are difficult to manufacture. Historically, diffraction, and spherical and chromatic aberration limit the resolution of the TEM to approximately $d = 100\lambda$. The conventional magnetic lenses are approximately 200 times poorer than optical lenses in a light microscope—roughly equivalent to viewing an object through the bottom of a beer glass (Hetherington, 2004). The breakthrough in resolution came with a change in hardware, that is, the use of nonround lenses, the principle of which was outlined by Scherzer in the mid-1930s (Scherzer, 1936). This advance was then followed by the presentation of a feasible design by Rose in 1990 (Rose, 1990) and the rapid development of electron-optical hardware components and experimental demonstrations by Haider, Urban, and Krivanek in the late 1990s (Haider et al., 1995; Zach and Haider, 1995; Krivanek et al., 1997, 1999). Now, the experimental resolution limit relative to wavelength has been reduced to approximately $d = 20\lambda$ (i.e., the resolution is 50 pm with a wavelength of 2 pm at an accelerating voltage of 300 kV).

Despite this tremendous progress in resolution, for imaging beam-sensitive weak-phase biological specimens and electric and magnetic fields, which are pure phase objects, only poor phase contrast can be achieved in conventional electron micrography. As the electron wave passes through a sample, the electron scatters, producing an exit wavefront that is rich in information. Using the wave nature of electrons, a wide range of solid properties, from electric and magnetic field strengths to specimen thickness, strain maps and mean inner potentials, can be extrapolated from the electron's phase and mapped at the nanoscale, or even at the atomic level. Therefore, accurate sensitive imaging of the electron phase signal at high resolution is a long-term goal that engineers continue to pursue in the field of electron microscopy.

Electron holography, the principle of which is based on the wave nature of electrons, was originally proposed by Gabor in 1948 to overcome the deleterious effect of lens aberration (Gabor, 1948, 1949, 1951). Electron holography forms interference patterns (hologram) by the superposition of an electron wave passing through a sample with a reference electron wave; then, from the recorded hologram, an image wave (including amplitude and phase information) can be reconstructed. Because this phase recovery method is completely based on the coherence and interference of the wave, it requires high coherence of the electron beam and a stable reference beam to perform the holographic measurements. A review of the technical details can be found in Lichte and Lehmann (2007).

Ptychography is an alternative phase retrieval technique based on scanning coherent diffractive imaging, as originally proposed by Hoppe (1969), to obtain a direct (noniterative) solution of a crystallographic phase problem. Later, Rodenburg proposed combining ptychography with iterative algorithms to solve this problem, especially for extended noncrystalline samples (Rodenburg et al., 2007). Ptychography records a series of diffraction patterns (constituting a 4D-STEM dataset) as a function of the illumination position, and recovers the sample exit plane wave function using computational algorithms, as shown in Fig. 1C–F. Unlike holography, ptychography does not require a reference beam in the optical configuration, as the diffraction pattern of the field emerging from the object itself acts as an interferometer. Ptychography is considered a lens-less imaging method, which means that it can obtain images without the usage of good quality lenses (such as aberration correctors) and thus, the resolution when using this method is ultimately determined by the diffraction limit.

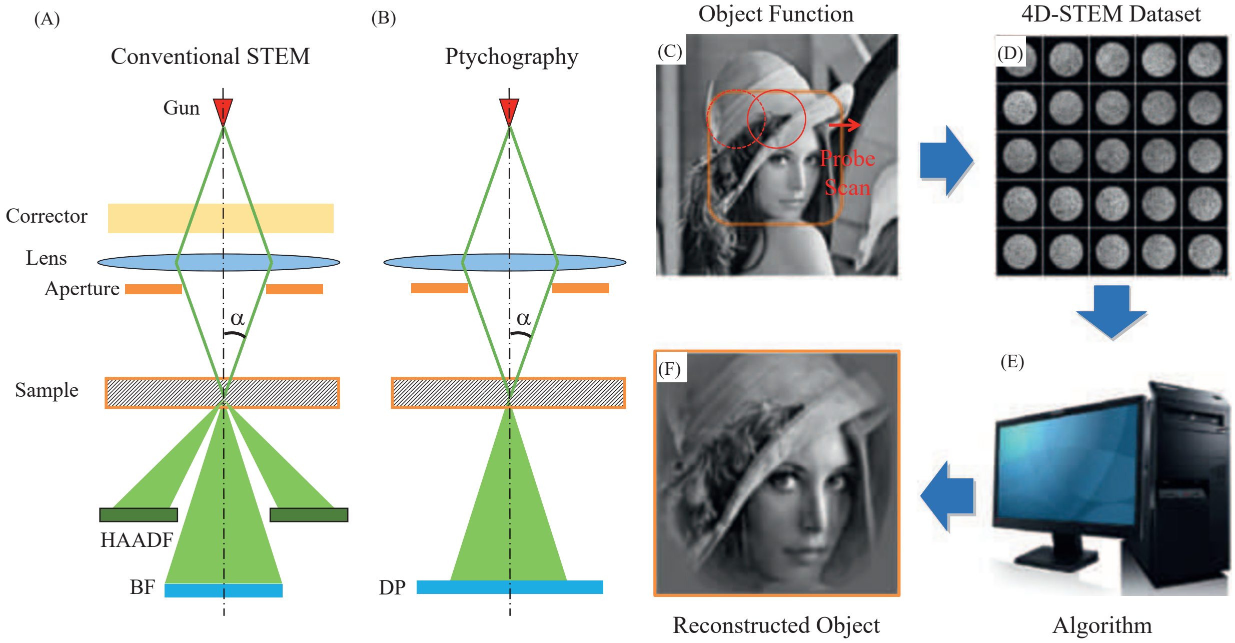

Fig. 1 Experimental setups of (A) conventional STEM mode and (B) ptychography. (c–f) Workflow of ptychography.

The key advantage of ptychography is the capability of reconstructing the entire wavefield (including amplitude and phase) scattered by an object that is considered to be lost in the context of other imaging methods, such as incoherent STEM imaging. Unlike defocused phase contrast TEM, ptychography is a post-acquisition imaging process, where the image is reconstructed in silico. Therefore, the algorithms control the resulting information transfer. The algorithms can be based on either direct methods (e.g., SSB, Rodenburg et al., 1993) or iterative methods (e.g., ePIE, Maiden and Rodenburg, 2009). Furthermore, the resulting image is free from the aberrations of the probe-forming optics, which is not the case for other scanning-type phase microscopies, such as differential phase contrast (DPC) imaging (Rose, 1976).

The recent rise of the popularity of ptychography is due to the new generation of direct electron detectors (Tate et al., 2016; Ballabriga et al., 2013; Ryll et al., 2016), as ptychography requires electron detectors that have readout speeds comparable to the STEM scanning rate (μs to ms timescales for each pixel) and a large dynamic range to record the complete distribution of transmitted electrons, including the low-intensity signals at high angles. In principle, almost every forward scattered electron that has interacted with the object can be counted. With fast electron detectors, ptychography offers the most efficient phase recovery and robustness under low electron dose conditions (Yang et al., 2016a; Pennycook et al., 2019; Pelz et al., 2017) in comparison to other conventional imaging modes (e.g., HAADF, ABF, DPC, and TEM) both in STEM (Yang et al., 2015) and TEM (Pennycook et al., 2019), which leads to significant potential for its application in beam-sensitive samples in the physical (dos Reis et al., 2018) and biological sciences (Pelz et al., 2017; Zhou et al., 2020).

A number of scholarly reviews provide details of the history and theories of ptychography (Rodenburg and Maiden, 2019; Rodenburg, 2008). In light of the current developments of ptychography within the past decade, our intention in this chapter is to provide a brief overview of the associated algorithms (Section "Ptychography algorithms") and optical configurations (Section "Optical configuration"), to draw attention to the latest applications (Section "Recent applications") and technological advancements (Section "Recent advances in technical development") based on ultra-fast detectors and to identify challenges and future perspectives (Section "Conclusion: Multidimensional ptychography").

Ptychography algorithms

Typical ptychography is based on scanning diffractive imaging, which is compatible with STEM mode, as shown in Figs. 1B and 2 with relevant notation. A convergent electron probe called the probe function, $a(\vec{R})$, is formed at the object plane with an aperture $A(\vec{K})$. After passing through the object, $o(\vec{R})$, the wave function at the exit plane, called the exit wave, $\psi_{exit}(\vec{R}, \overrightarrow{R_p})$, can be expressed by the product of the probe function and the object transmission function as

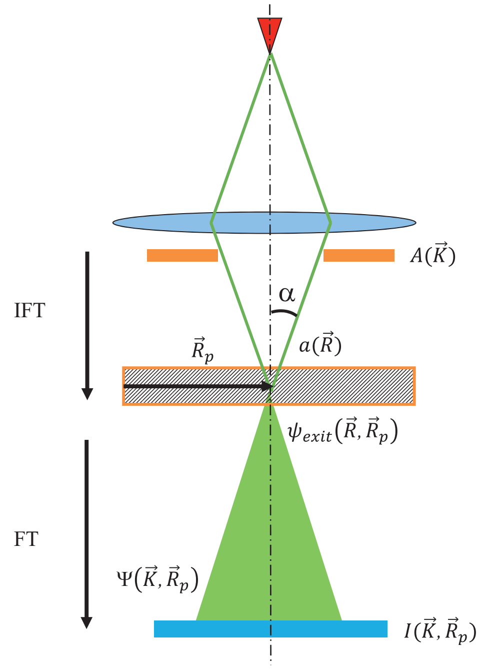

Fig. 2 Schematic illustration of ptychography in a STEM configuration and some of the notations used in the following equations. $\vec{K}$ and $\vec{R}$ represent coordinates in real space and Fourier space, respectively.

$$\psi_{exit}\left(\vec{R}, \overrightarrow{R_p}\right) = a\left(\vec{R} - \overrightarrow{R_p}\right) o\left(\vec{R}\right) \tag{1}$$

where $\overrightarrow{R_p}$ refers to the probe position and $\vec{R}$ represents coordinates in real space.

Then, the exit wave, $\psi_{exit}\left(\vec{R}, \overrightarrow{R_p}\right)$, propagates to the far-field plane and is recorded by the detector as a two-dimensional (2D) diffraction pattern for the position $\overrightarrow{R_p}$,

$$I\left(\vec{K}, \overrightarrow{R_p}\right) = \left|\Psi\left(\vec{K}, \overrightarrow{R_p}\right)\right|^2 = \left|FT_R\left(\psi_{exit}\left(\vec{R}, \overrightarrow{R_p}\right)\right)\right|^2 \tag{2}$$

As the probe is scanned on the object in a 2D array, at each probe position, a 2D diffraction pattern is recorded; thus, $I\left(\vec{K}, \overrightarrow{R_p}\right)$ is generated as a 4D data cube, the so-called 4D STEM dataset, which can be further analyzed and used to reconstruct the object transmission and probe functions using either direct methods or iterative methods, as described below.

Direct methods

Single side band (SSB)

Rodenburg first proposed the SSB method (Rodenburg et al., 1993), where the specimen is treated using the weak phase object approximation (WPOA). Hence, the object transmission function can be written as (Rodenburg et al., 1993)

$$o\left(\vec{R}\right) = 1 - io_s\left(\vec{R}\right), \left|o_s\left(\vec{R}\right)\right| \ll 1 \tag{3}$$

where $o_s\left(\vec{R}\right)$ is real, is much smaller than unity, and is proportional to the projected atomic potential. By performing a Fourier transform of $I\left(\vec{K}, \overrightarrow{R_p}\right)$ with respect to probe positions $\overrightarrow{R_p}$, under the WPOA, $G\left(\vec{K}, \overrightarrow{Q_p}\right)$ can be expressed as (Pennycook et al., 2015)

$$\begin{aligned} G\left(\vec{K}, \overrightarrow{Q_p}\right) &= \left|A\left(\vec{K}\right)\right|^2 \delta\left(\overrightarrow{Q_p}\right) + A\left(\vec{K}\right) A^*\left(\vec{K} + \overrightarrow{Q_p}\right) O_S^*\left(-\overrightarrow{Q_p}\right) \\ &\quad + A\left(\vec{K} - \overrightarrow{Q_p}\right) A^*\left(\vec{K}\right) O_s\left(\overrightarrow{Q_p}\right) \\ &= \left|A(\vec{K})\right|^2 \delta\left(\overrightarrow{Q_p}\right) + O_S\left(\overrightarrow{Q_p}\right)\left(A\left(\vec{K} - \overrightarrow{Q_p}\right) A^*\left(\vec{K}\right) - A\left(\vec{K}\right) A^*\left(\vec{K} + \overrightarrow{Q_p}\right)\right) \end{aligned} \tag{4}$$

There are three main terms, $A\left(\vec{K}\right)$, $A\left(\vec{K} - \overrightarrow{Q_p}\right)$, and $A\left(\vec{K} + \overrightarrow{Q_p}\right)$, the last two of which suggest the displacement of the aperture $A\left(\vec{K}\right)$ in the Fourier space with a shift $\pm\overrightarrow{Q_p}$. According to the value of the shift, $G\left(\vec{K}, \overrightarrow{Q_p}\right)$ contains double-overlap (DO) or triple-overlap (TO) regions, as shown in Fig. 3A (O'Leary et al., 2021). The amplitude and phase of the experimental $G\left(\vec{K}, \overrightarrow{Q_p}\right)$ from bilayer graphene in Fig. 3B show the interference at disk overlaps, which contains both the phase information of the specimen and the phase information due to aberrations in the probe forming lens. For the SSB, the lens is assumed to be aberration-free so that the object function, $o_s\left(\overrightarrow{R_p}\right)$, can be simply retrieved by the following steps. First, the amplitude and phase in one of the double overlap regions in $G\left(\vec{K}, \overrightarrow{Q_p}\right)$ (one side-band) are summed over all $\vec{K}$ for each $\overrightarrow{Q_p}$ to obtain $O_s\left(\overrightarrow{Q_p}\right)$. Second, an inverse Fourier transform of $O_s\left(\overrightarrow{Q_p}\right)$ with respect to probe positions $\overrightarrow{Q_p}$ is performed, allowing the transmission function in real space $o_s\left(\overrightarrow{R_p}\right)$ to be subsequently obtained.

The SSB algorithm can be used to achieve a resolution approximately twice the "conventional" resolution that can be obtained by using the same optical arrangement (Rodenburg et al., 1993). This algorithm has been adopted to reconstruct monolayer (O'Leary et al., 2021) and bilayer (Pennycook et al., 2015) graphene and aluminosilicate zeolite samples (O'Leary et al., 2020) (as shown in Fig. 4), in which case the contrast of the ptychographic reconstructions and dose efficiency are found to be greater than those of conventional imaging methods (Pennycook et al., 2019). In addition, the contrast transfer function (CTF) of SSB together with the factors that can affect the CTF was studied in Refs. (Yang et al., 2015; O'Leary et al., 2021).

Wigner distribution deconvolution (WDD)

As mentioned above, in SSB, the specimen is treated as a weak phase object, and the probe is assumed to be aberration-free. However, these two assumptions cannot always be satisfied; thus, at this time, it is difficult to achieve gratifying results with SSB. The WDD approach was first introduced in the early 1990s (Chapman, 1996; Rodenburg and Bates, 1992). In contrast to SSB, WDD is a full reconstruction that takes into account the nonlinear terms through a deconvolution approach and does not rely on the WPOA approximation, which allows a broader range of materials to be reconstructed (Yang et al., 2017). In addition, WDD is capable of measuring and correcting residual lens aberrations. $G\left(\vec{K}, \overrightarrow{Q_p}\right)$ can be written in the form of convolution (Yang et al., 2017)

$$G\left(\vec{K}, \overrightarrow{Q_p}\right) = A\left(\vec{K}\right) A^*\left(\vec{K} + \overrightarrow{Q_p}\right) \otimes O\left(\vec{K}\right) O^*\left(\vec{K} - \overrightarrow{Q_p}\right) \tag{5}$$

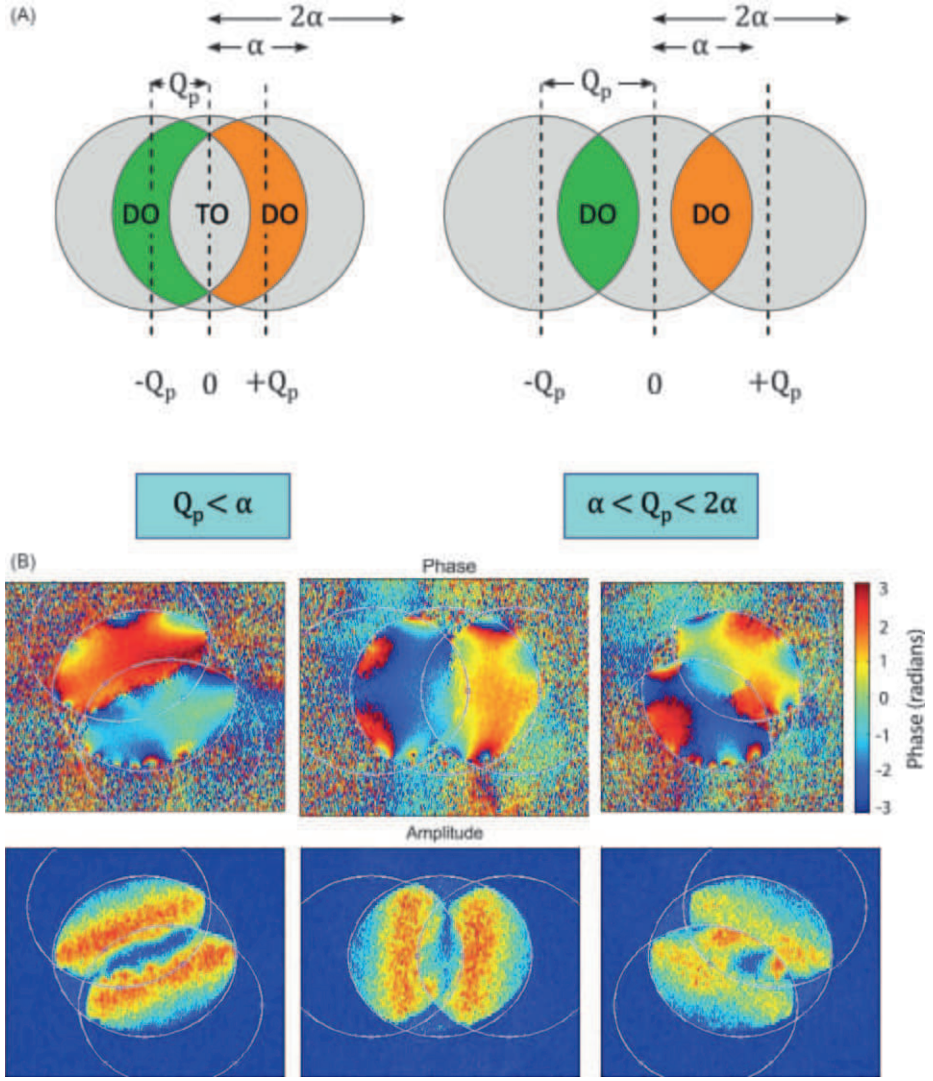

Fig. 3 (A) Schematic illustration of $G\left(\vec{K}, \overrightarrow{Q_p}\right)$ under the condition of $\left|\overrightarrow{Q_p}\right| < \alpha$ and $\alpha < \left|\overrightarrow{Q_p}\right| < 2\alpha$, where DO and TO represent the double and triple overlap regions (O'Leary et al., 2021). (B) The amplitude and phase of $G\left(\vec{K}, \overrightarrow{Q_p}\right)$ after applying the same process as that used in (A) on experimental 4D-STEM datasets collected from a sample of graphene. There are also "0" and "$\pm\overrightarrow{Q_p}$" disks, as indicated by white circles, and double and triple overlap regions (Pennycook et al., 2015).

where the symbol ⊗ denotes convolution. If we carry out an inverse Fourier transform of $G\left(\vec{K}, \overrightarrow{Q_p}\right)$ with respect to $\vec{K}$, we can obtain

$$\begin{aligned} H\left(\vec{R}, \overrightarrow{Q_p}\right) &= IFT_K\left(G\left(\vec{K}, \overrightarrow{Q_p}\right)\right) \\ &= \chi_a\left(\vec{R}, -\overrightarrow{Q_p}\right) \cdot \chi_o\left(\vec{R}, \overrightarrow{Q_p}\right) \end{aligned} \tag{6}$$

where χ is the Wigner distribution function. Next, terms related to the probe-forming aperture function can be separated from the reconstructed results using

$$\chi_o\left(\vec{R}, \overrightarrow{Q_p}\right) = \chi_a^*\left(\vec{R}, -\overrightarrow{Q_p}\right) H\left(\vec{R}, \overrightarrow{Q_p}\right) / \left(\left|\chi_a\left(\vec{R}, -\overrightarrow{Q_p}\right)\right|^2 + \varepsilon\right) \tag{7}$$

By doing so, residual lens aberrations can be corrected. Then, Eq. (8) can be applied to obtain $O\left(\overrightarrow{Q_p}\right)$ and the inverse Fourier transform can be performed to obtain $O\left(\overrightarrow{R_p}\right)$

$$O\left(\overrightarrow{Q_p}\right) = D^*\left(0, -\overrightarrow{Q_p}\right) / \sqrt{(D(0,0))} \tag{8}$$

where $D\left(\vec{K}, \overrightarrow{Q_p}\right) = FT_R\left(\chi_o\left(\vec{R}, \overrightarrow{Q_p}\right)\right) = O\left(\vec{K}\right) O^*\left(\vec{K} - \overrightarrow{Q_p}\right)$.

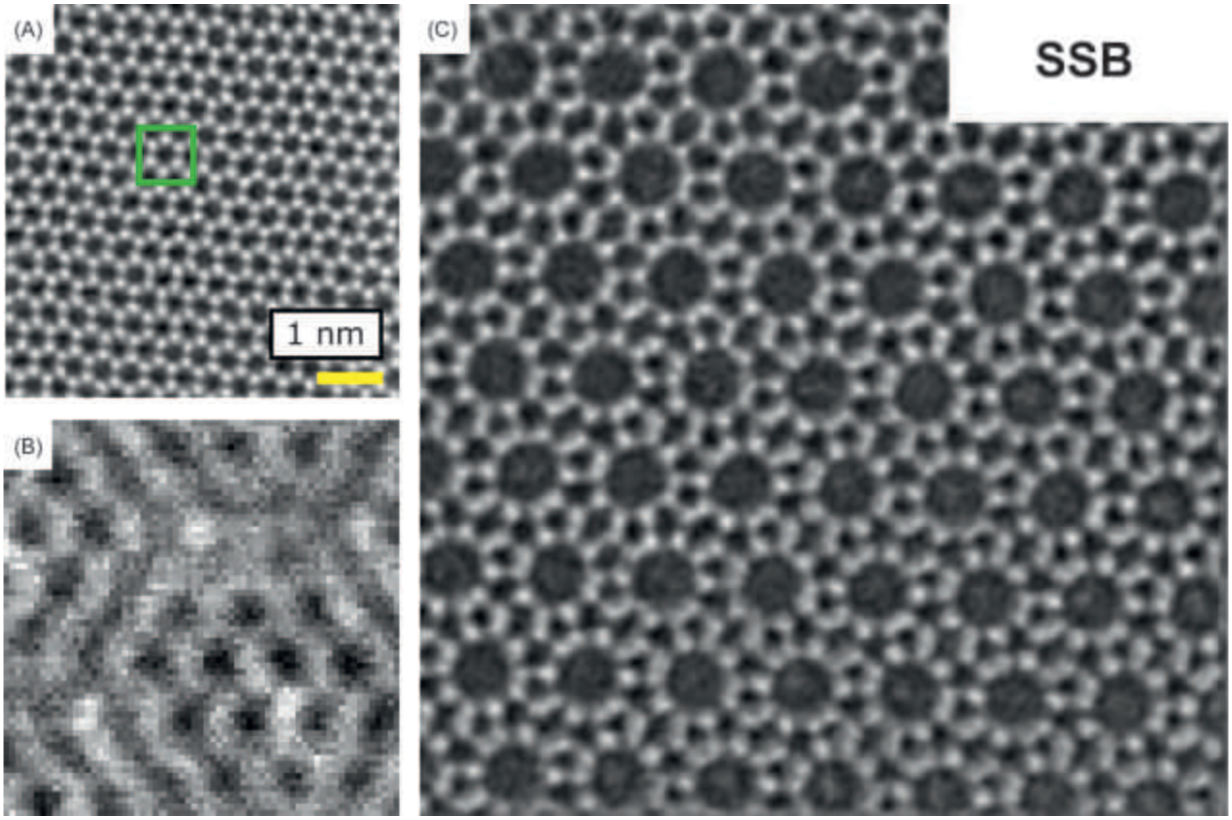

Fig. 4 Ptychographic reconstructed phase results of (A) monolayer graphene (O'Leary et al., 2021), (B) bilayer graphene (Pennycook et al., 2015), and (C) ZSM-5 (O'Leary et al., 2020).

Since WDD was proposed, it has been demonstrated that by using a Wigner distribution, the complex value of the specimen function at a resolution dictated by the largest collection angle can be obtained. Because this is much larger than the width of the objective lens transfer function of the microscope, the technique offers a practical means of overcoming the long-standing resolution problem in electron microscopy (Nellist and Rodenburg, 1994; Nellist et al., 1995; Bates and Rodenburg, 1989; Rodenburg and Bates, 1992). WDD has been used to reconstruct phase images of $BiFeO_3$ (Yang et al., 2017), GaN (Yang et al., 2017), and carbon fullerenes (Yang et al., 2016b) at atomic resolution. In addition, as shown in Fig. 5A and B, compared to the reconstructed phase result of gold nanoparticles using the SSB algorithm, the reconstructed result using the WDD algorithm delivers better contrast and higher quantitative phase values because the WPOA is not suitable for gold nanoparticles (Yang et al., 2017). In addition, WDD is able to measure and correct the residual lens aberrations in the phase image through post-acquisition processing, and thus, a higher resolution image can be achieved (shown in Fig. 5C–F) (Yang et al., 2017, 2016b). WDD has also been used to suppress noise (Lee and Barbastathis, 2016; Li et al., 2014).

Even though WDD no longer relies on the WPOA, it still assumes the exit wave to be the product of the probe function and the object transmission function, which makes WDD not strictly applicable to dynamical electron scattering (Yang et al., 2016b). Dynamical electron scattering effects are discussed in Section "Multiple scattering". Direct methods tend to be applied in focused probe ptychography (Section "Focused and defocused probe ptychography"), which is compatible with the current STEM optical configuration, whereas a defocused probe configuration (Section "Focused and defocused probe ptychography") is usually implemented with iterative schemes. The following section introduces iterative algorithms.

Iterative algorithms

In general, iterative algorithms rely on the application of measured constraints in the object plane and the far-field (diffraction) plane of intensity information, and the wave function propagation between these two planes is given by the Fourier transform shown in Fig. 6. The process used to find solutions consists of four steps: (1) forward propagate a complex guess object function with a random phase to the diffraction plane by Fourier transform; (2) perform Fourier constraint by replacing the modulus of the computed diffraction pattern with the measured modulus and retain the calculated phase; (3) backwards propagate to the object plane by inverse Fourier transform; (4) perform object constraint and use the calculated phase as a new estimation for the next iteration. These steps are repeated "iteratively" until convergence is achieved.

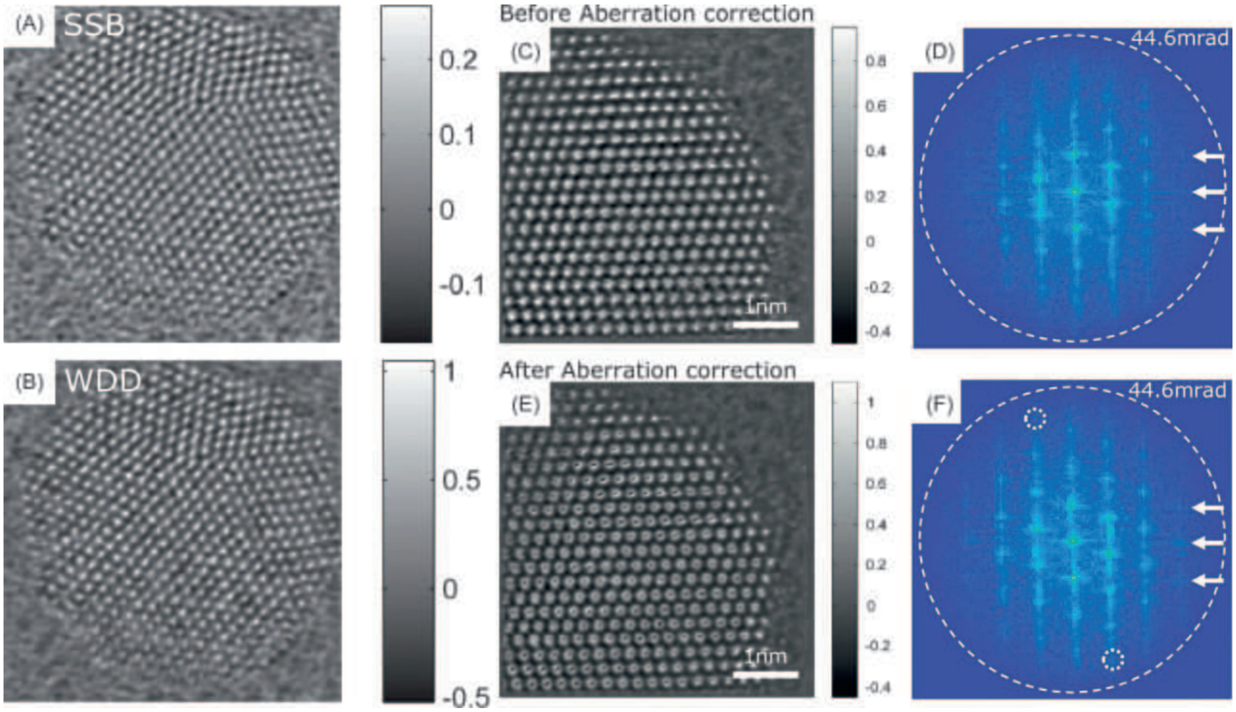
(A) SSB
0.2
0.1
0
-0.1
(B) WDD
1
0.5
0
-0.5
Before Aberration correction
(C)
1nm
0.8
0.6
0.4
0.2
0
-0.2
-0.4
After Aberration correction
(E)
1nm
1
0.8
0.6
0.4
0.2
0
-0.2
-0.4
(D)
44.6mrad
(F)
44.6mrad

Fig. 5 The ptychographic reconstructed phases of Au nanoparticles using (A) SSB and (B) WDD are compared, and the results show that WDD delivers better contrast when the sample no longer satisfies the WPOA. (C) and (E) show the reconstructed phase results of Au nanoparticles using WDD before and after aberration correction. (D) and (F) are the Fourier transform results of (C) and (E), respectively. (C–F) demonstrate that WDD can be used to measure and correct residual aberrations, and thus, a higher resolution can be achieved (Yang et al., 2017).

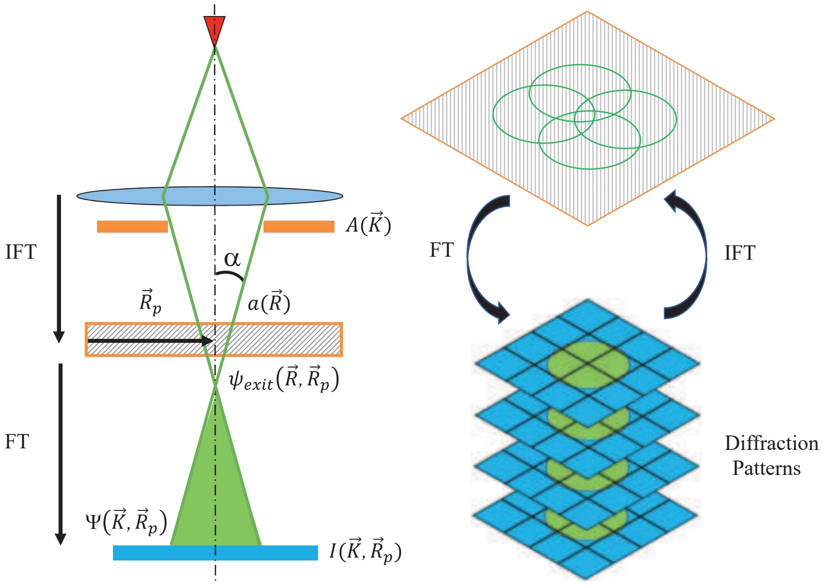
IFT
$A(\vec{K})$
α
$\vec{R}_p$
$a(\vec{R})$
$\psi_{exit}(\vec{R},\vec{R}_p)$
FT
$\Psi(\vec{K},\vec{R}_p)$
$I(\vec{K},\vec{R}_p)$
FT
IFT
Diffraction Patterns

Fig. 6 Schematic illustration of how iterative algorithm works.

The earliest iterative scheme was proposed by Gerchberg and Saxton (1972) and later developed by Fienup (1982). To solve for the object using a single diffraction pattern, a priori knowledge that the object is sufficiently small and isolated must be applied. Several demonstrations of high-resolution imaging with X-ray or electron optics have been reported (Zuo et al., 2003; Miao et al., 1999), but only for samples containing isolated objects, which limits the wider application of this technique. To overcome this limit, Rodenburg first proposed combining the iterative scheme with ptychography to solve for extended noncrystalline samples in particular (Faulkner and Rodenburg, 2005, 2004; Rodenburg and Faulkner, 2004), called the ptychographic iterative engine (PIE)

(Rodenburg et al., 2007). As shown in Fig. 6, by shifting the probe to different positions with partial overlap between neighboring illuminated areas, a series of diffraction patterns can be collected. The partial overlap (Bunk et al., 2008) largely increases the redundancy (Maiden et al., 2011) of the dataset, thus helping the algorithm to converge.

However, PIE still requires a priori knowledge of the incident illumination or probe function. Due to the high redundancy in ptychographic data, this requirement was eliminated with the difference map (DM) algorithm (Thibault et al., 2008, 2009) and the extended PIE (ePIE) (Maiden and Rodenburg, 2009), where both the object function and the illumination function can be extracted from a ptychographic dataset. Such redundancy has been continuously exploited in recent years. There are a number of required experimental conditions, such as accurate knowledge of the probe scanning position (Maiden et al., 2012b; Zhang et al., 2013), noise-free data (Godard et al., 2012; Thibault and Guizar-Sicairos, 2012), and fully coherent illumination sources (Thibault and Menzel, 2013), and the assumption of thin samples (Godden et al., 2014) can be relaxed in recent advanced algorithms. In Section "Recent advances in technical development", we discuss certain respects of these advanced technical developments. In this section, we give a brief introduction to the basics of the ePIE and DM algorithms.

Ptychographic iterative engine

The theory of the PIE technique can be found in an earlier work (Rodenburg and Faulkner, 2004). Unlike PIE, ePIE starts with initial guesses of both the probe function and the object function (Maiden and Rodenburg, 2009). The reconstruction steps of ePIE are shown in Fig. 7. The algorithm also follows the conventional iteration framework, which consists of the four steps described above. Two major modifications are introduced in the fourth step: both the probe function and the object function are updated using update functions in Eqs. (9) and (10), respectively; for the next iteration, the probe is moved to the next position in the dataset, and the newly updated object function is used as the initial estimate.

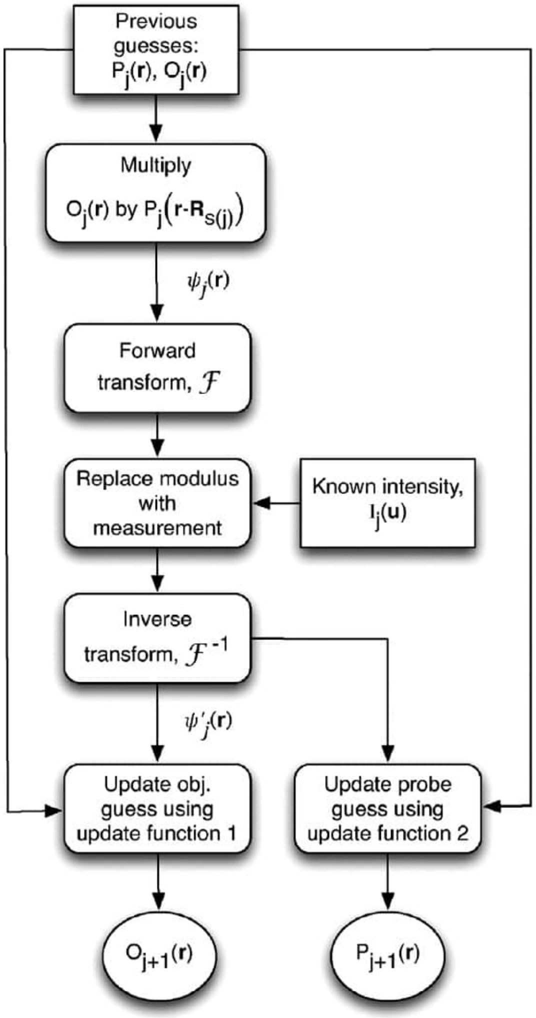
Previous guesses: $P_j(\mathbf{r})$, $O_j(\mathbf{r})$
Multiply $O_j(\mathbf{r})$ by $P_j(\mathbf{r}-\mathbf{R}_{s(j)})$
$\psi_j(\mathbf{r})$
Forward transform, $\mathcal{F}$
Replace modulus with measurement
Known intensity, $I_j(\mathbf{u})$
Inverse transform, $\mathcal{F}^{-1}$
$\psi'_j(\mathbf{r})$
Update obj. guess using update function 1
Update probe guess using update function 2
$O_{j+1}(\mathbf{r})$
$P_{j+1}(\mathbf{r})$

Fig. 7 Flowchart of the ePIE algorithm (Maiden and Rodenburg, 2009).

$$o_{j+1}\left(\vec{R}\right) = o_j\left(\vec{R}\right) + \alpha \frac{a_j^*\left(\vec{R} - \overrightarrow{R_p}\right)}{\left|a_j\left(\vec{R} - \overrightarrow{R_p}\right)\right|^2_{max}} \left(\psi_{new,j}\left(\vec{R}\right) - \psi_{old,j}\left(\vec{R}\right)\right) \tag{9}$$

$$a_{j+1}\left(\vec{R}\right) = a_j\left(\vec{R}\right) + \beta \frac{o_j^*\left(\vec{R} + \overrightarrow{R_p}\right)}{\left|o_j\left(\vec{R} + \overrightarrow{R_p}\right)\right|^2_{max}} \left(\psi_{new,j}\left(\vec{R}\right) - \psi_{old,j}\left(\vec{R}\right)\right) \tag{10}$$

Because a high degree of redundancy can be introduced into the recorded data due to the use of multiple diffraction patterns, instead of a single pattern, as well as the overlap between adjacent probes, the work by Maiden et al. (2011) demonstrated that when using ePIE, the super-resolution information can be extrapolated beyond the aperture of the detector. An electron microscopy work by Hue et al. (2011) demonstrated that ePIE is a very robust algorithm capable of updating the object and the probe at the same time, is resistant to noise, and is able to reconstruct strong phase objects, as shown in Fig. 8.

Difference map (DM)

The DM algorithm proposed by Elser (2003) is one of the iterative projection algorithms. There are two important concepts in the iterative projection algorithms. One is the constraint sets, which refer to a group of points that satisfies a certain condition. The other is the projection functions, which are used to find a point in the corresponding set that has a minimum distance from the initial point. Iterative projection algorithms aim to solve the phase problem by utilizing projection functions to find a point that exists in two constraint sets simultaneously, as illustrated in Fig. 9. In electron ptychography, one of these two constraint sets is the Fourier Constraint Set (FCS), and the other tends to be the Overlap Constraint Set (OCS).

FCS refers to a set of points whose modulus after Fourier transformation equals the square root of the intensity of the recorded diffraction patterns. The OCS states that each view can be factorized as a probe and an object function, and any view that can be decomposed into the product of a "probe" and an "object" function with a known displacement can be regarded as being in the same OCS. Detailed reconstruction steps of the difference map algorithm can be found in Elser (2003) and Thibault et al. (2009).

One of the advantages of the DM algorithm is its ability to reconstruct the object and probe function simultaneously by utilizing the FCS and the OCS (Thibault et al., 2008, 2009), which can realize a significant improvement in image quality. Fig. 10 shows the

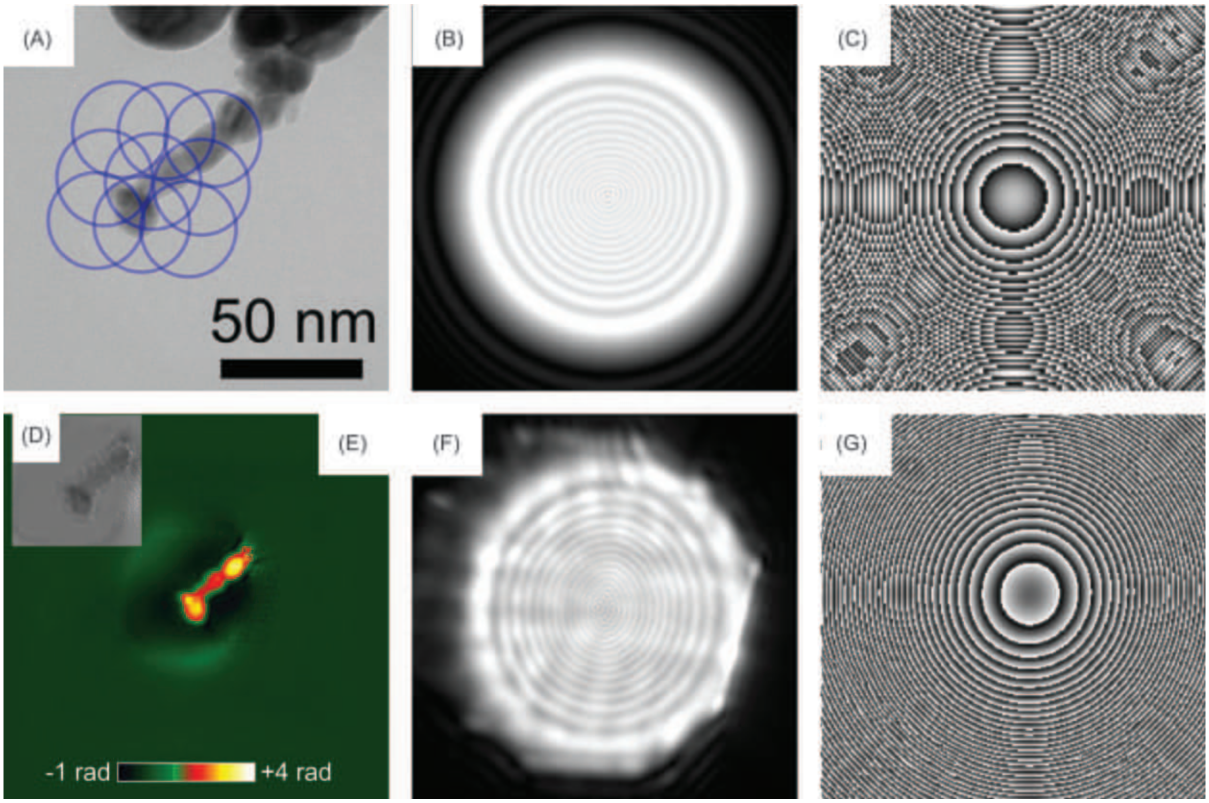

Fig. 8 ePIE-reconstructed phase results of FeNi particle aggregates. (A) TEM bright field image of FeNi particles, with blue circles representing the probe positions when collecting 4D-STEM datasets. The probe's initial guess (B) amplitude and (C) phase. After using the ePIE algorithm, the reconstructed amplitude and phase results of the object and probe are shown in (D–E) and (F–G), respectively (Hue et al., 2011).

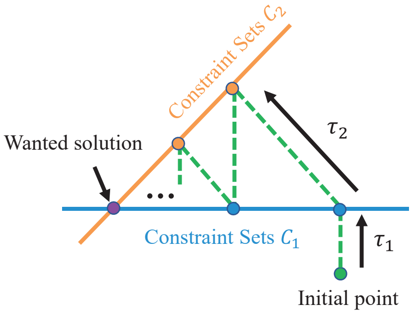

Fig. 9 Schematic illustration of how the iterative projection algorithms solve the phase problem. *Orange* and *blue lines* represent two different constraint sets. By iteratively utilizing projection functions, which find the closest point in the corresponding constraint set to the initial point, the point that exists in both constraint sets can be found.

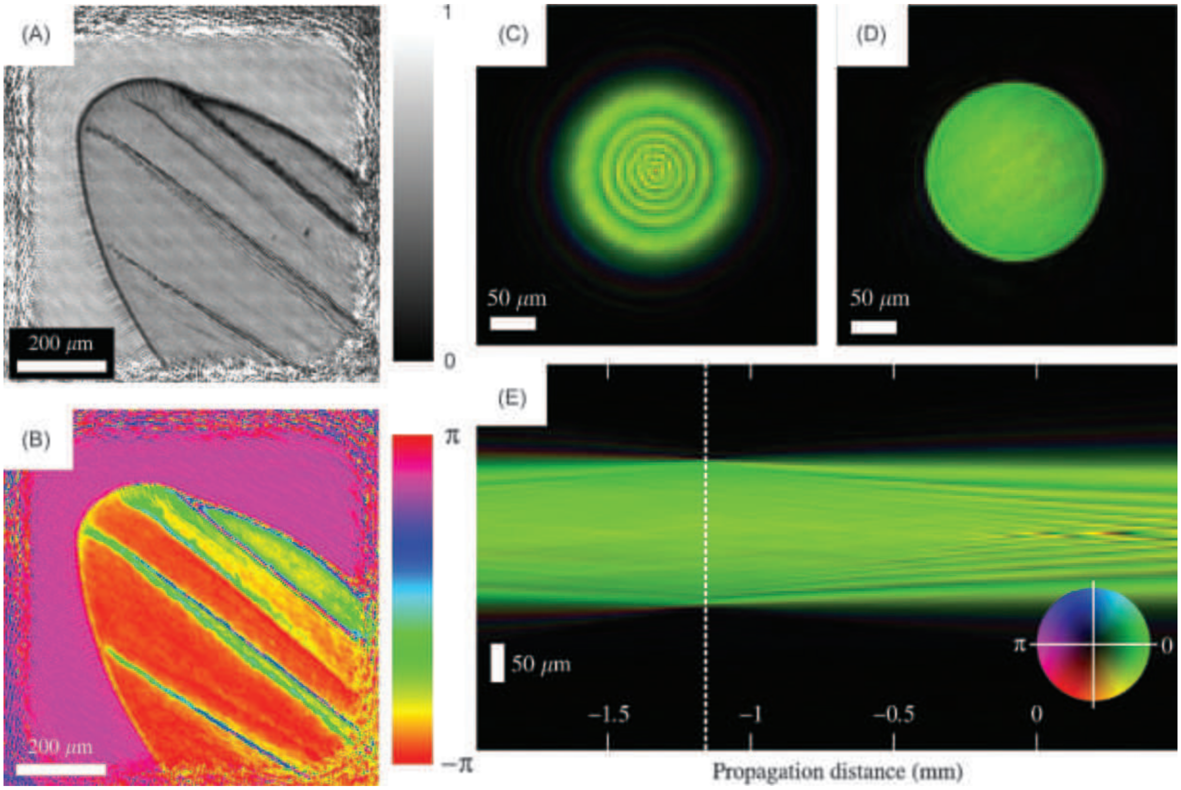

Fig. 10 Scanning X-ray diffraction microscopy (SXDM) reconstruction of the insect wing (A) amplitude and (B) phase. (C–E) Simultaneously reconstructed probe function. (C) Reconstructed probe with the brightness indicating amplitude and hue indicating phase. (D) Computed image after the reconstructed probe propagates freely to the plane where the aperture was placed. (E) Longitudinal cut of the propagated wavefield (Thibault et al., 2009).

simultaneously reconstructed phase results of the object and probe functions in scanning X-ray diffraction microscopy. However, the applications of this algorithm have only been demonstrated with X-rays (Thibault et al., 2008).

Optical configuration

There are three fundamental requirements to perform ptychographic experiments (Li and Maiden, 2018). First, the experiment needs a finite-size illumination area that can be shifted with respect to an object either by scanning the illumination or by translating the object through positional grid. Second, a detector can be placed at any plane downstream of the object, although it is normally located at the Fourier plane. Third, the shifting process itself can facilitate direct methods to a solution of the diffraction phase, whereas for iterative approaches, adjacent illumination positions must be partially overlapped. A sufficient degree of overlap leads to the high redundancy in the dataset, which then allows the reconstruction to converge at a unique phase solution (Bunk et al., 2008; Maiden et al., 2011) and thus relaxes the required experimental conditions of ptychography. This makes the method extremely versatile and diverse in terms of experimental setups. The following section briefly introduces a few mainstream optical configurations based on existing electron microscopes.

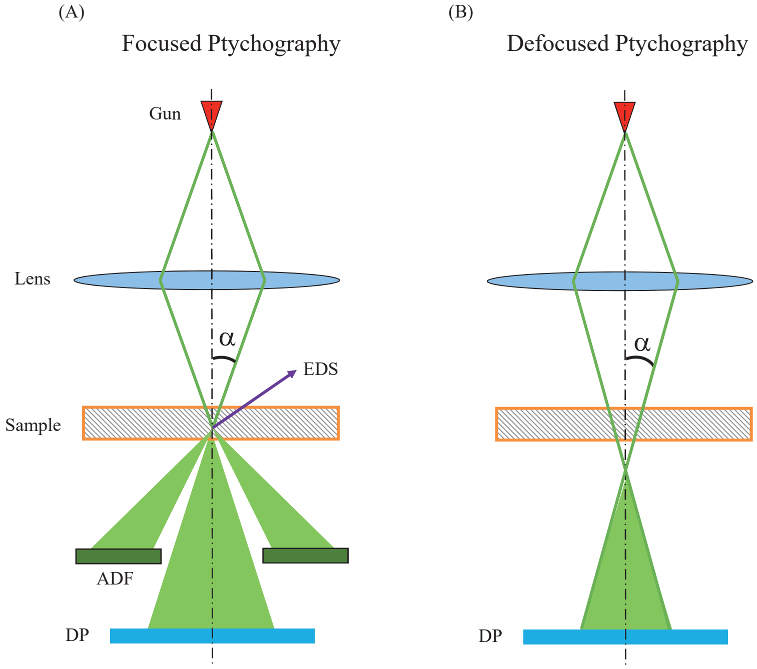

Fig. 11 Optical configurations of (A) focused-probe ptychography and (B) defocused-probe ptychography.

Focused and defocused probe ptychography

As shown in Fig. 11, both focused and defocused probe ptychography are compatible with the current STEM optical configurations. Placing an ultra-fast detector in the far-field plane to record diffraction patterns would be sufficient for a current STEM instrument to be able to perform ptychographic experiments.

Using an in-focused probe in the object plane (Fig. 11A), focused ptychography has the advantage of coupling with current aberration-corrected STEM capabilities at the atomic scale, including HAADF imaging to extract *Z*-contrast images (Yang et al., 2016b) and spectroscopy with characteristic X-rays, secondary electrons, and auger electrons, to analyze the elemental composition of the specimen. However, since a detector must be placed within the optic axis, which blocks electrons from entering electron energy loss spectrometer (EELS), the major tradeoff to using ptychography is the complete loss of any ability to use the inelastic electrons, which contain rich elemental composition and bonding information at atomic resolution (typically constituting one of the main rationales for using aberration-corrected STEM). To overcome this issue, hollow ptychography was proposed by Song et al. (2018), in which a hollow-type detector can be used. As a result, hollow ptychography can be performed with EELS to simultaneously provide a high-efficiency phase together with spectroscopic information in a single experiment and is compatible with many 4D-STEM techniques (Ophus, 2019).

The focused configuration also comes with some limits. Inferred from the procedure of SSB or WDD, the scanning step size that is equal to the pixel size in the reconstructed images must be small enough for atomic resolution imaging. As a result, the data volume for the acquisition of a large field of view can increase dramatically. Second, as the electron beam is focused into a fine spot on the sample, to sufficiently reach a low dose condition (i.e., 500 e/Å^2), the beam current must theoretically be reduced to approximately 0.1–0.01 pA, which is not tremendously lower than the typical beam currents (1–50 pA) used in normal STEM operation. This fact results in practical difficulties in locating the sample position and focusing the probe.

In contrast, the defocused setup, as shown in Fig. 11B, allows the size of the illumination on the object to be flexibly adjusted by the defocus value so that the beam current can be distributed to a wide region in a controlled manner while ensuring that the total electron dose is largely reduced. The large illumination region also enables a coarse scanning step size to be used, which can significantly reduce the total number of scanning positions and hence the data volume used in the reconstruction for a wide field of view. Note that when using iterative approaches, the resolution of the reconstruction is not compromised by the use of a large step size because it is determined by the maximum collection angle of the detector (Wang et al., 2017; Jiang et al., 2018).

Therefore, the focused and defocused configurations have their own advantages. The former can obtain simultaneous multichannel signals from conventional detectors and spectrometers at a high spatial resolution, whereas the latter can facilitate low-dose imaging to reach a dose suitable for beam-sensitive materials such as biological specimens.

Fourier ptychography

In both focused and defocused ptychography, the sample is scanned with a spatially confined electron probe, and the object is shifted relative to the probe with partial overlap between neighboring illuminated areas. Then, the diffraction patterns are recorded in the far-field plane. Since the object plane is considered to be in real space and the 4D-STEM diffraction datasets are collected in Fourier space, this kind of ptychography can also be referred to as real space ptychography. In reciprocity, the diffraction pattern in Fourier space can be treated as the object while the images in real space are collected as 4D-STEM datasets. Fourier ptychography was also proposed by Hoppe, shortly after his work on ptychography. As its name suggests, Fourier ptychography is the reciprocal analog of real space ptychography since the probe function and the object transmission function are in Fourier space.

Given that a plane wave $e^{i\overrightarrow{K_p}\cdot\vec{R}}$ is illuminated on the object, $o\left(\vec{R}\right)$, an exit wave $\psi_{exit}\left(\vec{R}\right)$ is formed. According to the WPOA approximation, the exit wave can be defined as

$$\psi_{exit}\left(\vec{R}\right) = o\left(\vec{R}\right)\cdot e^{i\overrightarrow{K_p}\cdot\vec{R}}. \tag{11}$$

The exit wave then continues to propagate to the focal plane, where an aperture is placed. After passing through the aperture, the wavefield $\Psi\left(\vec{K}\right)$ becomes:

$$\Psi\left(\vec{K}\right) = FT_R\left(\psi_{exit}\left(\vec{R}\right)\right)\cdot A\left(\vec{K}\right) = O\left(\vec{K}+\overrightarrow{K_p}\right)\cdot A\left(\vec{K}\right). \tag{12}$$

When the wave propagates to the detector plane, the detector records the intensity of the wavefield, which is given as

$$I\left(\vec{R}\right) = \left|FT_K\left(\Psi\left(\vec{K}\right)\right)\right|^2. \tag{13}$$

There are several differences with this approach, compared to conventional ptychography. First, the probe function and the object transmission function in conventional ptychography become the aperture function and the object's Fourier spectrum in the Fourier domain, respectively. Second, the diffraction patterns are captured in real space, while in conventional ptychography, diffraction patterns are captured in Fourier space. Third, the movement of the electron source, which modifies the vector $\overrightarrow{K_p}$ in plane wave $e^{i\overrightarrow{K_p}\cdot\vec{r}}$, causes the Fourier spectrum of the object to shift $O\left(\vec{K}+\overrightarrow{K_p}\right)$; however, in conventional ptychography, the shift of the object relative to the probe is controlled by scanning coils, which change the direction of the scanning probe.

Fourier ptychography can reduce hardware requirements, such as the dynamic range of the detector and coherence of electron guns. Fourier ptychography has already been demonstrated in TEM (Haigh et al., 2009), although it is generally called tilt-series reconstruction and has shown an ability to extend the ultimate resolution of the latest generation of aberration-corrected TEMs by 41% relative to that achievable using conventional axial imaging, as shown in Fig. 12.

There are many other derivatives of ptychography, such as near-field ptychography (Robisch et al., 2015; Stockmar et al., 2013), Bragg ptychography (Hruszkewycz et al., 2012, 2017; Godard et al., 2011; Pfeifer et al., 2006), selected area ptychography (Maiden et al., 2015), and single shot ptychography (Sidorenko and Cohen, 2015). Each has a unique experimental setup and requirements but shares the same underlying principle. As these setups have not yet been widely implemented on electron microscopes, they will not be introduced in detail here.

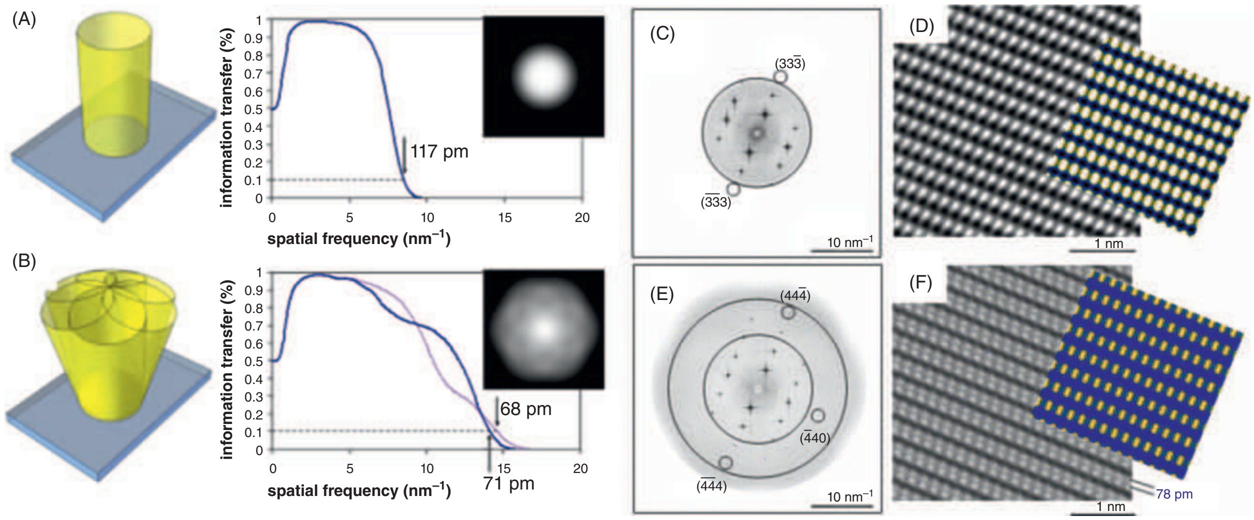

Fig. 12 Schematic illustration of geometry and information transfer for (A) focal series and (B) tilt series. Reconstructed exit wave function using (C–D) focal series and (E–F) tilt-series experimental data collected from ⟨112⟩ silicon (Haigh et al., 2009).

Recent applications

Since ptychography was first proposed, it has been widely used with X-ray optics, including the study of both engineered (Yu et al., 2015; Wilke et al., 2012) and biological (Lima et al., 2013; Giewekemeyer et al., 2010; Wilke et al., 2015; Hemonnot et al., 2016) materials. In electron microscopy, recent developments in regard to coherent electron guns, computing power and, in particular, ultra-fast detectors have significantly accelerated the application of ptychography techniques. With the advantages that it offers, ptychography has great potential in the following application areas.

First, compared to other phase-retrieval or imaging techniques, ptychography has an important advantage of overcoming the limitations of the coherence envelope (the "information limit") of electron microscopy. Super-resolution ptychography was first demonstrated by Nellist et al. in 1995 (Nellist et al., 1995) with a resolution of 0.136 nm from crystalline Si (see Fig. 13A and B). The atomic resolutions achieved from various samples, such as boron nitride cones (Putkunz et al., 2012), cerium dioxide nanocrystals (D'Alfonso et al., 2014; Morgan et al., 2013) and lanthanum hexaboride (Wang et al., 2017), were approximately 0.84 Å because electrons only within the bright-field disk were used due to the low dynamic range and sensitivity of conventional charge-coupled devices (CCDs). Usage of the signal at higher scattering angles beyond the bright-field disk was demonstrated by Humphry et al. (2012) by resolving lattices in gold nanoparticles on a 30-kV SEM. Recently, using a newly developed electron detector with a high dynamic range and speed (Jiang et al., 2018), Jiang et al. achieved an Abbe diffraction-limited resolution of 0.39 Å in 2D MoS_2 at 80 kV, as shown in Fig. 13C–F. Now, the experimental resolution limit relative to the wavelength is reduced to approximately $d = 10\lambda$ ($\lambda = 4$ pm at 80 kV), which outperforms the state-of-the-art electron microscope with aberration correctors. Although in principle the resolution of ptychography is determined by the diffraction limit for the wavelength of the radiation used, thermal diffuse scattering that arises from the vibrations of atoms around their equilibrium positions (lattice vibrations) may ultimately impose the image resolution for the materials being investigated.

Second, electron ptychography offers a more efficient phase contrast transfer function (PCTF) than any other phase imaging techniques used in STEM, such as BF, ABF, or DPC (Yang et al., 2015), as well as high sensitivity to low-Z elements. Being capable of visualizing light and heavier atoms simultaneously, which is a challenging objective for ADF, electron ptychography is becoming a popular method for detecting low-Z atoms in crystals (Wang et al., 2017; Yang et al., 2016b; Wen et al., 2019). Using the direct method of WDD, the work by Yang et al. (2017) resolved Ga-N dumbbells and atomic columns of oxygen in GaN and $BiFeO_3$ crystals, respectively. Wen et al. (2019) identified C and O surface atoms in a 2D MoS_2 monolayer, and Chen et al. (2019)

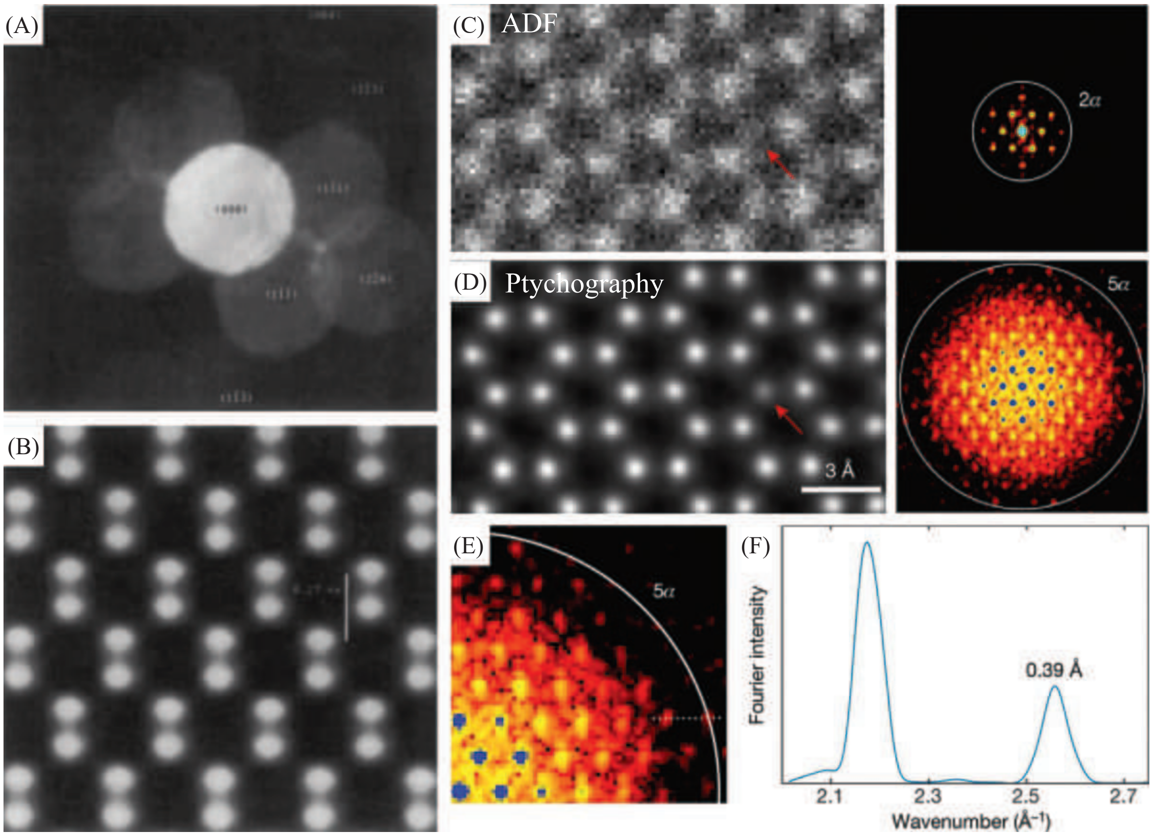

Fig. 13 Ultra-high resolution. Atomic resolution image of (A, B) silicon, demonstrating a resolution of 0.136 nm (Nellist et al., 1995) and (C–F) monolayer MoS2, demonstrating a resolution of 0.39 Å (Jiang et al., 2018).

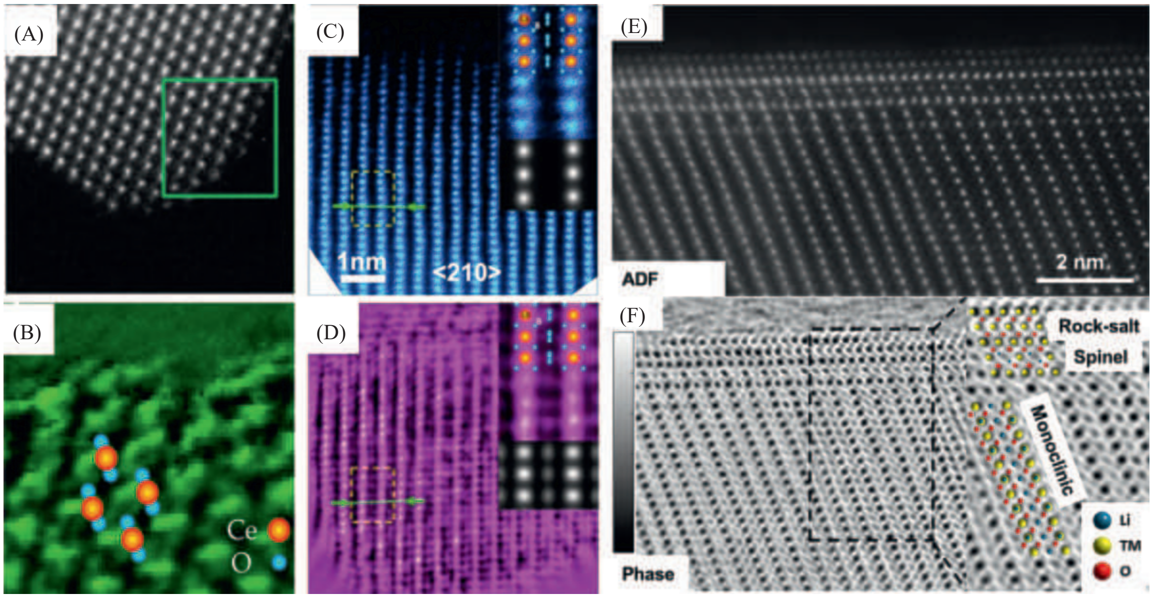

Fig. 14 Oxygen atoms resolved in CeO_2 by (A) HAADF imaging and (B) ptychographic reconstruction. Boron atoms resolved in LaB_6 by (C) HAADF imaging and (D) ptychographic reconstruction (Wang et al., 2017). Lithium atoms resolved in $Li_{1.2}Mn_{0.6}Ni_{0.2}O_2$ particles by (E) HAADF imaging and (F) ptychographic reconstruction (Lozano et al., 2018).

located interstitial boron dopants in a Pd lattice. Similarly, using an iterative approach such as ePIE, Wang et al. showed O columns in a CeO_2 crystal and further demonstrated that both boron ($Z_B = 5$) and lanthanum ($Z_{La} = 57$) atomic columns can be resolved simultaneously in the LaB_6 crystal in phase images (Wang et al., 2017), as shown in Fig. 14A–D. Recently, lithium ($Z_B = 3$) atomic columns were visualized in Li-rich cathode materials, as investigated by Lozano et al. (2018) using WDD (Fig. 14E and F). Elements as light as lithium in the periodic table have been clearly visualized in the ptychographic phase at atomic resolution. Given its high phase sensitivity, it can be foreseen that electron ptychography, in the near future, will yield an experimental reconstructed phase at atomic resolution with high phase sensitivity that will be sufficient to detect the lightest element in the universe, hydrogen, in materials such as hydrides.

Third, electron ptychography is robust even under low dose conditions. Unlike STEM ADF and BF imaging (Fig. 1A), which can only detect a small fraction of the transmitted electrons, electron ptychography collects most of the electrons in the diffraction plane (Fig. 1B) so that an image can be formed during the post-acquisition process. Compared to STEM phase imaging methods such as DPC and ABF, ptychography provides the highest signal-to-noise ratio of imaging for weak phase objects (Seki et al., 2018). In addition, ptychography shows better phase images than the equivalent TEM phase images in the presence of partial coherence (Pennycook et al., 2019). Overall, ptychography is a high dose efficiency atomic resolution imaging technique. In earlier work, such as Putkunz et al. (2012), D'Alfonso et al. (2016), and Humphry et al. (2012), the dose of ptychography was set in the range of 10^6–10^4 $e^-/Å^2$ to ensure atomic resolutions were achieved with conventional CCDs. The introduction of ultra-fast detectors (Tate et al., 2016; Ballabriga et al., 2013) enabled the usage of focused ptychography to obtain the atomic structural information of lithium oxide battery materials (Lozano et al., 2018) and all-inorganic perovskite solar cells ($CsPbBr_3$) (dos Reis et al., 2018) without beam damage at a dose of 10^4–10^3 $e^-/Å^2$. By using a defocused configuration (Fig. 11B), the dose can be further decreased under certain circumstances, and the reconstruction can be better than that of focused probe geometry at a low dose, as theoretically shown by Jiang et al. (2018). Song et al. (2019) and Chen et al. (2020) experimentally demonstrated high resolution (better than 1.6 Å) at a low dose of ~400 $e^-/Å^2$ using defocused electron ptychography on 2D monolayer MoS_2 (Fig. 15A–H) and WS_2, respectively. In terms of algorithm development, Pelz et al. (2017) proposed the use of nonconvex Bayesian optimization to solve the ptychographic phase-retrieval problem. Their theoretical calculations suggested that the dose requirements for imaging biological macromolecules with subnanometer resolution could be satisfied (Fig. 15I–N).

Given that electron ptychography is a technique with ultra-high resolution and high dose efficiency, and is sufficiently sensitive to be able to detect low-Z elements, it provides a promising alternative method for cryo-EM imaging of biological samples. Zhou et al. (2020) demonstrated the first cryo-electron ptychography (Cryo-EPty) experiments for viral particles imaging, as shown in Fig. 16, and showed that ptychography provides tunable, continuous wideband information transfer, including low spatial frequencies, which is superior to conventional phase contrast imaging. The authors also produced high phase contrast images of viral particles even at a low dose of 5.7 $e^-/Å^2$, and demonstrated the ability to image bio-samples over a wide field of view at the micrometer scale. It can be anticipated that Cryo-EPty will open a new avenue for high resolution and high contrast structural biological imaging by combining current state-of-the-art single particle analysis (SPA) and tomography in cryo-EM.

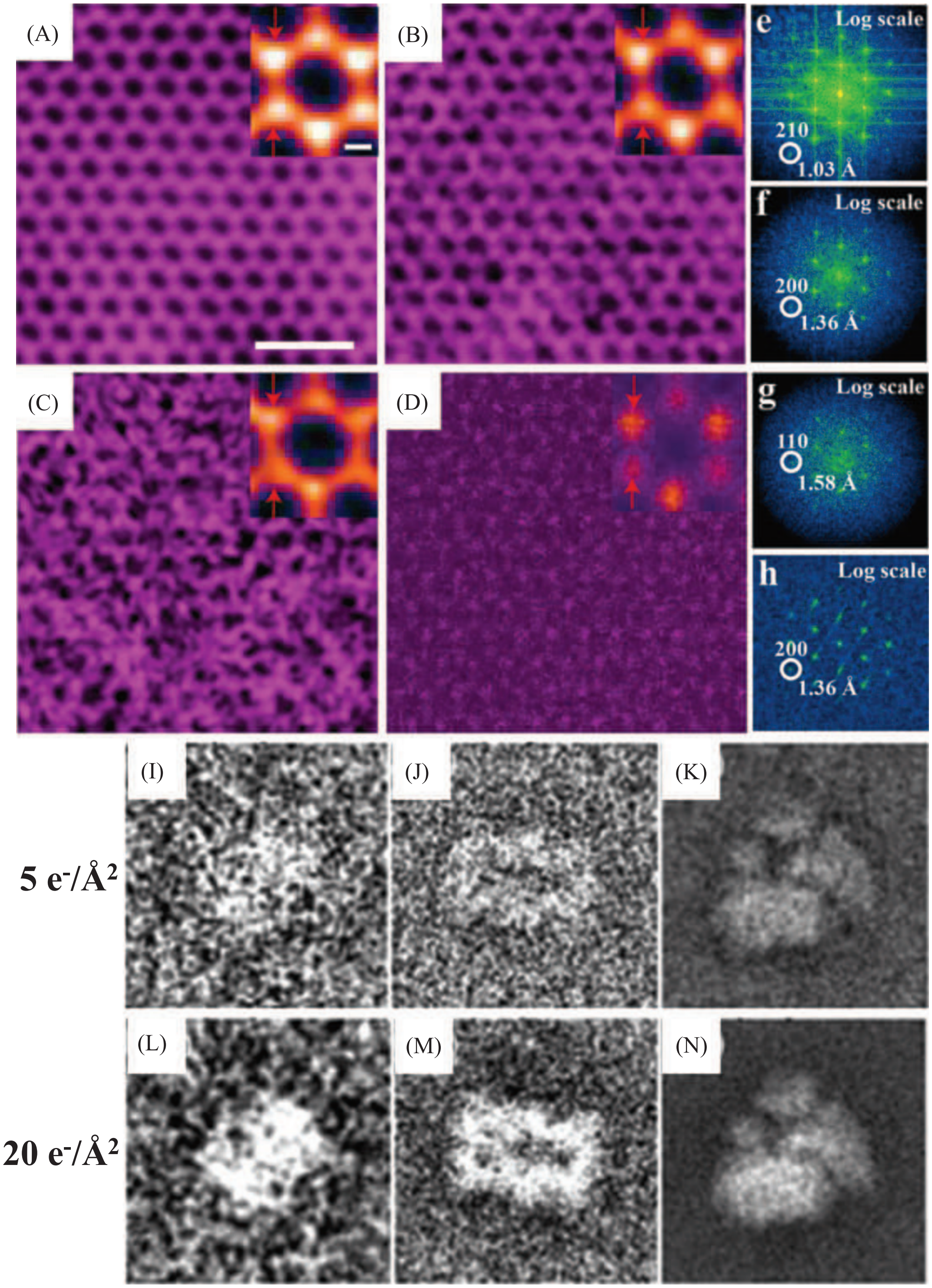
(A)
(B)
e
Log scale
210
1.03 Å
f
Log scale
200
1.36 Å
(C)
(D)
g
Log scale
110
1.58 Å
h
Log scale
200
1.36 Å
(I)
(J)
(K)
5 e-/Å2
(L)
(M)
(N)
20 e-/Å2

Fig. 15 Robustness under low dose conditions. (A–H) MoS_2 (Song et al., 2019), (I–N) Simulations of biological macromolecule (Pelz et al., 2017).

Recent advances in technical development

Although ptychography has shown numerous advantages and broad applications, there are still many challenges to tackle. Some of the challenges arise from microscope systems, such as the partial coherence of electron sources and instabilities of scanning systems, and others of which are associated with samples themselves, such as large sample thicknesses and a wide range of spatial frequencies. This section introduces the recent advances in technical development that aim to overcome these issues.

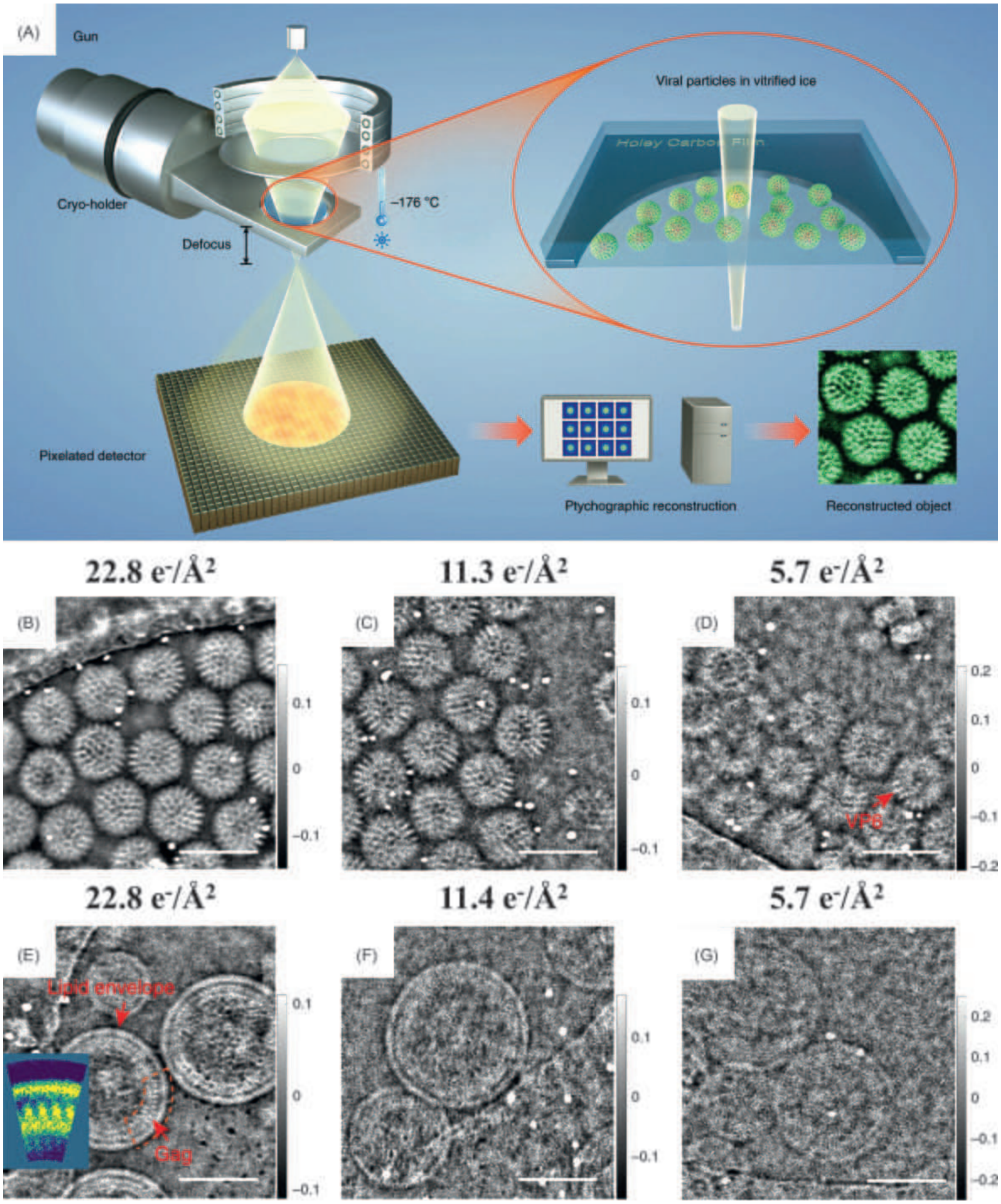
(A)
Gun
Viral particles in vitrified ice
Holey Carbon Film
Cryo-holder
−176 °C
Defocus
Pixelated detector
Ptychographic reconstruction
Reconstructed object
22.8 e⁻/Å²
11.3 e⁻/Å²
5.7 e⁻/Å²
(B)
0.1
0
−0.1
(C)
0.1
0
−0.1
(D)
0.2
0.1
0
−0.1
−0.2
VP8
22.8 e⁻/Å²
11.4 e⁻/Å²
5.7 e⁻/Å²
(E)
Lipid envelope
Gag
0.1
0
−0.1
(F)
0.1
0
−0.1
(G)
0.2
0.1
0
−0.1
−0.2

Fig. 16 Cryo-electron ptychography for viral particles imaging at low dose (Zhou et al., 2020).

Multiple states

Partial coherence determines the limit of resolution that can be achieved in both conventional TEM and STEM modes (Nguyen et al., 2014; de Jong and Van Dyck, 1993). Partial coherence also has a critical influence on the quality of ptychographic reconstructed results, as finite spatial coherence weakens the spatial resolution and introduces more artifacts (Stachnik et al., 2015). In recently produced electron microscopes, even though highly coherent electron guns are usually used and the electron probe in ptychographic reconstruction can be assumed to be a pure coherent state under certain circumstances, nonetheless elimination of the incoherence effect is crucial to improve the quality of ptychographic results.

To address this issue, mixed-state ptychography was proposed, and has, as of today, been demonstrated in X-ray (Thibault and Menzel, 2013) and electron ptychography (Cao et al., 2018, 2016). Partial coherence can be considered a combination of a series of

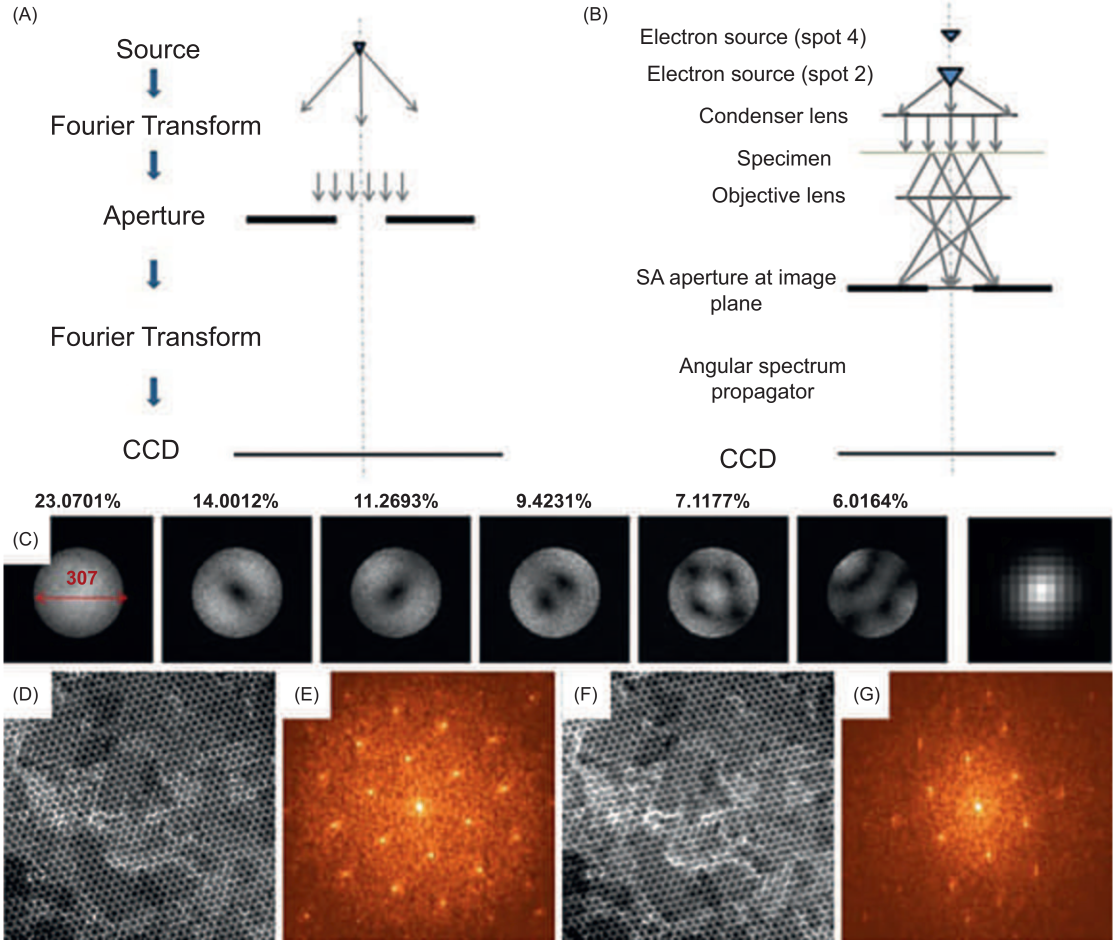

Fig. 17 (A) Idealized optical configuration. (B) Experimental setups; associated datasets were collected using different spot sizes and convergence angles. (C) Orthogonal modes and effective source (right-most tile), the contribution percentage of each mode is labelled above (Cao et al., 2016). Ptychographic reconstructed results of monolayer WS_2 at a dose of 58,000 $e^-/Å^2$; using (D–E) mixed-state ptychography and (F–G) single-state ptychography (Chen et al., 2020).

orthogonal modes, which propagate through optical facilities independently as pure states (Whitehead et al., 2009). Cao et al. (2016) showed that after decomposing the electron probe into a series of orthogonal modes, as shown in Fig. 17C, conventional ptychographic algorithms can be adopted, except that the probe function in the ptychographic reconstruction becomes a combination of different modes. Chen et al. (2020) further compared the reconstructed results from single-state and mixed-state ptychography and showed that the mixed-state approach can potentially improve the quality of the reconstructed result in terms of resolution, dose efficiency, contrast, signal-to-noise ratio, and precision, as shown in Fig. 17D–G. Because ptychography is also able to account for many of the different factors that result in decoherence-like effects in measured diffraction patterns, such as a finite electron source size, chromatic aberration, sample vibration, and rapid instabilities of the image-forming system, use of a mixed-state approach is greatly beneficial for ptychographic reconstructions.

Probe position errors

Ptychography does not rely on high-quality lenses; instead, the resolution and accuracy of the resultant reconstructions are limited by the precision with which the electron probe positions can be measured with respect to the sample, as shown in Fig. 11 (Maiden et al., 2012b). Simulation work by Hue et al. (2011) showed that even a small error in the probe position has a strong influence on the reconstruction, with probe position errors creating a mesh pattern that can lead to incorrect overall solution. Therefore, the accuracy of the probe position is crucial for producing high-quality ptychographic reconstructions.

Due to thermal drift and hysteresis in the probe scanning coils, errors in the probe position are inevitable. When using a well-controlled scanning system, the errors caused by hysteresis in the scanning coils can be reduced; yet, the thermal drift of the sample remains. As a result, the integration of post-processing position-correction algorithms into ptychographic iterations becomes increasingly necessary and essential for high-resolution reconstructions.

A number of position-correcting methods have been developed for ePIE and DM. For example, Maiden et al. proposed the position-correcting ptychographic iterative engine (pcPIE) (Maiden et al., 2012b), which integrates a set of position correction vectors into the inaccurately measured positions compared to conventional ePIE. Zhang et al. proposed unknown-position ePIE (Xu et al., 2020), which uses normalized root-mean-square-error (NRMSE) as an indicator for identifying drift points and automatically adjusts the feedback parameters. An approach based on optimization with respect to the summed-square error was also applied to the DM algorithm (Beckers et al., 2013). Using a gradient-descent-based algorithm (Guizar-Sicairos and Fienup, 2008), the object, the illumination beam, and the translation parameters can be jointly optimized.

Multiple scattering

Fundamentally ptychography is based on a 2D multiplicative approximation to model the interaction of the probe and the object, which assumes that the exit wave is the product of the probe function and the object transmission function (Eq. (1)). However, this approximation breaks down at modest specimen thicknesses due to their larger interaction cross-section with the electron beam, which causes significant multiple scattering events to occur. As a result, to minimize multiple scattering, the illumination should be optimized and a suitable sample thickness should be employed to obtain a reasonable reconstruction (Liu et al., 2009).

To overcome this issue, Maiden et al. (2012a) adapted a multislice approach (Kirkland, 1998; Cowley and Moodie, 1957) that is widely used to account for multiple scattering events in image simulations and incorporated an inverse multislice (invMS) method into ptychographic reconstruction algorithms, whereby the exit surface wave function of an object is calculated slice by slice using a series of multiplications and Fresnel propagations between the slices as the wave is transmitted through the sample.

This invMS ptychography has been implemented in visible light (Godden et al., 2014) and X-ray imaging (Suzuki et al., 2014; Tsai et al., 2016). In electron microscopy, Gao et al. (2017) found that this method can provide depth-sectioned information from a 3D complex transmission function of a thick sample (Fig. 18A–H). Recently, Chen et al. (2021) recovered a linear phase response versus thickness and pushed the lateral resolution close to the intrinsic atomic size, limited by the thermal fluctuations of the atoms themselves (Fig. 18I–L). InvMS electron ptychography provides a powerful tool for determining the 3D structures of crystalline samples, for example, locating single dopants.

Low-frequency information transfer

Objects (cells, proteins, particles, etc.) naturally tend to contain information at many different spatial scales (or frequencies) from very fine (atomic lattice) to very coarse (overall shape). The goal of an ideal imaging system is to form an image that contains information from all scales simultaneously. The CTF describes how information is transferred at different frequencies through optical systems (Wade, 1992).

Compared to defocused phase-contrast TEM, ptychography has a wider, tunable, and continuous CTF in which either direct solutions (O'Leary et al., 2021; Yang et al., 2015) (Fig. 19A) or iterative approaches (Zhou et al., 2020) (Fig. 19D) are used for weak phase objects. In general, there are no zero crossings in the CTF such that contrast reversals are completely avoided at varying defocus conditions, which allows the phase to be directly interpretable. The bandpass of the CTF in the spatial frequency domain can also be tuned by adjusting the convergence angle, α, which enables information of low and high spatial frequencies to be transferred in a controllable manner. One can simply decrease α to enhance information transfer in the low-frequency region, thereby improving overall contrast without inducing rapid oscillations in the CTF at high frequencies and causing resolution degradation. Unlike phase contrast TEM, the method of contrast enhancement by varying α does not sacrifice resolution, which has been a major limitation of defocused phase contrast TEM imaging used in cryo-EM.

Another method of contrast enhancement is to introduce a prespecimen phase plate in the probe forming aperture in STEM to form 4D-STEM data with a focused probe. This approach is called ptychographic matched illumination detector interferometry STEM (PMIDI-STEM) (Yang et al., 2016a). By combining with noniterative ptychography, PMIDI-STEM enables an improved enhancement of the contrast transfer at low spatial frequencies for 2D imaging. The advantage of contrast enhancement using ptychography is particularly important for biological cryo-EM imaging because low spatial frequencies are inaccessible using conventional phase-contrast imaging (as shown in Fig. 19E–G).

Conclusion: Multidimensional ptychography

Electron ptychography has been successfully applied in reconstruction of the 2D phase information of object transmission functions. This method has many advantages, such as higher resolution and better signal-to-noise ratio, and it is more sensitive to low-Z elements than conventional imaging methods. In the future, the capabilities of electron ptychography can be further extended to other dimensions, such as the third dimension, time, and energy domains, as shown in Fig. 20.

TEM images are 2D projections of 3D objects, which in some cases makes the interpretation of the results difficult without information pertaining to the third dimension (optical axis). The most widely used 3D imaging methods are electron tomography (ET) (Baumeister et al., 1999; Midgley and Dunin-Borkowski, 2009) and SPA (Henderson and Unwin, 1975; Unwin and Henderson, 1975), which have played vital roles in 3D imaging for materials and biological science.

The combination of ptychography and tomography has been experimentally demonstrated with X-ray (Diaz et al., 2014; Holler et al., 2014, 2017; Dierolf et al., 2010; Chen et al., 2013) and electron beams (Ding et al., 2022). As ptychography can provide each projected image with a higher resolution that can be used as input data for tomography, both in-plane and out-of-plane resolutions

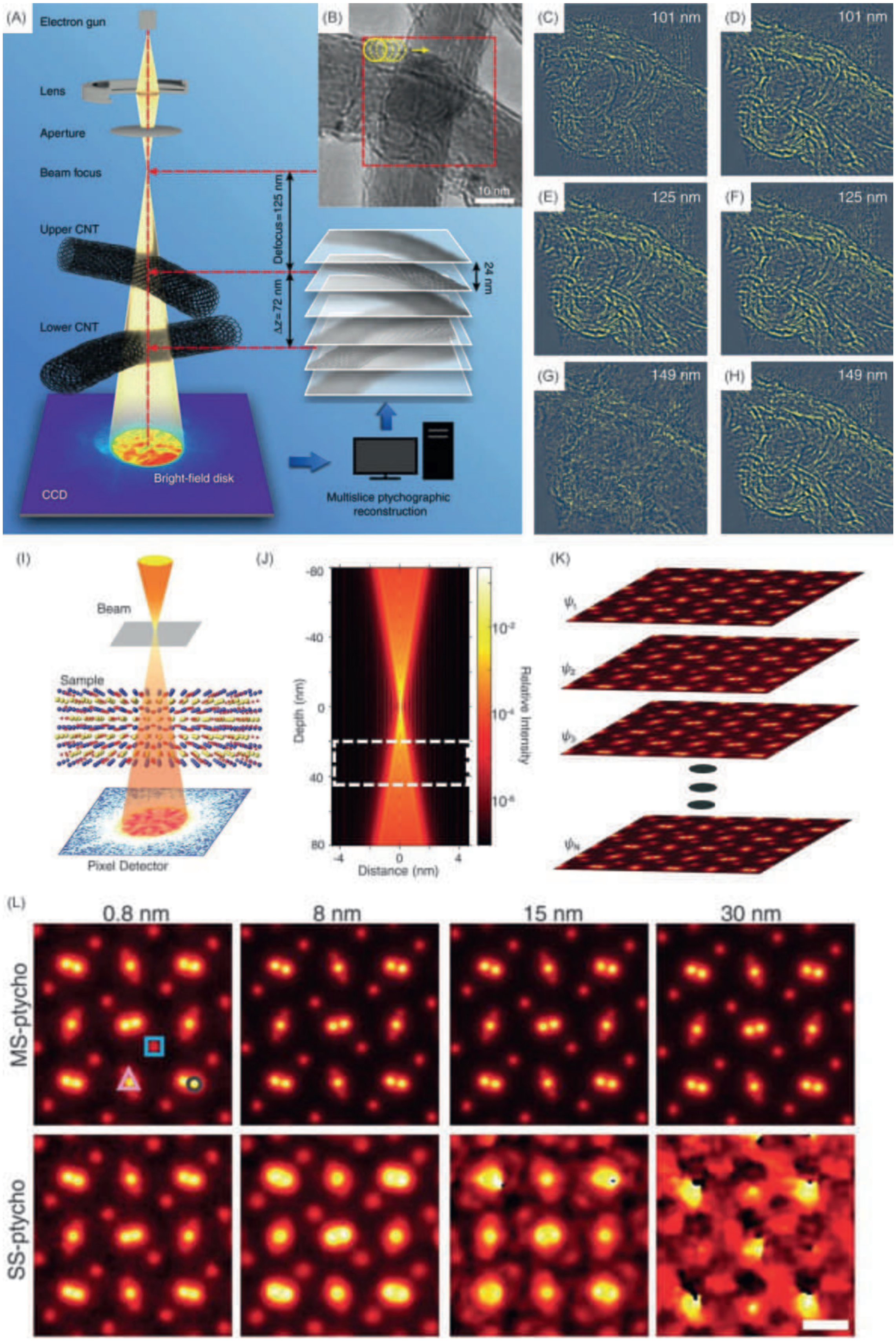
(A)
Electron gun
Lens
Aperture
Beam focus
Upper CNT
Lower CNT
CCD
Bright-field disk
Defocus=125 nm
Δz=72 nm
24 nm
Multislice ptychographic reconstruction
(B)
10 nm
(C)
101 nm
(D)
101 nm
(E)
125 nm
(F)
125 nm
(G)
149 nm
(H)
149 nm
(I)
Beam
Sample
Pixel Detector
(J)
-80
-40
0
40
80
Depth (nm)
-4
0
4
Distance (nm)
10^{-2}
10^{-4}
10^{-6}
Relative Intensity
(K)
ψ_1
ψ_2
ψ_3
ψ_N
(L)
0.8 nm
8 nm
15 nm
30 nm
MS-ptycho
SS-ptycho

Fig. 18 Multislice ptychography method used for reconstructing three-dimensional information of (A–H) carbon nanotubes (CNTs) (Gao et al., 2017) and (I–L) crystalline $PrScO_3$ (Chen et al., 2021).

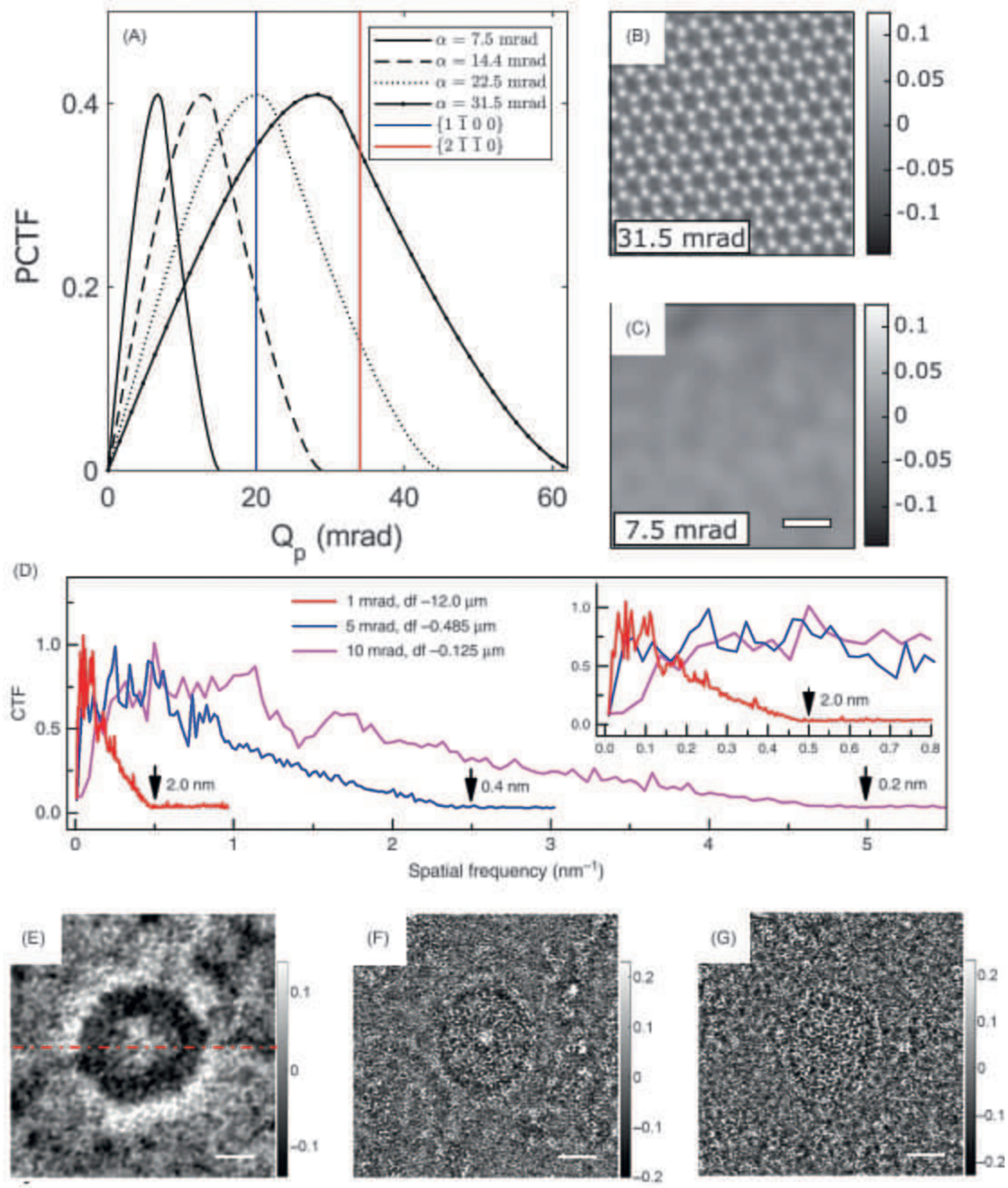

Fig. 19 (A) Phase contrast transfer functions (PCTFs) of ptychography using the SSB algorithm for various convergence semiangles were calculated. (B) and (C) show the ptychographic reconstructed results under convergence semiangle of 31.5 mrad and 7.5 mrad, respectively (O'Leary et al., 2021). (D) Simulated PCTFs of ptychography using the ePIE algorithm for various convergence semiangles. Poisson noise was added. (E–G) Experimental reconstructed phase results of adenovirus with convergence semiangle of 1.37, 4.68, and 10 mrad (Zhou et al., 2020).

can be improved. In particular, with the advantage of high contrast and high dose efficiency, electron ptychographic tomography holds great promise for the high-resolution 3D structural imaging of biological and nonbiological components simultaneously, which has been a great challenge for TEM tomography due to the inherently low contrast of biological components.

In light of recent 2D high-contrast Cryo-EPty work performed on viral particles (Zhou et al., 2020), ptychographic SPA (Pei et al., 2021; Pei et al., 2023) could help reduce the particle numbers required for 3D reconstruction and facilitate 3D classification of bio-structures of either low concentration or low symmetry.

With a pulsed electron beam source and ultrafast detector, single-shot and dynamic TEM have been designed and implemented to study dynamics in condensed matter systems and biological processes with micro- to attosecond temporal resolution. However, owing to the nature of the scanning mode and the limited read-out speed of detectors, the temporal resolution of ptychography remains poor. The limitations of ptychography have stimulated attempts to develop time-resolved methods in recent years.

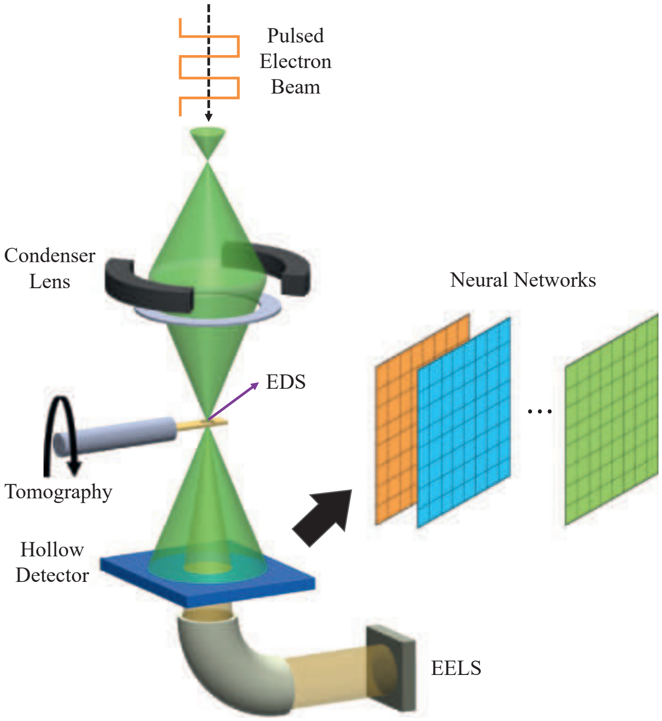

Fig. 20 Schematic illustration of future ptychography.

Single-shot ptychography was proposed for light optics (Sidorenko and Cohen, 2015), whereby instead of scanning the specimen point by point, pinholes are used to form multiple probe beams and illuminate the specimen simultaneously with partial overlap between neighboring illuminated areas so that ptychographic datasets are collected in a single exposure. Based on this, time-resolved imaging by multiplexed ptychography was developed for rapid dynamic imaging with pulsed laser beams (Wengrowicz et al., 2019; Sidorenko et al., 2017). In electron optics, the multiple electron beam system has been used to increase the throughput of microscopy and lithography applications. Therefore, based on current techniques, the integration of a multiple electron beam source with ptychography would be possible, which would facilitate time-resolved electron ptychography with a pulsed electron beam for dynamical studies both in the materials and life sciences.

Electrons can interact either elastically or inelastically with a sample, and the inelastically scattered electrons contain a wealth of information, such as the chemistry, band structure, and dielectric properties of the sample. Due to the constraints of detector geometry in electron ptychography, the inelastically scattered electrons in the energy-loss domain cannot be accessed.

A new "hollow" detector was devised, as shown in Fig. 20, to enable electron ptychography to couple with existing EELS designs to provide structural and elemental information simultaneously. Once dedicated "hollow" pixelated STEM detectors are commercially available, the configuration of "hollow"-type ptychography (Song et al., 2018) with EELS and other 4D-STEM (Ophus, 2019) capabilities (Fig. 20) will likely be widely used, becoming a powerful tool for the collection of multichannel signals and extraction of multidimensional information from samples.

Big data and artificial intelligence (AI) are at the forefront of technological advances in the digital world. Ptychography itself is a data-driven microscopic technique that can be further integrated with AI and machine learning (Nguyen et al., 2018; Wengrowicz et al., 2020; Guan and Tsai, 2019), for example, to obtain better reconstruction results using considerably less time (Kappeler et al., 2017). With the rapid generation of vast datasets across a range of multiple dimensions, permitted by continuous advances in EM instrumentation, AI-enhanced electron ptychography will emerge as one of the potentially disruptive themes in electron microscopy underpinning materials development for quantum computing, renewable energy, and the life sciences.

References

Ballabriga R, Alozy J, Blaj G, Campbell M, Fiederle M, Frojdh E, Heijne EHM, Llopart X, Pichotka M, Procz S, Tlustos L, and Wong W (2013) The Medipix3RX: A high resolution, zero dead-time pixel detector readout chip allowing spectroscopic imaging. *Journal of Instrumentation* 8: C02016.

Bates RHT and Rodenburg JM (1989) Sub-ångström transmission microscopy: A Fourier transform algorithm for microdiffraction plane intensity information. *Ultramicroscopy* 31: 303–307.

Batson PE, Dellby N, and Krivanek OL (2002) Sub-ångstrom resolution using aberration corrected electron optics. *Nature* 418: 617–620.

Baumeister W, Grimm R, and Walz J (1999) Electron tomography of molecules and cells. *Trends in Cell Biology* 9: 81–85.

Beckers M, Senkbeil T, Gorniak T, Giewekemeyer K, Salditt T, and Rosenhahn A (2013) Drift correction in ptychographic diffractive imaging. *Ultramicroscopy* 126: 44–47.

Bunk O, Dierolf M, Kynde S, Johnson I, Marti O, and Pfeiffer F (2008) Influence of the overlap parameter on the convergence of the ptychographical iterative engine. *Ultramicroscopy* 108: 481–487.

Cao S, Kok P, Li P, Maiden AM, and Rodenburg JM (2016) Modal decomposition of a propagating matter wave via electron ptychography. *Physical Review A* 94.

Cao S, Maiden AM, and Rodenburg JM (2018) Image feature delocalization in defocused probe electron ptychography. *Ultramicroscopy* 187: 71–83.

Chapman HN (1996) Phase-retrieval X-ray microscopy by Wigner-distribution deconvolution. *Ultramicroscopy* 66: 153–172.

Chen B, Guizar-Sicairos M, Xiong G, Shemilt L, Diaz A, Nutter J, Burdet N, Huo S, Mancuso J, Monteith A, Vergeer F, Burgess A, and Robinson I (2013) Three-dimensional structure analysis and percolation properties of a barrier marine coating. *Scientific Reports* 3: 1177.

Chen T, Ellis I, Hooper TJN, Liberti E, Ye L, Lo BTW, O'Leary C, Sheader AA, Martinez GT, Jones L, Ho PL, Zhao P, Cookson J, Bishop PT, Chater P, Hanna JV, Nellist P, and Tsang SCE (2019) Interstitial boron atoms in the palladium lattice of an industrial type of nanocatalyst: Properties and structural modifications. *Journal of the American Chemical Society* 141: 19616–19624.

Chen Z, Odstrcil M, Jiang Y, Han Y, Chiu MH, Li LJ, and Muller DA (2020) Mixed-state electron ptychography enables sub-angstrom resolution imaging with picometer precision at low dose. *Nature Communications* 11: 2994.

Chen Z, Jiang Y, Shao Y-T, Holtz Megan E, Odstrčil M, Guizar-Sicairos M, Hanke I, Ganschow S, Schlom Darrell G, and Muller David A (2021) Electron ptychography achieves atomic-resolution limits set by lattice vibrations. *Science* 372: 826–831.

Cowley JM and Moodie AF (1957) The scattering of electrons by atoms and crystals. I. A new theoretical approach. *Acta Crystallographica* 10: 609–619.

D'Alfonso AJ, Morgan AJ, Yan AWC, Wang P, Sawada H, Kirkland AI, and Allen LJ (2014) Deterministic electron ptychography at atomic resolution. *Physical Review B* 89.

D'Alfonso AJ, Allen LJ, Sawada H, and Kirkland AI (2016) Dose-dependent high-resolution electron ptychography. *Journal of Applied Physics* 119: 054302.

de Jong AF and van Dyck D (1993) Ultimate resolution and information in electron microscopy II. The information limit of transmission electron microscopes. *Ultramicroscopy* 49: 66–80.

Diaz A, Guizar-Sicairos M, Poeppel A, Menzel A, and Bunk O (2014) Characterization of carbon fibers using X-ray phase nanotomography. *Carbon* 67: 98–103.

Dierolf M, Menzel A, Thibault P, Schneider P, Kewish CM, Wepf R, Bunk O, and Pfeiffer F (2010) Ptychographic X-ray computed tomography at the nanoscale. *Nature* 467: 436–439.

Ding Z, Gao S, Fang W, Huang C, Zhou L, Pei X, Liu X, Pan X, Fan C, Kirkland AI, and Wang P (2022) Three-dimensional electron ptychography of organic–inorganic hybrid nanostructures. *Nature Communications* 13: 4787.

Dos Reis R, Yang H, Ophus C, Ercius P, Bizarri G, Perrodin D, Shalapska T, Bourret E, Ciston J, and Dahmen U (2018) Determination of the structural phase and octahedral rotation angle in halide perovskites. *Applied Physics Letters* 112.

Elser V (2003) Phase retrieval by iterated projections. *Journal of the Optical Society of America A* 20: 40–55.

Faulkner H and Rodenburg JM (2004) Movable aperture lensless transmission microscopy: A novel phase retrieval algorithm. *Physical Review Letters* 93: 023903.

Faulkner HML and Rodenburg JM (2005) Error tolerance of an iterative phase retrieval algorithm for moveable illumination microscopy. *Ultramicroscopy* 103: 153–164.

Fienup JR (1982) Phase retrieval algorithms: A comparison. *Applied Optics* 21.

Gabor D (1948) A new microscopic principle. *Nature* 161: 777–778.

Gabor D (1949) Microscopy by reconstructed wave-fronts. *Proceedings of the Royal Society of London. Series A: Mathematical and Physical Sciences* 197: 454–487.

Gabor D (1951) Microscopy by reconstructed wave fronts: II. *Proceedings of the Physical Society. Section B* 64: 449.

Gao S, Wang P, Zhang F, Martinez GT, Nellist PD, Pan X, and Kirkland AI (2017) Electron ptychographic microscopy for three-dimensional imaging. *Nature Communications* 8: 163.

Gerchberg RW and Saxton WO (1972) A practical algorithm for the determination of phase from image and diffraction plane pictures. *Optik* 35: 237–250.

Giewekemeyer K, Thibault P, Kalbfleisch S, Beerlink A, Kewish CM, Dierolf M, Pfeiffer F, and Salditt T (2010) Quantitative biological imaging by ptychographic x-ray diffraction microscopy. *Proceedings of the National Academy of Sciences of the United States of America* 107: 529–534.

Godard P, Carbone G, Allain M, Mastropietro F, Chen G, Capello L, Diaz A, Metzger TH, Stangl J, and Chamard V (2011) Three-dimensional high-resolution quantitative microscopy of extended crystals. *Nature Communications* 2: 568.

Godard P, Allain M, Chamard V, and Rodenburg J (2012) Noise models for low counting rate coherent diffraction imaging. *Optics Express* 20: 25914–25934.

Godden TM, Suman R, Humphry MJ, Rodenburg JM, and Maiden AM (2014) Ptychographic microscope for three-dimensional imaging. *Optics Express* 22: 12513–12523.

Guan Z and Tsai EH (2019) *Ptychnet: Fast and high quality phase retrieval for ptychography.* Brookhaven National Lab (BNL). Upton, NY (United States).

Guizar-Sicairos M and Fienup JR (2008) Phase retrieval with transverse translation diversity: A nonlinear optimization approach. *Optics Express* 16: 7264–7278.

Haider M, Braunshausen G, and Schwan E (1995) Correction of the spherical aberration of a 200 kV TEM by means of a hexapole-corrector. *Optik (Stuttgart)* 99: 167–179.

Haigh SJ, Sawada H, and Kirkland AI (2009) Atomic structure imaging beyond conventional resolution limits in the transmission electron microscope. *Physical Review Letters* 103: 126101.

Hemonnot CY, Reinhardt J, Saldanha O, Patommel J, Graceffa R, Weinhausen B, Burghammer M, Schroer CG, and Koster S (2016) X-rays reveal the internal structure of keratin bundles in whole cells. *ACS Nano* 10: 3553–3561.

Henderson R and Unwin PNT (1975) Three-dimensional model of purple membrane obtained by electron microscopy. *Nature* 257: 28–32.

Hetherington C (2004) Aberration correction for TEM. *Materials Today* 7: 50–55.

Holler M, Diaz A, Guizar-Sicairos M, Karvinen P, Farm E, Harkonen E, Ritala M, Menzel A, Raabe J, and Bunk O (2014) X-ray ptychographic computed tomography at 16 nm isotropic 3D resolution. *Scientific Reports* 4: 3857.

Holler M, Guizar-Sicairos M, Tsai EH, Dinapoli R, Muller E, Bunk O, Raabe J, and Aeppli G (2017) High-resolution non-destructive three-dimensional imaging of integrated circuits. *Nature* 543: 402–406.

Hoppe W (1969) Beugung im inhomogenen Primarstrahlwellenfeld. I. Prinzip einer Phasenmessung von Elektronenbeungungsinterferenzen. *Acta Crystallogr. Sect. A* 25: 495–501.

Hruszkewycz SO, Holt MV, Murray CE, Bruley J, Holt J, Tripathi A, Shpyrko OG, Mcnulty I, Highland MJ, and Fuoss PH (2012) Quantitative nanoscale imaging of lattice distortions in epitaxial semiconductor heterostructures using nanofocused X-ray Bragg projection ptychography. *Nano Letters* 12: 5148–5154.

Hruszkewycz SO, Allain M, Holt MV, Murray CE, Holt JR, Fuoss PH, and Chamard V (2017) High-resolution three-dimensional structural microscopy by single-angle Bragg ptychography. *Nature Materials* 16: 244–251.

Hue F, Rodenburg JM, Maiden AM, and Midgley PA (2011) Extended ptychography in the transmission electron microscope: Possibilities and limitations. *Ultramicroscopy* 111: 1117–1123.

Humphry MJ, Kraus B, Hurst AC, Maiden AM, and Rodenburg JM (2012) Ptychographic electron microscopy using high-angle dark-field scattering for sub-nanometre resolution imaging. *Nature Communications* 3: 730.

Jia C-L, Mi S-B, Urban K, Vrejoiu I, Alexe M, and Hesse D (2008) Atomic-scale study of electric dipoles near charged and uncharged domain walls in ferroelectric films. *Nature Materials* 7: 57–61.

Jiang Y, Chen Z, Han Y, Deb P, Gao H, Xie S, Purohit P, Tate MW, Park J, Gruner SM, Elser V, and Muller DA (2018) Electron ptychography of 2D materials to deep sub-angstrom resolution. *Nature* 559: 343–349.

Kappeler A, Ghosh S, Holloway J, Cossairt O, and Katsaggelos A (2017) *Ptychnet: CNN Based Fourier Ptychography.* IEEE International Conference on Image Processing (ICIP).

Kirkland EJ (1998) *Advanced Computing in Electron Microscopy*, vol. 12. Springer.

Krivanek OL, Dellby N, Spence AJ, Camps RA, and Brown LM (1997) Aberration correction in the STEM. In: *Electron Microscopy and Analysis 1997*. CRC Press.

Krivanek OL, Dellby N, and Lupini AR (1999) Towards sub-Å electron beams. *Ultramicroscopy* 78: 1–11.

Lee J and Barbastathis G (2016) Denoised Wigner distribution deconvolution via low-rank matrix completion. *Optics Express* 24: 20069–20079.

Li P and Maiden AM (2018) Ten implementations of ptychography. *Journal of Microscopy* 269: 187–194.

Li P, Edo TB, and Rodenburg JM (2014) Ptychographic inversion via Wigner distribution deconvolution: Noise suppression and probe design. *Ultramicroscopy* 147: 106–113.

Lichte H and Lehmann M (2007) Electron holography—basics and applications. *Reports on Progress in Physics* 71: 016102.

Lima E, Diaz A, Guizar-Sicairos M, Gorelick S, Pernot P, Schleier T, and Menzel A (2013) Cryo-scanning x-ray diffraction microscopy of frozen-hydrated yeast. *Journal of Microscopy* 249: 1–7.

Liu C, Walther T, and Rodenburg JM (2009) Influence of thick crystal effects on ptychographic image reconstruction with moveable illumination. *Ultramicroscopy* 109: 1263–1275.

Lozano JG, Martinez GT, Jin L, Nellist PD, and Bruce PG (2018) Low-dose aberration-free imaging of li-rich cathode materials at various states of charge using electron ptychography. *Nano Letters* 18: 6850–6855.

Maiden AM and Rodenburg JM (2009) An improved ptychographical phase retrieval algorithm for diffractive imaging. *Ultramicroscopy* 109: 1256–1262.

Maiden AM, Humphry MJ, Zhang F, and Rodenburg JM (2011) Superresolution imaging via ptychography. *Journal of the Optical Society of America. A, Optics, Image Science, and Vision* 28: 604–612.

Maiden AM, Humphry MJ, and Rodenburg JM (2012a) Ptychographic transmission microscopy in three dimensions using a multi-slice approach. *JOSA A* 29: 1606–1614.

Maiden AM, Humphry MJ, Sarahan MC, Kraus B, and Rodenburg JM (2012b) An annealing algorithm to correct positioning errors in ptychography. *Ultramicroscopy* 120: 64–72.

Maiden AM, Sarahan MC, Stagg MD, Schramm SM, and Humphry MJ (2015) Quantitative electron phase imaging with high sensitivity and an unlimited field of view. *Scientific Reports* 5: 14690.

Miao J, Charalambous P, Kirz J, and Sayre D (1999) Extending the methodology of X-ray crystallography to allow imaging of micrometre-sized non-crystalline specimens. *Nature* 400: 342–344.

Midgley PA and Dunin-Borkowski RE (2009) Electron tomography and holography in materials science. *Nature Materials* 8: 271–280.

Morgan AJ, D'Alfonso AJ, Wang P, Sawada H, Kirkland AI, and Allen LJ (2013) Fast deterministic single-exposure coherent diffractive imaging at sub-Ångström resolution. *Physical Review B* 87.

Muller DA, Kourkoutis LF, Murfitt M, Song JH, Hwang HY, Silcox J, Dellby N, and Krivanek OL (2008) Atomic-scale chemical imaging of composition and bonding by aberration-corrected microscopy. *Science* 319: 1073–1076.

Nellist PD and Rodenburg JM (1994) Beyond the conventional information limit: the relevant coherence function. *Ultramicroscopy* 54: 61–74.

Nellist PD, Rodenburg JM, and Mccallum BC (1995) Resolution beyond the 'information limit' in transmission electron microscopy. *Nature* 374: 630–632.

Nguyen DT, Findlay SD, and Etheridge J (2014) The spatial coherence function in scanning transmission electron microscopy and spectroscopy. *Ultramicroscopy* 146: 6–16.

Nguyen T, Xue Y, Li Y, Tian L, and Nehmetallah G (2018) Deep learning approach for Fourier ptychography microscopy. *Optics Express* 26: 26470–26484.

O'Leary CM, Allen CS, Huang C, Kim JS, Liberti E, Nellist PD, and Kirkland AI (2020) Phase reconstruction using fast binary 4D STEM data. *Applied Physics Letters* 116.

O'Leary CM, Martinez GT, Liberti E, Humphry MJ, Kirkland AI, and Nellist PD (2021) Contrast transfer and noise considerations in focused-probe electron ptychography. *Ultramicroscopy* 221: 113189.

Ophus C (2019) Four-dimensional scanning transmission electron microscopy (4D-STEM): From scanning nanodiffraction to ptychography and beyond. *Microscopy and Microanalysis* 25: 563–582.

Pei X, Zhou L, Kim J, Boyce M, Huang H, Liberti E, Nellist P, Zhang P, Stuart D, Kirkland A, and Wang P (2021) Ptychographic single particle analysis for biological science. *Microscopy and Microanalysis* 27: 190–192.

Pei X, et al. (2023) Cryogenic electron ptychographic single particle analysis with wide bandwidth information transfer. *Nature Communications* 14(1): 3027.

Pelz PM, Qiu WX, Bucker R, Kassier G, and Miller RJD (2017) Low-dose cryo electron ptychography via non-convex Bayesian optimization. *Scientific Reports* 7: 9883.

Pennycook TJ, Lupini AR, Yang H, Murfitt MF, Jones L, and Nellist PD (2015) Efficient phase contrast imaging in STEM using a pixelated detector. Part 1: experimental demonstration at atomic resolution. *Ultramicroscopy* 151: 160–167.

Pennycook TJ, Martinez GT, Nellist PD, and Meyer JC (2019) High dose efficiency atomic resolution imaging via electron ptychography. *Ultramicroscopy* 196: 131–135.

Pfeifer MA, Williams GJ, Vartanyants IA, Harder R, and Robinson IK (2006) Three-dimensional mapping of a deformation field inside a nanocrystal. *Nature* 442: 63–66.

Putkunz CT, D'Alfonso AJ, Morgan AJ, Weyland M, Dwyer C, Bourgeois L, Etheridge J, Roberts A, Scholten RE, Nugent KA, and Allen LJ (2012) Atom-scale ptychographic electron diffractive imaging of boron nitride cones. *Physical Review Letters* 108: 073901.

Robisch AL, Kröger K, Rack A, and Salditt T (2015) Near-field ptychography using lateral and longitudinal shifts. *New Journal of Physics* 17.

Rodenburg JM (2008) Ptychography and related diffractive imaging methods. In: Hawkes PW (ed.) *Advances in Imaging and Electron Physics*, pp. 87–184. Elsevier.

Rodenburg JM and Bates RHT (1992) The theory of super-resolution electron microscopy via Wigner-distribution deconvolution. *Philosophical Transactions of the Royal Society of London. Series A: Physical and Engineering Sciences* 339(1655): 521–553.

Rodenburg JM and Faulkner HML (2004) A phase retrieval algorithm for shifting illumination. *Applied Physics Letters* 85: 4795–4797.

Rodenburg J and Maiden A (2019) Ptychography. In: *Handbook of Microscopy*. Springer.

Rodenburg JM, Mccallum BC, and Nellist PD (1993) Experimental tests on double-resolution coherent imaging via STEM. *Ultramicroscopy* 48: 304–314.

Rodenburg JM, Hurst AC, Cullis AG, Dobson BR, Pfeiffer F, Bunk O, David C, Jefimovs K, and Johnson I (2007) Hard-x-ray lensless imaging of extended objects. *Physical Review Letters* 98: 034801.

Rose H (1976) Nonstandard imaging methods in electron microscopy. *Ultramicroscopy* 2: 251–267.

Rose H (1990) Outline of a spherically corrected semiaplanatic medium-voltage transmission electron microscope. *Optik* 85: 19–24.

Ryll H, Simson M, Hartmann R, Holl P, Huth M, Ihle S, Kondo Y, Kotula P, Liebel A, Müller-Caspary K, Rosenauer A, Sagawa R, Schmidt J, Soltau H, and STRüDER, L. (2016) A pnCCD-based, fast direct single electron imaging camera for TEM and STEM. *Journal of Instrumentation* 11: P04006.

Scherzer O (1936) Über einige Fehler von Elektronenlinsen. *Zeitschrift für Physik* 101: 593–603.

Seki T, Ikuhara Y, and Shibata N (2018) Theoretical framework of statistical noise in scanning transmission electron microscopy. *Ultramicroscopy* 193: 118–125.

Sidorenko P and Cohen O (2015) Single-shot ptychography. *Optica* 3.

Sidorenko P, Lahav O, and Cohen O (2017) Ptychographic ultrahigh-speed imaging. *Optics Express* 25: 10997–11008.

Song B, Ding Z, Allen CS, Sawada H, Zhang F, Pan X, Warner J, Kirkland AI, and Wang P (2018) Hollow electron ptychographic diffractive imaging. *Physical Review Letters* 121: 146101.

Song J, Allen CS, Gao S, Huang C, Sawada H, Pan X, Warner J, Wang P, and Kirkland AI (2019) Atomic resolution defocused electron ptychography at low dose with a fast, direct electron detector. *Scientific Reports* 9: 3919.

Stachnik K, Mohacsi I, Vartiainen I, Stuebe N, Meyer J, Warmer M, David C, and Meents A (2015) Influence of finite spatial coherence on ptychographic reconstruction. *Applied Physics Letters* 107.

Stockmar M, Cloetens P, Zanette I, Enders B, Dierolf M, Pfeiffer F, and Thibault P (2013) Near-field ptychography: Phase retrieval for inline holography using a structured illumination. *Scientific Reports* 3: 1927.

Suzuki A, Furutaku S, Shimomura K, Yamauchi K, Kohmura Y, Ishikawa T, and Takahashi Y (2014) High-resolution multislice x-ray ptychography of extended thick objects. *Physical Review Letters* 112: 053903.

Tate MW, Purohit P, Chamberlain D, Nguyen KX, Hovden R, Chang CS, Deb P, Turgut E, Heron JT, Schlom DG, Ralph DC, Fuchs GD, Shanks KS, Philipp HT, Muller DA, and Gruner SM (2016) High dynamic range pixel array detector for scanning transmission electron microscopy. *Microscopy and Microanalysis* 22: 237–249.

Thibault P and Guizar-Sicairos M (2012) Maximum-likelihood refinement for coherent diffractive imaging. *New Journal of Physics* 14.

Thibault P and Menzel A (2013) Reconstructing state mixtures from diffraction measurements. *Nature* 494: 68–71.

Thibault P, Dierolf M, Menzel A, Bunk O, David C, and Pfeiffer F (2008) High-resolution scanning x-ray diffraction microscopy. *Science* 321: 379–382.

Thibault P, Dierolf M, Bunk O, Menzel A, and Pfeiffer F (2009) Probe retrieval in ptychographic coherent diffractive imaging. *Ultramicroscopy* 109: 338–343.

Tsai EH, Usov I, Diaz A, Menzel A, and Guizar-Sicairos M (2016) X-ray ptychography with extended depth of field. *Optics Express* 24: 29089–29108.

Unwin PNT and Henderson R (1975) Molecular structure determination by electron microscopy of unstained crystalline specimens. *Journal of Molecular Biology* 94: 425–440.

Wade RH (1992) A brief look at imaging and contrast transfer. *Ultramicroscopy* 46: 145–156.

Wang P, Zhang F, Gao S, Zhang M, and Kirkland AI (2017) Electron ptychographic diffractive imaging of boron atoms in LaB6 crystals. *Scientific Reports* 7: 2857.

Wen Y, Ophus C, Allen CS, Fang S, Chen J, Kaxiras E, Kirkland AI, and Warner JH (2019) Simultaneous identification of low and high atomic number atoms in monolayer 2D materials using 4D scanning transmission electron microscopy. *Nano Letters* 19: 6482–6491.

Wengrowicz O, Peleg O, Loevsky B, Chen BK, Haham GI, Sainadh US, and Cohen O (2019) Experimental time-resolved imaging by multiplexed ptychography. *Optics Express* 27: 24568–24577.

Wengrowicz O, Peleg O, Zahavy T, Loevsky B, and Cohen O (2020) Deep neural networks in single-shot ptychography. *Optics Express* 28: 17511–17520.

Whitehead LW, Williams GJ, Quiney HM, Vine DJ, Dilanian RA, Flewett S, Nugent KA, Peele AG, Balaur E, and Mcnulty I (2009) Diffractive imaging using partially coherent x rays. *Physical Review Letters* 103: 243902.

Wilke RN, Priebe M, Bartels M, Giewekemeyer K, Diaz A, Karvinen P, and Salditt T (2012) Hard X-ray imaging of bacterial cells: nano-diffraction and ptychographic reconstruction. *Optics Express* 20: 19232–19254.

Wilke RN, Hoppert M, Krenkel M, Bartels M, and Salditt T (2015) Quantitative X-ray phase contrast waveguide imaging of bacterial endospores. *Journal of Applied Crystallography* 48: 464–476.

Xu W, Lin H, Wang H, and Zhang F (2020) Reconstruction method of a ptychographic dataset with unknown positions. *Optics Letters* 45: 4634–4637.

Yang H, Pennycook TJ, and Nellist PD (2015) Efficient phase contrast imaging in STEM using a pixelated detector. Part II: Optimisation of imaging conditions. *Ultramicroscopy* 151: 232–239.

Yang H, Ercius P, Nellist PD, and Ophus C (2016a) Enhanced phase contrast transfer using ptychography combined with a pre-specimen phase plate in a scanning transmission electron microscope. *Ultramicroscopy* 171: 117–125.

Yang H, Rutte RN, Jones L, Simson M, Sagawa R, Ryll H, Huth M, Pennycook TJ, Green ML, Soltau H, Kondo Y, Davis BG, and Nellist PD (2016b) Simultaneous atomic-resolution electron ptychography and Z-contrast imaging of light and heavy elements in complex nanostructures. *Nature Communications* 7: 12532.

Yang H, Maclaren I, Jones L, Martinez GT, Simson M, Huth M, Ryll H, Soltau H, Sagawa R, Kondo Y, Ophus C, Ercius P, Jin L, Kovacs A, and Nellist PD (2017) Electron ptychographic phase imaging of light elements in crystalline materials using Wigner distribution deconvolution. *Ultramicroscopy* 180: 173–179.

Yu YS, Kim C, Shapiro DA, Farmand M, Qian D, Tyliszczak T, Kilcoyne AL, Celestre R, Marchesini S, Joseph J, Denes P, Warwick T, Strobridge FC, Grey CP, Padmore H, Meng YS, Kostecki R, and Cabana J (2015) Dependence on crystal size of the nanoscale chemical phase distribution and fracture in LixFePO(4). *Nano Letters* 15: 4282–4288.

Zach J and Haider M (1995) Correction of spherical and chromatic aberration in a low voltage SEM. *Optik (Stuttgart)* 98: 112–118.

Zhang F, Peterson I, Vila-Comamala J, Diaz A, Berenguer F, Bean R, Chen B, Menzel A, Robinson IK, and Rodenburg JM (2013) Translation position determination in ptychographic coherent diffraction imaging. *Optics Express* 21: 13592–13606.

Zhou L, Song J, Kim JS, Pei X, Huang C, Boyce M, Mendonca L, Clare D, Siebert A, Allen CS, Liberti E, Stuart D, Pan X, Nellist PD, Zhang P, Kirkland AI, and Wang P (2020) Low-dose phase retrieval of biological specimens using cryo-electron ptychography. *Nature Communications* 11: 2773.

Zuo JM, Vartanyants I, Gao M, Zhang R, and Nagahara LA (2003) Atomic resolution imaging of a carbon nanotube from diffraction intensities. *Science* 300: 1419–1421.

Momentum-resolved scanning transmission electron microscopy

Knut Müller-Caspary[a] **and Florian F Krause**[b], [a]Department of Chemistry and Centre for NanoScience, Ludwig-Maximilians-Universität München, Munich, Germany; [b]Institute of Solid State Physics, University of Bremen, Bremen, Germany

© 2024 Elsevier Ltd. All rights reserved.

Introduction **95**
Multidimensionality in STEM **96**
Momentum-resolved STEM **97**
Terminology **97**
A momentum-resolved STEM example **98**
First-moment STEM **98**
Theory and methodology 98
Practical aspects 99
Mapping electrical properties **100**
Basic concept 100
Partial coherence 102
Mapping charges and potentials 102
Polarization and meso-scale electric fields 103
Angle-resolved STEM **104**
Methodology 104
Applications 105
Impact of inelastic scattering **106**
Conclusion **107**
Prospects **107**
Acknowledgments **108**
References **108**

Abstract

Momentum-resolved scanning transmission electron microscopy (MR-STEM) refers to the recording of a full diffraction pattern for each scan point of a scanning electron probe. The resulting four-dimensional datasets not only overcome the limited flexibility of established detector geometries determined by hardware but also transform formerly challenging methods into widespread imaging modes. After briefly reviewing multidimensionality aspects in STEM, a unique terminology for MR-STEM is introduced. The concept of first-moment STEM (FM-STEM) is derived robustly from fundamental quantum mechanics, followed by a detailed description of practical aspects related to ultrafast pixelated detectors. FM-STEM delivers the average lateral momentum of the electron beam. The article works out how atomic electric fields can be measured in thin specimens, and outlines methodologies for measuring polarization-induced electric fields in thick ones. By angular multirange analysis, it is elucidated how MR-STEM can yield specimen thickness and composition simultaneously. A brief assessment of inelastic scattering effects on MR-STEM closes this article.

Key points

This article provides the following concepts:

- Introduction to multidimensionality in STEM.
- Establishing momentum-resolved STEM as a versatile four-dimensional imaging technique.
- Mathematical derivation and experimental demonstration of momentum transfer mapping based on first-moment STEM.
- Atomic and polarization-induced electric field measurements by employing Ehrenfest's theorem.
- Angle-resolved STEM concept to separate local composition, thickness, and strain effects in an angular multirange analysis.
- Discussion of the impact of inelastic scattering on momentum-resolved STEM.
- Future prospects.

Introduction

Scanning transmission electron microscopy (STEM) has recently crossed the border to probe subatomic details thanks to aberration correction. At such length scales, partly reaching down below 50 pm, formerly paradigmatic questions as to chemical composition

https://doi.org/10.1016/B978-0-323-90800-9.00209-2

or lattice strain become secondary, in favor of studying electric properties with sub-bond-length resolution. In fact, the dramatic improvement of the spatial resolution is only one of several prerequisites to address these challenges because established detection and evaluation schemes provide insufficient information.

On the hardware side, ultrafast cameras led to a revolution of standard STEM acquisition in that a full diffraction pattern can be recorded at each scan point of the probe. This unique combination of real- and diffraction space information constitutes the focus of this article, momentum-resolved STEM (MR-STEM).

A paramount requirement to profit from the new wealth of available data is the development of methods to draw scientific conclusions about local physical properties such as electrostatic fields, potential, charge distributions, polarization, as well as chemical composition and structure.

To stay within the scope and maintain complementarity to the other chapters of this volume, this article covers the most important *direct* and *contemporary* methodologies. In particular, MR-STEM is introduced as a generic setup, before first moment imaging, electric field, potential and charge density mapping, polarization measurement, and composition quantification by angular multirange analysis are presented in detail. The impact of inelastic scattering on these methods is shortly discussed.

Electron ptychography concepts and related phase retrieval schemes, which are also based on momentum-resolved data, will not be discussed in this article. The reader is referred to pertinent literature to study those. Similarly, this document excludes methods that draw information from the geometry of diffraction patterns, such as strain and electric field measurements by nano-beam electron diffraction, which are well-represented in existing literature.

Multidimensionality in STEM

By shifting a focused beam and thereby subsequently probing different volumes of a specimen, STEM is inherently capable of simultaneously delivering a multitude of signals at high spatial resolution. Besides the two real-space dimensions of the scan, *multidimensionality* in STEM is an ambiguous term that can include energy-dispersive X-ray (EDX) or electron energy loss spectra (EELS), secondary or back-scattered electron signals, as well as cathodoluminescence data, to name a few established detection schemes. Most importantly, STEM originally employs detectors positioned in the Fraunhofer diffraction plane covering different portions of solid angles. The most prominent imaging modes are bright- and annular dark field (BF, ADF) STEM as depicted in Fig. 1. They employ disk or ring-shaped detectors centered around the optical axis and deliver coherent and incoherent scattering details, respectively. By segmenting (annular) BF detectors, differential phase contrast (DPC) (Dekkers and de Lang, 1978) STEM constitutes a long-standing tradition in providing contrast due to magnetic (Chapman et al., 1978), electric (Lohr et al., 2012; Shibata et al., 2012), and weakly scattering features (Rose, 1977; Lazić et al., 2016; Lazić et al., 2022).

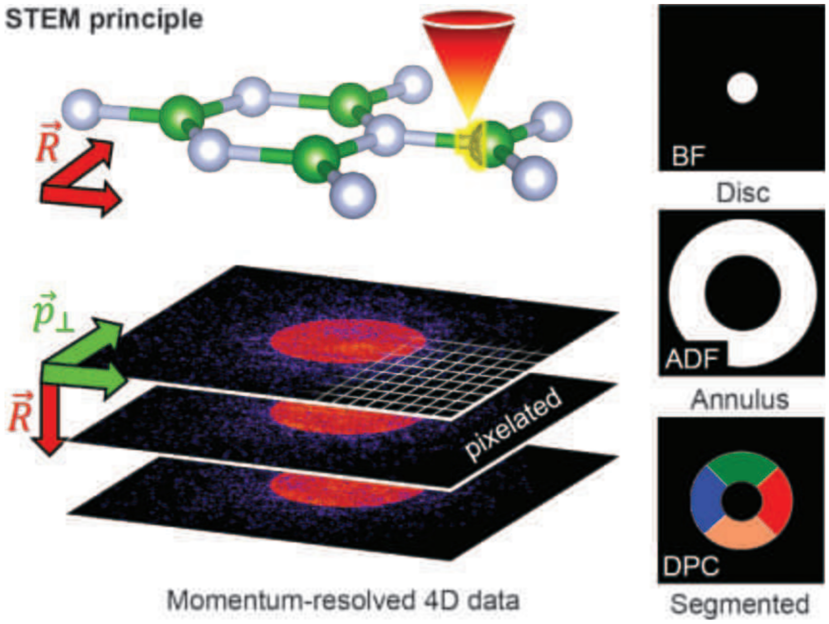

Fig. 1 Scanning transmission electron microscopy (STEM) setup and detection schemes. In aberration-corrected STEM, an electron probe is focused to subatomic diameter and rastered across the specimen. In momentum-resolved STEM (MR-STEM), a full diffraction pattern is recorded at each scan point, yielding a four-dimensional data set. This drastically enhances versatility of the STEM technique as compared to conventional bright field (BF), annular dark field (ADF) or differential phase contrast (DPC) imaging employing much simpler detector geometries.

Momentum-resolved STEM

Given the versatile physical insights dedicated detector geometries offer as to the local chemistry, electrical, magnetic, and structural properties, it is a natural advancement to record the data *momentum-resolved*. This means that a detailed diffraction pattern is recorded at each scan point which allows for maximum flexibility to generate any dedicated contrast a posteriori during the evaluation using software. As illustrated in Fig. 1, the momentum-resolved imaging mode hence produces a four-dimensional dataset $I(\vec{R}, \vec{p}_\perp)$ consisting of two raster coordinates $\vec{R}$ of the probe in real space, and two diffraction coordinates $\vec{p}_\perp$, which is why this imaging mode is occasionally referred to as *4D STEM*.

Obviously, a critical requirement to put any STEM technique into practice is the availability of high-speed detectors, as the dwell time per raster point is given by a detector's minimal exposure time. For example, a conventional ADF STEM detector is commonly read out at MHz rates. Although charge-coupled devices (CCDs) emerged in the late 1980s (Spence and Zuo, 1988), frame rates remained in the few-Hz range for decades, and allowed for rather conceptual proofs (Rodenburg et al., 1993) than practical applications. First ultrafast CCD-based cameras with kHz frame rates were introduced to STEM in 2012 (Müller et al., 2012), quickly followed by a variety of technologies in the coming years (Plackett et al., 2013; Müller-Caspary et al., 2015; Tate et al., 2016; Jannis et al., 2022; Ryll et al., 2016). Acquisition speeds rapidly increased to frame rates of several kHz, thus putting a variety of new diffraction-based STEM methods into practice which are based on momentum-resolved data acquisition.

Terminology

The multitude of accessible dimensions renders the term *4D STEM* rather ambiguous. Therefore, *scanning diffraction* or MR-STEM specifies the physical dimensions more accurately, and the latter term will be used throughout this article. MR-STEM is a broad term that describes any experiment where diffraction patterns are recorded at sufficiently high sampling in momentum space as a function of the position of a scanning STEM probe.

We will elucidate the significance of *first moment STEM* (FM-STEM) for the average momentum transferred to the electron beam by virtue of the interaction with electric fields below. FM-STEM refers to the first moment of the scattered intensity distribution (Waddell and Chapman, 1979) at each scan point, which is identical to the average momentum (transfer) occurring in the specimen. It is also called *center of mass* (COM) imaging. These two terms often appear in conjunction with, but need to be distinguished from direct electric or magnetic field mapping, which is only reliable if certain conditions are fulfilled, as will be detailed below.

In the style of rotationally symmetric BF and ADF detectors, the 2π-azimuthal integrals of diffracted intensities taken in dependence of the scattering angle ϑ are subject to *angle-resolved STEM* (AR-STEM). Strain, chemical composition, specimen thickness, or inelastic scattering can leave unique fingerprints in the radial intensity that can be used for the characterization of specimens via the comparison with simulations.

Fig. 2 depicts the three coordinate frames used in this work. Capital $\vec{R} = (X, Y)$ denotes the scan coordinate in a 2D plane perpendicular to the optical axis. The STEM probe might exhibit a defocus Δf measured perpendicular to $\vec{R}$ with $\Delta f < 0$ inside the specimen. Fourier-transforming a measured signal with respect to $\vec{R}$ provides its representation in terms of spatial frequencies of the scan denoted by $\vec{Q} = (U, V)$. Positions inside the specimen, for example, atom positions or the positions on which electric field and electrostatic potential depend, are given by real-space coordinates $\vec{r} = (x, y, z)$. Fourier-transforming in 2D with respect to

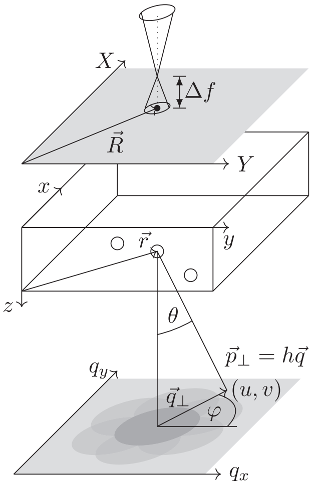

Fig. 2 The coordinate systems used in this article: x and y are used as lateral real-space coordinates perpendicular to the optical axis while z measures position in beam direction. Positions inside the specimen are therefore given by $\vec{r} = (\vec{r}_\perp, z) = (x, y, z)$. $\vec{r}_\perp$ gives the lateral component. $\vec{q}_\perp = (u, v)$ is the related reciprocal coordinate, that is used in the diffraction pattern. The position of the probe, measured in the x-y-system, is denoted as $\vec{R} = (X, Y)$.

$\vec{r}_\perp = (x, y)$ yields the conjugate diffraction coordinate system with spatial frequency vector $\vec{q}_\perp = (u, v)$ perpendicular to the optical axis, and the respective momentum $\vec{p}_\perp = h \cdot \vec{q}_\perp$ with Planck's constant h. The momentum transfer is related to the scattering angle by $p_\perp = h\lambda^{-1} \sin \vartheta \approx h\lambda^{-1}\vartheta$ with the electron wavelength λ and the approximation being valid for small angles.

A momentum-resolved STEM example

The versatility of MR-STEM is demonstrated by means of an experimental atomically resolved scan of an AuPd nanowire in Fig. 3. The scan covers 255 × 130 scan pixels and consists of 33150 diffraction patterns recorded in 26 s, of which one is shown in Fig. 3A. As an inset, the azimuthal integral is depicted for this particular scan point, being the basis for AR-STEM. Integrating intensity inside the Ronchigram yields the BF signal in (B), and taking only the central pixel delivers Fig. 3C. This can be considered equivalent to a conventional TEM image acquired under parallel illumination according to the theorem of reciprocity (Cowley, 1969; Krause and Rosenauer, 2017). Note that this is an aberration-corrected CTEM image acquired without a corrector for the imaging unit of the microscope. Different evolution of chemical and structural contrast in dependence of the detector acceptance angles becomes obvious from the low-angle ADF (LAADF) and the high-angle (HAADF) images in Fig. 3D and E.

Whereas, in principle, data in Fig. 3A–E are available also without an MR-STEM setup, Fig. 3F maps the first moment vector field color-coded. As will be shown below, the FM-STEM signal reflects the momentum transfer $\langle \vec{p}_\perp \rangle$, which points toward the atomic nuclei for scan points close to an atom due to the positive charge of the nucleus, being only partially screened by the electrons there. That atoms are sinks of momentum transfer is obvious from Fig. 3G, where div $\langle \vec{p}_\perp \rangle$ is shown. In sufficiently thin specimens, Figs. 3F and G are proportional to the projected electric field and charge density, respectively.

First-moment STEM

Theory and methodology

For each scan position $\vec{R}$ a real-space exit wave $\psi(\vec{r}_\perp, \vec{R})$ is present at the exit face of the specimen. FM-STEM targets the measurement of the average transverse momentum of this wave. Therefore, the expectation value $\langle \vec{p}_\perp(\vec{R}) \rangle$ is of central importance, which can be calculated in two equivalent ways. Firstly one can calculate the real-space integral

$$\langle \vec{\mathrm{p}}_\perp(\vec{\mathrm{R}}) \rangle = -\mathrm{i}\hbar \iint_{-\infty}^{\infty} \psi^*(\vec{\mathrm{r}}_\perp, \vec{\mathrm{R}}) \left[\vec{\nabla}_\perp \psi(\vec{\mathrm{r}}_\perp, \vec{\mathrm{R}}) \right] \mathrm{dxdy}, \tag{1}$$

which involves the (lateral) momentum operator $-\mathrm{i}\hbar\vec{\nabla}_\perp$ acting as a gradient on the complex wave function, which is not observable. ψ^* denotes the complex conjugate of ψ. Secondly, the transition to momentum space can be made, where the momentum operator takes the simple form of the vector $h\vec{q}_\perp$. Then the expectation value reads

$$\begin{aligned} \langle \vec{\mathrm{p}}_\perp(\vec{\mathrm{R}}) \rangle &= h \iint_{-\infty}^{\infty} \tilde{\psi}^*(\vec{q}_\perp, \vec{R}) \vec{q}_\perp \tilde{\psi}(\vec{q}_\perp, \vec{R}) \, \mathrm{d}u\mathrm{d}v \\ &= h \iint_{-\infty}^{\infty} \tilde{\psi}^*(\vec{q}_\perp, \vec{R}) \tilde{\psi}(\vec{q}_\perp, \vec{R}) \vec{q}_\perp \, \mathrm{d}u\mathrm{d}v \\ &= h \iint_{-\infty}^{\infty} |\tilde{\psi}(\vec{q}_\perp, \vec{R})|^2 \cdot \vec{q}_\perp \, \mathrm{d}u\mathrm{d}v, \end{aligned} \tag{2}$$

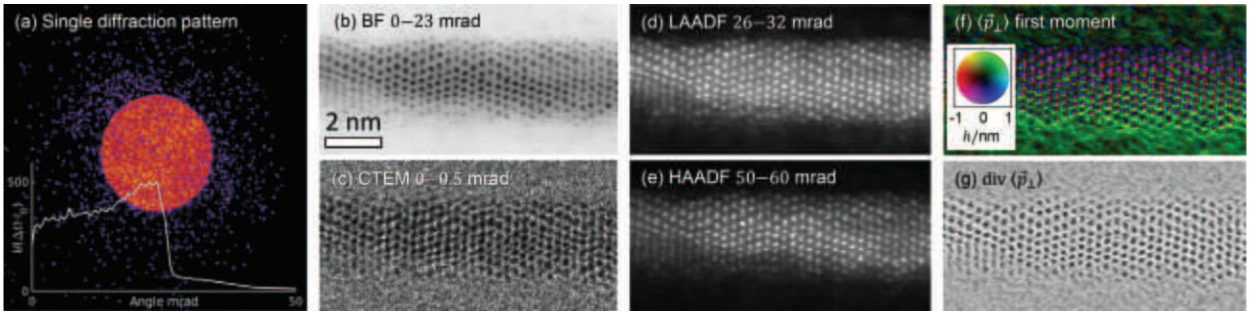
(a) Single diffraction pattern
500
0
0
Angle mrad
50
(b) BF 0–23 mrad
2 nm
(c) CTEM 0–0.5 mrad
(d) LAADF 26–32 mrad
(e) HAADF 50–60 mrad
(f) $\langle \vec{p}_\perp \rangle$ first moment
-1 0 1
ħ/nm
(g) div $\langle \vec{p}_\perp \rangle$

Fig. 3 Momentum-resolved STEM experiment (Au nanowire). A diffraction pattern as in (A) is recorded at each raster position in STEM. The inset shows the azimuthal average forming the basis for AR-STEM. (B) Bright field image from integrating the whole Ronchigram. (C) Image formed by the central pixel of the Ronchigram only, being equivalent to a CTEM image by reciprocity. (D, E) Low- and high-angle ADF images. (F) First moment showing the local momentum transfer and (G) divergence of the momentum transfer, showing atoms as sinks of the vector field in (F). The data have been recorded with a Medipix3 detector with 256 × 256 camera pixels at 120 keV.

with $\tilde{\psi}(\vec{q}_\perp)$ denoting the 2D Fourier transform of $\psi(\vec{r}_\perp)$ with respect to x, y. $|\tilde{\psi}(\vec{q}_\perp, \vec{R})|^2$ is the probability density to detect an electron at diffraction coordinate $\vec{q}_\perp$ with the STEM probe at position $\vec{R}$. It is identical to the normalized diffraction intensity $I(\vec{q}_\perp, \vec{R})$ so that Eq. (2) can be written as

$$\langle \vec{\mathrm{p}}_\perp(\vec{\mathrm{R}})\rangle = \mathrm{h} \iint\limits_{\infty}^{\infty} \vec{\mathrm{q}}_\perp \mathrm{I}(\vec{\mathrm{q}}_\perp, \vec{\mathrm{R}})\, \mathrm{d}u\mathrm{d}v, \tag{3}$$

which is more intuitive and states the central relation for FM-STEM.

The integrals in Eq. (3) equal the first moment of $I(\vec{q}_\perp, \vec{R})$, or simply its COM. The expectation value of the momentum is hence related to the diffraction pattern by this straightforward mathematical operation and it is due to this relation that FM-STEM is oftentimes referred to as COM. The expression (3) is exact and condenses the possibly very complex intensity distribution in diffraction space to a single vector with fundamental physical meaning.

Practical aspects

Eq. (3) means that the first moment in diffraction space is a robust measure of the average lateral momentum $\langle \vec{p}_\perp(\vec{R})\rangle$. This is rather a fundamental statement from basic quantum mechanics than being a specific STEM measurement methodology. However, translating these theoretical considerations to the experiment one can see that recording diffracted intensities in MR-STEM provides access to the average momentum transferred to the electron beam by the specimen.

An actual MR-STEM setup records the diffraction pattern only up to a cutoff frequency q_c, usually on a discrete pixel array. Therefore, Eq. (3) is in practice approximated by

$$\langle \vec{p}_\perp(\vec{R})\rangle \approx h \sum_{q_\perp \le q_c} \vec{q}_\perp I(\vec{q}_\perp, \vec{R}) \tag{4}$$

for a discretely sampled normalized $I(\vec{q}_\perp, \vec{R})$. FM-STEM has initially been mentioned conceptually in the 1970s by Waddell and Chapman (Waddell and Chapman, 1979). However, the realization of Eq. (4) employed typically only four segments for practical reasons, leading to the DPC setups with annular or disk-shaped detectors divided into four segments. In this regard, FM-STEM is the natural evolution of the traditional DPC techniques, making full use of the exhaustive detail of an MR-STEM measurement.

The approximate character of Eq. (4) should be kept in mind when selecting experimental parameters. First, given a certain camera hardware, the camera length determines the cutoff q_c and the reciprocal space sampling. Fortunately, it was shown that the sum in Eq. (4) converges very quickly, typically at spatial frequencies well below twice the Ronchigram radius (Müller-Caspary et al., 2016). The reason for this is that thermal diffuse scattering (TDS) makes the dominant contribution for high angles at room temperature, but does not contribute to the first moment significantly (Müller et al., 2014; Winkler et al., 2020).

Second, if $I(\vec{q}_\perp, \vec{R})$ is only sampled discretely, the pixel size has impact on the precision. However, a few tens of pixels along the Ronchigram diameter suffice in many cases, but this depends on the intended precision and used dose. Some nonpixelated detection schemes exist in the style of position-sensitive detectors (Müller-Caspary et al., 2015) or direct first moment detectors (Schwarzhuber et al., 2018).

Third, $I(\vec{q}_\perp, \vec{R})$ was defined normalized. Therefore, attention needs to be drawn to the normalization of experimental MR-STEM data. Denoting the raw measured signal by $J(\vec{q}_\perp, \vec{R})$, there has to be some normalization scheme

$$I(\vec{q}_\perp, \vec{R}) = \frac{1}{J_0} J(\vec{q}_\perp, \vec{R}). \tag{5}$$

Following Eqs. (3), (4), and (5), the normalization factor J_0 has to be chosen in such a way that $I(\vec{q}_\perp, \vec{R})$ is the probability density of detecting an electron with lateral momentum $h\vec{q}_\perp$. In the strict sense, this normalization can only be performed accurately if all electrons are detected, that is, if q_c in Eq. (4) is large enough to include the total scattered intensity. In practice, however, J_0 can only be calculated from recorded and hence limited diffraction patterns. Electrons having been scattered beyond the detector are missing especially at high camera lengths or in strongly scattering regions of the specimen. Usually,

$$J_0 = \sum_{q_\perp \le q_c} J(\vec{q}_\perp, \vec{R}) \tag{6}$$

is just calculated from the diffraction patterns themselves, implicitly assuming that the first moment of all unrecorded electrons is the same as that of the recorded ones. This assumption usually holds true, especially if q_c is chosen sufficiently large. Note that in this case J_0 can also vary throughout the different raster points an MR-STEM dataset. To sum up the previous three aspects, it is advisable to minimize errors by choosing a camera length that maximizes q_c while maintaining sufficiently dense sampling of the bright field region to which the first moment is most sensitive.

A fourth aspect of FM-STEM experiments results from the vectorial nature of $\langle \vec{p}_\perp(\vec{R})\rangle$ and is purely geometrical. The first moment of the diffraction pattern is determined within the coordinate frame of the pixel array of the camera, and then mapped against the scan position $\vec{R}$ to display and analyze this vector field. Because the scan frame can be rotated arbitrarily in STEM according to, for example,

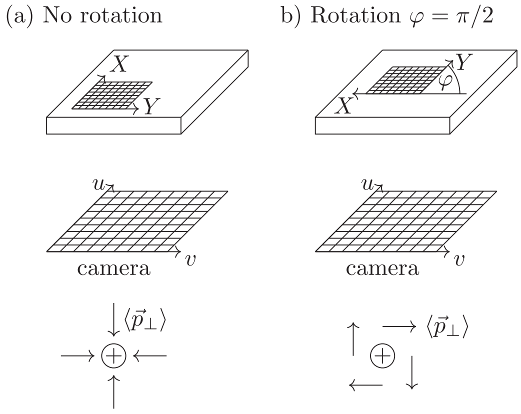
(a) No rotation
b) Rotation $\varphi = \pi/2$
X
Y
φ
u
v
camera
$\langle \vec{p}_\perp \rangle$

Fig. 4 Relative rotation of scan and diffraction frame. For the vectorial analysis of MR-STEM data, for example, for FM-STEM, a potential rotation between the coordinate frames for $\vec{R}$ and $\vec{q}_\perp$ needs to be accounted for; otherwise a radial field (A) appears falsely as a rotational one in (B).

the specimen geometry, a correction of the relative rotation between the different coordinate systems is necessary in nearly all cases (Zweck et al., 2023). Note that missing this aspect can turn a radial field into a curl field as schematically demonstrated in Fig. 4.

Fifth, besides the rotation, the origin of $\vec{q}_\perp$ is crucial. Choosing it in such a way that the first moment of the incoming electron beam is zero, it equals the average momentum *transferred* to the probe via interaction with the specimen, as implicitly assumed in the terminology above already. A practical way to determine the origin is to acquire an additional MR-STEM scan without any specimen taken under otherwise identical conditions, and to subtract it from the actual measurement so as to also remove any potential movement of the diffraction pattern induced by the scan engine.

Mapping electrical properties

Basic concept

For any quantum mechanical operator $\hat{o}$, the time evolution of its expectation value is given by the Ehrenfest theorem,

$$\frac{\mathrm{d}}{\mathrm{d}t}\langle \hat{o} \rangle = \frac{\mathrm{i}}{\hbar}\left\langle \left[\hat{H}, \hat{o}\right] \right\rangle + \left\langle \frac{\partial \hat{o}}{\partial t} \right\rangle, \tag{7}$$

including the Hamiltonian $\hat{H} = \frac{\hat{p}_\perp^2}{2m_e} - e\hat{V}(\vec{r})$ with electron mass m_e, elementary charge e, and the potential $\hat{V}$. For the static case and $\hat{o} = \hat{p}_\perp$

$$\left\langle \frac{\partial \hat{p}_\perp}{\partial t} \right\rangle = 0, \tag{8}$$

as well as

$$[\hat{p}_\perp^2, \hat{p}_\perp] = [\hat{p}_\perp \hat{p}_\perp, \hat{p}_\perp] = \hat{p}_\perp [\hat{p}_\perp, \hat{p}_\perp] + [\hat{p}_\perp, \hat{p}_\perp]\hat{p}_\perp = 0. \tag{9}$$

The remaining commutator in Eq. (7) reads, in real-space representation and after applying the product rule for $\vec{\nabla}_\perp$ acting on the product of $\hat{V}$ and ψ:

$$\left[-e\hat{V}(\vec{r}), \frac{\hbar}{\mathrm{i}}\vec{\nabla}_\perp\right] = e\frac{\hbar}{\mathrm{i}}\vec{\nabla}_\perp \hat{V}(\vec{r}) = -e\frac{\hbar}{\mathrm{i}}\vec{E}_\perp. \tag{10}$$

It was used that, in electrostatics, the negative gradient of the potential equals the electric field $\vec{E}$, here considering only lateral components. Inserting Eq. (10) into Eq. (7) gives

$$\frac{\mathrm{d}\langle \vec{\mathrm{p}}_\perp \rangle}{\mathrm{d}t} = -e\left\langle \vec{E}_\perp \right\rangle. \tag{11}$$

In a semiclassical picture, the beam electrons move along the z-direction with a velocity of

$$v_e = \frac{h}{\lambda m_e \gamma}, \tag{12}$$

where γ is the relativistic Lorentz factor and m_e is the mass of the electron. This allows for the substitution $\mathrm{d}z = v_e \mathrm{d}t$ within the time interval $\mathrm{d}t$, yielding

$$\mathrm{d}\langle \vec{p}_\perp \rangle = -\frac{e}{v_\mathrm{e}}\cdot\left\langle \vec{\mathrm{E}}_\perp \right\rangle \mathrm{d}z. \tag{13}$$

This fundamental relation can also be derived rigorously in quantum mechanical manner within the paraxial approximation. Integrating both sides and explicitly writing the xy integral $\langle \vec{E}_\perp \rangle$ results in

$$\begin{aligned} \langle \vec{p}_\perp \rangle &= -\frac{e}{v_e}\cdot \int_{-\infty}^{\infty} \left\langle \psi | \vec{E}_\perp | \psi \right\rangle \mathrm{d}z \\ &= -\frac{e}{v_e}\cdot \iiint_{-\infty}^{\infty} \vec{E}_\perp(\vec{r})\cdot|\psi(\vec{r})|^2 \, \mathrm{d}x \, \mathrm{d}y \, \mathrm{d}z. \end{aligned} \tag{14}$$

We have thereby gained a direct relation between field and momentum transfer. However, both $\vec{E}_\perp$ and the squared wave function depend on all three specimen coordinates, and the intensity distribution inside the specimen is generally not known. Eq. (14) states that the lateral momentum transfer is essentially determined by weighting the local lateral field components $\vec{E}_\perp$ with the local squared wave function, being proportional to the intensity. Critically, $\vec{E}_\perp$ and ψ are not independent from each other: Potential gradients due to, for example, the presence of atoms, shape the wave function possibly heavily on its propagation through the specimen, as is known from Bloch wave (Bethe, 1927) or multislice (Cowley and Moodie, 1957) solutions of the Schrödinger equation.

Until here the derivation was exact, but in order to separate field and intensity from each other, at least with respect to the z-integration along the electron beam direction, either prior additional knowledge of the beam propagation is required, or approximations need to be made. For optically very thin objects, one can neglect any change of the probe intensity in direct space, that is, assume that the shape of the probe intensity does not change while going through the specimen. Mathematically this approximation manifests in $|\psi(\vec{r})|^2 \approx |\psi(\vec{r}_\perp)|^2$ for all z-coordinates. The z-integration in (14) then involves $\vec{E}_\perp(\vec{r})$ only and yields

$$\langle \vec{p}_\perp \rangle \approx -\frac{e}{v_e}\cdot \iint_{-\infty}^{\infty} \vec{E}^P_\perp(x,y)\cdot|\psi(\vec{r}_\perp)|^2 \, \mathrm{d}x \, \mathrm{d}y \tag{15}$$

with the projected electric field

$$\vec{E}^P_\perp(x,y) := \int_{-\infty}^{\infty} \vec{E}_\perp(x,y,z) \, \mathrm{d}z, \tag{16}$$

usually measured in units of Volts because of the z-integration.

So far, the derivation comprised an arbitrary wave function and did not incorporate the scanning concept. The normalized intensity $I_\mathrm{P}(\vec{r}_\perp)$ of the coherent probe, centered on the optical axis, can be calculated if the shape and the position of the probe-forming aperture, as well as the aberrations are known. The scanning process shifts this probe by $\vec{R}$ such that the intensity reads

$$\left|\psi(\vec{r}_\perp, \, \vec{R})\right|^2 = I_\mathrm{P}(\vec{r}_\perp - \vec{R}), \tag{17}$$

which can be inserted in Eq. (15) to obtain

$$\begin{aligned} \langle \underset{\perp}{\vec{p}}(\vec{R}) \rangle &\approx -\frac{e}{v_e} \iint_{-\infty}^{\infty} I_\mathrm{P}(\vec{r}_\perp - \vec{R}) \, \vec{E}^P_\perp(\underset{\perp}{\vec{r}}) \, \mathrm{d}x \, \mathrm{d}y \\ &= -\frac{e}{v_e} I_\mathrm{P} \star \vec{E}_P. \end{aligned} \tag{18}$$

This central equation relates the measured momentum transfer $\langle \vec{p}_\perp \rangle$ in Eqs. (3) and (4) to the lateral electric field $\vec{E}^P_\perp$, projected along beam direction, by a formal cross-correlation $\star$ with I_P the intensity of the STEM probe. This can be understood intuitively, too: The first moment measured in thin specimens is directly proportional to the electric field broadened by the probe shape. With very small probes realizable thanks to aberration correction, this can be an excellent tool to measure fields down to the subatomic scale. In a further derivation within the framework of the phase object approximation, it can also be shown that the average momentum transfer is similarly proportional to the gradient of a phase object (Winkler et al., 2020; Müller-Caspary et al., 2017).

The result in Eq. (18) deserves several remarks. First, the cross-correlation with the probe intensity puts a limit to the spatial resolution for the measurement of $\vec{E}^P_\perp$. Second, the probe intensity is the governing quantity, rather than the wave function as would be the case for other BF-STEM techniques or electron ptychography. Third, FM-STEM-based electric field mapping as derived here puts DPC STEM on an accurate basis as long as, forth, dynamical scattering and propagation can be neglected. This aspect involves the thickness, composition, and crystallographic orientation of the specimen, the acceleration voltage, convergence angle of the STEM probe determined by $A(q_\perp)$ and aberrations $\chi(\vec{q}_\perp)$. Consequently, no general rule can be given up to which thickness Eq. (18) retains a desired accuracy. In a gold crystal, FM-STEM results as in Fig. 3F would not allow for a quantifiable conversion to electric fields anymore, whereas long-range electric stray fields in vacuum can extend hundreds of nanometers along z before Eq. (18)

becomes inaccurate. Fifth, real-space averaging strategies have been developed to separate long-range polarization fields in crystals from atomic contributions (Müller-Caspary et al., 2019), as will be outlined below. Despite the analytical clarity of Eqs. (2) and (4) it is nevertheless advisable to conduct dynamical simulations to investigate the impact of microscope and specimen parameters, and multiple scattering.

Partial coherence

Until now the fully coherent case was considered. However, when comparing real FM-STEM-based electric field measurements with simulations in well-defined systems such as mono-/bilayer 2D materials, it turns out that cross-correlating the electric field with the normalized probe intensity I_P yields too sharply peaked electrical fields. In that respect, partial spatial and temporal coherence need to be taken into account.

In STEM, partial spatial coherence results in an incoherent broadening of the probe. To account for it, one needs to calculate the momentum transfer $\left\langle \vec{p}_\perp \right\rangle$ according to Eq. (15) for different probe positions $\vec{R}_\perp$ and form an average weighted by the effective source extent $w_s(\vec{R}_\perp)$.

Partial temporal coherence can similarly be included by calculating $\left\langle \vec{p}_\perp \right\rangle$ for various probe defoci Δf and forming a weighted average according to the defocus spread $w_t(\Delta f)$.

Looking closely at Eq. (15), we realize that only I_P depends on $\vec{R}$ and Δf. Hence both the temporal and spatial averaging can be pulled into the correlation integral and only be applied to the probe intensity. Partial coherence can thus be elegantly included into Eq. (15) by simply replacing the totally coherent probe intensity with

$$\begin{aligned} I_{PC}(\vec{r}_\perp) \quad &= \iiint I_P(\vec{r}_\perp - \vec{R}, \Delta f) \\ &\times w_s(\vec{R}) w_t(\Delta f)\ \mathrm{d}\Delta f\ \mathrm{d}X \mathrm{d}Y. \end{aligned} \tag{19}$$

Note that I_{PC} is the actual probe intensity incident on the specimen surface and is in principle accessible to a direct measurement, for example, by taking an image of the probe without any sample on a camera, if the imaging system allows for it.

Mapping charges and potentials

In summary, the measurement of the first moment $\langle \vec{p}_\perp(\vec{R}) \rangle$ in diffraction patterns can be directly related to the local electric field in thin specimen, whereas the intensity distribution of the STEM probe, determined by the size of the objective aperture, aberrations, as well as partial spatial and temporal coherence, limits the spatial resolution. In essence, one can hence define

$$\vec{E}_\perp^{P,m}\left(\vec{R}\right) = -\frac{v}{e} \cdot \langle \vec{p}_\perp\left(\vec{R}\right) \rangle \tag{20}$$

to be the *measured* projected electric field in Volts. By the laws of electrostatics, its divergence is proportional to the measured projected charge density in Cm^{-2},

$$\varrho^{P,m}\left(\vec{R}\right) = \varepsilon_0 \cdot \mathrm{div} \vec{E}_\perp^{P,m}\left(\vec{R}\right) = -\frac{\varepsilon_0 v}{e} \cdot \mathrm{div} \langle \vec{\mathrm{p}}_\perp\left(\vec{\mathrm{R}}\right) \rangle, \tag{21}$$

which is shown in Fig. 5D for the WSe_2 experiment. Furthermore, the electrostatic electric field is the negative gradient of the electrostatic potential, $\vec{E} = -\vec{\nabla}\phi$. Inserting into Eq. (21), the measured projected electrostatic potential can thus be obtained by solving Poisson's equation

$$\Delta \phi^{P,m}\left(\vec{R}\right) = -\frac{1}{\varepsilon_0} \varrho^{P,m}\left(\vec{R}\right) \tag{22}$$

starting from a given charge density. For example, the integration can be performed by expressing the Laplacian as finite differences in an iterative five or nine-point stencil scheme, as was done to generate Fig. 5C.

Another option is to integrate the electric field directly, for which the most direct approach would be to calculate $\phi^{P,m}(\vec{R})$ from cumulative potential energy differences $\vec{E}_\perp^{P,m}(\vec{R}) \cdot \Delta \vec{R}$ with $\Delta \vec{R}$ connecting adjacent scan pixels. However, the presence of noise causes this integration scheme to be very unstable except for simulated data. An alternative consists of making use of the Fourier transform, where the gradient operator transforms into the multiplication with $\vec{Q}$, in analogy to the real- and Fourier space representations of the momentum operator in Eqs. (1) and (2), respectively. It is straight forward to show that

$$\phi^{P,m}\left(\vec{R}\right) = \mathcal{F}^{-1}\left\{ \frac{\vec{Q}}{2\pi \mathrm{i} Q^2} \cdot \mathcal{F}\left[\vec{E}_\perp^{P,m}\right]\left(\vec{Q}\right) \right\}\left(\vec{R}\right) \tag{23}$$

provides the potential distribution except for the DC component $Q = 0$, essentially via scalar multiplication of the 2D Fourier transforms of the electric field components with $\vec{Q}/Q^2$, followed by an inverse Fourier transform of the result.

It is instructive to elucidate the differences between integrations based on Eqs. (22) and (23), respectively. Since the former starts from the second, the latter from the first derivative, different knowledge about the boundary conditions is needed. In particular,

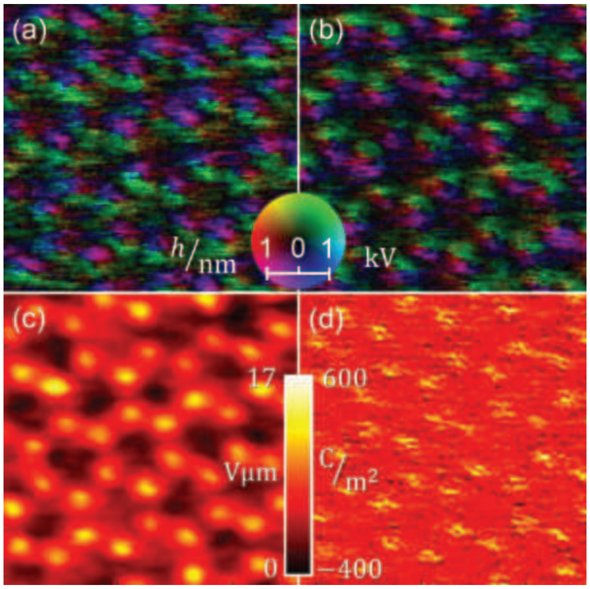

Fig. 5 First moment-based electrical properties of a WSe_2 bilayer. An MR-STEM scan with 256 × 256 scan pixels taken with 200 keV electrons with a probe-corrected instrument equipped with a Medipix 3 camera. Each panel shows the respective quarter of the scan. (A) Momentum transfer $\langle \vec{p}_\perp(\vec{R}) \rangle$ from first moments in units of Planck's constant per nm, from Eq. (4). (B) Measured electric field, that is, $-\frac{v_e}{e}\langle \vec{p}_\perp(\vec{R}) \rangle$. (C) Measured electrostatic potential determined from the measured electric field. (D) Measured charge density.

solving Poisson's equation takes only those charges into account which lie inside the scanned region, whereas integrating the electric field directly includes the effects from charges outside, too. However, the Fourier integration in Eq. (23) imposes periodic boundary conditions. In any case, $\phi^{P,m}(\vec{R})$ can only be determined up to an additive constant.

Polarization and meso-scale electric fields

The physical properties of nanotechnological devices such as laser diodes or field effect transistors are often governed by electric fields that vary at length scales in the nanometer range. Important examples are pn junctions as well as spontaneous and piezoelectric fields in semiconductor optoelectronics which, by the quantum-confined Stark effect, have dramatic impact on the emission properties. Furthermore, controlling ferroelectric polarizations at the nanoscale gained rapid interest in the field of information technology. Consequently, the capability to quantify such meso-scale electric fields is a key component for understanding the structure-property-functionality relationships.

At first glance, electric field measurement at the meso-scale seems less complicated than dealing with subatomic fields as in Fig. 5 because the requirements for the spatial resolution appear less strict. However, any interaction of relativistic electrons with the specimen is determined by the full electrostatic potential built up by atomic and possible meso-scale components. At a second glance, the situation is hence much more complicated because atomic and meso-scale components need to be separated. In addition, both contributions have significantly different orders of magnitude. Atomic fields as measured in Fig. 5B are in the V/pm range assuming specimen thicknesses in the nm range. Contrary, typical polarization-induced electric fields are of the order 10 MV/cm, that is, approximately three orders of magnitude smaller.

On the one hand, rather thick specimens should thus be used to measure meso-scale fields so as to transfer sufficient momentum. On the other hand, Eq. (18) is only valid up to a thickness of a few atomic layers in matter, where atomic electric fields vary rapidly at the scale of the probe and distort it significantly (MacLaren et al., 2015; Müller-Caspary et al., 2017).

Nevertheless, the correlation in Eq. (18) can be replaced simply by $\vec{E}_P$ if $\vec{E}_P$ doesn't show lateral gradients at the scale of the intensity $|\psi(\vec{r})|^2$ in the specimen. This suggests to write $\vec{E}_P$ as the sum of a constant part $\vec{E}_{\mathrm{ext}}$ and (atomic) contributions that vary at the scale of the interaction volume diameter and are affected by dynamical scattering. Then, the momentum transfer reads

$$\langle \vec{p}_\perp\left(\vec{R}\right)\rangle = -\frac{e}{v}\cdot\vec{E}_{\mathrm{ext}}\cdot t + \langle \vec{p}_\perp\left(\vec{R}\right)\rangle_{\mathrm{dyn}}, \tag{24}$$

where t is the specimen thickness.

One approach to solve for $\vec{E}_{\mathrm{ext}}$ makes use of symmetry considerations in crystals. For a single scan point $\vec{R}$, the dynamic part $\langle \vec{p}_\perp(\vec{R})\rangle_{\mathrm{dyn}}$ is intuitively unpredictable when the specimen thickness is large. For example, a complex vector field $\langle \vec{p}_\perp(\vec{R})\rangle$ can result where atomic sites are no more sinks of momentum transfer, as illustrated schematically in Fig. 6A. Assuming the presence of an

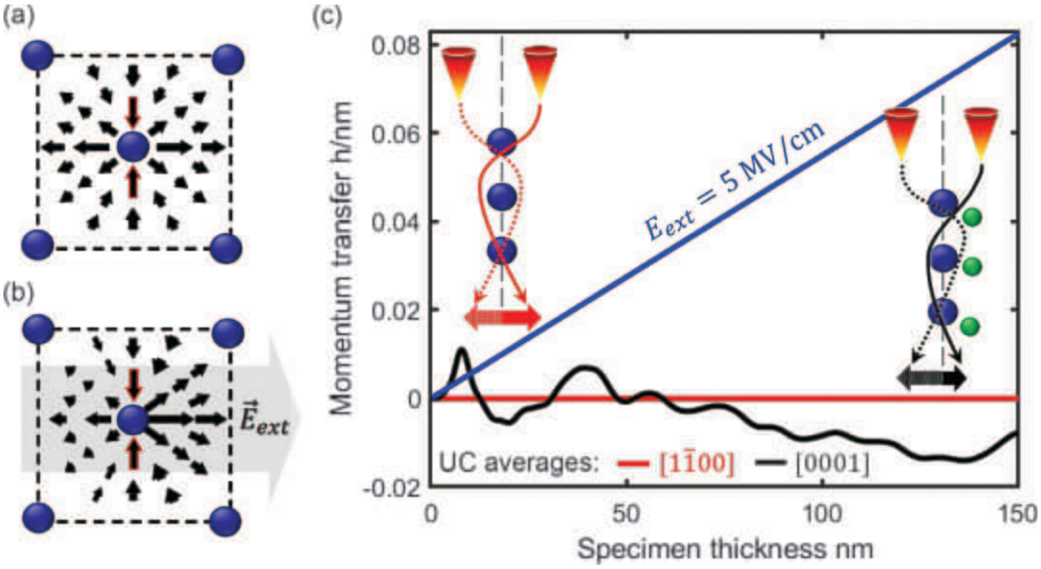

Fig. 6 Unit cell averaging concept for meso-scale electric field measurement. (A) Due to dynamical scattering, the momentum transfer distribution across a unit cell can be counter-intuitive, but is symmetric in centrosymmetric geometries. The unit cell average of atomic-scale contributions thus vanishes such that (B) a superimposed constant external field (exaggerated) remains as a residual. (C) Systematic error $\vec{\delta}$ for w-GaN is obtained by multislice assuming $[11\bar{2}0]$ zone axis and 300 keV electron energy. The unit cell (UC) average of the momentum transfer along the nonpolar direction vanishes; hence $\delta_{1\bar{1}00} = 0$ (*red*) opposite to δ_{0001} measured along the polar direction. The broken symmetry is sketched in the insets. A constant electric field of 5 MV/cm causes the momentum transfer shown in *blue*.

inversion center for the moment, any scan point has nevertheless a counterpart in the unit cell with a momentum transfer having the opposite sign. In other words, the unit cell average of $\langle \vec{p}_\perp(\vec{R}) \rangle_{\text{dyn}}$ must vanish in respective structures. Consequently, averaging $\langle \vec{p}_\perp(\vec{R}) \rangle$ in Eq. (24) over all scan points in a unit cell delivers $\vec{E}_{\text{ext}}$ according to Fig. 6B, assuming that the usually tiny amount of mistilt introduced by the constant component has negligible effects on the dynamical scattering.

Unfortunately, polarization effects emerge as a consequence of symmetry breaking, for example, in ferro- and piezoelectric materials and materials with spontaneous polarization. In addition to the desired dependence on $\vec{E}_{\text{ext}}$, the unit cell average of $\langle \vec{p}_\perp(\vec{R}) \rangle$ can involve a systematic error $\vec{\delta}$ arising from the fact that averaging $\langle \vec{p}_\perp(\vec{R}) \rangle_{\text{dyn}}$ is finite, and we find

$$\left[\langle \vec{p}_\perp(\vec{R}) \rangle\right]_{\text{UC}} = -\frac{e}{v} \cdot \vec{E}_{\text{ext}} t + \vec{\delta}(t), \tag{25}$$

where $[\ldots]_{\text{UC}}$ denotes the unit cell average. The measurement of polarization-induced electric fields thus involves the estimation of $\vec{\delta}$, which is usually done via multislice simulations (Müller-Caspary et al., 2019; Strauch et al., 2023).

As an example, Fig. 6C shows $\delta_{1\bar{1}00}$ (*red*) and δ_{0001} (*black*) thickness-dependent for wurtzite-type GaN. Since the $[1\bar{1}00]$ direction is nonpolar, this component vanishes in the unit cell average for symmetry reasons despite strong dynamical scattering, as sketched in the left inset. On the contrary, δ_{0001} takes finite values of more than $1\,\frac{h}{\text{nm}}$ due to the polarity generated by the Ga-N dumbbells, as illustrated on the right. Despite that, the blue curve shows that a superimposed polarization-induced electric field $\vec{E}_{\text{ext}}$ of a few MV/cm dominates the momentum transfer from a specimen thickness of a few tens of nanometers on and can hence be measured (Müller-Caspary et al., 2019).

Angle-resolved STEM

Methodology

Another prominent technique that allows for the condensation of the four-dimensional MR-STEM datasets into a more concise form while still preserving critical information is AR-STEM. Here, the MR-STEM data are azimuthally averaged in momentum space, yielding a radial intensity distribution

$$I_{\text{rad}}(q_\perp, \vec{R}) = \frac{1}{2\pi} \int I\left(q_\perp \cos\varphi, q_\perp \sin\varphi, \vec{R}\right) \, d\varphi. \tag{26}$$

It is also common practice to use the scattering angle $\vartheta = \lambda q_\perp$ rather than the spatial frequency modulus $q_\perp$.

Similarly to how FM-STEM can be seen as a progression of DPC-STEM, AR-STEM is an evolution of the traditional STEM ring detectors. It formally increases the number of rings to the continuous limit, even though in practice only a discrete sampling of the diffraction pattern is achievable, as discussed above.

Combining MR-STEM with AR-STEM is a natural fit, as the integral in Eq. (26) can be translated into a discrete sum

$$I_{\mathrm{rad}}(q_\perp, \vec{R}) \approx \frac{1}{n_{q_\perp}} \sum_{q'_\perp \approx q_\perp} I(\vec{q}\,'_\perp, \vec{R}), \tag{27}$$

where $n_{q_\perp}$ is the number of pixels summed up for a certain $q_\perp$. The criterion which pixels $q'_\perp$ are to be summed for a given $q_\perp$, denoted slightly informal here by $q_\perp \approx q'_\perp$, is chosen depending on the resolution and signal-to-noise ratio of the MR-STEM dataset, and the desired sampling of the scattering angle.

This sum results in a three-dimensional dataset that retains the two-dimensional spatial resolution of the MR-STEM scan and allows for the analysis of specific scattering angle ranges. The angular multirange analysis enables the determination of specimen properties such as chemical composition and homogeneity, or geometrical thickness by comparison to simulated reference data (Müller-Caspary et al., 2016; Grieb et al., 2021). The multitude of angle ranges that can be chosen *a posteriori* from a sufficiently sampled I_{rad} enables the simultaneous measurement of several specimen properties while at the same time artifacts from, for example, inhomogeneous detector sensitivity or diffraction pattern distortion can be avoided or reduced (Krause et al., 2016). This puts it a clear advantage over conventional STEM with a single or at least only few detectors.

For completeness, further AR-STEM capable setups are to be mentioned. One example is the positioning of an iris aperture in front of a conventional circular or annular detector, which allows to acquire different angle ranges by choosing the iris opening (Müller-Caspary et al., 2016; Grieb et al., 2021). The characteristic of this concept is the inherent rotational averaging during the acquisition. In that case, the azimuthal information is not recorded so that information is only available in dependence of the momentum modulus. However, acquisition speeds in the MHz range can be reached using established ring detectors which are much higher compared to common kHz frame rates in frame-based MR-STEM experiments.

Applications

Fig. 7 illustrates the possibilities of AR-STEM for quantitative evaluation: Multislice simulations of Ga(NAs) with varied specimen thickness and nitrogen concentration predict a scattering angle range from 42 to 66 mrad, in which the radial intensity is very sensitive to a change of the nitrogen content, and another interval between 82 and 141 mrad, in which the intensity is nearly independent of the composition but only depends on the specimen thickness. Hence, these two intervals can be used for the simultaneous evaluation of both specimen thickness and nitrogen concentration in a dedicated AR-STEM experiment.

The experimental results of this concept are shown in Fig. 8. From the radial AR-STEM intensity $I_{\mathrm{rad}}(\vartheta)$, the intensities in these two intervals are calculated by integration. A subsequent comparison to the simulated reference data yields the quantitative composition and thickness with atomic resolution, clearly revealing a nitrogen-rich layer. While this specific evaluation could, in theory, also be executed with two dedicated conventional ring detectors of appropriate geometry, AR-STEM has the significant advantage that the choice of the angle interval can be made and changed after the measurement, possibly on the basis of observations made in it.

An example for such an adaptive evaluation is given in Fig. 9: A GaN/InGaN layer was investigated with AR-STEM. In this material system, it is common to observe intensity alterations near the layer interfaces. The cause of these are strain effects due to the different covalent radii of In and Ga. However, their inclusion into reference simulations is tedious and an evaluation with atomic resolution is impossible without substantial additional effort. Here, the AR-STEM images immediately reveal that there is a scattering angle range near 36 mrad in which the effect nearly vanishes. Using this interval, therefore, enables a much easier and quicker evaluation.

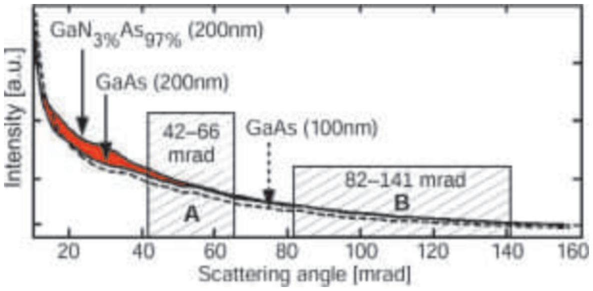

Fig. 7 Simulated AR-STEM intensity for GaNAs: The plot shows two radial intensity curves for pure GaAs of 100 and 200nm thickness, respectively, and another for 200-nm thick $\mathrm{GaN}_{3\%}\mathrm{As}_{97\%}$. In the higher angle range B, the nitrogen concentration has very little influence on the intensity, which is primarily determined by the thickness. For lower angles, however, the N concentration causes the massive difference marked in *red*. This gives the interval A a high sensitivity for the composition (Müller-Caspary et al., 2016).

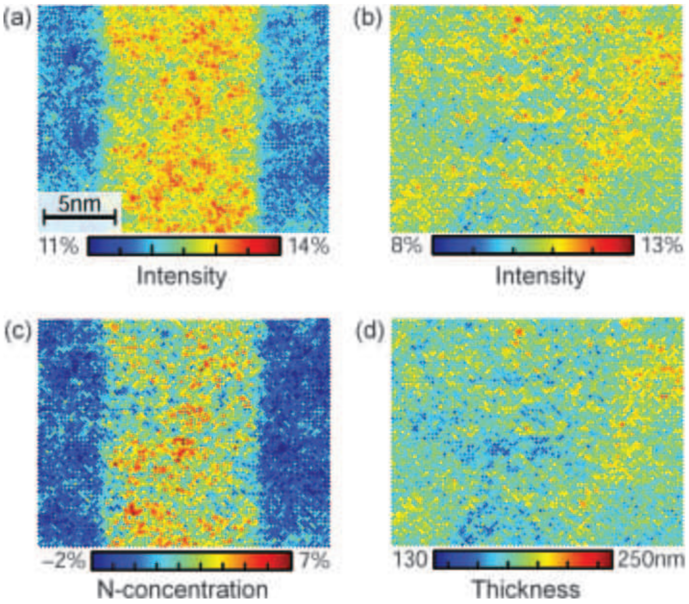

Fig. 8 An exemplary quantitative evaluation of an AR-STEM measurement: (A) and (B) show the integrated intensity images of a GaAs/GaNAs nanostructure from the two intervals marked in Fig. 7, recorded using an iris aperture-based AR-STEM setup. By comparison to the simulated reference data, both N concentration (C) and specimen thickness (D) are determined (Müller-Caspary et al., 2016).

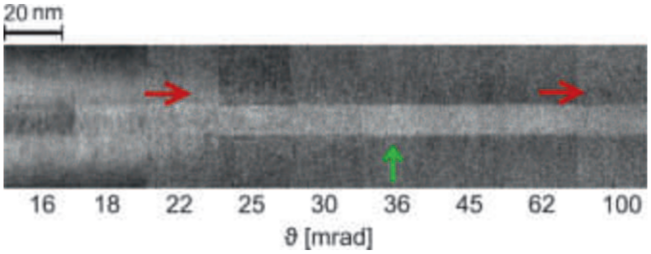

Fig. 9 AR-STEM image of a GaN/InGaN nanostructure: Small and large scattering angles ∂ show intensity variations in areas of pure GaN next to the layer in the center (*red arrows*). These are caused by strain effects due to the larger lattice constant in the layer complicating quantitative evaluation. For scattering angles around 36mrad, the effect disappears (*green arrow*). The given angles mark the center of the respective angle intervals used to form the images (Grieb et al., 2022).

Impact of inelastic scattering

The different evaluation schemes for MR-STEM data sets introduced above were primarily discussed in the context of elastic electron-sample interactions, where the specimen is completely represented simply by an electrostatic potential. In practice, however, electrons that have undergone inelastic interactions, that is, exchanged energy with the specimen, make up a significant fraction of the detected signal. In many cases they are even in the majority. The predominant inelastic interactions are related to energy transfer to phonons, that is, collective oscillations of the crystal lattice, and plasmons, that is, oscillations of the electron gas.

Fortunately, the inclusion of these two scattering mechanisms into the formalism used in the previous sections is possible. For phonons, this can be done through the so-called *frozen phonon* (FP) formalism. In brief, this means that instead of using one electrostatic specimen potential, where atoms are assumed to reside on their ideal positions, the calculations are done for multiple potentials, where the atoms have been displaced according to the thermodynamic probability distribution. The resulting images and signals including phonon scattering are then found by averaging over all these different displacement configurations. Going into detail here is beyond the scope of this article, but the interested reader is referred to Wang (1998), Van Dyck (2009), Krause et al. (2018), and Forbes et al. (2010).

The inclusion of plasmons is generally more complicated and more computationally demanding. However, to assess its influence on MR-STEM and subsequent evaluations, it can be shown that the effect of plasmon scattering on each diffraction pattern can in very good approximation be modeled by a convolution (⊗)

$$I_{\text{plasmon}}(\vec{q}_\perp) \propto I_{\text{elast.}}(\vec{q}_\perp) \otimes \sqrt{\frac{1}{q_\perp^2 + q_{\text{plasmon}}^2}}. \tag{28}$$

The quantity q_{plasmon} is the modulus of a characteristic plasmon scattering wave vector that is typically much smaller than the reciprocal lattice vectors of a crystal. Whereas there is a lot to account for in detail, it can be instantly seen that the elastic intensity is convolved with a sharp and rotationally symmetric function. For more details, Beyer et al. (2020), Robert et al. (2022), and Verbeeck et al. (2005) are recommended.

In the light of these descriptions, it can be concluded that the influence of inelastic scattering on FM-STEM is rather small and oftentimes negligible: As the convolution of an arbitrary diffraction pattern with any rotationally symmetric function will preserve the original COM, there will be no effect of inelastic scattering as long as these models hold true. Even if asymmetric contributions are taken into account, they are generally much smaller and their effect is hence still not significant.

For AR-STEM, the situation is very different: The approximately rotationally symmetric inelastic scattering redistributes intensity from the bright field center (low scattering angles) toward the outer rim of the diffraction pattern (high scattering angles). The radial intensity is therefore altered critically. Especially phonon scattering makes up the major part of scattering into high angles and cannot be neglected. Fortunately the FP methodology outlined above allows for a relatively straightforward inclusion in reference simulations.

The inclusion of plasmons into quantitative AR-STEM simulations is much more challenging. While Eq. (28) can be applied, the knowledge of several constants is critical for its quantitative application, especially the total plasmon scattering cross-section and the exact plasmon dispersion relation. Although these values are tabulated for common materials, they are often not known precisely enough to achieve full quantitative agreement between simulation and experiment.

Nevertheless, plasmon scattering can have a grave influence: Especially for smaller scattering angles, neglecting them can lead to a significant underestimation—in some cases by a factor of up to 2 (Müller-Caspary et al., 2016; Beyer et al., 2020). If, therefore, an accurate simulation including plasmons cannot be realized, this angle range has to be avoided for quantitative evaluations. The maximum scattering angle that is impacted significantly by plasmons is dependent on specimen material and orientation. However, as a rule of thumb, scattering angles less than 25mrad above the convergence angle should be avoided. In fact, this is the reason why interval A in Fig. 7 was chosen as shown there, even though smaller angles seem to promise an even better sensitivity to the nitrogen concentration.

Conclusion

In MR-STEM, a detailed diffraction pattern is recorded in dependence of the position of a scanning electron probe. This enables a high degree of flexibility in that virtual detectors can be defined after the acquisition in software and are not given by a rigid a-priori detector setup anymore. Besides traditional imaging schemes that produce conventional TEM, thickness- and Z-contrast now with dedicated, optimized disk- and ring detector geometries, MR-STEM enables completely new imaging modes.

A prominent method is FM-STEM, which yields the average lateral momentum (transfer) of the electron wave after the interaction with the specimen by assigning the COM of each diffraction pattern to the respective scan coordinate. This vector field can be directly related to the electric field under certain conditions. If the specimen is thin enough that one can assume that the intensity distribution of the probe is preserved, the momentum transfer is proportional to the correlation between electric field and probe intensity. Usually this approximation is valid for 2D materials only, or specimen with a thickness of a few nanometers. The unit cell average of the momentum transfer can be used as a measure of an external, for example, polarization-induced electric field, whereas systematic errors arising from a broken inversion symmetry need to be assessed in simulations.

In AR-STEM, azimuthal averaging in diffraction patterns condenses the MR-STEM dataset to its radial scattering information. Because specific specimen properties can leave fingerprints in characteristic scattering angles, this can either allow for the simultaneous measurement of a multitude of specimen properties by an angular multirange analysis, or it can help to avoid unwanted contrast mechanisms such as lattice deformations or contamination. With the nearly complete registration of scattering, MR-STEM necessitates a careful look at inelastic effects such as plasmon excitations, especially at small scattering angles.

Prospects

The multidimensional concept of MR-STEM puts high demands on the data acquisition speed and the computational performance to evaluate four-dimensional datasets, both to be improved for efficient and versatile in situ data evaluation. On the technological side, even faster cameras with MHz rate read-out would be desirable to achieve established STEM acquisition speeds. Due to the limited dose, MR-STEM datasets become rather sparse then, such that single-event-based recording and processing schemes seem to pave a promising way. Methodologically, electric field mapping at atomic and meso-scale has still large unlocked potential to be explored since the most interesting applications in solid-state physics require precisions and accuracies that allow for the detection of bonding effects and polarization-induced electric fields in a robust manner. In addition, the role of inelastic scattering, primarily due to plasmons, appears critical for a quantitative understanding of the whole MR-STEM dataset. Recording MR-STEM data energy-dependent or even energy-resolved, and developing efficient simulation schemes for inelastic scattering provide promising future directions, and surely one of the biggest challenges in this field.

Acknowledgments

We thank our colleagues Dr. Benjamin März and Dr. Tim Grieb for providing experimental data, and Max-Leo Leidl for his professional typographical support. The authors thank Andreas Rosenauer, Josef Zweck, Sandra Van Aert, and Johan Verbeeck for the scientific creativity and inspiration in their groups as a catalyst for the MR-STEM development during the past decade.

References

Bethe H (1927) Über die Streuung von Elektronen an Krystallen. *Die Naturwissenschaften* 15: 786–788.

Beyer A, Krause FF, Robert HL, Firoozabadi S, Grieb T, Kükelhahn P, Heimes D, Schowalter M, Müller-Caspary K, Rosenauer A, and Volz K (2020) Influence of plasmon excitations on atomic-resolution quantitative 4D scanning transmission electron microscopy. *Scientific Reports* 10: 17890.

Chapman J, Batson P, Waddell E, and Ferrier R (1978) The direct determination of magnetic domain wall profiles by differential phase contrast electron microscopy. *Ultramicroscopy* 3: 203–214.

Cowley JM (1969) Image contrast in a transmission scanning electron microscope. *Applied Physics Letters* 15: 58–59.

Cowley JM and Moodie AF (1957) The scattering of electrons by atoms and crystals. I. A new theoretical approach. *Acta Crystallographica* 10: 609–619.

Dekkers NH and de Lang H (1978) A calculation of bright field single-atom images in STEM with half plane detectors. *Optik* 51: 83–92.

Forbes BD, Martin AV, Findlay SD, D'Alfonso AJ, and Allen LJ (2010) Quantum mechanical model for phonon excitation in electron diffraction and imaging using a Born-Oppenheimer approximation. *Physical Review B* 82: 104103.

Grieb T, Krause FF, Müller-Caspary K, Firoozabadi S, Mahr C, Schowalter M, Beyer A, Oppermann O, Volz K, and Rosenauer A (2021) Angle-resolved STEM using an iris aperture: Scattering contributions and sources of error for the quantitative analysis in Si. *Ultramicroscopy* 221: 113175.

Grieb T, Krause FF, Müller-Caspary K, Ahl J-P, Schowalter M, Oppermann O, Hertkorn J, Engl K, and Rosenauer A (2022) Angle-dependence of ADF-STEM intensities for chemical analysis of InGaN/GaN. *Ultramicroscopy* 238: 113535. https://doi.org/10.1016/j.ultramic.2022.113535.

Jannis D, Hofer C, Gao C, Xie X, Beché´ A, Pennycook T, and Verbeeck J (2022) Event driven 4D STEM acquisition with a Timepix3 detector: Microsecond dwell time and faster scans for high precision and low dose applications. *Ultramicroscopy* 233: 113423.

Krause FF and Rosenauer A (2017) Reciprocity relations in transmission electron microscopy: A rigorous derivation. *Micron* 92: 1–5.

Krause FF, Schowalter M, Grieb T, Müller-Caspary K, Mehrtens T, and Rosenauer A (2016) Effects of instrument imperfections on quantitative scanning transmission electron microscopy. *Ultramicroscopy* 161: 146–160.

Krause FF, Bredemeier D, Schowalter M, Mehrtens T, Grieb T, and Rosenauer A (2018) Using molecular dynamics for multislice TEM simulation of thermal diffuse scattering in AlGaN. *Ultramicroscopy* 189: 124–135.

Lazić I, Bosch EG, and Lazar S (2016) Phase contrast stem for thin samples: Integrated differential phase contrast. *Ultramicroscopy* 160: 265–280.

Lazić I, Wirix M, Leidl ML, de Haas F, Mann D, Beckers M, Pechnikova EV, Müller-Caspary K, Egoavil R, Bosch EGT, and Sachse C (2022) Single-particle cryo-EM structures from iDPC-STEM at near-atomic resolution. *Nature Methods* 19: 1126–1136. https://doi.org/10.1038/s41592-022-01586-0. 01586.

Lohr M, Schregle R, Jetter M, Wächter C, Wunderer T, Scholz F, and Zweck J (2012) Differential phase contrast 2.0—Opening new "fields" for an established technique. *Ultramicroscopy* 117: 7–14.

MacLaren I, Wang L, McGrouther D, Craven AJ, McVitie S, Schierholz R, Kovács A, Barthel J, and Dunin-Borkowski RE (2015) On the origin of differential phase contrast at a locally charged and globally charge-compensated domain boundary in a polar-ordered material. *Ultramicroscopy* 154: 57–63.

Müller-Caspary K, Oelsner A, and Potapov P (2015) Two-dimensional strain mapping in semiconductors by nano-beam electron diffraction employing a delay-line detector. *Applied Physics Letters* 107: 072110.

Müller-Caspary K, Oppermann O, Grieb T, Krause FF, Rosenauer A, Schowalter M, Mehrtens T, Beyer A, Volz K, and Potapov P (2016) Materials characterisation by angle-resolved scanning transmission electron microscopy. *Scientific Reports* 6: 37146.

Müller K, Ryll H, Ordavo I, Ihle S, Struder¨ L, Volz K, Zweck J, Soltau H, and Rosenauer A (2012) Scanning transmission electron microscopy strain measurement from millisecond frames of a direct electron charge coupled device. *Applied Physics Letters* 101: 212110.

Müller-Caspary K, Grieb T, Müßener J, Gauquelin N, Hille P, Schörmann J, Verbeeck J, Aert SV, Eickhoff M, and Rosenauer A (2019) Electrical polarization in AlN/GaN nanodisks measured by momentum-resolved 4D scanning transmission electron microscopy. *Physical Review Letters* 122: 106102.

Müller K, Krause FF, Beche A, Schowalter M, Galioit V, Löffler S, Verbeeck J, Zweck J, Schattschneider P, and Rosenauer A (2014) Atomic electric fields revealed by a quantum mechanical approach to electron picodiffraction. *Nature Communications* 5: 5653.

Müller-Caspary K, Krause FF, Grieb T, Löffler S, Schowalter M, Béché A, Galioit V, Marquardt D, Zweck J, Schattschneider P, Verbeeck J, and Rosenauer A (2017) Measurement of atomic electric fields and charge densities from average momentum transfers using scanning transmission electron microscopy. *Ultramicroscopy* 178: 62–80. ({FEMMS} 2015).

Plackett R, Horswell I, Gimenez EN, Marchal J, Omar D, and Tartoni N (2013) Merlin: A fast versatile readout system for Medipix3. *Journal of Instrumentation* 8: C01038.

Robert HL, Diederichs B, and Müller-Caspary K (2022) Contribution of multiple plasmon scattering in low-angle electron diffraction investigated by energy-filtered atomically resolved 4D-STEM. *Applied Physics Letters* 121: 213502. https://doi.org/10.1063/5.0129692.

Rodenburg JM, McCallum BC, and Nellist PD (1993) Experimental tests on double-resolution coherent imaging via STEM. *Ultramicroscopy* 48: 304–314.

Rose H (1977) Nonstandard imaging methods in electron microscopy. *Ultramicroscopy* 2: 251–267.

Ryll H, Simson M, Hartmann R, Holl P, Huth M, Ihle S, Kondo Y, Kotula P, Liebel A, Müller-Caspary K, Rosenauer A, Sagawa R, Schmidt J, Soltau H, and Strüder L (2016) A pnCCD-based, fast direct single electron imaging camera for TEM and STEM. *Journal of Instrumentation* 11: P04006.

Schwarzhuber F, Melzl P, Pollath¨S, and Zweck J (2018) Introducing a non-pixelated and fast centre of mass detector for differential phase contrast microscopy. *Ultramicroscopy* 192: 21–28.

Shibata N, Findlay SD, Kohno Y, Sawada H, Kondo Y, and Ikuhara Y (2012) Differential phase-contrast microscopy at atomic resolution. *Nature Physics* 8: 611–615.

Spence JCH and Zuo JM (1988) Large dynamic range, parallel detection system for electron diffraction and imaging. *Review of Scientific Instruments* 59: 2102–2105.

Strauch A, März B, Denneulin T, Cattaneo M, Rosenauer A, and Müller-Caspary K (2023) Systematic errors of electric field measurements in ferroelectrics by unit cell averaged momentum transfers in STEM. *Microscopy and Microanalysis* 29: 499–511. https://doi.org/10.1093/micmic/ozad016.

Tate MW, Purohit P, Chamberlain D, Nguyen KX, Hovden R, Chang CS, Deb P, Turgut E, Heron JT, Schlom DG, Ralph DC, Fuchs GD, Shanks KS, Philipp HT, Muller DA, and Gruner SM (2016) High dynamic range pixel array detector for scanning transmission electron microscopy. *Microscopy and Microanalysis* 22: 237–249.

Van Dyck D (2009) Is the frozen phonon model adequate to describe inelastic phonon scattering? *Ultramicroscopy* 109: 677–682.

Verbeeck J, van Dyck D, Lichte H, Potapov P, and Schattschneider P (2005) Plasmon holographic experiments: Theoretical framework. *Ultramicroscopy* 102: 239–255.

Waddell EM and Chapman JN (1979) Linear imaging of strong phase objects using asymmetrical detectors in STEM. *Optik* 54: 83–96.

Wang ZL (1998) The Frozen-Lattice approach for incoherent phonon excitation in electron scattering. How accurate is it? *Acta Crystallographica Section A* 54: 460–467.

Winkler F, Barthel J, Dunin-Borkowski RE, and Müller-Caspary K (2020) Direct measurement of electrostatic potentials at the atomic scale: A conceptual comparison between electron holography and scanning transmission electron microscopy. *Ultramicroscopy* 210: 112926.

Zweck J, Schwarzhuber F, Pöllath S, and Müller-Caspary K (2023) Advanced processing of differential phase contrast data: Distinction between different causes of electron phase shifts. *Ultramicroscopy* 250: 113752. https://doi.org/10.1016/j.ultramic.2023.113752.

Confocal optical sectioning microscopy[☆]

J Sanderson[a], **MJ Solomon**[b], **and M Kogan**[b], [a]Mary Lyon Centre, MRC Harwell, Harwell Campus, Oxfordshire, United Kingdom; [b]University of Michigan, Ann Arbor, MI, United States

© 2024 Elsevier Ltd. All rights reserved.

This is an update of M.J. Solomon, M. Kogan, Confocal Optical Microscopy, Editor(s): Franco Bassani, Gerald L. Liedl, Peter Wyder, Encyclopedia of Condensed Matter Physics, Elsevier, 2005, Pages 229–235, ISBN 9780123694010, https://doi.org/10.1016/B0-12-369401-9/00581-7.

Introduction 109
Principle of confocal optical microscopy 109
Confocal laser scanning microscopy 110
Nipkow spinning disc confocal microscopy 111
Limits of optical resolution 112
Model materials for confocal imaging 113
Quantitative image processing for confocal microscopy 113
Applications in condensed matter physics 113
Conclusion 114
Further reading 114

Abstract

Confocal optical sectioning microscopy is a direct visualization method using fluorescent labels that is increasingly applied in condensed matter physics to study the structure and dynamics of complex fluids. The technique, developed for imaging cells and thick biological tissues, is borrowed from the life sciences. The focus of this article is the theory and practice of confocal microscopy in materials science. The instruments used to optically section through samples are described, together with their advantages and limitations. Auxiliary methods, such as fluorescent particle synthesis and quantitative image processing, are also summarized. Finally, current applications of confocal optical microscopy in condensed matter physics are discussed.

Key points

- Understand why fluorescently-stained specimens form blurred images
- Learn why optical sectioning is required
- Understand how optical sectioning is performed
- Learn about the different types of confocal microscopes

Introduction

Standard optical microscopy techniques, including microscopy by bright field and epifluorescence illumination, fail for the optically dense specimens that are typical of applications in materials science and condensed matter physics.

The origin of the optical density is often a combination of scattering due to strong refractive index contrast, emission due to high fluorophore density, or attenuation due to the long optical path of an object plane located deep in the specimen. This problem was first encountered and addressed in the life sciences. There, methods were sought to image deep into cellular tissue without the need for laborious sectioning. While sectioning is laborious, it also precludes examination of living tissues. More importantly fluorescent labels are *self-luminous*: the fluorescently-labeled specimen emits signal throughout its entire volume, which often exceeds the depth of field of the microscope objective (the depth of field is the axial depth of the space on both sides of the object plane within which the object can be moved without detectable loss of sharpness in the image, and within which features of the object appear acceptably sharp in the image while the position of the image plane is maintained). The consequence is the out-of-focus fluorescent signal emitted by the specimen blurs those in-focus details in the image.

Principle of confocal optical microscopy

Optical sectioning is achieved by point illumination and point detection. By restricting the illumination to a pinhole, rather than illuminating the entire field of view at once, as in widefield microscopy, it becomes possible to build up a blur-free image in three

---

[☆] *Change History:* November 2022. J Sanderson updated the chapter.

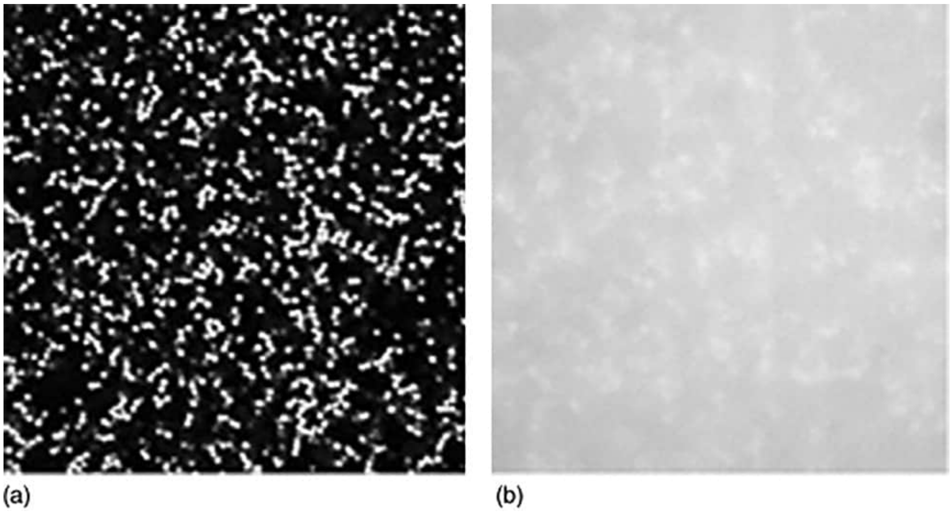

Fig. 1 A depletion gel of fluorescent poly(methyl methacrylate) colloids ~1.9 μm in diameter dispersed in a refractive index and density-matched solvent imaged with a 1.4 NA objective by (a) confocal fluorescence and (b) epifluorescence microscopy. The comparison demonstrates the image-forming capability of confocal microscopy for the optically dense specimens that are characteristic of condensed matter physics and materials science.

dimensions. The detection pinhole rejects light not originating from the vicinity of the object plane. The entire image is built up point-by-point in each frame, as the diffraction-limited spot of the illuminating beam rasters across the frame or the stage is moved, rather like reading words in lines along a page of script in a book.

The term "confocal" is a portmanteau of the words "conjugate focus" since the projection of the illumination pinhole, the plane of focus within the specimen and the back-projection of the detector pinhole are all situated at conjugate focal planes.

When the confocal detection scheme is combined with the capability to move the object plane through the specimen, to create so-called "z-stacks," a powerful technique for the imaging of three-dimensional (3D) volumes is made possible.

While fluorescence imaging is the most common application of confocal microscopy, visualization of structure by scattered or reflected light is also feasible. Fig. 1 shows the difference in image forming capability for a gelled colloidal suspension (volume fraction of 10%) imaged by confocal and epifluorescence microscopy.

The direct visualization of image volumes by confocal microscopy has been applied in many areas of condensed matter physics. In experimental statistical mechanics, application of quantitative image processing to 3D intensity maps generated by confocal microscopy has been used to quantify the thermodynamic and structural properties of glasses and gels comprised of colloidal particles. The field-induced and template-induced crystallization of novel colloidal phases has been observed and quantified. The 3D structure of mesoporous phases has been discovered. The diffusivity of fluorescent probes in polymer networks has been quantified. Particle tracking routines applied to time series of confocal image volumes have observed cooperative motion in colloidal suspensions. These observations can be used to understand the fundamental origins of glass transition.

These applications require understanding of the spatial and temporal resolution of confocal microscopy, the use of image processing tools to quantify acquired image volumes, and synthesis of model materials suitable for confocal imaging. These issues are discussed in subsequent sections. First, the configurations commonly used in confocal microscopy are described.

Confocal laser scanning microscopy

The conceptual idea of rejecting out-of-focus emission from the detector by adding an aperture (usually referred to as the "pinhole") to the detection system has been implemented in two principal ways. Fig. 2a shows the single-beam raster-scanning confocal laser scanning microscope (CLSM).

The confocal aperture is adjusted to optimize the trade-off between axial resolution and optical section thickness inherent to confocal microscopy. In the CLSM configuration, the image is collected pointwise with a single detector, usually a photodiode or photomultiplier tube. A PMT is used because these enhance the weak signal and can also very rapidly collect single points of light emitted as signal. Using an sCMOS or CCD detector would be far too slow.

In order to ensure sufficient emission from the excitation focal point in the objective plane, laser illumination is used. Scanning mirrors manipulate the path of an expanded, spatially filtered source so that the illuminated point is rastered across the object plane. The speed of the galvanometrically-actuated scanning mirrors determines the acquisition rate of a 2D image. At current capabilities a line scan can be executed at rates up to ~1 kHz. Thus, a 512 × 512 pixel scan can be acquired in less than one second. 3D image volumes are acquired by piezoelectric actuation of the specimen relative to the objective. This actuation can be conducted with nanoscale resolution and micrometer-scale repeatability. A 1024 × 1024 × 200 3D scan, a typical dataset, requires a few minutes with a good CLSM.

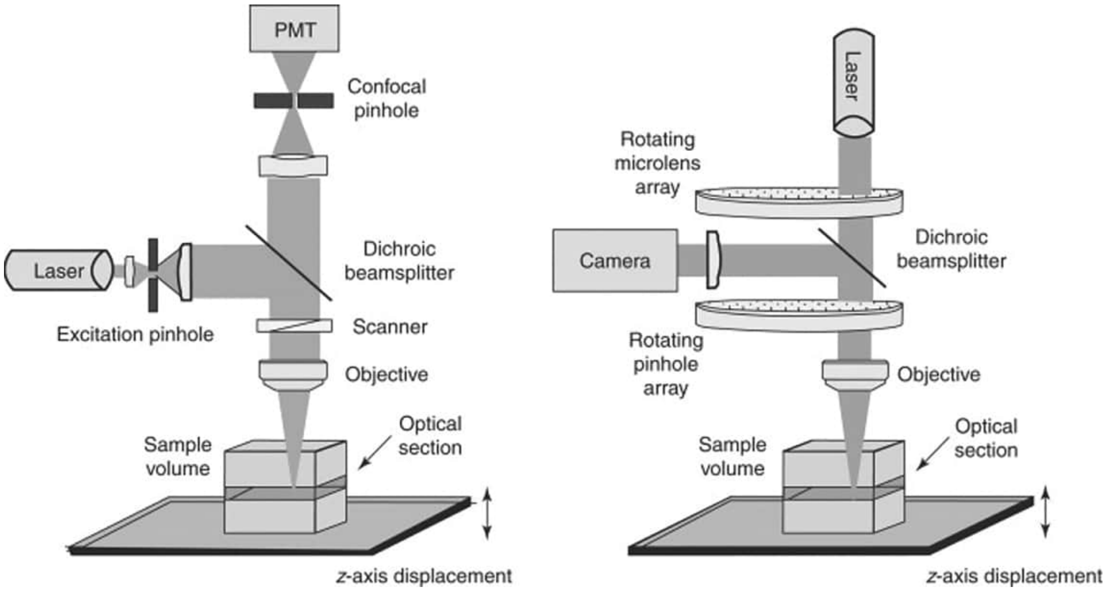

Fig. 2 Schematics of the: (a) confocal laser scanning microscope and (b) Nipkow spinning disc confocal microscope.

The confocal imaging system is used in conjunction with the components of a standard optical microscope. In particular, the microscope objectives and specimen preparation for CLSM and optical microscopy are identical. Just as in widefield epifluorescence technique, in CLSM the excitation and emission illumination traverse the microscope objective in reverse directions. Typically, a dichromatic beam splitter ensures that only emission from the specimen passes to the detector optics. Alternatively, an acousto-optic beam splitter (AOBS) provides flexibility in selecting transmission bands. The CLSM is commonly used in non-confocal fluorescence mode to first locate and focus the specimen. Switching to laser-scanning confocal mode, the detection system must then separate the emission spectrum into bands corresponding to the wavelength ranges relevant to the multiple fluorophores. This decomposition can be accomplished with a cascade of dichroic filters. Alternatively, after the confocal pinhole, the emission can be spectrally resolved with a prism and adjustably filtered with mechanical slits before detection with a photomultiplier tube. While fluorescence visualization is a frequent application of CLSM, some situations require analysis of reflected or scattered light. This method, called reflection CLSM, is of particular interest for measurements of topography in materials science and solid-state electronics.

Variations on the design of Fig. 2a include substitution of the confocal pinhole for a confocal slit. This configuration allows faster scanning with reduced resolution.

Nipkow spinning disc confocal microscopy

The pointwise scanning of CLSM imposes a significant limitation upon the image acquisition speed of this method. The Nipkow spinning disc confocal microscope, now more often called the spinning disc microscope, shown in Fig. 2b, is an alternate method that can achieve video rate imaging. Current configurations use two synchronized discs rotating at a rate that scans the image at 360 frames s^{-1}. One disc is patterned with an array of many thousands of pinholes. The pinhole diameter is optimized for high numerical aperture (NA) objectives (optimization for $NA = 1.4$ is typical). The excitation illumination is chopped by the pinhole array. A second rotating disc, located prior to the pinhole disc, consists of a microlens array. Each microlens focuses excitation light onto a corresponding pinhole, thereby significantly increasing the excitation intensity supplied to the specimen. The pinhole spacing relative to its diameter is optimized to reduce collection of the emission signal from one pinhole by a neighboring one. Thus, the pinhole disc has inherently low transmission efficiency without incorporation of the microlens array.

Because the primary excitation is subdivided into a number of sources by the pinhole disc, multiple points of the objective plane are simultaneously interrogated. Emission from the specimen propagates through the rotating pinhole array in the reverse sense. In this case, each pinhole serves as the confocal aperture. The emission paths are diverted to the detection system by a dichroic beamsplitter. A sCMOS or CCD array images the emission paths in widefield mode. The read-out rate of the digital camera detector is currently the limiting step in the time required to acquire a 2D image. 3D image volumes are acquired by relative actuation of specimen and objective, just as for CLSM.

At full frame resolution, image acquisition rates for spinning disc confocal microscopy are at least an order of magnitude faster than CLSM. However, because the primary incident laser source is subdivided into a number of beams, the excitation supplied to a particular point in the object plane is typically less than CLSM. In addition, the confocal aperture is not adjustable as is the case in the CLSM.

Limits of optical resolution

Confocal microscopy presents unique opportunities for 3D imaging of microstructure; however, the method is an optical one and thus resolution limits are dictated by the wavelength of light. Here, two limits of optical resolution are considered. The first, resolution in the object plane (lateral optical resolution), is governed by the Rayleigh resolution criterion. The second, resolution perpendicular to the object plane (axial optical resolution or optical section thickness), is dictated by the point spread function. The effect of confocal aperture diameter on resolution is also assessed.

According to the Rayleigh criterion, the resolution limit occurs when where the central maximum of the Airy pattern of one point emitter is directly overlapping with the first minimum of the Airy pattern of the adjacent point emitter. In other words, the minimum resolvable separation between the points is the radius of the Airy disc. For unpolarized light, this lateral optical resolution is $0.61\lambda/\mathrm{NA}$ where λ is the wavelength of light and NA is the numerical aperture of the objective. For $\mathrm{NA} = 1.4$, lateral resolution is $\sim 0.2\ \mu\mathrm{m}$ and this is the best resolution currently possible for optical microscopy. The Rayleigh criterion is a useful estimate of lateral resolution in both widefield and confocal microscopy.

In confocal microscopy, the criterion for axial object resolution commonly adopted is that two points oriented perpendicular to the object plane can be resolved if the first minima in their point spread functions (evaluated along the optical axis) are distinct. This criterion has the same physical basis as the one for the Rayleigh resolution and leads to a characteristic axial optical resolution of $2\lambda/(\mathrm{NA})^2$. For $\mathrm{NA} = 1.4$, axial resolution is $\sim 0.5\ \mu\mathrm{m}$, slightly greater than twice the lateral object resolution.

These resolution criteria are the best achievable. Actual microscopes achieve lower resolution due to polarization effects and nonidealities. For example, the confocal aperture diameter has a profound effect on optical section thickness. In scanning devices, this fixed diameter is adjusted to optimize the trade-off between image intensity and axial resolution. Units scaled on characteristics of the diffraction point spread function are a convenient basis to specify the aperture diameter and its performance. The dimensionless lateral scale in the image plane is then $(2\pi/\lambda)(\mathrm{NA}/M)r_a$, where M is the magnification in the image plane and r_a is a particular image plane dimension such as the aperture radius.

Calculations and experiments for confocal visualization show that the optimal confocal section thickness is attained with a confocal aperture dimension that corresponds to one Airy diffraction disc (cf. dimensional scaling above). Aperture reduction below this value yields only small improvement in resolution at the expense of reduced image intensity. As the confocal aperture is opened, progressively greater amounts of out-of-focus emission are admitted to the detector; however, resolution deteriorates. One way in which this effect has been quantified is by imaging a plane reflective coating. In this experiment, the full-width at half maximum (FWHM) of the axial intensity, a practical measure of the optical thickness and axial resolving power, doubles as the aperture is increased from one Airy disc to two. Fig. 3 displays images that show the qualitative effect of confocal aperture on image intensity and resolution as the aperture is opened for a colloidal crystal of interest to soft condensed matter physics and materials science.

The resolving power of a confocal microscope is marginally improved over that of a widefield microscope because the overall image PSF is the product of both illumination and detection PSFs. Therefore resolving power is improved by closing down the pinhole, but at the expense of rejecting most of the emitted signal. By collecting the rejected light with a high-sensitivity multi-channel detector, the emitted signal can be processed to improve the signal-to-noise ratio and resolving power in the image. This technique is called "pixel reassignment," and is of increasing importance in the life sciences.

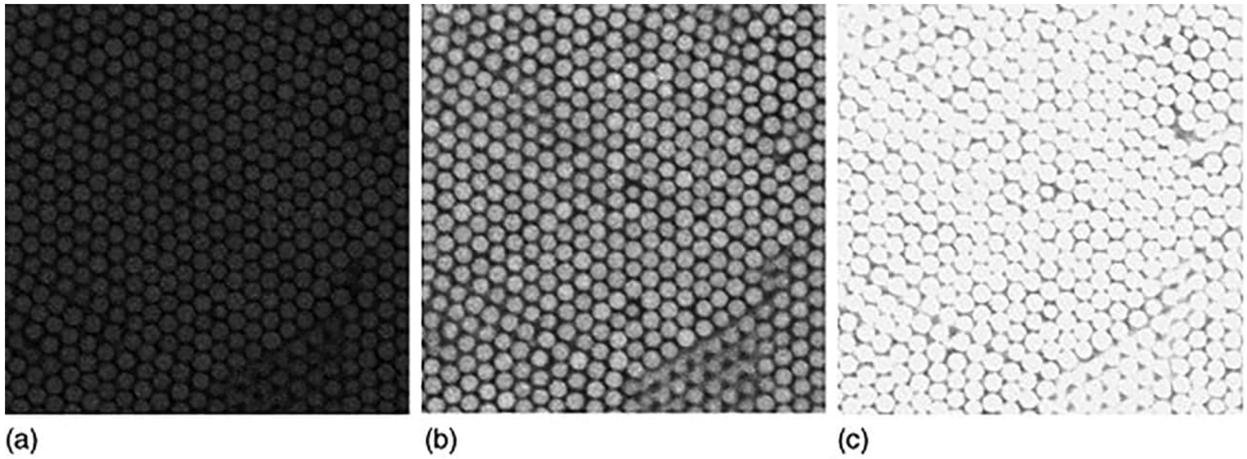

Fig. 3 The effect of pinhole aperture on the image-forming capability of confocal laser scanning microscopy. In optical units nondimensionalized on the size of the Airy diffraction disc, the images are for confocal apertures of 0.5, 1.0, and 2.0 (from left to right). The specimen is a colloidal crystal of colloidal poly(methyl methacrylate), diameter $\sim 1.9\ \mu\mathrm{m}$, in a refractive index and density-matched solvent for which electrostatic interactions between the colloids have been screened by the addition of an organic salt.

Model materials for confocal imaging

Most applications of confocal microscopy in condensed matter physics have used fluorescent imaging. The need to incorporate fluorophores into structures to be imaged imposes a constraint on materials that can be studied. Thus, studies of experimental statistical mechanics and self-assembly using colloidal models require methods for syntheses of monodisperse colloidal particles. Determination of bulk behavior requires imaging deep within the sample, where effects of the sample boundary are minimized. To accomplish such imaging, the particle and suspending medium must be at least approximately refractive index matched; otherwise scattering reduces the intensity and image-forming quality of the emitted signal returned to the detector.

A common approach to this challenge is to synthesize monodisperse colloids to which an oligomeric stabilizing layer is grafted to the particle surface. This steric layer ensures colloid stability in mixtures of organic solvents that match the refractive index of the colloid. A number of strategies exist to incorporate fluorescent dyes into silica or poly(methyl methacrylate) colloids during particle syntheses. For polymer colloids, the post-synthesis method of colloid swelling and dye absorption is also possible; however, these processes change the potential interactions between the colloids in ways that are poorly understood.

In addition to refractive index matching, solvent mixtures are often selected to match the density of particle and solvent so as to minimize colloid sedimentation (or flotation). Such particle motion, even when small, can destroy fragile gel or crystalline structures that arise due to the physical interactions between particles. Sedimentation also interferes with the study of Brownian and cooperative particle motion by particle tracking.

Long duration kinetic and dynamic studies require fluorescent dyes that are resistant to photobleaching. In the life sciences, the limitation of cytotoxity on dye concentration means that photobleaching is an important factor in dye selection. While the situation is less severe in condensed matter physics (because cytotoxic effects are absent), recent work has favored more photostable dyes, such as Alexa Fluor, DyLight, Cy dyes—to name a few—over traditional ones such as fluorescein and rhodamine.

Quantitative image processing for confocal microscopy

The 3D map of fluorescent intensity provided by confocal microscopy is a powerful qualitative indicator of complex fluid behavior. An even more fruitful approach is to use image processing to extract quantitative measures of structure and dynamics from the fluorescence maps. In 2D microscopy, a number of approaches for the interrogation of particle locations using edge detection and thresholding have been developed. Alternatively, particles can be identified from local intensity maxima and their locations then refined to subpixel resolution according to the distribution of brightness in the vicinity of the maxima. This latter approach, although computationally intensive, is readily extendable to the 3D particle location problem and has thus found wide application in confocal microscopy of colloidal systems. While estimates of the errors in particle location for these routines vary widely, the most significant determinant of the precision and accuracy of particle location is the delocalizing effect of Brownian motion on the timescale of image volume acquisition. For time series acquired at a rate such that the typical particle displacement is much less than the mean separation between particles, algorithms have been developed that reliably link particle locations in each frame into trajectories. The trajectory analysis yields dynamic information about Brownian and cooperative motion of the particles.

Once particle centroids and trajectories have been located, the information contained in the confocal image volumes is transformed into output of the same format that would result from a computer simulation of a corresponding model system. (In a typical image volume of $40 \times 40 \times 20\ \mu\text{m}^3$ resolved by a high-resolution objective, the number of micrometer-sized particles is of order 10^4. This number is not too different from the state-of-the-art computer simulation.) Thus, all the tools of statistical mechanics developed for the analysis of molecular, Brownian, and Stokesian dynamics simulations can be applied to the experimental results. This formal correspondence between experiment and simulation offers an unusually rich avenue for direct comparison between the two. Fig. 4 displays the results of quantitative image processing of a depletion colloidal gel comprised of monodisperse fluorescent poly(methyl methacrylate) colloids of diameter $\sim 1.9\ \mu\text{m}$. The projections of the confocal image volume in two orthogonal planes qualitatively demonstrate the degree to which image processing methods locate the imaged particles.

Applications in condensed matter physics

The qualitative fluorescence imaging and 3D sectioning capability of confocal microscopy have found wide application in the qualitative characterization of microstructure in colloidal suspensions, polymer gels, immiscible blends, and composites. Recently, the additional step of generating quantitative measures of complex fluid structure and dynamics from confocal microscopy has been taken. In this brief summary, the focus is on these new developments. These advances have been driven by three recent steps forward: (1) methods to synthesize monodisperse fluorescent colloidal particles have been discovered; (2) confocal microscopy, borrowed from the life sciences, has been applied to image materials comprised of colloidal particles; (3) techniques of quantitative image processing have been developed to extract the locations and trajectories of the colloidal particles.

Confocal microscopy has been used to interrogate the phase behavior of concentrated colloidal suspensions interacting through screened electrostatic forces. The self-assembly of colloidal particles into ordered crystals is a step in one method to produce photonic materials. The effect of an applied electric field on colloidal crystal structure has also been discovered. The nucleation and growth of crystal nuclei in colloidal suspensions has been directly visualized. The particle correlation function and coordination

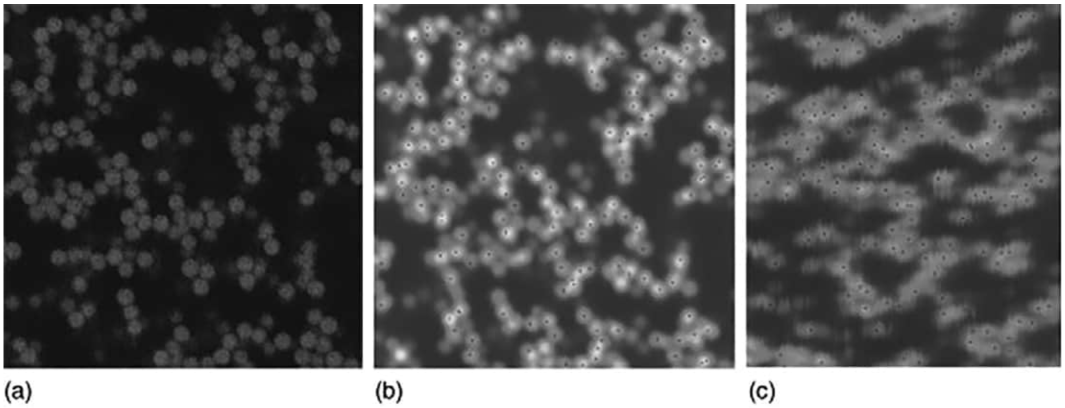

Fig. 4 Illustration of methods for quantitative image processing. Image (a) is a representative 2D slice from a 3D image volume of a depletion gel of poly(methyl methacrylate) colloids (volume fraction of 10%, diameter 1.9 μm) imaged by CLSM. Image (b) shows a projection of ~20 2D lateral slices with an overlay of particle locations found within that volume by quantitative image processing. Image (c) shows a similar projection, but now in a plane that includes the axial direction of the microscope. Note that the optical resolution in the axial direction is reduced relative to the lateral direction because of the different characteristics of the 3D point spread function along the optical axis and in the objective plane.

number of hard-sphere glasses have also been quantified by direct visualization with confocal microscopy. Short-range attractive forces, included by conformational changes of grafted steric layers or by the depletion interactions induced by nonadsorbing polymer, lead to the assembly of amorphous gel structures. The clusters and voids that comprise these structures have been directly visualized with CLSM. Cooperative particle dynamics in the vicinity of the colloidal hard-sphere glass transition have been visualized by time-resolved confocal microscopy. The thermal fluctuations of gel backbone segments have likewise been quantified as have the flow-induced structures of colloidal gels as they are subjected to shear and compressional flow. These direct visualization studies of structure and dynamics in colloidal systems by confocal optical microscopy represent a new and fruitful approach to understand the behaviors of complex fluids that are of broad interest in soft condensed matter physics and materials science.

Conclusion

Confocal optical sectioning microscopy is a direct visualization method of viewing detail in thick fluorescent specimens that would otherwise form blurred images.

Fluorescent labels are *self-luminous*: the fluorescently-labeled specimen emits signal throughout its entire volume, which often exceeds the depth of field of the microscope objective. The consequence is the out-of-focus fluorescent signal emitted by the specimen blurs those in-focus details in the image.

Optical sectioning is so-called because point illumination and point-detection are used to “slice” the sample with light to image deep into cellular tissue without the need for laborious mechanical sectioning. An aperture (usually referred to as the “pinhole”) in the detection system prevents the out-of-focus signal from being collected. The confocal aperture is adjusted to optimize the trade-off between axial resolution and optical section thickness inherent to confocal microscopy.

The pointwise scanning of CLSM imposes a significant limitation on the image acquisition speed of this method. The Nipkow spinning disc confocal microscope, now more often called the spinning disc microscope, is an alternative method that can achieve video rate imaging.

The Rayleigh criterion is a useful estimate of lateral resolution in both widefield and confocal microscopy. The resolving power of a confocal microscope is marginally improved over that of a widefield microscope because the overall image PSF is the product of both illumination and detection PSFs. Resolving power is improved by closing down the pinhole, but at the expense of rejecting most of the emitted signal. By collecting the rejected light with a high-sensitivity multi-channel detector, the emitted signal can be processed to improve the signal-to-noise ratio and resolving power in the image. This technique is called “pixel reassignment.”

Further reading

Dinsmore AD, Weeks ER, Prasad V, Lvitt AC, and Weitz DA (2001) Three-dimensional confocal microscopy of colloids. *Applied Optics* 40(24): 4152–4159.
Gasser U and Zhou B (2021) Accurate detection of spherical objects in a complex background. *Optics Express* 29(23): 37048–37065.
Kurita R, Ruffner DB, and Weeks ER (2012) Measuring the size of individual particles from three-dimensional imaging experiments. *Nature Communications* 3: 1127.
Pawley JB (ed.) (2006) *Handbook of Biological Confocal Microscopy*, 3rd ed. New York: Springer-Verlag.
Sanderson J (2020) Fundamentals of microscopy. *Current Protocols in Mouse Biology* 10: e76.
Sanderson J (2022) Chapter 5, Confocal microscopy. In: Nechyporuk-Zloy V (ed.) *Principles of Light Microscopy: From Basic to Advanced.* Vienna: Springer-Nature. pp. 105–138. (see https://doi.org/10.1007/978-3-031-04477-9_5).
Van Blaaderen A (1998) From the de Broglie to visible wavelengths: Manipulating electrons and photons with colloids. *MRS Bulletin* 39–43.
Richards JA, Martinez VA, and Arlt J (2021) Particle sizing for flowing colloidal suspensions using flow-differential dynamic microscopy. *Soft Matter* 17(14): 3945–3953.

Cyclotron resonance in metals, with a focus on quasiparticle scattering rates

John Singleton, [a]National High Magnetic Field Laboratory, Pulsed-Field Facility, Los Alamos National Laboratory, Los Alamos, New Mexico, United States; [b]University of Oxford Department of Physics, The Clarendon Laboratory, Oxford, United Kingdom

© 2024 Elsevier Ltd. All rights reserved.

This is an update of J. Singleton, Cyclotron Resonance: Metals, Editor(s): Franco Bassani, Gerald L. Liedl, Peter Wyder, Encyclopedia of Condensed Matter Physics, Elsevier, 2005, Pages 343–355, ISBN 9780123694010, https://doi.org/10.1016/B0-12-369401-9/01119-0.

Introduction 116
Landau quantization: A brief description 117
Cyclotron resonance in elemental metals and simple metallic alloys 118
Experimental considerations 118
Extraction of scattering rates 118
Layered metals and degenerate semiconductor systems 121
Fermi surfaces and resonant cavity techniques 121
Extraction of the apparent scattering rates in layered metals 123
Cyclotron resonance in semiconductors, candidate topological insulators and other low carrier-density systems 123
Experimental details: quasistatic measurements 123
Experimental techniques: Pulsed measurements 125
Extraction of apparent scattering times 125
Contributions to the apparent scattering rate in layered metals, semiconductor heterostructures and other similar systems 126
Comparisons with other methods 126
The importance of spatial inhomogeneities 127
Scattering times in angle-dependent magnetoresistance oscillations 128
Many-body effects I: Systems with two interacting carrier populations 128
Many-body effects II: Which effective mass does cyclotron resonance measure? 129
Effects related to cyclotron resonance 130
Conclusion 130
Acknowledgments 130
References 130

Abstract

This article covers the observation of cyclotron resonance in a wide range of materials and systems that may be loosely defined as metals; they possess Fermi surfaces. While all involve magnetic fields and (mostly) cryogens, details of the experimental techniques used are dictated by the carrier densities and skin depths of these “metals,” and range from simple transmission to complicated resonant cavities. A primary focus of this article is the extraction of the carrier scattering rate from cyclotron resonance, and various methods to recover the desired information from the raw data are described. The scattering rates thus deduced provide the purest gauge of the Landau-level width, and can be used to show how it is affected by various types of carrier scattering. Other techniques yield different values for the scattering rate, and the reasons for this are discussed. Finally, I describe the influence of many-body effects on the cyclotron-resonance lineshape and the effective mass measured, and give a brief summary of techniques related to cyclotron resonance.

Key points

- To introduce Landau quantization and cyclotron resonance.
- To explain the materials and systems—ranging from graphene and semiconductor heterostructures to elements, with cuprates, organic metals etc. in between—that are classified as “metals” and studied using cyclotron resonance.
- To describe the types of apparatus used to observe cyclotron resonance in these “metals,” and how the apparatus is chosen based on their carrier densities.
- To describe how quasiparticle scattering rates may be extracted reliably from the various cyclotron resonance experiments.
- To show why the quasiparticle scattering rates measured using cyclotron resonance differ from those deduced using other techniques.
- To give a brief description of the effective mass measured in cyclotron resonance, and how it is affected by many-body effects.
- To give brief descriptions of other phenomena related to cyclotron resonance.

Introduction

Landau quantization may occur when electrons in a solid are subjected to a magnetic field (Ashcroft and Mermin, 1976; Singleton, 2001). The excitation of electrons from one Landau level to another by photons results in a resonant contribution to the magnetic-field-dependent, high-frequency conductivity. It is this phenomenon that is known as *cyclotron resonance*. This article is chiefly concerned with the electronic *scattering rate* τ_{CR}^{-1} that can be deduced from a cyclotron resonance experiment; this is associated with the finite energy width of the Landau levels caused by their limited lifetime. By convention (Ashcroft and Mermin, 1976), the scattering rate is defined as the reciprocal of a notional scattering time τ_{CR}, which is sometimes also referred to as the "Landau-level lifetime." We shall see that simple-minded first analysis of a cyclotron resonance experiment often yields an *apparent* scattering rate, which may bear little relationship to the actual scattering processes present; it can contain contributions due to experimental factors that mask the true result. Apparent cyclotron scattering rates will be distinguished throughout by the use of the subscript "M," which stands for "measured"; thus we have the symbol τ_{CRM}^{-1}.

Another concern will be the relationship of τ_{CR}^{-1} to the *apparent* scattering rates deduced from other techniques such as de Haas-van Alphen (or Shubnikov-de Haas) oscillations ($\tau_{\mathrm{dHvA}}^{-1}$) and measurements of the electronic conductivity σ (τ_{σ}^{-1}). We shall see that τ_{CR}^{-1} is preferable to $\tau_{\mathrm{dHvA}}^{-1}$ as a guide to the true energy width of the Landau levels due to scattering. We shall also find that there can be considerable differences between τ_{CR} and τ_{σ}.

In order to keep the discussion as general as possible, we shall refer generally to electrons in a solid as "quasiparticles." This enables the descriptions that follow to encompass not only both carrier types (electrons, holes) but also systems in which effects such as electron-electron and electron-phonon interactions are significant and describable by Landau Fermi-liquid theory (Gross et al., 1991).

This article deals with cyclotron resonance in metals; the most fundamental definition of a metal is "a solid with a Fermi surface" (Shoenberg, 1984; Singleton, 2001). From the point-of-view of cyclotron resonance, this broad class of materials must be separated into three groups;

1. metals with a high electron density, including elements (Cu, Al etc.) (Häussler and Welles, 1966; Lindholm and Le Page, 1969) and simple alloys (e.g., AuZn, AuBe) (Shoenberg, 1984);
2. intermediate-electron-density systems, often of reduced dimensionality, such as certain oxides [e.g., "high T_c" cuprate superconductors (Harrison and Chan, 2022; Post et al., 2021), Sr_2RuO_4 (Rzepniewski et al., 2002)], crystalline organic metals (Hill, 1997, 2000; Mola and Hill, 2000; Schrama et al., 2001) and iron-based superconductors (Kimata et al., 2012);
3. low-electron-density systems, including graphene (Russell et al., 2018), topological insulators (Kamenskyi et al., 2020; Mohelský et al., 2020), degenerate semiconductors (Moss and Balkanski, 1994; Singleton, 2001), and semiconductor heterojunctions (Langerak et al., 1988).

The distinction between these three groups results from the ease with which light of the appropriate frequency to excite cyclotron resonance (usually in the GHz to THz range) can penetrate the sample. With the relatively recent advent of high quality epitaxial films, 10s of nm thick, of materials such as cuprates (Post et al., 2021), the boundary between the second and third categories has blurred a little, but nevertheless it is logical for the rest of the article to be arranged as follows. The section "Landau quantization; A brief description" presents a brief introduction to Landau quantization. "Cyclotron resonance in elemental metals and simple metallic alloys" deals with experimental techniques for elemental metals and the extraction of true scattering rates from the apparent rate produced by fitting experimental data. Intermediate- and low-electron-density systems are dealt with in the section "Layered metals and degenerate semiconductor systems"; the experimental techniques and the extraction of scattering rates from data are treated in separate subsections. However, the causes of the difference between τ_{CR} and τ_{dHvA} are similar in both types of "metal," and so are treated in a common subsection. [Note that, as this article focuses on the extraction of scattering rates from cyclotron resonance, "Layered metals and degenerate semiconductor systems" describes only Faraday geometry measurements (i.e., those in which the radiation propagates parallel to the applied magnetic field). The alternative (and more complex) Voigt configuration is discussed by McKnight and Drew (1981) and Otteneder et al. (2021) and references therein]. Systems containing two or more distinct types of quasiparticles are described in "Many-body effects I: systems with two interacting carrier populations"; the interactions may lead to a single cyclotron resonance rather than two distinct resonances (Cole et al., 1997). Finally, "Many-body effects II: Which effective mass does cyclotron resonance measure?" covers the distinctions between the effective masses measured in different experiments, and "Effects related to cyclotron resonance" mentions two effects closely related to cyclotron resonance.

The history of this subject begins in the 1950s. To avoid recent converts to cyclotron resonance having to "reinvent the wheel" (not always successfully, as some recent papers have shown), literature covering almost the whole of this period is summarized and cited in the text.

In all that follows, I assume that the materials under study are not very magnetic, so that the magnetic induction $B \approx \mu_0 H$, the applied magnetic field, to a good precision. Almost all cyclotron resonance measurements are performed at cryogenic temperatures, for reasons that will become obvious below. Finally, as a significant number of equations is necessary to give a quantitative understanding of the physics involved, Table 1 provides a reference list of the most frequently used symbols in this Chapter.

Table 1 Tabulation of selected symbols.

Symbol	*Definition*
A	Cross-sectional area of the Fermi surface
$\mathbf{B}$	Magnetic induction
E	Energy of a quasiparticle
$\mathbf{E}$	Electric field
j	A general integer used as a label
$\mathbf{k}$	Quasiparticle wavevector quantum number
$k_{\|}$	The component of **k** parallel to **B**
l	Landau-level quantum number
m^*_{CR}	Cyclotron effective mass
m^*	The quasiparticle mass measured in a de Haas-van Alphen experiment
ν	Frequency of photons used to excite cyclotron resonance
q	Quasiparticle charge: $q = \pm e$
σ, σ_{ij}	Conductivity, general element of conductivity tensor
$t_\perp$, $t_{\|}$	Transfer integrals
t	Time
$\mathbf{v}$	Quasiparticle velocity
τ_{CR}	Scattering time associated with Landau-level broadening
τ_{CRM}	Apparent scattering time from a cyclotron resonance measurement
τ_{dHvA}	Apparent scattering time deduced from a de Haas-van Alphen measurement
τ_σ	Scattering rate inferred from a zero-field conductivity measurement
ω	Angular frequency of photons used to excite cyclotron resonance
ω_{c}	Cyclotron (angular) frequency
Z	Surface impedance

Landau quantization: A brief description

To gain a qualitative understanding of the principles of the various measurement techniques for cyclotron resonance, it is useful to consider the semiclassical equation of motion of a quasiparticle of charge q, energy E and wavevector quantum number **k**, subjected to the Lorentz force (Ashcroft and Mermin, 1976, Singleton, 2001):

$$\hbar \frac{\mathrm{d}\mathbf{k}}{\mathrm{d}t} = q\mathbf{v} \times \mathbf{B}. \tag{1}$$

Here **B** is the magnetic induction and **v** is the quasiparticle's velocity, defined as

$$\mathbf{v} = \frac{1}{\hbar} \nabla_{\mathbf{k}} E(\mathbf{k}), \tag{2}$$

where $\nabla_{\mathbf{k}}$ is the gradient operator in k-space. Eqs. (1) and (2) imply that (i) the component of **k** parallel to **B** is constant; and (ii) $\frac{\mathrm{d}\mathbf{k}}{\mathrm{d}t}$ is perpendicular to $\nabla_{\mathbf{k}} E(\mathbf{k})$. This means that the quasiparticle path is one of constant energy.

The Fermi surface is of course a surface of constant energy (Shoenberg, 1984). Under the action of a magnetic field, quasiparticles on the Fermi surface will remain on that surface while moving on paths which lie in planes perpendicular to the magnetic field (see Fig. 1). The bandstructure of solids is such that in many cases, a constant energy path of this kind will form a closed orbit (or *cyclotron orbit*) of cross-sectional area (in k-space) A (Fig. 1). Standard texts (Ashcroft and Mermin, 1976; Singleton, 2001) show that the angular frequency ω_{c} associated with this periodic orbit is

$$\omega_c = \frac{qB}{m^*_{\mathrm{CR}}}, \tag{3}$$

where

$$m^*_{\mathrm{CR}} = \frac{\hbar^2}{2\pi} \frac{\partial A\left(E, k_{\|}\right)}{\partial E}. \tag{4}$$

The quantity defined in Eq. (4) is known as the *cyclotron mass* or *cyclotron effective mass*.

From a quantum-mechanical point-of-view, the cyclotron orbital frequency corresponds to the quantization of the quasiparticle's motion in the plane perpendicular to **B**, resulting in an energy spectrum

$$E\left(\mathbf{B}, k_{\|}\right) = (l + \phi)\hbar\omega_c + E\left(k_{\|}\right). \tag{5}$$

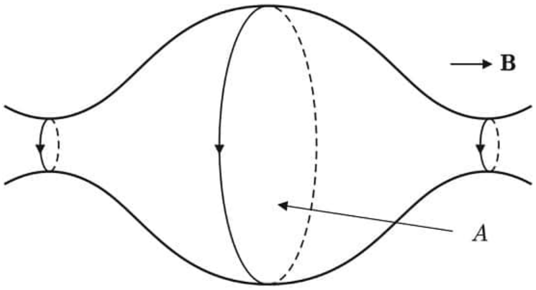

Fig. 1 Orbits on a Fermi-surface section are in planes perpendicular to **B**. The *k*–space cross-sectional area of a Fermi-surface orbit is denoted by *A* (shown in this diagram for the largest one). As will be discussed below, *extremal* orbits, such as the smallest and largest paths around the Fermi surface in this Figure, dominate the cyclotron-resonance spectrum. After Singleton J (2001) Band Theory and Electronic Properties of Solids, Oxford: Oxford University Press, Chapters 8 and 9.

Here l is an integer ($l = 0, 1, 2\ldots.$) known as the Landau quantum number, ϕ (~ 1) is a phase factor and $E(k_{||})$ is the energy associated with the unaffected wavevector $k_{||}$ in the direction parallel to $\mathbf{B}$. The quantization of the quasiparticle's energy in the plane perpendicular to $\mathbf{B}$ is known as *Landau quantization*, and the energy levels defined by l are called *Landau levels*.

Cyclotron resonance occurs when a photon promotes a quasiparticle from a full state in one Landau level to an empty state in another Landau level. Owing to the fact that photons of the appropriate energy carry very little momentum, such transitions conserve $k_{||}$. Hence, cyclotron resonance occurs when the photon energy ($h\nu$ or $\hbar\omega$) equals $\hbar\omega_c$, or, in some cases, integer multiples of $\hbar\omega_c$ (see below).

Cyclotron resonance in elemental metals and simple metallic alloys

Experimental considerations

The field components of electromagnetic radiation decay with distance z into a conducting material as exp.($-z/\delta$), where $\delta = \left(\frac{1}{2}\sigma\omega\mu_r\mu_0\right)^{-\frac{1}{2}}$ is the *skin depth* or anomalous skin depth; here σ is the conductivity of the material (Bleaney and Bleaney, 2013), $\mu_r\mu_0$ is its permeability and ω is the angular frequency of the radiation. Traditional metals have rather high conductivities (Ashcroft and Mermin, 1976); moreover, typical effective masses in metals combined with the magnetic fields readily available in laboratories have meant that frequencies $\omega/2\pi \sim 1$–100 GHz have tended to be applied in cyclotron resonance experiments. This combination of factors results in a small skin depth; hence, radiation cannot penetrate far into the crystal (Bleaney and Bleaney, 2013). These considerations dictate the geometry of the cyclotron resonance measurement (see Fig. 2); such an configuration is often referred to as *the Azbel′–Kaner geometry* (Häussler and Welles, 1966; Singleton, 2001).

The magnetic field is applied parallel to a surface of the crystal, which is placed in a region of oscillating electric field in a resonant cavity; the *E*-field $\mathbf{E}$ of the radiation is arranged to be perpendicular to the quasistatic magnetic field $\mathbf{B}$ and parallel to the surface. Examination of Eqs. (1) and (2) shows that the projection of an electron's real-space orbit in a plane perpendicular to $\mathbf{B}$ is the same shape as its k-space orbit rotated by $\pi/2$ radians. The paths of electrons on closed Fermi-surface orbits are therefore helices with axes parallel to $\mathbf{B}$ in real space.

If the angular frequency of the radiation $\omega = j\omega_c$, where j is an integer, then the electrons on a helical path corresponding to the cyclotron frequency ω_c will receive a "kick" from the radiation's electric field every time they come within a skin depth of the surface; this results in absorption of energy. Usually ω is kept constant and the field is swept, so that absorptions, seen as resonances in the surface impedance, are uniformly spaced in $1/B$ (see Fig. 3).

Extraction of scattering rates

Häussler and Welles (1966), Lindholm and Le Page (1969) and others have demonstrated that a magnetic field which is very accurately parallel to a very flat sample surface is required for a successful measurement; if this is not the case, the helical electron paths drift in and out of the skin depth, causing a smearing of the features in the surface impedance. If the surface is flat, and the magnetic field accurately parallel to it, then the surface impedance Z becomes

$$Z \propto \frac{e^{i\frac{\pi}{3}}}{s}, \quad \text{with} \quad s^3 \approx \sum_j p_j R(\lambda_j) + R_{\mathrm{NR}} \tag{6}$$

to reasonable accuracy. Here the index j labels the various Fermi-surface orbits involved; in practice, it is found that only *extremal orbits* make a significant resonant contribution (Shoenberg, 1984). Extremal orbits are defined by $\mathrm{d}m^*_{\mathrm{CR}}/\mathrm{d}k_{\parallel} = 0$; frequently these are

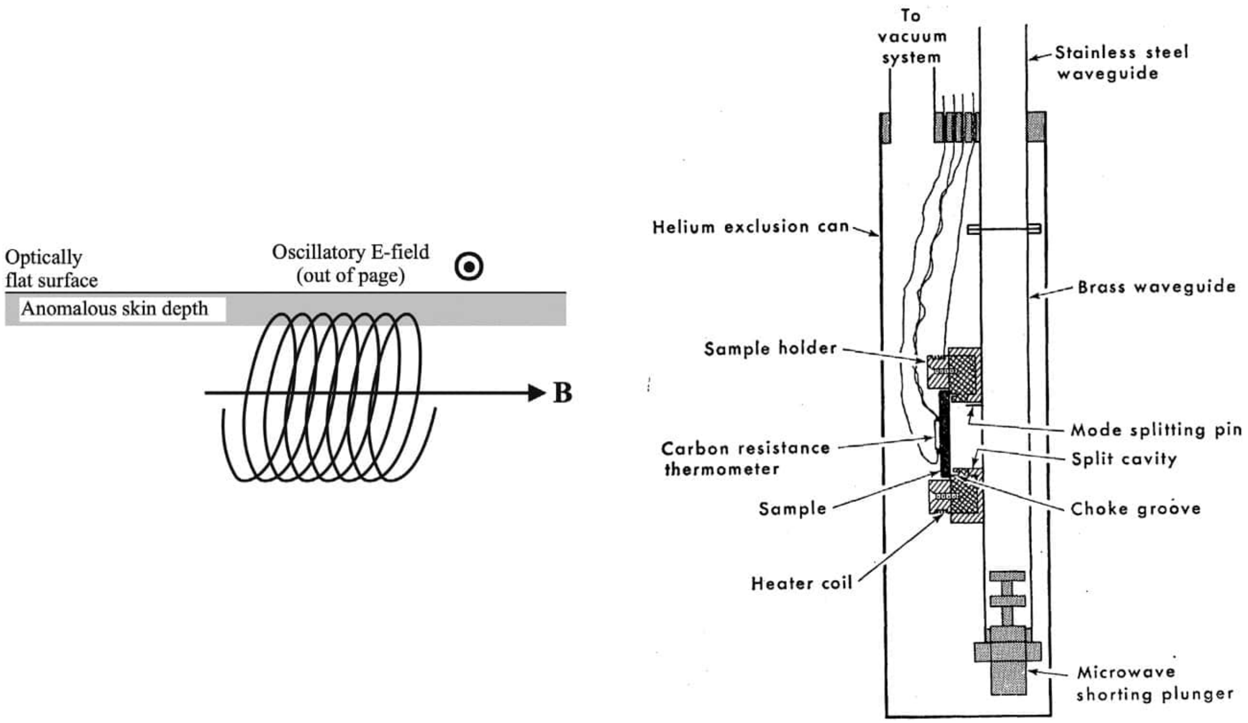

Fig. 2 Left: geometry of a cyclotron resonance experiment in a metal. The shaded region indicates the skin depth for the radiation; the helical orbits of the electrons are shown schematically (from Singleton, 2001). Right: a practical implementation of the Azbel'–Kaner technique. The sample acts as one wall of a microwave resonant cavity; the whole apparatus is immersed in a liquid helium dewar which sits inside an iron-yoked electromagnet. After Häussler P, and Welles SJ (1966) Determination of relaxation times in cyclotron resonance in copper. *Physics Review* 152: 675.

just the maximum- and minimum-area closed orbits for a particular direction of the magnetic field (see Fig. 1.) In such regions, a large number of electrons have almost identical masses (and thus almost identical ω_c), providing a large contribution to Z. The term R_{NR} encompasses non-resonant processes, while the resonant contributions are described by the function λ_j (Lindholm and Le Page, 1969);

$$\lambda_j = 2\pi \frac{\omega}{\omega_{cj}} \left(\frac{1}{\omega \tau_{j\,\mathrm{CRM}}} + \mathrm{i} \right). \tag{7}$$

Note that a cyclotron frequency ω_{cj} and an apparent scattering time $\tau_{j\mathrm{CRM}}$ has been identified for the j^{th} orbit. As long as the electronic dispersion relationship is nearly parabolic close to the Fermi surface, $R(\lambda_j)$ takes the simple form

$$R(\lambda_j) = \frac{1}{1 - \mathrm{e}^{-\lambda_j}}. \tag{8}$$

In practice, the sample orientation is chosen so that only one or two extremal orbits are possible, simplifying the features observed in Z; an example is shown in Fig. 3.

The above expressions for Z have been used to fit experimental data under a variety of valid approximations; typical examples are given in Häussler and Welles (1966), Lindholm and Le Page (1969) and references therein. It is found that the apparent scattering time $\tau_{j\mathrm{CRM}}$ encompasses several contributions:

$$\frac{1}{\tau_{j\,\mathrm{CRM}}} = C_{\mathrm{ms}j}\omega + C_{\mathrm{sr}j}\omega^{1/3} + \frac{1}{\tau_{\mathrm{imp}j}} + \frac{1}{\tau_{\mathrm{phonon}j}} + \frac{1}{\tau_{\mathrm{e}-\mathrm{e}j}}. \tag{9}$$

The first two terms on the right-hand side of Eq. (9) are due to so-called "mass spread" ($C_{\mathrm{ms}j}\omega$) and the effects of surface roughness ($C_{\mathrm{sr}j}\omega^{1/3}$). The former term has the following origin; as has been mentioned above, the resonance spectrum is dominated by extremal orbits about the Fermi surface, defined by $\mathrm{d}m^*_{\mathrm{CR}}/\mathrm{d}k_\parallel = 0$. In such regions, a large number of electrons have almost identical masses (and thus almost identical ω_c), providing a large contribution to Z. The fact that higher derivatives of m^*_{CR} do not vanish in real Fermi surfaces causes "mass-spread"; a distribution of cyclotron frequencies leads to a smearing of the resonant features which at first sight looks as though it is due to scattering. This effect is represented by the term $C_{\mathrm{ms}j}\omega$ in Eq. (9).

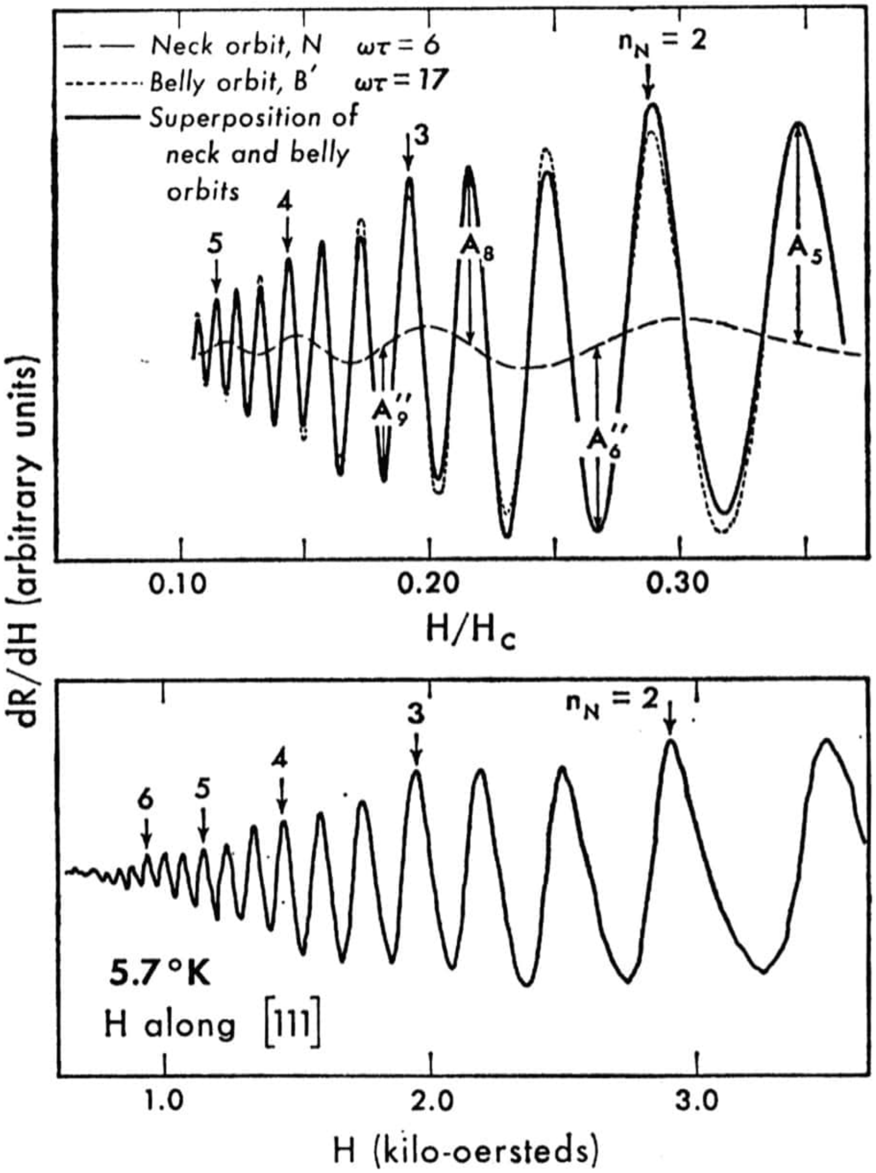

Fig. 3 Combined cyclotron resonance signals from extremal belly orbits *B*′ and neck orbits *N* in Copper; the field is in the [111] direction. The upper curve is a theoretical simulation that shows the two contributions separately (dashed and dotted curves) and combined (solid curve). The lower part of the figure shows experimental data. The fortuitous factor of 3 between the cyclotron periods of the two orbits facilitates separation of the two contributions. After Häussler P, and Welles SJ (1966) Determination of relaxation times in cyclotron resonance in copper, *Physics Review* 152: 675.

Because both the mass-spread and surface roughness terms consist of a constant times ω raised to a small power, they may be distinguished from the other (frequency-independent) contributions by measuring the surface impedance at more than one frequency.

The last three (frequency independent) terms in Eq. (9) are caused by the actual scattering mechanisms; their sum is $\tau_{\mathrm{CR}j}^{-1}$. A weighted average of all of the electron-impurity scattering processes leads to the term $\tau_{\mathrm{imp}j}$, while $\tau_{\mathrm{phonon}j}$ and $\tau_{\mathrm{e-e}j}$ are due to electron-phonon scattering and electron-electron scattering events respectively. The three terms may be distinguished by observing their temperature dependences;

$$\frac{1}{\tau_{\mathrm{imp}j}} = \text{constant}, \quad \frac{1}{\tau_{\mathrm{phonon}j}} \propto T^3 \quad \text{and} \quad \frac{1}{\tau_{e-ej}} \propto T^2. \tag{10}$$

The origins of the temperature power laws for these mechanisms is dealt with in standard texts (e.g., Ashcroft and Mermin, 1976; Singleton, 2001).

Layered metals and degenerate semiconductor systems

Fermi surfaces and resonant cavity techniques

The past 40 years has witnessed continuous great interest in layered materials; there are many correlated-electron systems which have very anisotropic electronic bandstructure. Examples include the "high-T_c" cuprates (Harrison and Chan, 2022; Post et al., 2021), iron-based superconductors (Mancini and Citro, 2017), crystalline organic metals and superconductors (Lebed, 2007; Singleton, 2000), and layered ruthenates (Rzepniewski et al., 2002) and manganites (Kimura and Tokura, 2000). In the context of the current discussion, such systems have two distinctive features.

1. Typically, their quasiparticle densities are rather lower than those in elemental metals; hence their skin depths tend to be larger, and the effects of screening are reduced (Rzepniewski et al., 2002; Schrama et al., 2001).
2. These systems may often be described by a tight-binding Hamiltonian in which the ratio of the average interlayer transfer integral $t_\perp$ to the average intralayer transfer integral $t_{||}$ is $\ll 1$. This results in very anisotropic electronic properties (Goddard et al., 2004; Singleton, 2000).

Fig. 4 shows the cross-section of the Fermi surface of a typical (and simple) example, the organic superconductor κ-(BEDT-TTF)$_2$Cu(NCS)$_2$, parallel to the highly conducting planes. The Fermi surface consists of both open and closed sections; it is customary to label such sections "quasi-one-dimensional" and "quasi-two-dimensional" respectively (Singleton, 2000, 2001). The names arise because the Fermi surface is a surface of constant energy, and so Eq. (2) shows that the velocities of quasiparticles at the Fermi surface will be directed perpendicular to it. Therefore, referring to Fig. 4, quasiparticles on the closed Fermi-surface pocket can possess velocities which point in any direction in the (k_b, k_c) plane; they have freedom of movement in two dimensions and are said to be *quasi-two-dimensional*. By contrast, quasiparticles on the open sections have velocities predominently directed parallel to k_b and are *quasi-one-dimensional*.

Thus far we have only considered a cross-section through the Fermi surface parallel to the highly-conducting planes (Fig. 4). In the interlayer direction (also known as *the interplane* direction), the dispersion is very small, due to the small interlayer transfer integrals. For the purpose of this discussion, we choose a simple model of the quasiparticle dispersion, written as

$$E(\mathbf{k}) = E(k_x, k_y) - 2t_\perp \cos(k_z d) \tag{11}$$

where k_x, k_y and k_z are the components of the wave vector parallel (k_x, k_y) and perpendicular (k_z) to the conducting planes and $t_\perp$ is again the interlayer transfer integral [For examples of more realistic interlayer dispersion see e.g., Goddard et al., 2004 and Grissonnanche et al., 2021]. The presence of dispersion in the interlayer direction will result in a slight warping of the Fermi surface, shown schematically for a closed pocket in Fig. 5a.

As before, when a magnetic field is introduced, Eqs. (2) and (1) indicate that the k-space path of the quasiparticle is defined by the intersections of surfaces of constant energy with planes perpendicular to **B**. Therefore, for almost all directions of the magnetic field, quasiparticles on the closed sections of Fermi surface will be able to complete closed k-space orbits in the plane perpendicular to **B** (see Fig. 5(a)); in contrast, the quasiparticles on quasi-one-dimensional sections of Fermi surface will not complete closed orbits (see Fig. 5(b)).

The experimental detection of cyclotron resonance depends on the effect that the quasiparticle paths have on the high-frequency conductivity. Eq. (2) shows that the quasiparticle velocity must always be perpendicular to the Fermi surface. Hence, as the

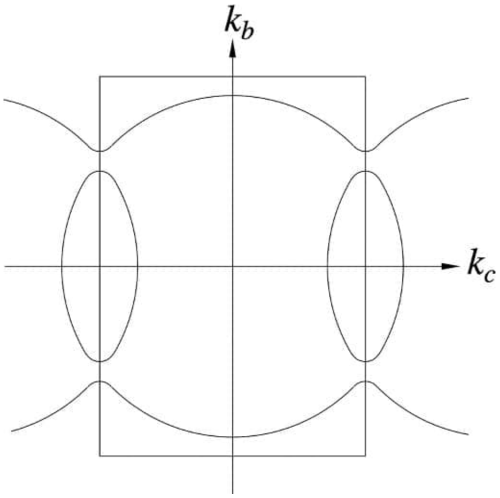

Fig. 4 Brillouin zone and Fermi-surface of κ-(BEDT-TTF)$_2$Cu(NCS)$_2$, showing the open, quasi-one-dimensional sections, and the closed, quasi-two-dimensional pocket (Singleton, 2001, 2000).

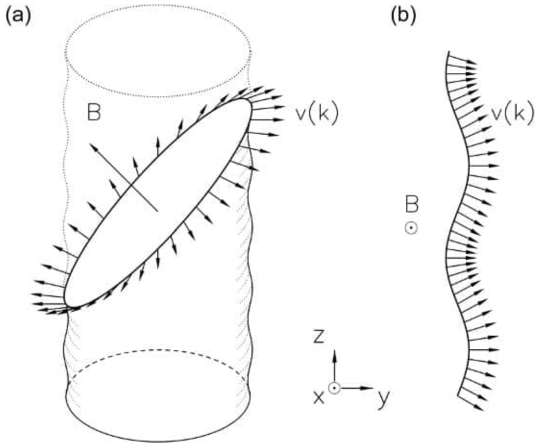

Fig. 5 (a) Schematic side view of the warping (corrugation) of a closed section of Fermi surface caused by finite interplane transfer integrals. The arrows indicate the velocities of a quasiparticle following a closed orbit about the Fermi surface in a plane perpendicular to the magnetic field **B**. (b) An open section of Fermi surface. In an in-plane magnetic field, quasiparticles will be driven across the Fermi surface, so that their velocities (shown by arrows) will rock from side to side. From Singleton J (2000) Studies of quasi-two-dimensional organic conductors based on BEDT-TTF using high magnetic fields. *Reports on Progress in Physics* 63(8): 1111.

quasiparticles traverse the orbits shown Fig. 5(a) and (b), the corrugations of the Fermi surface cause their velocity vectors to rock back and forth. It is the evolution of the quasiparticle velocities with time that affect the conductivity of the system, and thus enable cyclotron resonance to be detected. Cyclotron resonance is of course associated with the closed orbits of Fig. 5(a); the open orbits shown on Fig. 5(b) lead to a related resonant contribution to the high-frequency magnetoconductivity, known as a *Fermi-surface traversal resonance* (FTR). (To find out more about FTRs, see Schrama et al. (2001) and references therein.)

As mentioned above, the low electron densities of these materials compared to those in typical elemental metals results in a larger skin depth; hence, with careful planning, an experiment can be arranged in which a substantial fraction of a typical single-crystal sample (volume ~0.01–0.1 mm^3) can be penetrated by radiation with frequencies ~10–100 GHz. Therefore the experimental response is typically much more determined by the frequency-dependent *bulk conductivity*, rather than the surface impedance.

The evolution of the quasiparticle's velocity can be related to its contribution to the frequency-dependent conductivity of the metal using the frequency-dependent Boltzmann transport equation (also known as the Chambers Equation) (Nam et al., 2001; Schrama et al., 2001).

$$\sigma_{ij}(\omega) = \frac{e^2}{4\pi^3}\int d^3k\left[-\frac{\partial f_0(\mathbf{k})}{\partial E(\mathbf{k})}\right] v_i(\mathbf{k},0)\int_{-\infty}^{0} v_j(\mathbf{k},t)\cos(\omega t)e^{t/\tau}dt \tag{12}$$

Here, τ is a relaxation time (not necessarily the same as τ_{CR}), $v_i(\mathbf{k}, t)$ is the ith component of the velocity of a quasiparticle with wave vector $\mathbf{k}$ at time t and $f_0(\mathbf{k}) = (e^{(E(\mathbf{k})-E_F)/k_B T} + 1)^{-1}$ is the Fermi function. This is an integral (over all states at the Fermi surface) of the velocity-velocity correlation function for each Fermi-surface orbit.

The mechanism for detecting cyclotron resonance can be understood by examining Fig. 5(a). For a general direction of the magnetic field (as shown in Fig. 5) the corrugations of the Fermi cylinder will cause a quasiparticle's interplane (z) velocity to acquire an oscillatory component as it is driven round an orbit about the Fermi cylinder. These oscillatory interplane velocities contribute at a particular frequency (and, perhaps, its harmonics) to Eq. (12); hence they are detectable as resonances in the high-frequency interplane conductivity $\sigma_{zz}(\omega)$.

Note that if the corrugations are not exactly perpendicular to the cylinder axis, then even a magnetic field parallel to the cylinder axis (i.e., in the interplane z direction) will induce an oscillatory interplane component of the quasiparticle velocity and hence a resonant response in σ_{zz}. This resonant response in σ_{zz} occurs at integer harmonics of the cyclotron frequency, $j\omega_c$; these can be caused both by the orbit traversing j corrugations or by the presence of a non-sinusoidal corrugations.

Cyclotron resonance harmonics are also possible in the *intraplane* high-frequency conductivity components σ_{xx} and σ_{yy}; this results from Fermi-surface cross-sections that are non-elliptical (Nam et al., 2001). Unless the Fermi surface lacks inversion symmetry, this mechanism generates only *odd* harmonics. Both types of cyclotron resonance mechanism with their attendant harmonics have been reported in the layered perovskite Sr_2RuO_4 (Rzepniewski et al., 2002).

Cyclotron resonance in such materials is observed using millimeter-wave cavity perturbation techniques (see Fig. 6) such as those described in Schrama et al. (2001) and Mola and Hill (2000) (both applied to crystalline organic metals) and Kimata et al. (2012) (applied to the iron-based superconductor KFe_2As_2). Such measurements probe the bulk conductivity properties of anisotropic conductors. Changes in the dissipation of the cavity (Q factor) are measured as a function of an external quasistatic magnetic field **B** with the millimeter-wave frequency ν held constant. It is assumed that changes in the dissipation of the cavity are due to changes in the dissipation of the sample inside.

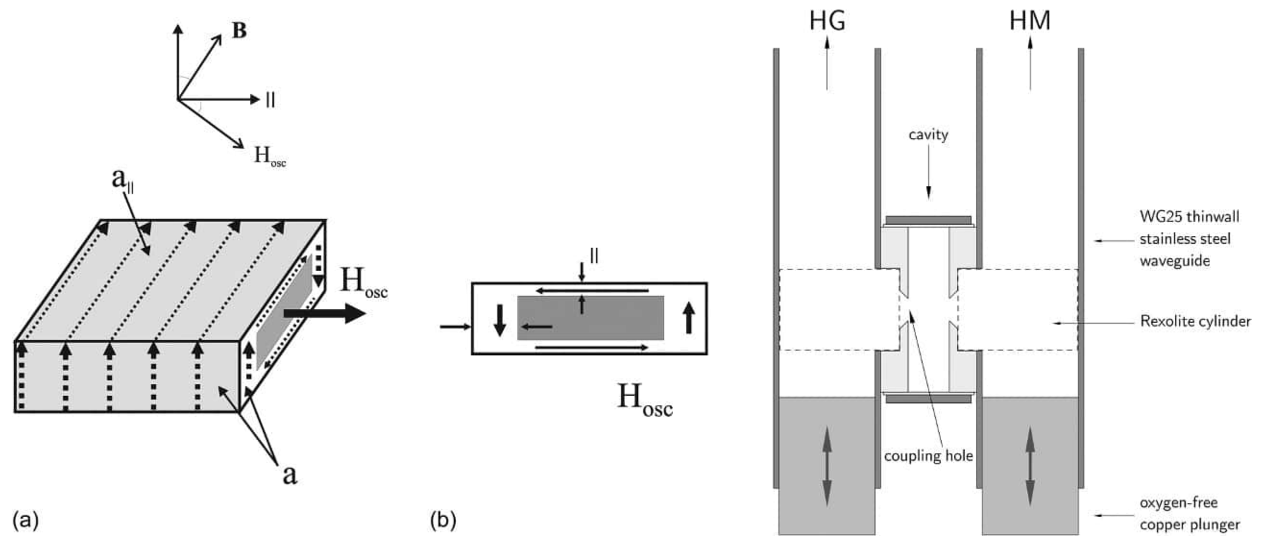

Fig. 6 Experimental configuration for cyclotron resonance in a layered metal (Schrama et al., 2001). Left: (a) the sample is placed in the cavity with the oscillating millimeter-wave field $\mathbf{H}_{osc}$ in the highly conducting planes (|| direction). (b) Both in-plane and interplane oscillating currents J_{osc} are induced. In the skin-depth regime in-plane currents flow within a surface layer of thickness $\delta_{||}$ parallel to large sample faces, and interplane currents flow within a thicker layer $\delta_{\perp}$ parallel to sample edges. Right: schematic of the vertical cross section of a rectangular cavity that can be used for cyclotron resonance measurements of a layered metal. The cavity is placed between two waveguides that lead to the source (HG) and detector (HM). The cavity is held in this position by two Rexolite cylinders of 3 mm diameter which are fitted in the recessed area around the coupling holes and which extend through the holes (3 mm diameter) in the waveguides. The sample is placed on a thin mylar film in the cavity center, in the *H*-field antinode of the TE_{102} mode of the cavity. The advantage of such a cavity system is that it allows the cavity and the sample to be rotated in the vertical quasistatic magnetic field (provided by either a superconducting or a Bitter magnet); because the cavity rotates, the sample remains in the same high-frequency electrodynamic environment. Hence, the magnetic-field-orientation dependence of the cyclotron resonance can be studied. (The mechanism for rotating the cavity has been omitted for clarity.)

The sample is placed in the cavity such that the millimeter-wave magnetic field $\mathbf{H}_{osc}$ is polarized parallel to the sample's highly conducting planes (perpendicular to the *c*-axis) (see Fig. 6). The response of an anisotropic conductor in this electromagnetic environment is understood by examining the polarizations of the currents induced in the sample by $\mathbf{H}_{osc}$. For $\mathbf{H}_{osc}$ parallel to the (*a*, *b*) plane (the highly-conducting plane), both in-plane and interlayer currents are induced (Fig. 6). These currents flow within a distance $\sim\delta$ (here δ is the skin depth) from the sample's edges and faces (Fig. 6(b)). The in-plane ($\delta_{||}$) and interlayer ($\delta_{\perp}$) skin depths give information about σ_{zz} and a combination of σ_{xx} and σ_{yy} respectively.

(All of the above applies to measurements of single crystals. With the more recent availability of epitaxial films, tens of nm thick, of materials such as cuprate superconductors, simple transmission measurements are also possible (Post et al., 2021): see the section "Experimental techniques: Pulsed measurements".)

Extraction of the apparent scattering rates in layered metals

As described by Schrama et al. (2001) and Mola and Hill (2000), changes in the *Q* factor of the resonant cavity can be related via the skin depths to changes in the components of the sample's conductivity tensor. Generally, the most reliable method of extracting the apparent scattering time is to fit the high-frequency conductivity directly (Edwards et al., 2003; see Fig. 7); for example, McKenzie and Moses (1999) and Moses and McKenzie (1999) suggest an interlayer conductivity

$$\frac{\sigma_{zz}(\omega)}{\sigma_{zz}(\omega=0)}=\sum_{-\infty}^{\infty}\frac{\left[J_j(k_F c\tan\theta)\right]^2}{1+(\omega-j\omega_c\cos\theta)^2\tau_{\mathrm{CRM}}^2} \tag{13}$$

for layered materials with weak interlayer coupling that has been successfully applied to organic conductors. Here *j* is an integer, J_j is the *j*th Bessel function, *c* is the interlayer lattice spacing, k_{F} is the Fermi wavevector and θ is the angle between the magnetic field and the normal to the conducting planes. Note that the apparent scattering time τ_{CRM} is always a fit parameter in such methods.

Cyclotron resonance in semiconductors, candidate topological insulators and other low carrier-density systems

Experimental details: quasistatic measurements

The number densities of carriers in semiconductor samples are much lower than those in metals, so that the radiation can completely penetrate even large crystals (Moss and Balkanski, 1994; Singleton, 2001). Similar considerations apply to topological insulators such as Bi_2Te_3 (see Kamenskyi et al. (2020) and Mohelský et al. (2020) and references therein), where the desired surface states are often accompanied by a low density of quasiparticles in the bulk of the sample. In systems such as graphene

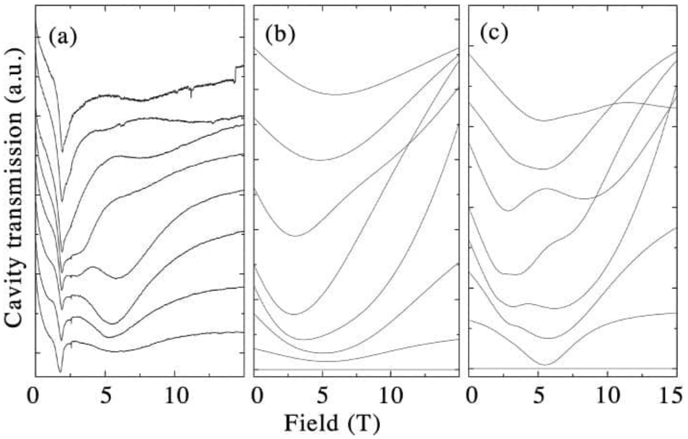

Fig. 7 (a) Cyclotron resonance data for the quasi-two-dimensional organic conductor β''-(BEDT-TTF)$_2$SF$_5$CH$_2$CF$_2$SO$_3$. The data are in the form of cavity transmission vs. magnetic field; the frequency of the measurement is 71 GHz, and the temperature is 1.5 K. Field sweeps for several orientations θ of the cavity and sample in the quasistatic field are shown (see Fig. 6); $\theta = 0$ corresponds to the field being perpendicular to the highly-conducting planes of the sample. The sharp slope downwards and small minimum at low fields are associated with the superconducting-to-normal transition of the sample and a background feature in the cavity response. The small sharp feature is the conduction-electron spin resonance of the sample. The cyclotron resonances are the broader features at higher fields. (b) A model of the data using Eq. (13) with k_F calculated for this particular sample orientation and $\tau_{CRM} = 1.22 \times 10^{-12}$; the latter value was derived from a simple treatment (see Eq. (15)) of Shubnikov-de Haas oscillations from the same sample. Note how the predicted resonances are too broad. (c) A repeat of (b) for $\tau = 7 \times 10^{-12}$ s; note how the predicted resonance widths are similar to the experimental ones. All panels show curves for $\theta = 0$ (lowest), 10, 20, 30, 40, 50, 60 and 70 degrees (highest). After Edwards RS, Herlach F, and Miura N (2003) High magnetic fields, science and technology, Vol. 2, Theory and Experiments, Singapore: World Scientific.

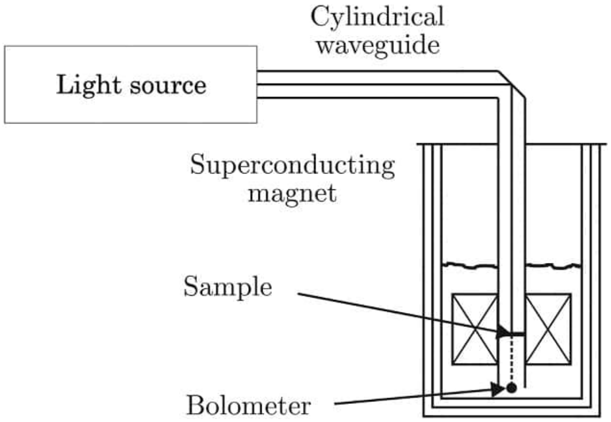

Fig. 8 Simplified schematic of a cyclotron resonance experiment in a semiconductor or other low-carrier-density metal. The light source may be monochromatic (e.g., optically-pumped FIR laser, backward-wave oscillator), in which case the field is swept. Alternatively, a broadband Fourier-transform infrared spectrometer may be used with the applied magnetic field held constant. The field is shown applied parallel to the light propagation direction, i.e., the Faraday geometry, as is the case for the vast majority of cyclotron resonance studies. Transmitted radiation is detected by the bolometer. In practice, the sample will usually be inside a re-entrant flow cryostat to allow the cyclotron resonance to be measured as a function of sample temperature. After Singleton J (2001) Band Theory and Electronic Properties of Solids, Oxford: Oxford University Press, Chapters 8 and 9.

(see, e.g., Russell et al. (2018) and citations therein) or semiconductor heterostructures or superlattices (Langerak et al., 1988; Moss and Balkanski, 1994), the quasiparticles inhabit a few layers (or even just a single layer) of ~nm thickness so that the overall *number* of carriers in a sample is very small; again, the radiation fills the whole sample. In all of these cases, a simple transmission arrangement is often adopted (see Fig. 8). Experiments are carried out either by using a fixed-frequency source [such as an optically-pumped far-infrared laser, which can give a number of monochromatic laser lines in the wavelength range 30–1000 μm (Langerak et al., 1988), or a free-electron laser (FEL) (Vaughan et al., 1996)] and sweeping the magnetic field [see Fig. 9(a)], or by fixing the magnetic field and varying the energy of the radiation [see Fig. 9(b)] using, e.g., a Fourier-transform infrared spectrometer. The magnetic field is provided either by a superconducting magnet ($B \lesssim 18$ T) or, in user facilities, by a Bitter or polyhelix magnet.

As the whole of the cyclotron orbit experiences the electric field of the radiation (*c.f.* the situation in metals; see above), the quantum-mechanical selection rule for the Landau-level quantum number ($\Delta l = \pm 1$) holds. Thus the resonance condition is

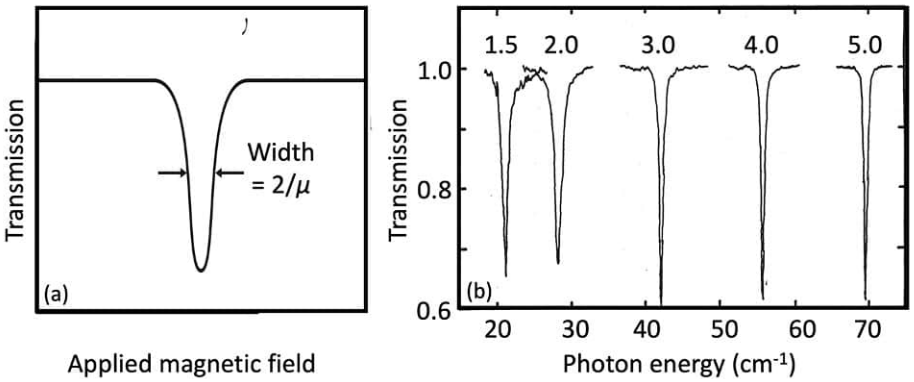

Fig. 9 (a) Illustration of cyclotron resonance in a swept-field, monochromatic light-source experiment. In a simple semiconductor system, the full width at half maximum of the resonance in such measurements is $2/\mu$, where μ is the mobility (see discussion). (b) Cyclotron resonances in a GaAs-(Ga,Al)As heterojunction at $T = 4.2$ K; the magnetic field has been applied perpendicular to the two-dimensional electron layer, which has an areal carrier density $\approx 9 \times 10^{10}$ cm^{-2}. The data have been recorded by fixing the magnetic field at 1.5, 2, 3, 4, and 5 T (the resonances in the figure have the corresponding field labeled above them); at each field, a Fourier-transform infrared spectrometer has then been used to record the transmission of the sample as a function of energy. Figure redrawn from Singleton J (2001) Band Theory and Electronic Properties of Solids, Oxford: Oxford University Press, Chapters 8 and 9.

$$h\nu \equiv \hbar\omega = \hbar\omega_c = \frac{\hbar eB}{m^*_{\mathrm{CR}}}, \tag{14}$$

where ν (ω) is the frequency (angular frequency) of the radiation.

As stated in the Introduction, in degenerate semiconductor systems (e.g., heterojunctions) and candidate topological insulators, free carriers are present even at low temperatures; typical cyclotron resonance data are shown for the former in Fig. 9(b). However, it is worth mentioning that in lightly doped semiconductor samples, the carriers must be excited into the bands by either raising the temperature to cause the impurities to ionize (but not so far as to broaden the Landau levels) or by additionally illuminating the sample with above-band-gap radiation (Bleaney and Bleaney, 2013; Moss and Balkanski, 1994; Singleton, 2001).

Experimental techniques: Pulsed measurements

As an alternative to the quasistatic optical methods described in the previous section, ultrashort pulsed lasers are used to generate broadband pulses of THz radiation. This *THz time-domain spectroscopy* (THz-TCDS) technique has been combined with both constant and pulsed magnetic fields to observe cyclotron resonance. Fig. 10 shows an experimental set-up in which a small pulsed magnet is incorporated into the free-space beam path of a THz-TDS spectrometer (Post et al., 2021). The field is applied parallel to the light propagation direction (i.e., the Faraday geometry). To rapidly detect the THz waveform at peak field, a THz-TDS system based on electronically controlled optical sampling (ECOPS), wherein the timing delay between the two ultrafast optical pulse trains that drive the THz emitter and receiver can be electronically modulated very quickly. When synchronized to the magnetic field, the THz waveform can be recorded at multiple field values during a single magnet pulse.

Following standard procedures, the measured THz electric field is Fourier transformed to yield the frequency-dependent complex optical transmission. The incorporation of two linear polarizers, P1 and P2, allows the sample's complex conductivity to be extracted from the transmission data in right- and left-circularly polarized bases, which correspond to $\sigma_{\mathrm{r}}(\omega)$ and $\sigma_{\mathrm{l}}(\omega)$, the cyclotron-active and -inactive modes, respectively. The direct measurement of both real and imaginary components of the frequency-dependent conductivity is unique to THz-TCDS—it is not possible with conventional Fourier-transform infrared spectroscopy—and permits the resolution of small cyclotron frequency shifts, even when $\omega_c\tau < 1$.

Examples of THz-TCDS applied to cyclotron resonance of a candidate topological insulator $\mathrm{Pb}_{0.5}\mathrm{Sn}_{0.5}$ and a thin film of a cuprate superconductor are given in Cheng et al. (2019) and Post et al. (2021) respectively.

Extraction of apparent scattering times

In some situations where both the scattering time (or mobility) and the density of the carriers are low (e.g., bulk degenerate semiconductors), the measured linewidth of the cyclotron resonance can give information about the true scattering rate τ_{CR}^{-1} directly. Via the uncertainty principle, the scattering induces a frequency uncertainty $\Delta\omega_c \sim \tau_{\mathrm{CR}}^{-1}$. If the experiment is a fixed-frequency, swept-field one, this translates to an uncertainty (i.e., resonance width) in magnetic field of $\Delta B = \Delta\omega_c m^*_{\mathrm{CR}}/q \sim m^*_{\mathrm{CR}}/q\tau_{\mathrm{CR}}$. Provided that $m^*_{\mathrm{CR}} \approx$ the effective mass for linear motion (and this is often true in direct-gap semiconductors like GaAs) it is apparent that ΔB is of order the reciprocal of the carrier mobility. More precise derivations show that the full width at half maximum is in fact twice the reciprocal of the mobility.

However, in systems such as GaAs-(Ga,Al)As heterojunctions, where both the scattering time (or mobility) and the equivalent three-dimensional carrier density in the two-dimensional layer are relatively large, there is a very marked contribution to the cyclotron resonance linewidth due to the impedance mismatch between the vacuum and the carriers (Langerak et al., 1988). The effect is illustrated in Fig. 11; often this "mismatch" contribution to the linewidth eclipses that due to scattering. The problem can be

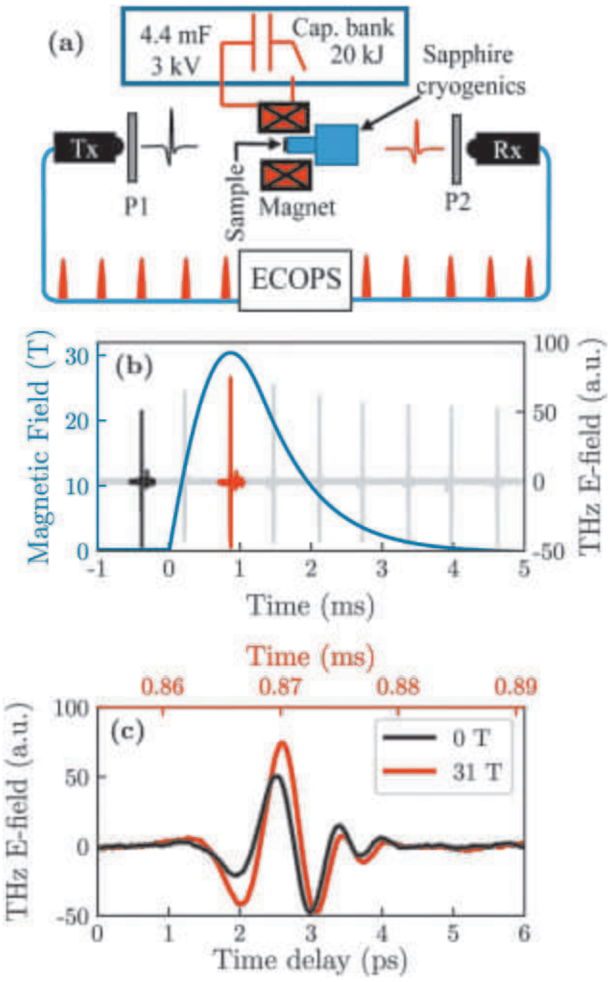

Fig. 10 (a) Experimental schematic of an ECOPS-based THz-TCDS spectrometer adapted for cyclotron resonance. A small pulsed magnet powered by a 20 kJ capacitor bank is incorporated into the beam path. Broadband THz optical pulses generated by the transmitter are linearly polarized (by P1) and focused through the sample in the magnet bore. They are then directed through a second polarizer (P2) and detected by the gated receiver (Rx). Parabolic collimating and focusing mirrors are not shown. (b) The field profile of a 31 T magnet pulse (blue, left axis) is plotted along with the simultaneously measured THz electric field (right axis). (c) THz electric field measured at zero field (black) and at 31 T (red). The upper x axis shows actual laboratory time. The ECOPS system sweeps the effective time delay through 5 ps in $\approx 30\ \mu$s. After Post KW, Legros A, Rickel DG, Singleton J, McDonald R, He X, Bozovic I, Xu X, Shi X, Armitage NP, Crooker S (2021) Observation of cyclotron resonance and measurement of the hole mass in optimally doped La2–xSrxCuO4, *Physical Review B* 103: 134515.

ameliorated by evaporating a surface metallic layer of carefully-chosen thickness on the sample (Watts et al., 1992), but the most reliable method to extract the apparent scattering rate is to perform a full modeling of the transmission or reflectivity of the sample (Langerak et al., 1988) as carried out in Fig. 11.

A similar approach is used with the THz-TCDS data; the scattering time is extracted via a direct fit of the cyclotron resonance lineshape (Cheng et al., 2019; Post et al., 2021).

Contributions to the apparent scattering rate in layered metals, semiconductor heterostructures and other similar systems

Comparisons with other methods

A measure of the scattering rate in metallic systems is often derived from the rate at which magnetic quantum oscillations (such as de Haas-van Alphen oscillations) grow in amplitude with increasing magnetic field; the dominant term in the Lifshitz-Kosevich formula (Shoenberg, 1984) describing this phenomenon is $\exp[-14.7 m^{*}_{\mathrm{CR}} T_{\mathrm{D}}/B]$ (SI units). The constant describing the phase-smearing of the oscillations due to Landau-level broadening is the so-called *Dingle temperature*, T_{D}.

If one were to assume that T_{D} is due *solely* to scattering (i.e., the energy width of the Landau levels detected by the de Haas-van Alphen effect is associated only with their finite lifetime due to scattering) then T_{D} would be related to the scattering rate $\tau^{-1}_{\mathrm{dHvA}}$ by the expression

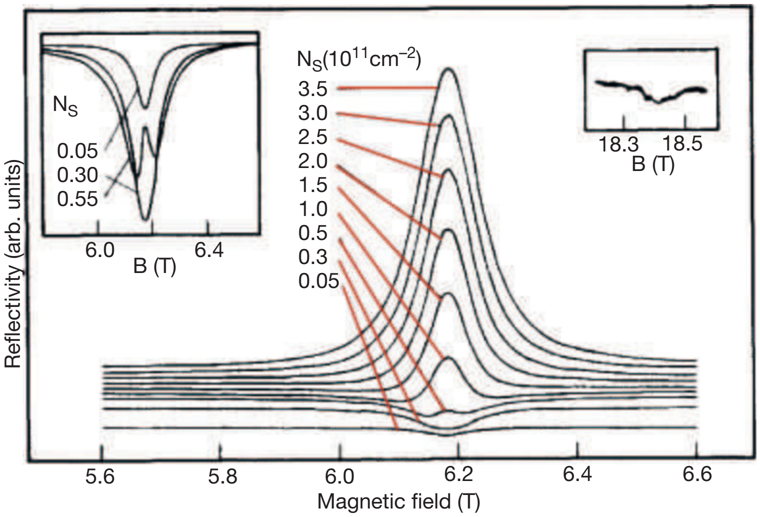

Fig. 11 Model calculations for the reflectivity of a GaAs-(Ga,Al)As heterojunction at a photon energy $\hbar\omega = 10.43$ meV for several values of the areal electron density N_s; each calculation is displaced vertically for clarity. The cyclotron resonance shows up as a dip in the reflectivity signal at low N_s but becomes a peak at higher carrier densities. Note that although the scattering rate is kept constant ($\tau = 10.6$ ps), the full width at half-maximum of the resonance grows with increasing N_s. Similar effects are seen in the transmission of the sample. The left-hand inset shows an expansion of the low-density part of the main figure; the right-hand inset contains experimental data for a photon energy of 31.05 meV and $N_s = 0.3 \times 10^{11}$ cm^{-2}. After Langerak CJGM, Singleton J, van der Wel PJ, Perenboom JAAJ, Barnes DJ, Nicholas RJ, Hopkins MA, and Foxon CTB (1988) Carrier-concentation-dependent electron-LO-phonon coupling observed in GaAs-(Ga,Al)As het-erojunctions by resonant-polaron cyclotron resonance, *Physical Review B* 38: 13133; see also Post KW, Legros A, Rickel DG, Singleton J, McDonald R, He X, Bozovic I, Xu X, Shi X, Armitage NP, Crooker S (2021) Observation of cyclotron resonance and measurement of the hole mass in optimally doped La2–xSrxCuO4, *Physical Review B* 103: 134515.

$$T_D = \frac{\hbar}{2\pi k_B \tau_{\mathrm{dHvA}}}. \tag{15}$$

In many experimental works, it is assumed that the τ_{dHvA} deduced from T_{D} in this way is a true measure of scattering rate; we shall see shortly that *it is not*!

Another measure of the scattering rate can be found by measuring the zero-magnetic-field electrical conductivity; in layered systems, one must be careful to ensure that this is the *intralayer* component of the conductivity (Singleton, 2000). If there is a dominant single carrier type of known density n, then the Drude expression $\sigma = nq^2\tau_\sigma/m^*$ can be used to estimate τ_σ. It is universally found that $\tau_\sigma \geq \tau_{\mathrm{dHvA}}$; in some cases such as semiconductor heterojunctions, τ_σ can be one to two orders of magnitude greater than τ_{dHvA}.

Finally, if these scattering times are compared with the τ_{CRM} deduced from cyclotron resonance experiments, the following is found;

$$\tau_\sigma \geq \tau_{\mathrm{CRM}} \geq \tau_{\mathrm{dHvA}}. \tag{16}$$

For some layered metals (Hill, 1997, 2000), the τ_{CRM} measured in cyclotron resonance has been found to be four to ten times larger than τ_{dHvA}. Another example is shown in Fig. 7, where the insertion of the scattering rate inferred from Shubnikov-de Haas oscillations (Fig. 7(b) into a model for the cyclotron resonance produces linewidths that are much too broad. A more realistic linewidth is obtained with a longer scattering time (Fig. 7(c)).

The importance of spatial inhomogeneities

The difference between any measurement of Landau-level broadening and the scattering rate deduced from a conductivity measurement is easy to grasp; a quasiparticle will be removed from a Landau-level eigenstate by *any* scattering event, small- or large-angle. Conversely, small-angle scattering events hardly affect the conductivity, because they cannot randomize a quasiparticle's excess forward momentum (see Fig. 12 and standard texts [e.g., Ashcroft and Mermin (1976), Singleton (2001)]. In the most thoroughly-studied systems of reduced dimensionality, semiconductor heterostructures and Si MOSFETs, it is found that $\tau_\sigma \approx \tau_{\mathrm{dHvA}}$ in systems in which large-angle scattering (e.g., due to impurities in the conducting channel) dominates. On the other hand, in systems in which small-angle scattering (e.g., due to remote impurities) is pre-eminent, $\tau_\sigma \gg \tau_{\mathrm{dHvA}}$. Having seen this, the remaining task is to explain how two measurements of Landau level width (cyclotron resonance and de Haas-van Alphen effect) can yield such different answers.

At least some of the difference between τ_{CRM} and τ_{dHvA} turns out to be due to spatial inhomogeneities or potential fluctuations. Screening is less effective in systems containing low densities of quasiparticles (such as layered metals or semiconductor heterojunctions) (Harrison and Singleton, 2001), compared to that in elemental metals; hence variations in the potential experienced by

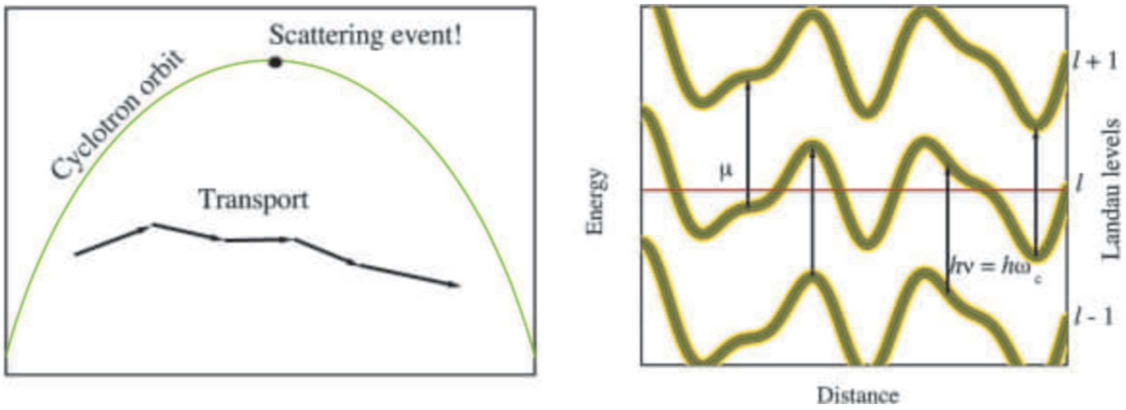

Fig. 12 Left: schematic of the difference in scattering rates in Landau quantization and electrical conductivity. *Any* scattering event (small- or large-angle) during the cyclotron orbit terminates that particular Landau state. By contrast, small-angle scattering is not effective at randomizing the quasiparticle's excess forward momentum in a transport (conductivity) measurement. Right: a cartoon of the effect of spatial inhomogeneities on Landau-level widths and energies. The variations in the potential experienced by the electrons make the Landau levels (shaded curves) move up and down in energy as one moves through the sample. As the field is swept, the levels will move up through the chemical potential μ and depopulate, resulting in the de Haas-van Alphen and Shubnikov-de Haas effects. The Dingle Temperature essentially parameterizes the movement of the *total energy width of a Landau level* through μ; hence it will measure a width that includes the energy variation due to inhomogeneities. By contrast, cyclotron resonance (shown by vertical arrows) is a "vertical" transition; it will measure just the true width of the Landau levels due to scattering (represented by shading).

the quasiparticles can lead to a spatial variation of the Landau-level energies (see Fig. 12). Even in the (hypothetical) complete absence of scattering, Harrison and Singleton (2001) (for example) shows that this spatial variation would give the Landau level a finite energy width (see Fig. 12) and therefore lead to an apparent Dingle temperature

$$T_D = \frac{\bar{x}[1-\bar{x}]F'(\bar{x})^2 a}{\pi k_B m^*}\sqrt{\frac{\hbar e^3}{2F}}. \tag{17}$$

Here F is the magnetic-quantum-oscillation frequency, and $F' = \mathrm{d}F/\mathrm{d}x$; x represents the (local) fractional variation of the quasiparticle density due to the potential fluctuations and $\bar{x}$ is its mean.

The Dingle temperature measured in experiments will therefore usually represent a combination of the effects described by Eqs. (15) and (17). Hence the simple-minded use of Eq. (15) to yield τ_{dHvA} from T_{D} will tend to result in a parameter that is an overestimate of the true scattering rate (see Fig. 12). By contrast, cyclotron resonance (shown by vertical arrows in Fig. 12) is a "vertical" transition (due to the very low momentum of the photon); it will measure just the true width of the Landau levels due to scattering (represented by shading).

Scattering times in angle-dependent magnetoresistance oscillations

Angle-dependent magnetoresistance oscillations are observed by measuring the resistance of a sample as it rotates in a fixed magnetic field (Blundell and Singleton, 1996; Lebed, 2007; Singleton et al., 2007); the technique is popular in the anisotropic materials (e.g., cuprates (Grissonnanche et al., 2021), organic metals etc.) discussed in this Section. Though some AMRO-like phenomena occur due to field-induced dimensional crossovers (Lebed, 2007), the majority of AMRO data are modeled using the Boltzmann transport equation (i.e., the zero-frequency version of Eq. (12)) (Blundell and Singleton, 1996; Goddard et al., 2004). This is an integral over all states at the Fermi surface of the velocity-velocity correlation function for each Fermi-surface orbit; it can change dramatically as the direction of the magnetic field is changed, because this alters the paths of all the orbits (see Fig. 13).

The scattering time is an input parameter in simulations of AMRO, and it is found that $\tau_{\mathrm{AMRO}} > \tau_{\mathrm{dHvA}}$. For example, experiments on the same single crystal of the organic superconductor κ–(BEDT-TTF)$_2$Cu(NCS)$_2$ revealed $\tau_{\mathrm{dHvA}} \approx 2.3$ ps (Goddard et al., 2004) and $\tau_{\mathrm{AMRO}} \approx 3.5$ ps (Singleton et al., 2007) under similar conditions of temperature and field. Part of this difference is likely to occur because the field-induced paths across the Fermi surface are less affected by small-angle scattering than are Landau-level states [see Fig. 12(a)]. In addition, whereas the effects of spatial inhomogeneities contribute to the apparent Landau-level width [see Fig. 12(b)], they may well be averaged out by the ensemble of Fermi-surface orbits that determine AMRO features (Blundell and Singleton, 1996). Similar considerations apply in the modeling of linear magnetoresistance in correlated-electron systems [see Singleton, 2020 and references therein].

Many-body effects I: Systems with two interacting carrier populations

Cyclotron resonance data can sometimes be difficult to interpret in systems containing two distinct quasiparticle populations that interact. An example is given by p-doped GaAs-(Ga,Al)As heterojunctions, containing two hole spin subbands with differing

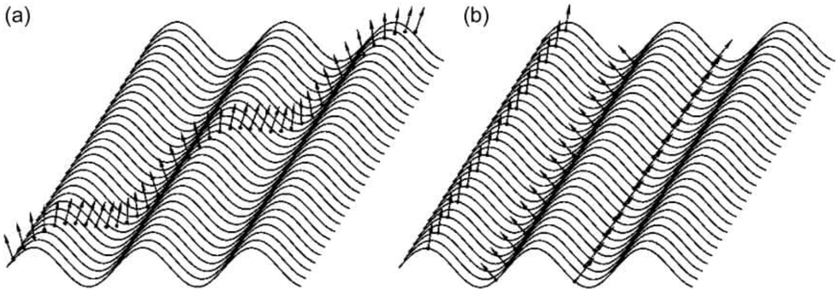

Fig. 13 Illustration of the field-induced motion of quasiparticles across a quasi-one-dimensional Fermi-surface section. The magnetic field lies at two different angles in the plane of the Fermi surface; as discussed earlier (see Eq. 1), the quasiparticles move across the Fermi surface in a plane perpendicular to the magnetic field. The quasiparticle velocities are directed perpendicular to the Fermi surface (see Eq. 2) and are shown as arrows. The velocity is more effectively averaged when electrons are not traveling along the axis of the Fermi-surface corrugation (a) than when they are (b). Analogous phenomena are produced by field-induced orbits on quasi-two-dimensional Fermi surfaces.

effective masses. One would expect two distinct cyclotron resonances; however, depending on temperature, photon energy and field, a single resonance is frequently observed. This results from the interactions between the two types of quasiparticle; the overall energy of the system is reduced if these interactions constrain both populations to have the same cyclotron frequency.

Cole et al. (1997) gives expressions for the high-frequency magnetoconductivity $\sigma(\omega)$ that can be very generally used to treat such situations; they allow the scattering rates and effective masses for each type of quasiparticle to be extracted, and also enable their interactions to be quantified.

Many-body effects II: Which effective mass does cyclotron resonance measure?

Cyclotron resonance is potentially a very interesting measure of the interactions in narrow-bandwidth metallic systems. In a translationally-invariant system, the mass m^*_{CR} measured in a cyclotron resonance experiment should not contain any contribution from the interactions between the carriers themselves; this is known as *Kohn's theorem* (Baym and Pethick, 2004; Post et al., 2021). In the language of Fermi-liquid theory, in such a situation, cyclotron resonance measures the dynamical mass $m_{\lambda\mathrm{CR}}$, whereas a thermodynamic measurement such the de Haas-van Alphen oscillations reveals the effective mass m^*, which also contains contributions from the Coulomb interactions between the quasiparticles (Gross et al., 1991).

A simple bandstructure calculation essentially uses ions and molecules which are rigidly fixed in a perfectly periodic arrangement to obtain a periodic potential and hence the bands. However, the ions and/or molecules in a substance will in general be charged, or at the very least possess a dipole moment; as an electron passes through the solid, it will tend to distort the lattice around it owing to the Coulomb interactions between the ions and molecules and its own charge. This leads to the electron being accompanied by a strain field as it moves through the substance; alternatively one can consider the electron being surrounded by virtual phonons. This affects the way in which the electron can move through the substance and usually acts to increase the apparent mass.

In the following, for consistency we deal with the orbitally averaged (cyclotron) mass; other "effective masses" (e.g., for linear motion) will be renormalized in an analogous way. If m_{bCR} is the cyclotron mass calculated in the bandstructure calculations, then the electron-lattice interactions discussed above will result in a cyclotron dynamical mass, $m_{\lambda\mathrm{CR}}$, where

$$m_{\lambda\mathrm{CR}} \approx (1+\lambda)m_{\mathrm{bCR}}, \tag{18}$$

where λ is an electron-phonon coupling constant.

The interactions between the electrons themselves must also be taken into account. As electrons are highly charged, they will repel each other; therefore, as an electron is moved across a sample under consideration by an external force, in effect there will be a backflow of electrons caused by this repulsion. Thus, it is "harder" to move electrons about than expected, i.e., their apparent effective mass is heavier than $m_{\lambda\mathrm{CR}}$. The effective masses m^* measured in experiments such as the de Haas-van Alphen effect include this contribution from the interactions between the electrons, so that

$$m^* \approx \left(1+\frac{F_{\mathrm{s}}^1}{3}\right)m_{\lambda}, \tag{19}$$

where F_{s}^1 is a constant known as a Fermi liquid parameter. (For a more detailed discussion of such effects, see Baym and Pethick (2004), Gross et al. (1991) and references therein.)

In practice, however, real systems do not possess translational invariance. Although the mass m^*_{CR} measured in a cyclotron resonance experiment does generally *differ* from that obtained from the de Haas-van Alphen effect (m^*), the simple expectations of Eq. (19) often do not hold; in one or two instances [see e.g., Rzepniewski et al., 2002], m^*_{CR} was even found to be *greater than* m^*. Nevertheless, a comparison between a cyclotron resonance experiment and the de Haas-van Alphen effect is often a good guide to the strength of the interactions in a system.

Effects related to cyclotron resonance

There are one or two effects related to cyclotron resonance that go beyond the scope of this article but which should nevertheless be mentioned for completeness. One is *surface cyclotron resonance*, an effect due to excitation of quasiparticles between levels caused by crossed electric and magnetic fields at the surface of a sample. Interested readers are referred to Koch and Jensen (1969) and Merkt (1985) and references therein. A second is the *Fermi-surface traversal resonance* due to the magnetic-field-induced motion of quasiparticles across open sections of Fermi surface; a discussion and relevant literature are given by Schrama et al. (2001).

Conclusion

Providing that a proper treatment of the sample's high-frequency magnetoconductivity is used, then the scattering rate τ_{CRM}^{-1} deduced from a cyclotron resonance experiment is a good measure of the energy width of the Landau levels due to their finite lifetime. In other words, $\tau_{\mathrm{CRM}} \approx \tau_{\mathrm{CR}}$. By contrast, the *apparent* scattering rate deduced from a simple-minded treatment of de Haas-van Alphen and Shubnikov-de Haas oscillations can contain significant contributions from spatial inhomogeneities. Finally, the scattering rate τ_{σ}^{-1} measured in a zero-field conductivity experiment can be very significantly different from τ_{CR}^{-1} because the two measurements are sensitive to different types of scattering process.

The scattering rates deduced from cyclotron resonance therefore provide the purest gauge of the Landau-level width. Once this has been realized, cyclotron resonance can be used to give quantitative details of the quasiparticle scattering mechanisms [e.g., Häussler and Welles, 1966; Vaughan et al., 1996; Post et al., 2021]. Cyclotron resonance is also an invaluable gauge of the importance of many-body effects [e.g., Rzepniewski et al., 2002]. Moreover, with the right choices of field and wavelength, cyclotron resonance can provide a measurement of the effective mass in systems where the scattering rate is too large for the de Haas-van Alphen or Shubnikov-de Haas oscillations to be visible [e.g., Post et al., 2021].

At present (2022), the combination of far-infrared optical equipment and high magnetic fields necessary for cyclotron resonance is relatively rare; examples tend to be concentrated at national high-field user facilities. Nevertheless, as new correlated-electron systems continue to be made, and as new approaches such as THz-TCDS become more widely used, the technique should have an important role in condensed-matter science for years to come.

Acknowledgments

Work at the National High Magnetic Field Laboratory on the high-frequency magnetoconductivity of metals is supported by National Science Foundation Cooperative Agreement No. DMR- 1644779, the Department of Energy (DOE) and the DOE BES program "Science at 100 T." Development of high-frequency techniques has been greatly aided by grant LDRD-ER 20200285. Oxford University is thanked for the provision of a visiting professorship that greatly facilitated some of the work described in this Chapter.

References

Ashcroft NW and Mermin ND (1976) *Solid State Physics*. New York: Holt, Rinehart and Winston.
Baym G and Pethick C (2004) *Landau Fermi-Liquid Theory*. Weinheim: Wiley-VCH.
Bleaney BI and Bleaney B (2013) *Electricity and Magnetism*. Oxford: Oxford Classic Texts, Oxford University Press.
Blundell SJ and Singleton J (1996) Semiclassical description of angle-dependent magnetoresistance oscillations in quasi-one-dimensional metals. *Physical Review B* 53: 5609.
Cheng B, Taylor P, Folkes P, Rong C, and Armitage NP (2019) Magnetoterahertz response and faraday rotation from massive dirac fermions in the topological crystalline insulator Pb0:5Sn0:5Te. *Physical Review Letters* 122: 097401.
Cole BE, Peeters FM, Ardavan A, Hill SO, Singleton J, Batty W, Chamberlain JM, Polisskii A, Henini M, and Cheng T (1997) Collective cyclotron modes in high-mobility two-dimensional hole systems in GaAs—(Ga, Al)As heterojunctions: I. Experiments at low magnetic fields and theory. *Journal of Physics. Condensed Matter* 9: 3163.
Edwards RS, Herlach F, and Miura N (2003) High magnetic fields, science and technology. In: *Theory and Experiments*, vol. 2. Singapore: World Scientific.
Goddard PA, Blundell SJ, Singleton J, McDonald RD, Ardavan A, Narduzzo A, and Schlueter JA (2004) Angle-dependent magnetoresistance of the layered organic superconductor κ-$(ET)_2Cu(NCS)_2$: Simulation and experiment. *Physical Review B* 69: 174509.
Grissonnanche G, Fang Y, Legros A, Verret S, Laliberte F, Collignon C, Zhou J, Graf D, Goddard PA, Taillefer L, and Ramshaw BJ (2021) Linear-in temperature resistivity from an isotropic Planckian scattering rate. *Nature* 595: 667.
Gross EKU, Runge E, and Heinonen O (1991) *Many Particle Theory*. Bristol: Adam Hilger.
Harrison N and Chan MK (2022) Magic gap ratio for optimally robust fermionic condensation and its implications for high-T_c Superconductivity. *Physical Review Letters* 129: 017001.
Harrison N and Singleton J (2001) On the de Haas-van Alphen effect in inhomogeneous alloys. *Journal of Physics. Condensed Matter* 13: L463.
Häussler P and Welles SJ (1966) Determination of relaxation times in cyclotron resonance in copper. *Physics Review* 152: 675.
Hill SO (1997) Semiclassical description of cyclotron resonance in quasi-two-dimensional organic conductors: Theory and experiment. *Physical Review B* 55: 4931.
Hill SO (2000) Electrodynamics of quasi-two-dimensional BEDT-TTF charge-transfer salts. *Physical Review B* 62: 8699.
Kamenskyi DL, Pronin AV, Benia HM, Martovitskii VP, Pervakov KS, and Selivanov YG (2020) Bulk cyclotron resonance in the topological insulator Bi_2Te_3. *Crystals* 10: 722.
Kimata M, Terashima T, Kurita N, Satsukawa H, Harada A, Kodama K, Takehana K, Imanaka Y, Takamasu T, Kiho K, Lee C, Kito H, Eisaki H, Iyo A, Fukazawa H, Kohori Y, Harima H, and Uji S (2012) Cyclotron Resonance in Fe-based Superconductor KFe_2As_2. *Journal of Physics Conference Series* 400: 022054.
Kimura T and Tokura Y (2000) Layered magnetic manganites. *Annual Review of Materials Science* 30: 451.
Koch JF and Jensen JD (1969) Magnetic-field-induced surface states in bismuth. *Physics Review* 184: 643.

Langerak CJGM, Singleton J, van der Wel PJ, Perenboom JAAJ, Barnes DJ, Nicholas RJ, Hopkins MA, and Foxon CTB (1988) Carrier-concentation-dependent electron-LO-phonon coupling observed in GaAs-(Ga,Al)As het-erojunctions by resonant-polaron cyclotron resonance. *Physical Review B* 38: 13133.

Lebed A (2007) *The Physics of Organic Superconductors and Conductors, Springer Series in Materials Science 110*. Berlin: Springer.

Lindholm DA and Le Page J (1969) Determination of anisotropic relaxation times in copper by cyclotron resonance. *Physics Review* 187: 861.

Mancini F and Citro R (eds.) (2017) *The Iron Pnictide Superconductors: An Introduction and Overview, Springer Series in Solid-State Sciences (SSSOL, Volume 186)*. Springer.

McKenzie RH and Moses P (1999) Periodic orbit resonances in layered metals in tilted magnetic fields. *Physical Review B* 60: 11241(R).

McKnight SW and Drew HD (1981) Breakdown of screening in Voigt cyclotron resonance. *Journal of Physics C: Solid State Physics* 14: 5367.

Merkt U (1985) Surface cyclotron resonance on InSb in Voigt configuration. *Physical Review B* 32: 6699.

Mohelský I, et al., Mohelský I, Dubroka A, Wyzula J, Slobodeniuk A, Martinez G, Krupko Y, Piot BA, Caha O, Humlicek J, Bauer G, Springholz G, and Orlita M (2020) Landau level spectroscopy of Bi_2Te_3. *Physical Review B* 102: 085201.

Mola M and Hill SO (2000) Instrumentation for millimeter-wave magnetoelectrodynamic investigations of low-dimensional conductors and superconductors. *The Review of Scientific Instruments* 71: 186.

Moses P and McKenzie RH (1999) Comparison of coherent and weakly incoherent transport models for the interlayer magnetoresistance of layered Fermi liquids. *Physical Review B* 60: 7998.

Moss TS and Balkanski M (1994) *Optical Properties of Semiconductors*. Amsterdam: Elsevier. Chapters 6, 7 and 11.

Nam MS, et al., Nam M-S, Blundell SJ, Ardavan A, Symington JA, and Singleton J (2001) Fermi surface shape and angle-dependent magnetoresistance oscillations. *Journal of Physics. Condensed Matter* 13: 2271.

Otteneder M, Sacre D, Yahniuk I, Budkin GV, Diendorfer K, Kozlov DA, Dmitriev IA, Mikhailov NN, Dvoretsky SA, Bel'kov VV, Knap W, and Ganichev SD (2021) Terahertz magnetospectroscopy of cyclotron resonances from topological surface states in thick films of $Cd_xHg_{1-x}Te$. *Physica Status Solidi B* 258: 2000023.

Post KW, Legros A, Rickel DG, Singleton J, McDonald R, He X, Bozovic I, Xu X, Shi X, Armitage NP, and Crooker S (2021) Observation of cyclotron resonance and measurement of the hole mass in optimally doped $La_{2-x}Sr_xCuO_4$. *Physical Review B* 103: 134515.

Russell BJ, Zhou B, Taniguchi T, Watanabe K, and Henriksen EA (2018) Many-particle effects in the cyclotron resonance of encapsulated monolayer graphene. *Physical Review Letters* 120: 047401.

Rzepniewski E, Edwards RS, Singleton J, Ardavan A, and Maeno Y (2002) Cyclotron resonance in the superconductor Sr_2RuO_4. *Journal of Physics. Condensed Matter* 14: 3759.

Schrama JM, Singleton J, Edwards RS, Ardavan A, Rzepniewski E, Harris R, Goy P, Gross M, Schlueter JA, Kurmoo M, and Day P (2001) Millimetre-wave measurements of the bulk magnetoconductivity of anisotropic metals: application to the organic superconductors κ-(BEDT-TTF)$_2$Cu(NCS)$_2$ and β\-(BEDT-TTF)$_2$SF$_5$CH$_2$CF$_2$SO$_3$ (BEDT-TTF $\equiv$ bis(ethylene-dithio)tetrathiafulvalene). *Journal of Physics. Condensed Matter* 13: 2235.

Shoenberg D (1984) *Magnetic Oscillations in Metals*. Cambridge: Cambridge University Press.

Singleton J (2000) Studies of quasi-two-dimensional organic conductors based on BEDT-TTF using high magnetic fields. *Reports on Progress in Physics* 63(8): 1111.

Singleton J (2001) *Band Theory and Electronic Properties of Solids*. Oxford: Oxford University Press. Chapters 8 and 9.

Singleton J (2020) Temperature scaling behavior in the linear magnetoresistance observed in high-temperature supercon-ductors. *Physical Review Materials* 4: 061801(R).

Singleton J, Goddard PA, Ardavan A, Coldea AI, Blundell SJ, McDonald RD, Tozer S, and Schlueter JA (2007) Persistence to high temperatures of interlayer coherence in an organic superconductor. *Physical Review Letters* 99: 027004.

Vaughan TA, Nicholas RJ, Langerak CJGM, Murdin BN, Pidgeon CR, Mason NJ, and Walker PJ (1996) Direct observation of magnetophonon resonances in Landau-level lifetimes of a semiconductor heterostructure. *Physical Review B* 53: 16481.

Watts M, Auer I, Nicholas RJ, Harris JJ, and Foxon CTB (1992) Electron lifetime in the low field limit: A microwave cyclotron resonance study. In: Landwehr G (ed.) *High Magnetic Fields in Semiconductor Physics. Springer series in Solid State Sciences*, vol. 101, p. 581. Berlin: Springer.

Cyclotron resonance: Semiconductors

G Timothy Noe II[a], **David R Leadley**[b], **and John Singleton**[a], [a]National High Magnetic Field Laboratory, Pulsed-Field Facility, Los Alamos National Laboratory, Los Alamos, New Mexico, United States; [b]Department of Physics, University of Warwick, Coventry, United Kingdom

© 2024 Elsevier Ltd. All rights reserved.

This is an update of D.R. Leadley, Cyclotron Resonance: Semiconductors, Editor(s): Franco Bassani, Gerald L. Liedl, Peter Wyder, Encyclopedia of Condensed Matter Physics, Elsevier, 2005, Pages 356–367, ISBN 9780123694010, https://doi.org/10.1016/B0-12-369401-9/00654-9.

Preamble **133**
Cyclotron resonance: Basic description **133**
General considerations 133
Magnetoplasmon modes 134
Experimental techniques **135**
Swept field, fixed frequency 135
Very high (megagauss) and very low fields 135
Fourier transform spectroscopy 135
Terahertz time-domain spectroscopy 136
Free-electron lasers 138
Optically detected cyclotron resonance 139
Effective mass measurements **141**
Field-orientation dependence of the cyclotron effective mass 141
Nonparabolicity from bandstructure 142
Nonparabolicity due to polaron coupling 143
Shifts and coupling of the resonance **143**
Subband structure 144
Frequency-shifted CR 144
Landau level hybridization 144
Spin splitting 145
Fractional quantum Hall effect 146
Magneto-excitons vs. cyclotron resonance **146**
Conclusion **148**
Acknowledgments **148**
References **149**

Abstract

This article covers the observation of cyclotron resonance (CR) in semiconductors and semiconductor heterostructures. The experimental techniques employed involve magnetic fields, far-infrared radiation sources, and (mostly) cryogens. The fields may be swept, static, pulsed or even destructive, while the radiation sources range from broadband Fourier-transform spectrometers and fs laser techniques to monochromatic or quasi-monochromatic electron tubes and molecular-gas- and free-electron lasers. A primary focus of this article is the extraction of the carrier effective mass from CR, and how the measured value is affected by magnetic field, carrier density, temperature, illumination, and details of the bandstructure. Resonant and nonresonant interactions with excitations such as longitudinal optic and homopolar phonons also affect the CR spectra, and descriptions will be given as to how the strength of these electron-phonon interactions can be inferred from the data. Finally, other effects that shift or alter the CR spectra, such as coupling to subbands in heterostructures, and spin splitting, will be described.

Key points

- To introduce Landau quantization and cyclotron resonance.
- To explain how these relate to salient details of the semiconductor systems studied.
- To describe the types of apparatus used to observe cyclotron resonance in these semiconductor systems.
- To give a brief description of the effective mass measured in cyclotron resonance, and how it is affected by many-body and other effects.
- To describe how bandstructure and coupling to excitations such as optic phonons lead to nonparabolicity; and how this is measured using cyclotron resonance.
- To give brief descriptions of other phenomena observed using cyclotron resonance, such as coupling to subbands in -reduced-dimensionality systems, spin splitting and resonant polaron coupling.

https://doi.org/10.1016/B978-0-323-90800-9.00218-3

Preamble

Periods in human civilization are frequently classified by the materials used to make the most advanced and vital tools and weapons; hence, we have the Stone Age, Bronze Age, Iron Age, etc. Following the same reasoning, one might say that we are presently (2023) living in the Semiconductor Age (Orton, 2009). Very many manufactured items, ranging from toasters to cars, from light bulbs to smartphones, from laptops to cruise missiles (and so on), depend on electronic and opto-electronic devices based on semiconductors (Miller, 2022). It is therefore very important to be able to characterize semiconductor materials, in particular their bandstructure and the scattering processes that affect the electrons and holes (Landwehr and Rashba, 1991; Orton, 2009; Singleton, 2001). At the simplest level, this involves measuring the electron and hole effective masses and their mobilities. The masses describe the curvatures of the conduction and valence band extrema, and how fast the charge carriers can be accelerated; the mobilities parameterize how soon the accelerated carriers will be scattered (Singleton, 2001). Cyclotron resonance (CR) has played, and continues to play, an important role in determining these quantities in bulk (three-dimensional or 3D) and layered (two-dimensional (2D) or quasi 2D) semiconductors (Landwehr and Rashba, 1991; Goryca et al., 2019). However, CR is capable of giving much more, for example, information about the interactions of electrons with each other and the with host lattice.

This article reviews the basic mechanism of CR and describes how it may be observed experimentally. Subsequently, it discusses information that can be obtained from the CR position and linewidth. In particular, it addresses the issue of how the effective mass m^*_{CR} measured in CR relates to the band-edge value m^*_0 and how energy-level crossings, polaron coupling, spin splitting, and collective interactions affect the CR spectrum.

Cyclotron resonance: Basic description

General considerations

In magnetic induction B, the electronic energies become quantized into Landau levels (LLs) with energies (Singleton, 2001, 2023)

$$E_l(B, k_{||}) = \left(l + \frac{1}{2}\right)\hbar\omega_{\mathrm{c}} \pm \frac{1}{2} g\mu_{\mathrm{B}} B + E(k_{||}). \tag{1}$$

Here, l is an integer, and

$$\omega_{\mathrm{c}} = \frac{eB}{m^*_{\mathrm{CR}}} \tag{2}$$

is the cyclotron (angular) frequency. The second and third terms in Eq. (1) are respectively the spin splitting, with g, the Landé g-factor, and $E(k_{||})$, the energy of motion in the direction parallel to the applied B; here, $k_{||}$ is the wavevector quantum number parallel to B. Note that, just as in free space, the electron energy in the direction of B is unaffected; moreover, ω_{c} is the exact analog of the classical free-electron cyclotron frequency eB/m_{e}, but with the effective mass m^*_{CR} replacing m_{e}, the free-electron mass.

As described elsewhere (Landwehr and Rashba, 1991; Singleton, 2001, 2023; Yoshioka, 2002), Landau levels have a field-dependent degeneracy; hence, in a degenerate semiconductor system, the number of occupied LLs varies with B. This is parameterized by the *filling factor*, ν. However, care is needed, because the definition of ν depends on the system under study (and to a certain extent, the workers involved!); it may include spin and valley degeneracy. For example, a single, full LL might be labelled $\nu = 1$ in a bulk semiconductor (or metal) where the spin splitting is small compared to $\hbar\omega_{\mathrm{c}}$; that is, the definition includes both spin-split halves of the LL (Singleton, 2023). By contrast, in a high-mobility GaAs heterojunction, where the spin splitting is very clearly resolved, a full LL would usually be indicated by $\nu = 2$; each spin-split half of the LL is counted separately (Yoshioka, 2002). In a Si MOSFET, where valley degeneracy is also present, the situation would be described as $\nu = 4$ (Landwehr and Rashba, 1991).

The cyclotron effective mass, m^*_{CR}, is an orbitally averaged effective mass (Singleton, 2001). Since the free carrier density in degenerate semiconductor systems is much smaller than the atomic density, the electron or hole states are only occupied close to the band extrema. Consequently, the Fermi surface(s) occupies/occupy only a small fraction of the Brillouin zone (Lax, 1958). Under these conditions, the Fermi-surface sections are roughly ellipsoidal so that m^*_{CR} can be simply related to the effective masses for linear motion (i.e., transport) in various directions (Lax, 1958; Singleton, 2001).

CR occurs when electrons are excited between adjacent LLs by absorbing a photon of energy $\hbar\omega = \hbar\omega_{\mathrm{c}}$; the selection rule is thus $\Delta l = \pm 1$. Most of the examples in this Chapter involve degenerate semiconductors, where the optical transitions are between filled and empty, or partially filled and partially empty LLs in either the conduction *or* the valence band. Nondegenerate semiconductors are also studied by CR; LLs in both conduction and valence bands are populated using cross-bandgap radiation. The latter situation is also described briefly below.

Most CR experiments are conducted in the Faraday geometry, where the direction of propagation of the radiation is parallel to B. Hence, the oscillating electric and magnetic fields are polarized in the plane perpendicular to the static magnetic field (Landwehr and Rashba, 1991). Another consequence of the relatively low free carrier density in degenerate semiconductors is that the skin depth is large;

almost the same oscillating electric field will be present throughout the sample (Singleton, 2023). Hence, the radiation couples to the center of mass motion of the electrons or holes and is insensitive to carrier-carrier interactions, a proposition known as *Kohn's theorem*.

As mentioned above, the CR transition has the selection rule $\Delta l = \pm 1$, which accounts for the unit of angular momentum absorbed from the photon; it is also spin preserving, and, because of the tiny photon momentum, does not alter $k_{||}$. Semiclassically, electrons and holes will perform cyclotron orbits in opposite directions, and this suggests a way to distinguish between them using circularly polarized radiation. Conduction-band electrons are excited to higher LLs by σ^+ circularly polarized radiation (this is termed *electron-active*;) hole CR will generally only be excited by oppositely handed σ^- circularly polarized light, though σ^+ may excite transitions between heavy and light hole levels in the valence band (Landwehr and Rashba, 1991).

Scattering of the charge carriers means that the LLs are broadened; this is reflected in the CR linewidth, which can be used as a quantitative measure of the sample quality (Singleton, 2023). If the average carrier scattering rate is τ^{-1}, then a well-resolved CR is likely to be observable if $\omega_c \tau \gtrsim 1$, a condition can be interpreted semiclassically as an average carrier completing at least one cyclotron orbit before scattering (Landwehr and Rashba, 1991; Singleton, 2001). The mobility μ is expressed as $\mu = e\tau/m^*$, allowing for the differences between m^* (the effective mass for linear motion) and m^*_{CR} (an orbitally averaged effective mass), the magnetic field needed for clear observation of CR can be written as $B \gtrsim \frac{1}{\mu}$. For example, for a carrier mobility of $\mu = 10^3\ \mathrm{cm}^2\ \mathrm{V}^{-1}\ \mathrm{s}^{-1}$, $B \gtrsim 10\,\mathrm{T}$ to observe a clear CR. (Conditions affecting CR linewidth are described in more detail in a companion chapter (Singleton, 2023).)'

These limitations due to scattering rate mean that CR in semiconductors is normally measured at low temperature (4.2 K or less), where the mobility is highest. Similarly, CR in low-mobility semiconductors is only recorded using the highest available magnetic fields (Puhlmann et al., 1998).

Further broadening of the CR line can arise from dielectric mismatch, especially within layered structures and at frequencies close to poles in the dielectric response (Langerak et al., 1988). In some cases, this can completely mask the effects of broadening due to scattering and even change the line from the clean Lorentzian of Fig. 1 to a differential shape, from which it is much more difficult to extract the true resonance position. This effect can often be corrected for by modeling the dielectric response of the particular sample being investigated (Langerak et al., 1988).

Magnetoplasmon modes

The former description of CR as a resonant absorption is completely adequate in most cases, but is an oversimplification. The CR absorption spectrum can be calculated within linear response theory as being proportional to the real part of the dynamical conductivity (Kushwaha, 2001). As we will see below, CR is generally studied using far-infrared (FIR) radiation. Such illumination causes a long-wavelength perturbation of the electron plasma, which has a collective response. In a magnetic field, the plasma excitation modes occur close to integer multiples of ω_c. The lowest of these is referred to as the magnetoplasmon mode, and at small wave vector k, is equivalent to forming a magnetic exciton comprising the excited electron in the upper LL and the hole remaining in the lower LL. The excitation has an energy $E(k) = \hbar\omega_c + \delta E(k)$, where the second term represents the magnetoexciton binding energy due to electron correlations (Kushwaha, 2001). Pure CR corresponds to the $k \to 0$ limit of the magnetoplasmon, in which limit $\delta E(k) \to 0$ as a consequence of Kohn's theorem (Singleton, 2023).

Band nonparabolicity reflects the fact that the semiconductor is not truly translationally invariant, but is made up of discrete atoms. More obviously, translational invariance is broken by lattice defects, impurities, and the interfaces and composition variations in heterostructures and other 2D systems. Consequently, $k \neq 0$ modes may be allowed to mix with the pure CR mode at $k = 0$. Coupling to other plasmon modes of the electron gas is then possible, especially when a metallic grating is applied to the surface of the semiconductor in order to impose spatial periodicity on the FIR excitation and thereby select particular wave vectors (Kushwaha, 2001).

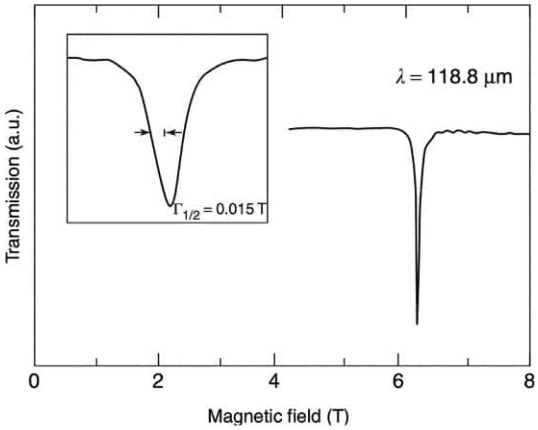

Fig. 1 Typical FIR transmission through a high-mobility GaAs 2DEG showing a very narrow CR. Permission from Hopkins MA, Nicholas RJ, Brummell MA, Foxon CT, and Harris JJ (1987) Cyclotron resonance study of non-parabolicity and screening in GaAs-GaAlAs heterojunctions. *Physical Review B* 36: 4789

Experimental techniques

The CR condition for a particular specimen can be satisfied either by applying monochromatic radiation of a fixed frequency and varying the magnetic field, or by fixing the field and varying the radiation frequency (Landwehr and Rashba, 1991; Singleton, 2023).

Swept field, fixed frequency

Quasistatic magnetic fields of up to $B = 45\text{T}$ are generated in resistive and hybrid magnets provided at national user facilities (see the webpages of the various national magnet laboratories for up-to-date information on maximum fields). On a smaller scale, commercial superconducting magnets can provide $B \approx 17 - 21\text{T}$, though the advent of reliable cuprate superconductor tape promises higher fields in the near future. At the other extreme, nondestructive pulsed-field magnets can give $B \approx 100\text{T}$; as we shall see below, even higher fields are possible in destructive pulsed magnets (Puhlmann et al., 1998). All of these different ways of providing swept magnetic fields have been used with monochromatic FIR to observe CR in semiconductors.

Typical semiconductor electron and hole masses lie in the range $0.01 \lesssim m^*_{CR}/m_e \lesssim 1$ (Landwehr and Rashba, 1991). Taken with the above routinely accessible fields of $B \sim 10\text{T}$, this means that FIR sources with wavelengths $10 \lesssim \lambda \lesssim 1000\,\mu\text{m}$ are required. Suitable monochromatic FIR can be obtained from a molecular gas laser pumped by a CO_2 laser operating at 9–11 μm (Jacobsson, 1989); typical lasing media are low-pressure vapors of methanol, formic acid, etc. or their deuterated variants. Though hundreds of lines can be obtained from such optically pumped FIR lasers, many experiments are limited to around 20 strong lines (Langerak et al., 1988), with 118.8μm being one of the most popular. Owing to strong atmospheric absorption of many of these FIR lines, radiation is usually conveyed from the laser to the magnet cryostat assembly using evacuated, cylindrical brass light pipes. Transmitted FIR is frequently detected by a carbon or Ge bolometer in the cryostat with the sample; noise is reduced using a lock-in amplifier synchronized with mechanical chopping of the laser (Langerak et al., 1988). Interference due to internal reflections from the back and front surfaces of the sample can result in distorted CR line shapes; to prevent this, samples are usually wedged by a few degrees (Langerak et al., 1988; Michels et al., 1996). The stability of the laser output over the course of the sweep of the magnetic field can be an issue, but this is ameliorated by taking the ratio of signals from the transmission bolometer and one that records the incident radiation. It is also possible to detect the CR through changes in the resistance of the sample being investigated in a photoconductivity measurement. Measurements at high fields can also be made in the "quantum limit," where only one LL is initially populated, as opposed to the classical limit at low fields. Between these limits, studies have been made of the effect of filling factor v on the line width, which can oscillate with the density of available initial and final states (Landwehr and Rashba, 1991).

Very high (megagauss) and very low fields

At pulsed magnetic fields in the megagauss regime ($B \sim 100$ T), the more powerful CO_2 laser can be used directly; other possible sources include H_2O, CO, and HeNe lasers. At these shorter wavelengths, fast (Hg,Cd)Te photovoltaic detectors can be used to detect the rapid change in IR intensity. Magnetic fields of up to 180 T are produced using the single-turn-coil technique pioneered at ISSP Tokyo (Puhlmann et al., 1998; Cole et al., 1997). A low-inductance capacitor bank is discharged through the coil to give currents of order 2 MA for ≈ 7μs. The maximum field is set by the capacitance and voltage of the bank and the coil diameter, which is typically about 10 mm. Though the coil explodes violently outwards, the cryostat and sample are (mostly!) left intact and the experiment can be repeated. Data from the detector and a pickup coil are transmitted via optical fiber to a shielded room where they are recorded on a fast multichannel digitizer. The pick-up voltage allows the field to be calibrated each time to an accuracy better than 2%. A set of typical CR recordings are shown for several II–VI semiconductors in Fig. 2.

Even higher fields, beyond 600 T, can be obtained using the electromagnetic flux-compression technique (Puhlmann et al., 1998). A pulsed current through an outer primary coil seeds a magnetic field and induces an opposing secondary current within an inner copper ring. The repulsive forces generated rapidly squeeze the ring, causing it to implode and compress the trapped magnetic flux density to a very high value. Unfortunately, the entire cryostat and sample are destroyed in this one-shot experiment! However, the extreme fields mean that CR can be studied in materials with large scattering rates, such as the dilute magnetic semiconductor $In_{1-x}Mn_xAs$, where heavy doping with magnetic impurities reduces the mobility. Data are shown in Fig. 2 for a temperature-dependent study of CR in CdS (Imanaka et al., 1998). Notice that at room temperature the CR peak is over 100 T wide.

By contrast, CR has also been observed at very low fields (20 mT), in very high quality GaAs/(Ga,Al)As heterojunctions where the mobility exceeds 10^6 cm^2 V^{-1} s^{-1} using microwave radiation from 17 to 90 GHz Gunn diodes. At these low fields, the cyclotron radius is ∼2 μm, which enables potential fluctuations in the sample to be observed on this macroscopic scale.

Fourier transform spectroscopy

The advent of reliable high-field superconducting magnets and Fourier transform infrared (FTIR) spectrometers in the late 1980s has provided a useful alternative to the swept-field CR measurements. In this technique, the FIR source is a mercury vapor lamp, heated metal wire or globar producing a broad spectrum of radiation. The radiation is sent through a Michelson interferometer before passing through the sample and being detected by a cooled Si bolometer. By rapidly scanning the moving mirror in the interferometer and recording the FIR intensity as a function of its position, an interferogram is produced. This is then fast-Fourier

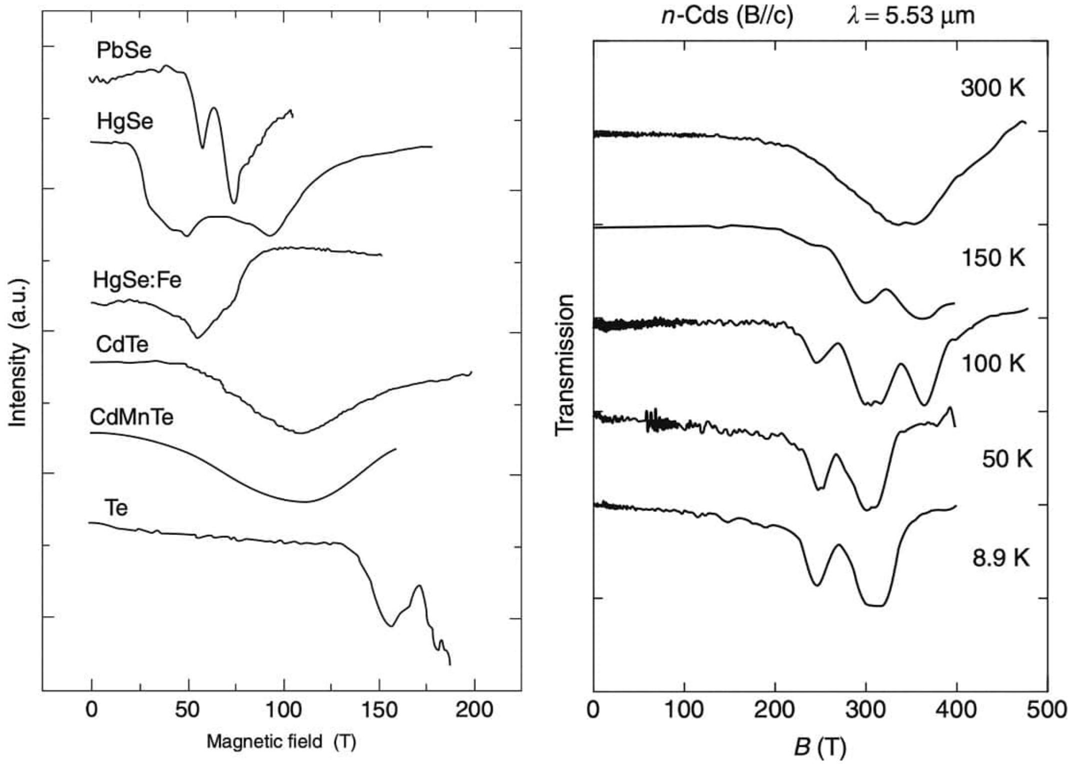

Fig. 2 Left: FIR transmission through a variety of II–VI semiconductors using a CO_2 laser with single-turn coils. Right: Temperature dependence of IR transmission through *n*-CdS at 5.53µm using ultrahigh magnetic fields. The electron CR line at 300 K is replaced by other lines related to impurity and phonon-coupled CR as the temperature is reduced. Left: Permission from Puhlmann N, Portugall O, Barczewski M, Stolpe I, Müller HU, and von Ortenberg M (1998) Multi-megagauss spectroscopy in the visible and infrared wavelength range. *Physica B: Condensed Matter* 246–247: 323–327. Right: Permission from Imanaka Y, Miura N, and Nojiri H (1998) Anomalous temperature dependence of the cyclotron mass in n-type CdS at ultra-high magnetic fields. *Physica B: Condensed Matter* 246–247: 328–332.

transformed to yield a transmission spectrum with a resolution of ~0.1 cm^{-1} (~0.01 meV). Each scan only takes a fraction of a second, but can be repeated many times to increase the signal-to-noise ratio. Intensity variation in the source spectrum and detector response can be removed by taking the ratio of spectra with and without the sample present. In practice, a set of transmission spectra are usually recorded as the magnetic field is stepped through the range of interest (Fig. 3) and differences are detected from the ratio of adjacent spectra. As a result of FTIR spectroscopy, the CR can be followed continuously as a function of magnetic field or energy, which allows detailed measurements of band nonparabolicity and subband structure to be made (Michels et al., 1995).

Terahertz time-domain spectroscopy

As an alternative to the continuous wave (CW) optical methods described in the previous sections, ultrafast pulsed lasers are used to generate and detect broadband pulses of THz radiation (Baydin et al., 2021). THz time-domain spectroscopy (THz-TDS) techniques have been combined with both constant and pulsed magnetic fields to observe CR in semiconductors.

Methods to generate THz radiation include using the output beam of an ultrafast laser to induce optical rectification in a nonlinear crystal such as ZnTe, GaSe, or $LiNbO_3$. Photoconductive antennas can also be employed; here the ultrafast laser pulse excites carriers in a material such as low-temperature grown GaAs. These carriers are then accelerated by a bias voltage, leading to a short current pulse ~1 ps that generates electromagnetic radiation in the THz frequency range.

Depending upon the method of generation and the pulse duration of the original ultrafast laser pulse, THz radiation in the frequency range 0.1–100 THz is generated. Detection methods include free space electro-optic sampling based on the Pockels effect, where the electric field of a THz pulse induces birefringence in a nonlinear crystal such as ZnTe. By analyzing the polarization of a detection pulse through the nonlinear crystal, the amplitude and phase of the THz electric field can be determined at a particular time. The THz electric field can then be mapped out as a function of time by varying the time delay between the detection pulse and the THz pulse; normally this is accomplished via mirrors on a mechanical translation stage.

THz-TDS allows for the direct measurement of both the amplitude and phase of the THz electric field as opposed to other techniques that only measure the intensity of radiation. The simultaneous direct measurement of both the amplitude and phase of the THz electric field transmitted through a sample allows one to determine both the real and imaginary part of the frequency-dependent conductivity without using techniques involving the Kramers–Kronig relations. Because THz-TDS techniques generally

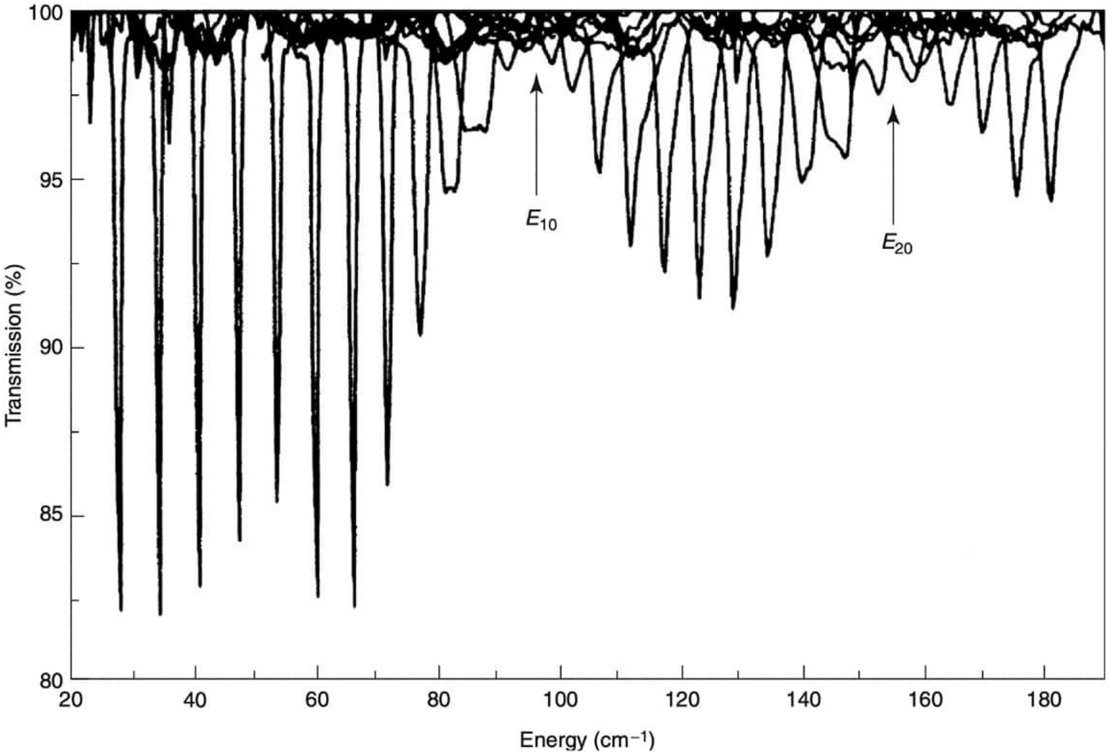

Fig. 3 Series of FTIR spectra from 2 to 14 T at 0.5 T steps for a GaAs heterojunction at 3.5 K. The *arrows* indicate resonant intersubband coupling at 12.4 and 20 meV. Permission from Michels JG, Nicholas RJ, Summers GM, Symons DM, Foxon CT, and Harris JJ (1995) Influence of light on the confinement potential of GaAs/Al$_x$Ga$_{1-x}$As heterojunctions. *Physical Review B* 52: 2688

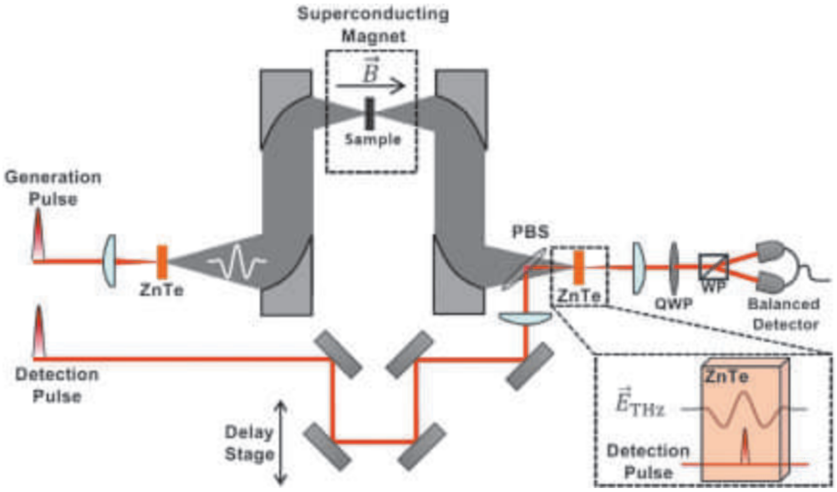

Fig. 4 A THz-TDS system incorporating a superconducting magnet in the free space beam path of the THz radiation. A delay stage is used to vary the time delay between a transmitted THz pulse and a detection pulse to record the amplitude and phase of a broadband THz electric field waveform. The polarization state of the detection pulse is analyzed using a quarter-wave plate (QWP) and a Wollaston prism (WP) to determine the THz electric field at each delay time. Permission from Baydin A, Makihara T, and Peraca NM (2021) Time-domain terahertz spectroscopy in high magnetic fields. *Frontiers of Optoelectronics* 14: 110–129.

utilize lasers that operate in the near-infrared range, it is also possible to optically pump carriers across the bandgap of semiconducting samples before the THz pulse arrives in an optical pump/THz probe experiment.

Fig. 4 shows an experimental set-up in which a direct current (DC) superconducting magnet is incorporated into the free-space beam path of a THz-TDS spectrometer (Baydin et al., 2021). The field is applied parallel to the light propagation direction (i.e., the Faraday geometry). CR in a high-mobility two-dimensional electron gas (2DEG) in GaAs has been measured using THz-TDS to determine the cyclotron coherence time directly, without the need for lineshape analysis and bypassing the saturation effect where

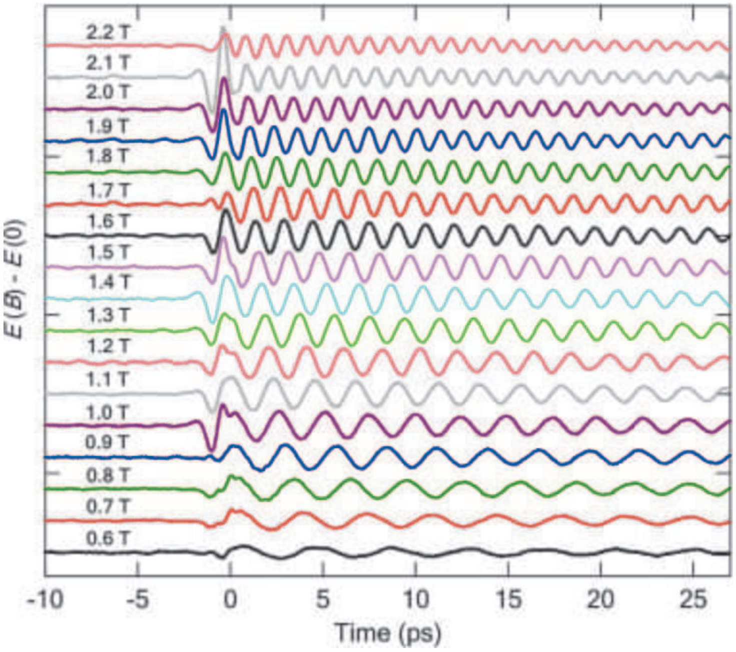

Fig. 5 Magnetic-field-dependent CR oscillations in a high mobility 2DEG in GaAs at low temperatures. Permission from Wang X, Hilton DJ, Reno JL, Mittleman DM, and Kono J (2010) Direct measurement of cyclotron coherence times of high-mobility two-dimensional electron gases. *Optics Express* 18: 12354–12361

the linewidth measured by FTIR is larger than the true linewidth (Wang et al., 2010). By subtracting the THz electric field that is transmitted through a 2DEG sample at 0 T from the transmitted THz radiation at finite *B*, one is left with an exponentially damped sinusoidal wave,

$$E(t) = A\exp(-t/\tau_{\mathrm{CR}})\sin(\omega_c t + \theta_0), \tag{3}$$

where A is the electric field amplitude, τ_{CR} is the CR decay time, ω_c is the CR angular frequency, and θ_0 is the starting phase of the oscillation. Fig. 5 shows CR oscillations in a high-mobility 2DEG in GaAs at various applied magnetic field strengths. Furthermore, it was discovered that in such a 2DEG system, the CR decay rate increased linearly with electron density, illuminating the role of many-body effects in CR decoherence via superradiant damping (Zhang et al., 2014).

Recently, THz-TDS studies in topological insulator $Pb_{0.5}Sn_{0.5}Te$ have revealed two types of carriers which display different CR dispersions, helping to further understand bulk states in Dirac and Weyl semimetals (Cheng et al., 2019).

In order to perform THz-TDS in pulsed magnetic fields, one must vary the time delay between the THz pulse and the detection pulse much faster than can be achieved with a mechanical delay stage. Two THz-TDS methods have been demonstrated to measure CR in pulsed magnetic fields. Electronically controlled optical sampling (ECOPS) utilizes two ultrafast lasers with nominally identical repetition rates (inverse of the time between consecutive pulses), except that one of the lasers (the "slave") incorporates a piezo-electric crystal to electronically modify the laser cavity length and hence repetition rate. By sweeping the repetition rate of the 'slave' laser in a close range around the fixed repetition rate of the 'master' laser, one can generate a set of two pulses at electronically controllable time delays with respect to each other. One is used to generate THz radiation, and the other is used for detection. ECOPS THz-TDS systems can be used to measure a THz waveform within a time window ~10s μs, which is suitable for use with pulsed magnets whose magnetic field strength varies on ms timescales. This method has been employed to measure CR in a high-mobility 2DEG in GaAs using a mini-coil pulsed magnet (Noe et al., 2014).

Single-shot THz-TDS techniques utilize a single laser where time delay information is encoded across the intensity profile of the detection pulse that is used to measure the THz radiation. The time delay information can be encoded by reflecting the detection pulse off of an echelon mirror. Different portions of the detection pulse will arrive at the detection crystal at slightly different times. The intensity profile of the detection pulse is finally imaged onto a two-dimensional camera providing a space-to-time mapping of the THz electric field. The measurement time is identical to the time delay range of the THz electric field measurement (~10s ps) meaning this technique is suitable for magnetic field pulses of any duration presently used for high magnetic field research. In an intrinsic Si sample, CR has been measured by single-shot THz-TDS after optically pumping carriers across the Si band gap in magnetic fields of up to 30 T (Noe et al., 2016).

Free-electron lasers

The limitation of the restricted number of lines from an optically pumped FIR laser can also be overcome by using a FIR free-electron laser (FEL) as a source for CR (Langerak et al., 1998a, b; Van Bockstal et al., 1998). FELs consist of an electron accelerator, an

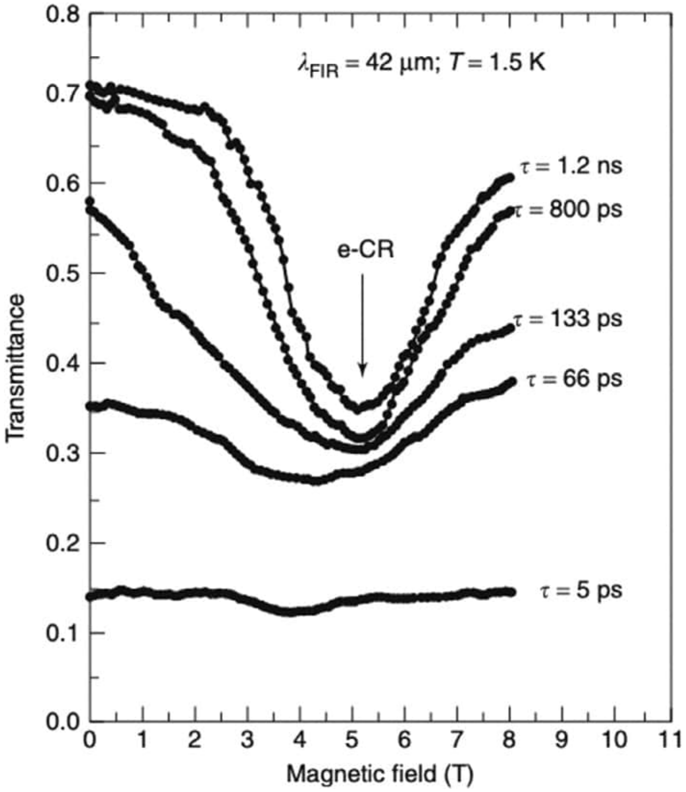

Fig. 6 Picosecond time-resolved CR in InSb using micro- pulses from an FEL. Initially, the very high density of photocreated electrons produces a very wide CR due to carrier scattering; only after ~1 ns is equilibrium restored. Permission from Kono J, Chin AH, Mitchell AP, Takahashi T, and Akiyama H (1999) Picosecond time-resolved cyclotron resonance in semiconductors. *Applied Physics Letters* 75: 1119

undulator in which the electrons emit radiation, and an optical resonator. By adjusting the undulator and electron energy, the output can be tuned over a rather large range (a factor ~3–20 in frequency); without changing the accelerator energy, the FIR frequency can be scanned over a factor ~2. Most FEL systems are driven by repetitively pulsed electron accelerators, and the resulting electron bunch structure (often a train of picosecond-duration micropulses within a 0.01–5 µs macropulse that is repeated at ~10 Hz) may be useful in time-resolved experiments (Fig. 6) (Kono et al., 1999). Over the past two decades, FELs have been colocated with high-magnetic-field facilities (Ramian, 2022) with such experiments in mind.

Optically detected cyclotron resonance

Rather than monitoring the FIR absorption directly, optically detected cyclotron resonance (ODCR) detects the variation in photoluminescence (PL), excited by a laser pumping electrons across the bandgap, due to FIR illumination (Michels et al., 1994). ODCR has some useful benefits: (i) undoped samples can be studied since the pump laser provides carriers; (ii) the conduction and valence band can be studied simultaneously; and (iii) the CCD arrays or photomultiplier tubes that are used to detect PL offer great sensitivity. ODCR is detected using the response of the PL intensity to chopped FIR; the signal is recorded either as the magnetic field is swept or the PL energy varied at fixed field. ODCR is clearly only suited to direct bandgap semiconductors that have a strong PL signal.

ODCR studies in bulk GaAs show the free-electron CR and also reveal transitions from the ground to excited states of donor-bound impurities (Fig. 7). Chemical shifts due to different donor atoms also appear with improved resolution compared to photoconductivity measurements. It is thought that the FIR illumination liberates electrons from donor sites to the conduction band, increasing the impact ionization of bound excitons and thus reducing the PL signal, which is predominantly due to excitonic recombination. The free electron luminescence makes a much smaller contribution to the PL. In magnetic field, charged excitons (or trions—labeled X^-) also have an energy quantized into a set of LLs, and CR between these can be used to extract the trion effective mass and lifetime (Michels et al., 1994).

In quantum wells, the ODCR signal is strongly dependent on the filling factor and, when the cyclotron energy exceeds the inter-subband separation, can show a complete transfer of luminescence intensity from the ground to second subband at resonance.

A development of ODCR is far-infra-red-modulated photoluminescence (FIRM-PL) whereby the whole PL spectrum is recorded at a fixed magnetic field, by dispersing the luminescence signal onto a CCD with typically a 1 m spectrometer (Chang and Nicholas, 1999). Two series of such spectra are taken as the magnetic field is stepped, with and without FIR radiation, and the CR contribution to each of the PL lines can be seen in their difference (Fig. 8). By studying these differences, as functions of magnetic field, PL, and

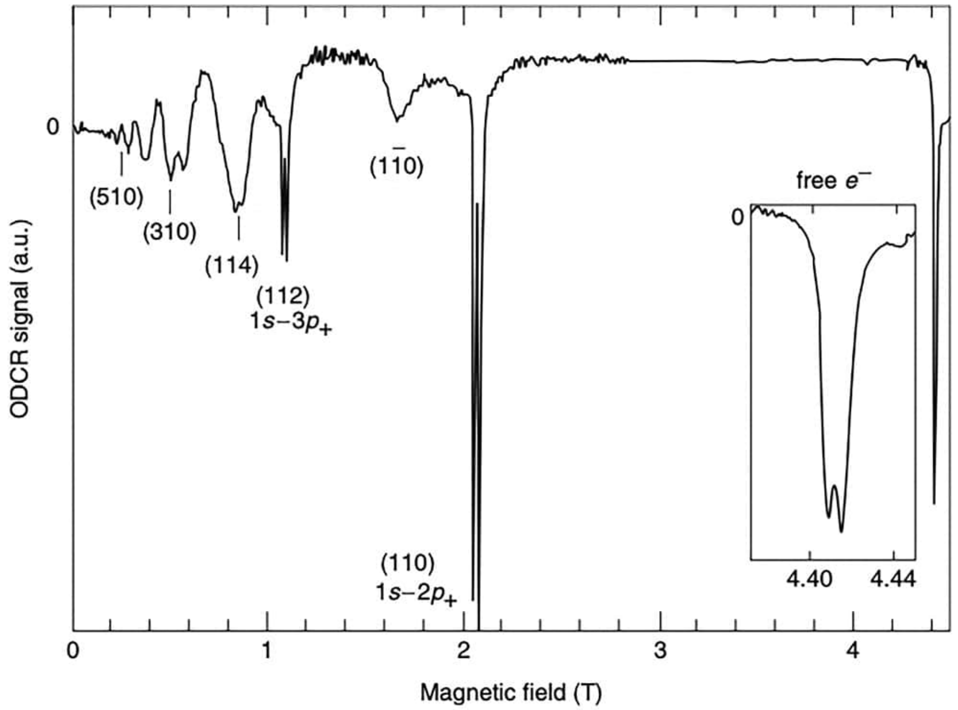

Fig. 7 ODCR signal from bulk GaAs for an FIR wavelength of 163μm, showing free-electron CR at 4.4 T (with a spin-split peak) and excitonic transitions at lower fields. Permission from Michels JG, Warburton RJ, Nicholas FR, and Stanley CR (1994) An optically detected cyclotron resonance study of bulk GaAs. *Semiconductor Science and Technology* 9: 198

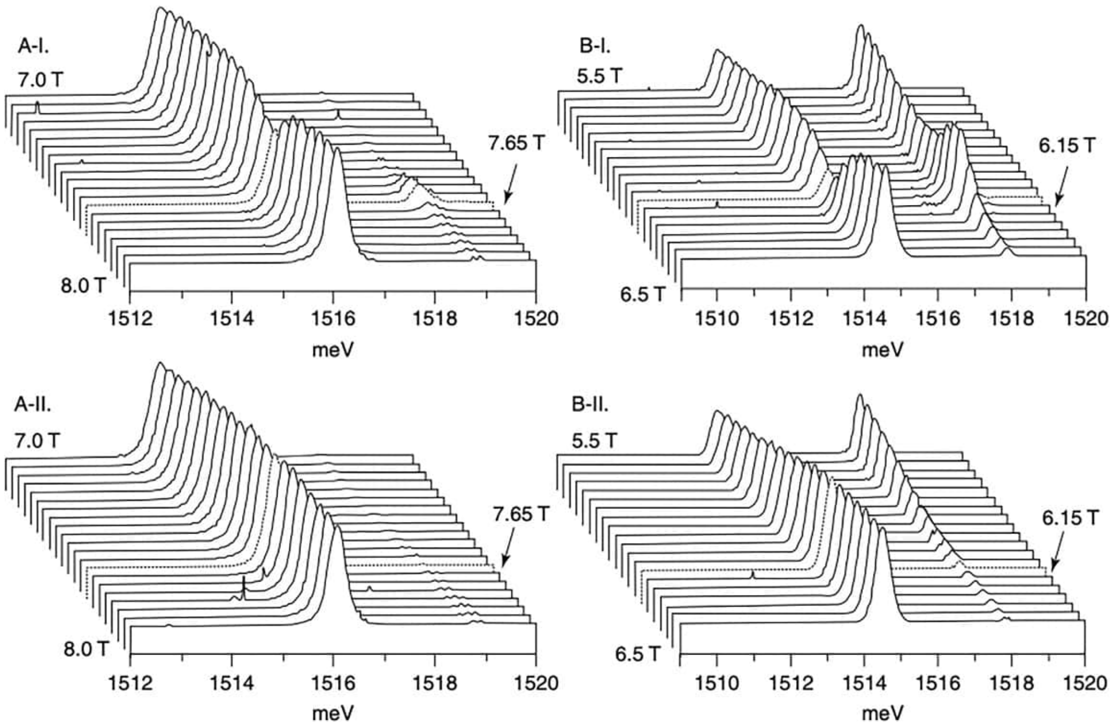

Fig. 8 FIRM-PL: PL spectra of a GaAs 2DEG with (I) and without (II) FIR radiation at (A) 96.5μm and (B) 118.8μm taken over a 1 T range about the CR position, indicated by *arrows*. Note the transfer of PL intensity from the E_0 to E_1 lines at resonance. Permission from Chang CC and Nicholas RJ (1999) A far infrared modulated photoluminescence (FIRM-PL) study of cyclotron resonance in a 2D electron gas in GaAs/Al$_x$Ga$_{1-x}$ As heterojunctions. *Semiconductor Science and Technology* 14: 768

FIR power, much can be learned about the energy levels and carrier dynamics within the semiconductor. However, such data must be interpreted carefully to account for the changes in carrier distribution and increases in nonradiative recombination due to FIR heating.

Effective mass measurements

Measurable features of a CR include the peak position, intensity, and linewidth. The integrated intensity of a CR line can be used to obtain the density of carriers responsible for the absorption, and the line width (after suitable correction) gives a measure of their mobility. The CR position is primarily used to extract the effective mass, m^*_{CR} (see Eqs. 1 and 2), which is often a function of the field orientation and the FIR energy (Lax, 1958; Landwehr and Rashba, 1991; Singleton, 2001).

Field-orientation dependence of the cyclotron effective mass

Although a spherically symmetric effective mass is a reasonable approximation for the conduction band minima of materials such as GaAs and InSb (Singleton, 2001), the bands in many semiconductors are much more anisotropic. In such cases, the effective mass is expressed as an inverse-mass tensor (Landwehr and Rashba, 1991; Singleton, 2001)

$$\left(\frac{1}{m^*}\right)_{i,j} = \frac{1}{\hbar^2}\left(\frac{\partial^2 E}{\partial k_i \partial k_j}\right), \tag{4}$$

where k_i and k_j are components of the wavevector quantum number $\mathbf{k}$. CR measures an average of the effective mass about a cyclotron orbit perpendicular to the applied magnetic field. Hence, by rotating the sample to different angles with respect to the magnetic field, and recording the CR spectra, the anisotropy can be mapped out. Practically, the rotation axis is perpendicular to the applied magnetic field, and usually chosen to be a one of the three principal crystalline axes. Frequently the experiment will be performed for two different planes of rotation. A pioneering example of this technique applied to Ge and Si (Dresselhaus et al., 1955) is shown in Fig. 9. Such data were instrumental in working out the bandstructures of these technologically important elements, and CR continues to be used to characterize new materials in a similar manner (Landwehr and Rashba, 1991; Goryca et al., 2019).

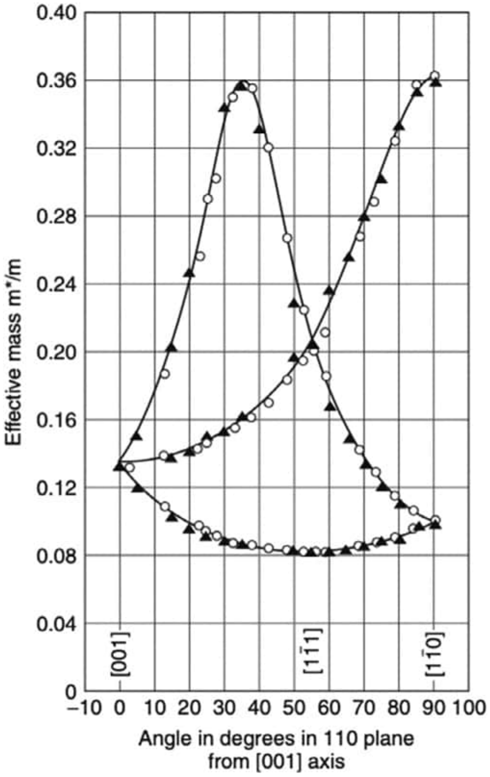

Fig. 9 Effective mass of electrons in Ge measured by CR for different crystalline directions. Solid lines are calculations. Permission from Dresselhaus G, Kip AF, and Kittel C (1955) Cyclotron resonance of electrons and holes in silicon and germanium crystals. *Physics Review* 98: 368

The anisotropy can become very large in reduced-dimensionality semiconductor systems such as semiconductor heterostructures and monolayers containing 2DEGs. Sometimes the confinement leads to almost perfect two-dimensional behavior of the CR, with the effective mass increasing as $1/\cos\theta$ as the field is tilted by an angle θ away from the normal to the layers. In other systems, the incorporation of strain into pseudomorphic layers, for example in Si-$\mathrm{Si}_{1-x}\mathrm{Ge}_x$ or GaAs-$\mathrm{In}_x\mathrm{Ga}_{1-x}\mathrm{As}$ (Landwehr and Rashba, 1991), produces a more complex anisotropy, especially in the valence band where heavy and light hole bands show considerable mixing. Hence, CR has been used as a valuable tool for checking bandstructure calculations, especially for p-type quantum wells (Cole et al., 1997).

Nonparabolicity from bandstructure

An energy-independent effective mass requires a perfectly parabolic band; in other words, one in which $E \propto k^2$. In real solids, however, bands have a finite energy width, and therefore both maxima and minima; between these, the electron dispersion relationship *must* inevitably deviate from parabolicity and the effective mass becomes a function of energy (Singleton, 2001).

However, most semiconductor applications involve electrons in states near to the band extrema, and some simplifying approximations can be made. First, at energies very close to the band extrema, the electronic dispersion relationship can frequently be approximated as a parabola. Then, at slightly higher energies, the nonparabolicity can in many cases be treated as a perturbation, For example, for the energies typically used in CR ($h\nu \lesssim 30$ meV), the nonparabolicity of the conduction band of many direct-gap semiconductors (such as InSb and GaAs) can be parameterized using the following expression (Hopkins et al., 1987; Peeters, 2004), derived using five-band **k**.**p** theory:

$$m^*_{\mathrm{CR}} = m_0\left\{1 + \frac{2K_2}{E_{\mathrm{g}}}\left([l+1]\hbar\omega_{\mathrm{c}} + \langle T_z\rangle\right)\right\}. \tag{5}$$

Here, $\langle T_z\rangle$ is the kinetic energy parallel to the magnetic field, l is the initial Landau-level quantum number, E_{g} is the bandgap and K_2 parameterizes the nonparabolicity. K_2 is usually negative, so that m^*_{CR} increases with energy. This increase is observed (Fig. 10) by changing the FIR frequency; when the CR transition occurs at higher field, ω_{c} is greater and the final state is higher in the band. Similarly, in high-mobility systems, transitions between different LLs may be resolved as distinct lines with for example, the $l = 1 - 2$ transition occurring at a higher field than the $l = 0 - 1$.

Nonparabolicity may also result in an effective mass that is a function of carrier density; as the Fermi energy increases, the initial LL quantum number l of the CR transition moves to progressively higher values (and thus higher m^*_{CR}), a phenomenon known as the Moss-Burnstein effect (Hopkins et al., 1987; Landwehr and Rashba, 1991). The observed mass may also increase with temperature. Two mechanism are involved here; electrons are thermally excited to higher LLs and thermal motion contributes to an increased $\langle T_z\rangle$. Another important contribution to $\langle T_z\rangle$ is the confinement energy in heterostructures, which generally results in 2D systems having larger m^*_{CR} than the corresponding bulk semiconductor in otherwise identical CR experiments.

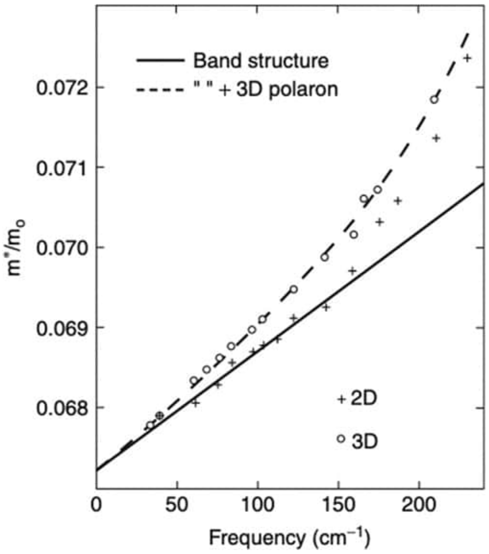

Fig. 10 Energy dependence of m^*_{CR} in 3D and 2D GaAs, showing the bandstructure and polaron contributions to nonparabolicity. The 3D results are shifted up by 0.0012 for comparison. Adapted from Hopkins MA, Nicholas RJ, Brummell MA, Foxon CT, and Harris JJ (1987) Cyclotron resonance study of non-parabolicity and screening in GaAs-GaAlAs heterojunctions. Physical Review B 36: 4789; Peeters FM (2004) Theory of electron-phonon interactions in semiconductors. In: Herlach F and Miura N (eds.) High Magnetic Fields: Science and Technology, vol. 2. pp. 23–45. New Jersey: World Scientific; Langerak CJGM, Singleton J, van der Wel PJ, Perenboom JAAJ, Barnes DJ, Nicholas RJ, Hopkins MA, Foxon CTB (1988) Carrier-concentation-dependent electron-LO-phonon coupling observed in GaAs-(Ga, Al)As heterojunctions by resonant-polaron cyclotron resonance. *Physical Review B* 38: 13133

Nonparabolicity due to polaron coupling

In polar semiconductors, there is an additional contribution to the nonparabolicity from polaron coupling (Fig. 10), which may be of similar magnitude to that due to the band structure (Devreese, 2007; Devreese and Alexandrov, 2009; Langerak et al., 1988; Peeters, 2004). When an electron or hole moves through a polar solid, it attracts or repels the charged ions around it; the associated strain field accompanying the carrier affects its self-energy and effective mass. The composite quasiparticle is known as a *polaron*, and may be regarded as a carrier dressed by virtual longitudinal optic (LO) phonons. We will see below that as the carrier energy approaches the LO phonon energy, $\hbar\omega_{\mathrm{LO}}$, the coupling becomes resonant, producing a strong effect on the Landau levels.

However, at carrier energies $\ll \hbar\omega_{\mathrm{LO}}$, the polaron has an effective mass m_λ^* that is larger than that expected from the underlying bandstructure (m^*) (Devreese, 2007; Devreese and Alexandrov, 2009; Langerak et al., 1988; Peeters, 2004),

$$m_\lambda^* = m^*\left(1 + \frac{\alpha}{6}\right), \tag{6}$$

where α is the Fröhlich coupling constant; for example, $\alpha = 0.07$ in GaAs and 1.2 in ZnO. In addition, the nonparabolicity is increased by an amount

$$\Delta K_{2,\mathrm{pol}} = -\frac{3\alpha E_{\mathrm{g}}}{40\hbar\omega_{\mathrm{LO}}}. \tag{7}$$

This explains the apparent discrepancy between the calculated $K_2 = -1.4$ in GaAs, expected from the bandstructure, with the actual value $K_2 = -1.8$ observed in CR measurements of low-electron-density samples (Fig. 10).

While the above mass and nonparabolicity enhancements are clearly observed in bulk semiconductors, they can be screened out in a degenerate 2DEG at low temperatures, reappearing at higher temperatures once the screening becomes less efficient (Fig. 11).

Polaron coupling becomes especially important as $\omega_{\mathrm{c}} \to \omega_{\mathrm{LO}}$; anticrossing occurs between the second LL and first LL plus an LO phonon (Fig. 12), opening an energy gap and bending the energy levels (Devreese, 2007; Devreese and Alexandrov, 2009; Langerak et al., 1988; Peeters, 2004). The two branches of the upper level can be traced out using CR at energies above and below the reststrahlen band; however, close to this region, careful interpretation of the CR lineshape is required to account for internal reflections, especially in layered heterostructures (Langerak et al., 1988; Singleton, 2023). In addition to resonant polaron coupling to LO phonons, a similar but weaker effect is observed in layered semiconductors due to homopolar optic phonons that modulate the layer thickness and couple to the carriers via a deformation potential (Howell et al., 1989).

Besides changing the CR energy, electron–phonon scattering can affect the CR linewidth. Inter-Landau level transitions may occur via phonon absorption/emission when $\omega_{\mathrm{LO}} = j\omega_{\mathrm{c}}$, where j is an integer. This effect is known as magnetophonon resonance (MPR), and is visible in semiconductors such as GaAs at temperatures of 80–200 K, where there is a favorable balance between LL width and optic phonon population. MPR is usually observed in transport measurements, but may also be seen as a modulation of the CR linewidth (Brummell et al., 1988).

Shifts and coupling of the resonance

We have already seen that the CR position can be altered by electron–phonon interactions. This section discusses some other mechanisms that may move and broaden CR spectra.

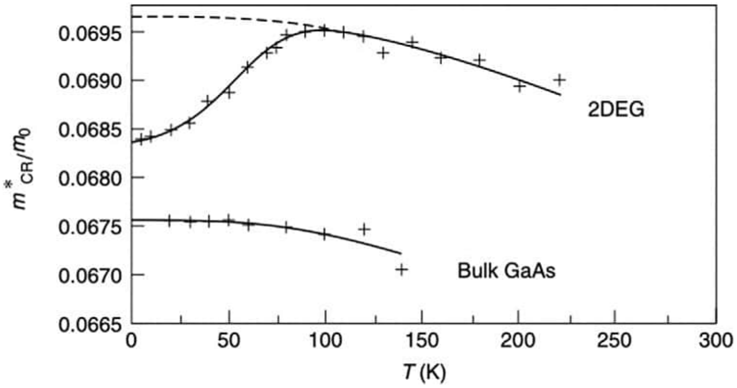

Fig. 11 Comparison of the temperature dependence of m^*_{CR} in 3D and 2D GaAs. Temperature-dependent screening of the polaron CR contribution in 2D is seen in the difference between the dashed extrapolation from high temperature and the data. Note the increase due to confinement in 2D. Permission from Hopkins MA, Nicholas RJ, Brummell MA, Foxon CT, and Harris JJ (1987) Cyclotron resonance study of non-parabolicity and screening in GaAs-GaAlAs heterojunctions. *Physical Review B* 36: 4789

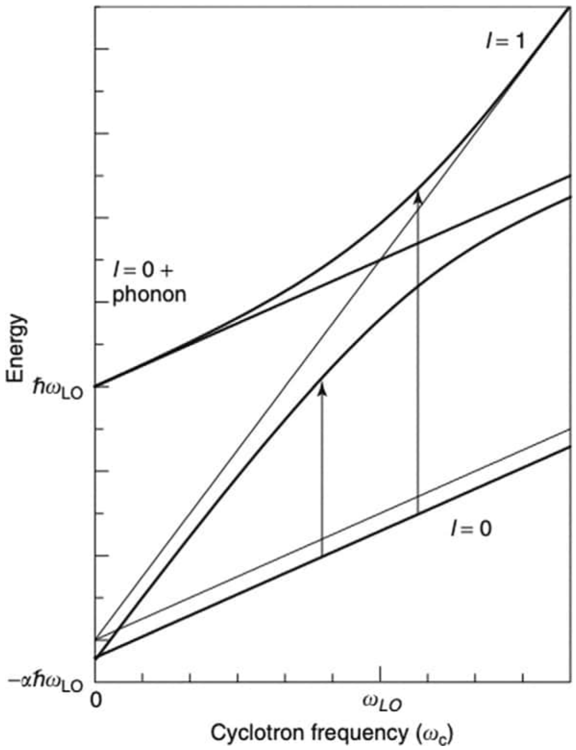

Fig. 12 Schematic representation of the polaron coupling between the first two LLs. *Dashed lines* show the unperturbed levels, *arrows* are the CR transitions. Adapted from Peeters FM (2004) Theory of electron-phonon interactions in semiconductors. In: Herlach F and Miura N (eds.) High Magnetic Fields: Science and Technology, vol. 2. pp. 23–45. New Jersey: World Scientific; Devreese JT (2007) Fröhlich polarons from 0D to 3D: Concepts and recent developments. *Journal of Physics: Condensed Matter* 19: 255201.

Subband structure

Reduced-dimensionality systems such as heterojunctions and quantum wells may have several electric subbands, due to confinement. Transitions between LLs of different subbands are usually forbidden, but the presence of a magnetic field component in the 2D plane mixes these states, permitting resonant subband-Landau-level coupling (RSLC) between, for instance, the $l = 1$ LL of the lowest E_0 subband and the $l = 0$ LL of the next E_1 subband. Thus, subband energies can be detected in tilted field CR as a discontinuity in m_{CR} as a function of energy or field, accompanied by an increase in CR linewidth at the RSLC condition (Fig. 3). This method has been used to determine the energy levels for a wide variety of structures, including heterojunctions, quantum wells, and superlattices (see e.g., Landwehr and Rashba, 1991; Michels et al., 1994; Winkler, 1996; Zawadzki and Pfeffer, 2004). In high-quality samples, the CR splits to reveal transitions to the upper and lower branches, and shows a transfer of oscillator strength from one to the other on passing through the resonance. In contrast to direct inter-subband transitions, which require the light to be polarized perpendicular to the interface and which exhibit a significant depolarization shift, in CR, the light is polarized parallel to the interface (even in tilted fields due to the high dielectric constant of most semiconductors) and depolarization shifts are very small.

Frequency-shifted CR

If carriers are bound to a harmonic potential Δ, then the CR angular frequency can be shifted from ω_c to ω

$$(\hbar\omega)^2 = (\hbar\omega_c)^2 + \Delta^2. \tag{8}$$

This occurs in for example, n-ZnO and n-CdS, where electrons may become bound in shallow traps (i.e., *not* bound impurity states). The effect has also been seen in quantum wells, where fluctuations in well width lead to carriers being confined to islands of lower potential (Merkt, 1996). For shifted CR to be observed, the localization length needs to be greater than the cyclotron radius, but not so large that the perturbation is the same for the initial and final state.

Landau level hybridization

An interesting example of LL hybridization occurs in heterojunctions in which the conduction band minimum in one semiconductor is below the valence band maximum in the other (i.e., InAs-GaSb heterojunctions). This leads to a semimetallic system with spatially separated electron and hole gases, unless the structure contains narrow quantum wells, where the additional confinement uncrosses the energy gap to produce a semiconducting arrangement (Singleton, 2001).

In the semimetallic examples, CR can be observed between both electron and hole LLs, and by following their position as a function of magnetic field, the relevant band-edge energies can be found. Strong oscillations of the CR linewidth and amplitude have been also observed; these disappear when the electron and hole layers are separated by a thin barrier. Maxima in linewidth occur whenever electron LLs and hole LLs cross, at which point energy gaps arise from hybridization of the electron and hole LLs. The hybridization only happens when the electron and hole wave functions can overlap by tunneling through the interface; this is why a thin barrier suppresses the effect (Warburton et al., 1996 and references therein). Similar hybridization phenomena have been seen in coupled GaAs quantum wells that form symmetric and antisymmetric wave functions.

Spin splitting

Eq. (1) shows that there are separate LL fans for each spin state. In a nonparabolic band, the spin-preserving CR transitions will be at different energies for spin-up and spin-down carriers, enabling the g-factor to be measured. As has been discussed elsewhere (Singleton, 2023), FIR-induced transitions are in general not sensitive to electron-electron interactions in a homogeneous layer (Kohn's theorem), so the g-factor measured in CR gives the single-particle value, and not the enhanced value detected in transport measurements.

The g-factor splitting is small in wide-gap materials (Zawadzki and Pfeffer, 2004), such as GaAs ($g = 0.44$), and spin-split CR is only observed in the quantum limit (see below). However, spin split CR is readily seen in narrow-gap semiconductors, such as InSb (Fig. 13), where the proximity of conduction and valence bands leads to strong nonparabolicity as well as a large g-factor (Khodaparast et al., 2004a). For InAs, with $g = -15$, the spin energy gap is so large that at low electron density and temperature, only the lower spin state is populated and only one CR line is observed, but once the second spin level becomes populated at higher temperature (or density), the second line appears. The onset of the second line can be used as a measure of carrier density (Landwehr and Rashba, 1991).

Dilute magnetic semiconductors, such as $\mathrm{In}_{1-x}\mathrm{Mn}_x\mathrm{As}$, have ferromagnetic phases below $\approx$50 K. The ferromagnetic exchange between Mn ions is believed to be hole mediated, and strongly affects both the conduction and valence band parameters due to the narrow bandgap. Megagauss hole CR, in Fig. 14, shows lines that shift to lower fields and intensify as the ferromagnetic phase is

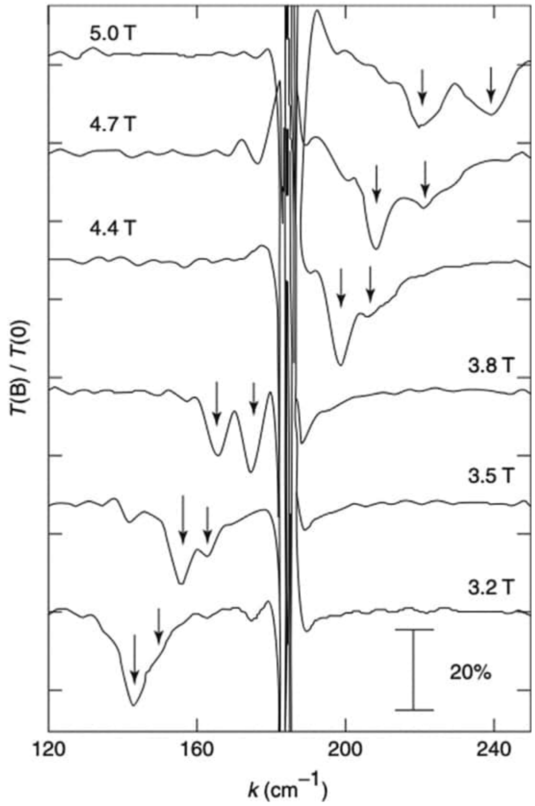

Fig. 13 FIR spectra showing clearly resolved spin splitting in InSb quantum wells on either side of the reststrahlen band due to InSb-like optic phonons close to 180 cm^{-1}. Permission from Khodaparast GA, Meyer RC, Zhang XH, Kasturiarachchi T, Doezema RE, Chung SJ, Goel N, Santos MB, and Wang YJ (2004a) Spin effects in InSb quantum wells. *Physica E: Low-Dimensional Systems and Nanostructures* 20: 386–391

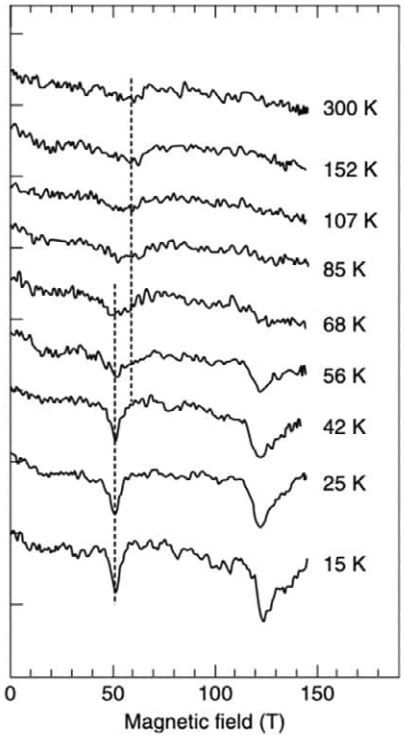

Fig. 14 CR spectra at 10.6μm from a InMnAs/GaSb heterojunction in magnetic fields of up to 150 T. On cooling through the ferromagnetic transition at 55 K, an additional line appears. Permission from Khodaparast GA, Kono J, Matsuda YH, Ikeda S, Miura N, Wang YJ, Slupinski T, Oiwa A, Munekata H, Sun Y, Kyrychenko FV, Sanders GD, and Stanton CJ (2004b) High-field cyclotron resonance studies of InMnAs-based ferromagnetic semiconductor heterostructures. *Physica E: Low-Dimensional Systems and Nanostructures* 21: 978–982

entered, consistent with the additional Mn exchange field increasing the spin splitting. In this regime, **k.p** calculations show that the spin splitting depends on temperature, magnetic field, and Mn concentration leading to a *g*-factor that varies from − 20 to + 100 (Khodaparast et al., 2004b). CR experiments proved vital in validating and refining such calculations.

Though spin–split electron CR is commonly observed in bulk GaAs (Mayer and Rössler, 1991), it has only been seen in 2DEGs at very low electron filling factors ($\nu < 10$) (Michels et al., 1996). At this very low filling factor and 100 mK, only the lowest transition occurs close to the position expected in bulk GaAs. On warming, the upper spin level becomes thermally populated and two lines appear by 1 K, with their relative intensities in accord with Boltzmann statistics based on the spin splitting expected in a single-particle picture. For $\frac{1}{10} \leq \nu \leq \frac{1}{6}$, this regime starts to break down, revealing a smaller splitting than expected. Finally, for $\frac{1}{6} \leq \nu \leq 2$, one CR line is seen that shifts from the position of the lower spin transition by up to half the spin splitting as the temperature increases. These results have been explained by a model whereby the cyclotron motions of the two spin states are coupled by the Coulomb interaction, which depends on the total electron density. The CR spectrum reflects hybridized spin-up/spin-down states, with the position of the single peak determined by the relative spin population (Cooper and Chalker, 1994).

A similar situation arises in Si, where two-and fourfold degenerate valleys possess different effective masses. Again, only a single CR line is observed until the system is considerably perturbed by uniaxial stress. Attempts to explain this rely on electron–electron interactions coupling the single-particle states (Landwehr and Rashba, 1991; see also Cole et al., 1997, and references therein).

Fractional quantum Hall effect

Throughout the temperature and field regime where fractional quantum Hall effect (FQHE) features are seen in transport experiments on GaAs-(Ga,Al)As heterojunctions (Yoshioka, 2002), there are no detectable deviations of the CR mass or line width, showing that CR is not affected by the electron correlations responsible for the FQHE (Michels et al., 1996).

Magneto-excitons vs. cyclotron resonance

An exciton is a bound electron-hole pair that can be created when a photon of energy greater than the bandgap of a semiconductor is absorbed (Singleton, 2001). Upon absorption of the photon, an electron is promoted from the valence band into the conduction band and a positively charged hole is left behind. The electron and hole can be bound via the Coulomb interaction. An exciton is analogous to the hydrogen atom, but it has a smaller binding energy due to the smaller reduced mass of the exciton and screening due to the dielectric environment of the lattice (Singleton, 2001).

Excitons have a series of bound states which modify the optical response near the band edge of semiconductors. These can be readily observed via absorption measurements when the binding energy is greater than the thermal energy. An applied magnetic field will modify the energy of the exciton. In the low magnetic field limit, the energy of the magneto-excitons shows a diamagnetic shift and Zeeman splitting similar to that of the hydrogen atom. In the high magnetic field limit, however, the effect of the magnetic field will dominate, and the magneto-exciton energies show a linear magnetic field dependence similar to the LLs of free electron-hole pairs.

The quantitative evolution of the exciton energy dependence on magnetic field depends on basic parameters of the exciton such as the binding energy, reduced mass, Bohr radius, and g-factor; therefore, analyzing the absorption spectra of semiconductors as a function of applied magnetic field can provide valuable information about the basic properties of excitons in semiconductors (Singleton, 2001). This has been extensively achieved over many decades for traditional III-V and II-VI semiconductors in both bulk samples and quasi-2D heterostructures. Recently, after advances in the synthesis of monolayer transition-metal dichalcogenide (TMD) semiconductors, magneto-optical measurements have been used to determine the basic excitonic properties including the exciton mass, size, and binding energy for these novel materials (Goryca et al., 2019) which are expected to possess unique optoelectronic properties due to their valley-specific optical selection rules. Pulsed magnetic fields of up to 60 T are necessary to determine the excitonic properties due to the heavy carrier masses and large exciton binding energies in monolayer TMD semiconductors.

CR is specifically used to describe the transitions between adjacent LLs for free electrons or holes; therefore, it is not appropriate to describe transitions between bound states of magneto-excitons as CR. However, there are cases where the distinction is not precisely clear. When an electron-hole pair have an energy higher than the binding energy, the electron and hole can be ionized, meaning they are no longer bound to one another although they may still be correlated. Disassociation of excitons can occur by thermal excitation, optical excitation of a large number of carriers, or by applying a gate voltage to electrostatically dope the semiconductor. With strong optical excitation in a semiconductor, the large number of electrons and holes results in an excitonic Mott transition from an insulating excitonic gas to an electron-hole plasma with increasing electron-hole density; excitons are only stable in the dilute limit where the Bohr radius is much smaller than the interexciton distance. Furthermore, with a transient optical excitation pulse, there can be a dynamically changing scenario where photoexcited electrons and holes first exist in an unbound state but later combine to form excitons.

THz-TDS has been used to measure the magneto-terahertz response of electron-hole pairs while varying the temperature, excitation strength (electron-hole density), and time delay between an optical pump pulse and the THz pulse (Zhang et al., 2016). Fig. 15 shows the magnetic field dependence of the real part of the photoinduced conductivity in undoped GaAs quantum wells. 15 ps after nonresonant photoexcitation, electron-CR and heavy hole-CR features are clearly identified, with linearly dependent energies as a function of applied magnetic field. At 1 ns after photo-excitation, intraexciton transitions are revealed, exhibiting a quadratic magnetic field dependence. Density dependent measurements revealed that magneto-excitons are more stable against a Mott transition at higher electron-hole densities when experiencing a high applied magnetic field.

Recently, optical absorption measurements at high magnetic fields have been performed in both a p-doped (Li et al., 2020) and a n-doped (Li et al., 2022) monolayer of WSe_2. Because of the valley-specific optical selection rules in monolayer TMD

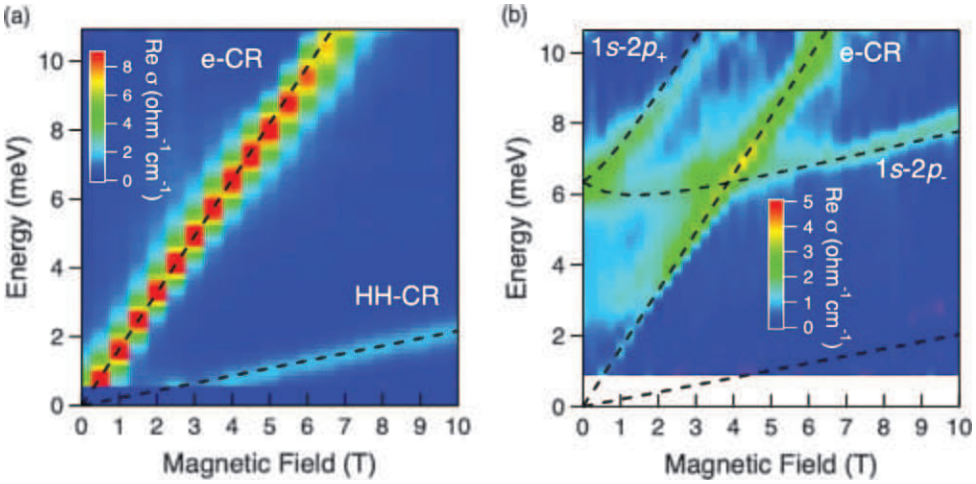

Fig. 15 Real part of the conductivity in the THz range for optically excited electron-hole pairs in undoped GaAs quantum wells. (A) At 15 ps after excitation, electron- and heavy hole-cyclotron resonance dominates the spectra. (B) At 1 ns after excitation, intraexciton transitions are observed. Permission from Zhang Q, Wang Y, Gao W, Long Z, Watson JD, Manfra MJ, Belyanin A, and Kono J (2016) Stability of high-density two-dimensional excitons against a Mott transition in high magnetic fields probed by coherent terahertz spectroscopy. *Physical Review Letters* 117: 207402

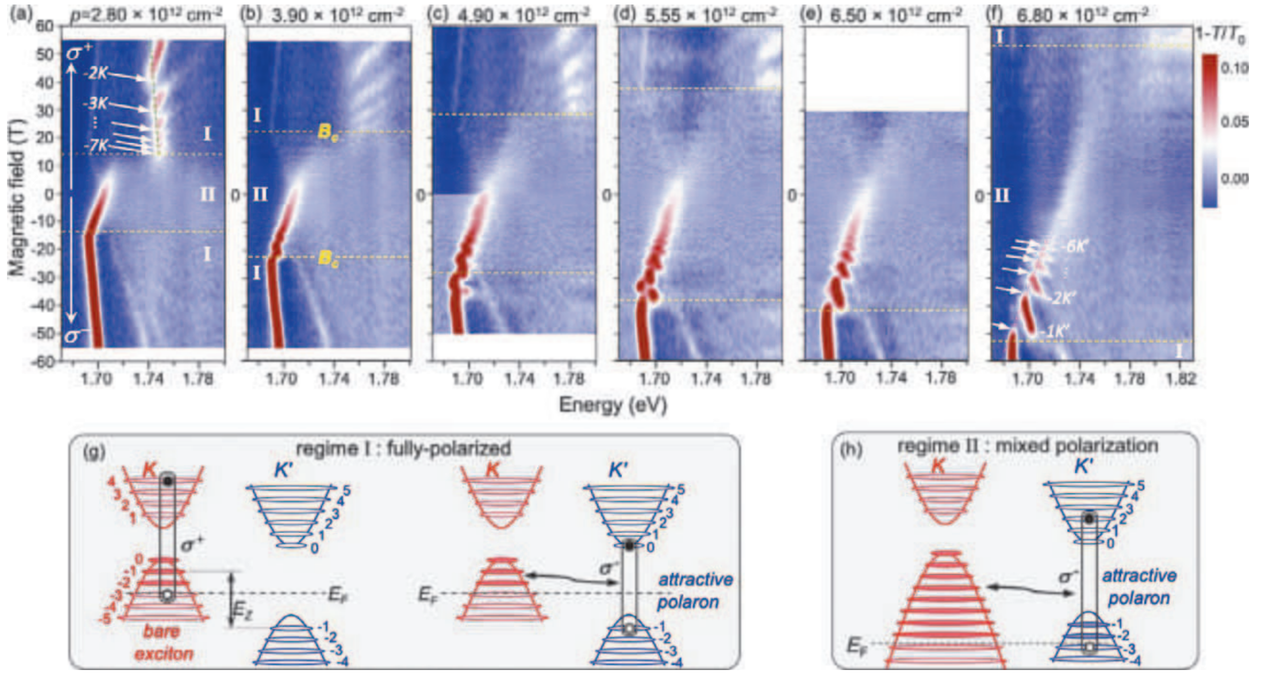

Fig. 16 Circularly polarized absorption spectra of hole-doped monolayer TMD WSe$_2$ provide a method to unambiguously determine the filled Landau levels in both the K and K' valleys. By tuning the carrier density, the 2DHG can become unstable against changes in LL filling and spontaneously valley polarize, as seen in (D) around 40 T. Permission from Li J, Goryca M, Wilson NP, Stier AV, Xu X, Crooker SA (2020) Spontaneous valley polarization of interacting carriers in a monolayer semiconductor. *Physical Review Letters* 125: 147602.

semiconductors, one can selectively probe the K(K′) valley with σ^+ (σ^-) circularly polarized light. At zero magnetic field, the K and K′ valleys are degenerate in energy; however this degeneracy can be lifted by an external magnetic field which breaks time-reversal symmetry. With the use of a single circular polarizer one can probe optical transitions in both the K and K′ valley simply by changing the direction of the applied magnetic field. Fig. 16 shows optical absorption spectra up to 60 T in a doped monolayer of WSe$_2$. Excitons are excited into the Fermi sea of free carriers and the resultant spectra display remarkable features depending on the doping level and magnetic field. In some cases, the 2D hole gas (2DHG) is unstable against changes in LL filling and becomes valley polarized. These studies highlight the importance of electron-electron interactions in monolayer TMDs.

Conclusion

CR in semiconductors has been discussed with an emphasis on the various experimental techniques that can be employed and the information that can be extracted. CR has been applied to a wide variety of different bulk materials and heterostructures, including elemental semiconductors, wide and narrow gap III–Vs, II–VIs, and dilute magnetic systems.

Though only a limited number of examples have been given here, the same principles apply to all materials. Whenever better material becomes available, CR reveals more about the band structure; as experimental facilities push toward higher fields, the technique can be extended to more imperfect crystals and structures.

This article has concentrated on FIR absorption as a measurement technique for CR. Transitions from higher to lower LLs have been shown to produce emission at the CR energy in a variety of studies over the past 40 years. Indeed, CR laser action has been demonstrated (Unterrainer et al., 1990). While such emission has often been touted for spectroscopic applications, it is beyond the scope of the present article.

Acknowledgments

Work at the National High Magnetic Field Laboratory on semiconductors is supported by National Science Foundation Cooperative Agreement No. DMR- 1644779, the Department of Energy (DOE) and the DOE BES program “Science at 100 T”. Development of high-frequency techniques has been greatly aided by grant LDRD-ER 20200285. Oxford University is thanked by JS for the provision of a visiting professorship that greatly facilitated some of the work described in this Chapter.

References

Baydin A, Makihara T, and Peraca NM (2021) Time-domain terahertz spectroscopy in high magnetic fields. *Frontiers of Optoelectronics* 14: 110–129.

Brummell MA, Leadley DR, Hopkins MA, and Nicholas RJ (1988) Cyclotron and magnetophonon resonance in semiconductor heterostructures. *Physica Scripta* T23: 73–81.

Chang CC and Nicholas RJ (1999) A far infrared modulated photoluminescence (FIRM-PL) study of cyclotron resonance in a 2D electron gas in GaAs/Al$_x$Ga$_{1-x}$ As heterojunctions. *Semiconductor Science and Technology* 14: 768.

Cheng B, Taylor P, Folkes P, Rong C, and Armitage NP (2019) Magnetoterahertz response and Faraday rotation from massive Dirac fermions in the topological crystalline insulator Pb$_{0.5}$Sn$_{0.5}$Te. *Physical Review Letters* 122: 097401.

Cole BE, Chamberlain JM, Henini M, Cheng T, Batty W, Wittlin A, Perenboom JAAJ, Ardavan A, Polisskii A, and Singleton J (1997) Cyclotron resonance in ultra-low-hole-density narrow p-type GaAs/(Al, Ga)As quantum wells. *Physical Review B* 55: 2503.

Cooper NR and Chalker JT (1994) Theory of spin-split cyclotron resonance in the extreme quantum limit. *Physical Review Letters* 72: 2057.

Devreese JT (2007) Fröhlich polarons from 0D to 3D: Concepts and recent developments. *Journal of Physics: Condensed Matter* 19: 255201.

Devreese JT and Alexandrov AS (2009) Fröhlich polaron and bipolaron: Recent developments. *Reports on Progress in Physics* 72: 066501.

Dresselhaus G, Kip AF, and Kittel C (1955) Cyclotron resonance of electrons and holes in silicon and germanium crystals. *Physics Review* 98: 368.

Goryca M, Li J, and Stier AV (2019) Revealing exciton masses and dielectric properties of monolayer semiconductors with high magnetic fields. *Nature Communications* 10: 4172.

Hopkins MA, Nicholas RJ, Brummell MA, Foxon CT, and Harris JJ (1987) Cyclotron resonance study of non-parabolicity and screening in GaAs-GaAlAs heterojunctions. *Physical Review B* 36: 4789.

Howell DF, Nicholas RJ, Langerak CJGM, Singleton J, Janssen TJBM, and Chevy A (1989) Two-dimensional magnetopolaron coupling to both homopolar and longitudinal optic phonons in the layer compound InSe. *Journal of Physics: Condensed Matter* 1: 7493.

Imanaka Y, Miura N, and Nojiri H (1998) Anomalous temperature dependence of the cyclotron mass in n-type CdS at ultra-high magnetic fields. *Physica B: Condensed Matter* 246–247: 328–332.

Jacobsson S (1989) Optically pumped far infrared lasers. *Infrared Physics* 29: 853–874.

Khodaparast GA, Meyer RC, Zhang XH, Kasturiarachchi T, Doezema RE, Chung SJ, Goel N, Santos MB, and Wang YJ (2004a) Spin effects in InSb quantum wells. *Physica E: Low-Dimensional Systems and Nanostructures* 20: 386–391.

Khodaparast GA, Kono J, Matsuda YH, Ikeda S, Miura N, Wang YJ, Slupinski T, Oiwa A, Munekata H, Sun Y, Kyrychenko FV, Sanders GD, and Stanton CJ (2004b) High-field cyclotron resonance studies of InMnAs-based ferromagnetic semiconductor heterostructures. *Physica E: Low-Dimensional Systems and Nanostructures* 21: 978–982.

Kono J, Chin AH, Mitchell AP, Takahashi T, and Akiyama H (1999) Picosecond time-resolved cyclotron resonance in semiconductors. *Applied Physics Letters* 75: 1119.

Kushwaha MS (2001) Plasmons and magnetoplasmons in semiconductor heterostructures. *Surface Science Reports* 41: 1–416.

Landwehr G and Rashba EI (eds.) (1991) Landau level spectroscopy. In: *Modern Problems in Condensed Matter Sciences*, vol. 27. Amsterdam: North-Holland.

Langerak CJGM, Singleton J, van der Wel PJ, Perenboom JAAJ, Barnes DJ, Nicholas RJ, Hopkins MA, and Foxon CTB (1988) Carrier-concentation-dependent electron-LO-phonon coupling observed in GaAs-(Ga, Al)As heterojunctions by resonant-polaron cyclotron resonance. *Physical Review B* 38: 13133.

Langerak CJGM, Li L, Van Bockstal L, Ardavan A, van de Pol MJ, van der Meer AFG, Herlach F, Mueller HU, Nicholas RJ, and Singleton J (1998a) The polaron effect in GaAs-(Al, Ga)As studied with a pulsed-field magnet: Free-electron-laser combination. *Physica B: Condensed Matter* 246–247: 400.

Langerak CJGM, Singleton J, Li L, Van Bockstal L, Ardavan A, van der Pol AJ, van der Meer AFG, Herlach F, Mason N, Nicholas RJ, and Walker PJ (1998b) Experiments on semiconductor systems using a pulsed-field-magnet free-electron-laser combination. *Physica B: Condensed Matter* 256: 339.

Lax B (1958) Experimental investigations of the electronic band structure of solids. *Review of Modern Physics* 30: 122–154.

Li J, Goryca M, Wilson NP, Stier AV, Xu X, and Crooker SA (2020) Spontaneous valley polarization of interacting carriers in a monolayer semiconductor. *Physical Review Letters* 125: 147602.

Li J, Goryca M, and Choi J (2022) Many-body exciton and intervalley correlations in heavily electron-doped WSe2 monolayers. *Nano Letters* 22: 426–432.

Mayer H and Rössler U (1991) Spin splitting and anisotropy of cyclotron resonance in the conduction band of GaAs. *Physical Review B* 44: 9048–9051.

Merkt U (1996) Cyclotron resonance of localized electron systems in the magnetic quantum limit. *Physical Review Letters* 76: 1134.

Michels JG, Warburton RJ, Nicholas FR, and Stanley CR (1994) An optically detected cyclotron resonance study of bulk GaAs. *Semiconductor Science and Technology* 9: 198.

Michels JG, Nicholas RJ, Summers GM, Symons DM, Foxon CT, and Harris JJ (1995) Influence of light on the confinement potential of GaAs/Al$_x$Ga$_{1-x}$As heterojunctions. *Physical Review B* 52: 2688.

Michels JG, Daly MS, Gee P, Hill S, Nicholas RJ, Singleton J, Summers GM, Warburton RJ, Foxon CT, and Harris JJ (1996) Cyclotron resonance and spin states in GaAs/GaAlAs heterojunctions: Experiment and theory. *Physical Review B* 54: 13807–13815.

Miller C (2022) *Chip War*. New York: Scribner.

Miura N, Osada T, and Takeyama S (2003) Research in super-high pulsed magnetic fields. *Journal of Low Temperature Physics* 133: 139–158.

Noe GT, Zhang Q, Lee J, Kato E, Woods GL, Nojiri H, and Kono J (2014) Rapid scanning terahertz time-domain magnetospectroscopy with a table-top repetitive pulsed magnet. *Applied Optics* 53: 5850–5855.

Noe GT, Katayama I, Katsutani F, Allred JJ, Horowitz JA, Sullivan DM, Zhang Q, Sekiguchi F, Woods GL, Hoffmann MC, Nojiri H, Takeda J, and Kono J (2016) Single-shot terahertz time-domain spectroscopy in pulsed high magnetic fields. *Optics Express* 24: 30328–30337.

Orton JW (2009) *The Story of Semiconductors*. Oxford: Oxford University Press.

Peeters FM (2004) Theory of electron-phonon interactions in semiconductors. In: Herlach F and Miura N (eds.) *High Magnetic Fields: Science and Technology*, vol. 2, pp. 23–45. New Jersey: World Scientific.

Puhlmann N, Portugall O, Barczewski M, Stolpe I, Müller HU, and von Ortenberg M (1998) Multi-megagauss spectroscopy in the visible and infrared wavelength range. *Physica B: Condensed Matter* 246–247: 323–327.

Ramian G (2022) *List of operational FELs*. http://sbfel3.ucsb.edu/www/vl_fel.html. (accessed 24.12.22).

Singleton J (2001) *Band Theory and Electronic Properties of Solids*. Oxford: Oxford University Press.

Singleton J (2023) Cyclotron resonance. In: *Encyclopaedia of Condensed Matter Physics*. Elsevier.

Unterrainer K, Kremser C, Gornik E, Pidgeon CR, Ivanov YL, and Haller EE (1990) Tunable cyclotron-resonance laser in germanium. *Physical Review Letters* 64: 2277.

Van Bockstal L, Li L, Langerak CJGM, van de Pol MJ, De Keyser A, van der Meer AFG, Ardavan A, Singleton J, Nicholas RJ, Herlach F, Bogaerts R, Müller HU, and von Ortenberg M (1998) Infrared spectroscopy with a pulsed high field magnet at a free electron laser. *Physica B: Condensed Matter* 246–247: 208–212.

Wang X, Hilton DJ, Reno JL, Mittleman DM, and Kono J (2010) Direct measurement of cyclotron coherence times of high-mobility two-dimensional electron gases. *Optics Express* 18: 12354–12361.

Warburton RJ, Brar B, Gauer C, Wixforth A, Kotthaus JP, and Kroemer H (1996) Cyclotron resonance of electron-hole systems in InAs/GaSb/AlSb. *Solid-State Electronics* 40: 679–682.

Winkler R (1996) Cyclotron resonance and subband-Landau level coupling in 2D electron and hole gases. *Surface Science* 361-362: 411–414. And references therein.

Yoshioka D (2002) The Quantum Hall Effect. *Springer Series in Solid-State Sciences.* Berlin Heidelberg: Springer-Verlag.

Zawadzki W and Pfeffer P (2004) Spin splitting of subband energies due to inversion asymmetry in semiconductor heterostructures. *Semiconductor Science and Technology* 19: R1–R17.

Zhang Q, Arikawa T, Kato E, Reno JL, Pan W, Watson JD, Manfra MJ, Zudov MA, Tokman M, Erukhimova M, Belyanin A, and Kono J (2014) Superradiant decay of cyclotron resonance of two-dimensional electron gases. *Physical Review Letters* 113: 047601.

Zhang Q, Wang Y, Gao W, Long Z, Watson JD, Manfra MJ, Belyanin A, and Kono J (2016) Stability of high-density two-dimensional excitons against a Mott transition in high magnetic fields probed by coherent terahertz spectroscopy. *Physical Review Letters* 117: 207402.

Scattering, inelastic: Electron

Dimitri D Vvedensky[a] **and Mehmet Erbudak**[b], [a]The Blackett Laboratory, Imperial College London, London, United Kingdom; [b]Solid State Physics, ETHZ, Zürich, Switzerland

© 2024 Elsevier Ltd. All rights reserved.

This is an update of M. Erbudak, D.D. Vvedensky, Scattering, Inelastic: Electron, Editor(s): Franco Bassani, Gerald L. Liedl, Peter Wyder, Encyclopedia of Condensed Matter Physics, Elsevier, 2005, Pages 205–211, ISBN 9780123694010, https://doi.org/10.1016/B0-12-369401-9/00644-6.

Introduction 150
Cross-section for inelastic scattering 151
Interband transitions 151
Plasmon excitations 152
Vibrations at surfaces 153
Excitation of core electrons 155
(e$^-$, 2e$^-$) Scattering 156
Conclusion 159
References 159

Abstract

An interaction event between an electron and a target material is called inelastic if the electron loses some or all of its energy. The general theory of the inelastic scattering cross-section is first developed before being specialized to interband transitions, plasmon excitations, vibrations at surfaces, core-electron excitations, and (e^-, $2e^-$) scattering. Examples are provided to illustrate how the elementary excitations of each method provide information about the atomic structure and electronic properties of materials, often in conjunction with density-functional calculations.

- Differential cross-section for inelastically scattered electrons, including dielectric formulation for interband transitions.
- Extensions to plasma excitations, vibrations at surfaces, excitations of core electrons, and (e^-, $2e^-$) scattering.
- Example of each application of inelastic electron scattering.
- Discussion of theoretical and computational approaches to inelastic scattering, including symmetry analysis, identification of paths in multiple scattering, and density functional methods.

Introduction

Inelastic electron scattering phenomena are used to obtain information on the electronic properties and atomic structure of materials. An interaction event between an electron and a target material is called inelastic if the electron loses some or all of its energy. Otherwise, the event is called elastic. Any energy loss by the electron is equal to the energy gained by the material and is characteristic of the type of scattering event. The measurement of an inelastic event determines the energy transferred and the rate of this transfer, which provides physical information about the elementary excitations of the material.

Inelastic interactions can be grouped according to different energy transfer regimes that form the basis of the principal experimental techniques. Historically, inelastic electron scattering was developed prior to the availability of continuous energy sources from dedicated storage rings. In fact, under certain circumstances, electronic excitations are equivalent to photon excitations in that they can be described within a common conceptual and theoretical framework.

An electron is an elementary particle with a mass m and, owing to its wave nature, has a de Broglie wave number $k = p/\hbar$, where $\boldsymbol{p} = m\boldsymbol{v}$ is the momentum of the electron, $\boldsymbol{v}$ is its velocity, and $\hbar$ is Plank's constant divided by 2π. The kinetic energy is expressed classically by $E = \frac{1}{2}mv^2$, where $v = |\boldsymbol{v}|$. Electrons have a negative charge e and a nonclassical angular momentum (spin). These properties play a central role in the interactions between electrons and their environment and constitute the basis of a wide range of spectroscopic techniques.

Owing to their unique properties, there are both advantages and disadvantages to using electrons as a probe in analytical applications. Spin-polarized or spin-averaged beam of electrons are readily created, electrons can be accelerated to any energy, and focused on a target at will. After they interact with the target material, electrons can be analyzed according to their intensity, momentum, energy, and spin polarization. In the final state, there are, even in an idealized single-scattering event, two electrons that arbitrarily share the initial energy. These electrons are indistinguishable, which makes the interpretation of the results especially challenging.

Cross-section for inelastic scattering

Electron-atom scattering is the cradle of today's understanding of the quantum mechanics of many solid-state interactions. Electron–solid interactions, however, not only present a wealth of phenomena to aid the development of modern physics, but have also made spectroscopies based on electronic excitations one of the major sources of information on atomic and electronic structure and on the elemental composition of materials. To account for all electronic interactions, a first-principles theory should be developed, though a semiclassical approach often suffices.

The strength of the electronic interaction depends on the electronic energy and the materials, which endows the energy dependence of a type of event with dynamical information about the interaction. If the interaction is weak, the energy $\hbar\omega$ lost by the electron and the associated momentum transfer $\boldsymbol{q}$, involve the creation of a single excitation with an energy $\hbar\omega$ and momentum $\boldsymbol{q}$. In this case, the Born approximation (Merzbacher, 1961) is valid, so the initial (i) and final (f) states of the electron are given by plane waves:

$$\psi_i = e^{i\boldsymbol{k}_i \cdot \boldsymbol{r}} \qquad \psi_f = f(\boldsymbol{k}_i)e^{i\boldsymbol{k}_f \cdot \boldsymbol{r}}, \tag{1}$$

where $f(\boldsymbol{k}_i)$ is the scattering amplitude. The interaction between the electron and the environment is described by a Hamiltonian containing the energy of the unperturbed sample, the energy of the electron, and the Coulomb potential $V(\boldsymbol{r})$ between the sample and the electron. During the interaction, energy and momentum are conserved,

$$E_i - E_f = \hbar\omega, \qquad \boldsymbol{k}_f - \boldsymbol{k}_i = \boldsymbol{q}. \tag{2}$$

Using Fermi's golden rule (Merzbacher, 1961), the differential scattering cross-section can be expressed as

$$d\sigma = \frac{2\pi}{\hbar}|\langle\phi_f\psi_f|V|\psi_i\phi_i\rangle|^2\delta(E_i - E_f)d\boldsymbol{k}, \tag{3}$$

where ϕ_i and ϕ_f are the wave functions of the target before and after the scattering, respectively.

When an electron scatters from an atom, the interaction only with the other electrons can be inelastic because no energy is transferred to the nucleus by Coulomb scattering. The most general type of energy transfer in electronic excitations produces a transition from an occupied to an unoccupied state separated by an energy equal to the energy loss of the primary electron. The differential cross-section of such a transition is obtained by integrating Eq. (3) to obtain

$$\frac{d^2\sigma}{dEdq} = \frac{8\pi}{q^3k_i^2}\left(\frac{e^2m^2}{\hbar^2}\right)^2|\langle\phi_f|e^{-i\boldsymbol{q}\cdot\boldsymbol{r}}|\phi_i\rangle|^2. \tag{4}$$

The cross-section $N(E) \propto d\sigma/dE$ is dominated by processes for which the momentum transfer is small. If $\boldsymbol{q}\cdot\boldsymbol{r} \ll 1$, then $e^{-i\boldsymbol{q}\cdot\boldsymbol{r}} \approx 1 - i\boldsymbol{q}\cdot\boldsymbol{r}$, and the dipole approximation used in optics becomes applicable to inelastic electron scattering:

$$\frac{d^2\sigma}{dEdq} = \frac{8\pi}{q}\left(\frac{e^2}{\hbar^2 v_i}\right)^2|\langle\phi_f|\boldsymbol{n}\cdot\boldsymbol{r}|\phi_i\rangle|^2, \tag{5}$$

where $v_i = \hbar k_i/m$, $\boldsymbol{q} = q\boldsymbol{n}$, and $\boldsymbol{n}$ is the unit normal vector along $\boldsymbol{q}$.

Interband transitions

The validity of the dipole approximation means that the scattering cross-section can be related to the dielectric properties of the target material. The dielectric response,

$$\varepsilon(\boldsymbol{q},\omega) = \varepsilon_1(\boldsymbol{q},\omega) + i\varepsilon_2(\boldsymbol{q},\omega), \tag{6}$$

depends on the energy transfer $\hbar\omega$ and the momentum transfer $\boldsymbol{q}$ defined in (2). Electrons interacting with the target produce a longitudinal perturbation over the long-range dipole fields. These fields attenuate the electron intensity through the absorptive part ε_2 of the dielectric constant. Since the field is screened by $1/\varepsilon$, the electron-loss function can be written as the sum of surface and bulk contributions (Raether, 1965; Froitzheim, 1977):

$$\begin{aligned} N(E) &\propto -\mathrm{Im}\left[\frac{S}{1+\varepsilon(\boldsymbol{q},\omega)} + \frac{B}{\varepsilon(\boldsymbol{q},\omega)}\right] \\ &\equiv -\mathrm{Im}\left[\frac{1}{\tilde{\varepsilon}(\boldsymbol{q},\omega)}\right], \end{aligned} \tag{7}$$

where S and B are weighting factors for the surface and bulk, respectively. The cross-section $N(E)$, therefore, contains fundamental information on the dielectric behavior of the bulk and the surface of the sample. A direct link between electron energy losses and the effective dielectric function defined in (7) is provided by the Kramers–Kronig relation (Jackson, 1975; Schattschneider and Jouffey, 1995),

$$\mathrm{Re}\left[\frac{1}{\tilde{\varepsilon}(\boldsymbol{q},\omega)}\right] = 1 + \frac{2}{\pi}\int_0^\infty \frac{\mathrm{Im}[1/\tilde{\varepsilon}(\boldsymbol{q},\omega)]}{\omega'^2 - \omega^2}\omega' d\omega', \tag{8}$$

which gives

$$\tilde{\varepsilon}(\boldsymbol{q},\omega) = \frac{\mathrm{Re}[1/\tilde{\varepsilon}(\boldsymbol{q},\omega)] - i\mathrm{Im}[1/\tilde{\varepsilon}(\boldsymbol{q},\omega)]}{[1/\tilde{\varepsilon}(\boldsymbol{q},\omega)]^2}. \tag{9}$$

The practical advantage of energy-loss measurements over optics lies in the fact that they cover a larger energy range than experiments with photons, which facilitates a more complete evaluation of (8). The electron energy-loss function, in fact, depends on the joint density of states (DOS), defined as the convolution of the occupied initial states and the unoccupied final states that are separated by the energy loss and are coupled by the matrix element. The optical function contains the transverse properties of the solid, which may be different from the longitudinal properties accessible to electron energy-loss spectroscopy. The differences between the traverse and the longitudinal responses are negligible for small momentum transfer $\boldsymbol{q}$ (the random phase approximation). For higher values of $\boldsymbol{q}$, multipole transitions are well resolved in electron-induced transitions, but are strictly forbidden in optics.

Inelastic interactions are responsible for the intensity attenuation of electrons within a bulk material. The characteristic quantity for the penetration depth of the electrons is called the mean free path Λ the value of which depends on the available excitations at a particular energy. For the range of energies ~30–100 eV, Λ has values comparable to interatomic distances (Schnatterly, 1979). Thus, the experiments contain information mainly on the surface properties (the S-term in Eq. 7). In optics, on the other hand, photons penetrate deeply into the target material, so the information is dominated by the bulk DOS (the B-term in Eq. 7). Transitions that are characteristic of the surface (e.g., surface states, adsorbates) help to distinguish between bulk and surface excitations.

Plasmon excitations

The cross-section in (7) attains peak values for $\varepsilon_1 = 0$ and $\varepsilon_2 = 0$. This condition corresponds to no charge-density fluctuations caused by the incident electrons. A longitudinal plasma wave along the crystal produces long-range Coulomb forces between positive and negative charges and excites collective excitations. These are called plasmons in the case of a quasi-free electron gas. The plasmon energy is obtained from the Fourier modes of the electron density,

$$\rho(\boldsymbol{r}) = \sum_{\boldsymbol{k}} \rho_{\boldsymbol{k}} e^{-i\boldsymbol{k}\cdot\boldsymbol{r}}. \tag{10}$$

The $\rho_{\boldsymbol{k}}$ are amplitudes for harmonic density fluctuations obeying,

$$\frac{d^2\rho_{\boldsymbol{k}}}{dt^2} + \omega_p^2 \rho_{\boldsymbol{k}} = 0, \tag{11}$$

in which ω_p is the Langmuir frequency,

$$\omega_p = \left(\frac{n_e e^2}{\varepsilon_0 m}\right)^{\frac{1}{2}}, \tag{12}$$

n_e is the bulk charge density, ε_0 is the permittivity of free space, and the energy loss due to plasmon creation is $\hbar\omega_p$. Plasmons are quantized excitations, so the energy loss is $n\hbar\omega_p$, where n is a positive integer.

Plasmon energies can be used to extract changes in the electron density that accompany changes of the electronic properties or the volume of a solid. For example, the alloy Al-3 at.% Ag shows a transition from a high-temperature phase, where Al and Ag form a homogeneous solid solution, to a regime ~ 400°C where Ag atoms precipitate as Ag_2Al clusters. The formation of these precipitates can be monitored by observing the plasmon energies of Al across the transition. With Ag atoms homogeneously distributed in the bulk, more volume is available at Al atoms, resulting in a lower effective electron density, thus shifting the plasmon to lower values.

The spectra in Fig. 1 show that, at 480°C, the plasmon energy is reduced from 15.8 to 15.5 eV signaling a 3.8% volume reduction. At temperatures below 440°C, Ag_2Al precipitates form that are largely decoupled from the aluminum matrix, thus leaving the volume and electron density unaltered from their values in pure Al. Thus, there is no change in the plasmon energy.

Fig. 2 shows high-resolution electron energy-loss spectroscopy (HREELS) measurements of the π and $\sigma + \pi$ plasmons for the indicated monolayers of epitaxial graphene prepared on a Si-terminated 6H-SiC(0001) crystalline wafer by solid state graphitization. The spectra were recorded under identical conditions with the momentum transfer parallel to the surface ($q = 0.1$Å).

The frequencies of the two collective excitation modes shift to higher energies and the peaks broaden as the thickness of the epitaxial layers increases. The changes in the plasmon peaks provide information about how the electronic structure changes with increasing epitaxial thickness. In particular, the 6.3 eV loss peak of the 3-4 monolayers of epitaxial graphene is close to that of graphite. Alternatively, the intensity of the $\sigma + \pi$ mode becomes weaker with deceasing number of epitaxial layers. The loss peak at

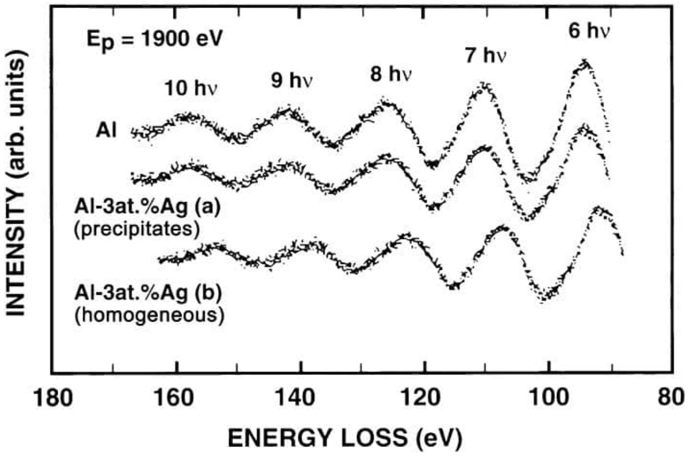

Fig. 1 Energy losses in Pure Al and Al–3 at.% Ag with (A) Ag_2Al precipitates, and (B) Ag atoms homogeneously distributed at 480°C. To accurately determine the plasmon energy, the measurements are extended up to the tenth plasmon loss. Reprinted with permission from Wetli E, Erbudak M, and Schultess T (1994) Segregation and dissolution of Ag-rich clusters at the (100) surface of Al-3 at.%Ag. *Physical Review B* 49: 14628–14631; © American Physical Society.

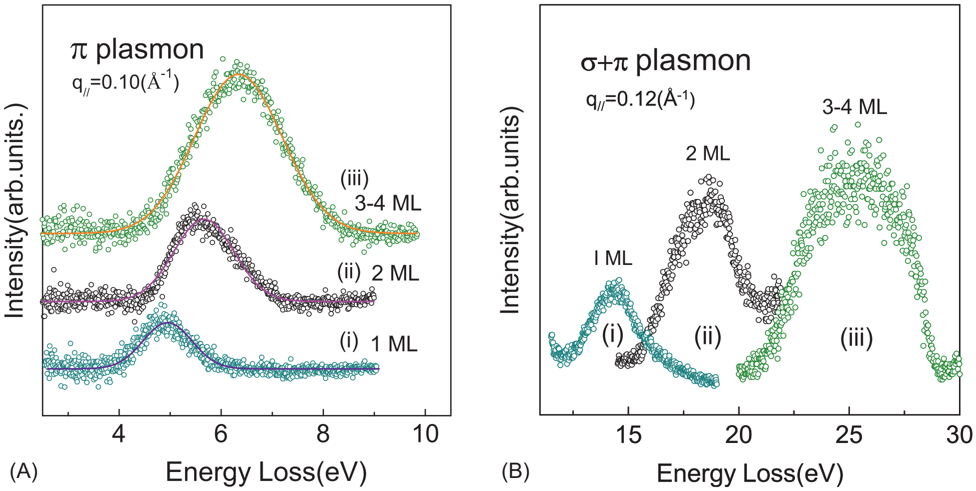

Fig. 2 The (A) π plasmon peak and (B) $\sigma + \pi$ plasmon peak for (i) monolayer, (ii) bilayer, and (iii) 3-4 monolayers of epitaxial graphene. The *solid line* is a Gaussian fit to the data. Reprinted with permission from Lu J, Ping Loh K, Huang H, Chen, W, and Wee ATS (2009) Plasmon dispersion on epitaxial graphene studied using high-resolution electron energy-loss spectroscopy. *Physical Review B* 80: 113410; © American Physical Society.

14.5 eV of the $\sigma + \pi$ plasmon peak for single layer epitaxial graphene can be viewed as a limiting case when the out-of-plane mode vanishes, leaving only the in-plane mode.

There are detailed investigations of the dependence of plasmon excitations on the momentum transfer. For increasing values of $\boldsymbol{q}$, the peak in the loss function moves to higher energies until the excitation decays into electron-hole pairs. In semiconductors, electron-hole pairs form a hydrogenic bound state called excitons which, for a material with an indirect band gap, such as Si, have a very long lifetime because the recombination process requires the emission of a phonon to conserve momentum.

Fig. 3 shows the dispersion of π-plasmon energies for epitaxial graphene with different thicknesses. Single layer and bilayer epitaxial graphenes show linear dispersions with q while the 3-4 monolayer structure shows a parabolic dispersion. The linear dispersion of monolayer epitaxial graphene is related to the unique band structure near the K-point of the Brillouin zone. The parabolic dispersion associated with 3-4 layers of epitaxial graphene is similar to the π plasmon dispersion of graphene.

Vibrations at surfaces

Electrons moving near the surface of a solid can excite localized and collective vibrations. The major experimental achievement in the measurement of these vibrations has been the development of near-monochromatic primary-electron beams and, additionally,

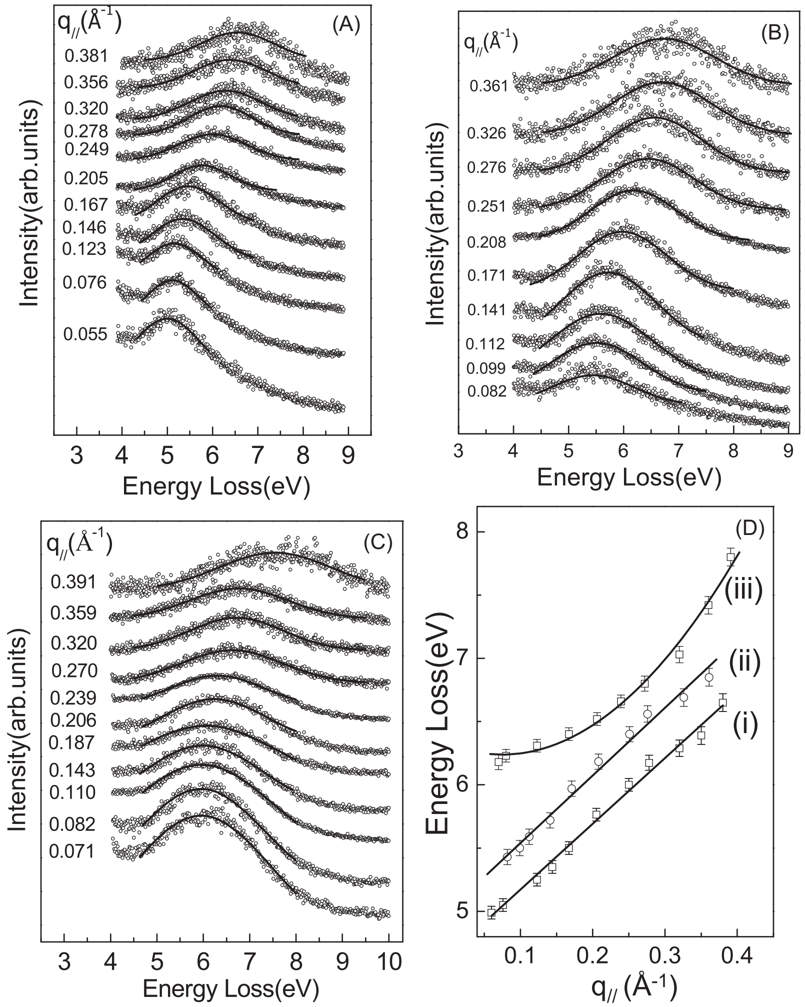

Fig. 3 Measured loss functions associated with the π plasmons of (A) single layer, (B) bilayer, and (C) 3-4 monolayer epitaxial graphene. The data are taken from $q = 0.05$Å to $q = 0.4$Å. The corresponding dispersion curves are shown in (D), for (i) single layer, (ii) bilayer, and (iii) 3-4 layers of epitaxial graphene. Reprinted with permission from Lu J, Ping Loh K, Huang H, Chen, W, and Wee ATS (2009) Plasmon dispersion on epitaxial graphene studied using high-resolution electron energy-loss spectroscopy. *Physical Review B* 80: 113410; ©American Physical Society.

the detection of reflected electrons with a resolution of the order of vibrational energies (a few meV). On Si(111), one of the most intensively studied surfaces, the local arrangement of atoms at and near the surface including the stretching of Si-Si bonds, has been obtained from surface phonon measurements and found to be consistent with the dimer-adatom-stacking fault model.

Adsorbates are foreign atoms that are bound to sites with a particular point-group symmetry of the surface structure. If the dipole image charge of the adsorbate has a component normal to the surface, the adsorbate can be excited into vibrational states while the modes with their dipole moment parallel to the surface are screened by a factor $1/(1+\varepsilon)^2$. These selection rules are similar to those governing infrared transitions. One can determine the local symmetry by observing the number of vibrational modes. The local geometry is modeled by a rigid substrate against which the adsorbates vibrate (Ibach and Mills, 1982).

Fig. 4 shows some fundamental types of bonding arrangements. In (A), an adsorbate atom is placed at a top position, directly above a surface atom. This site would produce a single low-energy mode. In (B), the same atom is placed in a bridge position, equidistant between two substrate atoms. Energy loss would be observed at an even lower value than (A), corresponding to the normal vibrational component. If the chemical bonding were not symmetrical, then one would observe two peaks at similar energy losses. Generally, a lowering of the adsorption symmetry, such as uneven bonding, increases the number of vibrational modes (Ibach and Mills, 1982).

For molecular adsorbates (Fig. 4C and D), a high-energy loss would be due to the stretching mode of the atoms in the molecule while a low-energy loss would be due to the vibration of each atom against the substrate or the entire molecule. Hence, for molecular adsorption, one always expects at least two modes. Observation of a single mode is, therefore, evidence for the dissociative adsorption of a molecule. Apart from the number modes, the vibrational energy contains information about the chemical bond. An adsorption site on top of a substrate atom results in a higher force constant compared to an adsorbate at a bridge or hollow site, where the bond strength is shared by several atoms.

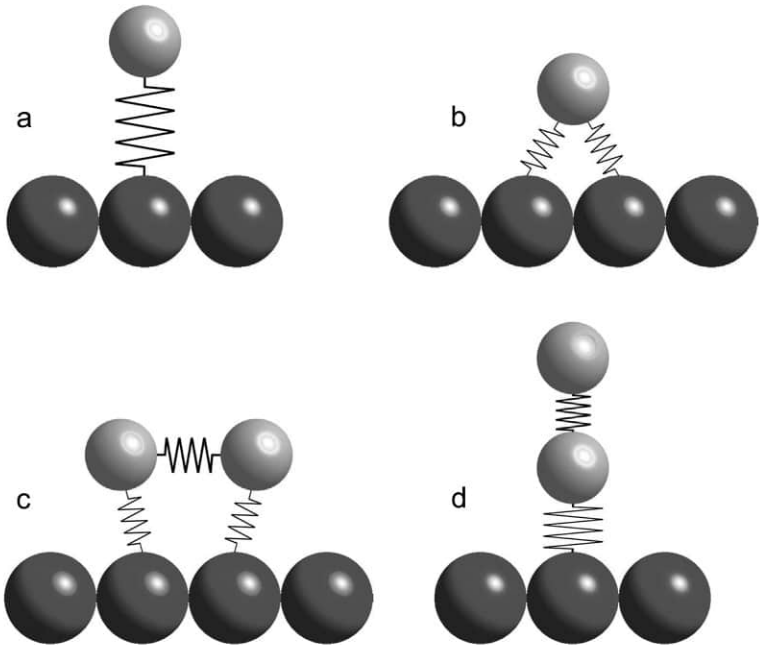

Fig. 4 Schematic description of four typical adsorption states for (A) an atop and (B) a bridge site for single atoms, and (C) a bridge site and (D) and atom site for a diatomic molecule. The springs represent chemical bonds of different strengths.

Excitation of core electrons

A special case of interband transitions is the excitation of core electrons with a binding energy E_B. The primary electron can transfer any amount of energy $E_L \leq E_i$ to the core electron. By measuring the energy loss of the primary electron, one knows the kinetic energy of the core electron after scattering, that is, how far above E_F the core electron has been excited. The excitation into states at E_F corresponds to zero kinetic energy and, hence, $E_L = E_B$. This is called the absorption edge. It is characteristic of a particular element and its chemical state and can thereby be used as a tool for chemical analysis.

Core states have almost no overlap between neighboring atoms, leading to extremely narrow bandwidths. Therefore, the energy-loss spectrum at and above the absorption edge is indicative of the unoccupied DOS at the site of the excited atom with an orbital angular momentum determined by the symmetry of the final state (Tinkham, 1964). If the final states are far above E_F, the modulations in the spectra result from single scattering, which can be used to extract local structural information near the excited atom. This is known as extended energy-loss fine structure (EELFS); the optical analog is extended X-ray absorption fine structure (EXAFS). The information obtained is a radial distribution function with peaks at the distances of nearest neighbors (Prinz and Koningsberger, 1986; Vvedensky, 1992; Rehr and Albers, 2000).

Closer to the absorption edge, the interpretation of the energy-loss near-edge fine structure (ELNES) spectrum requires a multiple scattering treatment, as in the near-edge X-ray-absorption fine structure (NEXAFS) in optics. In this regime, the type of information obtained includes bond angles between the excited atom and its nearest neighbors (Prinz and Koningsberger, 1986; Vvedensky, 1992; Rehr and Albers, 2000).

Nanotubes provide an illustration of such measurements. The chemical and physical properties can be manipulated by incorporating atoms or molecules within the tubes. Fig. 5 shows a high-resolution electron micrograph of an isolated single-wall nanotube containing C_{82} fullerenes and a schematic representation of the structure. The image reveals single Gd atoms encapsulated in the fullerene cages.

Fig. 6 displays spatially resolved ELNES spectra of the C *K*-edge (1*s* initial state) and the Gd *N*-edge (4d-initial state). Thus, it is possible to detect and identify single Gd atoms encaged in a complex C environment. Core-electron binding energies may show a chemical shift because the electronic charge density is redistributed in chemical bonding, thereby shifting the binding energy. The core electron binding energy of Gd shows a downward shift compared to the neutral Gd metal, which suggests a charge transfer from Gd to a C atom.

Detecting the local environment of Si in a graphene lattice has elements of local symmetry, as for lattice vibrations, and on the local bonding environment. Because of multiple scattering, and therefore, multi-atom correlations, ELNES is sensitive to both of these quantities. This goes far beyond the average local radial distribution function, a single-scattering quantity, obtained in EELFS. Si is one of the most common impurities in graphene grown by chemical vapor deposition or thermal decomposition. Thus, a better understanding of this impurity is desirable for the integration of graphene-based devices onto a silicon platform.

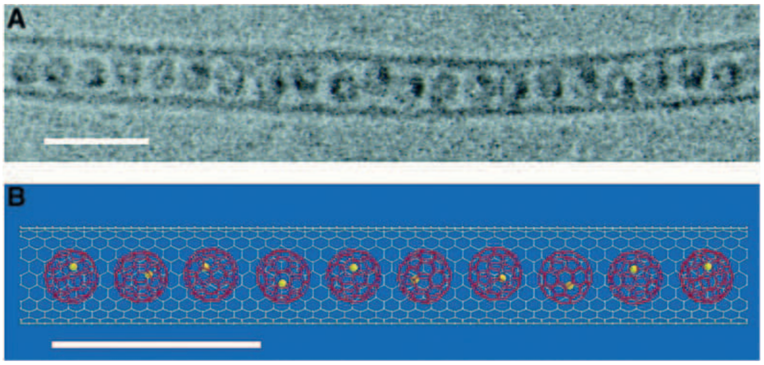

Fig. 5 (A) Electron micrograph of an isolated nanotube incorporated with a chain of Gd-metallofullerenes, and (B) a schematic representation of the structure. *Horizontal bars* represent a length of 3 nm. Reprinted with permission from Suenaga K, Tencé M, Mory C, Colliex C, Kato H, et al. (2000) Element-selective single atom imaging. *Science* 290: 2280–2282; ©AAAS.

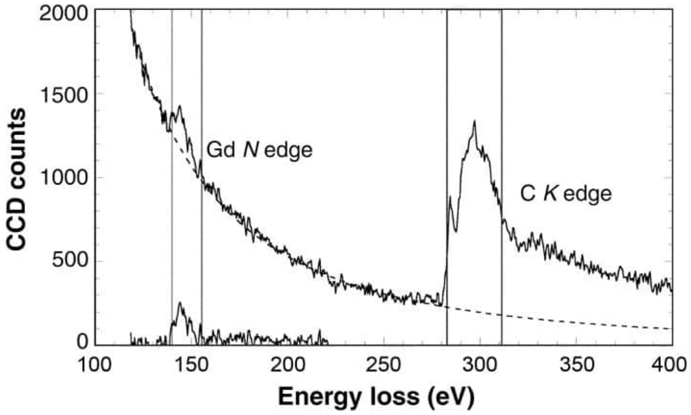

Fig. 6 Electron energy-loss spectra near the Gd *N*-edge and C *K*-edge obtained from an isolated nanotube incorporated with a chain of Gd-metallofullerenes. Reprinted with permission from Suenaga K, Tencé M, Mory C, Colliex C, Kato H, et al. (2000) Element-selective single atom imaging. *Science* 290: 2280–2282; ©AAAS.

Fig. 7 shows the local environment of a threefold- and a fourfold-bonded Si in a graphene lattice, the corresponding ELNES measurements, and relaxed density-functional calculations. The *L*-edge ($2p$ initial state) reflects the excitation to unoccupied $3d$ states. The observed differences in the ELNES of the two coordinations are a direct indication of the occupancy of the $3d$ states due to the different coordinations. In particular, the peak at 105 eV and the shoulder at ~101 eV for the threefold coordinated site were reproduced by the calculations. Moreover, the absence of the peak at 105 eV but the presence of weaker peaks at ~102 eV and 107 eV were also confirmed by the calculations.

The relaxed structures of the threefold and fourfold coordinated Si impurities in graphene are shown in Fig. 7A. The calculations used a 200-atom graphene supercell using the Vienna *Ab-Initio* Software Package (VASP) (Hafner, 2008). For the threefold coordinated site, the silicon atom is displaced outward from the graphene surface. The fourfold Si impurity site, however, stays largely in the plane of the graphene. The threefold calculations are consistent with previous calculations while the fourfold calculations agree with conclusions drawn from experimental data.

(e$^-$, 2e$^-$) Scattering

A general, yet simple, case of electron–atom or electron–solid interactions is considered in this section. Denoting the energy and momentum of the primary electron by superscript 1 and those of the target by superscript 2, the initial values (subscript i) are

$$\begin{array}{lll} \text{primary electron:} & E_i^{(1)}, & \boldsymbol{k}_i^{(1)} \\ \text{target:} & E_i^{(2)}, & \boldsymbol{k}_i^{(2)}. \end{array} \tag{13}$$

The corresponding final states (subscript f) are

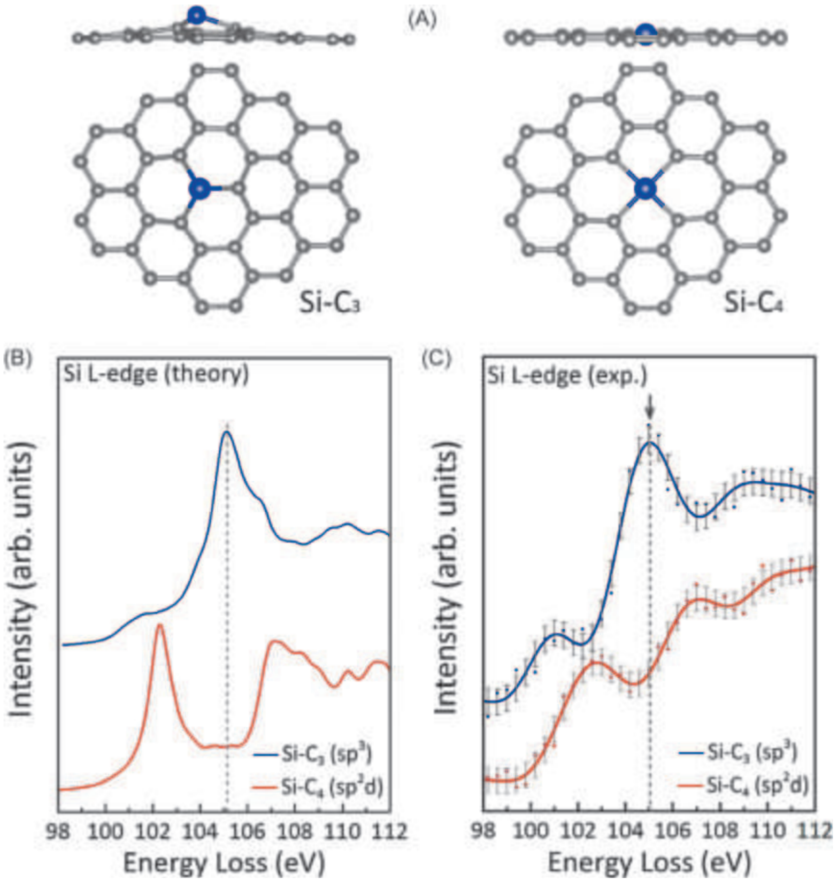

Fig. 7 (A) Three-dimensional relaxed structures for the three-fold and four-fold Si defect structures in graphene. The Si atom is indicated in *blue* and the C atoms in graphene *gray*. (B) Calculated Si *L*-edge spectra for the three-fold (top) and four-fold (bottom) coordinated Si defect structures in graphene. (C) Measured ELNES for the three-fold (top) and four-fold (bottom) coordinated Si defect structures. Adapted from Zhou W, Kapetanakis MD, Prange MP, Pantelides ST, Pennycook SJ and Idrobo J-C (2012) Direct determination of chemical bonding of individual impurities in graphene. *Physical Review Letters* 109: 206803; ©American Physical Society.

$$\begin{array}{lll}\text{primary electron:} & E_f^{(1)}, & \boldsymbol{k}_f^{(1)} \\ \text{target:} & E_f^{(2)}, & \boldsymbol{k}_f^{(2)}.\end{array} \tag{14}$$

In the limit of large energy and momentum transfer, $E_f^{(1)}$ and $E_f^{(2)}$ are well above the band structure regime, so the unoccupied DOS is parabolic and does not impose additional structure upon the measurement. This interaction regime is the basis of (e^-, $2e^-$) spectroscopy for solids (McCarthy and Weigold, 1991; Artamonov et al., 1997). For atomic or molecular targets (e^-, $2e^-$), spectroscopy provides information about the wave function density in momentum space by measuring the momentum distribution of the bound electron as a function of the momentum transfer. For crystalline targets, both the momentum density and the energy dispersion of valence electrons can be determined. Since the momentum of any ejected electron can be measured, the results are not confined to the first Brillouin zone.

In a binary collision between a high-energy electron and a band electron, the conservation of energy and of momentum requires that

$$\begin{aligned} E_i^{(1)} &= E_f^{(1)} + E_f^{(2)} + E_i^{(2)}, \\ \boldsymbol{k}_i^{(1)} &= \boldsymbol{k}_f^{(1)} + \boldsymbol{k}_f^{(2)} + \boldsymbol{k}_i^{(2)}. \end{aligned} \tag{15}$$

There is, however, a continuous spectrum of single- and multiple-scattering events leads to $E_f^{(1)} + E_f^{(2)}$. To single out the event for which both conservation equations hold, the particles must be recorded in coincidence.

Fig. 8A shows the geometry of primary electrons impinging on a solid sample. A binary collision event is depicted in which a target electron acquires energy and is ejected from the back of the sample together with the primary electron. For simplicity, the scattering event is shown with coplanar initial and final wave vectors. In general, the 2π azimuthal distribution relative to the primary-electron incidence is measured to access the details of the initial state (Fig. 8B). Energy conservation requires the binary

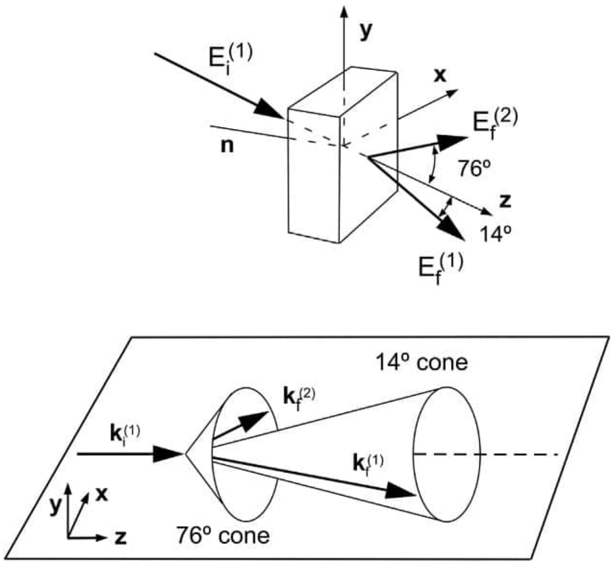

Fig. 8 Schematic illustration of energy conservation in an (e^-, $2e^-$) experiment. (A) Geometry of primary electrons impinging on a sample, and (B) the 2π azimuthal distribution relative to the primary-electron incidence. Adapted with permission from Cai YQ, Vos, M, Stoner, P, Kheifets AS, MacCarthy IE, et al. (1995) Direct imaging of the valence electronic structure of solids by (*e*, 2*e*) spectroscopy. *Solid State Communications* 95: 25–29.

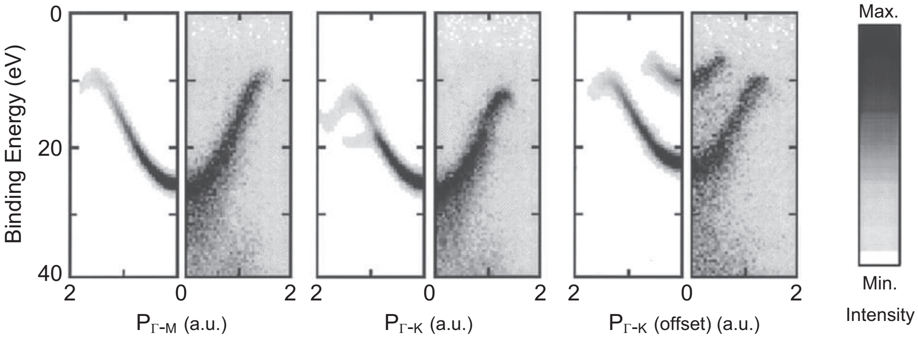

Fig. 9 Measured intensity (right half of each panel) as a function of binding energy and momentum of graphite along Γ-*M* (left), Γ–*K* (center), and offset Γ–*K* (right). Shown with these measurements are the results of density functional calculations (left half of each panel). Adapted with permission from Vos C, Fang Z, Canney S, Kheifets A, McCarthy IE, and Weigold E (1997) Energy-momentum density of graphite by (*e*, 2*e*) spectroscopy. *Physical Review B* 56: 963–966; ©American Physical Society.

collision event to take place as close to the surface as possible, so inelastic interactions after the principal collision are not considered. Consequently, the spectroscopic results are characteristic of the near surface region of the target material.

Fig. 9 shows an energy-band dispersion in graphite along the indicated directions in the Brillouin zone. Graphite has four populated bands, three of σ-type and one of π-type. No intensity is expected in the Γ–M and Γ–K directions from the π-band because the band is derived from C 2*p* orbitals will have a node at $q_z = 0$. Along the Γ–M direction, the lowest σ band, σ_1 disperses upward and crosses the first Brillouin zone boundary at $q = 0.8$ a.u. In the second Brillouin zone, the second σ band, σ_2, is populated and the small splitting between σ_1 and σ_2 is not resolved. The σ_2 band continues to a maximum at $q = 1.6$ a.u., where the occupation of this band decreases and no intensity is observed above this maximum.

Along the Γ–K direction, the σ_1 band reaches the Brillouin zone boundary at a somewhat larger momentum ($q = 0.9$ a.u.), where the population changes from the σ_1 band to the third σ_3 band. Continuing to the third Brillouin zone, the σ_3 band reaches a maximum at M for momentum $q \approx 1.3$ a.u. The momentum density decreases beyond this point and the band turns over in the experimental density plot. Finally, with a nonzero offset $q_z = 0.41$ a.u., we expect the π band to be occupied. Two parabolas are observed, one for the π band and one for the σ band. The offset excludes zero momentum, so the measured bottom of the σ band has moved up in energy accordingly.

All of the foregoing features are reproduced by density functional calculations, using a linear muffin-tin orbital (LMTO) model, convoluted with a 2 eV energy broadening and 1 eV momentum broadening, which are shown in Fig. 8.

Conclusion

Electron energy-loss spectroscopy is based on the measurement of electrons that have lost energy to a target specimen due to inelastic collisions. Several examples of such measurements have been provided: interband transitions, plasmon excitations, vibrations at surfaces, core-level spectroscopy, and (e^-, $2e^-$) scattering. When combined with transmission electron microscopy (TEM), electron energy-loss spectroscopy is capable of a spatial resolution down to the atomic level (Spence, 2006; Egerton, 2009, 2011; Krivanek et al., 2014). This is seen in Figs. 5–7. Another advance is the combined use of scanning tunnelling microscopy and TEM (Suenaga and Koshino, 2010) to differentiate between different bonding environments near, for example, a graphene edge.

Theoretical and computational studies supplement electron energy-loss experiments. These take the form of selection rules for atomic, molecular, and solid-state systems (Tinkham, 1964), a multiple scattering analysis of the dominant paths (Vvedensky and Pendry, 1985), or a full density functional calculation (Hafner, 2008). Fig. 7 provides an example of the latter type of calculation. By comparing fully relaxed structures with ELNES measurements, the symmetry of the site should be determined along with any relaxation out of the graphene plane. Thus, density functional calculations expand the spatial range of ELNES measurements to below atomic length scales.

References

Artamonov OM, Samarin SN, and Kirschner J (1997) (*e*, 2*e*) Electron spectroscopy of surfaces. *Applied Physics A* 65: 535–542.

Egerton RF (2009) Electron energy-loss spectroscopy in the tem. *Reports on Progress in Physics* 72: 016502.

Egerton RF (2011) *Electron Energy-Loss Spectroscopy in the Electron Microscope*. New York: Springer.

Froitzheim H (1977) Electron energy loss spectroscopy. In: Ibach H (ed.) *Electron Spectroscopy for Surface Analysis. Topics in Current Physics*, vol. 4, pp. 205–250. Berlin: Springer.

Hafner J (2008) Ab-initio simulations of materials using VASP: Density-functional theory and beyond. *Journal of Computational Chemistry* 29: 2044–2078.

Ibach H and Mills DL (1982) *Electron Energy Loss Spectroscopy and Surface Vibrations*. New York: Academic Press.

Jackson JD (1975) *Classical Electrodynamics*, second ed. New York: Wiley.

Krivanek OL, Lovejoy TC, Dellby N, Aoki T, Carpenter RW, Rez P, Soignard E, Zhu J, Batson PE, Lagos MJ, Egerton RF, and Crozier PA (2014) Vibrational spectroscopy in the electron microscope. *Nature* 514: 209–212.

McCarthy IE and Weigold E (1991) Electron momentum spectroscopy of atoms and molecules. *Reports of Progress in Physics* 54: 789–879.

Merzbacher E (1961) *Quantum Mechanics*, third ed. New York: Wiley.

Prinz R and Koningsberger K (1986) *X-Ray Absorption: Principles, Applications and Techniques of EXAFS, SEXAFS, and XANES*. New York: Wiley.

Raether H (1965) Solid state excitations by electrons. In: Höhler G (ed.) *Springer Tracts in Modern Physics*, vol. 38, pp. 85–157. Berlin: Springer.

Rehr JJ and Albers RC (2000) Theoretical approaches to x-ray absorption fine structure. *Reviews of Modern Physics* 72: 621–654.

Schattschneider P and Jouffey B (1995) Plasmons and related excitations. In: Reimer L (ed.) *Energy-Filtering Transmission Electron Microscopy. Springer Series in Optical Sciences*, vol. 71, pp. 151–224. Springer-Berlin.

Schnatterly SE (1979) Inelastic electron scattering spectroscopy. In: Ehrenreich H, Seitz F, and Turnbull D (eds.) *Solid State Physics*, vol. 34. New York: Academic Press.

Spence JCH (2006) Absorption spectroscopy with sub-angstrom beams: ELS in STEM. *Reports on Progress in Physics* 69: 725–758.

Suenaga K and Koshino M (2010) Atom-by-atom spectroscopy at graphene edge. *Nature* 468: 1088–1090.

Tinkham M (1964) *Group Theory and Quantum Mechanics*. New York: MacGraw-Hill.

Vvedensky DD (1992) Theory of x-ray absorption fine structure. In: Fuggle JC and Inglesfield JE (eds.) *Unoccupied Electronic States. Topics in Applied Physics*, vol. 69, pp. 139–201. Berlin: Springer.

Vvedensky DD and Pendry JB (1985) Comment on “experimental study of multiple scattering in x-ray-absorption near-edge structure”. *Physical Review Letters* 54: 2725.

Raman spectroscopy: Nanostructures

Xin Zhang and Ping-Heng Tan, State Key Laboratory of Superlattices and Microstructures, Institute of Semiconductors, Chinese Academy of Sciences, Beijing, China

© 2024 Elsevier Ltd. All rights reserved.

Introduction 160
Overview 161
Raman spectroscopy basics 161
Phonons in nanostructures 163
Confined vibration modes 163
Interface vibration modes 167
Surface vibration modes 167
Folded vibration modes 168
Resonance Raman scattering in nanostructures 170
Conclusion 171
Acknowledgment 171
References 171

Abstract

Raman spectroscopy provides information on the structure, electronic and vibrational properties of crystals by the inelastic photon scattering effect. It has been a fast and nondestructive characterization tool with high spatial and spectral resolutions, which is preferential to nanostructures. The classical and quantum theory of Raman scattering effect is introduced, with the emphasis on the basic features of a Raman spectrum. Phonons in nanostructures are first exampled by the case of a semiconductor superlattice and then extended into other systems based on their Raman spectra. The applications of resonance Raman scattering are demonstrated by studying the phonon dispersion, electronic structure and enhancement of interlayer shear phonon in carbon materials.

Key points

- Classical and quantum ways to understand Raman scattering effect
- Key parameters of a Raman spectrum
- Size impacts on Raman scattering in nanostructures
- Various types of phonons subject to nanostructures
- Resonant Raman scattering effects

Introduction

Light interacts with matter in many different ways (Fox, 2010). The photons which make up the light may be absorbed or scattered or directly pass through without any interactions with the medium. Scattering specifies the phenomenon in which the light changes direction and is said to be inelastic (elastic) if the frequency of the scattered light is changed (unchanged). The phenomenon of inelastic light scattering was first postulated by Smekal (1923) and first observed experimentally in 1928 by Raman and Krishnan in molecules (Raman and Krishnan, 1928) referred to as Raman scattering since then. Over nearly one century, Raman scattering effect has been widely used to provide information on chemical structures and physical properties of materials (Jorio et al., 2011; Tan, 2019; Toporski et al., 2018), through its spectroscopy measurements (so-called Raman spectroscopy). To obtain a Raman spectrum requires a specialized apparatus with the capability to resolve a relatively weak Raman signal that is much close in energy to the elastically scattered light. Thanks to the developments of advanced apparatus (Demtroder, 2003) like lasers, charge-coupled detectors, optical filters, etc., modern Raman spectroscopy (Smith and Dent, 2019) becomes an essential tool to study the electronic (Schuller, 2006) and vibrational (Stroscio and Dutta, 2001) properties of nanostructures.

Nanostructure features a typical size in the range 1～100 nm in either one (called two-dimensional system, 2D system), two (one-dimensional system, 1D system), three dimensions (zero-dimensional system, 0D system), as exampled by a quantum well, quantum wire and quantum dot (Davies, 1997), respectively. Notably, nanoplate (quasi-2D system), nanowire (quasi-1D system) and nanocrystal (quasi-0D system) are regularly used as the typical size is larger than (but close to) the characteristic length understudied. The reduced size of nanostructure distinguishes its Raman scattering effect from the bulk case (Zhang, 2012), from the aspects of the energy dispersion, momentum conservation and symmetry of vibration modes. As the quantized electrons are

https://doi.org/10.1016/B978-0-323-90800-9.00013-5

confined in a square/parabolic quantum well, there are similar quantized phonons that are confined within a phonon quantum well, as illustrated in Fig. 2(b). In addition, as the surface-to-volume is significantly increased in nanostructures, various types of surface/interface-associated phonons appear. The constraints by momentum conservation in Raman scattering process are degraded as the momentum uncertainty ($\Delta q \leq \hbar/\Delta r$) inevitably increases due to the reduced size in nanostructures. It will include those phonons with momentum lying within Δq to participate in the Raman scattering events. The symmetry of vibration mode, which determines if the mode is Raman active or not, is reduced as the dimensionality of nanostructures decreases. It may allow the observation of those forbidden modes in bulk cases. On the other hand, the quantized electrons feature a large density of states, which is readily exploited to enhance those weak Raman signals in both nanostructures and bulk structures. It is enabled by the resonance electronic transition (Cardona, 1975; Jorio et al., 2011), so-called resonance Raman scattering (RRS), which greatly enhances the electronic transition and electron-phonon scattering rates.

Overview

The section "Raman Spectroscopy basics" provides the fundamental theory for Raman scattering effect in both classical and quantum ways from which the general features of a specific Raman spectrum are summarized. The various types of vibration modes are introduced in the section "Phonons in nanostructures" which covers the confined, interface, surface and folded vibration modes, first introduced by an exampled superlattice (SL) and then expanded into other typical nanostructures. The third section is given to "Resonance Raman scattering in nanostructures" which specifies the contributions of resonance electronic transition to the Raman intensity enhancements and the applications to study the phonon dispersion, electronic structure and enhancement of interlayer shear phonon in carbon-related materials.

Raman spectroscopy basics

Raman scattering effect can be understood simply by the classical electromagnetic theory (Cardona, 1975; Jorio et al., 2011). An incident electric field E when applied to a solid will induce a polarization P resulting $P = \varepsilon_0 \chi E$, with ε_0 and χ the permittivity and the electronic susceptibility of the medium, respectively. χ is to measure the ability of the incident electric field to shake the electrons of atoms in the solid, as illustrated in Fig. 1(a), which is naturally modulated by the lattice vibration with a frequency ω_q in the solid,

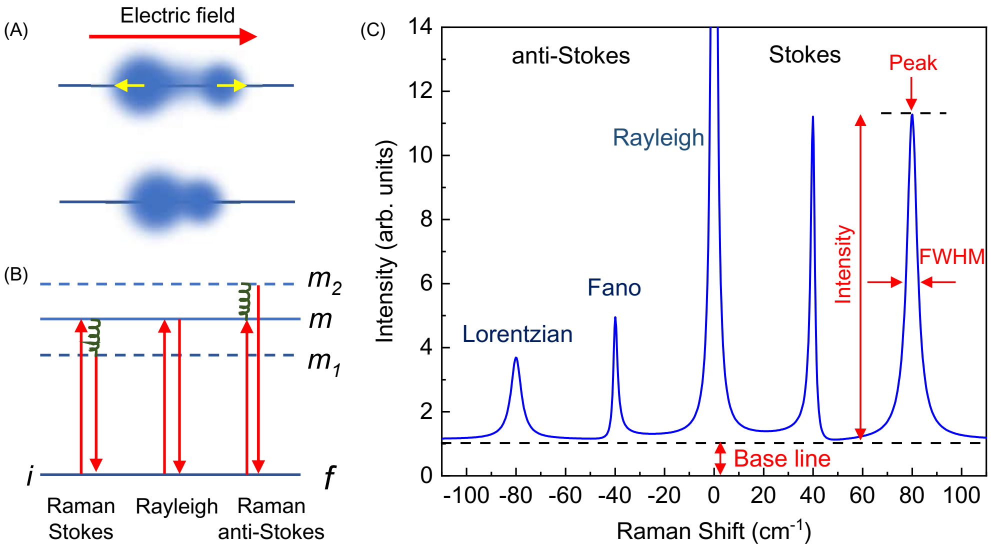

Fig. 1 (a) Schematics show how the lattice vibration changes the electronic susceptibility χ of the diatomic linear chain. When the two atoms get closer and far away along the chain direction, it will be respectively harder and easier for the electric field to shape the electron clouds. (b) Schematics show the third-order process to describe the Raman scattering process in crystals. The horizontal line is the electronic energy level and the solid (dashed) line is the real (virtual) state. The large upwards $i \rightarrow m$ and downwards m (including m_1 and m_2) $\rightarrow f$ arrows represent photon absorption and emission by electrons, while the small downwards ($m \rightarrow m_1$) and upwards ($m \rightarrow m_2$) arrows represent respectively the electron losing (obtaining) energy to (from) the lattice by an electron-phonon scattering event, accordingly known as Raman Stokes (anti-Stokes) process. Rayleigh scattering refers to the case without any energy changes of the electron in m state. (c) One artificial Raman spectrum to show the spectral features and the typical parameters. Rayleigh (at 0 cm^{-1}) intensity is always much stronger and it has to be filtered out for any Raman measurements. The Stokes processes ($>$0 cm^{-1}) are normally stronger than the anti-Stokes processes ($<$0 cm^{-1}) due to phonon creation/annihilation statistics. Raman peaks have a Lorentz lineshape featured by Peak, Intensity and the full width at half maximum (FWHM). In specific cases, the Raman features exhibit a Breit-Wigner-Fano (BWF) lineshape. Notably, the real Raman spectrum contains a baseline determined by the noise performance of the measurement system.

to the first-order, $\chi = \chi_0 + \left(\frac{\partial\chi}{\partial Q}\right)_0 Q(\omega_q)$, with $Q(\omega_q) = Q \sin \omega_q t$ the atomic displacements. In light scattering experiments, E is oscillating at an optical frequency ω_i, $E = E_0 \sin \omega_i t$. The polarization induced by electric field now becomes

$$P = \varepsilon_0 \chi_0 E_0 \sin \omega_i t + \frac{A}{2}\left[\cos\left(\omega_i - \omega_q\right)t - \cos\left(\omega_i + \omega_q\right)t\right] \tag{1}$$

with $A = \varepsilon_0 \left(\frac{\partial\chi}{\partial Q}\right)_0 Q E_0$. Eq. (1) points out that light will be scattered both elastically at a frequency ω_i (Rayleigh scattering) and inelastically, being downshifted (emission of a phonon) by the vibration frequency ω_q in the solid (Raman Stokes process) or upshifted (absorption of a phonon) by the same frequency ω_q (Raman anti-Stokes process). The differential Raman scattering cross section is obtained by (Cardona, 1975)

$$\frac{d\sigma}{d\Omega} = \frac{\omega_s^4}{(4\pi)^2 c^4}\left|\widehat{e}_L \cdot \left(\frac{\partial\chi}{\partial Q}\right)_0 Q(\omega_q) \cdot \widehat{e}_S\right|^2 \tag{2}$$

where the optical frequency of scattered light $\omega_s = \omega_i \pm \omega_q$ as indicated in Eq. (1), c the speed of light in the medium, $\widehat{e}_L$ $(\widehat{e}_S)$ the unit vector representing the polarization of the incident (scattered) light. The Raman tensor can be further defined from Eq. (2), as $R = \left(\frac{\partial\chi}{\partial Q}\right)_0 \widehat{Q}(\omega_q)$, with $\widehat{Q} = Q/|Q|$ the unit vector, which is a third-order tensor. The full list of Raman tensors to seven types of crystal systems can be found in textbooks (Jorio et al., 2011; Zhang, 2012). Raman tensor is key to probe the symmetry of lattice vibration, implemented in polarized Raman spectroscopy measurements.

A quantum mechanical description of Raman scattering effect is based on the so-called Fermi's Golden Rule, which is used to calculate the transition probability per unit time when considering the optical properties of solids (Fox, 2010; Jorio et al., 2011). W_{if} describes a transition from an initial state $|i\rangle$ to a final one $|f\rangle$, which results

$$W_{if} \cong \frac{2\pi}{\hbar}|\langle f|H'|i\rangle|^2 \rho(E_f)\delta(E_f - E_i) \tag{3}$$

with H' the Hamiltonian to account for the interaction between the electromagnetic radiation and the crystal, $\rho(E_f)$ density of final states assuming the discrete initial state. In the first-order Raman scattering process, as shown in Fig. 1(b), H' includes three types of interactions, which can be interpreted as three steps: (1) the incident light excites the electron from an initial state $|i\rangle$ with energy E_i, to a higher energy state $|m\rangle$ with energy E_m from a laser (E_L). The solid line of state $|m\rangle$ represents a real electronic state, allowing a resonant light absorption process. (2) The electron is further scattered by a phonon to a "virtual" state (dashed line) $|m_1\rangle$ (Stokes) or $|m_2\rangle$ (anti-Stokes). Noted virtual states are usually displayed by dashed lines and, within perturbation theory, they are described by a linear combination of the electron eigenstates of the system with a large energy uncertainty and a small lifetime to compensate for the uncertainty principle. (3) The scattered electron finally decays back to the state $|i\rangle$ by emitting the scattered light. Noted the whole system is now labeled as the state $|f\rangle$ since additional phonon is emitted or absorbed with respect to the initial state $|i\rangle$. The differential Raman scattering cross section is accordingly obtained by third-order perturbation theory (Jorio et al., 2011) which gives

$$\frac{d\sigma}{d\Omega} \propto |\langle f|H'|i\rangle|^2 = \left|\sum_{m,m'} \frac{M^{op}(k_i - q, im')M^{ep}(q, m'm)M^{op}(k_i, mi)}{(E_L - \Delta E_{mi})(E_L - \hbar\omega_q - \Delta E_{m'i})}\right|^2 \tag{4}$$

in which $\Delta E_{m'i} = (E_{m'} - E_i) - i\gamma$, where m and m' denote the two excited intermediate states, γ denotes the broadening factor of the resonance event, M^{op} and M^{ep} respectively denote the electric dipole matrix elements of the electron-photon and the electron-phonon interactions. A high-order Raman process, having the various transition diagrams (Yu and Cardona, 2010), can be described by high-order perturbation theory. The denominator in Eq. (4) determines the resonance condition in RRS, which is classified as an incident resonance when $E_L = E_m - E_i$, or a scattered resonance when $E_L - \hbar\omega_q = E_{m'} - E_i$. The resonance effect is essential to the observations of measurable Raman signals from nano-scale systems. A plot of Eq. (4) as a function of E_L gives the Raman excitation profile which is essential to provide the information about the electronic structure of nanostructures (Cardona, 1975).

A Raman spectrum is a plot of the intensity of the scattered light as a function of Raman shift, $\omega = \omega_i - \omega_s$, which is $\pm\omega_q$ according to Eq. (1). Thus, the spectrum exhibits a pair of peaks on the sides of the Rayleigh line, as shown in Fig. 1(c), but either one (usually the Stokes one) or both are recorded depending on the Raman filters available in the practice Raman spectrum measurements. The phonon excitation can be considered as a harmonic oscillator damped by the interaction with other excitations in the medium. Therefore, the Raman spectrum usually features a forced damped harmonic oscillator with a Lorentzian curve given by

$$I(\omega) = \frac{I_0}{\pi\Gamma_q}\frac{1}{\left(\omega - \omega_q\right)^2 + \Gamma_q^2} \tag{5}$$

in the limit where the frequency $\omega_q \gg \Gamma_q$, with Γ_q the inverse of the lifetime for a phonon, usually expressed by the full width at half maximum intensity (FWHM), FWHM $= 2\Gamma_q$. In specific cases, such as lattice vibration couples to an electronic continuum, the Raman lineshape can deviate from the simple Lorentzian curve and exhibit a so-called Breit-Wigner-Fano (BWF) lineshape, which is given by

$$I(\omega) = I_0 \frac{\left[1 + (\omega - \omega_0)/q\Gamma\right]^2}{1 + \left[(\omega - \omega_0)/\Gamma\right]^2} \tag{6}$$

where $1/q$ is a measure of the interaction of a discrete level (phonon) with a continuum of states (the electrons). ω_0 is the BWF peak frequency at maximum intensity I_0, and Γ is the half width of the BWF peak. A pair of BWF peaks with $1/q > 0$ is plotted in Fig. 1(c). Such effect is observed in the ultralow-frequency Raman spectra of a multilayer graphene (Tan et al., 2012), as shown in Fig. 6(d). From Eq. (2), the differential Raman scattering cross section for Stokes and anti-Stokes are obtained by (Cardona, 1975)

$$\begin{aligned}\frac{d\sigma_S}{d\Omega} &\propto \langle Q(\omega_q)Q^*(\omega_q)\rangle \propto (n+1)\\ \frac{d\sigma_{aS}}{d\Omega} &\propto \langle Q^*(\omega_q)Q(\omega_q)\rangle \propto n\end{aligned} \tag{7}$$

where $n = (\exp(\hbar\omega_q/k_BT) - 1)^{-1}$ is Bose-Einstein distribution function for the phonon with energy $\hbar\omega_q$. So the intensity of Raman Stokes process is much stronger than the anti-Stokes case by noticing

$$\frac{\sigma_S}{\sigma_{aS}} \propto \exp\left(\frac{\hbar\omega_q}{k_BT}\right) \gg 1 \tag{8}$$

Finally, energy and momentum conservations can respectively be found from Eq. (3), expressed by $\delta(E_f - E_i)$, and Eq. (4), by $k_s = k_i - q$, i.e., $q \sim 0$ because k_i is much small compared to the dimensions of Brillouin zone (BZ). It is why the first-order Raman process can only probe phonons near the BZ center (Γ point). The Raman frequency of this type of vibration is not dependent on E_L, which was normally taken as the general rule for Raman spectroscopy.

In practice, an efficient collecting system is always required to pick up the relatively weak Raman signals from the strong Rayleigh line. We recommend the book "Modern Raman Spectroscopy: A Practical Approach," written by Ewen Smith and Geoffrey Dent (Smith and Dent, 2019), which can serve as an excellent introduction to the Raman measurement system and the most advanced developments. As complementary, our original work to probe the ultra-low frequency Raman spectra of multilayer graphenes can be referred to as a standard tutorial to introduce the latest advancements to detect those Raman peaks extremely closed to Rayleigh line (Tan et al., 2012).

Phonons in nanostructures

Different types of phonons in nanostructures can be exampled by an SL, as illustrated in Fig. 2(a), which are categorized as the confined optical modes in barrier and well, the macroscopic and microscopic interface modes, and the folded acoustic mode (Tan et al., 2004; Zhang, 2012). The new 1D out-of-plane periods of SL along the growth direction shrink the BZ by folding both the optical and acoustic phonons into a smaller BZ with respect to the bulk case, as shown by Fig. 5(a). Because of the distinctive optical and acoustic vibrations, the folded optical phonons are mostly confined in the alternating layers (confined optical modes), in contrast, the folded acoustic phonons are extended into all of the constitutes of an SL (Fig. 5(a)). As a typical complementary to semiconductor SLs developed in the 1980s, a twisted bilayer system from a 2D material (2DM) holds in-plane artificial periods which create an interesting folding effect on its phonon dispersion (Fig. 5(e)). The confined acoustic and optical modes appear in the case of a strongly confined nanostructure, like nanowire, nanorod and nanocrystal which are normally known as surface vibration modes (Fig. 4). Interface vibration mode is unique in an SL with the macroscopic one from the excited states of the confined optical modes and the microscopic one localized at the interface (which is also known as surface vibration mode). The macroscopic interface modes find their general dispersive behaviors on the layer thickness in multilayer 2DMs (Fig. 3(b)) and distinctive decouples between in-plane and out-of-plane phonons in a 2D van der Waals heterostructures (vdWHs) (Fig. 3(c)). In addition, interface modes apply to the sample-substrate structure (Fig. 3(d)) and the hybrid nanostructures, as exampled by dot-in-rods in Fig. 4(d).

Confined vibration modes

Analogs to the quantization of electrons in a potential well, the frequency of lattice vibration in a "phonon potential well" is well quantized and strongly depends on the length of the potential well. Fig. 2(b) shows the calculated z component of displacements (U_z) for the highest GaAs-like LO modes, LO_1, LO_2, LO_3, in a $(GaAs)_{20}/(AlAs)_{20}$ SL, which are strictly confined in the GaAs layer (Rücker et al., 1992). The profile formed by the displacements of either Ga or As atoms is the same as the quantized electronic wavefunction in a square potential well with the nodes increasing in a sequence of 0,1,2,3, … (Fig. 2(b)). The confined optical modes within the well layers of quantum well structures were firstly observed in $GaAs/Ga_{1-x}Al_xAs$ SLs (Jusserand et al., 1984). The frequencies of Raman peaks associated with confined phonons show blueshift as decreasing the thickness of GaAs layer, indicated by the pitch arcs labeled by 1, 2, 3, 4 which corresponds to the different confined orders, as shown in Fig. 2(b). The spatial confinement effects on the vibrations in nanostructures are further studied in GaAs/AlAs quantum wire (Comas et al., 1993), silicon nanowire (Piscanec et al., 2003), carbon nanotube (Dresselhaus et al., 2005; Jorio and Saito, 2021), Ge nanocrystal (Bottani et al., 1996), etc. Special attention is paid to the case of nanostructures with intrinsic polarization, such as SiC nanorods (Feng et al., 1988), where the long-range Coulomb interaction results in a Raman spectrum featuring a non-crystallize structure.

Carbon nanotube with a hollow core is different from the semiconductor nanowire but clearly shows the confinement effects. The carbon-related materials involve an optical phonon between the two dissimilar carbon atoms in the unit cell, featuring one single

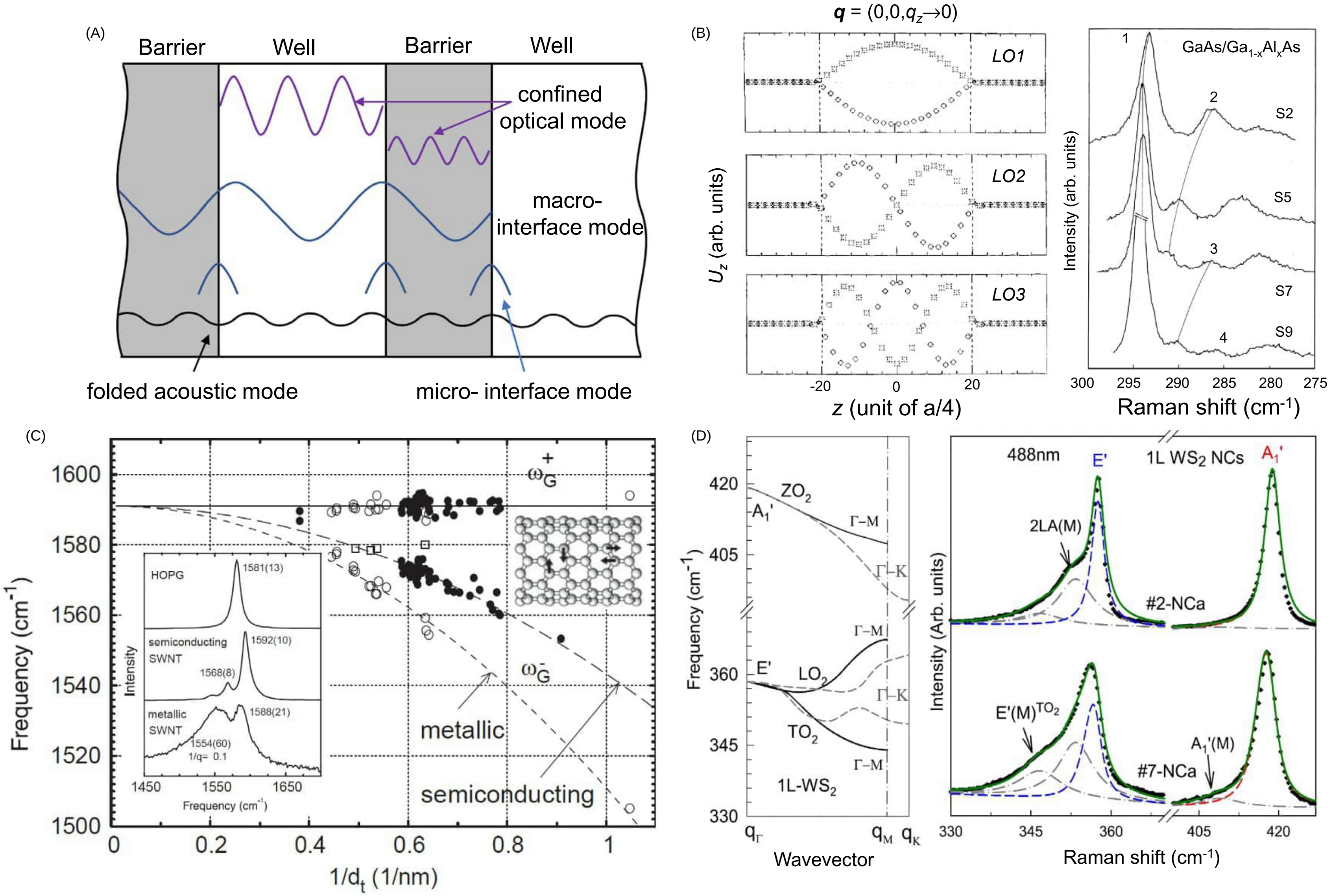

Fig. 2 (a) Five types of vibration modes in a semiconductor superlattice (SL), including the confined optical modes in both barrier and well, the macroscopic (macro-) and microscopic (micro-) interface modes, and the folded acoustic mode. (b) Left: atomic displacements (U_z) of the topmost GaAs-like modes of a (001)-oriented $(GaAs)_{20}/(AlAs)_{20}$ SL for $q = (0, 0, q_z \to 0)$. The GaAs layer is centered at $z = 0$; the dashed vertical lines mark the As interface planes. Diamonds, stars, and asterisks indicate the positions of Ga, Al, and As planes, respectively. Right: Raman spectra of GaAs/$Ga_{1-x}Al_xAs$ SLs in the GaAs optical frequency range. The pitch arcs labeled by 1, 2, 3, 4 correspond to the different confined orders. (c) Frequency as a function of $1/d_t$ for the two most intense G-band features (${}_{G}^{-}$ and ${}_{G}^{+}$) from isolated SWNTs. Insets: Left: the G-band for highly oriented pyrolytic graphite (HOPG), one semiconducting SWNT and one metallic SWNT. Right: atomic vibrations of G-band in SWNT. (d) Left: The phonon branches of 1L-WS_2 related with the E′ and A_1′ modes. Right: The experimental (crosses) and fitted (green solid lines) results of two 1L-WS_2 nanocrystals (NCs) with different domain sizes. The blue and red dashed lines are the calculated curves of the E′ and A_1′ modes, respectively, and the gray dashed-dotted lines are fittings with Lorentzian peaks to the zone-boundary peaks. The spectra are normalized to A_1′ mode. Panel (a): Reproduced from Zhang S.-L. (2012) *Raman Spectroscopy and its Application in Nanostructures*. John Wiley & Sons Ltd. Left Panel (b): Reproduced from Rücker et al. (1992) *Physical Review B* 45: 6747–6756. Right Panel (b): Reproduced from Jusserand et al. (1984) *Physical Review B* 30: 6245–6247. Panel (c): Reproduced from Dresselhaus et al. (2005) *Physics Reports* 409(2): 47–99. Panel (d): Reproduced from Shi et al. (2016) *2D Materials* 3(2): 025016.

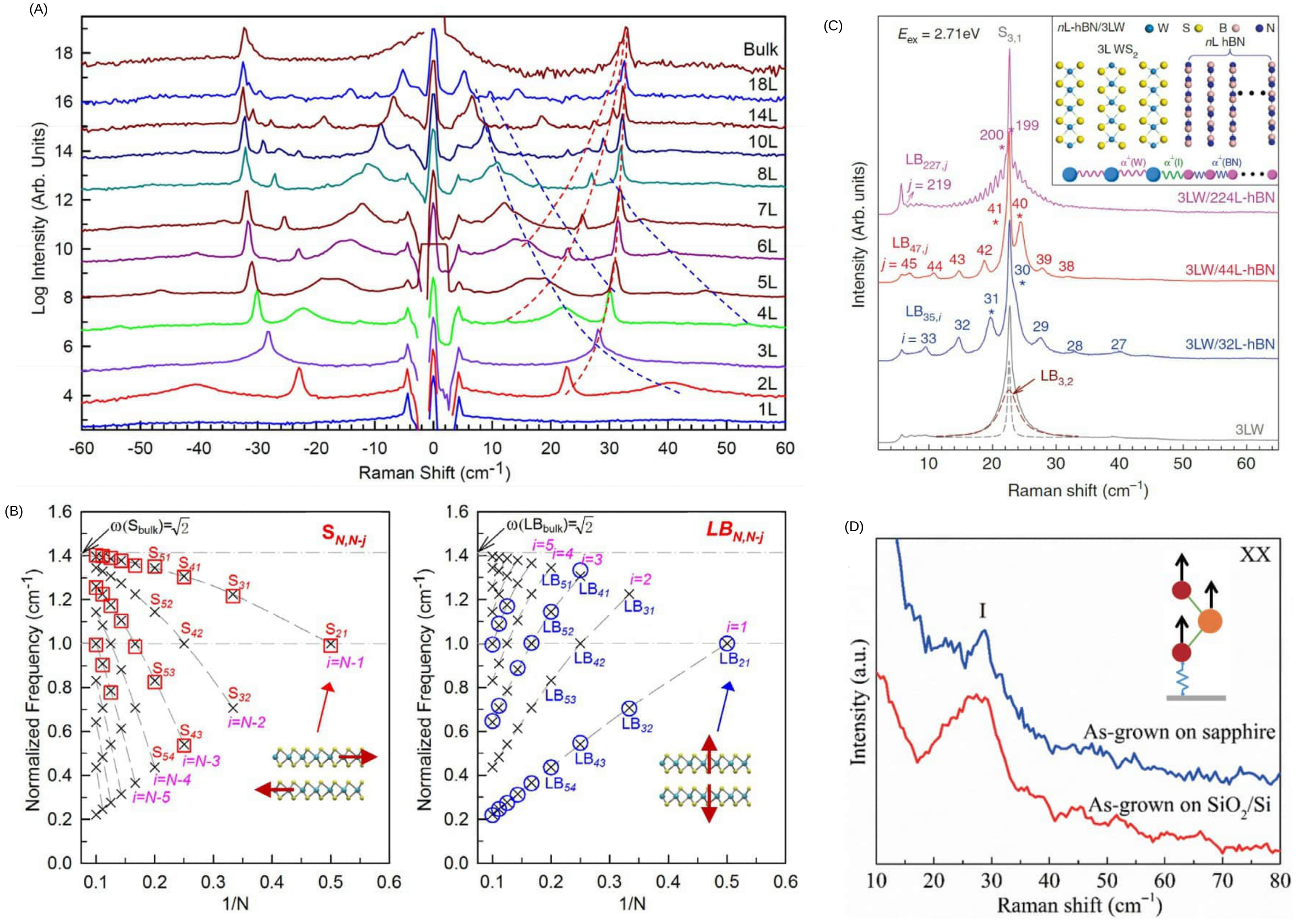

Fig. 3 (a) Stokes and anti-Stokes Raman spectra of *N*L- ($N = 1$ -8 , 10, 14 and 18) and bulk MoS$_2$ between −60 and 60 cm^{-1}. Red and blue dashed lines are guides for the eyes for the frequency trends of the S and LB modes. (b) Fan diagram of the frequencies of interlayer shear (S, Left) and layer-breathing (LB, Right) modes, in a multilayer 2DM as a function of inverse layer number (1/N), with $\omega(S_{2,1})$ and $\omega(LB_{2,1})$ normalized to unity. The subscript $(N, N-j)$ refers to the $(N-j)$th mode of *N* in a descending sequence. These modes are categorized as branches ($j = N-1, N-2, \ldots$) for the S modes and the branches ($j = 1, 2, \ldots$) for the LB modes. The squares and circles are experimental results from multilayer MoS$_2$. The atomic insets draw the interlayer S and LB modes in bilayer MoS. Two horizontal dashed lines denote the normalized frequency in bilayer and bulk. (c) Raman spectra of a trilayer WS$_2$ (3LW) and its heterostructure with a 32 layer, 44 layer and 224 layer hBN, respectively denoted by 3LW/32 L- hBN($\theta_t = 23.5^{\circ}$), 3LW/ 44L- hBN($\theta_t = 23.5^{\circ}$) and 3LW/ 224L- hBN($\theta_t = 17.2^{\circ}$). Inset shows the schematic diagram of a linear chain model for the LB modes in *N*L- hBN/3LW. (d) XX-polarized low-frequency Raman spectra of CVD-grown monolayer WS samples on different substrates. Inset: Schematic diagram of the displacement pattern for the interface (I) mode. Panel (a): Reproduced from Zhang et al. (2015) *Chemical Society Reviews* 44: 2757–2785. Panel (b): Reproduced from Zhang et al. (2016) *Nanoscale* 8: 6435–6450. Panel (c): Reproduced from Lin et al. (2019) *Nature Communications* 10(1): 2419. Panel (d): Reproduced from Xiang et al. (2021), *Nano Research* 14(11): 4314–4320.

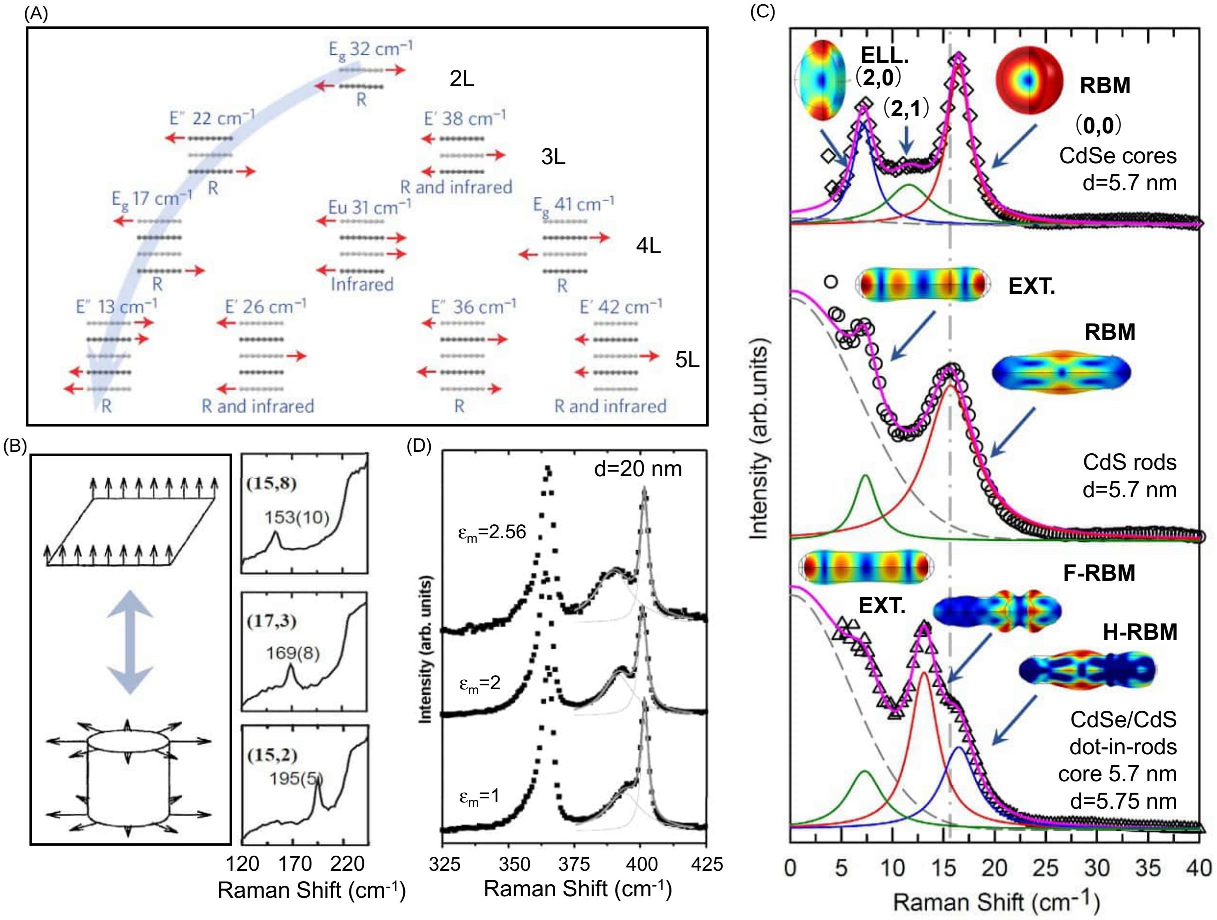

Fig. 4 (a) Symmetry, frequencies and normal mode displacement for each shear mode in multilayer graphene. The Raman-active (R) and infrared-active modes are identified. The arrow denotes the branch of interface vibration modes. (b) Top: The out-of-plane tangential acoustic mode at $k = 0$ (left) in monolayer graphene gives rise to a radial breathing mode (RBM) in the carbon nanotube with non-zero frequency (right). Bottom: RBM Raman spectra for three semiconducting isolated SWNTs of the indicated (n, m) values. (c) Raman spectrum of CdSe nanodot (top), CdS nanorods (middle) and CdSe/CdS dot-in-rods (bottom). Insets show the COMSOL calculations of the deformation. (n, l) is used to assign the ellipsoidal (ELL.) and spheroidal modes of CdSe nanodot. (d) Raman spectra of GaP nanowires with the most probable diameter, $d = 20$ nm, recorded in three different media with different dielectric constants (ε_m). The low, middle and high frequency bands are identified respectively with the TO, SO, and LO phonons. The solid lines represent Lorentzian line shapes used to fit the SO and LO bands. Panel (a): Reproduced from Tan et al. (2012) *Nature Materials* 11(4): 294–300. Top Panel (b): Reproduced from Saito et al. (1998) *Physical Properties of Carbon Nanotubes*. Imperial College Press. Bottom Panel (b): Reproduced from Dresselhaus et al. (2005) *Physics Reports* 409(2): 47–99. Panel (c): Reproduced from Miscuglio et al. (2016) *Nano Letters* 16(12): 7664–7670. Panel (d): Reproduced from Gupta et al. (2003) *Nano Letters* 3(12): 1745–1750.

Lorentzian peak at 1582 cm^{-1} (G-band) for graphite (Dresselhaus et al., 2005; Jorio and Saito, 2021). In contrast, the G-band in a single-wall carbon nanotube (SWNT) consists of two main components, one vibrating along SWNT (LO phonon), locating at ~1590 cm^{-1}(G$^+$), another one vibrating along the circumferential direction of the SWNT (TO phonon), lying at ~1570 cm^{-1}(G$^-$), as shown by the inset in Fig. 2(c). Notably, the lineshape of G-peak is highly sensitive to whether the SWNT is metallic (BWF lineshape) or semiconducting (Lorentzian lineshape), as shown by inset in Fig. 2(c). As SWNT curvature increases, i.e., decreasing the SWNT diameter d_t, the frequency of G$^-$ follows a monotonically descending trend both for metallic and semiconducting SWNTs as a result of the stronger spatial confinement. But it does not influence the G$^+$ peak since it is vibrating along SWNT without any confinements.

The extreme spatial confinements in (quasi-) 0D system, such as quantum dots and nanocrystals (NCs), make the contributions of the confined phonons to its Raman spectrum mixed with the relaxation of the fundamental momentum conservation of $q \sim 0$ required in the Raman scattering process (Sui et al., 1992; Yoshikawa et al., 1995; Zi et al., 1996). It allows those phonons near Γ point in BZ to participate in the scattering process, where the specific phonon dispersion is needed to be included to discuss the lineshape of Raman peaks. In practice, a phonon confinement model (originally proposed by Richter, Wang and Ley, known as RWL model) is widely used (Richter et al., 1981), which gives the Raman intensity in NCs with a domain size L_D as

$$I(\omega) = \int \frac{|C(0,q)|^2}{(\omega - \omega_q)^2 + (\Gamma_0/2)^2} d^3q \tag{9}$$

where $|C(0,q)| = \exp(-q^2L_D^2/2\alpha)$ is the Fourier coefficient of a phonon weighting function, with α an adjustable confinement coefficient, Γ_0 is the natural broadening, ω_q is the phonon dispersion curve. The integration is over the BZ. Note, under the circumstance of a Raman peak contributed by a pair of phonon branches which are degenerated at Γ point, as shown in Fig. 2(d) for LO_2 and TO_2, the integration must take them into account. The lineshapes of Raman peaks in NCs are exampled by 2D NCs in monolayer WS_2 (Shi et al., 2016), as shown in Fig. 2(d). The Raman spectra of two 1L-WS_2 NCs in the energy range of the two first-order peaks E' and A_1' are plotted, as well as the good fits including the predictions from Eq. (9). The extracted L_D are 10 nm (#2-NCs) and 2.3 nm (#7-NCs). It indicates a downshift in frequency and an asymmetrical broadening toward lower frequency as L_D decreases. However, an opposite behavior is recovered for A_1' mode in 1L-WSe_2NCs, as a result of its opposite trends of ZO_2 phonon branch away from Γ point in the BZ.

Interface vibration modes

The rapidly developed 2DMs hold a set of unique interface vibrations modes, which are referred to as the interlayer shear (S) and layer-breathing (LB) modes (Zhang et al., 2013, 2015). S and LB modes correspond to the relative motions of the atomic planes which are parallel and perpendicular to the basal plane, respectively. These modes are considered as quasi-acoustic phonons because the atomic vibrations within each layer are in-phase, while the interlayer vibrations are out-of-phase. It indicates that their typical frequencies are relatively small than the optical phonons in 2DMs, as illustrated in Fig. 3(a) for the case of MoS_2. In addition, those modes are highly dispersive as layer number increases. For an N-layer (NL) 2DM, there are (N-1) pairs of S modes and (N-1) pairs of LB modes, which are in sequence denoted as $S_{N,N-j}$ and $LB_{N,\ N-j}$ $(j = 1, 2, \ldots, N-1)$ with $S_{N,\ 1}(LB_{N,\ 1})$ the one with the highest frequency. The frequencies of S and LB modes as a function of thickness are well documented by a linear chain mode (LCM) among which each layer of 2DM is simplified as a single ball with an effective mass μ. LCM gives an analytic expression as (Zhang et al., 2016)

$$\begin{aligned}\omega\left(S_{N,N-j}\right) &= \omega(S_{bulk})\sin(j\pi/2N)\\ \omega\left(LB_{N,N-j}\right) &= \omega(LB_{bulk})\sin(j\pi/2N)\end{aligned} \tag{10}$$

where $\omega(S_{bulk}) = \sqrt{\alpha_0^{||}/\pi^2c^2\mu}$ and $\omega(LB_{bulk}) = \sqrt{\alpha_0^{\perp}/\pi^2c^2\mu}$ with c the speed of light, μ the mass per unit area in monolayers, and $\alpha_0^{|}(\alpha_0^{\perp})$ the force constants per unit area for the S (LB) mode. Fig. 3(b) shows the branches $(j = N-1, N-2, \ldots)$ for the S modes and the branches $(j = 1, 2, \ldots)$ for the LB modes by the scaled $\omega(S_{2,1}) = \omega(LB_{2,1}) = 1$. The normalized experimental frequencies of the S (squares) and LB modes (circles) in NL-MoS_2 by the corresponding $\omega(S_{2,1})$ and $\omega(LB_{2,1})$ perfectly match with the calculations based on LCM. The robust link between $\omega(S_{N,\ N-j})$ (and $\omega(LB_{N,\ N-j})$) and N makes itself an accurate and effective method to identify the thickness of a specific multilayer 2DM.

Interface vibration modes also apply to vdWHs which combine two different 2DMs, but have distinctive features with respect to natural 2DMs. Fig. 3(c) shows the Raman spectra of the vdWHs formed by interfacing a trilayer WS_2 (3LW) with N Layer hBN (NL-hBN, $N = 32$, 44, and 224), as compared with that of a standalone 3LW (Lin et al., 2019). The S mode in vdWHs is localized within 3LW ($S_{3,1}$) consitituent, in contrast, the LB modes are well extended over the entire layers of the vdWHs, exhibiting bulk-like phonon features. It is surprising to observe more than 30 LB modes in 3 LW/224L-hBN vdWHs, which are resonantly enhanced by electronic transitions related to the C exciton of the 3LW. Accordingly, the electron-phonon coupling (EPC) in 3LW/224L-hBN vdWHs happens between localized electrons confined within WS_2 constituents and bulk-like LB phonons involving all of the layers, named a cross-dimensional EPC. In addition, the specific frequency of LB phonons is well reproduced by extending LCM to include the interface force constant. The built-up cross-dimensional EPC in vdWHs allows new access to manipulate both the designable phonon excitations and the coupling to the localized electronic states by changing the constituents and interface engineering.

Surprisingly, the strong interaction between 2DM and its supported substrate behaviors is just like a spring to active the sample-substrate interface vibration modes, as shown in Fig. 3(d). The low-frequency Raman spectra of 1L-WS_2 samples as grown on both sapphire and silicon substrates clearly show an interface mode with its frequency close to ~ 30 cm^{-1} (Xiang et al., 2021). The distinguish of its origin from those low-frequency interlayer S and LB modes is by noticing the monolayer feature of WS_2 sample. It is shown that the strong sample-substrate interface stems from the unavoidable interface tensile strain introduced in the process of CVD growth, which is not supposed to exist in 2DMs obtained by mechanical exfoliation. Statistically, the frequencies of interface vibration peaks are quite similar for various as-grown WS_2 flakes, ruling out the possible sample-dependent phonon behaviors. These results introduce low-frequency Raman spectroscopy as an effective tool in probing sample-substrate interactions which are naturally subject to 2DMs.

Surface vibration modes

Surface vibration modes, as the microscopic interface mode of an SL (Fig. 2(a)), specify those modes strongly localized near the surface. In the multilayer 2DMs, the interlayer vibrations introduced above hold a branch of surface modes, as illustrated in Fig. 4(a) by the dashed line for multilayer graphenes, where the atomic displacements become much more surface-confined as the number of layers increases (Tan et al., 2012). The corresponding frequency in the bulk case must be zero as expected from the descending trend of the branch. Another example of surface mode is the radial breathing mode (RBM) of a SWNT, which corresponds to the coherent vibration of the carbon atoms in the radial direction, as if the tube were "breathing" (Saito et al., 1998), as shown in Fig. 4(b). It can be constructed by the roll-up of an out-of-plane transverse acoustic phonon (oTA) at Γ point in the BZ of monolayer graphene. RBM features are unique to carbon nanotubes and occur with frequencies between 120 and 350 cm^{-1} for SWNTs for diameters in the range 0.7 nm $< d_t <$ 2 nm (Dresselhaus et al., 2005), as shown in Fig. 4(b). The relation of RBM frequency (ω_{RBM}) on d_t is expressed by $\omega_{RBM} = A/d_t + B$ with A and B parameters determined experimentally. The reciprocal dependency of ω_{RBM} on d_t is a result of spatial confinements along the circumferential direction of the SWNT. RBM features find the applications to study d_t, to probe the electronic structure through its intensity (I_{RBM}) and to perform an (n, m) assignment of a single isolated SWNT from analysis of both d_t and I_{RBM}, as to be introduced in the section "Resonance Raman scattering in nanostructures."

In contrast to the long SWNT, there are both RBMs and confined extensional (EXT.) vibration modes vibrating along the long axis of the nanorod, (Miscuglio et al., 2016), as illustrated in Fig. 4(c). Different from SWNT, ω_{RBM} of a nanorod is described by

$$\omega_{RBM} = \frac{2\tau_n}{D}\sqrt{\frac{E(1-v)}{\rho(1+v)(1-2v)}} \tag{11}$$

with D the diameter of the nanorod, ρ the mass density, E the Young modulus, v the Poisson ratio, and τ_n the nth root of the equation $\tau J_0(\tau) = (1-2v)/(1-v)J_1(\tau)$. $J_0(\tau)$ and $J_1(\tau)$ are Bessel functions. The frequency of the confined EXT. mode is given by

$$\omega_{EXT} = \frac{2n+1}{L}\pi\sqrt{E_{||}/\rho} \tag{12}$$

where L is the nanorod length, $E_{\|}$ is the Young modulus along the long axis of the nanorod. The factor (2n + 1) with $n = 0, 1, 2, \ldots$, accounts for the number of confined modes. The confined EXT. mode has a smaller frequency ($\sim$7.5 cm^{-1}) with respect to the RBM ($\sim$15.7 cm^{-1}) because of the fewer confinements in the long axis. To hybrid nanorod with a nanodot to form the dot-in-rods (like CdSe/CdS core-shell) structure is prominent for light-emitting applications (Bruchez et al., 1998). The dot-in-rods hybrid structure has interesting impacts on the confined surface vibrations (Miscuglio et al., 2016). Unlike nanorods, the fundamental acoustic vibrations of a nanodot are separated into ellipsoidal (ELL.) and spheroidal modes (RBMs), whose frequencies can be obtained by Lamb's theory and assigned by the radial (n) and angular quantum (l) numbers. Accordingly, $l = 0$ represents the spheroidal modes with their frequencies expressed by

$$\omega_{RBM,n} = S_n\frac{2c_L}{D} \tag{13}$$

where c_L is longitudinal sound velocity, D is the diameter of the sphere, and the first two coefficients for $n = 1, 2$ are $S_1 = 2.87$ and $S_2 = 6.16$. The Raman spectrum of a CdSe nanodot (D$\sim$5.7 nm) is shown in Fig. 4(c) with each mode explicitly assigned by a (n, l). Noted its $\omega_{RBM,\ 0}\sim$16.5 cm^{-1} is much close to that in CdS nanodot ($\omega_{RBM}\sim$15.7cm^{-1}). Fig. 4(c) shows the Raman spectrum of a CdSe/CdS dot-in-rods, with $D\sim$5.7 nm for CdSe dot and $D\sim$5.75 nm for CdS rod. The Raman peak of the confined EXT. mode is much similar to that of the nanorod. It can be attributed to the nonlocality of this vibration that extends over the full rod volume and therefore is less affected by the local modification of the core. However, the RBM peak is divided into a fundamental RBM (F-RBM) and a high-order RBM (H-RBM). As illustrated by the inset in Fig. 4(c), F-RBM shows a symmetric dilatation/contraction motion located in the central region of the rod, while H-RBM exhibits a symmetric oscillation off-center of the rod. The splitting of F-RBM and H-RBM increases with increasing core size. This can be understood in the way that dot-in-rods architecture leads to a reduction of the sound velocity in the core region of the rod. Dot-in-rods architecture can be exploited as a tool to tune exciton-phonon coupling in nanocrystal heterostructures.

Surface optical (SO) vibration modes were first predicted by Fuchs and Kliewer (1965) and first observed by Ibach using inelastic electron scattering (Ibach, 1970). The dispersion relation of a SO mode in an infinitely long cylindrical wire can be written (in the limit $q \gg \omega/c$)

$$\omega_{SO}^2 = \omega_{TO}^2 + \frac{\omega_p^2}{\varepsilon_\infty + \varepsilon_m f(x)} \tag{14}$$

with $x = qr$, where ω_{TO} is the TO mode frequency at zone center, ω_p is the screened ion plasma frequency given by $\omega_{LO}^2 = \omega_{TO}^2 + \omega_p^2/\varepsilon_\infty$, ε_∞ is the high-frequency dielectric constant of bulk materials, ε_m is the dielectric constant of the overlaying media to wire, $d = 2r$ is the wire diameter, and $f(x)$ is obtained from the eigenvalue equation

$$f(x) = \frac{I_0(x)K_1(x)}{I_1(x)K_0(x)} \tag{15}$$

with $I_j(x)$ and $K_j(x)$ are Bessel functions. Raman spectra of GaP nanowires in air ($\varepsilon_m = 1$), dichloromethane ($\varepsilon_m = 2$), and aniline ($\varepsilon_m = 2.65$) are plotted in Fig. 4(d) (Gupta et al., 2003). They feature two sharp peaks, which are identified with the TO ($q = 0$) and LO ($q = 0$) modes, in reasonable agreement with bulk crystalline GaP, and a third one assigned to SO by its sensitivity to the interfaced external medium. Noted, unlike the surface acoustic modes discussed above, the observation of SO mode here is enabled by an inherent length scale ($\sim$40 nm) in the nanowires due to either the self-oscillating nature of the filament cross section or polynuclear growth (Gupta et al., 2003).

Folded vibration modes

Folded vibrations modes in a binary SL stem from the new 1D out-of-plane translational periods of the alternating layers (Cardona and Guntherodt, 1989), i.e., $L = n_1a_1 + n_2a_2$, where $d_1 = n_1a_1$ and $d_2 = n_2a_2$ are layer thickness for AlAs and GaAs, as

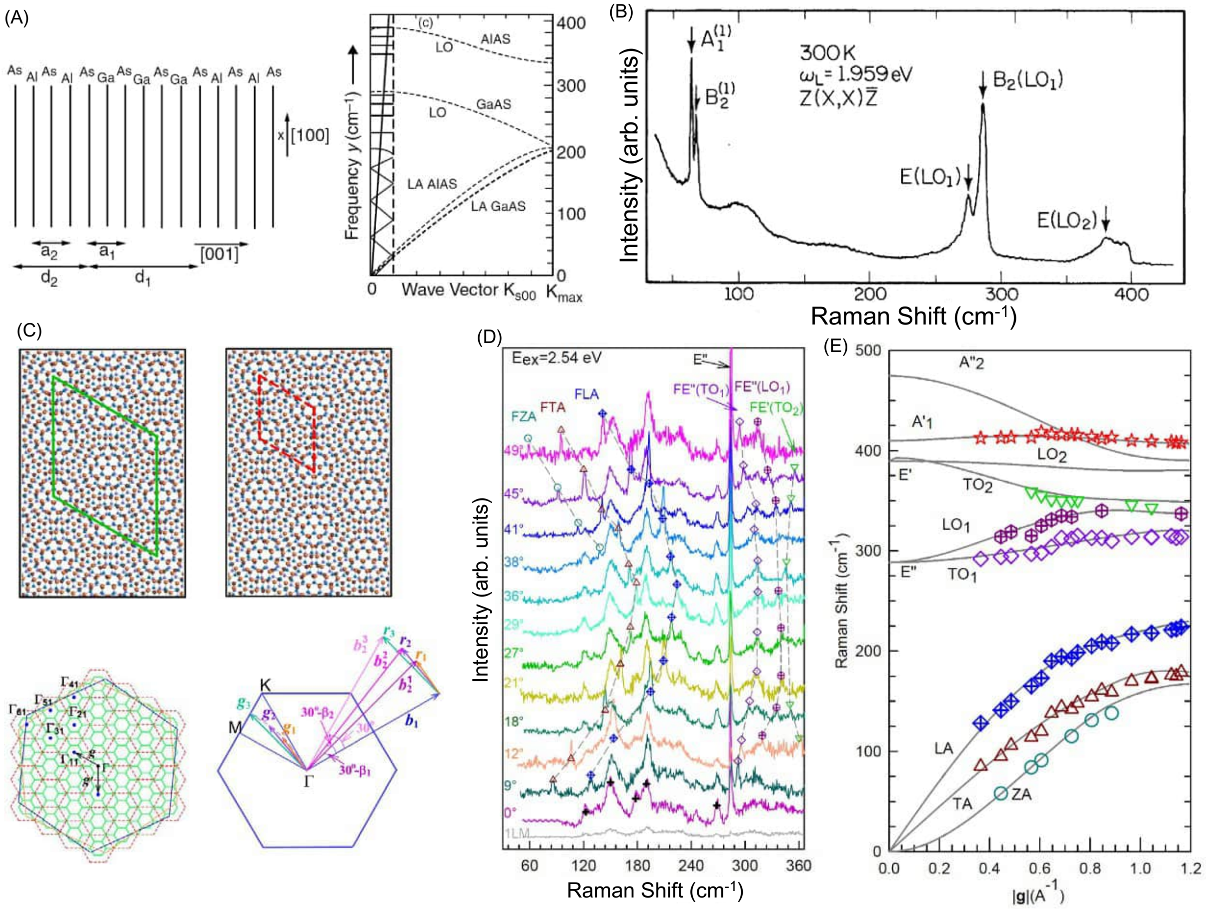

Fig. 5 (a) Sketch of GaAs/AlAs SL structure and dispersion curves of a photon (oblique solid line) and longitudinal phonons of bulk GaAs and AlAs (dashed line) and SL (solid line) (b) Raman spectrum of SL GaAs/AlAs. $A_1^{(1)}$ and $B_2^{(1)}$ are assigned to the folded acoustic phonons. (c) Top: Crystallographic SL and moiré pattern in (5,7)-tBLM with $\theta = 10.99^\circ$. Dashed (red) and solid (green) parallelogram corresponds to the moiré unit cell and crystallographic SL unit cell of the tBLMs, respectively. Bottom (left): the reciprocal lattice of (5,7)-tBLMs. The large blue and orange hexagons are the first BZ of top and bottom MoS_2 layers, and the dashed (red) and solid (green) hexagons represent the Wigner-Seitz cells of the reciprocal lattices corresponding to the moiré and crystallographic SL, respectively. Bottom (right): Schematic diagram of moiré basic vectors (g_i, $i = 1, 2, 3$) for $\theta \leq 30^\circ$. (d) Raman spectra of tBLMs in the region of 50–365 cm^{-1}. Different shapes and color symbols represent the Raman modes in different phonon branches. The Raman spectra of 1LM and 3R-BLM ($\theta = 0^\circ$) are plotted for comparison. (e) The comparison of calculated and experimental frequencies of moiré phonons dependent on $|\mathbf{g}|$. Panel (a): Reproduced from Zhang S.-L. (2012) *Raman Spectroscopy and its Application in Nanostructures*. John Wiley & Sons Ltd. Panel (b): Reproduced from Colvard et al. (1980) *Physical Review Letters* 45: 298–301. Panels (c–e): Reproduced from Lin et al. (2018) *ACS Nano* 12(8): 8770–8780.

shown in Fig. 5(a) for $n_1 = 3$ and $n_2 = 2$, respectively. The original BZ in bulk case, $-\pi/a$ to π/a, now is folded into a small one in SL, $-\pi/L$ to π/L. The folded optical phonons in AlAs and GaAs are strongly confined within each layer (confined vibration modes). But the acoustic phonons which are similar to each other in AlAs and GaAs produce ($p = n_1 + n_2$) folded phonons, as illustrated in Fig. 5(a) for $p = 8$. Interestingly, the non-intersect optical and acoustic branches in bulk GaAs and AlAs now overlap with each other, which makes the acoustic phonon Raman active in the GaAs/AlAs SL. Fig. 5(b) shows the Raman spectrum of a GaAs/AlAs SL which presents a folded acoustic doublet ($A_1^{(1)}$and $B_2^{(1)}$) (Colvard et al., 1980).

Instead of the 1D out-of-plane translational periods along the growth direction in the semiconductor SL, as drawn in Fig. 5(a), in-plane 2D translational periods are recently discovered in the twisted bilayer (tBL-) 2DMs (Cao et al., 2018), as firstly exampled by graphene and then rapidly extended to other 2DMs. It is achieved by rotating (with an angle θ) the two crystal networks in bilayer system with respect to each other. Fig. 5(c) shows the crystallographic and moiré SLs for tBL-MoS_2 with $(m, n) = (5,7)$, denoted as (5,7)-tBLM (Lin et al., 2018). The corresponding $\theta = 10.99^\circ$ is obtained based on the relation $\cos\theta = (m^2 + 4mn + n^2)/2(m^2 + mn + n^2)$. The lattice constants for crystallographic (L) and moiré (L^M) SLs are receptively, $L = a_0 \mid m - n \mid /2 \sin(\theta/2)$ and $L^M = a_0/2 \sin(\theta/2)$. They are equal for the case of $|m - n| = 1$. The Wigner-Seitz cells corresponding to crystallographic and moiré SLs are shown in Fig. 5(c), which clearly divide the first BZs of top and bottom monolayers into the small hexagons. The magnitude of the moiré reciprocal lattice vector ($\mathbf{g}$) is obtained by $|\mathbf{g}| = 2b \sin(\theta/2)$, with $b = 4\pi/\sqrt{3}a_0$. The trace of $\mathbf{g}$ in the first BZ of the monolayer MoS_2 (1LM) as a function of θ is demonstrated in Fig. 5(c). It indicates that the phonons of 1LM with $\mathbf{q} = \mathbf{g}$ are folded back to the Γ points in the Wigner-Seitz cells and accordingly become Raman active. The Raman spectra of tBLM with θ ranging from 0° to 49° are shown in Fig. 5(d). Seven series of θ-dependent Raman modes are identified as folded vibration modes associated with ZA, TA, LA, E″(TO$_1$), E″(LO$_1$), E′(TO$_2$) and A$_1$′ branches in 1LM, accordingly assigned as FZA (F stands for "folded"), FTA, FLA, FE″(TO$_1$), FE″ (LO$_1$), FE′ (TO$_2$) and FA$_1$′, respectively. Fig. 5(e) shows the experimental frequencies of moiré phonons mapped onto the theoretical dispersion curves traced by **g**. The good agreement indicates that the moiré phonons can serve as a fingerprint to determine θ of the tBLMs.

Similar to the confined folded optical phonons in each alternating quantum potential well, as shown in Fig. 2(a), the optical phonons of tBL-2DMs are confined within the in-plane moiré potential well. The strength of confinements becomes extremely strong as θ gets much close to zero, as exampled by the tBL-graphene (tBLG) with $\theta = 0.987^{\circ}$ (it corresponds to $L^M/a_0 \sim 3328$). It makes the G-band due to the stretching of the C—C bonds highly localized at those regions referred to as AB- and BA-stacked domains, strain solitons (SP) and topological points (AA) (Gadelha et al., 2021). To probe those G-bands, including G_r^+ from SP region and G_r^- from AA region, needs a nano-Raman spectroscope. These strongly confined moiré phonons are helpful to understand phonon-related effects at atomic and nanometric scales, such as Jahn-Teller effects (Angeli et al., 2019; Shinozuka, 2021) and electronic Cooper pairing (Lian et al., 2019; Wu et al., 2018b).

Resonance Raman scattering in nanostructures

RRS is key to detecting those Raman peaks subject to weak intensities in both bulk cases and nanostructures. But RRS in nanostructures may show distinctive or even anomalous features. As discussed in the section "Raman spectroscopy basics," Raman shift is not dependent on the exploited incident laser wavelength, which is considered as one general rule for Raman scattering effect. Fig. 6(a) shows the Raman spectra of monolayer graphene under different excitation energies, whose 2D-band (Note 2D is not referred as "two-dimensional," but double of D-band in frequency.) is linearly dispersive as E_L increases, with a slope of $\sim$100 cm^{-1}eV^{-1}, in contrast to the G-band (Wu et al., 2018a). The microscopic intra-valley and inter-valley scattering

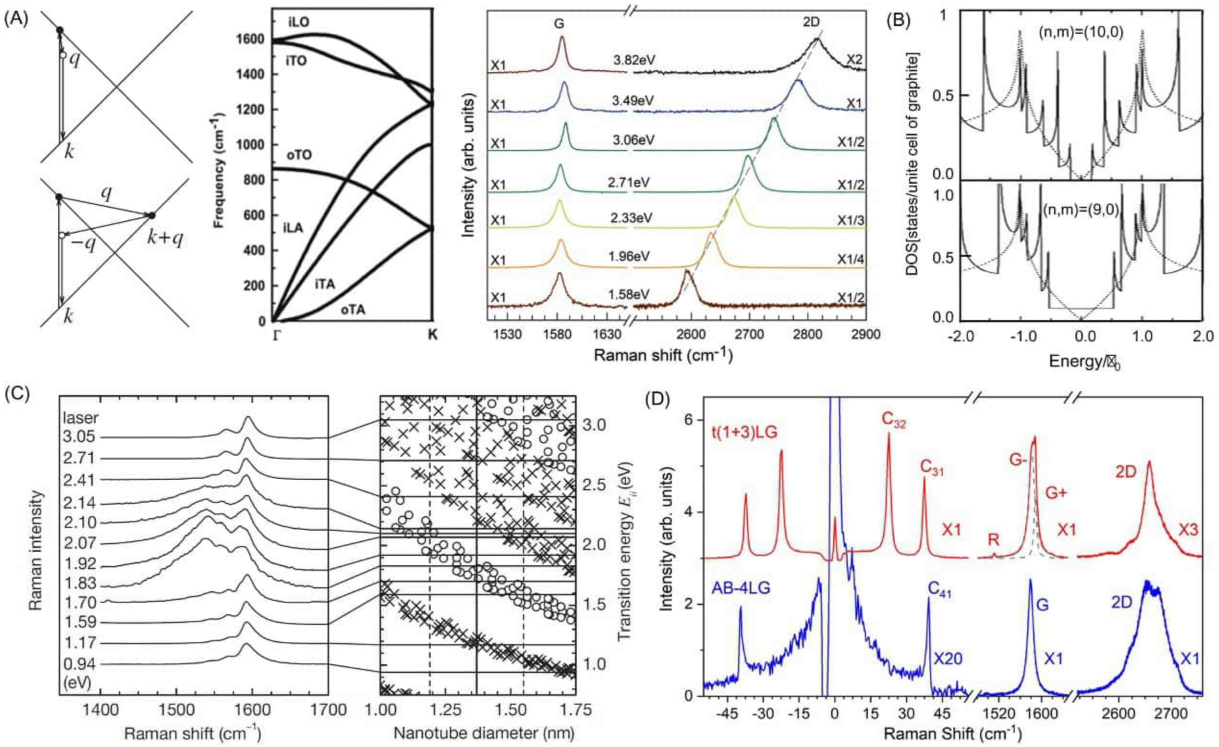

Fig. 6 (a) Left: One-phonon first-order and two-phonons second-order, resonance Raman spectral processes in monolayer graphene. Middle: Phonon dispersion of monolayer graphene. Right: Raman spectra of monolayer graphene measured at various excitations in the G- and 2D-bands regions. (b) The electronic 1D density of states (DOS) per unit cell for two (*n*,0) zigzag nanotubes: (up panel) the (9,0) nanotube which has metallic behavior, (bottom panel) the (10,0) nanotube which has semiconducting behavior. Also shown is the DOS for the graphene sheet. (c) Left: Raman spectra of the tangential G-band modes of SWNT bundles measured with several different laser lines, on a sample with $d_t = 1.37 \pm 0.18$ nm. Right: Resonant transition energies E_{ii} vs d_t. The vertical solid line is the average d_t and the vertical dashed lines denote the d_t distribution width. Crosses are for semiconducting SWNTs and open circles for metallic SWNTs. (d) Raman spectra of AB-stacked 4LG and t(1 + 3)LG in the regions of C, R-, G- and 2D-bands. C$_{31}$ and C$_{32}$ denote the observed shear modes in t(1 + 3) LG, which is from the 3LG constituent, in contrast to C$_{41}$ in AB-stacked 4LG. The dashed lines are fit to G-band, which features two subpeaks, G$^-$ and G$^+$, in t(1 + 3) LG. Panel (a): Reproduced from Wu et al. (2018) *Chemical Society Review* 47: 1822–1873. Panel (b): Reproduced from Saito et al. (1998) *Physical Properties of Carbon Nanotubes*. Imperial College Press. Panels (a (left and middle) and c): Reproduced from Jorio et al. (2011) *Raman Spectroscopy in Graphene Related Systems*, Weinheim: Wiley-VCH Verlag GmbH & Co. KGaA.

processes for G- and 2D-bands are shown in Fig. 6(a) (Jorio et al., 2011). G-band belongs to one-phonon (the degenerate TO/LO) first-order. scattering process with $q \sim 0$ (Γ point). 2D-band involves a two-phonon (two TO near K point) second-order scattering process, which has a $q \sim 2k \sim$ K (BZ boundary). $E_L = (E_m - E_i)$, proportional to$k$, applies to all the vertically electronic transitions, which is responsible for the strong Raman intensity observed in monolayer graphene which just has one atomic layer. On the other hand, ω_q of TO phonon is linearly increased as q gets away from the K point due to Kohn anomaly (Lazzeri and Mauri, 2006) (Fig. 6(a)). Accordingly, the increasing E_L (i.e., k) will lead to an increase in ω_q through the momentum conservation law $q \sim 2k$. Notably, q involved in the Stokes and anti-Stokes for the 2Dband are different from each other, creating a frequency discrepancy between its Stokes and anti-Stokes components (Cong et al., 2018; Tan et al., 1998) due to the dispersive feature of TO phonon (Thomsen and Reich, 2000). Such a frequency discrepancy had been widely detected in bulk graphite, graphite whiskers, and multi-walled carbon nanotubes.

The above discussion indicates the RRS in nanostructures is tightly associated with their electronic transitions which are mediated by the density of states (DOS). Of particular interest has been the 1D DOS in a carbon nanotube (Saito et al., 1998), as exampled by metallic (9,0) and semiconducting (10,0) zigzag nanotubes in Fig. 6(b). The DOS has a value of zero for the semiconducting nanotubes at $E = 0$ but is non-zero (and small) for the metallic nanotubes. The comparison between the 1D DOS for nanotubes and the 2D DOS for a graphene layer is included in Fig. 6(b). Nanotube exhibits lots of sharp peaks, which leads to the DOS-enhanced electronic transition as compared with graphene. A pair of sharp peaks in symmetry with respect to $E = 0$ specifies the resonance transition energy E_{ii}. Fig. 6(c) shows the Raman spectra of G-band modes of carbon nanotube bundles measured under different laser lines (Pimenta et al., 1998). The lineshapes indicate the presence of both semiconducting and metallic carbon nanotubes in bundles. Kataura plot was proposed to interpret the RRS effects in nanotubes, where Kataura and co-workers displayed the optical transition energies for each (n, m) SWNT as a function of tube diameter d_t (Kataura et al., 1999), as shown in Fig. 6(c). As demonstrated by the links between the Raman spectra and Kataura plot, RRS in bundles resonantly probes the SWNT with different d_t. Only those SWNTs with E_{ii} closed to the laser energy E_L are present in the Raman spectra. Alternatively, as indicated by the vertical lines in Fig. 6(c), G-band of a SWNT with a fixed d_t will not show up unless $E_L = E_{ii}$. In this way, RRS finds its valuable role to study the confined electronic structure in nanostructures.

The shear mode of multilayer graphenes is usually denoted as the C mode (Tan et al., 2012; Wu et al., 2014), which features a BWF line shape in AB-stacked multilayer graphene, as exampled by a four-layer graphene (AB-4LG) in Fig. 6(d). It is attributed to the quantum interference between the C mode and a continuum of electronic transitions near K point (Tan et al., 2012). As shown in Fig. 6(d), the intensity of C_{41} is much weak than G-band due to its small strength of electron-phonon coupling. However, the intensities of the S modes in a twisted (1 + 3) LG, labeled as t(1 + 3) LG, are comparable to the G-band. They are enhanced by the RRS processes mediated by the pairs of parallel electronic bands, induced by the intralayer twisting. This intensity enhancement of the S mode masks the weak BWF profile to give an overall Lorentzian profile, even though there is no band gap opening near K point in t(1 + 3) LG (Wu et al., 2014).

Conclusion

Raman spectroscopy has been used to study the science of nanostructures, recovering more and more fundamental aspects of their electronic and vibrational properties. In this encyclopedia, we firstly introduce the basics to understand the Raman scattering effect and the general features of a Raman spectrum. Followed is given to the phonon in nanostructures based on their Raman spectra, which is firstly exampled by a semiconductor SL and then extended to other cases. Of particular interest is RRS in nanostructures, which can be exploited to significantly enhance the weak Raman peaks and to probe the confined electronic structures. The rapid developments of Raman spectroscopy applied into nanostructures are readily beneficial from the non-stop improvements in experimental techniques, such as the nano-Raman spectroscope and the available laser lines for RRS. For the future perspectives, developing the specific Raman spectroscopy to allow the measurements of nanostructures under extreme environments, such as ultra-high pressure, ultra-strong magnetic field, extreme low-temperature, is desirable to find/address more and more fundamental questions, about electron-electron correlation, excitonic effects and electron-phonon interactions, etc., and the new physics in nanostructures.

Acknowledgment

We acknowledge support from the National Natural Science Foundation of China (Grant No. 11874350 and 12174381) and CAS Key Research Program of Frontier Sciences (Grant nos. ZDBS-LY-SLH004 and XDPB22).

References

Angeli M, Tosatti E, and Fabrizio M (2019) Valley Jahn-Teller effect in twisted bilayer graphene. *Physical Review X* 9: 041010.
Bottani CE, Mantini C, Milani P, Manfredini M, Stella A, Tognini P, Cheyssac P, and Kofman R (1996) Raman, optical-absorption, and transmission electron microscopy study of size effects in germanium quantum dots. *Applied Physics Letters* 69(16): 2409–2411.
Bruchez M, Moronne M, Gin P, Weiss S, and Alivisatos AP (1998) Semiconductor nanocrystals as fluorescent biological labels. *Science* 281(5385): 2013–2016.

Cao Y, Fatemi V, Fang S, Watanabe K, Taniguchi T, Kaxiras E, and Jarillo-Herrero P (2018) Unconventional superconductivity in magic-angle graphene superlattices. *Nature* 556(7699): 43–50.

Cardona M (1975) *Light Scattering in Solids*. Berlin Heidelberg: Springer-Verlag.

Cardona M and Guntherodt G (1989) *Light Scattering in Solids V: Superlattices and Other Microstructures.* Berlin Heidelberg: Springer-Verlag.

Colvard C, Merlin R, Klein MV, and Gossard AC (1980) Observation of folded acoustic phonons in a semiconductor superlattice. *Physical Review Letters* 45: 298–301.

Comas F, Trallero-Giner C, and Cantarero A (1993) Optical phonons and electron-phonon interaction in quantum wires. *Physical Review B* 47: 7602–7605.

Cong X, Wu JB, Lin ML, Liu XL, Shi W, Venezuela P, and Tan PH (2018) Stokes and anti-Stokes Raman scattering in mono- and bilayer graphene. *Nanoscale* 10: 16138–16144. https://doi.org/10.1039/C8NR04554B.

Davies JH (1997) *The Physics of Low-dimensional Semiconductors: An Introduction.* Cambridge University Press.

Demtroder W (2003) *Laser Spectroscopy: Basic Concepts and Instrumentation*, 3rd edn. Berlin Heidelberg: Springer-Verlag.

Dresselhaus M, Dresselhaus G, Saito R, and Jorio A (2005) Raman spectroscopy of carbon nanotubes. *Physics Reports* 409(2): 47–99.

Feng ZC, Mascarenhas AJ, Choyke WJ, and Powell JA (1988) Raman scattering studies of chemical-vapor-deposited cubic SiC films of (100) Si. *Journal of Applied Physics* 64(6): 3176–3186.

Fox M (2010) *Optical Properties of Solids*, 2nd edn. Oxford University Press.

Fuchs R and Kliewer KL (1965) Optical modes of vibration in an ionic crystal slab. *Physics Review* 140: A2076–A2088.

Gadelha AC, Ohlberg DAA, Rabelo C, Neto EGS, Vasconcelos TL, Campos JL, Lemos JS, Ornelas V, Miranda D, Nadas R, Santana FC, Watanabe K, Taniguchi T, van Troeye B, Lamparski M, Meunier V, Nguyen V-H, Paszko D, Charlier J-C, Campos LC, Cançado LG, Medeiros-Ribeiro G, and Jorio A (2021) Localization of lattice dynamics in low-angle twisted bilayer graphene. *Nature* 590(7846): 405–409.

Gupta R, Xiong Q, Mahan GD, and Eklund PC (2003) Surface optical phonons in gallium phosphide nanowires. *Nano Letters* 3(12): 1745–1750.

Ibach H (1970) Optical surface phonons in zinc oxide detected by slow-electron spectroscopy. *Physical Review Letters* 24: 1416–1418.

Jorio A and Saito R (2021) Raman spectroscopy for carbon nanotube applications. *Journal of Applied Physics* 129(2), 021102.

Jorio A, Saito R, Dresselhaus G, and Dresselhaus MS (2011) *Raman Spectroscopy in Graphene Related Systems.* Weinheim: WILEY-VCH Verlag GmbH & Co. KGaA.

Jusserand B, Paquet D, and Regreny A (1984) “Folded” optical phonons in GaAs/$Ga_{1-x}Al_xAs$ superlattices. *Physical Review B* 30: 6245–6247.

Kataura H, Kumazawa Y, Maniwa Y, Umezu I, Suzuki S, Ohtsuka Y, and Achiba Y (1999) Optical properties of single-wall carbon nanotubes. *Synthetic Metals* 103(1): 2555–2558. International Conference on Science and Technology of Synthetic Metals.

Lazzeri M and Mauri F (2006) Nonadiabatic kohn anomaly in a doped graphene monolayer. *Physical Review Letters* 97: 266407.

Lian B, Wang Z, and Bernevig BA (2019) Twisted bilayer graphene: A phonon-driven superconductor. *Physical Review Letters* 122: 257002.

Lin M-L, Tan Q-H, Wu J-B, Chen X-S, Wang J-H, Pan Y-H, Zhang X, Cong X, Zhang J, Ji W, Hu P-A, Liu K-H, and Tan P-H (2018) Moiré phonons in twisted bilayer MoS_2. *ACS Nano* 12(8): 8770–8780.

Lin M-L, Zhou Y, Wu J-B, Cong X, Liu X-L, Zhang J, Li H, Yao W, and Tan P-H (2019) Cross-dimensional electron-phonon coupling in van der Waals heterostructures. *Nature Communications* 10(1): 2419.

Miscuglio M, Lin M-L, Di Stasio F, Tan P-H, and Krahne R (2016) Confined acoustic phonons in colloidal nanorod heterostructures investigated by nonresonant raman spectroscopy and finite elements simulations. *Nano Letters* 16(12): 7664–7670.

Pimenta MA, Marucci A, Empedocles SA, Bawendi MG, Hanlon EB, Rao AM, Eklund PC, Smalley RE, Dresselhaus G, and Dresselhaus MS (1998) Raman modes of metallic carbon nanotubes. *Physical Review B* 58: R16016–R16019.

Piscanec S, Cantoro M, Ferrari AC, Zapien JA, Lifshitz Y, Lee ST, Hofmann S, and Robertson J (2003) Raman spectroscopy of silicon nanowires. *Physical Review B* 68: 241312.

Raman CV and Krishnan KS (1928) A new type of secondary radiation. *Nature* 121(3048): 501–502.

Richter H, Wang Z, and Ley L (1981) The one phonon Raman spectrum in microcrystalline silicon. *Solid State Communications* 39(5): 625–629.

Rücker H, Molinari E, and Lugli P (1992) Microscopic calculation of the electron-phonon interaction in quantum wells. *Physical Review B* 45: 6747–6756.

Saito R, Dresselhaus G, and Dresselhaus MS (1998) *Physical Properties of Carbon Nanotubes*. Imperial College Press.

Schuller C (2006) *Inelastic Light Scattering of Semiconductor Nanostructures: Fundamentals and Recent Advances.* Berlin Heidelberg: Springer-Verlag.

Shi W, Lin M-L, Tan Q-H, Qiao X-F, Zhang J, and Tan P-H (2016) Raman and photoluminescence spectra of two-dimensional nanocrystallites of monolayer WS_2 and WSe_2. *2D Materials* 3(2): 025016.

Shinozuka Y (2021) *Electron-Lattice Interactions in Semiconductors*, 1st edn. Jenny Stanford Publishing.

Smekal A (1923) Zur quantentheorie der dispersion. *Naturwissenschaften* 11: 873.

Smith E and Dent G (2019) *Modern Raman Spectroscopy: A Practical Approach*, 2nd edn. John Wiley & Sons Ltd.

Stroscio MA and Dutta M (2001) *Phonons in Nanostructures*. Cambridge University Press.

Sui Z, Leong PP, Herman IP, Higashi GS, and Temkin H (1992) Raman analysis of light-emitting porous silicon. *Applied Physics Letters* 60(17): 2086–2088.

Tan P-H (2019) *Raman Spectroscopy of Two-Dimensional Materials*. Springer International Publishing AG.

Tan PH, Bougeard D, Abstreiter G, and Brunner K (2004) Raman scattering of folded acoustic phonons in self-assembled Si/Ge dot superlattices. *Applied Physics Letters* 84: 2632–2634. https://doi.org/10.1063/1.1691171.

Tan PH, Deng YM, and Zhao Q (1998) Temperature-dependent Raman spectra and anomalous Raman phenomenon of highly oriented pyrolytic graphite. *Physical Review B* 58: 5435–5439. https://doi.org/10.1103/PhysRevB.58.5435.

Tan PH, Han WP, Zhao WJ, Wu ZH, Chang K, Wang H, Wang YF, Bonini N, Marzari N, Pugno N, Savini G, Lombardo A, and Ferrari AC (2012) The shear mode of multilayer graphene. *Nature Materials* 11(4): 294–300.

Thomsen C and Reich S (2000) Double resonant Raman scattering in graphite. *Physical Review Letters* 85: 5214–5217. https://doi.org/10.1103/physrevlett.85.5214.

Toporski J, Dieing T, and Hollricher O (2018) *Confocal Raman Microscopy*, 2nd edn. Springer International Publishing AG.

Wu J-B, Zhang X, Ijäs M, Han W-P, Qiao X-F, Li X-L, Jiang D-S, Ferrari AC, and Tan P-H (2014) Resonant Raman spectroscopy of twisted multilayer graphene. *Nature Communications* 5(1): 5309.

Wu J-B, Lin M-L, Cong X, Liu H-N, and Tan P-H (2018a) Raman spectroscopy of graphene-based materials and its applications in related devices. *Chemical Society Reviews* 47: 1822–1873.

Wu F, MacDonald AH, and Martin I (2018b) Theory of phonon-mediated superconductivity in twisted bilayer graphene. *Physical Review Letters* 121: 257001.

Xiang Q, Yue X, Wang Y, Du B, Chen J, Zhang S, Li G, Cong C, Yu T, Li Q, and Jin Y (2021) Unveiling the origin of anomalous low-frequency Raman mode in CVD-grown monolayerWS_2. *Nano Research* 14(11): 4314–4320.

Yoshikawa M, Mori Y, Obata H, Maegawa M, Katagiri G, Ishida H, and Ishitani A (1995) Raman scattering from nanometer-sized diamond. *Applied Physics Letters* 67(5): 694–696.

Yu PY and Cardona M (2010) *Fundamentals of Semiconductors: Physics and Materials Properties*, 4th edn. Berlin Heidelberg: Springer-Verlag.

Zhang S-L (2012) *Raman Spectroscopy and its Application in Nanostructures*. John Wiley & Sons Ltd.

Zhang X, Han WP, Wu JB, Milana S, Lu Y, Li QQ, Ferrari AC, and Tan PH (2013) Raman spectroscopy of shear and layer breathing modes in multilayerMoS_2. *Physical Review B* 87: 115413.

Zhang X, Qiao X-F, Shi W, Wu J-B, Jiang D-S, and Tan P-H (2015) Phonon and raman scattering of two-dimensional transition metal dichalcogenides from monolayer, multilayer to bulk material. *Chemical Society Reviews* 44: 2757–2785.

Zhang X, Tan Q-H, Wu J-B, Shi W, and Tan P-H (2016) Review on the raman spectroscopy of different types of layered materials. *Nanoscale* 8: 6435–6450.

Zi J, Buscher H, Falter C, Ludwig W, Zhang K, and Xie X (1996) Raman shifts in Si nanocrystals. *Applied Physics Letters* 69(2): 200–202.

Scattering techniques, Compton[☆]

B Barbiellini[a,b] **and A Bansil**[b], [a]LUT University, Lappeenranta, Finland; [b]Northeastern University, Boston, MA, United States

© 2024 Elsevier Ltd. All rights reserved.

This is an update of P.E. Mijnarends, A. Bansil, Scattering Techniques, Compton, Editor(s): Franco Bassani, Gerald L. Liedl, Peter Wyder, Encyclopedia of Condensed Matter Physics, Elsevier, 2005, Pages 182–193, ISBN 9780123694010, https://doi.org/10.1016/B0-12-369401-9/00646-X.

Introduction **174**
Theory 174
Instrumentation 178
Multiple scattering 180
Data analysis 181
Comparison with theory 181
Conclusion **185**
References **186**

Abstract

Compton scattered X-rays carry fingerprints of the electron momentum distribution in the target material. The chapter starts with a historical overview of the Compton scattering technique and its development as a solid-state spectroscopy. This is followed by sections addressing theoretical underpinnings, instrumentation, and issues related to data handling of the Compton spectra. We conclude by presenting a few illustrative examples that highlight applications of the Compton scattering spectroscopy to metals, alloys, and other complex materials.

Key points

- Introduce the X-ray Compton scattering and related techniques as solid-state spectroscopies for probing ground-state electronic structures and Fermi surfaces of materials.
- Provide an overview of the theory of X-ray Compton scattering.
- Highlight the key role synchrotron light sources are playing in advancing the Compton scattering technique, including the development of the magnetic Compton scattering technique based on using circularly polarized light for probing spin-dependent properties of materials.
- Provide illustrative examples of the applications of the Compton scattering techniques, including their application as an advanced characterization tool for investigating functional materials such as the Li-ion battery materials.

Nomenclature

$B(r)$	Reciprocal form factor (–)
c	Speed of light ($\mathrm{ms^{-1}}$)
e	Charge of the electron (C)
E_0	Energy of incident photon ($\mathrm{kg\ m^2\ s^{-2}}$)
E_1	Energy of scattered photon ($\mathrm{kg\ m^2\ s^{-2}}$)
E_C	Energy at top of Compton profile ($\mathrm{kg\ m^2\ s^{-2}}$)
E_F	Fermi energy ($\mathrm{kg\ m^2 s^{-2}}$)
h	Planck's constant ($\mathrm{kg\ m^2\ s^{-1}}$)
$\hbar$	Planck's constant/2p ($\mathrm{kg\ m^2\ s^{-1}}$)
J	Compton profile ($\mathrm{kg^{-1}\ m^{-1}\ s}$)
k	Wave vector ($\mathrm{m^{-1}}$)
k_0	Momentum of incident photon ($\mathrm{kg\ ms^{-1}}$)
k_1	Momentum of scattered photon ($\mathrm{kg\ ms^{-1}}$)

[☆] *Change History*: September 2022. B Barbiellini and A Bansil have prepared the update. The new Fig.12 has been added. The Section "Comparison with Theory" has been expanded. Key points, Conclusion and References have been added. Minor stylistic improvements have been implemented throughout the text.

K	Reciprocal lattice vector (m^{-1})
$\boldsymbol{m}$	Electronic rest mass (kg)
$\boldsymbol{n}$	Occupation function (–)
$\boldsymbol{p}_0$	Initial momentum of electron (kg m s^{-1})
$\boldsymbol{p}_1$	Momentum of recoil electron (kg m s^{-1})
$\boldsymbol{p}_x, \boldsymbol{p}_y, \boldsymbol{p}_z$	Components of electron momentum (kg ms^{-1})
$\boldsymbol{p}_\mathrm{F}$	Fermi momentum (kg m s^{-1})
$\boldsymbol{P}_c, \boldsymbol{P}_1$	Stokes parameters (–)
$\boldsymbol{q}$	Scattering vector (m^{-1})
$\boldsymbol{r}_0$	Classical electron radius (m)
$\boldsymbol{t}_{1/2}$	Radioactive half-life (s)
Z	Total number of electrons (–)
$\boldsymbol{\alpha}, \boldsymbol{\alpha}_0$	Emission angle of recoil electron (rad)
$\boldsymbol{\beta}$	Sample orientation (rad)
$\boldsymbol{\lambda}$	Wavelength (m)
$\boldsymbol{v}$	Frequency (s^{-1})
$\boldsymbol{\rho}$	Momentum density (kg^{-3} m^{-3} s^{3})
$\boldsymbol{\sigma}$	Cross section (m^{2})
$\boldsymbol{\phi}$	Scattering angle (rad), crystal wave function (m$^{-3/2}$)
$\boldsymbol{\chi}$	Momentum wave function (kg$^{-3/2}$ m$^{-3/2}$ s$^{3/2}$)
$\boldsymbol{\psi}$	Wave function (m$^{-3/2}$)
$\boldsymbol{\Omega}$	Solid angle (sterrad)
$\boldsymbol{\varepsilon}_0$	Initial energy of electron (kg m^{2} s^{-2})
$\boldsymbol{\varepsilon}_1$	Energy of recoil electron (kg m^{2} s^{-2})

Introduction

"Compton scattering" (Cooper et al., 2004) refers to a collision between a photon and a charged particle, often an electron, in which the photon loses a substantial fraction of its energy. The use of words "photon" and "collision" suggests a corpuscular nature of light, that is, that light may be viewed as a stream of particles with well-defined energies and momenta. The first indications that light can lose a part of its energy when scattered in this manner appeared at the beginning of the twentieth century. Convincing evidence was provided by the pioneering experiments in the 1920s by Arthur Compton after whom the effect has been named.

This was not the first time the suggestion had been made that light may behave as a particle. The photoelectric effect, in which a material irradiated by light can be seen to emit electrons, was earlier explained by Einstein by postulating that light of frequency v consists of particles called light quanta (and later photons), each with energy hv, where h is Planck's constant. For a given material, the photoemitted electrons possess energies, which depend on the frequency (or equivalently the wavelength, $\lambda = c/v$, where c is the speed of light), but not on the intensity of the incident light. Above a certain wavelength no electron emission is possible, as is observed to be the case, because a photon does not carry enough energy to overcome the binding energy of the electron to the material. Compton scattering, which views the photon-electron scattering to behave rather like billiard balls colliding with other billiard balls, thus reinforced Einstein's explanation of the photoelectric effect.

An outline of this chapter is as follows. The following section gives an overview of the theory of Compton scattering. The equations for energy and momentum transfer and the cross section for the Compton scattering process are given. Various forms of Compton scattering are discussed: (1) Compton scattering from the charge distribution of electrons in a material; (2) magnetic Compton scattering; and (3) (γ, $e\gamma$) scattering, in which additional information is obtained by measuring the properties of the recoil electron in addition to those of the scattered photon. The third section addresses issues of instrumentation. In keeping with current trends, the emphasis is on experiments using synchrotron radiation facilities around the world, which provide bright sources of X-rays. The fourth section touches upon the effect of multiple scattering of a Compton scattered photon within the sample, which complicates the interpretation of data. The fifth section turns to methods of analyzing Compton scattering data. In those cases where an adequate dataset is available, one can in principle obtain the three-dimensional momentum density of the many-body electronic ground state of the material. Much insight has been gained into the electronic structure and bonding properties in wide classes of materials via comparisons of measured Compton scattering data with the corresponding ab initio computations. The last section concludes with a presentation of a few illustrative examples of such comparisons.

Theory

Consider first a collision between a photon and a stationary electron in free space. The incident photon has momentum $\boldsymbol{k}_0$ and energy $E_0 = |\boldsymbol{k}_0|c$. As a result of the collision, the electron recoils with momentum p_1 and relativistic energy $\varepsilon_1 = [(p_1c)^2 + m^2c^4]^{1/2}$, while the momentum and energy of the scattered photon are $\boldsymbol{k}_1$ and $E_1 = |\boldsymbol{k}_1|c$, respectively. Energy and momentum conservation laws then yield

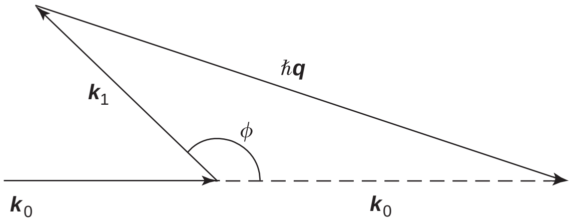

Fig. 1 Momentum conservation diagram for Compton scattering of an incident photon of momentum $\boldsymbol{k}_0$ from a free electron at rest. $\boldsymbol{k}_1$ is the momentum of the scattered photon, q the scattering vector, and ϕ the scattering angle.

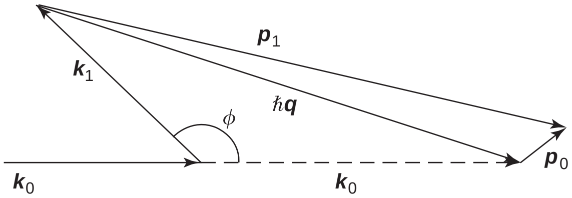

Fig. 2 Momentum conservation diagram for Compton scattering of an incident photon of momentum $\boldsymbol{k}_0$ from an electron with momentum $\boldsymbol{p}_0$. Upon recoiling, the electron has a momentum $\boldsymbol{p}_1$. The initial momentum $\boldsymbol{p}_0$ is typically much smaller than $\boldsymbol{p}_1$.

$$\varepsilon_1 + E_1 = E_0 + mc^2 \tag{1}$$

$$\boldsymbol{p}_1 + \boldsymbol{k}_1 = \boldsymbol{k}_0 \tag{2}$$

Eq. (2) shows that the momentum gained by the recoiling electron, $\boldsymbol{p}_1 = \boldsymbol{k}_0 - \boldsymbol{k}_1 \equiv \hbar \boldsymbol{q}$, is the same as the momentum lost by the photon, which, after division by $\hbar$, is called the scattering vector $\boldsymbol{q}$ (Fig. 1). Eliminating the electron momentum $\boldsymbol{p}_1$ from Eqs. (1) and (2) gives

$$E_0 - E_1 = \frac{E_0 E_1}{mc^2}(1 - \cos\phi) \tag{3}$$

Recalling the relation $\lambda = hc/E$ for photons, this can be written as

$$\lambda_1 - \lambda_0 = \frac{h}{mc}(1 - \cos\phi) \tag{4}$$

The quantity $h/mc \sim 0.00243$ nm, called the Compton wavelength of the electron, is the natural unit of length in quantum electrodynamics. The shift in wavelength is seen from Eq. (4) to be independent of the energy of the incident photon. Therefore, this shift can be more easily detected by using high-energy radiation since the percentage change in wavelength is then larger. Eq. (3) can also be rewritten as

$$E_1 = \frac{E_0}{1 + (E_0/mc^2)(1 - \cos\phi)} \tag{5}$$

This equation shows that for X- or γ-rays of energy E_0 comparable to $mc^2 \sim 511$ keV, the energy loss at large scattering angles ϕ is a substantial fraction of the initial energy E_0.

It is important to note that the energy conservation (Eq. (1)) neglects changes in the potential energy of the system, that is, the potential energy of the electron is assumed to be the same before and after the collision. In scattering from atoms, molecules, and solids, this approximation is valid only if the energy transferred in the scattering process is much larger than the relevant binding energies involved. Moreover, for high energy transfers, the scattering process is a fast one in that the duration of the interaction is too short for the system to rearrange itself. This is called the "impulse approximation," and it is at the heart of much of the interpretation of the Compton scattering spectra from materials (Kaplan et al., 2003). In the deeply inelastic regime, where the "impulse approximation" is valid, Compton scattering provides a direct probe of the many-body ground state of the electronic system.

In the more realistic case of a moving electron with initial momentum p_0 and energy $\varepsilon_0 = [(p_0 c)^2 + m^2 c^4]^{1/2}$, the energy and momentum conservation conditions are

$$\varepsilon_1 + E_1 = \varepsilon_0 + E_0 \tag{6}$$

$$\boldsymbol{p}_1 + \boldsymbol{k}_1 = \boldsymbol{p}_0 + \boldsymbol{k}_0 \tag{7}$$

The scattering vector (Fig. 2) once again is $\hbar \boldsymbol{q} \equiv \boldsymbol{k}_0 - \boldsymbol{k}_1 = \boldsymbol{p}_1 - \boldsymbol{p}_0$. Here, ε_0 and ε_1 cannot be eliminated simultaneously from Eqs. (6) and (7) to obtain an equation involving just the photon kinematics. However, elimination of $\boldsymbol{p}_1$ leads to the expression

$$(E_0 - E_1)(\varepsilon_0 + \varepsilon_1) = \left(\hbar^2 q^2 + 2\hbar p_0 \cdot q\right)c^2 \tag{8}$$

Substituting $\varepsilon_0 = \varepsilon_1 = mc^2$ in Eq. (8), one obtains the useful nonrelativistic relation

$$E_0 - E_1 = \frac{\hbar^2 q^2}{2m} + \frac{\hbar \boldsymbol{p}_0 \cdot \boldsymbol{q}}{m} \tag{9}$$

The term $\hbar^2 q^2/2\,m$ is called the Compton shift, while the term $\hbar \boldsymbol{p}_0 \cdot \boldsymbol{q}/m$ has the character of a Doppler shift in that this term is proportional to the velocity component of the electron along the direction of q. It is customary to choose p_z as the component of the initial electron momentum along the scattering vector so that $p_z = \boldsymbol{p}_0 \cdot \boldsymbol{q}/q$. If $p_z = 0$, then Eq. (9) becomes

$$E_0 - E_C = \frac{\hbar^2 q^2}{2m} \tag{10}$$

where E_C is the energy corresponding to the top of the Compton profile.

In the relativistic case Eq. (8) immediately yields

$$p_z = \frac{(E_0 - E_1)(\varepsilon_0 + \varepsilon_1) - \hbar^2 q^2 c^2}{2\hbar q c^2} \tag{11}$$

The scattering vector squared is

$$\begin{aligned} \hbar^2 q^2 &= k_0^2 + k_1^2 - 2k_0 k_1 \cos\phi \\ &= \left(E_0^2 + E_1^2 - 2E_0 E_1 \cos\phi\right)/c^2 \end{aligned} \tag{12}$$

Substituting (12) into (11), one obtains

$$p_z = \frac{(E_0 - E_1)\varepsilon_0 - E_0 E_1 (1 - \cos\phi)}{c\sqrt{E_0^2 + E_1^2 - 2E_0 E_1 \cos\phi}} \tag{13}$$

The width of the Compton profile is very narrow compared with E_C so that $E_C \approx E_1$, and one can use the leading order nonrelativistic approximation $\varepsilon_0 = mc^2$ to obtain the following equation:

$$\frac{p_z}{mc} \approx \frac{E_0 - E_1 - (E_0 E_1/mc^2)(1 - \cos\phi)}{\sqrt{E_0^2 + E_1^2 - 2E_0 E_1 \cos\phi}} \tag{14}$$

This expression allows one to convert the energy scale of the Compton profile to a momentum scale. Conventionally, a minus sign is added to the left-hand side of (13) and (14), so that positive values of p_z correspond to the high-energy side of the profile. Notice also that the energy and momentum of the electron do not occur on the right-hand side of Eq. (14). In a typical Compton scattering experiment the kinematics of the recoil electron is not measured, so that the data are in effect integrated over the p_x- and p_y-components and p_z is the only electron momentum component measured.

The double differential scattering cross section for spin-dependent Compton scattering from a material containing a collection of moving electrons is (Cooper et al., 2004)

$$\frac{\mathrm{d}^2\sigma}{\mathrm{d}\Omega \mathrm{d}E_1} = \left(e^2/mc^2\right)^2 (m/2\hbar q)(E_1/E_0) \times \left\{ fJ(p_z) + (\cos\phi - 1)P_c \hat{\boldsymbol{\sigma}}\left[(\boldsymbol{k}_0 \cos\phi + \boldsymbol{k}_1)/mc\right] J_{\mathrm{mag}}(p_z) \right\} \tag{15}$$

where

$$f = 1 + \cos^2\phi + \left[(E_0 - E_1)/mc^2\right](1 - \cos\phi) + P_l \sin^2\phi \tag{16}$$

and P_c and P_l denote the Stokes parameters which give the degree of circular and linear polarization, respectively, of the incident beam, $\hat{\boldsymbol{\sigma}}$ is a unit vector along the direction of magnetization, and e^2/mc^2 is the classical electron radius r_0. Eq. (15) is valid at low energies, but at high energies the factor $m/2\hbar q$ should be replaced by the more accurate expression

$$m/2\hbar q\left[1 + E_0/mc^2(1 - \cos\phi)\right]$$

Due to the presence of the factor $(\boldsymbol{k}_0 \cos\phi + \boldsymbol{k}_1)/mc$, the magnetic part of the cross section increases with the photon energy.

The first term in the cross section of Eq. (15) is proportional to the so-called Compton scattering profile $J(p_z)$ due to charge scattering, which is defined as the projection of the total ground-state momentum density $\rho(p) = \rho^{\uparrow}(p) + \rho\downarrow(p)$ onto the scattering vector $\boldsymbol{q}$ which was chosen as the z-axis, or, in other words,

$$J(p_z) = \int\int \left[\rho^{\uparrow}(p) + \rho^{\downarrow}(p)\right] \mathrm{d}p_x\, \mathrm{d}p_y \tag{17}$$

Here, $\rho^{\uparrow(\downarrow)}(\boldsymbol{p})$ denotes the momentum density of electrons with spin up (down) in a magnetic material. In a nonmagnetic material, of course $\rho^{\uparrow}(\boldsymbol{p}) = \rho^{\downarrow}(\boldsymbol{p})$. The momentum density, which is the probability distribution of electrons in momentum space, is given as (Barbiellini and Bansil, 2001)

$$\rho(p) = \sum_i n_i |\chi_i(p)|^2 \tag{18}$$

where

$$\chi_i(p) = (2\pi\hbar)^{-3/2} \int \psi_i(r) e^{-ip\cdot r/\hbar} dr \tag{19}$$

is the Fourier transform of the wave function $\psi_i(\boldsymbol{r})$ and the summation runs over all (spin-dependent) states i. A property of the Fourier transform is that $\psi_i(\boldsymbol{r})$ and $\chi_i(\boldsymbol{p})$ weight inverse regions of configuration space: the valence electrons, which tend to lie farther away from the nuclei contribute to $\chi_i(\boldsymbol{p})$ at low momenta, whereas the tightly bound core electrons contribute at higher momenta. Also, since $\chi_i(\boldsymbol{p})$ is the Fourier transform of $\psi_i(\boldsymbol{r})$, it contains the same fundamental information as $\psi_i(\boldsymbol{r})$. Thus, the momentum density describes the electronic system as well as the more familiar charge density. The occupation number n_i gives the number of electrons populating the ith state. In the absence of correlations between the electrons, $n_i = 1$ for an occupied state and $n_i = 0$ when the state is empty. Integrating the Compton profile $J(p_z)$ over p_z is equivalent to integrating the momentum density $\rho(\boldsymbol{p})$ over the entire $\boldsymbol{p}$-space, which from the properties of the Fourier transform is the same as the integral of the real-space charge density. But the integral of the charge density (appropriately normalized) obviously is the number of electrons Z per formula unit. This observation makes it possible to normalize the Compton profile on an absolute scale. However, it is emphasized that the simple relationship given by Eq. (17) between the Compton profile and the electron momentum density (EMD) only exists by the grace of the impulse approximation (Kaplan et al., 2003).

The second term in formula (15), which can be measured due to the circular polarization P_c of the incident radiation, contains the magnetic Compton scattering profile:

$$J_{\text{mag}}(p_z) = \int\int \left[\rho^{\uparrow}(p) - \rho^{\downarrow}(p)\right] dp_x \, dp_y \tag{20}$$

which, like the $J(p_z)$ of Eq. (17), is a projection along p_z, except that $J_{\text{mag}}(p_z)$ involves the difference (rather than the sum) of the up- and down-spin momentum densities. $J_{\text{mag}}(p_z)$ is thus related to the ground-state momentum distribution of the electrons with unpaired spin. The magnetic term in the cross section (15) is typically smaller than the charge scattering term proportional to $J(p_z)$ by a few orders of magnitude. This is due firstly to the factor of $(\boldsymbol{k}_0 \cos\phi + \boldsymbol{k}_1)/mc \approx E/mc^2$, since the photon energy is usually only a fraction of mc^2, and secondly because the integral of the magnetic Compton profile $\int J_{\text{mag}}(p_z)dp_z$ equals the number of electrons with unpaired spin, which is much less than the total number of electrons Z. The magnetic effect, however, increases with photon energy. It is to be noted that, in contrast to the scattering of polarized neutrons, magnetic Compton scattering only involves the electron spin, and does not depend on the orbital moment.

It is helpful to consider the momentum density of the noninteracting free-electron gas at 0 K. In this case, electrons occupy all available energy levels up to the Fermi energy E_F. Since $E = p^2/2m$, the occupied states fill a sphere in momentum space, the Fermi sphere, of radius $p_F = \sqrt{2mE_F}$, which is called the Fermi momentum. Thus, $n_i = 1$ and $n_i = 0$ inside and outside the Fermi sphere, respectively. It is then easily shown from Eq. (17) that the Compton profile is given by the area of the slice of the Fermi sphere at $p = p_z$ (Fig. 3):

$$\begin{aligned} J(p_z) &= 2\pi\left(p_F^2 - p_z^2\right) & p_z &\le p_F \\ J(p_z) &= 0 & p_z &> p_F \end{aligned} \tag{21}$$

which has the shape of an inverted parabola. The factor of 2 in $J(p_z)$ here accounts for the spin degeneracy of free-electron states. Eq. (21) describes the basic shape of $J(p_z)$ associated with the loosely bound conduction electrons in metals. The contribution of the more tightly bound core electrons varies smoothly and extends to much higher momenta, so that the total Compton profile

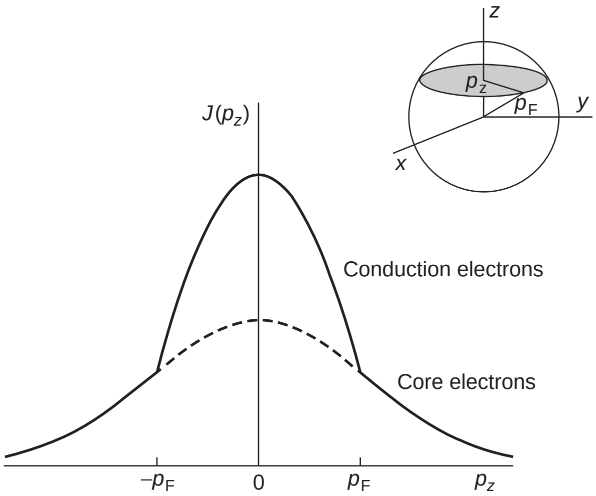

Fig. 3 Schematic Compton profile $J(p_z)$ for a hypothetical metal with two core electrons and one free conduction electron per atom. The parabolic contribution of the free electron is given by the area of the slice (for different p_z values) through the Fermi sphere of radius p_F as shown in the inset.

possesses the shape of an inverted parabola sitting on top of the broader core contribution (Fig. 3). The positions of the two kinks in $J(p_z)$ at $p_z = \pm p_F$ mark the Fermi momentum p_F. In a measured Compton profile these kinks will only appear as rapid changes in slope around the Fermi momentum because of finite experimental resolution. The width of the rapidly varying portion of the Compton profile is a direct result of the spreading of the electrons throughout the Fermi sphere due to Pauli's exclusion principle and the associated Fermi–Dirac statistics of electrons, which forbids more than one electron (of a given spin) to occupy any energy level.

In a real electron gas, electrons interact through Coulomb forces, so that electronic motions become correlated in the sense that an individual electron no longer moves independently of the positions of other electrons. The Coulomb interaction kicks some electrons out of the Fermi sphere, even at zero temperature, and in the process free-electron (noninteracting) states above the Fermi momentum become partially occupied at the expense of states inside the Fermi sphere. The occupation numbers thus become smaller than 1 below E_F and nonzero above E_F, and the momentum distribution becomes more spread out. This effect of electron correlations can be identified in experimental Compton scattering profiles.

In a crystal, electrons experience a periodic potential due to the presence of the underlying lattice. The energy spectrum of the crystal can be shown to consist of groups of levels or bands, where eigenstates within each band are characterized by the wave vector $\boldsymbol{k}$, which is restricted to lie within the first Brillouin zone. The crystal wave function $\phi_i(\boldsymbol{k})$ for the ith band for wave vector $\boldsymbol{k}$ contains momentum contributions not only at $\boldsymbol{p} = \hbar\boldsymbol{k}$, but also at momenta $\boldsymbol{p} = \hbar(\boldsymbol{k} + \boldsymbol{K})$, where $\boldsymbol{K}$ is any one of the group of reciprocal lattice vectors associated with the real space crystal lattice (there should be no confusion with the photon momenta $\boldsymbol{k}_0$ and $\boldsymbol{k}_1$ introduced earlier). The periodic potential thus has the effect of broadening the valence electron momentum distribution somewhat like the effect of electron correlations. Moreover, the Fermi surface breaks in the momentum density of the crystal will generally occur not only at the momenta p_F, but also at all the Umklapp images of the Fermi surface at momenta $p_F + \hbar\boldsymbol{K}$ with appropriate weights.

The twofold integration of $\rho(\boldsymbol{p})$ in Eq. (17) reflects the fact that in a standard Compton experiment, only the characteristics of the incoming and outgoing photons are measured and those of the recoiling electrons are ignored. It is obviously attractive to devise a way of measuring the three-dimensional momentum density $\rho(\boldsymbol{p})$. This is possible if the kinematics of the recoil electron is measured in coincidence with that of the Compton scattered photon. This is referred to as a $(\gamma, e\gamma)$ experiment since here one measures the cross section for the process in which a γ-ray photon scatters into a photon and an electron. Fig. 4 clarifies the various momenta involved. The recoil electron is emitted at an angle α (this angle does not necessarily lie in the plane defined by $\boldsymbol{k}_0$, $\boldsymbol{k}_1$, and $\hbar\boldsymbol{q}$) with respect to the primary beam direction. The angle α_0 for an electron initially at rest is given by

$$\cot\alpha_0 = \left(1 + E_0/mc^2\right)\tan(\phi/2) \tag{22}$$

The components p_x and p_y of the initial electron momentum $\boldsymbol{p}_0$ cause the recoil electron to end up in solid angles closely around the direction α_0, where it can be detected with the aid of a position-sensitive detector. As before, p_z can be determined from the Doppler broadening formula (13). Alternatively, one may measure the energy of the recoil electron by a time-of-flight method in coincidence with that of the photon. It should be emphasized that if the coincidence condition is not imposed, the energy distribution of the scattered photons as well as that of the recoil electrons is each proportional to the Compton profile. Only by observing the photon and the electron in coincidence does one obtain $\rho(\boldsymbol{p})$. Since electrons interact strongly with matter, $(\gamma, e\gamma)$ experiments require very thin samples in order to minimize the scattering of the recoil electrons.

A technique closely related to $(\gamma, e\gamma)$ scattering is $(e, 2e)$ scattering in which an incoming electron generates two outgoing electrons, the scattered and the recoiling one, and the kinematics of the two outgoing electrons is measured in coincidence. Electron scattering is even more of a problem in such an experiment. Finally, inverse Compton scattering in which a photon takes up energy by collision with an energetic electron plays a role in astrophysics.

Instrumentation

In its simplest form, a Compton scattering experiment involves a source of X- or γ-rays of a well-defined energy (or at least with a strong monochromatic component in its energy spectrum), a sample, an energy analyzer, and a detector to register the scattered radiation (Fig. 5). Along its path, the radiation is narrowly collimated by systems of parallel Soller slits to achieve an accurate

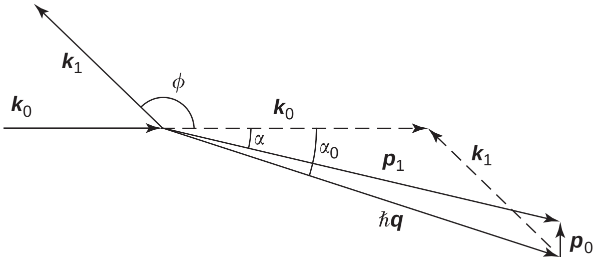

Fig. 4 Momentum conservation diagram for $(\gamma, e\gamma)$ scattering, where various momenta have been defined previously in Figs. 1 and 2. α_0 refers to the limiting case where the electron is initially at rest.

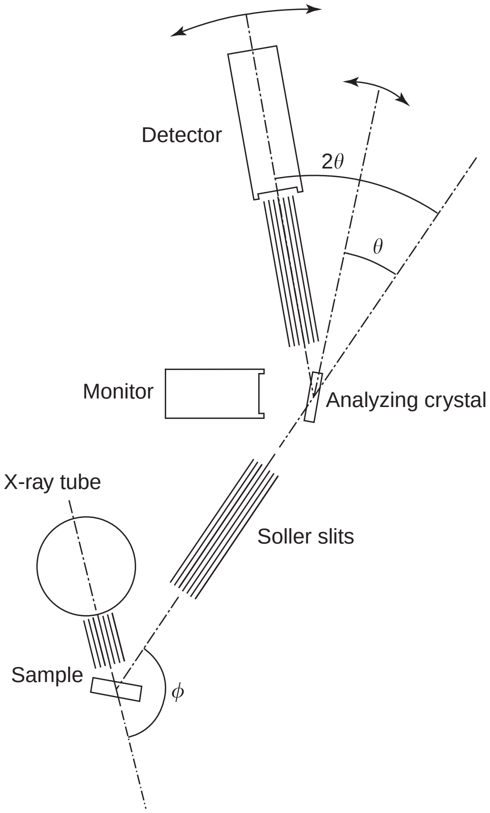

Fig. 5 Schematic setup of an X-ray Compton scattering experiment.

definition of the various angles and thus of the energy of the scattered radiation. The scattered photons are energy-analyzed by Bragg reflection from an analyzing crystal (usually LiF or Si) and detected with the aid of a scintillation detector. In such a setup, the Compton profile is obtained via a step-by-step energy scan, and the experiment therefore suffers from long data collection times and possible instabilities due to temperature variations, electronic drift, and other effects. Improvement is achieved by replacing the analyzer-detector combination with a high-resolution high-purity or lithium-drifted germanium solid-state detector, which registers the entire spectrum simultaneously, at the expense, however, of resolution.

When an X-ray tube is used, the energy of the incoming radiation is limited to several tens of keV (Mo or Ag anode) or at most to ~60 keV for the **K**α1 line of a tungsten anode. The flux from X-ray tubes is often too low to allow the use of a primary monochromator, and the scattered spectrum therefore consists of contributions from the **K**α1 and **K**α2 lines, in addition to other parts of the spectrum, which complicates the interpretation of the measured profiles. Over the years, the count rates have improved with the development of more powerful X-ray tubes, sometimes with rotating anodes, and the use of large samples in combination with bent analyzing crystals, which focus the broad scattered beam onto the detector, thereby allowing radiation with a larger divergence angle to be used. Momentum resolutions for this type of setup vary between 0.15 and 0.5 a.u. full-width-at-half-maximum (1 a.u. of momentum equals 1.9929×10^{-24} kg m s^{-1}), depending on the details of the instrumental design.

The relatively low energy of the radiation provided by X-ray tubes limits Compton experiments to materials with low Z values, since at these energies Compton scattering increases as Z while the competing photoelectric absorption increases as Z^5. Also, at low photon energies, the impulse approximation, which requires the energy transferred in the scattering process to be large compared to the binding energies involved, ceases to be valid for high Z atoms. Higher-energy radiation is needed to circumvent these limitations. γ-ray sources using radioactive isotopes offer the advantage of providing radiation of a high, single energy, and often possess a long half-life $t_{1/2}$. Examples include ^{241}Am (60 keV, $t_{1/2} = 425$ years), ^{198}Au (412 keV, 2.7 days), and ^{137}Cs (667 keV, 30 years). In combination with a solid-state detector, these sources allow the simultaneous detection of the entire Compton scattered spectrum in an apparatus without moving parts. Shielding is a serious problem at these high energies and limits the maximum scattering angle that can be used. An annular shape of the source with the scattered beam passing through the center of the ring can offer a solution. Scattering in the source itself should be kept low since it produces a tail at the low-energy side of the Compton line, which must be corrected for in data-handling procedures. For this purpose, a source material with a high specific activity should be used. The best momentum resolution of ~0.40 a.u. that can be achieved with γ-ray sources is substantially worse than that of a high-resolution X-ray setup using an analyzing crystal. This is an important consideration in some investigations since a high momentum resolution of ~0.1 a.u. or better is generally needed for observing Fermi surface signatures in the Compton spectra.

The most versatile source of X-rays is synchrotron radiation, which is produced by the acceleration of charged particles, most commonly electrons, going around a circular orbit. The synchrotron radiation beam has a small angular divergence and is emitted in the forward direction by the orbiting particles, rather like the searchlight beam in a lighthouse. Photons emitted in the orbital plane are linearly polarized, while those emitted above and below this plane are circularly polarized. The energy range over which an intense flux of linearly or circularly polarized photons is produced can be extended by increasing the acceleration of the orbiting particles over a small portion of their trajectory. This can be achieved with the aid of a suitably designed insertion device, an "undulator" or "wiggler," which introduces a small wiggle in the particle orbit. In a symmetric wiggler the two directions of circular polarization cancel, so the insertion device should contain a certain degree of asymmetry. Since the energy spectrum of synchrotron radiation is "white," a monochromator must be used to "cut" a monochromatic slice from this spectrum. Perfect Si or Ge single crystals with a rocking curve of width comparable to the beam divergence are often used as monochromators. These must be cooled to maintain stability in the presence of an intense heat load of several 100 W to a few kW to which they are exposed. The scattered beam is analyzed using a curved analyzing crystal and focused onto a detector. The high intensity of radiation may in some cases cause overloading of the detector electronics. Fig. 6 shows a Compton setup in used at ESRF in Grenoble, France. Another setup suitable for heavy element materials is available at the BL08W beamline at the SPring-8 synchrotron facility (Japan) (Sakurai and Itou, 2004).

Typical synchrotron fluxes at the sources used for Compton scattering vary between 10^{10} and a few times $10^{1.3}$ photons s^{-1}, while initial photon energies range from 10 keV to >250 keV. Such fluxes are sufficiently high for carrying out several different types of experiments. For example, using unpolarized or linearly polarized light, conventional Compton profiles for electronic structure studies may be measured with a resolution of 0.10–0.15 a.u. or better. If the initial radiation is circularly polarized, the presence of the spin-dependent term in the scattering cross section of Eq. (15) enables one to measure the magnetic momentum density of electrons with unpaired spin in ferromagnetic or ferrimagnetic media (since Compton scattering is an incoherent process, no magnetic effect is observed in antiferromagnetic materials). Since the synchrotron beam decays exponentially in time, the magnetization of the sample or the circular polarization (helicity) of the photons should be reversed every 10 s or so in the pattern (+ − − +). A high circular polarization is achieved at the expense of a high flux. In view of the smallness of the magnetic effect and the importance of good statistics, resolution has therefore to be traded against intensity and much of the currently existing magnetic Compton scattering work is limited to a resolution of ~0.4 a.u. or worse.

Finally, the way is open to $(\gamma, e\gamma)$ spectroscopy. As discussed in the second section, by measuring the recoiling electron in coincidence with the scattered photon, it is possible to determine the three-dimensional momentum density $\rho(\boldsymbol{p})$ of the electrons in a material. $(\gamma, e\gamma)$ measurements are only feasible with an intense flux of high-energy (about 150 keV) photons. Measurements of $\rho(\boldsymbol{p})$ on very thin (17–25 nm thick) graphite samples have been performed in this way with a momentum resolution of 0.60 (0.85) a.u. in the $p_z(p_x)$-direction (Sattler et al., 2001). A better resolution has been obtained with a time-of-flight spectrometer. In cases where the extremely low cross section of the process makes it necessary to integrate over the energy distributions of the recoil electron as well as the scattered photon, one is left with information only on the perpendicular components p_x and p_y of the initial electron momentum. The quantity measured is then a once-integrated, two-dimensional distribution of the EMD like a two-dimensional angular correlation distribution of photons from positrons annihilating in a solid (Barbiellini et al., 2003).

Multiple scattering

Multiple scattering refers to events in which the Compton scattered photon is further scattered one or more times within the sample before it escapes to the detector. The presence of multiple scattering events in the measured Compton profile complicates the analysis of the data. Generally, the multiple scattering contribution tends to broaden the profile somewhat, but its detailed energy dependence on sample geometry and thickness is complex. The effect can be reduced by choosing a thin sample, but that also results in a reduction in the intensity of the primary Compton scattering events of interest. Attempts to measure a Compton profile for various thicknesses followed by extrapolation to zero thickness suffer from the nonlinear dependence of multiple scattering on sample thickness. The most reliable results are obtained using an iterative Monte Carlo approach to simulate the effect of multiple scattering under the specific experimental conditions.

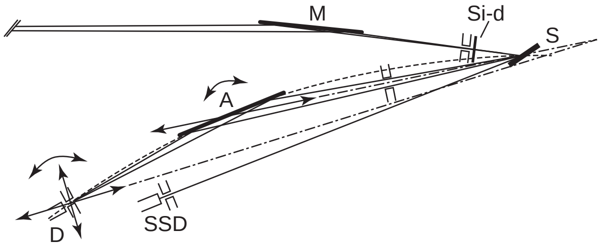

Fig. 6 Drawing of the scanning spectrometer at ESRF, Grenoble, France. The beam reflected by the monochromator (M) is collimated by the entrance slit, and the beam scattered by the sample (S) is collimated by the aperture slit. The sample, analyzer crystal (A), and the detector slit lie on the dashed circle. The detector (D) is an NaI scintillation counter. A Si-diode (Si-d) and a Ge detector (SSD) are used for monitoring. The arrows indicate translations and rotations of the analyzer and detector. The monochromator part of the figure is scaled down by a factor of 10. Courtesy of V Honkimaki.

Data analysis

Although all electrons contribute equally to the Compton profile, one is usually interested in the properties of the smaller group of valence electrons, which are mainly responsible for bonding as they undergo substantial changes when the material is formed by bringing the atoms together. The tightly bound core electrons are relatively unaffected and their contribution to the Compton profile is isotropic. One way to highlight the contribution of valence electrons in analyzing Compton data is to consider differences $\Delta J(p_z)$ between the Compton profiles measured along various pairs of directions of the scattering vector from an oriented monocrystalline specimen, for example, $\Delta J(p_z) \equiv [J_{100}(p_z) - J_{110}(p_z)]$, for the directional difference between the [100] and [110] profiles. The advantage is that the contributions from core electrons, background, and correlation effects (to the extent these are isotropic) cancel in $\Delta J(p_z)$ and the anisotropies related to the valence electrons become clearer.

As seen in the second section, the Compton profile in a crystal generally contains kinks (with appropriate weights) at the Fermi momentum p_F as well as at the images of the Fermi surface at higher momenta induced by the periodic crystalline potential. These kinks originate from breaks in the underlying three-dimensional momentum density $\rho(p)$. They can be made more clearly visible by considering the first or even the second derivative of the Compton spectrum.

Relation (17), which defines the Compton profile $J(p_z)$ as a two-dimensional integral of the momentum density $\rho(\boldsymbol{p})$, may alternatively be viewed as an integral equation for determining the three-dimensional function $\rho(\boldsymbol{p})$. The problem can then be formulated as one of "inverting" relation (17) or "reconstructing" $\rho(\boldsymbol{p})$ from a given set $J_\beta(p_z)$ of profiles corresponding to different orientations (scattering vectors) β of a monocrystalline sample. For this purpose, two approaches are commonly used. One is to expand $\rho(\boldsymbol{p})$ into a series of appropriately chosen directional harmonics. These can be the spherical harmonics, but often the crystal lattice possesses an inherent point symmetry, in which case harmonics of a higher symmetry (called lattice harmonics) are advantageous to use since one needs a smaller number of such harmonics. The expansion coefficients in this series can be expressed as Hankel or Bessel transforms of linear combinations of the set of profiles $J_\beta(p_z)$. This method is particularly useful if the momentum density $\rho(\boldsymbol{p})$ and the Fermi surface are not too far from being spherical. Methods of the second category disregard the point symmetry and solve the problem by Fourier transform techniques. The reconstruction itself can be performed in either the $\boldsymbol{p}$- or the r-space. In the latter case one considers the reciprocal form factor $B(r)$ by taking the Fourier transform of $\rho(\boldsymbol{p})$ (Cooper et al., 2004):

$$B(r) = \int \rho(\boldsymbol{p}) \exp\left(i\boldsymbol{p}\cdot\boldsymbol{r}/\hbar\right) d\boldsymbol{p} \tag{23}$$

from which it is easily shown that

$$B(z) = \int_{-\infty}^{\infty} J(p_z) \exp\left(ip_z z/\hbar\right) \mathrm{d}p_z \tag{24}$$

Thus, the one-dimensional Fourier transform of a Compton profile with the scattering vector along a given direction β equals $B_\beta(\boldsymbol{r})$ along a ray in that same direction in $\boldsymbol{r}$-space through the origin. $B_\beta(\boldsymbol{r})$ can thus be obtained along different rays in r-space from the set of Compton profiles $J_\beta(p_z)$. It is then a simple matter to find the three-dimensional function $B(\boldsymbol{r})$ via interpolation, followed by an inverse Fourier transformation of $B(\boldsymbol{r})$,

$$\rho(\boldsymbol{p}) = (2\pi\hbar)^{-3} \int B(\boldsymbol{r}) \exp\left(-i\boldsymbol{p}\cdot\boldsymbol{r}/\hbar\right) \mathrm{d}r \tag{25}$$

to find the momentum density $\rho(\boldsymbol{p})$.

A useful theorem (the "Lock-Crisp-West" (LCW) theorem) connects the momentum density $\rho(\boldsymbol{p})$ with the occupation density $n(\boldsymbol{k})$, which represents the number of filled electron states at wave vector $\boldsymbol{k}$:

$$n(\boldsymbol{k}) = \sum_K \rho(\hbar\boldsymbol{k} + \hbar\boldsymbol{K}) \tag{26}$$

where the summation is over the reciprocal lattice vectors $\boldsymbol{K}$. The occupation density $n(\boldsymbol{k})$ is a periodic function of $\boldsymbol{k}$, that is, $n(\boldsymbol{k}) = n(\boldsymbol{k} + \boldsymbol{G})$ for any reciprocal vector G. The theorem states that the occupation density at wave vector k is obtained by folding the momentum density at all corresponding points $\boldsymbol{p} = \hbar(\boldsymbol{k} + \boldsymbol{K})$ in the higher Brillouin zones back into the first zone.

Comparison with theory

The methods discussed in the preceding section have all been used extensively in analyzing Compton data. Insight into wide classes of materials has been gained via comparisons between experimental Compton spectra and the corresponding first-principles electronic structure computations. In this connection, many reliable techniques based on the local (spin) density approximation of density-functional theory have been developed for treating crystalline systems during the last few decades such as the (linearized) augmented plane wave (LAPW) method, the linearized muffin-tin orbital (LMTO) method, and the Korringa-Kohn-Rostoker (KKR) method (Cooper et al., 2004). The KKR method is based on the use of multiple scattering theory and possesses the advantage that it can be generalized straightforwardly to treat the electronic structure and momentum densities in substitutionally disordered (random solid solution) phases of alloys within the KKR-CPA scheme (Bansil, 1979a; Bansil, 1979b; Bansil et al., 1981;

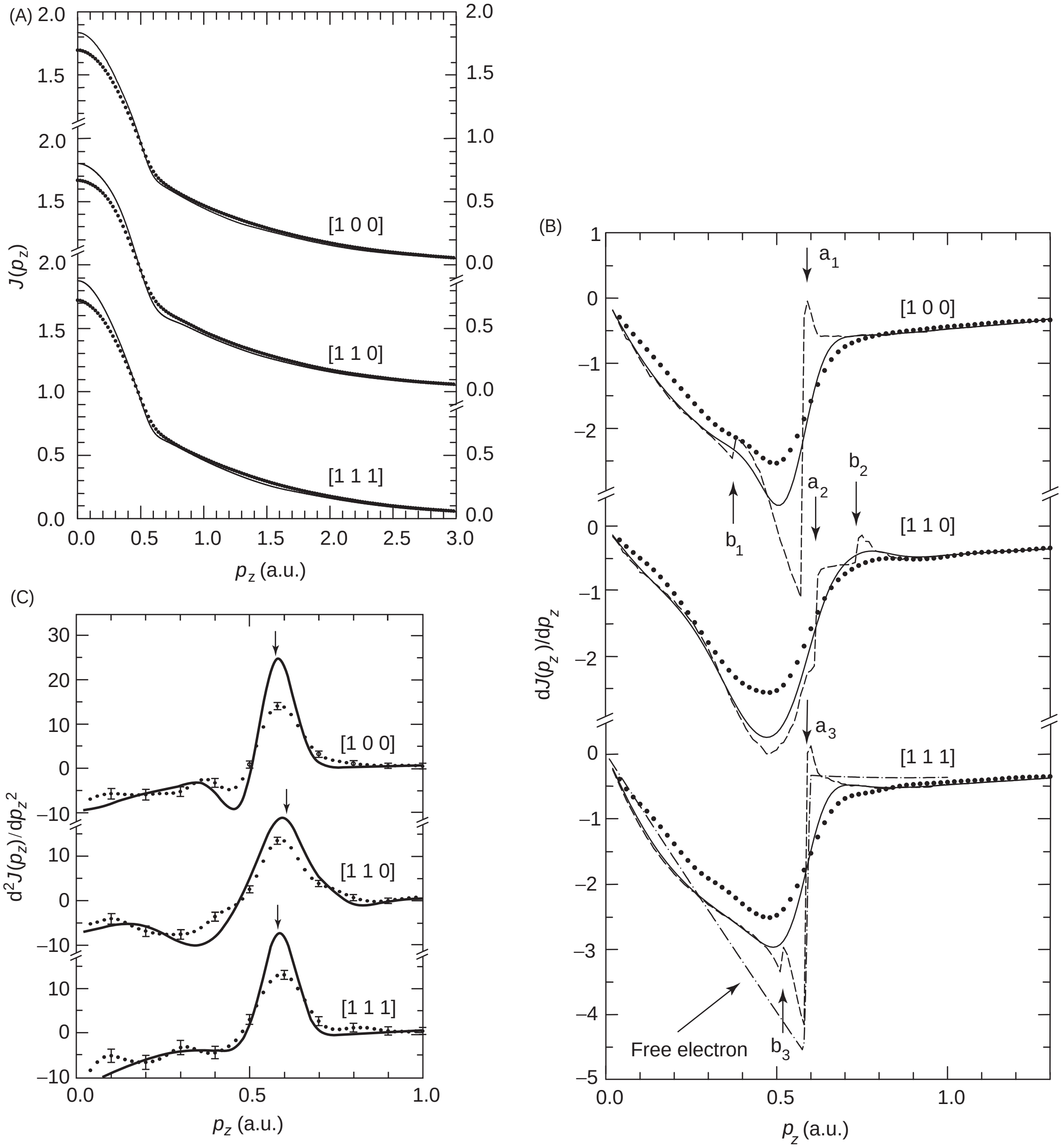

Fig. 7 (a) Measured (. . . .) and computed (——) Compton profile along the three principal symmetry directions of lithium. (b) First derivatives of the profiles. Theoretical profiles are shown with (——) and without (——) resolution broadening of 0.12 a.u. The structures marked a_1–a_3 and b_1–b_3 are Fermi surface breaks. The free-electron result is given for the [111] case. (c) Second derivatives of profiles. Arrows mark the theoretical Fermi radii. Reprinted figure with permission from Sakurai Y, Tanaka Y, Bansil A, Kaprzyk S, Stewart AT, et al. (1995) *Physical Review Letters* 74: 2252–2255; © American Physical Society.

Bansil et al., 1999; Mijnarends and Bansil, 1990). A few illustrative examples of comparison between theory and experiment are presented now. These results will also serve to highlight some of the general features of the Compton spectra that have been discussed throughout this chapter.

Fig. 7 (Sakurai et al., 1995) shows the Compton profiles for lithium (Li). The measured and computed Compton profiles for the scattering vector lying along three high-symmetry directions are shown in Fig. 7a. All profiles have been normalized so that the area under each of the profiles equals the number of electrons (three) in Li. The first derivatives of the profiles in Fig. 7b show that unbroadened theory curves (long dashes) contain breaks at Fermi radii (a_1–a_3) and one set of associated images at $\boldsymbol{p}_F + \hbar\boldsymbol{K}$(b_1 – b_3). The resolution broadening of 0.12 a.u. (full-width-at-half-maximum) washes out the breaks b_1–b_3 as seen from the solid lines. The first derivative for the free-electron profile of Eq. (21), shown for reference only along the [1 1 1]-direction by the dot-dashed line, makes it clear that the momentum density in even a relatively simple system such as Li is modified significantly from the free-electron behavior due to solid-state effects. In addition, note how differences in the results for the three directions, that is, the anisotropy of the profile, are more evident in Fig. 7b compared to Fig. 7a. The actual Fermi surface radii a_1–a_3 are more easily

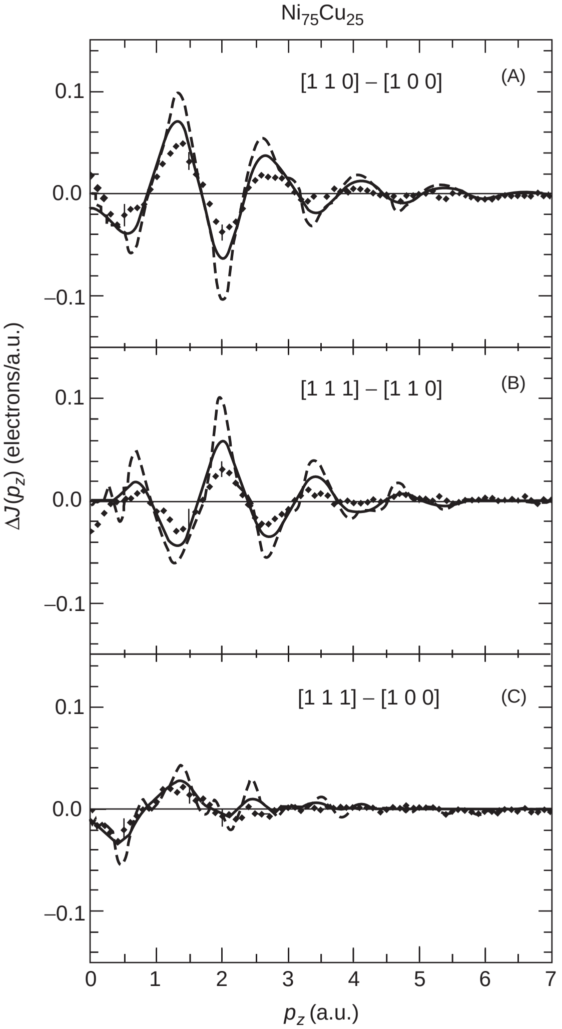

Fig. 8 Directional difference profiles for the disordered alloy $Ni_{75}Cu_{25}$. The experimental (◆) results are compared with theoretical profiles with (——) and without (—) the experimental resolution of 0.4 a.u. Reprinted figure with permission from Bansil A, Kaprzyk S, Andrejczuk A, Dobrzynski L, Kwiatkowska J et al. (1998) *Physical Review B* 57: 314–323; © American Physical Society.

determined from the second derivatives of Fig. 7c and are denoted in the theory curves by arrows. The Fermi surface of lithium is a distorted sphere, somewhat elongated along the ⟨1 1 0⟩ directions. The agreement between theory and experiment is good overall, although the theoretical distribution and particularly the Fermi surface breaks are broader in the experiment. This discrepancy reflects the residual electron correlation effects that are not treated accurately in the conventional band theory picture underlying the computations of Fig. 7 (Sakurai et al., 1995; Stutz et al., 1999; Tanaka et al., 2001; Matsumoto et al., 2001; Kwiatkowska et al., 2006; Hämäläinen et al., 1996; Huotari et al., 2000).

Fig. 8 (Bansil et al., 1998) considers directional anisotropies with the example of an alloy. The results here are for a solid solution of $Ni_{75}Cu_{25}$. The maximum value of the anisotropy $\Delta J(p_z)$ is typically one to two orders of magnitude smaller than the Compton peak intensity. The experimental data in Fig. 8 were taken using a γ-ray source with a momentum resolution of 0.4 a.u. (FWHM), under which all Fermi surface signatures in the data are essentially washed out. Despite some differences in detail, the undulations in $\Delta J(p_z)$ are similar in theory and experiment. The presence of oscillations in $\Delta J(p_z)$ extending to rather high momenta is indicative of interactions in the solid state (Bansil et al., 1998).

Fig. 9 (Matsumoto et al., 2001) takes up an example where a reconstruction technique has been applied to obtain the Fermi surface of the alloy Al–3 at.%Li. Here nine Compton profiles with scattering vectors in the (110) plane were measured and Fourier-transformed to obtain a projection of the momentum density $\rho(\boldsymbol{p})$ onto the (1 1 0) plane. Using the LCW folding procedure of (26) over a selected set of $\boldsymbol{K}$'s then yields the projected image of the Fermi surface shown in Fig. 9. The presence of the Fermi surface outside the indicated geometrical boundaries of the first Brillouin zone is clearly seen. The theoretical maps in the figure have been obtained from nine corresponding computed profiles following procedures which were identical to those used to treat the experimental data.

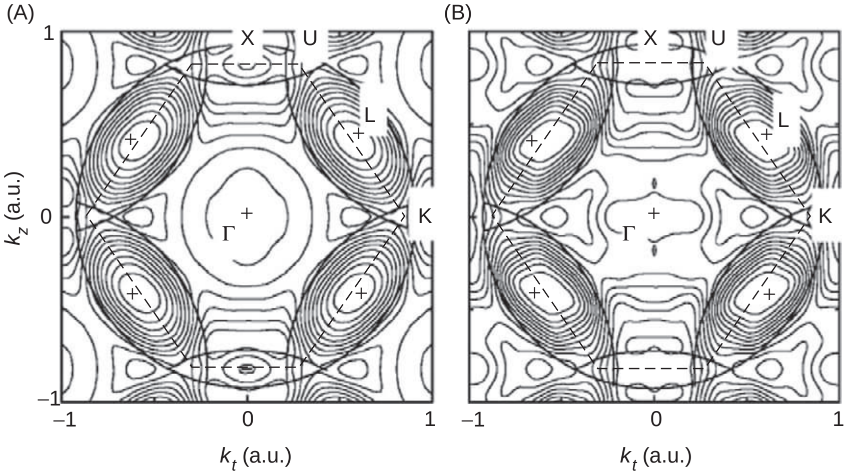

Fig. 9 Contour maps of the (a) theoretical and (b) experimental (1 1 0)-plane-projected occupation number densities for Al–3 at.%Li, obtained by LCW folding. Resolution broadening (0.12 a.u.) is included in the theory. The dashed lines mark the first Brillouin zone. The plus signs indicate high-density regions. Reprinted figure with permission from Matsumoto I, Kwiatkowska J, Maniawski F, Itou M, Kawata H, et al. (2001) *Physical Review B* 64: 045121; © American Physical Society.

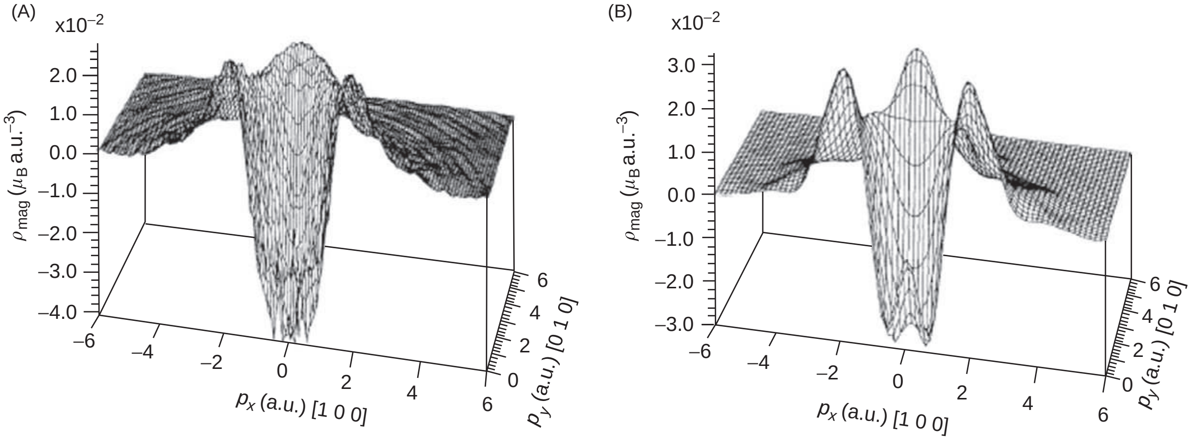

Fig. 10 (a) Cross section of the (001) plane containing the point $\boldsymbol{p} = 0$ through the reconstructed experimental magnetic momentum density $\rho_{mag}(\boldsymbol{p})$ in iron. (b) Corresponding computed magnetic momentum density broadened by the resolution of 0.76 a.u. Reprinted figure with permission from Tanaka Y, Sakai N, Kubo Y, and Kawata H (1993) *Physical Review Letters* 70: 1537–1540; © American Physical Society.

Fig. 10 (Tanaka et al., 1993) presents the magnetic momentum density of the electrons with unpaired spin in iron. In this study Compton profiles were measured for 14 orientations of an iron single crystal. By reversing the magnetization, two profiles were obtained for each of the 14 orientations; their differences yielded 14 magnetic Compton profiles. The Fourier transforms of these 14 profiles were used to map the reciprocal magnetic form factor $B_{mag}(r)$ along the lines of Eq. (24). The inverse transform of (23) was then performed to obtain the magnetic momentum density $\rho_{mag}(\boldsymbol{p})$ of Fig. 10a, which is seen to display a large negative momentum density at low momenta. Fig. 10b depicts the corresponding theoretical results and shows a similar general behavior of the computed momentum density.

An example of a complex material is given in Fig. 11 (Li et al., 2004). The magnetic Compton profile from the double-layer manganite $La_{1.2}Sr_{1.8}Mn_2O_7$ for the scattering vector along the [110] direction is shown. Measurements were carried out at a temperature of 5 K under an external magnetic field of 7 T along [110]. The theoretical profile computed within the first-principles band theory picture is seen after resolution broadening (thick line) to be in good accord with experiments. The shape of the profile in Fig. 11 can be analyzed in terms of the reciprocal form factor $B(\boldsymbol{r})$ given by the one-dimensional Fourier transform of the profile, see Eq. (24). By interpreting $B(\boldsymbol{r})$ as the autocorrelation function of the ground-state wavefunction, one can obtain a handle on the shapes and occupancies of various magnetic orbitals in the system. In particular, the $B(\boldsymbol{r})$ along the [110] direction is found to display a distinct dip at around 0.1 nm; the value (B_{min}) of $B(\boldsymbol{r})$ at the minimum can be related to the occupancy of the 3d(x^2-y^2) molecular orbital involved in the Mn—O bonding as discussed in reference (Li et al., 2004). Studies such as those of Fig. 11 illustrate the ability of magnetic and non-magnetic Compton scattering to analyze the phase diagrams of complex materials (Barbiellini et al., 2009) as a function of doping.

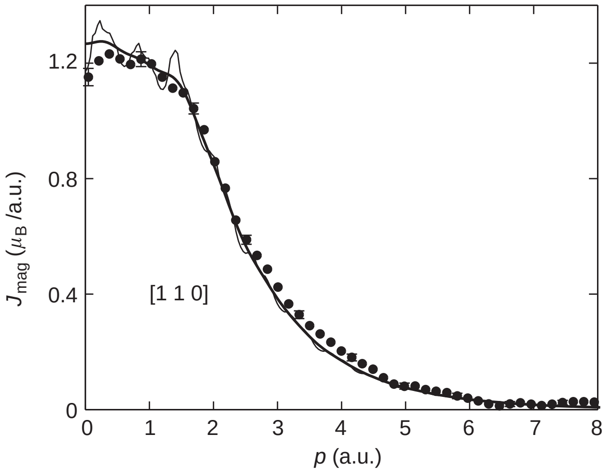

Fig. 11 Experimental (●) and theoretical magnetic Compton profiles along [110] direction in the double layer manganite $La_{12}Sr_{18}$ Mn_2O_7. Measurements were carried out at 5 K under a magnetic field of 7 T. The theoretical profile is shown with (—) and without (**—**) resolution broadening of 0.4 a.u. All profiles are normalized such that the area gives the measured magnetic moment of 3.4 μ_B/Mn atom. Reprinted figure with permission from Li Yinwan, Montano PA, Mitchell JF, Barbiellini B, Mijnarends PE et al. (2004) *Physical Review Letters* 93: 207206; © American Physical Society.

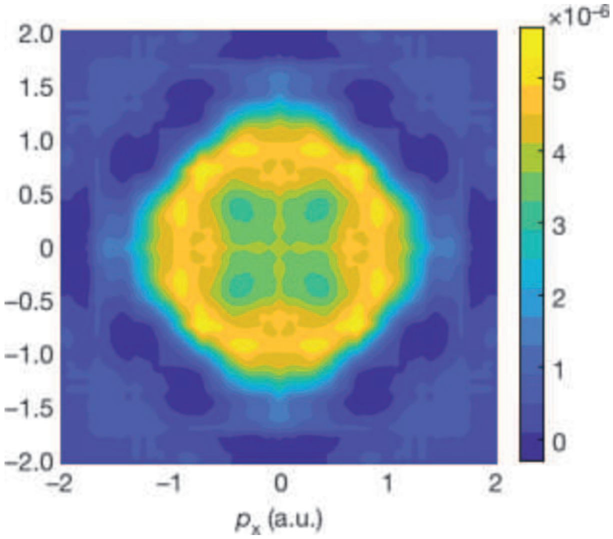

Fig. 12 Momentum density of the O(*2p*) redox orbitals involved in the O^{2-}/O^{-} anionic process in $Li_xTi_{0.4}Mn_{0.4}O_2$. The image has been obtained by subtracting the momentum density corresponding to $x = 0.4$ from that of $x = 0$. Reprinted figure with permission from Hafiz et al. (2021) *Nature* 594: 213; © Springer-Nature.

In fact, Compton scattering studies of $La_{2-x}Sr_xCuO_4$ single crystals have directly imaged the character of the doped holes in this high transition-temperature superconductor. At low doping levels, the O-*2p* character of the hole is much stronger than the Cu-*3d* character but at high doping levels the Cu-*3d* orbital becomes dominant (Sakurai et al., 2011). Along this line, Compton scattering has been used to study reduction-oxidation (redox) reactions in cathode materials for lithium batteries (Suzuki et al., 2015; Barbiellini et al., 2016; Hafiz et al., 2017), where the octahedron formed by a transition metal atom and six oxygen atoms plays a key role like the CuO_6 building block in the copper-oxide superconductors. Very recently, Compton scattering uncovered a new redox mechanism involving oxygen reduction in Li-rich cathodes (Hafiz et al., 2021) and yielded new insight into the nature of the transition-metal redox as well as oxygen redox processes and provided a visual image of the redox orbitals involved in the two cases via tomographic reconstruction. Fig. 12 illustrates the momentum density of the oxygen redox orbital in $Li_xTi_{0.4}Mn_{0.4}O_2$. In this way, Compton scattering is providing a new spectroscopic window for in situ, in operando probing of redox orbitals in working batteries, and a novel pathway for rational design of improved battery materials.

Conclusion

This review discusses the X-ray Compton scattering and related techniques as solid-state spectroscopies for probing ground-state electronic structures and Fermi surfaces of materials. An overview of the theory of X-ray Compton scattering is provided. The key role of synchrotron light sources in advancing the Compton scattering technique, including the development of the magnetic Compton scattering technique based on using circularly polarized light for probing spin-dependent properties of materials is highlighted. Illustrative applications of the Compton scattering techniques, including their application as an advanced characterization tool for investigating functional materials such as the Li-ion battery materials are presented.

References

Bansil A (1979a) Coherent-potential and average t-matrix approximations for disordered muffin-tin alloys. I. Formalism. *Physical Review B* 20(10): 4025.

Bansil A (1979b) Coherent-potential and average t-matrix approximations for disordered muffin-tin alloys. II. Application to realistic systems. *Physical Review B* 20(10): 4035.

Bansil A, Rao RS, Mijnarends PE, and Schwartz L (1981) Electron momentum densities in disordered muffin-tin alloys. *Physical Review B* 23(8): 3608.

Bansil A, Kaprzyk S, Andrejczuk A, Dobrzyński L, Kwiatkowska J, Maniawski F, and Żukowski E (1998) Compton study of Ni_{75} Cu_{25} and Ni_{75} Co_{25} disordered alloys: Theory and experiment. *Physical Review B* 57(1): 314.

Bansil A, Kaprzyk S, Mijnarends PE, and Toboła J (1999) Electronic structure and magnetism of $Fe_{3-x}V_xX$ ($X=$ Si, Ga, and Al) alloys by the KKR-CPA method. *Physical Review B* 60(19): 13396.

Barbiellini B and Bansil A (2001) Treatment of correlation effects in electron momentum density: Density functional theory and beyond. *Journal of Physics and Chemistry of Solids* 62(12): 2181–2189.

Barbiellini B, Dugdale SB, and Jarlborg T (2003) The EPMD-LMTO program for electron–positron momentum density calculations in solids. *Computational Materials Science* 28(2): 287–301.

Barbiellini B, Koizumi A, Mijnarends PE, Al-Sawai W, Lin H, Nagao T, Hirota K, Itou M, Sakurai Y, and Bansil A (2009) Role of oxygen electrons in the metal-insulator transition in the magnetoresistive oxide $La_{2-2x}Sr_{1+2x}Mn_2O_7$ probed by Compton scattering. *Physical Review Letters* 102(20): 206402.

Barbiellini B, Suzuki K, Orikasa Y, Kaprzyk S, Itou M, Yamamoto K, Wang YJ, Hafiz H, Yamada R, Uchimoto Y, and Bansil A (2016) Identifying a descriptor for d-orbital delocalization in cathodes of Li batteries based on x-ray Compton scattering. *Applied Physics Letters* 109(7): 073102.

Cooper MJ, Mijnarends PE, Shiotani N, Sakai N, and Bansil A (eds.) (2004) *X-Ray Compton Scattering*. Oxford: Oxford University Press.

Hafiz H, Suzuki K, Barbiellini B, Orikasa Y, Callewaert V, Kaprzyk S, Itou M, Yamamoto K, Yamada R, Uchimoto Y, Sakurai Y, Sakurai H, and Bansil A (2017) Visualizing redox orbitals and their potentials in advanced lithium-ion battery materials using high-resolution x-ray Compton scattering. *Science Advances* 3(8): e1700971.

Hafiz H, Suzuki K, Barbiellini B, Tsuji N, Yabuuchi N, Yamamoto K, Orikasa Y, Uchimoto Y, Sakurai Y, Sakurai H, Bansil A, and Viswanathan V (2021) Tomographic reconstruction of oxygen orbitals in lithium-rich battery materials. *Nature* 594(7862): 213–216.

Hämäläinen K, Manninen S, Kao CC, Caliebe W, Hastings JB, Bansil A, Kaprzyk S, and Platzman PM (1996) High resolution Compton scattering study of Be. *Physical Review B* 54(8): 5453.

Huotari S, Hämäläinen K, Manninen S, Kaprzyk S, Bansil A, Caliebe W, Buslaps T, Honkimäki V, and Suortti P (2000) Energy dependence of experimental Be Compton profiles. *Physical Review B* 62(12): 7956.

Kaplan IG, Barbiellini B, and Bansil A (2003) Compton scattering beyond the impulse approximation. *Physical Review B* 68(23): 235104.

Kwiatkowska J, Barbiellini B, Kaprzyk S, Bansil A, Kawata H, and Shiotani N (2006) Anomalous electronic correlations in the ground state momentum density of Al_{97} Li_3. *Physical Review Letters* 96(18): 186403.

Li Y, Montano PA, Mitchell JF, Barbiellini B, Mijnarends PE, Kaprzyk S, and Bansil A (2004) Temperature-dependent orbital degree of freedom of a bilayer manganite by magnetic Compton scattering. *Physical Review Letters* 93(20): 207206.

Matsumoto I, Kwiatkowska J, Maniawski F, Itou M, Kawata H, Shiotani N, Kaprzyk S, Mijnarends PE, Barbiellini B, and Bansil A (2001) Two-dimensional folding technique for enhancing Fermi surface signatures in the momentum density: Application to Compton scattering data from an Al-3 at.% Li disordered alloy. *Physical Review B* 64(4): 045121.

Mijnarends PE and Bansil A (1990) The Korringa-Kohn-Rostoker method and momentum density calculations in solids. *Journal of Physics: Condensed Matter* 2(4): 911.

Sakurai Y and Itou M (2004) A Cauchois-type X-ray spectrometer for momentum density studies on heavy-element materials. *Journal of Physics and Chemistry of Solids* 65(12): 2061–2064.

Sakurai Y, Tanaka Y, Bansil A, Kaprzyk S, Stewart AT, Nagashima Y, Hyodo T, Nanao S, Kawata H, and Shiotani N (1995) High-resolution Compton scattering study of Li: Asphericity of the Fermi surface and electron correlation effects. *Physical Review Letters* 74(12): 2252.

Sakurai Y, Itou M, Barbiellini B, Mijnarends PE, Markiewicz RS, Kaprzyk S, Gillet JM, Wakimoto S, Fujita M, Basak S, Wang YJ, Al-Sawai W, Lin H, Bansil A, and Yamada K (2011) Imaging doped holes in a cuprate superconductor with high-resolution Compton scattering. *Science* 332(6030): 698–702.

Sattler T, Tschentscher T, Schneider JR, Vos M, Kheifets AS, Lun DR, Weigold E, Dollinger G, Bross H, and Bell F (2001) Anisotropy of the electron momentum density of graphite studied by (γ, e γ) and (e, 2 e) spectroscopy. *Physical Review B* 63(15): 155204.

Stutz G, Wohlert F, Kaprolat A, Schülke W, Sakurai Y, Tanaka Y, Ito M, Kawata H, Shiotani N, Kaprzyk S, and Bansil A (1999) Electron momentum-space densities and Fermi surface of $Li_{100-x}Mg_x$ ($0 <\sim x <\sim 40$) alloys: Compton scattering experiment versus theory. *Physical Review B* 60(10): 7099.

Suzuki K, Barbiellini B, Orikasa Y, Go N, Sakurai H, Kaprzyk S, Itou M, Yamamoto K, Uchimoto Y, Wang YJ, Hafiz H, Bansil A, and Sakurai Y (2015) Extracting the redox orbitals in Li battery materials with high-resolution x-ray compton scattering spectroscopy. *Physical Review Letters* 114(8): 087401.

Tanaka Y, Sakai N, Kubo Y, and Kawata H (1993) Three-dimensional momentum density of magnetic electrons in ferromagnetic iron. *Physical Review Letters* 70(10): 1537.

Tanaka Y, Sakurai Y, Stewart AT, Shiotani N, Mijnarends PE, Kaprzyk S, and Bansil A (2001) Reconstructed three-dimensional electron momentum density in lithium: A Compton scattering study. *Physical Review B* 63(4): 045120.

Scattering: Inelastic scattering technique—Brillouin[☆]

Tomasz Blachowicz, Institute of Physics—Center for Science and Education, Silesian University of Technology, Gliwice, Poland

© 2024 Elsevier Ltd. All rights reserved.

This is an update of T. Blachowicz, M. Grimsditch, Scattering, Inelastic: Brillouin, Editor(s): Franco Bassani, Gerald L. Liedl, Peter Wyder, Encyclopedia of Condensed Matter Physics, Elsevier, 2005, Pages 199–205, ISBN 9780123694010, https://doi.org/10.1016/B0-12-369401-9/00643-4.

Introduction 187
Brief history of BLS 188
Origin of BLS 188
Scattering geometries and frequency analysis 188
Examples 188
Determination of elastic constants of a bulk crystal 188
Measurements of spectral features in liquids 190
Glasses 190
Gases 191
Surface acoustic modes in thin layers 191
Observation of bulk and surface spin waves in metallic superlattices 191
Recent trends and future direction of research 192
Conclusion 192
Acknowledgments 193
Further reading 193

Abstract

Interaction of laser light with natural acoustic phonons in materials can be used for non-destructive measurement of elastic parameters of materials. The Brillouin scattering technique is used for both basic research and applied efforts for all kinds of physical states: gases, liquids and solids. The article defines the scattering phenomenon itself, discusses the basic metrological elements and reviews the results of experimental work, mainly from the perspective of material research.

Key points

- Non-destructive materials characterization.
- Measurements of elastic properties of materials.
- Spectroscopy of acoustic phonons.
- Single acoustic phonon creation and annihilation.
- Light scattering of magnons in the hypersonic range of frequencies.

Introduction

Brillouin scattering (BLS), in its historical sense, is the inelastic scattering of light by acoustic phonons. It thus provides information on the elastic properties of the scattering medium and it has been used to study gases, liquids, crystals, polymers, glasses, semiconductors, nontransparent thin layers, and superlattices. BLS yields information similar to that obtained using ultrasonic techniques but it has certain advantages when dealing with small samples, reactive samples, or in cases where contact with a transducer poses experimental difficulties (e.g., high temperatures and pressures). The Fabry-Perot interferometer (FP) is, par excellence, the instrument of choice to achieve the 1–100 GHz resolution required in typical BLS experiments. Because of this, BLS has become synonymous for all experiments performed with an FP independent of whether the scattering is produced by acoustic phonons, by magnons, or by electronic states. Here we will use BLS in this broader context.

This article provides a brief historical review and a condensed description of the origin of the effect. Also, some key experimental aspects are briefly described. The emphasis of this article is to illustrate, via specific examples, the range of problems that can be investigated using BLS. This will include the determination of elastic constants with emphasis on its application under adverse experimental conditions (temperature, size and pressure), as well as its application to magnetic systems and electronic levels.

[☆] *Change History*: July 2022. T Blachowicz updated the text. The update modified only text and references. Mentioned about new results and ideas in the field providing adequte citations.

Brief history of BLS

The term Brillouin light scattering (BLS) was derived from the theoretical prediction made by L Brillouin in 1914 of a possible inelastic interaction between light and sound. The description of light-scattering experiments was published in his Ph.D. dissertation. A similar prediction was made independently in 1926 by L I Mandelstam. The first experiment was performed by E Gross in 1930. BLS spectroscopy developed rapidly in the early 1960s as lasers became available. The first light-scattering experiments in pure liquids were done by G B Benedek, et al. in 1964. The technique remained almost an academic curiosity until the multi-passed and later the tandem FP, both introduced by J Sandercock, enabled the weak Brillouin signals to be observed in the presence of the usually overwhelming intensity of the elastically scattered light. At that point, BLS became a powerful and versatile tool for material characterization. This article describes how it has made significant contributions to a wide range of problems in condensed matter physics.

Origin of BLS

Any excitation that produces a time-varying change in the polarizability of a medium (for a longitudinal sound wave this is related to the change in refractive index caused by the densification and rarefaction produced by the wave) interacts with electromagnetic radiation via the polarizability α. The polarization of the medium induced by the electromagnetic wave becomes

$$\mathbf{P}(\mathbf{r}, t) = [\langle\alpha\rangle + \delta\,\alpha\,(\mathbf{r}, t)]\,\mathbf{E}_0\,e^{i\,(\mathbf{k}_i\cdot\mathbf{r}\,-\,\omega_0\,t)}.$$

and it can be shown that this leads to the re-radiation of electromagnetic waves with frequencies $\omega_0 \pm \omega_{phon}$. The origin of the polarizability changes ($\delta\alpha$) is different for different excitations: bulk phonons modulate the polarizability via elasto-optic effects (strain-induced changes in refractive index), surface phonons produce polarizability changes as the interface moves into and out of the vacuum (known as the ripple mechanism), and magnons interact via magneto-optic contributions.

Interference between the radiation emanating from throughout the sample leads to the condition that only excitations with wave-vector $\mathbf{q}$ that satisfy

$$\mathbf{q} = \mathbf{k}' - \mathbf{k},$$

where $\mathbf{k}$and $\mathbf{k}'$ are the wave-vectors of the incident and scattered radiation, respectively, will produce scattered radiation. Since $\mathbf{k}$and $\mathbf{k}'$ are determined by the directions of the incident and scattered radiation, it is clear from the above equation that in a given experiment only excitations with a fixed wave vector will be probed. This also makes it clear that the geometry chosen for the experiment is crucial for analyzing the resulting data.

Scattering geometries and frequency analysis

There are a number of scattering geometries that are often used in Brillouin experiments; these are shown schematically in Fig. 1. Not only does each scattering geometry select different q values but it is clear that geometries (a), (b) and (c) are only suitable for transparent materials while geometries (d) and € can be used even if the sample is not transparent. The (e) geometry is a variant of the back-scattering geometry (d). The magnitude of the wave vector probed in each geometry, calculated from the $\mathbf{q} = \mathbf{k}' - \mathbf{k}$ equation, is also indicated in Fig. 1. In these expressions $|\mathbf{k}| = 2\pi/\lambda$ (with λ the wavelength of the incident radiation, and n the refractive index of the medium). In opaque materials, only the component of q parallel to the surface is conserved so that the $\mathbf{q} = \mathbf{k}' - \mathbf{k}$ equation yields only the value of $\mathbf{q}$ in the surface plane $\mathbf{q}_\mathbf{S}$. Typically, the choice of scattering geometry depends on the nature of the sample and the constraints of the experiment being performed; for example, cryostat, magnet, or furnace. In the laboratory, the incident radiation depicted in Fig. 1 is usually delivered by a laser. Since the frequency shifts are small, it normally requires a laser operating in a single longitudinal cavity mode. The scattered radiation is typically collected by a high quality lens (often a camera lens). Frequency analysis of the scattered light is accomplished using an Fabry-Perot interferometer. In all but a few cases, experiments rely on the high contrast provided by multi-passed and/or tandem instruments. These very delicate instruments are technically complex. Excellent reviews on their operation and fabrication exist in the literature (see the "Further reading" section).

Examples

To highlight BLS, a selection of examples are discussed. First, the classical application is described: the determination of elastic constants in a bulk transparent material. In this subsection, references to examples are provided where the determination of c_{ij} has been done at high temperatures and high pressures. Then examples of BLS applied to liquids, glasses, opaque materials (surface wave BLS), magnetic materials (magnons) and electronic levels are given.

Determination of elastic constants of a bulk crystal

Fig. 2 shows a Brillouin spectrum obtained from a diamond crystal in the backscattering geometry shown in Fig. 1C. Since the diamond surface was (111) and since the phonons probed in the experiment propagate along the surface normal, the peaks observed in Fig. 2 correspond to phonons along the [111] direction. Along this direction the longitudinal sound velocity is

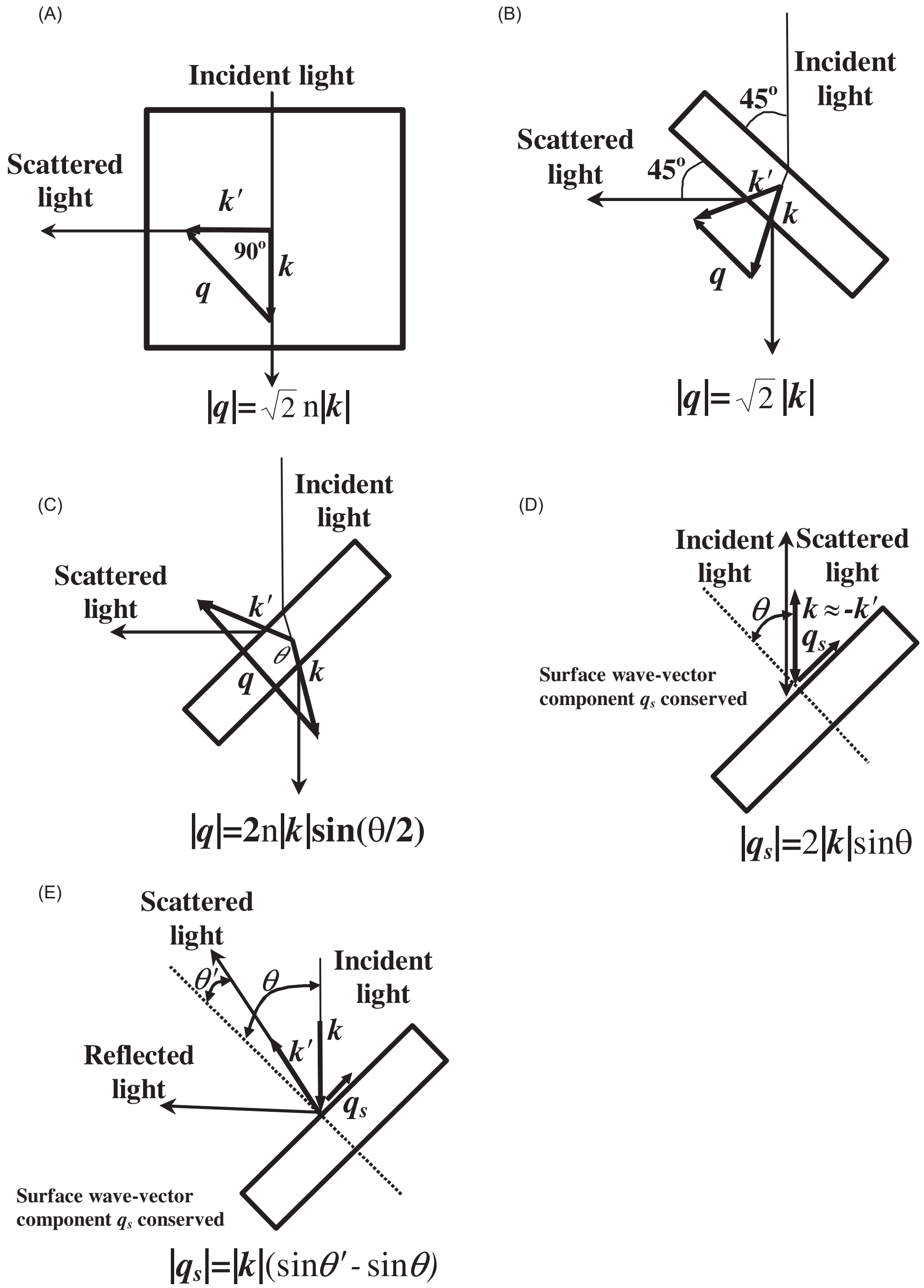
(A)
Incident light
Scattered light
k′
90°
k
q
|q|=√2 n|k|
(B)
Incident light
45°
Scattered light
45°
k′
k
q
|q|=√2 |k|
(C)
Incident light
Scattered light
k′
θ
q
k
|q|=2n|k|sin(θ/2)
(D)
Incident light
Scattered light
θ
k ≈ -k′
q_s
Surface wave-vector component q_s conserved
|q_s|=2|k|sinθ
(E)
Scattered light
θ′
θ
Incident light
Reflected light
k
k′
q_s
Surface wave-vector component q_s conserved
|q_s|=|k|(sinθ′ - sinθ)

Fig. 1 Scattering geometries: (A) a bulk-type analysis of excitations inside a transparent material using 90 degrees geometry, (B) a thin transparent layer—this geometry is sensitive to excitations propagating in the plane of the sample, (C) a transparent layer with near-normal incidence—this geometry is sensitive to wave vectors perpendicular to a sample surface, (D) a back-scattering geometry in an opaque material which is sensitive to in-plane, surface wave vectors, and (E) a variant of geometry (D), where $\mathbf{k}'$ is not along the direction of the incident light, is also used for studying surface excitations. For geometries (A) and (C) the material refractive index n is required for data analysis.

$v_L = \sqrt{(c_{11} + 2c_{12} + 4c_{44})/3\rho}$ and the velocity of the (degenerate) transverse phonons is $v_T = \sqrt{(c_{11} - c_{12} + c_{44})/3\rho}$. The peaks in Fig. 2 have therefore been labeled as L and T, respectively.

Since diamond crystals are large enough to be cut and polished with any desired orientation, it is clear that from a combination of measurements in different scattering geometries and/or crystal orientations the whole set of elastic constants can be determined. In Table 1, the c_{ij} of diamond determined by both Brillouin scattering and by ultrasonic techniques are listed. The results of both techniques are in very good agreement but it is interesting to note that while the BLS measurements were performed on crystals of around 1/3 carat, the ultrasonic measurements used a 22 carat diamond.

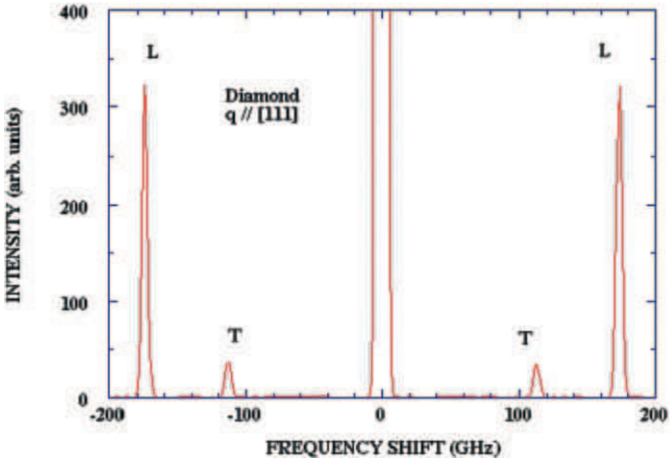

Fig. 2 Brillouin spectrum from a diamond crystal in the geometry from Fig. 1C. The longitudinal (L) and transverse (T) phonons propagate along the [111] direction.

Table 1 Elastic constants of diamond and boron nitride.

Material and method	c_{11} *(GPa)*	c_{12} *(GPa)*	c_{44} *(GPa)*
Diamond, BLS	1076	125	577
Diamond, ultras	1079	124	578
Boron nitride, BLS	820	190	480

In cases where large, transparent crystals are available, it is clear form Table 1 that BLS has no particular advantage over ultrasonic techniques. However, when only small samples are available the BLS technique becomes the technique of choice. Single crystals of cubic Boron Nitride (BN), for example, cannot be grown as single crystals larger than ≈500 μm. In this case, BLS becomes the technique of choice and yields the c_{ij} also included in Table 1.

The preceding section outlines how BLS can be used to determine c_{ij}. At ambient conditions c_{ij} can often be determined more accurately using ultrasonic techniques. In some cases, however, BLS becomes a much more versatile tool than ultrasonics. Such cases usually involve samples, where transducer bonding is difficult, as it was mentioned above, high pressure and/or high temperature experiments, or cases where chemical reactivity becomes severe. For example, the temperature dependence of the c_{11} and c_{44} elastic constants of $Ba_{1-x}La_xF_{2+x}$ over the range 300–1600 K was determined by P E Ngoepe and J D Comins who found a linear decrease that they attributed to anharmonicity. A case involving high pressures is represented by measurements of liquid and solid argon in a diamond anvil cell up to 70 GPa.

Measurements of spectral features in liquids

BLS can also be used to determine the elastic response of liquids. In contrast to solids, however, where the unshifted peak is dominated by the effects of impurities and surface scattering, in pure liquids the central peak is due to entropy fluctuations. The intensity of the unshifted component is related to that of the shifted BLS peaks via the Landau-Placzek ratio, C_p/C_v-1, where C_p and C_v are the specific heats at constant pressure and volume, respectively. In pure liquids, therefore, BLS can be used to study the intensity and shape of the central peak. Frequency broadening of this peak can be caused by fluctuations in the orientation of anisotropically polarizable molecules or by diffusive processes governed by the equations of hydrodynamics. In liquids, it is also possible to investigate relaxation and damping effects via the phonon lifetime that translates into changes in the shape and line-width of the phonon peaks. The same approach cannot usually be applied to most bulk crystals, because of a very low damping that results in line widths below the experimental resolution. However, in temperature regions where structural phase transitions occur, damping processes influence Brillouin line widths enough so that the changes are detectable, for example, in molten and crystalline alkali halides, during order-disorder transitions in mixed crystals, or during ferroelastic phase transitions in some crystals.

Glasses

BLS has been extensively used to investigate the transition for liquid to solid in materials that do not crystallize: for example, silica, $Rb_{1-x}(NH_4)_x/H_2PO_4$ (10–300 K), $Rb_x(NH_4)_y/H_2PO_4$ (20–80 K), and $Ca(NO_3)/KNO_3$ (320–640 K). Across the transition region, the phonons in these materials become highly damped and the resulting line shapes can be interpreted in terms of the underlying mechanism of the glass transition. These types of investigations are also of practical importance, because these materials are often used in fiber optics technology and in optoelectronic devices.

Gases

BLS in gases detects local fluctuations that lead to frequency shifts in the 0.1–1 GHz range. These shifts can also be viewed as a Doppler shift from the motion of individual atoms. In this context, BLS has also been used to investigate how the phonon spectrum evolves as a gas is pressurized to become a fluid. This evolution reflects the hydrodynamic transformation as the thermal mean free path for atomic motion becomes comparable and then shorter than the wavelength at which the medium is being probed by the scattering of visible light. These experiments can also be interpreted in terms of the hydrodynamic equations of motion. Investigations of CO_2 up to 8 atm pressure, and Xe over the range 0.022–0.66 atm are two instances where this phenomenon has been investigated.

Surface acoustic modes in thin layers

Light scattering from acoustic excitations in opaque materials results from a purely surface-induced mechanism, viz. phonon-induced thermal ripples. In these cases, the scattering geometries (d) and (e) in Fig. 1 must be employed. In a semi-infinite medium, the strongest coupling is to Rayleigh waves (reminiscent of waves in the ocean) with some weaker features induced by bulk waves reflecting from the free surface. In thin films and layered structures, however, it is also possible to couple to modes that are localized within the layers or at the interfaces; these modes are generally referred to as Sezawa modes. If the medium is not completely opaque, it is possible to couple to the phonons via both the ripple and elasto-optic mechanisms. In these cases, unusual interference effects are possible.

Fig. 3 shows a BLS spectrum from a Co/Cu superlattice built from 60 bilayers of 1 nm Co/0.8 nm Cu in which the Rayleigh and Sezawa modes are observed. The experiment was carried out using a Sandercock-type tandem 3-pass interferometer. From these results, the effective elastic properties of the superlattice can be extracted.

In cases where the surface layers become much thinner than the wavelength of light, the medium again becomes equivalent to a homogeneous solid. In these cases, Brillouin scattering has been a very efficient and reliable tool for determining the effective elastic constants of the heterogeneous solid. For example, R Danner et al. in the Ni/V superlattice, for different layer thicknesses from the range of 1.85 nm to 63.3 nm, proved that this b.c.c./f.c.c. system reveals softening of elastic parameters. J A Bell with co-workers measured effective elastic constants in the Mo/Ta superlattice ($c_{11}, c_{13}, c_{33}, c_{44}$) with an elementary spatial bilayer thickness ranging from 0.7 nm to 20 nm.

Observation of bulk and surface spin waves in metallic superlattices

Brillouin scattering can also be used to investigate the magnetic properties of materials via their magnetic excitations—magnons. In this sense, the information it yields is similar to that obtained in Ferromagnetic Resonance (FMR) experiments. However, contrary to FMR that probes the infinite wavelength excitations, Brillouin scattering probes excitations with wavelengths comparable to the wavelength of light. As for phonons, magnons can be subdivided into surface-like and bulk-like excitations. Expressions relating the magnon frequencies to the magnetic properties of the material- magnetization, anisotropies, applied field, and gyromagnetic ratio—can be quite complex and often cannot be rendered in analytical form.

The Brillouin scattering technique has also been used to investigate the nature of magnetic excitations in nonconventional materials. In the case of the Co/Cu superlattice described in the previous paragraph, which is built from alternating magnetic and nonmagnetic materials, bulk-like collective excitations resulting from coupling between spin waves across the nonmagnetic spacer are detected (Fig. 4). Additionally, a surface-like mode propagating on the surface of the sample was also found. The experiment was

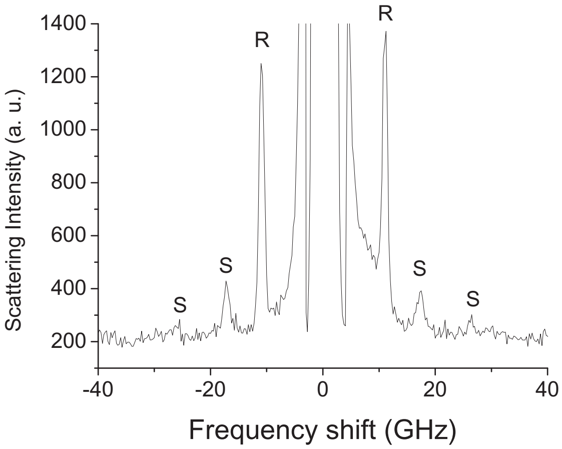

Fig. 3 BLS from surface acoustic phonons in the Co/Cu superlattice. Descriptions: R: the Rayleigh surface mode; S: Sezawa or higher-order Rayleigh modes. The measurement was carried out for (s-s) polarizations of the incident and scattered light.

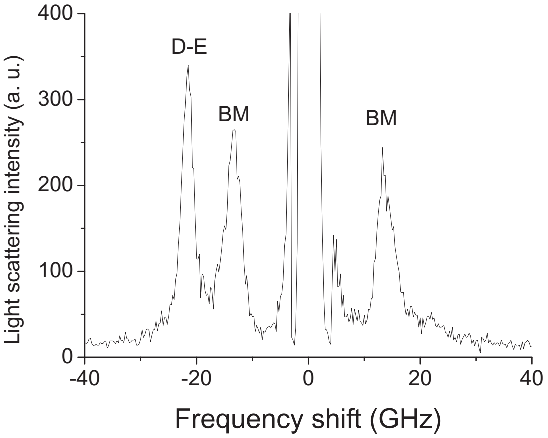

Fig. 4 BLS from spin waves in a multilayered Co/Cu system. Descriptions: D-E: Damon-Eshbach surface mode; BM: (bulk magnon) collective excitations of a bulk-like nature resulting from coupling between spin waves through the nonmagnetic spacer layer. The measurement was carried out for (s-p) polarizations of the incident-scattered light.

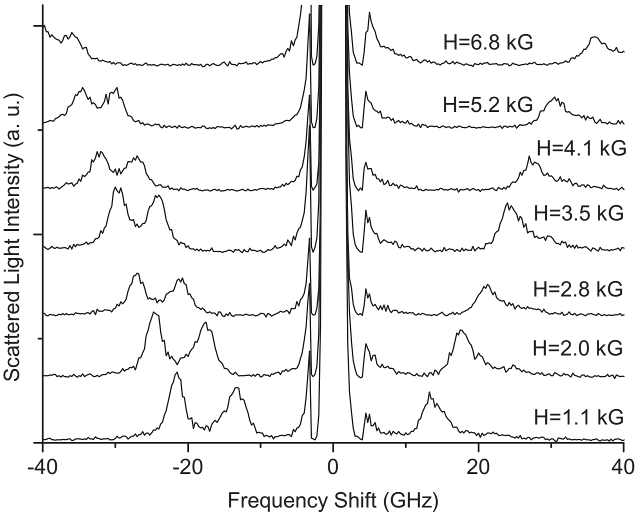

Fig. 5 A set of Brillouin spectra measured for different magnetic field intensities in the Co/Cu superlattice. The peaks that appear only on the left side (Stokes signals) result from scattering from a unidirectional surface-like spin wave (D-E mode from Fig. 4).

carried out with a tandem 3-pass spectrometer, with (s-p) polarization of the incident and scattered light, and a constant magnetic field lying in the sample plane. Fig. 5 provides results for different magnetic field intensities, from which the gyromagnetic ratio and saturation magnetization can be determined.

Recent trends and future direction of research

New research directions related to the BLS method are aimed at biomedical applications—on the one hand—and to applications in magnetoelectronics. The progress in the first area is related to the discovery of Virtual Imaged Phased Array (VIPA) by Scarelli and Yun, also developed by Palombo and Fioretto in viscoelastic media. In recent studies of low dimensional magnetic structures it was possible to observe determine interfacial Dzyaloshinskii-Moriya interactions sensed as asymmetry between BLS Stokes and anti-Stokes peaks position. These studies were intensively carried out by Maziewski, Geniusz and others, enabling the study of materials useful for the formation of skyrmions.

Conclusion

Inelastic Brillouin light scattering is a non-destructive measurement technique applicable to the study of the acoustic properties of materials in the hypersonic range. Although the phenomenon itself was discovered relatively long ago, measurements of acoustic phonons in gases, liquids and solids, including low-dimensional structures, are regularly performed in scientific laboratories. This method, using mainly sophisticated interferometric techniques, is constantly developed and has found applications in the study of magnetoelectronic materials and magnonic excitations in the hypersonic range of frequencies, and importantly, has recently been used in the study of biological and medical samples.

Acknowledgments

I would like to express my gratitude to the people who were my mentors, directly or indirectly, in particular to Marcos Grimsditch (Argonne National Laboratory) for many remote discussions and sharing of research results, to Gernot Güntherodt during my experimental works at RWTH Aachen and to John Sandercock for his support in many moments of my scientific work.

Further reading

Bell JA, Bennett WR, Zanoni R, Sttegeman GI, Falco CM, et al. (1987) Elastic constants of Mo/Ta superlattices measured by Brillouin Scattering. *Physical Review B* 35: 4127–4130.

Benedek GB, Lastovka JB, Fritsch K, and Greytak T (1964) Brillouin scattering in liquids and solids using low-power lasers. *Journal of the Optical Society of America* 54: 1284–1285.

Blachowicz T (1998) Numerical calculations of the rotational contributions to a scattering coefficient in the piezoelectric $LiTaO_3$ crystal. *Journal of the Optical Society of America* B15: 2599–2606.

Blachowicz T (2003) *Brillouin Spectroscopy in Crystal Lattices. Acoustic and Spin Waves*. Gliwice: Silesian University of Technology Press.

Blachowicz T, Pyka M, Kleszczewski Z, Swirkowicz M, and Lukasiewicz T (2002) Doping effects of Cu ions on the elastic properties of the $LiNbO_3$ crystal uncovered by Brillouin scattering. *Solid State Communications* 123: 317–319.

Blachowicz T, Beghi M, Beschoten B, Güntherodt G, Dieker H, et al. (2007) Crystalline phases in the $GeSb_2Te_4$ alloy system: Phase transitions and elastic properties. *Journal of Applied Physics* 102: 093519. 1–6.

Brillouin L (1922) Diffusion de la Lumière et des rayonnes X par un corps transparent homogéne; Influence de l'agitation thérmique. *Annales de Physique* 17: 88.

Broz A, Harrigan M, Kasten R, and Monkiewicz A (1971) Light scattered from thermal fluctuations in gases. *Journal of the Acoustical Society of America* 49: 950–953.

Danner R, Huebener RP, Chun CL, Grimsditch M, and Schuller IK (1986) Surface acoustic waves in Ni/V superlattices. *Physical Review B* 33: 3696–3701.

Dhiman AK, Matczak M, Gieniusz R, Sveklo I, Kurant Z, Guzowska U, Stobiecki F, and Maziewski A (2021) Thickness dependence of interfacial Dzyaloshinskii-Moriya interaction, magnetic anisotropy and spin waves damping in Pt/Co/Ir and Ir/Co/Pt trilayers. *Journal of Magnetism and Magnetic Materials* 519: 167485.

Grimsditch MH (1989) Brillouin scattering from metallic superlattices. In: Cardona M and Güntherodt G (eds.) *Light Scattering in Solids, Superlattices and Other Microstructures*. vol. 5, pp. 285–302. Berlin: Springer.

Grimsditch MH and Ramdas AK (1975) Brillouin scattering in diamond. *Physical Review B* 11: 3139–3148.

Grimsditch MH, Zouboulis ES, and Polian A (1994) Elastic constants of boron nitride. *Journal of Applied Physics* 76: 832–834.

Gross EF (1930) Change of wave-length of light due to elastic heat waves at scattering in liquids. *Nature* 126: 201.

Hyunjung K, Ramdas AK, Rodriguez S, Grimsditch MH, and Anthony TR (1999) Magnetospectroscopy of acceptors in “blue” diamonds. *Physical Review Letters* 83: 3254–3257.

Kuok MH, Lim HS, Ng SC, Liu NN, and Wang ZK (2003) Brillouin study of the quantization of acoustic modes in nanospheres. *Physical Review Letters* 90: 255502. 1–4.

Mandelstam LI (1926) K voprosu o rasseănii sveta neodnorodnoj sredoj. *Zhurnal Russkovo Fiziko-Khimicheskovo Obshchestva* 58: 381.

Ngoepe PE and Comins JD (1986) Measurements of elastic constants in super-ionic $B_{1-x}La_xF_{2+x}$. *Journal of Physics C: Solid State Physics* 19: L267–L271.

Palombo F and Fioretto D (2019) Brillouin light scattering: Applications in biomedical sciences. *Chemical Reviews* 119: 7833–7847.

Sandercock JR (1982) Trends in Brillouin scattering: Studies of opaque materials, supported films, and central modes. In: Cardona M and Güntherodt G (eds.) *Light Scattering in Solids, Recent Results*. vol. 3, pp. 173–206. Berlin: Springer.

Scarcelli G and Yun SH (2012) In vivo brillouin optical microscopy of the human eye. *Optics Express* 20: 9197–9202.

Shimizu H, Tashiro H, Kume T, and Sasaki S (2001) High-pressure elastic properties of solid argon to 70GPa. *Physical Review Letters* 86: 4568–4571.

Signoriello G and Beghi MG (2008) Exploitation of Brillouin spectroscopy for the characterization of a silica film. *Sensor Letters* 6: 130–136.

Scattering, inelastic: X-ray (methods and applications)

ChJ Sahle, A Bosak, NB Brookes, M Krisch, and F Sette, ESRF, The European Synchrotron, Grenoble, France

© 2024 Elsevier Ltd. All rights reserved.

This is an update of M. Krisch, F. Sette, Scattering, Inelastic: X-Ray (Methods and Applications), Editor(s): Franco Bassani, Gerald L. Liedl, Peter Wyder, Encyclopedia of Condensed Matter Physics, Elsevier, 2005, Pages 220–226, ISBN 9780123694010, https://doi.org/10.1016/B0-12-369401-9/00649-5.

Introduction 195
Theoretical aspects 196
IXS from electronic excitations 197
NIXS from electrons 197
IXS from valence electrons 198
IXS from core electrons (X-ray Raman scattering) 198
Resonant inelastic X-ray scattering 199
RIXS from valence electrons 201
RIXS from core electrons 201
Spin selective RIXS – > nonresonant XES 201
Dichroism effects in RIXS – > RIXS-mcd 201
IXS from phonons 202
Phonons in crystalline materials 203
High-frequency dynamics in liquids and glasses 203
Deep IXS 203
Conclusion 204
References 204

Abstract

Inelastic X-ray scattering (IXS) methodology has matured considerably in the past two decades providing a suite of tools for the study of electronic, dynamic, and magnetic response functions. We provide an introductory overview of IXS techniques most commonly available at modern X-ray light sources. Following a general introduction and the description of the theoretical framework, we discuss IXS from electronic excitations, both resonant and nonresonant, IXS from phonons and collective ion excitations. Conclusions and a short outlook round up this contribution.

Key points

- In an inelastic X-ray scattering experiment, energy and momentum are transferred from an X-ray photon to the sample.
- IXS measures the dynamical structure factor S(q,w), that is, the nonzero frequency correlations in materials.
- Depending on the amount of energy and momentum transferred and whether an experiment is performed at or off resonance, IXS is sensitive to electronic-, magnetic-, and/or lattice-degrees of freedom.
- Modern X-ray light sources have enabled rapid progress in IXS techniques over the last three decades.
- IXS has become truly complementary to inelastic neutron scattering.

Nomenclature

a	Inter particle separation (m)
a_c	Radial extent of core electron wave function (m)
A	Vector potential of the electromagnetic field (kg m^2 C^{-1}s^{-2})
b	Neutron scattering length (1/m)
c	Speed of light (ms^{-1})
E	Energy transfer (eV)
e	Electron charge (C)
e	Photon polarization vector
e_k	Kinetic energy of the photoelectron (eV)

E_c	Core-level binding energy (eV)
E_I	Energy of initial state
E_F	Energy of final state
E_N	Energy of intermediate state
$f(Q)$	Atomic form factor
G	Reciprocal lattice vector (m^{-1})
$\hbar$	Reduced Planck's constant (J s)
J	Exchange integral (eV)
j_n	Bessel function of order n
k	Wave vector (m^{-1})
k_B	Boltzmann constant ($\mathrm{J\,K}^{-1}$)
L	Angular momentum (J s)
M	Atom or ion mass (kg)
m	Electron mass (kg)
n	Electron density (m^{-3})
p	Momentum operator of scattered electrons ($\mathrm{kg\,m\,s}^{-1}$)
Q	Momentum transfer vector (m^{-1})
Q	Modulus of momentum transfer (m^{-1})
q	Reduced momentum transfer vector (m^{-1})
$\mathbf{q}$	Modulus of reduced momentum transfer (m^{-1})
r	Position operator of the electron (m)
r_0	Classical electron radius (m)
R	Position operator of the ion (m)
S	Total spin moment (μ_B)
$S(Q, \omega)$	Dynamical structure factor (eV^{-1})
T	Temperature (K)
U	Electron-core hole interaction (eV)
v	Sound velocity (ms^{-1})
W	Debye–Waller factor
Z	Number of electrons in an atom
Γ	Lifetime broadening width (eV)
$\varepsilon(Q, \omega)$	Dielectric function
Θ_S	Scattering angle (deg)
ξ	Structural correlation length (m)
ρ	Electron density of states (1/eV)
σ	Cross section (m^2)
σ_n	Phonon eigenvector of mode n
τ	Structural relaxation time (s)
Φ	External potential (V)
χ	Polarization function ($\mathrm{C}^{-2}m^{-2}$)
ω	Angular frequency of radiation (s^{-1})
Ω	Solid angle (rad^2)

Introduction

Inelastic X-ray scattering (IXS) experiments, including both energy and direction (momentum) analysis of the scattered photons, provide an important spectroscopic tool in the study of dynamical electronic-, magnetic-, and lattice degrees of freedom of matter (Hämäläinen and Manninen, 2001; Schülke, 2007; Ament et al., 2011). Two branches of IXS exist: resonant inelastic X-ray scattering (RIXS) and nonresonant inelastic X-ray scattering (NIXS). Within these branches, the different methods can roughly be classified according to the amount of energy and momentum transferred to the sample system and the nature of the excitation.

The different excitations and relative energy scales are schematically illustrated in Fig. 1. IXS from collective ion excitations aims at the study of phonons and phonon-like excitations. It is complementary to inelastic neutron scattering (INS), and has proven to be particularly powerful in cases where INS techniques cannot be applied. Electron dynamics and electronic excitations are studied in various regimes using NIXS. Compton scattering (which will not be further discussed in detail, see contribution by A. Bansil) allows one to determine the electron momentum distribution. IXS from valence and core electrons bears a very close resemblance to electron-energy-loss spectroscopy, X-ray absorption, and photoemission techniques, and gives access to single-particle or collective,

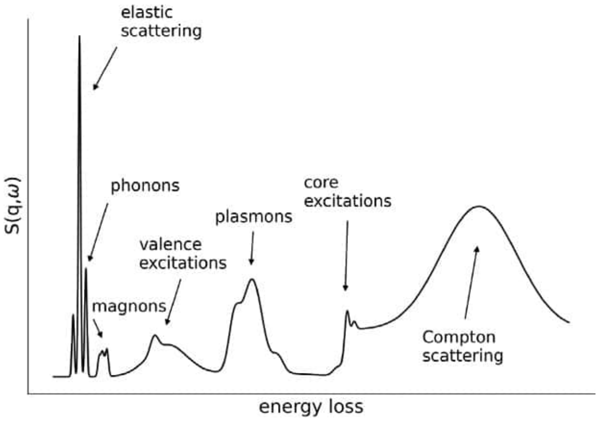

Fig. 1 Schematic X-ray excitation spectrum $S(q, \omega)$ as a function of energy transfer.

electron (plasmon) excitations. Low-energy electronic-, orbital-, and spin-degrees of freedom are probed using resonant IXS. Especially spin degrees of freedom are not easily accessible using nonresonant inelastic scattering. Furthermore, RIXS is element and valence selective.

Despite the fact that most of the IXS techniques were developed several decades ago, they gained their full maturity only after the outstanding properties of electron storage ring-based X-ray sources, in terms of source brilliance and energy tunability, became apparent and modern highly efficient IXS spectrometers with large resolving power became available. IXS experiments are performed over a very large spectral range – from the vacuum-ultraviolet over the soft X-ray range into the hard X-ray regime. Consequently, the associated instrumentation is very diversified, and is based on diffraction gratings for the low energy range, whereas perfect Bragg crystal optics are utilized in the X-ray range. All IXS techniques benefit from the very small beam sizes, in the order of a few tens of micrometers or less, that can presently be obtained at third-generation synchrotron sources (in contrast to milli- to centimeter-sized neutron beam sizes). In the hard X-ray range, these small photon beams even enable IXS at extreme conditions, such as high pressure and high temperature (Rueff and Shukla, 2010).

Theoretical aspects

The basic kinematics of the inelastic scattering process are depicted in Fig. 2. The incident photon of energy $\hbar\omega_1$ and momentum $\hbar\mathbf{k}_1$ are scattered from the sample into a photon of energy $\hbar\omega_2$ and momentum $\hbar\mathbf{k}_2$. The process is therefore characterized by the energy transfer $E = \hbar\omega_1 - \hbar\omega_2$ and the momentum transfer $\hbar\mathbf{Q} = \hbar\mathbf{k}_1 - \hbar\mathbf{k}_2$. Here, the polarization transfer is not considered. In cases where the energy transfer is much smaller than the incident photon energy, $\mathbf{Q}$ is solely controlled by the scattering angle Θ_s, and is given by the following expression:

$$Q = 2k_1 \sin(\Theta_s/2)$$

The Hamiltonian, describing the electron–photon interaction in the scattering process, is composed, in the weak relativistic limit, of four terms. Neglecting the much weaker magnetic couplings, only two terms have to be retained:

$$H_{\text{int}} = \sum_j \frac{e}{2mc^2}\mathbf{A}_j^2 + \sum_j \frac{e}{mc}\mathbf{A}_j\mathbf{p}_j$$

where $r_0 = e^2/mc^2$ is the classical electron radius, $\mathbf{A}$ is the vector potential of the electromagnetic field, and $\mathbf{p}$ is the momentum operator of the scattering electrons. The sum extends over all the electrons in the system j. Treating the scattering process in the lowest order perturbation theory, representing the vector potential $\mathbf{A}$ in terms of photon creation and annihilation operators, and assuming that both the initial and the final photon states can be represented by plane waves, one obtains, for the double differential cross (DDCS)

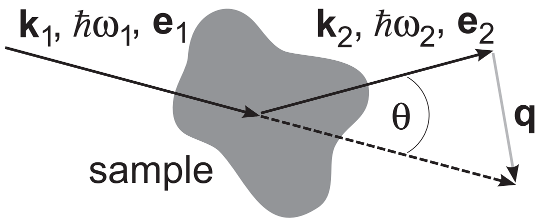

Fig. 2 Kinematics of the scattering process.

$$
\begin{aligned}
\frac{d^2\sigma}{d\Omega d\omega_2} = r_0^2\left(\frac{\omega_2}{\omega_1}\right)\sum_F \Bigg| &\left\langle F\Big|\sum_j e^{i(\mathbf{k}_2-\mathbf{k}_1)\mathbf{r}_j}\Big|I\right\rangle(\mathbf{e}_1\cdot\mathbf{e}_2) \\
&-\frac{1}{m}\sum_N\left\{\frac{\langle F|\mathbf{e}_2\cdot\sum_j\mathbf{p}_j e^{-i\mathbf{k}_2\mathbf{r}_j}|N\rangle\langle N|\mathbf{e}_1\cdot\sum_j\mathbf{p}_j e^{i\mathbf{k}_1\mathbf{r}_j}|I\rangle}{E_N-E_I-\hbar\omega_1-0.5i\Gamma_N}+\frac{\langle F|\mathbf{e}_1\cdot\sum_j\mathbf{p}_j e^{i\mathbf{k}_1\mathbf{r}_j}|N\rangle\langle N|\mathbf{e}_2\cdot\sum_j\mathbf{p}_j e^{-i\mathbf{k}_2\mathbf{r}_j}|I\rangle}{E_N-E_I+\hbar\omega_2}\right\}\Bigg|^2\times\delta(E_F-E_I-\hbar\omega)
\end{aligned}
\tag{1}
$$

where $\mathbf{e}_1$ and $\mathbf{e}_2$ are the polarization vectors of the incident and scattered photon, respectively, and Γ_N is the lifetime broadening of the intermediate state $|N\rangle$. The δ-function ensures energy conservation. The DDCS is proportional to the number of incident probe particles scattered within an energy range $\Delta E(\Delta\hbar\omega_2)$ and wave vector transfer variation ΔQ into a solid angle $\Delta\Omega$. If the interference terms are neglected, the cross section is composed of three contributions. The first term, derived from the $\mathbf{A}^2$-term in first-order perturbation, describes nonresonant IXS. The second and the third terms are derived from the $\mathbf{p}\cdot\mathbf{A}$-term in second-order perturbation. The second term describes an absorption process followed by an emission process, coupled via a resonant intermediate state $|N\rangle$, leading to an increase of the cross section, whenever the energy of the incident photon is close to an absorption edge of the element under study. The third term can be neglected in practical cases.

(1) *Validity of the adiabatic approximation.* In the adiabatic limit, one can separate the quantum state $|S\rangle$ of a system into the product of an electronic part, $|S\rangle_e$, which depends only parametrically on the nuclear coordinates, and a nuclear part, $|S\rangle_n$: $|S\rangle = |S\rangle_e|S\rangle_n$. This approximation is valid in particular if exchanged energies are small with respect to the excitation energies of electrons in bound core states as is the case for phonon excitations. In this approximation, one neglects the portion of the total electron density contributing to the delocalized bonding states in the valence band region.
(2) Limitation to the case for which the electronic part of the total wave function is not changed by the scattering process, and therefore the difference between the initial state $|I\rangle = |I\rangle_e|I\rangle_n$ and the final state $|F\rangle = |F\rangle_e|F\rangle_n$ is due only to excitations associated with atomic density fluctuations.

More in-depth introductions to the theory of resonant and NIXS can be found in, for example, Sinha (2001), Schülke (2007), De Groot and Kotani (2008), and Haverkort (2010).

IXS from electronic excitations

In the following, the various IXS processes, which arise from electronic excitations (with the exception of Compton scattering) are discussed. These can be roughly divided into two main fields according to the corresponding piece of the DDCS: (1) nonresonant IXS and (2) resonant IXS. In contrast to spectroscopies utilizing electron detection, IXS experiments are bulk sensitive and, if performed in the hard X-ray regime, allow one to study systems under extreme conditions such as very high temperatures and pressures.

NIXS from electrons

The cross section for nonresonant IXS is derived from the $\mathbf{A}^2$ term of the interaction Hamiltonian and constitutes the first term in the expression of the DDCS. The DDCS can be factorized into two parts, the first describes the coupling of the scattering probe to the system, and the second contains the properties of the system in the absence of the perturbing probe:

$$\frac{d^2\sigma}{d\Omega d\omega_2} = r_0^2(\mathbf{e}_1\cdot\mathbf{e}_2)^2\left(\frac{\omega_1}{\omega_2}\right)S(\mathbf{Q},\omega) = \left(\frac{d\sigma}{d\Omega}\right)_{\mathrm{Th}}S(\mathbf{Q},\omega)$$

where $(d\sigma/d\Omega)_{\mathrm{Th}}$ is the Thomson scattering cross section. The dynamical structure factor $S(\mathbf{Q},\omega)$ contains the information about electronic excitations via the imaginary part of the dielectric response function $1/\varepsilon(\mathbf{Q},\omega)$:

$$\frac{1}{\varepsilon(\mathbf{Q},\omega)} = 1 + \frac{4\pi e^2}{Q^2}\chi(\mathbf{Q},\omega),$$

where $\chi(\mathbf{Q},\omega)$ connects the Fourier-transformed induced charge $n_{\mathrm{ind}}(\mathbf{Q},\omega)$ with the Fourier transform of the external potential $\Phi_{\mathrm{ext}}(\mathbf{Q},\omega)$:

$$n_{\mathrm{ind}}(\mathbf{Q},\omega) = -e\chi(\mathbf{Q},\omega)\Phi_{\mathrm{ext}}(\mathbf{Q},\omega)$$

The basic ingredient of the polarization function is the so-called Lindhard polarization function, which describes the polarization of a homogeneous electron system by taking into account all single-particle excitation processes (particle–hole excitations) mediated by the momentum transfer, assuming that they are allowed by Pauli's principle, but neglecting the interaction of the particle and the hole with the surrounding electron fluid as well as any interaction between the particle and the hole left behind. A first step of approximating the Lindhard polarization function is the so-called random phase approximation (RPA) where, in addition to the external potential, the potential due to the induced polarization also acts on the system.

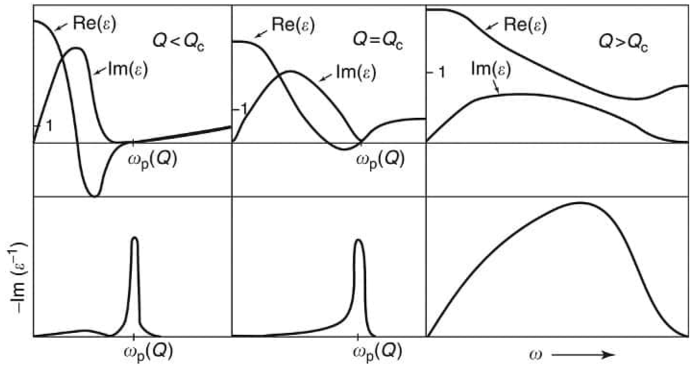

Fig. 3 Upper panel: real and imaginary part of the RPA dielectric function $\varepsilon_{\mathrm{RPA}}(Q, \omega)$ for $Q < Q_c$, $Q = Q_c$, and $Q > Q_c$. Lower panel: corresponding imaginary part of $-\varepsilon_{\mathrm{RPA}}{}^{-1}(Q, \omega)$. (Adapted from M. Krisch, F. Sette, Scattering, Inelastic: X-Ray (Methods and Applications), Editor(s): Franco Bassani, Gerald L. Liedl, Peter Wyder, Encyclopedia of Condensed Matter Physics, Elsevier, 2005, pp. 220–226, with permission)

IXS from valence electrons

Fig. 3 shows three characteristic $S(\mathbf{Q}, \omega)$ spectra along with the real and imaginary parts of the dielectric function $\varepsilon(\mathbf{Q}, \omega)$. The evolution of the spectra can be understood by inspection of $\varepsilon(\mathbf{Q}, \omega)$ and $Im[\varepsilon(\mathbf{Q}, \omega)^{-1}]$ for three different regimes of the momentum transfer Q. Within the RPA formalism, a sharp structure in the $S(\mathbf{Q}, \omega)$ appears at a frequency $\omega = \omega_p$, the plasma frequency of the system, when $Re[\varepsilon(\mathbf{Q}, \omega)]$ has a zero passage and simultaneously $Im[\varepsilon(\mathbf{Q}, \omega)]$ is close to zero. This behavior persists up to the so-called critical momentum transfer Q_c, for which the zero passage of $Re[\varepsilon(\mathbf{Q}, \omega)]$ coincides with the high-energy cutoff of $Im[\varepsilon(\mathbf{Q}, \omega)]$. In the above regime of $Q < Q_c$, the plasmon dispersion can be determined. For $Q > Q_c$, the plasmons can decay into particle–hole excitations, and a much larger spectral range yields a significant contribution to the $S(\mathbf{Q}, \omega)$. A comparison of the experimental spectra with relevant calculations gives an insight into electron correlation and band-structure effects. Moreover, IXS allows one to determine the bandgap of semiconductors or insulators, and—in the case of an indirect gap—its relative momentum. Furthermore, IXS spectra recorded in the particle–hole excitations regime provide information about the combined electron density of states. Finally, one gains access to the off-diagonal response of the dynamical structure factor by performing the IXS experiment in the presence of a standing-wave field, generated by the coherent superposition of an incident and diffracted wave vector when the sample is positioned in Bragg reflection conditions (Schülke and Kaprolat, 1991).

IXS from core electrons (X-ray Raman scattering)

One often refers to NIXS from core electrons or X-ray Raman scattering spectroscopy if the final state $|F\rangle$ of the electron system is characterized by a hole in a core level and an electron in a continuum state above the Fermi level. Within the RPA, the dynamical structure factor takes the following form:

$$S(\mathbf{Q}, \omega) = \left(\frac{\hbar Q^2}{4\pi e^2 n}\right) \sum_{k', \nu'} \left| \langle \mathbf{k}'\nu | \exp(i\mathbf{Q}\cdot\mathbf{r}) | c \rangle \right|^2 \times \delta(\hbar\omega + E_c - E(\mathbf{k}', \nu)),$$

where $|c\rangle$ is a core state with energy E_c and $E(\mathbf{k}', \nu)$ is the energy of a one-electron Bloch state with reduced wave vector $\mathbf{k}'$ and band index ν. The characteristics of the electronic transition are controlled by the transition operator $\exp(i\mathbf{Q}\cdot\mathbf{r})$.

XRS from core electrons of low Z materials is analogous to soft X-ray absorption spectroscopy (XAS) as long as the momentum transfer Q is small compared with the radial extent a_c of the wave function of the core electron involved in the inelastic scattering process (Mizuno and Ohmura, 1967). A Taylor expansion of the transition operator yields

$$\exp(i\mathbf{Q}\cdot\mathbf{r}) \approx 1 + i\mathbf{Q}\cdot\mathbf{r} - \frac{1}{2}(\mathbf{Q}\cdot\mathbf{r})^2 + \mathcal{O}((\mathbf{Q}\cdot\mathbf{r})^3),$$

where the leading term $i\mathbf{Q}\cdot\mathbf{r}$ is equivalent to the dipole transition operator for X-ray absorption if the momentum transfer $\mathbf{Q}$ in XRS takes the role of the photon polarization vector $\mathbf{e}$ in XAS. At finite momentum transfer $|\mathbf{Q}| \gg a_c$, the Taylor expansion breaks down and, instead, a multipole expansion of the transition operator in terms of spherical harmonics yields:

$$\exp(i\mathbf{Q}\cdot\mathbf{r}) = \sum_{k=0}^{\infty} \sum_{m=-k}^{k} i^k (2k+1) j_k(Qr) \times C_{km}^{*}(\Theta_Q, \phi_Q) \times C_{km}(\Theta_r, \phi_r)k,$$

where j_k are kth-order spherical Bessel functions containing the dependence of $S(\mathbf{Q}, \omega)$ on the modulus of the exchanged momentum Q and $C_{km} = \sqrt{4\pi/(2k+1)}Y_{km}$ are renormalized spherical harmonics, which describe the $\mathbf{Q}$-directional dependence of the transition operator. Three-dimensional representations of the angular part of the transition operators by means of a coherent sum over all terms $\sum_m C_{km}(\Theta_r, \phi_r)$ are shown for monopole ($k = 0$), dipole ($k = 1$), quadrupole ($k = 2$), octupole ($k = 3$), hexadecapole ($k = 4$), and triakontadipole ($k = 5$) operators in Fig. 4.

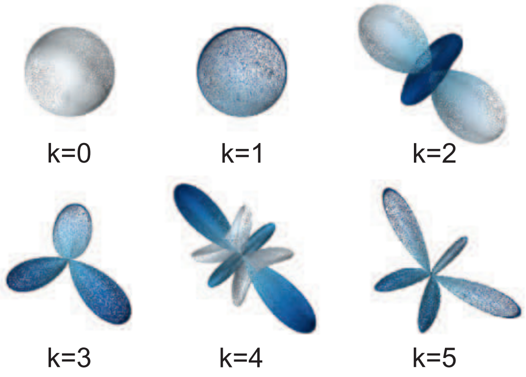

Fig. 4 Three-dimensional representations of the angular part of the transition operators: monopole ($k = 0$), dipole ($k = 1$), quadrupole ($k = 2$), octupole ($k = 3$), hexadecapole ($k = 4$), and triakontadipole ($k = 5$) operators.

The sensitivity of XRS to systems with higher than twofold rotational symmetry as opposed to XAS (dipole transitions) is immediately obvious based on the complex shape of these operators and is taken advantage of for studying linear dichroism in cubic systems (Gordon et al., 2009). If the initial state has spherical symmetry (*s*-orbitals), the angular dependence of XRS edges directly reflects the shape and orientation of the final state (e.g., *d*-orbitals in transition metal oxides and/or *f*-orbitals in the lanthanides) (Yavaş et al., 2019).

As a further consequence of the presence of these higher order multipole terms at large momentum transfer $\hbar Q$, the electric dipole selection rule, defining the final state symmetry, which can be reached in an absorption process, is relaxed and XRS can be used to extract the local core-excited electronic density of states $\rho(\hbar\omega)_L$ via

$$S(Q,\omega) \propto \sum_L M(\hbar\omega)_L \rho(\hbar\omega)_L,$$

with the matrix elements $M(\hbar\omega)_L$ for the given angular momentum channel $L = (l, m)$ (Soininen et al., 2006).

A great advantage of XRS over conventional XAS is that while in XAS the incident photon energy has to be tuned to the absorption edge energy under consideration, in XRS this role is taken by the energy transfer, thus leaving a certain freedom in the choice of the incident photon energy. This is schematically illustrated in Fig. 5. XRS therefore allows one to perform soft X-ray absorption studies in the hard X-ray regime, with the advantage of probing truly bulk properties and study systems which are not compatible with an ultrahigh vacuum environment, necessary in the soft X-ray regime. This is especially true for samples contained in complex *in situ* environments, such as diamond anvil cells for high pressure studies. The nonresonant character also renders the core excitation spectra practically free of artifacts such as self- or over-absorption and easier to treat theoretically as the transitions are describable by one-electron operators.

Resonant inelastic X-ray scattering

The cross section for resonant inelastic X-ray scattering (RIXS) is derived from the **p**·**A**-term in the interaction Hamiltonian, and constitutes the second term of the DDCS. It is a second-order optical process, in which a core electron is excited by an incident X-ray photon of energy $\hbar\omega_1$ into empty states above the Fermi level. This excited state then decays, and the deep core hole is filled by an

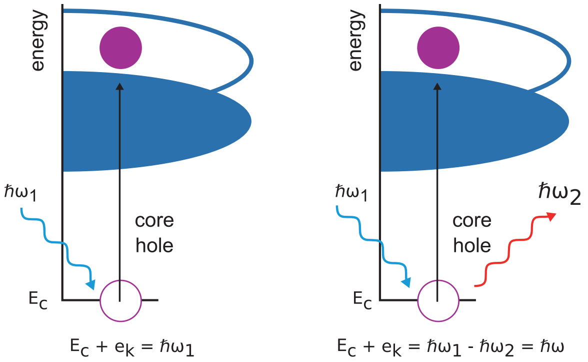

Fig. 5 Schematic representation of the X-ray absorption (left) and X-ray Raman scattering (right) process. E_c denotes the binding energy of a core level, and e_k is the kinetic energy of the photoelectron.

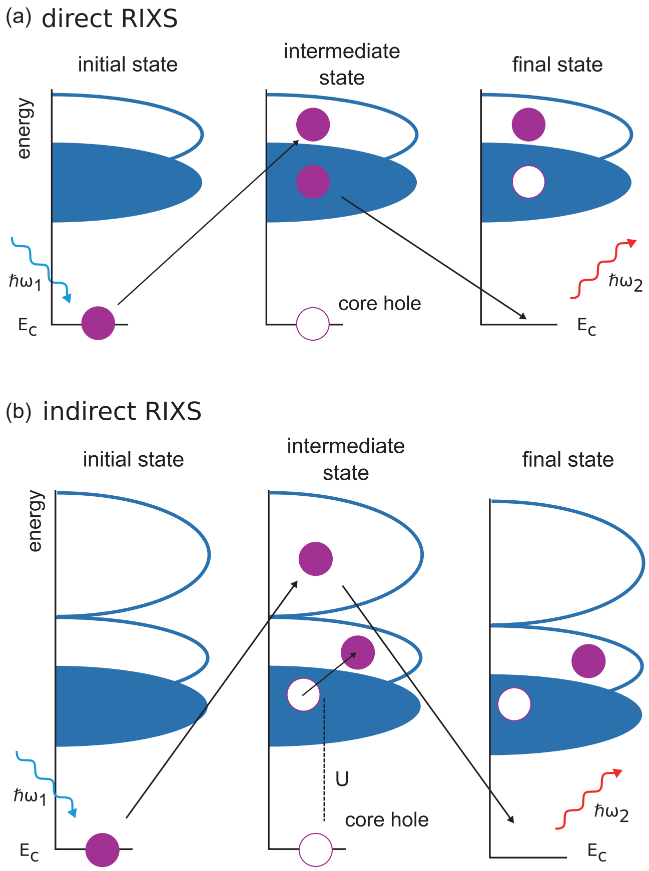

Fig. 6 Schematic representation of the RIXS process for direct RIXS (A) and indirect RIXS (B).

electron from a shallower core level or the valence band under emission of a photon of energy $\hbar\omega_2$ (see Fig. 6). In the most common case, both the excitation and de-excitation steps involve electric dipolar transitions. If the intermediate core-excited states are closely located in energy, interference between the absorption and emission process is possible (Revelli et al., 2019). The success of RIXS rests on the fact that elementary excitations, such as plasmons and charge-transfer excitations, excitons, and intra-orbital excitations (e.g., *dd* excitations), collective magnetic excitations, such as magnons and bi-magnons, as well as phonons down to the meV energy scale can be probed with a cross section that is enhanced due to the resonant nature of the RIXS process. Also, the electron–phonon coupling can be measured since it is related to the intensity of the phonons as measured by RIXS (Rossi et al., 2019). Depending on how energy and momentum are transferred during the lifetime of the intermediate state, two different RIXS mechanisms are usually differentiated: direct RIXS and indirect RIXS. In direct RIXS (Fig. 6A), a core electron is resonantly excited into an empty state above the Fermi level and a different electron from an occupied valence level fills the core hole leaving the system in a final state with an electron–hole excitation of energy $\hbar\omega = \hbar\omega_1 - \hbar\omega_2$ and momentum $\hbar Q = \hbar Q_2 - \hbar Q_1$. In indirect RIXS (Fig. 6B), on the other hand, the excited and decaying electrons are identical and the excitation is created via shake-up processed due to the strong electron-core hole interaction (U) in the intermediate state. The cross section for indirect RIXS is, therefore, considerably lower than that for direct RIXS.

Dynamics in the time domain can be assessed if the intermediate state undergoes a transition (emission or absorption of a phonon) in the time interval between the excitation and the emission step (Björneholm et al., 1997). The rate for this transition can then be directly compared to the core hole decay rate, and information about the time development in the range of the core hole lifetime can be obtained. Well above the absorption threshold, the IXS process can be regarded as a decoupled two-step process, and is commonly dubbed X-ray fluorescence.

In general, a simple one-electron picture is not sufficient to account for all the observed phenomena. Especially for open shell systems, such as transition metals or rare earths, a many-body description has to be invoked. Despite these complexities, RIXS is a very powerful spectroscopic tool, thanks to its high degree of selectivity. It is element and angular momentum selective (via its resonant intermediate state and the transition selection rules, respectively). Site selectivity with respect to identical atomic species in different chemical environments can be obtained by choosing an excitation energy so that a core electron is promoted to an unoccupied state which has a strong localization on that particular site. Detecting the scattered X-rays with angular selectivity adds further information: in solids band-structure information can be obtained, whereas for molecules, the symmetry of molecular states can be studied. Furthermore, exploiting the unique polarization properties of synchrotron-based X-ray sources, linear and circular dichroism phenomena can be studied. As in the case of nonresonant IXS, the various applications can be roughly classified according to the transferred energy.

RIXS from valence electrons

These experiments aim at detecting low-lying electronic excitations such as interband, *d-d*, and charge-transfer excitations. To perform these experiments at resonance with a characteristic absorption edge bears several advantages: (1) the resonant enhancement of the cross section of typically two orders of magnitude allows one to study essentially all compounds of interest while nonresonant IXS is practically limited to low Z materials; (2) the presence of (an) intermediate state(s) and eventual interference effects between them make the RIXS process highly selective in terms of angular momentum selection rules and geometrical considerations when the experiment is performed on single crystals. For example, the shape of resonantly excited valence fluorescence spectra from single crystals depends strongly on the energy of the incident photon and the momentum transfer $\mathbf{Q}$ (both direction and size), which is a direct consequence of momentum conservation, stating that $\mathbf{Q}$ must be equal to the vector difference $\mathbf{k}_e - \mathbf{k}_h$ between the Bloch vectors of the excited electron and those of the hole left behind, modulo a reciprocal lattice vector G. This Bloch $\mathbf{k}$-selective RIXS allows, in principle, one to obtain band-structure information although attention has to be paid to the relaxation processes in the intermediate state (Ma et al., 1992; Enkisch et al., 1999).

The momentum transfer dependence of RIXS can further be used to probe elementary excitations, such as excitons and orbitons, and collective excitations, such as plasmons, across the Brillouin zone. Even for transition metal L-edges, lying in the soft X-ray regime, large portions of reciprocal space are often accessible. Access to spin-flip excitations and, therefore, to collective spin excitations such as magnons is possible if the intermediate state is split by spin–orbit interaction and the dispersion of magnetic excitations can be probed (Braicovich et al., 2010). Recent advances in experimental setups and theory have helped to establish RIXS as a complementary technique to inelastic neutron scattering with the advantage of being able to measure small samples and samples containing strong neutron absorbers such as iridium.

RIXS from core electrons

Since the final state of the RIXS process is characterized by a hole in a shallow core level (or the valence band), spectral features narrower than the intermediate state lifetime width can be observed (Hämäläinen et al., 1991; Krisch et al., 1995). The ultimate resolution is limited by the final-state lifetime width. If these final state RIXS features are associated with different excitation channels (located at different energies in the intermediate state), they will resonate at different incident photon energies. RIXS, therefore, can reveal different excitation channels that are completely obscured in the corresponding X-ray absorption spectrum due to the large core hole lifetime width. This allows, for example, one to determine the energy position and the relative strength of weak quadrupolar ($2p - 4f$) transitions in rare-earth compounds. Absorption spectroscopy-like experiments utilizing this mechanism are often coined high-energy resolution fluorescence detected (HERFD) XAS or simply resonant X-ray emission spectroscopy (RXES).

Spin selective RIXS – > nonresonant XES

The shape of X-ray fluorescence spectra of elements, which contain an open electronic shell (e.g., transition metals or rare earths), shows characteristic shoulders or satellites which reflect the energies of the different electronic configurations of the excited atom. Besides the Coulomb interactions between the electrons occupying different orbital configurations, there are some interactions that have a magnetic origin, in particular in cases where the excited atom has valence electrons with unpaired spin giving rise to a magnetic moment. These exchange interactions between the magnetic electrons of the valence shell and the core electrons in the orbital where the photon emission process has left a core hole lead to features in the emission spectrum of dominant spin character. The energy separation is related to the strength of these interactions, which are largest when the hole is in an orbital with the same principal quantum number n of the magnetic electrons. In a simple picture, the X-ray emission is separated into high- and low-spin states whose energy separation is proportional to the exchange integral J and $(2S + 1)$, where S is the total spin moment of the magnetic shell, and whose intensity ratio is given by $S/(S + 1)$. Changes in the magnetic state (induced, e.g., by pressure, temperature, or doping) can therefore be witnessed by changes in the X-ray emission lineshape. By its nature, this method does not need a long-range magnetic order, and it is sensitive to the local (atomic) magnetic spin moment of a specific valence orbital. As a consequence, however, the method cannot discriminate between ferro-, antiferro-, ferri-, and paramagnetism.

Dichroism effects in RIXS – > RIXS-mcd

Resonant IXS and fluorescence spectral shapes are sensitive to both the polarization of incident and scattered photons. In ferromagnetically aligned samples, the emission spectra therefore display dichroic effects, in close analogy to X-ray absorption spectroscopy utilizing circular or linear polarized X-rays. RIXS from valence electrons, excited with circular polarized X-rays, provides information on the occupied spin density (Krisch et al., 1996; Sikora et al., 2010), whereas RIXS from core electrons allows one to reveal the magnetic character of the predominant features composing the emission line. The X-ray emission linear magnetic dichroism effect represents the angular dependence of the X-ray emission cross section with respect to the magnetization axis. For a given configuration, the sizes of these dichroic effects are proportional to the magnetic moment of the involved magnetic shell (Thole et al., 1992).

IXS from phonons

The study of atomic dynamics in condensed matter systems at momentum transfers Q and energies characteristic of collective motions is traditionally the domain of neutron scattering spectroscopy. There are, however, situations where the use of photons has important advantages over neutrons (Burkel, 2000; Baron, 2016, 2019). The most significant is that there are no kinematic limitations: for IXS, any energy transfer can be reached for a given momentum transfer, whereas for INS, due to the neutron mass and typical neutron energies, the small-Q range is not accessible. This is depicted in Fig. 7 for different scattering angles Θ_S.

In its most general form, the DDCS can be written as

$$\frac{d^2\sigma}{d\Omega d\omega_2} = r_0^2(\mathbf{e}_1\cdot\mathbf{e}_2)^2\left(\frac{\omega_2}{\omega_1}\right)\sum_{I_n,F_n}P_{I_n}\times\left|\langle F_n|\sum_j f_j(\mathbf{Q})e^{i\mathbf{Q}\cdot\mathbf{R}_j}|I_n\rangle\right|^2\times\delta(\hbar\omega+\hbar\omega_2-\hbar\omega_1)$$

where $|I_n\rangle(|F_n\rangle)$ are the initial (final) nuclear states, P_{I_n} represents the thermal population of the initial states, and $f_j(\mathbf{Q})$ is the atomic form factor of the jth particle whose center-of-mass position is at $\mathbf{R}_j$. With respect to the INS cross section, the following aspects are noteworthy.

1. X-rays couple to the electrons of the system with a cross section proportional to the square of the classical electron radius, $r_0 = 2.82\times10^{-15}$ m, that is, with a strength comparable to the neutron-nucleus scattering cross section b^2.
2. The IXS cross section is proportional to $f_i(\mathbf{Q})$. In the limit $Q\to0$, the form factor is equal to the number of electrons in the scattering atom, Z; for increasing values of Q, the form factor decays with decay constants of the order of the inverse of the atomic wave function dimensions of the electrons in the atom.
3. For elements with Z>4 and typical X-ray energies of 10–30 keV, photoelectric absorption is the main attenuation process. Far away from any absorption resonances, it is roughly proportional to Z^4, leading therefore to a reduction of the cross section for heavier elements.
4. The cross section for X-rays is highly coherent; therefore, only static or quasistatic structural and/or chemical disorder contributions have to be considered. Finally, it is noted that the instrument resolution function for IXS is independent of the energy and momentum transfer.

For the particular case of IXS from phonons at a given temperature T, the dynamical structure factor for one-phonon contribution becomes

$$S(\mathbf{Q},\omega)\propto\sum_n F_n(\mathbf{Q},\omega)G_n(\mathbf{Q})$$

$$F_n(\mathbf{Q},\omega)=[\delta(\omega-\omega_n(\mathbf{q}))-\delta(\omega+\omega_n(\mathbf{q}))]\times\left[\omega_n(\mathbf{q})(1-\exp(-\tfrac{\hbar\omega}{k_B T}))\right]^{-1}$$

$$G_n(\mathbf{Q})=\left|\sum_j \mathbf{Q}\cdot\boldsymbol{\sigma}_n^j(\mathbf{q})\frac{f_j(\mathbf{Q})}{\sqrt{M_j}}\exp\left[-W_j(\mathbf{Q})+i\mathbf{Q}\cdot\mathbf{R}_j\right]\right|^2$$

where ω_n is the phonon eigenfrequency for mode n, and $\boldsymbol{\sigma}_n$ is the eigenvector for mode n in periodic notations. Here, $\mathbf{q}=\mathbf{Q}-\mathbf{G}$ is the reduced momentum transfer with the reciprocal lattice vector $\mathbf{G}$, and W_j is the Debye–Waller factor.

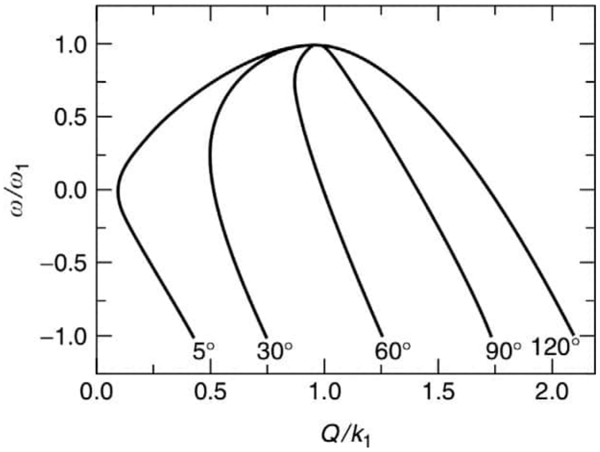

Fig. 7 Accessible energy–momentum transfer regions for inelastic neutron scattering for different scattering angles Θ_S, reported normalized to the incident neutron energy $\hbar\omega_1$ and incident neutron momentum $\hbar k_1$.

If the energy resolution of the experiment is much larger than the energy scale of the phonons, that is, if no energy analysis is applied, the formalism of so-called thermal diffuse scattering reduces to

$$S(\mathbf{Q}) \propto \sum_j \frac{1}{\omega_n(\mathbf{q})} \coth\left[\frac{\hbar\omega_n(\mathbf{q})}{2k_B T}\right] G_n(\mathbf{Q}).$$

While the energy-related information is not directly recoverable via the measurement of thermal diffuse scattering, it can provide valuable indications about the regions of interest in reciprocal space to be explored by energy-resolved IXS. In simple cases, the phonon dispersion can be derived directly from the q-dependence of the thermal diffuse scattering intensity (Xu and Chiang, 2005).

Preliminary calculations of lattice dynamics, even semi-quantitative, are highly beneficial for the experiment planning, as intensity and contrast for a given phonon can be optimized with the knowledge of eigenfrequencies and eigenvectors (thus selection rules).

Phonons in crystalline materials

The capability of providing micrometer-sized X-ray beams opens up the possibility of studying systems available only in small quantities down to a few 10^{-6} mm^3. These comprise novel or advanced materials such as superconductors for which sufficient crystalline quality and homogeneous doping can only be obtained for tiny crystals, by far too small to be studied by INS. Moreover, materials can be studied under very high pressures ($>$100 GPa) using diamond anvil cells, thus allowing important insights into the dynamics close to structural phase transitions and the pressure evolution of elastic properties. IXS from phonons in single crystalline materials provides the same information as coherent INS, and all aspects of lattice dynamics in terms of symmetry considerations, phonon eigenvectors, and selection rules are identical. One exception, however, concerns the relative intensity of the phonons in a multi-species system (with j different atom species in the unit cell), which can be very different due to the different weight of the atomic form factor $f_j(\mathbf{Q})$ with respect to the neutron scattering length b_j.

For polycrystalline materials, only the modulus of Q is well defined, and in general the $S(Q, \omega)$ spectrum will contain contributions from all the phonon branches. The density-of-states limit is reached, if a fine sampling of a sufficiently large Q-space is performed. On the other hand, if Q is confined within the first Brillouin zone, $Q = q$, only phonon modes which have a longitudinal symmetry component are excited, allowing the determination of an orientation-averaged acoustic phonon dispersion.

High-frequency dynamics in liquids and glasses

The absence of kinematic limitations for IXS has allowed one to access a previously unexploited region in $Q - \omega$ space, the so-called mesoscopic region, in which the momentum transfer $\hbar Q$ approaches the inverse of the interparticle separation a (Sette et al., 1998). This Q-range is particularly important because here the collective dynamics undergoes a transition from a hydrodynamic to a microscopic single-particle behavior. Numerous IXS studies in glasses have identified—despite qualitative differences—several common features in the high-frequency dynamics.

1. Propagating acoustic-like excitations exist up to a maximum Q-value Q_m ($Q_m a \approx 1-3$), depending on the fragility of the system.
2. The excitations are well defined and display a linear dispersion $\hbar\omega(Q)$. An extrapolation toward the $Q \rightarrow 0$ limit yields the macroscopic sound velocity.
3. The width $\Gamma(Q)$ of the inelastic peaks follows a power law, $\Gamma = DQ^{\alpha}$ with $\alpha = 2$ within the current experimental accuracy.
4. The value of D does not depend significantly on temperature, indicating that this broadening in the high-frequency region does not have a dynamic origin, but is instead due to static disorder.

For liquids, the dynamical structure factor is strongly affected, if the probed distances ($l = 2\pi/Q$) are comparable to those that characterize structural correlations among particles (over typical correlation lengths ξ), and times ($t = 1/\omega$) comparable to the lifetime t of these correlations. In this case, one observes a positive sound dispersion $v(Q)$ from its low-frequency ($\omega = 2\pi v \ll 1/\tau$) adiabatic value $v(0)$ to the high-frequency ($\omega \gg 1/\tau$) elastic value v_∞. A quantitative analysis of the $S(Q, \omega)$ can be performed within the framework of a generalized Langevin equation formalism using the memory function approach. This allows the reliable extraction of v_∞, relaxation times, and relaxation strengths.

Deep IXS

Quantitative information on the atomic momentum distribution can be obtained at sufficiently large momentum transfers, where the core electrons of the system under study recoil almost freely with an effective mass equal to the atomic mass (Monaco et al., 2002). These conditions are met, if the electron dynamics is instantaneous compared to the atomic one and if the atoms have an appropriate quantity of electronic charge on a length scale smaller than $1/Q$. Deep IXS provides a complementary technique to deep INS, and is particularly valuable for polyatomic or polyisotopic systems, for which the relative contrast between the different atomic/isotopic species in the sample is different for INS and IXS.

Conclusion

IXS provides a range of experimental techniques for the study of dynamic electronic-, magnetic-, and lattice degrees of freedom. The advent of synchrotron X-ray sources provided a fertile ground for the exploration of a wide range of IXS techniques that were then definitely established as powerful spectroscopic tools at third-generation synchrotron X-ray sources, truly complementary to inelastic neutron scattering techniques. The advent of fourth-generation synchrotron X-ray sources, close to the diffraction limit, will nurture further developments both experimentally and theoretically. In particular studies in operando and studies of minute amounts of samples at extreme conditions of pressure and temperature, electric and magnetic fields and set-ups allowing for time-resolution will allow exploring so far uncharted territory with broad applications in fields such as materials science, chemistry, catalysis, and earth and planetary sciences. In parallel, IXS at free-electron lasers is expected to offer additional opportunities with particular emphasis in the study of time-resolved phenomena.

References

Ament LJP, Van Veenendaal M, Devereaux TP, Hill JP, and van den Brink J (2011) Resonant inelastic X-ray scattering studies of elementary excitations. *Reviews of Modern Physics* 83(2): 705.

Baron AQR (2016) High-Resolution inelastic X-Ray scattering I: Context, spectrometers, samples, and superconductors. In: Jaeschke EJ, Khan S, Schneider JR, and Hastings JB (eds.) *Synchrotron Light Sources and Free-Electron Lasers: Accelerator Physics, Instrumentation and Science Applications*, pp. 1643–1719. Cham: Springer International Publishing.

Baron AQR (2019) High-resolution inelastic X-Ray scattering part II: Scattering theory, harmonic phonons, and calculations. In: Jaeschke E, Khan S, Schneider JR, and Hastings JB (eds.) *Synchrotron Light Sources and Free-Electron Lasers: Accelerator Physics, Instrumentation and Science Applications*, pp. 1–38. Cham: Springer International Publishing.

Björneholm O, Sundin S, Svensson S, Marinho RRT, de Brito AN, Gel'Mukhanov F, and Ågren H (1997) Femtosecond dissociation of core-excited HCl monitored by frequency detuning. *Physical Review Letters* 79(17): 3150.

Braicovich L, Van den Brink J, Bisogni V, Moretti Sala M, Ament LJP, Brookes NB, De Luca GM, Salluzzo M, Schmitt T, Strocov VN, et al. (2010) Magnetic excitations and phase separation in the underdoped $La_{2-x}Sr_xCuO_4$ superconductor measured by resonant inelastic X-ray scattering. *Physical Review Letters* 104(7): 077002.

Burkel E (2000) Phonon spectroscopy by inelastic X-ray scattering. *Reports on Progress in Physics* 63(2): 171.

De Groot F and Kotani A (2008) *Core level spectroscopy of solids*. CRC Press.

Enkisch H, Kaprolat A, Schülke W, Krisch MH, and Lorenzen M (1999) Bloch k-selective resonant inelastic scattering of hard X rays at valence electrons of Ni in NiAl. *Physical Review B* 60(12): 8624.

Gordon RA, Haverkort MW, Gupta SS, and Sawatzky GA (2009) Orientation-dependent X-ray Raman scattering from cubic crystals: Natural linear dichroism in MnO and CeO_2. *Journal of Physics Conference Series* 190(1): 012047.

Hämäläinen K and Manninen S (2001) Resonant and non-resonant inelastic X-ray scattering. *Journal of Physics. Condensed Matter* 13(34): 7539.

Hämäläinen K, Siddons DP, Hastings JB, and Berman LE (1991) Elimination of the inner-shell lifetime broadening in X-ray-absorption spectroscopy. *Physical Review Letters* 67(20): 2850.

Haverkort MW (2010) Theory of resonant inelastic X-ray scattering by collective magnetic excitations. *Physical Review Letters* 105(16): 167404.

Krisch MH, Kao CC, Sette F, Caliebe WA, Hämäläinen K, and Hastings JB (1995) Evidence for a quadrupolar excitation channel at the L III edge of gadolinium by resonant inelastic X-ray scattering. *Physical Review Letters* 74(24): 4931.

Krisch MH, Sette F, Bergmann U, Masciovecchio C, Verbeni R, Goulon J, Caliebe W, and Kao CC (1996) Observation of magnetic circular dichroism in resonant inelastic X-ray scattering at the L_3 edge of gadolinium metal. *Physical Review B* 54(18): R12673.

Ma Y, Wassdahl N, Skytt P, Guo J, Nordgren J, Johnson PD, Rubensson JE, Boske T, Eberhardt W, and Kevan SD (1992) Soft-X-ray resonant inelastic scattering at the C K edge of diamond. *Physical Review Letters* 69(17): 2598.

Mizuno Y and Ohmura Y (1967) Theory of X-ray Raman scattering. *Journal of the Physical Society of Japan* 22(2): 445–449.

Monaco G, Cunsolo A, Pratesi G, Sette F, and Verbeni R (2002) Deep inelastic atomic scattering of X rays in liquid neon. *Physical Review Letters* 88(22): 227401.

Revelli A, Moretti Sala M, Monaco G, Becker P, Bohatý L, Hermanns M, Koethe TC, Fröhlich T, Warzanowski P, Lorenz T, et al. (2019) Resonant inelastic X-ray incarnation of Young's double-slit experiment. *Science Advances* 5(1): eaav4020.

Rossi M, Arpaia R, Fumagalli R, Moretti Sala M, Betto D, Kummer K, De Luca GM, van den Brink J, Salluzzo M, Brookes NB, et al. (2019) Experimental determination of momentum-resolved electron-phonon coupling. *Physical Review Letters* 123(2): 027001.

Rueff J-P and Shukla A (2010) Inelastic X-ray scattering by electronic excitations under high pressure. *Reviews of Modern Physics* 82(1): 847.

Schülke W (2007) *Electron dynamics by inelastic X-ray scattering*, vol. 7. OUP Oxford.

Schülke W and Kaprolat A (1991) Nondiagonal response of Si by inelastic-X-ray-scattering experiments at Bragg position: Evidence for bulk plasmon bands. *Physical Review Letters* 67(7): 879.

Sette F, Krisch MH, Masciovecchio C, Ruocco G, and Monaco G (1998) Dynamics of glasses and glass-forming liquids studied by inelastic X-ray scattering. *Science* 280(5369): 1550–1555.

Sikora M, Juhin A, Weng T-C, Sainctavit P, Detlefs C, De Groot F, and Glatzel P (2010) Strong K-edge magnetic circular dichroism observed in photon-in-photon-out spectroscopy. *Physical Review Letters* 105(3): 037202.

Sinha SK (2001) Theory of inelastic X-ray scattering from condensed matter. *Journal of Physics. Condensed Matter* 13(34): 7511.

Soininen JA, Mattila A, Rehr JJ, Galambosi S, and Hämäläinen K (2006) Experimental determination of the core-excited electron density of states. *Journal of Physics. Condensed Matter* 18(31): 7327.

Thole BT, Carra P, Sette F, and van der Laan G (1992) X-ray circular dichroism as a probe of orbital magnetization. *Physical Review Letters* 68(12): 1943.

Xu R and Chiang TC (2005) Determination of phonon dispersion relations by X-ray thermal diffuse scattering. *Zeitschrift für Kristallographie Crystalline Materials* 220(12): 1009–1016.

Yavaş H, Sundermann M, Chen K, Amorese A, Severing A, Gretarsson H, Haverkort MW, and Tjeng LH (2019) Direct imaging of orbitals in quantum materials. *Nature Physics* 15(6): 559–562.

Nuclear resonant scattering☆

Wolfgang Sturhahn, Division of Geological and Planetary Sciences, California Institute of Technology, Pasadena, CA, United States

© 2024 Elsevier Ltd. All rights reserved.

This is an update of W. Sturhahn, Scattering, Nuclear Resonant, Editor(s): Franco Bassani, Gerald L. Liedl, Peter Wyder, Encyclopedia of Condensed Matter Physics, Elsevier, 2005, Pages 227–234, ISBN 9780123694010, https://doi.org/10.1016/B0-12-369401-9/00650-1.

Introduction **205**
Properties of nuclear resonances **206**
Scattering processes **207**
NRIXS **208**
Cross section 209
Observation 210
Phonon density of states 210
SMS 211
Level splitting 211
Index of refraction 212
Experimental procedure **213**
Conclusion **214**
Acknowledgments **214**
References **214**

Abstract

Nuclear resonant scattering (NRS) is a set of experimental techniques that use synchrotron radiation (SR) to excite well-defined resonances in atomic nuclei. Studies using NRS require isotopes with large nuclear resonant cross sections and transition energies matching high intensity SR sources. NRS methods typically use timing techniques which makes observation of NRS from isotopes with very short lifetimes technically difficult and resonant energy widths of the order of 10 neV are favorable. Nuclear resonant inelastic x-ray scattering (NRIXS) for the study of lattice dynamics and synchrotron Mossbauer spectroscopy (SMS) for the study of hyperfine interactions have become of practical importance during the past decade at highly brilliant SR facilities.

SMS is elastic forward scattering without nuclear recoil, i.e., without lattice excitation, and provides information about the electronic environment of the resonant nuclei analogous to conventional Mossbauer spectroscopy. The use of very collimated synchrotron radiation permits focusing to micrometer levels and easy manipulation of x-ray polarization.

NRIXS is used for the study of lattice vibrations and provides us with a spectrum of the phonons experienced by the resonant isotope. Most importantly one determines the phonon density of states (PDOS.) In contrast to other experimental techniques, NRIXS gives direct access to the partial and projected PDOS of the resonant isotope only. Complete isotope selectivity is truly unique in the area of lattice dynamics research.

Both techniques have been applied very successfully in studies at Mbar-pressure, biophysics research, and nanostructures. For applied studies, highly flexible and tested evaluation softwares, CONUSS for SMS and PHOENIX for NRIXS, are available as open source free of charge at https://www.nrixs.com.

Key points

- Nuclear resonant scattering with synchrotron radiation
- Coherent elastic nuclear resonant scattering
- Incoherent inelastic nuclear resonant scattering
- Nuclear resonant scattering at future synchrotron radiation sources

Introduction

Nuclear resonant scattering (Nrs) is a set of experimental techniques that use synchrotron radiation (SR) and well-defined resonances in atomic nuclei (Gerdau et al., 1985). Dynamics of the neutrons and protons cause a spectrum of these resonances for every nucleus except hydrogen. A nucleus can be created in an excited state by radioactive decay of a parent nucleus, or it can be

---

☆*Change History*: July 2022. W Sturhahn prepared the article and all updates/additions. Introduction, references, and outlook were updated from previous Encyclopedia article. Relevant website and key points were added

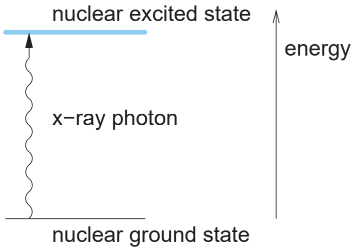

Fig. 1 Resonant excitation of a nucleus. The energy width of the excited state is typically 12 orders of magnitude smaller than the energy of the photon. Nuclei show the most narrow resonances in the x-ray regime.

brought into an excited state by collision with energetic particles (electrons, protons, neutrons, etc.) or the absorption of a photon. The latter process, a resonant excitation, becomes important if the energy of the photon is very close to the energy difference between the nuclear ground state and a nuclear excited state (see Fig. 1). Studies using NRS require isotopes with large nuclear resonant cross sections and transition energies that can be matched with high intensity by SR sources. NRS methods use timing techniques, and the observation of NRs from isotopes with very short lifetimes is technically difficult. Therefore, energy widths of the excited state of the order of 10^{-8}eV are favorable. Large values potentially result in higher counting rates in scattering experiments but also lead to shorter natural life times.

Spectroscopic techniques with nuclear resonances are based on either the use of radioactive sources or parent nuclei, e.g., Mössbauer spectroscopy and time-perturbed angular correlation (TPAC), or the direct excitation with photons, e.g., nuclear magnetic resonance (NMR) or the SR-based NRS described here. Nuclear resonant inelastic x-ray scattering (NRIXS) for the study of lattice dynamics and synchrotron Mössbauer spectroscopy (SMS) for the study of hyperfine interactions have become of practical importance during the past decade at highly brilliant SR facilities (Gerdau and de Waard, 1999/2000; Sturhahn, 2004; Langouche and Yoshida, 2021). SMS includes scattering processes that occur without recoil, i.e., without participation of lattice vibrations, and provides information about the electronic environment of the resonant nuclei analogous to conventional Mössbauer spectroscopy. The use of very collimated synchrotron radiation permits focusing to micrometer levels and easy manipulation of x-ray polarization. SMS has been applied very successfully to problems in high-pressure and biophysics research. In the study of magnetism, the strategic use of the isotopes ^{57}Fe (resonant) and ^{56}Fe (nonresonant) opened unique possibilities for analysis of thin films and nanostructures.

NRIXS is used for the study of lattice vibrations and provides us with a spectrum of the phonons experienced by the resonant isotope. Most importantly one determines the phonon density of states (PDOS.) In contrast to other experimental techniques, NRIXS gives direct access to the partial and projected PDOS of the resonant isotope only (Sturhahn et al., 1995). This complete isotope selectivity is truly unique in the area of lattice dynamics research. For example, materials surrounding the sample that do not contain resonant nuclei do not produce background, and this feature permitted high-pressure experiments in the Mbar regime that were impossible before (Sturhahn and Jackson, 2007). Many proteins contain only a few iron atoms at their biologically active sites; NRIXS studies using ^{57}Fe were conducted on several model compounds for such proteins, as well as on the proteins themselves. Among the thousands of atoms, NRIXS selects only the iron vibrations and thus permits detailed studies of protein dynamics related to these active sites. The same reasoning applies to studies of thin films and buried interfaces. Also for nanoparticles and disordered alloys, the NRIXS method has been applied very successfully. In those cases, as well as for amorphous materials, phonon dispersions are difficult or impossible to measure, but the PDOS still gives valuable information.

For both techniques, highly flexible and tested evaluation software, CONUSS for SMS and PHOENIX for NRIXS, are available as open source free of charge at https://www.nrixs.com.

Properties of nuclear resonances

X-ray scattering is usually treated solely with the electronic charge and spin. A justification is provided by classical electrodynamics in terms of the Thomson-scattering cross section, which is a factor of $(Z\,m/M)^2 \approx 10^{-7}$ smaller for the nucleus than for the electron shell. Here m, M are the masses of electron and nucleus, respectively, and Z is the atomic number. Based on this, it seems appropriate to ignore scattering contributions from the nucleus. However, the above argument fails if the time scale of internal nuclear dynamics matches the energy of the x-ray photon, i.e., the nucleus experiences a resonant excitation. Then the nuclear resonant cross section is calculated as

$$\sigma_N = \frac{\lambda^2}{2\pi}\,\frac{1}{1+\alpha}\,\frac{2I'+1}{2I+1}, \tag{1}$$

where λ is the wavelength of the resonant x rays, α is the internal conversion coefficient, and I, I' are the spins of nuclear ground and excited state. Values of α for relevant nuclear transitions range from 1 to 1000. The nuclear resonant cross section can become very large, e.g., the 14.4 keV nuclear transition of ^{57}Fe gives (with $\lambda = 86\,\mathrm{pm}$, $\alpha = 8.6$, $I = 1/2$, $I' = 3/2$) a value of $\sigma_N = 2.56\,\mathrm{Mbarn}$ and a ratio of $\sigma_N/\sigma_{pe} \approx 450$, where σ_{pe} is the photoelectric cross section. Fig. 2 displays nuclear resonant cross sections and nuclear level widths for isotopes with resonances below 150 keV. Higher transition energies are less favorable because the intensity of SR

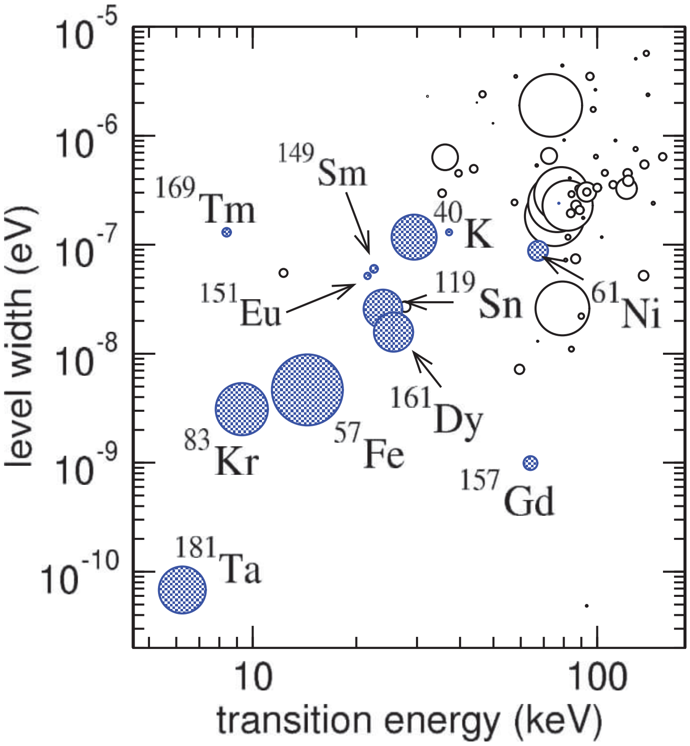

Fig. 2 Level widths of nuclear resonances below 150 keV. The size of the symbols is proportional to the nuclear resonant cross section. Prominent isotopes that have been used in NRS experiments are identified.

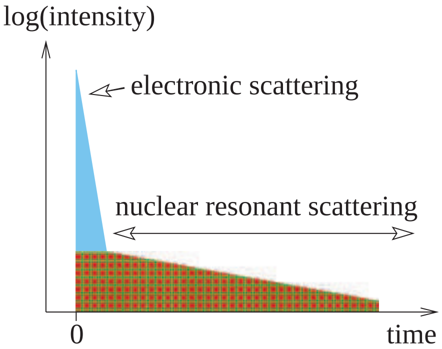

Fig. 3 Scattered intensity versus time. At zero time, a SR pulse excites a sample containing a nuclear resonant isotope. Electronic scattering is prompt whereas the response of the resonant nuclei is delayed. Time discrimination is the key to distinguishing nuclear and electronic scattering.

sources decreases, and x-ray optics, as well as detectors, become less efficient. Even though the nuclear resonant cross section is very large, the extraordinarily narrow energy width of these resonances leads to small energy-integrated cross section. For example, the best energy resolutions of x-ray optics are of the order $\delta E \approx 100\mu\text{eV}$, and a resonant enhancement over a neV scale would remain unresolved and unnoticed because $\sigma_N\Gamma \ll \sigma_{pe}\delta E$. Therefore NRS experiments require special observation techniques.

A sample containing resonant nuclei responds to a SR pulse on a time scale defined by the lifetime of the nuclear state τ. The value of τ is inversely related to the nuclear level width via $\tau\Gamma = \hbar$. Whereas values for τ are in the ns-μs range, the duration of a SR pulse is typically less than 100 ps. All electronic scattering of x rays occurs typically on the time scale of femtoseconds, virtually instantaneous compared to nuclear resonant contributions. A "time-discrimination trick," which is illustrated in Fig. 3, can cleanly separate nuclear resonant signals from other scattering contributions. The use of this time-discrimination trick makes NRS techniques possible.

Scattering processes

A schematic of the excitation process of a nuclear resonance is shown in Fig. 1. For a description of NRS, the de-excitation pathways must also be considered. The classification of elastic-inelastic and coherent-incoherent scattering processes is based on analysis of the initial and final quantum state of the scatterer symbolized by

$$|\Phi_i\rangle|\gamma_i\rangle \rightarrow |\Phi_n\rangle \rightarrow \left|\Phi_f\right\rangle\left|\gamma_f\right\rangle. \tag{2}$$

States of the x-ray field and the scatterer are described by $|\gamma\rangle$ and $|\Phi\rangle$, respectively. The intermediate state exists without x-ray photons. An inelastic scattering process is characterized by different energies of initial and final photon states, which implies an energy transfer to the scatterer. A meaningful definition of coherent and incoherent scattering can only be given for a collection of atoms, for which we may write

$$|\Phi_i\rangle = |\chi_i\rangle \prod_j \left|\phi_i^{(j)}\right\rangle. \tag{3}$$

Here $|\phi^{(j)}\rangle$ symbolizes a core state, i.e., the state of nucleus and inner electron shell, of atom j. The collective state of itinerant electrons and lattice vibrations is written as $|\chi\rangle$.

A classification of scattering processes using this nomenclature is presented in Fig. 4. Coherent processes leave all core states $|\phi^{(j)}\rangle$ unchanged. The scattering atom can in principle not be identified, and the situation is analogous to a quantum mechanical multi-slit experiment. The change of just one atom's state serves as an indicator, and the process will be incoherent. In particular, SMS is based on the coherent elastic process, whereas NRIXS originates from incoherent processes. Coherent inelastic scattering by resonant nuclei is of negligible strength. The almost purely incoherent character of inelastic NRS simplifies the interpretation of NRIXS data and presents a clear distinction to inelastic neutron scattering where incoherent and coherent processes often occur with similar strength.

NRIXS

The resonant absorption of an x-ray photon can lead to a simultaneous change of nuclear state and vibrational quantum state of the solid as illustrated in Fig. 5. Three energy scales determine the properties of this process: the transition energy of several keV; the phonon energies of the order of meV; the nuclear level width of less than μeV. The energies are different by many orders of magnitude, and energy eigenstates are very well described by simple combination of nuclear states and phonon states, e.g., $|g\rangle\,|\,1\rangle$ is a quantum state with the nucleus in the ground state and one phonon present. If we investigate the vibrating nucleus with monochromatic x rays, we would observe transitions with nuclear transition energy E_0 described by $|g\rangle\,|\,n\rangle \rightarrow \,|\,e\rangle\,|\,n\rangle$ and m-phonon creation of the type $|g\rangle\,|\,n\rangle \rightarrow \,|\,e\rangle\,|\,n+m\rangle$ leading to upshifted transition energies $E_0 + m\varepsilon$, where ε is the energy of the phonon. Also m-phonon annihilation of the type $|g\rangle\,|\,n\rangle \rightarrow \,|\,e\rangle\,|\,n-m\rangle$ with $n \geq m$ leads to downshifted transition energies $E_0 - m\varepsilon$. The absorption behavior is quantitatively described by the excitation probability density $S(E)$. The value of $S(E)\,d\,E$ gives the probability that the nucleus can be excited by x rays in the energy range $[E, E + d\,E]$. The phonon-creation/annihilation side bands of $S(E)$ are analogous to the Stokes and anti-Stokes lines observed by optical spectroscopies. The ratio $S(\text{-}E)/S(E)$ is universally given by the Boltzmann factor, i.e., $S(-E) = \exp\,[-\beta E]S(E)$, with $\beta = 1/(k_B T)$, temperature T, and Boltzmann's constant k_B. This relationship is known as "detailed balance" and is an intrinsic feature of all NRIXS spectra. The partial PDOS is extracted by a mathematical inversion procedure from $S(E)$. Here "partial" refers to the selection that has taken place by observing only vibrations of the resonant isotope.

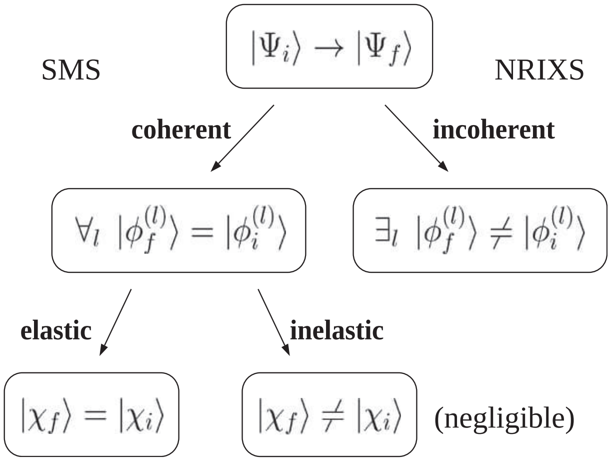
$|\Psi_i\rangle \rightarrow |\Psi_f\rangle$
SMS
NRIXS
coherent
incoherent
$\forall_l\ |\phi_f^{(l)}\rangle = |\phi_i^{(l)}\rangle$
$\exists_l\ |\phi_f^{(l)}\rangle \neq |\phi_i^{(l)}\rangle$
elastic
inelastic
$|\chi_f\rangle = |\chi_i\rangle$
$|\chi_f\rangle \neq |\chi_i\rangle$
(negligible)

Fig. 4 Classification scheme for scattering processes. Incoherent scattering implies energy transfer unless some core states are degenerate. Coherent inelastic NRS is of negligible strength.

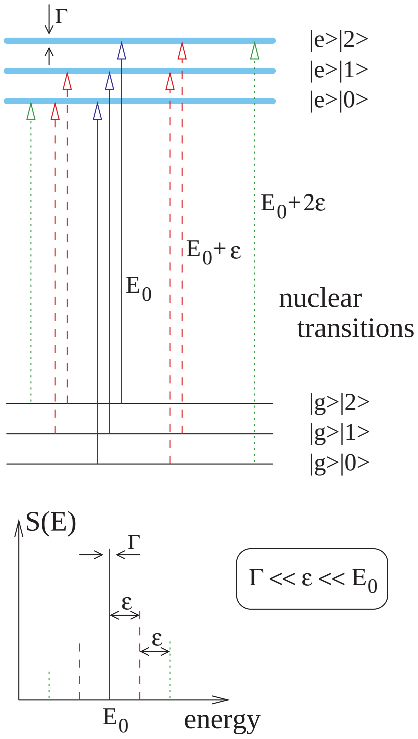

Fig. 5 The influence of atomic vibrations on the nuclear level scheme. The nucleus is embedded in an Einstein solid with a specific phonon energy ε.. This leads to sidebands in the excitation probability density $S(E)$ corresponding to phonon creation or annihilation.

Cross section

Excitation probabilities can be calculated with Fermi's Golden Rule which gives us the transition rate Λ_{ni} for changes from the initial state $|\Phi_i\rangle = |\chi_i\rangle|\phi_i\rangle$ to an intermediate state $|\Phi_n\rangle = |\chi_n\rangle|\phi_n\rangle$ under the influence of a monochromatic x-ray field of energy $\overline{E}$, amplitude $\mathbf{a}$, and wave vector $\boldsymbol{k}$

$$\Lambda_{ni} = \frac{2\pi}{\hbar}\left|\left\langle \Phi_n\middle|\widehat{H}_{int}\middle|\Phi_i\right\rangle\right|^2 \delta\left(E_{ni} - \overline{E}\right). \tag{4}$$

The energy difference of the states is given by E_{ni}, and the interaction Hamiltonian can be expressed by

$$\widehat{H}_{int} = \mathrm{e}^{\mathrm{i}k\cdot\hat{\mathbf{r}}}\mathbf{a}\cdot\widehat{\mathbf{J}}(-k), \tag{5}$$

where $\widehat{\boldsymbol{J}}$ is the spatial Fourier transform of the nuclear current operator in the center of mass frame, and the position of the center of mass is given by r. We obtain for the cross section

$$\sigma(E, \boldsymbol{k}) = \frac{1}{|\mathbf{a}|^2}\sum_n \langle\Lambda_{ni}\rangle_i = \frac{\pi}{2}\sigma_N \Gamma S(E, k), \tag{6}$$

where $E = \overline{E} - E_0$ is the energy of the incident x rays relative to the nuclear transition energy. The angle brackets indicate an average over all initial states that may be present, usually a thermal distribution. The last term is defined by

$$S(E, \boldsymbol{k}) = \int \frac{dt}{2\pi\hbar}\mathrm{e}^{\mathrm{i}Et/\hbar}\left\langle \mathrm{e}^{\mathrm{i}k\cdot\widehat{r}(t)}\mathrm{e}^{-\mathrm{i}k\cdot\widehat{r}(0)}\right\rangle. \tag{7}$$

This is the excitation probability density mentioned earlier, and here it is expressed as a self-correlation function of the position of a resonant isotope. For solid materials, $S(E, \boldsymbol{k})$ shows a sharp peak with width Γ around the nuclear transition energy E_0, i.e., around $E = 0$. This peak originates in recoilless absorption of x rays by the nucleus which is also known as the Mössbauer effect. In fact, we may write $\Gamma S(0) = f$, the Lamb-Mössbauer factor or probability for recoilless absorption. The value of f varies approximately between 0.05 and 0.9 for solids at room temperature but vanishes for liquids and gases. The estimate for absorption "on resonance" is then.

$$\sigma(0) \approx \frac{\pi}{2}\sigma_N f. \tag{8}$$

With the exception of the elastic peak, we expect $S(E)$ to be a smooth function in energy extending over an energy range that may be estimated by the Debye energy Θ. From Eq. (7) we obtain $\int S(E)dE = 1$, and with this normalization we can estimate for the "off resonance" region $\Theta S(E) \approx 1 - f$ providing

$$\sigma(E \neq 0) \approx \frac{\pi}{2}\sigma_N(1-f)\frac{\Gamma}{\Theta}. \tag{9}$$

A quantitative estimate for ^{57}Fe in metallic form gives in units of the photoelectric cross section

$$\sigma(0) \approx 560\sigma_{pe} \quad \sigma(E \neq 0) \approx 0.0002\sigma_{pe}. \tag{10}$$

The change of cross section by six orders of magnitude when moving away from the transition energy is dramatic. The large "on resonance" value permits conventional energy-resolved Mössbauer spectroscopy. The observation of the phonon sidebands via the small "off resonance" value requires the use of time discrimination.

Observation

Let us imagine a resonant nucleus that was somehow excited. The nucleus will decay into the ground state either by emission of an x-ray photon or by transferring the excitation energy to the electron shell. In the latter case, an electron is expelled, and the hole is quickly filled by other electrons with the emission of fluorescence x rays. All these decay products are emitted with some delay relative to the time of excitation of the nucleus, and the average delay time is given by the natural lifetime. Fig. 3 illustrates the time evolution of the scattered intensity of a material containing resonant nuclei after excitation with a SR pulse. If the energy of the incident x ray is close to the nuclear transition energy, nuclei are excited, and delayed emission of x rays can be observed. If only the delayed photons are counted while tuning the energy of the incident x-ray pulses, we expect to measure an event rate that is proportional to $\sigma(E)$. The normalized data then provide $S(E)$. An example of data collected from a metallic foil of ^{57}Fe is shown in Fig. 6. The low background shows that the time-discrimination trick removes all non-nuclear scattering of the x rays very effectively.

Phonon density of states

In many cases, an expansion of the interatomic potential around the equilibrium positions of the atoms in a solid is quite accurately described by a quadratic dependence on the atomic displacements. In this quasi-harmonic approximation, the equation of motion for the atomic motions can be integrated. The excitation probability can then be rewritten in a physically meaningful way as

$$\begin{aligned} S(E) &= f\delta(E) + \sum_{n=1} S_n(E) \\ S_1(E) &= \frac{fE_R}{E(1-\exp(-\beta E))}g(|E|) \\ S_n(E) &= \frac{1}{nf}\int S_{n-1}(E')S_1(E-E')dE', \end{aligned} \tag{11}$$

where the individual terms S_n correspond to n-phonon contributions. The delta-distribution term describes elastic scattering. The probability for this process is described in terms of the Lamb-Mössbauer factor f. The probability dP_1 to create $(E > 0)$ or annihilate

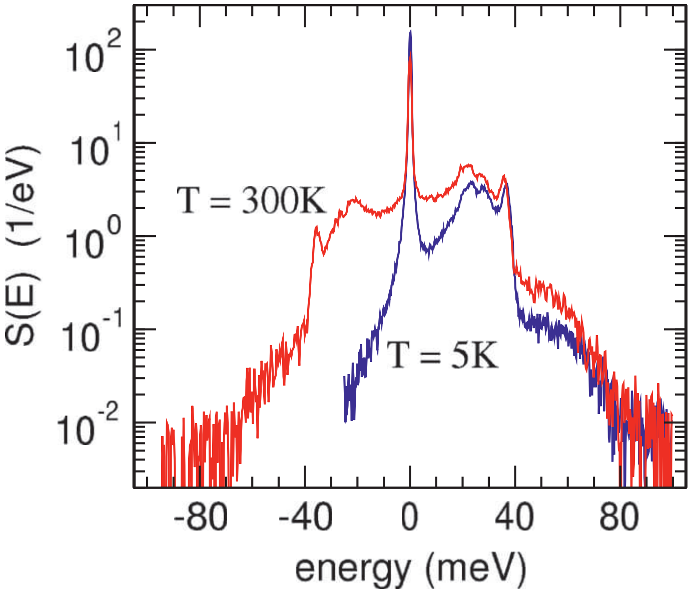

Fig. 6 Phonon excitation probability density from NRIXS data of an iron foil at two temperatures. Energy zero corresponds to the nuclear transition energy of 14.4125 keV of the ^{57}Fe isotope. At low temperatures phonon annihilation (negative energy values) is inhibited.

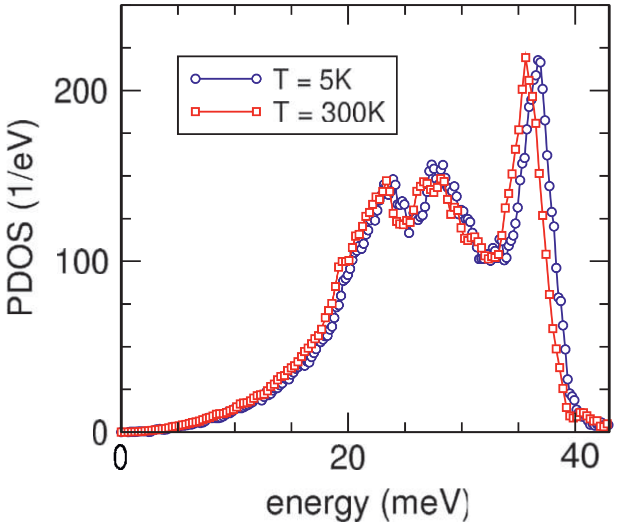

Fig. 7 The PDOs of iron metal (bcc) at two temperatures. The curves show 3 *g* calculated from the data shown in Fig. 6 using Eq. (11).

($E > 0$) one phonon of energy E is given by the first-order term, i.e., $dP_1 = S_1(E)dE$. The second-order term incorporates the participation of two phonons with energies that add to E. For a given inverse temperature β, all terms in Eq. (11) are generated from the PDOS $g(E)$. The measurement provides $S(E)$, and an inversion of Eq. (11) gives $g(E)$. In Fig. 7, we show the PDOS of iron metal.

SMS

In solids the probability that NRs occurs without change in the vibrational state is often appreciable and was introduced previously as the Lamb-Mössbauer factor f. In terms of the phonon excitation probability density of Eq. (7), we have $f = \Gamma S(0)$ with corresponding transitions indicated in Fig. 5. Now that vibrational transitions are excluded, slight energy differences of the nuclear levels become visible and measurable. The nuclear level splitting is caused by the electronic environment and is known as hyperfine interaction. The exclusion of phonon excitations results in elastic coherent scattering. This process is described by a differential scattering cross section that is strongly peaked in certain directions and in particular the direction of the incident x rays (nuclear forward scattering.)

Level splitting

Fig. 8 shows a ^{57}Fe nucleus under the influence of an electric field gradient (EFG) or a magnetic field. The energy levels of the isolated nucleus are twofold and fourfold degenerate, respectively. The presence of an EFG, which is created by the electronic environment and couples to the quadrupole moment of the nucleus, partly removes the degeneracy. In case of an axially symmetric EFG, the energy splitting for spin quantum numbers $I > 1/2$ and $m = -I, \ldots, I$ is given by

$$E_m = \Delta \frac{3m^2 - I(I+1)}{2I(2I-1)}, \tag{12}$$

where Δ is called the electric quadrupole splitting. For the ^{57}Fe case, we obtain a characteristic two-line pattern with$E_{\pm 3/2} - E_{\pm 1/2} = \Delta$.

The presence of the magnetic field imprints unidirectional symmetry, which removes the degeneracy completely. The energy splittings are given by

$$E_m = -\mu B \frac{m}{I} \quad m = -I, \ldots, I, \tag{13}$$

where μ, I are the magnetic moment, spin of the nuclear state, B is the magnetic field at the nucleus, and m is the spin-projection quantum number. The 14.4125 keV transition of ^{57}Fe has M1 multipolarity, and the individual transitions shown in Fig. 8 follow dipole selection rules, i.e., $|m_e - m_g| \leq 1$. This results in a characteristic six-line pattern.

In addition to the interactions discussed above, one expects a renormalization of the energy of nuclear levels due to the presence of s-electrons in the nuclear volume. The observable result is a slight shift of the transition energy that is proportional to the density of the s-electrons in the nuclear volume. This so-called isomer shift can only be measured by comparison of different materials, e.g., for ^{57}Fe the isomer shift is usually given relative to ^{57}Fe nuclei in iron metal at ambient conditions.

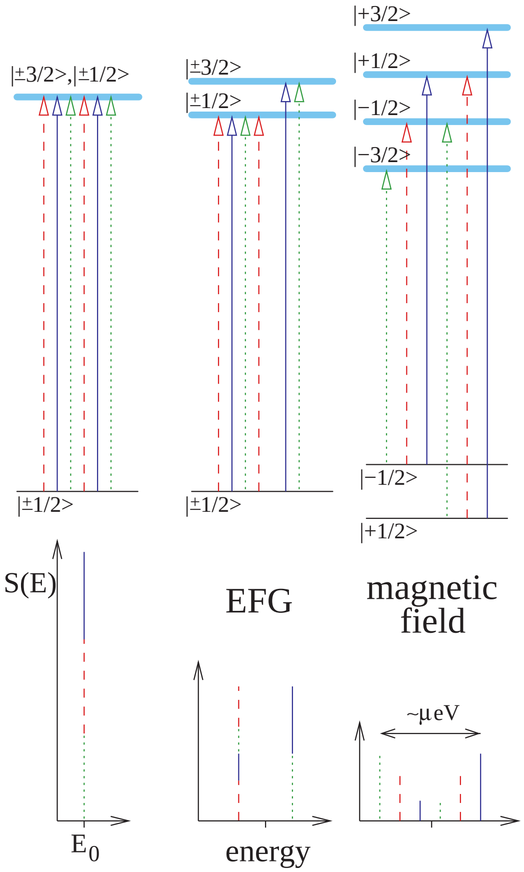

Fig. 8 Nuclear level splitting of ^{57}Fe by interactions with electrons. The presence of an EFG or a magnetic field leads to several nuclear transitions separated by up to several μeV. The ground and excited state have spin quantum numbers of 1/2 and 3/2, respectively.

Index of refraction

SMS is an elastic coherent process, and all possible nuclear sublevels can be excited simultaneously by a short x-ray pulse with sufficient bandwidth. The different nuclear transitions are then analogous to a set of oscillators with slightly different energies that are excited in phase at a given instant. Shortly after the x-ray pulse has passed, the de-excitation begins, also in phase, but soon the increasing phase difference leads to destructive interference and then again to a constructive interference. This process leads to oscillations in the emission of the scattered radiation that depend directly on the nuclear level splitting and thus on the hyperfine interactions.

In a transmission geometry, SMS is usually described by an energy-dependent contribution to the index of refraction

$$n(E) = \frac{\hbar c}{2E} \rho \sigma_N f \sum_l \frac{W_l}{z_l(E) - \mathrm{i}}, \tag{14}$$

where ρ is the number density of resonant nuclei, σ_N is the nuclear resonant cross section, and f is the Lamb-Mössbauer factor. The sum is over all sublevels of nuclear ground and excited states. The function $z_l = 2(E_l - E)/\Gamma$ depends on the energy difference between excited and ground states E_l and the nuclear level width Γ. The weight of each resonance is given by W_l with the normalization $\sum_l W_l = 1$. The weights depend on the directions of the hyperfine fields relative to the direction and the polarization of the SR. For simplicity we ignore their tensor character. Then the transmission of monochromatic x rays of energy E through a sample of thickness D is given by

$$T(E) = T_0 \exp\left[-\eta \sum_l \frac{W_l}{z_l^2(E) + 1} \right], \tag{15}$$

where $\eta = \rho \sigma_N f D$ is called "effective thickness" of the platelet. The factor T_0 accounts for electronic absorption. The time response to a *SR* pulse is expressed by

$$\frac{\mathrm{d}I}{\mathrm{d}t} = T_0 \tau \left| \mathscr{F}\left(\exp\left[\mathrm{i}\frac{\eta}{2} \sum_l \frac{W_l}{z_l(E) - \mathrm{i}} \right] - 1 \right) \right|^2, \tag{16}$$

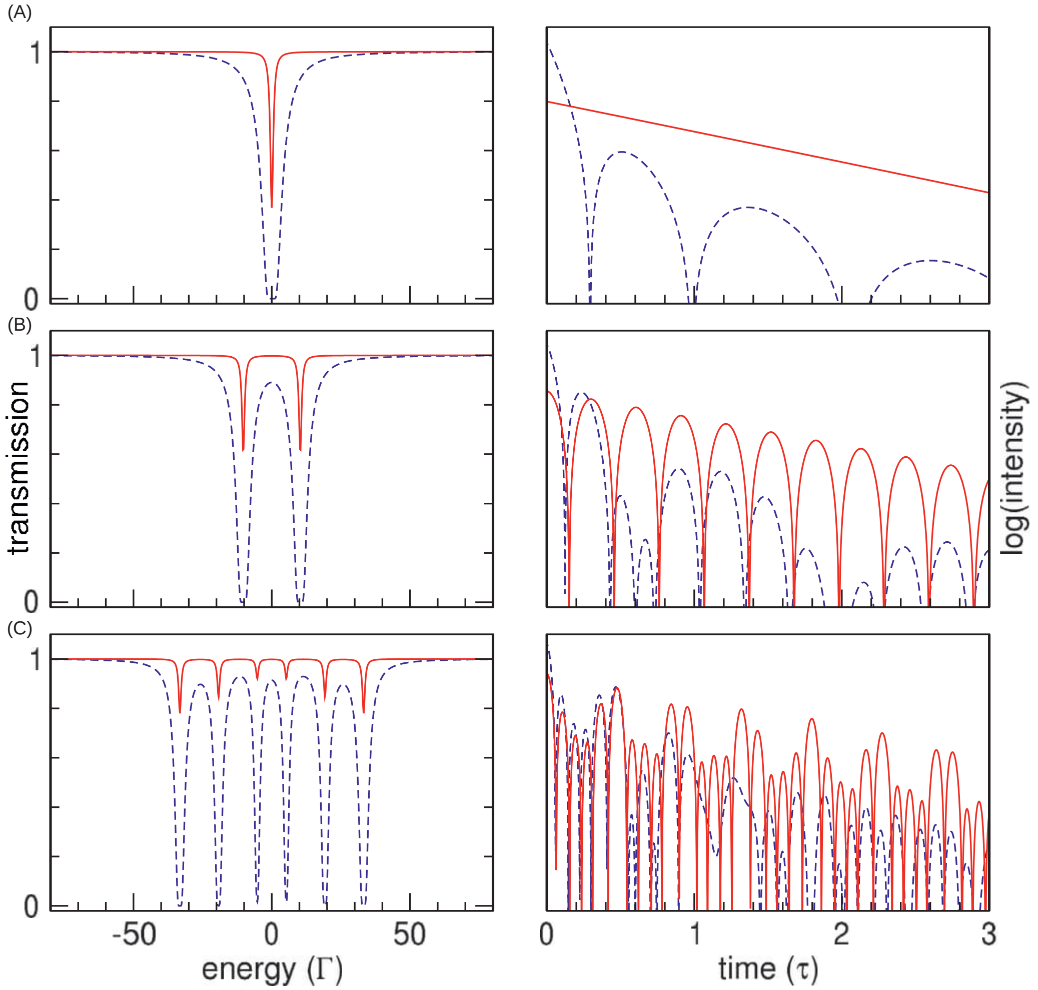

Fig. 9 SMS spectra in energy and time. Calculations used Eqs. (15) and (16) with small ($\eta = 1$, solid lines) and large ($\eta = 50$, dashed lines) effective thicknesses. Panel (A) displays the case without hyperfine fields; panels (B) and (C) show spectra characteristic for an EFG and a magnetic field, respectively. Time spectra (right side) were normalized to identical area.

where $\mathcal{F}$ symbolizes Fourier transformation. The primary application of SMS is the determination of hyperfine interaction parameters. The transmission spectra are easier to interpret if the effective thickness is small. Large values of η lead to a self-absorption effect, i.e., a broadening of the absorption lines in the energy spectra and a faster decay in the time spectra accompanied by aperiodic oscillations. The influence of the effective thickness is demonstrated in Fig. 9 by calculations using Eqs. (15) and (16).

Experimental procedure

A schematic of the typical experimental setup that can be found at third-generation SR facilities is shown in Fig. 10. The x-ray source consists of electron bunches that are orbiting in the storage ring and periodically pass through an undulator. The x rays are monochromatized in two steps using a premonochromator and a high-resolution monochromator.

For NRIXS measurements, the energy bandwidth determines the resolution of the phonon spectra of the samples. The high-resolution monochromator is tuned around the nuclear transition energy, and the x rays excite the nuclei in the sample. The re-emitted radiation is observed with an avalanche photodiode detector that is placed as close as possible to the sample but away from any strong coherent scattering directions. The integrated delayed counting rate is recorded.

For SMS measurements, the energy bandwidth should be as small as practicably achievable with reasonable efficiency. The high-resolution monochromator is tuned to the nuclear transition energy and kept as stable as possible. X rays that are transmitted through the sample excite the resonant nuclei coherently and are observed with an avalanche photodiode detector that is placed far enough away from the sample to avoid contamination from incoherent scattering. The delayed events are mapped as a function of elapsed time between arrival of a SR pulse and detection of transmitted x-ray photon - this constitutes the time spectrum of the nuclei in the sample.

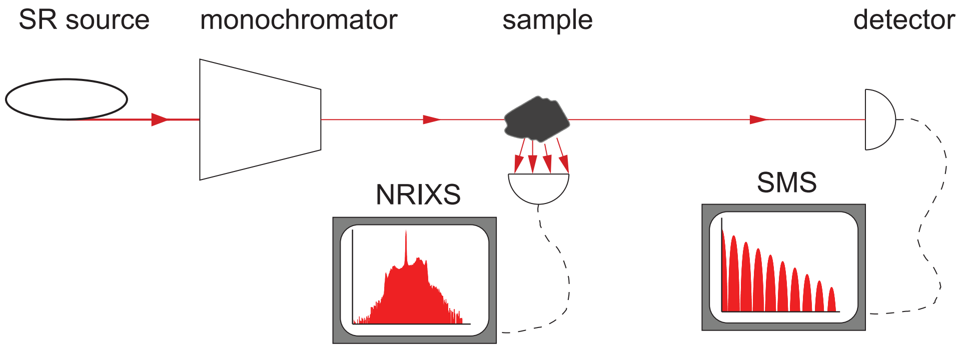

Fig. 10 Experimental setup for NRIXS and SMS.

Conclusion

The discovery of NRS using a synchrotron radiation source by Gerdau et al. (1985) was followed by an intense development phase that was fueled by availability of new third-generation SR facilities. A variety of NRS techniques was explored during the earlier period but mostly SMS and NRIXS introduced in this section have survived the test of practicality. SMS and NRIXS find unique applications to a variety of problems in condensed-matter physics, material science, geophysics, biophysics, and chemistry. Early NRS studies showed that its SR based form greatly benefitted from a new, translational approach: time resolved instead of energy resolved measurements, the latter familiar in traditional Mössbauer spectroscopy. This advance resulted from the time structure of SR, which is emitted as a sequence of very short x-ray pulses of typically less than 100 ps duration. Time resolved spectra are almost background-free and therefore show a vastly superior signal-to-noise ratio compared to energy resolved measurements leading to unique applications.

Todays evolution of SR sources is focused on optimized x-ray brilliance realized in either "ultimate storage rings" or "X-ray lasers." Experiments at the latter source are extremely access limited and will probably not play a major role for NRs techniques. The first source is an upgrade of existing SR facilities to achieve the smallest possible electron emittance in the storage ring and, in combination with optimized undulators, very high x-ray brilliance with significant transverse coherence. This often seems to require a time structure that puts NRS experiments at a disadvantage: x-ray pulse spacings that are too small for time-resolved studies. This leaves experimenters with time-integrated techniques with substantially reduced signal-to-noise ratios for SMS and reduced counting rate for NRIXS experiments. These issues are partially compensated by the improved x-ray properties that permit improvements in x-ray optics.

NRS techniques are adapting to x-ray source developments and SMS and NRIXS as introduced in this section are expected to dominate the selection. NRS may be considered a *gem* under a multitude of spectroscopic techniques and certainly contributes to the diversity of SR-based x-ray spectroscopies.

Acknowledgments

I am grateful for valuable discussions with J.M. Jackson and T.S. Toellner.

References

Gerdau E and de Waard H (eds.) (1999/2000) Nuclear resonant scattering of synchrotron radiation. *Hyperfine Interactions* 123–125.
Gerdau E, Rüffer R, Winkler H, Tolksdorf W, Klages CP, and Hannon JP (1985) Nuclear Bragg diffraction of synchrotron radiation in yttrium iron garnet. *Physical Review Letters* 54: 835.
Langouche G and Yoshida Y (eds.) (2021) *Modern Mössbauer Spectroscopy*. Springer Nature Singapore. ISBN: 9789811594229, 9811594228.
Sturhahn W (2004) Nuclear resonant spectroscopy. *Journal of Physics: Condensed Matter* 16: S497.
Sturhahn W and Jackson J (2007) Geophysical applications of nuclear resonant spectroscopy. In: Ohtani E (ed.) *Advances in High-Pressure Mineralogy*, 157–174. Special Paper 421.
Sturhahn W, Toellner TS, Alp EE, Zhang X, Ando M, Yoda Y, Kikuta S, Seto M, Kimball CW, and Dabrowski B (1995) Phonon density of states measured by inelastic nuclear resonant scattering. *Physical Review Letters* 74: 3832.

Relevant website

https://www.nrixs.com—NRIXS Evaluation Software.

Scattering, Rayleigh

Roberto Piazza, Department of Chemistry, Materials Science and Chemical Engineering, Politecnico di Milano, Milano, Italy

© 2024 Elsevier Ltd. All rights reserved.

This is an update of R. Piazza, V. Degiorgio, Scattering, Rayleigh, Editor(s): Franco Bassani, Gerald L. Liedl, Peter Wyder, Encyclopedia of Condensed Matter Physics, Elsevier, 2005, Pages 234–242, ISBN 9780123694010, https://doi.org/10.1016/B0-12-369401-9/00648-3.

Introduction 215
Molecular Rayleigh scattering 216
Scattering and fluctuations 216
Rayleigh scattering from pure fluids and fluid mixtures 217
Simple liquids 217
Liquid mixtures and solutions 218
Quantum fluids 218
Scattering from dispersed particles 219
Statement of the problem 219
The optical theorem (OT) 219
Scattering regimes 220
Interacting particles 224
The complex refractive index for interacting particles 225
Dynamic Rayleigh scattering 226
Conclusion 226
Acknowledgment 227
References 227

Abstract

This review discusses the physical origin of elastic scattering of radiation (Rayleigh Scattering, RS), its relation to fluctuations in fluids and fluid mixtures, its role in the investigation of dispersions of colloidal particles. Particular emphasis is put on the Optical Theorem, which allows to relate the total RS cross section to the real and imaginary part of the refractive index. Recent advances concerning RS from degenerate quantum gases, from correlated fluids, and from suspensions of interacting particles, are presented. Finally, a brief introduction to quasi-elastic RS is given, also known as Dynamic Light Scattering, is given, together with a mention of novel techniques that blend scattering and imaging.

Introduction

Rayleigh scattering (RS) is the elastic spreading of electromagnetic radiation from bound electrons, after they have been excited to virtual states far from resonances. Therefore, it differs from resonant fluorescence, molecular Raman scattering, and Brillouin scattering in condensed media, which are discussed elsewhere in this encyclopedia. Thomson scattering can be seen as a particular case of RS from free electrons, but is not further discussed in this article (neither is its relativistic Compton counterpart). Molecular RS plays a primary role in atmospheric optics accounting for the blue color of the sky and a large number of optical phenomena ranging from rainbows to fogbows, glories, halos, coronae, blue sun and moon, and the white color of clouds and snow, to cite only a few. A comprehensive discussion of atmospheric scattering has been made by Minnaert (1954) and, more recently, by Lynch and Livingston (1995).

Yet, the most interesting applications of RS arguably concern scattering from mesoscopic objects, either in the form of aerosols or suspensions of colloidal particles with a size ranging from a few nanometers to a few micrometers. Scattering from pollutant airborne particles has, for instance, crucial consequences on re-irradiation of solar energy from the lower atmosphere. Measurements of the scattering properties of dispersed particles yield primary information on colloid size, morphology, and interactions. Chances of obtaining photonic bandgap crystals often rely on the peculiar scattering properties of metal-coated colloids. Finally, by exploiting radiation forces associated to scattering, particles can be easily manipulated using noninvasive “optical tweezers,” allowing one to design template surfaces of interest in photonics. Although, fluid systems are primarily dealt with, it is also important to point out that the attenuation due to RS sets severe limits to the useful wavelength range for light propagation in optical fibers.

This article is organized as follows. After a basic analysis of elastic molecular scattering, the key role of fluctuations in RS from condensed media is pointed out, and a fluctuation approach to shortly derive RS from simple fluids and mixtures is applied. The final and largest part is devoted to particle RS and its exploitation. Besides specific applications, however, the main message of which an attempt is made to convey is the following: “every deviation of light from rectilinear propagation, including diffraction and even geometrical refraction, can be ultimately seen as a consequence of Rayleigh scattering.” As will be seen, the optical theorem, linking the refractive index to scattering properties, and the large particle limit of Mie scattering, yielding classical diffraction and eventually geometric optics, justify this strong statement.

Molecular Rayleigh scattering

First, recall the basic geometry of a scattering experiment. As incident field, what will always be taken is a plane wave linearly polarized along $\hat{\mathbf{n}}_i$ having a wave vector $\mathbf{k}_i$, with $|\mathbf{k}_i| = k = 2\pi/\lambda$, where λ is the wavelength in the medium. Measurements consist in detecting the light scattered along the direction set by the wave vector $\mathbf{k}_s$ that, together with $\mathbf{k}_i$, fixes the scattering plane. Since Rayleigh scattering is elastic, one must have $|\mathbf{k}_s| = k$, hence the scattering vector $\mathbf{q} \doteq \mathbf{k}_i - \mathbf{k}_s$ has magnitude $q = (4\pi/\lambda)\sin(\vartheta/2)$, where ϑ is the angle in the scattering plane between $\mathbf{k}_i$ and $\mathbf{k}_s$, while the azimuth angle with respect to the normal to the scattering plane will conversely be denoted by φ. In some measurements, a specific polarization component of the scattered field along $\hat{\mathbf{n}}_s$ may be selected with a polarizer.

The simplest way to estimate elastic scattering is the elegant dimensional argument originally devised by Rayleigh[1] that, restated in modern terms, goes as follows. If the size of the scattering objects is much smaller than λ, so that they essentially 'see' a spatially uniform, time-varying field, the scattered and incident fields will be proportional. Their dimensionless ratio E_s/E_i may in principle depend on λ, the speed of light c, the volume V of a scatterer, the dielectric constants ε_p, ε_m of the materials constituting the particle and the surrounding medium, and the distance r of the observation point from the scattering volume. Since c is the only quantity that contains time, it should not appear in E_s/E_i. Similarly, ε_p and ε_m must appear only as a homogenous function f of the ratio $\varepsilon_p/\varepsilon_m$. Since molecular polarizability α is linearly proportional to V, so must be E_s. Finally, in the radiation zone the scattered field will be a spherical wave, so that $E_s \propto r^{-1}$. Therefore, the simplest dimensionless combination is $E_s/E_i = Vr^{-1}\lambda^{-2}f(\varepsilon_p/\varepsilon_m)$, and for the scattered intensity one must have

$$I_s = \frac{V^2}{r^2\lambda^4} f^2\left(\frac{\varepsilon_p}{\varepsilon_M}\right) I_0, \tag{1}$$

giving both a strong preferential scattering of short wavelengths (accounting for the hue of the sky and for the sun reddening at dawn and setting) and the remarkable dependence on molecular volume (yielding, for spheroidal molecules, a sixth power dependence on the radius).

For a molecular scatterer of size $d \ll \lambda$, a formal analysis can be performed by solving the Helmholtz equation for the vector potential in far-field (radiation) zone $r \gg \lambda \gg d$, expanding the solution in multipoles, and retaining only the lowest (electric dipole) order. Within this approximation, the incident field induces a dipole $\mathbf{p} = \boldsymbol{\alpha} \cdot \mathbf{E_i}$, where in general the molecular polarizability $\boldsymbol{\alpha} = \alpha_{ij}$ is a tensor (so that $\mathbf{p}$ and $\mathbf{E_i}$ are not necessarily parallel). The induced dipole irradiates a spherical wave at the same frequency and with amplitude given by

$$\mathbf{E}_s(\mathbf{r}) = \frac{k^2}{4\pi\varepsilon_0}(\hat{\mathbf{r}} \times \mathbf{p} \times \hat{\mathbf{r}})\frac{\exp(ikr)}{r}. \tag{2}$$

If, for simplicity, one assumes that the molecule has a scalar polarizability α, so that $p \equiv |\mathbf{p}| = \alpha\mathbf{E_i}$, the scattered intensity (irradiance) is given by

$$I_s = \frac{\varepsilon_0 c}{2}\overline{\mathbf{E}_i^*\mathbf{E}_i} = \frac{\pi^2\alpha^2\sin^2\gamma}{\varepsilon_0^2\lambda^4 r^2} I_0 \tag{3}$$

where I_0 is the incident intensity, and γ is the angle between $\mathbf{p}$ and the direction of propagation of the scattered field.

This simple classical analysis is fully adequate for treating most of the problems involving molecular RS. For what concerns quantum effects, what must be first noticed is that RS is a two-photon process requiring full quantization of the radiation field. A simple quantum analysis of RS can be made starting from two-level Bloch equations, or from a more general multi-level perturbation theory leading to the Kramers-Heisenberg formula, which has the advantage of treating on the same footing Rayleigh, Thomson, and inelastic Raman scattering, and accounts also for quantum corrections to classical RS cross-sections (see Loudon, 2000). Nevertheless, far from resonances these corrections are negligible, so that a fully classical approach will be used in what follows.

Scattering and fluctuations

The former single-scatterer approach to RS may however be misleading, since it misses a crucial point. Indeed, a *uniform* distribution of molecules will not scatter light *at all*, since the phases of the scattered fields are uniformly distributed in $[0, 2\pi]$. Therefore, the total scattered field vanishes for all except the forward direction where, adding to the incident beam, leads to a phase delay of the transmitted beam modifying (as shall be better seen below) the refractive index of the medium. Exceptions are ordered arrays of scatterers, where Bragg peaks appear due to breaking of continuous translational symmetry. Scattering therefore always require *fluctuations*.

A very general approach to the problem can be made by treating the scattering medium as a continuum where, in order to account also for optical anisotropy effects, local dielectric (and therefore, refractive index) fluctuations are introduced by means of a tensor $\delta\varepsilon(\mathbf{r}, t)$, and deriving a wave-propagation equation in weakly inhomogeneous media. By assuming that the scattered field is much smaller than the incident field, the dielectric fluctuations in spatial Fourier components can be decomposed as

---

[1] Lord Rayleigh (John William Strutt) developed his theory in a series of papers, culminating in a final masterpiece, see Rayleigh (1899).

$$\delta\varepsilon(\mathbf{q},t) = \int \delta\varepsilon(\mathbf{r},t)\mathrm{e}^{\mathrm{i}\mathbf{q}\cdot\mathbf{r}}\mathrm{d}^3r, \tag{4}$$

where **r** gives the position of the scattering element with respect to an arbitrary origin O in the scattering volume. The instantaneous scattered field amplitude reaching a detector placed at a distance R from O, after passing through a polarizer with transmitting axis set along $\widehat{\mathbf{n}}_\mathbf{f}$, is given by

$$E_s^{if}(R,t) = -\frac{k^2E_0}{4\pi\varepsilon_0 R}\delta\varepsilon_{if}(q,t)\mathrm{e}^{\mathrm{i}(k_sR-\omega t)}, \tag{5}$$

where $\delta\varepsilon_{if} \equiv \widehat{\mathbf{n}}_\mathbf{i}\cdot\delta\varepsilon(\mathbf{q},\,\mathbf{t})\cdot\widehat{\mathbf{n}}_\mathbf{f}$. The time-averaged detected intensity is

$$I_s^{if}(\mathbf{q}) = \frac{k^4I_0}{16\pi^2\varepsilon_0^2R^2}\left\langle\left|\delta\varepsilon_{if}\right|^2\right\rangle, \tag{6}$$

and is therefore proportional to the mean square fluctuations of the dielectric constant with the same spatial frequency **q**.

In order to find a connection with the molecular approach, which is particularly useful when dealing with scattering from dispersed particles, it can simply be assumed that the local dielectric constant depends explicitly only on the local molecular number density $\rho(\mathbf{r},t)$ (see the next section for a discussion) writing $\delta\varepsilon(\mathbf{r},t) = \boldsymbol{\alpha}(t)\rho(\mathbf{r},t)$, where $\boldsymbol{\alpha}(t)$ is the molecular polarizability tensor, which depends on time too because of molecular rotations (See section "Scattering from dispersed particles" for details). Expressing the local density fluctuations as a sum of delta functions over the molecular positions $\mathbf{r}_i(t)$ as $\delta\rho(\mathbf{r},\,t) = \sum_i\delta(\mathbf{r}-\mathbf{r}_i)-\overline{\rho}$, where $\overline{\rho}$ is the average number density, and putting $\alpha_{if}(t) \equiv \widehat{\boldsymbol{n}}_f\cdot\boldsymbol{\alpha}(\mathbf{q},t)\cdot\widehat{\boldsymbol{n}}_f$, one can immediately see that

$$\delta\varepsilon_{if}(\mathbf{q},t) = \alpha_{if}(t)\left\{\sum_i \exp\left[i\mathbf{q}\cdot\mathbf{r}_i(t)\right] - N\delta(q)\right\},$$

where the second term (coming from $\overline{\rho}$) is simply the scattering contribution at $q = 0$ from the N molecules.

Provided that molecular orientations and translations are uncorrelated (so that the amplitude and phase averages factorize), from Eq. (6) one therefore obtains

$$I_s^{if}(\mathbf{q}) = \frac{k^4NI_0}{16\pi^2\varepsilon_0^2R^2}\left\langle\left|\alpha_{if}\right|^2\right\rangle S(q), \tag{7}$$

where

$$S(q) = N^{-1}\sum_{i,j}\left\langle \exp\left[\mathbf{iq}\cdot\left(\mathbf{r_i}-\mathbf{r_j}\right)\right]\right\rangle \tag{8}$$

is the static *structure factor*. To make things clearer, consider an ideal gas where particle positions are uncorrelated. Then $\langle\exp[\mathbf{iq}\cdot(\mathbf{r_i}-\mathbf{r_j})]\rangle = \delta_{ij}$, so that $S(q) = 1$ and I is proportional to N. Notice that this apparently 'trivial' scaling with N, holds true only because (Poisson) density fluctuations in an ideal gas are proportional to $\sqrt{N}$: for interacting systems, it is no longer so.

Rayleigh scattering from pure fluids and fluid mixtures

Simple liquids

In liquids, fluctuations of the local dielectric constant can be expanded in terms of any two thermodynamic variables whose fluctuations are uncorrelated (see Landau et al., 1990), like for instance temperature T and density ρ. Since experimentally, for most simple liquids, $(\partial\varepsilon/\partial T)_\rho \approx 0$, RS is in fact mostly due to density fluctuations. In order to derive RS effects in simple fluids, it is however more convenient taking pressure p and entropy S as independent variables, and using of a fluctuating hydrodynamics approach. This amounts to linearizing for small fluctuations the continuity, Navier-Stokes, and heat equations and finding their normal modes (Berne and Pecora, 1976).

Since in the continuity equation ρ is coupled to the fluid velocity **v** only through $\nabla\cdot\mathbf{v}$, density fluctuations are uncoupled to transverse velocity modes, which therefore cannot be detected by light scattering. In addition to two propagating pressure modes (corresponding to absorption or excitation of sound waves, giving rise to Brillouin scattering), the solution of linearized mode equations yields a thermal diffusive mode, corresponding to the frequency-unshifted Rayleigh peak having a width $\Delta\omega = D_Tq^2$, where D_T is the thermal diffusivity, and an amplitude proportional to the difference $c_p - c_v$ of the specific heats at constant pressure and volume. For many liquids, and in particular for water, $c_p - c_v$ is rather small, and therefore RS fairly weak.[2]

It is also useful to point out that the structure factor defined in (8) can directly be linked to structural correlations (Piazza, 2017). Introducing the density autocorrelation function for a homogeneous (but not necessarily isotropic) fluid

---

[2] In spite of a widespread belief, the bluish appearance of thick water layers or ice blocks is not primarily due to scattering, but to a much stronger absorption effect due to an overtone vibrational peak close to the red edge of the visible spectrum. Indeed, D_2O, where the shifts to higher λ due to isotope effects, is much more transparent.

$$G(\mathbf{r}) = \langle \rho(0)\rho(\mathbf{r})\rangle - \rho^2,$$

where $\rho(\mathbf{r})$ is the local density, with $\rho = \langle \rho(\mathbf{r})\rangle$, one indeed has

$$S(\mathbf{q}) = \frac{1}{\rho}\int G(\mathbf{r}) \exp(\mathrm{i}\mathbf{q}\cdot\mathbf{r}) \mathrm{d}^3 r, \tag{9}$$

so that $S(\mathbf{q})$ is essentially the (inverse) spatial Fourier transform of $C(\mathbf{r})$. Since the latter is related to the pair distribution function $g(\mathbf{r})$, the probability density per unit volume of finding two particles at a distance $\mathbf{r}$, by

$$G(\mathbf{r}) = \rho\delta(\mathbf{r}) - \rho^2[g(\mathbf{r}) - 1)],$$

where the first term s the self-correlation of the local density, one finds

$$S(\mathbf{q}) = 1 + \rho\int [g(\mathbf{r}) - 1] \exp(\mathrm{i}\mathbf{q}\cdot\mathbf{r}) \mathrm{d}^3 r \tag{10}$$

It is however important to recall that the typical q-range over which structural features of simple fluids develop is much larger than the range probed by light scattering, which therefore essentially measures only $S(0) = \rho k_B T \chi_T$, where $\chi_T = (1/\rho)(\partial P/\partial\rho)^{-1}$ is the isothermal compressibility. As discussed in what follows, the situation is however very different for suspensions of mesoscopic particles, where the structural spatial scales are often of the order λ.

Liquid mixtures and solutions

In liquid mixtures or molecular solutions new modes appear due to the presence of an additional conserved variable, namely the concentration c of one of the two species, adding a hydrodynamic mass diffusion equation. The analysis is much simpler if pressure fluctuation, and therefore effects on Brillouin peaks, are neglected (see Berne and Pecora, 1976), so that the problems amount to solving by Laplace transform the linearized form of the coupled equations for the fluctuations δc, δT

$$\begin{aligned} \frac{\partial(\delta c)}{\partial t} &= D\left[\nabla^2(\delta c) + \frac{k_T}{T}\nabla^2(\delta T)\right] \\ \frac{\partial(\delta T)}{\partial t} - \frac{1}{c_p}K_T\left(\frac{\partial\mu}{\partial c}\right)\frac{\partial(\delta c)}{\partial t} &= D_T\nabla^2(\delta T), \end{aligned} \tag{11}$$

where D is the mass diffusion coefficient, μ is the chemical potential of the mixture, and k_T is the thermal diffusion ratio, quantifying coupling of mass and heat transport through the Soret effect. Solution of (11) yields two diffusive modes where thermal and concentration fluctuations are in general mixed: in practice, however, since $D \ll D_T$ (for most liquids $D_T \simeq 10^{-3}$ cm^2 s^{-1}, while D varies between 10^{-5} cm^2 s^{-1} for simple mixtures and 10^{-6} – 10^{-8} cm^2 s^{-1} for macromolecular solutes) the two modes are almost decoupled. The peak due to concentration fluctuation has an extremely narrow width $\Delta\omega = Dq^2$ and an amplitude proportional to $(\partial\mu/\partial c)^{-1}$. The role played by density fluctuations in simple fluids is then taken by concentration fluctuations. For dilute solutions, this means that RS is proportional to the osmotic compressibility.

Quantum fluids

Although this paper mainly addresses classical systems, it is worth giving some basic ideas concerning the scattering properties of fluids at temperatures and densities where quantum degeneracy effects become relevant. Particularly interesting is the strong suppression of RS in ultracold Fermi gases, an effect predicted several decades ago (see, for instance, Javanainen and Ruostekoski, 1995) but only very recently observed (see DeMarco and Thywissen, 2021 and references therein).

Grasping the physical origin of this effect, often dubbed "Pauli blocking of light scattering", is not difficult. At temperatures $T \ll T_F$, where T_F is the Fermi temperature, the Fermi-Dirac distribution is very close to a step function, and fermions "pile up" occupying the single-particle energy states up to the Fermi energy $\varepsilon_F = k_B T_F = \hbar^2 k_F^2/2m$, where $k_F \simeq (6\pi\rho/g_s)^{1/3}$ is the Fermi momentum at particle number density ρ and $g_s = 2s + 1$ is the spin degeneracy. Particles lying well within the "Fermi sea", namely with a momentum k_0 consistently lower than k_F, will never be able to scatter radiation at wave vector q if the transferred momentum $\hbar q < k_F - k_0$, simply because they cannot find any available free state.[3] Hence, RS is strongly suppressed and can occur only close to the Fermi surface.

A more quantitative way to explain the effect is based on considering that the Pauli exclusion principle introduces effective repulsions between fermions, even when they do not interact via "real" forces. As a consequence, a system of independent fermions will display pair correlations manifested by specific features of the structure factor. In the weakly-degenerate limit $\rho\Lambda^3 \ll 1$, where $\Lambda = h/\sqrt{2\pi m k_B T}$ is the thermal wavelength for fermions of mass m at temperature T, the pair correlation function becomes

---

[3] Currently, ultracold fermions at densities exceeding 10^{15} cm^{-3} can be reached, corresponding to a Fermi momentum of the order of 2×10^5 cm^{-1}. In the visible range, this is far larger that the maximum scattering wave vector $4\pi/\lambda$.

$$g(r) = 1 - \exp\left(-2\pi r^2/\Lambda^2\right), \tag{12}$$

namely, $g(r)$ just display an "antibunching hole" up to interparticle distances of the order of Λ, which is the quantum equivalent of a hard-core repulsion for a classical system.[4] The corresponding structure factor,

$$S(q) = 1 - \frac{\rho\Lambda^3}{2\sqrt{2}} \exp\left[-\frac{(q\Lambda)^2}{8\pi}\right], \tag{13}$$

has then a shallow minimum at $q = 0$ yielding an isothermal compressibility that coincides with the value obtained from the equation of state for a weakly-degenerate Fermi gas $P = nk_BT\left(1 + \rho\Lambda^3/4\sqrt{2}\right)$.

Analytic expressions for $g(r)$ and $S(q)$ for lower temperature do exist, but in the case of fermions they are valid only for negative values of the chemical potentials, namely for $T \gg T_F$. Yet, the asymptotic limits for $T \to 0$ in Bosse et al. (2011) and numerical results in Tsutsui and Kita (2016) confirm that a system of highly degenerate fermions scatter almost no radiation in a q-range that extends up to Λ^{-1}, while recent experiments by Margalit et al. (2021), where temperatures down to $T \approx 0.2T_F$ were investigated, have indeed shown a reduction of RS up to 40%.

Scattering from dispersed particles

Statement of the problem

The important case of elastic scattering from dispersed particles is discussed here, first considering only particles made of an optically isotropic material, that is with a scalar polarizability. In far field, the scattered field $E_s(r,t)$ is an amplitude-modulated spherical wave, which can be written as

$$E_s(r, t) = s(\vartheta, \varphi)\frac{\exp\left[\mathrm{i}(kr - \omega t)\right]}{\mathrm{i}kr}E_0, \tag{14}$$

where $s(\vartheta,\varphi)$ is a dimensionless (single-particle) *scattering function*, which is in general a complex quantity, $s \doteq f(\vartheta,\varphi)\exp\left[\mathrm{i}\phi(\vartheta,\varphi)\right]$.[5] The scattered intensity can therefore be written in terms of the incident intensity I_0 as

$$I = \frac{f(\vartheta, \varphi)^2}{k^2r^2}I_0. \tag{15}$$

By integrating r^2I_S over the solid angle Ω, the scattering cross-section for a single particle is therefore found to be

$$\sigma_s = \frac{1}{k^2}\int f^2(\vartheta, \varphi)\mathrm{d}\Omega. \tag{16}$$

If, besides scattering, the particle absorbs part of the radiation with an absorbtion cross-section σ_a, the total extinction cross section will be given by $\sigma_{ext} = \sigma_s + \sigma_a$.

The previous definition can be generalized to account for scattering from optically anisotropic particles by writing

$$\begin{bmatrix} E_s^{\perp} \\ E_s^{\parallel} \end{bmatrix} = \frac{\exp\left[\mathrm{i}k(r-z)\right]}{\mathrm{i}kr}\begin{bmatrix} s_1 & s_2 \\ s_3 & s_4 \end{bmatrix}\begin{bmatrix} E_i^{\perp} \\ E_i^{\parallel} \end{bmatrix} \tag{17}$$

where z is the particle coordinate along the direction of the incident beam with respect to an arbitrary origin. Specific forms for the scattering matrix $[s_{ij}]$ are dictated by particle symmetry: for instance, it is diagonal for spherical particles made of an optically isotropic material and symmetric for nonchiral particles (van de Hulst, 1968).

The optical theorem (OT)

A simple, but extremely useful relation, which holds true not only for electromagnetic radiation but also for matter waves (Newton, 1976), connects the total scattering cross section to the scattering amplitude in the forward direction. The effect on the transmitted wavefront of the transit though a scattering medium can be expressed by stating that the forward scattering pattern consists in a faithful reproduction of the incident field that spatially superimposes with the transmitted radiation, but with a different phase. The interference between this "simulacrum" of the incident field and the portion of the field which passes through the medium without being scattered yields *both* its phase delay in traversing the medium (thus fixing its refractive index) and, adding any structural correlations, and (b) the incident to the non-radiative power loss due to absorption, field "seen" by a particle coincides with the exterthe power reduction of the transmitted field. For nal radiation, which loosely means that "multiple what concerns power loss, this is explicitly treated scattering" effects are negligible. If these condiby the so-called *Optical Theorem* (OT).

---

[4] For a weakly-degenerate Bose gas, the corresponding expression is $g(r) = 1 + \exp\left(-2\pi r^2/\Lambda^2\right)$, which conversely shows the boson propensity to "bunching" (Jeltes et al., 2007). It is however worth noticing that this result is somehow academic, since it is valid only for elementary massless bosons. Massive bosons are necessarily *composite*, namely, atoms with an even number of neutrons that definitely show a hard-core *repulsion* when their electronic clouds overlap.

[5] By factoring out an imaginary unit, which is related to the Gouy phase shift accumulated in far-field between a spherical and a plane wave, the amplitude function coincides in the short-wavelength limit (aside from polarization effects) with a standard normalized diffraction pattern (van de Hulst, 1968).

Consider again the simple case of a plane wave with incident wave vector $\mathbf{k}_i$, and polarized with the electric field along $\mathbf{n}_i$, which encounters a scattering and absorbing medium confined in a finite region of space around the origin. Then, the OT states that the extinction cross section is given by

$$\sigma_{ext} = \frac{4\pi}{k^2}(\mathbf{n}_i \cdot \mathbf{n}_s)\,\mathrm{Re}\,[S(\mathbf{k}_s = \mathbf{k}_i)], \tag{18}$$

where $S(\mathbf{k}_s = \mathbf{k}_i)$ is the *overall* scattering function of the medium in the forward direction $\mathbf{k}_i$. This rather surprising result, which basically shows that evaluating the total extinction (due to scattering and, possibly, absorption) of the radiation traversing the medium requires to know *only* the forward scattering amplitude, can be rather easily obtained Jackson (1998) by considering that, at steady state, the change in the total energy density within a spherical region containing the whole scattering medium is solely due to the dissipative absorption processes taking place within it, and by equating the latter to the outward flux of the incident plus scattered energy.

The forward scattering amplitude, however, contains more information than what simply conveyed by the OT, since the effects of propagation can be fully embodied into a complex refractive index $\tilde{n} = n + in'$, whose real and imaginary parts are respectively related to dispersion and power loss. Then, *both* n and n' can be formally linked to the real and imaginary parts of $S(\mathbf{k}_s = \mathbf{k}_i)$. Yet, such a relation is of little practical interest unless one is able to evaluate $S(\mathbf{k}_s = \mathbf{k}_i)$ in terms of the specific microscopic scattering and absorption events taking place in the medium. In the general case, this a formidable task leading to cumbersome and rather impractical results. Nevertheless, for particle suspensions the complex refractive index of the whole dispersion can indeed be related to the scattering properties of the individual scatterers provided that (a) the particles interact very weakly, so they do not display any structural correlations, and (b) the incident field "seen" by a particle coincides with the *external* radiation, which loosely means that "multiple scattering" effects are negligible. If these conditions are met, then for a thin slab of a medium consisting of a dispersion of N identical isotropic scatterers illuminated by a monochromatic plane wave Eq. (18) reduces to

$$\sigma_{ext} = \frac{4\pi N}{k^2}\,\mathrm{Re}\,[s(0)], \tag{19}$$

where $s(0)$ is the amplitude of the field scattered in the forward direction $\theta = 0$ by each *single* particle (van de Hulst, 1968).

The former simpler relation can be obtained by considering that for independent particles σ_{ext} is the sum of the single-particle cross sections, while in the forward direction (and *only* in this direction) the scattering amplitudes are additive too, because all scattering contributions add in phase, regardless of the particle positions. By evaluating the phase shift in propagation through the slab, the real and imaginary parts of the effective refractive index of the medium are then easily found to be

$$\begin{cases} n = 1 - \dfrac{2\pi\rho}{k^3}\mathrm{Im}[s(0)] \\ n' = \dfrac{2\pi\rho}{k^3}\,\mathrm{Re}\,[s(0)] \end{cases} \tag{20}$$

Hence the intensity of a plane wave propagating in the medium along z decreases as $I = I_0 \exp(-\gamma z)$, where the extinction coefficient

$$\gamma = 2kn' = \frac{4\pi\rho}{k^2}\,\mathrm{Re}\,[s(0)] = \frac{\sigma_{ext}}{V} \tag{21}$$

is simply the extinction cross section per unit volume.

Scattering regimes

The full solution of the electromagnetic scattering for particles of arbitrary size and composition is very elaborate, even for the simplest case of homogeneous spheres. It is however useful considering some specific approximation yielding simple explicit expressions for the scattering function. For what follows, an important distinction is between the *external* incident field and the *internal* field within the particle. The refractive indices of the particle and of the surrounding medium ("solvent") shall be denoted by n_p and n_s, the wavelength of the incident radiation *in vacuum* (so the wave vector is $k_{ext} = 2\pi n_s/\lambda_0$ for the external field, and $k_{int} = 2\pi n_p/\lambda_0$ within the particle) by λ_0, and a characteristic particle size by a.

Particles small compared to the wavelength. This what is called the Rayleigh regime in the strict sense. The defining requirement is that *both* the external *and* the internal fields are essentially uniform over the particle size. This means that the phase shifts ak_{ext} and ak_{int} have to be small, or $a \ll \lambda_0/2\pi n_s$, $a \ll \lambda_0/2\pi n_p$ (the second condition is generally more restrictive - notice in particular that it excludes strongly absorbing particles, whatever their size). The situation is then completely analogous to molecular Rayleigh scattering. If the particle is made by an optically isotropic material, so that its polarizability is scalar, the amplitude of the scattered field is given by Eq. (3) while, by integrating Eq. (3) and dividing by the incident intensity, the scattering cross section is found as

$$\sigma_s = k^4\alpha^2/6\pi\varepsilon_0^2. \tag{22}$$

A note of caution concerns however particle polarizability, which has to be interpreted as the *excess* optical polarizability with respect to an equal solvent volume. Noticing that, when the incident field is vertically polarized (perpendicular to the scattering plane), $\gamma \equiv \pi/2$, while if it is horizontally polarized $\gamma = \pi/2 - \vartheta$, the full scattering matrix is found to be

$$\mathbf{s} = \frac{\mathrm{i}k^3\alpha}{4\pi\varepsilon_0}\begin{bmatrix} 1 & 0 \\ 0 & \cos\vartheta \end{bmatrix}. \tag{23}$$

Specific expressions for the polarizability can be found by solving the electrostatic problem for a uniform field. For instance, for dielectric spheres of radius a, made of a material with dielectric constant ε_p,

$$\alpha = 4\pi\varepsilon_0 \frac{\varepsilon_p/\varepsilon_s - 1}{\varepsilon_p/\varepsilon_s + 2} a^3 = 4\pi\varepsilon_s \frac{n_p^2 - n_s^2}{n_p^2 + 2n_s^2} a^3 \tag{24}$$

Since $s(0) = \mathrm{i}k^3\alpha/4\pi\varepsilon_0$, from the OT one has $\sigma_{ext} = (k/\varepsilon_0)\,\mathrm{Im}\,(\alpha)$, so that a reduction of the incident power should occur only for absorbing particles. This inconsistency derives from neglecting the Lorentz radiation reaction field, which is actually the *only* mechanism for power loss in the absence of non-radiative dissipation (Snider and Garcia-Lopez, 2006). Taking into account this contribution yields an imaginary term in the particle polarizability, which is modified as

$$\alpha \to \tilde{\alpha} = \alpha\left(1 + \mathrm{i}\frac{2}{3}k^2\alpha\right). \tag{25}$$

Note that the additional term is *quadratic* in α. Taking into account radiation reactions, one finds that the complex refractive index $\tilde{n}$ of systems of point-like particles at number density ρ is exactly related to the modified polarizability defined in Eq. (25) by a *generalized Clausius-Mossotti (or Lorentz-Lorenz) relation*

$$\frac{\tilde{n}^2 - 1}{\tilde{n}^2 + 2} = \frac{4\pi}{3}\tilde{\alpha}\rho \tag{26}$$

It is useful to expand (26) at second order in $\tilde{\alpha}\rho$. Using (25) and equating the real and imaginary parts, one obtains

$$\begin{cases} n = 1 + 2\pi\alpha\rho + \dfrac{2}{3}(\pi\alpha\rho)^2 \\ n' = \dfrac{4\pi}{3}\rho k^3\alpha^2 \end{cases} \tag{27}$$

The real part coincides with the expansion at 2nd order of the usual Clausius-Mossotti formula, whereas the dissipative radiation-reaction term contribute *only* to attenuation. When this result is inserted into Eq. (20), it yields an explicit expression for the single-particle scattering amplitude

$$s_0(0) = \frac{2}{3}k^6\alpha^2 - \mathrm{i}k^3\alpha, \tag{28}$$

and the correct extinction cross section $\sigma_{ext} = (8\pi/3)N\alpha^2k^4$ for RS from N independent particles with a size much smaller than λ.

Optically anisotropic particles. The previous result can be extended to small optically anisotropic particles. For simplicity, it is assumed that the particle is made of an uniaxial birefringent material. The polarizability tensor, referred to the particle optical principal axes X, Y, Z, has only two independent components, that shall be denoted as $\alpha_\| \equiv \alpha_X$ and $\alpha_\perp \equiv \alpha_Y = \alpha_Z$. Assuming for convenience x as the direction of the scattered field and z as the normal to the (x, y) scattering plane, the two most common experimental configurations are the VV and VH geometries. In both of them the incident field is vertically polarized, but while in the VV scheme the vertical component I_{VV} of the scattered intensity is measured, the orthogonal ("depolarized") I_{VH} component is detected in the VH scheme. I_{VV} and I_{VH} can be found by evaluating $\hat{\mathbf{n}}_\mathbf{z}\cdot\boldsymbol{\alpha}\cdot\hat{\mathbf{n}}_\mathbf{z}$ and $\hat{\mathbf{n}}_\mathbf{y}\cdot\boldsymbol{\alpha}\cdot\hat{\mathbf{n}}_\mathbf{z}$, after the particle polarizability tensor has been re-expressed in the laboratory fixed frame, in terms of the average particle polarizability $\overline{\alpha} = \left(\alpha_\| + 2\alpha_\perp\right)/3$ and of the particle optical anisotropy $\beta = \alpha_\| - \alpha_\perp$.

Defining $\overline{n}_p^2 = \overline{\alpha}/V + 1$ and (provided that the optical anisotropy is small) $\Delta n = \beta/2\overline{n}V$, and assuming that $\overline{n}_p \approx n_s$, the final expression, after subtracting the solvent polarizability $\alpha_s = (n_s^2 - 1)V$, is

$$\begin{aligned} I_{VV} &= CV\overline{n}_p^2\left[\left(\overline{n}_p - n_s\right)^2 + (4/45)(\Delta n)^2\right] \\ I_{VH} &= CV\overline{n}_p^2(\Delta n)^2/15. \end{aligned} \tag{29}$$

Note that I_{VV} can be written

$$I_{VV} = I_{coh} + 4/3 I_{VH} \tag{30}$$

where I_{coh}, which comes from the isotropic part of the polarizability tensor, depends only on the average refractive index of the particles.

Fig. 1 shows the experimental results for optically anisotropic particles in water (for an extensive discussion see Degiorgio et al., 1994). Since both I_{VH} and the second term at the r.h.s. of the expression for I_{VV} do not depend on n_s, a residual scattered intensity is present even in "best index matching" conditions $n_s = \overline{n}_p$. These contributions are the direct analogous, in depolarized RS, of the

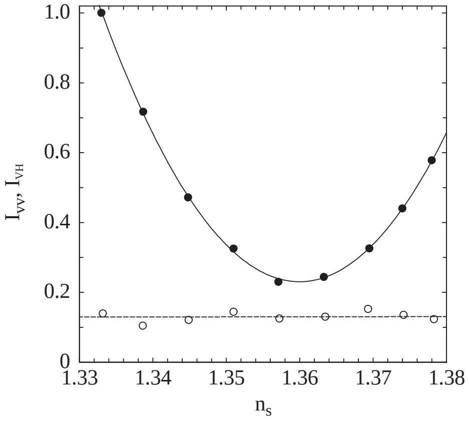

Fig. 1 Experimental values for I_{VV}(●) and I_{VH}(○), normalized to their values for water suspensions, as a function of the solvent refractive index n_s for optically anisotropic colloidal spheres made of the partially-crystalline polymer perfluoro-alkylvinylether (PFA). The parabolic fit to I_{VV} yields an average particle refractive index $\bar{n}_P \simeq 1.36$ and an optical anisotropy $\Delta n \simeq 0.03$. As discussed in the text, I_{VH} does not depend on n_s. From Piazza R and Degiorgio V (2005) Scattering, Rayleigh. In: *Encyclopedia of Condensed Matter Physics*, Bassani F, Liedl GL and Wyder P (ed.), vol. 5, pp. 234–242, Elsevier.

incoherent cross-section for neutron scattering. Notice that, although the depolarized scattering component cannot of course interfere with the orthogonally incident beam, the OT states that the sole *polarized* component still suffice to yield the *total* scattering cross section, including that due to depolarized scattering. The reason for this correct but apparently paradoxical result is discussed in Degiorgio et al. (2009).

Rayleigh-Gans-Debye (RGD) scattering. Most dispersed particles do not fulfill the strict requirements of the "pure" Rayleigh regime. A much more useful approximation can be obtained by letting the incident field vary, even appreciably, over the particle length scale, but requiring that the internal field does not appreciably differ from the incident one, both in amplitude and in phase. Weak amplitude changes simply imply $|n_p - n_s| \ll 1$, while tuning of the phases requires the optical path with or without the particles to be comparable, or

$$\frac{2\pi}{\lambda}|n_p - n_s|a \ll 1, \tag{31}$$

which, for $a > \lambda/2\pi$ is the more restrictive criterium framing the Rayleigh-Gans-Debye (RGD) regime. Notice that even particle with size $a \gg \lambda$ may satisfy (31), provided that there are sufficiently "faint". Equating the internal and external fields amounts to neglecting effects on any given volume element δV of the fields scattered by the surrounding, so that the RGD regime is the equivalent of the First Born Approximation in quantum scattering. Each δV can therefore be considered as an independent elementary Rayleigh scatterer, and the total scattered field is obtained by summing overall volume elements, taking in due account the phase of each scattering contribution.[6] Summing up overall volume elements, and allowing for nonuniformity of the particle refractive index by expressing $n_p = n_p(\mathbf{r})$, one obtains

$$\begin{bmatrix} s_1(\vartheta) \\ s_2(\vartheta) \end{bmatrix} = \frac{i n_s k^3 V}{2\pi} F(q) \begin{bmatrix} 1 \\ \cos(\vartheta) \end{bmatrix}, \tag{32}$$

where

$$F(q) = \frac{1}{V}\int_V \left[n_p(\mathbf{r}) - n_s\right] \exp(i\mathbf{q}\cdot\mathbf{r}) \mathrm{d}^3 r. \tag{33}$$

By introducing the "characteristic function" $\chi(\mathbf{r}) = 1$ if $\mathbf{r} \in V$ and zero otherwise, $F(q)$ is seen to be the spatial Fourier transform of the distribution of the refractive index mismatch. For the special case of a particle with uniform refractive index distribution and vertical incident polarization, the scattered intensity is then given by

$$I(q) = I_0 \frac{V^2 k^4}{4\pi^2 R^2}\left(n_p - n_s\right)^2 P(q), \tag{34}$$

where

---

[6] Note that the phase shift of a wave scattered by an element placed at $\mathbf{r}$ compared to the contribution from a volume element centered around an arbitrary origin is $\Delta\varphi = \mathbf{k}_i \cdot \mathbf{r} - \mathbf{k}_s \cdot \mathbf{r} = \mathbf{q} \cdot \mathbf{r}$.

$$P(q) = \frac{1}{V^2}\left|\int_V \exp\left(\mathbf{i}\mathbf{q}\cdot\mathbf{r}\right)\mathrm{d}^3r\right|^2, \tag{35}$$

called the particle *form factor*, is readily seen to represent an "intraparticle" structure factor. The scattering pattern in the RGD approximation can therefore be evaluation by a straight geometrical integration: for homogeneous spheres, for instance, $F(q)$ is simply proportional to the spherical Bessel function $J_{3/2}(qa)$, and analytical expression can be found also for ellipsoids, long rods, and thin disks. RDG scattering considerably extends the class of particles for which an easy analysis is feasible. A particularly interesting situation is colloidal fractal aggregation induced by the addition of salt. Fractal clusters grow with time, soon becoming much larger than λ, but they also became more and more "tenuous". Therefore, their average refractive index becomes more and more matched with the solvent, and it can be shown that, asymptotically, RGD conditions are always fulfilled.

Finally, note that the expression for the scattering matrix in the Rayleigh-Gans-Debye approximation suffers from the same problem found in the pure Rayleigh (small particle) limit. To get a consistent expression for the extinction coefficient, the particle polarizability should again be modified according to Eq. (25).

Mie scattering. The exact solution for RS from an arbitrary sphere was obtained in 1908, with a real mathematical *tour de force*, by Mie (1908). Here only the main features of the results are described and some of their general traits commented. First, the general solution is fixed by only two parameters, namely $m = n_p/n_s$ and the dimensionless size $x = ka = 2\pi n_s a/\lambda$, and is formally given by

$$s_1 = -\sum_n \frac{2n+1}{n(n+1)}\left(a_n\pi_n + b_n\tau_n\right) s_2 = -\sum_n \frac{2n+1}{n(n+1)}\left(a_n\tau_n + b_n\pi_n\right), \tag{36}$$

where

$$\pi_n(\vartheta) = P_n^1(\cos\vartheta)/\sin\vartheta \; \tau_n(\vartheta) = dP_n^1(\cos\vartheta)/d\vartheta$$

give, in terms of the associate Lagrange functions $P_n^1(\cos\vartheta)$, the angular distribution of the scattered light. The amplitude coefficients a_n and b_n are complicated functions of m and x. What is important to point out, however, is that their leading behavior is $a_n \sim x^{2n+1}$, $b_n \sim x^{2n+3}$, so that, for small particles, taking into account only the first terms in the summation is sufficient. By increasing n, the functions π_n and τ_n display in a polar diagram an increasing number of lobes, changing in direction and sign with n. For large particles, therefore, the sum of many terms tends to cancel out scattering at most angles. The only exceptions are the lobes that are present for all n around $\vartheta = 0°$ and $\vartheta = 180°$, the latter however alternating in sign. As a result, large particle tend to scatter predominantly forward, with a residual back-scattering cone.[7] For *very* large particles, the forward lobe has a width $\Delta\vartheta \sim \lambda/a$, witnessing the merging of Mie scattering with classical diffraction theory. Fig. 2 compares the full Mie and approximate RGD solutions for polystyrene latex spheres in water.

The coefficients a_n and b_n are finite for all real values of x. However, for strongly and absorbing particles, they often present complex poles with very small values of the imaginary part. These 'quasi-resonances' lead to strong enhancement of specific modes, and are responsible for the beautiful colors often observed in suspensions of metallic colloids (Bohren and Huffman, 1983).

By exploiting the OT, the total extinction cross-section can be obtained directly as a sum over the coefficients a_n, b_n:

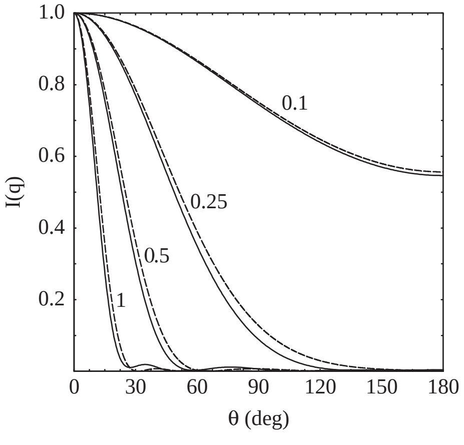

Fig. 2 Normalized scattering intensity versus scattering angle ϑ for polystyrene spheres ($n_p = 1.59$) in water for $\lambda_0 = 633$ nm. For each value of the ratio a/λ, indicated close to the curves, the full and dotted line are, respectively, the numerical result from Mie theory and corresponding RGD analytical solution. From Piazza R and Degiorgio V (2005) Scattering, Rayleigh. In: *Encyclopedia of Condensed Matter Physics*, Bassani F, Liedl GL and Wyder P (ed.), vol. 5, pp. 234–242, Elsevier.

---

[7] This is why, for instance, one gets dazzled by backlighted drops on a windshield. Ful colors often observed in suspensions of metallic colloids (Bohren and Huffman, 1983).

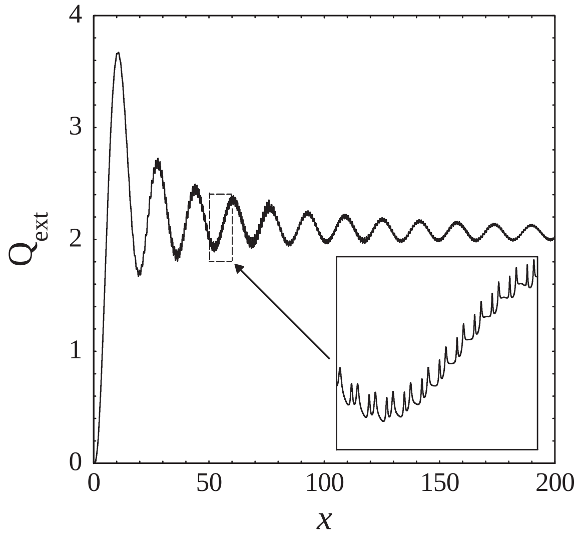

Fig. 3 Extinction factor $Q_{ext} = \sigma_{ext}/\pi a^2$ for polystyrene spheres in water as a function of x (varied by fixing $\lambda = 560$ nm and increasing a). The steep rise at small x corresponds to the RGD regime, $Q \sim x^4$, while the rich sub-structure at higher x, shown in the inset, derives from the large number of contributing Mie modes. "Blue moon" effects may take place in the regions where $dQ_{ext}/dx < 0$. From Piazza R and Degiorgio V (2005) Scattering, Rayleigh. In: *Encyclopedia of Condensed Matter Physics*, Bassani F, Liedl GL and Wyder P (ed.), vol. 5, pp. 234–242, Elsevier.

$$\sigma_{ext} = \frac{2\pi}{k^2}\sum_n (2n+1)\,\mathrm{Re}\,(a_n + b_n). \tag{37}$$

For small particles, σ_{ext} goes as λ^{-4} as in the RGD approximation, but by increasing x it tends to level off with substantial oscillations. In particular, for a specific (narrow) particles size-range, it may happen that in the visible region σ_{ext} *increases* with λ (see Fig. 3): this takes places for instance, when volcanic bursts eject in the atmosphere huge quantities of large particles, giving rise to the effect of blue sun or moon (as the name suggests, a rare event indeed).

The strong propensity to forward scattering for large particles also allows explaining a puzzling fact about extinction. As shown in Fig. 3, in the limit $x \to \infty$, Eq. (37) yields a value for σ_{ext} which is the *double* of the particle geometric cross-section $\sigma_g = \pi a^2$, namely the particle subtracts from the incident beam twice the expected power. This is not an artefact, but a real effect: what happens, however, is that half of the scattered power is concentrated in the forward lobe, so that it is collected by any finite-size detector as the eye. Such an intuitive geometrical optic concept as "shadow" is therefore based on subtle scattering effects.

A final consideration concerns transfer of momentum by radiation pressure, which is of primary importance both for optical levitation and for particle trapping by laser tweezers. For non-absorbing particles, it is easy to show that the radiation pressure is given by

$$p_{rad} = I_0\left(\sigma_s/\sigma_g\right)\left(1 - \langle\cos\vartheta\rangle\right),$$

where $\langle\cos\vartheta\rangle$ is an average over the scattering pattern distribution. For $a \ll \lambda$ one has $\langle\cos\vartheta\rangle \simeq 0$, and the radiation pressure increases approximately as a^4. However, for very large particles $\sigma_s/\sigma_g \to 2$ and $\langle\cos\vartheta \to 1\rangle$, so that radiation pressure decreases. Depending on size and material composition of the particle, there is therefore an optimal λ for efficient momentum transfer.

The limit of geometrical optics. A brilliant results by van de Hulst (1968) yields a rigorous link between scattering and simple "ray optics". Namely, in the limit $x \gg 1$, a term of order n in the Mie expansion is mapped into a ray passing at a distance $(n+1)\lambda/2\pi$ from the particle centre.[8] The Mie coefficients can then be split into two equal part leading, respectively, to diffuse refraction-reflection effects and to the forward diffraction cone. Obviously, classic ray optics is found to be incorrect near caustics and focal point.

Interacting particles

Interparticle interactions may consistently change the amount of radiation scattered by a particle dispersion. As a rule of thumb, attractive forces increase, while repulsive interactions decrease, the intensity of the scattered light. This can easily be grasped by recalling that RG is proportional to the (osmotic) compressibility of a fluid mixture, a result that still approximately holds for dispersions of particles that are not too big compared to λ.

---

[8] The number of "distinguishable" rays must be finite: a single "ray", to be meaningful must be straight over a length $\ell \geq \lambda$, so that, because of diffraction, it must have a minimum spot area of the order of λ^2.

More precisely, for a dispersion of particles at small but finite number density ρ interacting via an isotropic potential $U(r)$, the intensity of $I_0(\rho)$ light scattered in the forward direction is proportional to

$$I_0(c) \propto \rho(1 + 2B_2\rho)^{-1}, \tag{38}$$

where

$$B_2 = -2\pi \int_0^\infty r^2 \left(1 - e^{-U(r)/k_B T}\right) dr, \tag{39}$$

is the 2nd order (virial) coefficient of the expansion of the suspension osmotic pressure in terms of ρ. The contrasting effect of attractive vs. repulsive interactions is then evident from the opposite sign of the Boltzmann factor in Eq. (39).

For a suspensions of rigid particles that are not small compared to the wavelength (so that the scattering displays a nonnegligible q-dependence), the effect of interparticle interactions at any wave vectors can be obtained by writing the structure factor, Eq. (7), as a product of an internal contribution, which coincides with the form factor $P(q)$ in Eq. (33), times a purely *inter*particle term $S(q)$ coming from pair interactions, so to write $I(q) = I_0 P(q) S(q)$. It is worth emphasizing that such a "splitting" of the structure factors works only for *rigid* particles, whose size or shape is not altered by interparticle interactions, a conditions that is for instance often violated in dispersions of surfactant self-aggregates.

It is finally useful to point out that, if decoupling between translations and rotations holds, interactions affect only the "coherent" part I_{coh} in Eq. (30) for the scattering from optically anisotropic particles. Therefore I_{VV}, being independent from both solvent refractive index and interparticle forces, is just a sensitive probe of the local particle concentration.

The complex refractive index for interacting particles

As discussed above, interactions consistently modify the scattering cross-section of a colloidal dispersion. For instance, the intensity scattered by a suspension of charged particles can decrease by *orders of magnitude* by exposing the suspension by ion-exchange resins. One may therefore wonder whether Eq. (27) can be modified to properly account for the effect of interactions on the optical extinction, and if interparticle forces may possibly leave their signature on the real part of refractive index too. As anticipated in section "The optical theorem (OT)", this is in general an intractable problem. Nevertheless, Parola et al. (2014) have recently developed an *exact* treatment valid to second order in the particle polarizability for all values of particle concentration. A key result of this investigation is that the contribution from multiple scattering events, even when negligible at finite q, is conversely found to be crucial to figure out why the forward scattering amplitude, and therefore light extinction, depends on interparticle interactions.

For a suspension of homogeneous spherical particles at volume fraction ϕ, the model in Parola et al. (2014) yields the following general expression for the real part n of the refractive index and for the extinction coefficient γ

$$\begin{cases} n = 1 + 2\pi\phi\alpha_p + 2\pi\left(\frac{\pi}{3}\phi^2 + \mathrm{Re}\left[\tilde{C}\right]\phi\right)\alpha_p^2 \\ \gamma = 4\pi k\phi \mathrm{Im}\left[\tilde{C}\right]\alpha_p^2 \end{cases} \tag{40}$$

which contain the real and imaginary parts of a dimensionless correlation factor $\tilde{C}$ that depends in a rather complex way on an integral over q of the Fourier transform $g(q)$ of the pair distribution function. When interactions are negligible, Eq. (40) yields the Mie solution approximated to second order in polarizability. In the general case, the correlation contribution to the extinction coefficient depends only on those depends *only* on those values of p that are smaller than the maximum wave vector $2\,k$, corresponding to a scattering angle $\theta = \pi$, while effects on the real part of the refractive index are appreciable only when the peak the structure factor $S(q)$ falls within the accessible range $q \le 2k$. A striking example of the effect of interactions on the refractive index is shown in Fig. 4 for a dispersion of hard-sphere (HS) particles at volume fraction $\phi = 0.5$, which is approximately the maximum packing fraction for a HS fluid. In the absence of correlation effects, the suspension refractive index would simply given by $\langle n \rangle = \phi n_p + (1 - \phi)n_s = (n_s + n_p)/2$. Fig. 4 conversely shows that, in the region close to the peak of the structure factor $S(q)$ (evaluated at the maximum accessible scattering wave vector $q = 4\pi/\lambda$), the correlation contribution $\Delta n = n - \langle n \rangle$ is far from negligible. The plot also shows that for the values of λ/a indicated by the open dots, the refractive index increases with increasing λ, which is the hallmark of an "anomalous dispersion" region. Although no true absorption is present, the overall trend actually resembles the behavior of the refractive index of a Lorentz oscillator close to its natural resonance frequency, which suggests that, besides in resonant absorption, anomalous dispersion may occur in the presence of any process like scattering that leads to extinction of the incident field.

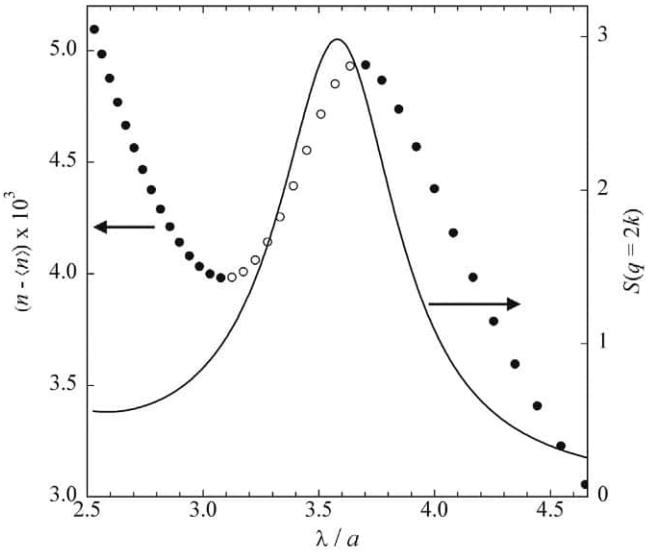

Fig. 4 Excess correlation contribution $\Delta n = n - \langle n \rangle$ versus the wavelength λ scaled to the particle radius a a suspension of hard-sphere (HS) particles at a volume fraction $\phi = 0.50$, according to the model in Parola et al. (2014). The full line is the structure factor of the HS fluid evaluated at the maximum experimentally detectable wave vector $q = 4\pi/\lambda$ while The open dots indicate the "anomalous dispersion" region.

Dynamic Rayleigh scattering

Rayleigh scattering from dispersed particles is not *exactly* elastic. Particles in suspensions undergo Brownian motion, so that the phase (and, for optically anisotropic particles, also the amplitude) of the scattered field in Eq. (2) depends on time. This leads to a spectral broadening $\Delta\omega$ due, in fact, to Doppler shift of the incident radiation by the moving scatterer. This shift is extremely small, typically $\Delta\omega/\omega \ll 10^{-9}$. Therefore, $\Delta\omega$ cannot be resolved even by sophisticated interferometric methods, since it is much smaller than the intrinsic spectral broadening on any source.

A brilliant solution is looking at *intensity* fluctuations measured by a quadratic detector (photodiode, photomultiplier, CCD). Quadratic detection introduced indeed a "replica" of the spectrum shifted to base band (as in homodyne radio systems) that can be easily extracted. Even more, this scheme does not require an incident light with strict temporal coherence (laser are actually used, but only because of their brilliance). This clever idea stands at the roots of intensity correlation spectroscopy (also called "Dynamic Light Scattering", DLS) methods, allowing to measure particle size from the behavior of the intensity time correlation function $g(t) = \langle I(0)I(t) \rangle$. A comprehensive analysis of the technique can be found in Berne and Pecora (1976), while a detailed review of recent advances in DLS and of its application to colloidal systems in Glatter (2018). Furthermore, novel ingenious intensity correlation schemes such as Differential Dynamic Microscopy (Cerbino and Trappe, 2008) and Photon Correlation Imaging (Duri et al., 2009) manage to provide space-resolved intensity correlation data, thus blending the powers of scattering and imaging. A review of these and related methods can be found in Piazza (2014).

Conclusion

Rayleigh scattering has been seen to stem from fluctuations of the refractive index. In a simple fluid, the latter are mostly due to spontaneous density fluctuations, and reflect structural correlations in the fluid via their proportionality to the structure factor $S(q)$, the Fourier transform of the density autocorrelation function. In a fluid mixture, the role of density is taken up by concentration, which implies that, for dilute solutions, RS is proportional to the osmotic compressibility. Quantum effects on RS are relevant even for weakly degenerate gases: For instance, in a gas of independent fermions, the Pauli exclusion principle introduces effective repulsions between the particle leading to a strong reduction of the scattered intensity.

Particularly interesting for applications in fields ranging from atmospheric optics to photonics is RS from dispersions of particles in the colloidal size range. To describe particulate systems, it is useful to introduce a dimensionless scattering function, or more generally a scattering matrix $s_{ij}(\vartheta, \varphi)$, whose specific form is dictated by the particle geometry and symmetry. A fundamental link between the total extinction cross-section and the scattering matrix in the forward direction is provided by the Optical Theorem. When the particles are noninteracting and scatter so weakly that multiple scattering is negligible, the single particle scattering function directly yield through the OT both the real and the imaginary part of the refractive index.

The form of the scattering matrix depends on the particle size and shape and on the polarizability of the constituting material. Depending on these parameters, one can tell apart different scattering regimes, ranging from isotropic scattering for particles much smaller than the wavelength, to Rayleigh-Gans scattering for "optically tenuous" particles, where the scattering angular pattern is given by the particle form factor, to the exact, albeit involved, solution obtained by Mie for spheres of any size a and particle polarizability that merges in the limit $ka \gg 1$ with geometrical optics. The intensity scattered by particles made of an optically anisotropic material displays a depolarized component that, at variance with the usual component polarized as the incident field, does not depend on the refractive index of the solvent and in therefore present in index-matching conditions too.

The intensity scattered by a colloidal suspension is however highly influenced by the presence of interparticle interactions, which enhance or depress concentration fluctuations depending on whether they are, respectively, attractive or repulsive. Interaction effects can be accounted for by expressing structural effects as a product of an internal form factor times a purely interparticle term, but this is true only for particle whose size or shape is not affected by interactions. Notably, for optically anisotropic particles the depolarized component is not affected by the presence of interparticle forces. A recent analysis, exact to second order in particle polarizability, has shown that the contribution from multiple scattering is crucial in determining how the forward scattering amplitude, and therefore light extinction, depends on interparticle interactions.

Finally, consideration of the tiny frequency shift that is present even for RS led to development of Dynamic Light Scattering, and more recently of other techniques exploiting correlations of the scattered intensity, which have become powerful methods for particle sizing and, more generally, in the investigation of the Brownian dynamics of colloidal fluids and soft materials.

Acknowledgment

This work is dedicated to the memory of Vittorio Degiorgio (1939–2021), a great scientist and mentor, who coauthored the first edition of this paper.

References

Berne B and Pecora R (1976) *Dynamic Light Scattering*. New York: Wiley.
Bohren C and Huffman D (1983) *Absorption and Scattering of Light by Small Particles*. New York: Wiley.
Bosse J, Pathak K, and Singh G (2011) Analytical pair correlations in ideal quantum gases: Temperature-dependent bunching and antibunching. *Physical Review Letters* 84: 042101.
Cerbino R and Trappe V (2008) Differential dynamic microscopy: Probing wave vector dependent dynamics with a microscope. *Physical Review Letters* 100: 188102.
Degiorgio V, Piazza R, Bellini T, and Visca M (1994) Static and dynamic light scattering study of fluorinated polymer colloids with a crystalline internal structure. *Advances in Colloid and Interface Science* 48: 61–91.
Degiorgio V, Potenza M, and Giglio M (2009) Scattering from anisotropic particles: A challenge for the optical theorem? *European Physical Journal E: Soft Matter and Biological Physics* 29: 379.
DeMarco B and Thywissen J (2021) No vacancy in the fermi sea. *Science* 374: 936–937.
Duri A, Sessoms D, Trappe V, and Cipelletti L (2009) Resolving long-range spatial correlations in jammed colloidal systems using photon correlation imaging. *Physical Review Letters* 102: 085702.
Glatter O (2018) *Scattering Methods and Their Application in Colloid and Interface Science*. Amsterdam: Elsevier.
Jackson JD (1998) *Classical Electrodynamics*, 3rd edn. New York: Wiley.
Javanainen J and Ruostekoski J (1995) Off-resonance light scattering from low-temperature bose and fermi gases. *Physical Review A* 52: 3033–3046.
Jeltes T, McNamara J, Hogervorst W, Vassen W, Krachmalnicoff V, Schellekens M, Perrin A, Chang H, Boiron D, Aspect A, and Westbrook C (2007) Comparison of the hanbury brown-twiss effect for bosons and fermions. *Nature* 445: 402–405.
Landau L, Lifshitz E, and Pitaevski L (1990) *Statistical Physics*. New York: Pergamon Press.
Loudon R (2000) *The Quantum Theory of Light*, 3rd edn. Oxford: Oxford University Press.
Lynch D and Livingston W (1995) *Color and Light in Nature*. Cambridge: Cambridge University Press.
Margalit Y, Lu Y-K, Top F, and Ketterle W (2021) Pauli blocking of light scattering in degenerate fermions. *Science* 374: 976–979.
Mie G (1908) Beiträge zur optik trüber medien, speziell kolloidaler metallösungen. *Annals of Physics (Berlin)* 25: 377–445.
Minnaert MJG (1954) *The Nature of Light and Colour in the Open Air*. New York: Dover Publications.
Newton R (1976) Optical theorem and beyond. *American Journal of Physics* 44: 639–642.
Parola A, Piazza R, and Degiorgio V (2014) Optical extintion, refractiverc index, and multiple scattering for suspensions of interacting colloidal particles. *The Journal of Chemical Physics* 141: 124902.
Piazza R (2014) Optical correlation techniques for the investigation of colloidal systems. In: Berti D and Palazzo G (eds.) *Colloidal Foundations of Nanoscience*, pp. 233–266. Amsterdam: Elsevier.
Piazza R (2017) *Statistical Physics*. Cham: Springer International.
Rayleigh L (1899) On the transmission of light through an atmosphere containing small particles in suspension, and on the origin of the blue of the sky. *The London, Edinburgh, and Dublin Philosophical Magazine and Journal of Science* 47(287): 375–384.
Snider A and Garcia-Lopez A (2006) The optical theorem and the rayleigh–gans power shortage. *IEEE Transactions on Antennas and Propagation* 54: 3840–3844.
Tsutsui K and Kita T (2016) Quantum correlations of ideal bose and fermi gases in the canonical ensemble. *Journal of the Physical Society of Japan* 85(11): 114603.
van de Hulst H (1968) *Light scattering by Small Particles*. New York: Plenum Press.

Shubnikov–de Haas and de Haas–van Alphen Techniques

W Biberacher, Walther-Meissner-Institut, Garching, Germany

© 2005 Elsevier Ltd. All rights reserved.

This is an update of W. Biberacher, Shubnikov–de Haas and de Haas–van Alphen Techniques, Editor(s): Franco Bassani, Gerald L. Liedl, Peter Wyder, Encyclopedia of Condensed Matter Physics, Elsevier, 2005, Pages 360–368, ISBN 9780123694010, https://doi.org/10.1016/B0-12-369401-9/00655-0.

Historical Introduction **228**
Basic Theoretical Models **229**
Landau Quantization 229
Lifshitz–Kosevich (LK) Formula 230
Other Oscillatory Quantities 231
Two-Dimensional Case 232
Analysis of Data 232
Special Cases **233**
Magnetic Interaction, Condon Domains 233
Magnetic Breakdown and Quantum Interference 233
Experimental Techniques **234**
Orders of Magnitude 234
de Haas–van Alphen Techniques 235
Pickup coil techniques 235
Torque method 235
Shubnikov–de Haas Techniques 236
Further Reading **236**

The de Haas–van Alphen (dHvA) and Shubnikov–de Haas (SdH) effects describe oscillatory components of the magnetization and conductivity, respectively, of a metal as a function of an applied magnetic field at low temperatures. The oscillations are periodic in a reciprocal magnetic field. It is the most accurate method to determine the contours of the Fermi surface of a metal or semimetal, but also gives information on other physical properties of electrons such as effective mass, scattering time, and spin-splitting factor.

Historical Introduction

The first experimental and theoretical manifestation of this effect dates back to 1930. In this year, L D Landau developed the quantum mechanical calculation of the diamagnetism of conduction electrons and mentioned the possibility of oscillatory effects there. But he believed, it was unobservable at that time. In the same year, L V Shubnikov and W J de Haas published an oscillatory behavior of the magnetoresistance in bismuth, and at the end of this year de Haas and P M van Alphen reported the observation of an oscillatory magnetization in the same material. Three years later, R Peierls developed a quantitative theory of the oscillations in Bi based on Landau's formulation of the energy levels of electrons in a magnetic field. In 1939, D Shoenberg determined the Fermi surface of Bi using the theoretical calculations of Landau. Shoenberg came to be the leading scientist in this field for several decades.

It was only around 1950 that general interest was seen in these oscillatory effects. In 1947, dHvA oscillations were detected in zinc, the first observation in a metal other than Bi. Soon after, it became clear that this effect could be observed in nearly every polyvalent metal, if crystals of high quality were available.

In the beginning of the 1950s, three important theoretical advances were made: first, the influence of the electron spin was worked out as a damping factor of the oscillation amplitude, second, R B Dingle could show that electron scattering broadens the Landau levels. This should change the oscillations in a way similar to a rise in temperature. The most important contribution was first published by L Onsager. He showed that the dHvA frequency is connected with the geometry of the Fermi surface and gives the extremal cross section of the Fermi surface perpendicular to the magnetic field. But this breakthrough could not be exploited immediately: at that time only low-frequency oscillations of the rather complex Fermi surfaces of polyvalent metals could be experimentally observed. On the other hand, band structure calculations were not yet good enough to show all details of a Fermi surface.

Around 1950, typical laboratory magnets produced fields up to 3 T. The very few water-cooled high-power magnets available at that time suffered from their instability. It was clear that higher and/or more stable magnetic fields are needed. Shoenberg, therefore, started working with pulsed fields up to 10 T and was soon able to observe high-frequency oscillations also in polyvalent metals, and even made the first observations in monovalent metals.

On the basis of prior theoretical work, I M Lifshitz and A M Kosevich developed a complete theory of the dHvA effect in 3D metals published in 1956. Together with improved band structure calculations starting from 1960, dHvA oscillations were investigated in all metals and compared with the theoretical band structure.

Although the basic investigations of the metallic elements are more or less completed, the dHvA and SdH effects are still of high use in the investigation of new compounds. Important examples are heavy fermion systems and low-dimensional conductors such as organic metals or artificially grown 2D electron systems.

https://doi.org/10.1016/B978-0-323-90800-9.00300-0

Basic Theoretical Models

Landau Quantization

The physical reason for the oscillatory effects in a magnetic field can be easily understood in the model of a free electron gas confined to a cube of length L. (The electron spin is neglected first.) The Schrödinger equation for free electrons in a magnetic field is given by

$$\frac{1}{2m_e}\left(\frac{\hbar}{i}\nabla - eA\right)^2 \Psi = E\Psi$$

where m_e is the electron mass, e is the electron charge, and $\boldsymbol{A}$ is the vector potential of the magnetic field $\boldsymbol{B}$. Landau showed in 1930, that for a magnetic field applied in the z-direction the energy is given by

$$E = \left(n + \frac{1}{2}\right)\hbar\omega_c + \frac{\hbar^2}{2m_e}k_z^2$$

with $n=0, 1, 2, \ldots$, $\omega_c = eB/m_e$ being the cyclotron frequency and $k_z = 2\pi n_z/L$ ($n_z = 0, \pm 1, \pm 2 + \cdots$) the wave vector in the z-direction. If one compares this to the solution of a free electron gas without a magnetic field, where $E = \hbar^2 k^2/2m_e$, it is seen that the wave vector in the x,y-plane perpendicular to the magnetic field is no longer quasicontinuous, but takes only discrete values

$$k_{x,y} = \sqrt{(n + 1/2)2m_e\omega_c/\hbar}$$

All permitted states lie on concentric tubes parallel to the magnetic field called Landau cylinders. The energy levels belonging to a certain n are highly degenerate. The degeneracy D is given by

$$D = \frac{eBL^2}{h}$$

This is the ratio between the magnetic flux BL^2 through the sample and the flux quantum h/e. The degeneracy is equal to the number of states contained in the adjacent interval of width $\hbar\omega_c$ of the electron spectrum in a zero field, that means, the adjacent states condense to the Landau tubes.

The cross-sectional areas of the Landau cylinders $S_k = \pi k_{x,y}^2$ are proportional to the applied magnetic field, that means, the Landau tube for a certain n increases as the field is increasing. In zero field, the electronic states are filled up to the Fermi level. In an increasing magnetic field, subsequent Landau levels pass through the Fermi energy and become depopulated (see Figure 1). This

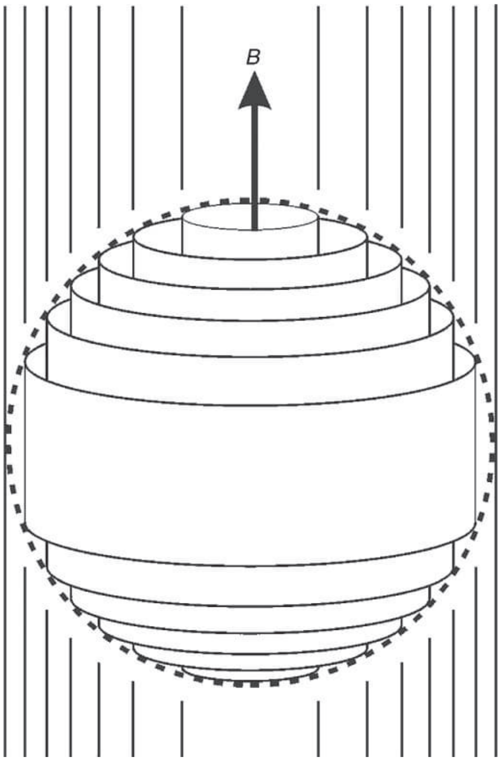

Figure 1 Schematic drawing of a spherical Fermi surface with Landau cylinders.

gives an oscillatory dependence to the free energy of the electronic system and to all other quantities derived from it. From the linear dependence of S_k on B, it can be easily derived that the oscillatory component must be periodic in $1/B$ with the frequency F of the oscillations given by the extremal cross section S_{extr} of the Fermi surface, as was first pointed out by Onsager:

$$F = \frac{h}{e} S_{\mathrm{extr}}$$

Lifshitz–Kosevich (LK) Formula

In 1956, Lifshitz and Kosevich published a theory of the magnetic susceptibility of conduction electrons in a metal with an arbitrary dispersion law. The oscillatory part of their solution turned out to be a complete description of the experimental results of the dHvA-oscillations measured in moderate magnetic fields and is still the standard to compare experiment with theory. They calculated the thermodynamic potential Ω of a gas of quasiparticles. The magnetization is then given by the thermodynamic relation:

$$M = -(\mathrm{grad}_B \Omega)_{T,\mu}$$

The contributions to the oscillatory part come exclusively from the vicinity of the extremal orbits of the Fermi surface. For a certain extremal orbit, the oscillatory magnetization M parallel to the applied magnetic field is given by

$$M \propto \frac{F}{m} \left(\frac{B}{\partial^2 \mathrm{A}_k / \partial k_z^2} \right)^{1/2} \infty \sum_{p=1} \frac{1}{p^{3/2}} R_{\mathrm{T}} R_{\mathrm{D}} R_{\mathrm{S}} \times \sin\left[2\pi p \left(\frac{F}{B} - \gamma \right) \pm \frac{\pi}{4} \right]$$

F is the dHvA frequency, m is the cyclotron mass, $\partial^2 A_k / \partial k_z^2$ is the curvature of the cross-sectional area of the Fermi surface at the extremal orbit along the field direction, the factors R_{T}, R_{D}, and R_{S} are damping factors according to impurity scattering, temperature and spin, and γ is a value close to 0.5. The sign of the phase $\pi/4$ is dependent on the geometry: if the extremal orbit is a minimum, the sign is +; for a maximum, it is –. In normal situations, the cyclotron energy $h\omega_c$ is much smaller than the Fermi energy and the oscillatory magnetization is dominated by the first harmonic in the summation over p.

In general, Fermi surfaces can be quite complicated and contain more than one extremal orbit. In that case, the total oscillatory component is a sum over all the contributions, each of which follows the LK formula, but with different parameters.

Without the reduction factors R_{i} the LK formula gives the idealized situation, where finite temperature, finite electron relaxation time, electron spin and other complications are neglected. At finite temperature, the occupation probability of a certain state with energy E is given by the Fermi Dirac function:

$$f(E) = \frac{1}{(1 + \exp((E - E_{\mathrm{F}})/kT))}$$

where k is the Boltzmann constant and E_{F} is the Fermi energy. This is a step function for T=0 K but is smeared out by kT around E_{F} at finite temperature. This smearing leads to a reduction of the dHvA amplitude by the temperature reduction factor R_{T}:

$$R_{\mathrm{T}} = \frac{2\pi^2 pkmT/\hbar eB}{\sinh(2\pi^2 pmkT/\hbar eB)}$$

Typical dependencies of the reduction factor on the temperature at a magnetic field of 15 T are given in Figure 2 for several values of the normalized cyclotron mass m/m_{e}.

Real crystals are always imperfect in some respect. This leads to a finite relaxation time τ of electrons, which is equivalent to a broadening of the Landau levels. If this broadening is described by a Lorentzian distribution, the reduction of the oscillation amplitude is given by

$$R_{\mathrm{D}} = \exp\left(\frac{-\pi p}{\omega_c \tau} \right)$$

This directly shows that the relaxation time must be long enough for the electron to complete a cyclotron orbit. The effect of impurities is similar to an increase in sample temperature. The reduction factor is generally given as

$$R_{\mathrm{D}} = \exp\left(-\frac{2\pi^2 pmkT_{\mathrm{D}}}{\hbar eB} \right)$$

with T_{D} being the so-called Dingle temperature, $T_{\mathrm{D}} = h/2\pi k\tau$. The influence of T_{D} on the oscillation amplitude is shown in Figure 3 for free electrons (m=m_{e}). In samples with Dingle temperatures higher than a few kelvin, oscillations are hard to detect. Additional damping can be caused by sample and field inhomogeneities, mosaic spread, bending and strain on the sample, etc.

In a magnetic field, the spin degeneracy of the energy levels is lifted and each Landau level is split into two at energies $E \pm \frac{1}{2}\Delta \mathrm{E}$ where

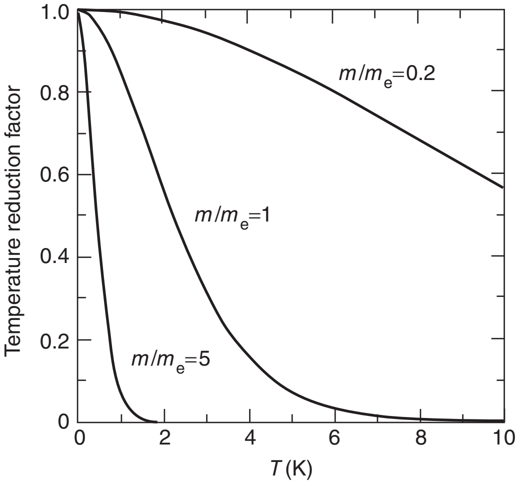

Figure 2 Temperature reduction factor of the fundamental frequency according to the Lifshitz–Kosevich theory at a magnetic field of 15 T for different values of the cyclotron mass.

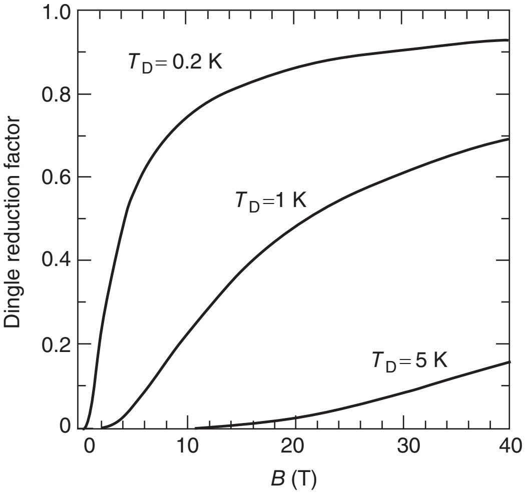

Figure 3 Dingle reduction factor of the fundamental frequency according to the Lifshitz–Kosevich theory for different values of the Dingle temperature. The cyclotron mass is set equal to the free electron mass.

$$\Delta E = g\mu_B B$$

Here $\mu_B = e\hbar/2m_e$ is the Bohr magneton and g is the spin-splitting factor, which takes the value 2.0023 for free electrons. On increasing the field, the split Landau levels pass the Fermi surface at different field values. Therefore, a phase difference between these two oscillations arises and leads to a reduction of the amplitude by

$$R_S = \cos\left(\frac{1}{2}p\pi g m/m_e\right)$$

For free electrons the spin reduction factor is just $(-1)^p$, since the spin-splitting is equal to the Landau level spacing. In special cases, if $pgm/m_e = 1, 3, 5, \ldots$, R_S becomes zero and the oscillation amplitude vanishes. This is called a spin-zero. The relation also shows that in the spin-zero of the fundamental frequency (p=1), the second harmonic becomes maximal.

Other Oscillatory Quantities

The standard method for the determination of Fermi surfaces of metals is the dHvA effect. But as mentioned above, the dHvA oscillations were derived from oscillations of the thermodynamic potential Ω. Therefore, it is clear that all other physical properties derived from Ω show an oscillatory behavior in a high magnetic field and there are many experimental investigations of these effects. Examples are the specific heat, magnetostriction, elastic properties, and the chemical potential. Oscillations of the chemical potential play an important role in quasi-two-dimensional (Q2D) systems as discussed later. In 3D systems, they are usually weak and can be neglected in most cases. Another important quantity, which can be derived from the thermodynamic potential or calculated in a similar way, is the density of states at the Fermi energy.

There are oscillatory effects which cannot be described by thermodynamic relations alone since they involve nonequilibrium properties. The most famous example for it is the SdH effect, the oscillatory property of the magnetoresistance. As mentioned above, magneto-oscillations were first observed in the magnetoresistance of Bi in 1930. But it turned out that the SdH effect is very weak in normal metals and hard to detect there. In recent years the SdH effect has been of high importance, since it is easy to observe in Q2D electron systems such as quantum well structures or organic metals.

The theory of the SdH effect is complicated since it involves the problem of electron scattering in a magnetic field. In 1959, E N Adams and T D Holstein calculated the oscillatory conductivity for two different scattering mechanisms and found similar results in both cases. They concluded that the exact nature of scattering is not very crucial. Their result for the case of phonon scattering and high quantum number is the following:

$$\frac{\widetilde{\sigma}}{\sigma} = \frac{R_{\mathrm{T}} \frac{5}{2} \widetilde{N}}{N_0}$$

where $\widetilde{\sigma}$ is the oscillatory part of the conductivity, σ the steady conductivity, R_{T} the temperature reduction factor and $\widetilde{N}, N_0$ are the oscillating and steady parts of the density of states at the Fermi energy, respectively. This result can be understood qualitatively by an argument of Pippard: the probability of scattering is proportional to the number of states in which the electrons can be scattered. Therefore, the conductivity is related to the oscillations of the density of states. The SdH effect is described by the same reduction factors as the dHvA effect. R_{S} and R_{D} are already involved in $\widetilde{N}$. Finally, one should mention that the oscillatory part of the density of states and thus the oscillatory conductivity is proportional to the derivative of the magnetization $\mathrm{d}M/\mathrm{d}B$.

Two-Dimensional Case

The above mentioned theories for the dHvA and SdH effect were calculated for an isotropic case, that is, for a spherical Fermi surface. It turned out that they can also describe anisotropic systems with ellipsoidal or even warped cylindrical Fermi surfaces well. But in the pure 2D case, the theory is no longer applicable. From a theoretical point of view, it turned out that the 2D case is in some respect more difficult to calculate than the 3D one, and up to now, analytic solutions are available only for limiting cases.

Typical examples for Q2D electron systems are layered metallic compounds. The energy spectrum is usually given by

$$E_k = \frac{\hbar^2}{2m}\left(k_x^2 + k_y^2\right) - 2t\cos(k_z d)$$

with t being the interlayer transfer integral, k_z the wave vector perpendicular to the layers, and d the interlayer distance. This yields a cylindrical Fermi surface with a slightly oscillating cross section along the k_z direction (warping). In the case of $2t > h\omega_c$, the system can be well described within the LK theory. In that case, there exists a minimal and a maximal cyclotron orbit and one expects two nearby frequency components in the dHvA spectrum (see Figure 4).

When the transfer integral becomes comparable to the Landau level separation, the LK theory is no longer appropriate and for $2t < h\omega_c$, the system is very near to the pure 2D case. In that case, the whole Fermi surface is extremal and one expects large oscillations. It is also clear that the assumption of a field independent chemical potential is, generally speaking, no longer valid. For a constant number of electrons, one would rather expect jumps in the chemical potential periodic in $1/B$. In the extreme 2D case, the Fermi energy lies between two Landau levels. The chemical potential is fixed to the highest occupied Landau level and when this level is depopulated by increasing the field, the chemical potential will jump to the next lower Landau level. A sawtooth form of the magnetization oscillations is expected for that case and was indeed observed in artificially grown 2D electron gases. The other limiting case of a fixed chemical potential can be fulfilled by oscillations of the total number of electrons due to an infinite reservoir. This situation is probably given in some organic metals where a Q1D band is present beside the 2D one.

Analysis of Data

In a typical experimental investigation of the quantum oscillations, the first quantity to derive is the oscillation frequency. The oscillatory signal measured in a certain interval of the magnetic field and plotted against $1/B$ is transformed by a Fourier transformation into a power spectrum. This gives the frequencies of the different extremal orbits of the Fermi surface and – if present – their higher harmonics. Repeating this procedure for different field directions allows one to reproduce the complete Fermi surface. One should mention that the frequency only gives the cross section of the extremal orbit, but cannot show the deviations from a circular form.

A comparison with the LK theory gives further information. If the oscillation amplitude is measured at different temperatures, a least-square fit of the temperature reduction factor to the experimental data directly yields the effective cyclotron mass m of this extremal orbit. The magnetic field dependence of the oscillation amplitude at constant temperature is given by the product of the Dingle factor R_{D} and B^n, where n depends on the experimental method. Knowing the effective mass m from the temperature dependence, one can extract the Dingle temperature by a least-square fit of the field dependence.

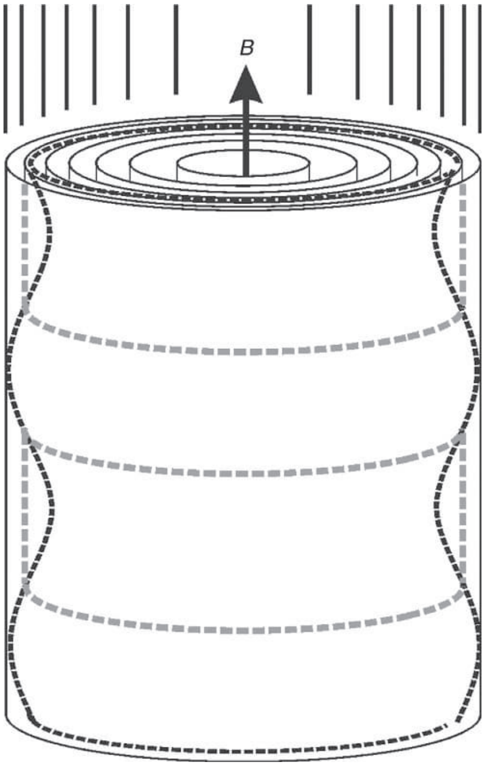

Figure 4 Slightly warped cylindrical Fermi surface (black dashed line) of a Q2D metal with Landau cylinders. The magnetic field is applied perpendicular to the conducting plane.

Finally, the spin reduction factor R_S can be used to determine the spin-splitting factor g. In most cases, there is an intrinsic ambiguity in the determination of the g-factor and only a series of possible values can be derived. A special situation is given in the layered organic metals. Due to the relatively high effective mass m and the angular dependence of m, usually a whole series of angles appears, where the oscillation amplitude vanishes due to R_S. This allows one to determine the product gm/m_e without ambiguity.

Special Cases

Magnetic Interaction, Condon Domains

Normally, the oscillating part of the magnetization $\mu_0\tilde{M}$ is much smaller than the applied magnetic field B_a. Therefore, in the LK theory the inner magnetic field B_i was taken as the applied field B_a. In some cases (very pure metals with large Fermi surfaces, low temperature), this assumption is no longer valid as was first observed by Shoenberg in very pure samples of gold. To analyse his data, he started with the LK-equation for the first harmonic and replaced B by B_i. He could show that the condition

$$a = \mu_0 \left| \frac{\mathrm{d}\tilde{M}}{\mathrm{d}B} \right| < 1$$

must be fulfilled for the LK theory to be fully applicable. If the factor a is smaller than 1 but of the same order of magnitude, the observed oscillations show an increased harmonic content and, if several different orbits are involved, the occurrence of combination frequencies is expected. In these cases, one has to take into account the demagnetization factor n of the sample shape also.

If the factor a becomes larger than 1, the magnetization of the sample is no longer a single-valued quantity of the applied field. This is thermodynamically unstable and leads to jumps in the magnetization. As first proposed by Condon, under this condition a sample with a demagnetization factor $n>0$ will split up into magnetic domains with two different values of the magnetization. The existence of these domains could be shown by NMR and muon spin rotation experiments. Up to now, clear evidences for Condon domains are reported in high-quality samples of silver, beryllium, white tin, aluminum, and lead.

Magnetic Breakdown and Quantum Interference

The Fermi surface of a metal can be completely described within the first Brillouin zone. Any constant energy surface exceeding this zone belongs to higher bands and can be folded back to the first Brillouin zone. It was therefore very exciting, when in the beginning of the 1960s, Priestly reported the observation of a dHvA orbit in Mg, which was considerably larger than the hexagonal cross section of the Brillouin zone. The explanation for this observation was given by Cohen and Falicov, who pointed out that electrons could tunnel from one band to another, if the bandgap E_g between these two bands is sufficiently small and the magnetic field strong enough. It is evident that this could happen, when the bandgap is comparable to or smaller than the Landau level separation $\hbar\omega_c$, but Blount could show that the much weaker condition

$$\hbar\omega_c \geq \frac{E_g^2}{E_F}$$

is valid, with E_F being the Fermi energy. Since typically $E_g/E_F < 1$, magnetic breakdown could happen in quite low magnetic fields.

For the theoretical description of magnetic breakdown, a simple hypothetical model of a free electron gas in a 1D crystal potential was introduced as shown in Figure 5. At the zone boundary, a small gap opens and the Fermi surface consists of a closed (α-orbit) and an open part. At very high magnetic fields, electrons can tunnel through the gap and a new much larger closed orbit (β-orbit) is observed. At intermediate magnetic fields, a complicated spectrum with sum and difference frequencies of α- and β-orbits will appear. The case – first thought as hypothetical – was in the meantime verified in artificial heterostructures and in organic metals such as $(BEDT\text{-}TTF)_2Cu(NCS)_2$ and is of high interest at present.

In systems, where magnetic breakdown is present, one often finds a striking difference in the frequency spectrum of dHvA and SdH oscillations. The SdH oscillations typically show additional frequencies not present in dHvA. These differences can often be described by quantum interference effects as introduced first by R W Stark and C B Friedberg: it is possible to have magnetic breakdown between orbits, along which electrons move in the same direction; if electrons moving from point A to B can travel along two different paths connected by magnetic breakdown, interference effects yield an oscillatory contribution in transport measurements with the frequency determined by the area between the two paths. Since this represents not a closed orbit, these frequencies are not detected in thermodynamic quantities such as dHvA oscillations.

Experimental Techniques

Orders of Magnitude

Quantum oscillations are periodic in the reciprocal magnetic field. Therefore, the unit of the oscillation frequency is tesla (T). Typical values range from a few T to ~50000 T. Low-frequency oscillations are easier to detect and can be often observed up to temperatures of 10–20 K. The observation of high-frequency oscillations requires usually low temperatures ($T<4$ K), and high and homogeneous magnetic fields. (The oscillation period of a 50 kT frequency amounts to 20 μT at $B=1$ T.) The observation of oscillations in the heavy fermion compounds needs dilution fridge temperatures for detection. This can be easily verified by calculation of the temperature reduction factor R_T with high effective cyclotron masses.

Optimal relative amplitudes of the oscillatory magnetization $\mu_0 M/B$ are $\sim 10^{-5}$, which is comparable to steady susceptibilities of weakly magnetic materials. The sensitivity of magnetization experiments is often improved by measuring dM/dB (see below). The oscillations in the resistivity are experimentally observed mainly in semimetals and under magnetic breakdown conditions. In recent years, the SdH effect plays an important role in layered metals and quantum well structures. In both cases, the oscillatory amplitude can exceed the background resistance in high magnetic field considerably.

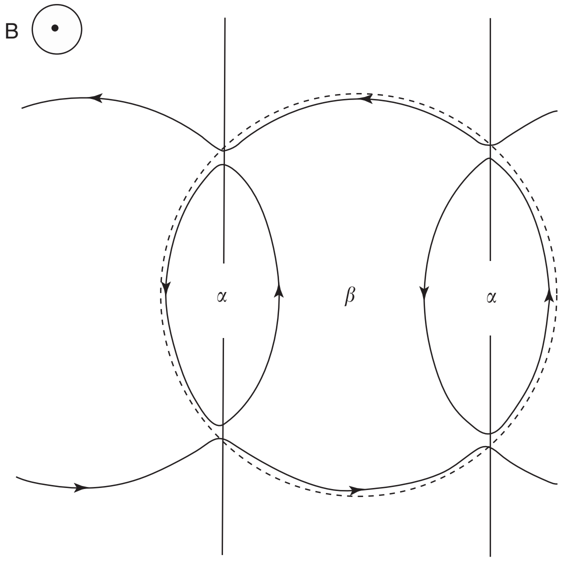

Figure 5 Model Fermi surface for magnetic breakdown: at small fields the carriers are fixed to the closed α-orbit or the open orbit above and below, at high magnetic fields the carriers can tunnel through the gap and a larger closed orbit (β-orbit, dashed line) becomes dominant.

Magnetic fields are typically produced nowadays by superconducting magnets. The maximum field available in laboratories lies between 8 and 20 T. Higher steady magnetic fields can be obtained in some high-field magnet laboratories running high-power (typically, 10–25 MW)-resistive or superconducting-resistive hybrid magnets. These laboratories are usually open for users and can offer magnetic fields between 20 and 45 T. For even higher magnetic fields, some pulsed field facilities are operated. For the study of metallic samples, they can produce magnetic field pulses of duration between a few ms and 1–2 s with maximal fields between 35 and 70 T.

de Haas–van Alphen Techniques

The above mentioned magnitude of the oscillatory effect shows that the standard techniques for measuring small magnetic susceptibilities are often sufficient for the observation of the dHvA effect. But for observation in less favorable circumstances, techniques with very high sensitivity are needed. It should also be mentioned that the high degree of field homogeneity required for the observation of high-frequency oscillations makes the Faraday method less suitable. The two mostly used methods are discussed in the following.

Pickup coil techniques

This technique is similar to the well-known mutual inductance method for AC-susceptibility measurements. The sample is placed in a pickup coil system consisting of two identical coils connected in series with opposite signs so that the voltage induced by a changing magnetic field is zero. If a sample is placed in one of the coils, the induced voltage will be

$$U \propto (\mathrm{d}M/\mathrm{d}B)(\mathrm{d}B/\mathrm{d}t)$$

The proportionality constant is determined by the geometry. For the arrangement of the two balanced coils, many possibilities exist. Due to limited space of high homogeneity in a magnet, the two coils are often wound one after the other on the same coil core. In the standard laboratory method, the applied magnetic field B is superimposed by an oscillatory contribution $b(t)=b_0\cos(\omega t)$, with typical frequencies ω lying between 20 Hz and a few kHz. The oscillation amplitude b_0 can be appropriately chosen for the system under consideration. It should be smaller or comparable to the period of the dHvA oscillation. The modulation field method allows the use of phase-sensitive detection via lock-in amplifiers, which considerably improves the signal-to-noise ratio. In addition, this allows detection at different harmonics of the modulation frequency.

The signal amplitude of the different harmonic contributions A_p of the LK theory is given by

$$U_p^{(k)} \propto k\omega J_k\left(\frac{2\pi pFb_0}{B^2}\right)A_p$$

for detection at the kth harmonic of the modulation signal, J_k is the kth order Bessel function. Some disadvantage of this method is the fact that the weight of the harmonics is changed: in case of high harmonic content, the observed waveform deviates from the real one and has to be recalculated. On the other hand, this can be used for suppressing a certain harmonic by working near the corresponding Bessel function zero, and therefore having increased sensitivity for other weak oscillations.

The changing magnetic field may be also produced by a pulsed magnetic field. In that case, the induced voltage is first amplified and then recorded by a fast data acquisition system. In both methods, a self heating of the sample due to eddy currents must be avoided.

Torque method

If the Fermi surface of a given metal deviates from spherical symmetry, that is, if the characteristic frequency F of an extremal orbit is dependent on the field orientation, there exists a torque about any axis perpendicular to the magnetic field given by

$$\tau = -\frac{1}{F}\frac{\mathrm{d}F}{\mathrm{d}\theta}BVM$$

where, θ determines the angle between the magnetic field B and a characteristic direction in the plane perpendicular to the torque axis, V is the volume of the sample, and M is the parallel magnetization as given by the LK formula. The torque vanishes for some symmetry directions of the crystal, where either $\mathrm{d}F/\mathrm{d}\theta$ vanishes or two related parts of the Fermi surface cancel each other. In practice this is often not a problem, since the missing angular range is very small and can be easily interpolated. In case of large oscillations, the torque should be measured by a feedback system to avoid problems due to slight changes of the sample orientation (torque interaction). A strong advantage of this method is the robust and easy set-up and the ease of calibrated measurements. Calibrated measurements are of importance for determining the curvature factor of the extremal orbit in the LK formula. A typical example of an oscillatory magnetic torque is shown in Figure 6.

The torque method is one of the first techniques applied by Shoenberg already in 1939, but is still in use in many cases. Whereas the first experiments used the torsion of a wire and optical detection, most of the present devices are based on capacitive detection of the torque. In a simple arrangement, the sample is placed on a small platform on a cantilever. The displacement of the platform is determined by a measurement of the capacitance between the platform and a fixed plate. Adding a calibration coil to the platform allows calibrated measurements. Nowadays, such cantilever spring torquemeters can be fabricated from a silicon wafer using lithographic techniques. Miniature devices of this kind were even used in pulsed field experiments.

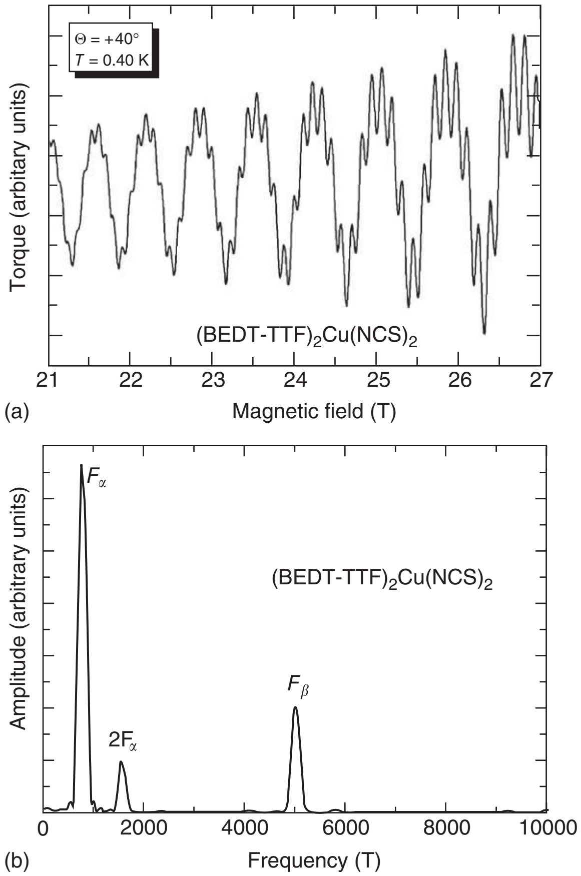

Figure 6 (a) Magnetic torque oscillations in very high magnetic fields showing magnetic breakdown. The sample is a small (m=80 μg) single crystal of the organic Q2D metal κ-(BEDT-TTF)$_2$Cu(NCS)$_2$. The tilt angle between the direction of magnetic field and the normal to the conducting layers is 40°. (b) Corresponding Fourier transform of the data in (a). The spectrum clearly shows the first and second harmonic of the α-orbit and the breakdown frequency F_β (see Figure 5).

Shubnikov–de Haas Techniques

Measurements of resistance always require a four wire arrangement: a current is applied to the sample via two contacts and the voltage drop between two other contacts is measured. For absolute measurements of the resistivity, the sample should be in a well-defined geometry to assure homogeneous current flow. The application of an AC- current with typical frequencies between 10 and a few hundred Hz allows phase-sensitive detection via a lock-in amplifier. For low-temperature experiments, the current must be small enough to avoid self-heating of the sample.

As mentioned above, the SdH effect is hard to detect in pure metallic elements. At present many SdH studies are carried out in 2D systems. In artificially produced 2D layers, the geometry is easy to adjust by using suitable masks. The typical arrangement is a rectangular bar with current contacts at both short sides and typically two additional contacts on both sides for voltage measurements. This allows one to measure the resistance and Hall effect at the same time. (For the calculation of the conductivity of a pure 2D system, both quantities are needed). In bulk-layered metals the in-plane resistance is often difficult to determine, since the crystals are usually very tiny and the arrangement of well-defined contacts with a homogeneous current distribution is difficult to accomplish. Therefore, most researchers use the interplane resistance for the determination of the SdH effect in these compounds. In that case, a current and a voltage contact are placed on both the large sides of a crystal. Due to very high anisotropy in the resistance (10^3 and more) in these compounds, the interplane resistivity is measured with high accuracy.

Further Reading

Abrikosov AA (1988) *Fundamentals of the Theory of Metals.* Amsterdam: North-Holland.
Gordon A, Vagner ID, and Wyder P (2003) Magnetic domains in non-ferromagnetic metalsthe non-linear de Haas-van Alphen effect. *Advances in Physics* 52: 385–454.
Joint R and Taillefer L (2002) The superconducting phases of UPt$_3$. *Reviews of Modern Physics* 74: 235–294.
Pippard AB (1989) *Magnetoresistance in Metals.* Cambridge: Cambridge University Press.
Shoenberg D (1984) *Magnetic Oscillations in Metals.* Cambridge: Cambridge University Press.
Wosnitza J (1996) *Fermi Surfaces of Low-Dimensional Organic Metals and Superconductors.* Berlin: Springer.

Core photoemission from graphene to silicene☆

Paola De Padova[a,b], **Paolo Perfetti**[a], **and Guy Le Lay**[c], [a]Consiglio Nazionale delle Ricerche-ISM, Roma, Italy; [b]Istituto Nazionale di Fisica Nucleare-Laboratori Nazionali di Frascati—INFN-LNF, Frascati, Italy; [c]Aix Marseille Université, CNRS, PIIM UMR 7345, Marseille, France

© 2024 Elsevier Ltd. All rights reserved.

This is an update of P. Padova, P. Perfetti, Core Photoemission, Editor(s): Franco Bassani, Gerald L. Liedl, Peter Wyder, Encyclopedia of Condensed Matter Physics, Elsevier, 2005, Pages 240–251, ISBN 9780123694010, https://doi.org/10.1016/B0-12-369401-9/00683-5.

Introduction 237
Overview of core photoemission spectroscopy 239
Key issues on core photoemission spectroscopy and its application to important examples, namely the elemental two-dimensional (2D) materials graphene and kagome silicene 239
C 1*s* and Si 2*p* core levels of graphene and kagome silicene 240
C 1*s* of graphene on SiC(0001) and Ni(111) 241
Si 2*p* and Al 2*p* core-levels from ($\sqrt{3} \times \sqrt{3}$)/(3 × 3) kagome silicene on an Al(111) substrate 243
Conclusion 244
References 244
Further reading 245

Abstract

Core-level photoemission has been and remains one of the most powerful spectroscopic techniques for studying the structure and properties of condensed matter. With the advent of high-resolution instrumentation, for both electron analyzers and photon sources, coupled to large accelerating machines such as synchrotrons, core photoemission spectroscopy (CPS) has revealed its great potential, notably in the study of surfaces and interfaces prepared in ultra-high vacuum.

Through peak fitting procedures, CPS performed on graphene and its first Xene siblings (two-dimensional elemental artificial materials), namely, silicene, we will retrace remarkable discoveries, where core-level photoemission has played a major role.

Key points

- Fundamentals on core photoemission spectroscopy
- Illustrative examples: core levels in graphene and kagome silicene
- Conclusions

Introduction

Core photoemission spectroscopy (CPS) is considered as one of the most significant techniques for studying the physical-chemical properties of atoms, molecules and solids, within the general context of the study of matter. Historically, to position the birth of the photoemission phenomenon, it is necessary to go back in time to the distant 1887–1888, with the first experiments performed by Heinrich Hertz (Hertz, 1887) and Wilhelm Hallwachs (Hallwachs, 1888), and successfully explained by Albert Einstein in 1905 upon invoking the quantum nature of light (Einstein, 1905), through his famous formula for the photoelectric effect:

$$E_k = h\upsilon - |E_B| - \Phi \quad (1)$$

where E_K is the kinetic energy of the photoemitted electron, $h\upsilon$ is the energy of the incoming photon, E_B, for instance, the one-electron binding energy (BE) of a core-level, and Φ the work function of the emitting material.

Basically, a photoemission experiment is based on the photoelectric effect (Einstein, 1905), where, typically, in condensed matter physics, a solid surface is irradiated by a beam of monochromatic photons, and the kinetic energy of the emitted electrons analyzed.

In the ultraviolet (UV) spectral energy range, of the photons, (10–100) eV, the photoemission spectroscopy is called UPS. With X-ray radiation in the (100–1000) eV range it is called soft X-ray photoemission spectroscopy (SXPS), and, for higher energies it is called XPS or electron spectroscopy for chemical analysis (ESCA). Conventional quasi-monochromatic discrete light sources such as

---

☆*Change History:* March 2023. PD Padova, P Perfetti, GL Lay. All authors changed the title, and according with template, they arranged the reported sections. All authors decided the text. All authors decided the included figures. All figures are new, except the Fig. 2, which is similar to Fig. 1A of the old chapter Core Photoemission, and now is also in color. All sections, now, are different, although the content of the basic photoemission principles, written in another way, are similar.

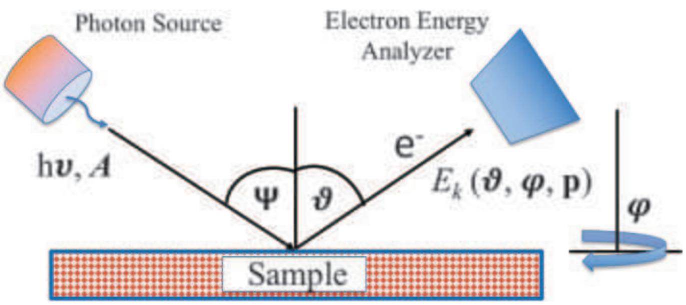

Fig. 1 Schematic illustration of a photoemission spectroscopy experiment.

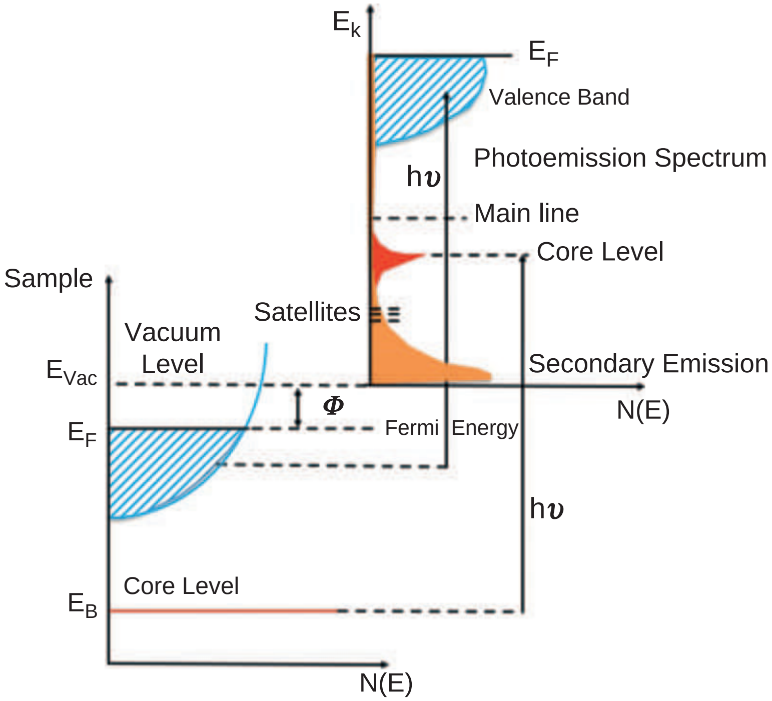

Fig. 2 Schematic relation of the energy-level diagram and energy distribution of the photoemitted electrons upon *hυ* photon excitation. The solid sample is a metal exhibiting core levels, valence-conduction bands (here, they are the same) and secondary emission in absence of electron-electron interaction. Main line and satellites account for electron-electron interactions.

the helium gas-discharge lamp, for energies in the UV range (He I: 21.23 eV; He II: 40.82 eV), and the characteristic lines emitted by the frequently used aluminum (Al-K_α: 1486.6 eV) and magnesium (Mg-K_α: 1253.6 eV) anodes, are very often present in laboratories, whereas continuous electromagnetic spectral radiation, from energy of few eV up to thousands eV, is available at the large synchrotron facilities, located in many different countries around the world.

As is simply schematized in Fig. 1, the light (vector potential $\boldsymbol{A}$), impinging on the surface of a solid sample (or on a liquid or a gas), produces by the photoelectric effect excited electrons, which are collected and analyzed in their kinetic energy, E_K, and momentum $\boldsymbol{p}$ (wave vector $\boldsymbol{p}/\hbar$) in an electrostatic electron energy analyzer.

In an angle-resolved photoemission experiment of solids, interfaces and thin films, the polarization of the light is a useful property, so that the important parameters to be measured are E_K, of the photoemitted electrons, and the angle of emission with respect to the direction of the incident light ($\Psi + \vartheta$) and the surface (ϑ, φ); ϑ, and φ are the polar and azimuth angles, respectively, under which the electrons leave the surface. The binding energy of the outgoing electrons can be obtained by measuring their kinetic energy E_K, and, if knowing the work function of the material, simply by applying Einstein's formula (1). The momentum p is determined by the E_K, through the relation $E_K = \frac{p2}{2m}$ for free electrons.

Let us, briefly, illustrate the relation between the energy levels of a solid and the energy distribution of the photoemitted electrons through of the scheme displayed in Fig. 2, where various contributions, including a core level, are highlighted. In this simple case the sample is a metal, therefore its Fermi energy E_F lies at the top of the occupied states within the valence-conduction band (VB/CB). E_F is separated from the vacuum energy level E_{vac} by the metal work function ϕ.

When the photoabsorption process takes place in a core level with a binding energy E_B ($E_B = 0$ at E_F), photoelectrons with kinetic energy given by the formula (1), can be detected in the vacuum, giving rise to the CLS (core level photoemission) process. The energy distribution of the photoemitted electrons, i.e., their number N(E) per energy interval, corresponds, as a first approximation, to a replica of the electron energy distribution in the solid.

This is a real crucial point in photoemission spectroscopy, since it interestingly provides the features of the energy distribution of electrons in a material.

We present in this article diverse applications of core photoemission spectroscopy in the current investigations of 2D elemental materials, typically, graphene and silicene. Their study constitutes, nowadays, one of the most interesting topics in condensed matter physics and chemistry.

Overview of core photoemission spectroscopy

For a fundamental and exhaustive theoretical treatment of the photoemission process, we refer to important literature (Cardona and Ley, 1978; De Padova and Perfetti, 2005; Feuerbacher et al., 1978; Hüfner, 2003). Here, we just report the basic principles for fully understanding the power of this old, but unique, spectroscopic technique, as well as for conducting and/or analyzing a photoemission experiment in the context of condensed matter with particular emphasis on the investigation of graphene and silicene on well-characterized surfaces.

Photoemission spectroscopy (PES) investigates the occupied valence/conduction electronic bulk and surface states of materials, as well as their localized core-levels, which are fingerprints of their constitutive atomic species. Hence, core-level photoemission spectroscopy, which highlights the elementary atomic specificity of matter, constitutes an irreplaceable tool for the investigation of the physical-chemical properties in materials science.

It is convenient to consider the so-called *sudden-approximation*, to understand the transition probabilities from an occupied state to an empty state promoted by a photoemission process, regulated by the Fermi "*golden-rule*," when the Hamiltonian changes so rapidly that the reaction times of the system in its entirety, are too short to cause relaxation effects, which would lead to observable perturbations in the photoemission spectra. In PES a system with N electrons in the initial state, is left after one-electron excitation in a final state containing N-1 electrons and a hole, such that the energy of the outgoing electron is usually affected by the interaction of the surrounding ionized system that has been left behind. If this interaction is negligible (in the regime of *sudden-approximation*) and the photoelectron kinetic energy, $E_{k,}$ is high enough, it can be derived directly by the Einstein relation (1). In the one-electron approximation, it is assumed that the N-1 electrons of the orbitals will be in the same final state $<f|$ as in the initial state $|i>$, under the so-called "*frozen-orbital approximation.*"

In general, in a CPS process, the probed photocurrent is expressed through the representative relation:

$$I \propto \sum_{f,i,k} | < \phi_{\mathrm{f,Ek}} | \boldsymbol{r} | \phi_{\mathrm{i,k}} > |^2 \sum_{s} | c_{\mathrm{s}} |^2 \, \delta \left(E_{f,k} + E_{\mathrm{s}} (N-1) - E_0 (N) - h\nu \right), \tag{2}$$

where it is supposed that the final state with N-1 electrons possesses s excited states with energy $E_s(N\text{-}1)$; E_0 is the ground energy state of the N electrons, and $E_{f,k}$ is the kinetic energy of the photoelectron promoted from the initial state $|\phi_{\mathrm{i,k}}>$ to the final state $<\phi_{\mathrm{f,Ek}}|$, while $|c_{\mathrm{s}}|^2$ is the probability that the removal of one electron from the ground-state orbital $|\phi_{\mathrm{i,k}}>$, is followed by the excitation of s states in the N - 1 electron system. The Dirac delta function in relation (2) ensures the energy conservation in the transition of the electron from its initial state to the final one, leading, in addition to the "*main-line*," also to a certain number of possible "*satellite-peaks*," sometimes called "*shake-up lines*," which derive from the excitations induced by the interaction of the remaining photoionizated system with the potential that arises after the creation of a core-hole. This is especially true when a strong interaction occurs between electrons and the core-hole potential, since the charge density of the *valence* electrons would be affected, eventually rearranged, placing the system in an excited state. As a consequence, the core binding energy appears at higher E_{B}, (*main-line*), and new features take place at lower binding energy (*satellite-peaks*). A very well-established case concerns metallic Ni, where the 3*d*, 3 *s*, and the 2*p* ($2p_{3/2}$ and $2\mathrm{p}_{1/2}$ doublet) core levels, are affected (Hüfner and Wertheim, 1975).

Very useful in the interpretation of photoemission spectra is the so-called "*three-step model*," where the intensity of the photocurrent measured with an electron energy analyzer is considered to result from three independent processes: (i) the optical excitation of an electron considered as a pure bulk transition between an initial and a final Bloch state of the crystal; (ii) the propagation of the excited electron toward the surface; and (iii) the escape of the electron from the solid into the vacuum (De Padova and Perfetti, 2005; Feuerbacher et al., 1978; Hüfner, 2003).

Key issues on core photoemission spectroscopy and its application to important examples, namely the elemental two-dimensional (2D) materials graphene and kagome silicene

Some qualitative information on the nature of a PES spectrum can be obtained, without any calculations, considering that there is a noticeable difference between valence and core levels spectra. Actually, the binding energy of a core level is independent of the exciting wave vector, due to the localization of its core wave function.

This leads to consider a core photoemission spectrum in the simplest way, where the measured peak is constituted by a Voigt function (the convolution between a Gaussian and a Lorentzian function). Their σ_{G} and Γ_{L} widths, representing, the overall broadening (especially instrumental and phonon broadening) and the inverse of the core-hole state lifetime, respectively.

However, a number of fundamental effects have to be taken into account in the interpretation of CPS, since they can significantly affect the core level spectrum.

These are initial-state effects ΔE_0, and final-state effects, ΔE_f. If we define the binding energy E_B of a core level as the difference between the total energy of the non-perturbed state of N electrons in its fundamental state as E_0 (N), and the energy of the state formed by the hole and the N-1 electrons remaining after the photoexcitation process as E_f $(N$-1), then $E_B = E_f$ $(N$-1) - E_0 (N).

By defining ΔE_B as the difference between the measured binding energy and the binding energy of an electron in its fundamental state in an isolated atom, then $\Delta E_B = \Delta E_0 + \Delta E_f$.

The physical meaning of these two separate contributions is at the heart of CPS.

Initial-state effects ΔE_0 on the core electron binding energy E_B are mainly due to a change in the electrostatic interactions, between the core electrons and those of the outer shells, determined by the variations in charge distribution. Three fundamental contributions can affect ΔE_0: (i) the charge transfer upon formation of chemical bonds for the same atomic species in different compounds: (ii) the atomic arrangement, where an atom can be isolated, be in a molecule or solid, or sit at a surface with different bulk and surface configurations (causing either bond charge transfer or valence-electron distribution changes); (iii) the "*Madelung contribution*," especially present in ionic compounds, related to the charge transfer between the emitter atom and its neighbor ones. The surface atoms that experience a reconstruction and/or a charge transfer give rise to a binding energy shift, named surface core-level shift (SCLS), while the binding energy changes between two different chemical compounds of the same atom is called "chemical shift."

Final-state effects ΔE_f are associated with the electrons of the outer shells, which "feel" a higher charge of the nucleus, due to the creation of a hole. They relax, by decreasing both the total final energy and the photoelectron binding energy. In the Koopmans' approximation, the photoelectron binding energy is that of the orbital from which it was removed, considering the relaxation energy of the remaining electrons during the photoemission process negligible and, therefore, $\Delta E_f = 0$.

Intra-atomic relaxation is typical of isolated atoms, not depending on the atoms surrounding the emitter. Examples of this mechanism are the appearances in the photoemission spectra of the above mentioned "*shake-up lines.*"

Extra-atomic relaxation concerns the effects of the relaxation energy of valence electrons on the binding energy of the excited atom core orbital. This effect can be strongly influenced by the type of chemical bond the emitter atom forms with the surrounding atoms. The binding energy shift, thus, depends on the effective screening capacity of the hole induced by the relaxing electrons. For *s* and *p* electrons this shift is expected to be higher than for the more localized *d* electrons.

In metals the relaxation process is often due to electron-hole pair excitations at the Fermi level, leading to a typical asymmetric core lineshape at the lower kinetic energy side. It can be also due to the creation of bulk and/or surface plasmons, collective electron oscillations upon the ions lattice potential. In the first case, the curve that represents the core level lineshape best in the fitting procedure is the Doniach-Sunjic function. In the photoemission process, this can be defined as an intrinsic phenomenon, to be distinguished from the extrinsic interactions related to scattering events. These scattering events are responsible of the smooth background of secondary electrons, on which the intrinsic primary photoelectron contribution is superimposed. They form a huge structure, monotonically decreasing after its maximum located at ~2 eV low kinetic energy.

The core-level lineshape in CPS can be affected by various contributions. The intrinsic core-hole lifetime is related to its recombination time through the Lorentzian width.

According to the Heisenberg uncertainty principle, the shorter the recombination time, the greater the uncertainty with which the energy of the emitted core electron is known. Recombination channels in a solid can be radiative (emission of fluorescence photons), or non-radiative (Auger processes, where electrons characteristic of the atomic species accompany the primary photoemission process). Both processes are responsible for the core-level lifetime. Their cross sections depend on the atomic number Z of the atomic species; the fluorescence channel is dominant at large Z.

A feature to be counted as a final-state effect is linked to the excitation of low-energy phonons, which leads to the phonon broadening of the core-level lineshape. Besides, the instrumental resolution depends mainly on the monochromator and the electron energy analyzer. Typically it is considered as a convolution of two Gaussian contributions and the overall Gaussian width takes this into account.

Finally, a very important issue that needs to be dealt with, is the electron escape depth (typically, in monolayers) versus its kinetic energy (eV), related to the so-called "universal curve" for electrons, and, consequently, the bulk or surface sensitivity. Photo-excited electrons, in a PES experiment, lose energy when travelling toward the surface. Many of them are unable to escape into the vacuum, and, hence, cannot be detected. The probability $S(E_k, x)$ that an electron photoexcited at a distance x from the surface, escapes with kinetic energy E_k, has an exponential dependence, following, in a first approximation the relation $S(E_k, x) \propto \exp.[-x/\lambda(E_k)]$, where $\lambda(E_k)$ is the electron escape depth. The "*universal curve*" traces the escape depth $\lambda(E_k)$ as a function of E_k for numerous materials, establishing the dependence of the emitted electron escape depth with its kinetic energy. $\lambda(E_k)$ can vary from tens of angströms, at very low kinetic energy, to a minimum of ~3 *Å* for $E_k \sim 50$ eV, and then slowly grows again up to ~20–30 *Å* at $E_k = 1000$ eV.

At the end of this section, we just briefly mention the importance of thorough core level investigations in photoelectron diffraction, for detailed crystallographic structure determinations (Woodruff and Bradshawi, 1994; Woodruff, 2021).

C 1*s* and Si 2*p* core levels of graphene and kagome silicene

This year marks the 75th anniversary of synchrotron light experimentally observed. Since 1946 the physicist Herbert Pollack, at the General Electric Research Laboratory in Schenectady (New York, USA), guided the assembly of a circular accelerator for driving electrons at relativistic energies. One year later, in 1947, the radiation from electrons, the synchrotron light, obtained by *bremsstrahlung*, was visually observed at the General Electric 70-Mev synchrotron (Elder et al., 1947), and rightfully entered in science (Margaritondo, 2022).

Today, it has become an indispensable tool for physics, chemistry, biology, cultural heritage, medicine and many other human science activities, where advance knowledge of materials and fundamental matter requires for scientific answers. Through the ability to continuously tune the photon's energy from UV light to soft and to hard x-rays, its polarization state and high brightness, synchrotron light is a formidable ally in the investigation of CPS.

An interesting aspect offered by synchrotron radiation in the study of core levels is the possibility of highlighting in the CPS spectra the characteristics of the surface features of a solid versus its bulk counterpart, upon considering the dependence of $S(E_k, x)$ of the photoexcited electron as a function of its kinetic energy, by choosing the energy of the impinging photons. Since the surface and the bulk atoms may not be equivalent due to their different physical/chemical environment and/or structural ordering, their contributions may appear at different core-level binding energies. Noteworthy, is that in CPS, these surface/bulk effects can be further enhanced by exploiting the angle Ψ, at which the surface is hit by the photons, and, above all, the angle at which the electrons emitted by the sample are analyzed at the detection angle ϑ. One passes from more bulk-mode to more surface sensitive mode upon changing from normal emission to emission at grazing angles (for the experiment geometry see Fig. 1).

Having described the photoemission process and its use in experiments, is now time to present some applications. The next two paragraphs summarize the main results obtained in CPS on graphene and silicene, the prominent representatives among all elemental 2D materials.

C 1s of graphene on SiC(0001) and Ni(111)

Graphene, a one-atom thick carbon layer, arranged in a honeycomb lattice, is the first natural, sheet obtained by peeling graphite, among the nowadays large family of 2D elemental materials. Graphene is extensively prepared in both its suspended freestanding form, and by epitaxial growth on different supporting substrates. Its pioneers Andre K. Geim and Kostantin Novoselov, were awarded the 2010 Nobel Prize, in physics "*for groundbreaking experiments regarding the two-dimensional material graphene*."

The substrates most commonly used for the epitaxial growth of graphene are Pt(111) (Otero et al., 2010; Sutter et al., 2009; Vinogradov et al., 2011), Ir(111) (Coraux et al., 2008; N'Diaye et al., 2006, 2008; Vinogradov et al., 2011), Cu(111) (Gao et al., 2010), Ru(0001) (Marchini et al., 2007; Sutter et al., 2008), Rh(111) (Preobrajenski et al., 2008), Ni(111) (Mittendorfer et al., 2011; Park et al., 2019), as well as SiC(0001) (Emtsev et al., 2008), and SiC(111)/Si(111) (Ouerghi et al., 2010). In some ways, they can be defined as more or less weakly or strongly interacting with the graphene overlayer. Among the substrates considered to have a weak interaction one has Ir(111) (Coraux et al., 2008, N'Diaye et al., 2006, 2008, Vinogradov et al., 2011), Cu(111) (Gao et al., 2010), and Pt(111) (Sutter et al., 2009; Otero et al., 2010). On the contrary, Ru(0001) (Sutter et al., 2008; Marchini et al., 2007), Rh(111) (Preobrajenski et al., 2008), and above all Ni(111) (Mittendorfer et al., 2011, Park et al., 2019), SiC(0001) (Emtsev et al., 2008) and SiC(111)/Si(111) (Ouerghi et al., 2010), are recognized as promoting a strong interaction between their surface and the overlying graphene layer.

The C 1*s* core level is the emblem of the versatile carbon element, capable of hybridizing in various forms, namely *sp* hybridization favoring 1D linear chain-like configurations, as well as sp^2 and sp^3 hybridizations, which permit 2D planar honeycomb, and 3D tetragonal crystalline structures, respectively. This leads, for example, to a narrow single C 1*s* core level, located at 284.5 eV BE, in the case of cleaved highly oriented pyrolytic graphite (Sette et al., 1990). Instead, for the clean diamond C(111) surface, which is 2 × 1 reconstructed (Morar et al., 1986), it leads, in addition to the bulk component actually located at 285.00 eV BE (i.e., higher BE than for graphite), to the appearance of a clear surface component, located at 284.20 eV BE, distinct from the bulk component by 0.8 eV. Thus, a BE difference of 0.5 eV is found for the bulk components of the C 1*s* core levels, for the sp^2 and sp^3 carbon hybridizations. Instead, for the hydrogen-covered C(111)2 ×1 surface, the bulk and surface peaks fall at nearly the same energy, because the outermost carbon atoms, which are bonded to hydrogen, with an electronegativity similar to that of carbon, find themselves, practically, in a bulk-like (1×1) configuration (Morar et al., 1986).

Ultrathin graphite layers (so-called few layer graphene (FLG)), present two different behaviors when grown on each of the two polar surfaces of a SiC single crystal, namely, the Si-terminated and interacting (0001) surface, and the quite-inert C-terminated $(000\overline{1})$ surface (Emtsev et al., 2008).

In the first case, the growth of the carbon layer exhibits, already from the very beginning, a $(6\sqrt{3} \times 6\sqrt{3})R30^\circ$ graphene-like surface reconstruction, on SiC(0001) (Emtsev et al., 2008). Fig. 3 displays the corresponding C 1 *s* core level (Emtsev et al., 2008).

The interaction between this graphene-like carbon layer with the underlying surface is quite strong giving rise to a structured C 1 *s* core-level as clearly visible on the two spectra of Fig. 3 The strong coupling of some of the C atoms in the $(6\sqrt{3} \times 6\sqrt{3})R30^\circ$ reconstructed layer with the substrate has its signature in the C 1 *s* core level, through the presence of two surface components S1 and S2 at 284.75 eV and 285.55 eV binding energy, respectively, in addition to the SiC bulk component, located at 283.70 eV BE, (Emtsev et al., 2008). Note that the intensity ratio between the two surface components S1:S2 ∼ 0.5, is essentially the same, irrespective of the inelastic mean free path of the photoelectrons, which changes from 2.9 to 4.5 Å, for measurements performed at 350 eV and 510 eV photon energy, respectively. This proves that the C atoms responsible for the two surface components, S1 and S2, are lying in the same plane (Emtsev et al., 2008). S1 was attributed to one-third of the carbon atoms in the surface layer, which strongly interact with the dangling bonds of the underlying SiC(0001) surface. S2, located at higher binding energy, was assigned to the remaining two-thirds, only bound to C atoms within the layer.

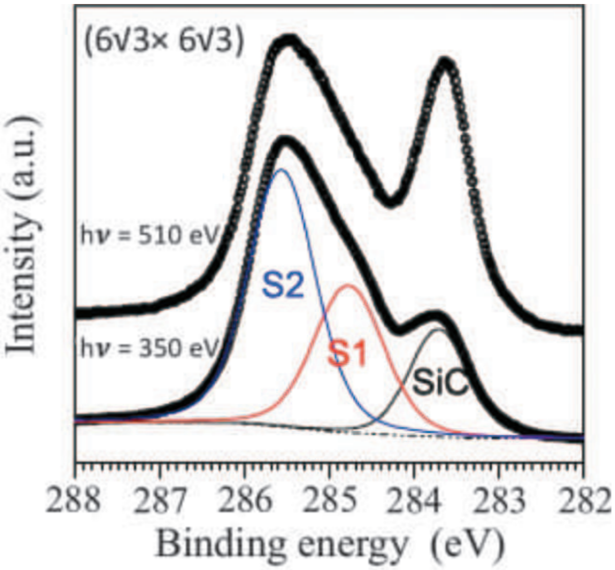

Fig. 3 C 1*s* core-level spectra of the SiC(0001)-(6√3 × 6 √ 3)*R*30° reconstruction recorded at 350 eV and 510 eV photon energies. Adapted from Fig. 3 with permission from Emtsev KV, Speck F, Seyller T, and Ley L (2008) Interaction, growth, and ordering of epitaxial graphene on SiC{0001} surfaces: A comparative photoelectron spectroscopy study. *Physical Review B* 77: 155303–155310. Copyright (2008) by the American Physical Society.

In the case of graphene grown on the inert C-terminated SiC(000$\bar{1}$) surface, the C 1*s* spectrum exhibits two completely separate peaks, the bulk one and that attributed to graphene located at 284.5 eV (Emtsev et al., 2008), like for the C 1*s* core-level from cleaved highly oriented pyrolytic graphite (Sette et al., 1990).

Another striking case concerns the single layer of graphene grown on the surface of the clean Ni(111) surface prepared by repeated cycles of Ar^+ ion sputtering and annealing at ~ 700 °C, in an ultra-high vacuum (UHV) chamber. Graphene was grown in C_2H_2 gas at low pressure, about $(1.0–5.0) \times 10^{-6}$ Torr, keeping the sample at ~700 °C (Park et al., 2019).

Fig. 4 shows the corresponding C 1*s* spectra is acquired with synchrotron radiation at 360 eV photon energy. Two different peaks related to C in graphene, directly grown on the Ni(111) surface, and after Au intercalation, are clearly distinguished (Park et al., 2019).

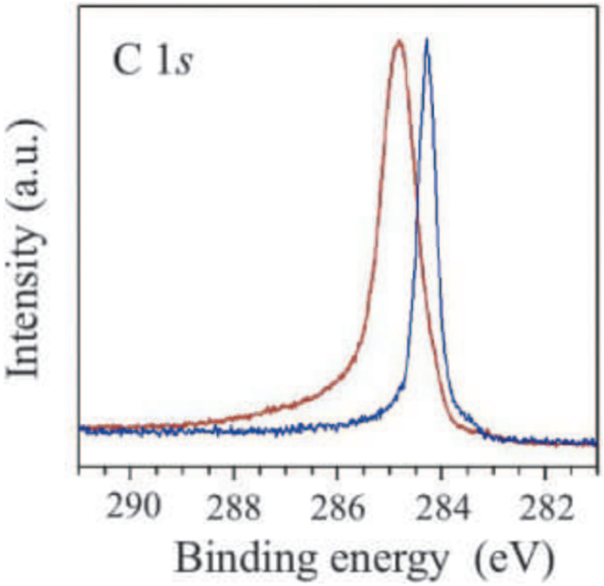

Fig. 4 C 1*s* core level spectra recorded at 360 eV photon energy from a graphene/Ni(111) interface (red-line), and after gold intercalation (blue-line; graphene/Au/Ni(111)). Adapted from Fig. 1 of Park Y, Jung D, Hwang H-N, Hwang C-C (2019) Electronic structure of the Au-intercalated graphene/Ni(111) surface. *Current Applied Physics* 19: 215–218. Copyright (2018), with permission from Elsevier.

As can be observed, in the first case the C 1*s* peak is located at ~ 284.8 eV and broadened because of the presence of unresolved components, due to the interaction between the carbon and nickel atoms. Conversely, the C 1*s* spectrum acquired when Au atoms are intercalated below the graphene sheet reflects its disconnection from the nickel substrate. This narrow peak (blue-line) is shifted toward lower binding energy by ~ 0.50 eV. The C 1*s* full width at half maximum (FWHM) is ~ 0.84 eV in the first case, and markedly less ~ 0.58 eV, in the second case, indicating the restoration of the graphene sublattice symmetry (Park et al., 2019). Note that, in this last case, the electronic properties of graphene, including the characteristic Dirac cone, are regained, demonstrating simultaneously the absence of interaction with the Au intercalated atoms and the loss of the interaction with the nickel surface (Park et al., 2019).

Si 2p and Al 2p core-levels from (√3 × √3)/(3 × 3) kagome silicene on an Al(111) substrate

The first trans-graphene artificial elemental 2D materials is called silicene. It is a new allotropic form of silicon, constituted of one sheet of Si atoms arranged in a honeycomb (but buckled) lattice, similarly to graphene (Feng et al., 2012; Lin et al., 2012; Vogt et al., 2012). The possible existence of silicene was theoretically predicted (Takeda and Shiraishi, 1994; Guzmán-Verri and Lew Yan Voon, 2007; Lebègue and Eriksson, 2009; Cahangirov et al., 2009), and experimentally realized for the first time in 2012 on a silver single crystal (111) surface, where a 3 × 3 reconstructed silicene overlayer epitaxially matched a Ag(111) 4 × 4 supercell (in short named (3 × 3)/(4 × 4)) reconstruction) (Vogt et al., 2012). Soon after, silicene was subsequently synthesized on different substrates (Fleurence et al., 2012; Meng et al., 2013; Stępniak-Dybala and Krawiec, 2019). Interestingly, the linear dispersions at the high symmetry K/K′ points of the surface Brillouin zone (SBZ) and after band folding have been revealed (Avila et al., 2013; Du et al., 2014; Feng et al., 2012, 2016; Lin et al., 2012; Meng et al., 2013; Tsoutsou et al., 2013; Vogt et al., 2012; Davila and Le Lay, 2022).

Strikingly, silicon can form amazing 2D structures showing its versatility, as can be ascertained after the discovery of an exotic kagome structure of silicene, where Si atoms arrange in a large superstructure.

Kagome-like silicene was recently synthesized on aluminum (111) substrates at room temperature (RT) (Sassa et al., 2020). Evidence of such an exotic 2D Si allotrope was given through low energy electron diffraction, scanning tunneling microscopy observations, high-resolution core-level, and angle-resolved photoelectron spectroscopy measurements, along with density functional theory calculations (Sassa et al., 2020). Kagome-silicene is (√3 × √3) reconstructed, epitaxially matching an Al(111)(3 × 3) supercell (in short (√3 × √3)/(3 × 3)).

Impressive corresponding Si 2*p* and Al 2*p* core-levels are shown in Fig. 5A and B, in both bulk- and surface-sensitive conditions. By a simple visual observation of these spectra, it is possible to get numerous information, directly obtainable from the core photoemission process.

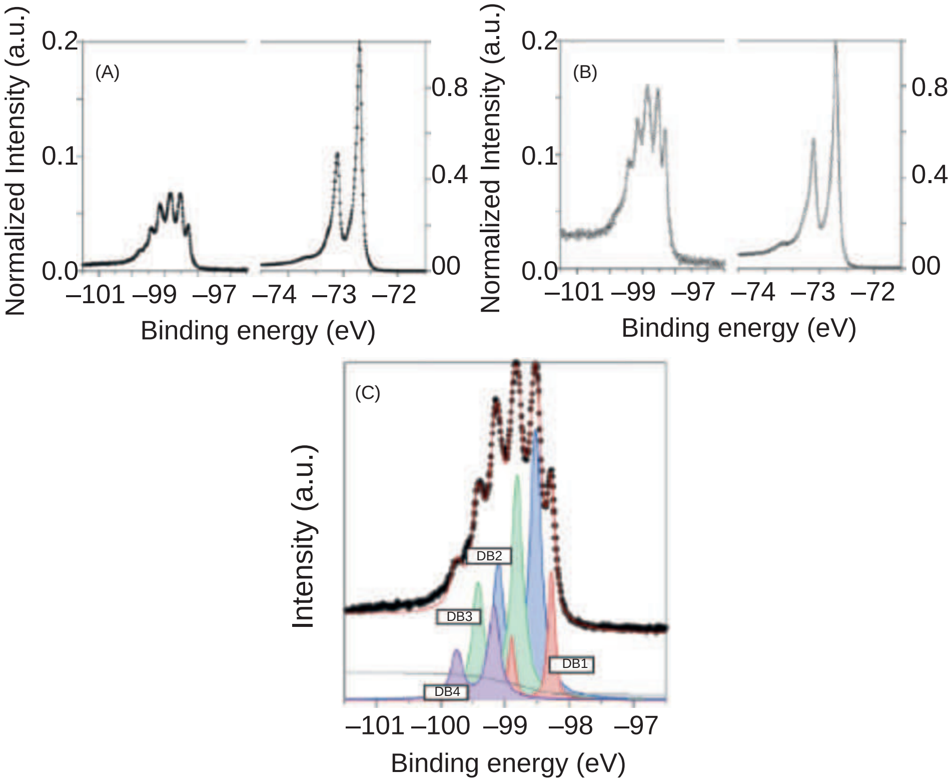

Fig. 5 Si 2*p* and Al 2*p* core-level spectra from kagome silicene synthesized on an Al(111) surface, obtained with synchrotron at 136 eV photon energy, in normal (A) and 60° off-normal (B) emission; (C) is the deconvolution of the Si 2*p* core-level in normal emission (A). Experimental data (black dots); fit curve (solid red line) with the DB1, DB2, DB3 and DB4 doublets. Adapted from Fig. 3 of Sassa Y, Johansson FOL, Lindblad A, Yazdi MG, Simonov K, Weissenrieder J, Muntwiler M, Iyikanat F, Sahin H, Angot T, Salomon E, Le Lay G (2020) Kagome-like silicene: A novel exotic form of two-dimensional epitaxial Silicon. *Applied Surface Science* 530: 147195.

Firstly, the Si 2*p* core level comprises several components associated to different adsorption sites on the Al surface. Secondly, upon passing from bulk to surface conditions, it is clear that all silicon atoms lie on top of the aluminum surface. Indeed, all Si 2*p* structures are enhanced in intensity with respect to the Al 2*p* peak intensity in surface-sensitive conditions, evidencing the surface location of all silicon sites (Sassa et al., 2020).

A thorough analysis was further performed through a least-square fitting procedure, as shown in Fig. 5C, with four components DB1, DB2, DB3 and DB4, lying on a Shirley background (continuous black line) (Sassa et al., 2020). Each component is a doublet (DB) with a spin–orbit splitting of ~600 ± 10 meV and a branching ratio of 0.50. Each doublet was built using two Voigt functions with a full width at half maximum (FWHM) of 170 ± 30 meV for DB1 and 285 ± 30 meV for DB2, DB3 and DB4 (Sassa et al., 2020).

Having presented and discussed several remarkable results, it is worth emphasizing at the end of this section that core level photoemission spectroscopy is an extremely powerful investigation tool, which makes it possible to discriminate even just slightly different chemical, physical, and crystallographic environments of specific atomic entities.

Conclusion

This chapter offers a broad overview on core photoemission spectroscopy. For a complete fundamental theoretical treatment of the photoemission process, the reader is referred to specialized texts such as those cited in Refs. (Cardona and Ley, 1978; Feuerbacher et al., 1978; Hüfner, 2003).

Here, we have given the basics by way of striking examples, namely graphene on silicon carbide and nickel, as well as kagome silicene on aluminum. The measurement of the C 1*s*, Si 2*p*, and Al 2*p* core levels in state-of the-art conditions, and their thorough analysis shows the power of core photoemission spectroscopy, and its prominent utility, not only in surface physics, but more generally, in materials science.

However, clearly, the complete interpretation of photoemission spectra must go hand in hand with results from other complimentary methods, such as scanning tunneling microscopy, low energy electron diffraction, Auger electron spectroscopy, etc., and, overall, with first principles theoretical calculations of the involved atomic structures.

At present, a high-resolution core-level measurements can be easily performed at most synchrotron radiation facilities, where different photon energies can be used, in conjunction with optimized experimental geometries.

Now, such measurements concern more and more appealing studies of samples of great interest, such as the artificial 2D Xenes.

Hence, this spectroscopy, which is one of the best performing ones in the field of materials science, has reached its maturity both for fundamental researches and applied studies.

Further developments, typically for investigations in near ambient conditions, and in the time domain, which are already realized in practice, e.g., for catalytic studies in operando conditions, especially using novel 2D materials, undoubtedly promise a bright future to core photoemission.

References

Avila J, De Padova P, Cho S, Colambo I, Lorcy S, Quaresima C, Vogt P, Resta A, Le Lay G, and Asensio MC (2013) Presence of gapped silicene-derived band in the prototypical (3 × 3) silicene phase on silver (111) surfaces. *Journal of Physics: Condensed Matter* 25: 262001–262008.
Cahangirov S, Topsakal M, Aktürk E, Sahin HS, and Ciraci S (2009) Two- and one-dimensional honeycomb structures of silicon and germanium. *Physical Review Letters* 102: 236804–4.
Cardona M and Ley L (1978) *Photoemission in Solids I*, 1st edn New York Heidelberg Berlin: Springer-Verlag.
Coraux J, N'Diaye AT, Busse C, and Michely T (2008) Structural coherency of graphene on Ir(111). *Nano Letters* 8: 565–570.
Davila ME and Le Lay G (2022) Silicene: Genesis, remarkable discoveries, and legacy. *Materials Today Advances* 16: 100312–100313.
De Padova P, Perfetti P, Bassani F, and Liedl GL (2005) In: Wyder P (ed.) *Core photoemission*, pp. 240–251. Encyclopedia of Condensed Matter Physics: Elsevier Academy Press.
Du Y, Zhuang J, Liu H, Xu X, Eilers S, Wu K, Cheng P, Zhao J, Pi X, See KW, Peleckis G, Wang X, and Dou SX (2014) Tuning the band gap in silicene by oxidation. *ACS Nano* 8: 10019–7.
Einstein A (1905) Uber einen die Erzeugung und Verwandlung des Lichtes betreffenden heuristischen Gesichtspunkt. *Ann. Phys.* 132–148.
Elder FR, Gurewitsch AM, Langmuir RV, and Pollock HC (1947) Radiation from electrons in a synchrotron. *Physics Review* 71: 829–830.
Emtsev KV, Speck F, Seyller T, and Ley L (2008) Interaction, growth, and ordering of epitaxial graphene on SiC{0001} surfaces: A comparative photoelectron spectroscopy study. *Physical Review B* 77: 155303–155310.
Feng B, Ding Z, Meng S, Yao Y, He X, Cheng P, Chen L, and Wu K (2012) Evidence of silicene in honeycomb structures of silicon on Ag(111). *Nano Letters* 12: 3507–3511.
Feng Y, et al. (2016) Direct evidence of interaction-induced Dirac cones in a monolayer silicene/Ag(111) system. *Proceedings. National Academy of Sciences. United States of America* 113: 14656–14661.
Feuerbacher B, Fitton B, and Willis RF (1978) *Photoemission and the Electronic Properties of Surfaces*, 1st edn Chichester, New York, Brisbane, Toronto: John Wiley & Sons Ltd.
Fleurence A, Friedlein R, Osaki T, Kawai H, Wang T, and Yamada-Takamura Y (2012) Experimental evidence for epitaxial silicene on diboride thin films. *Physical Review Letters* 108: 245501–245505.
Gao L, Guest JR, and Guisinger NP (2010) Epitaxial graphene on Cu(111). *Nano Letters* 10: 3512–3516.
Guzmán-Verri GG and Lew Yan Voon LC (2007) Electronic structure of silicon-based nanostructures. *Physical Review B* 76: 075131–10.
Hallwachs W (1888) Uber den Einfluß des Lichtes auf electrostatisch geladene Körper. *Annalen der Physik und Chemie.* 269: 301–312.
Hertz HR (1887) Uber einen Einfluß des ultravioletten Lichtes auf die electrische Entladung. *Annalen der Physikund Chemie* 267: 983–1000.
Hüfner S (2003) *Photoelectron Spectroscopy Principles and Applications*, 3rd edn. Berlin, Heidenberg, New York, Hong Kong, London, Milan, Paris, Tokyo: Springer.
Hüfner S and Wertheim GK (1975) Multielectron effects in the XPS spectra of Ni. *Physics Letters A* 51: 299–300.

Lebègue S and Eriksson O (2009) Electronic structure of two-dimensional crystals from ab initio theory. *Physical Review B* 79: 115409–4.

Lin C, Arafune R, Kawahara K, Tsukahara N, Minamitami E, Kim Y, Takagi N, and Kawai M (2012) Structure of silicene grown on Ag(111). *Applied Physics Express* 5: 045802–045803.

Marchini S, Günther S, and Wintterlin J (2007) Scanning tunneling microscopy of graphene on Ru(0001). *Physical Review B* 76: 075429.

Margaritondo G (2022) Who were the founders of synchrotron radiation? Historical facts and misconceptions. *Journal of Vacuum Science and Technology A* 40: 033204–033211.

Meng L, Wang Y, Zhang L, Du S, Wu R, Li L, Zhang Y, Li G, Zhou H, Hofer WA, and Gao H-J (2013) Buckled silicene formation on Ir(111). *Nano Letters* 13: 685–690.

Mittendorfer F, Garhofer A, Redinger J, Klimeˇs J, Harl J, and Kresse G (2011) Graphene on Ni(111): Strong interaction and weak adsorption. *Physical Review B* 84: 201401(R)–4.

Morar JF, Himpsel FJ, Hollinger G, Jordan JL, Hughes G, and Mc Feely FR (1986) C 1s excitation studies of diamond (111). I. Surface core levels. *Physical Review B* 33: 1340–33.

N'Diaye AT, Bleikamp S, Feibelman PJ, and Michely T (2006) Two-dimensional Ir cluster lattice on a graphene Moire ´on Ir(111). *Physical Review Letters* 97: 215501–215504.

N'Diaye AT, Coraux J, Plasa TN, Busseand C, and Michely T (2008) Structure of epitaxial graphene on Ir(111). *New Journal of Physics* 10: 043033–16.

Otero G, González C, Pinardi AL, Merino P, Gardonio S, Lizzit S, Blanco-Rey M, Van de Ruit K, Flipse CFJ, Méndez J, de Andrés PL, and Martín-Gago JA (2010) Ordered vacancy network induced by the growth of epitaxial graphene on Pt(111). *Physical Review Letters* 105: 216102–216104.

Ouerghi A, Kahouli A, Lucot D, Portail M, Travers L, Gierak J, Penuelas J, Jegou P, Shukla A, Chassagne T, and Zielinsk M (2010) Epitaxial graphene on cubic SiC(111)/Si(111) substrate. *Applied Physics Letters* 96: 191910–191913.

Park Y, Jung D, Hwang H-N, and Hwang C-C (2019) Electronic structure of the Au-intercalated graphene/Ni(111) surface. *Current Applied Physics* 19: 215–218.

Preobrajenski AB, Ng ML, Vinogradov AS, and Mårtensson N (2008) Controlling graphene corrugation on lattice-mismatched substrates. *Physical Review B* 78: 073401–073404.

Sassa Y, Johansson FOL, Lindblad A, Yazdi MG, Simonov K, Weissenrieder J, Muntwiler M, Iyikanat F, Sahin H, Angot T, Salomon E, and Le Lay G (2020) Kagome-like silicene: A novel exotic form of two-dimensional epitaxial Silicon. *Applied Surface Science* 530: 147195.

Sette F, Wertheim GK, Ma Y, Meigs G, Modesti S, and Chen CT (1990) Life time and screening of the C1s photoemission in graphite. *Physical Review B* 41: 9766–41.

Stępniak-Dybala A and Krawiec M (2019) Formation of silicene on ultrathin Pb(111) Films. *Journal of Physical Chemistry C* 123: 17019–17025.

Sutter PW, Flege JI, and Sutter EA (2008) Epitaxial graphene on ruthenium. *Nature Materials* 406–411.

Sutter P, Sadowski JT, and Sutter E (2009) Graphene on Pt(111): Growth and substrate interaction. *Physical Review B* 80: 245411–10.

Takeda K and Shiraishi K (1994) Theoretical possibility of stage corrugation in Si and Ge analogs of graphite. *Physical Review B* 50: 14916–14922.

Tsoutsou D, Xenogiannopoulou E, Golias E, Tsipas P, and Dimoulas A (2013) Evidence for hybrid surface metallic band in (4 × 4) silicene on Ag(111). *Applied Physics Letters* 103: 231604–231605.

Vinogradov NA, Schulte K, Ng ML, Mikkelsen A, Lundgren E, Mårtensson N, and Preobrajenski AB (2011) Impact of atomic oxygen on the structure of graphene formed on Ir(111) and Pt(111). *Journal of Physical Chemistry C* 115: 9568–9577.

Vogt P, De Padova P, Quaresima C, Avila J, Frantzeskakis E, Asensio MC, Resta A, Ealet B, and Le Lay G (2012) Silicene: Compelling experimental evidence for graphenelike two-dimensional silicon. *Physical Review Letters* 108: 155501–155505.

Woodruff DP (2021) Photoelectron diffraction: Early demonstrations and alternative modes. *Journal of Vacuum Science and Technology A* 39: 040801–040809.

Woodruff DP and Bradshawi AM (1994) Adsorbate structure determination on surfaces using Photoelectron. *Reports on Progress in Physics* 57: 1029–1080.

Further reading

Fukaya Y, Mochizuki I, Maekawa M, Wada K, Hyodo T, Matsuda Y, and Kawasuso A (2013) Structure of silicene on a Ag(111) surface studied by reflection high energy positron diffraction. *Physical Review B* 88: 205413–205414.

Huang S, Kan W, and Yang L (2013) Electronic structure and quasiparticle bandgap of silicene structures. *Applied Physics Letters* 102: 133106–5.

Harmonic generation frequency conversion[☆]

Marco Bellini, Istituto Nazionale di Ottica (CNR-INO), Florence, Italy; LENS and Department of Physics & Astronomy, University of Firenze, Florence, Italy

© 2024 Elsevier Ltd. All rights reserved.

This is an update of M. Bellini, Harmonic Generation Frequency Conversion, Editor(s): Franco Bassani, Gerald L. Liedl, Peter Wyder, Encyclopedia of Condensed Matter Physics, Elsevier, 2005, Pages 303–311, ISBN 9780123694010, https://doi.org/10.1016/B0-12-369401-9/00678-1.

Introduction	246
Nonlinear polarization and susceptibilities	247
Second harmonic generation	248
Phase-matching	249
Quasi phase-matching	251
High-order harmonic generation	252
The three-step model	253
Phase-matching in high-order harmonic generation	254
Conclusion	255
References	256

Abstract

The generation of coherent light at frequencies that are integer multiples of those of ordinary laser sources may give access to useful and often unexplored spectral regions. Here, we briefly describe the basics of harmonic generation, which relies on the nonlinear interaction between matter and intense laser fields, to extend the range of the accessible electromagnetic spectrum toward shorter and shorter wavelengths.

Key points

- The generation of coherent light at frequencies that are multiples of those emitted by laser sources is briefly described.
- Basic elements are given of the processes involved in the nonlinear interaction between matter and laser light.
- The generation of the second harmonic and the phenomenon of phase-matching are described in some detail.
- High-order harmonics are introduced, with a simple physical picture and hints of their phase-matching properties.

Introduction

The ability to manipulate the frequency of laser light is essential for extending the range of possible spectroscopic investigations of matter in its different forms. Although the number of available laser lines is continuously growing, thanks to the introduction of new active materials operating in different spectral ranges, the extension toward the short-wavelength region of the electromagnetic spectrum would have been seriously limited without the advent of harmonic generation techniques, which rely on the nonlinear interaction between matter and intense laser light to generate new optical frequencies at integer multiples of the pump frequency.

With ordinary light sources, the electric fields associated to radiation are normally very small when compared to the typical local fields (of atomic, molecular, or crystal origin) inside materials. The electrons in atoms or the nuclei in molecules just explore the bottom of their potential wells (where the shape is approximately parabolic) under the influence of the external optical field, and their motion is harmonic with the same frequency of the forcing light (see Fig. 1).

The oscillating dipoles in the material are the sources of re-emitted radiation, whose spectral content is thus the same as the incident one. Many properties of light propagation in matter (such as refraction, reflection, dispersion, scattering, and birefringence) can be readily explained in this regime of linear optics. However, when the light field is so intense that it becomes a non-negligible fraction of the internal field, the linear approximation breaks down and the electrons or nuclei start exploring the anharmonic parts of their potential wells. In this regime, their motion is no longer harmonic and can be expanded in a Fourier series containing frequencies at integer multiples of the forcing frequency. Such new frequencies are also present in the radiation field emitted by the material and constitute the harmonics of the fundamental driving field.

[☆] *Change History*: September 2022. M Bellini updated the chapter. Compared to the first edition of this chapter, several new references have been added and slight changes have been made throughout the entire text. A new equation (24) has been included and a new paragraph appears at the end of the "Phase-matching in high-order harmonic generation" section. A conclusion section is also present at the end of the chapter.

https://doi.org/10.1016/B978-0-323-90800-9.00068-8

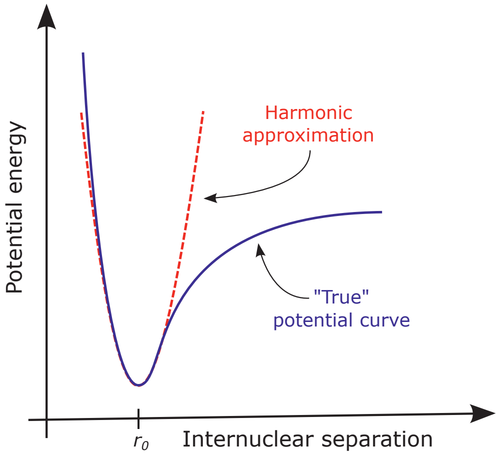

Fig. 1 Potential energy curve illustrating the vibrational motion of nuclei in a molecule. The bottom of the curve can be well approximated by a parabolic potential and the motion is harmonic if only small-amplitude oscillations are induced by an external field.

In this article, the basics of harmonic generation are presented concisely, with an attempt to illustrate the fundamental physical mechanisms that are responsible for the processes at play (Shen, 2003; Boyd, 2019). A few examples are then given: from the simple case of second harmonic generation (SHG), dating back to the dawn of the laser era (Franken et al., 1961), to the production of high-order harmonics (McPherson et al., 1987; Ferray et al., 1988) in the extreme ultraviolet (XUV) and soft X-rays, which relies on the high peak intensities available to the current pulsed laser systems.

Nonlinear polarization and susceptibilities

When incident light is sufficiently off-resonance, its interaction with matter does not induce any change in the population of the energy eigenstates of the material system (i.e., no absorption takes place), but only provokes a perturbation of the motion of electric charges within the atoms or molecules. In this non-resonant process, the material is transparent to the incident radiation, but the change in charge distribution due to the oscillating light field results in an induced electric dipole moment which, in turn, acts as a new source to emit secondary electromagnetic waves: the induced polarization P is thus the source term that has to be introduced in Maxwell's equations, leading to the inhomogeneous wave equation

$$\nabla^2 \mathrm{E} - \frac{1}{c^2}\frac{\partial^2}{\partial t^2}\mathrm{E} = \mu_0 \frac{\partial^2}{\partial t^2}\mathrm{P}, \tag{1}$$

for describing the subsequent field evolution. The general form for the component at frequency ω of the polarization vector P can be written as

$$\mathrm{P}(\omega) = \sum_n \mathrm{P}^{(n)}(\omega), \tag{2}$$

where the nth-order polarization has the following expression:

$$\mathrm{P}^{(n)}(\omega) = \epsilon_0 \chi^{(n)}(\omega_1, \omega_2, \ldots, \omega_n)\mathrm{E}(\omega_1)\mathrm{E}(\omega_2)\ldots\mathrm{E}(\omega_n) \tag{3}$$

and

$$\omega = \sum_{i=1}^{n} \omega_i \tag{4}$$

The quantities $\chi^{(n)}(\omega_1, \omega_2, \ldots, \omega_n)$ are known as the nonlinear optical susceptibilities of order n of the medium, and they are $(n+1)$th-order tensors relating an n-fold product of vector components E_j to a certain component of the nth-order polarization $\mathrm{P}^{(n)}(\omega)$.

In the ordinary linear regime, the Fourier component at frequency ω of the polarization for a medium reduces to

$$\mathrm{P}^{(1)}(\omega) = \epsilon_0 \chi^{(1)}(\omega)\mathrm{E}(\omega) \tag{5}$$

with the obvious meaning that, in this first-order approximation, the polarization at a given frequency is linearly proportional to the incident field Fourier component at the same frequency: a monochromatic incident light can only induce a monochromatic secondary wave at the same frequency. For anisotropic media, $\chi^{(1)}(\omega)$ is a 3 × 3-element second-order tensor, whereas it reduces to a complex function of the frequency for isotropic materials.

In the general case, the expression for $P^{(n)}(\omega)$ shows that, thanks to *n*th-order nonlinearities, it is possible to mix *n* incident waves at different frequencies to obtain an induced polarization, and thus some re-emitted radiation, at a different frequency: light at frequencies corresponding to sums and differences among the frequencies of the incoming beams can be produced this way. In the particular case where only one field at frequency ω enters the material, a susceptibility of order *n* can produce new radiation at *n*ω, the *n*th harmonic of the incident field.

The ratio of two successive orders of polarization can be roughly estimated as

$$\left|\frac{P^{(n+1)}}{P^{(n)}}\right| = \frac{\left|\chi^{(n+1)}\right||E|}{\left|\chi^{(n)}\right|} \approx \left|\frac{E}{E_m}\right| \tag{6}$$

where E is the amplitude of the applied optical field, and E_m is the characteristic value of the internal electric field in the material. If the main mechanism contributing to the nonlinear polarization is the distortion of the electronic cloud of an atomic or molecular system (as in the case of optical harmonic generation), then E_m is the average magnitude of the binding field experienced by the electrons ($\sim 10^{11}$ Vm^{-1} for the hydrogen atom). For ordinary light sources, the ratio $|E = E_m|$ is normally so small that nonlinear polarization terms can be safely neglected. However, when laser light of high spectral intensity is used, the laser field may become a non-negligible fraction of the material field, and the second, third, and higher-order nonlinear terms, may start playing an important role, causing part of the incident light to be converted into the corresponding harmonic. From the above expression, one can also infer that the *n*th-order polarization, hence the field emitted at *n*ω is proportional to the *n*th power of the ratio between *E* and E_m (normally much smaller than 1), so that the probability of generating higher harmonics is expected to drop exponentially with the corresponding order in this perturbative approach.

From the fact that the susceptibility tensors must remain unchanged upon the symmetry operations allowed for the medium, one can simply conclude that for all isotropic media and centrosymmetric crystals, the even-order susceptibilities $(\chi^{(2)}, \chi^{(4)}, \ldots, \chi^{(2n)})$ must be zero. Consequently, the generation of even-order harmonics is only possible in materials lacking inversion symmetry, whereas odd-order nonlinear effects can be exhibited by any media, although at different degrees of efficiency.

If the field amplitudes do not change much in a propagation length shorter than a wavelength (the so-called slowly varying amplitude approximation) and if nonlinearities are not too strong (so that the field amplitude at the pump frequency stays almost constant throughout the interaction), then one can find a simple expression for the wave equation of the plane-wave field and the induced nonlinear polarization P^{NL} oscillating at the new frequency ω′

$$\frac{\partial}{\partial z}E(z,\omega') = -\frac{i\mu_0\omega'^2}{2k'}P^{NL}(z,\omega')e^{i\Delta kz}, \tag{7}$$

where one assumes linearly polarized light (for reducing to a scalar equation) and collinear propagation along the *z* direction. The phase term $e^{i\Delta kz}$ accounts for the phase drift between the induced polarization and the generated electric field at ω′, and depends on the mismatch in their propagation vectors

$$\Delta k = k' - k_p \tag{8}$$

where $k_p = \sum_i \omega_i n(\omega_i)/c$ and $k' = \omega' n(\omega')c$, with $n(\omega)$ the material refractive index at frequency ω.

In the case of harmonic generation of order *q*, this factor reduces to

$$\Delta k = k(q\omega) - qk(\omega) \tag{9}$$

Second harmonic generation

As a simple example, let us consider the case of second-order nonlinearity for the generation of radiation at twice the frequency of the incoming light (Franken et al., 1961). As seen above, symmetry considerations impose the process to take place in non-centrosymmetric crystals only. The polarization vector

$$P^{(2)}(2\omega) = \epsilon_0\chi^{(2)}(\omega,\omega)E_1(\omega)E_1(\omega) \tag{10}$$

is the source term that has to be inserted in the wave equation and leads to the following expression for the variation of the field amplitude at the second harmonic $E_2(z)$:

$$\frac{\partial}{\partial z}E_2(z) = -\frac{i\omega d}{cn(2\omega)}E_1^2(z)e^{i\Delta kz} \tag{11}$$

where *d* corresponds to the component of the $\chi^{(2)}(\omega, \omega)$ tensor appropriate for the particular geometry of the laser-crystal interaction and

$$\Delta k = k(2\omega) - 2k(\omega) = \frac{4\pi}{\lambda}[n(2\omega) - n(\omega)] \tag{12}$$

is the phase mismatch factor, which takes into account the different phase velocities of the waves at ω and 2ω. If a negligible absorption and little production of the wave at 2ω are assumed, so that the pump field amplitude E_1 at frequency ω can be considered as almost constant, then the coupled wave equation can be integrated straightforwardly:

$$E_2(z) = -\frac{i\omega d}{cn(2\omega)} E_1^2(0) \int_0^L e^{i\Delta kz} dz \tag{13}$$

with the integration extending over the length L of the nonlinear medium. Assuming no initial second harmonic field, that is $E_2(0) = 0$, the integration yields:

$$E_2(L) = -\frac{\omega d}{cn(2\omega)} E_1^2(0) \frac{e^{i\Delta kL} - 1}{\Delta k} \tag{14}$$

and the output intensity of the second harmonic is thus proportional to

$$I_2(L) \propto d^2 I_1^2(0) L^2 \frac{\sin^2(\Delta kL/2)}{(\Delta kL/2)^2}. \tag{15}$$

Some simple observations can be made about this result: the amount of generated second harmonic light is proportional to the square of the intensity at the fundamental frequency; the efficiency is proportional to $|\chi^{(2)}|^2$ and to L^2, but also contains a sinc^2 term involving L and Δk. The dependence of the emitted intensity at the harmonic frequency on the propagation distance and phase-mismatch is quite general and does not depend on the particular harmonic order considered. As seen above, passing to higher harmonic orders normally involves a rapidly decreasing value of the nonlinear coefficient d and a different power dependence on the incident intensity I_1, but both the L^2 and the sinc^2 terms remain unchanged and play an important role in the harmonic generation of any order.

Only in the optimal conditions of phase-matching, with $\Delta k = 0$, does the efficiency actually scale quadratically with the medium length, and longer crystals are seen to produce more second harmonic. Note, however, that in these conditions the coupling between the fundamental wave and the second harmonic may become so strong that the depletion of E_1 while it propagates along z has to be taken into account, and some of the assumptions made above are no longer valid. In this so-called depleted-pump regime, a set of coupled equations for the pump field at ω and for the second harmonic field at 2ω has to be solved, and one finds that a complete transfer of the pump energy into the second harmonic field can be achieved.

Phase-matching

In the general case where $\Delta k \neq 0$, the intensity of the second harmonic field generated in a nonlinear crystal varies periodically along the z-axis with a period $2\pi/\Delta k$, and at a propagation distance of

$$L_C = \frac{\pi}{\Delta k} = \frac{\lambda}{4} \frac{1}{n(2\omega) - n(\omega)} \tag{16}$$

it reaches the first maximum, at a peak efficiency inversely proportional to Δk (see Fig. 2).

The physical explanation for this effect is related to the fact that, due to dispersion, the incident wave at frequency ω and the second harmonic wave at 2ω propagate in the medium with different phase velocities ($v_1 = c/n(\omega)$ for the fundamental and $v_2 = c/n(2\omega)$ for the second harmonic). Consequently, the two waves fall out of step with increasing distance in the crystal and the second harmonic waves generated at different places do no longer superpose in phase: after a distance L_C, destructive interference starts developing and it becomes complete, with the full disappearance of the wave at 2ω, at a distance of $2L_C$. L_C is the coherence length for SHG and defines the medium thickness for optimized conversion efficiency under the conditions of $\Delta k \neq 0$. Large Δk values lead to small SHG peak intensities and rapid variations with the distance, so that efficiency is severely limited for crystal lengths longer than L_C.

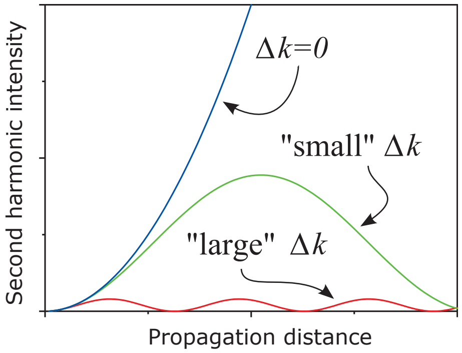

Fig. 2 Intensity of the second harmonic field vs. propagation distance in the nonlinear medium. A quadratic growth is obtained for perfect phase-matching conditions ($\Delta k = 0$), while oscillations of decreasing amplitude and period arise for increasing Δk.

The condition of $\Delta k = 0$ is referred to as the phase-matching condition and is achieved when $n(2\omega) = n(\omega)$. For ordinary waves in a medium with positive dispersion

$$n(2\omega) > n(\omega), \tag{17}$$

so one always gets $\Delta k \neq 0$, unless special conditions are met. In a birefringent material, different polarizations see different refractive indices. "Ordinary" and "extraordinary" refractive indices can be different by up to ~ 0.1 for SHG crystals, so one can satisfy the phase-matching condition by choosing the extraordinary polarization for one wave and the ordinary polarization for the other. For a negative uniaxial crystal ($n_o > n_e$), one can achieve phase-matching at a particular frequency ω if the relation $n_o(\omega) = n_e(2\omega)$ is satisfied (see Fig. 3).

Since the extraordinary index n_e depends on the propagation angle θ with respect to the optical axis of the crystal, one can phase-match the fundamental and second harmonic waves at different ω just by adjusting the angle of incidence on the crystal: the phase-matching condition in this case becomes $n_o(\omega) = n_e(2\omega, \theta_m)$, where θ_m is the so-called phase-matching angle. A geometric representation of this situation is obtained by plotting the refractive index curves for the ordinary and extraordinary waves at the fundamental and second harmonic frequencies (see Fig. 4). In such a representation, the refractive index n_e or n_o for each wave can be found at the crossing of the curves with the k-vector. In the negatively uniaxial crystal case, the point of intersection between the n_o circle at ω with the n_e ellipse at 2ω determines the phase-matching angle θ_m.

Note that in the quantum mechanical view of SHG, two photons of energy $\hbar\omega$ are absorbed during the excitation of the medium to a virtual state, and a single photon with an energy $2\hbar\omega$ is immediately re-emitted when the medium de-excites toward the ground state. In this framework, the phase-matching condition has the simple meaning of photon momentum conservation

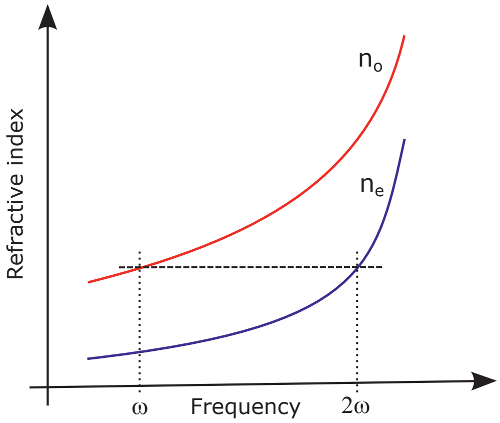

Fig. 3 Phase-matching condition for a negative uniaxial crystal occurring for a particular frequency ω. In reality, the two curves for n_o and n_e represent the maximum and the minimum attainable index of refraction in the crystal, and the whole range in between the two curves can be covered by the extraordinary index n_e by changing the angle between the propagation vector and the optical axis of the medium. So, by choosing the appropriate angle, phase-matching can be obtained for different frequencies.

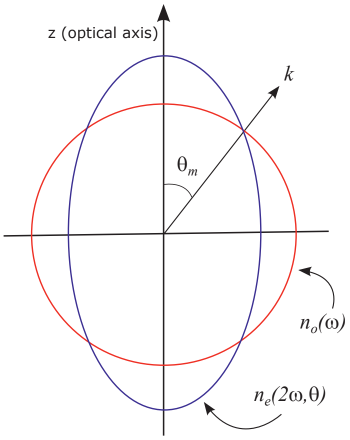

Fig. 4 Geometric construction for the determination of the phase-matching angle θ_m in a negative uniaxial crystal.

$$k_1 + k_1 = k_2 \tag{18}$$

between the initial and the final states of the system.

Although it was discussed in the particular case of SHG, phase-matching is a much more general issue and is always present in all nonlinear optical phenomena where waves at new frequencies are to be generated with the highest possible efficiency. In the most general case of n waves with wave vectors k_i participating in the nonlinear process, one has to make sure that the total photon momentum is conserved in the interaction by satisfying the condition

$$\sum_{i=1}^{n} k_i = 0 \tag{19}$$

Quasi phase-matching

As seen above, when perfect phase-matching is not achieved, the fundamental and second harmonic fields slip out of phase after a propagation distance L_C and the conversion efficiency oscillates without growing monotonically with L^2 as it should do in the case of $\Delta k = 0$ (Fig. 5). A clever solution to improve the conversion efficiency would consist in properly adjusting the phase of the nonlinear polarization after each coherence length (Armstrong et al., 1962). Ideally, one should flip the sign of the nonlinear coefficient (and thus the sign of the polarization) with a periodicity L_C. Under these circumstances, the nonlinear intensity would keep growing monotonically, although less rapidly than in the case of perfect phase-matching, and long interaction lengths could be used to boost the conversion efficiency.

Such a quasi-phase-matching (QPM) condition can be achieved in so-called periodically-poled materials (Hum and Fejer, 2007), generally ferroelectric crystals ($LiNbO_3$ is among the most frequently used) where regions of periodically reversed polarization domains are permanently written by applying strong spatially-shaped static electric fields (Fig. 6).

If technological limitations do not allow one to realize the right spacing between the inverted domains (it is currently difficult to obtain poling periods much smaller than ~5 μm), a higher-order QPM can be obtained by flipping the nonlinear coefficients every 3 (third-order QPM), 5 (fifth-order QPM), or any odd number of coherence lengths. However, the conversion efficiencies in these cases are clearly lower than those achieved with first-order QPM.

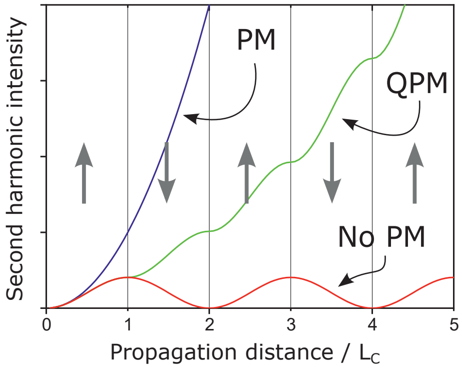

Fig. 5 Intensity of the second harmonic field vs. propagation distance in different phase-matching conditions. For QPM, the sign of the nonlinear coefficient of the crystal is reversed every coherence length L_C in order to get a monotonous increase of the second harmonic intensity. The perfect phase-matched condition (PM) and the mismatched situation (no PM) are also shown.

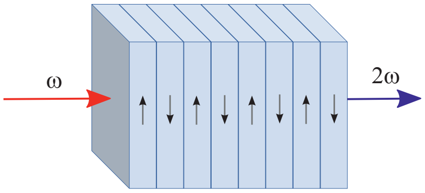

Fig. 6 Schematic of SHG in a periodically poled crystal with several layers of alternately-oriented domains.

High-order harmonic generation

Current amplified pulsed laser systems can routinely reach peak intensities of $\sim 10^{15}$–10^{20} W cm^{-2} and, in these situations, the perturbative approach used above to model the nonlinear response of materials to radiation is no longer adequate. As a matter of fact, at a peak intensity of 3.5×10^{16} W cm^{-2}, the amplitude of the oscillating laser electric field corresponds to the field that binds an electron to the proton in the ground state of a hydrogen atom. The assumption that successive terms of the expansion of medium polarization in powers of the incident field get progressively smaller with the order clearly cannot hold in these conditions.

The most impressive consequence of the breakdown of the perturbative approach is the deviation from the expected exponential decay of the intensity of successive harmonic orders (see Fig. 7). The appearance of a so-called plateau, a region of the spectrum where several harmonics are generated with almost constant efficiency, is the characteristic feature of high-order harmonic generation (HHG) in gases (Ferray et al., 1988; McPherson et al., 1987).

Here, short and intense laser pulses are typically focused in a pulsed gas jet (see Fig. 8) to produce coherent radiation in the extreme ultraviolet (XUV) and soft X-rays, a wavelength range (1–100 nm) where the lack of coherent sources has greatly limited the possibility of spectroscopic investigation, so far.

As a consequence of the isotropy of the gaseous medium, only odd-order harmonics are generated, and one finds that the region of efficient production of high harmonics is limited by a so-called cutoff. The most energetic photons generated in the process possess a cutoff energy E_{cutoff}, which is found to follow the simple law (Krause et al., 1992):

$$E_{cutoff} \approx I_P + 3.2U_P \tag{20}$$

where I_P is the ionization potential of the atoms in the gas jet, and U_P is the ponderomotive energy, which corresponds to the mean kinetic energy acquired by an electron in one cycle of oscillation in the laser field:

$$U_P = \frac{e^2E^2}{4m\omega^2} \tag{21}$$

with e and m the electron charge and mass, respectively, E the amplitude of the laser field, and ω its frequency. It is evident that high laser intensities and high ionization potentials are required in order to reach very short wavelengths. Indeed, rare gas atoms and

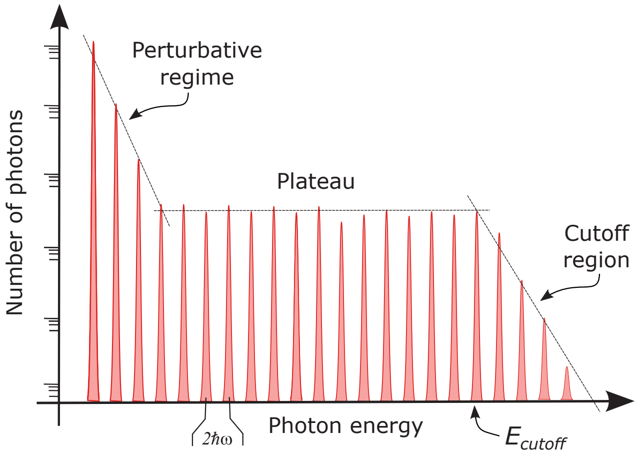

Fig. 7 Schematic view of the typical behavior of high-order harmonic spectra. Only odd-order harmonic photons are generated, with successive harmonics separated by twice the energy of the pump laser photons. The first harmonics follow the predictions of the perturbative approach, with intensities exponentially decreasing with the order. Then, a plateau is formed and extends up to E_{cutoff}.

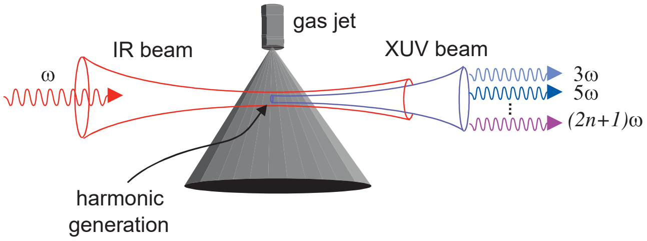

Fig. 8 Typical scheme for HHG in a gas jet.

ultrashort pulses of very high peak intensity are normally used to generate high harmonics. A further advantage of using hard-to-ionize gases and short pulses is given by the requirement that neutral atoms survive long enough to experience the full peak pulse intensity instead of being completely ionized at the leading edge of the pulse itself. If $W(I)$ is the atomic ionization rate and τ_p the pulse duration, then the maximum effective intensity useful to produce harmonic photons is the so-called saturation intensity I_s, approximately given by the relation $W(I_s)\tau_p = 1$. $W(I)$ being a monotonously increasing function of I, higher saturation intensities can be reached with shorter laser pulses and, of course, with light noble gases having higher ionization potentials.

The three-step model

The standard picture of the HHG process can be easily visualized from a semiclassical perspective in a single-atom approach (Corkum, 1993): in every half optical cycle of the laser pulse, electrons undergo tunnel ionization through the potential barrier formed by the atomic potential and by the electric field potential of the laser itself; after being accelerated in the ionization continuum by the field, they may come back to the ion core and recombine to emit harmonic photons that release the accumulated kinetic and ionization energy (see Fig. 9).

Some of the most relevant features of harmonic radiation can be simply obtained by using this single-atom picture and solving the classical equations of motion for an electron, freed with zero velocity at different moments in an oscillating electric field. Depending on the phase of the field at the moment of ionization, the electron can either escape from the parent ion or oscillate in the field and come back to the original position after a fraction of the optical period T. Only electrons ionized within $T/4$ after each field maximum contribute to the harmonic emission by recombining with the ion and converting their kinetic and potential energy into photons (see Fig. 10).

The experimentally found cutoff law can be simply obtained by noting that the maximum return kinetic energy (brought back by electrons that escape slightly after each field maximum every half optical cycle) corresponds to $\sim 3.17U_p$ (see Fig. 11). For the generation of harmonics with photon energies below the cutoff limit, there are always two different trajectories (corresponding to two different release times within each half cycle) that the electron can follow in the continuum, such that it returns to the ion core with the correct energy. These two trajectories, although giving rise to photons with the same energy, may correspond to quite different permanence times of the electrons under the influence of the laser field, and some of the spatial and temporal characteristics (phase-matching relations, defocusing, and frequency modulation) of the emitted harmonic radiation will thus be strongly affected (Gaarde et al., 1999; Bellini et al., 1998).

Harmonic emission during a single pump pulse is thus seen to be composed of a train of XUV photon bunches, essentially released twice every optical cycle of the laser field. This temporal structure translates into the characteristic spectral structure of high-order harmonics, with peaks corresponding to the odd orders, separated by twice the laser frequency.

The semiclassical model also offers a simple explanation for other experimentally observed characteristics of harmonic radiation. A linear polarization of the laser is needed to make sure that the electron oscillating in the field may "hit" the ion and recombine with it when it comes back after the oscillation in the continuum; experiments have shown that just a small degree of ellipticity is sufficient to

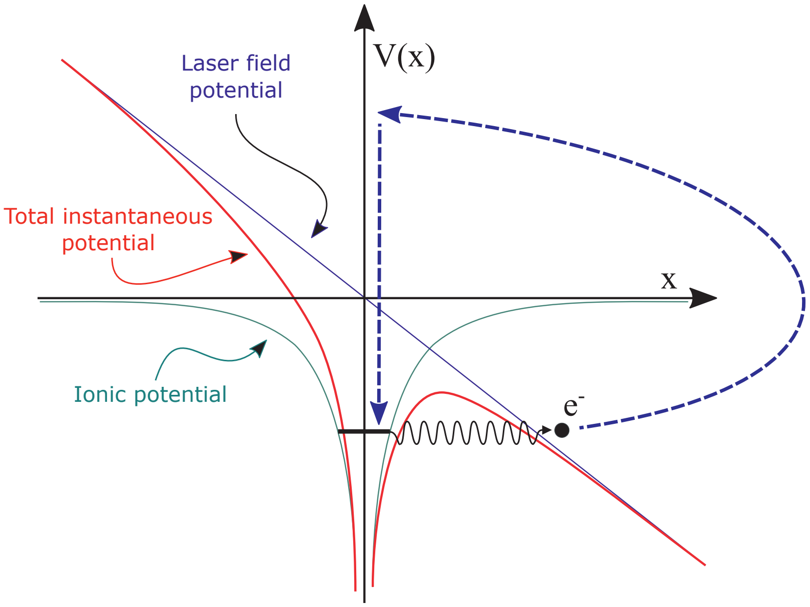

Fig. 9 The three-step model for HHG. Electrons are first tunnel-ionized by the intense laser field, then they are accelerated during an optical cycle and finally recombine with the parent ion, thus releasing the accumulated kinetic energy in the form of harmonic photons.

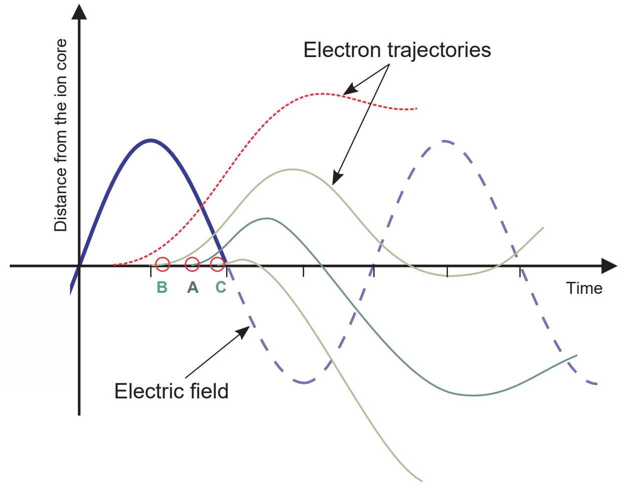

Fig. 10 Schematic representation of the main electron trajectories involved in the HHG process (only the first half optical cycle is considered for simplicity, but things repeat with a *T*/2 periodicity). Electrons that are ionized when the absolute value of laser field amplitude is growing, just escape from the ion and do not contribute to the process, while electrons released after the peak can come back to the core position and recombine to emit harmonic photons. Electrons ionized in *A* return with the maximum kinetic energy (related to the slope of the trajectory as it crosses the horizontal axis) and generate the most energetic photons in the cutoff region. Electrons released in *B* and *C* follow different trajectories in the continuum but return with the same kinetic energy (same slope at axis crossing), thus both contribute to the generation of the same harmonic.

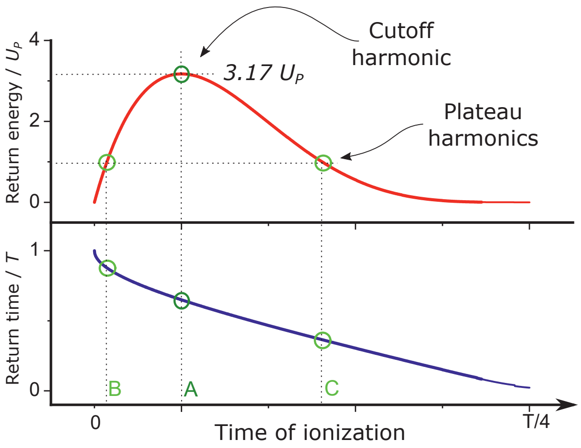

Fig. 11 Upper curve: plot of the return kinetic energy for electrons ionized at different times during the optical cycle. The origin of the time axis is fixed at the peak of the field amplitude for each half optical cycle. A single trajectory, corresponding to electrons emitted in *A*, is responsible for the emission of a cutoff harmonic, while two distinct trajectories (originating in *B* and *C*) contribute to the generation of a harmonic in the plateau. Lower curve: time (here indicated as the "return time") that the electrons spend oscillating in the continuum before re-combining with the ion. Plateau harmonics mainly come from two classes of electrons with distinct return times.

completely inhibit the generation of harmonics. It is also clear that, although the expressions for E_{cutoff} and U_p seem to favor long-wavelength pump pulses for the generation of high harmonics, actually, the longer time that it takes for the electron to return to the ion (proportional to the pump laser wavelength) implies a significant spreading of the electron wave packet during its oscillation and a final lower overlap with the ion wave function, which in turns causes the probability of recombination to decrease.

Phase-matching in high-order harmonic generation

The three-step model is an excellent way to understand the single-atom response of the gas medium to the intense electric fields of the laser. However, when the global response of the system is considered, propagation effects have to be included (Balcou et al., 1999). Phase-matching is again an essential condition for the efficient generation of high-order harmonics to take place. In this case, the fundamental and the harmonic field can fall out of phase for several reasons: besides the usual dispersion in the neutral gaseous medium (which may, however, contain both linear and nonlinear contributions, due to the high intensities involved), the geometrical dephasing due to the focusing of the Gaussian laser beam can introduce an additional phase shift, as well as the dispersion introduced by the generated free electrons, and the so-called dipole-phase variation. In order to achieve a sufficiently high conversion efficiency, the phase shift between the polarization of the qth harmonic and the generated harmonic field has to be kept as constant as possible over all the interaction region.

As for the dispersion by the neutral medium, the corresponding phase shift on a propagation distance z has the usual form

$$\Delta\phi_{ND} = \frac{2\pi qz}{\lambda}\,[n(q\omega) - n(\omega)] \tag{22}$$

and the refraction indices at the two frequencies clearly depend both on the gas density in the jet and on the fraction of neutral atoms left after the partial ionization by the laser pulse. The dispersion caused by free electrons produced in the interaction becomes important as soon as the intensity approaches the saturation intensity I_s and has to be accounted for by introducing the index of refraction

$$n_{el}(\omega) = \sqrt{1 - \frac{\omega_P^2}{\omega^2}} \tag{23}$$

where ω_P is the so-called plasma frequency, which is related to the local free-electron density n_e as

$$\omega_P = \sqrt{\frac{n_e e^2}{m\varepsilon_0}}. \tag{24}$$

The corresponding phase shift is thus approximately given by

$$\Delta\phi_{el} \approx \frac{z\omega_P^2}{2cq\omega}\left(q^2 - 1\right) \tag{25}$$

The on-axis phase shift across the focus of a Gaussian beam is $\phi(z) = \tan^{(-1)}(2z/b)$, where b is the laser confocal parameter. The phase shift due to this geometrical effect is then

$$\Delta\phi_G = (1 - q)\tan^{-1}(2z/b) \tag{26}$$

Finally, one finds that the laser-induced polarization has an intrinsic intensity-dependent phase that arises from the phase of the wave function of the electrons generating a particular harmonic. The two main electronic trajectories contributing to the dipole moment of a given plateau harmonic induce a phase that is proportional to the intensity of the driving laser field, and to the amount of time the electron has spent in the continuum (Gaarde et al., 1999; Corsi et al., 2006). For each trajectory (labeled by j), this leads to an intensity-dependent variation of the phase

$$\Delta\phi_{D,j} = -\alpha_j I(z,t) \tag{27}$$

summing up to a total dipole phase:

$$\Delta\phi_D = \sum_j \Delta\phi_{D,j}. \tag{28}$$

All these contributions to the phase slip between the induced polarization and the generated harmonic field combine to give a total phase mismatch

$$\Delta\phi = \Delta\phi_{ND} + \Delta\phi_{el} + \Delta\phi_G + \Delta\phi_D \tag{29}$$

that should not vary too much across the medium length. Unfortunately, most of the above terms have a complicated dependence on the detailed spatio-temporal dynamics of the atom—laser interaction, and the task of keeping $\Delta\phi$ fixed is normally a very difficult one, unless special simplifications can be made in order to neglect one or more of the contributions to the total phase-mismatch. Using collimated laser beams or propagation in hollow fibers can null the geometrical phase shift, whereas keeping a low ionization level can eliminate the free-electron contribution to dispersion. When the experimental conditions are achieved so that positive and negative terms partially cancel out in the expression for $\Delta\phi$, a strong enhancement in the conversion efficiency of a particular high-order harmonic can be obtained.

Recently, it has been shown that quasi phase-matching can be achieved also in the generation of high-order harmonics. A periodic modulation in the diameter of the hollow fibers (Gibson et al., 2003; Paul et al., 2003) or in the gas density (Pirri et al., 2008) in the interaction region where harmonics are produced have proved effective in strongly and selectively enhancing the yield of particular harmonic orders.

Conclusion

In this chapter, I concisely introduced some of the main concepts illustrating the conversion of the electromagnetic field frequency by means of harmonic generation. I briefly outlined the underlying physical mechanisms governing this phenomenon and gave some specific examples for the generation of the second harmonic and for the other extreme condition of high-order harmonics. Harmonic generation techniques, relying on the nonlinear response of matter (from natural crystals to artificial photonic structures and gas jets) to intense light, date back to the early days of the laser era and have since revolutionized the way we produce coherent light for applications in spectral regions that currently extend from the microwaves to the X-rays.

References

Armstrong JA, Bloembergen N, Ducuing J, and Pershan PS (1962) Interactions between light waves in a nonlinear dielectric. *Physics Review* 127: 1918–1939.

Balcou P, Dederichs AS, Gaarde MB, and L'Huillier A (1999) Quantum-path analysis and phase matching of high-order harmonic generation and highorder frequency mixing processes in strong laser fields. *Journal of Physics B: Atomic, Molecular and Optical Physics* 32: 2973–2989.

Bellini M, Lyngå C, Tozzi A, Gaarde MB, Hansch TW, and L'Huillier A (1998) Temporal coherence of ultrashort high-order harmonic pulses. *Physical Review Letters* 81: 4.

Boyd RW (2019) *Nonlinear Optics*, 4 edn. Academic Press is an imprint of Elsevier: San Diego.

Corkum PB (1993) Plasma perspective on strong field multiphoton ionization. *Physical Review Letters* 71: 1994–1997.

Corsi C, Pirri A, Sali E, Tortora A, and Bellini M (2006) Direct interferometric measurement of the atomic dipole phase in high-order harmonic generation. *Physical Review Letters* 97: 023901.

Ferray M, L'Huillier A, Li XF, Lompre LA, Mainfray G, and Manus C (1988) Multiple-harmonic conversion of 1064 nm radiation in rare gases. *Journal of Physics B: Atomic, Molecular and Optical Physics* 21: L31–L35.

Franken PA, Hill AE, Peters CW, and Weinreich G (1961) Generation of optical harmonics. *Physical Review Letters* 7: 118–119.

Gaarde MB, Salin F, Constant E, Balcou P, Schafer KJ, Kulander KC, and L'Huillier A (1999) Spatiotemporal separation of high harmonic radiation into two quantum path components. *Physical Review A* 59: 1367–1373.

Gibson EA, Paul A, Wagner N, Tobey R, Gaudiosi D, Backus S, Christov IP, Aquila A, Gullikson EM, Attwood DT, Murnane MM, and Kapteyn HC (2003) Coherent soft X-ray generation in the water window with quasi-phase matching. *Science* 302: 95–98.

Hum DS and Fejer MM (2007) Quasi-phasematching. *Comptes Rendus Physique* 8: 180–198.

Krause JL, Schafer KJ, and Kulander KC (1992) High-order harmonic generation from atoms and ions in the high intensity regime. *Physical Review Letters* 68: 3535–3538.

McPherson A, Gibson G, Jara H, Johann U, Luk TS, McIntyre IA, Boyer K, and Rhodes CK (1987) Studies of multiphoton production of vacuum-ultraviolet radiation in the rare gases. *Journal of the Optical Society of America B: Optical Physics* 4: 595–601.

Paul A, Bartels RA, Tobey R, Green H, Weiman S, Christov IP, Murnane MM, Kapteyn HC, and Backus S (2003) Quasi-phase-matched generation of coherent extreme-ultraviolet light. *Nature* 421: 51–54.

Pirri A, Corsi C, and Bellini M (2008) Enhancing the yield of high-order harmonics with an array of gas jets. *Physical Review A* 78: 011801.

Shen YR (2003) *The Principles of Nonlinear Optics*. Wiley Classics Library edn Hoboken, NJ: Wiley-Interscience.

Valence photoemission[☆]

G Margaritondo, Ecole Polytechnique Fédérale de Lausanne, (EPFL), Lausanne, Switzerland

© 2024 Elsevier Ltd. All rights reserved.

This is an update of G. Margaritondo, Valence Photoemission, Editor(s): Franco Bassani, Gerald L. Liedl, Peter Wyder, Encyclopedia of Condensed Matter Physics, Elsevier, 2005, Pages 279–286, ISBN 9780123694010, https://doi.org/10.1016/B0-12-369401-9/00682-3.

Introduction 257
The information content 258
Photoemission with synchrotron sources 259
Techniques requiring high-brightness synchrotron sources 262
Valence photoemission of correlated systems 262
Conclusion 264
References 264

Abstract

The basic features of this family of techniques are discussed, beginning with its historical development. Angle-resolved (band mapping) and angle-integrated techniques are analyzed as well as a series of experimental approaches requiring powerful photon sources such as undulators at synchrotrons or free electron lasers. Such techniques include photon polarization spectroscopy, experiments with variable photon energy, photoemission resonances and techniques affected by low signal levels such as time-resolved photoemission, two-photon photoemission, spectromicroscopy and spin-polarized photoemission. Finally, high-resolution photoemission studies of superconductors and of other highly correlated systems are briefly discussed.

Key points

- The photoelectric effect
- Information content of photoemission spectroscopy
- Role of synchrotron sources
- High brightness: special techniques
- Correlated systems

Introduction

The photoelectric effect (Hertz, 1887) is the basis of some of the most powerful techniques for analyzing the electronic structure of condensed-matter systems. These are the approaches collectively called “photoemission spectroscopy” (Cardona and Ley, 1978–1979; Hufner, 2003, 2010; Lynch and Olson, 1999; Prince, 2003; Rabalais, 1977; Van Howe and Schattke, 2003; Margaritondo, 2023; De Padova, 2023; Margaritondo, 2005).

Even before the development of such techniques, the photoelectric effect had a fundamental (and often not correctly understood) impact on the development of modern science. The main milestones after Hertz’s result were the discovery of the electron (Thompson’s, 1897), Einstein’s hypothesis on the photon (Einstein, 1905), and Millikan’s (reluctant) experimental validation of Einstein’s hypothesis (Millikan, 1918).

Einstein derived the photon hypothesis with a purely thermodynamic argument and used it to predict the frequency threshold in the photoelectric effect, which was not experimentally verified until the late 1910s. The photoelectric effect contributed in this way to the experimental foundations of quantum physics. This was of course a very significant element in the development of modern physics.

The next scientific impact of the photoelectric effect was its practical use in spectroscopy, which came almost 40 years later. The reason for this long delay is the confinement of the photoelectric effect to the region near the surface of the photoelectron-emitting solid. In order to become a photoelectron, the electron must absorb a photon and increase its energy above the photoelectric threshold, i.e., the energy barrier that keeps it in the solid. Since the threshold is of the order of several eV’s, the photon must be in the x-ray or ultraviolet spectral range. Photons of these energies can penetrate quite deep in the solid before being absorbed.

However, the electrons excited by absorbing them can travel only over a very short distance before losing energy. As a consequence, photoelectrons originate only from a very thin slab near the surface of the sample. And they carry information on the electronic structure of that slab, which includes a very few atomic planes.

[☆] *Change History*: November 2022. G Margaritondo updated the chapter. All sections and figures were updated.

If the surface is contaminated, the information reflects the properties of the solids mixed with those of the contaminant. To avoid this problem, a clean surface can be obtained by several different methods such as cleaving, scraping, and in situ growth. However, the surface does not stay clean for a reasonable time unless it is kept under ultrahigh vacuum (pressure $< 10^{-9}$ Pa). This kind of vacuum could not be routinely achieved before the 1960s: this explains the long delay in the practical use of the photoelectric effect for photoemission spectroscopy.

After solving the contamination problem, photoemission spectroscopy initiated a strong and steady expansion. This growth was accelerated in the late 1960s by the advent of synchrotron radiation sources (Hwu and Margaritondo, 2021; Margaritondo, 1988, 2003). With their help, photoemission became a leading tool for probing the electronic structure of solids and of condensed systems in general.

The information content

Solid-state photoemission explores the electronic states inside the specimen. An electron quantum state $|\boldsymbol{k}>$ in a crystalline solid is defined, according to the Bloch theorem, by the "crystal momentum" k-vector $\boldsymbol{k}$. This vector cannot be directly measured if the electron is inside the solid: only indirect information can be obtained, for example from optical experiments.

After an electron becomes a free photoelectron in vacuum, its state $|\boldsymbol{k_o}>$ can be measured. In fact, the magnitude of the k-vector $\boldsymbol{k}_o$ is given by the free-photoelectron (kinetic) energy K: $|\boldsymbol{k}_o| = (2m_oK)^{1/2}2\pi/h$ (where m_o is the electron mass). And the direction of $\boldsymbol{k}_o$ is that of the free photoelectron motion.

From the measured properties of $|\boldsymbol{k_o}>$ one can derive those of the initial state $|\boldsymbol{k}>$ inside the solid. The main steps are the following. One must measure K with a suitable energy analyzer. And one must also determine the direction of $\boldsymbol{k}_o$ by using an analyzer with angular resolution. Finally, one must connect the measured information on $|\boldsymbol{k_o}>$ to the properties of $|\boldsymbol{k}>$: this is not an easy task.

In fact, the connection is determined by the photoemission process, which is a complex combination of different phenomena interfering with each other. Historically, the task was conceptually simplified (Puff, 1964; Berglund and Spicer, 1964) by considering the overall process as the combination of different *independent* steps: excitation of the electron from the state $|\boldsymbol{k}>$ upon absorption of a photon, transfer of the excited electron to the surface and then emission in vacuum.

This simplified vision created the conceptual background of modern photoemission spectroscopy, whose strategy is schematically illustrated by Fig. 1: photons of a specific energy $h\nu$ are used to bombard the ultraclean surface of the solid under investigation and to transform electrons in the quantum state $|\boldsymbol{k}>$ into photoelectrons. The photoelectrons are collected and their flux per unit time is measured as a function of the kinetic energy K. This approach can be used to study both core electrons and valence electrons: our present discussion, however, is limited to the latter case.

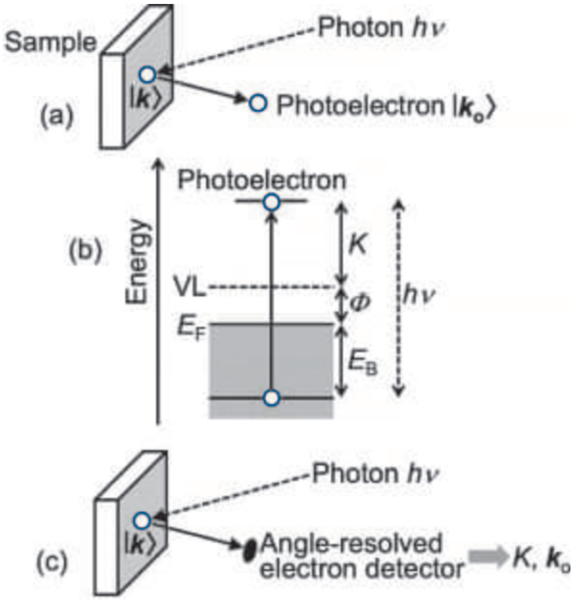

Fig. 1 (A) The photoelectric effect, the foundation of photoemission spectroscopy. (B) The kinetic energy K of a photoelectron is determined according to Eq. (1) by the photon energy $h\nu$, by the work function Φ and by the initial energy of the electron in the solid or binding energy E_B; VL is the vacuum level; and E_F is the Fermi level. (C) In angle-resolved photoemission, photoelectrons are collected selecting their direction of emission. This determines not only the energy of the photoelectron but all the properties of its k-vector $\boldsymbol{k}_o$. Reproduced from Margaritondo G (2005) Encyclopedia of Condensed Matter Physics, 1st edn. Amsterdam: Elsevier, 279–286.

In the early stage of the history of photoemission spectroscopy, the experiments collected photoelectrons without selecting their direction. This is no longer true today, when the technique of preference is "angle-resolved photoelectron spectroscopy" or ARPES.

Fig. 1B illustrates the essential features of the photoelectron energy analysis in the case of a metallic solid, with electrons distributed in energy up to the "Fermi level" E_F. The zero of the photoelectron kinetic energy is called the "vacuum level" (VL): this is the minimum energy required for an electron to leave the solid. The distance between VL and E_F is the "work function," Φ. The kinetic energy K of a photoelectron is given by Einstein's equation (Einstein, 1905):

$$K = h\nu - E_B - \Phi, \tag{1}$$

where E_B, the energy distance between the electron in the solid and E_F, is called the "binding energy."

Eq. (1) shows that by measuring K and knowing Φ and $h\nu$ one can extract the initial energy of the electron, E_B. This is the first information about the initial state $|\boldsymbol{k}>$ of the electron in the solid.

Consider now angle-resolved photoemission (Fig. 1C), which measures the photoelectron direction completing the information on the final state $|\boldsymbol{k_o}>$. How can this be connected to the initial state $|\boldsymbol{k}>$? Eq. (1) provides the answer for the energy. But the answer for the direction is not immediate.

In particular, the passage from the solid to vacuum changes the k-vector component perpendicular to the surface. One must thus estimate this change. Several clever schemes were developed to solve this problem.

The situation is simplified when the system under investigation has a two-dimensional (or one-dimensional) character – for example, it is a layered solid or a crystal surface. In that case, only the parallel component of $\boldsymbol{k}$ matters, which (in most cases) is equal to the parallel component of $\boldsymbol{k}_o$.

Angle-resolved photoemission experiments can thus experimentally determine both the electron energy E_B and its momentum vector $\boldsymbol{k}$. Thus, they probe the 3-dimensional $E_B(\boldsymbol{k})$ function in different directions. For crystalline solids, this function is the so-called "band structure."

Using angle-resolved photoemission to derive $E_B(\boldsymbol{k})$ is known as "band mapping." Fig. 2 shows an example of band mapping, including the raw photoemission data and a portion of the corresponding derived $E_B(\boldsymbol{k})$ function.

As mentioned, in the early and most elementary version of photoelectron spectroscopy photoelectrons were detected without selecting their direction, i.e., using an electron energy analyzer with a large detection area that mixed together a broad range of directions. This was practically unavoidable when the signal level was too low for angle-resolved photoemission. Furthermore, angular scrambling automatically occurs for polycrystalline samples and, to some extent, for sample surfaces cleaned by scraping.

In all these cases, plots of the photoelectron distribution in energy (energy distribution curves or EDC's) reproduce the electron "density of states," in the solid. This information is valuable to test the theoretical results on the electronic structure – but is of course reduced with respect to angle-resolved photoemission.

Photoemission with synchrotron sources

So far, we only mentioned photoemission experiments performed as a function of the electron energy and direction. However, several other parameters can be controlled during a valence-electron photoemission experiment, enhancing the extracted information. These parameters notably include the energy, polarization and direction of incidence of the photon, as well as the photoelectron spin polarization.

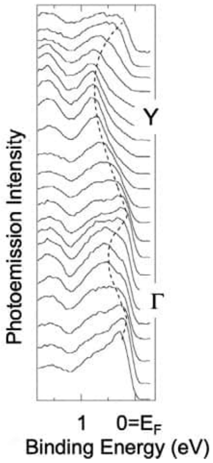

Fig. 2 An example of the band-mapping technique (Zwick et al., 1998): Angle-resolved photoemission spectra for the material TTF-TCNQ. Note the dispersing peak in the *low-binding energy region.* Reproduced with permission from Zwick F, Jérome D, Margaritondo G, Onellion M, Voit J and Grioni M (1998) *Physical Review Letters* 81: 2974–2977, © 1998 APS.

Controlling the above parameters requires a suitably high signal level, i.e., a high flux of photoelectrons. In turn, this corresponds to a high intensity of the photon beam. In modern photoemission, this is achieved using as photon sources synchrotrons of free electron lasers (Hwu and Margaritondo, 2021), which offer superior flux and brightness. This is particularly important in techniques with chronically low signal levels such as spin-polarized photoemission.

Furthermore, synchrotron sources emit polarized photons. And they also offer the possibility to "tune" the photon energy within the x-ray and ultraviolet range required for photoemission.

The photon polarization can be directly exploited to probe the symmetry of the valence electronic states. The theoretical background of this approach is the following. We have seen that the emission of photoelectrons requires excitation by photon absorption. For a given initial electronic state, the excitation may or may not be allowed depending on the symmetry of the initial and final electron state as well as on the photon polarization (and direction). Therefore, the symmetry of the initial electronic state can be identified by carefully analyzing the photon polarization dependence of the photoemission spectra.

In essence, the analysis is similar to that of (ultraviolet or x-ray) optical absorption spectra. Since the excited electron is in a high-energy, free-electron-like state, the photon polarization effects are mostly determined by the symmetry of the initial state. And can indeed be used to identify it. Fig. 3 shows an early example of this simple and powerful approach.

Interesting photoemission experiments are also performed using the circular polarization of special synchrotron sources such as the "helical wigglers." These experiments provide very valuable information, notably about magnetic systems.

Using the conceptual separation of the photoemission process in independent steps, one can also understand its dependence on the photon energy. The photoelectron emission is determined by the excitation probability for the first step, which in turn is determined by the corresponding Fermi's optical "matrix element." The matrix element depends both on the initial state and on the final state of the excitation.

When analyzing a given initial state with energy E_B, different photon energies correspond to different final states and, therefore, to different matrix element values. This influences the intensity of the spectral features. Such "matrix element effects" can significantly modify the photoemission spectra, producing in some cases spurious and potentially misleading features.

As a general rule, when the electrons are optically excited to high energies by high-energy photons, their states become free-electron-like and the matrix element effects are negligible. However, most valence-electron photoemission experiments are conducted with low photon energies (15–30 eV) and are not immune from such effects. Indeed, the use of low *hν*'s is preferable since by lowering *hν* the transition probability tends to increase leading to higher signal levels. Furthermore, for a constant resolving power $h\nu/\Delta h\nu$ of the photon source, the absolute photon energy resolution $\Delta h\nu$ becomes better for smaller *hν*'s.

As a consequence, matrix element effects must be considered in the data analysis. To avoid mistakes, one must take photoemission spectra at several different photon energies and compare the results.

This requires a photon source with tunable photon energy, that is, a synchrotron source. Specifically, a synchrotron source based on a "bending magnet" emits a broad band of *hν*'s, from which the desired photon energies can be filtered with a monochromator.

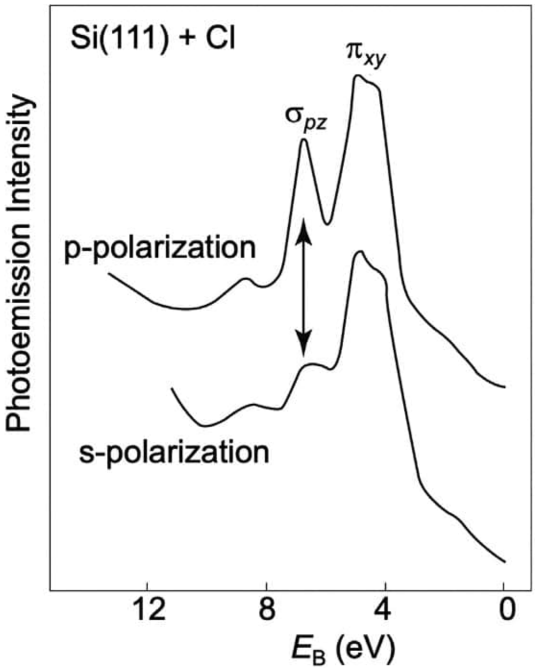

Fig. 3 Photon polarization effects in the (angle-integrated) photoemission spectra of a cleaved Si(111) surface covered by chemisorbed chlorine. Note the strong decrease of the feature at $E_B = 6–7$ eV as the photon polarization changes from p to s. By analyzing the data in terms of the optical excitation induced by photon absorption, the symmetry of the initial electronic state corresponding to this feature was identified as σ_{pz}. (Schluter et al., 1976). Reproduced with permission from Schluter M, Rowe JE, Margaritondo G, Ho KM, and Cohen ML (1976) *Physical Review Letters* 37: 1632–1635, © 1976 APS.

An "undulator" source provides a narrow band of photon energies centered at a tunable value; however, further monochromatization is required for photoemission experiments.

In addition to the identification of matrix element effects, the control of the photon energy provided by synchrotron sources opens up many other experimental opportunities. Consider, for example, the surface sensitivity of photoemission experiments. We have mentioned that photoelectrons are only emitted from a thin slab near the sample surface. The thickness of this slab, called "escape depth," changes with the photoelectron kinetic energy K (see Fig. 4), which in turn depends (Eq. 1) on the photon energy.

Therefore, by changing the photon energy and therefore K one can increase or decrease the surface sensitivity. Roughly speaking, experiments with K-values higher than 100 eV or lower than 50 eV tend to be less surface-sensitive than experiments with K-values ranging between 50 and 100 eV. Thius is useful to distinguish surface effects from bulk effects.

The photon energy tunability is also helpful in identifying the symmetry of the initial electronic states in the solid. Matrix element effects can, in fact, be exploited for "labeling" such states. This is a rather complex task. But it can be strongly simplified by the presence of "photoemission resonances."

Such resonances are very rapid and strong variations of the intensity of certain photoemission features when the photon energy is changed. A resonance typically occurs for photon energies near a core-level absorption threshold of a given element and affects valence states related to the same element. Therefore, a resonating photoemission feature can be immediately attributed to the corresponding element. Fig. 5 shows an example of this powerful approach.

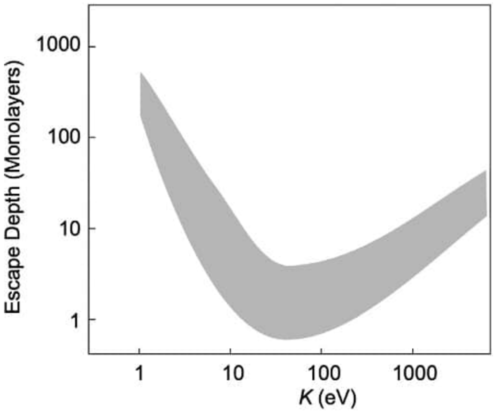

Fig. 4 The escape depth of photoelectrons plotted as a function of the kinetic energy is slightly different from material to material. For all samples, however, the depth falls in the shaded area and exhibit a minimum (corresponding to the maximum surface sensitivity of photoemission experiments) at $K = 50$–100 eV. Reproduced from Margaritondo G (2005) Encyclopedia of Condensed Matter Physics, 1st edn. Amsterdam: Elsevier, 279–286.

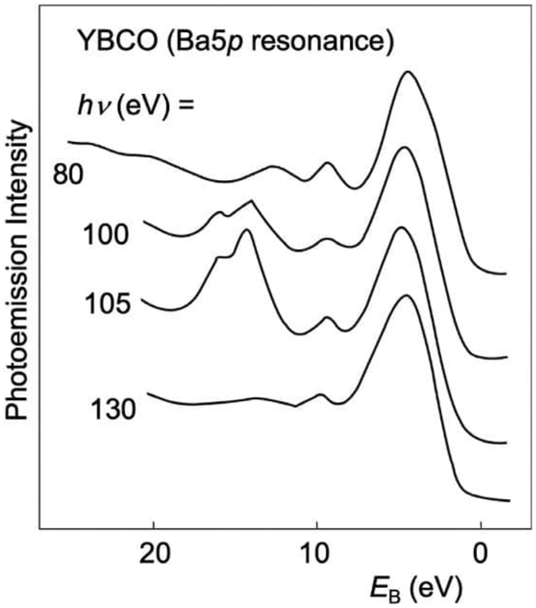

Fig. 5 Photoemission spectra for the YBCO high-temperature superconductor reveal a resonating feature at $E_B = 14$–18 eV when the photon energy varies near the Ba5p absorption edge. This photoemission resonance immediately identifies the feature as due to Ba-related electronic states (Onellion et al., 1987). Reproduced with permission from Onellion M, Chang Y, Niles DW, Joynt R, Margaritondo G, Stoffel G, and Tarascon JM (1987) Physical Review B 36: 819–821, © 1987 APS.

The tunability of synchrotron sources is also exploited in specialized photoemission techniques in which the photon energy is continuously changed rather than kept constant. One should note, in particular, G. J. Lapeyre's constant initial state (CIS) technique, in which both $h\nu$ and the kinetic energy K of the photoelectron are scanned while keeping constant their difference. According to Eq. (1), this implies that $E_B = h\nu - K - \Phi$ stays constant. Therefore, the detected photoemission intensity reflects the properties of the final states of the excitation rather than those of the initial state. This technique can thus be used to explore final (empty) valence states.

Techniques requiring high-brightness synchrotron sources

We already mentioned the importance of the very high flux and brightness of synchrotron sources for techniques with intrinsically low signal levels. Consider, for example, the difficulties in achieving high lateral resolution in a photoemission experiment. In general, the experiments are performed without lateral resolution: the detector collects photoelectrons from a rather large sample area in order to reach a reasonable signal level. This implies that the investigated electronic structure is averaged over the same area. In the case of inhomogeneous samples, the averaging could lead to misleading results.

High lateral resolution is therefore desirable, transforming "photoemission spectroscopy" into "photoemission spectromicroscopy." The corresponding decrease in signal level, however, must be compensated by using a high-brightness synchrotron source, such as an undulator.

The same requirement is present for time-resolved photoemission. In a standard photoemission experiment, the signal is accumulated over a certain period of time to reach an acceptable signal-to-noise ratio. This is of the order of several seconds per data point and of several minutes per spectrum, impeding studies of time-dependent phenomena over a shorter time scale.

The great interest of such phenomena triggered a substantial effort – based again on high-brightness sources – to decrease the data-taking time. The most spectacular results are now achieved with short laser pulses. The required photon energies for photoemission are obtained by multiplying the photon energy of low-$h\nu$ ultrashort laser pulses with nonlinear optical devices. In recent years, however, high-$h\nu$ pulses were directly delivered by ultraviolet and x-ray free electron lasers.

Ultrashort photon pulses can be used to directly excite photoelectrons. Another possible approach, called "two-photon photoemission," consists of using a low- $h\nu$ laser pulse to bring valence electrons into an excited state and then to use a high-$h\nu$ pulse to extract them as photoelectrons, as shown in Fig. 6. This approach is used to study the dynamic properties of excited states. Techniques in this class can reach the picosecond or sub-picosecond time range. Their impact is currently enhanced by the use of free electron lasers.

Spin-polarized photoemission is another valence-electron technique that is chronically affected by low signal levels. Experiments discriminating the spin polarization of the photoelectrons require special detectors with typically limited effectiveness. These difficulties notwithstanding, spin-polarized photoemission has evolved to become one of the most important subfields in this domain, providing extremely valuable information, for example on the valence states of magnetic systems.

Valence photoemission of correlated systems

The discovery of high-temperature superconductors and many subsequent experimental and theoretical results increased the need of experimental probes to study electron correlation. Photoemission was able to play a crucial role, primarily because of a substantial increase in its energy resolution.

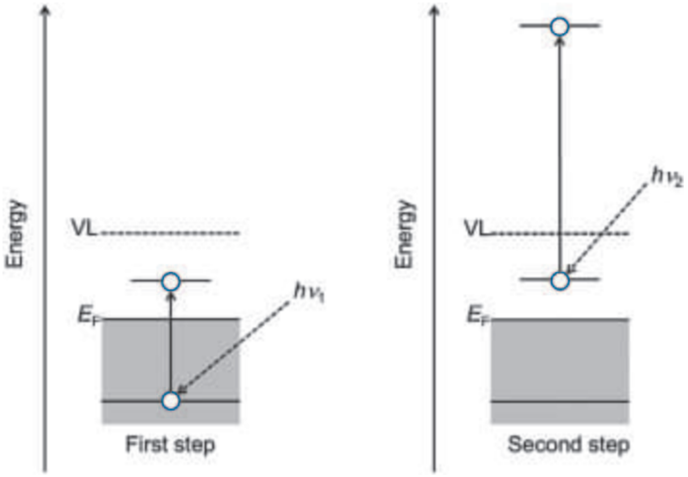

Fig. 6 Schematic illustration of a two-step photoemission process involving a low-energy laser photon ($h\nu_1$) that brings a valence electron into an excited state and a synchrotron (or free electron laser) high-energy photon ($h\nu_2$) to extract it as a photoelectron. Reproduced from Margaritondo G (2005) Encyclopedia of Condensed Matter Physics, 1st edn. Amsterdam: Elsevier, 279–286.

Roughly speaking, phenomena related to the formation of chemical bonds affect valence electrons within 10–20 eV of the Fermi level. Except in specialized cases, their study with photoemission techniques does not require an energy resolution better than ≈100 meV.

On the contrary, correlation phenomena occur on a smaller energy scale. A typical example is provided by the superconducting gap, which even for high-temperature superconductors does not typically exceed a few tens of meV. The study of such phenomena requires energy resolutions beyond 50 meV – and in some cases of 1–2 meV or better.

Experimental systems capable of achieving these performances were developed and used to explore superconductors as well as other correlated systems. Fig. 7A shows a typical result of these experiments: the opening of the superconducting gap during the phase transition of the high-temperature superconductor bismuth strontium copper oxide (BCSCO).

Note the high-energy edge in the normal-state spectrum, corresponding to the Fermi level. In the superconducting state, the edge recedes revealing the opening of the superconducting gap. Furthermore, the spectrum exhibits other interesting features – such as the strong quasiparticle peak immediately below the gap and the subsequent "dip'" - that have generated much interest.

Fig. 7B shows another example of the valuable information that can be extracted with high-resolution photoemission. Superconducting-state spectra taken along different directions reveal different values of the gap, ruling out theoretical models that predict isotropy.

Correlated systems can sometimes exhibit rather "exotic" phenomena departing from the standard frameworks of solid-state physics. This framework is Landau's "Fermi liquid," in which the free electrons of a Fermi gas are replaced by dressed quasiparticles with electron-like properties. The soundness of this theoretical foundation is evident in most photoemission results: for example, the spectrum of metallic samples (Fig. 8; Perfetti, 2002) typically exhibits a Fermi-level cutoff reflecting the edge of the Fermi–Dirac distribution.

However, high-resolution photoemission experiments on low-dimensional systems sometime reveal phenomena departing from the Fermi-liquid framework. Fig. 8, for example, also includes photoemission spectra of one-dimensional materials that, although metallic, do not exhibit a Fermi-edge cutoff.

Experiments in this domain explore alternate theoretical frameworks that could replace the Fermi liquid in highly correlated low-dimensional systems, such as the "Luttinger liquid." Such frameworks lead to exotic notions, such as the replacement of the holes of the Fermi liquids with spin-carrying "spinons" and charge-carrying "holons."

Correlation affects not only the initial state but the entire photoemission process. The simplest approach to analyze photoemission results treats the electrons (or the Fermi-liquid quasiparticles) as a gas of independent particles. The emitted photoelectrons are thus also treated as isolated entities.

This is not really correct, in particular for correlated systems: the photoemission process should be rigorously treated as the transition from a many-body correlated state to another many-body state plus a free electron. This, of course, complicates the theoretical treatment, but also enhances the quality and quantity of information that can be extracted from photoelectrons.

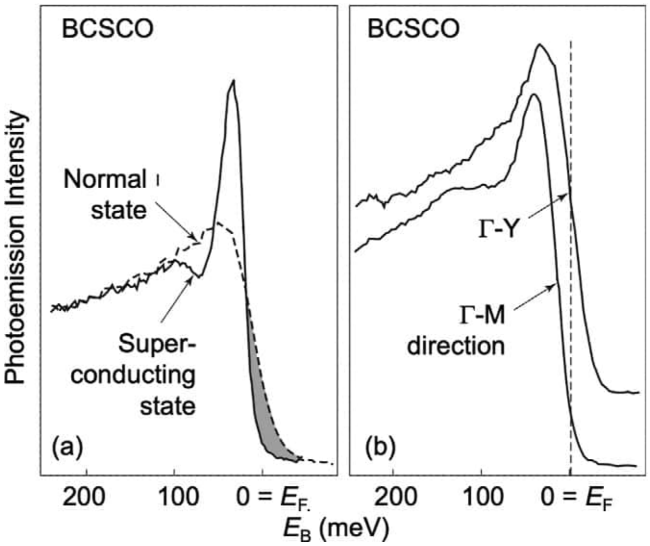

Fig. 7 (A) High-resolution photoemission spectra taken on the high-temperature superconductor BCSCO at temperatures corresponding to the normal and superconducting state reveal the opening of the superconducting gap (shaded area) (Hwu et al., 1991). (B) Superconducting-state spectra taken for the same compound along different crystallographic directions reveal the anisotropy of the superconducting gap (Kelley et al., 1994). (A) Reproduced with permission from Hwu Y, Lozzi L, Marsi M, La Rosa S, Winokur M, Davis P, Onellion M, Berger H, Gozzo F, Lévy F, and Margaritondo G (1991) *Physics Review Letters* 67: 2573–2577, © 1991 APS. (B) Reproduced with permission from Kelley RJ, Ma J, Quitmann C, Margaritondo G, and Onellion M (1994) *Physical Review B* 50: 590–593, © 1994 APS.

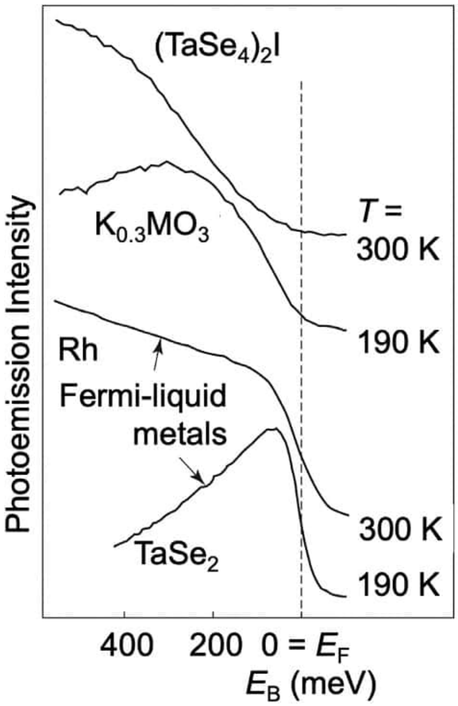

Fig. 8 Bottom: photoemission spectra of three-dimensional and two-dimensional metals exhibit a clear edge at the Fermi level, as predicted for Fermi liquids. Top: one-dimensional metals sometimes depart from this framework. Reproduced from Perfetti L (2002) Ph.D. thesis, EPFL: Lausanne.

Conclusion

Forty years after the development of the theoretical background for the photoelectric effect, the advent of ultrahigh-vacuum techniques solved the problem of surface contamination and opened the door to the leading role of photoemission techniques as probes of valence electrons in solids. In their simplest versions, such techniques explored the properties of the electronic states in the specimen, specifically the density of states with angle-averaged photoemission and the band structure of crystalline solids with angle-resolved photoemission.

The advent of synchrotron sources and, more recently, of free electron lasers boosted the capabilities of valence photoemission beyond this limited domain. His led to a variety of novel approaches including spin-polarized photoemission, time-resolved photoemission, spectromicroscopy, constant initial state (CIS) spectroscopy, the study of photoemission resonances and others.

After the discovery of high-temperature superconductors, high-energy resolution photoemission started to explore phenomena beyond the Fermi-liquid framework. This was made possible by a concentrated and successful effort to improve the energy resolution. The results most notably included the detection and analysis of the high-temperature superconducting gap, in particular its spatial asymmetry.

References

Berglund CN and Spicer WE (1964) *Physics Review* 136: A1030–A1044.
Cardona M and Ley L (eds.) (1978–1979) *Photoemission in Solids*. Heidelberg: Springer. 2 volumes.
De Padova P (2023) *Encyclopedia of Condensed Matter Physics*, 2nd edn, Oxford: Elsevier. Chapter 00313.
Einstein A (1905) *Ann. Phys.* 17: 132–148.
Hertz H (1887) *Ann. Phys.* 2267: 983–1000.
Hufner S (2003) *Photoelectron Spectroscopy: Principles and Applications*, 3rd edn, Heidelberg: Springer.
Hufner S (2010) *Very High Resolution Photoelectron Spectroscopy*. Heidelberg: Springer.
Hwu Y and Margaritondo G (2021) *Journal of Synchrotron Radiation* 28: 1014–1029.
Hwu Y, Lozzi L, Marsi M, La Rosa S, Winokur M, Davis P, Onellion M, Berger H, Gozzo F, Lévy F, and Margaritondo G (1991) Electronic spectrum of the high-temperature superconducting state. *Physics Review Letters* 67: 2573–2577.
Kelley RJ, Ma J, Quitmann C, Margaritondo G, and Onellion M (1994) *Physical Review* B50: 590–593.
Lynch DW and Olson CG (1999) *Photoemission Studies of High Temperature Superconductors*. Cambridge: Cambridge University Press.
Margaritondo G (1988) *Introduction to Synchrotron Radiation*. New York: Oxford University Press.
Margaritondo G (2003) *Elements of Synchrotron Radiation for Chemistry, Biology and Medical Research*. New York: Oxford University Press.
Margaritondo G (2005) *Encyclopedia of Condensed Matter Physics*, 1st edn. Amsterdam: Elsevier, pp. 279–286.
Margaritondo G (2023) *Encyclopedia of Condensed Matter Physics*, 2nd edn Oxford: Elsevier. Chapter 00394.
Millikan RA (1918) *Physics Review* 7: 355–390.

Onellion M, Chang Y, Niles DW, Joynt R, Margaritondo G, Stoffel NG, and Tarascon JM (1987) *Physical Review* B36: 819.

Perfetti L (2002) *Angle Resolved Photoelectron Spectroscopy on Strongly Correlated Electron-Phonon Systems, Ph.D. Thesis*. Lausanne: EPFL.

Prince KC (2003) *Photoelectron Spectroscopy of Solid Surfaces*. Singapore: World Scientific.

Puff H (1964) *Physica Status Solidi* 4: 125–138.

Rabalais JW (1977) *Principles of Ultraviolet Photoelectron Spectroscopy*. Hoboken: Wiley.

Schluter M, Rowe JE, Margaritondo G, Ho KM, and Cohen ML (1976) *Physical Review Letters* 37: 1632–1635.

Thompson JJ (1897) *Philosophical Magazine* 44: 293–316.

Van Howe MA and Schattke WM (eds.) (2003) *Solid-State Photoemission and Related Methods: Principles and Practices*. Hoboken: Wiley.

Zwick F, Jérome D, Margaritondo G, Onellion M, Voit J, and Grioni M (1998) *Physical Review Letters* 81: 2974–2977.

Spectroscopy: Impedance spectroscopy and mobility spectra[☆]

Rosario A Gerhardt, Georgia Institute of Technology, Atlanta, GA, United States

© 2024 Elsevier Ltd. All rights reserved.

This is an update of R.A. Gerhardt, Impedance Spectroscopy and Mobility Spectra, Editor(s): Franco Bassani, Gerald L. Liedl, Peter Wyder, Encyclopedia of Condensed Matter Physics, Elsevier, 2005, Pages 350–363, ISBN 9780123694010, https://doi.org/10.1016/B0-12-369401-9/00685-9.

Introduction 269
Equivalent circuits 269
Time constants and frequency dependence 271
Temperature dependence and conductivity curves 271
Multiple parallel processes appearing on the impedance plane 274
Microscopic interpretation 276
Polarization mechanisms 276
Relaxation and resonance frequency spectra 279
The Debye relaxation 279
Cole-Cole, Davidson-Cole and Havriliak-Negami relaxations 280
Various representations of the dielectric function 281
Multiplane analysis of several multiple process combinations 282
Temperature dependence 282
Data analysis 293
Electromagnetic simulation software 293
Recent advances (what to expect in the future) 295
Conclusion 295
Multimedia 296
Acknowledgments 296
References 296

Abstract

This article describes impedance spectroscopy and its relationship to dielectric properties (IS/DS). Impedance spectroscopy is generally interpreted in terms of equivalent circuits that can represent different electrical paths present in a material or device. Details about the simplest equivalent circuit models that can be used to interpret results is presented as well as suggestions on how to maximize the information that one can obtain from the ac measurements. IS/DS is often used to determine the conductivity of many materials and devices and therefore it is important to be able to separate effects caused by surface phenomena from bulk processes.

[☆] *Change History*: August 2022. RA Gerhardt updated the article has been substantially revised and only a few of the original images are included. And have referenced the original article published in 2005 multiple times.

https://doi.org/10.1016/B978-0-323-90800-9.00021-4

Graphical Abstract

(A) Real and Imaginary impedance and complex plot for an RC circuit, (B) Real and Imaginary impedance for an RL circuit, (C) Complex impedance plots for two parallel RC circuits in series where the capacitors are three orders of magnitude apart and the resistances vary as shown, (D) Complex impedance, complex permittivity, real and imaginary permittivity for a material with four different resistivity values and the same relaxation ratio.

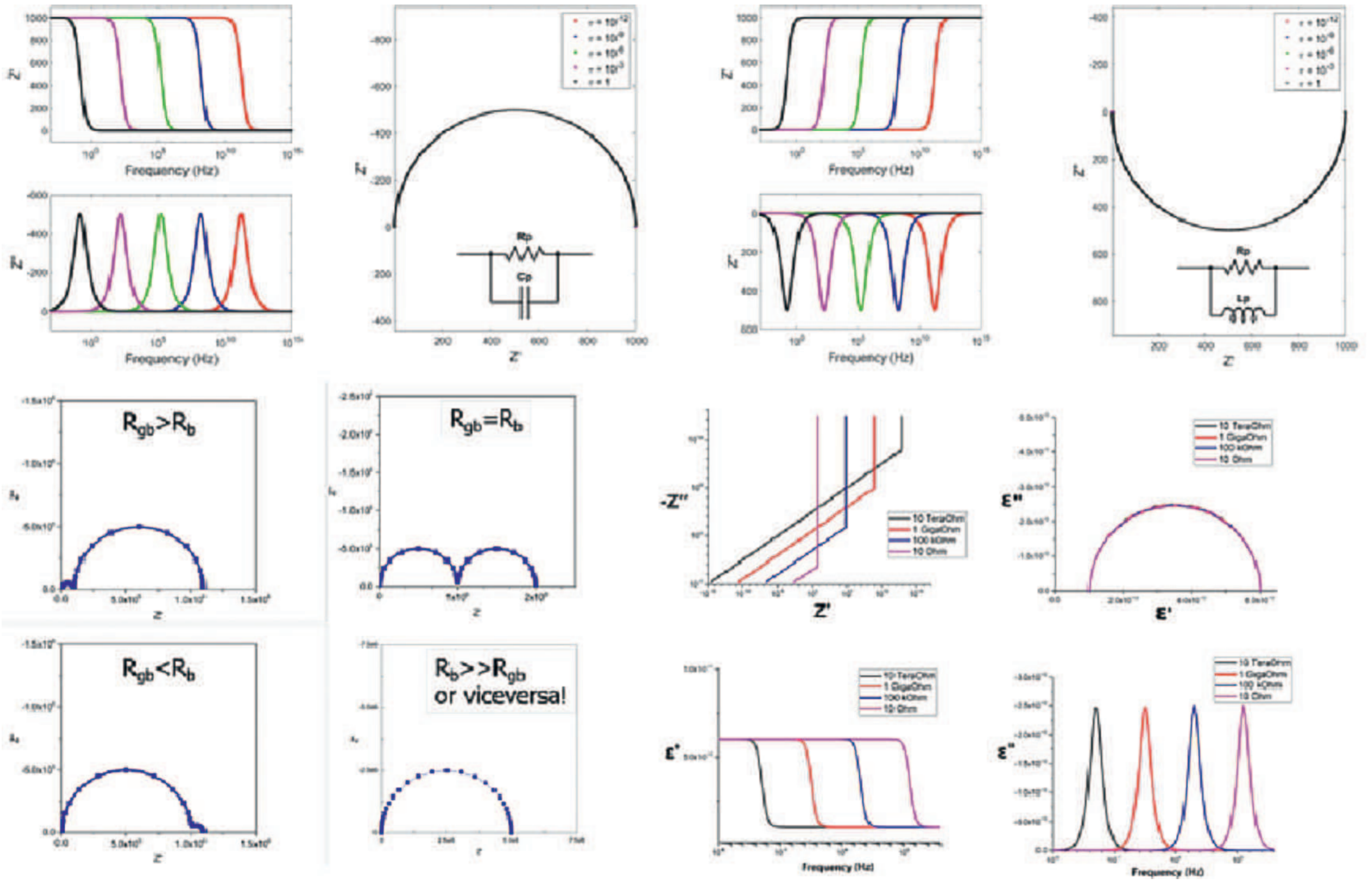

Glossary

Cole-Cole plots This is the name given to plots of imaginary permittivity vs. real permittivity (mostly ε'' vs. ε') which can also be labeled as complex permittivity plots or frequency explicit plots. The original name came from a publication by Cole and Cole (1942) that described excursions from an ideal Debye relaxation behavior which result in complex ε^* with the center of the semicircle origin sitting $\alpha\pi/2$ below the x-axis.
Frequency explicit plots Often referred to as Bode plots where one plots the real or imaginary component of a given function versus the frequency on a log scale.
IS/DS This is the combined approach of analyzing impedance spectra in terms of both impedance spectroscopy and dielectric spectroscopy.
Multiplane analysis In order to capture all of the phenomena that may be present in a material or device, it is necessary to conduct multiplane analysis to ensure that all processes are detected. Multiplane analysis refers to obtaining fitted data in terms of impedance, admittance, permittivity and electric modulus simultaneously. Data fitting using only impedance plane can often miss details only revealed by the other functions.
Negative dielectric constant All materials can undergo polarization of different charged species under the application of an ac field. Negative dielectric constant is mostly observed in conducting materials such as metals and highly conducting semiconductors, metamaterials and piezoelectrics. See some examples that are given in the text.
Nyquist plots This is the name given to plots of the imaginary vs real component (mostly Z'' vs. Z') which can also be labeled as complex impedance plots or frequency implicit plots.
Quadrants Since impedance and dielectric properties consist of real and imaginary parts, it is possible for the properties to carry a sign. By convention, parallel RC circuits are displayed in the 1st quadrant making sure to label the y-axis with a negative sign. In contrast, parallel RL circuits show up in the 4th quadrant where both the real and imaginary components are both positive.
Relaxation ratio This is the ratio that relates the low frequency permittivity to the high frequency permittivity that can help monitor the effect of the presence of a dipolar relaxation or a molecular relaxation in a Debye type process (Cao and Gerhardt, 1990) and its transformation to long range conductivity (Gerhardt, 1994). The relaxation ratio r can be written as $r = C_2/C_1 = \varepsilon_{s/}\varepsilon_{\infty}$. It is different from $\Delta\varepsilon = \varepsilon_s - \varepsilon_{\infty.}$
Space-charge behavior Space charge behavior may occur at any interface in a given material or device. The most common space charge phenomena refer to electrode contact space charge behavior caused by ohmic or non-ohmic Schottky type interfaces. Space charge type interfaces may also appear in multilayer films, polycrystalline materials, at the filler-matrix interfaces in polymer and ceramic composites as well as in semiconductors and metamaterials.
Time constant This is a number which is characteristic of a given electrical/optical/magnetic process that gives rise to a relaxation or resonance and can be obtained via equivalent circuit data fitting or knowledge of the expected complex resistivity, complex dielectric properties (including index of refraction) or complex magnetic properties. See simulations in the supplementary for some examples.

Key points

(1) Background on impedance spectroscopy.
(2) Complex impedance and frequency dependent real and imaginary impedance.
(3) Parallel and series equivalent circuits and their time constants.
(4) Relationships between impedance and electrical conductivity.
(5) Temperature dependence of electrical conductivity in materials.
(6) Relationships between impedance and dielectric permittivity and other dielectric functions (admittance, electric modulus)
(7) Polarization; microscopic source of frequency dependence.
(8) Debye relaxation model and the Debye time constant.
(9) Cole-Cole, Davidson-Cole and Havriliak-Negami Dielectric Models.
(10) Resonance behavior observed.
(11) How to distinguish multiple processes present by conducting multiplane analysis.
  - A Debye type relaxation as a function of relaxation ratio.
  - A Debye process accompanied by a parallel leakage.
  - A simple conducting process represented by a parallel RC circuit.
  - A simple conducting process represented by a parallel RL circuit.
  - A solid state ionic material with different response at the grain boundaries than within the bulk grains.
  - A semiconducting material with space charge polarization at the electrode/material interface.
  - A highly conducting nanomaterial or device.
  - Bulk and interfacial responses in multiphase systems.

Introduction

Impedance Spectroscopy is a technique that has seen revolutionary changes in the last 50 years as a result of the development of computer automation, swift data analysis, design of better frequency response analyzers and the ability to acquire data over many different frequency ranges (Gerhardt, 2005; Gerhardt, 2022). Most commercially available equipment today can collect real and imaginary impedance data from frequencies as low as a few microHerz and as high as a few GHz. Due to the large variance in material resistivities (e.g., $\rho > 10^{12}$ Ω-cm for insulators and $< 10^{-3}$ Ω-cm for semiconductors), different manufacturers specialize in the characterization of specific material types and the equipment specifications can vary widely.

Impedance spectroscopy, also referred to as IS/DS because of its close relationship to dielectric spectroscopy (Gerhardt, 1994), involves the measurement of the current (I), voltage (V) and phase angle (θ) over a wide frequency range so that the impedance vector (Z^*) may be defined as follows:

$$Z^*(\omega) = V(\omega)/I(\omega) \tag{1}$$

where $V(\omega) = V_m \sin(\omega t)$, $I(\omega) = I_m \sin(\omega t + \theta)$, $\omega = 2\pi f$, f is the linear frequency and θ is the phase difference between the current and the voltage.

Measurements can also be carried out in the time domain and then Fourier transformed into the frequency domain (Macdonald, 1987). Each measurement mode has advantages and disadvantages. The frequency domain is ideally suited for determining the steady state response of the object under test whereas the time domain is better suited for detecting time-dependent phenomena. This article will focus on frequency domain measurements.

Equivalent circuits

It is customary to analyze the measured impedance response in terms of the possible equivalent circuit components that can give rise to the frequency response observed. The circuit elements of interest are capacitors, represented by C, resistors, represented by R, and inductors, represented by L. Most dielectric materials can be represented by a parallel RC circuit, whereas others are better represented by a series RC circuit. The presence of magnetic components introduces inductive elements, and one may expect that series or parallel RL circuits may represent such materials (Gerhardt, 2005).

It is useful to remember that if elements are in series, it is easier to write the impedance response. On the other hand, if the circuit elements are in parallel, it is more convenient to write the admittance and then convert it to the impedance. For example, the impedance of a series RC circuit is written as:

$$Z^* = R + [1/j\omega C] \tag{2}$$

whereas the impedance of a parallel RC circuit is given by:

$$Z^* = 1/Y^* \tag{3}$$

where $Y^* = (1/R) + j\omega C$.

Most modern equipment includes some version of software that can be used to fit the most appropriate equivalent circuit to the experimentally measured results. However, the reader is urged to consider the physical mechanisms that may have contributed to the experimental data before concluding that a derived R or C is representative of the bulk of the material or device being measured (See section on data analysis below for more details).

Table 1 lists the simplest equivalent circuits and their corresponding impedance equations (modified from Gerhardt, 2005). Data acquired can be plotted in terms of frequency explicit and frequency implicit impedance plots. The frequency implicit plots are better known as complex plots because the imaginary impedance is plotted versus the real impedance. These plots are often referred to as Nyquist plots or Cole-Cole plots and result in the formation of semicircles only under certain conditions. Table 1 also displays complex plots for each of the simplest equivalent circuits listed and are drawn with imaginary impedance in the first quadrant where Z'' is negative as shown. Note that not all circuits display semicircles and when they do they can appear in any of the four quadrants (more about this later). Frequency explicit plots are often referred to as Bode plots. They are just simply real (Z') or imaginary impedance (Z'') plotted versus frequency. The magnitude of the impedance vector, which is equal to.

$$|Z^*| = \left[Z'^2 + Z''^2\right]^{1/2} \tag{4}$$

and the phase angle θ are also plotted versus the measured frequency. The magnitude of the impedance vector is useful for quickly assessing the presence of resistive components (flat with frequency), capacitive components (decrease with increasing frequency) and inductive components (increase with increasing frequency) (Gerhardt, 2013). See Fig. 1A for representative frequency explicit plots for a perfect resistor, a perfect capacitor and a perfect inductor as well as the corresponding phase angle vs frequency shown in Fig. 1B (modified from Gerhardt, 2022). Phase angles are zero for resistors, −90 degrees for capacitors and +90 degrees for inductors and should follow the same designation of the four quadrants.

Table 1 Equivalent circuits for selected circuits with impedance equations and complex plots.

Resistor	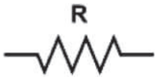	$Z^* = R$	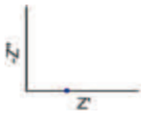
Capacitor	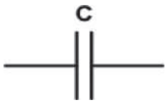	$Z^* = 1/j\omega C$	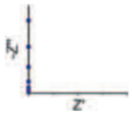
Inductor	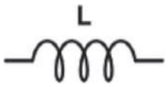	$Z^* = j\omega L$	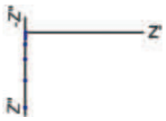
RC parallel	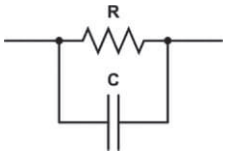	$Z^* = 1/\ (1/R + j\omega C)$	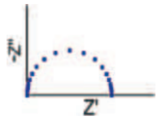
RC series	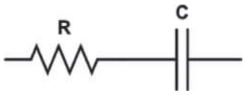	$Z^* = R + (1/j\omega C)$	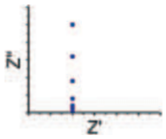
RL parallel	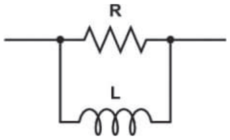	$Z^* = 1/(1/R + 1/j\omega L)$	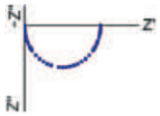
RL series	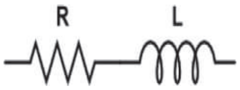	$Z^* = R + j\omega L$	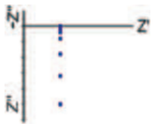
LC series	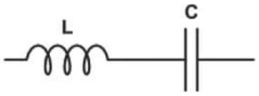	$Z^* = j\omega L + 1/j\omega C$	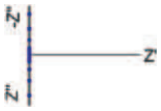
LC parallel	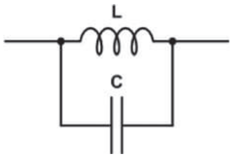	$Z^* = 1/(1/j\omega L + j\omega C)$	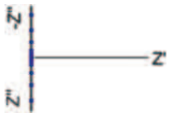
LCR series	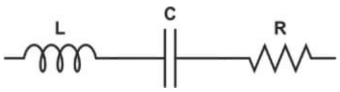	$Z^* = \omega L+(1/j\omega C) + R$	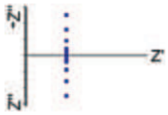

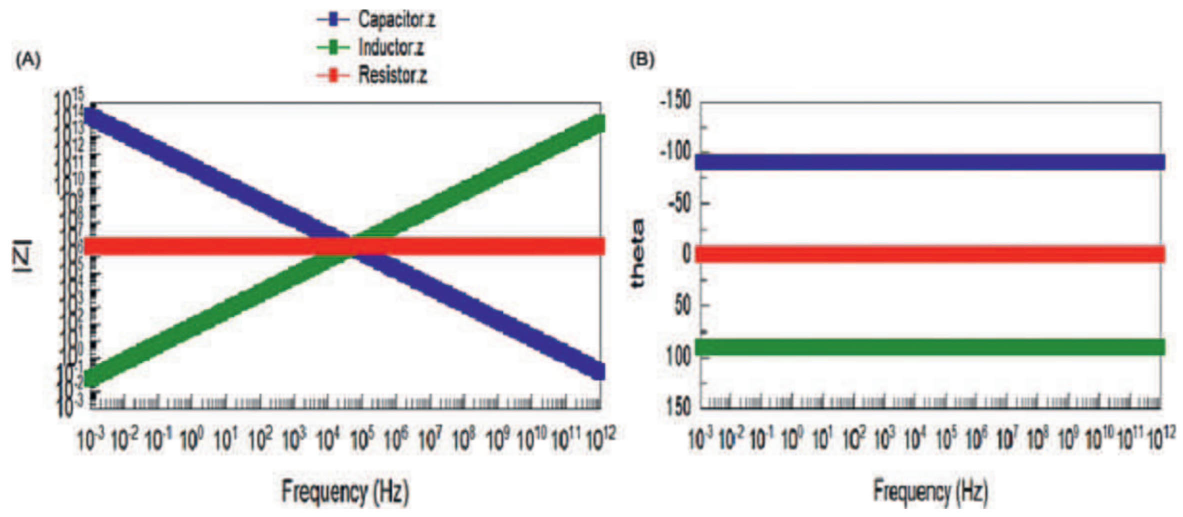

Fig. 1 (A) Representative impedance magnitude response. (B) Representative impedance phase angle plotted response for a perfect resistor, a perfect capacitor, and a perfect inductor as a function of frequency. Modified from Gerhardt RA (2022) What is impedance and dielectric spectroscopy? *IEEE Instrumentation and Measurement Magazine*, 14–20.

Time constants and frequency dependence

In reality one will never experimentally observe single circuit elements by themselves but instead they will appear in combination with other circuit elements as depicted in Table 1. One of the most important concepts one needs to understand is that parallel RC and parallel RL circuits will always show a semicircle in the complex impedance plane when their time constants $\tau = R_pC_p$ or L_p/R_p allow it to appear within the frequency range of the measurements. By established convention, a parallel RC circuit will display a semicircle in the first quadrant if the imaginary Z'' axis is labeled as negative. In contrast, a parallel RL circuit will display an upside down semicircle in the fourth quadrant (Gerhardt, 2005). Fig. 2 displays the Nyquist plots once again and the corresponding real and imaginary impedance plotted vs log frequency (f) highlighting the parallel RC and parallel RL time constants, where the apex of the semicircle is equal to $\omega\tau =$, $\omega = 2\pi f_p$, and f_p is the frequency where a peak will appear in the imaginary impedance. In contrast, series RC and series RL circuits will never show a semicircle in the complex impedance plane (as shown in Table 1 and described by Gerhardt, 2005). Instead, they will show a semicircle in the complex admittance plane with time constants $\tau = R_sC_s$ or L_s/R_s for the series RC circuit and the series RL circuit respectively.

Fig. 3 displays the complex impedance, complex admittance as well as the real and imaginary admittance plotted versus log frequency for the series RC, series RL and series RLC circuits. The RLC circuit shows both capacitive and inductive behavior as in the series RC and series RL circuit. As a result, the imaginary part of the RC and RL circuits will carry opposite signs as shown in Fig. 3C, F and I. Additionally, the RLC circuit does have an additional time constant associated with the LC combination which is equal to $\tau_{LC} = 1/(LC)^{1/2}$ which provides the frequency where the transition from the series RC or RL occurs (not shown because LC circuits do not result in semicircles) (Gerhardt, to be published).

Temperature dependence and conductivity curves

A generalized equation for conductivity (σ) for all types of materials (Schaffer et al., 1999; Buchanan, 2004) relates the number of charge carriers (N) to their charge (q) and their mobility (μ) as in

$$\sigma = \sum_{i=1}^{n} (N_i|qi|\mu_i) \tag{5}$$

where i refers to the i^{th} charge carrier. Since conductivity is inversely proportional to resistivity, we often use the value of resistance R obtained through impedance or admittance measurements to calculate the conductivity by incorporating the geometrical dimensions of the sample (Bauerle, 1969). Note that impedance and admittance do not always represent the same physical mechanism as will be described in more detail later. More often, the activation energy for conduction, in a given system, is obtained by taking the intercept of the impedance or admittance semicircle with the real axis, as displayed in Figs. 2A and 3B, as a function of temperature and then converting that to conductivity and plotting the calculated conductivity versus inverse temperature (for semiconductors and insulators or resistivity vs. T for metallic conductors). Either type of analysis is only accurate when the resistance and capacitance of the electrical processes being measured are both independent of frequency. A truly bulk response will always have constant R and C at a given temperature. This is not the case for space charge polarization under biasing conditions or diffusion controlled processes. In both of these cases, the number of mobile charge carriers will change the values of R and may also affect the value of C.

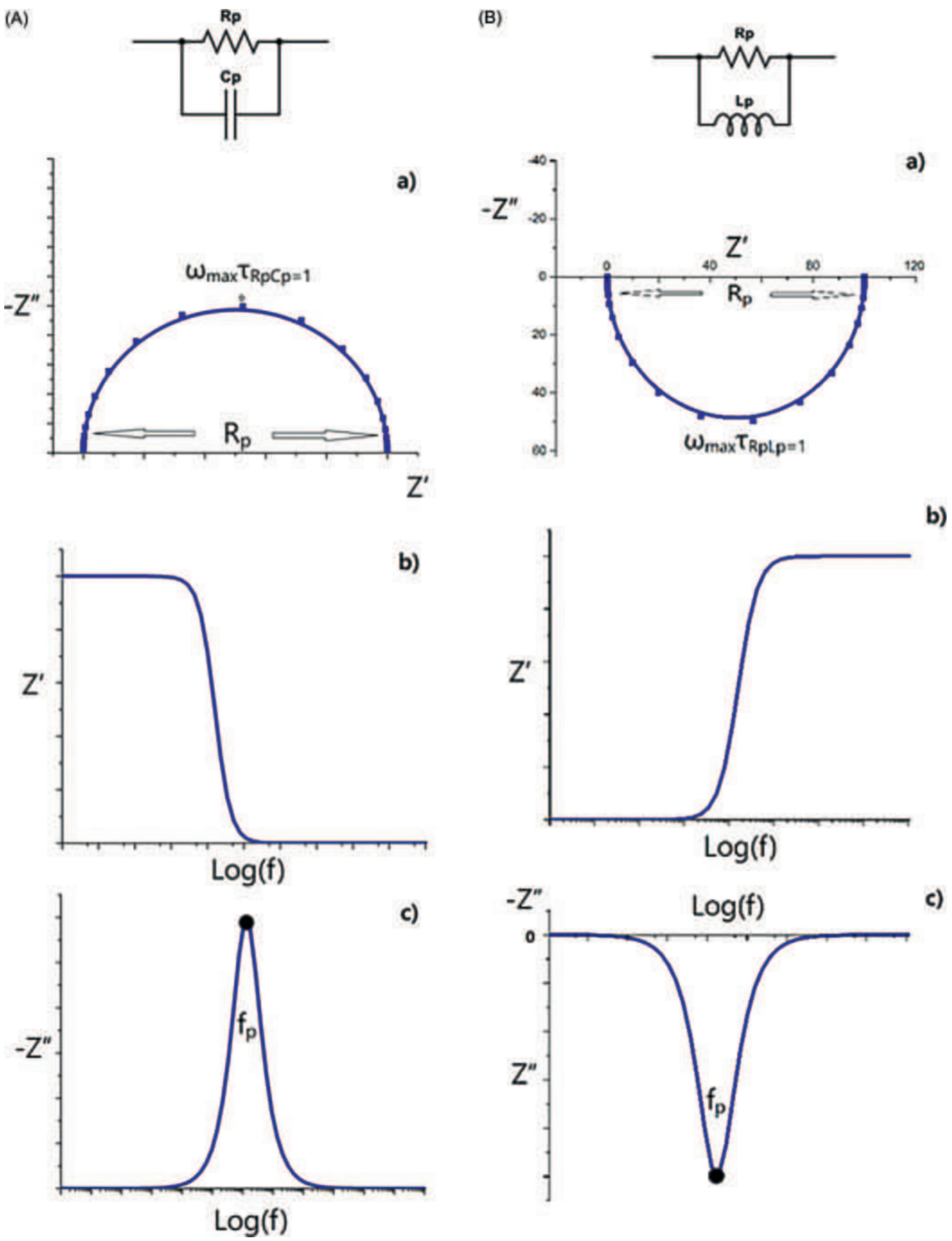

Fig. 2 Representative complex impedance, real impedance and imaginary impedance for (A) a parallel RC circuit, (B) a series RC circuit.

Furthermore, many materials and devices contain more than one electrical path and one cannot immediately assign the intercept of the semicircle on the impedance plane as given in Figs. 2 and 3 to the bulk behavior one is seeking to obtain. It is necessary to determine if the process giving rise to such semicircles is truly due to the bulk of the material by obtaining the geometric capacitance/inductance using the time constant formalisms given in the previous section. Additionally, one needs to conduct 4-probe dc measurements to ensure that the values obtained refer to the dc conductivity (Wang and Nowick, 1980) of the phase of interest and not to contact effects with the electrode or grain boundary phases in the material.

In the absence of impurities or other factors that could affect the measured conductivity, the temperature dependence is given by the temperature dependencies listed in Table 2 (compiled from Schaffer et al., 1999, Buchanan, 2004). For metallic materials, it is customary to use the resistivity ρ (T) at a given temperature in terms of the coefficient of resistivity α at a reference temperature T_0 with the reference resistivity ρ_0. The conductivity of semiconductors is related to the size of the band gap (E_g) and the conductivity of insulators can depend on the diffusivity D_{ion} of the ionic species that dominates the process which may control the transport of

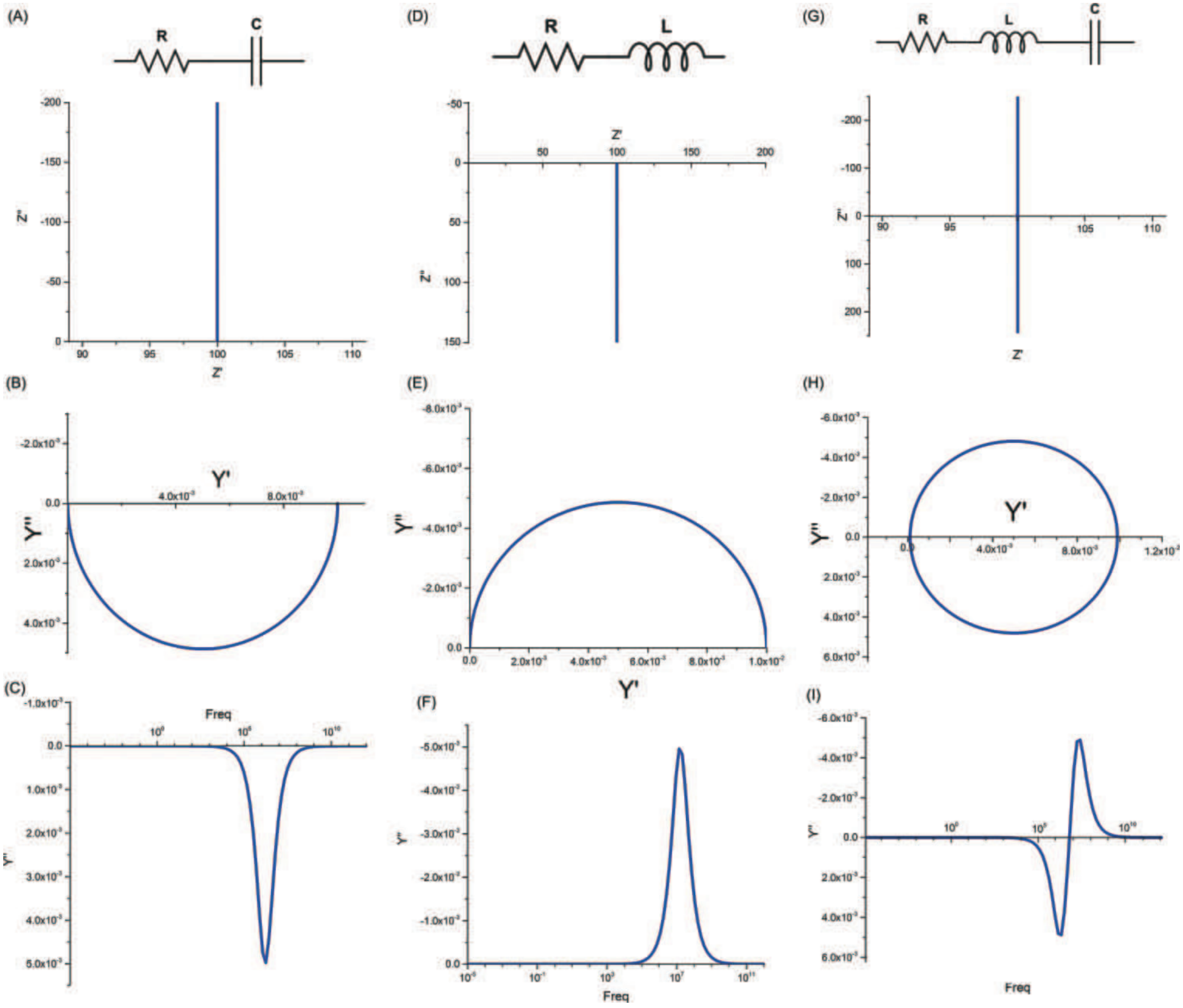

Fig. 3 Representative complex impedance plots, complex admittance plots and imaginary admittance plots for a series RC circuit (A, B and C), a series RL circuit (D, E and F) and a series RLC circuit (G, H and I).

Table 2 Conductivity for different material types.

Type	*Charge carriers*	*Carrier charge*	*Mobility*	*Temperature dependence*
Metallic	Electrons, Constant N	Constant q	$\mu \propto 1/T$	$\rho_T = \rho_0 [1 + \alpha (T-T_0)]$
Semiconductor	Electrons and holes	$q_e = q_h$	$\mu_e \propto 1/T$	$\sigma_{int} = \sigma_{o,in} \exp.[-E_g/2kT]$
Intrinsic	$N_e = N_h$		$\mu_h \propto 1/T$	$\sigma_{n\text{-type}} = \sigma_n \exp\text{-}(E_g - E_d/kT)$
Extrinsic	$N = N_o \exp.[-E_g/2kT]$ $N_e = N_d \exp. -(E_g - E_d)/kT$ $N_h = N_a \exp. -E_a/kT$			$\sigma_{p\text{-type}} = \sigma_p \exp\text{-}(E_a/kT)$
Insulator	Electrons, holes	q_e	$\mu_e \propto 1/T$	
Electronic carriers		q_h	$\mu_h \propto 1/T$	
Ionic carriers	Anions, cations	q_{ion}	$\mu_{ion} = D_{ion}q_{ion}/kT$	$\sigma \propto D_0 \exp. (-Q/RT)$

that ion. There are of course many additional more complex dependences associated with the presence of controlled impurities such as temperatures where donors and acceptors affect the properties of semiconductors (Kasap, 1997), defect association which can modify the conductivity behavior of ionic conductors (Gerhardt-Anderson and Nowick, 1981; Barsoum, 2019), the formation of polarons when electronic defects attach themselves to ionic defects (Austin and Mott, 1969) as well as Cooper pairs in superconductors (Varlamov et al., 1999) and other types of charge carriers in more complex cases which are discussed in more detail in other chapters of the encyclopedia.

Multiple parallel processes appearing on the impedance plane

Before moving onto describing the relationship of impedance with dielectric permittivity, it is important to first discuss what is expected to happen when more than one process shows up in the measured spectra. The presence of more than one semicircle in the complex impedance plane generally signifies the presence of more than one parallel RC circuit in series (Gerhardt and Nowick, 1986; Gerhardt, 2005). However, as seen earlier, it is also possible to see semicircles due to parallel RL circuits and other combinations although semicircles due to parallel RL will appear in the fourth quadrant as shown in Fig. 2B (Gerhardt, 2013; Muhlbauer et al., 2013). Reasons for getting more than one semicircle in the complex impedance plane can include: (1) a solid state ionic material with different response at the grain boundaries than within the bulk grains (Gerhardt et al., 1986; Guo and Maier, 2001); (2) a semiconducting material with space charge polarization at the electrode/material interface (Bertram and Gerhardt, 2009; Snaith and Grätzel, 2007); and (3) the presence of inductive behavior in an otherwise conducting material (Muhlbauer et al., 2013) and (4) bulk response and interfacial responses in multiphase systems (Bertram and Gerhardt, 2011a,b; Pruyn and Gerhardt, 2015).

In Fig. 4, different combinations of two parallel RC circuits in series are presented where the capacitances of process 1 and process 2 are kept constant at 1 pF and 1 nF respectively. The physical meaning of each of these circuit elements is, however, quite different for each of these cases. Table 3 lists some of the possible physical processes that may be responsible for the multiple semicircles obtained. In Fig. 4A the case where $R_1 > R_2$ is depicted whereas in Fig. 4B $R_1 = R_2$ and in Fig. 4C $R_1 < R_2$. In Fig. 4D, which can represent either the case where $R_1 \gg R_2$ or $R_1 \ll R_2$, one can only detect a single semicircle even though we started out with two processes. This makes it clear that when the difference between the relaxation times of the two processes present is small, one of the processes may be overshadowed by the other in the impedance plane (Gerhardt, 2005). It is more common to see the case of $R_1 > R_2$ nowadays (Fig. 4A) that most everyone works with nanocrystalline materials (Maier, 2004; Kosacki and Anderson, 2001) than it was earlier (Gerhardt and Nowick, 1986) when the bulk grains were on the micrometer scale and the grain boundaries were expected to be on the nanometer scale (Fig. 4C). Even if the two regions have the same resistance as was reported for YSZ materials due the high content of the dopants (Gerhardt-Anderson and Nowick, 1985), differences in the capacitance would still give rise to both semicircle being visible as seen in Fig. 4B. A similar situation will occur if we were to fix the resistance value and vary the capacitance (not shown). In fact, working with nanomaterials has made it more difficult to separate the grain boundary response from that of the bulk since the capacitances of the grain boundaries are on the same order of magnitude as those of the bulk nanograins, in contrast to earlier work which focused on micron-sized specimens that gave rise to capacitances that were three orders of magnitude apart (Gerhardt et al., 1986). All of these figures illustrate that only looking at the impedance plane may prevent identification of the presence of a second process. It may also be possible to reveal the presence of more than one process when the magnitude of the spectra are quite different, if one uses logarithmic scales, as suggested by Jonscher (1983) and demonstrated by Muhlbauer and Gerhardt (2013).

When making measurements of a semiconducting or a conducting material, it is important to pay attention to whether the electrode contact is ohmic or not (Ou et al., 2003; Hwang et al., 1997). If the electrode contact is non-ohmic or the charge transfer between the semiconductor and the electrode is inefficient, then an additional semicircle may be observed, which may be related to the space charge polarization at that interface and not be representative of the bulk of the material one is trying to characterize. Fig. 5A and B show the complex impedance graphs simulations for a semi-insulating material in contact with a blocking electrode (after Etsell and Flengas, 1970). Fig. 5A shows the response for a given size electrode for the same material with the same dimensions where the time constant does not change but the size of the semicircle does (Kumar and Gerhardt, 2012), whereas

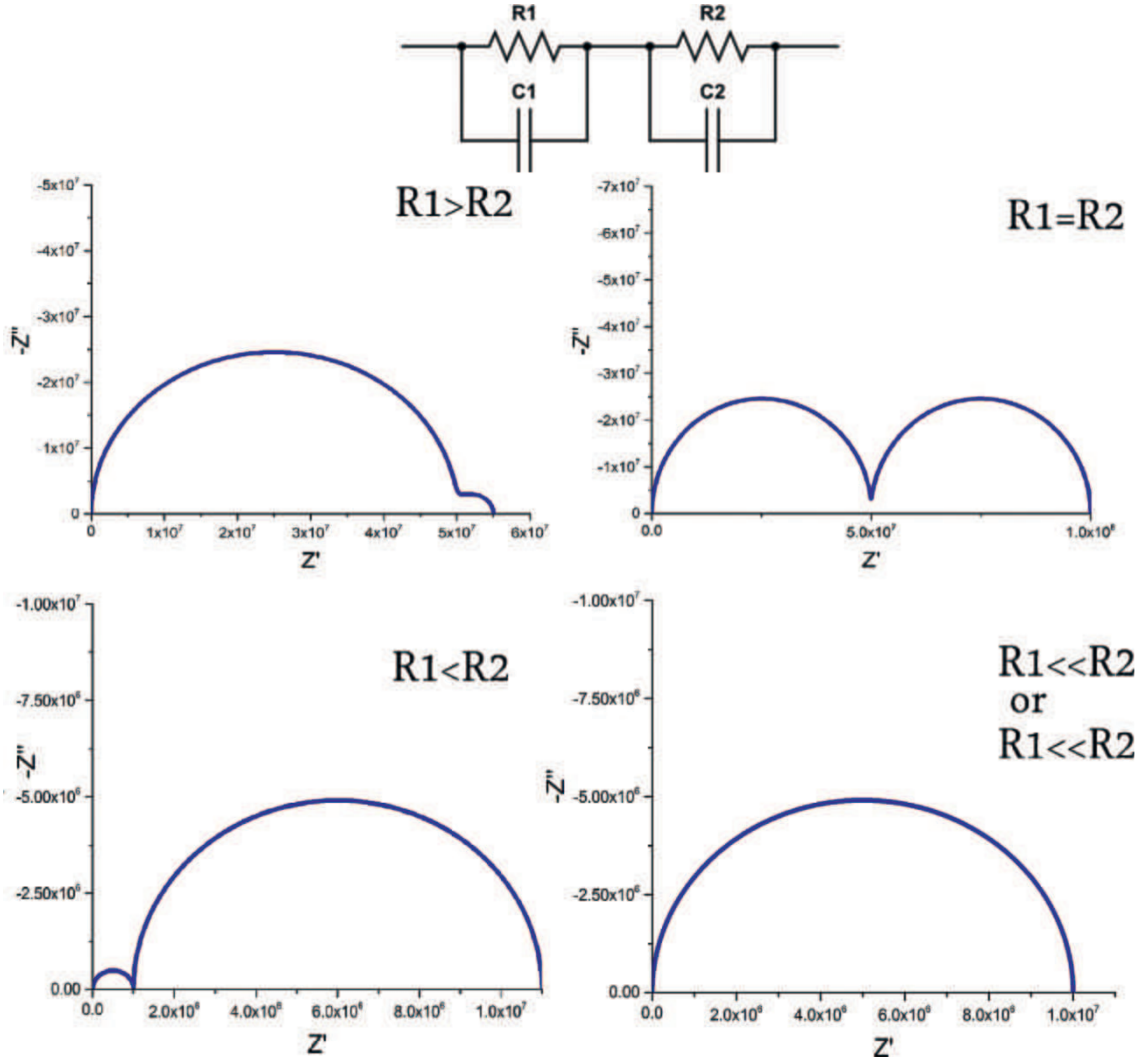

Fig. 4 (A) Two parallel RC circuits in series is the simplest equivalent circuit needed to represent the various two physical process systems described in Table 3. In all cases, $C_1 = 1$ pF and $C_2 = 1$ nF. (A) Complex impedance plot for a two-process system where $R_2 < R_1$ (B) Complex impedance for $R_1 = R_2$. (C) Complex impedance plot for a two process system where $R_2 > R_1$. (D) Complex impedance plot for a two-process system where $R_2 \gg R_1$. Note that R_1 is not easily detected in this case and that the impedance plot is dominated by R_2. Modified from Gerhardt RA (2005) Impedance spectroscopy and mobility spectra. In: Bassani G, Liedl G, Wyder P (Eds.). *Encyclopedia of Condensed Matter Physics*. Elsevier Press, pp. 350–363.

Fig. 5B displays the effect of changing the electrode size for a given material which affects the semicircle due to the electrode but not the response of the bulk material (Mebane and Gerhardt, 2006). Another way to detect these changes is to use a superimposed dc bias which will decrease the size of a blocking contact (Bertram and Gerhardt, 2009).

In Fig. 6, combinations of parallel RC and parallel RL circuits in series are displayed (modified from Gerhardt, 2013). These spectra are not as commonly observed as the parallel RC circuits in series described in the preceding paragraphs but they have become a lot more common place when characterizing conducting nanomaterials such as carbon nanotubes (Muhlbauer et al., 2013; Muhlbauer and Gerhardt, 2013; Muhlbauer et al., 2014; Muhlbauer and Gerhardt, 2021) and ITO thin films (Joshi and Gerhardt, 2013; Xia and Gerhardt, 2016) as well as solar cell devices (Panigrahi et al., 2016) and even memristors (Bisquert, 2021; Bou and Bisquert, 2021). In Fig. 6, the graphs were chosen to illustrate the effect of changing the R values so that we can compare the case where $R_{RL} = R_{RC}$ to when the resistance is larger for the RL circuit vs the RC circuit ($R_{RL} > R_{RC}$) and viceversa ($R_{RL} < R_{RC}$). It is clear that when the two R values are the same, a complete impedance circle is always observed (Gerhardt, 2013). These graphs can truly change in appearance quite rapidly so only cases where the two semicircles can be seen are shown. Fig. 6 shows arrows to indicate which way frequency increases. When $R_{RL} < R_{RC}$, it can be seen that the smaller semicircle related to the R_{RL} appears at low frequencies when the time constant $\tau_{RL} > \tau_{RC}$ whereas it appears at higher frequencies when the time constants are

Table 3 Relationships between dielectric functions.

$Z^* = 1/JWC_0\varepsilon^*$	$E^* = 1/JWC_0Z^*$
$Y^* = JWC_0\varepsilon^*$	$Y^* = 1/Z^*$
$M^* = 1/\varepsilon^*$	$M^* = JWC_0Z^*$
$\mathrm{TAN}\ \delta = \varepsilon''/\varepsilon'$	$\mathrm{TAN}\ \delta = Z''/ZZ'$

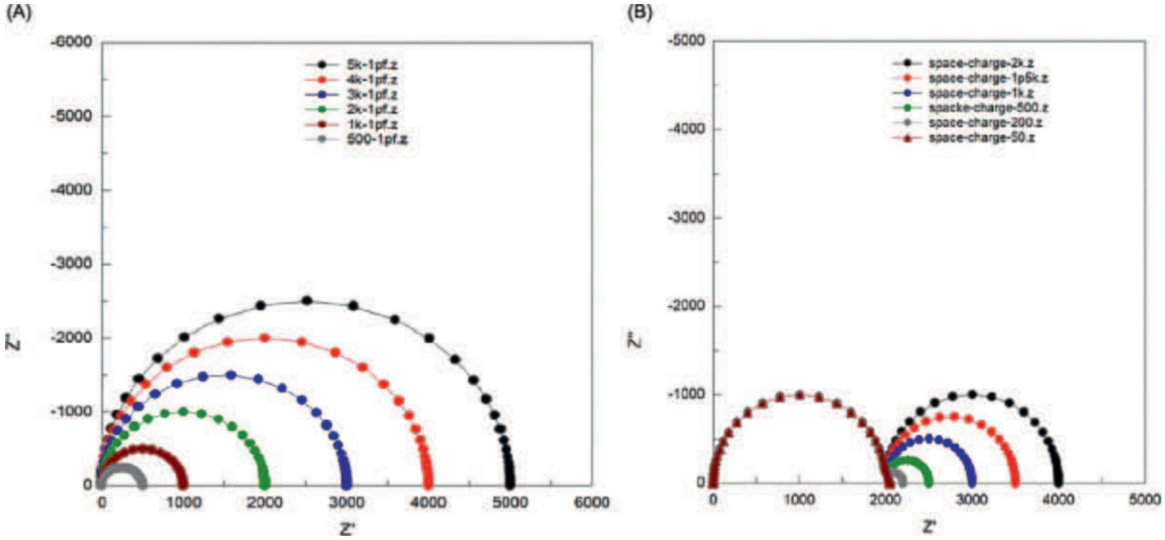

Fig. 5 (A) displays a situation where a blocking electrode is used and the size of the measured semicircle changes with it overshadowing the bulk response. (B) Case where both bulk and space charge due to blocking electrode are visible but can be minimized by varying electrode size which shows that only space charge semicircle is affected.

$\tau_{RL} < \tau_{RC}$ (Gerhardt, 2013). The opposite is observed for when $R_{RL} > R_{RC}$ where the smaller semicircle related to the R_{RC} appears at lower frequencies when the time constant $\tau_{RL} < \tau_{RC}$ while the smaller semicircle due to R_{RC} appears at higher frequencies when $\tau_{RL} > \tau_{RC}$. The reader is referred to the online version where a movie is displayed that presents a more gradual change between these very different cases.

Microscopic interpretation

If one is interested in determining what electrical process has given rise to a particular set of impedance spectra, it is useful to remember that all materials are made up of charged entities at various length scales (see Fig. 7 for an example). At the atomic level, we have protons and electrons. At the molecular level, we may have anions, cations or charged molecules. At the nano- meso- and micro-structural levels within a single material, we may also have charged interfaces (space charge at electrode surface or internal interfaces). The interface between the contacting electrode and the material surface often results in space charge polarization (Kao, 2004). Hence, the impedance response measured is dictated by the total number of impediments to the current flow that an ac signal encounters on its way from the high to the low voltage electrode. The impedance response measured is then a function of the frequency of the applied field, how that field interacts with each polarization process present in the material, and whether it is commensurate with the dimensions of the permanent or temporary dipoles formed and the strength of the signal.

Polarization mechanisms

Fig. 8 schematically displays the real and imaginary permittivity response of a material as a function of the applied frequency (Gerhardt, 2005). Upon the application of an electric field, atomic or electronic polarization are easily detectable in the optical frequency range, and this results in the resonance response displayed. Polarization strength is proportional to the number of electrons present (Kao, 2004) and is governed by the equation below

$$\mathrm{P} = \mathrm{Zqd} \tag{6}$$

where Z is atomic number, q is the charge constant $= 1.609 \times 10^{-19}$ coulombs/m and d is the distance.

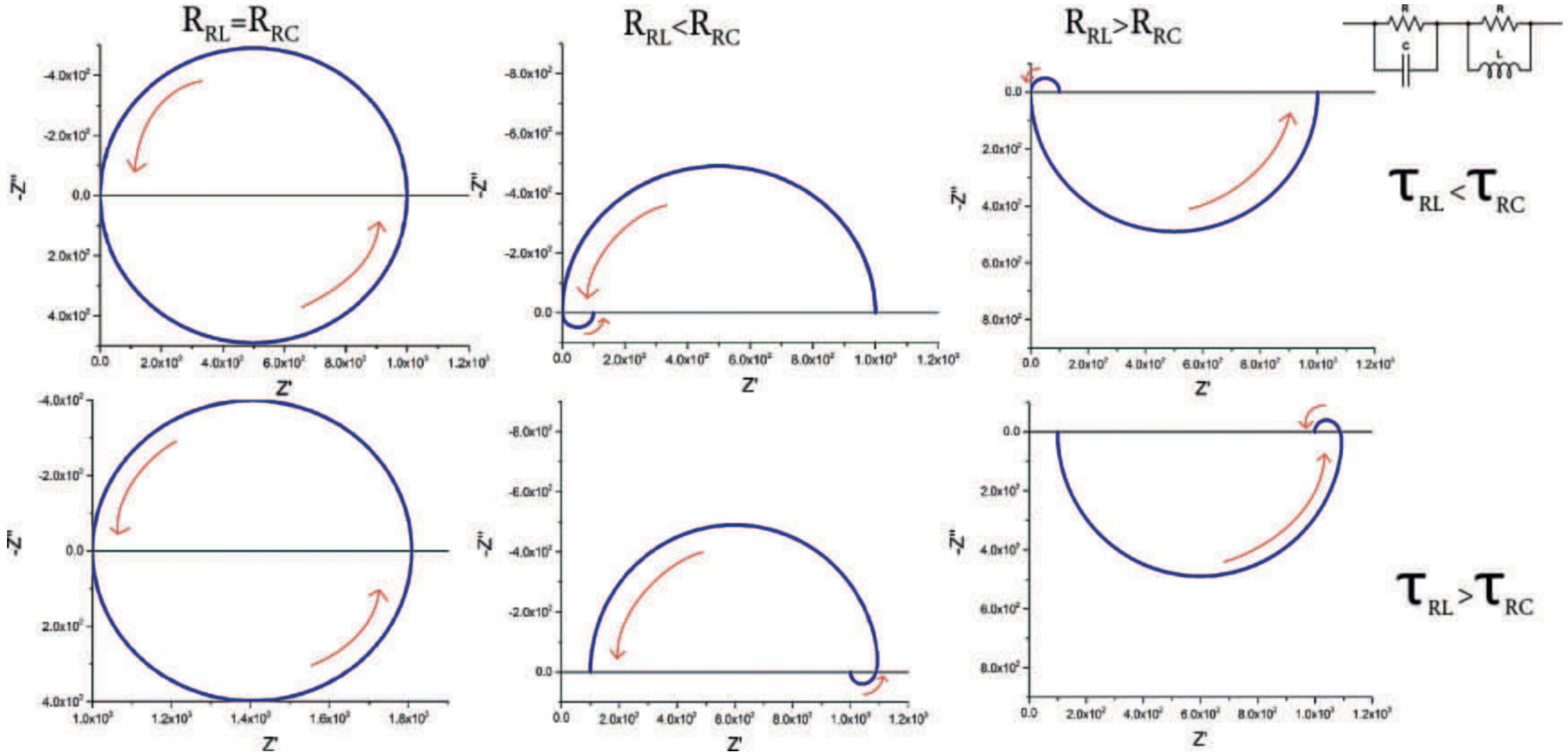

Fig. 6 Effect of resistance when a parallel RC circuit is followed by a parallel RL circuit. When $R_1 = R_2$, one obtains a complete circle whereas the location of each RC or RL component varies depending on whether the time constant for the RC circuit is higher or lower than that of the RL circuit. Modified from Gerhardt RA (2013) Impedance and dielectric spectroscopy of nanoparticulate films and composites. *Nanotech 2013 Conference Proceedings*, Paper 1433.

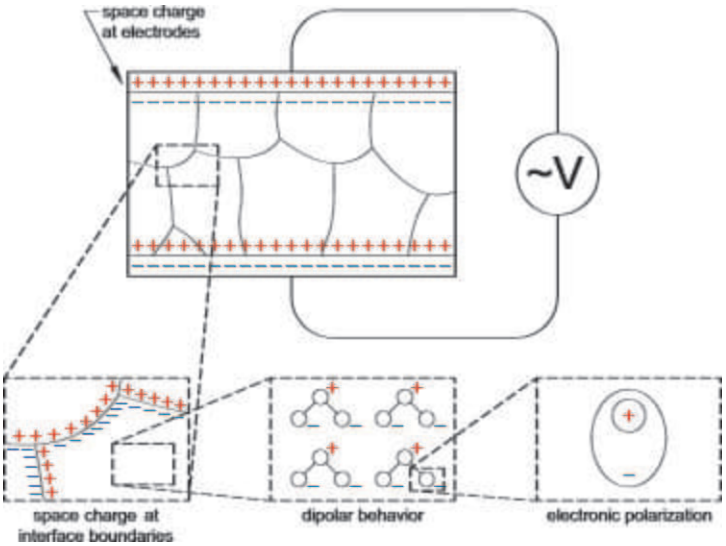

Fig. 7 Schematic of the cross section of a specimen subjected to an ac voltage showing the presence of several polarization mechanisms: electrode-specimen polarization, grain-to-grain interfaces in the bulk of the material, presence of permanent dipoles, ionic and electronic polarization. Modified from Gerhardt RA (2005) Impedance spectroscopy and mobility spectra. In: Bassani G, Liedl G, Wyder P (Eds.). *Encyclopedia of Condensed Matter Physics*. Elsevier Press, pp. 350–363.

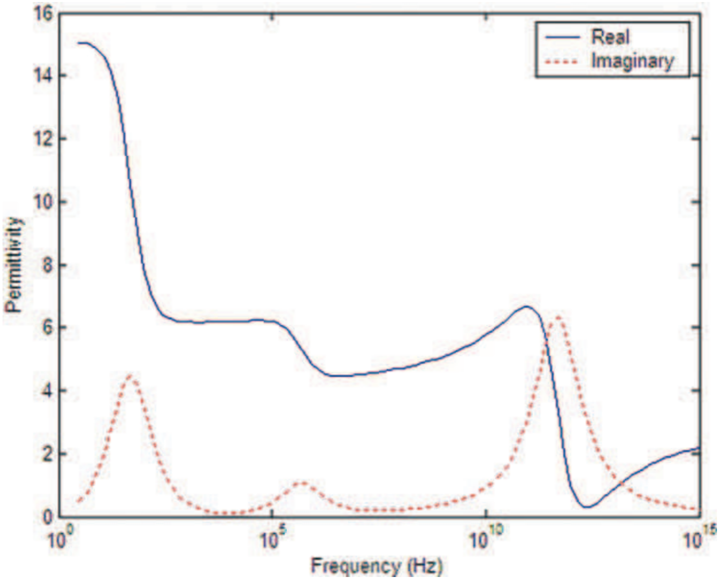

Fig. 8 Simulated real and imaginary permittivity curves for a material that contains two dielectric relaxation processes and a single resonance process. Note that change in the real part results in the formation of a peak in the imaginary part. Modified from Gerhardt RA (2005) Impedance spectroscopy and mobility spectra. In: Bassani G, Liedl G, Wyder P (Eds.). *Encyclopedia of Condensed Matter Physics*. Elsevier Press, pp. 350–363.

At the molecular level, dipole polarization can be due to temporary or permanent dipoles present in a material. Permanent dipoles are present in those materials that possess a different center of positive charge from that of a negative charge. This includes all ferroelectrics below their Curie temperature, all polar polymer molecules, and all polar liquids such as water. It may also occur by aliovalent doping of compounds which results in specific defects (Chadwick, 2007; Anderson and Nowick, 1981; Nowick and Berry, 1972). Temporary dipoles may occur in weakly bound polymers (Block and North, 1970) or in the electrostatic attachment of nanowires to patterned substrates (Kumar et al., 2005). Molecular temporary dipoles also occur in ionically bonded materials, such as many oxides and fluorides (Figueroa et al., 1984).

Space charge polarization occurs whenever the electrical response at an interface is dominated by pile up of charge carriers at that interface (Kao, 2004). This commonly occurs at the interface between the contacting electrode and the material under test, and is often assumed to only occur at very low frequencies. If the electrode contact is non-ohmic or if the charge transfer resistance is high, the space charge polarization will overshadow any other processes that may be present in the material. Space charge polarization may also occur at the interfaces between grains of phases with very different electrical properties (Balke et al., 2010; Figueroa et al., 1984) or at the grain boundaries of a single-phase material, if the defect concentration is high or if there is segregation of impurities into or away from the boundaries (Gerhardt et al., 1986; Guo and Maier, 2001; Hughes et al., 2018). Space charge polarization at the interfaces between two different materials is generally expressed in terms of the Maxwell-Wagner two-layer condenser model (Von Hippel, 1954). These equations will be discussed in the multiple relaxation process section.

Space charge polarization at electrode-material interfaces is often diffusive in nature and can be represented by the Warburg impedance (Barbero and Lelidis, 2017). This gives rise to a linear dependence of the conductivity on the frequency of the measurement, as described in the equation below:

$$Z^* = [A/(D\omega)^s](1 - j) \tag{7}$$

where A is a constant related to the valence state of the diffusing species and the concentration gradient, and s represents the diffusion exponent. For perfect diffusion controlled response, $s = ½$. This is often seen as a straight line at 45 degrees from the real impedance axis (Macdonald, 1987; Muralidharan, 1997). Many studies dealing with diffusion controlled interfaces have been studied in fuel cells (Kulikovsky, 2016), batteries (Cruz-Manzo and Greenwood, 2020), solar cells (Omar and Abdullah, 2014; Romero et al., 2019) and supercapacitors (Buller et al., 2005) where liquid electrolytes are often used to make electrical contact.

Relaxation and resonance frequency spectra

The Debye relaxation

The frequency dispersion that allows transformation of the dielectric response from one polarization mechanism to another is known as dielectric relaxation. The Debye equation describes this for essentially all relaxation processes even though it was originally developed to represent dielectric relaxation in polar liquids (Hill and Dissado, 1985):

$$\varepsilon^* = \varepsilon_\infty + (\varepsilon_s - \varepsilon_\infty)/[1 + j\omega\tau_D] \tag{8}$$

where ε_∞ represents the high frequency dielectric permittivity, ε_s is the lowest frequency dielectric permittivity (sometimes referred to as the static permittivity), ω is the angular frequency and τ_D the relaxation time for the Debye process.

The frequency implicit complex permittivity graphs and the real and imaginary parts of the permittivity are plotted vs frequency in Fig. 9 (modified from Cao and Gerhardt, 1990). It is clear that a complete semicircle is observed for the Debye process while the real part of permittivity displays a sigmoidal shaped curve that changes from the low frequency ε_s to the high frequency ε_∞ that results in the formation of an imaginary ε'' peak in the frequency explicit graph, where the Debye time constant can be obtained by taking $\omega\tau_D = 1$ and $\omega = 2\pi f_p$ at the apex of the complex permittivity semicircle and identify the frequency at which it will appear in

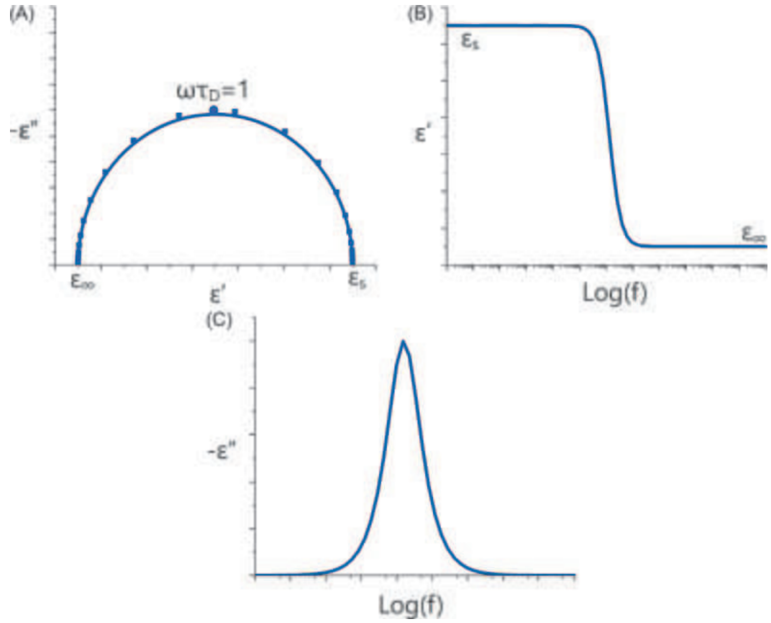

Fig. 9 Simulated complex permittivity, real and imaginary permittivity for the ideal Debye case. Modified from Cao W, Gerhardt R (1990) Calculation of various relaxation times and conductivity for a single dielectric relaxation process. *Solid State Ionics* **42**: 213–221.

the imaginary permittivity graph. This same equation can be used to represent any of the relaxation processes that were depicted in Fig. 8 making sure to replace to use different values of the high frequency ε_∞ and the low frequency ε_s for the different processes.

Cole-Cole, Davidson-Cole and Havriliak-Negami relaxations

Since most materials do not behave in an ideal manner, a number of modifications to the Debye equation have been taken. Cole-Cole were the first to have modified the Debye equation to account for deviations from the ideal Debye response. Cole and Cole (1942) introduced the α parameter as follows:

$$\varepsilon^* = \varepsilon_\infty + (\varepsilon_s - \varepsilon_\infty)/\left[1 + (j\omega\tau_D)^{1-\alpha}\right] \tag{9}$$

where $\alpha < 1$ shows up as a depression angle $\alpha\pi/2$ below the real ε' axis. Davidson and Cole introduced the β parameter, which accounts for deviations from ideality in the highest frequency region of the Debye relaxation (Davidson and Cole, 1950) that shows up as an inclined $\beta\pi/2$. This modification is written as follows:

$$\varepsilon^* = \varepsilon_\infty + (\varepsilon_s - \varepsilon_\infty)/[1 + j\omega\tau]^\beta \tag{10}$$

To account for both spreading of the relaxation time and deviations from ideality at high frequency, Havriliak and Negami (1967) combined the two parameters, as shown below:

$$\varepsilon^* = \varepsilon_\infty + (\varepsilon_s - \varepsilon_\infty)/\left[1 + (j\omega\tau)^{1-\alpha}\right]^\beta \tag{11}$$

The Havriliak and Negami equation is often used to characterize dielectric polymers because their response can be quite non-ideal (Havriliak and Negami, 1967). The differences between the Debye, Cole-Cole and Davidson-Cole relaxation equations are illustrated in Fig. 10. Some of these deviations can be accounted for by the use of the constant phase element (CPE), which is often used to account for non-ideal behavior (Brug et al., 1984; Boukamp, 2020).

Resonance behavior

Resonance spectra are hardly ever discussed in the context of impedance spectroscopy. This is because ionic and electronic resonance generally occur at frequencies near the optical range and are best detected with optical spectroscopic methods such as IR, UV and visible spectroscopy methods (Zhang, 2009) as well as spectroscopic ellipsometry (Fujiwara, 2007). NMR (Hatada and Kitayama, 2004) and EPR (Goldfarb and Stoll, 2018) methods are also superb at detecting ionic resonances. Nevertheless, it is possible to observe resonance phenomena when making impedance measurements. Resonance behavior that occurs at the lower frequencies of impedance measurements is normally associated with parasitics in the measurement circuitry but may also be due to non-linear response of materials such as in ferroelectrics (Gerhardt et al., 1996) and ferromagnetics (Valenzuela, 2001) as well as in metamaterials applications (Li et al., 2014). An equation that can generate a resonance response is given by

$$\varepsilon^* = \varepsilon'_\infty + ½\left(\varepsilon'_s - \varepsilon'_\infty\right)/[(1 - (\omega/\omega_{res})) + (\beta/\omega_{res})] \tag{12}$$

where ε'_s and ε'_∞ are the permittivities at frequencies much lower and much higher than the resonant frequency ω_{res}, and β represents the strength of the restoring force that gives rise to resonance (Jonscher, 1983). Fig. 11 displays the frequency explicit and frequency implicit graphs of the dielectric resonance equations for two different cases. It is to be noted when a dielectric resonance occurs, one gets to observe a negative dielectric constant at certain frequencies as shown in Fig. 11 (Jonscher, 1983). This also occurs for transitions in piezoelectrics (Appleby et al., 2014) or where there is a barrier being overcome (Joshi et al., 2020).

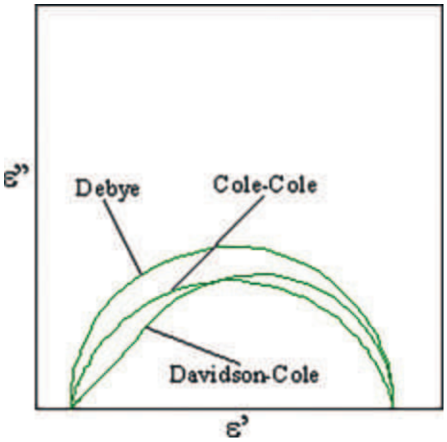

Fig. 10 Simulated complex permittivity plots for representative Debye, Cole-Cole, and Davidson-Cole relaxations described by Eqs. (8–10) (Gerhardt, 2005).

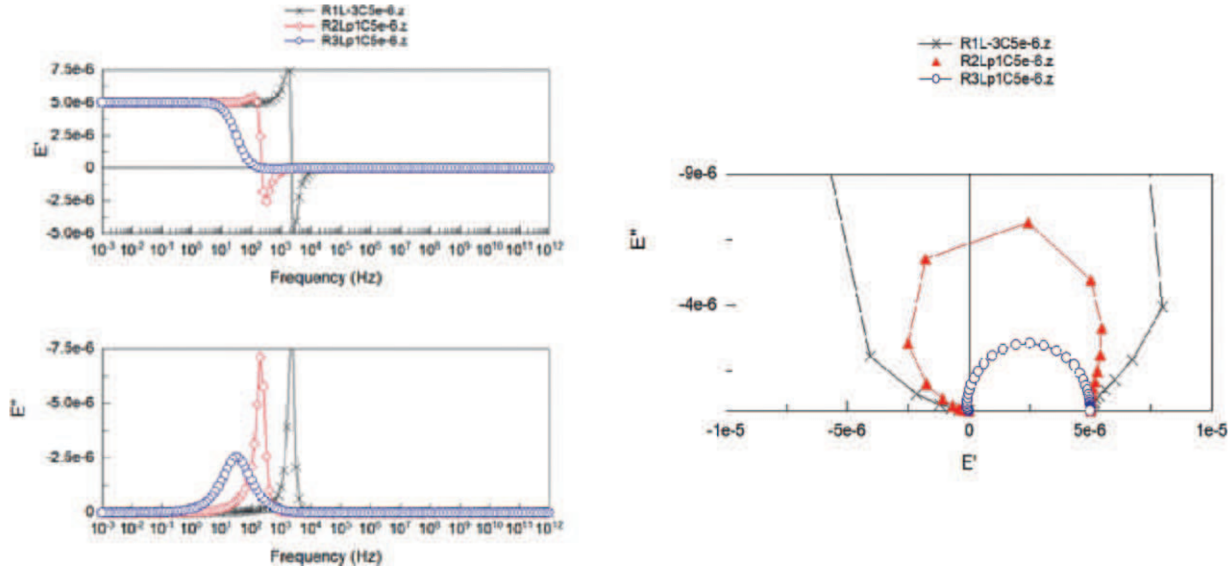

Fig. 11 (A) Frequency explicit real and imaginary permittivity plots for a resonance process. (B) Frequency implicit complex permittivity plot for a resonance process. Modified from Gerhardt RA (2005) Impedance spectroscopy and mobility spectra. In: Bassani G, Liedl G, Wyder P (Eds.). *Encyclopedia of Condensed Matter Physics*. Elsevier Press, pp. 350–363.

Various representations of the dielectric function

A fact not often recognized is that the dielectric relaxation equation originally developed by Debye for relaxation in polar liquids provides another way to interpret impedance data (Gerhardt, 2005). This is possible because dielectric permittivity is inversely related to impedance, as shown below:

$$Z^* = 1/j\omega C_o \varepsilon_r{}^* \tag{13}$$

Therefore, it follows that measured impedance data can be converted into permittivity and vice-versa provided that the geometric capacitance, C_0, of the sample measured is known and is multiplied by the relative permittivity, $\varepsilon_r{}^*$. It needs to be mentioned that many references do not use the 'r' subscript although the value needs to be unitless because it is normalized by the geometric capacitance. Recalling that admittance, Y^*, is the inverse of impedance and that electric modulus, M^*, is the inverse of permittivity, it then becomes possible to analyze the SAME measured data in four different formalisms without the use of any adjustable parameters (Cao and Gerhardt, 1990). Table 4 lists all the important relationships between these four dielectric functions. Performing the conversions mentioned is advantageous because polarization or conductivity processes that may be hidden in the impedance, for example, may become fully detectable in the admittance plane or permittivity plane because their frequency dependence are different (Gerhardt to be published).

As was shown in Fig. 3A and D, the complex impedance for a series RC circuit and a series RL circuit do not show semicircles. Instead, they show semicircles in the complex admittance graphs, displayed in Fig. 3B and E. The main difference being the quadrant in which they appear. For the circuits containing a capacitance and a resistance, they appear in the first quadrant for the impedance for the parallel RC (see Fig. 2A) but the fourth quadrant for the admittance for the series RC (See Fig. 3B), whereas for those containing an inductance, they appear in the fourth quadrant for the parallel RL impedance (Fig. 2B) but the first quadrant for the series RL admittance (see Fig. 3E).

It turns out that when we observe semicircles in any of the complex graphs, they are always paired with peaks in their corresponding imaginary functions as was already shown in Figs. 2 and 3 for the parallel and series RC and RL circuits and Fig. 9 for the Debye relaxation. When the semicircles represent the same physical processes, then they will show peaks in related imaginary

Table 4 Possible physical processes for two parallel RC circuits in series.

	R_1	C_1	R_2	C_2
Ionic conductor	Bulk	Bulk	Grain to grain interface	Grain to grain interface
Semiconductor	Bulk	Bulk	Electrode interface	Electrode interface
Multiphase 1	Bulk	Bulk	Interphase Boundary	Interphase Boundary
Multiphase 2	Main phase	Main phase	Second phase	Second phase

functions. For example, for long range dc conductivity, the frequency at which the peaks can appear in the imaginary functions will be the same for the impedance and the electric modulus so that $f_{Z''} = f_{M''}$ (Gerhardt, 1994), whereas for ac conductivity $f_{Y''} = f_{\varepsilon''}$ (Cao and Gerhardt, 1990; Gerhardt, 1994). When only dielectric relaxation occurs and no measurable conductivity can be obtained, then the only functions of interest will be ε'', tan δ and M'' (Gerhardt, 1994). There is not enough room to describe the many different processes that may occur in all types of materials and devices in this short introductory article. Nevertheless, the importance of using multiplane analysis cannot be ignored as it is often the only way for the analysis to reveal all of the possible processes present in a given sample or device. Such an analysis will often reveal the true richness of the IS/DS measurements by helping identify electrical/optical/magnetic processes occurring in many materials and devices. A few examples will be given in the multiple processes section that will demonstrate that each equivalent circuit type will have their own unique signatures, not just those described in the Debye relaxation papers (Cao and Gerhardt, 1990; Gerhardt, 1994). In fact, Hodge, Ingram and West gave some examples of multilayer samples in the 70s (Hodge et al., 1976). Several review articles will be appearing in the near future focusing on several of the many additional electrical/optical/magnetic applications.

While conversions to all of the different functions can be made without any adjustable parameters, it should be emphasized that these mathematical transformations need to be done with caution as the data on either extreme of the frequency range of a given impedance analyzer will tend to carry a higher error (Boukamp, 1993). Hence, taking the inverse can amplify the size of the errors. Nevertheless, it is an extremely useful tool for determining the most appropriate model that can help identify the relaxation process or processes present more easily than just looking at one of the functions. Moreover, once the relaxation process has been identified, the data can then be used to obtain the activation energy for that particular process.

Multiplane analysis of several multiple process combinations

If we refer back to Figs. 4–6, it should not be surprising to realize that most experimentally measured spectra will be made up of more than one relaxation process. Additional examples can include: (1) a Debye-type dielectric polarization process, (2) A Debye process with a parallel leakage current; (3) a simple semi-insulating process represented by a parallel RC circuit, (4) a simple conducting process represented by a parallel RL circuit, (5) a solid state ionic material with different response at the grain boundaries than within the bulk grains, (6) a semiconducting material with space charge polarization at the electrode/material interface, (7) a highly conducting nanomaterial and (8) bulk and interfacial responses of multiphase systems. Before describing each of these different processes, we need to describe how to obtain the activation energy via the temperature dependences observed.

Temperature dependence

Most relaxation/conductivity phenomena in insulators, ionic conductors and semiconductors are thermally activated (Nowick and Berry, 1972). As a result, the relaxation time can be expressed in terms of an Arrhenius-type temperature dependence:

$$\tau = \tau_o \ \exp.(E/kT) \tag{14}$$

where τ_o is the relaxation time at infinite temperature, E is the activation energy for the relaxation process in eV, k is Boltzmann's constant and T is temperature in degrees Kelvin. In addition, when a relaxation process occurs, $\omega_{max}\tau = 1$ regardless of which function it appears in. Therefore, one can use the frequency at which a peak occurs at a given temperature as a way to determine the activation energy for that process. Fig. 12A schematically displays a dielectric loss (tan $\delta = \varepsilon''/\varepsilon'$) process that changes peak frequency as temperature is changed. The linearized version of Eq. (14) converted to peak frequency f_p is used to obtain the activation energy as depicted in Fig. 12B.

Similarly, conductivity processes may display peaks in the imaginary impedance or imaginary admittance, which could then be used to estimate the activation energy for those processes in the same fashion as described above. The supplementary videos show several cases of the time constants for a parallel RC, a parallel Rl, two parallel RC processes in series and two parallel RL processes in series to show how the time constant can affect the phase angle and the imaginary part of the impedance. More often, the activation energy for conduction, in a given system, is obtained by taking the intercept of the impedance semicircle with the real axis, as displayed in Figs. 2–6, and converting that to conductivity after taking the geometric dimensions into account and plotting the calculated conductivity versus inverse temperature. Either type of analysis is only accurate when the resistance and capacitance of the relaxation processes being measured are both independent of frequency. A truly bulk response will always have constant R and C at a given temperature. This is not the case for space charge polarization under biasing conditions or diffusion controlled processes. In both of these cases, the number of mobile charge carriers will change the values of R and may also affect the value of C.

1) A Debye-type dielectric polarization process

Before describing a dielectric polarization with a parallel leakage current, it is useful to describe the Debye relaxation in more detail. As described in references (Cao and Gerhardt, 1990, Gerhardt, 1994) and others, the Debye relaxation process can be affected by the strength of the dielectric relaxation, referred to as the relaxation ratio r, which is equal to $\varepsilon_S/\varepsilon_{\infty.}$ (Cao and Gerhardt, 1990). In Fig. 13, the effect of this relaxation ratio on the ability of the dielectric process to begin showing some measurable impedance is displayed for several r values.

In addition to the Debye equation presented in Eq. (7), it is also possible to represent the Debye relaxation in terms of equivalent circuits, where a series R_1C_2 circuit is in parallel with a starting C_1 where $r = C_2/C_1$ and the Debye relaxation time constant is equal

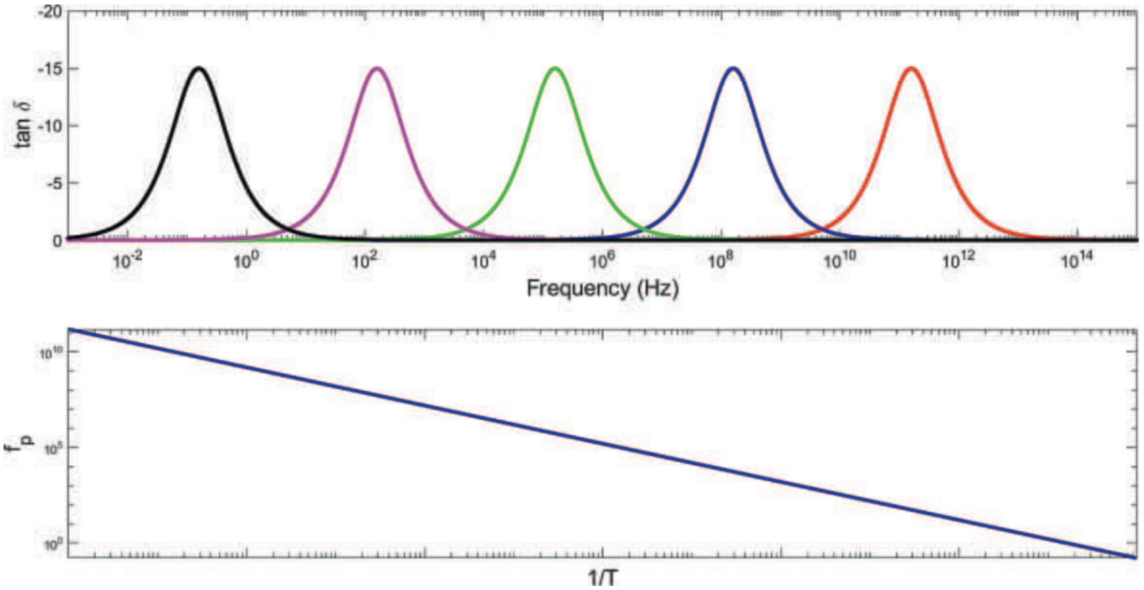

Fig. 12 (A) Schematic of a dielectric loss (tan δ process at different temperatures). Loss peaks shift to higher frequency (f_{max}) as the temperature is increased. (B) Plot of f_{max} versus the reciprocal temperature allows determination of the activation energy for the dielectric loss process.

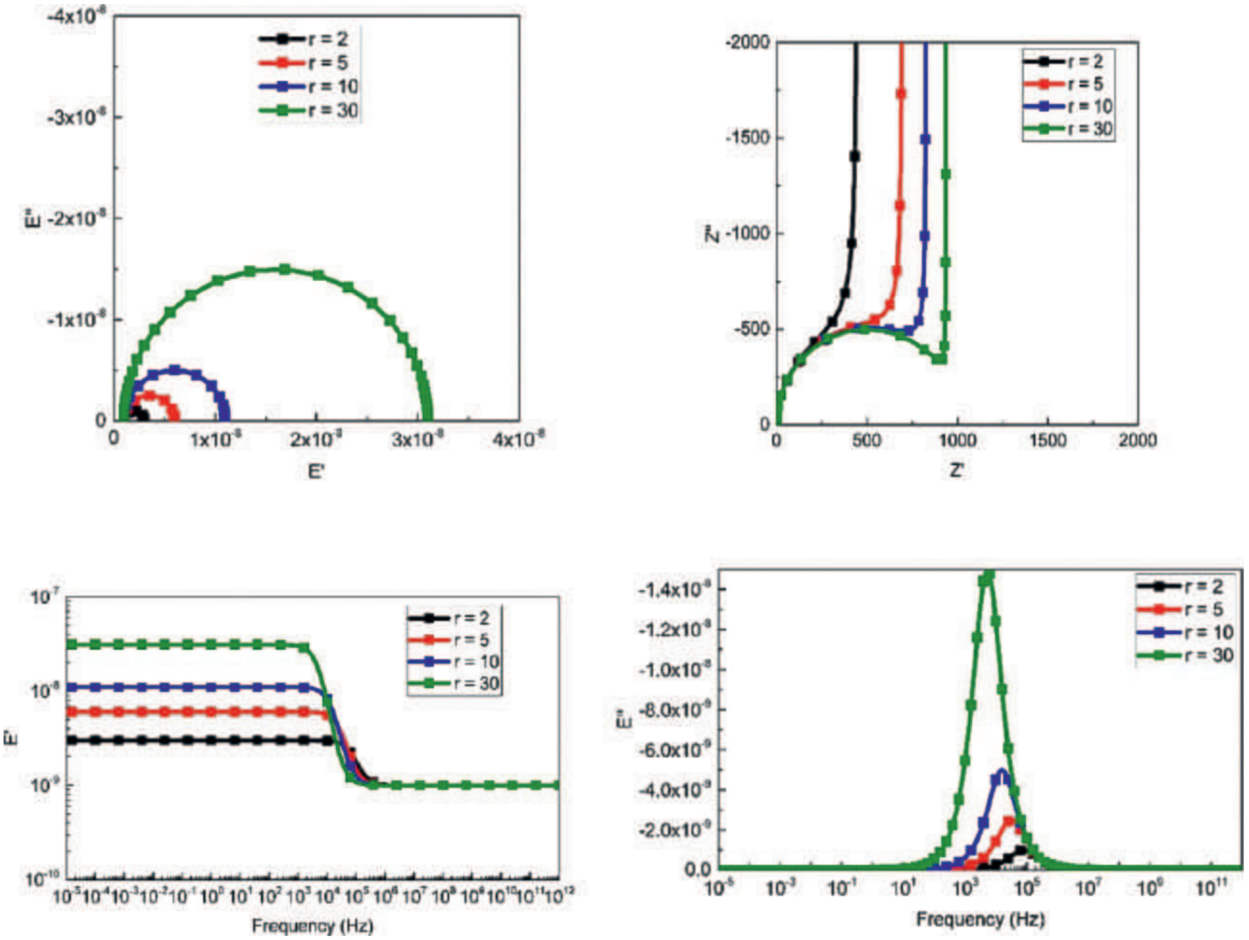

Fig. 13 Effect of relaxation ratio (r) on the complex permittivity and frequency explicit real and imaginary permittivity (A) Complex permittivity semicircle increases in size when εs increases (B) Real permittivity plotted vs. frequency show sigmoidal shaped curves accompanied by a peak in the imaginary permittivity function that increase in height as the value of r increases (C) As the relaxation ratio r increases, one can see the formation a more complete semicircle in the complex impedance graph.

to R_1C_2. This is shown in Fig. 13A. As the value of the relaxation ratio increases from 2 up to 1000, one can detect the onset of the formation of a semicircle in the complex impedance plane and a peak in the imaginary impedance as displayed in Fig. 13B and D. It should be mentioned that dielectric loss peaks (similar to those shown in Fig. 13C) by themselves do not give rise to a long range conductivity process because the path is always dominated by the higher valued capacitor C_2 which results in a fastly increasing imaginary impedance as in Fig. 13B. This is also seen in Fig. 13D as well as part (d) in the graphical abstract where the complex impedance is shown on a log scale to demonstrate the effect of the bulk impedance of the sample (R_1) while keeping the relaxation ratio constant. The dielectric loss peak is seen to shift to lower frequencies as the bulk resistance of the sample increases.

2) A Debye process with a parallel leakage path

If we now add a parallel leakage path by adding an additional resistor R_2 as in Fig. 14, we can better observe the ability of a leakage path to dominate the spectra measured as it can convert to a simple conducting process governed by the parallel combination of R_2C_1. This is shown in Fig. 14, where the no leakage Debye case with the same values of R_1, C_1 and C_2 is also included for

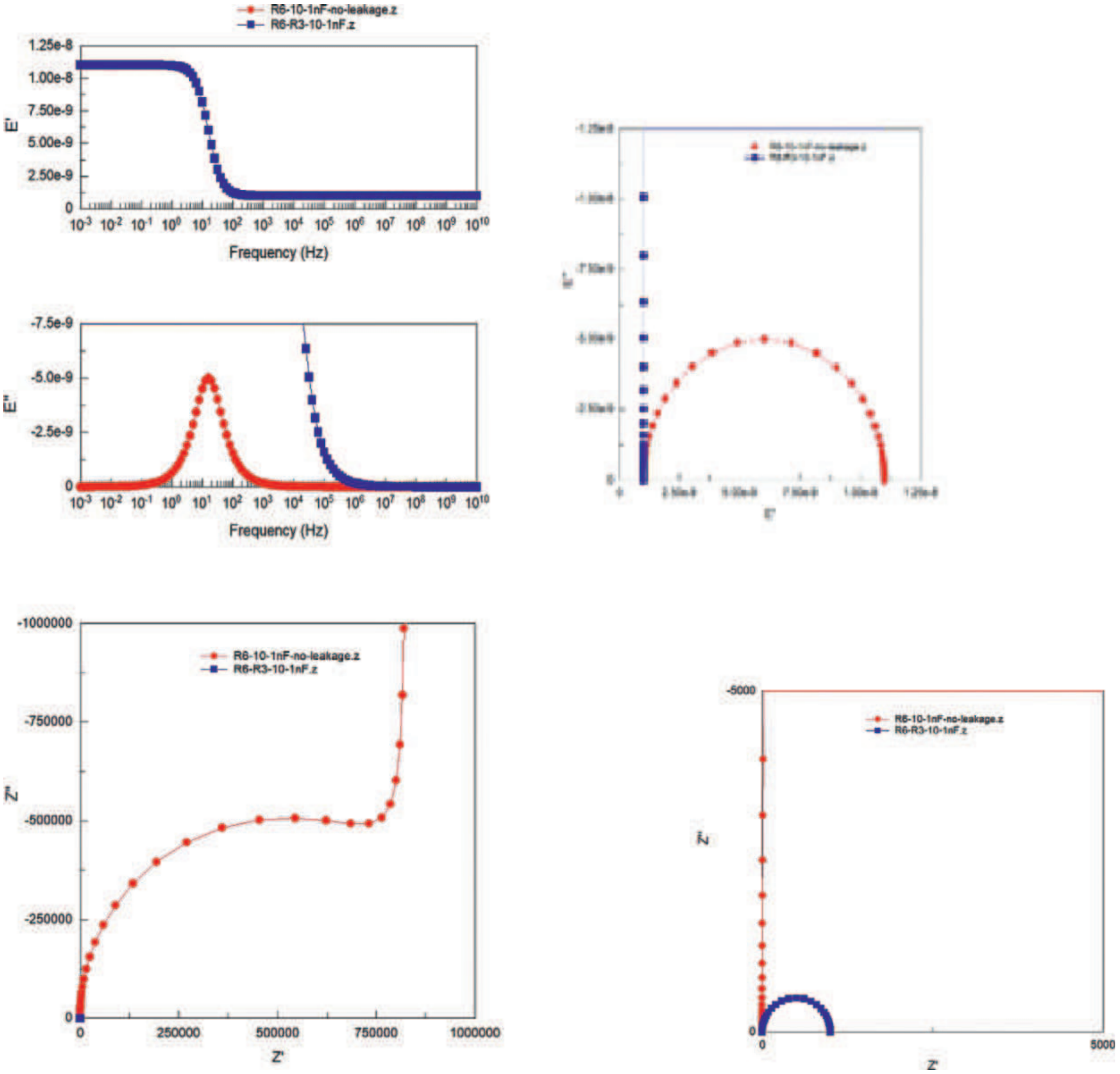

Fig. 14 Comparison of the response of a material with a Debye relaxation process with and without a leakage path. (A) Real and imaginary permittivity vs. frequency showing that the real component does not change but that the imaginary component shows a huge difference. (B) The complex permittivity still shows a semicircle for the purely Debye case while the leakage case no longer shows a complex permittivity semicircle. (C) The leakage case is totally dominated by the leakage path whereas the purely Debye case shows a semicircle shunted by a straight line dominated by the low frequency capacitance (D) the real and imaginary impedance vs. frequency graphs do show the appearance of a relaxation for both cases but displayed graphs only clearly show the frequency dependence for the pure Debye case as the other curves are a lot smaller and cannot be detected using the scale shown. Modified from Gerhardt RA (2005) Impedance spectroscopy and mobility spectra. In: Bassani G, Liedl G, Wyder P (Eds.). *Encyclopedia of Condensed Matter Physics.* Elsevier Press, pp. 350–363.

comparison. Fig. 14A shows that both the regular Debye case with no leakage and the one with a leakage path overlap in the real part of the permittivity but the similarity ends there as in the imaginary permittivity, the presence of the leakage path results in a fastly increasing imaginary ε'' that completely swamps the dielectric peak that one can see for the Debye case with no leakage. This is also detectable in the complex permittivity graph in Fig. 14B, where complex permittivity shows the semicircle for the Debye process while it is no longer available for the case with a leakage path. It is easy to see that when a clearly defined impedance semicircle is observed due to the presence of the leakage path, we no longer can see a semicircle in the permittivity plane especially if the bulk resistance is large as shown in Fig. 14C, where the bulk resistance is 1 MΩ. Furthermore, the complex impedance responses for the case with the leakage can vary widely as shown in Fig. 14D. The effect of the leakage path can also be included in the regular Debye equation where the easiest way to represent this is to add a leakage current, σ, term as follows:

$$\varepsilon^* = \varepsilon_\infty + \{(\varepsilon_S - \varepsilon_\infty)/[1 + j\omega\tau]\} - j\sigma/\omega \tag{15}$$

The corresponding equivalent circuit will contain a series RC circuit in parallel with a leakage resistor, which is also in parallel with the bulk capacitance as described above.

3) A simple conducting process represented by a parallel RC circuit

To fully illustrate the case of a material or device with some measurable dc conductivity, the easiest model to use is the RC in parallel. Fig. 15 demonstrates how the four dielectric functions appear when we only have such a circuit. It is clear that both the impedance and electric modulus show a semicircle (in opposite quadrants), whereas the dielectric permittivity and the admittance do not show any frequency dependence. This is one of the reasons why for a long time, no one interested in measuring ionically conducting materials ever thought of looking at the permittivity as one could not find any interesting trends. See the section of parallel RC circuits in series for more details.

4) A simple conducting process represented by a parallel RL circuit

A similar situation is obtained for much more conducting or highly conducting semiconductors which can usually be represented by an RL in parallel. Fig. 16 displays the complex graphs for all of the dielectric functions. Only the complex impedance shows a semicircle in the 4th quadrant in this case while the admittance shows no frequency dependence. The electric modulus and the dielectric permittivity both show negative values for the real components. This should not be surprising since very conducting materials can also get polarized due to the presence of electron clouds (Kao, 2004). Many other conducting materials can also be represented by an RL circuit in series (Muhlbauer et al., 2014; Pruyn and Gerhardt, 2015; Bertram and Gerhardt, 2009) but they often contain additional circuit elements. Some additional information may be found in a recent article (Gerhardt, 2022) and its accompanying tutorial.

5) A solid state ionic material with different response at the grain boundaries than within the bulk grains

The simplest equivalent circuit to represent an ionically conducting material contains two parallel RC circuits in series, as was shown in Fig. 4. The physical meaning for each of the four options shown is quite different. Table 3 listed some of the possible physical processes that may be represented in each of these cases.

Irrespective of the source of the frequency dependence, when the difference between the relaxation times of the two processes present is small, i.e., less than one or two orders of magnitude, or either the R or C are very small or large, one of the processes may be overshadowed by the other in the impedance plane as was demonstrated in Fig. 4D. This is when multiplane analysis should be used, as different processes can be best displayed in different dielectric functions, according to their R,C and L values. To illustrate this point, Fig. 17 is presented below.

Fig. 4A–D displayed the complex impedance spectra for a bulk ionic conductor with $C_1 = 1$ pF, which has different electrical responses at the grain boundaries (with $C_2 = 1$ nF) depending on the ratio of the bulk resistance $R_1 = R_g$ and the effective resistance at the grain boundaries labeled $R_2 = R_{gb.}$ (modified from Gerhardt, 2005). The following cases were included: (1) $R_g = R_{gb}$, (2) $R_g < R_{gb}$, (3) $R_g \ll R_{gb}$, (4) $R_g > R_{gb}$ and (5) $R_g \gg R_{gb}$. These figures illustrate that only looking at the complex impedance plane may prevent identification of the presence of a second process.

Taking the impedance graphs from Fig. 4D which correspond to cases 3 and 5 that do not provide any indication that a second process may be there and converting them to admittance, dielectric permittivity and electric modulus clearly reveals the existence of more than one process, one can obtain Fig. 17A–D for case 3. Furthermore, plotting the Bode plots also highlights the presence of two processes in some cases. The imaginary functions are generally dominated by the process with the largest value but it is easy to see that more than one process can be seen for impedance and electric modulus. As discussed in the earlier section, overlapping time constants have become a lot more common as the capacitances of nanophase materials ($\sim$ nF) have similar values to those of the grain boundary regions (also $\sim$ nF). This makes it more challenging to identify the different processes that may be present in a given nanomaterial. However, using logarithmic scales, as suggested by Jonscher (1983) may also reveal the presence of more than one process when the time constants are either too close together to be seen on a linear scale or the magnitude of one of the R,C and L components are too far apart. As stated before, one can always consider graphing them on a logarithmic scale if necessary. The videos shown in the supplementary illustrate how the difference in the time constants for each process can be used to detect the presence of more than one process but often it is necessary to transform the data into all four dielectric functions for a more complete assessment.

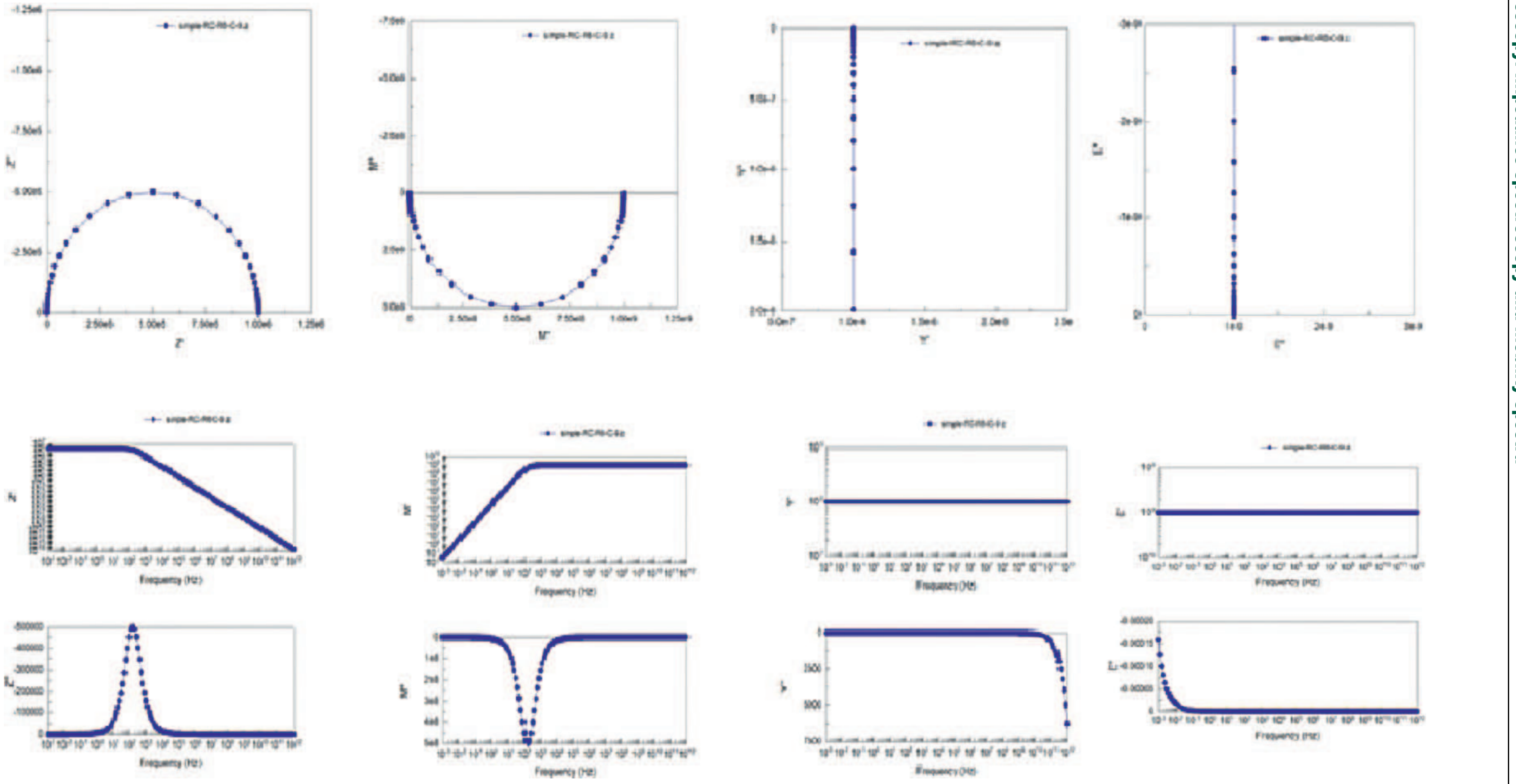

Fig. 15 Complex plots and Bode plots for a parallel RC circuit displaying all dielectric functions (Z*, Y*, M* and ε*) showing how the same equivalent circuit can appear totally different when looked at by converting to the other dielectric functions.

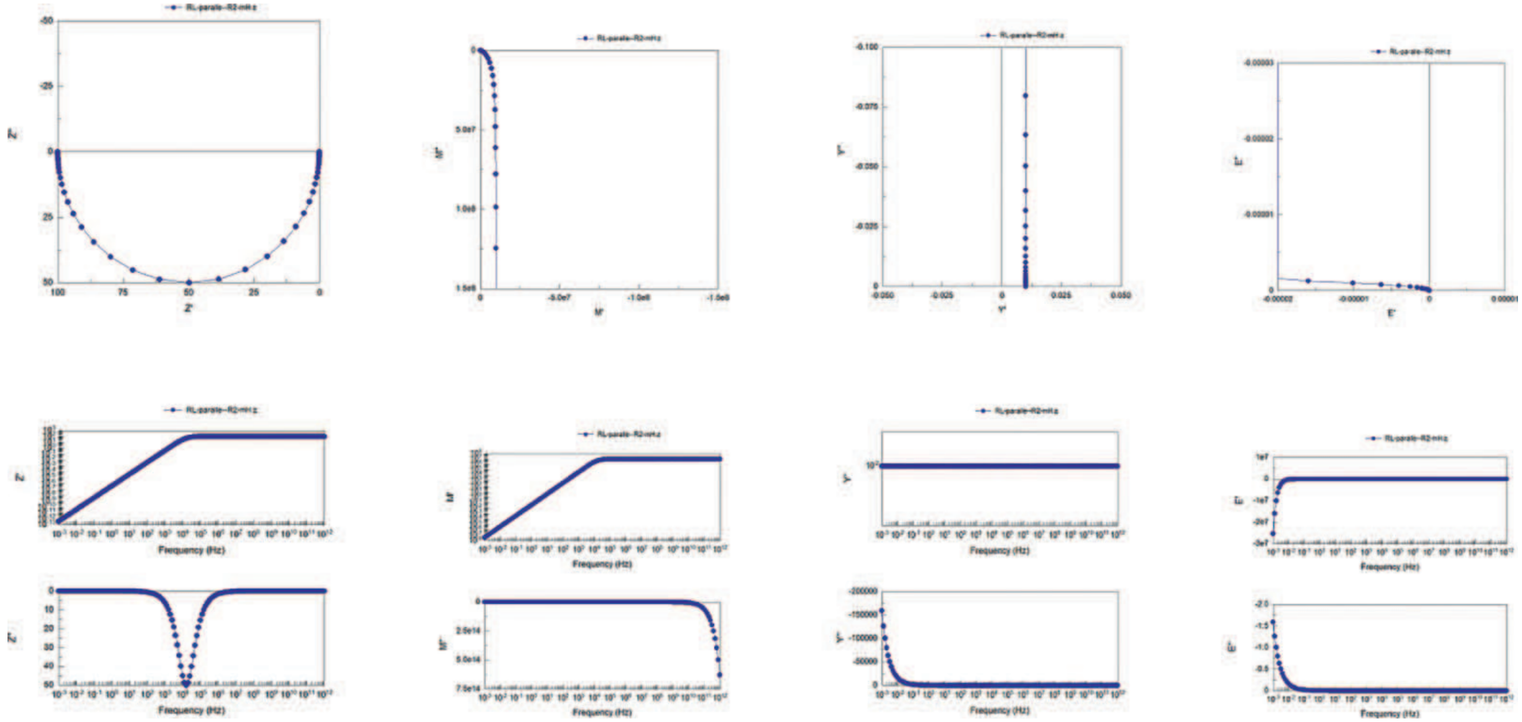

Fig. 16 Complex plots and Bode plots for a parallel RL circuit displaying all dielectric functions (Z^*, Y^*, M^* and ε^*) showing how the same equivalent circuit can appear totally different when looked at by converting to the other dielectric functions.

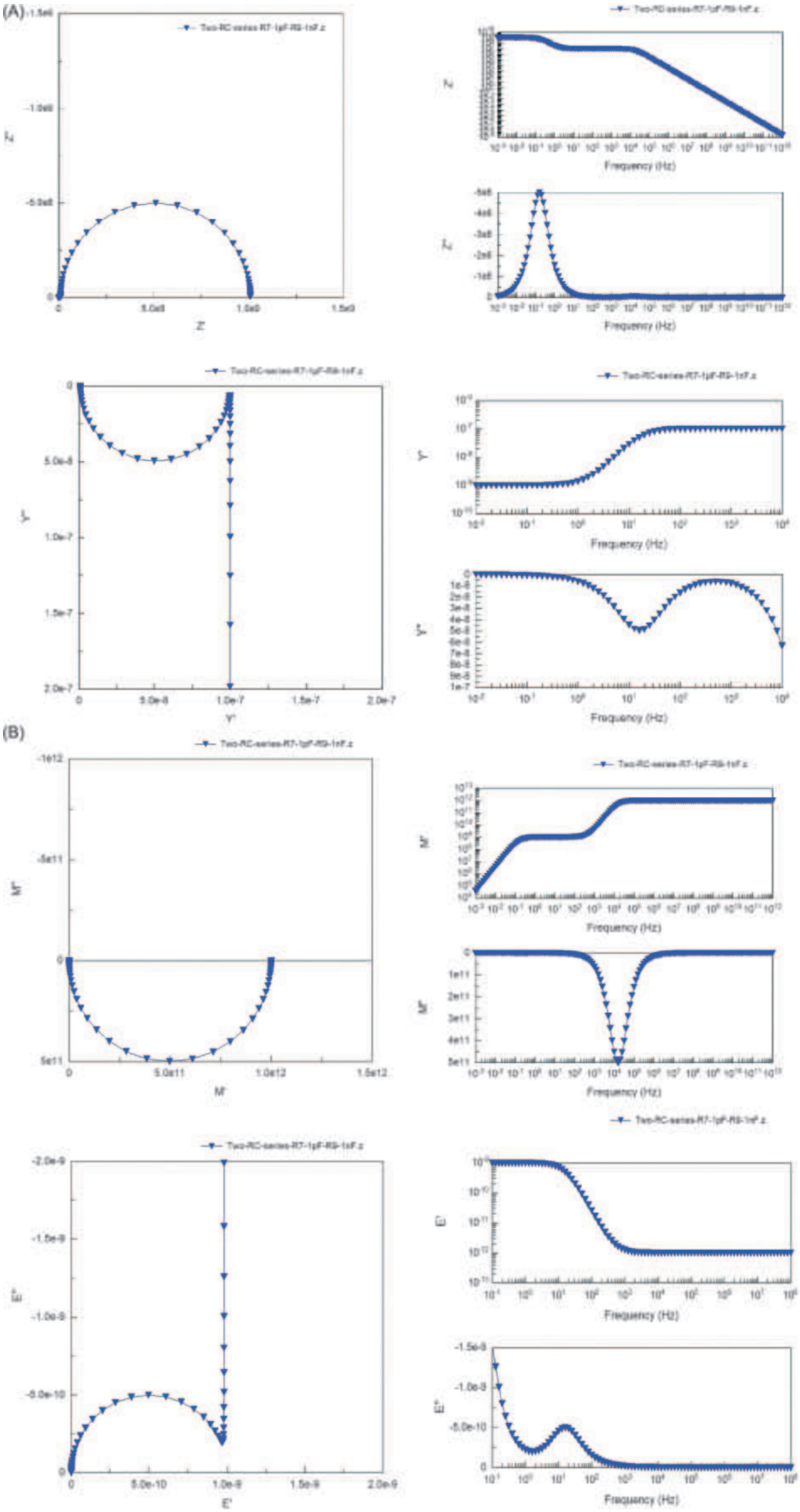

Fig. 17 Complex plots and Bode plots for two parallel RC circuits in series, where R_1 represents the bulk phase and has a much smaller resistance than the grain boundary phase in a semi-insulating material such as an ionic conductor. These graphs demonstrate that in this instance it is necessary to look at the frequency explicit plots to detect the presence of the second process. (A) Complex impedance same as Fig. 4D and its corresponding real and imaginary impedance. (B) Complex admittance and its corresponding real and imaginary admittance, (C) complex electric modulus and its corresponding real and imaginary electric modulus, (D) complex permittivity and its corresponding real and imaginary permittivity.

6) A semiconducting material with space charge polarization at the electrode/material interface

When making measurements of a semiconducting material, it is important to pay attention to whether the electrode contact is ohmic or not. If the electrode contact is non-ohmic or the charge transfer between the semiconductor and the electrode is inefficient, then an additional semicircle may be observed, which may be interpreted to be related to the space charge polarization at that interface. Fig. 18A and B present the simulation of the complex impedance and Bode plots of impedance graphs for a semiconductor in contact with a blocking electrode (Jamnik and Maier, 2001). Fig. 18A displays two curves. The semicircle closest to the origin coincides in both curves while the other semicircle does not. When the semicircles don't change, the response can be said to be representative of the bulk of the material (this needs to be confirmed by determining the geometric capacitance of the measured device). The Bode plots in Fig. 18B also highlight the difference between the two cases and can sometimes be used to confirm that one has more than one process occurring even if only one semicircle is visible. When electrode contact effects dominate, changing the size of the electrodes is one way to minimize the contact effects (Mebane and Gerhardt, 2006), changing the electrode material to get better matching with the surface potential of the material being electrode is another (Ou et al., 2003). Finally, if it is not possible to get a high quality ohmic contact, one can resort to superimposing a dc bias to decrease the Schottky barrier height (Bertram and Gerhardt, 2009), which will affect the barrier term but not the bulk term. The values of the circuit elements used for generating Fig. 18 were taken from an article by Mebane (Mebane and Gerhardt, 2006) where the size of the electrodes minimized the Schottky barrier error on the electrodes and thus resulted in a decrease in the size of the contact semicircle. This is also shown in one of the videos where the second semicircle (related to the electrode contact) decrease. Contact effects are quite common for semiconducting materials such as SiC (Huang et al., 2020) which usually forms Schottky barriers in contact with most metallic materials, but has recently been found to make good ohmic contact with Ni (He et al., 2019). Interestingly both types of contacts are desirable as certain applications may benefit from having a Schottky contact.

7) A highly conducting nanomaterial

For materials such as carbon nanotubes, graphene, indium tin oxide (ITO) or conducting polymers, it is not uncommon to observe a plethora of diverse responses as a function of the film thickness (Xia and Gerhardt, 2016; Sethuraman and Gerhardt, 2021), concentration of the active conducting species (Muhlbauer and Gerhardt, 2013; Jiang and Gerhardt, 2021; Sarı et al., 2006) and details about the substrate characteristics (Xia et al., 2019; Sethuraman and Gerhardt, 2021). More details regarding conducting materials and their electrical response (Jonscher, 1983). The images presented in Fig. 6, where combinations of parallel RC and parallel RL circuits in series were presented, can all occur in these types of materials. The case for the RL time constant being less than the RC time constant will be discussed here as it has been observed the most when these materials are in transition from a semi-insulating condition to a more conducting condition (Muhlbauer et al., 2014; Muhlbauer and Gerhardt, 2021). As discussed in the previous section (3), truly conducting materials will give rise to an RL in series after transitioning from an RL in parallel.

Fig. 19A depicts the simulation of a complex impedance graph for a carbon nanotube film in the process of transitioning from a semi-insulating film to a more conducting film (Muhlbauer and Gerhardt, 2021). The model here has been simplified in order to match with the simpler combination of RC and RL components where the time constant for the RL portion is less than that for the RC portion that was shown in Fig. 6. Hence the parallel RL portion appears at the lowest frequencies and shows up in the 4th quadrant. This type of behavior is observed in many other nanomaterial conducting films and devices made with films with nanodimensions.

Fig. 19B displays the real and imaginary impedance where both the inductive and the capacitive portions can be detected. They are then transformed into the admittance graphs shown in Fig. 19C and D, the electric modulus graphs in Fig. 19E and F and Fig. 19G and H for the permittivity. It is easy to see that the admittance is fairly comparable to the inverse of the impedance, while the electric modulus is also showing the same trends as the inverse of the dielectric permittivity. The most important item to note is that one can detect the presence of a negative permittivity or negative capacitance in Fig. 19H. When the films are made to contain more layers, the material response becomes much more conductive and the equivalent circuit further simplifies to a series RL (Muhlbauer and Gerhardt, 2021; Gerhardt, 2022). The videos provided also include cases that combine parallel RC and parallel RL in series and demonstrate all arrangements displayed in Fig. 6.

8) Bulk response and interfacial responses of multiphase systems

Many of the nanomaterial films are essentially composite films which initially incorporate the properties of the underlying substrate (Muhlbauer et al., 2013; Kumar and Gerhardt, 2012) and then eventually result in a response which is only related to the film itself once it becomes thick enough. The situation is again different for the impedance response of a multiphase bulk material where one can expect at least two different frequency dependent regions, one related to the matrix or majority phase and the other to the filler or minority phase. A lot of work has been done to characterize the electrical properties of polymer composites (Watt and Gerhardt, 2020a; Watt and Gerhardt, 2020b; Capozzi et al., 2008; Sullivan et al., 2014) and ceramic composite materials (Bertram and Gerhardt, 2009; Runyan et al., 2001b; Rudzik and Gerhardt, 2020) where the matrix is generally insulating and the filler is usually conducting and the results are found to be quite dependent on the size, shape and distribution of the two phases and the formation of percolating paths (Runyan et al., 2001a; Gerhardt et al., 2001).

The two-layer condenser, first proposed by Maxwell and Wagner to represent a layered material, contains layers of a material with conductivity σ_1 and dielectric permittivity ε_1 that are placed with alternating layers of a material with conductivity σ_2 and

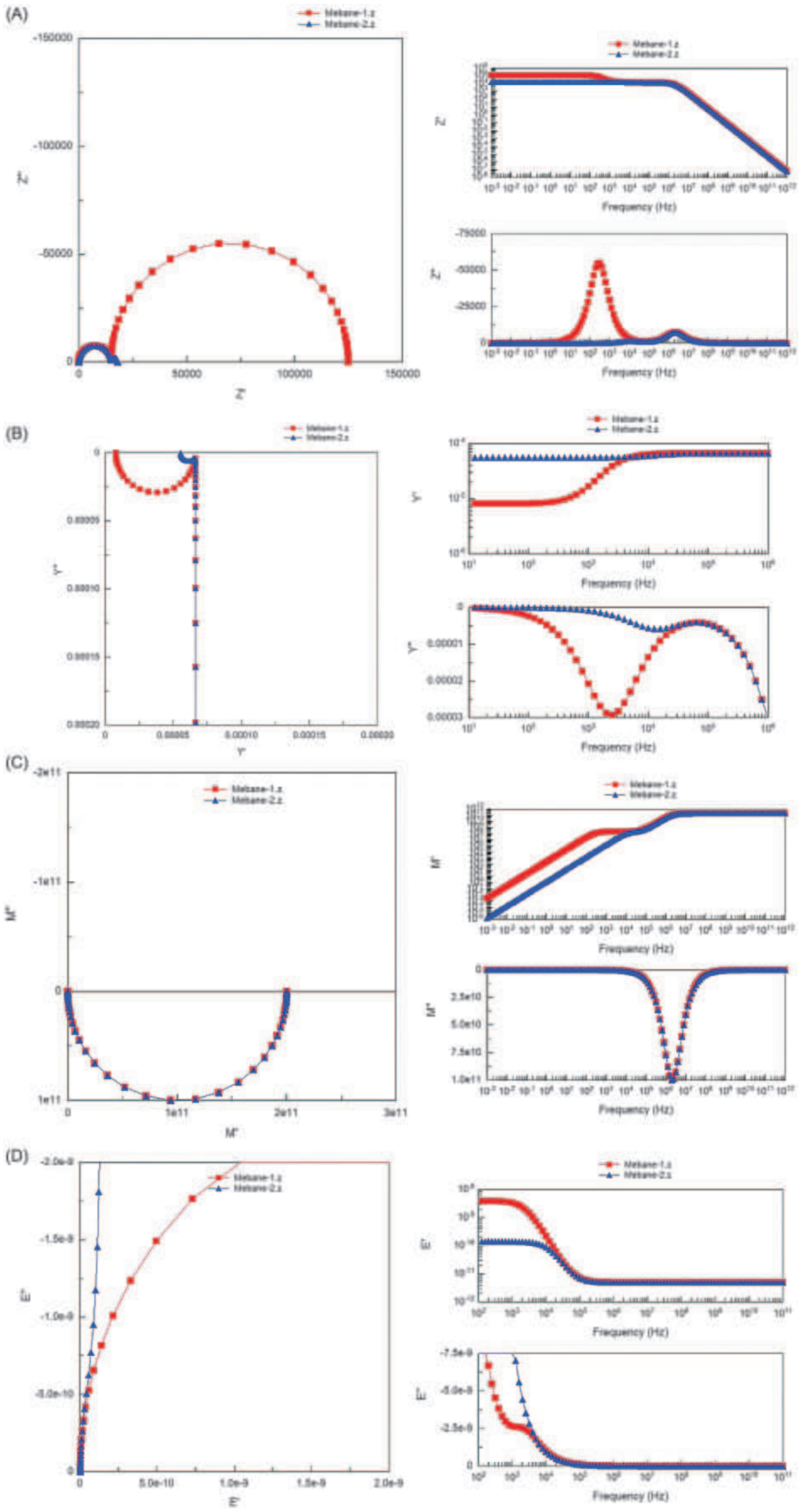

Fig. 18 Complex plots and Bode plots for two parallel RC circuits in series, where R_1 represents the electrical response of a bulk semiconductor phase and has a much smaller resistance than the blocking electrode. These graphs demonstrate that in this instance it is necessary to look at the frequency explicit plots to detect the presence of the second process. (A) Complex impedance same as Fig. 5A and its corresponding real and imaginary impedance. (B) Complex admittance and its corresponding real and imaginary admittance, (C) complex electric modulus and its corresponding real and imaginary electric modulus, (D) complex permittivity and its corresponding real and imaginary permittivity.

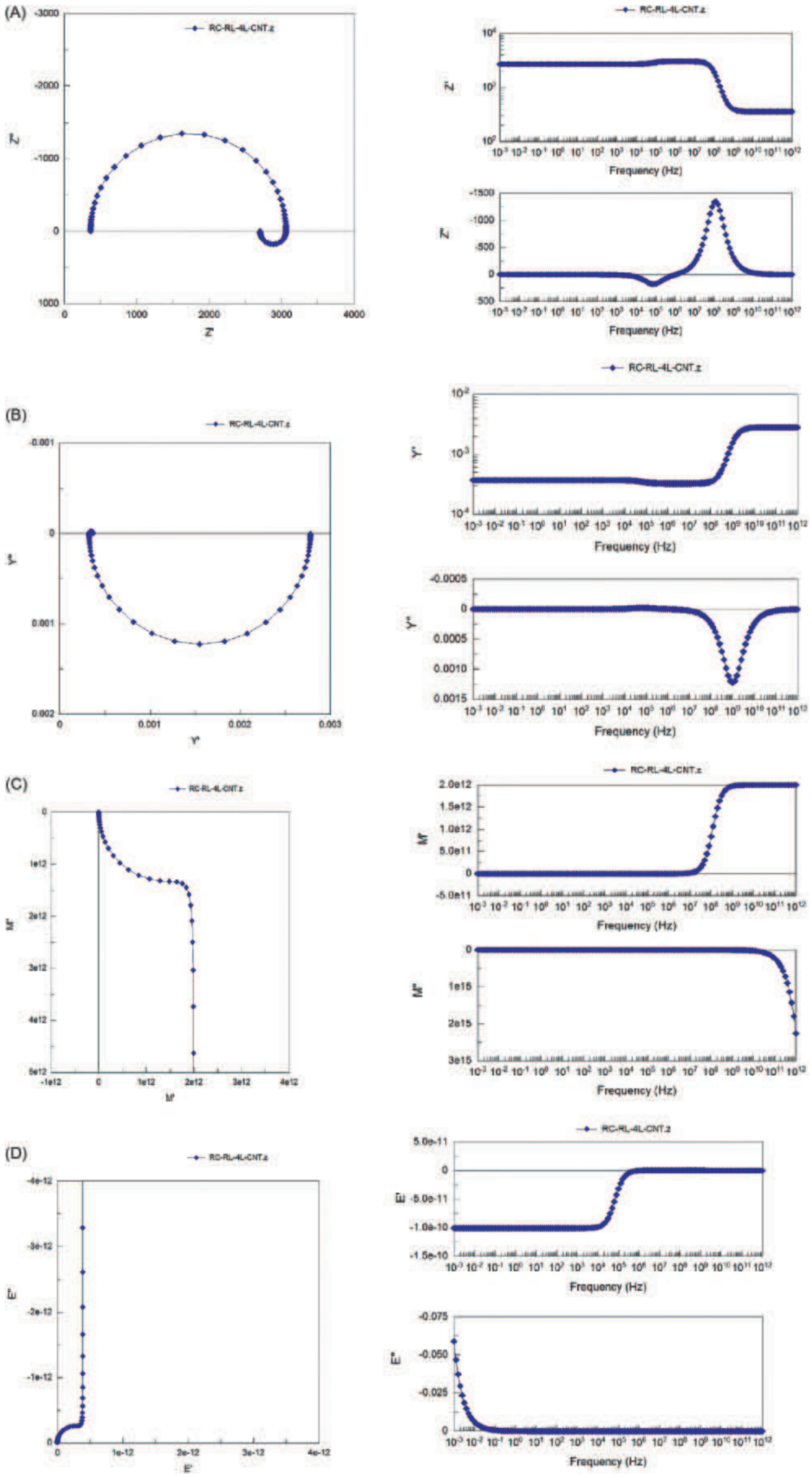

Fig. 19 Complex plots and Bode plots for a parallel RC circuit in series with a parallel RL circuit, where the resistance for the capacitive circuit is larger than the resistance for the inductive circuit. The RC circuit represents the behavior of the highly conducting nanomaterial film combined with the properties of the substrate while the inductive circuit displays the more conductive nature of the thin film nanomaterial. (A) Complex impedance (shown in Fig. 6) and its corresponding real and imaginary impedance displaying the capacitive circuit in the first quadrant and the inductive circuit in the 4th quadrant. (B) Complex admittance and its corresponding real and imaginary admittance the exact opposite as the impedance, (C) The complex electric modulus and its corresponding real and imaginary electric modulus display a partial semicircle shunted by a straight line which is also repeated for the complex permittivity and its corresponding real and imaginary permittivity displayed in (D). Major difference is seen in the real part of the permittivity where a negative dielectric permittivity is displayed.

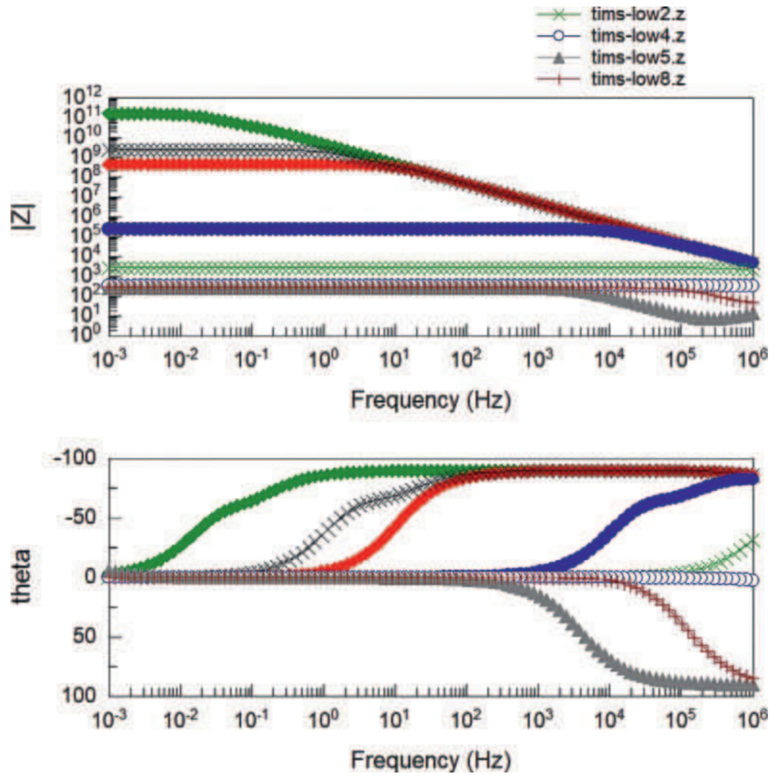

Fig. 20 Impedance magnitude |Z| and phase angle plotted vs. frequency for a series of insulator-conductor composites as a function of increasing conducting phase. |Z| graph needs to be plotted on a log scale so all measured values can be easily seen because of the large changes in impedance value. The phase angle displays the changeover from a capacitive dominated response to an inductive dominated response when the conducting nanoparticles are fully connected.

dielectric permittivity ε_2 and thicknesses of d_1 and d_2 (Von Hippel, 1954). This gives rise to the Maxwell-Wagner dielectric relaxation equations given below:

$$\varepsilon'_{M\text{-}W} = (\varepsilon_\infty)^{M\text{-}W}\left\{1 + \left[k/\left(1 + \omega^2\tau^2\right)\right]\right\} \tag{16}$$

where $k = [(\varepsilon_s)^{M\text{-}W}\text{-}(\varepsilon_\infty)^{M\text{-}W}]/(\varepsilon_\infty)^{M\text{-}W}$ and $\tau = [\varepsilon_1 d_2 + \varepsilon_2 d_1]/[\sigma_1 d_2 + \sigma_2 d_1]$ and

$$\varepsilon''_{M\text{-}W} = (\varepsilon_\infty)^{M\text{-}W}\left\{[\tau/\omega\tau_1\tau_2] + \left[k\omega\tau/\left(1 + \omega^2\tau^2\right)\right]\right\} \tag{17}$$

It should go without saying that quite different spectra will be obtained depending on what the values of σ_1, ε_1, σ_2, ε_2 are. The basic interpretation is that the response at the highest frequencies represents the "effective" response of the bulk of the material whereas the response at the lowest frequencies takes into account the interfaces between the two materials (Pruyn and Gerhardt, 2011). It should be added that it may be necessary to consider additional processes such as defect relaxation within the more insulating type material and/or additional space charge polarization processes at the interfaces of the more conducting material.

Because many insulating materials have resistivity $>10^{12}\Omega$-cm and conducting materials have resistivity less than $10^2\Omega$-cm, this leads to the possibility of seeing a 10 order of magnitude change or more in the measured properties, especially around the composition region where percolation occurs (Runyan et al., 2001b; Gerhardt et al., 2001). The easiest way to deal with such an enormous change in properties is to plot the impedance magnitude and phase angle vs. frequency as was done in Fig. 1. The impedance magnitude will allow visualizing the huge changes in the resistivity (impedance) more easily than the complex plots, while the phase angle will allow identification of capacitive and inductive responses quickly because of the sign difference.

Fig. 20 demonstrates this for a series of ceramic composites consisting of an insulating matrix filled with conducting nanoparticles. The values used here were taken from a study where borosilicate glass filled with antimony doped tin oxide nanoparticles were fabricated and their impedance behavior was characterized (Pruyn and Gerhardt, 2015). This is one of the first instances where the properties of the individual phases were measured separately by compressing powders of the constituent phases and measured in situ (Pruyn and Gerhardt, 2011) and then those values were used to determine the expected response of the fabricated composite materials. The behavior observed in this figure is quite representative of the behavior of insulator-conductor composites consisting of any material type that can undergo large changes in their electrical response. The large changes can be caused by some compositional variation (Rudzik and Gerhardt, 2020), some polymer conformation (Alig et al., 2007), some type of atmosphere control during measurements (Dong and Gerhardt, 1998), annealing prior to measurements (Joshi and Gerhardt, 2013) or some fabrication variations that can change the arrangement of the precursor phases (Gupta et al., 2006; Ou et al., 2006a; Ou et al., 2006b; Sullivan et al., 2016; Jin and Gerhardt, 2017; Watt and Gerhardt, 2020a). Characterizing the impedance properties of other materials such as hybrid organic-inorganic materials, metamaterials, biomaterials as well as superconductors as a function of composition, heat treatment or excitation with magnetic or optical signals would benefit from detailed studies. In fact the measurements could even be used to understand low temperature physics phenomena such as metal-superconductor transitions or insulator-superconductor transitions (Çavdar et al., 2011; Huang et al., 2022) to help the fields of spintronics, magnetoresistance and quantum devices.

Data analysis

Some guidelines have already been provided in the earlier sections, but some additional details will be given here. The most important concept is that of the geometric capacitance. The correct way to obtain the capacitance of a conducting process is to use the intercept of the impedance curve with the real axis to obtain, R, for that process (Gerhardt, 2005). To obtain the capacitance, the peak frequency must be identified (as was schematically shown in Fig. 2A) so that the following equation can be used:

$$C = 1/2\pi f_p R \tag{18}$$

Similarly, if one wishes to obtain the inductance of a conducting process represented by a parallel RL circuit as shown in Fig. 2B then we would locate the peak frequency and use the following equation

$$L = R/2\pi f_p \tag{19}$$

If one is interested in characterizing the bulk electrical properties of a given material or device, the measured capacitance/inductance should be on the same order of magnitude as that expected for the physical dimensions of the sample or device measured. This means that if such an analysis gives a capacitance/inductance that is not in agreement with the expected values, then the measured data is NOT related to the bulk of the material or the device and is most probably related to some type of space charge polarization mechanism (see equivalent circuit combinations in Table 5).

Table 6 lists the expected capacitances for materials with different dielectric constants and different thicknesses (Gerhardt, 2005). A detailed paper focused on the effect of the size of the electrodes and the thickness of the materials on capacitance and resistance was published in Kumar and Gerhardt (2012). Results revealed that changing the physical dimensions of the electrode contacts and thickness of the samples can change the value of the individual values of R and C while the time constant remains the same (Kumar and Gerhardt, 2012). Additional confirmation that a measured process is related to a bulk process can be obtained by varying the applied voltage or changing the size of the electrode contacts. The response for a bulk process should remain the same, irrespective of the values of the experimental parameters whereas space charge processes will show large changes as discussed in the section on the effect of space charge polarization at the electrode/material interface. Instead, if they scale with these variables, it may be possible to separate electrode contact effects from internal interface effects.

In cases where the impedance is so large that the intercept with the real axis is not available experimentally, the capacitance of the material will only be able to be obtained from either the real dielectric permittivity or the real electric modulus spectra. In most cases, the permittivity value is almost constant as a function of frequency (Cao and Gerhardt, 1990; Kumar and Gerhardt, 2012). The only time that a semicircle will appear in both the permittivity and the electric modulus is when there is a dipolar type relaxation present as was shown in the section describing a Debye relaxation with and without a leakage path (see Figs. 13 and 14).

Separating individual processes present in the bulk becomes a little bit more difficult. For example, separating dipolar relaxation from ionic conductivity in a good ionic conductor is not possible at temperatures where the ionic conductivity is high (Von Hippel, 1954) as demonstrated in Fig. 14. However, carrying out measurements at lower temperatures will suppress the ionic conductivity and allow detection of defect dipole relaxation (Nowick and Berry, 1972; Gerhardt et al., 1987). Likewise, if a material has a large fraction of electronic conductivity and only a small fraction of ionic conductivity, detecting the latter is almost impossible within a single set of experiments. In such cases, the usage of blocking electrodes and/or controlled atmospheres during the measurements should enhance or diminish a particular type of charge carrier (Etsell and Flengas, 1970; Dong and Gerhardt, 1998) that will aid in the data interpretation.

Electromagnetic simulation software

In recent years, a large number of commercially available software packages have become available. Many of the software packages come complete with electrostatics and electromagnetics modules. They are used mostly to model the performance of devices, but physical arrangements of structures (at various length scales) are also possible. Most commercially available simulation software is finite element based (FEA) or finite time difference based (FTDT). Some progress has been made on implementing these packages to help simulate impedance data at the microstructural level, but much more work needs to be done before they become commonplace. Several examples of numerical simulations applied to impedance measurements can be found in work by the author's research group (Kumar and Gerhardt, 2012; Jin and Gerhardt, 2014; Jin et al., 2016; Jin and Gerhardt, 2017). Additionally there are many additional COMSOL simulation proceedings papers that range from biomedical applications to antennas to resonators and beyond in the more than 2600 articles as of March 2022 located at https://www.comsol.com/papers-presentations. Simulations

Table 5 Equivalent circuits for some simple cases.

		Possible Time Constants
Debye relaxation	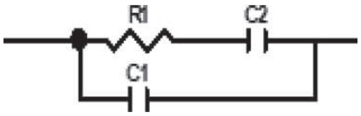	Series R_1C_2 Parallel R_1C_1
Debye relaxation with leakage path	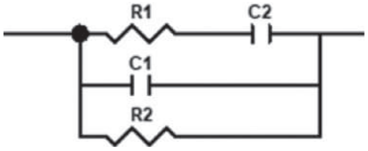	Series R_1C_2 Parallel R_1C_1 Parallel R_2C_1 Parallel R_2C_2
Semi-insulating conductor	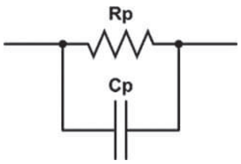	Parallel R_PC_P
High conductivity conductor	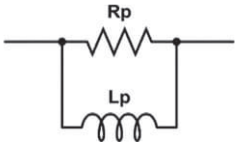	Parallel R_PL_P
A solid state ionic material with different grain boundary responses	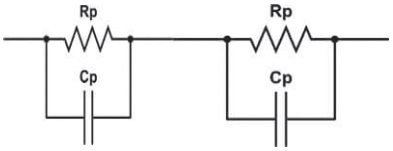	Parallel $R_{P1}C_{P1}$ Parallel $R_{P2}C_{P2}$ Series $R_{P1}C_{P2}$ Series $R_{P2}C_{P1}$
A semiconductor with space charge electrodes	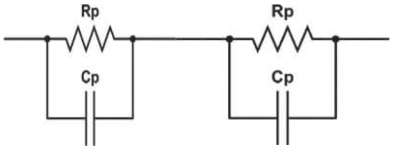	Parallel $R_{P1}C_{P1}$ Parallel $R_{P2}C_{P2}$ Series $R_{P1}C_{P2}$ Series $R_{P2}C_{P1}$
A highly conducting nanomaterial	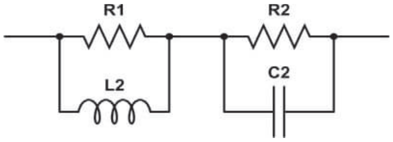	Parallel R_1L_2 Parallel R_2C_2 Series R_1C_2 Series R_2L_2
Bulk and interfacial effects in multiphase systems	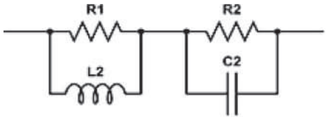 or 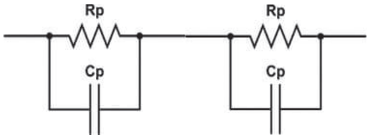	Any combination as above

Table 6 Effect of physical dimensions on measured capacitance for a film with different thicknesses.

Dielectric constant	*Physical dimensions* *t(m) with A= $5 \times 10^{-5}m^2$*	*Measured capacitance (F)*
2	1×10^{-3}	8.85×10^{-13}
2	1×10^{-6}	8.85×10^{-10}
2	1×10^{-9}	8.85×10^{-07}
10	1×10^{-3}	4.43×10^{-12}
10	1×10^{-6}	4.43×10^{-09}
10	1×10^{-9}	4.43×10^{-06}
100	1×10^{-3}	4.43×10^{-11}
100	1×10^{-6}	4.43×10^{-08}
100	1×10^{-9}	4.43×10^{-05}
1000	1×10^{-3}	4.43×10^{-10}
1000	1×10^{-6}	4.43×10^{-07}
1000	1×10^{-9}	4.43×10^{-04}

directly related to impedance and dielectric spectroscopy as discussed here can also be found in papers by Kumar and Gerhardt (2009), Jin et al. (2016), Gerhardt and Jin (2015), Jin and Gerhardt (2017), Xia et al. (2019) and Jiang and Gerhardt (2021).

Recent advances (what to expect in the future)

Impedance spectroscopy of solid state materials continues to be used in a wide variety of fields and the number of applications continues to grow. Besides being useful as a way to determine the bulk electrical properties of materials and devices, it can also be used as a way to determine: (1) sensitivity and selectivity of gas sensors (Huang et al., 2014); (2) the degree of biocompatibility of new biomedical implants (Lau, 2017); (3) methods of quality control (Rath and Gerhardt, 2022; Titus et al., 2022); and (4) non-destructive characterization of materials used in electronics (Ramachandran et al., 2015), monitoring in structural applications (Ozer and Feng, 2020) and more.

More recent developments include magneto-impedance measurements (Tang, 2022), photostimulated-impedance measurements (Drisko et al., 2019) and bioimpedance measurements of tissue (Khalil et al., 2014). These new methods will be a great help to the burgeoning fields of spintronics, giant magnetoresistance, electro-optical devices and biomedical engineering. In addition, impedance measurements can be taken at all length scales and help detect different electric processes in materials, devices and structures. Localized measurements have been acquired using macro-, micro- and nano-sized electrodes for a number of years (Fleig and Maier, 1999; Kalinin and Bonnell, 2002; Descoteaux et al., 2020). However, simultaneous impedance and topographical data acquisition in an AFM/STM with different scanning probes has the potential to revolutionize the usage of impedance spectroscopy in the future (Kalinin et al., 2006; Rodriguez et al., 2006; Jesse et al., 2007; Balke et al., 2010; Gramse et al., 2014; Gruverman et al., 2019). Single frequency impedance amplitude and phase image scans have been collected using tapping mode or conductive AFM mode (Kalinin and Bonnell, 2002; Peng et al., 2008; Bertram and Gerhardt, 2009; Waddell et al., 2009; Xia and Gerhardt, 2016) and are being related to topographical images in order to understand what role different features play. The main challenge is that the smaller the probe is, the higher the impedance will be, making it difficult to acquire data as a function of frequency as the equipment specifications can be exceeded easily (Gerhardt, 2022). The band excitation mode of data acquisition (Jesse et al., 2007) is potentially one way to bypass that barrier but there are still some challenges. It is anticipated that with further developments in probe tips and measurement set ups as well as integration of multiple tools such as AFMs embedded in SEMs, AFM imaging in STEMs, nano-IR probes as well as continued testing of different measurement tools on the AFM, many more exciting experiments will be conducted.

Conclusion

Attempts to simplify the many facets of impedance spectroscopy have been made throughout this manuscript. The author has purposely excluded discussion of more complex equivalent circuits, as these only modify the basic concepts described here and more detailed examples can be found in the published literature for specific materials and devices. Instead, great effort was made to describe the importance of using all four dielectric functions to help derive understanding about the electrical processes being probed in solid state materials starting with the relationships between impedance and dielectric properties that have been the hallmark of the author's work (Cao and Gerhardt, 1990; Gerhardt, 1994). As such quite a few references from the author's own work were cited for additional context. For more short examples the reader is referred to a chapter by Bonanos et al. (2005) and three MRS conference proceedings books that the author was responsible for editing. These were published in print but are now all available on the MRS online proceedings by individual papers (Gerhardt et al., 1996; Gerhardt et al., 1998; Gerhardt et al., 2002).

Electrochemical impedance spectroscopy (EIS), which is mainly used to study corrosion of metallic materials (Scully et al., 1993), and is the basis for understanding electrical phenomena in the components of batteries, fuel cells and supercapacitors, was mostly excluded. There are excellent edited books and monographs (Lvovich, 2012; Scully et al., 1993; Orazem and Tribollet, 2017) that describe the use of liquid electrolytes that are necessary for many of these applications and others. It is also important to mention the two additional impedance edited books (Macdonald, 1987; Barsoukov and Macdonald, 2005) as well as the seminal work in dielectric spectroscopy by Von Hippel (1954) and Jonscher (1983, 1996) should be studied in more detail. Readers are urged to carefully review the extensive published literature in the subject matter of their own research interest, keeping in mind some of the guidelines presented here.

Multimedia

All videos provided for the online version of this article were generated by Yifan Jin and Rosario A. Gerhardt using a generalized equation method (Jin and Gerhardt, 2022). Videos 1–10 in the online version at https://doi.org/10.1016/B978-0-323-90800-9.00021-4 include the effect of changing the time constant in all parallel RC and RL individual cases as well as the series combinations of the parallel RCs, RLs or RC and RL combinations.

Acknowledgments

The author is indebted to the Georgia Institute of Technology for giving her the opportunity to teach a full semester course every couple of years on the subject of impedance and dielectric spectroscopy for the last 30 years and to the many students who have taken her class and have contributed to her developing a better understanding of the subject matter. Additionally, the author would like to acknowledge the funding agencies that have supported her research work over the years (NSF, DOE, NASA), as well as to the many graduate students and collaborators she has interacted with. Finally, thanks to Goizueta Foundation Chair position for affording her the luxury of carving her own unique path in research.

References

Alig I, Lellinger D, Dudkin SM, and Po˝tschke P (2007) Conductivity spectroscopy on melt processed polypropyleneemultiwalled carbon nanotube composites: Recovery after shear and crystallization. *Polymer* 48: 1020–1029.

Anderson MP and Nowick AS (1981) Relaxation peaks produced by defect complexes in cerium dioxide doped with trivalent cations. *Journal de Physique, Colloque* 42: C5-823–C5-828.

Appleby DJR, Ponon NK, Kwa KSK, Zou B, Petrov PK, Wang T, Alford NM, and O'Neill A (2014) Experimental observation of negative capacitance in ferroelectrics at room temperature. *Nano Letters* 14: 3864–3868.

Austin AG and Mott NF (1969) Polarons in crystalline and non-crystalline materials. *Advances in Physics* 18(71): 41–102.

Balke N, Jesse S, Kim Y, Adamczyk L, Tselev A, Ivanov IN, Dudney NJ, and Kalinin SV (2010) Real space mapping of Li-Ion transport in amorphous Si anodes with nanometer resolution. *Nano Letters* 10(9): 3420–3425.

Barbero G and Lelidis I (2017) Analysis of Warburg's impedance and its equivalent electric circuits. *Physical Chemistry Chemical Physics* 19: 24934–24944.

Barsoukov E and Macdonald JR (eds.) (2005) *Impedance Spectroscopy: Theory, Experiment, and Applications*, 2nd edn John Wiley.

Barsoum M (2019) *Fundamentals of Ceramics*. *Series in Materials Science and Engineering*. CRC Press. ch. 7.

Bauerle JE (1969) Study of solid electrolyte polarization by a complex admittance method. *Journal of Physics and Chemistry of Solids* 30(12): 2657–2670.

Bertram BD and Gerhardt RA (2009) Room temperature properties of electrical contacts to alumina composites containing silicon carbide whiskers. *Journal of Applied Physiology* 105: 074902.

Bertram BD and Gerhardt RA (2011a) Properties and applications of ceramic matrix composites reinforced with silicon carbide whiskers composites. In: Gerhardt RA (ed.) *Properties and Applications of Silicon Carbides*, pp. 197–230. In-Tech Publications.

Bertram BD and Gerhardt RA (2011b) Effects of frequency, percolation, and axisymmetric microstructure on the electrical response of hot-pressed Alumina–Silicon carbide whisker composites. *Journal of the American Ceramic Society* 94(4): 1125–1132.

Bisquert J (2021) A frequency domain analysis of the excitability and bifurcations of the FitzHugh–Nagumo neuron model. *The Journal of Physical Chemistry Letters* 12(45): 11005–11101.

Block H and North AM (1970) Dielectric relaxation in polymer solutions. *Advances in Molecular Relaxation Processes* 1(4): 309–374.

Bonanos N, Steele BCH, and Butler EP (2005) Applications of impedance spectroscopy. In: Barsoukov E and Macdonald JR (eds.) *Impedance Spectroscopy: Theory, Experiment, and Applications*, 2nd edn. John Wiley.

Bou A and Bisquert J (2021) Impedance spectroscopy dynamics of biological neural elements: From memristors to neurons and synapses. *The Journal of Physical Chemistry B* 125(35): 9934–9949.

Boukamp BA (1993) Practical application of the Kramers-Kronig transformation on impedance measurements in solid state electrochemistry. *Solid State Ionics* 62: 131–141.

Boukamp BA (2020) Distribution (Function) of relaxation times, successor to complex non-linear least squares analysis of electrochemical impedance spectroscopy? *Journal of Physics: Energy* 2(4): 042001.

Brug GJ, Van Den Eeden ALG, Sluyters-Rehbach M, and Sluyters JH (1984) The analysis of electrode impedances complicated by the presence of a constant phase element. *Journal of Electroanalytical Chemistry* 176: 275–295.

Buchanan RC (ed.) (2004) *Ceramic Materials for Electronics*, 3rd edn. Marcel Dekker. chs. 1 and 2.

Buller S, Thele M, De Doncker RDAA, and Karden E (2005) Impedance-based simulation models of supercapacitors and Li-Ion batteries for power electronic applications. *IEEE Transactions on Industry Applications* 41: 3.

Cao W and Gerhardt R (1990) Calculation of various relaxation times and conductivity for a single dielectric relaxation process. *Solid State Ionics* 42: 213–221.

Capozzi CJ, Li Z, Gerhardt RA, and Samuels RJ (2008) Impedance spectroscopy and optical properties of polymethylmethacrylate/indium tin oxide nanocomposites with 3-dimensional voronoi microstructures. *Journal of Applied Physics* 104(11): 114902/1–114902/10.

Çavdar S, Koralay H, and Altında S (2011) Effect of vanadium substitution on the dielectric properties of glass ceramic Bi-2212 superconductor. *Journal of Low Temperature Physics* 164: 102–114.

Chadwick AV (2007) Transport in defective ionic materials: From bulk t nanocrystals. *Physica Status Solidi* 204: 631–641.

Cole KS and Cole RH (1942) Dispersion and absorption in dielectrics II. Direct current characteristics. *Journal of Chemical Physics* 10(2): 98–105.

Cruz-Manzo S and Greenwood P (2020) An impedance model based on a transmission line circuit and a frequency dispersion Warburg component for the study of EIS in Li-ion batteries. *Journal of Electroanalytical Chemistry* 871: 11430.

Davidson DW and Cole RH (1950) Dielectric relaxation in glycerine. *The Journal of Chemical Physics* 18(10): 1417.

Descoteaux M, Sunnerberg JP, and Staii C (2020) Quantitative characterization of dielectric properties of nanoparticles using electrostatic force microscopy. *AIP Advances* 10: 115118.

Dong M and Gerhardt RA (1998) Frequency and temperature dependence of the dielectric properties of ferroelectric materials. In: *1998 Annual Report Conference on Electrical Insulation and Dielectric Phenomena (Cat. No. 98CH36257)* 327–330.

Drisko JA, Feldman AD, Quinlan F, Booth J, Orloff N, and Long C (2019) Impedance tuning with photoconductors to 40 GHz, IEEE microwave and wireless components letters. *IET Optoelectronics* 13: 177–182.

Etsell TE and Flengas SN (1970) The electrical properties of solid oxide electrolytes. *Chemical Reviews* 70(3): 339–376.

Figueroa D, Fontanella J, Wintersgill M, Chadwick A, and Andeen C (1984) Dielectric relaxation, ionic conductivity and activation volumes in cubic lead fluoride doped with alkali-metal cations. *Journal of Physics C: Solid State Physics* 17(25): 4399.

Fleig J and Maier J (1999) Microcontact impedance measurements of individual highly conductive grain boundaries: General aspects and application to AgCl. *Physical Chemistry Chemical Physics* 1: 3315–3320.

Fujiwara H (2007) *Spectroscopic Ellipsometry: Principles and Applications*, 1st edn. John Wiley.

Gerhardt R (1994) Dielectric and impedance spectroscopy revisited: Distinguishing localized relaxation from long range conductivity. *Journal of Physics and Chemistry of Solids* 55(12): 1491–1506.

Gerhardt RA (2005) Impedance spectroscopy and mobility spectra. In: Bassani G, Liedl G, and Wyder P (eds.) *Encyclopedia of Condensed Matter Physics*, pp. 350–363. Elsevier Press.

Gerhardt RA (2013) Impedance and dielectric spectroscopy of nanoparticulate films and composites. In: *Nanotech 2013 Conference Proceedings, Paper 1433*.

Gerhardt RA (2022) What is impedance and dielectric spectroscopy? In: *IEEE Instrumentation and Measurement Magazine* 14–20.

Gerhardt R and Nowick AS (1986) The grain boundary conductivity effect in ceria doped with various trivalent cations. Part I: Electrical behavior. *Journal of the American Ceramic Society* 69(9): 641–646.

Gerhardt RA and Jin Y (2015) Simulation of the impedance response of materials with more than one electrical path. In: *COMSOL Multiphysics Users Workshop Proceedings* from Boston, October 8, 2015.

Gerhardt R, Nowick AS, Mochel ME, and Dumler I (1986) The grain boundary conductivity effect in ceria doped with trivalent cations. Part II: Microstructure and microanalysis. *Journal of the American Ceramic Society* 69(9): 647–651.

Gerhardt R, Lee WK, and Nowick AS (1987) Dielectric and anelastic relaxation in Sc doped Ceria. *Journal of Physics and Chemistry of Solids* 48(6): 563–570.

Gerhardt RA, Taylor SR, and Garboczi EJ (eds.) (1996) *Electrically based microstructural characterization*, *MRS Symposium Proceedings* In: vol. 411.

Gerhardt RA, Alim MA, and Taylor SR (eds.) (1998) *Electrically based microstructural characterization II*, *MRS Symposium Proceedings* In: vol. 500.

Gerhardt RA, Runyan J, Sana C, McLachlan DS, and Ruh R (2001) Electrical Properties of BN matrix composites—Part III: Observations near percolation threshold in BN-B$_4$C composites. *Journal of the American Ceramic Society* 84(10): 2335–2342.

Gerhardt RA, Washabaugh AP, Alim MA, and Choi GM (eds.) (2002) *Electrically based microstructural characterization III*, *MRS Symposium Proceedings* In: vol. 699.

Gerhardt-Anderson R and Nowick AS (1981) Ionic conductivity of CeO$_2$ with trivalent dopants of different ionic radii. *Solid State Ionics* 5: 547–550.

Gerhardt-Anderson R and Nowick AS (1985) The role of dopant ionic radius in 02- conducting solid electrolytes. In: Simkovich G and Stubican VS (eds.) *Transport in Non-Stoichiometric Compounds*, *NATO ASI Series*, vol. 129, pp. 111–124.

Goldfarb D and Stoll S (eds.) (2018) *EPR Spectroscopy: Fundamentals and Methods*. John Wiley.

Gramse G, Kasper M, Fumagalli L, Gomila G, Hinterdorfer P, and Kienberger F (2014) Calibrated complex impedance and permittivity measurements with scanning microwave microscopy. *Nanotechnology* 25: 145703.

Gruverman A, Alexe M, and Meier D (2019) Piezoresponse force microscopy and nanoferroic Phenomena. *Nature Communications* 10: 1661.

Guo X and Maier J (2001) Grain boundary blocking effect in Zirconia: A schottky barrier analysis. *Journal of the Electrochemical Society* 148(3): E121.

Gupta S, Ou R, and Gerhardt RA (2006) Effect of fabrication method on the electrical properties of ABS/carbon black composites. *Journal of Electronic Materials* 35(2): 224–229.

Hatada K and Kitayama T (2004) *NMR Spectroscopy of Polymers*. *Springer Laboratory Series*. Springer.

Havriliak S and Negami S (1967) A complex plane representation of dielectric and mechanical relaxation processes in some polymers. *Polymer* 8: 161–210.

He Y, Lv H, Tang X, Song Q, Zhang Y, Guo T, He X, Zhang Y, and Zhang Y (2019) Ohmic contacts simultaneously formed on n-type and p-type 4H-SiC at low temperature. *Journal of Alloys and Compounds* 805: 999–1003.

Hill RM and Dissado (1985) Debye and non-Debye relaxation. *Journal of Physics C: Solid State Physics* 18: 3829.

Hodge IM, Ingram MD, and West AR (1976) Impedance and modulus spectroscopy of poly-crystalline solid electrolytes. *Journal of Electroanalytical Chemistry* 74(2): 125–143.

Huang L, Jiang P, Wang D, Luo Y, Li M, Lee H, and Gerhardt RA (2014) A novel paper-based flexible ammonia gas sensor via silver and SWNT-PABS inkjet printing. *Sensors and Actuators B: Chemical* 197: 308–313.

Huang L, Tao H, Ma Y, and Gu X (2020) A barrier model for metal-SiC contact system. *Superlattices and Microstructures* 140: 106475.

Huang EW, La Nave G, and Phillips PW (2022) Discrete symmetry breaking defines the Mott quartic fixed point. *Nature Physics* 18: 511–516.

Hughes LA, Marple M, and van Benthem K (2018) Electrostatic fields control grain boundary structure in SrTiO$_3$. *Applied Physics Letters* 113: 041604.

Hwang HA, Kirkpatrick KA, and Mason TO (1997) Experimental limitations in impedance spectroscopy: Part IV. Electrode contact effects. *Solid State Ionics* 98: 93–104.

Jamnik J and Maier J (2001) Generalised equivalent circuits for mass and charge transport: Chemical capacitance and its implications. *Physical Chemistry Chemical Physics* 3: 1668–1678.

Jesse S, Kalinin SV, Proksch R, Baddorf AP, and Rodriguez BJ (2007) The band excitation method in scanning probe microscopy for rapid mapping of energy dissipation on the nanoscale. *Nanotechnology* 18: 435503.

Jiang KS and Gerhardt RA (2021) Fabrication and supercapacitor applications of multiwall carbon nanotube thin films. *Journal of Carbon Research* 7(4): 70.

Jin Y and Gerhardt RA (2014) Prediction of the percolation threshold and electrical conductivity of self-assembled antimony-doped tin oxide nanoparticles into ordered structures in PMMA/ATO nanocomposites. *ACS Applied Materials and Interfaces* 6(24): 22264–22271.

Jin Y and Gerhardt RA (2017) Fabrication and simulation of semi-transparent and flexible PMMA/ATO conductive nanocomposites obtained by compression molding at different temperatures and pressures. *AIP Advances* 7: 055004.

Jin Y and Gerhardt RA (2022) New Simplified Simulation Method for Predicting Impedance Behavior of Multiple Circuits. In: *IEEE I2MTC Poster Presentation*.

Jin Y, Xia N, and Gerhardt RA (2016) Enhanced dielectric properties of polymer matrix composites with BaTiO$_3$ and MWCNT hybrid fillers using simple phase separation. *NanoEnergy* 30: 407–416.

Jonscher AK (1983) *Dielectric Relaxation in Solids*. Chelsea Dielectrics Press.

Jonscher AK (1996) *Universal Relaxation Law: A Sequel to Dielectric Relaxation in Solids*. Chelsea Dielectrics Press.

Joshi SM and Gerhardt RA (2013) Effect of annealing atmosphere and temperature on the electrical properties of spin coated colloidal indium tin oxide films. *Journal of Materials Science* 48(3): 1465.

Joshi SM, Xia N, Gerhardt RA, Berta Y, Woods E, Tian M, and Ding Y (2020) Detection of plasmonic behavior in colloidal ITO thin films by impedance spectroscopy. *MRS Communications* 10(2): 278–285.

Kalinin SV and Bonnell D (2002) Scanning impedance microscopy: From impedance spectra to impedance images. In: *MRS Conference Proceedings 699, Published online in 2020*.

Kalinin SV, Rodriguez BJ, Jesse S, Shin J, Baddorf AP, Gupta P, Jain H, Williams DB, and Gruverman A (2006) Vector piezoresponse force microscopy. *Microscopy and Microanalysis* 12: 206–220.

Kao KC (2004) *Dielectric Phenomena in Solids With Emphasis on Physical Concepts of Electronic Processes*. Academic Press.

Kasap SO (1997) *Principles of Electrical Engineering Materials and Devices*. McGraw-Hill. ch. 5.

Khalil SF, Mohktar MS, and Ibrahim F (2014) The theory and fundamentals of bioimpedance analysis in clinical status monitoring and diagnosis of diseases. *Sensors (Basel)* 14(6): 10895–10928.

Kosacki I and Anderson HU (2001) Grain boundary effects in nanocrystalline mixed conducting films. In: Jürgen Buschow KH, Cahn RW, Flemings MC, Ilschner B, Kramer EJ, Mahajan S, and Veyssière P (eds.) *Encyclopedia of Materials: Science and Technology*, pp. 3609–3617. Elsevier.

Kulikovsky KK (2016) PEM fuel cell impedance at open circuit. *Journal of the Electrochemical Society* 163: F319.

Kumar S and Gerhardt RA (2009) Numerical study of the electrical properties of insulating thin films deposited on a conductive substrate. In: *COMSOL Users Workshop Proceedings, Boston* .

Kumar S and Gerhardt RA (2012) Numerical study of the electrical properties of insulating thin films deposited on a conductive substrate: Model development, effect of film thickness and electrode size. *Measurement Science and Technology* 23: 035602. (pp. 17).

Kumar S, Rajaraman S, Gerhardt RA, Wang ZL, and Hesketh PJ (2005) Tin oxide nanosensor fabrication using AC dielectrophoretic manipulation of nanobelts. *Electrochimica Acta* 51(5): 943–951.

Lau EW (2017) Leads and electrodes for cardiac implantable electronic devices. In: *Clinical Cardiac Pacing, Defibrillation and Resynchronization Therapy*, 5th edn, 313–351.

Li S, Gao J, Cao X, Li W, Zhang Z, and Zhang D (2014) Wideband, thin, and polarization-insensitive perfect absorber based the double octagonal rings metamaterials and lumped resistances. *Journal of Applied Physics* 116: 043710.

Lvovich VF (2012) *Impedance Spectroscopy: Applications to Electrochemical and Dielectric Phenomena*. John Wiley & sons.

Macdonald JR (ed.) (1987) *Impedance Spectroscopy: Emphasizing Solid Materials and Systems*. John Wiley. ch. 2.

Maier J (2004) *Physical Chemistry of Ionic Materials: Ions and Electrons in Solids*. John Wiley.

Mebane DS and Gerhardt RA (2006) Interpreting impedance response of silicon carbide whisker/alumina composites through microstructural simulation. *Journal of the American Ceramic Society* 89(2): 538–543.

Muhlbauer RL and Gerhardt RA (2013) Determining in-plane and thru-plane percolation thresholds for carbon nanotube thin films deposited on paper substrates using impedance spectroscopy. *Materials Research Society Symposium Proceedings* 1549: 1032.

Muhlbauer RL and Gerhardt RA (2021) Impedance spectroscopy of short multiwalled carbon nanotube networks deposited on a paper substrate: Tracking the evolution of in-plane and thru-plane electronic properties. *Journal of Materials Science* 56(4): 3256–3267.

Muhlbauer RL, Joshi SM, and Gerhardt RA (2013) The effect of drying technique on the electrical resistance of multiwalled carbon nanotube thin films on paper substrates with different pore size. *Journal of Materials Research* 28(12): 1617–1624.

Muhlbauer RL, Pruyn TL, Puckett WT, and Gerhardt RA (2014) Effect of graphitic filler size and shape on the microstructure, electrical percolation behavior and thermal properties of nanostructured multilayered carbon films deposited onto paper substrates. *Journal of Materials Research* 29(3): 472.

Muralidharan VS (1997) Warburg impedance—Basics revisited. *Anti-Corrosion Methods and Materials* 44(1): 26–29.

Nowick AS and Berry BS (1972) *Anelastic Relaxation in Crystalline Solids*. Academic Press.

Omar A and Abdullah H (2014) Electron transport analysis in zinc oxide-based dye-sensitized solar cells: A review. *Renewable and Sustainable Energy Reviews* 31: 149–157.

Orazem ME and Tribollet B (2017) *Electrochemical Impedance Spectroscopy*, 2nd edn John Wiley.

Ou R, Samuels R, and Gerhardt RA (2003) A structure-electrical property study of anisotropic polyaniline films. *Journal of Polymer Science Part B: Polymer Physics* 41(8): 823–841.

Ou R, Cui G, Gerhardt RA, and Samuels RJ (2006a) Effect of stretching on the structure and electrical conductivity of doped and undoped poly(phenylene vinylene) thin films. *Electrochimica Acta* 51(8-9): 1728–1735.

Ou R, Gupta S, Parker CA, and Gerhardt RA (2006b) Fabrication and electrical conductivity of PMMA/CB composites: Comparison between an ordered carbon black-nanowire segregated structure and a randomly dispersed carbon black nanostructure. *The Journal of Physical Chemistry. B* 110(45): 22362–22370.

Ozer E and Feng MQ (2020) Structural health monitoring. In: *Start-Up Creation*, 2nd edn. Elsevier.

Panigrahi J, Vandana SR, Batra N, Gope J, Sharma M, Pathi P, Srivastava SK, Rauthan CMS, and Singh PK (2016) Impedance spectroscopy of crystalline silicon solar cell: Observation of negative capacitance. *Solar Energy* 136: 412–442.

Peng C, Thio YS, and Gerhardt RA (2008) Conductive paper via self-assembly of polyelectrolytes and ITO nanoparticles. *Nanotechnology* 19: 505603. (pp. 10).

Pruyn TL and Gerhardt RA (2011) Characterization of ceramic powders during compaction using electrical measurements. *Advances in Bioceramics and Porous Ceramics IV: Ceramic Engineering and Science Proceedings* 32(6): 199–210.

Pruyn TL and Gerhardt RA (2015) Detection of different interfaces in percolated networks of ATO borosilicate glass composites by impedance spectroscopy. *Journal of the American Ceramic Society* 98(1): 154–162.

Ramachandran K, Pruyn TL, Huang T, Wang Y, Gerhardt RA, Sundaram V, and Tummala R (2015) Investigation of copper plated-through-holes in glass fiber reinforced epoxy substrates using AC impedance spectroscopy. *Journal of Materials Science* 26(4): 2563–2570.

Rath M and Gerhardt RA (2022) Repeatability and reproducibility of electrical measurements of spark-plasma-sintered alumina-SiCw composites. In: *IEEE I2MTC Conference Proceedings*.

Rodriguez BJ, Kalinin SV, Shin J, Jesse S, Grichko V, Thundat T, Baddorf AP, and Gruverman A (2006) Electromechanical imaging of biomaterials by scanning probe microscopy. *Journal of Structural Biology* 153: 151–159.

Romero B, Del Pozo G, Arredondo B, Martín-Martin D, Hernández-Balaguera E, and López González MC (2019) Characterization of organic and perovskite solar cells by impedance spectroscopy. In: *SPIE Proceedings Volume 11095, Women in Renewable Energy (WiRE)* 110950N.

Rudzik TJ and Gerhardt RA (2020) Effect of SPS current and voltage on the microstructure and electrical properties of borosilicate glass—ITO composites. *Advanced Engineering Materials* 22(5): 1901431.

Runyan J, Gerhardt RA, and Ruh R (2001a) Electrical properties of BN matrix composites—Part I: Analysis of the McLachlan equation in modeling the conductivity of BN-B_4C and BN-SiC composites. *Journal of the American Ceramic Society* 84(7): 1490–1496.

Runyan J, Gerhardt RA, and Ruh R (2001b) Electrical properties of BN matrix composites—Part II: Dielectric relaxations in boron nitride- silicon carbide composites. *Journal of the American Ceramic Society* 84(7): 1497–1503.

Sarı B, Go˘k A, and Sahın D (2006) Synthesis and properties of conducting polypyrrole, polyalkylanilines, and composites of polypyrrole and poly(2-ethylaniline). *Journal of Applied Polymer Science* 101: 241–249.

Schaffer JP, Saxena A, Antolovich SD, Sanders TH Jr., and Warner SB (1999) *The Science and Design of Engineering Materials*, 2nd edn. McGraw-Hill Publishers. ch. 10.

Scully JR, Silverman DC, and Kendig MW (1993) *Electrochemical Impedance: Analysis and Interpretation*. ASTM International.

Sethuraman S and Gerhardt RA (2021) Controlling the electrical, optical and morphological properties of sol-gel spin-coated indium tin oxide films. *AIP Advances* 11: 105117.

Snaith HJ and Grätzel M (2007) Electron and hole transport through mesoporous TiO_2 infiltrated with spiro-MeOTAD. *Advanced Materials* 19: 3643–3647.

Sullivan EM, Oh YJ, Gerhardt RA, Wang B, and Kalaitzidou K (2014) Understanding the effect of polymer crystallinity on the electrical conductivity of exfoliated graphite nanoplatelet/polylactic acid composite films. *Journal of Polymer Research* 563: 1–9.

Sullivan EM, Gerhardt RA, Wang B, and Kalaitzidou K (2016) Effect of compounding method and processing conditions on the electrical response of exfoliated graphite nanoplatelet/polylactic acid nanocomposite films. *Journal of Materials Science* 51(6): 2980–2990.

Tang J (2022) *Magnetic Impedance Testing, Online Research Description*. Uconn.edu.

Titus R, Gerhardt RA, and Fowler JE (2022) Quality Control Testing of Interdigitated Circuits With Impedance Spectroscopy. In: *IEEE I2MTC Poster Presentation*.

Valenzuela R (2001) Impedance spectroscopy in ferromagnetic materials. *MRS Online Proceedings Library* 699: 21.

Varlamov AA, Balestrino G, and Milani Livanov EV (1999) The role of density of states fluctuations in the normal state properties of high Tc superconductors. *Advances in Physics* 48(6): 655–783.

Von Hippel AR (1954) *Dielectrics and Waves*. John Wiley & Sons.

Waddell J, Ou R, Capozzi CJ, Gupta S, Parker CS, Gerhardt RA, Seal K, Kalinin SV, and Baddorf AP (2009) Detection of percolating paths in polyhedral segregated network composites using electrostatic force microscopy and conductive atomic force microscopy. *Applied Physics Letters* 95: 233122.

Wang DY and Nowick AS (1980) The “Grain-Boundary Effect” in doped ceria solid electrolytes. *Journal of Solid State Chemistry* 35: 325–333.

Watt MR and Gerhardt RA (2020a) Effect of processing method on the morphology and MWNT-polymer networks. *Materials Research Express* 7: 015075.

Watt MR and Gerhardt RA (2020b) Factors that affect network formation in carbon nanotube composites and their resultant electrical properties. *Journal of Composites Science* 4(3): 100.

Xia N and Gerhardt RA (2016) Fabrication and characterization of highly transparent and conductive indium tin oxide films with different solution-based methods. *Materials Research Express* 3: 116408.

Xia N, Lauter V, and Gerhardt RA (2019) Three-dimensional nanoscale sensing of porosity in solution-processed indium tin oxide multilayer thin films. *ACS Applied Nanomaterials* 2(2): 726–735.

Zhang JZ (2009) *Optical Properties and Spectroscopy of Nanomaterials*. World Scientific.

Plasmon-enhanced Raman spectroscopy: Principles and applications☆

Giulia Rusciano, Department of Physics E. Pancini, University of Naples “Federico II”, Napoli, Italy

© 2024 Elsevier Ltd. All rights reserved.

Introduction **300**
Understanding PERS enhancement **302**
Electromagnetic enhancement 302
Plasmons supported by a nanosphere in the quasi-static approximation 303
Mie theory: Size and shape effects 304
The plasmonic dimer 305
Chemical enhancement 305
Main PERS features **306**
Plasmonic enhancement 306
Spatial resolution 307
SERS for sensitive analytes detection **307**
Plasmonic nanostructures for SERS 308
Suspension of metallic NPs 308
Metal NPs immobilized on a support 309
Nanostructures fabricated directly on bulk metal substrates 310
TERS: Hot Spot *On Demand* **310**
TERS probes nanofabrication and preservation 311
Overview of selected PERS applications and conclusion **312**
References **314**

Abstract

Plasmon-enhanced Raman spectroscopy (PERS), including surface-enhanced Raman spectroscopy (SERS) and tip-enhanced Raman spectroscopy (TERS), has experienced an incredible development over the past 20 years, thanks to its chemical selectivity, elevated sensitivity and spatial resolution well below the diffraction limit. These features have busted the application of PERS to many fields of science, such as material characterization, biochemistry, biomedicine and surface analysis. In this chapter, the basis of plasmonic enhancement are described, together with the main aspects related to the design and the fabrication of proper metallic nanostructures supporting localized surface plasmon resonance (LSPR). Finally, some relevant applications of PERS will be illustrated.”

Key points

- Understanding PERS enhancement
- Surface Enhanced Raman Spectroscopy
- Tip Enhanced Raman Spectroscopy
- Fabrication of active plasmonic nanostructures
- Selected PERS applications

Introduction

When a laser light illuminates a sample, the interaction between photons and matter can assume different forms (Demtröder, 2003). By considering, for instance, a molecular sample, photons can be simply transmitted through the sample, conserving their energy and momentum. Alternatively, if their energy matches the energy gap between two electronic or roto-vibrational levels of the molecules, photons can be absorbed, and, eventually, re-emitted as fluorescence. Finally, photons can be scattered elastically or inelastically. In elastic scattering, photon energy is conserved, so that the frequency v, and therefore the wavelength λ, of the scattered light is equal to that of the incoming light. Depending by the size a of the scattering particle with respect to λ, elastic scattering is referred as Rayleigh ($a \ll \lambda$), Mie ($a \sim \lambda$) or geometric scattering ($a \gg \lambda$). In the inelastic scattering process, instead, photons energy is not conserved, and photons can either lose energy or gain energy from the interaction with scattering molecules (Vandenabeele, 2013). In a quantum picture, the energy exchange between incident photons and molecules occurring in scattering processes can be

---

☆*Change History*: February 2023. G Rusciano is involved in preparing the update. Updated queries and changed Figures 4, 6, 7, 11 and 12.

https://doi.org/10.1016/B978-0-323-90800-9.00041-X

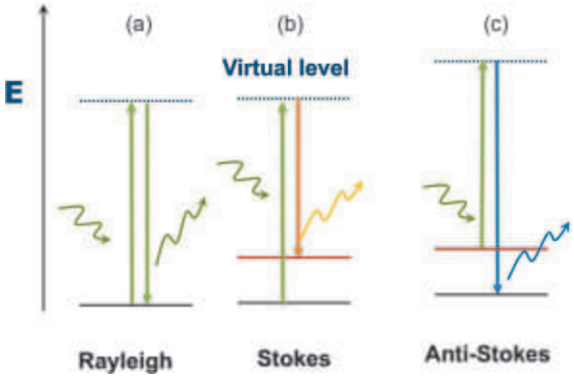

Fig. 1 Energy transfer process in Rayleigh (A), Stokes (B) and Anti-Stokes (C) Raman Scattering.

described in terms of the excitation of molecules from the ground state to a virtual state followed by a nearly simultaneous de-excitation toward a lower energy level (see Fig. 1). From the virtual state, most of molecules return back to the ground state through the emission of photons having the same energy as the incident photon (*Rayleigh scattering*). However, about 1 over 10^6 scattering processes follows a different path, involving a molecule decay from the virtual state toward an excited vibrational level (*Stokes scattering*). In this case, the photon energy is lower than that of the incident one and the energy defect ΔE is released to the internal (vibrational) energy of the molecule. The energy difference between the initial and final vibrational levels (Raman shift), expressed in wavenumbers $\tilde{\nu}(\mathrm{cm}^{-1})$, is given through the relation:

$$\tilde{\nu} = \frac{1}{\lambda_{inc}} - \frac{1}{\lambda_{scat}} \tag{1}$$

in which λ_{inc} and λ_{scat} are the wavelengths of the incident and Raman scattered photons, respectively. As result, the photon red-shift due to Stokes scattering is intrinsically connected to the molecule energy diagram. Finally, molecules starting from an excited vibrational level can be excited to the virtual state and decay to the ground state (*anti-Stokes scattering*). This process produces photons with energy higher that of the incoming photons: the energy defect is now transferred from molecules to photons. Since the number of molecules in an excited vibrational level decreases as $e^{-\Delta E/KT}$ (according to the Boltzmann statistic), anti-Stokes scattering is much less probable than Stokes scattering (typically by a factor around 1000). The spectral analysis of the inelastically scattered radiation is the subject of Raman spectroscopy (RS). Typically, Raman analysis is usually limited to the observation of the Stokes scattering (red-shifted photons), due to the higher cross-section with respect to anti-Stokes scattering.

From an experimental point of view, a Raman spectrum is typically obtained by dispersing the scattered photons by means of diffraction gratings and recording the so-dispersed radiation by means of a sensitive CCD camera. Since different molecules have bonds vibrating at well-defined frequencies, it turns out that the Raman spectrum consists of quite sharp peaks representing the actual *chemical fingerprint* of the molecule. This features clearly explains the wide diffusion of RS for the identification of analytes and the study of their evolution resulting from external stimuli or from the interaction with the environment. In particular, RS has revealed a powerful tool for the analysis of bio-systems, thanks to the relatively low Raman cross-section of water, which enables the observation of analytes in aqueous environment (Butler et al., 2016). The RS Achille's heal is the low Raman cross section (of the order of 10^{-30} cm^2/mol), which makes it prone to be hidden by the contribution of other optical process, in particular fluorescence (cross section of the order 10^{-18} cm^2/mol). To overcome this issue, Raman scattering can be amplified by exploiting the enhancement of Raman cross-section which occurs when the frequency of the Raman probe is close to the frequency of an electronic transition. Such enhancement is typically in the 10^3 - 10^6 range. This effect, which greatly improves the sensitivity of Raman spectroscopy, is referred as Resonance Raman scattering (RRS) (Demtröder, 2003; Efremov et al., 2008). RRS has been observed for several classes of biologically important molecules, such as metalloporphyrins and carotenoids, which have strong electronic transitions in the visible region, due to the presence of chromophors. In this condition, Raman scattering from the chromophoric moiety is greatly enhanced with respect to the contribution from the surrounding protein matrix. Raman signals intensity can be also increased by taking advantage from nonlinear effects which arise from induced polarization dependent by second and higher order electric field strength terms. Such terms, which become important for samples illuminated by high-power lasers (usually pulsed lasers) are at the basis of nonlinear Raman-based techniques (o Hamaguchi, 2009; Harvey et al., 1981), including stimulated Raman scattering (SRS), hyper Raman (HR), coherent anti-Stokes Raman spectroscopy (CARS), coherent Stokes Raman spectroscopy (CSRS), stimulated Raman gain (SRG) and inverse Raman scattering (IRS). Such techniques can be advantageous when the quantum yield for the generation of fluorescence is particularly high so that fluorescence signal swamps the weak Raman signal.

A huge step forward to the diffusion of Raman spectroscopy in research laboratories is due to the lucky marriage of spectroscopy and plasmonic, which has generated Plasmon-Enhanced Raman Spectroscopy (PERS). The key event in this regard occurred in 1974 during Raman analysis of pyridine molecules on a rough silver electrodes by Fleischmann and co-workers (Fleischmann et al., 1974). The authors observed an anomalous enhancement of Raman signal from such molecules, which was initially ascribed to the accumulation of molecules on the electrode surface. The connection of Raman signal enhancement to enhanced fields arising from localized surface plasmons in nanostructured metals came only several years later, thanks to the contribution by several groups

(Albrecht and Creighton, 1977; Jeanmaire and Van Duyne, 1977), including the fundamental contribution by Moskovits (Moskovits, 1978). Nowadays we know that an enhancement (up to 14 orders of magnitudes) of the Raman signal can be observed when the analyte is close to proper nano-sized metallic particles (NPs). This phenomenon is called Surface-Enhanced Raman Scattering (SERS) and, since its discovery, its use as analytical technique has grown exponentially (Han et al., 2022; Langer et al., 2020).

As a matter of facts, as the SERS 50*th* birthday approaches, thousands of SERS-related papers have been published, which report the SERS theoretical basis (although still not fully understood), the design and fabrication of newly conceived enhancing substrates, and SERS application in several fields. Notably, thanks to the huge enhancement of SERS, the detection limit has reached the single molecule (SM) level. The remaining limitation of SERS, related to the diffraction-limited character of optical techniques, has been overcome by the fruitful combination of SERS analysis with scanning probe microscopy (SPM). The resulting technique is named Tip-Enhanced Raman Spectroscopy (TERS) (Pienpinijtham et al., 2022; Verma, 2017). In TERS, the near field scanning probe tip is covered with proper metallic NPs, so that it behaves as a sort of optical nano-antenna, giving place to huge amplification of the optical field as for SERS but only in proximity of the tip apex. In a sense, we can say that a nanosized SERS substrate is put *on-demand* to the desired position. Such approach has been first reported in 2000 by two almost simultaneous papers from the groups of R. Zenobi and S. Kawata (Hayazawa et al., 2000; Stöckle et al., 2000). Following these pioneer works, TERS is becoming a fundamental tool for nanoscale analysis and its range of application spans from bio-related investigations to the analysis of 2D materials and catalyzed chemical reactions. In this contribution, we first introduce the basic principles of plasmonic enhancement, by illustrating the case of a single NP and that of a plasmonic dimer. A special attention will be devoted for illustrating some fundamental approaches for the fabrication and the characterization of plasmonic nanostructures. Finally, we will illustrate some state-of art applications of both SERS and TERS, with a special look to promising research trends.

Understanding PERS enhancement

It is widely accepted that the PERS enhancement can be attributed to two main enhancement mechanisms: electromagnetic and chemical enhancement. The Electromagnetic enhancement is generally the dominant contribution, providing a global enhancement factor up to 10^{11}. It is due to the coupling of the incident electromagnetic radiation field with the localized surface plasmons, which derive from the excitation of collective oscillations of electrons. Chemical enhancement originates from the interactions between the metal NP and the target molecule and contributes to the enhancement with a factor of the order of 10^2 - 10^3. Formally, the Raman and PERS signals can be related by the relation:

$$P_{PERS} = G_{PERS} \cdot P_{Raman} = G_{EM} \cdot G_{Chem} \cdot P_{Raman} \tag{2}$$

being P_{SERS} and P_{Raman} the PERS and Raman signals, while G_{EM} and G_{Chem} are the electromagnetic and chemical gain factors. The origin of these two contributions is described below.

Electromagnetic enhancement

The interaction of metal nanoparticles with electromagnetic radiation is largely ruled by the metal free electrons in the nanostructure. To figure out the main features of such interaction, let us consider a metal NP irradiated by a laser beam. Driven by the external field, such electrons are forced to be displaced with respect to the positive ions of the crystal structure, globally leading to a dipolar charge distribution. In turn, the Coulombic attraction between the displaced electrons and the positive charges works against this displacement, acting as a restoring force. As result, under the combined action of both forces, free electrons in the nanostructure are forced to oscillate, in a fashion quite similar to the mechanical analog of the mass-spring oscillator. This collective oscillation of electrons, which is inherently localized into the NP structure, is refereed as localized surface plasmon (LSP). Fig. 2A illustrates the LSP in the case of a spherical NP. As in the classical mass-spring system, a resonance effect can take place, if the forcing frequency is

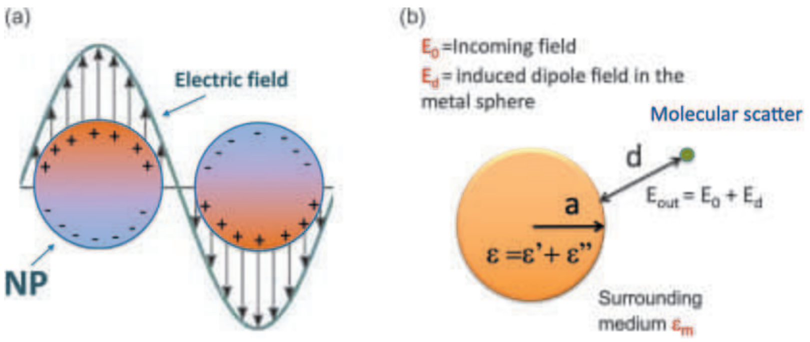
(a)
Electric field
NP
(b)
E_0=Incoming field
E_d = induced dipole field in the metal sphere
Molecular scatter
d
a
$E_{out} = E_0 + E_d$
$\varepsilon = \varepsilon' + \varepsilon''$
Surrounding medium ε_m

Fig. 2 (A) Schematic illustration of collective electron oscillations in a spherical NP induced by an external electric field. (B) Sketch of the geometry describing the interaction of a molecular scatter with a metal NP at distance d.

properly chosen. The LSP resonance (LSPR) gives rise to a strongly enhanced optical near-field, which is the key issue to explain the huge enhancement of the scattered field in PERS. It is not difficult to imagine that LSPR are strictly connected to NP size and shape. In the following, we will discuss the rising of such resonances starting from the simple case of a spherical nanoparticles with radius a much smaller than the incoming beam wavelength λ. Therefore, additional levels of complexity will be added, by relaxing the $a \ll \lambda$ hypothesis and considering nanoparticles with different shapes. Finally, we will consider the plasmonic dimer, the simplest system of interacting plasmonic NPs, which is the building block of all plasmonic nanoassemblies for SERS and TERS applications.

Plasmons supported by a nanosphere in the quasi-static approximation

In order to capture the essential features of LSPR, it is useful to consider the case of a metal NP interacting with an electromagnetic field in the so-called quasi-static approximation, which holds when $a \ll \lambda$, so that all the effects of retardation can be neglected. In this frame, all points in the NP respond simultaneously to the applied field, so that electric field is static around the particle. From a mathematical point of view, the Helmholtz equation for the potential Φ reduces to the easy-to-handle Laplace equation:

$$\nabla^2\Phi = 0 \tag{3}$$

Finally, the electric field can be calculated from the relation:

$$\mathbf{E} = -\nabla\Phi \tag{4}$$

For the seek of simplicity, we can assume a static electric field $\mathbf{E}_0$ directed along the x-direction of a cartesian reference system, having the origin at the NP center. After a proper evaluation of the boundary condition for Φ on the NP surface, it can be shown that the electric field inside $\mathbf{E}_{in}$ and outside the NP $\mathbf{E}_{out}$ assume the form:

$$\mathbf{E}_{in}(\mathbf{r}) = \frac{3\varepsilon_m}{\varepsilon + 2\varepsilon_m}\mathbf{E}_0 \tag{5}$$

$$\mathbf{E}_{out}(\mathbf{r}) = \mathbf{E}_0 + \frac{3\hat{\mathbf{r}}(\hat{\mathbf{r}}\cdot\mathbf{p}) - \mathbf{p}}{4\pi\varepsilon_0\varepsilon_m}\frac{1}{r^3} \tag{6}$$

being

$$\mathbf{p} = 4\pi\varepsilon_0\varepsilon_m a^3\frac{\varepsilon - \varepsilon_m}{\varepsilon + 2\varepsilon_m}\mathbf{E}_0 \tag{7}$$

In Eq. (7), ε_0 is the vacuum permittivity, ε the complex dielectric constant of the NP and, finally, ε_m is the real dielectric constant of the (non-absorbing) material in which the NP lies. Notably, from Eq. (5), it is clear that the electric field inside the NP results to be homogeneous, a condition which can be sustained only if $a \ll \lambda$. Even more important, it is worth underling that the second term in Eq. (6) corresponds to field of a dipole located at the center of the NP and induced by the external field $\mathbf{E}_0$. According to Eq. (7), the polarizability assumes the form:

$$\alpha = 4\pi a^3\frac{\varepsilon - \varepsilon_m}{\varepsilon + 2\varepsilon_m} \tag{8}$$

In general, the dielectric constant of a material is a complex, frequency dependent quantity $\varepsilon = \varepsilon' + i\varepsilon''$. Intriguingly, both fields in Eqs. (5) and (6) are enhanced when the condition:

$$\varepsilon + 2\varepsilon_m \sim 0 \tag{9}$$

holds (Fröhlich condition). This resonance condition corresponds to the excitation of non-propagating surface plasmon, localized around the nanoparticle (LSPR). Clearly, the achievement of resonance depends from both NP and surrounding medium dielectric constants, which confers an intrinsic sensitivity to environment to all plasmon based approaches. Eq. (9) can be satisfied in the visible and NIR region by several metals (and, in particular, noble metals) which exhibit, in selected spectral ranges, a negative ε' and $\varepsilon'' \sim 0$ (low losses), as illustrated in Fig. 3. For this reason, they are widely employed in LSPR applications. In particular, silver

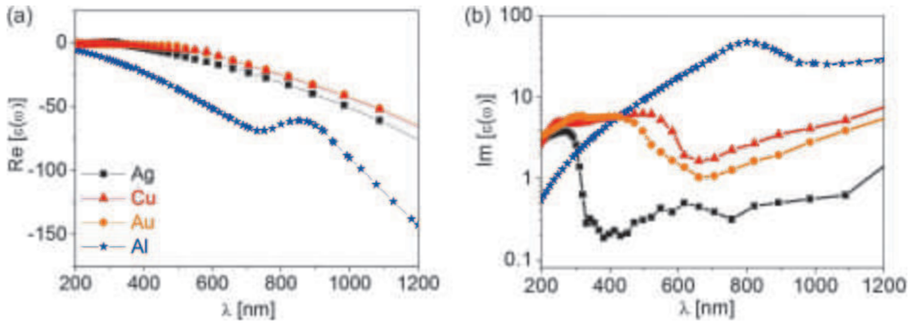

Fig. 3 Real (A) and imaginary (B) part of the dielectric constants of selected metals in the 200– 1200 nm spectral region. Adapted from ref. Pilot R, Signorini R, Durante C, Orian L, Bhamidipati M, and Fabris L (2019) *Biosensors* 9(2), 10.3390/bios9020057.

exhibits a quite broad plasmonic response covering both visible and NIR region. Similarly, gold is also very used, even if at wavelengths below ~500 nm, its plasmonic efficiency is affected by high interband losses. However, gold is sometimes preferred to silver due to its low reactivity to external agents. The plasmonic properties of metallic nanostructures are typically checked by measuring the extinction cross section σ_{ext}, which takes into account the contribution from both scattering and absorption cross sections ($\sigma_{ext} = \sigma_{sc} + \sigma_{abs}$). On the other hand, the scattering cross section can be obtained starting from the polarizability according to (Maier, 2007):

$$\sigma_{sc} = \frac{k^4}{6\pi} \cdot |\alpha|^2 = \frac{8\pi k^4}{3} a^6 \cdot \left|\frac{\varepsilon - \varepsilon_m}{\varepsilon + 2\varepsilon_m}\right|^2 \tag{10}$$

being $k = 2\pi\lambda$ the wavevector modulus in the surrounding medium. Similarly, the absorption cross section is provided by the relation:

$$\sigma_{abs} = 4\pi k a^3 \cdot Im\left|\frac{\varepsilon - \varepsilon_m}{\varepsilon + 2\varepsilon_m}\right| \tag{11}$$

It is worth noticing that the resonance condition described by Eq. (9) holds for both absorption and scattering (and therefore also for extinction). However, σ_{abs} scales with a^3 whereas σ_{sc} scales with a^6. As result, extinction is dominated by scattering for 'large' NPs, and by absorption for 'small' NPs.

Now, let us assume that a molecular scatter is positioned at distance d from the NP (Fig. 2B). Starting from Eq. (6), it can be easily demonstrated that the ratio $A(\nu_L)$ between the moduli of the total $\mathbf{E}_{out}$ field and the incoming field $\mathbf{E}_0$ scales according to:

$$A(\nu_L) \sim \frac{\varepsilon(\nu_L) - \varepsilon_m(\nu_L)}{\varepsilon(\nu_L) + 2\varepsilon_m(\nu_L)} \left(\frac{a}{a+d}\right)^3 \tag{12}$$

being ν_L the frequency of the incoming beam. In Eq. (12) we have explicitly indicated the frequency dependence of the dielectric constants ε and ε_M. On the other hand, also the scattered beam at frequency ν_s is enhanced, so that globally the plasmonic contribution G_{EM} to signal enhancement scales according to:

$$G_{EM} \sim \left|\frac{\varepsilon(\nu_L) - \varepsilon_m(\nu_L)}{\varepsilon(\nu_L) + 2\varepsilon_m(\nu_L)}\right|^2 \cdot \left|\frac{\varepsilon(\nu_s) - \varepsilon_m(\nu_s)}{\varepsilon(\nu_s) + 2\varepsilon_m(\nu_s)}\right|^2 \cdot \left(\frac{a}{a+d}\right)^{12} \tag{13}$$

Mie theory: Size and shape effects

A salient feature of Eq. (7) is that polarizability (and the resonance condition of Eq. (9) ruling scattering cross section) is independent from the NP size. This somewhat counter-intuitive outcome (a larger NP should radiate more) is clearly due to quasi-static approximation in which Eqs. (5) and (6) were obtained. A more general solution is provided by the Mie theory (Maier, 2007; Mulvaney, 1996), a full electrodynamic solution to the scattering problem. Within this theory, the extinction cross section can be obtained as a series of multipole oscillation according to (Maier, 2007, Mulvaney, 1996):

$$\sigma_{ext} = \frac{2\pi}{k^2} \sum_{n=1}^{n=\infty} (2n+1)\, Re\,(a_n + b_n) \tag{14}$$

In Eq. (14) a_n and b_n are the scattering coefficients, which are function of the NP radius a and the incoming beam wavelength λ and can be described in terms of the Ricatti-Bessel functions. In this frame, the effects of retardation, including radiative damping, are taken into account and the resonance condition for LSPR excitation is much more complex, showing explicitly a size-dependence. Fig. 4A illustrates this behavior for the case of Au—NP in water (Link and El-Sayed, 1999). Clearly, as the radius increases, LSPR resonances shift to the red and broaden, as consequence of the overlapping contribution from higher order multipolar excitation (Haynes and Van Duyne, 2001). Notably, in the case $a \ll \lambda$, only the first terms of Eq. (14) contributes significatively to σ_{ext}, so that it assumes the simpler form:

$$\sigma_{ext} = \frac{24\pi^2 a^3 \varepsilon_m^{3/2}}{\lambda} \frac{\varepsilon''}{(\varepsilon' + 2\varepsilon_m)^2 + \varepsilon''^2} \tag{15}$$

and the resonance condition return to that obtained in the case of quasi-static approximation.

The Mie-based approach is quite effective also to describe the scattering from non-spherical NPs. As a general rule, when the NP geometry is distorted from that of a sphere, additional resonances appear for each axis of the asymmetric particle (Reguera et al., 2017; Sherry et al., 2006). Moreover, LSPR exhibits a dependence from the field polarization. For instance, in the case of gold nanorods, LSPRs split into two different modes: the longitudinal mode, which corresponds to free electrons oscillation along the major axes, and a transverse mode, due to oscillation perpendicular to the major axes (Tong et al., 2009). The first mode exhibits a red-shift as the nanorod aspect ratio increases, whereas the second mode undergoes a blue shift in the same condition.

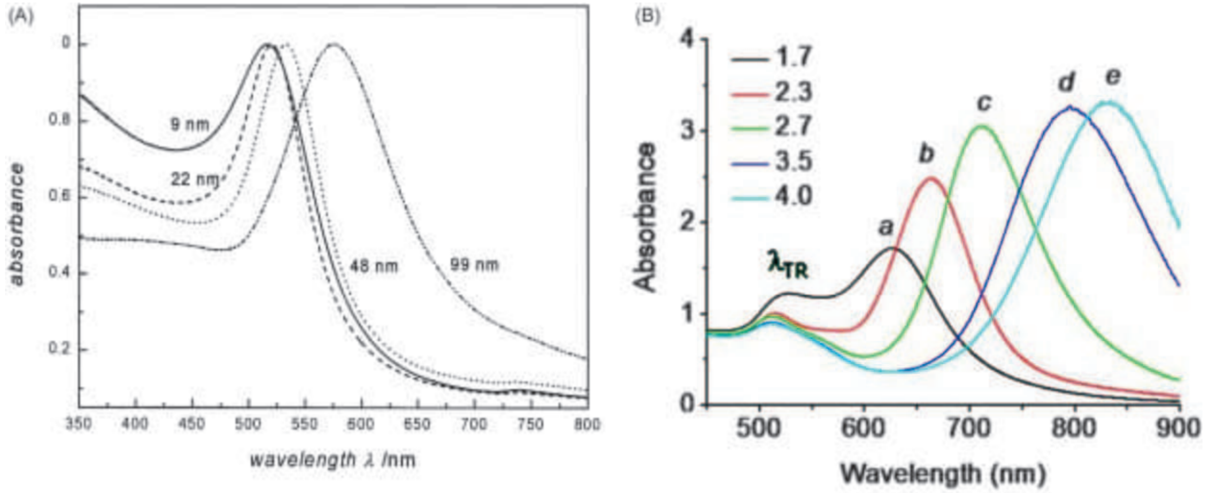

Fig. 4 (A) UV–vis absorption spectra of 9, 22, 48, and 99 nm gold nanoparticles in water. All spectra are normalized at their absorption maxima, which are at 517, 521, 533, and 575 nm, respectively. (B) Optical absorption spectra of Au nanorods with different aspect ratios (indicated in the labels) in the visible and near IR region. (A) Reproduced from ref. Link S and El-Sayed MA (1999) *The Journal of Physical Chemistry B* 103(21): 4212. (B) Adapted from ref. Tong L, Wei Q, Wei A, and Cheng J-X (2009) *Photochemistry and Photobiology* 85(1): 21.

The plasmonic dimer

Single, isolated particles do not exhibit very large enhancement of the electromagnetic field, so that their practical utility in sensing platform is limited. Much higher enhancement can be achieved in the junction between two NPs (Fig. 5A). Such highly localized regions are usually referred as *hot spots* and are the basic structure of extended SERS substrates (Etchegoin and Le Ru, 2008). The essential features of the coupling mechanism among NPs can be enucleated by considering the simple case of two spherical NPs placed at distance *d*, usually referred as *plasmonic dimer*. In such system, coupling effect becomes important when *d* is decreased up to a distance comparable to the NP radius. It is possible to demonstrate that the plasmon resonance of such system can be described as result of the 'hybridization' of the elementary plasmons of the single NPs, as described in ref. (Deng et al., 2018). The hybrid modes of such system are depicted in Fig. 5. In particular, for an incoming beam polarization parallel to the dimer axis, the in-phase coupling forms a 'bonding state' with a red-shifted resonance, and the out-of-phase coupling represents an 'antibonding state' with a blue-shifted resonance.

Chemical enhancement

The chemical enhancement (CE) is a short-range effect that arises from the fact that molecule geometry and its electronic structure is affected by the interaction with the metallic surface. As result, the Raman cross-sections of a given vibrational mode can be, in general, different with respect to those of the free molecule. Accordingly, the CE is described by the relation:

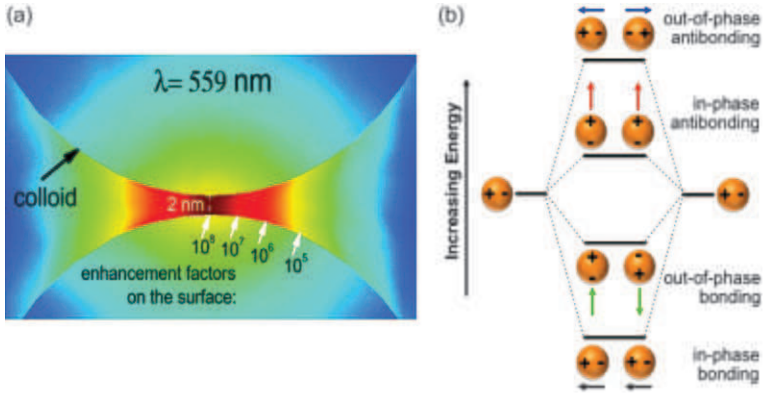

Fig. 5 (A) Enhancement factor distribution in the region of the gap (2 nm) between two gold colloids (radii = 30 nm) calculated in the electrostatic approximation with finite-element modeling (for polarization along the vertical axis of the dimer). (B) Scheme of the plasmon hybridization model of a symmetric dimer, depicting in-phase/out-of-phase bonding/antibonding combinations of dipole moments. The arrows in the scheme indicate the dipole moments of the individual particles. (A) Reproduced from ref. Etchegoin PG and Le Ru EC (2008) *Physical Chemistry Chemical Physics* 10: 6079 with permission from the Royal Society of Chemistry. (B) Reprinted from ref. Deng T-S, Parker J, Yifat Y, Shepherd N, and Scherer NF (2018) *The Journal of Physical Chemistry C* 122(48): 27662.

$$G_{Chem} = \frac{\sigma_k^{ads}}{\sigma_k^{\text{free}}} \tag{16}$$

being σ_k^{ads} and σ_k^{free} the Raman cross-sections of the k^{th} vibrational mode of the adsorbed and of the free molecule, respectively. Although G_{PERS} is dominated by the electromagnetic contribution, chemical enhancement also plays a significant role, ruling the shape of PERS spectra in terms of both bands intensities ratios and Raman shifts. The strength of the perturbation induced on the molecule energy pattern depends by the kind of molecule-surface interaction. Physisorption (i.e. physical adsorption, driven by Van der Waals forces) gives rise only to a slightly modification of molecular structure. On the other hand, chemisorption (i.e. chemical adsorption, leading to the formation of a chemical bond between the molecule and the surface), induces a strong perturbation of the molecule energy diagram. Due to the variety and complexity of this scenario, although many relevant studies can be found in literature (Birke et al., 2010; Chen et al., 2010; Jensen et al., 2008; Kneipp, 2016; Mullin et al., 2012; Otto, 2005), a fully comprehensive theory to explain the CE has not been developed yet. Generally speaking, theoretical description of CE is usually performed by using a computational approach based on density functional theory (DFT) or by a modeling approach, in which only the features that are expected to play a role for the molecule-surface interaction are taken into account. In both cases, it is widely recognized that three different mechanisms contribute to CE:

- *Non-resonant chemical effect*. In this case, the molecular orbitals lay at energies far away from the Fermi level of the metal and the interaction between the molecule and the metal does not lead to the formation of new electronic states. Nevertheless, such interaction may induce an appreciable change of molecule polarizability, that is mirrored as a slight modification of the Raman shifts and of the intensities of the vibrational modes. Usually, DFT computational methods are used to evaluate the non-resonant chemical effect.
- *Resonant charge transfer chemical effect*. The interaction between the molecule and the metal leads to the creation of a new state, referred as charge transfer (CT) state. If the Raman probe energy is in resonance or pre-resonance with this state, some Raman modes can be strongly enhanced. In particular, Raman modes coupled to the allowed electronic transitions exhibit a quite relevant enhancement (resonant Raman enhancement). Typically, resonant enhancement is described by a computational approach.
- *Transient CT mechanism*. In this case, the chemical effect originates from a 'transient' charge transfer mechanism, based on a temporary electron transfer between the metal and the molecule. The description of the molecule-surface interaction by time-dependent evolution in the intermediate anionic state of the adsorbate is analogous to intramolecular Franck-Condon resonance Raman scattering.

Main PERS features

Plasmonic enhancement

As previously mentioned, the plasmonic amplification, defined by Eq. (2), can reach 14 orders of magnitude, allowing the detection of single molecules. From an experimental point of view, such amplification is evaluated by tacking into account the number of scatters contributing to both spontaneous (N_{spont}) and enhanced (N_{SERS} or N_{TERS}) Raman signals. In particular, in the case of SERS G_{SERS} is provided by the relation:

$$G_{SERS} = \frac{I_{SERS}/N_{SERS}}{I_{\text{spont}}/N_{\text{spont}}} \tag{17}$$

For a liquid sample, N_{spont} can be estimated starting from the relation $N_{spont} = cN_A \cdot V_{eff}$, where c is the sample molar concentration, N_A is the Avogadro number and V_{eff} is the effective excitation volume. On the other hand, N_{SERS} can be estimated from the surface density σ and the laser spot area A_{spot} according to $N_{SERS} = \sigma \cdot A_{spot}$. For TERS, the enhancement factor G_{TERS} can be estimated by the relation:

$$G_{TERS} = \left(\frac{I_{tip}}{I_0} - 1\right)\frac{A_{spot}}{A_{NF}} \tag{18}$$

being I_{tip} and I_0 the Raman intensities obtained when the tip approaches to or is retracted from the sample, respectively, and A_{NF} is the near-field area (area explored by the tip). Typically, the enhancement produced by a single metallic colloidal particle (on a substrate or on the tip apex) is of the order of 10^3, while much higher values can be obtained in the so-called 'hot-spots,' i.e. highly partially localized regions exhibiting giant field enhancement. As previously mentioned, the gap between the two NPs of a dimer is able to create such enhancing region. The role of such kind of hot-spots in plasmonic enhancement was accurately explored by Le Ru et al. (Le Ru et al., 2006), examining the field distribution in a dimer system, consisting in a couple of 30 nm silver NPs separated by a 2 nm. It was assumed that the dimer was excited by a laser beam with polarization parallel to the dimer axis. It was also assumed a uniform distribution of molecules on the surface of the two NPs. Clearly, an intense field region is created in the gap whereas only moderate field intensities can be experienced by molecules located elsewhere. In these conditions, it can be shown that the statistical distribution of probabilities to find a certain enhancement G_{EM} exhibits a typical long-tail behavior. Intriguingly, a single molecule in a hot spot with a G_{EM} of 10^{10} provides the same Raman signal as 10^7 molecules experiencing a G_{EM} of 10^3! This simple estimation clearly highlights the necessity to fabricate plasmonic structures with a high hot-spots density.

Spatial resolution

A salient feature of plasmonic enhancement is its dependence from the distance between the metal nanostructure and the analyte. A rough estimation of such dependence is described in Eq. (13), obtained for the case of a scattering dipole in the quasi-static approximation, yielding to a d^{-12} dependence. This very short range character is somewhat mitigated in real systems. From an experimental point of view, such distance-dependence, which clearly rules the ultimate spatial resolution of plasmon-based techniques, was obtained in a SERS-based experiment by Masango et al. (Masango et al., 2016). In it, the authors used Al_2O_3 multilayers deposited by atomic layer deposition on a Ag substrate as 'spacers' between the probe molecules and substrate. In particular, the SERS from pyridine deposited on Al_2O_3 was acquired as function of the Al_2O_3 layer thickness (Fig. 6A). In this case, a d^{-10} distance dependence was observed, which also takes into account the number of molecules contributing to the signal (which scales as d^2). The dependence from distance was also investigated in a TERS experiment from Hartschuh et al. (Hartschuh et al., 2003). In this case, the authors measured the TERS signal from a single-walled carbon nanotubes (SWCN) as a function of the tip-SWCN gap. In this case, an inverse power low was observed, with the signal halved in ~10 nm.

SERS for sensitive analytes detection

As previously mentioned, the sensitivity of SERS can reach the SM level (Le Ru and Etchegoin, 2012; Le Ru et al., 2006). For this reason, SERS-based approaches are currently emerging as reliable techniques for analyte detection at low-concentration level (below nM range). At this purpose, two different approaches can be adopted (Pilot et al., 2019; Schlücker, 2014). The first, quite simple, relies on the direct detection of analytes, which are placed on proper SERS substrates (e.g. by analyte solution dipping or substrate immersion in the analyte solution). In this case, analyte presence and quantification is performed on the basis of the observation of the enhanced analyte spectrum. Such detection scheme is typically applied for analytes dissolved in pure water, but it becomes quite complicate for analytes in complex environments (such as biological matrices), in which the analytes spectral features can be masked by interfering species. In this case, indirect detection protocols can be applied, involving the use SERS labels (or tags), which are typically molecules exhibiting an high Raman cross-section (such as organic dyes), engineered to bind selectively to the analyte. In this case, analyte detection and quantification is performed on the basis of the SERS-tag spectrum. For SERS detection in complex matrices and at very low analyte concentration, separation and capturing techniques are also employed (Pilot et al., 2019). In particular, samples pretreatments by chromatographic approaches have been widely employed to separate (and also concentrate) analyte molecules. Immunoassays type approaches, tacking advantage of antibodies capability to selectively bind specific analytes (antigens), has been also applied as capturing tool for analyte detection (*SERS immunoassay*). They can be applied in both direct and indirect SERS detection approach. In the first case, the SERS substrate is functionalized with a specific antibody able to bind the analyte of interest, which is identified by its own spectral features, as well as by the changing of antibody spectral features due to binding to antigen molecules. Among indirect detection schemes, it is worth mentioning the approach illustrated in Fig. 7, for the detection of cancer biomarkers (Krasnoslobodtsev et al., 2015). It is based on the use of a gold capture surface (Fig. 7A) and an extrinsic Raman labels (ERL, Fig. 7B). Capture surface is prepared on a template stripped gold (TSG) substrate, successively modified with specific antibodies using thiolated linker molecules (DSP). ERLs are gold nanoparticles also modified with the same specific antibodies along with Raman reporter molecules (RRMs). The capture surface specifically binds and concentrates analytes from the

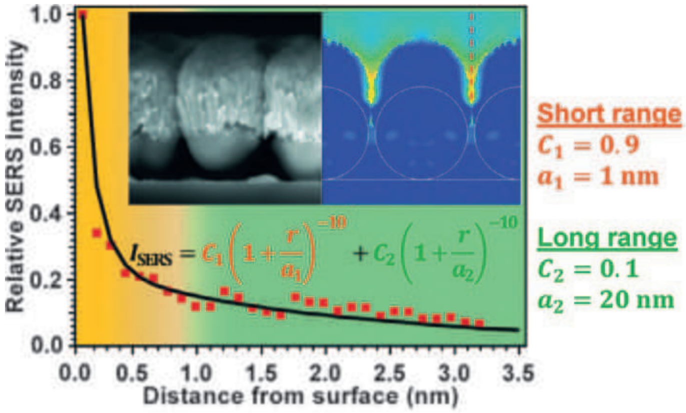

Fig. 6 SERS signal of the probe molecule as a function of the distance from the surface. A short and a long-range component are identified, associated with the morphological features of the silver substrate. The inset shows a SEM image of the substrate together with a simulation of the electric field. Reproduced from ref. Masango SS, Hackler RA, Large N, Henry A-I, McAnally MO, Schatz GC, Stair PC, and Van Duyne RP (2016) *Nano Letters* 16(7): 4251, pMID: 27243108.

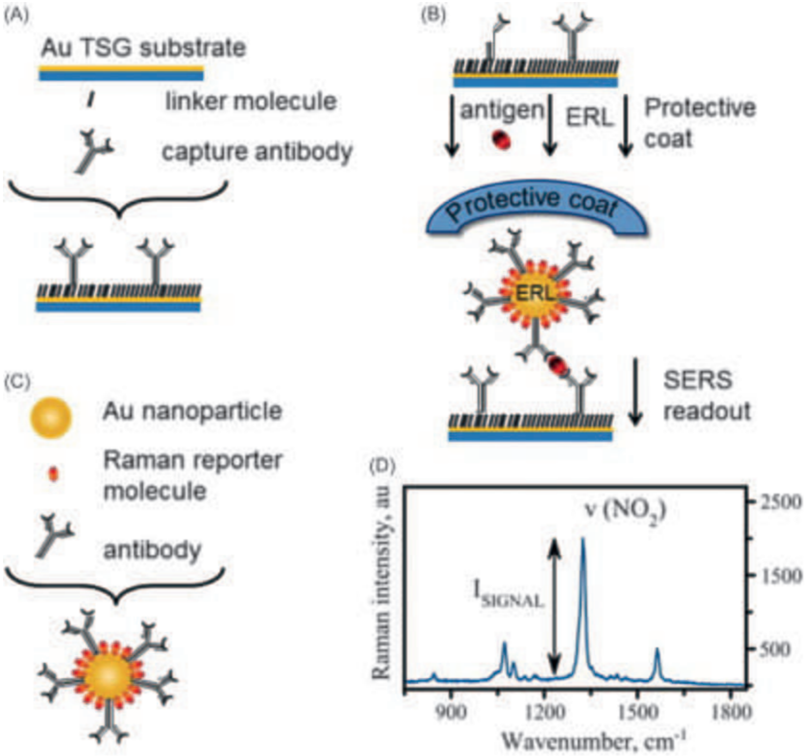

Fig. 7 SERS-sandwich based immunoassay: (A) A gold capture substrate modified with linker molecules and antibodies. (B) Gold nanoparticles (ERLs) functionalized with Raman reporter molecules (RRM's) and specific antibodies. (C) Sandwich immunoassay where antibodies on the capture surface first bind antigens and subsequently bind ERL. (D) The sandwiched assay produces SERS readout with several characteristic bands from NBT Raman reporter molecules. The most prominent is $\nu(\mathrm{NO_2})$ - a symmetric nitro stretch at 1336 cm^{-1}. Adapted from ref. Krasnoslobodtsev AV, Torres MP, Kaur S, Vlassiouk IV, Lipert RJ, Jain M, Batra SK, and Lyubchenko YL (2015) *Nanomedicine: Nanotechnology, Biology and Medicine* 11(1): 167.

sample (Fig. 7C). Exposure of this substrate to a solution containing ERLs results in binding of an ERL to the capture surface via antibody-antigen interaction in a *sandwich* format (Fig. 7C). Sample analysis produces readout signal associated to the Raman reporter molecules (Fig. 7D). Similar approaches have been used for a sensitive and selective detection of relevant chemical biomolecules (Kunushpayeva et al., 2020; Porter et al., 2008).

Plasmonic nanostructures for SERS

Starting from the simple dimer structure described above, we can go on with complexity, by increasing the number of NPs involved in the plasmonic coupling, a process which leads to a more or less uniform system of interacting NPs, i.e. a SERS substrate (Stewart et al., 2008). Generally speaking, a reliable SERS substrate should exhibit a high density and uniform distribution of hot spots regions. Typically, for SM studies, the presence of intense hot-spots is highly desired, while uniformity is an indispensable feature for analytical applications. The variety of SERS substrates reported in recent years is enormous and obviously it is not possible to review the whole field herein. Nevertheless, SERS substrates can be grouped in three main categories: (i) metal NPs in suspension (ii) metal NPs immobilized on a (usually solid) support; (iii) nanostructures fabricated directly on bulk metal substrates. In the following, we brief review these approaches.

Suspension of metallic NPs

Spherical silver and gold NPs are among the widest employed SERS substrates for the analysis of systems in aqueous environment (Turkevich et al., 1953). Differently from the counterpart of immobilized NPs, they can be also injected (or spontaneously endocytized) into cells, acting therefore as plasmonic reporters from the inner cellular compartments (Dreaden et al., 2012; Lee and Meisel, 1982). Such NPs are typically produced by reduction of a precursor salt with sodium citrate in water. It is worth mentioning that silver NPs produced according to the recipe reported by Lee and Meisdler (Lee and Meisel, 1982) is one of the first substrates revealing an enhancing capability adequate for SM investigations and, after 30 years from its introduction, it continues to be used in a large variety of experiments. Plasmonic NPs can also be fabricated by laser ablation (Amendola and Meneghetti, 2009). In this case, a pulsed laser is focused on metal target placed in aqueous environment so that NPs generated by heating and photoablation of the target are directly transferred in the aqueous solution. The enhancing capability of colloidal systems can be easily exploited by inducing NPs aggregation, which creates numerous hot-spots in the interparticles regions. This can be achieved by adding a salt (such as KCl and $NaNO_3$) to the solution. In such condition, the increase in the ionic strength of the solution reduces the screening of the charges at the NPs surface, inducing aggregation (Pamies et al., 2014). NPs aggregation in a confined region can be also achieved by using Optical Tweezers, which allow NPs trapping thanks to the gradient force generated by strongly focused laser beams (Foti et al., 2018). Notably, due to the complexity of aggregated NPs system, the plasmonic response can cover the whole visible-NIR spectral region.

Metal NPs immobilized on a support

A wide employed approach for the fabrication of SERS substrates relies on the assembly of pre-formed NPs (or NPs precursors) on a solid support. Recently, relatively ordered NPs arrays have been also deposited on flexible substrates such as paper or polymeric fibers (T. Vicente et al., 2018). An efficient approach for the production of an array of closely spaced, but physically separated, objects with optimal SERS properties was reported by the group of M.J. Natan (Freeman et al., 1995; Grabar et al., 1996). Briefly, a glass surface, silanized with (3-Aminopropyl)trimethoxysilane (APTMS), was immersed in an aqueous suspension of silver or gold NPs. Thanks to the strong interaction between the APTMS-NH_2 groups (exposed to the liquid phase), NPs self-assemble on the surface. In this way, the NPs spontaneous coalescence, occurring in the simple NPs solution drop casting on the surface, is prevented. By this approach, large area SERS surfaces (in the order of cm^2) can be produced, with good enhancement and reproducibility. Quasispherical gold NPs arranged on a APTMS- functionalized glass surface were also obtained by Lee et al. (Lee et al., 2017). In this case, a solution containing HAuCl, polyvinylpyrrolidone (PVP) and ethylene glycol were deposited on the surface, after which the Au-salt photoreduction was carried out by exposing the sample to a strongly focused femtosecond laser. In this way, SERS active surface are easily achieved by direct laser writing, which allows the production of the desired pattern with a spatial resolution in the micron range. Dense and ordered SERS nanopatterns can be obtained tacking advantage of the self-assembly of block copolymer (BCP) (Cho et al., 2012; Zito et al., 2015). The BCPs are macro-molecules composed of different types of polymer chains linked one to another with a covalent bond. Under certain conditions, BCPs tend to self-organize into aggregates of diverse morphologies such as spheres, cylinders or lamellae (see Fig. 8). Therefore, by chemically loading such aggregates with metal NPs, controlled NPs distributions can be obtained. Electrochemical techniques, including electrochemical roughening (ER) and the electrochemical deposition (ED), are also reliable methods for NPs deposition (Figueredo-Sobrinho et al., 2016; Fleischmann et al., 1974; Pilot et al., 2019). In ER, a short positive pulse is applied to a metal electrode, followed by a second pulse at a more negative potential. In this way, the first pulse causes the dissolution of small amount of metal from the initially smooth surface, while the second pulse induces the redeposit of the metal back onto the electrode. In ED, a proper application of electrical potential allows the deposit and adhesion of ions of the deposition material in the electrolyte to one of the electrodes. Usually, apart the metal salt to be deposited, an inert supporting electrolyte is added for sustaining and buffering the ionic conductivity, as well as proper ligands for controlling NPs shape and sizes.

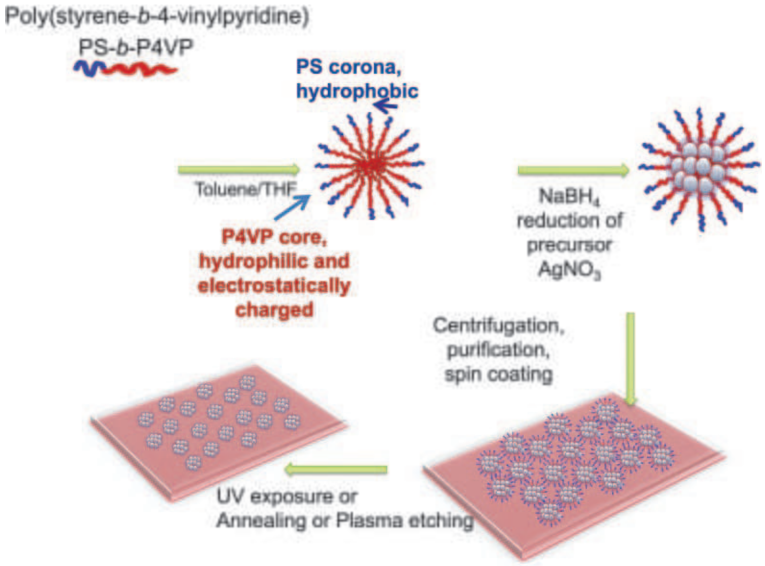
Poly(styrene-b-4-vinylpyridine)
PS-b-P4VP
PS corona, hydrophobic
Toluene/THF
P4VP core, hydrophilic and electrostatically charged
NaBH$_4$ reduction of precursor AgNO$_3$
Centrifugation, purification, spin coating
UV exposure or Annealing or Plasma etching

Fig. 8 Steps involved for the fabrication of plasmonic template by BCP self-assembly, as described in ref. (Zito et al., 2015). The experimental approach is based on the self-assembling of PolyStyrene-*block*-Poly-4-VinylPyridine (PS-b-P4VP) micelles loaded with silver Ag-NPs. Briefly, micelle were prepared by tacking advantage of the hydrophobic character of PS and the hydrophilic character of P4VP, which is not soluble in non-polar solvents. Micelles were spined on a glass coverslip by spin coating. This procedure leads to the formation of a single micelles layer. Subsequently, the polymer is removed by UV radiation that induces the photo-fragmentation and subsequent evaporation of the polymer, thus leaving only the nano-cluster of silver NPs.

Nanostructures fabricated directly on bulk metal substrates

A wide class of techniques for SERS substrates fabrication can be classified as top-down approaches, involving the creation of nanostructures directly on a bulk metallic support by various lithographic techniques (Kahl et al., 1998; Kanipe et al., 2016; Zhu et al., 2011), such as electron lithography (EBL) (Kahl et al., 1998; Romanato et al., 2011), interference lithography (IL) (Lu and Lipson, 2010) and soft-lithography (SL) (Qin et al., 2010). EBL allows the production of substrates theoretically engineered to optimize the enhancement, in a tens of nm. EBL is based on the use of an electron sensitive polymer (the resist) on which the desired nanopattern is 'written' by an electron beam. This latter locally modifies the resist solubility rendering it more (positive resist) or less soluble (negative resist). After that, the resist is immersed in a proper solvent which removes the soluble portion of the resist. In this way a mask is created, which can be used to create the metallic pattern on a bulk metal surface. For instance, reactive ion etching (RIE) can be used to etch the surface parts not covered by the resist mask, or the metal can be deposited straight on the surface, followed by removal of the polymer (lift-off). EBL approach is very expensive and also time-consuming, so that it is not suitable for fabricating large area substrates. In IL, the mask is designed on a photoresponsive polymer, exposed to the periodically modulated path created by two interfering laser beams. Then, the process follows the same steps as in EBL. Clearly, the mask preparation phase is much easier with respect to EBL, but only periodic structures can be created, with a gap which is to approximately half of the wavelength of the radiation used. Soft lithographic methods allow the fabrication of large area substrates (up to $\sim$1 cm^2) (Rogers and Nuzzo, 2005), with good SERS performances, in a cheaper and more easily accessible way with respect to traditional lithographic methods, like photolithography and EBL. In the last years, solid-state dewetting (SSD) of thin (initially smooth) films has emerged as an easy tool for the production of SERS substrates (Capaccio et al., 2021; Kang et al., 2015). In SSD, a metallic layer deposited on a substrate by physical vapor deposition or sputtering. Such layer is in an unstable or metastable state because of the relatively high energies of the metal surface at the film-substrate interface. This no-equilibrium condition leads the metal layer to break up and agglomerate in nano-islands (dewet) following the application of a proper perturbation (such as a cold plasma), even at temperatures well below the metal's melting point.

TERS: Hot Spot *On Demand*

Many problems at the frontiers of materials science and biotechnology require a spatial resolution that is well below the diffraction-limited regime of conventional optical techniques. TERS offers the opportunity to fulfill this request (Cao and Sun, 2022; Deckert-Gaudig et al., 2017; Kumar et al., 2015; Pienpinijtham et al., 2022; Schultz et al., 2020; Shao and Zenobi, 2019; Verma, 2017; Zhang et al., 2016). As anticipated in a former paragraph, TERS relies on the combination of near-field scanning probe microscopy and enhanced Raman spectroscopy. In TERS, in fact, the metal (or metallized) near field scanning probe behaves as a sort of optical nano-antenna, that gives place to huge amplification of the optical field as for SERS but only in proximity of the tip apex (Fig. 9). Therefore, due the short-range character of plasmon resonance, the enhanced Raman signal can be acquired with a spatial resolution which is only limited by the tip geometry. Since the radius of curvature of scanning probe tips can be very small (of the order of a few nm), the obtained spatial resolution is well below the light diffraction limit and scattering can be excited in a nano-sized region, selected 'on demand' by the SPM system.

Moreover, TERS acquires simultaneously the topographic structure of the scanned surface. TERS can be combined with both Scanning Tunnelling Microscopy (STM) and Atomic Force Microscopy (AFM). In this latter case, the AFM probe is rendered active from the plasmonic point of view by decoration with a proper metallic nanotexture, following experimental approaches similar to that employed for SERS substrate fabrication. Historically, the first TERS realization dates back to 2000 by Kawata and co-workers

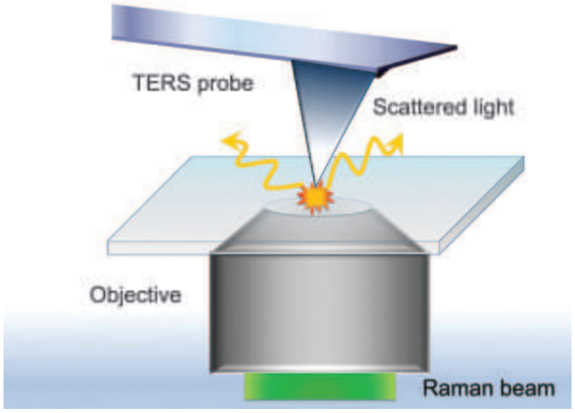

Fig. 9 Basic principle of TERS, combining the chemical sensitivity of SERS and the high lateral resolution of SPM.

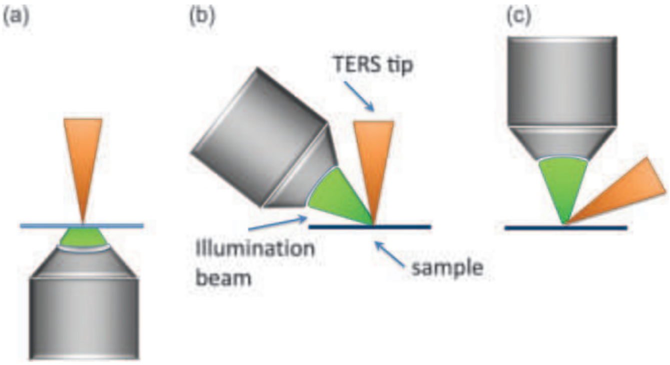

Fig. 10 Common illumination and detection geometries for TERS. (A) Bottom-illumination. (B) Side-illumination. (C) Top-illumination.

(Hayazawa et al., 2000), shortly followed by Zenobi's group (Stöckle et al., 2000). These pioneering studies have well elucidated the main TERS features: a very high sensitivity (due to the near-field plasmonic enhancement) combined with an elevated spatial resolution, obtained by the scanning probe-based approach. Both these characteristics make TERS a unique tool, for instance, to directly localize and identify proteins and their conformation in a complex (e.g., native) environment. In addition, it represents an excellent tool for detecting biomolecules that are adsorbed, layered, or assembled on a large variety of surfaces and interfaces. There are three main TERS illumination and collection setups (Gao et al., 2018), referred as *bottom*, *side*, and *top* configurations, which are illustrated in Fig. 10. The main difference among them is the position of the microscope objective relative to the sample. In the case of the bottom illumination and collection (Fig. 10A), a radially polarized beam is used to illuminate the gap between the tip and the sample. The use of a radial polarization is used for both increasing the beam focalization and to produce a stronger longitudinal electric field along the tip axes. The disadvantage of this setup is that only transparent samples can be measured. By using the side illumination and collection configuration (Fig. 10B), non transparent samples can be also examined. In this case, a long working distance objective is used to focus the light on the tip. Clearly, in this configuration, the focal point is widened due to the angle of the lighting beam, which leads to a larger far field contribution. Finally, in top illumination and collection configuration (Fig. 10C), the laser illuminates the sample perpendicular to the surface. However, tilted tips have to be used to avoid shadow effects. For thin samples, the *gap-mode* configuration can be used (Wang et al., 2020). In it, the sample is placed on a flat metallic substrate (e.g. a gold substrate) and the plasmonic field is created in the gap between the tip and the substrate. In general, the tip can be also relatively smooth, being the plasmonic ruled by the tip-substrate gap. This configuration is ideally suited for SM investigations.

TERS probes nanofabrication and preservation

TERS probes are usually made by silver or gold. Au-probes present a longer lifetime but are less enhancing than Ag-probes. STM-TERS tips are typically obtained by electrochemical etching process (Lopes et al., 2013). Even though the plasmonic performances can significantly vary from one tip to the other, such easy and cheap approach makes the trade-off acceptable for most cases. For this reason, most of the research on TERS tip fabrication is focused on AFM-TERS tips. The most employed approach for the fabrication of such tips relies on the deposition of a silver/gold film on commercial AFM probes. Silicon probes and nitride probes are typically used, with the first type preferred due to the redshift of resonances as the refractive index of the material increases. By selecting accurately the process parameters (metallic layer thickness, deposition time, etc.), a granular metallic structure can be achieved, providing a dipolar excitation at the tip apex. Depending by the grains size and their peculiar arrangement near the tip apex, active TERS probe in the visible and NIR region can be achieved. Silver grains on a SiO_2 ($n = 1.5$) surface exhibit a resonance which is blue shifted with respect to that deposited on a Si surface ($n = 4$), so that for TERS analysis in the blue-green region, AFM Si tips are often oxidized by thermal annealing. Fig. 11A reports a TERS tip obtained by the group of Kawata, in which a 60 nm film was evaporated on a SiO_2 tip (Hayazawa et al., 2012). In this case, a clear granular patter was obtained. A smoother metal film is instead obtained in the case of metal deposition by sputtering. As result, the plasmon activity of such tips is reduced, and their use is limited by the gap-mode configuration. Recently, Capaccio et al. reported an experimental procedure to strongly increase the roughness of Ag-sputtered probes by solid-state dewetting. The resulting tips exhibit a coral-like nanopattern (shown in Fig. 11C) and quite wide spectral response (Capaccio et al., 2020). Clearly, both evaporation and sputtering leads to a random distribution of NPs at the tip apex and, therefore, to a quite variable plasmon response. To fix this issue, numerous approaches have been reported to precisely attach a single properly designed NP to the tip apex. To this category it is worth mentioning the NPs positioning at the apex of an AFM probe by dielectrophoretic (DEF) forces reported in ref. (Leiterer et al., 2015) or the picking-up of gold NPs by using an AFM tip pre-coated with a glue, reported in ref. (Okamoto and Yamaguchi, 1997). Self-assembling of block-copolymers was also used to get a uniform distribution of NPs on a commercial AFM-tips, following an experimental approach similar to that used to produce hyper-uniform SERS substrates (Zito et al., 2016). Focused Ion Beam (FIB) based approaches were reported for the fabrication of TERS probes (Maouli et al., 2015; Umakoshi et al., 2016). Fig. 11 reports an AFM

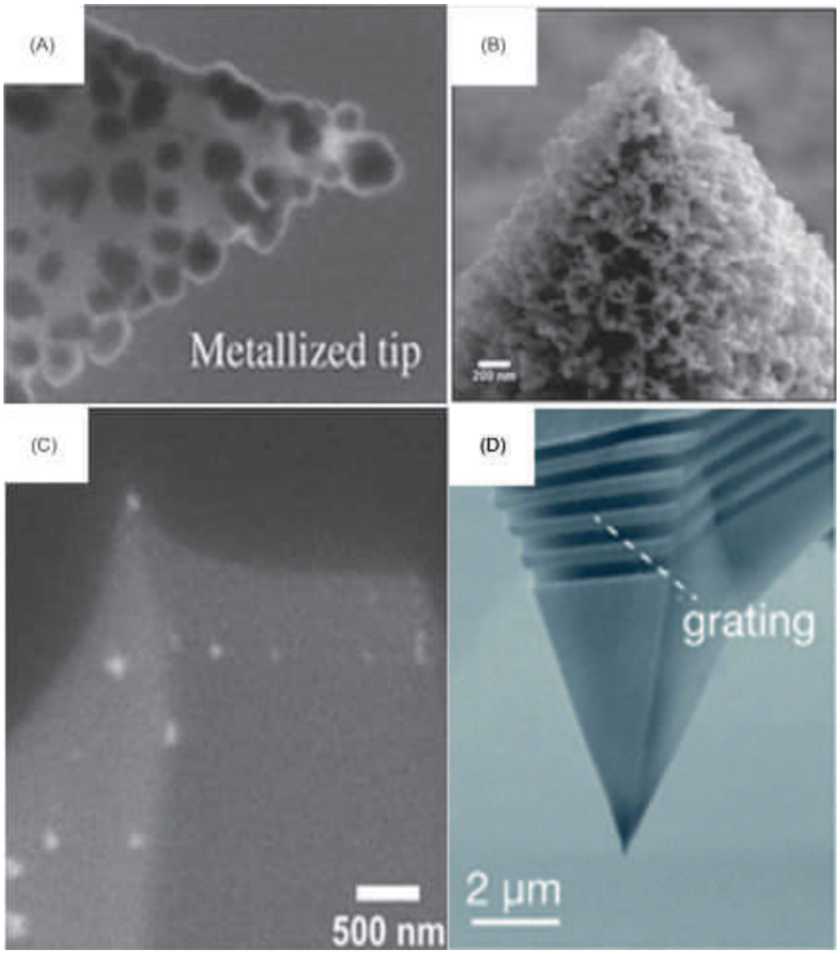

Fig. 11 SEM images of TERS probes obtained by thermal evaporation (A) (Hayazawa et al., 2012), solid-state dewetting (B) (Capaccio et al., 2020), NPs attachment by DEF (C) (Leiterer et al., 2015), FIB (D) (Umakoshi et al., 2016).

cantilever on which a grating structure was patterned by FIB (Umakoshi et al., 2016). Such structure allows propagation of surface plasmon polariton along the tip axis and emission at the tip apex. In such a way, remote excitation becomes possible, leading to a consistent reduction of the far-field background. Clearly, FIB-based approaches are quite expensive and time consuming, so that it is not applicable for the production of a large number of tips.

A significant issue in TERS analysis relies on tip preservation for environmental contamination. This issue is particularly important for the analysis in liquid environment, where the attachment of molecules present in solution to the tip apex (or the tip edge) can significantly deteriorate the acquired signal. Moreover, detachment of the metal NPs from the tip can also occur, which leads to tip loss. More importantly, even in TERS measurements in air (and probe storage in air) suffer from degradation, although to a lesser extent. For this reason, storage in N_2 is recommended (Deckert-Gaudig et al., 2017). Appropriate coating with a robust and inert layer can significantly extend tips lifetime. This is the case of SiO_2 and Al_2O_3 (Deckert-Gaudig et al., 2017) layer. However, such coatings leads to a plasmon resonance shift and to some reduction of the plasmonic enhancement.

Overview of selected PERS applications and conclusion

SERS analysis has been performed on a large variety of molecules (including dyes) and macromolecules, especially for biomedical applications. It is possible to find in literature excellent reviews reporting a wide overview of SERS based applications (Han et al., 2022; Langer et al., 2020; Schlücker, 2014) that cannot be fully discussed in the following. DNA/RNA and their sequences are among the most investigated samples. As a matter of facts, detection of DNA sequences has clear applications for the detection and identification pathogens and early cancer detection. For instance, direct detection of RNA extracted from urine samples has revealed a reliable tool to detect prostate cancer with high specificity and accuracy (Sivanesan et al., 2014). More frequently, DNA is revealed by using an indirect detection approach (Ngo et al., 2013; Wabuyele and Vo-Dinh, 2005; Wang et al., 2017). A protocol for miRNA detection, combining microfluidic with SERS and fluorescence analysis, has been developed by Wang et al, based on the development of a *molecular beacon* targeting miRNA (Wang et al., 2017). Such approach holds promise for the investigation of miRNA-related diseases. A particular miRNA, miR-21, was detected by a SERS sandwich-based approach by Guven et al. (Guven et al., 2014). Such miRNA constitutes an important biomarker, being over-expressed in several cancers. The author demonstrate a sensitivity for miR-21 detection under the nM level. In addition to DNA/RNA samples, a SERS sandwich-like approach was also used to detect relevant protein-based samples. This is the case of the approach developed by Wang et al. (Wang et al., 2011) to detect a pancreatic cancer biomarker, MUC4. In particular, SERS signals from gold nanoparticles functionalized with MUC4 antibody have proved to be an effective diagnostic tool for the detection of MUC4 from serum samples of patients. PSA, a wellknown prostate cancer biomarker, was instead detected by using Au-NPs functionalized with aptamers specific for detecting PSA. The developed protocol revealed a limit of detection at 5 pg/mL (Yoon et al., 2010). SERS analysis has been used to analyze cells and selected cellular compartments. Clearly, the most obvious compartment to be analyzed is the cellular membrane. As a matter of facts, by placing the cell on a solid SERS substrate, the only cellular compartment that 'feels' the plasmonic enhancement is that in contact with the substrate, i.e. the cytoplasmatic membrane (Zito et al., 2015). Such approach has been used to investigate the over-expression of carbonic anhydrase IX (CAIX) protein in SKOV3 cells (Rusciano et al., 2019). This protein is typically over-expressed in cells undergoing malignant transformations, so that such analysis can be used as a sensitive approach for early cancer detection. For the investigation of internal compartment, silver or gold colloids are used as SERS substrate, with the latter preferred due to their higher biocompatibility. Targeting to the selected compartment can be performed, to a certain extent, by a proper selection of NPs size and functionalization. Such approach has been used for the analysis of the endosomal system in eukaryotic cells (Kneipp et al., 2006). In this case, ~50 nm Au-NPs, endocytosed by cells, provided information of the nanoenvironment explored by cells, including the local pH value. Cancer cells obtained from biopsies were also investigated using colloidal NPs (González-Solís et al., 2013), which allowed the identification of chemical constituents, like phenylalanine, tyrosine, and tryptophan, and DNA bases. Particularly interesting is the use of SERS for the detection and identification of microorganisms such as bacteria, spores and viruses (Efrima and Bronk, 1998; Isticato et al., 2013; Kearns et al., 2017; Mosier-Boss, 2017; Wang et al., 2010; Witkowska et al., 2018), often even at strain level (Witkowska et al., 2018). For instance, it has been demonstrated that SERS spectra obtained by using Ag-nanorods arrays as SERS substrates, allow identification of strain of respiratory viruses, using extremely small samples amount (Shanmukh et al., 2006). A silver substrate, coated with antibiotics, was instead used by Waluk for detection of pathogenic bacteria, such as *Escherichia coli*, *Salmonella enterica*, and *Staphylococcus epidermidis* from blood samples (Sivanesan et al., 2014). The outcome of this study holds for the diagnosis of diseases related to clinically relevant pathogens.

As for SERS, TERS analysis spans over a wide variety of samples, including molecules, nanomaterial and 2D-materials. Interested readers are invited to refer to the many excellent reviews that can be find in literature (Deckert-Gaudig et al., 2017; Kumar et al., 2015; Pienpinijtham et al., 2022; Schultz et al., 2020; Shao and Zenobi, 2019; Verma, 2017; Zhang et al., 2016). Among bio-related samples, RNA and DNA have been widely investigated by TERS (Bailo and Deckert, 2008; Hennemann et al., 2010; Treffer et al., 2011). In particular, it was demonstrated the possibility to identify the contribution to the TERS signal of single bases when moving stepwise along single strands (Bailo and Deckert, 2008). Moreover, the investigation of hydrogen bonding between adenine and thymine is possible (Domke et al., 2007). These studies hold promise for the future identification of defects and local bonding in DNA strands. CNTs, and in particular single walled nanotubes (SWNT), are among the most employed samples (Hartschuh et al., 2003). This is mainly due the quite high Raman scattering cross section of SWNT, which allows the reduction of the TERS signal integration time and of the sample drift effects which deteriorates the simultaneously acquired topographic image. From the spectroscopic point of view, the observation of the G-band (graphitic-like mode at ~1580 cm^{-1}) and the D-band (defect-related band at ~1350 cm^{-1}) provide information on the purity and the presence of the defects in the tube. At the same time, the low frequency radial breathing mode can be used to estimate the CNT radius. Intriguingly, from the observation of the spectral shift of G-band along a CNT, it is possible to reconstruct the local stress field of the tube, due to the tube bending. It is clear that such shift is completely hidden by diffraction limited spontaneous Raman analysis (Hartschuh et al., 2005). Notably, in 2014 Chen et al. (Chen et al., 2014) have obtained the simultaneous chemical and structural analysis of individual carbon nanotubes (CNTs) by STM-TERS with 1.7 nm spatial resolution at ambient condition. Such impressive resolution can be improved when working with a low-temperature ultrahigh-vacuum scanning tunnelling microscope, reaching 0.7 nm (Liao et al., 2016). In 2019, a resolution at angstrom level has been demonstrated in UHV at cryogenic temperature by Zhang et al. (Zhang et al., 2019). In particular, the authors the possibility to get full Raman images of individual vibrational modes at the angstrom level for a single Mg-porphine molecule, revealing distinct characteristics of each vibrational mode in real space (see Fig. 12). Another field of application of TERS relies on the monitoring of chemical reaction. To the best of our knowledge, this issue was accomplished for the first time by Lantman et al. (van Schrojenstein Lantman et al., 2012), who investigated the dimerization of p-nitrothiophenol (p-NTP) adsorbed flat on a gold substrate by gap-mode AFM-TERS. In particular, dimerization was induced by a laser at 532 nm, while TERS signal was acquired by excitation at 633 nm. The possibility to monitor surface reaction by chemical interrogation of individual atomic adsorbates on a surface was instead demonstrated in ref. (Li et al., 2022). In particular, it is shown that single oxygen adatoms on a boron monolayer can be identified and mapped via ultrahigh vacuum STM-TERS with ~0.48 nm spatial resolution and single bond (B-O) sensitivity.

An emerging area of TERS is surely the nanoscale analysis of biological interfaces, including the membranes of bacteria, viruses and spores (Ashton et al., 2011; Neugebauer et al., 2006, 2007; Olschewski et al., 2015; Rusciano et al., 2014), as well as biofilms. In this case, AFM-TERS analysis is performed, which typically provides a lower resolution, but is much more versatile, allowing investigation also in aqueous environment. Clear, operation in such environment adds an additional level of difficulty, due to the

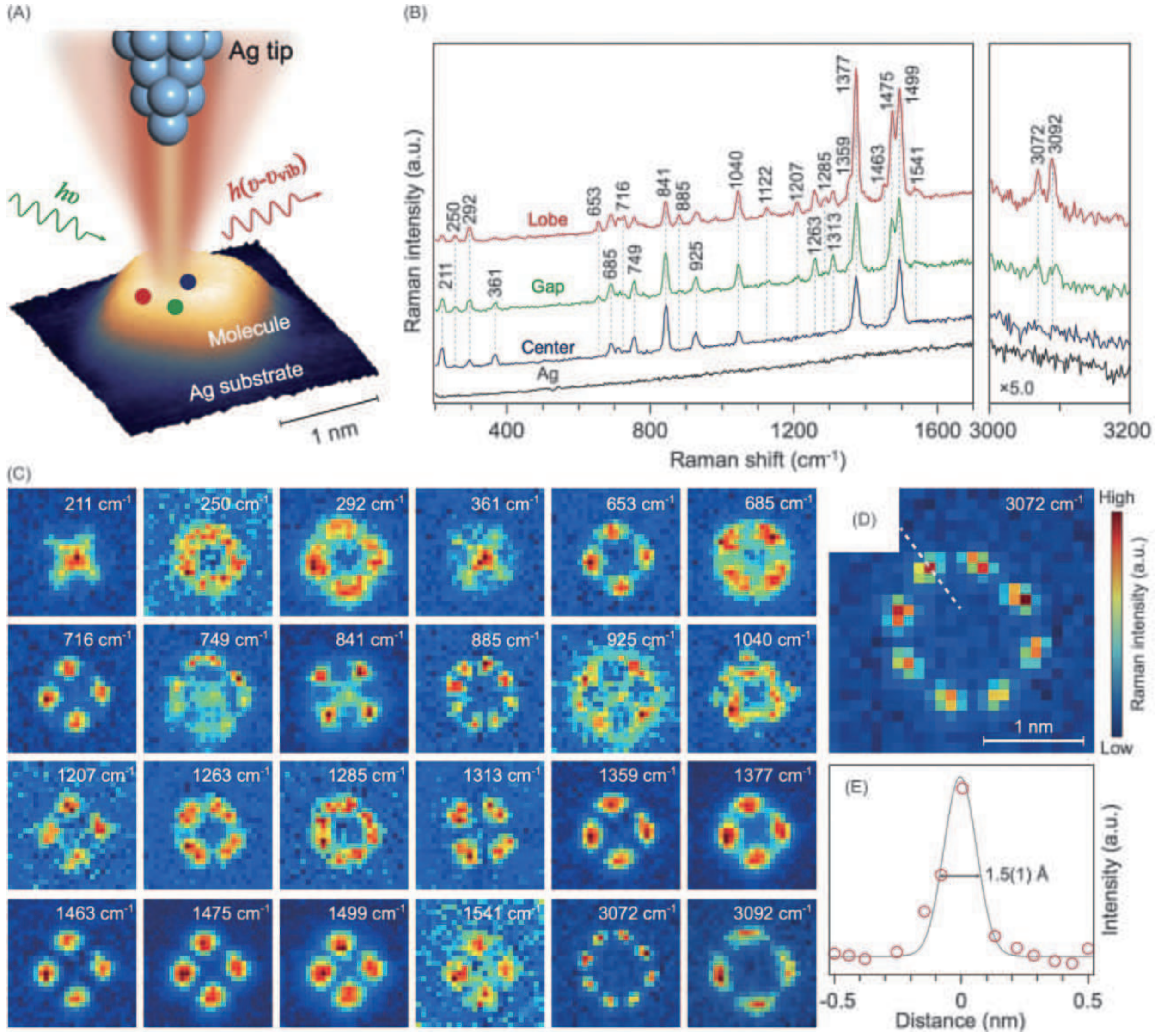

Fig. 12 Angstrom-resolved Raman images of distinct vibrational modes for a single molecule by scanning Raman picoscopy. (A) Schematic diagram of SRP technique. The nanocavity defined by the silver tip and substrate generates a strong and highly confined plasmonic field, which is used for the excitation and emission enhancement of the Raman signals from a single molecule. (B) Typical Raman spectra acquired at representative positions labeled in (A): lobe (red), gap (green) and center (blue). (C) SRP spatial mapping images corresponding to the peaks labeled in (B), revealing different spatial distribution patterns for different Raman modes. (D) SRP image at 3072 cm^{-1} used for the estimation of spatial resolution. (E) Line profile of Raman signal intensities corresponding to the dashed line in (D), exhibiting a lateral spatial resolution down to 0.15 nm. Adapted from ref. Zhang L, Yang B, Ghafoor A, Zhang Y, Zhang Y-F, Wang R-P , Yang J-L, Luo Y, Dong Z-C, and Hou JG (2019) *National Science Review* 6: 1169.

much faster tip contamination and degradation. Typically, protective layer on the tips reduce this problem, as demonstrated for the analysis of calcium alginate fibers (Hayazawa et al., 2012). Moreover, the necessity to handle with complex spectra, multivariate approaches (such as Principal Component Analysis, PCA) can help to pick-up relevant information. This approach was demonstrated in ref. (Rusciano et al., 2014), in which PCA was successfully applied for the analysis of spores surface.

References

Albrecht MG and Creighton JA (1977) *Journal of the American Chemical Society* 99(15): 5215.
Amendola V and Meneghetti M (2009) *Physical Chemistry Chemical Physics* 11: 3805.
Ashton L, Lau K, Winder CL, and Goodacre R (2011) *Future Microbiology* **6**(9): 991. pMID: 21958140.
Bailo E and Deckert V (2008) *Angewandte Chemie International Edition* 47(9): 1658.
Birke RL, Znamenskiy V, and Lombardi JR (2010) *The Journal of Chemical Physics* 132(21), 214707.

Butler HJ, Ashton L, Bird B, Cinque G, Curtis K, Dorney J, Esmonde-White K, Fullwood NJ, Gardner B, Martin-Hirsch PL, Walsh MJ, McAinsh MR, Stone N, and Martin FL (2016) *Nature Protocols* 11(4): 664.

Cao Y and Sun M (2022) *Reviews in Physics* 8: 100067.

Capaccio A, Sasso A, Tarallo O, and Rusciano G (2020) *Nanoscale* 12: 24376.

Capaccio A, Sasso A, and Rusciano G (2021) *Scientific Reports* 11(1): 22295.

Chen H, McMahon JM, Ratner MA, and Schatz GC (2010) *The Journal of Physical Chemistry C* 114(34): 14384.

Chen C, Hayazawa N, and Kawata S (2014) *Nature Communications* 5(1): 3312.

Cho WJ, Kim Y, and Kim JK (2012) *ACS Nano* **6**(1): 249. pMID: 22117916.

Deckert-Gaudig T, Taguchi A, Kawata S, and Deckert V (2017) *Chemical Society Reviews* 46: 4077.

Demtröder W (2003) Laser Raman spectroscopy. In: *Laser Spectroscopy: Basic Concepts and Instrumentation*, pp. 499–530. Berlin, Heidelberg: Springer Berlin Heidelberg. Chap. 1.

Deng T-S, Parker J, Yifat Y, Shepherd N, and Scherer NF (2018) *The Journal of Physical Chemistry C* 122(48): 27662.

Domke KF, Zhang D, and Pettinger B (2007) *Journal of the American Chemical Society* **129**(21): 6708. pMID: 17480079.

Dreaden EC, Alkilany AM, Huang X, Murphy CJ, and El-Sayed MA (2012) *Chemical Society Reviews* 41: 2740.

Efremov EV, Ariese F, and Gooijer C (2008) *Analytica Chimica Acta* 606(2): 119.

Efrima S and Bronk BV (1998) *The Journal of Physical Chemistry B* 102(31): 5947.

Etchegoin PG and Le Ru EC (2008) *Physical Chemistry Chemical Physics* 10: 6079.

Figueredo-Sobrinho FAA, Santos LPM, Leite DS, Craveiro DC, Santos SH, Eguiluz KIB, Salazar-Banda GR, Maciel CD, Coutinho-Neto MD, Homem-de Mello P, de Lima-Neto P, and Correia AN (2016) *Physical Chemistry Chemical Physics* 18: 7242.

Fleischmann M, Hendra P, and McQuillan A (1974) *Chemical Physics Letters* 26(2): 163.

Foti A, D'Andrea C, Villari V, Micali N, Donato MG, Fazio B, Maragò OM, Gillibert R, Lamy de la Chapelle M, and Gucciardi PG (2018) *Materials* 11(3). https://doi.org/10.3390/ma11030440.

Freeman RG, Grabar KC, Allison KJ, Bright RM, Davis JA, Guthrie AP, Hommer MB, Jackson MA, Smith PC, Walter DG, and Natan MJ (1995) *Science* 267(5204): 1629.

Gao L, Zhao H, Li T, Huo P, Chen D, and Liu B (2018) *International Journal of Molecular Sciences* 19(4). https://doi.org/10.3390/ijms19041193.

González-Solís J, Luévano-Colmenero G, and Vargas-Mancilla J (2013) *Laser Therapy* 22(1): 37.

Grabar KC, Smith PC, Musick MD, Davis JA, Walter DG, Jackson MA, Guthrie AP, and Natan MJ (1996) *Journal of the American Chemical Society* 118(5): 1148.

Guven B, Dudak FC, Boyaci IH, Tamer U, and Ozsoz M (2014) *Analyst* 139: 1141.

Han XX, Rodriguez RS, Haynes CL, Ozaki Y, and Zhao B (2022) *Nature Reviews Methods Primers* 1(1): 87.

Hartschuh A, Sánchez EJ, Xie XS, and Novotny L (2003) *Physical Review Letters* 90: 095503.

Hartschuh A, Qian H, Meixner AJ, Anderson N, and Novotny L (2005) *Nano Letters* **5**(11): 2310. pMID: 16277474.

Harvey A, et al. (1981) *Chemical Applications of Nonlinear Raman Spectroscopy*. Academic Press.

Hayazawa N, Inouye Y, Sekkat Z, and Kawata S (2000) *Optics Communications* 183(1): 333.

Hayazawa N, Yano T-A, and Kawata S (2012) *Journal of Raman Spectroscopy* 43(9): 1177.

Haynes CL and Van Duyne RP (2001) *The Journal of Physical Chemistry B* 105(24): 5599.

Hennemann LE, Meixner AJ, and Zhang D (2010) *Spectroscopy* 24: 428026.

Isticato R, Sirec T, Giglio R, Baccigalupi L, Rusciano G, Pesce G, Zito G, Sasso A, De Felice M, and Ricca E (2013) *PLoS One* 8(9): 1.

Jeanmaire DL and Van Duyne RP (1977) *Journal of Electroanalytical Chemistry and Interfacial Electrochemistry* 84(1): 1.

Jensen L, Aikens CM, and Schatz GC (2008) *Chemical Society Reviews* 37: 1061.

Kahl M, Voges E, Kostrewa S, Viets C, and Hill W (1998) *Sensors and Actuators B: Chemical* 51(1): 285.

Kang M, Park S-G, and Jeong K-H (2015) *Scientific Reports* 5(1): 14790.

Kanipe KN, Chidester PPF, Stucky GD, and Moskovits M (2016) *ACS Nano* **10**(8): 7566. pMID: 27482725.

Kearns H, Goodacre R, Jamieson LE, Graham D, and Faulds K (2017) *Analytical Chemistry* **89**(23): 12666. pMID: 28985467.

Kneipp K (2016) *The Journal of Physical Chemistry C* 120(37): 21076.

Kneipp J, Kneipp H, McLaughlin M, Brown D, and Kneipp K (2006) *Nano Letters* **6**(10): 2225. pMID: 17034088.

Krasnoslobodtsev AV, Torres MP, Kaur S, Vlassiouk IV, Lipert RJ, Jain M, Batra SK, and Lyubchenko YL (2015) *Nanomedicine: Nanotechnology, Biology and Medicine* 11(1): 167.

Kumar N, Mignuzzi S, Su W, and Roy D (2015) *EPJ Techniques and Instrumentation* 2(1): 9.

Kunushpayeva Z, Rapikov A, Akhmetova A, Sultangaziyev A, Dossym D, and Bukasov R (2020) *Sensing and Bio-Sensing Research* 29: 100355.

Langer J, Jimenez de Aberasturi D, Aizpurua J, Alvarez-Puebla RA, Auguié B, Baumberg JJ, Bazan GC, Bell SEJ, Boisen A, Brolo AG, Choo J, Cialla-May D, Deckert V, Fabris L, Faulds K, García de Abajo FJ, Goodacre R, Graham, Haes AJ, Haynes CL, Huck C, Itoh T, Käll M, Kneipp J, Kotov NA, Kuang H, Le Ru EC, Lee HK, Li J-F, Ling XY, Maier SA, Mayerhofer T, Moskovits M, Murakoshi K, Nam J-M, Nie S, Ozaki Y, Pastoriza-Santos I, Perez-Juste J, Popp J, Pucci A, Reich S, Ren B, Schatz GC, Shegai T, Schlücker S, Tay L-L, Thomas KG, Tian Z-Q, Van Duyne RP, Vo-Dinh T, Wang Y, Willets KA, Xu C, Xu H, Xu YSY, Zhao B, and Liz-Marzán LM (2020) *ACS Nano* **14**(1): 28. pMID: 31478375.

Le Ru EC and Etchegoin PG (2012) *Annual Review of Physical Chemistry* **63**(1): 65. pMID: 22224704.

Le Ru EC, Etchegoin PG, and Meyer M (2006) *The Journal of Chemical Physics* 125(20), 204701.

Lee PC and Meisel D (1982) *The Journal of Physical Chemistry* 86(17): 3391.

Lee MR, Lee HK, Yang Y, Koh CSL, Lay CL, Lee YH, Phang IY, and Ling XY (2017) *ACS Applied Materials & Interfaces* **9**(45): 39584. pMID: 29020445.

Leiterer C, Deckert-Gaudig T, Singh P, Wirth J, Deckert V, and Fritzsche W (2015) *Electrophoresis* 36(9–10): 1142.

Li L, Schultz JF, Mahapatra S, Lu Z, Zhang X, and Jiang N (2022) *Nature Communications* 13(1): 1796.

Liao M, Jiang S, Hu C, Zhang R, Kuang Y, Zhu J, Zhang Y, and Dong Z (2016) *Nano Letters* **16**(7): 4040. pMID: 27348072.

Link S and El-Sayed MA (1999) *The Journal of Physical Chemistry B* 103(21): 4212.

Lopes M, Toury T, de La Chapelle ML, Bonaccorso F, and Giuseppe Gucciardi P (2013) *Review of Scientific Instruments* 84(7), 073702.

Lu C and Lipson R (2010) *Laser & Photonics Reviews* 4(4): 568.

Maier S (2007) *Plasmonics—Fundamentals and Applications*. Springer.

Maouli I, Taguchi A, Saito Y, Kawata S, and Verma P (2015) *Applied Physics Express* 8(3), 032401.

Masango SS, Hackler RA, Large N, Henry A-I, McAnally MO, Schatz GC, Stair PC, and Van Duyne RP (2016) *Nano Letters* **16**(7): 4251. pMID: 27243108.

Mosier-Boss PA (2017) *Biosensors* 7(4): 51.

Moskovits M (1978) *The Journal of Chemical Physics* 69(9): 4159.

Mullin J, Valley N, Blaber MG, and Schatz GC (2012) *The Journal of Physical Chemistry A* **116**(38): 9574. pMID: 22946645.

Mulvaney P (1996) *Langmuir* 12(3): 788.

Neugebauer U, Rösch P, Schmitt M, Popp J, Julien C, Rasmussen A, Budich C, and Deckert V (2006) *ChemPhysChem* 7(7): 1428.

Neugebauer U, Schmid U, Baumann K, Ziebuhr W, Kozitskaya S, Deckert V, Schmitt M, and Popp J (2007) *ChemPhysChem* 8(1): 124.

Ngo HT, Wang H-N, Fales AM, and Vo-Dinh T (2013) *Analytical Chemistry* **85**(13): 6378. pMID: 23718777.

o Hamaguchi H (2009) In: Laane J (ed.) *Frontiers of Molecular Spectroscopy*, pp. 13–34. Amsterdam: Elsevier.

Okamoto T and Yamaguchi I (1997) *Japanese Journal of Applied Physics* **36**: L166. Part 2, No. 2A.

Olschewski K, Kämmer E, Stöckel S, Bocklitz T, Deckert-Gaudig T, Zell R, Cialla-May D, Weber K, Deckert V, and Popp J (2015) *Nanoscale* 7: 4545.

Otto A (2005) *Journal of Raman Spectroscopy* 36(6–7): 497.

Pamies R, Cifre JH, Espín VF, Collado-González M, Baños FGD, and de la Torre J (2014) *Journal of Nanoparticle Research* 16(4): 2376.

Pienpinijtham P, Kitahama Y, and Ozaki Y (2022) *Nanoscale* 14: 5265.

Pilot R, Signorini R, Durante C, Orian L, Bhamidipati M, and Fabris L (2019) *Biosensors* 9(2). https://doi.org/10.3390/bios9020057.

Porter MD, Lipert RJ, Siperko LM, Wang G, and Narayanan R (2008) *Chemical Society Reviews* 37: 1001.

Qin D, Xia Y, and Whitesides GM (2010) *Nature Protocols* 5(3): 491.

Reguera J, Langer J, Jiménez de Aberasturi D, and Liz-Marzán LM (2017) *Chemical Society Reviews* 46: 3866.

Rogers JA and Nuzzo RG (2005) *Materials Today* 8(2): 50.

Romanato F, Pilot R, Massari M, Ongarello T, Pirruccio G, Zilio P, Ruffato G, Carli M, Sammito D, Giorgis V, Garoli D, Signorini R, Schiavuta P, and Bozio R (2011) *Microelectronic Engineering* **88**(8): 2717. proceedings of the 36th International Conference on Micro- and Nano-Engineering (MNE).

Rusciano G, Zito G, Isticato R, Sirec T, Ricca E, Bailo E, and Sasso A (2014) *ACS Nano* **8**(12): 12300. pMID: 25415422.

Rusciano G, Sasso E, Capaccio A, Zambrano N, and Sasso A (2019) *Scientific Reports* 9(1): 1832.

Schlücker S (2014) *Angewandte Chemie International Edition* 53(19): 4756.

Schultz JF, Mahapatra S, Li L, and Jiang N (2020) *Applied Spectroscopy* 74(11): 1313. pMID: 32419485.

Shanmukh S, Jones L, Driskell J, Zhao Y, Dluhy R, and Tripp RA (2006) *Nano Letters* **6**(11): 2630. pMID: 17090104.

Shao F and Zenobi R (2019) *Analytical and Bioanalytical Chemistry* 411(1): 37.

Sherry LJ, Jin R, Mirkin CA, Schatz GC, and Van Duyne RP (2006) *Nano Letters* 6(9): 2060. pMID: 16968025.

Sivanesan A, Witkowska E, Adamkiewicz W, Dziewit L, Kaminska A, and Waluk J (2014) *Analyst* 139: 1037.

Stewart ME, Anderton CR, Thompson LB, Maria J, Gray SK, Rogers JA, and Nuzzo RG (2008) *Chemical Reviews* **108**(2): 494. pMID: 18229956.

Stöckle RM, Suh YD, Deckert V, and Zenobi R (2000) *Chemical Physics Letters* 318(1): 131.

Tong L, Wei Q, Wei A, and Cheng J-X (2009) *Photochemistry and Photobiology* 85(1): 21.

Treffer R, Lin X, Bailo E, Deckert-Gaudig T, and Deckert V (2011) *Beilstein Journal of Nanotechnology* 2: 628.

Turkevich J, Stevenson PC, and Hillier J (1953) *The Journal of Physical Chemistry* 57(7): 670.

Umakoshi T, Saito Y, and Verma P (2016) *Nanoscale* 8: 5634.

van Schrojenstein Lantman EM, Deckert-Gaudig T, Mank AJG, Deckert V, and Weckhuysen BM (2012) *Nature Nanotechnology* 7(9): 583.

Vandenabeele P (2013) Theoretical aspects. In: *Practical Raman Spectroscopy—An Introduction*, pp. 1–38. John Wiley & Sons, Ltd. Chapter 1.

Verma P (2017) *Chemical Reviews* **117**(9): 6447. pMID: 28459149.

Vicente AT, Araújo A, Mendes MJ, Nunes D, Oliveira MJ, Sanchez-Sobrado O, Ferreira MP, Águas H, Fortunato E, and Martins R (2018) *Journal of Materials Chemistry* C **6**: 3143.

Wabuyele MB and Vo-Dinh T (2005) *Analytical Chemistry* **77**(23): 7810. pMID: 16316192.

Wang Y, Lee K, and Irudayaraj JMK (2010) *Journal of Physical Chemistry C* 114: 16122.

Wang G, Lipert RJ, Jain M, Kaur S, Chakraboty S, Torres MP, Batra SK, Brand RE, and Porter MD (2011) *Analytical Chemistry* **83**(7): 2554. pMID: 21391573.

Wang Z, Zong S, Wang Z, Wu L, Chen P, Yun B, and Cui Y (2017) *Nanotechnology* 28(10), 105501.

Wang R, He Z, Sokolov AV, and Kurouski D (2020) *The Journal of Physical Chemistry Letters* **11**(10): 3815. pMID: 32340446.

Witkowska E, Korsak D, Kowalska A, Janeczek A, and Kamińska A (2018) *Analytical and Bioanalytical Chemistry* 410(20): 5019.

Yoon K-J, Hwang H, Eom I-Y, Hahn J-H, and Jung YM (2010) *Bulletin of the Korean Chemical Society, Pyo, Dongjin* 31(5): 1215.

Zhang Z, Sheng S, Wang R, and Sun M (2016) *Analytical Chemistry* **88**(19): 9328. pMID: 27571253.

Zhang L, Yang B, Ghafoor A, Zhang Y, Zhang Y-F, Wang R-P, Yang J-L, Luo Y, Dong Z-C, and Hou JG (2019) *National Science Review* 6: 1169.

Zhu W, Banaee MG, Wang D, Chu Y, and Crozier KB (2011) *Small* 7(13): 1761.

Zito G, Rusciano G, Pesce G, Dochshanov A, and Sasso A (2015) *Nanoscale* 7: 8593.

Zito G, Rusciano G, Vecchione A, Pesce G, Di Girolamo R, Malafronte A, and Sasso A (2016) *Scientific Reports* 6: 31113.

Optical tweezers: Theory and practice

Giuseppe Pesce, Physics Department “E. Pancini”, University of Naples “Federico II”, Naples, Italy

© 2024 Elsevier Ltd. All rights reserved.

Introduction 317
Theory of optical trapping 318
Geometrical ray optics regime 319
Dipole approximation regime 320
Electromagnetic theory 321
Three regimes but common features 322
Brownian motion in optical tweezers 323
Experimental setup and calibration techniques 323
Equipartition theorem 324
Potential analysis 325
Mean square displacement analysis 325
Autocorrelation analysis 325
Applications 326
Single molecule and single cell mechanics 326
Statistical physics and colloidal interactions 327
Optical tweezers in air and in vacuum 328
Conclusion 329
References 330

Abstract

Optical Tweezers, as the name suggest, are a tool to grab and hold an object using the light, that is without mechanical contact. The possibility for the manipulation of many different samples using only the light from a laser beam opened the way to a variety of experiments. Optical Tweezers, are nowadays employed in a multitude of applications demonstrating its relevance. Since the pioneering work of Arthur Ashkin, where he used a single strongly focused laser beam, ever more complex experimental set-ups are required in order to perform novel and challenging experiments. Here we provide a comprehensive discussion of the theoretical background and experimental techniques. We start by giving an overview of the theory of optical forces: first, we consider optical forces in approximated regimes when the particles are much larger (ray optics) or much smaller (dipole approximation) than the light wavelength; then, we, briefly, discuss the full electromagnetic theory of optical forces with a focus on T-matrix methods. Then, we describe the important aspect of Brownian motion in optical traps and how they are calibrated. Finally, we provide a review of some of the many experiments considering the perspective for future research.

Key points

- Introduction to optical forces
- Calculation of optical forces in the electromagnetic theory
- Description of experimental setups
- Calibration of Optical Tweezers
- Applications

Introduction

Evidences that the light can exert a force on matter are known since Johannes Kepler described the origin of comet tails as a consequence of the rays of the sun in 1619 (Kepler, 1619). After Maxwell’s theory of electromagnetism in the late 19th century it was possible to describe the radiation pressure of light along the direction of its propagation (Poynting, 1884). Later, some experiments to detect the mechanical effects of light were performed (Nichols and Hull, 1901; Lebedev, 1901; Beth, 1936), who succeeded in detecting the radiation pressure acting on macroscopic objects However, the magnitude of these effects was so small to be consider them irrelevant for any practical use (Ashkin, 2000). Indeed, after the invention of the laser (Townes, 1999) the light forces came back to the attention of scientists, mainly for the possibility to cool and confine atoms (Ashkin, 1970a,b).

Optical tweezers were proposed and demonstrated by Arthur Ashkin (Ashkin et al., 1986; Jones et al., 2015), who has been awarded the 2018 Nobel Prize in Physics (half of the prize). Optical Tweezers are essentially a tightly focused laser beam that can hold and manipulate a microscopic particle in the high-intensity region that is formed at the focal spot. The magnitude of the

https://doi.org/10.1016/B978-0-323-90800-9.00153-0

forces generated can vary from tens of piconewton down to few femtonewtons. Before Optical Tweezers tiny forces were exterted by Atomic Force Microscopes but limited to few tens of piconewtons. It is clear that Optical Tweezers extended the range of applicability of already existing techniques, like Atomic Force Microscopy, toward weaker forces and, therefore, opened to a myriad of new experiments.

First experiments demonstrated optical trapping and manipulation on individual tobacco mosaic virus and *Escherichia coli* bacterium (Ashkin et al., 1990). Later, the use of optical force spectroscopy to characterize the mechanical properties of biomolecules and motor proteins was developed (Block et al., 1990; Bustamante et al., 1994; Finer et al., 1994). Optical traps allowed biophysicists to observe the forces and dynamics of nanoscale motors at the single-molecule level (Bustamante et al., 2003; Neuman and Nagy, 2008). Since then, optical tweezers have also proven useful in many other areas of physics (Grier, 2003; Molloy and Padgett, 2002; Pesce et al., 2005, 2011; Dholakia et al., 2008; Jonáš and Zemánek, 2008; Juan et al., 2011; Dholakia and Čižmár, 2011; Padgett and Bowman, 2011; Padgett and Di Leonardo, 2011; Polimeno et al., 2018), nanotechnology (Maragó et al., 2013), chemistry (Yi et al., 2006), soft matter (Löwen, 2001; Petrov, 2007; Fusco et al., 2007), and nanothermodynamics (Gieseler and Millen, 2018).

Optical tweezers are not only able to manipulate microscopic objects, but, as it will be described below, are force transducer since their force, at first approximation, is the same of a spring, that is, proportional to the displacement from the equilibrium position. Thus, they can be used to measure the external forces applied to the trapped object. This is the basis of a new kind of scanning probe microscopy using an optically trapped particle as a probe. This technique was later called photonic force microscopy (Ghislain and Webb, 1993; Florin et al., 1997).

The range of optical tweezers applicability has been greatly expanded by the use of advanced beam-shaping techniques, where the structure of an optical beam is altered by a diffractive optical element (Dufresne and Grier, 1998), e.g., to produce multiple optical traps at definite positions (Dholakia and Čižmár, 2011; Padgett and Bowman, 2011). With this techniques it is also possible to generate more complex trapping configuration, e.g., using Laguerre-Gaussian beams, which can produce torques by the transfer of *orbital angular momentum* (He et al., 1995; Simpson et al., 1996; Piccirillo et al., 2013).

Theory of optical trapping

The conservation of electromagnetic momentum during the scattering process is the basis of the force exerted by light on matter. The general understanding of optical forces is related to approximations based on the ratio between the radiation wavelength and the size of the object illuminated. In fact, when the particle size is much bigger or much smaller than the wavelength of the light, the calculation of the force exerted is greatly simplified. In this case there are two well defined regimes: the geometrical ray optics regime (Ashkin, 1992; Callegari et al., 2015), the dipole approximation regime (Chaumet and Nieto-Vesperinas, 2000). However, when the particle dimensions are comparable with the optical wavelength, that is, the so called intermediate regime, a complete wave-optical modeling of the particle-light interaction is necessary for calculating the optical forces. The Lorenz-Mie theory can be used, for spherical particles, to generate accurate numerical results for essentially any size and refractive index (van de Hulst, 1957; Gouesbet and Gréhan, 2011). Fig. 1 provides an illustration of the range of sizes, shapes and inhomogeneous structures and compositions of objects that have been successfully manipulated in optical tweezers.

In the case of more complex non-spherical particles, e.g., elongated particles, optically anisotropic particles, and inhomogeneous particles (Borghese et al., 2007a) the theory is much more complex. In optical trapping experiments complex objects from tens of nanometers to tens of micrometers are manipulated, and cells, biological structures, metallic, dielectric or hybrid structures are often

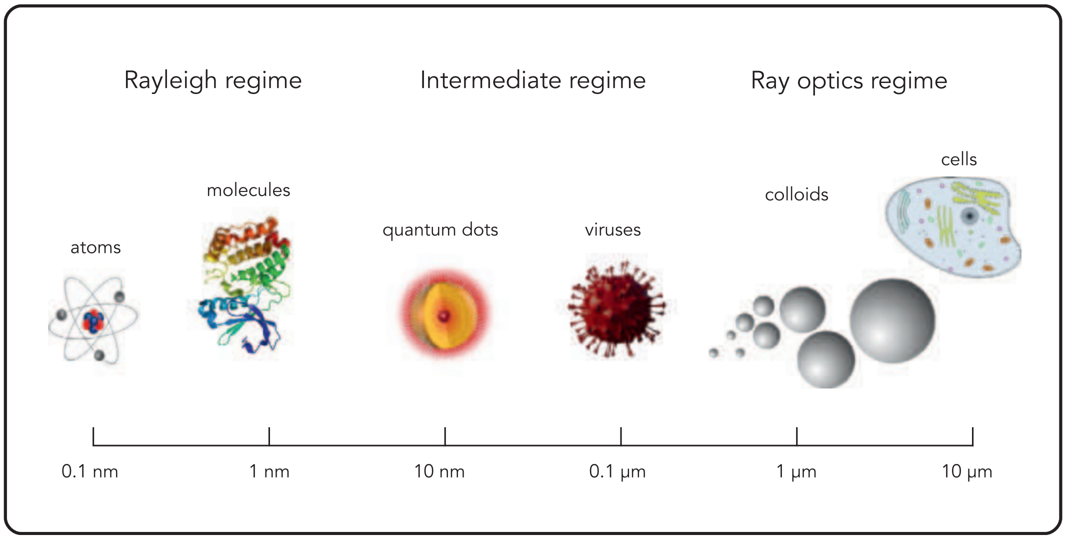

Fig. 1 Typical objects that can be trapped in optical manipulation experiments. The trapping wavelengths are in the visible or near-infrared spectral region.

in the middle of the two extreme regimes or from spherical shapes. Thus, in most cases full electromagnetic calculations need to be used to have a correct prediction of the optical trapping behavior.

Geometrical ray optics regime

In many physical problems, approximations are a valuable source of physical insight that can give answers to complex problems. The range of validity of these approximate approaches is determined by the *size parameter* of the particle, defined as:

$$\zeta = 2\pi a n_{\mathrm{m}} / \lambda_0, \tag{1}$$

where a is the characteristic size of the particle (e.g., the radius in the case of a sphere), λ_0 the trapping wavelength in vacuum, and n_{m} the refractive index of the surrounding medium. Ray optics is valid when $\zeta \gg 1$ and, furthermore, its accuracy increases as the size-parameter grows (Ashkin, 1992; Callegari et al., 2015). By comparison, all exact theories for non-spherical particles becomes unpractical when the size parameter exceeds a certain threshold. This makes ray optics an extremely useful and effective approach when dealing with large (relative to the optical wavelength) particles.

Let us consider a particle with a refractive index n_{p}, immersed in a homogeneous, non magnetic, non dissipative medium with refractive index $n_{\mathrm{m}} < n_{\mathrm{p}}$, and illuminated by a laser beam with vacuum wavelength λ_0 and hence wavenumber $k_{\mathrm{m}} = 2\pi n_{\mathrm{m}}/\lambda_0$ in the medium surrounding the particle. In the ray optics regime, the optical field may be described as a collection of N rays, each of which is associated with a portion, P_{i}, of the incident power, $P = \sum_{\mathrm{i}} P_{\mathrm{i}}$, and carries a linear momentum $n_{\mathrm{m}} P_{\mathrm{i}}/c$.

When a single ray impinges on the surface of a dielectric object sphere at a certain angle, a small portion of the power associated to the ray is reflected by the surface while the remaining portion (most of the total power) is refracted inside the sphere. Therefore, let r_i, r_r and r_t be the incident, the reflected and the transmitted rays respectively (see Fig. 2). After being transmitted, r_t travels inside the sphere until it reaches the surface. Again, a small portion will be reflected inside the sphere and the large portion will be transmitted outside. The ray that remains inside the sphere will reach, again, the surface and another scattering event occurs. It is clear that these processes will have place until all the total power of the impinging ray r_i has run off the sphere. Considering these multiple reflection and refraction events the optical force can be calculated directly as (Callegari et al., 2015):

$$\mathbf{F}_{\mathrm{ray}} = \frac{n_{\mathrm{m}} P_{\mathrm{i}}}{c} \hat{\mathbf{r}}_{\mathrm{i}} - \frac{n_{\mathrm{m}} P_{\mathrm{r}}}{c} \hat{\mathbf{r}}_{\mathrm{r},0} - \sum_{j=1}^{+\infty} \frac{n_{\mathrm{m}} P_{\mathrm{t},j}}{c} \hat{\mathbf{r}}_{\mathrm{t},j}, \tag{2}$$

where $\hat{\mathbf{r}}_{\mathrm{i}}$,$\hat{\mathbf{r}}_{\mathrm{r},j}$ and $\hat{\mathbf{r}}_{\mathrm{t},j}$ are unit vectors representing the direction of the incident ray and the j^{th} reflected and transmitted rays, respectively, calculated using Fresnel's reflection and transmission coefficients. Generally, most of the momentum transferred from the ray to the particle is due to only the first two scattering events, especially for small angle of incidence.

The force $\mathbf{F}_{\mathrm{ray}}$ in Eq. (2) has components only in the plane of incidence (Fig. 2) and can be split in two perpendicular components. The component in the direction of the incoming ray $\hat{\mathbf{r}}_{\mathrm{i}}$ represents the *scattering force*, $\mathbf{F}_{\mathrm{ray,\ s}}$, that pushes the particle in the direction of the incoming ray ($\hat{\mathbf{r}}_{\mathrm{i}}$). The component perpendicular to the incoming ray is the *gradient force*, $\mathbf{F}_{\mathrm{ray,\ g}}$, that pulls the particle in a direction perpendicular to that of the incoming ray ($\hat{\mathbf{r}}_{\perp}$).

The scattering and gradient forces of a circularly polarized ray on a sphere were derived by Ashkin (1992):

$$F_{\mathrm{scat}} = \frac{n_m P_i}{c}\left[1 + R\cos 2\theta_i - T^2 \frac{\cos(2\theta_i - 2\theta_r) + R\cos 2\theta_i}{1 + R^2 + 2R\cos 2\theta_r}\right], \tag{3}$$

$$F_{\mathrm{grad}} = \frac{n_m P_i}{c}\left[R\sin 2\theta_i - T^2 \frac{\sin(2\theta_i - 2\theta_r) + R\sin 2\theta_i}{1 + R^2 + 2R\cos 2\theta_r}\right], \tag{4}$$

where R and T are the Fresnel reflection and transmission coefficient, and θ_i and θ_r are the incidence and transmission angle relative to the scattering of the incident beam.

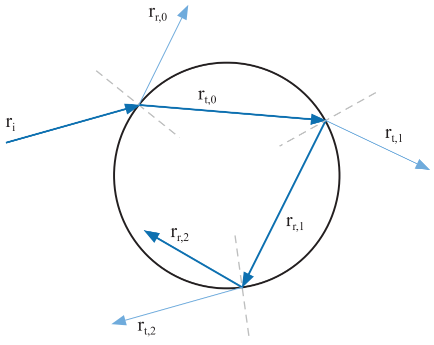

Fig. 2 Multiple scattering of a light ray impinging on a sphere, for simplicity is depicted the incident plane only. All the reflected and transmitted rays as well as the optical force associated to that light ray lie on this plane.

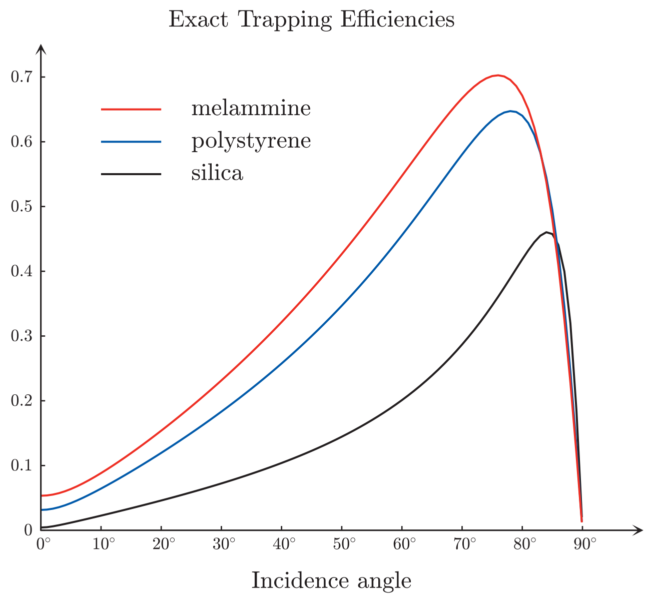

Fig. 3 Trapping efficiencies for a ray impinging on a sphere in water taking into account all scattering events. The results are shown for the most common material used for synthetic particles.

Instead of the force, is more convenient to use the trapping efficiency, a dimensionless quantity defined as $Q = c/(n_m P_i)$. The trapping efficiencies permit one to quantify how effectively momentum is transferred from the light ray to the particle, the theoretical maximum value that they can reach is 2, corresponding to complete reflection of a ray at normal incidence. Fig. 3 shows the trapping efficiencies of the total force (scattering and gradient forces) for a sphere of different materials in water. It is interesting to note also that these results are independent of the size of the sphere.

To have the total force exerted by the light on the particle, we have to take into account all the rays constituting a highly-focused laser beam, that is a set of many rays that converge at a very large angle. This means that the total force acting on the particle is the sum of all the contributions from each ray forming the beam. For a single-beam optical trap, the focused rays will produce a restoring force proportional to the particle's displacement from an equilibrium position that lies close to the beam waist. Hence, in one direction, x, for very small displacements, we have a harmonic response of the type $F_x \approx -\kappa_x x$, where κ_x is the spring constant or trap stiffness in the x direction and the origin of the axis is taken at the trap equilibrium position.

Dipole approximation regime

When the particle size are much smaller than the wavelength of the light it is possible to assume that they can be approximated as small dipoles, and that fields are homogeneous inside the particles. This sets a range of validity that is expressed by two conditions (Mishchenko et al., 2002):

$$\zeta \ll 1,$$

$$|m|\zeta \ll 1,$$

where $m = n_\mathrm{p}/n_\mathrm{m}$ is the relative refractive index between the particle, n_p, and the surrounding medium. Note that the condition (ii) needs to be considered with care for instance when dealing with materials with high refractive index.

An incident electromagnetic field $\mathbf{E}_\mathrm{i}$ induces an electric dipole moment, $\mathbf{p}$, that, for sufficiently small fields, can be expressed in terms of the particle polarizability as

$$\mathbf{p} = \alpha_\mathrm{p}(\omega)\mathbf{E}_\mathrm{i}, \tag{5}$$

where α_p is the complex polarizability of the particle relative to the surrounding medium given by Draine and Goodman (1993).

Without entering in details that are extensively treated in literature (Pesce et al., 2020; Jones et al., 2015), the particle experiences a time varying force whose average is essentially the sum of three contributions that depend on the gradient of the square modulus of the electric field, the time averaged Poynting vector of the electromagnetic field $\mathbf{S}_\mathrm{i}$ and the time averaged spin density (Albaladejo et al., 2009b; Gao et al., 2017) respectively:

$$\mathbf{F}_\mathrm{DA} \propto \nabla |E_\mathrm{i}|^2 + \sigma_\mathrm{ext}\mathbf{S}_\mathrm{i} - \sigma_\mathrm{ext}\nabla \times \mathbf{s}_\mathrm{d}, \tag{6}$$

where $\sigma_\mathrm{ext} = k\,\mathrm{Im}\,\{\alpha_\mathrm{p}\}/\varepsilon_\mathrm{m}$ is the particle extinction cross-section and ε_m the relative permittivity of the medium. The first term in Eq. (6) is the *gradient force*:

$$\mathbf{F}_{\text{grad}}(\mathbf{r}) = \frac{1}{4}\alpha'_{\text{p}}\nabla|E_{\text{i}}(\mathbf{r})|^2. \tag{7}$$

This force is responsible for confinement in optical tweezers. It arises from the potential energy of a dipole immersed in the electric field, and hence it is a conservative force. Since the intensity of the electric field is $I_{\text{i}} = \frac{1}{2}cn_{\text{m}}|E_{\text{i}}|^2$, we can re-write the gradient force in terms of the gradient of intensity as

$$\mathbf{F}_{\text{grad}}(\mathbf{r}) = \frac{1}{2}\frac{\alpha'_{\text{p}}}{cn_{\text{m}}}\nabla I_{\text{i}}(\mathbf{r}). \tag{8}$$

Therefore, particles with positive polarizability, i.e., particles whose refractive index is higher than that of the surrounding medium, are attracted toward the high-intensity region of the optical field (Ashkin et al., 1986), and particles with negative polarizability, i.e., particles whose refractive index is lower than that of the surrounding medium, are repelled by the high-intensity regions, such as at the focal spot of a focused beam.

The second term is the *radiation pressure* or *scattering force*:

$$\mathbf{F}_{\text{scat}}(\mathbf{r}) = \frac{n_{\text{m}}\sigma_{\text{ext}}}{c}\mathbf{S}_{\text{i}}(\mathbf{r}). \tag{9}$$

It arises from the transfer of momentum from the field to the particle as a result of scattering and absorption processes, as is revealed by the fact that $\mathbf{F}_{\text{scat}}$ is proportional to the extinction cross-section σ_{ext}. This force points in the direction of the Poynting vector, $\mathbf{S}_{\text{i}}$ (Ashkin, 1970a). However, note that this direction not always coincides with the direction of the local field propagation (Bliokh et al., 2014; Triolo et al., 2017).

The last term in Eq. (6) is the so-called *spin-curl force* (Albaladejo et al., 2009a; Gao et al., 2017):

$$\mathbf{F}_{\text{spin}}(\mathbf{r}) = -\frac{1}{2}\sigma_{\text{ext}}c\nabla \times \mathbf{s}_{\text{d}}(\mathbf{r}). \tag{10}$$

In order for this force to arise, the polarization of the field must be non-homogeneous, which may occur, e.g., in the case of high numerical aperture focusing. This force is relatively small compared to the gradient and scattering forces and, therefore, does not usually play a major role in optical trapping experiments. However, it may yield larger effects when considering higher-order optical beams with inhomogeneous polarization patterns such as superpositions of circularly polarized Hermite-Gaussian beams (Marqués, 2014) or cylindrical vector beams (Volpe et al., 2004; Donato et al., 2012; Skelton et al., 2013). Noticeably, these two last terms represent the *non-conservative* components of the optical force.

Electromagnetic theory

The intermediate regime is characterized by a size of the particle that is comparable to the optical wavelength. In the intermediate regime, the dipole and geometrical optics approximations are not strictly valid. Therefore, a full wave-optical modeling of the interaction between light and particles (i.e., light scattering) is required to calculate optical forces and torques. Starting from the laws of conservation of linear and angular momentum, it is possible to derive the resulting optical force and torque from the distribution of the scattered fields. In particular, by exploiting the conservation of linear momentum, the time-averaged optical force exerted by monochromatic light on a particle is found to be (Mishchenko, 2001; Nieminen et al., 2001; Saija et al., 2005; Borghese et al., 2007b):

$$\mathbf{F}_{\text{rad}} = \int_S \overline{\mathbf{T}}_{\text{M}} \cdot \hat{\mathbf{n}}\, dS, \tag{11}$$

where the integration is carried out over a surface S surrounding the scattering particle. The vector $\hat{\mathbf{n}}$ is the (outwards) unit vector normal to the S, and $\overline{\mathbf{T}}_{\text{M}}$ is the time-averaged Maxwell stress tensor which describes the mechanical interaction of an electromagnetic field with matter, which needs to be defined carefully (Pfeifer et al., 2007). For harmonic fields this quantity is defined in terms of the total fields complex amplitudes, $\mathbf{E}_{\text{t}}$ and $\mathbf{B}_{\text{t}}$, as

$$\overline{\mathbf{T}}_{\text{M}} = \frac{1}{2}\varepsilon_{\text{m}}\,\text{Re}\left[\mathbf{E}_{\text{t}} \otimes \mathbf{E}_{\text{t}}^* + \frac{c^2}{n_{\text{m}}^2}\mathbf{B}_{\text{t}} \otimes \mathbf{B}_{\text{t}}^* - \frac{1}{2}\left(|\mathbf{E}_{\text{t}}|^2 + \frac{c^2}{n_{\text{m}}^2}|\mathbf{B}_{\text{t}}|^2\right)\mathbf{I}\right], \tag{12}$$

where $\otimes$ represents the dyadic (outer) product, $\mathbf{I}$ is the unit dyadic, and the fields $\mathbf{E}_{\text{t}} = \mathbf{E}_{\text{i}} + \mathbf{E}_{\text{s}}$ and $\mathbf{B}_{\text{t}} = \mathbf{B}_{\text{i}} + \mathbf{B}_{\text{s}}$ are the total electric and magnetic fields resulting from the superposition of the incident $(\mathbf{E}_{\text{i}}, \mathbf{B}_{\text{i}})$ and scattered $(\mathbf{E}_{\text{s}}, \mathbf{B}_{\text{s}})$ fields. Similarly, by exploiting the conservation of angular momentum, the time-averaged radiation torque is found to be (Borghese et al., 2006)

$$\mathbf{T}_{\text{rad}} = -\int_S \left(\overline{\mathbf{T}}_{\text{M}} \times \mathbf{r}\right) \cdot \hat{\mathbf{n}}\, dS. \tag{13}$$

In the far-field region, the expressions for the radiation force and torque can be significantly simplified. By performing the integration over a spherical surface of very large radius, $r \to \infty$, fast decaying terms in the integration may be neglected and the radiation force and torque are (Mishchenko, 2001; Nieminen et al., 2001; Saija et al., 2005; Borghese et al., 2007b)

$$\mathbf{F}_{\mathrm{rad}} = -\frac{\varepsilon_{\mathrm{m}} r^2}{4} \int \left[|\mathbf{E}_{\mathrm{s}}|^2 + \frac{c^2}{n_{\mathrm{m}}^2} |\mathbf{B}_{\mathrm{s}}|^2 + 2\,\mathrm{Re}\left\{ \mathbf{E}_{\mathrm{i}} \cdot \mathbf{E}_{\mathrm{s}}^* + \frac{c^2}{n_{\mathrm{m}}^2} \mathbf{B}_{\mathrm{i}} \cdot \mathbf{B}_{\mathrm{s}}^* \right\} \right] \hat{\mathbf{r}}\, d\Omega, \tag{14}$$

$$\mathbf{T}_{\mathrm{Rad}} = -\frac{\varepsilon_{\mathrm{m}} r^3}{2}\,\mathrm{Re}\left\{ \int \left[(\hat{\mathbf{r}} \cdot \mathbf{E}_{\mathrm{t}})(\mathbf{E}_{\mathrm{t}}^* \times \hat{\mathbf{r}}) + \frac{c^2}{n_{\mathrm{m}}^2} (\hat{\mathbf{r}} \cdot \mathbf{B}_{\mathrm{t}})(\mathbf{B}_{\mathrm{t}}^* \times \hat{\mathbf{r}}) \right] d\Omega \right\}, \tag{15}$$

where the integration is now carried out over the full solid angle ($\Omega = 4\pi$). These expressions are the starting point for the electromagnetic calculations of optical forces and torques in optical trapping in the intermediate size regime as well as for inhomogeneous and non-spherical scatterers. The key point is to solve the scattering problem by calculating the scattered fields and consequently the Maxwell stress tensor, from which the optical force and torque can be found, as in Eqs. (11) and (13). However, the calculations of forces and torques in this regime can be a complicated and cumbersome procedure (Borghese et al., 2007a); thus various approaches have been developed to handle this problem (Simpson, 2014; Nieminen et al., 2014). Among the different methods, one successful approach is based on the calculation of the transition matrix (T-matrix) (Borghese et al., 2007a); this is particularly useful and computationally effective because it is possible to exploit the rotation and translation properties of the T-matrix to obtain at once optical forces and torques for different positions and orientations of the trapped particles (Nieminen et al., 2001, 2011; Saija et al., 2005, 2009; Borghese et al., 2006, 2007b, 2008; Simpson and Hanna, 2006, 2007; Simpson et al., 2007).

In Fig. 4, we compare the results for the transversal trapping stiffness κ_x for a spherical particle held by an optical tweezers as a function of the particle radius a obtained with the exact electromagnetic calculations (solid line) with those obtained with geometrical optics (dashed line) and with dipole approximation (dotted line). Interestingly, the agreement is quite good also beyond the range of particle sizes where the approximations are strictly valid.

Three regimes but common features

Although the theory is complicated and one has to make use of approximations or numerical calculations there are some general features that are always valid for a single beam optical tweezers:

- the force is dependent on the laser power, the higher the power the stronger the force;
- the force is dependent on the particle size;
- the stable trapping condition occurs when the gradient force is greater than the scattering one;
- the particle refractive index must be greater (within certain limits) than the surrounding medium;
- for small displacements from the equilibrium position the force is proportional to the displacement and the potential is harmonic;
- the trapping stiffness along the direction of the propagation of the light is less than those in the radial direction and the typical ratio is 0.2–0.4 depending on the focusing properties.

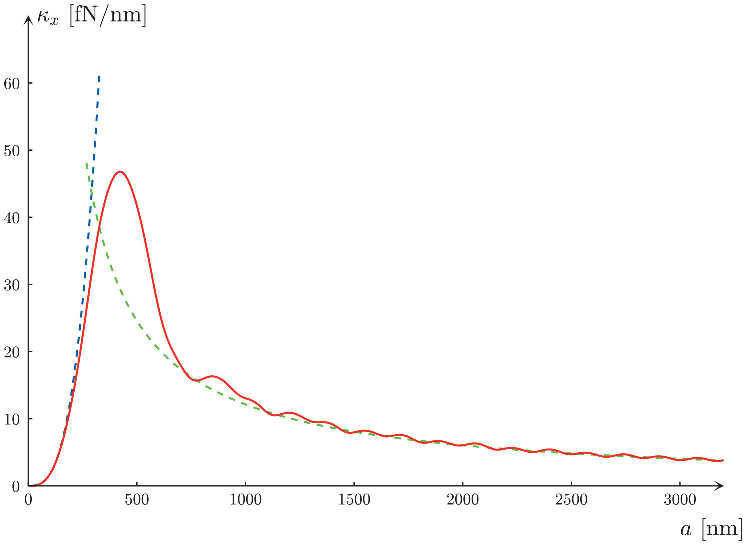

Fig. 4 The red solid line represents the exact electromagnetic calculation. The dipole approximation (dashed blue line) works for small spheres ($a \ll \lambda_0$). The geometrical optics approximation (dashed green line) works for large spheres ($a \gg \lambda_0$). The calculations refer to a polystyrene particle with refractive index of 1.59 immersed in water, trapped by a 10 mW infrared laser ($\lambda_0 = 1064$ nm) using an objective with 1.2 NA.

Brownian motion in optical tweezers

The names Optical Tweezers and Optical Manipulation could lead to misunderstanding, especially for people less expert in this field. The term "trapped particle" does not mean that the particle is at rest, immobilized by the "tweezers." It is important to have in mind that the scenario is that of microscopic world where the fluctuations of the molecules of the surrounding medium are relevant and affect the motion of the trapped particles. In other words the term "trapped" should be regarded as a "confinement" in space more or less strong.

The motion of microscopic particle in a fluid is, the result of the random collisions between the particle and the fluid molecules and is called Brownian motion after the botanist Robert Brown, who gave the first detailed account, in the early 19th century, examining aqueous suspensions of pollen grains, he found that microscopic particles contained within these grains were always in rapid oscillatory motion (Brown, 1828). Brownian motion never ceases even for a system isolated from external perturbations, i.e., it is a phenomenon that happens at thermodynamic equilibrium and is not due to external perturbations. Brownian motion increases as the particle becomes smaller, as the viscosity of the fluid decreases and as the temperature increases, while, at least to a first approximation, it does not depend on the composition and mass of the particle. The resulting Brownian trajectories are very irregular, composed of translations and rotations, to the point that they appear to have no tangent, their velocity is not well-defined and the motion of a particle at one particular instant is independent of the motion of that particle at any other instant.

Therefore when a particle is trapped by an Optical Tweezers it continues to move due to the fluctuations of the medium, but the motion is constrained within a certain volume whose size depends by the trapping stiffness.

Brownian motion can be described as such a random walk: when a particle in a fluid receives an impulse due to a collision with a solvent molecule, its velocity changes, but, if the fluid is very viscous, this change is quickly dissipated so that the net result of an impact is a displacement of the particle; this kind of behavior is typical of systems in the *low Reynolds number regime* (the Reynolds number, *Re*, is the ratio of inertial to viscous forces) (Purcell, 1977). The cumulative effect of multiple collisions is to produce the random walk of the particle.

The precise form of a Brownian motion is obviously not predictable, since it depends on a sequence of random events. However, analyzing the Brownian motion of several particles, it is possible to identify some average properties, which are deterministic. For example, the *average particle* displacement after h time steps is zero because in each time step the displacement has zero mean. However, the mean particle displacement does not deliver a lot of information about the random walk, but there are other, more informative, average properties. Some of these properties are the basis of the optical tweezers calibration and will briefly discussed below, for a more detailed treatment the reader could refer to the wide literature (Jones et al., 2015; Pesce et al., 2020).

Experimental setup and calibration techniques

The first experimental realization of an optical tweezers was based on a laser beam passing through an objective lens from the bottom, in this way the laser light pushed a particle against the gravitational force realizing optical levitation. A few year later Arthur Ashkin and coworkers demonstrated optical trapping in three dimensions with a setup comprised mainly of three parts: (i) a laser and a microscope whose objective lens tightly focuses the beam realizing the trapping condition, (ii) an imaging system and (iii) a detection system.

Usually a conventional commercial light microscope is used to built an optical tweezers. There are some advantages but also some drawbacks. Commercial microscopes can be modified to host a dichroic mirror before the objective lens to deflect the trapping laser beam into the lens and at the same time to transmit the illumination light to a camera to image the sample. They are easy to use and are optimized to reduce any aberration or distortion of the sample images, but they may be relatively difficult to customize, for example, to add a position sensitive device. Moreover, the optics are usually optimized for visible light and therefore some issues arise when infrared laser sources are used. Finally, commercial microscopes do not offer the level of mechanical stability required for the most sensitive nanometer-scale experiments. Despite the difficulties in the design and construction of a home-made microscope, choosing this option is increasingly popular. These microscopes can be built directly with standard optomechanical components or with the use of a user-designed frame. In these microscopes the access to any part is very easy and with the proper choice of materials and design the mechanical stability is extremely high. It is also worth noting that home-made microscopes are often significantly less expensive than commercial ones (Pesce et al., 2015).

As we discussed above, particle in an optical trap is subjected to elastic forces, i.e., the restoring force is proportional to the displacement of the optically trapped particle from the center of the optical trap, provided this displacement is not large.

The calibration of an optical tweezers entails the determination of the value of the optical trap stiffness, which in general depends on the properties of both the light beam and the particle. The calibration of an optical tweezers is essential to use it as a microscopic force transducer, i.e., to measure and exert forces in the femtonewton and piconewton range.

In principle, the stiffness could be determined from the properties of the focused laser beam and the trapped particle (Neto and Nussenzveig, 2000; Rohrbach, 2005; Dutra et al., 2014; Arzola et al., 2019). Nevertheless, this is in general a cumbersome task because an exact description of the focused beam and its interaction with particles depends on several parameters that are very difficult to know accurately and may vary drastically even within the same experiment. Therefore, the development and improvement of in-situ calibration methods have been very important to extend the practical applications of optical tweezers.

The calibration methods can be classified as either passive or active. Passive methods use information about the Brownian trajectory of a particle trapped in a static optical tweezers, while active methods are based on the analysis of the response of the particle to a known time-dependent perturbation exerted by an external force.

It is worth to be noticed that all methods used to calibrate optical tweezers rely on the knowledge of the particle position in units of length (i.e., meters). However, the detection devices used in optical tweezers setups (e.g., CCD cameras, quadrant photodiodes or position sensitive detectors) provide, usually, signals in pixels or volts. This point is little considered and very often neglected and usually the viscosity of the medium where the particles to be trapped are dispersed is considered as known variable. This, of course, is reasonable in many cases, but it is important to keep in mind that it is necessary to determine the conversion factor from pixels or volts to meters. For CCD camera, the pixel-to-meter conversion factor can be determined by standard microscopy techniques (e.g., by using a target with know dimensions) (Pesce et al., 2015; Jones et al., 2015). For quadrant photodiodes or position sensitive detectors, the volt-to-meter conversion factor can be determine by scanning an optically trapped particle across a (much weaker) detection beam, but this means that at least two beams are required. It is also possible to perform this calibration self-consistently using only the position signal of an optically trapped particle acquired by a photodetector, when the diffusion coefficient D of the particle is know (e.g., when the particle radius, the medium viscosity and the temperature are known). The basic idea is that the knowledge of D determines the scaling factor of the functions of the particle position used in the calibration process.

In the following there is a brief resume of the main calibration techniques used, for a detailed description the readers could refer to the wide literature, see (Pesce et al., 2015; Jones et al., 2015; Gieseler et al., 2021) and references therein, Fig. 5 shows typical calibration for a spherical colloidal particle trapped by a single beam optical tweezers.

Equipartition theorem

The potential associated with an optical trap is to a very good first approximation harmonic, i.e.,

$$U(x) = \frac{1}{2}\kappa_x\left[x - x_{\mathrm{eq}}\right]^2, \tag{16}$$

where κ_x is the trap stiffness and x_{eq} is the equilibrium position. Once this hypothesis has been verified, it is possible to use the equipartition theorem, which states that

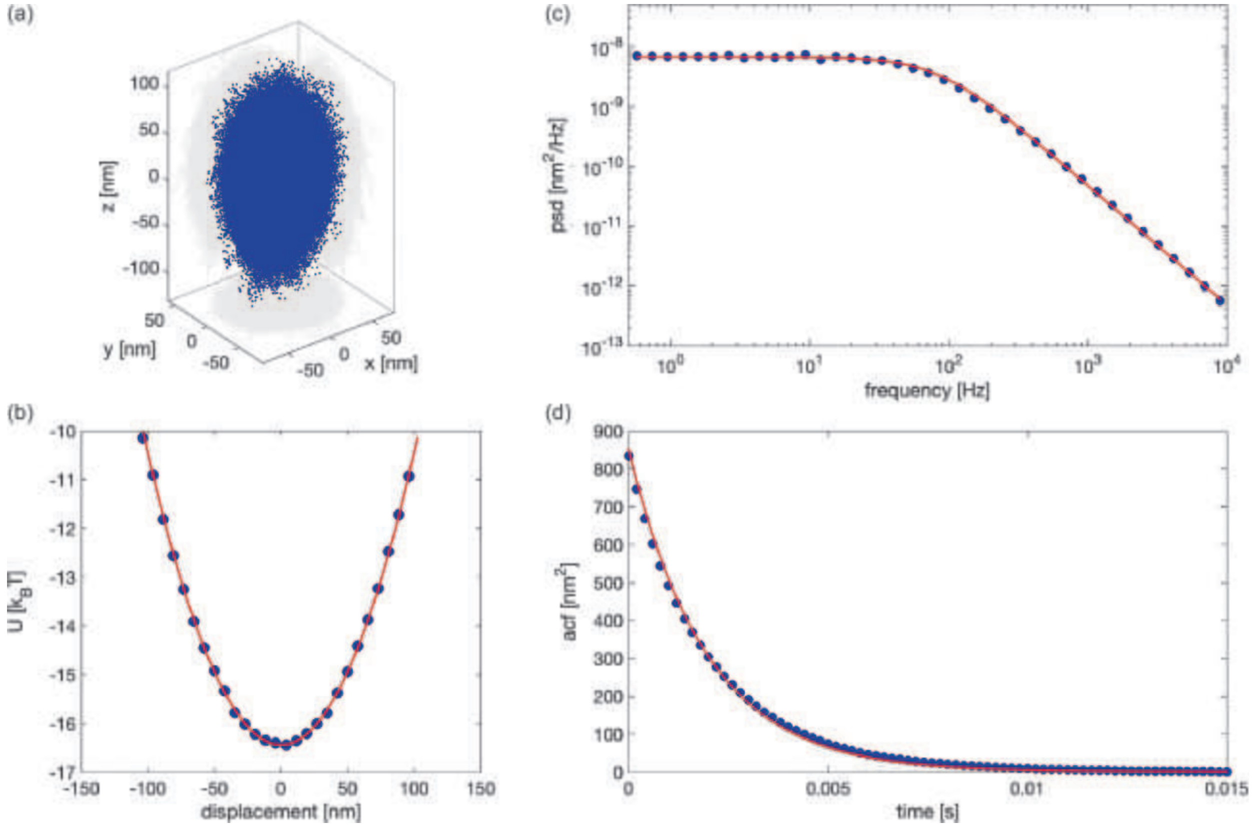

Fig. 5 (a) Positions of a 1 μm polystyrene particle trapped by a 1060 nm laser with a power of 3.7 mW, the stiffness along the z axis is weaker than those in the radial direction and the shape is ellipsoidal. Analysis of the trap with the three most common techniques (only the z-axis is shown): (b) potential analysis, (c) power spectral density and (d) autocorrelation function. The blue dots are the experimental data and in red the fit using the equations discussed in the section.

$$\langle U(x)\rangle = \frac{1}{2}\kappa_x\left\langle \left(x - x_{\mathrm{eq}}\right)^2 \right\rangle = \frac{1}{2}k_{\mathrm{B}}T, \tag{17}$$

where instead of the ensemble average one can also employ a time average because of the ergodicity of the system.

As in the determination of the potential described above, the experimental data points need to sample the probability distribution so that they do not need to be acquired at high frequency rate or with a fixed time step as long as a sufficient number of independent points is acquired. It is the easiest and simplest method nevertheless the estimation of trapping stiffness is also prone to systematic errors due to the presence of uncorrelated noise (Florin et al., 1998) and it is limited to harmonic potentials.

Potential analysis

This method can be used for any conservative force, in fact, for such a force, it is possible to define a potential at equilibrium $U(x)$ such that $F(x) = -dU(x)/dx$. The probability to find the particle in a specific position x is given by the Maxwell-Boltzmann distribution:

$$\rho(x) = \rho_0 e^{-\frac{U(x)}{k_B T}} \tag{18}$$

where ρ_0 is a normalization factor. Inverting Eq. (18) allows one to obtain the potential function from the probability density function:

$$U(x) = -k_B T\, ln\,(\rho(x)/\rho_0) + U_0 \tag{19}$$

where U_0 is a constant. In practice, acquiring a large number of positions (Pesce et al., 2015; Jones et al., 2015; Gieseler et al., 2021) using the CCD camera or the Quadrant Photodiode (provided these device have been calibrated to give the position in length units) it is very easy to construct and histogram that represents the probability density function and inverting the result according to Eq. (19) the potential of the optical trap. It is worth to be note that, differently from the methods presented in the following, this method does not assume that the optical tweezers potential is harmonic and, therefore, can be used to verify the hypothesis that the optical potential is harmonic, or to probe more complex potentials, but it does not give any information on the dynamics of the trapped particle like the diffusion coefficient.

Mean square displacement analysis

The Mean Square Displacement (MSD) quantifies how a particle moves from its initial position: for ballistic motion, the MSD is proportional to t^2, for diffusive motion it is proportional to t, and for a trapped particle it saturates to a constant value. For the case of an optically trapped particle the MSD is given by

$$\mathrm{MSD}_x(\tau) = \overline{[x(t+\tau) - x(t)]^2} = 2\frac{k_{\mathrm{B}}T}{\kappa_x}\left[1 - e^{-\frac{|\tau|}{\tau_0}}\right], \tag{20}$$

where κ_x is the trap stiffness and $\tau_0 = \gamma/\kappa_x$ is the trap characteristic time. The $\mathrm{MSD}_x(\tau)$ features a transition from a linear growth corresponding to a free diffusion behavior at short time scales ($\tau \ll \tau_0$) to a plateau due to the confinement al long time scales ($\tau \gg \tau_0$).

As for the Equipartion method, this technique only applies to harmonic potentials, the computation of MSD is very slow due to the large number of operations and since the experimental errors are correlated, the estimation from least squares results more involved.

Autocorrelation analysis

Another method often employed in characterizing an optical tweezers is the analysis of the Autocorrelation Function (ACF) of the particle position (Bechhoefer and Wilson, 2002; Viana et al., 2002; Gibson et al., 2008). This method is particularly suited when one wishes to deconvolve a more complex time-domain dynamics of the trapped particle from its tracking signal, e.g., in the case of non-conservative effects (Volpe and Petrov, 2006; Volpe et al., 2007; Pesce et al., 2009) and dynamics of non-spherical particles. The position ACF provides a measure of the time it takes for the particle to "forget" its earlier position. As the stiffness increases, the particle undergoes a stronger restoring force and this time decreases. The position ACF is given by

$$C_x(\tau) = \frac{k_{\mathrm{B}}T}{\kappa_x}e^{-\frac{|\tau|}{\tau_{\mathrm{to},x}}}, \tag{21}$$

where κ_x is the trap stiffness and $\tau_{\mathrm{to},\,x} = \gamma/\kappa_x$ is the trap characteristic time. The experimental ACF can be fitted by a least squares method to the theoretical ACF (Jones et al., 2015) to obtain an estimation of κ_x. By repeating this analysis on several experimental series it is possible to obtain an average value and an uncertainty for $\kappa_x^{(\mathrm{ex})}$, as well as for the $C_{x,\,k}$.

Applications

In the following, we present a review of the most relevant applications of Optical Tweezers, since their first experimental demonstration, with particular emphasis to the most recent and exciting experiments.

Single molecule and single cell mechanics

The capability of measuring tiny forces was immediately used in biology to study the thermodynamics and kinetics of intramolecular (Woodside and Block, 2014; Schönfelder et al., 2016) or intermolecular interactions (Manosas et al., 2017), to exploit the molecular motors (Spudich et al., 2011), and fundamental problems in nonequilibrium physics (Ritort, 2008; Ciliberto, 2017) as well as the study of elastic properties of biopolymers (Camunas-Soler et al., 2016) and in general to study single-molecule mechanics (Ritort, 2006; Deniz et al., 2007; Neuman et al., 2007; Moffitt et al., 2008; Neuman and Nagy, 2008; Zhang et al., 2013; Capitanio and Pavone, 2013; Miller et al., 2017).

The first seminal works on single-molecule manipulation appeared, as said above, few year after the demonstration of Ashkin (Ashkin et al., 1986) almost 30 years ago (Block et al., 1990; Bustamante et al., 1994; Finer et al., 1994) and since then, the number of applications of single-molecule mechanics has been continuously increasing. Some of the most used experimental schemes are reported in Fig. 6. It is worth noticing that in recent years, the research in this specific field is, also, oriented to step further toward a considerable increase in throughput. In fact, optical tweezers despite providing a superior accuracy with respect to other manipulation and force techniques like magnetic tweezers and atomic force microscopy, suffer the limitation of their still sophisticated setups that can conduct a single experiment at time, mostly with the presence of operators. Desirable future developments will be the parallelization of measurements in optical tweezers either using holographic techniques (Grier and Roichman, 2006), combining single-molecule fluorescence with force-measurement techniques (Candelli et al., 2011; Cordova et al., 2014; Whitley et al., 2017), controlled force resistive pulse sensing (Keyser et al., 2006; Bulushev et al., 2014), and plasmonic trapping (Juan et al., 2011). Finally, a major step would be to apply force spectroscopy techniques to ex-vivo and in-vivo conditions.

Single molecule mechanics is essentially divided in two groups. In the first one can find experiments intended to shed light on the fundamental physics and chemistry problems using large biomolecules as model systems, i.e., polymer physics, chemical reactions, nonequilibrium physics. In the second group the experiments aimed to enlighten specific biological questions like for instance the mechanics of maintenance and regulatory enzymes in the genome, the energetics and kinetics of DNA hybridization.

The literature comprises many specific reviews addressing these fields, see for example (Ritort, 2006; Deniz et al., 2007; Neuman et al., 2007; Moffitt et al., 2008; Neuman and Nagy, 2008; Zhang et al., 2013; Capitanio and Pavone, 2013; Miller et al., 2017; Bustamante et al., 2021). In these reviews it is evident, for the reader, that the single-molecule field is far to be exhausted and the way is still long.

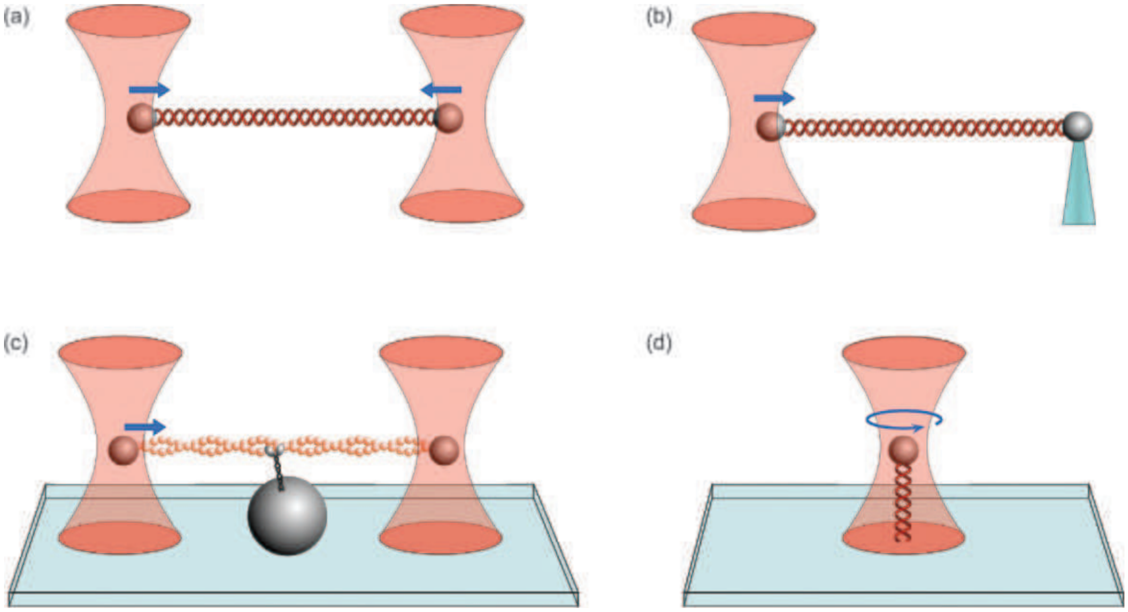

Fig. 6 Some examples of single molecules experiment. (a) a dDNA filament is attached to two beads trapped in different optical traps and stretched; (b) the same experiment as in (a), but in this case the force measurement is easier since one of the two beads is immobilized by a pipette so that the force is measured only by one optical trap; (c) an actin filament is stretched by two optical traps and a bead stuck to a coverslip has a myosin molecules on its surface, providing ATP to the solution the myosin molecule starts to move on the actin filament and its steps result in pulling of the bead on the left trap (see (Finer et al., 1994)); (d) the trapped particle can be put on rotation and the twisting elasticity of the dDNA strand can be measured (Deufel et al., 2007; Ma et al., 2018).

The possibility to trap microscopic objects immediately opened the way to optical manipulation inside living cells (Ashkin and Dziedzic, 1987; Ashkin et al., 1987). In 1989 Block and coworkers (Block et al., 1989) measured the force exerted by a trapped bacteria demonstrating the possibility to trap living organisms.

The manipulation of single cells with optical tweezers has not been extensively investigated as single-molecule manipulation. This is due, essentially, to the fact the living cells have particular shapes, can be deformed and the pulling forces are difficult to quantify. In addition, single cell manipulation with optical tweezers is achievable only on cells in suspension (such as red blood cells, lymphocytes, senescent, stem cells), since adherent cells are more difficult to manipulate. It is important to note that until now single cell manipulation experiments have been carried out in in-vitro environments, it is necessary to expand these techniques to ex-vivo conditions that offer more interesting and relevant possibilities to study cell biology. The recent advances in optical manipulation and techniques like deep learning are promising not only for biology but also for their implications in physiology and medicine.

Statistical physics and colloidal interactions

Despite the huge success of optical manipulation in the world of biology, the very breakthrough has occurred in the physics world with manipulation of particles to study their interactions in a variety of situations. A system composed of particles dispersed in a continuum medium (such as water) is usually named "colloidal system." The size of particles can range from 10 nm up to 10 μm. These particles undergo a continuous motion, the Brownian motion (Brown, 1828; Dhont, 1996) due to the never ending collisions with the solvent molecules. Their properties can be described by statistical physics ensembles, therefore, this make colloidal systems an ideal model to study statistical physics.

The classical description and concepts of statistical physics, like for example entropy, work and heat, in recent years, have been extended to single stochastic trajectories for systems in contact with a heat bath and driven arbitrarily far from thermal equilibrium by means of a well-specified experimental protocol (Seifert, 2012). This new area, called stochastic thermodynamics, gives several relationships between the fluctuating quantities which generalize the classical macroscopic laws of thermodynamics and describe the non-equilibrium energetics of many microscopic systems, such as colloidal particles, polymers, biomolecules, molecular motors, biochemical networks, and microelectromechanical systems (Ciliberto et al., 2013; Ciliberto, 2017). Therefore, stochastic thermodynamics is a solid theoretical framework for applications ranging from single-molecule biomechanics to optimization protocols and the efficiency of microscopic heat engines (see Fig. 7 for an example of two microscopic engines).

Colloidal suspensions have been used to investigate phase transitions between gas, liquid, solid, and crystalline phases (Anderson and Lekkerkerker, 2002; Pusey and Van Megen, 1986), crystal nucleation (Auer and Frenkel, 2001; Elliot et al., 2001; Gasser et al., 2001), glassy states (Pham et al., 2002), and vapor-liquid interfaces (Aarts et al., 2004). They have been also employed in industry to stabilize emulsions (oil in water and water in oil) and foams (Gonzenbach et al., 2006; Zanini et al., 2017). Colloidal interactions play a key role in all these applications, from food industry (Dickinson and McClements, 1995) to nanotechnology (Zerrouki et al., 2008).

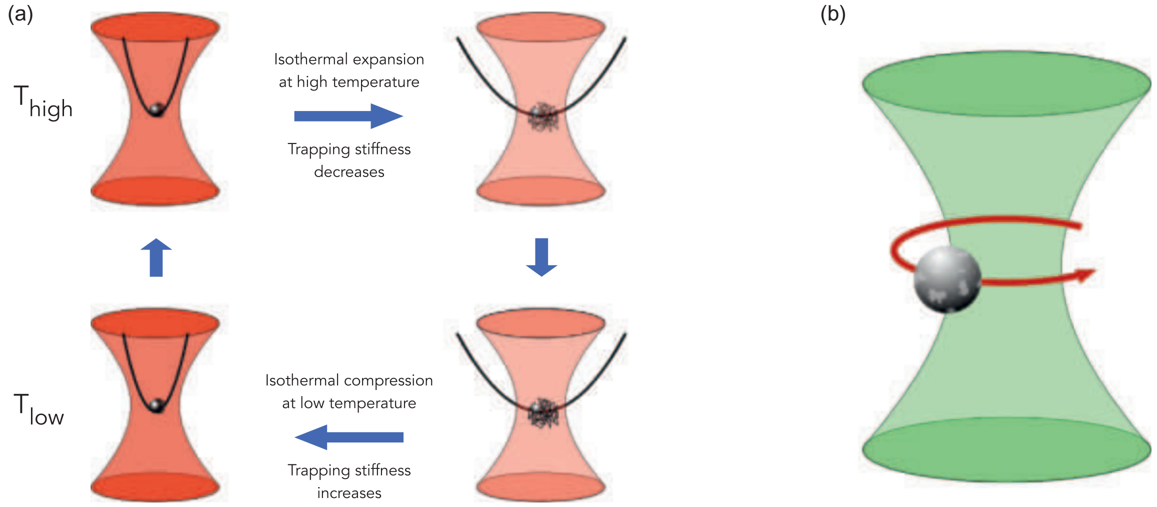
(a)
T_{high}
Isothermal expansion at high temperature
Trapping stiffness decreases
T_{low}
Isothermal compression at low temperature
Trapping stiffness increases
(b)

Fig. 7 Examples of microscopic engine. (a) A Stirling engine is a heat engine that is operates between different temperatures, resulting in a net conversion of heat energy to mechanical work. Blickle and Bechinger (2012) realized a microscopic version of a Stirling machine using optical tweezers. In that system an isothermal compression was realized changing the trap stiffness keeping the temperature of the medium constant while the instantaneous temperature changing (isochoric process) was realized using an infrared laser beam tuned to the absorption peak of water. (b) A particle immersed in a critical mixture interacts with the laser beam and is attracted toward the center of the beam. The particle has inhomogeneities that hare heated by the laser and the increase in the temperature generates a local phase demixing that exerts a force against the trapping force. Once the equilibrium between these forces has been reached the particle rotate around the laser beam Schmidt et al. (2018).

According to Einstein's description of Brownian motion, particles diffusion is characterized by a particle Mean Square Displacement increasing linearly in time (Fickian), and by a Gaussian displacement distribution. However, ground-breaking experiments on colloidal tracers in biological fluids revealed the existence of a third type of diffusion, which is simultaneously Fickian but non-Gaussian. This phenomenon has been, very recently, investigated using a particular optical manipulation system based on optical speckle field (Pastore et al., 2021, 2022).

The main colloidal interactions are: Van der Waals forces, double-layer forces, DLVO theory forces, steric and depletion forces, Critical Casimir forces and hydrodynamic interactions. Optical tweezers provide an ideal tool for probing these interactions.

Critical Casimir forces have a key role in nanoscience and nanotechnology since are quite strong (piconewton range), have an action in the nanometer range, can be fine tuned modifying the temperature of the ensemble or the particle surface chemistry. It is possible to use these forces to manipulate micro and nano-objects or to assemble micro and nano-devices (Marino et al., 2016; Nguyen et al., 2017), but also to drive nanomachines (Schmidt et al., 2018) at the nano and micro-meter scale.

Other colloidal interactions have also been studied using optical tweezers. A direct measurement of Van der Waals have been performed between two isolated optically trapped rubidium atoms (Beguin et al., 2013), this interesting experiment opened the way to the atomic modeling of micro- and nano-structured devices (Woods et al., 2016). Double layer forces can also play an important role in nanotechnology due to their ability to tune the transport and deposition rate of micro and nano-sized particles. Steric forces are important in crucial in chemistry, biochemistry, and pharmacology, since they tune the rates and the activation energies of most chemical reactions. Depletion forces are extensively used to stabilize colloidal solutions by flocculation, to produce the programmable self-assembly of colloidal nanostructures (Cademartiri and Bishop, 2014), and to drive cellular organization (Marenduzzo et al., 2006).

Optical tweezers in air and in vacuum

It is worth to remember that Arthur Ashkin developed the theory and started experiments to manipulate atoms in vacuum (Ashkin, 1970a; Ashkin and Dziedzic, 1977, 1976, 1971). The enormous explosion of research in liquids put in shadows the possibility to manipulate particles in air or, more challenging, in vacuum. The first experiment in air was demonstrated only 10 years after the seminal paper of Ashkin (Ashkin et al., 1986), since then optical tweezers have been employed mainly to study aerosol droplets (Hopkins et al., 2004; Reiner et al., 2006; Power et al., 2012; Cotterell et al., 2014; Haddrell et al., 2017; Kalume et al., 2018).

Nowadays, optical manipulation is oriented toward trapping nanoparticles in high vacuum. This allows to study a well isolated system and to cool the trapped object to very low temperature. It is clear that this paves the way to observe and study the quantum behavior of a macroscopic object, that is much larger than atoms or molecules, at room temperature (Romero-Isart et al., 2010; Chang et al., 2010; Barker and Shneider, 2010).

Such experiments are very interesting and challenging since to observe quantum effects it is necessary to reduce the residual motion of the trapped particle. This must be decreased to the level of single quantum excitation, that is it must be reduced by more than seven order of magnitude. Excellent and promising results have been already obtained by several groups using, mainly, feedback systems (Tebbenjohanns et al., 2019, 2020; Jain et al., 2016; Gieseler et al., 2012; Conangla et al., 2019) or cavity cooling schemes (Delić et al., 2019; Windey et al., 2019; Meyer et al., 2019). Fig. 8 depicts the mechanism based on these two different approaches to reduce the residual motion of levitated particles.

The quantum ground state is the most important goal since it is the fundamental to prepare these system in non-classical quantum states. For non classical systems like atom, ions, molecules and elementary particles this has been already reached (Haroche, 2013; Wineland, 2013; Tüxen et al., 2010; Hornberger et al., 2012). In the case of massive trapped particles in vacuum only very recently it has been claimed (Delić et al., 2020).

Using nanoparticles in quantum regime has the great advantage of their simpler mechanical mode structure with respect to conventional mechanical oscillators that have a series of vibrational modes. Inside nanoparticles, the frequencies of bulk modes are several orders of magnitude higher than those of the center of mass motion. Therefore, usually, one observes only three modes corresponding to the center of mass motion in each dimension.

Optically levitated particles have unique properties not available in traditional nanomechanical resonators. For example, its mechanical properties can be changed rapidly in situ by simple adjustments in the trapping light. This allows to perform free-fall experiments, which provide new opportunities in force sensing (Geraci and Goldman, 2015; Hebestreit et al., 2018) and quantum physics (Stickler et al., 2018). Unlike traditional clamped mechanical resonators, a levitated particle can rotate freely (Arita et al., 2013; Kuhn et al., 2015, 2017; Rahman and Barker, 2017). The rotation can be accelerated to GHz frequencies, faster than any other object (Ahn et al., 2018; Reimann et al., 2018), simply by changing the trapping laser polarization from linear to circular. At these fast rotations, the centrifugal stress is close to the ultimate tensile strength of the material. Hence, levitated particles can be utilized to test material limits on the nanoscale or to study friction at a fundamental level (Manjavacas et al., 2017; Zhao et al., 2012).

These experiment require an extremely high control of all the parameters involved and among these, it is worth to notice the tuning of the interaction of the trapped particle with the environment. Therefore it is clear that trapped nanoparticles in vacuum are suitable to test single particle thermodynamics (Gieseler and Millen, 2018), a field also known as stochastic thermodynamics (Seifert, 2012). Many studies in this field have already been conducted in the *overdamped* regime with optically trapped particles in a liquid medium. In contrast, levitated particles can also operate in the *underdamped* regime and have enabled the first observation of ballistic Brownian motion (Li et al., 2010), the first quantitative measurement of the Kramers turnover (Rondin et al., 2017),

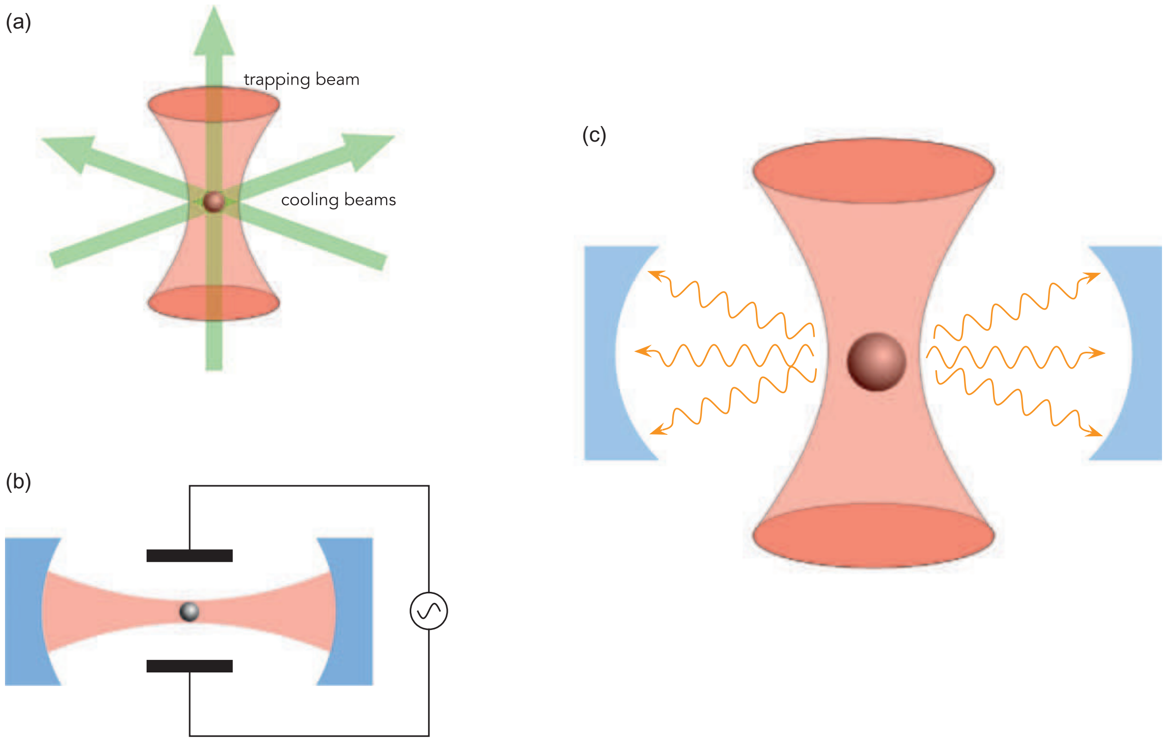

Fig. 8 A levitated microparticle or nanoparticle is an excellent system for precision measurements since it is very well isolated from the environment. These systems could also be used to study macroscopic quantum mechanics, to do that it is necessary to cool the particle to near their quantum limit, which is in the microkelvin regime for typical trapping potentials. The two main cooling methods are based on feedback or on an optical cavity. Feedback cooling, essentially, uses external forces like: (a) additional optical forces (Li et al., 2011) or, (b) electric forces (Millen et al., 2015). These forces are modulated according to the position of the trapped particle, to eliminate its residual motion. These techniques are limited by the position detection system. (b) Cavity cooling, instead, is based on the effect that an optical cavity, when slightly blue detuned with respect of the trapping laser frequency, allows the photons that have adsorbed mechanical energy from the particle to escape, leading to a decrease of the temperature of the particle (Delić et al., 2019; Windey et al., 2019).

experimental tests of fluctuation theorems (Gieseler et al., 2014a; Hoang et al., 2018), and fundamental tests of thermodynamic laws (Debiossac et al., 2020).

Since the nanoparticles are isolated from the environment these systems have a very large mechanical quality factor and, hence, the thermo-mechanical noise of these nanomechanical resonators is very low. Thus, trapped nanoparticles in vacuum can be used as nanomechanical sensors for force (Ranjit et al., 2016; Hempston et al., 2017; Blakemore et al., 2019), torque (Hoang et al., 2016), and acceleration (Monteiro et al., 2017). Applications of these sensors are envisioned to detect exotic forces (Rider et al., 2016; Moore et al., 2014), such as non-Newtonian gravity (Geraci and Goldman, 2015), Casimir forces (Canaguier-Durand et al., 2011; Manjavacas et al., 2017; Nie et al., 2013) and torques (Xu and Li, 2017), and gravitational waves (Arvanitaki and Geraci, 2013).

Finally they are also suited to study nonlinear nanomechanical phenomena (Lifshitz and Cross, 2008; Gieseler et al., 2014b; Ricci et al., 2017), in fact, levitated particles are the first systems where nonlinear effects have been witnessed already at the level of thermal fluctuations (Gieseler et al., 2013).

Conclusion

Optical tweezers were proposed by pioneering work by Arthur Ashkin in the 1970s, since then, these tools have been employed in a broad range of applications in life sciences, physics, and engineering. These include accurate force and torque measurement at the femtonewton level, microrheology of complex fluids, single micro- and nanoparticle spectroscopy, single-cell analysis, and statistical-physics experiments. Accordingly to the increasing difficulties and challenges of the experiments, Optical Tweezers have been developed into more and more sophisticated instruments to manipulate microscopic objects contactless with unrivaled precision and accuracy.

In this chapter, the fundamental aspects of the theory have been discussed and some of the most relevant applications have been presented.

After about 35 years the first demonstration the interest is still high and new routes and techniques are under development. The use of metamaterial to construct compact counterparts to a wide variety of classical refractive or reflective optical components this will allow a strong decrease of the size of current optical tweezers setup that can be easily integrated into more complex devices. Combining optical tweezers with other detection and measurement techniques will certainly improve their versatility and capability. The recent advances in machine learning will be combined with optical manipulation setups to develop autonomous measurement systems to respond to high demand to increase the output, that currently is still strongly dependent on the presence of trained personnel.

References

Aarts DGAL, Schmidt M, and Lekkerkerker HNW (2004) Direct visual observation of thermal capillary waves. *Science* 304: 847–850.
Ahn J, Xu Z, Bang J, Deng Y-H, Hoang TM, Han Q, Ma R-M, and Li T (2018) Optically levitated nanodumbbell torsion balance and GHz nanomechanical rotor. *Physical Review Letters* 121: 033603.
Albaladejo S, Marqués MI, Laroche M, and Sáenz JJ (2009a) Scattering forces from the curl of the spin angular momentum of a light field. *Physical Review Letters* 102: 113602.
Albaladejo S, Marqués MI, Scheffold F, and Sáenz JJ (2009b) Giant enhanced diffusion of gold nanoparticles in optical vortex fields. *Nano Letters* 9: 3527–3531.
Anderson VJ and Lekkerkerker HNW (2002) Insights into phase transition kinetics from colloid science. *Nature* 416: 811–815.
Arita Y, Mazilu M, and Dholakia K (2013) Laser-induced rotation and cooling of a trapped microgyroscope in vacuum. *Nature Communications* 4: 2374.
Arvanitaki A and Geraci AA (2013) Detecting high-frequency gravitational waves with optically levitated sensors. *Physical Review Letters* 110: 071105.
Arzola AV, Chvátal L, Jákl P, and Zemánek P (2019) Spin to orbital light momentum conversion visualized by particle trajectory. *Scientific Reports* 9: 4127.
Ashkin A (1970a) Acceleration and trapping of particles by radiation pressure. *Physical Review Letters* 24: 156–159.
Ashkin A (1970b) Atomic-beam deflection by resonance-radiation pressure. *Physical Review Letters* 25: 1321–1324.
Ashkin A (1992) Forces of a single-beam gradient laser trap on a dielectric sphere in the ray optics regime. *Biophysical Journal* 61: 569–582.
Ashkin A (2000) History of optical trapping and manipulation of small-neutral particle, atoms, and molecules. *IEEE Journal of Selected Topics in Quantum Electronics* 6: 841–856.
Ashkin A and Dziedzic JM (1971) Optical levitation by radiation pressure. *Applied Physics Letters* 19: 283–285.
Ashkin A and Dziedzic JM (1976) Optical levitation in high vacuum. *Applied Physics Letters* 28: 333–335.
Ashkin A and Dziedzic JM (1977) Feedback stabilization of optically levitated particles. *Applied Physics Letters* 30: 202–204.
Ashkin A and Dziedzic JM (1987) Optical trapping and manipulation of viruses and bacteria. *Science* 235: 1517–1520.
Ashkin A, Dziedzic JM, Bjorkholm JE, and Chu S (1986) Observation of a single-beam gradient force optical trap for dielectric particles. *Optics Letters* 11: 288–290.
Ashkin A, Dziedzic JM, and Yamane T (1987) Optical trapping and manipulation of single cells using infrared laser beams. *Nature* 330: 769–771.
Ashkin A, Schütze K, Dziedzic JM, Euteneuer U, and Schliwa M (1990) Force generation of organelle transport measured in vivo by an infrared laser trap. *Nature* 348: 346–348.
Auer S and Frenkel D (2001) Prediction of absolute crystal-nucleation rate in hard-sphere colloids. *Nature* 409(6823): 1020–1023.
Barker PF and Shneider MN (2010) Cavity cooling of an optically trapped nanoparticle. *Physical Review A* 81: 023826.
Bechhoefer J and Wilson S (2002) Faster, cheaper, safer optical tweezers for the undergraduate laboratory. *American Journal of Physics* 70: 393–400.
Beguin L, Vernier A, Chicireanu R, Lahaye T, and Browaeys A (2013) Direct measurement of the van der Waals interaction between two Rydberg atoms. *Physical Review Letters* 110: 263201.
Beth RA (1936) Mechanical detection and measurement of the angular momentum of light. *Physics Review* 50: 115–125.
Blakemore CP, Rider AD, Roy S, Wang Q, Kawasaki A, and Gratta G (2019) Three-dimensional force-field microscopy with optically levitated microspheres. *Physical Review A* 99: 023816.
Blickle V and Bechinger C (2012) Realization of a micrometre-sized stochastic heat engine. *Nature Physics* 8: 143–146.
Bliokh KY, Bekshaev AY, and Nori F (2014) Extraordinary momentum and spin in evanescent waves. *Nature Communications* 5: 3300.
Block SM, Blair DF, and Berg HC (1989) Compliance of bacterial flagella measured with optical tweezers. *Nature* 338: 514–518.
Block SM, Goldstein LSB, and Schnapp BJ (1990) Bead movement by single kinesin molecules studied with optical tweezers. *Nature* 348: 348–352.
Borghese F, Denti P, Saija R, and Iatí MA (2006) Radiation torque on nonspherical particles in the transition matrix formalism. *Optics Express* 14: 9508–9521.
Borghese F, Denti P, and Saija R (2007a) *Scattering from Model Nonspherical Particles*. Berlin: Springer.
Borghese F, Denti P, Saija R, and Iatí MA (2007b) Optical trapping of nonspherical particles in the t-matrix formalism. *Optics Express* 15: 11984–11998.
Borghese F, Denti P, Saija R, Iatí MA, and Maragó OM (2008) Radiation torque and force on optically trapped linear nanostructures. *Physical Review Letters* 100: 163903.
Brown R (1828) A brief account of microscopical observations made in the months of june, july and august, 1827, on the particles contained in the pollen of plants; and on the general existence of active molecules in organic and inorganic bodies. *Philosophical Magazine* 4: 161–173.
Bulushev RD, Steinbock LJ, Khlybov S, Steinbock JF, Keyser UF, and Radenovic A (2014) Measurement of the position-dependent electrophoretic force on DNA in a glass nanocapillary. *Nano Letters* 14: 6606–6613.
Bustamante C, Marko JF, Siggia ED, and Smith S (1994) Entropic elasticity of lambda-phage DNA. *Science* 265: 1599–1600.
Bustamante C, Bryant Z, and Smith SB (2003) Ten years of tension: Single-molecule DNA mechanics. *Nature* 421: 423–427.
Bustamante CJ, Chemla YR, Liu S, and Wang MD (2021) Optical tweezers in single-molecule biophysics. *Nature Reviews Methods Primers* 1(1): 25. ISSN 2662-8449.
Cademartiri L and Bishop KJM (2014) Programmable self-assembly. *Nature Materials* 14: 2–9.
Callegari A, Mijalkov M, Gököz AB, and Volpe G (2015) Computational toolbox for optical tweezers in geometrical optics. *Journal of the Optical Society of America B: Optical Physics* 32(5): B11–B19.
Camunas-Soler J, Ribezzi-Crivellari M, and Ritort F (2016) Elastic properties of nucleic acids by single-molecule force spectroscopy. *Annual Review of Biophysics* 45: 65–84.
Canaguier-Durand A, Gérardin A, Guérout R, Neto PAM, Nesvizhevsky VV, Voronin AY, Lambrecht A, and Reynaud S (2011) Casimir interaction between a dielectric nanosphere and a metallic plane. *Physical Review A* 83: 032508.
Candelli A, Wuite GJL, and Peterman EJG (2011) Combining optical trapping, fluorescence microscopy and micro-fluidics for single molecule studies of DNA–protein interactions. *Physical Chemistry Chemical Physics* 13: 7263–7272.
Capitanio M and Pavone FS (2013) Interrogating biology with force: Single molecule high-resolution measurements with optical tweezers. *Biophysical Journal* 105: 1293–1303.
Chang DE, Regal CA, Papp SB, Wilson DJ, Ye J, Painter O, Kimble HJ, and Zoller P (2010) Cavity opto-mechanics using an optically levitated nanosphere. *Proceedings of the National Academy of Sciences* 107: 1005–1010.
Chaumet PC and Nieto-Vesperinas M (2000) Time-averaged total force on a dipolar sphere in an electromagnetic field. *Optics Letters* 25(15): 1065–1067.
Ciliberto S (2017) Experiments in stochastic thermodynamics: Short history and perspectives. *Physical Review X* 7: 021051.
Ciliberto S, Gómez-Solano R, and Petrosyan A (2013) Fluctuations, linear response, and currents in out-of-equilibrium systems. *Annual Review of Condensed Matter Physics* 4: 235–261.
Conangla GP, Ricci F, Cuairan MT, Schell AW, Meyer N, and Quidant R (2019) Optimal feedback cooling of a charged levitated nanoparticle with adaptive control. *Physical Review Letters* 122: 223602.
Cordova JC, Das DK, Manning HW, and Lang MJ (2014) Combining single-molecule manipulation and single-molecule detection. *Current Opinion in Structural Biology* 28: 142–148.

Cotterell MI, Mason BJ, Carruthers AE, Walker JS, Orr-Ewing AJ, and Reid JP (2014) Measurements of the evaporation and hygroscopic response of single fine-mode aerosol particles using a bessel beam optical trap. *Physical Chemistry Chemical Physics* 16: 2118–2128.

Debiossac M, Grass D, Alonso JJ, Lutz E, and Kiesel N (Mar 2020) Thermodynamics of continuous non-markovian feedback control. *Nature Communications* 11(1): 1360. ISSN 2041-1723.

Delić UCV, Reisenbauer M, Grass D, Kiesel N, Vuletić V, and Aspelmeyer M (2019) Cavity cooling of a levitated nanosphere by coherent scattering. *Physical Review Letters* 122: 123602.

Delić U, Reisenbauer M, Dare K, Grass D, Vuletić V, Kiesel N, and Aspelmeyer M (2020) Cooling of a levitated nanoparticle to the motional quantum ground state. *Science* 367: 892–895.

Deniz AA, Mukhopadhyay S, and Lemke EA (2007) Single-molecule biophysics: At the interface of biology, physics and chemistry. *Journal of the Royal Society Interface* 5: 15–45.

Deufel C, Forth S, Simmons CR, Dejgosha S, and Wang MD (2007) Nanofabricated quartz cylinders for angular trapping: DNA supercoiling torque detection. *Nature Methods* 4: 223–225.

Dholakia K and Čižmár T (2011) Shaping the future of manipulation. *Nature Photonics* 5: 335–342.

Dholakia K, Reece P, and Gu M (2008) Optical micromanipulation. *Chemical Society Reviews* 37: 42–55.

Dhont JKG (1996) *An Introduction to Dynamics of Colloids*. Elsevier.

Dickinson E and McClements DJ (1995) *Advances in Food Colloids*. Springer Science & Business Media.

Donato MG, Vasi S, Sayed R, Jones PH, Bonaccorso F, Ferrari AC, Gucciardi PG, and Maragó OM (2012) Optical trapping of nanotubes with cylindrical vector beams. *Optics Letters* 37: 3381–3383.

Draine BT and Goodman J (1993) Beyond clausius-mosotti: Wave propagation on a polarizable point lattice and the discrete dipole approximation. *The Astrophysical Journal* 405: 685–697.

Dufresne ER and Grier DG (1998) Optical tweezer arrays and optical substrates created with diffractive optics. *The Review of Scientific Instruments* 69: 1974–1977.

Dutra RS, Viana NB, Neto PAM, and Nussenzveig HM (2014) Absolute calibration of forces in optical tweezers. *Physical Review A* 90: 013825.

Elliot MS, Haddon SB, and Poon WCK (2001) Direct observation of pre-critical nuclei in a metastable hard-sphere fluid. *Journal of Physics. Condensed Matter* 13(23), L553–L368.

Finer JT, Simmons RM, and Spudich JA (1994) Single myosin molecule mechanics: Piconewton forces and nanometre steps. *Nature* 368: 113–119.

Florin E-L, Pralle A, Hörber JH, and Stelzer EH (1997) Photonic force microscope based on optical tweezers and two photon excitation for biological applications. *Journal of Structural Biology* 119: 202–211.

Florin E-L, Pralle A, Stelzer EHK, and Horber JKH (1998) Photonic force microscope calibration by thermal noise analysis. *Applied Physics A: Materials Science & Processing* 66: S75–S78.

Fusco S, Borzacchiello A, Miccio L, Pesce G, Rusciano G, Sasso A, and Netti PA (2007) High frequency viscoelastic behaviour of low molecular weight hyaluronic acid water solutions. *Biorheology* 44: 403–418.

Gao D, Ding W, Nieto-Vesperinas M, Ding X, Rahman M, Zhang T, Lim C-T, and Qiu C-W (2017) Optical manipulation from the microscale to the nanoscale: Fundamentals, advances and prospects. *Light: Science & Applications* 6(9): e17039.

Gasser U, Weeks ER, Schofield A, Pusey PN, and Weitz DA (2001) Real-space imaging of nucleation and growth in colloidal crystallization. *Science* 292(5515): 258–262.

Geraci A and Goldman H (2015) Sensing short range forces with a nanosphere matter-wave interferometer. *Physical Review D* 92: 062002.

Ghislain LP and Webb WW (1993) Scanning-force microscope based on an optical trap. *Optics Letters* 18: 1678–1680.

Gibson GM, Leach J, Keen S, Wright AJ, and Padgett MJ (2008) Measuring the accuracy of particle position and force in optical tweezers using high-speed video microscopy. *Optics Express* 16(19): 14561–14570.

Gieseler J and Millen J (2018) Levitated nanoparticles for microscopic thermodynamics–a review. *Entropy* 20: 326.

Gieseler J, Deutsch B, Quidant R, and Novotny L (2012) Subkelvin parametric feedback cooling of a laser-trapped nanoparticle. *Physical Review Letters* 109: 103603.

Gieseler J, Novotny L, and Quidant R (2013) Thermal nonlinearities in a nanomechanical oscillator. *Nature Physics* 9: 806–810.

Gieseler J, Quidant R, Dellago C, and Novotny L (2014a) Dynamic relaxation of a levitated nanoparticle from a non-equilibrium steady state. *Nature Nanotechnology* 9: 358–364.

Gieseler J, Spasenović M, Novotny L, and Quidant R (2014b) Nonlinear mode coupling and synchronization of a vacuum-trapped nanoparticle. *Physical Review Letters* 112: 103603.

Gieseler J, Gomez-Solano JR, Magazzù A, Castillo IP, García LP, Gironella-Torrent M, Viader-Godoy X, Ritort F, Pesce G, Arzola AV, Volke-Sepúlveda K, and Volpe G (Mar 2021) Optical tweezers—From calibration to applications: A tutorial. *Advances in Optics and Photonics* 13(1): 74–241.

Gonzenbach UT, Studart AR, Tervoort E, and Gauckler LJ (2006) Ultrastable particle-stabilized foams. *Angewandte Chemie, International Edition* 45: 3526–3530.

Gouesbet G and Gréhan G (2011) *Generalized Lorenz-Mie Theories*. Springer Verlag.

Grier DG (2003) A revolution in optical manipulation. *Nature* 424: 810–816.

Grier DG and Roichman Y (2006) Holographic optical trapping. *Applied Optics* 45: 880–887.

Haddrell AE, Miles REH, Bzdek BR, Reid JP, Hopkins RJ, and Walker JS (2017) Coalescence sampling and analysis of aerosols using aerosol optical tweezers. *Analytical Chemistry* 89(4): 2345–2352.

Haroche S (2013) Nobel lecture: Controlling photons in a box and exploring the quantum to classical boundary. *Reviews of Modern Physics* 85: 1083–1102.

He H, Friese MEJ, Heckenberg NR, and Rubinsztein-Dunlop H (Jul 1995) Direct observation of transfer of angular momentum to absorptive particles from a laser beam with a phase singularity. *Physical Review Letters* 75: 826–829.

Hebestreit E, Frimmer M, Reimann R, and Novotny L (2018) Sensing static forces with free-falling nanoparticles. *Physical Review Letters* 121: 063602.

Hempston D, Vovrosh J, Toroš M, Winstone G, Rashid M, and Ulbricht H (2017) Force sensing with an optically levitated charged nanoparticle. *Applied Physics Letters* 111: 133111.

Hoang TM, Ma Y, Ahn J, Bang J, Robicheaux F, Yin Z-Q, and Li T (2016) Torsional optomechanics of a levitated nonspherical nanoparticle. *Physical Review Letters* 117: 123604.

Hoang TM, Pan R, Ahn J, Bang J, Quan HT, and Li T (2018) Experimental test of the differential fluctuation theorem and a generalized Jarzynski equality for arbitrary initial states. *Physical Review Letters* 120: 080602.

Hopkins RJ, Mitchem L, Ward AD, and Reid JP (2004) Control and characterisation of a single aerosol droplet in a single-beam gradient-force optical trap. *Physical Chemistry Chemical Physics* 6: 4924–4927.

Hornberger K, Gerlich S, Haslinger P, Nimmrichter S, and Arndt M (2012) Colloquium: Quantum interference of clusters and molecules. *Reviews of Modern Physics* 84: 157–173.

Jain V, Gieseler J, Moritz C, Dellago C, Quidant R, and Novotny L (2016) Direct measurement of photon recoil from a levitated nanoparticle. *Physical Review Letters* 116: 243601.

Jonáš A and Zemánek P (2008) Light at work: The use of optical forces for particle manipulation, sorting, and analysis. *Electrophoresis* 29: 4813–4851.

Jones PH, Maragò OM, and Volpe G (2015) *Optical tweezers: Principles and applications*. Cambridge University Press.

Juan ML, Righini M, and Quidant R (2011) Plasmon nano-optical tweezers. *Nature Photonics* 5: 349–356.

Kalume A, Wang C, Santarpia J, and Pan Y-L (Aug 2018) Study of single airborne particle using laser-trapped submicron position-resolved temporal Raman spectroscopy. *Chemical Physics Letters* 706: 255–260. ISSN 0009-2614.

Kepler J (1619) *De Cometis libelli tres. Augsburg.*

Keyser UF, Koeleman BN, Van Dorp S, Krapf D, Smeets RMM, Lemay SG, Dekker NH, and Dekker C (2006) Direct force measurements on DNA in a solid-state nanopore. *Nature Physics* 2: 473–477.

Kuhn S, Asenbaum P, Kosloff A, Sclafani M, Stickler BA, Nimmrichter S, Hornberger K, Cheshnovsky O, Patolsky F, and Arndt M (2015) Cavity-assisted manipulation of freely rotating silicon nanorods in high vacuum. *Nano Letters* 15: 5604–5608.

Kuhn S, Kosloff A, Stickler BA, Patolsky F, Hornberger K, Arndt M, and Millen J (2017) Full rotational control of levitated silicon nanorods. *Optica* 4: 356–360.

Lebedev P (1901) Untersuchungen über die Druckkräfte des Lichtes. *Annalen der Physik* 311: 433–458.

Li T, Kheifets S, Medellin D, and Raizen MG (2010) Measurement of the instantaneous velocity of a Brownian particle. *Science* 328: 1673–1675.

Li T, Kheifets S, and Raizen MG (2011) Millikelvin cooling of an optically trapped microsphere in vacuum. *Nature Physics* 7: 527–530.

Lifshitz R and Cross MC (2008) Nonlinear dynamics of nanomechanical and micromechanical resonators. In: *Rev. Nonlinear Dynamics Complexity*, 1–52.

Löwen H (2001) Colloidal soft matter under external control. *Journal of Physics. Condensed Matter* 13: R415–R432.

Ma J, Tan C, and Wang MD (2018) *Single-Molecule Angular Optical Trapping for Studying Transcription Under Torsion*. New York, NY: Springer New York. ISBN: 978-1-4939-8556-2301–332.

Manjavacas A, Rodríguez-Fortuño FJ, García de Abajo FJ, and Zayats AV (2017) Lateral Casimir force on a rotating particle near a planar surface. *Physical Review Letters* 118: 133605.

Manosas M, Camunas-Soler J, Croquette V, and Ritort F (2017) Single molecule high-throughput footprinting of small and large DNA ligands. *Nature Communications* 8: 304.

Maragó OM, Jones PH, Gucciardi PG, Volpe G, and Ferrari AC (2013) Optical trapping and manipulation of nanostructures. *Nature Nanotechnology* 8: 807–819.

Marenduzzo D, Finan K, and Cook PR (2006) The depletion attraction: An underappreciated force driving cellular organization. *The Journal of Cell Biology* 175: 681–686.

Marino E, Kodger TE, ten Hove JB, Velders AH, and Schall P (2016) Assembling quantum dots via critical Casimir forces. *Solar Energy Materials & Solar Cells* 158: 154–159.

Marqués MI (Sep 2014) Beam configuration proposal to verify that scattering forces come from the orbital part of the poynting vector. *Optics Letters* 39(17): 5122–5125.

Meyer N, de los Rios Sommer A, Mestres P, Gieseler J, Jain V, Novotny L, and Quidant R (2019) Resolved-sideband cooling of a levitated nanoparticle in the presence of laser phase noise. *Physical Review Letters* 123: 153601.

Millen J, Fonseca PZG, Mavrogordatos T, Monteiro TS, and Barker PF (Mar 2015) Cavity cooling a single charged levitated nanosphere. *Physical Review Letters* 114: 123602.

Miller H, Zhou Z, Shepherd J, Wollman AJM, and Leake MC (2017) Single-molecule techniques in biophysics: A review of the progress in methods and applications. *Reports on Progress in Physics* 81: 024601.

Mishchenko MI (2001) Radiation force caused by scattering, absorption, and emission of light by nonspherical particles. *Journal of Quantitative Spectroscopy and Radiation Transfer* 70: 811–816.

Mishchenko MI, Travis LD, and Lacis AA (2002) *Scattering, absorption, and emission of light by small particles*. Cambridge, United Kingdom: Cambridge University Press.

Moffitt JR, Chemla YR, Smith SB, and Bustamante C (2008) Recent advances in optical tweezers. *Annual Review of Biochemistry* 77: 205–228.

Molloy JE and Padgett MJ (2002) Lights, action: Optical tweezers. *Contemporary Physics* 43: 241–258.

Monteiro F, Ghosh S, Fine AG, and Moore DC (2017) Optical levitation of 10-ng spheres with nano-g acceleration sensitivity. *Physical Review A* 96: 063841.

Moore DC, Rider AD, and Gratta G (2014) Search for millicharged particles using optically levitated microspheres. *Physical Review Letters* 113: 251801.

Neto PAM and Nussenzveig HM (2000) Theory of optical tweezers. *Europhysics Letters* 50: 702–710.

Neuman KC and Nagy A (2008) Single-molecule force spectroscopy: Optical tweezers, magnetic tweezers and atomic force microscopy. *Nature Methods* 5: 491–505.

Neuman KC, Lionnet T, and Allemand J-F (2007) Single-molecule micromanipulation techniques. *Annual Review of Materials Research* 37: 33–67.

Nguyen TA, Newton A, Kraft DJ, Bolhuis PG, and Schall P (2017) Tuning patchy bonds induced by critical Casimir forces. *Materials* 10: 1265.

Nichols EF and Hull GF (1901) A preliminary communication on the pressure of heat and light radiation. *Physics Review* 13: 307–320.

Nie W, Lan Y, Li Y, and Zhu S (2013) Dynamics of a levitated nanosphere by optomechanical coupling and Casimir interaction. *Physical Review A* 88: 063849.

Nieminen TA, Rubinsztein-Dunlop H, Heckenberg NR, and Bishop AI (2001) Numerical modelling of optical trapping. *Computer Physics Communications* 142: 468–471.

Nieminen TA, Loke VL, Stilgoe AB, Heckenberg NR, and Rubinsztein-Dunlop H (2011) T-matrix method for modelling optical tweezers. *Journal of Modern Optics* 58: 528–544.

Nieminen TA, du Preez-Wilkinson N, Stilgoe AB, Loke VLY, Bui AAM, and Rubinsztein-Dunlop H (2014) Optical tweezers: Theory and modelling. *Journal of Quantitative Spectroscopy and Radiation Transfer* 146: 59–80.

Padgett M and Bowman R (2011) Tweezers with a twist. *Nature Photonics* 5: 343–348.

Padgett M and Di Leonardo R (2011) Holographic optical tweezers and their relevance to lab on chip devices. *Lab on a Chip* 11: 1196–1205.

Pastore R, Ciarlo A, Pesce G, Greco F, and Sasso A (2021) Rapid fickian yet non-gaussian diffusion after subdiffusion. *Physical Review Letters* 126: 158003. https://doi.org/10.1103/PhysRevLett.126.158003. https://link.aps.org/doi/10.1103/PhysRevLett.126.158003.

Pastore R, Ciarlo A, Pesce G, Sasso A, and Greco F (2022) A model-system of fickian yet non-gaussian diffusion: Light patterns in place of complex matter. *Soft Matter* 18: 351–364.

Pesce G, Sasso A, and Fusco S (2005) Viscosity measurements on micron-size scale using optical tweezers. *Review of Scientific Instruments* 76: 115105.

Pesce G, Volpe G, Luca ACD, Rusciano G, and Volpe G (2009) Quantitative assessment of non-conservative radiation forces in an optical trap. *Europhysics Letters* 86: 38002.

Pesce G, Mandracchia B, Orabona E, Rusciano G, Stefano LD, and Sasso A (2011) Mapping electric fields generated by microelectrodes using optically trapped charged microspheres. *Lab on a Chip* 11: 4113–4116.

Pesce G, Volpe G, Maragó OM, Jones PH, Gigan S, Sasso A, and Volpe G (2015) Step-by-step guide to the realization of advanced optical tweezers. *Journal of the Optical Society of America B: Optical Physics* 32: B84–B98.

Pesce G, Jones PH, Maragó OM, and Volpe G (2020) Optical tweezers: Theory and practice. *The European Physical Journal Plus* 2190-5444135(12): 949.

Petrov DV (2007) Raman spectroscopy of optically trapped particles. *Journal of Optics A: Pure and Applied Optics* 9: S139–S156.

Pfeifer RNC, Nieminen TA, Heckenberg NR, and Rubinsztein-Dunlop H (2007) Momentum of an electromagnetic wave in dielectric media. *Reviews of Modern Physics* 79: 1197–1216.

Pham KN, Puertas AM, Bergenholtz J, Egelhaaf SU, Moussaıd A, Pusey PN, Schofield AB, Cates ME, Fuchs M, and Poon WCK (2002) Multiple glassy states in a simple model system. *Science* 296: 104–106.

Piccirillo B, Slussarenko S, Marrucci L, and Santamato E (2013) The orbital angular momentum of light: Genesis and evolution of the concept and of the associated photonic technology. *La Rivista del Nuovo Cimento* 36(11): 501–555.

Polimeno P, Magazzu A, Iati MA, Patti F, Saija R, Degli Esposti Boschi C, Donato MG, Gucciardi PG, Jones PH, Volpe G, and Maragó OM (2018) Optical tweezers and their applications. *Journal of Quantitative Spectroscopy and Radiation Transfer* 2018: 131–150.

Power R, Reid JP, Anand S, McGloin D, Almohamedi A, Mistry NS, and Hudson AJ (2012) Observation of the binary coalescence and equilibration of micrometer-sized droplets of aqueous aerosol in a single-beam gradient-force optical trap. *The Journal of Physical Chemistry. A* 116: 8873–8884.

Poynting JH (1884) On the transfer of energy in the electromagnetic field. *Philosophical Transactions. Royal Society of London* 175: 343–361.

Purcell EM (1977) Life at low Reynolds number. *American Journal of Physics* 45: 3–11.

Pusey PN and Van Megen W (1986) Phase behaviour of concentrated suspensions of nearly hard colloidal spheres. *Nature* 320(6060): 340–342.

Rahman ATMA and Barker PF (2017) Laser refrigeration, alignment and rotation of levitated yb 3+: Ylf nanocrystals. *Nature Photonics* 11: 634–639.

Ranjit G, Cunningham M, Casey K, and Geraci AA (2016) Zeptonewton force sensing with nanospheres in an optical lattice. *Physical Review A* 93: 053801.

Reimann R, Doderer M, Hebestreit E, Diehl R, Frimmer M, Windey D, Tebbenjohanns F, and Novotny L (2018) Ghz rotation of an optically trapped nanoparticle in vacuum. *Physical Review Letters* 121: 033602.

Reiner JE, Crawford AM, Kishore RB, Goldner LS, Helmerson K, and Gilson MK (2006) Optically trapped aqueous droplets for single molecule studies. *Applied Physics Letters* 89: 013904.

Ricci F, Rica RA, Spasenović M, Gieseler J, Rondin L, Novotny L, and Quidant R (2017) Optically levitated nanoparticle as a model system for stochastic bistable dynamics. *Nature Communications* 15141.

Rider AD, Moore DC, Blakemore CP, Louis M, Lu M, and Gratta G (2016) Search for screened interactions associated with dark energy below the 100 μ m length scale. *Physical Review Letters* 117: 101101.

Ritort F (2006) Single-molecule experiments in biological physics: Methods and applications. *Journal of Physics. Condensed Matter* 18: R531–R583.

Ritort F (2008) Nonequilibrium fluctuations in small systems: From physics to biology. *Advances in Chemical Physics* 137: 31–123.

Rohrbach A (2005) Stiffness of optical traps: Quantitative agreement between experiment and electromagnetic theory. *Physical Review Letters* 95(16): 168102.

Romero-Isart O, Juan ML, Quidant R, and Cirac JI (2010) Toward quantum superposition of living organisms. *New Journal of Physics* 12: 033015.

Rondin L, Gieseler J, Ricci F, Quidant R, Dellago C, and Novotny L (2017) Direct measurement of kramers turnover with a levitated nanoparticle. *Nature Nanotechnology* 12: 1130–1133.

Saija R, Iatí MA, Giusto A, Denti P, and Borghese F (2005) Transverse components of the radiation force on nonspherical particles in the t-matrix formalism. *Journal of Quantitative Spectroscopy and Radiation Transfer* 94: 163–179.

Saija R, Denti P, Borghese F, Maragó OM, and Iatì MA (2009) Optical trapping calculations for metal nanoparticles: Comparison with experimental data for Au and Ag spheres. *Optics Express* 17: 10231–10241.

Schmidt F, Magazzù A, Callegari A, Biancofiore L, Cichos F, and Volpe G (2018) Microscopic engine powered by critical demixing. *Physical Review Letters* 120: 068004.

Schönfelder J, De Sancho D, and Perez-Jimenez R (2016) The power of force: Insights into the protein folding process using single-molecule force spectroscopy. *Journal of Molecular Biology* 428: 4245–4257.

Seifert U (2012) Stochastic thermodynamics, fluctuation theorems and molecular machines. *Reports on Progress in Physics* 75: 126001.

Simpson SH (2014) Inhomogeneous and anisotropic particles in optical traps: Physical behaviour and applications. *Journal of Quantitative Spectroscopy and Radiation Transfer* 146: 81–99.

Simpson SH and Hanna S (2006) Numerical calculation of inter-particle forces arising in association with holographic assembly. *Journal of the Optical Society of America. A* 23: 1419–1431.

Simpson SH and Hanna S (2007) Optical trapping of spheroidal particles in gaussian beams. *Journal of the Optical Society of America. A* 24: 430–443.

Simpson NB, Allen L, and Padgett MJ (1996) Optical tweezers and optical spanners with laguerre-gaussian modes. *Journal of Modern Optics* 43(12): 2485–2491.

Simpson SH, Benito DC, and Hanna S (2007) Polarization-induced torque in optical traps. *Physical Review A* 76: 043408.

Skelton SE, Sergides M, Saija R, Iatì MA, Maragó OM, and Jones PH (Jan 2013) Trapping volume control in optical tweezers using cylindrical vector beams. *Optics Letters* 38(1): 28–30.

Spudich JA, Rice SE, Rock RS, Purcell TJ, and Warrick HM (2011) Optical traps to study properties of molecular motors. *Cold Spring Harbor Protocols* 2011(11): pdb–top066662.

Stickler BA, Papendell B, Kuhn S, Schrinski B, Millen J, Arndt M, and Hornberger K (2018) Probing macroscopic quantum superpositions with nanorotors. *New Journal of Physics* 20: 122001.

Tebbenjohanns F, Frimmer M, Militaru A, Jain V, and Novotny L (2019) Cold damping of an optically levitated nanoparticle to microkelvin temperatures. *Physical Review Letters* 122: 223601.

Tebbenjohanns F, Frimmer M, Jain V, Windey D, and Novotny L (Jan 2020) Motional sideband asymmetry of a nanoparticle optically levitated in free space. *Physical Review Letters* 124: 013603.

Townes CH (1999) *How the Laser Happened: Adventures of a Scientist*. Oxford University Press.

Triolo C, Cacciola A, Patanè S, Saija R, Savasta S, and Nori F (2017) Spin-momentum locking in the near field of metal nanoparticles. *ACS Photonics* 4(9): 2242–2249.

Tüxen J, Gerlich S, Eibenberger S, Arndt M, and Mayor M (2010) Quantum interference distinguishes between constitutional isomers. *Chemical Communications* 46: 4145–4147.

van de Hulst HC (1957) *Light Scattering by Small Particles*. Courier Dover Publications.

Viana NB, Freire RTS, and Mesquita ON (Apr 2002) Dynamic light scattering from an optically trapped microsphere. *Physical Review E* 65: 041921.

Volpe G and Petrov D (2006) Torque detection using brownian fluctuations. *Physical Review Letters* 97: 210603.

Volpe G, Singh GP, and Petrov D (2004) Optical tweezers with cylindrical vector beams produced by optical fibers. *Proc. SPIE 5514, Optical Trapping and Optical Micromanipulation*. vol. 5514, pp. 283–292. SPIE.

Volpe G, Volpe G, and Petrov D (2007) Brownian motion in a nonhomogeneous force field and photonic force microscope. *Physical Review E* 76: 061118.

Whitley KD, Comstock MJ, and Chemla YR (2017) High-resolutio "Fleezers": Dual-trap optical tweezers combined with single-molecule fluorescence detection. *Methods in Molecular Biology* 183–256.

Windey D, Gonzalez-Ballestero C, Maurer P, Novotny L, Romero-Isart O, and Reimann R (2019) Cavity-based 3d cooling of a levitated nanoparticle via coherent scattering. *Physical Review Letters* 122: 123601.

Wineland DJ (2013) Nobel lecture: Superposition, entanglement, and raising schrödinger's cat. *Reviews of Modern Physics* 85: 1103.

Woods LM, Dalvit DAR, Tkatchenko A, Rodriguez-Lopez P, Rodriguez AW, and Podgornik R (2016) Materials perspective on Casimir and van der Waals interactions. *Reviews of Modern Physics* 88: 045003.

Woodside MT and Block SM (2014) Reconstructing folding energy landscapes by single-molecule force spectroscopy. *Annual Review of Biophysics* 43: 19–39.

Xu Z and Li T (2017) Detecting Casimir torque with an optically levitated nanorod. *Physical Review A* 96: 033843.

Yi C, Li C-W, Ji S, and Yang M (2006) Microfluidics technology for manipulation and analysis of biological cells. *Analytica Chimica Acta* 560: 1–23.

Zanini M, Marschelke C, Anachkov SE, Marini E, Synytska A, and Isa L (2017) Universal emulsion stabilization from the arrested adsorption of rough particles at liquid-liquid interfaces. *Nature Communications* 8: 15701.

Zerrouki D, Baudry J, Pine D, Chaikin P, and Bibette J (2008) Chiral colloidal clusters. *Nature* 455(7211): 380–382.

Zhang X, Ma L, and Zhang Y (2013) High-resolution optical tweezers for single-molecule manipulation. *The Yale Journal of Biology and Medicine* 86: 367–383.

Zhao R, Manjavacas A, García de Abajo FJ, and Pendry JB (2012) Rotational quantum friction. *Physical Review Letters* 109: 123604.

Angle-resolved photoemission of topological materials

Jaime Sánchez-Barriga[a,b], **Oliver J Clark**[a,c], **and Oliver Rader**[a], [a]Helmholtz-Zentrum Berlin für Materialien und Energie, Berlin, Germany; [b]IMDEA Nanoscience, Madrid, Spain; [c]School of Physics and Astronomy, Monash University, Clayton, VIC, Australia

© 2024 Elsevier Ltd. All rights reserved.

Introduction **335**
Topological insulators **335**
Prototypical strong topological insulators 335
Hexagonal warping 336
Spin and orbital texture and final-state effects 340
Thin limit 342
Magnetic topological insulators **342**
Topological crystalline insulators and weak topological insulators **345**
Dirac semimetals **345**
Nonmagnetic Weyl semimetals **347**
Magnetic Weyl semimetals and kagome systems **350**
Case study: Transition metal dichalcogenides **350**
Dirac cones in inversion symmetric TMDs 351
Weyl phases in inversion asymmetric TMDs 353
Thin limit 354
Topological nodal-line semimetals **356**
Topological chiral semimetals **357**
Correlated topological insulators **359**
Topological superconductors **360**
Ultrafast experiments **360**
Conclusion **362**
Acknowledgment **363**
References **363**

Abstract

Topological materials have gained significant attention in condensed matter physics due to their unique electronic and transport properties. Three-dimensional (3D) topological materials are characterized by robust electronic states that are protected by symmetries and exhibit peculiar spin textures. They offer a rich platform for future information technology including spintronics and topological quantum computing. Here, we review the investigation by angle-resolved photoelectron spectroscopy (ARPES) of topological phases such as strong topological insulators, topological crystalline insulators, magnetic topological insulators, and 3D Dirac, Weyl, nodal, and chiral semimetals and address the status of correlated topological insulators and topological superconductors. A special emphasis is laid on examples from the transition metal dichalcogenide family. Moreover, insights from ultrafast pump-probe experiments are reviewed and a brief outlook is provided.

Key points

- ARPES plays a pivotal role as the primary experimental method for investigating the electronic structure and topology of 3D topological materials.
- ARPES reveals topologically protected surface states as well as their origin in the bulk band structure due to its surface and bulk sensitivity, wave vector resolution in 3D, and sensitivity to symmetries.
- Spin resolution and circular dichroism in ARPES offer valuable information about degeneracies, spin-momentum locking, and spin and orbital textures but final-state effects need to be considered.
- ARPES enables conclusions on fundamental aspects of topological materials, such as band inversion, spin-orbit interaction, and the Berry phase.
- The use of ARPES provides insights into exchange splittings, superconducting pairing symmetries, and the robustness of topological surface states, including surface band bending, interface properties, and quantization effects.

https://doi.org/10.1016/B978-0-323-90800-9.00274-2

- ARPES has unambiguously identified examples for several classes of topological materials with correlated topological insulators and topological superconductors still outstanding.
- Transition metal dichalcogenides introduce additional flexibility in the study of topological materials and offer unique opportunities for exploration.
- ARPES allows conclusions on scattering channels and aids in understanding the behavior of spin and charge carriers in topological materials.
- The application of ultrafast pump-probe ARPES allows for the investigation of unoccupied states, their spin texture, and the dynamics of interactions between bulk and surface states, especially under external stimuli like infrared light. It can be utilized to study the creation of charge and spin-polarized currents as well as the emergence of exotic photon-dressed states in topological materials.
- The development of micro- and nano-ARPES techniques opens up possibilities for studying smallest crystallites and domains while additional in-operando options allow to study the effects of current, voltage, and strain and will enable the exploration of topological phase diagrams comprehensively.

Introduction

Topological phases of matter are an important research area in condensed matter physics due to their unique electronic and transport properties. In direct analogy the broader mathematical concept describing objects, the topology of a system’s electronic structure remains unchanged unless the system undergoes a topological phase transition. A change of the number of holes in the object corresponds then to a change in parameters such as the quantity of gapless states in the electronic structure. As such, the electronic states characterizing a nontrivial topological phase are extremely robust and insensitive to smooth changes in material parameters. Most typically, in 3D (2D) systems, these states manifest as highly conductive Dirac cone-like surface (edge) states with unconventional spin textures. Indeed, 2D topological phases such as the quantum Hall, the quantum spin Hall, and the quantum anomalous Hall insulator have been discovered and investigated through their quantized lossless 1D edge channel transport. Similarly, 3D topological phases have mainly been identified by angle-resolved photoelectron spectroscopy (ARPES) studies into the associated topologically protected surface states spanning across the topologically nontrivial band gap, or between so-called “Weyl nodes” which serve as sources of topological charge.

ARPES provides energy and momentum-resolved information about the occupied electronic structure, allowing for the detection of the electronic states that are characteristic of topological insulators (TIs) and other topologically nontrivial systems. The method is highly surface sensitive, thus providing direct access to the protected surface states in addition to the bulk band structure, which are connected through the bulk-boundary correspondence (i.e., the symmetry-mandated presence of surface or edge states at the interface between nontrivial and trivial media). The 3D momentum resolution enables direct observations regarding dimensionality, and ARPES can be combined with spin detection techniques to resolve characteristic spin textures. Moreover, ARPES can be used in time-resolved experiments, allowing for the investigation of the dynamics of topological electronic states under different conditions, such as in response to external perturbations.

While ARPES was crucial in the characterization of the early 3D TIs, further topological classifications have since been populated with experimental evidence of materials exhibiting nontrivial band topology beyond that of the strong TIs, including topological crystalline insulators, 3D Dirac semimetals, and Weyl semimetals and other topological systems, each possessing unique electronic properties and spin textures. Together, topologically nontrivial materials are at the forefront of the research and development of next-generation information technologies with electronic, spintronic,and quantum computing applications.

In the present chapter, we will address the different types of topological materials in the light of their investigation by ARPES. We will highlight where ARPES can provide insight and which aspects of topological materials facilitated or enabled key ARPES experiments. Likewise, topological materials for which ARPES data are not available are not discussed. For an introduction to the ARPES method, the reader is referred to excellent reviews such as the one by Comin and Damascelli (2015). A recent introduction to ARPES with a chapter on topological materials was published by Zhang et al. (2022) while the review by Lv et al. (2019) of ARPES of topological materials has a focus on instrument aspects. ARPES of quantum materials including topological materials has been reviewed by Sobota et al. (2021) and spin-resolved ARPES of topological materials by Dil (2019). Topological materials are introduced in other capters of the present volume as well as in prominent review articles (Hasan and Kane, 2010; Qi and Zhang, 2011). Further review articles are pointed out in the individual paragraphs below.

Topological insulators

Prototypical strong topological insulators

3D TIs behave as a bulk insulator and a surface conductor simultaneously. Their insulating bulk property is due to an inverted band structure between the valence band and the conduction band, typically mediated by the spin–orbit interaction, and their metallic surface is due to gapless surface Dirac cones with spin-momentum locked spin textures, protected by time-reversal symmetry. This is the situation of strong TIs in the $\mathbb{Z}_2$ class (Hasan and Kane, 2010; Qi and Zhang, 2011).

The bulk-boundary correspondence, responsible for the enforced existence of these topological surface states (TSSs), ensures a coupling between the bulk and the surface. This can be exploited in the verification and characterization of the topological properties of a material. The number of band inversions within the bulk corresponds directly to the number of Fermi-level crossings of individual spin subbands at the surface. Therefore, the topology of a material can be directly determined from the enumeration of Fermi-level crossings along the relevant momentum paths in ARPES data, further cementing the technique as an invaluable tool in the characterization of ground-state electronic structures.

A strong 3D TI phase was experimentally discovered by ARPES and spin-resolved ARPES in the $Bi_{1-x}Sb_x$ semiconducting alloy system, demonstrating the existence of nontrivial band topology in a 3D material for the first time (Hsieh et al., 2008). The topological classification, as subsequently confirmed (Nishide et al., 2010; Benia et al., 2015), was identified by a nontrivial $\mathbb{Z}_2$ topological invariant $\nu_0 = 1$, describing an odd number of Dirac cones, distinguishing strong $\mathbb{Z}_2$ TIs from trivial or topologically weak materials where the number of Dirac cones is instead even or zero ($\nu_0 = 0$).

In ARPES, the distinct properties of a 3D TI can be experimentally verified by observing the circular Fermi surface contours around time-reversal invariant momenta or by directly observing their Dirac-like energy-momentum dispersion and spin texture. For a strong $\mathbb{Z}_2$ TI, these signatures must be consistent with an odd number of Fermi-level crossings on the surface, an odd number of band inversions in the bulk, and Dirac-cone TSSs with a chiral, momentum-locked spin texture that fulfill a Berry phase of π. This condition also holds in the cases where the band inversion does not occur at the Fermi level, instead requiring the quantification of crossings in the constant energy contour where the inversion takes place. However, the system will not benefit from the conductive surface states in transport.

The most prominent examples of strong $\mathbb{Z}_2$ TI materials are Bi_2Se_3,Bi_2Te_3, and Sb_2Te_3 which were theoretically predicted (Zhang et al., 2009) and subsequently experimentally verified by ARPES (Bi_2Se_3 by Xia et al., 2009 and Chen et al., 2009 and Sb_2Te_3 by Wang et al., 2010) and spin-resolved ARPES (Bi_2Te_3 by Hsieh et al., 2009). An overview of the topologically nontrivial electronic structure of these materials is highlighted in Fig. 1 following their first theoretical prediction. The real-space crystal structure of these compounds consists of 2D van der Waals bonded layers of formula units X-M-X-M-X (X = Se, Te; M = Bi, Sb). Compared with the $Bi_{1-x}Sb_x$ alloy series, these layered stoichiometric compounds possess a much simpler electronic structure with only one bulk-band inversion, a considerably wide band gap (which has been characterized as direct in Bi_2Se_3 using ARPES; Nechaev et al., 2013), and surface states that form a single gapless Dirac cone at the $\overline{\Gamma}$ point of the surface Brillouin zone.

As shown in Fig. 1 for Bi_2Se_3, these gapless TSSs are directly observed in ARPES as single band features which disperse linearly between the bulk valence and conduction bands across the topologically nontrivial band gap of $\approx$0.3 eV, a value exceeding the energy scale of room temperature. The 2D nature of TSSs is verified by their lack of dispersion with the electron wave vector k_z perpendicular to the surface, which in ARPES is varied by the photon energy, in contrast to bulk bands that are permitted to disperse in 3D. The bulk band gap is caused by strong spin–orbit coupling driving a band inversion at the bulk Γ point. The resulting single Dirac cone TSS exhibits a pronounced linear energy-momentum dispersion, $E(k_x, k_y) \propto |k|$, and a chiral spin texture in which electron spins are locked perpendicular to their linear momenta and parallel to the surface plane. This spin texture was first measured by spin-resolved ARPES on Bi_2Te_3 (Hsieh et al., 2009). Extensive spin-resolved ARPES measurements (Pan et al., 2011; Souma et al., 2011; Xu et al., 2011; Jozwiak et al., 2011) identified and confirmed the predicted ground-state spin structure of the TSS in Bi_2Se_3, as shown in Fig. 2. These measurements revealed an in-plane spin orientation tangential to the Dirac cone, with a left-handed chirality that reverses direction below the spin-degenerate Dirac point. For Sb_2Te_3, the spin texture of the lower Dirac cone has been probed (Pauly et al., 2012).

Bi_2Se_3 and Bi_2Te_3 are intrinsically n-doped so that the chemical potential is in the bulk conduction band while Sb_2Te_3 is slightly p-doped. With ternary compounds $(Sb_{1-x}Bi_x)_2Te_3$ (Kong, 2011) and quaternary compounds $(Bi_{1-x}Sb_x)_2(Te_{1-y}Se_y)_3$ (Arakane et al., 2012) a fully bulk-insulating or intrinsic 3D-TI phase is achieved leading to surface-dominated conduction in electrical transport at room temperature. Moreover, the quaternary compound allows to control the energy of the Dirac point in the bulk band gap. ARPES is very useful to judge the effect of the doping, though surface band bending has to be taken into account (Analytis, 2010).

Hexagonal warping

In a topologically nontrivial analog of a free electron gas, a TSS would be entirely circular. In real systems, this is often not the case, with the shape of the surface state able to reflect the underlying crystal symmetries (Fu, 2009). The degree of warping is correlated to the localization of the orbitals composing the band inversion and the topological state. In the Bi_2Se_3 material class, this manifests in a hexagonal warping of the constant energy contours of the surface state, usually developing apexes along the $\overline{\Gamma}$–$\overline{K}$ direction. This warping, which is captured by the third-order correction to the Rashba Hamiltonian, opens an otherwise symmetry-forbidden out-of-plane spin component along the $\overline{\Gamma}$–$\overline{K}$ direction.

Indeed, ARPES has discovered a snowflake-like, hexagonally warped constant energy surface for Bi_2Te_3 (Chen et al., 2009) (see Fig. 3). This opens possibilities for realizing a number of interesting phenomena, such as a surface quantum Hall effect under applied magnetic fields parallel to the surface, anisotropic surface scattering, or the formation of spin-density waves. As shown in Fig. 3, the hexagonal warping causes a strong anisotropy between the energy-momentum dispersions of the TSS along the $\overline{\Gamma}$–$\overline{\mathrm{K}}$ and $\overline{\Gamma}$–$\overline{\mathrm{M}}$ directions of the surface Brillouin zone, as observed by ARPES.

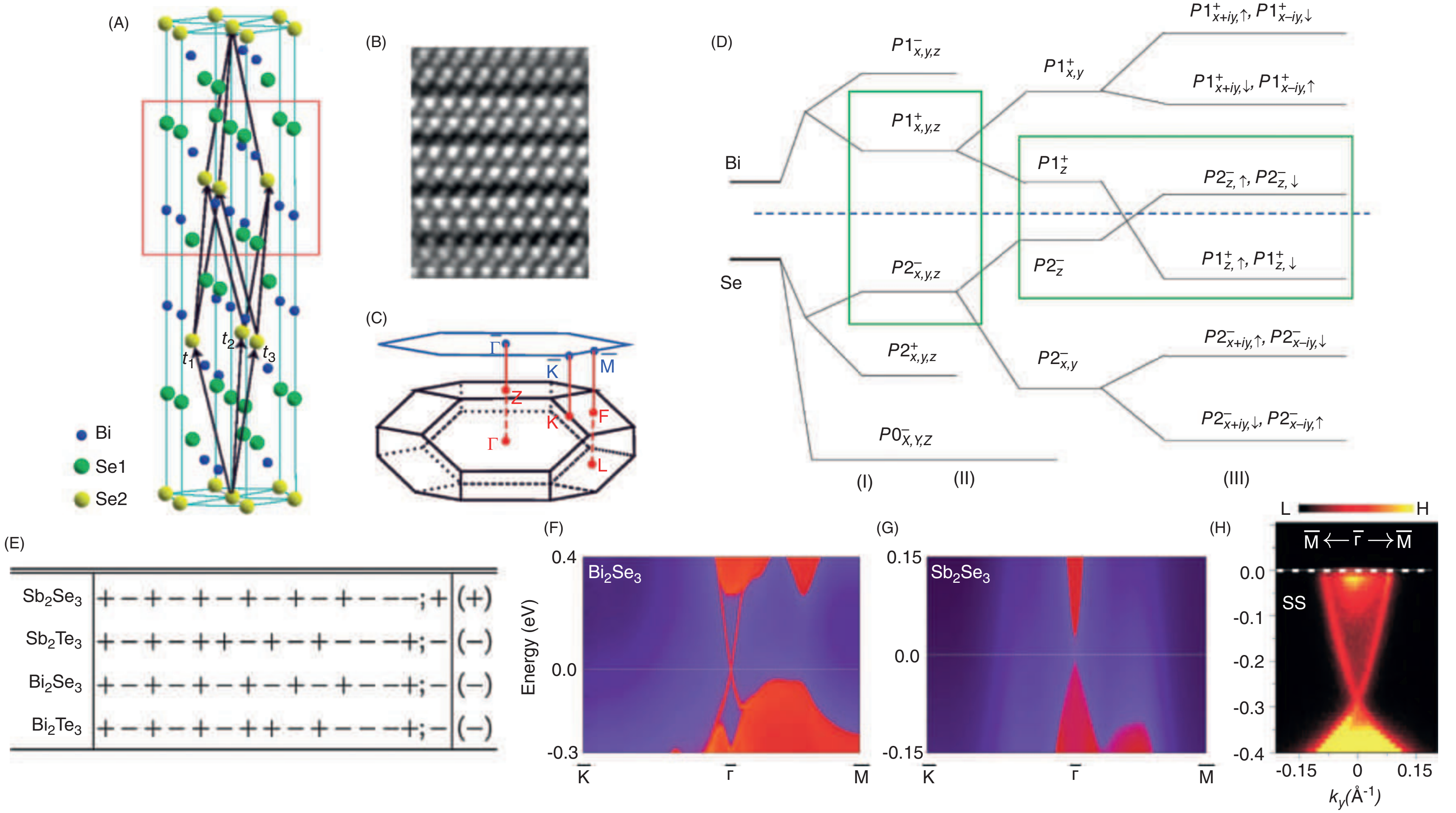

Fig. 1 Prototypical topological insulator Bi_2Se_3. (A) The structure consists of quintuple layers (*red box*) as seen by (B) transmission electron microscopy. Bi_2Se_3 shows a single Dirac cone surface state at the center of the (C) surface Brillouin zone. (D) The band inversion occurs due to the spin–orbit interaction included in the rightmost column. (E) The parity of the band at the Γ point for the four materials Sb_2Se_3, Sb_2Te_3, Bi_2Se_3, and Bi_2Te_3. The parities of fourteen occupied *s* and *p* bands are shown, and of the lowest unoccupied band. The product of the parities for the 14 occupied bands is given in parentheses on the right of each row. All of these systems, except for Sb_2Se_3, which has the lowest spin–orbit interaction, are topological insulators. (F,G) Surface band structure calculations show a Dirac cone surface state for Bi_2Se_3 and not for Sb_2Se_3. (H) Observation of the Dirac cone of Bi_2Se_3 by ARPES at $h\nu = 22$ eV. Panels (A), (C)–(G) From Zhang H, Liu C-X, Qi X-L, Dai X, Fang Z, and Zhang S-C (2009) Nature Physics 5: 438; (B) from Springholz G, et al., unpublished; (H) from Xia Y, Qian D, Hsieh D, Wray L, Pal A, Lin H, Bansil A, Grauer D, Hor YS, Cava RJ, and Hasan MZ (2009) Nature Physics 5: 398.

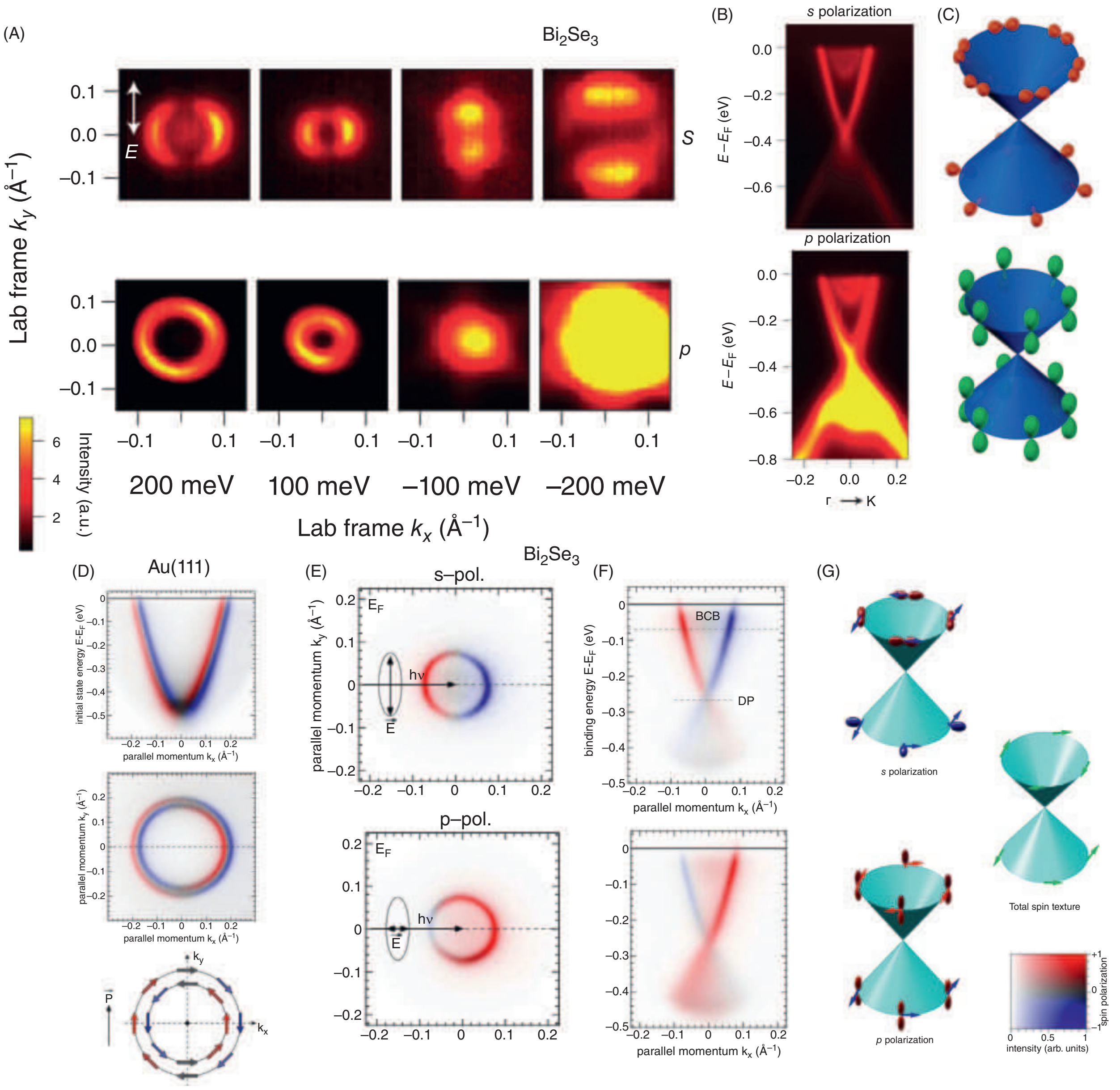

Fig. 2 Orbital-dependent spin texture of Bi$_2$Se$_3$. The photoemission signal of (A) constant energy surfaces and (B) band dispersion of (C) the Dirac cone depends on the direction of the polarization vector (**E** marked in panel (A)) (Cao et al., 2013). With s-polarized light, the orientation of in-plane $p_{x,\,y}$ orbitals can be determined using experimental geometries where a crystal mirror plane is along or perpendicular to the orbital axis. With p-polarized light predominantly p_z orbitals are probed. (C) The result of the experiments in (A,B) is given in a sketch. (B) The intensity asymmetry for p-polarized light is due to the finite incidence angle of the light. (D–F) Modern spin-resolved photoemission instruments provide complete spin-resolved constant energy surfaces and band dispersions. This is shown for (D) the Rashba-split surface state on Au(111) (Tusche et al., 2015), which shows spin-momentum locking but is not topological. (G) Spin-resolved ARPES has shown that the different *p*-orbital components have spin textures of opposite in-plane orientations (Xie et al., 2014) which is demonstrated with state-of-the-art data in panels (E,F) (Meyerheim and Tusche, 2018). The overall spin texture corresponds to the one of p_z orbitals probed by p-polarized light. Panels (A–C) from Cao Y, Waugh JA, Zhang X-W, Luo J-W, Wang Q, Reber TJ, Mo SK, Xu Z, Yang A, Schneeloch J, Gu GD, Brahlek M, Bansal N, Oh S, Zunger A, and Dessau DS (2013) Nature Physics 9: 499; (D) from Tusche C, Krasyuk A, and Kirschner J (2015) Ultramicroscopy 159: 520–529; (E, F) from Meyerheim HL and Tusche C (2018) Physica Status Solidi (RRL) 12: 1800078; and (G) from Xie Z, He S, Chen C, Feng Y, Yi H, Liang A, Zhao L, Mou D, He J, Peng Y, Liu X, Liu Y, Liu G, Dong X, Yu L, Zhang J, Zhang S, Wang Z, Zhang F, Yang F, Peng Q, Wang X, Chen C, Xu Z, and Zhou XJ (2014) Nature Communications 5: 3382.

Following the first theoretical description of this effect, the influence of hexagonal warping on the band dispersion and spin texture of the TSS in Bi$_2$Te$_3$ was confirmed by spin-resolved ARPES measurements (Souma et al., 2011). The experiments revealed a left-handed 3D spin texture with an out-of-plane spin component oscillating around the Fermi surface and an in-plane spin component tangentially following the snowflake contour (Chen et al., 2009) resulting from strong warping. The measured out-of-plane spin polarization was found to increase in magnitude with higher binding energy, to reverse sign with an angular

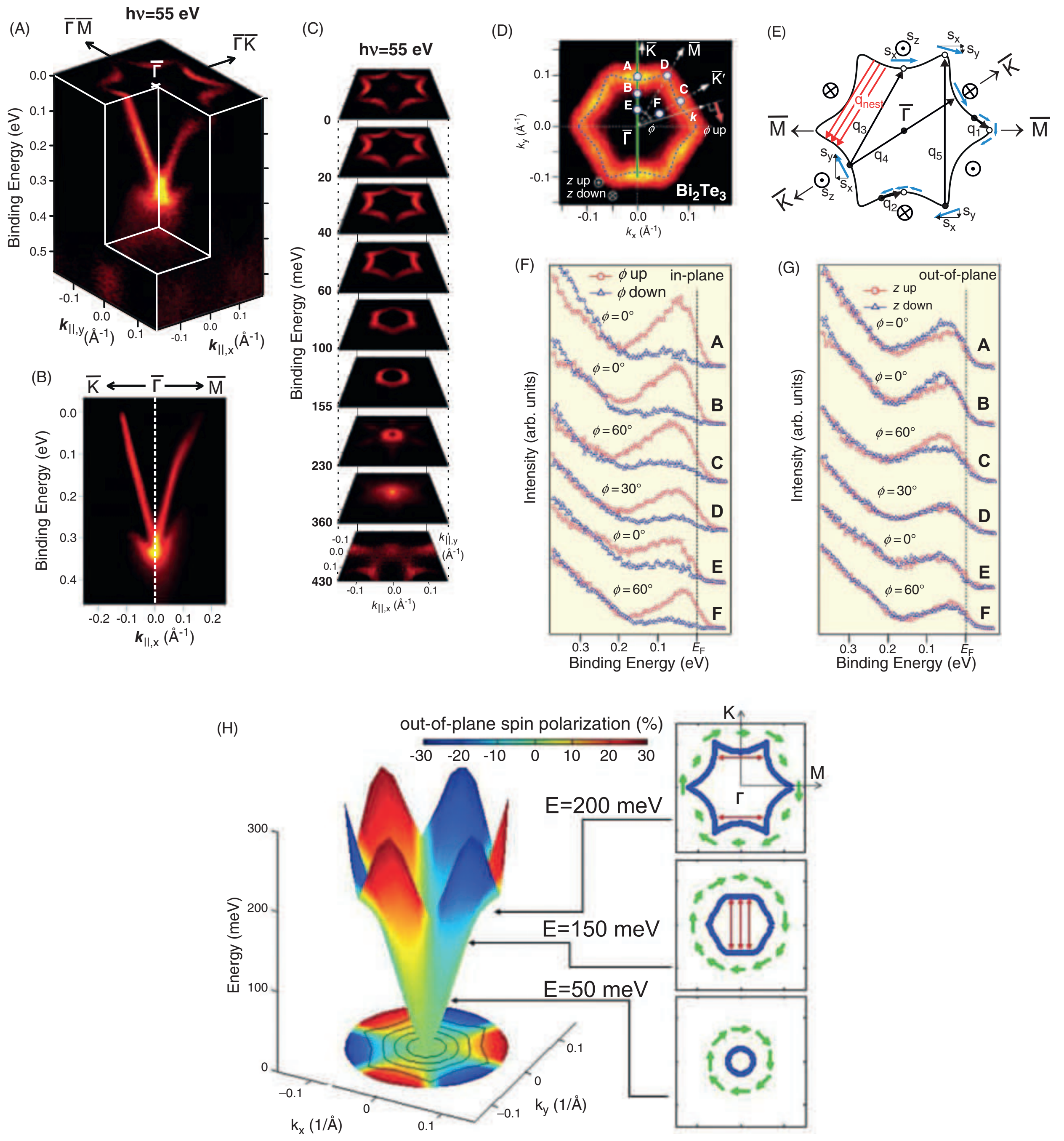

Fig. 3 Hexagonal warping in Bi$_2$Te$_3$. The warping was observed in ARPES at first by Chen et al. (2009). (A–C) Band dispersions and constant-energy surfaces showing the evolution of a circular Dirac cone to a strongly warped one at the Fermi energy. The warping is outward along the $\overline{\Gamma}-\overline{M}$ direction. (D–G) Influence of warping on the spin texture. (D) Constant-energy surface depicting the positions in momentum space of (F,G) spin-resolved measurements for (F) in-plane and (G) out-of-plane spin. (E) Scattering channels based on the spin texture which affect the lifetime broadening. (H) Emergence of the out-of-plane spin polarization from density functional theory calculation (Hasan et al., 2009). Panels (A–C,E) from Sánchez-Barriga J, Scholz MR, Golias E, Rienks E, Marchenko D, Varykhalov A, Yashina LV, and Rader O (2014a) Physical Review B 90: 195413; (D,F,G) from Souma S, Kosaka K, Sato T, Komatsu M, Takayama A, Takahashi T, Kriener M, Segawa K, and Ando Y (2011) Physical Review Letters 106: 216803; (H) from Hasan MZ, Lin H, and Bansil A (2009) Physics 2: 108.

periodicity of $\pi/3$ around the hexagonally distorted constant-energy contours, and vanish along the $\overline{\Gamma}$–$\overline{M}$ direction due to mirror symmetry (Souma et al., 2011). The influence of warping on the spin orientation was predicted to alter the channels for quasiparticle scattering (Fu, 2009), and ARPES measurements (Sánchez-Barriga et al., 2014a) showed that it introduces an anisotropy in the lifetime broadening of the TSS, which is larger along the $\overline{\Gamma}$–$\overline{K}$ direction.

Warping effects can also be induced in systems which possess many bands with significant k_z dispersion, regardless of the strength of the coupling to underlying bulk symmetries. In these cases, the surface electronic structure adopts unconventional band dispersions to avoid the energy cost associated with becoming resonant with the bulk bands (see, for example, both topologically trivial and nontrivial surface states in transition metal dichalcogenide (TMD) systems in Section "Case study: Transition metal dichalcogenides").

Spin and orbital texture and final-state effects

It has frequently been suggested that circular dichroism in the angular distribution (CDAD) of ARPES encodes direct information regarding the spin texture of TSSs (Wang et al., 2011). Circularly polarized light couples, however, mainly to the orbital angular momentum. This is being employed, for example, in x-ray magnetic circular dichroism (XMCD) and in soft-X-ray absorption experiments, where the selection rules for total angular momentum are exploited to access both the spin and orbital magnetic moment (van der Laan and Figueroa, 2014). While one could argue that CDAD may give information on the spin texture where it coincides with the orbital texture (Dil, 2019), it would be desirable to conclude from CDAD the orientation of the orbital moment relative to the spin (Park et al., 2012; Jung et al., 2011). The CDAD of the TSS of Bi_2Te_3 varies, however, strongly with the photon energies and changes sign several times (Scholz et al., 2013). Similar behavior indicating that the CDAD is a final-state effect was observed for Rashba-type spin textures in topologically trivial materials (Ärrälä et al., 2013; Crepaldi et al., 2014). One-step model photoemission calculations including the final state reproduced the sign changes in the CDAD and indicated also a behavior with photon energy different from that of the in-plane spin polarization (Scholz et al., 2013).

A combination of complementary techniques is often required for a full, unambiguous characterization. While initially spin-resolved ARPES experiments provided contradictory values for the in-plane spin polarization of the TSS, for example, in Bi_2Se_3 there is agreement that the measured in-plane spin polarization matches the theoretical prediction of ~50%, reduced from 100% due to spin–orbit interaction (Yazyev et al., 2010). By studying the response of the measured spin properties to incident light and its polarizations, it is possible to gain further experimental insight into the spin texture of TSSs. Several experimental and theoretical works have investigated the effect of varying photon energy and light polarization on the chiral spin texture of TSSs, which has revealed that it can be decomposed into individual orbital contributions from different atomic layers. Through an analysis of the initial states and their orbital character, it has been demonstrated that the total spin texture of the TSS in Bi_2Se_3 is a linear combination of the distinct spin textures associated with each individual orbital component, namely, the two opposite spin textures deriving from the out-of-plane p_z and in-plane $p_{x,\ y}$ orbitals, see Fig. 2. This phenomenon can be attributed to strong spin–orbit coupling, and the resulting spin textures compiled from the orbital-specific contributions were coined "coupled spin-orbital textures" (Zhang et al., 2013; Cao et al., 2013; Zhu et al., 2013). Since the dominant orbital character in the wave function of the TSS is p_z, this leads to a partial reduction in the magnitude of total spin polarization (<100%).

This property has been compared for the more isotropic Dirac cone of Bi_2Te_2Se and the warped Dirac cone of Bi_2Te_3 (Bentmann et al., 2021). For the isotropic Dirac cone, the measured momentum distribution of the photoemission intensity and the spin was found to qualitatively reflect the orbital composition and orbital-projected in-plane spin polarization, respectively. This was also observed for the in-plane spin polarization of Bi_2Te_3. However, the out-of-plane spin polarization of Bi_2Te_3 has been found to change with photon energy (Seibel et al., 2016; Bentmann et al., 2021), which was qualitatively confirmed by one-step photoemission calculations (Bentmann et al., 2021).

Furthermore, due to the fact that the wave function of the TSS extends deep into the bulk (about 2 nm) and the orbital weights change with distance from the surface, the total spin texture can also be broken down into contributions from different atomic layers (Zhu et al., 2013). As a result, a layer-dependent spin-orbital texture is observed, with a significant out-of-plane p_z-orbital contribution within the first five atomic layers (Se-Bi-Se-Bi-Se, or a quintuple layer, about 1 nm) while only a relatively small in-plane $p_{x,y}$ contribution is present except for the fifth atomic layer. It has been argued that this layer dependence is responsible for the photon energy dependence of the spin polarization via quantum interference (Zhu et al., 2013, 2014).

A theoretical study suggested that the spin texture of the photoelectrons may differ from that of the TSSs due to a strong spin-flip effect during photoemission (Park and Louie, 2012). This effect was later experimentally confirmed by a spin-resolved ARPES experiment on Bi_2Se_3 using a 6-eV laser source (Jozwiak et al., 2013), see Fig. 4. This raised the question of whether the use of linearly or circularly polarized light will always rotate the spins of the Dirac cone in the photoemission process along the propagation direction of the incident light, controlling their orientation through the direction of light polarization. According to another spin-resolved ARPES experiment, the measured spin texture of photoelectrons reflects the total spin texture of the TSSs in the initial state (which for Bi_2Se_3 is in plane) for various geometries, photon energies, and light polarizations, indicating that the predicted final state spin-flip effect is a weak perturbation (Sánchez-Barriga et al., 2014b). The relative importance of this effect ultimately depends on the final state the electron.

As shown in Fig. 4 for Bi_2Se_3, these experimental findings were consistent with one-step model photoemission calculations demonstrating that when vacuum ultraviolet photons with linear or circular polarization are used under different incident geometries, the magnitude and direction of the measured photoelectron spin polarization remain unchanged and independent of the light polarization in the photon energy range 50–70 eV. Accordingly, the observed spin texture of the photoelectrons is consistent with the chiral, momentum-locked, in-plane spin texture of the TSS in the initial state, and the magnitude of total spin polarization corresponds to the theoretically predicted value in the ground state (≈50%). For very low photon energies of 6 eV, however, circularly polarized photons flip the photoelectron spins perpendicular to the surface and reverse the resulting out-of-plane spin texture of the photoelectrons with the sense of circular polarization (Jozwiak et al., 2013). The conditions for light-induced spin manipulation at low photon energies are determined by dipole selection rules, which allow transitions into *s*-like final

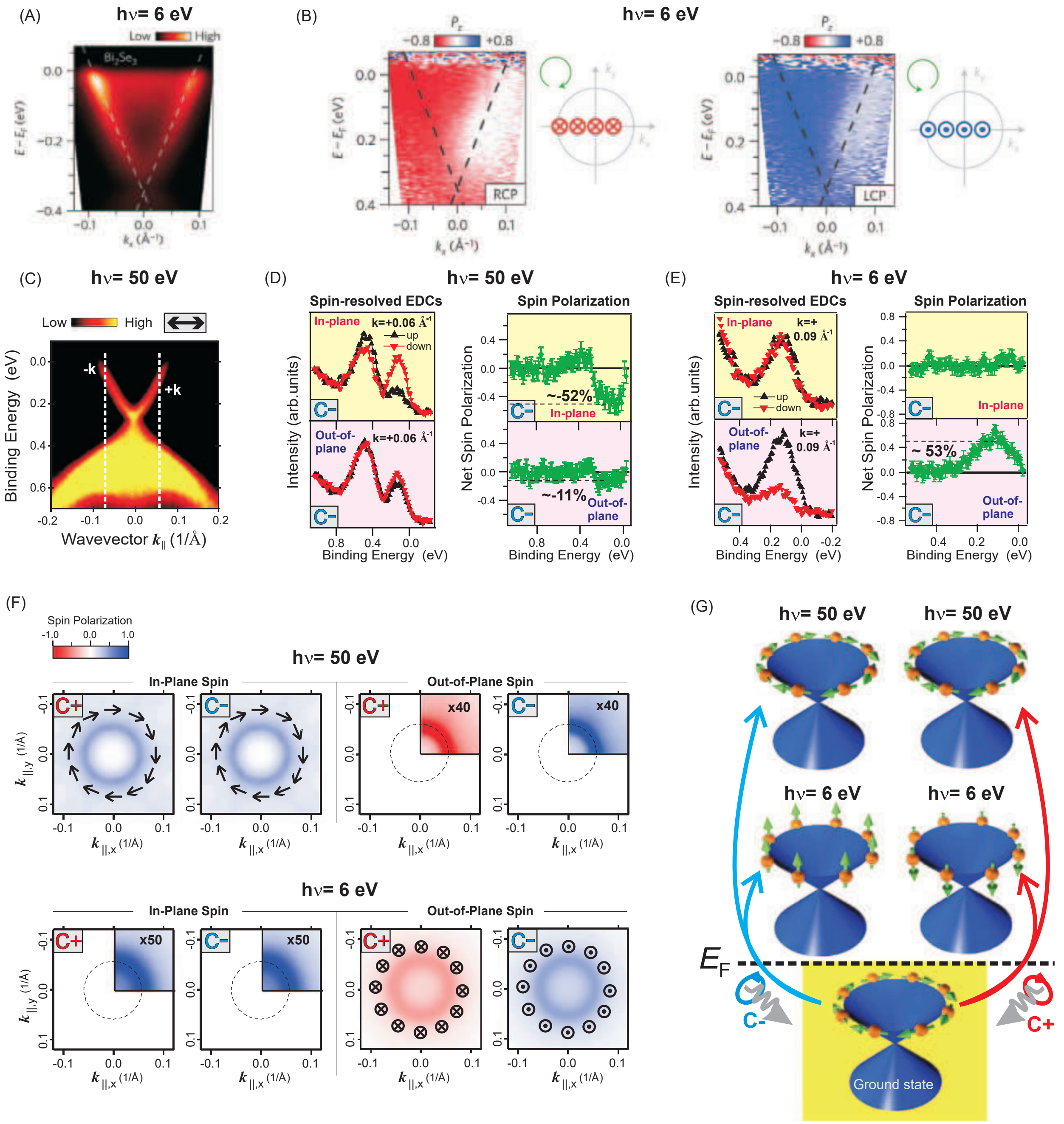

Fig. 4 Spin texture of photoelectrons from the Dirac cone of Bi_2Se_3. (A) ARPES dispersion using 6 eV laser light and (B,C) corresponding out-of-plane spin polarization for opposite circular light polarization. (C) Dispersion at 50 eV photon energy for linear light polarization and corresponding spin-resolved ARPES measurements for circular light polarization at (D) 50 eV and (E) 6 eV. (F) One-step-model photoemission calculations. At 50 eV, the photoelectron spin polarization corresponds to the in-plane ground-state spin texture while at 6 eV, the out-of-plane spin polarization reverses with the circular light polarization. (G) Simplified sketch of the experimental and theoretical results. Panels (A,B) from Jozwiak C, Park, C-H, Gotlieb K, Hwang C, Lee D-H, Louie SG, Denlinger JD, Rotundu CR, Birgeneau RJ, Hussain Z, and Lanzara A (2013) Nature Physics 9: 293; Panels (C–F) from Sánchez-Barriga J, et al. (2014b) Physical Review X 4: 011046.

states. However, this condition is not fulfilled for typical photon energies in the vacuum ultraviolet spectral range, where relevant transitions from the Dirac cone occur primarily into lower symmetry *d*-like final states. Therefore the original prediction is fulfilled at low laser energies despite the need for much higher photon energies to approximate free-electron-like final states. The final-state wave functions in both cases are the most symmetric and connected to the highest symmetry in the atomic case (i.e., an *s*-like final state wave function with angular momentum $l = 0$), which is necessary for light-induced spin manipulation. Thus, very low or very high photon energies in the X-ray spectral range are required for light-induced spin manipulation (Sánchez-Barriga et al., 2014b).

Thin limit

The effect of quantum confinement in topological insulators was initially investigated through ARPES experiments on Bi_2Se_3 bulk single crystals, demonstrating that inducing a sufficiently strong band bending is a feasible approach to achieve quantization of the bulk bands in the near surface region of a 3D TI (King et al., 2011). This is shown in Fig. 5A–C, which also demonstrates that the quantized subbands possess a Rashba-type spin splitting due to the surface potential well.

The weak van der Waals bonding of these compounds, leading to a relaxation of the requirement for lattice matching, allows for the growth of ultrathin films on various substrates by molecular-beam epitaxy (MBE), providing unprecedented control over thickness and composition. This advantage enables experimental investigations into the influence of chemical substitution, quantum-size effects, and dimensionality of topological properties. One example is the observation of a gap opening at the surface Dirac point in ultrathin TI films by ARPES, which demonstrates a topological phase transition driven by surface-to-surface tunneling between Dirac cones with opposite spin textures located on opposing film surfaces (Zhang et al., 2010), see Fig. 5D. This has been studied by spin-resolved ARPES (Neupane et al., 2014; Landolt et al., 2014). As demonstrated in Fig. 5E–G, this surface-to-surface coupling modulates the spin texture of the TSS with reducing thickness.

Magnetic topological insulators

Since $\mathbb{Z}_2$ TIs are protected by time-reversal symmetry, a spontaneous magnetization can lead to a magnetic exchange gap at the Dirac point. If the Fermi energy is aligned to the exchange gap, a quantum anomalous Hall effect can occur. Other desirable consequences include the topological magnetoelectric effect, axion insulator, dissipationless electronics and spintronics based on edge states, and the possibility for constructing topological quantum bits, see the review by Tokura et al. (2019).

The ARPES perspective has focused on the verification and measurement of the exchange gap relative to the position of the Fermi energy as well as investigation of the resulting hedgehog-type spin texture. The magnetic exchange gap was indirectly probed by the observation of the quantum anomalous Hall effect (Chang et al., 2013). From the thermal activation of dissipation-free transport, this gap is in the range of only 50–100 μeV in V- and Cr-doped TIs, orders of magnitude lower than the principal limit set by the Curie temperature (Chang et al., 2015).

Spectroscopic investigations relied on scanning tunneling spectroscopy and ARPES. Early work suffered from a lack of evidence for the closing of the gap above the Curie temperature, a test that, due to stability issues, is easier in ARPES than in scanning tunneling spectroscopy. Another prerequisite for the exchange gap is a perpendicular magnetic anisotropy (see, e. g., Henk et al., 2012), typically not present in Bi_2Se_3-based systems. The reason for the latter is that the spin–orbit interaction has to be high enough so that the magnetocrystalline anisotropy overcomes the shape anisotropy, and this can be achieved by replacing Se by the heavier Te (Rienks et al., 2019). The comparatively lower spin–orbit interaction has also been suggested as a reason why the Bi_2Se_3 systems are susceptible toward the opening of impurity-induced gaps at the Dirac point that are not of magnetic origin (Rienks et al., 2019).

Among early studies that fulfill some of these criteria, scanning tunneling spectroscopy of $Cr_{0.08}(Bi_{0.1}Sb_{0.9})_{1.92}Te_3$ reported substantial disorder in the size of the exchange gap (Lee et al., 2015), which might be responsible for the low operating temperature of the quantum anomalous Hall effect. ARPES of insulating V-doped $(Bi,Sb)_2Te_3$ epitaxial films showed that the Dirac point is degenerate with the bulk valence band and it was concluded that this limits the achievable temperature of the quantum anomalous Hall effect (Li et al., 2016). No exchange gap could be found by ARPES down to 7 K (Li et al., 2016) and down to 1 K (Golias et al., 2021). In both cases, the Dirac point was observed ≈50 meV below the Fermi level. Cr-doped $(Bi,Sb)_2Te_3$ was studied by ARPES at 12 K and no exchange gap was found also after increasing the chemical potential through surface *n*-doping by potassium (Kim et al., 2021).

Mn-doped Bi_2Te_3 has perpendicular magnetic anisotropy (Hor et al., 2010) and was later identified as consisting of a natural $MnBi_2Te_4/(Bi_2Te_3)_m$ heterostructure (Rienks et al., 2019), similar to its selenide counterpart (Hagmann et al., 2017; Hirahara et al., 2017). $MnBi_2Te_4$ contains a Mn layer in the center of a 7-layer unit (septuple layer). The Mn concentration and the number, m, of Bi_2Te_3 quintuple layers can be related by X-ray diffraction. For 6% Mn (i.e., $m = 2$ to 3), a gap at the Dirac point of 90 meV was measured by peak fitting in ARPES at 1 K and of 56 meV at 6.5 K by spin-resolved ARPES which closes at the Curie temperature (Rienks et al., 2019). This is shown in Fig. 6. The closing of the gap at the Curie temperature has been confirmed in two other cases: For a gap of 70 meV at 8 K for 3 and 5 net ferromagnetic quintuple layers of $MnBi_2Te_4$ (Trang et al., 2021) and for $MnBi_8Te_{13}$ (i.e., $m = 3$) with septuple layer termination for a 28 meV gap at 7 K (Lu et al., 2021). For $MnBi_6Te_{10}$ ($m = 2$), three different terminations can be distinguished from the band dispersions (Klimovskikh et al., 2020). Very similar results are obtained by Gordon et al. (2019) and Hu et al. (2020) with mass gaps of the order of 100 meV when $MnBi_4Te_7$, $MnBi_6Te_{10}$, and $MnBi_8Te_{13}$ are terminated by one layer of Bi_2Te_3, see Fig. 6.

A single septuple layer $MnBi_2Te_4$ has been characterized by ARPES as ferromagnetic trivial insulator (Gong et al., 2019) with a bandgap >780 meV (Trang et al., 2021). This septuple layer $MnBi_2Te_4$ becomes again topological when in a heterostructure with 4 quintuple layers Bi_2Te_3 and another septuple layer $MnBi_2Te_4$ (Li et al., 2022).

In stoichiometric bulk $MnBi_2Te_4$, the Mn layers couple antiferromagnetically to form an antiferromagnetic TI (Otrokov et al., 2019; Gong et al., 2019). The magnetic gap in $MnBi_2Te_4$ (Otrokov et al., 2019) has been the subject of controversy: Chen et al. (2019)

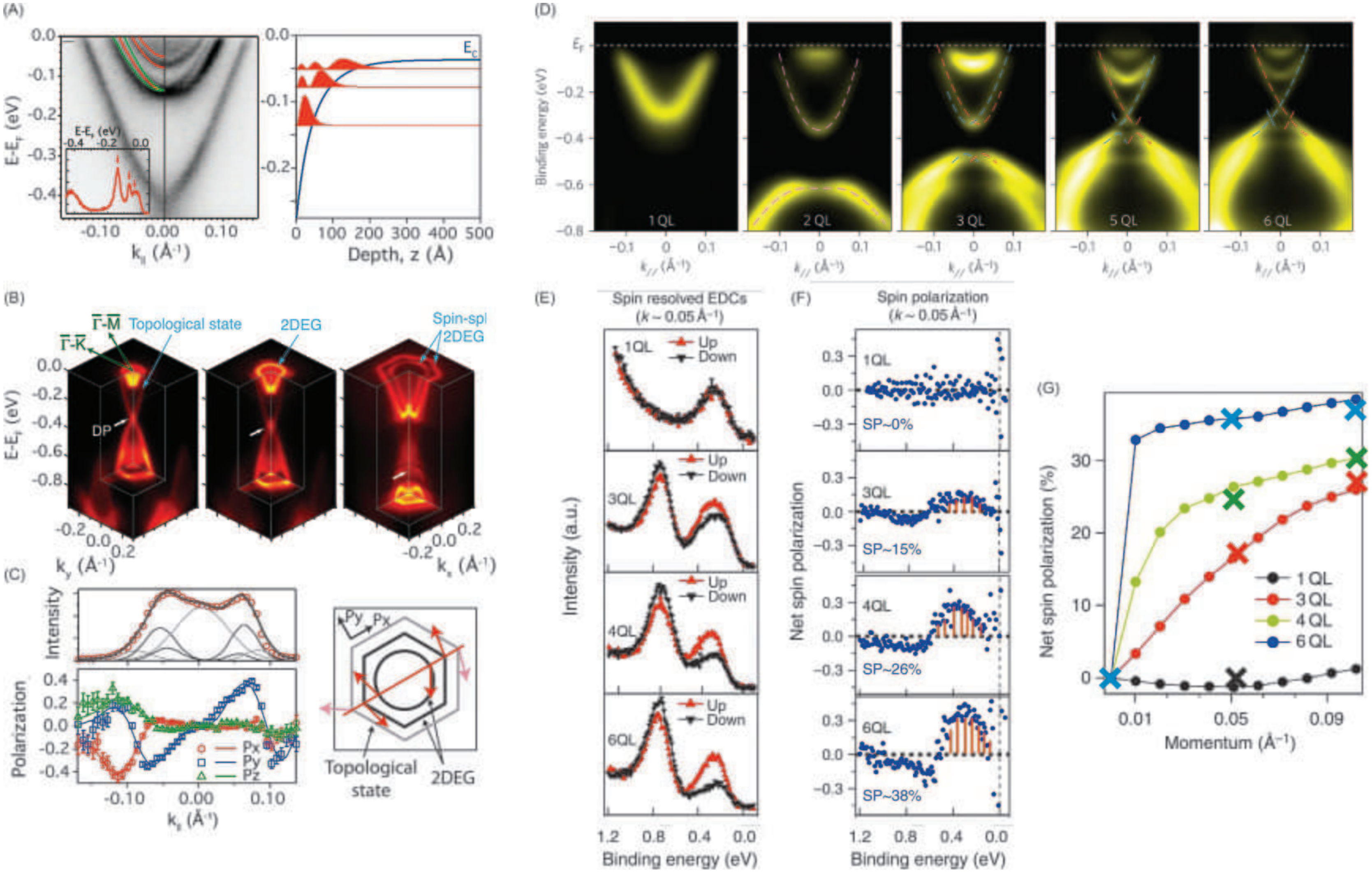

Fig. 5 Quantum-size effects in Bi$_2$Se$_3$. (A) Formation of a 2D electron gas (2DEG) at the surface of a bulk crystal due to surface band bending. Quantum-well states are formed. (B) Formation of spin-split 2D Rashba states with increasing band bending. (C) Spin-resolved ARPES showing the Rashba splitting. (D–G) Topological phase transition as a function of thickness, in 5-atomic-layer units (quintuple layer, QL). (D) Dispersion and (E,F) spin polarization affected by interaction between top and bottom surfaces. (G) Summary of calculated (*circles*) and measured (*crosses*) spin polarization as a function of thickness. Panels (A–C) from King PDC, Hatch RC, Bianchi M, Ovsyannikov R, Lupulescu C, Landolt G, Slomski B, Dil JH, Guan D, Mi JL, Rienks EDL, Fink J, Lindblad A, Svensson S, Bao S, Balakrishnan G, Iversen BB, Osterwalder J, Eberhardt W, Baumberger F, and Hofmann P (2011) Physical Review Letters 107: 096802; (D) from Zhang Y, He K, Chang C-Z, Song C-L, Wang L-L, Chen X, Jia J-F, Fang Z, Dai X, Shan W-Y, Shen S-Q, Niu Q, Qi X-L, Zhang S-C, Ma X-C, and Xue Q-K (2010) Nature Physics 6: 584–588; (E–G) from Neupane M, Xu S-Y, Sankar R, Alidoust N, Bian G, Liu C, Belopolski I, Chang T-R, Jeng H-T, Lin H, Bansil A, Chou F, and Hasan MZ (2014) Nature Communications 5: 3786.

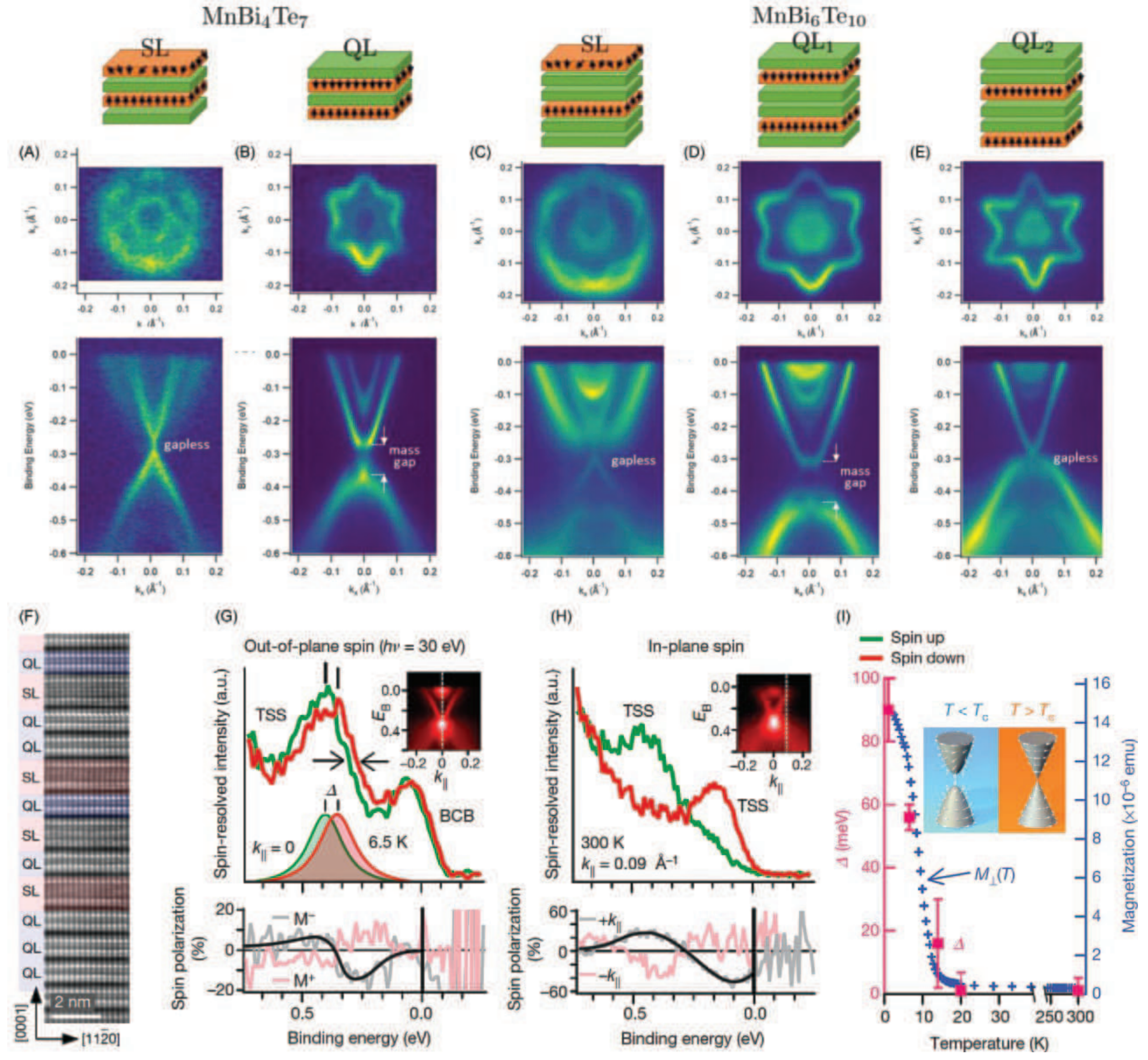

Fig. 6 Natural heterostructures MnBi$_2$Te$_4$/(Bi$_2$Te$_3$)$_m$. (A–E) Terminations with Bi$_2$Te$_3$ quintuple layers (QL) and MnBi$_2$Te$_4$ septuple layers (SL) have distinct features. (B,D) The Dirac cone appears gapped for 1 QL termination due to hybridization effects. (F) In thin films, the distribution of SL units is random, as seen in transmission electron microscopy. For 6% Mn ($m = 2$ to 3), the Dirac cone (topological surface state, TSS) shows (G) an exchange gap with out-of-plane spin texture which (H) away from the Dirac point develops into the spin-momentum-locked in-plane spin texture. (I) The gap closes at the Curie temperature and follows the macroscopic out-of-plane magnetization. Panels (A)–(E) from Gordon KN, Hongyi S, Chaowei H, Linn AG, Haoxiang L, Yuntian L, Pengfei L, Mackey S, Qihang L, Ni N, and Dessau D (2019) arXiv:1910.13943; (F)–(I) from Rienks EDL, Wimmer S, Sánchez-Barriga J, Caha O, Mandal PS, Růžička J, Ney A, Steiner H, Volobuev VV, Groiss H, Albu M, Kothleitner G, Michalicka J, Khan SA, Minár J, Ebert H, Bauer G, Freyse F, Varykhalov A, Rader O, and Springholz G (2019) Nature 576: 423.

found a vanishing gap and exchange split bulk states. It is possible that Mn-Bi intermixing (Zeugner, 2019) is responsible for differences in magnetic structure between different samples of MnBi$_2$Te$_4$ as well as those of MnBi$_2$Te$_4$/(Bi$_2$Te$_3$)$_m$.

Epitaxial films of MnSb$_2$Te$_4$ are ferromagnetic TIs with Curie temperatures up to 50 K. The ferromagnetic order contrasts predictions of antiferromagnetism but is explained by Mn excess of the order of 5%. A slight *p*-doping prevents ARPES from measuring the gap at the Dirac point, but in scanning tunneling spectroscopy, the gap is seen to vanish near the Curie temperature (Wimmer et al., 2021).

Among new materials, EuSn$_2$As$_2$ was characterized as antiferromagnetic TI by time-resolved ARPES above the Fermi level (Li et al., 2019a). The Weyl semimetal phase of MnSb$_2$Te$_4$ (Murakami et al., 2019) and MnBi$_2$Te$_4$ (Li et al., 2019b) has not yet been reached without external magnetic field. FeBi$_2$Te$_4$ has recently been synthesized (Saxena et al., 2020), and CrBi$_2$Te$_4$ and CrBi$_2$Te$_2$Se$_2$ have been predicted as magnetic TIs (Petrov et al., 2021).

Topological crystalline insulators and weak topological insulators

In contrast to the Dirac cones in strong TIs which are protected by time-reversal symmetry, a second class, known as topological crystalline insulator (TCI) exhibit Dirac cones protected by the crystal symmetry itself, see the review by Ando and Fu (2015). An example is the rock-salt-structured $Pb_{1-x}Sn_x(Se,Te)$ series, see Fig. 7. Dirac-cone TSSs have been observed by ARPES for SnTe (Tanaka et al., 2012), $Pb_{0.6}Sn_{0.4}Te$ (Xu et al., 2012), and the $Pb_{1-x}Sn_xSe$ series (Dziawa et al., 2012). They possess a chiral spin texture and spin-momentum locking. Since TCIs are protected by individual crystal symmetries and bear a weak topological index, the quantum phase transition in TCIs is vulnerable to external perturbations (Hsieh et al., 2012; Ando and Fu, 2015).

For TCIs, the decisive role of the crystal symmetry renders the topological protection dependent on the specific crystal face (Fu, 2011). The topological invariants allow for an even number of Dirac cones (Fu and Kane, 2007; Fu, 2011). $Pb_{1-x}Sn_xSe$ and $Pb_{1-x}Sn_xTe$ represent a mirror-symmetry-protected TCI phase with fourfold valley degeneracy (Fu and Kane, 2007; Hsieh et al., 2012) in which the trivial-to-TCI phase transition is reached for sufficiently large Sn contents and with reducing temperature (Tanaka et al., 2012; Xu et al., 2012; Dziawa et al., 2012). Upon cooling, the lattice contracts and the enhanced orbital overlap leads to an inverted bulk band gap, which, via bulk-boundary correspondence, gives rise to an even number of spin-polarized Dirac cone surface states with spin-momentum locking, as confirmed experimentally by ARPES (Dziawa et al., 2012) and spin-resolved ARPES (Wojek et al., 2013), see Fig. 7A–F. Since the TSSs in TCIs are only protected by crystal symmetry, they are an ideal platform for manipulating the topological properties. Due to their high sensitivity to external perturbations, the topological phase transition can be controlled by varying pressure, hybridization in ultrathin film geometries, magnetic interactions, or by breaking of mirror symmetry by strain, electrostatic fields, and ferroelectric lattice distortions (Hsieh et al., 2012; Assaf et al., 2014; Tang and Fu, 2014; Zeljkovic et al., 2015; Plekhanov et al., 2014). These properties offer an advantage for topology control not available in $\mathbb{Z}_2$-TIs, such as to open a gap at particular Dirac points by quantum confinement or unidirectional strain. For SnTe, a topological phase transition from a TCI to a $\mathbb{Z}_2$-TI by a lattice distortion has been predicted (Plekhanov et al., 2014). Bi doping of $Pb_{1-x}Sn_xSe$ (111) epilayers induces a quantum phase transition from a TCI to a strong $\mathbb{Z}_2$-TI by lifting the fourfold valley degeneracy via a sublattice shift and rhombohedral distortion along the [111] direction. The phase transition was confirmed by ARPES through the number of gapless Dirac cones (Mandal et al., 2017).

Up to now, most experimental work has been performed on *p*-type bulk single crystals exploiting the natural (001) cleavage plane of the IV-VI compounds, whereas for other surface orientations and actual devices, epitaxial TCI film structures are required. To this end, the (111) orientation is particularly interesting due to the polar nature of its surface. For instance, control of the Fermi level and carrier concentration leading to a giant Rashba effect was achieved for Bi- and Sb-doped TCI $Pb_{1-x}Sn_xTe$ (111) films (Volobuev et al., 2017). Similarly, control of both the topological phase transition and the structure inversion asymmetry additionally was achieved for TCI quantum wells in thin $Pb_{1-x}Sn_xSe$ films grown on $Pb_{1-y}Eu_ySe$ barriers (Rechciński et al., 2021), see Fig. 7G.

The TCIs presented above depend on a symmorphic mirror plane. Symmorphic symmetries preserve the origin whereas nonsymmorphic spatial symmetries translate the origin by a rational fraction of the lattice vector. This leads to new classes of topological crystalline insulators (Liu et al., 2014a), for example, such that lead to a symmetry-protected surface Dirac point that is not pinned to a specific point (Fang and Fu, 2015). In time-reversal invariant nonsymmorphic TIs, instead of surface Dirac fermions, the appearance of surface fermions with hourglass-shaped dispersion was predicted where two pairs of branches switch their partners (Wang et al., 2016b). This behavior was predicted for KHgX (X = As, Sb, and Bi) (Wang et al., 2016b) and was demonstrated by ARPES for the (010) surface of KHgSb (Ma et al., 2017; Liang et al., 2017).

Besides TCIs there is another topological class which leads to TSSs only on particular surfaces. These are weak TIs which are not protected by crystal symmetries but by time-reversal symmetry in the same way as strong topological insulators. They can be considered as 2D quantum spin Hall insulators stacked in 3D. The side surfaces are often difficult to prepare in experiment which renders their confirmation difficult despite several theoretical predictions, e. g. for PbTe/SnTe superlattices (Yang et al., 2014). Bi_1Te_1, which is a superlattice of 2 quintuple layers of Bi_2Te_3 and one Bi bilayer, has been predicted to be a dual TI, i.e., in this case a TCI and a weak TI. The TSS on the top surface, protected by mirror symmetry, has been confirmed by ARPES but not the TSS on the side surface protected by time-reversal symmetry following the picture of the stacked 2D quantum Hall insulator (Eschbach, 2017). Another prediction for a weak TI concerns β-Bi_4I_4 (Liu et al., 2016). β-Bi_4I_4 consists of stacked molecular chains and shows in ARPES a 1D Dirac cone surface state (Autès et al., 2016). The system has naturally cleavable top and side surfaces. By spatially resolved ARPES, a quasi-1D Dirac cone was found at the side surface (100) whereas the top surface (001) shows no TSS (Noguchi et al., 2019).

Dirac semimetals

3D Dirac semimetals emerge at the quantum critical point of a topological phase transition between a trivial insulator and a $\mathbb{Z}_2$-TI (Wang et al., 2012b). Closing the bulk band gap in a TI gives rise to a 3D Dirac semimetal phase that can be viewed as the bulk analog of graphene, which is a 2D Dirac semimetal. For Bi_2Se_3, for example, moving across the topological quantum phase diagram would be done theoretically by continuous control of the spin-orbit coupling strength (Brahlek et al., 2012; Wu et al., 2013).

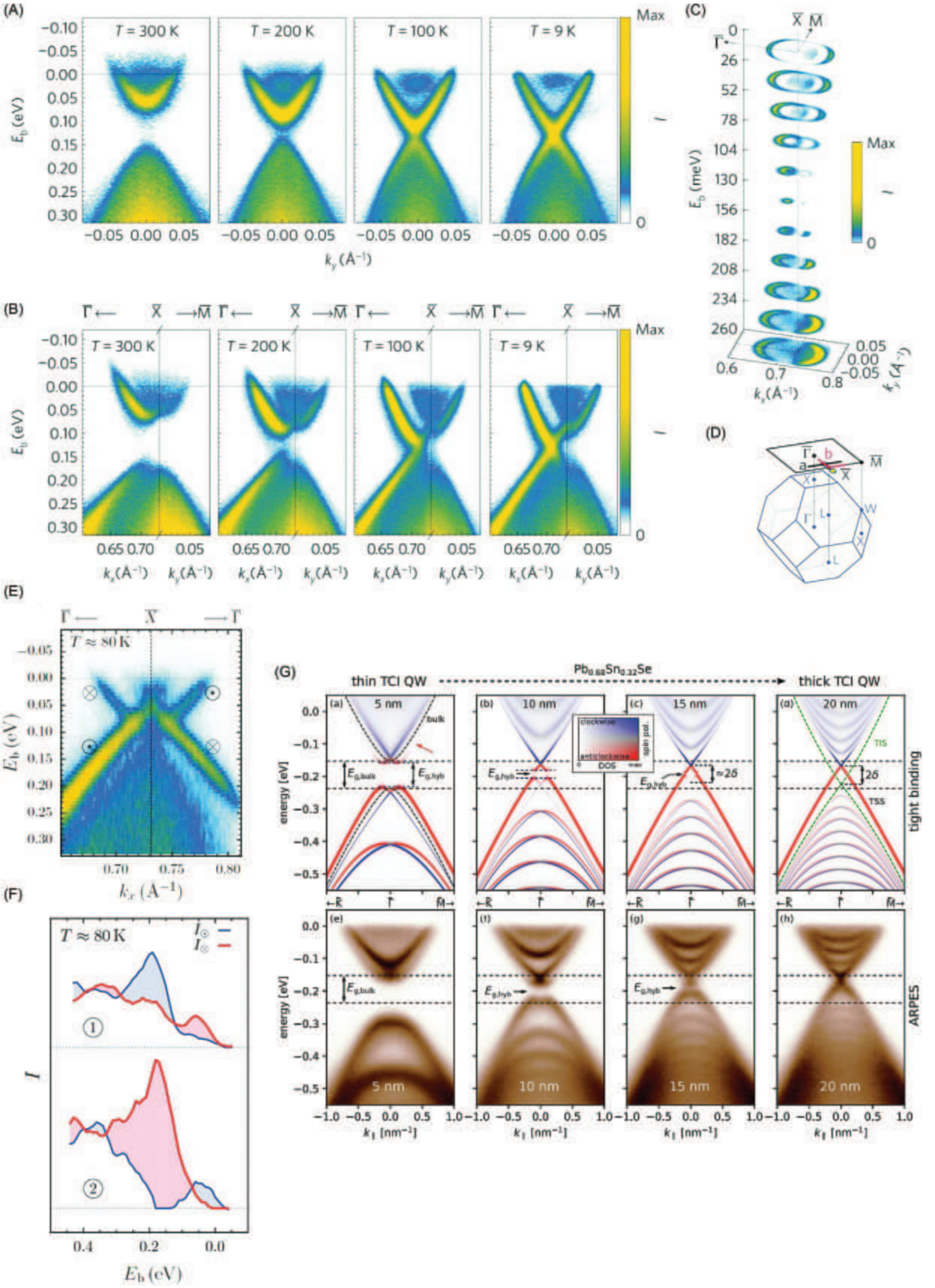

Fig. 7 Topological crystalline insulator (Pb,Sn)Se. (A,B) Temperature-driven topological phase transition from a trivial (300 K) to a topological crystalline insulator (low temperature). (C) Constant-energy surfaces showing the Dirac cone in the topological phase. (D) Corresponding surface and bulk Brillouin zone. (E) Dispersion and (F) spin-resolved ARPES of the in-plane spin texture of the topological state showing spin-momentum locking. (G) Thickness-dependent topological phase transition in Pb$_{1-x}$Sn$_x$Se. Panels (A–D) from Dziawa P, Kowalski BJ, Dybko K, Buczko R, Szczerbakow A, Szot M, Lusakowska E, Balasubramanian T, Wojek BM, Berntsen MH, Tjernberg O, and Story T (2012) Nature Materials 11: 1023–1027; (E,F) from Wojek BM, Buczko R, Safaei S, Dziawa P, Kowalski BJ, Berntsen MH, Balasubramanian T, Leandersson M, Szczerbakow A, Kacman P, Story T, and Tjernberg O (2013) Physical Review B 87: 115106; (G) from Wojek BM, Buczko R, Safaei S, Dziawa P, Kowalski BJ, Berntsen MH, Balasubramanian T, Leandersson M, Szczerbakow A, Kacman P, Story T, and Tjernberg O (2013) Physical Review B 87: 115106.

A linear bulk band crossing exactly at the quantum critical point between topologically trivial and nontrivial phases could be accurately described as a Dirac semimetal, with a single fourfold degenerate 3D Dirac point and linear energy dispersions along all three orthogonal momentum directions. Appropriate tuning of the chemical potential in this case would result in a point-like Fermi surface. However, this crossing point could be destroyed by minute perturbations, pushing the Dirac semimetal to either side of the topological transition to produce a finite gap, see Fig. 8A. Experimentally realized topological Dirac semimetals instead employ intrinsic rotational crystalline symmetries to prevent hybridization between crossing bands, ensuring the formation of robust bulk Dirac points.

Yang and Nagaosa (2014) presented a general framework for classifying stable 3D Dirac semimetals in systems characterized by the presence of time-reversal, inversion, and uniaxial rotational symmetries. Two distinct classes of 3D Dirac semimetals are identified in their study. In one class, the Dirac semimetal exhibits a single Dirac point at a time-reversal invariant momentum on the rotation axis where the band crossing is ensured by the lattice symmetry, see Fig. 8B. In contrast, the other class of Dirac semimetals features a pair of Dirac points on the rotation axis symmetric about the time-reversal invariant momentum, see Fig. 8C. Here, the Dirac points are formed through a band inversion and this class is accompanied by a quantized topological invariant and commonly referred to as 3D topological Dirac semimetals. A further spectroscopic signature is the presence of Fermi arc surface states connecting between bulk Dirac points in topological DSMs (Wang et al., 2012b, 2013b), which were at first discussed in the context of 3D Weyl semimetals (Wan et al., 2011). When the Dirac point acquires a mass gap because of symmetry breaking, the 3D topological Dirac semimetal can turn into either a 3D strong TI or a 3D TCI.

Experimentally, Cd_3As_2 (Borisenko et al., 2014; Ali et al., 2014a; Neupane et al., 2014) and Na_3Bi (Liu et al., 2014b; Xu et al., 2013b) were the first 3D topological Dirac semimetals that were confirmed by ARPES. A highly linear bulk band crossing forming a 3D Dirac cone projected at the Brillouin zone center of the (001) surface of Cd_3As_2 has been observed down to photon energies of about 22 eV (Neupane et al., 2014). A systematic confirmation along all three orthogonal momentum directions followed for Cd_3As_2 and Na_3Bi (Borisenko et al., 2014; Ali et al., 2014a; Neupane et al., 2014; Liu et al., 2014b; Xu et al., 2015c), see Fig. 8. ARPES and spin-resolved ARPES experiments on Na_3Bi revealed a double Fermi arc surface structure, which is spin polarized and confirms the topological protection (Xu et al., 2015c), see Fig. 8L. It has been proposed that Cd_3As_2 and Na_3Bi would transition into a TI state if they are distorted (Wang et al., 2012b, 2013b). This is another interesting aspect that concerns the protection of the 3D Dirac points by the symmetry of the lattice, potentially enabling the switching on and off of their contribution to transport by external perturbations, such as strain or other structural distortions (Wang et al., 2012b, 2013b). Such a topological phase transition would ideally require an intrinsic mechanism by which to induce a structural distortion to be easily accessible by ARPES. Au_2Pb is thought to be a candidate for this purpose, as it naturally undergoes several structural phase transitions with reducing temperature (Schoop et al., 2015).

Breaking inversion or time-reversal symmetry, or both, in a 3D Dirac semimetal is predicted to be a fruitful platform for the observation of topological phase transitions. A direct consequence is that the 3D Dirac points will split into Weyl points of opposite chirality in momentum space.

Nonmagnetic Weyl semimetals

3D Weyl semimetals are a nontrivial state of matter with peculiar low-energy excitations and transport properties (Wan et al., 2011; Balents, 2011; Burkov and Balents, 2011; Hosur and Qi, 2013; Weng et al., 2015; Armitage et al., 2018; Narang et al., 2021). They combine a quasi-relativistic dispersion, which is linear in momentum in all three spatial directions with topological protection (Soluyanov et al., 2015; Huang et al., 2015; Bansil et al., 2016) and exhibit extremely high carrier mobilities, which could enhance the efficiency of future electronic devices (Yang et al., 2011; Sun et al., 2016). Due to their nontrivial topology, 3D Weyl semimetals host spin-polarized topological Fermi arcs at the surface while being metallic in the bulk (Armitage et al., 2018; Narang et al., 2021; Soluyanov et al., 2015; Huang et al., 2015). They offer a rich platform for the realization of an unusually large magnetoresistance (Shekhar et al., 2015) and applications in future electronics and spintronics (Sun et al., 2016).

A 3D Weyl semimetal phase arises from breaking time-reversal symmetry or inversion symmetry in a 3D Dirac semimetal. If in addition the spin–orbit interaction is sufficiently strong such that the bulk bands remain in the inverted regime and gapless, each fourfold degenerate bulk Dirac point in a topological 3D Dirac semimetal will split into two 3D Weyl points of opposite chirality. Hence, for each original Dirac point in the 3D Dirac semimetal, breaking any of the two symmetries leads to a pair of twofold degenerate 3D Weyl cones that are topologically protected and exhibit quasi-relativistic energy dispersion in 3D momentum space. Consequently, the spin-polarized Fermi arcs connecting bulk Dirac points no longer form closed loops in the 3D Weyl semimetal phase. Instead, the surface Fermi arcs connect pairs of 3D Weyl points with opposite chirality, and form open loops when projected on the surface Brillouin zone. The Weyl nodes themselves act as channels through the bulk of the crystal to the opposite surface, thus ensuring a globally closed contour of Fermi arcs. In line with this, Weyl points arise as pairs with opposite chirality. Indeed, the chirality associated with each Weyl point is a topological property defined as a topological charge given by a nonvanishing Chern number, i.e., topological invariant, which means that the Weyl cones can only be moved in energy and momentum space, or tilted, rather than being gapped by external perturbations.

In the case of 3D Weyl semimetals, a minimal setting corresponds to the situation of a 3D Dirac semimetal, but in which time-reversal symmetry is broken while inversion symmetry is preserved. When only inversion symmetry is present, a 3D Weyl point at k

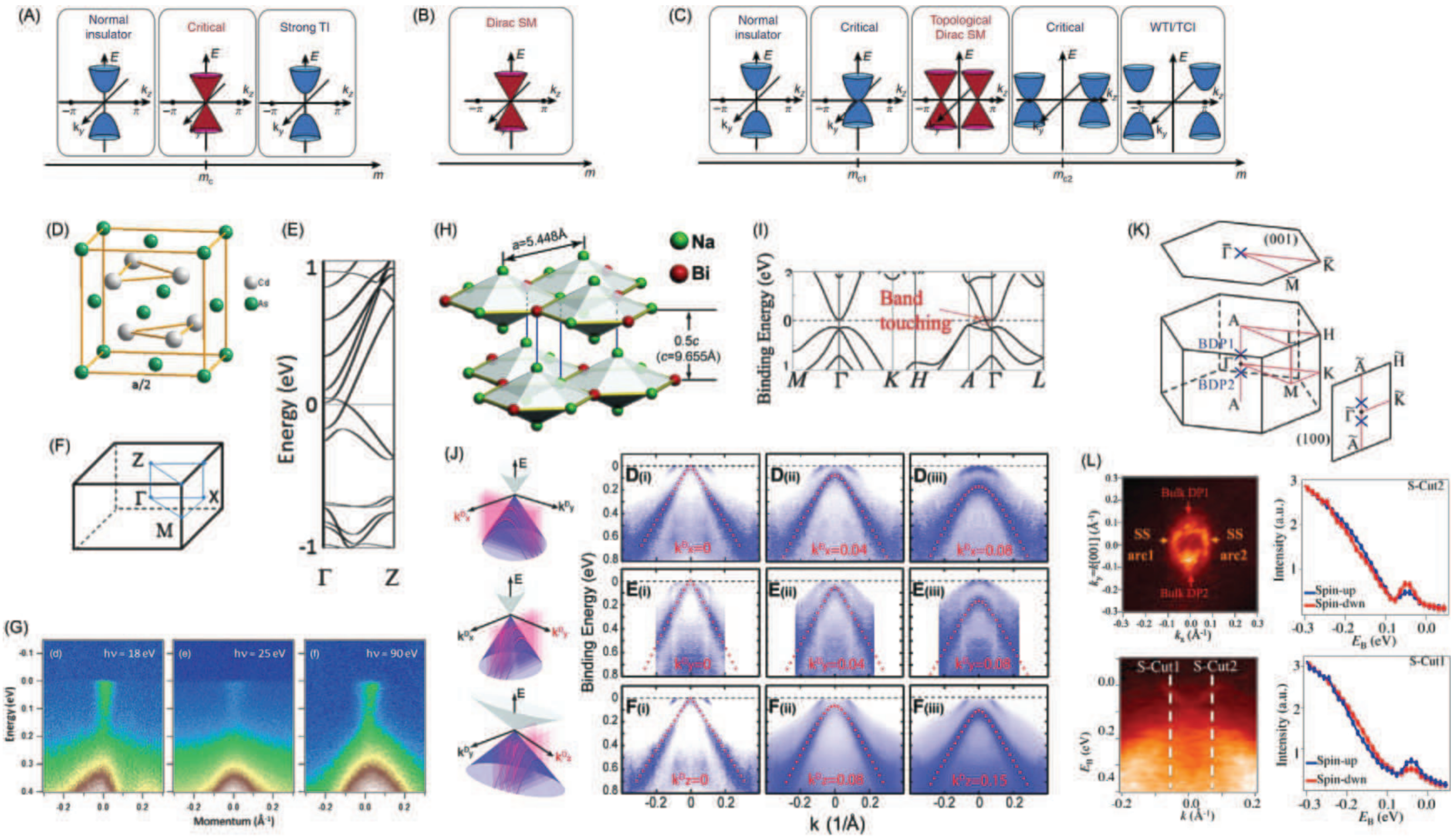

Fig. 8 3D Dirac semimetals Cd_3As_2 and Na_3Bi. Phase transition upon variation of control parameter m leading to a 3D Dirac semimetal by (A) accidental band crossing or with (B) additional protection by rotational symmetry. (C) Topological 3D Dirac semimetal by band inversion and protection by rotational symmetry. (D–G) Cd_3As_2 of C_3 symmetry shows the (E) predicted 3D Dirac points in (G) ARPES along the $\Gamma - Z$ direction. (H–L) Na_3Bi of C_4 symmetry shows (I) 3D Dirac points along the $\Gamma - A$ direction which are seen in (J) ARPES by variation of the momentum along all three directions. (K) The projected Dirac points are separated at the (100) surface where (L) two Fermi arcs are observed which exhibit opposite spin polarization. Panels (A–C) from Yang B-J and Nagaosa N (2014) Nature Communications 5: 4898; panels (D–G) from Borisenko S, Gibson Q, Evtushinsky D, Zabolotnyy V, Büchner B, and Cava RJ (2014) Physical Review Letters 113: 027603; panels (H–J) from Liu ZK, Zhou B, Zhang Y, Wang ZJ, Weng HM, Prabhakaran D, Mo, S-K, Shen ZX, Fang Z, Dai X, Hussain Z, and Chen YL (2014b) Science 343: 864; and panels (K,L) from Xu S-Y, Liu C, Kushwaha SK, Sankar R, Krizan JW, Belopolski I, Neupane M, Bian G, Alidoust N, Chang T-R, Jeng H-T, Huang C-Y, Tsai W-F, Lin H, Shibayev PP, Chou F, Cava RJ, and Hasan MZ (2015c) Science 375: 294.

must necessarily be accompanied by a partner node at $-k$ that carries the opposite topological charge at the same energy. This configuration allows for a minimum number of Weyl points with opposite chirality. In contrast, when only inversion symmetry is broken, time-reversal symmetry requires that these two Weyl points at opposite momenta carry the same topological charge. In this situation, because the total topological charge within the entire Brillouin zone should vanish, another pair of Weyl points with the opposite topological charge is additionally required to achieve charge neutrality. A natural consequence is that the Weyl nodes in 3D Weyl semimetals without inversion symmetry must necessarily exist in multiples of four. This fact also provides a convenient way to investigate a variety of interesting effects associated with topological charge redistribution, such as the efficient generation of optically driven spin-polarized currents from highly tilted Weyl cones or other photoinduced responses like the photovoltaic chiral magnetic effect or the gyrotropic magnetic effect.

The first materials confirmed experimentally were inversion-symmetry breaking 3D Weyl semimetals of the TaAs family, primarily by ARPES (Yang et al., 2015; Xu et al., 2015b; Liu et al., 2016b). Predicted materials with a stable 3D Weyl semimetal phase of this family of compounds included TaAs, TaP, NbAs, and NbP. These materials belong to the class of type-I Weyl semimetals, which have point-like Fermi surfaces at the Weyl nodes. As shown in Fig. 9, surface Fermi arcs connecting pairs of 3D Weyl points projected onto the surface Brillouin zone and the linear energy-momentum dispersion of bulk states were systematically identified by extensive ARPES measurements (Yang et al., 2015; Xu et al., 2015b; Liu et al., 2016b). In addition to photon-energy-dependent ARPES, the surface and bulk character of the different states were confirmed by low-energy surface-sensitive ARPES and soft-X-ray bulk-sensitive ARPES, the latter of which enabled the observation of the 3D Weyl nodes in isolation.

One important aspect facilitating the experimental verification of topological order is the influence of increasing spin–orbit coupling strength on the electronic properties of these compounds. As seen in the comparison between ARPES measurements of the Fermi surface and band dispersions of NbP, TaP, and TaAs, shown in Fig. 9, increasing the spin–orbit strength increases both the separation between the Weyl nodes in momentum space and the splitting of the band dispersions, which causes a splitting of the Fermi arcs while retaining the overall topology of the Fermi surface (Liu et al., 2016b). While this observation by itself provides

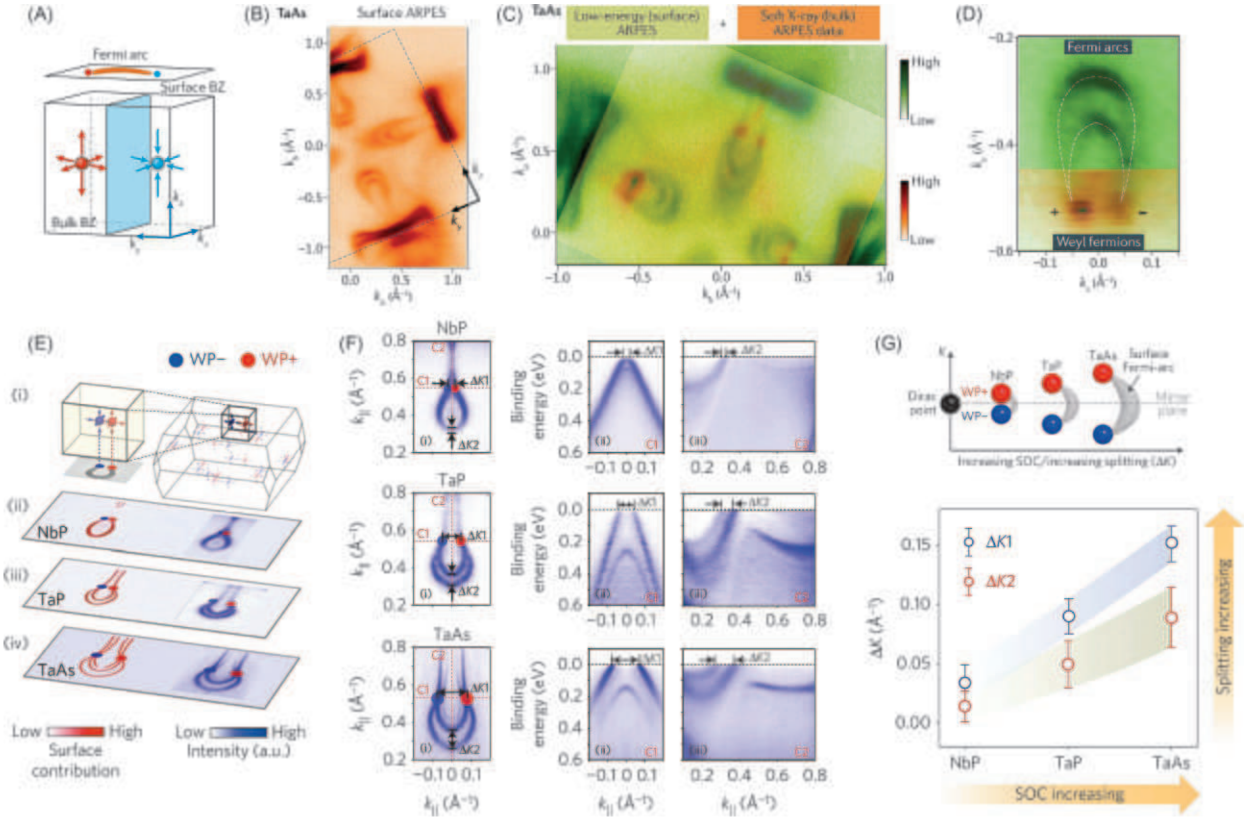

Fig. 9 3D Weyl semimetals. (A) Schematic bulk and surface Brillouin zone (BZ) depicting the projection of 3D Weyl points of opposite chirality on the surface along with the surface Fermi arc. (B–D) Fermi surface by ARPES of TaAs measured (B) with surface-sensitive ARPES. (C,D) The corresponding superposition with bulk-sensitive soft-X-ray ARPES (*red* in C and D) depicting the bulk Weyl points (WP) projected onto the surface along with the surface Fermi arcs (*green* in C and D). (D) Zoom in on the region of the surface Fermi arcs where the positive and negative signs indicate the chiralities of the Weyl points. (E–G) Comparison of different pnictide Weyl semimetals. From NbP through TaAs, the splitting between the Weyl points and the length of the surface Fermi arcs increases. This splitting increases with the spin-orbit coupling (SOC). Panels (A–D) from Xu S-Y, Belopolski I, Alidoust N, Neupane M, Bian G, Zhang C, Sankar R, Chang G, Yuan Z, Le C-C, Huang S-M, heng H, Ma J, Sanchez DS, Wang B, Bansil A, Chou F, Shibayev PP, Lin H, Jia S, and Hasan MZ (2015b) Science 349: 613–617 and (E–G) from Liu ZK, Yang LX, Sun Y, Zhang T, Peng H, Yang HF, Chen C, Zhang Y, Guo YF, Prabhakaran D, Schmidt M, Hussain Z, Mo S-K, Felser C, Yan B, and Chen YL (2016b) Nature Materials 15: 27.

additional evidence for the Weyl semimetal state, it also allows to experimentally identify groups of Weyl nodes with zero net chirality, establishing an independent criterion for the experimental verification of topological order.

By combination of bulk-sensitive soft-X-ray ARPES, spin resolution, and CDAD, it has been possible to observe large spin and orbital-angular-momentum polarizations in TaAs (Ünzelmann et al., 2021). From the winding of the orbital angular momentum, the Weyl points have been confirmed as Berry flux monopoles (Ünzelmann et al., 2021).

Type-II Weyl semimetals exhibit strongly tilted 3D Weyl cones in energy-momentum space, resulting in a Fermi surface where the upper and lower cones form electron and hole pockets that connect at the Weyl points. In consequence, type-II Weyl semimetals undergo peculiar Lifshitz transitions. The original prediction included the layered material WTe_2, known for its large, nonsaturating magnetoresistance, as well as $MoTe_2$ which we will discuss in Section "Weyl phases in inversion asymmetric TMDs." Moreover, ARPES found also evidence for a type-II Weyl semimetal in $TaIrTe_4$ (Koepernik et al., 2016; Haubold et al., 2017) and LaAlGe (Xu et al., 2017b).

Magnetic Weyl semimetals and kagome systems

The alternate route towards the creation of topological Weyl semimetals from Dirac semimetals is to instead break time-reversal symmetry by the application of an external magnetic field or through a spontaneous magnetization. In the ferromagnetic Heusler compound Co_2MnGa, linear bulk band dispersions were observed, which intersect in a nodal line near the Fermi energy (Belopolski et al., 2019) and are spin polarized (Sumida et al., 2020). Another such crossing at higher binding energy is spanned by a surface state in the shape of a drumhead supporting the assignment of the system to a Weyl semimetal (Belopolski et al., 2019). $YbMnBi_2$ is a magnetic system with a canted antiferromagnetic structure. By comparison to the control system $EuMnBi_2$, Weyl points and a Fermi surface arc have been observed and the system was classified as time-reversal-symmetry breaking type-II Weyl semimetal (Borisenko et al., 2019).

Insulating kagome materials can exhibit spin liquid phases as a result of magnetic frustration. The same interferences determine the electronic structure, which is particularly interesting for metallic systems. With spin–orbit coupling and spontaneous magnetization, a two-dimensional kagome lattice leads to a 2D Chern insulator phase with quantized anomalous Hall conductance (Xu et al., 2015a). The resulting 2D Dirac cones have been observed by ARPES in Fe_3Sn_2 (with Fe_3Sn kagome layers between Sn layers) and in FeSn (Kang et al., 2020b). A gap in the 2D Dirac cone in Fe_3Sn_2 observed by ARPES has been assigned to spin–orbit interaction (Ye et al., 2018). Depending on the stacking of the kagome layers, the system can transform into a magnetic 3D Weyl semimetal. $Co_3Sn_2S_2$ consists of a Co_3Sn kagome layer and a S_2 honeycomb layer and was identified by ARPES as such a magnetic Weyl semimetal (Liu et al., 2019; Morali et al., 2019; Xu et al., 2018c).

The kagome magnet RMn_6Sn_6 with rare-earth element R, in which Mn forms the kagome layer, is promising for the realization of different quantum phases due to a variety of magnetic structures. In the system YMn_6Sn_6, a Dirac cone dispersion was seen by Li et al. (2021b). Another signature of the kagome lattice is a flat (i.e., minimally dispersive) band. Such a flat band is observed $\approx$0.25 eV below the Fermi level in FeSn (Kang et al., 2020b), and similar flat bands appear in paramagnetic CoSn near the Fermi energy (Liu et al., 2020; Kang et al., 2020a). These observations are interesting since a flat band on the kagome lattice carries a finite Chern number, enabling a fractional quantum Hall state.

Case study: Transition metal dichalcogenides

With time, it is becoming apparent that nontrivial band topology, along with Dirac and Weyl nodes, is far from contained to the handful of compounds within which the first examples were found. Conversely, topological band properties are ubiquitous, generic features of band structures found across nature. Indeed, computational studies tasked with scouring the electronic structures of all existing solids for nontrivial band topology predict that more than one quarter of all existing solids have an inverted band gap somewhere within their electronic structures (e.g., Vergniory et al., 2019).

No material family better exemplifies the plethora of topological phases only recently verified to exist in previously well-studied compounds than the TMDs, a materials family exhibiting numerous examples of nontrivial band topology, bulk Dirac points, and Weyl points, often simultaneously, and alongside many other desirable properties for next-generation device fabrication. The TMDs are a family of >30 stable compounds with the formula MX_2, where M is a transition metal and $X \in \{S, Se, Te\}$. Each of these van der Waals layered materials stabilizes in one or more of the following structures: 1T ($P3\overline{m}1$), 2H (P63/mmc), 3R (R3m) or in one of several distorted trigonal structures (triclinic ($\overline{P}1$), monoclinic (β, $P2_1/m$) and orthorhombic (γ, $Pmn2_1$)), here collectively referred to as 1T′. A subset of these is schematized on the left hand side of Fig. 10 (Chen et al., 2021).

The thermodynamically favored structural phase of a TMD defines the crystal field splitting of the transition metal *d*-orbital manifold, which, together with the electron filling factor, determines many of the ground-state electronic properties of the TMDs (Chhowalla et al., 2013). For 2H (and 3R) structured TMDs (D_{3h}), the *d*-orbital manifold is split into three energetically separated subsets (a_1, e, and e' from low energy to high) located between the bonding and antibonding chalcogen *p*-orbital manifolds and are found predominantly in groups V (d^1 metals) and VI (d^2 semiconductors). 1T- and 1T′-structured TMDs instead have the *d*-orbital manifold split in two (t_{2g} and e_g) with examples found in groups IV (1T d^0 semiconductors), V (1T d^1 metals), VI (1T′ (monoclinic/orthorhombic) d^2 metals), VII (1T′ (triclinic) d^3 metals), IX (1T d^5 metals), and X (1T d^6 (semi)metals). For the latter two cases, M-M bonds are preferentially formed over M-X bonds, placing the Fermi level within the antibonding *p*-orbital manifold. Both 1T and 2H

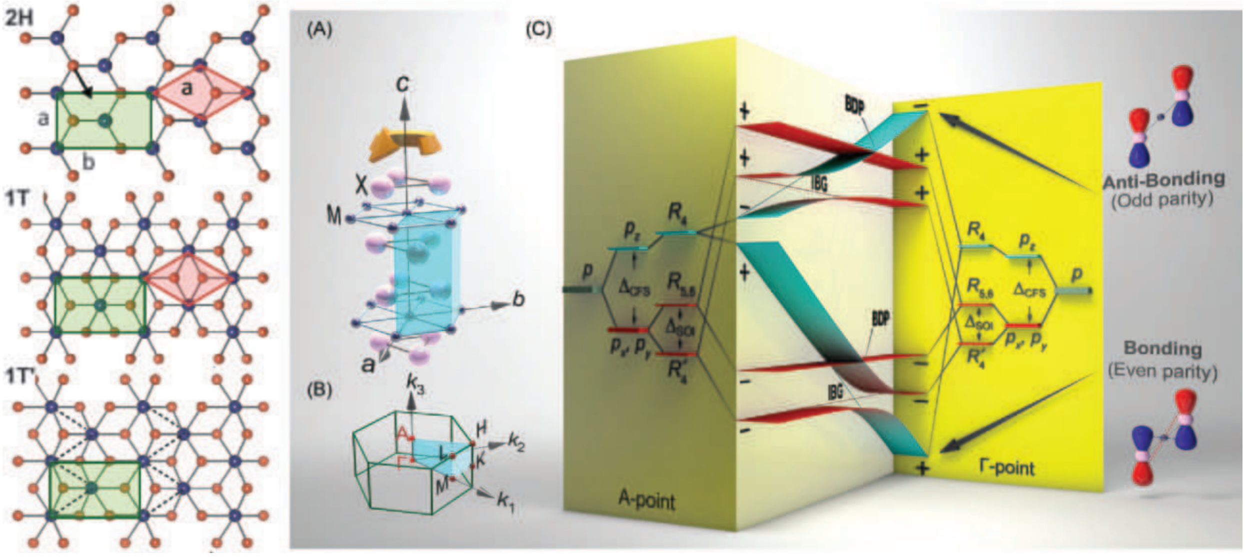

Fig. 10 Structural and electronic properties of transition metal dichalcogenides. Left panel: Top-down crystal structures of single-layer transition metal dichalcogenides with 2H, 1T, and 1T' (monoclinic/orthorhombic) structures from high to low. Primitive unit cells are indicated with *orange shaded areas*. $1 \times \sqrt{3}$ supercells, from which the primitive unit cell of the 1T' structure is derived, are indicated with *green shaded areas*. (A–C) Mechanism underpinning the formation of bulk Dirac points and inverted band gaps in 1T structured TMDs. Crystal structure and Brillouin zone for a 1T TMD, with the C_{3v} rotational axis, and high symmetry momenta highlighted. (C) Effect of bonding–antibonding splitting, crystal field splitting and the spin–orbit interaction on the *p*-orbital manifold. Resulting bulk Dirac points (BDPs) and inverted band gaps (IBGs) are labeled. Left panel: Taken directly from Chen K, Deng J, Yan Y, Shi Q, Chang T, Ding X, Sun J, Yang S, and Liu JZ (2021) npj Computational Materials 7: 79; (C) reproduced directly from Clark OJ, Mazzola F, Markovic I, Riley JM, Feng J, Yang B-J, Sumida K, Okuda T, Fujii J, Vobornik I, Kim TK, Okawa K, Sasagawa T, Bahramy MS, and King PDC (2019) Electronic Structure 1: 014002.

d^1 metallic systems contain charge density instabilities, with the signatures of back-folded bands clearly seen by several spectroscopic techniques including ARPES (Ritschel et al., 2015; Rossnagel et al., 2005; Wang et al., 2021b; Feng et al., 2018; Chen et al., 2022; Nakata et al., 2021; Borisenko et al., 2009; Terashima et al., 2003). These phases are often precursors to superconductivity at low temperatures (Koley et al., 2020; Xi et al., 2016; Liu et al., 2016a; Sahoo et al., 2020), a property also shared by many of the metallic d^5 and d^6 TMDs (Park et al., 2021; Zheng et al., 2020; Ryu, 2015). Perhaps most famously, the d^2 2H semiconductors are the central focus of the burgeoning field of valleytronics owing to their graphene-like honeycomb lattice structure (Fig. 10) and thus their layer and momentum-locked Rashba-split valence band maxima (see e.g., the seminal photoluminescence studies Mak et al., 2010 and Xiao et al., 2012).

The topological properties of these materials only began to draw attention in 2015 with the prediction and subsequent verification of type-II Weyl nodes and Fermi arcs in the d^2 1T′ (orthorhombic, γ)-structured tellurides, $MoTe_2$ and WTe_2 (see the review by Das et al., 2019), establishing the TMD family as among the first hosts of type-II Weyl semimetals. In addition to this wide array of TMD properties deriving primarily from the transition metal *d*-orbital manifold, remarkably, the 1T and 2H TMDs were additionally found to host TSSs and/or bulk Dirac points, the hallmarks of TIs and Dirac semimetals, respectively. In contrast to the Weyl phases of the 1T′-TMD subset, these topological properties stem entirely from within the chalcogen *p*-orbital manifold and are thus largely insensitive to the choice of the transition metal (Bahramy et al., 2018). Nontrivial band topology and/or bulk Dirac crossing points can therefore be found across the entire 1T and 2H TMD subclasses. Already, the topologically nontrivial TMDs have been shown to be of practical interest, with "giant" or nonsaturating magnetoresistance observed in both TMD Dirac and Weyl semimetals (see e.g., Ali et al., 2014b; Pavlosiuk and Kaczorowski, 2018), and tunable, high-efficiency THz detection realized in numerous group-X Dirac semimetals (e.g., Cheng et al., 2023; Guo et al., 2020).

The type of the protected crossings available to each TMD compound (2D Dirac, 3D Dirac or Weyl) is determined only by whether an axis of rotational symmetry and/or an inversion center is present within the crystal structure. In the 1T- and 2H-structured TMDs, the C_{3v}-symmetric k_z axis is capable of protecting any formed bulk Dirac points against perturbations including spin–orbit coupling (Yang and Nagaosa, 2014). By lifting inversion (or time-reversal) symmetry in such a way that the rotational axis is preserved, Dirac nodes could be transformed into Weyl points in the usual way. In contrast, the 1T′ (γ) structured TMDs possess neither a sufficient rotational axis nor inversion symmetry. In this scenario, Weyl points can be instead formed at the intersection of electron- and hole-like states at low symmetry *k*-vectors and are unrelated to the Dirac points in their 1T-structured counterparts. These two cases will be briefly overviewed below.

Dirac cones in inversion symmetric TMDs

The mechanism underpinning the simultaneous formation of bulk Dirac points and TSSs in bulk 1T and 2H structured TMDs has been extensively discussed in Bahramy et al. (2018) and Clark et al. (2019), thus explaining the preexisting observations of a TSS in $PdTe_2$ (Liu et al., 2015), and bulk Dirac points in $PtTe_2$ (Yan et al., 2017) and $PtSe_2$ (Huang et al., 2016a). This mechanism, applied to a 1T-TMD crystal structure, is schematized in Fig. 10 (Clark et al., 2019). In short, the bonding (B) and antibonding (AB) sets of the chalcogen p-orbitals are each split into three doubly degenerate bands by the combined influence of the trigonal (C_{3v}) crystal field and the spin–orbit interaction: The p_z-derived R_4 and the $p_{x,y}$-derived R_4' and $R_{5,\,6}$, where the subscript denotes the irreducible representation. In van der Waals stacked systems, out-of-plane hopping across the van der Waals gap is in general larger for p_z orbitals due to the larger spatial extent into the gap. The out-of-plane bandwidth (// k_z) of p_z-derived bands in momentum space is therefore larger than that of the pair of $p_{x,y}$-derived bands, making crossings between the six p-derived bands along k_z (3 for each AB and B sets) highly likely. Around half of these crossings will be between bands of different irreducible representations, producing C_{3v} lattice symmetry protected bulk Dirac points (Yang and Nagaosa, 2014). The rest will hybridize to open up band gaps, which may be topologically nontrivial depending on the parity of the involved bands, which in real TMD systems typically correlates with the sign of group velocity of each band between the Γ and A high-symmetry points. The result is a ladder of 3D and 2D Dirac cones, centered at the $\overline{\Gamma}$ point of the surface Brillouin zone and stacked along the energy axis.

The bulk Dirac points produced by this mechanism occur at low symmetry k points between Γ and A and, as a result, typically exhibit anisotropic band dispersions in three dimensions, thus violating the Lorentz symmetry intrinsic to the Dirac fermion analogs in high energy physics. Instead, their dispersion is tilted, with the type of Dirac cone determined by whether the two branches of the cone have different (type-I) or the same (type-II) sign of the group velocity in analogy to the tilted Weyl cones of type-II Weyl semimetals.

Clear ARPES and/or density functional theory evidence for topological ladders has been reported in the 1T systems PdTe$_2$ (Liu et al., 2015; Noh et al., 2017; Bahramy et al., 2018; Clark et al., 2018, 2019), PtTe$_2$ (Yan et al., 2017), PtSe$_2$ (Huang et al., 2016a; Bahramy et al., 2018), NiTe$_2$ (Xu et al., 2018a; Ghosh et al., 2019; Mukherjee et al., 2020; Nurmamat et al., 2021), CrTe$_2$ (Ou et al., 2022; Li et al., 2021c), HfSe$_2$ (Clark et al., 2022), CoTe$_2$ (Chakraborty et al., 2023), and IrTe$_2$ (Bahramy et al., 2018; Fei et al., 2018; Jiang et al., 2020; Nicholson et al., 2021). The differences in the composition of the topological ladder depend largely on the starting energetics of the six doubly degenerate p-derived bands: a combination of the B–AB splitting (determined by the degree of orbital overlap), the crystal field strength, and the chalcogen spin–orbit coupling strength. For example, in PdTe$_2$ (Fig. 11A–C Bahramy et al., 2018; Clark et al., 2018), the bandwidth of the p_z-derived AB-R_4 band is large enough to cross through both the

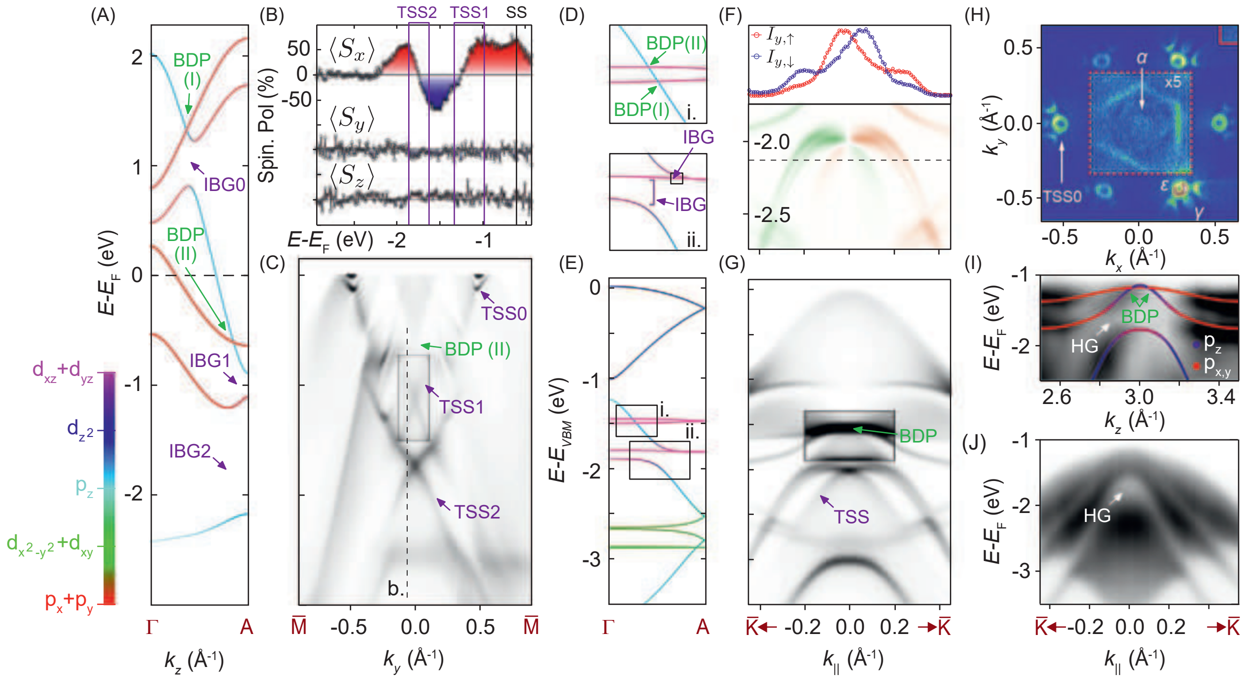

Fig. 11 Topological ladders in bulk transition metal dichalcogenides. Compilation of ARPES and spin-resolved ARPES findings on (A–C) 1T-PdTe$_2$ (Clark et al., 2018; Bahramy et al., 2018), (D–G) 2H-WSe$_2$ (Bahramy et al., 2018), (H) 1T-NiTe$_2$ (Mukherjee et al., 2020) and (I,J) 1T-HfSe$_2$ (Clark et al., 2022). Orbitally-projected density functional calculations in (A,D,E) share the color bar inset on the left, though the transition metal d-orbital contribution is neglected in (A). Calculations in (D) are zoom-ins of the indicated regions in (E). Circular dichroic spectrum in (F) is a zoom-in of the TSS region in (G) to better resolve the TSS. Highlighted (*black box*) region in (C) is performed with a higher photon energy to optimize matrix elements of TSS1. Highlighted regions in (G) and (H) have an increased image contrast only. *Dashed lines* in (C) and (F) indicate the energy ranges and approximate momentum positions for the spin-resolved energy and momentum distribution curves in (B) and (F), respectively (refer to original publications for details). Inverted band gaps (IBGs), trivial hybridization gaps (HG), Type-I/II bulk Dirac points (BDPs (I/II)), and topological surface states (TSSs) are labeled throughout. *(A–C) Adapted from* Clark OJ, Neat MJ, Okawa K, Bawden L, Markovi I, Mazzola F, Feng J, Sunko V, Riley JM, Meevasana W, Fujii J, Vobornik I, Kim TK, Hoesch M, Sasagawa T, Wahl P, Bahramy MS, and King PDC (2018) *Physical Review Letters* 120: 156401 *and* Bahramy MS, Clark OJ, Yang B.-J, Feng J, Bawden L, Riley JM, Marković I, Mazzola F, Sunko V, Biswas D, Cooil SP, Jorge M, Wells JW, Leandersson M, Balasubramanian T, Fujii J, Vobornik I, Rault J, Kim TK, Hoesch M, Okawa K, Asakawa M, Sasagawa T, Eknapakul, T, Meevasana W, and King PDC (2018) *Nature Materials* 17: 21. *(D–G) Adapted from* Bahramy MS, Clark OJ, Yang B.-J, Feng J, Bawden L, Riley JM, Marković I, Mazzola F, Sunko V, Biswas D, Cooil SP, Jorge M, Wells JW, Leandersson M, Balasubramanian T, Fujii J, Vobornik I, Rault J, Kim TK, Hoesch M, Okawa K, Asakawa M, Sasagawa T, Eknapakul, T, Meevasana W, and King PDC (2018) *Nature Materials* 17: 21. *(H) Adapted from* Mukherjee S, Jung SW, Weber SF, Xu C, Qian D, Xu X, Biswas PK, Kim TK, Chapon LC, Watson MD, Neaton JB, and Cacho C (2020) *Scientific Reports* 10: 12957. *(I,J) Adapted from* Clark OJ, Dowinton O, Bahramy MS, and Sánchez-Barriga J (2022) *Nature Communications* 13: 4147.

AB and B sets of $p_{x,y}$-derived bands as well as the oppositely dispersing B-R_4 band, thus creating a total of two bulk Dirac points and three TSSs at $\overline{\Gamma}$. In contrast, in HfSe$_2$ (Fig. 11I,J; Clark et al., 2022), the smaller chalcogen and larger van der Waals spacing lead to a much reduced bandwidth of the p_z-derived bands and no overlap between the B- and AB-derived p-orbital manifolds. The result is a topologically trivial hybridization gap and a single type-II bulk Dirac cone formed along Γ-A within the p-orbital manifold, though it is particularly noteworthy that the pair of type-II bulk Dirac points (symmetric about A) comprises the valence band maximum of this compound (Clark et al., 2022).

Although typically buried deep within the valence bands due to the energetic positioning of the chalcogen manifold, similar physics was found in the 2H-structured TMDs WSe$_2$, NbSe$_2$, and TaSe$_2$ (Bahramy et al., 2018). The 2H-structured variants have an extra consideration: by doubling the size of the unit cell along the c-axis, the number of distinct p-derived bands also doubles, thus providing twice the opportunities for bulk Dirac point and inverted band gap formation. For example, in 2H-WSe$_2$, pairs of very closely spaced (in energy and momentum) inverted band gaps and bulk Dirac points (which are necessarily of opposite types due to opposite group velocity of the two halves of a back folded $p_{x,y}$-derived band) are predicted by density functional theory, with a TSS verified by spin-resolved ARPES (Bahramy et al., 2018), see Fig. 11D–G. The observable surface state has its dispersion heavily influenced by the restricting nature of the surrounding small k_z-projected band gap to produce a Rashba-like dispersion. This is a common phenomenon across these materials, with both trivial and TSSs adopting highly usual dispersions due to the presence of only narrow channels left unexplored by the bulk electronic structure. This is particularly clear in PdTe$_2$ (Clark et al., 2018, 2019) and NiTe$_2$ (Mukherjee et al., 2020), where an inverted band gap above the Fermi level spawns a topological state with a dispersion maximally warped by the dense k_z-projected bulk manifold, eventually crossing the Fermi level along $\overline{\Gamma}$–$\overline{\text{M}}$ (Fig. 11C,H) with a highly complex in-plane spin texture (Clark et al., 2018; Mukherjee et al., 2020).

In conjunction with the Weyl semimetals within the TMD family, the surface and bulk Dirac physics of the rotationally symmetric subclass establishes the TMDs as an ideal platform to study all types of topological band structure, and their interplay with other material-specific properties. It is noteworthy that the generality of topological ladders to the rotationally symmetric material class as a whole is a direct consequence of the single-orbital manifold nature of the various band inversions contained within, and demonstrates an insensitivity of this nontrivial band topology to changes in spin-orbit coupling strength, d-orbital manifold overlap, and unit cell size. This is in sharp contrast to systems with band inversions between two distinct orbital manifolds, for example in the Bi$_2$Se$_3$ series, wherein the band inversions can be unwound by sufficiently altering the energetic separation of the Bi p and Se p-orbital manifolds, for example, through reducing the spin–orbit coupling strength.

Despite the robustness of the topological phases, the composition and energetics of the topological ladders in TMDs have been shown theoretically to be highly tunable through any perturbation altering the relative hopping parameters within the chalcogen sublattice, such as through alloying or through strain/compression (Bahramy et al., 2018; Huang et al., 2016a; Xiao et al., 2017; Clark et al., 2019). Of particular interest experimentally is the case of IrTe$_2$, which possesses a type-II bulk Dirac cone 100 meV above the Fermi level as well as two inverted band gaps located at higher binding energy (Bahramy et al., 2018; Fang et al., 2013; Nicholson et al., 2021). Tantalizingly, this compound also undergoes several temperature-driven structural phase transitions from 280 K, eventually finding a 6×1 ground state (see Nicholson et al., 2021 and references within). While the ground state typically has nanoscale domain sizes, the application of 0.1% strain along the a-axis stabilizes this 6×1 phase sufficiently to probe in isolation with ARPES.

In principle, this change of symmetry should lift the protection of the bulk Dirac points due to the loss of C_{3v} rotational symmetry, suggesting the possibility to exploit the structural transition as a temperature-controlled switch for bulk Dirac transport in this compound (Yang and Nagaosa, 2014). In contrast, it was not only observed that some signatures of the bulk Dirac point seem to endure this breaking of symmetry, but also that the energetics of the Dirac node fall below E_F in the 6×1 phase and become the dominant interlayer transport channel (Nicholson et al., 2021). This temperature-controlled Lifshitz transition is accompanied by the corresponding nonsaturating linear magnetoresistance (Zhang et al., 2019b). Alternatively, a similar Lifshitz transition can be achieved in the high-temperature trigonal structure by doping with Pt (Fei et al., 2018; Jiang et al., 2020), which remains superconducting for Pt concentrations <0.4, a range that includes the composition where the bulk Dirac point is at E_F (Fei et al., 2018; Jiang et al., 2020). These studies provide a proof of principle for tunable topological phases in TMDs in general, and highlight the ever-growing phase space available for *in situ* manipulation of electronic structures with ARPES.

This single-orbital manifold origin responsible for both the robustness and tunability of these Dirac nodes is not limited to the TMD family. Prior predictions of type-II bulk Dirac points near the Fermi level in both the VAl$_3$ (Chang et al., 2017b) and YPd$_2$Sn (Guo et al., 2017) families can be understood within this same framework, with the bulk Dirac points protected by fourfold rotational symmetries in analogy to the threefold symmetry-protected Dirac crossings in the TMDs. More recently, PdTe, like PdTe$_2$, was found to host a series of p-orbital derived band crossings along the Γ–A direction of its P63/mmc-type Brillouin zone by ARPES (Yang et al., 2023). While the presence of only one chalcogen per unit cell precludes any topologically nontrivial hybridization gaps within the p-orbital manifold, a type-I bulk Dirac point is formed within 100 meV of E_F. Crucially, unlike in the dichalcogenides, there is a possibility to realize a surface termination wherein pairs of bulk Dirac points formed along A-Γ-A do not project to the same point in the surface Brillouin zone, enabling the experimental characterization of Fermi arcs spanning between bulk Dirac points.

Weyl phases in inversion asymmetric TMDs

The first examples of topological phases found in the TMDs were the cases of the distorted type-II Weyl semimetals γ-WTe$_2$ and γ-MoTe$_2$ introduced in Section "Nonmagnetic Weyl semimetals." Despite being the first topological phases predicted in the TMDs, the experimental verification proved much more challenging than that of the Dirac phases inherent to the inversion symmetric TMDs. Where the topological ladders in, for example, the group-X TMDs are ideal for direct observation in ARPES due to the large energy and momentum scales involved, the Weyl nodes in $MoTe_2$ and WTe_2 occur at low symmetry points between electron and hole pockets, which disperse almost parallel to each other in the vicinity of the produced type-II Weyl points, thus leaving energetically narrow channels for Fermi arcs to disperse at all relevant k-points. Moreover, these crossings, protected by time-reversal symmetry, are located above the Fermi level, which precludes imaging them directly with conventional ARPES (Soluyanov et al., 2015; Das et al., 2019). This, combined with multiple surface terminations, the presence of trivial surface states alongside the predicted Fermi arcs (Bruno et al., 2016) and a perceived extreme sensitivity of the Weyl nodes to strain and pressure (Soluyanov et al., 2015; Bruno et al., 2016), made an unambiguous classification of bulk $MoTe_2$ and WTe_2 and a complete mapping of Fermi arc spin textures difficult by purely spectroscopic means (Das et al., 2019). Nevertheless, there is now significant spectroscopic evidence for Fermi arc surface states (and thus type-II Weyl points) in these compounds (Wu et al., 2016b; Wang, 2016; Sánchez-Barriga et al., 2016b; Bruno et al., 2016; Tamai et al., 2016; Jiang et al., 2017; Xu et al., 2018b; Huang et al., 2016b; Wan et al., 2022), with further evidence from transport experiments consistent with the presence of type-II Weyl points (Hosur and Qi, 2013; Udagawa and Bergholtz, 2016; Li et al., 2017). In addition, both of these compounds have been shown to be highly tunable. For example, the extremely large magnetoresistance in WTe_2, originating from a perfect compensation of charge carriers (Ali et al., 2014b; Alekseev et al., 2012; Das et al., 2019), is significantly amended following Lifshitz transitions that can be driven with temperature (Wu et al., 2015; Pletikosić et al., 2014) or pressure (Kang et al., 2015). In $MoTe_2$, a structural transition from the orthorombic (γ) Weyl semimetal phase into the monoclinic (β) phase occurs above 240 K (Xu et al., 2018b; He et al., 2018). This transition restores the inversion symmetry inherent to the undistorted 1T phase into the system, but not the threefold rotational symmetry. This combination thus precludes the presence of the type-II Weyl nodes found in the γ phase as well as the bulk Dirac nodes of the kind found across the 1T-TMDs (Yang and Nagaosa, 2014). The compound remains interesting for its topological properties, however, as β-type 1T′-TMDs are theoretically predicted to contain higher order nontrivial band topology (Tang et al., 2019; Wang et al., 2019). This same γ-β transition can be induced in 1T′-WTe_2 with ultrafast THz radiation (Sie et al., 2019).

In addition to the Weyl physics in the 1T′ TMDs, each bulk Dirac point in the 1T and 2H TMDs has the capacity to have its degeneracy reduced by breaking time-reversal or inversion symmetries, so long as the underpinning C_3 symmetry remains intact. While this has not yet been shown explicitly, this could be achieved by lifting time-reversal symmetry through the application of external magnetic fields or through the inclusion of magnetic dopants. Similarly, 1T-$CrTe_2$ may possess Weyl points intrinsically due to the combination of magnetic ground state (see, for example, Freitas et al., 2015; Zhang et al., 2021 for bulk and thin film variants) and a chalcogen p-orbital manifold, which is likely to share the k_z-mediated band inversions of its sister compounds. Alternatively, inversion symmetry can be explicitly broken through the fabrication of artificial TMD structures with inequivalent top and bottom chalcogen sublayers, such as in the so-called "Janus" TMDs (X_1-M-X_2, $X_1 \neq X_2$), although this is not necessarily a sufficient criterion to form Weyl nodes, with Dirac (fourfold) and triple (threefold) degenerate points maintained or formed in density functional theory studies of bulk Janus TMDs (Xiao et al., 2018; Bahramy et al., 2018). The creation of bulk Janus TMDs remains largely theoretical due to the logistics of such a precise sample growth (Yin et al., 2021; Griffith et al., 2023), though monolayer Janus TMDs in 1H, 1T, and 1T′ structures have been successfully synthesized (Tang and Kuo, 2022; Li et al., 2018a; Zhang et al., 2017; Trivendi et al., 2020; Zheng et al., 2022; Gan et al., 2022) but have yet to be measured by ARPES.

Thin limit

While bulk TMDs offer a rich platform in which to study and induce a wide array of novel physics, next-generation electronic or spintronic devices harnessing TMD materials are likely to turn to their few-layer variants both for easier control through gating (Nguyen et al., 2019b; Lei et al., 2022) and for optimized integration with other materials (Ji and Choi, 2022; Pham et al., 2022). Fortunately, the van der Waals nature of TMD systems makes them ideal for epitaxial growth via MBE on a wide array of substrates, including graphene, which is both highly conducting and largely inert (see e.g. the following ARPES studies: Zhang et al. (2021), Ou et al. (2022), Coelho et al. (2019), Feng et al. (2018), Biswas et al. (2021), Dreher et al. (2012), Watson et al. (2021), and Antonelli et al. (2022). Similarly, numerous methods of mechanically exfoliating monolayers from bulk single crystals are possible, rendering high quality films, which can be integrated into devices, though the size of such films is typically on the order of 20 μm. The development of nano-ARPES (i.e., ARPES with focused light spots smaller than 1μm) and angle-resolved photoelectron emission microscope (PEEM) beamlines worldwide has therefore proven crucial for the systematic characterization of these exfoliated TMD flakes and their devices (Grubisic-Cabo et al., 2023; Stansbury et al., 2021; Pei et al., 2022; Khalil et al., 2023; Nguyen et al., 2019b; Jones et al., 2022), and for TMD thin films more generally which are often spatially inhomogeneous and suffer from rotational disorder. Moreover, MBE grown or exfoliated TMD flakes can be capped with amorphous Se and/or Te to prevent film degradation between growth chamber and ARPES ultra-high vacuum environments, or often simply annealed *in situ* without prior capping to remove surface contaminants.

For the 1T′-structured TMDs, thinning $MoTe_2$ down to the few layer limit (less than 12 nm) has been found to remove the structural transition to the inversion-symmetric monoclinic phase, thus providing access to the type-II Weyl nodes, usually found only within the low-temperature inversion asymmetric orthorhombic (γ) phase, at room temperature (He et al., 2018). In the single-layer limit, both $MoTe_2$ and WTe_2 become inversion symmetric (though inversion symmetry is removed with a small perpendicular electric field) since the β and γ phases differ only by their stacking pattern along the c-axis, and are therefore equivalent in the single layer (Rhodes et al., 2021; Shi et al., 2019). While a 2D analog of Weyl nodes may then not be expected, monolayer 1T′-WTe_2 has been shown to be an intrinsic two-dimensional TI via numerous experimental methods including

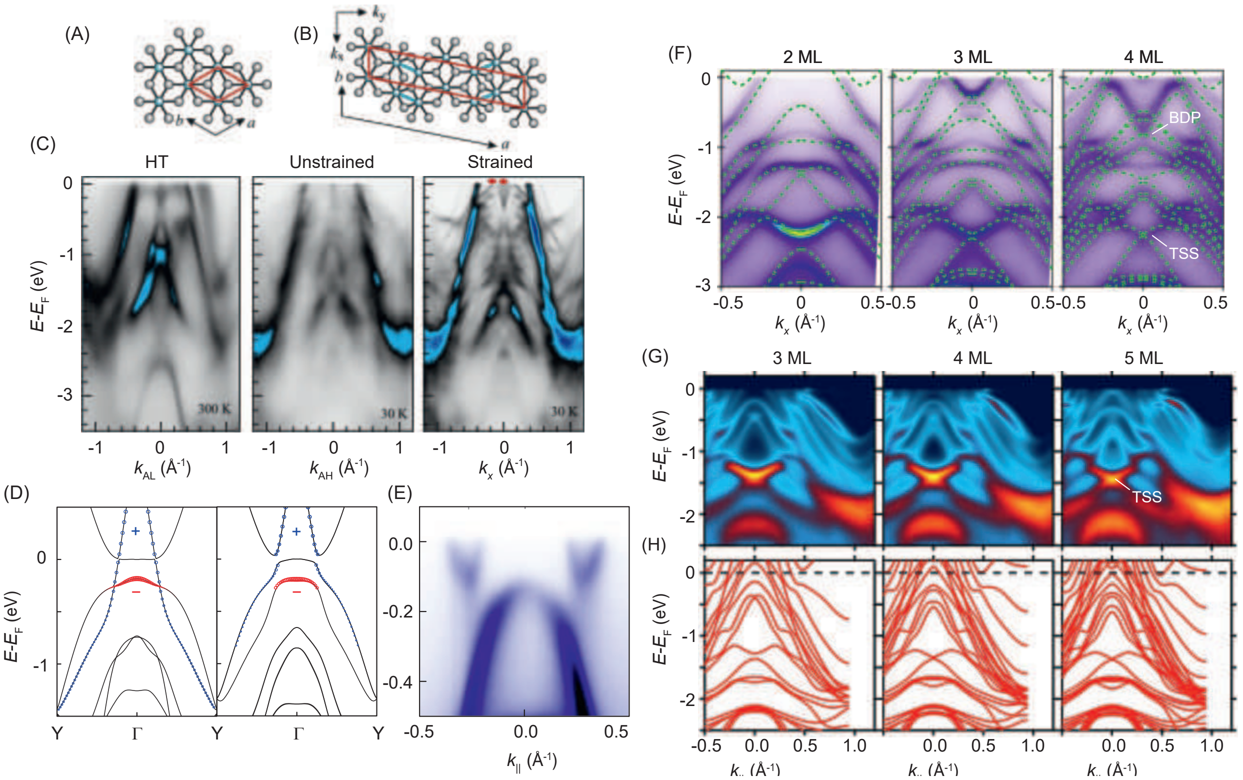

Fig. 12 Tunable topological phases in bulk and thin-film TMDs. (A–C) Temperature- and strain-dependent ARPES results on 1T–$IrTe_2$. (D,E) Band structure calculations and ARPES spectrum of (*n*-doped) monolayer 1T'–WTe_2. (F) Thickness-dependent ARPES of $PtTe_2$ thin films. (G,H) Thickness-dependent ARPES and density functional theory calculations of $NiTe_2$ thin films. (A) High and (B) low temperature structures of 1T–$IrTe_2$. (C) High-temperature (HT), low-temperature unstained and strained ARPES spectra of 1T–$IrTe_2$. The application of 0.1% strain both drives a Lifshitz transition of the Dirac bands and stabilizes the 6 × 1 ground state such that a single domain can be accessed. *Red arrows* indicate bands originating from the bulk Dirac cone in the high-temperature trigonal phase. Strain is applied along the *a*-axis. (D) Band structure calculations of monolayer 1T'–WTe_2 without (left) and with (right) spin–orbit coupling. The ± symbols indicate band parity at the Γ point. (E) ARPES spectrum of 1T'–WTe_2 along the Γ–Y direction. The sample has been dosed with K to facilitate clear observation of the conduction bands. (F) ARPES spectra and overlaid band structure calculations for 2, 3, and 4 monolayer (ML) 1T–$PtTe_2$ (refer to original publication for further film thicknesses). Bulk Dirac points (BDP) and a topological surface states (TSS) are labeled. (G) ARPES spectra for 3, 4, and 5 ML 1T–$NiTe_2$ (refer to original publication for further film thicknesses). The TSS is labeled. (H) Corresponding density functional theory calculations for the spectra in (G). (A–C) Adapted from Nicholson CW, Rumo M, Pulkkinen A, Kremer G, Salzmann B, Mottas, M-L, Hildebrand B, Jaouen T, Kim TK, Mukherjee S, Ma K, Muntwiler M, von Rohr, FO, Cacho C, and Monney C (2021) Communications Materials 2: 25; (D,E) adapted from Tang S, et al. (2017c) Nature Physics 13: 683–687; (F) adapted from Deng K, et al. (2019) Science Bulletin 654: 15; (G and H) adapted from Hlevyack J, et al. (2021) npj 2D Materials and Applications 5: 40.

ARPES (Fig. 12E), with inverted band gaps formed within the *d*-orbital manifold near the Fermi level generating topologically protected, conductive spin-polarized edge states around the perimeter of the semiconducting film (Tang et al., 2017c; Fei et al., 2017; Shi et al., 2019; Zhao et al., 2021).

For the 1T, and 2H-structured TMDs, one would not expect topological ladders of bulk and surface Dirac nodes to survive the thinning down to a single monolayer. Their formation, along the k_z-axis, relies on the intra- and interlayer hopping channels perpendicular to the surface plane, which are strongly reduced in the few layer limit. Indeed, no pristine monolayer TMDs have been found to host any Dirac nodes. For example, in its bulk 1T–$PtTe_2$ is metallic and hosts two bulk Dirac cones and three inverted band gaps at $\overline{\Gamma}$ (Yan et al., 2017). In its monolayer, it is a topologically trivial semimetal (Deng et al., 2019). However, the topological physics reappears abruptly as soon as 4 monolayers are reached, with clear TSS and "bulk" Dirac states observed by ARPES in MBE grown films (Fig. 12F) (Deng et al., 2019). A similar phenomenon was observed in semimetallic $NiTe_2$ films, where gapless TSS are found in five-layer samples, alongside conical bands deriving from the (near-E_F) type-II bulk Dirac cone in the bulk limit (Fig. 12G, H; Hlevyack et al., 2021). These studies suggest that the topological crossing points are not gradually unwound with reduced thickness, but rather that the hierarchy of band inversions is left intact along a discretized k_z-axis. The layer number needs only be sufficient to (a) access k_z sub-bands where bulk Dirac points form, and/or (b) access subbands on the nontrivial side of the k_z-mediated topological phase transitions which generate the surface Dirac nodes. As with all TIs, the film needs also to be sufficiently thick to avoid wavefunction interference of TSSs on opposing surfaces. Topological phases may also be induced in monolayer 1T–TMDs via chemical substitution. For example, in monolayer 1T–$PtSe_2$, a 2D topological insulating phase, unrelated to nontrivial band topology of the bulk, has been theoretically shown to be induced through Se–Hg substitution (with one nontrivial alloy naturally occurring), with the resulting topologically nontrivial edge states crossing the Fermi level (Crasto de Lima et al., 2023).

Altogether, the presence of both bulk Dirac nodes and nontrivial topology in the few-layer TMD limit opens avenues to incorporate topological physics in thin film heterostructures. For example, designer topological ladders, with selective control over the numbers, types, and energetics of Dirac nodes, may be engineered in 1T and 2H TMD heterostructures with a careful choice of TMD on a layer-by-layer basis. Such heterostructures could also open routes to drive correlated topological phases not possible in the bulk systems. In analogy to the induction of Mott gaps and superconductivity in bilayer graphene through the delicate control of the relative twist angle between the two monolayers (Cao et al., 2018), it has been shown how correlated phases are achievable in both twisted heterobilayer and homobilayer TMDs. In short, the moiré superlattice potential defined by the lattice mismatch between constituent layers enables hybridization channels between states that were previously well separated in momentum space, due to extreme back-folding into the reconstructed "mini" Brillouin zone. This produces flat bands from which correlated phases can emerge with the right band filling. Such flat bands have already been observed spectroscopically for numerous TMD heterostructures (Stansbury et al., 2021; Pei et al., 2022; Li et al., 2021a), with a correlated insulator phase experimentally found at half-band filling (Wang et al., 2020). While such findings already allude to technological applications such as the Mott field effect transistor, the coexistence of nontrivial band topology and these engineered correlated phases is yet to be explored, but is in reach, as demonstrated by the presence of topological states in monolayer WTe_2 (Tang et al., 2017c), monolayer $PtHg_xSe_{2-x}$ (Crasto de Lima et al., 2023) and 4–5 layer $PtTe_2$ (Deng et al., 2019) and $NiTe_2$ (Hlevyack et al., 2021).

Topological nodal-line semimetals

In analogy to the zero-dimensional nodes discussed in the previous sections, it is possible to produce one dimensional nodal lines along complete *k*-paths through a Brillouin zone (schematized in Fig. 13A). The hosting compounds, Dirac nodal line semimetals, often require additional crystalline symmetries with respect to Dirac and Weyl semimetals to ensure the protection of Dirac degeneracies over extended *k*-paths, at least in the absence of spin–orbit coupling. These nodal lines can take the form of nodal rings, chains, links, and knots (Kim et al., 2015; Fang et al., 2015; Bzdušek et al., 2016; Bi et al., 2017; Fu et al., 2019) and, while the nodal line stays ungapped (neglecting spin–orbit coupling) over the full momentum range, the Dirac node is free to move in energy. By now, many examples of nodal line semimetals have been theoretically predicted and/or experimentally confirmed with ARPES, including Mg_3Bi_2 (Chang et al., 2019), which possesses nodal lines only in the absence of spin–orbit coupling due to the presence of only time reversal and inversion symmetries, and $PbTaSe_2$ (Bian et al., 2016), Cu_3PdN (Yu et al., 2015), Ca_3P_2 (Xie et al., 2015), the CaP_3 family (Xu et al., 2017a), and $EuAs_3$ (Cheng et al., 2021), which host nodal lines protected in the absence of spin–orbit coupling due to reflection/mirror symmetries, and occasionally in the presence of spin–orbit coupling ($TaPbSe_2$), depending on the Brillouin zone path where the nodal line occurs and the presence of inversion symmetry. It is noteworthy that the addition of spin–orbit coupling transforms a subset of these compounds into Dirac semimetals with lattice-symmetry protected bulk Dirac points (Yu et al., 2015).

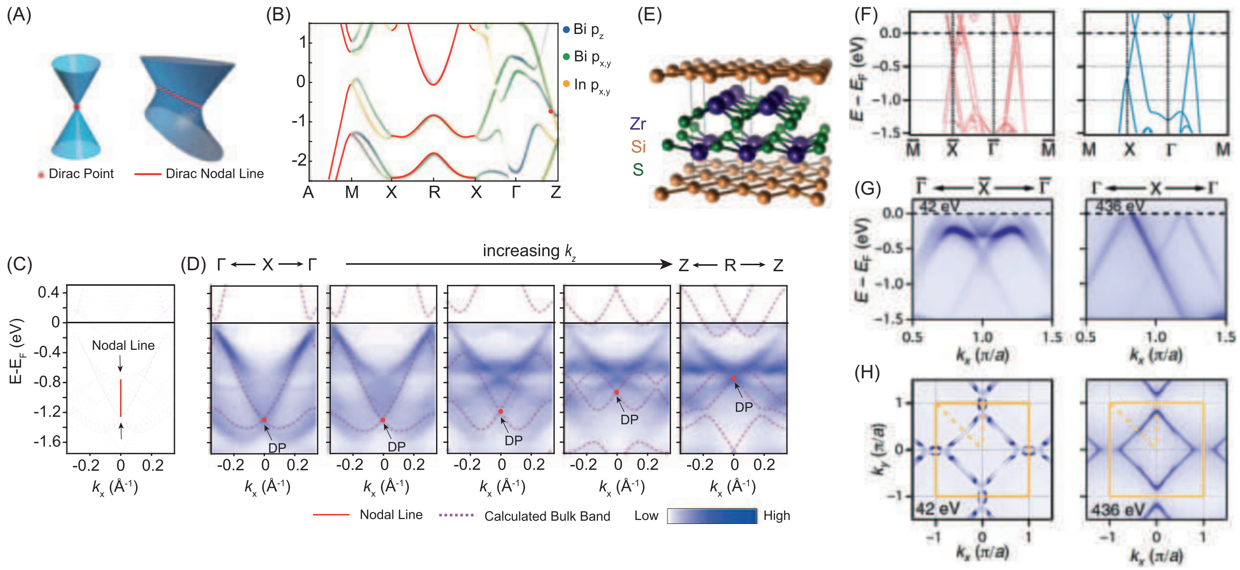

Fig. 13 Nodal lines and nodal surfaces in InBi and ZrSiS. (A) Schematic of a Dirac point and Dirac nodal line. (B) Band structure calculation for InBi. Dirac points and Dirac nodal lines are overlaid with *red markers/lines*. Other colorings indicate orbital character. (C) k_z integrated band structure calculations demonstrating the energy dispersion of the nodal line. (D) k_z-dependent datasets and overlaid band structure calculations demonstrating the continued presence of a protected Dirac crossing along the k_z path. (E) Crystal structure of nonsymmorphic ZrSiS. (F) Band structure calculations, (G) ARPES dispersions, and (H) ARPES Fermi surfaces of ZrSiS, for surface (left) and bulk (right) derived electronic structures. *Yellow squares* in (H) indicate the surface (bulk) Brillouin zones with the $\overline{M}$ (M) and $\overline{X}$ (X) points on the corners and edges, respectively. Adapted from (A–D) Ekahana SA, et al. (2017) New Journal of Physics 19: 065007; (E) Pezzini S, et al. (2018) Nature Physics 14: 178–183; and (F–H) Fu B-B, et al. (2019) Science Advances 5(5): aau6459.

There are instances where the nodal lines are resilient to spin–orbit coupling gapping along extended k-paths, however. These cases employ nonsymmorphic symmetry: a combination of a fractional lattice symmetry and either a glide plane or screw axis (Wu et al., 2022; Wang et al., 2016b; Yang et al., 2018). Nonsymmorphic compounds with nodal lines include InBi (Fig. 13B–D) (Ekahana et al., 2017), Pt(Sn, Pb)$_4$ (Wu et al., 2016a, 2022), and (Ta,Nb)$_3$SiTe$_6$ (Li et al., 2018b). Perhaps most extensively studied, however, is the Matlockite (P4/nmm) materials family, M$_1$M$_2$X, where $M_1 \in \{Zr, Hf, La, Na\}$, $M_2 \in \{Sb, Ge, Si\}$, and $X \in \{S, Se, Te\}$, which have been extensively characterized by ARPES (Schoop et al., 2016; Neupane et al., 2016; Chen et al., 2017; Topp et al., 2017; Hosen et al., 2017; Wang et al., 2016a; Yen et al., 2021; Cheng et al., 2019; Fu et al., 2019; Wang et al., 2021a; Lou et al., 2016). These compounds contain zero-dimensional Dirac nodes protected by the nonsymmorphic symmetry itself, which here results from a glide-mirror symmetry with respect to the Si layer in ZrSiS for example (Fig. 13E), and one-dimensional nodal lines protected by the combination of inversion and time-reversal symmetries (Schoop et al., 2016). The latter continuously connect Dirac crossings found along the high-symmetry X-Γ and Γ-M directions to form a line of Dirac degeneracies along low-symmetry paths near the Fermi level (Fig. 13F). The nodal line itself is not protected against spin–orbit coupling (unlike the nonsymmorphic symmetry protected Dirac nodes at higher binding energies), but in the case of ZrSiS, the small spin–orbit coupling strength renders only millivolt scale bandgaps (Fu et al., 2019; Yang et al., 2021). Note that this is different to the case of InBi (Fig. 13C and D), where the nonsymmorphic symmetry does fully protect the nodal lines even in the presence of strong spin–orbit coupling. More recently, it was predicted (Topp et al., 2017) and subsequently confirmed (Fu et al., 2019) that the nodal lines in ZrSiS form part of a nodal surface on the $k_z = 0$ and π contours of the Brillouin zone to produce a square-shaped bulk Fermi surface composed only of the near-Dirac degeneracies (Fig. 13G,H).

It is noteworthy that these systems host particularly rich surface electronic structures where the nonsymmorphic symmetries are broken. Indeed, in the ZrSiS family, the natural cleavage plane is between the Si layers, resulting in surface-derived “floating” pockets at the $\overline{X}$ point of the surface Brillouin zone, which accompany the Dirac nodal surface (Schoop et al., 2016; Topp et al., 2017; Fu et al., 2019; Yang et al., 2021), see Fig. 13F–H. These surface electronic structures can have rich properties of their own, including the formation of mirror-symmetry-protected crossings between pairs of Rashba-split surface states, which behave as 2D analogs of Weyl points (Marković et al., 2019).

Topological chiral semimetals

Chiral crystals are described by the 65 Sohncke space groups that contain only symmetry operations of the first kind (rotations and screwings), that is, they lack inversion, mirror, and roto-inversion symmetry. These have been suggested to host multifold fermions, which go beyond the Weyl, Dirac, and Majorana fermions of quantum field theory and of which the Weyl fermion is itself chiral. The discovered multiple degeneracies include three-, six-, and eight-band crossings stabilized by space group symmetries with spin–orbit coupling and time-reversal symmetry (Bradlyn et al., 2016).

The low-energy effective Hamiltonian describing, for example, the threefold crossing is a fermionic generalization of the Weyl Hamiltonian $H = \mathbf{k} \cdot \mathbf{S}$, where $\mathbf{k}$ is the momentum and the matrices S_i are the generators of the rotation group $SO(3)$ in the spin-1 representation. The bands of the multifold fermions bear a higher Chern number, ± 2 in the case of the threefold crossing, and also host a larger number of topologically protected surface Fermi arcs. The threefold fermions are predicted to show an anomalous negative magnetoresistance and a chiral anomaly different from that of single or double Weyl points. At large magnetic fields. the Landau-level spectrum displays two chiral modes with unusual momentum dependence (Bradlyn et al., 2016).

Threefold crossings have been observed before in MoP (Lv et al., 2017) and WC (Ma et al., 2018). Those, however, result from band inversion, and do not lead to defined Chern numbers. The multifold fermions, instead, do not require band inversion and occur at time-reversal invariant momenta. In contrast to Weyl fermions, they cannot move and annihilate and are therefore more robust as long as the relevant crystal symmetries are preserved. Single crossings of spin–orbit-coupled bands at time-reversal invariant momenta have been named Kramers–Weyl fermions (Chang et al., 2018).

In the presence of time-reversal symmetry, multifold fermions occur for several space groups. Among these groups, $P2_13$ (number 198) corresponds to a simple-cubic lattice where the sixfold degeneracy occurs at the R point (corner of the Brillouin zone) (Bradlyn et al., 2016). Space group 198 has been of particular interest because simple binary crystals are available such as transition metal monosilicides, monogermanides, monoaluminides, and monostannides. Specific predictions have been made, for example, for silicides (Tang et al., 2017; Chang et al., 2017a; Pshenay-Severin et al., 2018).

ARPES data have simultaneously been reported for PtAl (Schröter et al., 2019), CoSi (Rao et al., 2019; Takane et al., 2019; Sanchez et al., 2019), and RhSi (Sanchez et al., 2019). The associated large Chern numbers lead to multiple Fermi arcs. The chirality of the crystal structure can be deduced from the Fermi arc. Fig. 14A shows the comparison of the Weyl and Dirac fermion and multiple fermions: the chiral spin-1 fermion and the chiral double Weyl or charge-2 fermion. Fermi arcs span the surface projection of the high symmetry points at which the multifermions occur and, therefore, can span the whole surface Brillouin zone, depending on the surface. They are hence typically an order of magnitude longer than in Weyl semimetals, shown as sketch in Fig. 14B, and this is observed in ARPES (Schröter et al., 2019; Rao et al., 2019; Takane et al., 2019; Sanchez et al., 2019). For CoSi, a spin-1 fermion occurs at Γ (probed at soft-X-ray energies in Fig. 14F) and double Weyl fermions at the R points. The surface Fermi arcs span the whole (100) surface Brillouin zone from $\overline{\Gamma}$ to $\overline{M}$, see Fig. 14G,H). Their ARPES signature is independent of the photon energy due to their two-dimensionality (blue crosses 75 eV and red circles 110 eV in Fig. 14H).

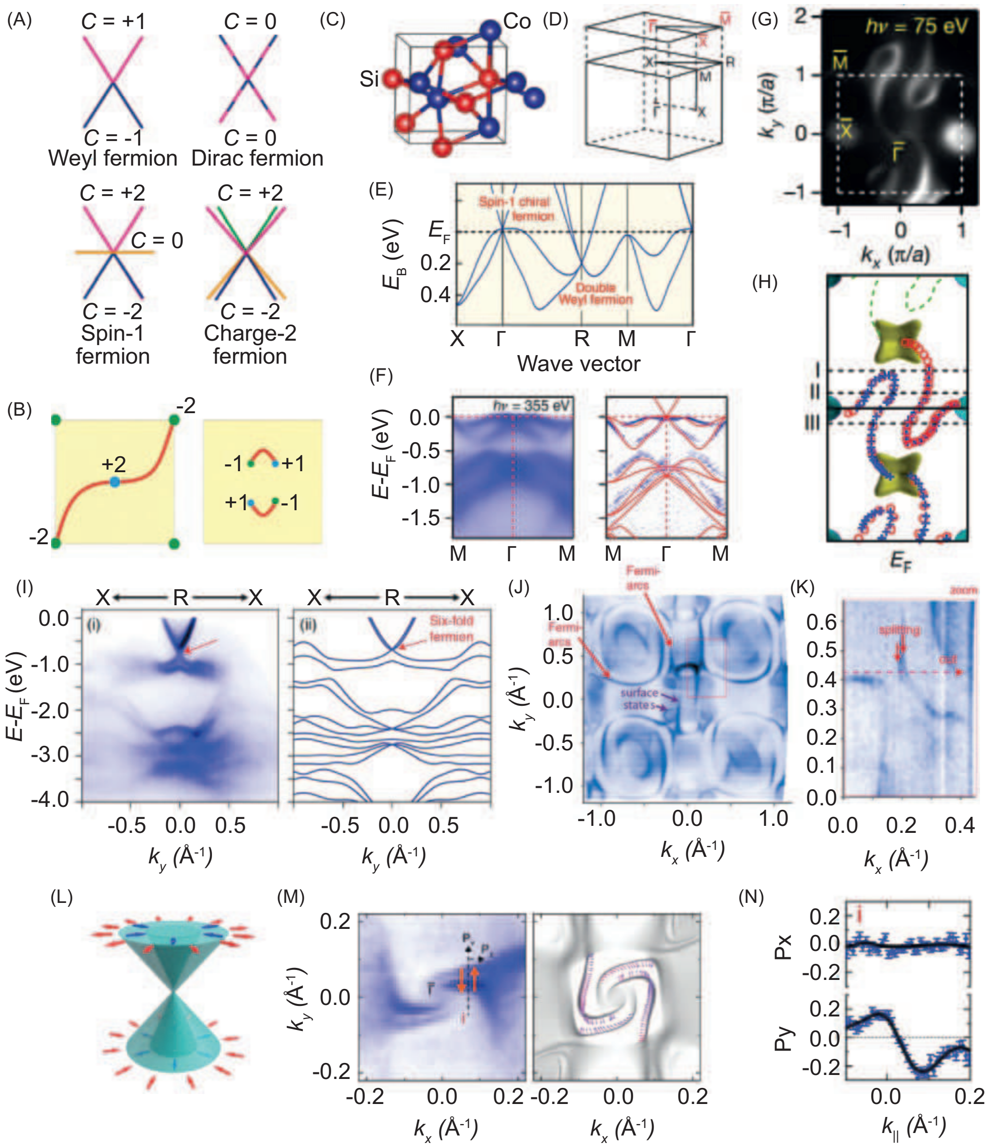

Fig. 14 Multifold fermions in topological chiral semimetals CoSi, PtAl, PdGa, and PtGa. (A) Examples of multifold fermions as compared to Weyl and Dirac fermions. (B) Since they are located at time-reversal invariant momenta, the surface Fermi arcs extend across the complete surface Brillouin zone (left), in contrast to the case of Weyl semimetals (right). (C–H) CoSi with (C) crystal structure, (D) bulk and surface Brillouin zone, and (E) band structure. (F) Bulk-sensitive ARPES data (355 eV) of the spin-1 chiral fermion. (G,H) Surface fermi arcs from data at two different photon energies (75 and 110 eV) superimposed on the calculated bulk Fermi surface. (I) In PtAl the large spin-orbit splitting of ~100 meV can be resolved. (J,K) Likewise, the surface Fermi arc of PdGa is split. (L) Spin texture of a multifold fermion. (M,N) Measurements of the spin texture of the surface Fermi arc of PtGa allow conclusions on parallel spin-momentum locking of the bulk multifold fermion. Panel (A,B,D–H) from Rao Z, Li H, Zhang T, Tian S, Li C, Fu B, Tang C, Wang L, Li Z, Fan W, Li J, Huang Y, Liu Z, Long Y, Fang C, Weng H, Shi Y, Lei H, Sun Y, Qian T, and Ding H (2019) Nature 567: 496; (C) from Takane D, Wang Z, Souma S, Nakayama K, Nakamura T, Oinuma H, Nakata Y, Iwasawa H, Cacho C, Kim T, Horiba K, Kumigashira H, Takahashi T, Ando Y, and Sato T (2019) Physical Review Letters 122: 076402; (I) from Schröter NBM, Pei D, Vergniory MG, Sun Y, Manna K, de Juan F, Krieger, JA, Süss V, Schmidt M, Dudin P, Bradlyn B, Kim TK, Schmitt T, Cacho C, Felser C, Strocov VN, and Chen Y (2019) Nature Physics 15: 759; (J–K) from Schröter NBM, Stolz S, Manna K, de Juan F, Vergniory MG, Krieger JA, Pei D, Schmitt T, Dudin P, Kim TK, Cacho C, Bradlyn B, Borrmann H, Schmidt M, Widmer R, Strocov VN, and Felser C (2020) Science 369: 179; (L–N) from Krieger JA, Stolz S, Robredo I, Manna K, McFarlane EC, Date M, Guedes EB, Dil JH, Shekhar C, Borrmann H, Yang Q, Lin M, Strocov VN, Caputo M, Pal B, Watson MD, Kim TK, Cacho C, Mazzola F, Fujii J, Vobornik I, Parkin SS, Bradlyn B, Felser C, Vergniory MG, and Schröter NBM (2022) arXiv:2210.08221.

For chiral semimetals with light elements, the spin-orbit splitting is small and not resolvable in ARPES. For PtAl, PdGa, and PtGa the spin-orbit coupling is, however, high and the splitting can be resolved in the bulk crossing of PtAl in Fig. 14I (Schröter et al., 2019) and in the Fermi surface arc of PdGa in Fig. 14J,K (Schröter et al., 2020). The splitting of the surface Fermi arc implies that four arcs connect the projections of the multifold fermions, which is consistent with them having a large Chern number with magnitude 4.

Topological chiral semimetals display a peculiar spin texture. We note that in Rashba systems, the presence of mirror symmetries render the spin perpendicular to the mirror plane for states with wave vector in the mirror plane because an in-plane spin reverses under mirror reflection. A radial spin texture, that is, parallel spin-momentum locking, has been predicted for chiral elemental semiconductors Te and Se (Hirayama et al., 2015). The Weyl nodes have been identified in Te by ARPES (Nakayama et al., 2017), and the radial spin texture was observed near the Fermi energy by spin-resolved ARPES for chiral Te (Sakano et al., 2020; Gatti et al., 2020), including its reversal for crystals with opposite chirality (Sakano et al., 2020). Gyrotropic effects, i.e., those that reverse with the crystal chirality, have been predicted for Te. A current along the trigonal axis induces a small parallel magnetization, which can be detected by Faraday rotation of transmitted light (Tsirkin et al., 2018).

Te does not exhibit topological semimetal behavior and the radial spin texture is not expected to be maintained in a large range of momentum space. However, theoretical studies have predicted the presence of a truly radial spin texture (Fig. 14L) and an isotropic parallel spin-momentum locking in chiral topological semimetals with single- and multifold band crossings (Chang et al., 2018; Lin et al., 2022). Spin-resolved ARPES investigations have been conducted on PtGa revealing parallel spin-momentum locking for the multifold fermions at Γ and R. This was possible through the spin texture of its topological Fermi arc surface states, which points orthogonal to the Fermi surface contour close to the projection of the bulk multifold fermion (Krieger et al., 2022). This is seen in Fig. 14M,N. Additionally, it has been demonstrated that the direction of spin polarization reverses with the chirality of the crystal (Krieger et al., 2022).

Correlated topological insulators

The topological materials discussed so far are classified based on their single-particle band structure and do not rely on electron correlation. Nonetheless, various research directions explore the connection between topology and strong correlation. One notable limitation of TIs identified thus far is the relatively small size of their inverted bulk band gaps, which restricts their practical use in semiconductor electronics. However, the Coulomb interaction can generate or augment band gaps to much greater magnitudes. In that case their gaps are centered about the Fermi level and do not require a certain stoichiometry such as in $(Bi,Sb)_2(Te,Se)_3$ compounds to become bulk insulating (Dzero and Galitski, 2013).

Generally the electron correlation is stronger among *d* and *f* electrons than for *s* and *p* electrons. In 5*d* transition metal oxides, both the spin–orbit interaction and the electron correlation are strong and of the same order of magnitude. According to a tight-binding model, Na_2IrO_3 has been predicted to be a quantum spin-Hall insulator, which is a 2D TI (Shitade et al., 2009). It is important to note that there are strongly correlated topological phases of matter that have no analog in band theory and hence do not lend themselves to an investigation of their nontrivial topology by ARPES. This applies to the topological Mott insulator (Raghu et al., 2008; Pesin and Balents, 2010) and extends to frustrated quantum magnetism (Balents, 2010; Reuther et al., 2012).

A prediction directly related to the band structure, and hence relevant for ARPES, applies to SmB_6, which has been predicted to be a topological Kondo insulator (Dzero et al., 2010; Alexandrov et al., 2013; Takimoto, 2011; Lu et al., 2013). The band gap in a Kondo insulator is caused by hybridization of itinerant conduction electrons, here *d* electrons, with localized electrons, here *f* electrons. Importantly, Dzero et al. realized that due to the odd parity of *f* states and even parity of *d* states, the precondition for band inversion is fulfilled (Dzero et al., 2010). Band calculations predicted SmB_6 as strong TI with an odd number of Dirac cones on the (100) cleavage plane (Alexandrov et al., 2013; Takimoto, 2011; Lu et al., 2013).

SmB_6 was the first established mixed valent compound and Kondo insulator and the predictions as TI prompted further experimental efforts (see the review by Allen, 2016). Surface transport experiments confirmed subsequently that at low temperatures only the surface remains metallic (Wolgast et al., 2013; Kim et al., 2013). In ARPES, surface states were found at the $\overline{\Gamma}$ and $\overline{X}$ points (Xu et al., 2013a; Jiang et al., 2013), as well as in quantum interference data (Li et al., 2014). ARPES data were consistent in the observation of a Fermi surface contour at $\overline{X}$ (Xu et al., 2013a; Jiang et al., 2013; Neupane et al., 2013; Frantzeskakis et al., 2013; Denlinger et al., 2013; Min et al., 2014). The dispersion of a Dirac cone was, however, not observed at $\overline{\Gamma}$ or at $\overline{X}$.

Hlawenka et al. (2018) demonstrated by core-level spectra two chemically pure terminations, consistent with earlier work (Denlinger et al., 2013). The boron and Sm terminations are also observed in scanning tunneling microscopy and differences in the assignment of scanning tunneling microscopy topographies in the literature have been explained by an element sensitivity due to the bias voltage (Herrmann et al., 2020). Hlawenka et al. (2018) observed that the $\overline{\Gamma}$ state has a massive dispersion for Sm termination and is sensitive to contamination indicating that it is topologically trivial. For the boron termination, it shows a Rashba splitting, which is incompatible with a topological state. Since one $\overline{\Gamma}$ and two $\overline{X}$ Dirac cones have been predicted at the surface (Alexandrov et al., 2013; Takimoto, 2011; Lu et al., 2013), it is actually unimportant for the topological assignment whether the contour at $\overline{X}$ is trivial.

The closing of the 5*d*-4*f* hybridization gap with increasing temperature has been observed in ARPES (Denlinger et al., 2013; Min et al., 2014; Hlawenka et al., 2018). It was found that the surface state at $\overline{X}$ is a surface shifted hybridized 5*d*-4*f* dispersion, which is shifted by 10 meV to higher binding energy for boron termination and by about the same amount to lower binding energy for Sm termination (Hlawenka et al., 2018). These shifts, which are consistently observed by scanning tunneling spectroscopy (Herrmann et al., 2020; Matt et al., 2020), are enough to bridge the bulk band gap and explain the robust surface metallicity despite the trivial character of the surface state at $\overline{X}$.

The results by Hlawenka et al. do not explain why Xu et al. (2014) observe a spin texture expected for a TSS for the $\overline{X}$ contour. A similar spin texture was reported for the nonpolar (111) surface (Ohtsubo et al., 2019). Ohtsubo et al. (2019) noted that the measurement temperatures of 15–20 K (Xu et al., 2014; Ohtsubo et al., 2019) would conflict with the gap energy scale by Hlawenka et al. if confirmed. A spin polarization has also been reported for YB_{12} as indication for a TSS (Hagiwara et al., 2016).

Another open question in SmB_6 concerns the umklapp features seen in ARPES. They are consistent with the (2×1) reconstruction of the Sm-terminated surface but appear also on the boron terminated surface, which shows only a (1×1) topography (Herrmann et al., 2020). In view of the trivial character of the observed $\overline{\Gamma}$ state, some researchers propose that the Fermi surface contour around $\overline{\Gamma}$, assigned so far to umklapp from the $\overline{X}$ contour (Xu et al., 2013a; Jiang et al., 2013; Hlawenka et al., 2018), is instead the missing Dirac cone to render SmB_6 topological (Ohtsubo et al., 2019; Thunström and Held, 2021; Li et al., 2020).

Recently, $FeSb_2$ has been proposed as another candidate for a topological Kondo insulator (Xu et al., 2020). Here, the Fe is mixed valent and the hybridization gap occurs with its *3d* states. The system also shows a conductivity plateau similarly to SmB_6. Other suggested compounds include Fe_2VAl, FeSi, and $FeGe_3$ (Xu et al., 2020; Tomczak, 2018).

Topological superconductors

ARPES has been playing an important role in the investigation of superconductors, in particular at high energy resolution to access the superconducting gap and determine the superconducting pairing symmetry, the pseudogap above the critical temperature, and other properties.

In a topological superconductor, the superconducting gap plays the role of the bulk gap in the TI, and the topological superconductor can be viewed as a TI with particle-hole symmetry (Roy, 2008; Schnyder et al., 2008; Qi and Zhang, 2011). The simplest scenario in which they can be expected to emerge is that where spin-polarized topological surface or edge states span across the Fermi level of a superconducting material (with the superconducting phase possessed either intrinsically or proximity induced). An overall antisymmetric pairing is then possible between electrons populating the TSS branches at $\pm k$. Alternatively, Rashba surface states in magnetic systems could produce similar results (Elliot, 2015; Sato and Ando, 2017). Indeed, time-reversal breaking topological superconductors could provide a platform for topological quantum computing making use of their non-Abelian statistics (Nayak et al., 2008). Proximity between a magnetic TI and an s-wave superconductor has, for example, been suggested for a topological quantum bit (Lian et al., 2018).

Intrinsic superconductors with E_F-pinned topological states at the Fermi level seem to be relatively sparse in nature. Of those that do exist, it is unlikely that an intrinsic superconducting phase can be present without (semi-)metallic ground states, thus precluding the use of genuine TIs for this purpose. Despite this, there are several candidate topological superconductors currently under investigation by ARPES. For the Fe-based superconductor Fe(Te,Se), a bulk band inversion involving strong spin–orbit interaction was predicted (Wang et al., 2015; Xu et al., 2016). This band inversion should lead to Dirac cone TSSs at $\overline{\Gamma}$ of $FeTe_{0.55}Se_{0.45}$ (100). By high-resolution laser ARPES, this surface state was recently reported (Zhang et al., 2018, 2019a). By superconducting proximity to the bulk, the Dirac cone is expected to open a superconducting gap. An isotropic superconducting gap was measured in the upper Dirac cone at $T = 2.4$ K (Zhang et al., 2018). It was recently argued, however, that $FeTe_{0.55}Se_{0.45}$ is a superconducting 3D Dirac semimetal hosting type-I and type-II Dirac points and that its electronic structure remains topologically trivial (Borisenko et al., 2020). Further increase in Te content would possibly create a band inversion, however, only with sub-meV sized gap (Borisenko et al., 2020). Similarly, the superconducting Dirac semimetal 1T–$PdTe_2$ has TSSs that cross the Fermi level, but scanning tunneling spectroscopy/microscopy and muon spin relaxation experiments have found only conventional superconducting pairing to date (Clark et al., 2018; Leng et al., 2019).

Ultrafast experiments

Time-resolved pump-probe ARPES experiments of topological matter allow for the study of unoccupied states, in particular TSSs, and the dynamics of excited charge carriers including their relaxation mechanisms (Sobota et al., 2012; Wang et al., 2012a), the spin texture of unoccupied states (Sánchez-Barriga et al., 2016; Jozwiak et al., 2016; Clark et al., 2021), and novel light-induced emergent phenomena (Wang et al., 2013a).

Upon ultrafast excitation of a TI with infrared (~1.5 eV) laser pulses of 50 fs, electrons from the Dirac cone and the bulk valence band are excited. Within a few 100 fs they occupy states above the Fermi level of the Dirac cone as well as the bulk conduction band, as seen with probe pulses of ~6 eV (Sobota et al., 2012; Wang et al., 2012a). For these experiments, conventional *n*-type Bi_2Se_3 has been used (Wang et al., 2012a) as well as special *p*-type Bi_2Se_3 samples (Sobota et al., 2012), see Fig. 15A. Immediately after the excitation, a thermalized electron distribution is reached in the TSS and in the bulk conduction band (Wang et al., 2012a). The thermalization, which can be probed at the Fermi-Dirac cutoff of the excited electron distribution, occurs due to electron–electron scattering. Since the maximum population of the TSS of *p*-type Bi_2Se_3 was reached at ~700 fs, higher-lying states are likely involved in the population (Sobota et al., 2012). The decay is noticeable after ~2 ps. This timescale is identified with energy transfer from the electrons to the lattice and thus characteristic for electron–phonon scattering in the bulk of Bi_2Se_3. The dynamics persist, however, at a timescale >10 ps. The reason is a second, slower component below the bulk conduction band edge. This slow component decays with the same timescale as the bulk conduction band population because the TSS is continuously filled by the slowly decaying bulk conduction band occupation (Sobota et al., 2012).

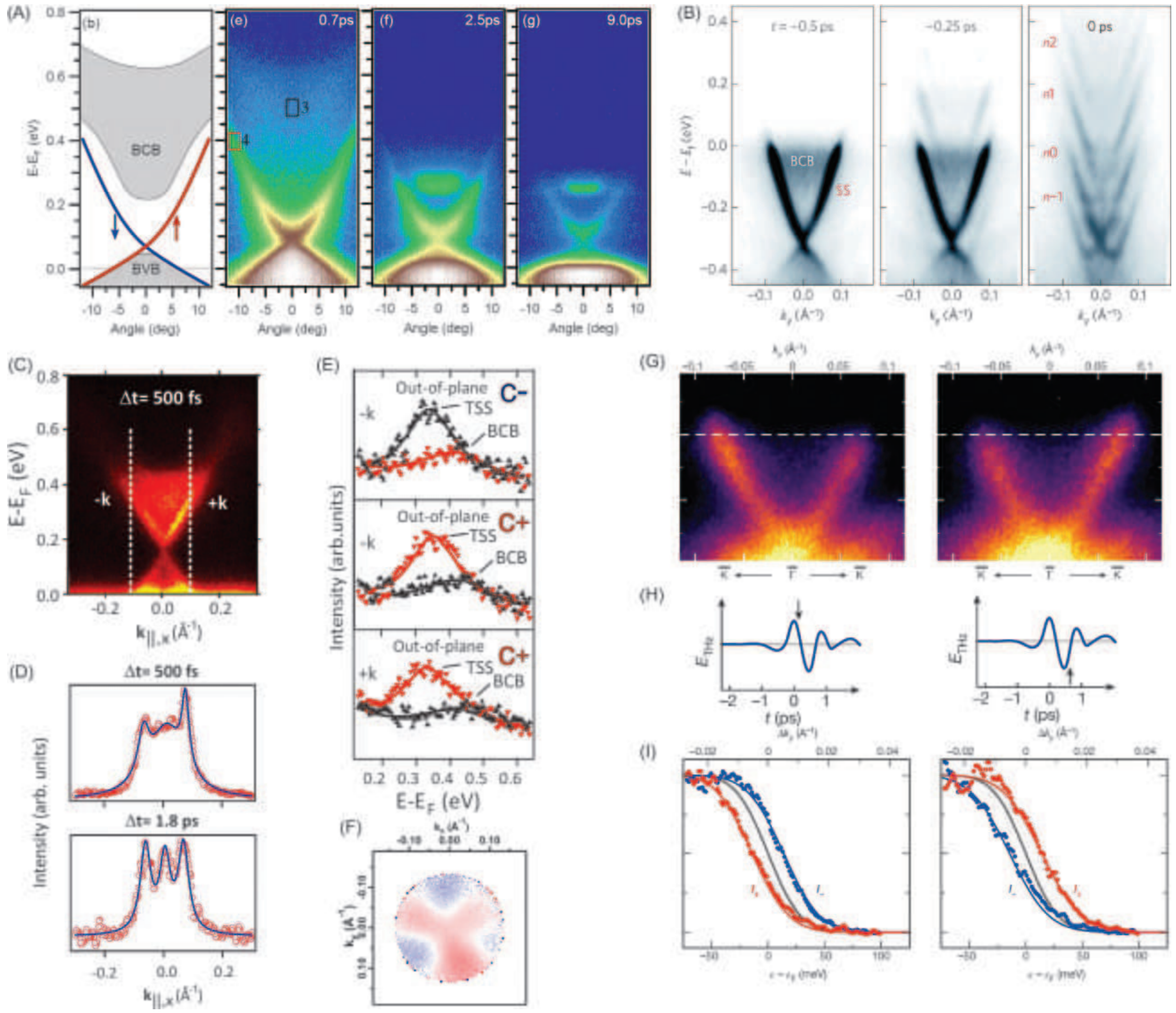

Fig. 15 Ultrafast pump-probe spectroscopy from Bi_2Se_3, Sb_2Te_3, and Bi_2Te_3. (A) Ultrafast populated unoccupied bulk conduction band states and the upper Dirac cone of p-type Bi_2Se_3 decay with a time constant that increases toward the Dirac point due to a bottleneck effect. (B) Bloch-Floquet states in Bi_2Se_3 due to coherent interaction of photons and electrons. Intensity of sidebands is maximum where pump and probe pulse maximally overlap ($t = 0$ ps). (C,E) Circularly polarized pump pulses create in Sb_2Te_3 a transient out-of-plane spin polarization in the Dirac cone determined by the light helicity, here shown for $t = 500$ fs. (C,D) Circular dichroism reveals that more electrons with momentum along $+k$ can be excited than along $-k$. (F) This asymmetry in the Dirac cone has for Bi_2Se_3 a threefold symmetry excluding a net effect on the (spin-polarized) photocurrent. (G–I) Acceleration of electrons in the TSS of Bi_2Te_3 by a THz pulse. The effect reverses with the sign of the electric field, shown in panel (H). (I) *Blue* (*red*) denotes the branch of the Dirac cone for negative (positive) momenta. Panel (A) taken from Sobota JA, Yang S, Analytis JG, Chen YL, Fisher IR, Kirchmann PS, and Shen Z-X (2012) Physical Review Letters 108: 117403; panel (B) from Mahmood F, Chan C-K, Alpichshev Z, Gardner D, Lee Y, Lee PA, and Gedik N (2016) Nature Physics 12: 306–310; panels (C–E) from Sánchez-Barriga J, Vergniory MG, Evtushinsky D, Aguilera I, Varykhalov A, Blügel S, and Rader O (2016b) Physical Review B 94: 161401(R); panel (F) from Ketterl AS, Otto S, Bastian M, Andres B, Gahl C, Minár J, Ebert H, Braun J, Tereshchenko OE, Kokh KA, Fauster T, and Weinelt M (2018) Physical Review B 98: 155406; panels (G–I) from Reimann J, Schlauderer S, Schmid CP, Langer F, Baierl S, Kokh KA, Tereshchenko OE, Kimura A, Lange C, Güdde J, Höfer U, and Huber R (2018) Nature 562: 396.

The combination of time- and spin-resolved ARPES allows to study the spin texture of unoccupied TSSs and the bulk conduction band. Again, *p*-type samples such as Sb_2Te_3 leading to an unoccupied upper and largely occupied lower Dirac cone (Zhu et al., 2015) are advantageous for studying the decay processes (Sánchez-Barriga et al., 2016). The spin texture forbids a vertical transition within the Dirac cone. For horizontal transitions involving phonons, the limitation is the maximum phonon energy, which is about 25 meV for Sb_2Te_3, similarly to Bi_2Se_3 (Hatch et al., 2011). The deceleration of the recombination due to lack of available states is sometimes referred to as electron bottleneck effect. It can be seen directly in the data as enhanced transient photoemission intensity above the Dirac point. Measured relaxation rates were 5–10 ps for Bi_2Se_3 (Sobota et al., 2012; Wang et al., 2012a), 50 ps for *p*-type $Bi_{2.2}Te_3$ (Hajlaoui et al., 2014), and 1.5 ps for Sb_2Te_3 (Sánchez-Barriga et al., 2016). Experiments with spin resolution allow to conclude whether spin manipulation with circularly polarized light, confirmed for continuous 6 eV ultraviolet light in Bi_2Se_3 (Jozwiak et al., 2013), will extend to the infrared range. Spin- and time-resolved ARPES of Sb_2Te_3 shows that a circularly polarized pump pulse turns the spins of the Dirac cone from in plane to out of plane in the transient state (Sánchez-Barriga et al., 2016), see Fig. 15C and E. Similarly to the direct photoemission experiment at 6 eV (Jozwiak et al., 2013; Sánchez-Barriga et al., 2014b) the spin orientation is determined by the light helicity (C+ and C−). This means that the spin manipulation does not only affect the final state of photoemitted electrons but also rotates the spin of electrons inside of the sample, an effect that could be employed for opto-spintronics (Sánchez-Barriga et al., 2016). This has been confirmed also for excitation into higher-lying surface states and resonances (Soifer et al., 2019). It was also possible to measure the decay of the spin polarization of the excited carriers which occurs twice as fast as the spin-averaged intensity, on a time scale of 0.4 ps as compared to 1 ps for the electron population (Sánchez-Barriga et al., 2016). The constant indirect filling of the bulk conduction band (Sobota et al., 2012) probably leads to a depolarization since it supplies unpolarized electrons from the bulk valence band (Sánchez-Barriga et al., 2016).

The above is also an example for the importance of the coupling of surface and bulk states. The coupling of surface resonances to the bulk was found to be comparatively weak for Sb_2Te_3 (Seibel et al., 2015) and Bi_2Se_3 (Cacho et al., 2015). For the *n*-doped systems Bi_2Se_3 and Bi_2Te_3, infrared light can excite electrons directly into higher lying surface resonances (Cacho et al., 2015), which plays a crucial role in the spin dynamics (Cacho et al., 2015; Sánchez-Barriga et al., 2017b).

When the stoichiometry is tuned to the bulk insulating state in $(Bi,Sb)_2Te_3$, the decay time increases dramatically from a few ps to several 100 ps (Sánchez-Barriga et al., 2017a; Sumida et al., 2017). A persistent photovoltage is observed and interpreted as caused by band bending (Sánchez-Barriga et al., 2017a). Thermalized electrons cannot diffuse from the surface state into the bulk while bulk holes diffuse to the surface. This special situation due to the intrinsically metallic surface has been suggested for use in photovoltaics (Sánchez-Barriga et al., 2017a). However, when Sb_2Te_3 is magnetically doped by V, the decay time decreases again strongly due to additional scattering paths, for example, at 0.33 eV above the Fermi level from ~3 ps to ~100 fs (Sumida et al., 2019).

In order to make use of TIs in spintronics, it is necessary to generate spin currents or spin-polarized currents, for example, for spin-transfer torques as generated in TI/ferromagnet interfaces (Mellnik et al., 2014). It has been reported that spin-polarized currents can be triggered and controlled by circularly polarized infrared radiation of 1.5 eV (McIver et al., 2012) but this result is awaiting confirmation by spectroscopic methods. The intensity enhancement in ARPES upon ultrafast excitation (Sobota et al., 2012; Wang et al., 2012a) becomes visibly asymmetric in electron momentum $k_{\|}$ for Sb_2Te_3 when the infrared light pulse is circularly polarized (Sánchez-Barriga et al., 2016), see Fig. 15C and D. Because of the locking of spin and linear momentum in the Dirac cone, this finding was interpreted as confirmation that an ultrafast spin-polarized current is excited by the circularly polarized infrared light (Sánchez-Barriga et al., 2016). With smaller excitation energies of 0.25 to 0.37 eV, the asymmetry in momentum is also strong but does not reverse by switching the light helicity (Kuroda et al., 2016). On the other hand, it has been pointed out for Bi_2Se_3 that the helicity-dependent asymmetry, that is, the circular dichroism, has at the Fermi energy a threefold asymmetry in the (k_x, k_y) momentum plane and, therefore, cannot lead to an overall spin-polarized current (Ketterl et al., 2018), see Fig. 15F.

Time-resolved ARPES has also been used to investigate carrier-wave-driven currents in the TSS (Reimann et al., 2018). With subcycle time resolution, the acceleration by the carrier wave of a THz pulse of electrons in the TSS of Bi_2Te_3 is probed. The branches appear shifted in energy and momentum with respect to each other marking the shift of the Fermi circle in momentum space, see Fig. 15G–I. The effect reverses when the electric field as marked in Fig. 15H changes sign. It is concluded that large ballistic mean free paths result from spin-momentum locking (Reimann et al., 2018).

Strong coupling of electronic states with photons can lead to Floquet–Bloch states, which are periodic in momentum and energy (Faisal and Kaminski, 1997). This has been demonstrated for the TSS of Bi_2Se_3 using intense ultrashort mid-infrared pulses the energy of which is below the bulk band gap (Wang et al., 2013a; Mahmood et al., 2016). It leads to the appearance of Dirac cone replicas above and below the original Dirac cone spaced by the driving photon energy, see Fig. 15B. Important for the confirmation as Floquet–Bloch states was the observation of hybridization gaps between these side bands (Wang et al., 2013a). In addition, a gap at the Dirac point was created using circularly polarized light and assigned to time-reversal symmetry breaking and the creation of a photoinduced quantum anomalous Hall phase (Wang et al., 2013a).

Conclusion

We end by highlighting a few aspects that we consider important for the future development of ARPES in topological materials.

The theoretical prediction of topological materials based on their band structure has recently been performed systematically (Bradlyn et al., 2017; Po et al., 2017; Kruthoff et al., 2017). Under the theory of topological quantum chemistry, band structures and symmetry groups are systematically analyzed by graph theory and group theory, respectively, and topologically nontrivial band structures can be systematically discovered. The nontrivial topology must be inherent in the band structure—as opposed to topological phases such as spin liquids—and electron correlation must be weak. ARPES will continue to directly verify these predictions and will contribute to explore the effects of electron correlation.

Micro- and nano-ARPES (see the review by Hofmann, 2021) will lift the constraints to grow large single crystals. Small crystalline domains or small single crystals can be studied but the surface preparation by cleaving will become more challenging and novel approaches will be required. Micro/nano-ARPES will also enable to distinguish differently stacked local regions in stacked 2D materials such as TMDs and MXenes (Gogotsi and Anasori, 2019).

In the general framework of future electronics, one can say that the transistor-based electronics, which is currently in use, faces limitations when it comes to further downsizing. Additionally, its operation relies on relatively uncomplicated materials.

In contrast, topological and other quantum materials possess distinct sensitivity to external influences. In the case of topological protection, this sensitivity can be extremely low. On the other hand, the sensitivity can be significantly high. In-operando ARPES can uncover such substantial state changes in response to electric current, bias voltage, electric field, temperature, and strain. In this way, topological phase transitions can be driven, and the effects may be leveraged in innovative devices. The phase space for the choice of the ideal material is enormously expanded in this way, and a material can be picked and further properties induced separately. This includes proximity effects as discussed above in the context of topological superconductivity. Dissipationless quantized edge states and functionalities required for topological quantum computations could thus be investigated in device-like structures.

Hence, another use of the high spacial resolution of micro/nano-ARPES will relate to in-operando use of ARPES (Hofmann, 2021). It has been shown for graphene and bilayer graphene stacked with h-BN that the effect of gating can be resolved (Joucken et al., 2019; Nguyen et al., 2019a; Curcio et al., 2020). It has also been achieved for the flat band of twisted bilayer graphene (Jones et al., 2020) and for WSe_2 (Nguyen et al., 2019a).

It would be a strong advantage to determine the nontrivial topology directly in ARPES. For topological matter simulated by ultracold atomic gases, the quantization of circular dichroism in photoabsorption was demonstrated as distinct differentiation between topologically trivial and nontrivial phases (Asteria et al., 2019). Deducing the Berry phase from the CDAD has been proposed and calculated for graphene (Liu et al., 2011; Gierz et al., 2012; Schüler et al., 2020), monolayer WTe_2 (Muechler et al., 2016), and bulk 2H–WSe_2 (Cho et al., 2018). It will be interesting to see how final-state effects can be treated and whether it will be possible to investigate arbitrary 3D materials.

Acknowledgment

We thank Sergey Borisenko and Niels B.M. Schröter for helpful discussions.

References

Alekseev PS, Dmitriev AP, Gornyi IV, Kachorovskii VYu, Narozhny BN, Schütt M, and Titov M (2012) *Physical Review Letters* 114: 156601.

Alexandrov V, Dzero M, and Coleman P (2013) *Physical Review Letters* 111: 226403.

Ali MN, Gibson Q, Jeon S, Zhou BB, Yazdani A, and Cava RJ (2014a) *Inorganic Chemistry* 53: 4062.

Ali MN, Xiong J, Flynn S, Tao J, Gibson QD, Schoop LM, Liang T, Haladolaaraschige N, Hirschberger M, Ong NP, and Cava RJ (2014b) *Nature* 514: 205–208.

Allen JW (2016) *Philosophical Magazine* 96: 3227.

Analytis JG (2010) *Physical Review B* 81: 205407.

Ando Y and Fu L (2015) *Annual Review of Condensed Matter Physics* 6: 361.

Antonelli T, et al. (2022) *npj Quantum Materials* 7: 98.

Arakane T, et al. (2012) *Nature Communications* 3: 636.

Armitage NP, Mele EJ, and Vishwanath A (2018) *Reviews of Modern Physics* 90: 015001.

Ärrälä M, Nieminen J, Braun J, Ebert H, and Lindroos M (2013) *Physical Review B* 88: 195413.

Assaf BA, Katmis F, Wei P, Chang C-Z, Satpati B, Moodera JS, and Heiman D (2014) *Physical Review B* 91: 195310.

Asteria L, Tran DT, Ozawa T, Tarnowski M, Rem BS, Fläschner N, Sengstock K, Goldman N, and Weitenberg C (2019) *Nature Physics* 15: 449–454.

Autès G, et al. (2016) A novel quasi-one-dimensional topological insulator in bismuth iodide β-Bi_4I_4. *Nature Materials* 15: 154–158.

Bahramy MS, Clark OJ, Yang B-J, Feng J, Bawden L, Riley JM, Marković I, Mazzola F, Sunko V, Biswas D, Cooil SP, Jorge M, Wells JW, Leandersson M, Balasubramanian T, Fujii J, Vobornik I, Rault J, Kim TK, Hoesch M, Okawa K, Asakawa M, Sasagawa T, Eknapakul T, Meevasana W, and King PDC (2018) *Nature Materials* 17: 21.

Balents L (2010) *Nature* 464: 199.

Balents L (2011) *Physics* 4: 36.

Bansil A, Lin H, and Das T (2016) *Reviews of Modern Physics* 88: 021004.

Belopolski I, Manna K, Sanchez DS, Chang G, Ernst B, Yin J, Zhang SS, Cochran T, Shumiya N, Zheng H, Singh B, Bian G, Multer D, Litskevich M, Zhou X, Huang S-M, Wang B, Chang T-R, Xu S-Y, Bansil A, Felser C, Lin H, and Hasan MZ (2019) *Science* 365: 1278.

Benia HM, Straßer C, Kern K, and Ast CR (2015) *Physical Review B* 91: 161406(R).

Bentmann H, Maaß H, Braun J, Seibel C, Kokh KA, Tereshchenko OE, Schreyeck S, Brunner K, Molenkamp LW, Miyamoto K, Arita M, Shimada K, Okuda T, Kirschner J, Tusche C, Ebert H, Minár J, and Reinert F (2021) *Physical Review B* 103: L161107.

Bi R, Yan Z, Lu L, and Wang Z (2017) *Physical Review B* 96: 201305(R).

Bian G, Chang T-R, Sankar R, Xu S-Y, Zheng H, Neupert T, Chiu C-K, Huang S-M, Chang G, Belopolski I, Sanchez DS, Neupane M, Alidoust N, Liu C, Wang B, Lee C-C, Jeng H-T, Zhang C, Yuan Z, Jia S, Bansil A, Chou F, Lin H, and Hasan MZ (2016) *Nature Communications* 7: 10556.

Biswas D, et al. (2021) *Nano Letters* 21: 1968.

Borisenko SV, Kordyuk AA, Zabolotnyy VB, Inosov DS, Evtushinsky D, Büchner B, Yaresko AN, Varykhalov A, Follath R, Eberhardt W, Patthey L, and Berger H (2009) *Physical Review Letters* 102: 166402.

Borisenko S, Gibson Q, Evtushinsky D, Zabolotnyy V, Büchner B, and Cava RJ (2014) *Physical Review Letters* 113: 027603.

Borisenko S, Evtushinsky D, Gibson Q, Yaresko A, Koepernik K, Kim T, Ali M, van den Brink J, Hoesch M, Fedorov A, Haubold E, Kushnirenko Y, Soldatov I, Schäfer R, and Cava RJ (2019) *Nature Communications* 10: 3425.

Borisenko S, Bezguba V, Fedorov A, Kushnirenko Y, Voroshnin V, Sturza M, Aswartham S, and Yaresko A (2020) *npj Quantum Materials* 5: 67.

Bradlyn B, Cano J, Wang Z, Vergniory MG, Felser C, Cava RJ, and Bernevig BA (2016) *Science* 353: aaf5037.

Bradlyn B, Elcoro L, Cano J, Vergniory MG, Wang Z, Felser C, Aroyo MI, and Bernevig BA (2017) *Nature* 547: 298–305.

Brahlek M, Bansal N, Koirala N, Xu S-Y, Neupane M, Liu C, Hasan MZ, and Oh S (2012) *Physical Review Letters* 109: 186403.

Bruno FY, et al. (2016) *Physical Review B* 94: 112112(R).

Burkov AA and Balents L (2011) *Physical Review Letters* 107: 127205.

Bzdušek T, Wu Q, Rüegg A, Sigrist M, and Soluyanov AA (2016) *Nature* 538: 75.

Cacho C, Crepaldi A, Battiato M, Braun J, Cilento F, Zacchigna M, Richter MC, Heckmann O, Springate E, Liu Y, Dhesi SS, Berger H, Bugnon P, Held K, Grioni M, Ebert H, Hricovini K, Minár J, and Parmigiani F (2015) *Physical Review Letters* 114: 097401.

Cao Y, Waugh JA, Zhang X-W, Luo J-W, Wang Q, Reber TJ, Mo SK, Xu Z, Yang A, Schneeloch J, Gu GD, Brahlek M, Bansal N, Oh S, Zunger A, and Dessau DS (2013) *Nature Physics* 9: 499–504.

Cao Y, et al. (2018) *Nature* 556: 43–50.

Chakraborty A, et al. (2023) *Physical Review B* 107: 085406.

Chang C-Z, Zhang J, Feng X, Shen J, Zhang Z, Guo M, et al. (2013) *Science* 340: 167.

Chang C-Z, Zhao W, Kim DY, Wei P, Jain JK, Liu C, Chan MHW, and Moodera JS (2015) *Physical Review Letters* 115: 057206.

Chang G, Xu S-Y, Wieder BJ, Sanchez DS, Huang S-M, Belopolski I, Chang T-R, Zhang S, Bansil A, Lin H, and Hasan MZ (2017a) *Physical Review Letters* 119: 206401.

Chang T-R, Xu S-Y, Sanchez DS, Tsai W-F, Huang S-M, Chang G, Hsu C-H, Bian G, Belopolski I, Yu Z-M, Yang SA, Neupert T, Jeng H-T, Lin H, and Hasan MZ (2017b) *Physical Review Letters* 119: 026404.

Chang G, Wieder BJ, Schindler F, Sanchez DS, Belopolski I, Huang S-M, Singh B, Wu D, Chang T-R, Neupert T, Xu S-Y, Lin H, and Hasan MZ (2018) *Nature Materials* 17: 978.

Chang T-R, et al. (2019) *Advanced Science* 6(4): 1800897.

Chen YL, Analytis JG, Chu J-H, Liu ZK, Mo S-K, Qi XL, Zhang HJ, Lu DH, Dai X, Fang Z, Zhang SC, Fisher IR, Hussain Z, and Shen Z-X (2009) *Science* 325: 178–181.

Chen C, Xu X, Jiang J, Wu S-C, Qi YP, Yang LX, Wang MX, Sun Y, Schröter NBM, Yang HF, Schoop LM, Lv YY, Zhou J, Chen YB, Yao SH, Lu MH, Chen YF, Felser C, Yan BH, Liu ZK, and Chen YL (2017) *Physical Review B* 95: 125126.

Chen YJ, Xu LX, Li JH, Li YW, Wang HY, Zhang CF, Li H, Wu Y, Liang AJ, Chen C, Jung SW, Cacho C, Mao YH, Liu S, Wang MX, Guo YF, Xu Y, Liu ZK, Yang LX, and Chen YL (2019) *Physical Review X* 9: 041040.

Chen K, Deng J, Yan Y, Shi Q, Chang T, Ding X, Sun J, Yang S, and Liu JZ (2021) *npj Computational Materials* 7: 79.

Chen P, Chan Y-H, Liu R-Y, Zhang HT, Gao Q, Fedorov A-V, Chou MY, and Chiang T-C (2022) *Physical Review B* 105: L161404.

Cheng Z, Zhang Z, Sun H, Li S, Yuan H, Wang Z, Cao Y, Shao Z, Bian Q, Zhang X, Li F, Feng J, Ding S, Mao Z, and Pan M (2019) *APL Materials* 7: 051105.

Cheng E, et al. (2021) *Nature Communications* 12: 6970.

Cheng L, Xiong Y, Kang L, Gao Y, Chang Q, Chen M, Qi J, Yang H, Liu Z, Song JCW, and Chia EEM (2023) *Science Advances* 9: eadd7856.

Chhowalla M, Shin HS, Eda G, Li L-J, Loh KP, and Zhang H (2013) *Nature Chemistry* 5: 263–275.

Cho S, Park J-H, Hong J, Jung J, Kim BS, Han G, Kyung W, Kim Y, Mo S-K, Denlinger J, Shim JH, Han JH, Kim C, and Park SR (2018) *Physical Review Letters* 121: 186401.

Clark OJ, Neat MJ, Okawa K, Bawden L, Markovi I, Mazzola F, Feng J, Sunko V, Riley JM, Meevasana W, Fujii J, Vobornik I, Kim TK, Hoesch M, Sasagawa T, Wahl P, Bahramy MS, and King PDC (2018) *Physical Review Letters* 120: 156401.

Clark OJ, Mazzola F, Markovic I, Riley JM, Feng J, Yang B-J, Sumida K, Okuda T, Fujii J, Vobornik I, Kim TK, Okawa K, Sasagawa T, Bahramy MS, and King PDC (2019) *Electronic Structure* 1: 014002.

Clark OJ, et al. (2021) Observation of a giant mass enhancement in the ultrafast electron dynamics of a topological semimetal. *Communications Physics* 4(165).

Clark OJ, Dowinton O, Bahramy MS, and Sánchez-Barriga J (2022) *Nature Communications* 13: 4147.

Coelho PM, et al. (2019) *Journal of Physical Chemistry C* 123(22): 14089–14096.

Comin R and Damascelli A (2015) In: Avella A and Mancini F (eds.) *Strongly Correlated Systems—Experimental Techniques. Springer Series in Solid-State Sciences*, vol. 180, pp. 31–72. Berlin, Heidelberg: Springer.

Crasto de Lima F, et al. (2023) *2D Materials* 10: 035001.

Crepaldi A, Cilento F, Zacchigna M, Zonno M, Johannsen JC, Tournier-Colletta C, Moreschini L, Vobornik I, Bondino F, Magnano E, Berger H, Magrez A, Bugnon P, Autès G, Yazyev OV, Grioni M, and Parmigiani F (2014) *Physical Review B* 89: 125408.

Curcio D, Jones AJH, Muzzio R, Volckaert K, Biswas D, Sanders CE, Dudin P, Cacho C, Singh S, Watanabe K, Taniguchi T, Miwa JA, Katoch J, Ulstrup S, and Hofmann P (2020) *Physical Review Letters* 125: 236403.

Das PK, et al. (2019) *Electronic Structure* 1: 014003.

Deng K, et al. (2019) *Science Bulletin* 654: 15.

Denlinger JD, Allen JW, Kang J-S, Sun K, Kim JW, Shim JH, Min B-I, Kim DJ, and Fisk Z (2013) *arXiv: 1312.6637v1*.

Dil JH (2019) *Electronic Structure* 1: 023001.

Dreher P, et al. (2021) *ACS Nano* 15(12): 19430–19438.

Dzero M and Galitski V (2013) *Journal of Experimental and Theoretical Physics* 117: 499.

Dzero M, Sun K, Galitski V, and Coleman P (2010) *Physical Review Letters* 104: 106408.

Dziawa P, Kowalski BJ, Dybko K, Buczko R, Szczerbakow A, Szot M, Łusakowska E, Balasubramanian T, Wojek BM, Berntsen MH, Tjernberg O, and Story T (2012) *Nature Materials* 11: 1023–1027.

Ekahana SA, et al. (2017) *New Journal of Physics* 19: 065007.

Elliot SR (2015) *Reviews of Modern Physics* 87: 137–163.

Eschbach M (2017) *Nature Communications* 8(14976). https://doi.org/10.1038/ncomms14976.

Faisal FM and Kaminski JZ (1997) *Physical Review A* 56: 748.

Fang C and Fu L (2015) *Physical Review B* 91: 161105(R).

Fang AF, Xu G, Dong T, Zheng P, and Wang NL (2013) *Scientific Reports* 3: 1153.

Fang C, Chen Y, Kee H-Y, and Fu L (2015) *Physical Review B* 92: 081201(R).

Fei Z, et al. (2017) *Nature Physics* 13: 677–682.

Fei FC, Bo XY, Wang PD, Ying JH, Li J, Chen K, Dai Q, Chen B, Sun Z, Zhang MH, Qu FM, Zhang Y, Wang QH, Wang XF, Cao L, Bu HJ, Song FQ, Wan XG, and Wang BG (2018) *Advanced Materials* 30: 1801556.

Feng J, et al. (2018) *Nano Letters* 18: 4493.

Frantzeskakis E, de Jong N, Zwartsenberg B, Huang YK, Pan Y, Zhang X, Zhang JX, Zhang FX, Bao LH, Tegus O, Varykhalov A, de Visser A, and Golden MS (2013) *Physical Review X* 3: 041024.

Freitas DC, Weht R, Sulpice A, Remenyi G, Strobel P, Gay F, Marcus J, and Núñez-Regueiro MN (2015) *Journal of Physics: Condensed Matter* 27: 176002.

Fu L (2009) *Physical Review Letters* 103: 266801.

Fu L (2011) *Physical Review Letters* 106: 106802.

Fu L and Kane CL (2007) *Physical Review B* 76: 045302.

Fu B-B, et al. (2019) *Science Advances* 5(5): aau6459.

Gan Z, et al. (2022) *Advanced Materials* 34(38): 2205226.

Gatti G, Gosálbez-Martínez D, Tsirkin SS, Fanciulli M, Puppin M, Polishchuk S, Moser S, Testa L, Martino E, Roth S, Bugnon P, Moreschini L, Bostwick A, Jozwiak C, Rotenberg E, Santo GD, Petaccia L, Vobornik I, Fujii J, Wong J, Jariwala D, Atwater HA, Rønnow HM, Chergui M, Yazyev OV, Grioni M, and Crepaldi A (2020) *Physical Review Letters* 125: 216402.

Ghosh B, et al. (2019) *Physical Review B* 100: 195134.

Gierz I, Lindroos M, Höchst H, Ast CR, and Kern K (2012) *Nano Letters* 12: 3900.

Gogotsi Y and Anasori B (2019) *ACS Nano* 13(8): 8491–8494.

Golias E, Weschke E, Flanagan T, Schierle E, Richardella A, Rienks EDL, Mandal PS, Varykhalov A, Sánchez-Barriga J, Radu F, Samarth N, and Rader O (2021) *Applied Physics Letters* 119: 132404.
Gong Y, Guo JW, Li JH, Zhu KJ, Liao MH, Liu XZ, Zhang QH, et al. (2019) *Chinese Physics Letters* 36: 076801.
Gordon KN, Hongyi S, Chaowei H, Linn AG, Haoxiang L, Yuntian L, Pengfei L, Mackey S, Qihang L, Ni N, and Dessau D (2019) *arXiv:1910.13943*.
Griffith MAR, et al. (2023) *Computational Materials Science* 218: 112004.
Grubisic-Cabo A, et al. (2023) *2D Materials*: 2301243.
Guo P-J, Yang H-C, Liu K, and Lu Z-Y (2017) *Physical Review B* 95: 155112.
Guo C, Hu Y, Chen G, Wei D, Zhang L, Chen Z, Guo W, Xu H, Kuo C-N, Lue CS, Bo X, Wan X, Wang L, Politano A, Chen X, and Lu W (2020) *Science Advances* 6: eabb6500.
Hagiwara K, Ohtsubo Y, Matsunami M, Ideta S-I, Tanaka K, Miyazaki H, Rault JE, Fèvre PL, Bertran F, Taleb-Ibrahimi A, Yukawa R, Kobayashi M, Horiba K, Kumigashira H, Sumida K, Okuda T, Iga F, and Kimura S-I (2016) *Nature Communications* 7: 12690.
Hagmann JA, Li X, Chowdhury S, Dong S-N, Rouvimov S, Pookpanratana SJ, Yu KM, Orlova TA, Bolin TB, Segre CU, Seiler DG, Richter CA, Liu X, Dobrowolska M, and Furdyna JK (2017) *New Journal of Physics* 19: 085002.
Hajlaoui M, Papalazarou E, Mauchain J, Perfetti L, Taleb-Ibrahimi A, Navarin F, Monteverde M, Auban-Senzier P, Pasquier CR, Moisan N, Boschetto D, Neupane M, Hasan MZ, Durakiewicz T, Jiang Z, Xu Y, Miotkowski I, Chen YP, Jia S, Ji HW, Cava RJ, and Marsi M (2014) *Nature Communications* 5: 3003.
Hasan MZ and Kane CL (2010) *Reviews of Modern Physics* 82: 3045.
Hasan MZ, Lin H, and Bansil A (2009) *Physics* 2: 108.
Hatch RC, Bianchi M, Guan D, Bao S, Mi J, Brummerstedt Iversen B, Nilsson L, Hornekaer L, and Hofmann P (2011) *Physical Review B* 83: 241303.
Haubold E, Koepernik K, Efremov D, Khim S, Fedorov A, Kushnirenko Y, van den Brink J, Wurmehl S, Büchner B, Kim TK, Hoesch M, Sumida K, Taguchi K, Yoshikawa T, Kimura A, Okuda T, and Borisenko SV (2017) *Physical Review B* 95: 241108(R).
He R, et al. (2018) *Physical Review B* 97: 041410.
Henk J, Flieger M, Maznichenko IV, Mertig I, Ernst A, Eremeev SV, and Chulkov EV (2012) *Physical Review Letters* 109: 076801.
Herrmann H, Hlawenka P, Siemensmeyer K, Weschke E, Sánchez-Barriga J, Varykhalov A, Shitsevalova NY, Dukhnenko AV, Filipov VB, Gabáni S, Flachbart K, Rader O, Sterrer M, and Rienks EDL (2020) *Advanced Materials* 29: 1906725.
Hirahara T, et al. (2017) *Nano Letters* 17: 3493–3500.
Hirayama M, Okugawa R, Ishibashi S, Murakami S, and Miyake T (2015) *Physical Review Letters* 114: 206401.
Hlawenka P, Siemensmeyer K, Weschke E, Varykhalov A, Sánchez-Barriga J, Shitsevalova NY, Dukhnenko AV, Filipov VB, Gabáni S, Flachbart K, Rader O, and Rienks EDL (2018) *Nature Communications* 9: 517.
Hlevyack J, et al. (2021) *npj 2D Materials and Applications* 5: 40.
Hofmann P (2021) *AVS Quantum Science* 3: 021101.
Hor YS, Roushan P, Beidenkopf H, Seo J, Qu D, Checkelsky JG, Wray LA, Hsieh D, Xia Y, Xu S-Y, Qian D, Hasan MZ, Ong NP, Yazdani A, and Cava RJ (2010) *Physical Review B* 81: 195203.
Hosen MM, et al. (2017) *Physical Review B* 95: 161101.
Hosur P and Qi X (2013) *Comptes Rendus Physique* 14: 857–870.
Hsieh D, Qian D, Wray L, Xia Y, Hor YS, Cava RJ, and Hasan MZ (2008) *Nature* 452: 970.
Hsieh D, Xia Y, Qian D, Wray L, Dil JH, Meier F, Osterwalder J, Patthey L, Checkelsky JG, Ong NP, Fedorov AV, Lin H, Bansil A, Grauer D, Hor YS, Cava RJ, and Hasan MZ (2009) *Nature* 460: 1101.
Hsieh TH, Lin H, Liu J, Duan W, Bansil A, and Fu L (2012) *Nature Communications* 3: 982.
Hu C, Ding L, Gordon KN, Ghosh B, Tien H-J, Li H, et al. (2020) *Science Advances* 6: eaba4275.
Huang S-M, Xu S-Y, Belopolski I, Lee C-C, Chang G, Wang B, Alidoust N, Bian G, Neupane M, Zhang C, Jia S, Bansil A, Lin H, and Hasan MZ (2015) *Nature Communications* 6: 7373.
Huang H, Zhou S, and Duan W (2016a) *Physical Review B* 94(12): 121117.
Huang L, et al. (2016b) *Nature Materials* 15: 1155.
Ji J and Choi JH (2022) *Nanoscale* 14: 10648–10689.
Jiang J, Li S, Zhang T, Sun Z, Chen F, Ye ZR, Xu M, Ge QQ, Tan SY, Niu XH, Xia M, Xie BP, Li YF, Chen XH, Wen HH, and Feng DL (2013) *Nature Communications* 4: 3010.
Jiang J, et al. (2017) *Nature Communications* 8: 13973.
Jiang J, et al. (2020) *APL Materials* 8: 061106.
Jones AJH, Muzzio R, Majchrzak P, Pakdel S, Curcio D, Volckaert K, Biswas D, Gobbo J, Singh S, Robinson JT, Watanabe K, Taniguchi T, Kim TK, Cacho C, Lanata N, Miwa JA, Hofmann P, Katoch J, and Ulstrup S (2020) *Advanced Materials* 32: 2001656.
Jones AJH, et al. (2022) *2D Materials* 9: 015032.
Joucken F, Avila J, Ge Z, Quezada-Lopez EA, Yi H, Le Goff R, Baudin E, Davenport JL, Watanabe K, Taniguchi T, Asensio MC, and Velasco J (2019) *Nano Letters* 19: 2682.
Jozwiak C, Chen YL, Fedorov AV, Analytis JG, Rotundu CR, Schmid AK, Denlinger JD, Chuang Y-D, Lee D-H, Fisher IR, Birgeneau RJ, Shen Z-X, Hussain Z, and Lanzara A (2011) *Physical Review B* 84: 165113.
Jozwiak C, Park C-H, Gotlieb K, Hwang C, Lee D-H, Louie SG, Denlinger JD, Rotundu CR, Birgeneau RJ, Hussain Z, and Lanzara A (2013) *Nature Physics* 9: 293.
Jozwiak C, Sobota JA, Gotlieb K, Kemper AF, Rotundu CR, Birgeneau RJ, Hussain Z, Lee D-H, Shen Z-X, and Lanzara A (2016) *Nature Communications* 7: 13143.
Jung W, Kim Y, Kim B, Koh Y, Kim C, Matsunami M, Kimura S-I, Arita M, Shimada K, Han JH, Kim J, Cho B, and Kim C (2011) *Physical Review B* 84: 245435.
Kang D, et al. (2015) *Nature Communications* 6: 7804.
Kang M, Fang S, Ye L, Po HC, Denlinger J, Jozwiak C, Bostwick A, Rotenberg E, Kaxiras E, Checkelsky JG, and Comin R (2020a) *Nature Communications* 11: 4004.
Kang M, Ye L, Fang S, You J-S, Levitan A, Han M, Facio JI, Jozwiak C, Bostwick A, Rotenberg E, Chan MK, McDonald RD, Graf D, Kaznatcheev K, Vescovo E, Bell DC, Kaxiras E, van den Brink J, Richter M, Ghimire MP, Checkelsky JG, and Comin R (2020b) *Nature Materials* 19: 163.
Ketterl AS, Otto S, Bastian M, Andres B, Gahl C, Minár J, Ebert H, Braun J, Tereshchenko OE, Kokh KA, Fauster T, and Weinelt M (2018) *Physical Review B* 98: 155406.
Khalil L, et al. (2023) *Nanotechnology* 34: 045702.
Kim D-J, Thomas S, Grant T, Botimer J, Fisk Z, and Xia J (2013) *Scientific Reports* 3: 3150.
Kim Y, Wieder BJ, Kane CL, and Rappe AM (2015) *Physical Review Letters* 115: 036806.
Kim CK, Denlinger JD, Kundu AK, Gu G, and Valla T (2021) *Journal of Applied Physics* 129: 083902.
King PDC, Hatch RC, Bianchi M, Ovsyannikov R, Lupulescu C, Landolt G, Slomski B, Dil JH, Guan D, Mi JL, Rienks EDL, Fink J, Lindblad A, Svensson S, Bao S, Balakrishnan G, Iversen BB, Osterwalder J, Eberhardt W, Baumberger F, and Hofmann P (2011) *Physical Review Letters* 107: 096802.
Klimovskikh II, Otrokov MM, Estyunin D, Eremeev SV, Filnov SO, Koroleva A, Shevchenko E, Voroshnin V, Rybkin AG, Rusinov IP, et al. (2020) *npj Quantum Materials* 5: 54.
Koepernik K, Kasinathan D, Efremov DV, Khim S, Borisenko S, Büchner B, and van den Brink J (2016) *Physical Review B* 93: 201101(R).
Koley S, Mohanta N, and Taraphder A (2020) *European Physical Journal B* 93: 77.
Kong D (2011) *Nature Nanotechnology* 6: 705–709. https://doi.org/10.1038/NNANO.2011.172.
Krieger JA, Stolz S, Robredo I, Manna K, McFarlane EC, Date M, Guedes EB, Dil JH, Shekhar C, Borrmann H, Yang Q, Lin M, Strocov VN, Caputo M, Pal B, Watson MD, Kim TK, Cacho C, Mazzola F, Fujii J, Vobornik I, Parkin SS, Bradlyn B, Felser C, Vergniory MG, and Schröter NBM (2022) *arXiv:2210.08221*.
Kruthoff J, de Boer J, van Wezel J, Kane CL, and Slager R-J (2017) *Physical Review X* 7: 041069.
Kuroda K, Reimann J, Güdde J, and Höfer U (2016) *Physical Review Letters* 116: 076801.

Landolt G, Schreyeck S, Eremeev SV, Slomski B, Muff S, Osterwalder J, Chulkov EV, Gould C, Karczewski G, Brunner K, Buhmann H, Molenkamp LW, and Dil JH (2014) *Physical Review Letters* 112: 057601.

Lee I, Kim CK, Lee J, Billinge SJL, Zhong R, Schneeloch JA, Liu T, Valla T, Tranquada JM, Gu G, and Davis JCS (2015) *Proceedings of the National Academy of Sciences of the United States of America* 112: 1316.

Lei Y, et al. (2022) *ACS Nanoscience Au* 2(6): 450–485.

Leng H, et al. (2019) *Physical Review B* 100: 224501.

Li G, Xiang Z, Yu F, Asaba T, Lawson B, Cai P, Tinsman C, Berkley A, Wolgast S, Eo YS, Kim D-J, Kurdak Ç, Allen JW, Sun K, Chen XH, Wang YY, Fisk Z, and Li L (2014) *Science* 346: 1208.

Li W, Claassen M, Chang C-Z, Moritz B, Jia T, Zhang C, Rebec S, Lee JJ, Hashimoto M, Lu D-H, Moore RG, Moodera JS, Devereaux TP, and Shen Z-X (2016) *Scientific Reports* 6: 32732.

Li P, Wen Y, He X, Zhang Q, Xia C, Yu Z-M, Yang SA, Zhu Z, Alshareef HN, and Zhang X-X (2017) *Nature Communications* 8: 2150.

Li R, et al. (2018a) *Small* 14: 45.

Li S, et al. (2018b) *Physical Review B* 97: 045131.

Li H, Gao S-Y, Duan S-F, Xu Y-F, Ke-Jia Z, et al. (2019a) *Physical Review X* 4: 041039.

Li J, Li Y, Du S, Wang Z, Gu B-L, Zhang S-C, He K, Duan W, and Xu Y (2019b) *Science Advances* 5: eaaw5685.

Li L, Sun K, Kurdak C, and Allen JW (2020) *Nature Reviews Physics* 2: 463.

Li E, et al. (2021a) *Nature Communications* 12: 5601.

Li M, Wang Q, Wang G, Yuan Z, Song W, Lou R, Liu Z, Huang Y, Liu Z, Lei H, Yin Z, and Wang S (2021b) *Nature Communications* 12: 3129.

Li S, et al. (2021c) *Physical Review B* 103: 045114.

Li Q, Xuan Trang C, Wu W, Hwang J, Cortie D, Medhekar N, Mo S-K, Yang SA, and Edmonds MT (2022) *Advanced Materials* 34: 2107520.

Lian B, Sun X-Q, Vaezi A, Qi X-L, and Zhang S-C (2018) *Proceedings of the National Academy of Sciences of the United States of America* 115: 10938.

Liang AJ, Jiang J, Wang MX, Sun Y, Kumar N, Shekhar C, Chen C, Peng H, Wang CW, Xu X, Yang HF, Cui ST, Hong GH, Xia Y-Y, Mo S-K, Gao Q, Zhou XJ, Yang LX, Felser C, Yan BH, Liu ZK, and Chen YL (2017) *Physical Review B* 96: 165143.

Lin M, Robredo I, Schröter NBM, Felser C, Vergniory MG, and Bradlyn B (2022) *Physical Review B* 106: 245101.

Liu C-C, et al. (2016) Weak topological insulators and composite Weyl semimetals: β-Bi4X4 (X = Br, I). *Physical Review Letters* 116: 014006.

Liu Y, Bian G, Miller T, and Chiang T-C (2011) *Physical Review Letters* 107: 166803.

Liu C-X, Zhang R-X, and VanLeeuwen BK (2014a) *Physical Review B* 90: 085304.

Liu ZK, Zhou B, Zhang Y, Wang ZJ, Weng HM, Prabhakaran D, Mo S-K, Shen ZX, Fang Z, Dai X, Hussain Z, and Chen YL (2014b) *Science* 343: 864.

Liu Y, Zhao J-Z, Yu L, Lin C-T, Liang A-J, Hu C, Ding Y, Xu Y, He S-L, and Zhao L (2015) *Chinese Physics Letters* 32: 067303.

Liu Y, Shao DF, Li LJ, Lu WJ, Zhu XD, Tong P, Xiao RC, Ling LS, Xi CY, Pi L, Tian HF, Yang HX, Li JQ, Song WH, Zhu XB, and Sun YP (2016a) *Physical Review B* 94: 045131.

Liu ZK, Yang LX, Sun Y, Zhang T, Peng H, Yang HF, Chen C, Zhang Y, Guo YF, Prabhakaran D, Schmidt M, Hussain Z, Mo S-K, Felser C, Yan B, and Chen YL (2016b) *Nature Materials* 15: 27.

Liu DF, Liang AJ, Liu EK, Xu QN, Li YW, Chen C, Pei D, Shi WJ, Mo SK, Dudin P, Kim T, Cacho C, Li G, Sun Y, Yang LX, Liu ZK, Parkin SSP, Felser C, and Chen YL (2019) *Science* 365: 1282.

Liu Z, Li M, Wang Q, Wang G, Wen C, Jiang K, Lu X, Yan S, Huang Y, Shen D, Yin J-X, Wang Z, Yin Z, Lei H, and Wang S (2020) *Nature Communications* 11: 4002.

Lou R, Ma J-Z, Xu Q-N, Fu B-B, Kong L-Y, Shi Y-G, Richard P, Weng H-M, Fang Z, Sun S-S, Wang Q, Lei H-C, Qian T, Ding H, and Wang S-C (2016) *Physical Review B* 93: 241104.

Lu F, Zhao J, Weng H, Fang Z, and Dai X (2013) *Physical Review Letters* 110: 096401.

Lu R, Sun H, Kumar S, Wang Y, Gu M, Zeng M, Hao Y-J, Li J, Shao J, and Ma X-M (2021) *Physical Review X* 11: 011039.

Lv BQ, Feng Z-L, Xu Q-N, Gao X, Ma J-Z, Kong L-Y, Richard P, Huang Y-B, Strocov VN, Fang C, Weng H-M, Shi Y-G, Qian T, and Ding H (2017) *Nature* 546: 627.

Lv B, Qian T, and Ding H (2019) *Nature Reviews Physics* 1: 609.

Ma J, et al. (2017) *Science Advances* 3: 16024.

Ma J-Z, He J-B, Xu Y-F, Lv BQ, Chen D, Zhu W-L, Zhang S, Kong L-Y, Gao X, Rong L-Y, Huang Y-B, Richard P, Xi C-Y, Choi ES, Shao Y, Wang Y-L, Gao H-J, Dai X, Fang C, Weng H-M, Chen G-F, Qian T, and Ding H (2018) *Nature Physics* 14: 349.

Mahmood F, Chan C-K, Alpichshev Z, Gardner D, Lee Y, Lee PA, and Gedik N (2016) *Nature Physics* 12: 306–310.

Mak KF, Lee C, Hone J, Shan J, and Heinz TF (2010) *Physical Review Letters* 105: 136805.

Mandal PS, Springholz G, Volobuev VV, Caha O, Varykhalov A, Golias E, Bauer G, Rader O, and Sánchez-Barriga J (2017) *Nature Communications* 8: 968.

Marković I, Hooley CA, Clark OJ, Mazzola F, Watson MD, Riley JM, Volckaert K, Underwood K, Dyer MS, Murgatroyd PAE, Murphy KJ, Fèvre PL, Bertran F, Fujii J, Vobornik I, Wu S, Okuda T, Alaria J, and King PDC (2019) *Nature Communications* 10: 5485.

Matt CE, Pirie H, Soumyanarayanan A, Yang H, Yee MM, Pengcheng C, Yu L, Larson DT, Paz WS, Palacios JJ, Hamidian MH, and Hoffman JE (2020) *Physical Review B* 101: 085142.

McIver JW, Hsieh D, Steinberg H, Jarillo-Herrero P, and Gedik N (2012) *Nature Nanotechnology* 7: 96.

Mellnik AR, Lee JS, Richardella A, Grab JL, Mintun PJ, Fischer MH, Vaezi A, Manchon A, Kim E-A, Samarthand N, and Ralph DC (2014) *Nature* 511: 449.

Meyerheim HL and Tusche C (2018) *Physica Status Solidi (RRL)* 12: 1800078.

Min C-H, Lutz P, Fiedler S, Kang BY, Cho BK, Kim HD, Bentmann H, and Reinert F (2014) *Physical Review Letters* 112: 226402.

Morali N, Batabyal R, Nag PK, Liu E, Xu Q, Sun Y, Yan B, Felser C, Avraham N, and Beidenkopf H (2019) *Science* 365: 1286.

Muechler L, Alexandradinata A, Neupert T, and Car R (2016) *Physical Review X* 6: 041069.

Mukherjee S, Jung SW, Weber SF, Xu C, Qian D, Xu X, Biswas PK, Kim TK, Chapon LC, Watson MD, Neaton JB, and Cacho C (2020) *Scientific Reports* 10: 12957.

Murakami T, Nambu Y, Koretsune T, Gu XY, Yamamoto T, Brown DM, and Kageyama H (2019) *Physical Review B* 100: 195103.

Nakata Y, Sugawara K, Chainani A, Oka H, Bao C, Zhou S, Chuang P-Y, Cheng C-M, Kawakami T, Saruta Y, Fukumura T, Zhou S, Takahashi T, and Sato T (2021) *Nature Communications* 12: 5873.

Nakayama K, Kuno M, Yamauchi K, Souma S, Sugawara K, Oguchi T, Sato T, and Takahashi T (2017) *Physical Review B* 95: 125204.

Narang P, Garcia CAC, and Felser C (2021) *Nature Materials* 20: 293.

Nayak C, Simon SH, Stern A, Freedman M, and Sarma SD (2008) *Reviews of Modern Physics* 80: 1083.

Nechaev IA, Hatch RC, Bianchi M, Guan D, Friedrich C, Aguilera I, Mi JL, Iversen BB, Blügel S, Hofmann P, and Chulkov EV (2013) *Physical Review B* 87: 121111(R).

Neupane M, Alidoust N, Xu S-Y, Kondo T, Ishida Y, Kim D-J, Liu C, Belopolski I, Jo YJ, Chang T-R, Jeng H-T, Durakiewicz T, Balicas L, Lin H, Bansil A, Shin S, Fisk Z, and Hasan MZ (2013) *Nature Communications* 4: 2991.

Neupane M, Xu S-Y, Sankar R, Alidoust N, Bian G, Liu C, Belopolski I, Chang T-R, Jeng H-T, Lin H, Bansil A, Chou F, and Hasan MZ (2014) *Nature Communications* 5: 3786.

Neupane M, Belopolski I, Hosen MM, Sanchez DS, Sankar R, Szlawska M, Xu S-Y, Dimitri K, Dhakal N, Maldonado P, Oppeneer PM, Kaczorowski D, Chou F, Hasan MZ, and Durakiewicz T (2016) *Physical Review B* 93: 201104.

Nguyen PV, Teutsch NC, Wilson NP, Kahn J, Xia X, Graham AJ, Kandyba V, Giampietri A, Barinov A, Constantinescu GC, Yeung N, Hine NDM, Xu X, Cobden DH, and Wilson NR (2019a) *Nature* 572: 220.

Nguyen PV, et al. (2019b) *Nature* 572: 220–223.

Nicholson CW, Rumo M, Pulkkinen A, Kremer G, Salzmann B, Mottas M-L, Hildebrand B, Jaouen T, Kim TK, Mukherjee S, Ma K, Muntwiler M, von Rohr FO, Cacho C, and Monney C (2021) *Communications Materials* 2: 25.

Nishide A, Taskin AA, Takeichi Y, Okuda T, Kakizaki A, Hirahara T, Nakatsuji K, Komori F, Ando Y, and Matsuda I (2010) *Physical Review B* 81: 041309(R).

Noguchi R, et al. (2019) *Nature* 566: 518–522.

Noh H-J, Jeong J, Cho E-J, Kim K, Min BI, and Park B-G (2017) *Physical Review Letters* 119: 016401.

Nurmamat M, et al. (2021) *Physical Review B* 104: 155133.

Ohtsubo Y, Yamashita Y, Hagiwara K, Ideta S-I, Tanaka K, Yukawa R, Horiba K, Kumigashira H, Miyamoto K, Okuda T, Hirano W, Iga F, and Kimura S-I (2019) *Nature Communications* 10: 2298.

Otrokov MM, Klimovskikh II, Bentmann H, Estyunin D, Zeugner A, Aliev ZS, Gass S, Wolter AUB, Koroleva AV, Shikin AM, Blanco-Rey M, Hoffmann M, Rusinov IP, Vyazovskaya AY, Eremeev SV, Koroteev YM, Kuznetsov VM, Freyse F, Sánchez-Barriga J, Amiraslanov IR, Babanly MB, Mamedov NT, Abdullayev NA, Zverev VN, Alfonsov A, Kataev V, Büchner B, Schwier EF, Kumar S, Kimura A, Petaccia L, Santo GD, Vidal RC, Schatz S, Kissner K, Ünzelmann M, Min CH, Moser S, Peixoto TRF, Reinert F, Ernst A, Echenique PM, Isaeva A, and Chulkov EV (2019) *Nature* 576: 416.

Ou Y, Yanez W, Xiao R, Stanley M, Ghosh S, Zheng B, Jiang W, Huang Y-S, Pillsbury T, Richardella A, Liu C, Low T, Crespi VH, Mkhoyan KA, and Samarth N (2022) *Nature Communications* 13: 2972.

Pan Z-H, Vescovo E, Fedorov AV, Gardner D, Lee YS, Chu S, Gu GD, and Valla T (2011) *Physical Review Letters* 106: 257004.

Park C-H and Louie SG (2012) *Physical Review Letters* 109: 097601.

Park SR, Han J, Kim C, Koh YY, Kim C, Lee H, Choi HJ, Han JH, Lee KD, Hur NJ, Arita M, Shimada K, Namatame H, and Taniguchi M (2012) *Physical Review Letters* 108: 046805.

Park S, Kim SY, Kim HK, Kim MJ, Kim T, Kim H, Choi GS, Won CJ, Kim S, Kim K, Talantsev EF, Watanabe K, Taniguchi T, Cheong S-W, Kim BJ, Yeom HW, Kim J, Kim T-H, and Kim JS (2021) *Nature Communications* 12: 3157.

Pauly C, Bihlmayer G, Liebmann M, Grob M, Georgi A, Subramaniam D, Scholz MR, Sánchez-Barriga J, Varykhalov A, Blügel S, Rader O, and Morgenstern M (2012) *Physical Review B* 86: 235106.

Pavlosiuk O and Kaczorowski D (2018) *Scientific Reports* 8: 11297.

Pei D, et al. (2022) *Physical Review X* 12: 021065.

Pesin DA and Balents L (2010) *Nature Physics* 6: 376.

Petrov EK, Ernst A, Menshchikova TV, and Chulkov EV (2021) *Journal of Physical Chemistry Letters* 12: 9076.

Pham PV, et al. (2022) *Chemical Reviews* 122(6): 6514–6613.

Plekhanov E, Barone P, Sante DD, and Picozzi S (2014) *Physical Review B* 90: 161108(R).

Pletikosić I, et al. (2014) *Physical Review Letters* 113: 216601.

Po HC, Vishwanath A, and Watanabe H (2017) *Nature Communications* 8: 50.

Pshenay-Severin DA, Ivanov YV, Burkov AA, and Burkov AT (2018) *Journal of Physics: Condensed Matter* 30: 135501.

Qi X-L and Zhang S-C (2011) *Reviews of Modern Physics* 83: 1057.

Raghu S, Qi X-L, Honerkamp C, and Zhang S-C (2008) *Physical Review Letters* 100: 156401.

Rao Z, Li H, Zhang T, Tian S, Li C, Fu B, Tang C, Wang L, Li Z, Fan W, Li J, Huang Y, Liu Z, Long Y, Fang C, Weng H, Shi Y, Lei H, Sun Y, Qian T, and Ding H (2019) *Nature* 567: 496.

Rechciński R, Galicka M, Simma M, Volobuev VV, Caha O, Sánchez-Barriga J, Mandal PS, Golias E, Varykhalov A, Rader O, Bauer G, Kacman P, Buczko R, and Springholz G (2021) *Advanced Functional Materials* 31: 2008885.

Reimann J, Schlauderer S, Schmid CP, Langer F, Baierl S, Kokh KA, Tereshchenko OE, Kimura A, Lange C, Güdde J, Höfer U, and Huber R (2018) *Nature* 562: 396.

Reuther J, Thomale R, and Rachel S (2012) *Physical Review B* 86: 155127.

Rhodes DA, et al. (2021) *Nano Letters* 21(6): 2505–2511.

Rienks EDL, Wimmer S, Sánchez-Barriga J, Caha O, Mandal PS, Růžička J, Ney A, Steiner H, Volobuev VV, Groiss H, Albu M, Kothleitner G, Michalicka J, Khan SA, Minár J, Ebert H, Bauer G, Freyse F, Varykhalov A, Rader O, and Springholz G (2019) *Nature* 576: 423.

Ritschel T, Trinckauf J, Koepernik K, Büchner B, v. Zimmermann M, Berger H, Joe YI, Abbamonte P, and Geck J (2015) *Nature Physics* 11: 328–331.

Rossnagel K, Rotenberg E, Koh H, Smith NV, and Kipp L (2005) *Physical Review B* 72: 121103.

Roy R (2008). ArXiv:0803.2868.

Ryu G (2015) *Journal of Superconductivity and Novel Magnetism* 28: 3275–3280.

Sahoo S, Dutta U, Harnagea L, Sood AK, and Karmakar S (2020) *Physical Review B* 101.

Sakano M, Hirayama M, Takahashi T, Akebi S, Nakayama M, Kuroda K, Taguchi K, Yoshikawa T, Miyamoto K, Okuda T, Ono K, Kumigashira H, Ideue T, Iwasa Y, Mitsuishi N, Ishizaka K, Shin S, Miyake T, Murakami S, Sasagawa T, and Kondo T (2020) *Physical Review Letters* 124: 136404.

Sánchez-Barriga J, Scholz MR, Golias E, Rienks E, Marchenko D, Varykhalov A, Yashina LV, and Rader O (2014a) *Physical Review B* 90: 195413.

Sánchez-Barriga J, et al. (2014b) *Physical Review X* 4: 011046.

Sánchez-Barriga J, Vergniory MG, Evtushinsky D, Aguilera I, Varykhalov A, Blügel S, and Rader O (2016) *Physical Review B* 94: 161401(R).

Sánchez-Barriga J, Battiato M, Golias E, Varykhalov A, Yashina LV, Kornilov O, and Rader O (2017a) *Applied Physics Letters* 110: 141605.

Sánchez-Barriga J, Battiato M, Krivenkov M, Golias E, Varykhalov A, Romualdi A, Yashina LV, Minár J, Kornilov O, Ebert H, Held K, and Braun J (2017b) *Physical Review B* 95: 125405.

Sanchez DS, Belopolski I, Cochran TA, Xu X, Yin J-X, Chang G, Xie W, Manna K, Süß V, Huang C-Y, Alidoust N, Multer D, Zhang SS, Shumiya N, Wang X, Wang G-Q, Chang T-R, Felser C, Xu S-Y, Jia S, Lin H, and Hasan MZ (2019) *Nature* 567: 500.

Sato M and Ando Y (2017) *Reports on Progress in Physics* 80: 076501.

Saxena A, Rani P, Nagpal V, Patnaik S, Felner I, and Awana VPS (2020) *Journal of Superconductivity and Novel Magnetism* 33: 2251.

Schnyder AP, Ryu S, Furusaki A, and Ludwig AWW (2008) *Physical Review B* 78: 195125.

Scholz MR, Sánchez-Barriga J, Braun J, Marchenko D, Varykhalov A, Lindroos M, Wang YJ, Lin H, Bansil A, Minrár J, Ebert H, Volykhov A, Yashina LV, and Rader O (2013) *Physical Review Letters* 110: 216801.

Schoop LM, Xie LS, Chen R, Gibson QD, Lapidus SH, Kimchi I, Hirschberger M, Haldolaarachchige N, Ali MN, Belvin CA, Liang T, Neaton JB, Ong NP, Vishwanath A, and Cava RJ (2015) *Physical Review B* 91: 214517.

Schoop LM, Ali MN, Straßer C, Topp A, Varykhalov A, Marchenko D, Duppel V, Parkin SSP, Lotsch BV, and Ast CR (2016) *Nature Communications* 7: 11696.

Schröter NBM, Pei D, Vergniory MG, Sun Y, Manna K, de Juan F, Krieger JA, Süss V, Schmidt M, Dudin P, Bradlyn B, Kim TK, Schmitt T, Cacho C, Felser C, Strocov VN, and Chen Y (2019) *Nature Physics* 15: 759.

Schröter NBM, Stolz S, Manna K, de Juan F, Vergniory MG, Krieger JA, Pei D, Schmitt T, Dudin P, Kim TK, Cacho C, Bradlyn B, Borrmann H, Schmidt M, Widmer R, Strocov VN, and Felser C (2020) *Science* 369: 179.

Schüler M, Giovannini UD, Hübener H, Rubio A, Sentef MA, and Werner P (2020) *Science Advances* 6: aay2730.

Seibel C, Bentmann H, Braun J, Minár J, Maass H, Sakamoto K, Arita M, Shimada K, Ebert H, and Reinert F (2015) *Physical Review Letters* 114: 066802.

Seibel C, Braun J, Maaß H, Bentmann H, Minár J, Kuznetsova TV, Kokh KA, Tereshchenko OE, Okuda T, Ebert H, and Reinert F (2016) *Physical Review B* 93: 245150.

Shekhar C, Nayak AK, Sun Y, Schmidt M, Nicklas M, Leermakers I, Zeitler U, Skourski Y, Wosnitza J, Liu Z, Chen Y, Schnelle W, Borrmann H, Grin Y, Felser C, and Yan B (2015) *Nature Physics* 11: 645.

Shi Y, et al. (2019) *Science Advances* 5(2): aat8799.

Shitade A, Katsura H, Kunes J, Qi XL, Zhang SC, and Nagaosa N (2009) *Physical Review Letters* 102: 256403.

Sie EJ, Nyby CM, Pemmaraju CD, Park SJ, Shen X, Yang J, Hoffmann MC, Ofori-Okai BK, Li R, Reid AH, Weathersby S, Mannebach E, Finney N, Rhodes D, Chenet D, Antony A, Balicas L, Hone J, Devereaux TP, Heinz TF, Wang X, and Lindenberg AM (2019) *Nature* 565: 61–66.

Sobota JA, Yang S, Analytis JG, Chen YL, Fisher IR, Kirchmann PS, and Shen Z-X (2012) *Physical Review Letters* 108: 117403.
Sobota JA, He Y, and Shen Z-X (2021) *Reviews of Modern Physics* 93: 025006.
Soifer H, Gauthier A, Kemper AF, Rotundu CR, Yang S-L, Xiong H, Lu D, Hashimoto M, Kirchmann PS, Sobota JA, and Shen Z-X (2019) *Physical Review Letters* 122: 167401.
Soluyanov AA, et al. (2015) *Nature* 527: 495–498.
Souma S, Kosaka K, Sato T, Komatsu M, Takayama A, Takahashi T, Kriener M, Segawa K, and Ando Y (2011) *Physical Review Letters* 106: 216803.
Stansbury CH, et al. (2021) *Science Advances* 7: eabf4387.
Sumida K, Ishida Y, Zhu S, Ye M, Pertsova A, Triola C, Kokh KA, Tereshchenko OE, Balatsky AV, Shin S, and Kimura A (2017) *Scientific Reports* 7: 14080.
Sumida K, Kakoki M, Reimann J, Nurmamat M, Goto S, Takeda Y, Saitoh Y, Kokh KA, Tereshchenko OE, and Güdde J (2019) *New Journal of Physics* 21: 093006.
Sumida K, Sakuraba Y, Masuda K, Kono T, Kakoki M, Goto K, Zhou W, Miyamoto K, Miura Y, Okuda T, and Kimura A (2020) *Communications Materials* 1: 89.
Sun Y, Zhang Y, Felser C, and Yan B (2016) *Physical Review Letters* 117: 146403.
Takane D, Wang Z, Souma S, Nakayama K, Nakamura T, Oinuma H, Nakata Y, Iwasawa H, Cacho C, Kim T, Horiba K, Kumigashira H, Takahashi T, Ando Y, and Sato T (2019) *Physical Review Letters* 122: 076402.
Takimoto T (2011) *Journal of the Physical Society of Japan* 80: 123710.
Tamai A, et al. (2016) *Physical Review X* 6: 031021.
Tanaka Y, Ren Z, Sato T, Nakayama K, Souma S, Takahashi T, Segawa K, and Ando Y (2012) *Nature Physics* 8: 800.
Tang E and Fu L (2014) *Nature Physics* 10: 964.
Tang X and Kuo L (2022) *Physica Status Solidi B* 259: 2100562.
Tang P, Zhou Q, and Zhang S-C (2017) *Physical Review Letters* 119: 206402.
Tang S, et al. (2017c) *Nature Physics* 13: 683–687.
Tang F, Po HC, Vishwanath A, and Wan X (2019) *Nature Physics* 15: 470–476.
Terashima K, Sato T, Komatsu H, Takahashi T, Maeda N, and Hayashi K (2003) *Physical Review B* 68: 155108.
Thunström P and Held K (2021) *Physical Review B* 104: 075131.
Tokura Y, Yasuda K, and Tsukazaki A (2019) *Nature Reviews Physics* 1: 126–143.
Tomczak JM (2018) *Journal of Physics: Condensed Matter* 30: 183001.
Topp A, et al. (2017) *Physical Review X* 7: 041073.
Trang CX, Li Q, Yin Y, Hwang J, Akhgar G, Di Bernardo I, Grubisić-Cabo A, Tadich A, Fuhrer MS, Mo S-K, Medhekar NV, and Edmonds MT (2021) *ACS Nano* 15: 13444.
Trivendi DB, et al. (2020) *Advanced Materials* 32: 50.
Tsirkin SS, Aguado Puente P, and Souza I (2018) *Physical Review B* 97: 035158.
Tusche C, Krasyuk A, and Kirschner J (2015) *Ultramicroscopy* 159: 520–529.
Udagawa M and Bergholtz EJ (2016) *Physical Review Letters* 117: 086401.
Ünzelmann M, Bentmann H, Figgemeier T, Eck P, Neu JN, Geldiyev B, Diekmann F, Rohlf S, Buck J, Hoesch M, Kalläne M, Rossnagel K, Thomale R, Siegrist T, Sangiovanni G, Sante DD, and Reinert F (2021) *Nature Communications* 12: 3650.
van der Laan G and Figueroa AI (2014) *Coordination Chemistry Reviews* 277-278: 95.
Vergniory MG, Elcoro L, Felser C, Regnault N, Bernevig BA, and Wang Z (2019) *Nature* 566: 7745.
Volobuev VV, Mandal PS, Galicka M, Caha O, Sánchez-Barriga J, Di Sante D, Varykhalov A, Khiar A, Picozzi S, Bauer G, Kacman P, Buczko R, Rader O, and Springholz G (2017) *Advanced Materials* 29: 1604185.
Wan X, Turner AM, Vishwanath A, and Savrasov SY (2011) *Physical Review B* 83: 205101.
Wan Y, et al. (2022) *Physical Review B* 105: 086421.
Wang G, et al. (2010) *Nano Research* 3: 874–880. https://doi.org/10.1007/s12274-010-0060-2.
Wang C (2016) *Physical Review B* 94: 24119(R).
Wang YH, Hsieh D, Pilon D, Fu L, Gardner DR, Lee YS, and Gedik N (2011) *Physical Review Letters* 107: 207602.
Wang YH, Hsieh D, Sie EJ, Steinberg H, Gardner DR, Lee YS, Jarillo-Herrero P, and Gedik N (2012a) *Physical Review Letters* 109: 127401.
Wang Z, Sun Y, Chen X-Q, Franchini C, Xu G, Weng H, Dai X, and Fang Z (2012b) *Physical Review B* 85: 195320.
Wang YH, Steinberg H, Jarillo-Herrero P, and Gedik N (2013a) *Science* 342: 453–457.
Wang Z, Weng H, Wu Q, Dai X, and Fang Z (2013b) *Physical Review B* 88: 125427.
Wang Z, Zhang P, Xu G, Zeng LK, Miao H, Xu X, Qian T, Weng H, Richard P, Fedorov AV, Ding H, Dai X, and Fang Z (2015) *Physical Review B* 92: 115119.
Wang X, et al. (2016a) *Advanced Electronic Materials* 2: 1600228.
Wang Z, Alexandradinata A, Cava RJ, and Bernevig BA (2016b) *Nature* 532: 189–194.
Wang Z, Wieder BJ, Li J, Yan B, and Bernevig BA (2019) *Physical Review Letters* 123: 186401.
Wang L, et al. (2020) *Nature Materials* 19: 861–866.
Wang Y, Qian Y, Yang M, Chen H, Li C, Tan Z, Cai Y, Zhao W, Gao S, Feng Y, Kumar S, Schwier EF, Zhao L, Weng H, Shi Y, Wang G, Song Y, Huang Y, Shimada K, Xu Z, Zhou XJ, and Liu G (2021a) *Physical Review B* 103: 125131.
Wang Z, Yin Q, Yan S, Wu L, Wu X, Li M, Song W, Liu Q, Ma H, Ji W, Lei H, and Wang S (2021b) *Physical Review B* 104: 155134.
Watson MD, et al. (2021) *2D Materials* 8: 015004.
Weng H, Fang C, Fang Z, Bernevig BA, and Dai X (2015) *Physical Review X* 5: 011029.
Wimmer S, Sánchez-Barriga J, Küppers P, Ney A, Schierle E, Freyse F, Caha O, Michalicka J, Liebmann M, Primetzhofer D, Hoffmann M, Ernst A, Otrokov MM, Bihlmayer G, Weschke E, Lake B, Chulkov EV, Morgenstern M, Bauer G, Springholz G, and Rader O (2021) *Advanced Materials* 42: 2102935.
Wojek BM, Buczko R, Safaei S, Dziawa P, Kowalski BJ, Berntsen MH, Balasubramanian T, Leandersson M, Szczerbakow A, Kacman P, Story T, and Tjernberg O (2013) *Physical Review B* 87: 115106.
Wolgast S, Kurdak C, Sun K, Allen JW, Kim D-J, and Fisk Z (2013) *Physical Review B* 88: 180405.
Wu L, Brahlek M, Valdés Aguilar R, Stier AV, Morris CM, Lubashevsky Y, Bilbro LS, Bansal N, Oh S, and Armitage NP (2013) *Nature Physics* 9: 410.
Wu Y, et al. (2015) *Physical Review Letters* 115: 166602.
Wu Y, Wang L-L, Mun E, Johnson DD, Mou D, Huang L, Lee Y, Bud'ko SL, Canfield PC, and Kaminski A (2016a) *Nature Physics* 12: 667.
Wu Y, et al. (2016b) *Physical Review B* 94: 12113 (R).
Wu H, et al. (2022) *npj Quantum Materials* 7: 31.
Xi X, Wang Z, Zhao W, Park J-H, Law KT, Berger H, Forró L, Shan J, and Mak KF (2016) *Nature Physics* 12: 139–143.
Xia Y, Qian D, Hsieh D, Wray L, Pal A, Lin H, Bansil A, Grauer D, Hor YS, Cava RJ, and Hasan MZ (2009) *Nature Physics* 5: 398.
Xiao D, Liu G-B, Feng W, Xu X, and Yao W (2012) *Physical Review Letters* 108: 196802.
Xiao RC, Gong PL, Wu QS, Lu WJ, Wei MJ, Li JY, Lv HY, Luo X, Tong P, Zhu XB, and Sun YP (2017) *Physical Review B* 96: 075101.
Xiao RC, Cheung CH, Gong PL, Lu WJ, Si JG, and Sun YP (2018) *Journal of Physics: Condensed Matter* 30: 245502.
Xie Z, He S, Chen C, Feng Y, Yi H, Liang A, Zhao L, Mou D, He J, Peng Y, Liu X, Liu Y, Liu G, Dong X, Yu L, Zhang J, Zhang S, Wang Z, Zhang F, Yang F, Peng Q, Wang X, Chen C, Xu Z, and Zhou XJ (2014) *Nature Communications* 5: 3382.
Xie LS, et al. (2015) *APL Materials* 3: 083602.

Xu S-Y, Xia Y, Wray LA, Jia S, Meier F, Dil JH, Osterwalder J, Slomski B, Bansil A, Lin H, Cava RJ, and Hasan MZ (2011) *Science* 332: 560–564.

Xu S-Y, Liu C, Alidoust N, Neupane M, Qian D, Belopolski I, Denlinger JD, Wang YJ, Lin H, Wray LA, Landolt G, Slomski B, Dil JH, Marcinkova A, Morosan E, Gibson Q, Sankar R, Chou FC, Cava RJ, Bansil A, and Hasan MZ (2012) *Nature Communications* 3: 1192.

Xu N, Shi X, Biswas PK, Matt CE, Dhaka RS, Huang YK, Plumb NC, Radovic M, Dil JH, Pomjakushina E, Conder K, Amato A, Salman Z, Paul DM, Mesot J, Ding H, and Shi M (2013a) *Physical Review B* 88: 121102.

Xu SY, Liu C, Kushwaha SK, Chang TR, Krizan JW, Sankar R, Polley CM, Adell J, Balasubramanian T, Miyamoto K, Alidoust N, Bian G, Neupane M, Belopolski I, Jeng HT, Huang CY, Tsai WF, Lin H, Chou FC, Okuda T, Bansil A, Cava RJ, and Hasan MZ (2013b) *arXiv:1312.7624*.

Xu N, Biswas PK, Dil JH, Dhaka RS, Landolt G, Muff S, Matt CE, Shi X, Plumb NC, Radović M, Pomjakushina E, Conder K, Amato A, Borisenko SV, Yu R, Weng H-M, Fang Z, Dai X, Mesot J, Ding H, and She M (2014) *Nature Communications* 5: 4566.

Xu G, Lian B, and Zhang S-C (2015a) *Physical Review Letters* 115: 186802.

Xu S-Y, Belopolski I, Alidoust N, Neupane M, Bian G, Zhang C, Sankar R, Chang G, Yuan Z, Lee C-C, Huang S-M, Zheng H, Ma J, Sanchez DS, Wang B, Bansil A, Chou F, Shibayev PP, Lin H, Jia S, and Hasan MZ (2015b) *Science* 349: 613–617.

Xu S-Y, Liu C, Kushwaha SK, Sankar R, Krizan JW, Belopolski I, Neupane M, Bian G, Alidoust N, Chang T-R, Jeng H-T, Huang C-Y, Tsai W-F, Lin H, Shibayev PP, Chou F, Cava RJ, and Hasan MZ (2015c) *Science* 375: 294.

Xu G, Lian B, Tang P, Qi X, and Zhang S (2016) *Physical Review Letters* 117: 47001.

Xu Q, et al. (2017a) *Physical Review B* 95: 045136.

Xu S-Y, Alidoust N, Chang G, Lu H, Singh B, Belopolski I, Sanchez DS, Zhang X, Bian G, Zheng H, Husanu M-A, Bian Y, Huang S-M, Hsu C-H, Chang T-R, Jeng H-T, Bansil A, Neupert T, Strocov VN, Lin H, Jia S, and Hasan MZ (2017b) *Science Advances* 3: 1603266.

Xu C, Li B, Jiao W, Zhou W, Qian B, Sankar R, Zhigadlo ND, Qi Y, Qian D, Chou F-C, and Xu X (2018a) *Chemistry of Materials* 30: 4823.

Xu N, et al. (2018b) *Physical Review Letters* 121: 136401.

Xu Q, Liu E, Shi W, Muechler L, Gayles J, Felser C, and Sun Y (2018c) *Physical Review B* 97: 235416.

Xu K-J, Chen S-D, He Y, and Shen Z-X (2020) *Proceedings of the National Academy of Sciences of the United States of America* 117: 15409.

Yan M, Huang H, Zhang K, Wang E, Yao W, Deng K, Wan G, Zhang H, Arita M, Yang H, Sun Z, Yao H, Wu Y, Fan S, Duan W, and Zhou S (2017) *Nature Communications* 8: 257.

Yang B-J and Nagaosa N (2014) *Nature Communications* 5: 4898.

Yang K-Y, Lu Y-M, and Ran Y (2011) *Physical Review B* 84: 075129.

Yang LX, Liu ZK, Sun Y, Peng H, Yang HF, Zhang T, Zhou B, Zhang Y, Guo YF, Rahn M, Prabhakaran D, Hussain Z, Mo S-K, Felser C, Yan B, and Chen YL (2015) *Nature Physics* 11: 728–732.

Yang G, et al. (2014) Weak topological insulators in PbTe/SnTe superlattices. *Physical Review B* 89: 085312.

Yang S-Y, Yang H, Derunova E, Parkin SSP, Yan B, and Ali MN (2018) *Advances in Physics: X* 3: 1414631.

Yang Y, et al. (2021) *Physical Review B* 103: 125160.

Yang XP, Zhong Y, Mardanya S, Cochran TA, Chapai R, Mine A, Zhang J, Sánchez-Barriga J, Cheng Z-J, Clark OJ, Yin J-X, Blawat J, Cheng G, Belopolski I, Nagashima T, Najafzadeh S, Gao S, Yao N, Bansil A, Jin R, Chang T-R, Shin S, Okazaki K, and Hasan MZ (2023) *Physical Review Letters* 130: 046402.

Yazyev OV, Moore JE, and Louie SG (2010) *Physical Review Letters* 105: 266806.

Ye L, Kang M, Liu J, von Cube F, Wicker CR, Suzuki T, Jozwiak C, Bostwick A, Rotenberg E, Bell DC, Fu L, Comin R, and Checkelsky JG (2018) *Nature* 555: 638.

Yen Y, Chiu C-L, Lin P-H, Sankar R, Chuang T-M, and Guo G-Y (2021) *New Journal of Physics* 23: 203019.

Yin W-J, Tan H-J, Ding P-J, Wen B, Li X-B, Teobaldi G, and Liu L-M (2021) *Advanced Materials* 2: 7543–7558.

Yu R, et al. (2015) *Physical Review Letters* 115: 036807.

Zeljkovic I, et al. (2015) *Nature Materials* 14: 318.

Zhang H, Liu C-X, Qi X-L, Dai X, Fang Z, and Zhang S-C (2009) *Nature Physics* 5: 438.

Zhang Y, He K, Chang C-Z, Song C-L, Wang L-L, Chen X, Jia J-F, Fang Z, Dai X, Shan W-Y, Shen S-Q, Niu Q, Qi X-L, Zhang S-C, Ma X-C, and Xue Q-K (2010) *Nature Physics* 6: 584–588.

Zhang H, Liu C-X, and Zhang S-C (2013) *Physical Review Letters* 111: 066801.

Zeugner A (2019) *Chemistry of Materials* 31: 2795–2806.

Zhang J, et al. (2017) *ACS Nano* 11(8): 8192–8198.

Zhang P, Yaji K, Hashimoto T, Ota Y, Kondo T, Okazaki K, Wang Z, Wen J, Gu GD, Ding H, and Shinxu S (2018) *Science* 360: 182.

Zhang P, Wang Z, Wu X, Yaji K, Ishida Y, Kohama Y, Dai G, Sun Y, Bareille C, Kuroda K, Kondo T, Okazaki K, Kindo K, Wang X, Jin C, Hu J, Thomale R, Sumida K, Wu S, Miyamoto K, Okuda T, Ding H, Gu GD, Tamegai T, Kawakami T, Sato M, and Shin S (2019a) *Nature Physics* 15: 41.

Zhang X, et al. (2019b) *Journal of Physics and Chemistry of Solids* 128: 245–250.

Zhang X, Lu Q, Liu W, Niu W, Sun J, Cook J, Vaninger M, Miceli PF, Singh DJ, Lian S-W, Chang T-R, He X, Du J, He L, Zhang R, Bian G, and Xu Y (2021) *Nature Communications* 12: 2492.

Zhang H, Pincelli T, Jozwiak C, Kondo T, Ernstorfer R, Sato T, and Zhou S (2022) *National Review* 2: 54.

Zhao W, et al. (2021) *Physical Review X* 11: 041034.

Zheng F, et al. (2020) *Physical Review B* 101: 100505.

Zheng T, et al. (2022) *ACS Nano* 16(3): 4197–4205.

Zhu Z-H, et al. (2013) *Physical Review Letters* 110: 216401.

Zhu Z-H, et al. (2014) *Physical Review Letters* 112: 076802.

Zhu S, Ishida Y, Kuroda K, Sumida K, Ye M, Wang J, Pan H, Taniguchi M, Qiao S, Shin S, and Kimura A (2015) *Scientific Reports* 5: 13213.

Metals and Metallic Alloys, Optical Properties of

F Forstmann, Freie Universität Berlin, Berlin, Germany

© 2005 Elsevier Ltd. All rights reserved.

This is an update of F. Forstmann, Metals and Metallic Alloys, Optical Properties of, Editor(s): Franco Bassani, Gerald L. Liedl, Peter Wyder, Encyclopedia of Condensed Matter Physics, Elsevier, 2005, Pages 392–403, ISBN 9780123694010, https://doi.org/10.1016/B0-12-369401-9/00595-7.

Reflection and Transmission 370
Surface Plasmon Polaritons 373
Plasma Waves in Metal Optics 375
Magnetooptics 379
Generalizations 380
"Left-Handed Materials," Optics for $\epsilon<0$ and $\mu<0$ 380
Further Reading 381

Reflection and Transmission

Metals are characterized by large electrical conductivity and shiny surfaces, that is, intense reflectivity. Because both properties are responses to electromagnetic fields, there is a close connection.

For a transparent discussion, Maxwell's equations which govern optics are presented, with polarization, magnetization, and current shown explicitly:

$$\nabla \times \boldsymbol{B} = \mu_0 \varepsilon_0 \frac{\partial \boldsymbol{E}}{\partial t} + \mu_0 \left(\boldsymbol{j} + \frac{\partial \boldsymbol{P}}{\partial t} + \nabla \times \boldsymbol{M}\right) \quad [1]$$

$$\nabla \cdot \boldsymbol{E} = \frac{1}{\varepsilon_0}(\rho - \nabla \cdot \boldsymbol{P}) \quad [2]$$

$$\nabla \times \boldsymbol{E} = -\frac{\partial B}{\partial t} \quad [3]$$

$$\nabla \cdot \boldsymbol{B} = 0 \quad [4]$$

Here, it is clearly seen that $-\nabla \cdot \boldsymbol{P}$ acts as a source of the electric field like any charge and $\partial \boldsymbol{P}/\partial t$ (and $\nabla \times \mathbf{M}$) creates $\boldsymbol{B}$ like any current. This is easily understood from the definition of the polarization $\boldsymbol{P}$ as the amount of charge penetrating a plane normal to $\boldsymbol{P}$ when the polarization is created. It is conventional to distinguish between true charges ρ and apparent charges $-\nabla \cdot \boldsymbol{P}$, true currents $\boldsymbol{j}$ and apparent currents $(\partial \boldsymbol{P}/\partial t + \nabla \times \boldsymbol{M})$. $\boldsymbol{P}$ is then considered due to the shift of bound charges (such as in an oscillator-model). But it is obvious that at very high frequencies with short shifts of all charges, the distinction between free and bound charges will not be possible any more. It is impracticable in metal optics. It is only a theoretical concept. One effectively deals with a total response to the electromagnetic fields and therefore with an effective response function: a complex dielectric function ε, a complex conductivity σ, or a complex polarizability $\chi = \varepsilon - 1$.

Next, linear isotropic responses are assumed:

$$\boldsymbol{j} = \sigma \boldsymbol{E}, \quad \boldsymbol{P} = \chi_p \varepsilon_0 \boldsymbol{E}, \quad \boldsymbol{M} = \chi_m \boldsymbol{H} \quad [5]$$

$$\boldsymbol{D} = \varepsilon_0 \boldsymbol{E} + \boldsymbol{P} = \varepsilon_0 \left(1 + \chi_p\right) \boldsymbol{E} = \varepsilon_0 \varepsilon_p \boldsymbol{E} \quad [6]$$

$$\begin{aligned} \boldsymbol{B} &= \mu_0 (\boldsymbol{H} + \boldsymbol{M}) = \mu_0 (1 + \chi_m) \boldsymbol{H} \\ &= \mu_0 \mu \boldsymbol{H}, \quad \varepsilon_0 \cdot \mu_0 = \frac{1}{c^2} \end{aligned} \quad [7]$$

The relation between polarizability and conductivity can be derived by reordering of eqns [1] and [2] to the more conventional form

$$\nabla \times \boldsymbol{H} = \frac{\partial \boldsymbol{D}}{\partial t} + \boldsymbol{j} = \frac{\partial}{\partial t} \boldsymbol{D}_{\text{eff}} \quad [8]$$

$$\nabla \cdot \boldsymbol{D} = \rho \quad [9]$$

$\boldsymbol{D}_{\text{eff}}$ is easily defined for each time Fourier component. A periodicity $e^{-i\omega t}$ for all optical fields is introduced (the minus sign is chosen arbitrarily, but it determines many signs from now on) and one gets from [8] and [3]

$$\nabla \frac{1}{\mu_0 \mu} \boldsymbol{B} = -i\omega \left(\varepsilon_0 \varepsilon_p - \frac{\sigma}{i\omega}\right) \boldsymbol{E} = -i\omega \boldsymbol{D}_{\text{eff}} \quad [10]$$

$$\nabla \times \boldsymbol{E} = +\mathrm{i}\omega \boldsymbol{B} \qquad [11]$$

$$\nabla \times (\nabla \times \boldsymbol{E}) = \nabla(\nabla\cdot\boldsymbol{E}) - \Delta\boldsymbol{E} = \frac{\omega^2}{c^2}\mu\left(\varepsilon_\mathrm{p} - \frac{\sigma}{\mathrm{i}\omega\varepsilon_0}\right)\boldsymbol{E} \qquad [12]$$

As explained at the beginning, the polarizability and the conductivity are found to be on the same footing in the wave equation [12] and therefore, the effective complex dielectric function is defined as

$$\varepsilon = 1 + \chi_\mathrm{p} - \frac{\sigma}{\mathrm{i}\omega\varepsilon_0}, \quad \boldsymbol{D}_\mathrm{eff} = \varepsilon_0\varepsilon\boldsymbol{E} \qquad [13]$$

In standard metal optics, it is argued that in conducting metals any charge ρ is quickly dissipated or screened and eqn [2] yields effectively $\nabla\cdot\mathrm{E}=0$. An estimate of the decay time of a charge can be got by putting eqn [9] into the continuity equation

$$\dot{\rho} = -\nabla\cdot\boldsymbol{j} = -\sigma\nabla\cdot\boldsymbol{E} = -\frac{\sigma}{\varepsilon_0\varepsilon_\mathrm{p}}\rho \qquad [14]$$

$$\rho = \rho_0\cdot\mathrm{e}^{-t/\tau}, \quad \text{with} \quad \tau = \frac{\varepsilon_\mathrm{p}\varepsilon_0}{\sigma} \qquad [15]$$

For silver with $\sigma = (0.016 \times 10^{-4}\Omega\mathrm{cm})^{-1}$ and, $\varepsilon_\mathrm{p} \approx 1$, the decay time $\tau \approx 10^{-19}\mathrm{s}$ and, therefore, charges decay faster than most optical fields vary. This estimate with the static conductivity is too optimistic. It is seen later that around $\omega \approx 10^{16}s^{-1}(\hbar\omega > 3.5\ \mathrm{eV})$ charge density waves, plasma waves with $\nabla\cdot\boldsymbol{E} \neq 0$, play a role in optics. But in the regime of visible optics with $\nabla\cdot\mathbf{E}=0$ and eqn [13], the level of standard optics was attained with transverse waves and the complex index of refraction

$$\tilde{n} = \sqrt{\varepsilon\mu} \qquad [16]$$

In most metals, $\mu\approx 1$ is a valid approximation. A treatment of the reflection from the surface of a metal with dielectric function ε_M facing a transparent medium (ε_1) yields the standard Fresnel formulas, which for later use are derived in a handy notation for wave vectors in the *xz*-plane, surface normal $||z$ into the metal:

$$\text{in medium1:} \quad \boldsymbol{E}(\boldsymbol{r},\omega) = \boldsymbol{E}_0\mathrm{e}^{\mathrm{i}(k_x x + qz)} + \boldsymbol{R}\mathrm{e}^{\mathrm{i}(k_x x - qz)} \qquad [17]$$

$$\text{in the metal:} \quad \boldsymbol{E}(\boldsymbol{r},\omega) = \boldsymbol{T}\mathrm{e}^{\mathrm{i}(k_x x + lz)} \qquad [18]$$

$$q = \sqrt{\frac{\omega^2}{c^2}\varepsilon_1\mu_1 - k_x^2}, \quad l = \sqrt{\frac{\omega^2}{c^2}\varepsilon_\mathrm{M}\mu_\mathrm{M} - k_x^2} \qquad [19]$$

p- and *s*-polarization are distinguished and so are ***E*** parallel or normal to the plane of incidence, here the *xz*-plane. Because ***R*** and ***T*** are orthogonal to their respective wave vectors, only the two *z*-components have to be determined for *p*-polarization (the two amplitudes for *s*-polarization). Therefore, the two standard boundary conditions are used:

$$\text{continuity of } E_\text{tangential} \text{ or } B_\text{normal} \qquad [20]$$

$$\text{continuity of } D_\text{eff,normal} \text{ or } H_\text{tangential} \qquad [21]$$

Here, an obvious problem is usually brushed under the carpet – what the continuity of the normal component of ***D*** from $\nabla\cdot\mathrm{D}=0$ (eqn [19] with $\rho=0$) or of $\boldsymbol{D}_\mathrm{eff}$ from $\nabla\cdot\mathrm{D}_\mathrm{eff}=0$ as eqn [8] or [10] tells us. Because this problem is difficult, one takes refuge in the continuity of H_tg which actually makes D_eff,normal continuous as a consequence of [8] or [10]. Continuity of H_tg requires (from [8]) all fields to be finite, here ***D***, and no singular surface currents. But the discontinuity of E_normal, which goes with the continuity of $D_\mathrm{eff,normal} = \varepsilon_0\varepsilon E_\mathrm{normal}$ and a discontinuous ε, requires singular surface charges, from eqn [2]. Arguing with bound charges $-\nabla\cdot\mathrm{P}$ does not help because $\chi_\mathrm{p}=0,\mathrm{P}=0$ is often a good description of the metal. Also the normal component of $\mathrm{j}=\sigma\mathrm{E}$ is discontinuous.

For frequencies in the visible approximation, [21] works. Around the eigenfrequency of the electrons, the plasma frequency ω_p, the charges, and the currents get so large that the problem behind boundary condition [21] must be solved. This is done in the section "Plasma waves in metal optics."

Boundary conditions [20] and [21] yield two linear equations for the reflection and transmission amplitudes. They are related to the reflection and transmission coefficients *r* and *t*:

$$p\text{–polarization}: \frac{R_z}{E_{0z}} = \frac{\varepsilon_\mathrm{M}q - \varepsilon_1 l}{\varepsilon_\mathrm{M}q + \varepsilon_1 l}, \quad \frac{T_z}{E_{0z}} = \frac{2q\varepsilon_1}{\varepsilon_\mathrm{M}q + \varepsilon_1 l} \qquad [22]$$

$$r=\left|\frac{R_z}{E_{0z}}\right|^2,\quad t=\frac{l\varepsilon_M}{q\varepsilon_1}\left|\frac{T_z}{E_{0z}}\right|^2 \qquad [23]$$

$$s\text{-polarization}:\ \frac{R}{E_0}=\frac{q\mu_M-l\mu_1}{q\mu_M+l\mu_1},\quad \frac{T}{E_0}=\frac{2q\mu_M}{q\mu_M+l\mu_1} \qquad [24]$$

$$r=\left|\frac{R}{E_0}\right|^2,\quad t=\frac{l\mu_1}{q\mu_M}\left|\frac{T}{E_0}\right|^2 \qquad [25]$$

In the infrared, the term $\sigma/(\omega\varepsilon_0$ in eqn [13] is much larger than 1. If $\mu_M\approx\mu_1$ and $\varepsilon_1=1$, the reflection coefficient for normal incidence ($k_x\rightarrow0$) can be expanded:

$$r=\left|\frac{\tilde{n}_M-1}{\tilde{n}_M+1}\right|^2\approx1-2\sqrt{2\frac{\omega\varepsilon_0}{\sigma}} \qquad [26]$$

This is called the Hagen–Rubens relation for the decrease of the metallic reflectivity due to the finite conductivity. It is a good approximation (with the static conductivity) for most metals in the infrared for $\lambda>10\mu m$.

For further discussion of the consequences of eqns [22]–[25], a model for the metallic response is considered, the Drude model, which approximates well the typical properties of metals. It considers only the conducting electrons. It could easily be supplemented by a Debye oscillator model for underlying bound electrons, the polarizability χ_p which could then simply be added as in eqn [13]. The Drude model is the equation of motion of the collection of electrons driven by the electric field and suffering a friction:

$$m\ddot{\boldsymbol{r}}=-e_0\boldsymbol{E}-m\gamma\dot{\boldsymbol{r}},\quad \boldsymbol{j}=-e_0n_0\dot{\boldsymbol{r}} \qquad [27]$$

$$\frac{\partial}{\partial t}\boldsymbol{j}=\frac{n_0e_0^2}{m}\boldsymbol{E}-\gamma\boldsymbol{j}=\omega_p^2\varepsilon_0\boldsymbol{E}-\gamma\boldsymbol{j} \qquad [28]$$

The plasma frequency is introduced here via the mean conduction electron density n_0:

$$\omega_p=\left(\frac{n_0e_0^2}{m\varepsilon_0}\right)^{1/2} \qquad [29]$$

and the friction constant $\gamma=1/\tau$ related to the collision time τ. The Drude model (eqn [28]) leads to the static conductivity

$$\sigma_{stat}=\frac{n_0e^2}{m\gamma}=\frac{n_0e^2}{m}\tau$$

but more relevantly here to the optical conductivity:

$$\sigma(\omega)=\frac{i\omega_p^2\varepsilon_0}{\omega+i\gamma} \qquad [30]$$

and from eqn [13] ($\chi_p=0$) to the typical metal dielectric function:

$$\varepsilon=1-\frac{\omega_p^2}{\omega^2+i\omega\gamma} \qquad [31]$$

From the static conductivity, one can derive an estimate for τ or $\gamma\approx10^{10}s^{-1}$, and find that at least for the visible frequencies, a good approximation is

$$\varepsilon(\omega)\approx1-\frac{\omega_p^2}{\omega^2} \qquad [32]$$

ε is negative for small frequencies ω, $\varepsilon=0$ at $\omega=\omega_p$, and approaches 1 for values smaller than 1 for large ω.

The negative values of ε are responsible for the high reflectivity. In eqn [19] l is purely imaginary and r=1 in [23] and [25] because the numerator and denominator are a conjugate complex. The imaginary l says that the electromagnetic waves do not travel inside the metal, but the fields decay exponentially with the penetration depth

$$d=\frac{1}{[l]}=\left|\left(\frac{\omega^2}{c^2}\mu\varepsilon\right)^{1/2}\right|^{-1}=\frac{\lambda_0}{2\pi|\varepsilon^{1/2}|} \qquad [33]$$

much smaller than the vacuum wavelength λ_0. At very low frequencies, ε is determined by γ (eqn [31]), varies little, and d decreases with growing frequency ("skin effect"). There is a turnover ("anomalous skin effect") when $|\varepsilon|$ decreases and approaches zero at ω_p (eqn [32]). At ω_p, l becomes real, the waves are transmitted inside the metal, and the metal becomes transparent.

This threshold of transparency, ω_p, is characterized by the density of conduction electrons in simple metals (eqn [29]). This transparency is not seen because the plasma frequencies lie in the near to far ultraviolet (for tables of plasma frequencies, see "Further reading" section).

Formally, metal optics is normally developed completely parallel to the optics of transparent media. Only the dielectric function is different. It is purely imaginary, $\sim\sigma$, in the infrared (eqn [13]), mainly real and negative in the visible (eqns [31] and [32]), has a zero at ω_p in the near ultraviolet beyond which the metal is transparent with an index of refraction smaller than 1 (eqn [32]). At frequencies below ω_p, electromagnetic fields decay exponentially inside the metal and the optical energy is reflected.

Due to the fact that ε always has some real and some imaginary part, the statements just made are approximate. Around ω_p, for instance, ε (eqn [31]) does not go exactly through zero, and there is a smooth transition from the wave vector $k = (\omega/c)\sqrt{\mu\varepsilon}$ being dominated by the imaginary part to the propagating frequencies with mainly real k, from the anomalous skin effect to transparency.

The approximation [27]–[32], essentially for nearly free electrons, does not work well for d-band transition metals or for the lanthanides. For these metals, a model must at least include a polarizable background leading to an additional χ_p as in eqn [13]. The screening by this background can shift the frequency for $\varepsilon(\omega)\approx 0$ drastically, for example, for silver, from $\hbar\omega_p = 9$ eV according to eqn [29] to the measured $\hbar\omega_p = 3.8$ eV.

In most frequency regions of interest in optics, one cannot determine the index of refraction $\tilde{n} = n(1+i\kappa) = \sqrt{\mu\varepsilon}$ from the angle of refraction and from light attenuation (absorption). One has to use the information in reflection. The difference in reflectivity of s- and p-polarized light is exploited in ellipsometry. When linearly polarized light with an (equal) s- and p-component is reflected from a metal surface, there generally appears a difference in phase and amplitude of the reflected components leading to elliptical polarization in the reflected beam. Measurements of the ellipse, the rotation angle of the main axis, and the difference of the two main axes, allow the determination of the real and imaginary part of $\tilde{n}$ or ε, because the reflection amplitudes eqns [22] and [24] contain the relations. The realm of variation of the phase on reflection can be easily estimated from the reflection amplitudes [22] and [24]. The transversality means $R_x = (q/k_x)R_z$ and $E_{0x} = -(q/k_x)E_{0z}$, $R_x/E_{0x} = -R_z/E_{0z}$. Then for normal incidence ($k_x \to 0$), s- and p-reflection amplitudes are the same:

$$\frac{R_x}{E_{0x}} = \frac{\sqrt{\varepsilon_1\mu_M} - \sqrt{\varepsilon_M\mu_1}}{\sqrt{\varepsilon_1\mu_M} + \sqrt{\varepsilon_M\mu_1}} \approx \frac{\tilde{n}_1 - \tilde{n}_M}{\tilde{n}_1 + \tilde{n}_M}$$
$$(\text{for } \mu_1 \approx \mu_M \approx 1 \text{ and} \tilde{n} = \sqrt{\varepsilon}) \qquad [34]$$

If the angle of incidence grows up to glancing incidence ($q \to 0$), the limits are: for p-polarization $R_x/E_{0x} \to 1$, for s-polarization $R/E_0 \to -1$, that is, a phase difference of π. Therefore, one can expect an angle θ, called "the principle angle of incidence," at which the phase difference is $\delta = \pi/2$, that is, circularly polarized light is reflected as linearly polarized. This angle for metals is reminiscent of the Brewster angle for nonmetallic reflectors, which is seen when the numerator in the p-reflection amplitude eqn [22] is zero. Strongly negative ε_M prohibits such a zero. A Brewster angle is also found for metals in the transparent region beyond ω_p, when the imaginary part of ε is small.

The measured effective dielectric functions ε or indices of refraction $\tilde{n}$ of many metals for different frequency regions can be found in several tables (see the "Further reading" section).

Because metal optics is often studied with very thin metal layers, it may be mentioned again that the distinction between nonpropagating and propagating waves is not sharp because l in eqn [19] always has a real and an imaginary part due to the complex ε. Formally, the fields inside the metal and the transmitted field are calculated as in standard optics : general solution on top, general solution inside, general solution below, and the four amplitudes (reflected, down and up inside, transmitted) determined from the four boundary conditions, [20] and [21] at each surface. This yields the exact fields everywhere. There is no use in summing an infinite series of scatterings from the top and bottom of the layer (and approximating this summation by one or two reflections).

The metal optics described so far is essentially a summary of the relevant chapters in the famous book of Born and Wolf, where extensions and details can be found (see the "Further reading" section).

Surface Plasmon Polaritons

In the region where $\varepsilon < 0$, the reflection amplitude eqn [22] has no zero in the numerator, therefore there is no Brewster angle; but the denominator can be zero (eqn [35]). For those values of ω and k_x, there can be reflected and transmitted amplitudes when the incident field vanishes: one finds eigensolutions of the system, which are called surface polaritons or surface plasmon polaritons (SPP) or surface plasmons. Their dispersion relation ω_s ($k_{\text{tangential}}$) or $k_{tg}(\omega_s)$ is found from eqns [22] and [19]:

$$\varepsilon_M(\omega_s)\sqrt{\frac{\omega_s^2}{c^2}\varepsilon_1\mu_1 - k_{tg}^2} + \varepsilon_1\sqrt{\frac{\omega_s^2}{c^2}\varepsilon_M(\omega_s)\mu_M - k_{tg}^2} = 0 \qquad [35]$$

$$k_{tg} = \frac{\omega_s}{c}\sqrt{\frac{\varepsilon_M(\omega_s)\varepsilon_1}{\varepsilon_M(\omega_s) + \varepsilon_1}}(\mu_M = \mu_1 = 1) \qquad [36]$$

The SPP dispersion relations [35] and [36] are best discussed with ε approximated by eqn [32]. For small frequencies ω_s, an expansion with respect to ω_s/ω_p yields

$$k_{\mathrm{tg}} = \frac{\omega_s}{c}\sqrt{\varepsilon_1}\left(1+\frac{1}{2}\varepsilon_1\frac{\omega_s^2}{\omega_{\mathrm{p}}^2}\right) \qquad [37]$$

while $k_{\mathrm{tg}} \to \infty$ when the denominator in [36] goes to zero at

$$\omega_{\mathrm{s}} \to \frac{\omega_{\mathrm{p}}}{\sqrt{1+\varepsilon_1}} \text{ or } \omega_{\mathrm{s}} \to \frac{\omega_{\mathrm{p}}}{\sqrt{2}} \text{ (for } \varepsilon_1 = 1) \qquad [38]$$

Solutions of eqn [36] for small k_{tg} and $\omega > \omega_{\mathrm{p}}$ are not eigenmodes but indicate the Brewster angle. The dispersion relation for the SPP is shown schematically in Figure 1.

One essential point is that $k_{\mathrm{tg}} > (\omega_{\mathrm{s}}/c)\sqrt{\varepsilon_1}$ (see eqn [37]), that is, the wavelength of the SPP is shorter than the wavelength of light at the same frequency in the medium 1 above the metal surface, the eigenmode lies "to the right of the light line $k = (\omega/c)\sqrt{\varepsilon_1}$." Therefore, according to eqn [19], the z-components q and l of the wave vector of the surface wave are imaginary; the electromagnetic fields decay exponentially toward both sides of the surface. The excitation energy in the eigenmode is bound to the surface and does not radiate away. On the other hand, this eigenmode cannot directly couple to, or be excited by the light incident on the surface, because even for grazing incidence, k_{tg} of the light is too small; the periodicity parallel to the surface does not match the one of the SPP. At very large k_{tg}, the eigenfrequency rises above the limit of eqn [38] in Figure 1. This is a real plasma effect and is treated in the following section.

These eigenmodes were first derived by Zenneck and Sommerfeld, who explained the transmission of radio waves along the ocean surface. At metal surfaces, they were first seen as energy losses of electrons scattered from metal layers. In optics, it is possible to couple to the SPP if the incident light comes through a prism which shortens λ or increases k. In Figure 1, the SPP dispersion is shown for a metal surface towards vacuum or air ($\varepsilon_1=1$). Also indicated is the "light line" $(\omega/c)\sqrt{\varepsilon_{\mathrm{prism}}} = k$. For angles of incidence φ with

$$k_x = \sin\varphi\frac{\omega}{c}\sqrt{\varepsilon_{\mathrm{prism}}} > \frac{\omega}{c} \qquad [39]$$

the light is totally reflected from the prism–air interface because l (eqn [19]) in air becomes imaginary. But when this prism surface is brought in close proximity to the metal surface, at the angle where k_x from [39] fulfills the dispersion relation of the SPP [36], the eigenmode is excited, it develops large fields, soaks up energy, and attenuates the total reflection of the prism. This attenuated total reflection (ATR) method has been widely used to study the SPPs as well as the properties of layers adsorbed on metal surfaces, because adsorbed layers shift the dispersion according to $\varepsilon_1 \neq 1$ in eqn [36]. The large fields near the metal surface, when the SPP is excited, have been used to excite molecules especially brought near the surface. On the other hand, a microscope has been built on the ATR principle in order to see structures in adsorbed layers, which appear in self-organized surface reactions. The SPP can be excited by one prism, then travel along the metal surface and be coupled out by a second prism, and the metal surface between the prisms can be manipulated.

The narrow coupling condition that k_x of the exciting light must fulfill the SPP dispersion eqn [36] is true when the metal surface is translationally invariant. Surfaces with some roughness or any local obstacles can scatter light especially strong near $\omega = \omega_{\mathrm{p}}/\sqrt{1+\varepsilon_1}$, where the density of eigenmodes is very high. If a periodic structure is established on the metal surface, for example, a grid of grooves, the related reciprocal lattice vectors can be added or subtracted to k_{tg} in order to overcome the restrictions for SPP excitation. Then refolding of $\omega_{\mathrm{s}}(k_{\mathrm{tg}})$ and gaps due to Bragg diffraction apply as in electron band structures, and there appear possibilities for coupling the SPPs to incident light. Also any irregularities, roughness, adsorbed molecules or metal clusters, which break the translational invariance of the surface, make excitation of surface modes possible. These often lead to extremely large fields around the imperfections. An example is surface-enhanced Raman scattering (SERS) from adsorbed molecules on silver.

Surface waves also play a role when light is transmitted through apertures smaller than the wavelength as in near-field microscopy. Recently, it was shown that light is transmitted through an array of narrow holes in a thick metal layer at a surprisingly

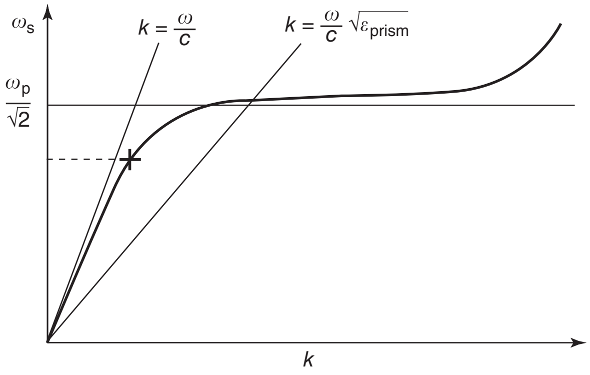
ω_{s}
$k = \frac{\omega}{c}$
$k = \frac{\omega}{c}\sqrt{\varepsilon_{\mathrm{prism}}}$
$\frac{\omega_{\mathrm{p}}}{\sqrt{2}}$
k

Figure 1 The surface plasmon dispersion. At "+" the wave in a prism can couple to the SPP in an ATR configuration.

large rate. Also, this phenomenon is explained via excitation of SPPs. The same mechanism leads to strong absorption at special frequencies in a system of grooves on a metal surface.

Generally, the excitation of SPPs leads to strong absorption of energy in the metal, to an attenuation of reflection, because the large fields of the eigenmode cause large currents and large losses in the metal. Occasionally, one finds high-energy transport at the excitation condition leading to strong scattering or even high transmission through narrow holes.

When the metal layer is thin enough, the two surfaces excite each other. Then the surface modes on both sides couple symmetrically or antisymmetrically, and the dispersion relations are changed.

Plasma Waves in Metal Optics

In 1953, Bohm and Pines discovered that the electrons in metals can sustain charge density waves with longitudinal electric fields. In an electron gas model of a metal, they found the dispersion relation for plasma waves:

$$\omega^2 = \omega_{\mathrm{p}}^2 + \beta k^2 \qquad [40]$$

The Drude model (eqn [28]) leads to plasma oscillations. Taking the divergence of eqn [28] and using the continuity equation and eqn [9] yields

$$\rho = -\omega_{\mathrm{p}}^2 \rho - \gamma \dot{\rho} \qquad [41]$$

that is, damped oscillations with the plasma frequency ω_{p}.

In addition to the electric field, the electrons are driven by a gradient in electron pressure, in density, in the local Fermi energy proportional to $(n_0)^{2/3}$. This pressure spreads out the electrons at metal surfaces and metal–metal interfaces leading to surface dipoles and contact potentials. In the Drude model, this additional force can be introduced by a term $-\beta\nabla\rho$:

$$\frac{\partial \boldsymbol{j}}{\partial t} = \omega_{\mathrm{p}}^2 \varepsilon_0 \boldsymbol{E} - \gamma \boldsymbol{j} - \beta \nabla \rho \qquad [42]$$

The coefficient $\beta = (3/5) v_{\mathrm{F}}^2$ in a free electron gas with Fermi velocity v_{F}. The expression for the high-frequency electron gas pressure was derived by Bloch. Equation [42] can be derived from a Boltzmann equation for the electron gas, and it is called the "hydrodynamic approximation" to a quantum mechanical treatment of the free electron gas. This extended Drude model describes plasma waves and makes it easy to include them in metal optics in the correct way.

First, the plasma waves are seen as eigensolutions of the system. Equation [41] is now supplemented to yield

$$\rho = -\omega_{\mathrm{p}}^2 \rho - \gamma \dot{\rho} + \beta \nabla \cdot (\nabla \rho) \qquad [43]$$

which is solved by a wave with the plasmon dispersion [40] when the damping γ is neglected. The mode is a charge density wave (analog to a longitudinal acoustic density wave) with longitudinal electric fields $\boldsymbol{E} || \boldsymbol{k}$. Transverse waves have necessarily $\rho = 0$ from eqn [9]. Therefore, the response, conductivity $\sigma_\perp$ and $\varepsilon_\perp$, is not affected by the new term in [42], and remains as in eqns [30] and [31]. But the longitudinal response is changed. For a plane wave pertubation $\sim \mathrm{e}^{\mathrm{i}(\boldsymbol{kr} - \omega t)}$, the continuity equation $(1/\mathrm{i}\omega)\nabla \cdot \boldsymbol{j} = \rho$ replaces ρ in eqn [42], and for longitudinal fields and currents,

$$\sigma_{\|}(k, \omega) = \frac{\mathrm{i}\omega \omega_{\mathrm{p}}^2 \varepsilon_0}{\omega^2 - \beta k^2 + \mathrm{i}\omega\gamma} \qquad [44]$$

and with the general relation [13]:

$$\varepsilon_{\|}(k, \omega) = 1 - \frac{\omega_{\mathrm{p}}^2}{\omega^2 - \beta k^2 + \mathrm{i}\omega\gamma} \qquad [45]$$

The response functions are now dependent on frequency ω and wave vector $\boldsymbol{k}$. This is the so-called nonlocal response (in time and now also in space), which is familiar in nonlocal metal optics.

What do Maxwell's equations tell one about longitudinal waves? Equation [3] shows that longitudinal plasma waves have no magnetic induction field, $\mathbf{B} = 0$. On the other hand, the longitudinal wave is a homogeneous solution of the wave equation [12]:

$$\nabla(\nabla \cdot \boldsymbol{E}) - \Delta \boldsymbol{E} = \frac{\omega^2}{c^2} \mu \varepsilon_{\|} \boldsymbol{E} \qquad [46]$$

For a wave with $\boldsymbol{E} || \boldsymbol{k}$, the left-hand side is zero and a nontrivial solution requires the general dispersion relation for plasmons

$$\varepsilon_{\|}(k, \omega) = 0 \qquad [47]$$

With eqn [45], neglecting the damping γ, [47] yields [40]. The hydrodynamic approximation (eqns [42], [44], and [45]) should be considered as the long wavelength, small k expansion of any sophisticated treatment of conduction electron response. For the purpose of optics, this approximation has been shown to be sufficient for the analysis of many experiments involving metal surfaces or metal layers at frequencies around the plasma frequency.

The longitudinal plasma waves are homogeneous solutions of Maxwell's equations according to eqn [46], and must therefore be included in the general solutions, which via boundary conditions yield the optical fields. Sauter was the first to point this out in 1964, and he suggested the third boundary condition, which is necessary at a free metal surface to determine the three amplitudes: of the reflected wave $\boldsymbol{R}$ (eqn [17]) and inside the metal of the transmitted transversal wave $\boldsymbol{T}$ (eqn [18]) and of the longitudinal wave $\boldsymbol{L}e^{i(k_x x+\eta z)}$, which completes the general solution [18].

Before the boundary conditions are discussed, the question of energy current is addressed. When it was brought up that the longitudinal waves should be excited on reflection at metal surfaces, it was objected that this additional channel of energy transport would have long been recognized if the suggestion was true. The wrong answer is that the plasma wave does not carry energy, because $\mathbf{B}=0$ and therefore, the Poynting vector $\mathbf{S}=0$. But the excitation of plasma waves becomes appreciable for frequencies of the order ω_p, which is in the UV where hardly any reflection measurements have been done. In addition, the energy current of the plasma wave is small because of the very small group velocity of plasmons:

$$\frac{\partial\omega}{\partial k} \approx \beta\frac{k}{\omega_p} \sim \frac{v_F^2}{c} \qquad [48]$$

The extension of the material equation [42] leads to an extension of Poynting's theorem: By taking the dot product of eqn [3] with $\boldsymbol{H}$ and subtracting the dot product of $\boldsymbol{E}$ with eqn [3], one obtains

$$-\frac{\partial}{\partial t}\left(\frac{1}{2}\boldsymbol{E}\cdot\boldsymbol{D}+\frac{1}{2}\boldsymbol{H}\cdot\boldsymbol{B}\right) = \nabla\cdot(\boldsymbol{E}\times\boldsymbol{H})+\boldsymbol{E}\cdot\boldsymbol{j} \qquad [49]$$

Multiplying the material equation of motion [42] by $\boldsymbol{j}$, the terms can be rearranged with the help of the continuity equation

$$\omega_p^2\varepsilon_0\boldsymbol{E}\cdot\boldsymbol{j} = \frac{\partial}{\partial t}\left(\frac{1}{2}\boldsymbol{j}^2\right)+\gamma\boldsymbol{j}^2+\nabla\cdot(\beta\rho\boldsymbol{j})+\frac{\partial}{\partial t}\left(\frac{1}{2}\beta\rho^2\right) \qquad [50]$$

which by replacing $\mathbf{E}\cdot\mathbf{j}$ in eqn [49] yields Poynting's theorem with plasma waves:

$$-\frac{\partial}{\partial t}\left(\frac{1}{2}\boldsymbol{E}\boldsymbol{D}+\frac{1}{2}\boldsymbol{H}\boldsymbol{B}+\frac{1}{2\omega_p^2\varepsilon_0}\boldsymbol{j}^2+\frac{1}{2\omega_p^2\varepsilon_0}\beta\rho^2\right) = \nabla\cdot\left(\boldsymbol{E}\times\boldsymbol{H}+\frac{1}{\omega_p^2\varepsilon_0}\beta\rho\boldsymbol{j}\right)+\frac{\gamma}{\omega_p^2\varepsilon_0}\boldsymbol{j}^2 \qquad [51]$$

On the left-hand side, the kinetic energy density of the electron current and the potential energy density connected with the density perturbation against the electron gas pressure are found. On the right-hand side, one has the energy current density in the plasma wave and the positive definite energy absorption due to the friction coefficient γ.

The problem of "additional boundary conditions" is taken up next. At first, the total response is described by ρ and $\mathbf{j}$, that is, formally $\chi_p=0, \mathbf{P}=0$. It has been mentioned already after eqn [21] that the standard boundary conditions, $D_{\text{eff,n}}$ and H_{tg} continuous, imply a discontinuity in E_n caused by singular surface charges, and from eqn [8], the denial of singular surface currents. With $\mathbf{j}=\sigma\cdot\mathbf{E}$, one also gets a finite normal component of the current up to the surface, which then disappears in a singular sink or source of charge in the surface plane. In nonlocal optics, the charges and currents are treated seriously in the plasma waves, and especially singular charges would lead to infinite pressures in eqn [42]. The model of the surface must be improved. Singular surface charges can only be avoided if the normal component of the current $\mathbf{j}$ is continuous (zero at a free surface). With finite charge densities everywhere, the normal component of $\boldsymbol{E}$ is also continuous. These two independent conditions replace the continuity of $D_{\text{eff,n}}$, which is then a consequence. Continuous $\boldsymbol{E}$ and continuous $\boldsymbol{D}_{\text{eff}}$ does not contradict eqn [13], because σ and ε are now tensors with $\varepsilon_\perp \neq \varepsilon_\|$.

At an interface with metal only on one side, one has one reflected wave amplitude in the dielectric, and a transverse and a longitudinal wave amplitude in the metal to be determined via three boundary conditions:

$$\text{(a) continuity of } E_{\text{tangential}} \qquad [52]$$

$$\text{(b) continuity of } E_{\text{normal}} \qquad [53]$$

$$\text{(c) } j_{\text{normal}} = \sigma_\perp E_{\perp\text{normal}}+\sigma_\| E_{\|\text{normal}} = 0 \qquad [54]$$

For the interface between two metals, a fourth amplitude via a fourth boundary condition must be determined because there are plasma waves in both metals. A reasonable requirement is that the interface should not be a singular sink or source of energy. This plausible assumption for our surface model leads to the continuity of the normal component of the energy current; so the boundary conditions at a metal–metal interface are

$$\text{(a) continuity of } E_{\text{tangential}} \qquad [55]$$

$$\text{(b) continuity of } E_{\text{normal}} \tag{56}$$

$$\text{(c) continuity of } j_{\text{normal}} = \sigma_\perp E_{\perp\text{normal}} + \sigma_\| E_{\|\text{normal}} \tag{57}$$

$$\text{(d) continuity of } \frac{\beta}{\omega_{\text{p}}^2 \varepsilon_0}\rho = \frac{\beta}{\omega_{\text{p}}^2}\nabla\cdot\boldsymbol{E} = \frac{\beta}{\omega_{\text{p}}^2}\boldsymbol{k}_\|\cdot\boldsymbol{E}_\| \tag{58}$$

The conductivity $\sigma_\perp$ for transverse fields is also from eqn [42] equal to eqn [30], and $\varepsilon_\perp$ is given by eqn [31]. With (a), (b), and (c), the Poynting vector is continuous; so the requirement [58] suffices to make the total normal energy current continuous. All boundary conditions lead to linear equations for the determination of the reflection and transmission amplitudes, therefore to no complication, in principle, compared to standard optics.

In this treatment of plasma waves in optics, the response functions $\sigma_\|$ and $\varepsilon_\|$ are dependent on frequency ω as well as on wave vector k or wavelength; hence, this kind of optics is called nonlocal optics. Equation [42] says that the current at r is not only driven by the electric field at **r** (local relation), but the charge density in the neighborhood determines the other force $\sim\nabla_\rho$. Charge density waves with larger gradients, larger k, oscillate faster according to eqn [40]. The standard local optics is an approximation which neglects charge densities altogether and does not treat the singular surface charges consistently which eqn [21] implies. This standard approximation is simpler and sufficient as long as the charge densities are small. At frequencies of the order of the plasma frequency, the charge densities get large due to resonant eigenmodes and must be treated consistently. The nonlocal optics can lead to results qualitatively different from standard optics and in agreement with the experiment.

A few examples of this nonlocal metal optics are discussed next. One can understand at the beginning that only when there are normal components of **E**, normal currents leading to oscillating charge densities near the surface, a plasma wave is optically excited. Therefore, only for *p*-polarization with the electric field parallel to the plane of incidence, this nonlocal extension of optics is necessary, and the plasmon gets a nonzero amplitude **L**.

In the case of reflection from a free metal surface, the extension of the treatment in eqns [17]–[23] takes the steps: the outgoing general solution [18] inside the metal is supplemented by the plasma-wave $+\boldsymbol{L}e^{i(k_x x+\eta z)}$ with η from

$$\varepsilon_\| = 0 = 1 - \frac{\omega_{\text{p}}^2}{\omega^2 - \beta\left(k_x^2 + \eta^2\right) + i\omega\gamma} \tag{59}$$

and with

$$\eta = \sqrt{\frac{1}{\beta}\left[\omega(\omega+i\gamma) - \omega_{\text{p}}^2\right] - k_x^2} \tag{60}$$

and for the longitudinal wave

$$L_x/L_z = k_x/\eta \tag{61}$$

The three boundary conditions [52]–[54] lead to three linear equations and to the reflection amplitude

$$\frac{R_z}{E_{0z}} = \frac{\varepsilon_\perp q - l + (\varepsilon_\perp - 1)k_x^2/\eta}{\varepsilon_\perp q + l - (\varepsilon_\perp - 1)k_x^2/\eta} \tag{62}$$

with $\varepsilon_\perp = \varepsilon_{\text{M}}$ and q, l from eqns [31], [19], and $\varepsilon_1 = 1$, $\mu_{\text{M}} = \mu_1 = 1$. The limit $\beta\to0$ leads back from [42] to local [28], in [60] to $\eta\to\infty$, and from [62] back to [22]. The difference between $r = |R_z/E_{0z}|^2$ from [62] and from [22] is shown in Figure 2. The excitation of plasma waves really reduces the reflectivity, but only above the plasma frequency and by a small amount. This case was outlined to demonstrate that this extension of metal optics is straightforward.

As in the previous section, one finds from the zero of the denominator of the reflection amplitude [62], the dispersion relation of the surface plasmon polariton

$$\varepsilon_\perp q + l - (\varepsilon_\perp - 1)k^2/\eta = 0 \tag{63}$$

For low frequencies, the last term of the order of $k\left(v_{\text{F}}\omega/c\omega_{\text{p}}\right)$ can be neglected and the dispersion agrees with [35]. But for $k \approx (\omega/c)\left(c/2\sqrt{\beta}\right)^{1/3}$, the frequency of the eigensolution [63] rises above $\omega_{\text{p}}/\sqrt{2}$, which was the limit for [35]. The approximate dispersion in this frequency range is from eqn [63]:

$$\omega_s \approx \frac{\omega_{\text{p}}}{\sqrt{2}} + k\frac{\sqrt{\beta}}{2} \tag{64}$$

This linear dispersion is often extrapolated toward k=0. In optics, this is wrong because then, the light line is crossed and light could couple to the eigenmodes which is not the case. For larger k, the increase of ω_{s} is stronger than linear which is indicated in Figure 2. This dispersion describes the essential facts of the experiments. Only the linear rise [64] is usually suppressed to a plateau due to a skin effect before the final rise, when at large k the electron gas pressure dominates.

The dispersion relation [64] was derived when Ritchie discovered this surface mode in 1957 from an electrostatic approximation to Maxwell's equations ($c\to\infty$) and called it the surface plasmon. When the charge densities in the plasma and Maxwell's equations

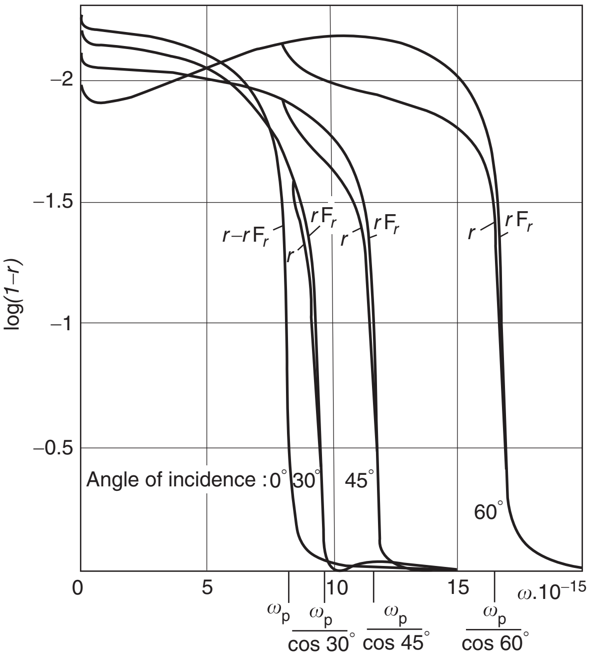

Figure 2 The reflectivity r with plasma waves, r_{Fr} standard Fresnel formula.

are treated correctly, it becomes clear that [35] and [64] are approximations to the dispersion [63] of a single kind of surface mode, which is then properly termed the "surface plasmon polariton" (SPP).

The reflection from a simple metal surface is changed so little by the inclusion of plasma waves in optics (Figure 2) that this is not the experiment to prove the necessity of nonlocal optics. The first relevant experiment was theoretically predicted by Melnyk and Harrison in 1968 and carried out by Lindau and Nilson in 1970. The transmittance through thin silver layers shows periodic minima when the plasma waves form standing waves in the layer and by the large amplitude, increase the absorption. It turns out that half a wavelength and even three and five halves of a wavelength fit into a layer of 100 Å. One can calculate from eqn [40] that this is the order of the plasma wavelength, while the transverse waves are more than ten times longer, so the experiment can only be explained by the optical excitation of plasma waves in the metal. Another example is shown in Figure 3. An electroreflection experiment measures the change in reflectivity $\Delta r/r$ when a strong (static or slowly oscillating) electric field changes the charge density at the metal surface. The optical calculations give qualitatively different results when standard local optics or nonlocal optics is employed. Only nonlocal optics describes the experiment. In the late 1970s and early 1980s, several examples were published with the same outcome (see the "Further reading" section.)

One can draw the general conclusions: standard optics must be extended to nonlocal optics when the optical frequency ω is around the plasma frequency $\left(0.5\omega_{\mathrm{p}} < \omega < 2\omega_{\mathrm{p}}\right)$ and when metallic layers, especially very thin ones (1 –1000 Å), are involved. The nonlocal optics discussed in this article gives the right answers in these cases.

The treatment of plasma waves in optics in this section is designed for a free electron gas model of a metal, where the total response can be described as conduction electron current density and charge density. The parameters, electron density n_0 and damping γ, could be taken from a fit of a model (eqn [31]) to measure dielectric data. This is a good approximation for most metals except the *d*-band transition metals. But silver is one of the best candidates for demonstrating the effects of nonlocal optics because its plasma frequency is easily accessible just above the visible at $\hbar\omega_{\mathrm{p}} = 3.8$ eV and the plasmons see little damping. The conduction electron density in silver is high and would lead to $h\omega \approx 9$ eV from eqn [29]. $\varepsilon=0$ is shifted to a lower frequency because of other "bound" electrons.

In such a situation, it has been successful to think of two responding electron systems, free and bound. The free conduction electrons follow eqn [42] while the bound ones are described by a polarizability χ_{p}. The total measured ε is then separated as in eqn [13]. An assumption of the conduction electron density (and the damping) allows the determination of χ_{p} from [13]. Then it is consistent to use in [53] and [56] the normal component of $\boldsymbol{D} = \left(1+\chi_{\mathrm{p}}\right)\varepsilon_0\boldsymbol{E}$. This procedure was used for Figure 3 and for many other comparisons with experiments on silver.

A final remark shall close this section: the response of a metal to electromagnetic fields is a vast field in solid-state theory where quite a number of theoreticians have invested their ingenuity. Here, a simple extension of standard optics was presented which can easily be applied by experimentalists also and has been successfully used for the analysis of several experiments. Around the plasma frequency, the predictions of nonlocal optics including plasma waves can be qualitatively different from the results of standard optics.

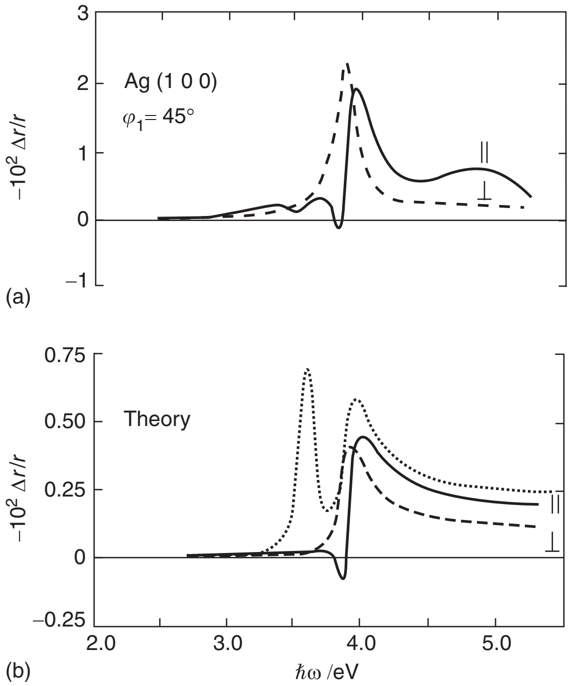

Figure 3 Electroreflection on silver. (a) Experiment for s(⊥) and *p*-polarized (||) light. (b) Theory, (——) nonlocal optics, (. . . . . .) standard optics.

Magnetooptics

The response of metals as well as other materials to electromagnetic waves is determined by the forces due to the electric field of the wave, because the Lorentz force due to the magnetic field is weaker by a factor v/c<1% with electron velocity of the order of the Fermi velocity. Magnetooptics considers the interaction of light with external magnetic fields or strong magnetizations in ferromagnets.

A system with a magnetic field or magnetization acquires a special symmetry with respect to time inversion ($\boldsymbol{E}, \boldsymbol{B}, \boldsymbol{H}, \boldsymbol{M} \rightarrow \boldsymbol{E}, -\boldsymbol{B}, -\boldsymbol{H}, -\boldsymbol{M}$). Onsager's relations require

$$\varepsilon_{ij}(E, B, H) = \varepsilon_{ji}(E, -B, -H) \qquad [65]$$

Therefore, optical effects introduced by (proportional to) $\boldsymbol{B}$ or $\boldsymbol{M}$ manifest themselves as antisymmetric tensor components in an otherwise symmetric dielectric tensor $\hat{\varepsilon}$.

It is briefly shown that an external magnetic field leads to antisymmetric ε-components in an extension of the Drude model (eqns [27] and [28]) and that the consequence in optics is a difference in index of refraction for right and left circularly polarized waves. This leads to the Faraday rotation of the plane of polarization for linearly polarized light in transmission and to the Kerr rotation in reflection.

The Lorentz force $-e_0(\dot{\boldsymbol{r}} \times \boldsymbol{B}_0)$, in an external magnetic field $\mathbf{B}_0$=(0,0,B_0 parallel to the *z*-axis, is added to the equation of motion [27]. To be more general, an elastic restoring force $-\omega_0^2\boldsymbol{r}$ is also added (for free electrons in metals $\omega_0 \rightarrow 0$):

$$m\ddot{\boldsymbol{r}} = -e_0E - m\gamma\dot{\boldsymbol{r}} - m\omega_0^2\boldsymbol{r} - e_0(\dot{\boldsymbol{r}} \times \boldsymbol{B}_0) \qquad [66]$$

With $\boldsymbol{r} \sim \exp(-\mathrm{i}\omega t)$ and $\boldsymbol{j} = -e_0n_0\dot{\boldsymbol{r}}$, one finds from [66] the conductivity tensor and obtains from eqn [13] the dielectric tensor:

$$\hat{\varepsilon} = \hat{1} + \omega_\mathrm{p}^2\begin{pmatrix} a & \mathrm{i}b & 0 \\ -\mathrm{i}b & a & 0 \\ 0 & 0 & c \end{pmatrix} = \varepsilon\begin{pmatrix} 1 & \mathrm{iQ} & 0 \\ -\mathrm{iQ} & 1 & 0 \\ 0 & 0 & \alpha \end{pmatrix} \qquad [67]$$

$$a = \frac{\omega_0^2 - \omega(\omega + \mathrm{i}\gamma)}{\left(\omega_0^2 - \omega(\omega + \mathrm{i}\gamma)\right)^2 - \omega^2\omega_c^2} \qquad b = \frac{\omega\omega_c}{\left(\omega_0^2 - \omega(\omega + \mathrm{i}\gamma)\right)^2 - \omega^2\omega_c^2} \qquad [68]$$

$$c = \frac{1}{\omega_0^2 - \omega(\omega + \mathrm{i}\gamma)} \qquad [69]$$

$\omega_c = eB_0/m$ is the cyclotron frequency proportional to B_0. Due to the external magnetic field, one finds an antisymmetric tensor added to an otherwise symmetric $\hat{\varepsilon}$.

The dielectric tensor is now employed on the right-hand side of the wave equation [12]. For a wave traveling in the z-direction parallel to $\boldsymbol{B}_0$

$$\begin{aligned} \left(\frac{\omega^2}{c^2}\varepsilon - k^2\right)E_x + \mathrm{i}Q\varepsilon\frac{\omega^2}{c^2}E_y &= 0 \\ -\mathrm{i}Q\varepsilon\frac{\omega^2}{c^2}E_x + \left(\frac{\omega^2}{c^2}\varepsilon - k^2\right)E_y &= 0 \end{aligned} \qquad [70]$$

$$\left(\frac{\omega^2}{c^2}\varepsilon(1 \pm Q) - k^2\right)\left(E_x \pm \mathrm{i}E_y\right) = 0 \qquad [71]$$

which yields

$$k_{\mathrm{r}}^2 = \frac{\omega^2}{c^2}\varepsilon(1+Q) \quad \text{for } E_x = \mathrm{i}E_y$$

(for right circular polarized light)

$$k_{\mathrm{l}}^2 = \frac{\omega^2}{c^2}\varepsilon(1-Q) \quad \text{for } E_x = -\mathrm{i}E_y$$

(for left circular polarized light)

or

$$n_{\mathrm{r}} = \sqrt{\varepsilon}\left(1+\frac{1}{2}Q\right) \quad \text{and} \quad n_{\mathrm{l}} = \sqrt{\varepsilon}\left(1-\frac{1}{2}Q\right) \qquad [72]$$

The increase of the effective ε or polarizability for right circular polarization can be understood for the simple model (eqn [66]) from the direction of the Lorentz force which increases the radius of the circular electron motion. When light travels through a piece of matter of length L, the waves accumulate a phase difference of

$$\delta = (k_{\mathrm{l}} - k_{\mathrm{r}})L = \frac{\omega}{c}L(n_{\mathrm{l}} - n_{\mathrm{r}}) = -\frac{\omega}{c}LQ \qquad [73]$$

The Faraday rotation of the plane of linear polarization is $\delta/2$. Because Q is proportional to ω due to the Lorentz force, the Faraday rotation is proportional to ω^2.

Generalizations

The dielectric tensor is more generally expressed as

$$\hat{\varepsilon} = \varepsilon\begin{pmatrix} 1 & \mathrm{i}Q_z & -\mathrm{i}Q_y \\ -\mathrm{i}Q_z & 1 & \mathrm{i}Q_x \\ \mathrm{i}Q_y & -\mathrm{i}Q_x & 1 \end{pmatrix} \qquad [74]$$

by the "Voigt vector" $\boldsymbol{Q} = \left(Q_x, Q_y, Q_z\right)$.

Then in the refraction indices (eqn [72]), Q is generalized: $Q \rightarrow \boldsymbol{Qk}/|\boldsymbol{k}|$, to the projection of $\boldsymbol{Q}$ on the direction of propagation $\boldsymbol{k}$. In the model and in transparent materials, $\boldsymbol{Q}$ is mainly real and one finds the Faraday rotation due to the real phase shift (eqn [73]). In ferromagnetic metals, the magnetooptical effects are larger by several orders of magnitude, but here, mainly the absorption, the imaginary part of $\boldsymbol{Q}$ is changed by the magnetization leading to elliptically polarized light in general.

Because ferromagnetism is rooted in the electron spin, a microscopic explanation of the magnetooptical effects in ferromagnets involves the spin–orbit coupling of the electron motion and the unequal number of spins parallel and antiparallel to $\boldsymbol{M}$.

For the investigation of magnetic properties of metallic layers, the magnetooptical Kerr effect (MOKE) in reflection has been developed into an efficient tool. With strong lasers, nonlinear optical response is also exploited (for detailed information see the "Further reading" section).

"Left-Handed Materials," Optics for $\varepsilon<0$ and $\mu<0$

Charge carriers exposed to oscillating electric fields show, in some frequency region, negative polarizability as a forced oscillator has a phase shift of π above resonance. Therefore, in simple metals $\varepsilon<0$ below the plasma frequency (resonance frequency $\omega_0 \rightarrow 0$) (eqns [31] and [32]). Then the index of refraction $n = \sqrt{\varepsilon}$ is imaginary, electromagnetic waves decay exponentially into the metal, do not propagate at all and the reflectivity goes to 1.

In 1968, V G Veselago pointed out that the wave propagation is really determined by the product $\varepsilon\mu$ (eqns [16] and [19]) and therefore, a system with $\varepsilon<0$ and $\mu<0$ in the same frequency region would be transparent again. One has, in principle, negative

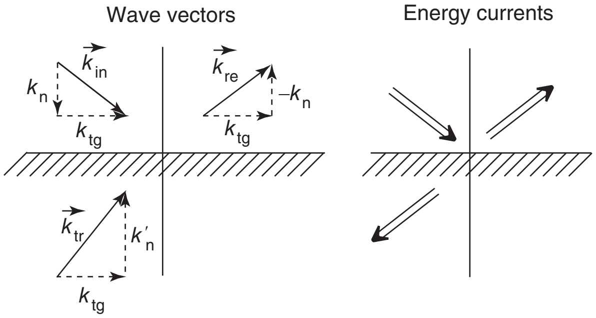

Figure 4 Refraction at a left-handed material.

magnetic polarizability in diamagnets (due to Lenz's rule) but usually the polarizabilities χ_m are extremely small ($\sim 10^{-6}$), and the susceptibility $\mu=1+\chi_m$ deviates little from 1 and does not go below 0.

Recently materials with $\mu<0$ have been manufactured. Therefore, the surprising optical properties are outlined. The term "left-handed material" (LHM) derives from the fact that Maxwell's equations (e.g., (eqn [3])) for a plane wave $\boldsymbol{k} \times \boldsymbol{E} = \omega \boldsymbol{B}$ and $\boldsymbol{H} = (1/\mu_0\mu)\boldsymbol{B}$ usually make the vectors **k**,**E**,H a right-handed tripod, while with $\mu<0$ the tripod gets left-handed. Consequently, normally the energy current $\mathbf{S}=\mathbf{E}\times\mathbf{H}$ is parallel to the wave vector $\boldsymbol{k}$. In LHMs, the Poynting vector is opposite to $\boldsymbol{k}$.

Refraction at an interface between material I ($\varepsilon_I > 0, \mu_I > 0$) and material II ($\varepsilon_{II} < 0, \mu_{II} < 0$) puts the refracted beam in II on the opposite side of the surface normal than usual. Therefore, diverging rays in I can converge in II which led to speculations about perfect lenses by slabs of LHMs. This uncommon refraction can be understood as follows:

$\mathbf{S}=\mathbf{E}\times\mathbf{H}$ is antiparallel to $\boldsymbol{k}$ in LHM II. Therefore, the correct homogeneous solution in II which carries the energy from the interface has a wave vector pointing towards the interface. The tangential components of all wave vectors are equal, so the refracted beam (i.e., the energy current) lies in II on the same side of the surface normal as the incoming beam in I (see Figure 4).

The subject of optics with LHMs has been revived after 2000 in connection with the investigation of the "optical" properties of conducting networks, three-dimensional wire mesh crystals. If the wavelength of the electromagnetic waves are much larger than the lattice spacing, the conducting network behaves like a metallic conductor with a low density plasma frequency and with a frequency region of negative ε according to eqn [32]. The necessary large diamagnetism is achieved by conducting rings in each cell of the lattice. In such a designed material, $\varepsilon<0$ and $\mu<0$ at frequency $\nu = 10.5$ GHz, $\lambda \approx 3$ cm, was demonstrated with $\varepsilon\mu = 7.28 \pm i0.54$. It was shown that the refraction is indeed as in Figure 4 (see the "Further reading" section).

Further Reading

Bennemann KH (ed.) (1998) *Nonlinear Optics in Metals*. Oxford: Clarendon Press.
Boardman AD (ed.) (1982) *Electromagnetic Surface Modes*. New York: Wiley.
Born M and Wolf E (1975) *Principles of Optics*. Pergamon Ch. XIII.
Bouhelier A, Renger J, Beversluis MR, and Novotny L (2003) *Journal of Microscopy* 210: 220.
Flaetgen G, Krischer K, Pettinger B, Doblhofer K, and Junkes H (1995) *Science* 269: 668.
Forstmann F and Gerhardts RR (1986) Metal optics near the plasma frequency. *Springer Tracts in Modern Physics* 109.
Palik ED (1985/1991) *Handbook of Optical Constants of Solids*, vols. I and II. London: Academic Press.
Raether H (1980) Excitation of plasmons and interband transitions of electrons. *Springer Tracts in Modern Physics* 88.
Raether H (1988) Surface plasmons on smooth and rough surfaces and on gratings. *Springer Tracts in Modern Physics* 111.
Shelby RA, Smith DR, and Schultz S (2001) *Science* 292: 77.

Nonlinear Optics

V Degiorgio and I Cristiani, Università di Pavia, Pavia, Italy

© 2005 Elsevier Ltd. All rights reserved.

This is an update of V. Degiorgio, I. Cristiani, Nonlinear Optics, Editor(s): Franco Bassani, Gerald L. Liedl, Peter Wyder, Encyclopedia of Condensed Matter Physics, Elsevier, 2005, Pages 105–113, ISBN 9780123694010, https://doi.org/10.1016/B0-12-369401-9/00677-X.

Introduction 383
Physical Origin of Nonlinearity 383
Second-Order Nonlinear Effects 384
Second-Harmonic Generation 384
Phase Matching 385
Parametric Amplification and Oscillation 386
Nonlinear Optical Materials 387
Third-Order Nonlinear Effects 388
Optical Kerr Effect 388
Optical switch 388
Self-focusing 388
Self-phase modulation 388
Four-Wave-Mixing and Optical Conjugation 388
Frequency-shifting scheme 389
Phase-conjugate mirror 389
Stimulated Raman and Brillouin Scattering 389
Further Reading 391

Nomenclature

$A(z)$	electric field slowly varying envelope
c	$(3\times10^8\,\mathrm{m\,s^{-1}})$ velocity of light in vacuum
d_{eff}	effective nonlinear coefficient
$E(r, t)$	electric field
g_R	Raman gain
I	intensity
k	electric field wave vector
l_c	second-harmonic generation coherence length
L_{SH}	characteristic second-harmonic generation length
n	index of refraction
n_e	extraordinary index of refraction
n_o	ordinary index of refraction
n_2	nonlinear refractive index
P_p	pump power
$P(r, t)$	macroscopic polarization
P_s	Stokes power
u_a	velocity of the acoustic wave
ε_0	$(8.85\times10^{-12}\,\mathrm{F\,m^{-1}})$ permittivity vacuum
λ	wavelength
Λ	spatial periodicity
μ_o	$(4\pi\times10^{-7}\,\mathrm{N\,A^{-2}})$ permeability vacuum
$\chi^{(1)}$	linear susceptibility
$\chi^{(2)}$	second-order susceptibility
$\chi^{(3)}$	third-order susceptibility
ω	angular frequency
ω_{as}	anti-Stokes frequency
ω_{pm}	phase-matching frequency
ω_s	Stokes frequency
ω_v	vibrational mode with angular frequency

Introduction

The propagation of optical waves inside a medium is described by the wave equation:

$$\nabla^2 \boldsymbol{E} = \frac{1}{c^2}\frac{\partial^2 \boldsymbol{E}}{\partial t^2} + \mu_o \frac{\partial^2 \boldsymbol{P}}{\partial t^2} \qquad [1]$$

where $\boldsymbol{E}(\boldsymbol{r}, t)$ is the electric field and $\boldsymbol{P}(\boldsymbol{r}, t)$ is the macroscopic polarization. Traditional optics is based on the simplified assumption that $\boldsymbol{P}$ is linearly related to $\boldsymbol{E}$ through a differential equation describing the noninstantaneous response of the medium. In the frequency domain, $\boldsymbol{P}(\boldsymbol{r}, \omega) = \varepsilon_0 \chi(\omega)\boldsymbol{E}(\boldsymbol{r}, \omega)$, where $\boldsymbol{E}(\boldsymbol{r}, \omega)$ and $\boldsymbol{P}(\boldsymbol{r}, \omega)$ are the electric field and polarization Fourier transforms, and $\chi(\omega)$ is the frequency-dependent electric susceptibility that is related to the index of refraction of the material through the expression: $n(\omega) = \sqrt{1+\chi(\omega)}$. Actually the relation between $\boldsymbol{P}$ and $\boldsymbol{E}$ is intrinsically nonlinear and can be considered approximately linear when the optical field is much smaller than the internal field seen by the electron. Whereas in the past the optical intensities available with conventional sources were too weak to explore optical nonlinearities, it is now very easy to generate nonlinear optical effects by exploiting laser beams. The term nonlinear optics should apply to all the physical situations in which the linear approximation is not adequate. This article is limited to a treatment of those nonlinear optical interactions that are nonresonant. Resonant interactions, such as those responsible for laser behavior, optical bistability, or electromagnetically induced transparency, are discussed elsewhere in this encyclopedia.

Nonlinear optics has enhanced the understanding of fundamental light–matter interactions and provided new powerful methods for the investigation of materials. At the same time, nonlinear optics has a strong impact on technology as it offers the way to develop coherent radiation sources, emitting at new frequencies that are not usually available with lasers, and offering tunability from ultraviolet to visible and near infrared. Important applications also concern optical devices performing the same functions provided at radio frequencies by electronic devices, such as modulators, switches, and logical circuits.

Physical Origin of Nonlinearity

A simple physical model describing the relation between $\boldsymbol{P}$ and $\boldsymbol{E}$ is represented by the Lorentz model that treats a bound electron as a harmonic oscillator. Clearly, the assumption that the electron is in a parabolic potential well is valid only for small displacements from the equilibrium position. As shown in Figure 1, if the exciting field is strong enough, the electron displacement will also probe a range of distances over which the potential is no longer parabolic. The potential can be written as a Taylor expansion in the displacement x: $V(x) = V_0+\alpha x^2+(1/2)\beta x^3+(1/3)\gamma x^4+\cdots$. It can be easily seen by a perturbative approach that the cubic term in $V(x)$ can give rise to a polarization term proportional to the square of the field, and the quartic term gives a term proportional to the cube of the field.

Note that a cubic term in $V(x)$ can exist only if the material structure is not centrosymmetric, as it happens with a crystal having a noncentrosymmetric unit cell or a system of oriented polar molecules. On the macroscopic scale the relation between $\boldsymbol{P}(\boldsymbol{r}, \omega)$ and $\boldsymbol{E}(\boldsymbol{r}, \omega)$ can be written as

$$\boldsymbol{P} = \varepsilon_0 \chi^{(1)}\boldsymbol{E}+\varepsilon_0 \chi^{(2)}\boldsymbol{E}^2+\varepsilon_0 \chi^{(3)}\boldsymbol{E}^3+\cdots \qquad [2]$$

Materials presenting a second-order nonlinearity, when illuminated with a beam at angular frequency ω, can generate a second-harmonic beam at frequency 2ω. If two beams at frequencies ω_1 and ω_2 are sent into the material, a third beam at the sum or difference frequency $\omega_3 = \omega_1 \pm \omega_2$ can be generated. Such a process is used in optical parametric amplifiers and oscillators. In the case of third-order materials, besides the generation of new frequencies through various frequency-mixing processes,

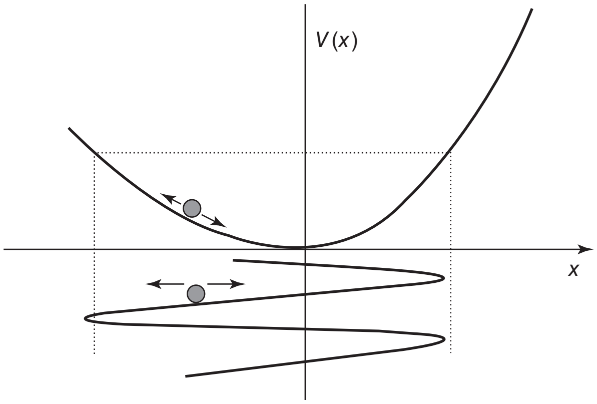

Figure 1 Particle motion in an asymmetric potential well under the action of a sinusoidal field: the oscillation is not symmetric; thus, it contains higher-harmonic contribution.

phenomena such the optical Kerr effect, self-focusing, self-phase modulation, and optical phase-conjugation can be observed and exploited for the realization of optical devices. In addition, stimulated Raman and Brillouin scattering also belong to the family of third-order effects.

Second-Order Nonlinear Effects

Second-Harmonic Generation

In order to illustrate the basic aspects of nonlinear interactions, it is better to start with the simplest situation: a second-order material illuminated by a monochromatic plane wave propagating along the z-axis – $E_1 \exp[i(\omega_1 t - k_1 z)]$. It is easy to see from eqn [2] that such a wave gives rise to a nonlinear polarization oscillating at $2\omega_1$. In turn, the nonlinear polarization, once inserted into eqn [1], behaves like a source for a second-harmonic (SH) optical wave. Limiting the consideration to stationary waves in the slowly-varying-envelope-approximation and expressing the pump and SH fields E_1 and E_2 as $E_1 = A_1(z)\exp(ik_1 z)$ and $E_2 = A_2(z)\exp(ik_2 z)$, respectively, the evolution of the SH generation phenomenon can be described through the following equations:

$$\begin{aligned}\frac{d}{dz}A_1(z) &= i\frac{\omega_1}{cn_1}d_{\text{eff}}A_2(z)A_1^*(z)\exp(-i\Delta kz)\\ \frac{d}{dz}A_2(z) &= i\frac{\omega_1}{cn_2}d_{\text{eff}}A_1^2(z)\exp(i\Delta kz)\end{aligned} \qquad [3]$$

where $d_{\text{eff}} = \chi^{(2)}/2$ is called the effective nonlinear coefficient, $\Delta k = k_2 - 2k_1$ is the wave vector mismatch, c is the light velocity, and n_1 and n_2 represent the refractive indices experienced by the pump and SH fields during the propagation through the nonlinear medium. It is important to remark that, in scientific literature, the nonlinear properties of materials are usually expressed in terms of the d_{eff} coefficient values. It can be seen from eqns [3] that the condition for efficient SH generation is: $\Delta k = 0$. Such a condition is called the phase-matching condition. It expresses the requirement that the nonlinear polarization wave travels at the same phase velocity as the SH wave. It should be noted that the process consists in an exchange of energy (and momentum) between waves in which the nonlinear medium acts as a catalyst. If the process is described by a quantum-mechanical approach, two photons of the fundamental wave are converted into an SH photon; the phase-matching condition corresponds to momentum conservation in the nonlinear process.

In the case $\Delta k = 0$, the propagation equations can be solved analytically, giving the SH intensity as a function of the propagation distance z:

$$I_2(z) = I_1(0)\tanh(z/L_{\text{SH}}) \qquad [4]$$

where the constant L_{SH} is inversely proportional to the nonlinear coefficient of the medium and to the square root of the input intensity. Equation [4] shows that the input intensity can be fully converted into the SH provided that the propagation distance is sufficiently long (the crystal length L should be larger than L_{SH}). As an example, by using a lithium niobate crystal with a second-order coefficient $d_{\text{eff}} = 5$ pm V^{-1} and a neodymium laser ($\lambda = 1064$ *nm*) beam with an intensity of 10 MW cm^{-2}, $L_{\text{SH}} = 1$ cm. When the phase-matching condition is not satisfied, $I_2(z)$ is an oscillating function of z (see Figure 2): the SH intensity achieves a maximum after a distance called coherence length $l_c = \pi/\Delta k$ and vanishes at $z = 2l_c$.

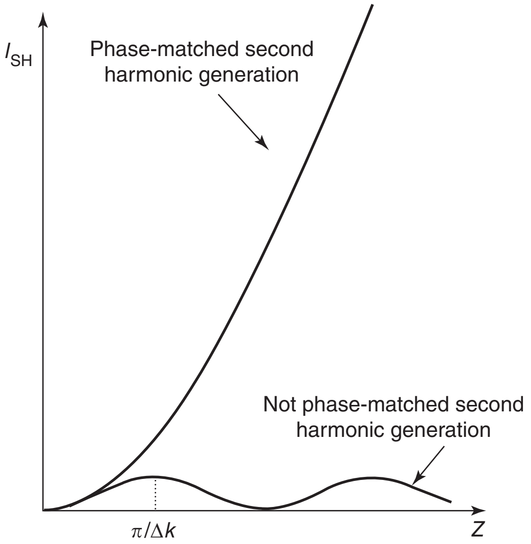

Figure 2 SH intensity as a function of propagation distance in a nonlinear crystal.

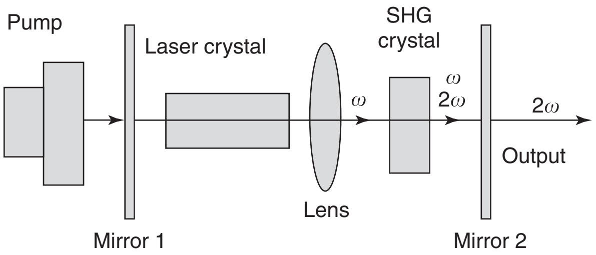

Figure 3 Scheme of an SH laser: mirrors 1 and 2 have high reflectivity for the frequency ω corresponding to the laser transition, but are transparent for 2ω.

SH generation of a laser beam becomes particularly efficient if the nonlinear crystal is placed inside a laser cavity (see Figure 3). At present, such an approach represents one of the most convenient methods of generating coherent green and blue light by using near infrared solid-state lasers. As an example, a 532 nm green light is efficiently generated by intracavity frequency doubling of a neodymium laser.

Phase Matching

Recalling that the modulus of $\boldsymbol{k}$ is related to the angular frequency by the relation $k = (\omega/c)n(\omega)$, the phase-matching condition $\Delta k = 0$ requires that the index of refraction of the second harmonic be equal to that of the fundamental. In normal cases, n is an increasing function of frequency, so that phase matching is not satisfied for beams having the same polarization. A very clever method of obtaining phase matching is that of exploiting the crystal birefringence to compensate for the material dispersion (see Figure 4). Recall that, in a crystal possessing an optical axis, the propagation velocity of a linearly polarized plane wave depends on its polarization direction: a wave polarized perpendicularly to the optical axis sees the "ordinary" index of refraction n_o, whereas a wave polarized along the optical axis sees the "extraordinary" index n_e. A typical nonlinear crystal is lithium niobate, a uniaxial crystal presenting negative birefringence, that is, $n_o > n_e$. It can be shown that there is a frequency ω_{pm} for which $n_o(\omega_{pm}) = n_e(2\omega_{pm})$. In such a situation, an ordinary input beam at frequency ω_{pm}, propagating perpendicularly to the optical axis, can be efficiently converted into an extraordinarily polarized SH beam. Noting that the index of refraction of the extraordinary beam can be changed continuously between n_o and n_e by changing the angle θ between $\boldsymbol{k}$ and the optical axis, ω_{pm} can be tuned by appropriately rotating the crystal.

Since the indices of refraction depend on temperature, it is possible to tune ω_{pm} finely by varying T. More degrees of freedom are added to the SH experiment if two input beams having the same frequency, but different direction or different polarization, are considered.

From the point of view of applications, a very important trend that emerged in recent years is that of considering nonlinear interactions in microstructured materials and in waveguides. It goes beyond the scope of this article to approach such a subject; however, mention may be made here that a microstructured material, in which the value of the $\chi^{(2)}$ coefficient varies with a spatial periodicity Λ, can exchange momentum with the propagating waves in multiples of the unit $2\pi/\Lambda$, so that, in principle, phase matching can be achieved at any desired frequency by appropriately choosing the period Λ (see Figure 5). Concerning waveguided

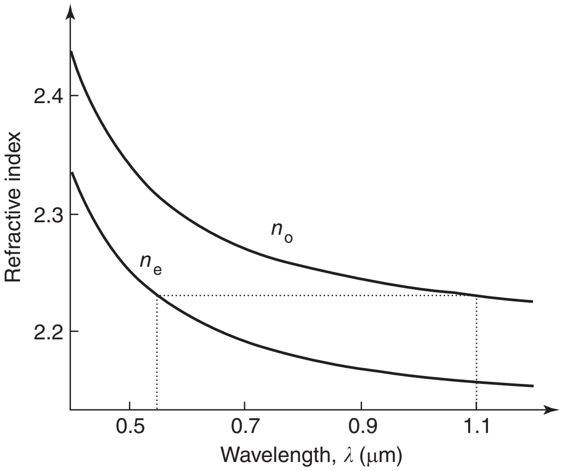

Figure 4 Birefringence phase matching.

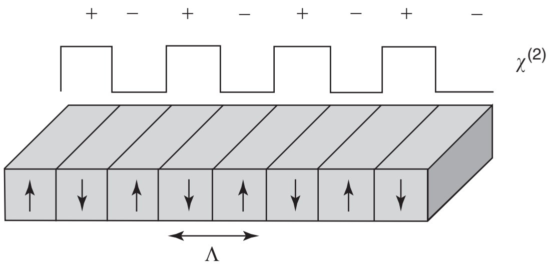

Figure 5 Periodically poled ferroelectric crystal presenting a uniform $\chi^{(1)}$ and an oscillating $\chi^{(2)}$.

propagation, the main difference with respect to bulk propagation is that the waveguide can support different spatial modes possessing different phase velocities even if they have the same frequency; such a "modal dispersion" also opens new possibilities of phase matching.

This section concludes with an important consideration: whereas the "ideal" phase-matching condition is $\Delta k = 0$, the "practical" condition in a crystal of finite length L is $\Delta kL < \pi$, or, equivalently, $l_c > L$. As a consequence, there is a frequency interval, centered on ω_{pm}, in which efficient SH generation can be achieved. The existence of a nonzero spectral acceptance makes it possible to use short pulses, instead of stationary beams, in nonlinear optical experiments.

Parametric Amplification and Oscillation

If two beams, possessing different frequencies ω_1 and ω_2, and different wave vectors $\boldsymbol{k}_1$ and $\boldsymbol{k}_2$, are sent into a second-order nonlinear crystal, the nonlinear polarization can give rise to new frequencies representing the SH of each beam or the sum/difference of the input frequencies. By choosing a specific phase-matching condition, only one process is selected among all possible processes. If the difference-frequency generation (DFG) is selected, and it is assumed that $\omega_1 > \omega_2$, a new beam at frequency $\omega_3 = \omega_1 - \omega_2$ and wave vector $\boldsymbol{k}_3$ is obtained, provided that the condition $\boldsymbol{k}_3 = \boldsymbol{k}_1 - \boldsymbol{k}_2$ is satisfied (see Figure 6).

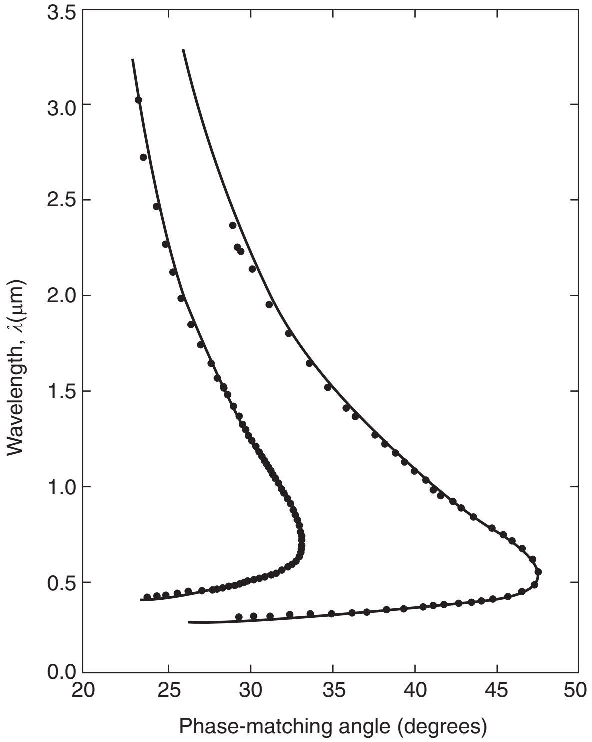

Figure 6 Tuning curves for an optical parametric oscillator pumped by the third- and fourth-harmonic of a neodymium laser. (Reproduced with permission from Cheng *et al.* (1988) *Applied Physics Letters* 53(3): 175–177.)

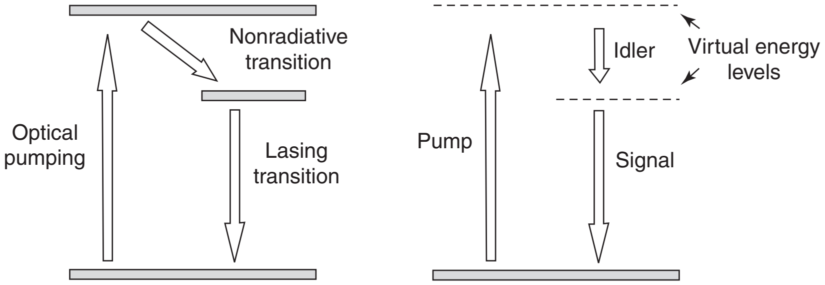

Figure 7 Comparison between the three-level laser, using real energy levels, and the optical parametric oscillator, using virtual levels.

All the phase-matching methods discussed in the previous section in connection with SH generation can also be applied to the sum/difference frequency generation. By using the same approach outlined for SH generation, it is easy to derive nonlinear propagation equations for the sum/difference fields having a structure similar to that of eqns [3]. In the DFG process, one photon at frequency ω_1 is annihilated and two photons at frequencies, respectively ω_3 and ω_2, are created, so that the process not only produces a new coherent beam at ω_3, but also amplifies the beam at ω_2. Such an amplification process is called parametric amplification. Whereas standard optical amplifiers work only at frequencies corresponding to transitions among energy levels, parametric amplifiers use transparent crystals and can work, in principle, over the whole transparency window of the crystal, provided that phase matching can be achieved (see Figure 7).

Recalling that an optical amplifier can become a laser oscillator once inserted into an optical cavity, a similar approach can transform the parametric amplifier into a parametric oscillator. Whereas in the laser case, the trigger to cavity oscillation comes from spontaneous emission from the upper level of the amplifying medium, the initial seed for parametric oscillation comes from parametric fluorescence, the process by which the "pump" photon at frequency ω_1 spontaneously breaks down into two photons at frequencies ω_2 (signal) and ω_3 (idler). Potentially, parametric fluorescence can yield any couple of frequencies satisfying energy conservation, the choice among all possible couples being determined by the phase-matching condition. The tuning of the parametric oscillator is generally achieved by rotating the crystal or by changing the operating temperature.

Nonlinear Optical Materials

The second-order processes described in the previous sections require the availability of noncentrosymmetric media. Such media are intrinsically anisotropic, so that the electric susceptibilities become tensorial quantities. In particular, $\chi^{(2)}$ is a third-order tensor, possessing 27 components χ_{ijk}. This fact makes the description of beam propagation inside the crystal and also the search for phase matching conditions rather complicated. Such descriptions are beyond the scope of this article; however, the following example is taken up: consider an input field polarized along the x-axis (this implies $j = k = 1$); birefringence phase matching requires that the generated nonlinear polarization lies along the z-axis (this implies $i = 3$), so that the useful component of the $\chi^{(2)}$ tensor is, in this case, χ_{311}. As a general consideration, the most powerful phase matching method, that is, birefringence phase matching, exploits nondiagonal components of $\chi^{(2)}$, whereas several interesting crystals present very large diagonal components of $\chi^{(2)}$. Such components can be exploited only if the phase-matching conditions are achieved by means of the periodical poling technique.

The commonly used second-order materials are inorganic crystals with oxygen polyedra, which can be viewed as ionic crystals where one of the ions is replaced by an oxygen polyedron in an ionized state, stabilized in a noncentrosymmetric configuration by the surrounding ions (usually of metal elements). Examples of such crystals are the ABO_3 type of ferroelectrics, such as $LiNbO_3$ and $KNbO_3$, borates, such as BaB_2O_4 and LiB_3O_5 (usually indicated, respectively, as BBO and LBO), and the isomorphic family with the generic formula $MTiOXO_4$, such as potassium titanyl phosphate $KTiOPO_4$ (usually indicated as KTP).

It is important to note that the requirements for nonlinear materials are not only suitable transparency and high nonlinearity, but also sufficient birefringence for phase-matching, high-optical-damage threshold, good thermal, mechanical, and chemical properties, and possibility of growing large crystals of good optical quality.

Families of crystals possessing a second-order nonlinearity larger than that of inorganic crystals are organic molecular crystals and heteropolar semiconductors. However, at present, they are less interesting for applications because the former has insufficiently good mechanical and chemical properties, whereas the latter is not birefringent. In addition, both families have a limited transparency range.

A possibility that is actively explored is that of starting from an amorphous material (such as a polymer or a silicate glass) and introducing an orientation of noncentrosymmetric molecular groups by heating at a temperature above the glass transition and applying an external field, usually an electric field (electrical poling).

Third-Order Nonlinear Effects

Optical Kerr Effect

If a third-order material illuminated by a monochromatic plane wave at frequency ω propagating along the z-axis is considered, it results from eqn [2] that such a wave gives rise to a nonlinear polarization oscillating at $3\omega_1$. In turn, the nonlinear polarization, once inserted into eqn [1], yields a third-harmonic (TH) optical wave. The entire treatment developed for SH generation, including the phase-matching considerations, can be easily translated to the TH case, and is not repeated here. Instead, the attention is on the polarization term having the expression

$$P(z,\omega) = \varepsilon_0\left[\chi^{(1)}E(z,\omega)+\chi^{(3)}\alpha|E(z,\omega)|^2E(z,\omega)\right] \qquad [5]$$

where α is a numerical factor that can assume values ranging from 1/2 to 3/2, considering different third-order phenomena. From eqn [5], it is possible to define an intensity-dependent susceptibility: $\chi_{\text{eff}}^{(1)} = \chi^{(1)}+\chi^{(3)}\alpha|E(z,\omega)|^2$. By recalling the relation between index of refraction and electric susceptibility and assuming that the nonlinear contribution is small in comparison with the linear one, one obtains

$$n_{\text{eff}} = n+n_2|E|^2 \qquad [6]$$

where $n_2 = \alpha\chi^{(3)}/\left(2\varepsilon_0 c\chi^{(1)}\right)$. A more careful analysis shows that the overall effect consists in an intensity-dependent deformation of the index ellipsoid of the medium. In particular, an initially isotropic material becomes uniaxial in the presence of a strong linearly polarized optical beam.

Equation [6] expresses the optical Kerr effect. Some phenomena due to such an effect are briefly discussed below.

Optical switch

The phase and the polarization of an optical signal going through a Kerr medium can be changed by illuminating the medium with a strong auxiliary (pump) beam. This opens the way to the realization of all-optical modulators and switches. If the Kerr effect is fast, as it happens when it is due to the displacement of electron clouds, the response time of the device can be as short as the duration of pump pulses (less than 1 ps).

Self-focusing

Considering a pump with a Gaussian transverse intensity profile (this is the output beam from a single-mode laser), the optical Kerr effect produces a transverse index-of-refraction profile that follows the shape of the beam. If n_2 is positive, a greater index of refraction is induced on-axis than in the wings of the beam, creating in this way, a positive lens that tends to focus the beam. This effect is called self-focusing. If the input power is larger than a threshold value, self-focusing can exactly balance diffraction, so that the beam propagates without changing its profile. This phenomenon is called self-trapping. If the input power is further increased, the beam will catastrophically focus, causing in many cases optical damage inside the medium. To conclude this short discussion about self-focusing, it should be mentioned that the effect is very usefully exploited in the so-called Kerr-lens passive mode-locking method for the generation of ultrashort laser pulses.

Self-phase modulation

Considering a beam with a time-dependent intensity profile (optical pulse), the optical Kerr effect gives rise to a self-induced nonlinear phase shift that is also time dependent. Generally speaking, this has the consequence of broadening the frequency spectrum of the optical pulse. It should be recalled that an optical pulse propagating in a linear dispersive medium has a time duration increasing progressively with the propagation distance. Among the various phenomena occurring during the nonlinear propagation of short pulses, it is worth mentioning the existence of optical solitons, that is, pulses of appropriate shape, intensity, and time duration that propagate without changing shape and duration in a medium presenting anomalous group-velocity dispersion. Such a phenomenon is made possible by a compensation between the effects of linear dispersion and self-phase modulation. Particularly important for applications to optical communications is the study of nonlinear propagation in single-mode optical fibers: although the nonlinearity of glass is very small, nonlinear effects can be significant because the intensity can be high and the propagation distance is very large.

Four-Wave-Mixing and Optical Conjugation

The term four-wave-mixing (FWM) refers to the interaction of four waves in a nonlinear medium via the third-order polarization. In the presence of three monochromatic beams at frequencies ω_1, ω_2, ω_3, a nonlinear polarization term oscillating at the frequency $\omega_4 = \omega_1+\omega_2-\omega_3$, with wave vector $\boldsymbol{k_4} = \boldsymbol{k_1} + \boldsymbol{k_2} - \boldsymbol{k_3}$, is generated:

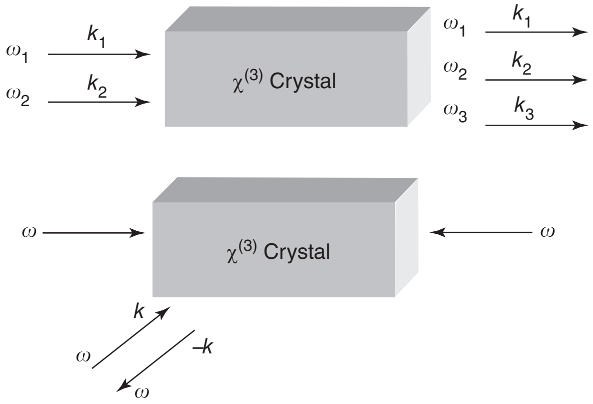

Figure 8 Schematic wave-mixing processes: frequency shifter and conjugated mirror.

$$P = \varepsilon_0\chi^{(3)}A_1A_2A_3^* \exp[i(\boldsymbol{k}_1+\boldsymbol{k}_2-\boldsymbol{k}_3)\cdot\boldsymbol{r}] \qquad [7]$$

Among the various phenomena originated by the nonlinear polarization of eqn [7], two particularly interesting processes are selected (see Figure 8).

Frequency-shifting scheme

In practical situations, a high-intensity beam (pump beam) at frequency $\omega_p = \omega_1$ is sent collinearly with the weak beam (signal beam) 2. The new beam 3 is also collinear, and has a frequency $\omega_3 = 2\omega_1 - \omega_2$. Note that $\omega_3 - \omega_1 = \omega_1 - \omega_2$, that is, ω_3 is the mirror image of ω_2 with respect to the pump frequency. If, for instance, the pump beam is continuous and the signal is a sequence of pulses, the frequency-shifted beam 3 is a temporal replica of the signal beam. It should be added that, in the absence of materials having a large $\chi^{(3)}$, it is usually more convenient to perform the same operation by using a cascade of two second-order processes in a $\chi^{(2)}$-material. Frequency-shifting devices can be usefully applied in optical communications systems.

Phase-conjugate mirror

If a degenerate case in which all the frequencies coincide is considered, $\omega_1 = \omega_2 = \omega_3 = \omega$, the new field has frequency $\omega_4 = \omega$ and wave vector $\boldsymbol{k}_4 = -\boldsymbol{k}_3$, that is, it counterpropagates with respect to beam 3. The nonlinear medium illuminated by beams 1 and 2 acts as a mirror for beam 3: this is what is called a phase-conjugate mirror. Such a mirror has some unique properties compared to an ordinary mirror. First of all, it functions as a retroreflector for any incident angle θ, within the acceptance angle of the experiment. Any phase change $\varphi(\boldsymbol{r})$ impressed on beam 3 by propagating, for example, through an inhomogeneous medium, will result in exactly the opposite phase $-\varphi(\boldsymbol{r})$ impressed on the reflected wave, in this way correcting the phase distortion during the back-propagation. In terms of energy balance, the FWM process subtracts one photon from beam 1 and one photon from beam 2, and adds one photon to beam 3 and one photon to beam 4. As a consequence, the reflection coefficient of the conjugated mirror is proportional to the product of the intensities of beams 1 and 2 and can even become larger than 1.

This section concludes with a brief discussion on third-order nonlinear materials. It is useful to distinguish between slow and fast nonlinearities. Slow nonlinearities involve the rotation and alignment of molecular groups under the action of an optical field, such as it may happen in liquid crystals. The effects are large, but the response time can be of the order of milliseconds or even longer. Fast nonlinearities involve the displacement of electron clouds, response times can be in the range of picoseconds but the effects are small. In order to enhance electronic nonlinearities one can operate near a resonance, but the drawback is that response times are now controlled by the material decay time. The most interesting materials are semiconductors or conjugated polymers, but, in practice, the largest fast third-order nonlinearities are obtained by using a cascade of second-order processes in a noncentrosymmetric material.

Stimulated Raman and Brillouin Scattering

Raman scattering is an inelastic light scattering process in which a quantum of excitation is exchanged between the optical field and the scattering medium. A typical case is that of a molecule possessing a vibrational mode with angular frequency ω_v, illuminated by a light beam at frequency ω. The spectrum of scattered light, observed at any scattering angle, will contain, besides the unshifted Rayleigh line at ω, also an additional line, called Stokes line, at frequency $\omega_s = \omega - \omega_v$. The energy difference between the incident and scattered photon is taken to excite the molecular vibration. If the illuminated medium includes molecules that are already in an excited vibrational state, the spectrum of scattered light will contain a third line, called the anti-Stokes line, at frequency $\omega_{as} = \omega + \omega_v$, describing a scattering event in which the molecule has given its vibrational energy to the scattered photon. Raman scattering may exist also in association with rotational energy levels of molecules. Besides localized molecular excitations, there are also collective excitations producing Raman scattering, such as optical phonons in crystals or plasma waves in an electron gas. It should be noted that not all elementary excitations are Raman active; there are selection rules, usually different from those controlling radiative transitions.

Stimulated Raman scattering (SRS) is observed when two light beams, at frequencies ω and ω_s, are sent into the medium. The Stokes photons generated by SRS are emitted with the same wave vector as that of the incident Stokes field and added coherently to that field. The result is that the field at ω_s is amplified, and, at the same time, more molecules are excited to the vibrational level. SRS can be used not only to amplify a signal at ω_s, but also to generate a coherent wave at ω_s. In fact, if a powerful beam at ω is sent into the medium, it will create Stokes photons by spontaneous Raman scattering, and the created Stokes photons can constitute the seed for an amplification process yielding an intense coherent Stokes field. Note that the spontaneous Stokes photons are emitted isotropically in space, whereas the stimulated Stokes beam will appear in a specific direction satisfying the criterion of maximum overlap between the pump and the Stokes beam. In practice, SRS is observed only in the forward and backward directions.

The growth of the Stokes field along the direction z is described by the equation

$$P_S(z) = P_S(0)\exp\left[\int_0^z g_R P_p(z)\mathrm{d}z\right] \qquad [8]$$

where g_R (in units of $\mathrm{m\,W^{-1}}$) is called the Raman gain and $P_p(z)$ is the pump power. SRS is a third-order process; in fact, it can be shown that g_R is proportional to the imaginary part of $\chi^{(3)}$.

If the scattering medium is placed inside an optical cavity, one can build a Raman laser. The Raman laser is different from a normal laser because the pump frequency ω_p can be arbitrary, whereas in normal lasers ω_p must correspond to a transition between the ground level and an excited level of the active medium. As shown in Figure 9, the energy transfer between pump and Stokes can be so efficient that a sequence of Stokes lines of decreasing frequency can be coherently generated. Raman lasers utilizing optical fibers as active medium represent very efficient and powerful sources of coherent radiation: as an example, fiber Raman lasers pumped by a neodimium-laser ($\lambda = 1064$ nm) and working on the fifth Stokes line can emit at a wavelength ~1500 nm with an overall efficiency of 30%.

Any medium at a nonzero temperature presents local fluctuations in the thermodynamic variables that give origin to light scattering. It is assumed that the incident light is characterized by a wave vector $\boldsymbol{k}$ and an angular frequency ω. In the case of a solid or liquid, the frequency spectrum of scattered light contains an unshifted line (due to nonpropagating density fluctuations) and two lines, called Brillouin lines, centered at frequencies $\omega \pm \omega_B$ that are due to density fluctuations propagating as spontaneous acoustic waves. If the scattering direction is fixed, hence the wave vector of the scattered field, $\boldsymbol{k}'$, only those spontaneous waves possessing a

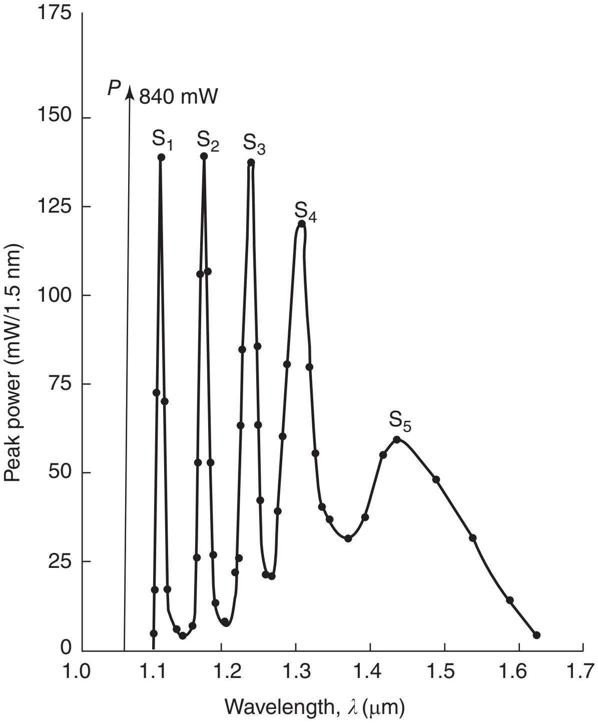

Figure 9 Generation of a sequence of Stokes lines in an optical fiber by stimulated Raman scattering. (Reproduced with permission from Cohen *et al.* (1978) *IEEE Journal of Quantum Electronics* QE-14(11): 855–859.)

wave vector $\boldsymbol{K} = \pm(\boldsymbol{k}' - \boldsymbol{k})$ contribute to light scattering in that direction. The frequency shift ω_B of the Brillouin lines corresponds to the frequency of the acoustic phonon which is exchanged in the scattering process. Recalling that the velocity of acoustic waves is given by $u_a = \omega_B/K$, the Brillouin frequency shift can also be seen as a Doppler shift due to diffraction from a traveling phase grating. Although Raman shifts are typically in the range of several terahertz, Brillouin shifts are of the order of some gigahertz.

Stimulated Brillouin scattering (SBS) can occur in a way fully similar to that of SRS. Only the interaction $\boldsymbol{K} = -(\boldsymbol{k}' - \boldsymbol{k})$, corresponding to the situation in which the incident wave reinforces the spontaneous acoustic wave, can give rise to a stimulated effect, generating a coherent wave at the frequency $\omega - \omega_B$. In practice, SBS is observed only in the backward scattering direction. It is interesting to mention that the backward Brillouin wave behaves as the phase conjugate of the pump wave. Therefore SBS can create a phase-conjugate mirror, similar to FWM, but in a simpler way, because only one beam is required.

Further Reading

Agrawal GP (1995) *Nonlinear Fiber Optics*, 2nd edn. New York: Academic Press.
Boyd RW (1992) *Nonlinear Optics*. New York: Academic Press.
Degiorgio V and Flytzanis C (eds.) (1995) *Nonlinear Optical Materials: Principles and Applications*. Amsterdam: IOS Press.
Sutherland RL (2003) *Handbook of Nonlinear Optics*. New York: Dekker.

Surfaces, Optical Properties of

R Del Sole and P Chiaradia, Università di Roma, Rome, Italy

© 2005 Elsevier Ltd. All rights reserved.

This is an update of R. Del Sole, P. Chiaradia, Surfaces, Optical Properties of, Editor(s): Franco Bassani, Gerald L. Liedl, Peter Wyder, Encyclopedia of Condensed Matter Physics, Elsevier, 2005, Pages 144–150, ISBN 9780123694010, https://doi.org/10.1016/B0-12-369401-9/00601-X.

Introduction 392
Results Obtained with SDR 392
Results Obtained with RAS 393
Results Obtained with Ellipsometry 396
Other Experimental Techniques 396
Theory 396
Conclusion 398
Further Reading 398

Introduction

In this article, an overview of the application of linear optical spectroscopies in surface science is given. From a historical point of view, optical methods were important in the very first development of surface-state spectroscopy of clean semiconductor surfaces at the end of the 1960s, when progress in both vacuum technology and surface diagnostics made it possible to reproducibly obtain well-characterized clean surfaces. In fact, optical transitions between filled and empty surface states of intrinsic type were discovered at that time in Ge(1 1 1)2×1 and Si(1 1 1)2×1 by differential reflectance with multiple internal reflections. These results demonstrated the existence of intrinsic (electronic) surface states for the first time in a direct way rather than indirectly from electrical measurements. In the subsequent years, many other surface-sensitive spectroscopies were successfully applied to investigate surface states at the cleavage faces of semiconductors as well as at other clean surfaces.

Generally speaking, in order to study surface optical properties, one has to extract the optical signal originating from the surface from the overwhelming bulk term. For example, in the surface differential reflectivity (SDR), this is accomplished by measuring a change of reflected-light intensity induced by either contamination (usually oxidation or hydrogenation) or chemisorption of foreign atoms. Instead, in reflectance anisotropy spectroscopy (RAS), which is also named reflectance difference spectroscopy (RDS), one measures the reflectance difference for light linearly polarized along two (orthogonal) axes of symmetry at the surface of cubic semiconductors. Since, in general, the surface has a lower symmetry than the bulk, an anisotropy signal originating from the surface is often measured.

When performed with polarized light, SDR yields information on all surface optical transitions (both isotropic and anisotropic) but requires a reference surface, which is obtained by modifying the sample in an irreversible way. On the other hand, RAS does not require any reference surface but is obviously limited to detection of anisotropic transitions only.

The interpretation of the optical experiments is, in general, not straightforward. Hence, the full potentiality of surface optical spectroscopy can be exploited only by a strong interplay of experimental and theoretical work.

At the beginning of the twentieth century, the so-called three-layer model (ambient–surface layer–substrate) was introduced by Drude to describe the surface optical properties from a phenomenological point of view. However, the first steps of the modern theory of surface optical spectroscopy started in 1971, when McIntyre and Aspnes expanded the reflectivity formula for the three-layer model to first order in the surface-layer thickness, obtaining a simple result, suitable for a clear physical interpretation. Realistic and *ab initio* calculations of surface optical properties have later been carried out, even including (in recent years) the electron–hole interaction. At present, the theory is fully developed, but its application to complex surfaces is hampered by the limitations of computational capabilities.

In the following, some relevant results obtained with surface optical spectroscopies, mainly SDR, RAS, and ellipsometry, are briefly described, together with their theoretical interpretations.

Results Obtained with SDR

One of the best-known semiconductor surfaces is the cleavage face of silicon, namely Si(1 1 1)2×1, whose reconstruction is described by the chain model developed in 1981 by Pandey. The optical properties of this surface have been extensively investigated over the years, in particular with reflectance techniques. Figure 1 shows the so-called absorption constant in the near infrared due to transitions between filled and empty surface states possessing a dangling-bond character, at Si(1 1 1)2×1. These pioneering results (1971) were obtained by applying the method of multiple internal reflections to cleaved samples in order to amplify the small surface effect. They proved the semiconducting character of the surface, in spite of the fact that the ideal (1 1 1) face should be metallic, with an energy gap of ~0.45 eV. Similar results were obtained in 1968 for Ge(1 1 1)2×1.

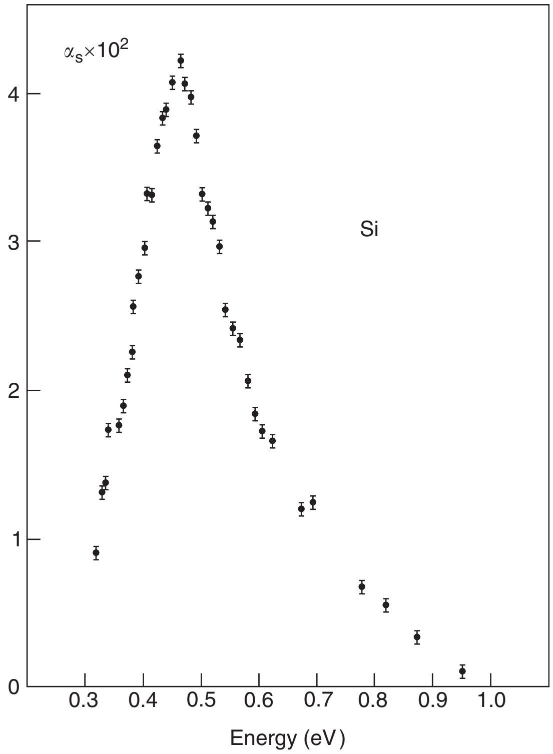

Figure 1 Absorption constant vs. photon energy for Si(1 1 1)2×1. (From Chiarotti G, Nannarone S, Pastore R, and Chiaradia P (1971) *Physical Review B* 4; 3398.)

The results of Figure 1 were compatible with Haneman's model, in which the lack of equivalency of surface atoms was explained by a charge transfer associated with a partial dehybridization, due to their up and down displacement with respect to the surface plane. These results were indeed interpreted in the framework of that model. However, when the chain model appeared many years later, its pronounced one-dimensional character suggested a strong anisotropy of the optical properties, at variance with what was predicted by Haneman's model. Indeed, this prediction was confirmed by another experiment with linearly polarized light. Figure 2 shows the surface reflectance peak (analogous to the absorption peak of Figure 1) for light polarized parallel and perpendicular to the chains of surface atoms at single domain Si(1 1 1)2×1. The results, recently confirmed by RAS, point out that this peak is totally anisotropic, thus providing a convincing evidence for the chain model.

In 1999, Rohlfing and Louie carried out a calculation of the optical properties of this surface, according to the method of the Bethe–Salpeter equation to account for the electron–hole interaction. The result (see Figure 3) has suggested that the experimental peak in Figure 2 is due to a bound exciton, with the electron and hole in two surface-state bands with a binding energy of 0.27 eV.

Results Obtained with RAS

RAS was developed as a modulation technique distinct from SDR (in USA) by Aspnes and in Russia by Safarov, independently, in the mid-1980s.

In the beginning, Aspnes mainly studied optical anisotropies of real surfaces of elemental semiconductors, in particular, Si substrates for technological applications. These anisotropies, ~1%, are not related to intrinsic surface states. They are, instead, associated to a lower symmetry of the subsurface region with respect to the (cubic) bulk, which perturbs the bulk-state wave functions, a situation often described as "bulk states modified by the surface." Figure 4 shows an example of these surprising anisotropies in the case of oxidized Si(1 1 0).

It is seen in Figure 4 that the line shape of the surface anisotropy clearly mimics the imaginary part of the bulk dielectric function of Si. While oxidized Si(1 1 0) now has become a standard for calibration of RAS apparatuses, the interpretation of spectra, such as those of Figure 4, is still an intriguing matter. After some controversies on the origin of the spectrum in Figure 4, the last calculations carried out, including the electron–hole interaction by Bechstedt and co-workers, have finally shown that it can be explained in terms of surface effects on the bulk resonant exciton underlying the E1 peak, close to 3.4 eV.

Since optical techniques can be performed in metal organic chemical vapor deposition (MOCVD) environments as well in vacuum, RA spectra during growths of GaAs(0 0 1) by both molecular beam epitaxy and MOCVD have been compared. As a result, a striking correspondence has been found between RAS signals characteristic of surface reconstructions in vacuum and those obtained in an MOCVD reactor at atmospheric pressure of hydrogen in suitable conditions. Figure 5 shows this correspondence, demonstrating that local ordering is the same in the two cases.

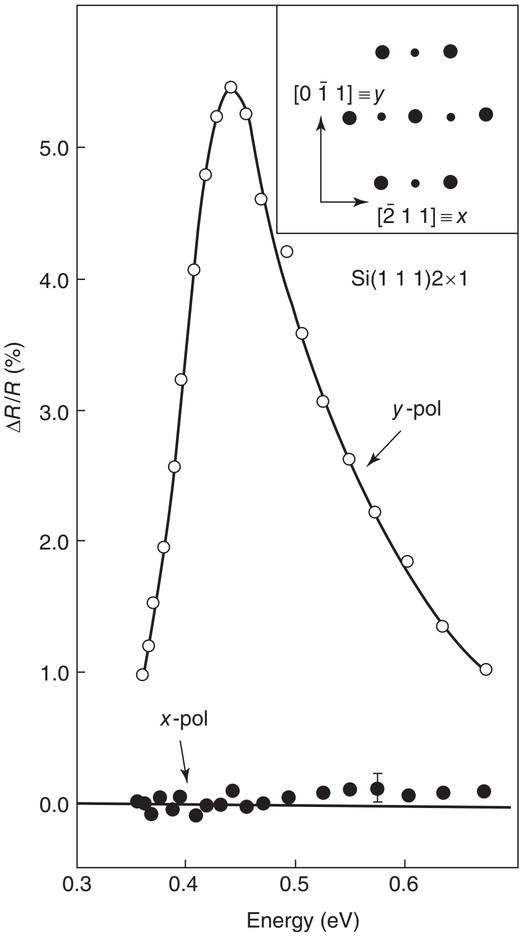

Figure 2 Differential reflectivity spectra of a single domain Si(1 1 1)2×1 surface, for light polarized along the [–211]=x and [0–11]=y directions. The LEED pattern is sketched in the inset. (From Chiaradia P, Cricenti A, Selci S, and Chiarotti G (1984) *Physical Review Letters* 52: 1145.)

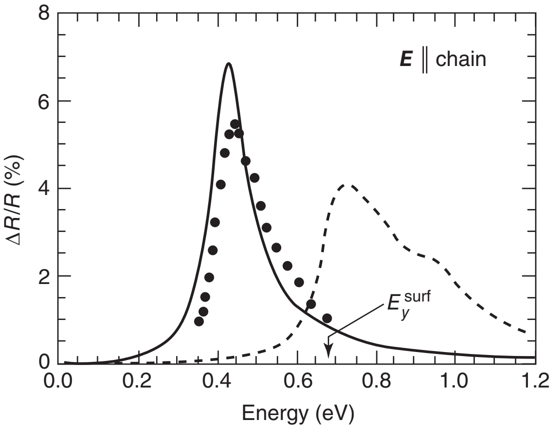

Figure 3 Surface contribution to reflectance of Si(1 1 1)2×1 for light polarized along the chains of surface atoms. – – – –: one-electron *GW* calculation; ———: including excitonic and local field effects; ● ● ● ●: experiment. (Reproduced with permission from Rohling M and Louie S G (1999) *Physical Review Letters* 83: 856.)

Calculations have been carried out for various reconstructions of GaAs(0 0 1), using both semi-empirical and *ab initio* methods, in order to understand the origin of the observed structures. A good explanation of the RAS of the As-rich reconstructions has been obtained. Most of the RAS structures arise from transitions across surface-perturbed bulk states. However, on the (2×4) reconstruction, a combined energy loss and RAS experimental work have recently revealed true surface-state transitions at ~2.5 eV, well below the first bulk critical point. The optical properties of the Ga-rich (0 0 1) surface, instead, are not yet completely understood. In recent years, interesting RAS investigations have been performed on other semiconductor surfaces, both clean and covered with

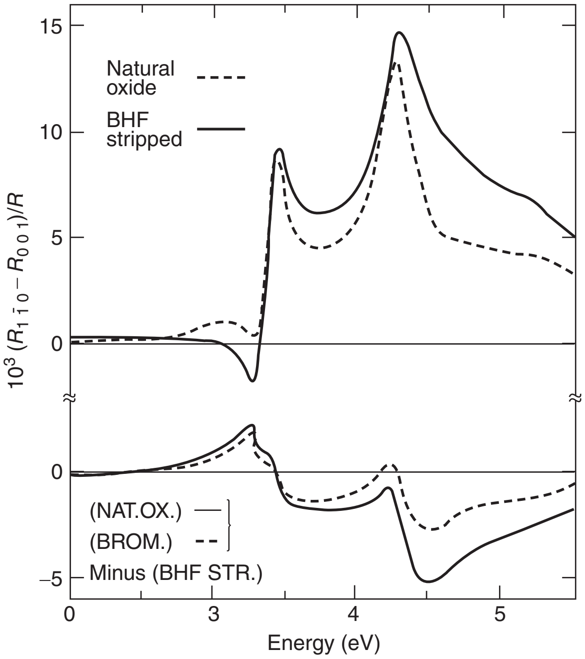

Figure 4 Top: Reflectance anisotropy spectra for a naturally oxidized Si(1 1 0) surface before and after stripping with buffered HF acid. Bottom: changes in the stripped-surface spectrum upon air oxidation and upon exposure to Br_2 in methanol. (Reproduced with permission from Aspnes DE (1985) *Journal Vacuum Science and Technology B* 3: 1498.)

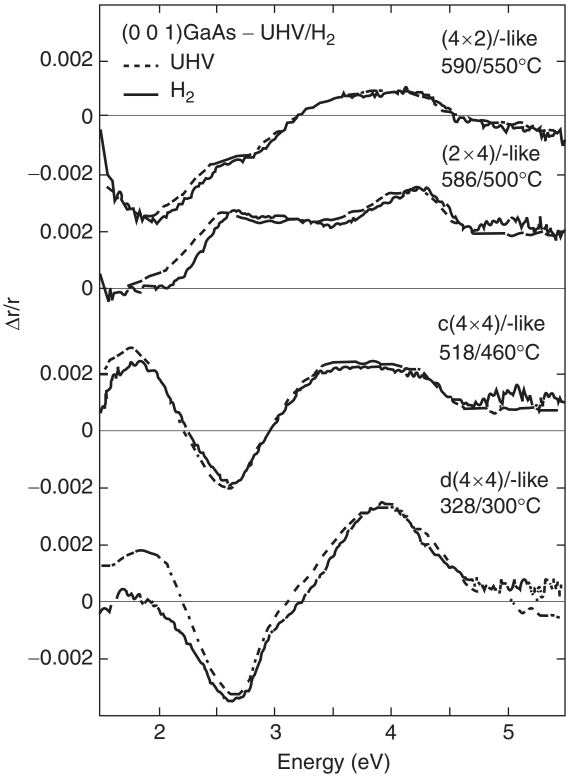

Figure 5 Reflectance anisotropy spectra of the primary reconstructions of GaAs(1 0 0) in UHV and atmospheric pressure of hydrogen, at the indicated temperatures. (Reproduced with permission from Kamiya I, Aspnes DE, Tanaka H, Florez LT, Harbison JP, and Bhat R (1992) *Physical Review Letters* 68: 627.)

monolayers of alkali atoms, by the groups of Richter and Paget. Also, organic molecules deposited on different substrates have been studied by RAS, especially by Weightman and Chiaradia-Goletti. Moreover, RAS shows promise to yield valuable information on low-dimensional systems (quantum wires and dots) and nanostructures (carbon nanotubes, polymers, etc.).

Results Obtained with Ellipsometry

Ellipsometry measures changes in the polarization parameters of light upon reflection from a surface. These parameters are: the relative phase Δ and the relative amplitude ratio arctan Ψ of the two components of linearly polarized light, parallel and perpendicular to the plane of incidence,

$$r^{\mathrm{p}}/r^{\mathrm{s}} = \tan\Psi\exp(\mathrm{i}\Delta) \tag{1}$$

From the spectral dependence of Δ and Ψ, the optical constants n and k are obtained by making use of the Fresnel formulas for the reflection coefficients r^{p} and r^{s}.

When surface properties are studied by ellipsometry, a differential method has to be used, as in the case of SDR. Thus, the changes $\delta\Delta$ and $\delta\Psi$ of the ellipsometric parameters are recorded upon adsorption of a gas. Under simplifying hypotheses, in the framework of the usual three-layer model, the optical constants of the surface are eventually obtained.

Starting from the pioneering work of Mayer in the 1970s, ellipsometry has been applied to derive the surface optical constants of a number of clean semiconductor surfaces. Especially, various crystallographic faces of Si and Ge, as well as the cleavage faces of GaP, GaAs, and ZnO, and also a number of metallic surfaces have been investigated by this technique.

In spite of the seemingly greater complexity in the data reduction, the results obtained by ellipsometry are practically coincident with those obtained by reflection-based methods, as demonstrated, for instance by the spectra of Figure 6, reporting the dielectric anisotropy obtained from both RAS and ellipsometry data for GaAs(0 0 1) 2×4.

Other Experimental Techniques

Many other optical techniques have contributed in the past to the development of surface physics. Although some of them have fallen into disuse, they deserve to be mentioned here: surface photoconductivity, surface photovoltage, photothermal displacement spectroscopy, and surface photoluminescence. A review of the main results obtained by means of these techniques, especially in the field of clean semiconductor surfaces, can be found in the literature.

Theory

Theoretical work is needed in order to fully exploit the potentiality of surface optical spectroscopy. Three steps are involved in the theory: (1) the determination of one-electron wave functions; (2) the calculation of the dielectric susceptibility, possibly including many-body interactions; and (3) the solution of light-propagation equations. The last problem was solved in a quite simple way at the end of the 1970s. The surface contribution to reflectivity (i.e., the reflectance difference with and without the surface layer) can be calculated according to the formula:

$$\Delta R/R = 4\left(\frac{\omega}{c}\right)\cos\theta\,\mathrm{Im}\left\{\frac{\Delta\varepsilon_{yy}}{(\varepsilon_b-1)}\right\} \tag{2}$$

for s-light incident from vacuum in the xz-plane and polarized in the y direction.

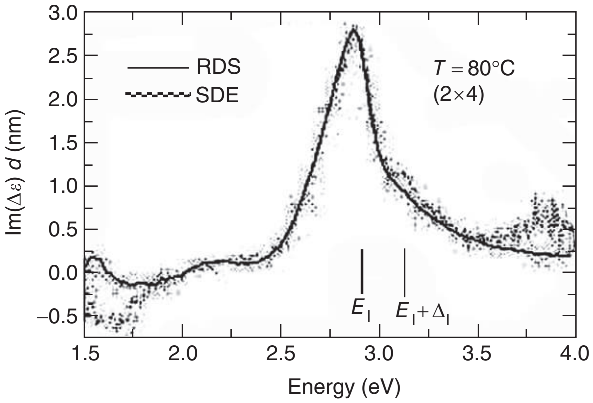

Figure 6 Dielectric anisotropy of GaAs(1 0 0) 2×4, as obtained from reflectance difference spectroscopy (RDS) and from surface differential ellipsometry (SDE). (Reproduced with permission from Wassermeier M, Behrend J, Ploog KH, Zettler JT, Stahrenberg K, and Richter W (1996) *Physical Review B* 53: 13542.)

Here, θ is the angle of incidence, and

$$\Delta\varepsilon_{yy} = \int_{-\infty}^{\infty} \mathrm{d}z \int_{-\infty}^{\infty} \mathrm{d}z' \left[\varepsilon_{yy}(z,z') - \delta(z,z')\varepsilon_0(z)\right] \qquad [3]$$

$\varepsilon_0(z) = \theta(-z) + \varepsilon_b\theta(z)$ is the zeroth-order dielectric constant yielding Fresnel formulas, and $\varepsilon_{yy}(z,z')$ is the relevant component of the nonlocal dielectric tensor of the solid–vacuum interface.

For a microscopic evaluation of surface optical properties, one has to calculate eqn [3]. If excitonic and local-field effects are neglected, $\varepsilon_{yy}(z,z')$ can be computed from one-electron wave functions. It is usually evaluated mimicking the semi-infinite crystal by a slab of several (from 10 to 30) atomic layers. In this case, the right-hand side of eqn [3] is related to the slab dielectric function. Within the single-particle scheme, its imaginary part is simply related to the transition probability induced by the radiation between slab states:

$$\varepsilon^{(2)}_{yy}(\omega) = (8\pi^2 e^2/m^2\omega^2 A)\sum_{k}\sum_{\mathrm{v,c}} \left|p^{y}_{\mathrm{v,c}}(k)\right|^2 \times \delta(E_c(k) - E_v(k) - \hbar\omega) \qquad [4]$$

where $p^{y}_{\mathrm{vc}}(\boldsymbol{k})$ is the matrix element of the y-component of the momentum operator between initial (v) and final (c) slab states at the point $\boldsymbol{k}$ in the two-dimensional Brillouin zone (BZ), and A is the sample area. The real part is computed via the Kramers–Kronig relation.

One more ingredient entering eqn [2] is the bulk dielectric function, whose imaginary part is analogous to eqn [4], where, now, eigenstates and eigenvalues of the infinite crystal, together with three-dimensional $\boldsymbol{k}$ vectors, are involved. The study of the optical response of surfaces within the single-particle picture amounts then to calculating (1) the single-particle spectrum and (2) the transition probability between occupied and unoccupied states, both for the perfect crystal and for the crystal with a surface.

If the dielectric susceptibility $\varepsilon_{yy}(z,z')$ is assumed to be local, and a three-step model is hypothesized for its z dependence, the formula of McIntyre and Aspnes mentioned in the section "Introduction" is recovered.

The one-electron states appearing in eqn [4] should be obtained, strictly speaking, within the theory of Green's functions, by solving the quasiparticle Schrödinger-like equation. In this framework, electrons move in a potential which is the sum of the ion potential, the Hartree potential due to the electronic charge density, and of a nonlocal energy-dependent self-energy, which accounts for exchange-correlation (XC) effects due to the interaction with the other electrons. The so-called *GW* approximation to the self-energy, developed by Hedin in 1965, completes the recipe for a rigorous calculation of band energies in solids. Calculations carried out starting in the 1980s have yielded band energies in agreement within 0.1 eV with experimental values for semiconductors.

GW calculations of the electronic structure of solids are computationally very demanding. Hence, as in the past, before the advent of vector computers, even now for complex systems, simpler – yet less accurate – methods are being used. Semi-empirical methods include the tight-binding and pseudopotential methods, where the matrix elements of the Hamiltonian (in the former case) or of the total potential (in the latter case) between basis functions (local orbitals in the former case, plane waves in the latter) are fitted to reproduce bandgaps at some high-symmetry points of the BZ, obtained from experiments. An *ab initio* method often used to determine the band structure of solids is the density-functional theory (DFT), where the XC self-energy is substituted by a local energy-independent XC potential, which is a functional of the electron density. Optical spectra calculated for bulk semiconductors within the one-electron approximation yield only qualitative agreement with experimental spectra, no matter which method – semi-empirical or *ab initio*, *GW*, or DFT – is used. This is because the excitonic and local-field effects are neglected. When these are considered, the discrepancies disappear, as it was shown first by Hanke and Sham in 1980 with a tight-binding calculation. *Ab initio* calculations of the optical properties of bulk solids including the electron–hole interaction and local-field effects yield quantitative agreement with experiments.

The most used methods to calculate surface optical properties are those relying on the single-particle approximation, ranging from the simplest (less accurate) ones (such as semi-empirical tight binding) to the rigorous quasiparticle *GW* method. Anyway, if the electron–hole interaction is not included, one can expect only a qualitative description of the spectra. The inclusion of the electron–hole interaction in the calculation of excited spectra leads one to consider a two-particle problem (the Bethe–Salpeter equation) rather than a single-particle problem (the Schrödinger-like equation for quasiparticles). Hence, the computational cost increases dramatically and makes the method usable, at present, only for simple surfaces.

The semi-empirical tight-binding method, for its computational speed, has been the first method used for calculating surface optical properties in 1986, when it was successfully applied to Si(1 1 1)2×1 and explained the strong optical anisotropy shown in Figure 1. In spite of its limitations, this method has yielded, in many cases, results in qualitative agreement with experiments and has helped in clarifying the atomic and electronic structure of a number of surfaces.

Ab initio methods have been developed in the last decade within DFT local-density approximation (DFT-LDA), by expanding the wave functions in plane waves and using nonlocal norm-conserving pseudopotentials. Finally, a rigorous one-electron calculation of surface optical properties should rely on the Green's function approach, with the electron self-energy calculated according to the *GW* approximation. These approaches are much more demanding than semi-empirical tight binding from the computational point of view, since a great number of plane waves are needed to represent slab wave functions.

As an example, the case of GaAs(1 1 0) is discussed. First-principles calculations including self-energy corrections according to the *GW* approximation have been carried out for this surface and are shown in Figure 7. They are compared to room temperature (RT) experiments carried out by Esser and co-workers. Calculations show that the experimental peak at 2.7 eV has a substantial

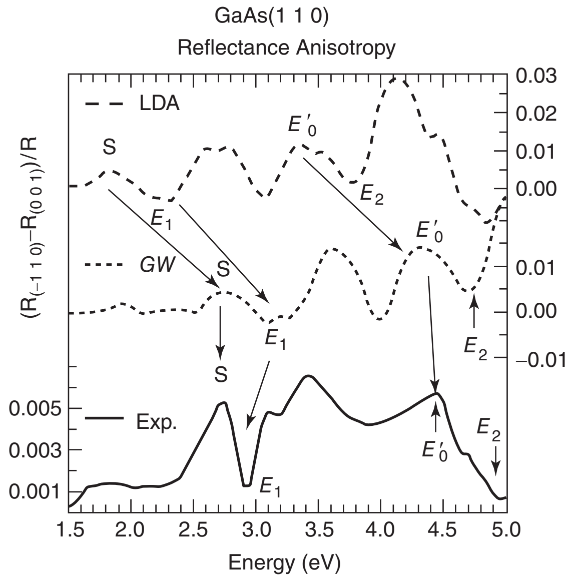

Figure 7 Reflectance anisotropy of GaAs(1 1 0). Upper curve: DFT-LDA calculation. Middle curve: *GW* calculation. Lower curve: RT experiment. (After Del Sole R, Palummo M, and Pulci O (2004) In: Cricenti A (ed.) *Epioptics*-7, p. 1. World Scientific.)

(∼50%) contribution arising from transitions across surface states, while all other structures are due to transitions across surface-perturbed bulk states. The reflectance anisotropy calculated in this way has the main structures in very good agreement with experimental ones as far as energy positions are concerned, while the DFT-LDA calculation, also shown in Figure 7, is considerably red-shifted, as a consequence of the DFT "gap problem." Differences in line shapes are still present, which are expected to be fixed by introducing excitonic and local-field effects in the calculations.

Finally, the inclusion of the electron–hole interaction can be performed by solving the Bethe–Salpeter equation at surfaces. The first calculation of this kind, carried out by Rohlfing and Louie for Si(1 1 1)2×1 in 1999, is shown in Figure 3. As it was mentioned before, the SDR peak at 0.45 eV is ascribed to a surface-state bound exciton, which takes over most of the oscillator strength of the transitions across the dangling-bond (DB)-like surface states. As a consequence, these transitions become very weak and are hardly visible in the experimental spectra. Another application of this technique has been done by Bechstedt and co-workers in 2002 for Si(1 0 0):H, which explained the line shape of the RAS spectrum of Figure 4 as due to a polarization-dependent quenching of bulk excitonic effects close to 3.4 eV.

Conclusion

Optical spectroscopy has become, in the last decades, an important tool for surface analysis, of great sensitivity to structural changes and versatility. The theoretical understanding of the results is becoming more and more satisfactory, thanks to the application of advanced many-body techniques to the simulation of surface optical properties. Nevertheless, some problems are still open: the most obvious is the extension of these techniques to complex surfaces (those with higher-order reconstructions), which is hampered by the current computational limitations. Less obvious problems are those related to the electron–phonon interaction, which affects surface optical line shapes in a drastic way, and to the complex morphological structure of surfaces, arising from steps, multiple domains, and defects, whose study is now at an initial stage.

Further Reading

Aspnes DE (1993) *Thin Solid Films* 233: 1–8.

Bassani F and Pastori-Parravicini G (1975) *Electronic States and Optical Transitions in Solids*. Oxford: Pergamon.

Chiaradia P (1996) In: Chiarotti G (ed.) *Physics of Solid Surfaces*, Landolt Boernstein, Group III "Condensed Matter," vol. 24, p. 29, subvolume d, (Interaction of Radiation with Surfaces and Electron Tunneling.)

Chiaradia P and Del Sole R (1999) *Surface Review and Letters* 6: 517.

Chiarotti G (1994) *Surface Science* 299/300: 541.

Halevi P (ed.) (1995) Photonic probes of surfaces. *Electromagnetic Waves: Recent Developments and Research*. Amsterdam: North-Holland/Elsevier.

Herman MA, Richter W, and Sitter H (2004) *Epitaxy*. Berlin: Springer.

X-Ray Topography☆

JB Hartwig[a], **J Härtwig**[a], **and SN Aqida**[b], [a]ESRF, Grenoble, France; [b]Ahmad Universiti Malaysia Pahang, Pekan, Malaysia

© 2016 Elsevier Inc. All rights reserved.

This is an update of J.B. Hartwig, J. Härtwig, S.N. Aqida, X-Ray Topography, Reference Module in Materials Science and Materials Engineering, Elsevier, 2016, ISBN 9780128035818, https://doi.org/10.1016/B978-0-12-803581-8.01228-5.

Introduction 399
Principle of the Topographic Techniques 399
Some Results of Dynamical Theory 401
Effect of Imperfections: Contrast Mechanisms 402
Diffraction Topographic Techniques 404
Synchrotron Radiation Topography: Real-Time Investigations and Coherence-Related Effects 405
Simulations of X-Ray Topographs 406
Conclusion 407
References 407
Further Reading 407

Nomenclature

$\boldsymbol{b}$	Burgers vector of a dislocation (m)
C_p	Polarization factor (X-ray diffraction)
F_h	Structure factor associated with the reciprocal vector h
r_0	Classical electron radius (2.8×10^{-15} m)
$\boldsymbol{u}(\boldsymbol{r})$	Displacement vector
V_c	Volume of the unit cell (m^3)
$\delta\boldsymbol{\theta}(\boldsymbol{r})$	Effective misorientation (rad)
θ_B	Bragg angle (rad)
λ	Wavelength (m)
Λ_0	Extinction distance (dynamical theory) (m)
ω_h	Intrinsic width of the diffraction curve (dynamical theory) (rad)

Introduction

A major use of X-rays, ever since they were discovered over a century ago, has been and still is the visualization of the inside of systems, opaque for other probes. Whatever the imaging process used, it implies an inhomogeneous response of the sample to the beam. Recently, X-ray imaging techniques have dramatically progressed, in connection with the improvements in sources (synchrotron radiation), detectors, and computer image processing. Among these new features, three-dimensional imaging with spatial resolution in the micrometer range (microtomography), the sensitivity enhancement associated with phase contrast imaging, and new X-ray microbeam-based imaging approaches such as fluorescence or diffraction microtomography are discussed below.

This section is devoted to another way of obtaining X-ray images, based on Bragg diffraction: the 'X-ray topographic' techniques (the 'historical' name is retained: it is widely used, but misleading because it suggests that these techniques are surface techniques, whereas very often they are used to probe the bulk of single-crystal samples). They were mostly developed in the late 1950s and 1960s to visualize defects and distortions in crystals. Work performed on silicon made the routine production of large perfect crystals, as used by the microelectronics industry, possible. These techniques are nondestructive and sensitive to a large range of distortions (typically in the $10^{-3}-10^{-8}$ range). Understanding the main contrast mechanisms implies knowing how crystal imperfections modify the diffraction behavior of the underlying perfect crystal. The dynamical theory of diffraction describes this behavior. The specific contributions of synchrotron radiation (and, briefly, neutrons) are outlined.

☆*Change History*: July 2015. S.N. Aqida added abstract; added key words; expanded text with additional review materials; updated list of further reading; added list of reference; and update 'Change History' section.

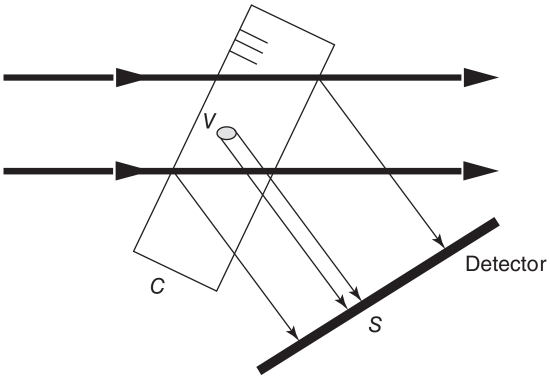

Figure 1 Principle of the topographic methods.

Principle of the Topographic Techniques

X-ray topography is an imaging technique for single crystals based on Bragg diffraction. The local variations of the amplitude or direction of the diffracted beam provide information on crystal inhomogeneities such as defects, domains, or phases. This information is often averaged out, and lost, when using usual diffraction methods.

Figure 1 schematically represents the main idea of all the diffraction imaging methods. The single-crystal sample C is set to diffract a fraction of the incoming beam, according to Bragg's law, $2d \sin\theta_B = \lambda_h$. The diffracted beam is recorded on a position-sensitive detector (usually X-ray films, nuclear plates or, increasingly, CCD cameras equipped with a high-resolution scintillator). If a small volume *V* within C behaves differently from the matrix, intensity variations ('contrast') can be produced on an area *S* of the two-dimensional image produced by the diffracted beam. This contrast only occurs if the platelet-shaped crystal displays inhomogeneities.

The inhomogeneities that can be visualized using X-ray diffraction topography include defects such as dislocations (Figure 2), twins, domain walls, inclusions, impurity distribution, and macroscopic deformations, such as bending or acoustic waves, present within the single-crystal sample.

Figure 3 is an example of such a topographic image. It shows the image recorded using the 444 reflection from a flux-grown platelet-shaped gallium-substituted yttrium iron garnet crystal ($Y_3Ga_xFe_{5-x}O_{12}$, with $x \sim 1$, Ga – YIG) using the MoKα_1 radiation from a standard X-ray generator.

In addition to a distorted region on the upper corner, associated with the crystal fixation, various features are observable on this topograph: dislocations, growth striations and growth sectors, magnetic domains, dissolution bands, and the initial stage of a crack.

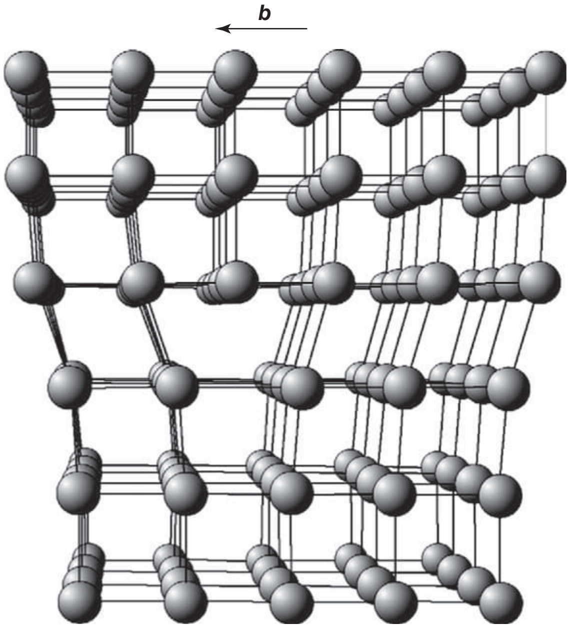

Figure 2 Schematic drawing of a dislocation, characterized by its line direction (the border of the incomplete atomic plane in this case) and the Burgers vector *b* (in this case – 'edge' dislocation – horizontal and perpendicular to the line direction).

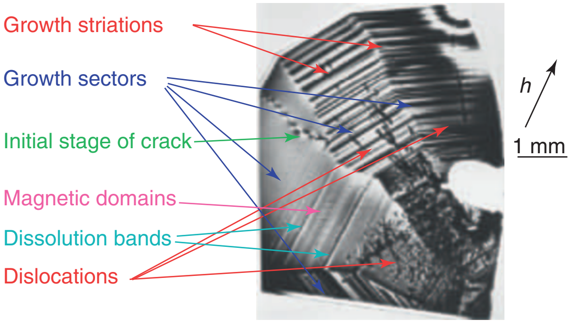

Figure 3 Topograph of a flux-grown Ga–YIG crystal.

These features are observed because they entail a distortion of the crystalline lattice. It is worth giving the typical value of these distortions, which include either a lattice rotation $\delta\theta$, or a lattice parameter variation $\Delta d/d$, or a combination of both. For the growth striations, which are the main observable features, this distortion is in the 10^{-4} range, whereas the variation of magnetostriction associated with the magnetic domains, as well as the distortion between growth sectors, are in the 10^{-6} range. The distortion associated with dislocations is a function of the distance to the core; at the level of the image border, it is in the 10^{-5} range. Large contrast on the image can, therefore, correspond to rather weak distortions, showing that these techniques are very sensitive.

Some Results of Dynamical Theory

A few results of the dynamical theory, necessary to understand the contrast mechanisms, are given below. The discussion is restricted to symmetrical transmission geometry as shown in **Figure 1**.

In the case of a monochromatic plane wave beam, and a perfect crystal set in Bragg diffraction position (**Figure 1**), two 'wavefields' propagate within the crystal if the direction of the incident beam propagation vector lies within an angle ω_h around the exact Bragg position (ω_h the intrinsic width of the diffraction curve, often called the Darwin width, being of the order of $10^{-5}-10^{-6}$ rad:

$$\omega_h = \left(2\lambda^2 C_{\mathrm{p}} |F_h| r_0\right) / (\pi V_{\mathrm{c}} \sin 2\theta_{\mathrm{B}}) \qquad [1]$$

where C_{p} is the polarization factor ($C_\pi = \cos 2\theta_{\mathrm{B}}$ for π polarization, i.e., for the electric field vector $\boldsymbol{E}$ in the scattering plane, and $C_\sigma = 1$ for ∝ polarization, i.e., for E perpendicular to this plane), r_0 is the 'classical electron radius' (2.8×10^{-15} m), V_{c} is the unit cell volume, and F_h is the structure factor corresponding to the Bragg reflection used. A wavefield corresponds to the superposition of one diffracted and one forward-diffracted wave, coupled because the perfect crystal is set for Bragg diffraction. These waves decouple outside the crystal, producing two beams, parallel to the incident and diffracted directions, respectively (**Figure 4**).

In the case of a monochromatic spherical wave, wavefields propagate and interfere within the whole 'Borrmann' fan or Borrmann triangle ABC (**Figure 4**). The characteristic coupling length between wavefields is ⊠$_0$ (extinction length, or Pendellösung period), which corresponds, in the case considered, to the distance necessary for most of the energy participating in the diffraction process to move from the transmitted to the diffracted direction, or vice versa:

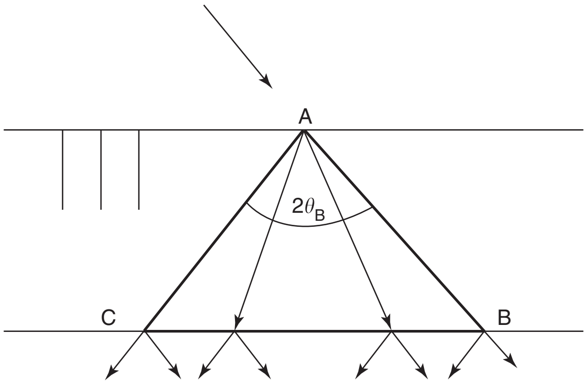

Figure 4 Propagation of wavefields within the 'Borrmann' triangle ABC in the case of a perfect crystal.

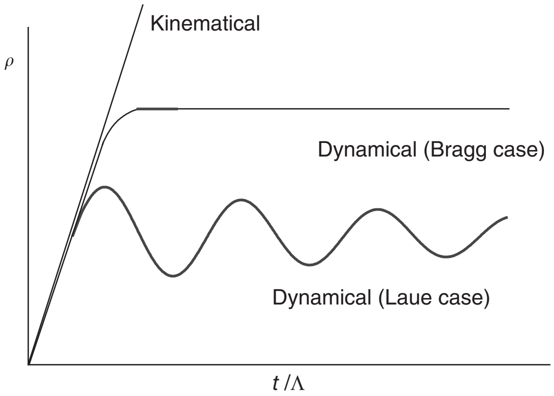

Figure 5 Reflecting power ρ of a nonabsorbing perfect crystal as a function of the reduced thickness t/Λ_0 for the transmission ('Laue') and reflection ('Bragg') cases. The kinematical approximation limit is also shown.

$$\Lambda_0 = (\pi V_c \cos\theta_B)/(\lambda C_p|F_h|r_0) \qquad [2]$$

Typical values of Λ_0 are in the 1 – 100 μm range.

If the crystal is rotated in a monochromatic beam, or if the beam is polychromatic, the diffracted power is a function of this 'variable' (angle, or wavelength), leading to the integrated reflectivity ρ, defined as the area under the diffraction curve. Figure 5 shows ρ for a nonabsorbing perfect crystal, as a function of t/Λ_0, t being the thickness of the platelet-shaped crystal, for both the transmission ('Laue') and reflection ('Bragg') cases. These curves show that

- ρ is proportional to t for $t \ll \Lambda_0$ ('kinematical' limit of the dynamical theory);
- ρ is nearly constant for $t \gg \Lambda_0$, the saturation value being proportional to $|F_h|$; and
- ρ displays an oscillatory behavior in the Laue case (the image produced by a low-absorption wedge-shaped crystal will, therefore, exhibit 'equal thickness' fringes associated with the maxima and minima of the curve, and to the varying thickness of the crystal). Its saturation value, for $t \gg \Lambda_0$, is half of the one corresponding to the Bragg case.

Effect of Imperfections: Contrast Mechanisms

For a nonabsorbing plate-shaped crystal illuminated by a parallel and polychromatic beam (a good approximation for the simplest and presently the most usual topographic technique, white beam synchrotron radiation topography), within a very simplified approach, the direction and intensity of the locally diffracted intensity depends upon

- the structure factor F_h;
- the angle θ formed by the considered lattice planes, and the incident beam; and
- Y, a parameter that incorporates the modifications introduced by the crystal inhomogeneities on the perfect-crystal dynamical theory results.

The beams diffracted by two neighboring regions I and II of the sample produce contrast on the topograph if

- $(F_h)_I \neq (F_h)_{II}$, where the differences can either reside in the modulus or the phase or the structure factor. This structure factor contrast is the main contrast mechanism in neutron diffraction topography of magnetic domains, the magnetic structure factor often being different for the various domains (Figure 6);
- $\theta_I \neq \theta_{II}$, that is, regions I and II are misoriented – subgrains, domains, etc. – one with respect to the other: this is orientation contrast; Figure 7 shows, for instance, white or black thick lines, corresponding to the separation, or superposition, of the images of subgrains;
- $Y_I \neq Y_{II}$, the two regions display extinction contrast.

Imperfections modify the perfect-crystal behavior described by the dynamical theory. They can hide the interference fringes, or lead to locally enhanced or reduced diffracted intensity, depending on the absorption conditions. New images can occur through the decoupling of a wavefield and the creation of new wavefields at a defect.

In the low-absorption case, the predominant contrast mechanism is the so-called direct-image process. Assume again (Figure 1) that a polychromatic, extended beam impinges on a crystal such that a small crystal volume V contains a defect (inclusion, dislocation, etc.) associated with a distortion field, which decreases with growing distance from the defect core. A wavelength range $\Delta\lambda/\lambda = \omega_h/(\tan\theta_B)(\sim 10^{-4})$ participates in diffraction by the 'perfect' matrix crystal, whereas regions around the defect are at the Bragg

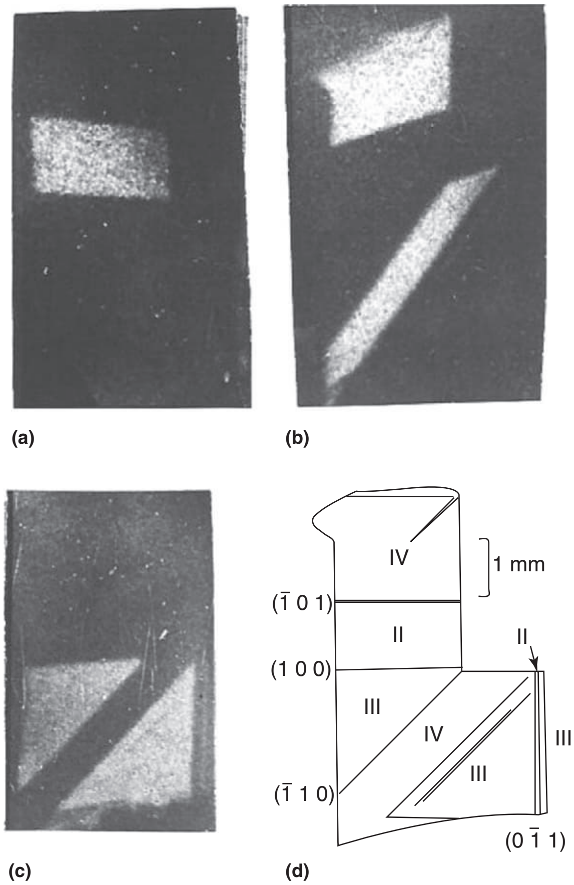

Figure 6 The observation, by neutron diffraction topography of antiferromagnetic domains in NiO is an example of ‘structure factor contrast.’ These domains are characterized by their propagation vector, which lies along one of the four equivalent 1 1 1 directions; each type of domain has a nonzero magnetic structure factor for the Bragg reflection corresponding to its propagation vector, and zero for the other three magnetic reflections: (a) 1,1, – 1, (b) – 1,1,1, (c) – 1,1, – 1, and (d) drawing of the domain configuration – type I is missing in the investigated crystal. These images were recorded – exposure times $\sim$ 10 h – using a ^{157}Gd screen acting as n - β converter and X-ray film; ‘white’ means more illuminated.

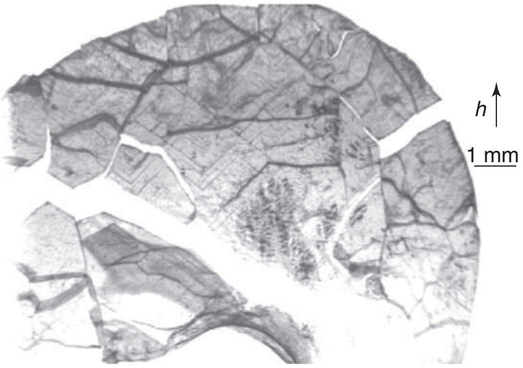

Figure 7 White beam topograph of an Fe – 3%Si crystal, $E \approx 25$ keV, showing orientation contrast associated with subgrains. A fir-tree magnetic domain pattern is also visible.

position for components of the incoming beam which are outside this spectral range. The defect thus leads to additional diffracted intensity on the detector.

The regions that produce the direct image of a given defect are some distance away from the core of the defect. This distance depends not only on the nature of the defect, but also on the diffraction process itself. The lattice distortion acts on diffraction through an angle, the effective misorientation $\delta\theta$, which reflects the change in the departure from the Bragg angle that is associated with the existence of the defect:

$$\delta\theta(r) = -(\lambda/\sin 2\theta_B)\partial(\boldsymbol{h} \times u(r))/\partial(s_h) \quad [3]$$

where $\boldsymbol{h}$ is the undistorted reciprocal lattice vector, $\boldsymbol{u}(\boldsymbol{r})$ is the displacement vector, and $\partial/\partial(s_h)$ is the differentiation along the reflected beam direction. It was shown that the width of the direct image corresponds to the contribution of regions such that $\delta\theta$ is of the order of ω_h. This can be understood when considering that the regions where the distortion is $<\omega_h$ are within the diffraction range of the perfect crystal, and that those where the distortion is $\gg\omega_h$ have a negligible contribution for the considered Bragg diffraction spot. This leads to 'intrinsic' image widths, for an edge dislocation such as the one schematized in Figure 2, $\sim\Lambda_0|\boldsymbol{b}\cdot\boldsymbol{h}|/4$ ranging in the 1–100 μm scale, and therefore implies a limitation on the density of defects that can be resolved on a topograph ($\sim 10^4 - 10^5$ cm^{-2} for dislocations).

This also implies that direct images are only seen in crystals that are thick enough. Indeed, the dynamical theory predicts a width ω_h for thin ($t < \Lambda_0/\pi$) crystals inversely proportional to the thickness. If the crystal is thin, only very distorted regions with a strongly reduced volume – and consequently reduced diffracted intensity – can contribute to the direct image, which cannot therefore be observable.

The effective misorientation $\delta\theta$ allows, in addition, determining on which reflections a given defect can produce an image. Equation [3] shows that $\delta\theta = 0$ if u is perpendicular to h. The defect is not visible on the corresponding topographs. A dislocation, for instance, is usually not visible when $\boldsymbol{h}\cdot\boldsymbol{b} = 0$, $\boldsymbol{b}$ being the Burgers vector. The invisibility criteria are powerful ways of characterizing the defects.

The effective misorientation can also be written as a function of the local variation in the rotation $\delta\phi$ of the concerned lattice planes and the local relative variation in the lattice parameter, $\Delta d/d$, as

$$\delta\theta = -(\Delta d/d)\tan\theta_B \pm \delta\varphi \quad [4]$$

when taking absorption into account, the situation can change drastically. Direct images do not occur in the high-absorption case ($\mu t > 10$), and are replaced by dips in the intensity corresponding to the disruption of a dynamical-theory-related effect, the anomalous transmission (also called the Borrmann effect). Both types of images ('additional' intensity and 'dips') are simultaneously present on the topographs, as well as interference fringes ('dynamical' and 'intermediary' images) for samples with intermediate absorption ($\mu t \sim 2-5$).

Diffraction Topographic Techniques

As already discussed, Bragg diffraction imaging may be used either in transmission or in reflection. In addition, the beam can be extended or restricted, and the image can be an integrated or a nonintegrated one.

Figure 1 shows an extended, divergent, and/or nonmonochromatic beam illuminating the whole sample, or a large area. This results in an image which can, to a first approximation corresponding to the predominance of the direct images, be considered as the projection of the defect distribution along the diffracted beam direction. The incident beam can also be restricted to a small width (typically 10–20 μm) in the scattering plane. In the same first approximation, this produces an image of those defects intercepted by the blade-shaped incident beam, hence the name 'section' topograph.

A better definition of the extended/restricted beam distinction is based on the width of the Borrmann triangle, $w_B = 2t\sin\theta_B$ in the symmetrical Laue case, t being the crystal thickness. The extended beam, or projection topograph, situation corresponds to the case where the width w of the incoming beam in the scattering plane is such that $w \gg w_B$. The restricted beam, or section topograph, case corresponds to $w < w_B$.

In the section topography, the position of the direct images within the image can be used to extract the depth of the related defects in the crystal, one edge of the image corresponding to the entrance face of the sample, the other to the exit surface. In very good crystals, with small or moderate absorption, the same interference effect that leads to the oscillations shown in Figure 5, produces interference fringes, called Kato's fringes. These fringes are very sensitive to crystal distortion, and their modification is one of the first indications of a departure from the perfect-crystal situation (see Figure 11).

The use of a polychromatic beam with a sufficiently wide bandwidth often offers advantages. Several reflections are recorded simultaneously, which is very helpful when characterizing defects or phenomena, and misoriented regions within a sample diffract at once, each region finding a wavelength λ that satisfies the local Bragg condition. This 'white beam' version of diffraction topography is identical to the well-known Laue technique, except that the incident beam is broad. Each Bragg spot is now a topograph. This is an integrated wave diffraction image, because it results from the superposition of contributions from a range of wavelengths. It is mainly sensitive to the variations of lattice plane orientation $\delta\phi$, which produce a change in the diffracted beam direction, and not to $\Delta d/d$. 'White beam' topography is widely used at synchrotron radiation facilities. The exposure time is often of the order of a fraction of a second, and it is possible to follow the evolution of any one of the Bragg spots in 'real time,' using a CCD camera equipped with a scintillator.

White-beam X-ray topography (WBXRT) have been used to study formation micro-cracks and associated strain fields produced by nano-indentations in Si wafers (Allen *et al.* 2010). Oriwol *et al.* (2013) revealed dislocation pile-ups and formation of smallangle subgrain boundaries with spacing between dislocations up to 28 nm in block-cast multicrystalline silicon using WBXRT.

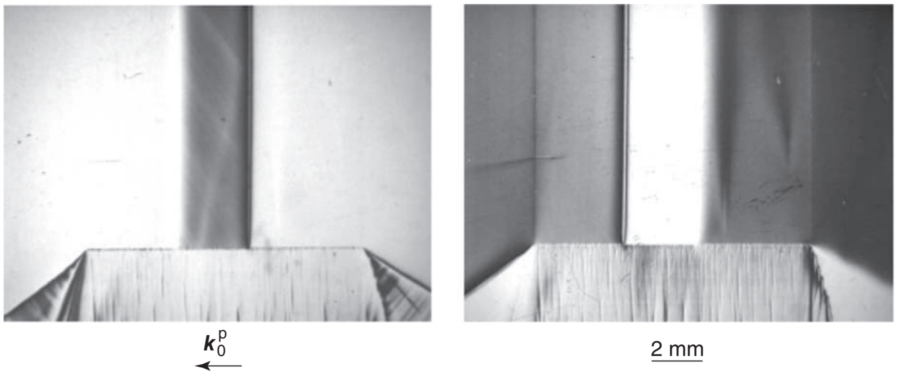

Figure 8 Bragg case plane wave topographs of a quartz plate with nonhomogeneous distributions of impurity atoms in different growth sectors and in the seed plate (rectangle in the middle part), $40\bar{4}0$ reflection, $E = 8.04778$ keV, k_0^p is the projection of the wave vector of the incident wave on the crystal surface; the topographs were recorded at ~ 40% of the maximum intensity on the low-angle side (left image) and ~ 20% of the maximum intensity on the high-angle side (right image) of the rocking curve.

The incident beam on the sample can also be monochromatized. This 'monochromatic wave' nevertheless displays a range of wavelengths ($\Delta\lambda/\lambda$) as well as an angular divergence ω. Let ω_c be the diffraction width of the crystal (which reduces to ω_h in the case of a 'perfect' crystal). If the divergence ω (and/or $(\Delta\lambda/\lambda)\tan\theta_B) > \omega_c$, the image is still an integrated wave topograph.

If ω (and $(\Delta\lambda/\lambda)\tan\theta_B \ll \omega_h$, the technique is called plane wave topography. It is not only suited to detect weak deformations ($10^{-6}-10^{-8}$ range), but also to obtain images of defects such as dislocations (see Figure 9) with much more details than in the case of direct images. Its use allows a quantitative analysis, because the local diffracted intensity is closely related to the effective misorientation. An example of the use of 'plane wave' topography is shown in Figure 8: the seed of the investigated quartz crystal and the various growth sectors exhibit different impurity contents, which result in small variations of the lattice parameter (in the $10^{-5}-10^{-7}$ range).

If an image is recorded at an angular position very far away (typically a few ω_c) from the center of the diffraction curve, the main contribution to Bragg diffraction originates from the distorted regions, and not from the perfect-crystal matrix. This allows reducing the 'intrinsic' width of the images and is known, by analogy with electron microscopy, as weak beam topography (Figure 9).

Synchrotron Radiation Topography: Real-Time Investigations and Coherence-Related Effects

Synchrotron radiation is now widely used for X-ray imaging. The typical exposure time to record a synchrotron radiation topograph is a fraction of a second. It is therefore possible to investigate evolving phenomena such as the movements of defects, boundaries during first-order phase transitions, or domains. Specific sample environments (cryostat, furnace, electric or magnetic field, strain, etc.) are added for each particular experiment. Image subtraction can help emphasize changes with respect to a reference state.

In recent studies, synchrotron radiation X-ray topography has been an effective technique for characterizing crystal quality, dislocations and imperfections in crystalline thin films. The topographies revealed crystalline imperfections in strained Si layer where several centimeters in size macule pattern and crosshatch patterns were observed on supercritical-thickness strained

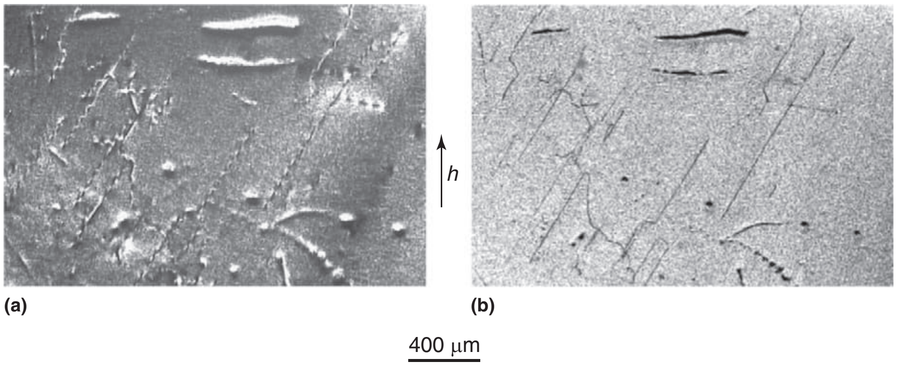

Figure 9 1 1 1 topographs of a Ge crystal recorded using the beam (35 keV) produced by an Si 1 1 1 monochromator: (a) top of the rocking curve, and (b) on the high-angle tail of the rocking curve ('weak beam' image).

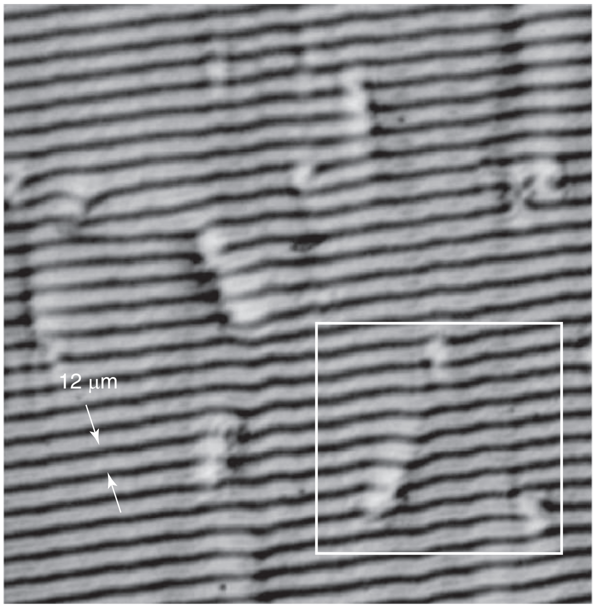

Figure 10 Stroboscopic topograph showing the propagation of surface acoustic waves – 12 μm wavelength – in a $LiNbO_3$ crystal. Wave front distortions caused by the interaction of the waves with dislocations are visible. One dislocation region is framed. (Courtesy of E. Zolotoyabko.)

silicon-on-insulator (SC-sSOI) wafers (Shimura *et al.* 2012). In Jussila *et al.* (2013) works, synchrotron radiation topographs indicated misfit dislocations which lead to critical thickness and crystal quality of $GaP_{0.98}$ $N_{0.02}$ layers grown on GaP substrates evaluation. Furthermore, the technique was also used to trace changes in density of microdefects and dislocation structure of grown $ZnGeP_2$ crystals (Verozubova *et al.,* 2014).

It is possible to investigate quicker phenomena if they are periodic, through stroboscopic imaging. Choppers located on the beam path and synchronized with periodic magnetic or electric fields were used to investigate phenomena such as the motion of magnetic domains or the evolution of conduction channels, in the $10^{-2}-10^{-3}$ s range. Stroboscopic experiments on bulk or surface acoustic waves, in the $10^{-8}-10^{-9}$ s range, were performed using the pulsed structure of the synchrotron radiation source itself (Figure 10).

The small source sizes and the large source-to-sample distances, which are now common features of modern synchrotron radiation facilities, lead to highly coherent X-ray beams, which can be used for diffraction topography. In this case surface inhomogeneities, or porosities, can be imaged in the diffracted beam even when they do not produce a strain field through their Fresnel diffraction image. Recording images at various sample-to-detector distances allow retrieving the phase jump involved in these images. The use of Bragg diffraction imaging with a coherent beam can even, in special cases, produce structural information at the atomic level, even though the spatial resolution of the images is on a much larger scale of micrometers. For instance, diffraction topographs of ferroelectric crystals, using a coherent beam, give access to a very elusive microstructural piece of information: how ferroelectric domains are connected across the domain wall and, in particular, how they match at the atomic level.

Simulations of X-Ray Topographs

The information provided by the topographs allows a detailed quantitative analysis. This is performed through simulations. The simulation process requires introducing a deformation field with free parameters that will be refined by comparing the simulated image to the experimental one. Depending on how rapidly the distortions (expressed by the effective misorientation $\delta\theta r$) change locally within the crystal, this may be done using diffraction theories with various complexities. In the case of Figure 8, the Braggcase plane wave topographs of a quartz plate with nonhomogeneous distributions of impurity atoms, the local application of the dynamical theory for perfect crystals already provides very good results. In this case, the diffracted intensity can be approximated by the simple formula $I_h = I_M R_N(\theta_A - \delta\theta)$, where R_N is the rocking curve of the setup, I_M is a normalization factor, and θ_A is the Bragg angle in a crystal part assumed as the perfect reference one. This means that the contrast depends on the position of the 'working point,' which is determined, through the parameter $\delta\theta(r)$, by the local Bragg angle on the perfect reference-rocking curve. For faster varying deformations (Figure 11), a geometric-optical approximation may be chosen. The most general case requires a wave-optical approach, which is necessary to calculate, for instance, the contrast of a dislocation. The algorithms give very good results for the plane wave case.

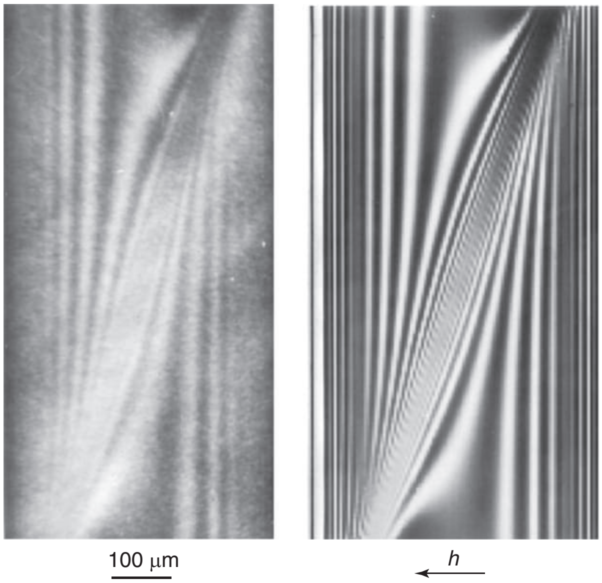

Figure 11 Measured (left) and calculated (right) 422 section topographs of a 565 μm thick silicon crystal with the edge of a 150 nm silicon oxide film, $E = 17.48$ keV.

Conclusion

X-ray diffraction topography is an invaluable tool to characterize single crystals and investigate many-crystal physics phenomena (creation of defects, domains, phase transitions, vibrations, etc.), whereas neutron topography remains a unique tool for the investigation of magnetic crystals, and more specially the antiferromagnetic ones. The scope of X-ray topography, when coupled with synchrotron radiation, extended to unexpected topics through the use of coherent beams or by *in situ* experiments, where the material, in an adequate sample environment device, is imaged while an external parameter (temperature, stress, etc.) is changed. Some of the applications, of course, require a better spatial resolution. A possibility of overcoming this limitation is to use an X-ray lens to magnify the image before the detector. Promising attempts are being made using parabolic compound refractive lenses, asymmetrically cut crystals, or bent mirrors (Kirkpatrick-Baez setup).

References

Allen D, Wittge J, Zlotos A, et al. (2010) Observation of nano-indent induced strain fields and dislocation generation in silicon wafers using micro-Raman spectroscopy and white beam X-ray topography. *Nuclear Instruments and Methods in Physics Research B* 268: 383–387.

Jussila H, Nagarajan S, Sintonen S, et al. (2013) Evaluation of critical thickness of GaP0.98N0.02 layer on GaP substrate by synchrotron X-ray diffraction topography. *Thin Solid Films* 534: 680–684.

Oriwol D, Carl E-R, Danilewsky AN, et al. (2013) Small-angle subgrain boundaries emanating from dislocation pile-ups in multicrystalline silicon studied with synchrotron white-beam X-ray topography. *Acta Materialia* 61: 6903–6910.

Shimura T, Shimokawa D, Matsumiya T, et al. (2012) Synchrotron X-ray topography of supercritical-thickness strained silicon-on-insulator wafers for crystalline quality evaluation and electrical characterization using back-gate transistors. *Current Applied Physics* 12: 69–74.

Verozubova GA, Okunev AO, and Gribenyukov AI (2014) Bulk growth of ZnGeP2 crystals and their study by X-ray topography. *Journal of Crystal Growth* 401: 782–786.

Further Reading

Authier A (ed.) (2001) *Dynamical Theory of X-Ray Diffraction*. New York: Oxford University Press.

Authier A, Lagomarsino S, and Tanner BK (eds.) (1996) *X-Ray and Neutron Dynamical Diffraction – Theory and Applications*. New York: Plenum.

Bowen DK and Tanner BK (eds.) (1980) *Characterization of Crystal Growth Defects by X-Ray Methods*. New York: Plenum.

Bowen DK and Tanner BK (eds.) (1998) *High Resolution X-Ray Diffractometry and Topography*. London: Taylor and Francis.

Dittrich H and Bieniok A (2012) Reference module in Chemistry, Molecular Sciences and Chemical engineering encyclopedia of electrochemical power sources. In: Garche J (ed.) *Measurement methods – Structural properties: X-ray and neutron diffraction*, pp. 718–737. Elsevier.

Laser radiation sources☆

Antonio Agnesi and Giancarlo Reali, Dipartimento di Ingegneria Industriale e dell'Informazione, Università degli Studi di Pavia, Pavia, Italy

© 2024 Elsevier Ltd. All rights reserved.

This is an update of A. Agnesi, G. Reali, A. Tomaselli, Laser Radiation Sources, Editor(s): Franco Bassani, Gerald L. Liedl, Peter Wyder, Encyclopedia of Condensed Matter Physics, Elsevier, 2005, Pages 67–77, ISBN 9780123694010, https://doi.org/10.1016/B0-12-369401-9/00758-0.

Introduction 408
Creating population inversion and laser beam properties 410
Interaction of light with matter 411
1 Rate-equation approximation and the laser amplifier 413
Laser resonators and beam modes 414
Single mode continuous laser operation 417
Laser types: Important laser active media 418
Laser transients: *Q*-switching pulse generation 420
Laser transients: Mode-locking and ultra-short pulse generation 421
Conclusion 424
References 424

Abstract

The basic principles of laser operation are presented starting with the semiclassical light-matter interaction model. Main properties of laser resonators and spatial modes are summarized. Laser amplifiers and laser oscillators operating in continuous-wave as well as in pulsed regimes, such as Q-switching and mode-locking, are discussed. The most important laser devices available today for industrial and scientific applications are also briefly presented.

Key points

- Electronic transitions
- Semiclassical/rate
- Equations model
- Laser amplifier
- Spatial modes
- cw laser
- Laser types
- Pulsed laser regimes

Introduction

LASER is the acronym for Light Amplification by Stimulated Emission of Radiation. This Section and the next one will introduce the basic concepts in a most traditional way (Siegman 1986; Yariv 1989; Milonni and Eberly 2010; Svelto 2010). Stimulated emission can be obtained from a medium prepared in a non-thermal distribution of its energy-level populations (Fig. 1).

In a solid-state material, for example, this is achieved through the absorption of light at an appropriate pumping wavelength.

The laser medium can be practically everything, but for definiteness in the following reference is made to a solid-state matrix, contributing a background refractive index η, enclosing atoms which under pumping will be all set in a same final state, so that a homogenous lineshape of their laser transition is also understood, for simplicity. For the same reason, laser manifolds will not be considered and they will be treated as single levels. Since Nd:YAG is a widely used solid-state laser material, numerical examples will refer to it in the following.

A laser can be either an amplifier or an oscillator, in which an optical feedback is provided in order to allow the device to generate the laser beam from its own internally generated optical seed.

When a laser system is properly designed and operated, it is able to generate coherent light of extraordinary quality, in terms of spectral purity, directionality and power. The properties of the generated beam are precisely the reason of the importance of laser devices in scientific, biomedical, and industrial applications.

☆*Change History*: September 2022. A Agnesi and G Reali are involved in the revison. All figures have been reworked and uploaded. Few minor typos corrected in the main text. Sections "Laser types" and "Laser transients: Q-switching pulse generation" have been added (not present in the original chapter). Section "Laser transients: Mode-locking and ultra-short pulse generation" has also been a little expanded in its last part. Also the section "Conclusions" was added.

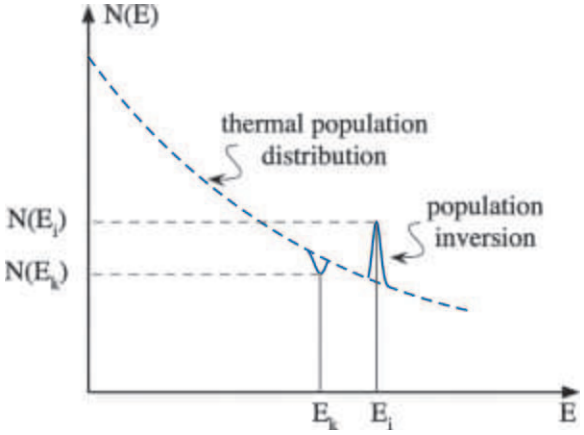

Fig. 1 Selective population inversion ($N_i > N_k$) deviating from thermal population distribution (dashed curve).

The basic interactions involved in laser operation proceed via the processes of (induced) absorption, spontaneous emission, and stimulated (or induced) emission. Spontaneous emission needs a quantum treatment, and in addition to providing, for a fraction of it, the seed into the right cavity mode that can start the laser action, represents an incoherent and completely uncorrelated contribution with respect to the coherent stimulated terms, and ultimately, it is responsible for the phase and amplitude fluctuations of laser systems.

For the induced processes instead, it is possible to resort to much simpler balance equations, first devised by Einstein, that describe how light is transported through the system. The basic idea of transport or rate equations approach is to add or subtract the quasi-resonant photon energies $\hbar\omega$ from the field as it travels through the atomic population, of densities N_2, N_1, that make transitions between levels separated by $\hbar\omega_0$. This is schematically shown in Fig. 2.

Accordingly, the incident optical intensity S (energy per unit area per unit time), that sweeps across a volume of unit cross-sectional area and thickness dz, containing N_2dz and N_1dz atoms in upper and lower levels interested by the interaction, will be changed as

$$\frac{\partial S}{\partial z} + \frac{1}{c}\frac{\partial S}{\partial t} = \sigma(N_2 - N_1)S \tag{1}$$

where σ (in units of length^2) is the induced transition cross-section, equal for both the events. The overall change in (1) will be according to the sign of $(N_2 - N_1)$. For positive sign, the medium behaves as an amplifier of light, while in the opposite case of negative population inversion, that is under ordinary thermal equilibrium conditions, only absorption can be realized and the optical intensity decreases in going across the medium.

In recognition of the amplifier condition, it is usual to define the gain coefficient (in units of length^{-1}) as

$$g = \sigma(N_2 - N_1) \tag{2}$$

so that, considering a steady-state ($\partial/\partial t = 0$) situation in (1),

$$\frac{dS}{dz} = gS. \tag{3}$$

In case of constant gain coefficient, equation (3) is easily solved, giving an exponential optical intensity growth,

$$S(z) = e^{gz}S(0). \tag{4}$$

An amplifier medium is used in laser oscillators, which are the basic laser devices. In their simplest configuration, they are set up enclosing the gain medium in a linear cavity formed by two (plane or curved) mirrors as shown in Fig. 3, of which one, of partial reflectivity R, provides the useful output coupling.

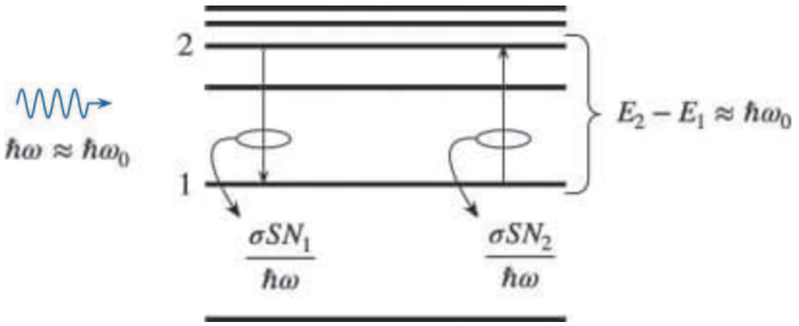
2
1
$\hbar\omega \approx \hbar\omega_0$
$E_2 - E_1 \approx \hbar\omega_0$
$\frac{\sigma S N_1}{\hbar\omega}$
$\frac{\sigma S N_2}{\hbar\omega}$

Fig. 2 Schematic of the interaction of two atomic levels with a quasi-resonant photon flux for an allowed transition.

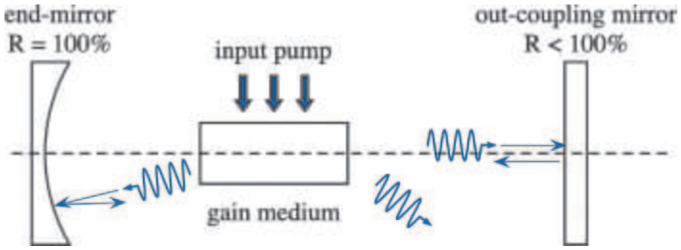

Fig. 3 Optical laser cavity, with the pictorial description of its operation. Only almost axially emitted photons are trapped inside it.

The purpose is to trap only the almost axially emitted part of spontaneous emission seeds and redirect it along the axis so that it can be amplified and filtered through the combined action of the stimulated emission in the gain medium and the selective modal structure of the optical cavity. These iterated actions build up the self-sustained intense, highly monochromatic and directional laser beam. A simple gain-loss balance analysis of the mode in the optical cavity (or resonator) immediately provides the threshold lasing condition. Following the history of gain and losses of the oscillating mode along a full round-trip, and requiring self-reproducibility at the end of it, results:

$$e^{2g\ell}R(1-L_i)=1. \tag{5}$$

where ℓ is the gain medium length, R is the output coupling mirror reflectivity, and L_i are the double-pass passive cavity losses. This defines the threshold gain for the laser oscillator:

$$g_{th}=-\frac{ln\,(R)+ln\,(1-L_i)}{2\ell}, \tag{6}$$

above which stimulated laser action initiates. A second important condition, which sets a constraint on the change of phase of the oscillating mode after a round-trip, will be derived later.

Creating population inversion and laser beam properties

In order to create a population inversion, the closed two-level system illustrated in Fig. 2 cannot work "as is," since the nature of up-down stimulated transitions and their relation (same cross-section) prevents the possibility of using the same channel for both excitation and generation, in case of optical pumping. The minimum number of required levels is thus three, and a more general four-level system may perform even better, depending on the relative magnitudes of the relaxation rates of the level populations and on the selective actions of the pumping system. Fig. 4 clarifies the kinematics of the level populations in a four-level system.

In the most favorable case, a four-level system is one in which upper laser level 2 is fed at a rate that almost coincides with the rate at which level 3 is fed, due to a very fast, nonradiative relaxation from 3 to 2; in addition, the lower laser level 1 is constantly drained off, keeping it essentially empty, by its fast decay to lower laying levels.

Pumping efficiency and resonator design are the most important problems in laser engineering, since on their optimization depend the properties of the generated laser beam. (Thermal effects handling is also another important issue of high power laser systems).

Once the active medium has been chosen, and the application the laser is aimed at has suggested the operating regime (continuous wave, long pulses, short pulses, etc...), power, monochromaticity and spectral purity, coherence and directionality are essentially controlled by pumping and by the optical resonator. An overall parameter which can be used, for example, to

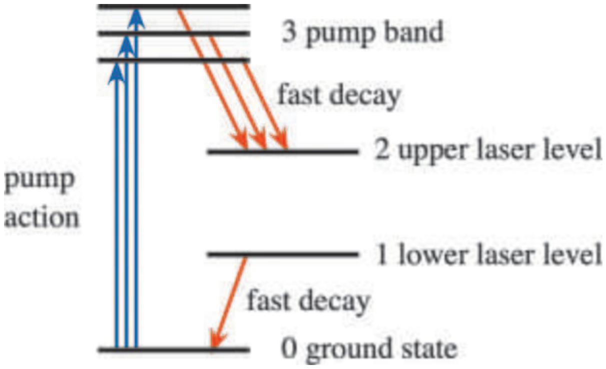

Fig. 4 A four-level laser, with the indication of the most relevant energy exchanges: the pump, and the fast decays into the upper laser level and out of the lower laser level, which favor an efficient creation of the population inversion.

compare laser light and standard generated light (Sun, lamp, discharge, etc…), is the brightness which summarizes all the above properties.

As a rule, laser emission is not at a single frequency near the ω_0 of the laser transition. Because of natural lifetime and interactions of the active atoms with the surrounding environment, gain effects, and photon lifetime, there is a sizable spectral broadening $\Delta\omega$ of the emitted light. Still, laser light is far better than all other light sources. As an example, Nd:YAG, one of the most widely used solid-state laser materials, lases at 1064 nm, corresponding to $\omega_0 \approx 1.8 \times 10^{15}\ \mathrm{s}^{-1}$, and may have spectral purity $\Delta\omega/\omega \approx 10^{-9}$ or better, several order of magnitudes smaller than any unfiltered thermal light source, for which that figure approaches 1.

Since the stimulated emission forces all photons in exactly the same quantum state, coherence persists until the radiating polarization, set up in the laser material, remains temporally and spatially correlated, and is not disturbed by any spurious effects like collisions with the environment. Collisions essentially determine the coherence time, which is connected to the degree of monochromaticity of the emitted light, $\tau_{coh} \approx 1/\Delta\omega$.

To a large extent, spatial coherence is formed by the transverse modal structure of the resonator, from which the beam derives its directionality. Spatial coherence and directionality are the properties that allow the beam to be brought, with very low spill-out energy, to a tight focus, an essential requirement in most laser applications. Diffraction theory shows that the lowest order, Hermite-Gauss mode of a stable resonator diverges with an angle $\vartheta_{0x} = \lambda/(\pi w_{0x})$, where w_{0x} is the beam waist (its lowest radius) in a x-direction perpendicular to z-propagation direction; a same expression holds for the y-direction. This is the lowest divergence among beams with same beam waist. It can be shown that higher order modes (and, more generally, a real beam made up of a mixture of these) with same waist diverge with an angle $\Theta_x = M_x^2\vartheta_{0x}$, greater that the lowest order mode by a factor of M_x^2, called the spatial beam quality factor (Koechner 2006); this expression can be used as an operative definition of the factor M_x^2, which always is >1 for any real beam (a same expression holds for the y-direction).

High intensities and low divergence can be put together to define laser brightness, the power emitted per unit area per unit solid angle. The concept applies in general to any source of radiation; in case of lasers, it assumes a very simple form:

$$B = \frac{P}{A \times \Omega} \sim \frac{P}{(w_{0x}w_{0y})(\Theta_x\Theta_y)} \sim \frac{P}{\lambda^2\left(M_x^2 M_y^2\right)} \tag{7}$$

and can be used as an indicator of the laser quality.

The fact that laser brightness is directly proportional to power is one of the reasons for research in the area of short and ultrashort pulse generation. Another reason is that very short pulses allow to investigate very short phenomena, in the same way as very small spots allow to see and work out very small details.

Interaction of light with matter

In order to understand the mechanisms that govern the generation of laser light, it is useful to analyze in some detail the results of the semi-classical treatment of light-matter interaction, using a simple two-level system as toy model (Yariv 1989; Milonni and Eberly 2010).

An incident optical field $\vec{E}\left(\vec{r}, t\right)$ on a quantum system, possessing a set of stationary levels and eigenfunctions, $\left\{E_i, \phi_i\left(\vec{r}\right)\right\}$, is assumed to be almost resonant with two levels 2 and 1 with energy separation $\hbar\omega_0 = (E_2 - E_1)$, so that all the other levels can be ignored. Levels 2 and 1 are also assumed to have a well defined parity, and to be connected by a dipole-allowed transition. The time-dependent interaction is described by the second term of the hamiltonian $H = H_0 + H_1$, where, in the dipole approximation, $H_1 = -\vec{p}\cdot\vec{E}$ and the optical field is linearly polarized along $\hat{\varepsilon}$ and has the form $\vec{E} = \hat{\varepsilon}E_0(t)\,cos\,(\omega t)$ with a slowly time-varying amplitude.

The solution is assembled in the form $\psi\left(\vec{r}, t\right) = c_1(t)\phi_1\left(\vec{r}\right) + c_2(t)e^{-i\omega t}\phi_2\left(\vec{r}\right)$. Defining the dipole matrix elements $\vec{p}_{ij} = \int d^3r\phi_i^*\left(\vec{r}\right)\vec{p}\phi_j\left(\vec{r}\right)$, neglecting rapidly varying terms, introducing the detuning $\Delta = (\omega_0 - \omega)$, and the Rabi frequency $\Omega = \left(\vec{p}_{ij}\cdot\hat{\varepsilon}\right)E_0(t)/\hbar$, the amplitude equations result:

$$\begin{aligned} i\frac{dc_1}{dt} &= -\frac{1}{2}\Omega^* c_2 \\ i\frac{dc_2}{dt} &= \Delta c_2 - \frac{1}{2}\Omega c_1 \end{aligned} \tag{8}$$

These are used to form the set of equations obeyed by the density matrix

$$\rho = \begin{bmatrix} \rho_{11} & \rho_{12} \\ \rho_{21} & \rho_{22} \end{bmatrix} = \begin{bmatrix} c_1c_1^* & c_1c_2^* \\ c_2c_1^* & c_2c_2^* \end{bmatrix}. \tag{9}$$

with closure condition $\rho_{11} + \rho_{22} = |c_1|^2 + |c_2|^2 = 1$, which provides a most compact means to calculate the expectation values of quantum observables, $<A> = Tr\{\rho A\}$. In their final form, the equations for the ρ_{ij} are:

$$\begin{aligned}\frac{d\rho_{11}}{dt} &= -\frac{i}{2}(\Omega\rho_{12}-\Omega^{*}\rho_{21})\\ \frac{d\rho_{2}}{dt} &= -\frac{d\rho_{11}}{dt}\\ \frac{d\rho_{12}}{dt} &= i\Delta\rho_{12}+\frac{i}{2}\Omega(\rho_{22}-\rho_{11})\end{aligned} \tag{10}$$

These equations describe the evolution of the laser population densities and of the induced polarization in a material, introduced through the macroscopic variables:

$$\begin{aligned}N_1 &= N\rho_{11}\\ N_2 &= N\rho_{22}\\ \vec{P} &= N\int d^3r\psi^{*}\left(\vec{r}\right)\vec{p}\psi\left(\vec{r}\right) = N\left(\rho_{12}\vec{p}_{21}e^{-i\omega t}+c.c.\right)\end{aligned} \tag{11}$$

with N the total population density participating in the interaction, and where $\vec{p}_{ii}=0$ has been used. Introducing the slowly varying macroscopic polarization, $\vec{P}(t)=1/2[\hat{\varepsilon}P(t)e^{-i\omega t}+c.c.]$, and comparing it with the third of equations (11),

$$P(t) = 2N\left(\vec{p}_{12}\cdot\hat{\varepsilon}\right)\rho_{21} \tag{12}$$

is obtained. The macroscopic equations thus result:

$$\begin{aligned}\frac{dN_1}{dt} &= -\frac{1}{2\hbar}\text{Im}\left(E_0^{*}P\right) = -\frac{dN_2}{dt}\\ \frac{dP}{dt} &= -i\Delta P - i\frac{\left|\vec{p}_{12}\cdot\hat{\varepsilon}\right|^2}{\hbar}(N_2-N_1)E_0\end{aligned} \tag{13}$$

These equations describe the dynamics of an ensemble of isolated two-level atoms. In this form, they do not yet reflect some very important features that extend this ensemble into a working model of laser, such as the existence of relaxation processes through collisions or radiative decays, and especially the possibility of pumping energy into the system to get population inversion, $(N_2-N_1)>0$. The inclusion of these physical effects is possible by making a phenomenological fix of the equations (13) based on physical considerations; this is illustrated in Fig. 5.

The main effects to be included are: (i) pumping rates into levels 2 and 1, R_2, and R_1, respectively; (ii) dampings of levels 2 and 1 due to inelastic collisions and radiative decays, γ_2 and γ_1, respectively; (iii) damping due to elastic collisions, which only affect induced polarization, γ_{ph}. Taking all these effects into account leads to:

$$\begin{aligned}\frac{dN_1}{dt} &= R_1-\gamma_1 N_1-\frac{1}{2\hbar}\text{Im}\left(E_0^{*}P\right)\\ \frac{dN_2}{dt} &= R_2-\gamma_2 N_2+\frac{1}{2\hbar}\text{Im}\left(E_0^{*}P\right)\\ \frac{dP}{dt} &= -(\gamma+i\Delta)P-i\frac{\left|\vec{p}_{12}\cdot\hat{\varepsilon}\right|^2}{\hbar}(N_2-N_1)E_0,\end{aligned} \tag{14}$$

where $\gamma=\gamma_{ph}+(\gamma_1+\gamma_2)/2$ is the damping rate for the induced polarization.

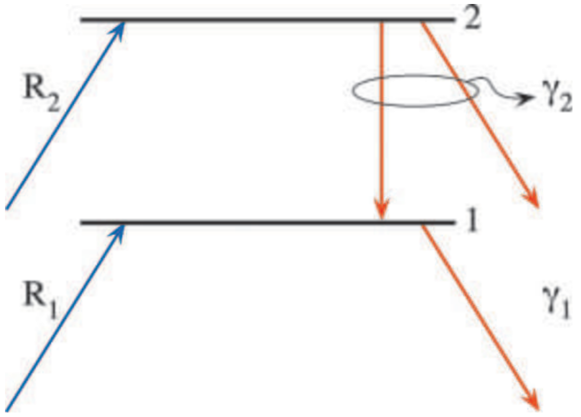

Fig. 5 Pumping and decays that make the "two-level" model a "real" laser model.

1 Rate-equation approximation and the laser amplifier

It happens quite often that in laser materials γ is much larger than all the other rates, so that the induced polarization rapidly reaches a steady-state and follows adiabatically the changes of the field and the atomic populations. In this "rate-equation approximation", it is possible to set $dP/dt = 0$, resulting in:

$$P(t) = -i\frac{\left|\vec{p}_{12}\cdot\hat{\varepsilon}\right|^2}{\hbar(\gamma+i\Delta)}(N_2-N_1)E_0(t). \tag{15}$$

This can be substituted back into the population equations to give the final rate equations (Siegman 1986; Yariv 1989; Koechner 2006; Milonni and Eberly 2010; Svelto 2010):

$$\begin{aligned}\frac{dN_1}{dt} &= R_1 - \gamma_1 N_1 + W(N_2-N_1)\\ \frac{dN_2}{dt} &= R_2 - \gamma_2 N_2 - W(N_2-N_1)\\ W &= \frac{\pi|p_{12}|^2|E_0(t)|^2}{6\hbar^2}\frac{\gamma/\pi}{\gamma^2+\Delta^2}\end{aligned} \tag{16}$$

A factor of 3, due to angular averaging, has been included in the last of (16) to account for random local dipole orientations with respect to the electric field, $\overline{\left|\vec{p}_{12}\cdot\hat{\varepsilon}\right|^2} = |p_{12}|^2/3$.

It is recognized that the expression of W, which represents the rate at which the inversion is changed, can be written as:

$$W = \frac{\sigma S}{\hbar\omega}, \tag{17}$$

where the photon flux is

$$\frac{S}{\hbar\omega} = \frac{c\varepsilon_0\eta|E_0(t)|^2}{\hbar\omega}$$

and where η is the average, background refractive index of the material. From (17) the expression for the induced transition cross-section is obtained:

$$\sigma = \frac{\pi|p_{12}|^2\omega}{6c\varepsilon_0\eta\hbar}\frac{\gamma/\pi}{\gamma^2+\Delta^2}. \tag{18}$$

A quantum mechanical calculation of the spontaneous emission rate A provides the explicit form:

$$A = \frac{1}{\tau_{sp}} = \frac{\omega_0^3\eta|p_{12}|^2}{3\pi\varepsilon_0\hbar c^3}, \tag{19}$$

which, used in (18) to eliminate $|p_{12}|^2$, with the consideration that $\gamma << \omega_0$, leads to the most popular form of the transition cross-section ($\lambda = \lambda_0/\eta$ is the laser wavelength in the laser material):

$$\sigma(\omega) = \frac{\lambda^2}{8\tau_{sp}}\frac{\gamma/\pi}{\gamma^2+\Delta^2} = \frac{\lambda^2}{8\tau_{sp}}\mathscr{L}(\omega). \tag{20}$$

$\mathscr{L}(\omega)$ is the normalized Lorentzian lineshape, obtained in the homogeneous broadening hypothesis. This expression can be used, for example, to get a numerical estimate of the cross-section of Nd:YAG using available data, $\tau_{sp} = 230$ μs, $\gamma = 2\pi \times 120$ *GHz*, $\eta = 1.82$. The computation gives $\sigma \approx 3.5 \times 10^{-19}$ cm^2, which catches with its most quoted value, a good result for this simple model.

Thus, the laser gain introduced in equation (2) results

$$g(\omega) = \frac{\lambda^2}{8\tau_{sp}}\mathscr{L}(\omega)(N_2-N_1). \tag{21}$$

In more general and realistic situations, the lineshape has different widths and shapes, and can be largely inhomogeneous, if all the atoms do not have the same center transition frequency (as, for example, in Nd:glass).

From rate equations, it is immediately clear that the population inversion depends on optical intensity S, since W depends on it. In a strict four-level system, previously illustrated, in which pumping into lower laser level is suppressed, $R_1 = 0$, and the decay from the lower laser level is assumed to be very fast, these rate equations unveil this feature very clearly, when solved for the steady-state. The result in this case is:

$$N_2 - N_1 = \frac{R_2/\gamma_2}{1 + S/S_{sat}} = \frac{(N_2 - N_1)_0}{1 + S/S_{sat}}, \tag{22}$$

where $(N_2 - N_1)_0 = R_2/\gamma_2$ is the inversion at low optical intensity, when $S/S_{sat} < < 1$, and $S_{sat} = (\hbar\omega\gamma_2/\sigma)$ is the saturation intensity. The gain thus becomes:

$$g(\omega) = \frac{\sigma(\omega)(N_2 - N_1)_0}{1 + S/S_{sat}} = \frac{g_0(\omega)}{1 + S/S_{sat}}. \tag{23}$$

where the small signal gain g_0 has been introduced with an obvious identification.

An immediate application of (23) is its use into (3) to obtain the general behavior of a single-mode amplifier. The equation

$$\frac{dS}{dz} = \frac{g_0(\omega)}{1 + S/S_{sat}} S. \tag{24}$$

has general solution of the following form:

$$\frac{S(z) - S(0)}{S_{sat}} + ln\left(\frac{S(z)}{S(0)}\right) = g_0 z. \tag{25}$$

where $S(0)$ is the input intensity. The exponential growth of equation (4) is thus obtained only for intensities small compared with the saturation intensity. At the opposite limit, when the first term of the left-hand side of (25) dominates, the intensity difference grows only linearly with the length, as $g_0 S_{sat} z$. If multiplied by the effective area A_{eff} of the beam, and noting that $P_{ex} = g_0 S_{sat} = R_2 \hbar\omega$ is the available power density from the gain medium, $g_0 S_{sat} A_{eff}\, z$ is seen to be the maximum extractable power from the amplifier, which is only attained working in saturation regime. In Fig. 6 the plots of the "growth rate" $= (1/S)(dS/dz)$ and the "power extraction rate" $= dS/dz$ show that the growth rate is maximum for small S and drops to zero for large S, while an exactly specular behavior is followed by the power extraction.

Finally, it is useful to summarize these considerations into the definition of a figure of merit for the amplifier, its internal efficiency:

$$\eta_{int} = \frac{S(z) - S(0)}{R_2 \hbar\omega_p z} = \frac{S(z) - S(0)}{R_2 \hbar\omega z} \frac{\hbar\omega}{\hbar\omega_p} = \frac{S(z) - S(0)}{R_2 \hbar\omega z} \eta_S. \tag{26}$$

where $P_p = R_2 \hbar\omega_p$ is the pump power density available in the amplifier, and η_S is the Stokes efficiency.

Laser resonators and beam modes

The importance and the advantages of making high quality beams are so overwhelming that laser research has dedicated a lot of efforts in studying optical resonators, which are the devices used to provide the oscillator feedback and to spatially shape the laser beams. In a laser, the cavity is set up of (flat or curved) mirrors, surrounding the gain medium, which select only the light emitted approximately along the resonator axis, and reflect it back and forth several times, thus providing the necessary feedback that sustains the laser action. What characterizes a laser from other coherent devices at longer wavelengths (in the far IR and microwave

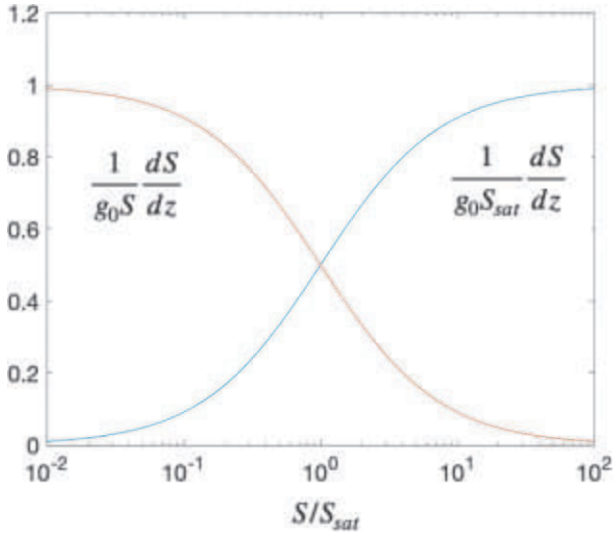

Fig. 6 Growth rate and power extraction rate plots as a function of intensity normalized to the saturation intensity.

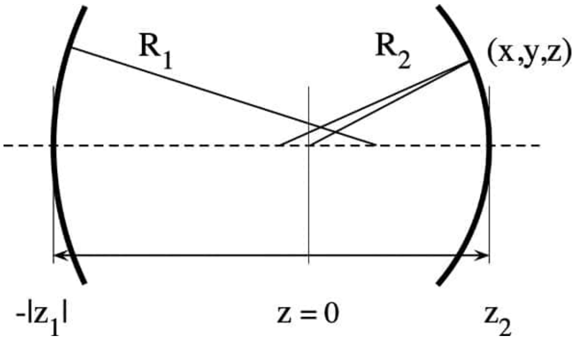

Fig. 7 Empty laser resonator used to discuss the modes of a stable cavity laser. R1 and R2 are the curvature radii of the two confining mirrors, one of which eventually has a partial reflectivity to allow outcoupling of the laser field.

ranges) is that an open resonator is needed to limit the number of possible oscillating modes which fits under the gain linewidth of the laser medium, and get temporally coherent radiation. In addition to the feedback action, the most important function of the resonator is the transverse spatial shaping of the radiated field, and the optical spatial quality of a beam is generated by using the transverse modal structure of the resonator. Optical resonators can be grouped into two classes: stable resonators are characterized by having closed ray paths, while unstable resonators have no closed paths, and are mainly used in high gain laser systems. Only stable resonators will be briefly described, while the book by Siegman (1986) provides a complete authoritative review on resonator subject. The empty linear resonator shown in Fig. 7 will be used to illustrate the sustained resonator modes.

With this geometry, it is possible to select the fundamental TEM_{00} mode because the higher-order modes suffer significantly greater losses.

The structure of these modes can be found by solving the wave equation, which governs the propagation of beams whose transverse (i.e., (x, y)) dependence is less rapid than their z–dependence. Recognizing these different spatial rates, the complex quasi-monochromatic field amplitude is written as

$$E(x, y, z, t) = E_0 u(x, y, z) e^{i(kz-\omega t)} \tag{27}$$

where the spatial shape $u(x, y, z)$ is a slowly varying function in its variables with respect to e^{ikz}, and satisfies the following parabolic wave equation (also known in optics as paraxial wave equation):

$$2ik\frac{\partial u}{\partial z} + \left(\frac{\partial^2 u}{\partial x^2} + \frac{\partial^2 u}{\partial y^2}\right) = 0 \tag{28}$$

It can be shown that, if a (unit amplitude) beam with Gaussian shape

$$u(x, y, 0) = \exp\left(-\frac{x^2 + y^2}{w_0^2}\right) \tag{29}$$

is chosen as initial condition at its narrowest point in $z = 0$ (w_0 is correspondingly called the beam waist), then the solution for arbitrary z is given by:

$$u(x, y, z) = \frac{1}{1 + i\left(2z/kw_0^2\right)} \exp\left(-\frac{x^2 + y^2}{w_0^2 + i2z/k}\right) \tag{30}$$

After defining new quantities (illustrated in Fig. 8): $z_0 = kw_0^2/2$, the Rayleigh range or confocal parameter; $R(z) = z + z_0^2/z$, the beam radius of curvature; $w(z) = w_0[1 + (z/z_0)^2]^{1/2}$, the beam radius; equation (30) can be put into the more transparent form:

$$u(x, y, z) = \frac{w_0}{w(z)} \exp\left(-\frac{x^2 + y^2}{w^2(z)} + ik\frac{x^2 + y^2}{2R(z)} - i\tan^{-1}\left(\frac{z}{z_0}\right)\right) \tag{31}$$

The fundamental, TEM_{00} mode of the laser beam is thus:

$$E_{00}(x, y, z, t) = E_0(t)e^{i(kz-\omega t)} \times \frac{w_0}{w(z)} \exp\left(-\frac{x^2 + y^2}{w^2(z)} + ik\frac{x^2 + y^2}{2R(z)} - i\tan^{-1}\left(\frac{z}{z_0}\right)\right) \tag{32}$$

Higher order transverse modes can also be found, and they are given, in terms of the complete Hermite-Gauss set functions, so that

$$\begin{aligned} E_{mn}(x, y, z, t) &= E_0(t)e^{i(kz-\omega t)} H_m\left(\sqrt{2}x/w(z)\right) H_n\left(\sqrt{2}y/w(z)\right) \\ &\times \frac{w_0}{w(z)} \exp\left(-\frac{x^2 + y^2}{w^2(z)} + ik\frac{x^2 + y^2}{2R(z)} - i(m + n + 1)\tan^{-1}\left(\frac{z}{z_0}\right)\right) \end{aligned} \tag{33}$$

The first few transverse mode distributions are pictorially shown in Fig. 9.

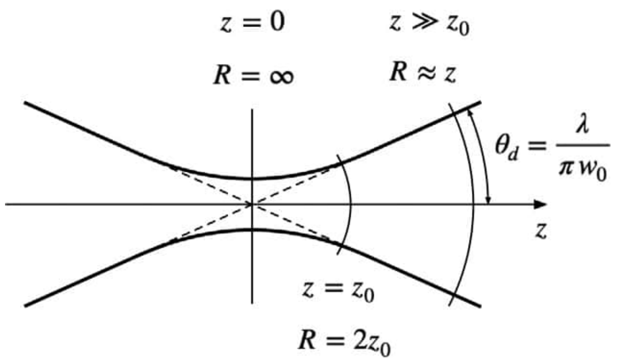

Fig. 8 Geometrical meaning of the beam parameters defined in the text.

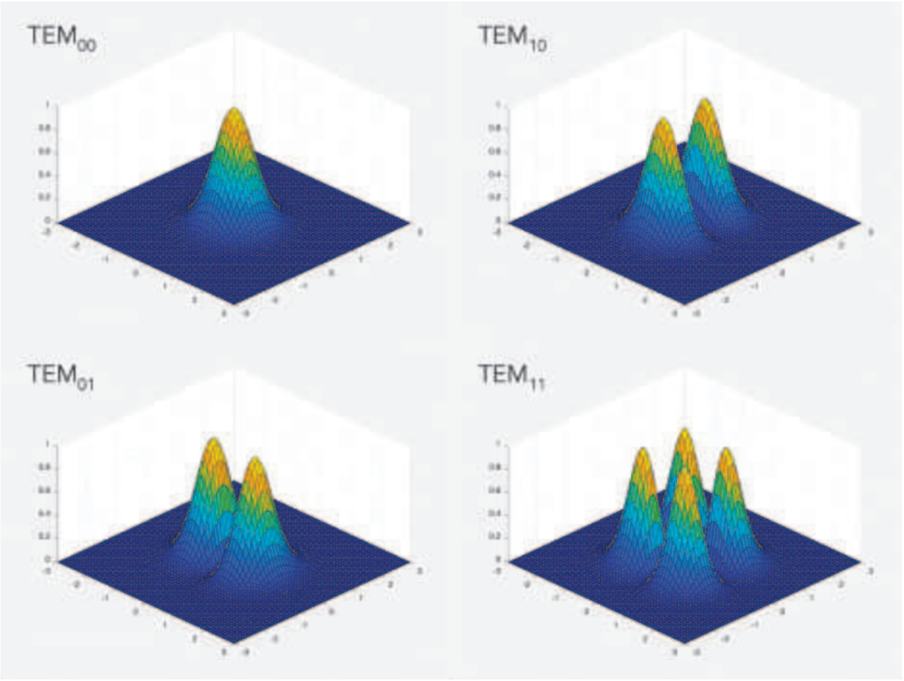

Fig. 9 Patterns of first low-order Hermite-Gauss modes.

Imagine now that the resonator of Fig. 7 has mirrors at $z_1 < 0$ and $z_2 > 0$, with radii of curvature $R_1 = -R(z_1), R_2 = R(z_2)$, respectively. A point (x, y, z) on mirror 2 satisfies the equation

$$R_2^2 = x^2 + y^2 + (R_2 - z_2 + z)^2 \tag{34}$$

which can be rewritten as

$$z_2 - \frac{(z - z_2)^2}{2R_2} = z + \frac{x^2 + y^2}{2R_2} \tag{35}$$

The paraxial wavefront of constant phase φ almost coincides (within the lowest order) with the mirror at z_2 when evaluated on the mirror surface:

$$\varphi = k\left\{z_2 - \frac{x^2 + y^2}{2R_2} - \frac{(z - z_2)^2}{2R_2}\right\} + k\frac{x^2 + y^2}{2R_2} - (m + n + 1)\tan^{-1}\left(\frac{z}{z_0}\right) - \omega t \tag{36}$$

and the beam strikes the mirrors perpendicularly and propagates back and forth along the cavity. The losses due to phase mismatch can be canceled by tuning the wave-number $k = \omega/c$ so that the total phase change of the beam between the mirrors is an integer number l of π:

$$l\pi = \frac{\omega L}{c} - (m + n + 1)\left\{\tan^{-1}\left(\frac{z_2}{z_0}\right) - \tan^{-1}\left(\frac{z_1}{z_0}\right)\right\} \tag{37}$$

where $L = (z_2 + |z_1|)$ is the cavity length. The frequency satisfying (37) for given values of (l, m, n) is called ω_{lmn} (l is the longitudinal mode index; m, n are the transverse mode indices) and the corresponding field is called the TEM_{mn} transverse mode. The larger the transverse indices (m, n) are, the less the wavefronts coincide with the mirrors' curvatures, which means that there is the tendency (if not otherwise managed) to have larger losses and the suppression of higher order transverse modes in favor of the lowest order one. A change between two nearby longitudinal mode frequencies with same (m, n) is given by:

$$\Delta\omega_{lmn} = \omega_{(l+1)mn} - \omega_{lmn} = \frac{\pi c}{L} \tag{38}$$

while varying the transverse mode indices at fixed l results:

$$\delta\omega_{lmn} = \frac{c}{L}\delta(m+n)\left\{\tan^{-1}\left(\frac{z_2}{z_0}\right) - \tan^{-1}\left(\frac{z_1}{z_0}\right)\right\} \tag{39}$$

where $\delta(m+n)$ is the change in $(m+n)$. It is not hard to see, for example, in the case when $z_0 >> z_2, |z_1|$, that the transverse mode structure appears as a fine structure of the longitudinal mode spectrum.

It should be noted that, if the resonator is loaded with a gain medium of length ℓ, its length L must be replaced by the optical length $L' = L + (\eta - 1)\ell$, so that the phase condition (37) contains the refractive index of the gain medium $\eta(\omega, S)$, which depends on frequency as well as on laser beam intensity. This should alert that the exact longitudinal mode position is also a function of the working power of the laser.

Single mode continuous laser operation

Laser oscillators can be operated in various regimes. Some of them can be easily studied using the laser rate equations previously introduced:

$$\begin{aligned}\frac{dN_1}{dt} &= -\gamma_1 N_1 + \frac{\sigma S}{\hbar\omega}(N_2 - N_1)\\ \frac{dN_2}{dt} &= R_2 - \gamma_2 N_2 - \frac{\sigma S}{\hbar\omega}(N_2 - N_1)\\ \frac{\partial S}{\partial z} + \frac{1}{c}\frac{\partial S}{\partial t} &= \sigma S(N_2 - N_1) - \frac{\gamma_c}{c}S + \frac{R_{sp}}{c}\end{aligned} \tag{40}$$

where the added spontaneous emission rate R_{sp} reminds the origin of the starting laser seed, and a loss term for the laser field has been inserted to account for both useful mirror output coupling and residual, undesirable losses due to intracavity absorption and scattering. According to (6), these are collectively given by

$$\frac{\gamma_c}{c} = -\frac{ln(R) + ln(1 - L_i)}{\ell} \approx \frac{(1-R) + L_i}{\ell}, \tag{41}$$

where the last expression applies in the low-loss limit. In many common situations the intensity S is approximately uniform along the cavity axis. Assuming this approximation, and taking into account the different lengths of the gain medium, ℓ, and of the cavity, L, the final form of (40) becomes:

$$\begin{aligned}\frac{dN_1}{dt} &= -\gamma_1 N_1 + \frac{\sigma S}{\hbar\omega}(N_2 - N_1)\\ \frac{dN_2}{dt} &= R_2 - \gamma_2 N_2 - \frac{\sigma S}{\hbar\omega}(N_2 - N_1)\\ \frac{dS}{dt} &= \frac{c\sigma\ell}{L}S(N_2 - N_1) - \gamma_c S + R_{sp}\end{aligned} \tag{42}$$

which are the single-mode rate-equations (Siegman 1986; Yariv 1989; Koechner 2006; Svelto 2010; Milonni and Eberly 2010).

Under steady-state conditions, the rates of change of both population inversion and intensity is set to zero, and neglecting the small R_{sp} contribution, from (42) it follows:

$$\begin{aligned}g(\omega, S) &= \frac{g_0(\omega)}{1 + S/S_{sat}}\\ 0 &= \left[\frac{c\ell}{L}g(\omega S) - \gamma_c\right]S\end{aligned} \tag{43}$$

where the first equation gives the saturated gain already derived in (23), with $S_{sat} = \hbar\gamma_2/\sigma$, and $g_0 = \sigma(N_2 - N_1)_0 = \sigma R_2/\gamma_2$. Below threshold the optical intensity remains zero until the pumping rate has grown high enough to bring the small signal gain at the threshold. Thus, g_0 grows linearly with the pump rate, and at threshold it results:

$$\begin{aligned}\frac{c\ell}{L}g_{th} &= \frac{c\ell}{L}g_{0th} = \frac{c\ell}{L}\frac{\sigma R_{2th}}{\gamma_2} = \gamma_c\\ R_{2th} &= \frac{L}{c\ell}\frac{\gamma_2\gamma_c}{\sigma}\end{aligned} \tag{44}$$

Above threshold, $g(\omega, S)$ remains clamped to its threshold value, since $S \neq 0$ and, under the steady-state hypothesis, it cannot be

$$\left[\frac{c\ell}{L}g(\omega, S) - \gamma_c\right]S > \left[\frac{c\ell}{L}g_{0th} - \gamma_c\right]S = 0. \tag{45}$$

Thus it follows that

$$\frac{g_0}{1 + S/S_{sat}} = g_{0th}. \tag{46}$$

and, for the internal intensity,

$$S = S_{sat}\left(\frac{g_0}{g_{0th}} - 1\right) = S_{sat}\left(\frac{R_2}{R_{2th}} - 1\right). \tag{47}$$

Far above threshold, this becomes $S \approx (\ell/L)(cR_2\hbar\omega/\gamma_c)$.

The resonator output intensity is, in the low-loss limit of (41):

$$S_{out} = (1-R)S = \frac{\ell}{L}(1-R)S_{sat}\left[\frac{2g_0\ell}{(1-R)+L_i} - 1\right]. \tag{48}$$

which is plotted in Fig. 10 as a function of the output coupling T.

The factor of 2 multiplying the gain coefficient is due to the fact that in a two-mirror resonator the gain medium is traversed twice per round-trip.

From this figure it is clear that there is an optimum working point, obtained maximizing S_{out} with respect to the output coupling at fixed small signal gain (that is, at fixed pump rate):

$$\begin{aligned} T^{opt} &= L_i\left(\sqrt{\frac{2g_0\ell}{L_i}} - 1\right) \\ S_{out}^{opt} &= \frac{\ell}{L}S_{sat}\left(\sqrt{2g_0\ell} - \sqrt{L_i}\right)^2, \end{aligned} \tag{49}$$

which represents the working condition for well-engineered continuous wave laser systems.

Laser types: Important laser active media

In this Section, an overview of laser materials is provided (Svelto 2010). Laser action has been demonstrated from X-rays to THz domain, while the first historical demonstration of electromagnetic radiation amplification by stimulated emission was done with a microwave device, a "maser."

Free-electron lasers (FELs) actually exploit a kind of coherent radiation amplification which cannot be strictly modeled as it was done in the previous Sections, for a general four-level or three-level laser. In FELs a beam of relativistic electrons is sent through a periodic, spatially-modulated orthogonal magnetic field which causes transversal charge acceleration, producing narrow-angle radiation emission in the beam direction. FELs are complex, yet unique scientific tools for production of intense beams of spatially

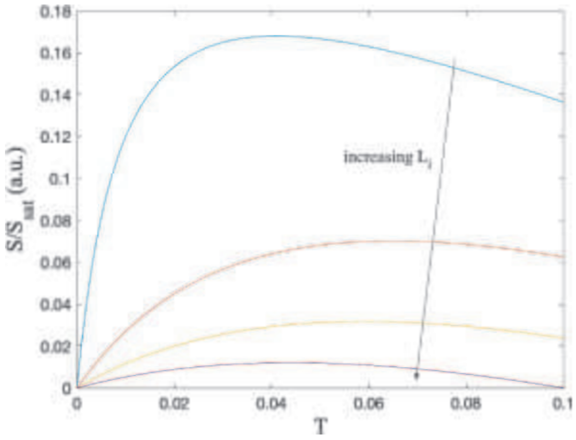

Fig. 10 Output intensity as a function of outcoupling transmission.

and temporally coherent radiation from a resonant cavity, at wavelengths not accessible with other laser technologies, especially on the short-wavelengths side of the electromagnetic spectrum. Additionally, tuning parameters such as electrons speed and magnetic field strength make FELs the most broadly tunable source of coherent radiation, in principle, from X-rays to far-infrared.

Excimer lasers are traditionally important for UV radiation generation, which finds applications in microelectronics and surgery. As in most gas lasers the excitation occurs through electric discharge, in this particular case producing transient "artificial" molecules of rare gases and halogens such as XeCl, KrF, etc. which decay in short (picosecond) time releasing an UV photon. These lasers usually work at atmospheric pressure to produce high energy UV pulses up to multi-kHz repetition rate.

Although the visible spectrum was covered for a long time by gas lasers such as Ar-ions, Kr-ions, copper-vapors and HeNe, exploiting dipole-allowed electronic transitions, in the last decades solid-state and semiconductor laser technologies became more popular for many applications due to their higher efficiency and reliability, less expensiveness, maintenance-free operation and greater compactness of the devices.

Semiconductor lasers are now commercially available with wavelength ranging from the UV to the THz. In these devices an electrical current produces coherent radiation at junctions between different types of semiconductors, through carrier recombination, often exploiting the advantages of quantum well structures at the junction. Electronic transitions can be either interband (for the most energetic photons, UV to near-infrared) or intraband, like in quantum cascade lasers (wavelengths $>2\ \mu\text{m}$). Semiconductor laser engineering allows to design practical devices which can emit at any desired wavelength in this broad range. However, single-spatial-mode emission as well as single-frequency operation is possible only for modest power $<1\ W$, whereas more powerful devices (up to hundred watts) needed for medical and industrial applications have increasingly poor beam quality.

Thus high-power semiconductor lasers at convenient wavelengths are frequently used to pump solid-state lasers, which in turn act as brightness amplifiers, absorbing very-low-spatial-quality radiation and emitting diffraction-limited radiation at longer wavelength, normally at good efficiency, up to $\sim 90\%$ in some cases.

A particular technology implementing a multiwatt semiconductor laser with excellent spatial and spectral features is the optically-pumped semiconductor laser: an ordinary current-driven high-power multimode semiconductor laser pumps a semiconductor disk in a laser resonator, with a mode size $\sim \sqrt{\lambda L}$ allowing both multiwatt operation and diffraction-limited performance. Intracavity second harmonic generation with nonlinear crystals is generally exploited to reach the visible range, with excellent power stability performance unlike solid-state lasers. These are potentially affected by relaxation oscillations started by the nonlinear conversion process due to their long fluorescence lifetime.

Solid-state lasers are workhorse technology for most industrial, medical and scientific applications. Rare-earth ions such as Nd^{3+} and Yb^{3+} (four-level and quasi-three-level, respectively), with suitable hosts (typically crystals like YAG, YVO_4 and many others) are used for laser emission at $\sim 1\ \mu\text{m}$ wavelength, where sources up to $\sim$kW-class (continuous-wave) and ~ 100 W average power in pulsed operation (either nanosecond, picosecond and even femtosecond pulse duration) are available commercially for demanding industrial applications. Er^{3+}/Yb^{3+} solid-state three-level lasers are used mainly for laser ranging and medical applications at the eyesafe wavelength around 1.5 μm. Tm^{3+} and Ho^{3+} three-level lasers emit light at $\sim 2\ \mu\text{m}$ which is an important wavelength for laser surgery (strong absorption by water and organic tissues). Additionally they are becoming increasingly important for mid-IR technology, also through wavelength extension using optical parametric generation with nonlinear crystals.

Vibronic laser materials based on transition metal ions like $Ti^{3+}:Al_2O_3$ and Cr^{2+}:ZnSe or Cr^{2+}:ZnS exploit exceptional spectral broadening due to strong electron-phonon interactions. They feature the broadest tuning range of ~ 0.65–1.1 μm and ~ 2–3.5 μm, respectively, allowing direct generation of the shortest pulses possible from a given laser material. $Ti^{3+}:Al_2O_3$ lasers are very common tools for ultrafast science, enabling a variety of advanced applications including ultrafast spectroscopy, nonlinear microscopy and precision metrology with frequency combs. Cr^{2+}-doped lasers extend such concepts and technologies to the mid-IR, also enabling important new sensing applications.

A most remarkable technology is that of fiber lasers, based on either Yb^{3+} ($\sim 1\ \mu\text{m}$ wavelength range), Er^{3+}/Yb^{3+} ($\sim 1.5\ \mu\text{m}$), or Tm^{3+}/Ho^{3+} ($\sim 2\ \mu\text{m}$). Although "solid-state" in nature, waveguiding in optical fibers enables high compactness, robustness and alignment-free operation, as well as the ability to manage high-power absorption over long lengths. These features spurred a quick and extraordinary development of the fiber laser technology in the last 20 years.

As a side note, the huge market for telecom application ($\sim 1.5\ \mu\text{m}$ wavelength range) drove fast and exceptional development of fiber- and semiconductor-laser technologies in the 1990s, which greatly benefited many other industries, for example, making available laser diodes of increasing reliability and performance for pumping solid-state lasers.

Presently, fiber lasers are challenging solid-state laser technology also in many traditional applications where pulsed laser emission is required, and for which they were intrinsically limited due to the difficulty to propagate intense pulses (of nanosecond or picosecond duration) in small fiber cores. In fact, recent developments of special photonic-crystal fibers, with increasingly large mode area, or hollow fibers, in which the pulse propagates in air, are dramatically reducing the performance gap with traditional solid-state laser technology in these increasingly expanding area of applications.

Finally, kW-class continuous-wave Yb^{3+} fiber laser has become nowadays the technology of choice for the heaviest industrial applications such as in the automotive, in many cases replacing or completely displacing away CO_2 lasers (another notable example of gas laser, based on molecular vibrational transitions at ~ 10-μm wavelength).

Laser transients: *Q*-switching pulse generation

In this Section and the next one, time-dependent, transient laser effects are briefly discussed. There are distinctly two ways to generate powerful pulses, and which one is chosen depends on applications.

When high power and high energy are required, Q-switching operation is the preferred technique. This consists in keeping the Q of the optical cavity low at the beginning of the pump action, so that the population inversion can grow to a very high level. When this is achieved, the cavity Q is suddenly restored to its original value, allowing an abrupt growth of the field to a high power concentrated in a short pulse. Q-switching can be discussed within the single-mode approximation of the previous paragraph using the equations (42), even if fast transients always tend to bring many longitudinal modes into oscillation. Generally this technique leads to nanosecond pulse durations, with single-pulse energies up to several hundreds of millijoules or even joules.

Since the growth of the laser pulse starting from spontaneous emission, as well as the gain dynamics, are fast with respect to both fluorescence decay and pump rate (for continuous-wave pumping), the equations (42) describing single-mode Q-switching in a linear, standing-wave resonator can be simplified as (Siegman, 1986; Koechner, 2006)

$$\frac{d\Gamma}{dt} = -\frac{S}{S_{sat}}\Gamma \tag{50}$$

$$T_R\frac{dS}{dt} = (2\Gamma - L_i - \ln(1/R))S \tag{51}$$

with $\Gamma = \int g dz$ being the single-pass unsaturated gain exponent, integrated along the amplifier. T_R is the round-trip time.

Here we concentrate on active Q-switching, where loss modulation is basically instantaneous, and is provided by an electrical modulator (typically electro-optic or acousto-optic).

Assuming continuous-wave pumping, in general, these equations can be readily solved to give the output pulse energy E_o and the pulse duration τ_o:

$$E_o = E_{sat}\frac{\ln(1/R)}{L_i + \ln(1/R)}(\Gamma_i - \Gamma_f) \tag{52}$$

$$\tau_o = \frac{\Gamma_i - \Gamma_f}{\Gamma_i - \Gamma_{th}[1 + \ln(\Gamma_i/\Gamma_{th})]}T_c \tag{53}$$

being Γ_i the initial gain when Q-switching occurs, Γ_f the residual gain after the pulse is emitted, $2\Gamma_{th} = L_i + \ln(1/R)$ the threshold gain for continuous-wave operation, and $T_c = T_R/[L_i + \ln(1/R)]$ the photon lifetime in the un-pumped resonator. The saturation energy is $E_{sat} = S_{sat}A\tau_{sp}$, where A is the beam cross section in the amplifier.

A third equation relates initial and final gains:

$$\Gamma_i - \Gamma_f + \Gamma_{th}\ln(\Gamma_f/\Gamma_i) = 0 \tag{54}$$

Integrating the difference of the first two equations (42), to give the time evolution of the population inversion between two Q-switching pulses, one finds a fourth equation, which allows to eventually calculate Γ_i and Γ_f:

$$\Gamma_i = \Gamma_0 - (\Gamma_0 - \Gamma_f)\exp\left(-\frac{1}{f\tau_{sp}}\right) \tag{55}$$

where f is the repetition rate of the Q-switching pulses, determined by the active modulator. Γ_0 is clearly the gain at $f = 0$, due to the continuous-wave pump rate R_2.

Since in general all lasers are designed to operate well above threshold, in continuous-wave regime, we may assume $\Gamma_0 \gg \Gamma_{th} > \Gamma_f$, yielding a simple expression for the pulse energy as a function of f:

$$E_o \sim E_{sat}\Gamma_0\eta_o\left[1 - \exp\left(-\frac{1}{f\tau_{sp}}\right)\right] \tag{56}$$

where $\eta_o = (\ln(1/R))/(L_i + \ln(1/R))$ is the output coupling efficiency. At low repetition rate, the preferred regime for high-energy Q-switched lasers, $f \ll 1/\tau_{sp}$, $\Gamma_i \sim \Gamma_0$ and the output pulse energy and duration is $E_o \sim E_{sat}\Gamma_0\eta_o$ and $\tau_o \sim T_c$, respectively.

High-frequency Q-switching is used instead for many industrial applications such as fast material processing and laser sensing. In this regime $f \gg 1/\tau_{sp}$ and one can use a convenient asymptotic approximation of equations (52) and (53) to obtain the key laser parameters:

$$E_o \sim \frac{E_{sat}\Gamma_0}{f\tau_{sp}} \tag{57}$$

$$\tau_o \sim \frac{8T_R\tau_{sp}}{\Gamma_0}f \tag{58}$$

However, there exists a maximum possible frequency f, which is related to the build-up time of the pulse from starting noise, which is emitted isotropically and is amplified most effectively along the solid angle determined by the amplifier length and the cross-section of the pumped region. In general, it turns out that

$$\tau_b = \frac{25T_c}{\Gamma_0/\Gamma_{th} - 1} \tag{59}$$

This is generally one order of magnitude longer than the pulse width. Applying again the high-frequency approximation, τ_b becomes

$$\tau_b \sim \frac{50T_R\tau_{sp}}{\Gamma_0} f \tag{60}$$

The obvious condition that must be satisfied is $\tau_b < 1/f$, which eventually sets the highest frequency of operation:

$$f < \sqrt{\frac{\Gamma_0}{50T_R\tau_{sp}}} \tag{61}$$

It is thus seen that the pulse duration increases proportionally to f, and the energy decreases like $1/f$.

A completely different behavior is obtained with passive Q-switching. In this case, a saturable absorber is used instead of an electric modulator.

Saturable absorbers most frequently employed for Q-switching are Cr:YAG crystals (for 1-μm lasers) and SESAMs (SEmiconductor Saturable Absorber Mirrors), which will be mentioned also for the generation of much shorter pulses, in the next Section.

If proper material and laser design conditions are met, such nonlinear absorber saturates its losses before the laser amplifier is depleted, providing a relatively slow but effective Q-switching action. This kind of Q-switching will not be described in detail here, however the most important results are summarized as follows:

- the pulse energy is constant, $E_o \sim AS_{sat}\tau_{sp}2q_0$, basically fixed by the round-trip saturable loss modulation q_0
- pulse width is also constant, $\tau_o \sim 3.5T_R/q_0$
- pulse repetition rate increases linearly with pump power
- a maximum repetition frequency exists also in this case, due to $\tau_b < 1/f$

It is clear that relatively short pulses down to ~100 ps can be more easily generated with microchip lasers ($T_R \sim$ few picoseconds) operating in passive Q-switching, with the unique advantage of constant pulsewidth over their frequency range. In fact, the smallest electric modulators allows miniature Q-switched lasers as short as few centimeters, giving pulse duration slightly longer in principle: since in this last case $\tau_o \sim T_c$, pulses as short as few hundreds picosecond are still possible, but the duration increases with the frequency.

A consequence of (61) (and a similar expression for passive Q-switching) is that repetition rates as high as ~1 MHz are possible with very short laser resonators.

Laser transients: Mode-locking and ultra-short pulse generation

In this Section, a different technique is discussed for the generation of ultra-short pulses, which find broad popularity in scientific, biomedical, and also, more recently, in industrial applications.

Short and ultrashort pulses generated by lasers have durations from few tens of picoseconds (10^{-12} s) to well below femtoseconds (10^{-15} s). Laser media that allow such a short pulses need to have wide spectral bandwidths to sustain their generation, since, according to Fourier relation, $\Delta\omega\tau_p \approx 2\pi$. The gain bandwidth is usually a fraction of the available spectral bandwidth $\Delta\omega_g$. For example, the full bandwidth of the Nd:YAG allows pulses of ≈5 ps, while for many other solid-state laser materials they can definitely be well below that.

The technique that allows to achieve this performance is named "Mode-Locking," and can be implemented either passively, exploiting the saturable absorption properties of some nonlinear materials, or actively, by the use of externally driven acousto-optic or electro-optic (loss or phase) modulators.

For example, it has been shown that most of the fluorescence (or spectral) bandwidth is readily exploited by passive mode-locking. In such conditions the generated pulses are almost Fourier-limited, with duration $\tau_p \approx 2\pi/\Delta\omega_g$, and with a number of longitudinal modes locked in phase $N \approx \Delta\omega_g/(\pi c/L') = \Delta\omega_g T_R/2\pi = T_R/\tau_p$, where L' is the optical length of the cavity and T_R is the round-trip time.

At the beginning of the mode-locking process, only a few of these longitudinal modes experience a net gain above threshold, and they tend to oscillate uncorrelated in laser free-running operation. At this initial stage, the output intensity has a noisy pattern. It is only when the modes are forced by the modulating device to maintain a fixed phase relationship to each other that the output as a function of time can vary in a well-defined manner. Under these conditions, the laser switches to the mode-locking regime.

Thus, mode-locking corresponds to correlating the spectral amplitudes and phases, so that the initial randomness is removed and a localized radiation pattern emerges, that circulates in the laser cavity with a repetition-rate of one per round-trip. This appears at the output as a pulse train, that can be continuous or a modulated bunch, depending on the pumping modalities. The conditions for obtaining stable mode-locking operation and well-formed ultrashort pulses are not trivial, and are reviewed in detail by Keller (2003).

For the purpose of illustrating the principle, continuously pumped active mode-locking is presented based on a time-domain model essentially due to Haus (1984), which is able to capture the main features of laser mode-locking. The model is not concerned with the starting mechanism itself, and assumes an already formed light pulse traveling inside the cavity. Looking for the conditions of self-reproducibility, let the field be

$$\vec{E} = \hat{\varepsilon}E(t), \tag{62}$$

with

$$E(t) = \frac{1}{\sqrt{2\pi}}\int_{-\infty}^{\infty} A(\omega)e^{-i\omega t}d\omega. \tag{63}$$

$E(t)$ and $A(\omega)$ are Fourier transforms of each other, representing pulse envelopes in their domains at some position into the cavity.

Assuming a linear laser cavity of length L, containing a gain medium of length ℓ and a gain coefficient with a frequency dependence $g(\omega) = g_0/[1 + (\omega - \omega_0)^2/\Delta\omega_g^2]$, where (in this case) g_0 is the saturated gain coefficient at the center frequency ω_0 of the gain medium, after one passage in the gain medium $A(\omega)$ becomes $\exp\{g_0\ell/[1 + (\omega - \omega_0)^2/\Delta\omega_g^2]\}A(\omega)$.

The unavoidable cavity losses (either passive or due to output coupling) can be modeled introducing a loss coefficient per unit length, so that the overall losses can be thought of as $\alpha_i L_i$, with L_i an appropriate loss medium length. A passage through it produces the change $\exp(-\alpha_i L_i)A(\omega)$.

Finally, the essential element in the mode-locked laser is the modulator, for example, an active, externally driven acousto-optic device of loss coefficient α_m and length L_m, producing a time dependent loss $\alpha_m L_m[1 - cos(\omega_m t)]$ at the modulation frequency ω_m. This is best described in the time domain, affecting directly the field envelope after a passage through it: $\exp\{\alpha_m L_m[1 - cos(\omega_m t)]\}E(t)$.

By taking the appropriate Fourier transforms to describe all the actions in the time domain, and assuming low net gain as well as low losses so that only first order terms in their expanded expressions are kept, after one round-trip time T_R, at the same space position we have:

$$E(t + T_R) = \left[1 + 2g_0\ell\left(1 + \frac{1}{\Delta\omega_g^2}\frac{d^2}{dt^2}\right) - 2\alpha_i L_i - 2\alpha_m L_m(1 - \cos(\omega_m t))\right]E(t). \tag{64}$$

Steady-state operation requires self-reproducibility, $E(t + T_R) = E(t)$, and for this to happen it needs

$$\omega_m = \frac{2\pi}{T_R}.$$

Since the pulse tends to adjust itself for minimum losses, the modulation function can be expanded up to its first nonzero contributed term, getting the final form of the mode-locking equation:

$$\left[\frac{d^2}{dt^2} - \frac{\alpha_m L_m \omega_m^2 \Delta\omega_g^2}{2g_0\ell}t^2 + \Delta\omega_g^2\left(1 - \frac{\alpha_i L_i}{g_0\ell}\right)\right]E(t) = 0. \tag{65}$$

This is written in a way that evidences its similarity with the Schroedinger equation of one-dimensional harmonic oscillator:

$$\left[\frac{d^2}{dx^2} - \frac{m^2\omega^2}{\hbar^2}x^2 + \frac{2mE}{\hbar^2}\right]\psi(x) = 0. \tag{66}$$

As for (66), equation (65) has Hermite-Gauss solutions of integer order n:

$$E_n(t) = H_n(2\pi t/\tau_p)\exp\left[-(2\pi t/\tau_p)^2/2\right]. \tag{67}$$

with

$$\begin{gathered} \frac{2\pi}{\tau_p} = \left(\frac{\alpha_m L_m \omega_m^2 \Delta\omega_g^2}{2g_0\ell}\right)^{1/4} \\ \left(1 - \frac{\alpha_i L_i}{g_0\ell}\right) = (2n + 1)\left(\frac{2\pi}{\tau_p \Delta\omega_g}\right)^2. \end{gathered} \tag{68}$$

Since as a rule the gain barely exceeds the loss ($g_0\ell/\alpha_i L_i \approx 1$), the last relation in (68) can be put into a more transparent form as follows:

$$\begin{aligned} \frac{g_0\ell}{\alpha_i L_i}\left(1 - \frac{\alpha_i L_i}{g_0\ell}\right) &= \left(\frac{g_0\ell - \alpha_i L_i}{\alpha_i L_i}\right) \\ &= (2n + 1)\left(\frac{2\pi}{\tau_p \Delta\omega_g}\right)^2 \frac{g_0\ell}{\alpha_i L_i} \\ &\approx (2n + 1)\left(\frac{2\pi}{\tau_p \Delta\omega_g}\right)^2 \end{aligned} \tag{69}$$

which represents the excess gain over the threshold gain for continuous operation, needed to sustain a mode-locked Hermite-Gauss pulse of order n. Higher orders need more gain.

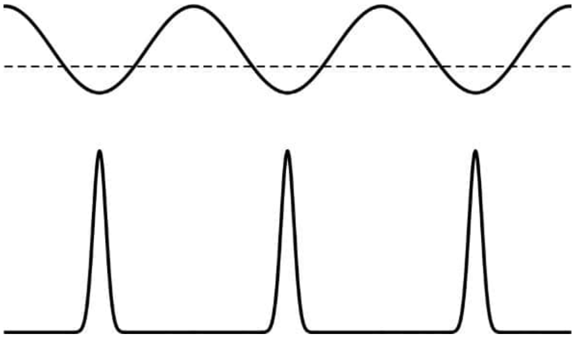

Fig. 11 Gain and losses in an actively mode-locked laser, and its generated pulse train. The dotted line sets the net gain of the laser for continuous operation, and the extra, modulated loss are shown in full line above it. With periodicity of a round-trip time, a temporal window is opened in which the net gain is positive, and the pulses can go through, as shown in full line at the bottom. Pulse duration not to scale with round-trip time in the figure.

Gain saturation leads to the stability of lowest order Gaussian pulse, and to instability of higher order solutions. If just the right net gain to excite the fundamental ($n = 0$) solution is supplied, higher order ones do not have enough gain to start. If the supplied gain is in excess to this amount so that higher order solutions can also start, the amplitude of the lowest order grows faster to the point that it saturates the gain which settles to its steady-state value, switching off the higher order solutions.

It is thus seen from (67) that the pulse is Gaussian in shape; furthermore from the first of (68) it is seen that the pulsewidth has a power dependence on both the modulation depth and the gain bandwidth. Fig. 11 illustrates qualitatively the interplay of gain and losses in an actively mode-locked laser, and its Gaussian envelope pulses.

Actually, passive mode-locking is definitely more used in practice, owing to its superior performance and simplicity, since reliable fast saturable absorbers exist for a wide range of lasers (solid-state, semiconductors and fibers) (Keller 2003).

"Fast" means that the absorber is supposed to recover its initial, unperturbed state, in much less than one round-trip time T_R. Kerr-lens mode-locking is based on optical Kerr effect, which modifies the refractive index nearly instantaneously with respect to the pulse envelope (typical electronic response $\sim 10^{-15}$ s): this affects the spatial focusing/defocusing of the intra-cavity beam which, in combination with an aperture provides the necessary loss modulation for many solid-state femtosecond lasers. Another application of the third-order "fast" nonlinearity, ubiquitous to all transparent materials, is the nonlinear polarization rotation, which is most often employed in ultrafast fiber lasers.

The most popular mode-locking concept today is certainly the SESAM (semiconductor saturable absorber mirror), used for a variety of lasers, wavelengths and pulse durations (from picoseconds to few femtoseconds). Its detailed design may vary according to the desired performance, however the general principle is based on semiconductor engineering of quantum well absorbers fabricated at low temperature, such that the lifetime of the excited carriers is squeezed from the nanoseconds to the picoseconds, and the saturable modulation loss can be precisely tuned within the range from $\sim 1\%$ to few tens %.

Passive mode-locking allows to exploit nearly all the available net gain bandwidth, producing pulses of few picoseconds in relatively narrowband solid-state materials such as Nd-doped crystals: $\tau_p \sim 1/\Delta\omega_g$. Active mode-locking produces instead longer pulses, due to the mild and broad time-window of the sinusoidal modulation compared to the fast, self-adaptive modulation window which compresses pulses more effectively, until a balance with bandwidth narrowing in the amplifier is achieved.

An important condition ensuring stability of continuous-wave-pumped picosecond mode-locking against spontaneous Q-switching requires that the intracavity circulating pulse energy be $E_c > \sqrt{E_{sat,A}E_{sat,L}q_0}$, given the saturation energies of the absorber and of the laser material, and the round-trip modulation loss $\sim$ few %. Such instabilities cannot be excluded in principle, since typically $E_{sat,\,A} \ll E_{sat,\,L}$. The stability condition basically requires that the absorber be fully saturated at each round-trip, leaving no room for a slow growth of self-Q-switching over many round-trips.

In femtosecond lasers, dispersive effects and self-phase modulation cannot be neglected, however the main results for passive mode-locking still apply:

- full gain bandwidth exploitation possible, provided the laser design is carefully optimized
- possible instabilities are suppressed if the circulating energy exceed a certain threshold

Such threshold is small compared to the case of no dispersion (picosecond domain), since an intrinsic passive feedback helps stabilize the pulse energy: as the pulse energy starts to grow due to gain fluctuations, for example, self-phase modulation would broaden the pulse spectrum thus reducing the gain due to finite gain bandwidth.

Spectral broadening via self-phase modulation is more effective in femtosecond rather than picosecond lasers, since it is proportional to (peak power)/(pulse duration). Peak power is generally limited by optical damaging practical considerations, therefore shorter pulses can produce much broader spectra.

Conclusion

Since the discovery of laser action in ruby in 1960, a broad variety of lasers has been demonstrated over the years, with many of them finding important practical applications that overall cover a very large portion of the electromagnetic spectrum from X-rays to the THz.

Laser light can be manipulated to enhance its spectral and spatial coherence properties: the invention of unstable resonators (Siegman 1986) has made possible high-power diffraction-limited lasers, while sophisticated electronically-stabilized ultra-narrow bandwidth lasers have become essential tools in many exciting applications, such as gravitational wave detection. Furthermore, even the quantum nature of laser light is presently being exploited for practical applications such as cryptography and next-generation quantum computing.

In this Chapter we have presented the basic principles and the most important operating regimes and properties of lasers. These represent the basis for a more advanced investigation and further exploitation of technical tools and methods in laser design and modeling.

It should be remarked that, along with laser physics and technology, nonlinear optics rapidly evolved, for obvious reasons: besides the interest in the rich variety of theoretical aspects that can be tested also experimentally for the first time due to the very unique properties of the laser light, nonlinear optical effects, such as harmonic generation, wave mixing, stimulated scatterings, self-focusing and so on, have evolved into many technologically important applications. In particular, due to their very nature, fiber lasers display and take advantage of an epiphany of nonlinear optical effects.

References

Haus HA (1984) *Waves and Fields in Optoelectronics*. London: Prentice-Hall.

Keller U (2003) Recent developments in compact ultrafast lasers. *Nature* 424: 831–838.

Koechner W (2006) *Solid-State Laser Engineering*, 6th ed. New York: Springer.

Milonni PW and Eberly JH (2010) *Laser Physics*, 2nd ed. New York: Wiley.

Siegman AE (1986) *Lasers*. Mill Valley: University Science Books.

Svelto O (2010) *Principles of Lasers*, 5th ed. New York: Springer.

Yariv A (1989) *Quantum Electronics*, 3rd ed. New York: Wiley.

Synchrotron radiation☆

G Margaritondo, Ecole Polytechnique Fédérale de Lausanne, (EPFL), Lausanne, Switzerland

© 2024 Elsevier Ltd. All rights reserved.

This is an update of G. Margaritondo, Synchrotron Radiation, Editor(s): Franco Bassani, Gerald L. Liedl, Peter Wyder, Encyclopedia of Condensed Matter Physics, Elsevier, 2005, Pages 150–157, ISBN 9780123694010, https://doi.org/10.1016/B0-12-369401-9/00634-3.

Introduction: X-ray sources **425**
The relativistic basis of synchrotron sources **426**
Main properties of synchrotron sources **428**
Different types of synchrotron sources **429**
Wigglers 429
Undulators 429
Helical wigglers 430
Free-electron lasers 430
The overall picture 431
Practical use of synchrotron sources **431**
Conclusion **432**
Further reading **432**

Abstract

Electron accelerators such as synchrotrons and storage rings are the best sources of X-rays and ultraviolet photons for research and technological applications. The physical mechanisms for all these sources use relativistic effects to increase the emission and its photon energies, and require an electron (or positron) beam moving at relativistic speed. The specific implementation of this strategy is reviewed here for different types of synchrotron or synchrotron-related sources: bending magnets, wigglers, undulators, helical wigglers, and free-electron lasers (FELs).

Introduction: X-ray sources

X-rays and ultraviolet photons are very extensively used not only for medical applications but also in research and technology. They are the basic ingredients of a wide variety of techniques ranging from microscopy and spectroscopy to imaging and structural analysis. The reason for their broad usefulness is quite fundamental: they possess photon energies and wavelengths that match basic magnitudes such as the binding energy of valence or core electrons and the length of chemical bonds.

As a consequence, the development of powerful X-ray and ultraviolet sources has been for many decades a high priority for research in many different disciplines. Progress in this field, however, has been rather slow until the advent in the late 1960s of the sources in the class broadly labeled as “synchrotrons.”

A conventional, non-synchrotron source emits X-rays or ultraviolet photons by bringing electrons to an excited state and then exploiting their radiative decay. Considering the photon energies to be emitted, the process must involve core electrons. Its effectiveness is limited: for example, pumping core electrons to an excited state requires putting a high power in the system (e.g., by bombarding it with electrons)—but the power is limited by the possible thermal damage to medium.

Furthermore, the photon emission occurs over a broad angular range. This limits the collimation of the source and its usefulness in experiments that require not only a high photon flux but also a high intensity and/or a high coherence.

The best parameter to characterize the source quality is the so-called brightness or brilliance, b. Roughly speaking (Fig. 1), this parameter is proportional to the flux F and inversely proportional to the source area A and to the (solid) angular range of emission Ω:

$$b = \text{constant} \times F/(A\Omega) \qquad (1)$$

(more precisely, F is the number of photons per second emitted in a given bandwidth of 0.1%; A is the product of the horizontal and vertical source sizes; Ω is the product of the horizontal and vertical angular spreads of the emitted photon beam).

A limited flux and a large angular range result in a small brightness. Limited brightness was a major problem in the experimental use of X-rays and ultraviolet photons until the advent of synchrotrons. For example, with a synchrotron source of today certain crystallographic experiments take a few minutes, whereas before they required days or months or were impossible.

For visible light, high brightness is obtained from lasers. This is not easy for X-rays: as discussed later, the effectiveness of the lasing mechanisms decreases and the fabrication of optical cavities is problematic. Only in recent years high-peak-brightness X-ray free electron lasers have been realized, triggering a new revolution.

☆*Change History*: September 2022. G Margaritondo updated all sections. All figures were redrawn and therefore updated.

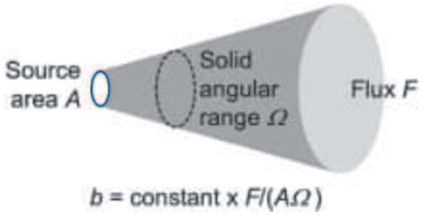

Fig. 1 The brightness b is the parameter which is most often used to characterize the quality of photon sources, including synchrotron sources.

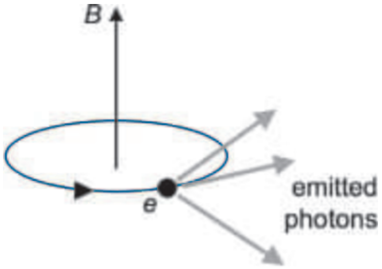

Fig. 2 The emission of photons by an electron during its cyclotron motion is a good starting point to analyze the mechanism of synchrotron sources. The analysis, however, must be performed for a motion at relativistic speed, $v \approx c$.

Before the advent of FELs, the X-ray sources in the broad "synchrotron" class had solved the problem of increasing the flux and the brightness with a radically different approach with respect to the classical sources (that still dominate medical applications). This strategy was based on a clever use of relativistic effects and required the electrons or positrons moving at a speed close to the speed of light, c. The light mass of such particles made them easier to accelerate and therefore more effective in emitting X-rays than heavier particles such as protons.

The relativistic basis of synchrotron sources

Consider (Fig. 2) a very simple emitter of electromagnetic waves: an electron moving along a circular orbit under the action of a constant magnetic B-field (cyclotron motion). The emitted photon energy $h\nu$ is determined by the cyclotron frequency, which in classical physics is given by $\nu = eB/(2\pi m_o)$, where e and m_o are the charge and the rest mass of the electron. This result derives, as it is well known, from the balance between the Lorentz force and the mass multiplied by the centripetal acceleration. The typical emitted photons have rather low energies with respect to X-rays.

Imagine, however, the same phenomenon when the speed v of the circulating electron becomes close to the speed of light. In an inertial reference frame moving with the same velocity as the electron at a given time (hereafter called the "electron frame"), the transverse Lorentz force evB of the B-field becomes a transverse electrostatic force of magnitude γevB, where the relativistic γ-factor (the energy of the moving electron divided by $m_o c^2$) is:

$$\gamma = \left(1 - \left(v^2/c^2\right)\right)^{-1/2}. \tag{2}$$

As a consequence, relativistic dynamics predicts a cyclotron frequency $\gamma eB/(2\pi m_o)$, which is γ times larger than the aforementioned classical result. The emitted photon energy in the electron reference frame is also multiplied by this factor, shifting toward the ultraviolet and X-ray spectral domains.

This shift toward shorter wavelengths and larger photon energies is further enhanced if one observes the emission in the reference frame of the laboratory. Imagine, for example, that the emitted photon energy is measured in the laboratory frame along the direction of the electron velocity. Since the source (the electron) is in motion, the photon energy is affected by the Doppler effect, which for electromagnetic waves is a relativistic phenomenon.

In the "forward" direction of the electron (source) velocity, the Doppler effect multiplies the photon energy by a factor $[(1 + v/c)/(1 - v/c)]^{1/2} = \gamma\ (1 + v/c)$. In the extreme relativistic case $v^2/c^2 \approx 1$, this factor is close to 2γ. Overall, therefore, relativity increases the classical emitted photon energy for the cyclotron motion by a factor $\approx \gamma(2\gamma) = 2\gamma^2$.

The mechanism just described is active in the photon emission by "bending magnets" (Fig. 3). These are the dipole magnets that keep the electrons circulating in a closed orbit within the vacuum chamber of an accelerator such as a storage ring. The deflection of the electron trajectory causes a (centripetal) acceleration and therefore the emission of electromagnetic waves. The mechanism is roughly equivalent to that of a portion of a cyclotron trajectory orbit, and the characteristics of the emission are also similar although a rigorous description requires a more sophisticated electrodynamics treatment.

In the first approximation, in fact, the center of the photon energy spectrum emitted by a bending magnet is close to $2\gamma^2$ multiplied by the classical photon energy given by the cyclotron frequency, $h\nu = heB/(2\pi m_o)$. For a typical B-field of 1T, the

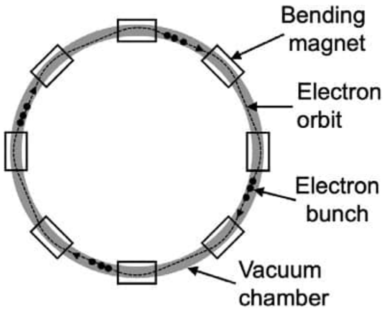

Fig. 3 (Dipole) bending magnets are used to keep electrons (grouped in bunches) circulating along closed orbits in the vacuum chamber of a storage ring (top view).

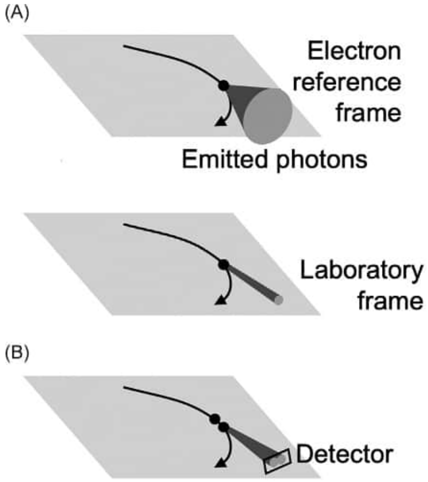

Fig. 4 (A) The emission of photons by an electron, whose trajectory is deviated by a bending magnet, occurs over a wide angular range in the electron reference frame. Relativity drastically reduces this angular range when the emission is observed in the laboratory frame. (B) In practice, however, the angular collimation is only present for the vertical direction. In the horizontal direction, electrons at different points of the orbits emit in different directions and the horizontal angular range is set by the portion of the orbit "seen" by the detector.

classical photon energy would be $\approx 4 \times 10^{-23}$ J or ≈ 0.2 meV, well below the ultraviolet and X-ray range. If one takes a typical electron energy of 1 GeV in a storage ring, the γ -value is $\approx 2 \times 10^3$, the factor $2\gamma^2$ is $\approx 4 \times 10^6$, and the relativistic emission becomes $\approx 2 \times 10^2$ eV, which falls indeed in the X-ray range.

As discussed later, all types of synchrotron sources exploit this combination of relativistic effects to shift their emission into the ultraviolet and X-ray ranges. In addition to the spectral shift, relativity has other beneficial effect: a shrinkage of the angular spread of the emission and a corresponding increase in the brightness.

This angular-range shrinkage can be easily understood. As shown in Fig. 4A, a photon emitted in the vertical plane, when observed from the reference frame of the emitting electron, can travel in a direction quite far from that of the electron velocity (the "forward" direction). When seen from the laboratory frame, the photon direction changes becoming very close to the same "forward" direction.

The reason is that the relativistic Lorentz transformations include a γ-factor for the "forward" direction coordinate, whereas the transverse direction coordinates are invariant. When calculating the angle between the photon direction and the "forward" direction as the ratio of the two velocity components, the γ-factor appears in the denominator but not in the numerator. This confines the emission within an angular range $\approx 1/\gamma$ from the "forward" direction. Because of the large value of γ, this relativistic effect strongly collimates the emission, enhancing the brightness.

Note, however, that for bending magnets the angular collimation is only present in the vertical direction. In the horizontal direction (Fig. 4B), the angular range depends on the portion of the electron orbit "seen" by the detector.

Finally, it should be noted that the brightness (Eq. 1) is also enhanced because relativity boosts the emitted power. Electrodynamics shows that the power emitted by an accelerated charge is proportional to the square of the acceleration. The relativistic transformation of the transverse acceleration includes a factor γ^2, which becomes γ^4 for the square of the acceleration and for the emitted power. Thus, large γ-values boost the emitted power.

Main properties of synchrotron sources

Based on the above discussion, we can summarize the main properties of bending magnets and other synchrotron sources as follows:

- *Spectral domain*: centered in the ultraviolet and X-ray region because of the relativistic factor $\approx 2\gamma^2$ in the emitted photon energies.
- *Bandwidth*: a bending magnet emits over a wide photon energy range. The reason can be understood by considering an emitting electron as it passes through the bending magnet. Due to the angular collimation of the emission, the electron can be imagined as a torchlight with a very narrow beam. A detector (Fig. 5A) is illuminated by this "torchlight" for a very short time. The corresponding bandwidths of frequencies and photon energies (according to the Fourier theorem and/or to the uncertainty principle) are inversely proportional to the illumination time and therefore quite broad. A detailed theory shows that for a bending magnet the photon energy bandwidth is close to the relativistic "cyclotron" photon energy $\approx 2\gamma^2 heB/(2\pi m_o)$ so that the relative bandwidth $\Delta h\nu/(h\nu) \approx 1$. Overall, the emitted spectrum of a bending magnet can be roughly imagined as a broad peak with center close to $\approx 2\gamma^2 heB/(2\pi m_o)$ and $\Delta h\nu/(h\nu) \approx 1$. In some other types of synchrotron sources such as the undulators (see Fig. 5B and the discussion later), the bandwidth is narrow rather than broad as in bending magnets. As shown in Fig. 6, a log–log plot of this peak gives the familiar synchrotron spectrum.
- *Collimation*: the vertical emission is limited to an angular range $\approx 1/\gamma$.
- *Flux*: high and proportional to γ^4.
- *Brightness*: very high because of the high flux and strong collimation. In addition, the brightness is also enhanced by the small source area A (Eq. 1). The effective A is determined by the transverse section of the electron beam circulating in the accelerator. In modern storage rings as well as in other accelerators, the trajectories of the electrons are controlled with extreme accuracy. This strongly limits A boosting the brightness.
- *Coherence*: the lateral coherence of a source of electromagnetic radiation increases as the product of the source size times the angular range decreases, until it reaches the "diffraction limit" (for which the product roughly equals the wavelength). Thus, the same geometric factors that influence the brightness (Eq. 1) also determine the lateral coherence. For a bending magnet, the high angular collimation in the vertical direction produces high lateral coherence in the same direction. The longitudinal coherence is determined by the relative bandwidth $\Delta h\nu/(h\nu)$ and, for a bending magnet, it is quite limited. However, the longitudinal coherence can be increased by reducing the bandwidth with a monochromator.
- *Polarization*: for a bending magnet, the limited angular range confines the emission to directions close to the (horizontal) plane of the storage ring. From the corresponding viewpoints, the emitting electrons (Fig. 7, right) appear to move along a horizontal line, and their emission is linearly polarized with the photon electric field in the horizontal plane. Slightly out of the plane (Fig. 7, middle), the observed electron motion appears to follow an elliptical curve and the emitted light possesses a circularly polarized component. As discussed later, other synchrotron sources are also linearly or elliptically polarized.

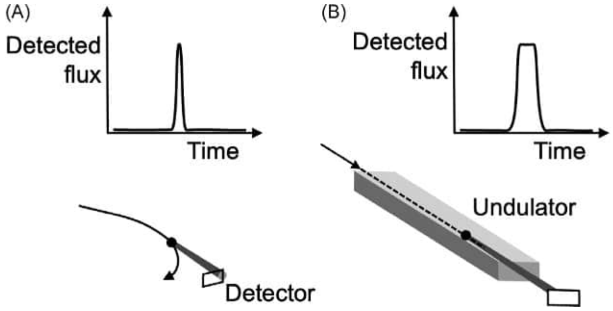

Fig. 5 (A) An electron going through a bending magnet emits photons that illuminate the detector only during a short time pulse. This corresponds to a broad photon energy bandwidth. (B) An electron passing through an undulator, instead, illuminates the detector continuously producing a longer pulse and a narrow bandwidth. The undulator bandwidth is further decreased by other factors.

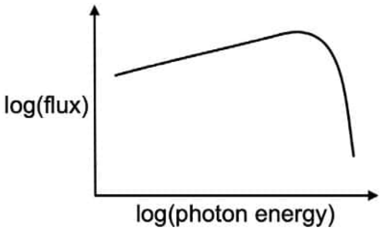

Fig. 6 In first approximation, the spectrum emitted by a bending magnet can be imagined as a broad peak. The conventional way to show the spectrum, however, is a log–log plot that transforms a peak-like line shape into the familiar spectrum of bending-magnet synchrotron sources.

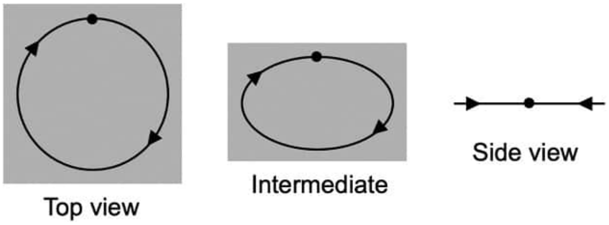

Fig. 7 The polarization of the bending magnet emission can be understood by considering how electrons moving in a storage ring appear from different points of view. For example, in the ring plane (side view) the motion appears linear and the emission is linearly polarized.

- *Time structure*: The electrons circulate around a storage ring grouped in bunches. Every time a bunch passes through a source point such as a bending magnet, a pulse of photons is emitted. Thus, the time structure of a synchrotron source consists of short pulses separated by longer "dark" intervals. The parameters of the time structure depend on those of the storage ring, and the pulse duration can reach in some cases the picosecond range.

Different types of synchrotron sources

The previous discussion primarily dealt with bending magnet sources. Other types of synchrotron sources exist and are briefly reviewed here.

Wigglers

A wiggler (Fig. 8) is a periodic sequence of dipole magnets inserted in an otherwise straight portion of a storage ring. It produces a series of transverse "wiggles" in the electron path, each roughly equivalent to a portion of the trajectory in a bending magnet. Thus, the emission approximately corresponds to that of a series of bending magnets.

The positive aspects of a wiggler with respect to a bending magnet are mainly two. First, the flux and the brightness are multiplied with respect to a single bending magnet by the number of wiggles. Second, the B-field strength can be selected to tune the emission spectrum to a desired value (e.g., to very high photon energies in the hard-X-ray range). This is not possible for bending magnets since their field strength is dictated by the task of keeping the electrons in a closed trajectory around the ring.

Undulators

An undulator is a device similar to a wiggler except that the B-field strength is weaker and the "wiggles" along the electron trajectory are less pronounced. As a consequence, the emission properties are quite different from those of wigglers or bending magnets.

Roughly speaking, the "wiggles" in this case produce angular deviations smaller than $1/\gamma$ with respect to the axis of the undulator. Since the angular spread of the emission is $\approx 1/\gamma$, the emission corresponding to one "wiggle" illuminates the subsequent wiggles, producing coherent interference. As a result, the emitted peak intensity increases with the square of the number of wiggles rather than being proportional to it.

The photon energy spectrum of an undulator is also quite different from that of a wiggler or a bending magnet. First, the bandwidth is much narrower. The reason (Fig. 5B) is that for weak wiggles the detector is illuminated during the entire passage of the electron-torchlight through the undulator. The resulting long pulse corresponds to a narrow photon energy bandwidth. This effect is further enhanced by other factors. In essence, therefore, an undulator concentrates the emitted flux into a narrow bandwidth, achieving very high brightness.

This narrow bandwidth is centered at a photon energy which is determined by the undulator period (see Fig. 9). The physical explanation is rather simple: in the reference frame of an electron moving at relativistic speed through the undulator, the periodic transverse B-field is observed as the combination of a periodic transverse B-field plus a transverse periodic electric field perpendicular to the B-field, both moving at a speed $\approx c$. In other words, it appears as an electromagnetic wave.

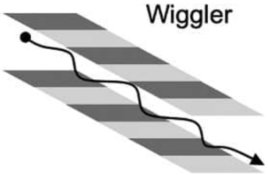

Fig. 8 A wiggler is a periodic series of magnets inserted along a straight section of the storage ring. The magnets cause lateral undulations or "wiggles" of the electrons with respect to their otherwise straight trajectory. The resulting photon emission is similar to that of a series of bending magnets.

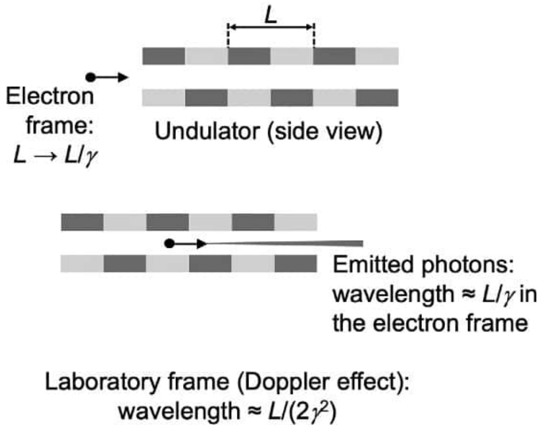
L
Electron frame: $L \rightarrow L/\gamma$
Undulator (side view)
Emitted photons: wavelength ≈ L/γ in the electron frame
Laboratory frame (Doppler effect): wavelength ≈ $L/(2\gamma^2)$

Fig. 9 Schematic explanation of how the two relativistic effects (Lorentz contraction of the undulator period and Doppler shift) determine the "central" emitted wavelength and photon energy of an undulator.

The electron backscatters this "wave": this is the mechanism of synchrotron radiation emission. What is the wavelength of the backscattered wave? Obviously, it is related to the undulator period, L. However, in its reference frame the electron "sees" L shortened by a factor γ because of the relativistic "Lorentz contraction." When observed in the laboratory frame, the wavelength is further decreased by a factor $\approx 2\gamma$ by the Doppler effect, becoming $\approx L/(2\gamma^2)$. The corresponding photon energy is $\approx 2\gamma^2 hc/L$.

In addition to this photon energy, the undulator also emits higher harmonics corresponding to its integer multiples. As the B-field increases, the sequence of higher harmonic merges into one broad spectrum corresponding to the wiggler emission.

The fundamental-harmonic photon energy $\approx 2\gamma^2 hc/L$ of an undulator is shifted when the emission is detected along a direction other than the undulator axis, or when the B-field changes. The reason is similar in both cases: at an angle θ from the "forward" direction, the Doppler factor is no longer $\approx 2\gamma$ and becomes a function of θ. Similarly, as the B-field increases the transverse wiggles decrease the electron speed along the undulator axis and effectively modify the γ-factor in the Doppler shift.

Taking both effects into account, the first harmonic photon energy of the undulator changes from $2\gamma^2 hc/L$ to.

$$h\nu \approx \left(2\gamma^2 hc/L\right)/\left(1 + K^2/2 + \gamma^2\theta^2\right), \tag{3}$$

where the K-factor is proportional to B. Eq. (3) has a very important impact on the operation of undulator sources: by changing the B-field (e.g., the gap between permanent magnets), one can tune the emitted photon energy to a desired value.

Contrary to bending magnets, undulators achieve high angular collimation not only on the vertical direction but also horizontally. In fact, during the entire emission process, the electron stays in a straight trajectory except for small transverse wiggles, and this limits the horizontal angular divergence. This also implies that the lateral coherence is high both vertically and horizontally.

Finally, the undulator emission is linearly polarized with the electric vector in the horizontal plane. The reason is that, when observed from the point of view of the detector, an emitting electron looks like an oscillating charge along a horizontal line.

Helical wigglers

For many applications of synchrotron sources, it is necessary to have elliptical polarization. Such a polarization does exist (Fig. 7) in the out-of-plane emission of bending magnets. However, the emitted intensity strongly decreases as the direction diverges from the horizontal plane. Therefore, bending magnets can only provide elliptically polarized radiation of weak intensity.

Dedicated sources for elliptical polarization are based on special magnet arrays that force the electrons to move along a periodic helical path rather than simply undulating in the transverse direction. Such devices can operate either in the wiggler mode ("helical wigglers") or as undulators.

Free-electron lasers

Standard synchrotron sources are not based on lasers mechanism: they do possess laser-like properties such as high collimation, brightness, and coherence, but they are not lasers. Indeed, their emission mechanism is not based on optical amplification by stimulated emission as for a conventional laser.

There exists, however, a special class of synchrotron-related sources that operate with optical amplification, even though they are not based on stimulated emission: the free-electron lasers (FELs). They operate either as emitters of infrared radiation or as very powerful X-ray sources.

The realization of X-ray lasers is complicated also because optical cavities, which are standard components of conventional lasers, are not available. Formed by two reflecting or partially reflecting surfaces, the cavity increases the path of photons and the effects of optical amplification. However, reflection is very weak for X-rays, so lasing must be achieved without an optical cavity and requires strong optical amplification.

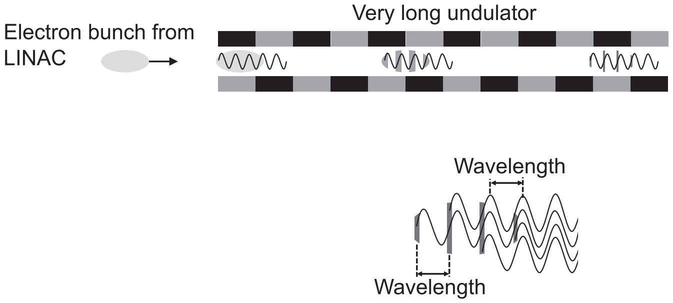
Electron bunch from
LINAC
Very long undulator
Wavelength
Wavelength

Fig. 10 Top: The main components of a FEL are a LINAC and a very long undulator. We see here a relativistic electron bunch produced by the LINAC entering the undulator and emitting a wave, which then travels with the bunch interacting with it. This interaction reshapes the bunch creating periodic "slices." Bottom: The slice periodicity coincides with the wavelength, so the electrons in the slices emit waves in a coordinated fashion, causing optical amplification.

The basic ingredients of an FEL for X-rays are a linear electron accelerator (LINAC) and a very long undulator. The LINAC produces electron bunches of high energy. When a bunch enters the undulator, it starts emitting waves that then travel with the bunch. The electrons and the wave interact reshaping the bunch.

Note that the interaction disappears at the wave nodes, so the reshaping must produce a periodic structure. One can demonstrate that this structure consists of very thin "slices" with period equal to the wavelength. As seen in Fig. 10, electrons in these slices emit in a coordinated fashion, and this causes the optical amplification.

Although conceptually simple, this mechanism is very difficult to implement for short-wavelength X-rays. This is why X-ray FELs were realized only five decades after those for infrared radiation. And it also explains why an ordinary undulator or wiggler in a synchrotron source does not act as an FEL.

Several FELs for X-rays are now in operation in different countries, producing very exciting results. One important property of these sources is the time structure, consisting of pulses with duration determined by the passage of each electron bunch. The time scale is in the femtosecond range or even shorter, opening the door to the analysis of many important fast phenomena.

One should note, however, that FELs for X-rays cannot replace synchrotron sources based on storage rings. In fact, their very high peak brightness and ultrashort pulses, although suitable for specific applications, are not useful when longer pulses or a quasi-constant emission are required.

The overall picture

The different types of synchrotron or synchrotron-related sources, either already implemented or under development, provide extreme flexibility in matching the needs of a wide variety of applications. Fig. 11 is a summary overview of the characteristics of the emission of the main different machines.

Practical use of synchrotron sources

Synchrotron sources ceased long ago to be exotic instruments only used by a tiny minority of physicists. They have become instead standard instruments used by a large part of the research community in many diverse disciplines. Dozens of facilities are in operation in many countries, most of them at no cost for qualified users performing nonproprietary research. Additional programs often provide support to users for travel and lodging expenses.

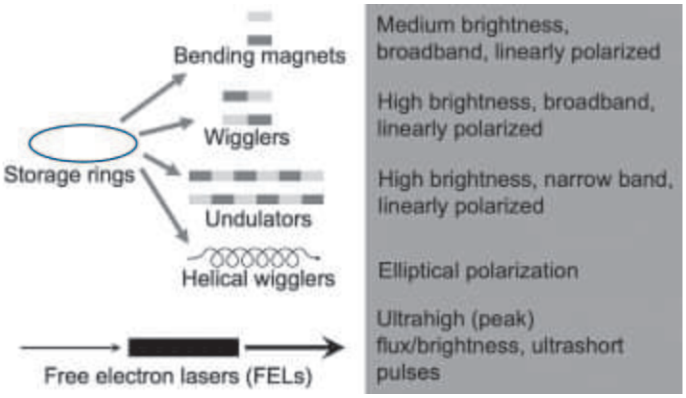
Bending magnets
Wigglers
Storage rings
Undulators
Helical wigglers
Free electron lasers (FELs)
Medium brightness, broadband, linearly polarized
High brightness, broadband, linearly polarized
High brightness, narrow band, linearly polarized
Elliptical polarization
Ultrahigh (peak) flux/brightness, ultrashort pulses

Fig. 11 The main different types of synchrotron radiation sources.

Each synchrotron facility serves its users with a variety of instruments. Roughly speaking, the core of the facility is an accelerator such as a storage ring with its injection and control systems. The emitted photons are collected by beamlines that improve the photon beam characteristics (e.g., by selecting a narrow band of photon energies with suitable monochromators) and convey them to experimental chambers.

In the accelerator, the electrons must circulate under ultrahigh vacuum. Many of the beamlines are also under vacuum since no window can be used to separate them from the accelerator without sharply decreasing the photon beam intensity.

The typical operation cycle of a synchrotron facility begins with the injection of electrons (or positrons) in the accelerator. If this is a storage ring, the electron beam keeps circulating and emitting photons for hours or days as the energy lost through photon emission is restored by radiofrequency cavities. Natural losses steadily reduce the circulating electron beam until a new injection and the beginning of a new operation cycle. In many facilities, the injection is performed continuously so that the electron beam can circulate with no time limitations except for maintenance and equipment modifications.

Conclusion

Relativity enables high-energy electrons accelerated by magnetic devices to emit X-rays with exceptional properties: extreme flux, brightness and collimation, selected wavelengths, polarization, and coherence. The resulting synchrotron radiation sources constitute now a worldwide network of facilities with unprecedented magnitude in terms of instrumentation and user population. In recent years, new research opportunities were opened up by a variant of this class of X-ray emitters, the “free electron lasers,” with exceptional peak brightness and ultrashort pulses.

Further reading

Bonifacio R, De Salvo L, Pierini P, Piovella N, and Pellegrini C (1994) Spectrum, temporal structure, and fluctuations in a high-gain free-electron laser starting from noise. *Physical Review Letters* 73: 70–73.
Bordovitsyn VA (1999) *Synchrotron Radiation Theory and its Development, Series on Synchrotron Radiation Techniques and Applications*. vol. 5. Berlin: Springer.
Carroll FE (2002) Tunable monochromatic X-rays: A new paradigm in medicine. *American Journal of Roentgenology* 179: 583–590.
D’Amico KL, Terminello LJ, and Shuh DK (eds.) (1996) *Synchrotron Radiation Techniques in Industrial, Chemical, and Materials Science*. New York: Plenum.
Duke PJ (2000) *Synchrotron Radiation: Production and Properties*. New York: Oxford University Press.
Hwu Y and Margaritondo G (2021) Synchrotron radiation and X-ray free-electron lasers (X-FELs) explained to all users, active and potential. *Journal of Synchrotron Radiation* 28: 1014–1029.
Margaritondo G (1988) *Introduction to Synchrotron Radiation*. New York: Oxford University Press.
Margaritondo G (2003) *Elements of Synchrotron Radiation for Chemistry, Biology and Medical Research*. New York: Oxford University Press.
Mills DM (ed.) (2002) *Third-Generation Hard X-Ray Synchrotron Radiation Sources: Source Properties, Optics, and Experimental Techniques*. Hoboken: Wiley.
Mobilio S, Boscherini F, and Meneghini C (2015) *Synchrotron Radiation Basics, Methods and Applications*. Berlin: Springer.
Sham TK (2002) *Chemical Applications of Synchrotron Radiation (Advanced Series in Physical Chemistry, V 12A–12B)*. Singapore: World Scientific.
Wiedemann H (2002) *Synchrotron Radiation*. Heidelberg: Springer.
Willmott P (2011) *An Introduction to Synchrotron Radiation Techniques and Applications*. New York: Wiley.
Winick H (1995) *Synchrotron Radiation Sources: A Primer*. Singapore: World Scientific.
Winick H and Doniach S (1980) *Synchrotron Radiation Research*. New York, London: Plenum Press.

Radiation sources: X-ray sources

A Pifferi, CNR—Institute of Crystallography, Rome, Italy

© 2024 Elsevier Ltd. All rights reserved.

This is an update of A. Pifferi, X-Ray Sources, Editor(s): Franco Bassani, Gerald L. Liedl, Peter Wyder, Encyclopedia of Condensed Matter Physics, Elsevier, 2005, Pages 323–329, ISBN 9780123694010, https://doi.org/10.1016/B0-12-369401-9/00631-8.

Introduction 433
Natural sources (astronomy) 434
Conventional sources 434
X-ray tube 434
Sealed tube and rotating anode sources 436
X-ray tube based on carbon nanotube field emitters 437
Synchrotron sources 438
Bending magnets 438
Wigglers 439
Undulators 439
Fourth generation light sources 440
Laser plasma X-ray sources 441
Conclusion 442
References 442

Abstract

Since their discovery in 1895, X-rays have become a vital tool to determine the chemical and atomic structure of materials. It is currently used in many fields, including biological systems and human beings. X-ray technology has tremendously evolved from the first commercial x-ray tube built by Carl Heinrich Florenz Müller in 1896 to the modern synchrotron sources, allowing increasingly precise and sophisticated analyses in hard and soft matter.

In this chapter, after brief notes on cosmic ray sources, the devices capable of producing X-rays from vacuum tubes up to modern particle accelerators for the production of Synchrotron Radiation (SR) and Free Electron Lasers (FEL) are described.

Key points

- **Astrophysics** is a science that employs the methods and principles of physics and chemistry in the study of astronomical objects and phenomena
- **Atomic particle** All matter consists of atoms that contain a nucleus and orbiting electrons
- **Brehmsstrahlung** braking radiation; refers to any radiation produced by deceleration of a particle
- **Bending Magnet** Device used to bend the electron beam produced by an accelerator tube
- **CNT** Carbon Nano Tube
- **Laser Plasma** is a product of the very complicated process of laser-matter interaction
- **Synchrotron** is a particular type of cyclic particle accelerator
- **Undulator** is a device similar to a wiggler except that the B-field strength is more limited
- **Wiggler** is a series of magnets designed to periodically laterally deflect ('wiggle') a beam of charged particles
- **XFEL** Free Electron Laser sources that produce radiation with brightness several orders of magnitude higher then undulators on third-generation rings
- **X-ray** form of ionizing radiation
- **XRF** X-Ray Fluorescence is an analysis technique that can be applied to most inorganic materials

Introduction

X-rays are forms of ionizing radiations, i.e., they have enough energy to ionize atoms and molecules in matter, including the biological one represented by cells and tissues. They are electromagnetic radiations having a wavelength (λ) between 10 and 0.01 nm, frequency from about 3×10^{16} to 3×10^{19} Hz and having energy between 0.1 and 100 KeV.

"X-rays" was the name given by W. C. Roentgen to the highly penetrating rays that are produced when high-energy electrons strike a metal target. On November 8, 1895, he noted for the first time this phenomenon and on December 28, 1895, Roentgen astonished the scientific world with his preliminary report "Ueber eine neue Art von Strahlen" (Roengten, 1895) given to the president of the Wurzburg Physical-Medical Society (along with experimental radiographs and by the X-ray image of his wife's hand). A few weeks later C.H.F. Muller was able to construct in his factory in Hamburg the first commercial X-ray tube for one of local hospitals. This was a milestone of what was become a major technical industry. Röntgen received the Nobel Prize in Physics in 1901 for this discovery. X-ray technology is one of the most important inventions of the nineteenth century. It plays a major role in our daily life. X-rays are nowadays one of the most powerful tools to investigate hard and soft matter.

There are numerous applications of X-rays in the various fields of science and medicine. In addition to radiography, in the medical field, applications for Computed Axial Tomography (ACT), Micro tomography are known. In biology and chemistry, X-rays are used for structural determination of both inorganic and biological molecules by X-ray diffraction from crystals (Giacovazzo, 2002). Baggage inspection is based on X-ray imaging in checkpoints of airports or sensitive areas, to control the structural integrity of aircrafts and transports or more generally, to inspect the insights of materials subjected to mechanical/thermal stress. In the food industry, X-ray are used to check for the presence of extraneous objects inside the packaging. In the field of Cultural Heritage to analyze paintings, archaeological finds, or to carry out elemental analyses in pigments or in metals using Fluorescence X (XRF). Of course, different types of radiation sources have been studied and developed for each application.

In nature, as it turned out later, there are sources of X-rays generated by cosmic processes or nuclear particles decay phenomena.

Natural sources (astronomy)

X-ray source, in astronomy, are cosmic objects that emit radiation at X-ray wavelength (Britannica, 2018). Since the Earth's atmosphere absorbs X-rays from space, detectors and telescopes capable of measuring the weak emissions generated by celestial bodies have been launched into space (high above Earth's atmosphere) The sun was the first celestial object for which radiations in the range of X-rays wavelengths were measured (1949). The radiations coming from the sun are substantially weak and it is notable only because its proximity to the Earth. Only 30 years later with the launch of the HEAO 2 satellite better known as the Einstein Observatory (Giacconi et al., 1979), more than 150 stars emitting X radiation were observed.

In Astronomy, X-rays come from material that has been heated to extreme temperatures by a small number of physical processes:

(1) Accretion: material falls within the gravitational potential of a celestial body, potential energy is converted into kinetic energy, and via different processes (collisions, friction) into heat, and the heated material cools then by emitting X-rays. Common environments where accretion occurs are binary stars, in particular those containing "stellar remnants," i.e., white dwarfs (Pravdo et al., 1986), neutron stars (Morton, 1964), and black holes (Wilkins et al., 2021). Because of their extreme densities, material is accelerated to 1000s of km/s (white dwarfs) to highly relativistic velocities (neutron stars, black holes), which then facilitates heating material to very high temperatures. However, also young (single) stars that are still in the process of formation accrete from a proto-stellar disc, and the most luminous X-ray sources are super-massive black holes (millions to billions of solar masses) in the centers of most (maybe all) galaxies, accreting interstellar dust/gas.

   In terms of heating processes, there are two main branches:

   - Shock-heating of material that is abruptly decelerated, e.g. in the case that it hits the stellar "surface" (=atmosphere), which is the case if the accreting star has a sufficiently strong magnetic field (young some white dwarfs, most neutron stars). Material cools via thermal bremsstrahlung.
   - In the case of no/weak magnetic fields of the accreting object, an accretion disk (flat structure) forms, material drifts inwards, angular momentum is transported outwards, and gravitational energy is gradually converted into heat via friction. Temperatures in the inner discs around white dwarfs, neutron stars, and black holes reach temperatures where they emit X-rays (again, material simply cools, and emits thermal bremsstrahlung).

   So the process of generating the X-rays in these systems is fairly general, and does not depend too much on the detailed properties of the accreting object.

(2) High-energy processes within the outer layers of stars, generally called "stellar activity," such as e.g. in the sunspots. These are related to magnetic phenomena (twisted field lines, magnetic reconnection). As such, the Sun is an X-ray source—and some other stars are much more active and X-ray luminous.

Conventional sources

X-ray tube

Whenever a charged particle is accelerated or decelerated, it emits energy in the form of photons. This process takes place within an X-ray tube to create X-rays. At one end of the tube is the source of electrons or the cathode and at the other end of the tube is the metal target, or anode. To produce X-rays, electrons are accelerated from the cathode to the anode with a high voltage. When the electrons hit the anode, they are quickly stopped. This rapid change in speed causes the emission of X-ray photons. These X-rays are commonly called brehmsstrahlung or "braking radiation."

Bremsstrahlung is the German word for slowing down or braking. Bremsstrahlung is an electromagnetic radiation produced by the deceleration of a charged particle, deflected by another charged particle, typically an electron by the atomic nucleus. Assuming

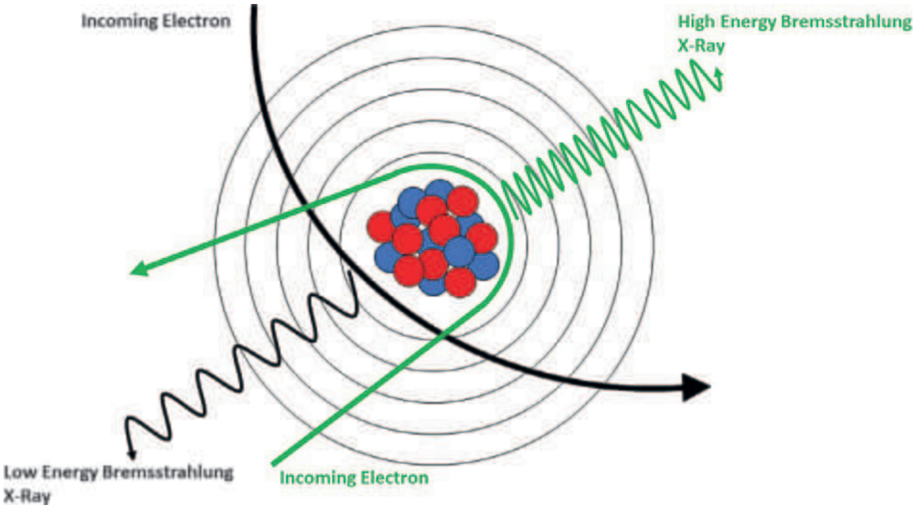
Incoming Electron
High Energy Bremsstrahlung X-Ray
Low Energy Bremsstrahlung X-Ray
Incoming Electron

Fig. 1 Radiation produced by an electron passing through an atom and being deflected by the nucleus.

that there are charged particles in a piece of matter and that a high-speed electron passes close to it, the trajectory of the latter will be deflected due to the electric field around the atomic nucleus, as shown in the image (Fig. 1).

The moving particle, when deflected, loses kinetic energy and, to satisfy the energy conservation principle, emits radiation in the form of a photon; bremsstrahlung radiation is characterized by a continuous distribution of radiation that becomes more intense (and moves towards higher frequencies) with the increase in the energy of the bombarding electrons (braked particles).

An electron that completely avoids the orbital electrons on passing through an atom of the target may travel sufficiently close to the nucleus of the atom to come under its influence. Since the electron is negatively charged and the nucleus is positively charged, there is an electrostatic force of attraction between them. As the electron approaches the nucleus, it is influenced by a nuclear force much stronger than the electrostatic attraction. As it passes by the nucleus, it is slowed down and deviated in its course, leaving with reduced kinetic energy in a different direction. This loss in kinetic energy reappears as an X-ray photon.

If all the energy carried by an electron is transformed into radiation, the energy of an X-ray photon is

$$E_{max} = h\nu_{max} = eV$$

Where h is the Plank's constant, ν_{max} the photon frequency. The indication max indicates that this is the maximum possible energy, e is the charge of the electron and V the acceleration potential. If the frequency is substituted with the wavelength, the above expression becomes

$$h\nu_{max} = hc/\lambda_{min} = eV \quad \text{and} \quad \lambda_{min} = hc/eV = 12398/V$$

The energy contained in each bremsstrahlung photon emitted from an X-ray tube extends from that associated with the peak electron energy all the way down to zero. In other words, when an X-ray tube is operated at 70 kVp, bremsstrahlung photons with energies ranging from 0 to 70 keV are emitted, creating a typical continuous X-ray emission spectrum. Since total conversion of the electron energy into radiation is not a highly probable event, the radiation of the highest intensity is obtained at a longer wavelength compared to λ_{min} (1.5 times). Fig. 2 shows some X-ray continuous spectra as a function of the accelerating voltage.

If the bombarding electrons have sufficient energy, they can knock an electron out of an inner shell of the target metal atoms. Then electrons from higher states drop down to fill the vacancy, emitting X-ray photons with precise energies determined by the electron energy levels. These X-rays are called characteristic X-rays. In summary, transitions of orbital electrons from outer to inner shells produce characteristic X-rays. Since the electron binding energy for every element is different, the characteristic X-rays produced by the various elements are also different. This type of X-radiation is called characteristic radiation because it is characteristic of the target element. The effective energy characteristic X-rays increases with increasing atomic number of the target element. The characteristic lines of this type of spectrum are called K, L and M and correspond to the transition from higher energy orbital to the K,L,M orbital. When the two orbital involved in the transition are adjacent then the line is called α, if they are separated by another shell the line is called β (Fig. 3).

For example, K electrons for tungsten anode have binding energies of 69.5 keV, and L electrons are bound by 12.1 keV. Therefore, the characteristic X-ray emitted has energy

$$69.5 - 12.1 = 57.4 \text{ keV}$$

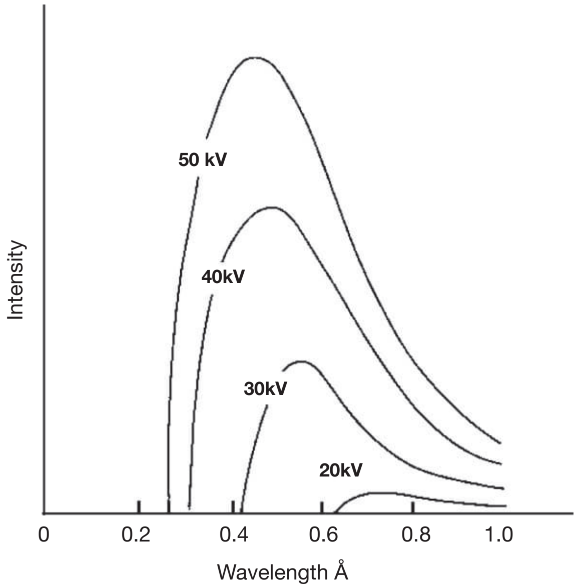

Fig. 2 X-Ray radiation spectra as a function of accelerating voltage.

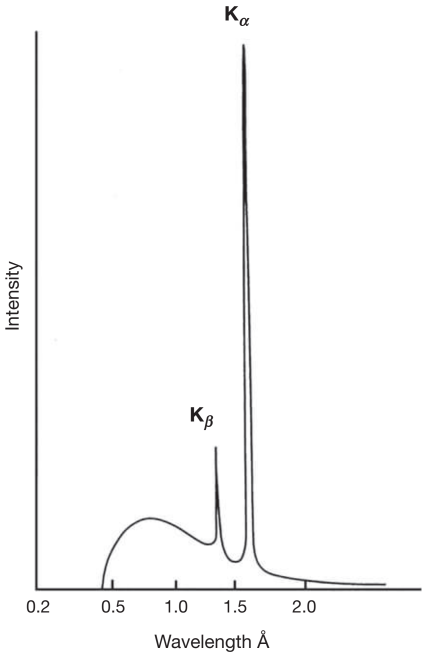

Fig. 3 Characteristic lines K_α and K_β of Cu spectra superimposed on the brehmsstrahlung.

Sealed tube and rotating anode sources

The X-ray tube is a large diode valve, which is designed to produce fast moving electrons and then cause the electrons to decelerate rapidly in a vacuum environment. A conventional generator consists of a high-voltage power supply electronically controlled applied between the anode and the cathode. In Fig. 4 the sketch of a sealed tube is showed.

It consists of a cathode with a filament that emits the electrons that are accelerated under vacuum by the high voltage. The electrons hit the anode and produce the characteristic X-ray spectrum relative to the metal of the anode. The high vacuum is necessary because the presence of gas molecule would decrease the efficiency of the tube. Normally this type of sources is highly inefficient because only 0.1% of power used is transformed into X-ray, the rest is dissipated as heat. In the rotating anode the anode has a cylindrical shape and to increase the efficiency of the X-ray beam the anode is continuously rotated. Thus, the electron beam

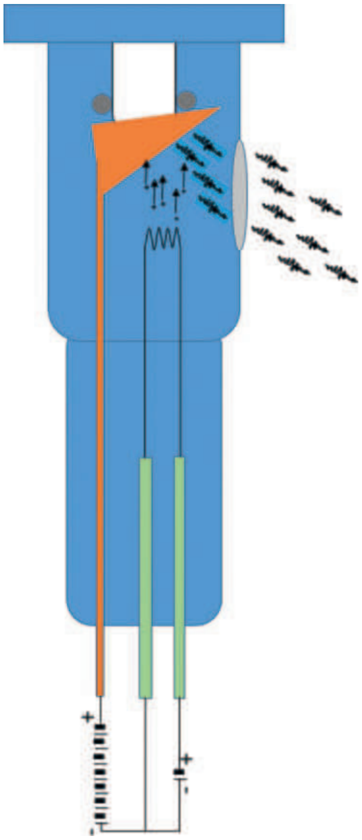

Fig. 4 Sketch of a sealed X-ray tube.

hits the metal of the anode in different positions permitting a better dissipation of heat. The increasing of the intensity of the beam may be quite an order of magnitude in respect to a sealed tube.

The intensity of a K line can be calculated using the equation:

$$I_K = Bi(V - V_K)^{1.5}$$

Where B is a constant, i the electrical current, and V_K the excitation potential of the K series. If the accelerating potential $V = 4V_K$ is applied the Kα line is 90 times more intense then the white radiation of the equivalent wavelength (I_W). In this condition the ratio I_K/I_W is a maximum.

X-ray tube based on carbon nanotube field emitters

Over the last few decades, the technology for manufacturing X-ray sources has not substantially changed. Different types of generators have been developed according to the applications for which X-rays are used, i.e., in high definition medical diagnostics, safety inspection or high throughput industrial control processes (Parmee et al., 2015). The thermionic sources are limited due to the slow temporal response and the size and spatial amplitude of diffusion. For these reasons, new types of field emission X-ray sources have been studied.

In the tubes with Thermionic Emission (TE) the electrons are produced from a metallic filament, often consisting of Tungsten, which when crossed by an electric current heat it to a temperature above 1000 °C. Since the emission is strictly dependent on the temperature of the filament, as the temperature of the emitter increases the electrons able to overcome the surface barrier increase. In such tubes the filament current is controlled analogically. One of the disadvantages of this type of technology is the large production of heat that must generally be disposed of by cooling with the circulation of water or coolants. A second limitation consist in the slowness of the response when it is necessary to rapidly vary the intensity of the electron beam to increase or decrease the intensity of the X-ray beam. This slowness is due to the inertia in the heating or cooling of the filament.

Field Emissions (FE) offer several significant benefits. FE sources are often physically more compact than TE systems. The emission process occurs at room temperature and therefore does not require a heat sink. FE is a tunneling process and consequently provides almost instantaneous emission. The rise times are of the order of the microseconds as opposed to the TE that are of the order of milliseconds.

CNT-based emitters have several advantages over thermionic electron sources (Heo et al., 2012). The advantages are in the fact of having little heat generation compared to a thermionic tube, an important characteristic for creating small sources. They are simple to make and easily electronically controlled to generate pulses even of high frequency. Finally, they allow generating high current densities for electron and X-ray microscopy devices.

Synchrotron sources

Synchrotron radiation (SR) is emitted when charged particles moving with relativistic speeds are forced to follow curved trajectories in magnetic fields. The first visual observation of SR was in 1948 from the General Electric synchrotron in the USA during investigations into the design and construction of accelerators suitable for the production of very high-energy electrons. Over the next 50 years, an explosive growth in the building of accelerators optimized for SR production has turned this interesting radiative energy into a valuable research tool (Winik, 1995).

Whenever charged particles undergo an acceleration they emit electromagnetic radiation. An electron oscillating at radio-frequencies in an antenna emits radio waves. When electrons are subjected to an acceleration perpendicular to their velocity, for example when they pass through a magnetic field, their direction is changed and they begin to travel in a circular path. Charged particles moving under the influence of an accelerating field emit electromagnetic radiation. The energy of this radiation is dependent on the velocity of the particle. The total instantaneous power P emitted by an electron moving on a circular orbit is

$$P = \frac{2e^2cE^4}{3R^2(m_0c^2)^4} = \frac{2e^2c\gamma^4}{3R^2} \tag{1}$$

where P is the energy emitted per unit time, e is the particle charge, c the speed of light, E the energy of the particle, m_0 its mass at rest and R the bending radius of the orbit. The emitted radiation has very different characteristics in dependence of the velocity v of the particle. If $v \ll c$ the emitted pattern is identical to the well-known dipole radiation field (Fig. 5a). When the speed increases to almost light velocity the whole power is compressed into a narrow cone in forward direction tangentially to the orbit (Fig. 5b). The radiation emitted is called synchrotron radiation. The quantity γ in eqn. 1, which is the ratio of the total energy to the rest energy of the particle, is of considerable importance since it is related to the opening angle $\Delta\Psi$ of the cone of radiation in the perpendicular plane of the orbit by:

$$\Delta\Psi \cong 1/\gamma$$

where $\Delta\Psi$ is expressed in radians.

A storage ring synchrotron consist of an arrangements of devices where charged particles travel at essentially the speed of light in evacuated pipes under the influence of magnets which are positioned around a closed orbit (Winik, 1995). Acceleration is achieved by the application of radio frequency electric fields at RF cavities along the circumference of the ring. The magnetic fields grow synchronously with the acceleration in order to keep the particles on the constant radius path. Such accelerators can be used with protons or electrons, and even with heavier positive ions. The particles travel in the closed loop for periods of several hours while synchrotron radiation spread out from all curved parts of the orbit.

In general, three kinds of magnets are used to make the necessary magnetic fields: bending magnets, wigglers and undulators.

Bending magnets

In bending magnets, a simple dipole structure is used to constrain the electrons in a curved path. The radiation emitted is extremely intense and extends over a broad wavelength range from the infrared through the visible and ultraviolet, and into the soft and hard

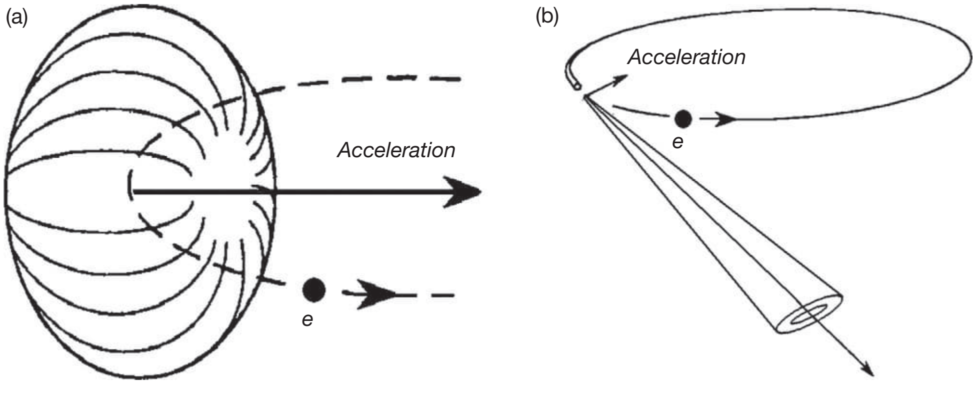

Fig. 5 Emission pattern of radiation from centripetally accelerated electrons: (a) non relativistic case $v \ll c$. (b) relativistic case $v \cong c$.

X-ray regions of the electromagnetic spectrum. A typical output curve for a bending magnet source has a smooth spectral distribution with a broad maximum near the so-called critical wavelength. This critical wavelength depends on the square of the energy of the electrons and the bending radius in the dipole. In practical units of angstroms, it can be calculated as:

$$\lambda c = 18.64/\left(B * E^2\right),$$

where B (the dipole field) is in Tesla and E (the ring energy) is in GeV. The critical wavelength (or energy) has the property that one-half of the power radiated is above this wavelength and one-half below.

Wigglers

High-field wiggler magnets are often used as sources in order to increase the flux at shorter wavelengths. We can best think of a wiggler as a sequence of bending magnets of alternating polarities which gives a 2 N enhancement in the flux, where N is the number of poles (Fig. 6). Each magnet bends the electron beam through an angle large compared with mc^2/E. The properties of wiggler SR are thus very similar to that of dipole radiation with a reduction in the critical wavelength because of the higher field. For superconducting wiggler magnets a value of 6 Tesla, as opposed to around 1.2 Tesla for conventional dipoles, would be typical. The characteristics of the synchrotron radiation from the wiggler are the same one as from the bending magnet, and so, the critical energy play a determinant role. To reach the same spectral range as from the bending magnets the magnetic flux density within the wigglers must be the same as within the bending magnets, if the magnetic field in the wiggler is higher than the ring bending magnet field, the wiggler spectrum extend to higher photon energy. The photon flux as well as the central intensity of the radiation emitted by the wiggler is the same as from the bending magnet but more intensive by a factor Np, where Np is the number of poles within the wiggler.

Undulators

An undulator magnet is similar to a wiggler, in that it is also a succession of alternating magnetic poles (Fig. 7a). However, in this case the angle of bend in each pole is of the order of mc^2/E, so that the small angular divergence due to the emission pattern of synchrotron radiation is not significantly increased. The radiation emitted at the various poles interferes coherently resulting in the emission of a pencil-shaped beam (Fig. 7b) peaked in narrow energy bands at the harmonics of the fundamental energy. For N poles, the beam's opening angle decrease by a factor $N^{1/2}$ and thus the intensity per solid angle increases as N^2.

Fig. 8 shows the performance in terms of brilliance of bending magnets, wigglers and undulators for a 6 GeV Energy synchrotron with a current in the ring of 100 mA.

Synchrotron radiation characteristically is highly polarized and continuous. Its intensity and frequency are directly related to the strength of the magnetic field and the energy of the charged particles affected by the field. Accordingly, the stronger the magnetic field and the higher the energy of the particles, the greater the intensity and frequency of the emitted radiation. The high intensity, broad spectral range and other properties such as collimation, polarization, pulsed-time structure, partial coherence, make synchrotron radiation a powerful tool for basic and applied studies in biology, chemistry, medicine, and physics, as well as in applications to technology such as X-ray lithography, micromechanics, materials characterization and analysis. Brilliance of

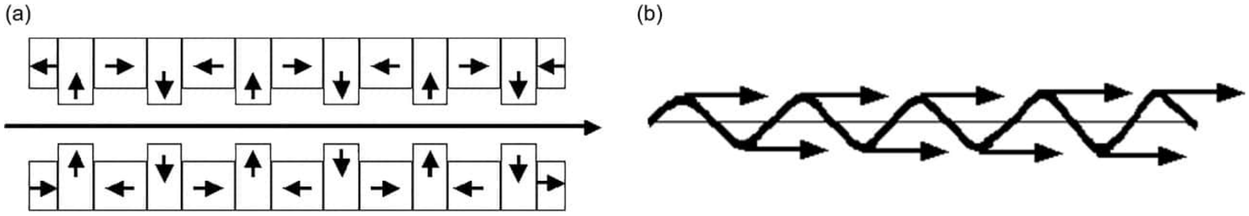

Fig. 6 (a) The arrangement of magnets within an wiggler. Horizontal arrows indicate permanent magnet vertical arrows indicate magnetic steel. (b) The trajectory of an electron beam within a wiggler. The arrows symbolize the emitted synchrotron radiation.

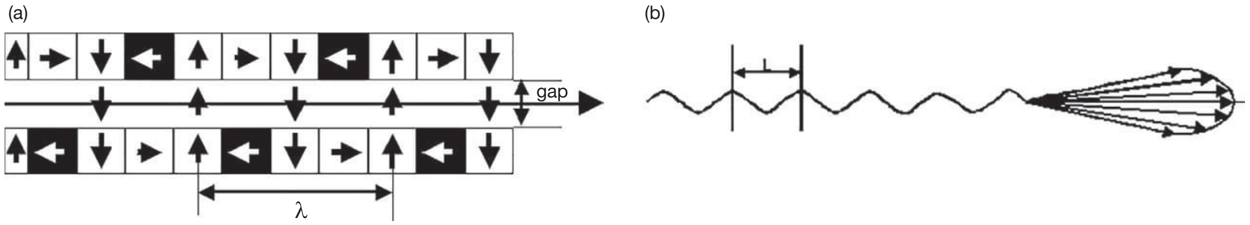

Fig. 7 (a) The arrangement of magnets within an undulator. (b) The characterization of the undulator radiation. L is the period length.

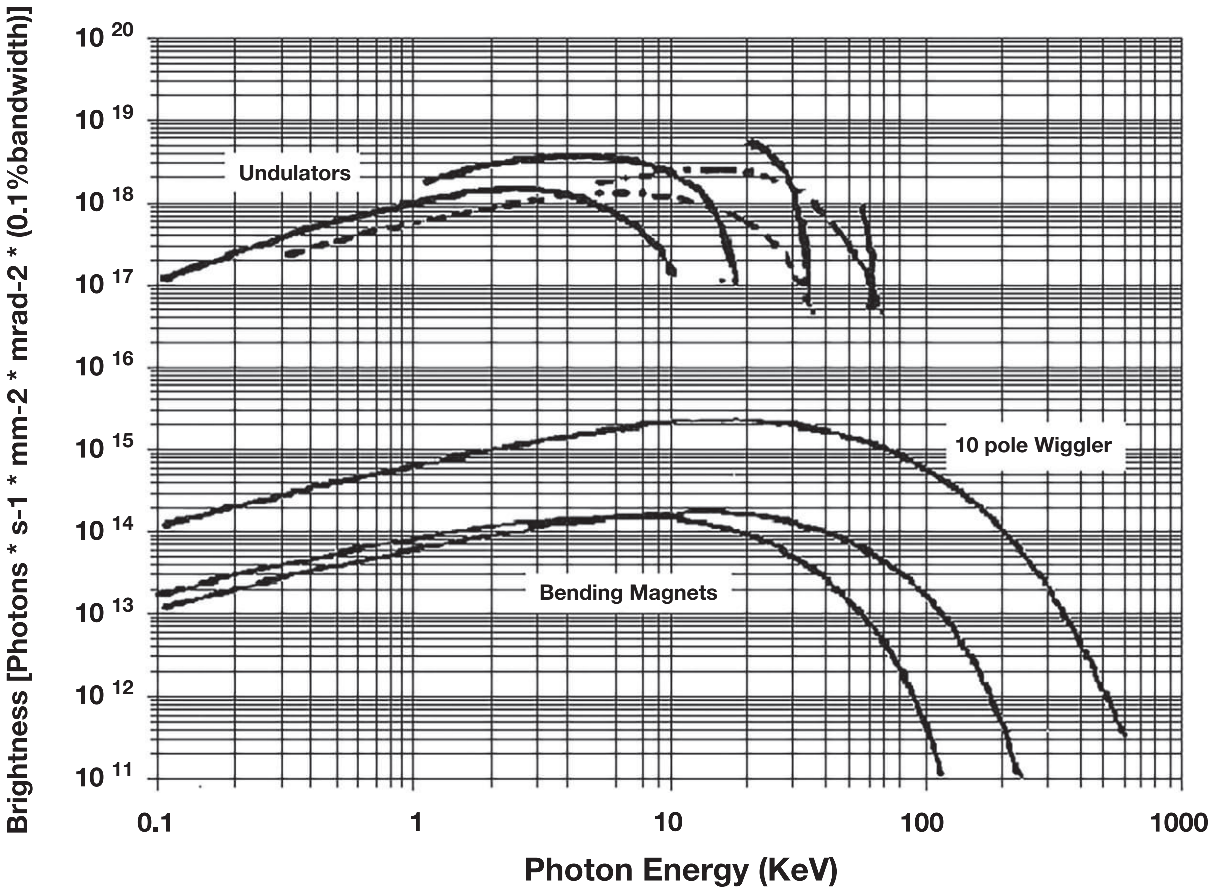

Fig. 8 Plot of Brilliance versus Photon Energy for a storage ring of 6 GeV Energy and 100 mA current.

synchrotron sources, up to $\sim 10^{10}$ larger than X-ray tube, mostly due to much smaller angular divergence. This is important because many experiments use small samples (e.g. protein crystals!) that can use only a tiny fraction of radiation emitted by tube. Much higher intensity make possible to observe very weak signals not observable with tube source, much tighter angular collimation is especially important for small samples, e.g. protein crystals, high pressure applications, etc. (Giacovazzo, 2002). By the use of special optical elements, such as monochromators, single energies can be selected among the continuous spectrum of Synchrotron Radiation; this energy tunability is of extremely importance especially for experiments driven near the absorption edge of specific elements.

Fourth generation light sources

The development of Fourth Generation Light Sources has been pointed out on Free Electron Lasers (FELs) (Pellegrini and Stöhr, 2003; Pant, 2015; Freund and Antonsen, 2018). Such sources produce radiation with brightness several orders of magnitude higher then undulators on third-generation rings. Graph in Fig. 9 shows the trend of the growth of the brilliance of X-ray sources starting from the beginning of the XX Century.

Radiation from a FEL has much in common with radiation from a conventional optical laser, such as high power, narrow bandwidth and diffraction limited beam propagation. One of the main differences between the two lasers is the gain medium: in a conventional laser the amplification comes from the stimulated emission of electrons bound to atoms, either in a crystal, liquid dye or a gas, whereas the amplification medium of the FEL are "free" (unbound) electrons. The free electrons are stripped from atoms in an electron gun and are then accelerated to relativistic velocities. While the electrons are propagating in an undulator the interaction with an electromagnetic radiation field leads to an exponential growth of the radiation emitted by the electrons. This amplification of radiation is initiated by an increasingly pronounced longitudinal density modulation of the electron bunch. The initial radiation field can be an external one, e.g. a seed laser, or an "internal" field, i.e., the spontaneous emission of the undulator. In the latter case it is called a SASE (Self Amplified Spontaneous Emission) FEL. Oscillating through the undulator, the electron bunch then interacts with its own electromagnetic field created via spontaneous emission. Depending on the relative phase between radiation and electron oscillation, electrons experience either a deceleration or acceleration: electrons that are in phase with the electromagnetic

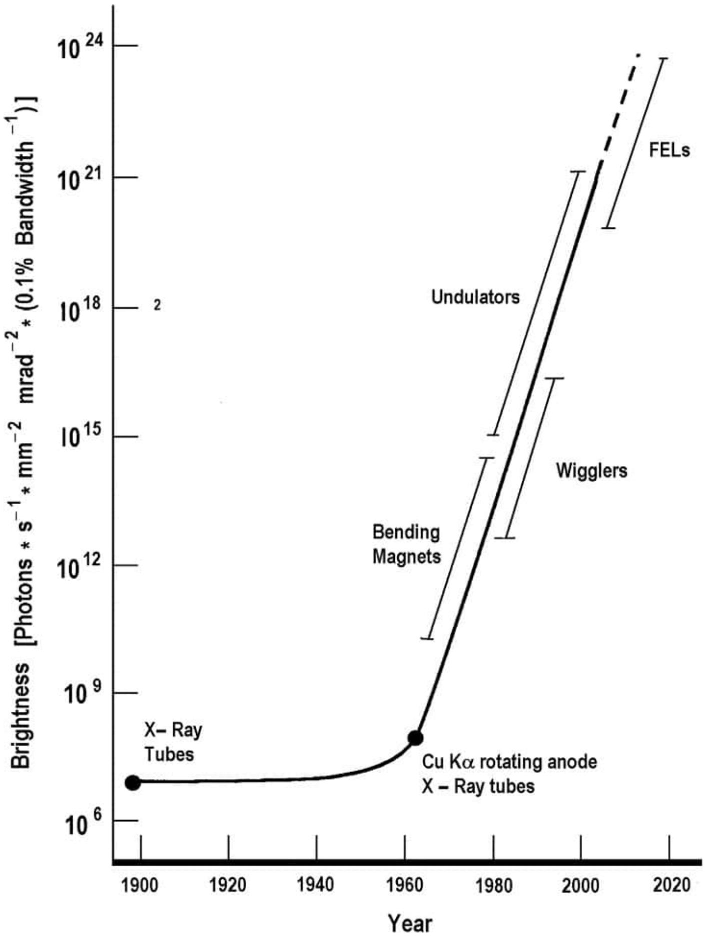

Fig. 9 Trend of the Brightness of X-ray sources plotted starting from the beginning of 1900.

wave are retarded while the ones with opposite phase gain energy. Through this interaction a longitudinal fine structure, the so-called micro bunching, is established which amplifies the electromagnetic field. The longitudinal distribution of electrons in the bunch is "cut" into equidistant slices with a separation corresponding to the wavelength λ_{ph} of the emitted radiation, which causes the modulation. More and more electrons begin to radiate in phase, which results in an increasingly coherent superposition of the radiation emitted from the micro-bunched electrons. The more intense the electromagnetic field gets, the more pronounced the longitudinal density modulation of the electron bunch and vice versa. The characteristics of FEL radiation are high power, short pulse length (pico to femtoseconds), narrow bandwidth, spatial coherence and wavelength tunability. Of particular importance are detectors capable of measuring such fast and intense signals (Knoll, 2012; Antonelli et al., 2013). Technology is constantly advancing in the construction of these devices.

Laser plasma X-ray sources

The concept for X-ray lasers goes back to the 1970s, when physicists realized that laser beams amplified with ions would have much higher energies than beams amplified using gases. Nuclear explosions were even envisioned as a power supply for these high-energy lasers. In X-ray lasers (Umstadter, 2015), a pulse of light strikes a target, stripping its atoms of electrons to form ions and pumping energy into the ions ("exciting" or "amplifying" them). As each excited ion decays from the higher energy state, it emits a photon. Many millions of these photons at the same wavelength, amplified in step, create the X-ray laser beam. Compact short-pulse high-power X-ray sources can be produced by focusing on a solid target ultra short laser pulses of low or moderate energy (from several to ten or a hundred millijouls) but of high intensity ($\geq 10^{15}$ Wcm^{-2}). For example, subpicosecond laser pulses can produce X-ray pulses of high power and short duration (in the picosecond range). With respect to hard and soft X-ray emission, such laboratory X-ray sources offer the following advantages over conventional X-ray sources such as synchrotrons: a greater compactness, an easier access, a lower cost, a shorter pulse length and a smaller source size.

Conclusion

The future of the research in the field of X-ray sources will be more and more bonded to the possibility to manipulate optically the radiation and to obtain a selective detection of the photons in order to perform ever more accurate spatial and temporal analysis. The use of these new methodologies of detection is already allowing to develop new X-ray sources and to study new physical phenomena until now inaccessible.

References

Antonelli M, et al. (2013) Fast synchrotron and FEL beam monitors based on single-crystal diamond detectors and InGaAs/InAlAs quantum well devices. *Nuclear Instruments and Methods in Physics Research Section A: Accelerators, Spectrometers, Detectors and Associated Equipment* 730.

Britannica T (2018) Editors of encyclopaedia. In: *"X-ray Source." Encyclopedia Britannica, September 12.* https://www.britannica.com/science/X-ray-source.

Freund HP and Antonsen TM (2018) Principles of free-electron lasers. Cham: Springer. https://doi.org/10.1007/978-3-319-75106-1.

Giacconi, et al. (1979) The Einstein (HEAO 2) X-ray observatory. *The Astrophysical Journal* 2301: 540–550.

Giacovazzo C (ed.) (2002) *Fundamentals of Crystallography, IUCr.* New York, USA: Oxford University Press Inc.

Heo SH, et al. (2012) A vacuum-sealed miniature X-ray tube based on carbon nanotube field emitters. *Nanoscale Research Letters* 7(2): 258.

Knoll GF (2012) *Radiation Detection and Measurement.* New York, USA: John Wiley & Sons.

Morton DC (1964) Neutron stars as X-ray sources. *Nature* 201: 1308–1309.

Pant K (2015) Free electron lasers. In: *Laser Physics and Technology*, 151–164. https://doi.org/10.1007/978-81-322-2000-8_7.

Parmee RJ, et al. (2015) X-ray generation using carbon nanotubes. *Nano Convergence* 2(2015).

Pellegrini C and Stöhr J (2003) X-ray free-electron lasers—Principles, properties and applications. *Nuclear Instruments and Methods in Physics Research Section A: Accelerators, Spectrometers, Detectors and Associated Equipment* 33–40.

Pravdo SH, Marshall FE, White NE, and Giommi P (1986) X-rays from the magnetic white dwarf PG 1658 + 441. *The Astrophysical Journal* 300: 819.

Roengten W (1895) *Ueber eine neue Art von Strahlen. Vorläufige Mitteilung. Aus den Sitzungsberichten der Würzburger Physik.-medic.* Gesellschaft Würzburg 137–147.

Umstadter DP (2015) All-laser-driven Thomson X-ray sources. *Contemporary Physics* 56(4): 417–431.

Wilkins DR, Gallo LC, Costantini E, Brandt WN, and Blandford RD (2021) Light bending and X-ray echoes from behind a supermassive black hole. *Nature* 595(7869): 657–660.

Winik H (1995) *Synchrotron Radiation Sources.* World Scientific. Winick Editor.

Neutron sources☆

P Böni, Physik-Department E21, Technische Universität München, Garching, Germany

© 2024 Elsevier Ltd. All rights reserved.

This is an update of A. Furrer, Neutron Sources, Editor(s): Franco Bassani, Gerald L. Liedl, Peter Wyder, Encyclopedia of Condensed Matter Physics, Elsevier, 2005, Pages 69–75, ISBN 9780123694010, https://doi.org/10.1016/B0-12-369401-9/00633-1.

Introduction **443**
Neutron scattering for condensed matter research **444**
Historical evolution of neutron sources **446**
Production of neutrons **446**
Fission sources 447
Spallation sources 448
Compact neutron sources 449
Halo neutrons 450
Neutron energies and properties **451**
Moderation of neutrons **452**
Neutron beam transport **454**
Conclusion **455**
Acknowledgments **457**
References **457**

Abstract

Neutrons are a very elusive and versatile probe for the investigation of the microscopic properties of materials in basic research and for technological applications. In the following we provide an overview of the status and the future of high-flux neutron sources and the progress made in the development of the extraction of intense neutron beams for experiments using advanced neutron optics based on high-performance supermirrors. Despite the significant progress made during the last years, the maximum neutron flux seems to saturate at a peak flux of the order of 10^{17} – 10^{18} neutrons per cm^2 and per s.

Key points

- Performance of neutron sources
- Neutron scattering for condensed matter research
- Historical evolution of neutron sources
- Production of neutrons
- Neutron energies and properties
- Moderation of neutrons
- Neutron beam transport
- Prospects for future neutron sources

Introduction

Neutron scattering (Furrer et al., 2009; Shirane et al., 2002) is one of the key scattering techniques for the investigation of the static and dynamic properties of materials in solid state physics. In addition, neutrons are also a valuable tool for imaging of materials, (Kardjilov et al., 2018) for solving fundamental questions in particle physics, (Chupp et al., 2019; Dubbers and Schmidt, 2011) and for irradiation (Tarantini et al., 2006) and activation experiments (Greenberg et al., 2011). Clearly, the quality and the precision of experiments with neutrons are determined by the available neutron flux.

The history of neutron sources has seen a tremendous increase of the thermal neutron flux density Φ_{th} of fission reactors from 10^7 cm^{-2} s^{-1} in 1942 at the Chicago Pile CP1 to $\simeq 10^{15}$ cm^{-2} s^{-1} at the HFR at the ILL in 1972 (ILL, 1986). Since then, due to limitations in the power density, no further progress has been reported (Fig. 1). Indeed, for the production of one neutron, an energy of approximately 200 MeV is released.

In contrast, the spallation process releases only about 20 MeV per neutron thus allowing to increase Φ_{th} by approximately an order of magnitude. For pulsed neutron beams produced by spallation, peak flux densities of the order of $\widehat{\Phi}_{th} \simeq 10^{17}$ cm^{-2} s^{-1} can

---

☆*Change History:* November 2022. P Böni updated the chapter.

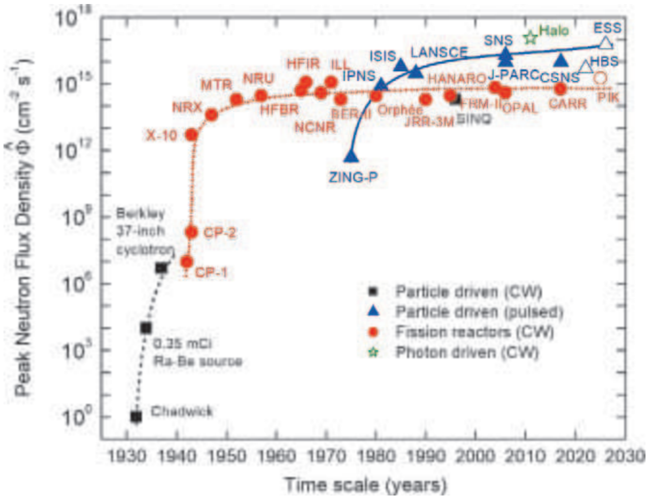

Fig. 1 Peak neutron flux density $\widehat{\Phi}_{th}$ of some typical neutron sources. Inserted are also the performances of the recently proposed accelerator-based sources namely the source based on halo neutrons, i.e., neutrons in highly excited states orbiting the nucleus at large radii (Habs et al., 2011) and the compact source HBS (Brückel and Gutberlet, 2020; Gutberlet et al., 2020). Open symbols indicate neutron sources that are not yet in operation or are in a conceptual phase. After Böni P, and Petry W (2018) Neutron science with highly brilliant beams, Chapter 20. In Bolton P, Parodi K, and Schreiber J. (Eds.), *Applications of Laser-Driven Particle Acceleration*, pp. 314–330. CRC-Press Taylor & Francis Group: Boca Raton, FL, USA. ISBN 9781498766418. https://www.crcpress.com/Applications-of-Laser-driven-Particle-Acceleration/Bolton-Parodi-Schreiber/p/book/9781498766418. (Please note that the figure has been modified when compared with the cited one.)

be achieved. At the spallation sources SNS at Oak Ridge National Laboratory (SNS, 2019) and J-PARC in Tokai (JPARC, 2019) a peak flux density of $\simeq 2 \cdot 10^{16}$ cm^{-2} s^{-1} has been realized, which is expected to be surpassed by the future European Spallation Source (ESS, 2019) by about a factor of three. Similarly as for reactors, the maximum flux density is converging too, namely toward a value $\widehat{\Phi}_{th} \simeq 10^{17}$cm^{-2} s^{-1} (Fig. 1).

Therefore, the prospects of increasing $\widehat{\Phi}_{th}$ significantly are rather grim and future progress has to be achieved by other means, for example by optimizing all components, which bring the neutrons from the source to the experiment. This situation is in strong contrast to synchrotron sources and free electron lasers which witness a steady increase in photon flux by orders of magnitude during the recent years (Shin, 2021). Further progress in increasing the neutron flux significantly seems to be possible only by the development of new concepts of neutron production, for example by direct conversion of particle beams into cold or thermal neutrons circumventing the moderation process.

In the following we start by summarizing the unique character of neutron scattering for the investigation of the static and dynamic properties of condensed matter followed by a survey of the historical evolution of neutron sources and an introduction into the basic principles of neutron production and their properties. The next chapter deals with the moderation of the neutrons reducing their original energy from the MeV to the meV range. Finally we discuss means for the extraction and the transport of neutrons from the moderator to the experiments followed by a discussion of future prospects of neutron sources in the concluding section.

Neutron scattering for condensed matter research

The principle of the scattering of particles by a sample is the same for most kinds of radiation. The geometry of a scattering experiment is shown in Fig. 2. Incident particles (neutrons, photons, electrons, etc.) having a wavevector $\mathbf{k}_i$ and a flux density Φ

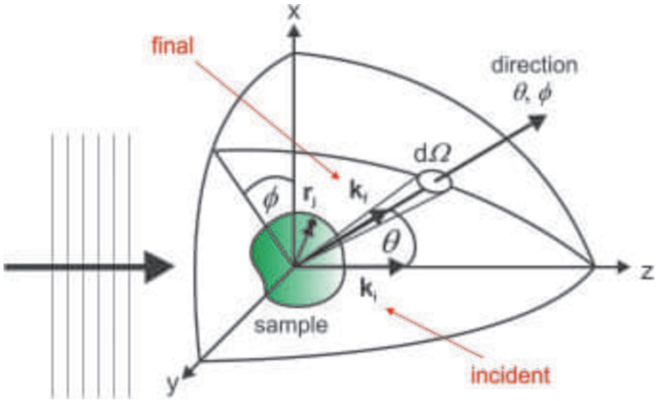

Fig. 2 Geometry for a scattering experiment. A plane wave of radiation that propagates along the *z*-direction is scattered by the sample into a solid angle $d\Omega$.

(unit: $m^{-2}\ s^{-1}$) are scattered by the sample into the solid angle $d\Omega = \sin\theta d\theta d\phi$ (unit: sr). Then the number of particles scattered per second into $d\Omega$ with wavevector $\mathbf{k}_f$ is given by

$$I = \Phi\left(\frac{d\sigma}{d\Omega}\right)d\Omega \quad \left(\frac{1}{\mathrm{s}}\right). \tag{1}$$

Here, I and $d\sigma/d\Omega$ designate the intensity (s^{-1}) as measured by a detector covering a solid angle $d\Omega$, and the differential cross section ($m^2 sr^{-1}$), respectively.

In inelastic scattering experiments, the detector also measures the energy of the radiation, i.e., the double differential cross section (units: $m^2\ J^{-1} sr^{-1}$)

$$I = \Phi\left(\frac{d^2\sigma}{d\Omega dE}\right)d\Omega_f dE_f. \tag{2}$$

can be determined. It contains information on the dynamical properties of the sample. Clearly, a high flux density Φ is essential to obtain reasonable counting statistics within a short time due to the selection of the energy. We note that the momentum and energy transfer to the sample are given by

$$\mathbf{Q} = \mathbf{k}_i - \mathbf{k}_f \tag{3}$$

$$E = E_i - E_f. \tag{4}$$

For the definition of the **Q**- and E-transfer during the course of an experiment, the range of the solid angle, Ω_i, and of the energy, E_i, of the incident radiation has to be restricted to $d\Omega_i$ and dE_i, respectively. To measure an optimum intensity, these quantities should be comparable with the resolution of the detecting system that is given by $d\Omega_f$ and dE_f. Note that $d\Omega_i$ and $d\Omega_f$ define the uncertainty of $\mathbf{k}_i$ and $\mathbf{k}_f$, namely $d\mathbf{k}_i$ and $d\mathbf{k}_f$, respectively and therefore the uncertainty of the transferred momentum $d\mathbf{Q}$.

Obviously, for measuring inelastic scattering, a high brilliance Ψ of the incident radiation

$$\Psi = \frac{d^4N}{dA\,dt\,d\Omega\,dE} \quad \left(\frac{1}{\mathrm{m^2\,s\,sr\,J}}\right) \tag{5}$$

is required. Here, N designates the number of neutrons. In terms of wavelength, the brilliance is given by

$$\Psi_\lambda = \frac{d^4N}{dA\,dt\,d\Omega\,d\lambda} \quad \left(\frac{1}{\mathrm{m^2 s\ sr\,Å}}\right) \tag{6}$$

Knowing Ψ, the spectral flux density $\varphi(E)$ can be calculated by integrating Ψ about the solid angle encompassed by the neutrons illuminating the sample, i.e.,

$$\varphi = \Psi\Delta\Omega_i \quad \left(\frac{1}{\mathrm{m^2\,s\,J}}\right). \tag{7}$$

Finally the flux density at the sample is given by

$$\Phi = \Psi\Delta\Omega_i\Delta E_i = \varphi\Delta E_i \quad \left(\frac{1}{\mathrm{m^2\,s}}\right), \tag{8}$$

i.e., for a high **Q**- and E-resolution, Φ becomes very small.

Let us estimate the number of neutrons per second impinging a sample during the course of a typical inelastic neutron scattering experiment. We assume the following configuration: $\lambda_i = 5\,\text{Å}$, $\Delta\lambda_i = 0.05\,\text{Å}$ and $\Delta\Omega_i = 4 \cdot 10^{-4}$sr. Taking the spectral flux density of cold neutrons from the "Blue Book" of the FRM II (see also Fig. 10), (FRM II, 2011), i.e., $\varphi_c = 1.2 \cdot 10^{13}\ cm^{-2}\ s^{-1}\ \text{Å}^{-1}$ (corresponding to $\Psi_c \simeq 1 \cdot 10^{12}\ cm^{-2}\ s^{-1}\text{Å}^{-1}sr^{-1}$) one obtains for a beam size of 1 cm^2 an intensity of $I = 2 \cdot 10^7 s^{-1}$.

For the development of new materials and processes, a detailed knowledge of the microscopic processes on an atomic scale is required and scattering techniques are obviously a powerful means to obtain microscopic information about the static and dynamic properties of the sample.

Among all the scattering techniques, neutrons have outstanding properties. The most relevant, unique character of thermal neutrons, which can hardly be matched by any other experimental technique, can be summarized as follows:

(i) Neutrons interact with the nuclei and are therefore sensitive to light and heavy atoms. Moreover, isotopic substitution enables adjustment of the scattering contrast thus allowing for example to highlight the functionality of parts of large macromolecules.
(ii) The wavelength of thermalized neutrons is of order of atomic lengths, thereby ideally suited to make visible these dimensions.
(iii) The energy of thermal neutrons is of order of the energy of elementary excitations in condensed matter. Therefore the dynamic properties of materials, which are relevant at room temperature, can be measured with high accuracy.
(iv) As neutrons have no charge, their penetration depth is large for most materials. Therefore, the volumetric properties of materials can be identified. Moreover, studies under extreme conditions such as high pressure and high magnetic fields can be performed.
(v) In first order the interaction of neutrons with matter is a nuclear process, i.e., it depends on the particular isotope thereby allowing a distinction of isotopically labeled molecules in an environment of chemically identical molecules.
(vi) Because of the weak interaction strength, neutrons do not cause significant radiation damage and the cross sections can be interpreted in most cases in terms of linear response theory. In addition, the data can be put on an absolute scale facilitating the interpretation.

(vii) Neutrons carry a magnetic moment and are thus very sensitive to the static and dynamic magnetic properties of materials.
(viii) Finally, thermal neutrons might be absorbed by a nucleus and induce a nuclear reaction, thereby creating radio isotopes.

The quality and precision of neutron scattering experiments is primarily determined by the counting rate and, therefore, by the brilliance of the neutron source and the transport system bringing the neutrons to the sample. Although about half of our world is made up of neutrons, they are tightly bound in the atomic nucleus and quite difficult to set free. Facilities that accomplish this task in a manner useful for scientific and technological applications are called neutron sources.

Historical evolution of neutron sources

Because free neutrons have only a lifetime of about 15 min (Greene and Geltenbort, 2016), they have to be released for applications continuously by means of nuclear reactions. Table 1 lists some processes that can be used for the production of neutrons. Clearly, for a high brilliance, reactions with a minimal deposited heat are preferred in order to reduce the power generation.

Neutrons were observed for the first time by Chadwick in 1932 (Chadwick, 1932). He illuminated beryllium with alpha particles, which are released during the decay of natural polonium. Indeed, most early neutron sources for neutron physics research used alpha radiation.

In order to increase the neutron flux, nuclear fission reactors were invented. Initially, they were constructed for research in nuclear industry rather than for neutron scattering that was a kind of unforeseen spin off. The development started in 1942 with the Chicago Pile 1 that yielded a thermal neutron flux density $\Phi_{th} = 10^7\ \mathrm{cm}^{-2}\ \mathrm{s}^{-1}$ (CP-1, USA) and had its climax in 1972 when the high-flux reactor at the Institute Laue-Langevin (ILL) in Grenoble was taken into operation yielding $\Phi_{th} = 1.2 \cdot 10^{15}\ \mathrm{cm}^{-2}\ \mathrm{s}^{-1}$. This facility was dedicated for neutron scattering and the study of the fundamental properties of the neutron.

Meanwhile, pulsed sources, starting with Alvarez's use of an rf-pulsed cyclotron, and in particular electron accelerators that produce neutrons through bremsstrahlung have been increasingly applied for research with slow neutrons. In addition, pulsed reactors have been developed. However, all these facilities could not really compete with the overall performance of the HFR reactor (ILL), or the HFIR (Oak Ridge) and HFBR (Brookhaven) in the US, except perhaps the pulsed reactor IBR-2 at Dubna (Russia) that produces thermal peak flux densities up to $\widehat{\Phi}_{th} = 10^{16}\mathrm{cm}^{-2}\ \mathrm{s}^{-1}$ in pulses several hundred microseconds long.

Today the most intense pulsed neutron sources are based on powerful proton accelerators that produce high peak flux densities by spallation (Andersen et al., 2020). Presently the world-wide leading facilities are the SNS in Oak Ridge (USA) and J-PARC in Tokai (Japan), which provide a peak flux density of the order of $10^{16}\ \mathrm{cm}^{-2}\ \mathrm{s}^{-1}$ with short pulse lengths of the order of 50 μs and a repetition rate of 60 Hz. Next-generation pulsed neutron sources, such as ESS (Lund, Sweden) and STS-SNS (Oak Ridge) with a peak flux density approaching $10^{17}\mathrm{cm}^{-2}\ \mathrm{s}^{-1}$ are presently under construction or in the planning phase.

Production of neutrons

The primary goal of a neutron source is the release of as many neutrons as possible in a volume as small as possible to achieve a high brilliance Ψ. These requirements go along with the important demand that the heat deposition going along with the neutron release has to be minimized, since cooling problems are a limiting factor in practically all neutron source designs (see Fig. 1). In this respect fusion (Taylor et al., 2007) is by far the most optimal process for neutron production as can be seen from Table 1, followed by spallation and fission. Fusion may be the technique of neutron production in the far future, but today the two most commonly used reactions are (i) nuclear fission in ^{235}U with thermal neutrons and (ii) spallation by protons with an energy of about 1 GeV. In the next section we are going to introduce four concepts for neutron production.

Table 1 Neutron yields and deposited energy for some neutron-producing reactions (Furrer, 2005).

Reaction	*Incident energy (MeV)*	*Yield (n/event)*	*Deposited heat (MeV/n)*
T(d, n)	0.2	$8 \cdot 10^{-5}$n/d	2500
W(e, n)	35	$1.7 \cdot 10^{-2}$n/e	2000
^{9}Be(d, n)	15	$1.2 \cdot 10^{-2}$n/d	1200
^{235}U(n, f) (fission)	$3 \cdot 10^{-8}$	$\simeq$1 n/fission	200
(T, d) fusion	$\simeq$0.014	$\simeq$1 n/fusion	3
Pb spallation	1 GeV	$\simeq$20n/p	23
^{236}U spallation	1 GeV	$\simeq$40n/p	50

The energy of the incident neutrons for fission corresponds to the energy of a thermal neutron. The incident energy of 14 keV for the fusion reaction corresponds to the temperature of the plasma at the minimum near the triple product (Lawson, 1955, 1957).
After Furrer A (2005) Neutron sources. In Bassani F, Liedl GL, and Wyder P (Eds.), *Encyclopedia of Condensed Matter Physics*, pp. 69–75. Elsevier: Oxford. ISBN 978-0-12-369401-0. https://doi.org/10.1016/B0-12-369401-9/00633-1. https://www.sciencedirect.com/science/article/pii/B0123694019006331.

Fission sources

Fission of the uranium isotope 235 by the capture of thermal neutrons is still the most frequently used process for the provision of high-intensity neutron beams. The reaction can be made self-sustaining because it is exothermal and releases typically $\eta_f = 2.42$ neutrons per fission process, i.e., more neutrons than needed to sustain a chain reaction. At capture, the resulting deformation of the U causes the nucleus to break into two fragments (Fig. 3). Most neutrons are released directly during this process while 0.65% of the neutrons are released with a delay of a few tens of seconds from the daughter nuclei. The delayed neutrons are an important feature of the fission process because they enable a critical arrangement to be run in a controlled fashion.

The spectral distribution of the fission neutrons can be parametrized by the normalized Watt spectrum (Fig. 4)

$$f_W(E)dE = C \sinh\left(\sqrt{bE}\right) e^{-\alpha E} dE. \tag{9}$$

The parameters are given by $a = 1.0124$ MeV^{-1}, $b = 2.1893$ MeV^{-1}, and $C = 0.4524$ MeV^{-1} (Emendörfer and Höcker, 1969). f_W can also be well approximated by a Maxwell-Boltzmann distribution with a thermal energy $Eth = k_B T = 1.29$ MeV

$$f(E)\,dE = 2\left(\frac{E}{\pi (k_B T)^3}\right)^{1/2} e^{-E/k_B T} dE. \tag{10}$$

Because the wavelength of the fission neutrons is not matched to atomic distances in materials, they are not useful for neutron scattering as explained in section "Moderation of neutrons."

Let us estimate the neutron production per second as follows

$$N_f = \eta_f \frac{P}{E_f}, \tag{11}$$

where P is the thermal power of the reactor and $E_f = 200$ MeV is the energy released during a fission process (Table 1). Obviously, the neutron production scales with P. Assuming a power of 20 MW and $\eta_f = 2.42$ one obtains $N_f = 1.5 \cdot 10^{18}$ s^{-1}. One of the neutrons is required for maintaining the chain reaction and some neutrons are lost due to absorption and leakage, leaving essentially one neutron per fission process left over for experiments, i.e., $N_f^{eff} = 6.2 \cdot 10^{17}$ s^{-1}. Usually, the fuel element is placed inside a tank of about 2500 L of D_2O yielding an equilibrium neutron density of $n_f \simeq 2.4 \cdot 10^{11}$cm^{-3}. Obviously, due to limitation

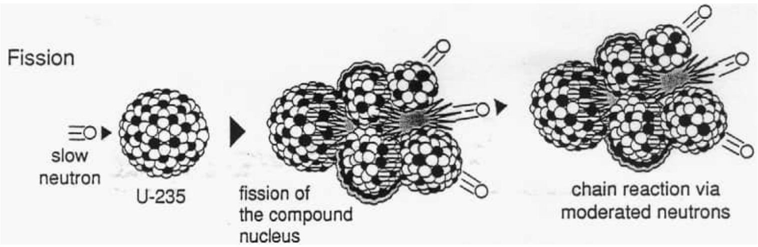
Fission
slow neutron
U-235
fission of the compound nucleus
chain reaction via moderated neutrons

Fig. 3 Schematic representation of the fission process of ^{235}U. From Furrer A (2005) Neutron sources. In Bassani F, Liedl GL, and Wyder P (Eds.), *Encyclopedia of Condensed Matter Physics*, pp. 69–75. Elsevier: Oxford. ISBN 978-0-12-369401-0. https://doi.org/10.1016/B0-12-369401-9/00633-1. https://www.sciencedirect.com/science/article/pii/B0123694019006331.

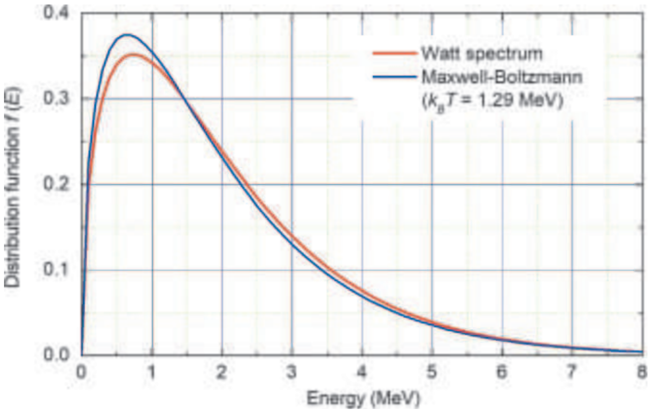

Fig. 4 Fast fission spectrum of ^{235}U. The Watt spectrum can be well approximated by a Maxwell-Boltzmann distribution function with a thermal energy $E_{th} = 1.29$ MeV.

in the heat transfer, the power of neutron sources is limited. This is the reason, why the proposal to construct a high-brilliance neutron source with a power of 300 MW, the Advanced Neutron Source (ANS) in the US, was canceled in 1995 (Rush, 2015).

Spallation sources

The term "spallation" is applied to a sequence of events that occur when heavy target nuclei are bombarded with high energy particles with a de Broglie wavelength $\lambda_{dB} = \sqrt{h^2/(2mE)}$, which is shorter than the diameter of the nuclei (Fig. 5). Therefore, collisions can take place with individual neutrons and protons inside the nuclei and large amounts of energy are transferred to them which, in turn, can hit other neutrons and protons within the same nucleus. The net effect of this intra-nuclear cascade is twofold: Firstly, energy is more or less evenly distributed over the nucleus leaving it in a highly excited state; secondly, energetic neutrons and protons may leave the nucleus and carry the cascade on to neighboring nuclei (inter-nuclear cascade) or escape from the target. The excited nucleus left behind will start to evaporate neutrons and to a lesser extent protons.

The low-energy part of the spectrum of these evaporation neutrons is quite similar to the one resulting from fission (Eq. 9), but as a consequence of the neutron escape during the intra-nuclear cascade, the spectrum extends to energies up to that of the incident particles that is of the order of 2 GeV. The release of spallation neutrons takes place within less than 10^{-15} s after the nucleus is hit, so that the time distribution of spallation neutrons is exclusively determined by the time distribution of the driving particle pulse.

Modern spallation sources are usually driven by protons from a linear accelerator (linac). The process starts at the front end of the linac with the creation of negatively charged hydrogen ions by powerful ion sources. As they are electrically charged these hydrogen ions can be accelerated by radio frequency cavities to kinetic energies in the GeV range, which corresponds to about 90% of the speed of light. When this highly energetic particle stream exits the linac, the hydrogen ions are stripped off their electrons by letting them pass through a thin carbon foil, turning the hydrogen ions into protons. The pulse length of the proton bunches is typically $t_{linac} \simeq 1$ ms.

If short neutron pulses are required, as for example for short-pulse spallation sources (SPSS), such as ISIS, SNS, or J-PARC, the protons are fed into a compressor ring (typical diameter 200 m), which accumulates the protons from a large number of successive bunches as delivered by the linac into single high intensity proton pulses. For this purpose an assembly of magnets bends each accelerated proton bunch onto a circular orbit such that the next bunch of protons arrives exactly when the previous has gone once around. In this way all these bunches pile up.

After about 1000 revolutions sufficient intensity is accumulated, and the full proton pulse with a pulse length of $t_{SP} \simeq 1\ \mu$s is extracted and propelled toward the target, which is usually a solid target (Ta, W) or a liquid metal (mercury or a lead-bismuth eutectic mixture (Latge et al., 2016) to take up the beam power of the order of 1 MW. This whole process from the creation of the hydrogen ions to the arrival of the highly energetic protons at the target occurs with a pulse repetition rate in the range 10–100 Hz in order to achieve an optimal neutron economy in scattering experiments. As explained in section "Moderation of neutrons" after moderation, the pulse length of the neutrons will be with 50 – 150 μs much longer than the proton pulse due to the slowing down process in the moderator.

At SNS, assuming a power $P = 1$ MW, an energy of about 20 kJ is deposited per proton pulse within about 1 μs corresponding to an instantaneous power $P_{SP} \simeq 20$ GW leading to a strong erosion of the liquid metal container by cavitation (Naoe et al., 2020). Moreover, very large space charges develop in the accumulation ring thus limiting further progress with this technology.

As suggested by Mezei (1997), a given beam power can be achieved at significant lower costs if the protons emerging from a linac are directly used for the spallation process. The long pulse of the order of ms allows to deposit a much higher beam energy per pulse

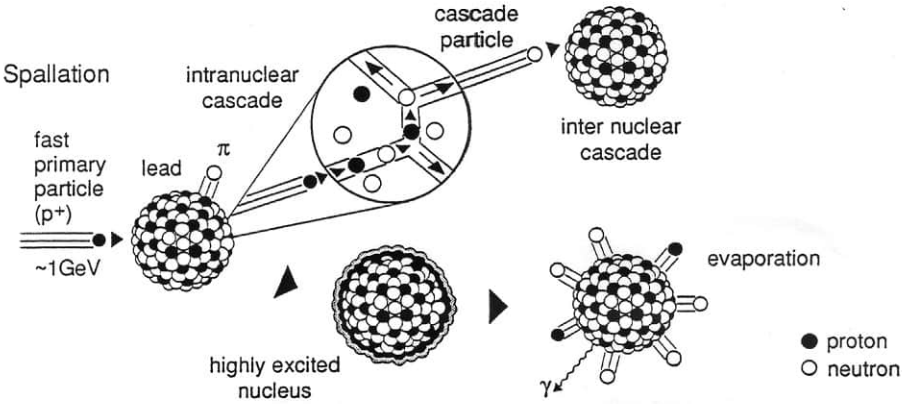

Fig. 5 Schematic representation of the spallation process of heavy nuclei. From Furrer A (2005) Neutron sources. In Bassani F, Liedl GL, and Wyder P (Eds.), *Encyclopedia of Condensed Matter Physics*, pp. 69–75. Elsevier: Oxford. ISBN 978-0-12-369401-0. https://doi.org/10.1016/B0-12-369401-9/00633-1. https://www.sciencedirect.com/science/article/pii/B0123694019006331.

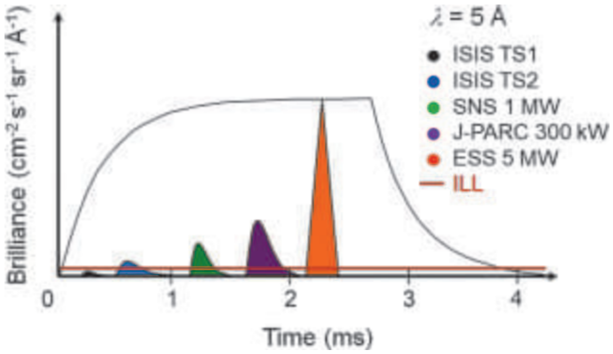

Fig. 6 Time structure of neutron pulses as produced at a SPSS and at a long-pulse spallation source (LPSS). At the ESS (ESS, 2019) the neutron pulses have a length of 2.86 ms. If shorter pulses are required they can be selected by chopping the beams (triangle in orange). After Andersen K (2013) *Reactor & Spallation Neutron Sources Website*. https://www.oxfordneutronschool.org/2013/Lectures/Andersen-Neutron_Sources.pdf.

on the target thus leading to a higher neutron flux density (Fig. 6). If shorter neutron pulses are required, they can be selected according to the requirements of the experiments by using choppers thus providing a tremendous flexibility (Andersen et al., 2020).

For example, the future neutron source ESS with a power of 5 MW will deliver pulses with an energy of 360 kJ and a length of 2.86 ms at a repetition rate of 14 Hz to a rotating target made from tungsten (Andersen, 2013). Therefore, the instantaneous power is only 0.13 GW per proton pulse, i.e., about two orders of magnitude smaller than for a SPSS. Still, the dissipation of heat from the target will be a factor limiting the flux density of long pulse spallation sources (Fig. 1).

Compact neutron sources

Nuclear reactors and spallation sources for research are usually only available at large neutron scattering centers due to the complexity of their operation and the large financial investments. An alternative route to obtain brilliant neutron beams is based on nuclear reactions using low energy electron, proton or deuteron beams hitting a target composed of light or heavy elements (Fig. 7). Because of the low nuclear inventory of these facilities, nuclear licensing is less critical and the shielding requirements are small.

One of the first accelerator based facilities started operation in Bariloche (Argentina) in 1969 (Rodríguez Palomino et al., 2013). An electron linac accelerated electrons up to 25 MeV at a current of 30 μA, which were directed on a Pb target yielding a neutron beam with an intensity of approximately 6×10^{11} s^{-1}. Since then, due to significant scientific and technological advances in accelerator and target technology, the particle currents could be strongly increased, i.e., up to 50–100 mA thus providing neutron beams with a high brilliance. The pulsed beams have typically a frequency between 10 and 300 Hz that can be adjusted to the needs of the experiment.

Compact neutron sources are in operation in the US and in Japan since the 90s (Table 2). A detailed overview can be found in the paper by Anderson et al. (2016) Recently, several projects for compact accelerator driven neutron sources have been proposed in Europe such as HBS at JCNS and SONATE at LLB (ELENA, 2022; Table 2).

At most existing facilities, protons are accelerated to energies of the order of 10 MeV providing currents of a few tens of mA on a Be target. Recently, Rücker et al. proposed the reaction (Rücker et al., 2016).

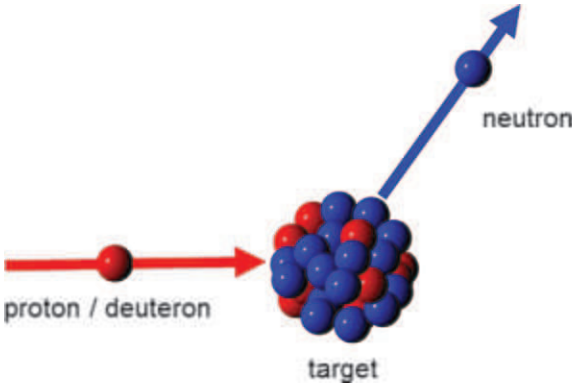

Fig. 7 Neutrons are released from a target nucleus after being hit by protons or deuterons with an energy of the order of 10–70 MeV. From https://elena-neutron.iff.kfa-juelich.de/neutron-facilities/.

Table 2 List of some existing and projected compact accelerator based neutron sources.

Facility	*Current (mA)*	*Voltage (MeV)*	*Beam*	*Target*	*Remarks startup*
Linac, Bariloche	0.03	25	e	Pb	Shut down
Rodríguez Palomino et al. (2013)					
HUNS, Hokaido					1974
Furusaka et al. (2014)					
LENS, Indiana	25	13	p	Be	2005
Lavelle et al. (2008)					
RANS-Riken, Wako	10	7	p	Be	2013
Ikeda et al. (2019)	10	7	p	Be	2013
CPHS, Beijing	50	13	p	Be	2013
Xiao et al. (2015)	50	13	p	Be	2013
HBS, Jülich	100	70	p	Ta	Proposal
Gutberlet et al. (2020)					
Brückel and Gutberlet (2020)					
LvB, Mirrotron	20	8	p	Li	Proposal
Mirrotron (2022)					
NEPIR, LNL	0.75	70	p	Be/W	Proposal
ARGITU, Bilbao	32	31.5	p	Be	Proposal
Pérez et al. (2020)					
SONATE, LLB	60	30	p	Be	Proposal
Ott et al. (2020)					

$$^{9}\mathrm{Be} + \mathrm{d} \rightarrow \mathbf{n} + {}^{10}\mathrm{Be}. \tag{12}$$

The released neutrons will be thermalized in small moderators with a thickness $t \simeq 1$ cm. They can be individually designed for the foreseen application such as for diffraction, spectroscopy, SANS, imaging, etc. It is expected that the performance of instruments at these compact accelerator driven neutron sources may become competitive with existing medium-flux neutron sources (Fig. 1).

The Jülich High Brilliance Neutron Source (HBS) represents one of the most advanced projects to deliver neutron beams with a high brilliance (Brückel and Gutberlet, 2020). Here, a proton beam with a high current of 100 mA is accelerated to an energy of 70 MeV and directed to several target stations which provide neutrons for moderators, which are optimized for the various beam lines. The use of a Ta target instead of Be increases the yield per proton by a factor of 2–3, i.e., a neutron intensity of the order of 10^{15} s^{-1} is expected. At a beam current of 100 mA, a neutron flux density of the order of $5 \cdot 10^{14}\,\mathrm{cm}^{-2}\,\mathrm{s}^{-1}$ may be obtained. Therefore, beamlines at the HBS are expected to be competitive with beamlines at present day research reactors of medium size spallation sources (Brückel and Gutberlet, 2020).

Halo neutrons

Conventional neutron sources suffer from at least two drawbacks: Firstly, the neutrons are emitted essentially into a solid angle of 4π when they are produced by the nuclear reaction and slowed down in the moderator. Therefore, only a fraction of $\simeq 10^{-5}$ of the produced neutrons can be extracted from the moderator and brought to an experiment. Secondly, the size of the neutron source is much larger than typical sample volumes, which are of the order of a few cubic centimeters. Ideally, a neutron source should be designed emitting thermal neutrons as a beam in a well defined direction.

A concept proposed by Habs et al. is based on the idea of producing neutrons by means of the emission of low energy neutron beams from neutron halo isomers of stable nuclei (Habs et al., 2011). These isomers may provide beams with a high brilliance. As shown in Fig. 8, a narrow-band γ - beam with a high intensity hits target nuclei and excites neutrons to a halo state, i.e., to an energy level directly below the ionization threshold. Finally, low energy neutrons from these long-lived states (100 ps - μs) can be released in pulses or quasi-continuously by photons in the visible or X-ray regime along the direction of the electric field vector, for

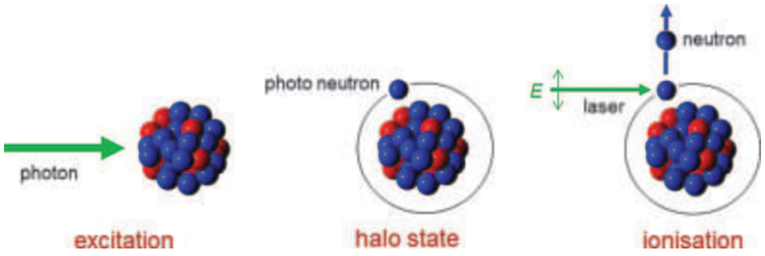

Fig. 8 Neutrons are released from target nuclei in two steps: excitation of photo neutrons by γ - photons from an ERL followed by ionization by a laser-photons.

example by a laser. The γ - rays can be produced by Compton back-scattering of laser beams off brilliant electron beams as produced by energy recovery linacs (ERL) (Hajima et al., 2009).

According to Habs et al. (2011), using present day technology, an up to a 10^2- to 10^6 - fold increase in brilliance may be achieved when compared with fission and spallation sources, respectively, using accelerator technology that will become available in the near future.

Because the targets for neutron production have only a diameter of typically a few tens of mm, the total number of produced neutrons per second (or pulse) will be much smaller when compared with conventional sources, however, much more confined in space leading to an exceptionally high brilliance.

As has been witnessed for sources of synchrotron radiation, the further development of accelerators, for example by laser-driven technology, will help to increase the brilliance even further. Clearly, to make this concept work, suitable neutron halo isomers, i.e., nuclei that allow neutron excitation much beyond the nuclear core radius, have to be identified. A list of suitable rare-earth nuclei has been proposed (Habs et al., 2011).

Neutron energies and properties

The energy range of the neutrons available in neutron sources spans many orders of magnitude. Table 3 provides a summary of denominations commonly used to label various regimes of neutron energy.

Table 4 summarizes the basic properties of the neutron as well as some useful physical constants and relations regarding thermal neutrons.

Table 3 Neutrons classified by their energy, velocity, and wavelength.

Classification	*Energy (meV)*	*Velocity (m/s)*	*Wavelength (Å)*
Ultra cold (UCN)	≤ 0.1	<140	>28
Very cold (VCN)	0.1–0.5	140–310	13–28
Cold	0.5–5	310–980	4–13
Thermal	5–100	980 – 4′400	0.9–4
Hot (epithermal)	100–1000	4′400 – 14′000	0.29–0.9
Resonant	$10^3 – 10^5$	14′000 – 140′000	0.029–0.29
Classification	*Energy (MeV)*	*Velocity (km/s)*	*Wavelength (fm)*
Intermediate	10^{-3} – 0.5	440–9800	40–900
Fast	0.5–10	9′800 – 44′000	9–40
Very fast	10–50	44′000 – 98′000	4–9
High energy	50 – 10^4	98′000 – 1.4 Mio	0.29–4
Relativistic	$>10^4$	$\geq$1.4 Mio	$\leq$0.29

Neutrons with energies up to approximately 1 eV are typically used for neutron scattering, imaging, and fundamental physics. The high energy neutrons (50 MeV–10 GeV) are also called ultra fast neutrons.

Table 4 Neutron properties and important constants.

Parameter	*Variable*	*Numerical value*	*Unit*
Mass	m_n	$1.674927498 \times 10^{-24}$	kg
Charge	Q	0	C
Spin	S_n	1/2	
Magnetic moment	μ_n	$-9.662365 \cdot 10^{-27}$	J/T
		−1.9130427	μ_N
Nuclear magneton	μ_N	$5.05078370 \cdot 10^{-27}$	J/T
		$3.15245126 \cdot 10^{-5}$	meV/T
		7.62259329	MHz/T
Lifetime of neutron Zyla et al. (2020)	τ	879.4	s
Boltzmann constant	k	$1.3806504 \cdot 10^{-23}$	J/K
		0.08617087	meV/K
Elementary charge	e	$1.602176634 \cdot 10^{-19}$	C
Planck constant	h	$6.62607015 \cdot 10^{-34}$	Js
		$4.13566770 \cdot 10^{-12}$	meV s
Composition	quarks	udd	

For the calculation of the conversion factors, the parameters E, λ, k, and v are given in meV, Å, Å^{-1}, and km, respectively.
Conversion factors: $E = 81.81 \cdot \lambda^{-2} = 2.072 \cdot k^2 = 5.227 \cdot v^2$
Energy scales: 1 meV = 0.242 THz = 8.07 cm^{-1} = 11.6 K.

Moderation of neutrons

As discussed in section "Production of neutrons," the energy of neutrons released by nuclear reactions is in the MeV range, whereas neutrons with an energy of meV are required for most experiments. Therefore, an energy shift by about 9 orders of magnitude is necessary that can be accomplished by collisions of neutrons with light nuclei in a moderator.

In research reactors, the fast neutrons are thermalized in a moderator that surrounds the fuel element. Part of the neutrons are used to maintain the chain reaction and the others are extracted by beam tubes pointing into the moderator (Fig. 9). The preferred moderator is D_2O due to its low absorption and the small mass of the deuterium atoms yielding an efficient thermalization within about 21 collisions. Usually, the volume of the moderator is large thus bringing the neutrons close to the thermal equilibrium. To reduce the background of fast neutrons, the beam tubes are arranged tangential to the fuel element.

At short-pulse spallation and compact neutron sources, the neutrons should be thermalized within as short a time as possible to guarantee short neutron pulses. Therefore, hydrogen containing materials such as water, H_2 or methane encompassing small volumes of a few liters are used to provide the short required thermalization times (Fig. 9). Usually, the neutrons do not reach a thermal equilibrium yielding a pronounced tail of epithermal neutrons, which are useful for certain experiments.

Currently, the trend goes toward small "high-brilliance moderators," such as the flat pancake shaped para-hydrogen moderator at the ESS (Andersen et al., 2018; Zanini et al., 2019) or the finger-moderators (Cronert et al., 2016) for compact accelerator-or photon based neutron sources (Carpenter, 2019). The small shape yields not only an increase in brilliance, it also provides an enhanced emission of neutrons in particular directions.

In the following we assume that the neutrons attain a thermal equilibrium with the moderator. Therefore, the velocity distribution of the neutrons is given by the Maxwell-Boltzmann distribution function (compare with Eq. (10))

$$f(v)\cdot dv = 4\pi\left(\frac{m_n}{2\pi kT}\right)^{3/2} v^2 e^{-\frac{m_n v^2}{2kT}} dv \tag{13}$$

where m_n is the mass of the neutron. $f(v)dv$ is the number of neutrons within a velocity interval dv having a velocity v. Moderators are usually kept at room temperature and this is why the extracted neutrons are called thermal neutrons.

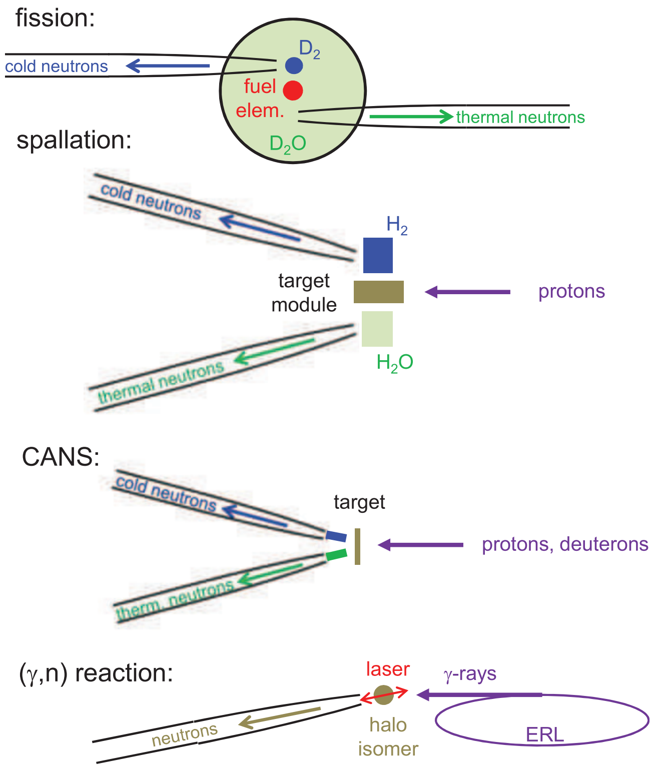

Fig. 9 Moderator configurations for four types of neutron sources. The moderators for fission sources are large to bring the neutrons close to the thermal equilibrium. To warrant a short pulse width at spallation sources and CANS, small moderators are used yielding under-moderated beams. The volumes of the targets anticipated for the (γ, n) reaction are of the order of 1 mm^3 yielding highly brilliant beams. Neutron guides may be used to extract neutrons. For full illumination, their entrance has to be moved as close as possible to the neutron source.

The yield of experiments requiring cold neutrons can be significantly improved by shifting the velocity spectrum of the neutrons to smaller energies by inserting a vessel containing liquid D_2 and H_2 with a temperature $20\text{ K} \leq T \leq 50\text{ K}$ into the D_2O moderator of a reactor or placing it close to the target of a spallation target (Fig. 9). For hot neutrons, a block of graphite with a temperature $T \simeq 2000$ K is inserted into the D_2O moderator. By choosing the adequate neutron spectrum the experiments with neutrons can be optimally tailored to the particular experimental requirements.

We have shown in section "Neutron scattering for condensed matter research," that the number of detector counts during the course of an experiment is directly proportional to the spectral neutron flux density φ or the brilliance Ψ, which are related to each other according to Eq. (7).

Knowing the neutron density n, the flux density is given by

$$\Phi = n\langle v\rangle = n\int_0^\infty vf(v)dv. \tag{14}$$

Hence the spectral flux density is given by

$$\varphi = \frac{d\Phi}{dv} = nvf(v). \tag{15}$$

Inserting the Maxwell-Boltzmann equation yields

$$\varphi(v)dv = 4\pi n\left(\frac{m_n}{2\pi kT}\right)^{3/2} v^3 e^{-\frac{m_n v^2}{2kT}}dv \quad \left(\frac{1}{\text{cm}^3}\right), \tag{16}$$

i.e., knowing the neutron density, the temperature of the moderator, and assuming the neutrons to be in thermal equilibrium one can easily calculate φ. Finally, assuming that the neutrons are emitted isotropically, the brilliance $\Psi = \varphi/(4\pi)$ is obtained.

In neutron scattering experiments, it is often more convenient to express φ in terms of energy and wavelength

$$\varphi(E)dE = 2n\left(\frac{2}{\pi(kT)^3 m_n}\right)^{1/2} Ee^{-E/kT}dE \quad \left(\frac{1}{\text{cm}^2\text{SJ}}\right) \tag{17}$$

and

$$\varphi(\lambda)d\lambda = -8n\left(\frac{kT}{2\pi m_n}\right)^{1/2}\frac{\lambda_T^4}{\lambda^5}\cdot e^{-\frac{\lambda_T^2}{\lambda^2}}d\lambda \quad \left(\frac{1}{\text{cm}^2\ s\text{Å}}\right), \tag{18}$$

respectively, where $\lambda_T = \frac{h}{\sqrt{2m_n kT}}$.

Fig. 10 shows the calculated spectra of the FRM II for hot, thermal and cold neutrons vs λ for moderator temperatures of 2000 K, 293 K, and 50 K, respectively. It is seen that using a neutron density $n_t = n_c = 2.4 \cdot 10^{11}$ (see section "Fission sources") reproduces the spectral flux density of thermal and cold neutrons at the FRM II quite well (FRM II, 2011). For the hot spectrum, a reduced density $n_h = 2.4 \cdot 10^{10}$ had to be used. The deviations between the simple calculation and the measured spectra may be caused by the fact that there is still a significant contribution of under-moderated neutrons and that neutrons are scattered in and out of the cold and hot moderators. Anyway, the overall agreement is quite impressive.

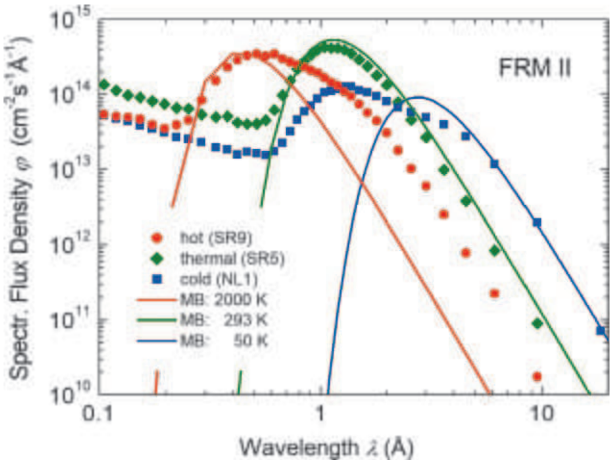

Fig. 10 The spectral flux density $\varphi(\lambda)$ is shown for neutrons emerging from a cold (50 K), thermal (293 K) and hot (2000 K) moderator. The calculations (solid lines) are based on the assumption that the neutrons are in thermal equilibrium with the moderator. A neutron density $n_c = n_t = 2.4 \cdot 10^{11}\ \text{cm}^{-3}$ is assumed for the cold and thermal flux density. For the hot flux density $n_h = 2.4 \cdot 10^{10}\ \text{cm}^{-3}$ is assumed. The data is in reasonable qualitative agreement with the measured φ of the FRM II (solid symbols) (FRM II, 2011). Note that the brilliance Ψ is obtained by dividing φ by 4π.

Neutron beam transport

After moderation of the neutrons, it is necessary to transport them to the experiment positions, except for irradiation experiments, which are usually performed in-pile. Because conventional neutron sources radiate isotropically, they have to be surrounded by heavy biological shielding to protect the users. Beam tubes containing neutron optical components are inserted into the shielding to allow the neutrons to leave the moderator surface. It is essential that the beam tubes are arranged tangentially to the fuel or target region of the neutron source in order to reduce unwanted radiation, i.e., fast neutrons and γ - photons.

Originally, neutron beams were extracted by means of beam tubes (Fig. 11(a)), which did not contain any neutron optical components, yielding beams with a triangular divergence distribution with a width

$$\alpha_{BT} = \arctan\,(H/L) \simeq 1^{\circ} \tag{19}$$

when typical values for beam tubes, i.e., $H = 100$ mm and $L = 6'000$ mm, are used. Because of the resulting small solid angle, the neutron flux density available at the instrument position is drastically reduced by about five orders of magnitude when compared with the isotropic flux within the moderator, which is emitted into 4π. If the experiment is placed far away from the biological shielding, the flux decreases further by the squared inverse distance.

The flux at the instrument positions can be considerably improved by using neutron guides (Fig. 11(b)) (Maier-Leibnitz and Springer, 1963). A neutron guide works via total reflection of neutrons from the smooth walls of the guide material (Fermi et al., 1946). Total reflection occurs for scattering angles less than the critical angle of reflection θ_c, which is given by

$$\theta_c = \lambda\sqrt{\frac{\rho b}{\pi}}, \tag{20}$$

where ρ and b are the atom number density and the coherent scattering length of the wall material, respectively. Among common materials, nickel is the best choice with a critical angle $\theta_c = \kappa\lambda$, where $\kappa = 0.099\ \deg/\text{Å} = 0.00173\,\text{rad/Å}$.

The angular acceptance of a neutron guide can be dramatically increased by coating the walls with so-called supermirror, which consists of a sequence of layers of variable thickness with alternating high positive and negative scattering length density (Mezei, 1976, 1992). Typical materials are Ni and Ti. Supermirror can be characterized by a number m defining the increase of $\theta_{c,m} = m\theta_c$ compared to nickel. According to Fig. 11(b), the divergence of the extracted neutrons is given by

$$\alpha_{SM} = 2m\kappa\lambda. \tag{21}$$

Of course, supermirror-coated guides are most efficient for neutrons with a large wavelength. For example, for $\lambda = 2\,\text{Å}$ and a coating $m = 4$ one obtains $\alpha_{BT} \simeq 1.6^{\circ}$ if reflection losses are neglected. If they are included, a trapezoidal divergence distribution is obtained (Fig. 11(b)). When compared to a beam tube, the gain in flux density when compared with an extraction by a beam tube is increased by a factor of $1.6^2 \simeq 2.5$. At present $m \simeq 8$ can be routinely achieved (Fig. 12) (Schanzer et al., 2016) resulting in a rather dramatic increase in neutron flux when compared with a conventional beam tube even for neutrons with a small λ. Further improvements in neutron extraction are achieved by means of elliptic or parabolic guides if their entrance can be properly illuminated (Böni, 2008).

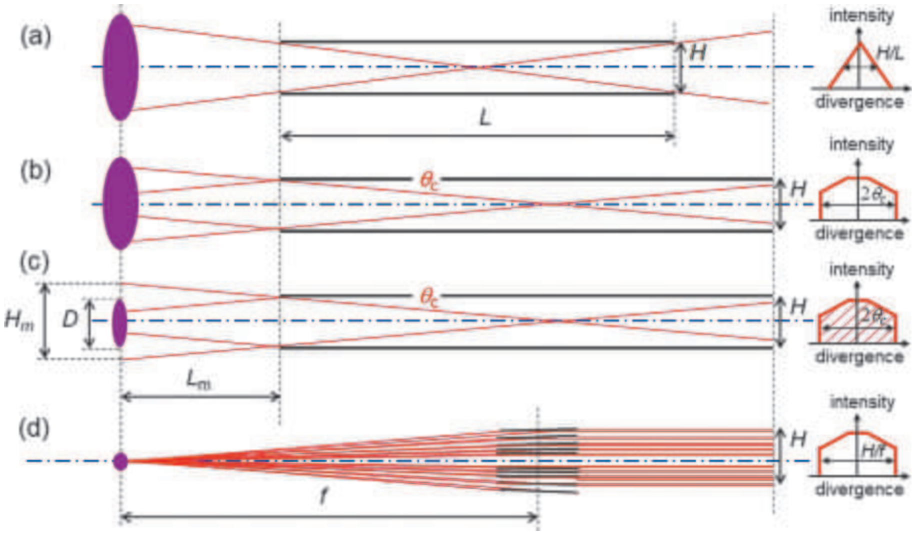

Fig. 11 Beam extraction from a moderator using a beam tube (a), a fully illuminated neutron guide (b), an under-illuminated neutron guide (c), or a parabolic nested mirror optics (NMO). A NMO yields about a four times higher flux density than a neutron guide with identical supermirror coating. The figures on the right hand side show the divergence distribution of the extracted neutron beam.

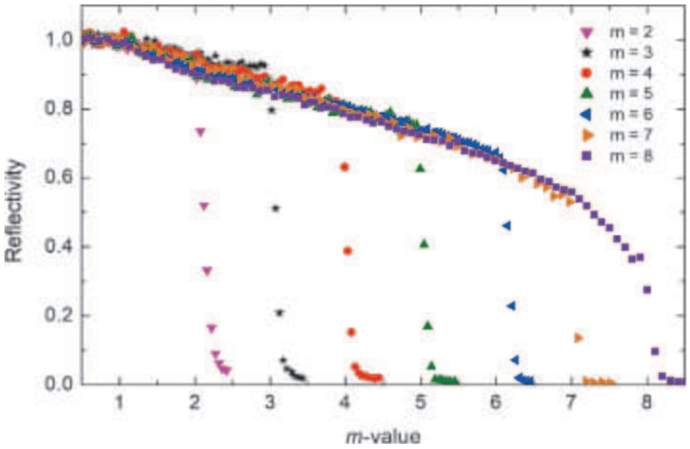

Fig. 12 Reflectivity profiles of supermirrors with *m*-values $2 \leq m \leq 8$. The slope of *R* is largely independent of the *m*-value indicating a stable interface roughness, which is essentially constant for all layers From Schanzer C, Schneider M, and Böni P (2016) Neutron optics: Towards applications for hot neutrons. *Journal of Physics: Conference Series* 746: 012024-(1-7). http://iopscience.iop.org/article/10.1088/1742-6596/746/1/012024/pdf.

The current trend toward small "high-brilliance moderators", such as the ones proposed for ESS and for compact accelerator based neutron sources, seems to be an obstacle for an efficient neutron extraction because of under-illumination of the guide entrance. According to Fig. 11(c), the wavelength dependent footprint (shown in one dimension) of transportable neutrons at the moderator position is given by

$$H_m = H + 2L_m \tan \theta_{c,m} \simeq H + 2L_m m\kappa\lambda. \tag{22}$$

Clearly, as soon as the size of the moderator, *D*, becomes smaller than H_m, illumination losses will occur leading to a dilution of the phase space of the neutrons indicated by the hatched trapezoid in Fig. 11(c). Therefore, the transfer of the brilliance from the source to the experiment is reduced. Hence, *D* has to be significantly larger than the size of the neutron guide for full illumination.

As proposed by Herb et al. (2022) the problem of under-illumination can be resolved by using an arrangement of nested elliptic or parabolic mirrors, which in contrast to elliptic guides or Montel mirrors provide an imaging of the moderator. As shown in Fig. 11(d), each mirror reflects neutrons emerging from a small angular range in the beam direction. All mirrors are fully illuminated and transform the incident divergent beam into a low-divergence beam that can be transported efficiently by a neutron guide which suffers only small reflection losses due to the small angles of reflection. Finally, the neutron beam can be refocused by nested mirrors at the position of the experiment.

The maximum divergence that is accepted by a parabolic system is given by

$$\alpha_{\mathrm{NMO}} = \frac{H}{f} = 4m\kappa\lambda = 2\alpha_{SM}, \tag{23}$$

which is twice as large as achieved for an extraction by a conventional neutron guide. Therefore, an approximately fourfold increase in flux density is achieved. Moreover, the phase space is more compact. Even hot neutrons can be efficiently extracted using nested mirrors (Herb et al., 2022). It may well be that parabolic nested mirrors turn out to become the most efficient technique for neutron extraction presently available.

Conclusion

An ever growing scientific community uses neutrons in various disciplines of condensed matter research and fundamental physics, however, the currently active neutron sources (see Table 5) will not be able to supply the future demand at least not in Europe, where the number of neutron facilities has significantly decreased due to the recent shut-down of the Orphée reactor, BER II, and R-2 (Table 5). Moreover, further shut-downs of reactors taken into operation in the last century will happen in the near future. Most of these medium-flux neutron sources, which are indispensable (i) for experiments requiring a medium flux, (ii) for the education of scientists in neutron physics, and (iii) for the development of instrumentation will be sorely missed and cannot simply be replaced by the European Spallation Source ESS in Lund. Thus new sources, such as accelerator based compact neutron sources (CANS), are indispensable to ensure the continuity and further developments in neutron scattering. In contrast to Europe (with the exception of FRM II), new sources have been taken into operation in the US, Asia, and Australia in this century.

The history of the evolution of the neutron flux at fission sources was impressive until the high-flux reactor in Grenoble was commissioned. Since then a leveling off is observed that is caused by the technical difficulty of removing the heat from the reactor

Table 5 An incomplete list of neutron sources.

Startup	*Facility*	*Location*	*Power (MW)*	*Peak flux density (cm^{-2}s^{-1})*	*Type*	*Status*
1932	Chadwick	Cambridge		1		Shut down
1934	0.35 mCi RaBe source			10,000		Shut down
1937	37′ cyclotron	Berkley		$5 \cdot 10^{6}$		Shut down
1942	CP-1	Chicago	200 W	$1 \cdot 10^{7}$	Fission, CW	1943
1943	CP-2	Chicago	Few kW	$2 \cdot 10^{8}$	Fission, CW	Shut down
1943	X-10	Oak Ridge	4	$5 \cdot 10^{12}$	Fission, CW	1963
1947	NRX	Chalk River	42	$4 \cdot 10^{13}$	Fission, CW	1993
1952	MTR	Arco (Idaho)	40	$2 \cdot 10^{14}$	Fission, CW	1970
1956	DIDO/PLUTO	Harwell	25	$1.2 \cdot 10^{14}$	Fission, CW	1990
1957	NRU	Chalk River	120	$3 \cdot 10^{14}$	Fission, CW	2018
1957	FRM-I	Garching	4	$6.6 \cdot 10^{12}$	Fission, CW	200
1957	LVR-15	Rez	10	$1 \cdot 10^{14}$	Fission, CW	in oper.
1957	Saphir	Würenlingen	10	$1 \cdot 10^{14}$	Fission, CW	1994
1958	FRG-1	Geesthacht	5	$1.4 \cdot 10^{14}$	Fission, CW	2010
1958	BER I	Berlin	0.05	$1 \cdot 10^{12}$	Fission, CW	1972
1959	BNC	Budapest	10	$2.1 \cdot 10^{14}$	Fission, CW	in oper.
1959	WWR-M	Gatchina	18	$4.5 \cdot 10^{14}$	Fission, CW	in oper.
1959	MNR	McMaster	5	$1 \cdot 10^{14}$	Fission, CW	in oper.
1960	Diorit	Würenlingen	30	$8 \cdot 10^{13}$	Fission, CW	1977
1960	R-2	Studsvik	50	$1 \cdot 10^{14}$	Fission, CW	
1960	DR-3	Risø	10	$1.2 \cdot 10^{14}$	Fission, CW	2000
1962	BR3	Mol	125	$1 \cdot 10^{15}$	Fission, CW	in oper.
1962	FRJ-2	Jülich	23	$3 \cdot 10^{14}$	Fission, CW	2006
1963	HOR	Delft	2.3	$4.5 \cdot 10^{13}$	Fission, CW	in oper.
1965	HFBR	Brookhaven	60	$5 \cdot 10^{14}$	Fission, CW	1996
1965	SAFARI-1	Pelindaba	20	$2 \cdot 10^{14}$	Fission, CW	in oper.
1966	HFIR	Oak Ridge	85	$1.2 \cdot 10^{15}$	Fission, CW	in oper.
1966	MURR	Missouri	10	$6 \cdot 10^{14}$	Fission, CW	in oper.
1969	NCNR	Gaithersburg	20	$4 \cdot 10^{14}$	Fission, CW	in oper.
1971	ILL	Grenoble	58.4	$1.2 \cdot 10^{15}$	Fission, CW	in oper.
1973	BER II	Berlin	10	$2 \cdot 10^{14}$	Fission, CW	2019
1974	ZING-P	Argonne	0.5	$5 \cdot 10^{11}$	Spall. pulsed	Shut down
1980	KENS	Tsukuba	0.003	$3 \cdot 10^{14}$	Spall. pulsed	2006
1980	Orph´ee	Saclay	14	$3 \cdot 10^{14}$	Fission, CW	2019
1981	IPNS	Argonne	0.007	$8 \cdot 10^{14}$	Spall. pulsed	2008
1984	IBR-2	Dubna	2	$1 \cdot 10^{16}$	Fission, pulsed	in oper.
1985	ISIS	Didcot	0.16	$6 \cdot 10^{15}$	Spall. pulsed	in oper.
1985	Dhruva	Trombay	100	$1.8 \cdot 10^{14}$	Fission, CW	in oper.
1988	LANSCE	Los Alamos	800	$3 \cdot 10^{15}$	Spall. pulsed	in oper.
1990	JRR-3 M	Tokai	20	$2 \cdot 10^{14}$	Fission, CW	in oper.
1995	HANARO	Daejeon	30	$3 \cdot 10^{14}$	Fission, CW	in oper.
1996	SINQ	Villigen	1	$2 \cdot 10^{14}$	Spall. CW	in oper.
2004	FRM-II	Garching	20	$7 \cdot 10^{14}$	Fission, CW	in oper.
2006	SNS	Oak Ridge	1.4	$2 \cdot 10^{16}$	Spall. pulsed	in oper.
2006	J-PARC	Tokai	0.7	$1 \cdot 10^{16}$	Spall. pulsed	in oper.
2006	OPAL	Lucas Heights	20	$4 \cdot 10^{14}$	Fission, CW	in oper.
2017	CSNS	Dongguan	100		Spall. pulsed	in oper.
2017	CARR	Beijing	60	$6 \cdot 10^{14}$	Fission, CW	in oper.
2025	PIK	Gatchina	100	$1.5 \cdot 10^{15}$	Fission, CW	und. constr.
2025	R-10	Bariloche	20	$4 \cdot 10^{14}$	Fission, CW	und. constr.
2026	ESS	Lund	5	$5 \cdot 10^{16}$	Spall. pulsed	und. constr.
2032	SNS-STS	Oak Ridge	2.8		Spall. pulsed	Funded
	HBS	Jülich	7	$8.5 \cdot 10^{14}$	CANS pulsed	Proposed
	Inertial Fusion			$7 \cdot 10^{18}$	(T,d) fusion	Proposed
	Halo			$1.2 \cdot 10^{17}$	Photon, CW	Proposed
	Halo			$5 \cdot 10^{22}$	Photon, pulsed	Proposed

The column “Peak flux density” provides the perturbed or unperturbed thermal peak flux density. For continuous sources, the peak flux density $\widehat{\Phi}_{th}$ is equal to the average flux density Φ_{th}. The column “status” provides information on the status of the neutron source, namely shut down (the year is given if known to the author), in operation, under construction, funded, or proposed.

core (Fig. 1). A similar trend is observed for spallation sources, where the power may be limited to about 5–10 MW. Therefore, not much progress in the neutron flux can be expected by further developments on the source side. Only completely new concepts for neutron production, such as the fusion reaction (Taylor et al., 2007) or using halo isomers (Habs et al., 2011), can help to increase the flux significantly (Table 5) This situation is very different in comparison to X-ray synchrotron radiation where the flux is steadily increasing by orders of magnitude (Shin, 2021).

Due to the limitation of the flux density, most progress in increasing the performance of beam lines for neutron physics has been achieved by the development of new instrumental concepts and the improved transport of neutrons by neutron guides using supermirror. The use of nested mirror optics may prove to be the most efficient means for extracting neutrons from small high-brilliance moderators and focusing of neutrons. Here, a brilliance transfer of 25–70% may be achieved (Herb et al., 2022).

While most intensity gains are due to the increase of the divergence of the neutron beams, this development seems also to be limited because the ever increasing number of required layers for achieving a large *m*-value for supermirror, which is of the order of 16′000 atomically smooth layers for mirrors with $m = 8$, the ever increasing absorption by the layers is a limiting factor for increasing *m* further. Moreover, many experiments, such as studies of strongly correlated electron systems require high resolution in momentum *and* energy, thus preventing the use of neutron beams with a large divergence. Therefore, without the discovery of new concepts for neutron production, neutrons will indeed remain a flux limited probe making them very elusive and valuable.

Acknowledgments

I acknowledge the strong support of Albert Furrer for this work and providing his manuscript. It is with great pleasure to thank Thomas Gutberlet for useful discussions about Compact Accelerator-driven Neutron Sources and Christoph Herb and Oliver Zimmer for the collaboration in the field of nested mirror optics.

References

Andersen K (2013) Reactor & Spallation Neutron Sources Website. https://www.oxfordneutronschool.org/2013/Lectures/Andersen-Neutron_Sources.pdf.

Andersen KH, Bertelsen M, Zanini L, Klinkby EB, Schönfeldt T, Bentley PM, and Saroun J (2018) Optimization of moderators and beam extraction at the ESS. *Journal of Applied Crystallography* 51(2): 264–281. https://doi.org/10.1107/S1600576718002406.

Andersen KH, Argyriou DN, Jackson AJ, Houston J, Henry PF, Deen PP, Toft-Petersen R, Beran P, Strobl M, Arnold T, Wacklin-Knecht H, Tsapatsaris N, Oksanen E, Woracek R, Schweika W, Mannix D, Hiess A, Kennedy S, Kirstein O, Årsköld SP, Taylor J, Hagen ME, Laszlo G, Kanaki K, Piscitelli F, Khaplanov A, Stefanescu I, Kittelmann T, Pfeiffer D, Hall-Wilton R, Lopez CI, Aprigliano G, Whitelegg L, Moreira FY, Olsson M, Bordallo HN, Martín-Rodríguez D, Schneider H, Sharp M, Hartl M, Nagy G, Ansell S, Pullen S, Vickery A, Fedrigo A, Mezei F, Arai M, Heenan RK, Halcrow W, Turner D, Raspino D, Orszulik A, Cooper J, Webb N, Galsworthy P, Nightingale J, Langridge S, Elmer J, Frielinghaus H, Hanslik R, Gussen A, Jaksch S, Engels R, Kozielewski T, Butterweck S, Feygenson M, Harbott P, Poqué A, Schwaab A, Lieutenant K, Violini N, Voigt J, Brükel T, Koenen M, Kämmerling H, Babcock E, Salhi Z, Wischnewski A, Heynen A, Désert S, Jestin J, Porcher F, Fabrèges X, Fabrèges G, Annighofer B, Klimko S, Dupont T, Robillard T, Goukassov A, Longeville S, Alba-Simionesco C, Bourges P, Le Bouffy JG, Lavie P, Rodrigues S, Calzada E, Lerche M, Schillinger B, Schmakat P, Schulz M, Seifert M, Lohstroh W, Petry W, Neuhaus J, Loaiza L, Tartaglione A, Glavic A, Schütz S, Stahn J, Lehmann E, Morgano M, Schefer J, Filges U, Klauser C, Niedermayer C, Fenske J, Nowak G, Rouijaa M, Siemers DJ, Kiehn R, Müller M, Carlsen H, Udby L, Lefmann K, Birk JO, Holm-Dahlin S, Bertelsen M, Hansen UB, Olsen MA, Christensen M, Iversen K, Christensen NB, Rønnow HM, Freeman PG, Hauback BC, Kolevatov R, Llamas-Jansa I, Orecchini A, Sacchetti F, Petrillo C, Paciaroni A, Tozzi P, Zanatta M, Luna P, Herranz I, del Moral OG, Huerta M, Magán M, Mosconi M, Abad E, Aguilar J, Stepanyan S, Bakedano G, Vivanco R, Bustinduy I, Sordo F, Martínez JL, Lechner RE, Villacorta FJ, Šaroun J, Lukáš P, Markó M, Zanetti M, Bellissima S, del Rosso L, Masi F, Bovo C, Chowdhury M, De Bonis A, Di Fresco L, Scatigno C, Parker SF, Fernandez-Alonso F, Colognesi D, Senesi R, Andreani C, Gorini G, Scionti G, and Schreyer A (2020) The instrument suite of the European spallation source. *Nuclear Instruments and Methods in Physics Research Section A: Accelerators, Spectrometers, Detectors and Associated Equipment* 0168-9002957: 163402. https://doi.org/10.1016/j.nima.2020.163402.

Anderson IS, Andreani C, Carpenter JM, Festa G, Gorini G, Loong C-K, and Senesi R (2016) Research opportunities with compact accelerator-driven neutron sources. *Physics Reports* 0370-1573654: 1–58. https://doi.org/10.1016/j.physrep.2016.07.007. Research opportunities with compact accelerator-driven neutron sources.

Böni P (2008) New concepts for neutron instrumentation. *Nuclear Instruments and Methods in Physics Research Section A: Accelerators, Spectrometers, Detectors and Associated Equipment* 0168-9002586(1): 1–8. https://doi.org/10.1016/j.nima.2007.11.059.

Brückel T and Gutberlet T (2020) *Conceptual Design Report Jülich High Brilliance Neutron Source (hbs)*. vol. 8. Forschungszentrum Jülich GmbH, Schriften des Forschungszentrums Jülich, Reihe Allgemeines/General. 197 S. Jülich, 2020.

Carpenter JM (2019) The development of compact neutron sources. *Nature Reviews Physics* 2522-58201(3): 177–179. https://doi.org/10.1038/s42254-019-0024-8. tex. copyright: 2019 The Publisher.

Chadwick J (1932) The existence of a neutron. *Proceedings of the Royal Society of London A* 136: 692–708. https://doi.org/10.1098/rspa.1932.0112.

Chupp TE, Fierlinger P, Ramsey-Musolf MJ, and Singh JT (2019) Electric dipole moments of atoms, molecules, nuclei, and particles. *Reviews of Modern Physics* 91: 015001. https://doi.org/10.1103/RevModPhys.91.015001.

Cronert T, Dabruck JP, Doege PE, Bessler Y, Klaus M, Hofmann M, Zakalek P, Rücker U, Lange C, Butzek M, Hansen W, Nabbi R, and Brückel T (2016) High brilliant thermal and cold moderator for the HBS neutron source project Jülich. *Journal of Physics Conference Series* 1742-6588746: 012036. https://doi.org/10.1088/1742-6596/746/1/012036. 1742–6596.

Dubbers D and Schmidt MG (2011) The neutron and its role in cosmology and particle physics. *Reviews of Modern Physics* 83: 1111–1171. https://doi.org/10.1103/RevModPhys.83.1111.

ELENA (2022) ELENA Website. https://elena-neutron.eu.

Emendörfer D and Höcker KH (1969) *Theorie der kernreaktoren*. Mannheim, Wien, Zürich: Bibliographisches Institut.

ESS (2019) ESS Website. http://www.europeanspallationsource.se.

Fermi E, Zinn WH, Los Alamos National Laboratory, and U. S. Atomic Energy Commission (1946) *Reflection of Neutrons on Mirrors*. United States: Atomic Energy Commission. MDDC. Manhattan District. https://books.google.de/books?id=IKsY9gzauzUC.

FRM II (2011) BlueBook of the FRM *II* 2011. http://cdn.frm2.tum.de/fileadmin/stuff/instruments/BlueBook/exp-fac_cs4_Januar2011_verlinkt2.pdf.

Furrer A (2005) Neutron sources. In: Bassani F, Liedl GL, and Wyder P (eds.) *Encyclopedia of Condensed Matter Physics*, pp. 69–75. Oxford: Elsevier. ISBN: 978-0-12-369401-0. https://doi.org/10.1016/B0-12-369401-9/00633-1.

Furrer A, Mesot J, and Strässle T (2009) *Neutron Scattering in Condensed Matter Physics*. World Scientific Publishing Company.

Furusaka M, Sato H, Kamiyama T, Ohnuma M, and Kiyanagi Y (2014) Activity of hokkaido university neutron source, huns. *Physics Procedia* 1875-389260: 167–174. https://doi.org/10.1016/j.phpro.2014.11.024. 3rd International Meeting of the Union for Compact Accelerator-driven Neutron Sources, UCANS III, 31 July–3 August 2012, Bilbao, Spain, the 4th International Meeting of the Union for Compact Accelerator- driven Neutron Sources, UCANS IV, 23–27 September 2013, Sapporo, Hokkaido, Japan.

Greenberg RR, Bode P, and De Nadai Fernandes EA (2011) Neutron activation analysis: A primary method of measurement. *Spectrochimica Acta Part B: Atomic Spectroscopy* 0584-854766(3): 193–241. https://doi.org/10.1016/j.sab.2010.12.011.

Greene GL and Geltenbort P (2016) The neutron enigma. *Scientific American* 314(4): 37–41. https://doi.org/10.1038/scientificamerican0416-36.

Gutberlet T, Rücker U, Mauerhofer E, Zakalek P, Cronert T, Voigt J, Baggemann J, Li J, Doege P, Böhm S, Rimmler M, Felden O, Gebel R, Meusel O, Podlech H, Barth W, and Brückel T (2020) Sustainable neutrons for today and tomorrow—The jülich high brilliance neutron source project. *Neutron News* 31(2–4): 37–43. https://doi.org/10.1080/10448632.2020.1819132.

Habs D, Gross M, Thirolf PG, and Böni P (2011) Neutron halo isomers in stable nuclei and their possible application for the production of low energy, pulsed, polarized neutron beams of high intensity and high brilliance. *Applied Physics B* 103: 485–499. https://doi.org/10.1007/s00340-010-4276-3.

Hajima R, Kikuzawa N, Nishimori N, Hayakawa T, Shizuma T, Kawase K, Kando M, Minehara E, Toyokawa H, and Ohgaki H (2009) Detection of radioactive isotopes by using laser compton scattered γ-ray beams. *Nuclear Instruments and Methods in Physics Research Section A: Accelerators, Spectrometers, Detectors and Associated Equipment* 0168-9002608(1, Suppl): S57–S61. https://doi.org/10.1016/j.nima.2009.05.063. Compton sources for X/γ rays: Physics and applications.

Herb C, Zimmer O, Georgii R, and Böni P (2022) Nested mirror optics for neutron extraction, transport, and focusing. *arXiv* 23. https://doi.org/10.48550/arXiv.2202.07899. 2202.07899 [physics].

Ikeda S, Otake Y, Kobayashi T, and Hayashizaki N (2019) Design of 500 mhz linear accelerator for a compact neutron source, rans-iii. *Nuclear Instruments and Methods in Physics Research Section B: Beam Interactions with Materials and Atoms* 0168-583X461: 186–190. https://doi.org/10.1016/j.nimb.2019.09.051.

ILL (1986) *Yellow Book of the ILL 1986*. Institut Laue Langevin.

JPARC (2019) JPARC Website. http://www.j-parc.jp/index-e.html.

Kardjilov N, Manke I, Woracek R, Hilger A, and Banhart J (2018) Advances in neutron imaging. *Materials Today* 1369-702121(6): 652–672. https://doi.org/10.1016/j.mattod.2018.03.001.

Latge C, Wohlmuther M, Dai Y, Gavillet D, Gessi A, Guertin A, Hammer B, Heinitz S, Henry J, Konstantinovic M, Lindau R, Fazio C, Maloy S, Neuhausen J, Saito S, Park K, Schumann D, Thomsen K, Türler A, and Wagner W (2016) Megapie: The world’s first high-power liquid metal spallation neutron source. *Thorium Energy for the World*. https://doi.org/10.1007/978-3-319-26542-1˙41.

Lavelle CM, Baxter DV, Bogdanov A, Derenchuk VP, Kaiser H, Leuschner MB, Lone MA, Lozowski W, Nann H, Przewoski BV, Remmes N, Rinckel T, Shin Y, Snow WM, and Sokol PE (2008) Neutronic design and measured performance of the low energy neutron source (lens) target moderator reflector assembly. *Nuclear Instruments and Methods in Physics Research Section A: Accelerators, Spectrometers, Detectors and Associated Equipment* 0168-9002587(2): 324–341. https://doi.org/10.1016/j.nima.2007.12.044.

Lawson JD (1955) *Some Criteria for a Useful Thermonuclear Reactor*. A.E.R.E. GP/R 1807 1–12.

Lawson JD (1957) Some criteria for a power producing thermonuclear reactor. *Proceedings of the Physical Society. Section B* 70(1): 6–10. https://doi.org/10.1088/0370-1301/70/1/303.

Maier-Leibnitz H and Springer T (1963) The use of neutron optical devices on beam-hole experiments on beam-hole experiments. *Journal of Nuclear Energy. Parts A/B. Reactor Science and Technology* 0368-323017(4): 217–225. https://doi.org/10.1016/0368-3230(63)90022-3.

Mezei F (1976) Novel polarized neutron devices: supermirror and spin component amplifier. *Communications on Physics (London)* 1(3): 81–85.

Mezei F (1992) Polarizing supermirror devices: Some new developments. In: Majkrzak CF and Wood JL (eds.) *Neutron Optical Devices and Applications*. vol. 1738, pp. 107–115. SPIE. https://doi.org/10.1117/12.130623.

Mezei F (1997) Long pulse spallation sources. *Physica B: Condensed Matter* 0921-4526234-236: 1227–1232. https://doi.org/10.1016/S0921-4526(97)00271-8. Proceedings of the First European Conference on Neutron Scattering.

Mirrotron (2022) Mirrotron Website. https//mirrotron.com/en.

Naoe T, Kinoshita H, Kogawa H, Wakui T, Wakai E, Haga K, and Takada H (2020) *Mitigation of Cavitation Damage in J-PARC Mercury Target Vessel*. vol. 28, 1–6. https://doi.org/10.7566/JPSCP.28.081004.

Ott F, Menelle A, and Alba-Simionesco C (2020) The SONATE project, a French CANS for materials sciences research. In: *European Physical Journal Web of Conferences, Volume 231 of European Physical Journal Web of Conferences* 01004. https://doi.org/10.1051/epjconf/202023101004.

Pérez M, Sordo F, Bustinduy I, Muñoz JL, and Villacorta FJ (2020) Argitu compact accelerator neutron source: A unique infrastructure fostering r&d ecosystem in euskadi. *Neutron News* 31(2–4): 19–25. https://doi.org/10.1080/10448632.2020.1819140.

Rodríguez Palomino LA, Blostein JJ, and Dawidowski J (2013) Performance of the second deep inelastic neutron scatering spectrometer at the bariloche electron linac. *Journal of Instrumentation* 8(08): P08016.

Rücker U, Cronert T, Voigt J, Dabruck JP, Doege PE, Ulrich J, Nabbi R, Beßler Y, Butzek M, Büscher M, Lange C, Klaus M, Gutberlet T, and Brückel T (2016) The jülich high-brilliance neutron source project. *The European Physical Journal Plus* 131(19): 1–14. https://doi.org/10.1140/epjp/i2016-16019-5.

Rush JJ (2015) US neutron facility development in the last half-century: A cautionary tale. *Physics in Perspective* 17: 1–21. https://doi.org/10.1007/s00016-015-0158-8.

Schanzer C, Schneider M, and Böni P (2016) Neutron optics: Towards applications for hot neutrons. *Journal of Physics: Conference Series* 746(1): 012024. http//stacks.iop.org/1742-6596/746/i=1/a=012024.

Shin S (2021) New era of synchrotron radiation: fourth-generation storage ring. *AAPPS Bulletin* 31(21): 1–16. https://doi.org/10.1007/s43673-021-00021-4.

Shirane G, Shapiro SM, and Tranquada JM (2002) *Neutron scattering with a triple-axis spectrometer: Basic techniques*. Cambridge University Press. https://doi.org/10.1017/CBO9780511534881.

SNS (2019) SNS Website. http://neutrons.ornl.gov/facilities/SNS/.

Tarantini C, Aebersold HU, Braccini V, Celentano G, Ferdeghini C, Ferrando V, Gambardella U, Gatti F, Lehmann E, Manfrinetti P, Marr´e D, Palenzona A, Pallecchi I, Sheikin I, Siri AS, and Putti M (2006) Effects of neutron irradiation on polycrystalline $mg^{11}b_2$. *Physical Review B* 73: 134518. https://doi.org/10.1103/PhysRevB.73.134518.

Taylor A, Dunne M, Bennington S, Ansell S, Gardner I, Norreys P, Broome T, Findlay D, and Nelmes R (2007) A route to the brightest possible neutron source? *Science* 315(5815): 1092–1095. https://doi.org/10.1126/science.1127185.

Xiao Y, Chen Z, Yang Y, and Wang X (2015) Development progress of the neutron imaging station in cphs. *Physics Procedia* 1875-389269: 96–103. https://doi.org/10.1016/j.phpro.2015.07.014. Proceedings of the 10th World Conference on Neutron Radiography (WCNR-10) Grindelwald, Switzerland October 5–10, 2014.

Zanini L, Andersen KH, Batkov K, Klinkby EB, Mezei F, Schönfeldt T, and Takibayev A (2019) Design of the cold and thermal neutron moderators for the European Spallation Source. *Nuclear Instruments and Methods in Physics Research Section A: Accelerators, Spectrometers, Detectors and Associated Equipment* 0168-9002925: 33–52. https://doi.org/10.1016/j.nima.2019.01.003.

Zyla PA, Barnett RM, Beringer J, Dahl O, Dwyer DA, Groom DE, Lin CJ, Lugovsky KS, Pianori E, Robinson DJ, Wohl CG, Yao WM, Agashe K, Aielli G, Allanach BC, Amsler C, Antonelli M, Aschenauer EC, Asner DM, Baer H, Sw Banerjee L, Baudis CW, Bauer JJ, Beatty VI, Belousov SB, Bettini A, Biebel O, Black KM, Blucher E, Buchmuller O, Burkert V, Bychkov MA, Cahn RN, Carena M, Ceccucci A, Cerri A, Chakraborty D, Sekhar Chivukula R, Cowan G, D'Ambrosio G, Damour T, de Florian D, de Gouvêa A, De-Grand T, de Jong P, Dissertori G, Dobrescu BA, D'Onofrio M, Doser M, Drees M, Dreiner HK, Eerola P, Egede U, Eidelman S, Ellis J, Erler J, Ezhela VV, Fetscher W, Fields BD, Foster B, Freitas A, Gallagher H, Garren L, Gerber HJ, Gerbier G, Gershon T, Gershtein Y, Gherghetta T, Godizov AA, Gonzalez-Garcia MC, Goodman M, Grab C, Gritsan AV, Grojean C, Grünewald M, Gurtu A, Gutsche T, Haber HE, Hanhart C, Hashimoto S, Hayato Y, Hebecker A, Heinemeyer S, Heltsley B, Hernandez-Rey JJ, Hikasa K, Hisano J, Höcker A, Holder J, Holtkamp A, Huston J, Hyodo T, Johnson KF, Kado M, Karliner M, Katz UF, Kenzie M, Khoze VA, Klein SR, Klempt E, Kowalewski RV, Krauss F, Kreps M, Krusche B, Kwon Y, Lahav O, Laiho J, Lellouch LP, Lesgourgues J, Liddle AR, Ligeti Z, Lippmann C, Liss TM, Littenberg L, Lourengo C, Lugovsky SB, Lusiani A, Makida Y, Maltoni F, Mannel T, Manohar AV, Marciano WJ, Masoni A, Matthews J, Meißner UG, Mikhasenko M, Miller DJ, Milstead D, Mitchell RE, Mo¨nig K, Molaro P, Moortgat F, Moskovic M, Nakamura K, Narain M, Nason P, Navas S, Neubert M, Nevski P, Nir Y, Olive KA, Patrignani C, Peacock JA, Petcov ST, Petrov VA, Pich A, Piepke A, Pomarol A, Profumo S, Quadt A, Rabbertz K, Rademacker J, Raffelt G, Ramani H, Ramsey-Musolf M, Ratcliff BN, Richardson P, Ringwald A, Roesler S, Rolli S, Romaniouk A, Rosenberg LJ, Rosner JL, Rybka G, Ryskin M, Ryutin RA, Sakai Y, Salam GP, Sarkar S, Sauli F, Schneider O, Scholberg K, Schwartz AJ, Schwiening J, Scott D, Sharma V, Sharpe SR, Shutt T, Silari M, Sjöstrand T, Skands P, Skwarnicki T, Smoot GF, Soffer A, Sozzi MS, Spanier S, Spiering C, Stahl A, Stone SL, Sumino Y, Sumiyoshi T, Syphers MJ, Takahashi F, Tanabashi M, Tanaka J, Taševský M, Terashi K, Terning J, Thoma U, Thorne RS, Tiator L, Titov M, Tkachenko NP, Tovey DR, Trabelsi K, Urquijo P, Valencia G, Van de Water R, Varelas N, Venanzoni G, Verde L, Vincter MG, Vogel P, Vogelsang W, Vogt A, Vorobyev V, Wakely SP, Walkowiak W, Walter CW, Wands D, Wascko MO, Weinberg DH, Weinberg EJ, White M, Wiencke LR, Willocq S, Woody CL, Workman RL, Yokoyama M, Yoshida R, Zanderighi G, Zeller GP, Zenin OV, Zhu RY, Zhu SL, Zimmermann F, Anderson J, Basaglia T, Lugovsky VS, Schaffner P, and Zheng W (2020) Review of particle physics. *Progress of Theoretical and Experimental Physics* 2050-39112020(8): 08. https://doi.org/10.1093/ptep/ptaa104.

Electron and positron sources

D Alesini[a], **M Ferrario**[a], **and A Variola**[b], [a]Laboratori Nazionali di Frascati (L.N.F) of Istituto Nazionale di fisica Nucleare (I.N.F.N), Frascati, Roma, Italy; [b]Sezione di Roma1 of Istituto Nazionale di Fisica Nucleare (I.N.F.N), c/o Dipartimento di Fisica, Edificio, G. Marconi, Roma, RM, Italy

© 2024 Elsevier Ltd. All rights reserved.

This is an update of S. Tazzari, M. Ferrario, Electron and Positron Sources, Editor(s): Franco Bassani, Gerald L. Liedl, Peter Wyder, Encyclopedia of Condensed Matter Physics, Elsevier, 2005, pp. 42–52, ISBN 9780123694010, https://doi.org/10.1016/B0-12-369401-9/00632-X.

Introduction **461**
Basic beam dynamics elements 461
Electron sources **462**
Time structure of electron beams 463
Electron guns 463
Thermoionic cathodes 463
Photo cathodes 465
Field emission cathodes 466
Beam manipulation systems 467
Frontiers in electron sources development 468
Positron sources **469**
Slow positrons 469
Moderation 470
Photoproduction 471
Positron capture 471
Photon production separation 472
Generation by lasers 473
Conclusion **473**
References **473**

Abstract

Particle accelerators and sources are currently used for scientific, technological and medical applications. These devices provide low or high energy, charged or neutral particle beams employed as a function of their physical characteristics, like the current, the density, the beam duration, size and divergence. Electron sources play an important role in this context because they are easy particles to produce and because relatively simple technological systems of reasonable cost can be used to generate electron beams. Positron sources, have recently acquired an increasing interest in medical science and material diagnostics. In this chapter, the concept of particle source and the main designs and characteristics of electron and positron sources will be illustrated.

Key points

- Introduction of the particle source concept and the associated quality parameters
- Time structure of the electron beams
- Description of the different type of electron guns
- Description of the electron beams manipulation systems
- Overview of the future developments in electron sources
- Description of the positron production mechanisms
- Radioactive sources and energy moderation mechanism
- Positron photoproduction and beams separation
- Description of the main positron sources capture systems.

List of symbols

B, B_n	Brightness, normalized brightness
β	Reduced velocity v/c
c	Speed of light

https://doi.org/10.1016/B978-0-323-90800-9.00224-9

γ	Lorentz factor
γ_{ph}	High energy photon
e	Electron charge
e^-, e^+	Electron, positron
E_o	Particle rest energy
E	Energy
E_e	Electron energy
ε, ε_n	Emittance, normalized beam emittance
I	Beam current
I_b, $\widehat{I}_b$	Bunch current, peak bunch current
m_o	Particle rest mass
m_e	Electron rest mass
N	Number of particles
p, n	Proton, neutron
$\vec{P}$, $\vec{P}_o$	Momentum, nominal beam momentum
$\vec{p}$	Relative momentum deviation $\vec{P} - \vec{P}_o$
q	Charge
Q	Quality factor
QE	Quantum efficiency
r_e	Classical electron radius
s	Longitudinal coordinate
σ	Cross section
τ	Bunch duration
v	Velocity
V	Voltage
$e\phi_w$	Work function
$e\phi_{eff}$	Effective work function
ω_L	Laser frequency, laser photon energy
X_o	Radiation length
x, y	Horizontal, vertical coordinates
z	z stands for either x or y
Z	Atomic number

Introduction

A particle source is a device producing *particle beams* with well-defined and controlled intensity, divergence, mean energy and energy spread. Electron beams are used in science and technology to both investigate and modify matter, and as components of several electric and electronic devices. They are produced directly via *thermal*, photo or *field emission processes*. Positrons are mainly used in science and produced directly in radioactive decays or indirectly via *photon annihilation* in electron-positron pairs. Different types of sources are used for different applications.

Once produced, particle beams are accelerated by DC or alternating (RF) *electric field*, handled and transported using *electric* or *magnetic* components equivalent to lenses and prisms for light beams transport systems. One therefore speaks of *beam optics*. Because particles are charged, space charge, radiation and other possible forces between particles, including those mediated by the beam environment, have to be taken into account in addition to optical aberrations.

The main parameters characterizing a particle beam are energy E, energy spread ΔE, momentum, current I and brightness B. The beam current is defined as $I = qN\beta c$, q being the particle charge, βc the particle velocity and N the number of beam particles. Brightness is a measure of the current flowing through the unit area and solid angle and ultimately of the current that, for given energy spread and optics, can be focused onto a spot of given size: for given current, the higher the brightness the smaller the spot, down to the diffraction limit. A brief introduction to beam dynamics, given below, is required to precisely define the relations between these parameters.

Basic beam dynamics elements

The equivalent of the optical axis in a beam *optical* transport system is the trajectory followed by an ideal *reference particle* having the nominal beam momentum $\vec{P}_o$ and initial position $\vec{x}_o$ at the center of the magnetic quadrupoles. Position and momentum of the generic beam particle are defined relative to those of the reference particle and described by a point in the six dimensional phase space whose coordinates (x, p_x, y, p_y, s, p_s) are functions of the coordinate s along the trajectory, the reference particle always occupying the origin. Introducing the familiar from optics angular coordinates x', y', the prime indicating the derivative with respect to s the 6-D phase space reduces to $[x, \beta\gamma x', y, \beta\gamma y', s, p_s]$, with γ the reference particle *Lorentz factor*.

Let us now consider an ideal paraxial beam of N non-interacting particles (forces between particles negligibly small), subject only to external conservative forces (no radiation) with constant or slowly varying momentum P_0 and p_x, $p_y \ll P_0$. In this case the transverse $[x, \beta\gamma x', y, \beta\gamma y']$ and longitudinal $[s, p_s]$ phase space projections become (to first order in the coordinates) uncoupled and it can then be shown (*Liouville's theorem*) that the volume and area respectively occupied by the beam particles in each of the two projections are constants of motion. From the invariance of the beam occupied area in $[s, p_s]$ there follows that $\triangle E/I$ is a constant of motion. In transverse phase space let first consider a cylindrically symmetric beam with radius r and angular half aperture θ: the occupied volume $(\beta\gamma)^2 \triangle S \triangle \Omega \approx \pi^2(\beta\gamma r\theta)^2 \approx \pi^2\varepsilon_n^2$, with $\triangle S$ the beam cross section and $\triangle\Omega$ the beam subtended solid angle, is invariant and so is the here defined quantity ε_n called energy-*normalized* (or *reduced*) beam *emittance*. Note that because the invariant quantity is $\beta\gamma r\theta$, the physical emittance $\varepsilon = \pi^2(r\theta)^2$, which is in practice the relevant quantity, becomes smaller as the beam is accelerated. The *normalized brightness* is defined as $B_n = I/\pi^2\varepsilon_n^2$ and is seen to be none other but the normalized phase space current density. As one intuitively expects, the smaller the beam radius and angular aperture the brighter the beam. More generally, when motions in x and y are uncoupled, the *horizontal* and *vertical* normalized emittances, $\beta\gamma \int z' dz = \pi\varepsilon_{nz}$ (z stands for x or y), are also separately constant. The corresponding normalized brightness value is $B_n = I/\pi^2(\varepsilon_{nx} \cdot \varepsilon_{ny})$. Here the factor π in the definition of ε_{nz} arises from the beam boundary in two dimensional phase space being an ellipse in the simple case of external forces linear in the particle displacements. For a Gaussian beam with standard deviations $\sigma_z(s)$ and $\sigma'_z(s)$ (z standing for either x or y) the most used expression is $\varepsilon_{nz} = \beta\gamma\sigma_z\sigma'_z$.

When dealing with non-ideal, irregular beam shapes and current densities, it becomes useful to introduce the *rms* (or *average*) normalized beam emittance $\pi\varepsilon_{nz}^{(rms)}(s) = \sqrt{\langle z^2\rangle\langle(\beta\gamma z')^2\rangle - \langle z\beta\gamma z'\rangle^2}$, the expression $4\pi\varepsilon_{nz}^{(rms)}$ being used by most authors to define the actual "beam stay clear" envelope in physical transverse space. The corresponding *rms* beam brightness is $B_n^{(rms)} = I/(16\pi^2\varepsilon_{nx}^{(rms)}\varepsilon_{ny}^{(rms)})$.

Note finally that when in real life one has to deal with nonlinear optical elements and internal forces the *rms* normalized emittances are no longer invariant. They will in general depend on the beam local current density, tending to blow up during beam acceleration and transport and thereby spoiling $B_n^{(rms)}$. A great amount of theoretical and experimental work has and is therefore been devoted to methods and techniques to minimize the final output brightness deterioration particularly of high current sources. Last, keeping the beam energy spread small is also important particularly to reduce chromatic aberrations; the ratio of $B_n^{(rms)}$ to the beam relative momentum (energy) spread $\triangle p/P_0$, called *rms* normalized *spectral brightness* or *brilliance*, B_{ns}, quantifies this aspect.

Also note that the brightness is often defined in literature either incorrectly, simply as a current density $B = \triangle I/(\triangle S \triangle \Omega)$, or correctly, in normalized form, as $B_{nV} = I/(\triangle S \triangle \Omega V)$, qV being the reference particle kinetic energy. B_{nV} and the adimensional energy dependence definition B_n are related through equation $B_n = (E_0/q)B_{nV}$, with E_0 the particle rest energy.

Electron sources

Electron sources are used to drive a great variety of devices such as power tubes, klystrons, electron microscopes, X rays vacuum tubes and linear accelerators (linacs) for industrial, medical and scientific applications (Gilmour, 2011; Faircloth, 2021). The main objective of an electron source and, more generally, of an electron injector, is therefore to generate an electron beam with a current, longitudinal and transverse particles distribution, and energy, suitable for a specific application.

The general structure of an electron injector is given in Fig. 1, where the three main components are put in evidence: the cathode, the pre-acceleration and beam manipulation systems. The cathode is the source of electrons and can be furthermore divided into three main categories based on the emission mechanism: thermoionic, photo-electric or field emission cathode (Dowell, 2008). Immediately after the source the beam is pre-accelerated by continuous (DC) or radiofrequency (RF) electric fields. The systems composed by the cathode and the pre-acceleration system is usually called electron gun. In the beam manipulation section, electric or magnetic fields are used to make a beam "conditioning" in the transverse and longitudinal planes matching the beam to

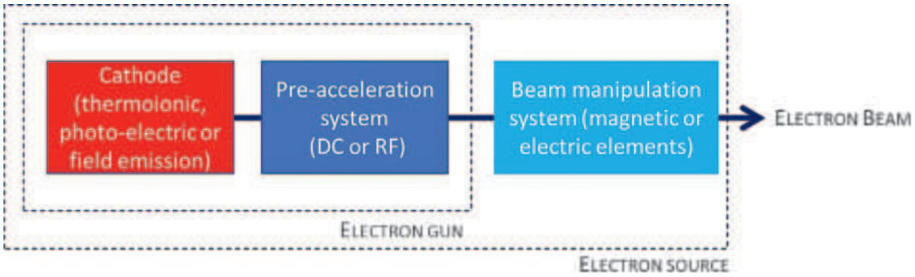
Cathode (thermoionic, photo-electric or field emission)
Pre-acceleration system (DC or RF)
Beam manipulation system (magnetic or electric elements)
ELECTRON BEAM
ELECTRON GUN
ELECTRON SOURCE

Fig. 1 General structure of an electron injector.

subsequent beamline systems or acceleration stages. In particular, in this section, the effects of space charge forces or aberrations have to be properly compensated to avoid degradation of the beam quality.

Time structure of electron beams

The electron beam at the output of a source has the typical beam time structure shown in Fig. 2: the beam is a train of macro-pulses, with duration T_P and repetition frequency $f_{rep} = 1/T_{rep}$. The macro pulse can be a continuous beam or a train of bunches. The second case refers to the RF electron sources and the relatively short bunches have a bunch spacing T_B with a repetition frequency $f_B = 1/T_B$ that is a is a subharmonic of the RF accelerating field frequency $f_{RF} = 1/T_{RF}$. The ratio $DC = T_P/T_{rep}$ is called Duty Cycle and is typically expressed in percent. Pulsed electron sources have Duty Cycles from a fraction of percent up to several percent, while continuous sources have, by definition, a Duty Cycle equal to 100%. In the case of a RF injector operating continuous mode we usually refer to a CW (Continuous Wave) operation.

Electron guns

An electron gun consists of a cathode, the primary emitter of low energy electrons, and of a system to pre-accelerate the electrons and shape them into a beam. The three fundamental emission processes are: thermoionic emission, photo-electric emission and field emission (Dowell, 2008; Faircloth, 2021).

The electron temperature of the emission process determines the lower limit of the achievable beam emittance that is often called the thermal emittance (or intrinsic emittance), due to the Maxwell-Boltzmann (MB) distribution of thermoionic emitters.

The electron emission process can be understood looking at the behavior of the electric potentials at the cathode surface that is given by three main term: the work function, the image charge potential and the applied electric field as given by the formula:

$$e\varphi = e\phi_w - \frac{e^2}{16\pi\varepsilon_0 z} - eE_z z$$

Where $e\phi_w$ is the material work function (the minimum energy needed to remove an electron from a solid to a point immediately outside of the solid surface), E_z is the applied electric field and z is the distance from the surface. The graphical representation of the electric potential is given in Fig. 3. Electrons with energies larger than the work function can be emitted, as in the case of thermoionic and photo-emission, while those with lower energy can tunnel through the barrier as in the case of field emission. In this last case if the barrier height is lowered by an external electric field, the process is called Schottky emission.

Thermoionic cathodes

The first way to extract electrons is to heat a material to a high temperature (Herring and Nichols, 1949). When the material is heated, electrons can populate excited states above the Fermi level according to the Fermi-Dirac distribution. Electrons with an energy greater than the Work Function ($e\phi_w$) can escape the surface of the cathode. The thermoionic emission is the resulting flow of electrons extracted from the heated material. The application of a negative voltage helps to extract electrons from the surface (and accelerates them) also providing focusing forces.

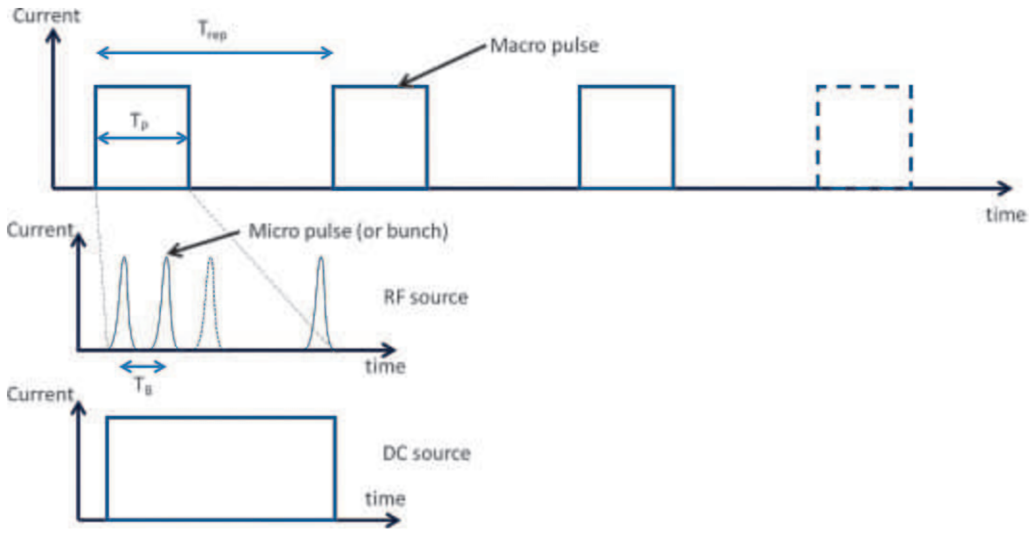

Fig. 2 Typical time structure of an electron beam at the output of a source.

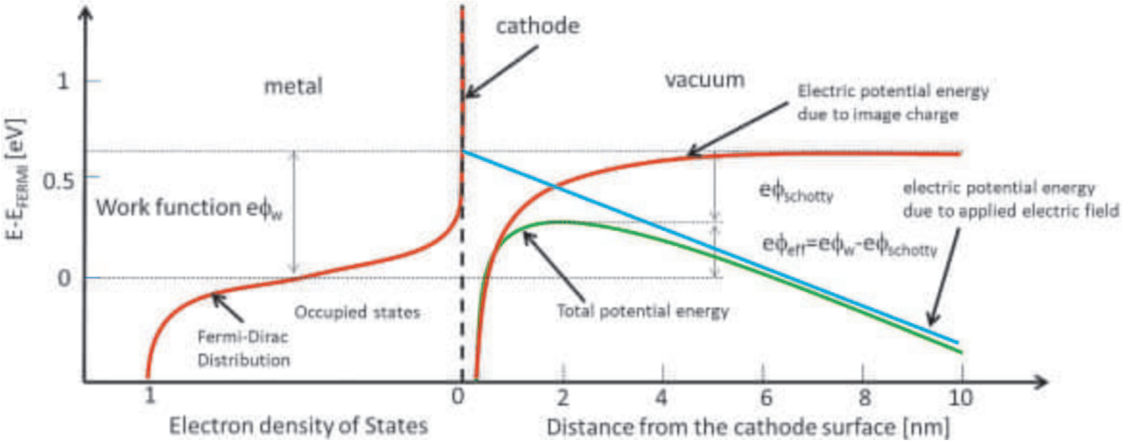

Fig. 3 Potential energy barrier near the cathode surface within 10 nm of a metallic surface (right) and density of occupied states (left).

The theoretical maximum extracted current density is given by the Richardson-Dushman equation:

$$J_{RD} = AT^2 e^{\left(-\frac{e\phi_w}{k_B T}\right)}$$

where $A \cong 120[A/cm^2K^2]$ is a constant, T is the temperature and $k_B = 8.6 \cdot 10^{-5}[eV/K]$ is the Boltzmann constant. The exponential dependence from the temperature, illustrates how thermoionic current rises rapidly with temperature, and with decreasing work function.

For this reason, cathode material should have relatively low work function and/or high melting temperature. Typical materials are Tungsten ($e\phi_w = 4.53$ eV) that is heated at temperature above 2000 W, or low work function composite, such as LaB_6 crystals that has a lower work function (2.66 eV) and is heated at 1500–2000 K. Typical reachable Richardson-Dushman density currents are $J_{RD} = 10–100$ A/cm^2.

Thermoionic guns can be metal filaments (typically W) directly heated with current flowing in the filament itself, or disc-shaped thermoionic emitters with a retro heating system, as given in Fig. 4. Depending on their main application they can be loosely classified into low DC current, high brightness devices, designed for "micro-applications" such as electron microscopy, material analysis and processing, micro lithography, micro machining and medium-high average (DC or pulsed) current sources to drive devices such as klystrons and linacs for scientific and industrial applications.

For the first class of applications currents from nA up to μA and extremely low emittances are required. Since, for thermoionic cathodes, the thermal contribution to the normalized emittance scales as $\varepsilon_{th} \approx \sigma_x \sqrt{k_B T / m_e c^2}$, where σ_x is the rms spot size of the source and T is the cathode absolute temperature, "needle" cathodes are used in combination with DC accelerating system that allows also to collimate, collect and focus the beam (Wehnelt cylinder). The use of high accelerating fields allows also to lower the

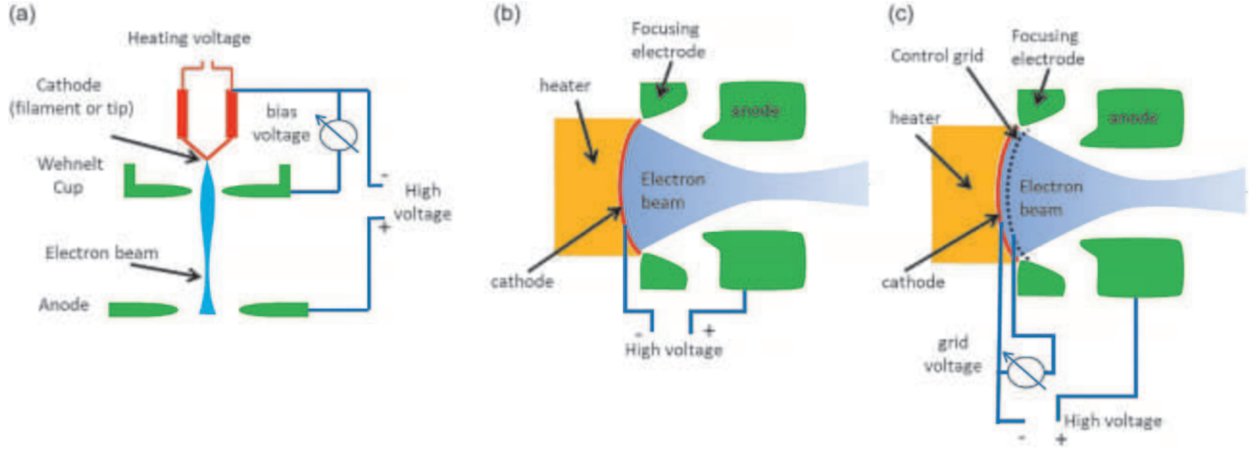
(a)
Heating voltage
Cathode (filament or tip)
bias voltage
Wehnelt Cup
-
High voltage
+
Electron beam
Anode
(b)
Focusing electrode
heater
anode
Electron beam
cathode
-
+
High voltage
(c)
Control grid
Focusing electrode
heater
anode
Electron beam
cathode
grid voltage
High voltage
-
+

Fig. 4 Different types of thermoionic cathodes: (a) W filament for micro applications; (b) diode system for high current devices; (c) triode system for low and medium current sources such as linacs for industrial and scientific applications.

operating temperature due to the Schottky effect, reducing the required working temperature T and making for longer cathode lifetime. Nanometer size spots at the sample can be obtained with very small normalized emittances ($\varepsilon_n \approx 10^{-2} - 10^{-5}\mu m$) with resulting normalised brightness that exceed $10^{12} A/(m \cdot rad)^2$ and energies from a few tens up to few hundreds of keV and energy spread in the 10^{-5}range.

For the second class of applications the cathodes consist of a high melting-point metal disc coated with a low work function material and indirectly heated by a filament. The most used material is Ba or Sr oxide coated tungsten having a work function of $\approx 1.6\ eV$ and capable of $10 - 20\ A \cdot cm^2$ at temperatures of $\approx 1500\ K$. Because, in the high temperature and high voltage environment the coating tends to be removed rather rapidly by desorption, sputtering and evaporation, dispenser cathodes have been developed made of porous tungsten impregnated with oxide which slowly diffuses towards the cathode surface, continuously replacing the removed material. Operated in good vacuum ($\leq 10^{-7} hPa$) a dispenser cathode can typically reach useful lifetimes in the order of 40000 hours. The gun voltage and current specifications vary widely, depending on the application, from the 10 – 100 kV/ 1 – 10A of Linac guns to the 100 – 500 kV/ 100 – 500A of klystron guns. Pulsed beam configurations are obtained by pulsing either the anode voltage (diode configuration) or a grid between the cathode and the anode (triode configuration). The first technique is generally used for high voltage, high current klystrons. In this case, between the cathode and the anode the beam is transversely focused using external solenoids that allow to keep under control the beam emittance increase due to space charge forces. Triode configurations are, indeed, used for low and medium voltage sources such as linacs for industrial and scientific applications. Thermoionic cathodes basically emit a continuous beam that can be modulated by pulsing either the anode or the grid voltage at the level of several ns up to ms level. To allow RF acceleration in the further stages of the linac, the beam has then to be manipulated, as illustrated in the following sections, using special RF cavities that allow to bunch the beam.

For this class of thermoionic guns the self-generated beam field reduces the effective voltage on the cathode, thus limiting the beam intensity with respect to the ideal Richardson-Dousmann theoretical value. This regime is called space charge limited Child-Langmuir regime and the maximum current which can be extracted from the cathode can be expressed as: $I = P \cdot V^{3/2}$, being P a constant, characteristic of the device geometry, called perveance. Its measurement unit is the perv = $A/V^{3/2}$ and typical values are few μperv.

Cathode and anode geometries are also designed following the criteria firstly developed by Pierce that proposed to adopt spherical shapes to provide radial focusing forces and increase the beam quality in term of uniformity and emittance (Pierce, 1949). Normalized emittance and brightness values lie typically in the $\varepsilon_n \approx 10^{-3} - 10^{-1} m$ and $B_n \approx 10^8 - 10^{11} A/(m \cdot rad)^2$ range respectively.

Photo cathodes

In the photo emission process, the cathode is illuminated by a laser pulse, electrons within the material can absorb the energy of photons and, if this energy is larger than the material work function, the electrons can be ejected (DuBridge, 1933). The photo-electric emission in several material is described by the Spicer's three step model (Spicer, 1958): the photon absorption by the electron, the electron transport to the surface and the escape through the barrier. The model allows to theoretically derive the two main important quantities that characterize a photo-cathode: the quantum efficiency (QE) that is defined as the number of emitted electrons per photon impinging on the cathode, and the normalized intrinsic (or thermal) emittance (ε_{th}) that represents the minimum possible achievable emittance value for a given injector. This second quantity, for a metallic cathode, is given by:

$$\varepsilon_{th} \approx \sigma_x \sqrt{\frac{\hbar\omega - e\phi_{eff}}{3 m_e c^2}}$$

where σ_x is the rms laser spot size, $e\phi_{eff}$ is the effective work function and includes the effect of Schottky reduction of the barrier in the presence of an applied electric field (E_z): $e\phi_{eff} = e\phi_w - e\phi_{Schottky} = e\phi_w - e\sqrt{eE_z/4\pi\varepsilon_0}$. Photocathode materials can be metal or semiconductors. For a semiconductor cathode $e\phi_w$ in the formula has to be substituted with the sum of the valence-conduction bandgap energy (EG) and electron affinity (EA) (Dowell et al., 2010).

Metal photocathodes (typically Cu, Mg, Nb and Pb) are robust, can operate at relatively high operation pressures ($<10^{-8}$ mbar), and due to the high work function, require UV photons ($\sim$250 nm). They typically have QE, in the 10^{-4}–10^{-5} range. An interesting and significant increase in QE occurs when the metal is coated with a few angstroms of CsBr. In this case QE can be enhanced by a factor of 50. The theoretical thermal emittance ($\varepsilon_{th}/\sigma_x$) for metallic cathodes is in the range 0.5–1 μm/mm(rms).

Semiconductor cathodes are typically alkali-telluride (as the most common Cs_2Te) or alkali-antimonide materials. They can reach QE larger than 5% and intrinsic emittances comparable with the metallic one but they have to operate at very low pressure ($<10^{-9}$ mbar) to avoid deterioration of their performances. Also for these cathodes UV photons are requires. Multi-alkali antimonide semiconductors (Na_2KSb or K_2CsSb) show QE larger than 10% but have to operate at extremely low pressure ($<10^{-10}$ mbar) to avoid contamination and maintain their performances. The last family of semiconductors is represented by the negative electron affinity (NEA) cathodes (as GaAs) that can operate with longer laser wavelength (500–800 nm) and, illuminated with polarized light, allow for 80–90% polarized beams.

The last key factor of photo-cathodes is the temporal response of photo-emitted electrons with respect to the laser pulse. Metallic cathodes have response time lower than a picosecond while semiconductor typically higher than few picoseconds.

As already pointed out in the previous section, thermoionic cathodes basically emit a continuous beam that can be modulated and properly bunched. On the contrary with photocathodes, the beam micro-structure can be directly generated by modulating the

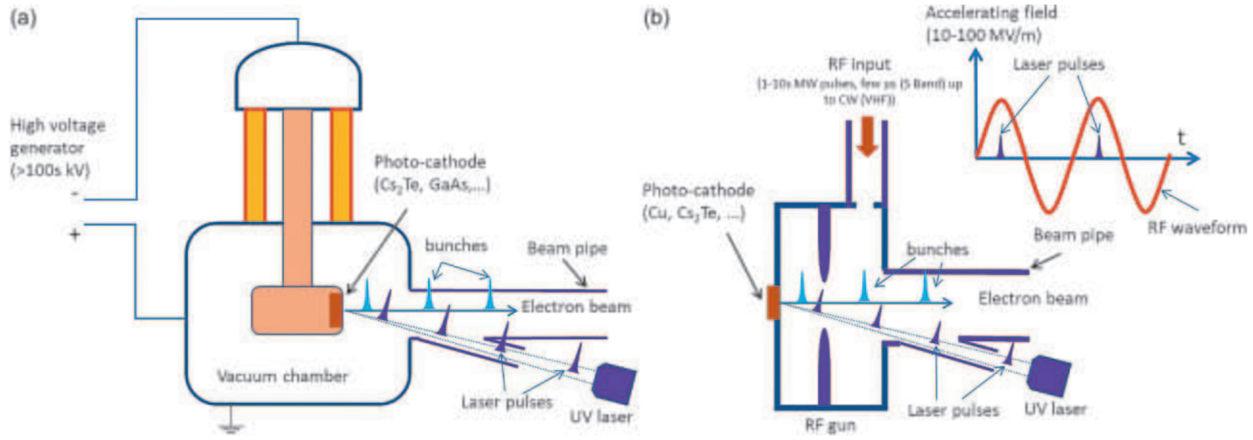
(a)
High voltage generator (>100s kV)
-
+
Photo-cathode (Cs$_2$Te, GaAs,...)
bunches
Beam pipe
Electron beam
Vacuum chamber
Laser pulses
UV laser
(b)
Accelerating field (10-100 MV/m)
RF input
(1-10s MW pulses, few μs (S Band) up to CW (VHF))
Laser pulses
t
Photo-cathode (Cu, Cs$_2$Te, ...)
RF waveform
Beam pipe
bunches
Electron beam
RF gun
Laser pulses
UV laser

Fig. 5 Schematic layouts of photo-guns: (a) DC; (b) RF.

drive laser pulse length, shape, spot size, and intensity on a pulse-to-pulse basis. This characteristic allows the generation of short (<ps for metallic cathodes as example) electron bunches that can be also further compressed in the other stages of the acceleration. This allows to drive free electron laser (FEL) and Compton based sources and to implement techniques such as laser and plasma-wave acceleration for a future generation of compact particle accelerators. For ps bunches with charge larger than few tens of pC, the space charge forces, that scale with the peak current and $1/\gamma^2$, tend to blow out the beam emittance and, for this reason, the beam has to be accelerated to relativistic energies as fast as possible. This is done through DC or RF accelerating fields, as illustrated in Fig. 5. In DC photo-guns the generated electron beam is accelerated by static electric field between the photo-cathode and the anode. Voltages in the 100–400 kV range and accelerating field lower than 10 MV/m are typically implemented. Larger voltages cannot be applied because of the risk of electric-field breakdown in the vacuum chamber. This limits the maximum performances in term of achievable peak current and charge density, related to the reachable cathode peak field, but allow operation at very high Duty Cycle up to CW. In room temperature RF guns the cathode is integrated in an accelerating cavity with oscillating electromagnetic fields (Rao and Dowell, 2014). They typically operate in S band (3 GHz) in pulsed regime with Duty Cycle less than 1% and cathode peak field in the range of 100 MV/m with output energies of several MeV (Alesini et al., 2018). L band (1 GHz) guns with cathode peak field <60 MV/m have been developed for high Duty Cycle (>1%) accelerators (Dwersteg et al., 1997). RF guns operating at lower frequency (VHF Band, ~200 MHz) have been also design and implemented for CW operation because of the larger sustainable average dissipated power with ~20 MV/m cathode peak field and output energies ~1 MeV (Sannibale et al., 2012).

In high Duty Cycle guns (DC or RF), cathodes are semiconductor because of the lower average energy required for the laser system impinging the cathode itself (Smolenski et al., 2009; Gulliford et al., 2013). This requires an extremely good vacuum performances and operating pressure to guarantee the cathode lifetime (Musumeci et al., 2018).

A strong R&D activity is now in progress in several laboratories and is related to the development of superconducting RF guns (Arnold and Teichert, 2011; Petrushina et al., 2020). The potentialities of these type of guns are related to the fact that they can, in principle, operate with high cathode peak fields, in CW mode, with cathode peak field larger than 100 MV/m, but there are limitations due to the applicable magnetic field (necessary for beam emittance compensation processes) and insertion of photo-cathodes in a superconducting operating system.

High cathode peak field guns (>80–100 MV/m) have also to cope with the charge emitted by field emission and called "dark current" because is emitted from the cathode surface and cavity wall even without laser (Shu et al., 2021). This current is emitted in the negative RF half-wave in all RF periods and can drive a total charge in the RF pulse that superimposed to the photo-emitted bunch current. Cleaning procedures and surface treatments have to be implemented in order reduce this dark current thus avoiding activation of components, damages of instrumentation and background for experiments.

Field emission cathodes

Field emission (FE) occurs under the influence of very high electric field at the level of 10^7–10^9 V/m (Murphy and Good, 1956). Under the effect of such high electric field, electrons near the Fermi level quantum mechanically tunnel through the barrier and useful emission currents can be achieved. The Fowler-Nordheim theory describes this process. Because of the relatively low current but extremely high reachable brightness, they are used, typically, as source of ultra-high resolution scanning (transmission) electron microscopes (S(*T*)EM) (Krysztof, 2021).

A field emission cathode is, typically, a tungsten needle with radius smaller than 100 nm settled on a Tungsten hook with a negative bias voltage of several kVs applied to the cathode and electric fields that can overcome the 10^9 V/m values. With these sources, it is possible to obtain a current density of 10^5 A/cm^2 (that is orders of magnitude larger than that of a thermoionic emission).

FE guns can be Cold Field Emitters (CFE), Thermal Field Emitters (TFE), Schottky Field Emitters (SFE). In CEF the emission derives from a few nanometers area and it is independent from the source temperature. The beam is focused and accelerated by two anodes with a bias voltage of few 3–5 kV. A bias voltage of several tens of kVs between the second anode and the cathode accelerates the electrons at the required energy. Even if the total current is relatively small (1–10 μA), the brightness is particularly high ($>10^{12}$ A/(mrad)^2) thanks to the very small beam dimensions at the source and the beam dimensions at the sample can reach the nm level. TFE have the same properties of CFE, but they work at high temperatures thus reducing the noise and beam instabilities even at not perfect vacuum conditions. In SFE field emitters are coated with low working function materials such as ZrO_2 and the thermoionic emission is combined with field emission. Vacuum level is not as demanding as that one of CFE, but an ultrahigh vacuum allow for long-term stability, preventing poisoning of the ZrO_2 cathode. The larger source spot size in SFE is compensated by larger currents that can exceed the 50 μA level thus reaching comparable brightness.

Beam manipulation systems

After the guns, the emitted beam is focused and bunched to allow applications or further stages of acceleration. We can refer to these systems as beam manipulation devices. They have different configurations depending on the cathode type and applications.

In thermoionic guns used as sources of low energy (<10 MeV) industrial linacs, the continuous beam at few tens of keV, is directly injected in radiofrequency accelerating structures that have the first accelerating cells designed in order to capture a large fraction of the continuous beam current, allowing, also, bunching, as illustrated in Fig. 6a. For this reason this part of the linac is called "buncher." The bunching cells can be either integrated or separated with respect to the other stages of acceleration (Kutsaev, 2021). Typical few μs continuous beams at a repetition rate of few hundred Hz, are bunched in a microstructure having a bunch distance equal to the rf period used for the other stages of acceleration (typically 0.1–0.3 ns for operation in S and C Band). This relatively simple scheme allows to obtain capture efficiencies up to 40–50% with energy spreads of several percent and long bunch tails that are generated in the bunching process.

To improve the beam quality in term of bunch length and energy spread, "pre-bunchers" can be also adopted, as schematically illustrated in Fig. 6b. This is the case of high energy linacs used for scientific applications for which thermoionic gridded cathodes are used at voltages in the 100–200 kV range. Pre-bunchers are standing wave RF structures that modulate the energy of the continuous beam out from the gun. The energy modulation results in a velocity modulation and, after a drift space, in a density modulation, allowing a better capture of the beam. Other techniques implement choppers that are RF deflecting cavities sweeping, transversely, the continuous beam. The swept beam is then collimated and a microstructure with extremely good beam quality, in term bunch tails and energy spread, can be achieved.

The typical beam parameters, in term of emittances (in the range 0.1–1 μm), bunch length (several tens of ps with relatively long tails) and energy spread 1–5% that can be obtained in thermoionic-based linacs are not compatible with scientific applications that require extremely good beam performances. We refer, in particular, to linacs for FEL and high brilliance Compton sources where normalized emittances lower than 1 μm, energy spread of <0.1%, and bunch length < 1 ps with peak bunch current of few kA are required.

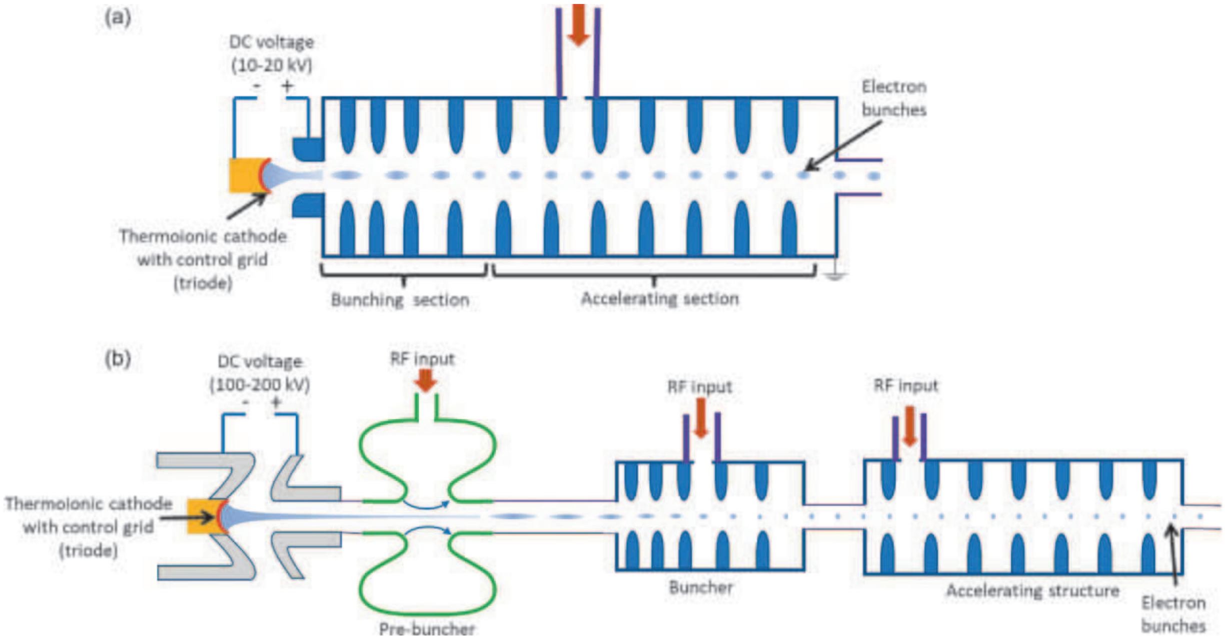

Fig. 6 Schemes of thermoionic based injectors for low energy industrial linacs (a) and high energy, high beam quality linacs for scientific applications (b).

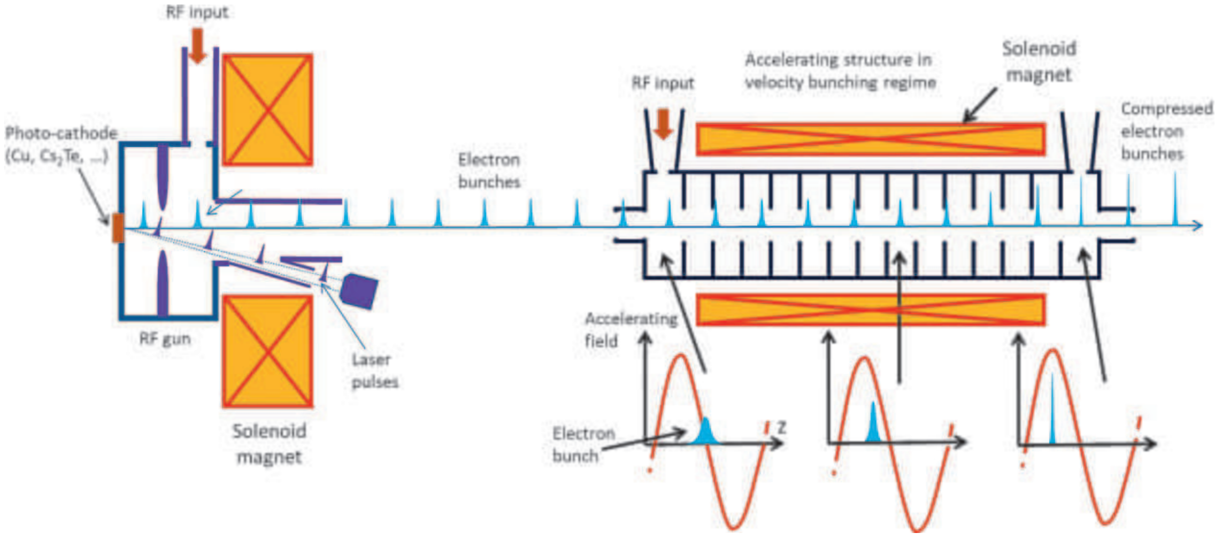

Fig. 7 Conceptual layout of an RF photo-injector with velocity bunching.

To reach these parameters RF photo-guns are typically used. A laser pulse, of a suitable wavelength, extracts the electrons from the cathode, embedded in the cavity. An external RF power source (klystron) excites the cavity accelerating mode so that the photo-electrons are immediately accelerated by the RF electric field on the cathode and all along the gun beam axis. Under the combined action of the RF accelerating field and of an external focusing solenoidal magnetic field, the dynamics of the electron beam, that has a typical charge of 0.1–1 nC, is guided and controlled and the effects of space charge, properly compensated (Serafini and Rosenzweig, 1997). The conceptual scheme is reported in Fig. 7.

Presently, the RF technology mostly used for RF Guns is the S-band (3 GHz). The S-band is used in particular, for facilities operating at low rep rate (frep $\leq \sim$ 100 Hz) low duty cycle ($<0.1\%$) single bunch, while lower frequency technologies (L-band, VHF) are used for higher rep rates and multi bunch linacs. According to beam dynamics studies, the higher the peak electric field on the cathode, the better the quality of the beam emerging from the gun. In this respect the S-band represents the state-of-the-art, providing typical peak fields of $\approx$120 MV/m on the cathode. Even taught larger values would be very much desirable to furtherly improve the beam quality, it was found experimentally to be very difficult to go beyond 120 MV/m in S-band based injectors. The limitation comes from the unacceptable increase of the RF breakdown rate (BDR) that is a complex phenomenon which depends on many aspects, such as conditioning time and strategy, construction quality, surface cleanliness, residual pressure. Synchronization systems have, also, to be carefully implemented to avoid jitters between the laser and the RF that results in unstable operation and oscillations in the beam parameters. Typical energies out from and RF photo-guns are in the range 1–7 MeV with normalized emittances in the range 1–2 μm, bunch length of few ps and peak bunch currents $<$100 A. In the case of multi bunch operation or high Duty Cycle facilities as, for example, the injectors for the energy recovery linacs, also DC photo-gun are used. As already pointed out, in this case, the cathode peak field cannot reach the value of RF photo-injectors and the extracted charge has to be reduces to avoid emittance increase due to space charge.

To further increase the bunch peak current after the rf gun, the longitudinal phase space can be manipulated. There are basically three techniques that can be used to this purpose: velocity bunching, ballistic bunching (Anderson et al., 2005) and magnetic compression (Di Mitri, 2018). In the first case the few MeV bunch is injected in an RF accelerating structure off-crest (typically at the zero crossing of the RF accelerating field) so that the head and tail are accelerated all along the structure with an head-tail different energy gain that results in a velocity modulation and a consequent reduction of the bunch length. The emittance is kept under control by adding focusing solenoids around the accelerating sections. Fig. 7 report this scheme of compression. The ballistic bunching mechanism work similarly but with a single standing wave cavity that kick the head and tail of the bunch immediately after the gun. This kick is converted into density modulation after a drift space as in the case of pre-buncher cavities for thermoionic guns. In the magnetic compression the bunch receive a head-tail energy chirp in the acceleration process and a magnetic chicane transform this energy chirp in longitudinal particle position variation thus allowing compression. The first two methods typically work at output energies from the gun of few MeV while the third one at energies above the 100 MeV level.

Frontiers in electron sources development

Frontiers in the research of electron guns include new types of RF injectors operating at very high cathode peak field ($>$150–200 MV/m) and high RF frequency (C band, 6 GHz), that allow to obtain extremely high-brightness beams with repetition rates up to 1 kHz (Alesini et al., 2022). Other schemes are exploring the possibility to integrate field emission cathodes (as carbon nanotubes) in RF guns avoiding the use of lasers or thermoionic processes (Faillace, 2015). The R&D activity involve also plasma gun based on laser driven plasma wake accelerators to be capable of GV/m electric fields, micrometer spot sizes, and femtosecond-long bunches. The schemes foresee a high intensity laser pulse that, injected in a gas (H2 as example) ionizes the gas itself thus creating an accelerating plasma wave able to directly generate and accelerate ~100 fs, <0.1 nC bunches with peak currents up to the kA. The technology research is also oriented to realizations of superconducting guns that, as already pointed out, allow to simultaneously achieve CW operation and extremely high cathode peak field.

Positron sources

At present, positrons beams are used in different fields and applications. At non relativistic energy (thermal sources) they can be very effective as probe for defect spectroscopy and detection in metals, semiconductors and isolators (Giley et al., 2006). In this framework the very high sensitivity is given by the attractive potential of the negative charged impurities. Slow positrons are also used for experimental activities in the field of electron-positrons plasmas, Positronium (Ps) decay and spectroscopy, Ps_2 molecule formation, Positron Annihilation induced Auger spectroscopy (PAES), Bose Einstein condensate and gamma ray production (gamma ray laser) thanks to the e^+- e^- 0.511 keV annihilation line at rest (Dupasquier et al., 2009). In the relativistic and ultra-relativistic regimes positrons beams are used in the framework of the high energy physics positrons-electrons (e^+- e^-) colliders. In this context leptons are particularly suited for the reduced background noise in respect to hadron colliders. Moreover e^+- e^- very high luminosity colliders are used to explore the intensity frontier in fundamental particle physics (Chaikovska et al., 2022). In the past, thanks to the suppression of the positive ions instability positrons had also be used in storage rings as synchrotron radiation sources, where a positron source was available (Besson et al., 1989).

Slow positrons

Slow positrons are usually produced by radioactive sources. As far as the positrons are concerned, the efficient process is the β^+ decay (Chehab, 1989) that, taking into account the conservation of charge, can be considered as the decay of a nucleus proton in a neutron with the emission of a positron and an electron neutrino:

$$\mathrm{p} \rightarrow \mathrm{n} + \mathrm{e}^+ + \nu_\mathrm{e}$$

resulting in a reaction in which an atomic nucleus decreases by one his atomic number:

$${}^{A}_{z}Y + \left[{}^{A}_{Z-1}K\right]^- + e^+ + \nu_e$$

Since the neutron mass is ~1 MeV bigger than the proton mass, this reaction is forbidden for isolate protons. The proton decay can be seen only in the nucleus, where the final daughter state has respectively greater binding and lower total energy in respect to the mother state. In this framework the total energy released in the β^+ decay must be higher than twice the electron mass,

$$Q = m\,({}_{Z}X) - m\,({}_{Z+1}X) - 2m_e$$

where m and m_e are respectively the mass of the generic atomic nucleus X and of the electron e, and Z is the nucleus atomic number. Typical positron emission spectrum is asymmetric bell shaped (see Fig. 8) with energies that typically go up to one MeV and large energy spread of hundreds of keV. Due to the handling requirements of radioactive sources usually long half time isotopes are

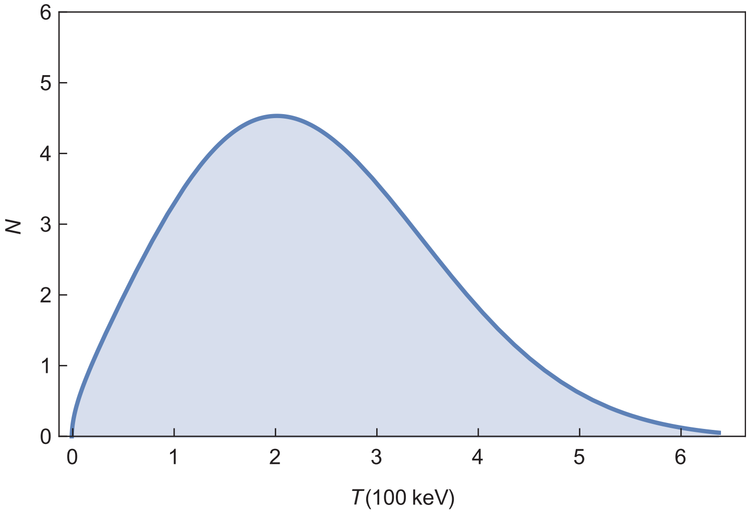

Fig. 8 Typical spectral distribution of positrons emitted by beta decay.

preferred like ^{22}Na (2.6 years) and ^{58}Co (71 days). ^{22}Na sources emission also presents a good positron emission efficiency resulting in the primary technique for producing low energy positrons by radioactive beta decays. Available sources give a maximum activity in the order of some GBq, from one to four.

Nuclear reactors can also be used to trigger p-n or n-γ reactions to produce positrons emitting isotopes (Ottewitte, 1987). Thanks to the high neutron flux it is possible to have typical reactions like

$$ {}_{z}A + n \rightarrow {}_{Z\mp1}A + \gamma $$

followed by the decay

$$ {}_{Z\mp1}A \rightarrow {}_{Z*1}B + \beta^{+} + \nu $$

A typical example is the reaction $^{63}\mathrm{Cu} + \mathrm{n} \rightarrow {}^{64}\mathrm{Cu} + \gamma_{\mathrm{ph}}$ decaying in $^{64}\mathrm{Cu} \rightarrow {}^{64}\mathrm{N} + \beta^{+} + \nu$. Other suitable positrons beams producing isotopes are, for example, ^{83}Sr, ^{76}Br. ^{72}As, ^{84}Rb, ^{26}Al and others, with different characteristics decay time, positron producing efficiency and reaction products.

Also p-n reactions can trigger positron production via some characteristics decay like:

$$ \mathrm{p} + {}_{Z}A \rightarrow n + {}_{Z}B $$

followed by

$$ {}_{Z}B \rightarrow {}_{Z}B + e^{+} $$

like for example:

$$ \mathrm{p} + {}^{17}\mathrm{O} \rightarrow {}^{17}\mathrm{F} + \mathrm{n} \text{ that gives} {}^{17}\mathrm{F} \rightarrow {}^{17}\mathrm{O} + \mathrm{e}^{+}. $$

In this framework the total rate of positron production is given by:

$$ \frac{dN_{e^{+}}}{dt} = B\,\sigma\,\varphi\,V\,N $$

Where B is the β^{+} branching ratio in respect to the disintegration events, σ is the positrons production cross section (for example in the reaction $\mathrm{p} + {}^{17}\mathrm{O} \rightarrow {}^{17}\mathrm{F} + \mathrm{n}$; $^{17}\mathrm{F} \rightarrow {}^{17}\mathrm{O} + \mathrm{e}^{+}$ its value is ~200 mb), φ is the thermal neutron flux, V the target volume and N its atom density. Thanks to the huge thermal neutron flux present in the nuclear reactors it is possible to increase the positron rate of orders of magnitude. Nevertheless, the difficulty in accessing nuclear plants in respect to a radioactive source is a basic limitation for this production scheme.

Moderation

All sources mentioned emit slow positrons isotropically and distributed in a large energy spectrum. Since all the applications require quasi monochromatic beams (and with a good directivity) it is possible either to have a spectrometer energy selection or to cool the emitted positrons in a thermal positron cloud that can be re-accelerated a posteriori by an applied electrostatic or electromagnetic field. The spectrometric selection is a classical and reliable scheme, but it suffers from a very poor efficiency due to the losses in the angle-energy selection. On the other side, it is possible to decrease the positron energy by introducing a solid or gaseous moderator with higher efficiency $\xi = N_{\mathrm{e+slow\ positron\ available}}/N_{\mathrm{e+fast\ positron\ emitted}}$. The cooling in gas is basically given by the positron energy loss due to molecular rotational and vibrational excitation. Appropriate gases are chosen so that positron annihilation cross section is low in a selected energy range. On the other side, the energy range in which these cross sections are high is fast passed due to the high probability for appropriate inelastic scattering processes. For example, the annihilation process like the positronium formation has a threshold at 8.5 eV, above this threshold thermal cooling is very effective due to rotational and vibrational excitations, thus reducing the positronium formation with the consequent positron annihilation. Below the threshold the positrons gas continues to cool thanks to the molecular interactions. Due to the high excitations cross sections mixtures of SF_6, CF_4 and CO_2 gases with N_2 are often employed as gas moderators.

The cooling in solid is mainly given by a first energy loss due to multiple inelastic scattering in the material bulk. After thermalization there is a finite probability for them to diffuse to the solid surface. When the solid has a negative work function for the positrons, they can be emitted perpendicularly with a spectrum peaked around the corresponding positron work function. The process efficiency is mainly limited by the backscattering reflection in the solid or by the positron loss processes like annihilation with bulk electrons or positronium formation. Typical solid moderators are realized in Tungsten (W with efficiency of 10^{-4} with a 0.3 eV energy distribution) or Nichel (Ni). With the techniques of solid rare-gas moderators, obtained by freezing Neon gas onto a metal surface at cryogenic temperature (8 K) (Mills and Gullikson, 1986), it is possible to increase the moderator efficiency to $\xi = 10^{-2}$. To increase the emission in a given direction it is also possible to integrate the radioactive source in systems made of a high Z reflection material to enhance the directivity of the emitted flux. A typical example, with the source integrated in the front of a tungsten support, is illustrated in Fig. 9.

The total efficiency of the moderator process gives the final available slow positrons flux, which, for radioactive sources, can go up to 10^{6} e^{+}/s whereas it can achieve 10^{8}–10^{9} useful e^{+}/s for the reactors isotopes.

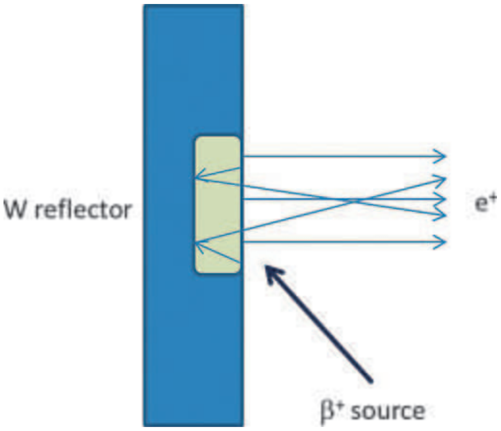

Fig. 9 Possible configuration β^+ source—W reflector to increase the source available flux.

To create at rest positron plasma (Jørgensen et al., 2005), buffer gas moderation can be inserted in a series of electrostatic electrodes with applied potential providing a longitudinal confinement and surrounded by a solenoidal field for the transverse one. After a first cooling phase the gas is extracted and the positrons are further respectively cooled and compressed by emitting photons by cyclotron radiation in the solenoidal field and by an applied torque given by a sinusoidal electric field imposed on splitted electrodes (rotating wall technique) (Danielson et al., 2006). At the end the cold positron plasma can be extracted by kicking the electrostatic potential of the last electrode. With this technique it was possible to merge cold positrons and antiprotons producing the first anti Hydrogen atoms at cryogenic temperature.

Photoproduction

As far as high relativistic and high intensity positron beams are concerned, their production is provided by the conversion of gamma rays, with energy higher than the electron-positron mass threshold $E > 1.022$ MeV, in the nuclear potential of the atoms of a target. The most popular scheme foresees a relativistic primary electron beam impinging on the target. The "primary" beam electrons interact with the target nucleus and they produce a high flux of soft and hard gamma rays by bremsstrahlung. These are subsequently converted in e^+- e^- pairs by the process $\gamma_{ph} + A \rightarrow A' + e^- + e^+$ with a cross section, similar to the bremsstrahlung one (Donahue, 1991) directly proportional to the square of the classical electron radius re and of the atomic number Z of the material and to a "screening effect" complex function $F(\gamma_{ph}, Z)$. This is known as the Bethe-Heitler process, to be distinguished from the trident process where the pair production takes place directly in the nucleus ($e \rightarrow e^- + e^- + e^+$), triggered by the electron coulomb field. Also in this case the cross section is proportional to the square of r_e and Z and to a complex function of γ. Usually the primary beam has energies in the range of 150–300 MeV with $0.3\text{–}3.10^{10}$ electrons per bunch, but in a high energy laboratory the positron production has also been performed at 3.7 and 33 GeV (Variola, 2014).

The mean free path for a high energy photon to convert in one pair in a solid is given by (7/9) X_0 where X_0 is the characteristic radiation length of the material (Tanabashi et al., 2018). The produced pairs immediately start to contribute to the γ_{ph} production with consequent other pairs conversions triggering the development of an electromagnetic shower with typical production yield in the order of few % GeV^{-1}. On the other side, low energy positrons lose their energy by ionization thermalizing in the material so contributing to the average heating. The equilibrium between cascade production and energy losses gives an optimized target length for the positron production around $3X_0$ for a primary beam of 1 GeV and it scales approximately as $\text{Ln}[\gamma]$. The target has to be designed to withstand both the average thermal stress and the high thermo-mechanical stress given by the temperature derivative in the target, expressed by the Peak Energy Deposition Density (PEDD), so avoiding the target failure. Typical melting temperature are 1940° for Ti, 3695° for W and 3460° for Re. PEDD threshold is given by experiments, a typical value shows 35 J/g for a $6X_0$ $W^{25}Re$ target (Bharadwaj et al., 2001). Due to the high melting point often ^{74}W, $^{76}W^{24}Re$ but also Ta have been preferred for positron sources (Chaikovska et al., 2022). To reduce the thermal deposition different design have been proposed like wire targets and granular targets based on 2 mm W spheres. When the thermal load is unsustainable by solid target different solutions have also been introduced, like liquid lead or Ti^6Al^4V rotating targets. In the last case the choice of Ti targets are justified by the reduced activation issues in low Z materials.

Positron capture

Energy losses and multiple scattering result in a loss of "memory" of the phase space characteristic of the primary beam providing high values of the 6D emittance of the final e^+ beam. To avoid very important losses at the source it is therefore mandatory to immediately insert a focusing system reducing the angular spread to the detriment of the geometrical size. This system is based on a decreasing solenoidal B field with high initial peak values at the target (up to 10 T) reduced to a constant value (typical value between 0.25 and 0.5 T). If this field reduction is adiabatic the system is called Adiabatic Matching Device, if the transition is abrupt it is known as Quarter Wave Transformer (QWT). Angular and radial acceptance of these systems is function of the peak and lower filed, of the particle momenta and of the geometrical system aperture (Chehab, 1989):

QWT

$$R = \frac{2\pi^2}{3}\left(\frac{eB_2a}{2}\right)^2\left(1-\left(1-\frac{1}{Sin^2\chi+\left(\frac{B_1}{B_2}\right)^2Cos^2\chi}\right)^{\frac{3}{2}}\right); \mathrm{A} = \frac{eB_1a}{2P}\left(1+\frac{B_2}{B_1}\right)$$

AMD

$$R = \frac{2\pi^2}{3}\left(\frac{eB_2a}{2}\right)^2; \mathrm{A} = \frac{e\sqrt{B_1B_2}}{P}a$$

Where R and A are the radial and the angular acceptance, B_1 and B_2 are respectively the maximum and the minimum magnetic field, a is the accelerating section iris radius (geometrical acceptance), P is the scalar momentum and χ is the rotation Larmor angle

$$\chi = \int \frac{eB}{2P}dz$$

Other focusing systems are based on Lithium lenses providing a very high B field azimuthal field at the target location. The focal strength is mainly limited by the maximum achievable current in the lens. The other technical limitation is given by the compatibility of lithium lenses in an ultrahigh vacuum environment.

After the transverse compression the longitudinal one is performed by a series of accelerating sections (longitudinal lenses) enclosed by solenoids providing the constant low B field to avoid positron losses due to the high divergence of the positron beam. Different RF longitudinal compression schemes are possible starting the positron capture in either accelerating or decelerating phase. At the end of the longitudinal and transverse positron capture typical positron fluxes range from 10^{10} to 10^{12} e^+/s.

Photon production separation

To further reduce the thermal deposition in the target the photon-primary electron beam separation is introduced in the positron source design. Taking into account a separated gamma source, with a consequent conversion of only the produced gamma rays beam, this excludes the heating given by the primary beam energy losses in the target. The basic scheme is illustrated in Fig. 10.

In this framework different schemes are taken into account. The first considers a very high energy primary beam injected in a helical undulator channel with a variable K (function of energy). This scheme allows the production of a large amount of gammas per primary electron bunch and at the same time provides photon circular polarization that will subsequently be transferred to the positron helicity. The main drawback is that to obtain the proper gamma energy for positron production it is mandatory to provide a very high energy primary beam (in the order of few hundreds GeV) (Adolphsen et al., 2013).

To reduce the primary beam energy to some GeV, another scheme takes into account the production of high energy gamma rays by Compton backscattering in dedicated facilities (Omori et al., 2006). High density electron beam collides with high intensity laser pulses resulting in a beam of backscattered gammas. Depending on the required photon energy it is possible to tune the frequency of the impinging lasers. Typical wavelengths are 515, 800 and 1030 nm. This solution has the advantage of the tunability and the polarization selection. The drawback is the low flux given by the Compton cross section resulting in less efficient positrons production.

Another explored configuration is given by the production of a "soft" gamma ray spectrum by channeling emission in a oriented crystal (Artru et al., 2005). The primary beam is sent to a crystal (typically W, Ge or Si) aligned on the $\langle 111\rangle$, or the $\langle 110\rangle$ axis. If the angle of incidence is lower than a characteristic critical angle $\theta_c = \sqrt{\frac{2V}{E}}$ with E the beam energy and V the potential given by the

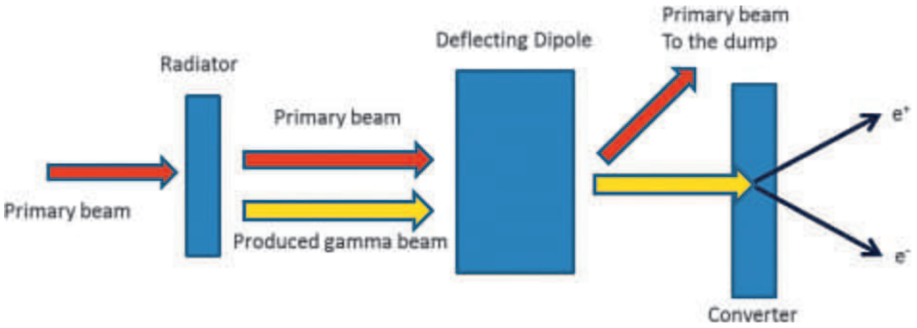

Fig. 10 The photon flux separation scheme is illustrated. The primary beam, after the emission of the gamma rays in the radiator, is discarded to a dump by a deflecting dipole. Only the produced gammas are subsequently converted in pairs.

atomic rows in the crystal, the particles undergoes a motion and a radiation emission similar to the wiggler one with periods of the order of several atomic separation distances. This scheme strongly enhances the production (factor ~5) in the soft part of the gammas spectrum in respect to the bremsstrahlung one. This allows a more efficient positron production in the energy range suitable for conversion and post capturing by the capture system. In this configuration it is not possible to provide polarized positrons.

Low intensity beams of polarized positrons are also obtainable by polarized bremsstrahlung, where the "classical" production scheme is performed with polarized electrons. Only selecting a small part of the produced positrons energy spectrum results in a good polarization degree, therefore reducing the achievable maximum current.

Generation by lasers

The increased capability of lasers system to deliver very short pulse length and higher peak power and intensity also opens the way to a new scheme of positron generation (Sarri et al., 2022). When a pulse of high intensity impinges on a solid target the electrons are accelerated in the very intense field and their quivering results in an acquired energy of:

$$E = m_e\left[1 + \left(\frac{eE_L}{m_e\omega_L}\right)\right]$$

Where m_e is the electron mass and ω_L and E_L are respectively the laser frequency and field. For a 10^{20} W/cm^2 class laser the electrons are accelerated up to energy of few MeV, sufficient for pairs' conversion in the target nuclei. This can be done through the two main primary processes respectively the Bethe-Heitler or the Trident one. The former dominates for thick high Z radiators, the latter for thin target (for example less than 30 μm for a gold foil). Promising experiments show that for a 120 J–$6\cdot10^{19}$ W/cm^2 laser on targets, a production of $2\cdot10^{10}$ e^+/sr was obtained with a positron population peak energy of 4–7 MeV and a spread of ~some tenths %.

More ambitious is the direct production of pairs in vacuum where the laser field must exceed the Schwinger critical field, 10^{28} W/cm^2. This is not achievable at the present status of technology, but production of high energy and highly collimated positron pairs have been produced in laser assisted experiments. In this experiment a "drive" 29.2 GeV electron beam undergoes Compton backscattering in an intense 0.6 J–527 nm laser field (Burke et al., 1997). The produced high energy gamma ray triggered the Breit-Wheeler process $\gamma_{ph} + \gamma_{ph} \rightarrow e^+ + e^-$ in its nonlinear form $\gamma_{ph} + n\omega_L \rightarrow e^+ + e^-$ (with ω_L = laser photon energy), interacting with many photons of the laser field. In this framework a low positron number per collision was produced (about 100). For a higher flux to be achieved for this very high brilliance source, a Lorentz parameter $\eta > 1$ (where the single Compton backscattering events become a coherent emission) and the Schwinger threshold with the laser need to be attained. In this scenario the emitted photon is fully in quantum regime (energy bigger than me) and there is an exponential increase of the emitted γ to the laser field interaction probability for positron emission.

Conclusion

Nowadays electron and positron sources provide high quality particle beams to different users communities. Their main quality parameters are represented by the beam emittance and brightness taking into account the occupied phase space and the beam intensity. Electrons are present in nature, their sources are based on emission mechanisms. On the other side positron sources needs either radioactive decay processes or secondary beams production, either by primary electron or photons beams. This makes electron source much more diffuse thanks also to their relative reduced costs. Electrons are also, at present, the most used particles for the generation of photons beams for the applied science, like in Synchrotron and Compton sources. At present many applications indicates the needs to conceive sources providing high average current but maintaining good values of the emittance. This requires not only in maximizing the production rates but also in providing more and more efficient beam manipulation systems, able to collect, shape and accelerate the produced beams.

References

Adolphsen, et al. (2013) *The International Linear Collider Technical Design Report—Volume 3.II: Accelerator Baseline Design*. arXiv:1306.6328.

Alesini D, et al. (2018) Design, realization, and high-power test of high gradient, high repetition rate brazing-free S-band photogun. *Physical Review Accelerators and Beams* 21(11): 112001.

Alesini D, et al. (2022) The new C band gun for the next generation RF photo injectors. In: *Proc. of the 13th Int. Particle Acc. Conf. IPAC2022, Bangkok, Thailand JACoW Publishing*, ISBN: 978-3-95450-227-1. https://doi.org/10.18429/JACoW-IPAC2022-MOPOMS021.

Anderson SG, et al. (2005) Velocity bunching of high-brightness electron beams. *Physical Review Special Topics—Accelerators and Beams* 8: 014401.

Arnold A and Teichert J (2011) Overview on superconducting photoinjectors. *Physical Review Special Topics—Accelerators and Beams* 14: 024801.

Artru X, et al. (2005) Summary of experimental studies at CERN on a positron source using crystal effects. *Nuclear Instruments and Methods in Physics Research Section B* 240: 762.

Baptiste K, et al. (2009) A CW normal-conductive RF gun for free electron laser and energy recovery linac applications. *Nuclear Instruments and Methods in Physics Research* A599: 9–14.

Besson JC, et al. (1989) Super-ACO: Results on a positron low emittance ring. *Review of Scientific Instruments* 60(7): 1373–1376.

Bharadwaj V, et al. (2001) Analysis of beam-induced damage to the SLC positron production target. In: *Proceedings of the 2001 Particle Accelerator Conference, Chicago, IL, U.S.A., 18–22 June*, pp. 2123–2125.

Burke D, et al. (1997) Positron production in multiphoton light-by-light scattering. *Physical Review Letters* 79(9): 1626.

Chaikovska I, et al. (2022) Positron sources: From conventional to advanced accelerator concepts-based colliders. *Journal of Instrumentation* 17: P05015.

Chehab R (1989) *Positron Sources, CAS—CERN Accelerator School: 3rd General Accelerator Physics Course, CERN, Geneva.* https://doi.org/10.5170/CERN-1989-005.105.

Danielson JR, et al. (2006) Plasma manipulation techniques for positron storage in a multicell trap. *Physics of Plasmas* 13: 123502.

Di Mitri S (2018) Bunch-length compressors. In: *Proceedings of the CAS–CERN Accelerator School: Free Electron Lasers and Energy Recovery Linacs, Hamburg, Germany, 31 May–10 June 2016, Edited by R. Bailey, CERN Yellow Reports: School Proceedings, Vol. 1/2018, CERN-2018-001-SP (CERN, Geneva).*

Donahue RJ (November 1991) *Alternative Positron-Target Design for Electron-Positron Colliders, SLAC-PUB-5702, LBL-30724.*

Dowell D (2008) *USPAS Course on High Brightness Electron Injectors for 4th Generation Light Sources, UC Santa Cruz.* Santa Rosa, CA. https://uspas.fnal.gov/materials/08UCSC/Lecture2_EmissionStatisticsCathodeEmittance.pdf.

Dowell DH, et al. (2010) *Nuclear Instruments and Methods in Physics Research* A622: 685–697.

DuBridge LA (1933) *Physical Review* 43: 0727.

Dupasquier A, et al. (2009) Physics with many positrons. In: Dupasquier A, Mills AP Jr, and Brusa RS (eds.) *Fisica con molti positroni: Proceedings of the International School of Physics "Enrico Fermi": Course CLXXIV : Varenna on Lake Como, Villa Monastero 7–17 July.*

Dwersteg B, et al. (1997) RF gun design for the TESLA VUV free electron laser. *Nuclear Instruments and Methods in Physics Research Section A: Accelerators, Spectrometers, Detectors and Associated Equipment* 393(1–3): 93–95. https://doi.org/10.1016/S0168-9002(97)00434-8.

Faillace L (2015) Experimental results of carbon nanotube cathodes inside RF environment. In: *6th International Particle Accelerator Conference IPAC2015, Richmond, VA, USA JACoW Publishing*, ISBN: 978-3-95450-168-7. https://doi.org/10.18429/JACoW-IPAC2015-WEAD2.

Faircloth DC (2021) Particle sources. In: *Proceedings of the CERN–Accelerator–School: Introduction to Accelerator Physics.* https://doi.org/10.48550/ARXIV.2103.13231.

Giley DW, et al. (2006) Positron annihilation as a method to characterize porous materials. *Annual Review of Materials Research* 36: 49–79. Published Amsterdam; Washington, DC : IOS Press, 2010.

Gilmour AS (2011) *Klystrons, Traveling Wave Tubes, Magnetrons, Crossed-Field Amplifiers, and Gyrotrons*. Artech.

Gulliford C, et al. (2013) Demonstration of low emittance in the Cornell energy recovery linac injector prototype. *Physical Review Special Topics—Accelerators and Beams* 16: 073401.

Herring C and Nichols M (1949) Thermoionic emission. *Reviews of Modern Physics* 21: 185.

Jørgensen LV, et al. (2005) (ATHENA Collaboration), New source of dense, cryogenic positron plasmas. *Physical Review Letters* 95: 025002.

Krysztof M (2021) Field-emission electron gun for a MEMS electron microscope. *Microsystems & Nanoengineering* 7: 43. https://doi.org/10.1038/s41378-021-00268-9.

Kutsaev SV (2021) Electron bunchers for industrial RF linear accelerators: Theory and design guide. *The European Physical Journal Plus* 136: 446. https://doi.org/10.1140/epjp/s13360-021-01312-3.

Mills AP and Gullikson EM (1986) Solid neon moderator for producing slow positrons. *Applied Physics Letters* 49: 1121–1123.

Murphy EL and Good RH (1956) Thermionic emission, field emission, and the transition region. *Physical Review* 102: 1464. https://doi.org/10.1103/PhysRev.102.1464.

Musumeci P, et al. (2018) Advances in bright electron sources. *Nuclear Instruments and Methods in Physics Research A* 907: 209–220.

Omori T, et al. (2006) Efficient propagation of the polarization from laser photons to positrons through Compton scattering and electron-positron pair creation. *Physical Review Letters* 96: 114801.

Ottewitte EH (1987) Large scale positron production for physics needs via fission reactors. *AIP Conference Proceedings* 156(1): 209–221.

Petrushina I, et al. (2020) High-brightness continuous-wave electron beams from superconducting radio-frequency photoemission gun. *Physical Review Letters* 124: 244801.

Pierce JR (1949) *Theory and Design of Electron Beams*. New York: D. Van Nostrand.

Rao T and Dowell DH (2014) *An Engineering Guide To Photoinjectors.* https://doi.org/10.48550/ARXIV.1403.7539.

Sannibale F, et al. (2012) Advanced photoinjector experiment photogun commissioning results. *Physical Review Special Topics - Accelerators and Beams* 15(10): 103501.

Sarri G, et al. (2022) Plasma-based positron sources at EuPRAXIA. *Plasma Physics and Controlled Fusion* 64: 044001.

Serafini L and Rosenzweig JB (1997) Envelope analysis of intense relativistic quasilaminar beams in rf photoinjectors: mA theory of emittance compensation. *Physical Review E* 55(6): 7565–7590. https://doi.org/10.1103/PhysRevE.55.7565.

Shu G, et al. (2021) Dark current studies of an L-band normal conducting RF gun. *Nuclear Instruments and Methods in Physics Research A* 1010.

Smolenski K, et al. (2009) Design and performance of the cornell ERL DC photoemission gun. *AIP Conference Proceedings* 1149: 1077.

Spicer WE (1958) Photoemissive, photoconductive, and optical absorption studies of alkali-antimony compounds. *Physics Review* 112: 114–122. https://doi.org/10.1103/PhysRev.112.114.

Tanabashi M, et al. (2018) (ParticleDataGroup), Review of particle physics. *Physics Review* D98: 030001.

Variola A (2014) Advanced positron sources. *Nuclear Instruments and Methods in Physics Research Section A* 740: 21–26.

The fundamental laws of thermodynamics; Role of surroundings in heat and work transfer

Jurgen M Honig, Department of Chemistry, Purdue University, West Lafayette, IN, United States

© 2024 Elsevier Ltd. All rights reserved.

This is an update of J.M. Honig, Thermodynamic Properties, General, Editor(s): Franco Bassani, Gerald L. Liedl, Peter Wyder, Encyclopedia of Condensed Matter Physics, Elsevier, 2005, Pages 164–173, ISBN 9780123694010, https://doi.org/10.1016/B0-12-369401-9/00711-7.

Introduction 475
The zeroth law, temperature, and equations of state 475
Force, heat, work, and the First Law of Thermodynamics 476
Heat transfer, entropy, and the Second Law of Thermodynamics 477
Cyclic processes: The Clausius inequality 478
Efficiencies of cyclic engines: Kelvin and Planck statements 479
Deficit functions and their use in setting up functions of state 479
Standard formulation for differentials of state functions: Maxwell relations 480
The Third Law of Thermodynamics: Unattainability of zero temperature 481
Thermodynamics of anisotropic media 482
Application of thermodynamic concepts 483
Reprise and extension of fundamentals 484
Performance of work 485
Conclusion 486

Abstract

A review of the four fundamental laws of thermodynamics is provided, together with an extension to anisotropic media. The role of surroundings in systematizing heat and work transfers is emphasized.

Key points

- Generation of a universal temperature scale
- The Zeroth law of thermodynamics
- Definition of Heat and Work
- Ramifications of the first law of thermodynamics
- Definition of entropy and the second law of thermodynamics
- The Clausius inequality
- Efficiencies of operation of cyclic engines
- Use of deficit functions
- Functions of state under various operating conditions
- Maxwell relations
- Cross derivatives and their use
- The third law of thermodynamics, nonachievement of zero temperature
- Properties of anisotropic media
- Effect of surroundings on properties of materials

Introduction

A general overview of thermodynamic principles is provided herein, with emphasis on topics that are useful in dealing with materials properties. The theory is extended to deal with anisotropic media. Thermodynamic operations are elucidated by considering the effects of surroundings, thereby eliminating the standard inequalities that are in common use.

The zeroth law, temperature, and equations of state

The venerable field of thermodynamics rests on four basic laws that are discussed in turn.

The zeroth law asserts that "two bodies in equilibrium with a third are in equilibrium with each other." This seemingly obvious statement of transitive properties has important ramifications: consider systems 1 and 2 surrounded by walls that effectively isolate them from the rest of the universe, but allow them to be independently subject to mechanical deformations via pressures P_1 and P_2 (forces per unit area) that deform their volumes V_1 and V_2. While the systems are separated, these four quantities may be varied independently. However, when joined together and allowed to equilibrate, it is an experience of mankind that only three of the four variables may be independently altered. This is expressed mathematically by the relation $\beta_3\ (P_1, V_1, P_2, V_2) = 0$. Repeat the process for systems 1 and 3, leading to the expression $\beta_2\ (P_1, V_1, P_3, V_3) = 0$. Then by the zeroth law, $\beta_1\ (P_2, V_2, P_3, V_3) = 0$ on combining systems 2 and 3. As long as mutual equilibrium prevails after each combination, system 3 remains unaltered in its union with either system 1 or 2; one can then solve for P_3 in the functions β_2 and β_1 to express $P_3 = \Phi_1\ (P_2, V_2, V_3) = \Phi_2\ (P_1, V_1, V_3)$, from which the following difference function is constructed: Φ_1 (P2, $V_2, V_3) - \Phi_2\ (P_1, V_1, V_3) \equiv \lambda\ (P_1, V_1, P_2, V_2; V_3) = 0$. Unfortunately, a glaring inconsistency now emerges: the functional dependence of λ on V_3 is absent from the function $\beta_3 = 0$; also, it makes no sense to refer to λ in system 3 when combining systems 1 and 2. To resolve this impasse, let V_3 occur in Φ_1 and Φ_2 so as to cancel out when their difference is constructed. This may be achieved in most general terms by writing $\Phi_1 = f_2\ (P_2, V_2)\ h\ (V_3) + q\ (V_3)$ and $\Phi_2 = f_1\ (P_1, V_1)\ h\ (V_3) + q\ (V_3)$, where h and q are arbitrary functions of V_3. Substitution of the last two equations in the function λ then leads to the relation

$$f_1(P_1, V_1) = f_2(P_2, V_2) \tag{1a}$$

Similarly, consistent with the zeroth law,

$$f_1(P_1, V_1) = f_3(P_3, V_3) \tag{1b}$$

Reference is now made only to the variables appropriate to each separate system. Eqs. (1a), (1b) thus characterize the equilibration process, and they permit one to consider system 1 as a reference standard that determines whether systems 2 and 3 are in equilibrium, according as system 1 is or is not changed when it comes successively in contact with systems 2 and 3. Clearly, the functional interrelation specified by $f_1\ (P_1, V_1)$ is of great significance; therefore, a short-hand notation symbol τ_1, termed the "empirical temperature function" is provided for this function. The relationship $\tau_i = f_i\ (P_i, V_i)$ is known as an "equation of state" for system *i*. One can thus characterize the empirical temperature of a given system through measurements of its pressure and/or volume. While it has been worked here with mechanical variables, other experimental measurements could have been used in a similar fashion to construct empirical temperatures. Many different methods for monitoring temperature have been employed; these are described in review articles on the subject. Only the use of a gas thermometer is briefly discussed here. Other commonly used techniques include measurements of electrical resistivity, thermocouple voltages, paramagnetic susceptibility, pyrometers, and thermal expansion; a description of these and other techniques would be beyond the confines of this article.

The labeling of τ_i as "temperature" obviously introduces a link between physical properties and human sensory perceptions of "hotness levels." The ordering of different hotness levels requires a quantification scheme via an empirical temperature scale; one may employ the equation of state of any suitable material as one indicator of hotness; an enormous multitude of other indicators has been applied for the same purpose. For present purposes, Boyle's law $f(P, V) = PV = \text{constant} \equiv \tau$ is adopted, which applies to an ideal gas, such as He at low pressure and at a constant temperature well above its critical point. The PV product can then be used as a measure of hotness. A useful quantification scheme is the so-called "Celsius" scale that assigns the values $\tau = 0\ ^\circ\text{C}$ (the original intent, but nowadays assigned a value 0.01 °C) and $\tau = 100\ ^\circ\text{C}$ to water that is equilibrated, respectively, with ice and with steam at 1 bar. Let V, V_0, and V_{100} be the volume of He gas at a fixed, low pressure and at temperatures τ, 0 °C and 100 °C respectively; then τ is specified by

$$\begin{aligned} \tau = 100(V - V_0)/(V_{100} - V_0) = 100\,\text{V}/(V_{100} - V_0) \\ - 100V_0/(V_{100} - V_0) \equiv T + T_0 \end{aligned} \tag{2}$$

A straight line plot of τ versus V based on the above two assigned points extrapolates to an intercept $T_0 \equiv -100V_0/(V_{100} - V_0)$ which has been found to have the value −273.15 °C, where the volume V of the ideal gas would vanish, if the gas could be maintained at lowest temperatures. (Actually, the third law, discussed below, shows that a perfect gas cannot exist at very low temperatures. This, however, does not prevent introducing the ideal gas concept as an excellent approximation to properties of a real gas, and then extrapolating its characteristics to the ultralow temperature range, showing what its properties would be if the gas could be maintained in that range. The extrapolation to $V = 0$ suggests that there exists a natural lower limit to the hotness levels, and that an absolute temperature scale may be set up by adding 237.15 to the Celsius scale. One thereby establishes the "thermodynamic temperature scale" $T\ (\text{K}) = \tau(^\circ\text{C}) + 273.15$.

Force, heat, work, and the First Law of Thermodynamics

In preparation for the next step, let xi represent a "deformation or thermodynamic coordinate" (such as volume, pressure, temperature, mole number, and the like) that characterizes the thermodynamic state of a given system, and let f_i represent any causative agent by which this particular state may be altered; this is taken to be the "thermodynamic force." Then, the element of work of type *i* performed "on a system" by its surroundings is specified by $f_i\text{d}x_i$; if more than one force brings about a change in x_i, the various contributions must be summed. f_i must remain sufficiently small so as to avoid turbulent or dissipative effects, otherwise, a whole host of extrathermodynamic variables would be required to characterize the process. One thus deals with reversible processes that involve only infinitesimal displacements of a system from equilibrium. Also, the force itself may depend on the displacement and may or may not be collinear with the deformation coordinate. These situations are addressed by expressing the work performed on the system when changing its state from $\boldsymbol{x}_1$ to $\boldsymbol{x}_2$ as $W_i = \int_{x_1}^{x_2} f_i(\boldsymbol{x}_i) \cdot d\boldsymbol{x}_i$, where the force is taken to be a vector and the dot vector product has been introduced. In general, such a line integral depends on the chosen path that takes the system from state $\boldsymbol{x}_1$ to $\boldsymbol{x}_2$, whence this is also the case for the differential quantity $\text{đW} = f_i(\boldsymbol{x}_i) \cdot d\boldsymbol{x}_i$. To emphasize this point, the special symbol đ has been used. It is obviously awkward to have to deal with path-dependent entities; hence, one searches for functions that depend only on the initial and final states of a given process; such entities are known as "functions of state." In the present example, a path-independent work performance may be generated if the force is representable as the gradient of a potential, so that $f = -\nabla\varphi$, whence

$$
\begin{aligned}
-\mathrm{W_i} &= -\int_{\mathrm{x_1}}^{\mathrm{x_2}} \mathrm{f_i}(\mathbf{x_i}) \cdot \mathrm{d}\mathbf{x_i} \\
&= \int_{\mathrm{x_1}}^{\mathrm{x_2}} \nabla\phi \cdot \mathrm{dx_i} = \phi(\mathrm{x_2}) - \phi(\mathrm{x_{1.}})
\end{aligned}
$$

is indeed seen to depend only on the initial and final values of ϕ. The presence of the minus sign indicates that in going from a higher potential $\phi(\boldsymbol{x}_2)$ to a lower potential $\phi(\boldsymbol{x}_1)$, the system does work on the surroundings, the negative of work done by the surroundings on the system.

Mathematical formulations of commonly encountered types of work are briefly listed, but the list is not exhaustive: (1) mechanical pressure – volume work: $\text{đW} = -P\,\mathrm{d}V$; (2) enlargement of surface area A: $\text{đW} = -\sigma\,\mathrm{d}A$, where σ is the surface tension; (3) gravitational work involved in lifting mass $M\,\mathrm{d}n$ (M is the gram-molecular mass and n is the mole number) through a height z: $\text{đW} = gzM\,\mathrm{d}n$, where g is the gravitational constant; (4) electrostatic work (in Gaussian units): $\text{đW} = \int d^3r\boldsymbol{E} \cdot \frac{d\boldsymbol{D}}{4\pi} = -\int_V d^3r\boldsymbol{P} \cdot d\boldsymbol{E}_0$, where $\boldsymbol{E}$, $\boldsymbol{D}$, $\boldsymbol{P}$, $\boldsymbol{E}_0$ are, respectively, the electrostatic field in the presence of the sample, the electric displacement vector, the polarization vector, and the preexisting electrostatic field prior to sample insertion. The first integral must be taken over all space; the second extends over the volume of the sample, since $\boldsymbol{P}$ vanishes outside the confines of the specimen; (5) magnetic work (in Gaussian units): $\text{đW} = \int d^3r\boldsymbol{H} \cdot d\boldsymbol{B}/4\pi = \int_V d^3r\boldsymbol{H}_0 \cdot d\boldsymbol{M}$. Here, $\boldsymbol{H}$, $\boldsymbol{B}$, $\boldsymbol{H}_0$, and $\boldsymbol{M}$ are, respectively, the applied magnetic field in the presence of the sample, the magnetic induction, the applied magnetic field prior to insertion of the sample, and the magnetic moment vector. The above shows that work performance can always be determined from first principles; alternatively, it may be measured experimentally. This is of importance in what follows.

"The first law of thermodynamics" states in part that when work $W|_a$ is performed adiabatically (that is, on a system impervious to changes in temperature of the surroundings) thereby changing its state from $\boldsymbol{x}_1$ to $\boldsymbol{x}_2$, then this change is independent of the type of work performed and independent of the path taken to effect this change. In these circumstances, one deals with a function of state, termed energy, here designated as U, that characterizes the $\boldsymbol{x}_1$ to $\boldsymbol{x}_2$ transformation via $\Delta U \equiv U_2 - U_1 = W|_a$. If now, the same process is carried out under nonadiabatic conditions, the $\Delta U = W$ equivalence no longer holds, thus seemingly impairing the usefulness of the energy concept. However, in the nonadiabatic process, additional changes take place that need to be considered.

The first law of thermodynamics asserts that there exists a function of state U, termed the internal energy, such that, for any process whatsoever that takes a system from an initial state $\boldsymbol{x}_n$ to a final state $\boldsymbol{x}_f$, the difference $\Delta U \equiv U_f - U_n$ depends solely on the thermodynamic coordinates $\boldsymbol{x}_n$ and $\boldsymbol{x}_f$ and is independent of the path connecting these states. ΔU can be determined experimentally, or theoretically from $W|_a$. In nonadiabatic changes between the same states, ΔU remains exactly the same, but now the work performance W is different: $\Delta U - W \neq 0$. It is then expedient to introduce a deficit function Q, termed heat transfer, that reinstates the equality in the form: $Q - (\Delta U - W) = 0$. One thus arrives at the following formulation for the first law of thermodynamics:

$$
\Delta U = Q + W \quad \text{or} \quad \mathrm{d}U = \text{đQ} + \text{đW} \tag{3}
$$

where the second formulation applies to an infinitesimal stage of the process; d and đ are used when one deals with infinitesimal processes that are not or are path dependent. Thus, Q and W are two different manifestations of energy in transit across the boundary separating the system from its surroundings. $Q > 0$ (< 0) increases (decreases) the energy of the system via an inflow (outflow) of heat; similarly, for the work transfer $W > 0$ (< 0). While Q, W, đQ, dW generally are path dependent, their sum in Eq. (3) is not. Thus, given a set of n thermodynamic variables $\boldsymbol{x} = \{x_1, x_2, \ldots, x_n\}$, the function of state U has the differential form of an analytic function:

$$
\mathrm{d}U = \sum_{j=1}^{n} \left(\partial U/\partial x_j\right) \mathrm{d}x_j \tag{4}
$$

Clearly, if processes occur totally within the system, there is no transfer of heat or work across the boundaries; then $\Delta U = 0$, which is an expression of the law of conservation of energy in an isolated system. This also disposes off the possibility of having a perpetual motion taking place.

Heat transfer, entropy, and the Second Law of Thermodynamics

The next law has been phrased in several different ways: the most common versions involve the statements enunciated by Kelvin and by Planck; these are derived below from more general principles. They are generally presented in elementary textbook discussions that build up to the second law. There is nothing wrong logically with this procedure. However, intellectually it is rather unsatisfactory to base a fundamental thermodynamic principle on statements concerning the operation of a heat engine.

A more general formulation was provided by Carathéodory: in every neighborhood of any state of an adiabatically isolated system, there exist other states that cannot be accessed from it by any process. This statement really provides the proper theoretical background to the second law, but considerable mathematical sophistication is needed to show how this statement leads to the concept of entropy. Here, one can simplify matters by noting that just as one connected an adiabatic performance of work to the establishment of a function of state, a transfer of heat can also be used to the same end. Effectively, the first part of the second law of thermodynamics is equivalent to the statement that a reversible infinitesimal transfer of heat to a system $\text{đ}Q|_r$, though path dependent, is related by a scaling (or integrating) factor λ to a new differential function of state, the empirical entropy s, via $\text{đ}s = \text{đ}Q|_r/\lambda$.

The determination of λ is accomplished through a set of tight arguments by considering the process of combining two systems A and B into a compound unit C. Let the heats transferred to the surroundings in an infinitesimal process be designated by $\text{đ}Q_a$ and $\text{đ}Q_b$ for the component parts, and by $\text{đ}Q_c$ for the compound system, $\text{đ}Q_a + \text{đ}Q_b = \text{đ}Q_c$. Then, according to the second law,

$$ds_c = (\lambda_a/\lambda_c)ds_a + (\lambda_b/\lambda_c)ds_b \tag{5}$$

Let the deformation coordinates of A and B be given by $x_1, x_2, \ldots, x_{n-1}, t$ and $y_1, y_2, \ldots, y_{m-1}, t$ respectively, where t is the common empirical temperature of the compound system. Mathematically, one can then solve for x_{n-1} in terms of $x_1, x_2, \ldots, x_{n-2}, t, s_a$ and for y_{m-1} in terms of $y_1, y_2, \ldots, y_{m-2}, t, s_b$. It is now asserted that: (1) s_c must be independent of $x_1, x_2, \ldots, x_{n-2}; y_1, y_2, \ldots, y_{m-2}$; and t. If this were not so, Eq. (5) would necessarily contain terms involving the differential quantities $dx_1, dx_2, \ldots, dy_{m-2}, dt$ (see Eq. 4). (2) The ratios λ_a/λ_c and λ_b/λ_c cannot depend on these variables; otherwise, statement (1) would be contradicted. (3) λ_c cannot depend on $y_1, y_2, \ldots, y_{m-2}$; for, if it did, then λ_a in Eq. (5) would have to depend on these same coordinates in such a manner as to cancel out from the ratio λ_a/λ_c, for consistency with statement (2) and (1). However, λ_a cannot possibly depend on the y-coordinates appropriate to system B. By the same reasoning, λ_c must be independent of $x_1, x_2, \ldots, x_{n-2}$. (4) Furthermore, λ_a and λ_b cannot depend on $x_1, x_2, \ldots, x_{n-2}$ and $y_1, y_2, \ldots, y_{m-2}$, respectively. For, according to (3) these variables are missing from λ_c, whence the ratios λ_a/λ_c and λ_b/λ_c must also be free of these variables, to remain consistent with (1), (2), and (3). However, this argument does not apply to t, which is common to A, B, and C. (5) As a consequence of (1)–(4), the functions λ_a, λ_b, and λ_c can involve at the most, the variables (s_a, t), (s_b, t), and (s_a, s_b, t), respectively. (6) The functional dependences mentioned in (5) must have the form $\lambda_a = \varphi_a(s_a)T(t)$, $\lambda_b = \varphi_b(s_b)T(t)$, and $\lambda_c = \varphi_c(s_a, s_b)T(t)$, in which $T(t)$ is a common though arbitrary function of the empirical temperature t; this function cancels from the ratios λ_a/λ_c and λ_b/λ_c in Eq. (5), in consonance with requirement (2). In summary, it is found that

$$\begin{aligned}
\text{đ}Q_a &= T(t)\varphi_a(s_a)ds_a \equiv T(t)dS_a \\
\text{đ}Q_b &= T(t)\varphi_b(s_b)ds_b \equiv T(t)dS_b \\
\text{đ}Q_c &= T(t)\varphi_c(s_a, s_b)ds_c \equiv T(t)dS_c
\end{aligned} \tag{6}$$

where S in $dS_a \equiv \varphi_a(s_a)ds_a$, etc., is termed the metrical entropy. As described earlier, one can select any arbitrary function for T; T is thus taken to be identical with the thermodynamic temperature scale of Eq. (2). Further, equilibrium conditions have been assumed throughout, so that all processes must be executed reversibly. Thus, one is led to the result

$$\text{đ}Q|_r = T\,dS \tag{7}$$

which relates the state function S to the reversible transfer of heat across the boundaries of the system.

Now, the corollary of the second law is introduced as follows: For any process in a system in (adiabatic), isolation, the entropy of the final state is never less than that of the initial state. Thus, $dS|_a \geqslant 0$; the equality holds at equilibrium, and the inequality applies to processes taking place totally within an isolated system; thus, the entropy increases in such processes and reaches a maximum when equilibrium is attained.

Cyclic processes: The Clausius inequality

The relation between entropy and heat transfer is clarified by considering a process in which a system is taken reversibly from an initial state n to a final state f, involving a heat exchange $\text{đ}Q|_r^{n-f}$. This is to be compared to the heat exchange $\text{đ}Q|_i^{n-f}$ accompanying an irreversible process connecting the same states. From the first law, it is found that $\text{đ}Q|_i^{n-f} - \text{đ}Q|_r^{n-f} = -\text{đ}W|_i^{n-f} + dW|_r^{n-f}$; dU, being a function of state, has been cancelled out. The above difference cannot vanish, since the two paths must necessarily differ. Thus, the algebraic sum must be either positive or negative. (1) Suppose $\text{đ}Q|_i^{n-f} - \text{đ}Q|_r^{n-f} \equiv -\text{đ}Q|_i^{n-f} + \text{đ}Q|_r^{f-n} < 0$, so that $-\text{đ}W|_i^{n-f} + \text{đ}W|_r^{n-f} = -\text{đ}W|_i^{n-f} - \text{đ}W|_r^{f-n} < 0$; that is, in going around one cycle (n-f-n), work has been performed on the system and an equivalent amount of heat has been transferred by the system to the surroundings. No other changes have taken place. (2) On the other hand, if the algebraic sum $\text{đ}Q|_i^{n-f} + \text{đ}Q|_r^{f-n}$ is assumed to be positive, a similar reasoning shows that during the cycle, heat has been introduced into the system, and an equivalent amount of work is obtained. To choose between the alternatives, consider the n–f process for which $\text{đ}Q|_i^{n-f} \equiv \text{đ}Q|_i$, $\text{đ}Q|_r^{n-f} = T\,dS$. Then, under alternative (1) $T\,dS > \text{đ}Q|_i$ in all circumstances, including the case where the n–f process is performed adiabatically, in which case $T\,dS|_a > 0$. No contradictions have been encountered. By contrast, in alternative (2) $T\,dS|_a < 0$, a conclusion that is unacceptable. One obtains the important result:

$\text{đ}Q|_i < T\,dS = \text{đ}Q_r$. Thus, in a reversible n-f process, the entropy change is matched by a heat transfer $\text{đ}Q|_r/T$. If the same change is achieved irreversibly, the entropy change is the same but the heat transferred is smaller, the difference between $\text{đ}Q|_r$ and $\text{đ}Q|_i$ being made up by effects beyond experimental control. Also, for any process $\text{đ}W|_i < \text{đ}W|_r$ the maximum amount of work attainable involves a reversible process. Lastly, for finite changes, $S_f - S_n \geqslant \int_n^f \text{đ}Q/T$; then, for a cyclic process where $S_f = S_n$, $\oint dS = \oint \text{đ}Q/T \leqslant 0$. This latter result, which is consistent with $\text{đ}Q|_i < \text{đ}Q|_r$, is known as the Clausius inequality. The above brings up the problem of defining the temperature during irreversible processes; this is generally handled in two ways. One is to assume that the system is anchored to a huge reservoir whose temperature remains essentially fixed, while assuming that the heat transfer is sufficiently rapid to have that temperature also prevail in the system. The second is to note that in irreversible processes, for which departures from equilibrium are "small" (the linear regime of irreversibility), the temperature remains locally defined but varies with position. For more drastic departures from equilibrium, the temperature concept becomes more problematic.

Efficiencies of cyclic engines: Kelvin and Planck statements

One can now deal with the efficiency of any engine that operates in cycles while attached to a hot and a cold reservoir maintained at temperatures T_h and T_c, respectively. All changes in the universe then occur solely in the surroundings. Let the heat transferred per cycle at the cold and hot junctions be $Q_\text{c} > 0$ and $Q_\text{h} > 0$, respectively; for the engine to operate, one requires $Q_\text{h} - Q_\text{c} > 0$, so that less heat is rejected at the cold end than was transferred into the engine at the hot end. Correspondingly, $W = -(Q_h - Q_c) < 0$ represents the amount of work transferable to the surroundings. The efficiency η is defined by the ratio of work output/heat input. The Clausius inequality as applied to the present process reduces to the sum $\sum_i Q_i/T_i = Q_h/T_h - Q_c/T_c \leqslant 0$; this may be converted to the inequality

$$-\mathrm{Q_c}/\mathrm{Q_h} \leqslant -\mathrm{T_c}/\mathrm{T_h}$$

Then,

$$\begin{aligned}\eta &= -W/Q_\text{h} = 1 - Q_\text{c}/Q_\text{h} \leqslant 1 - T_\text{c}/T_\text{h} \\ &= (T_\text{h} - T_\text{c})/T_\text{h} \equiv \eta_\text{Carnot}\end{aligned} \tag{8}$$

The following are to be noted: (1) The generality of the approach; no mention is made of what types of cyclic engines are inserted between the two reservoirs. (2) The efficiency relates to the isothermal transfer of heat across the hot and cold junctions. (3) The efficiency for irreversible processes is less than that for reversible ones. (4) The efficiency is never unity since one cannot operate at the unattainable limits (see below) of $T = 0$ or $T \to \infty$. Thus, the efficiency never exceeds the Carnot efficiency η_Carnot. (5) η depends solely on the temperature of the "boiler" and "condenser" and, the bigger the temperature difference between them, the larger the efficiency is.

Statement (4) leads to Kelvin's statement of the second law: it is impossible to devise an engine operating in cycles that produces no effect other than to extract heat from a reservoir and to perform an equal amount of work. Also, one may infer the Clausius statement of the second law: it is impossible to devise a machine operating in cycles that transfers heat from a colder to a hotter body without producing other changes in the universe. If this were false, one could transfer heat without loss from the cold to the hot reservoir, so that $-Q_h/T_h + Q_c/T_c \leqslant 0$ with $Q_\text{c} = Q_\text{h}$, which would lead to the contradiction that $T_h/T_c \leqslant 1$.

Deficit functions and their use in setting up functions of state

The following discussion is much simplified by converting the Clausius inequality to an equality through the use of a deficit function $\text{đ}\varepsilon > 0$, such that $\text{đ}Q|_r - \text{đ}\varepsilon = \text{đ}Q|_i$; similarly, $\text{đ}W|_r + \text{đ}\varepsilon = \text{đ}W|_i$. In a closed universe consisting of system (energy U) and surroundings, (energy $\mathrm{U_0}$) the first law leads to the expression $dU + dU_0 = 0 = \text{đ}Q|_i + \text{đ}W|_i + \text{đ}U_0$, so that

$$T\,\mathrm{d}S - \text{đ}\varepsilon + \text{đ}\mathrm{W}|_\mathrm{i} - \mathrm{d}U = T\,\mathrm{d}S + \text{đ}\mathrm{W}|_\mathrm{r} - \mathrm{d}U = 0 \tag{9}$$

One imposes small deviations from the equilibrium, under a variety of constraints, and subsequently allows the system to relax to its original state. Such small deviations are symbolized by δ. Several cases are considered here:

(1) The system is totally isolated; then $\delta Q = \delta W = \delta U = 0$, and Eq. (9) reduces to $T\delta S = \delta\varepsilon \equiv T\delta\theta \geqslant 0$. Here, $\delta\theta = \delta\varepsilon/T$ has been introduced as the entropy associated with the execution of irreversible processes that are not subject to external control. It is seen immediately that in an irreversible process taking place in an isolated system, the entropy can only increase, a point made earlier. When processes cease and equilibrium prevails, the entropy has achieved a maximum value.

(2) If one allows isoenergetic processes to occur, where $\delta U = 0$ but $\delta Q = \delta W \neq 0$, then Eq. (9) reads as $T\delta S = \delta\varepsilon + \delta Q|_i = \delta Q|_r$, which merely reinforces the fact that changes in entropy are tracked by reversible heat transfers. Also, if irreversible processes occur, the heat transfer is smaller; the entropy generated by processes outside experimental control is transferred as energy $\delta\varepsilon$.

(3) In isothermal processes for which $\delta T = 0$, Eq. (9) specializes to the form

$$\delta(U - TS) \equiv \delta A = \delta W|_\mathrm{i} - \delta\varepsilon = \delta W|_\mathrm{r} \tag{10}$$

where a new function of state, the Helmholtz free energy $A \equiv U - TS$ has been generated. This is tracked either by the performance of reversible work or by work over which the experimenter has control plus a component not under his control. If no work is performed, $\delta A = -\delta\varepsilon \leqslant 0$: any spontaneous process under the specified conditions reduces the Helmholtz free energy. When the processes have run their course and equilibrium prevails, A is at a minimum.

(4) One next considers the isothermal-isobaric conditions for which $\delta T = \delta P = 0$. It is now expedient to write $\delta\varepsilon = \delta\varepsilon_m + \delta\varepsilon_t$, where the two terms refer to mechanical (P—V) and nonmechanical types of work; it may be shown that $\delta\varepsilon_m \geqslant 0$ and $\delta\varepsilon_t \geqslant 0$ separately. Eq. (9) now becomes

$$\delta(U - TS + PV) \equiv \delta G = \delta W_\mathrm{t}|_\mathrm{i} - \delta\varepsilon_\mathrm{t} = \delta W_\mathrm{t}|_\mathrm{r} \tag{11}$$

wherein one introduces a new function of state, the Gibbs free energy $G \equiv U - TS + PV$. This quantity is tracked by reversible work other than mechanical ones; in irreversible processes, the work is augmented by energy transfers not subject to control. In the absence of work, $\delta G = -\delta\varepsilon_t \leqslant 0$, showing that under the stated conditions, the Gibbs free energy diminishes in spontaneous processes until it achieves a minimum at equilibrium.

(5) Isentropic phenomena: here, S is fixed, so that from Eq. (9)

$$\delta U = -T\delta\theta + \delta W|_\mathrm{i} = \delta W|_\mathrm{r} \tag{12}$$

which merely repeats the first law, as specialized to adiabatic conditions. In the absence of work, $\delta U = -T\delta\theta \leqslant 0$, so that under the stated conditions, the energy is reduced and tends to a minimum at equilibrium.

(6) For isentropic-isobaric conditions (P and S fixed), Eq. (9) specializes to

$$\delta(U + PV) \equiv \delta H = \delta W_\mathrm{t}|_\mathrm{i} - \delta_\varepsilon = \delta W_\mathrm{t}|_\mathrm{r} \tag{13}$$

where yet another function of state, the enthalpy $H \equiv U + PV$, tracked by nonmechanical work, generally augmented by irreversibility effects, has been constructed. When no work is performed under the stated conditions, $\delta H = -T\delta\theta \leqslant 0$, so that once more H diminishes in irreversible phenomena and achieves a minimum at equilibrium.

Among the most frequently used functions of state is the chemical potential, derived from Eq. (11) as $\mu = (\partial G/\partial n_i)_{T,\,P,\,n_{j\neq i}}$, where n_i represents the mole number of species i in the system. The utility of this function arises in part because it involves T and P as independent variables; these are precisely the quantities that are readily subject to experimental control. The second useful feature hinges on the fact that at equilibrium, μ is a minimum. Different phases are associated with different chemical potentials that vary differently with T and P. The phase among competing phases that prevails under a given set of conditions is the one with the lowest μ. As conditions change, the relative values of μ for the different possible phases are also altered, and a transition from one phase to another takes place whenever the chemical potential of a particular phase falls below that of a previously stable phase. Two phases coexist under conditions where their chemical potentials are the same. This very general subject area has vast ramifications that cannot be explored here.

Standard formulation for differentials of state functions: Maxwell relations

The above functions of state are summarized in Table 1. They lead to the various standard differential forms displayed in part A; note that all work other than mechanical has been excluded. If other types of work are to be included, one must adjoin to these equations, the appropriate work differentials (refer to those listed above).

Table 1 Standard formulations for thermodynamic functions of state and resulting relations.

A. Legendre transformations

From the definitions for $H = U + PV$, $A = U - TS$, $G = U - TS + PV$, and the fundamental relation for dU, one obtains

$\mathrm{d}U = T\,\mathrm{d}S - P\,dV \quad \mathrm{d}A = -S\,dT - P\,dV$ (I.1, I.3)

$\mathrm{d}H = T\,\mathrm{d}S + V\,\mathrm{d}P \quad \mathrm{d}G = -S\,\mathrm{d}T + V\,\mathrm{d}P$ (I.2, I.4)

If work other than mechanical is involved, those terms must also be included.

B. First derivatives

$T = (\partial U/\partial S)_V = (\partial H/\partial S)_P \quad V = (\partial H/\partial P)_S = (\partial G/\partial P)_T$ (I.5, I.6)

$S = -(\partial A/\partial T)_V = -(\partial G/\partial T)_P \quad P = -(\partial U/\partial V)_S = -(\partial A/\partial V)_T$ (I.7, I.8)

C. Cross-derivatives, Maxwell relations

$(\partial T/\partial V)_S = -(\partial P/\partial S)_V \quad (\partial S/\partial P)_T = -(\partial V/\partial T)_P$ (I.9, I.10)

$(\partial T/\partial P)_S = (\partial V/\partial S)_P \quad (\partial S/\partial V)_T = (\partial P/\partial T)_V$ (I.11, I.12)

The process of generating the differentials dH, dA, and dG from dU is called a Legendre transformation. These differential functions of state are very useful in determining the thermodynamic properties of systems. Taking first derivatives leads to the results shown in part B; by taking cross derivatives in either order, one obtains the so-called Maxwell relations shown in part C. Once the equation of state $P = P(T, V)$ or $V = V(T, P)$ is known, one can integrate (I.10) and (I.12) to find S as a function of T and V or T and P. Alternatively, one may employ Eq. (I.7) if A or G are known, for example, from statistical mechanics.

Other deductions are found by substituting $S = S(T, V)$ or $S = S(T, P)$ into $U(S,V)$ or $H = H(S, P)$ to obtain $U = U(S(V, T), V) = U(T, V)$, and

$$
\begin{aligned}
H &= H(S(P,\ T), P) = H(T, P), \text{ so that}\\
dU &= T(\partial S/\partial T)_V \, dT + \left[T(\partial S/\partial V)_T - P\right] dV\\
&= (\partial U/\partial T)_V \, dT + (\partial U/\partial V)_T \, dV
\end{aligned} \tag{14a}
$$

$$
\begin{aligned}
dH &= T(\partial S/\partial T)_P \, dT + \left[T(\partial S/\partial P)_T + V\right] dP\\
&= (\partial H/\partial T)_P \, dT + (\partial H/\partial P)_T \, dP
\end{aligned} \tag{14b}
$$

Comparing the coefficients leads to the results

$$
\begin{aligned}
(\partial U/\partial T)_V &= T(\partial S/\partial T)_V \equiv C_V\\
(\partial H/\partial T)_P &= T(\partial S/\partial T)_P \equiv C_P
\end{aligned} \tag{15a}
$$

$$
\begin{aligned}
(\partial U/\partial V)_T &= T(\partial S/\partial V)_T - P\\
&= T(\partial P/\partial T)_V - P(V, T)
\end{aligned} \tag{15b}
$$

$$
\begin{aligned}
(\partial H/\partial P)_T &= T(\partial S/\partial P)_T + V\\
&= -T(\partial V/\partial T)_P + V(P, T)
\end{aligned} \tag{15c}
$$

The appropriate Maxwell relations have been introduced on the right-hand side of Eqs. (15b), (15c). The symbols C_P and C_V represent the heat capacities at constant pressure and volume; these are readily measurable as a function of temperature. This permits the determination of U and H as a function of T, with either V or P as a parameter. Eqs. (15b), (15c) are known as caloric equations of state; insertion of the equations of state $P(T,V)$ or $V(T,P)$ into these relations, followed by integration, enables one to determine $U = U(T, V)$ and $H = H(T, P)$. Also, from (15a), after measurements of C_V or C_P as a function of T, followed by integration, one can determine $S = S(T, V)$ or $S = S(T, P)$. In a series of lengthy but elementary steps listed in all textbooks, one finds that $C_P - C_V = \alpha^2 VT/\beta$, with $\alpha \equiv V^{-1}(\partial V/\partial T)_P$ representing the isobaric expansion coefficient, and $\beta \equiv -V^{-1}(\partial V/\partial P)_T$, the isothermal compressibility of the material. This difference relation is of importance because it is easier to measure C_P experimentally, whereas the quantity useful in theoretical analysis is C_V. Lastly, insertion of Eq. (I.7) into $A = U - TS$ leads to $A = U + T(\partial A/\partial T)_V$; similarly, $G = H + T(\partial G/\partial T)_P$. These are known as "Gibbs–Helmholtz equations," which may be converted into the partial differential forms involving $(\partial A/\partial T)_V = A/T - U/T$ and $(\partial G/\partial T)_P = G/T - H/T$, whose solution, after insertion for U or H yields A or G.

Eq. (I.7) is particularly useful in determining the entropy when the dependence of A or G on T is known from other sources. Eqs. (I.10), (I.12) permit substitution for entropy derivatives in terms of information derived from the equations of state.

The Third Law of Thermodynamics: Unattainability of zero temperature

The "third law of thermodynamics" deals with events as $T \rightarrow 0$, where dQ/T might diverge. One first demonstrates that zero temperature is unattainable. Consider the general case where z represents a deformation coordinate and Z is the conjugate variable, such that the first law assumes the form $dS = T^{-1}[\, dU + Z\, dz] = T^{-1}\{(\partial U/\partial T)dT + [Z + (\partial U/\partial z)]dz\}$. Below, one needs the result of the cross differentiation of this expression with respect to T and z, namely $Z + (\partial U/\partial z) = T(\partial Z/\partial T)$. Special interest now attaches to the case $dS = 0$, since only under adiabatic conditions, one can hope to reach the lowest possible temperature. Imposing this requirement leads to

$$
dT = \{[Z + (\partial U/\partial z)]/(\partial U/\partial T)\} dz \tag{16}
$$

This relation shows that any change in deformation coordinates under isentropic (adiabatic) conditions necessarily changes the temperature of the system. Insertion of the cross differentiation result leads to the requirement

$$
\begin{aligned}
dT &= -T\left[(\partial Z/\partial T)_z/(\partial U/\partial T)_z\right] dz\\
&= -\left[T(\partial Z/\partial T)_z/C_z\right] dz\\
&= -(T/C_z)(\partial S/\partial z)_T \, dz,
\end{aligned} \tag{17}
$$

where Eq. (I.12) with the correspondences P, Z, and V; z was introduced on the right-hand side. Whether $T = 0$ can be achieved or not, thus, hinges on the properties of $(\partial Z/\partial T)_z$ and of (T/C_z) at exceedingly low temperatures. In the experience of mankind, both quantities approach zero as $T \to 0$, but $(\partial Z/\partial T)_z$ does so more rapidly than does C_z/T. Thus, the limit $T = 0$ is unattainable. Moreover, $(\partial S/\partial z)_T \to 0$ in this limit, which is an important statement that becomes part of the third law.

Based on these findings, one can now state the third law of thermodynamics which asserts that as $T \to 0$, the entropy of any system tends toward a least value when the system is in its lowest energy state and, as the thermodynamic coordinates are altered, approaches this value with zero slope. The wording implies that the system must actually have reached its equilibrium state, hence, its lowest energy, on cooling to the lowest possible temperature. Contrary to statements in some textbooks, it is not claimed that $S \to 0$ as $T \to 0$. Liquid mercury under ambient pressure, disordered solid solutions or amalgams, random elemental isotopic abundances, are common counter examples. However, if in any given process these types of ground states are left undisturbed, it is effectively permissible to set $S = 0$ at $T = 0$, much as the gravitational energy of a quiescent system at sea level is assigned an energy zero.

Thermodynamics of anisotropic media

Lastly, the deformation of anisotropic solids is considered. Let $\boldsymbol{s}(\boldsymbol{r})$ and $\boldsymbol{s}(\boldsymbol{r} + \mathrm{d}\boldsymbol{r})$ be the displacement vectors that move element A, originally at $\boldsymbol{r}$, to $\boldsymbol{r} + s(\boldsymbol{r})$, and neighboring element B, originally at $\boldsymbol{r} + \mathrm{d}\boldsymbol{r}$ to new locations. For small displacements, $\boldsymbol{s}(\boldsymbol{r} + d\boldsymbol{r}) \approx \boldsymbol{s}(\boldsymbol{r}) + d\boldsymbol{r} \cdot \nabla s(\boldsymbol{r})$. Here, $\nabla \boldsymbol{s}(\boldsymbol{r})$ is a matrix (a tensor) with columns $\partial s_x(\boldsymbol{r})/\partial x$, $\partial s_x(\boldsymbol{r})/\partial y$, and $\partial s_x(\boldsymbol{r})/\partial z$, and similarly with $s_y(\boldsymbol{r})$ and $s_z(\boldsymbol{r})$. Now, any matrix with entries M_{ij} may be rewritten as $M_{ij} = (1/2)(M_{ij} + M_{ji}) + (1/2)(M_{ij} - M_{ji})$, involving a symmetric ($\boldsymbol{e}_s$) and an antisymmetric component, $\boldsymbol{e}_a$. The matrix for $\nabla s(\boldsymbol{r}) = \boldsymbol{e_s} + \boldsymbol{e_a}$ is shown for e_s in Table 2, with entries $e_{ij} = (1/2)[\partial s_i/\partial \boldsymbol{r_j} + \partial s_j/\partial \boldsymbol{r_i}]$. For the $\boldsymbol{e}_a$ entries, the "+ " sign is replaced by " −," so that the diagonal elements of $\boldsymbol{e}_a$ vanish.

Consider now a dilatation of a solid in which element A at $\boldsymbol{r}$ is displaced by $s(r)$ to A', and a neighboring element B at $\boldsymbol{r} + \mathrm{d}\boldsymbol{r}$ is displaced to B' by $s(\boldsymbol{r} + \mathrm{d}\boldsymbol{r})$. The A'—B' separation distance is then $dr' = dr + [s(r + d\boldsymbol{r}) - \boldsymbol{s}(\boldsymbol{r})] \approx d\boldsymbol{r} + d\boldsymbol{r} \cdot \nabla \boldsymbol{s}(\boldsymbol{r}) = d\boldsymbol{r} + d\boldsymbol{r} \cdot (\boldsymbol{e_s} + \boldsymbol{e_a})$. Note that $\boldsymbol{e_a}$ represents a pure rotation; on rotating the coordinate system by $-e_a$, one obtains $dr' = dr + dr \cdot e_s$ in the rotated system. Here, dr is the row vector [dx, dy, dz] and the $\boldsymbol{e}_s$ matrix is shown in Table 2.

A linear dilatation along x is then specified by $dx' = (1 + \boldsymbol{e_{xx}})dx + \boldsymbol{e_{yx}}\ dy + \boldsymbol{b}\ dz$, with similar expressions for dy' and dz'. Thus, the diagonal element e_{xx} of Table 2 indicates the fractional lengthening of the solid along the x-axis, and similarly, for y and z. Angular dilatations, on the other hand, involve a displacement dl whereby $\hat{\boldsymbol{i}}.\boldsymbol{dl}$ originally perpendicular to $\hat{j}\boldsymbol{dl}$ ($\hat{\boldsymbol{i}}$ and $\hat{j}$ are orthogonal unit vectors along x and y) now change into $A_x \equiv \hat{\boldsymbol{i}}\, \boldsymbol{dl} + \hat{\boldsymbol{i}}\, dl \cdot \boldsymbol{e_s} = \hat{i}(1 + e_{xx})dl + \hat{j}e_{xy}\, \boldsymbol{dl} + \hat{k}e_{xz}\, \boldsymbol{dl}$, and $A_y \equiv \hat{j}\, dl + \hat{j}\, dl \cdot e_s = \hat{i}e_{yx}\, dl + \hat{j}(1 + e_{yy})dl + \hat{k}e_{yz}\, dl$. The angle between

A_x and A_y in the x-y-plane is specified by

$$\cos \phi_{xy} = \frac{\left(\hat{\boldsymbol{i}}\, \mathrm{d}l + \hat{\boldsymbol{i}}\, \mathrm{d}l \cdot \boldsymbol{e}_s\right) \cdot \left(\hat{\boldsymbol{j}}\, \mathrm{d}l + \hat{\boldsymbol{j}}\, \mathrm{d}l \cdot \boldsymbol{e}_s\right)}{\left|\hat{\boldsymbol{i}}\mathrm{d}l + \hat{\boldsymbol{i}}\mathrm{d}l \cdot \boldsymbol{e}_s\right| \times \left|\hat{\boldsymbol{j}}\, \mathrm{d}l + \hat{\boldsymbol{j}}\, \mathrm{d}l \cdot \boldsymbol{e}_s\right|} \tag{18}$$

When the appropriate entries for $\boldsymbol{e}_s$ are introduced and an expansion is carried out to first order in e_{ij}, one obtains (after a large number of elementary steps) $cos\phi_{xy} \approx 2e_{xy}$. Now, introduce the deviation from the right angle by $\Omega_{xy} = \pi/2 - \phi_{xy}$, so that $cos\phi_{xy} \approx \Omega_{xy} \approx 2e_{xy}$. Similarly, $\Omega_{xz} \approx 2e_{xz}$, $\Omega_{yz} \approx 2e_{yz}$.

It is conventional to introduce a more compact notation for the strain components, as shown in part B of Table 2; also, one sets up six components of a stress tensor $\boldsymbol{\sigma}$ that induces the strain. Here, $\sigma_i = [\partial(U/V)/\partial e_i]_{S,\, ej \neq i}$; these are listed in part C of Table 2. The element of work is then given by $V\sum_i \sigma_i\, \boldsymbol{de_i}$.

Table 2 Matrix entries for deformation of anisotropic materials.

A. Entries to the symmetric strain tensor

$$\boldsymbol{e} = \begin{vmatrix} e_{xx}e_{xy}e_{xz} \\ e_{yx}e_{yy}e_{yz} \\ e_{zx}e_{zy}e_{zz} \end{vmatrix} \begin{array}{ll} e_{xx} = (\partial s_x/\partial x) & e_{xy} = (1/2)\left[(\partial s_x/\partial y) + \left(\partial s_y/\partial x\right)\right] = e_{yx} \\ e_{yy} = \left(\partial s_y/\partial y\right) & e_{xz} = (1/2)[(\partial s_x/\partial z) + (\partial s_z/\partial x)] = e_{zx} \\ e_{zz} = (\partial s_z/\partial z) & e_{yz} = (1/2)\left[(\partial s_z/\partial y) + \left(\partial s_y/\partial z\right)\right] = e_{zy} \end{array}$$

B. Conventional notation for strain components

$e_1 \equiv e_{xx}$, $e_2 \equiv e_{yy}$, $e_3 \equiv e_{zz}$

$e_4 \equiv 2e_{xy} = 2e_{yx}$, $e_5 \equiv 2e_{xz} = 2e_{zx}$, $e_6 \equiv 2e_{yz} = 2e_{zy}$

C. Conventional notation for stress components

$\sigma_1 \equiv \sigma_{xx}$ pressure along x $\sigma_4 \equiv \sigma_{xy} = \sigma_{yx}$ pressure $\perp x$ along y or vice versa

$\sigma_2 \equiv \sigma_{yy}$ pressure along y $\sigma_5 \equiv \sigma_{xz} = \sigma_{zx}$ pressure $\perp x$ along z or vice versa

$\sigma_3 \equiv \sigma_{zz}$ pressure along z $\sigma_6 \equiv \sigma_{yz} = \sigma_{zy}$ pressure $\perp y$ along z or vice versa

Table 3 Maxwell relations for anisotropic solids; constant *V*.

$\frac{1}{V}\left(\frac{\partial S}{\partial e_i}\right)_T = -\left(\frac{\partial \sigma_i}{\partial T}\right)_{e_i}$	$\frac{1}{V}\left(\frac{\partial S}{\partial \sigma_i}\right)_T = \left(\frac{\partial e_i}{\partial T}\right)_{\sigma_i}$	(III.1, III.2)
$\frac{1}{V}\left(\frac{\partial S}{\partial \sigma_i}\right)_{e_i} = \left(\frac{\partial e_i}{\partial T}\right)_S$	$\frac{1}{V}\left(\frac{\partial S}{\partial e_i}\right)_{\sigma i} = -\left(\frac{\partial \sigma_i}{\partial T}\right)_S$	(III.3, III.4)

With these definitions, the above concepts are embedded in thermodynamics by writing the differential of the energy (of the strained relative to the unstrained body) as

$$\mathrm{d}U = T\,\mathrm{d}S + V\sum_{i=1}^{6}\sigma_i\,\mathrm{d}e_i \tag{19}$$

One should note the positive sign ahead of the second term: work is done by the system as the strain is diminished. Next, the enthalpy, by $H = U - \sum_{i=1}^{6}\sigma_i(Ve_i)$ is introduced. The enthalpy differential is then given by

$$\begin{aligned}\mathrm{d}H &= \mathrm{d}U - V\sum_{i=1}^{6}e_i\,\mathrm{d}\sigma_i - V\sum_{i=1}^{6}\sigma_i\,\mathrm{d}e_i \\ &= T\,\mathrm{d}S - V\sum_{i=1}^{6}e_i\,\mathrm{d}\sigma_i\end{aligned} \tag{20}$$

From (19) and (20), Maxwell relations may be constructed in the usual manner; these are listed in Table 3: integration then specifies the entropy of the solid in its dependence on σ_i, or on e_i under different conditions (for details, see the "Further reading" section).

Moreover, from the definition of the stress tensor, it follows that

$$\left(\partial\sigma_i/\partial e_j\right)_{S,e_{j\neq i}} \equiv c_{ij}\Big|_S = \left(\partial\sigma_j/\partial e_i\right)_{S,e_{j\neq i}} \equiv c_{ji}\Big|_S \tag{21a}$$

$$\left(\partial\sigma_i/\partial e_j\right)_{T,e_{j\neq i}} \equiv c_{ij}\Big|_T = \left(\partial\sigma_j/\partial e_i\right)_{T,e_{j\neq i}} \equiv c_{ji}\Big|_T \tag{21b}$$

which are known as isentropic and isothermal elastic stiffness coefficients. The inverse $(\partial\sigma_i/\partial e_j)_{S,\ \sigma_{j\neq i}}$ or $(\partial\sigma_i/\partial e_j)_{T,\ \sigma_{j\neq i}}$ represent isentropic and isothermal compliance coefficients. There also exist six thermal strain coefficients $\alpha_i \equiv (\partial e_i/\partial T)_{\sigma j}$ and six thermal stress coefficients $\delta_i \equiv (\partial\sigma_i/\partial T)_{ej}$ that deal with the temperature variations of the respective coefficients.

This completes the brief survey of commonly used coefficients that characterize the deformation of anisotropic elastic solids.

Application of thermodynamic concepts

The basic concepts developed above find many applications in condensed matter physics. Several important uses are briefly listed. Prominent among these is the determination of heat capacities of materials as a function of temperature, from which the energy, enthalpy, and entropy may be found by integration of Eq. (15a).

An entire subdiscipline deals with phase equilibria, phase diagrams, phase transitions, and related aspects. All these topics are ultimately based on the properties of the chemical potential, briefly alluded to in an earlier section of the present article. Phase diagrams obtained from empirical measurements are of cardinal importance in the entire manufacturing process and industrial output of chemicals in developed countries.

Another subdiscipline deals with the properties of matter, energy, and entropy flow, as determined by irreversible thermodynamics.

Thermal properties of materials represent another area of great contemporary interest. Here, the properties of anisotropic media discussed above, represent the proper theoretical background for a rationalization of experimental results.

Results based on the third law of thermodynamics provide the basic theoretical framework for interpreting a large number of studies dealing with properties of materials at ultralow temperatures. The operation of cyclic engines, described briefly above, is another area where thermodynamics plays an important role. Lastly, by considering the various different types of work alluded to in the introduction to the first law, one can extend the above thermodynamic principles to new areas, such as electromagnetic properties, surface adsorption phenomena, curved surfaces, radiation, processes in gravitational fields, and the like. Their detailed discussion must be left to specialized monographs. They form the foundation for explaining many physical characteristics of condensed matter, such as magnetic and electrical properties, the interaction of condensed phases with electromagnetic radiation, and interfacial phenomena.

Reprise and extension of fundamentals

It is instructive to extend the earlier discussion of the laws of thermodynamics by including the significant role of the surroundings, and featuring the distinction between reversible and irreversible heat transfers and work performance. To this end we study the interaction of a system, uniformly characterized by independent variables T, V, n_j, with its surroundings, characterized by the variables T_0, V_0, $n_{0,j}$. The surroundings are assumed to be so vast as to remain essentially constant, or respond to the system in a reversible manner, even when the system itself undergoes irreversible processes. All irreversible processes are assumed to occur such that in an infinitesimal advance the thermodynamic variables of the system change nearly uniformly during their interaction with the external world. The system and surroundings of the compound unit are separated by a thin barrier, across which quantities such as the temperature change from T to T_0. Processes within this small interface are ignored. Analogous remarks apply to all other intensive variables, such as pressure or chemical potential.

Even though the above restrictions are somewhat unrealistic the corresponding processes are instructive. Examine first a reversible process (r) that involves heat exchanges between system and surroundings, both at constant volume and composition. During an infinitesimal step the corresponding entropy change, d_rS_u in the universe is the sum of the entropy change dS of the system, and the compensating entropy change d_rS_0 of the surroundings at the temperature T almost equal to T_0. In the present case there is no net change in entropy in the compound system:

$$d_rS_u \equiv dS(T,\, V,\, n_j) + d_rS_0(T,\, V_0,\, n_{0,j}) = 0. \tag{22a}$$

Next, let the same change of the system take place irreversibly (i) while the reservoir, operating reversibly, remains at temperature T_0. The irreversible operation occurs under conditions that can still be maintained at a more – or - less uniform average value T. Since entropy is a function of state of the system, $dS(T,V,n_j)$ is the same as before, but the entropy change in the surroundings, $d_iS_0(T_0,V_0,n_{0,j})$, is now different. According to the Second Law the entropy of the universe can only increase, so that

$$d_iS_u \equiv dS(T,\, V,\, n_j) + d_iS_0(T_0,\, V_0,\, n_{0,j}) > 0. \tag{22b}$$

The use of inequalities is always awkward; we avoid several problems by introducing an entropy deficit function $\text{đ}\theta > 0$ that converts Eq. (22b) into an equality:

$$d_iS_u \equiv dS(T, V, n_j) + d_iS_0(T_0, V_0, n_{0,j}) - \text{đ}\theta = 0. \tag{22c}$$

We encounter a notational problem here: $d_iS_0(T_0,V_0,n_{0,j})$ refers to a reversible process in the surroundings in response to an irreversible process in the system.

So far $\text{đ}\theta$ is simply a bookkeeping device. However, it acquires meaning when we subtract Eq. (22a) from Eq. (22c) to write

$$d_iS_0(T_0, V_0, n_{0,j}) - d_rS_0(T, V_0, n_{0,j}) = \text{đ}\theta \tag{22d}$$

whereby $\text{đ}\theta$ represents the entropy difference in the surroundings when the infinitesimal step $dS(T,V,n_j)$ within the system is carried out irreversibly as opposed to reversibly.

The system + surroundings form a closed unit, so that the infinitesimal heat (đ_iQ) lost (gained) irreversibly by the system operating at temperature T is gained (lost) by the surroundings (đ_rQ_0) operating reversibly at temperature T_0. Thus, necessarily, $-\text{đ}_iQ = \text{đ}_rQ_0$. It is only in the limit $T - T_0 \to 0$ that the heat transfer from or to the system can be carried out reversibly.

During the reversible step (r) at the common temperature T the infinitesimal entropy change of the system is given by $dS \equiv d_rS = \text{đ}_rQ/T$; hence, by Eq. (22a), the entropy change in the surroundings is specified by

$$\text{đ}_rS_0 = -dS = -\text{đ}_rQ/T. \tag{23a}$$

For the same step executed irreversibly (i), with the temperature of the system at T and that of the surroundings at T_0, the heat exchange $\text{đ}_iQ = -\text{đ}_rQ_0$ produces an entropy change in the surroundings as

$$d_iS_0 = \text{đ}_rQ_0/T_0 = -\text{đ}_iQ/T_0, \tag{23b}$$

where we invoked the reversibility of all processes in the reservoir.

On inserting Eqs. (23a) and (23b) into Eq. (22d) we obtain the fundamental relation

$$\text{đ}_iQ = (T_0/T)\text{đ}_rQ - T_0\text{đ}\theta = T_0\,(dS - \text{đ}\theta) < (T_0/T)\text{đ}_rQ. \tag{24a}$$

The inequality is self-evident for the case where heat is transferred into the system; here đ_iQ and đ_rQ are both positive, with $T < T_0$. Moreover, this result must apply for any $T < T_0$, and particularly, to the limiting case $T = T_0$. One thereby obtains a tighter constaint, as a string of inequalities:

$$\text{đ}_iQ < \text{đ}_rQ < (T_0/T)\text{đ}_rQ, \tag{24b}$$

where the first inequality is a version of the **Clausius Inequality**. Implicit in the above is the assumption that in the limiting case $đ\theta$ does not necessarily vanish: as an example, consider the case where the reversible heating of the system triggers a spontaneous reaction totally within the sample.

When heat is transferred out of the system, with $T > T_0$, Eq. (24a) shows that $đ_iQ$ is more negative than $(T_0/T)đ_rQ$. This result applies as well to any $T > T_0$, and thus, to the limiting case $T = T_0$. We then recover a string of increasingly less negative quantities going from left to right in Eq. (24b).

Eq. (24a) may be restated in the equivalent form

$$đ_iQ = đ_rQ + (T_0/T - 1)\, đ_rQ - T_0 đ\theta, \tag{24c)]}$$

where the last two terms specify the difference between the heat transferred irreversibly in the infinitesimal step, $đ_iQ$, and that transferred reversibly, $đ_rQ$, in executing the same step.

When the temperature of the system and reservoir differ only infinitesimally, $T \approx T_0$, Eq. (24c) reduces to

$$đ_iQ = đ_rQ - Tđ\theta = T(dS - đ\theta). \tag{24d}$$

Here $Tđ\theta$ may be interpreted as the difference in heat transfers executed reversibly and irreversibly under these limited conditions, as may happen if an otherwise reversible heat transfer into the system triggers additional irreversible phenomena totally within the system. Eq. (24d) shows directly that the irreversible heat transfer is less positive or more negative than its reversible counterpart.

One may also turn Eq. (24a) around to read

$$dS = đ_iQ/T_0 + đ\theta > đ_iQ/T_0, \tag{24e}$$

which shows explicitly that in irreversible processes the total entropy change in the system is only partially accounted for by the exchange of heat. Note that it is the well established temperature of the reservoir that always enters the expression. The above should be contrasted with the usual relation $dS = đ_rQ/T$, in which the entropy change is completely tracked by the reversible heat transfer at the common temperature T. Eq. (24e) represents the Clausius Inequality.

Eq. (24e) merits further careful scrutiny. In the above infinitesimal step that carries the system from state A to state B, dS is always the total concomitant entropy change. In the absence of any work or compositional changes the only channel for outside communication is the transfer of heat, as shown by the first term on the right. This then dictates that the $đ\theta$ term represents the additional contribution to dS arising from purely reconfigurations of the system that are outside the control of the experimenter.

Performance of work

Next, we reintroduce the First Law of Thermodynamics. Because the energy E is a function of state we set

$$dE = đ_rQ + đ_rW = đ_iQ + đ_iW, \tag{25a}$$

where W is the work performed during the process. On eliminating $đ_iQ$ between Eqs. (24c), and (25a) we may solve for

$$đ_iW = đ_rW - (T_0/T - 1)\, đ_rQ + T_0đ\theta = đ_rW - (T_0 - T)dS + đ\varepsilon, \tag{25b}$$

where $T_0đ\theta \equiv đ\varepsilon$ represents the infinitesimal difference in work performance under reversible as opposed to irreversible conditions. A special case of interest involves processes that are carried out under conditions where T and T_0 differ only infinitesimally, so that

$$đ_iW = đ_rW + T_0đ\theta \equiv đ_rW + đ\varepsilon. \tag{25c}$$

We now note that the last two terms on the right in Eq. (25b) differ in sign from those in Eq. (24c) and therefore are positive. This leads to the inequality

$$đ_iW > đ_rW, \tag{25d}$$

which indicates, in accord with intuition, that work executed in carrying out a particular process irreversibly always exceeds work carried out reversibly, whether work is done on or by the system. In the latter case less useful work is obtained from the system operating irreversibly.

Another significant feature of the present analysis is found by solving Eq. (25b) for

$$đ\theta = (đ_iW - đ_rW)/T_0 + (1 - T/T_0)dS. \tag{26}$$

This relation expresses the contribution of irreversible phenomena to the infinitesimal entropy change, in terms of quantities that may be measured or calculated. It requires monitoring the entropy change in the system while carrying out a given process reversibly. Also, one needs to determine the work for executing the same change reversibly and irreversibly. Work executed in any given process may always be determined experimentally; the work involved in a reversible process may be calculated. Thus, the right hand side of Eq. (26) is experimentally accessible.

Conclusion

A brief review of the four basic laws of thermodynamics has been provided, based on standard operations covered in the literature. Much of the present discussion is based on the distinction between reversible and irreversible phenomena. This is followed by discussion with special emphasis on the interaction between the system and its surroundings, thus obviating the need of inequalities in discussing the exchange of heat and work. For more detailed information of all the topics raised above the reader is directed to the vast accumulation of articles and books that have accumulated of over 160 years, calling for a firm grasp of the fundamental principles.

Irreversible thermodynamics as applied to basic electron transport theory in solids[☆]

Jurgen M Honig, Department of Chemistry, Purdue University, West Lafayette, IN, United States

© 2024 Elsevier Ltd. All rights reserved.

This is an update of J.M. Honig, Irreversible Thermodynamics and Basic Transport Theory in Solids, Editor(s): Franco Bassani, Gerald L. Liedl, Peter Wyder, Encyclopedia of Condensed Matter Physics, Elsevier, 2005, Pages 34–43, ISBN 9780123694010, https://doi.org/10.1016/B0-12-369401-9/00712-9.

Introductory comments **488**
Elementary description of heat and mass transport **488**
Transfer of heat between two different systems 488
Heat transfer equations 488
Transfer of energy and mass between two different regions 489
Phenomenological equations 489
Basic principles of mass, energy, and entropy balances **490**
Mass balance equation 490
Energy balance equations 490
Entropy balance relations 490
Phenomenological equations for thermoelectric effects; Onsager's reciprocity conditions 491
Thermoelectric phenomena 491
Thermoelectric transport coefficients 492
Peltier and Thomson effects 493
Transport effects in magnetic fields 493
Phenomenological equations for thermomagnetic phenomena 493
Transport coefficients for thermomagnetic phenomena 494
Identification of phenomenological coefficients 495
Transport in two-band (electron–hole) conductors 495
Use of constraints to identify transport coefficients 495
Conclusion **496**
Acknowledgment **496**
Reference **496**

Abstract

An overview of basic ideas in irreversible thermodynamics as they apply to electron transport phenomena in solids is provided; the theory is thus not presented in its full generality. The discussion is limited to systems that are at rest, remain at constant volume, undergo no chemical changes, are isotropic, and for which steady-state conditions hold. In these circumstances, the ordinary time differential operator d/dt and its partial counterpart, $\partial/\partial t$, are equivalent, and the tensorial notation can be dispensed with. Readers who desire a full introduction to irreversible phenomena should consult the listings under "Further reading" section. The discussion is also limited to the linearized regime, in which departures from equilibrium are small, such that intensive variables such as temperature, pressure, concentration, chemical potential, and the like retain their significance locally. However, these variables are presumed to vary with position in such a manner that their gradients are small compared to their values averaged over the system.

Key points

- Heat transfer is governed by Fourier's Law, Eq. (5).
- The entropy change associated with heat transfer is specified by Eq. (8).
- The mass transfer, energy change, and entropy change during heat transfer is specified by Eqs. (10), (14), (16) respectively.
- Thermoelectric processes are described in terms of Seebeck coefficients, Eq. (25), Peltier effects, Eqs. (27a)–(27e), and Thomson coefficients.
- Magnetic field effects are displayed in Eqs. (28a)–(28d), subject to the Casimir-Onsager relations.
- Special are discussed in detail: Ohm's Law in magnetic fields, the Hall effect, the Ettingshausen effect, the adiabatic and isothermal Hall effects, thermal conductivity, thermoelectric phenomena via the Seebeck coefficient, the Nernst effect, the Righi-Leduc coefficients.
- Various transport coefficients of Eqs. (28a)–(28d) are re-expressed in terms of the coefficients specified above via Eq. (35).

[☆] *Change History*: September 2022. JM Honig updated the chapter.

- One-band transport coefficients are generated by Eqs. (36a)–(36d).
- Transport coefficients for p-n band solids are assembled in Table 1.
- Transport coefficients in the limit of small magnetic fields are assembled in Table 2.

Introductory comments

An overview of basic ideas in irreversible thermodynamics as they apply to electron transport phenomena in solids is provided; the theory is thus not presented in its full generality. The discussion is limited to systems that are at rest, remain at constant volume, undergo no chemical changes, are isotropic, and for which steady-state conditions hold. In these circumstances, the ordinary time differential operator d/dt and its partial counterpart, $\partial/\partial t$, are equivalent, and the tensorial notation can be dispensed with. Readers who desire a full introduction to irreversible phenomena should consult the listings under "Further reading" section. The discussion is also limited to the linearized regime, in which departures from equilibrium are small, such that intensive variables such as temperature, pressure, concentration, chemical potential, and the like retain their significance locally. However, these variables are presumed to vary with position in such a manner that their gradients are small compared to their values averaged over the system.

Elementary description of heat and mass transport

Transfer of heat between two different systems

To begin with, a heuristic introduction of basic concepts characterizing relaxation processes that lead toward establishment of equilibrium conditions is given. Consider two isolated regions in space, designated by (and at) temperatures T' and T''; when brought into contact (see Fig. 1), and on allowing the intervening partition to become slightly diathermic, heat is slowly transferred between the compartments. If the enlarged unit remains isolated, and the interfacial phenomena are ignored, the energies, E' and E', of the two subsystems are additive, as are the entropies $S'(E', V')$ and $S''(E'', V'')$. Assume further that the volumes V' and V'' remain fixed. Then the first and second laws of thermodynamics lead to the relations

$$\mathrm{d}E' + \mathrm{d}E'' = 0 \tag{1a}$$

$$dS = (\partial S'/\partial E')_{V'} dE' + (\partial S''/\partial E'')_{V'} dE'' \geqslant 0 \tag{1b}$$

On account of Eq. (1a) and with $(\partial E/\partial S)_V = T$, where T is the temperature of the bulk of the system, Eq. (1b) becomes

$$dS = (1/T'' - 1/T') dE'' \geqslant 0 \tag{2}$$

which immediately establishes the requirement $T' = T''$ as a necessary condition for thermal equilibrium. Moreover, according to the second law, as equilibrium is established, the total entropy of the isolated compound system increases toward a maximum, consistent with the remaining constraints. Hence, the time derivative of the total entropy, $\dot{S} \equiv (dS/dt)$, may be written as

$$\dot{S} = (1/T'' - 1/T')(dE''/dt) \geqslant 0 \tag{3}$$

In the present case, no work has been performed and no material has been transferred; therefore, all energy changes involve solely a transfer of heat between the two subsystems. It is then appropriate to identify $\mathrm{d}E''/\mathrm{d}t$ with the rate of heat transfer Q across the boundary. Hence, Eq. (3) is rewritten as $\dot{S} = \Delta(1/T)\dot{Q}$. Next, a heat flux is defined by $J_Q \equiv \dot{Q}/A$, where A is the cross section of the partition. In the experiment, the temperatures T' and T'' remain nearly constant within both compartments, except near the common boundary, where the change from T' to T'' occurs over a small distance l perpendicular to the partition (see Fig. 1). The product Al roughly defines a volume V in the boundary region over which the temperature changes. One can then write $\dot{S} = \Delta(1/T) V J_Q / l$. In the limit of small l, the ratio $\Delta(1/T)/l$ becomes the gradient of inverse temperature, $\nabla(1/T)$. The ratio $\dot{S}/V$ is the rate of entropy production per unit volume, $\dot{\theta}$, in the heat transfer region. This gives, finally,

$$\dot{\theta} = \nabla(1/T) J_Q \geqslant 0 \tag{4}$$

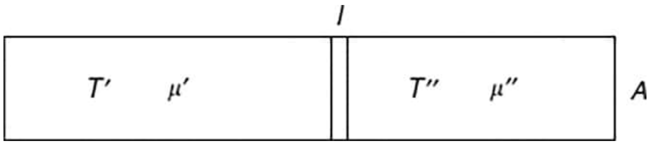

Fig. 1 Two bodies of cross section A at temperatures T' and T'' and at chemical potentials μ' and μ'' are in tenuous contact. Changes in T and μ occur over a small distance/straddling the boundary. When no mass transfer occurs, the chemical potentials are irrelevant.

Heat transfer equations

The above discussion is very suggestive. The rate of entropy generation is seen to be a product of two conjugate variables, namely, a heat flux, J_Q, and a generalized force, $F_T \equiv \nabla(1/T)$; hence, schematically $\dot{\theta} = F_T J_Q \geqslant 0$. Note that in Eqs. (3) and (4), and with the directions indicated in Fig. 1, $\dot{\theta} > 0$ means either that $F_T > 0$, $I_Q > 0$, with $T'' < T'$, or that $F_T < 0$, $J_Q < 0$, with $T'' > T'$. In either case, heat flows from the hotter to the cooler side. When $\dot{\theta} = 0$, equilibrium prevails; J_Q and F_T both vanish. It is then plausible to claim that the heat flux is "driven" by the existence of a temperature gradient (actually, a gradient in inverse temperature).

Next, a relation between J_Q and F_T is established, which requires extrathermodynamic information, such as a microscopic transport theory or experimental considerations. Close to the equilibrium, a linear relation $J_Q = L_T F_T$ is assumed to prevail between force and flux, where L_T is a parametric function independent of J_Q or F_T. The proportionality factor is known as a phenomenological or macroscopic coefficient. The essential correctness of this very primitive approach may be checked by noting that

$$J_Q = L_T \nabla(1/T) = -(L_T/T^2)\nabla T \equiv -\kappa \nabla T \tag{5}$$

where $\kappa \equiv L_T/T^2$ is the thermal conductivity, and one recovers the *Fourier law* of heat conduction.

Transfer of energy and mass between two different regions

The above approach will now be generalized. Consider two compartments at different temperatures that contain the same material at two different mole numbers n' and n''. The 2 units are joined and the intervening partition is rendered slightly porous, allowing the very gradual transfer of energy and of mole numbers (Fig. 1). As long as the compartmental volumes are unchanged, one can invoke the fundamental relation

$$\mathrm{d}S = (\partial S'/\partial E')_{V',n'}\mathrm{d}E' + (\partial S''/\partial E'')_{V'',n''}\mathrm{d}E'' + (\partial S/\partial n')_{V',E'}\mathrm{d}n' + (\partial S/\partial n'')_{V'',E''}\mathrm{d}n'' \tag{6}$$

Since $\mathrm{d}S = \mathrm{d}E/T - (\mu/T)\mathrm{d}n$, where μ is the chemical potential, and with $\mathrm{d}E'' = -\mathrm{d}E'$, $\mathrm{d}n'' = -\mathrm{d}n'$, the above may be recast as

$$dS = (1/T'' - 1/T')dE'' - (\mu''/T'' - \mu'/T')dn'' \geqslant 0 \tag{7a}$$

from which it follows that at equilibrium, $T' = T''$ and $\mu' = \mu''$, consistent with well-established thermodynamic principles. The earlier procedure can be extended by introducing two fluxes, namely $J_E \equiv \mathrm{d}E''/A\,\mathrm{d}t$ and $J_n \equiv \mathrm{d}n''/A\,\mathrm{d}t$, as well as two generalized forces, $F_T \equiv \Delta(1/T)/l \equiv \nabla(1/T)$ and $F_n \equiv \Delta(\mu/T)/l \equiv \nabla(\mu/T)$, appropriate for small distances, l, across the junction. Eq. (7a) thus becomes

$$\dot{\theta} = J_E \nabla(1/T) - J_n \nabla(\mu/T) \tag{7b}$$

The minus sign in this equation can also be rationalized via a sufficiency argument. To ensure that $\dot{\theta} > 0$, both terms in the expression need to be positive. Referring to Fig. 1, assume that $J_E > 0$ (i.e., energy flows left to right); to keep the first term positive it is necessary that $T'' < T'$, as before. In order to render the second term positive, one requires that $(\mu''/T'' - \mu'/T')J_n < 0$. Assume that $J_n > 0$ (particles flow from left to right), which then requires the multiplier to be negative, so that $\mu'/T' > \mu''/T''$, or $\mu'/\mu'' > T'/T'' > 1$, implying that the particle flux occurs from the region of higher chemical potential to one of lower chemical potential.

Phenomenological equations

The relation $T\,\mathrm{d}S = \mathrm{d}E - \mu\mathrm{d}n$ is now introduced, reformulated after time differentiation as $TJ_S = J_E - \mu J_n$, valid in the absence of any mechanical pressure-volume work (V' and V'' remain fixed). Using Eq. (7b), the rate of entropy production per unit volume may be written as

$$\dot{\theta} = -\frac{1}{T}\{J_S \nabla T + J_n \nabla\mu\} \geqslant 0 \tag{8}$$

Such a relation is of fundamental importance, in that it specifies $\dot{\theta}$ as a sum of products that involve conjugate flux-force pairs, namely, $(J_S, -T^{-1}\nabla T)$ and $(J_n, -T^{-1}\nabla\mu)$. These quantities are of great importance in the formulation of the so-called linear phenomenological equations (PEs), valid for small departures from equilibrium. These are constructed so as to relate the two fluxes Js and Jn to the two forces $(1/T)\nabla T$ and $(1/T)\nabla\mu$ in the following linear form:

$$J_S = (L_{11}/T)\nabla T + (L_{12}/T)\nabla\mu \tag{9a}$$

$$J_S = (L_{21}/T)\nabla T + (L_{22}/T)\nabla\mu \tag{9b}$$

The minus signs have been absorbed in the L coefficients. One should note the implied superposition principle: both forces contribute to both fluxes. The L_{ij} are known as phenomenological or macroscopic coefficients; L_{11} and L_{22} connect the fluxes to their principal driving forces, while L_{12} and L_{21} give rise to interference effects that are studied in detail below.

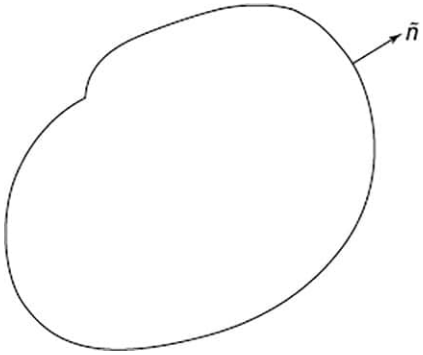

Fig. 2 Boundary of a system, with the unit vector pointing opposite to the inward flow of energy, entropy, or mass.

Basic principles of mass, energy, and entropy balances

Mass balance equation

The very heuristic approach presented so far, while leading to correct results, ought really to be supplanted by a more rigorous (though simplified) derivation of Eqs. (9a) and (9b). One can begin with the conservation law

$$\mathrm{d}\rho_k/\mathrm{d}t = -\nabla\cdot\boldsymbol{J}_k \tag{10}$$

wherein the total rate change in concentration ρ_k of species k within the system (Fig. 2) is given by the imbalance between the influx and outflow of species k across the boundaries; the minus sign arises because the normal unit vector in Fig. 2 faces outward.

Energy balance equations

In order to introduce relations for energy balance, one can follow the convention by changing from energy or mass per unit volume to energy per unit mass and mass fraction. This is indicated by overbars such as $\overline{u}$,$\overline{e}$,$\overline{\psi}$,$\overline{n}_k$, as introduced below. Further, let species k interact with a stationary external potential $\overline{\psi}_k$ (e.g., electrons in an electrostatic potential); then operating on both sides of Eq. (10) with $\sum_{(k)}\overline{\psi}_k$ and setting $\sum_{(k)}\overline{\psi}_k\rho_k \equiv \overline{\psi}\rho$, and using the vector calculus involving a scalar function a and a vector function v, $\nabla\cdot av = a\nabla\cdot v + v\cdot\nabla a$, one obtains

$$\mathrm{d}(\rho\overline{\psi})/\mathrm{d}t = -\nabla\cdot\sum_k \overline{\psi}_k\boldsymbol{J}_k + \sum_k \boldsymbol{J}\cdot\nabla\overline{\psi}_k \tag{11}$$

As a third step, one introduces the conservation law for total energy density $\rho\overline{u}$ (energy cannot be generated or destroyed locally):

$$\mathrm{d}(\rho\overline{u})/\mathrm{d}t = -\nabla\cdot\boldsymbol{J}_U \tag{12}$$

The total energy density can be separated into $\overline{u} = \overline{e} + \overline{\psi}$, where $\overline{e}$ is the internal energy per unit mass. Correspondingly,

$$\boldsymbol{J}_U = \boldsymbol{J}_Q + \sum_k \overline{\psi}_k\boldsymbol{J}_k \tag{13}$$

This nomenclature is appropriate; the net total energy flux density $\nabla\cdot\boldsymbol{J}_U$ consistently reflects the performance of work, potential energy changes, and heat flows. The first two effects are subsumed in the term $\nabla\cdot\sum_k\overline{\psi}_k\boldsymbol{J}_k$; the rest is contained in the net heat flux, $-\nabla\cdot\boldsymbol{J}_Q\cdot$. Next, subtracting (11) from (12) and introducing Eq. (13), yields an expression for the overall rate of change of internal energy

$$\mathrm{d}(\rho\overline{e})/\mathrm{d}t = -\nabla\cdot\boldsymbol{J}_Q - \sum_k J_k\cdot\nabla\overline{\psi}_k \tag{14}$$

This involves not only the customary divergence term but also the last term, which represents a source term that arises from the interaction of species k with the external potential $\overline{\psi}_k$.

Entropy balance relations

The entropy balance equations can be introduced by using the expression (for $\mathrm{d}V = 0$) $T\mathrm{d}S = \mathrm{d}E - \sum_k \mu_k\, \mathrm{d}n_k$ to write

$$T(\,\mathrm{d}(\rho s)/\mathrm{d}t) = (\mathrm{d}(\rho\overline{e})/\mathrm{d}t) - \sum_k \overline{\mu}_k(\,\mathrm{d}\rho_k/\mathrm{d}t) \tag{15a}$$

On insertion of Eqs. (14) and (10), one obtains

$$\frac{\mathrm{d}(\rho\overline{s})}{\mathrm{d}t} = \frac{1}{T}\left\{ -\nabla\cdot\boldsymbol{J}_Q - \sum_k \boldsymbol{J}_k\cdot\nabla\overline{\psi}_k + \sum_k \overline{\mu}_k\nabla\cdot\boldsymbol{J}_k \right\} \tag{15b}$$

The above may be rearranged by repeated application of the vector identity cited earlier; standard manipulations lead to the final result

$$\begin{aligned}\frac{\mathrm{d}(\rho\bar{s})}{\mathrm{d}t} &= -\nabla\cdot\left\{\left(J_Q - \sum_k \bar{\mu}_k \boldsymbol{J}_k\right)/T\right\} \\ &\quad -\left(1/T^2\right)\boldsymbol{J}_Q\cdot\nabla T + \left(1/T^2\right)\sum_k \bar{\mu}_k \boldsymbol{J}_k\cdot\nabla T \\ &\quad -(1/T)\sum_k \boldsymbol{J}_k\cdot\nabla\left(\bar{\mu}_k + \bar{\psi}_k\right)\end{aligned} \tag{16}$$

Although this looks complicated, it is amenable to a simple interpretation which is based on the entropy balance equation in the form $d(\rho\bar{s})/dt = -\nabla\cdot J_S + \dot{\theta}$. Comparison with Eq. (16) shows that it is appropriate to consider the quantity in curly brackets as a flux vector, so that

$$\boldsymbol{J}_S = \frac{1}{T}\left(J_Q - \sum_k \bar{\mu}_k \boldsymbol{J}_k\right) \tag{17}$$

is an entropy flux vector. The remaining terms are then to be identified as source terms θ in the entropy balance equation. This allows one to express the contribution of local events to the entropy generation rate as

$$\dot{\theta} = -(1/T)J_S\cdot\nabla T - (1/T)\sum\nolimits_k J_k\cdot\nabla\bar{\zeta}_k \geqslant 0 \tag{18}$$

where the generalized chemical potential has been introduced as $\bar{\zeta} \equiv \bar{\mu} + \bar{\psi}$ For isotropic materials in the absence of external potentials, Eq. (18) reduces to Eq. (8). This establishes the proper background for constructing the PEs, Eqs. (9a) and (9b), precisely in the same manner as was done earlier.

Phenomenological equations for thermoelectric effects; Onsager's reciprocity conditions

A very important characteristic of Eqs. (9a) and (9b) is the fact that the Onsager reciprocity relations, $L_{ij} = L_{ji}$ apply to such equations, so long as conjugate flux-force pairs are employed in formulating Eqs. (9a) and (9b). For proofs, the reader is referred to the literature; a simpler version, applicable to processes under steady-state conditions, was provided by Tykody (n.d.).

Thermoelectric phenomena

Eqs. (9a) and (9b) can be specialized to characterize interactions between heat flow and electric currents in a conductor, known as thermoelectric effects; this topic has been treated elsewhere in great detail (see the "Further reading" section). Consider a rectangular bar clamped between two thermal reservoirs at different temperatures (Fig. 3). The electron flow in the conductor is established by charging external condenser plates; this cumbersome method is used here (though not in actual practice) to avoid distracting complications from leads that normally connect the sample to the current source. Using the dissipation function, Eq. (18) with $k = n$, substituting $\bar{\zeta} = \bar{\mu} - e\bar{\varphi}$ in place of $\bar{\mu}$, and then replacing the electron flux vector $\boldsymbol{J}_n$ by the current density $\boldsymbol{J} = (-e)\boldsymbol{J}_n$, where $-e$ is the charge on the electron and $\bar{\varphi}$ is the electrostatic potential per electron mass, the dissipation relation can be written as $\dot{\theta} = J_S\cdot\left(-T^{-1}\nabla T\right) + J\cdot\left(-T^{-1}\nabla\left(\bar{\zeta}/e\right)\right)$. One can identify, from this relation, the proper fluxes and forces, so as to construct the phenomenological relations for an isotropic material (the vector notation can then be dropped):

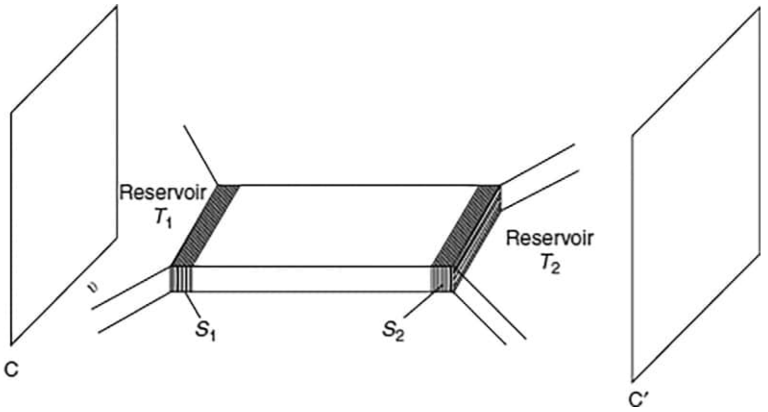

Fig. 3 Idealized setup for detection of thermoelectric effects. The solid is clamped between two thermal reservoirs at temperatures T_1 and T_2; S_1 and S_2 are removable strips for thermal insulation. Current flow is activated through charging of the condenser plates C and C'.

$$J_S = -(L_{SS}/T)\nabla T + (L_{Sn}/T)\nabla(\zeta/e) \tag{19a}$$

$$J = -(L_{nS}/T)\nabla T + (L_{nn}/T)\nabla(\zeta/e) \tag{19b}$$

with $L_{nS} = L_{Sn}$. In doing so, one has also switched from $\overline{\zeta}$ to ζ, absorbing the mass factor and the minus sign in L_{Sn} and L_{nn}.

Thermoelectric transport coefficients

By imposing a variety of constraints, the above expressions can be attributed to physical significance:

(1) Set $\nabla T = 0$ and eliminate $\nabla(\zeta/e)$ between (19a) and (19b) to obtain $J_S/J = L_{Sn}/L_{nn} = -J_S/eJ_n$; since $J_S/J_n \equiv S^*$ is the total entropy carried per electron, one obtains

$$L_{Sn}/L_{nn} = -S^*/e \tag{20}$$

Next, consider Eq. (19b) with $\nabla T = 0$. For a homogeneous sample $\nabla\mu = 0$; Eq. (19b) then reduces to $J = (L_{nn}/T)\ \nabla\ (-\phi) = (L_{nn}/T)\ E$, where E is the electrostatic field. Thus, one recovers.

Ohm's law $J = \sigma E$, where σ is the electrical conductivity. This leads to the identification

$$L_{nn}/T = \sigma, \quad J = \sigma\nabla(\zeta/e) \quad (\nabla T = 0) \tag{21}$$

(2) If current flow is suppressed, set $J = 0$, solve Eq. (19b) for $\nabla(\zeta/e)$, and substitute the result in Eq. (19a); this yields

$$J_S = -(1/T)\left[L_{SS} - L_{nS}^2/L_{nn}\right]\nabla T \quad (J = 0) \tag{22}$$

Now, as shown in Eq. (17), in the absence of current flow the entropy flux may be replaced by J_Q/T; thus, one recovers *Fourier's law* of heat conduction, $J_Q = -\kappa\nabla T$, with the thermal conductivity given by

$$\kappa = L_{SS} - L_{nS}^2/L_{nn} \tag{23}$$

An additional contribution to κ arises from the lattice thermal conductivity that is not included here.

(3) In the more general case when $J > 0$, one may still eliminate $\nabla(\zeta/e)$ between Eqs. (19a) and (19b) to obtain

$$J_S = -(S^*/e)J - (\kappa/T)\nabla T = S^* J_n - (\kappa/T)\nabla T \tag{24}$$

This shows that the total electronic entropy flux involves the entropy transport $S^* J_n$ as well as heat transport through the motion of the electrons.

(4) A second result arises by imposing the condition $J = 0$ and solving Eq. (19b) for

$$\nabla(\zeta/e) = (L_{nS}/L_{nn})\nabla T \equiv \alpha\nabla T \tag{25}$$

Here, one encounters a new prediction: the imposition of a temperature gradient necessarily establishes a gradient in the electrochemical potential. The proportionality factor, here designated as α, is called the *Seebeck coefficient*, or less desirably, the thermoelectric power. It is measured by connecting the ends of the sample in a temperature gradient to a voltmeter under open circuit conditions, and by determining the resulting temperature difference with, for example, a thermocouple. Comparison with Eq. (20) shows that $\alpha = -S^*/e = \nabla(\zeta/e)/\nabla T \approx \Delta(\zeta/e)/\Delta T$. Eq. (19a) may thus be rewritten as

$$J_S = \alpha J - (\kappa/T)\nabla T \tag{26}$$

The three phenomenological coefficients may now be solved in terms of the three experimental parameters α, κ, and σ, so as to express the PEs in their final form

$$J_S = -\left(\sigma\alpha^2 + \kappa/T\right)\nabla T + \alpha\sigma\nabla(\zeta/e) \tag{27a}$$

$$J = -\sigma\alpha\nabla T + \sigma\nabla(\zeta/e) \tag{27b}$$

Eq. (27b) represents a further generalization of Ohm's law, showing how the current density is affected by the presence of a temperature gradient. The apparent differences in sign involving $\alpha\sigma$ arise because there is a corresponding sign difference in Eqs. (19a) and (19b). Thus, Onsager's relations are indeed satisfied.

A physical explanation of the *thermoelectric effect* is based on the fact that electrons at the hot end have a larger thermal velocity along the downstream direction than that associated with electrons at the cold end along the upstream direction. Consequently, a net accumulation of electrons takes place at the cold end, leaving an effective positive charge at the hot end.

Hole conductors may be treated by the same approach: a rather lengthy analysis shows that one may simply replace $-e$ by $+e$; for n-type carriers $\alpha < 0$, whereas for *p*-type materials $\alpha > 0$. The results otherwise carry over without change. Thermoelectric effects thus provide a means for distinguishing between *n*- and *p*-type charge transport.

Peltier and Thomson effects

Two other thermoelectric effects encountered in the literature are only briefly mentioned. The so-called *Peltier effects* arise when current is passed through an isothermal junction of two dissimilar materials (1 and 2), resulting in the production of heat. The explanation is based on Eq. (13), with $k = 1$, and ψ and $\mu \to \zeta$. An electrochemical potential is continuous across the junction; also, the current density is conserved. Hence, in passing from region 1 to region 2,

$$J_{U2} - J_{U1} = J_{Q2} - J_{Q1} = T(J_{S2} - J_{S1}) = T(\alpha_2 - \alpha_1)J \tag{27c}$$

where Eqs. (17) and (26) and $\nabla T = 0$ have been used. The *Peltier coefficient* is defined as

$$\Pi \equiv (J_{Q2} - J_{Q1})/J = T(\alpha_2 - \alpha_1) \tag{27d}$$

showing the relation between n and a. On the other hand, if current flows through a conductor with an established temperature gradient, the heat generated in line element dx (in excess of the Joule heating effect) is proportional to the current and to the temperature gradient, as expected: $\dot{Q}/dx \propto I\nabla_x T$. On introducing a proportionality factor, τ, the so-called *Thomson coefficient*, one obtains

$$J_{Qx} = \tau J_x \nabla_x T \tag{27e}$$

For an extended derivation and discussion of these effects refer to the literature.

Transport effects in magnetic fields

Now consider the effects that operate in the presence of a magnetic field, H, aligned with the z-axis. Provision is made in the sample for current and heat flow in the x and y directions (Fig. 4).

Phenomenological equations for thermomagnetic phenomena

A study of the thermoelectric and thermomagnetic interactions resulting in the presence of magnetic fields is useful. The effects introduced by the electric leads will be ignored. For this purpose the choice of $(J_s, \nabla T)$ and $(J, \nabla(\zeta/e))$ as conjugate variables is extended; the $1/T$ factors and minus signs are absorbed into the phenomenological coefficients. Three new points must be taken into account: (1) since the observed effects occur along two dimensions, $(J_S^x, \nabla_x T)$, $(J_S^y, \nabla_y T)$, $(\nabla_x(\zeta/e), J^x)$, $(\nabla_y(\zeta/e), J^y)$ are introduced as conjugate flux-force pairs. (2) For later convenience, J_S^x, J_S^y, $\nabla_x(\zeta/e)$, $\nabla_y(\zeta/e)$ are considered as dependent variables, so that the PEs cited below appear in partially inverted form. Such a partial interchange of dependent and independent variables is a perfectly permissible mathematical step and greatly simplifies the subsequent analysis. (3) The Onsager reciprocity conditions must now be generalized to read (Casimir–Onsager relations) $L_{ij}(H) = \pm L_{ji}(-H)$, the adopted sign depending on whether or not the forces on the charged particles change sign when the magnetic field is reversed. Without loss of generality, the sequence of signs in Eq. (28a) is selected arbitrarily; the signs in the other equations are then determined by the augmented reciprocity relations. The above considerations lead to macroscopic PEs of the form

$$J_S^x = -L_{11}\nabla_x T - L_{12}\nabla_y T + L_{13}J^x + L_{14}J^y \tag{28a}$$

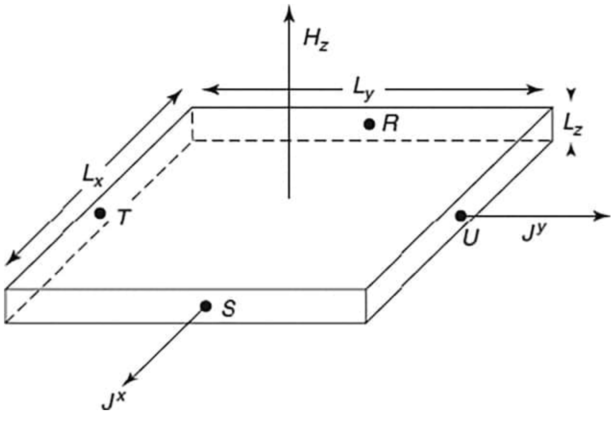

Fig. 4 Sample cut in a rectangular parallelepiped geometry and placed in a magnetic field H aligned with the z-axis. Current and heat pass into the solid through leads connected to R and S along x, and to T and U along y.

$$J_S^y = L_{12}\nabla_x T - L_{11}\nabla_y T - L_{14}J^x + L_{13}J^y \tag{28b}$$

$$\nabla_x(\zeta/e) = L_{13}\nabla_x T + L_{14}\nabla_y T + L_{33}J^x + L_{34}J^y \tag{28c}$$

$$\nabla_y(\zeta/e) = -L_{14}\nabla_x T + L_{13}\nabla_y T - L_{34}J^x + L_{33}J^y \tag{28d}$$

The above formulation permits a systematic investigation of the 560 possible thermoelectric and thermomagnetic effects. A selection of these is presented under a variety of headings.

Transport coefficients for thermomagnetic phenomena

(1) $J^y = \nabla_x T = \nabla_y T = 0$: isothermal conditions are maintained along x and y and no current is allowed to flow along y. The PEs then reduce to

$$\begin{aligned} J_S^x &= L_{13}J^x && \text{(a)} \\ J_S^y &= -L_{14}J^x && \text{(b)} \\ \nabla_x(\zeta/e) &= L_{33}J^x && \text{(c)} \\ \nabla_y(\zeta/e) &= -L_{34}J^x && \text{(d)} \end{aligned} \tag{29}$$

Expression (29c) is simply a reformulation of *Ohm's law*, $J^x = \sigma_I \nabla_x(\zeta/e)$, wherein $L_{33} \equiv \rho_I$ is the isothermal resistivity of the sample. Equation (29d) describes the *isothermal Hall effect*: a current in the longitudinal direction induces a transverse gradient in the electrochemical potential; for convenience, the magnitude of the magnetic field is explicitly introduced: it can be seen that

$$\nabla_y(\zeta/e) = -(L_{34}/H)J^x H \equiv \mathfrak{R}_I J^x H \tag{30}$$

where the magnitude of the effect is characterized by the Hall coefficient $\mathfrak{R} \equiv -L_{34}/H$. Eqs. (29a) and (29b) simply relate the entropy transport along x and y to current flux along x; L_{13} and L_{14} are determined below.

(2) $J^y = \nabla_x T = J_S^y = 0$: open-circuit conditions are imposed and no heat flow is allowed along y; isothermal conditions prevail along x. The PEs now reduce to

$$\begin{aligned} J_S^x &= -L_{12}\nabla_y T + L_{13}J^x && \text{(e)} \\ 0 &= -L_{11}\nabla_y T - L_{14}J^x && \text{(f)} \\ \nabla_x(\zeta/e) &= L_{14}\nabla_y T + L_{33}J^x && \text{(g)} \\ \nabla_y(\zeta/e) &= L_{13}\nabla_y T - L_{34}J^x && \text{(h)} \end{aligned} \tag{31}$$

Eq. (31f) shows that under these conditions, a longitudinal current flow produces a transverse temperature gradient; this is the so-called *Ettingshausen effect* $\nabla_y T = -(L_{14}/L_{11}H)J^x H$, with a coefficient specified by $\boxtimes \equiv \nabla_y T/J^x H = -L_{14}/L_{11}H$. Insertion of (31f) into (31g) yields the expression $\nabla_x(\zeta/e) = (L_{33} - L_{14}^2/L_{11})J^x$, which is Ohm's law under "adiabatic" conditions, with a *resistivity* $\rho_A = (L_{33} - L_{14}^2/L_{11})$. When (31f) is used in (31h), one obtains $\nabla_y(\zeta/e) = -[(L_{13}L_{14}/L_{11} + L_{34})/H]J^x H$, which represents the "adiabatic" Hall effect, with a corresponding coefficient $\mathfrak{R}_A \equiv -(1/H)[L_{13}L_{14}/L_{11} + L_{34}]$.

(3) Next, set $J^x = J^y = \nabla_y T = 0$: no current flows and the temperature is uniform along y. The PEs reduce to

$$\begin{aligned} J_S^x &= -L_{11}\nabla_x T && \text{(i)} \\ J_S^y &= L_{12}\nabla_x T && \text{(j)} \\ \nabla_x(\zeta/e) &= L_{13}\nabla_x T && \text{(k)} \\ \nabla_y(\zeta/e) &= -(L_{14}/H)H\nabla_x T && \text{(l)} \end{aligned} \tag{32}$$

Under these conditions, TJ_S^x and TJ_S^y represent heat fluxes. Eq. (32i) then specifies an "isothermal" heat flux (a contradiction in terms!) $TJ_S^x = -L_{11}T\nabla_x T$ that identifies the thermal conductivity $\kappa_I = TL_{11}$ in the absence of a transverse thermal gradient. Moreover, (32k) represents nothing other than the "isothermal" Seebeck effect, along x, for which the coefficient is given by $\alpha = L_{13}$. Furthermore, according to (32l), a T gradient along x produces a gradient in ζ along y. This is the so-called transverse Nernst effect, with a corresponding coefficient $N_I \equiv -L_{14}/H$.

(4) Another set of constraints of interest is given by $J^x = J^y = J_S^y = 0$. These reduce the PEs to

$$\begin{aligned} J_S^x &= -L_{11}\nabla_x T - L_{12}\nabla_y T && \text{(m)} \\ 0 &= L_{12}\nabla_x T - L_{11}\nabla_y T && \text{(n)} \\ \nabla_x(\zeta/e) &= L_{13}\nabla_x T + L_{14}\nabla_y T && \text{(o)} \\ \nabla_y(\zeta/e) &= -L_{14}\nabla_x T + L_{13}\nabla_y T && \text{(p)} \end{aligned} \tag{33}$$

Eq. (33n) shows that, in this case, the temperature gradient in the longitudinal direction induces one in the transverse direction; this is known as the Righi–Leduc effect, rewritten as

$$\nabla_y T = (L_{12}/L_{11}H)H\nabla_x T \equiv MH\nabla_x T \tag{34}$$

with a corresponding coefficient $M \equiv L_{12}/L_{11}H$. A second relation of interest is found by inserting Eq. (34) into (33m) and multiplying through by T; this yields $TJ_S^x = -T[L_{11} + L_{12}^2/L_{11}]\nabla_x T$, leading to the "adiabatic" thermal conductivity $\kappa = T(L_{11} + L_{12}^2/L_{11})$. Also, use of (34) in (33o) leads to $\nabla_x(\zeta/e) = (L_{13} + L_{14}L_{12}/L_{11})\nabla_x T$, which represents the adiabatic Seebeck effect, with a corresponding coefficient $\alpha_A = L_{13} + L_{14}L_{12}/L_{11}$. Lastly, combining (34) with (33p) yields $\nabla_y(\zeta/e) = (1/H)[-L_{14} + L_{13}L_{12}/L_{11}]H\nabla_x T$, which represents the adiabatic transverse Nernst effect, with a coefficient $N_\mathrm{A} = (1/H)[-L_{14} + L_{13}L_{12}/L_{11}]$.

The above procedure may be applied repeatedly to obtain other galvano-thermomagnetic effects; these are left to the reader to explore.

Identification of phenomenological coefficients

The principal inference of the discussion so far is that the various parameters L_{ij} of the PEs in Eqs. (28a)–(28d) can be rewritten in terms of experimentally determined parameters. These are:

$$\begin{array}{l} L_{33} = \rho_\mathrm{I} \quad (\mathrm{q}), \quad L_{34} = -\Re_\mathrm{I} H \quad (\mathrm{r}) \\ L_{11} = \kappa_\mathrm{I}/T \quad (\mathrm{s}), \quad L_{13} = \alpha_\mathrm{I} \quad (\mathrm{t}) \\ L_{14} = -N_\mathrm{I} H \quad (u), \quad L_{12} = \kappa_\mathrm{I} M_\mathrm{I} H/T \quad (\mathrm{v}) \end{array} \tag{35}$$

The subscript I has been introduced to indicate isothermal conditions, that is, $\nabla_y T = 0$. By inserting (35) into the PEs, a complete description of the galvano-thermomagnetic effects that are observable in the rectangular parallelepiped geometry of Fig. 4 has been obtained.

Transport in two-band (electron–hole) conductors

In conclusion, a limited set of galvano-thermomagnetic phenomena for a material in which both holes and electrons contribute to the conduction process can be considered. For this purpose, it is necessary to use the PEs in uninverted form, so that the partial currents can be summed to form the total current. Specializing to the case $J^y = \nabla_x T = \nabla_y T = 0$, the expressions involving J_S^x and J_S^y are not needed. In an obvious notation, the PEs for electron and hole conduction become, with due regard to the Casimir–Onsager conditions,

$$J_-^x = \Gamma_1 \nabla_x(\zeta/e) + \Gamma_2 \nabla_y(\zeta/e) \tag{36a}$$

$$J_-^y = -\Gamma_2 \nabla_x(\zeta/e) + \Gamma_1 \nabla_y(\zeta/e \tag{36b}$$

$$J_+^x = \Gamma_3 \nabla_x(\zeta/e) + \Gamma_4 \nabla_y(\zeta/e)) \tag{36c}$$

$$J_+^y = -\Gamma_4 \nabla_x(\zeta/e) + \Gamma_3 \nabla_y(\zeta/e) \tag{36d}$$

Use of constraints to identify transport coefficients

Consider first the one-band, n-type semiconductor, by setting $\Gamma_3 = \Gamma_4 = 0$. If $J_-{}^y = 0$ as well, (36a) and (36b) can be solved for:

$$J_-^x = \left[\left(\Gamma_1^2 + \Gamma_2^2\right)/\Gamma_1\right]\nabla_x(\zeta/e) \equiv \sigma_n \nabla_x(\zeta/e) \tag{37a}$$

which immediately identifies the n-type conductivity σ_n. One can also write

$$J_-^x = \left[\left(\Gamma_1^2 + \Gamma_2^2\right)/\Gamma_2\right]\nabla_y(\zeta/e) \tag{37b}$$

$D \equiv [(\sigma_n + \sigma_p)^2 + (H\sigma_n\sigma_p)^2(\Re_n + \Re_p)^2]\sigma_n$, σ_p are electrical conductivity of electrons and holes, respectively; $\Re_n$, $\Re_p$ are Hall coefficients of electrons and holes; ρ is the electrical resistivity; α_n, α_p are the Seebeck coefficient of electrons and holes, respectively; κ_n, κ_p are the thermal conductivity of electrons and holes, respectively; N_n, N_p are the transverse Nernst coefficients of electrons and holes, respectively; and H is the applied magnetic field. Note that $\alpha_n = -|\alpha_n|$, $\Re_n = -|\Re_n|$ are negative, while σ_n, σ_p, N_n, N_p are positive; hence $\Re$ and α tend to be small except in large applied magnetic fields.

which introduces the Hall coefficient for electrons as

$$\Re_n H = \Gamma_2/\left(\Gamma_1^2 + \Gamma_2^2\right) \tag{38}$$

Eqs. (37a) and (38) yield the result $\Gamma_2/\Gamma_1 = \sigma_n H \Re_n \equiv X_n$.

On elimination of Γ_2 using (38), $\Gamma_1 = \sigma_n/(1 + X_n^2)$. Similarly, $\Gamma_2 = \sigma_n X_n/(1 + X_n^2)$. Analogous operations for a hole conductor yield the results $\Gamma_4/\Gamma_3 = \sigma_p H \Re_p \equiv X_p$, $\Gamma_3 = \sigma_p/(1 + X_p^2)$, $\Gamma_4 = X_p/(1 + X_p^2)$. The total current density is then given by

$$J^x = J_-^x + J_+^x = \Gamma_a \nabla_x(\zeta/e) + \Gamma_b \nabla_y(\zeta/e) \tag{39a}$$

$$J^y = J_-^y + J_+^y = -\Gamma_b \nabla_x(\zeta/e) + \Gamma_a \nabla_y(\zeta/e) \tag{39b}$$

with $\Gamma_a \equiv \Gamma_1 + \Gamma_3$, $\Gamma_b \equiv \Gamma_2 + \Gamma_4$. Setting $J^x = 0$ and eliminating either $\nabla_y(\zeta/e)$ or $\nabla_x(\zeta/e)$ from Eqs. (39a) and (39b). One finds

Table 1 Galvano-thermomagnetic effects for a two-band *n-p* conductor in a magnetic field.

Electric resistivity:	$\rho = [(\sigma_n + \sigma_p) + H^2\sigma_n\sigma_p(\sigma_n\mathfrak{R}_n^2 + \sigma_p\mathfrak{R}_p^2)]/D$
Hall coefficient:	$\mathfrak{R} = [\mathfrak{R}_n\sigma_n^2 + \mathfrak{R}_p\sigma_p^2 + (H\sigma_n\sigma_p)^2(\mathfrak{R}_n\mathfrak{R}_p)(\mathfrak{R}_n + \mathfrak{R}_p)]/D$
Seebeck coefficient:	$\alpha = \big[(\sigma_n + \sigma_p)(\sigma_n\alpha_n + \sigma_p\alpha_p) + (H\sigma_n\sigma_p)^2(\mathfrak{R}_n + \mathfrak{R}_p)(\mathfrak{R}_n\alpha_p + \mathfrak{R}_p\alpha_n) + H^2\sigma_n\sigma_p(N_n - N_p)(\mathfrak{R}_n\sigma_n - \mathfrak{R}_p\sigma_p)\big]/D$
Thermal conductivity:	$\kappa = \kappa_n + \kappa_p + (T/D)\Big\{\Big[\sigma_n\sigma_p(\sigma_n + \sigma_p)(\alpha_n - \alpha_p)^2 - (N_n - N_p)\Big(\sigma_n\sigma_p H^2\Big)\Big] \times [(\sigma_n + \sigma_p)(N_n - N_p) - 2\sigma_n\sigma_p(\mathfrak{R}_n + \mathfrak{R}_p)(\alpha_n - \alpha_p)]\Big\}$

Table 2 Galvano-thermomagnetic effects to the limit of small applied magnetic fields: $H \rightarrow 0$.

$\sigma = \sigma_n + \sigma_p$,	$\alpha = \frac{\alpha_n\sigma_n + \alpha_p\sigma_p}{\sigma_n + \sigma_p}$
$\mathfrak{R} = \frac{\mathfrak{R}_n\sigma_n^2 + \mathfrak{R}_\rho\sigma_\rho^2}{(\sigma_n + \sigma_p)^2}$,	$\kappa = \kappa_n + \kappa_p + \frac{T\sigma_n\sigma_p(\alpha_n - \alpha_p)^2}{\sigma_n + \sigma_p}$

$$J^x = \frac{\Gamma_a^2 + \Gamma_b^2}{\Gamma_a}\nabla_x(\zeta/e) \quad \text{or} \quad \sigma = \frac{\Gamma_a^2 + \Gamma_b^2}{\Gamma_a} \tag{40a}$$

$$J^x = \frac{\Gamma_a^2 + \Gamma_b^2}{\Gamma_b}\nabla_y(\zeta/e) \quad \text{or} \quad \frac{1}{H\mathfrak{R}} = \frac{\Gamma_a^2 + \Gamma_b^2}{\Gamma_b} \tag{40b}$$

The last step consists in replacing Γ_a, Γ_b by $\Gamma_1, \ldots, \Gamma_4$, and introducing X_n, X_p, σ_n, $\mathfrak{R}_nH$, σ_p, $\mathfrak{R}_pH$. The steps are elementary but tedious. The results are listed in Tables 1 and 2.

A similar procedure may be used to determine the Seebeck coefficient and thermal conductivity of a two-band conductor. For detailed derivations, the reader is referred to the literature. The results are again displayed in Tables 1 and 2.

See notes in Table 1.

The principal points to be noted are (1) that the results are model-independent, and (2) that the contribution from electrons and holes in general are not simply additive.

Conclusion

This article has focused on the thermodynamic representation of irreversible effects as applied to electron transport phenomena in conductors. The advantage of this approach is its generality (aside from specific restrictions mentioned earlier); it does not depend on the adoption of a specific model for electron transport. The disadvantage is that the phenomenological parameters and transport coefficients remain unspecified. One may now invoke the microscopic transport theory to evaluate these quantities from first principles, at least in certain degrees of approximation, but this is a rather lengthy procedure beyond the scope of the present article. For additional information readers are encouraged to consult the literature that now extends to over 140 years and provides a text book example of a thoroughly explored research field.

Acknowledgment

The preparation of this article was supported on NSF Grant DMR 96 12130.

Reference

Tykody R Thermodynamics of the Steady State. New York: MacMillan ch. 5.

Thermodynamics: Phase transformations

John H Perepezko, Department of Materials Science and Engineering, University of Wisconsin-Madison, Madison, WI, United States

© 2024 Elsevier Ltd. All rights reserved.

This is an update of J.H. Perepezko, Phase Transformation, Editor(s): Franco Bassani, Gerald L. Liedl, Peter Wyder, Encyclopedia of Condensed Matter Physics, Elsevier, 2005, Pages 247–258, ISBN 9780123694010, https://doi.org/10.1016/B0-12-369401-9/00716-6.

Introduction **497**
Phase stability thermodynamics **498**
Equilibrium 498
Pure components 498
Classification of phase transformations 499
Alloy solutions 501
Phase transformation energetics 503
Phase stability hierarchy **504**
Nucleation—Controlled reactions 504
Competitive phase selection and metastability 504
Constrained equilibrium 505
Thermodynamics of nanoscale systems **506**
Advances in analysis **507**
Conclusion **508**
References **508**

Abstract

In the analysis of phase transformations, the thermodynamic evaluation of phase stability and the hierarchy of equilibrium conditions is essential in understanding the response of materials to changes in temperature, pressure, composition and size scales. For phase transformations driven by undercooling, overpressure or supersaturation metastable phases can develop during the phase selection involved in competitive nucleation and growth. During the early stage of reaction constrained equilibrium and nanoscale size effects can alter the relative phase stability. These important features of phase transformations are treated in terms of the governing thermodynamic relationships. Current developments are highlighted for the computational modeling of phase transformations and phase stability.

Key points

- Phase equilibrium thermodynamics and relative phase stability
- Hierarchy of equilibrium and metastability
- Nucleation-controlled reactions
- Competitive phase selection
- Constrained equilibrium
- Thermodynamics of nanoscale materials
- Advances in analysis

Introduction

A central focus of phase transformation thermodynamics is the examination of relative phase stability. Under most conditions, phase stability is considered in terms of the response of a material to changes in temperature, pressure, composition and size scale. The changes are often applied rapidly in order to establish undercoolings, overpressures and supersaturations, that place the initial stable phase in a metastable (or energized) condition. The relaxation of a metastable state to the stable state can proceed through a succession of various other metastable states, but the rate of the relaxation processes is usually limited by diffusional kinetics for thermally activated reactions (Turnbull, 1981). In general, it is often useful to identify also the rate limiting stage of a phase transformation reaction as either the nucleation or the growth stage since the thermodynamic analysis for each stage can be different (Christian, 1975; Porter and Easterling, 1992).

☆*Change History*: September 2022. JH Perepezko updated the text. Section 5 Advances in Analysis has been added.

https://doi.org/10.1016/B978-0-323-90800-9.00097-4

The essential thermodynamics that governs the relative phase stability for phase transformation reactions can be represented in analytical expressions for the Gibbs free energy as a function of temperature, pressure, composition and size scale and other appropriate variables (Lupis, 1983; Gaskell, 1995; Hillert, 1998). The relationships can also be presented in a graphical form that can facilitate the interpretation and visualization of the free energy changes, the metastable phase options and various reaction pathways that often occur in kinetic competition.

A useful concept for the study of phase transformation processes is the distinction between closed and open system processes (Martin and Bellon, 1984). In a closed system, an energized state is achieved through a rapid temperature, pressure or composition change to create a certain level of undercooling or supersaturation (i.e., a metastable state), which then releases the excess free energy during relaxation toward the equilibrium stable state. With an open system, the energized state is often attained by a continuous incremental excess energy input to an initial state through the incorporation of excess lattice defects or solute on a localized spatial scale and time interval that is short compared to the relaxation time so that the relaxation process can be influenced by external factors. Regardless of the type of phase transformation or synthesis method, there are common themes in the phase stability. The fundamental issues include the phase selection during the initial synthesis and the phase stability after synthesis and during subsequent treatment.

In order to treat the basic issues in phase stability within the limited coverage that is available, some of the key points are examined by considering selected thermodynamic relations for macroscopic systems and their modification for high interfacial area nanoscale systems. A central issue is the free energy change (i.e., driving free energy) associated with a phase transformation reaction. As a means of illustrating the use of the relevant thermodynamic concepts some examples are considered for the evaluation of the driving free energy and the ranking of different levels of metastability.

Phase stability thermodynamics

Equilibrium

There are a number of essentially equivalent approaches to describe thermodynamic equilibrium. For a closed system, the general conditions for equilibrium are represented by a maximum in entropy, S or a minimum in free energy, G with respect to a system variable, z where z can be a variable such as pressure, P, temperature, T or V as given by

$$dS/dz = 0 \text{ and } d^2S/dz^2 \leq 0 \tag{1}$$

or

$$dG/dz = 0 \text{ and } d^2G/dz^2 \geq 0 \tag{2}$$

These conditions prevail for either local minima that represents a metastable equilibrium or for an absolute minima that holds for a stable equilibrium as illustrated in Fig. 1.

Pure components

In the analysis of relative phase stability and the driving forces for different phase transformation reactions the Gibbs free energy, G, is the main quantity of interest. By definition, $G = H - TS = E + PV$ where H is the enthalpy, E is the internal energy, and PV represents the system work (Lupis, 1983; Gaskell, 1995; Hillert, 1998). For reactions between two phases, the free energy change is the difference, $\Delta G = \Delta H - T\Delta S$. For example, during solidification of a liquid, $G_s - G_l = (H_s - H_l) - T(S_s - S_l)$ or $\Delta G_f = \Delta H_f - T\Delta S_f$. At equilibrium, $\Delta G_f = 0$ so that $\Delta S_f = \Delta H_f/T_m$. If ΔS_f is taken as independent of T (i.e., neglecting the small heat capacity correction), then $\Delta G_f = \Delta H_f[1 - T/T_m] = \Delta H_f[T_m - T]/T_m = \Delta H_f\Delta T/T_m$ so that the driving free energy (i.e., driving force) available to accomplish the reaction is proportional to the undercooling, ΔT. The dependence of the molar free energy on temperature is illustrated in Fig. 2 for a liquid, a stable α phase and a metastable β phase where it is evident that the formation of the metastable β phase requires a minimum liquid undercooling below the stable α phase melting point of $\Delta T = T_m^{\alpha} - T_m^{\beta}$.

From the second law of thermodynamics several differential relations can be developed (i.e., Maxwell relations). The relation for the Gibbs free energy for a single phase is.

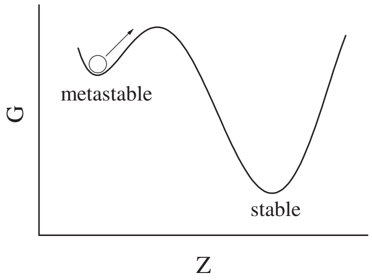

Fig. 1 Schematic comparison of metastable (i.e., local) and stable (i.e., absolute) equilibrium.

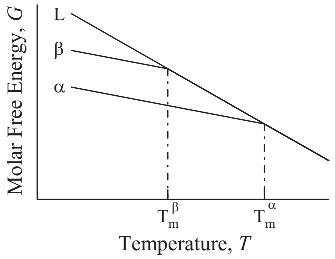

Fig. 2 Free Energy as a function of temperature for a single component. The melting point of the stable α phase $T_m\alpha$ and the metastable β phase $T_m\beta$ is indicated.

$$dG = VdP - SdT \tag{3}$$

For the liquid-solid case at equilibrium, dG = 0 and.

$$V_s dP - S_s dT = V_l dP - S_s dT. \tag{4}$$

Or

$$(dP/dT)_{eq} = [S_s - S_l]/[V_s - V_l] = \Delta S_f/\Delta V_f = [\Delta H_f/(\Delta V_f T_m)] \tag{5}$$

which is the Clapeyron equation for the pressure dependence of the melting point. When Eq. (3) is applied to other two-phase coexistence such as solid-liquid, solid-vapor and liquid-vapor equilibrium, the pressure–temperature phase diagram for a single component is developed as shown in Fig. 3. The solid lines represent the two-phase coexistence conditions where there is one degree of freedom according to the phase rule (i.e., p + f = c + 2 where p = the number of phases, f = the number of degrees of freedom and c = the number of components). The lines intersect at an invariant triple point where f = 0. It is useful to note that $(\partial G/\partial T)_P = -S$ and $(\partial G/\partial P)_T = V$ as illustrated in Fig. 2.

Classification of phase transformations

The pure component reactions that are depicted in Fig. 3 are often classified as first order phase transformations. At T_e, the equilibrium transformation temperature, $G^\alpha = G^\beta$, but the slopes are different (i.e., $d\ G^\alpha/dT \neq d\ G^\beta/dT$). This gives rise to a discontinuity in S,V and H at T_e and a singularity in heat capacity, $C_p = T(dS/dT) = T(d^2G/dT^2)$ as illustrated in Fig. 4.

During a second order phase transformation S, V and H are continuous at the transformation temperature or critical temperature, T_c (i.e., there is no latent heat), but there is a discontinuity in heat capacity as indicated in Fig. 4. Second order phase transformations are often associated with electronic effects such as the paramagnetic/ferromagnetic transition, but they can also be observed for certain order-disorder changes in alloys (Soffa and Laughlin, 1989).

The distinction between first and second order phase transformations also has an impact on the presentation of the equilibria in a phase diagram and the progress of a phase transformation (Porter and Easterling, 1992). For example, long range ordering of unlike atoms in a crystal lattice develops due to an attractive interaction between unlike atoms. During a first order reaction, the development of an ordered atomic arrangement initiates at separate regions as the temperature falls below T_e as shown in Fig. 5. A sharp interface separates the transformed (i.e., ordered) regions and the untransformed (i.e., disordered) regions. Across this interface there is a jump in the long-range order parameter, η that varies from zero for a random arrangement to unity for a perfectly ordered arrangement. The coexistence at T_e is represented on the phase diagram as a two-phase field between the ordered and the disordered phase. In contrast, during a second order reaction, the development of an ordered arrangement initiates throughout the volume at the critical temperature, T_c and develops with increasing values of η progressively as the temperature is lowered below T_c. There is no two-phase coexistence of an ordered and a disordered phase so that the phase diagram does not display a two-phase field. Instead, the phase diagram shows the locus of T_c as a function of composition.

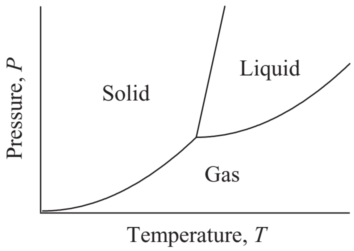

Fig. 3 A schematic pressure vs temperature diagram for a single component.

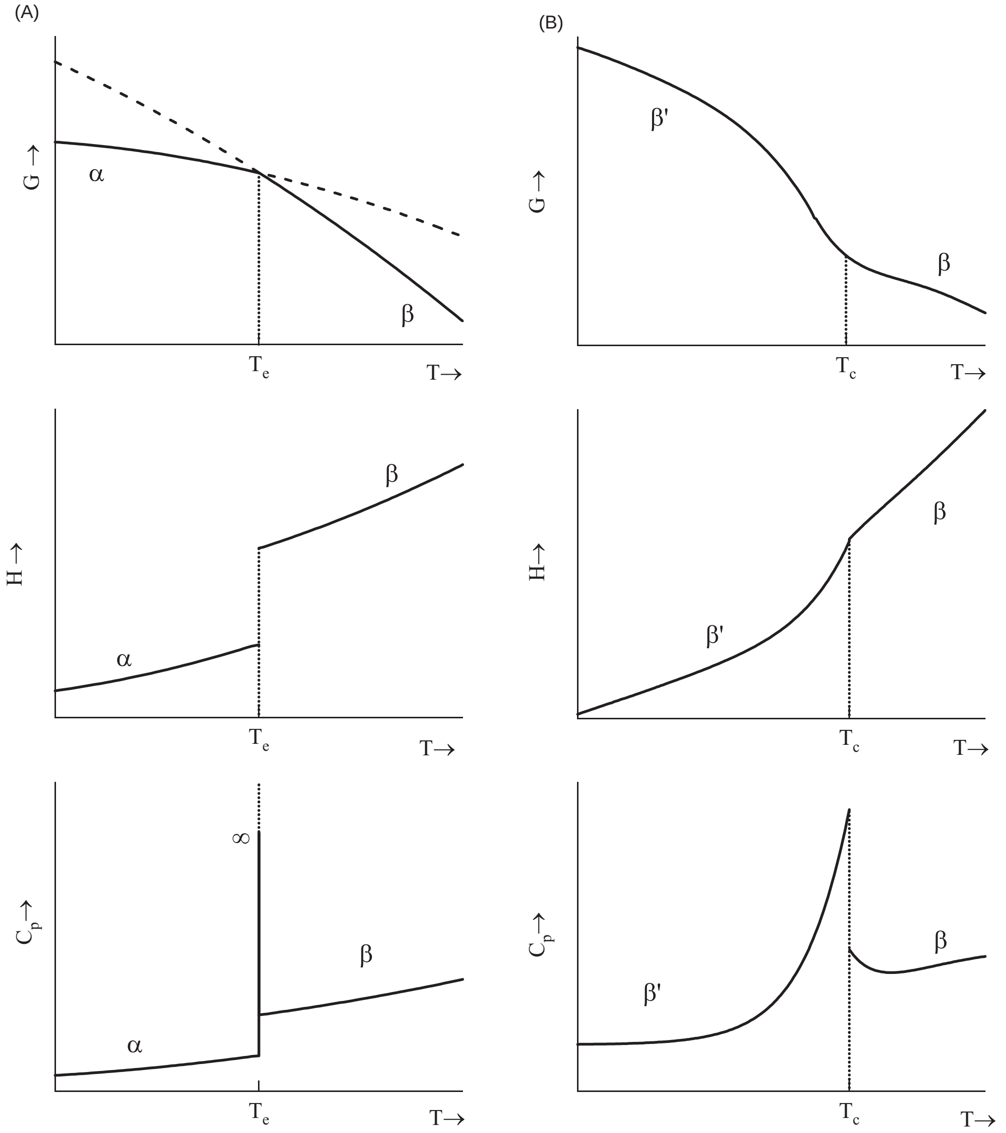

Fig. 4 The thermodynamic characteristics of (a) first-order and (b) second-order phase transformations.

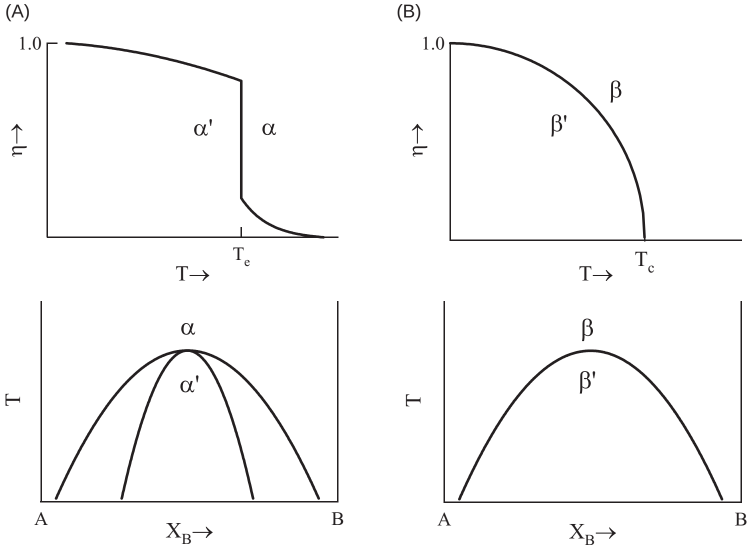

Fig. 5 Schematic illustration of the temperature dependence of η and the phase diagram characteristics for (a) first-order and (b) second-order phase transformations.

Alloy solutions

For alloy solutions, the chemical terms for the free energy are included by adding the partial molar free energy for each component, i or j to Eq. (3) as

$$dG = VdP - SdT + (\partial G/\partial n_i)_{T,P,nj}\, dn_i + (\partial G/\partial n_j)_{T,P,ni} dn_{j,} \tag{6}$$

where n is the number of moles. The partial molar free energy represents the chemical potential, μ_i, that is defined as

$$(\partial G/\partial n_i)_{T,P,nj} = \mu_i = \mu_i{}^0 + RT\ln a_{i,} \tag{7}$$

where μ_i^0 is the standard state chemical potential, R is the gas constant and a_i is the activity that is the product of an activity coefficient, γ_i and the mole fraction, X_i (note that for a binary solution $X_i + X_j = 1$). For an alloy solution at constant T and P with a given composition X_0 in an A-B system the molar free energy is.

$$G = (1 - X_0)\mu_A + X_0\mu_B \tag{8}$$

and as indicated in Fig. 6, Eq. (8) describes the tangent to the G vs X_B curve at X_0. For reaction between two coexisting solution phases such as liquid and solid in an alloy with overall composition X_0.

$$\Delta G = (1 - X_0)\left(\mu_A{}^s - \mu_A{}^l\right) + X_0\left(\mu_B{}^s - \mu_B{}^l\right), \tag{9}$$

At equilibrium, $\Delta G = 0$ so that $(\mu_A^s = \mu_A^l) = (\mu_B^s = \mu_B^l)$ and the two phases share a common tangent.

For the examination of interactions in solutions it is often useful to represent the free energy change for mixing of pure components to form a solution, ΔG_m, in terms of an enthalpy of mixing, ΔH_m and a mixing entropy, ΔS_m. The simplest model is based upon an ideal solution where there are no nearest neighbor interactions so that $\Delta H_m = 0$ and $\gamma_i = 1$ and the ideal entropy of mixing is given by

$$\Delta S_m = -R[(1 - X_B)\ln(1 - X_B) + X_B \ln X_B]. \tag{10}$$

Most real solutions are not ideal. When the departure from ideal behavior is modest so that the molar volume change upon mixing to form a solution is negligible, the enthalpy of mixing can be represented in terms of the nearest neighbor pairwise interaction energies E_{AA}, E_{BB} and E_{AB} as

$$\Delta H_m = ZN_a X_A X_B [E_{AB} - 0.5(E_{AA} + E_{BB})] \tag{11}$$

or

$$\Delta H_m = \Omega X_A X_B, \tag{12}$$

where Z is the lattice coordination number, N_a is the Avogado number and $\Omega = ZN_a[E_{AB} - 0.5(E_{AA} + E_{BB})]$ is a constant for a regular solution. The entropy of mixing is given by the ideal solution expression (Eq. 8) to yield.

$$\Delta G_m = \Delta H_m - T\,\Delta S_m = \Omega X_A X_B + RT[(1 - X_B)\ln(1 - X_B) + X_B \ln X_B]. \tag{13}$$

The composition dependence of ΔG_m is shown in Fig. 7 for different values of Ω and temperature. For exothermic solutions, $\Omega < 0$ and mixing results in a free energy decrease at all temperatures. In this case the preference for unlike atom pairings results in a tendency for the development of ordering in the solid solution. When $\Omega > 0$, however, the behavior can change with temperature. At high temperatures $T\Delta S_m$ is greater than ΔH_m for all compositions and the free energy curve has a positive curvature at all points. At low temperatures however, $T\Delta S_m$ can be smaller than ΔH_m and ΔG_m displays a change in curvature with a negative curvature near the pure component compositions that changes to a positive curvature (i.e., unstable solutions) in the central composition range. The positive value of Ω indicates a preference for pairings of like atoms and results in a tendency for the development of clustering in the solid solution.

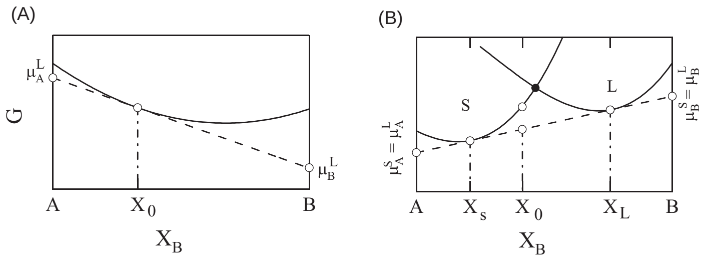

Fig. 6 Schematic free energy vs composition diagrams for a binary alloy as (a) a single phase liquid solution with the component chemical potentials μ_A^L and μ_B^L determined by the pure component intersections with the tangent to the G vs X_B curve at X_0 and as (b) a two-phase liquid-solid equilibrium with common tangent points at X_S and X_L.

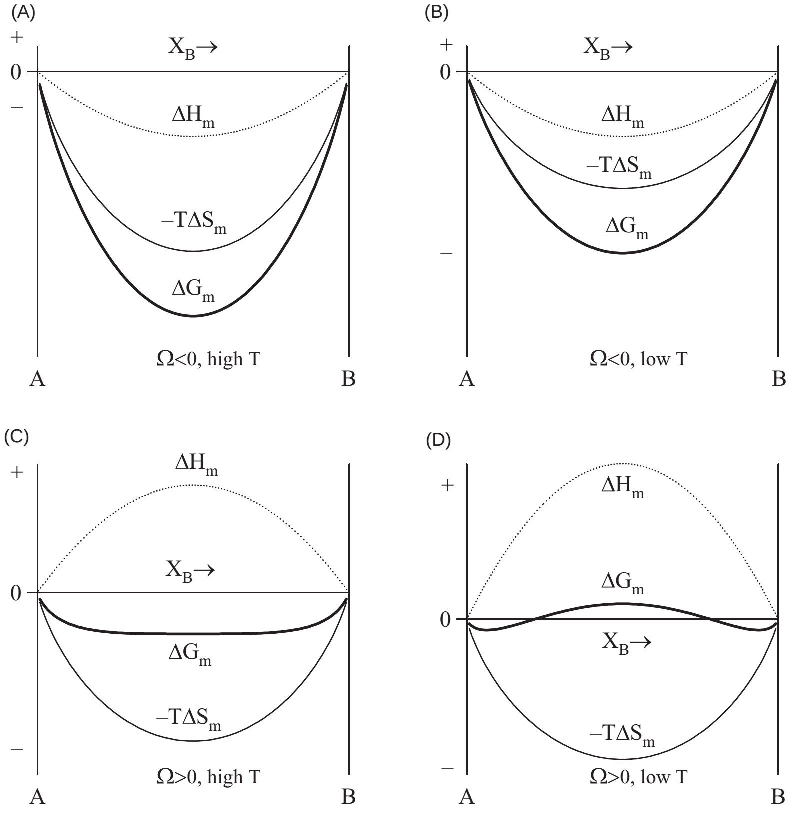

Fig. 7 The influence of temperature and ΔH_m on ΔG_m.

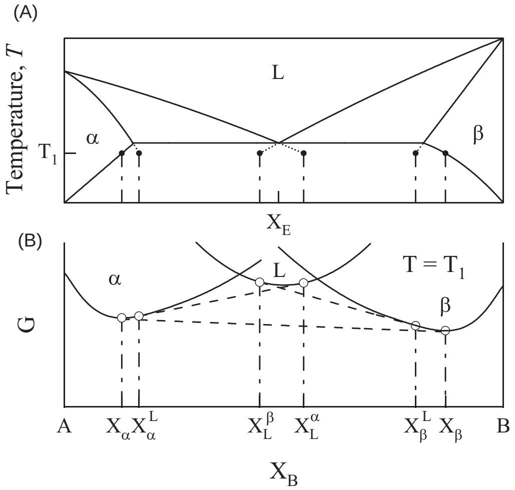

Fig. 8 Schematic phase diagram (a) and free energy vs composition diagram (b) for a binary alloy that exhibits a eutectic reaction: L → α + β. The relationship between the phase boundaries on the phase diagram and the common tangents is illustrated for a temperature T_1 where both a stable α + β and the metastable L + α and L + β two-phase equilibria could occur for different kinetic conditions. The location of the T_0 points are indicated by filled circles.

The composition dependence of ΔG_m yields a concave curve when $\Delta H_m < 0$ as illustrated in Fig. 6a. In addition, in Fig. 6b, the equilibrium condition of the equality of the chemical potential for each component in the coexisting phases is illustrated by the common tangent construction. The various phase equilibria that are defined by a collection of free energy vs compositions diagrams at different temperatures are the basis of the equilibrium phase diagram. As demonstrated in the schematic diagram in Fig. 8, the common tangent points on the free energy vs composition diagram define the tie lines between coexisting phases at each temperature on the phase diagram. Within the two-phase regions defined by the common tangents the free energy curves intersect. The point of intersection defines the limit to partitionless transformation. For liquid compositions to the left of the intersection (i.e., A-rich compositions) there is a free energy decrease for a composition invariant or partitionless solidification. For liquid

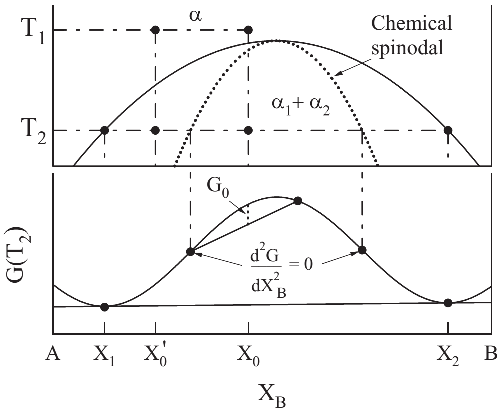

Fig. 9 Alloys between the spinodal points are unstable and can decompose into two coherent phases α_1 and α_2 without overcoming an activation energy barrier. Alloys between the miscibility gap and the spinodal are metastable and can decompose only after nucleation of the other phase.

compositions to the right of the intersection a partitionless solidification is impossible since the free energy would increase. The locus of the intersection points as a function of temperature is often called a T_0 curve (Hillert, 1998).

When $\Delta H_m > 0$, the composition dependence of ΔG_m displays a change in curvature as noted in Fig. 7 and presented in more detail in Fig. 9. As shown in Fig. 9, the phase diagram for a solution with $\Delta H_m > 0$ exhibits a miscibility gap at low temperature where a homogeneous solution, α decomposes into two solutions α_1 and α_2. Due to the change in curvature of the G vs X_B curve, there is a fundamental change in the stability of solutions within the miscibility gap and a resultant change in the mechanism of the decomposition mechanism (Cahn, 1961, 1968). For example, solutions with compositions within the range between X_1 and the turning point (i.e., where $d^2G/dX_B^2 = 0$) or between the turning point and X_2 are metastable since $d^2G/dX_B^2 > 0$. This signifies that fluctuations in composition that are necessary to accomplish the decomposition reaction result in an increase in free energy that represents a barrier to the reaction. For these solutions, a nucleation process is required to initiate the decomposition reaction. In contrast, solutions with compositions between the turning points are unstable since $d^2G/dX_B^2 < 0$. In this case fluctuations in composition are spontaneous since they lead to a reduction in free energy. The demarcation between metastable and unstable solutions within the miscibility gap is represented by the spinodal curve that refers to the locus of temperatures and compositions where $d^2G/dX_B^2 = 0$.

Phase transformation energetics

An important application of the thermodynamic description of phase stability is the representation of the free energy change that accompanies a phase transformation (i.e., the driving free energy). A change of phase requires a departure from equilibrium as the system develops a supersaturation or an undercooling that represents the driving free energy as indicated in Fig. 10. For a dilute

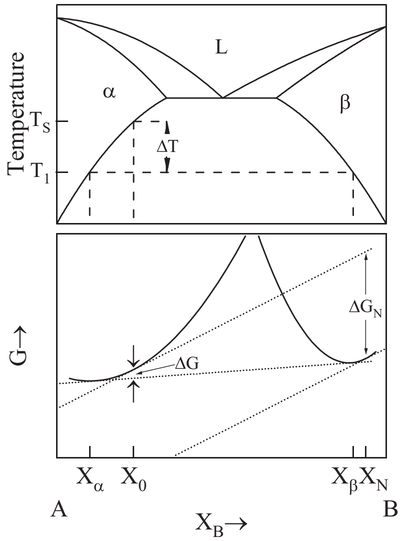

Fig. 10 Schematic illustration for the development of a supersaturation $[X_0/X_\alpha]$ as an α phase alloy of composition X_0 is undercooled by an amount ΔT below the α phase solvus boundary. During the initial formation of a β phase precipitate, the maximum driving free energy for nucleation, ΔG_N is given by the parallel tangent construction.

solution where the activity can be represented by the mole fraction, the free energy change associated with a precipitation reaction where the α phase composition changes from X_0 to X_α as pure β develops at temperature T_1 is given by

$$\Delta G = RT_1 \ln (X_0/X_\alpha). \tag{14}$$

Since the solvus phase boundary composition, X_s, may be represented as

$$X_S = \exp(\Delta S_S)\ \exp(-\Delta H_S/RT) \tag{15}$$

where ΔS_S is the entropy for solution and ΔH_S is the enthalpy of solution, the free energy change for precipitation can be expressed as

$$\Delta G = \Delta H_S \Delta T/T_S \tag{16}$$

demonstrating again that a supersaturation can be expressed in terms of an equivalent undercooling. It should be noted that the expressions in Eqs. (12) or (14) refer to the overall ΔG for the reaction, $\alpha(X_0) \rightarrow \alpha(X_\alpha) + \beta(X_\beta)$. During the initial nucleation stage when a small quantity of β forms, the α matrix composition is not changed much from the X_0 value. In this case the maximum driving free energy for nucleation of β, ΔG_N is given by the separation between the tangent to the G_α curve at X_0 and a parallel tangent to the G_β curve as illustrated in Fig. 10. The tangent to the G_β curve occurs at the composition X_N that is the favored composition for a β nucleus (i.e., the composition with the largest driving free energy) (Hillert, 1998).

Similarly, for a phase transformation involving the decomposition of an initial phase such as the liquid with composition X_E in Fig. 8 into two phases such as α of composition X_α and β of composition X_β the ΔG for reaction can be evaluated from Eq. (8). The free energy change is given by the separation between the tangent to the G_L curve at X_E and the common tangent to the G_α and G_β curves as

$$\Delta G = \left(\mu_\alpha{}^B - \mu_L{}^B\right)X_E + \left(\mu_\alpha{}^A - \mu_L{}^A\right)(1 - X_E) \tag{17}$$

Phase stability hierarchy

Nucleation—Controlled reactions

Throughout the analysis of transformation behavior, it is commonly recognized that nucleation control is an important part of the initial stage of a reaction. Under nucleation control a strong temperature dependence of the product phase selection and number density can develop and lead to a nanoscale microstructure. Nucleation limitations in diffusion reactions, especially those involved in reactive diffusion also represent a form of nucleation control that is important in nanostructure synthesis. In terms of alloy metastability, nucleation control is important in allowing access to metastable states. In effect, the observation of nucleation control is directly related to the factors that promote the development of large undercooling or supersaturation, enable the expression of kinetic transitions through competitive phase selection and result in the refinement of the product size to the nanoscale level (Boettinger and Perepezko, 1993).

Competitive phase selection and metastability

A common theme in the development of new microstructural options by phase transformations is the occurrence of metastable structural states. Often, the reactions that occur during the freezing of undercooled liquids or during other rapid transformations are viewed as non-equilibrium processes (Boettinger and Perepezko, 1993; Perepezko and Boettinger, 1983). However, it is also evident that some of the departures from full equilibrium can be considered in terms of different levels of metastability. In fact, a hierarchy of equilibrium can be identified based upon the severity of the kinetic constraints that affect the capability of a material to relax toward full equilibrium during processing. As the rate of reaction becomes faster, kinetic constraints that can arise from nucleation and growth limitations associated with an equilibrium product phase formation can develop and can expose alloy metastability that often coincides with nanostructure synthesis. For the suppression of the equilibrium phase or the formation of a kinetically favored metastable phase, it is still possible to analyze reactions in terms of a metastable equilibrium that is used locally at interfaces. The transition from stable to metastable equilibrium is illustrated in Fig. 11 where the kinetic suppression of an equilibrium γ phase (Fig. 11a) yields a metastable eutectic involving the α and β phases. Moreover, it is expected that the application of the appropriate local equilibrium can be used when the processing involves nanoscale structures. Under extreme conditions, loss of interfacial equilibrium for either a stable or metastable phase can develop when even interfacial relaxation becomes too slow. With the loss of interfacial equilibrium, thermodynamics can still be used to restrict the possible range of compositions that can exist at an interface at various temperatures since the selection must yield a net reduction in the free energy of the system. One way to represent the thermodynamic restrictions is based upon the application of T_0 curves which represent the locus of temperatures and compositions where the free energies of two phases are equal as illustrated in Fig. 6 for liquid and solid phases and thus define the limiting condition for partitionless transformation. For example, as interfacial equilibrium is lost, the liquidus and solidus boundaries in Fig. 11b collapse to the T_0 curves. With isomorphous systems that exhibit complete solubility the T_0 curve is continuous with composition (Fig. 11c) while for alloys based upon components with different structures each crystal phase has a T_0 curve (Fig. 11d). At temperatures and compositions above the T_0 curves solute partitioning is required for solidification (Fig. 11d). Because of the diffusional constraint due to solute partitioning, a crystallization reaction can be inhibited by quenching

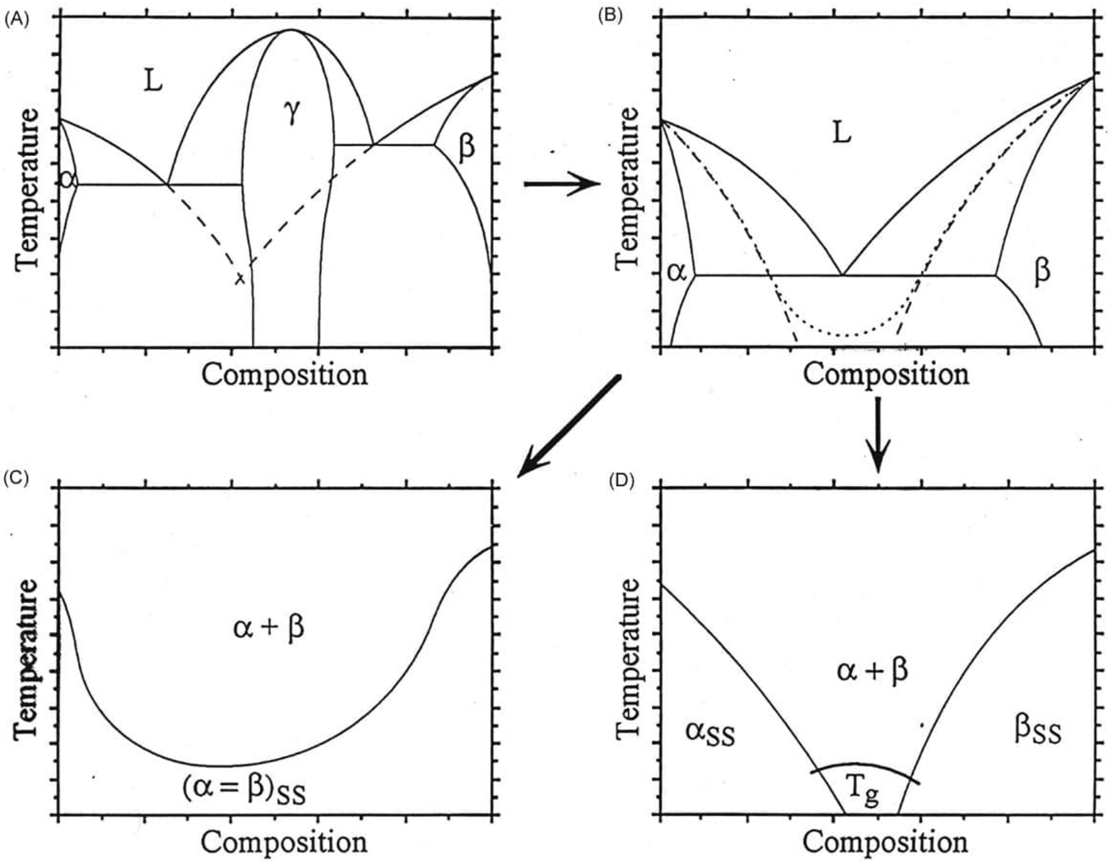

Fig. 11 Schematic illustration of some of the levels in the hierarchy of equilibrium. The equilibrium phase diagram of a system with an intermediate phase is given in (a) Included are the metastable extensions of the liquidus and solidus curves for the primary solution phases (dashed). Solidification under metastable equilibrium conditions can result in a bypassing of the intermediate phase to yield a metastable eutectic phase diagram between α and β. The T_0 curves for the primary solutions are included in (b). The extensions of these curves to temperatures below the metastable eutectic are indicated as dashed curves. In (c) the primary phases have the same structure so that a complete single phase solid solution is formed. If the primary phases have different crystal structures and low mutual solubility, then the T_0 curves might not intersect. Such a situation favors glass formation in the composition range where the T_g curve is greater than the T_0 curves in (d).

to promote glass formation. Within the overall hierarchy of stability the systematic examination of the different levels of kinetic constraints can provide useful insight into the thermodynamic analysis of alloy metastability and phase selection.

Constrained equilibrium

There are a number of important cases where phase transformation reactions proceed under various constraints that can involve externally imposed conditions or internally generated limitations. A common example is the development of a metastable phase because of favorable nucleation and growth kinetics compared to the stable phase. This is a kinetically constrained equilibrium. Another kinetically constrained equilibrium can develop in alloys where one component exhibits a significantly higher diffusivity than the other components. This is commonly observed in alloy steels where the high diffusivity component is an interstitial component such as carbon and the other slow diffusivity components are substitutional species. The high diffusivity component is able to establish an equality of the chemical potential in the coexisting phases before the slow diffusivity components. This is called paraequilibrium (Hillert, 1998). Of course, since paraequilibrium is constrained kinetically, it will dissipate with time as the alloy approaches the stable equilibrium.

During the initial stages of a phase transformation reaction in the solid state or during deposition from the vapor, it is often observed that the product phase exhibits an epitaxial crystallographic relationship with the transforming phase or the substrate involving the interfacial matching of lattice planes and directions. The appearance of a crystallographic matching results in a reduction of the interfacial energy that in turn yields favorable nucleation kinetics. However, the matching is rarely perfect so that there remains a residual interfacial strain. The resulting elastic strain energy represents another component to the free energy. With progress of the reaction, the product phase grows and there is a loss of coherency and elastic strain energy.

The elastic strain energy is usually not partitioned equally between the transforming and product phase so that the constraint of lattice matching across the interphase interface alters the phase equilibrium. This constrained equilibrium is designated as coherent equilibrium (Cahn and Larchi, 1984; Johnson, 1999). Because the level of elastic strain energy depends on the volume, the influence of coherent equilibrium is a function of composition in the two phase region (i.e., relative amounts of phases). This yields new behavior that is beyond the scope of coverage in this discussion.

Thermodynamics of nanoscale systems

The nanoscale is often reported as a linear dimension but the important interfacial effects should be considered in terms of the interfacial area per unit volume (A/V). For example, for a sphere: $A/V = 3/r = 3 \times 10^7\ \mathrm{m}^{-1}$ for $r = 100$ nm.

This is significant!

Interfacial effects can be included in the free energy as

$$dG = VdP - SdT + \Sigma\mu_i dn_i + \Sigma\sigma_i dA_i, \tag{18}$$

where σ_i is the interfacial energy and A_i is the interfacial area.

The increment in free energy due to interfaces (Garvie, 1978; Trivedi, 1999) is represented by the Gibbs-Thompson relation in terms of the interface curvature κ, that is determined by the principal radii, r_i, as

$$\Delta G = \kappa\sigma = \left(r_1^{\ -1} + r_2^{\ -1}\right)\sigma \tag{19}$$

For a sphere, $\Delta G = 2\sigma/r$. The effect of curvature on the melting point and the relative phase stability is indicated in Fig. 12 where the dependence of melting point on curvature can be expressed from Eqs. (3) and (13) as

$$T_m(r) = T_m(\infty) - 2\sigma_{SL}V_m/(r\Delta S_f). \tag{20}$$

There are two key points that are illustrated in Fig. 12. First, the macroscopic melting points for the α and β phases i.e., $T_m\alpha$ and $T_m\beta$ decrease with increasing curvature. Secondly, the β phase that is metastable for macroscopic sizes becomes the stable phase with respect to α phase at high curvature values. Furthermore, the phase stability relations for a macroscopic scale system can be modified in different ways depending on the relative magnitude of σ for each phase for a nanostructured system. As illustrated in Fig. 13, when $\sigma_\alpha < \sigma_\beta$, the stability of α is enhanced at the nanoscale. However, when $\sigma_\beta < \sigma_\alpha$, there is a reversal of phase stability at the nanoscale. There are a number of examples of the reversal in relative phase stability when the size scale changes from macroscopic to nanostructured.

The excess free energy due to curvature that acts to control the relative phase stability in nanoscale materials also acts to modify other thermodynamic behavior. For example with the same analysis that was applied to express the curvature dependence of the melting point, the dependence of the solubility may be represented in terms of particle size. This behavior is illustrated in Fig. 14 where it is evident that the increase in chemical potential with decreasing particle size will act to drive a diffusive flux between neighboring articles in a particle size distribution such as that produced by a precipitation reaction (Porter and Easterling, 1992). An important consequence of the interparticle transport is the dissolution of the finest particles along with a concomitant increase in

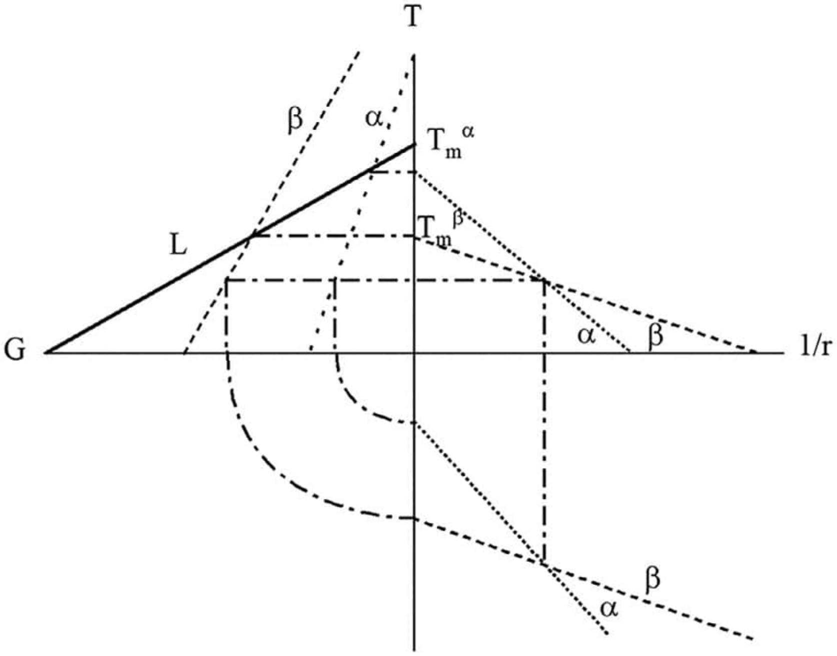

Fig. 12 Schematic illustration of the influence of curvature (1/r) on the melting point of the α phase and the β phase and on the relative phase stability when $[\sigma_{\alpha L}V_m/\Delta S_f^\alpha > \sigma_{\beta L}V_m/\Delta S_f^\beta]$.

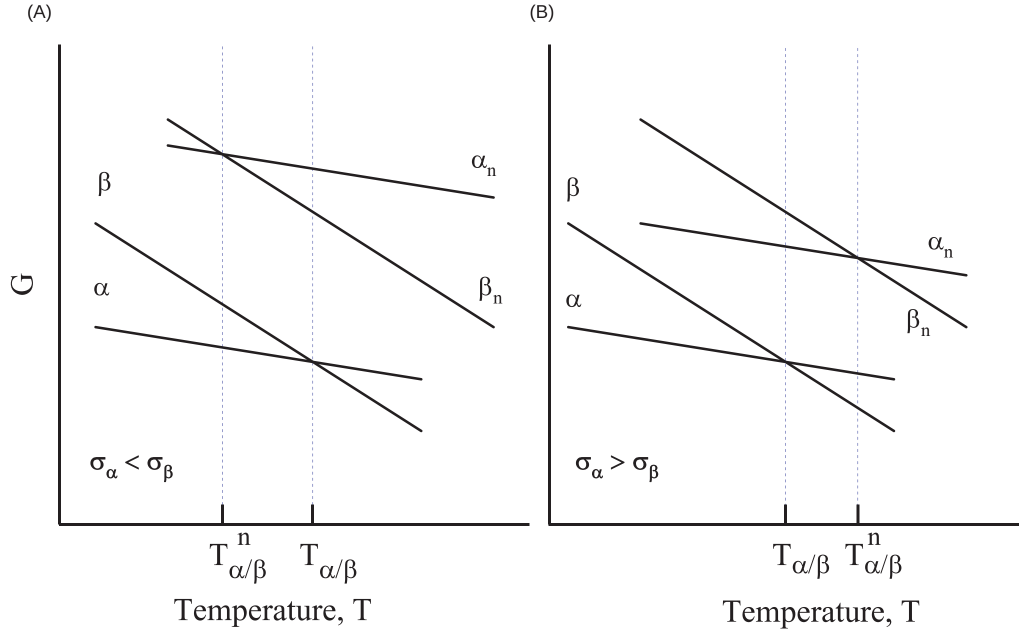

Fig. 13 Schematic Illustration of the modification of the stability of the α phase at the nanoscale. (a) when $\sigma_\alpha < \sigma_\beta$, there is an enhancement of α phase stability; (b) when $\sigma_\alpha > \sigma_\beta$, there is a reversal of phase stability between the α phase and the β phase.

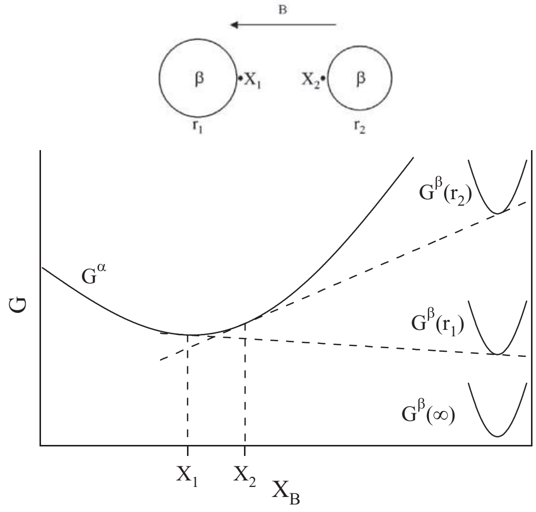

Fig. 14 Schematic free energy vs composition diagram demonstrating the influence of interface curvature of a β phase particle on the solubility.

the average particle size in the distribution (Christian, 1975). This coarsening behavior is central to the kinetic stability of a nanoscale microstructure.

A useful perspective on the different phase transformation reactions can be developed by considering the relative magnitudes of the driving free energies associated with each of the reactions. A partial summary of the representative magnitudes for the driving free energies for a selection of reactions is presented in Table 1. The listings in Table 1 indicate that for typical processes involving chemical changes or phase transitions the driving free energies range from a few to 100 KJ/mol. While the excess free energy associated with a nanoscale microstructure is only a few KJ/mol, this level is sufficient to alter the relative phase stability and to modify the path of kinetic reactions.

Advances in analysis

The analysis of phase stability during phase transformations has been advanced by a number of computational methods. The widely used Calphad approach (Saunders and Miodownik, 1998) is most effective in leveraging experimental data to provide a full evaluation of alloy phase stability. Moreover, the Calphad assessment provides the basis to evaluate the component mobilities that

Table 1 Comparison of the driving free energies for some phase transformation reactions.

Reaction process	*Free energy*	*Typical value (J/mol)* T = *1000 K*	*Remarks*
Crystallization polymorphic transition	$\Delta H_f \Delta T/T_m$	$3 \cdot 10^3$	
Mixing/interdiffusion	$RT(X_A \ln X_A + X_B \ln X_b)$	$5 \cdot 10^3$	Ideal solution behavior
Oxidation	$\Delta G^0 = -RT \ln K$	$5 \cdot 10^4$–$5 \cdot 10^6$	ΔG^0 formation of oxide K equilibrium constant
Sublimation/condensation	$\Delta H_v \Delta T/T_s$	10^4–10^5	ΔH_v—sublimation enthalpy T_s—sublimation temperature
Grain growth, coarsening	$2\sigma/r$	20 for $r = 1$ μm $2 \cdot 10^3$ for $r = 10$ nm	$\sigma = 1$ J/m^2
Precipitation	$RT \ln (X_\alpha/X_0)$	10^4	$X_\alpha/X_0 = 10$
Cold work (stored energy)	$\rho G\boldsymbol{b}^2$	10^2–10^3	G—shear modulus $\boldsymbol{b}$—Burgers vector ρ—shear modulus☆

can be used by programs such as Dictra or Pandat or other methods such as phase field analysis (Boettinger and Warren, 1996; Qin and Bhadeshia, 2010) to model phase transformation kinetics and microstructure evolution. For cases where there is a lack of data other approaches such as density functional theory (Argaman and Makov, 2000) can provide the missing phase stability analysis. All of these methods have provided unprecedented access to the rich variety of alloy phase stability and transformation behavior that has enabled a more effective and efficient design of alloys.

Conclusion

This chapter provides coverage of the essential features of phase transformation thermodynamics. From the initial definition of equilibrium conditions the discussion covers the thermodynamics of pure components and alloy systems. With the background on the basic thermodynamic factors involved in phase transformations the discussion focuses on the phase stability hierarchy concerning nucleation-controlled reactions, competitive phase selection and metastability. Two topics of contemporary interest in thin film systems and the early stage of phase transformations are discussed in terms of constrained equilibrium and the thermodynamics of nanoscale materials. The evolving approaches in the analysis of phase stability based upon density functional theory are highlighted as important developments.

References

Argaman N and Makov G (2000) Density functional theory: An introduction. *American Journal of Physics* 68: 69–79.

Boettinger WJ and Perepezko JH (1993) Fundamentals of solidification at high rates. In: Liebermann HH (ed.) *Rapidly Solidified Alloys: Processes, Structures, Properties, Applications*, pp. 17–78. New York: Marcel Decker Inc.

Boettinger WJ and Warren JA (1996) The phase field method: simulation of alloy dendritic solidification during recalesence. *Metallurgical and Materials Transactions A: Physical Metallurgy and Materials Science* 27A: 657–669.

Cahn JW (1961) On spinodal decomposition. *Acta Metallurgica* 9: 795–801.

Cahn JW (1968) Spinodal decomposition. *Transactions of AIME* 242: 166–180.

Cahn JW and Larchi F (1984) A simple model for coherent equilibrium. *Acta Metallurgica* 1915–1923.

Christian JW (1975) *The Theory of Transformations in Metals and Alloys*, 2nd edn. Oxford, UK: Pergamon Press.

Garvie RC (1978) Stabilization of the tetragonal structure in zirconia microcrystals. *The Journal of Physical Chemistry* 82: 218–224.

Gaskell DR (1995) *Introduction to the Thermodynamics of Materials*, 3rd edn. London, UK: Taylor & Francis.

Hillert M (1998) *Phase Equilibria, Phase Diagrams and Phase Transformations: Their Thermodynamic Basis*. Cambridge, UK: Cambridge University Press.

Johnson WC (1999) Influence of elastic stress on phase transformations. In: Aaronson HI (ed.) *Lectures on the Theory of Phase Transformations*, pp. 35–134. PA: TMS, Warrendale.

Lupis CHP (1983) *Chemical Thermodynamics of Materials*. Oxford, UK: Elsevier.

Martin G and Bellon P (1984) Driven alloys. *Solid-State Physics* 32: 189–331.

Perepezko JH and Boettinger WJ (1983) Use of metastable phase diagrams in rapid solidification. 19. In: Bennett LH, Massalski TB, and Giessen BC (eds.) *Mat. Res. Soc. Symp. Proc. Symposium E—Alloy Phase Diagrams*, pp. 223–240. Oxford, UK: Elsevier.

Porter DA and Easterling KE (1992) *Phase Transformations in Metals and Alloys*. New York: Chapman and Hall.

Qin RS and Bhadeshia HK (2010) Phase field method. *Materials Science and Technology* 26(7): 803–811.

Saunders N and Miodownik AP (1998) *Calphad Calculation of Phase Diagrams: a Comprehensive Guide*. Oxford: Elsevier.

Soffa WA and Laughlin DE (1989) Decomposition and ordering processes involving thermodynamically first-order order ➔ disorder transformationss. *Acta Metallurgica* 37(11): 3019–3028.

Trivedi RK (1999) Theory of capillarity. In: Aaronson HI (ed.) *Lectures on the Theory of Phase Transformations*, pp. 135–165. PA: TMS, Warrendale.

Turnbull D (1981) Metastable structures in metallurgy. *Metallurgical Transactions* 12A: 695–708.

Incommensurate phases

Gervais Chapuis, École Polytechnique Fédérale de Lausanne, Institute of Physics, Lausanne, Switzerland

© 2024 Elsevier Ltd. All rights reserved.

This is an update of J.M. Perez-Mato, Incommensurate Phases, Editor(s): Franco Bassani, Gerald L. Liedl, Peter Wyder, Encyclopedia of Condensed Matter Physics, Elsevier, 2005, Pages 364–374, ISBN 9780123694010, https://doi.org/10.1016/B0-12-369401-9/00717-8.

Introduction	509
Theoretical presentation of superspace for the description of aperiodic structures	510
The habit of Calaverite ($Au_{1-x}Ag_xTe_2$ with $x < 0.15$) or the macroscopic manifestation of incommensurate phases	513
Sodium carbonate Na_2CO_3	514
The luminescence of Europium containing scheelites	516
Structure evolution of the organic perovskite $CH_3NH_3PbI_3$ by thermal cycling around the phase transitions	518
Conclusion	520
Acknowledgments	520
References	521

Abstract

Incommensurately modulated crystalline phases are part of a more general family called aperiodic crystals. Their symmetry is treated within the theoretical framework of superspace groups that is a generalization of the 3D space groups that are used for conventional crystalline structures. Aperiodic structures are conveniently embedded in superspace with dimensions varying from $(3+1)$ to $(3+3)$D. They do occur in all types of material, organic and inorganic, metal and alloys, minerals and macromolecules under various pressure and temperature. Some examples of incommensurate structures are presented along with their chemical and physical properties.

Key points

- Incommensurate crystalline phases are part of a more general group of structures called *aperiodic* which do not exhibit the usual periodicity in three dimensions. They are however perfectly ordered structures as witnessed by essentially discrete diffraction pattern.
- The symmetry of incommensurate structures are described in superspace with dimensions varying from four to six.
- They exhibit interesting physical and chemical properties which can be exploited in material sciences.

Introduction

Incommensurate phases or more precisely incommensurately modulated crystalline phases are a relatively modern concept in crystallography. The concept was introduced in the 1970s following the discovery of a new class of materials which did not conform to the classical model of crystalline structures. The fingerprint of a classical crystalline structure placed in an incident beam with a adequate wavelength consists of a diffraction pattern where each diffracted beam can uniquely be associated to a three dimensional grid called reciprocal space. Thus every diffracted intensity $I(h_1,h_2,h_3)$ can unambiguously be associated to three integers h_1, h_2, h_3, which are called the Laue indices. The diffracted intensities can thus be analyzed in terms of parallel sections of two dimensional grid points. Each grid point is characterized by two integers and associated with the corresponding diffracted intensity.

The first observations of deviations from the classical model of crystals already appeared in the literature in the 1950s. First it was observed that the spins of magnetic materials did form helical structures with a pitch independent of the structural three dimensional periodicity. Later it was observed that some alloys exhibited additional diffraction spots which did not fit with the classical three dimensional grid points. These additional spots were called satellite reflections and were associated to a structural long range order independent of the three dimensional periodicity of the structure.

An important milestone in the origin of satellite reflections appeared in 1967 and was due to Korekava and Jagodzinski based on the study of the mineral Labradorite (Korekawa and Jagodzinski, 1967). The authors reported two types of satellites related to two scale length in the diffraction patterns of Labradorite. The first type of satellites (e-satellites) were associated with a periodicity of 50 Å whereas the second type of satellites (s-satellites) were attributed to a periodicity between 1400 and 1800 Å which are linked to the iridescence (or Schiller) effect characteristic of the mineral Labradorite. It was later shown that the s-satellites correspond to large alternating domains which are also subdivided in alternating subdomains corresponding to the e-satellites. Each domain contains various specific concentrations of Ca, Na, Al, and Si atoms.

At this point, the theory of satellite reflections was considered as an interesting topic but did not immediately contributed to new developments for one clear reason. The material specialists did not have the necessary tools to handle in a unified way the resolution of structures containing both main and satellite reflections. The missing link was a theoretical development of the symmetry characteristics to describe structures presenting satellite reflections. In other words, a generalization of the notion of space groups, which is so fundamental for the resolution of classical structures, had to be developed.

The first decisive publication on the symmetry of modulated structures, i.e., structures presenting satellite reflections in their diffraction patterns, was published by de Wolff (Dewolff, 1974). The author described for the first time the concept of superspace, i.-e., the symmetry tools to characterize modulated structures. The method to calculate the corresponding structure factors which are fundamental to solve the structure were also introduced in order to obtain the electron density of the structure. The resolution of the modulated structure of sodium carbonate, Na_2CO_3, was at the origin of this new development. We shall come back to this structure at a later stage. With further contributions by Yamamoto et al. (1985), the toolbox necessary to deal with the symmetry of modulated structures was completed and the method of solving them could be definitely established. Soon many examples of incommensurately modulated structures were published including minerals, metals, organic and inorganic structures.

The concept of modulated structures was further extended a decade later when Shechtman et al. discovered quasicrystalline structures (Shechtman et al., 1984). Incommensurately modulated structures and quasicrystals are parts of a larger group of materials called aperiodic crystals. In the next sections, we shall first introduce the theoretical background leading to superspace, an extension of the symmetry of crystalline structures adapted to aperiodic crystals and incommensurately modulated structures in particular. We shall then present a few examples of incommensurate structures and show how they affect some physical properties.

Theoretical presentation of superspace for the description of aperiodic structures

In classical structure, the positions of each atom is given relatively to the origin of the unit cell which in the most general case is characterized by six parameters namely the magnitudes of the three vectors $\mathbf{a}_1$, $\mathbf{a}_2$, and $\mathbf{a}_3$ and the corresponding angles α_1, α_2, and α_3. The cell parameters are obtained from X-rays, neutron or electron diffraction pattern of the crystal and it is therefore convenient to introduce the reciprocal cell parameters because diffraction phenomena are better analyzed in terms of reciprocal space.

Reciprocal cell vectors are defined according to the following scalar product, i.e., the orthogonality relation

$$\mathbf{a}_i \cdot \mathbf{a}_j^* = \delta_{ij} \tag{1}$$

with reciprocal vectors indicated by *. Here δ_{ij} is the Kronecker symbol which is 1 if $i = j$ and 0 if $i \neq j$. For classical crystals, i and j vary from 1 to 3. (Physicists usually includes a factor 2π in this relation. Crystallographers however prefer to omit this factor.)

Diffraction patterns of classical structures can be analyzed in terms of a three dimensional grid determined by the three reciprocal vectors. Each grid or lattice point is specified by the three integers h_1, h_2, and h_3 and the measured intensity of each diffracted beam can be uniquely associated to the reciprocal lattice vector.

$$\mathbf{h} = h_1\mathbf{a}_1^* + h_2\mathbf{a}_2^* + h_3\mathbf{a}_3^*. \tag{2}$$

The analysis of the diffraction pattern of the modulated structure γ-Na_2CO_3 illustrated in Fig. 1 shows the reconstructed layer with indices $h_1 2 h_3$ of the diffraction pattern. It is immediately clear that we do not observe a regular two dimensional disposition of grid points. The satellites reflections are all aligned along the vector $\mathbf{q}$ called the modulation vector. They are also equidistant. Each satellite row is centered around a lattice point located at the intersection of a grid (thin black lines) subtended by the reciprocal lattice vectors $\mathbf{a}_1^*$ and $\mathbf{a}_3^*$ located on the thick black lines. Based on the three vectors $\mathbf{a}_1^*$ and $\mathbf{a}_3^*$ and $\mathbf{q}$, every reflection in the layer $\mathbf{l}$ can be indexed with three integers.

$$\mathbf{l} = h_1\mathbf{a}_1^* + h_3\mathbf{a}_3^* + m\mathbf{q}. \tag{3}$$

When $m = 0$, $\mathbf{l}$ represents a main reflection whereas for $m \neq 0$, $\mathbf{l}$ represents a satellite reflection. Thus the complete diffraction pattern of γ-Na_2CO_3 can be indexed by four integers in the form.

$$\mathbf{H} = h_1\mathbf{a}_1^* + h_2\mathbf{a}_2^* + h_3\mathbf{a}_3^* + m\mathbf{q}. \tag{4}$$

The modulation vector $\mathbf{q}$ can be expressed in terms of threereciprocal lattice vectors $\mathbf{a}_1^*$ with coefficients α_i.

$$\mathbf{q} = \alpha_1\mathbf{a}_1^* + \alpha_2\mathbf{a}_2^* + \alpha_3\mathbf{a}_3^*. \tag{5}$$

The coefficients can be obtained experimentally. When at least one of them is irrational, the modulated structure is incommensurately modulated. This is often the case when the coefficients are temperature or pressure or composition dependent.

The increase of the number of reciprocal space vectors to fully characterize the diffraction pattern of modulated crystals requires an embedding in the so called superspace. In the particular case of γ-Na_2CO_3, we shall introduce the four new reciprocal basis vectors $\mathbf{a}_{S1}^*, \ldots \mathbf{a}_{S4}^*$ and express them in terms of external and internal components along the scheme given in Fig. 2. Once the reciprocal vectors are defined in superspace, we can use the orthogonality relations to find the corresponding direct space embedding for the description of the crystal structure,

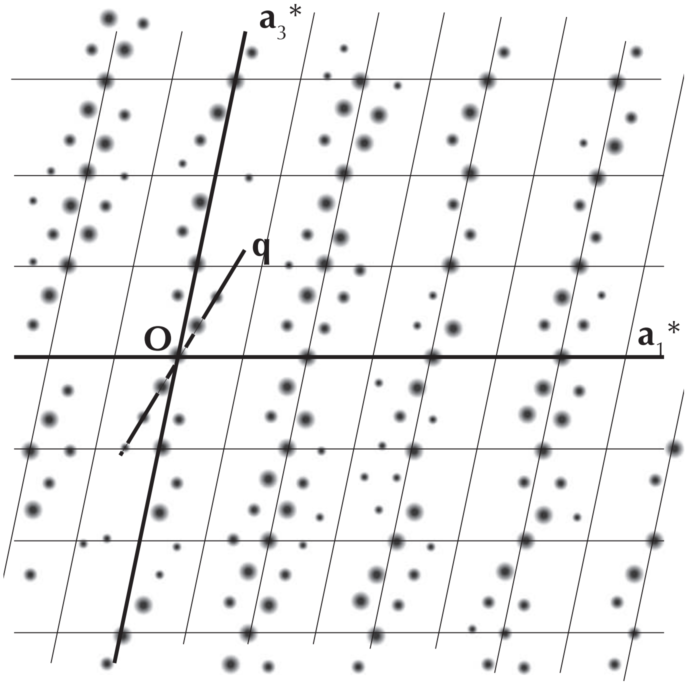

Fig. 1 The reconstructed $h_1 2 h_3$ reciprocal lattice plane from an experimental single crystal diffraction pattern of $\gamma - \mathrm{Na_2CO_3}$.

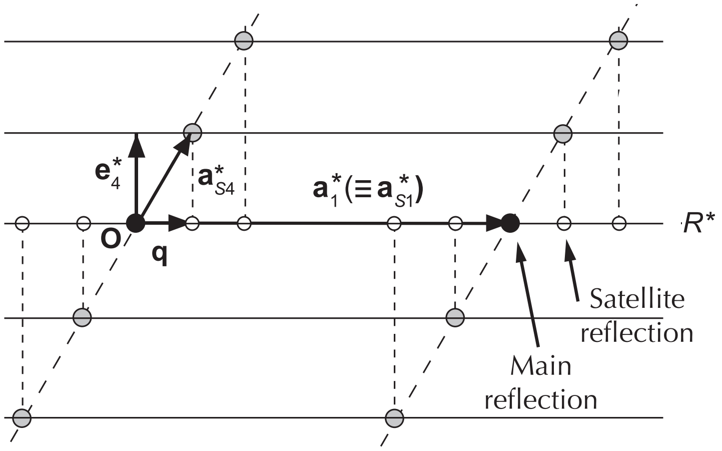

Fig. 2 Embedding of the 3D reciprocal space into superspace of dimension 3 + 1. The reciprocal space vector $\mathbf{a}_{S4}^*$ has an *external* component $\mathbf{q}$ and an *internal* component $\mathbf{e}_4^*$ normal to $\mathbf{a}_1^*$, $\mathbf{a}_2^*$, and $\mathbf{a}_3^*$.

$$\left.\begin{aligned} \mathbf{a}_{S1}^* &= \left(\mathbf{a}_1^*,\ 0\right) \\ \mathbf{a}_{S2}^* &= \left(\mathbf{a}_2^*,\ 0\right) \\ \mathbf{a}_{S3}^* &= \left(\mathbf{a}_3^*,\ 0\right) \\ \mathbf{a}_{S4}^* &= (\mathbf{q},\ 1) \end{aligned}\right\} \rightarrow \mathbf{a}_{Si} \cdot \mathbf{a}_{Sj}^* = \delta_{ij} \rightarrow \left\{\begin{aligned} \mathbf{a}_{S1} &= (\mathbf{a}_1,\ -\mathbf{q}\cdot\mathbf{a}_1) \\ \mathbf{a}_{S2} &= (\mathbf{a}_2,\ -\mathbf{q}\cdot\mathbf{a}_2) \\ \mathbf{a}_{S3} &= (\mathbf{a}_3,\ -\mathbf{q}\cdot\mathbf{a}_3) \\ \mathbf{a}_{S4} &= (0,\ 1). \end{aligned}\right. \tag{6}$$

In order to analyze the modulated structure, it is convenient to describe it in the superspace embedding as illustrated in Fig. 3. In this example, the modulation of the structure is a simple sinusoidal displacement with wavelength λ in the $\mathbf{a}_2$ direction. In other words $\mathbf{q} = \alpha_2 \mathbf{a}_2$. The wavelength satisfies the relation $\lambda = 1/\parallel \mathbf{q} \parallel$ and in general it is incommensurate relative to at least one of the cell constants $\mathbf{a}_i$. The structure can be analyzed in terms of $(\mathbf{a}_{Si}, \mathbf{a}_{S4})$ sections with $i = 1$ to 3. The directions $\mathbf{a}_i$ and $\mathbf{a}_{Si}$ are different if the scalar products $\mathbf{q}\cdot\mathbf{a}_i \neq 0$. We observe that the horizontal line "real crystal" or any other parallel line in Fig. 3(B) does reproduce the displacements of the atom with coordinates x_2 around its average position $\bar{x}_2$ indicated in Fig. 3(A). It is now straight forward to imagine the corresponding $(\mathbf{a}_{S1}, \mathbf{a}_{S4})$ section corresponding to Fig. 3(B). The scalar product $\mathbf{q}\cdot\mathbf{a}_1 = 0$ and consequently the shape of the periodic motif would be rectangular. With no modulation component in the $(\mathbf{a}_{S1}, \mathbf{a}_{S4})$ section, the shape of the modulation would be a straight line $x_1 = \bar{x}_1$.

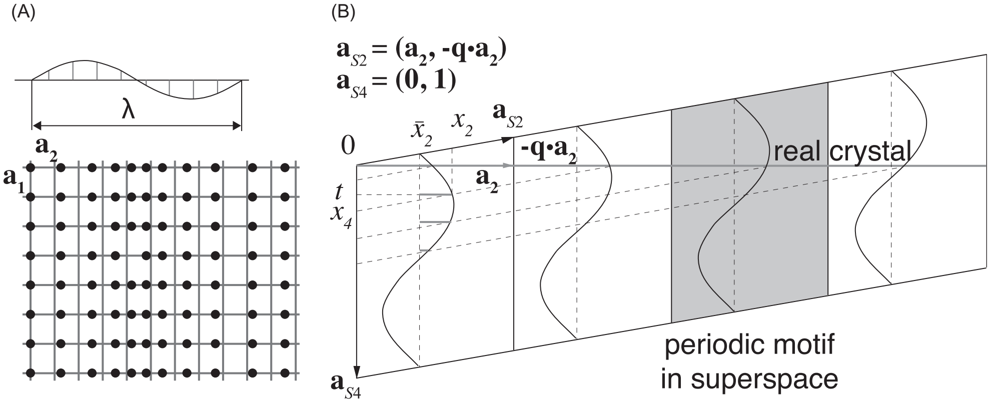

Fig. 3 Embedding of a modulated structure in 3 + 1 dimensions. The sinusoidal modulation along $\mathbf{a}_2$ given in (A) is extended in superspace according to the model indicated in (B). See the text for further information.

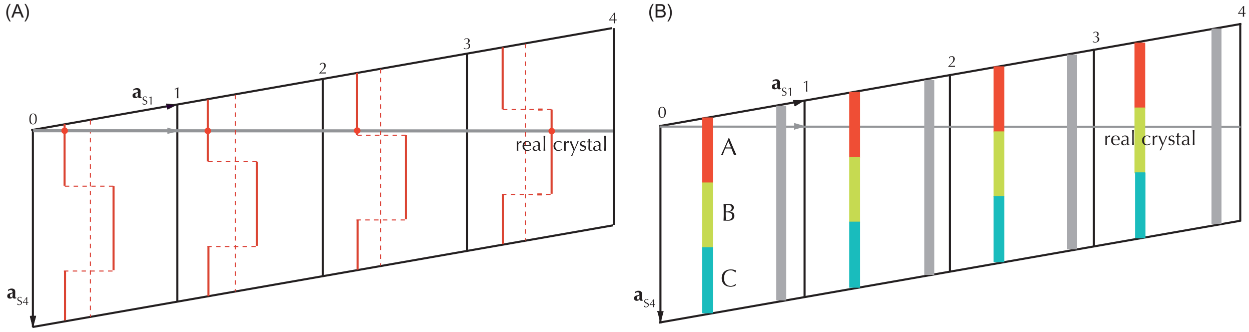

Fig. 4 Two examples of modulation functions. (A) Step function characterizing two possible locations of the same atom in the crystal structure. (B) Example of various stacking sequences for closed packed layers with three possible stacking positions A, B, or C.

For the description of modulated structures, we see from Fig. 3(B) that the x_4 component is ill suited for analyzing the relations between atomic positions. Therefore the variable t, which satisfies the relation

$$t = x4 - \mathbf{q} \cdot \mathbf{r}, \tag{7}$$

is preferred for practical purposes. Here $\mathbf{r}$ defines the position of an atom in the unit cell defined by $\mathbf{a}_1$, $\mathbf{a}_2$, and $\mathbf{a}_3$.

Since the introduction of the superspace, a large array of possible modulation functions have been successfully used. The most general modulation function can be approximated by a series of harmonic terms. Other possibilities like crenel or step functions as well as sawtooth and other functions have been successfully applied (Petříček et al., 2014) depending on the nature of the modulation function. Fig. 4 illustrates two possible types of modulated function.

With the example of γ-Na_2CO_3 the superspace model was derived in (3 + 1)D. Since the development of superspace many more examples were discovered requiring an extension of the superspace to higher dimensions. Modulated structure models can possibly exists up to (3 + 3)D. We recall that the first number in the parenthesis is the space (or external) dimension of the structure and the second number is the dimension of the internal space. The rank of the structure is the sum of both numbers. Icosahedral quasicrystals (QC) for example, are described in (3 + 3)D whereas decagonal QC are described in (3 + 2)D. Most of the incommensurately modulated phases are described in (3 + 1)D but there are a few examples of (3 + 2)D including composite structures. The modulated structure of Lazurite and the modulated structure presented in Section "Structure evolution of the organic perovskite $CH_3NH_3PbI_3$ by thermal cycling around the phase transitions" is a rare example of non-QC structures described in(3 + 3)D.

We have seen above that the reciprocal space of aperiodic crystal structures can be analyzed in terms of external (also called physical or parallel) and internal (also called perpendicular) space dimensions. Fig. 5, inspired from the publication of Yamamoto (Yamamoto, 1996), illustrates the principal differences between the three families of aperiodic crystal structures. For modulated crystals, the prominent main reflections are all located along R_E. In composites, two (or more) series of prominent reflections are aligned along lines crossing the origin whereas for QC, the prominent reflections do not exhibit any periodicity.

The structural resolution of aperiodic crystals and in particular modulated structures has made enormous progress in the past decades and excellent open software is readily available. The electron density of a (3 + 1)D modulated structure can be obtained from the Fourier transform of the structure factor which is given as

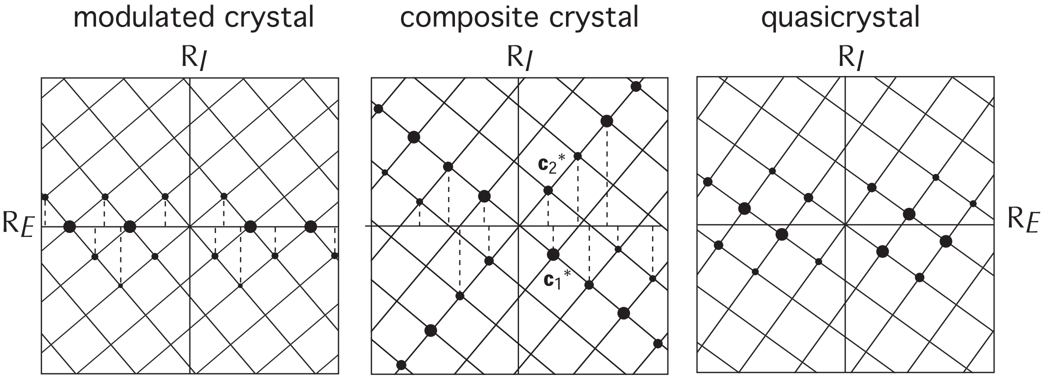

Fig. 5 Characteristics of aperiodic crystal families according to their reciprocal space embeddings. R_E and R_I indicate the external and internal space components.

$$F(\mathbf{H}) = \sum_j f_j(\mathbf{H})\ \exp\left(2\pi i \mathbf{H}\cdot \mathrm{r}_j\right) \times \int_0^1 \mathrm{d}t\ p_j(t)\ \exp\left\{2\pi i\left(\mathbf{H}\cdot \mathbf{u}_j(t) + h_4 t\right)\right\}. \tag{8}$$

The first line of the equation is very similar to the structure factor of a classical 3D crystal with the reciprocal vector **H** defined in (4). The term $\mathbf{u}_j$ in the second line characterizes the displacement of the atom j along t defined in (7) from the average position $\mathbf{r}_j$. Here $h_4 = m$ defined in (4). The population parameter $p_j(t)$ for example, can express the presence or absence of the specific atom j in some portion of the structure or an atomic position substituted by another one.

The determination of the displacement function $\mathbf{u}_j$ is the subject of the structure resolution algorithms treated in another chapter of the present encyclopedia.

The crystallographic model of a modulated structure obtained by exploiting the diffraction measurements can be analyzed in terms of two-dimensional sections of the type $(\mathbf{a}_{Si}, \mathbf{a}_{S4})$ with i varying from 1 to 3. In general, many sections are needed in order to completely characterize the structure. The nature of the modulations is usually presented in forms of t-plots which give some information about all possible conformations occurring in the crystal space. It can be interatomic or contact distances and angles. It can also represent occupational or substitutional parameters or some other meaningful crystal chemical parameters. Due to the aperiodic nature of the crystal structure, only selected portions of the crystal structure can be illustrated. This differs from the classical crystal structure where the unit cell content suffices to fully represent the structure.

We cannot terminate this section without discussing the important topic of symmetry. The sine qua non condition to determine and refine a classical crystal structure is to know its space group. There are 230 of them in 3D. It is due to the work of de Wolff, Janner and Janssen (Janssen et al., 2018) that the field of aperiodic crystals could evolve by deriving the superspace groups up to rank 6, i.e., up to (3 + 3)D. Owing to the very large number of possible cases, the list of superspace groups can be directly accessed from the web (Stokes et al., 2011). There are 775 superspace groups in (3 + 1)D, 3′338 in (3 + 2)D and 12′584 in (3 + 3)D!

The theoretical derivation and the development of superspace group symmetry is beyond the scope of this chapter. The interested user may consult the references cited in (Janssen et al., 2018) for further reading.

In the next sections, we shall explore a selection of incommensurate structures which have been solved experimentally and relate them to some specific physical and chemical properties.

The habit of Calaverite ($Au_{1-x}Ag_xTe_2$ with $x < 0.15$) or the macroscopic manifestation of incommensurate phases

One of the most fundamental laws concerning the habit or shape of (macroscopic) crystals is Haüy's law stating that every crystal face can be uniquely characterized by three integer indices also called Miller indices. This law was so anchored among scientists since the beginning of the 18 century that none would dare to question the general validity of the law although some experimental data were at hand to disproof it. The discovery of X-rays diffraction in 1912 revealed the intimate relation between the Laue indices characterizing the diffracted beam and the Miller indices of the crystal faces.

The difficulties to index the crystalline faces of Calaverite where already mentioned well before the discovery of X-ray diffraction. The most important study on indexing Calaverite crystals appeared in 1931 by Goldschmid, Palache and Peacok (see Dam et al. (1985) and references cited therein). 105 specimens from various worldwide origins including 92 crystal forms lead to the conclusion that the law of rational indices was not of general validity! The authors were obviously right as it was later confirmed but the publication did not lead immediately to further developments. Only 52 years later, Amelincks and coworkers found by high resolution electron microscopy (HREM) that Calaverite exhibited an incommensurately modulated structure with the modulation vector $\mathbf{q} = (\alpha_1, 0, \alpha_3)$. This discovery led Dam, Janner and Donnay to use the 1931 data to propose a new indexation of the faces with integer indices corresponding to the rank of the structure, i.e., the minimal number of integer coefficients necessary to fully index the diffraction pattern. The rank of Calaverite being four, every reciprocal vector **H** associated with each diffracted beam must satisfy the following relation.

$$\mathbf{H} = h_1\mathbf{a}_1^* + h_2\mathbf{a}_2^* + h_3\mathbf{a}_3^* + m\mathbf{q} \tag{9}$$

with

$$\mathbf{q} = \alpha_1\mathbf{a}_1^* + 0\mathbf{a}_2^* + \alpha_3\mathbf{a}_3^*. \tag{10}$$

This approach was very successful and led to the new characterization of the faces illustrated in Fig. 6. It was first realized that the crystals of Calaverite were twins and moreover, the components α_1 and α_3 of the modulation vector could be deduced from the optical goniometer measurements with a precision close to the values obtained by modern diffractometer measurements. The ultimate confirmation of the incommensurate nature appeared 3 years later when Schutte and de Boer (ref. cited in Dam et al. (1985)) published the complete resolution of the structure in the superspace formalism.

The study shows that the structure of the incommensurate Calaverite consists of parallel edge sharing layers of Te octahedra centered with (Au, Ag). The layers are stacked in the third dimension. The origin of the incommensurate modulation is due to an ordered substitution of Ag atoms which is independent of the lattice parameters.

What can be said on the stability of the crystal faces of Calaverite? Fig. 6 shows that most of the indices of the faces correspond to satellite reflections, i.e., $m \neq 0$. Only three of them correspond to main reflections ($m = 0$). In other words, faces corresponding to main or satellite reflections do not distinguish themselves as far as their stability is concerned. Moreover, the example of the Calaverite faces is not an exception and many other examples are known (see Dam et al. (1985)).

Sodium carbonate Na_2CO_3

Sodium carbonate is a very interesting example illustrating the interplay between commensurate and incommensurate phases occurring at different temperatures. It is also interesting because of its role in establishing a new paradigm in crystallography, namely the concept of superspace to characterize the symmetry of incommensurate structures or more generally aperiodic crystal structures.

Let us first describe the general features the Na_2CO_3 structure (Brouns et al., 1964; Arakcheeva and Chapuis, 2005) illustrated in Fig. 7. The structure can be interpreted in terms of a series of identical layers staked in the third dimension. Each layer consists of graphite-like layers with C and Na atoms. Each C atom is linked to three Na atoms and similarly, each Na atom is linked to three C atoms. The three O atoms of the carbonate group form nearly equilateral triangles around C atoms. We shall not deal further with the O atoms as their role in the phase transition mechanisms are secondary. In other words, we shall essentially study the role of the second coordination spheres around C.

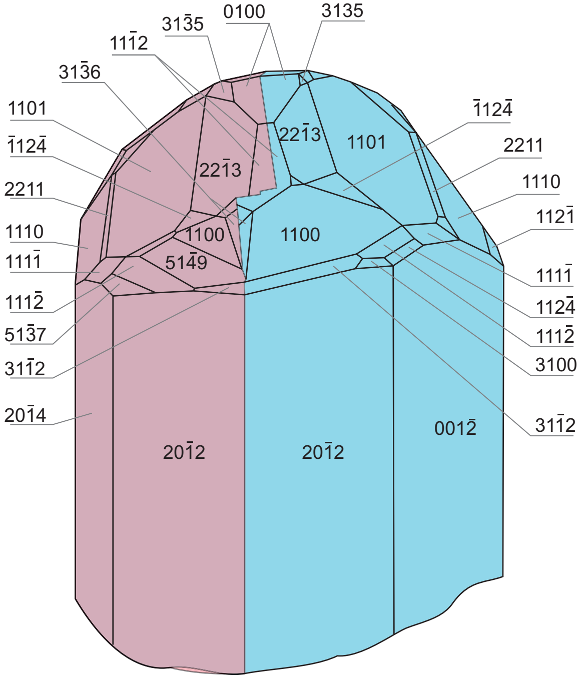

Fig. 6 The indexation of the twinned incommensurate structure of Calaverite in (3 + 1)D. Colors distinguish the twin components. The illustration is based on the figure published in (Dam et al., 1985).

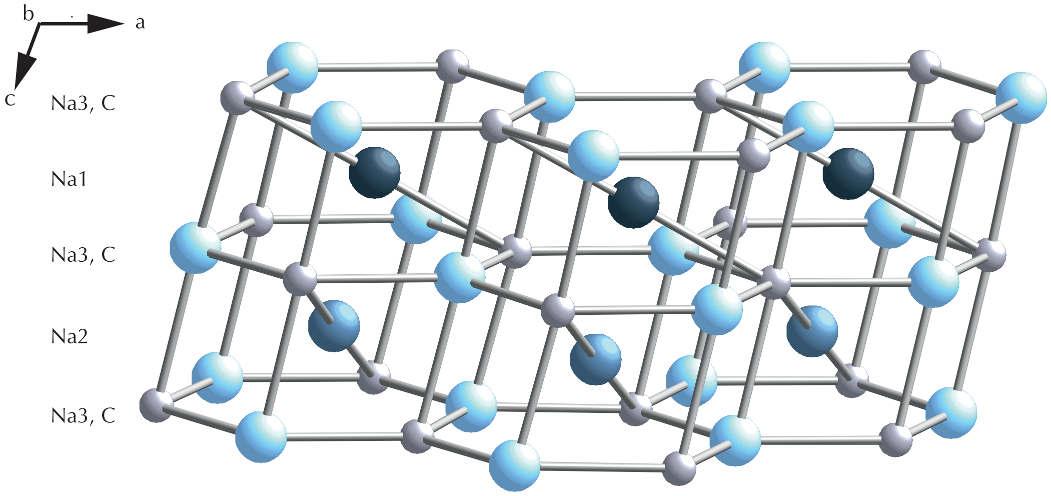

Fig. 7 A portion of the room temperature form of γ-Na_2CO_3 interpreted as a layer structure. Small and large spheres are C respectively Na atoms. O atoms are omitted for clarity.

In sodium carbonate, we can distinguish two types of sodium atoms, namely Na3 on one side and Na1 and Na2 on the other side. Na3 is part of the graphite-like layers whereas Na1 and Na2 are located halfway between the layers in alternating mode. From the chemical point of view, it turns out that Na3 behaves differently than Na1 and Na2. Thus, in this structure they can be interpreted as different chemical species.

Table 1 illustrates the sequence of second order phase transitions occurring between 754 and 170 K. The transition from the hexagonal α phase to the monoclinic β phase occurs following a shear deformation parallel to the graphite-like layer planes. Below 605 K, two incommensurate phases are observed resulting in the commensurate lock-in phase δ below 170 K.

We shall attempt to understand the nature of the incommensurate phase γ by analyzing various planar sections containing the C and Na atoms. The hexagonal high temperature phase α exhibits three mirror planes containing the hexagonal axis which are indicated by m_M and m_V in the inset of Fig. 8. The shear transformation occurring at the α to β transition results in the disappearance of two of the three mirror planes. Only mirror m_M remains. The right part of Fig. 8 represents the planar sections of the γ phase in the unique m_M plane which remains after the transition but also the planar section of the m_V (V for virtual) which only exists in the high temperature phase. The incommensurate γ phase consists of clusters which are similar to other phase portions at various temperatures. We can distinguish two main features, namely the regular section m_M indicated in Fig. 8 and the irregular section m_V. Only C-Na contact distances are indicated. Whereas the m_M section of phase γ is similar to the corresponding section of phase β, this is not the case of the other section m_V. Here the content of the m_V section of the incommensurate structure γ consists of different clusters which can be found at different temperatures but within the range of existence of phase β. Apparently, the regular structural motif observed in the m_M section cannot be realized in the m_V section. However, some parts of the motif can be accommodated locally in the form of clusters. This is at the origin of the incommensurate nature of the phase γ.

At this point, one may ask the question about the driving force behind the sequence of phase transitions occurring at different temperatures. It appears that the C atoms attempt to increase the number of C-Na contact distances by decreasing temperature. This is reflected in the coordination number of C-Na contacts distances less than 3.1 Å indicated in the above table. This number increases constantly for each phase starting from three in phase α to reach the number of seven in the lock-in phase δ.

The structural analysis of the incommensurate phases and the sequence of phase transitions occurring in sodium carbonate reveals two important characteristics which often occur in incommensurate structures. We observe first that two different types of Na atoms exists namely the ones (Na3) which are part of the graphite like layer structure. They behave in different ways if we compare their distances and geometries to the nearest or next nearest neighbors. On the other hand Na1 and Na2 are located between the graphite-like layers and play a different role during the phase transition mechanisms. This behavior is very well reflected in the Na-O distances. In the γ phase, the Na1-O and Na2-O distances vary from 2.3 to 2.4 Å whereas the Na3-O distances show a much larger spread varying between 2.5 and 2.9 Å. Such a structural differentiation between atoms of the same chemical species is not seldom in incommensurate structures. The host-guest type of high pressure BaIV structure (Arakcheeva et al., 2017) clearly distinguishes the guest Ba atoms located in the channels formed by the framework of the host Ba atoms. In this case, we are even dealing with a self host-guest structure.

Table 1 Phases and transition temperatures of Na_2CO_3.

α	*754* K	β	*605* K	γ′	*530* K	γ	*170* K	δ
hexag. CN: 3		monocl. 4		monocl. incom. 5		monocl. incom. 6–7		monocl. lockin 7

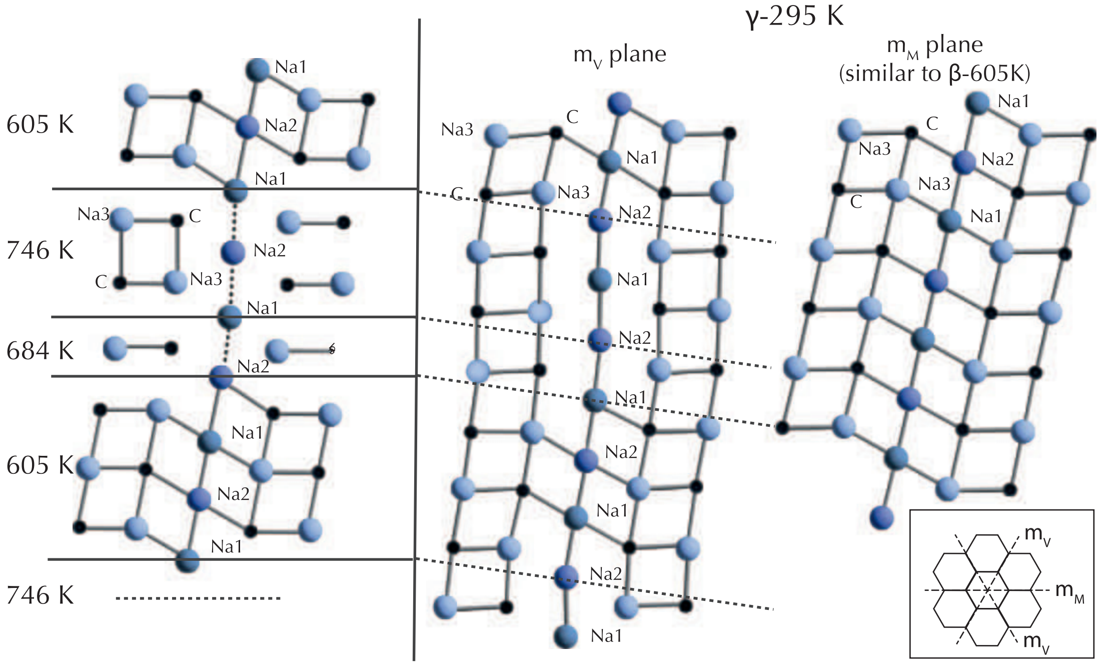

Fig. 8 Analysis of the incommensurate phase γ in terms of different planar sections. The three planar sections correspond to the three mirror planes occurring in the hexagonal phase α as indicated in the inset. During the shear transformation only one mirror plane remains, m_M, and the two others m_V disappear. Only contact distances smaller than 3.1 Å are represented. O atoms are omitted.

Another important aspect of incommensurate structures concerns the role not only of first nearest neighbors but also of the second nearest neighbors in the phase transition mechanisms (Arakcheeva et al., 2005). The example of Na_2CO_3 is characteristic but not unique. We have stressed above the important role of the second nearest neighbors of C atoms to drive the phase transition mechanism. Apparently the nearest neighbors of the C atoms, i.e., the O atoms, only play a secondary role in the driving force of the transition mechanism.

The luminescence of Europium containing scheelites

In this section we shall illustrate how the resolution of the incommensurate structures of a family of Europium containing scheelites did contribute to the understanding of their luminescent properties. Scheelite related compounds (SRC) with the general formula $M_n(XO_4)_m$ where M and X cover a large spectrum of elements are very stable and their preparation by solid state reactions are easy so that scheelites are found in many industrial applications including fuel cells and photocatalysts. In particular, Eu^{3+}-containing compounds exhibit interesting white-light-emitting diode properties. The study of a series of scheelites with the composition $Na_xEu_{(2-x)/3}{}^{3+}MoO_4(0 \leq x \leq 0.5)$ gives interesting insights into the important role of incommensurate structures in determining some physical properties of solids (Arakcheeva et al., 2012).

The general feature of the Eu containing scheelites is illustrated in Fig. 9. The unit cell is composed of two cubic face centered unit cells stacked along c. The positions of the Eu, Na atoms alternates with the MoO_4 tetrahedra.

The luminescent characteristics of a series of samples with x varying between 0 and 0.5 have been measured in order to correlate them with their structural properties. The large majority of the structures are incommensurately modulated and their structures could be solved from powder diffraction data. Due to the incommensurability of the structures only finite portions of them can be represented. Fig. 10 represents portions of the cationic part of the structures projected along c.

For each specific Na/Eu ratio we observe specific incommensurate structures, the characteristics of which can all be deduced from a single superspace group. The corresponding coefficients α and β of the modulation vectors $\mathbf{q} = \alpha\mathbf{a}^* + \beta\mathbf{b}^*$ vary by only a few percents depending on the composition. As a consequence of the modulation vector, the periodicity along c remains and the propagation of the modulation is confined to the (a,b) plane. The direction of $\mathbf{q}$ is indicated in Fig. 10. In all the structures, except for the Eu/Na ratio of 1, we observe parallel lines of extended domains normal to $\mathbf{q}$ representing either Eu (dark blue) or Na (light blue) domains but also vacancies (white stars).

The incommensurate structures exhibit an outstanding feature namely the presence of Eu dimers or clusters which play an important role in relation to the luminescent characteristics of these materials. The Eu-clusters are represented in the top right of Fig. 10 and form separate entities (surrounded by yellow ellipses in the figure) which are well distinguishable. Their number are specific for each chemical composition but are not related to the Eu/Na ratio.

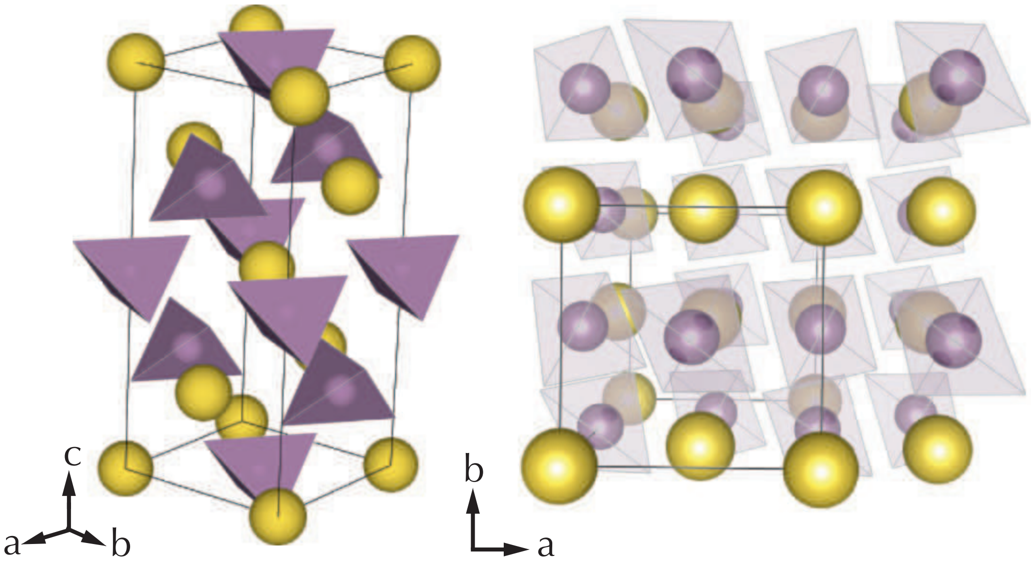

Fig. 9 Two representations of the of Na, Eu scheelite with MoO_4 tetrahedra. In the incommensurate structures, the yellow spheres show a well ordered distribution of the Na and Eu atoms and also their vacancies.

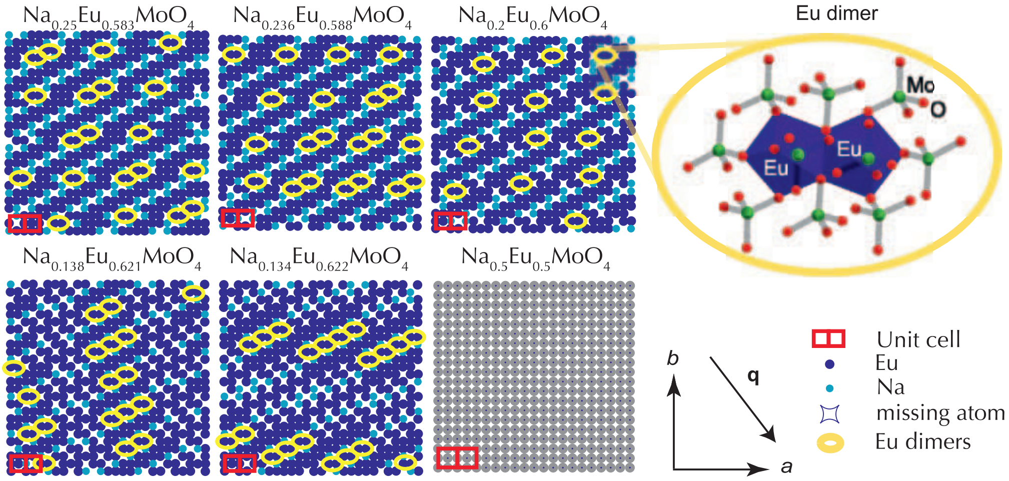
$Na_{0.25}Eu_{0.583}MoO_4$
$Na_{0.236}Eu_{0.588}MoO_4$
$Na_{0.2}Eu_{0.6}MoO_4$
Eu dimer
Mo
O
Eu
Eu
$Na_{0.138}Eu_{0.621}MoO_4$
$Na_{0.134}Eu_{0.622}MoO_4$
$Na_{0.5}Eu_{0.5}MoO_4$
b
q
a
Unit cell
Eu
Na
missing atom
Eu dimers

Fig. 10 Portions of the *ab* projections of the cationic part of $Na_xEu_{(2-x)/3}{}^{3+}MoO_4$. The unit cells of the structures based on the main reflections only are given in red. Eu atoms (dark blue) Na atoms (light blue) and vacancies (white stars) form different aggregates depending on the composition. One of them, the Eu dimer is represented on the top right. Gray atoms indicate disorder between Eu and Na atoms.

It turns out that a linear relation can be found between the percentage of Eu-clusters relative to the total number of Eu atoms. Fig. 11 illustrates some luminescent characteristics as function of the Eu-cluster percentage. Different characteristic measurements are represented, namely, the quantum yield, Q_L^{Eu}, obtained by ligand excitation at 273 K, the intrinsic quantum yield of Eu^{3+}, Q_{Eu}^{Eu}(meas), and the observed lifetimes τ_{obs} at 293 and 77 K as function of the relative amount of Eu clusters, $N_{Eu-cl}/N_{Eu-total}$ in $Na_xEu_{(2-x)/3}{}^{3+}MoO_4$.

An interesting question arises concerning the count of the relative number of Euclusters in an aperiodic structure. The distribution of the clusters represented in Fig. 10 rather show a random distribution if we consider that only portions of aperiodic structure are represented. For this purpose we can take advantage of the *t*-plots mentioned at the end of Section "Theoretical presentation of superspace for the description of aperiodic structures." The aim is to look at the domain of existence of Eu-Eu contact distances where each Eu has only one neighbor within a maximal specified distance. The extension of the domain in the corresponding *t*-plot yields the percentage of the Eu-clusters relative to the total amount of Eu present in the structure.

The study shows the important role played by incommensurate structures in revealing some structure-property relations. This is even more important regarding the fact that the satellite reflections are very weak in the case of $Na_xEu_{(2-x)/3}{}^{3+}MoO_4$ and therefore can easily be overseen if the powder diffractograms lack sufficient resolution. This is why many previous studies on the origin of the luminescence of Eu-scheelites failed by considering only periodic approximations of the crystal structures.

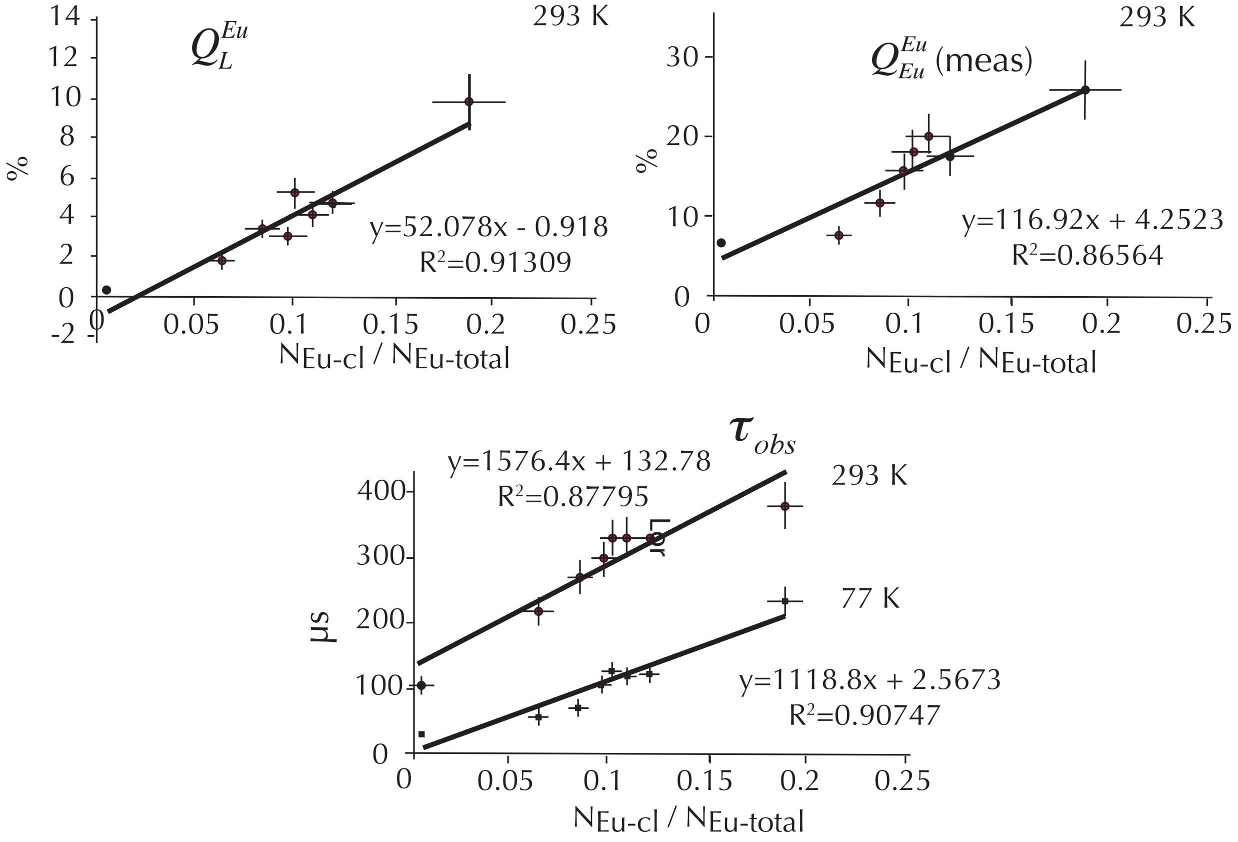

Fig. 11 Different luminescence characteristics namely the quantum yield, Q_L^{Eu}, obtained by ligand excitation at 273 K, the intrinsic quantum yield of Eu^{3+}, Q_{Eu}^{Eu}(meas), and the observed lifetimes τ_{obs} at 293 and 77 K are represented in function of the relative amount of Eu clusters, $N_{Eu-cl}/N_{Eu-total}$ in Na$_x$Eu$_{(2-x)/3}{}^{3+}$MoO$_4$.

The superspace formalism, which we used here to discover the linearity between luminescent properties and the relative content of Eu-clusters, exhibits another interesting property. The superspace formalism can be used as a predictive tool for the discovery of new physical properties in material science. In particular, it could be used to optimize the luminescent properties of some extended series of SRC by maximizing the number of clusters.

Structure evolution of the organic perovskite $CH_3NH_3PbI_3$ by thermal cycling around the phase transitions

Methyl ammonium lead iodide (MAPbI$_3$) is a very efficient light absorbing photovoltaic material with a broad spectrum of opto-electronic properties. Its properties have found applications in gas sensor, photodetectors, light-emitting diodes and solar cells in particular (Glushkova et al., 2019). Currently, MAPbI$_3$ based solar cells have reached the impressive level of 22% efficiency!

The physical properties strongly depend on the preparation methods and storage conditions, i.e., temperature and humidity. In addition, the crystal structure is subject to phase transitions which affect the electronic and photonic band structure, i.e. the transport properties. They are essentially two phase transitions occurring at low temperature (160 K) and high temperature (330 K).

In the temperature range from 100 to 352 K, we observe essentially two types of structural modifications occurring during the phase transitions. The first concerns the orientations of the C—N bonds which are linked to the inorganic framework by H-bonds between the N and I atoms. The room temperature pristine form of the organic perovskite $CH_3NH_3PbI_3$, methylammonium lead iodide, is tetragonal, space group *I* 422 and is illustrated in Fig. 12. Already at room temperature, a superposition of four different disordered C—N bonds can be observed. The second type of changes occurring during the transition mechanisms concerns a slight rotation of the octahedra about the tetragonal axis. Consequently each corner sharing octahedra in the plane rotates about the same amount but in the opposite direction. The two types of structural modifications are not independent and the H bonded links tend to adopt the best possible orientation depending on the closest contact distances with the iodine atoms.

Under standard operating conditions, solar cells with encapsulated MAPbI$_3$ layers can reach over 360 K crossing thus the transition temperature twice each day. A deep understanding of the repeated phase transition mechanisms is thus necessary in order to optimize the working conditions of the solar cells. The following study shows the effect on the structural modifications of the thermal cycling around the high temperature phase transition. It appears that MAPbI$_3$ does not return to the initial structural state but reaches an equilibrium structure which is specific for the phase transition temperature. The cycling around the high temperature

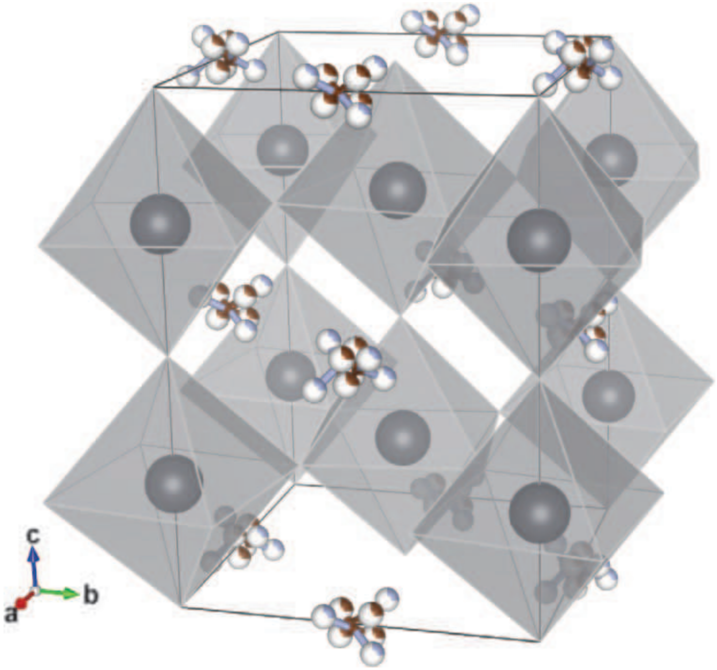

Fig. 12 The pristine structure of the organic perovskite CH_3-NH_3PbI_3, methylammonium lead iodide. The tetragonal form consists of a 3D grid of PbI_3 octahedra sharing common vertices with their nearest neighbors. The methylammonium (MA) groups represented here without hydrogens are located in the cavities formed by the framework of octahedra. In the tetragonal form, each MA site is disordered and consists of a superposition of four different C—N bonds orientations.

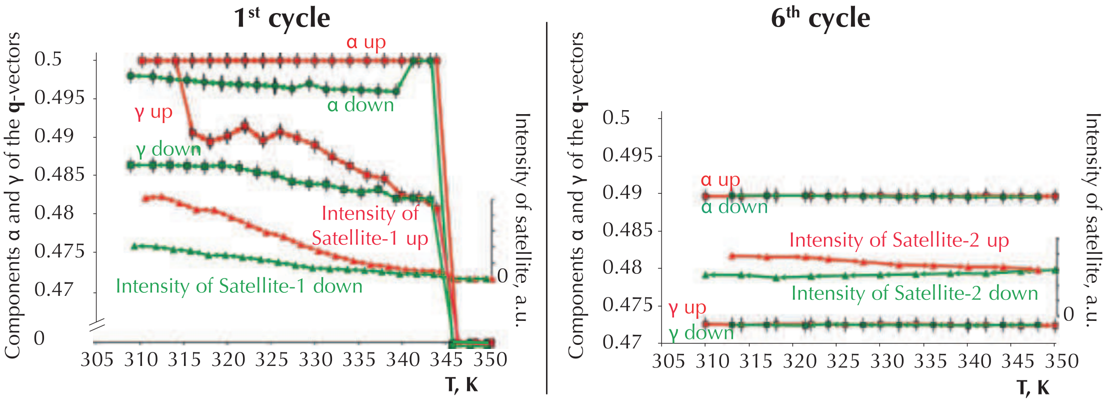

Modulation vectors: $\mathbf{q}_1 = \alpha\mathbf{a}^* + \alpha\mathbf{b}^*$, $\mathbf{q}_2 = -\alpha\mathbf{a}^* + \alpha\mathbf{b}^*$ and $\mathbf{q}_3 = \gamma\mathbf{c}^*$

Fig. 13 Evolution of the characteristics of two satellite reflections in the high temperature range of the phase transition depending on the number of cycling. The initial tetragonal structure transforms to an incommensurately modulated tetragonal phase which reaches equilibrium after a limited number of transitions.

phase transition gives rise to an incommensurately modulated phase reaching stability already after a few number of successive transitions as indicated in Fig. 13. Both left and right figures consist of two parts, α and γ components of the characteristic satellite reflection (left ordinate) and the intensities of the satellite (right ordinate). Up and down refers to the increase respectively decrease of the temperature around the phase transition. On the first cycling process, α remains rational by increasing temperature (red color) until the phase transition occurs. Above 340 K the value reaches 0. For γ on the other hand, the value decreases and becomes incommensurate reaching 0 above 340 K. By decreasing temperature (green color) both α and γ components remain incommensurate till the end of the first cycle. The sixth cycle shows that the incommensurate phase is well settled and no more variation of the α and γ components can be observed.

In order to see the effect of the modulation on the structure, a 30 nm square portion of the non-periodic structure is illustrated in Fig. 14 for two different temperatures. For clarity, the organic part of the structures has been omitted. Both figures show domains with the same periodicity. However, due to different intensities of the satellite reflections, the temperature dependent nano domains exhibit different amplitudes of the rotations of the lead iodide octahedra. In the temperature range between 310 and 350 K, we

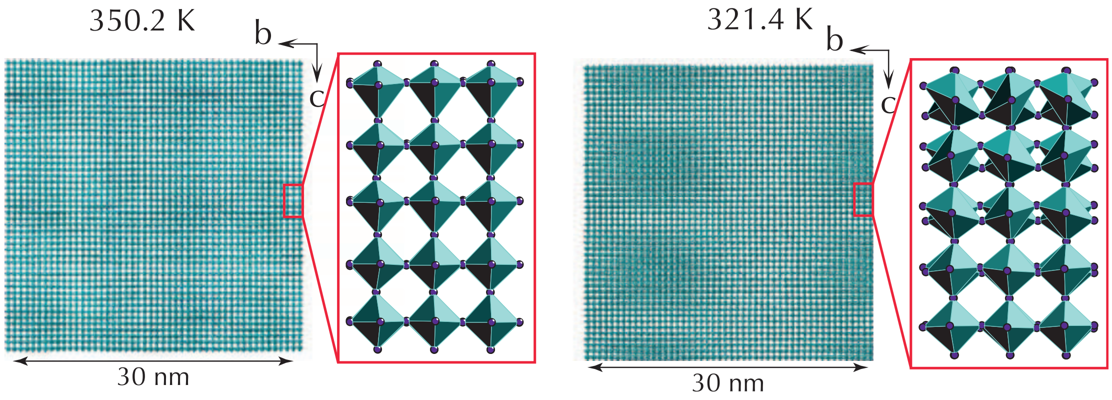

The (3+3)D superspace group is P4/mmm(α_1,α_1,0)0s0s(-α_1,α_1,0)0s00(0,0,γ_2)00ss (No. 123.3.174.104) with unit cell parameters: a = 6.309(3), c = 6.311(3) Å and modulation vectors: $\mathbf{q}_1$ = 0.4861$\mathbf{a}^*$ + 0.4861$\mathbf{b}^*$; $\mathbf{q}_2$ = -0.4861$\mathbf{a}^*$ + 0.0.4861$\mathbf{b}^*$ and $\mathbf{q}_3$ = 0.4718$\mathbf{c}^*$.

Fig. 14 Two portions of the incommensurate $MAPbI_3$ structure at different temperatures. We observe the formation of nano domains with the same periodicity given by the modulation vector **q**. The domains are essentially due to various tilt angles of lead iodide octahedra relative to the tetragonal unit cell vectors.

observe also a small linear temperature dependency of the lattice parameters which changes by less than 0.01 Å both in increasing and decreasing temperatures.

The interaction between the inorganic and organic parts of the structure is the principal cause of the phase transitions. The stability of the structure might be improved by some cationic substitution and indirectly influence the electronic properties of the material. Other approaches have been proposed, e.g., by introducing some inert gas into the framework of the structure leaving ample possibilities to improve the stability of the structure.

Conclusion

Only very limited aspects of incommensurately modulated structures could be illustrated in this presentation. Modulated structures are not rare, on the contrary they appear in all possible categories of materials from small molecules to macromolecules, in metals and alloys under high pressure and often in minerals. Before the discovery of aperiodic crystals and the introduction of the very powerful superspace tools, many structures were published as conventional 3D structures but often with "disordered" character. Some of them were later successfully reinterpreted in terms of well ordered incommensurately modulated structures. Many examples of scheelite structures as described in Section "The luminescence of Europium containing scheelites" fit into this scheme.

We have to stress at this point that incommensurate structures cannot be classified as disordered structures. On the contrary, they are very well ordered structures as indicated by the presence of discrete satellite reflections. This order goes beyond the 3D unit cell periodicity and mostly appears in terms of nano domains as exemplified in the case of $MAPbI_3$ described in Section "Structure evolution of the organic perovskite $CH_3NH_3PbI_3$ by thermal cycling around the phase transitions." It is however not excluded that the appearance of satellite reflections might be accompanied with the presence of diffuse scattering in the diffraction patterns, especially in cases of phase transitions where some dynamical rearrangements occur in the formation of nano domains depending on the temperature or pressure variation.

There is another interesting aspect concerning the utility of the superspace group concept. Initially the superspace was developed to characterize the symmetry of incommensurate structures. This concept however is a very powerful tool to predict and explore new structures with specific physical properties as described in reference (Arakcheeva and Chapuis, 2008). It is also very useful to describe families of compounds containing both commensurate (3D) and incommensurate (3 + n)D members. The interesting feature here is that only one single superspace group is sufficient to describe the complete series of members of the family characterized by a large range of elements, chemical composition and topology.

Acknowledgments

I would like to thank Dr. Alla Arakcheeva for suggestions and providing the figures of Section "Structure evolution of the organic perovskite $CH_3NH_3PbI_3$ by thermal cycling around the phase transitions."

References

Arakcheeva A and Chapuis G (2005) A reinterpretation of the phase transitions in Na_2CO_3. *Acta Crystallographica. Section B* 61(Pt 6): 601–607.

Arakcheeva A and Chapuis G (2008) Capabilities and limitations of a (3 + d)-dimensional incommensurately modulated structure as a model for the derivation of an extended family of compounds: Example of the scheelite-like structures. *Acta Crystallographica. Section B* 64(1): 12–25.

Arakcheeva A, Chapuis G, Petricek V, and Morozov V (2005) The role of second coordination-sphere interactions in incommensurately modulated structures, using β-$K_5Yb(MoO_4)_4$ as an example. *Acta Crystallographica. Section B* 61(Pt 4): 400–406.

Arakcheeva A, Logvinovich D, Chapuis G, Morozov V, Eliseeva SV, Buenzli J-CG, and Pattison P (2012) The luminescence of $Na_xEu^{3+}{}_{(2-x)/3}MoO_4$ scheelites depends on the number of Eu-clusters occurring in their incommensurately modulated structure. *Chemical Science* 3(2): 384–390.

Arakcheeva A, Bykov M, Bykova E, Dubrovinsky L, Pattison P, Dmitriev V, and Chapuis G (2017) Incommensurate atomic density waves in the high-pressure IVb phase of barium. *IUCrJ* 4(Pt 2): 152–157.

Brouns E, Visser JW, and deWolff PM (1964) An anomaly in the crystal structure of Na_2CO_3. *Acta Crystallographica* 17(5): 614.

Dam B, Janner A, and Donnay JDH (1985) Incommensurate morphology of calaverite (Aute2) crystals. *Physical Review Letters* 55(21): 2301–2304.

Dewolff PM (1974) The pseudo-symmetry of modulated crystal-structures. *Acta Crystallographica Section A* 30: 777–785.

Glushkova A, Mantulnikovs K, Giriat G, Semeniuk K, Forro L, Horvath E, and Arakcheeva A (2019) Effect of thermal cycling on the structural evolution of methylammonium lead iodide monitored around the phase transition temperatures. *Solar RRL* 3(7).

Janssen T, Chapuis G, and Boissieu M (2018) *Aperiodic Crystals: From Modulated Phases to Quasicrystals: Structure and Properties, International Union of Crystallography Monographs on Crystallography*, 2nd edn. Oxford: Oxford University Press.

Korekawa M and Jagodzinski H (1967) Die Satellitenreflexe des Labradorits. *Schweizerische Mineralogische und Petrographische Mitteilungen* 47: 269–278.

Petříček V, Dušek M, and Palatinus L (2014) Crystallographic computing system JANA2006: General features. *Zeitschrift für Kristallographie - Crystalline Materials* 229(5): 345–352.

Shechtman D, Blech I, Gratias D, and Cahn JW (1984) Metallic phase with long-range orientational order and no translational symmetry. *Physical Review Letters* 53(20): 1951–1953.

Stokes HT, Campbell BJ, and van Smaalen S (2011) Generation of (3 + d)-dimensional superspace groups for describing the symmetry of modulated crystalline structures. *Acta Crystallographica Section A* 67(1): 45–55.

Yamamoto A (1996) Crystallography of quasiperiodic crystals. *Acta Crystallographica Section A* 52: 509–560.

Yamamoto A, Janssen T, Janner A, and de Wolff PM (1985) A note on the superspace groups for one-dimensionally modulated structures. *Acta Crystallographica Section A* 41(6): 528–530. https://doi.org/10.1107/S0108767385001167.

Thermodynamics of information

Juan MR Parrondo, Departamento de Estructura de la Materia, Física Térmica y Electrónica and GISC, Universidad Complutense de Madrid, Madrid, Spain

© 2024 Elsevier Ltd. All rights reserved.

Introduction 522
Information 524
Shannon and thermodynamic entropies 525
Second law for feedback processes 527
Informational states and Landauer's principle 529
Restoring the second law 530
Information flows 532
Conclusion: What is information? 533
Acknowledgments 534
References 534

Abstract

As early as 1867, two years after the introduction of the concept of entropy by Clausius, Maxwell showed that the limitations imposed by the second law of thermodynamics depend on the information that one possesses about the state of a physical system. A "very observant and neat-fingered being," later on named *Maxwell demon* by Kelvin, could arrange the molecules of a gas and induce a temperature or pressure gradient without performing work, in apparent contradiction to the second law. One century later, Landauer claimed that "information is physical," and showed that certain processes involving information, like overwriting a memory, need work to be completed and are unavoidably accompanied by heat dissipation. Thermodynamics of information analyzes this bidirectional influence between thermodynamics and information processing. The seminal ideas that Landauer and Bennett devised in the 1970s have been recently reformulated in a more precise and general way by realizing that informational states are out of equilibrium and applying new tools from non-equilibrium statistical mechanics.

Introduction

The connection between information and thermodynamics was first revealed by the celebrated Maxwell demon, a gedanken experiment that Maxwell devised shortly after his discovery of the distribution of velocities in an equilibrium gas. The velocity distribution revealed that temperature is proportional to the average kinetic energy of molecules, but their speeds cover a wide range of values. Maxwell considered two gases, a hot one *A* and a cold one *B*, confined respectively in two containers separated by a wall or diaphragm. Then he imagined an external agent or demon as "a finite being who knows the paths and velocities of all the molecules by simple inspection but who can do no work except open and close a hole in the diaphragm by means of a slide without mass." In a letter to his friend Tait, dated December 11th 1867, Maxwell describes for the first time the operation of the demon:

> Let him first observe the molecules in *A* and when he sees one coming the square of whose velocity is less than the mean square velocity of the molecules in *B*, let him open the hole and let it go into *B*. Next, let him watch for a molecule of *B*, the square of whose velocity is greater than the mean square velocity in *A*, and when it comes to the hole let him draw the slide and let it go into *A*, keeping the slide shut for all other molecules. Then the number of molecules in *A* and *B* are the same as at first, but the energy in *A* is increased and that in *B* diminished, that is, the hot system has got hotter and the cold colder and yet no work has been done, only the intelligence of a very observant and neat-fingered being has been employed.

Maxwell published the idea, four years after the letter to Tait, in a section of his book, *Theory of Heat* (1871). The section is entitled "Limitation of the second law of thermodynamics." Later on, Lord Kelvin coined the name Maxwell's demon for this "neat-fingered being," and it has been subject of constant controversy until nowadays (Leff and Rex, 1990). The original Maxwell demon opened at least two important lines of research.

The first one is based on a simpler version of the Maxwell demon, also known as pressure demon. In this variant, the demon opens the door only when a particle from the left half of the container is moving to the right half, that is, he allows particles to cross only from left to right. By doing so, the demon accumulates particles in the rightmost half of the container, increasing its density and inducing a pressure difference that can be subsequently used to obtain work. Notice that, in principle, a simple valve, like the one depicted in Fig. 1, could do the same job as the demon. However, this naive idea does not work because the valve is subjected to thermal fluctuations that randomly open the gate and allow particles to cross in the "wrong" direction. In fact, there is a fundamental impossibility of rectifying thermal fluctuations due to the reversibility of microscopic dynamics (Ehrich et al., 2019). The celebrated Smoluchowsky-Feynman ratchet (Feynman et al., 1966; Smoluchowski, 1912) is another example of autonomous Maxwell demon, which cannot rectify thermal fluctuations from a single bath. Feynman went further and assumed

https://doi.org/10.1016/B978-0-323-90800-9.00174-8

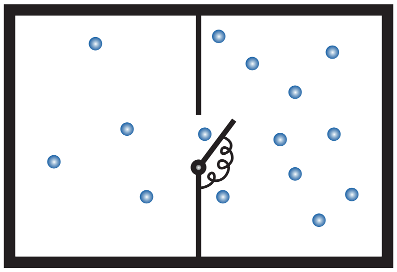

Fig. 1 The autonomous pressure Maxwell demon.

that the ratchet is immersed in a fluid at a temperature lower than the source of the fluctuations and proved that then the ratchet is indeed able to rectify and perform work. Nevertheless, the second law is not defeated since now the system is in contact with two thermal baths at different temperatures and the whole setup acts as a thermal machine. Feynman showed that the efficiency of such a motor cannot be higher than the Carnot efficiency, in agreement with the second law.[1] This approach can be applied to generic classical systems in contact with thermostats and/or chemostats. The idea has yielded a fruitful line of research on Brownian motors (Reimann, 2002), systems that exhibit systematic motion or perform work using gradients of temperature and/or chemical potential, with applications in biology and nanotechnology (Bustamante et al., 2001; Feng et al., 2021). The role of information in Brownian motors is not completely clear, although we introduce in Section "Information flows" the concept of information flows in autonomous systems, which allows one to analyze some of these machines as an exchange between information and entropy (Allahverdyan et al., 2009; Horowitz and Esposito, 2014).

The second line of research directly concerns the use of information by the original Maxwell's demon (Leff and Rex, 1990; Parrondo et al., 2015; Sagawa, 2012a,b). Two questions immediately arise form the fact that the demon can beat the second law using information. First, can we derive a quantitative relationship between the entropy decrease and the information that the demon possesses? Or, in other words, how the acquisition of information modifies the second law? Second, can we restore the validity of the second law by finding an entropy cost associated to the acquisition and/or manipulation of information by the demon? Thermodynamics of information addresses these two questions. However, it is convenient to analyze them separately. We discuss the first question in Section "Second law for feedback processes" and the second one in Section "Restoring the second law."

In 1929, Szilárd introduced a simplified version of the Maxwell demon known as the Szilárd engine (Szilárd, 1929), which is more suitable for the resolution of these issues. It consists of a single-molecule gas at temperature T in a box of volume V. This means that the molecule thermalizes at temperature T in any collision with the wall, i.e., the outgoing velocity is a random variable distributed according to the corresponding equilibrium distribution. An external agent or demon performs the cyclic operations sketched in Fig. 2. First, he inserts a piston at the middle point of the container and measures in which of the two halves the particles lies. With this information, the demon can realize a reversible isothermal expansion by opposing a force to the pressure P exerted by the single-molecule gas. In the expansion, the demon extracts a work

$$W_{\text{extract}} = \int_{V/2}^{V} P dV' = \int_{V/2}^{V} \frac{kT}{V'} dV' = kT \ln 2 \tag{1}$$

where we have used the equation of ideal gases, $PV' = NkT$, with $N = 1$, and k is the Boltzmann constant. Finally, the piston is removed and the cycle is completed. In principle, the insertion and removal of the piston can be performed without any energy expenditure.[2] Hence, the Szilárd engine is able to extract energy from a single thermal bath in a cycle, in apparent contradiction to the second law.

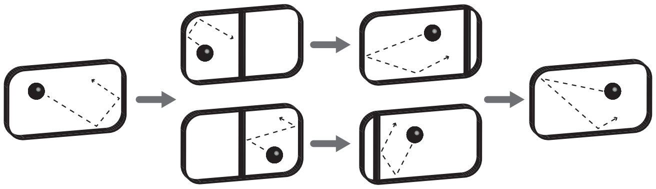

Fig. 2 The Szilárd engine.

---

[1] Feynman also proved that the thermal ratchet can reach Carnot efficiency in the limit of zero power. However, this result has been subject to some criticism: an autonomous thermal machine can reach Carnot efficiency only in the case of tight coupling between heat flow and mechanical work, something that it is not possible to reach in the original setup by Smoluchowsky and Feynman (Parrondo and Español, 1996).

[2] This is not true for a quantum particle at low temperature because, due the Heisenberg uncertainty principle, the kinetic energy increases when it is confined in one of the halves (Zurek, 1990).

Some aspects of the original Szilárd cycle are not completely clear, specially the application of the ideal gas equation to the pressure on the piston, which is due to single collisions. Nevertheless, these issues can be resolved and, moreover, the Szilárd engine can be implemented in any system exhibiting a symmetry breaking, like an Ising model (Parrondo, 2001). In fact, there are experimental realizations of the Szilárd engine in a variety of systems: single-electron circuits (Koski et al., 2014; Pekola and Khaymovich, 2019), Brownian particles in optical traps (Roldán et al., 2014), or Brownian rotors in electrostatic potentials (Toyabe et al., 2010).

The Szilárd engine, as the original Maxwell demon, utilizes the information gathered in the measurement to decrease the entropy of the system. While in the Maxwell demon the information involved and the decrease of entropy are difficult to assess, in the Szilárd engine both have a precise value: information is acquired in a single measurement per cycle with two equiprobable outcomes, left (L) or right (R), and the entropy decreases by $k \ln 2$. This is why most of the studies on the connection between thermodynamics and information are based on the Szilárd engine. In fact, the Szilárd engine partially solves the first question mentioned above. Before the measurement, the particle can be in any of the two halves and, after the measurement, it occupies only one. The measurement is equivalent to a compression from a volume V to $V/2$, which reduces the entropy of the gas by $k \ln 2$. Such a compression would need a work $kT \ln 2$, counterbalancing the work (1) extracted in the expansion, but apparently the measurement is able to perform the compression without any energy expenditure.

Thermodynamics of information refines and generalizes this argument (Parrondo et al., 2015). First, by incorporating concepts from information theory that quantify the information acquired in a measurement in a more precise and general way. Second, by realizing that the states resulting from measurements and other processes involving information are in general non-equilibrium states. Hence, thermodynamics of information can be considered as a branch of statistical mechanics that deals with a special class of non-equilibrium states bearing information.

The outline of this article is the following. In Section "Information," we review the concepts of information theory relevant to thermodynamics, like Shannon entropy and mutual information. We discuss in detail the relationship between Shannon entropy and thermodynamic entropy in Section "Shannon and thermodynamic entropies." In Section "Second law for feedback processes," we show how the acquisition of information affects the second law. The resulting modified second law for feedback processes—those that follows a protocol depending on the outcome of a measurement—is the answer to the first question that we have posed above. In Section "Informational states and Landauer's principle," we derive the thermodynamic cost of some processes involving information in memories and other information devices, like the celebrated Landauer principle (Landauer, 1961). These costs help us to solve the second question, i.e., the restoration of the original second law in the Szilárd engine and any generic isothermal feedback processes. This is discussed in Section "Restoring the second law," where we show that feedback processes obey the original second law when one accounts for the cost of measurement and/or restoring the demon's memory, generalizing Bennett's analysis of the Szilárd engine (Bennett, 1982). In Section "Information flows," we introduce a formalism that allows one to study information flows (Allahverdyan and Saakian, 2008; Horowitz and Esposito, 2014) in autonomous Maxwell demons. Finally, in Section "Conclusion: What is information?" we present our main conclusions and discuss the physical nature of information.

Information

In his seminal papers published in 1948 (Shannon, 1948), Shannon introduced a measure of the uncertainty or ignorance that one has about a random object or discrete random variable X, which can be a generic message in a communication channel, a file in a computer, or the microstate of a physical system. Shannon uncertainty, also known as Shannon entropy,[3] is defined as

$$S(X) = S[p_X] = -\sum_x p_X(x) \log p_X(x). \tag{2}$$

Here we have introduced two useful equivalent notations, namely, expressing the dependency of the uncertainty S on the random variable X or on its probability distribution $p_X(x)$. Uncertainty can be expressed in bits, if the logarithm in Eq. (2) is in base 2, in nats, if it is the natural logarithm, or in units of thermodynamic entropy if we multiply nats by, for instance, the Boltzmann constant k. In the rest of the article, we will assume that the Shannon entropy is expressed in physical units of energy divided by temperature, without the need of writing explicitly the Boltzmann constant. Finally, for continuous random variables, the sum in (2) must be replaced by an integral (Cover and Thomas, 2006).

It is customary to interpret Shannon uncertainty as a measure of information, and this is indeed appropriate in certain situations. For example, when we consider the information content of a given instance of the random variable X. However, when we talk about information, specially in physics, or, more precisely, about obtaining information from a system, we have in mind an inquiry about the state X of the system, which consists in the measurement of a quantity Y. When we measure Y, we acquire information about X that results in a decrease of its uncertainty. This decrease is precisely the amount of information that Y provides about X:

---

[3] In a famous conversation between Shannon and Von Neumann, the latter suggested Shannon to use the name entropy because (2) is similar to the definition of entropy in statistical mechanics and, more importantly, because "nobody really knows what entropy is." The conversation was reported by Shannon himself but later on he admitted that it probably never took place (Price, 1982).

$$I(X;Y) \equiv S(X) - S(X|Y) \tag{3}$$

which is called *mutual information* (Cover and Thomas, 2006; Shannon, 1948). Here $S(X|Y)$ is the uncertainty of the posterior probability distribution $p_{X|Y}(x|y)$ averaged over the possible outcomes $p_Y(y)$, i.e.,

$$\begin{aligned} S(X|Y) &\equiv \sum_y p_Y(y)\left[-\sum_x p_{X|Y}(x|y)\log p_{X|Y}(x|y)\right] \\ &= -\sum_{x,y} p_{XY}(x,y)\log p_{X|Y}(x|y). \end{aligned} \tag{4}$$

Using the relationship between conditional and joint probabilities (Bayes' formula): $p_{XY}(x,y) = p_{X|Y}(x|y)p_Y(y)$, we can write the mutual information as

$$I(X;Y) = \sum_{x,y} p_{XY}(x,y)\log\frac{p_{XY}(x,y)}{p_X(x)p_Y(y)}. \tag{5}$$

From this expression we can derive a number of interesting properties of the mutual information. First, mutual information is symmetric, i.e., Y provides the same information about X as X provides about Y. Second, using the properties of the logarithm, one can prove from Eq. (5) that $I(X;Y)$ is always positive and vanishes if and only if X and Y are statistically independent (Cover and Thomas, 2006). Hence, mutual information is a measure of the correlation between X and Y. Third, if we measure without error a quantity $Y = f(X)$, then $S(Y|X) = 0$ and $I(X;Y) = S(Y)$. In other words, the information provided by an error-free measurement is the uncertainty of the outcome.

Finally, Eq. (5) allows us to write the mutual information in three different ways:

$$\begin{aligned} I(X;Y) &= S(X) - S(X|Y) \\ &= S(Y) - S(Y|X) \\ &= S(X) + S(Y) - S(X,Y) \geq 0 \end{aligned} \tag{6}$$

where $S(X,Y)$ is the Shannon entropy or uncertainty of the joint probability distribution $p_{XY}(x,y)$. The last equality indicates that correlations make the entropy sub-additive:

$$S(X,Y) = S(X) + S(Y) - I(X;Y). \tag{7}$$

This expression will be useful when we consider the physical nature of Maxwell or Szilárd demons and interpret a measurement as the creation of correlations between the state of the demon and the state of the system.

Shannon and thermodynamic entropies

If Shannon uncertainty is identified as thermodynamic entropy, one immediately obtains from the definition of mutual information (3) that the entropy of a system X decreases by an amount $I(X;M)$ when we measure a quantity M. For instance, in the case of the Szilárd engine with error-free measurements, X is the micro-state of the global system, particle plus bath, which obviously includes the position of the particle, and $M = L, R$ (L for left, and R for right) is the outcome of the measurement, i.e., the half of the container where the particle lies after the insertion of the piston. Since M is a function of X and the two outcomes are equally probable, $I(X;M) = S(M) = k\ln 2$. Thus, the total entropy decreases by $k\ln 2$, and this decrease allows one to extract an energy $kT\ln 2$ from the thermal bath in the form of work by driving quasi-statically the system back to its initial state. This is a similar argument as the one that we sketched in Section "Introduction."

This explanation, however, requires a more careful consideration. The identification of Shannon and thermodynamic entropies is not correct, in general. The main reason is that the Shannon entropy $S[\rho(x,t)]$ of the probabilistic state of a classical system is invariant under Hamiltonian evolution. Here x denotes a micro-state of the system, i.e., the value of the positions and momenta of all its particles, and $\rho(x,t)$ is the probability density of observing a microstate x at time t. The same argument holds for quantum systems, replacing $\rho(x,t)$ by the density matrix $\rho(t)$ and the Shannon entropy by Von Neumann entropy, $\mathrm{Tr}(\rho\ln\rho)$ (Schumacher and Westmoreland, 2010). Here, we will restrict our discussion to classical systems, although it is not difficult to extend it to quantum systems (Esposito et al., 2010).

To observe an increase of Shannon entropy, as dictated by the second law for irreversible processes, one has to consider information losses that degrade the probabilistic state $\rho(x,t)$, like coarse-graining or the inaccessibility of detailed information about certain degrees of freedom.

A second important property of thermodynamic entropy is its connection with the energetics of a process through Clausius equation, which relates the temperature T to the increase of the entropy, δS, and the energy, δE, of a system[4]:

---

[4] Clausius originally introduced this equation as a definition of entropy. However, it is in fact a definition of temperature for systems at equilibrium, since energy and entropy are more fundamental magnitudes that can be obtained from dynamical properties, like the Hamiltonian and the phase space volume of regions of constant energy.

$$\delta S = \frac{\delta E}{T}. \tag{8}$$

This equation is crucial to find the limitations that the second law imposes on energy extraction from thermal reservoirs. For instance, if a system is in contact with a thermal bath at temperature T, according to Eq. (8) the total entropy production in a process is

$$\Delta S_{\text{tot}} = \Delta S - \frac{Q}{T} \geq 0 \tag{9}$$

where ΔS is the change of entropy in the system and Q is the energy transferred from the bath to the system. If an external agent manipulates the system performing a work W, the change of energy in the system is $\Delta E = Q + W$ and

$$T\Delta S_{\text{tot}} = T\Delta S - \Delta E + W = W - \Delta F \tag{10}$$

ΔF being the increase of free energy, $F = E - TS$, in the system. The second law $\Delta S_{\text{tot}} \geq 0$ for this isothermal process is equivalent to

$$W \geq \Delta F. \tag{11}$$

In particular, for a cycle $\Delta F = 0$ and the inequality, $W \geq 0$, tells us that it is impossible to extract energy from a thermal bath in a cyclic process.

For a system in contact with equilibrium thermal reservoirs, one can solve these two issues—namely, the invariance of Shannon entropy under Hamiltonian evolution and its connection with the energetics of a process—with the two following assumptions that specify the information available to an external observer (Esposito et al., 2010): first, the observer does not have access to the correlations between the system and the baths and, second, the only information about the state of the baths is their average energy. More precisely, the baths are described by thermal states with given average energies. In the case of a single bath with micro-states z, if the actual probabilistic state of the global system at time t is $\rho(x,z;t)$, this loss of information yields an effective state $\rho_{\text{obs}}(x,z;t)$ given by

$$\rho(x,z;t) \to \rho_{\text{obs}}(x,z;t) = \rho(x,t)\rho_{\text{B,eq}}(z;T(t)) \tag{12}$$

where $\rho(x,t)$ is the marginal probabilistic state of the system

$$\rho(x,t) = \int dz \rho(x,z;t) \tag{13}$$

and $\rho_{\text{B,eq}}(z;T)$ is the thermal state of the bath

$$\rho_{\text{B,eq}}(z;T) = \frac{e^{-\beta H_{\text{B}}(z)}}{Z_{\text{B}}(\beta)}. \tag{14}$$

Here $H_{\text{B}}(z)$ is the Hamiltonian of the bath, $\beta = 1/(kT)$ the inverse temperature, and $Z_{\text{B}}(\beta)$ the partition function. The temperature (t) in (12) is set as the one that verifies

$$\begin{aligned} E_{\text{B}}(t) &\equiv \int dxdz H_{\text{B}}(z)\rho(x,z;t) \\ &= \int dz H_{\text{B}}(z)\rho_{\text{B,eq}}(z;T(t)), \end{aligned} \tag{15}$$

i.e., both distributions have the same average bath energy $E_{\text{B}}(t)$ at any time t.

The replacement of the actual state $\rho(x,z;t)$ by the observable state $\rho_{\text{obs}}(x,z;t)$ solves the two aforementioned issues: the invariance of Shannon entropy under Hamiltonian evolution and the relationship between entropy and energy given by the Clausius equation (8). First, applying (7), we find that the replacement (12) increases the Shannon entropy:

$$S[\rho_{\text{obs}}(x,z;t)] - S[\rho(x,z;t)] = I(X;Z) + \Delta S_{\text{B}} \geq 0 \tag{16}$$

where $\Delta S_{\text{B}} = S[\rho_{\text{B,eq}}(z;T(t))] - S[\rho(z;t)]$. The inequality follows from the positiveness of the mutual information and the fact that the thermal state (14) is the one that maximizes the Shannon entropy under condition (15).

Consider a process where we manipulate the system, whose Hamiltonian $H(x;t)$ is now time-dependent. We also assume that initially system and bath are uncorrelated and the latter is at equilibrium, i.e., $\rho(x,z;0) = \rho(x,0)\rho_{\text{B,eq}}(z;T(0))$. Then, $\rho(x,z;0) = \rho_{\text{obs}}(x,z;0)$ and, since Shannon entropy is invariant under the Hamiltonian evolution, $S[\rho(x,z;t)] = S[\rho_{\text{obs}}(x,z;0)]$. Hence, from Eq. (16), we obtain the entropy production in the process:

$$S[\rho_{\text{obs}}(x,z;t)] - S[\rho_{\text{obs}}(x,z;0)] = I(X;Z) + \Delta S_{\text{B}} \geq 0. \tag{17}$$

This expression reflects the two information losses that we have introduced in (12): $(X;Z)$ is the information associated to the correlations between the system and the bath, whereas ΔS_{B} is the increase of Shannon entropy that results from replacing the actual state of the bath by a thermal state (Esposito et al., 2010). Each of these terms is positive and we recover a second law for the Shannon entropy $S[\rho_{\text{obs}}(x,z;t)]$. It is interesting to notice that both terms can be relevant in realistic situations, as shown in (Ptaszyński and Esposito, 2019a,b).

Alternatively, the entropy production can also be calculated by using the explicit form of the thermal state (14):

$$S[\rho_{\text{obs}}(x,z,t)] = S[\rho(x,t)] + k\beta(t)E_{\text{B}}(t) + k\ln Z_{\text{B}}(\beta(t)). \tag{18}$$

Since $E_{\text{B}} = -\partial \ln Z_{\text{B}}/\partial\beta$, the time derivative of the Shannon entropy of the observable state can be written as

$$\dot{S}[\rho_{\text{obs}}(x,z,t)] = \dot{S}[\rho(x,t)] + \frac{\dot{E}_{\text{B}}(t)}{T(t)}. \tag{19}$$

Integrating over the whole process with the initial condition discussed above, and taking into account that the bath is large enough so that the change of temperature is negligible,[5] we finally get

$$S[\rho_{\text{obs}}(x,z;t)] - S[\rho_{\text{obs}}(x,z;0)] = \Delta S - \frac{Q}{T} \tag{20}$$

where $Q = E_{\text{B}}(0) - E_{\text{B}}(t)$ is the net energy transferred from the bath to the system. From Eq. (17), we conclude that the entropy production, as expressed in Eq. (20), is positive. Thus, we recover the same expression for the entropy production as in (9), i.e., the loss of information implied by (12) is compatible with Clausius equation (8). The standard thermodynamic argument to derive (11) can now be applied to the *non-equilibrium free energy defined as:*

$$\mathcal{F}(\rho,H) \equiv \langle H(x)\rangle - TS[\rho(x)] \tag{21}$$

and yielding a bound to the work needed to complete an isothermal process:

$$W \geq \Delta\mathcal{F}. \tag{22}$$

This can be considered an extension of the second law (11) for isothermal processes involving non-equilibrium states, and reduces to the standard second law if the initial and final states are equilibrium, since the non-equilibrium free energy (21) is equal to the standard equilibrium one for thermal states like (14). Alternatively to our derivation based on information losses, (22) can be directly obtained from a master equation obeying local detailed balance (Esposito and Van den Broeck, 2011), which is the equation that describes systems in contact with reservoirs in the Markovian approximation.

The bound (22) is saturated for operationally reversible process, i.e., for processes where the system visits the same states as in the forward process when the protocol is reversed (Parrondo et al., 2015). This observation puts into question the utility of (22) for generic non-equilibrium states, since any irreversible relaxation to equilibrium prevents the bound to be reached. One strategy to overcome this issue consists in modifying instantaneously the Hamiltonian to convert the initial and final states into equilibrium states, although this protocol is a bit artificial and sometimes unrealizable.[6] However, the bound (22) can be tight as well for systems with slow and fast degrees of freedom. If there is a large separation of time scales and the fast degrees of freedom are equilibrated during the process, then the inequality (22) is met. As we will see in Section "Informational states and Landauer's principle," it turns out that this is the case of many relevant processes involving information.

Second law for feedback processes

In an isothermal feedback process, like the Szilárd engine, the external agent measures a magnitude M at a given time t_{m} and uses this information to complete an isothermal process. The measurement is characterized by the conditional probability $p_{M|X}(m|x)$, where m is the measurement outcome and x is the microscopic state of the system. This includes error-free measurements, where $p_{M|X}(m|x) = 1$ if $m = m\,(x)$ and zero otherwise, but it can also describe measurements affected by noise or any other source of inaccuracy. Using the measurement outcome, the observer updates the probabilistic state of the system $\rho_X(x,t_{\text{m}})$ according to Bayes rule

$$\rho_X(x,t_{\text{m}}) \to \rho_{X|M}(x|m) = \frac{p_{M|X}(m|x)\rho_X(x,t_{\text{m}})}{p_M(m)}. \tag{23}$$

Here we are assuming the most common case, where x is a continuous random variable and m is discrete, and use the Latin letter p for probability distributions and the Greek one ρ for probability densities. Nevertheless, the argument can be easily generalized to other cases. For a given outcome m, the updated state $\rho_{X|M}(x|m)$ is in general a non-equilibrium state, even if the state before the measurement, $\rho_X(x,t_{\text{m}})$, is equilibrium. We see here the first appearance of nonequilibrium states in processes involving information. The unconditional state of the system after the measurement is again

---

[5] Notice that we have to consider a time-dependent temperature to derive the variation of Shannon entropy in the bath in Eq. (19). However, this variation can be neglected when we integrate this equation, if the heat capacity of the bath is large enough.

[6] Any state $\rho(x)$ can be converted into an equilibrium state by setting the Hamiltonian equal to $H(x) = -kT\ln\rho(x)$. Notice however that such Hamiltonian can be difficult or impossible to realize as, for instance, when $\ln\rho(x)$ is not a quadratic function of velocities.

$$\sum_m p_M(m)\rho_{X|M}(x|m) = \rho_X(x, t_\mathrm{m}), \tag{24}$$

i.e., the measurement does not alter the system. In Section "Restoring the second law," we will establish this as a condition for an ideal classical measurement. Given an outcome m, the free energy after the measurement is

$$\mathcal{F}\left[\rho_{X|M}(x|m)H(x, t_\mathrm{m})\right] = \int dx H(x, t_\mathrm{m})\rho_{X|M}(x|m) - TS\left[\rho_{X|M}(x|m)\right] \tag{25}$$

where $H(x, t)$ is the Hamiltonian of the system at time t. Averaging over the possible outcomes we get the nonequilibrium free energy after the measurement

$$\mathcal{F}_\mathrm{post} = \sum_m p_M(m)\mathcal{F}\left[\rho_{X|M}(x|m)H(x, t_\mathrm{m})\right] = \int dx H(x, t_\mathrm{m})\rho(x, t_\mathrm{m}) - TS(X|M). \tag{26}$$

Using the definition of mutual information (7), we obtain that, as a consequence of the Bayes update, the nonequilibrium free energy of the system changes as

$$\Delta\mathcal{F}_\mathrm{meas} \equiv \mathcal{F}_\mathrm{post} - \mathcal{F}_{pre} = T[(S(X) - S(X|M)] = TI(X;M), \tag{27}$$

where $\mathcal{F}_\mathrm{pre} = \mathcal{F}[\rho(x, t_\mathrm{m}), H(x, t_\mathrm{m})]$ is the non-equilibrium free energy of the system immediately before the measurement.

We can now apply Eq. (22) to the subprocesses that take place before and after the measurement. The total work in the feedback process is bound as

$$W_{fb} \geq \mathcal{F}_{fin} - \mathcal{F}_\mathrm{post} + \mathcal{F}_{pre} - \mathcal{F}_\mathrm{init} = \mathcal{F} - \Delta\mathcal{F}_\mathrm{meas} \tag{28}$$

where $\Delta\mathcal{F} = \mathcal{F}_\mathrm{fin} - \mathcal{F}_\mathrm{init}$ and the subscripts, init, pre, post, fin, indicate respectively the states at the different stages of the process: initial and final, and immediately before and after the measurement (see Fig. 3). Combining (27) and (28), we finally obtain

$$W_\mathrm{fb} \geq \Delta\mathcal{F} - TI(X;M) \tag{29}$$

which is the second law for feedback processes. This result was derived by Sagawa and Ueda for classical and quantum systems (Sagawa and Ueda, 2008), although the relevance of mutual information in thermodynamics was first pointed out by Lloyd and Touchette (Lloyd, 1989; Touchette and Lloyd, 2000). It indicates that the work necessary to complete a process decreases by an amount $TI(X;M)$ if we use the information gathered in the measurement. In particular, for a cycle the work can be negative, i.e., we can extract a work $W_\mathrm{extract} = -W_\mathrm{fb}$ at least equal to $TI(X;M)$. The Szilárd engine, where $I(X;M) = k \ln 2$ is an explicit example that saturates the bound.

Notice that, due to (24), the unconditional non-equilibrium free energy of the system does not change in the measurement. The mutual information $I(X;M)$ in (27) and (29) appears because we average the conditional entropy over $p_M(m)$. The reason of averaging in this way is that, in a feedback process, the protocol depends on the outcome m, and so does the work. The bound (29) applies to the average work W_fb over all possible outcomes and protocols, each one obeying (22). If the information provided by the measurement is not used in the protocol from t_m to the final time of the process, then we recover the standard second law (22) with equilibrium free energies.

The bound (29) does not resolve the problem of reconciling the Szilárd engine with the original second law. However, it is an important result because it establishes a benchmark to the work that can be extracted in a feedback process. It also indicates that the mutual information $I(X;M)$ is a thermodynamic resource and can be used to define efficiencies for information and hybrid engines (Saha et al., 2021; Schmitt et al., 2015) and to compare the performance of information motors and of chemical or thermal machines (Horowitz et al., 2013). It is also interesting to explore which protocols saturate the bound (29). It is found that this happens for operationally reversible processes, those which visit the same states when the action of the external agent is reversed (Horowitz and Parrondo, 2011a). Notice however that the notion of reversibility of feedback processes requires a more careful discussion, since it is not trivial to define the time reversal of a measurement (Horowitz and Parrondo, 2011b; Horowitz and Vaikuntanathan, 2010).

The second law (29) can be further refined by deriving fluctuation theorems. These theorems are exact equalities that hold for any process even far from equilibrium, and from which the second law can be obtained as a corollary (Horowitz and Vaikuntanathan, 2010; Ponmurugan, 2010; Sagawa and Ueda, 2009, 2010, 2012).

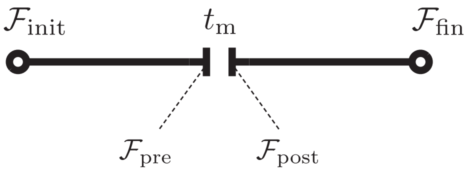
$\mathcal{F}_\mathrm{init}$
t_m
$\mathcal{F}_\mathrm{fin}$
$\mathcal{F}_\mathrm{pre}$
$\mathcal{F}_\mathrm{post}$

Fig. 3 Scheme of a basic feedback process with a single measurement.

Informational states and Landauer's principle

Information devices, like memories, processors, or the biochemical machinery of DNA and RNA, are systems that can adopt different informational states that have a long lifetime and are interchangeable. These states are, for example, the bits in a hard drive, which can be 0 or 1, or the bases of DNA, which can be any of the four nucleotides: cytosine, guanine, adenine or thymine.

These two properties, long lifetimes and interchangeability, imply some kind of effective symmetry breaking in the system: its phase space is partitioned into several regions where the system remains for a very long time. Each region is an informational state and the system is no longer ergodic in the whole phase space. Here, we refer to an effective lack of ergodicity when there is a huge separation between the time scales of the dynamics within the regions and of the jumps between regions. This type of effective ergodicity breaking occurs due to phase transitions in finite systems or to the presence of high energy barriers with a negligible probability to be crossed. A paradigmatic example is a Brownian degree of freedom in a double well potential, like the one depicted in Fig. 4.

In general, the phase space Γ of an information device is partitioned into a number of regions Γ_m, with $m = 1, 2, \ldots, \mathcal{M}$. We will assume that the dynamics within each region is very fast and that the system is in local equilibrium within every Γ_m. On the other hand, the system can be in any of the informational states with certain probability p_m that depends on the history, measurements, etc. We show an explicit example in Fig. 4, based on a Brownian particle or degree of freedom in a double well potential. By raising the barrier far above kT, we create a memory from (a) to (b). If the potential is symmetric, each informational state $m = L, R$ is populated with the same probability $p_L = p_R = 1/2$ and the system is in global equilibrium. However, if we change the energy of the wells, as in (c), populations do not change due to the high barrier but the equilibrium probabilities $p^{\mathrm{eq}}_{R,L}$ depart from 1/2. Hence, the system is no longer in global equilibrium. The informational state can also change due to a measurement, as in the transition from (c) to (d).

If the device is at temperature T, the state of the system is then given by

$$\rho(x) = \sum_m p_m \frac{e^{-\beta H(x)}}{Z_m} \chi_m(x) \tag{30}$$

where $x \in \Gamma$ is a micro-state, $H(x)$ is the Hamiltonian, $\chi_m(x)$ is the index function of Γ_m, i.e., $\chi_m(x) = 1$ if $x \in \Gamma_m$ and zero otherwise, and Z_m is the restricted partition function

$$Z_m \equiv \int_{\Gamma_m} dx e^{-\beta H(x)}. \tag{31}$$

The probability distribution $\{p_m\}$, with $m = 1, 2, \ldots, \mathcal{M}$ is arbitrary and defines a probabilistic informational state. The main characteristic of the information device is that it can adopt any probabilistic informational state and that an external agent can drive the system, as in Fig. 4, from one probabilistic informational state to another, writing or processing information in the device. A special probabilistic informational state is the one corresponding to global equilibrium $p_m = Z_m/Z$, where $Z = \sum_m Z_m$ is the global partition function.

The energetics of processes involving informational states can be analyzed using the non-equilibrium free energy (21), which for state (30) reads

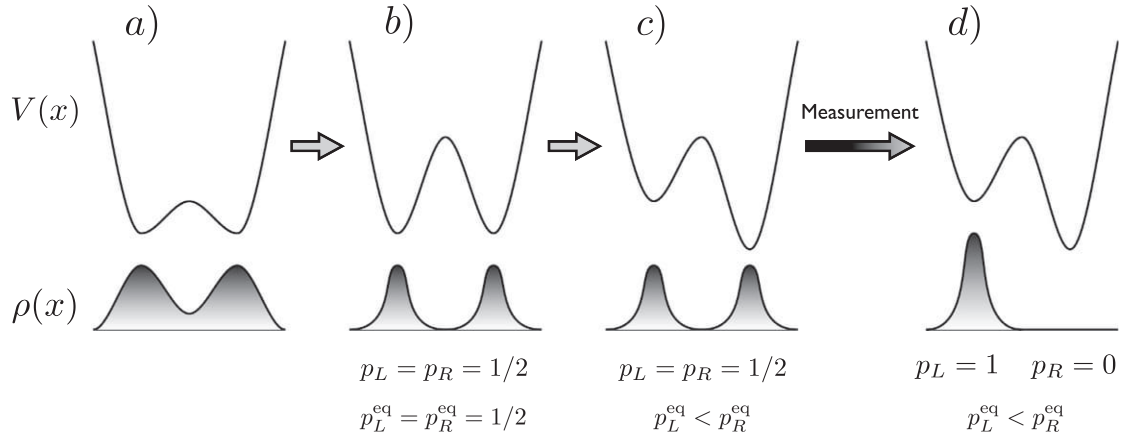
a)
b)
c)
d)
$V(x)$
Measurement
$\rho(x)$
$p_L = p_R = 1/2$
$p_L^{\mathrm{eq}} = p_R^{\mathrm{eq}} = 1/2$
$p_L = p_R = 1/2$
$p_L^{\mathrm{eq}} < p_R^{\mathrm{eq}}$
$p_L = 1 \quad p_R = 0$
$p_L^{\mathrm{eq}} < p_R^{\mathrm{eq}}$

Fig. 4 Informational states of a Brownian degree of freedom in a bistable potential. The rise of the barrier from (a) to (b) illustrates the creation of information (Roldán et al., 2014), whereas (c) and (d) show non-equilibrium probabilistic informational states, which are the result of the history and of a measurement, respectively.

$$\mathcal{F}(\rho, H) = \sum_m p_m F_m - TS(p_m) \tag{32}$$

where $F_m = -kT \ln Z_m$ is the restricted free energy and $S(p_m)$ is the Shannon entropy of the probabilistic informational state. As already mentioned, the non-equilibrium free energy equals the equilibrium one, $\mathcal{F}(\rho, H) = -kT \ln Z$ if the system is in global equilibrium. For a symmetric memory where $F_m = F_{\text{local}}$ is the same for all informational states m, we have

$$\mathcal{F}(\rho, H) = F_{\text{local}} - TS(p_m). \tag{33}$$

Now suppose that we manipulate a symmetric memory driving the system isothermally from a distribution p_m to p'_m. If the initial and final restricted free energies are equal, then the work needed to complete the process is bound by

$$W \geq T\left[S(p_m) - S(p'_m)\right]. \tag{34}$$

This equation tells us that we have to perform work to order a memory, $S(p'_m) < S(p_m)$, whereas we can extract work by disordering a symmetric memory $S(p'_m) > S(p_m)$.

Landauer's principle is a special case of Eq. (34). Landauer considered a simple process where a binary symmetric memory is initially in a random state $p_0 = p_1 = 1/2$, with $S(p_m) = k \ln 2$ and is driven to the informational state 0 with probability one, i.e., $p'_0 = 1$ and $p'_1 = 0$, with zero Shannon entropy. This process is called restore-to-zero, and is usually considered as the erasure of the initial random bit, although it is more appropriate to call it overwriting, since the initial unknown bit is replaced by a given one, 0 in our example. The work needed to complete Landauer's overwriting is

$$W \geq kT \ln 2 \tag{35}$$

which is the so-called Landauer's principle. The Landauer principle has been confirmed experimentally in different systems, like Brownian particles in optical traps (Berut et al., 2011) (see Proesmans et al., 2020 for a discussion on experimental results on the energetics of overwriting at finite speed). Landauer's overwriting is a special case of a logically irreversible operation, since the initial informational state of the memory (input) cannot be recovered from the final one (output). It is a common misunderstanding to interpret Landauer's principle as if logical irreversibility implied thermodynamic irreversibility. This is not true. If inequality (35) is met, the overwriting process is still logically irreversible but thermodynamically reversible because the decrease of entropy in the system is compensated by the increase of entropy in the thermal bath due to heat dissipation. Hence, the total entropy production is zero. See (Sagawa, 2014) for a detailed discussion on the relation between thermodynamic and logical reversibility.

On the other hand, if a memory has a low Shannon entropy, one can extract work by disordering it. The thermodynamics of these information reservoirs that can act as thermodynamic resources has been analyzed in detail by Barato and Seifert (2014), and by Wolpert (2019). Mandal and Jarzynski (2012) have devised a concrete realization of work extraction from an ordered memory using a kinetic model that reads the content of a tape.

Restoring the second law

We can now address the question of restoring the original second law in the Szilárd engine by considering the physical nature of the demon, who must possess a memory to register the measurement outcomes and is subjected to the thermodynamic limitations discussed in the previous section.

First, let us consider the energetics of a measurement. An ideal classical measurement consists of the interaction between a system and a measurement apparatus, which fulfills the following requirements: (i) system and apparatus are initially uncorrelated; (ii) the system is not affected by the interaction; and (iii) system and apparatus do not interact before and after the measurement, i.e., the Hamiltonian of the global system is $H_{\text{sys}}(x) + H_{\text{app}}(y)$, where x and y are microstates of the system and the apparatus, respectively. Let Y and Y' be the random variables denoting the state of the apparatus before and after the measurement, respectively, and $p_{M|X}(m|x)$ the conditional probability characterizing the measurement. We will further assume that the outcome is a function of the apparatus micro-state $M = m(Y')$ and that all the information about X is provided by the measurement outcome, i.e., $\rho_{X|Y}(x|y) = \rho_{X|M}(x|m(y))$.

If the initial state of the global system immediately before the measurement is

$$\rho_{XY}(x, y) = \rho_X(x)\rho_Y(y) \tag{36}$$

with non-equilibrium free energy

$$\mathcal{F}(X, Y) = \mathcal{F}(X) + \mathcal{F}(Y), \tag{37}$$

then the state after the measurement is

$$\rho_{XY'}(x, y) = \sum_m \rho_X(x) p_{M|X}(m|x) \rho_{Y'|M}(y|m) \tag{38}$$

where $\rho_{Y'|M}(y|m) = \rho_{Y'}(y)/p_M(m)$ if $m = m(y)$ and zero otherwise. The marginal probability density for the state of the system $\rho_X(x)$ does not change as a consequence of the measurement. This is why we can still denote the random variable corresponding to the

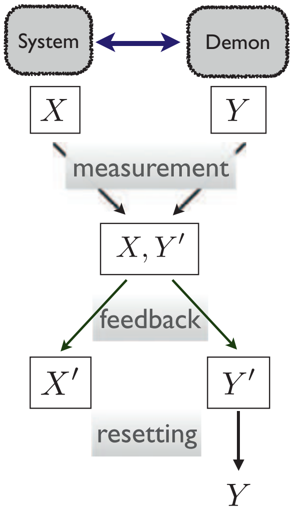

Fig. 5 Sketch of the operations in a feedback cycle.

state of the system as X, whereas the apparatus changes from Y to Y' (see Fig. 5). With these assumptions, it is not hard to prove that $I(X;Y') = I(X;M)$, since Y' provides information about X through the outcome M. Since the energy of the system does not change due to the measurement, the non-equilibrium free energy of the global system (X, Y') immediately after the measurement can be written as

$$\begin{aligned}\mathcal{F}(X,Y') &= \mathcal{F}(X) + \mathcal{F}(Y') + TI(X;Y') \\ &= \mathcal{F}(X) + \mathcal{F}(Y') + TI(X;M)\end{aligned} \tag{39}$$

where we have used Eq. (7) to express the total Shannon entropy $S(X, Y')$ in terms of the mutual information $I(X;Y')$. Hence, the work needed to complete the measurement is

$$W_{\text{meas}} \geq \Delta\mathcal{F} = \Delta\mathcal{F}_Y + TI(X;M) \tag{40}$$

where $\Delta\mathcal{F}_Y = \mathcal{F}(Y') - \mathcal{F}(Y)$. Since $I(X;M)$ is positive, we see that measuring or, more generally, creating correlations between two systems, increases the free energy and, if not counterbalanced by $\Delta\mathcal{F}_Y$, needs work and heat dissipation to be completed.

As discussed in Section "Second law for feedback processes," the demon can extract a work $W_{\text{extract}} = -W_{\text{fb}}$ with $W_{\text{fb}} \geq TI(X;M)$ if he uses the information acquired in the measurement in a cyclic process, where the system is driven back to its initial state X.

However, to complete the cycle, the apparatus must be also driven to its initial state Y. In doing so, the demon must perform a work

$$W_{\text{reset}} \geq \mathcal{F}(Y) - \mathcal{F}(Y') = -\Delta\mathcal{F}_Y. \tag{41}$$

The total work in the process is then

$$W_{\text{tot}} = W_{\text{meas}} + W_{\text{fb}} + W_{\text{reset}} \geq 0. \tag{42}$$

Hence, the validity of the second law for feedback processes is restored when the entropy costs of measurement and/or resetting the demon's memory are taken into account. This is the generalization of Bennett's analysis of the Szilard engine. Bennett discussed in (Bennett, 1982) a realization of the Szilard engine where $W_{\text{meas}} = 0$ and the demon must overwrite the outcome of the measurement performing a work $kT \ln 2$, as dictated by Landauer's principle. This is achieved if $\Delta\mathcal{F}_Y = -TI(X;M)$.

From the previous discussion, we see that the Szilárd engine can be interpreted as a relatively simple exchange between work and the free energy $TI(X;M)$ stored in the correlations between the system and the demon. For instance, if $\Delta\mathcal{F}_Y = 0$, the engine consists of creating correlations in the measurement, an operation that requires a work $TI(X;M)$ and increases the free energy by the same amount, and then destroying these correlations in the feedback, where the same amount of work is now extracted.

The previous discussion can be presented in terms of entropy, instead of free energy, and extended to continuous time. Consider now that both the system and the demon are random processes, $X(t)$ and $Y(t)$, respectively. The time derivative of Eq. (7) reads

$$\dot{S}(X(t), Y(t)) = \dot{S}(X(t)) + \dot{S}(Y(t)) - \dot{I}(X(t);Y(t)) \tag{43}$$

and the total entropy production can be written as

$$\dot{S}_{\text{prod}} = \dot{S}(X(t)) + \dot{S}(Y(t)) - \dot{I}(X(t);Y(t)) + \dot{S}_{\text{env}}(t) \geq 0 \tag{44}$$

where $\dot{S}_{\text{env}}(t)$ is the change per unit of time of the entropy of the environment at time t. For instance, if the system and/or the demon are in contact with several thermal baths at different temperatures T_i, then $\dot{S}_{\text{env}}(t) = -\sum_i \dot{Q}_i(t)/T_i$, where $Q_i(t)$ is the energy transfer per unit of time from the i-th bath to the system.

The scheme of Fig. 5 can be seen as the different stages of a continuous evolution. In the measurement, the system does not change, hence $\dot{S}(X(t)) = 0$ and the integration of (44) yields

$$\Delta S_Y - \Delta I + \Delta S_{\text{env}}^{(\text{meas})} \geq 0. \tag{45}$$

Here, ΔI is the mutual information developed in the measurement. Notice however that the measurement in this description is any interaction between X and Y that creates correlations between the two systems, keeping X constant. During feedback, the demon does not change, hence $\dot{S}(Y(t)) = 0$. If the feedback process is cyclic, $\Delta S_X = 0$, and if all the correlations created during the measurement are destroyed, then

$$\Delta I + \Delta S_{\text{env}}^{(\text{fb})} \geq 0. \tag{46}$$

Finally, during the demon resetting:

$$-\Delta S_Y + \Delta S_{\text{env}}^{(\text{reset})} \geq 0. \tag{47}$$

The sum of the three inequalities (45)–(47) yields the standard second law for the total entropy production

$$S_{\text{prod}} = \Delta S_{\text{env}}^{(\text{meas})} + \Delta S_{\text{env}}^{(\text{fb})} + \Delta S_{\text{env}}^{(\text{reset})} \geq 0. \tag{48}$$

Therefore, Eq. (44) comprises all our discussion on the Szilárd engine but also extends to generic dynamics where two systems evolve in time creating and destroying correlations (Horowitz and Esposito, 2014).

Information flows

The previous discussion holds for an arbitrary evolution. However, for (44) to be meaningful, the evolution must be driven by an external agent (without feedback), which switches on and off the coupling between system and demon in the measurement and resets the demon to its initial state. Otherwise the global system reaches a steady state where all terms in Eq. (44) vanish in average. Still, it is interesting to interpret as information engines autonomous motors that work in a non-equilibrium stationary state (NESS). For this purpose, it is useful to introduce the notion of *information flows* (Allahverdyan et al., 2009; Horowitz, 2015; Horowitz and Esposito, 2014):

$$\dot{I}_X(t) = \lim_{\tau \to 0^+} \frac{I(X(t+\tau); Y(t)) - I(X(t); Y(t))}{\tau} \tag{49}$$

and

$$\dot{I}_Y(t) = \lim_{\tau \to 0^+} \frac{I(X(t); Y(t+\tau)) - I(X(t); Y(t))}{\tau}. \tag{50}$$

In the NESS, $\dot{I}_X(t) + \dot{I}_Y(t) = \dot{I}(X(t); Y(y)) = 0$, and $\dot{I}_X(t) = -\dot{I}_Y(t)$. This is why these quantities can be considered flows of a conserved quantity, although this interpretation is valid only in the stationary regime.

If $\dot{I}_X(t)$ is positive then the motion of X, with Y fixed, increases the correlation between the two systems. Accordingly to our discussion in the previous section, we can interpret it as X measuring Y. On the other hand, if $\dot{I}_X(t) < 0$, the motion of system X destroys correlations, like a demon using information to complete a feedback process and converting the free energy stored in correlations into work.

When each system is coupled to separate baths, one can derive a second law for the entropy production in the stationary regime due to the dynamics of each system, X or Y:

$$-\dot{I}_X + \dot{S}_{env}^X \geq 0; \; \dot{I}_X + \dot{S}_{env}^Y \geq 0 \tag{51}$$

where $\dot{S}_{\text{env}}^{X,Y}$ is the entropy increase in the reservoir connected to system X and Y, respectively. These partial second laws have been derived for multipartite continuous and discrete Markovian systems (Horowitz and Esposito, 2014; Horowitz, 2015) and they allow us to analyze the energetics of autonomous motors from the point of view of information flows. In Horowitz and Esposito (2014), apply it to two coupled quantum dots in contact with reservoirs with different temperatures and/or chemical potentials, a device that can operate as a pump or a refrigerator. Information flows and Eq. (51) do not only provide an interesting interpretation of one of the dots acting as a Maxwell demon on the other, but are also useful to derive limitations to the energetics that go beyond the application of the standard second law to the whole device. It is possible as well to evaluate separately the efficiency of the exchange between entropy and information in each dot (Horowitz and Esposito, 2014). See also (Rosinberg and Horowitz, 2016) for an example of continuous classical degrees of freedom and (Ptaszyński and Esposito, 2019a,b) for an extension to quantum systems.

Information flows are related to other magnitudes that quantify the exchange of information among different systems. In the context of data analysis, Schreiber introduced the so-called *transfer entropy* (Schreiber, 2000) to find causal relationships between two time series, whereas Liang and Kleeman (2005) studied similar information transfers in dynamical systems. Although transfer entropies have been criticized as a tool to find causal relations (James et al., 2016), they have been proven useful to derive fluctuation theorems in bipartite systems (Hartich et al., 2014) and general causal networks (Ito and Sagawa, 2013). The relationship between transfer entropies and information flows has been studied in detail in (Allahverdyan et al., 2009; Cafaro et al., 2016; Horowitz, 2015; Horowitz and Sandberg, 2014; Kiwata, 2022).

Conclusion: What is information?

Thermodynamics of information makes a precise assessment of the effect of information on the second law and clarifies the thermodynamic cost of information operations. The key concept is the mutual information between the state of a system and the outcome of a measurement since, as shown in (7), it is equal to the decrease of Shannon entropy due to the measurement, but also to the difference, due to correlations, between the entropy of a composite system and the sum of the entropies of its parts. To relate Shannon entropy with the energetics of a process, we have introduced in Section "Shannon and thermodynamic entropies" the loss of information that one would expect when a system is in contact with reservoirs at equilibrium. This analysis yields the definition of another relevant concept: the non-equilibrium free energy (21), which determines the minimal work necessary to complete an isothermal process connecting non-equilibrium states.

We have shown that the states relevant to information processing are out of equilibrium, either because they are the result of a Bayesian update, like (23), or because they describe memories with arbitrary probabilistic informational states, as in (30). In both cases, non-equilibrium free energy establishes limitations to the energetics of isothermal processes involving information. These limitations are extensions of the second law to informational non-equilibrium states. In this framework, information appears as a novel thermodynamic resource and those extensions of the second law are indispensable to assess the efficiency of its exploitation.

We have also used non-equilibrium free energy to prove that the Szilárd engine and any isothermal feedback process are compatible with the standard second law of thermodynamics. For this purpose, we have considered the physical nature of the demon and, in doing so, we not only solve the fundamental question posed by Maxwell more than one century ago, but open as well the possibility of interpreting certain devices like motors, refrigerators and other chemical or thermal machines, as transducers that convert information into work and vice-versa. For this interpretation to hold, thermal fluctuations and correlations must be essential ingredients in the functioning of these machines. This is why information thermodynamics is closely related to—or can even be considered as a branch of—a recent field of research, stochastic thermodynamics, which studies the energetics of processes at the micro- and nano-scale, incorporating fluctuations (Peliti and Pigolotti, 2021; Sekimoto, 2010).

In this article, we have restricted ourselves mostly to classical systems. The reason is that, in an isothermal process, a quantum system rapidly adopts a state which is diagonal in the eigenbasis of the Hamiltonian. In these scenarios, coherences are lost and the system can be studied with the same tools as those developed for classical systems. In fact, most of the concepts that we have introduced in the previous sections can be straightforwardly extended to quantum systems. Nevertheless, in the last years there has been an increasing interest in phenomena that combine in a nontrivial way quantum and thermal effects (Anders and Esposito, 2017). Zurek (1990) and Lloyd (1997) already found distinctive aspects of the quantum Szilárd engine and Kim et al explored the effect of quantum statistics in multiparticle Szilárd cycles with bosons and fermions (Kim et al., 2011). The mutual information between quantum systems can be split into a classical and a purely quantum part due to entanglement, known as *quantum discord*, and whose role in quantum Maxwell demons have been analyzed in (Park et al., 2013; Zurek, 2003). Finally, some setups involving the coupling between two quantum states can be interpreted as Maxwell demons that use information. This is the case of the experiment reported in (Cottet et al., 2017) where the coupling between a transmon qubit and the radiation in a microwave cavity can be used to extract work.

From a more fundamental point of view, the interplay between information and matter is nowadays considered a crucial issue for our understanding of the physical world. In 1992, Wheeler summarized in the celebrated lemma "it from bit" (Wheeler, 1995) the idea that information is the basic concept upon which every physical theory should be built. Since then, a number of physicist and philosophers have attempted to follow this research program. Thermodynamics of information, on the other hand, pursues more modest goals but it does provide some insight on how information is implemented in physical systems. In this article we have seen two basic aspects of the physical nature of information. The first one is the characteristics of the informational states introduced in Section "Informational states and Landauer's principle," namely, long lifetimes and interchangeability. The second one is the interpretation of information in feedback engines as an exchange between work and the free energy $TI(X;Y)$stored in the correlations between two systems, X and Y. Each of these two aspects has yielded interesting lines of research. The first one explores the energetics of processes in systems where there is a huge separation of time scales (Roldán et al., 2014), whereas the second one has inspired the notion of information flows in autonomous systems (Horowitz and Esposito, 2014). We believe that any reflection about information as a fundamental concept in physics should account for and/or utilize these two aspects.

Acknowledgments

This article summarizes work done over more than 10 years and it would not have been possible without the interaction with many colleagues, friends, and students from different summer schools. A special mention deserve Jordan Horowitz, with whom I have done a great part of my contributions to the field, and Takahiro Sagawa, who has been one of the most active and influencing researchers in the recent application of stochastic thermodynamics to information processing. Together with Jordan and Takahiro, we wrote a review article (Parrondo et al., 2015), which shaped most of my ideas on the thermodynamics of information. The preparation of this review has been financially supported by the Spanish Government (Grant FLUID. Ref: PID2020-113455GB-I00) and the Foundational Questions Institute (FQXi) under the program "Information as Fuel" (Grant NanoQit. Ref FQXi-IAF19-01). I appreciate the hospitality of Natalia Ares at University of Oxford and discussions with the whole NanoQit team on the content and organization of this article. Finally, I am indebted to Jordan Horowitz, Takahiro Sagawa, and Massimiliano Esposito for their careful reading of the article and their helpful suggestions.

References

Allahverdyan AE and Saakian DB (2008) Thermodynamics of adiabatic feedback control. *Europhysics Letters* 81: 30003.

Allahverdyan AE, Janzing D, and Mahler G (2009) Thermodynamic efficiency of information and heat flow. *Journal of Statistical Mechanics: Theory and Experiment* 2009: P09011. https://doi.org/10.1088/1742-5468/2009/09/P09011. Publisher: IOP Publishing.

Anders J and Esposito M (2017) Focus on quantum thermodynamics. *New Journal of Physics* 19: 010201. https://doi.org/10.1088/1367-2630/19/1/010201.

Barato A and Seifert U (2014) Stochastic thermodynamics with information reservoirs. *Physical Review E* 90: 042150.

Bennett C (1982) The thermodynamics of computation—A review. *International Journal of Theoretical Physics* 21: 905–940. Reprinted in (Leff and Rex, 1990).

Berut A, Arakelyan A, Petrosyan A, Ciliberto S, Dillenschneider R, and Lutz E (2011) Experimental verifciation of landauer's principle linking information and thermodynamics. *Nature* 483: 187–189.

Bustamante C, Keller D, and Oster G (2001) The physics of molecular motors. *Accounts of Chemical Research* 34: 412–420.

Cafaro C, Ali SA, and Giffin A (2016) Thermodynamic aspects of information transfer in complex dynamical systems. *Physical Review E* 93: 022114. https://doi.org/10.1103/PhysRevE.93.022114. Publisher: American Physical Society.

Cottet N, Jezouin S, Bretheau L, Campagne-Ibarcq P, Ficheux Q, Anders J, Auffèves A, Azouit R, Rouchon P, and Huard B (2017) Observing a quantum Maxwell demon at work. *Proceedings of the National Academy of Sciences* 114: 7561–7564. https://doi.org/10.1073/pnas.1704827114. Publisher: Proceedings of the National Academy of Sciences.

Cover TM and Thomas JA (2006) *Elements of Information Theory*, 2nd edn. New York, NY: Wiley-Interscience.

Ehrich J, Esposito M, Barra F, and Parrondo JM (2019) Micro-reversibility and thermalization with collisional baths. *Physica A: Statistical Mechanics and its Applications* 122108. https://doi.org/10.1016/j.physa. 2019.122108.

Esposito M and Van den Broeck C (2011) Second law and landauer principle far from equilibrium. *Europhysics Letters* 95: 40004.

Esposito M, Lindenberg K, and den Broeck CV (2010) Entropy production as correlation between system and reservoir. *New Journal of Physics* 12: 013013. https://doi.org/10.1088/1367-2630/12/1/013013.

Feng Y, Ovalle M, Seale JSW, Lee CK, Kim DJ, Astumian RD, and Stoddart JF (2021) Molecular pumps and motors. *Journal of the American Chemical Society* 143: 5569–5591.

Feynman RP, Leighton RB, and Sands M (1966) *The Feynman Lectures on Physics*. vol. I. Addison-Wesley. Chap. 46.

Hartich D, Barato AC, and Seifert U (2014) Stochastic thermodynamics of bipartite systems: transfer entropy inequalities and a maxwell's demon interpretation. *Journal of Statistical Mechanics: Theory and Experiment* P02016.

Horowitz JM (2015) Multipartite information flow for multiple Maxwell demons. *Journal of Statistical Mechanics: Theory and Experiment* 2015: P03006. https://doi.org/10.1088/1742-5468/2015/03/P03006. Publisher: IOP Publishing.

Horowitz JM and Esposito M (2014) Thermodynamics with continuous information flow. *Physical Review X* 4: 031015.

Horowitz JM and Parrondo JMR (2011a) Designing optimal discrete-feedback thermodynamic engines. *New Journal of Physics* 13: 123019.

Horowitz JM and Parrondo JMR (2011b) Thermodynamic reversibility in feedback processes. *Europhysics Letters* 95: 10005.

Horowitz JM and Sandberg H (2014) Second-law-like inequalities with information and their interpretations. *New Journal of Physics* 16: 125007. https://doi.org/10.1088/1367-2630/16/12/125007. Publisher: IOP Publishing.

Horowitz JM and Vaikuntanathan S (2010) Nonequilibrium detailed fluctuation theorem for discrete feedback. *Physical Review E* 82: 061120.

Horowitz JM, Sagawa T, and Parrondo JMR (2013) Imitating chemical motors with optimal information motors. *Physical Review Letters* 111: 010602.

Ito S and Sagawa T (2013) Information thermodynamics on causal networks. *Physical Review Letters* 111: 180603.

James RG, Barnett N, and Crutchfield JP (2016) Information flows? A critique of transfer entropies. *Physical Review Letters* 116: 238701. https://doi.org/10.1103/PhysRevLett.116.238701. Publisher: American Physical Society.

Kim SW, Sagawa T, De Liberato S, and Ueda M (2011) Quantum Szilard engine. *Physical Review Letters* 106: 070401.

Kiwata H (2022) Relationship between Schreiber's transfer entropy and Liang-Kleeman information flow from the perspective of stochastic ther-modynamics. *Physical Review E* 105: 044130. https://doi.org/10.1103/PhysRevE.105.044130. Publisher: American Physical Society.

Koski JV, Maisi VF, Pekola JP, and Averin DV (2014) Experimental realization of a szilard engine with a single electron. *Proceedings of the National Academy of Sciences* 111: 13786–13789. https://doi.org/10.1073/pnas. 1406966111.

Landauer R (1961) Irreversibility and heat generation in the computing process. *IBM Journal of Research and Development* 5: 183–191. https://doi.org/10.1147/rd.53.0183.

Leff HS and Rex AF (eds.) (1990) *Maxwell's Demon: Entropy, Information, Computing*. New Jersey: Princeton University Press.

Liang XS and Kleeman R (2005) Information transfer between dynamical system components. *Physical Review Letters* 95: 244101. https://doi.org/10.1103/PhysRevLett.95.244101. Publisher: American Physical Society.

Lloyd S (1989) Use of mutual information to decrease entropy: Implications for the second law of thermodynamics. *Physical Review A* 39: 5378–5386.

Lloyd S (1997) Quantum-mechanical Maxwell's demon. *Physical Review A* 56: 3374–3382.

Mandal D and Jarzynski C (2012) Work and information processing in a solvable model of maxwell's demon. *Proceedings of the National Academy of Sciences of the United States of America* 109: 11641–11645.

Park JJ, Kim KH, Sagawa T, and Kim SW (2013) Heat engine driven by purely quantum information. *Physical Review Letters* 111: 230402.

Parrondo JMR (2001) The Szilard engine revisited: Entropy, macroscopic randomness, and symmetry breaking phase transitions. *Chaos* 11: 725–733.

Parrondo JMR and Español P (1996) Criticism of Feynman's analysis of the ratchet as an engine. *American Journal of Physics* 64: 1125–1130. https://doi.org/10.1119/1.18393.

Parrondo JMR, Horowitz JM, and Sagawa T (2015) Thermodynamics of information. *Nature Physics* 11: 131–139. https://doi.org/10.1038/nphys3230.

Pekola J and Khaymovich I (2019) Thermodynamics in single-electron circuits and superconducting qubits. *Annual Review of Condensed Matter Physics* 10: 193–212. https://doi.org/10.1146/annurev-conmatphys-033117-054120.

Peliti L and Pigolotti S (2021) *Stochastic Thermodynamics*. Princeton University Press.

Ponmurugan M (2010) Generalized detailed fluctuation theorem under nonequilibrium feedback control. *Physical Review E* 82: 031129. https://doi.org/10.1103/PhysRevE.82.031129.

Price R (1982) Oral-History:Claude E. Shannon. Engineering and Technology History Wiki (ETHW). https://ethw.org/Oral-History. Claude_E._Shannon.

Proesmans K, Ehrich J, and Bechhoefer J (2020) Finite-time landauer principle. *Physical Review Letters* 125: 100602. https://doi.org/10.1103/PhysRevLett.125. 100602.

Ptaszyński K and Esposito M (2019a) Thermodynamics of quantum information flows. *Physical Review Letters* 122: 150603. https://doi.org/10.1103/PhysRevLett.122. 150603.

Ptaszyński K and Esposito M (2019b) Entropy production in open systems: The predominant role of intraenvironment correlations. *Physical Review Letters* 123: 200603.

Reimann P (2002) Brownian motors: Noisy transport far from equilibrium. *Physics Reports* 361: 57–265.

Roldán E, Martínez IA, Parrondo JMR, and Petrov D (2014) Universal features in the energetics of symmetry breaking. *Nature Physics* 10: 457–461.

Rosinberg ML and Horowitz JM (2016) Continuous information flow fluctuations. *EPL (Europhysics Letters)* 116: 10007. https://doi.org/10.1209/0295-5075/116/10007. Publisher: IOP Publishing.

Sagawa T (2012a) Thermodynamics of information processing in small systems*. *Progress of Theoretical Physics* 127: 1–56. https://doi.org/10.1143/PTP. 127.1.

Sagawa T (2012b) *Thermodynamics of Information Processing in Small Systems*. Springer Theses Springer.

Sagawa T (2014) Thermodynamic and logical reversibilities revisited. *Journal of Statistical Mechanics: Theory and Experiment* 2014: P03025. https://doi.org/10.1088/1742-5468/2014/03/p03025.

Sagawa T and Ueda M (2008) Second law of thermodynamics with discrete quantum feedback control. *Physical Review Letters* 100: 080403.

Sagawa T and Ueda M (2009) Minimal energy cost for thermodynamic information processing: Measurement and information erasure. *Physical Review Letters* 102: 250602.

Sagawa T and Ueda M (2010) Generalized jarzynski equality under nonequilibrium feedback control. *Physical Review Letters* 104: 090602.

Sagawa T and Ueda M (2012) Fluctuation theorem with information exchange: Role of correlations in stochastic thermodynamics. *Physical Review Letters* 109: 180602.

Saha TK, Lucero JNE, Ehrich J, Sivak DA, and Bechhoefer J (2021) Maximizing power and velocity of an information engine. *Proceedings of the National Academy of Sciences* 118: e2023356118. https://doi.org/10.1073/pnas.2023356118.

Schmitt RK, Parrondo JMR, Linke H, and Johansson J (2015) Molecular motor efficiency is maximized in the presence of both power-stroke and rectification through feedback. *New Journal of Physics* 17. https://doi.org/10.1088/1367-2630/17/6/065011.

Schreiber T (2000) Measuring information transfer. *Physical Review Letters* 85: 461–464. https://doi.org/10.1103/PhysRevLett.85.461. Publisher: American Physical Society.

Schumacher B and Westmoreland M (2010) *Quantum Processes Systems, and Information*. USA: Cambridge University Press.

Sekimoto K (2010) *Stochastic Energetics. Volume 799 of Lecture Notes in Physics*. Berlin Heidelberg: Springer.

Shannon CE (1948) A mathematical theory of communication. *Bell System Technical Journal* 27: 379–423. https://doi.org/10.1002/j.1538-7305.1948.tb01338.x.

Smoluchowski Mv (1912) Experimentell nachweisbare, der Üblichen Thermodynamik widersprechende Molekularphenomene. *Physikalische Zeitschrift* 13: 1069.

Szilárd L (1929) über die entropieverminderung in einem thermody-namischen system bei eingriffen intelligenter wesen. *Zeitschrift für Physik* 53: 840–856. https://doi.org/10.1007/BF01341281. On the decrease of entropy in a thermodynamic system by the intervention of intelligent beings. Translated into English and reprinted in (Leff and Rex, 1990).

Touchette H and Lloyd S (2000) Information-theoreitc limits of control. *Physical Review Letters* 84: 1156–1159.

Toyabe S, Sagawa T, Ueda M, Muneyuki E, and Sano M (2010) Experimental demonstration of information-to-energy conversion and validation of the generalized Jarzynski equality. *Nature Physics* 6: 988–992.

Wheeler JA (1995) Toward "it from bit" In: Anandan JS and Safko JL (eds.) *Quantum Coherence and Reality*, p. 281. World Scientific. https://doi.org/10.1142/9789814533294.

Wolpert DH (2019) The stochastic thermodynamics of computation. *Journal of Physics A: Mathematical and Theoretical* 52: 193001. https://doi.org/10.1088/1751-8121/ab0850. Publisher: IOP Publishing.

Zurek W (1990) Maxwell's demon, Szilard's engine and quantum measurements. In: Leff HS and Rex AF (eds.) *Maxwell's Demon: Entropy, Information, Computing*. New Jersey: Princeton University Press.

Zurek W (2003) Quantum discord and Maxwell's demons. *Physical Review A* 67: 012320.

Quantum annealing and computation

Bikas K Chakrabarti[a] **and Sudip Mukherjee**[b,a], [a]Saha Institute of Nuclear Physics, Kolkata, India; [b]Barasat Government College, Kolkata, India

© 2024 Elsevier Ltd. All rights reserved.

Introduction 536
Simulated (classical) annealing 536
Quantum tunneling advantage for annealing 537
Quantum annealing in spin glasses 538
Quantum annealer using optical lattice in a cavity 540
Conclusion and further reading 541
Acknowledgments 542
References 542

Abstract

We introduce and review briefly the phenomenon of quantum annealing and analog computation. The role of quantum fluctuation (tunneling) in random systems with rugged (free) energy landscapes having macroscopic barriers are discussed to demonstrate the quantum advantage in the search for the ground state(s) through annealing. Quantum annealing as a physical (analog) process to search for the optimal solutions of computationally hard problems are also discussed.

Introduction

The idea of computation by decomposing the entire operation into elementary operations like addition, subtraction, etc., and eventually recasting the problem into just number crunching arithmetic, has been quite successful and popular. This has been possible because of the feasibility of binary digitization of the real numbers and availability of ever faster electronic logic gates (AND, OR, XOR, NOT, etc.).

The development and success of digital computers eclipsed the development of the analog computers, based on the dynamics of physical systems. Imagine a bowl on the table and you need to 'locate' its bottom point. Of course, one can calculate the local depths (from a reference height) everywhere along the inner surface of the bowl and search for the point where the local depth is maximum. However, as every one would easily guess, a much simpler and practical method could be to allow rolling of a marble ball along the inner surface of the bowl and wait for its resting location or position. Here, the physics of the forces of gravity and friction allows us to 'calculate' the location of the bottom-most (or minimum energy) point in an analog way! In principle, a similar trick would work for cases where the internal surface of the bowl has modulations, keeping the surface contour or the landscape valleys all tilted toward the same bottom point location. Problem comes when these valleys get separated by 'barriers', high enough.

Computationally hard problems, e.g., search of the ground state(s) of N-spin Sherrington-Kirkpatrick (SK) spin glass system (Sherrington and Kirkpatrick, 1975) involves locating the minima in a rugged landscape of size 2^N, or exponential in N. The (free) energy landscape becomes rugged with occasional barriers of N order, meaning that by flipping a countable few spins one can not get out of the local minimum. For that, one needs to flip a macroscopic number (of order N) to get out of the local minima. The same is true for the N-city Traveling Salesman Problem (see e.g., Kirkpatrick et al., 1983) where one has to find the minimum cost (or travel distance) tours for visiting all the cities, from among the $N!$ order possible tours. Here also, perturbing a tour of higher travel length (cost function), by rearranging the local visit sequence (of a few cities), will not lead to success and one has to take a global view of modifying the sequence of visits to a finite fraction of the cities (effectively by overcoming N order cost function barriers). Generally, for such minimum cost search from among exp.(N) or higher configurations (or tours), often separated by N-order (energy or cost function) barriers, the search time can not be bounded by any polynomial in N (NP-hard problems).

Simulated (classical) annealing

In the seminal paper by Kirkpatrick et al. (1983), a novel stochastic technique was proposed based on the metallurgical annealing technique: To search for the optimized cost (energy of the ground state 'crystal') at eventually vanishing noise (or temperature T), one starts from a high noise (T) 'melt' phase, and tune slowly the noise level. In this 'simulated noise' tuning process, the (classical) noise at any intermediate level of annealing allows for the acceptance with (Gibbs-like) probability determined by the change in cost or energy (scaled by the noise factor) of even higher cost (energy) fluctuations. As the noise level (T) is slowly reduced during the annealing, the gradually decreasing probability of accepting higher cost values allows the system to come out of the local minima valleys and to settle eventually in the 'ground state' of the system with lowest cost (energy) value. It has been a remarkably successful trick for 'practical' computational solutions of a large class of multi-variable optimization problems in reasonable

https://doi.org/10.1016/B978-0-323-90800-9.00057-3

convergence time. For NP-hard problems, however, the search or convergence time for reaching the lowest cost state or configuration grows exponentially with N.

The bottleneck could be identified soon. Extensive study of the dynamics of frustrated random systems like the SK model showed that its (free) energy landscape (in the spin glass phase) is extremely rugged and the barriers, separating the local valleys, often become N order for a N-spin glass. Same is true for N-city Traveling Salesman Problem. In the macroscopic size limit (N approaching infinity) therefore such systems become (effectively) non-ergodic or localized and the classical (thermal) fluctuations, like that in the simulated annealing, fail to help the system to come out of such high barriers (at random locations or configurations, not dictated by any symmetry) as the escape probability is of order exp.$(-N/T)$ only. Naturally the annealing time (inversely proportional to the escape probability), to get the ground state of the N-spin SK model, can not be bounded by any polynomial in N.

Quantum tunneling advantage for annealing

The indication (Ray et al., 1989) was that quantum fluctuations in the SK model can perhaps lead to some escape routes to ergodicity or quantum fluctuation induced delocalization (at least in low temperature region of the spin glass phase) by allowing tunneling through such macroscopically tall but thin barriers which are difficult to scale using classical fluctuations. This is based on the argument that escape probability (see e.g., the discussion in Mukherjee and Chakrabarti (2015)) due to quantum tunneling, from a single valley with single barrier of height V and width w, scales as $\exp\left(-\sqrt{V}w/\Gamma\right)$; where Γ represents the quantum fluctuation strength (or tunneling probability), while the classical (escape) probability is of order exp.$(-V/T)$ with T denoting the temperature of the system (see Fig. 1). This extra handle through the barrier width w (absent in the classical escape probability) helps in a major way in its vanishing limit. Indeed, for a single narrow ($w \to 0$) barrier of height N, when the tunneling parameter Γ is slowly tuned to zero, the annealing time to reach the ground state or optimized cost, will become N independent! It has led to some important clues. Of course, complications (due to localization) may still arise for many such barriers at random locations.

In the Quantum Annealing scheme, the cost function of a multivariable optimization problem is mapped on to the energy function corresponding to a classical (frustrated) Hamiltonian (H_0). A time dependent quantum (non-commuting) kinetic term ($\Gamma(t)H'$) is then added to the system. As H' does not commute with the H_0, it provides quantum dynamics to the overall system represented by the time dependent Hamiltonian $H(t) = H_0 + \Gamma(t)H'$ and the evolution of the system is given by the solution of the time dependent Schrödinger equation of the system

$$i\hbar\frac{\partial\psi}{\partial t} = \left[\Gamma(t)H' + H^0\right]\psi.$$

If $\Gamma(0)$ is taken to be very large, then ψ starts as the ground state of H', which is assumed to be known. As $\Gamma(t)$ starts decreasing slowly enough, following the quantum adiabatic theorem, the system will then be carried into the ground state of the instantaneous total Hamiltonian. At the end of the annealing schedule the kinetic term becomes zero ($\Gamma = 0$). Hence, one would expect the system to arrive at (one of) the ground state(s) of H_0, thereby giving the optimized value of the original cost function. We represent schematically the advantage of quantum annealing, compared to the classical one, using Fig. 2. This was first demonstrated in Kadowaki and Nishimori (1998) for random spin systems, by numerical solutions of the above Schrodinger equation for such systems. Indeed, the numerical results reported there for the annealing of a frustrated magnetic system (with less than 10 spins), are shown in Fig. 3, indicating the clear advantage of tuning the quantum fluctuation, compared to the classical (thermal) one. The

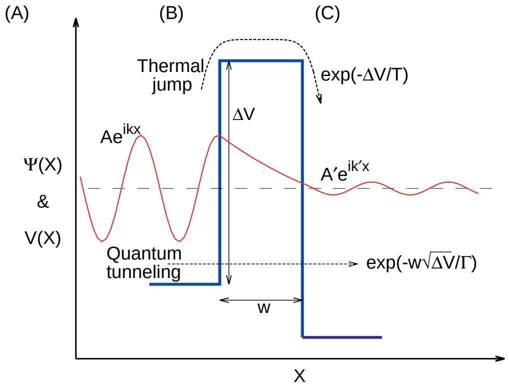

Fig. 1 Schematic diagram suggesting the advantage of quantum tunneling over thermal hopping across a potential barrier. For kinetic energy (E) greater than the barrier potential (V), compared to those in regions (A) and (C), the plane wave functions ($\psi(x) = A$ exp.(ikx) or $\psi(x) = A'$ exp.$(ik'x)$) are indicated with (real) wave vectors $k = \sqrt{E - V} \simeq k'$ in the two regions respectively. For region (B), the wave vector becomes imaginary (as $V > E$) and the consequent damping of the amplitude A in region (A) to A' in region (C), occurs while passing through region (B). For V of order N and E of order $N\Gamma$, the barrier transmission probability $(A'/A)^2$ scales as $\exp\left(-w\sqrt{N(1-\Gamma)}\right) \sim exp\left(-w\sqrt{N}/\Gamma\right)$.

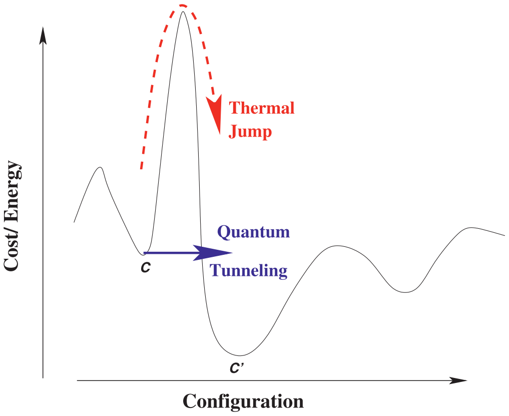

Fig. 2 Optimizing the cost function of a computationally hard problem (for example, search for the ground state energy of a spin glass or for the minimum travel distance in a traveling salesman problem), one has to get out of a shallower local minimum (indicated here by the configuration *C* of the spins in a spin glass or of a travel route of the salesman), to reach a deeper minimum (indicated here by *C*′). This requires jumps or tunneling like fluctuations in the dynamics. Classically one has to jump over the energy or the cost barriers separating them, while (as indicated in Fig. 1) quantum mechanically one can tunnel through the same. With increasing barrier height, thermal jump becomes extremely difficult. However, if the barrier is narrow enough, quantum tunneling can help the search problem much easily.

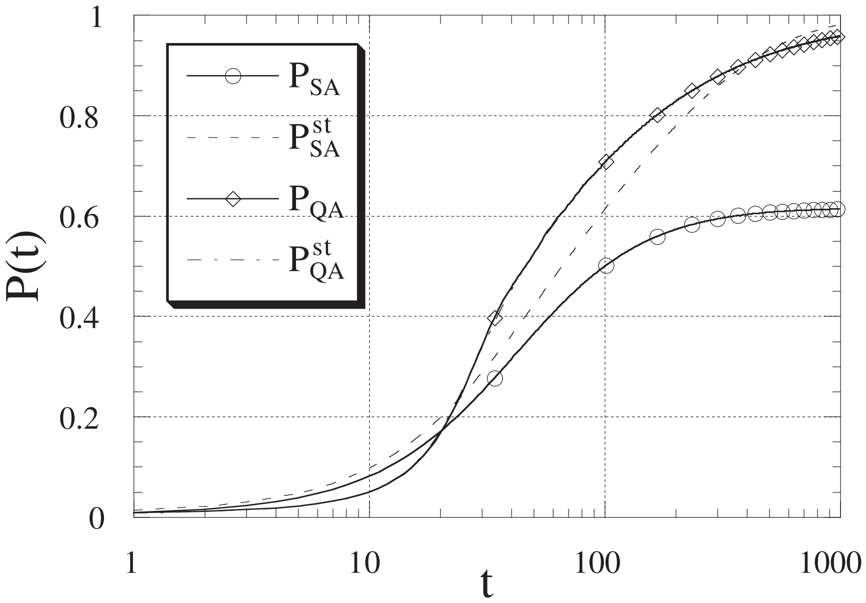

Fig. 3 Time dependence of the overlaps *P* (with the ground state) of the frustrated model with $\Gamma(t) = T(t) = 3/\sqrt{t}$ for classical and quantum annealing (subscripts 'SA' and 'QA' indicate simulated annealing and quantum annealing respectively, whereas superscript 'st' corresponds to quasistatic solution). From Kadowaki T and Nishimori H (1998) Quantum annealing in the transverse Ising model. *Physical Review E* 58: 5355.

successive experimental (Brooke et al., 1999) and theoretical (Farhi et al., 2001; Santoro et al., 2002) demonstrations led to the emergence of the field (Das and Chakrabarti, 2008).

Quantum annealing in spin glasses

Using Suzuki-Trotter mapping of the quantum SK model to the effective classical spin model, Monte Carlo studies were conducted and annealing through ergodic and nonergodic regions of the model was studied (Mukherjee and Chakrabarti, 2019). Determination of thee phase diagram of the quantum SK model, employing the Monte Carlo simulation (at finite temperatures) and exact diagonalization technique (at zero temperature) revealed some interesting features. To extract the critical behavior at finite temperatures, different sizes (number of Ising spins ranging from 20 to 180) were considered in (Mukherjee and Chakrabarti, 2019), keeping constant the ratio of Trotter size and the effective dynamical size of the number of spins. At zero temperature,

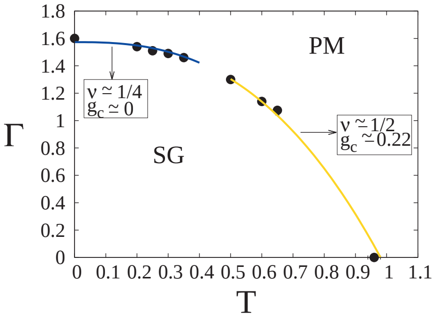

Fig. 4 Phase diagram of quantum SK spin glass model as estimated from the Monte Carlo simulation and exact diagonalization. The spin glass and paramagnetic phases are denoted by SG and PM respectively. The data points at $T = 0$ and $\Gamma = 0$ are associated with the purely quantum and classical phase transitions, respectively. The two observed different critical behaviors of the system are indicated by blue (with the Binder cumulant g_c near 0 and the correlation length exponent value near 1/4) and by yellow (with critical Binder cumulant g_c near 0.22 and correlation length exponent value near 1/2) lines. The crossover in the critical behavior occurs around $T = 0.49$ and $\Gamma = 1.31$. From Mukherjee S and Chakrabarti BK (2019) On the question of ergodicity in quantum spin glass phase and its role in quantum annealing. *Journal of the Physical Society of Japan* 88: 061004.

however, the maximum system size (for diagonalization study) had been of order 20 only. They found that from the quantum transition point ($T = 0, \Gamma_c \simeq 1.63$) to almost the point ($T = 0.45$, $\Gamma = 1.33$), the critical Binder cumulant value remained vanishingly small (it can indeed effectively vanish even for non-Gaussian fluctuation-induced phase transitions). In this range of the phase boundary, they found the correlation length exponent to be about 1/4 from the data collapse of Binder cumulant plots. In the rest of the phase boundary, the critical Binder cumulant value is about 0.22 and they observed a satisfactory data collapse with the correlation length exponent equal to 1/2. These two different values of the critical Binder cumulant and the correlation length exponent for the two different parts of the phase boundary indicate the classical to quantum crossover (at $T \simeq 0.49$ and $\Gamma \simeq 1.31$; see Fig. 4) occurs at a non-vanishing value of temperature in the quantum SK model.

Unlike in the pure system (also in non-frustrated random system), where the free-energy landscape is smoothly inclined toward the global minima (Landau scenario), in the SK spin glass the landscape is extremely rugged. In particular, the local minima are often separated by system size dependent energy barriers which induce nonergodicity and the consequent replica-symmetry-broken distribution of the order parameter. Therefore, at any finite temperature the thermal fluctuations are unable to help the localized system to come out or escape from the macroscopically high free-energy barriers to reach the ground state (by flipping finite fraction of spins). With the aid of the transverse field the system can tunnel through such free-energy barriers (Das and Chakrabarti, 2008; Mukherjee and Chakrabarti, 2015; Ray et al., 1989). As a consequence, at low temperatures, the phase transition is governed by the quantum fluctuation and the system essentially exhibits quantum critical behavior (see the discussion on "possible restoration of ergodicity through quantum tunneling" for appropriate parameter space in the quantum SK model (Leschke et al., 2021)).

Study on the nature of the order parameter distribution in the spin glass phase at finite temperatures through Monte Carlo simulations also showed (Mukherjee and Chakrabarti, 2019) that in the high-temperature (low-transverse-field) classical fluctuation dominated spin glass region, along with the peak at the most probable value of the order parameter, the distribution contains a long tail (extending up to the zero value of the order parameter). This tail did not vanish even in the large system size limit, which indicated that the order parameter distribution remains Parisi type (replica Symmetry broken), corresponding to the nonergodic region SG(NE) (Fig. 5A) of the spin glass phase. On the other hand, in the low temperature (large transverse field) region, where the order parameter distribution effectively converges to a Gaussian form (with a peak around the most probable value) in the infinite-system-size limit. This indicates the existence of a single (replica-symmetric) order parameter in this ergodic region SG(E) of the spin glass phase. At zero temperature, the extrapolated order parameter distribution function showed a clear tendency to become one with a sharp peak (around the most probable value) in the large-system-size limit, suggesting the conclusion that the ergodic and non-ergodic regions of the spin glass phase are separated by a line possibly originating from point ($T = 0$, $\Gamma = 0$) and extending up to the quantum-classical crossover point (T near 0.49 and Γ near 1.31) on the phase boundary (see Fig. 5A). In order to find the role of such quantum-fluctuation-induced ergodicity in the (annealing) dynamics, they studied the variation of the annealing time τ (required to reach close to the ground state(s)) with the system size following the schedules $T(t) = T_0(1\text{–}t/\tau)$ and $\Gamma(t) = \Gamma_0(1\text{–}t/\tau)$. Attempts were made to reach a desired preassigned very low energy state (near the ground state) at the end of the annealing dynamics (in time τ), keeping both T and Γ nonzero (but very small) at the end of the annealing schedule as the Suzuki-Trotter Hamiltonian (which governed the annealing dynamics) has singularities at both $T = 0$ and $\Gamma = 0$ (starting with T_0 and Γ_0 corresponding to the paramagnetic region of the phase diagram). They found (see Fig. 5B) that the average annealing time does not depend on the system size when annealing is carried out along paths that pass entirely through the ergodic region, whereas the annealing time becomes much larger and strongly size-dependent for paths that pass through the nonergodic region of the spin glass phase. These confirm the earlier observations (Mukherjee and Chakrabarti, 2015; Ray et al., 1989) regarding the annealing time behavior, occurring due to tunneling through macroscopically tall but thin free-energy barriers in the SK model. In fact, the temporal variations of the average spin autocorrelation at finite temperatures also showed distinct behavior in these two regions of the spin glass phase of the quantum SK model. While at high temperatures, in the classical fluctuation dominated (nonergodic)

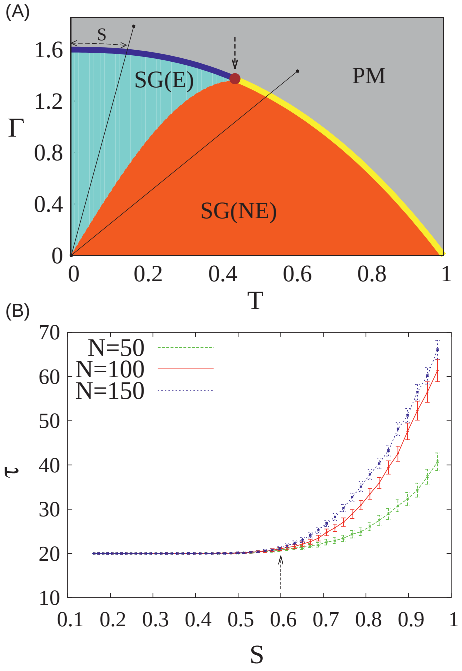

Fig. 5 (A) Schematic phase diagram of the quantum SK model. The spin glass and paramagnetic phases are denoted by SG and PM, respectively. Numerical results showed (Mukherjee and Chakrabarti, 2019) that the spin glass phase is further divided into two regions: ergodic spin glass phase SG(E) and nonergodic spin glass phase SG(NE). The quantum-classical crossover point in the critical behavior of the model is indicated by the red dot on the SG-PM phase boundary. The annealing behavior for the schedules $T(t) = T_0(1 - t/\tau)$ and $\Gamma(t) = \Gamma_0(1 - t/\tau)$, with T_0 and Γ_0 values corresponding to the paramagnetic phase are shown in (B). The Variation of annealing time τ with S, the length of the arc measured along the phase boundary (starting from the zero-temperature quantum transition point) to the intersection of the annealing line with the phase boundary. Low values of S correspond to the SG(E)-PM phase boundary, while higher values of S correspond to SG(NE)-PM boundary. The annealing time τ is clearly system size independent when the annealing path passes through the SG(E) region and increases rapidly with the system size when it pass through the SG(NE) region. From Mukherjee S and Chakrabarti BK (2019) On the question of ergodicity in quantum spin glass phase and its role in quantum annealing. *Journal of the Physical Society of Japan* 88: 061004.

region of the spin glass phase (SG(NE) region in Fig. 5A), one obtains very large values of the fitting relaxation times, the fitting relaxation times become order of magnitude smaller in the low temperature quantum fluctuation dominated region (SG(E) in Fig. 5A) presumably because of quantum tunneling (Mukherjee and Chakrabarti, 2019). These investigations clearly indicated the existence of a high-temperature (low-transverse-field) nonergodic region as well as a low-temperature (high-transverse-field) ergodic region in the spin glass phase. The line separating these two regions starts from $T = 0$, $\Gamma = 0$ and intersects the spin glass phase boundary at the quantum-classical crossover point (see Fig. 5A). The annealing behaviors are indicated in Fig. 5B, showing that the annealing time τ is practically independent of N when the annealing schedule (line) passes through the ergodic spin glass region (at low T and high Γ).

Quantum annealer using optical lattice in a cavity

Indeed, Starchl and Ritsch (2022) studied a minimal Bose-Hubbard type system containing two atoms inside a cavity-generated optical lattice induced by an external trapping potential and directly pumped by two laser beams resulting in photon scattering into two separate cavity modes. Introduction of an additional local energy shift for a specific lattice site allows creating a unique energy separated optimal ground state for the problem Hamiltonian. The main focus was to compare the full quantum mechanical model with the semi-classical model, where the field mode induced interactions are approximated by classical coherent fields. The investigation revealed strong differences between the quantum and semi-classical model, which can be cast into a sort of phase diagram separating a distinct parameter region where (partial) quantum annealing does not find the optimum in the semi-classical approach, while full quantum annealing does. They found strong evidence for the involvement of entanglement in two ways. First, Starchl and Ritsch (2022) confirmed the importance of vanishing entanglement at the end of the protocol and its influence on the minimal time needed for a successful simulation. Second, they identified a novel role of the maximum entanglement generated during the quantum annealing protocol in finding an optimal solution to the problem. They also studied the impact of different photon number cut-offs in the numerical quantum simulation. Most surprisingly they found improvement in the optimization success rate even for short simulation times when they used too low cut-off numbers to get a numerically accurate solution of the

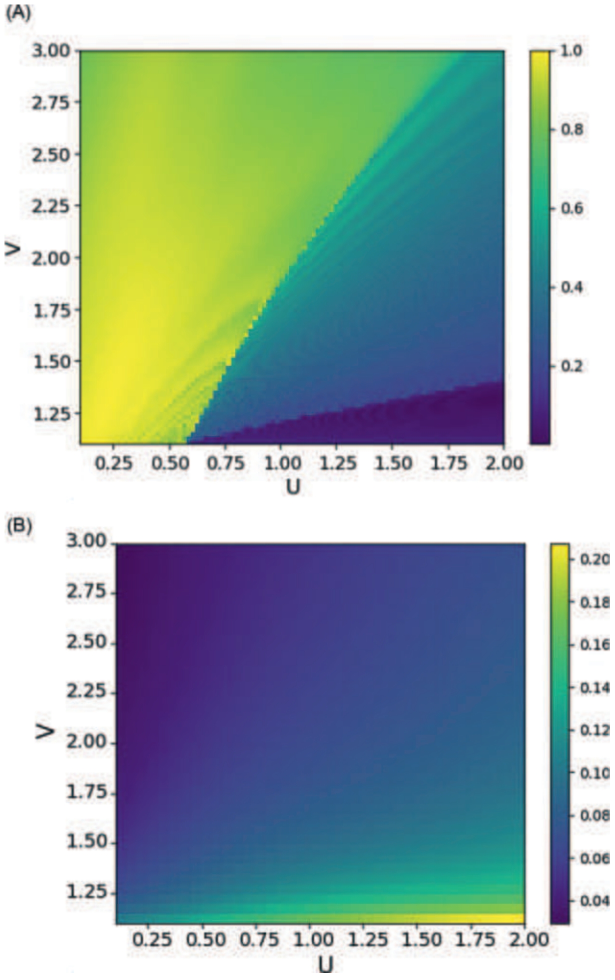

Fig. 6 (A) Color density plot showing the solution fidelity after an adiabatic sweep using a Hamiltonian description with a classical mean-field approximation of the photon cavity modes. The parameter *U* describes the particle-particle on-site repulsive interaction and the parameter *V* represents the total potential depth of the specifically shifted lattice site, to create an impurity with a unique optimal solution. Three regions are clearly visible, a green-yellowish one, where the correct solution of two-particle on the mentioned lattice site is found, a bluish region with finite overlap but non-optimal solution, and a dark purple region with minimal overlap to the optimal solution. (B) Color density plot for the same parameter range showing the maximum entropy generated during the adiabatic sweep. In comparison, a connection between low maximum entropy and high success probability can be seen. Courtesy, Starchl E and Ritsch H (2022) Unraveling the origin of higher success probabilities in quantum annealing versus semi-classical annealing. *Journal of Physics B: Atomic, Molecular and Optical Physics* 55: 025501; private communication.

Schrödinger equation. Using higher cut-off numbers and thus a better representation of the exact quantum dynamics seems to be more relevant only for longer simulation times with very high success rates (see Fig. 6). These observations indicate a clear quantitative improvement of the annealing process for a full quantum system compared to a semi-classical one.

Conclusion and further reading

Quantum Annealing is now a very well developed subject, both theoretically as well as experimentally (see e.g., Brooke et al. (1999); Das and Chakrabarti (2008)). The breakthrough implementation of quantum annealing, employing superconducting qubits in successive generations of the D-wave annealers (Johnson et al., 2011) since 2011 and their availability in the market, has helped the growth of analog quantum computing in a major way. In fact, the availability of commercial quantum annealing condensed matter devices (like the D-wave systems) have revolutionized quantum information processing and computing algorithms for optimization across many disciplines, and led to developments which were unthinkable about a decade back. We would refer the readers to a few recent studies to get further information and ideas. For discussions on quantum versus classical annealing the readers may consult Heim et al. (2015), while for discussions on the efficiency of quantum versus classical annealing in the context of learning problems, the readers may consult Baldassia and Zecchinaa (2018) (see Nath et al. (2021) for a recent review on machine learning using quantum annealing). For a discussion on fault-tolerant quantum heuristics in the context of combinatorial optimizations, one may consult Sanders et al. (2020), and Pelofske et al. (2022) for the indication of a major success using parallel quantum annealing algorithms. For a discussion on computer aided design of heterogeneous materials using quantum annealing algorithms, one may consult (Sahimi and Tahmasebi, 2021). For recent extensive discussions on both theoretical and experimental developments, the readers are referred to the books (Dutta et al., 2015; Tanaka et al., 2017) and reviews (Albash and Lidar, 2018; Hauke et al., 2020).

Acknowledgments

We are thankful to our colleagues Arunava Chakrabarti, Arnab Das and Purusattam Ray for their contributions at various stages of this development over last three decades, to Gabriel Aeppli, Amit Dutta, Uma Divakaran, Jun-ichi Inoue, Atanu Rajak, Thomas Rosenbaum, Diptiman Sen, Parongama Sen, Sei Suzuki, Ryo Tamura and Shu Tanaka for collaborations on this and closely related topics over the years, and to Elias Starchl for his comments on the manuscript and help with Fig. 6. BKC is grateful to the Indian Academy of Sciences for their support through a Senior Scientist Research Grant. SM thanks the SERB, DST (India) for partial financial support through the TARE scheme [file no.:TAR/2021/000170] (2022).

References

Albash T and Lidar A (2018) Adiabatic quantum computation. *Reviews of Modern Physics* 90: 015002.
Baldassia C and Zecchinaa R (2018) Efficiency of quantum vs. classical annealing in nonconvex learning problems. *Proceedings of the National Academy of Sciences of the United States of America* 115: 1457.
Brooke J, Bitko D, Rosenbaum TF, and Aeppli G (1999) Quantum annealing of a disordered magnet. *Science* 284: 779.
Das A and Chakrabarti BK (2008) Quantum annealing and analog quantum computation. *Reviews of Modern Physics* 80: 1061.
Dutta A, Aeppli G, Chakrabarti BK, Divakaran U, Rosenbaum TF, and Sen D (2015) *Quantum Phase Transitions in Transverse Field Spin Models: From Statistical Physics to Quantum Information*. Cambridge: Cambridge University Press.
Farhi E, Goldstone J, Gutmann S, Lapan J, Ludgren A, and Preda D (2001) A quantum adiabatic evolution algorithm applied to random instances of an NP-complete problem. *Science* 292: 472.
Hauke P, Katzgraber HG, Lechner W, Nishimori H, and Oliver WD (2020) Perspectives of quantum annealing: methods and implementations. *Reports on Progress in Physics* 83: 054401.
Heim B, Rønnow TF, Isakov SV, and Troyer M (2015) Quantum versus classical annealing of Ising spin glasses. *Science* 348: 215.
Johnson MW, Amin MHS, Gildert S, Lanting T, Hamze F, Dickson N, Harris R, Berkley AJ, Johansson J, and Bunyk P (2011) Quantum annealing with manufactured spins. *Nature* 473: 194.
Kadowaki T and Nishimori H (1998) Quantum annealing in the transverse Ising model. *Physical Review E* 58: 5355.
Kirkpatrick S, Gelatt CD, and Vecchi MP (1983) Optimization by simulated annealing. *Science* 220: 671.
Leschke H, Manai C, Ruder R, and Warzel S (2021) Existence of replica-symmetry breaking in quantum glasses. *Physical Review Letters* 127: 207204.
Mukherjee S and Chakrabarti BK (2015) Multivariable optimization: Quantum annealing and computation. *The European Physical Journal Special Topics* 224: 17.
Mukherjee S and Chakrabarti BK (2019) On the question of ergodicity in quantum spin glass phase and its role in quantum annealing. *Journal of the Physical Society of Japan* 88: 061004.
Nath RK, Thapliyal H, and Humble TS (2021) A review of machine learning classification using quantum annealing for real-world applications. *SN Computer Science* 2: 365.
Pelofske E, Hahn G, and Djidjev HN (2022) Parallel quantum annealing. *Scientific Reports* 12: 4499.
Ray P, Chakrabarti BK, and Chakrabarti A (1989) Sherrington-Kirkpatrick model in a transverse field: Absence of replica symmetry breaking due to quantum fluctuations. *Physical Review B* 39: 11828.
Sahimi M and Tahmasebi P (2021) Reconstruction, optimization, and design of heterogeneous materials and media: Basic principles, computational algorithms, and applications. *Physics Reports* 939: 1.
Sanders YR, Berry DW, Costa PCS, Tessler LW, Wiebe N, Gidney C, Neven H, and Babbush R (2020) Compilation of fault-tolerant quantum heuristics for combinatorial optimization. *PRX Quantum* 1: 020312.
Santoro GE, Martoňák R, Tosatti E, and Car R (2002) Theory of quantum annealing of an Ising spin glass. *Science* 295: 2427.
Sherrington D and Kirkpatrick S (1975) Solvable model of a spin-glass. *Physical Review Letters* 35: 1792.
Starchl E and Ritsch H (2022) Unraveling the origin of higher success probabilities in quantum annealing versus semi-classical annealing. *Journal of Physics B: Atomic, Molecular and Optical Physics* 55: 025501.
Tanaka S, Tamura R, and Chakrabarti BK (2017) *Quantum Spin Glasses, Annealing and Computation*. Cambridge: Cambridge University Press.

Molecular dynamics calculations: Machine learning☆

Albert P Bartók, Warwick Centre for Predictive Modelling, School of Engineering and Department of Physics, University of Warwick, Coventry, West Midlands, United Kingdom

© 2024 Elsevier Ltd. All rights reserved.

This is an update of L. Colombo, Molecular Dynamics Calculations, Editor(s): Franco Bassani, Gerald L. Liedl, Peter Wyder, Encyclopedia of Condensed Matter Physics, Elsevier, 2005, Pages 1–8, ISBN 9780123694010, https://doi.org/10.1016/B0-12-369401-9/00455-1.

Introduction 543
Molecular dynamics calculations 544
Molecular dynamics 544
Potential energy surfaces 544
Surrogate models 545
Machine learned interatomic potentials 546
Representations 546
Regression 548
Data generation 549
Applications 549
Organic molecules 550
Water 550
Amorphous silicon 550
Further use of machine learning in molecular dynamics 550
Conclusion 551
References 551

Abstract

Molecular dynamics calculations have been an essential tool to model the structural and dynamic properties of atomic systems. Apart from providing the experimental tool set for statistical mechanics, molecular dynamics simulations are routinely used to understand, interpret and predict microscopic processes in realistic materials. Machine learning techniques have helped to accelerate molecular dynamics in several ways: surrogate models, trajectory analysis, enhanced sampling, to name a few. This entry focusses largely on machine learning interatomic potentials (MLIPs), presenting their development grounded on ab initio methods and analytical potentials. The basic ingredients of the methodology is discussed through examples, and some concrete implementations are mentioned. Applications highlighting the new possibilities offered by MLIPs are shown, as well as some remarks on future directions.

Introduction

Molecular dynamics (MD) is a numerical technique used to simulate the motion of interacting atomic particles as well as to generate statistical ensembles of atomic configurations (Frenkel and Smit, 2002). While the motion of atomic particles cannot be obtained in an analytic form, except for the simplest cases, well established numerical integration techniques are routinely used to generate high resolution, arbitrarily long trajectories. The fundamental challenge of the field is the drive to increase the accuracy of the trajectory, inasmuch as to make simulations more realistic and predictive.

The key quantity that determines the quality of each integration step during a MD calculation is the interaction energy model between the particles. Traditionally, interactions have been approximated by simple analytical forms based on theoretical considerations, also known as force fields, and parameterized using experimental data or a few reference quantum mechanical calculations. With the development of quantum mechanical calculations, it has become feasible to evaluate atomic forces from solving the Schrödinger equation, and use these to propagate the atomic trajectories (Car and Parrinello, 1985; Payne et al., 1992). Termed ab initio molecular dynamics (AIMD), the technique is regarded as truly predictive (Brommer et al., 1992) within the approximations employed in the numerical solution of the quantum mechanical equations. This is in contrast to MD based on traditional or empirical force fields, which are generally used to interpret experimental phenomena or study generic statistical mechanics processes.

Very simplistically, the main limitation of AIMD is the lack of access to large time and length scales, due to the computational complexity and unfavorable scaling of ab initio methods, while empirical force fields lack accuracy and therefore predictive capability, because their simplified form remains only locally valid (Stillinger and Weber, 1985).

☆*Change History:* March 2023. AP Bartók updated the chapter.

It is useful to consider the reason empirical potentials have been typically formulated using simple analytical expressions with few free parameters. In the absence of reliable quantum mechanical data, only a few experimental data points have been available to find numerical values for the potential parameters, such as thermal data, elastic and vibrational properties or defect energies (Tersoff, 1988). Therefore, traditional potentials rely on the theoretical considerations encapsulated in the functional form.

Algorithmic developments (Becke, 2014), aided by a massive increase in computational power have made it possible to generate a large number of reliable reference data points using ab initio methods. This has largely coincided with an explosion in non-linear, non-parametric regression techniques, termed as machine learning (ML) (Mackay, 2003), allowing to define significantly more flexible functional form for atomic interactions, which can be fitted using reference ab initio data.

Even though MLIPs are typically slower to evaluate computationally than empirical force fields due to their more complex functional form, they remain linear scaling with system size and significantly faster than ab initio methods, while approaching ab initio accuracy in the fitting domain (Zuo et al., 2020). Another favorable feature of MLIPs is that they are extensible, inasmuch as their flexibility allows increasing their domain of validity by adding more reference data (Vandermause et al., 2020; Gubaev et al., 2019).

Apart from surrogate models for atomic interactions, ML techniques have found application in analyzing MD trajectories (Cheng et al., 2020) as well as aiding enhanced sampling techniques (Bonati et al., 2019). Regardless of the model representing the atomic interactions, analysis of the resulting trajectories benefits from unsupervised ML methods to discover patterns and processes.

In the following sections, I will review machine learning interatomic potentials, focusing on general concepts as well as practical implementations and highlighting a few applications. I will also discuss other uses of ML techniques in MD simulations and provide an outlook of the state-of-the-art and future challenges.

Molecular dynamics calculations

Molecular dynamics

In its simplest form, MD is based on Newtonian mechanics, solving the second order differential equations describing Newton's law of motion

$$m_i \ddot{\mathbf{r}}_i = \mathbf{F}_i \equiv -\nabla_{\mathbf{r}_i} E, \tag{1}$$

where m_i and $\mathbf{r}_i$ represent the mass and position of atom i, respectively, and E describes the potential energy of all the N interacting particles. The force acting on atom i, $\mathbf{F}_i$ is obtained as the negative gradient of the potential energy.

The underlying assumption is that atoms can be regarded as classical particles, ignoring their quantum nature, which is well justified in case of heavier nuclei (Marx and Parrinello, 1996). Lighter nuclei may require quantum mechanical treatment, some of which are also based on MD, such as the Path Integral Molecular Dynamics method, which are out of the scope of this entry, but MLIPs remain equally applicable.

Typical solutions of (1) are based on numerical integration schemes, which propagate the trajectory in discrete time steps Δt, collecting a time series of positions and velocities. Most often used are the Verlet or the closely related Velocity Verlet algorithms (Frenkel and Smit, 2002), which have advantages that they are stable, as errors in the integration are in the fourth order above; and the integration is time reversible, preserving this fundamental symmetry of Hamiltonian dynamics.

As the numerical integration is a well established technique, with a well controlled accuracy if the discretization time step is small enough, the quality of the trajectory is determined predominantly by the description of the atomic interactions. Also, for all but the simplest of models, the computational cost of a MD simulation is dominated by the evaluation of the atomic forces.

Potential energy surfaces

In our context, the interaction model is based on the Born-Oppenheimer approximation, applicable to problems where the degrees of freedom of the electrons and nuclei can be treated separately. The Born-Oppenheimer approximation assumes that the combined wave function of the electrons and nuclei Ψ, is separable in the form

$$\Psi(\mathbf{r}_{\mathrm{n},1}, \ \mathbf{r}_{\mathrm{n},2}, \ldots; \ \mathbf{r}_{\mathrm{e},1}, \ \mathbf{r}_{\mathrm{e},2}, \ldots) = \chi(\mathbf{r}_{\mathrm{n},1}, \ \mathbf{r}_{\mathrm{n},2}, \ldots)\psi(\mathbf{r}_{\mathrm{e},1}, \ \mathbf{r}_{\mathrm{e},2}, \ldots), \tag{2}$$

where $\mathbf{r}_{\mathrm{n,i}}$ and $\mathbf{r}_{\mathrm{e,j}}$ denote the Cartesian coordinates of the i-th nucleus and j-th electron, respectively. From this assumption follows that the electronic Schrödinger equation, with the electronic Hamiltonian $\hat{H}_{\mathrm{e}}$ parameterized by the coordinates of the nuclei, can be solved separately as

$$\hat{H}_{\mathrm{e}}(\mathbf{r}_{\mathrm{n},1}, \ \mathbf{r}_{\mathrm{n},2}, \ \ldots)\psi = E(\mathbf{r}_{\mathrm{n},1}, \ \mathbf{r}_{\mathrm{n},2}, \ \ldots)\psi, \tag{3}$$

resulting in a potential energy surface (PES) function which depends only on the coordinates of the nuclei, also known as the Born-Oppenheimer surface.

As the potential energy E is assumed to depend on the coordinates of the nuclei, the electronic degrees of freedom need not be explicitly considered, and the solution of (3) is often regarded as a black-box calculation.

A large proportion of atomic modelling problems can be characterized by the ground state wavefunction and therefore the Born-Oppenheimer approximation provides an accurate solution, therefore for the remainder of this entry I focus on the MD of classical particles interacting via a surrogate model of the Born-Oppenheimer surface.

Surrogate models

It is evident from the Born-Oppenheimer approximation that in case of an AIMD simulation, the particulars of the electronic structure are irrelevant, and only the forces based on the PES are used from the solution of the electronic Schrödinger equation to propagate the trajectory. The use of surrogate models for the PES, which bypass the explicit solution of the Schrödinger equation is therefore straightforward and widely used (Deringer et al., 2021).

For an isolated system with relatively few degrees of freedom, such as a small molecule, it is possible to create PES models that explicitly contain all atomic coordinates. Examples in include models for H_3^+ (Adamowicz and Pavanello, 2012), H_2O (Partridge and Schwenke, 1997) or CH_5^+ (Thompson et al., 2005). In isolated systems, symmetrized coordinates describing the entire entity are used to form basis functions, which are often physically motivated, and a fitting procedure to reference data is used to determine the parameters of basis functions and corresponding coefficients.

As an example, let us consider the model for describing the PES of the water molecule developed by Partridge and Schwenke (1997). A convenient representation of the geometry of the water molecule is provided by the length of the two O—H bonds (r_1, r_2) and the bond angle θ. As opposed to the representation given by the 9 Cartesian coordinates, the representation by bond lengths and angle eliminates the translational and rotational degrees of freedom, to which the PES is invariant, therefore these invariant features are built in when formulating E as a function $E(r_1, r_2, \theta)$. Partridge and Schwenke suggested the form

$$E(r_1,\ r_2,\ \theta) = E_a(r_1) + E_a(r_2) + E_b(r_{\mathrm{HH}}) + E_c(r_1,\ r_2,\ \theta) \tag{4}$$

where E_a takes the form of the Morse potential

$$E_a(r) = D\{\exp\left[-2a(r-r_0)\right] - 2\exp\left[-a(r-r_0)\right]\}, \tag{5}$$

E_b is a simple repulsive term given by

$$E_b(r) = A\exp(-br), \tag{6}$$

and the three-body term E_c is

$$\begin{aligned} E_c(r_1, r_2, \theta) = c_{000} + \exp\left[-\beta(r_1-r_e)^2\right]\exp\left[-\beta(r_2-r_e)^2\right] \\ \times\sum_{ijk} c_{ijk}\left(\frac{r_1-r_e}{r_e}\right)^i\left(\frac{r_2-r_e}{r_e}\right)^j\left[\cos\theta - \cos\theta_e\right]^k. \end{aligned} \tag{7}$$

The three-body component includes 245 terms, and coefficients were fitted using a least squares algorithm that minimized the difference between the model PES and 771 ab initio energies calculated at different geometries. It is remarkable that even though there is no reference to ML, the functional form is equivalent to those used in MLIPs, as we shall see later.

Extended systems pose a different challenge. As the formal definition of the PES function depends on 3 N Cartesian coordinates, with varying number of atoms the number of arguments of E changes, therefore a rigid functional form would be very restricted. While according to (2) the energy is an N-body quantity, the principle of nearsightedness of electronic matter proposed by Prodan and Kohn, 2005 suggests that there exists a locality which can be exploited to approximate the full N-body interaction energy by simpler terms.

A common approach to decompose the total energy into more manageable terms is to apply the many-body expansion (MBE) (Richard et al., 2014), where

$$E(r_1,\ r_2,\ \ldots,\ r_N) = \sum_i^N E_i^{(1)} + \sum_{i<j} E_{ij}^{(2)} + \sum_{i<j<k} E_{ijk}^{(3)} + \ldots \tag{8}$$

and we assume that (i) the expansion may be truncated at reasonably low orders; (ii) the individual terms are local, i.e. they tend to zero as pairwise distances increase. The MBE reduces the complexity by substituting a 3 N-dimensional function by functions of significantly lower, and constant, dimensionality as well as limiting the domain of each term by the locality assumption. It is important to note that long range interactions, such as dispersion or the Coulomb interaction, form an exception as truncation may lead to the omission of important physical effects, but there exists well-established methods to approximate these contributions to the total energy and only consider the local contributions within the MBE approximation.

Examples for models based on the MBE in condensed systems include the ubiquitous Lennard-Jones potential (Jones, 1924) for noble gases and the Stillinger-Weber potential (Stillinger and Weber, 1985) for silicon. The Lennard-Jones potential is based on truncation at the two-body term

$$E = \sum_{i<j} 4\varepsilon\left(\frac{\sigma^{12}}{r_{ij}^{12}} - \frac{\sigma^6}{r_{ij}^6}\right). \tag{9}$$

Indeed, Cao and Berne (1992) found that including many-body effects is quantitatively significant, although the qualitative structural features of noble gas clusters and liquid remain unchanged, justifying the truncation as an approximate model for interactions of noble gas atoms.

The Stillinger-Weber potential has the form of

$$E = \sum_{i<j} A\left(Br_{ij}^{-p} - r_{ij}^{-q}\right) \exp\left[\left(r_{ij} - a\right)^{-1}\right] + \\ \sum_{i<j<k} \lambda \exp\left[\gamma\left(r_{ij} - a\right)^{-1} + \gamma\left(r_{ik} - a\right)^{-1}\right]\left(\cos\theta_{ijk} + \frac{1}{3}\right)^2, \tag{10}$$

illustrating a truncation at the three-body term. Inspecting its functional form, it becomes apparent that the three-body term favors a tetrahedral arrangement, which is appropriate for the diamond phase, but unphysically destabilizes other, high-pressure phases, such as the β-tin or simple hexagonal phases (Pizzagalli et al., 2013). Other parameterizations or functional forms may remedy this particular failure, nevertheless the Stillinger-Weber potential illustrates the major limitation of the less flexible forms of traditional interatomic potentials.

Another ansatz for the total energy was obtained by Daw and Baskes (1983) and later by Finnis and Sinclair (1984) by considering a series of approximations to Density Functional Theory (DFT). Daw and Baskes (1983) wrote the total energy as

$$E(r_1, \ r_2, \ \ldots, \ r_N) = \sum_{i}^{N} E^{(n)}\left(\rho_i\right) + \sum_{i<j} E^{(2)}\left(r_{ij}\right), \tag{11}$$

where $E^{(\mathrm{n})}$ is an n-body term interpreted as the density dependent energy functional, where ρ_i is the local electron density at atom i and $E^{(2)}$ is a pair term. The electron density is approximated as a sum of static terms contributed by nearby atoms

$$\rho_i = \sum_{j} \rho\left(r_{ij}\right), \tag{12}$$

hence the n-body term is local. Finnis and Sinclair (1984) provided a connection with tight-binding theory.

Machine learned interatomic potentials

While the accuracy and transferability of AIMD, within the approximations employed in the underlying ab initio method, is unquestionable, it is clear that AIMD is limited in accessing time and length scales necessary to study certain phenomena. Slow processes require the collection of long trajectories, which have a correspondingly large computational cost. Plane-wave DFT (Martin, 2004), the most widely used ab initio method for MD scales cubically with system size, meaning that large systems that are necessary to minimize finite size effects quickly become out of reach, limiting system sizes to a few hundreds of atoms. Even linear-scaling DFT implementations have such a large prefactor that it is not practical to sample long MD trajectories.

Surrogate models, as introduced previously, offer a major increase in speed and a favorable linear scaling with system size due to the locality assumption.[1] A natural development is the use of flexible functional forms for the terms in the MBE represented by (8) or (11), which is enabled by regression techniques based on ML.

Representations

The first ingredient to realize a ML based force field model is to define representations that map Cartesian coordinates of atoms onto features that are invariant to basic symmetry operations, much in the spirit of the Partridge-Schwenke water model described in Section "Surrogate models". Such representations form the input variables of subsequent regression methods approximating the individual terms in the total energy expression. As the total energy of a system is invariant to rotations, translations, reflections and permutations of the indices of the same atomic species, it is convenient to build in these symmetries into the transformation that maps Cartesian coordinates, which do not obey these symmetries, onto invariant features or descriptors.

Further desirable properties of the transformation include smoothness, since the Born-Oppenheimer PES in most cases is a continuous and differentiable function of atomic coordinates – which is itself an necessary condition for most integrators used in MD simulations. For example, the representation formed by ordered list of interatomic distances may have the necessary invariances, but discontinuities in the Jacobian are introduced, meaning the forces derived from a model based on this representation would be discontinuous (Musil et al., 2021). However, descriptors can be constructed by choosing appropriate combinations of pair-wise distances, such as those provided by a suitably constructed neural network (Schütt et al., 2018).

The locality assumption can also be implemented at the level of the descriptors. If a descriptor is attributed to an atom, a cutoff function can limit its dependence to the neighboring atoms within a certain distance.

---

[1] We note that there exist efficient algorithms to evaluate long range interactions, for example by Essmann et al. (1995).

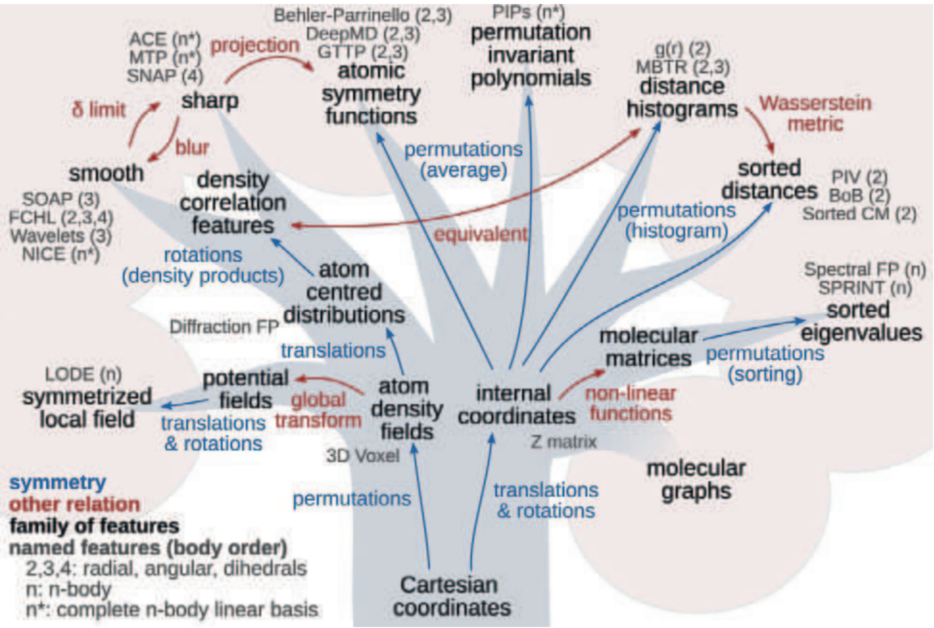
Behler-Parrinello (2,3)
DeepMD (2,3)
GTTP (2,3)
atomic symmetry functions
ACE (n*)
MTP (n*)
SNAP (4)
projection
sharp
δ limit
blur
smooth
SOAP (3)
FCHL (2,3,4)
Wavelets (3)
NICE (n*)
density correlation features
rotations (density products)
atom centred distributions
Diffraction FP
translations
PIPs (n*)
permutation invariant polynomials
permutations (average)
equivalent
g(r) (2)
MBTR (2,3)
distance histograms
Wasserstein metric
sorted distances
PIV (2)
BoB (2)
Sorted CM (2)
permutations (histogram)
Spectral FP (n)
SPRINT (n)
sorted eigenvalues
molecular matrices
permutations (sorting)
non-linear functions
LODE (n)
symmetrized local field
potential fields
translations & rotations
global transform
atom density fields
3D Voxel
internal coordinates
Z matrix
molecular graphs
permutations
translations & rotations
Cartesian coordinates
symmetry
other relation
family of features
named features (body order)
2,3,4: radial, angular, dihedrals
n: n-body
n*: complete n-body linear basis

Fig. 1 The family tree of descriptors, with equivalencies noted. Reproduced from Musil F, Grisafi A, Bartók AP, Ortner C, Csányi G, and Ceriotti M (2021) Physics-inspired structural representations for molecules and materials. *Chemical Reviews* 121(16):9759–9815. doi: 10.1021/acs.chemrev.1c00021. http://eutils.ncbi.nlm.nih.gov/entrez/eutils/elink.fcgi?dbfrom=pubmed&id=34310133&retmode=ref&cmd=prlinks, licensed under the CC-BY 4.0 License.

A large number of representations have been suggested, some of which are illustrated on Fig. 1. Particularly successful have been representations based on atomic densities. The atomic environment of atom i in an extended structure is characterized by the density field

$$\rho_i(\mathbf{r}) = \sum_j f_{\text{cut}}(r_{ij})\, g\left(\mathbf{r} - \mathbf{r}_{ij}|\right), \tag{13}$$

where f_{cut} is a suitably chosen cutoff function that enforces locality, allowing neighboring atoms to enter and exit the cutoff radius in a smooth fashion; g may be a function with compact support, such as the Dirac-delta or a Gaussian function. Neighbor density representations implement invariance to permutations due to the commutativity of the summation, invariance to translations as positions are relative to the central atom as well as locality by using the cutoff function. Invariance to rotations and reflections may be achieved by first considering a basis set expansion using spherical harmonics Y_{lm} and radial basis functions b_n as

$$\rho_i(\mathbf{r}) = \sum_{nlm} c^i_{nlm}\, Y_{lm}(\hat{\mathbf{r}})\, b_n(\mathbf{r}). \tag{14}$$

The power spectrum components are formed from the coefficients as

$$\mathbf{p}^i_{nn'l} \equiv \sum_{m=-l}^{l} c^{i\,*}_{nlm}\, c^i_{n'lm} \tag{15}$$

are invariant to rotations and reflections, and may be regarded as a basis set expansion of the histogram of three-body terms within the atomic neighborhood environment (Bartók et al., 2013). It is also possible to generate higher order correlations representing four- or more body terms, such as the bispectrum (Bartók et al., 2013; Drautz, 2019). Arbitrarily high body order correlations can be encoded in the Moment Tensors (Shapeev, 2016) and the Atomic Cluster Expansion framework (Drautz, 2019).

A related family of descriptors has been suggested by Behler and Parrinello, 2007, such as

$$G^{\text{radial}}_{i,n} = \sum_j \exp\left[-\eta_n\left(r_{ij} - r_n\right)^2\right] f_{\text{cut}}(r_{ij}) \quad \text{and} \tag{16}$$

$$G^{\text{angular}}_{i,n} = 2^{1-\varsigma_n} \sum_{jk} \left(1 + \lambda_n \cos\theta_{ijk}\right)^{\varsigma_n} \exp\left[-\eta_n\left(r^2_{ij} + r^2_{ik}\right)^2\right] f_{\text{cut}}(r_{ij}) f_{\text{cut}}(r_{ik}). \tag{17}$$

By constructing a set of these functions based on different η_n, r_n, ζ_n and λ_n values, a representation up to three-body correlations is obtained. It is clear from the construction of the Behler-Parrinello (BP) descriptors that they possess all the desirable invariant properties. It has also been shown (Musil et al., 2021) that the terms in the BP descriptors are equivalent, up to a basis transformation, to terms in the power spectrum in Eq. (15).

It is important to note, however, that important features of the atomic neighbor environment are omitted from descriptors based on up to three-body correlations, meaning that it is possible to construct two different atomic neighborhood environments, which are not related by rigid body symmetries, that have the same power spectrum of BP descriptors (Pozdnyakov et al., 2020). Conceivably, this shortcoming can lead to inaccurate surrogate models, as two identical representations can only map to equal energy terms. Descriptors encoding higher body correlations, such as ACE (Drautz, 2019), MTP (Shapeev, 2016), SNAP (Thompson et al., 2015) remedy this incompleteness of the representation.

Regression

The key innovation brought by ML to the field of interatomic potential development is the introduction of non-linear regression techniques and robust fitting methodologies. Each term in the MBE expression can be approximated by a high-dimensional function that depends on a descriptor, such as those illustrated in the previous section, allowing the use of arbitrarily high body-order expansion. Denoting a many-body energy function associated with an atomic site by ε parameterized by $\mathbf{w}$, the total energy of an N-atom system is expressed as

$$E = \sum_{i}^{N} \varepsilon(\mathbf{d}_i; \mathbf{w}), \tag{18}$$

where I ignored long-range contributions and used a generic descriptor vector $\mathbf{d}$ for each atom. Given a suitable database of reference ab initio data, consisting of total energies (E_I), forces etc. associated with atomic configurations, the regression problem can be formulated as the least square problem

$$\mathcal{L}_E = \sum_{I} \left[E_I - \sum_{i \in I} \varepsilon(\mathbf{d}_i; \mathbf{w}) \right]^2 \tag{19}$$

with analogous expressions for other microscopic ab initio quantities. Minimizing $\mathcal{L}$ with respect to $\mathbf{w}$ results in a surrogate model that interpolates between the reference data points, and thanks to the highly flexible functional form (*c.f.* high number of parameters in $\mathbf{w}$) is extensible when new points are added to the database.

Some descriptors presented in Section "Representations" provide a highly non-linear mapping, and as a consequence successful interatomic potential were obtained by simple linear regression, such as Moment Tensor Potentials (Shapeev, 2016), the Spectral Neighbor Analysis Potentials (Thompson et al., 2015) and ACE potentials (Drautz, 2019).

MLIPs based on other descriptors benefit from non-linear regression, such as Gaussian Process Regression (GPR) or artificial neural networks. GPR, schematically represented in Fig. 2, is a kernel method, and prediction of $\tilde{y}$ at an arbitrary input point $\mathbf{d}$ can be expressed as

$$\tilde{y}(\mathbf{d}) = \sum_{m=1}^{M} w_m k(\mathbf{d}, \mathbf{d}_m), \tag{20}$$

where M is a set of representative points and k is a kernel function, responsible for defining a similarity between two data points. A key ingredient in fitting the weights $\mathbf{w}$ is the use of regularization, formulated as an additional penalty term in the least squares problem

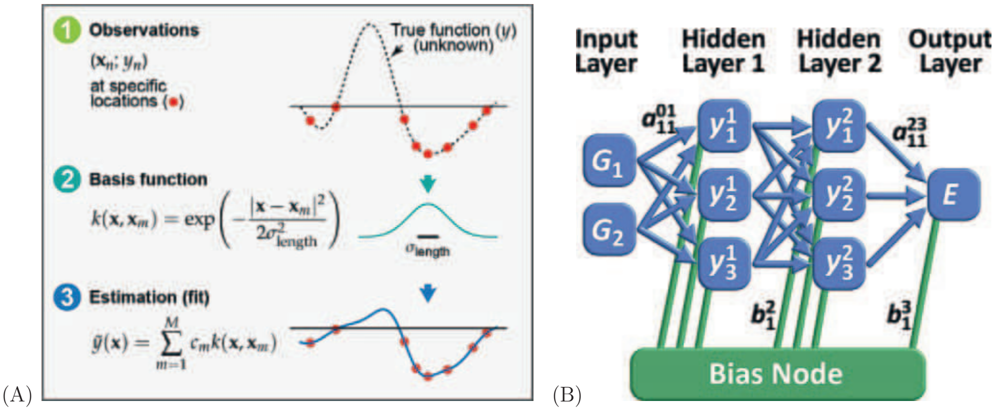

Fig. 2 Left panel (A): schematic of GPR. Right panel (B): a simple, fully connected neural network architecture. Figure (A) reproduced from Deringer VL, Bartók AP, Bernstein N, Wilkins DM, Ceriotti M, and Csányi G (2021) Gaussian process regression for materials and molecules. *Chemical Reviews* 121(16):10073–10141. doi: 10.1021/acs.chemrev.1c00022. http://eutils.ncbi.nlm.nih.gov/entrez/eutils/elink.fcgi?dbfrom=pubmed&id=34398616&retmode=ref&cmd=prlinks, licensed under the CC-BY 4.0 License. Figure (B) reprinted with permission from Behler J (2021) Four generations of high-dimensional neural network potentials. *Chemical Reviews* 121(16):10037–10072. ISSN 0009-2665. doi: 10.1021/acs.chemrev.0c00868. Copyright 2021 American Chemical Society.

$$R = \sum_{m,m'} w_m k(\mathbf{d}_m, \mathbf{d}_{m'}) w_{m'} \tag{21}$$

that is responsible for avoiding overfitting (Mackay, 2003). Non-linearity is introduced by the kernel function, also allowing the coupling of different descriptor elements, thereby increasing the effective body-order of the energy term, although not eliminating completely the issues caused by the incompleteness of descriptors (Pozdnyakov et al., 2020). Successful MLIP frameworks based on GPR include the Gaussian Approximation Potentials (GAP) (Bartók et al., 2010), symmetric Gradient Domain Machine Learning (sGDML) (Chmiela et al., 2019), or the interpolation scheme based on reproducing kernel Hilbert space by Koner and Meuwly (2020).

An alternative method that has been widely adopted is the regression technique based on artificial neural networks (ANNs). In this context, the mathematical form of ANNs is described by layers, where $\mathbf{y}^{\mathrm{k}}$ is the vector describing the k-th layer. Each layer is obtained from the previous one according to the formula

$$y_i^{k+1} = f\left(b_i^k + \sum_j^{n_k} W_{ij}^k y_j^k\right) \tag{22}$$

where $\mathbf{b}^{\mathrm{k}}$ and $\mathbf{W}^{\mathrm{k}}$ are free parameters called bias and weight, respectively; and f is the *activation* function (Mackay, 2003). Recursive evaluation of (22) with the descriptor vectors as the input layer $\mathbf{y}^0$ and the local energy terms ε as the output layer defines the functional form of the MLIP. A sketch of a simple ANN on Fig. 2 illustrates the interconnected nature of this construction. Similarly to kernel methods, a non-linear activation function f is responsible for mixing information from different descriptor elements, allowing the representation of higher body interactions. The fitting is performed by minimizing the difference between the predicted and ab initio reference properties with respect to the free parameters, a process which has been considerably streamlined in the last two decades (Nielsen, 2015).

Many MLIP frameworks are based on ANNs, for example the neural network potentials originally developed by Behler and Parrinello (Behler and Parrinello, 2007, Behler, 2021), SchNet (Schütt et al., 2018), SpookyNet (Unke et al., 2021), ANI (Smith et al., 2017), DeepMD (Zhang et al., 2018) or PhysNet (Unke and Meuwly, 2019) among others.

Data generation

A significant aspect of fitting MLIPs is generating the ab initio reference database. Unlike other applications in ML which operate with a fixed *training* data set, we can relatively easily choose data points and expand the original data set as required. Even the seminal work of Behler and Parrinello used an iterative approach to train a neural network potential, starting with an MLIP fitted on a data set obtained from configurations collected using ab initio MD. Performing subsequent MD, Monte Carlo and metadynamics (Laio and Parrinello, 2002) calculations using MLIPs, new configurations were added to the training set, and this procedure was repeated until a desired accuracy was achieved.

The problem of iterative database generation highlights the interpolative nature of MLIPs, as predictions that are concerning atomic environments outside of the fitting domain are uncontrolled. While most approaches suggest uncertainty quantification, which can be based on Bayesian error prediction available for GPR or ensemble techniques which are applicable to any fitting method, the primary aim is ascertain a ML model that is reliable across phases and includes defects, surfaces or any structural feature of interest. An attempt to generate a general MLIP for silicon was presented by Bartók et al. (2018), which necessitated a carefully assembled database that covered multiple crystalline, liquid and amorphous phases; surfaces; defects; as well as high-energy, unrealistic configurations which serve to avoid the ML model predicting unphysically low energy to "unseen" configurations. While useful to demonstrate the possibilities and potential accuracy of the MLIPs, it is clear that more automated protocols are required to reliably generate reference databases.

Later approaches include preforming quenches from high-temperature liquid to amorphous states in an iterative fashion, bootstrapping from a direct ab initio simulation, and continuing with MLIPs, adding configurations to the reference database if the accuracy of the ML property prediction compared to ab initio is above a predefined threshold (Deringer and Csányi, 2017). A similar iterative process, based on random structure search was suggested by Bernstein et al. (2019).

Active learning, where feedback from uncertainty quantification is used to select new training configurations offer a further step of automation was suggested by Gubaev et al. (2019), Jinnouchi et al. (2019), Smith et al. (2018), and Vandermause et al. (2020). In these frameworks a seamless switching between MD driven by a MLIP and ab initio calculations is realized that automatically computes new reference points and refits the MLIP as required.

Applications

With MLIPs being established as direct substitutes of ab initio MD simulations, the list of applications cannot be complete, so I will only focus on a few examples, which illustrate problems where ab initio accuracy was needed, but had been impractical before surrogate models based on ML were developed.

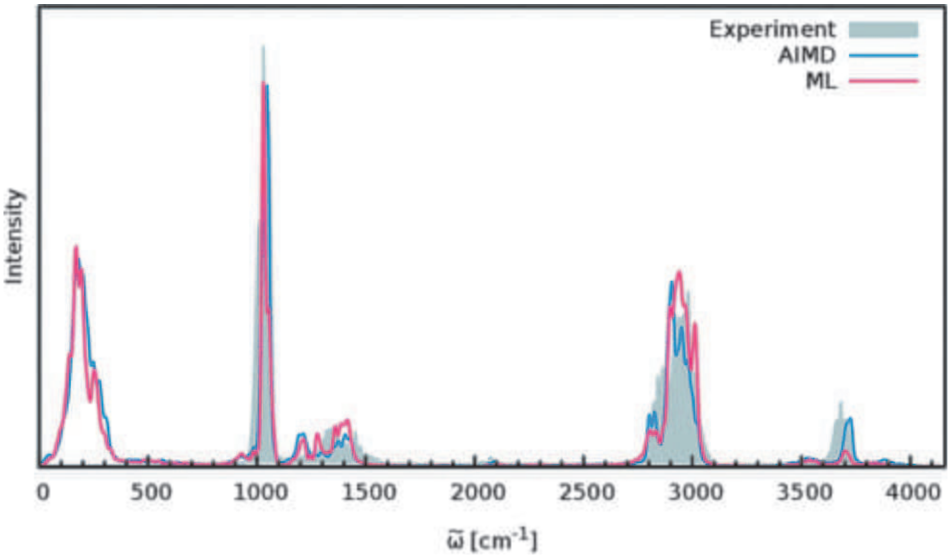

Fig. 3 Experimental (grey area) and simulated (DFT and MLIP, blue and red lines, respectively) IR spectrum of methanol. Figure reproduced from Gastegger M, Behler J, and Marquetand P (2017) Machine learning molecular dynamics for the simulation of infrared spectra. *Chemical Science* 8(10): 6924–6935. ISSN 2041-6520. doi: 10.1039/c7sc02267k, licensed under the CC-BY 4.0 License.

Organic molecules

A high-dimensional neural network potential was fitted by Gastegger et al. (2017) to model organic molecules, including the charge distribution. The Fourier transform of the dipole moment autocorrelation function, obtained from MD simulations, is proportional to the infrared (IR) spectrum. Gastegger et al. have shown that the results calculated from MLIP trajectories not only match those from ab initio simulations, but fit experiments very closely, as shown in Fig. 3.

While for such a small molecule as methane a benchmark calculation comparing the MLIP model to the reference ab initio method is feasible, it follows naturally that much larger systems are only available to model using the MLIP.

Water

Water has an exceptionally complex phase diagram, which has been a long-standing challenge to reproduce by computer simulations. Extensive sampling is required to map out the phase stability lines, which is impractical by ab initio MD due to the computational expense of such calculations. On the other hand, phase diagrams predicted using traditional interatomic potentials for water, such as the TIP4P/Ice model, are found to be inaccurate, especially at high pressures (Bore et al., 2022). Zhang et al. (2021) fitted a highly accurate Deep Potential model for water to construct a phase diagram with ab initio accuracy, which approximates the experimental phase diagram significantly closer, in a much broader range. Apart from validating the MLIP, the excellent agreement between the simulated and experimental phase diagrams highlight the accuracy of the reference DFT method, at an affordable computational cost.

Amorphous silicon

Determining realistic structural models of amorphous materials on the atomic level is challenging as characterization techniques lack the resolution to resolve the atomistic details of disordered structures. Simulations mimicking the experimental conditions at which amorphous compounds form require long time scales, which are require to model experimentally achievable cooling rates.

To model disorder on a sufficiently large length scale, large system sizes are needed. Direct ab initio simulations are out of reach, but ab initio may be required to generate realistic structural models that reproduce experimental observations. Deringer et al. (2020) showed that traditional interatomic potentials suggested for silicon are inadequate to model the liquid-amorphous transition. The authors used the GAP silicon model by Bartók et al. to model the formation of amorphous silicon in simulation cells containing 100,000 atoms at a cooling rate of 10^{11} Ks^{-1}. Pressurization simulations of the amorphous silicon structures further revealed the previously unknown mechanism of crystallization through a very high density amorphous phase.

Further use of machine learning in molecular dynamics

In addition to generating trajectories in a reliable and predictive fashion, ML tools assist studies based on MD in several ways. Firstly, often a vast amount of data is generated, which needs to be analyzed and interpreted. In addition to quantities traditionally used to characterize atomic configurations, such as radial and angular distribution functions or bond order parameters (Steinhardt et al., 1983), descriptors combined with unsupervised learning techniques can be applied. Dimensionality reduction techniques help visualization and classification of atomic configurations or atomic neighborhood environments (Cheng et al., 2020; Shires and

Pickard, 2021). Closely related, ML techniques can be used to discover patterns, for example Bonati et al. (2021) used deep learning to automatically find collective variables describing slow modes in MD simulations. By using enhanced sampling based on such collective variables, rare events can be modelled more efficiently. Noé et al. (2019) showed that ML may be used to bypass MD altogether in sampling configurations, by employing Boltzmann generators to create representative samples without running costly MD simulations. As an alternative to using Newton's laws of motion to propagate trajectories in time, *Deeptime* (Hoffmann et al., 2022) implements methods that predict the state of a system based on an earlier instance.

Conclusion

In this entry to the encyclopedia, I have provided a bird's-eye view of the state of using machine learning techniques to enhance molecular dynamics simulations. Given the dynamic nature of the field, my contribution cannot be regarded as complete, and the methods mentioned here are only intended as an illustration of the current state of the field. With pointers to more specific reviews and original publications, the reader should be able to orient themselves and get started.

Being very much an active area of research, I have largely omitted from the entry the current efforts to treat long-range interactions. I have not discussed efficiency, apart from contrasting the favorable linear scaling of MLIPs to the cubic scaling of plane-wave DFT and higher order of quantum chemistry approaches. There is a strong ongoing effort in the community to improve the speed of MLIPs without compromising the accuracy, which will enable even larger scale and hence more realistic simulations.

Like ML in general, ML applications for MD are under constant development, with the field expanding every day. However, the last two decades have shown the viability of MLIPs and other ML techniques used in simulations, which I hope I managed to convey in this entry.

References

Adamowicz L and Pavanello M (2012) Progress in calculating the potential energy surface of H3. *Philosophical Transactions of the Royal Society A: Mathematical, Physical and Engineering Sciences* 370(1978): 5001–5013. https://doi.org/10.1098/rsta.2012.0101. ISSN 1364-503X.

Bartók AP, Payne MC, Kondor R, and Csányi G (2010) Gaussian approximation potentials: the accuracy of quantum mechanics, without the electrons. *Physical Review Letters* 104(13). https://doi.org/10.1103/physrevlett.104.136403. 136403.

Bartók AP, Kondor R, and Csányi G (2013) On representing chemical environments. *Physical Review B* 87(18). https://doi.org/10.1103/physrevb.87.184115. 184115. ISSN 1550-235X.

Bartók AP, Kermode J, Bernstein N, and Csányi G (2018) Machine learning a general-purpose interatomic potential for silicon. *Physical Review X* 8(4): 041048. https://doi.org/10.1103/physrevx.8.041048. ISSN 2160-3308.

Becke AD (2014) Perspective: Fifty years of density-functional theory in chemical physics. *The Journal of Chemical Physics* 140(18). https://doi.org/10.1063/1.4869598. URL. 18A301. ISSN 0021-9606.

Behler J (2021) Four generations of high-dimensional neural network potentials. *Chemical Reviews* 121(16): 10037–10072. https://doi.org/10.1021/acs.chemrev.0c00868. ISSN 0009-2665.

Behler J and Parrinello M (2007) Generalized neural-network representation of high-dimensional potential-energy surfaces. *Physical Review Letters* 98(14). https://doi.org/10.1103/PhysRevLett.98.146401. 146401.

Bernstein N, Csányi G, and Deringer VL (2019) De novo exploration and selfguided learning of potential- energy surfaces. *npj Computational Materials* 5(1): 1–9. https://doi.org/10.1038/s41524-019-0236-6. ISSN 2057-3960.

Bonati L, Zhang Y-Y, and Parrinello M (2019) Neural networks-based variationally enhanced sampling. *Proceedings of the National Academy of Sciences* 116(36): 17641–17647. https://doi.org/10.1073/pnas.1907975116. ISSN 0027-8424.

Bonati L, Piccini G, and Parrinello M (2021) Deep learning the slow modes for rare events sampling. *Proceedings of the National Academy of Sciences* 118(44). https://doi.org/10.1073/pnas.2113533118. e2113533118. ISSN 0027-8424.

Bore SL, Piaggi PM, Car R, and Paesani F (2022) Phase diagram of the TIP4P/Ice water model by enhanced sampling simulations. *The Journal of Chemical Physics* 157(5). https://doi.org/10.1063/5.0097463. 054504. ISSN 0021-9606.

Brommer K, Needels M, Larson B, and Joannopoulos J (1992) Ab initio theory of the Si(111)-(7 x 7) surface reconstruction: A challenge for massively parallel computation. *Physical Review Letters* 68(9): 1355–1358. http://eutils.ncbi.nlm.nih.gov/entrez/eutils/elink.fcgi?dbfrom=pubmed&id=10046145&retmode=ref&cmd=prlinks.

Cao J and Berne BJ (1992) Many-body dispersion forces of polarizable clusters and liquids. *The Journal of Chemical Physics* 97(11): 8628–8636. https://doi.org/10.1063/1.463381. ISSN 0021-9606.

Car R and Parrinello M (1985) Unified approach for molecular-dynamics and density-functional theory CC-BY 4.0 License. *Physical Review Letters* 55(22): 2471–2474. http://link.aps.org/doi/10.1103/PhysRevLett.55.2471. https://creativecommons.org/licenses/by/4.0/.

Cheng B, Griffiths R-R, Wengert S, Kunkel C, Stenczel T, Zhu B, Deringer VL, Bernstein N, Margraf JT, Reuter K, and Csányi G (2020) Mapping Materials and Molecules. *Accounts of Chemical Research* 53(9): 1981–1991. https://doi.org/10.1021/acs.accounts.0c00403. ISSN 0001-4842.

Chmiela S, Sauceda HE, Poltavsky I, Müller K-R, and Tkatchenko A (2019) sGDML: Constructing accurate and data efficient molecular force fields using machine learning. *Computer Physics Communications* 240: 38–45. https://doi.org/10.1016/j.cpc.2019.02.007.

Daw M and Baskes M (1983) Semiempirical, quantum-mechanical calculation of hydrogen embrittlement in metals. *Physical Review Letters* 50(17): 1285–1288. http://link.aps.org/doi/10.1103/PhysRevLett.50.1285.

Deringer VL and Csányi G (2017) Machine learning based interatomic potential for amorphous carbon. *Physical Review B* 95(9). https://doi.org/10.1103/physrevb.95.094203. 094203–15. ISSN 2469-9950.

Deringer VL, Bernstein N, Csányi G, Mahmoud C, Ceriotti M, Wilson M, Drabold DA, and Elliott SR (2020) Origins of structural and electronic transitions in disordered silicon. *Nature* 1–19. https://doi.org/10.1038/s41586-020-03072-z.

Deringer VL, Bartók AP, Bernstein N, Wilkins DM, Ceriotti M, and Csányi G (2021) Gaussian Process Regression for Materials and Molecules. *Chemical Reviews* 121(16): 10073–10141. https://doi.org/10.1021/acs.chemrev.1c00022. http://eutils.ncbi.nlm.nih.gov/entrez/eutils/elink.fcgi?dbfrom=pubmed&id=34398616&retmode=ref&cmd=prlinks.

Drautz R (2019) Atomic cluster expansion for accurate and transferable interatomic potentials. *Physical Review B* 99(1): 1–15. https://doi.org/10.1103/physrevb.99.014104. ISSN 2469-9950.

Essmann U, Perera L, Berkowitz ML, Darden T, Lee H, and Pedersen LG (1995) A smooth particle mesh Ewald method. *The Journal of Chemical Physics* 103(19): 8577–8593. https://doi.org/10.1063/1.470117. ISSN 0021-9606.

Finnis MW and Sinclair JE (1984) A simple empirical N-body potential for transition metals. *Philosophical Magazine A* 50(1): 45–55. https://doi.org/10.1080/01418618408244210. ISSN 1460-6992.

Frenkel D and Smit B (2002) *Understanding Molecular Simulation: From Algorithms to Applications*, 2nd edn *Volume 1 of* Computational Science Series2nd edn, San Diego: Academic Press.

Gastegger M, Behler J, and Marquetand P (2017) Machine learning molecular dynamics for the simulation of infrared spectra. *Chemical Science* 8(10): 6924–6935. https://doi.org/10.1039/c7sc02267k. ISSN 2041-6520.

Gubaev K, Podryabinkin EV, Hart GLW, and Shapeev AV (2019) Accelerating high-throughput searches for new alloys with active learning of interatomic potentials. *Computational Materials Science* 156: 148–156. https://doi.org/10.1016/j.commatsci.2018.09.031.

Hoffmann M, Scherer M, Hempel T, Mardt A, de Silva B, Husic BE, Klus S, Wu H, Kutz N, Brunton SL, and Noé F (2022) Deeptime: A Python library for machine learning dynamical models from time series data. *Machine Learning: Science and Technology* 3(1). https://doi.org/10.1088/2632-2153/ac3de0. 015009.

Jinnouchi R, Lahnsteiner J, Karsai F, Kresse G, and Bokdam M (2019) Phase transitions of hybrid perovskites simulated by machine-learning force fields trained on the fly with Bayesian inference. *Physical Review Letters* 122(22): 225701. https://doi.org/10.1103/physrevlett.122.225701. ISSN 0031-9007.

Jones JE (1924) On the determination of molecular fields.—I. From the variation of the viscosity of a gas with temperature. *Proceedings of the Royal Society of London. Series A, Containing Papers of a Mathematical and Physical Character* 106(738): 441–462. https://doi.org/10.1098/rspa.1924.0081. ISSN 0950-1207.

Koner D and Meuwly M (2020) Permutationally Invariant, Reproducing Kernel-Based Potential Energy Surfaces for Polyatomic Molecules: From Formaldehyde to Acetone. *Journal of Chemical Theory and Computation* 16(9): 5474–5484. https://doi.org/10.1021/acs.jctc.0c00535. ISSN 1549-9618.

Laio A and Parrinello M (2002) Escaping free-energy minima. *Proceedings of the National Academy of Sciences* 99(20): 12562–12566. https://doi.org/10.1073/pnas.202427399. http://eutils.ncbi.nlm.nih.gov/entrez/eutils/elink.fcgi?dbfrom=pubmed&id=12271136&retmode=ref&cmd=prlinks.

Mackay D (2003) *Information Theory, Inference, and Learning Algorithms*. Cambridge University Press.

Martin RM (2004) *Electronic Structure: Basic Theory and Practical Methods*. Cambridge University Press. https://doi.org/10.1017/CBO9780511805769.

Marx D and Parrinello M (1996) Ab initio path integral molecular dynamics: Basic ideas. *The Journal of Chemical Physics* 104(11): 4077–4082. https://doi.org/10.1063/1.471221. ISSN 0021-9606.

Musil F, Grisafi A, Bartók AP, Ortner C, Csányi G, and Ceriotti M (2021) Physics-inspired structural representations for molecules and materials. *Chemical Reviews* 121(16): 9759–9815. https://doi.org/10.1021/acs.chemrev.1c00021. http://eutils.ncbi.nlm.nih.gov/entrez/eutils/elink.fcgi?dbfrom=pubmed&id=34310133&retmode=ref&cmd=prlinks.

Nielsen MA (2015) *Neural Networks and Deep Learning*. Determination Press.

Noé F, Olsson S, Köhler J, and Wu H (2019) Boltzmann generators: Sampling equilibrium states of many-body systems with deep learning. *Science* 365(6457). https://doi.org/10.1126/science.aaw1147. ISSN 0036-8075.

Partridge H and Schwenke DW (1997) The determination of an accurate isotope dependent potential energy surface for water from extensive ab initio calculations and experimental data. *The Journal of Chemical Physics* 106(11): 4618. https://doi.org/10.1063/1.473987. ISSN 00219606. http://link.aip.org/link/JCPSA6/v106/i11/p4618/s1&Agg=doi.

Payne M, Teter M, Allan D, Arias T, and Joannopoulos J (1992) Iterative minimization techniques for abinitio total-energy calculations - molecular-dynamics and conjugate gradients. *Reviews of Modern Physics* 64(4): 1045–1097. http://links.isiglobalnet2.com/gateway/Gateway.cgi?GWVersion=2&SrcAuth=mekentosj&SrcApp=Papers&DestLinkType=FullRecord&DestApp=WOS&KeyUT=A1992JV36300004.

Pizzagalli L, Godet J, Guénolé J, Brochard S, Holmstrom E, Nordlund K, and Albaret T (2013) A new parametrization of the Stillinger–Weber potential for an improved description of defects and plasticity of silicon. *Journal of Physics: Condensed Matter* 25(5): 055801. https://doi.org/10.1088/0953-8984/25/5/055801. ISSN 0953-8984.

Pozdnyakov SN, Willatt MJ, Bartók AP, Ortner C, Csányi G, and Ceriotti M (2020) Incompleteness of atomic structure representations. *Physical Review Letters* 125(16). https://doi.org/10.1103/physrevlett.125.166001. 166001.

Prodan E and Kohn W (2005) Nearsightedness of electronic matter. *Proceedings of the National Academy of Sciences* 102(33): 11635–11638. https://doi.org/10.1073/pnas.0505436102.

Richard RM, Lao KU, and Herbert JM (2014) Understanding the many-body expansion for large systems. I. Precision considerations. *The Journal of Chemical Physics* 141(1). https://doi.org/10.1063/1.4885846. 014108. ISSN 0021-9606.

Schütt KT, Sauceda HE, Kindermans PJ, Tkatchenko A, and Müller KR (2018) SchNet – A deep learning architecture for molecules and materials. *The Journal of Chemical Physics* 148(24). https://doi.org/10.1063/1.5019779. 241722–12. ISSN 0021-9606.

Shapeev AV (2016) Moment tensor potentials: A class of systematically improvable interatomic potentials. *Multiscale Modeling and Simulation* 14(3): 1153–1173. https://doi.org/10.1137/15m1054183. ISSN 1540-3459.

Shires BWB and Pickard CJ (2021) Visualizing energy landscapes through manifold learning. *Physical Review X* 11(4). https://doi.org/10.1103/physrevx.11.041026. 041026.

Smith JS, Isayev O, and Roitberg AE (2017) ANI-1: An extensible neural network potential with DFT accuracy at force field computational cost. *Chemical Science* 8(4): 3192–3203. https://doi.org/10.1039/c6sc05720a. ISSN 2041-6520.

Smith JS, Nebgen B, Lubbers N, Isayev O, and Roitberg AE (2018) Less is more: Sampling chemical space with active learning. *The Journal of Chemical Physics* 148(24): 241733. https://doi.org/10.1063/1.5023802. ISSN 0021-9606.

Steinhardt P, Nelson D, and Ronchetti M (1983) Bond-orientational order in liquids and glasses. *Physical Review B* 28(2): 784. http://prb.aps.org/abstract/PRB/v28/i2/p784_1.

Stillinger FH and Weber TA (1985) Computer simulation of local order in condensed phases of silicon. *Physical Review B* 31(8): 5262–5271. http://prb.aps.org/abstract/PRB/v31/i8/p5262_1.

Tersoff J (1988) Empirical interatomic potential for silicon with improved elastic properties. *Physical Review B* 38(14): 9902–9905. http://ukpmc.ac.uk/abstract/MED/9945814.

Thompson KC, Crittenden DL, and Jordan MJT (2005) CH5 +: Chemistry's chameleon unmasked. *Journal of the American Chemical Society* 127(13): 4954–4958. https://doi.org/10.1021/ja0482280. ISSN 0002-7863.

Thompson AP, Swiler LP, Trott CR, Foiles SM, and Tucker GJ (2015) Spectral neighbor analysis method for automated generation of quantum-accurate interatomic potentials. *Journal of Computational Physics* 285(C): 316–330. https://doi.org/10.1016/j.jcp.2014.12.018.

Unke OT and Meuwly M (2019) PhysNet: A neural network for predicting energies, forces, dipole moments, and partial charges. *Journal of Chemical Theory and Computation* 15(6): 3678–3693. https://doi.org/10.1021/acs.jctc.9b00181. ISSN 1549-9618.

Unke OT, Chmiela S, Gastegger M, Schütt KT, Sauceda HE, and Müller K-R (2021) *SpookyNet: Learning force fields with electronic degrees of freedom and nonlocal effects*. *Springer US*.1–14. https://doi.org/10.1038/s41467-021-27504-0. https://www.nature.com/articles/s41467-021-27504-0.pdf.

Vandermause J, Torrisi SB, Batzner S, Xie Y, Sun L, Kolpak AM, and Kozinsky B (2020) On-the-fly active learning of interpretable Bayesian force fields for atomistic rare events. *npj Computational Materials* 6(1): 1–11. https://doi.org/10.1038/s41524-020-0283-z. ISSN 2057-3960.

Zhang L, Han J, Wang H, Car R, and W. E. (2018) Deep Potential Molecular Dynamics: A Scalable Model with the Accuracy of Quantum Mechanics. *Physical Review Letters* 120(14): 143001. https://doi.org/10.1103/physrevlett.120.143001. ISSN 0031-9007.

Zhang L, Wang H, Car R, and W. E. (2021) Phase diagram of a deep potential water model. *Physical Review Letters* 126(23). https://doi.org/10.1103/physrevlett.126.236001. 236001.

Zuo Y, Chen C, Li X, Deng Z, Chen Y, Behler J, Csányi G, Shapeev AV, Thompson AP, Wood MA, and Ong SP (2020) Performance and cost assessment of machine learning interatomic potentials. *The Journal of Physical Chemistry. A* 124(4): 731–745. https://doi.org/10.1021/acs.jpca.9b08723. ISSN 1089-5639.

Materials informatics with machine learning

T Miyake and Y Ando, National Institute of Advanced Industrial Science and Technology, Tsukuba, Japan

© 2024 Elsevier Ltd. All rights reserved.

Introduction 553
Computational screening 553
Machine learning 554
Descriptor 555
Machine-learning potentials 556
Bayesian optimization 557
Gaussian process regression 557
Acquisition functions 558
Conclusion 558
References 558

Abstract

Materials Informatics is a research field in materials science and engineering that is based on data-driven methods. Materials informatics can accelerate materials research and help to gain a deeper understanding of materials. Machine learning is used to analyze materials data obtained by various computational or experimental means and to predict material properties.

Key points

- Machine-learning-aided computational screening for materials discovery
- Basic machine-learning techniques
- Machine-learning potential as a surrogate of first-principles calculations
- Bayesian optimization for efficiently exploring good candidates

Introduction

Over the past 100 years, numerous material data have been reported by researchers around the world. These data include atomic, molecular, and crystal structures, electronic states (density of states, band structure, etc.), and physical properties (optical, electrical, magnetic, mechanical, etc.). These literature data have been collected and various material databases were constructed. In addition, computer simulation methods, mainly first-principles electronic structure calculations, have been developed which makes it possible to create systematic computational data. The Materials Project, the Open Quantum Materials Database (OQMD), Automatic FLOW for Materials Discovery (AFLOW) and the Novel Materials Discovery (NOMAD) are among the well-known computational materials science databases.

These big data have enabled data-driven approaches in materials science. For example, high-throughput first-principles calculations for various crystal structures and chemical compositions are becoming a conventional tool to search for materials exhibiting desired properties. Machine learning is a powerful technique to accelerate this screening process. Another use of machine learning is to obtain useful information (e.g., controlling factors for material properties) from available data. Applications of machine learning are expanding into experimental measurement and synthesis.

Computational screening

First-principles calculations based on the density functional theory (DFT) are the standard method for quantitatively describing material properties. By inputting the chemical composition and initial structure, the optimized structure, total energy, band dispersion, density of states, and various other physical quantities (formation energy, bulk modulus, phonon dispersion, electrical conductivity, optical absorption spectrum, magnetic moment, dielectric function, etc.) can be calculated numerically. Since first-principles calculations are non-empirical methods, they can deal with not only existing materials but also hypothetical materials and predict their properties.

Advances in methodology, algorithms, and computer hardware have enabled exhaustive first-principles calculations for a wide variety of conditions. Typically, hundreds to tens of thousands of structural and chemical composition calculations can be

https://doi.org/10.1016/B978-0-323-90800-9.00198-0

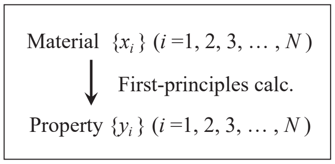
Material $\{x_i\}$ $(i=1, 2, 3, \ldots, N)$
First-principles calc.
Property $\{y_i\}$ $(i=1, 2, 3, \ldots, N)$

Fig. 1 Workflow of direct screening using first-principles calculation.

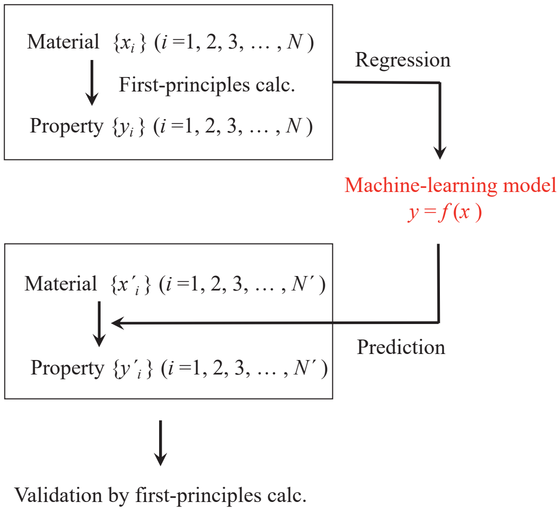
Material $\{x_i\}$ $(i=1, 2, 3, \ldots, N)$
First-principles calc.
Property $\{y_i\}$ $(i=1, 2, 3, \ldots, N)$
Regression
Machine-learning model
$y=f(x)$
Material $\{x'_i\}$ $(i=1, 2, 3, \ldots, N')$
Property $\{y'_i\}$ $(i=1, 2, 3, \ldots, N')$
Prediction
Validation by first-principles calc.

Fig. 2 Workflow of virtual screening using first-principles calculation and machine learning.

performed. By comparing the results of these calculations, the best material with the highest score for a given task can be found. This is called direct screening (Fig. 1). Direct screening has become a common method for material search since the beginning of the 2010s. For example, Nishijima et al. carried out direct screening of cathode materials for lithium-ion batteries (Nishijima et al., 2014). They performed first-principles calculations of thousands of materials for 630 compositions, based on the hypothesis that volume changes associated with lithium charging and discharging affect the cycle life, and proposed $Li(Fe_{1-x}Zr_x)(P_{1-2x}Si_{2x})O_4$. Experimental tests showed that the cycle life of the cell containing the proposed cathode outperforms the cell containing the standard cathode by a factor of 5.

While it is possible to perform first-principles calculations for more than a few thousand materials, the computational cost is high. Virtual screening speeds up screening by utilizing machine learning (Fig. 2). Suppose we have computational data $\{x^{(i)}, y^{(i)}\}$ $(i = 1, 2, \ldots, N)$, where $x^{(i)}$ is the i-th material, $y^{(i)}$ is its property and N is the number of the data. We construct a machine learning model $y = f(x)$ from the data. The model is then used to screen materials and select candidate materials. Screening by machine learning is much faster than direct screening but has limitations in prediction accuracy. Therefore, in the final stage of virtual screening, the properties of the narrowed-down candidate materials are calculated using first-principles calculations to validate the results.

Machine learning

There are several techniques in machine learning. Clustering divides given data into several groups (Fig. 3). Classification is another technique that divides data into groups. In classification, each group is pre-labeled. For example, classification into gases, liquids, and solids, or metals and insulators. In the case of clustering as shown in Fig. 3, on the other hand, we do not know what A, B, and C mean. Therefore, clustering is an unsupervised learning, while classification is classified as supervised learning.

Regression is a supervised learning technique that uses statistical methods to estimate the relationship between the independent variable (explanatory variable) and the dependent variable (objective variable). The former is the variable of interest, and the latter is the variable used to explain it. For example, suppose we are now interested in the property y of the material $\boldsymbol{x} = (x_1, x_2, \ldots, x_d)$. Here, $\boldsymbol{x}$ is a numerical representation of the material and is called descriptor in materials informatics. The objective of the regression is to find the relationship $y = f(\boldsymbol{x})$ (Fig. 4). Various regression methods exist, including linear regression, neural network, kernel method, random forest, and support vector regression. The simplest model is a linear model represented as follows,

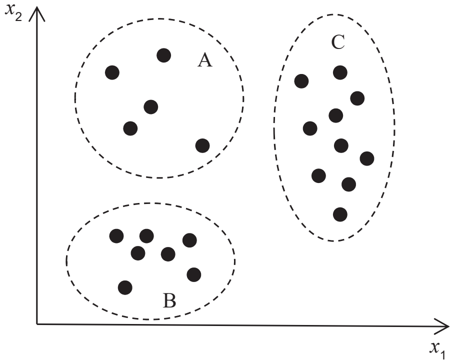

Fig. 3 Example of clustering. Data (black circles) on a two-dimensional (x_1–x_2) plane are divided into three groups, A, B and C.

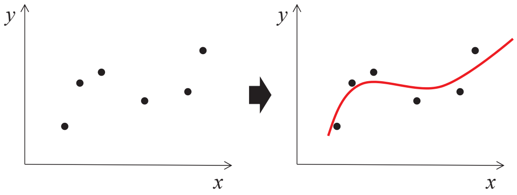

Fig. 4 Regression is a technique for estimating the relationship between the independent variable *x* and the dependent variable *y*. Dots represent data points and the red curve is a regression curve.

$$y = w_0 + w_1 x_1 + w_2 x_2 + \ldots + w_d x_d.$$

Here, the parameters $\boldsymbol{w} = (w_0, w_1, w_2, \ldots, w_d)$ are determined so that the loss function,

$$L = \sum_{i=1}^{N} \left\{ y^{(i)} - f\left(\boldsymbol{x}^{(i)}\right) \right\}^2,$$

is minimized. (The term linear means linear with respect to the parameter $\boldsymbol{w}$. A linear model need not be linear with respect to the variable $\boldsymbol{x}$.)

One measure of the accuracy of a machine-learning model is the coefficient of determination R^2, defined as

$$R^2 = 1 - \frac{\sum_{i=1}^{N} \{y^{(i)} - f(\boldsymbol{x}^{(i)})\}^2}{\sum_{i=1}^{N} \{y^{(i)} - \bar{y}\}^2},$$

where $\bar{y}$ is the average of $y^{(i)}$ with respect to i. The maximum value of R^2 is 1. The larger R^2 is, the better the data is reproduced.

If more parameters than the number of data are provided, the data can be reproduced perfectly. However, a model that perfectly fits data containing noise behaves in a complex manner and does not have high predictive power for $\boldsymbol{x}$ not included in the data. This problem is called overfitting. A desirable model (a highly predictive model) is one that is simple and reproduces the existing data. Regularization is used to construct such a model. Taking a linear model as an example, we add a second term on the right-hand side of the following equation,

$$L = \sum_{i=1}^{N} \left\{ y^{(i)} - f\left(\boldsymbol{x}^{(i)}\right) \right\}^2 + \lambda \sum_{j=1}^{d} |w_j|^p,$$

where λ is a hyperparameter. Hyperparameters are parameters that are predetermined before the model is trained. When $p = 2$, it is called a ridge, and a linear regression with $p = 1$ is called "Least Absolute Shrinkage and Selection Operator (LASSO)" regression. In LASSO, certain coefficients are forced to zero, effectively selecting a simpler model that does not include these coefficients.

Descriptor

The numerical representation of materials is not unique. Therefore, the design of descriptors adapted for predictions is a major challenge in materials informatics. A simple example of a descriptor is as follows. Consider a binary material *AB* composed of elements *A* and *B*. Using the properties of the element *A*, e.g., atomic number Z_A, ionic radius R_A, ionization energy I_A, and similar quantities of the element *B*, Z_B, R_B, I_B, the material *AB* can be represented as $(Z_A, R_A, I_A, Z_B, R_B, I_B)$. In general, a material descriptor has multiple components. Extracting the important descriptors from these is an important issue for understanding the controlling factors of material properties.

In materials simulation, the design of descriptors related to atomic structure is generally important. Conventionally, atomic structures are represented in crystalline or Cartesian coordinates. However, this is not suitable for machine learning with structural information as input. This is because the coordinates vector is variable with respect to symmetry operations. For example, the total energy for an atomic configuration should be invariant to rotational and translational operations. However, when coordinates vector is used as descriptors, symmetry operations change their values, i.e., they are considered different data and will give a different energy. Therefore, descriptors must be invariant to symmetry operations. Additionally, dimension of the descriptor increases monotonically as the number of particles increases. In general, the more input dimensions there are, the more difficult machine learning becomes.

Instead, there are two types of atomic structure descriptors: system-wide descriptors and local descriptors. System-wide descriptors are often used to compare the total energy of molecules or crystals. For example, the simplified molecular input line entry system (SMILES) allows molecular structures to be represented as string series (Weininger, 1988). Molecular graphs are graph representations of molecular bonding networks. Several molecular fingerprints have also been proposed that encode the presence or absence of substructures in a molecular system.

Local descriptors, on the other hand, are well suited for molecular dynamics calculations with machine learning. Symmetry functions are typical examples of local descriptors. Symmetry functions (Behler and Parrinello, 2007, and Behler, 2015) quantify the structural information around an individual atom in a way that is invariant to symmetry operations. For example, the symmetry function for distance is expressed by the following equation,

$$G_i = \sum_{j\neq i}^{all\ atoms} e^{-\eta\left(R_{ij}-R_s\right)^2} \cdot f_c\left(R_{ij}\right),$$

where R_{ij} is the distance between atoms i and j, η and R_s are hyperparameters, and $f_c(r)$ is the cutoff function. This equation approximately represents the number of atoms in a spherical shell of radius R_s. The symmetry function vector, which combines the chosen symmetry functions of several hyperparameters and the symmetry function with respect to angles, is the descriptor around that atom as input of machine-learning potentials.

Machine-learning potentials

A machine learning potential is a surrogate model of first-principles calculations that uses atomic structure as input and outputs energy and forces acting on atoms. First-principles calculations based on DFT simulate total energy of a material and the forces nonempirically. On the other hand, the computational cost is typically proportional to the cube of the number of atoms, making it unsuitable for large-scale and complex systems such as catalytic reactions on surfaces or amorphous materials. Material simulations using classical potentials based on physical models are computationally efficient, but it is difficult to treat complex materials system with high accuracy. The machine learning potential is a solution that takes advantage of both benefits (Fig. 5).

There are various machine-learning models used to design the potentials. A typical example is the neural network potential, originally published in Behler and Parrinello (2007), which introduces a structural descriptor called symmetry functions as input and an architecture of neural network segmented by individual atoms. The symmetry functions are a descriptor that represents the local structure around atoms, which is invariant to the physically required translational and rotational symmetry. The symmetry functions are an important factor for the general-purpose neural network potentials. The error function for optimizing the model can be made more accurate by including force and virial coefficients as well as energy differences. ANI-1 potential proposed in Smith et al. (2017) targeting organic molecules also employs Behler-Parrinello type neural networks. Gaussian Approximation potential (Bartók et al., 2010) and moment tensor potential (Shapeev, 2016) are based on different regression approach. From an information-science perspective, MEGNet (Chen et al., 2019), M3GNet (Chen and Ong, 2022), and PreFerred Potential (Takamoto et al., 2022) based on graph neural networks have also been developed.

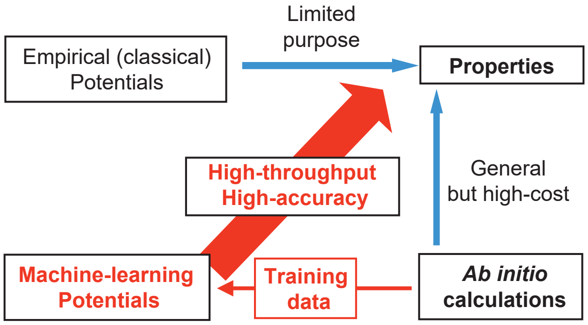
Empirical (classical) Potentials
Limited purpose
Properties
High-throughput High-accuracy
General but high-cost
Machine-learning Potentials
Training data
Ab initio calculations

Fig. 5 Concept of the machine learning potentials.

Bayesian optimization

Bayesian optimization (BO), also called Kriging or black box optimization, have been originally used to predict a best place where mineral resources would be found. Indeed, it is impossible to survey all land for mineral resources. Then, a strategy is required from the limited data to predict the best place where to survey next. BO is one of the techniques. Several applications have been reported in the field of materials science. For example, Fukazawa et al. studied the problem of finding superior compositions in terms of magnetization, Curie temperature, and formation energy for disordered phases of rare earth transition metal compounds (Fukazawa et al., 2019). The results showed that using Bayesian optimization, the probability of finding a composition that exhibits the top 10 properties out of 3630 compositions within 50 times is more than 95%, which is much more efficient than the random sampling case (12.9%).

Researchers often search for the best experimental conditions by grid search, which is time-consuming and requires a great deal of experience. Especially, novice researchers with new equipment have no choice but to spend a great deal to find the best conditions. Therefore, BO has attracted hot attention as a technique to overcome this problem. The essence of BO is to estimate the optimal next choice from the obtained data. It is not suitable for case with the low data accumulation cost, but it is powerful in cases where it is difficult to collect exhaustive data within a limited time and financial cost, such as in material search and process optimization for synthesis.

BO can be understood in terms of two important processes. One is "prediction from existing data" and the other is "evaluation of candidates based on the prediction results" (Fig. 6). The former is based on a nonparametric method commonly referred to as Gaussian process regression. Unlike the kernel regression, Gaussian process regression (GPR) is formulated based on probability theory, so it can simultaneously evaluate the ambiguity of the prediction or credibility. For the evaluation of candidates based on the prediction results, we use an "acquisition function" to evaluate the quality of candidates based on predictions and their ambiguity and suggests candidates for the next observation point. In the following subsections, GPR and acquisition functions are introduced in detail.

Gaussian process regression

Gaussian process regression (GPR) is a non-parametric regression technique based on probability theory. GPR uses a high-dimensional Gaussian distribution as the generator of the regression curve. For example, suppose that an N-dimensional vector is sampled from an N-dimensional Gaussian distribution. This vector can be regarded as a 1-dimensional point series. By controlling the correlation between the points, this 1D point series can be made to form a smooth curve. The function controlling the correlation between the points is called the kernel function.

In Gaussian process regression, the regression model is created using the conditional probabilities under observed data points. When a curve randomly generated from a high-dimensional Gaussian distribution is restricted under the constraint that passes through the observed points, the mean curve is the regression model, and the variance of the conditional random curve is defined as the interval of the credibility. Regression curve $E(x)$ and credibility interval $V(x)$ is expressed as follows:

$$E(x) = \mathbf{k}^T\left(\mathbf{K} + \sigma^2\mathbf{I}_n\right)^{-1}\mathbf{Y},$$

$$V(x) = k(x,x) - \mathbf{k}^T\left(\mathbf{K} + \sigma^2\mathbf{I}_n\right)^{-1}\mathbf{k},$$

where σ is an estimated error of the regression model, $\mathbf{I}_n$ is a n-dimensional identity matrix and $\mathbf{Y}$ is the vector of the obtained objective data, respectively. The vector $\mathbf{k}$ and matrix $\mathbf{K}$ are corresponding to the kernel function $k(x, y)$, and their elements are expressed by the following equations,

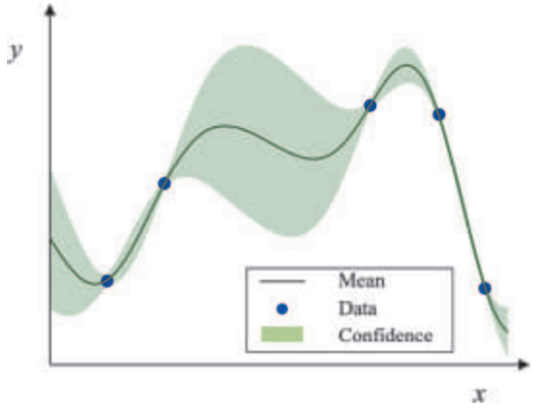

Fig. 6 Bayesian optimization determines the next search point by considering not only the mean value but also the probability distribution. The values of x, y respectively stand for a descriptor and a target variable.

$$k_i = \mathrm{k}(x_i, x), K_{ij} = k(\mathrm{x_i}, \mathrm{x_j}).$$

Acquisition functions

The acquisition function is an index for determining the next observation point. The Expected Improvement (EI) is a typical example of the acquisition function, which is the expectation value of improvement for target function y such as electronic conductivity. EI is given by following formula:

$$\mathrm{EI}(x) = \int_{-\infty}^{y_{\min}} dy(y_{\min} - y)N[E(x), V(x)],$$

where $y_{\min}$ is the minimum target value that have been already obtained, and N is normal distribution.

Another typical acquisition function is Lower confidence bound (LCB), which evaluates the next candidates taking the balance between exploration and exploitation into consideration. The basic strategy of the acquisition function for this minimization is to evaluate the point with the lowest expected value $E(x)$ of the objective function in terms of exploitation. In addition to this, from the perspective of exploration, the point where the prediction is ambiguous, i.e., the point where the credit interval (standard deviation) is large, is also considered. The acquisition of LCB is expressed as follows:

$$\mathrm{LCB}(x) = E(x) - \beta\sqrt{V(x)},$$

where β is the hyperparameter balancing the exploration and exploitation. In general, GP-UCB is often used where the parameters are automatically tuned.

Conclusion

Materials informatics has developed rapidly over the past decade. In the early days, the data handled by materials informatics were mainly computational data, but nowadays, data obtained by various experimental means are also treated. In general, the data available for materials development is limited, and the development of data creation techniques such as automated calculations and the introduction of robots is expected. In addition, the development of effective machine learning methods for small data and the utilization of materials expertise are also important issues.

References

Bartók AP, et al. (2010) Gaussian approximation potentials: The accuracy of quantum mechanics, without the electrons. *Physical Review Letters* 104: 136403.

Behler J (2015) Constructing high-dimensional neural network potentials: A tutorial review. *International Journal of Quantum Chemistry* 115: 1032–1050.

Behler J and Parrinello M (2007) Generalized neural-network representation of high-dimensional potential-energy surfaces. *Physical Review Letters* 98: 146401.

Chen C and Ong SP (2022) A universal graph deep learning interatomic potential for the periodic table. *Nature Computational Science* 2: 718–728.

Chen C, et al. (2019) Graph networks as a universal machine learning framework for molecules and crystals. *Chemistry of Materials* 31: 3564–3572.

Fukazawa T, et al. (2019) Bayesian optimization of chemical composition: A comprehensive framework and its application to $\mathrm{RFe_{12}}$-type compounds. *Physical Review Materials* 3: 053807.

Nishijima M, et al. (2014) Accelerated discovery of cathode materials with prolongated cycle life for lithium-ion battery. *Nature Communications* 5: 4553.

Shapeev AV (2016) Moment tensor potentials: A class of systematically improvable interatomic potentials. *Multiscale Modeling and Simulation* 14: 1153–1173.

Smith JS, et al. (2017) ANI-1: an extensible neural network potential with DFT accuracy at force field computational cost. *Chemical Science* 8: 3192–3203.

Takamoto S, et al. (2022) Towards universal neural network potential for material discovery applicable to arbitrary combination of 45 elements. *Nature Communications* 13: 2991.

Weininger D (1988) SMILES, a chemical language and information system. 1. Introduction to methodology and encoding rules. *Journal of Chemical Information and Computer Sciences* 28: 31–36.

Relevant websites

https://materialsproject.org—Materials Project
https://oqmd.org—Open Quantum Materials Database
https://www.aflowlib.org—Automatic FLOW for Materials Discovery
https://nomad-lab.eu—Novel Materials Discovery

Classical statistical mechanics

Davide Cassi, Dipartimento di Scienze matematiche, fisiche e informatiche, Università di Parma, Parma, Italy

© 2024 Elsevier Ltd. All rights reserved.

This is an update of D. Cassi, Statistical Mechanics: Classical, Editor(s): Franco Bassani, Gerald L. Liedl, Peter Wyder, Encyclopedia of Condensed Matter Physics, Elsevier, 2005, Pages 27–35, ISBN 9780123694010, https://doi.org/10.1016/B0-12-369401-9/00619-7.

Introduction **559**
Overview **560**
Macroscopic and microscopic variables 560
Time averages 560
Phase space averages 561
The statistical ensembles 561
The microcanonical ensemble 561
The canonical ensemble 563
The grand canonical ensemble 564
The perfect gas 565
Microcanonical ensemble 566
Canonical ensemble 566
Grand canonical ensemble 567
Key issues **567**
Statistical models 567
Classical spin models 568
Phase transitions ad universality classes 568
Statistical models on general networks 568
Conclusion **569**
References **569**

Abstract

We present the basics of classical statistical mechanics, starting from the time averages of the macroscopic variables. We then move on to the Gibbs approach based on the phase space averages and introduce the microcanonical, canonical and grand canonical ensembles, applying the corresponding distributions to the ideal gas case. Finally, we briefly discuss the most modern developments in classical statistical mechanics, which have led to the study of statistical models for phase transitions.

Key points

- Time averages
- Phase space averages
- Gibbs ensembles
- Microcanonical ensemble
- Canonical ensemble
- Grand canonical ensemble
- Perfect gas
- Statistical models and classical spin models

Introduction

Statistical mechanics was created in the second half of nineteenth century as a branch of theoretical physics with the purpose of deriving the laws of thermodynamic systems from the equations of motion of their elementary constituents, i.e. atoms and molecules.

Its commonly recognized fathers were Rudolf Clausius (1822–1888), who first interpreted the heath as kinetic energy of molecules, James Clerk Maxwell (1831–1879), who derived the velocity distribution of the molecules in an ideal gas and, most important, Ludwig Boltzmann (1844–1906), who gave the entropy the statistical meaning.

Statistical mechanics was also the field where quantum physics first revealed itself: indeed, in 1900, Max Plank proposed the quantization hypothesis to give a statistical interpretation of the black body radiation.

https://doi.org/10.1016/B978-0-323-90800-9.00017-2

Only 2 years later, Josiah Willard Gibbs (1839–1903) introduced the statistical-ensembles approach we commonly use today, allowing to extend statistical methods to a great variety of physical systems (Gibbs, 1902).

In the ’20 of the twentieth century, the application of statistical methods to quantum mechanical systems gave rise to a substantially new discipline which was called *quantum statistical mechanics*; the theory elaborated up to that time and all its further developments not involving quantum mechanics (e.g. the study of statistical models and the theory of phase transitions and critical phenomena) were accordingly called *classical statistical mechanics*.

Usually, statistical mechanics deals with equilibrium phenomena and it should be called, more precisely, *equilibrium statistical mechanics*. Non-equilibrium phenomena are typically more difficult to study, but several important statistical treatments of them exist, starting with the famous and seminal Boltzmann-equation. These topics of *non-equilibrium statistical mechanics* are generally discussed as specific subjects directly related to their applications (e.g. transport phenomena, relaxation phenomena). Here we follow this habit. In the next sections we introduce the basics of *classical equilibrium statistical mechanics* in a concise but complete way. For further information, the reader can consult many excellent textbooks (Gallavotti, 1999; Khinchin, 1960; Ma, 1985; Reichl, 1998; Ruelle, 1999; Thompson, 1988; Toda et al., 1983).

Overview

Macroscopic and microscopic variables

The physical systems studied by statistical mechanics are composed of a very large (typically 10^{23}) number N of particles or degrees of freedom. In classical mechanics, the (microscopic) state of a system is univocally identified by giving the generalized positions q and momenta p of all the constituents.

For clarity sake, in the following we shall focus on a systems composed of N pointlike particles. We denote the 6 N-tuple of all momenta and positions by (p, q) (or, when it is convenient to explicitly specify the number of particles, by $(p^{(N)}, q^{(N)})$), defining

$$(p, q) = \left(p^{(N)}, q^{(N)}\right) = \left(p_{1x}, p_{1y}, p_{1z}, \ldots, p_{Nx}, p_{Ny}, p_{Nz,} q_{1x}, q_{1y}, p_{1z}, \ldots, q_{Nx}, q_{Ny}, q_{Nz}\right).$$

The *microstate (p,q)* is therefore a point in the 6 N dimensional *phase space* Ξ_N, which is the set of all possible physical states of the system.

According to classical dynamics, the time evolution of a system is determined by its Hamiltonian *H(p,q)*, and its coordinates *(p(t),q(t))* satisfy the Hamilton equations

$$\frac{dp_i}{dt} = -\frac{\partial H}{\partial q_i} \quad \frac{dq_i}{dt} = \frac{\partial H}{\partial p_i}.$$

On the other hand, the macroscopic state (*macrostate*) of a system, which is the object of thermodynamics, is described by a very small number of macroscopic variables (e.g. volume, pressure, temperature); therefore it corresponds to many different microscopic states.

The macroscopic variables appearing in thermodynamic laws can be divided into two different categories: the mechanical (or, in more general systems, the magnetic, the electric etc.) and the statistical (or thermal) ones. The former can be calculated even for a single microstate from its *(p,q)* coordinates, i.e. they are functions *f(p,q)* of the points of the phase space (for example, the internal energy). The latter cannot be determined for a single microstate, but we need all the microstates belonging to a given macrostate in order to calculate them, i.e. they are functions of subsets of the phase space (for example, the entropy).

Time averages

A fundamental assumption of classical statistical mechanics concerns the characteristic times of microscopic vs. macroscopic dynamics. It is assumed that the microscopic dynamics is much faster than the macroscopic one, so that during a macroscopic measurement (the measurement of a macroscopic variable) the systems assumes many different microstates (indeed, for continuous coordinates, infinite microstates). Therefore, the measured value of a mechanical macroscopic variable M is to be considered the *time average* $\overline{m}_t$ of the corresponding microscopic one m:

$$\overline{m}_t = \frac{1}{t} \int_0^t m(\tau)\, d\tau \tag{1}$$

t being the measurement duration. Considering that t is typically very large with respect to all characteristic times involved in microscopic dynamics, one takes the $t \to \infty$ limit, defining the macroscopic variable M as

$$M = \lim_{t \to \infty} \overline{m}_t \tag{2}$$

Even with this simplifying assumption, the problem of determining M would require the solution of the equations of motion for the system, unless we introduce some further hypotheses. These are connected with the *statistical equilibrium* condition, i.e. to the experimentally observed time-independence of macroscopic variables: first, we must suppose the limit in (2) exist; then, we have to require the independence of M from the specific microstate (belonging to the given macrostate) assumed by the system at the instant $t = 0$, formally chosen as the beginning of the measurement.

Phase space averages

A crucial technical step in the development of classical statistical mechanics is the passage from time averages to phase-space averages. To introduce it, we consider that in classical mechanics every mechanical variable *m* is a function *m(p,q)* of the phase space coordinates *p* and *q*. Therefore, to calculate time averages we could simply ask how many times the system has visited each point in phase space (or, more precisely, an infinitesimal volume *dpdq* around that point); associating to every point *(p,q)* a weight $\rho(p,q)$ proportional to the number of visits, we can then obtain the time average of any variable *m* by computing its weighted average on the phase space points. These heuristic considerations can be mathematically formalized as follows (assuming all the conditions for the interchange of the integrals and the limit hold)

$$\begin{aligned} M &= \lim_{t\to\infty}\frac{1}{t}\int_0^t m(p(\tau),q(\tau))d\tau = \lim_{t\to\infty}\frac{1}{t}\int_0^t\left[\int m(p,q)\delta(p-p(\tau))\delta(q-q(\tau))dpdq\right]d\tau = \\ &= \int m(p,q)\left[\lim_{t\to\infty}\frac{1}{t}\int_0^t \delta(p-p(\tau))\delta(q-q(\tau))d\tau\right]dpdq \equiv \\ &\equiv \int m(p,q)\rho(p,q)dpdq \end{aligned} \tag{3}$$

where

$$\rho(p,q) \equiv \lim_{t\to\infty}\frac{1}{t}\int_0^t \delta(p-p(\tau))\delta(q-q(\tau))d\tau \tag{4}$$

with $dp \equiv dp_{1x}\cdots dp_{Nz}$ and $dq \equiv dq_{1x}\cdots dq_{Nz}$.

Notice that the introduction of $\rho(p,q)$ allows us to calculate the average values of any mechanical variable without knowing its dynamics: in other words, once $\rho(p,q)$ is known, we can completely neglect the time in all further calculations.

From the requirements introduced at the end of the last section, and from the generality of M, it follows that the function $\rho(p,q)$ only depends on and completely determines the macrostate it corresponds to. Therefore it must parametrically depend only on the restricted number of macroscopic variables defining that macrostate. The same requirements would imply that, for any starting point *(p,q)* belonging to the macrostate, the system visits all the microstates belonging to it and that the frequency of visits is $\rho(p,q)$. This property cannot be proven for a generic dynamical system, and it has to be considered as one of the fundamental assumptions of classical statistical mechanics.

The statistical ensembles

The calculation of $\rho(p,q)$ from its definition would imply the complete solution of the equations of motion with any initial condition. This is in practice impossible even for simple systems, due to the large number of degrees of freedom. In fact, $\rho(p,q)$ was determined in a general form once and for all by Gibbs for the most significant cases, on the basis of physical considerations and assumptions.

Gibbs followed an alternative approach. Instead of just one system, he considered a large set of physically identical systems at once, all having the same Hamiltonian but being in different microstates at a given time *t*, and he assumed they representative points *(p,q)* in phase space were distributed with a density $\rho(p,q)$. He called such a set a *statistical ensemble* and $\rho(p,q)$ its *distribution*. In other word, each system in the ensemble is, at time *t*, in a microscopic state *(p,q)* corresponding to the macroscopic state described by $\rho(p,q)$, with a probability given by $\rho(p,q)$ itself. Then he imposed the *statistical equilibrium condition* by requiring that the density of the points representing the systems in the phase space was left invariant during their time evolution. Finally, he proved that this condition is fulfilled if and only if

$$\rho(p,q) = f(H(p,q)) \tag{5}$$

i.e. if and only if $\rho(p,q)$ depends on the phase space coordinates *p* and *q* only through the Hamiltonian of the system.

Now, considering the typical macroscopic constraints characterizing a thermodynamic system, he identified three main general kinds of ensembles and, using (5) and some specific hypotheses, he calculated their distributions. Gibbs called these ensembles *microcanonical*, *canonical* and *grand canonical* and these names have been used ever since.

The microcanonical ensemble

Even if Gibbs first considered the canonical ensemble and then he derived the microcanonical one from it, the following formal development of statistical mechanics suggested inverting the order, to have a stronger connection with the microscopic dynamical equations.

The microcanonical ensemble describes a closed isolated system, i.e. a system which cannot exchange particles and energy with the external world, confined in a fixed volume. Therefore, the macroscopic variables characterizing it are the number of particles N, the volume V and the total energy E. Notice that all of them are mechanical variables: indeed, the microcanonical ensemble is the statistical ensemble which is most directly connected with a classical dynamical system. The variables N, V and E are also all extensive, i.e. they are asymptotically proportional to the number of degrees of freedom (usually 3N) for large N. Many physical properties of thermodynamic systems turn out to be simpler by taking the *thermodynamic limit* $N \to \infty$; in that case we shall require that the ratios of V and E to N (called the *specific volume* and the *specific energy* respectively) are constant in this limit:

$$\lim_{N\to\infty} \frac{V}{N}\, v; \qquad \lim_{N\to\infty} \frac{E}{N}\, \varepsilon \tag{6}$$

Due to its defining conditions, the energy of each system belonging to the microcanonical ensemble is constant during time evolution; in other words, its trajectory in phase space entirely lies on the hypersurface $H(p, q) = E$. The microcanonical distribution is obtained assuming $\rho(p, q)$ is constant on this hypersurface and zero elsewhere:

$$\rho^{\mu C}_{N,V,E}(p, q) = \frac{\varepsilon_0 \delta(E–H(p, q))}{\Gamma(N, V, E)} \tag{7}$$

where

$$\Gamma(N, V, E) = \varepsilon_0 \int \delta(E–H(p, q))dpdq \tag{8}$$

is the measure of the region of the phase space accessible to the system, i.e. it measures how large is the set of microstates corresponding to the given macrostate identified by N,V and E, and ε_0 is an arbitrary but fixed constant with the dimension of an energy, which is convenient to introduce to give Γ the dimension of a volume in phase space (without loss of generality, we can set it equal to 1).

The assumption leading to (7) means that the system, in its motion, explores "in a uniform way" the whole constant-energy hypersurface. Many attempts have been made during the last century to mathematically prove this hypothesis to be a consequence of general properties of Hamiltonian dynamical systems. However this problem, known as the *ergodic problem*, has not been solved but for a very restricted class of systems (typically hard-spheres gases), and we will consider the *ergodic hypothesis* a reasonable assumption leading to experimentally verifiable results.

Knowing the microcanonical distribution $\rho^{\mu C}_{N,\, V,\, E}(p, q)$, it is possible to calculate the average of any mechanical variable according to (3). However, we have no rule to calculate the fundamental thermal variables, such as the entropy S and the temperature T. In order to connect the microcanonical distribution with the thermodynamics, we have to introduce the most important postulate of all statistical mechanics, namely the Boltzmann relation, which derives the entropy from Γ:

$$S(N, V, E) = k_B \ln \frac{\Gamma(N, V, E)}{\Gamma_0} \tag{9}$$

where $k_B = 1.3807 \cdot 10^{-23} JK^{-1}$ is the Boltzmann constant and Γ_0 is a fixed but arbitrary number with the same dimensions as Γ. It represents a unit of measure for volumes in phase space and it is necessary to make the argument of the logarithm adimensional. Notice that it does not make the definition (9) ambiguous, since the entropy, like every thermodynamic potential, is always defined up to an arbitrary additive constant. As it is well known, this arbitrariness can be eliminated by introducing the so called *third principle of thermodynamics*, or *Nernst postulate*, according to which the entropy must vanish for $T \to 0$: this requirement univocally fix the value of Γ_0. Moreover, in order to have a coherent definition of $\Gamma_0$for different values of N when taking the thermodynamic limit, it is customary to choose once for all the unit of measure $\gamma$for the smallest phase space, corresponding to only one particle in one dimension, and then define $\Gamma_0(N)$ for a system of N particles (in three dimensions) as

$$\Gamma_0(N) = \gamma^{3N} \tag{10}$$

Considerations based on the semiclassical limit of quantum mechanics suggest then to chose $\gamma = h$, where h is the Plank constant, but this is outside the proper domain of classical statistical mechanics.

The Boltzmann relation cannot be mathematically proven and we have to consider it a postulate.

All that we can do is proving that, under some restrictive hypotheses, the *statistical entropy* defined by (9) has the same mathematical properties of the *thermodynamic entropy* defined by the differential relation $dS = dQ/T$. The fundamental of these hypotheses concerns the interactions between the particles in the system: they must decay rather fast with increasing distance. More precisely, supposing the interactions isotropic for simplicity sake, the interaction potentials $V(r)$ must decay faster than r^{-2} as $r \to \infty$. This means that we cannot apply equilibrium statistical mechanics to systems with (non negligible) gravitational interactions as well as to systems containing electrically charged particles and having non-zero total charge.

An important modification to (9) has to be introduced if the particles of the system are indistinguishable. Indeed, many years before the quantum concept of identical particles was introduced, Gibbs proved that Γ needs to be divided by $N!$ in order to preserve the asymptotic additivity of the entropy (his argument is commonly know as the *Gibbs paradox*):

$$S(N, V, E) = k_B \ln \frac{\Gamma(N, V, E)}{\Gamma_0 N!} \tag{11}$$

In the most general case, not all the particles are indistinguishable, but we can have N_1 indistinguishable particles of one kind, N_2 of a different kind and so on. If the system is composed of m different kinds of indistinguishable particles, with $\sum_{i=1}^{m} N_i = N$, (allowing even $N_i = 1$ for generality sake), the most general expression of the entropy is given by

$$S(N_1, \cdots, N_m, V, E) = k_B \ln \frac{\Gamma(N_1, \cdots, N_m, V, E)}{\Gamma_0 N_1! \cdots N_m!} \tag{12}$$

A slightly different definition of the microcanonical ensemble can be found in literature, according to which the systems belonging to the ensemble have energy between E and $E + \Delta E$ instead of exactly E. Assuming a constant distribution in the entire phase space region satisfying that constraint, and defining Γ to be the volume of this region, one can again define S using (12). It can be shown that in the thermodynamic limit the two definitions of the entropy are asymptotically equivalent and the corresponding distributions give the same thermodynamic behavior.

Eq. (12) is the starting point for deriving all the thermodynamics of the microcanonical ensemble. Applying basic thermodynamic relations we obtain

$$\frac{1}{T} = \left.\frac{\partial S}{\partial E}\right|_{V,N_1,\cdots,N_m} \tag{13}$$

$$\frac{P}{T} = \left.\frac{\partial S}{\partial V}\right|_{E,N_1,\cdots,N_m} \tag{14}$$

$$\frac{\mu_i}{T} = -\left.\frac{\partial S}{\partial N_i}\right|_{V,E} \tag{15}$$

giving the *temperature*, the *pressure* and the *chemical potentials* respectively.

The canonical ensemble

The most typical system studied in statistical mechanics is confined in a fixed volume and is closed, but it is not isolated and it can exchange energy with a thermal bath (or a *reservoir*) at a fixed temperature. It is described by the canonical ensemble and the macroscopic variables characterizing it are the number of particles N, the volume V and the temperature T.

We can consider it as a small but macroscopic subsystem of a closed isolated system, the remaining part of which acts as reservoir. Therefore, we can obtain the *canonical distribution* from the microcanonical one, calculating the distribution of a closed subsystem whose volume and number of particles in the thermodynamic limit satisfy

$$\lim_{N\to\infty} \frac{V}{N} = v; \qquad \lim_{N\to\infty} \frac{N}{N_{TOT}} = \lim_{N\to\infty} \frac{V}{V_{TOT}} = 0 \tag{16}$$

N_{TOT} and V_{TOT} being the number of particles and the volume of the whole closed isolated system.

Introducing, as usual, some suitable hypotheses (e.g. the ratio between the external surface of the subsystem and its volume must vanish in the thermodynamic limit) after some calculations we get

$$\rho^{C}_{N,V,T}(p,q) = \frac{e^{-\frac{H(p,q)}{k_B T}}}{Z(N,V,T)} \tag{17}$$

where

$$Z(N,V,T) = \int e^{-\frac{H(p,q)}{k_B T}} dp dq \tag{18}$$

is called the *canonical partition function*.

For the canonical ensemble, Z plays a role analogous to Γ for the microcanonical one: it is a sort of normalization factor which is not directly measurable but it is the starting point for deriving all the thermodynamic quantities. The basic relation connecting it to a thermodynamic potential is

$$F(N,V,T) = -k_B T \ln \frac{Z(N,V,T)}{Z_0} \tag{19}$$

F being the *Helmholtz free energy* and Z_0 an arbitrary constant with the same dimensions as Z, playing the same role of Γ_0 in (9); indeed, F too is defined up to an additive constant like S and the arbitrariness can be eliminated in the same way assuming the third principle of thermodynamics to hold. Moreover, the same considerations introduced for Γ_0, concerning the normalization in the thermodynamic limit and the presence of indistinguishable particles, apply. Accordingly, the general form of (19) becomes

$$F(N_1, \cdots, N_m, V, T) = -k_B T \ln \frac{Z(N_1, \cdots, N_m, V, T)}{Z_0(N) N_1! \cdots N_m!} \tag{20}$$

with

$$Z_0(N) = \gamma^{3N} \tag{21}$$

After determining F by (20), all the thermodynamics of the canonical ensemble can be easily deduced. The main thermodynamic equations we need are

$$S = -\left.\frac{\partial F}{\partial T}\right|_{V, N_1, \cdots, N_m} \tag{22}$$

$$P = -\left.\frac{\partial F}{\partial V}\right|_{T, N_1, \cdots, N_m} \tag{23}$$

$$\mu_i = \left.\frac{\partial F}{\partial N_i}\right|_{V,T} \tag{24}$$

$$E = F + TS \tag{25}$$

where E denotes the *internal energy* and coincides with the average value of the Hamiltonian.

The grand canonical ensemble

The case of a system occupying a fixed volume but exchanging particles and energy with the external world, at fixed temperature and chemical potentials, is described by the *grand canonical ensemble.* In the simplest situation, all the particles are of the same kind and a macrostate is as usual defined by three macroscopic variables, the volume V, the temperature T and the chemical potential μ (representing the energy increment due to the addition of a particle). However, a microstate is no longer represented by a point in a usual phase space. Indeed, the dimension of the phase space depends on the number of particles N, and here N is variable.

To face this problem, we have to introduce an extended space Ξ given by the union of the phase spaces Ξ_N corresponding to all possible N

$$\Xi = \bigcup_{N=0}^{\infty} \Xi_N \tag{26}$$

A point in this space is given by the 6 N + 1-tuple$(N, p^{(N)}, q^{(N)})$, i.e. by the number of particles N and a point in the corresponding phase space Ξ_N (notice that we have to include the case $N = 0$, corresponding to an empty system). For any N we have also to consider a specific Hamiltonian $H_N(p^{(N)}, q^{(N)})$ and, to have a coherent definition of volumes in phase spaces of different dimensions, we chose the volume unit $Z_0(N) = \gamma^{3N}$ according to (21).

To obtain the *grand canonical distribution,* we can follow a procedure similar to that we have used to derive the canonical distribution from the microcanonical one.

We consider a small but macroscopic subsystem of a closed isolated system, the remaining part of which acts as reservoir of energy and particles. The subsystem is open (it can exchange particles and energy with the external world), but it occupies a fixed volume V in space. We assume that, taking the thermodynamic limit,

$$\lim_{V \to \infty} \frac{V}{V_{TOT}} = 0 \tag{27}$$

where V_{TOT} is the volume of the whole closed isolated system, and that the ratio between the external surface of the subsystem and its volume also vanish in the thermodynamic limit.

After some algebra we obtain

$$\rho^{GC}_{\mu,V,T}\left(N, p^{(N)}, q^{(N)}\right) = \frac{e^{\frac{\mu N - H_N\left(p^{(N)}, q^{(N)}\right)}{k_B T}}}{\gamma^{3N} N! Z^{GC}(\mu, V, T)} \tag{28}$$

where

$$Z^{GC}(\mu, V, T) = \sum_{N=0}^{\infty} \frac{e^{\frac{\mu N}{k_B T}}}{\gamma^{3N} N!} \int e^{-\frac{H_N\left(p^{(N)}, q^{(N)}\right)}{k_B T}} dp^{(N)} dq^{(N)} \tag{29}$$

is the *grand canonical partition function* or *grand partition function.* The last expression can also be written as

$$Z^{GC}(\mu, V, T) = \sum_{N=0}^{\infty} \frac{z^N Z(N, V, T)}{\gamma^{3N} N!} \tag{30}$$

in terms of the canonical partition functions $Z(N, V, T)$ and of the *activity* z, defined by

$$z = e^{\frac{\mu}{k_B T}} \tag{31}$$

In the most general case of a system composed of m different kinds of indistinguishable particles, we have to introduce a different chemical potential for each kind of particle, therefore the macroscopic variables characterizing a macrostate are T,V, and the m chemical potentials$\mu_1, \cdots, \mu_m$.

As for the microstates, we have to specify the number $N_i$of particles of each kind $i = 1, \cdots, m$, and introduce the corresponding phase space $\Xi_{N_1,\cdots,N_m}$with coordinates $(p^{(N_1,\cdots,N_m)}, q^{(N_1,\cdots,N_m)})$. Accordingly, the extended space Ξ of (26) becomes

$$\Xi = \bigcup_{N_1=0}^{\infty} \cdots \bigcup_{N_m=0}^{\infty} \Xi_{N_1,\cdots,N_m} \tag{32}$$

and a point of Ξ is specified by the coordinates $(N_1, \cdots, N_m, p^{(N_1,\cdots,N_m)}, q^{(N_1,\cdots,N_m)})$ while the Hamiltonian acting on it is $H_{N_1,\cdots,N_m}(p^{(N_1,\cdots,N_m)}, q^{(N_1,\cdots,N_m)})$.

Using this notation, the grand canonical partition function is given by

$$\begin{aligned}&\rho^{GC}_{\mu_1,\cdots,\mu_m,V,T}\left(N_1, \cdots, N_m, p^{(N_1,\cdots,N_m)}, q^{(N_1,\cdots,N_m)}\right) = \\ &= \frac{e^{\frac{\sum_{i=1}^{m} \mu_i N_i - H_{N_1,\cdots,N_m}\left(p^{(N_1,\cdots,N_m)}, q^{(N_1,\cdots,N_m)}\right)}{k_B T}}}{\gamma^{3\sum_{i=1}^{m} N_i} N_1! \cdots N_m! Z^{GC}(\mu_1, \cdots, \mu_m, V, T)}\end{aligned} \tag{33}$$

with

$$\begin{aligned}&Z^{GC}(\mu_1, \cdots, \mu_m, V, T) = \\ &= \sum_{N_1=0}^{\infty} \cdots \sum_{N_m=0}^{\infty} \prod_{i=1}^{m} \frac{z_i^{N_i}}{\gamma^{3N_i} N_i!} \int e^{-\frac{H_{N_1,\cdots,N_m}\left(p^{(N_1,\cdots,N_m)}, q^{(N_1,\cdots,N_m)}\right)}{k_B T}} dp^{(N_1,\cdots,N_m)} dq^{(N_1,\cdots,N_m)}\end{aligned} \tag{34}$$

and

$$z_i = e^{\frac{\mu_i}{k_B T}} \tag{35}$$

The thermodynamics of the grand canonical ensemble can be derived from the basic equation

$$\Omega(\mu_1, \cdots, \mu_m, V, T) = -k_B T \ln Z^{GC}(\mu_1, \cdots, \mu_m, V, T) \tag{36}$$

where the thermodynamic potential $\Omega$is defined by

$$\Omega = -PV \tag{37}$$

The other thermodynamic quantities are obtained from Ω applying the relations

$$S = -\left.\frac{\partial \Omega}{\partial T}\right|_{V,\mu_1,\cdots,\mu_m} \tag{38}$$

$$N_i = -\left.\frac{\partial \Omega}{\partial \mu_i}\right|_{V,T} \tag{39}$$

$$E = \Omega + TS + \sum_{i=1}^{m} \mu_i N_i \tag{40}$$

where N_i denotes the average number of particles of kind i.

The perfect gas

The simplest and best known application of classical statistical mechanics concerns the so called perfect gas, i.e. a system of non-interacting particles. This is obviously an ideal case, since a complete absence of interaction would prevent a system from reaching the equilibrium, but we can consider it a good approximation for rarefied real gases, where the potential energy is negligible with respect to the kinetic energy. It also represents the natural starting point for the study of more complicated systems by perturbative techniques.

Choosing, for simplicity sake, a monatomic gas composed of indistinguishable pointlike particles of only one kind, the perfect gas Hamiltonian is

$$H_N\left(p^{(N)}, q^{(N)}\right) = \sum_{i=1}^{N} \frac{\mathbf{p}_i^2}{2m} \tag{41}$$

with $\mathbf{p}_i = (p_{ix}, p_{iy}, p_{iz})$ and m being the mass of each particle.

Microcanonical ensemble

Let us study first the case of a closed isolated system, described therefore by the microcanonical ensemble. We suppose the gas confined in a fixed space volume V and with a fixed energy E and number of particles N.

To calculate the thermodynamic properties of such a system we have first to determine its entropy according to (11) and to do that we need the measure $\Gamma(N, V, E)$ of the region of the phase space accessible to the system:

$$\Gamma(N, V, E) = \varepsilon_0 \int \delta(E - H(p, q))dpdq = \varepsilon_0 V^N \int \delta\left(E - \sum\nolimits_{i=1}^{N} \frac{\mathbf{p}_i^2}{2m}\right) d\mathbf{p}_1 \cdots d\mathbf{p}_N \tag{42}$$

After some straightforward steps we obtain

$$\Gamma(N, V, E) = \frac{\varepsilon_0 V^N (E)^{3N/2-1} (2m\pi)^{3N/2}}{\Gamma_{Eul}(3N/2)} \tag{43}$$

and, substituting in (11) and using (10),

$$S(N, V, E) = k_B \ln \frac{\varepsilon_0 V^N (E)^{3N/2-1} (2m\pi)^{3N/2}}{\Gamma_{Eul}(3N/2)\gamma^{3N} N!} \tag{44}$$

which, for $N \to \infty$ and using the definitions (6), gives the asymptotic expression

$$S(N, V, E) \approx k_B N \left(5/2 + \ln \frac{(4m\varepsilon\pi/3)^{3/2} v}{\gamma^3} \right) \tag{45}$$

Notice that the entropy (45) is extensive as expected, due to the Gibbs factor N! introduced in (11).

Finally, applying (13), (14) and (15), we obtain the usual thermodynamic equations for the perfect monatomic gas

$$\frac{1}{T} = \frac{3}{2} \frac{k_B}{\varepsilon} \tag{46}$$

$$\frac{P}{T} = \frac{k_B}{v} \tag{47}$$

$$\frac{\mu}{T} = -k_B \ln \frac{(4m\varepsilon\pi/3)^{3/2} v}{\gamma^3} \tag{48}$$

Notice that, due to the presence of the arbitrary normalization constant γ, the chemical potential is not univocally defined unless one introduces the third principle of thermodynamics or quantum mechanical arguments (see the comments to Eqs. (9), (10)).

Canonical ensemble

Let us now consider the perfect monatomic gas composed of N particles in a fixed volume V, in thermal equilibrium with a reservoir at temperature T. This system is described by the canonical ensemble and to calculate its thermodynamics we need the partition function Z defined in (18).

Calculating Z for the Hamiltonian (41) we obtain

$$\begin{aligned} Z(N, V, T) &= \int e^{-\frac{H(p,q)}{k_B T}} dpdq = V^N \int e^{-\sum_{i=1}^{N} \frac{\mathbf{p}_i^2}{2mk_B T}} d\mathbf{p}_1 \cdots d\mathbf{p}_N = \\ &= V^N (2\pi m k_B T)^{\frac{3N}{2}} \end{aligned} \tag{49}$$

and, applying (20) for $m = 1$ and $N \to \infty$,

$$F(N, V, T) = -k_B T \ln \frac{Z(N, V, T)}{N! \gamma^{3N}} \approx -k_B T N \ln\left(e v \left(2\pi m k_B T \gamma^{-2}\right)^{\frac{3}{2}}\right) \tag{50}$$

Again, the Helmholtz free energy is extensive due to the Gibbs factor N!

The main thermodynamic equations are then given by Eq. (22)–(25):

$$S = N k_B \ln\left(e^{\frac{5}{2}} v \left(2\pi m k_B T \gamma^{-2}\right)^{\frac{3}{2}}\right) \tag{51}$$

$$P = \frac{k_B T}{v} \tag{52}$$

$$\mu = -k_B T \ln\left(v\left(2\pi m k_B T \gamma^{-2}\right)^{\frac{3}{2}}\right) \tag{53}$$

$$E = \frac{3}{2} N k_B T \tag{54}$$

Grand canonical ensemble

Finally, we study the case of a perfect monatomic gas in a fixed volume V, exchanging energy and particles with a reservoir at fixed T and μ. Using expression (30) for the grand canonical partition function, with $Z(N,V,T)$ given by (49), we obtain

$$\begin{aligned} Z^{GC}(\mu, V, T) &= \sum_{N=0}^{\infty} \frac{z^N Z(N, V, T)}{\gamma^{3N} N!} = \sum_{N=0}^{\infty} \frac{z^N V^N (2\pi m k_B T)^{\frac{3N}{2}}}{\gamma^{3N} N!} = \\ &= e^{zV(2\pi m k_B T \gamma^{-2})^{\frac{3}{2}}} \end{aligned} \tag{55}$$

and, from (36) and (37),

$$\Omega = -PV = -k_B z V T^{\frac{5}{2}} \left(2\pi m k_B \gamma^{-2}\right)^{\frac{3}{2}} \tag{56}$$

while the thermodynamic relations given by Eq. (38)–(40) are

$$S = \left(\frac{5}{2} - \frac{\mu}{k_B T}\right) k_B z V \left(2\pi m k T_B \gamma^{-2}\right)^{\frac{3}{2}} \tag{57}$$

$$N = zV\left(2\pi m k_B T \gamma^{-2}\right)^{\frac{3}{2}} \tag{58}$$

$$E = \frac{3}{2} k_B T z V \left(2\pi m k_B T \gamma^{-2}\right)^{\frac{3}{2}} \tag{59}$$

The thermodynamic equations derived for the three ensembles have obviously different meanings, since they refer to different physical situations. Indeed, quantities which are fixed in one of the ensemble can be fluctuating in a different ensemble (e.g. E is fixed in the microcanonical and fluctuating in the other ensembles). However, if we consider the average values of the fluctuating quantities, all these equations becomes equivalent from a mathematical point of view, allowing a unified thermodynamic description. From a physical point of view this makes sense as far as the fluctuations around the average values are negligible with respect to the average values themselves or, in other words, as far as the *relative fluctuations* vanish.

This can be shown to happen usually in the thermodynamic limit, with the important exception of systems near critical point, where even the relative fluctuations typically diverge.

Key issues

Statistical models

Although classical statistical mechanics has as its starting point the time averages on the evolution of a system in phase space, Gibbs' innovative approach, over the course of the twentieth century, paved the way for applications that go beyond its initial scope.

The ensemble average, understood as the average over a set of microstates, each weighted with an appropriate probability, in fact, can be extended to very different systems than those initially described by Gibbs himself.

The key point is to replace the concept of microstate with that of configuration, where, by configuration, we mean the set of values assumed by the microscopic variables that describe the system.

An energy is associated with each configuration, through a function defined Hamiltonian, in analogy with the canonical case, even if, technically, it does not have the properties of the Hamilton function in classical mechanics. In particular, here the conjugate variables p and q do not exist in general, and it is not possible to derive the dynamics of the system from the Hamiltonian, as it happens instead in the canonical case. Indeed, in general these systems are studied without any reference to the dynamic properties, implying that the average on the configurations should be equivalent to the time average on a dynamics which is not explicitly defined. This implies, among other things, that the term corresponding to kinetic energy is normally missing in the Hamiltonian. This lack can also lead to surprising results compared to what is found in the canonical approach. Among these, one of the most interesting is the existence of systems with negative temperatures, which, among other things, have an experimental equivalent in population inversion systems, such as lasers (Ramsey, 1956). This phenomenon is found by applying microcanonical statistics to systems in which the number of configurations corresponding to a given energy decreases as the energy increases, an impossible situation in the presence of the kinetic term in the Hamiltonian. Since the temperature is given by the inverse of the derivative of entropy with respect to energy (13), it follows that this decrease, producing a negative derivative, gives rise to negative temperatures.

Statistical models, unlike classical statistical systems, are not born with the aim of calculating exactly the macroscopic physical quantities that characterize the system they describe. Their nature is approximate by definition: details are neglected, and we focus only on the essential aspects. Their importance lies in the fact that they are able to give very general qualitative (and in some cases also quantitative) predictions on the behavior of the real systems they approximate. The most typical example of application concerns phase transitions, in particular magnetic ones. In this case, the predictive power of these models derives from the properties of universality, which were highlighted mainly in the second half of the twentieth century.

To discuss in more detail the function and properties of statistical models, we now focus on perhaps the most representative case, namely spin models.

Classical spin models

In a classical spin model, each site *i* of a lattice is associated with a variable σ_i which represents the value of the spin at that site. These models were originally introduced to describe the magnetic behavior of crystalline structures but have since been extended to more general systems. A system configuration, in this case, is represented by the set of values assumed by the variables σ_i in each site and is symbolically indicated with $\{\sigma_i\}$.

Historically, the first spin model to be introduced was the Ising model (Lenz, 1920), in which each variable σ_i can only assume the values +1 and −1. Later, this approach was extended to more general models, in which the variables σ_i can assume a larger number of values or represent vector variables.

The typical Hamiltonian of a spin model can be written in the general form

$$H(\{\sigma_i\}) = -\sum_{i,j} J_{ij}\sigma_i.\sigma_j - \sum_i h_i.\sigma_i \tag{60}$$

where the variables σ_i can be scalars or vectors, $h_i$represents a local (magnetic) field of the same nature (scalar or vector) as the σi, and J_{ij}, called the coupling matrix, is a real symmetric matrix whose elements describe the interaction between the variables σ_i and σ_j.

Normally, the coupling matrix is determined by the geometry or topology of the structure on which the spin variables are located. On a lattice with first-neighbor interactions, for example, J_{ij}, $\neq 0$ only if *i* and *j* are nearest neighbor sites. In the simplest cases, commonly studied, we assume to have the same coupling between each pair of nearest neighbors and the same local magnetic field in each site: $J_{ij} = J$ and $h_i = h$, with $J > 0$ if the model describes a ferromagnetic system and $J < 0$ in the antiferromagnetic case.

In general, statistical models, and spin models in particular, despite their simplified nature, are not exactly soluble with analytical tools (Baxter, 2008; Mussardo, 2020), with an important exception represented by the Ising model on a two-dimensional lattice (Onsager, 1944). To study them one can resort to further analytical approximations, or to numerical simulations, as happens more frequently since the computing power of computers reached levels that were unthinkable a few decades ago.

Nevertheless, as mentioned previously, a series of rigorous theorems allows us to obtain very valuable and useful information on the behavior of these models and the systems they describe.

Phase transitions ad universality classes

The most important point concerns the universality property, according to which the behavior of the models as far as phase transitions are concerned, depends exclusively on the dimension of the lattice on which they are defined, and on the nature of the symmetry of the Hamiltonian (more precisely, on the transformations of the spin variables that leave the Hamiltonian invariant when $h = 0$). From a mathematical point of view, a ferromagnetic phase transition can only occur on infinite lattices and what we are going to say has to be understood as referring to this type of lattice. Discrete symmetry models (scalar spin variables), such as the Ising model, may exhibit ferromagnetic phase transitions, with non-zero spontaneous magnetization at zero magnetic field *h*, and at $T > 0$, if and only if the lattice dimension *d* is greater or equal to 2 (Peierls, 1936), while those with continuous symmetry can have ferromagnetic phase transitions at $T > 0$ if and only if the lattice dimension *d* is greater than or equal to 3 (Mermin and Wagner, 1966; Fröhlich et al., 1976). Furthermore, in the case of second order phase transitions and critical phenomena, also the critical exponents that describe the behavior of the system only depend on the lattice dimension and the symmetry of the Hamiltonian. The importance of these results, beyond their theoretical interest, also lies in their practical and applicative implications. In fact, if some relevant quantities do not depend on the details of the system, such as the exact value of the couplings or the presence of defects in a crystal lattice, but only on those extremely general characteristics which are the lattice size and the Hamiltonian symmetry, then it is possible to obtain those quantities by calculating them, analytically or numerically, for the simplest possible model that has the same characteristics.

All models exhibiting the same critical behavior form a universality class.

Using this terminology, we can say that the universality classes are only determined by the lattice dimension and the symmetry of the Hamiltonian and that, to know the critical exponents of a given model, it is sufficient to know those of any other model in the same universality class.

Statistical models on general networks

In more recent times, the study of statistical models has been extended from lattices to more complex structures represented by graphs or networks (Burioni et al., 2004). These models are useful for describing, for example, the behavior of non-crystalline structures such as amorphous materials, polymer gels, fractals, or generic disordered structures. In these cases, the concept of lattice size is missing, or it can be misleading, lacking translational invariance, from which most of the properties of crystal lattices derive. However, through a series of analytical studies, it was possible to identify some universal parameters, linked to the geometry or large-scale topology of the structures, which allow to extend the classification into universality classes also to these systems.

The key point for solving these problems consists in noting that the coupling matrix J_{ij} is in fact an algebraic description of the topology of the structure and can be used to describe not only the interactions between spins in statistical models, but also different physical phenomena, such as diffusion, harmonic oscillations or the electrical properties of the structure. Without going into details, we limit ourselves to saying that it is possible to define a new topological parameter, called the spectral dimension, $\tilde{d}$, defined, referring to the density of acoustic vibrational modes of the structure $\rho\ (\omega)$ at low frequencies ω, by the relation (Alexander and Orbach, 1982)

$$\rho(\omega) \sim \omega^{\tilde{d}-1} \tag{61}$$

The spectral dimension $\tilde{d}$ coincides with the usual dimension d in the case of lattices, while, in the more general case of connected real structures, it can assume real values between 1 and 3. It can be calculated, numerically and in some cases analytically, in the case of graph models, while it can be experimentally measured in the case of real structures, using neutron scattering, low temperature calorimetry and other related techniques.

The spectral dimension plays a similar role to the dimension d of lattices in the case of continuous symmetry models. The latter present phase transitions at $T > 0$ if and only if $\tilde{d} > 2$ (Cassi, 1992; Burioni et al., 1999) and the corresponding universality classes are determined by $\tilde{d}$ and by the symmetry of the Hamiltonian.

The case of discrete symmetry models, on the other hand, has not yet been completely solved. It is known for certain that, for these models, the spectral dimension is not the relevant parameter for determining phase transitions. There are some rigorous theorems that link the presence or absence of phase transitions to other topological parameters (Campari and Cassi, 2010, 2011), but a necessary and sufficient condition, similar to that determined by the spectral dimension in the case of continuous symmetries, has not yet been found. The field of research in this sector is still very open.

Conclusion

In the previous sections we examined the foundations of classical statistical mechanics, established in the nineteenth century through the definition of time averages. We then showed how Gibbs' innovative approach, based on the averages on the sets, has allowed an extremely more efficient formal evolution, and we applied the Gibbs statistical sets to the case of the perfect gas. Subsequently, we dealt with the more modern evolution of classical statistics which led to the study of so-called statistical models, which are particularly useful in the study of phase transitions and critical phenomena, both on the lattice and on more complex and irregular structures.

In recent years, the application of statistical models and the methods used for their study has been extended to increasingly vast sectors, which go beyond physics itself, such as economics, ecology, sociology, and others (Park et al., 2012; Fort, 2020; Chakrabarti and Sen, 2014). The basic idea consists in describing all the possible states of a generic system through a set of variables, introducing a function similar to the Hamiltonian that determines the probability of each state. In this case, the initial meaning of the Gibbs distributions and their relationship with thermodynamics is obviously lost. Nonetheless, the parallel with the results obtained for true physical models is extremely useful for understanding the behavior of these non-physical systems.

The main problem of classical statistical mechanics and its extensions remains the impossibility of obtaining exact analytical solutions for real systems, combined with the difficulty of numerically simulating systems with a realistic number of degrees of freedom. If until a few years ago the search for approximate analytical solutions was the guiding thread of many formal developments in this field, currently the computing power achieved thanks to High Performance Computing makes the numerical approach increasingly promising.

References

Alexander S and Orbach R (1982) Density of states on fractals: "fractons" *Journal de Physique, Lettres* 43: L625.

Baxter RJ (2008) *Exactly Solved Models in Statistical Mechanics*. New York: Dover.

Burioni R, Cassi D, and Vezzani A (1999) Inverse Mermin-Wagner theorem for classical spin models on graphs. *Physical Review E* 60: 1500.

Burioni R, Cassi D, and Vezzani A (2004) Random walks and physical models on infinite graphs: an introduction. In: Kaimanovich V (ed.) *Random Walks and Geometry*, pp. 35–72. Berlin: De Gruyter.

Campari R and Cassi D (2010) Generalization of the Peierls-Griffiths theorem for the Ising model on graphs. *Physical Review E* 81: 021108.

Campari R and Cassi D (2011) Absence of Spontaneous Magnetization for the Ising Model on Weakly Separable Graphs. *Modern Physics Letters B* 25: 801–811.

Cassi D (1992) Phase transitions and random walks on graphs: A generalization of the Mermin-Wagner theorem to disordered lattices, fractals, and other discrete structures. *Physical Review Letters* 68: 3631.

Chakrabarti BK and Sen P (2014) *Sociophysics: An Introduction*. Oxford: Oxford University Press.

Fort H (2020) *Ecological Modelling and Ecophysics*. Bristol: IOP Publishing.

Fröhlich J, Simon B, and Spencer T (1976) Infrared bounds, phase transitions and continuous symmetry breaking. *Communications in Mathematical Physics* 50(1): 79–95.

Gallavotti G (1999) *Statistical Mechanics*. Berlin: Springer-Verlag.

Gibbs JW (1902) *Elementary Principles in Statistical Mechanics*. New York: Scribner's sons.
Khinchin AI (1960) *Mathematical Foundations of Statistical Mechanics*. New York: Dover.
Lenz W (1920) Beitrag zum Verständnis der magnetischen Erscheinungen in festen Körpern. *Physikalische Zeitschrift* 21: 613–615.
Ma S-K (1985) *Statistical Mechanics*. Singapore: World Scientific.
Mermin ND and Wagner H (1966) Absence of ferromagnetism or antiferromagnetism in one- or two-dimensional isotropic heisenberg models. *Physical Review Letters* 17: 1133–1136.
Mussardo G (2020) *Statistical Field Theory: An Introduction to Exactly Solved Models in Statistical Physics*. Oxford: Oxford University Press.
Onsager L (1944) Crystal statistics. I. A two-dimensional model with an order-disorder transition. *Physics Review* 65: 117–149.
Park J-W, Kim CU, and Isard W (2012) Permit allocation in emissions trading using the Boltzmann distribution. *Physica A* 391: 4883–4890.
Peierls R (1936) On Ising's model of ferromagnetism. *Mathematical Proceedings of the Cambridge Philosophical Society* 32: 477.
Ramsey N (1956) Thermodynamics and statistical mechanics at negative absolute temperatures. *Physical Review* 103(1): 20–28.
Reichl L (1998) *A Modern Course in Statistical Physics*, 2nd edn. New York: Wiley-Interscience.
Ruelle D (1999) *Statistical Mechanics, Rigorous Results*. Berlin: Springer-Verlag.
Thompson CJ (1988) *Classical Equilibrium Statistical Mechanics*. Oxford: Clarendon Press.
Toda M, Kubo R, and Saito N (1983) *Statistical Physics I: Equilibrium Statistical Mechanics*. Berlin: Springer-Verlag.

Statistical mechanics: Quantum

Rosario Fazio[a] **and G Piccitto**[b], [a]The *Abdus Salam* International Centre for Theoretical Physics, Trieste, Italy; [b]Università di Catania, Catania, Italy

© 2024 Elsevier Ltd. All rights reserved.

This is an update of R. Fazio, G. Piccitto, Statistical Mechanics: Quantum, Editor(s): Franco Bassani, Gerald L. Liedl, Peter Wyder, Encyclopedia of Condensed Matter Physics, Elsevier, 2005, Pages 35–40, ISBN 9780123694010, https://doi.org/10.1016/B0-12-369401-9/00620-3.

Introduction 571
Conclusion 575
References 576

Abstract

Ensembles of identical quantum particles have statistical properties that deviate from the classical Boltzmann distribution. Quantum statistics drastically depend on the constituent particles being bosons or fermions, with tangible consequences on the properties of low-temperature quantum gases. We briefly review the properties of quantum statistics with some of their most spectacular consequences. The additional interaction between the particles enriches enormously the panorama leading to a huge variety of phenomena, two examples are magnetism or superconductivity.

Key points

- The statistical properties of ensembles of indistinguishable particles drastically depend on their nature, being bosonic or fermionic. Bose-Einstein condensation, the specific heat of solid at low temperatures, are only few important examples of the relevance of quantum statistics.
- The interplay of quantum effects and interactions in systems of many particles is at the heart of a multitude of macroscopic phenomena, ferromagnetism or superconductivity are only two examples of this sort.
- Phase transitions can occur also at zero temperature, driven by quantum fluctuations.

Introduction

One of the fundamental results in classical statistical mechanics is the Boltzmann distribution function (Huang, 1987). Given a system formed by a large number of identical particles and in contact with a thermal reservoir, it gives the probability for the system to have a given energy E. The Boltzmann distribution can be derived by counting the number of possible microscopic configurations which lead to the same energy and assuming that they occur with the same probability. Another crucial assumption, which seems perfectly justified in the classical world, is that the particles, albeit identical, are supposed to be distinguishable. This last hypothesis does not hold in the quantum world, as one of the postulates of quantum mechanics states that identical particles should be considered as indistinguishable (Eisberg and Resnick, 1985). The wave function of a system of identical particles should be unchanged, up to a phase factor, under a permutation of two of them. The standard argument to derive the statistics is to apply a permutation between two particles twice, that is, restoring the initial configuration. It immediately follows (the 2D case is not considered) that under a permutation, the wave function can remain unchanged (symmetric) or change sign (antisymmetric). These two cases define two different classes of particles named bosons and fermions, respectively. Bosons are particles with an integer spin, while for fermions, the spin assumes half-integer values. In both cases, the presence of a particle in a given state influences the probability of the other particles to be in that state; this is not the case in the hypothesis which leads to the Boltzmann distribution. Indistinguishability of identical particles and then quantum mechanical effects are intimately related to the fact that the wave functions of two particles have appreciable overlap. Decreasing the temperature T or increasing the density, ρ, of an identical particle system will lead to a wave packet overlap when the thermal de Broglie wavelength $\lambda_{\mathrm{dB}}(T) = \sqrt{2\pi\hbar^2/mk_{\mathrm{B}}T}$ becomes of the order or greater than the average distance between particles, $\lambda_{\mathrm{dB}}(T) \geqslant d \approx 1/\rho^{1/3}$. If P_1 is the probability of adding a classical particle to a state with n particles, from the symmetry properties of the wave functions, it is easy to show that in the case of fermions or bosons, this probability is respectively suppressed by a factor $(1 - n)$, or enhanced by a factor $(1 + n)$. The probability for two bosons to be in the same quantum state is enhanced; on the contrary, fermions obey the Pauli principle which forbids two fermionic particles to have the same quantum numbers.

In order to obtain the distribution function for fermions and bosons one can proceed as follows. Consider two energy states E_1 and E_2; the principle of detailed balance states that in equilibrium the ratio of transition rates between the two states is equal to the ratio of the populations of particles in the two states or, equivalently, to the ratio of the Boltzmann factors: $\Gamma_{2\to1}/\Gamma_{1\to2} = n_1/n_2 = \mathrm{e}^{-\beta E_1/\mathrm{e}^{-\beta E_2}}$. The probability of having n fermions/bosons in a given state can be expressed in terms of the Boltzmann distribution if the rates are properly modified so as to account for the suppression/enhancement factor due to the occupancy of the final state. The detailed balance condition can then be rewritten as $n_1(1 \pm n_1)/[n_2(1 \pm n_2)] = \mathrm{e}^{-\beta(E_1-E_2)}$ where $\beta = 1/k_\mathrm{B}T$, T is the temperature and k_B is the Boltzmann constant. From the previous equation it follows that the distribution functions for quantum particles are

$$n_{FD}(E) = \frac{1}{\mathrm{e}^{\beta(E-\mu)} + 1} \quad \text{for fermions} \tag{1}$$

$$n_{BE}(E) = \frac{1}{\mathrm{e}^{\beta(E-\mu)} - 1} \quad \text{for bosons} \tag{2}$$

In the previous equations the chemical potential μ fixes the average total number of particles. The functions $n(E)$ are named after the scientists who formulated them, as Bose–Einstein and Fermi–Dirac distribution functions. Eqs. (1) and (2) are represented in Fig. 1 for different values of the temperatures. At energies E much larger than $1/\beta$, the quantum statistics approaches the Boltzmann distribution; in the limit of high temperatures, the average occupation of each energy state is much smaller than one and the quantum effects can be ignored. Indeed for $n \ll 1$, the suppression/enhancement factor related to the quantum statistics can be ignored and thus the classical distribution function is recovered. In the low temperature limit, the quantum effects become dominant. Bose–Einstein statistics lies always above the Boltzmann distribution. The Fermi–Dirac distribution function is always less than one (due to the Pauli principle), and at zero temperature, drops abruptly from one to zero at the (so-called) Fermi energy E_F (coincident in this case with the chemical potential).

The differences in the distribution functions will reflect in the properties of Fermi and Bose systems at low temperatures. Although it is impossible to briefly review this huge field of investigation, it is nevertheless useful to recall a few brief important examples where quantum statistics plays a dominant role. In order to keep the presentation as simple as possible, perfect gases are considered, that is, the only contribution to the energy is due to the kinetic term while interaction between particles are disregarded. The fact that a direct interaction term is not present does not mean that the particles do not feel each other. As discussed already, indistinguishability implies that the probability for a particle to occupy a given state influences the probability of the other particles being in the same state. Let fermions be considered first. At zero temperature, from the Pauli principle, it follows that all states below a certain energy are occupied while all the states above it are empty. The energy of the highest occupied level is defined as the Fermi energy. A Fermi gas is said to be degenerate when its temperature is small compared to $E_\mathrm{F}/k_\mathrm{B}$; in the opposite limit of a non-degenerate gas, the properties are those of a classical gas and therefore, they are not discussed here. For a gas of N fermions contained in a volume V, the Fermi energy is given by

$$E_\mathrm{F} = \frac{\hbar^2}{2m}\left(\frac{3\pi^2 N}{V}\right)^{2/3} \tag{3}$$

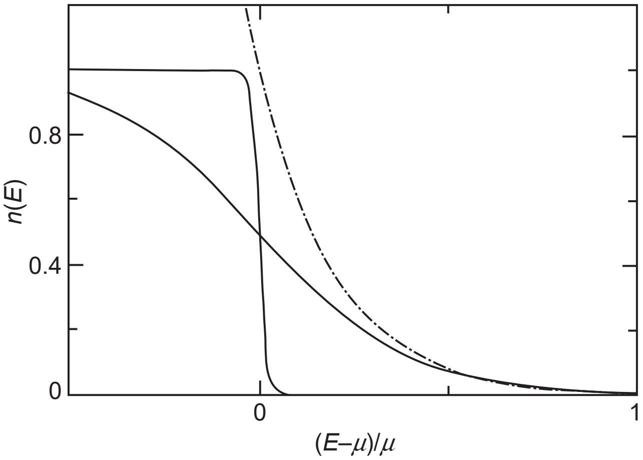

Fig. 1 The Fermi–Dirac distribution function (thin solid curve) is compared to the Boltzmann distribution (dashed-dotted curve) for a temperature of $T = 0.2\ \mu/k_\mathrm{B}$. The agreement with the classical distribution is good only for energies far above the Fermi energy. At low energies the Pauli principle prevents the double occupancy of the same state as it would follow from the classical analysis. For completeness, the Fermi-Dirac distribution is plotted also at lower temperature $T = 0.01\ \mu/k_\mathrm{B}$; it can be noted that it approaches a step function at zero temperature.

where $\hbar$ is the Planck constant divided by 2π, and m is the fermion mass. Another useful quantity to characterize the system is the density of states $N(\varepsilon)$, defined as the number of states which are present in an energy shell between E and $E + \mathrm{d}E$. For a Fermi gas, counting the states in the given shell results in a density of states

$$N(E) = \frac{V}{2\pi^2}\left(\frac{2m}{\hbar^2}\right)^{3/2} E^{1/2} \tag{4}$$

The chemical potential μ coincides with the Fermi energy at zero temperatures; on increasing T, it decreases and becomes negative (a 3D system is considered) at temperatures of the order of the Fermi temperature $T_\mathrm{F} = E_\mathrm{F}/k_\mathrm{B}$. Typical values of the Fermi energy for metals are such that at room temperature the ratio T/T_F is of the order of 10^{-2}. In this case, which is the most frequently encountered situation, the density of states can be assumed to be constant in an interval of the order of T centered in T_F. A good example to see deviations in the thermodynamic quantities due to quantum effects is to consider the heat capacity of a Fermi gas, such as electrons in a metal. One can recall the equipartition theorem which states that, for a monoatomic gas the heat capacity is constant and is 3/2. That is what is expected for a Fermi gas at temperatures higher than the Fermi temperature. In the low temperature limit, the only states which contribute to the heat capacity are those in a strip of width $k_\mathrm{B}T$ around the Fermi energy, that is, those in the energy region where the Fermi function is smeared. All the other electrons are effectively frozen due to the Pauli principle. The number of electrons thus contributing to the temperature dependence of the internal energy are of the order of NT/T_F, each of them having an energy of the order of $k_\mathrm{B}T$. A detailed calculation leads to the result $C_e = (\pi^2/2)Nk_\mathrm{B}T/T_\mathrm{F}$; it goes to zero linearly with temperature. It is possible to measure the electronic contribution to the heat capacity in metals at low temperature (typically of the order of kelvin) when the lattice contribution (which depends on T^3) can be disregarded. Another interesting example of the consequence of the Pauli principle in the thermodynamic quantities is the Pauli spin susceptibility, which measures the spin response of the electron system to an applied magnetic field. Using the same line of reasoning as before, it is evident that at low-temperature spin susceptibility, $\chi = N(E_\mathrm{F})$. Indeed the argument goes as follows: the number of spins which can be flipped by an applied magnetic field is a fraction of T/T_F around the Fermi energy because, due to the Pauli exclusion principle, the other spins cannot be flipped since the corresponding (spin-flipped) state is occupied. The susceptibility per spin is given by the Curie law $\sim 1/T$. From here it therefore follows that the Pauli result of a spin susceptibility is independent of temperature and proportional to the density of states at the Fermi energy. In the presence of electron-electron interaction and/or external potential, instead of the particles, one can describe the properties of the Fermi liquid by means of the long-lived quasiparticle excitations close to the Fermi energy (Abrikosov et al., 1975). The leading temperature dependence of the various observables is not modified (for example the heat capacity remains linear in the temperature dependence); however, the effect of the interaction enters in the renormalization of the parameters characterizing the Fermi liquid. Degenerate Fermi systems are observed in a variety of very different physical situations ranging from electrons in metals to electrons in white dwarfs. It is worth stressing at this point that the effect of interaction between electrons, or interaction of the electrons with the ions of the lattice does not always result in the renormalization of the parameters (such as effective mass).

A completely different behavior is observed in a gas of bosons at low temperatures. Here there is no Pauli blocking; on the other hand, for bosons, the probability of being in the same quantum state is enhanced as compared to the classical value. A very interesting phenomenon observed in the Bose system is that of the Bose–Einstein condensation. Below a given critical temperature, there is a macroscopic fraction of the particles which condense into the state with the lowest energy. In order to grasp the process of Bose–Einstein condensation, it is useful to understand the behavior of the chemical potential close to the transition temperature. (If the total number of bosons is not conserved, as for photons, the chemical potential is zero and the Bose–Einstein distribution coincides with the Planck distribution for the blackbody radiation.) As in the case of fermions, an ideal boson gas with a macroscopic fixed number N of particles of spin zero is considered. The density of states $N(E)$ of this system is given by Eq. (4). The factor 1/2 is due to the fact that the density of states per spin species is being considered. In order to avoid that some occupation number could be negative, the value of chemical potential must always be less than the ground-state energy which, for simple reasons is assumed to be equal to zero, $\mu < 0$ (see Eq. 2). The chemical potential depends on the number of particles and on the temperature. At zero temperature all the N particles are in the ground state; from this fact it is easy to show that for $T \to 0$, the chemical potential tends to the ground-state energy as $\mu = -k_\mathrm{B}T/N$. The particles are distributed among the ground state and all the excited states as

$$\begin{aligned} N &= \sum_i \frac{1}{\mathrm{e}^{\left(E_i-\mu\right)/k_\mathrm{B}T} - 1} = N_0(T) + \int_0^\infty N(E)\frac{1}{\mathrm{e}^{(E-\mu)/k_\mathrm{B}T} - 1}\,\mathrm{d}E \\ &= N_0(T) + N_\mathrm{ex}(T) \end{aligned} \tag{5}$$

The integral in Eq. (5) can be calculated and the result is

$$N = N_0(T) + \frac{V}{\lambda_{\mathrm{d}B}^3(T)} g_{3/2}\left(\mathrm{e}^{\mu/k_\mathrm{B}T}\right) \tag{6}$$

where $g_\eta(z) = \sum_{t=1}^{\infty} z^t/t^\eta$.

At "high" temperature the value $N_\mathrm{ex}(T)$ is of the same order of magnitude of N, and the population is distributed over all the states, each state being weakly occupied. Below a critical temperature $T_\mathrm{c} \propto \rho^{2/3}$, where ρ is the particle density, the ground state becomes macroscopically occupied and the fraction of particle in the ground state is

$$\frac{N_0(T)}{N} = 1 - \left(\frac{T}{T_c}\right)^{3/2} \tag{7}$$

The temperature T_c is the Einstein condensation temperature and satisfies the relation $N_{ex}(T_c) = N$; it is important to note that the critical temperature is usually several orders of magnitude higher than the level spacing between the ground state and the first excited state. The occurrence of a single quantum state macroscopically occupied is the key to the Bose–Einstein condensation. The experimental observation of Bose–Einstein has been recently realized with dilute alkali gases (Dalfovo et al., 1999).

Quantum statistical mechanics embraces a large class of situations where quantum effects do not necessarily stem from the quantum statistics of the constituent particles. There are a large number of situations where, though the particles are localized (therefore, the indistinguishability is not important), quantum mechanics plays a crucial role. Probably, among the most popular situations, the studies on localized spins interacting through an exchange coupling are mentioned. In this case, quantum effects emerge due to the quantum nature of the spin degree of freedom. The fact that different components of the spin do not commute reflects in a kind of quantum frustration. The impact of spin models in quantum statistical mechanics is not confined only to the theory of magnetism. More generally, pseudo-spin models should be considered as they cover a wider range of materials, for example, glasses and superconductors. They can be described in terms of fictitious spins located in a given network, in certain limits.

As it is already hinted in the previous paragraph, interaction between the particles is responsible for a huge variety of phenomena which will appear in many articles in this encyclopedia. In the brief description made of the properties of Fermi systems, it is mentioned that electron–electron interaction can be incorporated by means of renormalization of the physical parameters characterizing the fermion liquid. However, this is not always the case. Among the others, interaction between particles often leads to instabilities and consequently a phase transition to a condensed phase occurs (Goldenfeld, 1992). Examples of phase transitions are ferromagnetism, superconductivity, and charge/spin density waves, just to mention a few important cases. Phase transitions can be driven both by thermal fluctuations and by quantum fluctuations. In the former case, below a certain temperature the system orders spontaneously even in the absence of any applied field. The prototype example is the ferromagnetic transition; below the Curie temperature, the system will present a spontaneous magnetization even in the absence of any external magnetic field (Yosida, 1998). A quantum phase transition instead takes place at zero temperature, and it is driven by the changing of some parameter, for example, a coupling constant or an external field, of the system (Sachdev, 2000). In this case the thermodynamical properties, for example, the magnetization, are deeply connected to the dynamical ones since both derive from the quantum dynamics of the many-body system. Probably, the simplest example of a quantum phase transition can be described in a model of spin interacting via an (ferromagnetic) exchange coupling (with strong anisotropy in the x-direction) J_x, and subjected to an external magnetic field B (say along the z-direction). This model Hamiltonian, known as Ising model in a transverse field, appropriate for this model is

$$H = -\frac{J_x}{2}\sum_{\langle ij\rangle}\sigma_i^x\sigma_j^x - B\sum_i \sigma_i^z \tag{8}$$

where σ^a are the Pauli matrices ($a = x, y, z$). The interaction, in order to give an example, is chosen to be between nearest neighbors. In the limit of a large external field the spin will align along the z-direction. However, because of the quantum nature of the spin degree of freedom, the alignment along the direction of the external field prevents any kind of ordering along the x-direction due to the exchange interaction. By increasing the ratio between J_x/B, at a given critical value the spin will prefer to order along the x-direction, and the system will develop a nonzero magnetization along the x-direction. The transition to the ordered state can be induced at zero temperature solely by the variation of the parameter J_x/B and, as has already been said, is intimately related to the quantum properties of the spin. All the signals for the emergence of a phase transition are contained in the dynamical properties of the interacting spins. If the spins of the Ising model are arranged in a chain, this is one of the few exactly solvable models in quantum statistical mechanics. Here the case of a 3D lattice is considered and the quantum phase transition by means of the mean field approximation is discussed. It consists in replacing the interaction among the neighboring spins by an effective field which acts on each spin, that is, it consists in replacing of $\sigma_i^x = \langle\sigma_i^x\rangle + (\sigma_i^x - \langle\sigma_i^x\rangle)$, where the angular brackets $\langle\ldots\rangle$ mean the quantum statistical average, disregarding the quadratic fluctuations around the average internal field. The value of $\langle\sigma^x\rangle$ is determined self-consistently by imposing that the average value of the magnetization calculated with the approximated form of the Hamiltonian, which reads $H_{MF} = -(J_x z\langle\sigma^x\rangle/2)\sum\sigma_i^x - B\sum\sigma_i^z$ of, coincides with the mean field. In the previous equation, z is the number of nearest neighbors. This condition leads to the self-consistent equation

$$\langle\sigma^x\rangle = \langle\psi_{MF}|\sigma^x|\psi_{MF}\rangle \tag{9}$$

where the $|\psi_{MF}\rangle$ S is the ground-state wave function of the mean field Hamiltonian (only the case of zero temperature is considered). A numerical solution of Eq. (9) sketched in Fig. 2, shows the behavior that is briefly outlined. As it is beautifully described by Nielsen and Chuang in 2000 (Nielsen and Chuang, 2000), thanks to universality, most of the properties of a system close to a phase transition do not depend on the microscopic details of the model. For the example discussed, while the value of the critical field is indeed dependent on the exchange coupling, the behavior of the magnetization is only related to the dimensionality of the system and to the symmetry which is spontaneously broken.

As it should emerge from these remarks, quantum mechanics plays a different role in classical and quantum phase transitions. Let superconductivity as an example be taken in order to elucidate this point. A transition to the superconducting state is induced by the condensation of a pair of electrons (the Cooper pairs). The effective electron–electron attractive interaction (which in

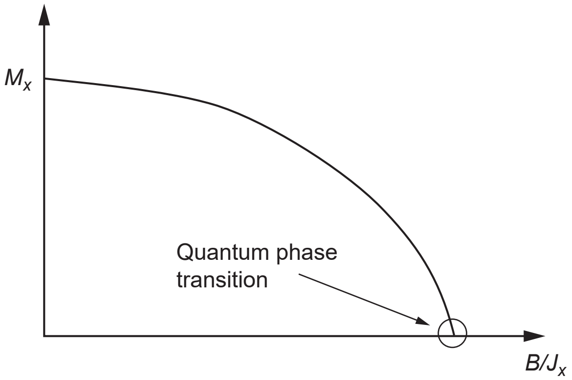

Fig. 2 A sketch of the magnetization, at zero temperature, along the *x*-axis is plotted against the ratio B/J_x. The spontaneous magnetization is different from zero only at sufficiently low fields. Close to the critical point the magnetization goes as $|\lambda - \lambda_\chi|^\beta$. In the mean field analysis discussed in the text $\beta = 1/2$.

conventional superconductors is mediated by the phonons) is responsible for the formation of the pairs. The formation of a bound state of two electrons is a Fermi surface effect, which relies on quantum mechanics. Although quantum mechanical effects are responsible for the instability to the superconducting state, the properties of the transition itself can be described by classical statistical mechanics. In a quantum phase transition, instead, the quantum fluctuations are primarily responsible for the transition itself, which is now related to a modification of the ground-state wave function.

This last paragraph represents a return to the theme in the introduction and a slight deviation from the traditional quantum statistical mechanics. The question of indistinguishability viewed from a different perspective, has stimulated a number of works in the newly born field of quantum information. The (anti-)symmetrized form of the wave function for a system composed by *N* (fermions) bosons implies that the many-body state cannot be written, even in the absence of any interaction, as a product of wave functions related to each single particle. The many-body wave function is said to be entangled (Vedral, 2003). Entanglement is the property of quantum states to exhibit correlation which cannot be accounted for by classical physics. It arises as a consequence of the principle of superposition in the presence of a Hilbert space with a tensor product structure. Entanglement denotes the nonlocal correlations that exist, even in the absence of direct interaction, between two (spatially separated) parts of a given quantum system. Since the early days of quantum mechanics, understanding the phenomenon of entanglement has been central to the understanding of the foundations of quantum theory. Besides its fundamental importance, a great deal of interest has been brought forth by its role in quantum information. Entanglement is believed to be the main ingredient of computational speed-up in quantum information protocols. In the case being discussed here, entanglement is of statistical origin. With the development of information theory, a great deal of attention has been devoted to the characterization and quantification of entanglement contained in a given quantum state. Although the progress has been impressive, a full characterization is still far from being completed. Parallel to understanding entanglement in systems of two-level systems (qubits) used for quantum information, research has touched the question on how to characterize entanglement in "traditional" condensed matter systems with the aim of finding a bridge between information science and condensed matter (Osterloh et al., 2002).

Conclusion

In order to understand more deeply the role of quantum mechanics in the collective properties of quantum many-body systems, probably conventional approaches in quantum statistical mechanics can be conveniently supplemented by the use of a variety of techniques developed in quantum information theory. As a final example, the attention devoted recently to the study of quantum phase transitions from a "quantum information" point of view is mentioned (Vidal et al., 2003; Osborne and Nielsen, 2002). Both classical and quantum phase transitions can indeed be formulated in the framework of Ginzburg–Landau approach. A crucial point that determines all the properties close to the transition is the fact that the systems behave cooperatively. Classical correlations between particles do not, however, imply that quantum correlations (entanglement) do follow the same behavior. As entanglement is one of the major resources in quantum computation, it is certainly important to be able to understand the properties and the amount of entanglement possessed by a large number of particles close to a quantum phase transition. The link between statistical mechanics and quantum information theory has been carried ahead in refining established methods for examining many-body interacting systems. An QJ; example is the entanglement preserving Density Matrix Renormalization Group, where a deep understanding of the entanglement properties of the many-body systems has helped in reformulating and generalizing this method Daley (Daley et al., 2004). A final mention is made of the attention which is being devoted to the possibility of using quantum spin networks, a traditional arena for quantum statistical mechanics, as quantum channels for transporting and/or manipulating quantum information.

References

Abrikosov AA, Gorgov LP, and Dzyaloshinski IE (1975) *Methods of Quantum Field Theory in Statistical Physics*. New York: Dover.

Daley AJ, Kollath C, Schollwoeck U, and Vidal G (2004) Time-dependent density-matrix renormalization-group using adaptive effective Hilbert spaces. *Journal of Statistical Mechanics: Theory and Experiment*: P04005.

Dalfovo F, Giorgini S, Pitaevskii LP, and Stringari S (1999) Theory of Bose-Einstein condensation in trapped gases. *Reviews of Modern Physics* 71: 463.

Eisberg R and Resnick R (1985) *Quantum Physics of Atoms, Molecules, Solids, Nuclei, and Particles*. New York: Wiley.

Goldenfeld N (1992) *Lectures on Phase Transitions and the Renormalization Group*. New York: Addison Wesley.

Huang K (1987) *Statistical Mechanics*. New York: Wiley.

Nielsen M and Chuang I (2000) *Quantum Computation and Quantum Communication*. Cambridge: Cambridge University Press.

Osborne TJ and Nielsen MA (2002) Entanglement in a simple phase transition. *Physical Review A* 66: 044301.

Osterloh A, Amico L, Falci G, and Fazio R (2002) Nature. *Scaling of entanglement close to a quantum phase transition* 416: 608.

Sachdev S (2000) *Quantum Phase Transitions*. Cambridge: Cambridge University Press.

Vedral V (2003) Entanglement and the second quantisation formalism. *Central European Journal of Physics* 1: 289–306.

Vidal G, Latorre JI, Rico E, and Kitaev A (2003) Entanglement in quantum critical phenomena. *Physical Review Letters* 90: 227902.

Yosida K (1998) *Theory of Magnetism*. Heidelberg: Springer.

Quantum biology: An overview

Neill Lambert[a] **and Franco Nori**[a,b,c], [a]Theoretical Quantum Physics Laboratory, Cluster for Pioneering Research, RIKEN, Wakoshi, Saitama, Japan; [b]Center for Quantum Computing, RIKEN, Wakoshi, Saitama, Japan; [c]Department of Physics, The University of Michigan, Ann Arbor, MI, United States

© 2024 Elsevier Ltd. All rights reserved.

Introduction 577
What is a quantum advantage? 577
Photosynthesis 578
Magnetoreception with radical pairs 580
Other contenders 581
Conclusion 582
References 582

Abstract

This is an overview of the field of quantum biology, focusing on the examples of light harvesting in photosynthesis and radical-pair-based avian magnetoreception. We briefly describe the history and motivation behind categorizing certain biological phenomenon as "quantum" in nature, and explain how these examples might satisfy this criterion.

Key points

- Define what we mean by "quantum" biology, particularly with regard to function and advantage.
- Describe photosynthesis in its basic form, and evidence for and against quantum coherence being important.
- Describe radical-pair-based magnetoreception, why it is classified as quantum, and the latest results in this field.

Introduction

The topic of quantum biology (Lambert et al., 2013a; Mohseni et al., 2014; Scholes et al., 2017; Cao et al., 2020) describes a broad range of potential biological phenomena which may rely on quantum effects to function. While the modern conception of quantum biology arose alongside the demonstration of electronic coherence in light-harvesting complexes in the early part of this century, its history extends back to early speculation by Erwin Schrödinger in his textbook "What is life?" (Schrödinger, 1944), and extensive work by the physical chemistry community in the latter half of the 20th century.

Despite this long pedigree, and immense attention from both the scientific and popular science communities, the existence of an uncontested and clear demonstration of a biological system whose function relies on quantum mechanics in some nontrivial way is still lacking. In this article we will describe the essential parts of the two primary examples of quantum biological systems, and summarize the latest results and progress in each case.

What is a quantum advantage?

Before considering explicit examples, it is useful to clarify under what circumstances, in terms of time scales and temperatures, we might expect quantum mechanics to be important in some biological process. Then, assuming such circumstances are tenable, we will explain why quantum mechanics may sometimes be advantageous over "classical" theories, and hence why it might fulfill some role in either making some biological function more optimal or enabling some functions that cannot exist classically at all.

The understanding and development of quantum mechanics in the 20th century began, generally speaking, with the problem of understanding atomic structure, and the wave–particle duality of light and matter. It was only at very small length and time scales that quantum mechanics appeared in a clear way, and gave rise to phenomena that could not be described with classical theories. The reason we do not see quantum mechanics at large length and time scales is typically attributed to "decoherence". In other words, in macroscopic systems, a large number of degrees of freedom interact with each other and eventually "smear out" any local quantum effects, giving rise to the observable classical world.

We can imagine focusing on some small part of a larger system, and asking the question of how that small "quantum system" is affected by the rest, which we call its environment. Under some reasonable assumptions, we expect that, after some time interacting with the environment, that small system will reach thermal equilibrium with said environment and thereafter can be described by a

https://doi.org/10.1016/B978-0-323-90800-9.00176-1

thermal mixture of quantum states. In a thermal state the interaction with the environment has obscured precisely which quantum state the system is in. Such a mixture can be described with an ensemble of possible quantum states in the form of a density matrix:

$$\rho(t \to \infty) = \sum_i \frac{e^{-\hbar\omega_i/k_B T}}{Z} |\psi_i\rangle\langle\psi_i| \tag{1}$$

This formula tells us that a certain quantum state $|\psi_i\rangle$ exists, in equilibrium, with probability $e^{-\hbar\omega_i/k_B T}/Z$, where ω_i is that state's energy, $\hbar$ is the reduced Planck's constant, k_B is Boltzmann's constant, T is the temperature, and Z is the partition function which normalizes these probabilities to one. Intuitively, such a thermal state can be considered as becoming classical at high temperatures because it has no coherence between eigenstates of the system ψ_i. Such eigenstates themselves however can, in principle, contain coherence (i.e., superpositions in a different basis). At very high temperatures $\hbar\omega_i \ll k_B T$, even these coherences start to be less relevant (an infinite temperature state has no coherence in any basis), and this "classical mixture" obscures any desirable quantum effects. These features give rise to the rule of thumb that quantum mechanical effects are difficult to observe in hot environments.

This is not the whole story, however, as in nonequilibrium situations, common in chemical and biological processes, this thermal equilibrium does not occur immediately. To quote Schrödinger, "living matter evades the decay to equilibrium" (Schrödinger, 1944). If, for example, the arrival of a photon gives rise to a process like electron transfer between a donor and an acceptor molecule, or the excitation of an electron in a molecule to a higher energy configuration, then it may take some time before this "quantum system" reaches equilibrium. How quickly any quantum effects that may then occur are washed away depends not on the temperature alone, but also on how strongly the surrounding environment affects that state. The spin of an electron, for example, is very weakly interacting with anything around it, and thus quantum coherence and correlations can persist for a long time. This weak interaction is what has given rise to the possibility of magnetoreception in radical pairs, as we will describe later.

If the energy difference between possible states in the biological system is either high enough to avoid thermalization, or the system is slow to reach equilibrium on some biologically relevant timescale, what kind of use might biological systems make of quantum mechanics? Why do we presume it to be useful in the first place? The potential for systems operating according to the laws of quantum mechanics gaining some advantage over equivalent classical ones largely comes from the field of quantum computing, through examples like Grover's search algorithm. More mundanely, superconductivity, lasing, and the transistor all rely on quantum effects in less direct ways, but all together suggest the idea that quantum physics can have functional roles, either to speed up certain processes (as is argued in photosynthesis) or enable them to function at all (as is argued in the radical pair mechanism for magnetoreception).

In quantum computing, any advantage that is gained typically relies on preserving coherence (and entanglement), which is another word for the existence of quantum superposition of multiple possible states in a desired basis or set of possible states (or irreducible correlated coherence between multiple systems). The intuition used in the field of quantum biology is then that if quantum coherence is observed on timescales relevant for some biological process then that coherence may potentially play a functional, and even advantageous, role. In the examples that follow, we will see that while arguments and evidence for such a functional role seem reasonable, unambiguously verifying it remains challenging.

Photosynthesis

Light harvesting in plants, algae, and some bacteria is a complex process involving many individual steps, from light absorption at an antenna complex (a pigment protein complex, made up of chlorophyll molecules which can absorb light, at appropriate frequencies, as electronic excitations), to, eventually, charge transfer at a reaction center, which is used to build up an electromagnetic potential across a cell membrane. This potential is then used, by a later process, to form adenosine triphosphate (ATP) and eventually sugars.

The steps between the absorption of energy by an antenna complex and the charge transfer at a reaction center can be understood in the following way. Initially, an electron in a single chlorophyll molecule is excited to a higher energy state. This molecule is in close proximity to other chlorophyll molecules, with which this excited electron interacts via a Coulomb force. This interaction induces the electron in the first molecule to return to its lower energy state, while an electron in the second molecule is excited (one can imagine, from a fundamental physics point of view, that this interaction is mediated by the emission and absorption of virtual photons). The goal of the complex then is to use this interaction between its constituent molecules to funnel energy toward the reaction center, which typically succeeds because of a downhill gradient in the chlorophyll excitation energies, and with the help of energy dissipation from the environment (largely thought to be harmonic motion of the nuclei within the molecules and the protein structure) .

The energies and timescales involved depend on the photosynthetic complex being studied, but in general the transfer of energy from antenna to reaction center takes on the order of 1–100 pico-seconds. The time scale at which excitations are lost due to, for example, an electron in a chlorophyl falling back to its original state is much slower, on the order of nano-seconds, and hence the efficiency, per unit of energy absorbed, of photosynthetic light harvesting is incredibly high (though some energy is inevitably lost in various substeps of the process, like the environmentally assisted downhill motion).

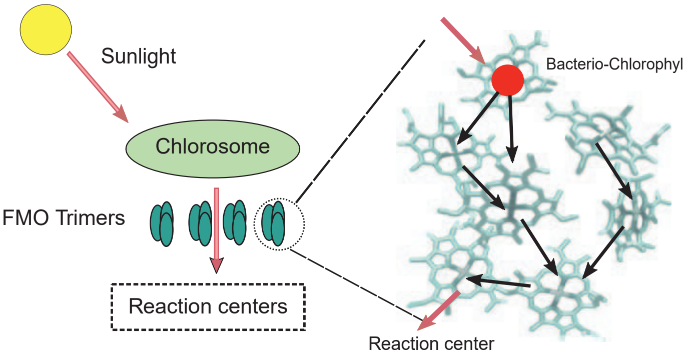

Fig. 1 A cartoon schematic of the Fenna-Matthews-Olson complex and its role in the light-harvesting apparatus of green sulfur bacteria. The FMO complex is a type of pigment-protein complex, which exists as a trimer. Within each part of the trimer there are seven (or potentially eight, according to recent research) Bacterio-Chlorophyll (BChl) molecules, which act as nodes in a energy-transport network. The trimers connect a large light-harvesting antenna, a chlorosome, to reaction centers. On the right we have illustrated how a localized excitation on a single BChl can be seen as hopping through the network in a classical fashion (the arrows indicated the strongest couplings between sites). An alternative orthodox semiclassical picture is of an excitation delocalized across the complex, but which then increases the probability of the excitation being close to the reaction center via a classical rate equation connecting delocalized eigenstates. The quantum picture sits between these two extremes, where the arrival of a semilocalized excitation does not immediately thermalize, but experiences temporal beating, or oscillations, on the same time scale that it takes for the excitation to arrive near the reaction center.

There are two traditional, classical, or semiclassical, pictures of this energy transport process:

- The site picture: In this limit (see Fig. 1), the excitation is localized on a single chromophore, and the motion between chromophores can be described by a classical rate equation. This picture may be valid when there is a large amount of disorder and the interaction with the environment is much stronger than the coupling between chromophores.
- The excitonic picture: In this limit, the excitation is delocalized across multiple pigments and is in, or close to being well described by, one of the eigenstates of the full Hamiltonian (though for larger complexes this seems unlikely, and the delocalization may just be across a few pigments). Any preparation in a state which is not an eigenstate (e.g., a superposition of eigenstates, or an excitation localized on a single chromophore, either because of direct illumination or due to the arrival of an excitation from another complex), very quickly thermalizes into its constituent eigenstates. Then, that mixture evolves toward a thermal mixture of even more eigenstates via an effectively classical rate equation. In this picture, an excitation arriving from the antenna complex will be higher in energy, and follow a downhill path, to arrive in a delocalized state which has a large probability of being in a chromophore near the reaction center. Interestingly, this thermalization and downhill energy flow still, fundamentally, relies on a quantum description of the complex and its interaction with the environment (Cao et al., 2020).

It has been this process of energy transfer that has been studied as a potential example of functional quantum biology (Scholes et al., 2017), for which some evidence suggests neither of the above two standard pictures are sufficient. The broad idea is that the movement of the electronic energy from absorption site, to the reaction center, can, potentially, be more efficient when there is both electronic coherence across multiple chlorophyll molecules (i.e., a delocalization of energy), and a nonnegligible lifetime of coherent oscillations between superpositions (i.e., not the instant thermalization typically assumed in the excitonic picture). Combined with the aforementioned downhill arrangement of eigenenergies, and interaction with the environment, these are expected to give a higher efficiency for the movement of energy to the reaction center.

The first observation of nonnegligible quantum coherent oscillations, persisting for hundreds of femto-seconds, between different excitonic (delocalized) states was in the Fenna-Mathews-Olsen (FMO) complex of green sulfur bacteria (Engel et al., 2007; Cheng and Fleming, 2009; Panitchayangkoon et al., 2010; Collini et al., 2010). The FMO complex is it itself a pigment-protein complex, comprising seven Bacterio-Chlorophyll molecules, but it largely acts as a wire, or transport route, between a much larger chlorosome antenna and a reaction center (see Fig. 1). The time for energy to move through a single FMO complex is roughly one pico-second; hence, quantum coherent oscillations persisting for hundreds of femto-seconds would suggest it could influence efficiency of the total light-harvesting process.

Superficially, the energies involved also suggest that such a hypothesis is reasonable. Ambient temperatures of 300 K, using our rule of thumb, correspond to frequencies on the order of 200 cm^{-1}, roughly the same magnitude as the difference between the excitation energies of the FMO complex and their couplings. The question of nonequilibrium dynamics allowing quantum effects to persist for hundreds of femto-seconds then depends on how strongly the electronic degrees of freedom interact with their environment, largely thought to be dominated by the aforementioned vibronic motion of nuclei.

Interestingly, no interaction with the environment at all is not beneficial for light harvesting, because a purely quantum model of the energy transfer, without an energy sink to assist in the downhill motion, would lead to localization of the energy on a few sites. Conversely, very strong interaction with the environment can also lead to localization (from the quantum mechanics perspective this is a type of Zeno effect, where the repeated observation of the location of the excitation by the environment prevents it from propagating). Intermediate ranges of interaction strength can optimize the efficiency of light harvesting and imply that quantum coherent interactions between the system and environment can occur. In addition, structured resonant modes in the environment may further enhance efficiency (Mourokh and Nori, 2015), and imply a nontrivial quantum role for “quantum environments” in light harvesting. For the electronic coherence oscillations to persist for hundreds of femto-seconds implies the environment sits in this sweet spot.

However, it is important to mention that experimental techniques used to demonstrate coherence in the FMO complex are complex, and conflicting results have been observed in attempts to repeat the observation of coherent oscillations. Recent work has shown that very long-lived oscillations seen in some examples may have arisen because vibronic environment oscillations modulate the energy of the electronic ground state (Duan et al., 2017), and not because of excited state electronic coherence as expected. Data in these newer experiments suggest that at room temperature the electronic excited state coherent oscillations only persist up to sixty femto-seconds.

These works give a different perspective on the role of quantum mechanics in light harvesting, and suggest that the orthodox excitonic model is the correct picture. In that picture, described above, the delocalized nature of the electronic states and the quantum nature of the interaction with the environment are what is important for maximizing the efficiency of the transport of energy in the FMO complex (Cao et al., 2020), but transient quantum coherent beating is unimportant. These results also suggest a more pragmatic approach to studying the role of quantum mechanics in light harvesting: quantum models are needed to accurately describe light harvesting, but it does not necessarily imply nature has evolved some mechanism to protect temporal quantum coherence to more efficiently harvest energy. Ultimately, these conflicting observations may need to be answered with more nuanced experimental approaches. Interestingly, novel approaches to spectroscopic studies of these systems involving quantum-enhanced sensing are being investigated (Scholes et al., 2017) as a way to achieve this goal, and artificial photosynthetic mimics of natural systems (Ghosh et al., 2011a, b) are being explored.

Magnetoreception with radical pairs

The mechanism by which some birds and insects navigate has fascinated scientists for decades, suggesting a hidden sense which humans either do not have or cannot access. In most cases, pinning down exactly how this sense functions has been difficult. Behavioral experiments on migratory birds have elaborated several key clues regarding their sensory apparatus (Hore and Mouritsen, 2016), some of which are:

- It acts as an inclination compass. In other words, it does not distinguish north from south, but instead is sensitive to the inclination of the magnetic field lines, which become more steep away from the equator.
- It is sensitive to the presence of certain frequencies of light, and thus might be “photo-activated”.
- It can be disrupted by broadband oscillatory electromagnetic fields.

Interestingly, many of these features can be explained by a chemical reaction process involving electron spin states in radical pairs (Schulten et al., 1978). Early work on the sensitivity of such chemical reactions *in vitro* only saw a response for magnetic fields much larger than the geomagnetic field of 50μT. In fact, sensitivity to very small magnetic fields was initially dismissed as impossible because the energy of electronic spin states in such a field is much smaller than the ambient temperature, suggesting any signal would be obscured by thermal effects.

The answer to this mystery of how sensitivity to very small fields might be maintained is, of course, again the transient, nonequilibrium nature of the processes involved, as we will describe below. Very recently experimental evidence was obtained of radical pair chemical reactions being sensitive to magnetic fields on the same order as the geomagnetic field (Kerpal et al., 2019). This observation, combined with recent progress in identifying specific host proteins in the form of certain types of cryptochromes in flavoproteins that occur in the eye of migratory birds (and the demonstration of their sensitivity to magnetic fields in vitro (Xu et al., 2021)) has put radical-pair-based magnetoreception back in the spotlight as a reasonable candidate example of quantum biology.

How exactly is this radical-pair-based reaction sensitive to the earth’s magnetic field, and why is it presented as an example of quantum biology in the first place? A radical is a molecule with a single unpaired electron, which can then behave “magnetically” because of the electron’s spin which, in a magnetic field, behaves like a quantized magnetic degree of freedom. Two radicals formed together, a radical pair, have an important property; they can be created in a highly correlated spin state, where the spin of the electron in a single molecule is not well defined (see Fig. 2). Essentially we do not know which spin is aligned up, and which is aligned down, so that they are described by a highly entangled superposition (in the form of a singlet or triplet state).

An important second property is that if this state changes in a certain way, for example, it changes from a singlet to a triplet state, the radical pair relaxes to a different chemical product than if it stayed in its original spin configuration. The logic then is that these two different “products” can give rise to biologically detectable signals, suggesting that if the singlet/triplet ratio depends on the alignment with the earth’s magnetic field, one would have a functioning magnetic compass.

The “quantum” part of this process is largely discussed in terms of the singlet-triplet states and how they are converted from one to the other. To elaborate further, it is useful to consider the schematic diagram in Fig. 2. As mentioned earlier, the initial singlet state of the radicals is that of a superposition of one of the electron spins pointing up, and the other down, for example,

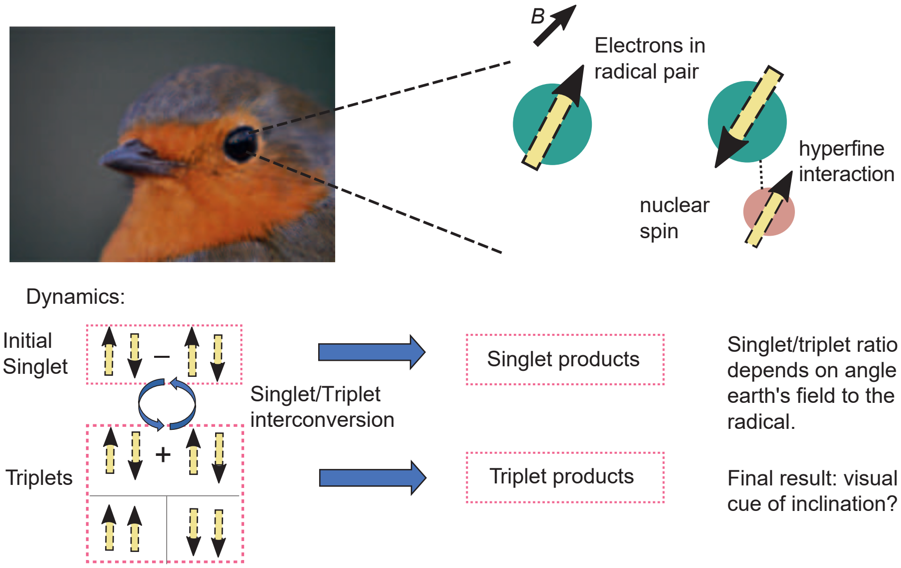
B
Electrons in radical pair
hyperfine interaction
nuclear spin
Dynamics:
Initial Singlet
−
Singlet/Triplet interconversion
Triplets
+
Singlet products
Triplet products
Singlet/triplet ratio depends on angle of earth's field to the radical.
Final result: visual cue of inclination?

Fig. 2 A cartoon schematic of the radical-pair mechanism for magnetoreception. Certain frequencies of light are thought to set off a process which creates radical pairs in cryptochrome within the eye of certain species. The two unpaired electrons in the radical retain their initial singlet correlation state. In the presence of inhomogeneous nuclear hyperfine interactions and the earth's magnetic field, the singlet state changes, converting into triplet states and back again. The radical can either decay back to its groundstate, when the electrons are in the singlet configuration, or into a different transient product, when they are in the triplet configuration. This is an irreversible process which is thought to lead to a biologically detectable signal. The ratio of singlet-triplet products depends on the angle of the external field, and may eventually give rise to a visual cue. (Here, a European robin, shown in a photo used in a modified form under creative commons licence v4.0 https://creativecommons.org/licenses/by/4.0/ from Alexis @ https://www.inaturalist.org/photos/30476121g)

$\psi_S = \frac{1}{\sqrt{2}}(|\uparrow\downarrow\rangle - |\downarrow\uparrow\rangle)$. In the presence of both the geomagnetic field and an anisotropic nuclear hyperfine interaction this state will interconvert with the triplet states ($\psi_{T_0} = \frac{1}{\sqrt{2}}[|\uparrow\downarrow\rangle + |\downarrow\uparrow\rangle]$, $\psi_{T_+} = |\uparrow\uparrow\rangle$, $\psi_{T_-} = |\downarrow\downarrow\rangle$).

This interconversion between singlet and triplet states occurs coherently, oscillating back and forth between the possibilities very quickly, and the degree to which this interconversion changes the probability of occupation of a particular state depends on the angle of the external geomagnetic relative to the anisotropic nuclear hyperfine interaction (though other mechanisms have been proposed (Lambert et al., 2013b)). At any given moment, it is possible for the radical pairs to decay, and form reaction products which depend on the spin state, and thus may give rise, as mentioned, to spin-dependent biologically detectable signals. The quantum aspects of this whole process then clearly lie in the highly entangled nature of the spin states, and the fast interconversion between said states.

There are several interesting technical points about this mechanism that connect back to behavioral experiments: (i) The candidate host of the radical pairs, cryptochrome, occurs in the eye, and is photo-activated. (ii) In addition, the expression of these cryptochromes (ErCry4 to be precise) in European robins peaks during migration season. (iii) To be magnetically sensitive, one of the radicals must have an anisotropic nuclear magnetic hyperfine interaction (to create a "local" magnetic field, otherwise both radicals are affected equally by the geomagnetic field, and no single-triplet interconversion can occur). (iv) Theoretical models have shown then that singlet-triplet ratio would be affected by broadband oscillatory magnetic fields, consistent with more of the aforementioned experiments (Leberecht et al., 2022).

While evidence then is increasing that radical pairs may be a viable candidate for the magnetic sensory apparatus, and a clear example of quantum biology, and that cryptochrome is the host of said pairs, there are still many open questions. There are debates regarding exactly which cryptochrome, and which radicals in said cryptochromes, is used to detect the earth's magnetic field (Leberecht et al., 2022; Wiltschko et al., 2021), whether dipolar and exchange interactions have a deleterious effect on the sensitivity (Kattnig et al., 2016), and whether more realistic models of nuclear hyperfine interactions can produce the required levels of sensitivity. If these, and other, open questions and debates can be resolved, it may well be that avian magnetoreception will be the first concrete example of nature taking advantage of quantum physics in a nontrivial manner.

Other contenders

The interest in quantum effects in light harvesting and magnetoreception has spurred a wider effort to reconsider the potential for quantum effects in other biological processes. For example, quantum tunnelling (Gray and Winkler, 2003; Stuchebrukhov, 2003) has been investigated for allowing new, or modifying existing, chemical reactions. In a classical picture, an electron or proton must overcome a potential energy barrier to transfer from a donor to an acceptor molecule, for example, but in the quantum picture the probability of this occurring can be modified by the chance of the wavefunction tunnelling through the potential barrier.

In a related idea, it has been suggested that the electron tunnelling through odorant molecules might play a role in our sense of smell (Turin, 1996). In the traditional picture, we can distinguish different odorants through their interaction with receptors which are sensitive to their shape. Some experiments suggest, however, that we can distinguish odorants with the same shapes, requiring an extra mechanism in the overall sensing apparatus. The electron tunnelling mechanism relies on interactions with certain vibrational degrees of freedom within the odorant molecule, which potentially provides additional discrimination between odorants. However, contradictory experiments suggest this may not be feasible (Keller and Vosshall, 2004). Similarly, ion channels, used to transport ions cross cell membranes (Vaziri and Plenio, 2010), and photoreceptors in the eye (Prokhorenko et al., 2011; Nagy et al., 2006), have been suggested as other biological processes which may be enhanced or made more discriminatory by the use of quantum tunnelling and quantum coherence.

Conclusion

Despite decades of work, a clear and irrefutable example of a biological system functioning with the aid of quantum mechanics in a nontrivial way is still lacking. Most biological processes occur on timescales where quantum effects are expected to be washed away, but the prospect of some fast nonequilibrium contribution of quantum effects is still in the realm of possibility. In photosynthetic light harvesting, while the persistent electronic beating observed in early experiments is contested, it still appears a delocalized quantum model, taking into account the quantum nature of the environment, is necessary for the correct description and understanding of the light-harvesting process. Similarly, for magnetoreception, despite the difficulties in isolating and studying the precise structures and mechanisms hypothesized to form the vital elements of the radical-pair mechanism, evidence is increasing that such a mechanism is at least feasible, and might explain the results obtained from behavioral studies.

References

Cao J, Cogdell RJ, Coker DF, Duan H-G, Hauer J, Kleinekathöfer U, Jansen TLC, Mančal T, Miller RJD, Ogilvie JP, Prokhorenko VI, Renger T, Tan H-S, Tempelaar R, Thorwart M, Thyrhaug E, Westenhoff S, and Zigmantas D (2020) Quantum biology revisited. *Science Advances* 6(14): eaaz4888. https://doi.org/10.1126/sciadv.aaz4888.

Cheng Y-C and Fleming GR (2009) Dynamics of light harvesting in photosynthesis. *Annual Review of Physical Chemistry* 60(1): 241–262. https://doi.org/10.1146/annurev.physchem.040808.090259.

Collini E, Wong CY, Wilk KE, Curmi PMG, Brumer P, and Scholes GD (2010) Coherently wired light-harvesting in photosynthetic marine algae at ambient temperature. *Nature* 463: 644. https://doi.org/10.1038/nature08811.

Duan H-G, Prokhorenko VI, Cogdell RJ, Ashraf K, Stevens AL, Thorwart M, and Miller RJD (2017) Nature does not rely on long-lived electronic quantum coherence for photosynthetic energy transfer. *Proceedings of the National Academy of Sciences* 0027-8424. 114(32): 8493–8498. https://doi.org/10.1073/pnas.1702261114.

Engel GS, Calhoun TR, Read EL, Ahn T-K, Mančal T, Cheng Y-C, Blankenship RE, and Fleming GR (2007) Evidence for wavelike energy transfer through quantum coherence in photosynthetic systems. *Nature* 446: 782. https://doi.org/10.1038/nature05678.

Ghosh PK, Smirnov AY, and Nori F (2011) Artificial photosynthetic reaction centers coupled to light-harvesting antennas. *Physical Review E* 84: 061138. https://doi.org/10.1103/PhysRevE.84.061138.

Ghosh PK, Smirnov AY, and Nori F (2011) Quantum effects in energy and charge transfer in an artificial photosynthetic complex. *The Journal of Chemical Physics* 134: 244103. https://doi.org/10.1063/1.3600341.

Gray HB and Winkler JR (2003) Electron tunneling through proteins. *Quarterly Reviews of Biophysics* 36: 341. https://doi.org/10.1017/s0033583503003913.

Hore PJ and Mouritsen H (2016) The radical-pair mechanism of magnetoreception. *Annual Review of Biophysics* 45(1): 299–344. https://doi.org/10.1146/annurev-biophys-032116-094545.

Kattnig DR, Sowa JK, Solov'yov IA, and Hore PJ (2016) Electron spin relaxation can enhance the performance of a cryptochrome-based magnetic compass sensor. *New Journal of Physics* 18(6): 063007. https://doi.org/10.1088/1367-2630/18/6/063007.

Keller A and Vosshall L (2004) A psychophysical test of the vibration theory of olfaction. *Nature Neuroscience* 7: 337. https://doi.org/10.1038/nn1215.

Kerpal C, Richert S, Storey J, Pillai S, Liddell PA, Gust D, Mackenzie SR, Hore PJ, and Timmel CR (2019) Chemical compass behaviour at microtesla magnetic fields strengthens the radical pair hypothesis of avian magnetoreception. *Nature Communications* 10: 3707. https://doi.org/10.1038/s41467-019-11655-2.

Lambert N, Chen Y-N, Cheng Y-C, Li C-M, Chen G-Y, and Nori F (2013) Quantum biology. *Nature Physics* 9(1): 10. https://www.nature.com/articles/nphys2474.

Lambert N, Liberato SD, Emary C, and Nori F (2013) Radical-pair model of magnetoreception with spin-orbit coupling. *New Journal of Physics* 15: 083024. https://doi.org/10.1088/1367-2630/15/8/083024.

Leberecht B, Kobylkov D, Karwinkel T, Döge S, Burnus L, Wong SY, Apte S, Haase K, Musielak I, Chetverikova R, Dautaj G, Bassetto M, Winklhofer M, Hore PJ, and Mouritsen H (2022) Broadband 75-85 MHz radiofrequency fields disrupt magnetic compass orientation in night-migratory songbirds consistent with a flavin-based radical pair magnetoreceptor. *Journal of Comparative Physiology. A* 208: 97–106. https://doi.org/10.1007/s00359-021-01537-8.

Mohseni M, Omar Y, Engel GS, and Plenio MB (2014) *Quantum Effects in Biology*. Cambridge: Cambridge University Press. https://doi.org/10.1017/CBO9780511863189.

Mourokh LG and Nori F (2015) Energy transfer efficiency in the chromophore network strongly coupled to a vibrational mode. *Physical Review E* 92: 052720. https://doi.org/10.1103/PhysRevE.92.052720.

Nagy A, Prokhorenko VI, and Miller RJD (2006) Do we live in a quantum world? Advances in multidimensional coherent spectroscopies refine our understanding of quantum coherences and structural dynamics of biological systems. *Current Opinion in Structural Biology* 16: 654. https://doi.org/10.1016/j.sbi.2006.08.012.

Panitchayangkoon G, Hayes D, Fransted KA, Caram JR, Harel E, Wen J, Blankenship RE, and Engel GS (2010) Long-lived quantum coherence in photosynthetic complexes at physiological temperature. *Proceedings of the National Academy of Science* 107(29): 12766–12770. https://doi.org/10.1073/pnas.1005484107.

Prokhorenko VI, Halpin A, Johnson PJM, Miller RJD, and Brown LS (2011) Coherent control of the isomerization of retinal in bacteriorhodopsin in the high intensity regime. *The Journal of Chemical Physics* 134: 085105. https://doi.org/10.1063/1.3554743.

Scholes GD, Fleming GR, Chen LX, Aspuru-Guzik A, Buchleitner A, Coker DF, Engel GS, van Grondelle R, Ishizaki A, Jonas DM, Lundeen JS, McCusker JK, Mukamel S, Ogilvie JP, Olaya-Castro A, Ratner MA, Spano FC, Whaley KB, and Zhu X (2017) Using coherence to enhance function in chemical and biophysical systems. *Nature* 0028-0836. 543(7647): 647–656. https://doi.org/10.1038/nature21425.

Schrödinger E (1944) *What is life? The Physical Aspect of the Living Cell.* Cambridge: Cambridge University Press, ISBN:0-521-42708-8.

Schulten K, Swenberg CE, and Weller AA (1978) A biomagnetic sensory mechanism based on magnetic field modulated coherent electron spin motion. *Zeitschrift fr Physikalische Chemie* 111: 1–5. https://doi.org/10.1524/zpch.1978.111.1.001.

Stuchebrukhov AA (2003) Long-distance electron tunneling in proteins. *Theoretical Chemistry Accounts* 110: 291.

Turin L (1996) A spectroscopic mechanism for primary olfactory reception. *Chemical Senses* 21: 773. https://doi.org/10.1134/S1054660X09170186.

Vaziri A and Plenio MB (2010) Quantum coherence in ion channels: Resonances, transport and verification. *New Journal of Physics* 12: 085001. https://doi.org/10.1088/1367-2630/12/8/085001.

Wiltschko R, Nießner C, and Wiltschko W (2021) The magnetic compass of birds: The role of cryptochrome. *Frontiers in Physiology* 1664-042X. 12: 667000. https://doi.org/10.3389/fphys.2021.667000.

Xu J, Jarocha L, T., Z.., Konowalczyk M, Henbest KB, Richert S, Golesworthy MJ, Schmidt J, Déjean V, Sowood DJC, Bassetto M, Luo J, Walton JR, Fleming J, Wei Y, Pitcher TL, Moise G, Herrmann M, Haijia Wu HY, Bartölke R, Käsehagen SJ, Horst S, Dautaj G, Murton PDF, Gehrckens AS, Chelliah Y, Takahashi JS, Koch K-W, Weber S, Solov'yov IA, Xie C, Mackenzie SR, Timmel CR, Mouritsen H, and Hore PJ (2021) Magnetic sensitivity of cryptochrome 4 from a migratory songbird. *Nature* 594: 535–540. https://doi.org/10.1038/s41586-021-03618-9.

Fundamental aspects of quantum biology

Elisabetta Collini, Department of Chemical Sciences, University of Padova, Padova, Italy; Padua Quantum Technologies Research Center, Padova, Italy

© 2024 Elsevier Ltd. All rights reserved.

Introduction 584
Historical overview 585
Elementary concepts of quantum mechanics: coherent superpositions of states, tunneling, and entanglement 585
Applications 586
Light-harvesting in photosynthesis and energy transport 586
Avian magnetoreception 588
Olfaction and tunneling 589
Quantum features of entire organisms 590
Conclusion 590
References 590

Abstract

Quantum mechanics and biology are seldom considered within the same framework because they seemingly belong to well-separated kingdoms. Quantum mechanics is the fundamental theory to describe the infinitesimally small objects, elucidating the physical properties of Nature at the scale of atoms and subatomic particles. Biology is the science of life, devoted to the study of the behavior of living organisms on a macroscopic scale, where the classical mechanics is the supreme ruler.

Quantum objects are small, cold, and well-controlled. Life is complex, disordered, ‘hot and wet.’

Although the impression that quantum mechanics is limited to the microworld governs the general understanding of science, recent experimental and theoretical studies challenge this neat dichotomy and demonstrate that natural macroscopic phenomena like photosynthesis, olfaction, and bird navigation can be investigated remarkably well through quantum mechanical formalisms. This is precisely what is now recognized as ‘quantum biology’: the application of quantum theory to aspects of biology for which classical physics fails to provide an accurate description.

Key points

- Define the research field of Quantum Biology
- Provide a brief historical overview of its developments
- Introduce to the non-experts the concepts of quantum mechanics needed to understand the advances in quantum biology
- Review the main research areas involved in quantum biology research, highlighting open questions, criticalities, and possible developments
- Discuss the latest developments and possible future perspectives

Introduction

Quantum biology is the study of applications of quantum mechanics to fundamental biologically relevant problems. It aims to bridge the apparently uncorrelated realms of quantum mechanics and biology (Arndt et al., 2009; Lambert et al., 2013; Brookes, 2017; Marais et al., 2018; McFadden and Al-Khalili, 2018).

Quantum mechanics is the fundamental theory that describes the microscopic world. It is a powerful tool to describe particles, atoms, and molecules but it gives way to classical physics on the macroscopic scale of sensible world where instead biology, the science of life, operates. Somewhere between molecules and macroscopic world lies a boundary where quantum behavior ends and the familiarity of classical physics begins (Huelga and Plenio, 2013). The impression that quantum mechanics is limited to the microworld permeates the general understanding of science. Yet this partitioning of the world is just a convenient way to simplify the description of the different phenomena and it is but a useful approximation of a world that is quantum at all scales.

Although quantum effects are perhaps harder to see in the macroworld, the reason for that has nothing to do with the size *per se* but with how quantum systems interact with one another. The feature of quantum mechanics that most distinguishes it from classical mechanics is the description of systems in terms of coherent superpositions of distinct physical states. In fact, such superposition states are very fragile in the presence of dissipation and rapidly collapse to a classical mixture exhibiting no unusual interference features. This is the so-called decoherence process. The predictions of quantum mechanics indeed converge to those of

https://doi.org/10.1016/B978-0-323-90800-9.00022-6

classical mechanics in the macroscopic world when a system moves to higher energies or–equivalently–larger quantum numbers. Larger objects tend to be more susceptible to decoherence than smaller ones, which justifies why biologists can usually get away with disregarding quantum mechanics (Joos and Zeh, 1985).

Strictly speaking, all biochemical compounds are quantum objects in the sense that they are made of atoms bound by quantum-mechanical forces. Therefore, one could claim that all of biology is in fact, a quantum mechanical process. In effect, the definition of quantum biology is more subtle since it is based on the idea of addressing the dynamical nature of biological processes, where a classical description is inadequate. For example, it was recently suggested that a good definition of quantum biology could be provided on the basis of the physical 'correctness' of the models used to describe biological processes and the capability of classical versus quantum mechanical approaches to explain their behavior (Marais et al., 2018).

In other words, the fundamental question of quantum biology is whether quantum mechanisms play a specific role in the functions of complex biological systems or if they are unable to maintain a quantum coherent state of sufficient duration to have a significant influence. Going even further, one could also wonder if quantum mechanisms can be suitably engineered in macroscopic artificial systems to steer the performances of artificial devices.

Historical overview

The idea that quantum phenomena may play a crucial role in macroscopic living systems dates back to the origin of quantum mechanics. In 1932, 10 years after being awarded the Nobel Prize, Niels Bohr gave a lecture entitled 'Light and Life' at the International Congress on Light Therapy in Copenhagen. In his lecture, he raised the question of whether quantum mechanics could contribute to the description and the scientific understanding of living systems and provided an occasion to reflect on the philosophical significance of developments in quantum theory for the life sciences (Bohr, 1933). This proposition fascinated a young physicist in the audience, Max Delbrück, one of the future fathers of molecular biology and Nobel Prize winner in 1969 for his discoveries in genetics (McKaughan, 2005). The original approach of Delbrück was also influenced by the seminal contribution by a luminary in quantum mechanics, Erwin Schrödinger. In 1944, Schrödinger wrote a book with the unusual title 'What is life?' based on a course of public lectures delivered in February 1943, under the auspices of the Dublin Institute for Advanced Studies, where he was Director of Theoretical Physics, at Trinity College, Dublin (Schrödinger, 1944). In this book, where he predicted several of the functional features of DNA, he posed essential questions about the possibility of describing biological phenomena with quantum mechanics.

Just as Bohr, Delbrück, and Schrödinger, other founders of quantum mechanics like Heisenberg and Wigner offered speculations on the topic: building upon their success in explaining the properties of non-living matter, they hoped their theory was powerful enough to justify the peculiar living state of matter too. This was prevalent to such an extent that in the late 1940s and 1950s, it was fashionable to suppose that quantum mechanics or some form of "post-quantum mechanics" held the key to the mystery of life.

It is precisely during those exciting years and in this cultural context that the word 'quantum biology' was coined for the first time by physicist Pasqual Jordan (Jordan, 1932).

After this period of initial enthusiasm, discussions on quantum biology have begun to diminish. In 1963, Per-Olov Löwdin proposed proton tunneling, an exquisitely quantum effect, as a possible mechanism for DNA mutation and mentioned this new field called "quantum biology" (Löwdin, 1966). In 1979, Alexander Davydov published what can be considered as the first textbook on quantum biology entitled "Biology and Quantum Mechanics" (Davydov, 1979).

However, it was only in the last two decades that relevant developments in experimental techniques such as ultrafast spectroscopy (Hybl et al., 1998; Collini, 2021), single-molecule spectroscopy (Moerner et al., 2015; Liebel et al., 2018), time-resolved microscopy (Huang et al., 2020) and single-particle imaging (Shashkova and Leake, 2017) allowed investigating the biological dynamics on increasingly small length and time scales. These new techniques captured a variety of processes contributing to the function of the living systems that strongly depend on a delicate interplay between quantum and classical physical effects and gave rise to the real dawn of quantum biology (Ball, 2011).

Elementary concepts of quantum mechanics: coherent superpositions of states, tunneling, and entanglement

The formulation of quantum mechanics proposed by Schrödinger describes the dynamics of microscopic systems through the use of wave mechanics. In this framework, the time evolution of the system is represented by the state vector $|\psi(t)\rangle$, which obeys the time-dependent Schrödinger equation: $i\hbar\frac{\partial|\psi(t)\rangle}{\partial t} = H(t)|\psi(t)\rangle$, where $\hbar$ is the reduced Planck constant and $H(t)$ is the so-called Hamiltonian operator, which accounts for the energy levels of the system and all the interactions taking place within the system (Zettili, 2022).

A particularly fascinating aspect of quantum theory is that, given a set of quantum states $|\psi_i\rangle$ describing the system, linear combinations of these states, $\sum_i a_i|\psi_i\rangle$, also belong to the Hilbert space that contains all the states available to the system. In these superpositions, each normalized orthogonal state $|\psi_i\rangle$ is weighted by the complex number a_i, such that $|a_i|^2$ is the probability of finding the system in that state. It is here that quantum mechanics departs from the classical world. The existence of superposition states in the quantum regime results in uniquely quantum-mechanical properties, which are often counterintuitive, like for example a cat being at the same time dead and alive (Castelvecchi, 2018).

For example, when the system is described by a superposition of two states: $\Psi = a_1|\psi_1\rangle + a_2|\psi_2\rangle$, the probability density P oscillates in time as: $P(t) = |\Psi|^2 = |\psi_1|^2 + |\psi_2|^2 + 2|\psi_1\psi_2|\, cos\,[(\omega_2 - \omega_1)t]$ where $\omega_i = E_i/\hbar$, with E_i being the energy associated with the i-th state. We refer to this state of the system that gives rise to this time-dependent oscillation in probability density as a coherent superposition state, or *coherence*. More generally, the oscillation term in the probability expression may also include a time-independent phase factor that arises from the complex expansion coefficients (Tokmakoff, 2020). The measured observables are related to this probability. It is precisely the presence of oscillations in the measured observable that acts as a smoking gun for the existence of quantum coherent mechanisms active during the system dynamics during light-harvesting and energy or charge transport (Collini, 2013).

The probabilistic approach of quantum mechanics also allows understanding another important quantum mechanical concept, the tunneling mechanism. The tunneling effect may be explained in terms of the Heisenberg uncertainty principle: the uncertainty in the exact location of a quantum system allows this system to break rules of classical mechanics and move in space without passing over the potential energy barrier (Zettili, 2022). Indeed, when a particle encounters a potential barrier that is higher than its kinetic energy, it will not be able to pass by any classical mechanism. Quantum mechanics, however, allows it to tunnel through this barrier. The tunneling probability strongly depends on the height, width, and shape of the potential barrier as well as on the particle's mass and kinetic energy. The tunneling of light particles like electrons and protons is rather ubiquitous in biology, especially in relation to enzymatic activity. Indeed, hydrogen transfer reactions and the manipulation of carbon-hydrogen bonds feature prominently in a wide range of biomolecular systems (Das et al., 2020).

When the superposition principle is extended to more than a single object or property, the notion of quantum entanglement is introduced. Quantum entanglement is one of the most important phenomena at the heart of the disparity between classical and quantum physics. It is a primary feature of quantum mechanics that is absent in classical mechanics. In simple terms, quantum entanglement is a special form of correlation between quantum states, such that, given an ensemble of particles, the quantum state of each particle cannot be described independently of the state of the others, including when the particles are separated by a large distance (Brody, 2020). There are several formal definitions and measures of entanglement (Vedral and Plenio, 1998) and this effect has so far been demonstrated for photons, superconducting circuits, nuclear spins in small molecules, spin noise in atomic ensembles, trapped ions, and other systems [see Nielsen and Chuang, 2000 and references therein]. Although these demonstration experiments are typically performed under strictly controlled environmental conditions, often including ultrahigh vacuum and ultralow temperatures, the concept of quantum entanglement has been brought up also in conditions more compatible with living organisms (Fassioli and Olaya-Castro, 2010; D'Acunto, 2022).

Applications

In this section, a brief outline of some of the cases in which quantum effects are thought to assist or enhance a biological function is presented. The discussion begins by describing the observations of quantum coherence (superpositions) at room temperature in excitation energy transport through photosynthetic systems. The latest research about the role this coherence might play in the efficiency of photosynthesis in various photosystems is presented together with a critical view of how this concept has been interpreted in the past two decades of investigations. The second example is the radical-pair model used to describe the magnetoreception sense of some avian species. This model invokes the role of quantum coherence and entanglement of singlet and triplet states during the magnetic compass action. Then, the possible interpretation of the sense of olfaction in terms of phonon-assisted inelastic tunneling and the long-range tunneling of electrons through proteins in redox reactions and enzyme catalysis will be presented. Finally, a recent development broadly classified as quantum biology and dealing with quantum features in entire organisms will be introduced, which is a burning issue for the quantum physics community.

It is important to immediately underline that the effective role of quantum mechanical phenomena in the described biological processes and the possible advantages that they can bring to the organisms in terms of improved functionality is still highly debated and is somewhat controversial. Especially in the last examples, the possibility that a macroscopic cognitive species could respond to quantum effects is fascinating, but caution should be paid in the interpretation of the available experiments because these effects are difficult to study and, in most cases, they remain at the level of speculations.

Light-harvesting in photosynthesis and energy transport

Broadly speaking, any process in which some kind of cellular energy is derived from light can be defined as photosynthetic. Key processes in photosynthesis are the absorption of solar energy by antenna complexes and the efficient transfer of excitation energy to photochemical reaction centers (RCs), where the energy is trapped in the form of a stable charge separation, which eventually is converted to chemical energy through a series of dark reactions (Blankenship, 2008). There is a remarkable variety of organisms carrying out photosynthesis, from the well-known green plants to microscopic forms of life such as algae and photosynthetic bacteria. While the structure of the RCs has mainly been retained across different organisms, a remarkable variety of antenna complexes have been identified from various classes of photosynthetic organisms, showing no apparent correlations in their structural organization or in terms of the pigments they utilize. This seems to suggest different evolutionary patterns for different antennas but also emphasizes the importance of the light-gathering process in general (Collini et al., 2009).

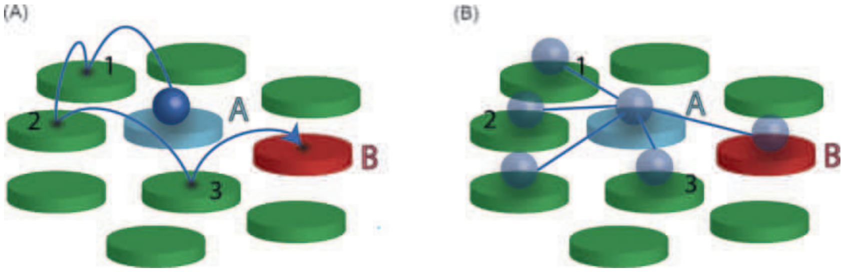

Fig. 1 Schematic of the classical and quantum-coherent wavelike mechanisms of excitation energy transfer. The disks represent the different pigments (chlorophylls or bacteriochlorophylls, for example) in an antenna complex. The photoexcitation initially excites one of the sites (A) and it is then transported across the network of molecules (1 to 3). Once it arrives at site B it can irreversibly enter the reaction center and start a charge-separation process. (A) Classical (Förster) energy transfer; the excitation energy jumps randomly between chromophores dissipating energy at each step. Excitation can be on one chromophore at a time. (B) Quantum-coherent energy transfer; the excitation energy is instantaneously quantum-mechanically shared among several chromophores. The system is described as a 'coherent' superposition.

The mechanism of energy transfer in light-harvesting is, in general, well established and well reproduced by the traditional approach that makes use of Förster resonance energy transfer theory (Olaya-Castro and Scholes, 2011). Förster's theory states that, when two molecules A and B are separated by a distance large compared to their size, their electronic coupling can be represented approximately as a dipole-dipole interaction between electric dipole transition moments. Förster theory holds when the electronic coupling is weak, meaning that it is small compared to the coupling to the environment. In this condition, the energy transfer happens after complete equilibration at the photoexcited state of the donor. In this way, any quantum effect between the donor and acceptor excited states is completely quenched by the interaction with the environment degrees of freedom and the energy transfer among several chromophores can be described as a sequence of 'jumps' (Fig. 1A). The Förster model yields simple exponential dynamics and provides an excellent qualitative fit of the observed population transfer rates for most systems.

However, in recent years many subtle aspects of the process, not accounted for in the traditional treatments, were found to be relevant - quantum coherence being one of them. Such subtleties have forced researchers to change the conventional way of thinking about energy transfer and led to the introduction of substantial changes to this basic model (Scholes, 2011; Collini, 2013; Ball, 2018).

The idea that quantum coherent mechanisms could contribute to the excitation energy transfer in photosynthesis was first proposed in 1938 by Franck and Teller (Franck and Teller, 1938). Rather than describing the energy migration among chromophores as a sequence of energy jumps like in the Förster model, they considered the diffusion of a so-called Frenkel exciton (Frenkel, 1931). When the electronic coupling becomes stronger compared to the interaction with the environment, the so-called "strong coupling" limit is reached, and the excitation energy transfer acquires the quantum-coherent character. In the strong coupling limit, the donor and acceptor electronic states mix strongly to produce new, delocalized states that are little perturbed by the interaction with the environment. Within these states, known indeed as Frenkel excitons, the energy is shared quantum mechanically among several chromophores. This is the so-called wavelike transfer (Fig. 1B) (Collini and Scholes, 2009; Olaya-Castro and Scholes, 2011; Scholes et al., 2014).

For many years, although intrigued by the idea of quantum-driven processes, scientists treated their presence mainly as some kind of academic curiosity, until when new technological advances in spectroscopy allowed recording direct experimental proof of quantum coherent dynamics in natural photosynthetic complexes. The first evidence for coherent mechanisms came through the measure of oscillations in pump-probe signals in the late 1990s (Edington et al., 1995; Savikhin et al., 1997). However, a turning point in the discussion was possible only with the development of two-dimensional electronic spectroscopy (2DES) (Hybl et al., 1998). Thanks to the time and frequency resolution of these techniques, it is possible to directly follow the evolution of quantum coherences in light-harvesting complexes and differentiate Förster-type energy transfer from quantum-coherent mechanisms (Hybl et al., 2001). The presence of cross-peaks in the 2D maps was associated with couplings between exciton states, while their oscillations along the third time dimension were assigned to electronic quantum coherence, i.e., the time evolution of coherent superpositions between exciton states (Collini, 2013, 2021; Bránczyk et al., 2014; Gelzinis et al., 2019). In 2007, two-dimensional (2D) electronic spectra recorded at 77 K for the Fenna-Matthews-Olson (FMO) complex isolated from photosynthetic green sulfur bacteria showed a striking quantum beating pattern explained by Engel et al. to arise from long-lived coherent superpositions of electronic states (Engel et al., 2007). In 2009, similar oscillatory signals were revealed for the main light-harvesting complex of higher plants (LHCII) and were interpreted as quantum-coherent energy transfer (Schlau-Cohen et al., 2009). These initial results were obtained at cryogenic temperatures. A few years later, a significant development came when the Engel (Panitchayangkoon et al., 2010) and Scholes (Collini et al., 2010) groups found independently similar coherent oscillations at physiological temperatures in FMO and the light-harvesting complexes of two species of marine cryptophyte algae, respectively. Since then, many photosynthetic pigment-protein complexes extracted from different organisms have been investigated in cryogenic and physiologically relevant conditions (see for example, Lambrev et al., 2020 and references therein).

These findings rejuvenated the long-standing discussion regarding relationships between the energy transfer efficiency and quantum features. In fact, the possibility that quantum coherent dynamics could boost the efficiency of biological light-harvesting systems and effectively funnel the energy transport has been discussed. Within this framework, it was proposed that coherence could improve robustness against energetic disorder or dynamical perturbations (Mohseni et al., 2008; Plenio and Huelga, 2008), be used as a strategy to overcome energy traps (Akihito and Fleming, 2009) or as a mechanism that may speed up the search for the lowest energy level (Engel et al., 2007). Even more bewildering is the possibility that the practical functionality of quantum coherent phenomena may be connected with the ability of natural systems to modulate their function under different environmental conditions through mechanisms related to quantum entanglement (Fassioli and Olaya-Castro, 2010; Scholes, 2011).

After the initial burst of enthusiasm, the increasing body of experimental observations and theoretical modeling and the growing comprehension of the spectroscopic observables suggested a more cautious approach. The case of FMO, probably the most studied and modeled complex, is a clear example of this trend. After numerous experiments and models both for and against the presence of long-lived electronic coherence, recent 2DES experiments suggested that these long-lived (in the ps time scale) coherences originate mainly from ground state vibrations and not from exciton-exciton superpositions, which decay in a faster timescale (within hundreds of fs) (Duan et al., 2017; Thyrhaug et al., 2018). However, experimental confirmation of excited-state vibronic coherence was also found and its role in excitation energy transfer in photosynthesis remains to be determined. It is thus clear that, despite two decades of investigations, the role of quantum (vibrational, vibronic, or electronic) coherence in light-harvesting remains a highly engaging albeit controversial issue (Christensson et al., 2012; Duan et al., 2017; Scholes et al., 2017; Cao et al., 2020).

There is, however, a general consensus in admitting that 2DES played an essential role in resolving the dynamics and pathways of energy and electron transport in various light-harvesting antenna systems and reaction centers with an unsurpassed level of detail. The investigation on the role of quantum effects in the dynamics of photosynthetic complexes, regardless of whether or not these effects are relevant in Nature, had the merit to trigger important new lines of research. Indeed, it is questionable whether quantum effects can be engineered into artificial systems designed *ad hoc* to control quantum coherent energy or charge transfer (Scholes et al., 2011).

Avian magnetoreception

Avian magnetoreception is a sense which allows some species of migrating birds to detect Earth's magnetic field to perceive direction, altitude, or location. This sense is used for orientation and navigation (Wiltschko and Wiltschko, 2012). It represents the second prominent example (beyond photosynthesis) typically invoked in quantum biology research.

A series of early behavioral experiments have revealed several important details about this sense: (i) it is photoreceptor based (i.e., it depends on the presence of specific frequencies of ambient light); (ii) it is sensitive to changes in the intensity of the external magnetic field and (iii) it is strongly disturbed by magnetic pulses and very weak external oscillating magnetic fields. To account for all these pieces of evidence, more than 40 years ago, Shulten et al. proposed the so-called radical-pair mechanism, graphically summarized in Fig. 2 (Schulten et al., 1978).

Although the exact details can be pretty complex, the process can be summarized in three steps. First, the initial photoexcitation stimulates electron transfer and a radical pair formation. A radical pair is typically a pair of bound molecules, each having an unpaired electron. These pairs are generated via photochemical processes in spin correlated states (i.e., singlets or triplets).

Once formed, the radical pair oscillates between singlet and triplet spin states before a final step of recombination and neural interpretation. When the system is in a singlet-triplet superposition, it experiences the influence of the Earth's magnetic field. Depending on that, different recombination products can be formed, which are biologically detectable. Thus, if the relative weights

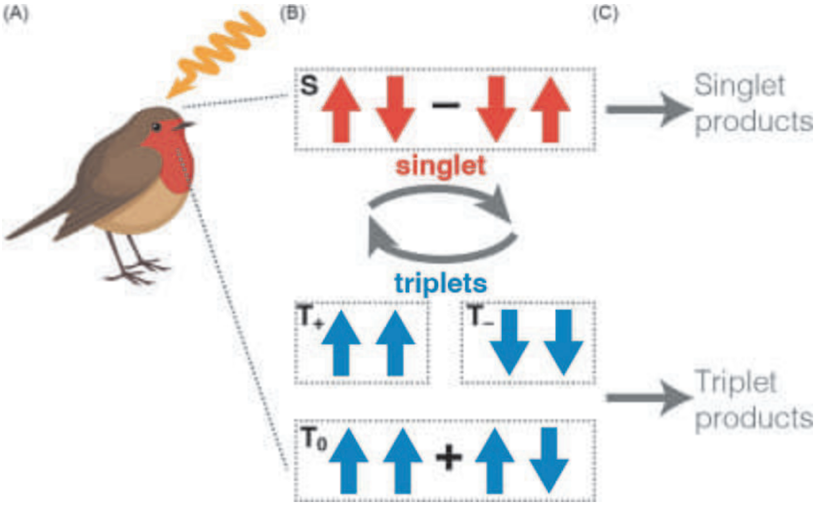

Fig. 2 The three main steps of the radical pair mechanism for avian magnetoreception. (1) Light-induced electron transfer from one radical-pair-forming molecule (for example, in a cryptochrome in the retina of a bird) to an acceptor molecule creates a radical pair. (2) The radical pair oscillates between singlet (S) and triplet (T_+, T_- and T_0) states under the influence of the Zeeman and hyperfine effects. (3) Spin-dependent recombination into the chemical products.

of the singlet and triplet states are sensitive to the angle of the Earth's magnetic field, the reaction products will reflect this sensitivity, leading to a magnetic compass.

The radical pair theory has given rise to numerous papers discussing the role of quantum coherence and entanglement of singlet and triplet states during the magnetic compass action (Zhang et al., 2015). It has been suggested that the incredible accuracy of the avian compass can only be justified as the result of genuinely quantum mechanical effects (Hiscock et al., 2016). However, there remains some doubt about whether the compass mechanism is indeed a quantum phenomenon or can be described using a semi-classical framework.

Olfaction and tunneling

Olfaction, i.e., the sense of smell, is traditionally explained in terms of a shape theory known as the "lock and key" model (Moncrieff, 1949; Amoore, 1963), which states that a particular odor can be smelled when both shapes of the odorant molecule and the corresponding receptor perfectly fit each other. Then, the sense of smell would depend only on the shapes of molecules. The model can be modified by introducing a distortion of the whole system to induce a more appropriate mutual fit ("hand and glove" model). A more refined demonstration of the idea requires that the receptors respond to only one structural feature, such as a functional group, instead of the main body of the odorant ("odotope" model) (Mori and Shepherd, 1994). There is plenty of evidence that supports these shape-based theories. Still, some findings are against them: structurally different odorants that smell similarly and structurally similar odorants that smell differently (Tirandaz et al., 2017).

Based on this observation, a controversial theory, first developed by Dyson in 1927 (Dyson, 1928) and then further developed by Wright (Wright, 1977) and by Turin (Turin, 1996), was proposed. It is based on the idea that the signature of the scent is due to the odorant's unique vibrational spectrum and not to its structure ("swipe card" model). Through fruit fly behavioral experiments, it was observed that molecules with the same shapes correspond to completely different smells (Turin, 1996). To explain this evidence, it was proposed that vibrational modes, different and characteristic for each molecule, play a crucial mediating role in signal transduction. Indeed, a mechanism has been proposed where the presence of a vibrational mode with energy compatible with the difference in energies between two energy levels on the receptor can promote the electron transfer via inelastic electron tunneling, triggering the ensuing odor recognition process. In other words, the signal transduction is described in terms of phonon-assisted inelastic tunneling of an electron from the donor to the acceptor sites of the receptor, mediated by the odorant molecule (Fig. 3). The specificity of the vibrational modes of molecules would guarantee a further level of selectivity to the process with respect to the "lock and key" model. More recently, this model was revised and expanded by Brookes (Brookes et al., 2007) and several arguments have been brought forth both in favor and disfavor of this theory, which still remains highly controversial (Eric et al., 2015; Pandey et al., 2021). Moreover, it should be noted that the vibrational theory of olfaction in principle can also be described using semi-classical approaches (Brookes et al., 2007), and, therefore, it is not clear to what extent this could be effectively considered as a quantum biology phenomenon.

Nonetheless, tunneling is an exquisitely quantum mechanical effect, studied since the dawn of quantum mechanics. Besides the controversial vibrational theory of olfaction, there are several other well-established examples of biological processes relying on long-range particle tunneling. For example, it is well known that electron and proton tunneling plays essential roles in redox reactions and enzyme catalysis, respectively (Gray and Winkler, 2003; Allemann and Scrutton, 2009). Indeed, it has been experimentally demonstrated that long-range electron transfer between redox centers in proteins separated by distances of 1–3 nm is crucial in respiration and photosynthesis (Moser et al., 2010). It is remarkable that such long-distance electron transfer

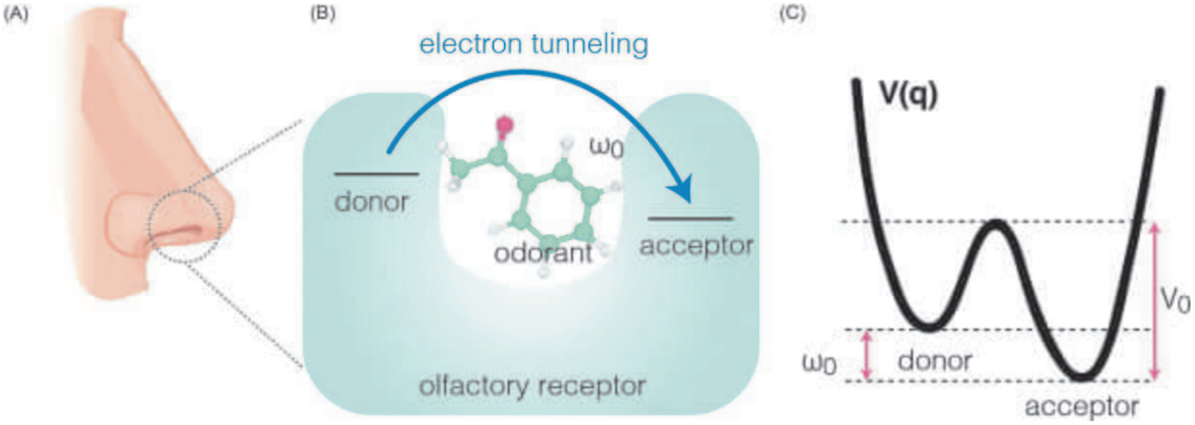

Fig. 3 Possible role of quantum effects in olfaction. (A) The sense of smell is activated when odorants are absorbed by odorant receptors in the olfactory receptor cells in the nasal cavity. (B) According to the vibrational theory of olfaction, the odorant, which has a characteristic vibrational frequency ω_0, binds to the olfactory receptor forming an electron-donor-acceptor complex. Electron tunneling from the donor to the acceptor is activated if the vibrational frequency of the odorant molecule matches the energy difference. (C) In this model, each odorant can be simulated as an asymmetric double-well potential V(q), where the minima correspond to the donor and acceptor states. The states can be inter-converted by the quantum tunneling through the barrier V_0 (Tirandaz et al., 2017).

in biology might be enabled by quantum mechanical tunneling, possibly mediated, also in this case, by the action of vibrations (Allemann and Scrutton, 2009; Hay and Scrutton, 2012). However, whether or not the electron-conducting proteins have explicitly evolved for coherent electron tunneling still remains a central open question (Moser et al., 2010; Brookes, 2017).

In summary, quantum tunneling is undoubtedly present in a large number of biological processes, but it is experimentally proven only on the level of small-scale chemical reactions.

Quantum features of entire organisms

While in previous examples, the attention was mainly focused on detecting quantum effects on biological processes at the microscopic level, very recently, experiments concerned with quantum features of entire organisms have been proposed. Building on a systematic body of work revealing wave properties of molecules with growing complexity (Gerlich et al., 2011), Lidzey et al. have devised an experiment to strongly couple living photosynthetic bacteria to light. Under certain assumptions, the results obtained could be interpreted as entanglement between the quantized light and light-sensitive parts of bacteria (Coles et al., 2017). Subsequent experiments involving a multi-cellular eukaryote interacting electrically with quantum bits were performed (Lee et al., 2021). The experimental setup consisted in placing a microscopic eukaryote (a tardigrade) between two superconducting qubits at an ultracold temperature so that entanglement between the tardigrade and its immediate environment was achieved, at least according to the authors' claim. While several other experts question the effective existence of any entanglement in this experiment, it undoubtedly represents a stepping stone to more ambitious goals and further discussions.

Conclusion

Quantum effects have been argued to exist in many biological processes. Although all the biological materials can be considered 'quantum' at the atomic level, the extent to which quantum mechanics may really affect the mechanism, dynamics, and efficiency of biological processes in physiologically relevant conditions has, for many years, mostly remained as a negligible curiosity.

Two prominent landmarks have started changing this opinion. First, the recent development of quantum information theory, revealing that quantum mechanics could, in some situations, do things better than an equivalent classical theory (for example speeding up a computation process). Thus, in the same way, it has been suggested that, for example, quantum transport of energy could be more efficient than classical transport. Second, the possibility to directly detect signatures of the dynamical evolution of such quantum coherences through recently developed spectroscopic techniques, allowing, in principle, the experimental verification of the role of quantum effects in biological processes.

To date, conclusive evidence of that is still lacking, and the presence, role, and even the experimental methods of detection of such quantum effects are under scrutiny and debate. The priority for advancing the field must be the design of novel experiments that directly test the quantum biology hypotheses. Indeed, most quantum biology investigations remain at the level of conjectures because of the number of restrictions and challenges to be overcome to observe and measure even the most straightforward quantum effect. Any conclusion is not possible without solid experimental proofs from complex living organisms. At this stage, the available experimental findings seem to be too conflicting to suggest that quantum mechanics can effectively explain all biological systems. However, there is enough evidence to suggest that this hypothesis is at least plausible.

It is not clear what opportunities may be presented in quantum biology, but it will be fruitful to pursue this idea. For example, it has been suggested that quantum biology might play a critical role in the future of medicine and in developing more efficient and robust innovative quantum technologies for solar energy, communication, and navigation that are fundamental in our everyday lives. Even if proven non-relevant in natural processes, the characterization of the role of quantum effects may result anyway valuable if the underlying principle can be applied regardless of whether biology exploits it.

References

Akihito I and Fleming GR (2009) Theoretical examination of quantum coherence in a photosynthetic system at physiological temperature. *Proceedings of the National Academy of Sciences* 106(41): 17255–17260. https://doi.org/10.1073/pnas.0908989106.

Allemann RK and Scrutton NS (2009) Quantum Tunnelling in Enzyme-Catalysed Reactions. *The Royal Society of Chemistry (RSC Biomolecular Sciences).* https://doi.org/10.1039/9781847559975.

Amoore JE (1963) Stereochemical theory of olfaction. *Nature* 199(4896): 912–913. https://doi.org/10.1038/199912b0.

Arndt M, Juffmann T, and Vedral V (2009) Quantum physics meets biology. *HFSP journal* 3(6): 386–400. https://doi.org/10.2976/1.3244985. 2009/11/09. HFSP Publishing.

Ball P (2011) Physics of life: The dawn of quantum biology. *Nature. England, England* 474(7351): 272–274. https://doi.org/10.1038/474272a.

Ball P (2018) *Is Photosynthesis Quantum-Ish?* Physics World.

Blankenship RE (2008) *Molecular Mechanisms of Photosynthesis.* Oxford: Wiley-Blackwell.

Bohr N (1933) Light and life. *Nature* 131(3308): 421–423. https://doi.org/10.1038/131421a0.

Bránczyk AM, et al. (2014) Crossing disciplines - A view on two-dimensional optical spectroscopy. *Ann. Phys.* 526(1–2): 31–49. https://doi.org/10.1002/andp.201300153. John Wiley & Sons, Ltd.

Brody J (2020) *Quantum Entanglement.* Boston: The MIT Press.

Brookes JC (2017) Quantum effects in biology: golden rule in enzymes, olfaction, photosynthesis and magnetodetection. *Proceedings of the Royal Society A: Mathematical, Physical and Engineering Science* 473(2201): 20160822. https://doi.org/10.1098/rspa.2016.0822.

Brookes JC, et al. (2007) Could Humans Recognize Odor by Phonon Assisted Tunneling? *Physical Review Letters* 98(3): 38101. https://doi.org/10.1103/PhysRevLett.98.038101. American Physical Society.

Cao J, et al. (2020) Quantum biology revisited. *Science Advances* 6(14): eaaz4888. https://doi.org/10.1126/sciadv.aaz4888.

Castelvecchi D (2018) Quantum puzzle baffles physicists. *Nature* 561: 446.

Christensson N, et al. (2012) Origin of long-lived coherences in light-harvesting complexes. *Journal of Physical Chemistry B* 116(25): 7449–7454. https://doi.org/10.1021/jp304649c.

Coles D, et al. (2017) A nanophotonic structure containing living photosynthetic bacteria. *Small* 13(38): 1701777.

Collini E (2013) Spectroscopic signatures of quantum-coherent energy transfer. *Chemical Society Reviews* 42(12): 4932–4947. https://doi.org/10.1039/c3cs35444j. The Royal Society of Chemistry.

Collini E (2021) 2D electronic spectroscopies towards quantum technology applications. *Journal of Physical Chemistry C* 125: 13096–13108. https://doi.org/10.1021/acs.jpcc.1c02693.

Collini E and Scholes GD (2009) Electronic and vibrational coherences in resonance energy transfer along MEH-PPV chains at room temperature. *Journal of Physical Chemistry A* 113(16): 4223–4241. https://doi.org/10.1021/jp810757x.

Collini E, et al. (2009) Electronic energy transfer in photosynthetic antenna systems. In: Burghardt I, et al. (ed.) *Energy Transfer Dynamics in Biomaterial Systems*, pp. 3–34. Berlin, Heidelberg: Springer-Verlag Berlin Heidelberg.

Collini E, et al. (2010) Coherently wired light-harvesting in photosynthetic marine algae at ambient temperature. *Nature* 463(7281): 644–647. https://doi.org/10.1038/nature08811. Nature Publishing Group.

D'Acunto M (2022) Quantum biology. π-π entanglement signatures in Protein-DNA interactions. In: *Physical Biology*. Bristol; Philadelphia, PA: Institute of Physics. https://doi.org/10.1088/1478-3975/ac5bda.

Das A, et al. (2020) Biological concepts for catalysis and reactivity: Empowering bioinspiration. *Chemical Society Reviews* 49(23): 8840–8867. https://doi.org/10.1039/d0cs00914h. Thomas Graham House, Science park, Milton rd, Cambridge CB4 0WF, Cambs, England: Royal Soc Chemistry.

Davydov AS (1979) *Biology & Quantum Mechanics*. Oxford: Pergamon Press.

Duan H-G, et al. (2017) Nature does not rely on long-lived electronic quantum coherence for photosynthetic energy transfer. *Proceedings of the National Academy of Sciences* 114(32): 8493–8498. https://doi.org/10.1073/pnas.1702261114.

Dyson G (1928) Some aspects of the vibration theory of odor. *Perfumery and Essential Oil Record* 19: 456–459.

Edington MD, Riter RE, and Beck WF (1995) Evidence for coherent energy transfer in allophycocyanin trimers. *The Journal of Physical Chemistry* 99(43): 15699–15704. https://doi.org/10.1021/j100043a001. American Chemical Society.

Engel GS, et al. (2007) Evidence for wavelike energy transfer through quantum coherence in photosynthetic systems. *Nature* 446(7137): 782–786. https://doi.org/10.1038/nature05678.

Eric B, et al. (2015) Implausibility of the vibrational theory of olfaction. *Proceedings of the National Academy of Sciences* 112(21): E2766–E2774. https://doi.org/10.1073/pnas.1503054112.

Fassioli F and Olaya-Castro A (2010) Distribution of entanglement in light-harvesting complexes and their quantum efficiency. *New Journal of Physics* 12(8): 85006. https://doi.org/10.1088/1367-2630/12/8/085006. IOP Publishing.

Franck J and Teller E (1938) Migration and Photochemical Action of Excitation Energy in Crystals. *The Journal of Chemical Physics* 6(12): 861–872. https://doi.org/10.1063/1.1750182. American Institute of Physics.

Frenkel J (1931) On the Transformation of light into Heat in Solids. I. *Physical Review* 37(1): 17–44. https://doi.org/10.1103/PhysRev.37.17. American Physical Society.

Gelzinis A, et al. (2019) Two-dimensional spectroscopy for non-specialists. *Biochimica et Biophysica Acta - Bioenergetics* 1860(4): 271–285. https://doi.org/10.1016/j.bbabio.2018.12.006. Elsevier B.V.

Gerlich S, et al. (2011) Quantum interference of large organic molecules. *Nature Communications* 2(1): 263. https://doi.org/10.1038/ncomms1263.

Gray HB and Winkler JR (2003) Electron tunneling through proteins. *Quarterly Reviews of Biophysics. England* 36(3): 341–372. https://doi.org/10.1017/s0033583503003913.

Hay S and Scrutton NS (2012) Good vibrations in enzyme-catalysed reactions. *Nature Chemistry* 4(3): 161–168. https://doi.org/10.1038/nchem.1223.

Hiscock HG, et al. (2016) The quantum needle of the avian magnetic compass. *Proceedings of the National Academy of Sciences* 113(17): 4634–4639. https://doi.org/10.1073/pnas.1600341113.

Huang L, Wong C, and Grumstrup E (2020) Time-resolved microscopy: A new frontier in physical chemistry. *The Journal of Physical Chemistry A* 124(29): 5997–5998. https://doi.org/10.1021/acs.jpca.0c05511. American Chemical Society.

Huelga SF and Plenio MB (2013) Vibrations, quanta and biology. *Contemporary Physics* 54(4): 181–207. https://doi.org/10.1080/00405000.2013.829687.

Hybl JD, et al. (1998) Two-dimensional electronic spectroscopy. *Chemical Physics Letters* 297(3): 307–313. https://doi.org/10.1016/S0009-2614(98)01140-3.

Hybl JD, Ferro AA, and Jonas DM (2001) Two-dimensional Fourier transform electronic spectroscopy. *Journal of Chemical Physics* 115(14): 6606–6622. https://doi.org/10.1063/1.1398579.

Joos E and Zeh HD (1985) The emergence of classical properties through interaction with the environment. *Zeitschrift fur Physik B: Condensed Matter* 59(2): 223–243. https://doi.org/10.1007/BF01725541.

Jordan P (1932) Die quantenmechanik und die grundprobleme der biologie und psychologie. *Naturwissenschaften* 20(45): 815–821. https://doi.org/10.1007/BF01494844.

Lambert N, et al. (2013) Quantum biology. *Nature Physics* 9(1): 10–18. https://doi.org/10.1038/nphys2474.

Lambrev PH, Akhtar P, and Tan HS (2020) Insights into the mechanisms and dynamics of energy transfer in plant light-harvesting complexes from two-dimensional electronic spectroscopy. *Biochimica et Biophysica Acta, Bioenergetics* 1861(4): Elsevier. 148050. https://doi.org/10.1016/j.bbabio.2019.07.005.

Lee KS, et al. (2021) Entanglement between Superconducting Qubits and a Tardigrade. *arxiv.org/abs/2112.07978*.

Liebel M, Toninelli C, and van Hulst NF (2018) Room-temperature ultrafast nonlinear spectroscopy of a single molecule. *Nature Photonics* 12(1): 45–49. https://doi.org/10.1038/s41566-017-0056-5.

Löwdin P-O (1966) Quantum Genetics and the Aperiodic Solid: Some Aspects on the Biological Problems of Heredity, Mutations, Aging, and Tumors in View of the Quantum Theory of the DNA Molecule. **Sponsored in part by the King Gustaf VI Adolf's 70-Years Fund for Swedish Culture, Knut and Alice Wallenberg's Foundation, and in part by the Cancer Institute of National Institutes of Health, under Contract CA 06850–01 with Uppsala University. In: *Advances in Quantum Chemistry*, pp. 213–360. Academic Press. https://doi.org/10.1016/S0065-3276(08)60076-3.

Marais A, et al. (2018) The future of quantum biology. *Journal of the Royal Society, Interface* 15(148). https://doi.org/10.1098/rsif.2018.0640.

McFadden J and Al-Khalili J (2018) The origins of quantum biology. *Proceedings of the Royal Society A-Mathematical Physical and Engineering Sciences* 6–9. Carlton House Terrace, London Sw1y 5AG, England: Royal Soc, 474 (2220) https://doi.org/10.1098/rspa.2018.0674.

McKaughan DJ (2005) The influence of niels bohr on max delbrück: Revisiting the hopes inspired by "light and life" *Isis* 96(4): 507–529. https://doi.org/10.1086/498591. The University of Chicago Press.

Moerner WE, Shechtman Y, and Wang Q (2015) Single-molecule spectroscopy and imaging over the decades. *Faraday Discussions* 184: 9–36. https://doi.org/10.1039/C5FD00149H. The Royal Society of Chemistry.

Mohseni M, et al. (2008) Environment-assisted quantum walks in photosynthetic energy transfer. *The Journal of Chemical Physics* 129(17). https://doi.org/10.1063/1.3002335. American Institute of Physics. 174106.

Moncrieff RW (1949) Recent developments in the chemistry of perfumes. *Endeavour* 8(30): 92–95. England.

Mori K and Shepherd GM (1994) Emerging principles of molecular signal processing by mitral/tufted cells in the olfactory bulb. *Seminars in Cell Biology* 5(1): 65–74. https://doi.org/10.1006/scel.1994.1009.

Moser CC, Anderson JLR, and Dutton PL (2010) Guidelines for tunneling in enzymes. *Biochimica et Biophysica Acta (BBA) - Bioenergetics* 1797(9): 1573–1586. https://doi.org/10.1016/j.bbabio.2010.04.441.

Nielsen M and Chuang I (2000) *Quantum Computation and Quantum Information*. Cambridge: Cambridge University Press.

Olaya-Castro A and Scholes GD (2011) Energy transfer from Förster–Dexter theory to quantum coherent light-harvesting. *International Reviews in Physical Chemistry* 30(1): 49–77. https://doi.org/10.1080/0144235X.2010.537060. Taylor & Francis.

Pandey N, et al. (2021) Vibration-based biomimetic odor classification. *Scientific Reports* 11(1): 11389. https://doi.org/10.1038/s41598-021-90592-x.

Panitchayangkoon G, et al. (2010) Long-lived quantum coherence in photosynthetic complexes at physiological temperature. *Proceedings of the National Academy of Sciences of the United States of America* 107(29): 12766–12770. https://doi.org/10.1073/pnas.1005484107.

Plenio MB and Huelga SF (2008) Dephasing-assisted transport: quantum networks and biomolecules. *New Journal of Physics* 10(11). https://doi.org/10.1088/1367-2630/10/11/113019. IOP Publishing. 113019.

Savikhin S, Buck DR, and Struve WS (1997) Oscillating anisotropies in a bacteriochlorophyll protein: Evidence for quantum beating between exciton levels. *Chemical Physics* 223(2): 303–312. https://doi.org/10.1016/S0301-0104(97)00223-1.

Schlau-Cohen GS, et al. (2009) Pathways of energy flow in LHCII from two-dimensional electronic spectroscopy. *The Journal of Physical Chemistry B* 113(46): 15352–15363. https://doi.org/10.1021/jp9066586. American Chemical Society.

Scholes GD (2011) Coherence in photosynthesis. *Nature Physics* 7(6): 448–449. https://doi.org/10.1038/nphys2013. Nature Publishing Group.

Scholes GD, et al. (2011) Lessons from nature about solar light harvesting. *Nature Chemistry* 3: 763. https://doi.org/10.1038/nchem.1145. Nature Publishing Group, a division of Macmillan Publishers Limited. All Rights Reserved.

Scholes GD, et al. (2014) Photosynthetic light harvesting: Excitons and coherence. *Journal of the Royal Society Interface* 11(92): 20130901. https://doi.org/10.1098/rsif.2013.0901.

Scholes GD, et al. (2017) Using coherence to enhance function in chemical and biophysical systems. *Nature* 543(7647): 647–656. https://doi.org/10.1038/nature21425. Nature Publishing Group.

Schrödinger E (1944) *What is Life?* Dublin: Cambridge University Press.

Schulten K, Swenberg CE, and Weller A (1978) A biomagnetic sensory mechanism based on magnetic field modulated coherent electron spin motion. *Zeitschrift für Physikalische Chemie* 111(1): 1–5. https://doi.org/10.1524/zpch.1978.111.1.001.

Shashkova S and Leake MC (2017) Single-molecule fluorescence microscopy review: Shedding new light on old problems. *Bioscience Reports* 37(4). https://doi.org/10.1042/BSR20170031. BSR20170031.

Thyrhaug E, et al. (2018) Identification and characterization of diverse coherences in the Fenna-Matthews-Olson complex. *Nature Chemistry* 10(7): 780–786. https://doi.org/10.1038/s41557-018-0060-5. Springer US.

Tirandaz A, Taher Ghahramani F, and Salari V (2017) Validity examination of the dissipative quantum model of olfaction. *Scientific Reports* 7(1): 4432. https://doi.org/10.1038/s41598-017-04846-8.

Tokmakoff A (2020) *Time Dependent Quantum Mechanics and Spectroscopy*. Chicago: University of Chicago. Available at: https://chem.libretexts.org/@go/page/107215.

Turin L (1996) A spectroscopic mechanism for primary olfactory reception. *Chemical Senses* 21(6): 773–791. https://doi.org/10.1093/chemse/21.6.773.

Vedral V and Plenio MB (1998) Entanglement measures and purification procedures. *Physical Review A* 57(3): 1619–1633. https://doi.org/10.1103/PhysRevA.57.1619. American Physical Society.

Wiltschko FR and Wiltschko W (2012) Chapter 8 - Magnetoreception. In: *Sensing in Nature. Advances in Experimental Medicine and Biology*, pp. 126–141. New York: Springer.

Wright RH (1977) Odor and molecular vibration: Neural coding of olfactory information. *Journal of Theoretical Biology* 64(3): 473–502. https://doi.org/10.1016/0022-5193(77)90283-1.

Zettili N (2022) *Quantum Mechanics: Concepts and Applications*, 3rd edn Chichester: John Wiley & Sons Inc.

Zhang Y, Berman GP, and Kais S (2015) The radical pair mechanism and the avian chemical compass: Quantum coherence and entanglement. *International Journal of Quantum Chemistry* 115(19): 1327–1341. https://doi.org/10.1002/qua.24943. John Wiley & Sons, Ltd.

Nature's novel materials: A review of quantum biology

Betony Adams[a,b,c] **and Francesco Petruccione**[a,b,d], [a]Quantum Research Group, University of KwaZulu-Natal, Durban, South Africa; [b]National Institute for Theoretical and Computational Sciences, Stellenbosch, South Africa; [c]The Guy Foundation, Dorset, United Kingdom; [d]School of Data Science and Computational Thinking and Department of Physics, Stellenbosch University, Stellenbosch, South Africa

© 2024 Elsevier Ltd. All rights reserved.

Introduction **594**
A brief history 594
Non trivial quantum effects 594
Methods and models 595
The biological context **596**
Quantum tunnelling 596
DNA 596
Enzymes 596
Receptors 596
Coherent transfer processes 597
Photosynthesis 597
Microtubules 598
Mitochondria 598
Spin dynamics 598
Spin chemistry 598
Avian navigation 598
Reactive oxygen species 599
Phosphorus nuclear spin 599
Chirality 600
New (and old) avenues of interest 600
Conclusion **601**
Funding and Acknowledgments **601**
References **601**

Abstract

Quantum biology is, most simply, the investigation of quantum effects in biological systems. While all matter is fundamentally quantum, quantum biology focuses on those quantum effects that result in properties of biological scale and relevance. It has long been argued that quantum effects are incompatible with biological systems, due to the likelihood of decoherence. But nature is a surprising and enterprising engineer. In this sense, quantum biology is the study of nature's materials and how they might sustain and enhance quantum effects, even in hot and wet environments. Quantum mechanics was developed in response to seemingly anomalous interactions between light and matter. It seems fitting that a great deal of the progress made in quantum biology in the last few decades has been on the topic of photosynthesis: the interaction of light with living matter. The interaction of electromagnetic radiation with matter is also at the heart of many other topics of quantum biology. This review is a broad overview of the current state of this research. While the underlying quantum effects are often similar—energy and charge transfer, tunnelling, spin dynamics—the biological contexts are varied and continue to grow. These contexts include enzyme catalysis, DNA mutation, receptor binding, photosynthesis, microtubule and mitochondrial function, magnetoreception, regulation of the production of reactive oxygen species, calcium ion storage and release and, potentially, consciousness. While there remain a number of reservations regarding quantum biology, progress made in this regard might further our understanding of both quantum and biological systems. With respect to the latter, advances in understanding biology might also contribute to a better understanding of physiology and the development of new therapeutics. But quantum biology might equally advance our understanding of quantum mechanics, by illustrating what quantum effects could look like in the novel materials out of which living systems are built.

Key points

- What is quantum biology?
- What are nontrivial quantum effects such as tunnelling, coherence, and entanglement?
- In what biological contexts do quantum effects occur?
- In what new biological contexts might quantum effects occur?

https://doi.org/10.1016/B978-0-323-90800-9.00268-7

Introduction

Of what special interest is quantum biology to the study of condensed matter physics? In quantum biology, much attention is paid to the problem of decoherence, which is the loss of quantum effects such as superposition or entanglement due to interaction between the quantum system and its environment. It is often stated that sustained quantum effects are unlikely to occur in biological systems because of the distinct properties of biological matter: the high physiological temperature, the relative disorder of protein environments. Quantum systems are fragile and biological systems are robust. While this may seem an argument against quantum biology, it is also an argument for why quantum biology is interesting, especially with regard to the study of matter. Nature is a novel materials engineer. Adaptability is a driving principle in biology. This seems evident not only on the scale of organisms but also with respect to the matter that constitutes biological systems. Consider the opsins, for instance. This group of proteins is light-sensitive due to the inclusion of the light-reactive chromophore retinal. While retinal absorbs at a given frequency, this absorption can be tuned by the particular protein it is attached to, allowing nature to repurpose a single chromophore to give us color vision across the visible spectrum (Wang et al., 2014; Hoffmann et al., 2006). In many different contexts, the protein environment seems one of nature's aces. The electronic properties of living matter are uniquely interesting. It has even been suggested that almost all biomolecules belong to a fundamentally new class of disordered conducting material, poised at the critical quantum state between metal and insulator (Vattay et al., 2015). While quantum theory might offer valuable insight into biological systems, the opposite is also true. A better understanding of nature's materials might show us new and surprising ways to control and manipulate quantum systems.

A brief history

Quantum biology is sometimes referred to as an emerging field of research. In reality its concerns are almost as old as quantum mechanics itself (McFadden and Al-Khalili, 2018). Quantum theory was first proposed as a way to explain anomalous interactions between light and matter (Zettili, 2009; Haken and Wolf, 1987). In the context of blackbody radiation, the departure of observed behavior from classical prediction was so extreme as to be called the ultraviolet catastrophe. In response, Planck postulated a minimum quantum of energy. This was followed by Einstein's explanation of the photoelectric effect (Zettili, 2009; Haken and Wolf, 1987). Light, it appeared, behaved as both a wave and a particle, that came to be known as the photon. Reciprocally, de Broglie postulated that matter, conventionally understood as being particulate, can also demonstrate wave-like effects such as interference, which was subsequently observed in the case of electrons. These ideas were later formalized by physicists such as Heisenberg and Schrödinger (Zettili, 2009; Haken and Wolf, 1987). While quantum physics was a response to the interaction of light with inanimate matter, many of its founding figures already expressed interest in what insights it might offer in the context of living systems. In 1944, Schrödinger published the book *What is Life? The Physical Aspect of the Living Cell*, which is often cited as the inspiration for the discovery of DNA (Schrödinger, 1944; Marais et al., 2018). Indeed, the term "quantum biology" was already in use as early as the 1930s, by Pascual Jordan (McFadden and Al-Khalili, 2018). The interaction of light with matter was central to the development of quantum theory. Light is also pivotal in the context of living matter. In 1932, Bohr, another figure central to the consolidation of quantum theory, gave a lecture entitled "Light and Life" (Bohr, 1933; Marais et al., 2018). It is perhaps no surprise then that much of the research in quantum biology is focused on photosynthesis: the interaction of light with biological systems. Indeed, the interaction of electromagnetic radiation with matter is also at the heart of other topics of quantum biology. For the most part, however, these speculations would have to remain theoretical until technology caught up with them.

Non trivial quantum effects

Questions around the quantum nature of biological matter may be as old as quantum theory itself (McFadden and Al-Khalili, 2018). But what is more recent is the distinction that is made between trivial and nontrivial quantum effects in biological systems. All matter obeys the laws of quantum mechanics (Zettili, 2009; Haken and Wolf, 1987; Marais et al., 2018). In this trivial sense, biology can be described as being quantum mechanical in the same way that all matter is quantum mechanical. Nontrivial quantum effects, on the other hand, might be thought of as those quantum processes that give rise to functional outcomes on a biological scale, potentially conferring some evolutionary advantage on the system in question (Marais et al., 2018; Al-Khalili and McFadden, 2014; Mohseni et al., 2013; Lambert et al., 2013). Tunnelling, for instance, is the nonzero probability that a quantum particle will pass through a barrier in a manner that is forbidden by classical physics (Zettili, 2009; Haken and Wolf, 1987). Historically, quantum tunnelling was the first of the so-called nontrivial effects to be proposed and observed in biological systems (McFadden and Al-Khalili, 2018; Löwdin, 1963). In 1963, Löwdin hypothesized that point mutations in DNA might be caused by proton tunnelling (Löwdin, 1963). Shortly afterwards, in 1966, DeVault and Chance observed electron tunnelling in enzymes (DeVault and Chance, 1966). In this review we will examine in more detail the advances made in understanding and identifying tunnelling in biological molecules in the context of both DNA mutation and enzymes as well as a number of other biological phenomena in which it may play a part.

The movement of charged particles such as protons and electrons is also the subject of quantum biology in the context of photosynthesis. Research suggests that photosynthetic networks use quantum coherence to maximize their transport of energy and charge (Engel et al., 2007; Brixner et al., 2005; van Grondelle and Novoderezhkin, 2011; Schlau-Cohen et al., 2009; Panitchayangkoon et al., 2010; Collini et al., 2010). Coherence follows from the wave description of matter, and measures how in phase two waves are. This phase difference gives rise to interference. In quantum mechanics, the superposition principle allows that for two quantum states describing a system, a linear combination of the two also describes the system (Zettili, 2009; Haken and Wolf, 1987). The coherence then quantifies the relationship between the states in this superposition. In biological terms, this means that energy or charge transport between sites in a photosynthetic network can behave collectively, spread out across sites rather than isolated to a single site. A great deal of experimental effort has been directed toward confirming this coherent transport (Engel et al., 2007; Brixner et al., 2005; van Grondelle and Novoderezhkin, 2011; Schlau-Cohen et al., 2009; Panitchayangkoon et al., 2010; Collini et al., 2010). In 2007, it appeared that long-lived quantum coherence in photosynthetic networks had been experimentally observed (Engel et al., 2007). This remains a matter of debate. We will examine this evidence further as well as outlining the case for energy and charge transfer outside of photosynthetic networks.

Of all the weird effects that quantum mechanics gives rise to, entanglement is possibly the strangest. Entanglement describes the nonclassical correlation between different quantum objects, the extent of which means that they cannot be considered separate systems but must be treated as a single system (Zettili, 2009; Haken and Wolf, 1987). In the biological context, entanglement is often invoked with respect to quantum spin. Spin, or spin angular momentum, describes the quantized response of a physical system, such as an electron or proton, to a magnetic field. While spin correlation and entanglement have been extensively reviewed in the context of avian navigation, there is emerging evidence that magnetic fields have an effect on biological systems in a wider context (Hore and Mouritsen, 2016; Rodgers and Hore, 2009; Cai et al., 2010; Gauger et al., 2011; Pauls et al., 2013). The interaction between spin and molecular chirality is also an important emerging subject in quantum biology, especially given the fact that biological molecules favor certain chiralities (Aiello et al., 2022).

Methods and models

While the founding figures of quantum mechanics speculated on the role that quantum effects might play in living systems, the field would remain mostly theoretical until experimental techniques were developed for the investigation of systems on such small time and length scales. Many of the relevant processes—such as energy transfer—happen on ultrafast timescales such as pico and femtoseconds. For a comparison of timescales relevant to quantum and biological processes, see Table 1. Developments in experimental techniques such as ultrafast spectroscopy, single-molecule spectroscopy, time-resolved microscopy, and single-particle imaging have contributed much to the recent accumulation of research in quantum biology (Marais et al., 2018; Kim et al., 2021). Most of this experimental investigation, however, has been in the context of photosynthetic systems. There has also been some suggestion that more tractable, hybrid or artificial models of these systems would be useful in advancing the field (Kim et al., 2021). It remains to be seen how techniques used fruitfully in investigating coherent energy and charge transfer processes might be applied to other contexts in quantum biology. For investigations into tunnelling, the widely adopted experimental approach is selective deuteration or the exploration of isotope effects, given that tunnelling is strongly dependent on the mass of the tunnelling quantum object. This approach is also used to investigate vibration-assisted tunnelling in olfaction and related phenomena, though caution is noted with respect to the possibility of contaminants skewing the results (Paoli et al., 2017). Direct evidence for radical pairs in avian magnetoreception is lacking, with most of the evidence being behavioral (Rodgers and Hore, 2009). However, a recent experiment has demonstrated autoluminescence in the context of radical pair dynamics, opening a new era in experimental techniques relating to radical pairs (Ikeya and Woodward, 2021).

Theoretically the field is more widely developed. A number of models have been used to describe the dynamics of quantum systems in biological environments. Many of which begin with a simple Hamiltonian describing the charge transport or spin dynamics. Classically, energy transport has been modeled using Förster resonance energy transfer (FRET) theory. Quantum Theoretical frameworks of this transport use a variety of approaches including Redfield theory and the numerically exact hierarchical equations of motion (HEOM) (Kim et al., 2021). In the case of the spin dynamics, the initial density matrix treatment of radical pair reactions initiated by Haberkorn has garnered discussion (Haberkorn, 1976; Tiersch et al., 2012; Kominis, 2015). A number of other open quantum systems approaches have been applied to the problem (Haberkorn, 1976; Tiersch et al., 2012; Kominis, 2015). Open systems approaches have also been applied to proton tunnelling in DNA (Slocombe et al., 2022). In modeling the effects of quantum tunnelling in enzymes, reaction rates following from transition state theory are modified by multiplication with a

Table 1 Timescales for different biological phenomena Rodgers and Hore (2009), Engel (2011), Tegmark (2000), Verpoorte et al. (2008), and Song et al. (2014).

Timescale	*Quantum effect*	*Biological processes*
Femto/picoseconds	Coherent transfer	Photosynthetic (microtubule) processes
Microseconds	Radical pair mechanism	Ion channel gating
Milliseconds	Spin effects	Enzyme catalysis, neural firing rates
Seconds to hours	Posner molecule model	Gene expression, protein synthesis, memory

The list of biological processes is not exhaustive but gives some idea of which quantum processes have comparable timescales with which biological processes. This does not mean that the particular quantum effect is necessarily implicated in the functioning of that biological process, only that their timescales overlap. We have included the more general "spin effects" as radical pairs may have up to millisecond lifetimes, while nuclear spins may relax faster than seconds. For biological processes that span many timescales, such as magnetoreception, the timescale of interest would be that of the appropriate chemical reaction and signal transduction.

tunnelling correction factor (Kim et al., 2021). Another theoretical approach widely employed in quantum biology is density functional theory, which is often used to calculate relevant parameters. Finally, a number of theoretical approaches use different measures of coherence—such as relative entropy—or entanglement—such as concurrence or negativity—in order to investigate how quantum a given biological system is (Le and Olaya-Castro, 2020; Player and Hore, 2018; Gauger et al., 2011). This is a very brief overview of the methods and models by which quantum biology is investigated. This review is meant as a broad introduction to the field and not as an exhaustive foray into the physics. For excellent overviews of the field of quantum biology see Al-Khalili and McFadden (2014), Mohseni et al. (2013), Marais et al. (2018), and Lambert et al. (2013). For a more detailed history of quantum biology see McFadden and Al-Khalili (2018). For a recent update at the physical details of the models applied in quantum biology, see Kim et al. (2021).

The biological context

Quantum tunnelling

DNA

It is difficult to overstate the role that deoxyribonucleic acid (DNA) plays in our understanding of biological systems. DNA carries the information by which essential proteins are synthesized. Within DNA, the genes that code for proteins consist of specific strings of the four nucleotides with bases: adenine, thymine, guanine, and cytosine. These bases form pairs—adenine with thymine, guanine with cytosine—that constitute the double helix of DNA (Kim et al., 2021). The specificity of this pairing is essential to DNA replication and protein synthesis. It is integral that each base binds only to its complementary base, despite being exposed to any of the possible bases. While DNA mutation has primarily been attributed to external factors such as radiation, it has also been suggested that structural changes to the base pairs may result in mismatched base-pair binding. This is because the bases can exist in a tautomeric form whose pair geometry mimics that of the correct base pairs (Kim et al., 2021; Slocombe et al., 2021). In 1963 the Swedish physicist Per-Olov Löwdin put forward the theory that proton tunnelling might facilitate DNA mutation due to the fact that tautomerization depends on proton relocation (Löwdin, 1963). Since then, there have been a number of attempts to accurately model these tunnelling effects using mathematical and computational techniques (Kim et al., 2021). Experimental evidence for tunnelling follows the well-established path of kinetic isotope effects involving deuterium substitution. Although the research suggests that there is such an effect, further evidence is necessary for confirmation. While the details of progress made in the field of proton tunnelling in DNA mutation are beyond the scope of this review, see Kim et al. for an excellent review (Kim et al., 2021).

Enzymes

While proton tunnelling is considered the first theoretical instance of tunnelling in biological systems, electron tunnelling was first observed in enzymes. DeVault and Chance observed a temperature-independent electron transfer reaction indicative of quantum tunnelling (DeVault and Chance, 1966). Today the study of tunnelling—both electron and proton—in enzymes is a well-developed field of research. Enzymes are large biological molecules, usually proteins, that are integral to the efficient function of biological systems, catalyzing many essential reactions. The action of enzymes on substrates is conventionally understood through transition state theory. This approach to modeling enzyme action includes an energy barrier between the reactants and products of a chemical reaction. The enzyme is thought to lower the necessary activation energy of a reaction (Kim et al., 2021; Sutcliffe and Scrutton, 2000). Quantum tunnelling offers an alternative mechanism for enzyme catalysis whereby the barrier is passed through rather than over (Zettili, 2009; Kim et al., 2021; Sutcliffe and Scrutton, 2000; Brookes, 2017). The contribution of quantum tunnelling to the reaction rate dominates at lower temperatures, where thermal activation no longer contributes (Sutcliffe and Scrutton, 2000; Kim et al., 2021; Brookes, 2017). It is well established that tunnelling is the mechanism of electron transfer in enzymes (Sutcliffe and Scrutton, 2000; Marcus and Sutin, 1985). For the considerably more massive proton, tunnelling in enzymes has elicited mixed responses. See Kim et al. for an overview of the subject (Kim et al., 2021). The kinetic isotope effect, in which rates of transfer are compared for isotopes, is one of the ways in which proton tunnelling might be measured experimentally. However, the kinetic isotope effect may also play a role in enzyme reactions as modeled by transition state theory. The temperature dependence of the kinetic isotope effect might then offer a way to measure the contribution of tunnelling to the rate acceleration. Pressure might also offer a means to measure tunnelling in enzymes, though the accuracy of its predictions remains to be seen (Kim et al., 2021). What is becoming clearer, however, is the contribution that the protein scaffold or, alternatively, water, might play in tunnelling processes (Klinman and Kohen, 2013; Thompson et al., 2021; Marković et al., 2020).

Receptors

Quantum tunnelling in the context of enzyme catalysis has generated a great deal of research, both theoretical and experimental. The hypothesis that tunnelling might also be implicated in the action of receptor binding and activation has been met with more skepticism, however. At the risk of simplification, receptor binding has conventionally been described as utilizing the "lock-and-key" mechanism, by which shape or conformation is the distinguishing factor for the binding of appropriate ligands to receptors (Tripathi and Bankaitis, 2017). In 1996, Turin, building on an idea by Dyson, proposed an alternative or augmented mechanism for one such set of receptors: olfactory G-protein coupled receptors (GPCRs) (Dyson, 1938; Turin, 1996). The theory is that olfactory receptors are activated by electron tunnelling, facilitated by the matching vibrational mode of the appropriate odorant. The standard way of testing the theory is to examine the effects of selectively deuterated odorants, whose different masses yield different vibrational spectra. Experiments have demonstrated that fruit flies appear to be able to differentiate these deuterated varieties, though insect olfactory receptors differ from mammalian G-protein-related olfactory receptors and results may not be generalizable (Franco et al., 2011; Horsfield et al., 2017). Lake whitefish and the American cockroach have also demonstrated an ability to differentiate between isotopes of amino acids and pheromones (Hoehn et al., 2015; Hara, 1977; Havens and Meloan, 1995). However, the theory remains a contentious one. In two recent paper, Gehrckens et al. address one of the primary objections to the theory: the lack of evidence for electron transfer in GPCRs. They present results that suggest that electron movement is possible in certain classes of these receptors (Gehrckens et al., 2019, 2021). While the vibrational theory of olfaction remains debatable, there have been attempts to generalize the theory to other classes of GPC receptors, which include those that mediate neurotransmission. Hoehn et al. focus on the neurotransmitter serotonin and its receptors (Hoehn et al., 2015, 2017). They investigate the vibrational spectra of endogenous and nonendogenous agonists that bind to the serotonin receptor. Their theoretical results show that serotonin shares an inelastic electron tunnelling spectral peak with other agonists that activate the serotonin receptor and that the intensity of this peak can be used to predict the potency of an agonist (Hoehn et al., 2015). These results however are not supported by subsequent experimental investigations (Hoehn et al., 2017). Classification schemes for GPCR binding ligands are well developed due to the fact that GPCRs are important pharmaceutical target. There are a variety of ways to classify molecules as potential ligands. Recent research suggests that vibrational spectra might also be used as a feature in classification, specifically in the case of adenosine and histamine receptor ligands (Chee and Oh, 2013; Chee et al., 2015; Oh, 2012). While there is some experimental evidence for different binding patterns of histamine and its deuterated counterpart, it is far from evident that this is due to tunnelling effects (Kržan et al., 2016). Despite a lack of definitive experimental evidence in support of vibration-assisted tunnelling in GPC receptors, the idea is an interesting one in the context of quantum biology. There has even been some interest in its application to spike protein binding in the context of the SARS-CoV-2 virus (Adams et al., 2022). In various different contexts—including tunnelling in enzymes as well as energy and charge transfer in photosynthesis—the role of the protein scaffold has been highlighted, in particular the vibrational or phonon character of the protein (Brookes, 2017). It appears that protein vibrations can facilitate charge transfer, for a detailed description of this in the context of photosynthesis, see Cao et al. (2020). This would seem to have implications for protein binding, including those proteins that constitute receptors.

Coherent transfer processes

Photosynthesis

Photosynthesis is the process by which organisms such as plants or bacteria convert energy from the sun into chemical energy. Light is harvested and its energy transferred by membrane-bound chromophore-protein complexes of light-harvesting complexes (LHC) to the reaction center (RC). Here, charge separation occurs and the energy is converted into a membrane potential. This energy and charge transfer is extremely efficient, which has led to the suggestion that there is quantum enhancement of the process. More specifically, it has been suggested that quantum coherence—specifically in the form of excitonic coherence or delocalization—contributes to this efficacy, facilitated by the geometry and coupling strengths of the network of chromophores between which transfer happens (Engel et al., 2007; Brixner et al., 2005; van Grondelle and Novoderezhkin, 2011; Schlau-Cohen et al., 2009; Panitchayangkoon et al., 2010; Collini et al., 2010). Classically this transfer is modeled as discrete hopping between the states of each individual site in the network, as described by FRET theory. Taking coherence into account, wavefunction overlap allows for an excitonic "best path" approach, potentially minimizing the disorder introduced by the protein environment. Theoretical approaches vary according to the specific parameters of the networks and the strength of coupling (Kim et al., 2021). It is important to be clear what is meant by coherence as the term appears often and in varying contexts in quantum biology. For an excellent discussion of what is meant by coherence in the context of photosynthesis see the paper by Cao et al. (2020). Experimental advances such as two-dimensional electronic spectroscopy (2DES) have allowed for more precise resolution of energy dynamics in chromophore networks. Experimentally, the signature of coherent transfer is often taken to the appearance of cross-peaks or quantum beats in the spectrum of a system, which represent the interaction between discrete sites. The Fenna-Matthews-Olson (FMO) complex, found in green sulfur bacteria, is often used as a model system for coherent transfer dynamics. In 2007, oscillating cross-peaks were detected in the FMO complex, suggesting coherence might indeed play a role in transfer processes in photosynthetic systems. The study, by Engel et al., is a landmark one in quantum biology, generating many subsequent studies as well as a great deal of debate as to exactly what the results signified (Engel et al., 2007; Kim et al., 2021). While the role of excitonic coherence in transfer processes remains a matter of debate, the role of vibronic coherence is of growing interest (Policht et al., 2022; Abramavicius and Valkunas, 2016). In contrast to the view that the noisy protein environment hinders energy transfer, the coupling of vibrational modes to energy levels has been suggested to enhance transfer processes. Environment-assisted enhancement effects have been supported by both theoretical and experimental results, with evidence for sustained coherence at physiologically relevant temperatures (Kim et al., 2021; Thyrhaug et al., 2018; Dean et al., 2016; Tiwari et al., 2013). In addition to vibration-assisted transfer, a number of studies have looked at whether the spin environment might enhance or disrupt transfer processes (Marais et al., 2013). Advances in experimental techniques have also led to the synthesis of tractable chromophore-scaffold complexes, which allow for better control of the transfer dynamics (Kim et al., 2021; Proppe et al., 2020; Lee et al., 2019). Progress in this direction could contribute to solar cell improvements and green energy technology, as could a better understanding of design principles employed by natural photosynthetic systems, to maximize the efficiency of energy transfer and charge separation (Romero et al., 2017).

Microtubules

The study of energy and charge transfer in the pigment-protein complexes of photosynthetic systems is by now well developed. These complexes are not unique to photosynthesis however. An emerging topic in quantum biology is the study of other contexts in which chromophores may play a role. In photosynthetic light harvesting complexes, the main chromophore of interest is chlorophyll. Biological systems have a host of other chromophores that absorb at different frequencies. Among these is tryptophan, which absorbs in the ultraviolet part of the spectrum (Celardo et al., 2019). Tryptophan is an essential part of tubulin proteins, which make up cytoskeletal filaments called microtubules. Microtubules are instrumental in many cellular processes, including cell division, motility, and intracellular transport (Hameroff and Penrose, 2014; Meunier and Vernos, 2012). Tubulin and microtubules have been central to the physical realization of theories about quantum consciousness. Penrose and Hameroff's Orchestrated objective reduction (Orch OR) theory posits microtubules as the site of quantum computations that give rise to consciousness. Among other things, the theory calls for collective behavior within microtubules, as envisioned by Fröhlich (Hameroff and Penrose, 2014; Penrose, 1989). Fröhlich condensation has long been of interest in the study of quantum effects in biological systems. Although it is generally maintained that classical Fröhlich regimes dominate in microtubules, arguments have been made for quantum fluctuations in Fröhlich condensates of biological matter (Zhang et al., 2019). As interest in vibrational coherence grows, phonon condensates are likely to offer a rich field of research. Recent experimental work supports that out-of-equilibrium collective oscillations are capable of activating long-range electrodynamic intermolecular forces in biological systems (Lechelon, 2022). Microtubules have also generated interest as a site for coherent energy transfer and the disruption of this transfer by drugs such as anesthetics. Craddock et al. suggest that the tryptophan residues present in the tubulin proteins that constitute microtubules are structurally and functionally capable of supporting the possibility of quantum coherent—particularly excitonic coherence—energy transfer (Craddock et al., 2014a, b). The particular geometry of tryptophan networks in tubulin proteins and microtubule filaments has led researchers to suggest ways in which biological materials might manipulate and amplify light, scaling up nanoscale effects by the collective behavior of the tryptophans. While evidence for superradiance in microtubules has been demonstrated using theoretical modeling and computational simulation, experimental verification is still under way (Celardo et al., 2019). The opposite process, superabsorption, is also a growing field of interest, with some evidence that natural design principles might contribute to the design of quantum technologies that maximize energy storage (Quach et al., 2022). Collective effects in light–matter interactions could also provide a way in which ultraweak endogenous photons might have measurable effects in biological systems.

Mitochondria

The presence of microtubule-based tryptophan networks capable of coherent transfer processes has also led to suggestions that mitochondria could funnel photons to microtubules (Kurian et al., 2017). Mitochondria are often termed the "power stations" of the cell due to the fact that they produce adenosine triphosphate (ATP), the molecule whose energy-rich bonds fuel the majority of cellular processes. It is becoming clear, however, that mitochondria play a pivotal role in signaling processes in the body, regulating signaling molecules such as reactive oxygen species (ROS) (Auten and Davis, 2009; Zorov et al., 2014; Nunn et al., 2016). Mitochondria are thought to be a primary site of endogenous photons, which result from oxidative processes in mitochondrial electron transport chains (Kumar et al., 2016; Cifra and Pospisil, 2014). These electron transport chains shuttle electrons through various complexes toward the aim of creating a proton gradient. In this sense they are similar to electron transport chains in photosynthesis. As such, some of the progress made by quantum biology in the context of photosynthesis and radical pair dynamics might be applied to mitochondria. Tunnelling has been reported in mitochondrial electron transport chains (Nunn et al., 2016; Bennett, 2019; Moser et al., 2006). Mitochondria have also been put forward as a site for the biological light–matter interactions that could underpin the mechanism of therapeutic photobiomodulation (Salehpour et al., 2019; Hamblin, 2018).

Spin dynamics

Spin chemistry

Spin chemistry first emerged as a field of research in the 1960s and 1970s to explain how spin and magnetic fields can change the outcome of chemical reactions. The radical pair mechanism was proposed as a way to explain chemically induced dynamic nuclear polarization (CIDNP) (Steiner and Ulrich, 1989; Hore et al., 2020). Radicals are molecules with unpaired electrons. A radical pair is two such radicals whose electron spins are correlated—which means they are related in a specific physical sense—either in a singlet or triplet state. The interaction of each radical of the pair with magnetic fields can convert the spin state between singlet and triplet. Chemical binding is restricted by the spin state, which means that a magnetic field can change the outcome of a chemical reaction by changing the spin state of the intermediate radical pair. This has come to be known as the radical pair mechanism (Steiner and Ulrich, 1989; Rodgers and Hore, 2009; Hore et al., 2020). Further interest in this mechanism has been generated by the fact that the singlet state, for example, is a maximally entangled state (Cai et al., 2010; Gauger et al., 2011).

Avian navigation

In 1978, following on progress made in the field of spin chemistry, (Schulten et al., 1978) suggested that the radical pair mechanism might be applied to the chemical reactions that occur in biological systems, specifically with respect to the avian compass, allowing birds to orient themselves using the weak geomagnetic field. It is generally accepted that birds do use the earth's magnetic field, in the very least as a partial navigational cue (Mouritsen and Ritz, 2005). The radical pair mechanism of avian magnetoreception is proposed to be photon-generated. In 2000, Ritz et al. (Ritz et al., 2000) suggested that cryptochromes, flavoprotein photoreceptors that resemble photolyases, were a potential candidate molecule for a radical pair-based compass. Since then, a great deal of research has attempted to narrow down which of the various types of cryptochrome is best suited to the purpose of magnetoreception (Ritz et al., 2010; Pinzon-Rodriguez et al., 2018; Liedvogel and Mouritsen, 2010; Günther et al., 2018; Wiltschko et al., 2021; Xu et al., 2021). This is one of many open questions, which include the role of the dipole and exchange interactions in the radical spin dynamics (Efimova and Hore, 2008). For the most part, only the effects of the external field—Zeeman effect—and the nuclear spin environment local to each radical—hyperfine effect—are taken into account in the commonly accepted models. Common models also primarily involve the interaction of two radicals, although three radical models have also been proposed to offer novel advantages (Babcock and Kattnig, 2021; Kattnig, 2017). Spin-to-chemical transduction is also up for debate. Spin effects in biological systems are likely widespread, but are also very much dependent on the fact that the appropriate reactions are spin-selective. In avian magnetoreception, it is still not entirely clear how the spin states translate into a signal interpretable to the birds, though some theoretical research suggests the spin-dependent visual modulation (Ritz et al., 2000). Given the ubiquity of radical creation in biological systems, it seems amiss that there are so few robust examples of magnetic field sensitivity in these systems. This may be because a number of conditions must be met in order for the radical pair mechanism to confer meaningful magnetic field sensitive spin selectivity. See the excellent review by Kim et al. for a detailed account of these conditions. The radical pair mechanism of avian navigation is theoretically well-developed. It is also supported by behavioral evidence such as the fact that it is a light-dependent, inclination compass, disrupted by oscillating electromagnetic fields (Rodgers and Hore, 2009; Thalau et al., 2004; Ritz et al., 2009; Engels et al., 2014). However, direct experimental evidence of radical pair-mediated magnetic effects in biological cells is still lacking. A recent experiment by Ikeya and Woodward is thus a pivotal one for the field. They demonstrate that flavin-based autofluorescence in cells is magnetic field sensitive. In particular, it is sensitive to weak magnetic fields, a hallmark of the radical pair mechanism. They explain these results as being due to the formation and spin-selective recombination of radical pairs (Ikeya and Woodward, 2021).

Reactive oxygen species

Despite the conditions laid out in Kim et al., spin-selective chemical reactions remain a fruitful field of study within quantum biology. Indeed, given the possible effects of broadband low-intensity radiofrequency electromagnetic radiation on the avian compass, the radical pair mechanism should be afforded more scrutiny in a wider biological context (Engels et al., 2014); if only to rule out the possibility that background electromagnetic radiation may play a role in disrupting important biological processes. Of growing interest is the role that radical reaction intermediates might play in the chemistry and biology of ROS. Reference to ROS is often made in terms of inflammation in biological systems. The term is used generically to define a wide variety of oxidant molecules. It should also be acknowledged that these molecules have very different properties and biological functions that range from signaling to causing cell damage (Sies et al., 2022). In this context, the radical pair mechanism might give some insight into the possible effects that magnetic fields might have on biological systems that are sensitive to the balance of ROS. Usselman et al. show how yields of ROS in live cells can be changed by radical pair dynamics, in particular coherent singlet-triplet mixing (Usselman et al., 2016, 2014). The signaling properties of ROS have been the subject of recent studies examining the effects of weak magnetic fields on stem cell differentiation (Hack et al., 2021). Van Huizen et al. report that weak magnetic fields alter stem cell proliferation and differentiation by changing ROS levels. The authors discuss the possibility of this being due to the radical pair mechanism. The data also demonstrate how weak magnetic fields can both increase and decrease new tissue formation. This has implications for regenerative medicine as well as the targeting of rapidly proliferating cells, as in the case of cancer (van Huizen et al., 2019). Oxygen radicals have also been implicated in the action of lithium in treating bipolar disorder (Zadeh-Haghighi and Simon, 2021). Following from the observation that lithium isotopes appear to have differing effects on animal behavior, Zadeh–Haghighi and Simon propose that this can be explained through the radical pair mechanism, specifically the role that nuclear spin plays in radical dynamics through the hyperfine effect (Zadeh-Haghighi and Simon, 2021). This is also used to explain the effects that lithium and magnetic fields have on circadian rhythms (Zadeh-Haghighi and Simon, 2022a). A version of this radical pair model has been applied in a number of other biological contexts, such as the differential anesthetic effects of xenon isotopes and microtubule reorganization (Smith et al., 2021; Zadeh-Haghighi and Simon, 2022b). These studies remain theoretical and it is yet to be seen if the radicals in question satisfy the conditions laid out by Kim et al. However, given the importance of radicals in biological systems and the growing ubiquity of environmental electromagnetic fields, the subject seems one that is set to grow in scope.

Phosphorus nuclear spin

Radicals are molecules with unpaired electrons. The radical pair mechanism is the result of correlated electron spins. Might nuclear spin pairs play any similar role in the biological context? Nuclear spin has played a central role advancing our understanding of physiology since the development of magnetic resonance imaging (MRI). A recent hypothesis suggests that nuclear spin may play a role in biological systems in more than only an imaging sense. Fisher hypothesizes that the spin of phosphorus nuclei might become entangled in the hydrolysis of pyrophosphate (Fisher, 2015). This entanglement can be preserved if the phosphates bind with spin-zero calcium ions, forming amorphous calcium phosphate or Posner molecules (Fisher, 2015). Phosphorus nuclei are an ideal qubit due to the fact that spin-half nuclei are only relaxed by interaction with other magnetic fields and not electric fields, due to their lack of quadrupolar moment (Fisher, 2015). Fisher contends that due to the rapid tumbling of Posner molecules in body fluid the spin coherence times could be as long as days (Swift et al., 2017). Furthermore, these long coherence times, coupled with the fact that the entanglement could change Posner binding and free calcium ion production, could give rise to "entangled" neural activation. In this way, entangled phosphorus might play a role in cognition and even consciousness. Fisher also offers an alternative explanation to the isotope dependence of lithium action. Given that lithium can be incorporated into Posner molecules, the nonzero nuclear spin of the different isotopes could have different effects on the spin dynamics of entangled phosphorus nuclei (Fisher, 2015; Swift et al., 2017; Weingarten et al., 2016). While experimental investigations of the hypothesis are still under way, various questions have been raised. Foremost among these would be whether nuclear spin entanglement plays any role in spin-selective chemical transduction. In Fisher's model, the entanglement-sensitive calcium ion production is particularly dependent on the symmetry of the Posner molecules. Research suggests, however, that Posner molecules might favor asymmetric structures (Agarwal et al., 2021). In such a case, it is unclear how nuclear spin dynamics would result in chemical and biological signaling. The long coherence times have also been debated. Player and Hore estimate that intramolecular dipole interactions would relax the nuclear spin within 37 minutes and likely even less (Player and Hore, 2018). Despite these caveats, the potential for nuclear spin processing in biological systems remains intriguing. In the quest to realize physical qubits for quantum computing, phosphorus nuclear spins have been a main contender, they may play an equally important role in biological computing. Phosphorus is important in many contexts in biological systems, not least of which is phosphorylation (Tony, 2012). There is also a proposal that nuclear spin could play a role in lipid membranes as well (Smolin, 2020). Should it turn out that coherence lifetimes are more likely of the order of seconds, this is still long enough to play a role in many important functions in biological systems.

Chirality

Symmetry and symmetry-breaking play an important role in physics. The same might be said for biology. Chirality is a measure of mirror symmetry, that is, the "handedness" of a molecule is described by its chirality. Molecules can exist as left or right-handed enantiomers that cannot be superimposed onto each other. Life, however, favors specific chiralities over others, a preference that is still not yet understood (Inaki et al., 2016). Enantiomers display distinct biological behaviors. For example, different enantiomers of odorants have different scents (Brenna et al., 2003; Brookes et al., 2009). An understanding of chiral effects in biological systems is also essential in the context of pharmaceuticals, where different enantiomers may have different pharmacological outcomes, as seen with thalidomide (Tokunaga et al., 2018). Chirality has become a topic of interest in quantum biology due to the phenomenon of chiral-induced spin selectivity (CISS). Charge transport through small chiral structures results in spin polarization due to the fact that the direction of movement favors a specific spin polarization (Naaman et al., 2019; Aiello et al., 2022). This has elicited excitement with respect to advancements in quantum technologies, see Naaman et al. and Aiello et al. for excellent, comprehensive reviews. At the same time, the centrality of charge transfer in many of the models of quantum biology means that a better understanding of room-temperature CISS effects could have profound implications for our understanding of biological systems. Aiello et al. outline some of the potential applications of chirality in quantum biology, including the chirality of cytoskeletal filaments and their capacity for superradiant effects. They also suggest a role for chirality in understanding how the immune system functions (Aiello et al., 2022). Intriguing results from Gaitanidis et al. reveal a novel biological signal of spontaneous radiofrequency emission in fruit flies (Gaitanidis et al., 2022). The authors suggest that the signal is due to spin-polarized electron currents undergoing radiative relaxation. Even more interestingly, this signal can be interrupted by the administration of chloroform anesthesia, which the authors consider initial proof that the signals originate in the nervous system (Gaitanidis et al., 2022). This implicates spin currents in the action of anesthetics and thus potentially consciousness, a result that appears to support an earlier study that showed electron spin changes under the effects of anesthetics (Turin et al., 2014). A recent study also suggests that CISS could be responsible for the differential viscosity of lactic acid enantiomers, a result that cannot be explained using classical molecular dynamics (Daplan et al., 2022). And finally, chirality has an effect on interactions between electromagnetic radiation and matter. Given that the interaction of radiation and matter is a primary preoccupation of quantum biology, chirality may feature in this context as well (Yuan et al., 2021).

New (and old) avenues of interest

This review has outlined active research in quantum biology and how this might be expanded to related biological contexts. The underlying quantum systems discussed in this review might also offer further insight across the spectrum of biological interests. Research has suggested that redox activity and proton gradients may have played a role in the origins of living systems (Lane, 2010). At the other end of the spectrum, it has also been suggested that most complex biological system, the brain, might be best understood using quantum theory (Hameroff and Penrose, 2014; Penrose, 1989). In 1989, the Nobel Prize winning physicist, Roger Penrose, suggested that consciousness might only be explained by quantum computations in the brain. His collaborator, anethesiologist Stuart Hameroff, suggested that microtubules and tubulin proteins could act as biological quantum bits or "qubits" (Hameroff and Penrose, 2014; Penrose, 1989). While the theory remains contentious, the question of whether quantum effects take place in the brain continues to generate research (Adams and Petruccione, 2020). The selectivity of ion channels, central to the efficient function of nerve cells, is still not fully understood. There has been some suggestion that quantum effects may play a role (Kim et al., 2021; Salari et al., 2017). The action and mechanism of anesthetics have also been investigated from various angles in the context of quantum biology (Smith et al., 2021; Turin et al., 2014; Adams and Petruccione, 2020; Craddock et al., 2015). Understanding anesthetics is a measurably material way in which to investigate consciousness. Other chemicals that have an effect on consciousness, such as serotonin and lithium, have also been the subjects of quantum biological research (Hoehn et al., 2015; Zadeh-Haghighi and Simon, 2021, 2022a; Fisher, 2015). In addition to this, the role that quantum effects may play in circadian rhythms and associated mental states, has been investigated (Zadeh-Haghighi and Simon, 2022a). Circadian rhythms or body clocks are essential in biological systems, with synchronization underlying the efficient function of many biological functions (Patke et al., 2020). Oscillatory dynamics also underpin the brain, although the origin and purpose of these brain waves remains unclear (Skinner, 2012). Re-examining oscillation and synchronization through the lens of quantum mechanics may offer new insights.

In addition to the big philosophical questions—what is life, what is consciousness—which might remain unanswered for some time, quantum biology might also offer practical interventions in the near future. Information gleaned from biological systems might very well be applied to the physiological and medical context as well. Indeed, the history of quantum biology and what might be called quantum physiology, show some close parallels. Bohr's "Light and Life" lecture was given as an address at the opening meeting of the International Congress on Light Therapy (Bohr, 1933). The therapeutic use of light won the Nobel Prize for physiology in 1903, as long ago as the origins of quantum theory (Pernow, 1997). More recently, however, light-matter interaction in the therapeutic context has been gathering impetus in both application and verification (Salehpour et al., 2019; Hamblin, 2018; Pooam et al., 2021). Quantum spin, too, has played an important role in the more recent history of medicine, with the invention of MRI. It now appears that spin might also play a role in the development of new therapies that exploit magnetic fields to control and manipulate signaling molecules in the body (van Huizen et al., 2019; Hack et al., 2021).

Conclusion

This review has been a short introduction to the current state of the field of quantum biology. We have not gone into too much detail with respect to each of the various areas of research. For these details, we hope the suggested reviews as well as the reference list will be instructive. What we did hope to communicate is the expanding scope and possible impact of quantum biology. There are still, no doubt, questions that remain to be answered. Take timescales for instance. How do ultrafast processes translate into effects on biologically relevant timescales? And related to this, how are coherence times preserved in the hot, wet, and disordered biological environment? What coherence times are sufficient for a biologically functional outcome? Despite these questions, however, research in quantum biology continues to reveal the possible ways in which electrons, protons, photons, and phonons play a fundamental role in living systems. Further study in this direction will hopefully shine light on the details of these systems. At the same time, quantum biology may offer insights into our understanding of quantum theory as applied in different materials. If nothing else, quantum biology—the study of quantum effects in biological matter—is an investigation into nature's genius for novel material engineering.

Funding and Acknowledgments

B.A and F.P. were supported by the South African Research Chair Initiative of the Department of Science and Technology and the National Research Foundation. B.A. was also supported by the National Institute for Theoretical and Computational Sciences. Many thanks to Professor Ilya Sinayskiy, Professor Clarice Aiello, and Dr. Ismael Galván for their excellent suggestions, corrections, and feedback.

References

Abramavicius D and Valkunas L (2016) Role of coherent vibrations in energy transfer and conversion in photosynthetic pigment-protein complexes. *Photosynthesis Research* 127(1): 33–47.

Adams B and Petruccione F (2020) Quantum effects in the brain: A review. *AVS Quantum Science* 2: 022901.

Adams B, Sinayskiy I, van Grondelle R, et al. (2022) Quantum tunnelling in the context of SARS-CoV-2 infection. *Scientific Reports* 12: 16929.

Agarwal S, Aiello CD, Kattnig DR, and Banerjee AS (2021) The dynamical ensemble of the Posner molecule is not symmetric. *Journal of Physical Chemistry Letters* 12(42): 10372–10379.

Aiello CD, Abendroth JM, Abbas M, Afanasev A, Agarwal S, Banerjee AS, Beratan DN, Belling JN, Berche B, Botana A, Caram JR, Celardo GL, Cuniberti G, Garcia-Etxarri A, Dianat A, Diez-Perez I, Guo Y, Gutierrez R, Herrmann C, Hihath J, and Wang QH (2022) A chirality-based quantum leap. *ACS Nano* 16(4): 4989–5035.

Al-Khalili J and McFadden J (2014) *Life on the Edge: The Coming of Age of Quantum Biology*. London: UK Bantam Press.

Auten R and Davis J (2009) Oxygen toxicity and reactive oxygen species: The devil is in the details. *Pediatric Research* 66: 121–127.

Babcock NS and Kattnig DR (2021) Radical scavenging could answer the challenge posed by electron-electron dipolar interactions in the cryptochrome compass model. *Journal of the American Chemical Society* 1(11): 2033–2046.

Bennett JP (2019) Medical hypothesis: Neurodegenerative diseases arise from oxidative damage to electron tunneling proteins in mitochondria. *Medical Hypotheses* 127: 1–4.

Bohr N (1933) The future of quantum biology. *Nature* 131: 421–423.

Brenna E, Fuganti C, and Serra S (2003) Enantioselective perception of chiral odorants. *Tetrahedron: Asymmetry* 14(1): 1–42.

Brixner T, Stenger J, Vaswani HM, Cho M, Blankenship RE, and Fleming GR (2005) Two-dimensional spectroscopy of electronic couplings in photosynthesis. *Nature* 434: 625.

Brookes JC (2017) Quantum effects in biology: Golden rule in enzymes, olfaction, photosynthesis and magnetodetection. *Proceedings of the Royal Society A* 473: 20160822.

Brookes JC, Horsfield AP, and Stoneham AM (2009) Odour character differences for enantiomers correlate with molecular flexibility. *Journal of the Royal Society Interface* 6: 75–86.

Cai J, Guerreschi GG, and Briegel HJ (2010) Quantum control and entanglement in a chemical compass. *Physical Review Letters* 104(22): 220502.

Cao J, et al. (2020) Quantum biology revisited. *Science Advances* 6(14): eaaz4888.

Celardo GL, Angeli M, Craddock TJ, and Kurian P (2019) On the existence of superradiant excitonic states in microtubules. *New Journal of Physics* 21: 023005.

Chee HK and Oh SJ (2013) Molecular vibration-activity relationship in the agonism of adenosine receptors. *Genome Informatics* 11(4): 282.

Chee HK, Yang J, Joung J, Zhang B, and Oh SJ (2015) Characteristic molecular vibrations of adenosine receptor ligands. *FEBS Letters* 589(4): 548.

Cifra M and Pospisil P (2014) Ultra-weak photon emission from biological samples: Definition, mechanisms, properties, detection and applications. *Journal of Photochemistry and Photobiology B: Biology* 139: 2–10.

Collini E, Wong CY, Wilk KE, Curmi PM, Brumer P, and Scholes GD (2010) Coherently wired light-harvesting in photosynthetic marine algae at ambient temperature. *Nature* 463: 644.

Craddock T, Priel A, and Tuszynski J (2014a) Are we more than quantum computers? *Journal of Integrative Neuroscience* 13: 293.

Craddock TJ, Friesen D, Mane J, Hameroff S, and Tuszynski J (2014b) A model for consciousness: Quantum field theory of mind-brain interaction. *Journal of the Royal Society Interface* 11(100): 20140677.

Craddock TJA, Hameroff SR, Ayoub AT, Klobukowski M, and Tuszynski JA (2015) Anesthetics act in quantum channels in brain microtubules to prevent consciousness. *Current Topics in Medicinal Chemistry* 15: 523.

Daplan E, Terranova U, and Turin L (2022) Anomalous viscosity of a racemate: A simple experiment demonstrating chirally induced spin selectivity. *Journal of Physical Chemistry Letters* 13: 4215–4219.

Dean JC, Mirkovic T, Toa ZS, Oblinsky DG, and Scholes GD (2016) Vibronic enhancement of algae light harvesting. *Chem* 1: 858–872.

DeVault D and Chance B (1966) Studies of photosynthesis using a pulsed laser: I. Temperature dependence of cytochrome oxidation rate in chromatium. Evidence for tunneling. *Biophysical Journal* 6: 825–847.

Dyson GM (1938) The scientific basis of odour. *Journal of the Society of Chemical Industry* 57: 647.

Efimova O and Hore PJ (2008) Role of exchange and dipolar interactions in the radical pair model of the avian magnetic compass. *Biophysical Journal* 94(5): 1565–1574.

Engel GS (2011) Quantum coherence in photosynthesis. *Procedia Chemistry* 3: 222.

Engel GS, Calhoun TR, Read EL, Ahn TK, Mancal T, Cheng YC, Blankenship RE, and Fleming GR (2007) Evidence for wavelike energy transfer through quantum coherence in photosynthetic systems. *Nature* 446: 782.

Engels S, et al. (2014) Anthropogenic electromagnetic noise disrupts magnetic compass orientation in a migratory bird. *Nature* 509: 353–356.

Fisher MPA (2015) Quantum cognition: The possibility of processing with nuclear spins in the brain. *Annals of Physics* 362: 593–602.

Franco MI, Turin L, Mershin A, and Skoulakis EM (2011) Molecular vibration-sensing component in *Drosophila melanogaster* olfaction. *Proceedings of the National Academy of Sciences of the United States of America* 108(9): 3797–3802.

Gaitanidis A, Sotgiu A, and Turin L (2022) Chapter 13—Spontaneous radiofrequency emission from electron spins within *Drosophila*: A novel biological signal. In: Fairclough SH and Zander TO (eds.) *Current Research in Neuroadaptive Technology*, pp. 235–253. Academic Press.

Gauger EM, Rieper E, Morton JJL, Benjamin SC, and Vedral V (2011) Sustained quantum coherence and entanglement in the avian compass. *Physical Review Letters* 106(4): 040503.

Gehrckens AS, Horsfield A, Skoulakis E, and Turin L (2019) Gated electron transport in rhodopsin and its relevance to GPCR activation. *bioRxiv*. https://doi.org/10.1101/650531.

Gehrckens AS, Horsfield AP, Skoulakis EMC, and Turin L (2021) Evidence for free radical drug ligands in class A G-protein coupled receptors. *bioRxiv*. 2021.08.30.458164.

Günther A, Einwich A, Sjulstok E, Feederle R, Bolte P, Koch KW, Solov'yov IA, and Mouritsen H (2018) Double-cone localization and seasonal expression pattern suggest a role in magnetoreception for European robin cryptochrome 4. *Current Biology: CB* 28(2). 211–223.e4.

Haberkorn R (1976) Density matrix description of spin-selective radical pair reactions. *Molecular Physics* 32: 1491.

Hack SJ, Kinsey LJ, and Beane WS (2021) An open question: Is non-ionizing radiation a tool for controlling apoptosis-induced proliferation? *International Journal of Molecular Sciences* 22(20): 11159.

Haken H and Wolf HC (1987) *Atomic and Quantum Physics*. Berlin Heidelberg: Springer-Verlag.

Hamblin MR (2018) Photobiomodulation for traumatic brain injury and stroke. *Journal of Neuroscience Research* 96(4): 731.

Hameroff S and Penrose R (2014) Consciousness in the universe: A review of the 'Orch OR' theory. *Physics of Life Reviews* 11(1): 39–78.

Hara J (1977) Olfactory discrimination between glycine and deuterated glycine by fish. *Experientia* 33(5): 618–619.

Havens BR and Meloan CE (1995) The application of deuterated sex pheromone mimics of the American cockroach (*Periplaneta americana*, L.), to the study of Wright's vibrational theory of Olfaction. In: *Food Flavors: Generation, Analysis and Process Influence. Developments in Food Science*, vol. 37, p. 497. Elsevier.

Hoehn RD, Nichols DE, McCorvy JD, Neven H, and Kais S (2017) Experimental evaluation of the generalized vibrational theory of G protein-coupled receptor activation. *Proceedings of the National Academy of Sciences of the United States of America* 114(22): 5595.

Hoehn R, Nichols D, Neven H, et al. (2015) Neuroreceptor activation by vibration-assisted tunneling. *Scientific Reports* 5: 9990.

Hoffmann M, et al. (2006) Color tuning in rhodopsins: The mechanism for the spectral shift between bacteriorhodopsin and sensory rhodopsin II. *Journal of the American Chemical Society* 128: 10808–10818.

Hore PJ and Mouritsen H (2016) The radical-pair mechanism of magnetoreception. *Annual Review of Biophysics* 5(45): 299–344.

Hore PJ, Ivanov KL, and Wasielewski MR (2020) Spin chemistry. *Chemical Physics* 152: 120401.

Horsfield AP, Haase A, and Turin L (2017) Molecular recognition in olfaction. *Advances in Physics: X* 2(3): 937–977.

Ikeya N and Woodward JR (2021) Cellular autofluorescence is magnetic field sensitive. *Proceedings of the National Academy of Sciences of the United States of America* 118(3). e2018043118.

Inaki M, Liu J, and Matsuno K (2016) Cell chirality: Its origin and roles in left-right asymmetric development. *Philosophical Transactions of the Royal Society of London. Series B, Biological Sciences* 371(1710): 20150403.

Kattnig DR (2017) Radical-pair-based magnetoreception amplified by radical scavenging: Resilience to spin relaxation. *The Journal of Physical Chemistry B* 121(44): 10215–10227.

Kim Y, Bertagna F, D'Souza EM, Heyes DJ, Johannissen LO, Nery ET, Pantelias A, Sanchez-Pedreño Jimenez A, Slocombe L, Spencer MG, et al. (2021) Quantum biology: An update and perspective. *The Qualitative Report* 3: 80–126.

Klinman JP and Kohen A (2013) Hydrogen tunneling links protein dynamics to enzyme catalysis. *Annual Review of Biochemistry* 82(1): 471–496.

Kominis IK (2015) The radical-pair mechanism as a paradigm for the emerging science of quantum biology. *Modern Physics Letters B* 29: 1530013.

Kržan M, Vianello R, Maršavelski A, Repič M, Zakšek M, Kotnik K, Fijan E, and Mavri J (2016) The quantum nature of drug-receptor interactions: Deuteration changes binding affinities for histamine receptor ligands. *PLoS One* 11(5): e0154002.

Kumar S, Boone K, Tuszyński J, Barclay P, and Simon C (2016) Possible existence of optical communication channels in the brain. *Scientific Reports* 6: 36508.

Kurian P, Obisesan TO, and Craddock T (2017) Oxidative species-induced excitonic transport in tubulin aromatic networks: Potential implications for neurodegenerative disease. *Journal of Photochemistry and Photobiology B: Biology* 175: 109–124.

Lambert N, Chen YN, Cheng Y, Li C, Chen G, and Nori F (2013) Quantum biology. *Nature Physics* 9: 10.

Lane N (2010) Why are cells powered by proton gradients? *Nature Education* 3(9): 18.

Le T and Olaya-Castro A (2020) Basis-independent system-environment coherence is necessary to detect magnetic field direction in an avian-inspired quantum magnetic sensor. *arXiv: Quantum Physics*.

Lechelon M (2022) Experimental evidence for long-distance electrodynamic intermolecular forces. *Science Advances* 8(7): eabl5855.

Lee SH, Shin DH, Park WR, Kim JY, Kang SO, and Joo T (2019) Strongly coupled phenazine-porphyrin dyads: Light-harvesting molecular assemblies with broad absorption coverage. *ACS Applied Materials and Interfaces* 11: 8000–8008.

Liedvogel M and Mouritsen H (2010) Cryptochromes—A potential magnetoreceptor: What do we know and what do we want to know? *Journal of the Royal Society Interface* 7 (supplement 2): S147–S162.

Löwdin P (1963) Proton tunneling in DNA and its biological implications. *Reviews of Modern Physics* 35: 724.

Marais A, Sinayskiy I, Kay A, Petruccione F, and Ekert A (2013) Decoherence-assisted transport in quantum networks. *New Journal of Physics* 15: 013038.

Marais A, et al. (2018) The future of quantum biology. *Journal of the Royal Society Interface* 15: 20180640.

Marcus RA and Sutin N (1985) Electron transfers in chemistry and biology. *Biochimica et Biophysica Acta* 811: 265–316.

Marković AK, et al. (2020) Hydrogen tunnelling as a probe of the involvement of water vibrational dynamics in aqueous chemistry? *Molecules* 25(1): 172.

McFadden J and Al-Khalili J (2018) The origins of quantum biology. *Journal of Physics Conference Series* 474: 20180674.

Meunier S and Vernos I (2012) Microtubule assembly during mitosis—From distinct originsto distinct functions? *Journal of Cell Science* 125: 2805.

Mohseni M, Omar Y, Engel GS, and Plenio MB (2013) *Quantum Effects in Biology*. Cambridge University Press.

Moser CC, Farid TA, Chobot SE, and Dutton PL (2006) Electron tunneling chains of mitochondria. *Biochimica et Biophysica Acta (BBA)—Bioenergetics* 1757(9–10): 1096–1109.

Mouritsen H and Ritz T (2005) Magnetoreception and its use in bird navigation. *Current Opinion in Neurobiology* 15(4): 406–414.

Naaman R, Paltiel Y, and Waldeck DH (2019) Chiral molecules and the electron spin. *Nature Reviews Chemistry* 3: 250–260.

Nunn AVW, Guy GW, and Bell JD (2016) The quantum mitochondrion and optimal health. *Biochemical Society Transactions* 44(4): 1101–1110.

Oh SJ (2012) Characteristics in molecular vibrational frequency patterns between agonists and antagonists of histamine receptors. *Genome Informatics* 10(2): 128.

Panitchayangkoon G, Hayes D, Fransted KA, and Engel GS (2010) Long-lived quantum coherence in photosynthetic complexes at physiological temperature. *Proceedings of the National Academy of Sciences of the United States of America* 107: 12766.

Paoli M, Münch D, Haase A, Skoulakis E, Turin L, and Galizia CG (2017) Minute impurities contribute significantly to olfactory receptor ligand studies: Tales from testing the vibration theory. *eNeuro* 4(3): 0070.

Patke A, Young MW, and Axelrod S (2020) Molecular mechanisms and physiological importance of circadian rhythms. *Nature Reviews Molecular Cell Biology* 21: 67–84.

Pauls JA, Zhang Y, Berman GP, and Kais S (2013) Quantum coherence and entanglement in the avian compass. *Physical Review E: Statistical, Nonlinear, and Soft Matter Physics* 87(6): 062704.

Penrose R (1989) *The Emperor's New Mind: Concerning Computers, Minds, and the Laws of Physics*. New York, US: Oxford University Press.

Pernow B (1997) De tre första nordiska nobelpristagarna i fysiologi eller medicin [The first three nordic nobel laureates in physiology or medicine]. *Svensk Medicinhistorisk Tidskrift* 1 (1): 147–168.

Pinzon-Rodriguez A, Bensch S, and Muheim R (2018) Expression patterns of cryptochrome genes in avian retina suggest involvement of Cry4 in light-dependent magnetoreception. *Journal of the Royal Society Interface* 15: 20180058.

Player TC and Hore PJ (2018) Viability of superoxide-containing radical pairs as magnetoreceptors. *Journal of the Royal Society Interface* 15(147): 225101.

Policht VR, et al. (2022) Hidden vibronic and excitonic structure and vibronic coherence transfer in the bacterial reaction center. *Science Advances* 8(1): eabk0953.

Pooam M, Aguida B, Drahy S, Jourdan N, and Ahmad M (2021) Therapeutic application of light and electromagnetic fields to reduce hyper-inflammation triggered by COVID-19. *Communicative and Integrative Biology* 14(1): 66–77.

Proppe AH, Ratner MA, Sattler WR, and Gray-Weale AA (2020) Bioinspiration in light harvesting and catalysis. *Nature Reviews Materials* 5: 828–846.

Quach JQ, et al. (2022) Superabsorption in an organic microcavity: Toward a quantum battery. *Science Advances* 8(2): eabk3160.

Ritz T, Adem S, and Schulten K (2000) A model for photoreceptor-based magnetoreception in birds. *Biophysical Journal* 78(2): 707–718.

Ritz T, et al. (2009) Magnetic compass of birds is based on a molecule with optimal directional sensitivity. *Biophysical Journal* 96: 3451–3457.

Ritz T, Yoshii T, Helfrich-Forster C, and Ahmad M (2010) Cryptochrome A photoreceptor with the properties of a magnetoreceptor? *Communicative and Integrative Biology* 3: 24.

Rodgers CT and Hore PJ (2009) Chemical magnetoreception in birds: The radical pair mechanism. *Proceedings of the National Academy of Sciences of the United States of America* 106(2): 353–360.

Romero E, Novoderezhkin V, and van Grondelle R (2017) Quantum design of photosynthesis for bio-inspired solar-energy conversion. *Nature* 543: 355–365.

Salari V, Naeij H, and Shafiee A (2017) Quantum interference and selectivity through biological ion channels. *Scientific Reports* 7: 41625.

Salehpour F, et al. (2019) Near-infrared photobiomodulation combined with coenzyme Q10 for depression in a mouse model of restraint stress: Reduction in oxidative stress, neuroinflammation, and apoptosis. *Brain Research Bulletin* 144: 213.

Schlau-Cohen GS, Calhoun TR, Ginsberg NS, Read EL, Ballottari M, Bassi R, van Grondelle R, and Fleming GR (2009) Pathways of energy flow in LHCII from two-dimensional electronic spectroscopy. *The Journal of Physical Chemistry B* 113: 15352.

Schrödinger E (1944) *What is Life? The Physical Aspect of the Living Cell*. Cambridge University Press.

Schulten K, Swenberg CE, and Weller A (1978) A biomagnetic sensory mechanism based on magnetic field modulated coherent electron spin motion. *Zeitschrift für Physikalische Chemie* 111: 1.

Sies H, et al. (2022) Defining roles of specific reactive oxygen species (ROS) in cell biology and physiology. *Nature Reviews Molecular Cell Biology* 23: 499–515.

Skinner F (2012) Cellular-based modeling of oscillatory dynamics in brain networks. *Current Opinion in Neurobiology* 22(4): 660–669.

Slocombe L, Al-Khalili JS, and Sacchi M (2021) Quantum and classical effects in DNA point mutations: Watson-Crick tautomerism in AT and GC base pairs. *Physical Chemistry Chemical Physics* 23: 4141–4150.

Slocombe L, Sacchi M, and Al-Khalili J (2022) An open quantum systems approach to proton tunnelling in DNA. *Communications on Physics* 5: 109. https://doi.org/10.1038/s42005-022-00881-8.

Smith J, Zadeh Haghighi H, Salahub D, and Simon C (2021) Radical pairs may play a role in xenon-induced general anesthesia. *Scientific Reports* 11: 6287.

Smolin L (2020) Natural and bionic neuronal membranes: Possible sites for quantum biology. *arXiv: Quantum Physics*.

Song H, Cannon WR, Beliaev AS, and Konopka A (2014) Mathematical modeling of microbial community dynamics: A methodological review. *Processes* 2: 711–752.

Steiner UE and Ulrich T (1989) Magnetic field effects in chemical kinetics and related phenomena. *Chemical Reviews* 89: 51–147.

Sutcliffe MJ and Scrutton NS (2000) Enzymology takes a quantum leap forward. *Philosophical Transactions. Series A, Mathematical, Physical, and Engineering Sciences* 358(1766): 367–386.

Swift MW, Van de Walle CG, and Fisher MPA (2017) Posner molecules: From atomic structure to nuclear spins. *Physical Chemistry Chemical Physics* 20(18): 12373–12380.

Tegmark M (2000) Importance of quantum decoherence in brain processes. *Physical Review E* 61(4): 4194.

Thalau P, Ritz T, Stapput K, Wiltschko R, and Wiltschko W (2004) Magnetic compass orientation of migratory birds in the presence of a 1.315 MHz oscillating field. *Naturwissenschaften* 92: 86–90.

Thompson EJ, Paul A, Iavarone AT, and Klinman JP (2021) Identification of thermal conduits that link the protein-water interface to the active site loop and catalytic base in enolase. *Journal of the American Chemical Society* 143(2): 785–797.

Thyrhaug E, Tempelaar R, Alcocer MJ, žídek K, Bína D, Knoester J, Jansen TL, and Zigmantas D (2018) Identification and characterization of diverse coherences in the Fenna-Matthews-Olson complex. *Nature Chemistry* 10: 780–786.

Tiersch M, Steiner UE, Popescu S, and Briegel HJ (2012) Open quantum system approach to the modeling of spin recombination reactions. *The Journal of Physical Chemistry A* 116(16): 4020–4028.

Tiwari V, Peters WK, and Jonas DM (2013) Electronic resonance with anticorrelated pigment vibrations drives photosynthetic energy transfer outside the adiabatic framework. *Proceedings of the National Academy of Sciences of the United States of America* 110: 1203–1208.

Tokunaga E, Yamamoto T, Ito E, et al. (2018) Understanding the thalidomide chirality in biological processes by the self-disproportionation of enantiomers. *Scientific Reports* 8: 17131.

Tony H (2012) Why nature chose phosphate to modify proteins. *Philosophical Transactions of the Royal Society B* 367: 2513–2516.

Tripathi A and Bankaitis VA (2017) Molecular docking: From lock and key to combination lock. *Journal of Molecular Medicine and Clinical Applications* 2(1). https://doi.org/10.16966/2575-0305.106.

Turin L (1996) A spectroscopic mechanism for primary olfactory reception. *Chemical Senses* 21(6): 773–791.

Turin L, Skoulakis EMC, and Horsfield AP (2014) Electron spin changes during general anesthesia in *Drosophila*. *Proceedings of the National Academy of Sciences* 111 (34): E3524–E3533.

Usselman RJ, Hill I, Singel DJ, and Martino CF (2014) Spin biochemistry modulates reactive oxygen species (ROS) production by radio frequency magnetic fields. *PLoS One* 9(3): e93065.

Usselman RJ, Chavarriaga C, Castello PR, Procopio M, Ritz T, Dratz EA, Singel DJ, and Martino CF (2016) The quantum biology of reactive oxygen species partitioning impacts cellular bioenergetics. *Scientific Reports* 6: 38543.

van Grondelle R and Novoderezhkin VI (2011) Quantum effects in photosynthesis. *Procedia Chemistry* 3(1): 198–210.

van Huizen AV, et al. (2019) Weak magnetic fields alter stem cell—Mediated growth. *Science Advances* 5(1): eaau7201.

Vattay G, Salahub D, Csabai I, Nassimi A, and Kaufmann SA (2015) Quantum criticality at the origin of life. *Journal of Physics Conference Series* 626: 012023.

Verpoorte R, Choi YH, Mustafa NR, and Kim HK (2008) Metabolomics: Back to basics. *Phytochemistry Reviews* 7: 525–537.

Wang W, Geiger JH, and Borhan B (2014) The photochemical determinants of color vision: Revealing how opsins tune their chromophore's absorption wavelength. *Bioessays* 36(1): 65–74.

Weingarten CP, Doraiswamy PM, and Fisher MPA (2016) A new spin on neural processing: Quantum cognition. *Frontiers in Human Neuroscience* 10: 541.

Wiltschko R, Nießner C, and Wiltschko W (2021) The magnetic compass of birds: The role of cryptochrome. *Frontiers in Physiology* 19(12): 667000.

Xu J, et al. (2021) Magnetic sensitivity of cryptochrome 4 from a migratory songbird. *Nature* 594: 535–540.

Yuan Z, Zhou Y, Qiao Z, Eng Aik C, Tu W, Wu X, and Chen Y (2021) Stimulated chiral light-matter interactions in biological microlasers. *ACS Nano* 15(5): 8965–8975.

Zadeh-Haghighi H and Simon C (2021) Entangled radicals may explain lithium effects on hyperactivity. *Scientific Reports* 11: 12121.

Zadeh-Haghighi H and Simon C (2022a) Radical pairs can explain magnetic field and lithium effects on the circadian clock. *Scientific Reports* 12: 269.

Zadeh-Haghighi H and Simon C (2022b) Radical pairs may play a role in microtubule reorganization. *Scientific Reports* 12: 6109.

Zettili N (2009) *Quantum Mechanics Concepts and Applications: Second Edition*. UK: John Wiley & Sons Ltd.

Zhang Z, Agarwal GS, and Scully MO (2019) Quantum fluctuations in the Fröhlich condensate of molecular vibrations driven far from equilibrium. *Physical Review Letters* 122: 158101.

Zorov DB, Juhaszova M, and Sollott SJ (2014) Mitochondrial reactive oxygen species (ROS) and ROS-induced ROS release. *Physiology Reviews* 94(3): 909–950.

Physics of protein folding

Patrícia FN Faísca, Departamento de Física and BioISI – Biosystems and Integrative Sciences Institute, Faculdade de Ciências, Universidade de Lisboa, Lisboa, Portugal

© 2024 Elsevier Ltd. All rights reserved.

Introduction 605
The native structure: Hierarchical organization and physical interactions 606
Knotted proteins 608
The protein folding transition 608
The thermodynamic hypothesis and the paradox of Levinthal 609
The energy landscape theory and folding funnels 610
Folding mechanisms 612
Folding kinetics 613
Folding and knotting 614
Conclusion 615
Acknowledgments 616
References 616

Abstract

The field of protein science is witnessing a revolution in the wake of recent breakthroughs such as the artificial intelligence (AI) system AlphaFold which can predict the three-dimensional structure of almost every globular protein from its protein sequence alone. Inevitably, there is some expectation that structure-prediction modelling approaches based on AI may also learn the physics of protein folding to the extent of predicting folding pathways. Motivated by these advances, we briefly review the thermodynamic, kinetic, and structural aspects governing the folding transition from an unfolded protein chain into its final native structure and discuss directions for future research.

Key points

- Non-expert introduction to protein folding physics
- Physically motivated review integrating classical and recent results
- Discussion of future research directions

Introduction

A protein is a heteropolymer of the 20 naturally occurring amino acids. Proteins can be broadly classified as fibrous or globular, depending on whether they play a functional or structural role in their host organism. A recent quantitative analysis of the proteome of model organism *Saccharomyces cerevisiae* estimates that the number of globular proteins per cell stands between 3 and 5.9×10^5 molecules (Ho et al., 2018). This number is likely higher for human cells (Flamholz et al., 2014).

Globular proteins are the cell's workhorses. They perform a variety of functions, the two most common being binding (binding proteins) and catalysis (enzymes). Proteins are also involved in signal transduction, transportation, regulation of gene expression, and enhancement of signaling efficiency and fidelity through binding to other proteins, and organizing binding partners into a functional unit (scaffold proteins), just to mention a few examples.

Following synthesis in the ribosome a linear polypeptide chain spontaneously self-assembles into a specific three-dimensional, soluble structure termed native structure. The term conformation refers to the spatial arrangement of the proteins atoms and the expression native conformation is often used when referring to the native structure. Sometimes the native structure embeds topological entanglements such as a physical knot (Dabrowski-Tumanski et al., 2018b). Moreover, it frequently involves the association of more than one chain as in the case of hemoglobin, the protein that transports oxygen in the blood, a tetramer formed by four polypeptide chains.

Proteins acquire their native structure through the physical process of protein folding and, if everything goes well, each protein sequence will always reproducibly fold into the same native structure in a biologically relevant timescale. However, errors in protein folding (resulting from mutations or adverse environmental conditions) may culminate in malformed proteins

https://doi.org/10.1016/B978-0-323-90800-9.00263-8

that expose patches of hydrophobic amino acids and frequently self-associate into insoluble fibrils called amyloids. These malformed proteins are the culprits of a class of debilitating (and sometimes deadly) diseases called conformational disorders. So far, more than 40 conformational disorders have been identified including the well-known Parkinson's and Alzheimer's diseases (Chiti and Dobson, 2006). Correct protein folding is therefore essential for the health and function of living organisms, and a complete understanding of the folding process has a considerably high societal impact since it would provide directions toward the cure of conformational disorders. On the other hand, from a physical (or fundamental) point of view, the comprehension of hierarchical organization, cooperative processes, and self-assembly is not complete without a complete understanding of protein folding.

When thinking about protein folding, the expression *protein-folding problem* often comes to mind (Dill and MacCallum, 2012). The latter is not actually a single problem, but rather encompasses three related questions: (a) the folding code: what balance of interatomic forces dictates the native structure of a given amino acid sequence? (b) the structure-prediction problem: can the protein's native structure be predicted from its amino acid sequence by means of computational methods? and (c) the folding process: what are the mechanisms that make a protein fold so quickly in the microsecond to millisecond timescale? (Or, how can order arise from disorder so fast?)

The challenge of solving protein folding prompted the development of computer technologies (i.e., specific machine architectures and software) that can simulate folding with realistic forcefields in a reasonable amount of time. The state-of-the-art is a machine called Anton (Dror et al., 2011), developed by D.E. Shaw Research, that performs multi-microsecond simulations in a single day for systems with more than 1 million atoms (surpassing the computational speed of commercial machines routinely used in research laboratories by two orders of magnitude) (Shaw et al., 2010).

Recently, a machine learning model called AlphaFold, which uses physical and biological knowledge about protein structure, has been regularly predicting the native structure to near experimental accuracy by taking the protein's amino acid sequence as an input (Jumper et al., 2021). The AlphaFold database (AlphaFold DB) (https://alphafold.ebi.ac.uk/) already provides access to over 200 million protein structure predictions, which is three orders of magnitude larger than the number of experimentally solved protein structures deposited in the Protein Data Bank (PDB) over the last 50 years. One can therefore claim that this remarkable breakthrough has already solved the structure-prediction problem. But are these models also learning the physics of protein folding, i.e., of how proteins dynamically fold into their native equilibrium structures as shown by experiments and predicted by simulations? Results reported so far are inconsistent. On the one hand, it has been claimed that AlphaFold has learned an energy potential function, suggesting that efficient machine-learning algorithms can disclose critical information about the physical interactions that ultimately lead to the native structure without being trained to do so (Roney and Ovchinnikov, 2022). However, it has also been shown that AlphaFold is not able to correctly produce folding pathways, providing worse predictions than the protein's chain length, a trivial, sequence-independent classifier of protein folding kinetics (Outeiral et al., 2022). The future will tell us if AlphaFold, and other similarly inspired methodologies, will be able to generate correct protein folding pathways and novel insights on protein folding principles (Chen et al., 2023).

Motivated by these latest advancements, here we summarize the status quo of protein folding physics, which encompasses the understanding of thermodynamics, kinetics and mechanisms underlying the transition of a disordered polypeptide chain into its final native ordered structure (Finkelstein and Galzitskaya, 2004).

The native structure: Hierarchical organization and physical interactions

The native structure is a specific three-dimensional structure that determines the protein's biological function. In cells, proteins are synthesized in a molecular machine called ribosome as linear chains of linked amino acids. There are 20 naturally occurring amino acids.

Each amino acid contains a basic amino group, a carboxylic acid group, a hydrogen atom, and an R-group (or side-chain group), which are all attached to a central carbon atom named alpha carbon, C_α. Depending on the structure and chemical properties of the R-groups, amino acids can be broadly classified as hydrophilic or hydrophobic. While the former includes electrically charged groups (acidic or basic groups that bear a full negative or positive charge, respectively), the latter are neutral and relatively non-polar.

Amino acids are linked together by a rigid C-N covalent bond termed peptide bond. The latter involves the carboxyl end of one amino acid and the amino group of the next. The term main chain (or protein backbone) is used to refer to the linked sequence of carbon, nitrogen, and oxygen atoms. The term primary structure is used to describe the linear (i.e., one-dimensional) sequence of amino acids linked together along the polypeptide chain (Fig. 1A). The peptide bond and its four adjacent bonds are coplanar forming an amide plane. Each amide plane can rotate around the C_α-C and the C_α-N bonds, and these rotations are described by the torsional angles φ and ϕ, respectively. Not all φ-ϕ combinations are possible because of steric clashes between backbone atoms. However, some favorable combinations allow the formation of hydrogen-bond interactions between the carbonyl oxygen and amide nitrogen of the main chain. Hydrogen bonds direct (and stabilize with 2–10 kcal/mol) the local structural arrangement of the polypeptide chain into the so-called elements of secondary structure, the most common being the alpha-helix and the

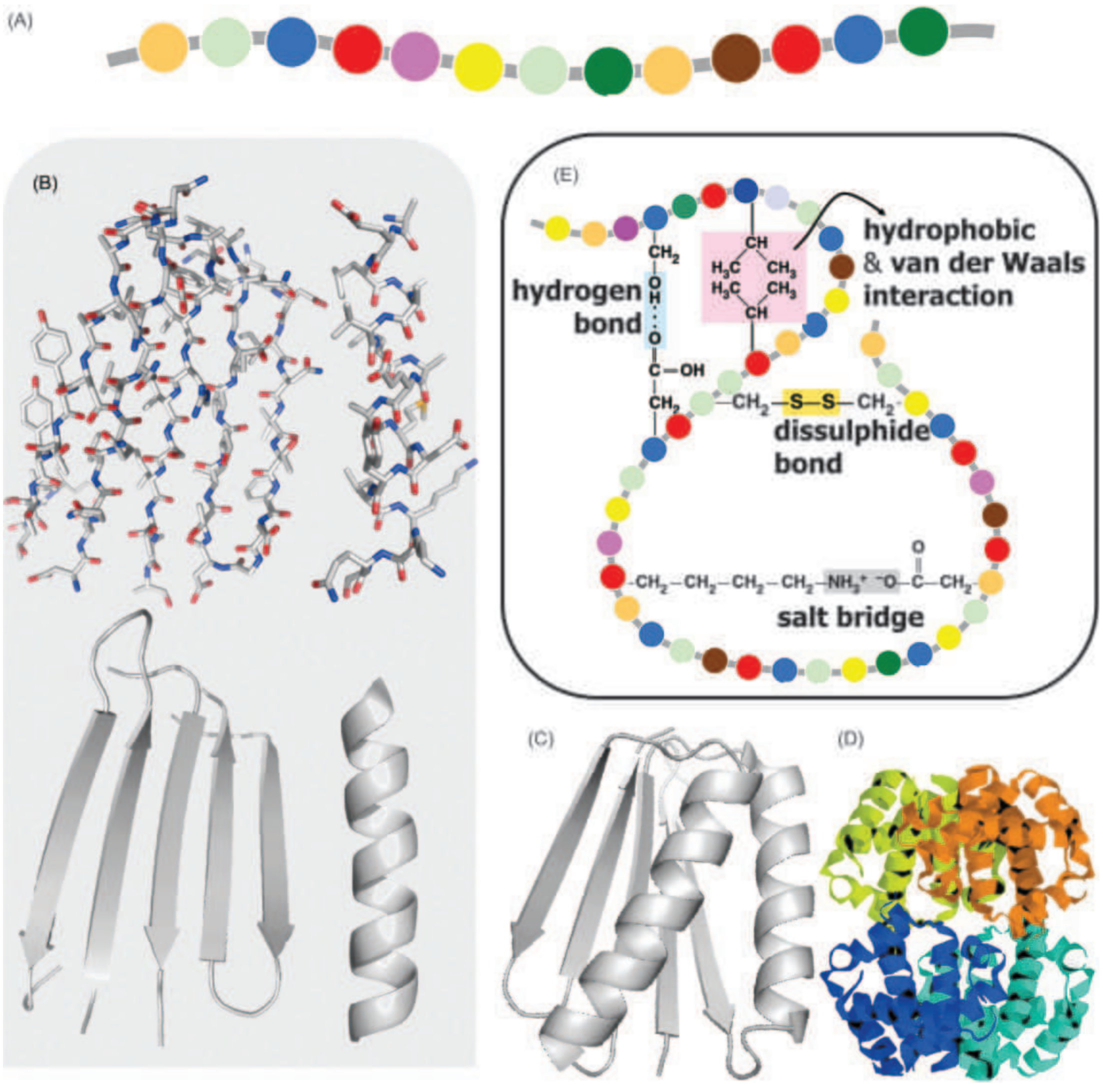

Fig. 1 Hierarchical structure of proteins. Primary structure (A). The two most common elements of secondary structure: the alpha-helix and the beta-strand displayed in full atomistic detail and in cartoon representation (B). Tertiary structure in cartoon representation (C). Quaternary structure of hemoglobin in cartoon representation (D). Interactions that stabilize protein structure (E).

beta-sheet (Fig. 1B). Hydrophobic interactions between non-polar amino acids drive the packing of secondary structural elements into the formation of the tertiary structure (Fig. 1C). The resulting protein structure exhibits a tightly packed core (the fraction of filled space inside proteins is 74%, i.e., almost the same as the maximum density packing of identical spheres), where the formation of weak van der Waals interactions between the side chains groups is highly optimized through side-chain packing.

Often the native structure coincides with the tertiary structure, but in many proteins it contains two or more polypeptide chains, being classified as a dimer or a higher order oligomer (trimer, tetramer, etc.). This level of structural arrangement is termed quaternary structure (Fig. 1D). It is important to note that in the quaternary structure each chain has its own secondary and tertiary structure. The tertiary and quaternary structure can be stabilized by disulfide bonds (a kind of reversible covalent bond formed between the thiol groups, -SH, of two cysteine amino acids), and salt-bridges (establishing between residues with ionizable side chains such as aspartic acid and histidine) (Darby and Creighton, 1995). Despite all these sources of energetic stability (Fig. 1E) the native state of proteins is only thermodynamically marginally stable (−10 kcal) regarding the unfolded state. The origins of marginal stability remain undetermined, but it has been argued that it enables proper function (Taverna and Goldstein, 2002).

When discussing protein structure, the term protein domain refers to a distinct functional and/or structural unit in a protein. A domain is responsible for a specific function or interaction. A domain is self-stabilizing and folds independently of the rest of the chain. A protein that is formed by one domain is termed a single-domain protein. A protein subunit, on the other hand, is a separate polypeptide chain of a protein that assembles with other polypeptide chains to form a protein complex (Wang et al., 2021).

Knotted proteins

Knotted proteins are proteins whose native structure embeds a physical (in opposition to a topological or closed) knot (Fig. 2A). The first knotted protein was reported in 1977 (Richardson, 1977) but it was only in 2000, after the development of efficient knot detection methods and loop closure procedures, that these tangled molecules came into the spotlight (Lua and Grosberg, 2006; Taylor, 2000). The most recent survey of the PDB indicates that there are about 1% of knotted entries (Dabrowski-Tumanski et al., 2018b), and a survey of the AlphaFold DB found that knots are present in 0.2% of the human proteome (Perlinska et al., 2023). Knotted proteins exhibit different levels of topological complexity, depending on the minimal number of crossings of the polypeptide chain on a planar projection of the knot (Fig. 2B). The simplest and most abundant type is the trefoil (or 3_1) knot, but there is one protein featuring the Stevedore's (or 6_1) knot (with 6 crossings) (Bölinger et al., 2010). Recently, the 6_3 knot was found in a human protein (Perlinska et al., 2023). An interesting example is that of protein UCH-L1, the most abundant in the human brain (Sjölin et al., 2022), which features the gordian (or 5_2) knot. Knots can be further classified as deep, when the minimal segment of the polypeptide chain that contains the knot (knotted core) is located at least 10 residues away from the termini, or shallow if this distance is smaller. Protein YibK, featuring a deep trefoil knot, is one of the most extensively studied knotted proteins (Fig. 2C–E).

Despite being statistically rare (Lua and Grosberg, 2006) these tangled molecules have attracted considerable attention, and the last decade witnessed a battery of experimental and computational studies dedicated to disclosing their folding and knotting mechanisms, and determine their biological function (Faísca, 2015; Jackson et al., 2017; Jackson, 2020).

The protein folding transition

In the 1930s, Anson and Mirsky observed that protein denaturation is a reversible process (Anson and Mirsky, 1934). Likewise, the refolding process observed after complete protein denaturation offers aoperational setup to study protein folding *in vitro*. Protein denaturation can be chemically induced (e.g., by means of a denaturing agent such as urea or guanidinium chloride) or thermally induced by increasing temperature. Calorimetric experiments framed on differential scanning calorimetry, where the heat capacity is measured as a function of temperature, show that thermal denaturation resembles a melting process, with the heat capacity peaking at the so-called melting temperature T_m (or denaturation temperature) (Fig. 3A). At T_m both the protein's energy and entropy increase sharply with temperature as intramolecular interactions break and the system gains conformational freedom.

The transition from folding to unfolding is described by a sigmoidal (or S-shaped) curve depicting the fraction of folded protein over temperature or denaturant concentration (Fig. 3B). An S-shaped curve indicates an abrupt change is some measurable property at the transition midpoint, T_m. If the width of the transition region is narrow, it means that many amino acids are involved in the process. In fact, S-shaped curves are a hallmark of cooperative physical processes, i.e., processes in which the elements composing the system act dependently of each other.

In the case of protein folding, the abrupt change upon denaturation led Anson and Mirsky to introduce the two-state approximation for the folding-unfolding transition to indicate the absence of intermediate states populated in thermal equilibrium at $T_{m.}$ Under this model, the folding process is a two-state cooperative transition. When the transition is two-state, the microscopic

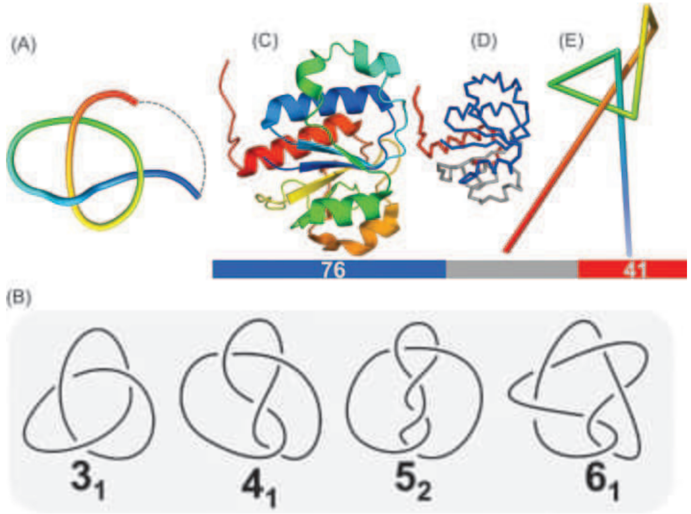

Fig. 2 Knotted proteins. A physical trefoil knot featuring a loop closure (A). Types of mathematical knots found in proteins (B). Native structure of YibK (PDB ID 2EFV) in cartoon representation (C). The ribbon representation highlights the knotted core in gray and knot tails in blue (76 amino acids long) and red (41 amino acids long) (D). Reduced representation of the native structure found with Taylor's algorithm (Taylor, 2000) (E).

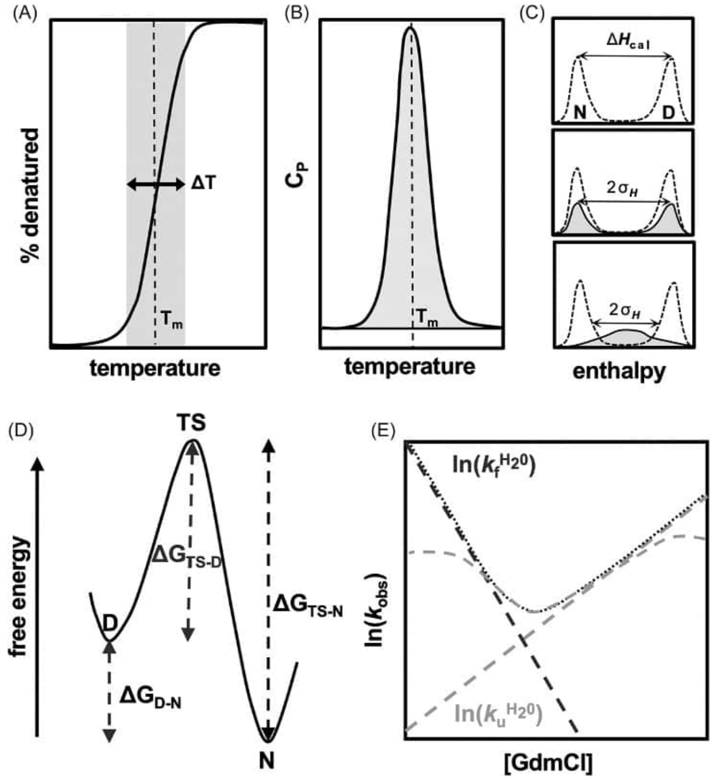

Fig. 3 The folding transition. Thermal denaturation curve with the transition midpoint indicating the melting temperature, T_m, and ΔT measuring the transition width (A). Heat capacity curve showing a peak of heat capacity at T_m (B). The area under the curve is a measure of ΔH_{cal}. Microscopic distribution of protein conformations over a measurable property expected for a two-state transition (C, top panel) with σ_H being the standard deviation of H. The latter decreases as the equilibrium population shifts from a bimodal to a unimodal distribution (C, mid and bottom panels). Free energy profile (projection of the free energy over a reaction coordinate, e.g., H) expected for a two-state transition (D). Dependence of the folding rate constant on the concentration of denaturant showing typical linear chevron behavior. The chevron roll-overs also displayed in the graph are an indication of the presence of intermediate states populating the folding transition (E).

distribution of protein conformations at T_m is bimodal, indicating that only the native and denatured states coexist in equilibrium at that temperature (Fig. 3C, top panel). A projection of the free energy into an appropriate property (e.g., the protein's energy or enthalpy) shows a free energy barrier separating the two thermodynamic states (Fig. 3D).

In experiments *in vitro*, the so-called calorimetric criterium is often used to determine if protein folding is an "all-or-none" two-state transition (Zhou et al., 1999). Accordingly, a transition is two-state when the ratio between the measured calorimetric enthalpy change, and the effective two-state van't Hoff enthalpy change ($\Delta H_{vH} = 2\sigma_H$) is unity (Fig. 3C) (Chan et al., 2004). However, it turns out that it is not a sufficient condition (Zhou et al., 1999). Indeed, for the transition to classify as two-state, the so-called chevron-plots (showing the dependence of folding and unfolding rate on the concentration of denaturant) must show strongly sloping linear refolding arms (Chan et al., 2004) (Fig. 3E). Most small (~with up to 120 amino acids), single-domain proteins fold thermodynamically via a two-state transition and with single-exponential kinetics (Jackson, 1998). Because of their simplicity, they became the preferred model systems to study protein folding.

The thermodynamic hypothesis and the paradox of Levinthal

In the 1950s, Cristian Anfinsen performed a series of experiments with protein ribonuclease A (RNase) that ended up launching the field of protein folding (Anfinsen, 1973). RNase is an enzyme with a chain length of 124 amino acids. Its native structure is stabilized by four disulfide bonds. Anfinsen used a reducing agent (called beta-mercaptoethanol) to break the disulfide bonds, and urea to disrupt the secondary structural elements and he noticed that the protein became biologically inactive, i.e., it denatured. Subsequently, by simultaneously removing the two chemical agents, he observed that the protein regained activity, i.e., it refolded back into its biologically active native conformation. Anfinsen concluded that since refolding occurred spontaneously, the native conformation in its normal physiological milieu (solvent, pH, ionic strength, presence of other components such as metal ions or prosthetic groups, temperature and other) is the one in which the Gibbs free energy of the whole system is the lowest; and since refolding did not requir the addition of other chemicals, the native conformation must be determined by the totality of interatomic interactions and hence by the amino acid sequence in a given environment. This, conclusion, known as Anfinsen's dogma, or thermodynamic hypothesis, granted Anfinsen the 1972 Nobel Prize in Chemistry.

In the late 1960s, Cyrus Levinthal noted that the number of atomistic-level conformations of a protein is massive (Levinthal, 1968, 1969). A lower bound estimate for this number can be obtained as follows. Assume that an amino acid can only be in two distinct conformations. In this case, a small protein with ~100 amino acids would have access to 2^{100} (or 10^{30}) conformations. Assume additionally that a conformational change occurs so fast that it only takes 1 ps for an amino acid to move between two conformations. If protein folding is really a two-state process without intermediate states, the time needed to fold (i.e., to find the native conformation that corresponds to the global minimum of the free energy) can be estimated from the time needed to randomly explore all possible conformations. This time is astronomically large. In fact, even for the simplest case considered above, it would take 2^{100} ps or 10^{10} years to find the native structure. But generally, small proteins fold fast in the timescale of milliseconds to seconds (Jackson, 1998). This quantitative argument is known as Levinthal's Paradox. According to Levinthal, the goal of achieving a global minimum of the free energy is not compatible with doing it fast, and in his own words 'if the final folded state turned out to be the one of lowest conformational energy, it would be a consequence of biological evolution, not of physical chemistry' (Levinthal, 1969).

Levinthal's paradox represents a landmark in the history of protein science because it prompted and stimulated research on the kinetics and mechanisms of protein folding: What is the physical mechanism according to which proteins acquire their native structure in a biological timescale? Levinthal himself proposed that folding should be under kinetic rather than under thermodynamic control. This means that the folding process should proceed through the population of specific intermediate states that form a folding pathway. In his view, the native structure should be - not the global free energy minimum - but a kinetically accessible minimum that is sufficiently deep to trap the protein's conformation in a thermodynamically stable state. In 1992, kinetic trapping was observed in the folding reaction of a designed protein, but the corresponding state was not biologically active (Baker and Agard, 1994). In 1996, a model for a kinetically controlled folding pathway as envisioned by Levinthal was suggested for protein Serpin Plasminogen Activator Inhibitor 1 (PAI-1), which forms a metastable active structure that converts slowly to the more stable but low-activity 'latent' conformation (Wang et al., 1996). While the possibility that folding may be under kinetic control for some model systems should not be ruled out, the fact that robust, stable proteins can be designed by focusing on the stability of the target structure, indicates that thermodynamics must generally outcast kinetics in protein folding (Baker, 2019). In fact, the analysis of early lattice models suggested a correlation between thermodynamic stability and kinetic accessibility of the native structure (Shakhnovich and Gutin, 1993) and, for some small proteins, thermodynamic stability, as measured by the free energy of folding (ΔG_U), correlates strongly with folding rate (Plaxco et al., 2000).

In recent years, folding intermediates have attracted considerable attention because of their potential to trigger the aggregation process. This has been shown in experiments *in vitro* (Le Marchand et al., 2018; Neudecker et al., 2012) and predicted by molecular simulations (Krobath et al., 2012; Estácio et al., 2014; Loureiro et al., 2017). We note, however, that such species are not necessarily intermediate states in the thermodynamic sense. Most often they are indeed transiently populated and difficult to detect experimentally (Chiti and Dobson, 2009).

The energy landscape theory and folding funnels

Computer power increased dramatically throughout the 1990s, which allowed researchers to use computer simulations to study protein folding. In particular, coarse grained models like lattice models (Fig. 4A) and off-lattice C-alpha models (Fig. 4B) combined with Monte Carlo sampling were, and still are (Especial and Faísca, 2021), very popular among the molecular biophysics community. These models contributed to establish basic principles of protein folding (Kmiecik et al., 2016).

A landmark computational study explored the behavior of random heteropolymer (RHP) sequences featuring the 20 naturally occurring amino acids in the context of a lattice model (Šali et al., 1994). It was found that 15% of the tested random sequences were able to find the native state (the maximally compact structure with the lowest energy) rapidly and reproducibly fold to it. What distinguished these proteinlike sequences from the non-folding ones was an energy gap between the native state and other unrelated conformations. Since natural protein sequences overcome the paradox of Levinthal, these results suggested that folding RHP are proteinlike sequences. Therefore, a necessary condition to fold fast is that the native state is a pronounced global minimum on the potential energy surface. Additionally, analytical calculations on lattice representations of hydrophobic (H)-polar (P) sequences predicted sharp cooperative transitions from unfolded conformations with very few HH interactions, to a native structure where the number of HH interactions are maximized (Dill et al., 1995). These results, and others alike, also indicated that folding does not proceed through a random search for the native structure because the number of accessible conformations decreases exponentially as the protein becomes progressively more compact through the establishment of native interactions. This behavior was theoretically described though the concept of folding funnel (Fig. 5), a major outcome of the so-called energy landscape theory developed by Wolynes and co-workers (Onuchic et al., 1997).

The energy landscape theory is a theoretical framework that conciliates Anfinsens's thermodynamic hypothesis with fast folding kinetics. It combined concepts from polymer physics with the theory of spin glasses and used insights from computer simulations of simple lattice models. The interested reader will find illuminating reviews on this subject in the works of Ken Dill and collaborators (Dill and Chan, 1997; Dill, 1999). Here, we breifly expose its main concepts and ideas.

The energy landscape is a multidimensional representation of the folding process where the vertical axis represents the internal free energy of a single conformation, while the multiple lateral axes represent the conformational coordinates (e.g., the dihedral bond angles, φ_1-ϕ_1, φ_2-ϕ_2, …). The internal free energy of one conformation accounts for everything (i.e., hydrogen bonds, salt bridges, torsion angle energies, hydrophobic and solvation free energies, etc.) except for the conformational entropy. It is called free

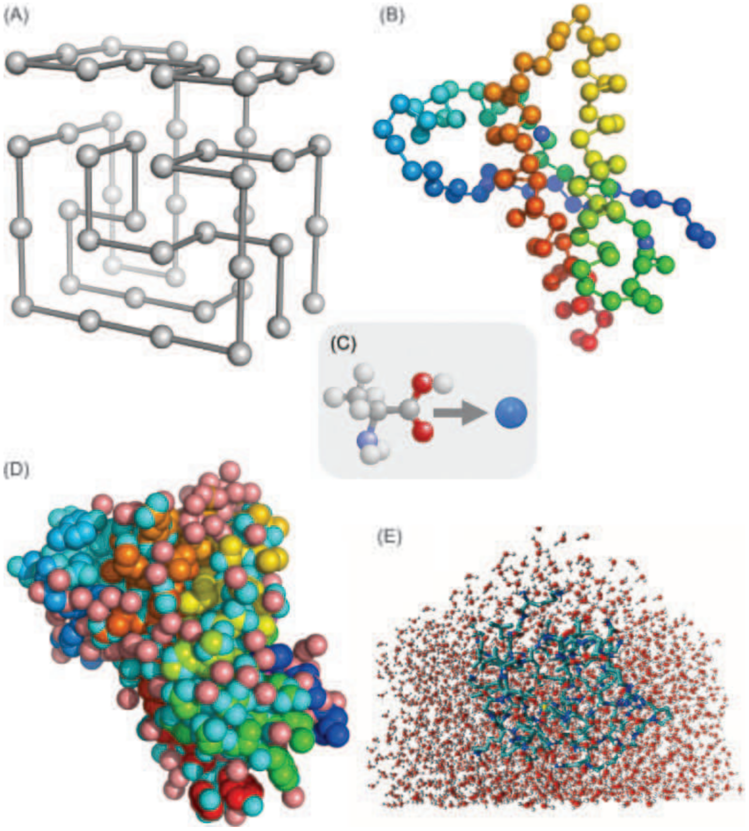

Fig. 4 Protein models with different granularity used in simulations of protein folding. In both the lattice model (A) and the C-alpha model (B) each amino acid is reduced to a bead of uniform size (C). The lattice model restricts the beads to occupy the vertices of a regular lattice, with the lattice spacing mimicking the peptide bond. In the C-alpha model the coordinates of the C-alpha atoms are taken from the PDB native structure and the distance between them is set to a fixed value. In the full atomistic model, all atoms are explicitly represented (D). In (A) and (B) protein energetics is mimicked with sequence-specific or structured based potentials, and conformational space is explored with Monte Carlo methods, Langevin Molecular Dynamics, or Discrete Molecular Dynamics. When the solvent is explicitly represented (E) the conformational space is explored with classical Molecular Dynamics, and energetics is based on a force field (GROMOS, CHARMM, AMBER etc.) that is empirically parametrized.

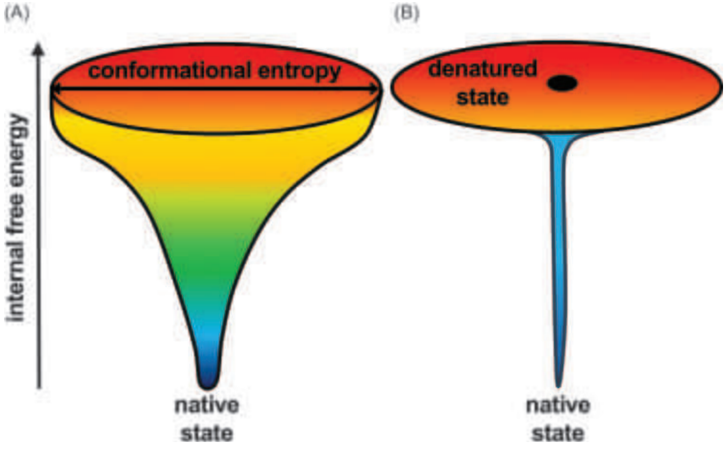

Fig. 5 The folding funnel. Diagrammatic representation of a perfectly funneled shaped energy landscape representing a fast two-state folding transition (A). Energy landscape illustrating the paradox of Levinthal (B). In this case only the denatured and native ensemble can be populated, and the search for the native structure is unbiased. The folding chain randomly explores all denatured conformations until it finds the only one that provides access to the native state.

energy (and not merely energy) because of the solvation terms, which involve entropy due to water ordering. A point in the free energy landscape represents a protein conformation, and geometrically closed conformations lay close to each other. For a certain value of the vertical axis (i.e., of the internal free energy) there is an ensemble of conformations corresponding to some conformational entropy. On the top of the funnel, the unfolded ensemble is the largest one, with the highest conformational entropy. The width of the funnel progressively shrinks down as folding progresses reflecting the fact that the number of accessible conformations progressively decreases as the chain approaches the native ensemble (i.e., the native conformation and nearby ones) at the bottom, with the lowest internal free energy (Fig. 5A). In the landscape perspective, folding is viewed as a succession of random conformational transitions starting from an arbitrary unfolded conformation. In its search for the native state the polypeptide chain will lower its internal free energy by shielding hydrophobic residues in the core, and by increasing its content in hydrogen bonds, number of salt-bridges, disulfide bonds etc. while it becomes progressively more compact (note that the paradox of Levinthal results from assuming an unbiased conformational search (Fig. 5B)). The funneled shape of the free energy landscape reflects the concomitant decrease in the chain's internal free energy and conformational entropy that occurs during folding. A chain navigating the folding funnel will rapidly attain the native state starting from an arbitrarily unfolded conformation by taking many possible routes (instead of populating a sequence of well-defined conformations as envisioned by Levinthal). Therefore, the folding process satisfies Anfinsen's thermodynamic hypothesis in a directed and rapid way. The folding funnel is, therefore, a conceptual insight that reconciles the thermodynamic hypothesis with the biological timescale of protein folding.

A rather provocative view, which challenges the traditional interpretation of protein folding, was recently proposed based on the so-called *excluding* interactions. The latter are steric clashes and unsatisfied hydrogen bond donors and acceptors which, despite being unspecific, can induce considerable chain organization. Conformations with disfavored interactions of this type will be largely excluded from equilibrium populations. Thus, under physical–chemical conditions that favor folding, excluding interactions substantially separate the accessible population. In doing so, they solve the problem of entropy loss (which is conventionally compensated by the formation of specific and stabilizing intramolecular interactions as outlined above) and also reduce the timescale of protein folding (Rose, 2021).

Folding mechanisms

The landscape perspective offers an ensemble view of protein folding that is, nevertheless, too generic to discriminate between the folding mechanism of different proteins. But what is the exact meaning of folding mechanism? In a recent review article (Nassar et al., 2021) Dill and co-workers provide a illuminating definition: a mechanism is a descriptor "of folding at a level that is sufficiently general and coarse-grained to apply to all proteins, and yet sufficiently granular to account for the differences across proteins." The idea that a mechanism is a sequence of physical events that bring a disordered unfolded chain into its ordered native structure is implicit in this statement.

Levinthal was one of the first researchers to propose a folding mechanism. The latter was based on the formation of nucleation sites, or local interactions that establish rapidly between residues which are close to each other along the chain (e.g., hydrogen bonds interactions that stabilize the secondary structural elements). The resulting secondary structural elements would then coalesce to form the tertiary structure. This is, in fact, the core idea behind the framework model (Wetlaufer, 1973), which envisions folding as a hierarchical process where the formation of secondary structure elements precedes the formation of the native structure. A different mechanism is the diffusion-collision model (Karplus and Weaver, 1979). In this case, the core part of protein folding are the diffusive encounters (or collisions) between metastable regions of the polypeptide chain that progressively leads to more stable intermediate states. In the 1970s, the so-called molten globule, an intermediate state that preserves the mean overall native structure but exhibits a looser packing and higher mobility at loops and termini, was proposed to be a common species in the folding process (Ptitsyn, 1995).

In the so-called hydrophobic collapse model (Dill, 1985), the initial event in protein folding is the collapse of the unfolded chain resulting from the hydrophobic effect. The formation of secondary structure occurs in this collapsed state and the packing of the sidechains eventually leads to the native structure.

However, perhaps one of the most popular folding mechanisms is the nucleation-condensation mechanism (reviewed in Faísca, 2009). As previously stated, small, single-domain proteins fold with a two-state thermodynamic transition, and their folding rate fits a single-exponential kinetic model. For these small proteins, folding is limited by the formation of a folding nucleus in the so-called transition state ensemble (i.e., the ensemble of conformations laying at the top of the free energy barrier). In the classical nucleation mechanism of first-order phase transitions the critical nucleus is a portion of the new phase, whereas in the folding transition the folding nucleus is a *specific set* of (local and non-local) intrachain interactions (Abkevich et al., 1994). The formation of the folding nucleus is rate-limiting. Thus, once it forms, the native structure is promptly achieved. Perhaps not surprisingly, Monte Carlo simulations of lattice models (in which intrachain contacts are straightforwardly and unequivocally determined), offered the first theoretical predictions for a nucleation mechanism. Experimentally, it is not possible to obtain a structurally resolved picture of the folding transition state using standardly used biophysical techniques due to its transient nature and being sparsely populated. Thus, a protein engineering technique termed ϕ-value analysis was developed to provide an indirect structural characterization from thermodynamic considerations (Itzhaki et al., 1995). The ϕ-value is defined as being the ratio between the change in the activation energy of folding ($\Delta\Delta G_{TS-D}$) and the change in the free energy of folding ($\Delta\Delta G_{N-D}$) upon performing a single-point mutation. For two-state proteins, a ϕ-value near unity means that the TS is perturbed upon mutation as much as the native state is perturbed. This is interpreted as if the mutated residue is in a native (or near native) conformation in the TS. Alternatively, a ϕ-value of zero means that the corresponding residue is as unstructured in the TS as it is in the denatured (D) state. The interpretation of fractional ϕ-values or non-classical ($\phi < 0$) or ($\phi > 1$) is not straightforward and may indicate partial contact formation or folding path heterogeneity (Best and Hummer, 2016).

By determining the ϕ-value of all the 64 protein residues in the single-domain protein chymotrypsin-inhibitor 2 (CI2), it was found that the folding nucleus comprises a set of predominantly local interactions stabilized by a few non-local ones, in line with the predictions from lattice simulations (Itzhaki et al., 1995). The lack of secondary and tertiary structure in the transition state was taken as evidence that they form concomitantly triggered by the folding nucleus. The nucleation-condensation mechanism appears to be common among many small, single-domain proteins, but it is unlikely that there is a unifying mechanism for protein folding. It has been proposed that an increased propensity to form stable elements of secondary structure, makes folding more hierarchical, eventually following a framework mechanism where the transition state is assembled from pre-formed secondary structural elements (Daggett and Fersht, 2003).

More recently, the use of a technique termed hydrogen-exchange pulse-labeling mass-spectrometry (HX MS) (Englander et al., 2016), which can detect and characterize local structure, even when it is only transiently present, has provided evidence that some proteins (including small ones such as Anfinsen's RNase) fold in a stepwise manner by populating distinct intermediates separated by kinetic barriers; these proteins fold through a folding pathway similar to that envisioned by Levinthal (Hu et al., 2013). The novel insight is that these intermediate states are formed by assembling small pieces (with about 20 residues) of secondary structure (helices, turns and beta-strands) termed *foldons*. Because of their small size, foldons resolve the timescale search problem. However, they are not individually stable being transiently populated, and need to accrete to gain stability and persist for a longer time. Interactions between foldons provide the free energy bias for the ordered addition of foldons in a stepwise pathway that sequentially builds the native protein. In this mechanism, known as the foldon funnel model, the free energy barrier is a consequence of the substantial entropy loss that results from ordered secondary structural elements, with the energetic gain due to native contacts not being enough to balance it (Rollins and Dill, 2014).

The folding mechanisms outlined above have been proposed by exploiting the folding of small proteins though simulations and *in vitro* experiments. However, research on larger, multidomain proteins is considerably less developed (Gershenson et al., 2020). Recent work suggests that even though these proteins can be broken down in smaller units by domain dissection (i.e., the identification of structural domains from the amino acid sequence by means of informatic methods), the folding of these component domains may not be independent. Consequently, the mechanisms guiding individual small, single-domain proteins may not be applicable to the universe of larger proteins (Hingorani and Gierasch, 2014). Moreover, there is evidence that the folding of large proteins *in vivo* may be context dependent, which means that *in vitro* and *in silico* studies may offer an incomplete, or even unrealistic, view of these processes as they happen in the living cell (Sorokina and Mushegian, 2018).

Folding kinetics

The question of understanding the mechanism(s) of protein folding is complemented by the question of understanding folding kinetics, i.e., the temporal laws and timescales that govern this self-assembly process.

As stated previously, many small, single-domain proteins fold rapidly (in the microsecond to millisecond time scale) via a two-state folding process where the only states populated in equilibrium are the native and the denatured states (Jackson, 1998). For these proteins, a plot of the natural logarithm of the rate constants for unfolding (lnk_U), and refolding (lnk_F), versus denaturant concentration, [D], is frequently linear (linear chevron plots) (Fig. 3E). The corresponding kinetics is termed single-exponential because folding speed is limited by the height of only one free energy barrier corresponding to the transition state (Fig. 3D).

The speed at which a protein folds is quite sensitive to temperature. Early studies on Monte Carlo simulations of lattice models predicted that there is an optimal folding temperature, i.e., a temperature at which folding is fastest (Faisca and Ball, 2002a). This temperature is typically lower than the melting temperature, i.e., in conditions that favor the population of the native state. However, away from this optimum, both at higher and lower temperatures the process gets increasingly slower. In the first case, the protein tends to behave like an RHP rapidly fluctuating between unfolded states. In the second case, there is a high probability for the chain to get trapped into metastable states and folding entails overcoming the corresponding kinetic barriers. This kind of temperature-rate dependence was also observed in experiments *in vitro* (Oliveberg et al., 1995) and, more recently, in living cells (Guo et al., 2012).

From a physics point of view it is more relevant to understand how the structural features of the protein determine its folding rate. One, the chain length, is simply the number of amino acids, N, in the primary structure. A seminal study, combining concepts from statistical mechanics of random heteropolymers, and results from simple lattice models, formulated the relation $k_f \sim \exp(N^{1/2})$ between the folding rate, k_f, and the chain length (France, 1995). A later study that considered experimentally determined folding times for 69 proteins and peptides with size ranging from 16 to 396 residues found a correlation of 0.74 between the logarithm of folding time and $N^{1/2}$, and a maximum value of ~0.78 as the exponent approaches 0(Naganathan and Muñoz, 2005).

A stronger correlation (of 0.91) was found between the logarithmic folding rates of a set of 24 small ($56 \le N \le 154$), single-domain proteins that fold with single-exponential kinetics and a parameter of native structure named relative contact order, CO (Plaxco et al., 2000). The latter is a measure of the average length of the backbone loops connecting contacting pairs of residues in the native structure,

$$CO = \frac{1}{LN} \sum_{i,j}^{N} \Delta_{ij} \, |i-j|,$$

where L is the total number of contacts, and $\triangle_{ij}=1$ if residues i and j are in contact and is 0 otherwise, $|i\text{-}j|$ is the backbone separation between residues i and j. A protein whose native structure is predominantly dominated by interactions between amino acids that are far away in sequence has a high-*CO*, whereas interactions that are predominantly local should render a low-*CO*. The relative contact order fails to predict the folding rates of short peptides and large multistate folding proteins (Ivankov et al., 2003), for which the chain length seems to be the major determinant of folding time (Galzitskaya et al., 2003). Thus, it is important to understand why the *CO* predicts the folding rates of small, single-domain proteins.

The first computational study that investigated the *CO*-rate correlation in the context of lattice models used a pairwise addictive potential and found a moderate correlation (0.70), but only for chains with number of amino acids $N \geq 54$ and high-contact order ($CO > 0.17$) (Faisca and Ball, 2002b). However, the folding rates underlined by this potential are far from exhibiting the six-order-magnitude difference observed in real small, single-domain proteins. A subsequent study, also framed on lattice simulations, suggested that the *CO*-rate dependency may require multi-body interactions (Kaya and Chan, 2003). Indeed, a coupling mechanism between local and non-local native interactions was able to render the folding transition more cooperative while simultaneously leading to highly dispersed folding rates, a necessary condition to observe a strong statistical correlation with the *CO*. Another lattice simulation study explored the CO-rate correlation in a set of model systems in which the effect of the *CO* in folding kinetics was isolated from other properties (e.g., native state stability) potentially affecting kinetics (Faísca et al., 2012). The considered model systems were designed to share the same native structure, but displayed different backbone connectivities and, therefore, different *CO* values. The results from this study suggest that the *CO*-rate correlation is a consequence of the fact that, in high-CO native structures, the contact order of the transition state ensemble closely mirrors that of the native state. This happens because in these high-CO structures the native topology is present in the transition state through the formation of a network of tertiary interactions that are distinctively long-ranged. Despite these and other alterative views (Makarov and Plaxco, 2003), no consensus was yet reached regarding the microscopic mechanism underlying the *CO*-rate correlation.

Folding and knotting

If understanding the folding process of topologically regular proteins is already challenging, doing it for deeply knotted proteins (which represent extreme cases of topological complexity) is even more difficult. However, the solution of the folding puzzle is not complete without solving the folding mechanism of knotted proteins.

Since it is not yet possible to obtain a structurally resolved picture of the knotting mechanism in laboratory experiments, molecular simulations have been playing a major role in providing theoretical predictions. According to the current picture, the knotting step occurs with highest probability in structurally consolidated (i.e., near native) conformations toward the final stage of the folding process. Two major knotting mechanisms have been observed in simulations: in one mechanism, the chain terminus that lays closer to the knotted core (i.e., the minimal segment of the chain that contains the knot), directly threads a loop formed by the remainder of the chain (Wallin et al., 2007; Faísca et al., 2010). In the alternative mechanism, the chain terminus arranges itself into a hairpin conformation that threads the loop, transiently forming a slipknot (Noel et al., 2013; Sułkowska et al., 2009) (Fig. 6).

Because the formation of the loop must precede the threading event, the folding process of knotted proteins is highly ordered. This means that if native or nonnative interactions are formed untimely, they must break and re-establish later. The folding process of knotted proteins is thus prone to backtracking, and knotted proteins tend to exhibit slower folding kinetics (Soler et al., 2014; King et al., 2010).

It has been shown by experiments *in vitro* using a cell-free translation system, i.e., a minimal kit containing the necessary machinery for transcription (the production of messenger RNA, mRNA, from a DNA template) and translation (where the ribosome, reads the mRNA and synthesizes a polypeptide chain with the correct amino-acid sequence), that deeply knotted proteins can spontaneously self-tie (Mallam and Jackson, 2012; Lim and Jackson, 2015). However, this type of experiments also showed that the folding rate of deeply knotted proteins can be increased by at least one order of magnitude through the addition of chaperonins. The latter are a class of cylindrical shaped complexes featuring an interior cavity that works as an infinite dilution chamber. Together with chaperones they assist folding *in vivo* (Saibil, 2013) (Fig. 7). According to the classical mechanism

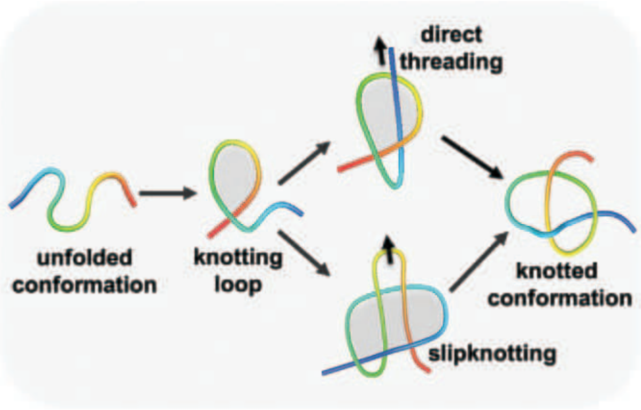

Fig. 6 Knotting mechanism. The knotting step involves the formation of the knotting loop by one portion of the polypeptide chain. The latter is directly threaded from one of the termini in the direct threading mechanism, or threaded by a hairpin forming a slipknotted conformation.

(also termed Anfinsen's passive model) the chaperonin accelerates folding by preventing off-pathway aggregation (Hayer-Hartl et al., 2016). However, this does not seem to be the case of knotted proteins, and it has been proposed that the chaperonin facilitates unfolding of kinetically and topologically trapped intermediates, or that it stabilizes interactions that promote knotting (Lim and Jackson, 2015). Computer simulations suggest that the steric confinement provided by the chaperonin decreases the entropic barrier to knotting (Soler et al., 2016), while intermolecular hydrophobic interactions established between the protein and the chaperonin surface decrease the melting temperature, which facilitates the unfolding of trapped intermediates (Especial et al., 2019). Additionally, it has been proposed, based on molecular simulations, that ribosomes can assist the folding of knotted proteins by actively forcing the positioning of the knotting loop in a way that allows for a penetration by the threading segment (Chwastyk and Cieplak, 2015; Dabrowski-Tumanski et al., 2018a).

Conclusion

The principles of protein folding have been established from results obtained for small, single-domain proteins (∼100 amino acids long) that fold fast, and in the absence of detectable intermediate states. These proteins, however, do not represent the majority of proteins in a cell's proteome, with the average protein featuring ∼450 amino acids. Moreover, these results derive from studies framed on computer simulations of single chains, and from experiments *in vitro* where folding occurs in ideal conditions, at high dilution, in the simulated environment of the test tube.

The cell offers a completely different environment, with the cellular cytoplasm being highly crowded, with macromolecular concentrations ranging between 200 and 400 mg/ml (Fig. 7A). It is inevitable to wonder whether these assumptions may be oversimplifying, in the sense that system size and cellular environment may change the analysis at a fundamental level (Frembgen-Kesner and Elcock, 2013; Ostrowska et al., 2019).

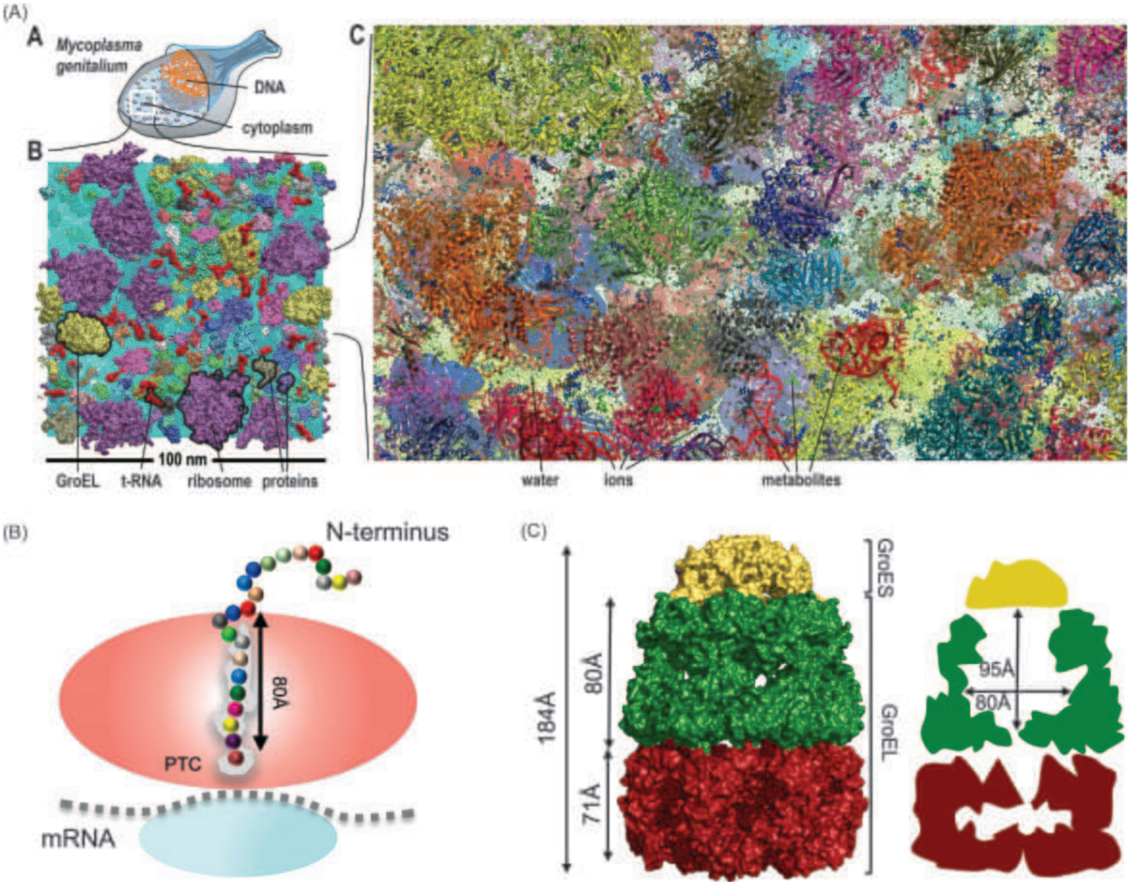

Fig. 7 Folding *in vivo*. Model of bacterial cytoplasm represented with atomistic detail and highlighting the presence of proteins, the chaperonin GroEL, the ribosome and t-RNA (A). Schematics of the ribosome's cross-sectional showing the exit tunnel, the channel through which nascent polypeptide chains emerge as they are synthesized, and the peptidyl transferase center (PTC), which catalyzes the two principal chemical reactions of protein synthesis: peptide bond formation and peptide release (B). Three-dimensional representation of the *E. coli* chaperonin GroEL-GroES complex (PDB ID: 1aon) (C) and cross-sectional view highlighting the cavity dimensions (D). The GroEL-GroES complex can accommodate proteins with up to 60 kDa (∼550 amino acids). (A) Reprinted from Yu I, Mori T, Ando T, Harada R, Jung J, Sugita Y, and Feig M (2016) Biomolecular interactions modulate macromolecular structure and dynamics in atomistic model of a bacterial cytoplasm. *eLife* 5: e19274 with permission (CC-BY license).

Large proteins, often comprising multiple domains and subdomains, are expected to have complex folding processes with multiple folding routes and populate stable intermediate states. Additionally, is more likely that their folding process is initiated during synthesis on the ribosome (Waudby et al., 2019) (Fig. 7B). Furthermore, recent experimental evidence supports the view that, for large proteins, folding may be context dependent, which means that it may be not exclusively governed by the primary sequence. Is it possible that different, still unidentified physical principles may be at play in the folding of large proteins?

In the cellular milieu protein molecules are exposed to excluded volume interactions and become highly vulnerable to establish intermolecular interactions with other molecular species. The combination of these effects may affect native state stability, which becomes context dependent, and not intrinsically determined by primary sequence. Is it possible that the crowded, diverse cellular environment may be more than a neutral background for folding? (Yu et al., 2016) As we have seen in the case of knotted proteins, cellular components (including the ribosome and the chaperonin) (Fig. 7C and D) do affect the folding process. It remains to be ascertained up to which extent the physical constraints they impose, and the intermolecular interactions they induce alter the folding process with consequences for the folding code and for the principles that govern protein folding.

Research in protein folding will be inevitably shaped, perhaps dominated, by these kinds of ever more complex questions. Hopefully, AI research will evolve into physics-informed AI, whereby physical models can be transformed into descriptors within a machine learning framework, offering a promising route to establish "fundamental laws" for protein folding (Chen et al., 2023).

Acknowledgments

Work supported by UID/MULTI/04046/2020 Research Unit grant from FCT, Portugal (through BioISI).

References

Abkevich VI, Gutin AM, and Shakhnovich EI (1994) Specific nucleus as the transition state for protein folding: Evidence from the lattice model. *Biochemistry* 33: 10026–10036.
Anfinsen CB (1973) Principles that govern the folding of protein chains. *Science* 181: 223–230.
Anson ML and Mirsky AE (1934) The equilibria between native and denatured hemoglobin in salicylate solutions and the theoretical consequences of the equilibrium between native and denatured protein. *Journal of General Physiology* 17: 399–408.
Baker D (2019) What has de novo protein design taught us about protein folding and biophysics? *Protein Science* 28: 678–683.
Baker D and Agard DA (1994) Kinetics versus thermodynamics in protein folding. *Biochemistry* 33: 7505–7509.
Best RB and Hummer G (2016) Microscopic interpretation of folding ϕ-values using the transition path ensemble. *Proceedings of the National Academy of Sciences* 113: 3263–3268.
Bölinger D, Sułkowska JI, Hsu H-P, Mirny LA, Kardar M, Onuchic JN, and Virnau P (2010) A Stevedore's protein knot. *PLoS Computational Biology* 6: e1000731.
Chan HS, Shimizu S, and Kaya H (2004) Cooperativity principles in protein folding. *Methods in Enzymology* 380: 350–379.
Chen S-J, Hassan M, Jernigan RL, Jia K, Kihara D, Kloczkowski A, Kotelnikov S, Kozakov D, Liang J, Liwo A, Matysiak S, Meller J, Micheletti C, Mitchell JC, Mondal S, Nussinov R, Okazaki K-I, Padhorny D, Skolnick J, Sosnick TR, Stan G, Vakser I, Zou X, and Rose GD (2023) Protein folds vs. protein folding: Differing questions, different challenges. *Proceedings of the National Academy of Sciences* 120: e2214423119.
Chiti F and Dobson CM (2006) Protein misfolding, functional amyloid, and human disease. *Annual Review of Biochemistry* 75: 333–366.
Chiti F and Dobson CM (2009) Amyloid formation by globular proteins under native conditions. *Nature Chemical Biology* 5: 15–22.
Chwastyk M and Cieplak M (2015) Cotranslational folding of deeply knotted proteins. *Journal of Physics: Condensed Matter* 27: 354105.
Dabrowski-Tumanski P, Piejko M, Niewieczerzal S, Stasiak A, and Sulkowska JI (2018a) Protein knotting by active threading of nascent polypeptide chain exiting from the ribosome exit channel. *The Journal of Physical Chemistry B* 122: 11616–11625.
Dabrowski-Tumanski P, Rubach P, Goundaroulis D, Dorier J, Sułkowski P, Millett KC, Rawdon EJ, Stasiak A, and Sulkowska JI (2018b) KnotProt 2.0: A database of proteins with knots and other entangled structures. *Nucleic Acids Research* 47: D367–D375.
Daggett V and Fersht AR (2003) Is there a unifying mechanism for protein folding? *Trends in Biochemical Sciences* 28: 18–25.
Darby N and Creighton TE (1995) Disulfide bonds in protein folding and stability. In: Shirley BA (ed.) *Protein Stability and Folding: Theory and Practice*. Totowa, NJ: Humana Press.
Dill KA (1985) Theory for the folding and stability of globular proteins. *Biochemistry* 24: 1501–1509.
Dill KA (1999) Polymer principles and protein folding. *Protein Science* 8: 1166–1180.
Dill KA and Chan HS (1997) From Levinthal to pathways to funnels. *Nature Structural & Molecular Biology* 4: 10–19.
Dill KA and Maccallum JL (2012) The protein-folding problem, 50 years On. *Science* 338: 1042–1046.
Dill KA, Bromberg S, Yue K, Chan HS, Ftebig KM, Yee DP, and Thomas PD (1995) Principles of protein folding — A perspective from simple exact models. *Protein Science* 4: 561–602.
Dror RO, Young C, and Shaw DE (2011) Anton, a special-purpose molecular simulation machine. In: Padua D (ed.) *Encyclopedia of Parallel Computing*. Boston, MA: Springer US.
Englander SW, Mayne L, Kan Z-Y, and Hu W (2016) Protein folding—How and why: By hydrogen exchange, fragment separation, and mass spectrometry. *Annual Review of Biophysics* 45: 135–152.
Especial JNC and Faísca PFN (2021) A specific set of heterogeneous native interactions yields efficient knotting in protein folding. *The Journal of Physical Chemistry B* 125: 7359–7367.
Especial J, Nunes A, Rey A, and Faísca PFN (2019) Hydrophobic confinement modulates thermal stability and assists knotting in the folding of tangled proteins. *Physical Chemistry Chemical Physics* 21: 11764–11775.
Estácio SG, Krobath H, Vila-Viçosa D, Machuqueiro M, Shakhnovich EI, and Faísca PFN (2014) A simulated intermediate state for folding and aggregation provides insights into ΔN6 β2-microglobulin amyloidogenic behavior. *PLoS Computational Biology* 10: e1003606.
Faísca PFN (2009) The nucleation mechanism of protein folding: A survey of computer simulation studies. *Journal of Physics: Condensed Matter* 21: 373102.
Faísca PFN (2015) Knotted proteins: A tangled tale of Structural Biology. *Computational and Structural Biotechnology Journal* 13: 459–468.
Faisca PFN and Ball RC (2002a) Thermodynamic control and dynamical regimes in protein folding. *The Journal of Chemical Physics* 116: 7231–7237.
Faisca PFN and Ball RC (2002b) Topological complexity, contact order, and protein folding rates. *The Journal of Chemical Physics* 117: 8587–8591.

Faísca PFN, Travasso RMD, Charters T, Nunes A, and Cieplak M (2010) The folding of knotted proteins: Insights from lattice simulations. *Physical Biology* 7: 016009.

Faísca PFN, Travasso RDM, Parisi A, and Rey A (2012) Why do protein folding rates correlate with metrics of native topology? *PLoS One* 7: e35599.

Finkelstein AV and Galzitskaya OV (2004) Physics of protein folding. *Physics of Life Reviews* 1: 23–56.

Flamholz A, Phillips R, and Milo R (2014) The quantified cell. *Molecular Biology of the Cell* 25: 3497–3500.

France DTJJPI (1995) From minimal models to real proteins: Time scales for protein folding kinetics. *Journal de Physique I* 5: 1457–1467.

Frembgen-Kesner T and Elcock AH (2013) Computer simulations of the bacterial cytoplasm. *Biophysical Reviews* 5: 109–119.

Galzitskaya OV, Garbuzynskiy SO, Ivankov DN, and Finkelstein AV (2003) Chain length is the main determinant of the folding rate for proteins with three-state folding kinetics. *Proteins: Structure, Function, and Bioinformatics* 51: 162–166.

Gershenson A, Gosavi S, Faccioli P, and Wintrode PL (2020) Successes and challenges in simulating the folding of large proteins. *Journal of Biological Chemistry* 295: 15–33.

Guo M, Xu Y, and Gruebele M (2012) Temperature dependence of protein folding kinetics in living cells. *Proceedings of the National Academy of Sciences* 109: 17863–17867.

Hayer-Hartl M, Bracher A, and Hartl FU (2016) The GroEL–GroES chaperonin machine: A nano-cage for protein folding. *Trends in Biochemical Sciences* 41: 62–76.

Hingorani KS and Gierasch LM (2014) Comparing protein folding in vitro and in vivo: foldability meets the fitness challenge. *Current Opinion in Structural Biology* 24: 81–90.

Ho B, Baryshnikova A, and Brown GW (2018) Unification of protein abundance datasets yields a quantitative *Saccharomyces cerevisiae* proteome. *Cell Systems* 6: 192–205.e3.

Hu W, Walters BT, Kan Z-Y, Mayne L, Rosen LE, Marqusee S, and Englander SW (2013) Stepwise protein folding at near amino acid resolution by hydrogen exchange and mass spectrometry. *Proceedings of the National Academy of Sciences* 110: 7684–7689.

Itzhaki LS, Otzen DE, and Fersht AR (1995) The structure of the transition state for folding of chymotrypsin inhibitor 2 analysed by protein engineering methods: Evidence for a nucleation-condensation mechanism for protein folding. *Journal of Molecular Biology* 254: 260–288.

Ivankov DN, Garbuzynskiy SO, Alm E, Plaxco KW, Baker D, and Finkelstein AV (2003) Contact order revisited: Influence of protein size on the folding rate. *Protein Science* 12: 2057–2062.

Jackson SE (1998) How do small single-domain proteins fold? *Folding and Design* 3: R81–R91.

Jackson S (2020) Why are there knots in proteins? *Contemporary Mathematics* 746: 129–174.

Jackson SE, Suma A, and Micheletti C (2017) How to fold intricately: Using theory and experiments to unravel the properties of knotted proteins. *Current Opinion in Structural Biology* 42: 6–14.

Jumper J, Evans R, Pritzel A, Green T, Figurnov M, Ronneberger O, Tunyasuvunakool K, Bates R, Žídek A, Potapenko A, Bridgland A, Meyer C, Kohl SAA, Ballard AJ, Cowie A, Romera-Paredes B, Nikolov S, Jain R, Adler J, Back T, Petersen S, Reiman D, Clancy E, Zielinski M, Steinegger M, Pacholska M, Berghammer T, Bodenstein S, Silver D, Vinyals O, Senior AW, Kavukcuoglu K, Kohli P, and Hassabis D (2021) Highly accurate protein structure prediction with AlphaFold. *Nature* 596: 583–589.

Karplus M and Weaver DL (1979) Diffusion–collision model for protein folding. *Biopolymers: Original Research on Biomolecules* 18: 1421–1437.

Kaya H and Chan HS (2003) Contact order dependent protein folding rates: Kinetic consequences of a cooperative interplay between favorable nonlocal interactions and local conformational preferences. *Proteins: Structure, Function, and Bioinformatics* 52: 524–533.

King NP, Jacobitz AW, Sawaya MR, Goldschmidt L, and Yeates TO (2010) Structure and folding of a designed knotted protein. *Proceedings of the National Academy of Sciences* 107: 20732–20737.

Kmiecik S, Gront D, Kolinski M, Wieteska L, Dawid AE, and Kolinski A (2016) Coarse-grained protein models and their applications. *Chemical Reviews* 116: 7898–7936.

Krobath H, Estácio SG, Faísca PFN, and Shakhnovich EI (2012) Identification of a conserved aggregation-prone intermediate state in the folding pathways of Spc-SH3 amyloidogenic variants. *Journal of Molecular Biology* 422: 705–722.

Le Marchand T, De Rosa M, Salvi N, Sala BM, Andreas LB, Barbet-Massin E, Sormanni P, Barbiroli A, Porcari R, Sousa Mota C, De Sanctis D, Bolognesi M, Emsley L, Bellotti V, Blackledge M, Camilloni C, Pintacuda G, and Ricagno S (2018) Conformational dynamics in crystals reveal the molecular bases for D76N beta-2 microglobulin aggregation propensity. *Nature Communications* 9: 1658.

Levinthal C (1968) Are there pathways for protein folding? *Journal de Chimie Physique* 65: 44–45.

Levinthal C (1969) How to fold graciously. In: Debrunnder JTP and Munck E (eds.) *, Mossbauer Spectroscopy in Biological Systems: Proceedings of a meeting held at Allerton House, Monticello, Illinois*, pp. 22–24. University of Illinois Press.

Lim NCH and Jackson SE (2015) Mechanistic insights into the folding of knotted proteins in vitro and in vivo. *Journal of Molecular Biology* 427: 248–258.

Loureiro RJS, Vila-Viçosa D, Machuqueiro M, Shakhnovich EI, and Faísca PFN (2017) A tale of two tails: The importance of unstructured termini in the aggregation pathway of β2-microglobulin. *Proteins: Structure, Function, and Bioinformatics* 85: 2045–2057.

Lua RC and Grosberg AY (2006) Statistics of knots, geometry of conformations, and evolution of proteins. *PLoS Computational Biology* 2: e45.

Makarov DE and Plaxco KW (2003) The topomer search model: A simple, quantitative theory of two-state protein folding kinetics. *Protein Science* 12: 17–26.

Mallam AL and Jackson SE (2012) Knot formation in newly translated proteins is spontaneous and accelerated by chaperonins. *Nature Chemical Biology* 8: 147–153.

Naganathan AN and Muñoz V (2005) Scaling of folding times with protein size. *Journal of the American Chemical Society* 127: 480–481.

Nassar R, Dignon GL, Razban RM, and Dill KA (2021) The protein folding problem: The role of theory. *Journal of Molecular Biology* 433: 167126.

Neudecker P, Robustelli P, Cavalli A, Walsh P, Lundström P, Zarrine-Afsar A, Sharpe S, Vendruscolo M, and Kay LE (2012) Structure of an intermediate state in protein folding and aggregation. *Science* 336: 362–366.

Noel JK, Onuchic JN, and Sulkowska JI (2013) Knotting a protein in explicit solvent. *The Journal of Physical Chemistry Letters* 4: 3570–3573.

Oliveberg M, Tan YJ, and Fersht AR (1995) Negative activation enthalpies in the kinetics of protein folding. *Proceedings of the National Academy of Sciences* 92: 8926–8929.

Onuchic JN, And ZL-S, and Wolynes PG (1997) Theory of protein folding: The energy landscape perspective. *Annual Review of Physical Chemistry* 48: 545–600.

Ostrowska N, Feig M, and Trylska J (2019) Modeling crowded environment in molecular simulations. *Frontiers in Molecular Biosciences*: 6.

Outeiral C, Nissley DA, and Deane CM (2022) Current structure predictors are not learning the physics of protein folding. *Bioinformatics* 38: 1881–1887.

Perlinska AP, Niemyska WH, Gren BA, Bukowicki M, Nowakowski S, Rubach P, and Sulkowska JI (2023) AlphaFold predicts novel human proteins with knots. *Protein Science* 32: e4631.

Plaxco KW, Simons KT, Ruczinski I, and Baker D (2000) Topology, stability, sequence, and length: Defining the determinants of two-state protein folding kinetics. *Biochemistry* 39: 11177–11183.

Ptitsyn OB (1995) Molten globule and protein folding. In: Anfinsen CB, Richards FM, Edsall JT, and Eisenberg DS (eds.) *Advances in Protein Chemistry*. Academic Press.

Richardson JS (1977) [beta]-Sheet topology and the relatedness of proteins. *Nature* 268: 495–500.

Rollins GC and Dill KA (2014) General mechanism of two-state protein folding kinetics. *Journal of the American Chemical Society* 136: 11420–11427.

Roney JP and Ovchinnikov S (2022) State-of-the-art estimation of protein model accuracy using AlphaFold. *Physical Review Letters* 129: 238101.

Rose GD (2021) Protein folding - seeing is deceiving. *Protein Science* 30: 1606–1616.

S˘ali A, Shakhnovich E, and Karplus M (1994) How does a protein fold? *Nature* 369: 248–251.

Saibil H (2013) Chaperone machines for protein folding, unfolding and disaggregation. *Nature Reviews Molecular Cell Biology* 14: 630–642.

Shakhnovich EI and Gutin AM (1993) Engineering of stable and fast-folding sequences of model proteins. *Proceedings of the National Academy of Sciences* 90: 7195–7199.

Shaw DE, Maragakis P, Lindorff-Larsen K, Piana S, Dror RO, Eastwood MP, Bank JA, Jumper JM, Salmon JK, Shan Y, and Wriggers W (2010) Atomic-level characterization of the structural dynamics of proteins. *Science* 330: 341–346.

Sjölin K, Kultima K, Larsson A, Freyhult E, Zjukovskaja C, Alkass K, and Burman J (2022) Distribution of five clinically important neuroglial proteins in the human brain. *Molecular Brain* 15: 52.

Soler MA, Nunes A, and Faísca PFN (2014) Effects of knot type in the folding of topologically complex lattice proteins. *The Journal of Chemical Physics* 141: 025101.

Soler MA, Rey A, and Faisca PFN (2016) Steric confinement and enhanced local flexibility assist knotting in simple models of protein folding. *Physical Chemistry Chemical Physics* 18: 26391–26403.
Sorokina I and Mushegian A (2018) Modeling protein folding in vivo. *Biology Direct* 13: 13.
Sułkowska JI, Sułkowski P, and Onuchic J (2009) Dodging the crisis of folding proteins with knots. *Biophysical Journal* 106: 3119–3124.
Taverna DM and Goldstein RA (2002) Why are proteins marginally stable? *Proteins: Structure, Function, and Bioinformatics* 46: 105–109.
Taylor WR (2000) A deeply knotted protein structure and how it might fold. *Nature* 406: 916–919.
Wallin S, Zeldovich KB, and Shakhnovich EI (2007) The folding mechanics of a knotted protein. *Journal of Molecular Biology* 368: 884–893.
Wang Z, Mottonen J, and Goldsmith EJ (1996) Kinetically controlled folding of the serpin plasminogen activator inhibitor 1. *Biochemistry* 35: 16443–16448.
Wang Y, Zhang H, Zhong H, and Xue Z (2021) Protein domain identification methods and online resources. *Computational and Structural Biotechnology Journal* 19: 1145–1153.
Waudby CA, Dobson CM, and Christodoulou J (2019) Nature and regulation of protein folding on the ribosome. *Trends in Biochemical Sciences* 44: 914–926.
Wetlaufer DB (1973) Nucleation, Rapid Folding, and Globular Intrachain Regions in Proteins. *Proceedings of the National Academy of Sciences* 70: 697–701.
Yu I, Mori T, Ando T, Harada R, Jung J, Sugita Y, and Feig M (2016) Biomolecular interactions modulate macromolecular structure and dynamics in atomistic model of a bacterial cytoplasm. *eLife* 5: e19274.
Zhou Y, Hall CK, and Karplus M (1999) The calorimetric criterion for a two-state process revisited. *Protein Science* 8: 1064–1074.

How protein fold: Insights from nuclear magnetic resonance spectroscopy

Anastasia Zhuravelva, School of Molecular and Cellular Biology, Faculty of Biological Sciences & Astbury Centre for Structural Molecular Biology, University of Leeds, Leeds, United Kingdom

© 2024 Elsevier Ltd. All rights reserved.

Introduction 619
Basic principles of NMR 621
NMR approaches to characterize protein folding 623
Challenges and limitations 629
Conclusion 630
Acknowledgments 630
References 630

Abstract

Many devastating diseases are linked to an imbalance in protein folding. Efficient and correct protein folding is crucial for protein functions, including catalysis, molecular recognition, molecular transport, and cellular signaling. Additionally, if protein folding is unsuccessful or the protein cannot remain in its folded state, the accumulation of misfolded species results in many pathological conditions, including neurodegenerative diseases, cancers, diabetes, and cardiovascular diseases. Not surprisingly, despite advances in our understanding of protein folding, it remains one of the fundamental questions in biology and biomedicine. Here, I discuss current experimental approaches for the characterization of protein folding using solution Nuclear Magnetic Resonance (NMR) spectroscopy.

Key points

- A non-expert introduction to the basic concepts of protein folding
- A non-expert review of the main strategies for the characterization of protein folding by NMR
- Discussion of the latest developments and limitations

Introduction

The understanding of protein folding (a process by which a polypeptide chain spontaneously folds to a specific 3D conformation called a native state) has provided critical insights into the fundamental principles of life and helped develop new therapeutics for protein-folding diseases. One of the central dogmas of the protein folding field, formulated by Christian Anfinsen in 1962 (Anfinsen et al., 1961; Anfinsen, 1972, 1973), states that the 3D structure of a protein is uniquely determined by its amino acid sequence and is stabilized by the non-covalent interactions between amino acids. As a result, in a physiological environment, the protein will spontaneously fold into its native conformation driven by the minimization of its free energy. However, given the complexity of a protein molecule, if a protein has to sample all possible conformations to find the free energy minimum, the time required for the protein to fold to its native conformation through a random search would be far longer than the age of the Universe. This paradox was first described by Cyrus Levinthal in 1969 (Levinthal, 1969), who questioned why proteins fold so quickly [the characteristic times for protein folding are μs–seconds (Kubelka et al., 2004)] and efficiently despite the vast number of possible conformations that they can adopt. It now has been widely accepted that while driven by the minimization of the protein's free energy (as described by Anfinsen's 'thermodynamic dogma'), proteins fold through a series of intermediate states called the protein folding pathway (Dill and Chan, 1997). Different proteins have different levels of complexity of their protein folding pathways (Mecha et al., 2022; Nassar et al., 2021) that range (depending on protein size and sequence) from a simple, one-step folding directly into a native state without passing through intermediate structures to the complex, multistep process that requires the formation of multiple intermediates. These intermediates are essential stepping stones toward the native structure, directing and facilitating the folding process (Brockwell and Radford, 2007).

In general, the protein folding pathway can be described in terms of a funnel-shaped protein folding landscape (Fig. 1) that represents the relationship between the protein's conformational space (entropy) and its free energy (Dill, 1985; Dill and Chan, 1997; Leopold et al., 1992; Tsai et al., 1999; Roder and Wales, 2022; Karplus, 2011). The protein folding process can be considered as a search for the native state (representing the lowest free energy and entropy minima) from a disordered state(s) (representing the highest free energy and entropy). Together with global minima (native states), the protein folding landscape also includes local minima that represent multiple, on-pathway intermediates (ones that contain native-like contacts and support protein folding), as well as off-pathway (non-productive) intermediates and misfolded/aggregation-prone states. By competing with the native state(s) and on-pathway intermediates kinetically and/or thermodynamically, the off-pathway states often determine the rate

https://doi.org/10.1016/B978-0-323-90800-9.00246-8

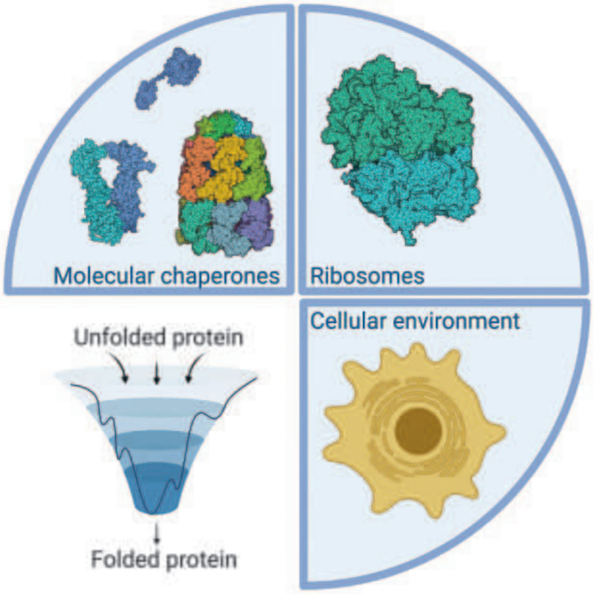

Fig. 1 *The complexity of protein folding:* The protein folding energy landscape consists of various folding intermediates that a protein can adopt before reaching its native (folded) state. As a nascent polypeptide chain emerges from the ribosome, it is exposed to the cellular environment that can significantly impact protein folding by modulation the stability of intermediates, promoting or hindering specific folding pathways, and influencing the kinetics of the folding process. Interactions with ribosomes and ribosome-associated chaperones can guide protein folding and prevent misfolding. The binding and release of molecular chaperones at different stages of folding ensure the fidelity of the folding process. Created with BioRender.com.

and efficiency of protein folding (Brockwell and Radford, 2007). Moreover, by decreasing the kinetic barriers of off-pathway reactions, the off-pathway states can favor protein aggregation, a (irreversible) process by which individual protein molecules come together to form large insoluble structures. These insoluble species are often thermodynamically more stable than native states (Mecha et al., 2022). The formation of such aggregates (e.g., amyloid fibrils) is thought to be a key factor in progression of many protein folding diseases, including Alzheimer's disease, Parkinson's disease and type II diabetes (Knowles et al., 2014; Chiti and Dobson, 2017; Hartl, 2017; Tittelmeier et al., 2020).

Many amylogenic proteins, including amyloid-β, tau, and α-synuclein, are fully or partially intrinsically disordered (Bowman et al., 2020; Pauwels et al., 2017). Unlike globular proteins that adopt one or few folded conformations, about 30–50% of eukaryotic proteins remain intrinsically disordered in solution or contain intrinsically disordered regions (IDRs) longer than 30 residues (Dunker et al., 2000; Bondos et al., 2021). How these proteins can perform specific biological functions without adopting a well-defined structure remains highly elusive. Interestingly, IDP conformational heterogeneity and flexibility are essential for IDP functions such cellular signaling and gene regulation as it enables multivalent interactions with several binding partners and IDP functional diversity (Uversky, 2021). The multifunctionality of many IDPs is based on their ability to fold into well-defined structures as a response to external triggers such as binding to small molecule ligands, communication with other proteins or post-translational modifications (Uversky, 2021; Wright and Dyson, 2009; Piersimoni et al., 2022). However, this conformational flexibility also has an important disadvantage as it increases the ability to misfold and aggregate.

Protein folding and misfolding are also influenced by mutations or/and environmental factors such as pH, temperature, pressure or salt concentrations. Understanding how environmental factors affect the folding process is a critical question to be addressed (Braselmann et al., 2013). Inside the living cell, the crowding environment, physiological and pathological stresses, and unspecific and specific interactions with other macromolecules and/or small molecules make protein folding even more complicating (Gershenson and Gierasch, 2011; Qin and Zhou, 2017; Hingorani and Gierasch, 2014; Braselmann et al., 2013). Unsurprisingly, most proteins require special folding machines called molecular chaperones that ensure efficient protein folding under normal and stress conditions (Hartl et al., 2011; Jayaraj et al., 2020; Wilson et al., 2023). Molecular chaperones are key players in protein quality control (PQC) that act at different stages of the protein folding process to ensure the formation of the native state(s) from a newly synthesized nascent chain. They also maintain the integrity of proteins by detecting misfolded proteins, refolding them or delivering them to the degradative enzymes (Torner et al., 2022; Tittelmeier et al., 2020). Not surprisingly, protein misfolding and aggregation are usually linked to a failure of the PQC machinery to maintain protein homeostasis inside the cells (Hartl, 2017; Hartl et al., 2011).

There are more than 300 types of molecular chaperones in human cells (Jayaraj et al., 2020) that work synergistically and sequentially to endure that proteins inside the cell are correctly folded and functional in health and under specific environmental and metabolic conditions (reviewed elsewhere (Hartl et al., 2011, Jayaraj et al., 2020)). For example, Hsp70 chaperones bind to newly synthesized nascent chains, preventing non-functional interactions and the formation of off-pathway intermediates (Mayer and Gierasch, 2019). Following Hsp70 acting, Hsp90 (Moran Luengo et al., 2019) and Hsp60 (Hayer-Hartl et al., 2016; Gestaut et al., 2019) chaperones recognize and interact with later folding intermediates, stabilizing them and providing a favorable environment for folding. Other molecular chaperones (e.g., Hsp104 and its prokaryotic homolog ClpB) play an important role in the degradation of misfolded proteins and aggregates, ensuring that these toxic species do not interfere with cellular processes (Lin et al., 2022; Fauvet et al., 2021). The molecular chaperones are dynamic molecular machines that undergo ATP-dependent (e.g., Hsp70, Hsp90, Hsp100) or ATP-independent (e.g., small heat shock proteins or sHSPs, trigger factor) conformational changes to control the affinity and specificity of binding to their client (unfolded) proteins (Balchin et al., 2016). Understanding the mechanisms by which molecular chaperones recognize their client protein substrate and synergistically assist their folding is another key research area in the field.

Nuclear Magnetic resonance (NMR) spectroscopy has been one of the central tools to characterize protein folding both *in vitro* and *in vivo* (Zhuravleva and Korzhnev, 2017; Cawood et al., 2021; Alderson and Kay, 2021; Dyson and Wright, 2005). Solution NMR is particularly powerful in the elucidation of molecular details about complex protein folding pathways, including the characterization of short-living intermediate states that populated during the protein folding process and transient aggregation-prone folded conformations (Alderson and Kay, 2021). Recent developments in fast acquisition methods (including non-uniform sampling and processing algorithms) allows real-time characterization of folding processes with the ms resolution (Kremer et al., 2011; Charlier et al., 2018a; Pinter and Schwalbe, 2020). Furthermore, the development of new labeling scheme (deuteration, methyl NMR, ^{19}F-labeling) and NMR experiments dedicated for characterization of large proteins (Arthanari et al., 2019), enables characterization of complexes between molecular chaperones and their unfolded protein clients (Karamanos and Clore, 2022), nascent chain folding on ribosomes (Waudby et al., 2022) and even inside the living cells (Luchinat et al., 2022). NMR, together with other state-of-the-art biophysical techniques, allows some of the complexity of protein folding now beginning to be unraveled. This report provides an overview for non-experts that discusses how solution NMR can be used to address key questions in the protein folding field. I highlight some recent NMR achievements that enable the characterization of the challenging and fascinating process of protein folding.

Basic principles of NMR

For the first time (in 1946), nuclear magnetic resonances were reported by Bloch et al. (1946) and Purcell et al. (1946). Since then, NMR has become one of the most powerful techniques to investigate inorganic and organic molecules and complex biological systems such as multidomain proteins, protein complexes, enzymes, allostery, dynamic interactions between macromolecules and more. The physical principles of NMR are based on the quantum mechanics of nuclear spin angular momentum and have been reviewed in detail elsewhere (Cavanagh et al., 2006). This chapter provides a brief, simplistic overview of the basic NMR terminology.

Spin magnetic momentum: Bio-NMR is a spectroscopic technique that allows observation of NMR active nuclei in biological macromolecules. Atoms with spin ½, such as ^{1}H, ^{13}C, ^{15}N, ^{19}F and ^{31}P, are usually used for bio-NMR due to their favorable relaxation properties. When a nucleus with a spin ½ is inserted into an external magnetic field B_0 (an NMR spectrometer), its spin magnetic momentum begins to move on a cone around the magnetic field, keeping a constant angle between the spin magnetic momentum and the field. The frequency of these motions (precession), called Larmor frequency, is proportional to the magnetic field and equal to:

$$\omega_0 = \frac{\Delta E}{\hbar} = -\gamma B_0,$$

whether γ is a characteristic constant for a given nucleus, called a gyromagnetic ratio; $\hbar$ is a Plank's constant; and ΔE is the energy level splitting of the spin in a magnetic field B_0 (called Zeeman splitting).

Chemical shift: Although atoms and molecules vigorously move around in solution, it has little effect on the precession of a spin angular momentum for a specific nucleus as it only depends on the magnetic field. However, due to these fluctuations, the surrounding electrons and nuclei produce a small, rapidly fluctuating magnetic field that is slightly different from the external (static) magnetic field in amplitude and direction. As a result, the local magnetic field around a specific nucleus rapidly fluctuates, resulting in a shielding effect which depends on electron density and electronegativity of neighboring groups. Consequently, a spin resonates at a unique (different from other spins of the same type) frequency that depends on its local (chemical) environment. These small, environment-induced differences are referred to as a chemical shift that can be defined as:

$$\delta = \frac{v - v_{ref}}{\omega_0} \times 10^6,$$

whether v is a resonance frequency of an atomic nucleus, v_{ref} is a reference frequency from a standard molecule, and ω_0 is the Larmor frequency of the corresponding atom type. Chemical shifts are independent of the static (external) magnetic field and measured in parts per million (ppm). Chemical shifts can be also converted to Hz (usually referred to ω) by multiplying the chemical shift value in ppm (δ) by ω_0. Because chemical shifts reflect the local (chemical) environment around a specific nucleus, they can be used to extract information about a molecule's local and global structure and dynamics. In turn, changes in chemical shits allow monitoring of chemical reactions (e.g., phosphorylation, ATP hydrolysis, etc.), binding to a small molecule ligand or a macromolecule, as well as structural and dynamic changes (e.g., due to local or global unfolding) upon external perturbations such as mutations, changes in temperature or pH, and ligand binding.

Relaxation: While in the absence of the magnetic field, all nuclear spin orientations are equally likely, when the external magnetic field is turned on, the bulk longitudinal (along the external field) magnetization is gradually built on with the relaxation time constant T_1. T_1 relaxation occurs due to angular fluctuations of relaxation-active interactions resulting in transitions that return the spin state back to equilibrium. Similarly, the longitudinal magnetization will gradually return to zero if the field is switched off. In turn, after being created by a radio frequency pulse, the transverse magnetization (that is perpendicular to the external field) follows a single exponential decay with the time constant T_2. This happens due to the loss of phase coherence in the xy plane over time. The T_2 relaxation limits the duration of the NMR acquisition as the detected signal decays to zero over time; in a frequency NMR spectrum, T_2 determines the broadness of the peak that has width is equal to $1/(\pi T_2)$. Many modern NMR techniques [e.g., amide- and methyl-TROSY (transverse relaxation optimized spectroscopy)] exploit favorable relaxation properties of specific transitions to improve the sensitivity and resolution of NMR spectra, enabling characterization of large biological molecules that have a small T_2 (fast relaxation) and, as a result, a low sensitivity if traditional techniques are used for their characterization. Because T_1 and T_2 depend on the size of a molecule, internal motions of a nucleus, and external parameters such as temperature and viscosity, their measurements have been widely used to characterize protein conformational dynamics.

Chemical exchange: Consider that the protein of interest can co-exist in two conformations: the ground (native) state A and a low-populated (folded intermediate) state B. The two states undergo conformational exchange $A \underset{k_{BA}}{\overset{k_{AB}}{\rightleftarrows}} B$ with the exchange constant: $k_{ex} = k_{AB} + k_{BA}$. To calculate the population of states A and B, we can use the Boltzmann distribution (Neudecker et al., 2009):

$$\frac{p_A}{p_b} = \frac{k_{AB}}{k_{BA}} = e^{-\frac{\Delta G_{A \to B}(T)}{RT}},$$

where $p_A = k_{BA}/k_{ex}$ and $p_B = k_{AB}/k_{ex}$ are the populations of states A and B, respectively; R is the gas constant; and T is the absolute temperature. If there is no exchange between these two states (or exchange is slow on the NMR timescale) and the populations of both states are sufficiently large to be observed by NMR, two peaks appear in an NMR spectrum with chemical shifts ω_A and ω_B. If the exchange between the A and B states is significantly faster than the difference between ω_A and ω_B (fast on the NMR timescale), the precession frequency of an observed spin will change between ω_A and ω_B, resulting in one peak in the NMR spectrum with a chemical shift equal to the population-weighted average of ω_A and ω_B. In the case of intermediate exchange (if the exchange rate is comparable with the difference between ω_A and ω_B), the exchange process significant increases the transverse relaxation rate constant ($R_2 = 1/T_2$), resulting in broadening of peaks in the NMR spectrum. Different NMR techniques can study this contribution in the transverse relaxation to extract information about rate constants of different exchange processes as well populations and chemical shifts of exchangeable states (Clore, 2022; Anthis and Clore, 2015).

Magnetization transfer: All modern bio-NMR techniques measure the response of nuclear spins to a radio frequency (rf) pulse that irradiates the sample with a frequency close to the Larmor frequency of the specific nucleus to create desired nuclear magnetization. Most NMR experiments consist of more than one rf pulse divided by variable delays during which the selected magnetization is allowed to evolve and transfer between NMR active nuclei in specific ways. This approach allows magnetization transfer between different atoms, enabling multidimensional homonuclear and heteronuclear bio-NMR experiments. In general, the magnetization can be transferred from one nucleus to another through either covalent bond(s) connecting two nuclei or space. Magnetization transfer through bond, known as scalar or J-coupling, plays a key role in 2D and multidimensional NMR, coupling different atoms of the same type (e.g., COSY and TOCSY experiments) or different types (most 2D and multidimensional bio-NMR experiments). Magnetization can be also transferred from one nucleus to another without direct covalent bonding through cross-relaxation or spin diffusion mechanisms. When two nuclei are close together (within 6–10 Å), the magnetic field of one nucleus can affect the magnetic polarization of the other nucleus. This effect can be measured by NMR, providing information about the distance between two nuclei (NMR nuclear Overhauser effects).

Isotope labeling: Not all nuclei are NMR active, and not all NMR active nuclei have spin ½. For example, ^{12}C has spin 0 (NMR inactive) as it has six protons and six neutrons; however, its stable isotope ^{13}C has seven neutrons and six protons with a net spin of ½. Similarly, ^{14}N has spin 1 (NMR active but unsuitable for bio-NMR); however, its stable isotope ^{15}N has a spin ½. Consequently, most of the modern bio-NMR approaches require ^{15}N and/or ^{13}C labeling (Fig. 2) because proton NMR has very limited applicability due to the complexity and overlapping issues of ^{1}H NMR protein spectra. Moreover, it is challenging (if even possible) to assign NMR peaks for any protein larger than 10 kDa using ^{1}H NMR only. Heteronuclear correlation experiments improve the resolution in protein NMR spectra, facilitating the resonance assignments and interpretation of NMR data. Uniform labeling of all ^{13}C and/or ^{15}N atoms is the most commonly used approach for small protein and isolated domains (up to 20–30 kDa). However, for larger systems (>30 kDa), deuteration is usually essential to obtain good quality NMR data. For larger proteins, ^{1}H-dependent relaxation mechanisms cause a significant broadening of NMR peaks and, as a result, a drastic decrease in peak intensities. Perdeuteration (uniform substitution of all or a significant part of ^{1}H atoms with ^{2}H), in turn, significantly suppresses these effects and enables the NMR characterization of 30–200 kDa protein systems, including multidomain proteins and protein-protein complexes. Furthermore, selective $^{13}CH_3$ labeling of methyl-containing side-chains in combination with a highly deuterated background enables NMR studies of protein complexes and oligomers up to 1 MDa (Tugarinov et al., 2006).

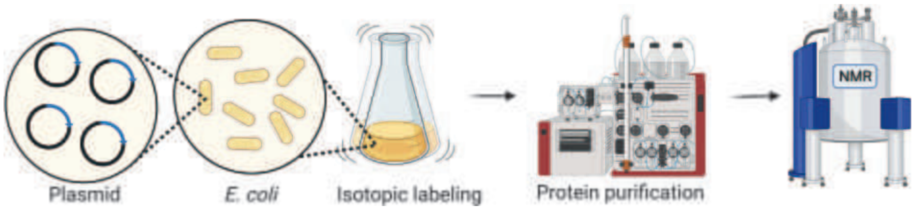

Fig. 2 *Isotopic Labeling Strategy for Protein NMR:* The protein of interest is expressed in a suitable host organism (usually *E. coli*) using a recombinant expression system; the protein needs to be produced in high yield to obtain sufficient material for NMR studies. The host organism is grown in an isotopically enriched medium. For example, ^{15}N-labeled proteins are produced by growing bacteria in a medium containing ^{15}N-labeled ammonium chloride; similarly, ^{13}C labeling is achieved by incorporating ^{13}C-labeled glucose. The isotopically labeled protein is then purified using standard techniques, such as affinity chromatography and size-exclusion chromatography, to remove other cellular components and impurities. The purified labeled protein is used for NMR experiments to provide information on protein conformation, structure, dynamics, and interactions. Created with BioRender.com.

NMR approaches to characterize protein folding

NMR for characterization of transiently populated intermediates: As discussed in Introduction, most proteins populate on- and off-pathway intermediates during their folding processes. These 'alternative' protein states are challenging to characterize due to their low populations, short life times, and conformational dynamics. However, while only transiently populated, these intermediates often play critical roles and define the efficiency of folding and, thus, protein function. Moreover, some of these intermediates have a toxic effect on a living cell or favor the formation of insoluble oligomers (Cawood et al., 2021). Consequently, understanding how and why these intermediates are formed during the folding process is an extremely challenging but fundamental task in the protein folding field. NMR is one of the most powerful techniques to tackle this challenge and has been successfully used to obtain detailed structural, kinetic and thermodynamic details about folding intermediates for several protein systems (Korzhnev and Kay, 2008; Cawood et al., 2021).

One way to characterize folding intermediate is to perform experiments under static conditions, often using destabilized protein variants, small concentrations of denaturants or high pressure or temperature to perturb the folding landscape and enable the equilibrium population of partially folded intermediates to achieve the detectible level. While, in some cases (if several sets of signals corresponding to the folded, unfolded, and intermediate states are observed in the NMR spectrum), it is possible to stabilize and characterize folding intermediates or misfolded species directly (Eliezer et al., 1998; Ropson and Frieden, 1992; Ferrolino et al., 2013; Bhatt et al., 2020; Low et al., 2008; Dreydoppel et al., 2022; Kakeshpour et al., 2021; Panova et al., 2019), such characterization of transiently(0.5–10%)-populated (as called invisible or dark) states are usually not possible due to sensitivity issues. Several NMR approaches have been developed to exploit μs-ms exchange between the major and excited (minor) states to transfer information (e.g., chemical shifts) about an 'invisible' minor state to the major state and then detect it (Fig. 3). There are three main

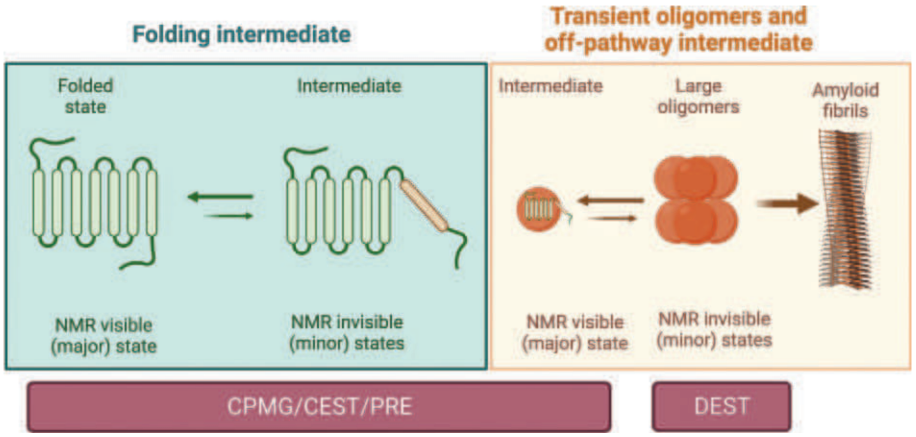
Folding intermediate
Transient oligomers and off-pathway intermediate
Folded state
Intermediate
Intermediate
Large oligomers
Amyloid fibrils
NMR visible (major) state
NMR invisible (minor) states
NMR visible (major) state
NMR invisible (minor) states
CPMG/CEST/PRE
DEST

Fig. 3 *Characterization minor, invisible protein states using advanced NMR techniques:* Folding intermediates are transient, partially folded conformations that populated during the folding process (left); they often have regions of native-like secondary structure, but their tertiary structure is not fully formed. They are typically short-lived and difficult to observe directly. Off-pathway intermediates, in turn, are conformations that deviate from the productive folding pathway, leading to non-native or misfolded states. They are often associated with the formation of higher-order protein structures such as non-functional oligomers and protein aggregates (right). Transient oligomers form through transient interactions between partially folded or misfolded intermediates. They can lead to non-native oligomeric structures, such as amorphous aggregates and amyloid fibrils. Characterization of transient oligomers can provide information about the factors and mechanisms governing protein aggregation. The advanced NMR techniques (such as CPMG, CEST, DEST, and PRE) can detect and characterize these minor protein states that are otherwise invisible to direct observation methods. Created with BioRender.com.

strategies to achieve this [reviewed in detail in (Clore, 2022, Anthis and Clore, 2015)]: (i) The relaxation dispersion (CPMG and R1ρ) experiments (partially) suppress the exchange contribution into the T_2 relaxation. The suppression level can be attenuated in the experiments, and the level of attenuation can be then fitted to extract exchange parameters, including exchange rates, populations of each states and their chemical shifts. (ii) Chemical exchange saturation transfer (CEST) is based on the saturation transfer between two exchangeable states. If the minor and major states have significantly different chemical shifts, the minor state can be selectively saturated (temporarily show no net magnetization) using rf irradiation; this saturation is transferred to the major state due to the exchange process, resulting in a signal attenuation for the major state. This attenuation can be used then to calculate the parameters of exchange. Dark state Exchange Saturation Transfer (DEST) uses the same principles but without the requirement to have different chemical shifts between the visible and invisible states. This can be achieved in case of exchange between a smaller (visible) state and a very large (invisible) oligomeric or aggregation state that has a very broad signal and, thus, can be saturated far away from the resonances of the visible state. (iii) Paramagnetic Relaxation Enhancement (PRE) measurements require a paramagnetic probe(s) to be introduced to the protein of interest (usually attached to a cysteine residue). Atoms located close (within ca. 24 Å) to the paramagnetic probe have enhanced T_2 relaxation. To characterize the minor (invisible) state by PRE, the distance between the paramagnetic probe and the observable site must be significantly shorter in the minor state than in the major state so that the enhanced relaxation in the minor state (but not in the major state) is extremely fast. As a result, even a small population ($<1\%$) of the minor state that interconverts with the major state, would affect the observable T_2 relaxation of the major state and can be, thus, detected.

These techniques have been successfully used to study folding mechanisms of several single-domain proteins, including detection and characterization of folding intermediates (Tollinger et al., 2001; Korzhnev et al., 2006, 2004, 2010, 2012; Neudecker et al., 2012; Tugarinov et al., 2015; Vallurupalli et al., 2019; Meinhold et al., 2022; Meinhold and Wright, 2011; Dyson and Wright, 2017; Tiwari et al., 2021). In addition, these techniques have been used to probe aggregation-prone conformations, misfolding and self-assembly processes that lead to the formation of large, non-functional aggregates (Alderson and Kay, 2021; Lim et al., 2013; Mukherjee et al., 2011; Karamanos et al., 2014, 2019; Kotler et al., 2019; Sekhar et al., 2015b; Culik et al., 2018; Wu and Baum, 2010; Fawzi et al., 2011). The information about folding/unfolding kinetics and thermodynamics can be mapped into folding pathways of the protein of interest, and, in some cases, NMR also provides structural details about transiently populated intermediated [reviewed in (Neudecker et al., 2009, Korzhnev and Kay, 2008, Zhuravleva and Korzhnev, 2017, Cawood et al., 2021)].

Hydrogen exchanges to probe folding intermediates and aggregates: Hydrogen exchange (HX) was one of the first tools to characterize protein folding and detect early folding intermediates (Hvidt and Nielsen, 1966; Schmid and Baldwin, 1979). Its combination with 2D amide NMR (Wagner and Wuthrich, 1982) further revolutionized the field, providing residue-resolved HX data. HX-NMR provides a residue-resolved protection map of NH groups that can be extrapolated into local flexibility and solvent accessibility, providing information about structural and dynamic features of different protein conformations (Anthis and Clore, 2015) or can be even used to predict a *de novo* tertiary structure (Marzolf et al., 2021; Nguyen et al., 2022).

In HX experiments (Fig. 4), the H- to D-exchange reaction of individual amide groups is monitored by placing the protein of interest into a D_2O buffer, allowing amide protons to exchange to deuterons (Bai, 2006). The rate of HX for individual NH atoms depends on both protein conformation and intrinsic amide hydrogen exchange rates and, thus, provide information about the solvent accessibility of individual NH groups and hydrogen bond stability. The exposure of an unfolded protein to D_2O results in very rapid HX. Because the formation of protein structure almost always involves H-bonding (that makes HX significantly slower), in a folded protein, the protons that are deeply buried (inaccessible for the solvent) have an intrinsic exchange rate (observed for unprotected amides) that is 10^6–10^9 times faster than the HX rate observed experimentally (Kuwajima et al., 2022). In turn, protons located in the flexible regions of a folded protein or partially unfolded state(s) are significantly less protected. Because HX experiments are performed under equilibrium conditions in which folded and unfolded (or partially folded states) are interconverting, the difference between intrinsic and observable HX rates for folded (stable) proteins depends on the rate of the event(s) that make NH groups are more accessible for exchange (exposed to the solvent and lack stable hydrogen-bonding). As a result, the level of protection (the ratio of the intrinsic rate to the observed rate) for individual NH groups in a protein provides information about the structural, thermodynamic and dynamic properties of the protein conformational ensemble.

While mass-spectrometry is also very powerful tool to monitor HX in proteins (James et al., 2022), the main advantage of NMR is the atomic resolution of HX data. Because deuterons are not observed in a 2D amide NMR spectrum (that contains peaks that correspond to individual amide groups in the protein), amide signals will decay after the protein is placed in D_2O because of the hydrogens exchange (Fig. 4). Deuterium incorporation for individual backbone amides can be extracted from a corresponding peak intensity. To obtain more detailed insights into the folding process, these experiments are often coupled with pressure changes or performed at different denaturant concentrations to perturb the folding landscape. While this approach has been now applied to characterize several protein systems [reviews in (Dyson and Wright, 2005) (Kuwajima et al., 2022)], it is only applicable for the characterization of exchange processes that are significantly slower that the time required to record an NMR spectrum. Recent advantages in NMR data acquisition [reviewed in (Felli and Brutscher, 2009, Quinn et al., 2018)] have shortened this time from 10–15 min to seconds. However, this time resolution is still not sufficiently fast for characterization of fast (μs-ms) folding steps. Alternative approaches to probe HX that occur on a sub-second timescale (Hwang et al., 1998; Brand et al., 2007; Chevelkov et al., 2010; Fitzkee et al., 2011; Grzesiek and Bax, 1993), involve the transfer of the ^1H magnetization from water molecules to the protein through hydrogen exchange [reviewed in (Anthis and Clore, 2015)].

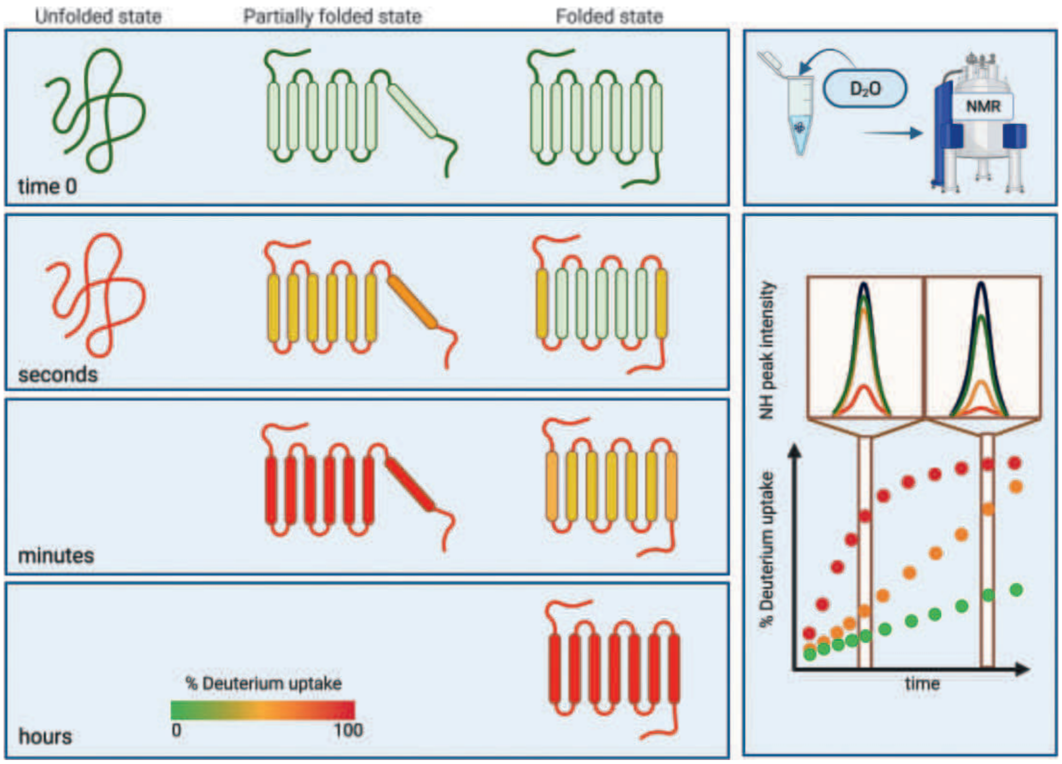

Fig. 4 *Basic principles of hydrogen-deuterium (HX) exchange and NMR-based analysis:* The rate of HX exchange depends on solvent accessibility, hydrogen bonding, and local structural dynamics. As a result, the rates of deuterium uptake vary significantly for folded, partially folded, and unfolded proteins (left). Unfolded proteins exhibit the fastest HX rates as they lack a well-defined secondary structure, leading to increased solvent exposure for the majority of backbone amide hydrogens. In the native folded state, proteins have well-defined secondary and tertiary structure, with many backbone amide hydrogens involved in hydrogen bonding, reducing accessibility to the solvent; these protected amide hydrogens exhibit slow HX rates. In turn, dynamic and disordered regions (e.g., loops) have faster HX rates. In partially folded states, such as folding intermediates, proteins possess protected regions with a native-like structure, while other (unprotected) regions may lack a well-define structure. Protection factors calculated from the HX exchange rates provide residue-specific information about the stability of local protein structure and can reveal the presence of intermediate states or alternative conformations. NMR can be employed (right) to extract HX information with residual resolution: When exposed to D_2O, amide hydrogen atoms on a protein are gradually replaced by deuterium atoms. 2D NMR experiments, such as HSQC (Heteronuclear Single Quantum Coherence), monitor the changes in peak intensities as a function of HX time. Residue-specific HX protection factors, derived from NMR data, provide insights into protein conformation and dynamic, folding pathways and interactions. Created with BioRender.com.

Pulse-labeling is another HX approach that overcomes the time-resolution limitations of traditional 2D amide experiments (Dobson et al., 1994; Kuwajima et al., 2022). For pulse-labeling techniques, HX only occurs for a brief amount of time and then is quenched by transferring the protein to conditions that preserve its protonation state. This could be achieved by either promoting fast folding to a native (slow exchange) state (Bai, 2006) or placing the protein in an aprotic (containing no protons) solvent such as dimethyl sulfoxide (DMSO) (Zhang et al., 1995; Nishimura et al., 2005). 2D or 3D NMR experiments can be then recorded to extract the amount of incorporated ^2H for individual amide groups. Importantly, the DMSO-quenched HX approach also overcomes one of the most critical limitations of NMR. While the majority of amide NMR techniques are only suitable for the characterization of relatively small (up to 30–40 kDa) protein systems, limited by the sensitivity and resolution of 2D amide NMR, the DMSO-quenched HX approach does not have this size limitation, enabling high-resolution HX data for large and challenging protein systems (Kuwajima et al., 2022). Moreover, because DMSO is very efficient in the solubilization of protein aggregates, including amyloid fibrils, the DMSO-quenched HX method has also been successfully used to obtain structural insights into the formation of insoluble aggregates and fibrils (Alexandrescu, 2001; Ippel et al., 2002; Hoshino et al., 2002; Vilar et al., 2012; Lee and Goto, 2012).

Real-time folding by NMR: An alternative approach to sample the protein folding landscape is to monitor the folding-unfolding transition under non-equilibrium conditions in real time (Fig. 5). This can be achieved by the dilution of solutions of chemical denaturants, salts, acids/bases, or by the temperature or pressure jump. The folding (or unfolding) process can then be monitored experimentally in real time. In this case, the time needed to perform these measurements should be significantly shorter than the observed process (Bartlett and Radford, 2009). Techniques such as fluorescence or circular dichroism combined with stopped-flow methods have been widely used for these measurements, providing insights into global folding/unfolding with high enough time resolution (Eaton et al., 2000; Roder et al., 2006). In principle, folded and (partially) misfolded states can be monitored by real-time NMR (Smith et al., 2015b) during a refolding process. Particularly, a set of consecutive NMR spectra need to be recorded to monitor changes in peak positions, broadening and/or intensities to obtain information about folded and (partially) unfolded states and

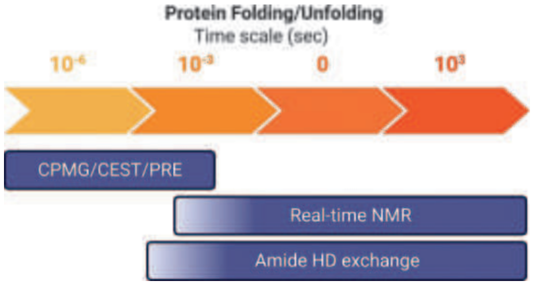

Fig. 5 *Protein folding timescales and NMR approaches for characterizing different folding steps:* Methods (such as CPMG, CEST and PRE) that probe μs-ms dynamics allow the characterization of rapidly exchanging folding intermediates and aggregation-prone species. Amide exchange experiments are employed to investigate the solvent accessibility and hydrogen bonding network, revealing information about protein stability and relatively long-lived folding intermediates. Real-time NMR methods are applied to monitor protein folding events on intermediate time-scale, providing insights into the formation of secondary and tertiary structures during the folding process. Created with BioRender.com.

characterize kinetics and thermodynamics of the folding-unfolding transition (Zeeb and Balbach, 2004). Using a similar approach, the formation of insoluble (invisible for NMR) oligomers from smaller (visible) protein states can also be characterized by monitoring the decay of NMR signal intensities for the visible state over time (Mishra et al., 2009).

While real-time NMR enables the atomic level of details, it is an intrinsically slow method; the long acquisition time has been the main limitation of this approach. However, recent advantages in NMR techniques (Felli and Brutscher, 2009; Quinn et al., 2018) have pushed boundaries and created new opportunities for the characterization of faster folding and misfolding processes with the second-time resolution as well as allowing structural characterization of relatively short-lived (few hours) intermediates (Rennella et al., 2012; Karamanos et al., 2016; Rao Kakita et al., 2018; Kumar and Balbach, 2015). These techniques use sparse data collection strategies and/or a shorter delay between experimental repetitions that is needed for magnetization recovery (Mobli et al., 2012; Hyberts et al., 2014; Smith et al., 2015b; Kumar and Balbach, 2015) that enables recording 2D and 3D spectra one-two order of magnitude faster than conventional NMR techniques (e.g., few seconds *vs* few minutes for a 2D spectrum). In some cases, if reversible folding is possible, fast acquisition techniques can be combined with a multiple folding-unfolding cycle during a single 2D or 3D experiment, when the NMR data acquisition is synchronized with a protein folding/unfolding reaction induced by pressure (Kremer et al., 2011; Charlier et al., 2018a) or temperature (Pinter and Schwalbe, 2020). These approaches further increase the time resolution to milliseconds, opening new opportunities to gain detailed information about the kinetics and thermodynamics of fast folding transitions and obtain structural features of on- and off-pathway intermediates populated at the early stages of folding (Charlier et al., 2018a,b; Dubois et al., 2020) or misfolding (Barnes et al., 2019).

NMR for the characterization of intrinsically disordered proteins: Together with small-angle X-ray scattering, electron paramagnetic resonance, mass spectrometry, and Förster resonance energy transfer, NMR enables the characterization of highly dynamic unfolded states and intrinsically disordered protein (IDP) systems, providing atomic insights into their conformational dynamics and interactions (Uversky, 2020; Dyson and Wright, 2021). Different NMR approaches for IDP characterization have been recently reviewed in Dyson and Wright (2019), Milles et al. (2018), Naudi-Fabra et al. (2021), Camacho-Zarco et al. (2022), Karamanos et al. (2022), Schneider et al. (2019). These approaches exploit the fact that fully unstructured proteins have drastically different NMR parameters compared to folded proteins, including the poor dispersion of chemical shifts, near zero residual dipolar coupling values (that report on an average of bond orientations with respect to the magnetic field), internal flexibility on the ns time-scale that affects their T_1 and T_2 relaxation rates, only local residual contacts that results in short-range NOEs and PREs. Any deviations of the experimental NMR parameters from those predicted for a fully unstructured state can be then used to calculate local propensities for the formation of transient secondary structure and long-range contacts (Fig. 6) (Dyson and Wright, 2005).

For several IDP systems that can adopt more ordered structures upon binding to their partners (Shammas et al., 2016) or posttranslational modifications (Bah and Forman-Kay, 2016), NMR has been successfully used to probe and characterize the induced folding process [reviewed in (Dyson and Wright, 2021) and (Mollica et al., 2016)]. On the other side, many IDPs remain disorder upon complex formation and their complexes cannot be described by a single conformational state [as called 'fuzzy' complexes (Tompa and Fuxreiter, 2008)]. Instead of a well-defined binding site, such IDPs contain several short interacting motifs; while each of these motifs has only weak binding affinity (enabling transient and reversible interactions), the presence of multiple motifs on the same protein molecule ensures high-affinity binding. Bio-NMR has played a crucial role in the characterization of such interactions [reviewed in (Ahmed and Forman-Kay, 2022)], including a recent study of a 'fuzzy' complex between two fully disordered IDPs (Borgia et al., 2018).

While NMR is a potent technique for IDP characterization, the correct quantitative interpretation of experimental data for such systems is a highly challenging task due to the heterogeneity and complexity of their conformational ensembles. Indeed, the IDP ensemble consists of many structurally heterogeneous and dynamic conformations rather than a small set of well-defined structures. While in most cases, these conformations are interconverting on the fast NMR timescale (faster than hundreds of microseconds), NMR reports on a population-weighted average over the ensemble of interconverting conformations (Kosol et al., 2013). Consequently, interpreting such complex experimental data requires generating a representative conformational ensemble.

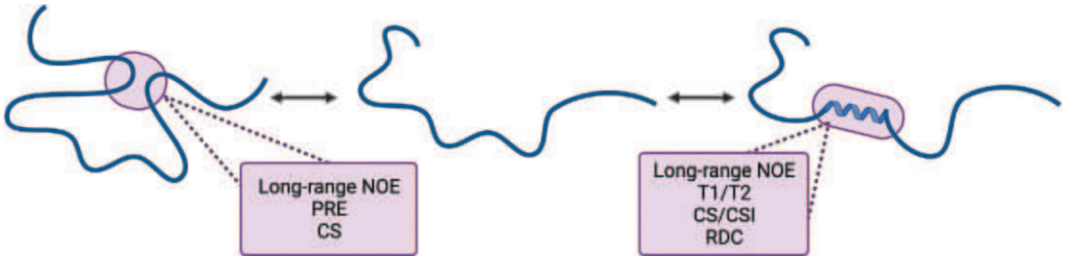

Fig. 6 Conformational ensemble characterization of intrinsically disordered protein using NMR techniques: Long-range NOE (Nuclear Overhauser Effects) and PRE (Paramagnetic Relaxation Enhancement) measurements can be used to identify through-space interactions within the conformation ensemble; RDC (Residual Dipolar Coupling) experiments, capturing weakly aligned protein molecules in an anisotropic medium, provide information on long-range order and secondary structure propensities; T1 and T2 measurements allow the assessment of local and global flexibility in the protein molecules; Chemical Shift Index (CSI) analysis uses chemical shift deviations from random coil values to predict secondary structure elements; Chemical Shift Perturbation (CSPs) analysis detects changes in chemical shifts upon mutations and/or environmental changes and reveals long-range interactions and structural and conformational changes in IDPs. Created with BioRender.com.

Assuming that all IDP conformations interconverting on the fast-experimental timescale (beyond the fast regime, an NMR observable no longer represents a population-weighted average), the conformational ensemble can be then defined as a set of relevant conformations and their respective populations that accurately describe the experimental data, including all (often transient) long-range and local interactions in the protein chain. There are two main approaches to derive ensemble models that correctly describe experimental data, discussed in details in (Karamanos et al., 2022; Camacho-Zarco et al., 2022; Gama Lima Costa and Fushman, 2022; Bonomi et al., 2017). In the first approach (reweighting methods), an initial *in sillico* set of protein structures (conformations) are generated. Initially, experimental data are predicted for all conformations from this set, assuming that they have equal probabilities of contributing to experimental observables. The real experimental data are used to refine the ensemble and find an appropriate weight (population) for each conformation. The main advantage of reweighting methods is that new experimental data can be added at any moment to refine the ensemble, minimizing computational cost, but the success of these methods largely depends on whether the initial set of structures realistically represents the real conformational ensemble. The second approach exploits restrained molecular dynamics (MD) simulations to include experimental data in the force field. Incorporating experimental data as restraints for MD simulations allows more enhanced sampling of the protein conformational space that is otherwise unavailable due to limited computations resources.

Because the number of degrees of freedom for IDPs are drastically larger than the number of independent experimental observables, often several conformational ensamples can fit the experimental data equally well. Consequently, to be able to capture all critical features of the heterogeneous IDP ensemble, the characterization of IDP usually requires an integrated structural approach that combines data from NMR and complementary biophysical techniques such as single-molecule fluorescence energy transfer (smFRET), electron magnetic resonance (EPR), small angle X-ray scattering (SAXS), fluorescence correlation spectroscopy (FCS), chemical cross-linking, electrospray ionization mass spectrometry, and others, (Karamanos et al., 2022; Camacho-Zarco et al., 2022).

Protein folding in the presence of molecular chaperones: During the folding process, proteins expose hydrophobic motifs that are essential for the formation of the folding core but can also favors off-pathway interactions and, thus, misfolding (Hartl et al., 2011). Molecular chaperones recognize these exposed hydrophobic motifs and/or these off-pathway interactions in a protein chain. Different molecular chaperones interact with a wide range of client proteins at different stages of their folding pathway, giving them different roles in assisting and maintaining protein folding. It has been widely accepted that molecular chaperones affect the conformation of their client proteins either by altering the folding landscape (e.g., by favoring on-pathway contacts and/or disfavoring non-productive contacts in the protein chain) (Jayaraj et al., 2020; Tittelmeier et al., 2020) or/and stabilizing a native state under conditions in which the native state is energetically unfavorable (Goloubinoff et al., 2018). However, only very recently we have started to understand how molecular chaperones perform this complex task (Sucec et al., 2021; Macosek et al., 2021). Because different conformations of molecular chaperones and their client proteins have distinct NMR fingerprints (chemical shifts, relaxation times, etc.), NMR has provided a unique opportunity to address these intriguing questions (Burmann and Hiller, 2015; Karamanos and Clore, 2022).

Recent developments in NMR techniques enable the detailed characterization of large, multicomponent protein systems, transient interactions and protein-protein complexes, and disordered protein conformations (Burmann and Hiller, 2015). As a result, the detailed characterization of chaperone interactions with their full-length protein clients for several cellular chaperones has been obtained in the last decade [reviewed in detail in (Karamanos and Clore, 2022) and (Hiller, 2021)]. For example, NMR studies of Hsp70 interactions with its full-length substrates revealed that the substrate-binding cleft of Hsp70 promiscuously recognizes multiple binding sites in the same protein sequence (Clerico et al., 2021; Rosenzweig et al., 2017), directly selecting the unfolded (extended) conformation of their client proteins by binding to the sites exposed during the early steps of the folding process (Landry et al., 1992; Sekhar et al., 2018; Lee et al., 2015). These Hsp70-client interactions reshape its clients' folding pathway by destabilizing off-pathway long-range contacts (Sekhar et al., 2016, 2015a). In turn, NMR characterizations of the bacterial Hsp60 GroEL demonstrated that this chaperone preferentially binds to late-folding intermediates (Landry et al., 1992; Goldberg et al., 1997) and stabilizes them relative to the fully folded and unfolded states (Libich et al., 2015); moreover, GroEL accelerates the transition rate between the fully folded states and folding intermediate (Libich et al., 2017).

NMR has also played a key role in the elucidation of transient ('fuzzy') interactions between molecular chaperones and their protein substrates. For example, the NMR characterization of Hsp90 demonstrated that this chaperone binds to their client proteins through an extended surface area reminiscent of 'fuzzy' complexes observed upon interactions between disordered proteins and their binding partners (Park et al., 2011a). It has been further demonstrated that these weak binding contacts that spread other Hsp90 structures enable more effective interactions with partially folded intermediates that expose hydrophobic and charged regions over a large surface area (Karagoz and Rudiger, 2015) (Moran Luengo et al., 2019). A similar multivalent ('fuzzy') binding mechanism has been also revealed by NMR for several ATP-independent chaperones, including bacterial trigger factor (Saio et al., 2014), Skp (Burmann et al., 2013; Salmon et al., 2016), SecB (Huang et al., 2016), Hsp40 (Jiang et al., 2019).

For the majority of molecular chaperones, their functions rely on ATP-dependent or ATP-independent conformational changes (e.g., changes in domain arrangements for Hsp70 and Hsp60 or oligomerization state for Hsp90 and small HSPs) that control binding to their client proteins and/or interactions with co-chaperones and other members of the protein quality control network. Without knowing the structural details of these conformational changes and interactions, our understanding of protein folding mechanisms would be incomplete. The large size of multidomain molecular chaperones was the main limitation for their NMR characterization until the early 2010s. For this reason, first NMR studies (for example, characterization of the isolated substrate-binding (Pellecchia et al., 2000) and nucleotide binding (Zhuravleva and Gierasch, 2011) domains of Hsp70 and the isolated domains of Hsp90 (Hagn et al., 2011)) were focused on characterization of isolated domains or truncated variants rather than on full-length chaperones. The methyl labeling approach that selectively labels $^{13}CH_3$ of methyl groups (Tugarinov et al., 2006) significantly enhances sensitivity due to the fast methyl group rotation and the presence of the three equivalent protons. As a result, this labeling scheme has made it possible to use NMR to characterize very large protein systems (Rosenzweig and Kay, 2014; Rossi et al., 2019) (up to 2 MDa) such as full-length chaperones and other protein quality control enzymes, enabling the comprehensive understanding of mechanisms for the regulation of their chaperone activity (Zhuravleva et al., 2012; Wieteska et al., 2017; Meng et al., 2018; Karagoz et al., 2011; Park et al., 2011b; Henot et al., 2022; Lopez et al., 2021; Faust et al., 2020; Rosenzweig and Kay, 2016; Rosenzweig et al., 2015).

Protein folding on ribosomes and in vivo: In *in vitro* studies, the refolding process usually starts with a relatively expanded state of a protein with the entire protein chain in solution. On contrast, *in vivo* protein folding starts co-translationally with the nascent chain still bound to the ribosome and molecular chaperones (Fig. 7). The rate of translation enables another level of control by providing a time delay for co-translational folding (Zhang and Ignatova, 2011) and reducing risk of formation of off-pathway contacts and misfolded species in the complex cellular environment (Rajasekaran and Kaiser, 2022; Braselmann et al., 2013). For most experimental techniques, the signal detection from the ribosome-bound nascent chain or in living cells is impossible due to the

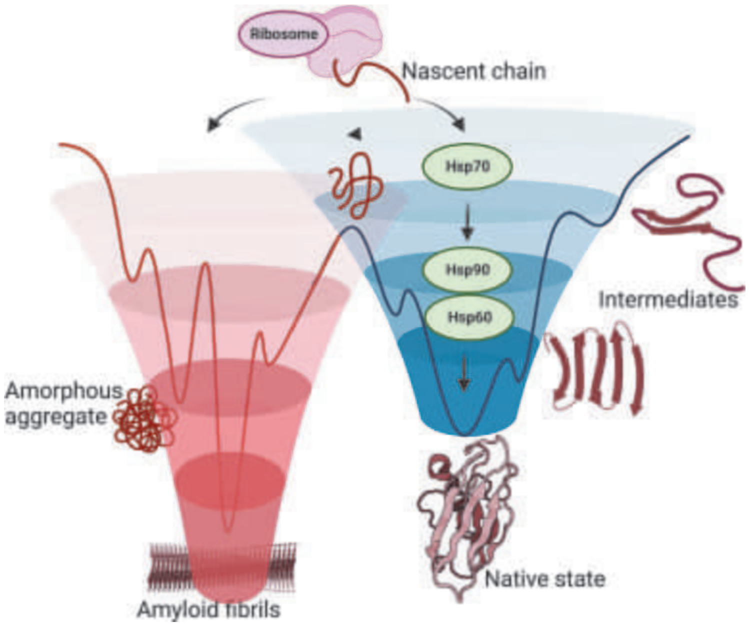

Fig. 7 Molecular chaperones and ribosomes in protein folding: A newly synthesized protein emerges from the ribosome, and the complex folding process begins. It involves the formation of on-pathway folding intermediates that lead toward the native states (blue). In turn, the formation of off-pathway intermediates can potentially lead to midfolded and aggregated species (red). Molecular chaperones assist protein folding by preventing the formation of non-native contacts and stabilizing on-pathway intermediates. Created with BioRender.com.

large background signal. New improvements in NMR sensitivity and selective labeling have provided unique opportunities to observe NMR signals under these conditions and, thus, assess the complexity of protein folding on ribosomes (Waudby et al., 2022, 2021) and/or *in vivo* (Luchinat and Banci, 2018; Luchinat et al., 2022; Selenko and Wagner, 2007) at the atomic level.

The characterization of ribosome-bound nascent chain is still a challenging task for solution NMR due to its large size (ca. 2 MDa) and low sample concentrations (few μM). However, because nascent chains are overall dynamic, they can be observed against the 2 MDa (invisible by NMR) ribosome; uniform ^{15}N or $^{13}CH_3$ methyl isotope labeling enables selective observation of the nascent chain (arrested at a specific chain length) against other ribosomal proteins. As a result, co-translational folding has been extensively studied by NMR in the last 15 years (Hsu et al., 2007, 2009; Cabrita et al., 2009, 2016; Eichmann et al., 2010; Waudby et al., 2018; Deckert et al., 2021; Burridge et al., 2021; Cassaignau et al., 2021; Ahn et al., 2022; Wang et al., 2019). By providing information about the population of folded and unfolded conformations as well as site-specific structural and dynamic features of each state and their dynamic interactions with the ribosome surface, these studies clearly demonstrated that interactions with the ribosome alter thermodynamics and kinetics of the protein folding energy landscape (Waudby et al., 2022).

In 2001 the first in-cell NMR study from Dötsch and co-workers (Serber et al., 2001) demonstrated that solution NMR is suitable for characterize protein behavior with atomic resolution inside the living cells. Methodological developments of in-cell NMR in the last 20 years have allowed characterization of a number of proteins [reviewed in (Luchinat and Banci, 2018), (Luchinat et al., 2022) and (Tochio, 2012)], including in-cell high-resolution structure of small proteins (Sakakibara et al., 2009; Ikeya et al., 2016; Tanaka et al., 2019), characterization of IDPs (Smith et al., 2015a; Theillet et al., 2016; Burmann et al., 2020; Lopez, 2023), protein folding and stability in cell (Inomata et al., 2009, 2017; Banci et al., 2011, 2013; Danielsson et al., 2015; Smith et al., 2016), in-cell protein interactions with ribosomes (Breindel et al., 2018), and interactions between different molecular chaperones and its client proteins (Burmann et al., 2020).

To be able to observe protein in cells without strong interreference from the background, two isotopically labeling approaches have been developed for in-cell NMR (Luchinat et al., 2022). The first approach requires the expression and labeling of the protein of interest directly in cells in which NMR experiments will be performed. However, enrichment with ^{15}N and/or ^{13}C, commonly used for these experiments, often results in a relatively large background signal due to unselective labeling of other cellular components. An alternative labeling approach can be used (Selenko and Wagner, 2007): The protein of interest is first labeled and purified elsewhere and then introduced into selected cells (e.g., bacteria, oocytes or mammalian cultured cells), resulting in background-free spectra. Another serious limitation of in-cell NMR is the presence of transient, unspecific interactions in crowded cells that can significantly compromise the quality of in-cell 2D and 3D NMR spectra (Wang et al., 2011; Mu et al., 2017; Burz et al., 2019). However, this limitation can be compensated by the choice of the cell type (Leeb et al., 2020; Thole et al., 2021), maintaining a consistence cellular background during the experiments, and using advanced NMR pulse-sequences that increase the efficiency of magnetization transfer (Burz et al., 2019). Alternatively, methyl NMR in combination with local deuteration, can be used to improve sensitivity (Dubey et al., 2021). Another approach to improve the quality of NMR spectra and increase the applicability of in-cell NMR to more complex systems is to exploit the high sensitivity of ^{19}F NMR spectroscopy [83% of ^{1}H (Arntson and Pomerantz, 2016)]. For ^{19}F NMR, fluorine-containing non-canonical amino acids are incorporated in the protein using fluorinated mimics of aromatic amino acids (Arntson and Pomerantz, 2016) or via an orthogonal translation system (Maranhao and Ellington, 2017), allowing background-free detection using 1D ^{19}F NMR spectra (Chan et al., 2022; Pham et al., 2023; Zhu et al., 2022; Luchinat et al., 2022).

Challenges and limitations

In the last 20 years, dramatic improvements in NMR methodology, hardware and software have opened new avenues for NMR: from automatic protein structure determination using deep learning algorithms (Klukowski et al., 2022) to real-time NMR analysis of living cells (Luchinat et al., 2022). As a result, solution NMR, combined with other structural and biophysical approaches, has become a key technique to address fundamental questions in structural biology, drug developments and biomedicine, including protein folding and misfolding. However, at this stage, several critical challenges have still to be addressed.

Characterization of the dynamic protein quality control network: During the folding process, a protein transiently and sequentially interacts with different molecular chaperones and other protein quality controls enzymes. In turn, the activity of molecular chaperones depends on highly dynamic conformational changes and transient interactions with co-chaperones and other chaperones. Moreover, this complex network of molecular chaperones is post-translationally controlled in real time (Nitika and Truman, 2017; Backe et al., 2020) to adjust the protein folding capacity in the constantly changing cellular environment. This complexity cannot be addressed with a single technique, including NMR.

Folding only of the small fraction of proteome has been characterized: NMR and other techniques have focused on the folding characterization of relatively small and well-behaved proteins (Braselmann et al., 2013). Larger proteins usually have a more complex folding pathway that contains several on- and off-pathway intermediates making experimental data analysis more complex and ambiguous. The combination of data obtained from solution NMR and other experimental techniques (electron microscopy, mass spectrometry, Förster resonance energy transfer, time-resolved X-Ray diffraction, and others) with deep learning algorithms similar to AlphaFold (Jumper and Hassabis, 2022), RoseTTAFold (Baek and Baker, 2022) and EVE (Frazer et al., 2021) is the obvious way to obtain a complete picture of how complex, multidomain proteins fold and/or how (partially) folded proteins interact with the protein quality control enzymes.

Sensitivity and size limitations: Despite the significant progress in NMR characterization of large proteins (Rosenzweig and Kay, 2014; Rossi et al., 2019) and the development of higher field strength (Quinn et al., 2018; Luchinat et al., 2021) that dramatically enhance sensitivity and resolution of NMR experiments, the atomistic characterization of large protein systems (such as protein complexes with ribosomes and/or molecular chaperones and co-chaperones) remains to be extremely challenging. While a single 1D and 2D NMR spectrum can be recorded using relatively low (μM) protein concentrations, more complex experiments that are usually used to assess protein structure and conformational dynamics require significantly higher (tens to hundreds μM) concentrations and longer (hours) experimental time. As a result, the success of an NMR characterization of complex systems still largely depends on protein behavior in an NMR tube, its stability and solubility.

Time- and cost-efficient NMR labeling and characterization: Protein characterization by NMR usually requires months of work for a well-trained NMR expert(s) that significantly limits the use of NMR by non-NMR research groups. Despite very promising progress (Li et al., 2021; Karunanithy and Hansen, 2021; Klukowski et al., 2022, 2023), the automation of different steps of NMR characterization (from the optimization of a labeling scheme and experimental conditions enabling sufficient spectra quality to automatic resonance peak assignments in NMR spectra and calculation of NMR parameters) is still under development.

Conclusion

Protein folding is a complex and dynamic process that depends on a protein amino acid sequence but is also controlled by the environment, including concentrations of salt and small-molecule metabolites, molecular crowding, unspecific binding to cellular components as well as specific interactions with ribosomes, molecular chaperones and other cellular proteins and macromolecules. Due to this multidimensional complexity, many aspects of protein folding still need to be better understood. Recent methodological advantages in NMR and isotopic labeling have been successfully addressing many of previous limitations, enabling the characterization of challenging systems such as large multidomain chaperone machines, transient complexes between chaperones and their protein substrates, highly dynamic intrinsically disordered and unfolded proteins and their interactions, short-lived folding intermediates and aggregation-prone species. Moreover, state-of-the-art achievements in computational methods have the potential to provide synergy links between sparse experimental data from NMR and other experimental techniques. In the long term, deep learning algorithms can be used to analyze large and complex datasets from different experimental techniques and identify patterns and relationships between the observed experimental data, protein folding landscape, its amino acid sequence and chaperone interaction pattern. Altogether, these developments are leading to unprecedented opportunities to understand the fundamental principles of the protein folding process in living cells with atomic details and opening new avenues for drug discovery and protein engineering.

Acknowledgments

The author acknowledges research support from Biotechnology and Biological Sciences Research Council (BBSRC BB/T000635/1 and BBSRC BB/M021874/1).

References

Ahmed R and Forman-Kay JD (2022) NMR insights into dynamic, multivalent interactions of intrinsically disordered regions: From discrete complexes to condensates. *Essays in Biochemistry* 66(7): 863–873.

Ahn M, Wlodarski T, Mitropoulou A, Chan SHS, Sidhu H, Plessa E, Becker TA, Budisa N, Waudby CA, Beckmann R, Cassaignau AME, Cabrita LD, and Christodoulou J (2022) Modulating co-translational protein folding by rational design and ribosome engineering. *Nature Communications* 13(1): 4243.

Alderson TR and Kay LE (2021) NMR spectroscopy captures the essential role of dynamics in regulating biomolecular function. *Cell* 184(3): 577–595.

Alexandrescu AT (2001) An NMR-based quenched hydrogen exchange investigation of model amyloid fibrils formed by cold shock protein A. *Pacific Symposium on Biocomputing*: 67–78.

Anfinsen CB (1972) The formation and stabilization of protein structure. *The Biochemical Journal* 128(4): 737–749.

Anfinsen CB (1973) Principles that govern the folding of protein chains. *Science* 181(4096): 223–230.

Anfinsen CB, Haber E, Sela M, and White FH Jr (1961) The kinetics of formation of native ribonuclease during oxidation of the reduced polypeptide chain. *Proceedings of the National Academy of Sciences of the United States of America* 47(9): 1309–1314.

Anthis NJ and Clore GM (2015) Visualizing transient dark states by NMR spectroscopy. *Quarterly Reviews of Biophysics* 48(1): 35–116.

Arntson KE and Pomerantz WC (2016) Protein-observed fluorine NMR: A bioorthogonal approach for small molecule discovery. *Journal of Medicinal Chemistry* 59(11): 5158–5171.

Arthanari H, Takeuchi K, Dubey A, and Wagner G (2019) Emerging solution NMR methods to illuminate the structural and dynamic properties of proteins. *Current Opinion in Structural Biology* 58: 294–304.

Backe SJ, Sager RA, Woodford MR, Makedon AM, and Mollapour M (2020) Post-translational modifications of Hsp90 and translating the chaperone code. *The Journal of Biological Chemistry* 295(32): 11099–11117.

Baek M and Baker D (2022) Deep learning and protein structure modeling. *Nature Methods* 19(1): 13–14.

Bah A and Forman-Kay JD (2016) Modulation of intrinsically disordered protein function by post-translational modifications. *The Journal of Biological Chemistry* 291(13): 6696–6705.

Bai Y (2006) Protein folding pathways studied by pulsed- and native-state hydrogen exchange. *Chemical Reviews* 106(5): 1757–1768.

Balchin D, Hayer-Hartl M, and Hartl FU (2016) In vivo aspects of protein folding and quality control. *Science* 353(6294): aac4354.

Banci L, Barbieri L, Bertini I, Cantini F, and Luchinat E (2011) In-cell NMR in E. coli to monitor maturation steps of hSOD1. *PLoS One* 6(8): e23561.

Banci L, Barbieri L, Bertini I, Luchinat E, Secci E, Zhao Y, and Aricescu AR (2013) Atomic-resolution monitoring of protein maturation in live human cells by NMR. *Nature Chemical Biology* 9(5): 297–299.

Barnes CA, Robertson AJ, Louis JM, Anfinrud P, and Bax A (2019) Observation of beta-amyloid peptide oligomerization by pressure-jump NMR spectroscopy. *Journal of the American Chemical Society* 141(35): 13762–13766.

Bartlett AI and Radford SE (2009) An expanding arsenal of experimental methods yields an explosion of insights into protein folding mechanisms. *Nature Structural & Molecular Biology* 16(6): 582–588.

Bhatt H, Ganguly AK, Sharma S, Kushwaha GS, Firoz Khan M, Sen S, and Bhavesh NS (2020) Structure of an unfolding intermediate of an RRM domain of ETR-3 reveals its native-like fold. *Biophysical Journal* 118(2): 352–365.

Bloch F, Hansen WW, and Packard M (1946) Nuclear induction. *Physics Review* 69: 147.

Bondos SE, Dunker AK, and Uversky VN (2021) On the roles of intrinsically disordered proteins and regions in cell communication and signaling. *Cell Communication and Signaling: CCS* 19(1): 88.

Bonomi M, Heller GT, Camilloni C, and Vendruscolo M (2017) Principles of protein structural ensemble determination. *Current Opinion in Structural Biology* 42: 106–116.

Borgia A, Borgia MB, Bugge K, Kissling VM, Heidarsson PO, Fernandes CB, Sottini A, Soranno A, Buholzer KJ, Nettels D, Kragelund BB, Best RB, and Schuler B (2018) Extreme disorder in an ultrahigh-affinity protein complex. *Nature* 555(7694): 61–66.

Bowman MA, Riback JA, Rodriguez A, Guo H, Li J, Sosnick TR, and Clark PL (2020) Properties of protein unfolded states suggest broad selection for expanded conformational ensembles. *Proceedings of the National Academy of Sciences of the United States of America* 117(38): 23356–23364.

Brand T, Cabrita EJ, Morris GA, Gunther R, Hofmann HJ, and Berger S (2007) Residue-specific NH exchange rates studied by NMR diffusion experiments. *Journal of Magnetic Resonance* 187(1): 97–104.

Braselmann E, Chaney JL, and Clark PL (2013) Folding the proteome. *Trends in Biochemical Sciences* 38(7): 337–344.

Breindel L, DeMott C, Burz DS, and Shekhtman A (2018) Real-time in-cell nuclear magnetic resonance: Ribosome-targeted antibiotics modulate quinary protein interactions. *Biochemistry* 57(5): 540–546.

Brockwell DJ and Radford SE (2007) Intermediates: ubiquitous species on folding energy landscapes? *Current Opinion in Structural Biology* 17(1): 30–37.

Burmann BM and Hiller S (2015) Chaperones and chaperone-substrate complexes: Dynamic playgrounds for NMR spectroscopists. *Progress in Nuclear Magnetic Resonance Spectroscopy* 86-87: 41–64.

Burmann BM, Wang C, and Hiller S (2013) Conformation and dynamics of the periplasmic membrane-protein-chaperone complexes OmpX-Skp and tOmpA-Skp. *Nature Structural & Molecular Biology* 20(11): 1265–1272.

Burmann BM, Gerez JA, Matecko-Burmann I, Campioni S, Kumari P, Ghosh D, Mazur A, Aspholm EE, Sulskis D, Wawrzyniuk M, Bock T, Schmidt A, Rudiger SGD, Riek R, and Hiller S (2020) Regulation of alpha-synuclein by chaperones in mammalian cells. *Nature* 577(7788): 127–132.

Burridge C, Waudby CA, Wlodarski T, Cassaignau AME, Cabrita LD, and Christodoulou J (2021) Nascent chain dynamics and ribosome interactions within folded ribosome-nascent chain complexes observed by NMR spectroscopy. *Chemical Science* 12(39): 13120–13126.

Burz DS, Breindel L, and Shekhtman A (2019) Improved sensitivity and resolution of in-cell NMR spectra. *Methods in Enzymology* 621: 305–328.

Cabrita LD, Hsu ST, Launay H, Dobson CM, and Christodoulou J (2009) Probing ribosome-nascent chain complexes produced in vivo by NMR spectroscopy. *Proceedings of the National Academy of Sciences of the United States of America* 106(52): 22239–22244.

Cabrita LD, Cassaignau AME, Launay HMM, Waudby CA, Wlodarski T, Camilloni C, Karyadi ME, Robertson AL, Wang X, Wentink AS, Goodsell L, Woolhead CA, Vendruscolo M, Dobson CM, and Christodoulou J (2016) A structural ensemble of a ribosome-nascent chain complex during cotranslational protein folding. *Nature Structural & Molecular Biology* 23(4): 278–285.

Camacho-Zarco AR, Schnapka V, Guseva S, Abyzov A, Adamski W, Milles S, Jensen MR, Zidek L, Salvi N, and Blackledge M (2022) NMR provides unique insight into the functional dynamics and interactions of intrinsically disordered proteins. *Chemical Reviews* 122(10): 9331–9356.

Cassaignau AME, Wlodarski T, Chan SHS, Woodburn LF, Bukvin IV, Streit JO, Cabrita LD, Waudby CA, and Christodoulou J (2021) Interactions between nascent proteins and the ribosome surface inhibit co-translational folding. *Nature Chemistry* 13(12): 1214–1220.

Cavanagh J, Skelton N, Fairbrother W, Rance M, and Palmer IA (2006) *Protein NMR Spectroscopy Principles and Practice*. Elsevier.

Cawood EE, Karamanos TK, Wilson AJ, and Radford SE (2021) Visualizing and trapping transient oligomers in amyloid assembly pathways. *Biophysical Chemistry* 268: 106505.

Chan SHS, Wlodarski T, Streit JO, Cassaignau AME, Woodburn LF, Ahn M, Freiherr von Sass GJ, Waudby CA, Budisa N, Cabrita LD, and Christodoulou J (2022) The ribosome stabilizes partially folded intermediates of a nascent multi-domain protein. *Nature Chemistry* 14(10): 1165–1173.

Charlier C, Alderson TR, Courtney JM, Ying J, Anfinrud P, and Bax A (2018a) Study of protein folding under native conditions by rapidly switching the hydrostatic pressure inside an NMR sample cell. *Proceedings of the National Academy of Sciences of the United States of America* 115(18): E4169–E4178.

Charlier C, Courtney JM, Anfinrud P, and Bax A (2018b) Interrupted pressure-jump NMR experiments reveal resonances of on-pathway protein folding intermediate. *The Journal of Physical Chemistry. B* 122(49): 11792–11799.

Chevelkov V, Xue Y, Rao DK, Forman-Kay JD, and Skrynnikov NR (2010) 15N H/D-SOLEXSY experiment for accurate measurement of amide solvent exchange rates: Application to denatured drkN SH3. *Journal of Biomolecular NMR* 46(3): 227–244.

Chiti F and Dobson CM (2017) Protein misfolding, amyloid formation, and human disease: A summary of progress over the last decade. *Annual Review of Biochemistry* 86: 27–68.

Clerico EM, Pozhidaeva AK, Jansen RM, Ozden C, Tilitsky JM, and Gierasch LM (2021) Selective promiscuity in the binding of E. coli Hsp70 to an unfolded protein. *Proceedings of the National Academy of Sciences of the United States of America* 118(41).

Clore GM (2022) NMR spectroscopy, excited states and relevance to problems in cell biology—Transient pre-nucleation tetramerization of huntingtin and insights into Huntington's disease. *Journal of Cell Science* 135(12).

Culik RM, Sekhar A, Nagesh J, Deol H, Rumfeldt JAO, Meiering EM, and Kay LE (2018) Effects of maturation on the conformational free-energy landscape of SOD1. *Proceedings of the National Academy of Sciences of the United States of America* 115(11): E2546–E2555.

Danielsson J, Mu X, Lang L, Wang H, Binolfi A, Theillet FX, Bekei B, Logan DT, Selenko P, Wennerstrom H, and Oliveberg M (2015) Thermodynamics of protein destabilization in live cells. *Proceedings of the National Academy of Sciences of the United States of America* 112(40): 12402–12407.

Deckert A, Cassaignau AME, Wang X, Wlodarski T, Chan SHS, Waudby CA, Kirkpatrick JP, Vendruscolo M, Cabrita LD, and Christodoulou J (2021) Common sequence motifs of nascent chains engage the ribosome surface and trigger factor. *Proceedings of the National Academy of Sciences of the United States of America* 118(52).

Dill KA (1985) Theory for the folding and stability of globular proteins. *Biochemistry* 24(6): 1501–1509.

Dill KA and Chan HS (1997) From Levinthal to pathways to funnels. *Nature Structural Biology* 4(1): 10–19.

Dobson CM, Evans PA, and Radford SE (1994) Understanding how proteins fold: The lysozyme story so far. *Trends in Biochemical Sciences* 19(1): 31–37.

Dreydoppel M, Balbach J, and Weininger U (2022) Monitoring protein unfolding transitions by NMR-spectroscopy. *Journal of Biomolecular NMR* 76(1-2): 3–15.

Dubey A, Stoyanov N, Viennet T, Chhabra S, Elter S, Borggrafe J, Viegas A, Nowak RP, Burdzhiev N, Petrov O, Fischer ES, Etzkorn M, Gelev V, and Arthanari H (2021) Local deuteration enables NMR observation of methyl groups in proteins from eukaryotic and cell-free expression systems. *Angewandte Chemie (International Ed. in English)* 60(25): 13783–13787.

Dubois C, Herrada I, Barthe P, and Roumestand C (2020) Combining high-pressure perturbation with NMR spectroscopy for a structural and dynamical characterization of protein folding pathways. *Molecules* 25(23).

Dunker AK, Obradovic Z, Romero P, Garner EC, and Brown CJ (2000) Intrinsic protein disorder in complete genomes. *Genome Inform Ser Workshop Genome Inform* 11: 161–171.

Dyson HJ and Wright PE (2005) Elucidation of the protein folding landscape by NMR. *Methods in Enzymology* 394: 299–321.

Dyson HJ and Wright PE (2017) How does your protein fold? Elucidating the apomyoglobin folding pathway. *Accounts of Chemical Research* 50(1): 105–111.

Dyson HJ and Wright PE (2019) Perspective: The essential role of NMR in the discovery and characterization of intrinsically disordered proteins. *Journal of Biomolecular NMR* 73(12): 651–659.

Dyson HJ and Wright PE (2021) NMR illuminates intrinsic disorder. *Current Opinion in Structural Biology* 70: 44–52.

Eaton WA, Munoz V, Hagen SJ, Jas GS, Lapidus LJ, Henry ER, and Hofrichter J (2000) Fast kinetics and mechanisms in protein folding. *Annual Review of Biophysics and Biomolecular Structure* 29: 327–359.

Eichmann C, Preissler S, Riek R, and Deuerling E (2010) Cotranslational structure acquisition of nascent polypeptides monitored by NMR spectroscopy. *Proceedings of the National Academy of Sciences of the United States of America* 107(20): 9111–9116.

Eliezer D, Yao J, Dyson HJ, and Wright PE (1998) Structural and dynamic characterization of partially folded states of apomyoglobin and implications for protein folding. *Nature Structural Biology* 5(2): 148–155.

Faust O, Abayev-Avraham M, Wentink AS, Maurer M, Nillegoda NB, London N, Bukau B, and Rosenzweig R (2020) HSP40 proteins use class-specific regulation to drive HSP70 functional diversity. *Nature* 587(7834): 489–494.

Fauvet B, Rebeaud ME, Tiwari S, De Los Rios P, and Goloubinoff P (2021) Repair or degrade: The thermodynamic dilemma of cellular protein quality-control. *Frontiers in Molecular Biosciences* 8: 768888.

Fawzi NL, Ying J, Ghirlando R, Torchia DA, and Clore GM (2011) Atomic-resolution dynamics on the surface of amyloid-beta protofibrils probed by solution NMR. *Nature* 480(7376): 268–272.

Felli IC and Brutscher B (2009) Recent advances in solution NMR: Fast methods and heteronuclear direct detection. *ChemPhysChem* 10(9–10): 1356–1368.

Ferrolino MC, Zhuravleva A, Budyak IL, Krishnan B, and Gierasch LM (2013) Delicate balance between functionally required flexibility and aggregation risk in a beta-rich protein. *Biochemistry* 52(49): 8843–8854.

Fitzkee NC, Torchia DA, and Bax A (2011) Measuring rapid hydrogen exchange in the homodimeric 36 kDa HIV-1 integrase catalytic core domain. *Protein Science* 20(3): 500–512.

Frazer J, Notin P, Dias M, Gomez A, Min JK, Brock K, Gal Y, and Marks DS (2021) Disease variant prediction with deep generative models of evolutionary data. *Nature* 599(7883): 91–95.

Gama Lima Costa R and Fushman D (2022) Reweighting methods for elucidation of conformation ensembles of proteins. *Current Opinion in Structural Biology* 77: 102470.

Gershenson A and Gierasch LM (2011) Protein folding in the cell: Challenges and progress. *Current Opinion in Structural Biology* 21(1): 32–41.

Gestaut D, Limatola A, Joachimiak L, and Frydman J (2019) The ATP-powered gymnastics of TRiC/CCT: An asymmetric protein folding machine with a symmetric origin story. *Current Opinion in Structural Biology* 55: 50–58.

Goldberg MS, Zhang J, Sondek S, Matthews CR, Fox RO, and Horwich AL (1997) Native-like structure of a protein-folding intermediate bound to the chaperonin GroEL. *Proceedings of the National Academy of Sciences of the United States of America* 94(4): 1080–1085.

Goloubinoff P, Sassi AS, Fauvet B, Barducci A, and De Los Rios P (2018) Chaperones convert the energy from ATP into the nonequilibrium stabilization of native proteins. *Nature Chemical Biology* 14(4): 388–395.

Grzesiek S and Bax A (1993) Measurement of amide proton exchange rates and NOEs with water in 13C/15N-enriched calcineurin B. *Journal of Biomolecular NMR* 3(6): 627–638.

Hagn F, Lagleder S, Retzlaff M, Rohrberg J, Demmer O, Richter K, Buchner J, and Kessler H (2011) Structural analysis of the interaction between Hsp90 and the tumor suppressor protein p53. *Nature Structural & Molecular Biology* 18(10): 1086–1093.

Hartl FU (2017) Protein misfolding diseases. *Annual Review of Biochemistry* 86: 21–26.

Hartl FU, Bracher A, and Hayer-Hartl M (2011) Molecular chaperones in protein folding and proteostasis. *Nature* 475(7356): 324–332.

Hayer-Hartl M, Bracher A, and Hartl FU (2016) The GroEL-GroES chaperonin machine: A nano-cage for protein folding. *Trends in Biochemical Sciences* 41(1): 62–76.

Henot F, Rioual E, Favier A, Macek P, Crublet E, Josso P, Brutscher B, Frech M, Gans P, Loison C, and Boisbouvier J (2022) Visualizing the transiently populated closed-state of human HSP90 ATP binding domain. *Nature Communications* 13(1): 7601.

Hiller S (2021) Molecular chaperones and their denaturing effect on client proteins. *Journal of Biomolecular NMR* 75(1): 1–8.

Hingorani KS and Gierasch LM (2014) Comparing protein folding in vitro and in vivo: Foldability meets the fitness challenge. *Current Opinion in Structural Biology* 24: 81–90.

Hoshino M, Katou H, Hagihara Y, Hasegawa K, Naiki H, and Goto Y (2002) Mapping the core of the beta(2)-microglobulin amyloid fibril by H/D exchange. *Nature Structural Biology* 9(5): 332–336.

Hsu ST, Fucini P, Cabrita LD, Launay H, Dobson CM, and Christodoulou J (2007) Structure and dynamics of a ribosome-bound nascent chain by NMR spectroscopy. *Proceedings of the National Academy of Sciences of the United States of America* 104(42): 16516–16521.

Hsu ST, Cabrita LD, Fucini P, Christodoulou J, and Dobson CM (2009) Probing side-chain dynamics of a ribosome-bound nascent chain using methyl NMR spectroscopy. *Journal of the American Chemical Society* 131(24): 8366–8367.

Huang C, Rossi P, Saio T, and Kalodimos CG (2016) Structural basis for the antifolding activity of a molecular chaperone. *Nature* 537(7619): 202–206.

Hvidt A and Nielsen SO (1966) Hydrogen exchange in proteins. *Advances in Protein Chemistry* 21: 287–386.

Hwang TL, van Zijl PC, and Mori S (1998) Accurate quantitation of water-amide proton exchange rates using the phase-modulated CLEAN chemical EXchange (CLEANEX-PM) approach with a Fast-HSQC (FHSQC) detection scheme. *Journal of Biomolecular NMR* 11(2): 221–226.

Hyberts SG, Arthanari H, Robson SA, and Wagner G (2014) Perspectives in magnetic resonance: NMR in the post-FFT era. *Journal of Magnetic Resonance* 241: 60–73.

Ikeya T, Hanashima T, Hosoya S, Shimazaki M, Ikeda S, Mishima M, Guntert P, and Ito Y (2016) Improved in-cell structure determination of proteins at near-physiological concentration. *Scientific Reports* 6: 38312.

Inomata K, Ohno A, Tochio H, Isogai S, Tenno T, Nakase I, Takeuchi T, Futaki S, Ito Y, Hiroaki H, and Shirakawa M (2009) High-resolution multi-dimensional NMR spectroscopy of proteins in human cells. *Nature* 458(7234): 106–109.

Inomata K, Kamoshida H, Ikari M, Ito Y, and Kigawa T (2017) Impact of cellular health conditions on the protein folding state in mammalian cells. *Chemical communications (Cambridge)* 53(81): 11245–11248.

Ippel JH, Olofsson A, Schleucher J, Lundgren E, and Wijmenga SS (2002) Probing solvent accessibility of amyloid fibrils by solution NMR spectroscopy. *Proceedings of the National Academy of Sciences of the United States of America* 99(13): 8648–8653.

James EI, Murphree TA, Vorauer C, Engen JR, and Guttman M (2022) Advances in hydrogen/deuterium exchange mass spectrometry and the pursuit of challenging biological systems. *Chemical Reviews* 122(8): 7562–7623.

Jayaraj GG, Hipp MS, and Hartl FU (2020) Functional modules of the proteostasis network. *Cold Spring Harbor Perspectives in Biology* 12(1).

Jiang Y, Rossi P, and Kalodimos CG (2019) Structural basis for client recognition and activity of Hsp40 chaperones. *Science* 365(6459): 1313–1319.

Jumper J and Hassabis D (2022) Protein structure predictions to atomic accuracy with AlphaFold. *Nature Methods* 19(1): 11–12.

Kakeshpour T, Ramanujam V, Barnes CA, Shen Y, Ying J, and Bax A (2021) A lowly populated, transient beta-sheet structure in monomeric Abeta(1-42) identified by multinuclear NMR of chemical denaturation. *Biophysical Chemistry* 270: 106531.

Karagoz GE and Rudiger SG (2015) Hsp90 interaction with clients. *Trends in Biochemical Sciences* 40(2): 117–125.

Karagoz GE, Duarte AM, Ippel H, Uetrecht C, Sinnige T, van Rosmalen M, Hausmann J, Heck AJ, Boelens R, and Rudiger SG (2011) N-terminal domain of human Hsp90 triggers binding to the cochaperone p23. *Proceedings of the National Academy of Sciences of the United States of America* 108(2): 580–585.

Karamanos TK and Clore GM (2022) Large chaperone complexes through the lens of nuclear magnetic resonance spectroscopy. *Annual Review of Biophysics* 51: 223–246.

Karamanos TK, Kalverda AP, Thompson GS, and Radford SE (2014) Visualization of transient protein-protein interactions that promote or inhibit amyloid assembly. *Molecular Cell* 55(2): 214–226.

Karamanos TK, Pashley CL, Kalverda AP, Thompson GS, Mayzel M, Orekhov VY, and Radford SE (2016) A population shift between sparsely populated folding intermediates determines amyloidogenicity. *Journal of the American Chemical Society* 138(19): 6271–6280.

Karamanos TK, Jackson MP, Calabrese AN, Goodchild SC, Cawood EE, Thompson GS, Kalverda AP, Hewitt EW, and Radford SE (2019) Structural mapping of oligomeric intermediates in an amyloid assembly pathway. *eLife* 8.

Karamanos TK, Kalverda AP, and Radford SE (2022) Generating ensembles of dynamic misfolding proteins. *Frontiers in Neuroscience* 16: 881534.

Karplus M (2011) Behind the folding funnel diagram. *Nature Chemical Biology* 7(7): 401–404.

Karunanithy G and Hansen DF (2021) FID-Net: A versatile deep neural network architecture for NMR spectral reconstruction and virtual decoupling. *Journal of Biomolecular NMR* 75(4-5): 179–191.

Klukowski P, Riek R, and Guntert P (2022) Rapid protein assignments and structures from raw NMR spectra with the deep learning technique ARTINA. *Nature Communications* 13(1): 6151.

Klukowski P, Riek R, and Guntert P (2023) NMRtist: An online platform for automated biomolecular NMR spectra analysis. *Bioinformatics* 39(2).

Knowles TP, Vendruscolo M, and Dobson CM (2014) The amyloid state and its association with protein misfolding diseases. *Nature Reviews. Molecular Cell Biology* 15(6): 384–396.

Korzhnev DM and Kay LE (2008) Probing invisible, low-populated States of protein molecules by relaxation dispersion NMR spectroscopy: An application to protein folding. *Accounts of Chemical Research* 41(3): 442–451.

Korzhnev DM, Salvatella X, Vendruscolo M, Di Nardo AA, Davidson AR, Dobson CM, and Kay LE (2004) Low-populated folding intermediates of Fyn SH3 characterized by relaxation dispersion NMR. *Nature* 430(6999): 586–590.

Korzhnev DM, Bezsonova I, Evanics F, Taulier N, Zhou Z, Bai Y, Chalikian TV, Prosser RS, and Kay LE (2006) Probing the transition state ensemble of a protein folding reaction by pressure-dependent NMR relaxation dispersion. *Journal of the American Chemical Society* 128(15): 5262–5269.

Korzhnev DM, Religa TL, Banachewicz W, Fersht AR, and Kay LE (2010) A transient and low-populated protein-folding intermediate at atomic resolution. *Science* 329(5997): 1312–1316.

Korzhnev DM, Religa TL, and Kay LE (2012) Transiently populated intermediate functions as a branching point of the FF domain folding pathway. *Proceedings of the National Academy of Sciences of the United States of America* 109(44): 17777–17782.

Kosol S, Contreras-Martos S, Cedeno C, and Tompa P (2013) Structural characterization of intrinsically disordered proteins by NMR spectroscopy. *Molecules* 18(9): 10802–10828.

Kotler SA, Tugarinov V, Schmidt T, Ceccon A, Libich DS, Ghirlando R, Schwieters CD, and Clore GM (2019) Probing initial transient oligomerization events facilitating Huntingtin fibril nucleation at atomic resolution by relaxation-based NMR. *Proceedings of the National Academy of Sciences of the United States of America* 116(9): 3562–3571.

Kremer W, Arnold M, Munte CE, Hartl R, Erlach MB, Koehler J, Meier A, and Kalbitzer HR (2011) Pulsed pressure perturbations, an extra dimension in NMR spectroscopy of proteins. *Journal of the American Chemical Society* 133(34): 13646–13651.

Kubelka J, Hofrichter J, and Eaton WA (2004) The protein folding 'speed limit'. *Current Opinion in Structural Biology* 14(1): 76–88.

Kumar A and Balbach J (2015) Real-time protein NMR spectroscopy and investigation of assisted protein folding. *Biochimica et Biophysica Acta* 1850(10): 1965–1972.

Kuwajima K, Yagi-Utsumi M, Yanaka S, and Kato K (2022) DMSO-quenched H/D-exchange 2D NMR spectroscopy and its applications in protein science. *Molecules* 27(12).

Landry SJ, Jordan R, McMacken R, and Gierasch LM (1992) Different conformations for the same polypeptide bound to chaperones DnaK and GroEL. *Nature* 355(6359): 455–457.

Lee YH and Goto Y (2012) Kinetic intermediates of amyloid fibrillation studied by hydrogen exchange methods with nuclear magnetic resonance. *Biochimica et Biophysica Acta* 1824(12): 1307–1323.

Lee JH, Zhang D, Hughes C, Okuno Y, Sekhar A, and Cavagnero S (2015) Heterogeneous binding of the SH3 client protein to the DnaK molecular chaperone. *Proceedings of the National Academy of Sciences of the United States of America* 112(31): E4206–E4215.

Leeb S, Sorensen T, Yang F, Mu X, Oliveberg M, and Danielsson J (2020) Diffusive protein interactions in human versus bacterial cells. *Current Research in Structural Biology* 2: 68–78.

Leopold PE, Montal M, and Onuchic JN (1992) Protein folding funnels: A kinetic approach to the sequence-structure relationship. *Proceedings of the National Academy of Sciences of the United States of America* 89(18): 8721–8725.

Levinthal C (1969) How to fold graciously. *Mössbaun Spectroscopy in Biological Systems Proceedings* 67(41): 22–24.

Li DW, Hansen AL, Yuan C, Bruschweiler-Li L, and Bruschweiler R (2021) DEEP picker is a deep neural network for accurate deconvolution of complex two-dimensional NMR spectra. *Nature Communications* 12(1): 5229.

Libich DS, Tugarinov V, and Clore GM (2015) Intrinsic unfoldase/foldase activity of the chaperonin GroEL directly demonstrated using multinuclear relaxation-based NMR. *Proceedings of the National Academy of Sciences of the United States of America* 112(29): 8817–8823.

Libich DS, Tugarinov V, Ghirlando R, and Clore GM (2017) Confinement and stabilization of Fyn SH3 folding intermediate mimetics within the cavity of the chaperonin GroEL demonstrated by relaxation-based NMR. *Biochemistry* 56(7): 903–906.

Lim KH, Dyson HJ, Kelly JW, and Wright PE (2013) Localized structural fluctuations promote amyloidogenic conformations in transthyretin. *Journal of Molecular Biology* 425(6): 977–988.

Lin J, Shorter J, and Lucius AL (2022) AAA+ proteins: One motor, multiple ways to work. *Biochemical Society Transactions* 50(2): 895–906.

Lopez JM (2023) Combined H-N cross-polarization and carbonyl detection NMR spectroscopy allow to record high-resolution, high-sensitivity spectra of alpha-synuclein in bacterial cells. *Methods in Molecular Biology* 2551: 449–460.

Lopez A, Dahiya V, Delhommel F, Freiburger L, Stehle R, Asami S, Rutz D, Blair L, Buchner J, and Sattler M (2021) Client binding shifts the populations of dynamic Hsp90 conformations through an allosteric network. *Science Advances* 7(51): eabl7295.

Low C, Weininger U, Neumann P, Klepsch M, Lilie H, Stubbs MT, and Balbach J (2008) Structural insights into an equilibrium folding intermediate of an archaeal ankyrin repeat protein. *Proceedings of the National Academy of Sciences of the United States of America* 105(10): 3779–3784.

Luchinat E and Banci L (2018) In-cell NMR in human cells: Direct protein expression allows structural studies of protein folding and maturation. *Accounts of Chemical Research* 51(6): 1550–1557.

Luchinat E, Barbieri L, Cremonini M, and Banci L (2021) Protein in-cell NMR spectroscopy at 1.2 GHz. *Journal of Biomolecular NMR* 75(2-3): 97–107.

Luchinat E, Cremonini M, and Banci L (2022) Radio signals from live cells: The coming of age of in-cell solution NMR. *Chemical Reviews* 122(10): 9267–9306.

Macosek J, Mas G, and Hiller S (2021) Redefining molecular chaperones as chaotropes. *Frontiers in Molecular Biosciences* 8: 683132.

Maranhao AC and Ellington AD (2017) Evolving orthogonal suppressor tRNAs to incorporate modified amino acids. *ACS Synthetic Biology* 6(1): 108–119.

Marzolf DR, Seffernick JT, and Lindert S (2021) Protein structure prediction from NMR hydrogen-deuterium exchange data. *Journal of Chemical Theory and Computation* 17(4): 2619–2629.

Mayer MP and Gierasch LM (2019) Recent advances in the structural and mechanistic aspects of Hsp70 molecular chaperones. *The Journal of Biological Chemistry* 294(6): 2085–2097.

Mecha MF, Hutchinson RB, Lee JH, and Cavagnero S (2022) Protein folding in vitro and in the cell: From a solitary journey to a team effort. *Biophysical Chemistry* 287: 106821.

Meinhold DW and Wright PE (2011) Measurement of protein unfolding/refolding kinetics and structural characterization of hidden intermediates by NMR relaxation dispersion. *Proceedings of the National Academy of Sciences of the United States of America* 108(22): 9078–9083.

Meinhold DW, Felitsky DJ, Dyson HJ, and Wright PE (2022) Transient on- and off-pathway protein folding intermediate states characterized with NMR relaxation dispersion. *The Journal of Physical Chemistry. B* 126(46): 9539–9548.

Meng W, Clerico EM, McArthur N, and Gierasch LM (2018) Allosteric landscapes of eukaryotic cytoplasmic Hsp70s are shaped by evolutionary tuning of key interfaces. *Proceedings of the National Academy of Sciences of the United States of America* 115(47): 11970–11975.

Milles S, Salvi N, Blackledge M, and Jensen MR (2018) Characterization of intrinsically disordered proteins and their dynamic complexes: From in vitro to cell-like environments. *Progress in Nuclear Magnetic Resonance Spectroscopy* 109: 79–100.

Mishra R, Geyer M, and Winter R (2009) NMR spectroscopic investigation of early events in IAPP amyloid fibril formation. *Chembiochem* 10(11): 1769–1772.

Mobli M, Maciejewski MW, Schuyler AD, Stern AS, and Hoch JC (2012) Sparse sampling methods in multidimensional NMR. *Physical Chemistry Chemical Physics* 14(31): 10835–10843.

Mollica L, Bessa LM, Hanoulle X, Jensen MR, Blackledge M, and Schneider R (2016) Binding mechanisms of intrinsically disordered proteins: Theory, simulation, and experiment. *Frontiers in Molecular Biosciences* 3: 52.

Moran Luengo T, Mayer MP, and Rudiger SGD (2019) The Hsp70-Hsp90 chaperone Cascade in protein folding. *Trends in Cell Biology* 29(2): 164–177.

Mu X, Choi S, Lang L, Mowray D, Dokholyan NV, Danielsson J, and Oliveberg M (2017) Physicochemical code for quinary protein interactions in Escherichia coli. *Proceedings of the National Academy of Sciences of the United States of America* 114(23): E4556–E4563.

Mukherjee S, Pondaven SP, and Jaroniec CP (2011) Conformational flexibility of a human immunoglobulin light chain variable domain by relaxation dispersion nuclear magnetic resonance spectroscopy: Implications for protein misfolding and amyloid assembly. *Biochemistry* 50(26): 5845–5857.

Nassar R, Dignon GL, Razban RM, and Dill KA (2021) The protein folding problem: the role of theory. *Journal of Molecular Biology* 433(20): 167126.

Naudi-Fabra S, Blackledge M, and Milles S (2021) Synergies of single molecule fluorescence and NMR for the study of intrinsically disordered proteins. *Biomolecules* 12(1).

Neudecker P, Lundstrom P, and Kay LE (2009) Relaxation dispersion NMR spectroscopy as a tool for detailed studies of protein folding. *Biophysical Journal* 96(6): 2045–2054.

Neudecker P, Robustelli P, Cavalli A, Walsh P, Lundstrom P, Zarrine-Afsar A, Sharpe S, Vendruscolo M, and Kay LE (2012) Structure of an intermediate state in protein folding and aggregation. *Science* 336(6079): 362–366.

Nguyen TT, Marzolf DR, Seffernick JT, Heinze S, and Lindert S (2022) Protein structure prediction using residue-resolved protection factors from hydrogen-deuterium exchange NMR. *Structure* 30(2): 313–320 e313.

Nishimura C, Dyson HJ, and Wright PE (2005) Enhanced picture of protein-folding intermediates using organic solvents in H/D exchange and quench-flow experiments. *Proceedings of the National Academy of Sciences of the United States of America* 102(13): 4765–4770.

Nitika and Truman AW (2017) Cracking the chaperone code: Cellular roles for Hsp70 phosphorylation. *Trends in Biochemical Sciences* 42(12): 932–935.

Panova S, Cliff MJ, Macek P, Blackledge M, Jensen MR, Nissink JWM, Embrey KJ, Davies R, and Waltho JP (2019) Mapping hidden residual structure within the Myc bHLH-LZ domain using chemical denaturant titration. *Structure* 27(10): 1537–1546 e1534.

Park SJ, Borin BN, Martinez-Yamout MA, and Dyson HJ (2011a) The client protein p53 adopts a molten globule-like state in the presence of Hsp90. *Nature Structural & Molecular Biology* 18(5): 537–541.

Park SJ, Kostic M, and Dyson HJ (2011b) Dynamic interaction of Hsp90 with its client protein p53. *Journal of Molecular Biology* 411(1): 158–173.

Pauwels K, Lebrun P, and Tompa P (2017) To be disordered or not to be disordered: Is that still a question for proteins in the cell? *Cellular and Molecular Life Sciences* 74(17): 3185–3204.

Pellecchia M, Montgomery DL, Stevens SY, Vander Kooi CW, Feng HP, Gierasch LM, and Zuiderweg ER (2000) Structural insights into substrate binding by the molecular chaperone DnaK. *Nature Structural Biology* 7(4): 298–303.

Pham LBT, Costantino A, Barbieri L, Calderone V, Luchinat E, and Banci L (2023) Direct expression of fluorinated proteins in human cells for (19)F in-cell NMR spectroscopy. *Journal of the American Chemical Society* 145(2): 1389–1399.

Piersimoni L, Abd El Malek M, Bhatia T, Bender J, Brankatschk C, Calvo Sanchez J, Dayhoff GW, Di Ianni A, Figueroa Parra JO, Garcia-Martinez D, Hesselbarth J, Koppen J, Lauth LM, Lippik L, Machner L, Sachan S, Schmidt L, Selle R, Skalidis I, Sorokin O, Ubbiali D, Voigt B, Wedler A, Wei AAJ, Zorn P, Dunker AK, Kohn M, Sinz A, and Uversky VN (2022) Lighting up Nobel Prize-winning studies with protein intrinsic disorder. *Cellular and Molecular Life Sciences* 79(8): 449.

Pinter G and Schwalbe H (2020) Refolding of cold-denatured barstar induced by radio-frequency heating: A new method to study protein folding by real-time NMR spectroscopy. *Angewandte Chemie (International Ed. in English)* 59(49): 22086–22091.

Purcell EM, Torrey HC, and Pound RV (1946) Resonance absorption by nuclear magnetic moments in a solid. *Physics Review* 69: 37.

Qin S and Zhou HX (2017) Protein folding, binding, and droplet formation in cell-like conditions. *Current Opinion in Structural Biology* 43: 28–37.

Quinn CM, Wang M, and Polenova T (2018) NMR of macromolecular assemblies and machines at 1 GHz and beyond: New transformative opportunities for molecular structural biology. *Methods in Molecular Biology* 1688: 1–35.

Rajasekaran N and Kaiser CM (2022) Co-translational folding of multi-domain proteins. *Frontiers in Molecular Biosciences* 9: 869027.

Rao Kakita VM, Bopardikar M, Kumar Shukla V, Rachineni K, Ranjan P, Singh JS, and Hosur RV (2018) An efficient combination of BEST and NUS methods in multidimensional NMR spectroscopy for high throughput analysis of proteins. *RSC Advances* 8(32): 17616–17621.

Rennella E, Cutuil T, Schanda P, Ayala I, Forge V, and Brutscher B (2012) Real-time NMR characterization of structure and dynamics in a transiently populated protein folding intermediate. *Journal of the American Chemical Society* 134(19): 8066–8069.

Roder K and Wales DJ (2022) The energy landscape perspective: Encoding structure and function for biomolecules. *Frontiers in Molecular Biosciences* 9: 820792.

Roder H, Maki K, and Cheng H (2006) Early events in protein folding explored by rapid mixing methods. *Chemical Reviews* 106(5): 1836–1861.

Ropson IJ and Frieden C (1992) Dynamic NMR spectral analysis and protein folding: Identification of a highly populated folding intermediate of rat intestinal fatty acid-binding protein by 19F NMR. *Proceedings of the National Academy of Sciences of the United States of America* 89(15): 7222–7226.

Rosenzweig R and Kay LE (2014) Bringing dynamic molecular machines into focus by methyl-TROSY NMR. *Annual Review of Biochemistry* 83: 291–315.

Rosenzweig R and Kay LE (2016) Solution NMR spectroscopy provides an avenue for the study of functionally dynamic molecular machines: The example of protein disaggregation. *Journal of the American Chemical Society* 138(5): 1466–1477.

Rosenzweig R, Farber P, Velyvis A, Rennella E, Latham MP, and Kay LE (2015) ClpB N-terminal domain plays a regulatory role in protein disaggregation. *Proceedings of the National Academy of Sciences of the United States of America* 112(50): E6872–E6881.

Rosenzweig R, Sekhar A, Nagesh J, and Kay LE (2017) Promiscuous binding by Hsp70 results in conformational heterogeneity and fuzzy chaperone-substrate ensembles. *eLife* 6.

Rossi P, Monneau YR, Xia Y, Ishida Y, and Kalodimos CG (2019) Toolkit for NMR studies of methyl-labeled proteins. *Methods in Enzymology* 614: 107–142.

Saio T, Guan X, Rossi P, Economou A, and Kalodimos CG (2014) Structural basis for protein antiaggregation activity of the trigger factor chaperone. *Science* 344(6184): 1250494.

Sakakibara D, Sasaki A, Ikeya T, Hamatsu J, Hanashima T, Mishima M, Yoshimasu M, Hayashi N, Mikawa T, Walchli M, Smith BO, Shirakawa M, Guntert P, and Ito Y (2009) Protein structure determination in living cells by in-cell NMR spectroscopy. *Nature* 458(7234): 102–105.

Salmon L, Ahlstrom LS, Horowitz S, Dickson A, Brooks CL 3rd, and Bardwell JC (2016) Capturing a dynamic chaperone-substrate interaction using NMR-informed molecular modeling. *Journal of the American Chemical Society* 138(31): 9826–9839.

Schmid FX and Baldwin RL (1979) Detection of an early intermediate in the folding of ribonuclease A by protection of amide protons against exchange. *Journal of Molecular Biology* 135(1): 199–215.

Schneider R, Blackledge M, and Jensen MR (2019) Elucidating binding mechanisms and dynamics of intrinsically disordered protein complexes using NMR spectroscopy. *Current Opinion in Structural Biology* 54: 10–18.

Sekhar A, Rosenzweig R, Bouvignies G, and Kay LE (2015a) Mapping the conformation of a client protein through the Hsp70 functional cycle. *Proceedings of the National Academy of Sciences of the United States of America* 112(33): 10395–10400.

Sekhar A, Rumfeldt JA, Broom HR, Doyle CM, Bouvignies G, Meiering EM, and Kay LE (2015b) Thermal fluctuations of immature SOD1 lead to separate folding and misfolding pathways. *eLife* 4: e07296.

Sekhar A, Rosenzweig R, Bouvignies G, and Kay LE (2016) Hsp70 biases the folding pathways of client proteins. *Proceedings of the National Academy of Sciences of the United States of America* 113(20): E2794–E2801.

Sekhar A, Velyvis A, Zoltsman G, Rosenzweig R, Bouvignies G, and Kay LE (2018) Conserved conformational selection mechanism of Hsp70 chaperone-substrate interactions. *eLife* 7.

Selenko P and Wagner G (2007) Looking into live cells with in-cell NMR spectroscopy. *Journal of Structural Biology* 158(2): 244–253.

Serber Z, Keatinge-Clay AT, Ledwidge R, Kelly AE, Miller SM, and Dotsch V (2001) High-resolution macromolecular NMR spectroscopy inside living cells. *Journal of the American Chemical Society* 123(10): 2446–2447.

Shammas SL, Crabtree MD, Dahal L, Wicky BI, and Clarke J (2016) Insights into coupled folding and binding mechanisms from kinetic studies. *The Journal of Biological Chemistry* 291(13): 6689–6695.

Smith AE, Zhou LZ, and Pielak GJ (2015a) Hydrogen exchange of disordered proteins in Escherichia coli. *Protein Science* 24(5): 706–713.

Smith MJ, Marshall CB, Theillet FX, Binolfi A, Selenko P, and Ikura M (2015b) Real-time NMR monitoring of biological activities in complex physiological environments. *Current Opinion in Structural Biology* 32: 39–47.

Smith AE, Zhou LZ, Gorensek AH, Senske M, and Pielak GJ (2016) In-cell thermodynamics and a new role for protein surfaces. *Proceedings of the National Academy of Sciences of the United States of America* 113(7): 1725–1730.

Sucec I, Bersch B, and Schanda P (2021) How do chaperones bind (partly) unfolded client proteins? *Frontiers in Molecular Biosciences* 8: 762005.

Tanaka T, Ikeya T, Kamoshida H, Suemoto Y, Mishima M, Shirakawa M, Guntert P, and Ito Y (2019) High-resolution protein 3D structure determination in living eukaryotic cells. *Angewandte Chemie (International Ed. in English)* 58(22): 7284–7288.

Theillet FX, Binolfi A, Bekei B, Martorana A, Rose HM, Stuiver M, Verzini S, Lorenz D, van Rossum M, Goldfarb D, and Selenko P (2016) Structural disorder of monomeric alpha-synuclein persists in mammalian cells. *Nature* 530(7588): 45–50.

Thole JF, Fadero TC, Bonin JP, Stadmiller SS, Giudice JA, and Pielak GJ (2021) Danio rerio oocytes for eukaryotic in-cell NMR. *Biochemistry* 60(6): 451–459.

Tittelmeier J, Nachman E, and Nussbaum-Krammer C (2020) Molecular chaperones: A double-edged sword in neurodegenerative diseases. *Frontiers in Aging Neuroscience* 12: 581374.

Tiwari VP, Toyama Y, De D, Kay LE, and Vallurupalli P (2021) The A39G FF domain folds on a volcano-shaped free energy surface via separate pathways. *Proceedings of the National Academy of Sciences of the United States of America* 118(46).

Tochio H (2012) Watching protein structure at work in living cells using NMR spectroscopy. *Current Opinion in Chemical Biology* 16(5-6): 609–613.

Tollinger M, Skrynnikov NR, Mulder FA, Forman-Kay JD, and Kay LE (2001) Slow dynamics in folded and unfolded states of an SH3 domain. *Journal of the American Chemical Society* 123(46): 11341–11352.

Tompa P and Fuxreiter M (2008) Fuzzy complexes: Polymorphism and structural disorder in protein-protein interactions. *Trends in Biochemical Sciences* 33(1): 2–8.

Torner R, Kupreichyk T, Hoyer W, and Boisbouvier J (2022) The role of heat shock proteins in preventing amyloid toxicity. *Frontiers in Molecular Biosciences* 9: 1045616.

Tsai CJ, Kumar S, Ma B, and Nussinov R (1999) Folding funnels, binding funnels, and protein function. *Protein Science* 8(6): 1181–1190.

Tugarinov V, Kanelis V, and Kay LE (2006) Isotope labeling strategies for the study of high-molecular-weight proteins by solution NMR spectroscopy. *Nature Protocols* 1(2): 749–754.

Tugarinov V, Libich DS, Meyer V, Roche J, and Clore GM (2015) The energetics of a three-state protein folding system probed by high-pressure relaxation dispersion NMR spectroscopy. *Angewandte Chemie (International Ed. in English)* 54(38): 11157–11161.

Uversky VN (2020) New technologies to analyse protein function: An intrinsic disorder perspective. *F1000Res* 9.

Uversky VN (2021) The protein disorder cycle. *Biophysical Reviews* 13(6): 1155–1162.

Vallurupalli P, Tiwari VP, and Ghosh S (2019) A double-resonance CEST experiment To study multistate protein conformational exchange: An application to protein folding. *Journal of Physical Chemistry Letters* 10(11): 3051–3056.

Vilar M, Wang L, and Riek R (2012) Structural studies of amyloids by quenched hydrogen-deuterium exchange by NMR. *Methods in Molecular Biology* 849: 185–198.

Wagner G and Wuthrich K (1982) Amide protein exchange and surface conformation of the basic pancreatic trypsin inhibitor in solution. Studies with two-dimensional nuclear magnetic resonance. *Journal of Molecular Biology* 160(2): 343–361.

Wang Q, Zhuravleva A, and Gierasch LM (2011) Exploring weak, transient protein—Protein interactions in crowded in vivo environments by in-cell nuclear magnetic resonance spectroscopy. *Biochemistry* 50(43): 9225–9236.

Wang X, Kirkpatrick JP, Launay HMM, de Simone A, Haussinger D, Dobson CM, Vendruscolo M, Cabrita LD, Waudby CA, and Christodoulou J (2019) Probing the dynamic stalk region of the ribosome using solution NMR. *Scientific Reports* 9(1): 13528.

Waudby CA, Wlodarski T, Karyadi ME, Cassaignau AME, Chan SHS, Wentink AS, Schmidt-Engler JM, Camilloni C, Vendruscolo M, Cabrita LD, and Christodoulou J (2018) Systematic mapping of free energy landscapes of a growing filamin domain during biosynthesis. *Proceedings of the National Academy of Sciences of the United States of America* 115(39): 9744–9749.

Waudby CA, Burridge C, and Christodoulou J (2021) Optimal design of adaptively sampled NMR experiments for measurement of methyl group dynamics with application to a ribosome-nascent chain complex. *Journal of Magnetic Resonance* 326: 106937.

Waudby CA, Burridge C, Cabrita LD, and Christodoulou J (2022) Thermodynamics of co-translational folding and ribosome-nascent chain interactions. *Current Opinion in Structural Biology* 74: 102357.

Wieteska L, Shahidi S, and Zhuravleva A (2017) Allosteric fine-tuning of the conformational equilibrium poises the chaperone BiP for post-translational regulation. *eLife* 6.

Wilson MR, Satapathy S, and Vendruscolo M (2023) Extracellular protein homeostasis in neurodegenerative diseases. *Nature Reviews Neurology* 19: 235–245.

Wright PE and Dyson HJ (2009) Linking folding and binding. *Current Opinion in Structural Biology* 19(1): 31–38.

Wu KP and Baum J (2010) Detection of transient interchain interactions in the intrinsically disordered protein alpha-synuclein by NMR paramagnetic relaxation enhancement. *Journal of the American Chemical Society* 132(16): 5546–5547.

Zeeb M and Balbach J (2004) Protein folding studied by real-time NMR spectroscopy. *Methods* 34(1): 65–74.

Zhang G and Ignatova Z (2011) Folding at the birth of the nascent chain: Coordinating translation with co-translational folding. *Current Opinion in Structural Biology* 21(1): 25–31.

Zhang YZ, Paterson Y, and Roder H (1995) Rapid amide proton exchange rates in peptides and proteins measured by solvent quenching and two-dimensional NMR. *Protein Science* 4(4): 804–814.

Zhu W, Guseman AJ, Bhinderwala F, Lu M, Su XC, and Gronenborn AM (2022) Visualizing proteins in mammalian cells by (19) F NMR spectroscopy. *Angewandte Chemie (International Ed. in English)* 61(23): e202201097.

Zhuravleva A and Gierasch LM (2011) Allosteric signal transmission in the nucleotide-binding domain of 70-kDa heat shock protein (Hsp70) molecular chaperones. *Proceedings of the National Academy of Sciences of the United States of America* 108(17): 6987–6992.

Zhuravleva A and Korzhnev DM (2017) Protein folding by NMR. *Progress in Nuclear Magnetic Resonance Spectroscopy* 100: 52–77.

Zhuravleva A, Clerico EM, and Gierasch LM (2012) An interdomain energetic tug-of-war creates the allosterically active state in Hsp70 molecular chaperones. *Cell* 151(6): 1296–1307.

Solid-State NMR Structural Studies of Proteins

CE Hughes and M Baldus, Max-Planck-Institute for Biophysical Chemistry, Göttingen, Germany

© 2005 Elsevier Ltd. All rights reserved.

This is an update of C.E. Hughes, M. Baldus, Solid-State NMR Structural Studies of Proteins, Editor(s): Franco Bassani, Gerald L. Liedl, Peter Wyder, Encyclopedia of Condensed Matter Physics, Elsevier, 2005, Pages 394–401, ISBN 9780123694010, https://doi.org/10.1016/B0-12-369401-9/00739-7.

Introduction 636
Interactions 636
Sample Preparation 637
Structural Analysis Using Solid-State NMR 638
Spectral Assignment 638
Secondary Structure 639
Tertiary Structure 639
Protein Orientations, Interactions, and Dynamics 640
Applications 640
Conclusion 641
Acknowledgments 643
Further Reading 643

Introduction

Unlike macroscopic scattering methods such as X-ray diffraction, electron microscopy, or neutron diffraction, nuclear magnetic resonance (NMR) delivers structural information indirectly by probing the local electronic and magnetic environment of a nuclear magnetic moment (spin) or by investigating spin–spin interactions, both in the presence of a static magnetic field. The choice of NMR methods to detect such interactions can be strongly related to the mobility of the molecule of interest. In fact, molecular motion, or more generally speaking, the overall molecular correlation time τ_c, can be used to classify the type of NMR techniques for studying structure at the atomic level. Solution-state NMR studies in proteins are usually applied to systems with an overall correlation time in the nanosecond regime, while solid-state NMR, the area of research discussed in this article, traditionally relates to long or infinite correlation times (Figure 1).

In general, an increase in molecular correlation time may result from large molecular size, interactions with an anisotropic environment or from a decrease in temperature. In the context of this article, such phenomena may be related to large proteins, proteins interacting with membranes, or protein aggregates that are indicated in a growing number of protein folding disease states. In all cases, the molecular correlation time becomes longer than the inverse of the magnetic resonance frequency and all possible molecular orientations in the magnetic field are sampled in the NMR frequency spectrum. Unlike in solution, the spectral resolution and the overall sensitivity of solid-state NMR are furthermore influenced by the size of the nuclear spin interactions. Recent progress in NMR instrumentation, in particular the combination of ultrahigh magnetic fields (i.e., above 14 T) with rapid sample rotation (discussed in more detail below) has considerably improved the use of solid-state NMR in biophysical applications.

So far, such conditions have not permitted a widespread application of high-resolution ^{1}H NMR spectroscopy, the most sensitive detection method in solution, but have greatly extended the possibilities for studying multiply or uniformly [^{13}C, ^{15}N]-isotope-labeled polypeptides with high sensitivity and adequate spectral resolution. In this article, an overview of the principal interactions that can be probed in NMR is provided, and a set of high-resolution solid-state NMR (HR-SSNMR) techniques that permit the detection of multiple structural parameters from a single protein sample or NMR data set, is introduced. In general, solid-state NMR spectra directly report on the conformational heterogeneity of the sample. Maximum spectral resolution is often obtained for proteins exhibiting a high degree of structural homogeneity. Hence, particular attention is placed on sample preparation and isotope labeling schemes. Finally, the possible range of applications of HR-SSNMR for the structural investigation of solid-phase (membrane) proteins is exemplified in three cases.

Interactions

The microscopic interactions that can be probed by NMR techniques are summarized in Figure 2 and encompass the chemical shielding, the quadrupolar coupling, the dipolar coupling, and the scalar coupling. The chemical shielding describes the interaction between a nucleus and the applied magnetic field, as mediated by the environment of the nucleus. It is observed as a shift in the resonant frequency, with isotropic and anisotropic contributions. In general, chemical shielding information can directly deliver information about the local electronic environment of a spin or the molecular coordination. In addition, for applications in polypeptides, the resulting resonance frequencies are not only diagnostic for each individual peptide residue but are also very sensitive to local backbone conformation.

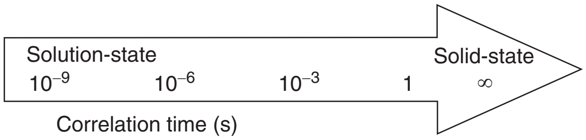

Figure 1 Typical ranges of molecular correlation times accessible to solution-state and solid-phase NMR.

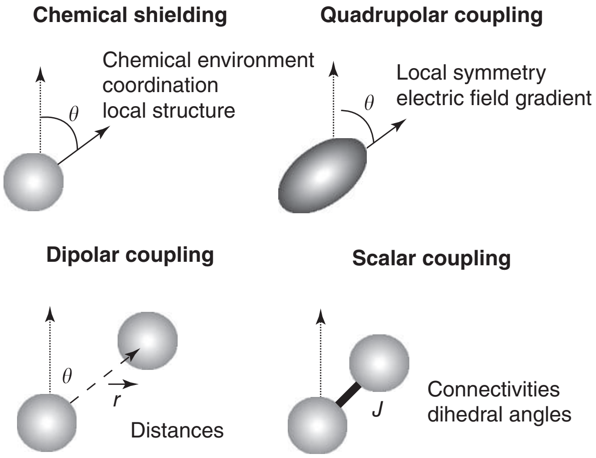

Figure 2 Summary of the four principal interactions probed by NMR. While chemical shielding and quadrupolar interactions involve only one-spin interactions, dipolar and scalar coupling refer to two-spin contacts.

The second interaction is the quadrupolar coupling, between the electric quadrupole moment of a nucleus and the electric field gradient at the nucleus. Only nuclei with a spin quantum number greater than 1/2 possess an electric quadrupole moment, making this interaction unimportant when dealing with spin-1/2 nuclei such as ^{1}H, ^{13}C, and ^{15}N. On the other hand, naturally abundant ^{14}N and deuteration with ^{2}H spins (both spin-1) may yield novel insights into the details of polypeptide structure and, in particular, dynamics. In addition to the interactions probing local chemical environments, two-spin interactions are invaluable tools for studying protein structure. For example, the dipolar coupling between pairs of nuclei, of either the same species (homonuclear) or different species (heteronuclear) directly reports on internuclear distances. This coupling is anisotropic in nature, having the same dependency upon spatial rotation as the anisotropic part of the chemical shielding. Finally, spin–spin interactions may be mediated by the through-bond coupling, also known as the scalar or *J*-coupling. This is an isotropic interaction between nuclei (homo- or heteronuclei) modulated by the bonding electrons. Both the dipolar and *J*-couplings can be exploited to transfer magnetization between nuclei, giving invaluable information about the proximity (dipolar) and bonding (*J*) of the nuclei.

In solutions, the rapid tumbling of molecules leads to an averaging out of the anisotropic interactions. In solids, these interactions remain and directly influence the detected NMR spectra. Because the dependence upon spatial rotation of both the chemical shift anisotropy (CSA) and the dipolar coupling is given by $3\cos^2\theta - 1$, where θ is the angle between the z principal axis of the interaction and the applied magnetic field, spinning a sample at an angle of 54.7° to the field axis results in a strong suppression of the anisotropic components of both interactions. The corresponding technique is known as magic-angle spinning (MAS). When MAS is combined with decoupling of the ^{1}H nuclei (whose dipolar couplings are larger and not generally removed by MAS) the line widths of many nuclei, including ^{13}C and ^{15}N, are narrowed toward values observed in solution-state NMR. By removing the dipolar and CSA interactions under ultrahigh magnetic fields (i.e., above 14 T), MAS makes the acquisition of high-resolution solid-state NMR spectra possible.

In addition, a variety of radio frequency (RF) NMR techniques have been developed to recover the structural information contained in the four interactions of Figure 2 under MAS conditions. Some of these NMR schemes rely solely on particular settings of the MAS rate and are called rotor-driven recoupling techniques. Other techniques, known as radio-frequency-driven polarization transfer techniques, employ a series of RF pulses to overcome the effects of MAS or chemical shift perturbations and allow the detection of specific structural parameters in high resolution.

Sample Preparation

In general, for HR-SSNMR based studies on proteins, [^{13}C, ^{15}N]-isotope labeling is mandatory. Labeling patterns ranging from the incorporation of specifically [^{13}C, ^{15}N]-labeled amino acids to uniform [^{13}C, ^{15}N] substitution are often most economically generated during bacterial growth in minimal media. In addition, chemical synthesis, such as fluorenylmethoxycarbonyl (Fmoc) chemistry, or cell-free approaches can be employed to produce isotope-labeled polypeptides. In both cases, structural studies using solid-state NMR can be performed using a variety of macroscopic sample preparations. For globular proteins, NMR experiments can be conducted after lyophilization and subsequent rehydration, which often increases the structural homogeneity of the sample. For the same purpose, precipitants such as polymers (e.g., polyethylene glycol, PEG) or organic solvents can be added that can lead to nano- or microcrystalline material. In the context of membrane proteins, structural studies have been conducted using frozen, detergent-solubilized specimens or liposomes in which the protein of interest has been reconstituted. Finally, fibrillized proteins have been extensively studied using solid-state NMR.

The highest sensitivity is usually achieved if the sample of interest is studied under MAS conditions using randomly oriented samples. In addition, macroscopically oriented samples, for example, mechanically oriented biopolymers or membrane-reconstituted peptides, aligned on thin polymer films, can be studied under fast MAS conditions. Furthermore, macroscopically oriented systems can also be investigated after orientation onto glass plates in static experiments or under MAS conditions.

Structural Analysis Using Solid-State NMR

Spectral Assignment

Of particular importance in the context of studying multiply or uniformly labeled proteins are polarization transfer methods employing scalar or dipolar two-spin interactions. Because of the isotropic character of the scalar coupling, polarization transfer mediated by through-bond interactions between two nuclei generally proceeds in an oscillatory manner, irrespective of the macroscopic orientation in the magnetic field (Figure 3a). In contrast, polarization transfer transmitted by through-space interactions under MAS conditions is dependent upon the orientation θ, of the dipolar vector in the static magnetic field. Integration over all possible molecular conformations can lead to a polarization transfer behavior, as depicted in Figure 3b, where positive and negative signal buildup corresponds to zero-quantum or double-quantum transfer, respectively.

An essential first step in NMR studies of multiply labeled proteins is the spectral assignment, based on the known amino acid sequence. Chemical shifts can be used to distinguish between general types of nuclei (e.g., ^{13}C nuclei in carbonyl (CO) and alpha (C_α) positions) but, for a full assignment, correlation experiments are necessary. These experiments generate two-dimensional (2D) spectra in which pairs of nuclei in close proximity are correlated. Two types of experiments exist, designed to establish intra- and inter-residue correlations. Different ^{13}C spin topologies of the amino acids give characteristic intra-residue correlation patterns, allowing the ^{13}C resonances to be assigned to the different residue types. Experiments for acquiring these correlation spectra may use single-quantum or double-quantum signal in an indirect dimension to separate out different contributions to the simple one-dimensional spectrum.

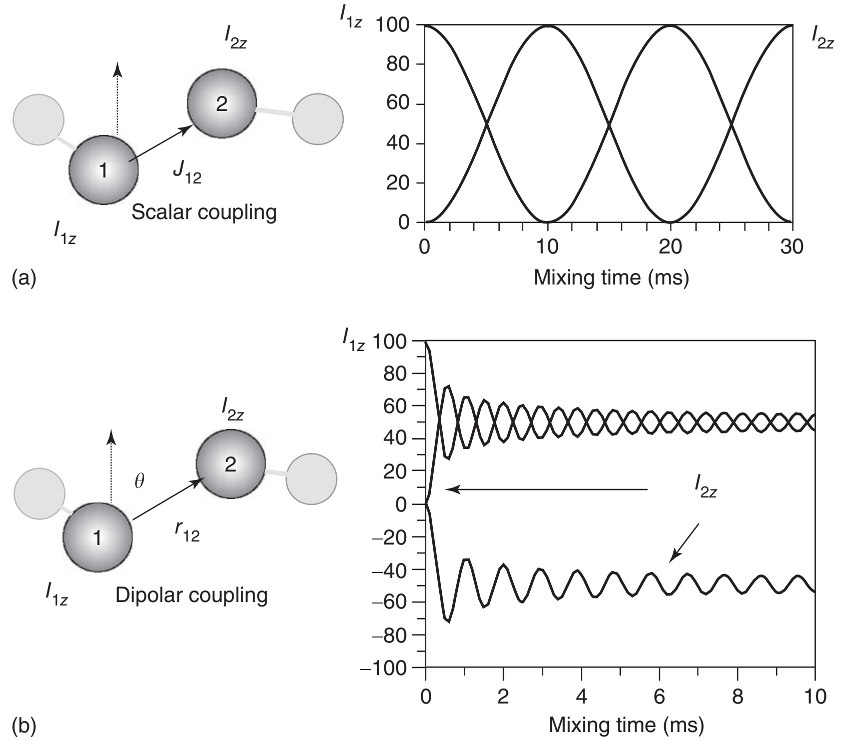

Figure 3 Analytical transfer functions for a two-spin system (denoted by the spin operators I_{1z} and I_{2z}) for the case of (a) the *J*-coupling and (b) the dipolar coupling. In both cases, the spin pair was initially prepared with magnetization only on spin 1. The transfer of polarization is subsequently monitored as a function of the mixing time (given in ms).

To acquire inter-residue information, ^{13}C nuclei can be correlated with ^{15}N nuclei in the same residue and the adjacent residues. This requires selective transfer of polarization between ^{13}C and ^{15}N in order to generate the desired indirect dimension and to ensure good resolution in the direct dimension. A common method involves two experiments, carried out on uniformly ^{13}C and ^{15}N labeled samples. In the first, magnetization is transferred from the backbone ^{15}N nuclei to the adjacent carbonyl (CO) ^{13}C and then, in a subsequent step, on to the α ^{13}C nuclei. This links the ^{15}N in residue *i* to the ^{13}C nuclei in residue *i*–1 (Figure 4, upper row) and is, in general, referred to as an NCOCA correlation experiment. In the second experiment, magnetization is transferred from the peptide bond ^{15}N nuclei to the nearest neighbor $^{13}C_\alpha$ spin, linking the ^{15}N and ^{13}C nuclei within the same residue. A subsequent (^{13}C, ^{13}C) transfer step leads to C_β resonance of the same residue corresponding to an NCACB-type experiment (Figure 4, lower row). From these two experiments, all backbone ^{13}C and ^{15}N nuclei of the polypeptide can be investigated.

Secondary Structure

The secondary structure of a protein encompasses the arrangement of the backbone atoms, depicted in Figure 5a. As the bond lengths are invariant, the secondary structure is largely defined by the torsional angles CO(i–1)–N(i)–C$_\alpha$(i)–CO(i) and N(i)–C$_\alpha$(i)–CO(i)–N(i+1), known as the φ and ψ angles, respectively. These may be measured in a variety of ways. A strong correlation exists between the ^{13}C chemical shifts at the C$_\alpha$ and C$_\beta$ positions and the values of φ and ψ. In particular, the two main backbone conformational types, the α-helix and the β-sheet, may be distinguished by comparing these ^{13}C chemical shifts to the average chemical shifts (so-called "random-coil" values) for each amino acid. An example of the strong correlation between, so-called, secondary chemical shifts $\Delta\delta$ and the torsion angle ψ is shown in Figure 5b for a U-[^{13}C, ^{15}N]-labeled sample of the SH3 domain from α spectrin.

Dihedral angle constraints may also be determined directly by experiments monitoring the relative orientation of the appropriate internuclear vectors. This encoding can be carried out by allowing the dipolar interactions to generate cross-peaks in a correlation spectrum characteristic of their relative orientation or by creating a multiple-quantum state that evolves under the influence of surrounding dipolar interactions. Distance measurements are also important for the determination of secondary structure. For example, the $H_\alpha(i)$–$H_N(i+1)$ distance is a sensitive measure of the ψ torsional angle and can be probed by indirect detection schemes in solid-state NMR. Specifically, ^{13}C and ^{15}N labeled samples can also be used to measure distances between residues, which are sensitive to the φ and/or ψ angles. In both cases, experiments are used which involve dipolar recoupling between the two nuclei of interest. The buildup of either magnetization transfer or double-quantum coherence depends upon the internuclear distance and may be analyzed by appropriate theoretical or numerical models to give a measure of the distance. Of particular importance for structural characterization of side chains are HCCH and HNCH torsional angles, both of which can be measured using the methods outlined above.

Tertiary Structure

In order to establish the overall fold of a protein, distances must be measured between separate parts of the peptide chain. For a long time, the determination of these long-range contacts represented a major challenge for solid-state NMR due to an effect known as dipolar truncation, where the strong, short-range dipolar interactions dominate weaker, long-range interactions. As a result, relay effects over several short-range interactions may determine the spin system dynamics. These problems are most serious for uniformly [^{13}C, ^{15}N]-labeled proteins. Three approaches have been recently suggested to circumvent these difficulties. One is to dilute the isotope labeling of the protein by, for example, block labeling. A second approach involves the use of selective recoupling methods that establish polarization transfer for particular two-spin systems only. Finally, useful information may be obtained from an analysis of (^{1}H, ^{1}H) contacts, which is common practice in solution-state NMR. Because of the limited spectral resolution in

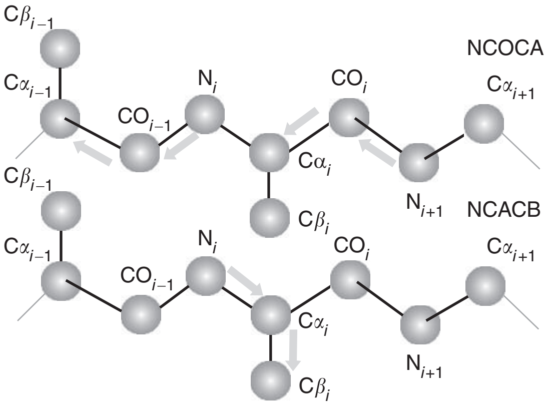

Figure 4 Graphical representation of NCOCA (upper row) and NCACB (lower row) correlation experiments that lead to spectral assignments in HR-SSNMR.

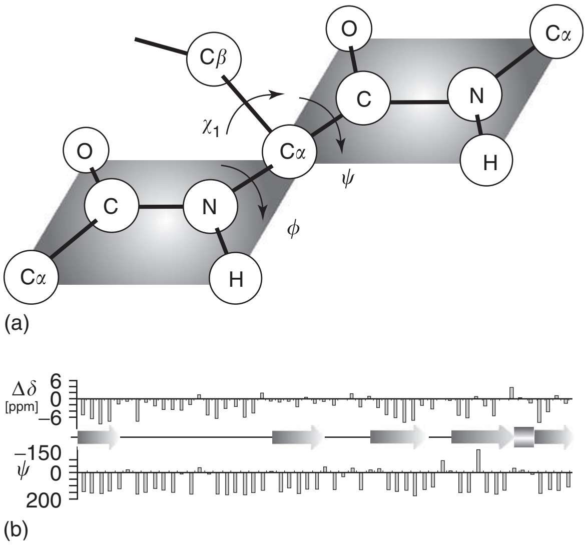

Figure 5 (a) The arrangement of atoms in the backbone of a protein. (b) The correlation between protein backbone structure, i.e., ψ, and secondary chemical shifts $\Delta\delta$ correlating C_α and C_β ^{13}C resonances obtained for the SH3 domain from α spectrin. $\Delta\delta$ is defined by the difference of observed (obs) and random coil (rc) C_α and C_β chemical shifts: $\Delta\delta=(\delta_{C\alpha}(obs)-\delta_{C\alpha}(rc))-(\delta_{C\beta}(obs)-\delta_{C\beta}(rc))$.

solid-state ^1H NMR spectra, such interactions may be encoded indirectly in high-resolution ^{13}C and/or ^{15}N spectral dimensions. Correspondingly, the 2D NMR experiments have been denoted by CHHC and NHHC correlation methods, respectively.

Similar to the solution-state, NMR structure determination in the solid state subsequently involves the calculation of families of molecular conformations that are consistent with the experimentally derived distance or angle constraints. The number and precision of these parameters determine the accuracy of the resulting 3D structure.

Protein Orientations, Interactions, and Dynamics

In addition to revealing structural information about the protein in a near-biological environment, the orientation of the protein with respect to a macroscopic reference frame (for example, one defined by the membrane bilayer for membrane peptides and proteins) can be investigated. The application of such methods often involves the NMR study of macroscopically aligned polypeptides and has resulted in several high-resolution structures of membrane-embedded systems. Furthermore, interactions between different proteins, proteins–ligand interactions (e.g., involving drugs, hormones, etc.), or monomer–monomer interactions in oligomeric proteins (quaternary structure) can, in principle, be investigated by high-resolution solid-state NMR.

Applications

In the following, three examples for the range of structural problems in immobilized proteins that can be addressed by high-resolution solid-state NMR are given. In Figure 6, results of 2D CHHC correlation experiment conducted on a uniformly [^{13}C, ^{15}N]-labeled sample of the 2×10.4 kDa dimeric form of the regulatory protein Crh in microcrystalline form are shown. Each correlation reflects close proton–proton contacts encoded in ^{13}C resonance frequencies. Three sections are highlighted where short, inter-residue (^1H, ^1H) distances are observed. A combination of these results with NC correlation experiments discussed earlier leads to NMR assignments of the largest protein studied by HR-SSNMR thus far and provides the basis for investigating the Crh folding pathway from a monomeric, soluble protein to a domain-swapped dimer observed in the microcrystalline state. Domain-swapping is a process by which one protein molecule exchanges a domain with an identical partner, and has been discussed as a general means for creating protein complexes and as a mechanism for misfolding and aggregation.

Solid-state NMR not only can report on the complete structure of a membrane protein but can also probe dynamics in the protein of interest. Both aspects have recently been investigated in the context of a uniformly [^{13}C, ^{15}N]-labeled version of the LH2 light-harvesting complex, one of the largest membrane systems studied by solid-state NMR to date (~150 kDa). Here, the application of ultrahigh magnetic fields (up to 750 MHz) was crucial to establish high-resolution conditions in the solid state. Two-dimensional (^{15}N, ^{13}C) correlation experiments (such as shown in Figure 7) were conducted to assign backbone and side-chain resonances at different temperatures. At −10°C, a variety of spectral assignments within the transmembrane sections of the protein were possible. Additional correlations occur at lower temperatures consistent with the immobilization of flexible loop regions of the protein. A more detailed structural study in membrane proteins could include (^{13}C, ^{13}C) or indirect (^1H, ^1H)

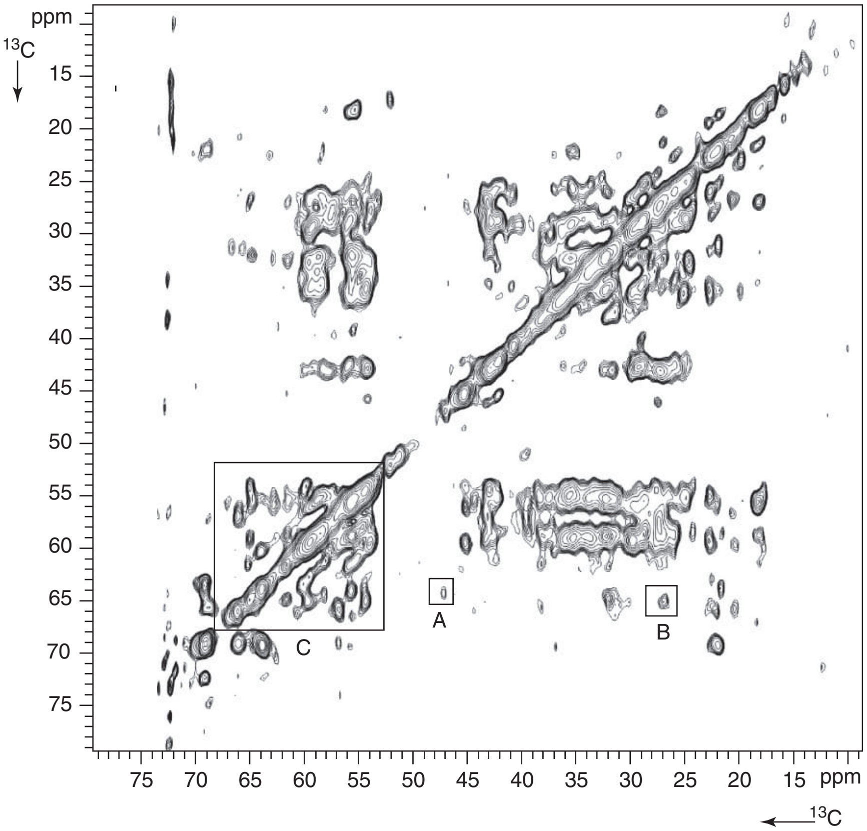

Figure 6 2D CHHC correlation experiment conducted on a uniformly [^{13}C, ^{15}N]-labeled sample of the 2×10.4 kDa dimeric form of the regulatory protein Crh. Each correlation reflects close proton–proton contacts encoded in ^{13}C resonance frequencies. Three sections are highlighted where short, inter-residue (^1H, ^1H) distances are observed: A – involving Gly49 and Ser46, B – Pro18 - Leu10, and C – a variety of C_α–C_α contacts.

correlation experiments possibly in conjunction with advanced isotope-labeling approaches, to determine the complete 3D structure of a membrane protein in the solid state.

To date, no structural information of a high-affinity ligand bound to a G-protein-coupled receptor (GPCR) is available. The recombinant expression of GPCRs in large quantities is usually difficult and must involve carefully optimized biochemical procedures. Restrictions regarding the availability of functional receptors also affect the quantities of ligand that can be studied. Moreover, the chemical environment including lipids and receptor protein can hamper the unambiguous spectral identification of a bound ligand in a solid-state NMR experiment. It has been recently shown how 2D solid-state NMR experiments can be used to detect microgram quantities of bound neurotensin, a 13-residue neuropeptide that binds in high affinity to the NTS-1 (101 kDa) receptor. For the 6-residue, biologically active, C-terminal sequence of neurotensin, a homonuclear (2Q, 1Q) correlation spectrum is sufficient to assign all C_α and C_β resonances of the uniformly [^{13}C, ^{15}N]-labeled ligand. These chemical shift assignments can be used to construct the backbone model of the ligand complexing with the receptor. Using the only high-resolution structure of a GPCR, rhodopsin, as a template, this information could be used to establish a molecular model for the binding pocket of NT(8-13) (Figure 8).

Conclusion

In many research fields, NMR methods have made important contributions to the present understanding of molecular structure and function. In particular, NMR has become a standard method for the characterization of 3D structure and dynamics of proteins that undergo fast molecular reorientations in solution. Such macroscopic sample conditions are, however, difficult to establish for protein aggregates, which are associated with a growing number of protein folding diseases. Moreover, integral membrane proteins, which constitute about 30% of all proteins, are often difficult to solubilize or crystallize in functional form. In all these cases, NMR techniques particularly designed for the study of solid-phase systems (“solid-state NMR”) offer unique possibilities to elucidate structural or dynamic parameters at atomic resolution.

In this article, a summary of high-resolution solid-state NMR methods that permit the detection of multiple structural parameters from a single protein sample or NMR data set is given. Recent applications in (membrane) proteins underline the growing potential of HR-SSNMR to provide exclusive insight into the microscopic details of biological functioning. Advances

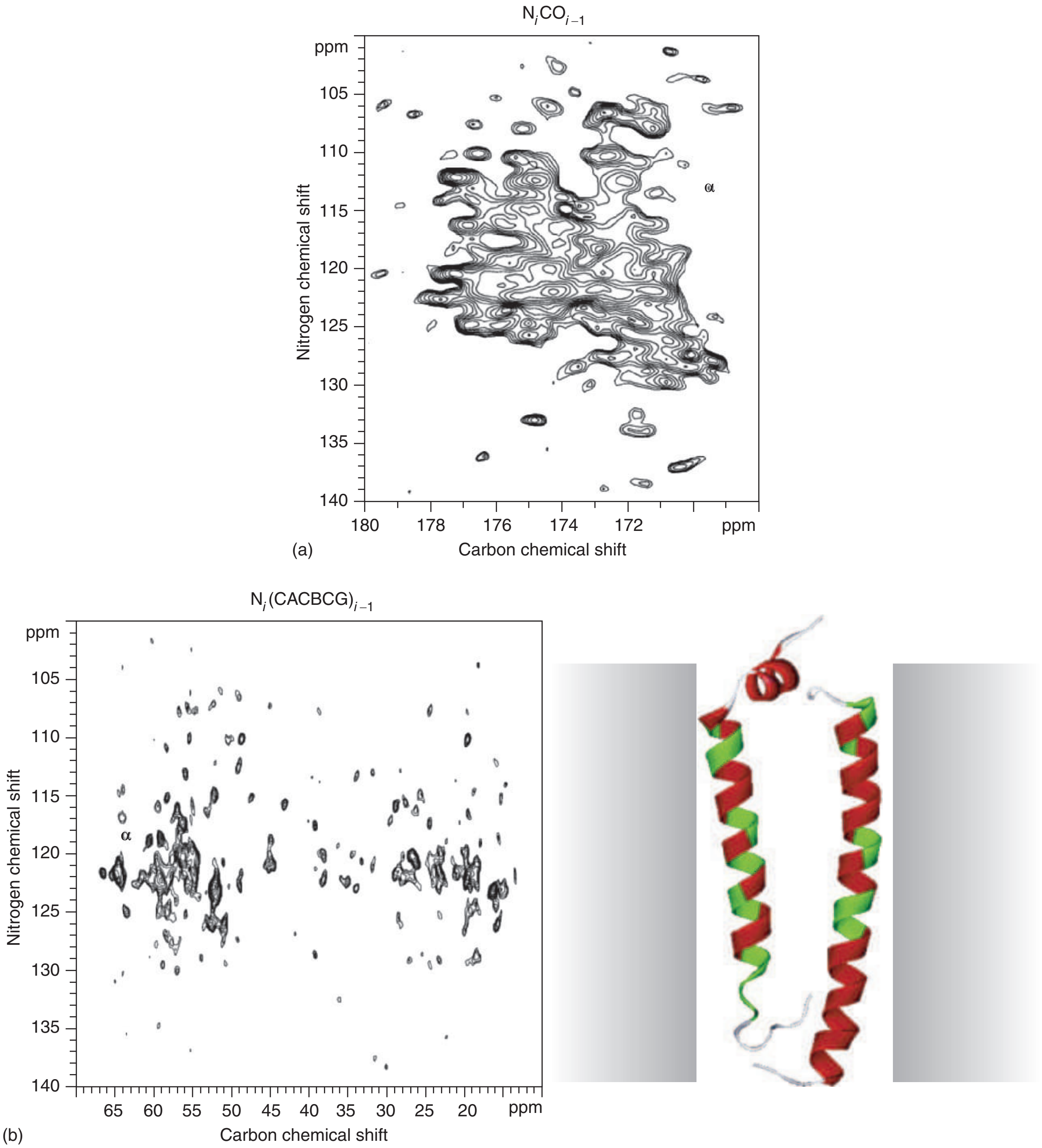

Figure 7 Combined NC-CC 2D transfer experiment on U-[^{13}C, ^{15}N]-labeled LH2 revealing a variety of N_iCO_{i-1} (a) and $N_i(CACBCG)_{i-1}$ (b) correlations. A schematic view of the backbone structure of the LH2 protomer complex embedded in a model membrane is shown. Assigned residues are indicated in green.

regarding sample preparation (for example, including modular labeling, *in vitro* expression, and intein technology) and improvements in NMR hardware instrumentation could open up additional areas of solid-state NMR research, such as the investigation of large protein–protein complexes or the complete 3D characterization of larger membrane proteins. Solid-state NMR studies of multiply labeled biomolecules will furthermore profit from improved procedures for calculating 3D structures, in particular, in the presence of ambiguous or a limited number of structural constraints. In general, protein motion does not hinder the application of solid-state NMR methods, providing a very efficient means of studying protein folding, flexibility, and function under biologically relevant conditions. Complementary to solution-state techniques and crystallographic methods, solid-state NMR can give detailed insight into protein structure and function.

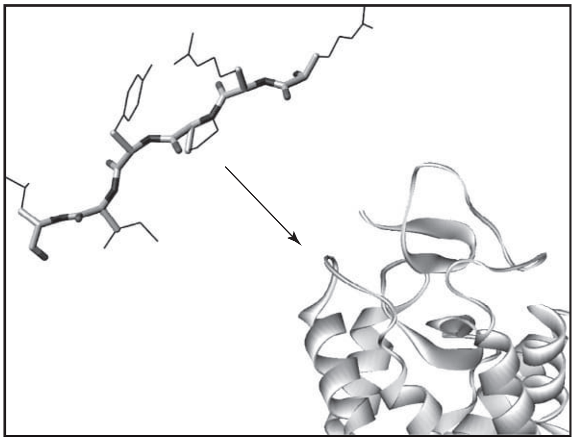

Figure 8 Schematic representation of the neurotensin NT(8-13) backbone structure, as obtained from solid-state NMR, and its interaction with a G-protein coupled receptor. For illustration, the only currently known GPCR structure (rhodopsin) is included.

Acknowledgments

The authors would like to thank their collaborators and group members who contributed to the work described here. This work has been funded in part by an Alexander-von-Humboldt fellowship for C.E.H.

Further Reading

Baldus M (2002) Correlation experiments for assignment and structure elucidation of immobilized polypeptides under magic angle spinning. *Progress in NMR Spectroscopy* 41: 1–47.
Cross TA and Opella SJ (1994) Solid-state NMR structural studies of peptides and proteins in membranes. *Current Opinion in Structural Biology* 4: 574–581.
Ernst RR, Bodenhausen G, and Wokaun A (1987) *Principles of Nuclear Magnetic Resonance in One and Two Dimensions*. Oxford: Clarendon.
Griffin RG (1998) Dipolar recoupling in MAS spectra of biological solids. *Nature Structural Biology* 5: 508–512.
Haeberlen U (1976) High resolution NMR in solidsselective averaging. In: Waugh JS (ed.) *Advances in Magnetic Resonance*. New York: Academic Press.
Levitt MH (2002) Symmetry-based pulse sequences in magic-angle spinning solid-state NMR. In: Grant DM and Harris RK (eds.) *Encyclopedia of Nuclear Magnetic Resonance: Supplementary Volume*, pp. 165–196. Chichester: Wiley.
McDowell LM and Schaefer J (1996) High-resolution NMR of biological solids. *Current Opinion in Structural Biology* 6: 624–629.
Mehring M (1983) *Principles of High Resolution NMR in solids*, 2nd edn. Berlin: Springer.
Thompson LK (2002) Solid-state NMR studies of the structure and mechanisms of proteins. *Current Opinion in Structural Biology* 12: 661–669.
Tycko R (2000) Solid-state NMR as a probe of amyloid fibril structure. *Current Opinion in Chemical Biology* 4: 500–506.

Protein Folding, Engineering of

SE Jackson, University of Cambridge, Cambridge, UK

© 2005 Elsevier Ltd. All rights reserved.

This is an update of S.E. Jackson, Protein Folding, Engineering of, Editor(s): Franco Bassani, Gerald L. Liedl, Peter Wyder, Encyclopedia of Condensed Matter Physics, Elsevier, 2005, Pages 418–425, ISBN 9780123694010, https://doi.org/10.1016/B0-12-369401-9/00382-X.

Introduction 644
Protein Engineering 644
Characterizing Folding Pathways: φ-Value Analysis 645
Interpretation of φ-Values 646
CI2 Protein-Engineering Results: The Nucleation–Condensation Mechanism 647
Barnase: Hierarchical Folding Mechanisms 647
Ultrafast Folders: The Engrailed Homeodomain 648
A Unifying Mechanism? 649
Computational Approaches 649
Further Reading 650

Introduction

Proteins are the most diverse of biological macromolecules, both in the structures they adopt and the functions they perform. Proteins are essential in all biological processes, acting as catalysts in the form of enzymes, in structural roles such as collagen and keratin in skin and hair, in the transport of small molecules such as oxygen by the protein hemoglobin, in the immune response in the form of antibodies, and in the regulation of all cellular processes acting as receptors and mediators of cellular signaling pathways.

Proteins are linear-chain polymers of amino acids, of which there are twenty naturally occurring building blocks. The condensation of the monomeric amino acid units into a polymer produces what is known as the polypeptide chain. Each protein has a specific sequence of amino acids which is encoded by the DNA of the gene for that protein. Proteins vary in length, the shortest are ~40–50 amino acids or residues long, whilst the longest, such as the giant muscle protein titin, can be over 10000 residues in length. Many proteins, however, are much smaller than this, typically between 200 and 300 amino acid units. This article focuses on how, relatively small proteins, that is to say those that are 100 residues or less in length, fold.

Proteins are produced in cells on ribosomes, the cellular machines for the synthesis of proteins. When it is first made, the polypeptide chain is in a highly flexible and conformationally dynamic state. In this state, the protein is referred to as being "unfolded" or "denatured" and it is not active. The polypeptide chain has to collapse into a specific, compact, and tightly packed folded state, known as the native state, before it can perform its physiological function.

The protein-folding field emerged in the early 1960s with the seminal work of Christian Anfinsen who showed that all the information necessary to specify the final three-dimensional structure of a protein was encoded in its primary amino acid sequence. How, after synthesis, an unfolded polypeptide chain collapses into a specific, compact, and tightly packed folded state, is the protein-folding problem. Up until the late 1980s, most of the work in the field focused on proteins with disulfide bonds or *cis*-prolines, as in these systems stable intermediates were observed which could be characterized experimentally. In these cases, folding is limited not by folding *per se*, but by the formation or rearrangement of disulfide bonds or isomerization of the prolyl peptide bond. Whilst these processes are interesting in themselves, they provide little information on the conformational changes occurring in the protein that result in the formation of a stable native state. In the late 1980s, protein engineering techniques were first employed along with rapid-reaction kinetics to characterize the folding pathways of a number of small proteins. In contrast to earlier studies, in these studies, the rate-limiting steps probed corresponded to folding and not some slower rearrangement or isomerization event. This approach to studying protein folding has now been widely adopted by the experimental protein-folding community and has provided data critical for the development of new protein-folding mechanisms and in benchmarking numerous computational studies. Here, the main features of the protein engineering methods are outlined and the work in this field over the last ten years, which has led to the determination of the energy landscapes for folding at atomic resolution for several small proteins, is summarized.

Protein Engineering

With the advent of recombinant DNA technology in the 1970s and 1980s came the ability to rationally and specifically engineer proteins. Over the past twenty years, these techniques have been considerably further developed and extended to include the use of the polymerase chain reaction (PCR), which now plays a major role in the manipulation of DNA. These methods enable many proteins from a variety of sources (e.g., human, yeast, bacterial, and archaebacterial) to be produced in large quantities in bacteria, generally *Escherichia coli*. This greatly facilitates the process of obtaining sufficient quantities of pure proteins for biophysical analysis. Further, these technologies allow one to engineer proteins with ease by modifying the genes (DNA) that encode for a specific protein. A number of different methods of engineering proteins can be adopted: site-directed mutagenesis can be used to replace one amino acid in a protein with any other at a specific position in the protein thereby producing a mutant protein with a single mutation (the protein with the naturally occurring sequence is known as the "wild type"). Alternatively, multiple mutations can be made either rationally or randomly; the latter is a powerful technique when combined with a selection screen for proteins with a particular property. Proteins can also be changed more radically in a variety of ways, for example, by changing the order in which structural units or motifs are connected, resulting in a mutant protein which has the same overall structure as the wild-type protein but with different connectivities between structural subunits. These mutant proteins are known as circular permutants. These methodologies are now routine and used widely by the protein-folding community. A review of the entire field is beyond the scope of this article. Here, the focus is primarily on the results that have come from single-site-directed mutagenic studies, which have had the biggest impact on the field of protein folding. In particular, the focus is on the methods of analyzing protein-folding pathways using protein-engineering approaches and the models that have resulted from such work.

Characterizing Folding Pathways: φ-Value Analysis

In order to understand how proteins fold, the structure and energetics of all states on the folding pathway need to be characterized. This includes the folded or native state, the unfolded or denatured state, as well as any intermediate states. Whereas, in the early years of protein folding it was thought that stable intermediate states were a prerequisite enabling the protein to fold on physiological timescales by reducing the amount of conformational space that needed to be sampled, in the early 1990s it was shown that a small protein, CI2, could fold very rapidly indeed without populating any such partially structured states. It is now well established that many small proteins fold in this so-called "two-state" fashion. In these cases, and others, one of the most important states to characterize on the folding pathway is the rate-limiting transition state which represents the energetic barrier to folding. Whilst the unfolded and folded states can be characterized directly using X-ray crystallography and multidimensional NMR techniques, the structure and energetics of the transition state can only be inferred from kinetic measurements. Fersht and co-workers have developed a method for analyzing folding transition states which is known as φ-value analysis and which uses protein-engineering approaches. The method is outlined below.

A point mutation is made to a protein and the kinetics of folding and unfolding are measured for both the wild-type protein and the mutant. In general, "nondisruptive deletions" are engineered such that the mutation removes a single interaction in the folded state of the protein and does not introduce any new interactions. In these cases, interpretation of φ-values is straightforward. The mutations usually destabilize the native state of the protein with respect to the denatured state (Figure 1). $\Delta\Delta G_{\mathrm{D-N}}$ is the difference in the free energy of unfolding (the energy difference between D, the denatured state, and N, the native state) between the wild type and the mutant, and a positive sign indicates that the mutation is destabilizing. It is straightforward to measure this difference under equilibrium conditions using a suitable probe of the folded state, frequently intrinsic fluorescence of aromatic amino acids or far-UV circular dichroism. In order to quantitate the effect of a mutation on the transition state for folding, then $\Delta\Delta G_{\ddagger-\mathrm{D}}$, the energy difference between the transition state (‡) and the denatured state, between the wild type and the mutant, also needs to be measured (Figure 1). For simple systems, such as CI2 which fold in a two-state manner, this value can be calculated from the unfolding data (by measuring the rate constant of unfolding, k_{U}, which is determined by the energy barrier for unfolding), or from the folding data using the rate constant for folding, k_{F}. A φ-value is defined as the ratio of $\Delta\Delta \mathrm{G}_{\ddagger-\mathrm{D}}$ to $\Delta\Delta G_{\mathrm{D-N}}$, which is a measure of the extent to which favorable interactions that the side chain of the mutated amino acid makes in the native state are formed in the transition state. Formal definitions of the different parameters are given below. Unfolding data can be used to calculate φ-values whether folding is two-state or not, as for small proteins no intermediate states are stable under unfolding conditions

$$\Delta\Delta G_{\ddagger-\mathrm{N}} = -RT\ln(k_{\mathrm{U}}/k'_{\mathrm{U}}) \qquad [1]$$

where k_{U} and k'_{U} are the rate constants of unfolding for the wild type and mutant, respectively. In this case, a φ-value is defined as follows:

$$\Phi = 1 - \Delta\Delta G_{\ddagger-\mathrm{N}}/\Delta\Delta G_{\mathrm{N-D}} \qquad [2]$$

For those small proteins that fold with two-state kinetics, φ-values can also be calculated from folding rate constants

$$\Delta\Delta \mathrm{G}_{\ddagger-\mathrm{D}} = -RT\ln(k_{\mathrm{F}}/k'_{\mathrm{F}}) \qquad [3]$$

where k_{F} and k'_{F} are the rate constants of folding for the wild type and mutant, respectively.

In this case, a φ-value is defined as follows:

$$\Phi = \Delta\Delta G_{\ddagger-\mathrm{D}}/\Delta\Delta G_{\mathrm{N-D}} \qquad [4]$$

For two-state systems, φ-values calculated from the unfolding and folding data are the same.

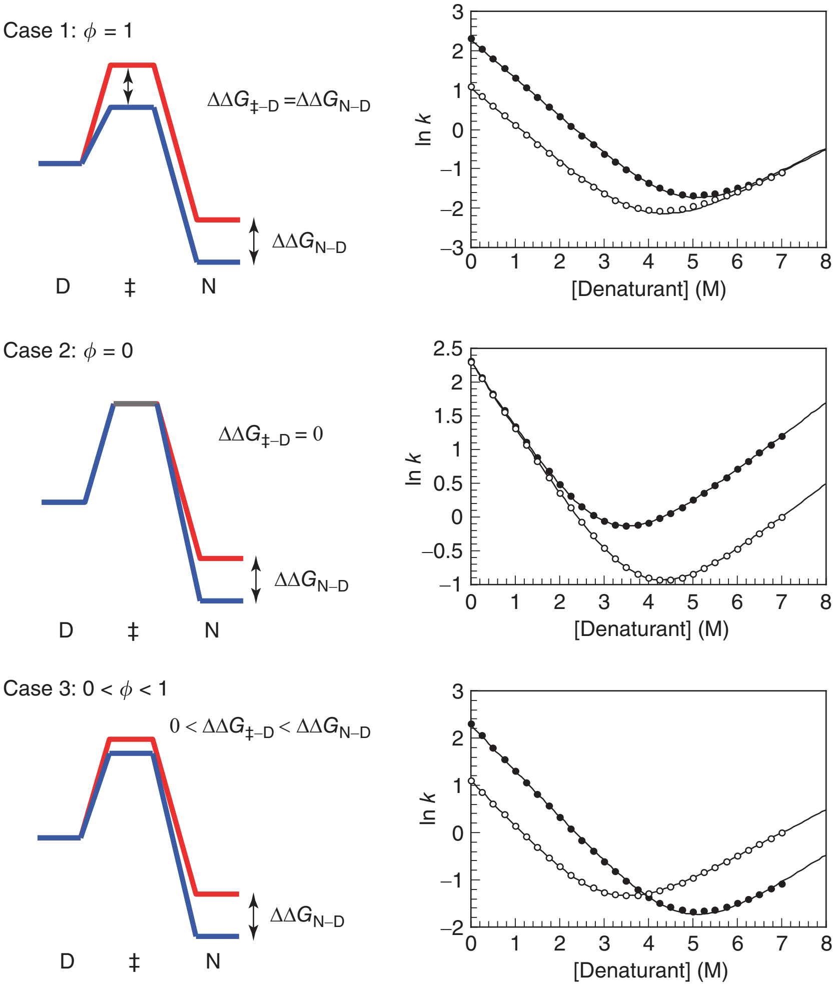

Figure 1 Free-energy diagrams showing the effect of a destabilizing mutation on the energy of the denatured (D), transition (‡), and native (N) state of a protein which folds with simple two-state kinetics. Case 1, when $\Delta\Delta G_{\ddagger-D}=\Delta\Delta G_{N-D}$ then $\varphi = 1$. In this case, the mutation affects the folding rate but not the unfolding rate – see the "chevron" plot of the rate constants for folding/unfolding as a function of denaturant concentration (right-hand side of figure). At low concentrations of the denaturant, the folding rate constant is measured and this decreases exponentially with increasing denaturant concentration, whilst at high concentrations of the denaturant, the unfolding rate constant is measured and this increases exponentially with increasing denaturant concentration. Case 2, $\Delta\Delta G_{\ddagger-D}=0$ then $\varphi = 0$. In this case, the mutation affects the unfolding rate but not the folding rate. Case 3, $0<\Delta\Delta G_{\ddagger-D}<\Delta\Delta G_{N-D}$ then $0 <\varphi<1$. In this case, the mutation affects both unfolding and folding rate constants. (Reprinted with permission from Daggett V and Fersht AR (2003) The present view of the mechanism of protein folding. *Nature Reviews. Molecular Cell Biology* 4: 497–502; © Macmillan Magazines Ltd.)

Interpretation of φ-Values

Briefly, $\varphi = 1$ when $\Delta\Delta G_{\ddagger-D}=\Delta\Delta G_{N-D}$, that is, the lost interaction energy upon mutation is the same in the native and transition states (Figure 1, case 1). In this case, the mutation affects only the rate of folding and not the rate of unfolding. φ-Values of 1 occur when the transition state is highly structured in the region of the mutation. Conversely, $\varphi = 0$ when $\Delta\Delta G_{\ddagger-D} = 0$, that is, when the mutation has no effect upon the energy of the transition state relative to the unfolded state (Figure 1, case 2). In this case, the mutation affects the rate of unfolding but has no effect on the rate of folding. φ-Values of 0 occur when the transition state is completely unstructured in the region of the mutation. Besides the values of 0 and 1, fractional φ-values are obtained when $0 <\Delta\Delta G_{\ddagger-D}<\Delta\Delta G_{N-D}$ (Figure 1, case 3). In this case, the mutation has an effect on both unfolding and folding rate constants. In general, fractional φ-Values are more difficult to interpret; however, in some cases, there is an approximately linear relationship between the φ-Value and the extent of formation of nonpolar contacts in the transition state relative to the native state. In these cases, φ-values are a good measure of the degree to which interactions of the mutated side chain are made in the transition state. An extensive description of the interpretation of φ-values and the assumptions and limitations of this method are not within the scope of this article and are discussed in detail elsewhere; see "Further reading."

In order to illustrate this method, the results of protein engineering and φ-value analysis on the small protein FKBP12 from the author's laboratory are discussed briefly below. FKBP12 is a small protein, the structure of which is shown in Figure 2**a**. Extensive

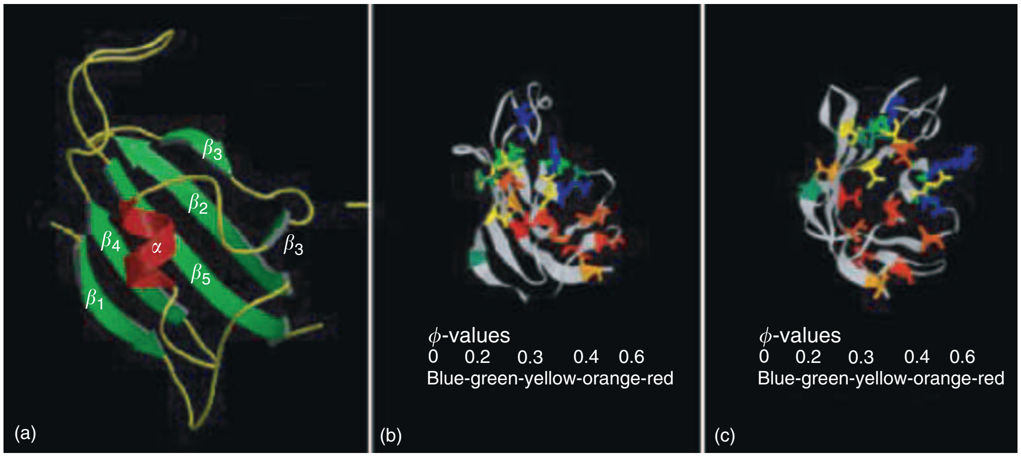

Figure 2 (a) Structure of the small, 106-residue protein FKBP12. Shown in red is the single α-helix, shown in green are the five β-strands which wrap around the helix to form the hydrophobic core. (b) Results of protein engineering studies and φ-value analysis. φ-values range from 0 (blue) to 0.6 (red). The side chains of the mutated residues are shown. (c) View of the φ-values and structure of FKBP12 rotated through 90°. (Reprinted with permission from Daggett V and Fersht AR (2003) The present view of the mechanism of protein folding. *Nature Reviews. Molecular Cell Biology* 4: 497–502; © Macmillan Magazines Ltd.)

protein engineering was performed on FKBP12 and the effect of mutations on the stability and kinetics of folding and unfolding of the protein was measured. Data were analyzed by the method described above and φ-values for many residues in the protein obtained. The results of these studies are summarized in Figures 2**b** and **2c,** which show the range of φ-values obtained and regions of the protein that have high values (are partially structured in the transition state) and those that have very low values (regions which are largely unstructured in the transition state). As expected, the φ-values vary between 0 and 1. In the case of FKBP12, no values of 1 were found, the highest value being 0.6. This is quite typical for small proteins. From Figure 2, it can be seen that residues with high values (>0.5) cluster together and form a folding nucleus (see discussion on nucleation–condensation mechanism). In FKBP12, the nucleus is formed by residues at the C-terminus of the α-helix and residues in the middle of the central β-strands which form part of the hydrophobic core. There is a gradation of φ-values moving away from this nucleus, and edge strands and end of the β-strands and loop regions frequently have values close to zero indicating that these regions are highly flexible and unstructured in the transition state. FKBP12 behaves in many ways like other small proteins including CI2 (see next section).

The resolution with which folding pathways can be determined using this approach has meant that it is now the most popular way of characterizing folding transition states experimentally and φ-values have now been measured for a number of proteins. Results from these studies from numerous folding groups fall broadly into one of three categories illustrated by the three examples given below. Together, these studies give a detailed picture of the ways in which proteins fold.

CI2 Protein-Engineering Results: The Nucleation–Condensation Mechanism

As discussed above, the small protein CI2 folds in a simple two-state manner without populating a stable intermediate state. Thus, mechanisms which require a stable intermediate to be present cannot be applied to this protein. Protein-engineering experiments have mapped in detail the structure of, and interactions present in, the transition state. As a result of these studies, the nucleation–condensation mechanism of protein folding was proposed by Fersht and co-workers in the mid-1990s. In this mechanism, the rate-limiting step of folding is the formation of a folding nucleus which can either involve a large part of the protein structure (in this case, the protein is said to have a diffuse nucleus) or comprise just a few elements of secondary structure (in this case, the nucleus is said to be localized). After the nucleus has formed, folding involves the rapid condensation of the rest of the native structure around the nucleus in an energetically downhill process. For CI2, the nucleus is quite diffuse, involving, to some degree, most regions of the protein. However, several residues in the α-helix and in the β-sheet are the most critical in stabilizing the transition state structure. In contrast to earlier proposed mechanisms, in the nucleation–condensation model, secondary and tertiary structures are formed concomitantly, the secondary structure being inherently unstable without the presence of some stabilizing tertiary interactions. NMR spectroscopy and molecular dynamic simulations have both shown that the denatured state of CI2 has little fixed structure and approximates well to a random coil. The complete folding pathway of CI2 is shown in Figure 3**a**.

Barnase: Hierarchical Folding Mechanisms

Barnase was the first protein to be subject to an extensive protein engineering and φ-value analysis and its folding pathway illustrates some key differences with CI2. Barnase is a larger protein, 110 residues in length, which, in contrast to CI2, folds with three-state kinetics demonstrating the presence of a kinetically significant, populated, intermediate state on the folding pathway. A close

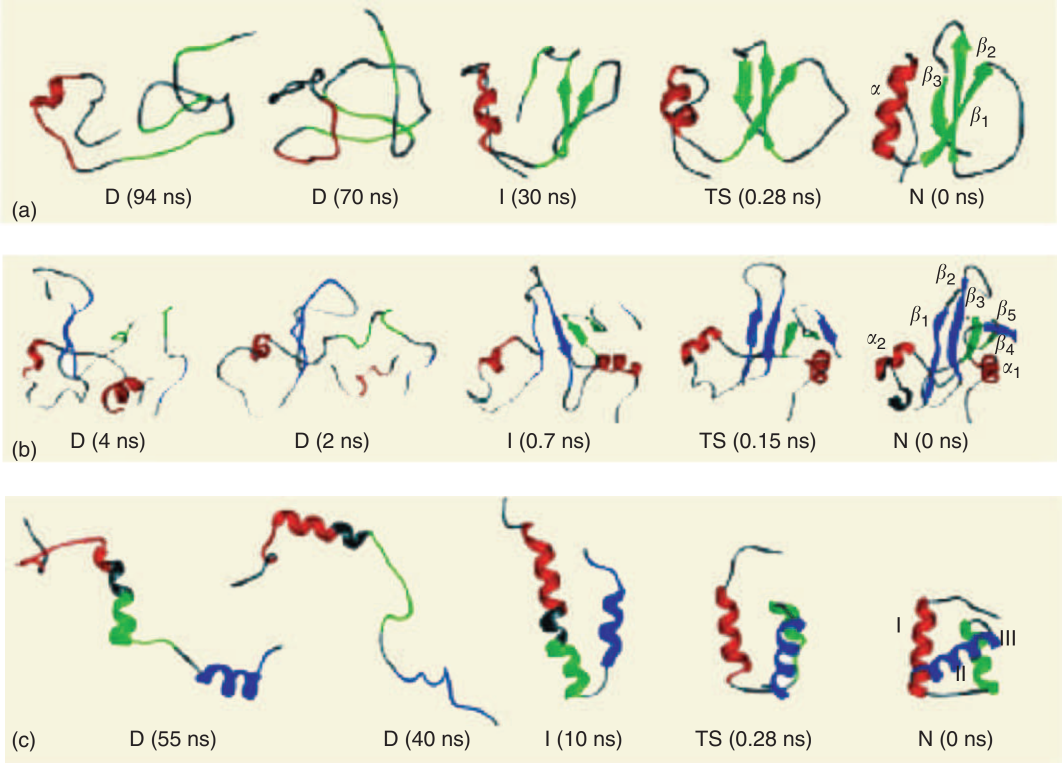

Figure 3 Schematic representations of the folding pathways of (a) CI2, (b) barnase, and (c) engrailed homeodomain. Results from protein-engineering studies and molecular dynamic simulations. (Reprinted with permission from Daggett V and Fersht AR (2003) The present view of the mechanism of protein folding. *Nature Reviews. Molecular Cell Biology* 4: 497–502; © Macmillan Magazines Ltd.)

analysis of the native structure of barnase shows that it has two structural subdomains. In contrast with CI2, barnase has a significant residual structure in the denatured state as probed by molecular dynamics simulations and NMR spectroscopy, that is, the denatured state is not a random coil and elements of both secondary and tertiary structure are transiently formed in this state. In barnase, the residual structure establishes a loose native-like topology in the denatured state which facilitates folding. From this state, the main hydrophobic core of the protein folds via a nucleation–condensation mechanism similar to CI2. The folding is nucleated by a residual fluctuating native-like helical structure in $\alpha1$ with a $\beta3$–$\beta4$ hairpin. The $\alpha1$, $\beta3$, and $\beta4$ elements of secondary structure form a scaffold or nucleus on which the remaining β-strands pack. This creates the metastable intermediate state observed in the kinetics. Further collapse and consolidation then occurs which brings residues involved in stabilizing the rate-limiting transition state together. During the formation of this nucleus, there is a refinement of packing interactions and consolidation of the interface between the two structural subdomains. Thus, barnase shows more hierarchical folding than CI2, with a gradual build-up of structure along the folding pathway. A schematic representation of the folding pathway of barnase is shown in Figure 3b.

Ultrafast Folders: The Engrailed Homeodomain

CI2 and barnase fold on the order of milliseconds to seconds at room temperature. Recently, proteins which fold with much faster rates have been identified and their folding pathways characterized using the techniques described above. The engrailed homeodomain from *Drosophila melanogaster* (En-HD) is a 61-residue, highly helical protein which folds on the microsecond timescale under physiological conditions. When unfolded in high concentrations of chemical denaturant or at very high temperatures, the unfolded state contains rather little residual secondary structure which is highly dynamic and fluctuating. Under more physiological conditions, however, at lower temperatures in the absence of denaturants, the denatured state has considerable residual structure with a high helical content and some long-range tertiary contacts. Combining experimental protein-engineering results with molecular dynamic simulations has provided a detailed picture of how this protein folds, Figure 3**c**. From the physiological denatured state (D), the transition state (‡) is formed by a reorientation of the helices and docking of them to form a partially packed hydrophobic core. In the final steps, the helices fully dock against each other and water is expelled from the hydrophobic core. En-HD folds by first forming relatively stable elements of secondary structure (in this case α-helices) which then diffuse and collide to form the tertiary structure and the native state. This is much like the framework model proposed by Ptitsyn and co-workers in the early days of protein folding.

A Unifying Mechanism?

Outlined above are the results of detailed experimental and computational studies on the folding pathways of three proteins. These three proteins are excellent examples illustrating the different mechanisms by which proteins can fold. It is useful to include a short history of the field of protein folding here, to show how recent work has established new folding mechanisms and shed light on mechanisms which were proposed in the early days of the field when high-resolution structural information on folding pathways was not yet available. The Holy Grail of folding is, of course, to unite these different mechanisms into a simple single mechanism applicable to all proteins. This unified mechanism is presented later after a brief discussion of individual mechanisms.

Wetlaufer was one of the first to propose a nucleation type of mechanism, that of nucleation growth, back in 1973. Here, an initial nucleus of local secondary structure forms and then the tertiary structure propagates rapidly from this. As this mechanism does not require the formation of stable intermediate states – and at that time all experimental studies were focused on proteins which folded slowly and had discrete intermediates (later some of these intermediates were shown to be misfolded species off the main folding pathway) – the nucleation-growth mechanism was not widely adopted. At that time, experimental studies were limited by suitable experimental techniques and rapid-reaction kinetics had not yet been applied to complex biological problems such as protein folding. In addition, protein engineering was still in its infancy. Other mechanisms were proposed and dominated in the 1970s and 1980s: the framework model in which secondary structure folds first, then diffuses and collides to form the three-dimensional native structure; the hydrophobic collapse model, in which the hydrophobic effect drives the formation of a compact state in which many hydrophobic side chains are excluded from the solvent water, rearrangement then takes place to form the fully folded structure. This model was extended and it was proposed that a secondary structure was formed during the collapse stage to form a "molten-globule"-like intermediate state. These molten-globule states have a native-like secondary structure but a liquid-like core in which side chains retain a high degree of mobility and in which fixed tertiary interactions are not yet formed. In the early 1990s, and as a direct result of protein-engineering studies and φ-value analysis by Fersht and coworkers on CI2, a new mechanism – the nucleation–condensation model – was proposed.

The results and models of the folding of CI2, barnase, and En-HD are typical of the range of results obtained for the folding of a number of small proteins. Despite apparent differences in the way in which these three proteins fold, Daggett and Fersht have recently proposed a unified mechanism of folding based on the nucleation–condensation model. In their view of folding, there is a spectrum of pathways available to a protein with the framework mechanism at one end of the spectrum and the hydrophobic collapse model at the other. The nucleation–condensation mechanism lies in the center of this spectrum and the two other models can be viewed as extreme cases. Proteins which have sequences with high intrinsic propensities for forming stable elements of secondary structure, such as the engrailed homeodomain, tend to fold with mechanisms which lie at one end of the spectrum and which approximate to a framework model. Proteins for which the conformational preferences for secondary structure are weak, such as CI2, tend to fold according to a nucleation–condensation mechanism in which secondary structural elements are stabilized by tertiary interactions in the transition state. Larger proteins with more than one structural subdomain, such as barnase, fold in a hierarchical fashion but each subdomain, however, folds with a mechanism which lies somewhere on the spectrum of mechanisms found for smaller proteins. It is interesting that, although the hydrophobic collapse model can be viewed as one extreme of the folding spectrum, there are no examples so far of small proteins which fold in this way. Theoretically, proteins may fold through a molten-globule-like intermediate if hydrophobic interactions are very strong.

Computational Approaches

It is clear from the discussions on CI2, barnase, and En-HD given above that results from computational studies in conjunction with experimental results of φ-values from protein-engineering studies have played a critical role in the development of new folding mechanisms and in increasing our knowledge of the complexities of the energy landscape for folding of small proteins. Although it is beyond the scope of this article, a few words on the main computational techniques used are included here. Many different computational approaches have been employed in the 1990s and applied to the protein-folding problem. These approaches range from rather coarse-grained models in which amino acids in the polypeptide chain are treated as beads on a string, a lattice-based structure is used, and simple pairwise potentials are employed. At the other end of the scale, all-atom molecular dynamic approaches have also been widely applied to the protein-folding problem. The different approaches, limited in different ways, have provided very complementary information on folding mechanisms and the fundamental questions regarding folding. Simple models and lattice-based approaches have provided support for nucleation-based mechanisms of folding, as well as being used to investigate cooperativity in folding. All-atom MD simulations are the most realistic of computational approaches but are restricted by the computational power and time necessary to simulate complex biological systems such as proteins (10000 plus atoms). With the exception of small structural motifs, such as β-hairpins, for which folding has been simulated using distributed computing techniques, simulations of folding itself are not possible. This problem has been circumvented by simulating unfolding processes using high temperatures to accelerate the unfolding event. In these cases, the potentials used correspond to lower temperatures, the effect of the high temperature merely being to speed up the process but not change the mechanism. Using the principle of microscopic reversibility, the unfolding and folding pathways must be identical under the same conditions. Thus, it has been possible to gain information on folding pathways using these techniques. Rigorous testing of this approach has been performed with multiple simulations of the same protein under different temperatures and conditions. Results of this type of testing have shown the technique to be robust. Further, this type of approach has now been benchmarked extensively against experimental data and shown to be reliable and accurate in predicting experimental results. From these simulations, ensembles of structures corresponding to the denatured, intermediate, and transition states have been identified and characterized for a significant number of small proteins. The data obtained from these simulations is very much complementary to that obtained from φ-value analysis, the one generating structures whilst the other provides information on the energetics of the system.

Recently, experimental and computational approaches have been combined and new methods developed by Vendruscolo, Paci and co-workers to probe in further detail the structures of, and interactions in, transition state ensembles. Experimental φ-values are used as restraints in simulations, in a manner similar to the use of NOE data in NMR structure determination, and computational approaches used to generate an ensemble of conformations corresponding to the transition state. The advantage over the MD unfolding simulations described above is that a large number of conformations can be generated rapidly. This approach has been successfully applied to the small 98-residue protein acylphophatase to characterize the network of interactions that stabilize the transition state and which are formed when a few key residues (the folding nucleus) form a native-like arrangement.

Further Reading

Daggett V and Fersht AR (2003) Is there a unifying mechanism for protein folding? *Trends in Biochemical Sciences* 28: 18–25.

Ferguson N and Fersht AR (2003) Early events in protein folding. *Current Opinion in Structural Biology* 13: 75–81.

Fersht AR (1999) *Structure and Mechanism in Protein Science*. London: Freeman.

Fersht AR and Daggett V (2002) *Cell* 108: 573–582.

Fersht AR, Matouschek A, and Serrano L (1992) The folding of an enzyme. 1. Theory of protein engineering analysis of stability and pathway of protein folding. *Journal of Molecular Biology* 224: 771–782.

Jackson SE (1998) How do small single-domain proteins fold? *Folding & Design* 3: R81–R90.

Matthews CR (1987) Effect of point mutations on the folding of globular proteins. *Methods in Enzymology* 154: 489–511.

Murphy KP (2001) *Protein Structure, Stability and Folding*. Totowa, NJ: Humana Press.

Pain RH (2000) *Mechanisms in Protein Folding*. New York: Oxford University Press.

Tanford C (1970) Protein folding, Part C. *Advances in Protein Chemistry* 24: 1–95.

Vendruscolo M and Paci E (2003) Protein foldingbringing theory and experiment closer together. *Current Opinion in Structural Biology* 13: 82–87.

Protein Folding and Aggregation

RA Broglia and G Tiana, Universitá degli Studi di Milano, Milan, Italy

© 2005 Elsevier Ltd. All rights reserved.

This is an update of R.A. Broglia, G. Tiana, Protein Folding and Aggregation, Editor(s): Franco Bassani, Gerald L. Liedl, Peter Wyder, Encyclopedia of Condensed Matter Physics, Elsevier, 2005, Pages 414–418, ISBN 9780123694010, https://doi.org/10.1016/B0-12-369401-9/00752-X.

Introduction 651
Models for Folding 651
Aggregation 654
Further Reading 655

Introduction

The protein folding problem concerns understanding how a protein of specified amino acid sequence ends up in a unique configuration which, among other things, determines its biological function. In physical terms: how does the one-dimensional information provided by the sequence of 20 different types of amino acids encodes for a unique and stable three-dimensional equilibrium conformation.

This problem has a clear biological and medical importance. The sequencing of the human genome provides information on the sequence of amino acids forming each of the hundreds of thousands of proteins which build our cells. The acquisition of sequence data by DNA sequencing is relatively quick, and vast quantities of data have become available through international efforts. On the other hand, the acquisition of three-dimensional data is still slow and is limited to proteins that either crystallize in a suitable form or are sufficiently small and soluble so that their structure can be determined by NMR in solution. Algorithms are thus required to translate the linear information into spatial information.

But the protein folding problem is quite intriguing also from a physical point of view. A protein is a system which is in a nearly-zero-entropy equilibrium state (usually referred to as "native" state; cf., e.g., Figure 1) in a wide range of temperatures (typically from 0°C to 60°C). Such equilibrium state has essentially no symmetries. The interactions within the protein are noticeably complicated and heterogeneous. Nonetheless, the protein does not display, as a rule, any competing low-energy states or kinetic traps (metastable states) typical of "frustrated" systems, but folds on a short call. The only feature typical of frustrated systems that survives in the case of proteins is the difficulty of predicting the ground state conformation from the knowledge of its elements (amino acids) and their interaction.

The goal of the physical approach to the protein folding problem is to understand the general principles of the folding mechanism of any protein. This implies that such a mechanism displays some amount of universality. There is indeed evidence that supports this scenario. In fact, aside from displaying a unique state of equilibrium (unique at the length scale of amino acids, i.e., 10^{-10} m) at biological temperatures, most proteins undergo a highly cooperative denaturation when the temperature is increased, similar to first-order phase transition (see Figure 2). The average folding time of proteins usually ranges from microseconds to seconds, and the distribution is usually a single- or multi-exponential, typical of a (or of few) Poissonian process. As a rule, proteins are very tolerant to point mutations. Mutations in a large number of sites have little or no effect on the folding properties of the protein, while each protein displays some key sites which, if mutated, lead to a large destabilization of the native state.

Typical cells contain around 20% proteins by weight. Consequently, evolution has provided proteins not only with the ability to fold on their own, but also to avoid aggregation, or to recognize other amino acid chains to perform their biological task. As in the case of oligomers, ordered assemblies of few single chains, which display the same features of unicity, stability, and fast folding of monomeric proteins.

Models for Folding

The simplest (and oldest) interpretation of the folding process consists of summarizing all possible conformations in a few macroscopic states, in the same way as is done to describe chemical reactions. Usually, the thermodynamically relevant states are the unfolded states (U), which contain all the conformations where the protein chain is unstructured; the native state (N), which corresponds by definition to a single conformation; and possibly some intermediate states ($I_1, I_2, \ldots$). The folding reaction is thus viewed as a chain of events $U \to I_1 \to I_2 \to \ldots \to N$, and the dynamics of the associated probabilities is described by a mean of master equations. The distribution of folding times results in a sum of a number of exponential terms of the type $e^{-t/\tau}$ equal to the number of jumps between states that the system has to do to reach the native state. The typical time τ needed to perform each of such jumps is determined, according to Kramer's theory, by the height of the free-energy barrier ΔF, which separates the two states, and has the form $\tau \propto \exp[\Delta F/kT]$. In the case of small globular proteins, experiments often detect a single timescale for folding, indicating a two-state process between states U and N.

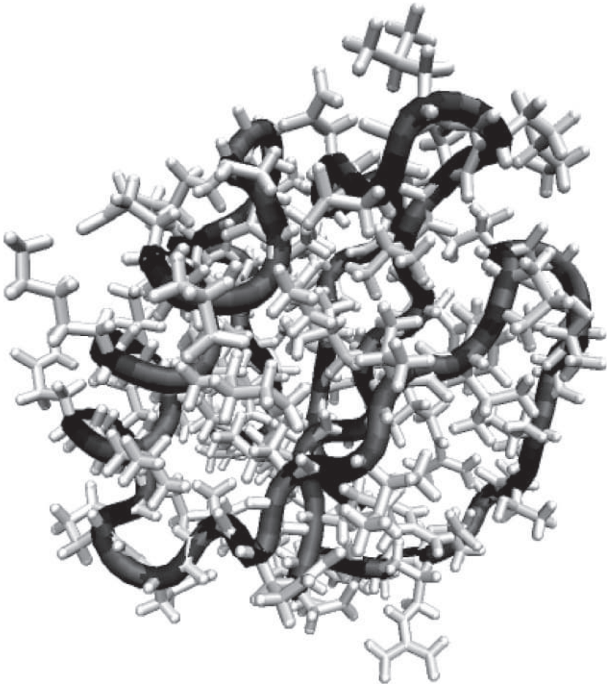

Figure 1 The native conformation of chymotrypsin inhibitor 2. The light gray parts highlight the arrangement of the atoms, which build a complicated network of interactions. In dark gray is highlighted the backbone of the protein.

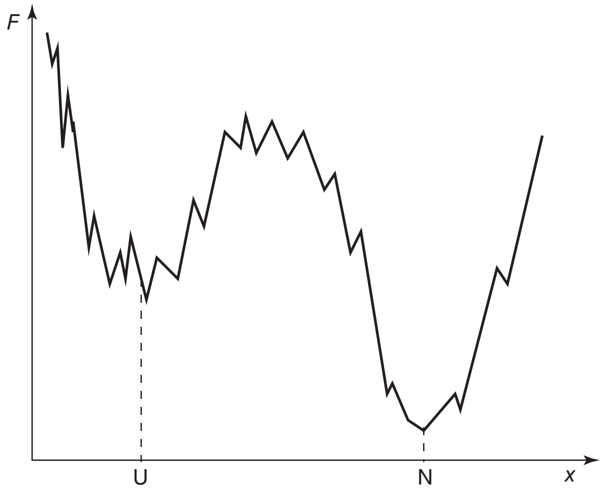

Figure 2 The typical free-energy landscape of a protein, plotted with respect to an arbitrary reaction coordinate *x*. Although the complexity of the interactions leaves some roughness in the landscape, evolution has shaped it in order to display two major wells separated by a barrier. The minimum associated with the native state (N) has essentially zero entropy and is stabilized by its attractive interactions, while the unfolded state (U) is mainly stabilized by its large entropy. As a consequence, when the temperature is increased, the free energy of the unfolded state decreases stabilizing it.

This simple model highlights the cooperativity of the folding process, determined by the presence of a major free-energy barrier, and provides good numerical estimates for the dependence of folding times on temperature and on mutations in protein sequence, but provides little insight into the molecular aspects of folding.

More recently, the focus has moved towards understanding the protein folding mechanism through a detailed description of the associated free energy landscape. A model which pursues this goal (the Go model) describes realistically the geometry of the protein but makes use of a simplified two-body potential function. Starting from the knowledge of the native conformation of the protein, two atoms are defined to be in (native) contact if their distance is smaller than a threshold. To such a conformation is ascribed a (negative) energy, and zero otherwise. This model, used in connection with computer simulations, is aimed at approximating the free energy with a careful entropic part and a simplified energetic part. Studying the folding of a number of small globular proteins with the help of the Go model, it is observed that the conformations associated with the top of the free-energy barrier separating the unfolded from the native conformation have well-defined structural properties, characterized by some important native contacts.

A different approach focuses attention on the energetic content of the free-energy function and, in particular, on the heterogeneity of the interaction arising from the presence of 20 kinds of different amino acids. It is known that physical systems displaying such a heterogeneity are associated, as a rule, with a rough energy landscape with many competing low-energy states. This picture is incompatible with that of proteins, which must display a unique ground state, well separated from the others, and as few metastable states as possible. The purpose of these models is to understand what makes a protein, characterized by a well-defined amino acid sequence, different from a generic heterogeneous system, whose paradigm is a random sequence of amino acids.

The starting point of energy-based models is the study of the thermodynamics of a random heteropolymer, which is an idealization of the peptide chain only characterized by stochastically independent contact energies. Being the sum of independent stochastic contributions, the total energy of the heteropolymer follows a Gaussian distribution, according to the Central Limit Theorem. Identifying this distribution with the distribution of conformational energies of the heteropolymer, the number of conformational states as a function of energy is

$$n(E) \propto \exp\left[-N_c \left(\frac{(E - N_c \varepsilon_0)^2}{2 N_c^2 \sigma_\varepsilon^2} - \ln \gamma \right) \right] \qquad [1]$$

where N_c is the number of contacts in the chain (assumed to be constant), ε_0 and σ_ε are the mean and the standard deviation over the 20 types of amino acids of the contact energies, and γ is the number of conformations that the chain can build per contact. Similar to the random energy model used in the field of spin glasses, the random heteropolymer model displays an entropy given by the relation $S(E) = N_c \ln \gamma - (E - N_c \varepsilon_0)^2 / (2 N_c \sigma^2)$ at energies above the threshold energy $E_c \equiv N_c \varepsilon_0 - N_c \sigma (2 \ln \gamma)^{1/2}$. On the other hand, below E_c the probability of finding any state of the heteropolymer is negligible, decreasing exponentially with the number of contacts N_c. Using the replica solution originally set up for spin glasses, it is possible to show that low-energy states are clustered in such a way that different clusters are separated by an energy barrier. This is a picture which can be hardly conciliated with that of proteins displaying a unique equilibrium state.

This simple model emphasizes a property of peptidic chains, that is the "frustration" due to the complicated interaction between 20 amino acids with different physical properties. "Frustration" implies the inability the system has to optimize all interactions at the same time, even in the lowest-energy state. A sequence of amino acids chosen at random is likely to be highly frustrated, and consequently not to display protein-like features. Within such a scenario, it is assumed that evolution selects protein sequences by minimizing the associated frustration. Setting this scenario within the framework of statistical mechanics, one can assume that protein-like sequences are those which display in some conformation an energy much lower than the sequence-independent threshold E_c, this conformation being the native state. In fact, if the native state is well below E_c, it does not have to compete with the other conformations whose energies are controlled by eqn [1]. Consequently, the native state will be unique and stable, more so, the larger the energy gap between the native state and E_c.

From the study of the models described above it emerges that the key ingredients of proteins to fold are their polymeric character and the heterogeneity of interactions. A powerful tool which allows to retain these two ingredients, although relaxing that of providing a detailed description of the protein geometry, is the lattice model. This model is based on two approximations: (1) the internal atomic structure of the amino acids is neglected and each of them is described as pointlike; (2) the amino acids move on the vertices of a cubic lattice of unitary side length. Accordingly, the conformational degrees of freedom are discrete. This is very convenient from a computational point of view and makes conformational entropy easy to handle, provided a contact potential is given. The simplest choice of such a potential has the form

$$U(\{r_i\}, \{\sigma(i)\}) = \sum_{ij} \varepsilon_{\sigma(i)\sigma(j)} \Delta(r_i - r_j) \qquad [2]$$

where r_i and $\sigma(i)$ are the position and type of the ith amino acid, $\Delta(r_i - r_j)$ being a contact function assuming the value 1 if the ith and the jth amino acids are in contact and zero otherwise, while $\varepsilon_{\sigma\tau}$ is the element of a 20×20 interaction matrix which measures the interaction energy between amino acids of type σ and τ. A widely used interaction matrix has been determined by Miyazawa and Jernigan from the statistical analysis of the contacts of a large database of proteins, assuming that the frequency with which a given contact appears in the database measures the strength of the contact energy between the corresponding amino acids.

Within the framework of the lattice model, it is possible to obtain a data set of sequences which fold into a selected native conformation starting from a random sequence displaying the observed composition (experimental ratio of the different types of amino acids), by swapping amino acids in such a way as to minimize the energy of the protein in the native conformation. This is a consequence of the fact that E_c does not depend on the details of the sequence, but only on its length. In other words, swapping amino acids does not change E_c, while the native energy can be decreased until it displays a large gap with respect to E_c.

A key result which emerges from such studies is that the stabilization energy of the protein is not distributed evenly throughout the native conformation, but is concentrated in a few, "hot" sites. This fact has remarkable consequences on the properties of the protein. First, it sheds light on the experimental fact that a protein is essentially insensitive to mutations in most of its sites. In fact, if a site different from the few "hot" sites is mutated, the change in native energy is not enough to fill the gap to the threshold energy E_c (which is not affected by the mutation), and consequently the protein retains its protein-like features. On the other hand, if a "hot" site is mutated, the energy of the resulting sequence in the native conformation can become larger than E_c. Consequently, the native state gets surrounded by a sea of unfolded conformation, losing its uniqueness.

Moreover, lattice model calculations indicate that "hot" sites build, as a rule, local elementary structures (LESs), that is fragments of the chain characterized by strong interactions between the "hot" sites which are close along the chain. Such LESs, which can be viewed as hidden, incipient secondary structures (like beta-sheets and alpha-helices) are very important for the folding dynamics because they bias the chain to the native state, according to a hierarchical scheme. Starting from a random conformation, LESs are formed very fast, because their stabilizing native contacts are close along the chain and, consequently, they do not need to explore a wide conformational space. Due to their large stabilization energy, LESs remain remarkably stable for the whole folding process. The rate-limiting step is then that of the assembly of LESs among themselves to build out their relative native contacts (the so-called "folding nucleus"). Being (quasi-) rigid entities, LESs make the chain effectively shorter. Furthermore, LESs interact among themselves with energies which are much larger than those with which single amino acids do. Consequently, it is unlikely that LESs form metastable structures, different from the native contacts designed by evolution. Once LESs have reached their mutual native positions, the conformational space of the protein is so restricted that the remaining amino acids fold immediately to their native position. Summing up, LESs provide an efficient way to squeeze out entropy from the initial random conformation in its way to the native state, avoiding metastable traps.

The uneven distribution of the stabilization energy and some hints about the events which take place on the folding trajectories of small real proteins can be studied by means of all-atom molecular dynamics simulations, combined with semi-empirical force fields. Results of such simulations, performed by considering specifically water, reveal the existence and allows the identification of "hot" sites. However, the simulation of the complete folding trajectory and the repetition of such simulations to obtain a statistically significant sample of the event is still computationally out of reach.

Aggregation

The term "aggregation" can mean a number of different processes, when applied to proteins. The simplest case is that of dimerization (or oligomerization), where two (or few) amino acid polypeptide chains assemble together into a conformation which displays all properties typical of the native state of monomeric proteins (e.g., uniqueness, stability, etc.). There are essentially three paradigms for this process. The best-understood is that of "exchange-domain" dimers, wherein two identical proteins have been induced by evolution to exchange part of their peptidic chain, giving rise to an interwined, symmetric conformation. The "lock-and-key" scenario is followed by those chains which first fold into monomeric native states and then assemble together, resulting at equilibrium in three populated states: denaturated, intermediate (single chain folded), and oligomeric (dock of single folded chains). On the other hand, "induced fit" oligomers first bind together in an unstructured conformation and subsequently find the native structure. While dimers (or oligomers) following the "exchange-domain" and the lock-and-key mechanism can still be described in terms of a few key sites (hot sites) controlling the whole process as in the case of single domain proteins, the "induced-fit" mechanism seems to be more subtle, implying a delicate balance between the contact energies at the interface and in the volume.

A mechanism similar to the lock-and-key mechanism can be used at larger scales, giving rise to micrometric, ordered structures. It is the case of tubulin, which builds microtubules in the cell, and actin, which builds muscle fibers. Aggregation can involve, under particular conditions, also proteins which usually fold to monomeric native conformations.

A cell contains 17–26% of proteins by weight, and in the cytoplasm there are $\sim 10^6$ peptide chains, separated by an average distance of 3 nm. It is thus likely that evolution has selected sequences not only to fold on their own, but also to avoid the interference of other proteins. Nonetheless, mutations, changes in the chemical environment, or other factors can make proteins aggregate into (usually) biologically inactive, eventually harmful, clumps.

Aggregates can be disordered clumps, kept together by unspecific interactions, or an ordered, elongated structure usually called a fibril (see Figure 3). There is strong evidence that a number of diseases are related to the deposit of fibrils in particular areas of the

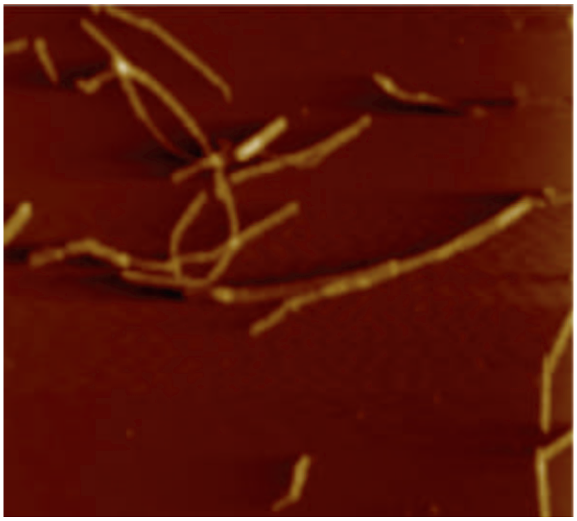

Figure 3 Fibrils made of insulin detected by atomic force microscopy. The length scale of the figure is μm.

human body (e.g., fibrils of beta-amyloid protein in the brain, in the case of Alzheimer's disease). Solid state NMR experiments have shown that, as a rule, fibrils contain parallel arrangements of specific U-like conformations of parts of the protein.

Aggregation is usually triggered by a nucleation event, and consequently the whole process can be separated into formation of the nucleus, that is, the minimum stable aggregate, and growth. Nucleation is a mechanism which reflects the entire thermodynamics of the solution, affected by the thermodynamic fluctuations of the solvent. For example, it has been shown that nucleation rate of sickle cell hemoglobin is strongly dependent on fluctuations associated with liquid–liquid demixing phase transition. Nucleation can be slowed down by stabilization of nonaggregating metastable states: light-scattering experiments and models based on molecular dynamics simulations indicate that micelle-like structures composed of a few beta-amyloid monomers compete with nuclei and discourage fibril formation. Also, the growth process often involves a nontrivial process which goes beyond mere diffusion. For example, the rate of elongation of beta-amyloid fibrils depends on temperature following an Arrhenius law, indicating that the binding of monomers to the end part of a fibril requires conformational changes.

Further Reading

Anfinsen CB (1973) Principles that govern the folding of protein chains. *Science* 181: 223.

Broglia RA, Shakhnovich EI, and Tiana G (2001) *Protein Folding, Evolution and Design*. Proceedings of the International School of Physics (E. Fermi). Amsterdam: IOS Press.

Broglia RA and Tiana G (2004) Lattice model of protein folding and of nonconventional drug design. *Journal of Physics: Condensed Matter* 16: R111.

Creighton TE (1992) *Protein Folding*. New York: W.H. Freeman.

Frauenfelder H and Wolynes PG (1994) Biomoleculeswhere the physics of complexity and simplicity meet. *Physics Today*, February 58.

Kusumoto Y, Lomakin A, Teplow DB, and Benedek G (1998) Temperature dependence of amyloid beta-protein fibrillazion. *Proceedings of National Academy of Sciences of the USA* 95: 12277.

Shakhnovich EI (1994) Proteins with selected sequences fold into unique native conformation. *Physical Review Letters* 72: 3907.

Vaiana SM, Palma-Vittorelli MB, and Palma MU (2003) Time scale of protein aggregation dictated by liquid–liquid demixing. *Proteins* 51: 147.

Protein Folding and Evolution☆

R Harada, Y Inagaki, and Y Shigeta, University of Tsukuba, Tsukuba, Japan

© 2016 Elsevier Inc. All rights reserved.

This is an update of R. Harada, Y. Inagaki, Y. Shigeta, Protein Folding and Evolution, Reference Module in Materials Science and Materials Engineering, Elsevier, 2016, ISBN 9780128035818, https://doi.org/10.1016/B978-0-12-803581-8.09800-3.

Introduction **656**
Basics of Protein Structure **656**
Early Studies on Protein Folding **657**
Complexity of the Protein-folding Problem **658**
Structure Prediction of Proteins by Empirical and Physical Models **658**
Protein Evolution **659**
Recent Topics in Protein-Folding Research **659**
A. Recent Progress in Single Protein-folding Experiments 660
B. Recent Progress in the Development of Models for Protein-Folding Simulations 660
C. Recent Trends in Hardware 660
D. Recent Progress in Conformational Sampling Methods 661
E. Importance of Robust Analysis Methods for Protein Folding 661
F. Towards Protein-Folding Simulation in Cellular Environments 662
Further Reading **662**

Introduction

Activities of life on Earth are carried out by proteins, which are synthesized according to the genome of the organism. A protein is a kind of molecular nanomachine, which takes an important role in biological functions such as (i) signal transduction, (ii) molecular recognition, (iii) catalyzing enzymatic reactions, and (iv) transporting molecules, ions, and electrons. Although the size of an individual protein molecule is typically several tens of nm, proteins form various structures that correspond to their inherent nature and the surrounding environment. Moreover, they cooperatively act on each other to maintain life. To understand their biological functions, one of the most important keyword is 'structure–function relationship'; this indicates that a particular protein has its native structure in physiological conditions, which enables it to carry out a certain function in those conditions. Thus, knowing the structure of a protein is essential to understanding the mechanism of its functionalities.

Since Kendrew and Perutz determined X-ray structures of myoglobin (1958) and hemoglobin (1960), both X-ray crystallography and nuclear magnetic resonance (NMR) experiments have so far described about 110 000 proteins at atomic resolution (Aug 2015). These structures are deposited in the Protein Data Bank (PDB), which is a convenient and freely available web service. However, the total number of proteins in organisms is thought to be about 10 000 000. Some of them are difficult to crystallize and are too big to have their structures measured by NMR experiments. Recently, electron microscope techniques have enabled measurements of the surface of large protein structures, but these experiments have yet to reach atomic resolution. Thus, it remains important to predict possible structures of proteins and their functions from a given amino acid (AA) sequence. During the last four decades, many theoreticians and experimentalists have worked to reveal the principles of protein-folding processes in nature. However, it is still difficult to do this and it is recognized as a fundamental problem in this field. In this commentary, we focus on giving the basics of the protein-folding problem and surveying both theoretical and experimental progress in the last 10 years.

Basics of Protein Structure

A protein comprises a one-dimensional sequence of 20 different AA residues with no branches. A small one typically consists of several tens of AAs and larger ones contain thousands of AAs, so that they form complicated macromolecular structures that range from 1000 to several hundred thousand atoms. Several subunits of the protein sometimes combine to form a complex of proteins. Moreover, some proteins contain small molecules, atomic groups, and ions as cofactors inside their structures to support complex structures and functions. For example, photosystem I (PS I) is a gigantic protein complex that consists of 11 subunits: [FeS] clusters, chlorophylls, β-carotenoids, phylloquinones, and so on. In PS I, a special pair of chlorophylls first harvest photon energy, then electron transfer occurs among [FeS], the other chlorophylls, β-carotenoids, and phylloquinones to promote reduction at the active site, a ferredoxin.

☆*Change History*: July 2015. Y. Shigeta, R. Harada, and Y. Inagaki made updates to the text and references. A new figure showing a folding funnel and structural changes was added.

In physiological conditions, a protein forms a steric structure according to its AA sequence. In the water-soluble proteins, polar and hydrophilic AAs are largely populated at the surface, while hydrophobic ones are inside the protein. Except for proline, the backbone structure formed by the AAs, –(O = C)–Cβ–(NH)–, is the same, so that some common structures are expected to appear in proteins. Indeed a helical structure is called an α-helix and a sheet-like structure a β-sheet, which are generally called the secondary structures. For these structures, a ϕ–φ plot of the backbone, which is often called a Ramachandran plot, indicates that these angles are extensively populated at specific regions, meaning it should be possible to predict protein structures, because these are not completely random. However, in actual proteins, these secondary structures are linked with loop regions and are three-dimensionally packed with particular alignments. These alignments are called ‘folds’ and there are tens of thousands of them. It should be noted here that different AA sequences occasionally adopt the same secondary structures and folds.

Early Studies on Protein Folding

In the 1960s, Anfinsen performed a refolding experiment using a ribonuclease A (RNase), where the RNase was initially reduced by β-mercaptoethanol to cleave disulfide (S–S) bonds. It was then denatured by concentrated urea solution to completely lose its native structure, and then the solution was diluted to the physiological condition to yield a reconstructed RNase that was indistinguishable from the native RNase. This landmark experiment led to a dogma: ‘the native structure of the protein is uniquely determined by the corresponding AA sequence and is thermodynamically the most stable structure.’ This dogma gives a thermophysical background to the protein-folding processes, and it has been supported widely by researchers in protein science. On the other hand, Levinthal proposed a thought experiment for the protein-folding dynamics. If a completely random-coil (unfolded) structure reaches the native structure randomly, it would require a longer time than the age of the universe, meaning that the protein-folding process may use unique routes (Levinthal’s paradox). On the basis of these ideas, many experiments were performed to find a two-state transition pathway from the random coil to the native structures. It was proven that relatively small proteins could fold rapidly with no intermediate states. On the other hand, some proteins consisting of more than 100 AAs slowly fold to the native structures via intermediate states called molten globule states. In a molten globule structure, the secondary structures and their folds are quite similar to the natural ones, although they lack particular three-dimensional tight packings among side chains compared with the natural ones. These processes are well explained by the frame model, in which: (a) the secondary structure first forms rapidly to reduce hydrophobic regions’ exposure to the aqueous solution, then (b) the secondary structures are aligned because of the long-range interactions among them, and finally (c) after the folds are fixed, fine adjustments among neighboring AAs occur to reach the native structure. However, the framework model does not always hold for all the protein-folding processes. For example, β-lacto-globulin, which is one of the whey proteins in cow’s and sheep’s milk, first forms several α-helices to become an intermediate state, and then the α-helices gradually collapse to reform the β-sheet-rich structure. These secondary transitions are occasionally found in a growth process of amyloids, and so might be a common process in protein folding.

From theoretical considerations, Go first applied a lattice model for the protein-folding problem and derived a consistency principle: the protein folds to the native structure because of a total, consistent balance of interactions among AAs. The lattice model and its variants are commonly called the Go Model. Later, Wolynes proposed a principle of minimal frustration, which is an expansion of Go’s consistency principle and states that the native structure has minimal frustration in interactions among AAs. Following these pioneering studies, the basic picture of the protein-folding process is now based on the existence of the folding funnel proposed by Onuchic, in which the energy landscape from the random-coil structure to the native one consists of downfolding

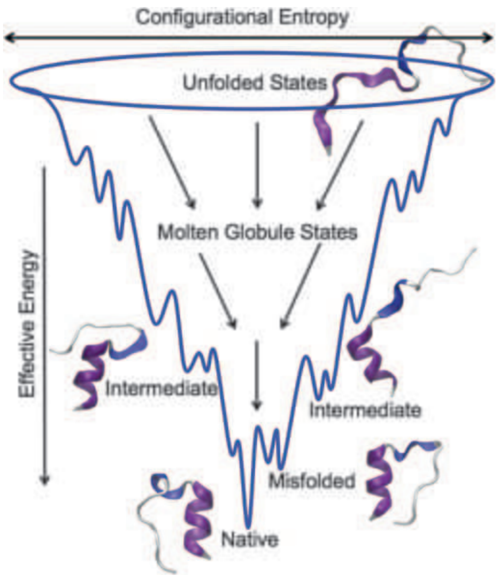

Figure 1 Schematic view of folding and corresponding folding structures.

with many local minima and the native structure is the global minimum in the landscape, resulting in spontaneous folding to the native structure (**Figure 1**). Because the free energy is the sum of entropic and enthalpic (potential energy) contributions, the relative stability of the random-coil and natural states is regulated by the competition between the two contributions. The random-coil state has various conformations with high potential energy, whereas the native one has a few conformations with the lowest potential energy, indicating the former is entropically and the latter is energetically favorable. Additions of denaturants and salts, changes in pH, concentration, and temperature, and so on cause changes in the relative stabilities among states, i.e., a change in the energy landscape, which sometimes leads to protein denaturation or an aggregation of proteins.

Complexity of the Protein-folding Problem

The history of the AA sequencer began when Edman established a sequential degradation technique from the N terminus of a given protein in 1950. In 1967, the first automated AA sequencer was described. Since 1990, analyses of complicated structures with posttranslational modifications have been achieved. Nowadays the process is quite fast and highly sensitive in determining the one-dimensional AA sequences. In spite of the availability of the AA sequence, as mentioned before, it is still difficult to predict the three-dimensional structure, even for small fast-folding proteins. Although secondary structures, such as α-helices and β-sheets, can be predicted from parts of a given AA sequence to some degree, a prediction of a fold is far from possible, except for special cases such as an α-bundle or a TIM barrel, because the long-range interactions among regions of AAs simultaneously affect the whole structure and both loop regions and side chains restrict alignment of these secondary structures.

The difficulty of predicting folds causes serious problems, because a fold occasionally affects the secondary structure. For example, two different mutants of a G protein, where 11 AAs consisting of an α-helix or a β-sheet in a part of the wild-type (WT) structure are replaced by the same sequence of 11 AAs, have the same fold as the WT, meaning that the same AA sequence takes either the α-helix or the β-sheet, depending on the situation. This kind of AA sequence is called a chameleon sequence. This suggests that the tertiary structure prediction rather than the secondary one is essentially inevitable for solving the protein-folding problem, because one AA sequence does not always correspond to a unique local secondary structure and has high flexibility in the conformational space. Other examples that partly violate Anfinsen's dogma, i.e., a diversity of conformations, are: (a) the same protein has two different structures depending on the crystal packing; (b) some proteins fold by forming a complex with other proteins as intrinsically disordered proteins; (c) molecular chaperons such as the GroEL/GroES complex support the folding of proteins; and (d) the same misfolded proteins aggregate to form an insoluble fibril-like macrostructure called an amyloid. In these ways, the mechanisms of the protein-folding processes are highly likely variable, and both empirical and nonempirical strategies, or mixtures of them, are indispensable for theoretical predictions.

Structure Prediction of Proteins by Empirical and Physical Models

A group of proteins having a close evolutionary relationship with 50% homology in their AA sequences is called a family, while one with 25% homology is a superfamily. Proteins within the same superfamily often share characteristics in their folds. As noted before, even if the AA sequences differ, the folds of two different AA sequences are occasionally the same. According to this heuristic, homology modeling, which considers that matching in individual parts of AA sequences is not important while that in the total AA sequence is, is often adopted for the structural modeling of a given protein, if structures of proteins in the same superfamily are available as scaffolds. After obtaining a rough structure of the given protein by homology modeling, the energy minimization of the modeled structure follows by adding side chains of AA residues, hydrogen atoms, and surrounding water molecules to yield the finer structure. Although homology modeling has succeeded in obtaining possible structures quickly and seems to be powerful, it has several drawbacks. The method can be adopted only when scaffolds (structures of proteins in the same superfamily) are available, and sometimes overlooks important structures for an AA sequence in the superfamily with a low homology. This is a common failure inherent in data-driven structure-modeling methods that require statistically sufficient numbers of samples to reduce the statistical error. At present, highly developed methods such as a template method, a 3D–1D method, and a fragment assembly method, which refer not only to AA sequences but also to known protein structures, have been widely used and some of them are freely available via their web sites.

As an approach to predict the native structure, computational simulations are powerful tools. In particular, molecular dynamics (MD) simulations with physics-based models have been widely used, not only to predict the native structure of a given protein from its AA sequence but also to trace the protein dynamics directly. Furthermore, MD simulations offer deep understanding of the dynamics that are important for biological functions. If the physical-based methods work properly, they provide valuable information beyond bioinformatics as follows: (a) predictions of conformational changes that are relevant to computational drug discovery; (b) understanding of enzymatic catalysis; (c) understanding of how proteins respond to ligand molecules as an allosteric effect; and (d) designing synthetic proteins that have noncanonical AAs. In the study of protein folding, MD simulations are indispensable for obtaining a complete and detailed picture of the mechanisms with atomic-level resolution, beyond the limits of temporal and spatial resolution of experimental techniques. However, there are several issues that must be tackled to achieve useful simulations of protein folding. They are mainly divided into three issues: (a) accurate models (including force fields) for MD simulations; (b) sufficient conformational sampling for reproducing the protein folding; and (c) robust data analyses for the big data generated by MD simulations as atomic trajectories to unveil the mechanisms of protein folding.

For structural prediction of a given protein, Critical Assessment of Structure Prediction (CASP), is famous for evaluating native structures. CASP is a community-wide, worldwide experiment for protein structure prediction. It has run every two years from 1994 to 2010. In CASP, predictors prepare a candidate for the native structure of a target protein within a few weeks. Herein, it is important that structural information of the target protein should be protected in a double-blind fashion, i.e., neither the predictors nor the organizers know the structure of the target protein when the predictions are made. Predictors use the available time to run their computer programs, which are usually based on protein sequences of known structure as templates. Templates can be found using sequence alignment methods. From CASP1 held in 1994 to the most recent CASP9 in 2010, structural prediction of the native structure of a given protein has gradually improved.

Protein Evolution

Although the basic processes in protein evolution are point mutations of individual AAs in a polypeptide chain, occasionally there are relatively remarkable changes such as insertions and/or deletions of a series of AAs. Moreover, the repetition or fusion of genes results in generating new proteins or the fusion of AA sequences, respectively. These modifications have accumulated over time, so AA sequences of current proteins are often different from those of primitive ones. In structural biology, one discusses protein evolution from the viewpoints of speciation and functional differentiation. The former means the evolution of homologous proteins with the same function but from different species. Studies of them are of great importance in knowing phylogenetic relations of proteins. On the other hand, the latter means the diversity of the proteins by acquiring different functions from the original ones. This kind of differentiation is thought to originate from AA mutations after the gene repetition to diverge into proteins with different functions. These analyses focus on the existing functionalities of proteins. In this review, we give a brief summary of the differentiation of proteins from the viewpoints of the protein structures and folding processes.

Proteins are not polymers that consist of random AA sequences, but are specific AA sequences that have been selected via evolution over a long period. The problem is: how have they been selected? There are two possible scenarios. One is that abiotic biopolymers (polypeptides) were synthesized in a proto-Earth or extraterrestrial environment. Most of those random AA sequences had no folding ability. However, some of them acquired the ability to fold by chance, and then protobionts harnessed them as biomaterials. Accidentally, these proteins helped the protobiont to survive hostile environments, and then the genes for these proteins might have been preserved for their descendants. The second scenario is that there were initially proteins with partial folding activity. The species with favorable functional proteins for existence were selected and handed their genes down to their descendants. Over generations, the proteins acquired proper folding activities with highly efficient functions. Because it is impossible to reproduce the whole evolutionary process that occurred on Earth, it is difficult to prove which hypothesis is correct or whether both of them are wrong. However, for the latter scenario, there is some collateral evidence. Szostak *et al.* succeeded in selecting proteins with Zn-binding activities from a library with random AA sequences. Among these proteins, they also found proteins with folding activity and showed that their crystal structures are quite similar to those of the wild-type versions. This means that they could identify folding proteins on the basis of the Zn-binding activity. Another ground for the latter scenario is that there are many proteins with indefinite structures in a physiological condition. These are the so-called intrinsically unfolded proteins (IUPs) or intrinsically disordered proteins (IDPs). As noted before, IUPs (IDPs) occasionally fold after binding to other proteins. Because they have characteristic AA sequences, a reverse search of their genetic codes was performed for a gene. It was found that about half of the coded proteins in a gene are IUPs (IDPs). They might have abilities to fold during extra-evolutionary processes and be helpful, or might become active to be adapted to other environments. The energy landscape of the IUP (IDP) has lugged and flat structures such that these proteins wander around many local minima (metastable structures). After binding to or interacting with other proteins, the energy landscape drastically changed to allow folding. This feature is quite different from ordinary folding proteins with their funnel-like folding energy landscape.

The next problem is whether the folding speeds of proteins are related to protein evolution. In a theoretical work that dealt with this problem, Gräter and his coworkers analyzed 92 000 proteins and 989 genomes, and showed with a mathematical model that the folding speed of the proteins became faster during the 40 billion years of evolution since life appeared on Earth. According to their results, it is suggested that (a) the folding speeds of proteins have accelerated from Archaea to multicellular eukaryotic organisms, (b) about 10.5 billion years ago, proteins with complicated structures appeared, resulting in a diversity of protein structures, and then folded proteins slowly developed, and (c) independent of alignment size, the folding speed of proteins became faster. One advantage of proteins folding faster is that it precludes their self-aggregation. These results conform well to the second protein evolution process mentioned above.

Recent Topics in Protein-Folding Research

With recent advances in single-molecule observation techniques, special-purpose computers, and the development of fast MD simulation codes, both the experimental and theoretical research in protein folding have made rapid progress over the past two decades. Below, we summarize the remarkable achievements in this field.

A. Recent Progress in Single Protein-folding Experiments

There are several experimental methods for predicting folding structures by experiments. ϕ-value analyses, which were originally developed in bioengineering, could predict a transition structure during a folding process at AA resolution. In this method, several AA mutations are introduced, and then the kinetics of the folding transition are measured for these mutants to evaluate the ϕ-value, which is a measure of the instability of a transition state following the introduction of the mutation. The ϕ-value is also defined as $\Delta\Delta G^{+}/\Delta\Delta G^{0}$, where $\Delta\Delta G^{+}$ and $\Delta\Delta G^{0}$ are the changes of activation energies and folding stabilization energies between the wild type and a mutant, respectively. Fersht investigated folding processes (transition state structures, kinetics, and so on) of small proteins with a two-state transition. The results obtained were explained well by those obtained using the Go-model. These facts indicate that two-state folding proteins have a funnel-like free energy landscape. As an extension of ϕ-value analyses, Sosnick proposed ψ-analyses, which might detect more structures in the folding processes of ubiquitin than would ϕ-value analyses. In any case, these analyses lack information about the dynamics of protein-folding processes.

To reveal the dynamics of protein-folding processes, fluorescent resonance energy transfer (FRET) experiments on a single free protein have become popular. In this method, two pigments are labeled on both the C- and N-terminals, and the fluorescent signals are measured over an extended time period. The time series of these signals contain information about the conformational dynamics of a given labeled protein from denatured to natural structures and vice versa. There are two experimental techniques used to observe the fluorescence signals. In one, the protein is fixed on an optical substrate, enabling measurements of the fluorescence signals of the single protein for a long time because the translational modes of the protein are rather restricted. However, the results may contain artifacts originating from interactions between the protein and the substrate. The other technique uses a confocal microscope that can reconstruct three-dimensional images of the fluorescence signals with high resolution. Because the residence time of a flowing sample in an observable region is not long term, the most crucial drawback of the latter method is a limitation on the observable time period. Nevertheless, recent developments in trapping the sample allow measurements for a relatively long time. For example, slow folding processes of a yeast cytochrome *c* (more than milliseconds) were observed from a quench signal caused by the FRET from a pigment to a heme. Other single-molecule experiments have also been developed. One of the most important single-molecule experiment technique is a mechanical unfolding induced by an atomic force microscope (AFM), which was first demonstrated by Mitsui, and then applied to a connectin by Rief. After their pioneering works, refolding processes followed by mechanical unfolding were extensively investigated.

Quite recently, X-ray free-electron laser experiments for detecting fast dynamics of a protein at the atomic resolution have been announced. It is strongly expected that these experiments, with the help of femtosecond spectroscopy, may open a new era in revealing protein-folding mechanisms ranging from femtoseconds to seconds in the forthcoming decade.

B. Recent Progress in the Development of Models for Protein-Folding Simulations

In recent progress in protein-folding simulations, force fields for the all-atom model have been updated extensively. Although further refinements might still be needed to improve accuracy, most current force fields are capable of folding proteins in good agreement with experimental data, indicating that semiempirical atomic force fields are accurate enough to simulate protein folding. However, it is expensive computationally to produce statistically reliable trajectories of protein folding to reach a typical folding time scale, i.e., milliseconds, because the time step for MD is typically 1 fs, so that 10^{12} iterations of the integration are required. Generally, the accessible time scale traced by the laboratory-level computer resources might be several hundreds of nanoseconds, which is far from the timescale for protein folding.

To extend the time scale of all-atom MD simulations, many coarse-grained (CG) models have been proposed and widely applied to large biological systems. There are two main families of CG models: the elastic network models (ENMs) and the Go models. In the ENMs, each residue of a given protein is spatially coarse grained as a particle, i.e., one bead per residue, where the interactions between the CG particles are defined as collections of harmonic springs. If a pairwise distance between two CG particles is small enough, their interaction is modeled with a harmonic spring. In the Go models, the local and nonlocal contacts are distinguished and the nonlocal pairwise potentials are represented by a dissociative function using the Lennard–Jones potential. The merits of CG MD are speed and low cost compared with all-atom MD, so that one can compute long-time dynamics of huge systems. The main demerits of CG MD are its low accuracy and lack of precise time scale. Thus, the results obtained from the CG MD simulations should be carefully compared with experimental data for validation.

C. Recent Trends in Hardware

As recent trends in specialized hardware developments, many techniques have been designed to reproduce protein folding. One way to enhance the conformational sampling of protein folding is simply to extend the simulation time period of the all-atom MD simulations. As a long-time MD simulation of protein folding, the first milestone might be a supercomputer simulation performed by Duan and Kollman in 1998 of the protein folding of the 36-residue villin headpiece in explicit solvent. In this simulation, a microsecond-order all-atom MD simulation sampled a snapshot that has 4.5 Å root mean square deviation measured from the NMR structure. Recently, as an example of progress in specialized hardware, a significant improvement in the computational efficiency of all-atom MD simulations has been achieved by a development of a specialized machine called 'ANTON' by D.E. Shaw's group. They performed all-atom MD simulations of some typically fast-folding miniproteins such as ubiquitin (76 residues) including explicit water, reaching the timescales of microseconds to milliseconds, resulting in reproductions of reversible folding and unfolding events as statistically reliable trajectories.

Along with specialized hardware, general-purpose graphics processing units (GPUs) and many-core architectures (Intel Xeon Phi) have frequently been used with all-atom MD simulation programs, because they are relatively cheaper than specialized hardware and useful for a variety of applications. In particular, many important algorithms have been implemented on GPU-based MD programs for accelerating all-atom MD, in which several orders of magnitude speedup over the CPU implementations have been achieved. Because the standard MD packages for biomolecules including AMBER, GROMACS, and NAMD have been implemented on GPUs, nowadays one can use them for long-time all-atom MD simulation of relatively large proteins.

D. Recent Progress in Conformational Sampling Methods

Before the emergence of ANTON, several enhanced sampling methods based on external biases were extensively proposed, where external perturbations are artificially imposed to promote the protein folding. These methods can be categorized into two types. The first approach is to sample transition pathways under the condition that two end-point structures, i.e., a set of reactant and product, are given *a priori.* The second category is to find a global minimum efficiently in the free energy landscape as the native state of a given protein, based on the accelerated dynamics without referring to the end-point structures. These important methods are briefly explained below.

For protein folding, the first approach might be convenient to reproduce folding events from an unfolded structure to the native structure of a given protein because the boundaries are fixed. For example, the transition path sampling method provides ensembles of transition pathways connecting a set of unfolded and native structures. As another example, the string method might be powerful in obtaining a relaxed folding pathway on a minimum free energy pathway (MFEP). In the string method, coarse-grained collective variables (CVs) describing the protein folding must be specified *a priori*. Based on the CVs, multiple images of an initial folding pathway are gradually relaxed to an optimal folding route on the MFEP. For the latter, replica exchange MD (REMD) and multicanonical MD (McMD) simulations are well-established methods, and are called generalized ensemble (GE) methods. In GE methods, the specifications of reaction coordinates (RCs), i.e., CVs, describing the protein folding are not required. As general RCs, temperature or the potential energy of a given protein are employed to perform the REMD and McMD. The ensembles generated by the GE can be reweighted to derive the Boltzmann ensemble at the target temperature. As examples of additional biased dynamics, targeted MD (TMD) or steered MD (SMD) provide sets of candidates of folding pathways with external restraints or forces for the native structure of a given protein. If the folding pathways generated by TMD or SMD have some hysteresis, the imposed restraints and forces might be inappropriate. As a self-updating biasing sampling method, meta-dynamics (MetaD) simulations have been widely used to reproduce rare events, including protein folding. In the MetaD, history-dependent external bias potentials along CVs have been imposed to reproduce the protein folding, leading to efficient folding into the native structure. One of the merits is that MetaD can simultaneously evaluate free energy differences among minima through single dynamics. However, a rather technical issue is how long one should continue the MetaD.

In any case, it might be difficult to restore details of the dynamics of protein folding from these methods, because all accelerated dynamics track trajectories with modified statistical treatments or with modified potentials, which are different from the real dynamics that are reproduced by naive long-time MD simulations by ANTON. In other words, the time series of detailed atomic trajectories are discarded in compensation for increasing the conformational sampling efficiencies. In this sense, it should be noted that these methods do not directly reproduce the dynamics of protein folding.

E. Importance of Robust Analysis Methods for Protein Folding

To extract the dynamics of protein folding, one might need analytical methods that are capable of reducing simulation data to their essential features without discarding physical insights. Nowadays, one can simulate the folding of relatively small proteins in explicit solvent at 100 ns per calculating day with GPU machines. These simulations provide long-time atomic trajectories as big data, however, and it is difficult to extract essential protein dynamics from them because of their high dimensionalities. For this problem, several analytical and numerical techniques in the fields of informatics and data analysis have been extensively applied, such as principal component analysis (PCA) and its variant, multivariate statistics (MS), time series data analyses, network-based models (NMs), and so on. The two former analyses/methods are used to find appropriate RCs that describe essential protein-folding dynamics, and the last one is called the Markov state model (MSM); these are well-established algorithms representing the first-order kinetics between a set of discrete states (microstates) projected onto a subspace spanned by the RCs. Once the appropriate RCs have been found, MSMs have been widely applied to yield the lifetimes of microstates by solving master equations for them, where conformational transitions among the microstates are represented by a transition matrix evaluated from the given trajectories. Because of the flexibility of MSMs, one must carefully confirm whether or not the kinetics obtained by the MSM correctly describe the protein-folding events by comparing the results with experimental evidence. Furthermore, a unique determination of the appropriate RCs is a nontrivial task, because it is difficult to use common CVs, for example those taken from PCAs, for reactant and product. Therefore, one must also carefully specify the appropriateness of RCs and check whether the analyses correctly explain the essential protein dynamics of interest.

F. Towards Protein-Folding Simulation in Cellular Environments

Most current protein-folding simulations assume that the protein folding occurs in a dilute aqueous solution. However, in practice, biological cells consist of many elements such as proteins, nucleic acids, lipids, metabolites, and ions, and the protein folding must be considered in these crowded environments that are significantly different from those typically encountered in experimental studies. Protein crowding appears to modulate the kinetic properties of the protein folding. Furthermore, crowded environments might shift the structural stabilities of native states after the protein folding. From the viewpoint of the effect of protein crowding, stability involves an entropic stabilization of the native state because of volume exclusion that is related to limits of the space for extended conformations, deriving compact and globular shapes that tend to be stabilized as native structures in the crowded environment. Theoretical studies with a hard-sphere model by Minton supported the stabilities derived by the excluded-volume effect. However, recent hydrogen-exchange NMR studies of several proteins in concentrated conditions and non-proteincrowder solutions showed that the structural stability of the protein depended strongly on the surrounding crowders, meaning that stabilities of proteins measured in dilute conditions are different from those for crowded (cellular) environments. Recent crowding simulations in explicit solvent reported by Feig *et al.* have supported these results and concluded that protein stabilities are affected by the surrounding crowder types, suggesting that the effect of crowding primarily depends on the nature of the protein–protein interactions with the surrounding crowder proteins. Therefore, the protein-folding process might be affected by the protein–protein interactions of the intermediates of the protein folding and shift away from the folding pathways in dilute solution. With our expanded computational resources, full atomic crowding simulations are feasible, but physically and computationally valid models that describe the protein folding under cellular environments are strongly desirable future work.

Further Reading

Anfinsen CB (1973) Principles that govern the folding of protein chains. *Science* 181: 223–230.

Debès C, Wang M, Caetano-Anollés G, and Gräter F (2013) Evolutionary optimization of protein folding. *PLoS Computational Biology* 9: , e1002861.

Dill KA, Banu Ozkan S, Shell MS, and Weikl TR (2008) The protein folding problem. *Annual Review of Biophysics* 37: 289–316.

Frauenfelder H, Sligar SG, and Wolynes PG (1991) The energy landscapes and motions of proteins. *Science* 254: 1598–1603.

Go N (1983) Theoretical studies of protein folding. *Annual Review Biophysical and Bioengineering* 12: 183–210.

Harada R, Takano Y, Baba T, and Shigeta Y (2015) Simple, yet powerful methodologies for conformational sampling of proteins. *Physical Chemistry Chemical Physics* 17: 6155–6173.

Harada R, Tochio N, Kigawa T, Sugita Y, and Feig M (2013) Reduced native state stability in crowded cellular environment due to protein-protein interactions. *Journal of American Chemical Society* 135: 3696–3701.

Hartl FU, Bracher A, and Hayer-Hartl M (2011) Molecular chaperones in protein folding and proteostasis. *Nature* 475: 324–332.

Hartl FU and Hayer-Hartl M (2009) Converging concepts of protein folding in vitro and in vivo. *Nature Structural & Molecular Biology* 16: 574–581.

Karplus M (1997) The Levinthal paradox: Yesterday and today. *Folding and Design* 2: S69–S75.

Keefe AD and Szostak J (2001) Functional proteins from a random-sequence library. *Nature* 410: 715–718.

Kuwajima K (1983) The molten globule state as a clue for understanding the folding and cooperativity of globular-protein structure. *Proteins* 6: 87–103.

Lindorff-Larsen K, Piana S, Dror RO, and Shaw DE (2011) How fast-folding proteins fold. *Science* 334: 517–520.

Minor DL Jr. and Kim PS (1996) Context-dependent secondary structure formation of a designed protein sequence. *Nature* 380: 730–734.

Ohgushi M and Wada A (1983) Molten-globule state: A compact form of globular proteins with mobile side-chains. *FEBS Letters* 164: 21–24.

Okamoto Y (2004) Generalized-ensemble algorithms: Enhanced sampling techniques for Monte Carlo and molecular dynamics simulations. *Journal of Molecular Graphics and Modelling* 22: 424–440.

Onuchic JN, Luthey-Schulten Z, and Wolynes PG (1997) Theory of protein folding: the energy landscape perspective. *Annual Review of Physical Chemistry* 48: 545–600.

Onuchic JN and Wolynes PG (2004) Theory of protein folding. *Current Opinion in Structural Biology* 14: 70–75.

Piana S, Lindorff-Larsen K, and Shaw DE (2013) Atomic-level description of ubiquitin folding. In: *Proceedings of the National Academy of Sciences of the United States of America 110* 5915–5920.

Ramachandran GN, Ramakrishnan C, and Sasisekharan V (1963) Stereochemistry of polypeptide chain configurations. *Journal of Molecular Biology* 7: 95–99.

Shaw DE, Maragakis P, Lindorff-Larsen K, et al. (2010) Atomic-level characterization of the structural dynamics of proteins. *Science* 330: 341–346.

Takada S (2012) Coarse-grained molecular simulations of large biomolecules. *Current Opinion in Structural Biology* 22: 130–137.

Ueda Y, Taketomi H, and Go N (1978) Studies on protein folding, unfolding, and fluctuations by computer simulation. II. A. Three-dimensional lattice model of lysozyme. *Biopolymers* 17: 1531–1548.

Yanagida T, Kitamura K, Tanaka H, Iwane AH, and Esaki S (2000) Single molecule analysis of the actomyosin motor. *Current Opinion in Cell Biology* 12: 20–25.

Zhou H-X (2008) Protein folding in confined and crowded environments. *Archives of Biochemistry and Biophysics* 469: 76–82.

Relevant Website

http://www.wwpdb.org. Protein Data Bank.

DNA and RNA, biophysical aspects

MD Frank-Kamenetskii, Boston University, Boston, MA, United States

© 2024 Elsevier Ltd. All rights reserved.

This is an update of M.D. Frank-Kamenetskii, DNA and RNA, Biophysical Aspects, Editor(s): Franco Bassani, Gerald L. Liedl, Peter Wyder, Encyclopedia of Condensed Matter Physics, Elsevier, 2005, Pages 463–472, ISBN 9780123694010, https://doi.org/10.1016/B0-12-369401-9/00386-7.

Introduction 663
Structures of DNA and RNA 665
Major helical structures of DNA 665
B-DNA 665
B′-DNA 667
A-DNA 667
Z-DNA 667
ps-DNA 667
RNA structure and function 667
DNA topology 668
Knots of DNA 668
DNA supercoiling 669
Structural transitions and unusual structures 670
DNA melting 670
B–Z transition 670
Cruciforms 670
Triplexes 671
Quadruplexes 671
Bent DNA 672
RNA unusual structures 672
Nanostructures and nanodevices from DNA and RNA 672
Biophysical methods to study DNA and RNA 673
Theoretical models 673
Gel electrophoresis 674
Single-molecule experiments with DNA and RNA 674
Further reading 674

Abstract

Biophysical aspects of DNA and RNA are covered. A brief introduction into DNA and RNA chemical structure is given. Main helical structures of DNA and RNA are described: A, B, B′, Z forms and parallel-stranded DNA. Special emphasis is given to a variety of functional RNA molecules. DNA topology, DNA supercoiling and DNA unusual structures induced by negative supercoiling (triplexes, cruciforms) are described. Theoretical models to study RNA and RNA are indicated. Nanostructures and nanodevices based on DNA and RNA are discussed and single molecule experiments with DNA are briefly covered.

Introduction

DNA and RNA together are known as nucleic acids. Their full names are deoxyribonucleic acid and ribonucleic acid, respectively. They play a crucial role in all living organisms because they are the key molecules responsible for storage, duplication, and realization of genetic information. They are both heteropolymeric molecules consisting of residues (nucleotides) of four types. Four RNA nucleotides are shown in Fig. 1. They consist of the phosphate group, sugar (called ribose) (these two elements are identical for all four nucleotides), and nitrous bases, which determine the type of the nucleotide. DNA nucleotides are very similar to RNA nucleotides. The main difference is that the right-handed OH group in sugar is replaced with just H (making deoxyribose). Three bases (A, G, and C) are the same for DNA and RNA. Only the fourth base is different: instead of uracil (U), DNA carries thymine (T) (see Fig. 2). The DNA chain is shown in Fig. 3.

In living nature, as is observed today, DNA plays the most important role because genetic information is stored and duplicated in the form of DNA in all living cells and organisms without any exceptions. Only in some viruses, which are not living creatures because they cannot reproduce themselves outside cells, the genetic information may be carried in the form of RNA molecules. A notable class of such viruses is retroviruses, which include many cancer-inducing viruses as well as HIV, the AIDS virus.A genetic message is “written down” in the form of a continuous text consisting of four letters (DNA nucleotides A, G, T, and C). This continuous text, however, is subdivided, in its biological meaning, into sections. The most significant sections are genes, parts of

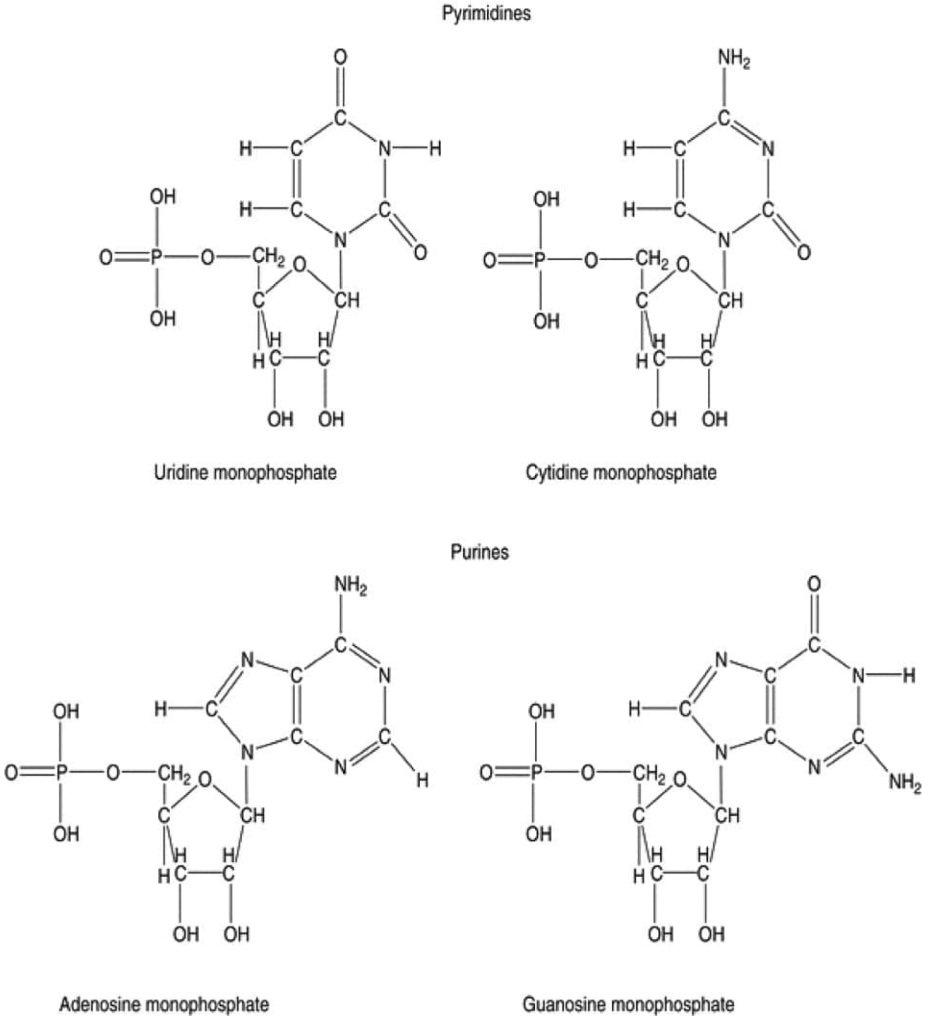
Pyrimidines
Uridine monophosphate
Cytidine monophosphate
Purines
Adenosine monophosphate
Guanosine monophosphate

Fig. 1 Chemical formulas of residues of RNA, i.e., of nucleotides. At the top are the pyrimidine nucleotides (U and C), and below, the purine nucleotides (A and G). Nucleotides within DNA differ in that, instead of the right-hand lower OH group, they simply have H. In addition, DNA, instead of the uridine nucleotide, includes the thymidine nucleotide whose top C—H group in the ring is replaced by the C—CH_3 group.

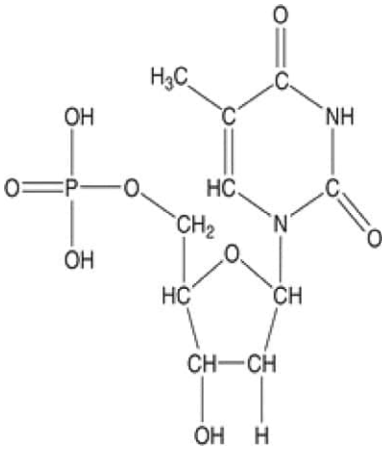

Fig. 2 Thymidine monophosphate is a thymine nucleotide that is part of DNA. The remaining three DNA nucleotides have similar structure, but each has a nitrous base of its own (the top group). These three bases (adenine, guanine, and cytosine) are identical in DNA and RNA (see Fig. 1).

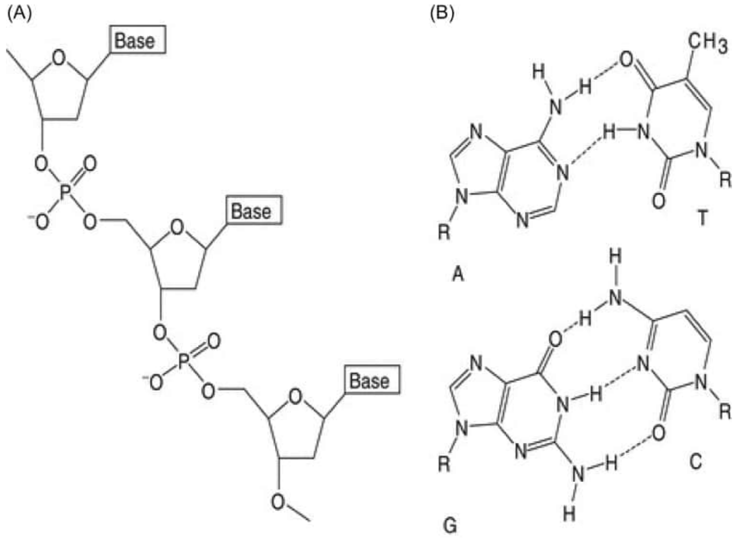

Fig. 3 (A) The DNA single strand and (B) the Watson–Crick complementary base pairs.

DNA, which carry information about the amino acid sequence of proteins. Whereas DNA stores and duplicates genetic information, RNA plays a key role in its realization, that is, in the process of synthesis of a protein molecule in accordance with the nucleotide sequence of the corresponding gene.

This process consists of two major steps. First an RNA copy of the gene is made with the help of a special enzyme, RNA polymerase. The process is called transcription and the RNA copy of the gene is called messenger RNA (mRNA). The mRNA is an exact copy of the gene, in which all thymines (T) are replaced with uracils (U). In the second step, called translation, mRNA is used as a template for protein synthesis in a special cell machinery, the ribosome. Ribosome is a complex aggregate of special ribosomal RNA (rRNA) and a number of proteins. It translates the nucleic acid text into amino acid language. In so doing, it uses a special dictionary, the genetic code. In the process of translation, a very important class of additional small RNA molecules plays a crucial role. These RNA molecules consist of about hundred nucleotides and are called transfer RNA (tRNA).

In this article, an overview of the present knowledge of physical structures of nucleic acids is provided. The most important structural transitions, such as DNA melting and B–Z transition, are explained. Special attention is paid to the topological properties of DNA, which play a significant role in its functioning within the cell. Theoretical models, which are most popular in the field of biophysics of DNA and RNA are also overviewed. Recently emerged areas of DNA and RNA biophysics, such as single-molecule experiments and DNA/RNA nanostructures are also considered.

Structures of DNA and RNA

Traditionally, the structural versatility of nucleic acids had been considered as much narrower than that of proteins. This viewpoint fitted well "the division of power" between nucleic acids and proteins in present-day living creatures. The major function of nucleic acids is to store and reproduce genetic information while proteins perform an innumerable variety of reactions within the cell and are also its main construction blocks. The discovery of ribozymes (RNA molecules capable of catalytic functions) and of the remarkable versatility of the RNA structure completely changed the attitude toward the pivotal question of which type of major biopolymers, proteins or nucleic acids, had been the prebiotic molecule, forefather of the living cell. Earlier, everybody believed that only protein could fulfill this function. Now, the common view is that this should be the RNA molecule (the RNA World concept).

Major helical structures of DNA

In spite of enormous versatility of living creatures, and, accordingly, variability of genetic texts which DNA molecules in different organisms carry, they all have virtually an identical physical spatial structure: the double-helical B form discovered by Watson and Crick in 1953. Sequences of the two strands of the double helix obey the complementary principle. This principle is the most important law in the field of nucleic acids, and, probably, the most important law of living nature. It declares that in the double helix, A always opposes T and vice versa, whereas G always opposes C and vice versa.

B-DNA

It (see Fig. 4A) consists of two helically twisted sugar-phosphate backbones stuffed with base pairs of two types, AT and GC. The helix is right-handed with 10 bp per turn. The base pairs are isomorphous (see Fig. 3): the distances between glycosidic bonds,

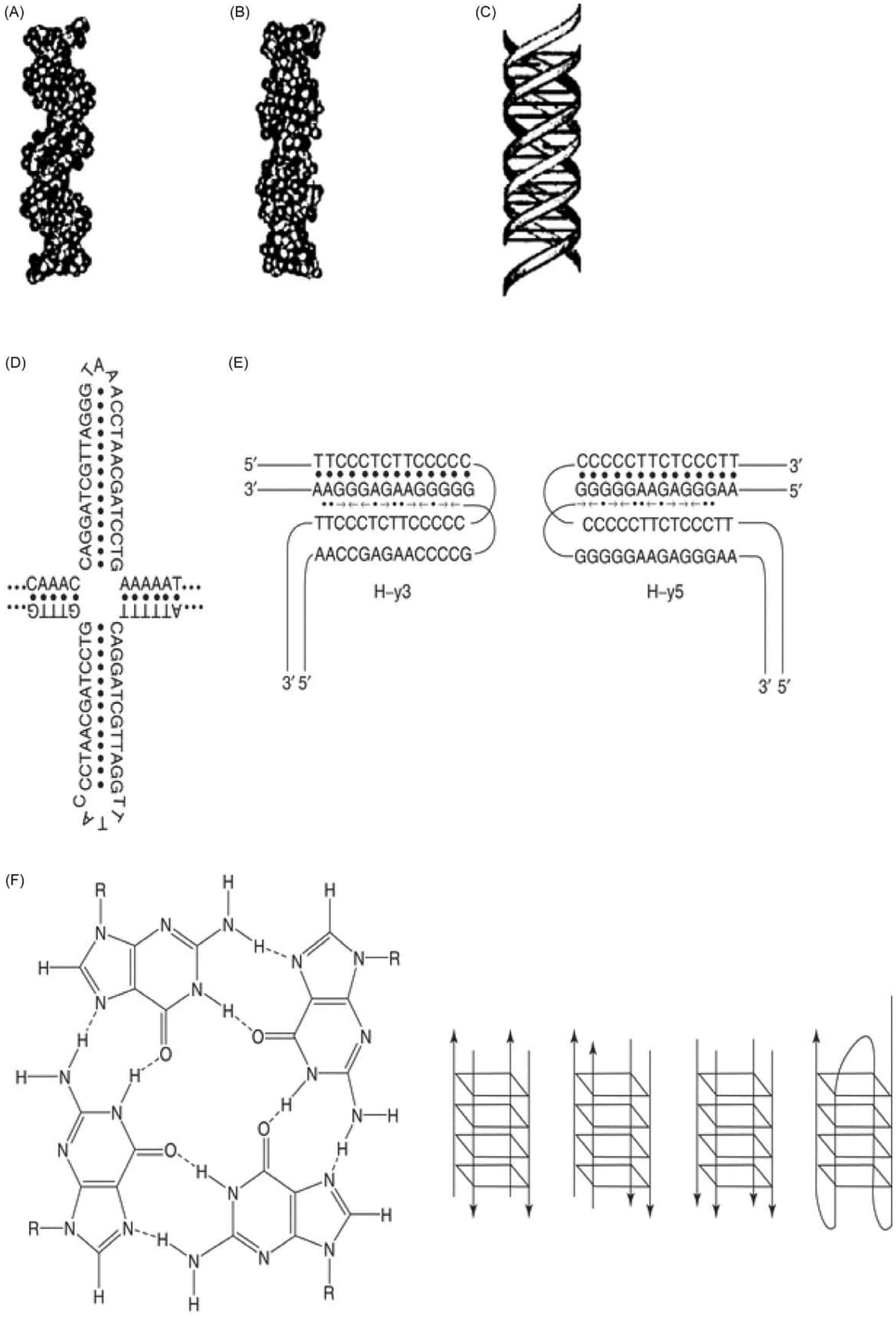
(A)
(B)
(C)
(D)
CAGGATCGTTAGGG
AA
ACCTAACGATCCTG
...CAAAC
...GTTTG...
AAAAAT...
TTTTTA...
CCTAACGATCCTG
CAGGATCGTTAGGT
TAC
(E)
5′
3′
TTCCCTCTTCCCCC
AAGGGAGAAGGGGG
TTCCCTCTTCCCCC
AACCGAGAACCCCG
H–y3
3′ 5′
CCCCCTTCTCCCTT
GGGGGAAGAGGGAA
CCCCCTTCTCCCTT
GGGGGAAGAGGGAA
H–y5
3′ 5′
(F)

Fig. 4 Schematics of (A) B-DNA and some unusual structures of DNA: (B) *Z*-DNA, (C) intermolecular triplex, (D) cruciform, (E) H-DNA, (F) G-quadruplex and its various folding modes.

which attach bases to sugar, are virtually identical for AT and GC pairs. Due to this isomorphism, the regular double helix is formed for an arbitrary sequence of nucleotides and the fact that DNA should form a double helix imposes no limitations on DNA texts. The surface of the double helix is by no means cylindrical. It has two very distinct grooves: the major groove and the minor groove. These grooves are extremely important for DNA functioning because in the cell, numerous proteins recognize specific sites on the DNA via binding with the grooves.

Each nucleotide has direction: if one treats sugar as a ring lying in the plane, then the CH_2 group will be above the plane (see Fig. 1). This carbon is designated as 5′ whereas the carbon atom connecting the sugar to the next nucleotide in the polynucleotide chain is designated as 3′. In the DNA double helix, the two strands have opposite directions.

In B-DNA, base pairs are planar and perpendicular to the axis of the double helix.

Under normal conditions in solution, often referred to as "physiological" (neutral pH, room temperature, ~200 mM NaCl), DNA adopts the B form. All available data indicate that the same is true for the totality of DNA within the cell. It does not exclude, however, the possibility that separate stretches of DNA carrying special nucleotide sequences would adopt other conformations.

B′-DNA

Up to now only one such conformation has been demonstrated, beyond any doubts, to exist under physiological conditions. When three or more A residues in one strand (and, accordingly, T's in the other DNA strand) are met, they adopt the B′ form. In many respects, the B′ form is similar to the classical B form. There are two main differences: base pairs in B′-DNA are not planar (they form a kind of propeller with the propeller twist of 20°) and the minor groove in B′-DNA is twice as narrow as in B-DNA.

A-DNA

Similar to B-DNA, the A form can be adopted by an arbitrary sequence of nucleotides. As in B-DNA, the two complementary strands in A-DNA are antiparallel and form right-handed helices. Normal DNA undergoes transition from the B to A form under drying. In A-DNA, the base pairs are planar but their planes form a considerable angle with the axis of the double helix. In so doing, the base pairs shift from the center of the duplex forming a channel in the center.

Z-DNA

It presents the most striking example of how different from the B form the DNA double helix can be (Fig. 4B). Although in *Z*-DNA the complementary strands are antiparallel as in B-DNA, unlike in B-DNA they form left-handed, rather than right-handed, helices. There are many other dramatic differences between *Z*- and B-DNA.

Not any sequence can adopt the Z form. To adopt the Z form, the regular alternation of purines (A or G) and pyrimidines (T or C) along one strand is strongly preferred. However, even this is not enough for *Z*-DNA to be formed under physiological conditions. Nevertheless, Z-DNA can be adopted by DNA stretches in cell due to DNA supercoiling (see below). The biological significance of Z-DNA, however, remains to be elucidated.

ps-DNA

The complementary strands in DNA duplex can be parallel. Such parallel-stranded (ps) DNA is formed most readily if both strands carry only adenines and thymines and their sequence excludes formation of the ordinary antiparallel duplex. If these requirements are met, the parallel duplex is formed under quite normal conditions. It is right-handed but the AT pairs are not regular Watson–-Crick ones, but rather so-called reverse Watson–Crick.

Some other sequences also can adopt parallel duplexes. For instance, at acidic conditions two strands carrying only C residues form parallel duplex consisting of hemiprotonated CC^+ base pairs (see the section "Quadruplexes"). However, any possible biological role of psDNA remains obscure.

RNA structure and function

Quite naturally, similarity between DNA and RNA in their chemical nature entails significant similarity in structures they adopt. RNA can also form the double helix with complementary base pairs AU and GC. However, the major RNA duplex conformation remains A-form rather than B-form.

In general, due to bulkier OH group in the sugar ring, the versatility of RNA duplexes is rather narrower than those of DNA.

In a cell, different types of RNA molecules (mRNA, rRNA, tRNA, etc.) exist as single strands. Of course, these strands are not unfolded, but fold into complex spatial structures. Mutually complementary stretches of the same molecules form numerous short duplexes, which are a major structural motif of RNA molecules. Single-stranded regions form loops of different types. Sometimes very complex folding patterns, called pseudoknots, are met.

Spatial structure plays an important role in RNA functioning. For instance, rRNA organized in complex spatial structure forms a scaffolding to which numerous ribosomal proteins attach to form the functional ribosome. The elucidation of the full 3D structure of the ribosome by X-ray crystallography has been one of the major achievements of biophysics and structural biology. Spatial structure at tRNA molecules are specially designed to permit them to fulfill the central role in the realization of the genetic code. One part of tRNA carries the anticodon, a trinucleotide complementary to a codon (a trinucleotide corresponding to one amino acid in the genetic code), whereas the amino acid, which corresponds to the codon in the genetic code, is attached to the 3′ terminus of the molecule.

More we learn about the living cell, more RNA molecules of different kinds emerge, which had been overlooked before and which proved to be extremely important. A totally new class of small RNAs was discovered at the turn of the century, which are involved in the RNA interference (RNAi) pathway and participate in the gene expression regulation on the level of mRNA. Most important of these small regulatory RNAs are small interfering RNAs (siRNAs) and micro RNAs (miRNAs). The RNAi pathway is present only in eukaryotes. Another groundbreaking discovery made already in 21st century was so-called CRISPR mechanism of bacterial immunity against bacteriophages. Here small ssRNA molecules, called CRISPR RNAs (crRNAs) or guide RNAs (gRNAs), recruit CRISPR associate (cas) endonucleases and guide them to the specific sites on dsDNA recognized by gRNAs via base pairing with one of two DNA strands. As a result, the cas protein inflicts the double strand break into target dsDNA. The CISPR-cas mechanism discovered in bacteria has been converted into the revolutionary CISPR-cas technology, which makes it possible to perform in vivo genome editing in eukaryotes, including humans.

DNA topology

DNA very often operates within the cell in the form of a closed circular molecule in which both strands form closed circles (Fig. 5). The physical properties and physiological behavior of closed circular (cc) DNA are different in many respects from those of linear DNA molecules. These differences stem from the fact that ccDNA acquires, as compared to linear DNA, a new fundamental feature, topology. There are two levels of DNA topology.

Knots of DNA

The double helix, as a whole, may form a simple circle (i.e., a trivial knot) or be knotted (see Fig. 6). Knotting of DNA may be conducted by random closure of linear molecules with "cohesive" ends (mutually complementary single-stranded overhangs). There are also different enzymes which do the job. The most important class of such enzymes is known as DNA topoisomerases II. The type of knot is the topological invariant, that is, it cannot be changed (converted to another type of knot) without breakage of both DNA strands. As a result, identical ccDNA molecules belonging to different knot types may be separated in gel.

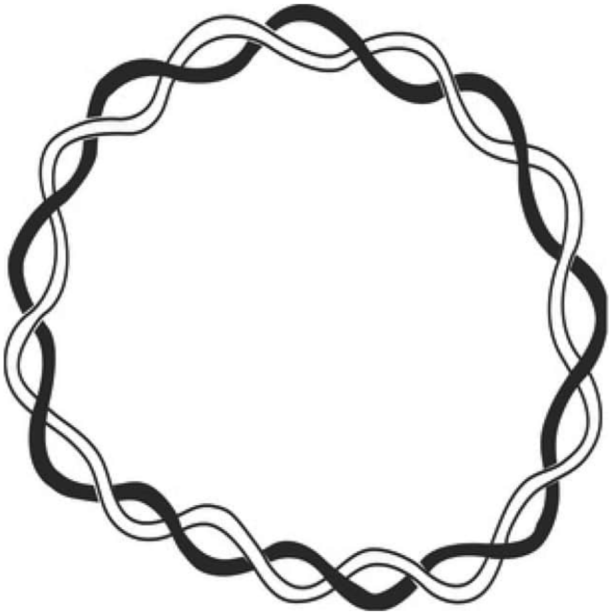

Fig. 5 In a ccDNA, two complementary strands form a linkage of a high order.

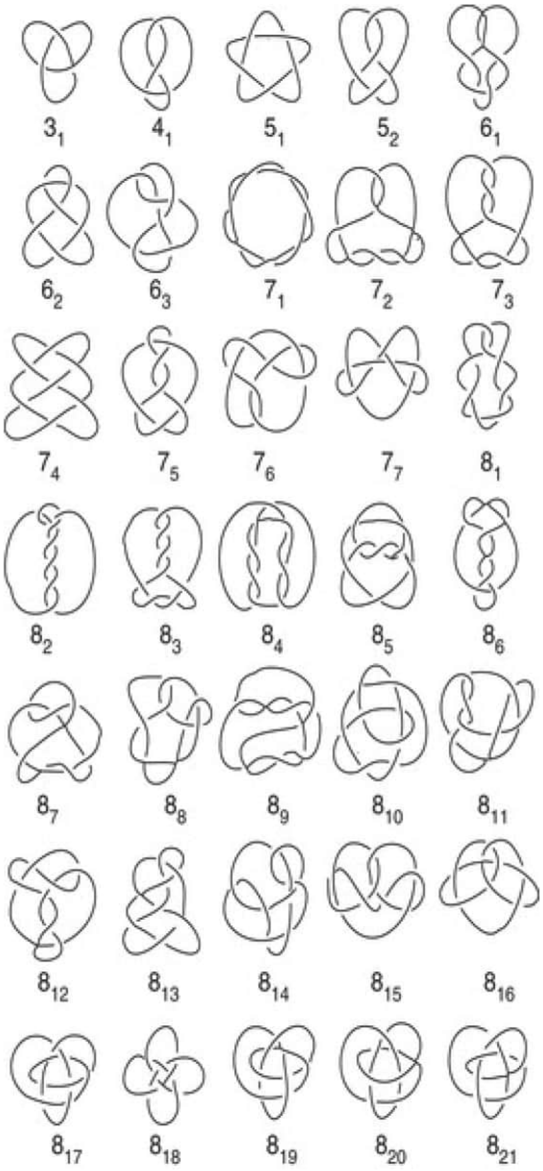

Fig. 6 Knots.

DNA supercoiling

The two complementary strands in ccDNA are topologically linked with one another (see Fig. 5). The degree of linkage, which is designated as *Lk*, the DNA linking number, is a topological invariant, which cannot be changed with any deformations of the DNA strands without strand breaks. The *Lk* value is easily calculated as the number of times one strand pierces the surface placed on the other strand. If N is the number of base pairs in DNA and γ_o is the number of base pairs per one turn of the double helix under given ambient conditions, then the difference:

$$\tau = Lk\text{–}N/\gamma_o \qquad (1)$$

is the number of superhelical turns in ccDNA under given conditions. If $\tau \neq 0$, then ccDNA cannot form a planar ring with the helical twist corresponding the γ_o value. Either the helical twist should change or the DNA molecule as a whole should writhe in space. Actually, with $\tau \neq 0$ both things happen: the DNA adopts the writhe, and its twist changes. The distribution of energy associated with DNA supercoiling (i.e., with $\tau \neq 0$) between twist and writhe is determined by the torsional and bending rigidities, which have been measured with good accuracy. Supercoiling is also significantly affected by replication and transcription. DNA topology plays an extremely important role in DNA functioning.

Structural transitions and unusual structures

If negative supercoiling in ccDNA becomes too high, the bending and torsional degrees of freedom may become insufficient to accommodate the superhelical energy. Under these circumstances, the integrity of the DNA double helix breaks down at its most "weak" sites. These sites, which have the potential to adopt structures significantly different from B-DNA, can undergo structural transitions into unusual (non-B-DNA) structures.

DNA melting

On heating or under superhelical stress, the DNA complementary strands separate forming single-stranded loops. In case of linear duplex molecules, the process ends up, at a high temperature, with complete separation of the two strands. The process has been studied comprehensively both experimentally and theoretically and is known as DNA melting (the terms denaturation or helix-coil transition are also used in literature). AT pairs have significantly lower stability than GC pairs.

With increasing temperature, long DNA sections melt out. Melting of each such section is a cooperative, all-or-none phenomenon. However, melting of a long enough molecule becomes a series of such cooperative processes, each occurring at its own temperature (Fig. 7). Roughly speaking, sections more enriched with GC pairs melt out at higher temperatures. Thus, DNA melting is not a classical phase transition because two different "phases," helical and melted, coexist with each other in one and the same molecule.

When two mutually complementary single-stranded DNA molecules are mixed, the process reverse to melting occurs. It is called renaturation, annealing or hybridization.

DNA melting is an exceptionally important phenomenon. It occurs in the cell when DNA replicates and when DNA polymerase "reads" the mRNA copy of the gene. Cycles of melting and annealing are utilized in the polymerase chain reaction (PCR) machines, which belong to the most remarkable tools of the current biotechnology revolution.

B–Z transition

Negative supercoiling favors the formation of Z-DNA most because, in this case, the maximal release of superhelical stress per 1 bp adopting a non-B-DNA structure is achieved. As a result, although under physiological conditions the Z form is energetically very unfavorable as compared with B-DNA, it is easily adopted in negatively supercoiled DNA by appropriate DNA sequences (with alternating purines and pyrimidines).

Cruciforms

Another structure readily formed under negative supercoiling is cruciform, which requires palindromic regions (see Fig. 4D). To form cruciform, a palindromic region should be long enough. For example, 6 bp long palindromes recognized by restriction enzymes do not form cruciforms under any conditions.

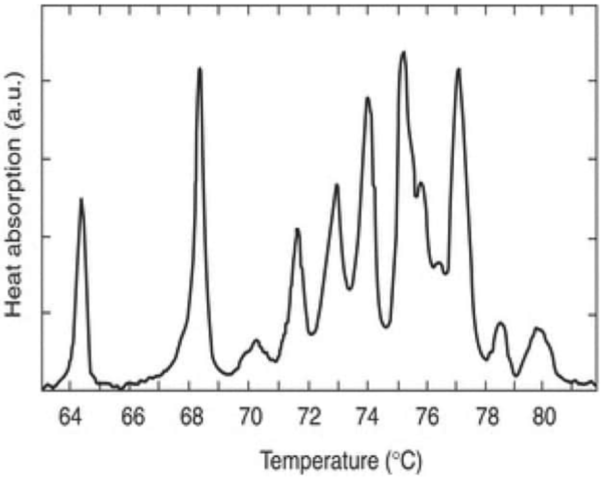

Fig. 7 Melting of DNA. This curve is also often called the differential melting curve. The curve was obtained for DNA that has the code name of ColE1 and contains 6646 base pairs.

Triplexes

Intramolecular triplex or H-DNA forms a special class of unusual structures, which are adopted under superhelical stress by sequences carrying purines (A and G) in one strand and pyrimidines (T and C) in the other, that is, homopurine–homopyrimidine sequences. The major element of H-DNA is triplex formed by a half of the insert adopting the H form and by one of two strands of the second half of the insert (Fig. 4E). Two major classes of triplexes are known: pyrimidine–purine–pyrimidine (YRY) and pyrimidine–purine–purine (YRR). Fig. 8 shows the canonical base-triads entering these triplexes.

Always two isomeric forms of H-DNA are possible, which are designated as H-y3, H-y5, H-r3, and H-r5 depending on which kind of triplex is formed and which half of the insert forms the triplex (see Fig. 4E).

Discovery of H-DNA stimulated studies of intermolecular triplexes, which may be formed between homopurine–homopyrimidine regions of duplex DNA and corresponding pyrimidine or purine oligonucleotides (Fig. 4C).

Quadruplexes

Of all nucleotides, guanines are most versatile in forming different structures. They may form GG pairs but the most stable structure, which is formed in the presence of monovalent cations (especially potassium), is G4 quadruplex (see Fig. 4F). G-quadruplexes may

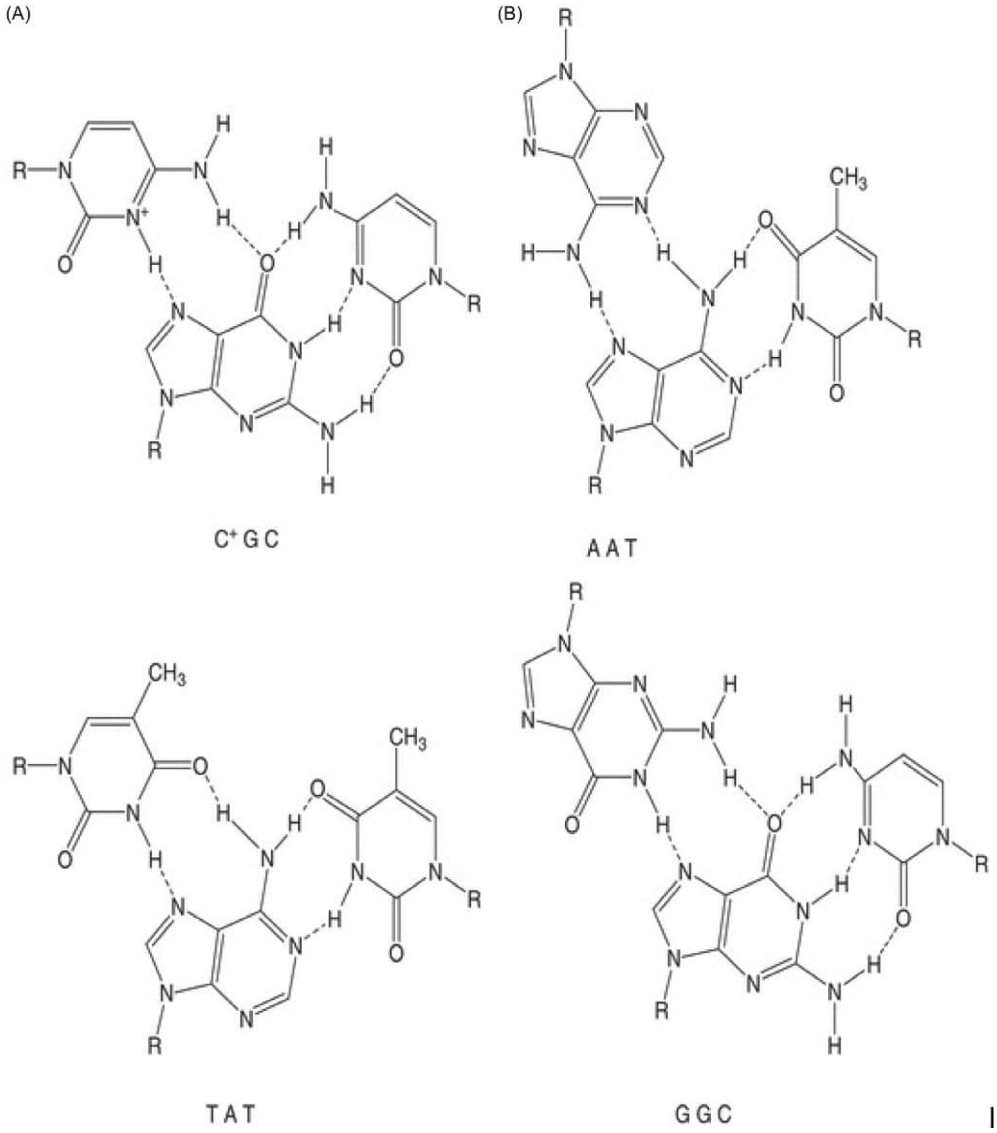

Fig. 8 The structure of (A) pyrimidine (TAT and C$^+$GC), and (B) purine (AAT and GGC) base triads of which the DNA triple helix is made. In YRY triplexes, the Y strand lying in the major groove of the duplex is parallel to the R strand of the Watson-Crick duplex and forms with it Hoogsteen pairs. In RYR triplexes, two R strands are anti-parallel to each other and are connected with each other via reverse Hoogsteen pairs.

exist in a variety of modifications: all-parallel, all-antiparallel, and others. As a result, G-quadruplexes are easily formed both inter- and intramolecularly, again with a variety of modifications. A remarkable variety of quadruplex structure was discovered for protonated cytosines. This structure, called i-motif, consists of two pairs of parallel stranded duplexes consisting of hemiprotonated CC^+ base pairs. In the final structure, two duplexes are mutually antiparallel and CC^+ base pairs from one ps duplex alternate with CC^+ base pairs from the other ps duplex. The structure is stable only at acidic pH because protonation is necessary.

Bent DNA

For an arbitrary sequence, the minimum energy conformation of the DNA double helix corresponds to the straight DNA axis. However, there is a notable exception to this rule. If three or more A nucleotides are located in a row in one of the DNA strands, the corresponding regions adopt the B′ structure. As a result, the DNA axis experiences a bend of 20° in such a region. DNA bending plays an important role in DNA functioning.

RNA unusual structures

Most DNA unusual structures have their analogs in the RNA world. Specifically, formation of triplexes was first demonstrated for artificial RNA chains. Solitary RNA base-triads are often met in tRNA structures. Triplexes are formed by mixed DNA–RNA hybrids and some of them are rather stable.

However, in general, studies of RNA unusual structures lag behind corresponding DNA structures because methods to study unusual structures are much better developed in the case of DNA than in the case of RNA.

Nanostructures and nanodevices from DNA and RNA

One of the most rapidly developing areas in DNA and RNA biophysics consists in using the remarkable ability of nucleic acid to self-assembly for creation of nanostructures and nanodevices. In so doing, virtually all unusual structures described above are extensively used: triplexes, quadruplexes, *Z*-DNA, etc., as well as the duplex. Specifically, a family of topological and pseudotopological nanostructures has been assembled as is shown in Fig. 9A–C. An example of a nanodevice (nanoactuator) is shown in Fig. 9D. By adding specially designed single-stranded DNA chains, the nanoactuator is transformed from the relaxed form shown in Fig. 9D to a straightened form in which the A strand is extended into a straight double helix.

A very ingenious method for making sophisticated DNA nanostructures has been invented, which makes it possible to create so-called DNA origami. Using special computer programs, DNA oligonucleotides are designed, which will bind to a long DNA molecule with the known sequence and fold it into the desired 3D structure. By this approach a huge variety of nanostructures are being created.

A special class of short ssRNA molecules, called aptamers, has been developed. These molecules are produced via special in vitro selection process, called SELEX, and they are selected on their ability to bind strongly to particular proteins. Aptamers find more and more applications.

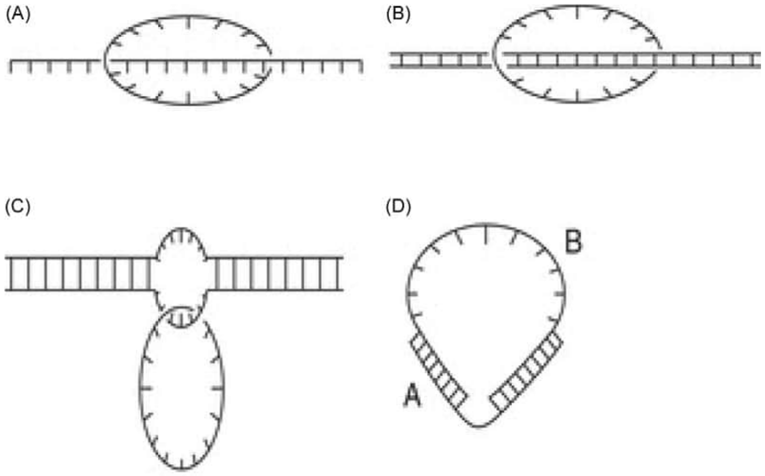

Fig. 9 Examples of DNA nanostructures: (A) padlock probe (pseudorotaxane), (B) sliding clamp (pseudorotaxane), (C) earring probe (pseudocatenane), and (D) nanoactuator.

Biophysical methods to study DNA and RNA

The whole arsenal of methods, which is traditionally used to study molecular structure, is applied to DNA and RNA. A leading position is occupied by X-ray crystallography, which provided us with a knowledge of details of the atomic structure of DNA and RNA. X-ray crystallography made it possible to solve the structure of the nucleosome, the main building block of chromosomes consisting of DNA and histone proteins, and of a major cellular machinery, ribosome, consisting of RNA and many proteins. The next method is proton NMR, which is especially valuable when biological molecules resist crystallization, a not uncommon problem with nucleic acids. An enormous body of data on the structure of DNA triplexes, quadruplexes, and various ribozymes was delivered by NMR. Electron microscopy (EM), cryo-EM and atomic force microscopy (AFM) have become indispensable in studying the DNA and its complexes with proteins. Most recently, a dramatic progress in single particle analysis of crio-EM images has made this approach a method of choice in elucidation of structure of large nucleoprotein assemblies, like ribosomes. All kinds of spectroscopy methods, UV, IR, Raman, and CD are very useful in studying conformational transitions in DNA and RNA. A special role is played by various fluorescence methods, which find more and more applications not only in biophysical studies, but also in biotechnology. Below, specific methods, which have been specially developed in the field of DNA and RNA biophysics are discussed.

Theoretical models

As in the study of any important physical object, a number of simplified theoretical models of nucleic acids exist, different models being used to analyze different properties. Fig. 10 presents schematics of some of these models.

The DNA double helix may be treated as an isotropic elastic rod (Fig. 10A). In the framework of this model, the DNA molecule is described by only three parameters: bending, torsional rigidities, and the diameter. The model has proved to be extremely useful for analyzing hydrodynamics and other properties of linear DNA, when it behaves as a usual polymeric molecule. It has also provided a comprehensive theoretical treatment of DNA topology of both levels: knotting and supercoiling. More recently, the model has been extensively used for quantitative analysis of the force-extension curves for DNA in single-molecule experiments (see below).

A quite different, but also very successful, model treats the DNA double helix as consisting of base pairs of two types: closed and open (Fig. 10B). This is the helix-coil model, which explains all major features of DNA melting quantitatively.

The polyelectrolyte model (Fig. 10C) treats DNA itself just as a charged cylinder but allows for mobile counter-ions surrounding the double helix.

To predict the RNA structure, a simplified model of RNA folding is widely used (Fig. 10D).

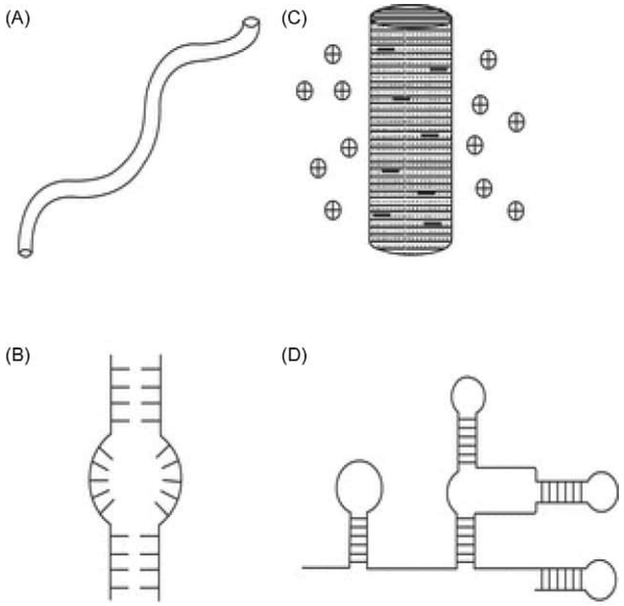

Fig. 10 Theoretical models of nucleic acids: (A) elastic-rod model, (B) helix-coil model, (C) polyelectrolyte model, and (D) model of RNA folding.

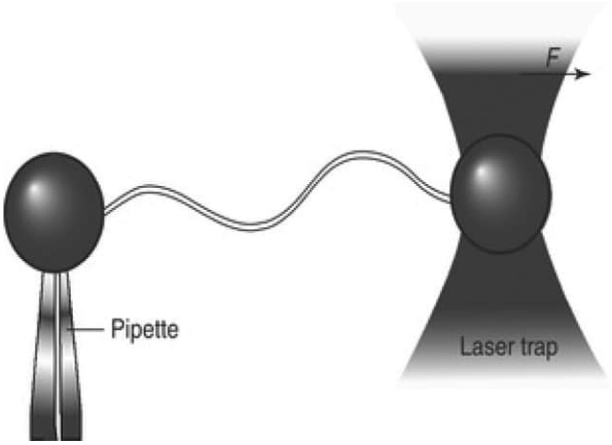

Fig. 11 Stretching a single DNA molecule with optical tweezers.

Gel electrophoresis

Gel electrophoresis is a simple technique, introduced in the early 1970s, which truly revolutionized the biophysical studies of DNA and RNA and, subsequently, the whole field of molecular biology. All developments in this field in the past 40 years are connected, directly or indirectly, with the gel electrophoresis method. Gel electrophoresis has pushed aside ultracentrifugation as the method to separate nucleic acids.

Gel electrophoresis differs from electrophoresis in solution only in the nature of the medium in which molecules are separated in the electric field. In case of gel electrophoresis the medium is the gel, a polymer network. The most popular in the field of nucleic acids are gels made of polyacrylamide or agarose. Originally, the great advantage of gels in the separation of nucleic acids was discovered purely empirically. The understanding came later after some ideas of P-J De Grennes were borrowed from polymer physics, namely the notion of reptation of polymer molecules.

Single-molecule experiments with DNA and RNA

In recent years, remarkable progress in the application of the single-molecule techniques to DNA and RNA studies has been achieved. There are many different formats for single-molecule experiments. For example, a DNA molecule consisting of about 50 kbp is attached via one terminus to a pipette tip equipped with a streptavidin-covered polymer bead. Streptavidin is a protein, which binds very strongly to a small molecule, biotin. The DNA terminus is covalently tagged with biotin to be attached to the streptavidin-covered bead. The other terminus is also attached to the polymer bead, but the bead is not fixed. Then, optical tweezers are used to drag the free bead with the DNA attached to it. As a result, a single DNA molecule can be stretched in a fully controllable manner and the force created in the process can be accurately measured (see Fig. 11).

These experiments have allowed, for the first time, measurement of the force–extension curves of ds and ss DNAs and comparison of the curves with theoretical predictions. One of the important directions of these studies include isothermal melting of DNA and RNA duplexes under the external force. The influence of the force on the performance of major enzymes working on DNA and RNA (DNA and RNA polymerases) has also been studied. A very important feature of single-molecule experiments consists in the fact that they introduce a new variable on which DNA and RNA structure critically depend, the external force.

Further reading

Bates AD and Maxwell A (2005) *DNA Topology*. Oxford, UK: Oxford University Press.
Bloomfield VA, Crothers DM, and Tinoco I (2000) *Nucleic Acids Structures, Properties, and Functions*. Sausalito, CA: University Science Books.
Frank-Kamenetskii MD (1997) *Unraveling DNA*. Cambridge, MA: Perseus Publishing.
Sinden RR (1994) *DNA Structure and Function*. San Diego, CA: Academic Press.
Vologodskii A (2015) *Biophysics of DNA*. Cambridge, UK: Cambridge University Press.

DNA and RNA, electronic and electric properties

Artur Erbe, Department of Nanoelectronics, Helmholtz-Zentrum Dresden-Rossendorf, Institute of Ion Beam Physics and Materials Research, Dresden, Germany

© 2024 Elsevier Ltd. All rights reserved.

Introduction 675
Conductance in organic molecules 676
Contacting techniques for DNA and RNA 677
Conducting atomic force microscopy 678
Break junctions 679
Electrodes at fixed distances 679
Electrical properties of single DNA and RNA molecules 679
Nanopores 682
DNA Origami 682
Conclusion 682
References 682

Abstract

DNA and RNA offer fascinating possibilities for the self-organization of complex patterns, which can be used in various combinations. Since this self-organization occurs at the nanometer scale, it can possibly offer ways for the creation of nanooptical or nanoelectronic devices. Therefore, the quest for conductivity of DNA or RNA has inspired a vast amount of experiments, which have led to a large number of diverse results. In the recent past, a coherent picture has emerged which describes charge transport along DNA or RNA in various environments. Based on this, electronic applications of these biomolecules have been developed.

Key points

- Electrical and electronic properties of DNA and RNA are reviewed.
- Theoretical models for understanding the electronic properties are discussed.
- Experimental techniques for measuring DNA and RNA electrically are presented.
- Experiments and theory on charge transport in DNA and RNA are reviewed.

Introduction

The electronic properties of biomolecules may lead to novel applications in the field of nanoelectronics, because self-organization of complex nanostructures can be encoded in the base sequence of the constituting molecules. Therefore, experimental and theoretical studies of such molecules will elucidate which applications can be targeted with such nanostructures. It is *a priori* not clear whether one might expect good charge conductance in DNA or RNA molecules or in ensembles composed of these molecules. This question thus triggered a large number of experiments in the late 1990s, which resulted in amazingly disparate results (Porath et al., 2000; Braun et al., 1998; Kasumov et al., 2001). It soon became clear that the reasons for the large variation of conductance values in DNA nanojunctions are given by the influence of the environment (Gutierrez et al., 2005) or the different conformation or base sequence of the DNA strands (Xu et al., 2004). Single-stranded DNA appears to be not conducting (Cohen et al., 2005) and sequences containing A-T base pairs are less conducting than sequences containing G-C pairs only (pG-pC DNA).

The complexity of the system makes understanding of the underlying charge mechanism rather difficult. Therefore a number of simplifying assumptions have been taken into account in order to describe the charge transport in DNA molecules. An overview of the models resulting in this approach is given in Section "Conductance in organic molecules." The main challenge of contacting single DNA molecules for charge transport measurements arises from the nanoscale dimensions of the structures. In the past decades, the field of molecular electronics has developed a large number of techniques to achieve such contacts (Metzger, 2015). Some of these techniques have been successfully applied for measuring charge transport as well. In addition, techniques for contacting DNA molecules have been developed, which rely on special properties of the DNA. An overview of the contacting

https://doi.org/10.1016/B978-0-323-90800-9.00237-7

techniques is given in Section "Contacting techniques for DNA and RNA." The outcome of the simulations and measurements of charge transport in DNA lead nowadays to a good understanding of the electronic nature of the DNA strands. An overview on these results is given in section "Electrical properties of single DNA and RNA molecules."

Conductance in organic molecules

Concepts for describing charge transport along DNA and RNA are not so different from concepts describing transport of charges in organic molecules. It is therefore constructive to first have a look at these general concepts before discussing special differences arising from the structure of RNA and DNA. The general idea of a charge transport experiment through a single DNA molecule is shown in Fig. 1A. A DNA molecule is connected via anchoring groups to two atomically sharp Au tips. Charge transport in organic molecules is typically measured on short length-scales, that is, Å up to few nm. At these length-scales, tunneling processes dominate, which can be described either by vacuum tunneling (Simmons, 1963) or by resonant tunneling through molecular orbitals, which can be aligned with Fermi energy E_F of the electrodes (Scott and Natelson, 2010) or offset by a certain energy ε_0 (Zotti et al., 2010). Longer molecules on the order of few nm to tens of nm exhibit a transition from tunneling to hopping behavior, which changes the length dependence of the conductance (Moreno-Garcia et al., 2013).

In case of simple tunneling, the tunnel current between two closely spaced electrodes depends linearly on the applied voltage and exponentially on the distance between the electrodes. The current density can be thus approximated by (Wang et al., 2003)

$$J \approx \left(\frac{(2m\Phi_B)^{1/2} e^2 \alpha}{h^2 d}\right) V \exp\left[-\frac{2(2m)^{1/2}}{\hbar}\alpha(\Phi_B)^{1/2} d\right]. \tag{1}$$

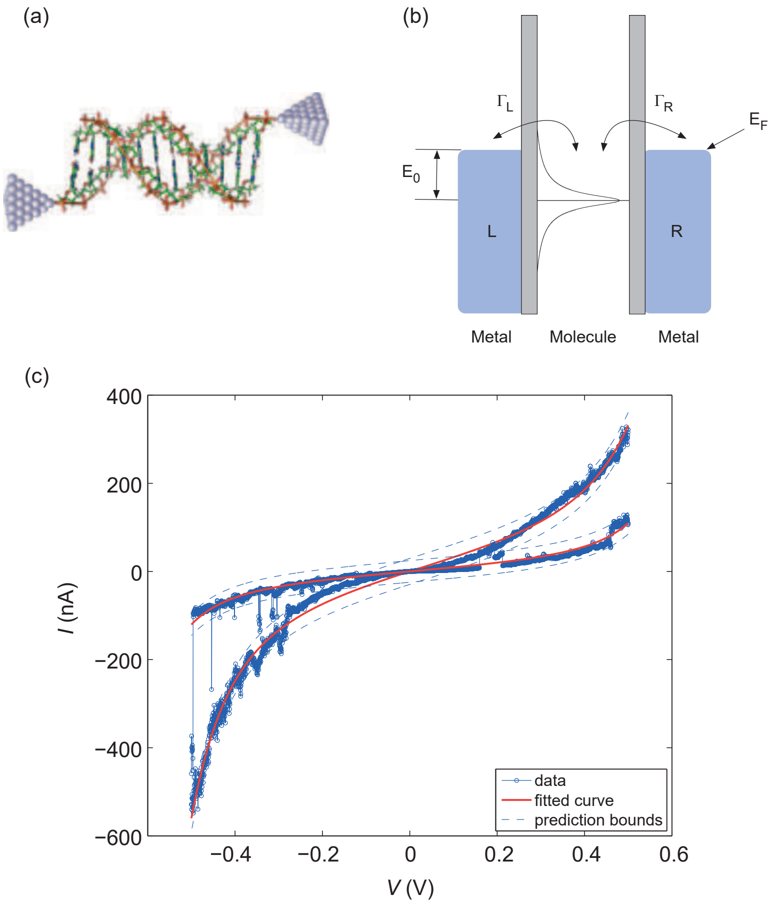

Fig. 1 Model of charge transport in molecular junctions (A) Sketch of metallic electrodes connected to DNA molecule (not to scale). (B) Energy diagram for the SLM. Electrons in the metallic electrodes on the left and right fill the available energy states according to Fermi statistics. The molecular state in the center is positioned at an energy ε_0 away from Fermi energy. The exact value of ε_0 depends on the molecular orbitals (highest occupied molecular orbital, HOHO, or lowest unoccupied molecular orbital, LUMO) and the charge transfer between the electrodes and the molecular orbitals. Whether charge transport is dominated by holes (HOMO-like) or electrons (LUMO-like) depends on the nature of the resonance closest to E_F. (C) *I-V*-curve measured using the mechanically controllable break junction technique (see Section "Break junctions") and fit to the SLM (*red*).

Here, m is the (reduced) mass of the electron, h and $\hbar$ are the Planck and reduced Planck constants, respectively, d is the distance between the electrodes, and Φ_B is the height of the tunneling barrier. The factor α accounts for deviations from the perfect rectangular shape of the barrier; it is 1 for a perfect rectangular barrier, otherwise less than unity. Some of the parameters in Eq. (1) depend on the exact shape of the contacts or the tunneling barrier in between. Since it is impossible to characterize the molecular junction on the atomic scale, comparisons of fit results with numerical simulations need to be evaluated in order to determine the fit parameters.

When increasing the bias voltage across the junction, the effective shape of the barrier is affected by the voltage drop. In this situation, approximations leading to Eq. (1) are no longer valid. In this regime, the current density is given by (Wang et al., 2003)

$$J \approx \left(\frac{4}{\pi^2 \hbar d^2}\right)\left\{\left(\Phi_B - \frac{eV}{2}\right) \times \exp\left[-\frac{2(2m)^{1/2}}{\hbar}\alpha\left(\Phi_B - \frac{eV}{2}\right)^{1/2} d\right]\right\}. \tag{2}$$

The transition between these two regimes can be identified when plotting $\ln(I/V^2)$ vs. $1/V$. This graph shows a clear minimum at the position at which the transition between both regimes happen. Assuming that at this position the energy of the charge carriers is larger than the height of the tunnel barrier, this minimum occurs at the voltage corresponding to the height of the barrier Φ_B (Huisman et al., 2009).

For conjugated molecules with a large conductance, a different view may be more appropriate (Fig. 1B). In this regime, one can assume that charge transport is mostly taking place in the delocalized orbitals of the molecule rather than by tunneling through vacuum. Transmission through the molecule then depends on the nature and number of levels, which are composed of the molecular orbitals. The contribution of these levels depends on their coupling to the electronic states in the electrodes at E_F. If the transmission through the molecule can be approximated by one single resonance with Lorentzian shape, the transmission through the molecular states can be approximated by (Zotti et al., 2010):

$$T(E,V) = \frac{4\Gamma_L\Gamma_R}{[E - E_0(V)]^2 + [\Gamma_L + \Gamma_R]^2} \tag{3}$$

Based on this assumption, which is also referred to as single-level model (SLM), the current through the molecular junction can be calculated via:

$$I(V) = \frac{2e}{h}\int_{-\infty}^{\infty} T(E,V)\left[f\left(E - \frac{eV}{2}\right) - f\left(E + \frac{eV}{2}\right)\right]dE \tag{4}$$

Eq. (4) can be used to fit the measured current–voltage (I–V) curve (Fig. 1C) and extract the single-level model parameters (SLM parameters ε_0 and Γ). This gives information on the energetic position of the channel transporting charge along the molecule and the electronic coupling to the electrodes.

For longer molecules, the assumption that a single state on the molecule transports the charge does not hold any more. In this situation, one needs to assume that a series of localized charge states exist along the molecule. Transport between these states occurs by hopping with an amplitude proportional to the hopping matrix element $t_{i,j}$, where i, j refer to the hopping sites ($1 \le i, j \le N$ for N hopping sites). When measuring the conductance of molecular junctions as a function of the length of the contacted molecule, one therefore finds a transition from the tunnelling behavior described by Eq. (1) or (4) to a hopping conductance (Choi et al., 2010).

Although these conductance models have been derived for organic molecules in general, they are still valid for contacts to single DNA or RNA molecules. The situation changes once ensembles of molecules are contacted because in this case, collective effects become more dominant. We therefore concentrate mostly on the behavior in single DNA doublestrand molecules. Some experiments at room temperature show transport along the molecules which resembles the SLM picture mentioned above. Other experiments show that transport at low temperatures may be along the backbone of the DNA because the base dependence found at room temperatures could not be found at low temperatures. All these experiments confirm the initial finding that the environment of the DNA has a major influence on the charge transport. We will therefore first discuss experimental techniques for contacting single DNA and RNA strands because the techniques determine the environment. Based on these techniques, we will then describe experimental results found on different molecules and discuss them in the framework of the techniques presented in this section.

Contacting techniques for DNA and RNA

Contacting single molecules can be achieved using a large variety of techniques. The main challenge in such experiments is given by the small size of the molecules, which requires structuring of the electrodes on sizes below 5 nm. No lithographic process is available for the creation of electrodes on such small length scales. Therefore additional steps need to be taken for including the molecules in such nanojunctions. The length of a single DNA strand can be much longer than typical organic molecules, sometimes exceeding even 100 nm. Therefore also direct contacting methods have been used for creating contacts, as well. Charge transport on such extended lengths is, however, suppressed in most cases.

Famous first experiments have been performed on DNA strands with fixed electrodes at lengths in the micrometer range (Fink and Schönenberger, 1999; Porath et al., 2000; Braun et al., 1998; Kasumov et al., 2001). It soon turned out that apart from the presence of the DNA itself, the conformation of the DNA and the exact conditions of the environment determine the conductance of the DNA nanojunctions (Endres et al., 2004). Several methods have been developed which allow the contacting of DNA single and double strands under more controllable conditions, and therefore the controlled characterization of the electrical properties of these structures.

Conducting atomic force microscopy

Conducting atomic force microscopy (c-AFM) offers the possibility to image surfaces on the nanoscale and at the same time measure their electrical properties. This method has first been used for conjugated organic molecules which were embedded in a matrix of nonconjugated, electrically insulating molecules (Cui et al., 2001). A monolayer of a mixture of these molecules was self-assembled on top of an atomically flat Au layer (substrate). For specifically contacting the conducting molecules with the c-AFM tip, these molecules were functionalized with thiol groups, to which Au nanoparticles could bind. When contacting these nanoparticles with the tip of the c-AFM, a metal–molecule–metal contact us formed between tip/nanoparticle on the one side and the conducting substrate on the other side. It is shown in Fig. 2A how the connection is achieved in case of DNA strands. The coupling to the Au nanoparticles could be achieved by binding a DNA strand to the particle, which is complementary to the strands, which are bound to the substrate (Cohen et al., 2005). Charge transport can then be measured through a single double-stranded DNA formed by this combination inside a matrix of single-stranded DNA.

The c-AFM technique can be used for the direct transport measurement along DNA molecules as well. The molecules are deposited on an insulating surface, for example, SIO_2. One end of the molecule is covered with metal creating one of the two contacts. The other contact is given by the tip of the c-AFM, which is used to scan and image the molecules and then to electrically contact them along the molecule. The setup allows for recording *I*–*V* curves at various points of the molecule (Stern et al., 2018; Livshits et al., 2014). This technique was used for metallized strands as well as for bare DNA on the surface.

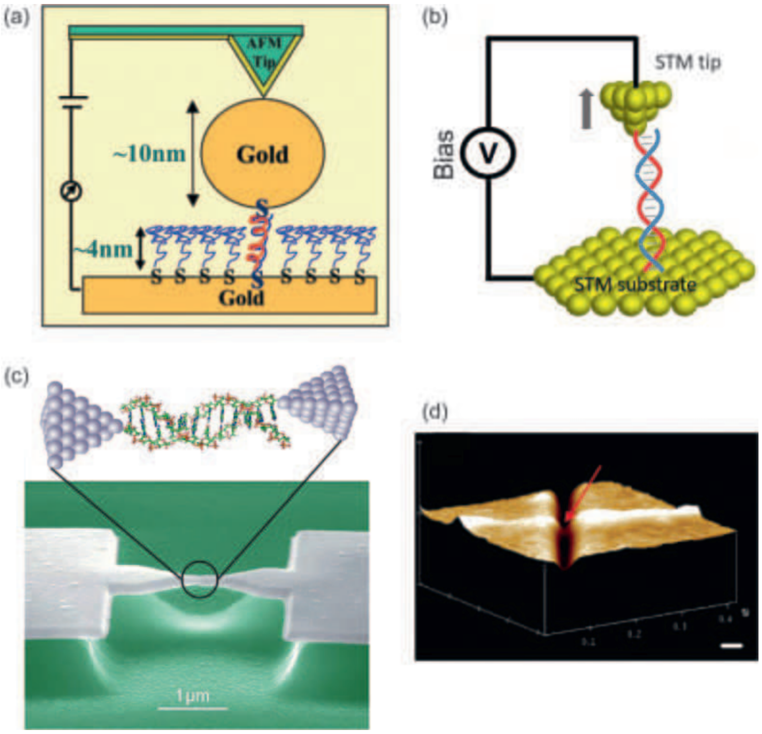

Fig. 2 Different contacting techniques: (A) Conductive atomic force microscopy (c-AFM). The AFM cantilever with a conductive tip is brought into contact with a metal particle in order to measure current through the metal particle and the ds-DNA to the metallic substrate. (B) STM breakjunction technique. The metallic STM tip is connected to a ds-DNA vial thiol bonds, the DNA is connected to the substrate via a thiol group at the other end of the strand. Contacts are repeatedly formed by pushing the tip into the substrate which is covered by molecules and retracting it again. During this procedure, the current through the molecule is measured at a fixed bias voltage. (C) Mechanically controllable break junction (MCBJ). An SEM image of a metallic, underetched nanobridge is shown. The bridge is placed on a flexible substrate and, upon bending, stretched until the contact between the metal atoms is lost. A ds-DNA can be connected to both tips (sketch above), the conductance and *I*–*V*-characteristics can be measured in this configuration. (D) Electrodes with fixed distance. DNA molecule between two metallic CNTs, which serve as contacts. The DNA is suspended in the gap between the CNTs, therefore interaction with the substrate is minimized. Scale bar 30 nm.
(A) Adapted with permission from Cohen H, Naaman R, and Porath D (2005) Direct measurement of electrical transport through single DNA molecules of complex sequence. Proceedings of the National Academy of Sciences of the United States of America 102(33): 11589–11593. https://doi.org/10.1073/pnas.0505272102. Copyright (2005) National Academy of Sciences, U.S.A. (B,C,D) Adapted with permission from Roy S, Vedala H, Roy AD, et al. (2008) Direct electrical measurements on single-molecule genomic DNA using single-walled carbon nanotubes. Nano Letters 8(1): 26–30. Copyright 2008 American Chemical Society.

Break junctions

Systematic studies of the influence of the primary structure of DNA on the conductance of DNA nanojunctions need statistical information based on a large number of measurements. Using the scanning tunneling microscope (STM) on metallic substrates with self-assembled monolayers of ds-DNA, contacts to the DNA can be formed repeatedly by pushing the tip into the substrate and pulling it back while measuring the conductance as a function of the distance *d* between the STM tip and the substrate (STM breakjunction technique). In this measurement, *G* decreases exponentially with increasing *d*, unless a conducting molecule is attached between tip and substrate and charge transport is observed along the molecule. In this case, *G* exhibits a plateau with a length roughly corresponding to the length of the molecule. Fig. 2B shows the situation in which the ds-DNA is completely stretched between the substrate and the tip. This situation would correspond to the final points in the plateau, before the DNA loses contact on one end and the resistance drops exponentially to zero upon further stretching. The plateau causes an accumulation of data points corresponding to the value of *G* on the plateau, which can be identified when the histograms of the occurrence of the conductance values are evaluated (Venkataraman et al., 2006). This method is well-known from the identification of single-atom contacts in metallic junctions (Scheer et al., 1998). The conductance of a molecular junction, however, is orders of magnitude lower than that of a metallic junction, indicating the off-resonant nature of the charge transport through the molecules. This method was successfully demonstrated for characterization of the dependence of the conductance of DNA strands on their base sequence (Xu et al., 2004). Fig. 2C shows an SEM image of the metallic bridge, which is used to contact the molecules. The main difference of this technique compared to STM breakjunctions lies in the slow speed at which the electrodes are moved apart, which results in lower statistics but larger stability for single measurements. It is therefore easier to record stable *I–V* curves using the mechanically controllable break junctions (MCBJs) as the STM breakjunctions. Using MCBJs, ds-DNA and G-quadruplex structures could be contacted using two tips with adjustable distance (Liu et al., 2013, 2010).

Electrodes at fixed distances

The pairing of base pairs was successfully used for integration of ds-DNA in between electrode with fixed distance. The main advantage of this approach is given by the fact that the difference between measurements on nonconducting ss-DNA and conducting ds-DNA can be directly seen using the same contacts. Examples for this approach are measurements using metal contacts and metallic carbon nanotubes (CNTs) (Guo et al., 2008). Fig. 2D shows an AFM image of a junction, in which a ds-DNA is connected to a gap in two suspended CNTs and can be clearly imaged. This approach can be further perfectioned by binding Au nanoparticles to both ends of the DNA molecule. This can be achieved in a similar way as was described for the c-AFM technique. The nanoparticles are bound to ss-DNA with a sequence, which is complementary to the end of the DNA to be measured. These nanoparticles are bound to both ends of the molecules, which can then be deposited on an insulating substrate. The main advantage of this approach is that the Au nanoparticles can be identified and contacted using electron beam lithography (Roy et al., 2008; Zhuravel et al., 2020).

Electrical properties of single DNA and RNA molecules

The experimental techniques described above facilitate the controlled measurement of DNA and RNA in a controlled environment. The results depend on the contacting technique, but most of the differences can be attributed to the variations in environmental conditions due to the different contacting methods. We therefore review the experimental results grouped by contacting method and compare the main conclusions with conclusions drawn from theoretical calculations.

The main results of initial characterization measurements based on STM and c-AFM techniques revealed nonlinear s-shaped curves in a resistance range from 100 kΩ to 1 GΩ. Typical examples of such curves are shown in Fig. 3A.The nonlinearity of the curve can be explained with transport along the ds-DNA in the presence of a characteristic energy gap. Such energy gaps are characteristic for semiconducting and organic micro-and nanostructures. One can therefore conclude from these experimental results that charge transport along ds-DNA occurs along delocalized orbitals, which are formed by the structure of the molecule. ss-DNA does not exhibit any measurable conductance and is therefore considered to be insulating (Cohen et al., 2005). This indicates that the secondary and the ternary structures of DNA are essential for the conductance of single DNA strands. The influence of the base sequence on charge transport can be seen when comparing sequences containing different amounts of G-C and A-T pairs. Using the STM break-junction method, it was experimentally shown that molecules consisting of G-C pairs exclusively (pG-pC DNA) are conducting with a resistance in the range of a few MΩ while molecules only built from A-T pairs (pA-pT DNA) have much higher resistance (Xu et al., 2004). In Fig. 3B conductance histograms for three different ds-DNA strands are shown. The histograms exhibit clear maxima at conductance values corresponding to transport through single molecules that are attached to the substrate and the tip, respectively, on both ends. The conductance decreases when A-T pairs are introduced into pG-pC molecules. Studies of the length dependence of charge transport along ds-DNA have shown a transition between tunneling at short distances and hopping at longer distances for strands containing A-T pairs, which does not appear for pure G-C strands up to 16 bases (Li et al., 2016). This transition can be seen in Fig. 3D, where the conductance of ds-DNA is plotted logarithmically as a function of the number of base pairs. A-T pairs inside otherwise pure G-C structures can therefore be regarded as tunnel barriers in a conducting channel.

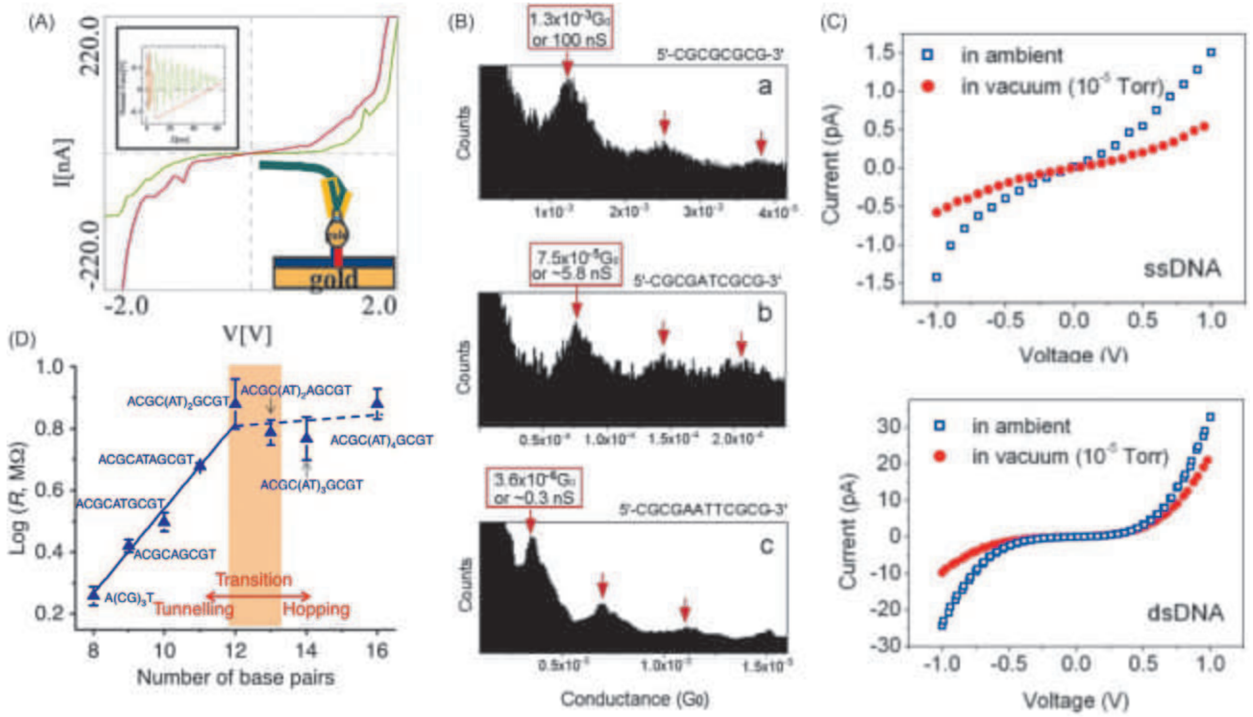

Fig. 3 Experimental results on charge transport through DNA molecules: (A) Nonlinear curve measured on ds-DNA using the c-AFM technique. (B) Histograms from opening curves measured using the STM breakjunction technique for ds-DNA with various base sequences. The lowest lying maximum in the histogram corresponds to junctions with single molecules. The resistance value at this maximum is therefore a measure for the metal-molecule-metal junction. The resistance is lowest for pC-pG wires. (C) Comparison between charge transport through ss-DNA and ds-DNA connected to CNTs (as shown in Fig. 2). (D) Transition between tunnelling and hopping for increasing number of AT base pairs in the ds-DNA. (A) Reprinted with permission from Cohen H, Naaman R, and Porath D (2005) Direct measurement of electrical transport through single DNA molecules of complex sequence. Proceedings of the National Academy of Sciences of the United States of America 102(33): 11589–11593. https://doi.org/10.1073/pnas.0505272102. Copyright (2005) National Academy of Sciences, U.S.A. (B) Reprinted with permission from Xu B, Zhang P, Li X, et al. (2004) Direct conductance measurement of single DNA molecules in aqueous solution. Nano Letters 4(6): 1105–1108. (C) Reprinted with permission from Roy S, Vedala H, Roy AD, Kim D, Doud M, Mathee K, Shin H, Shimamoto N, Prasad V, Choi W. (2008) Direct electrical measurements on single-molecule genomic DNA using single-walled carbon nanotubes. Nano Letters 8(1): 26–30. Copyright 2004 American Chemical Society.

The idea of transport through a single transport channel is further supported by measurements of G-C rich DNA fragments in MCBJ setups. At a fixed electrode distance, *I*–*V* curves were measured and compared to predictions by the SLM. In situations, in which a single ds-DNA strand binds to both electrodes, the transport can be fitted well to curves calculated based on (4). In analogy to measurements on single, organic molecules (Zotti et al., 2010), this can be seen as a hint that the base sequence creates a path for resonant tunneling of charges along the DNA. Measurements at varying electrode distances show a transition from pure tunneling at short distances to symmetric coupling with resonant tunneling at distances comparable to the DNA fragments to an asymmetric coupling at even larger distances. Further stretching of the junctions finally leads to a loss of conductance because the contact to the molecules is broken. This behavior can be modeled by assuming that first the contact between molecule and electrode is broken on one end, then the junction is stretched so far that the total tunnel current vanishes. Such a stretching behavior is modified when G-quadruplex structures are contacted. In these structures, the planes constituted by the G-bases can slide with respect to each other without losing the electronic coupling (Liu et al., 2010).

Theoretically, it has been confirmed that fluctuations of the molecular structure, which can be imposed by the presence of a solvent modify the coupling between the bases substantially (Gutierrez et al., 2009). Fig. 4A shows in a model presentation of this idea how the coupling of the sites to the phonon bath leads to additional energy states in the charging gap. Molecular dynamics simulations combined with quantum-chemical calculations and a model Hamiltonian approach were used to evaluate the contribution of different bases to the charge transport across the molecules. It turns out that transmission through pG-pC structures leads to a transmission close to E_F of Au while transmission through pA-pT structures occurs at considerably lower energies (see Fig. 4B). For extended structures, that is, long molecules, one can assume that transport between G bases occurs via hopping between the bases while parts with A-T pairs act as tunnel barriers. Fig. 4C depicts this transport behavior for pure poly G-C wires and poly G-C with partly A-T regions, respectively. The dominating effects on the transport behavior, however, are given by dynamical disorder, which is mainly caused by fluctuations of the DNA structure. Especially in liquid environment, which is needed to stabilize the double-helix structure of DNA, these fluctuations dominate the transport behavior. Fig. 4D shows simulated curves for pG-pC and pA-pT DNAs in a environment with fluctuations. The current is similar for both structures, indicating that the role of fluctuations in this regime is more dominant than the role of the base pair configuration.

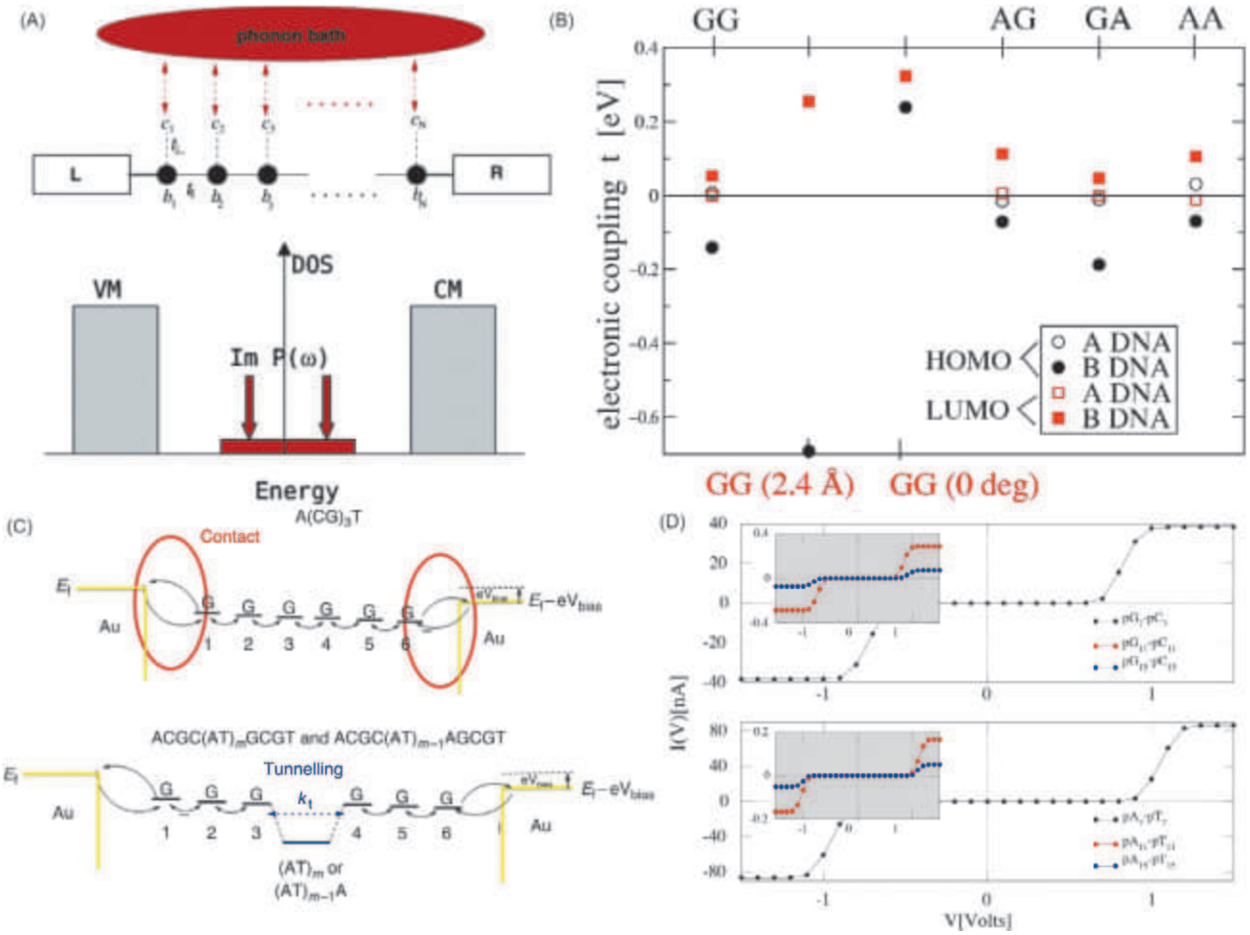

Fig. 4 Theory of charge transport in DNA: (A) Contact to the phonon bath creates midgap states which dominate charge transport at E_F. (B) Calculated electronic coupling between the different base pairs, showing that GG coupling occurs at the lowest energy and gives rise to the most efficient charge transport path. (C) Sketch of the difference between hopping along pG-pC wires and AT pairs, which act as tunnel barriers Li et al. (2016). (D) Comparison between calculated transport through pG-pC and pA-pT molecules. The overall current levels are similar, when fluctuations are taken into account. (A) Reprinted with permission from Gutierrez R, Mandal S, and Cuniberti G (2005) Quantum transport through a DNA wire in a dissipative environment. Nano Letters 5(6): 1093–1097. https://doi.org/10.1021/nl050623g. Copyright 2005 American Chemical Society. (B) Reprinted figure with permission from Endres RG, Cox DL, and Singh RRP (2004) Colloquium: The quest for high-conductance DNA. Reviews of Modern Physics 76: 195. Copyright 2004 by the American Physical Society. (D) Reprinted figure with permission from Gutierrez R, Caetano RA, Woiczikowski BP, et al. (2009). Charge transport through biomolecular wires in a solvent: Bridging molecular dynamics and model Hamiltonian approaches. Physical Review Letters 102(20): 208102. https://doi.org/10.1103/Phys- RevLett.102.208102. Copyright 2009 by the American Physical Society.

The role of fluctuations could be confirmed by comparing the behavior of pure RNA double strands with DNA:RNA hybrids in STM-breakjunction experiments (Chandra et al., 2022). Pure RNA double strands show similar conductance values as ds-DNA with similar base sequence. This confirms the idea that charge transport along these strands occurs mostly by hopping between different bases and is therefore determined by the intrastrand interactions between the bases. The variation of the conductance values is larger in case of RNA compared to DNA:RNA. MD simulations confirm that the origin of this phenomenon is most likely the different mechanical behavior of the two species.

The large conductance along G-bases can also be seen in other structures, for example, the so-called G-quadruplex structures. In MCBJ-breakjunction experiments, the resistance of the G-quadruplexes, which were contacted between two Au electrodes, as a function of distance between the electrodes could be recorded (Liu et al., 2010). Long plateaus at resistance values in between 100 kΩ and 10 MΩ indicate that the G-quadruplex can be stretched over several nm without changing the conductance of the junction. This can be explained by the overlap between G-bases in different layers of the quadruplex. It was found, however, that for G-quadruplexes lying on a conducting surface the energy gap, through which charge transport occurs, strongly depends on the position and therefore most likely on the geometric constraints of the molecule (Shapir et al., 2010). This was demonstrated by measuring scanning tunneling spectroscopy curves along G-quadruplex strands and categorizing the resulting curves in order to identify relevant energy states.

Using dimers consisting of ds-DNA and covalently bound Au nanoparticles. charge transport in long, freestanding, and dried ds-DNA could be measured (Zhuravel et al., 2020). In the absence of solvent effects, the measurements could be taken at various temperatures down to 5 K. In contrast to measurements in liquid environment, the transport shows no strong dependence on the base sequences of the DNA. It can be suppressed, however, by introducing defects ("nicks") in the strands. A single nick in one strand does not affect the current value at finite voltages, but if both strands are nicked at least once, the current is suppressed. These two findings in combination with the temperature dependence of the charge transport indicate that in this configuration the majority of the charge transport occurs by hopping along the backbone. This result is confirmed by ab initio electronic structure calculations and transport calculations.

Nanopores

Nanopores in electrically insulating membranes can be used for the detection of ionic currents between the two sides of the membranes (Xue et al., 2020). These ionic currents are influenced by the presence of a molecule, such as DNA or a protein. Therefore, changes in the amplitude of the ionic current give information on the electrical properties of the molecule inside the pore. By designing the pore geometry (length and diameter) properly, the resolution of this measurement technique can be brought to a stage at which single DNA bases can be detected (Manrao et al., 2012). In such experiments, the DNA is typically unzipped and guided through the pore at a speed which is low enough to distinguish the changes in ionic current above noise level. Recent improvements of this basic principle include fabrication of nanopores in artificial membranes, which improve selectivity and throughput (Xue et al., 2020). Nanopores have thus been a standard tool for DNA sequencing even on the commercial level (Mauger et al., 2020). The detection principle, as mentioned before, relies on the detection of ionic currents in the solution surrounding the DNA molecules and is therefore only weakly linked to the electronic properties of the DNA molecules themselves.

DNA Origami

As shown above, the conductance of double-stranded DNA with pG-pC base sequences indicates delocalized charge transport along the DNA with, however, comparably low transmission. The resulting resistance in the MΩ range is far too large for charge transport over long ranges. Therefore, electronic structures based on pure DNA molecules will unlikely be able to be used for the construction of large electronic circuits. The DNA origami method (Rothemund, 2006), however, allows the formation of arbitrary shapes on the nanoscale, which can be functionalized with conducting particles. Using this method, metallic nanostructures can be created, which can be used as wires for charge transport across lengths exceeding 100 nm (Bayrak et al., 2018; Aryal et al., 2018). More complex structures leading to junctions or nanogaps can be developed by implementing T-crossings and links between the different building blocks, for example, nanomolds which can be filled with semiconducting or metallic material (Ye et al., 2021). The deterministic self-assembly of the Origami structures then allows to include ds-DNA into these nanogaps with high precision. Therefore, this technique may ultimately lead to DNA electronics integrated in larger circuits, which are created using self-assembly. Apart from this, the conformational changes possible in DNA Origamis allow for reconfigurations in liquid environments. These dynamic changes in the position of conducting nanoparticles can be used for changing the optical properties of the assemblies and thus open vast possibilities in this area. For electronic readout, however, the liquid environment is typically detrimental. Therefore such applications are not within the scope of this article.

Conclusion

Charge transport along DNA and RNA molecules depends on the one hand on the structure of the DNA, for example, the base sequence and the conformation of the molecule, and on the other hand on the environment, which is mostly determined by the contacting techniques. Due to the development of reliable contacting techniques for single molecules, the understanding of charge transport in DNA and RNA could be advanced during the past two decades. Based on this experimental evidence one can conclude that charge transport at room temperature occurs by tunneling along the bases, with a coupling energy between the bases depending on the base. Fluctuations create states below the coupling energy similar to midgap states in semiconductors. At low temperatures, charge transport has been shown to be carried by the backbone of the molecule and is therefore independent of the base sequence. In all cases, the resistance of the DNA molecules is most likely too large for direct use in electronic applications. Therefore, concepts were developed to use self-organized nanostructures based on DNA, for example DNA Origamis. With these nanostructures, complex circuits can be built and bring DNA nanoelectronics closer to application.

References

Aryal BR, Westover TR, Ranasinghe DR, Calvopiña DG, Uprety B, Harb JN, Davis RC, and Woolley AT (2018) Four-point probe electrical measurements on templated gold nanowires formed on single DNA origami tiles. *Langmuir* 34: 15069–15077. https://doi.org/10.1021/acs.langmuir.8b02225.

Bayrak T, Helmi S, Ye J, Kauert D, Nano JK, et al. (2018) DNA-mold templated assembly of conductive gold nanowires. *Nano Letters* 18(3): 2116–2123. https://doi.org/10.1021/acs.nanolett.8b00344.

Braun E, Eichen Y, Sivan U, and Ben-Yoseph G (1998) DNA-templated assembly and electrode attachment of a conducting silver wire. *Nature* 391(6669): 775–778. https://doi.org/10.1038/35826.

Chandra S, Arachchillage KGGP, Kliuchnikov E, Maksudov F, Ayoub S, Barsegov V, and Vivancos JMA (2022) Single-molecule conductance of double-stranded RNA oligonucleotides. *Nanoscale* 14(7): 2572–2577. https://doi.org/10.1039/D1NR06925J.

Choi SH, Risko C, Delgado MCR, Kim B, Bredas J-L, and Frisbie CD (2010) Transition from tunneling to hopping transport in long, conjugated oligo-imine wires connected to Metals. *Journal of the American Chemical Society* 132(12): 4358–4368. https://doi.org/10.1021/ja910547c.

Cohen H, Naaman R, and Porath D (2005) Direct measurement of electrical transport through single DNA molecules of complex sequence. *Proceedings of the National Academy of Sciences of the United States of America* 102(33): 11589–11593. https://doi.org/10.1073/pnas.0505272102.

Cui XD, Primak A, Zarate X, Tomfohr J, Sankey OF, Moore AL, Moore TA, Gust D, Harris G, and Lindsay SM (2001) Reproducible measurement of single-molecule conductivity. *Science* 294: 571. http://www.google.com/search?client=safari&rls=en-us&q=Reproducible+Measurement+of+Single-Molecule+Conductivity&ie=UTF-8&oe=UTF-8.

Endres RG, Cox DL, and Singh RRP (2004) Colloquium: The quest for high-conductance DNA. *Reviews of Modern Physics* 76: 195.

Fink H-W and Schönenberger C (1999) Electrical conduction through DNA molecules. *Nature* 398: 407.

Guo X, Gorodetsky AA, Hone J, Barton JK, and Nuckolls C (2008) Conductivity of a single DNA duplex bridging a carbon nanotube gap. *Nature Nanotechnology* 3(3): 163–167. https://doi.org/10.1038/nnano.2008.4.

Gutierrez R, Mandal S, and Cuniberti G (2005) Quantum transport through a DNA wire in a dissipative environment. *Nano Letters* 5(6): 1093–1097. https://doi.org/10.1021/nl050623g.

Gutierrez R, Caetano RA, Woiczikowski BP, Kubar T, Elstner M, and Cuniberti G (2009) Charge transport through biomolecular wires in a solvent: Bridging molecular dynamics and model Hamiltonian approaches. *Physical Review Letters* 102(20): 208102. https://doi.org/10.1103/PhysRevLett.102.208102.

Huisman EH, Guedon CM, van Wees BJ, and van der Molen SJ (2009) Interpretation of transition voltage spectroscopy. *Nano Letter* 9(11): 3909–3913. https://doi.org/10.1021/nl9021094.

Kasumov AY, Kociak M, Gueron S, Reulet B, Volkov VT, Klinov DV, and Bouchiat H (2001) Proximity-induced superconductivity in DNA. *Science* 291(5502): 280–282.

Li Y, Xiang L, Palma JL, Asai Y, and Tao N (2016) Thermoelectric effect and its dependence on molecular length and sequence in single DNA molecules. *Nature Communications* 7(1): 11294. ISSN: 2041-1723. https://doi.org/10.1038/ncomms11294.

Liu S-P, Weisbrod SH, Tang Z, Marx A, Scheer E, and Erbe A (2010) Direct measurement of electrical transport through G-quadruplex DNA with mechanically controllable break junction electrodes. *Angewandte Chemie, International Edition* 49(19): 3313–3316. https://doi.org/10.1002/anie.201000022.

Liu SP, Artois J, Schmid D, Wieser M, Bornemann B, Weisbrod S, Marx A, Scheer E, and Erbe A (2013) Electronic transport through short dsDNA measured with mechanically controlled break junctions: New thiol-gold binding protocol improves conductance. *Physica Status Solidi B* 250(11): 2342–2348. https://doi.org/10.1002/pssb.201349158.

Livshits GI, Stern A, Rotem D, Borovok N, Eidelshtein G, Migliore A, Penzo E, Wind SJ, Di Felice R, Skourtis SS, Cuevas J-C, Gurevich L, Kotlyar AB, and Porath D (2014) Long-range charge transport in single G-quadruplex DNA molecules. *Nature Nanotechnology* 9(12): 1040–1046. https://doi.org/10.1038/nnano.2014.246.

Manrao EA, Derrington IM, Laszlo AH, Langford KW, Hopper MK, Gillgren N, Pavlenok M, Niederweis M, and Gundlach JH (2012) Reading DNA at single-nucleotide resolution with a mutant MspA nanopore and phi29 DNA polymerase. *Nature Biotechnology* 30(4): 349–353. ISSN: 1546-1696. https://doi.org/10.1038/nbt.2171.

Mauger F, Horgues C, Pierre-Jean M, Oussada N, Mesrob L, and Deleuze J-F (2020) Comparison of commercially available whole-genome sequencing kits for variant detection in circulating cell-free DNA. *Scientific Reports* 10(1): 6190. ISSN: 2045-2322. https://doi.org/10.1038/s41598-020-63102-8.

Metzger RM (2015) Unimolecular electronics. *Chemical Reviews* 115(11): 5056–5115. https://doi.org/10.1021/cr500459d.

Moreno-Garcia P, Gulcur M, Manrique DZ, Pope T, Hong W, Kaliginedi V, Huang C, Batsanov AS, Bryce MR, and Lambert C (2013) Single-molecule conductance of functionalized oligoynes: Length dependence and junction evolution. *Journal of the American Chemical Society* 135(33): 12228–12240. https://doi.org/10.1021/ja4015293.

Porath D, Bezryadin A, De Vries S, and Nature CD (2000) Direct measurement of electrical transport through DNA molecules. *Nature* 403: 635. https://doi.org/10.1063/1.1342553.

Rothemund PWK (2006) Folding DNA to create nanoscale shapes and patterns. *Nature* 440(7082): 297–302. https://doi.org/10.1038/nature04586.

Roy S, Vedala H, Roy AD, Kim D, Doud M, Mathee K, Shin H, Shimamoto N, Prasad V, and Choi W (2008) Direct electrical measurements on single-molecule genomic DNA using single-walled carbon nanotubes. *Nano Letters* 8(1): 26–30.

Scheer E, Agrait N, Cuevas JC, Yeyati AL, Ludoph B, Martin-Rodero A, Bollinger GR, van Ruitenbeek JM, and Urbina C (1998) The signature of chemical valence in the electrical conduction through a single-atom contact. *Nature* 394(6689): 154–157. https://kops.ub.uni-konstanz.de/xmlui/handle/id-13/browse?offset=1560&type=ddc&value=530.

Scott GD and Natelson D (2010) Kondo resonances in molecular devices. *ACS Nano* 4(7): 3560–3579. https://doi.org/10.1021/nn100793s.

Shapir E, Sagiv L, Molotsky T, Kotlyar AB, Felice RD, and Porath D (2010) Electronic structure of G4-DNA by scanning tunneling spectroscopy. *Journal of Physical Chemistry C* 114(50): 22079–22084. ISSN: 1932-7447. https://doi.org/10.1021/jp107952y.

Simmons CB (1963) Generalized formula for electric tunnel effect between similar electrodes separated by a thin insulating film. *Journal of Applied Physics* 34(6): 1793–1803.

Stern A, Eidelshtein G, Zhuravel R, Livshits GI, Rotem D, Kotlyar A, and Porath D (2018) Highly conductive thin uniform gold-coated DNA nanowires. *Advanced Materials* 30(26): 1800433. https://doi.org/10.1002/adma.201800433.

Venkataraman L, Klare JE, Tam IW, Nuckolls C, Hybertsen MS, and Steigerwald ML (2006) Single-molecule circuits with well-defined molecular conductance. *Nano Letters* 6(3): 458–462. https://doi.org/10.1021/nl052373+.

Wang W, Reed M, and Lee T (2003) Mechanism of electron conduction in self-assembled alkanethiol monolayer devices. *Physical Review B* 68(3): 035416. https://doi.org/10.1103/PhysRevB.68.035416.

Xu B, Zhang P, Li X, and Tao N (2004) Direct conductance measurement of single DNA molecules in aqueous solution. *Nano Letters* 4(6): 1105–1108.

Xue L, Yamazaki H, Ren R, Wanunu M, Ivanov AP, and Edel JB (2020) Solid-state nanopore sensors. *Nature Reviews Materials* 5(12): 931–951. ISSN: 2058-8437. https://doi.org/10.1038/s41578-020-0229-6.

Ye J, Aftenieva O, Bayrak T, Jain A, König TAF, Erbe A, and Seidel R (2021) Complex metal nanostructures with programmable shapes from simple DNA building blocks. *Advanced Materials* 33: 2100381. ISSN: 1521-4095. https://doi.org/10.1002/adma.202100381.

Zhuravel R, Huang H, Polycarpou G, Polydorides S, Motamarri P, Katrivas L, Rotem D, Sperling J, Zotti LA, Kotlyar AB, Cuevas JC, Gavini V, Skourtis SS, and Porath D (2020) Backbone charge transport in double-stranded DNA. *Nature Nanotechnology* ISSN: 1748-3395. 15(10): 836–840. https://doi.org/10.1038/s41565-020-0741-2.

Zotti LA, Kirchner T, Cuevas J-C, Pauly F, Huhn T, Scheer E, and Erbe A (2010) Revealing the role of anchoring groups in the electrical conduction through single-molecule junctions. *Small* 6(14): 1529–1535. https://doi.org/10.1002/smll.200902227.

Genetic Algorithms for Biological Systems

K Sneppen[a] **and S Maslov**[b], [a]Niels Bohr Institutet, Copenhagen, Denmark; [b]Brookhaven National Laboratory, Upton, NY, USA

© 2005 Elsevier Ltd. All rights reserved.

This is an update of K. Sneppen, S. Maslov, Genetic Algorithms for Biological Systems, Editor(s): Franco Bassani, Gerald L. Liedl, Peter Wyder, Encyclopedia of Condensed Matter Physics, Elsevier, 2005, Pages 251–256, ISBN 9780123694010, https://doi.org/10.1016/B0-12-369401-9/00376-4.

Introduction 684
Topology of Genetic Regulatory Networks 684
Combinatorics in Genetic Networks, and an Evolution Model 688
Further Reading 689

Introduction

Cells are controlled by the action of molecules upon molecules. Receptor proteins in the outer cell membrane sense the environment and may subsequently induce changes in the states of specific proteins inside the cell. These proteins then interact again and convey the signal further to other proteins and so forth, until some appropriate action is taken. The final results of such signaling may be a transcription regulation, thereby making more of some kinds of proteins.

The reader is reminded that proteins are produced from DNA through a two-step process, where first the DNA code is transcribed into mRNA by an RNA polymerase, and subsequently, the mRNA is translated into a protein by a ribosome. This is illustrated in Figure 1. The simplest way that one protein regulates the production rate of another protein is illustrated in Figure 2. The regulated protein may in turn regulate other proteins, and thereby be part of the transcription regulatory network. Regulatory genetic networks are essential for epigenetics and thus multicellular life, but are not essential for life. In fact, there exist prokaryotes with nearly no genetic regulation.

An interesting overall observation dealing with the architecture of genetic regulatory networks is that the fraction of proteins that regulate other proteins N_{reg}/N increases with total number of proteins N. In other words, the relative size of the bureaucracy increases with system size. In fact for prokaryotes, the fraction of regulators increases linearly with the system size, reaching ~10% for the prokaryote *Pseudomonas auriginosa* with its ~6000 genes. If a living cell could be understood as an essential core plus a number of modules (genes regulated together), each, for example, associated to respond to a corresponding external situation, then the fraction of regulators would be independent of the number of genes N. The fact that N_{reg}/N grows linearly with N indicates that each added gene or module should be regulated with respect to all other gene modules. Thus, already prokaryotic organisms show features of a highly integrated computational machine. Networks are indeed important, from the smallest hubs with feedback to the whole integrated circuitry.

Topology of Genetic Regulatory Networks

In Figure 3, the known regulatory network for the single-celled eukaryote, the yeast *Saccromyces cerevisia* is shown. One feature of regulatory networks is the wide distribution of directed arrows from individual proteins. There are many proteins which control only few other proteins, but there also exist some proteins which control the expression level of many other proteins. In fact, the distribution of proteins with a given number of neighbors (connectivity) K may (very crudely) be approximated by a power law

$$N(K) \propto 1/K^{\gamma} \qquad [1]$$

with exponent $\gamma \sim 1.5 \pm 0.5$ for the "out-degree" distribution of transcription regulators (see Figure 4). It is also to be noticed that the distribution of the number of proteins in which a given protein regulates, the "out-degree" differs from the narrower distribution of "in-degrees." Overall however, both of these distributions are broad, and one would like to develop an intuition to find possible reasons why life organizes its regulation in this way.

One aspect of a wide distribution of connectivity in signaling networks is the possible amplification of signals in the network. Thus on an average, a signal entering a node could be transmitted to a number of other nodes given by the amplification factor:

$$\begin{aligned}\mathcal{A} &= \frac{\langle K_{\mathrm{in}} K_{\mathrm{out}}(\text{given } K_{\mathrm{in}})\rangle}{\langle K_{\mathrm{in}}\rangle} \\ &= \frac{\langle K_{\mathrm{in}} K_{\mathrm{out}}\rangle}{\langle K_{\mathrm{in}}\rangle}\end{aligned} \qquad [2]$$

the last equality implies that the output connectivity is independent of the input connectivity. The above formula follows from following a signal that enters a node with probability proportional to K_{in}, and leaves along any of the K_{out} links. The equation is thus the average amplification factor in a randomly wired directed network. When $\mathcal{A} > 1$, signals tend to be exponentially amplified and thus, most signals will influence signaling over the entire network. For networks with degree distribution which is a power law, $\mathcal{A}$

https://doi.org/10.1016/B978-0-323-90800-9.00309-7

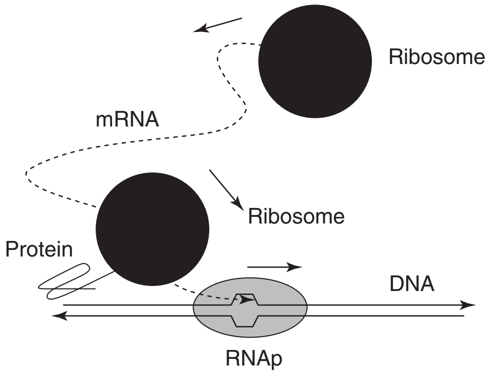

Figure 1 RNA polymerase (RNAp) moves along the DNA while transcribing it into an mRNA string. This mRNA is subsequently translated into a protein by a ribosome, here shown in black. The same mRNA may easily be translated into several proteins.

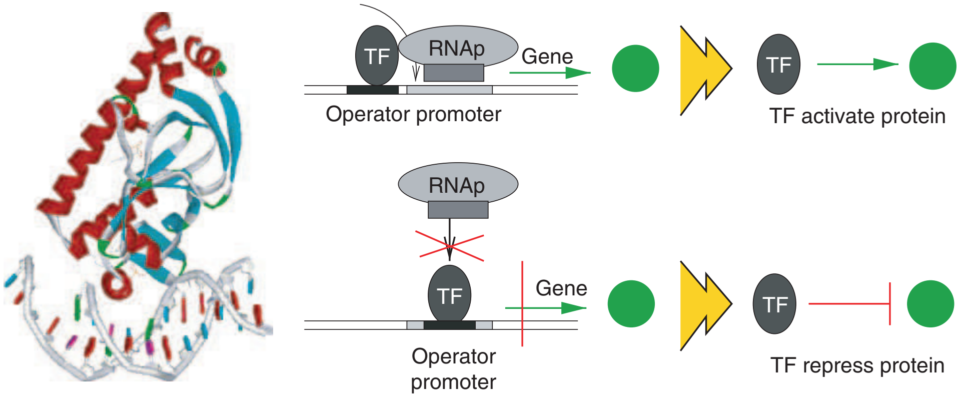

Figure 2 On left panel an example of a transcription factor is shown, the protein CAP that binds to a piece of DNA. On right panel is illustrated respective positive and negative regulation by a transcription factor (TF) on a protein shown as a green filled circle. The TF is a protein that binds to a region on the DNA called an operator (dark region on the DNA). The positive regulation is through a binding between the TF and the RNAp, that increases the chance that RNAp binds to the promoter that is shown as a medium dark region on the DNA strand. Negative regulation occurs when the operator is placed such that the bound TF prevents the RNAp from binding to the promoter. On the rightmost panels is shown how one typically draws the elementary regulation as an arrow in a regulatory network.

typically depends on the most highly connected node. Thus, highly connected nodes will be effective in transmitting a signal very fast to a substantial part of the whole system. This has obvious advantages, and may be one of the reasons why one also observes very highly connected nodes in both genetic and other signaling networks in living cells.

Power-law networks have also been proposed to be due to statistical processes, with little regard to functionality. One very widespread suggestion is the preferential attachment idea, that uses the fact that, if a network is growing by a mechanism where each new node is attached to nodes selected as being in the ends of already existing links in the network, then one obtains a steadily growing scale-free network. Another suggestion is the observation that even a nongrowing network can develop into a steady-state attractor with a scale-free degree distribution, if one assumes that a major element in the network rewiring dynamics is merging of old vertices and creation of new vertices. In the perspective of signaling networks, the latter model represents an on-going attempt to minimize the length of signaling pathways, competing with an on-going pressure to increase the protein diversity. In any case, traces of the actual evolution of networks can be quantified using the rather frequent gene duplication and associated protein homologs that one finds in any presently living organism. The overall lesson of such studies is that the genome of any organism is dynamic, and that reorganizations indeed are possible if they are functionally desirable.

The real reason for the observed broad distribution of edge degrees in biological networks should probably be seen in the perspective of where especially the highly-connected nodes sit in the network. To analyze this, a discussion on how to analyze network topologies beyond the degree distribution is taken up now. The key idea is to generate a random network, and then to compare this with the real network.

As was pointed out in the general context of complex scale-free networks, a broad distribution of degrees indicates that the degree itself is an important individual characteristic of a node and as such, it should be preserved in the randomized null-model network. In addition to degrees, one may choose to preserve some other low-level topological properties of the network in question. Any measurable topological quantity, such as, the total number of edges connecting pairs of nodes with given degrees, the number of loops of a certain type, the number and sizes of components, the diameter of the network, can then be measured in the real complex network and separately in its randomized version. One then concentrates only on those topological properties of the real network that significantly deviate from their null-model counterpart.

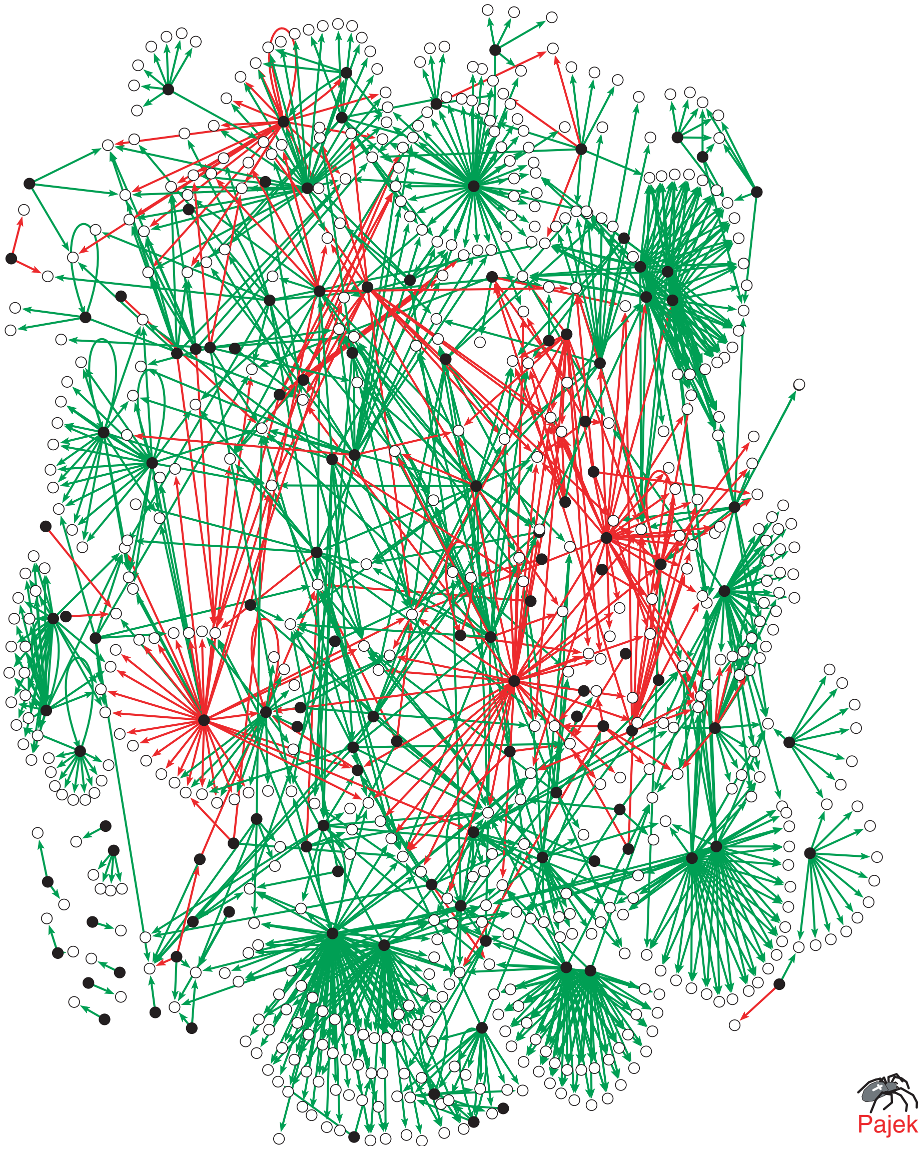

Figure 3 Presently known transcription regulations in yeast (*Saccromyces cerevisia*), with green arrows indicating positive regulation (activation) and red arrows indicating repression.

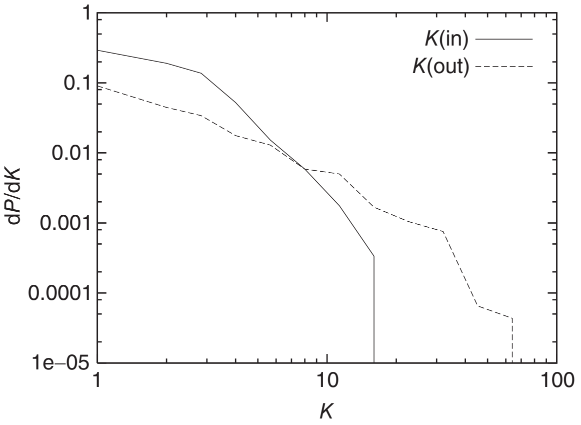

Figure 4 Statistics of regulation in the yeast *Saccromyces cerevisia*. (Data from Proteome.)

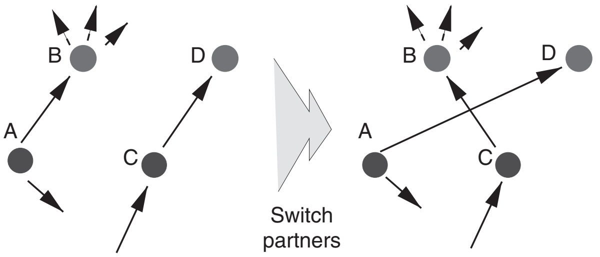

Figure 5 One step of the local rewiring algorithm. A pair of directed edges A→B and C→D. The two edges then switch connections in such a way that A becomes linked to D, while C to B, provided that none of these edges already exist in the network, in which case the move is aborted and a new pair of edges is selected. An independent random network is obtained when this is repeated a large number of times, exceeding the total number of edges in the system. This algorithm conserves both the in- and out-connectivity of each individual node. (Reproduced from Maslov S and Sneppen K (2002) Specificity and stability in topology of protein networks. *Science* 296: 910–913; American Association for the Advancement of Science.)

An algorithm giving rise to a random network with the same set of individual node degrees, as in a given complex network, was proposed by Maslov S and Sneppen K in 2002. It consists of multiple repetitions of the following simple switch move (elementary rewiring step) illustrated in Figure 5: "Randomly select a pair of edges A→B and C→D and rewire them in such a way that A becomes connected to D, while C to B."

To prevent the appearance of multiple edges connecting the same pair of nodes, the rewiring step is aborted and a new pair of edges is selected if one or two of the new edges already exist in the network. A repeated application of the above rewiring step leads to a randomized version of the original network. The set of MATLAB programs generating such a randomized version of any complex network can be downloaded from the internet.

Sometimes it is desirable that the null-model random network in addition to degrees of nodes, conserves some other topological quantity of the real network. In this case, one could supplement the random rewiring algorithm described above with the Metropolis acceptance/rejection criterion.

The "correlation profile" of any large complex network quantifies correlations between degrees of its neighboring nodes. The topological property of the network giving rise to its correlation profile is the number of edges $N(K_0, K_1)$ connecting pairs of nodes with degrees K_0 and K_1. To find out if in a given complex network the degrees of interacting nodes are correlated, $N(K_0, K_1)$ should be compared to its value $N_r(K_0, K_1) \pm \delta N_r(K_0, K_1)$ in a randomized network, generated by the edge rewiring algorithm. When normalized by the total number of edges E, $N(K_0, K_1)$ defines the joint probability distribution $P(K_0, K_1) = N(K_0, K_1)/E$ of degrees of interacting nodes. Any correlations would manifest themselves as systematic deviations of the ratio

$$R(K_0, K_1) = P(K_0, K_1)/P_r(K_0, K_1) \qquad [3]$$

away from 1. The correlation profile for the yeast regulatory network is shown in Figure 6. The statistical significance of such deviations can, in principle, be quantified by their Z-score

$$Z(K_0, K_1) = (P(K_0, K_1) - P_r(K_0, K_1))/\sigma_r(K_0, K_1) \qquad [4]$$

where $\sigma_r(K_0, K_1) = \Delta N_r(K_0, K_1)/N$ is the standard deviation of $P_r(K_0, K_1)$ in an ensemble of randomized networks.

The result of the above analysis is that there is a significant suppression of links between hubs, both for regulatory networks analyzed in Figure 6 and also for the protein networks measured in large-scale two-hybrid experiments on yeast. Similarly, by

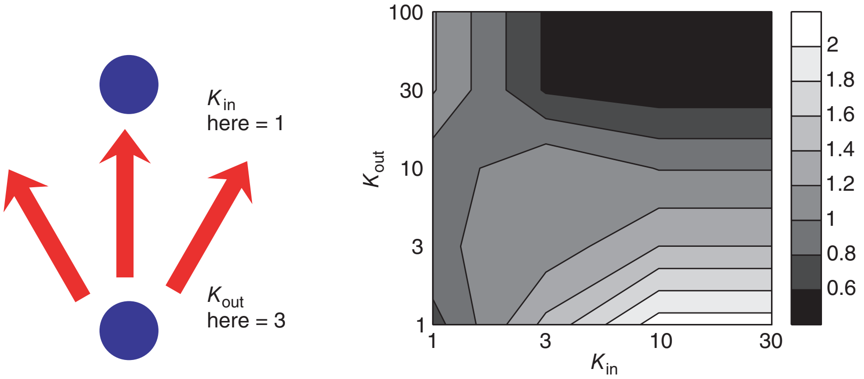

Figure 6 Correlation profile showing correlation between connected proteins in the regulatory network of yeast, quantified in terms of Z scores. The single output module is reflected in the abundance of high K_{out} controlling single K_{in} proteins. The dense overlapping regulons correspond to the abundance of connections between K_{out}~10 and K_{in}~3 proteins. Finally, the suppression of connections between highly connected proteins show that these tend to be on the periphery of the network. (Maslov S and Sneppen K (2002) Specificity and stability in topology of protein networks. *Science* 296: 910–913.)

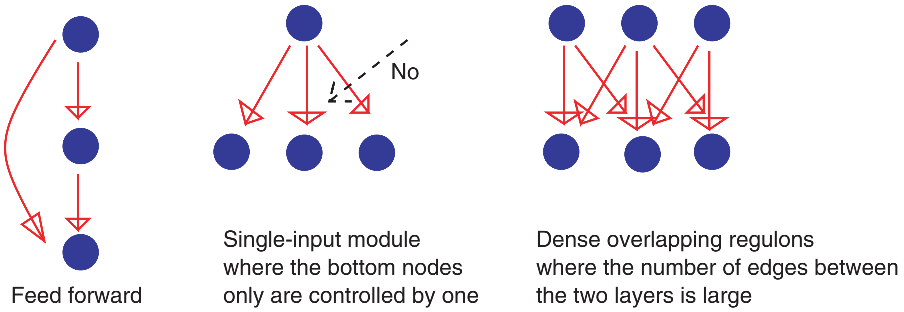
Feed forward
No
Single-input module where the bottom nodes only are controlled by one
Dense overlapping regulons where the number of edges between the two layers is large

Figure 7 Genetic control motifs which are found to be over represented in regulatory networks of both *E. coli* and yeast. (Milo R, Shenn-Orr S, Itzkovitz S, Kashtan N, and Chklovskii D (2002) Network motifs: simple building blocks of complex networks. *Science* 298: 824–827.)

defining higher-order occurrences of various local patterns of control, Shen-Orr and co-workers suggested some frequent motifs of gene control in 2002, as illustrated in Figure 7.

Finally, it may be mentioned that the tendency of highly connected proteins to be at the periphery of regulatory networks in itself teaches one something about the origin of broad connectivity distributions. To see this, one could consider the fact that a protein is a fairly simple unit, that presumably gives essentially the same information to each of its downstream targets. Thus, the feature that a hub protein sits on the periphery of the network and does not link to other hub proteins, presumably reflects a one-hub-one-function structure. As a corollary of this, one may suspect that the broad distribution of molecular networks is not an intrinsic property of the network, but rather reflects the broad distribution of external requirements that the surroundings of an organism puts on it. Some functions simply require many proteins, whereas many functions require only a few proteins. This scenario is also supported by the observation that there is essentially no correlation between connectivity of a regulatory protein and its importance measured by its chance to be essential in knock-out experiments. If highly connected proteins were involved in many functions, their likelihood of being essential would grow linearly with their connectivity. This is not the case, for the yeast transcription network: the chance that a transcription factor is lethal is independent of how many proteins it regulates!

To summarize the topological properties of regulatory and signaling networks, the broad connectivity distributions may very well reflect the widely different needs associated to widely different functions that a living cell needs to cope with as it changes its environment.

Combinatorics in Genetic Networks, and an Evolution Model

In addition to the topological properties, the regulation of genes also have a combinatorical part. This means that the regulation of a given gene may depend on the combination of the concentration of its regulators. An inspiring way to model such a combinatorical regulation was proposed already in 1969 by S Kauffman. In this very simplified approach, each gene was assigned a binary number, 0 or 1, that counts whether the gene was off or on. Each gene i was assumed to be on or off depending on some logical function of the state of the gene that regulated it. A very simple version of this Boolean rule would be the threshold network where the state of the gene i at time t is given by

$$\sigma(i,t) = \Theta\left(\sum A_{ij}\sigma(j, t-1)\right) \qquad [5]$$

where $\Theta(x)$ is zero for $x<0$ and $=1$ otherwise. The A_{ij} is nonzero for genes j that regulate gene i. A_{ij} is positive for activation, and negative for repression. For a large regulatory network, the above update defines a cellular automata in a geometry defined by the connectivity matrix. Starting in an arbitrary initial condition, the system will move through a sequence of states that at some point is bound to repeat itself. This is because the state space is finite and the update deterministic. Thus, much effort has been used to characterize the behavior of these attractors as a function of the connectivity pattern of the system. One simple result is that the system undergoes a percolation phase transition when the average connectivity is increased beyond a critical out-connectivity $\langle K_{\text{out}}\rangle \sim 2$. Above this transition, the attractors become very long (exponentially growing with system size) and the behavior is called chaotic.

The Boolean paradigm allows for modeling large-scale expression patterns of idealized regulatory networks. Thus, it also allows one to address how long-time evolution of rewiring and changes of combinatorical rules may constrain the evolution of such networks. In this regard, it is especially interesting to consider robustness as an evolutionary principle. One way to implement this is to "Evolve a new network from an old network by accepting rewiring mutations with a probability determined by the expression overlap."

This minimal-constraint scenario has no outside fitness imposed. Also, it ignores competition between networks, as it only compares a network with its predecessor. However, the model naturally selects networks which have a high overlap with neighbor mutant networks. This feature is associated to robustness, defined as the requirement that not only should the present network

work, but also mutations of the networks should work. In terms of network topology, this means a change in the wiring $\{A_{ij}\} \rightarrow \{A'_{ij}\}$ that takes place on a much slower timescale than the $\{\sigma_j\}$ updating using the Boolean dynamics itself.

The system that is evolved is the set of couplings A_{ij} in a single network. One evolutionary time-step of the network is:

1. Create a daughter network by (a) adding, (b) removing, or (c) adding and removing a weight in the coupling matrix A_{ij} at random, each option occurring with probability $p=1/3$. This means turning an $A_{ij}=0$ to a randomly chosen ± 1 or vice versa.
2. Select a random input state $\{\sigma_i\}$. Iterate simultaneously both the mother and the daughter system from this state until they either have reached and completed the same attractor cycle, or until a time where $\{\sigma_i\}$ differs between the two networks. In case their dynamics is identical, then replace the mother with the daughter network. In case their dynamics differs, keep the mother network.

The result of this type of modeling is an intermittent evolutionary pattern: occasionally the evolved network is trapped in states with few evolution paths away from it; sometimes it is, instead, in highly active regions of "network space," thus allowing fast readjustments of genome architecture. More important, the obtained network exhibits a less chaotic behavior than random ones. The computational structure thus emerging has a simplicity of form consistent with that obtained with real molecular networks by placing highly connected nodes on the periphery of the network. In the Boolean model networks explored here, the attractors for the networks are shorter, and there are more frozen regulators in a random network at the same average connectivity.

Further Reading

Barabasi A-L and Albert R (1999) Emergence of scaling in random networks. *Science* 286: 509.

Bornholdt S and Sneppen K (2000) Robustness as an evolutionary principle. *Proceedings of Royal Society of London B* 267: 2281–2286.

Davidson *et al.*, A genomic regulatory network for development. *Science* 295(5560): 1669–2002.

Derrida B and Pommeau Y (1986) Random networks of automataa simple annealed approximation. *Europhysics Letters* 1: 45–49.

deS Price DJ (1976) A general theory of bibliometric and other cumulative advantage processes. *Journal of American Society Information Science* 27: 292.

Kauffman SA (1969) Metabolic stability and epigenesis in randomly constructed genetic nets. *Journal of Theoretical Biology* 22: 437–467.

Kim BJ, Trusina A, Minnhagen P, and Sneppen K Self organized scale-free networks from merging and regeneration. nlin.AO/0403006.

Maslov S, Sneppen K, and Eriksen KA (2004) Upstream plasticity and downstream robustness in evolution of molecular networks. *BMC Evolutionary Biology* 4: 9.

Maslov S, Sneppen K, and Zaliznyak A (2004) Pattern detection in complex networkscorrelation profile of the internet. *Physica A* 333: 529–540.

Metropolis N, Rosenbluth AW, Rosenbluth MN, Teller AH, and Teller E (1953) Equation of state calculations by fast computing machines. *Journal of Chemical Physics* 21: 1087.

Newman MEJ, Strogatz SH, and Watts DJ (2001) Random graphs with arbitrary degree distributions and their applications. *Physical Review E* 64: 026118, 1.

Stover CK, Pham XQ, Erwin AL, Mizoguchi SD, and Warrener P (2000) Complete genome sequence of *Pseudomonas Aeruginosa PA01*, an opportunistic pathogen. *Nature* 406: 959.

The set of MATLAB programs can be downloaded at http://www.cmth.bnl.gov/maslov/matlab.htm

Ion Transport in Biological Membranes

M Baruscotti[a], **G Thiel**[b], **and A Moroni**[c], [a]Università degli Studi di Milano, Milan, Italy; [b]Darmstadt University of Technology, Darmstadt, Germany; [c]Università degli Studi di Milano, Milan, Italy

© 2005 Elsevier Ltd. All rights reserved.

This is an update of M. Baruscotti, G. Thiel, A. Moroni, Ion Transport in Biological Membranes, Editor(s): Franco Bassani, Gerald L. Liedl, Peter Wyder, Encyclopedia of Condensed Matter Physics, Elsevier, 2005, Pages 1–9, ISBN 9780123694010, https://doi.org/10.1016/B0-12-369401-9/00389-2.

Structure and Function of Transport Proteins 693
Selectivity 694
Gating 694
The Cell Membrane as an Equivalent Circuitry of Parallel Ion Channels with Variable Conductance: An Explanation for Complex Changes of Membrane Voltage 695
Further Reading 698

All living cells are surrounded by lipid membranes that are impermeable to ions and any large or charged molecules. With this, lipid barrier cells are able to separate a well-defined ionic environment inside the cell, the cytoplasm, from the extra cellular solution and also from internal compartments. The purpose of internal compartmentation is that biochemical reactions with different ionic requirements can occur simultaneously without interfering. A schematic representation of the main cellular compartments of a typical animal cell is illustrated in Figure 1. The maintenance of these compartments and the integrity of the membranes is an absolute requirement for cellular life.

As much as the separation of compartments by membranes is important for cell function, a tightly controlled and selective communication between the individual compartments is required. Such a communication cannot occur via simple diffusion across the lipid membrane, because this process is much too slow. Cells have therefore evolved specific transport proteins, which facilitate the diffusion of ions and solutes through the membrane in a selective and regulated fashion.

Ion channel proteins represent a very efficient mechanism of facilitated diffusion. Due to the architecture of the channel pore (see section "Structure and function of transport proteins"), these transporters allow ions to cross membranes at rates which approach diffusion in water.

Diffusion is a passive process and occurs energetically only downhill. However, cells often have to concentrate ions in different compartments and in order to do this they have to move ions against their concentration gradient (see Figure 1). To this purpose cells utilize a class of transport proteins, termed pumps, which drive active, energy-consuming transport across the membranes. Active transport of a solute against its concentration gradient is driven by the energy released in the hydrolysis of a high-energy molecule, ATP. The pumps are therefore also called ATPases.

Transport of solutes against their gradient does not necessarily require the presence of a primary active transport system. The movement of solutes can also be coupled to the movement of other molecules down their respective electrochemical gradients (secondary active transport). In this case, the potential energy stored in ionic gradients (by the ATPases) can be utilized to transport other solutes. An example for this type of transporter is the Na^+/glucose co-transport. The concentration of sodium $[Na^+]$ is kept low in the cytoplasm by the primary active transport system (the Na^+/K^+ ATPase). The glucose molecules are driven by secondary active transport by a Na^+/glucose co-transporter.

The best understood transporters to date, in terms of structure and function, are ion channels. This has two reasons. One reason is their key role in important physiological reactions such as nerve activity and muscle contraction. However, more significant for their understanding is their high turnover rate which allows them to be investigated at the single protein level. Two techniques, the planar lipid bilayer and the patch clamp technique, have greatly improved our understanding of ion transport through channels. The main features of the two methods are illustrated in Figure 2. The characteristic of the former approach is that the performance of a channel protein, even those from intracellular membranes, can be measured in a completely artificial system, in which all components such as the composition of the lipids and of the solutions are under the control of the experimenter, while the latter method allows one to measure channels in their native environment.

Both techniques report essentially the same kind of activity from ion channels. Figure 3 illustrates a typical patch clamp recording of single-channel fluctuations in a membrane. The channel fluctuates between an open and a closed state. When it opens, it gives rise to a current, measured in picoampere (pA), with the characteristic open-channel amplitude. A single-channel current of 1 pA as in Figure 3 corresponds to a flow of 6×10^6 ions per second.

In the simplest case, the conductance of an open channel behaves like an Ohmic resistor increasing linearly with the driving force. The slope of the current/voltage relation is a measure of the conductance of a channel. The conductance is characteristic of each individual channel proteins. In the case of potassium channels, they are in the range of picosiemens (pS).

The possibility of measuring and controlling the solution composition on both sides of the membrane allows examining the selectivity of these proteins. If a channel were perfectly selective for only one ion, the measured equilibrium voltage should match that predicted from the Nernst equation. Any other behavior indicates that the channel is either less selective or even, in the extreme case, not selective at all for a given ion. Channels of the latter kind have been described but they are a minority among the physiologically relevant channels, which are in general highly selective. Experiments performed in the way indicated above show,

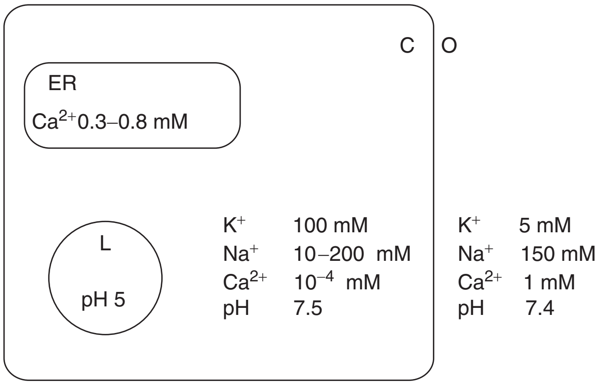
C
O
ER
Ca2+ 0.3–0.8 mM
L
pH 5
K+ 100 mM
Na+ 10–200 mM
Ca2+ 10−4 mM
pH 7.5
K+ 5 mM
Na+ 150 mM
Ca2+ 1 mM
pH 7.4

Figure 1 Concentration of main cations and pH in a typical animal cell and in some selected endo-compartments. O, external solution; C, cytoplasm; ER, endoplasmic reticulum; L, lysosome.

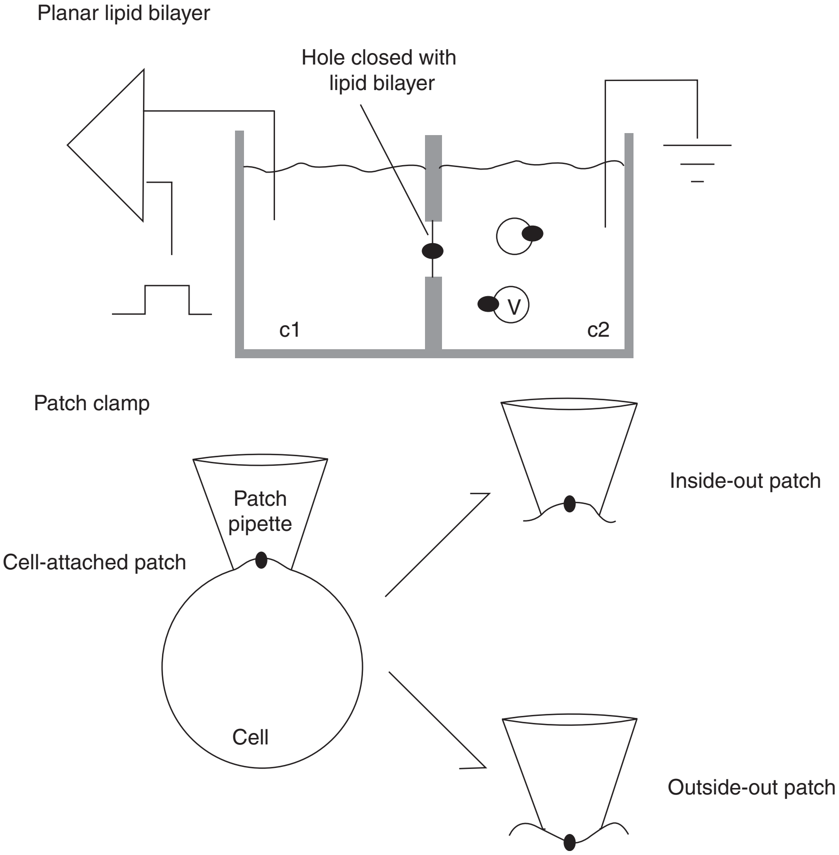
Planar lipid bilayer
Hole closed with lipid bilayer
V
c1
c2
Patch clamp
Patch pipette
Cell-attached patch
Cell
Inside-out patch
Outside-out patch

Figure 2 Sketch of main experimental techniques for single-channel recording. Planar lipid bilayer: two chambers (c1, c2) are connected by a small hole. This hole is sealed by a lipid bilayer reflecting a biological membrane. Vesicles (v) containing a channel protein (black dot) are made to fuse with this bilayer. This results in an incorporation of the channel protein into the bilayer. The activity of this channel can be recorded as a current between the two chambers. Patch clamp: A patch clamp pipette is sealed against the membrane of a cell. The current through a channel (here indicated by black dot) can be recorded. With different procedures, the membrane patch underneath the electrode can be isolated from the cell resulting in different orientations.

for example, that K^+ channel are 1000 times more selective to K^+ than to Na^+. According to their selectivity, ion channels are classified as K^+, Na^+, Ca^{2+}, Cl^-, and H^+ channels.

The current flow through a channel is determined by the open-channel amplitude and by the relative time the channel stays open. As illustrated in the characteristic example in Figure 3, all channels fluctuate in a stochastic manner between an open and a closed state. In the simplest case, the mean dwell time of the open and the closed states are single exponentials so that the probability of a channel to be open (P_o) is given by

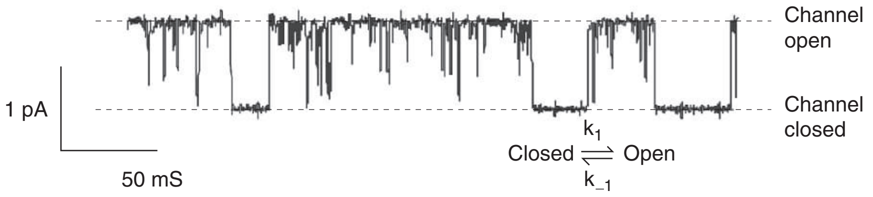

Figure 3 Example of single-channel fluctuations of K^+ channel. Opening of the channel pore allows a current flux of constant amplitude. The length which a channel spends in the open or closed state is variable. In the simplest case, the channel fluctuates in a stochastic manner with k_1 and k_{-1} between open and closed states.

$$P_o = \tau_o/(\tau_o + \tau_c) \qquad [1]$$

where τ_c and τ_o are the time constants for the closed and open times respectively.

While this simple kinetic model is suitable for the description of most channels, a detailed analysis of many ion channels has shown much more complex kinetic models. The analysis of the single-channel open and closed dwell times thus has led to models which include many more closed and open states organized in serial and/or parallel arrangement.

One of the important features of ion channels is that they are regulated. This guarantees that their activity is well integrated into the general physiological functions of a cell. In order to increase or decrease the current flux, channels increase or decrease their open probability, respectively. An increase in open probability can be achieved via a prolongation of the mean open dwell times or by a shortening of the mean closed dwell times or by both.

Several factors have been found to regulate ion channels in the physiological context. These include physical factors such as membrane voltage and mechanical stress. In addition, a large number of chemical modifications acting from either side of the membrane are known. Figure 4 illustrates as an example the regulation of channel activity performed by pH on one side of the membrane. The data show that lowering of the pH results in a prolongation of the closed times, while the open times are not affected. As a result, the activity of the channels drops in a pH-dependent manner. This is mostly due to a titratable amino acid in the channel protein. As in the case of modulation by pH, most channel proteins harbor specific binding sites for their modulators.

Several different channels have been found to be regulated by chemical modification. The more general factors known to regulate channel activity in the plasma membrane of cells from the cytoplasmic side are, for example, phosphorylation/dephosphorylation, Ca^{2+}, pH, and cyclic nucleotides.

So far, the function of ion channels only at the single-protein level have been seen. From this information, one can easily extrapolate to the behavior of the ensemble of many channels of the same type in the membrane. From the aforementioned channel function, it can be deduced that the time-averaged current (I) through a channel is given by the product of the single-channel current (i) and the open probability (P_o):

$$I = i^{*} P_o \qquad [2]$$

In this sense, the statistically weighted open-channel current is a perfect representation for the ensemble of the same kind of channels in a membrane. This only needs to be multiplied by the real number of channels in the membrane (N) to obtain the entire behavior of all channels in the membrane:

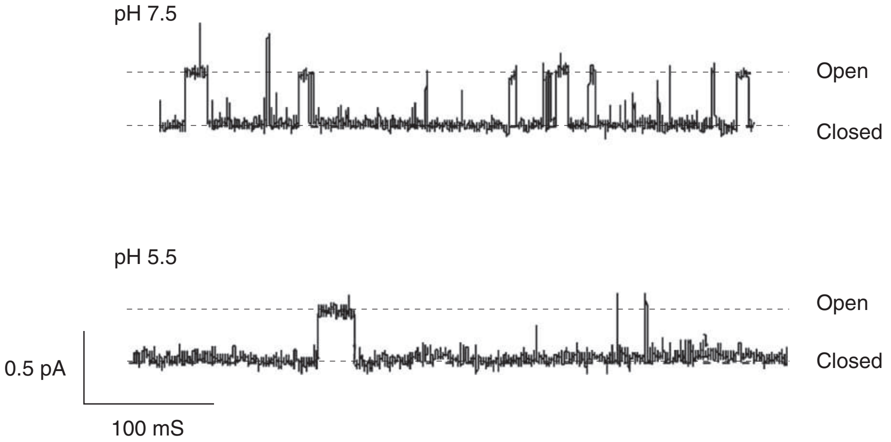

Figure 4 Effect of different pH on single K^+ channel gating. Activity of the same channel measured with a different pH on the cytoplasmic side of the membrane patch. Note that acidification increases the duration of the closed state.

$$I = i^{*} P_{o}{}^{*} N \quad [3]$$

From an experimental point of view, it is sometimes more convenient to measure and analyze directly the ensemble currents in a membrane without any attention to the single channels. This can be achieved as illustrated in Figure 5. In this patch clamp configuration, referred to as "whole cell" configuration, the sum of currents through the ensemble of ion channels in the membrane is recorded. But in essence, the data between the statistical analysis of a single channel and the recording of ensemble currents are interchangeable.

Structure and Function of Transport Proteins

The first information on how membrane transport devices work came from physiological flux measurements. Physiologists traditionally divided transport mechanisms into two classes, carriers and pores. Carriers were responsible for transport which at high substrate concentration reached saturation, while pores were identified as mediating membrane transport which did not show any saturation kinetics. A carrier was essentially viewed as a molecule diffusing back and forth across the membrane while carrying small molecules or ions bound to specific sites, whereas a pore was a narrow, water-filled tunnel, permeable to few ions and molecules small enough to fit through the hole.

The numerous membrane proteins which have been purified, and the related genes which have been cloned, show that the carrier proteins are too large to diffuse or spin around at the predicted rate. The new view of carrier transport is that the protein is fixed in the membrane while exposing the transport-binding sites alternatively at the two sides of the membrane by small motions. Although the first crystal structure of a carrier appeared in the year 2000, nevertheless the specific mechanisms by which several carrier devices (transporters and pumps) work still await to be proved combining different experimental approaches, such as electrophysiology, molecular biology, and crystallography.

The view of pores as water-filled tunnels has been firmly established for a class of proteins which is now known as ion channels. The early identification of these pores as proteins that span the membrane and the subsequent identification of the genes that codify for them have focused the work of electrophysiologists, biophysicists, and molecular biologists since the 1980s on ion channel structure–function relationships, creating a solid background of knowledge on how these channel proteins operate. The understanding of the structure and function of ion channels culminated in the landmark determination of the crystal structure of a K^{+}

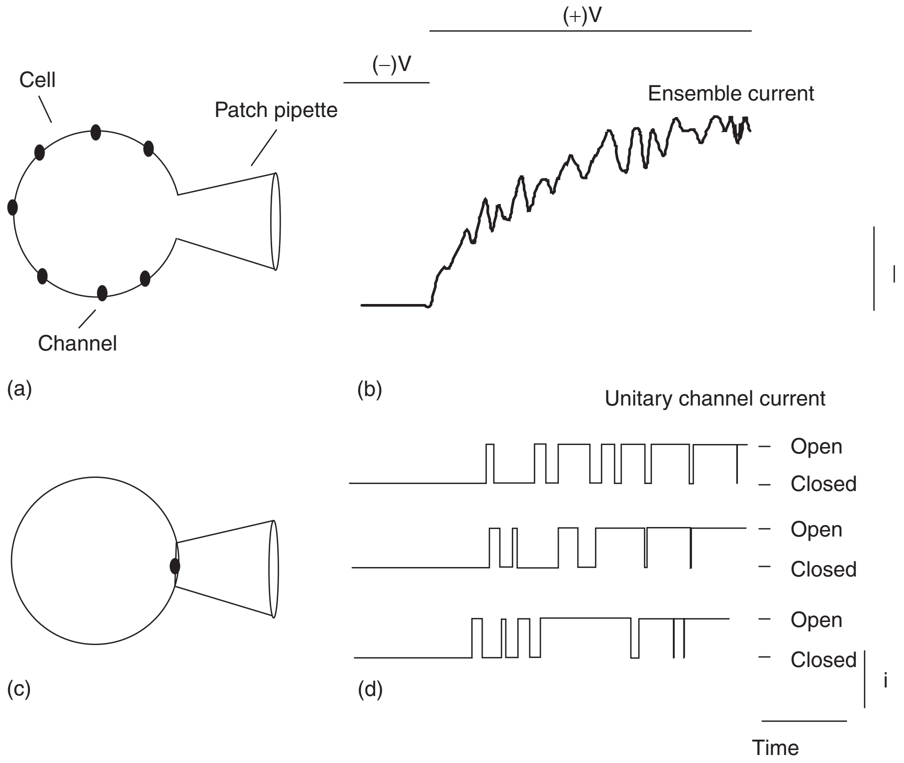

Figure 5 Relationship between single-channel activity and ensemble membrane current. Single-channel fluctuations (d) from a cell-attached recording (c, see Figure 2). The three simulated channel fluctuations are responses to a depolarizing voltage step (from (–)V to (+)V). The ensemble current (b) is obtained by averaging 30 sweeps as in (d). The same ensemble current (as in (b)) would be measured in the recording configuration illustrated in (a). Here the membrane underneath the patch pipette is ruptured to give a low resistance access to the cell interior.

channel, the bacterial channel KcsA, by Roderick MacKinnon. For his work on structure determination of several bacterial K^+ channels, MacKinnon received the Nobel Prize for chemistry in the year 2003.

The atomic structures of K^+ channels have especially improved the understanding of two main properties of ion channels: selectivity and gating.

Selectivity

A potassium channel can conduct K^+ ions one thousand times better than Na^+ ion. It is assumed that, in order to allow the protein channel to discriminate one ion from the other, the ions have to pass the cell dehydrated. In this situation, the atomic ray of Na^+ is smaller than that of K^+ (0.95 Å and 1.3 Å, respectively) implying that the Na^+ ions are not excluded on the basis of their dimension and that the selection process probably involves some kind of interaction with specific binding sites in the protein. The second striking characteristic of K^+ channels is that they pass K^+ ions at high speed, 10 e6, close to the diffusion limit. How can a protein interact with an ion and nevertheless allow its passage at the speed of ion diffusing in water? The atomic structure achieved for the bacterial potassium channel KcsA provides a deep understanding of K^+ selectivity and the ion conduction process.

Figure 6 reports the structure of the KcsA channel. The K^+ channel pore is formed by four identical subunits surrounding a central ion conduction pathway (two of the four subunits are shown in Figure 6a). Each subunit contains two transmembrane α-helices, termed inner (nearest the ion pathway) and outer helices, and a tilted shorter pore helix (in red) pointing toward the ion pathway and keeping in place the selectivity filter (in gold). The selectivity filter discriminates between potassium and other ions. It is the narrowest part of the ion permeation pathway, and is located in the extracellular third of the ion pathway. Inside the selectivity filter, the K^+ ion encounters four binding sites, which are created by evenly spaced layers of carbonyl oxygen atoms and a single layer of threonine hydroxyl oxygen atoms. At these sites a K^+ ion binds in a dehydrated state, surrounded by eight oxygen atoms from the protein, four "above" and four "below" each ion (Figure 6b). The arrangement of protein oxygen atoms in each binding site is very similar to the arrangement of water molecules around hydrated K^+ ion observed in the central cavity (Figure 6b). Potassium ions therefore diffuse from water into the selectivity filter where the energetic cost of dehydration is compensated. Sodium ions, on the other hand, do not enter the selectivity filter because the dehydrated Na^+ ions have a radius of 0.9 Å, and their coordination is precluded in this rigid structure. The precise ion coordination required for selectivity does not prevent their rapid diffusion through the pore. This is due to the fact that the selectivity filter contains more than one ion and the repulsion between closely spaced ions helps to overcome the affinity that each ion has for its binding site.

Gating

While the pore of a channel is designed to achieve minimal energy barriers to ensure a fast flow rate, other parts of the channel are responsible in determining whether the channels are open or closed, and they do so by propagating conformational changes to the ion-permeating pathway inside the pore. Potassium channels differ in relation to the various ways in which they are gated, that is, the way they change from a nonconductive to a conductive state. Some K^+ channels are ligand-gated, which means that the pore opening is energetically coupled to the binding of an ion, a small organic molecule, or even a small protein. Other K+ channels are voltage-gated, and the pore opening is energetically coupled to the movement of a charged voltage sensor within the membrane electric field. Diversity in gating is achieved by diverse structural domains attached in a modular fashion to the conserved pore domain. Binding of ligands as well as displacement of the voltage sensor by voltage changes must result in a global conformational change of the channel protein which is eventually transduced to the pore unit, causing the pore to open (and close). The recent

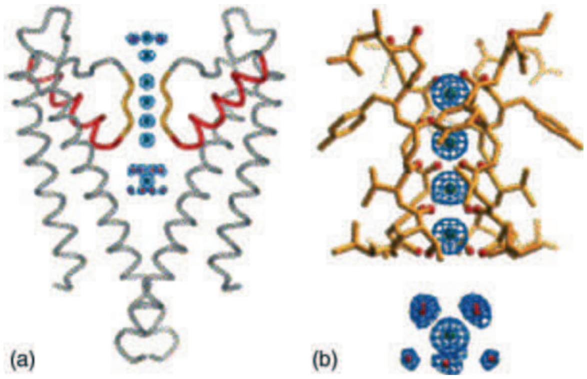

Figure 6 Ion conductance through a potassium channel pore, as deduced from the crystal structure of the bacterial channel KcsA. (a) Two of the four subunits from the pore of KcsA are shown, with the extra cellular side on top. Each subunit is formed by an outer helix that contacts the lipid membrane, an inner helix that faces the permeation pathway, a pore helix (red), and a selectivity filter (yellow). Blue mesh shows electron density for K^+ ions (green) and water molecules (red) along the pore. (b) Enlargement of the selectivity filter showing four dehydrated K^+ ions inside the filter and one hydrated K^+ ion outside (bottom). (Reprinted with permission from R MacKinnon (2003) Potassium channels. *FEBS Letters* 555: 62–65.)

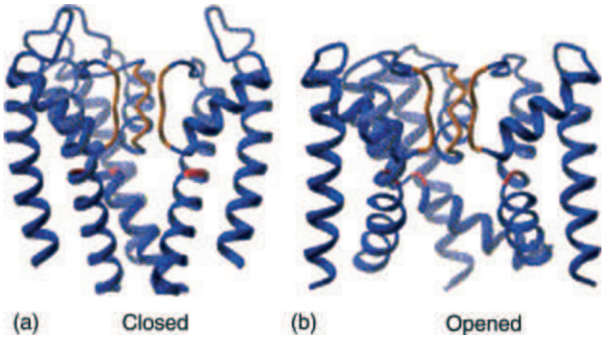

Figure 7 The pore gating of a potassium channel. Left: structure of the bacterial channel KcsA, crystallized in the closed conformation. Right: structure of the bacterial channel MthK crystallized in the open conformation. Three subunits are shown for each channel with the selectivity filter yellow and gating hinge in red. (Reprinted with permission from R MacKinnon (2003) Potassium channels. *FEBS Letters* 555: 62–65.)

crystallization of several K^+ channels (both in the open and closed conformation) has explained the conformational changes which underlie the pore opening in K^+ channels.

The pores of KcsA, crystallized in the closed configuration, and MthK, crystallized in the open configuration, are compared in Figure 7. The prominent difference between these two structures is the position of their inner helices. In KcsA they form a bundle at the cytoplasmic side of the pore that prevents free ion flow, while in MthK the inner helices are bent at a hinge point, allowing free ion flow between the cytoplasm and the selectivity filter. These structures are probably representative of the closed- and open-pore configurations of many different K^+ channels, as suggested by the amino acid conservation in the inner helices sequences of all K^+ channels (in particular of a glycine at the hingepoint) (Figure 7).

The Cell Membrane as an Equivalent Circuitry of Parallel Ion Channels with Variable Conductance: An Explanation for Complex Changes of Membrane Voltage

In this section, the functional roles of ion channel proteins are discussed with the aim of integrating their individual properties. This aims to explain their concerted contribution to the overall cell activity.

The concerted activity of ion channels may here be described for electrically excitable cells such as neurons and muscle cells. In general these cells can be found in two different conditions, namely at rest or excited. In the resting condition, the cell membrane voltage is stable over long periods of time; during electrical excitation, the cell undergoes a transient depolarization, a phenomenon called action potential (AP).

Both situations can be explained by a dynamic interplay of different ion channels in the plasma membrane. A physical model of the main elements in the plasma membrane of such a cell is presented in Figure 8 where an equivalent circuit of a cell membrane built on capacitance, variable resistors, and batteries is presented. In this simple circuit, each resistor represents a specific type of ion channel, that is for K^+ or Na^+, with a variable internal resistance. The branch with the conductance g_L represents the ensemble of other conductances such as channels for Cl^- and Ca^{2+}. The variability of the resistor reflects the ability of the ion channels to undergo changes in activity. An important detail of this model is that the activity of the channels is sensitive, in a distinct way, to

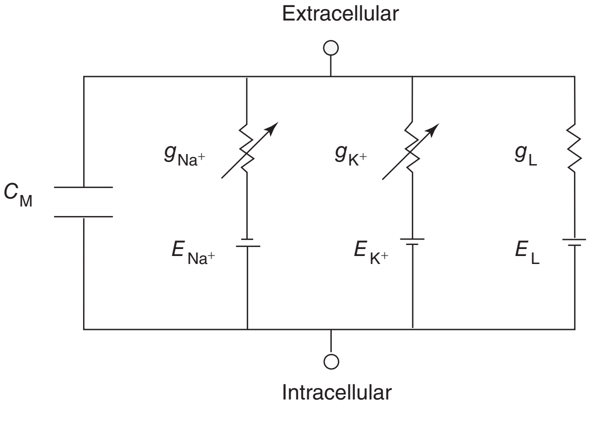

Figure 8 Electrical circuit representing the cell membrane. The lipid bilayer is modeled by a capacitance (C_M), while the different families of ionic channels are represented by conductances (g_x). The electromotive forces (E_X) generated by asymmetric ionic concentrations are included in the battery elements. Note that g_{Na} and g_K are variable conductances due to their time and voltage dependence.

voltage. Hence through the voltage coupling of the channels via the membrane, the activity of each channel has an effect on the activity of the others. Due to their different distribution across cell membranes, the main ionic species involved in electrical activity (i.e., Na^+, K^+, Ca^{2+}) have different thermodynamic equilibrium (see Figure 1). These electrochemical gradients are a source of potential energy. In the model they are represented by specific battery voltages, which are determined by the Nernst potential (E_X) of the respective ion. Cells consume this energy difference when ionic channels open and ions can freely diffuse. Due to its dielectric properties, the lipid component of the cell membrane is represented by a capacitor (C_M). Large and fast changes in the membrane voltage will hence cause currents to charge this capacitor.

At rest, cells have an internal potential of −60/−80 mV with respect to the extracellular environment. The precise value of the resting potentials is determined mainly by two factors: a relatively high K^+ (g_{K+}) and Cl^- (included in g_L) permeability of the cell membrane due to active K^+ and Cl^- channels and the respective battery voltages of E_{Cl}^{-} and E_{K+}. E_{Na+} does not contribute to the resting voltage since Na^+ channels are generally closed at rest ($g_{Na+}=0$). Hence, the membrane current (I) at rest can be described according to the Ohms law by

$$I = g_{K+}{}^{*}(V - E_{K+}) + g_{Cl}^{-}{}^{*}\left(V - E_{Cl}^{-}\right) \quad [4]$$

This resting state is drastically modified when cells become electrically active, that is, when they fire an AP. A simple physical description of an AP would be a wave of potential that travels at a rate of $1–100\,\mathrm{m}\,{}^{*}\mathrm{s}^{-1}$ along excitable membranes, and conveys information from one point to another. The peak of the moving wave corresponds to a physical location where the membrane polarity is inverted (the intracellular part is positive up to +40/+60 mV with respect to the external), while the adjacent regions are still (region ahead) or have already returned (region before) to the resting hyperpolarized value.

The Hodgkin and Huxley (HH) model presented the first mechanistic explanation of the AP. This original model has now undergone major revision; however, the basic ideas can still be used to unravel how the concerted work of different ionic channels can bring about the AP. HH's interpretation of the molecular mechanisms underlying the complex event of an AP consists of a voltage-coupled interplay of two conductances: the Na^+ and K^+ channels. The elements that confer the circuit its active properties (i.e., the capacity of generating an AP) are the variable conductances (g_x) which are disposed in parallel (Figure 8). In the original HH model, the number of conductances is limited to three: g_{Na} and g_K that are the true, time- and voltage-dependent components, and a fixed g_L that represents a pathway for leakage currents. The last elements to consider are the source of electromotive forces E_x which complete each conductance branch with the electrochemical energy associated with the specific ionic flow and determined by the Nernst equation. The two dominant elements, the Na^+ and K^+ channels, have very distinct voltage- and time-dependent properties which can be summarized as follows: the Na^+ channels open transiently very fast upon a depolarization of the membrane. The K^+ channels in contrast open slowly upon depolarization. Because of their electrocoupling, the activity of one reflects back on the other and vice versa. Once the appropriate set of time- and voltage-dependent variables for each channel is defined, the mathematical solution of the circuit will appropriately simulate the electrical activity of the cell.

A more intuitive description of an AP can be attempted by describing the events that take place in a membrane region that is invested by an AP wave. If one could take a look at the intracellular side of the membrane, a situation would be observed where an already depolarized, positively charged region, is followed by a region in an electrically resting state of about −70/−80 mV. This situation would generate a depolarizing flow of positive charges toward the negative region; this event is the key element in the generation of APs. If the depolarization is not strong enough, then the resting K^+ conductance will soon buffer this perturbation and reestablish the correct resting potential, but if the depolarization reaches a threshold it will trigger a cascade of events that generates an AP. This is the reason why biophysicists describe the AP as an all-or-nothing event. It has already been seen that a great number of ion channels are gated by voltage, and this concept is crucial to the understanding of the AP mechanism. The threshold corresponds to a critical value of potential at which Na channels start opening, and thus generate an inward-going current that further depolarizes the membrane by a positive feedback mechanism that drives the membrane potential toward the equilibrium of Na^+ ions (E_{Na}). This depolarization activates two additional events: the inactivation of Na^+ channels and the activation of K^+ channels. Na^+ channels are dually gated by voltage: the positive electric field acting on these transmembrane proteins initially induces a conformational change that forces the channels to an open, conductive state, but soon after the channels relax to a nonconductive state. The voltage-gated K^+ channels involved in the AP differ from the resting ones in that the former are normally closed at resting, but open upon depolarization. K^+ channels activate with a slower kinetics compared to that of Na^+ channels, and, according to the acting electrochemical gradient, they generate an outward-going K^+ ions efflux, that repolarizes the cell to the resting state, and thus terminate the AP signaling. The electrical activity of a cell can now be summarized in three general components: first, a trigger phase that moves the potential to the threshold; second, the activation of an inward-going current that rapidly depolarizes the cell, and finally the third part driven by a potassium outflow that terminates the electrical event. The above events are an over-simplification of a reality that is often more complex and thus adaptable; nature has evolved molecules with slightly different properties so that an array of elements is available to better accomplish the different functional requirements of excitable cells. Indeed APs can simply represent a piece of information that needs to be transferred from one point to another with high fidelity, but in many cases they must locally trigger crucial events such as a neurotransmitter release or a muscle contraction. Often, when spatial transferring of information is required, a simple system, based on limited population of channels (HH model), is perfectly fit for the function. Neuronal exocytosis and muscle contraction require the contribution of at least one more class of channels: the Ca^{2+} channel family. Ca^{2+} ions are key elements in inducing both the activation of the synaptic release machinery, and in allowing the physical interaction between the sliding filaments of muscle fibers.

Ion channels can be largely modulated by several effectors, for example calcium, second messengers such as cyclic nucleotides, phosphorylation, interaction with other proteins, and more (see above). As an example of the functional importance of these modulations, the activity of cardiac pacemaker cells are described here (Figure 9). These cells exhibit spontaneous voltage oscillations (Figure 9a) that determine the cardiac rate.

The most striking property of these cells is the slowly depolarizing or pacemaker phase (between arrows in Figure 9a) that, while moving the cell membrane toward the threshold (dotted line), allows for cardiac chamber refilling. This phase is generated by the intervention of several ionic channels and transporters, with the most important one being a specific current named I_f or pacemaker current. The I_f is modulated by the neural autonomic system that can increase (sympathetic branch) or decrease (parasympathetic branch) the current availability at any given potential (Figure 9b). The functional effect of this modulation is the modification of the slope of the diastolic depolarization that becomes steeper or shallower thus determining the autonomic-induced modulation of the heart rate (Figure 9a).

So far, the role of ion channels in underlying important physiological functions have been described; one can now appreciate why ion channels are important targets for drug-based therapy. Indeed in the year 2003, 15% of the top 100 best-selling drugs on the market were designed to specifically interfere with ion-channel proteins. Several diseases such as epilepsy, long QT syndrome, cystic fibrosis, myopathies (but the list is in constant expansion) have been found to depend on abnormalities of genes coding for these proteins. For this reason, a new group of diseases has now been named after their molecular origin channelopathies. A still far

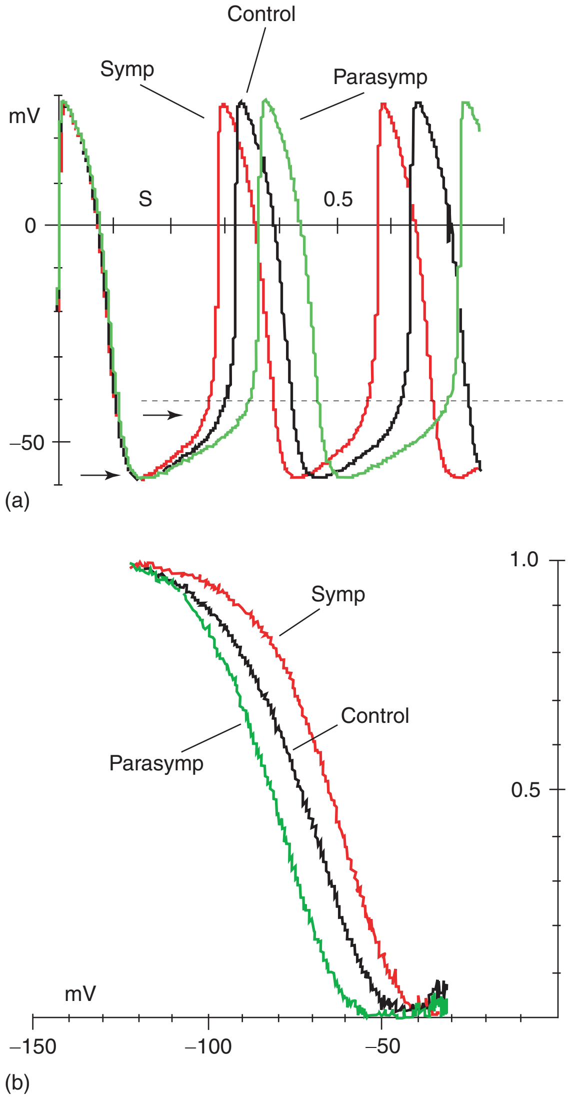

Figure 9 Heart rate modulation by autonomic system. (a) Spontaneous APs of pacemaker cells in control and during autonomic-induced modulation. (b) Fractional availability (*y*-axes) of the pacemaker current as a function of the applied voltage. The amount of available current modifies the slope of the pacemaker depolarization and thus the heart rate. (Modified with permission from Accili EA, Robinson RB, and Di Francesco D (1997) Properties and modulation of I_f in newborn versus adult cardiac SA node. *American Journal of Physiology, Heart and Circulatory Physiology* 272: H1549–H1552; and from Accili EA, Proenza C, Baruscotti M and Di Francesco D (2002) From funny current to HCN channels: 20 years of excitation. *News in Physiological Sciences* 17: 32–37; The American Physiological Society.)

to come, yet enticing possibility, is a strategy devised by ion-channel biologists which is based on the "use" of ion-channel proteins as molecular tools for therapy of cardiac rhythm alteration. To date, cardiac electronic pacemakers have been widely used in the treatment of rhythm disorders. However, recent research suggests the possibility of developing therapeutic approaches based on "biological pacemakers" in which the ability of generating spontaneous cardiac electric activity could be restored by manipulating the level of ion channels expressed in a specific desired region of the heart.

Further Reading

Ashcroft FM (2000) *Ion Channels and Disease*. San Diego: Academic Press.
Armstrong CM (1975) Ionic pores, gates, and gating currents. *Quarterly Reviews of Biophysics* 7: 179–210.
Colquhoun D and Hawkes AG (1981) *On the Stochastic Properties of Single Ion Channels*. Proceedings of the Royal Society of London. Series B 211: 205–235.
DiFrancesco D (1993) Pacemaker mechanisms in cardiac tissue. *Annual Review of Physiology* 55: 455–472.
Doyle DA, Morais Cabral J, Pfuetzner RA, Kuo A, Gulbis JM, Cohen SL, Chait BT, and MacKinnon R (1998) The structure of the potassium channelmolecular basis of K^+ conduction and selectivity. *Science* 280: 69–77.
Hamill OP, Marty A, Neher E, Sakmann B, and Sigworth FJ (1981) Improved patch-clamp techniques for high-resolution current recording from cells and cell-free membrane patches. *Pflügers Archive: European Journal of Physiology* 391: 85–100.
Hille B (2001) 3rd edn. *Ion Channels of Excitable Membranes*3rd edn., Sunderland, Massachussets, USA: Sinauer Associates, Inc.
Hille B, Armstrong CM, and MacKinnon R (1999) Ion channelsfrom idea to reality. *Nature Medicine* 10: 1105–1109.
Hodgkin AL and Huxley AF (1952) A quantitative description of membrane currents and its application to conduction and excitation in nerve. *Journal of Physiology, London* 117: 500–544.
Hodgkin AL and Keynes RD (1955) The potassium permeability of a giant nerve fibre. *Journal of Physiology, London* 128: 61–88.
Jiang Y, Lee A, Chen J, Ruta V, Cadene M, Chait BT, and MacKinnon R (2003) X-ray structure of a voltage-dependent K^+ channel. *Nature* 423: 33–41.
MacKinnon R (2003) Potassium channels. *FEBS Letters* 555: 62–65.
Miller C (1985) *Ion Channel Reconstitution*. New York: Plenum Press.
Neher E and Sakmann B (1992) The patch clamp technique. *Scientific American* 266: 44–51.
Sakmann B and Neher E (1995) *Single Channel Recording*. New York: Plenum.
Yellen G (1998) The moving parts of a voltage-gated ion channel. *Quarterly Reviews of Biophysics* 31: 239–295.

Electric and Magnetic Fields in Cells and Tissues☆

J Gimsa, University of Rostock, Rostock, Germany

© 2017 Elsevier Inc. All rights reserved.

This is an update of J. Gimsa, Electric and Magnetic Fields in Cells and Tissues, Reference Module in Materials Science and Materials Engineering, Elsevier, 2017, ISBN 9780128035818, https://doi.org/10.1016/B978-0-12-803581-8.00982-6.

Introduction 700
Mechanisms and Frequencies of Field Generation and Interaction 700
Passive Electric Properties of Biological Matter 701
Dispersions 701
Properties of Aqueous Media 702
Aqueous Electrolytes 702
Cytosolic Proteins 702
Passive Membrane Properties 703
Sectoral Capacitance 703
Lipid Region 704
Membrane Proteins 704
Bound Water 704
Impedance and AC-Electrokinetic Phenomena 704
The Induced Transmembrane Potential ($\Delta\Phi$) 705
Absorption 706
The Physiological Transmembrane Potential ($\Delta\Psi$) 706
Passive Magnetic Properties of Biological Matter 707
Generation and Effects of Magnetic Fields 707
Further Reading 708

Nomenclature

a	length of semiaxes of a (m)
a_i	length of influential radius along semiaxes a (m)
a_x	activity of ion species x (molL^{-1})
A	area (m^2)
B	magnetic flux density (T)
C	capacitance (F)
C_m	sectoral (area specific) capacitance (Fm^{-2})
d	distance (m)
D	electric displacement (Cm^{-2})
E	electric field strength (Vm^{-1})
F	Faraday constant (9.648456×10^4 Cmol^{-1})
f_{CM}	Clausius–Mossotti factor
g	area specific conductance (Sm^{-2})
j	$\sqrt{-1}$
m	dipole moment (Cm)
n	depolarizing factor
p	volume portion of suspended cells
P	power (W)
P_x	membrane permeability of ion species x (ms^{-1})
R	gas constant (8.314510 JK^{-1} mol^{-1})
r	radius (m)
T	temperature (K)
V	volume (m^3)
Z	impedance (Ω)
$\Delta\Phi$	induced transmembrane potential (V)
$\Delta\chi$	magnetic anisotropy

☆*Change History*: December 2015. J. Gimsa made updates to the text and updated the "Further Reading" section.

$\Delta\Psi$	physiological transmembrane potential (V)
ε	relative permittivity
ε_0	permittivity of vacuum (8.854×10^{-12} CV^{-1} m^{-1})
μ	magnetic permeability
μ_0	magnetic field constant (1.256×10^{-6} VsA^{-1}m^{-1})
σ	specific conductivity (Sm^{-1})
X	magnetic susceptibility
ω	circular frequency (Hz)
ω_c^{IMP}	characteristic circular frequency of the suspensions (Hz)
Asterisks (*)	indicate complex terms

Introduction

Electromagnetic phenomena play an important role at all hierarchical and structural levels of biological organisms and even in interactions among organisms and their orientation within the biosphere. Electromagnetic fields in cells and tissues may be inherent to the biological system or the result of natural or man-made exposure to such fields. Fields may interact with electrically passive or active biological structures. In both cases, the response by specific mechanisms will depend on field frequency and intensity. Whereas external fields may range from electrostatic fields up to Gamma-irradiation, the generation of fields in cells is limited in frequency range and intensity. The frequencies of physiologically generated electromagnetic fields range from 0 Hz for static (DC-) fields up to light frequencies for fluorescence effects driven by captured photons or ATP, as is the case with lightning bugs.

In this article, the electric and magnetic properties of biological matter will be considered for frequencies ranging from DC up to GHz. The focus will be electric phenomena, since the interaction with magnetic fields is usually weak for the generally low magnetic susceptibility of biological matter. Also impedance and AC electrokinetic techniques will be considered as methods that apply fields for exploring the passive properties of tissues and suspended cells. To focus on tissues and cells specific mechanisms discussed in relation to speculations of possible harmful effects of electromagnetic fields will not be considered. Neither will fields be considered beyond GHz in the far infrared or visible light ranges.

Mechanisms and Frequencies of Field Generation and Interaction

At the atomic and molecular levels, static electric fields associated to ions and dipole molecules are important for intermolecular forces. At the next higher structural level, static fields are found in electric double layers such as at the interfaces of membranes with aqueous electrolytes. Whereas these fields are part of the thermodynamic (electrochemical) equilibrium at the interface, the (nonequilibrium) physiological transmembrane potential of living cells is built up by ATP-driven ion pump proteins. Other nonequilibrium processes are found in electro-rheological effects as motion of fluids in or around cells and tissues, and in the deformation of tissue leading to a piezo-like effect, as in bones, for instance. Even though the transmembrane potential cannot usually be measured in the external medium, in some cases static fields can be detected around single cells or even organisms, for example, the DC potentials between various parts of an animal body or of plants. In lesions, wound potentials are found.

Cell excitation, as in nerve and muscle cells, is based on active electric cell properties. Voltage gated ion channel proteins play the key in the generation of membrane potential spikes. Spikefrequencies reach the kHz range. In excitable tissues, such as the brain, so called "field potentials," superimposed potentials generated by a great number of cells, are found. Such potentials are detected in medical diagnostics in electromyograms, electrocardiograms, or electroencephalograms (EMG, ECG, or EEG), for example. Between limbs, ECG potentials of several mV are detected.

Even though mechanical oscillations in the lower radio frequency range are common for ultrasound orientation of animals, the emission of electromagnetic fields by biological systems in the radio frequency range is unknown. Nevertheless, the hair cells of the inner ears of these animals or the sound detecting cells in insects must of course be capable of electrically processing these frequencies.

Beyond the radio frequency range, spectroscopic methods detect molecular properties. In the microwave and far infrared regions energy transitions (the absorption and emission of energy quanta) are particularly related to the rotation of molecules. Oscillations inherent to the molecules possess higher energies and are subsequently detected in the near infrared range. The highest energies are associated with the electrons of the molecules. The corresponding energy transitions are mediated by quanta of the visible and ultra-violet optical ranges.

It is generally believed that vibrations of molecules and the related oscillations of their electronic clouds are not synchronous and generate localized fields of low strength. Nevertheless, these fields mediate inter- and intramolecular interaction forces (van der Waals forces). Since physiological energy is steadily degraded by chemical reactions, which leads to a warming, living organisms radiate electromagnetic energy of the infrared frequency range into the environment.

The exploration of the properties of biological matter has always been connected to medical and biotech application of electromagnetic fields. For the response of cells to electric fields, both the passive properties of the different media as well as the active properties of various membrane proteins, such as ion pumps and exchangers, are of importance. The patch clamp technique has revolutionized the exploration of protein channels, another class membrane proteins. Muscle and nerve stimulations as well as hyperthermia are well established in medical therapy. Electric cell transfection by foreign DNA and the production of hybridom cells by fusion are based on membrane poration by large induced transmembrane potentials. New biotech applications such as the development of a lab-on-chip technology are based on a combination of single cell techniques and AC-electrokinetics.

Passive Electric Properties of Biological Matter

An electric field E passing through a medium is weakened by a factor that is given by the absolute value of its relative complex permittivity $|\varepsilon^*|$. The electric displacement D^* is constant:

$$D^* = \varepsilon^* \varepsilon_0 E \tag{1}$$

For such parameters, a phase shift may appear in between the exciting field or voltage and the resulting displacement or current. ε_0 Stands for the permittivity of vacuum. The asterisk denotes complex parameters. As a result the material parameters, for example, ε^*, consist of a real (ε'-in-phase) and an imaginary (ε''-out-of-phase) part. The capacitance of a medium with a relative permittivity ε^* that is located in between two parallel electrodes of distance d and area A is

$$C^* = \frac{1}{\varepsilon^* \varepsilon_0} \frac{A}{d} \tag{2}$$

For thin films like membranes a sectoral capacitance $C_m = C/A$ can be defined. When C_m values are given in the literature in most cases a possible frequency dependence is neglected. Often the passive electric properties of biological matter are described by its impedance Z^*, that is the generalized, frequency dependent resistance:

$$Z^* = \frac{1}{\sigma^*} \frac{d}{A} \tag{3}$$

This describes the impedance of a medium with a specific conductivity σ^* that is located in between two parallel electrodes of distance d and area A. In the simplest case, the medium is homogeneous and isotropic like aqueous electrolytes. In contrast, biological tissue is structured, for example, by cell membranes. This compartmentalization is the reason for structural dispersions.

Dispersions

The impedance of biological material is characterized by a variety of characteristic frequency dependent changes. These changes base on the fact that permittivity contributions of certain relaxation processes, which follow the external field at lower frequencies, disperse at higher ones. Consequently, the permittivity of biological material drops by several orders of magnitude over some frequency decades. A permittivity drop at a given frequency corresponds to a certain conductivity increase since the field-induced movement of bound charges can no longer be distinguished from the movement of charges, such as ions, that are already free to move at DC.

Researchers tried assigning the measured dispersions to certain biological structures on the different hierarchical levels and to classify the contributing processes. For classification, two different approaches were chosen – the dispersions were either sorted according to their physical nature, for example, as Maxwell–Wagner and Debye dispersions, or according to the frequency range wherein they occur. While Maxwell–Wagner dispersions base on the structuration of the material, Debye dispersions are related to the orientation of molecular dipoles. A classification according to frequencies yielded a scaling where the dispersions with increasing frequencies were assigned to the α-, β-, and γ-range (Fig. 1). It was assumed that well-defined processes are responsible in a certain dispersion range.

Despite their low frequencies, analysis of the α-dispersions in the sub-1 kHz frequency range is especially difficult. Many different processes may overlap, including such processes as electrode processes, hydrodynamic relaxation of electroosmotically induced convections within the measuring chamber and around the cells, membrane channels, cell orientation and deformation, as well as cell electrophoresis. The difficulty is that these phenomena are hard to separate, and concurrently influence suspension medium and cells (Fig. 2).

In tissues and cell suspensions the major contributions of the β-dispersion stem from structural polarizations as those of the cytoplasmic membrane or of internal membrane systems, as well as the polarization of the cytoplasm. It is to be noted that membrane and cytoplasmic dispersions are of different qualities. Whereas membrane dispersions are based on the capacitive bridging of the thin membrane film, the cytoplasmic dispersions are mediating the switching from a field distribution, according to the conductivities, to a distribution according to the permittivities of the bulk media. The structural dispersions may be influenced by the dispersion of other processes, such as the surface conductance or dipole relaxation of large molecules. In cellular systems, Debye dispersions of proteins usually occurring around 1 MHz are masked by the structural membrane dispersions.

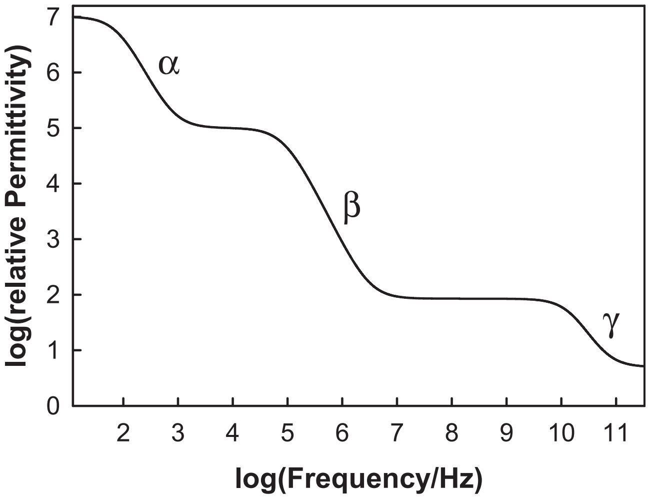

Fig. 1 Schematic frequency dependence of the relative permittivity of tissue or cell suspensions according to H.P. Schwan *et al.*

In the γ-range above 100 MHz, quick dissociation-association relaxation or Debye dispersions of small molecules or charged groups must be expected. The dielectric properties of proteins are believed to be important for their physiological function such as protein–protein association or the interaction with charged ligands. Dispersions between 200 MHz and 10 GHz were assigned to bound water and small molecules (δ-dispersion). Dispersion over 10 GHz can mainly be assigned to free water.

Properties of Aqueous Media

Aqueous Electrolytes

The intracellular space and the cytoplasm can be considered aqueous solutions of ions and organic molecules. Up to GHz frequencies, their properties are often simplified to those of aqueous electrolytes that can be described by frequency independent specific conductivities and permittivities. For electrolytes, the conductivity σ and relative permittivity ε are based on ionic conduction and the permittivity of water, respectively. Whereas the permittivity of water of 80 at 18 ° C shows a slight decrease with temperature and ion concentration, the conductivity may vary by orders of magnitude. For solutions of one salt, it can be calculated from salt concentration and equivalent conductivity. These relations are more complex for mixed solutions. Accordingly, the complex specific conductivity σ^* consists of the frequency-independent contribution of ion conduction and frequency-dependent displacement currents based on the water permittivity

$$\sigma^* = \sigma + j\omega\varepsilon\varepsilon_0 \tag{4}$$

where ω and j stand for the circular frequency of the field and $\sqrt{-1}$, respectively. After introduction of Eq. (4), Eq. (3) describes a system that consists of a resistor (for the ion current) in parallel to a capacitor (for the displacement current). Accordingly, the impedance of the medium steadily decreases with frequency.

Cytosolic Proteins

The cytoplasm of most cells is extremely rich in proteins influencing the electric properties. Proteins reduce the water concentration resulting in a reduced ion mobility and conductivity. The reduction factor may be higher than 2 in red cells. A second contribution comes from the proteins themselves. Because of their high dipole moments, they are the cause for extraordinary high permittivities at low frequencies. Nevertheless, their bulky structure is incapable of following the orientation force of an external field beyond a certain frequency. This is the reason for dielectric dispersions, that is, the decrease of ε, by the dielectric decrement, and a corresponding increase in σ, which are typically in the frequency range around 1 MHz. The dispersion in pure protein suspensions can be considered to be Debye dispersions, which were extensively investigated. In tissues and cell suspensions, protein dispersions are masked by the structural dispersions. Therefore, dispersions of cytoplasmic proteins were predominantly investigated after cell lysis or in cell free suspensions.

structural level ***theory***	**sketch of structure**	**dispersing effect**
MICROSCOPIC FORCES **- tissue** **- cell** **- membrane** **- electric double layer** **- intercellular fluid** ***- cytomechanics*** ***- hydrodynamics*** ***- double layer theory***	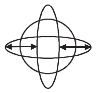	**- cell deformation**
	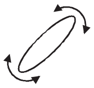	**- cell orientation**
	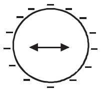	**- cell electrophoresis**
	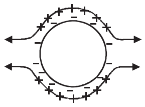	**- electroosmosis** **- chemical ion adsorption**
	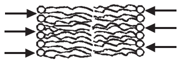	**- electrostriction of membranes**
STRUCTURAL EFFECTS **- membranes** **- compartment geometry** **- media** ***- La Place equation***	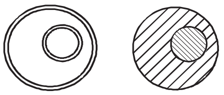	**- membrane polarization** **- bulk polarization**
MOLECULAR EFFECTS **- molecules** **- side chains** **- water clusters** **- bound water** **- bulk water** **- biochemical reactions** ***- dispersion theory*** ***- Debye theory*** ***- reaction kinetics*** ***- molecular models***	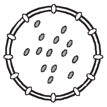	**- Debye polarization of membrane & cytoplasmic proteins**
	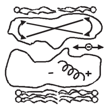	**- protein transport** **- protein conformation** **- side chain orientation**
	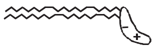	**- orientation & flexing of lipid head groups**
	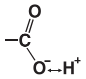	**- dissociation/association**
	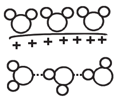	**- water cluster & molecule orientation** **- localization of partial charge**

Fig. 2 Polarization processes based on various biological structures. The size of the polarized structures and the physical nature of the dispersion processes determine their characteristic times and frequency dependencies. The first column summarizes the structural levels and theoretical approaches for describing dispersion processes. The sketches in the second column present examples for processes that are designated in the third column.

Passive Membrane Properties

Sectoral Capacitance

Membranes are known to be inhomogeneous and anisotropic. For a membrane, solely composed of a lipid double layer, a specific capacitance of $\sim 0.75 \times 10^{-3}$ F/m^2 can be estimated. Nevertheless, biological membranes are rich in membrane spanning proteins. Thus, protein and lipid areas form a parallel circuit of two capacitors, resulting in a specific capacitance of about 10^{-2} F/m^2 at frequencies below 1 MHz. Accordingly, protein regions present areas of higher specific capacitance. The various regions of the membrane, that is, bound water layers, lipid headgroup regions, the hydrophobic lipid chain regions as well as the orthogonal segments formed by transmembrane proteins, will exhibit a different frequency-dependent dielectric behavior. The glycocalix surface layer made up by charge-carrying polysaccharides that are bound to membrane lipids and proteins is of special importance for the α-dispersion.

Lipid Region

The lipid regions of membranes have an overall thickness of 4–5 nm with roughly 0.8 nm at each side being occupied by the headgroups. The hydrophilic headgroup regions contain the strong P–N dipoles, the ester bonds of the fatty acids and the glycerol backbones. Together with the associated water molecules, dipole potentials as high as 240 mV (positive at the membrane surface) are generated. In normal direction, the relative permittivity drops from ~78 in the bulk water to ~2 in the fatty acid chain region. The permittivity of ~30 in the headgroup region disperses with a decrement of ~28. In tangential direction, experimental and theoretical results hint on relative permittivities as high as 300 to 400 with a dispersion that is related to the in-plane orientation of the headgroups. For both orientations, dispersion occurs around 50 MHz resulting in a high frequency permittivity of ~2. Due to its low permittivity already at low frequencies, the fatty acid chain region is highly hydrophobic, forming the major energetic barrier for the permeation of ions and small polar molecules. For a spherical ion, this barrier arises from the difference of its electric surface potentials inside the lipid and aqueous phases, which differ by the quotient of the ε-values of the two phases.

Membrane Proteins

Intercalation of proteins in the membrane relies on a microenvironment of specific dielectric properties. Nonpolar amino acids form the protein surface where it is exposed to the lipid chain region. Highly polar protein groups as loops and tails of the polypeptide chains are exposed to aqueous surfaces. They possess a higher degree of molecular freedom suggesting higher permittivities. The peptide bonds of the membrane part of most proteins are very rigid. Their highly restricted mobility results in a low permittivity. Up to low kHz frequencies, the protein mediated ion transport is also of importance for electric protein properties.

Bound Water

The thickness of the bound water layers is ~0.5 nm, with 11–16 water molecules per lipid. About four water molecules per lipid are tightly bound and strongly oriented. More distant water molecules show a smoothly decreasing orientation profile. The average permittivity of the bound water layer is ~60. The dispersion frequency will depend on binding strength with higher frequencies for lower binding strengths.

Impedance and AC-Electrokinetic Phenomena

Impedance experiments provided the first proof for the existence of biological membranes. Impedance experiments analyze the frequency dependent electric response to an applied field to explore dielectric properties of tissues and cells. The electric response is based on the polarization of the sample structures, like suspended cells. Single cell polarization may lead to orienting, deforming, moving or rotating in AC-electrokinetics. The different motions depend on the different spatial properties of the field determining its interaction with the polarized cell. The frequency dependence of each effect is related to the frequency dependence of the polarizability of the various constituents of the cell. All effects are exploited in cell characterization methods: electroorientation, electrodeformation, dielectrophoresis, and electrorotation. For modeling the effects, the induced cell dipole moment is obtained by integrating over the local fields of all subcellular structures in the cell volume. As in the case of impedance, models for multishell spherical, cylindrical and ellipsoidal geometries are readily available.

Generally, the force experienced by the cell is related to the induced dipole moment m^*, which is the volume integral of the cell's polarization.

$$m^* = (m_a \;\; m_b \;\; m_c) = \varepsilon_e \varepsilon_0 V \left(f^{*a}_{CM} f^{*b}_{CM} f^{*c}_{CM} \right) E \tag{5}$$

Along the semiaxes, its frequency-dependent part is given by the components of the Clausius–Mossotti factor f^*_{CM}. Its a-component is given by

$$f^{*a}_{CM} = \frac{\varepsilon_i^* - \varepsilon_e^*}{\varepsilon_e^* + \left(\varepsilon_i^* - \varepsilon_e^*\right) n_a} \tag{6}$$

The permittivities of the external and internal media are marked by indices e and i, respectively. n_a is the depolarizing factor along semi-axis a. Depending on the ellipsoidal shape, n_a can vary from 0 to 1. Please note that Eq. (6) simplifies in structure to the left side of Eq. (7) for spherical objects with $n_a = 1/3$.

For an ellipsoidal cell with confocal layers, for each field frequency, a Maxwellian equivalent body can be found that exhibits the same complex dipole moment m^*. The equivalent body has homogeneous medium properties and a constant local field.

The impedance of suspensions of randomly orientated three-axial single-shell cells is described by the Maxwell–Wagner mixing equation, which can be written in the form

$$\frac{3\left(\sigma_S^*-\sigma_e^*\right)}{\sigma_S^*+2\sigma_e^*} = \frac{p}{3}\left(f_{CM}^{*a}+f_{CM}^{*b}+f_{CM}^{*c}\right) \tag{7}$$

where p is the volume portion of the suspended cells. $\sigma_S{}^*$ is the complex specific conductivity of the cell suspension, ie, the inverse of its specific impedance in Ωm. For objects oriented with semiaxis a in the external-field direction we obtain:

$$\frac{3\left(\sigma_S^*-\sigma_e^*\right)}{\sigma_S^*+2\sigma_e^*} = pf_{CM}^{a*} \tag{8}$$

The impedance of oriented single cells can be detected in microfluidic devices. For a population of suspended cells, synchronous reorientations will be detectable as impedance transitions. Such reorientation can be induced, for example, by electro-orientation in DC or AC fields, as well as in optical, acoustic or hydrodynamic fields. For the specific conductivity of a suspension of spherical cells ($a=r$), the analytical expression

$$\sigma_S^* = \sigma_e\frac{2\sigma_e+\sigma_i+2p(\sigma_i-\sigma_e)\omega rC_m^{spec}-2j\sigma_e\sigma_i(1-p)}{2\sigma_e+\sigma_i-p(\sigma_i-\sigma_e)\omega rC_m^{spec}-j\sigma_e\sigma_i(p+2)} \tag{9}$$

can be obtained. Neglecting the membrane conductance, it allows for deriving the characteristic circular frequency of the suspensions ω_c^{IMP} in the membrane dispersion frequency range

$$\omega_c^{IMP} = \frac{1}{rC_m}\,\frac{2\sigma_e\sigma_i}{2\sigma_e+\sigma_i}\left(\frac{2\sigma_e+\left(1-\frac{3}{4}p\right)\sigma_i}{2\sigma_e+\sigma_i}\right) \tag{10}$$

For infinite dilutions ($p=0$), the equation corresponds to Eq. (14) for spherical cells.

AC-electrokinetic methods yield similar information, as does impedance, though with a lower resolution with the latter. A rotating field induces a dipole moment, which rotates at the angular frequency of the external field. A spatial phase shift of the external field vector and the induced dipole moment, caused by any dispersion process, gives rise to a torque generating individual cell rotation. For example, the membrane dispersion generates a cell-typical electrorotation peak. Interestingly, the torque and therefore cell rotation is at maximum if relaxation time of the dispersion process and external field frequency match ($\omega=\omega_c$, see below). For their high resolution, dielectric single cell methods are of special value for cell characterization and the determination of the field distribution at the subcellular level. All AC-electrokinetic phenomena can also be used for cell or molecule manipulation. They form the basis for the lab on chip technology.

The Induced Transmembrane Potential (ΔΦ)

Electric cell transfection and cell fusion are routine biotech applications basing on membrane poration by high induced ΔΦ. For poration DC or AC fields have to be applied for a sufficiently long time or at a sufficiently low frequency, respectively. Pore induction is a strongly nonlinear process mimicking a "critical" membrane voltage of ~1 V corresponding to ~200 MV/m in the lipid phase. ΔΦ is proportional to the external field strength and depends on cell size, shape, orientation and electric cell properties.

Since the 1920s of the last century, physicists and chemists have been dealing with the potential induced on the surface of cavities or bodies, to describe the dependence of the local field deviation on the shape of the bodies or cavities. H. Fricke was the first to apply the physical knowledge on the depolarizing factors of ellipsoidal bodies or cavities to express the induced transmembrane potential ΔΦ. For a cell of the general ellipsoidal shape with semiaxes a, b, and c, at the pole of semiaxis a, a ΔΦ of

$$\Delta\Phi = \frac{1}{1-n_a}aE = a_{infl}E \tag{11}$$

is induced. a, n_a, and a_{infl} stand for the length of the semiaxis oriented in field direction, the depolarizing factor along semiaxis a, and the influential radius, respectively. Please note that only the field component, which is oriented along semi-axis a contributes to ΔΦ at pole a. The equation applies for the DC steady state and a cell with zero membrane conductance. Along each semi-axis, the parameter "influential radius" depends solely on the shape of the ellipsoidal body. For a vacuum body, it describes the distance between its center and that undisturbed equipotential plane, which touches the pole in the presence of the body.

For a sphere, $a=b=c=r$, and $n_a=n_b=n_c=1/3$ since the sum of the three factors along the three principal axes is always unity. Eq. (11) becomes the well known expression: $\Delta\Phi = \frac{3}{2}aE$. For axisymmetric cells $a=b$. The symmetry axis is c. For such spheroidal cells limited in shape by an infinitely thin disk and an infinitely long cylinder, respectively, the shape dependence can be sufficiently good described by

$$\Delta\Phi = \frac{a+2c}{a+c}aE \tag{12}$$

and

$$\Delta\Phi = \frac{\mathrm{a}+2c}{2}E \tag{13}$$

for a field oriented in *a*-direction and *c*-direction, respectively. At higher frequencies, the membrane impedance decreases by capacitive bridging. The characteristic frequency ω_{c} at which the induced potential is decreased by −3 dB is given by

$$\omega_c = \frac{1}{aC_m}\left(\frac{\sigma_e\sigma_i}{\sigma_e+\left(\frac{a_i}{a}-1\right)\sigma_i}+ag\right) \tag{14}$$

σ_i, σ_e, and g stand for the specific internal and external conductivities in S/m, and the area specific membrane conductance in S/m^2. The complete equation for $\Delta\Phi$ at pole a of the ellipsoidal cell is

$$\Delta\Phi = \frac{a_i}{\left(1+ag\left(\frac{1}{\sigma_i}+\frac{\frac{a_i}{a}-1}{\sigma_e}\right)\right)\sqrt{1+\frac{\omega^2}{\omega_C^2}}}E \tag{15}$$

with ω standing for the field frequency. Assuming a superposition of the $\Delta\Phi$ and the physiological $\Delta\Psi$ (see below) is the simplest way to explain the asymmetry in cell poration often found after dielectric membrane breakdown.

Absorption

An exposed system is only influenced by that part of the electromagnetic field energy that is absorbed (principle of Grotthus and Draper). For this reason, research on the impact of electromagnetic fields must focus on the mechanisms of absorption and the identification of the absorbing structures. Generally, the energy input into a given volume is described by Ohmic heating that is proportional to the square of the local field strength and the effective, specific conductivity of a certain medium. Magnetic absorption processes, also those based on quantum effects, such as on the spins of unpaired (radical-) electrons, can usually be neglected. Dispersions lead to subcellular field redistributions. Up to GHz-range frequencies, the local field distribution and thus local absorption greatly depend on the geometric structure and compartmentalization of a cell.

The local power dissipation (Ohmic heating) per volume element P/V in an AC-field is not directly proportional to the applied field but depends on the effective local field E_{eff}

$$\frac{P}{V} = \sigma E_{eff}^2 \tag{16}$$

The equation suggests that the power dissipation is described by a frequency independent specific DC-conductivity. In practice, the specific conductivity of structured media increases with frequency in correspondence to the permittivity decline given in Fig. 1.

Considerations show that the field strength in the external medium and thus absorption in the vicinity of the cell strongly depends on field frequency even for the simple single-shell geometry. The picture dramatically deviates from the classic one when assuming more realistic membrane and cytoplasmic properties based on their molecular structure. It suggests a possible role of the membrane in field absorption even at frequencies far above the membrane-dispersion frequency.

The Physiological Transmembrane Potential ($\Delta\Psi$)

Muscle activity or nerve excitation generate AC fields in the Hz and kHz ranges. The physiological transmembrane potential $\Delta\Psi$ is of special importance for this phenomenon. $\Delta\Psi$ generation is based on the special electric properties of biological membranes. $\Delta\Psi$ is defined as the difference of the potentials of the internal (index i) and external (index e) bulk media:

$$\Delta\Psi = \Psi_i - \Psi_e \tag{17}$$

Because of the surface potentials at the two membrane sides, fixed charges in the glycocalix and the dipole potentials of the lipid headgroups, the actual potential difference across the lipid phase of the membrane may strongly deviate from the $\Delta\Psi$. At specialized membranes like the thylakoid membranes of plant chloroplasts $\Delta\Psi$ may exceed −200 mV. Accordingly, the field strengths across the membrane under physiological conditions may be well above 10 MV/m. The membrane properties allow for the storage and transformation of electrochemical energy into chemical energy such as ATP, or in electrical energy as in nerve excitation or the electrical organs of fishes. $\Delta\Psi$ for resting neurons or muscle cells are in the range of −100 to −40 mV. Action potentials are typically in the range of 30 to 80 mV.

In excitable cells of vertebrate species, sodium and potassium ions are actively pumped outwardly and inwardly, respectively, leading to a roughly inverse distribution for the two ion species. In resting cells, the membrane permeability for potassium is much higher than for sodium. Consequently, $\Delta\Psi$ is determined by the potassium distribution. Since its concentration is much higher in the cytoplasm, random diffusion across the membrane via potassium channels leads to a net potassium loss and a negative charging of the cytoplasm. Nerve cells are rich in voltage-gated ion channel proteins. The transition from resting to action potential is driven by a sequential change in the membrane permeabilities for sodium ions and potassium ions. The relations are described by the Goldman equation:

$$\Delta\Psi = \frac{RT}{F}\ ln\ \frac{\mathrm{P_{Cl}}a^{i}_{\mathrm{Cl}}+\mathrm{P_{K}}a^{e}_{\mathrm{K}}+\mathrm{P_{Na}}a^{e}_{\mathrm{Na}}}{\mathrm{P_{Cl}}a^{e}_{\mathrm{Cl}}+\mathrm{P_{K}}a^{i}_{\mathrm{K}}+\mathrm{P_{Na}}a^{i}_{\mathrm{Na}}} \tag{18}$$

R, T, F, P, and a stand for the gas constant, the absolute temperature, the Faraday constant, permeability and ion activity, respectively. Indices i, e, Na, K, Cl designate internal and external bulk media, as well as the ion species sodium, potassium and chloride, respectively. Please note that for $\mathrm{P_K} \gg \mathrm{P_{Na}}$, $\mathrm{P_{Cl}}$ and $\mathrm{P_{Na}} \gg \mathrm{P_K}$, $\mathrm{P_{Cl}}$, the Goldman equation reduces to the Nernst equations for potassium and sodium, respectively. A feedback loop where the local membrane field alters the ion permeabilities of voltage-gated ion channel proteins is the basis for the propagation of cell excitation, for example, along the axon of a nerve cell.

Passive Magnetic Properties of Biological Matter

In analogy to the electric field, a static magnetic field of strength H causes a magnetic induction B of

$$B = \mu\mu_0 H \tag{19}$$

where μ and μ_0 are the relative permeability of the material and the magnetic field constant, respectively. Since the permeabilities of biological matter are very close to unity, it is reasonable to list susceptibilities $X = \mu - 1$ (**Table 1**).

The low magnetic susceptibility is the reason for the very weak interaction of static magnetic fields with biological matter. Most biological cells and tissues are diamagnetic ($\chi < 0$). Paramagnetic ($\chi > 0$) desoxygenized red cells are an exception.

The high structuration of biological tissues and cells is reflected in their magnetic anisotropy $\Delta\chi$, which describes the difference in the magnetic susceptibilities parallel and perpendicular to characteristic biological structures. This feature is especially pronounced in lipid membranes that can even be orientated by magnetic fields at flux densities larger than 1 T.

Biogenic magnetites (Fe_3O_4-crystals) are found in magnetostatic bacteria. The susceptibility of these ferromagnetic particles is as large as 10^6. The particles are the major component of magnetosomes, cell organells that are surrounded by a membrane. They enable the bacteria to orientate themselves along the vector of the geomagnetic field. To a lesser extent biogenic magnetites have also been found in different animals and even in the human brain. Nevertheless, it is still not clear as to whether magnetic fields can interfere with physiological processes in humans. The mechanisms of magnetic orientation of animals are not fully understood, either.

Generation and Effects of Magnetic Fields

Of course, all biological processes which involve charge movement generate endogenous magnetic fields. Such processes include the transmembrane transport of ions or charged compounds as well as the ion currents related to signal transduction in nerves and muscles. The displacement of ions and charged particles in the blood stream or the lymphatic system induces streaming potentials and in turn electric currents. Nevertheless, in no case does the induced magnetic flux densities exceed the pT-range (compare to 20–70 μT of the geomagnetic field). Currently, no hard experimental data is available on the coupling of external with endogeneous magnetic fields, subsequently influencing biologically relevant processes.

Exogenous low-frequency magnetic fields can induce electrical (eddy-) currents. Nevertheless, for effective induction, structures larger than single cells are required. Candidate structures are, therefore, the blood system and cells that are interconnected via gap

Table 1 Magnetic susceptibility of different matter

Material	$\chi/10^{-6}$
Air	0.264
Water	–9.04
Arterial blood	–9.3
Oxygenized red cells	–9.03
Desoxygenized red cells	3.88
Venous blood	–7.8
Lungs (air-filled to 15%)	–4.2
Muscle	–9.03
Liver	–8.26
Bone	–10
Biogenic Fe_3O_4-crystals	10^{12}

junctions, allowing for the formation of large induction loops. It can be estimated, that a flux density of at least 1 mT is necessary to effect biological functions of the brain or of the heart. Static and low-frequency fields may deflect moving charges by Lorentz's force. However, ions and charged compounds can only be significantly influenced at flux densities higher than 10^6 T. Nevertheless, in larger structures such as nerves or blood vessels crossing magnetic field lines, current induction may cause nerve excitations already at flux density exceeding 10 mT.

Magnetic fields can influence the spins of unpaired electrons, for example, of organic label molecules, and nuclei with a spin different from zero, for example, of hydrogen. To orientate the spins, typically static magnetic fields of 50 mT to 6 T and 340 mT to 1.25 T are applied in Nuclear Magnetic Resonance (NMR) for medical diagnostics (usually designated as Magnetic Resonance Tomography (MRT)) and Electron Spin Resonance (ESR), respectively. The field introduces an energy difference for the two possible spin orientations. The transition from the low-energy orientation to the higher one can be induced by resonant absorption of a radio-frequency field in the MHz to GHz ranges with a frequency corresponding to the energy difference of the two spin orientations. Either the absorption or the emission of the radio frequency field induced by the relaxation of the spin distribution is detect in the methods.

Static and low-frequency magnetic fields have been shown to influence chemical reactions which involve radical-pair intermediate states in electron transfer processes. The lifetime of triplet-singlet interconversions in such reactions have been altered at magnetic flux densities of 1 mT and beyond. This mechanism may as well apply to biochemical reactions. For the interaction of magnetic fields with biological processes, other mechanisms such as cyclotron resonance in protein channels and ion parametric resonance in macromolecules have also been proposed, but could not be verified so far.

Further Reading

Able KP (1994) Magnetic orientation and magnetoreception in birds. *Progress in Neurobiology* 42: 449–473.

Adey WR and Lawrence A (1984) *Nonlinear Electrodynamics in Biological Systems*. New York: Plenum Press.

Delgado AV (2001) *Interfacial Electrokinetics and Electrophoresis*. New York: Marcel Dekker Inc.

Edmonds DT (2001) *Electricity and Magnetism in Biological Systems*. Oxford University Press.

Gimsa J, Stubbe M, and Gimsa U (2014) A short tutorial contribution to impedance and AC-electrokinetic characterization and manipulation of cells and media: Are electric methods more versatile than acoustic and laser methods? *Journal of Electrical Bioimpedance* 5: 74–91.

Glaser R (2012) *Biophysics*. Berlin, Heidelberg, New York: Springer.

Grandolfo M, Michaelsom SM, and Rindi A (1983) *Advances in Biological Effects and Dosimetry of Low Energy Electromagnetic Fields*. New York, London: Plenum Press.

Grimnes S and Martinsen O (2014) *Bioimpedance and Bioelectricity Basics*. Academic Press.

Jones TB (1995) *Electromechanics of particles*. Cambridge, New York, Melbourne: Cambridge University Press.

Kortüm G (1962) *Kalorimetrie Photometrie und Spektrometrie*. Berlin, Göttingen, Heidelberg: Springer (in German).

Landau LD and Lifschitz EM (1985) *Elektrodynamik der Kontinua*. vol. 8. Berlin: Akademie-Verlag (in German).

Maret G, Boccara N, and Kiepenheuer J (1986) *Biophysical Effects of Steady Magnetic Fields*. Berlin: Springer-Verlag.

Neumann E, Sowers A, and Jordan C (1989) *Electroporation and Electrofusion in Cell Biology*. New York: Plenum Press.

Polk C and Postow E (1996) *CRC Handbook of Biological Effects of Electromagnetic Fields*, second ed Boca Raton: CRC Press.

Schütt W, Klinkmann H, Lamprecht I, and Wilson T (1991) *Physical Characterization of Biological Cells*. GmbH Berlin: Verlag Gesundheit.

Biological Effects of Electromagnetic Fields[☆]

C Marino, P Galloni, and C Merla, Casaccia Research Center, ENEA, Rome, Italy

© 2016 Elsevier Inc. All rights reserved.

This is an update of C. Marino, P. Galloni, C. Merla, Biological Effects of Electromagnetic Fields, Reference Module in Materials Science and Materials Engineering, Elsevier, 2016, ISBN 9780128035818, https://doi.org/10.1016/B978-0-12-803581-8.00983-8.

Introduction **709**
Bioeffects of Static Fields **710**
Cellular Models 711
Animal Models 711
Human Studies 711
Bioeffects of ELF Fields **711**
Cellular Models 711
Animal Models 712
Human Studies 713
Conclusion **713**
Bioeffects of IF Fields **713**
Cellular Models 714
Animal Models 714
Bioeffects of RF Fields **714**
Cellular Models 715
Animal Models 715
Human Studies 715
Conclusion **716**
Medical Applications **716**
Occupational Exposures **716**
Health Risk Assessment **716**
Further Reading **717**

Introduction

Research on biological and health effects of electromagnetic fields (EMFs) has been driven in the last few decades by public concerns about their potential detrimental effects. Up to date, an extensive application of EMFs, for both diagnostic and therapeutic purpose, has taken hold as well, moving the attention from the sole aspect of health protection.

EMFs sources are broadly diffused in the environment, varying both in emission intensity and frequency range (see **Figure 1** for EM spectrum visualization). Static fields (SF at 0 frequency or namely DC, see **Figure 1**) are naturally associated to the earth surface, weather changes, and solar activity. Nonnaturally derived fields come from household and office appliances, video displays, power transmission lines, industrial processes, and medical and research applications (Magnetic Resonance Imaging, MRI).

High voltage lines and all the electric devices are also the principal sources of extremely low frequency fields (ELF, <300 Hz, see **Figure 1**), operating at 50 Hz (Europe) or 60 Hz (America), commonly present in our daily life. Within particular occupational situations, such as industrial machines, induction ovens, or electrolytic cells, workers can be exposed to high electric or magnetic fields intensities.

Exposure to intermediate frequency (IF, $300\ \text{Hz} < f \leq 10\ \text{kHz}$, see **Figure 1**) fields has been so far limited to specific situations, but emerging technologies, such as anti-theft devices, badge readers, induction hotplates, or fluorescent bulbs, producing IF emissions, are now amply diffused.

In the radiofrequency (RF, $10\ \text{kHz} < f \leq 300\ \text{GHz}$, see **Figure 1**) range, natural sources are essentially represented by electrical discharges in the atmosphere and solar and cosmic radiation. Human exposure, along with domestic and indoor transmitters, lay essentially on portable wireless telecommunication systems; mobile phones remain the main source of exposure for brain tissues. RF EMF levels are not going to rise, having new technologies, like digital broadcasting, reduced EMF exposure from far field sources (radio and TV broadcasting and mobile phones base stations). The current tendency is to make use of devices at close contact with human body but of lower emissions, working at higher frequencies than GSM.

This classification does not rule out the fact that in real life the EMF exposure is often due to multiple sources acting contemporaneously at different frequencies. However, few available studies on combined exposure to EMF of different frequency ranges have been carried out and they do not provide sufficient information to challenge existing risk assessment; in addition, in most experiments an absence of effects has been reported.

[☆] *Change History*: February 2015. C. Marino, P. Galloni, and C. Merla replaced Table 1 with Figure 1. Several new sections have been added to the original version to make the article up to date. In the Further reading section, several references have been added to the former list.

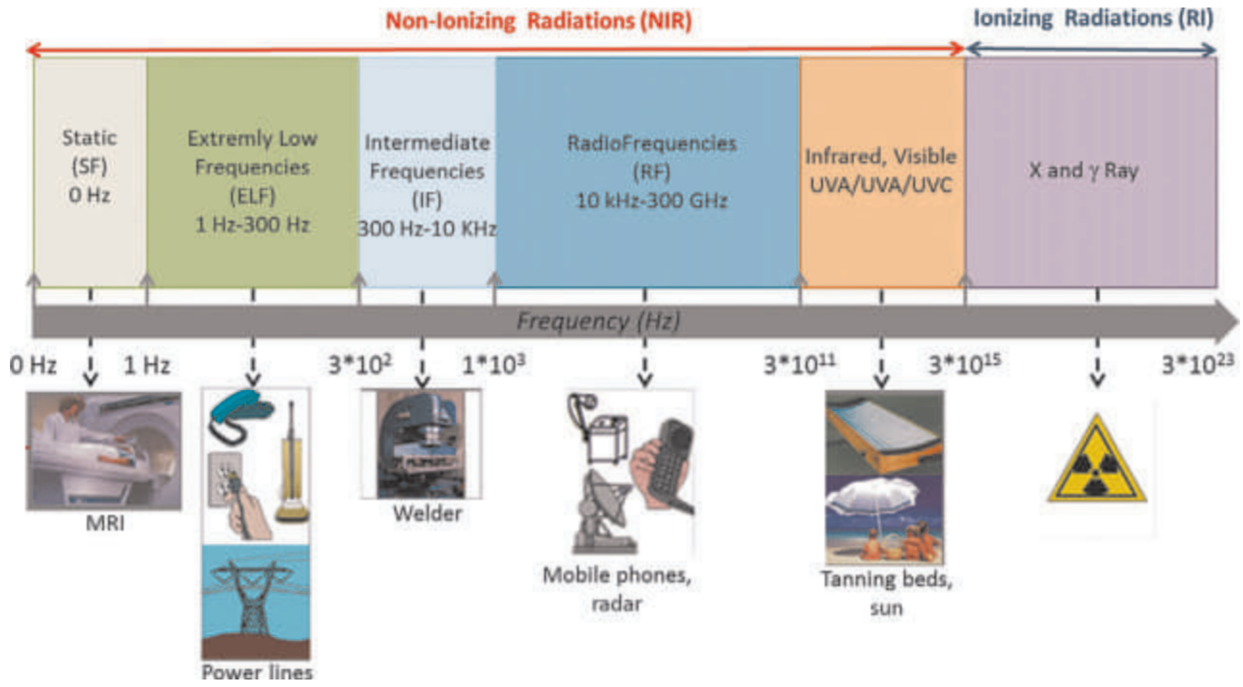
Non-Ionizing Radiations (NIR)
Ionizing Radiations (RI)
Static (SF) 0 Hz
Extremly Low Frequencies (ELF) 1 Hz-300 Hz
Intermediate Frequencies (IF) 300 Hz-10 KHz
RadioFrequencies (RF) 10 kHz-300 GHz
Infrared, Visible UVA/UVA/UVC
X and γ Ray
Frequency (Hz)
0 Hz
1 Hz
3*10²
1*10³
3*10¹¹
3*10¹⁵
3*10²³
MRI
Power lines
Welder
Mobile phones, radar
Tanning beds, sun

Figure 1 Scheme of non-ionizing and ionizing spectrum of radiations. Some sources of radiation are also sketched.

Another important issue is the combination of EMF exposure with other physical (e.g., ultrasound and ionizing radiation) or chemical agents. However, the reports on combined effects lack consistency and are not linked to specific experimental conditions. Therefore, further research is needed in order to clarify any relevance of combined exposures, especially to human cancer risk under real life exposure situations, and to explore the potentially beneficial (protective) effects of such exposures. In next paragraphs brief indication will be given also on these aspects when available.

Explicit distinctions must be made between the concepts of interaction, biological effect, and health hazard, consistent with the criteria used by international bodies when making health assessments: biological effects occur when fields interact to produce responses that may or may not be experienced by people. Deciding whether biological changes have health consequences depends, in part, on whether they are reversible, are within the range for which the body has effective compensation mechanisms, or are likely, taking into account the variability of response among individuals, to lead to unfavorable changes in health. World health organization (WHO) defines health as the state of complete physical, mental, and social well-being, and not merely the absence of disease or infirmity. Not all biological effects are hazardous: some may be innocuously within the normal range of biological variation and physiological compensation. Others may be beneficial under certain conditions, and the health implications of others may be simply indeterminate. In this document a health hazard is defined as a biological effect outside the normal range of physiological compensation and adverse to well-being.

It is known that EM interference with electromedical devices, such as cardiac pacemakers, leads to adverse health consequences, but this review is only concerned with direct effects of EMFs on living tissues.

The scientific approaches to health risk assessment related to non-ionizing EMFs are the same as in the ionizing range and toxicology in general, i.e., epidemiology, experimental studies on humans, animals, and cells in culture.

Many effects on biological systems exposed to EM fields have been reported. In the last 30 years, numerous experiments have been performed in laboratories worldwide to assess the biological effects of EM fields. This has led to the design and building of several types of exposure systems for *in vitro*, *in vivo*, and human studies. The goal is to expose the biological samples (mainly cell cultures and animals) to well-characterized fields under well-defined environmental conditions. Indeed, it is now internationally recognized that exposure setups have to be of sufficient quality to warrant that biological findings were not due to physical artifacts. Exposure setups, further, have to guarantee suitable arrangements for blind sham (i.e., without EM field) exposures. There have been many improvements in the design of exposure systems in recent years and most of the key parameters described below are well-characterized and controlled. However, standardization of these systems has only been achieved within some of the multi-center research programmes.

This article gives a review of the existing scientific knowledge on the biological and health effects of EMFs for the most part in the two main frequency ranges of concern: ELF and RF. A brief section will be devoted to the other frequency intervals as SF and IF sources for which only limited studies are up to now available.

Bioeffects of Static Fields

SF interact with moving charged particles, such as ions, and with magnetic moments arising from the orbital motions of electrons in atoms. SF can interact with paramagnetic elements in the body (metals and molecules as hemoglobin or ferritin) and modify chemical reaction rates. Most of the tissues in the body can conduct electricity, but in ordinary conditions currents flow only in particular tissues, as to say nerves, muscles, and excitable cells. Eddy currents can be induced by external SF if the biological tissue is moving in relation to the field, for example for body movements or blood flow. Manifest effects of interaction with SF are reported, including peripheral nerve stimulation, perturbation of the vestibular system (dizziness), magnetophosphenes, or metallic taste, but are often related to high levels of exposure (over 2–8 T to evoke vertigo and other sensory perceptions or peripheral nerve stimulations respectively).

Cellular Models

Strong SF (>0.2 T) have been tested in different *in vitro* systems for various exposure durations, evidencing that magnetic fields can orientate both cells and macromolecules. Genotoxic potential has been evaluated failing to show effects, while gene expression was reported to be up-regulated in different investigations. An increased sensitivity to harmful agents was reported in studies of combined exposure.

Animal Models

Cancer-related endpoints, reproduction, development, physiological, and behavioral responses have been studied after SF exposure *in vivo*. Concerning carcinogenicity, long-term investigations were performed only with relatively weak SF, drawing inconclusive results. Few high-quality studies with low intensity SF (<1 T) on fertility, growth, and development have been performed, showing no consistent adverse effects. Some effects were reported for studies on the cardiovascular system (evidencing, for example, generation of electric potentials across arteries), but their physiological consequences are unsure. Publications from a single laboratory evidenced behavioral and neural changes (i.e., vestibular disorder) for exposure above 4–7 T.

Human Studies

Epidemiological investigation, trials, and case-report studies do not suggest long-term adverse health effects due to SF exposure. A small evidence of increase in leukemia risk in electrolytic plants workers was reported. Only limited evidence exists (only one study) for an increase of metallic taste or vertigo in people working in MRI facilities.

Bioeffects of ELF Fields

In view of the interaction processes of fields with biological organisms (mainly induced electric fields at ELF), the effects of external magnetic fields, which penetrate the body, have been the main focus of the research projects. In contrast, external electric fields at ELF do not penetrate well the organism because of its conductivity. This is not true for direct stimulation of nerves and other excitable cells using electrodes. Electric fields (mainly E pulses of μs up to ms in duration) can also induce polarization of the cell membranes leading to specific effects such as electroporation.

Many mechanisms have been proposed through which living systems could interact with electric and magnetic fields at low frequencies. However, both laboratory studies and controlled human studies have provided evidence mainly for electrically-based phenomena that occur in the presence of ELF fields and that are present only during exposure to these fields. However, a great interest in direct magnetic field effects on biochemical reactions has recently undergone a further increase because of very accurate experimental evidences associated with avian magneto-reception involving Cryptochromes. These studies suggest the involvement of a radical pair in the reaction cascade and, hence, the plausible role of direct magnetic field effects.

Induced electric signals in tissues of the nervous and visual system of animals exposed to ELF electric and magnetic fields can produce effects that lead to field perception. The most notable effect that occurs in humans exposed to fields of moderate intensity is the induction of visual phosphenes. The neuronal circuits of the retina form a part of the CNS and thus the magneto-phosphene threshold may be taken as a realistic indicator of the threshold value for functional changes induced in other parts of the CNS. Threshold values at 20 Hz were estimated at approximately 100 mV m^{-1}. Direct effects on the peripheral nervous system occur only at relatively high levels of electrical stimulation (about 2 V m^{-1} and with increasing thresholds for frequencies above 1 kHz).

A variety of other potential mechanisms for interaction of ELF electric and magnetic fields with living systems have been proposed, but not demonstrated to produce effects that could significantly perturb normal biological functions. Examples of such interactions are the following: (1) magneto-chemical interactions with charge-transfer reactions which do not appear to influence biochemical pathways such as those involving electron transport; and (2) resonance interactions involving combined static and ELF fields in specific geometric configurations have not been shown to have significant biological effects, consistent with predictions based on well-founded physical arguments.

Cellular Models

There is a large and varied body of research literature on the ability of fields to cause changes in cellular models. *In vitro* studies were extensively performed and published up to 2000. More recent results suggest that, overall, the evidence for stimulation of cell division by ELF fields is at best equivocal. Neither is there clear evidence that ELF magnetic fields can alter calcium ion home-ostasis.

Finally, the data on several aspects of intracellular signaling do not consistently support the existence of field effects on these signaling pathways. Furthermore, the types of effects reported, when found, have been of a magnitude that gives little support to the conclusion that they are of consequence for human health.

Redox-related mechanisms have been mainly documented for ELF, studies proposed that exposure can stabilize free radicals increasing their lifetime and allowing a wider dispersion rather than their return to the basal level. Super oxide production in mouse macrophage was also detected after ELF exposure in a dose-dependent manner. Thus considering evidence from various authors, it seems plausible that reactive oxygen species (ROS) generation could be well-considered as an *in vitro* model for interaction between ELF and biological systems.

Animal Models

Overall, a large number of studies have been carried out, testing many different biological endpoints in a variety of animal species.

With regard to genotoxicity, there is no clear evidence that exposure to ELF magnetic fields presents an hazard. Relatively few animal studies have been carried out, however, and the subject has been more extensively investigated at the cellular level (see above). Similarly, no convincing evidence has been found from experimental studies supporting the hypothesis that exposure to power-frequency magnetic fields increases the risk of cancer.

Many studies have dealt with the reproductive and developmental effects of exposure to power frequency electric and magnetic field effects and VLF visual-display-frequency magnetic fields using chicks and mammalian species. Overall, the data do not support the hypothesis that low-frequency EMF exposures result in reproductive toxicity.

Generally, the evidence for an effect of exposure to power-frequency EMFs on melatonin levels and melatonin-dependent reproductive status is mostly negative in seasonally-breeding animals. In addition, no convincing effect on melatonin levels has been seen in a study of non-human primates chronically exposed to power-frequency EMFs. The interpretation of the outcome of studies on rat pineal and serum melatonin levels was more problematic: both positive and negative effects were reported in studies without apparent technical or analytical deficits.

With regard to possible effects on other hormones, with the possible exception of transient stress following the onset of ELF electric field exposure at levels significantly above perception thresholds, no consistent effects have been observed in levels of the stress-related hormones of the pituitary–adrenal axis, growth hormone levels, levels of hormones involved in controlling metabolic activity or those associated with the control of reproduction and sexual development. Results of these studies are inconsistent and contradictory, reporting no effects or either an increase or a decrease of the normal hormones concentration. There is little consistent evidence of any inhibitory effect of ELF EMF exposure on various aspects of immune system function including those relevant to cancer. In addition, there was no compelling evidence that hematological variables were affected by exposure to ELF fields.

In general, many studies of nervous system functions were either negative, or difficult to interpret because of weakness in experimental design or confounding by artifact. However, several studies suggest possible EMF effects on the opioid and cholinergic systems, along with concomitant changes in analgesia and in the acquisition and performance of spatial memory tasks. Effects on opioid and cholinergic systems should thus be further investigated.

Action of free radicals in brain under ELF exposure was fully analyzed in a recent review evidencing, in particular, redox and trophic responses in mouse brain and brain lipid oxidative damage. Moreover, antioxidant defense can be specifically deteriorated by ELF exposure thus amplifying oxidative stress both in young and aged rat brain. However, a direct link to health risk assessment of these results is difficult due to the limited number of conducted studies

Hypotheses relating ELF to neurodegenerative diseases are a relatively novel part of the EMF research area and, so far, only a modest number of studies have been performed if compared to cancer research field. A single study on animals, genetically modified rodents for amyotrophic lateral sclerosis (ALS), was performed to assess the possible effects of chronic exposure to ELF on the development of this neurodegenerative disease. Authors did not reveal any difference between exposed and control animals, providing no evidence of a link between ELF and ALS in an oxidative prone experimental model. Connection with Huntington's disease (HD) was also investigated *in vivo*. These data together other observations seem to support the hypothesis of a neuro-protective effect elicited by ELF on HD.

The potential sensitivity of people with epilepsy to EMF exposure is an important factor that should be considered. Exposure of animals to EMFs before testing has been reported to have an inhibitory effect on subsequent tests of epileptic-seizure sensitivity but the type of response was not consistent among different studies. Further investigation should be carried out of possible effects during exposure.

Moreover, ELF seems related to the offset and onset of evoked potentials, this suggests that the field was transduced like ordinary stimuli such as light and sound. However, the changes induced by ELF were governed by nonlinear and complex law for which the underlying mechanism still remains unknown.

There is convincing evidence that ELF electric fields can be perceived by animals, most likely as a result of surface charge effects; threshold values for both rats and baboons lie between about 5 and 15 $\mathrm{kV\ m^{-1}}$. Exposures above these thresholds are sufficient to be mildly aversive and will result in transient arousal but mostly disappear following prolonged exposure.

Largely consistent with earlier results, recent studies have reported that exposure to magnetic fields has no effect on activity or locomotion, but may affect the performance of spatial memory tasks (both deficits and improvements have been reported) and engender subtle increases in behavioral anxiety and stress. Other studies have investigated potential molecular and cellular mechanisms, and despite a number of studies continuing to report candidate mechanisms, particularly regarding effects on ROS, none that operate at levels of exposure found in the everyday environment has been firmly identified.

Human Studies

Small inconsistent changes have been described in circulating levels of leukocytes, but as with animals, the relevance to human health of these changes is not clear. No indication of a clear-cut cytogenetic effect was observed in the blood cells of exposed subjects. The circulating hormone levels in humans, including melatonin, are not adversely affected by exposure to power-frequency electric and/or magnetic fields. At the same time, two recent independent studies have examined the effects of occupational exposure to magnetic fields by examining peripheral blood of exposed workers. At best, these provide only weak evidence for a field-related effect on natural killer cell activity and antioxidant activity.

Positive results from studies on the power spectrum of different EEG frequency bands and on sleep structure have been performed at occupational exposure levels higher than general environmental levels.

In the light of cognitive and performance studies that show a large number of positive biological effects the need for further studies is warranted in order to clarify their significance for human health.

Some authors investigated the possible effects of fields generated by electric motors in incubators on autonomic function in newborn babies. Transient changes in the total power and spectral components of heart rate variability (HRV) were noted when the motors were running. Confirmatory studies are required to determine the significance of this observation. Others reported that HRV in adults was affected by exposure to very weak fields (around 2 μT). The direction of change was dependent on the frequency used. The majority of published cardiovascular changes stay within the range of normal biological variations; else, the study protocols and the results have not been successfully replicated in other laboratories.

More recently, it has been hypothesized that exposure to low frequency fields is associated with several neurodegenerative diseases. For Alzheimer's disease (AD) and ALS more studies have been published, while lack of data and inconsistency emerged for diseases as Parkinson (PD). Some of these reports concerning Alzheimer and ALS suggest that people employed in electrical occupations might have an increased risk. So far, no biological mechanism has been established which can explain this association, although it could have arisen because of confounders related to electrical occupations, such as electric shocks. However more sophisticated studies do not observed increasing of the risk. Hence, overall the evidence for the association between low frequency exposure and AD and ALS is inconclusive.

Only few new studies have been published since the previous opinion and they do not provide support to increase the risk for AD.

As perception of electric or magnetic fields has been reasonably well characterized, skin symptoms, headache, and mood disturbance claimed by working near computer screens or in proximity of other environmental ELF sources have not reliably been linked to any electromagnetic exposure produced by these devices. Also, reported studies do not indicate any ability of individuals who alleged electromagnetic hypersensitivity to react to any test-field situation, suggesting that other environmental or psycho-social factors should be considered for people suffering from this pathology.

Conclusion

There is today little scientific evidence suggesting that ELF EMF exposures pose a health risk. The strongest evidence for health effects comes from an association observed with childhood leukemia. In contrast, mechanistic studies and animal toxicology data fail to demonstrate any consistent pattern across studies, although sporadic findings of biological effects (including increased cancers in animals) have been reported.

This was at the basis of a classification performed by the International Agency for Research on Cancer in 2001, ranking ELF magnetic fields as possibly carcinogenic to humans (Group 2B) (IARC, 2002). The classifications essentially were based on the facts that epidemiological studies showed a consistent association between magnetic fields above approximately 0.3/0.4 μT and a doubling in risk for childhood leukemia, although chance, bias and confounding could not be ruled out as an explanation with reasonable confidence, but that experimental studies or mechanistic modeling provided little support for, or explanation of, these findings.

The lack of connection between human and experimental data (animal and mechanistic) severely complicates the interpretation of these results.

Bioeffects of IF Fields

For the purposes of risk assessment, IF fields have only been considered as a separate entity relatively recently. Largely depending on the definition of their frequency range, IF fields have been considered in various reviews and monographs alongside either low or high frequency fields. IF fields can induce electric fields and currents in the human body, much as it is seen with low frequency fields, but they can also induce heating effects in the body as in high frequency field exposures. Assessments of possible hazards at IF are based primarily on extrapolation from data on exposure to higher and lower frequencies. Very little useful epidemiological data are available. The existing evidence largely comes from older studies that tended to used job title as a surrogate for exposure. Groups studied include users of visual display units (VDUs) associated with personal computers and radio and telegraph operators. Outcomes studied included cancer as well as effects on the eye, the cardiovascular system and the reproductive system. Although no particular risks were identified, the quality of existing studies is limited. There have been some animal studies exploring the effects of IF fields from VDUs, particularly on reproduction and development. There are fewer studies on humans, although some studies have investigated effects of IF fields on skin. With the demise of cathode-ray based monitors, more recent work exploring health risks associated with computer use in humans has concentrated on ergonomic issues (and is not considered here). Despite some limited evidence from animal studies that have reported field-dependent effects on reproduction and development, there is no consistent or conclusive evidence of field-dependent adverse effects. Overall, it can be concluded that there was insufficient data for a health risk assessment, so the overall evaluation for all health endpoints has to be considered to be inadequate. Since then, an IARC Working Group has classified EMFs with a frequency range of 30 kHz to 300 GHz as being 'possibly carcinogenic to humans' (see Section 5).

Cellular Models

In vitro IF exposure of a single work on genotoxicity gives negative results as well as stress responses on glioblastoma cells. Negative effects was also obtained for global gene expression on human astroglia cell line.

Animal Models

A series of study of IF exposure effects on embryotic development was carried out recently with negative outcomes. Globally, no effects on reproductive outcome were documented in these studies.

Bioeffects of RF Fields

Concerns about health effects caused by exposure to RF are mainly related to mobile telephones and base stations, becoming a major societal issue in some countries, or at least among part of the population. Mobile (or cellular) telephony has developed very rapidly, followed and unseated in the last years by phones equipped for data services (smart phones, 3G). They are now part of the basic equipment of modern life and billions of such devices are in use worldwide. Stories about health risks from radiofrequency radiation (RFR) from mobile phones and base stations have become common in the media over the past 10 years.

Several systems are used in mobile telephony worldwide, all based on the same principle, i.e., 'cellular' mapping of the territory. In each cell, a base station (BTS) emits toward and receives signals from the mobile telephones active in that cell (up to around 50). There are, for example, 30 000 BTS in France used by three networks. The carrier frequency varies from 400 to 2100 MHz and the voice or data information is coded digitally either by frequency or phase modulation. Mobile telephones are two-way radio transmitters operating in the 400–2100 MHz frequency range. In the GSM system, for example, the peak power emitted is 2 W, but the time-averaged power is always below 1/8 of this value, as power control reduces emission to the lowest level required. About half of the emitted power is absorbed by the user's head, i.e., a maximum of 125 mW. Power absorption is expressed as specific absorption rate (SAR) in W kg^{-1}. New generation of smart phones include contemporarily a large number of communication protocols as GSM/GPRS/EDGE/UMTS/HSDPA/HSUPA/LTE spanning up to frequencies above 2450 MHz.

Major improvements have been achieved in measuring the SAR in liquid phantoms and calculating power distribution in the head using numerical phantoms over the last 10 years. Today, the worst-case SAR associated with the average GSM phone on the market is ca. 0.5 W kg^{-1}, i.e., 1/4 of the recommended local-exposure limit value. It is now known with certainty that temperature increases in the brain periphery caused by the waves emitted by mobile telephones does not exceed 0.1°C. As for smart phones, they are backward-compatible with older mobile phones networks, and usually operates with lower emissions than their precursors.

As a result of current changes in usage – increasing use of text and image messages and hands-free kits – mobile telephones are less frequently placed against the ear. This dramatically reduces exposure of the tissues in the head.

GSM base-station antennas have an emitting power of ca. 20 W. They are usually placed on rooftops and the emission beam is disc-shaped. Maximum exposure occurs on the ground, approximately 200 m from the BTS and it is almost zero at the bottom of the building or mast on which the antenna is mounted. Exposure of the public to the RFR emitted by base stations is typically 1/10 000 of the recommended limit in terms of incident power. There is a consensus in the scientific community that base stations do not represent an health hazard.

There is much scientific evidence, based on existing research, that warrants limiting exposure to high-level RFR due to the 'thermal effects' caused by heating of the tissues at SAR levels that correspond to a temperature elevation of a few degrees. However, this does not occur with mobile telephones. The search is thus for 'non-thermal' effects and most of the research activity has been aimed at defining the thresholds for these effects, with respect to existing exposure guidelines based on acute effects known to be due to heating.

Health risk assessment associated with RF benefits from a database spanning over 50 years: the WHO and IEEE databases list about 2000 peer-reviewed publications, from biophysical theoretical analyses to human epidemiological studies. The EHC

(Environmental Health criteria) Monograph by WHO, peer-reviewing all the literature on this subject from year 2000 is periodically realized.

The carcinogenicity of RF EMFs was assessed by a working group at IARC (International Agency for Research on Cancer), classifying them as 'possibly carcinogenic to humans (Group 2B),' after the examination of the relevant human, animal and cellular studies, mainly due to limited epidemiological evidence. A causal link between RF exposure and increased risk of cancer was considered possible, but chance, bias or confounding factors could not be excluded.

Cellular Models

A number of replication studies that addressed some positive findings on enzyme activity, gene expression, and DNA alteration have all proven negative so far. A wide range of short-term, low-level *in vitro* experiments have shown that exposure did not cause cell death, implying that RF is not a toxic agent. Furthermore, the weight of evidence available today (induction of DNA strand breaks, chromosome aberrations, micronuclei formation, DNA repair synthesis, sister chromatid exchange, and phenotypic mutation) supports the conclusion that RF is not genotoxic. However, the synergy of RF with chemical agents or other physical agents still needs further investigation.

Weak evidence is reported that RFR activates a stress response or production of ROS (free radicals) in human and animal cells under non-thermal conditions. The same outcome was evidenced about HSP (Heat Shock Proteins) production, cell proliferation, or apoptosis.

A few studies reported positive findings, often reversible, and linked to critical physical exposure parameters such as modulation, frequency and power 'windows,' field polarization, or background ELF fields.

Animal Models

A large number of animal experiments have been performed over the past 50 years, using various frequencies and modulations. It is clear from these data that the vast majority of the reported biological effects are due to heating. These effects result either from a rise in tissue or body temperature exceeding 1 ° C or in physiological and behavioral responses aimed at minimizing the total heat load.

Major improvements in exposure system design have made it possible to better characterize the SAR within the organism, and allow for either local exposure that mimics mobile telephone use (e.g., loop antenna, carousel) or whole-body exposure related to base-stations (e.g., Ferry's wheel, reverberation chamber, circular waveguide).

Results on most of the non-cancer endpoints have been negative (memory, EEG, hearing, etc.) except for data on the permeability of the blood–brain barrier, which was found to be increased by two research groups but not by several others.

Therefore, most of the major ongoing studies deal with cancer models. All of the long-term bioassays or sensitized studies have given negative results except for one using transgenic mice, genetically modified to increase the background incidence of lymphomas; an increased tumor incidence was found following GSM exposure. Most of more recent studies have not produced any persuasive evidence that RF fields are carcinogenic, even if a long-term low-level GSM exposure was reported to shorten life-span in rats, and increased lung tumor development was showed in mice co-treated with UMTS fields and chemical carcinogens during gestation and after weaning, such studies requiring confirmation. A large NTP (National Toxicology Program) study is ongoing, and unresolved questions about studies design and interpretation of results should be clarified through this study.

A number of studies on animals ranging from focus on learning and memory, on behavior, biochemical brain responses, sensory organs, neurogenesis, and cytotoxicity, to neurodegenerative diseases have been carried out. Different endpoints have been studied at various SAR-levels in both mice and rats. The few positive findings appears inconsistent and mostly at levels well above guideline values.

Since the issue that children are more sensitive than adults to the wireless telephones associated emissions has recently set in, important and well designed investigations of RF effects on pregnancy outcome, development of the offspring, and immunological parameters have been performed in the last years. Although one study suggested an association between early postnatal exposure and accelerated maturity in male rats, the evidence does not indicate that prenatal or early postnatal exposures are linked to acute adverse responses or the development of long-term harmful changes.

Human Studies

In spite of the obvious limitations of human experiments in terms of endpoints and exposure characterization, several investigations have been performed using various models. Findings have either been negative or difficult to replicate (sleep, EEG, cognitive functions, etc.).

No unequivocal increased risk of brain tumors, head and neck tumors, or other malignant diseases has been indicated by epidemiological studies on RF EMF exposure. Great interest regarding an increased risk of glioma and acoustic neuroma in heavy users (corresponding, as in the IARC 2013 Monograph, to half an hour of daily use over years or more) of mobile phones derived from early studies. Based on the most recent cohort and incidence time trend studies, it appears that the evidence for an increased risk of glioma became weaker while the possibility of an association with acoustic neuroma remains open.

Inconsistent results have been showed by neuro-physiological studies on possible effects on brain function in humans, including macrostructure of sleep, electroencephalography (EEG), event-related potentials, slow brain potentials, cognition, as well as regional blood flow and oxygenation changes. Although the associated biological mechanism and significance are still unclear, the former evidence that RF exposure may affect brain activities, as for EEG studies during wake and sleep state, is further supported by more recent studies. Overall, there is evidence that exposure to RF fields does not cause symptoms or affect cognitive function in humans.

Clearly, the main issue today is the potential greater sensitivity of children to mobile phone emissions. Their lifetime exposure, the fact that their CNS is still developing, and, possibly, increased RF absorption in the head, have led to concerns that cannot be easily resolved through laboratory investigations and numerical modeling. A large Danish study has reported results that suggest higher prevalence of some behavioral and health disorders in children. About that, some considerations must be taken into account: results are not confirmed in other studies; some methodological weaknesses are present; the exposure indicators such as frequency of mother's mobile phone use could not at all be relevant for fetal exposure *in utero*; attention deficit disorders have a clear hereditary component. By and large, the evidence for an association between behavioral disorders and RF exposure of the fetus is considered weak.

Few studies have investigated the possibility that exposure to low-level RF fields from mobile phones and other sources can affect male fertility, but none of the recent studies are particularly informative.

Conclusion

RFR can cause biological effects when exposure is sufficiently intense: possible injuries include cataracts, skin burns, deep burns, heat exhaustion, and heat stroke. They are mostly due to heating. There have been scattered reports of effects that do not appear to be due to temperature elevation: the 'non-thermal' effects. None of these effects have been independently replicated, and most have no obvious consequence to human health. Furthermore, there are no known biophysical mechanisms that suggest that such effects could occur.

Following the very rapid development of mobile telephony, a major research effort has been carried out worldwide (tens of millions of euros per year). Europe is most active (UK, Germany, Italy, and Finland, in particular), but many research groups are contributing from Japan, US, and Australasia.

Most governments have addressed the issue of mobile telephony and health and several international and national expert committees have written accurate summaries of current knowledge (see the list of the most recent reports in the 'Further reading' section). Their conclusions converge toward an absence of health effects related to mobile telephones, but all encourage continuing research in some areas.

In answer to the question: 'mobile telephony: is there evidence of harm?' one must conclude that the weight of scientific evidence does not support health concerns or indicate any health risk from mobile phones in normal use, nor that there is any accepted mechanism for potential health effects at the low levels associated with these devices. Findings to date, including epidemiological studies and laboratory studies of animals exposed both short-term and for their entire lifetimes, have not provided evidence that exposure causes cancer, or affects biological tissues in a manner that might lead to, or augment, any disease. However, some pending issues as the potentially greater sensitivity of children has been addressed using *in vivo* models as well as epidemiological investigations also still ongoing.

Medical Applications

Recently the therapeutic use of EMF in various medical applications has raised much attention within the scientific community.

The deep description of the effects and application of EMF in this area of research and clinics is beyond the scope of this article, even if some fundamental effect, as the ones related to RF or MW heating, nervous system stimulation and electrical membrane polarization to induced electroporation has been also previously discussed.

Occupational Exposures

Directive 2013/35/UE of June 26, 2013 on the minimum health and safety requirements regarding the exposure of workers to the risks arising from physical agents (EMFs) covers all known direct biophysical effects and other indirect effects caused by EMFs. However, the Directive currently only addresses short-term effects and does not concern possible long-term effects.

Health Risk Assessment

The process of health risk assessment by bodies such as ICNIRP (International Commission on Non-ionizing Radiation Protection), IEEE (Institute of Electrical and Electronics Engineers), IARC (International Agency for Research on Cancer), and WHO relies heavily on judging the quality of investigations. As stated above, the quality of exposure systems has greatly improved and can now be considered adequate. The use of well-grounded experimental protocols (sham-exposure, blinding of exposure and biological tests, positive controls) has become generalized. Moreover, it is now common practice in the field of bioelectromagnetics to ascertain that any positive results are replicated in at least one independent laboratory. In spite of these improvements, it should be noted that only a few top-level biology laboratories have engaged in this type of research, partly due to interferences created by societal and media pressure.

Within its EMF International Programme, WHO has reviewed the science and issued research recommendations. The main conclusion from these reviews is that EMF exposures below the limits recommended in the ICNIRP guidelines do not appear to have any known impact on health. However, there are still some key gaps in knowledge requiring further research to provide definitive health risk assessments are provided by the World Health Organization within the EMF Project and published into a dedicated Research Agenda.

Remaining uncertainties in the science database have led to pressure to introduce precautionary measures until gaps in knowledge are filled. If precautionary measures are introduced to reduce RFR levels, it is recommended that they should be voluntary and that health-based exposure limits be mandated to protect public health.

Further Reading

Consales C, Merla C, Marino C, and Benassi B (2012) Electromagnetic fields oxidative stress and neurodegeneration. *Int. Cell Biology* 2012: 1–16.

COST Action BM1309: European network for innovative uses of EMFs in biomedical applications (EMF-MED). Available at: http://cost-emf-med.eu/ (accessed 28.07.15).

COST Action EP4Bio^{2}Med: European network for development of electroporation-based technologies and treatments. Available at: http://www.electroporation.net/ (accessed 28.07.15).

Directive 2013/35/EU of the European Parliament and of the Council. Official Journal of the European Union L179/1.

EFHRAN Report. Risk analysis of human exposure to electromagnetic fields (revised), 2012. Project funded by Executive Agency for Health and Consumers Framework of the Programme of Community Action in the Field of Health 2008–2013.

EMF Health Risk Research, Lessons Learned and Recommendations for the Future, 2005. Monte Verità, Switzerland, 20–24 November 2005. Available at: http://www1.itis.ethz.ch/mv/ (accessed 28.07.15).

Health Protection Agency (HPA), 2008. Static Magnetic Fields. Report of the Advisory Group for Non-Ionizing Radiation, RCE-6.

IARC Monograph Vol 80 2002. On ELF Bioeffects. Available at: http://www.iarc.fr (accessed 28.07.15).

IARC (2013) Non-Ionizing Radiation, Part 2: Radiofrequency Electromagnetic Fields. In: *Monographs on the Evaluation of Carcinogenic Risks to Humans*, IARC Monograph Vol 102.

ICNIRP, International Commission on Non-Ionising Radiation Protection Statement (1998) Guidelines for limiting exposure to time varying electric, magnetic, and electromagnetic fields (up to 300 GHz). *Health Phys.* 74(4): 494–522.

ICNIRP, Exposure to Static and Low Frequency Electromagnetic Fields, Biological Effects and Health Consequences (0–100 kHz) – Review of the Scientific Evidence and Health Consequences. Available at: www.icnirp.de (accessed 28.07.15).

ICNIRP (2010) Guidelines for limiting exposure to timevarying electric, and magnetic, fields (1 Hz–100 kHz). *Health Phys.* 99: 818–836.

IEGMP Independent Expert Group, 2000. Mobile Phones and Health, c/o National Radiological Protection Board, Chilton, Didcot UK, ("Stewart Report". www.iegmp.org.uk).

INTERPHONE Study Group (2010) Brain tumour risk in relation to mobile telephone use: Results of the INTERPHONE international case-control study. *Int. J. Epidemiol.* 39: 675–694.

Kuhn S and Kuster N (2006) Handbook of biological effects of electromagnetic fields. In: Barnes FS and Greenebaum B (eds.) *Bioengineering and Biophysical Aspects of Electromagnetic Fields.* Boca Raton, FL: CRC Press.

Marino C, Lagroye I, Scarfi MR, and Zenon S (2011) Are the young more sensitive than adults to the effects of radiofrequency fields? An examination of relevant data from cellular and animal studies. *Prog. Biophys. Mol. Biol.* 107: 374–385.

Marsh JL, Armstrong TJ, Jacobson AP, and Smith RG (1982) Health effect of occupational exposure to steady magnetic fields. *Am. Ind. Hyg. Assoc. J.* 43(6): 387–394.

NIEHS (1998) Niesh report on health effects of exposure to power-line frequency electric and magnetic field. Available at:www.niehs.nih.gov/emfrapid/home.htm. Accessed 29 July 2015.

National Radiological Protection Board (NRPB). Available at: http://www.nrpb.org/ (accessed 29.07.15).

NRPB (2001) *ELF electromagnetic fields and the risk of cancer, Report of an Advisory Group on non-ionising radiation. Documents of the NRPB*Vol 12. #1, Chilton, Didcot ("Doll Report") UK.

Ritz T, Thalau P, Phillips J, Wiltschko R, and Wiltschko W (2004) Resonance effects indicate a radical-pair mechanism for avian magnetic compass. *Nature* 429: 177–181.

Sadetzki S, Langer CE, Bruchim R, et al. (2014) The MOBI-Kids study protocol: Challenges in assessing childhood and adolescent exposure to electromagnetic fields from wireless telecommunication technologies and possible association with brain tumor risk. *Front Public Health* 2(124): 1–10.

SCENIHR (Scientific Committee on Emerging and Newly Identified Health Risks), Potential health effects of exposure to electromagnetic fields (EMF), November 2013.

SCENIHR (2007) *Possible Effects of Electromagnetic Fields (EMF) on Human Health. Scientific Committee on Emerging and Newly Identified Health Risks*. European Commission, Health and Consumer Protection DG. Available at:http://ec.europa.eu/health/scientific_committees/emerging/index_en.htm. Accessed 29 July 2015.

SCENIHR (2009) *Health Effects of Exposure to EMF. Scientific Committee on Emerging and Newly Identified Health Risks*. European Commission, Health and Consumer Protection DG. Available at:http://ec.europa.eu/health/scientific_committees/emerging/index_en.htm accessed 29.07.15.

WHO International EMF Project (1996) Health and environmental effects of exposure to static and time varying electric and magnetic fields. Available at:www.who.int/%20peh-emf. Accessed 29 July 2015.

WHO Research Agenda. Available at: http://www.who.int/peh-emf (accessed 29.07.15).

Wiltschko R, Stapput K, Ritz T, Thalau P, and Wiltschko W (2007) Magnetoreception in birds: Different physical processes for two types of directional responses. *HFSP J* 1(1): 41–48.

Zanetti-Polzi L, Marracino P, Aschi M, et al. (2013) Modeling triplet flavin-indole electron transfer and interradical dipolar interaction: A perturbative approach. *Theor. Chem. Acc.* 132: 1393.

Metalloproteins, Structural Determination of ☆

C Luchinat and G Parigi, University of Florence, Florence, Italy

© 2016 Elsevier Inc. All rights reserved.

This is an update of C. Luchinat, G. Parigi, Metalloproteins, Structural Determination of, Reference Module in Materials Science and Materials Engineering, Elsevier, 2016, ISBN 9780128035818, https://doi.org/10.1016/B978-0-12-803581-8.00994-2.

Introduction 719
The Magnetic Susceptibility in Diamagnetic and Paramagnetic Systems 720
The Dipole–Dipole Interaction 721
Pseudocontact Shift Restraints 721
Relaxation Enhancement Restraints 722
Cross-Correlation between Curie and Dipole–Dipole Relaxation Restraints 723
Self-Orientation Residual Dipolar Coupling Restraints 723
Contact Shift (and Hyperfine Shift) Restraints 724
Collecting the Paramagnetism-Based Restraints 726
Solution Structure Determination Programs 728
Recovering Information on Structure Heterogeneity 728
Paramagnetic Tagging of Diamagnetic Proteins 729
Conclusion 729
Further Reading 729

Nomenclature

B_0	magnetic induction (kg $\mathrm{A^{-1}}$ $\mathrm{s^{-2}}$)
$E_{S,MS}$	Zeeman energy of the level (kg $\mathrm{m^2}$ $\mathrm{s^{-1}}$)
g_e	electron g factor
$\hbar$	Planck constant $h/2\pi$ (kg $\mathrm{m^2}$ $\mathrm{s^{-1}}$ $\mathrm{rad^{-1}}$)
H_0	external magnetic field (A $\mathrm{m^{-1}}$)
I	nuclear spin angular momentum
^1J	coupling constant ($\mathrm{s^{-1}}$)
k	Boltzmann constant (kg $\mathrm{m^2}$ $\mathrm{s^{-1}}$ $\mathrm{K^{-1}}$)
M	magnetization (A $\mathrm{m^{-1}}$)
M_S	one-electron spin angular momentum quantum number
N_A	Avogadro constant ($\mathrm{mol^{-1}}$)
r	distance (m)
$R_{1\mathrm{dia}}$	diamagnetic contribution to the longitudinal relaxation rate ($\mathrm{s^{-1}}$)
$R_{2\mathrm{dia}}$	diamagnetic contribution to the transverse relaxation rate ($\mathrm{s^{-1}}$)
$R_{1\mathrm{M}}$	paramagnetic contribution to the longitudinal relaxation rate ($\mathrm{s^{-1}}$)
$R_{2\mathrm{M}}$	paramagnetic contribution to the transverse relaxation rate ($\mathrm{s^{-1}}$)
S	electron spin angular momentum
$\mathbf{S}$	orientation tensor
T	temperature (K)
V_M	molar volume ($\mathrm{m^3}$ $\mathrm{mol^{-1}}$)
γ_I	nuclear magnetogyric radio (rad kg $\mathrm{A^{-1}}$ $\mathrm{s^{-3}}$)
δ	chemical shift
$\Delta\nu$	line width (Hz)
$\Delta\chi_{\mathrm{aX}}$	axial magnetic susceptibility anisotropy ($\mathrm{m^3}$)
$\Delta\chi_{\mathrm{rh}}$	rhombic magnetic susceptibility anisotropy ($\mathrm{m^3}$)
μ	magnetic moment (A $\mathrm{m^2}$)
μ_0	permeability of a vacuum (kg m $\mathrm{s^{-2}}$ $\mathrm{A^{-2}}$)
μ_B	electron Bohr magneton (A $\mathrm{m^2}$)
$\rho_{I(J)}$	contribution to longitudinal relaxation of nucleus I due to the coupling with nucleus J ($\mathrm{s^{-1}}$)
σ	dipolar shielding tensor

☆ *Change History*: June 2015. G. Parigi made a few minor changes in the previous text. Two new sections: 'Recovering Information on Structure Heterogeneity' and 'Tagging of Diamagnetic Proteins' were added and references have been changed.

https://doi.org/10.1016/B978-0-323-90800-9.00313-9

$\boldsymbol{\tau}_{\mathbf{c}}$	correlation time (s)
$\boldsymbol{\tau}_{\mathbf{M}}$	exchange time (s)
$\boldsymbol{\tau}_{\mathbf{r}}$	reorientational time (s)
$\boldsymbol{\tau}_{\mathbf{s}}$	electron relaxation time (s)
$\boldsymbol{\chi}$	magnetic susceptibility per molecule (m^3)
$\boldsymbol{\chi}_{\mathbf{v}}$	susceptibility per unit volume
$\boldsymbol{\omega}_{\boldsymbol{I}}$	nuclear Larmor frequency (rad s^{-1})
$\boldsymbol{\omega}_{\mathbf{S}}$	electron Larmor frequency (rad s^{-1})

Introduction

Nearly half of proteins in all living organisms contain a metal ion. Such metalloproteins may be diamagnetic or paramagnetic systems, depending on the nature of the metal ion and its spin state. The presence of a diamagnetic metal ion in the protein does not affect the NMR parameters appreciably, and the usual techniques for protein solution structure determination can be applied, with the additional problem of locating the metal ion. On the contrary, the presence of a paramagnetic metal ion largely perturbs the NMR parameters, as it affects both the signal line widths and the intensity of the Nuclear Overhauser Effects (NOEs). In fact, since the magnetic moment of an unpaired electron is 658.2 times larger than that of proton, the major magnetic interaction of any nucleus not far from the metal ion will be provided by the dipolar coupling with the unpaired electron rather than with other closer nuclei (**Figure 1**). Such interaction sizably increases both their longitudinal and transverse relaxation rates – two parameters strongly affecting the protein NMR spectra.

If R_{1M} and R_{2M} indicate the paramagnetic contributions to the longitudinal and transverse relaxation rates, respectively, the increase in nuclear signal line width due to the presence of a paramagnetic metal ion will be given by

$$\Delta\nu = R_{2M}/\pi$$

and the change in NOE intensity by

$$\frac{\eta_{I(J)}^{\text{para}}}{\eta_{I(J)}^{\text{dia}}} = \frac{\rho_{I(J)} + \rho_{I(\text{other})}}{\rho_{I(J)} + \rho_{I(\text{other})} + R_{1M}}$$

where $\rho_{I(J)}$ is the contribution to longitudinal relaxation of nucleus I due to the coupling with nucleus J and $\rho_{I(\text{other})}$ includes all other contributions to relaxation of nucleus I, with the exception of the coupling with nucleus J and with the paramagnetic center, R_{1M}.

The increase in line widths and the decrease of NOE intensities make it more difficult to collect data for structure calculations. For $R_{1M} > R_{1\text{dia}}$ and $R_{2M} > R_{2\text{dia}}$, the integrals of NOESY cross-peaks decrease linearly with R_{1M}, and the scalar coupling cross-peaks decrease quadratically with R_{2M}. However, the presence of a paramagnetic metal ion makes available a new class of structural restraints: the paramagnetism-based restraints. The amount of information related to these new restraints is often able to compensate the loss of information due to the effects described above. Paramagnetism-based restraints are derived from contact shifts (CSs), pseudo-CSs (PCSs), relaxation enhancements, residual dipolar couplings (RDCs) arising from partial metalloprotein self-orientation, cross-correlation between Curie relaxation and dipole–dipole nuclear relaxation (CCR).

The availability of the paramagnetism-based restraints may also make it convenient to use a paramagnetic metal ion in the place of a native diamagnetic metal or as a probe to be attached to a protein.

Paramagnetism-based restraints have also the advantage of being often quicker to obtain than the classical NOE restraints, especially for proteins of large size. Therefore, the development of protocols for their efficient use is of great perspective importance in order to increase the speed in solving protein structures and to obtain structures of large proteins employing NMR.

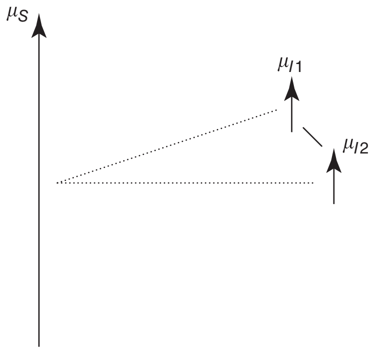

Figure 1 The magnetic interaction of a nuclear magnetic moment with the electron magnetic moment can be larger than that between two close nuclei, due to the larger electron magnetic moment.

The Magnetic Susceptibility in Diamagnetic and Paramagnetic Systems

All the paramagnetism-based effects indicated above originate from the dipolar coupling between protein nuclei and the unpaired electron(s) and/or from the presence of paramagnetic susceptibility, usually an anisotropic quantity, which is now introduced.

When a molecule is immersed in an external magnetic field $\boldsymbol{H}_0$, an induced magnetic moment is established along $\boldsymbol{H}_0$. A magnetization $\boldsymbol{M}$ thus arises, defined as the induced magnetic moment per unit volume, usually proportional to H_0

$$M = \frac{\chi_V B_0}{\mu_0}$$

where μ_0 is the permeability of free space and $B_0 = \mu_0(H_0 + M) \approx \mu_0 H_0$. In systems that do not contain paramagnetic ions, χ_V is the diamagnetic susceptibility, usually independent of B_0 and is negative.

In paramagnetic systems, χ_V is dominated by the paramagnetic susceptibility per unit volume, it is independent of B_0 and is positive. An average induced magnetic moment per particle, $\langle \mu \rangle$, is, in fact, established due to the different populations of the electron energy levels, as a consequence of the fact that the magnetic field splits the S manifold of a particle with spin S according to its M_S values (**Figure 2**). The magnetic susceptibility per molecule, χ, is defined as

$$\chi = \frac{V_\mathrm{M}\chi_\mathrm{V}}{N_\mathrm{A}} = \frac{V_\mathrm{M}\mu_0 M}{N_\mathrm{A} B_0} = \frac{\mu_0 \langle \mu \rangle}{B_0}$$

where V_M is the molar volume and N_A is the Avogadro constant.

The electron magnetic moment is related to the electron spin according to the following equation:

$$\boldsymbol{\mu} = -\mu_\mathrm{B} g_\mathrm{e} \boldsymbol{S}$$

where g_e is the electron g factor and μ_B is the electron Bohr magneton. The expectation value of $\boldsymbol{\mu}$ along the direction of the applied magnetic field z, is thus given by $-\mu_\mathrm{B} g_\mathrm{e} S_z$. Analogously, the average induced magnetic moment per particle is

$$\langle \mu \rangle = -\mu_\mathrm{B} g_\mathrm{e} \langle S_z \rangle$$

where $\langle S_z \rangle$, the expectation value of S_z, in the high-temperature approximation and in the limiting case where there is no contribution from the orbital magnetic moment, is given by

$$\langle S_z \rangle = -\frac{g_\mathrm{e}\mu_\mathrm{B} B_0}{3kT} S(S+1)$$

where k is the Boltzmann constant and T is the absolute temperature. Therefore, the Curie law is obtained:

$$\chi = \mu_\mathrm{B}^2 g_\mathrm{e}^2 \frac{\mu_0}{3kT} S(S+1)$$

If the orbital magnetic moment is considered, the magnetic susceptibility becomes anisotropic, and must be represented as a tensor. As a consequence, the average induced magnetic moment depends on the orientation of the $\boldsymbol{\chi}$-tensor with respect to the direction of the applied magnetic field:

$$\langle \boldsymbol{\mu} \rangle = \frac{\boldsymbol{\chi} \cdot \boldsymbol{B}_0}{\mu_0}$$

The energy of a magnetically anisotropic molecule, with average magnetic moment per particle $\langle \mu \rangle$, in a magnetic field is given by

$$E^\mathrm{aniso} = -\int_0^{\langle \mu \rangle} \boldsymbol{B}_0 \cdot d\langle \boldsymbol{\mu} \rangle = -\frac{\boldsymbol{B}_0 \cdot \boldsymbol{\chi} \cdot \boldsymbol{B}_0}{2\mu_0}$$

The fact that the energy is orientation dependent has an influence on the probability that the molecule orients along different directions.

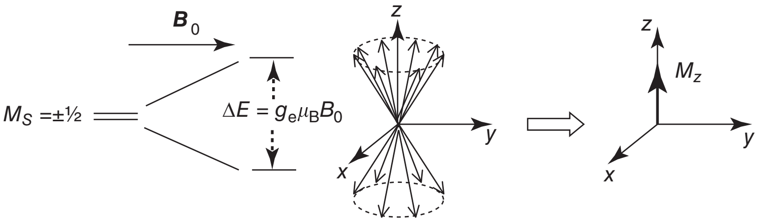

Figure 2 A magnetization arises due to the different population of the electron energy levels corresponding to $M_\mathrm{s} = ½$ and $M_\mathrm{s} = -½$.

The Dipole–Dipole Interaction

The point dipole–point dipole interaction between two particles possessing a magnetic moment is described by the Hamiltonian

$$H = -\frac{\mu_0}{4\pi}\left[\frac{3(\boldsymbol{\mu}_1\cdot\boldsymbol{r})(\boldsymbol{\mu}_2\cdot\boldsymbol{r})}{r^5} - \frac{\boldsymbol{\mu}_1\cdot\boldsymbol{\mu}_2}{r^3}\right]$$

where μ_1 and μ_2 are the interacting magnetic moments and $\boldsymbol{r}$ is the vector connecting the two point dipoles (**Figure 3**). The magnetic moment of the proton is related to its spin I by the relationship $\mu_I = h\gamma_1 I$ where γ_I is the proton magnetogyric ratio and $\hbar = h/2\pi$ is the Planck constant. Therefore, if the dominant interaction is between a proton and the average induced electron magnetic moment, the dipolar Hamiltonian can be written as

$$H = -\frac{\hbar\gamma_I}{4\pi}\left[\frac{3(\boldsymbol{I}\cdot\boldsymbol{r})(\boldsymbol{r}\cdot\boldsymbol{\chi}\cdot\boldsymbol{B}_0)}{r^5} - \frac{\boldsymbol{I}\cdot\boldsymbol{\chi}\cdot\boldsymbol{B}_0}{r^3}\right] = \hbar\gamma_1\boldsymbol{I}\cdot\boldsymbol{\sigma}\cdot\boldsymbol{B}_0$$

where $\boldsymbol{\sigma}$ is called dipolar shielding tensor. In case a reference system is chosen with axes coinciding with the main directions of the $\boldsymbol{\chi}$-tensor and origin on the metal ion, the dipolar shielding tensor is

$$\sigma = -\frac{1}{4\pi r^5}\begin{pmatrix} (3x^2-r^2)\chi_{xx} & 3xy\chi_{yy} & 3xz\chi_{zz} \\ 3xy\chi_{xx} & (3y^2-r^2)\chi_{yy} & 3yz\chi_{zz} \\ 3xz\chi_{xx} & 3yz\chi_{yy} & (3z^2-r^2)\chi_{zz} \end{pmatrix}$$

where χ_{xx}, χ_{yy}, and χ_{zz} are the principal components of the magnetic susceptibility tensor and x, y, and z are the coordinates of the nucleus in that reference system.

Pseudocontact Shift Restraints

The rotational average of the dipole–dipole interaction between the nucleus magnetic moment and the average induced electron magnetic moment causes a shift of the NMR signals, called PCS. It is calculated by taking the average of the values of the dipolar interaction energy along three principal directions, divided by the Zeeman energy $\hbar\gamma_I B_0$, and thus it is given by

$$\delta^{\text{pcs}} = -\frac{1}{3}Tr(\sigma)$$

Therefore, in the case where the reference frame coincides with the main directions of the $\boldsymbol{\chi}$-tensor, with the metal ion in the origin,

$$\delta^{\text{pcs}} = \frac{1}{12\pi r^3}\frac{(3x^2-r^2)\chi_{xx} + (3y^2-r^2)\chi_{yy} + (3z^2-r^2)\chi_{zz}}{r^2}$$

The latter equation can be written in spherical coordinates by using the ϑ and ϕ angles to specify the position of the nucleus in this reference frame,

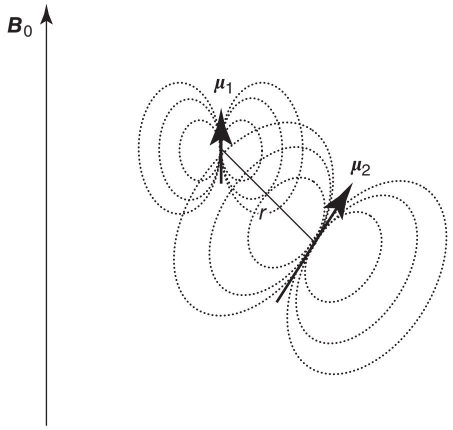

Figure 3 The dipole–dipole interaction between two magnetic moments. The nuclear magnetic moment is along $\boldsymbol{B}_0$, whereas the electron magnetic moment can be along a different direction due to the anisotropy of the magnetic susceptibility tensor.

$$\delta^{\text{pcs}} = \frac{1}{12\pi r^3}\left[\Delta\chi_{\text{ax}}\left(3\cos^2\vartheta - 1\right) + \frac{3}{2}\Delta\chi_{\text{rh}}\sin^2\vartheta\cos 2\phi\right]$$

where $\Delta\chi_{\text{ax}}$ and $\Delta\chi_{\text{rh}}$ are the axial and rhombic anisotropy parameters of the magnetic susceptibility tensor of the metal,

$$\Delta\chi_{ax} = \chi_{zz} - \frac{\left(\chi_{xx} + \chi_{yy}\right)}{2}, \Delta\chi_{rh} = \chi_{xx} - \chi_{yy}$$

It should be noted that the PCS depends only on the anisotropy of $\boldsymbol{\chi}$ and not on its magnitude. If the magnetic susceptibility is isotropic, the rotational average of the dipolar energy is zero, and no PCS occurs.

In conclusion, PCS restraints depend on the coordinates of the protein atom, on the values of the magnetic susceptibility anisotropies, and on the three Euler angles defining the principal frame of the magnetic susceptibility tensor. Figure 4 shows the form of the surface where a nucleus can stay, for a given positive (dark gray) or negative (light gray) value of the PCS and for a given magnetic susceptibility tensor, in the limiting cases of no ($\Delta\chi_{\text{rh}} = 0$) and maximal ($\Delta\chi_{\text{rh}} = 2\Delta\chi_{\text{ax}}/3$) rhombicity.

Relaxation Enhancement Restraints

The recovery to equilibrium of a nuclear spin system is characterized by two time constants, the longitudinal and the transverse relaxation times, indicated by T_1 and T_2, respectively, or by their inverse R_1 and R_2. The longitudinal relaxation time, also called spin–lattice relaxation time, is the time constant for the evolution of the component of the nuclear magnetization along the magnetic field direction toward its equilibrium value. The more numerous and efficient the mechanisms allowing the nuclear spin to jump from one nuclear energy level to another, the shorter the longitudinal relaxation time.

The transverse, or spin–spin, relaxation time is related to the lifetime of the magnetization component in the plane perpendicular to the magnetic field direction, which is zero at equilibrium. The mechanisms causing transverse relaxation comprise those causing longitudinal relaxation, but they are more numerous/efficient, and therefore $R_2 \geq R_1$.

The dipolar interaction energy between the electron spin magnetic moment and the proton magnetic moment can fluctuate in time due to changes in the metal–nucleus distance, for example, detachment of a coordinated molecule bearing the nucleus of interest, reorientation of the complex with respect to the external magnetic field, or changes in the M_z or M_{xy} components of the electron spin magnetic moment (electron relaxation). All these three processes represent mechanisms leading to nuclear relaxation, and thus causing the so-called paramagnetic enhancement of the longitudinal and transverse relaxation rates, $R_{1\text{M}}$ and $R_{2\text{M}}$, respectively.

The resulting equation for $R_{1\text{M}}$ is proportional to the average of the square of the dipolar interaction energy and to the appropriate spectral density functions:

$$R_{1\text{M}} = \frac{2}{15}\left(\frac{\mu_0}{4\pi}\right)^2 \frac{\gamma_I^2 g_e^2 \mu_B^2 S(S+1)}{r^6}\left[\frac{\tau_c}{1 + (\omega_I - \omega_S)^2\tau_c^2} + \frac{3\tau_c}{1 + \omega_I^2\tau_c^2} + \frac{6\tau_c}{1 + (\omega_I + \omega_S)^2\tau_c^2}\right]$$

where $\omega_I = \gamma_I B_0$ is the proton Larmor frequency, ω_S is the electron Larmor frequency ($\omega_S = 658.2\omega_I$), and τ_c is the correlation time related to the mechanisms responsible for relaxation

$$\left(\tau_c^{\text{dip}}\right)^{-1} = \tau_s^{-1} + \tau_r^{-1} + \tau_M^{-1}$$

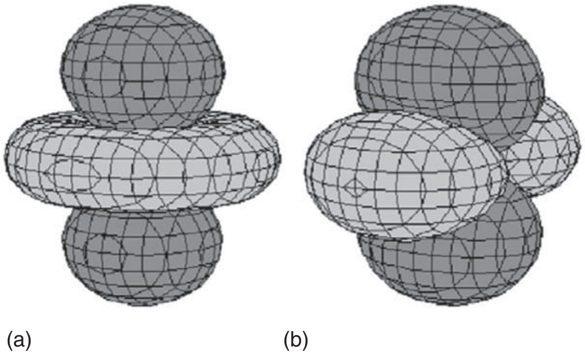
(a) (b)

Figure 4 Surface constraint for a nucleus with a positive (dark gray) or negative (light gray) PCS value in the case of (a) axial paramagnetic susceptibility tensor ($\Delta\chi_{\text{rh}} = 0$) or (b) maximal rhombicity ($\Delta\chi_{\text{rh}} = 2\Delta\chi_{\text{ax}}/3$) of the paramagnetic susceptibility tensor. The metal is located at the origin.

given by the shortest among the electron relaxation time τ_s, the reorientational time τ_r, and the exchange time τ_M. In metalloproteins, τ_c is generally equal to τ_s.

Analogously, the equation for nuclear transverse relaxation rate enhancement is

$$R_{2M} = \frac{1}{15}\left(\frac{\mu_0}{4\pi}\right)^2 \frac{\gamma_I^2 g_e^2 \mu_B^2 S(S+1)}{r^6}\left[4\tau_c + \frac{\tau_c}{1+(\omega_I-\omega_S)^2\tau_c^2} + \frac{3\tau_c}{1+\omega_I^2\tau_c^2} + \frac{6\tau_c}{1+(\omega_I+\omega_S)^2\tau_c^2} + \frac{6\tau_c}{1+\omega_S^2\tau_c^2}\right]$$

In the case of lanthanides and actinides, the term $g_J J(J+1)$, should replace $g_e S(S+1)$.

The former equations, calculated for systems without zero-field splitting and hyperfine coupling with the metal nucleus, are called Solomon equations. Such equations can be used to provide restraints for solution structure determination as they contain a dependence on the distance between the resonating nucleus and the unpaired electron(s) at the sixth power, thus being very effective for locating the metal ion in the protein frame and for determining nuclear–metal distances for protons close to the paramagnetic center.

The modulation of the dipole–dipole interaction of the nuclear spin with the average induced electron magnetic moment $\langle\mu\rangle$ provides a further relaxation contribution. This relaxation mechanism is usually called magnetic susceptibility relaxation or Curie spin relaxation. Such interaction, of course, cannot be modulated by the electron relaxation, since $\langle S_z\rangle$ is already an average over the electron spin states, and therefore the relevant correlation time is determined by τ_r (if τ_M is longer). The contributions to R_{1M} and R_{2M} provided by this mechanism (in the approximation of isotropic magnetic susceptibility) are

$$R_{1M} = \frac{2}{5}\left(\frac{\mu_0}{4\pi}\right)^2 \frac{\omega_I^2 g_e^4 \mu_B^4 S^2(S+1)^2}{(3kT)^2 r^6}\frac{3\tau_r}{1+\omega_I^2\tau_r^2}$$

$$R_{2M} = \frac{1}{5}\left(\frac{\mu_0}{4\pi}\right)^2 \frac{\omega_I^2 g_e^4 \mu_B^4 S^2(S+1)^2}{(3kT)^2 r^6}\left(4\tau_r + \frac{3\tau_r}{1+\omega_I^2\tau_r^2}\right)$$

In the case of lanthanides and actinides, the term $g_J^4\mu_B^4(J(J+1))^2$, or more properly the experimental μ_{eff}^4 value, when available, should replace $g_e^4\mu_B^4(S(S+1))^2$.

The effect of Curie relaxation on R_{2M}, and thus on line widths, is very important in paramagnetic metalloproteins, especially at high magnetic fields, due to the large value of the reorientation time τ_r, compared to the normally shorter electron relaxation time, which appears in the Solomon equation. The effect on R_{1M}, which does not contain nondispersive terms, is instead usually negligible.

Cross-Correlation between Curie and Dipole–Dipole Relaxation Restraints

Another kind of restraint is the cross-correlation arising between the dipole–dipole interaction between two nuclei (for instance, N and H in a protein amide bond) and the dipolar interaction between the magnetic moment of one of the two nuclei and the average induced electron magnetic moment, both the interactions being modulated by the reorientation time. Such cross-correlation contributes to nuclear relaxation.

As for the cross-correlation present in diamagnetic systems between the dipole–dipole interaction and the chemical-shielding anisotropy, the cross-correlation between Curie and dipolar relaxation causes a difference in the line width of the two doublet components of, for example, the amide H (or the amide N). This difference in line width for the amide H, in the approximation of isotropic magnetic susceptibility, is given by

$$\Delta\nu_{1/2}^{\mathrm{CCR}} = \frac{2}{15\pi}\left(\frac{\mu_0}{4\pi}\right)^2 \frac{B_0\gamma_H^2\gamma_N\mu_B^2 g_e^2\hbar S(S+1)}{r^3 r_{HN}^3 kT}\,\frac{3\cos^2\theta_{MHN}-1}{2}\left(4\tau_r + \frac{3\tau_r}{1+\omega_I^2\tau_r^2}\right)$$

where the angle θ_{MHN} is that between the proton–nitrogen direction and the proton–metal ion direction and r is the proton–metal ion distance.

CCR restraints thus structurally depend on the inverse of the metal-proton distance at the third power and on the metal–proton–nitrogen angle. Their magnitude increases with the magnetic field and with the metal magnetic susceptibility, rather than with its anisotropy. Coupling between CH or CC pairs can also give rise to cross-correlation with Curie relaxation.

Self-Orientation Residual Dipolar Coupling Restraints

The dipole–dipole interaction between the magnetic moments of two unlike nuclei is given by

$$H = -\frac{\mu_0}{4\pi}\frac{\hbar^2\gamma_A\gamma_B}{r_{AB}^2} I_z^A I_z^B\left(3\cos^2\gamma-1\right)$$

where r_{AB} is the distance between the two nuclei A and B and γ is the angle between the interspin vector $\boldsymbol{r}$ and the external magnetic field, along which both the nuclear magnetic moments are quantized. The isotropic rotational average value of the dipolar coupling is zero. However, in case the different orientations are not all equally populated, different weights must be considered for the different directions, and therefore an RDC arises

$$\Delta\nu^{\mathrm{rdc}} = \frac{\Delta E}{h} = -\frac{\mu_0 \hbar \gamma_A \gamma_B}{4\pi^2 r_{AB}^3}\left\langle \frac{3\cos^2\gamma - 1}{2} \right\rangle$$

This can be written as a function of an orientation tensor S:

$$\Delta\nu^{\mathrm{rdc}} = -\frac{\mu_0 \hbar \gamma_A \gamma_B}{8\pi^2 r_{AB}^3}\left[S_{zz}\left(3\cos^2\Theta - 1\right) + \left(S_{xx} - S_{yy}\right)\sin^2\Theta \cos 2\Phi\right]$$

where Θ is the angle between the AB vector and the z-axis of the orientation tensor, and Φ is the angle which describes the position of the projection of the AB vector on the xy-plane of the $\boldsymbol{S}$-tensor, relative to the x-axis.

As noted already, the presence of an anisotropic metal magnetic susceptibility induces PCS. It can also contribute to partial orientation of the molecule in high magnetic fields.

The degree of alignment of a molecule relative to a magnetic field can be described by the principal components of the orientation tensor $\boldsymbol{S}$, defined as

$$S_{ii} = \frac{\displaystyle\int \frac{3\cos^2\alpha - 1}{2}\exp\left[-\frac{E^{\mathrm{aniso}}(\alpha,\beta)}{kT}\right] d\cos\alpha\, \mathrm{d}\beta}{\displaystyle\int \exp\left[-\frac{E^{\mathrm{aniso}}(\alpha,\beta)}{kT}\right] d\cos\alpha\, \mathrm{d}\beta}$$

where α and β are the spherical angles describing the direction of $\boldsymbol{B}_0$ in the molecular frame and $E^{\mathrm{aniso}}(\alpha,\beta)$ is the anisotropic energy of the molecule in a field B_0. Therefore, one obtains

$$S_{ii} = \frac{3}{2}\frac{B_0^2}{15\mu_0 kT}\left(\chi_{ii} - \bar{\chi}\right)$$

The RDC due to paramagnetism can thus be expressed as a function of $\Delta\chi_{\mathrm{ax}}$ and $\Delta\chi_{\mathrm{rh}}$,

$$\Delta\nu_{\mathrm{rdc}}^{\mathrm{para}} = -\frac{1}{4\pi}\frac{B_0^2}{15kT}\frac{\gamma_A \gamma_B \hbar}{2\pi r_{AB}^3}\left[\Delta\chi_{\mathrm{ax}}\left(3\cos^2\Theta - 1\right) + \frac{3}{2}\Delta\chi_{\mathrm{rh}}\sin^2\Theta\cos 2\Phi\right]$$

where the angles Θ and Φ are defined in the principal frame of the paramagnetic susceptibility tensor. $\Delta\nu_{\mathrm{rdc}}^{\mathrm{para}}$ represents the difference in the measured ^1J values between the paramagnetic system and a diamagnetic analog.

The functional form for PCS and RDC is the same. It is, however, important to note that the angles in the equation for RDC define the orientation of the coupled nuclei independently of their position with respect to the metal ion. Figure 5 shows the surface restraint determined by a given value of the RDC and a given magnetic susceptibility tensor with no and maximal rhombicity.

Contact Shift (and Hyperfine Shift) Restraints

CSs are due to the presence of unpaired electron spin density onto the resonating nucleus, which occurs through direct spin delocalization and/or spin polarization. CSs contain structural information because they are somehow related to chemical bonds, although only in a few cases this information can be translated into structural constraints.

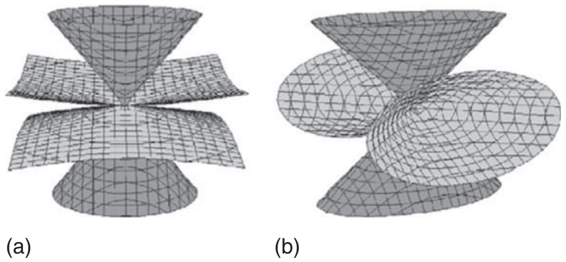
(a) (b)

Figure 5 Surface constraint for a nucleus with a positive (dark gray) or negative (light gray) RDC value in the case of (a) axial magnetic susceptibility tensor or (b) maximal rhombicity of the magnetic susceptibility tensor. The coupled nucleus is located on the origin.

In the case of $Fe_4S_4{}^{2+}$ clusters (**Figure 6(a)**), it has been found that the CS of the βCH_2 protons of coordinated cysteines depends on the FeSCH dihedral angle θ as

$$\delta^c = a\sin^2\theta + b\cos\theta + c$$

where $a \cong 10.3$, $b \cong -2.2$, and $c \cong 3.9$ ppm. The dominant dependence on $\sin^2\theta$ is ascribed to the fact that the spin density is in a p-orbital of the S-atom orthogonal to the Fe–S bond (**Figure 6(b)**). The relative values of the constant c with respect to a give an idea of the importance of the processes of electron delocalization through the σ-bond of Fe–S with respect to the π-bond of Fe–S. In these clusters, the observed hyperfine shifts are essentially CSs in origin.

The hyperfine shifts (given by the sum of contact and pseudocontact contributions) of heme methyl protons are given by the following heuristic equation in low-spin Fe(III) heme proteins containing a histidine and a cyanide as axial ligands, at 298 K,

$$\delta_i = a\sin^2(\gamma_i - \alpha) + b\cos^2(\gamma_i + \alpha) + c$$
$$a \cong 18.4, \quad b \cong -0.8, \quad c \cong 6.1$$

where γ_i is the angle between the metal–pyrrole II axis and the metal–ith-methyl direction, and α is the angle between the metal–pyrrole II axis and the direction of the histidine ring plane (**Figure 7**). In fact, the unpaired electron occupies one metal 3d-orbital that has the correct symmetry to form π-bonds with the axial ligand, and thus the contact contribution will be zero when the methyl protons lie in the nodal plane, and maximal when the methyl protons lie along the direction of the axial π-interaction, and thus $\delta_i^c \propto \sin^2(\gamma_i - \alpha)$. On the other hand, since the z-axis of the magnetic susceptibility tensor is always approximately perpendicular to the heme plane, the PCS is proportional to a function of the type $\delta^{pcs} \propto k\cos 2\phi - 1$, with the χ_x-axis rotated clockwise from the metal–pyrrole direction by an angle which is the same in magnitude, but opposite in direction, to the angle α. Therefore, $\phi = \gamma_i + \alpha$, and the equation given above is obtained.

Finally, the hyperfine shifts of methyl protons are given by the following heuristic equation in low-spin Fe(III) heme proteins containing two histidines as axial ligands:

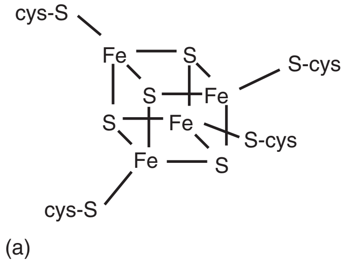

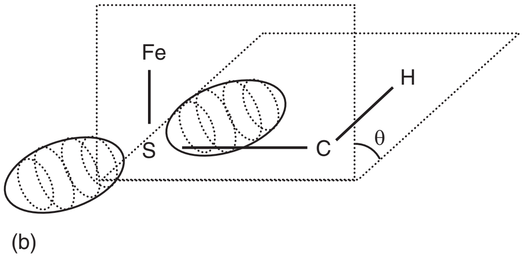

Figure 6 (a) Cybane-type Fe_4S_4 cluster. (b) Dihedral angle θ between the Fe–S–C plane and the S–C–H plane in the case of the spin density being in a p-orbital of the S-atom orthogonal to the Fe–S bond.

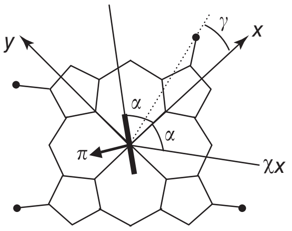

Figure 7 The γ angles for the four methyl groups (indicated with a dot) are defined as the angles between the metal–methyl *i*th vector and the *X*-axis, taken along the metal–pyrrole II direction. The angle α defines the direction of the histidine ring plane.

$$\delta_i = \cos\beta\left[a\sin^2(\gamma_i - \alpha) + b\cos^2(\gamma_i + \alpha) + c\right] + d\sin\beta$$

$$a \cong 38.8, \quad b \cong -10.5, \quad c \cong -1.1, \quad d \cong 9.4$$

where α is the angle between the bisector of the angle β and the metal–pyrrole II axis, and β is the acute angle between the two histidine planes.

Similar considerations can be made for Fe(II) heme proteins with a single histidine in an axial position, when the electron configuration is high spin and the shifts of the methyl protons are determined by a mixture of σ- and π-delocalization mechanisms.

Collecting the Paramagnetism-Based Restraints

The NMR parameters that can be obtained by performing NMR experiments are the chemical shift, the longitudinal relaxation rate, and the transverse relaxation rate. For a given nucleus, the chemical shift is defined as the resonating frequency of the nucleus with respect to a reference signal (in Hz). The chemical shifts result from the sum of two contributions: the diamagnetic shift, arising from the shielding of the observed nucleus from the external magnetic field due to electrons around, and the paramagnetic shift or hyperfine shift, which consist of the pseudocontact and the contact contributions:

$$\delta^{\text{exp}} = \delta^{\text{dia}} + \delta^{\text{c}} + \delta^{\text{pcs}}$$

As seen earlier, the contact contribution is present only for nuclei close to the paramagnetic center, since it can arise only if electron spin density can be delocalized on the investigated nuclei. Therefore, only the pseudocontact term can affect the hyperfine shift of amino acids that are not directly bonded to the metal center or H-bonded to the donor atoms.

In order to calculate δ^{pcs}, it is necessary to evaluate δ^{dia}. This can be done, to a good approximation, by performing the measurements on the analog diamagnetic protein, obtained by removing the paramagnetic metal ion, by substituting the metal ion with a diamagnetic metal with the same charge, or by reducing the paramagnetic metal to a diamagnetic state.

PCSs have been measured, among others, in many low-spin iron(III) heme-containing proteins (Figure 8 shows those measured in cytochrome b_5) and in lanthanide-substituted calcium-binding proteins (e.g., calmodulin, parvalbumin, and calbindin). As noted previously, their magnitude depends on the magnetic susceptibility anisotropy of the metal. Estimates of the latter are reported in Table 1 for some metal ions. Figure 9 shows the observed PCS in the protein calbindin D_{9k} after substitution of Ce(III), Yb(III), or Dy(III) in the C-terminal calcium-binding site. Metal ions characterized by a small magnetic anisotropy (e.g., Ce(III)) permit one to obtain values only for nuclei at short distances, whereas metal ions characterized by a large magnetic anisotropy (e. g., Dy(III)), although they do not provide information for nuclei close to the metal ion, due to the excessive line-broadening caused by Curie relaxation, permit the observation of values for nuclei that are much farther away from the metal.

Once the PCSs have been used to determine the magnetic susceptibility tensor and the structure is known, the contact contribution to the hyperfine shifts for atoms in amino acids close to the metal ion can be obtained. In fact, the pseudocontact contribution for such atoms can be calculated and subtracted from the hyperfine shift.

Coupled nuclei experience ^1J splittings of the observed nucleus signals. Such splittings can be measured in HSQC spectra or in J-modulated experiments, and are given by the sum of the diamagnetic ^1J contribution, due to the scalar coupling and diamagnetic RDC, and the paramagnetic contribution. The values for $\Delta\nu_{\text{rdc}}^{\text{para}}$ can be obtained after subtraction of the ^1J measured at the same field and temperature on the analog diamagnetic protein, obtained by removing the paramagnetic metal ion, by substituting the metal

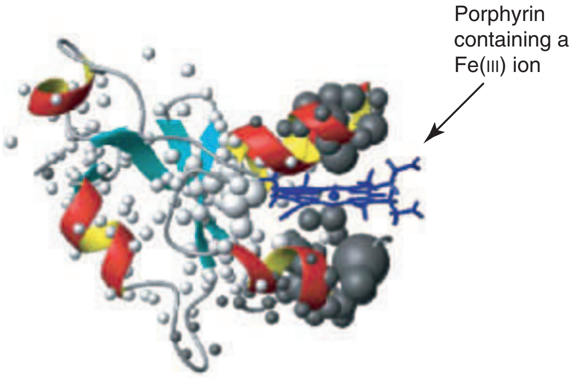

Figure 8 Observed PCS for the heme protein cytochrome b_5. The size of the balls is proportional to the magnitude of the negative (light gray) or positive (dark gray) PCS.

Table 1 Magnetic susceptibility and pseudo-contact shifts for some metal ion

	$\chi_{av}(10^{-32}\ m^3)$	$\Delta\chi_{ax}(\%)$	δ^{pcs} for $r = 10$ Å and $\theta = 0°$ (ppm)
Fe(III) HS	31	10	1.6
Fe(III) LS	3	80	1.3
Fe(II)	21	10	1.1
Co(II)	13	40	2.8
Ce(III)	5	35	0.9
Dy(III)	99	35	18.4
Yb(III)	15	45	3.6

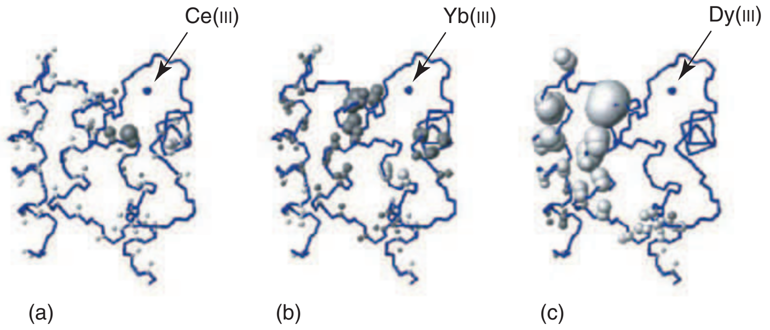

Figure 9 Observed PCS for the N and HN nuclei of the protein calbindin D_{9k} after substitution of (a) Ce(III), (b) Yb (III), or (c) Dy(III) in the C-terminal metal binding site. The size of the balls is proportional to the magnitude of the negative (light gray) or positive (dark gray) PCS.

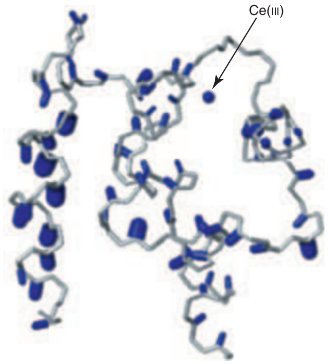

Figure 10 Observed self-orientation RDC for the HN atoms of the protein calbindin D_{9k} after substitution of Ce(III) in the C-terminal metal binding site.

ion with a diamagnetic metal with the same charge, or by reducing the paramagnetic metal to a diamagnetic state. Paramagnetic RDCs have been measured for many metalloproteins. Those related to the protein Ce(III)-calbindin D_{9k} are shown in Figure 10.

Relaxation rates are also measured as the sum of the diamagnetic and the paramagnetic contributions. Again, the diamagnetic contribution can be evaluated by performing measurements on the diamagnetic analog of the protein, by removing the paramagnetic metal ion or by substituting it with a diamagnetic one. Another way to estimate the diamagnetic contribution consists in taking an average among all the experimental relaxation rates that are below a given threshold value in the paramagnetic metalloprotein. In fact, R_{1M} is proportional to r^{-6}, and thus it becomes negligible for nuclei far from the paramagnetic center, whereas it is dominant for nuclei close to the paramagnetic center.

Transverse relaxation rates are related to signal line widths. The difference in the line width (in Hz) measured at half-height of, for example, the two components in the proton dimension of the HN doublet in the HSQC spectra of ^{15}N enriched paramagnetic metalloproteins is given by $\Delta\nu_{1/2}^{ccr}$, and it can be used as an additional restraint for protein solution structure determination. Figure 11**(a)** reports the observed values for amide proton cross-correlations between Curie and dipolar relaxation in the Ce(III)-substituted protein calbindin D_{9k}, and Figure 11**(b)** reports the CCR values observed in metaquomyoglobin.

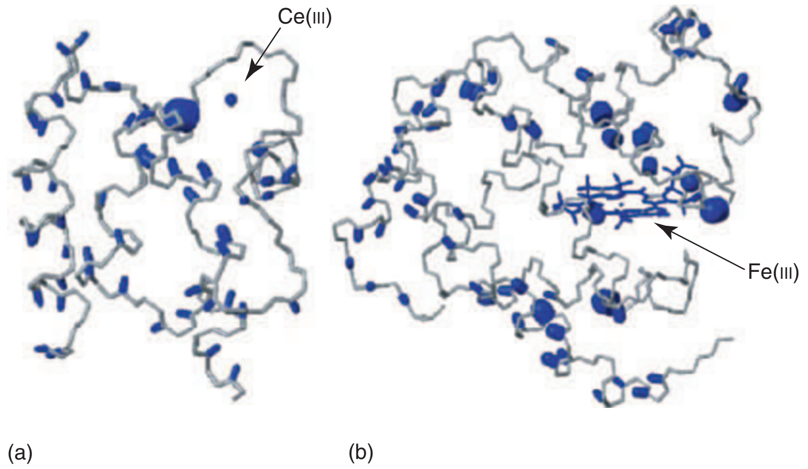

Figure 11 Observed CCR for the HN atoms (a) of the protein calbindin D_{9k} after substitution of Ce(III) in the C-terminal metal binding site, (b) of met-myoglobin, a heme protein containing high-spin Fe(III).

Solution Structure Determination Programs

Calculations of the solution structure of metalloproteins by employing paramagnetism-based restraints are normally performed using a modified version of the program CYANA, called PARAMAGNETIC CYANA, or the Xplor-NIH package. Both programs use molecular dynamics for energy minimization combined with a simulated annealing algorithm to calculate a family of structures starting from randomly generated conformers. Any metal ion and the relative magnetic susceptibility tensor axes are represented using pseudo-atoms as shown in Figure 12.

The paramagnetism-based restraints are introduced by calculating a pseudopotential E_l, for each class of new restraints

$$E_l = \sum_i w_i[\max(|X_{i,\mathrm{obs}} - X_{i,\mathrm{calc}}| - \mathrm{tol}_i, 0)]^2$$

to be added to the global target function, which is the quantity to be minimized. The index i runs over all experimental data of the considered class of restraints; tol indicates the tolerance, and w_i the weighting factor for that restraint. $X_{i,\ \mathrm{obs}}$ represents the experimental data and $X_{i,\ \mathrm{calc}}$ the calculated values in the present protein configuration according to the equations provided above.

PARAMAGNETIC CYANA and PARArestraints for Xplor-NIH use the PCS and RDC restraints by keeping fixed the values of the magnetic susceptibility anisotropies during the annealing process. These parameters ($\Delta\chi_{\mathrm{ax}}$ and $\Delta\chi_{\mathrm{rh}}$), which can be initially estimated from theoretical predictions, can be obtained by fitting the observed data on the protein structure (using, for instance, the program FANTEN). Therefore, both their values and the protein structure are actually obtained by a few cycles of structure calculations and fit on the protein structure, until convergence is reached.

Recovering Information on Structure Heterogeneity

Several proteins can experience some conformational variability, so that their structure cannot be represented by a single conformation. The paramagnetism-based restraints are very effecting in providing evidences of this conformational heterogeneity.

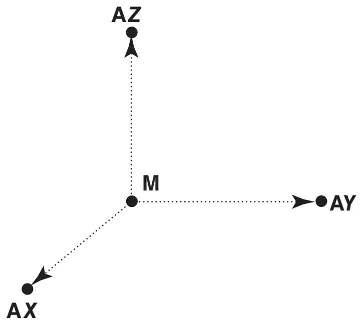

Figure 12 A pseudoresidue is defined containing pseudo-atoms needed to represent in the protein frame the position of the metal ion and the directions of the principal axes of the magnetic susceptibility anisotropy tensor.

The paramagnetic relaxation enhancements are averaged over conformations that interconvert at rates larger than the nuclear relaxation rate, and larger than the differences in nuclear chemical shifts among the different conformations. Due to the r^{-6} distance dependence, the contributions to R_{1M} and R_{2M} from conformations where r is small are much larger than from conformations where r is large. Experimental paramagnetic relaxation enhancements can thus monitor the occurrence of lowly populated protein conformations with nuclei much closer to the paramagnetic metal than in the highly populated states.

In the presence of conformational variability, PCSs and RDCs are averaged over the values corresponding to the different conformations sampled by the system (if the interconversion rate is larger than the differences in nuclear chemical shifts among the different conformations). The measurement of paramagnetic RDCs can provide a quick way to estimate the presence of conformational rearrangement between the protein domain containing a paramagnetic ion and any other domain. In fact, in rigid systems, the RDC-determined magnetic susceptibility anisotropy $\Delta\chi_{(ax)}$ must be the same for all domains, whereas, in the case of interdomain mobility, the RDCs of the domain without the metal provide a reduced magnetic susceptibility anisotropy, as a result of the conformational averaging.

Recovering the structural ensemble from average data is, in mathematical terms, an ill-posed inverse problem, which admits an infinite number of solutions. In fact, we can determine possible ensembles of conformations providing averaged PCS, RDC, and/or R_{1M} and R_{2M} values in agreement with the experimental data. However, there is an infinite number of ensembles which may agree equally well with the experimental data.

Ensemble averaging approaches can be used to estimate the extent of the conformational heterogeneity and retrieve some conformations which may be representatives of the protein structure variability. This can be done by recovering the maximum entropy solution or by recovering ensembles composed of the smallest number of conformations providing agreement with the experimental data. To evaluate how much a given conformation can contribute at most to the experimental average, the Maximum Occurrence (MaxOcc) of conformations can be determined. The MaxOcc is defined as the largest weight that a conformation can have within any ensemble and be still in agreement with the experimental data. Using an analogous approach, the MaxOcc can also be calculated for ensembles of conformationally close structures.

Paramagnetic Tagging of Diamagnetic Proteins

The information content of paramagnetism-based restraints is so effective that diamagnetic proteins are sometimes conveniently tagged with paramagnetic metal complexes, so that PCS and/or RDC data can be measured. Lanthanide tags are mostly used because many of them have the largest magnetic susceptibility anisotropy, and thus are those providing the largest PCSs and RDCs; furthermore, the whole series of lanthanide ions (diamagnetic as well as paramagnetic) can be replaced in the same position, so that multiple datasets of paramagnetic data can be easily obtained.

A lanthanide binding tag can be genetically encoded and expressed as fusion tag together with the protein, or can be a synthetic tag that ligates specific residues. Tag rigidity is an important requisite, because the internal mobility of a tag causes a reduction in the amplitude of the RDCs (which implies a smaller signal-to-noise ratio) and provides averaged PCSs perturbed by this mobility. Rigidity can be achieved (1) by two-point attachment of the tag to nonmobile residues on the surface of the protein, through disulfide bridges, after cysteine replacement of the protein residues at the desired binding positions; (2) by anchoring to the target protein in a first position via a disulfide bridge and in a second position through the N-terminal fusion, (3) by a single covalent bond and additional coordination of the paramagnetic ion by an amino acid of the protein, or (4) by a bulk metal ion binding cage attached through a single covalent bond.

Conclusion

It has been shown that paramagnetism-based restraints can provide relevant information for solution structure determination of paramagnetic metalloproteins, both around the metal ion and in the whole protein. CS can, in fact, identify the metal ligands and can provide dihedral angle restraints on the metal ligands. PCSs contain information on the coordinates of the metal ion and on the position of the protein atoms in the frame of the magnetic susceptibility tensor. Nuclear relaxation rates provide metal–nucleus distances. Cross-correlations contain information on distances and angles among the metal ion and coupled nuclei. Selforientation RDCs provide information on the orientations of internuclear vectors in the magnetic susceptibility frame. All these restraints are vital for obtaining information around the metal ion, where it is usually missing, and can actually be precious to increase the accuracy of the protein structure. Furthermore, it is demonstrated that they provide enough information to be an alternative to classical diamagnetic restraints for protein solution structure determination.

Further Reading

Berliner LJ and Reuben J (1993) *Biological Magnetic Resonance*. vol. 12, New York: Plenum, pp.1–78.
Bertini I, Luchinat C, and Parigi G (2001) *Solution NMR of Paramagnetic Molecules*. Amsterdam: Elsevier.
Bertini I, Luchinat C, and Parigi G (2002) Magnetic susceptibility in paramagnetic NMR. *Prog. Nucl. Magn. Reson. Spectrosc.* 40: 249–273.

Bertini I, Luchinat C, Parigi G, and Pierattelli R (2008) Perspectives in paramagnetic NMR of metalloproteins. *Dalton Trans.* 3782–3790.
Bertini I, McGreevy KS, and Parigi G (eds.) (2012) *NMR of Biomolecules: Towards Mechanistic Systems Biology*. Weinheim, Germany: Wiley-VCH.
Bertini I, Turano P, and Vila AJ (1993) NMR of paramagnetic metalloproteins. *Chem. Rev.* 93: 2833–2932.
Clore GM and Iwahara J (2009) Theory, practice, and applications of paramagnetic relaxation enhancement for the characterization of transient low-population states of biological macromolecules and their complexes. *Chem. Rev.* 109: 4108–4139.
Eaton DR, Fischer RD, Hawkins CJ, et al. (1973) *NMR of Paramagnetic Molecules*. New York: Academic Press.
Fragai M, Luchinat C, Parigi G, and Ravera E (2013) Conformational freedom of metalloproteins revealed by paramagnetism-assisted NMR. *Coord. Chem. Rev.* 257: 2652–2667.
Keizers PHJ and Ubbink M (2011) Paramagnetic tagging for protein structure and dynamics analysis. *Prog. Nucl. Magn. Reson. Spectrosc.* 58: 88–96.
Kurland RJ and McGarvey BR (1970) Isotropic NMR shifts in transition metal complexes calculation of the Fermi contact and pseudocontact terms. *J. Magn. Reson.* 2: 286–301.
La Mar GN (1995) *NMR of Paramagnetic Macromolecules*. Dordrecht NATO ASI series: Kluwer Academic.
Markley JL, Ulrich EL, Westler WM, and Volkman BF (2003) Macromolecular structure determination by NMR spectroscopy. *Methods Biochem. Anal.* 44: 89–113.
Ming L-J (2000) Nuclear magnetic resonance of paramagnetic metal centers in proteins and synthetic complexes. In: Que L Jr. (ed.) *Physical Methods in Bioinorganic Chemistry*, pp. 375–464. Sausalito, CA: University Science Books.
Osborne MJ, Crowe D, Davy SL, Macdonald C, and Moore GR (1997) NMR of paramagnetic proteins. *Methods Mol. Biol.* 60: 233–269.
Pintacuda G, John M, Su XC, and Otting G (2007) NMR structure determination of protein–ligand complexes by lanthanide labeling. *Acc. Chem. Res.* 40: 206–212.
Ravera E, Salmon L, Fragai M, Parigi G, Al-Hashimi H, and Luchinat C (2014) Insights into domain–domain motions in proteins and RNA from solution NMR. *Acc. Chem. Res.* 47: 3118–3126.
Turner DL, Brennan L, Chamberlin SG, Louro RO, and Xavier AV (1998) Determination of solution structures of paramagnetic proteins by NMR. *Eur. Biophys. J. Biophys. Lett.* 27: 367–375.

Photosynthesis, Physics of[☆]

JL Herek, FOM Institute for Atomic and Molecular Physics, Amsterdam, The Netherlands
FT Mahi, Trinity College Dublin, Dublin, Ireland

© 2017 Elsevier Inc. All rights reserved.

This is an update of J.L. Herek, F.T. Mahi, Photosynthesis, Physics of, Reference Module in Materials Science and Materials Engineering, Elsevier, 2017, ISBN 9780128035818, https://doi.org/10.1016/B978-0-12-803581-8.00996-6.

Introduction 731
Photosynthetic Machinery 731
Harvesting Light 732
Antenna Action: Energy Transfer 733
Energy Conversion and Storage 736
From Natural to Artificial Photosynthesis 737
References 738
Further Reading 738

Introduction

Photosynthesis is the transformation of light energy into fuel that drives essential life processes in a variety of organisms. The physics of photosynthesis is photophysics: the collection and handling of sunlight and its conversion to a more stable form of energy. The subsequent utilization of this light energy involves a series of chemical reactions, which taken together comprise the global biological function of photosynthesis. In this article, the focus is on the fundamental steps of photosynthesis. The article begins by looking at the nanoscale machines involved, and then follows the path of an absorbed photon of sunlight as it journeys through the photosystem until eventually being converted into chemical potential.

It is worth bearing in mind that the total time of this phase of photosynthesis is not more than 100 ps, yet it is packed with numerous small steps, each of which has now been resolved in exquisite detail. Since the 1980s, photosynthetic complexes have been crystallized and analyzed to the atomic level. At the same time, lasers have been replacing the Sun in laboratory studies with increasingly better time resolution, such that one can now initiate and follow the flow of energy and charge in real time. This combination of detailed structural and dynamic information has opened a new window on photosynthesis, revealing the importance of these fundamental physical processes on the overall biological function.

Photosynthetic Machinery

Photosynthesis occurs in plants, algae, and some bacteria. The photosynthetic apparatus of all these organisms contains two key components responsible for the primary photophysics: light-harvesting (LH) complexes and reaction centers (RCs). Both are sophisticated pigment–protein structures located within cell membranes, and while they are necessarily coupled, each has a unique task. The light-harvesting complexes capture photons and transfer the solar energy both within and between complexes until it reaches the reaction centers, where this energy is then used to shuttle electrons across the photosynthetic membrane.

The essential components of photosynthesis can be viewed as nanoscale machines arranged in a complex web (rather than a linear assembly line operation) for optimal performance. Fig. 1 shows the photosynthetic apparatus responsible for collection and conversion of solar energy for the case of purple nonsulfur bacteria. These primitive organisms serve as prototype species for studies of the physics of photosynthesis. Unlike plant systems, the various components of the photosynthetic apparatus in these bacteria can be easily isolated and purified. In some species, these components have been crystallized, allowing atomic-level structural information to be extracted. Also, the genetic makeup of these systems is known, allowing site-specific mutagenesis in which individual amino acids in the protein matrix can be altered. Such mutants are invaluable in studies aimed at detailed structure–function relations.

Fig. 1 shows schematically a top-down look at the photosynthetic membrane of purple bacteria, based on real structural data. The ring-like structures are light-harvesting (LH) complexes. These complexes contain cylindrical aggregates of alpha-helical proteins (not shown) that span the lipid bilayer membrane and noncovalently bind the pigment molecules in circular or elliptical arrays. Nestled within one of these rings is another pigment–protein complex, the so-called reaction center (RC). This complex contains two branches with near mirror symmetry, also spanning the photosynthetic membrane. The overall supramolecular aggregate of peripheral light-harvesting complexes LH2 and core complexes containing the RC and surrounding LH1 complex is called the photosynthetic unit (PSU), though the ratio of LH2 to LH1-RC varies according to growth conditions such as temperature and light intensity.

[☆] *Change History*: May 2016. F.T. Mahi added Abstract, Keywords, Figures and expanded text with additional review materials. Updated the list of references.

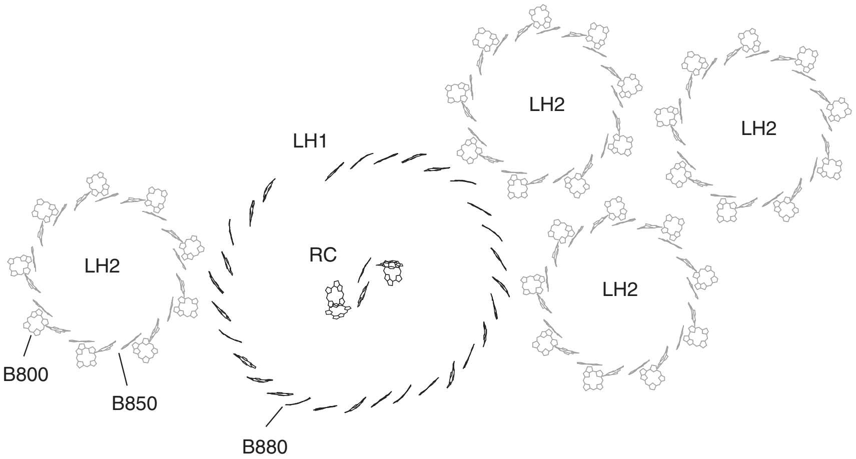

Fig. 1 Schematic representation of the photosynthetic machinery of purple nonsulfur bacteria, based on crystallographic data. For clarity, the protein and carotenoid molecules are omitted. The peripheral light-harvesting complex LH2 contains two circular aggregates of bacteriochlorophyll molecules, labeled B800 and B850 according to their characteristic absorption maxima at 800 and 850 nm. Likewise, the larger core light-harvesting complex LH1 contains a broken ellipse of aggregated bacteriochlorophylls, the B880 ring. Nestled within the LH1 complex is the photosynthetic reaction center (RC). The supramolecular aggregate of LH2, LH1, and RC complexes is called the photosynthetic unit.

In the intricate network of molecules arranged within the protein matrix, the function is determined by the location. While a chlorophyll molecule in the reaction center plays an essential role in photochemistry, a chlorophyll molecule located in an antenna complex functions in a completely different manner. These functions are described in the following sections.

Harvesting Light

The first step of photosynthesis is the collection of sunlight. How is light captured by living things? Illuminated molecules may either reflect or absorb incident light. Molecules that are especially capable of absorbing light in the visible region of the spectrum and give color to living things are called pigments. The pigments of photosynthesis are primarily chlorophylls, of which there are many different varieties. These molecules efficiently absorb light in the red and blue regions of the solar spectrum, while reflecting away most of the green (hence the predominance of this color in Nature). In addition, a variety of other less-abundant pigments enhance the light-absorbing capabilities of photosynthetic organisms by capturing other regions of the visible spectrum. Carotenoids, for example, have strong absorption in the blue-green region, but reflect away the yellow to red wavelengths. These pigments are largely responsible for the autumn "colorama," showcasing the presence of the carotenoids that becomes gloriously apparent as the chlorophyll in the leaves of the trees begins to break down.

When a molecule absorbs a photon of visible light, one of its electrons is promoted to a higher energy state. The molecule is then said to be in an electronic excited state. The wavelengths of light that are capable of creating excited states for a given molecule are given by an absorption spectrum. In Fig. 2, the absorption spectra of chlorophyll and carotenoid molecules are shown, in comparison with the solar irradiance spectrum on Earth. The entire visible range of light (400–700 nm) as well as much of the near-infrared (up to 1000 nm) is used to drive photosynthesis in different organisms.

Understanding the excited states in photosynthesis is a key area of biophysics research, as it is from these states that all physical processes such as energy transfer and trapping as well as chemical reactions may occur. The nature of the excited state depends not only on the characteristic properties of the individual molecule, but also on its specific location within the photosynthetic complex. Interactions between neighboring pigments and, to some extent, the surrounding protein can shift the excited-state energies and thereby affect dynamics. For example, in photosynthetic purple bacteria, the primary pigment is bacteriochlorophyll. The main absorption of this pigment when isolated in solution is at ~780 nm. In the photosynthetic unit, however, the absorption band shifts according to its location (and corresponding function): in the peripheral light-harvesting complex (LH2), there are two distinct binding sites for bacteriochlorophyll, giving rise to absorption bands at 800 and 850 nm, respectively. These binding sites are correspondingly labeled B800 and B850; see Fig. 1. In the B800 ring, the individual pigments are well separated (by ~20 Å), and the spectral properties are determined mainly by weak interactions with the protein environment. In the B850 ring, however, the pigments are tightly packed in a "waterwheel" arrangement; the further red-shifted absorption of the molecules here is due to the much stronger excitonic coupling between adjacent pigments. The ring structure also enhances absorption and acts as an energy storage unit. In the LH1 core light-harvesting complex, which directly couples to the reaction center, the bacteriochlorophyll absorb

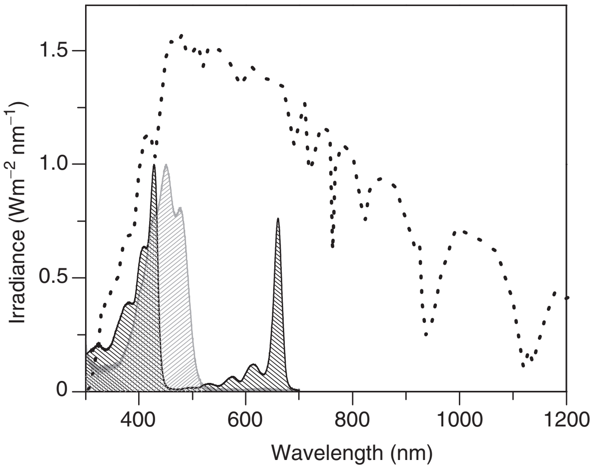

Fig. 2 Solar irradiance spectrum and absorption spectra of photosynthetic pigments. Dotted curve: Intensity profile of sunlight measured on the Earth's surface. Black hatch: Absorption spectrum of chlorophyll, the most abundant photosynthetic pigment in Nature. Gray hatch: Absorption spectrum of the carotenoid beta-carotene, an accessory pigment. The spectra of the pigments are in absorption units (scale not shown).

at 880 nm, and have an arrangement similar to the B850 ring. This tuning of absorption properties with location is crucial to the overall function of photosynthesis, creating an energy hierarchy that efficiently funnels light energy into the reaction center.

Grieco *et al.* (2015) has investigated and presented a new model for the excitation energy distribution in plant thylakoids. Also assigned a role to the fraction of Light Harvesting Complex II denoted as "extra-LHCII." Extra LHCII ensures energetic connectivity between Photo System II (PSII) and Photo System I (PSI). The whole LHCII constitutes an antenna "lake" in which PSII and PSI are embedded. LHCII phosphorylation is a regulator, but not a necessity, for the connectivity. Fig. 3 illustrates the process.

Antenna Action: Energy Transfer

While the reaction center is the hotspot for photosynthetic energy conversion, by itself it can only capture a few photons per second (given its absorption cross section, the solar flux, and its overlap with the solar irradiance spectrum). Yet, the turnover time of the reaction center function is of the order of 10 ms, that is, it is capable of a much higher throughput. Hence, an antenna system evolved to catch extra photons and feed them to the reaction center.

Antenna networks are highly regulated to maximize the efficiency of energy collection while at the same time avoiding photodamage that can occur when too much light is absorbed. These functions occur by rapid and directional energy transfer reactions. Following absorption of solar light, the pigment molecules are in electronically excited states. In principle, this excitation energy may then be used directly to drive a chemical reaction. However, in photosynthesis, the energy is first transferred between many molecules, over quite large distances, before it arrives at the site of action.

The antenna system increases the amount of sunlight that can be absorbed compared to a single pigment, thereby increasing the number of photons available for photochemistry. A photosynthetic antenna is analogous to a satellite dish, collecting energy from a large area and concentrating it at a small receiver site (the reaction center), thereby greatly increasing the signal strength. Antenna networks contain an additional 100–10,000 pigments per reaction center. Molecules located in the antenna do not perform any chemistry, but simply transfer the collected energy between each other in a well-defined and efficient manner. For optimal functioning, energy collected by the antenna pigments must reach the reaction center within ~100 ps; hence, the transfer between individual pigments should be of the order of 1 ps or less. This transfer process is purely physical and is governed by the energetic interactions between molecules.

Advances in ultrafast laser spectroscopy have allowed detailed measurements of these energy transfer dynamics in real time. In the laboratory, a femtosecond laser replaces the sun and initiates the process of interest. As the absorption of the antenna pigments is determined by their location, the laser may be tuned to be resonant with a given molecule, thereby isolating a specific energy transfer step. For example, in the LH2 complex of purple bacteria, the B800 to B850 energy transfer can be targeted by tuning an excitation pulse to 800 nm, and then probing the arrival of energy by monitoring the buildup of the transient absorbance signal at 850 nm with a second delayed femtosecond pulse. By varying the timing of the probe pulse, the dynamics of the process may be followed at discrete time steps, which, when combined, yield a kinetics trace.

All photosynthetic systems have an inherent energy gradient that dictates the flow of energy among the pigments. In purple bacteria, this is given by B800→B850→B880→RC (note that the valuable contributions of carotenoids, which perform accessory

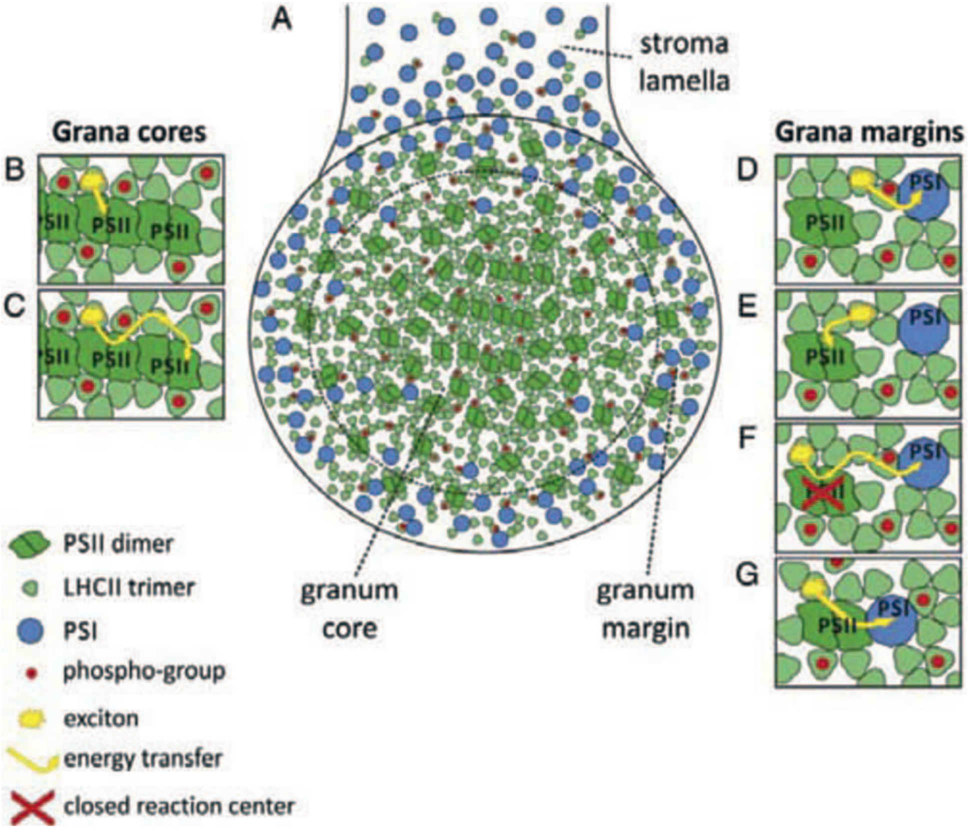

Fig. 3 Schematic representation of the distribution of photosystems and their antennae in the thylakoid membrane (A) and the possibilities of excitation energy flow in the PSII and LHCII rich grana core ((B)–(C)) and in the more exposed domains with high amount of PSI also ((D)–(F)). (A) PSII–LHCII complexes and the PSI complexes are enriched in the grana core and peripheral domains of thylakoid disks, respectively. Both PSII and PSI are present at peripheral areas of the grana disks. A considerable amount of LHCII trimers is interposed between the photosystems and all LHCII trimer populations are partially phosphorylated (for clarity, the phosphorylation of PSII is not shown). (B) Light is absorbed by an LHCII trimer, thus forming an excitation energy packet (exciton) that is transferred to an open PSII center. (C) Exciton moves from LHCII to a closed PSII and subsequently reaches an open PSII through LHCII connectivity. Toward the peripheral areas of the grana disks ((D)–(F)), the probability that exciton can move through LHCII connectivity to PSI increases. In the absence of LHCII phosphorylation, the probability that exciton can enter to PSI is low. The LHCII phosphorylation, however, modulates the molecular interaction in the antenna lake to enhance energy trapping by PSI (D). (G) PSII and PSI can be in contact, allowing direct energy spillover from PSII to PSI.

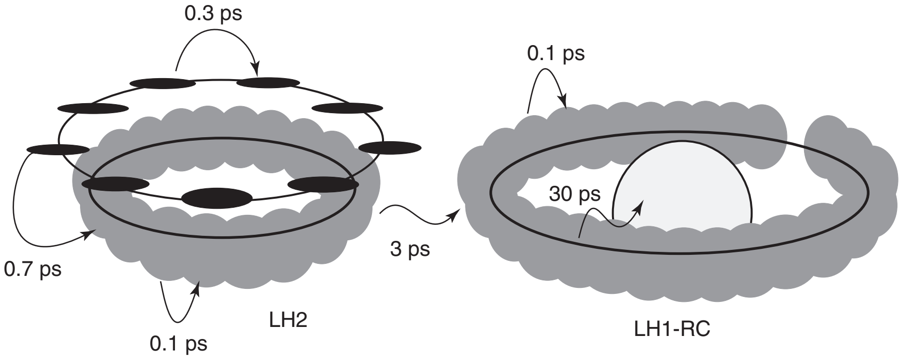

Fig. 4 Energy transfer times between the various pigments in the photosynthetic units of purple bacteria.

light harvesting in addition to other important functions, are ignored). The associated time constants for these transfer steps are shown in Fig. 4. The lifetime of an isolated antenna complex, decoupled from the reaction center, is of the order of 1 ns. During this time, the excitation energy moves freely among the lowest-energy pigments of the antenna network, until eventually dissipated by nonradiative relaxation processes. In the full photosynthetic unit, where antennas are connected to reaction centers, the excitation is trapped within 30–50 ps. Hence under physiological conditions, nearly all the energy is utilized for photochemistry.

Excitation transfer in biological systems has usually been described as an incoherent hopping process following the theory of Förster. It is hard to overestimate the physical insight obtained by this approach. At the same time, a number of experimental observations for photosynthetic pigment–proteins do not fit into this picture and call for a more general description of the problem. The incoherent Förster description of electronic energy transfer assumes that the interaction between the involved molecules is very weak. In the opposite limit of strong interaction between the molecules, a molecular exciton description is appropriate. In this limit, the excited states of the individual molecules combine to exciton states common for all the interacting molecules (the aggregate), the excitation is coherently delocalized over a number of pigment molecules and the absorption spectrum exhibits a prominent exciton band structure. Time evolution in the exciton picture occurs via phonon-induced relaxation between exciton levels. These two descriptions, incoherent hopping and exciton relaxation, are the two qualitatively different limiting cases of the general process of excitation dynamics. What description should be chosen for a particular observation depends on the system properties and the experimental conditions. It may happen that the real situation is somewhere in between these two limiting cases, in which case the analysis is particularly challenging.

The important factor in deciding which process(es) occur is the ratio of the coupling between electronic transitions (V) and the disorder (Δ). The disorder may be either static (spectral inhomogeneity) or dynamic (electron–phonon interaction). If V/Δ is much less than unity, then the interactions are considered very weak and energy transfer occurs in the incoherent Förster hopping regime. In the opposite case, if $V/\Delta \gg 1$, the interaction is very strong and the exciton picture is used. In both cases, the transfer rate can be calculated using the first-order perturbation theory leading to the Fermi Golden rule. In the hopping description, the electronic coupling (V) acts as a perturbation; in the exciton picture, an electron–phonon coupling (dynamic disorder) is the perturbation.

In the weak coupling incoherent limit, the rate of energy transfer (energy hopping) from a donor to an acceptor molecule is determined by three different molecular properties: the electronic coupling between donor and acceptor (V), the overlap of donor fluorescence and acceptor absorption spectra (J), and the relative orientation of the molecules (κ), and given by

$$K_{\mathrm{ET}} \sim V^2 J \kappa^2$$

A few things should be noted. The electronic coupling (V) has two contributions, one short-range electron-exchange interaction (which decays exponentially with the intermolecular distance R) and one long-range Coulombic interaction (which scales as R^{-6}). These two cases are described in **Fig. 5**. The interaction accounted for in the Förster mechanism and implicated by the transition dipoles is the generally dominating dipole–dipole contribution to the Coulombic interaction; higher multipole terms are also generally present, but of much less importance for molecules with strong transition dipole moments (eg, strongly allowed optical transitions). The electron exchange term in the interaction may become important at very short distances, when there is overlap of the donor and acceptor molecular orbitals. This is the so-called Dexter mechanism, and in particular for molecules with forbidden optical transitions, it may become important. Energy transfer in photosynthetic antenna complexes between the lowest forbidden excited state of carotenoid molecules and the lowest excited state of chlorophyll molecules has been discussed in terms of the Dexter mechanism.

In the exciton picture, the excitation energy is delocalized over the interacting pigment molecules. However, the extent of delocalization is determined by the V/Δ ratio, and in a real system, exciton delocalization is generally smaller than the physical size of the molecular aggregate. The localization process may also have a dynamic part due to the dynamic contribution to the disorder Δ, and the exciton thereby changes its size in time. The relevant aspects of the energetics and dynamics in the exciton limit are the exciton level structure, the dynamics of exciton relaxation among the set of exciton levels, the extent and dynamics of delocalization of the exciton, and the motion of the whole exciton over the aggregate of interacting molecules. The energies of the exciton states are obtained from the Hamiltonian of the interacting molecules and the dynamics may be obtained from the density matrix of the system.

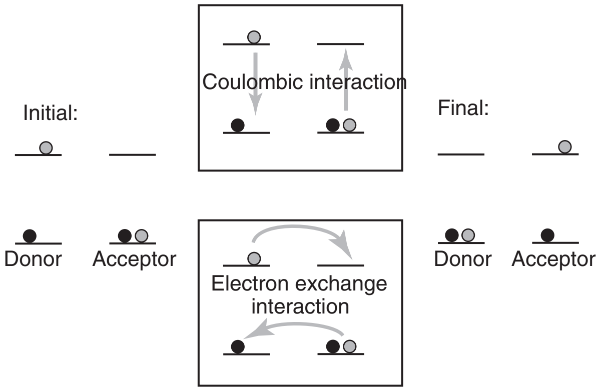

Fig. 5 Interactions governing excitation energy transfer. The Coulombic interaction promotes simultaneous deactivation of the donor and excitation of the acceptor. The electron exchange interaction involves transfer of excitation energy via direct exchange of electrons between donor and acceptor molecules.

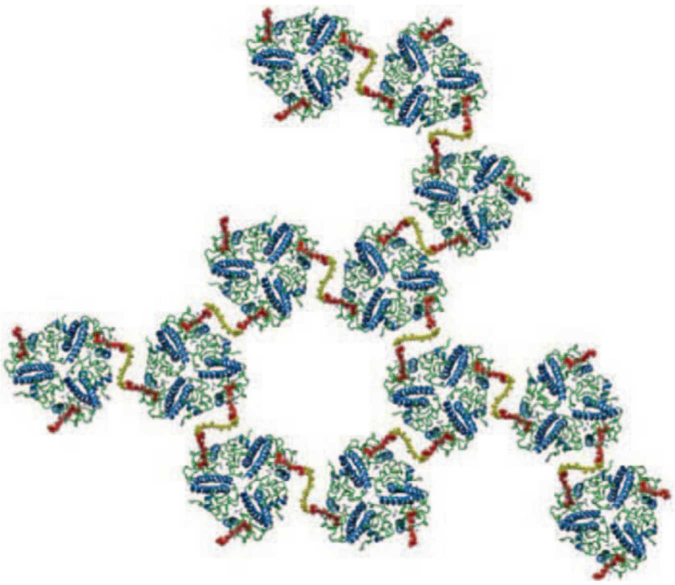

Fig. 6 Model of one of the possible supramolecular structures formed by LHCII under the presence of exogenous Vio. Endogenous neoxanthin displayed in red color and exogenous Vio displayed in yellow color.

Janik *et al.* (2016) studied the effect of violaxanthin and zeaxanthin, two main carotenoids of the xanthophyll cycle, on molecular organization of LHCII, the principal photosynthetic antenna complex of plants, in a model system based on lipid –protein membranes, by means of analysis of 77K chlorophyll a fluorescence and "native" electrophoresis. Violaxanthin was found to promote trimeric organization of LHCII, contrary to zeaxanthin which was found to destabilize trimeric structures. Moreover, violaxanthin was found to induce decomposition of oligomeric LHCII structures formed in the lipid phase and characterized by the fluorescence emission band at 715 nm. Both pigments promoted formation of two-component supramolecular structures of LHCII and xanthophylls. The violaxanthin-stabilized structures were composed mostly of LHCII trimers, while the zeaxanthin-stabilized supramolecular structures of LHCII showed more complex organization which depended periodically on the xanthophyll content. The effect of the xanthophyll cycle pigments on molecular organization of LHCII was analyzed based on the results of molecular modeling and discussed in terms of a physiological meaning of this mechanism. Supramolecular structures of LHCII stabilized by violaxanthin, prevent uncontrolled oligomerization of LHCII, potentially leading to excitation quenching, therefore can be considered as structures protecting the photosynthetic apparatus against energy losses at low light intensities. Fig. 6 illustrates the process.

Energy Conversion and Storage

Electron transfer reactions are Nature's solution to the problem of converting the short-lived energy of electronically excited molecules into a more stable form of energy, which can, in addition, be transformed into various energy-rich substances with practically unlimited storage potential. Nature has devised highly efficient systems that optimize electron transfer processes while at the same time avoiding back-reactions and quenching processes.

When the excitation energy reaches the photosynthetic reaction center, it launches a sequence of electron transfer reactions that create a charge-separated state in which positive and negative charges are separated over the lipid bilayer membrane. Energy stored in this manner can then be used to pump protons across the membrane. The resulting proton motive force drives the synthesis of energy-rich compounds such as adenosine triphosphate (ATP). ATP is thermodynamically stable for a sufficiently long time to serve as the "fuel" for many subsequent biochemical processes. Once stored in the form of ATP, the energy can be used in the cell at any arbitrary instant for transport, synthesis, or other chemical reactions that require input energy.

Again, of all the photosynthetic organisms, the reaction center of anoxygenic purple bacteria is best understood. Though in contrast to the wide variety in the configurations of antenna complexes, the reaction centers of bacteria and plants share a rather common structural and functional motif. The reaction center consists of a number of protein subunits that form a scaffold (not shown) to hold the photochemically active molecules. While a number of these molecules are identical or similar to the (bacterio) chlorophyll pigments found in the antenna, here the molecules are called cofactors to distinguish their different function. The structure of the reaction center from *Rhodobacter sphaeroides* is shown in Fig. 7. The cofactors are bacteriochlorophylls (P and B in

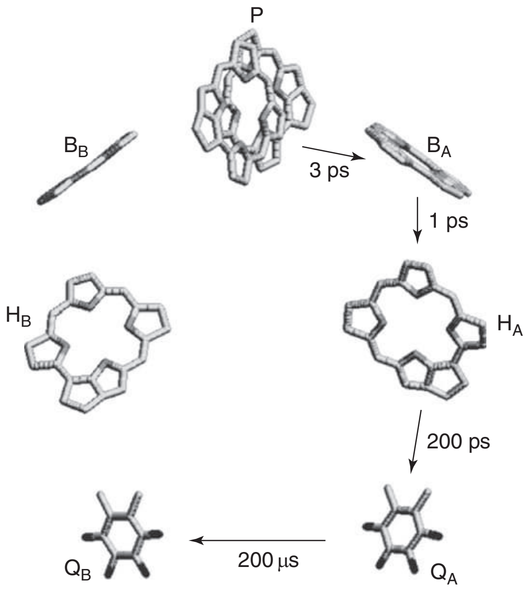

Fig. 7 X-ray structure of the active molecules in the reaction center from the photosynthetic purple bacteria *Rhodobacter sphaeroides*, showing the pathway and time constants of electron transport via the active branch A.

Fig. 7), bacteriopheophytins (H), quinones (Q), and an iron atom (located between the quinones; not shown). The cofactors are arranged into two nearly symmetric branches (A and B), joined at the top by the so-called "special pair" of bacteriochlorophyll molecules that are located so close together as to form a super molecule or dimer.

When the excitation energy collected by the antenna network finally arrives at the reaction center, it initiates a cascade of electron transfer reactions. These reactions have been visualized by a variety of spectroscopic techniques, in particular ultrafast transient absorption spectroscopy, often combined with genetic manipulations of the native structure to better elucidate structure–function relations. Upon light irradiation, the excited dimer (P) transfers an electron to the bacteriochlorophyll (B_A) and the bacteriopheophytin (H_A) on the A side of the branch within a few ps. The resulting radical pair ($P^+H_A^-$) decays in about 200 ps moving the electron onward to the quinones.

The most striking feature of the reaction center activity is the unidirectional transport down branch A (the active branch), despite the apparent twofold symmetry of the structure. The electron is 200 times more likely to follow branch A than branch B. Although considerable experimental and theoretical efforts have tackled this discrepancy, it remains as one of the most intriguing puzzles in the primary processes of photosynthesis.

The high quantum yield of primary charge separation (as much as 0.95 in some systems) comes with a price: a lower energetic yield. The final radical pair state of the bacterial RC contains 0.55 eV, which is only 40% of the excited state energy of the primary electron donor (or around a third of the average photon energy absorbed by the antenna). Perhaps the energetic efficiency of the RC could be improved upon in synthetic RC-like structures, though model systems (consisting of electron donor and acceptor molecules connected by covalent links) have shown quantum efficiencies of 30% or less. Most likely, the rigidity of the protein surrounding the donor and acceptor pigments is essential to achieve such high quantum efficiency.

From Natural to Artificial Photosynthesis

An understanding of how Nature works will allow one to use the basic principles for other purposes. The most obvious application of artificial photosynthesis is the conversion of sunlight to useful forms of energy, such as electricity by photovoltaic devices or fuel by photochemical reactors. Modern solar cells are already being built on principles gleaned from natural photosynthesis. Sensitized semiconductor materials are environmentally friendly and becoming cost-effective alternatives to silicon. Solar cells based on this material utilize sensitizer molecules that act as antenna pigments to collect sunlight in a wide spectral region and funnel the solar energy into the semiconductor by way of an electron transfer process. Ongoing research will lead to the development of new, more efficient solar light-harvesting technologies that not only mimic Nature, but perhaps also surpass it.

House *et al.* (2015) investigated that the artificial photosynthesis converts and stores solar energy through solar fuels. Dyesensitized photoelectrosynthesis (DSPEC) cells are used for artificial photosynthesis. In a DSPEC, molecular assemblies absorb light and carry out chemical catalysis. Higher efficiencies and stabilities are required for useful devices. Fig. 8 shows some examples of energy storage technologies and their relative stages of development.

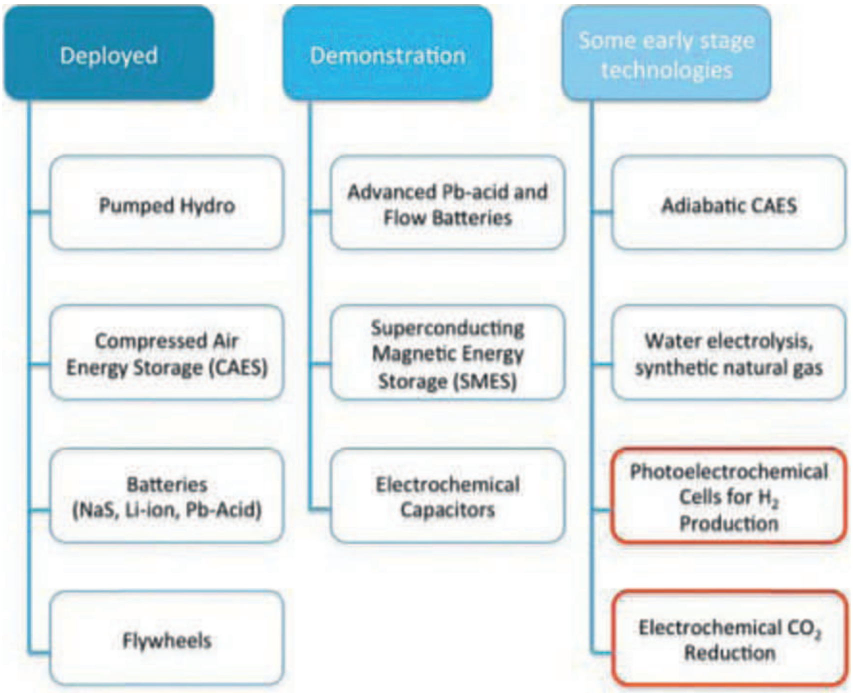
Deployed
Demonstration
Some early stage technologies
Pumped Hydro
Compressed Air Energy Storage (CAES)
Batteries (NaS, Li-ion, Pb-Acid)
Flywheels
Advanced Pb-acid and Flow Batteries
Superconducting Magnetic Energy Storage (SMES)
Electrochemical Capacitors
Adiabatic CAES
Water electrolysis, synthetic natural gas
Photoelectrochemical Cells for H_2 Production
Electrochemical CO_2 Reduction

Fig. 8 Examples of energy storage technologies and their relative stages of development. Technologies based on artificial photosynthesis are highlighted in red.

References

Grieco M, Suorsa M, Jajoo A, Tikkanen M, and Aro EM (2015) Light-harvesting II antenna trimers connect energetically the entire photosynthetic machinery – Including both photosystems II and I. *Biochimica et Biophysica Acta (BBA) – Bioenergetics* 1847(6–7): 607–619.
House RL, Murakami Iha NY, Coppo RL, et al. (2015) Artificial photosynthesis: Where are we now? Where can we go? *Journal of Photochemistry and Photobiology C: Photochemistry Reviews* 25: 32–45.
Janik E, Bednarska J, Zubik M, et al. (2016) The xanthophyll cycle pigments, violaxanthin and zeaxanthin, modulate molecular organization of the photosynthetic antenna complex LHCII. *Archives of Biochemistry and Biophysics* 592: 1–9.

Further Reading

van Amerongen H, van Grondelle R, and Valkunas L (2000) *Photosynthetic Excitons*. Singapore: World Scientific.
Amesz J and Hoff AJ (1996) *Biophysical Techniques in Photosynthesis*. Dordrecht: Kluwer.
Blankenship E (2002) *Molecular Mechanisms of Photosynthesis*. Oxford: Blackwell Science.
Hall DO and Rao K (1999) *Photosynthesis*, sixth ed London: Cambridge University Press.
Ke B (2001) *Photosynthesis Photobiochemistry and Photobiophysics*. Dordrecht: Kluwer.
May V and Kühn O (2000) *Charge and Energy Transfer Dynamics in Molecular Systems*. Berlin: Wiley-VCH.
Ritz T, Damjanovic A, and Schulten K (2002) The quantum physics of photosynthesis (review). *ChemPhysChem* 3: 243–248.
Sundstrom V, Pullerits T, and van Grondelle R (1999) Photosynthetic light-harvesting reconciling dynamics and structure of purple bacterial LH2 reveals function of photosynthetic unit (review). *The Journal of Physical Chemistry B* 103: 2327–2346.

Biomedical Materials

JR Jones and LL Hench, Imperial College, London, United Kingdom

© 2005 Elsevier Ltd. All rights reserved.

This is an update of J.R. Jones, L.L. Hench, Biomedical Materials, Editor(s): Franco Bassani, Gerald L. Liedl, Peter Wyder, Encyclopedia of Condensed Matter Physics, Elsevier, 2005, Pages 108–116, ISBN 9780123694010, https://doi.org/10.1016/B0-12-369401-9/00405-8.

The Need for Biomedical Materials **739**
Bone Defects **739**
A New Direction 740
Biomedical Materials **740**
Bioactive Materials 740
Composites 741
Scaffolds for Bone Repair **741**
The Criteria for an Ideal Scaffold 741
Polymer Scaffolds 742
Bioactive Ceramic Scaffolds 742
Bioactive Glass Scaffolds 743
Spectroscopy and Biophotonics **744**
Fourier Transform Infrared Spectroscopy 744
Bio-Raman Spectroscopy and Biophotonics 745
Conclusion **745**
Acknowledgments **746**
Further Reading **746**

The Need for Biomedical Materials

Improving healthcare and technology are increasing life expectancy but as one ages the body parts cannot maintain their function. Tissues such as bone and cartilage are needed to support the aging body even though the cells that produce them become less active with age. The heart, kidneys, and liver have to operate for much longer than ever before. This entry discusses how biomedical materials and biophysics techniques are being used in the development of regenerative medicine procedures. The aim of regenerative medicine is to regenerate diseased and damaged tissue to its original state and function.

Bone Defects

Bone is a natural composite of collagen (polymer) and bone mineral (ceramic). Collagen is a triple helix of protein chains, a complex structure that has high tensile and flexural strength and provides a framework for the bone. Bone mineral is a crystalline calcium phosphate ceramic (hydroxyapaptite (HA), $Ca_{10}(PO_4)_6(OH)_2$) that provides stiffness and the high compressive strength of the bone. The two most important types of bone are cortical and cancellous bone. Cortical bone is a dense structure with high mechanical strength and is also known as compact bone. Cancellous or trabecular bone is an internal porous supporting structure present in the ends of long bones such as the femur or within the confines of the cortical bone in short bones. The trabecular bone is a network of struts (trabeculae) enclosing large voids (macropores) with 55–70% interconnected porosity.

The mechanism for natural bone generation/regeneration in the body is the secretion of extracellular matrix by osteogenic cells (osteoblasts), which have developed (differentiated) from stem cells. The extracellular matrix is collagen type I, which mineralizes to form bone mineral, creating a composite of orientated collagen fibrils and apatite. The bone is remodeled in response to its local loading environment by the body. Osteoclasts are cells that resorb old bone and bone that is not required (i.e., not under any load), while osteoblasts lay down new bone.

Osteoporosis is a disease where bone resorption occurs faster than new bone is produced, causing the trabeculae to become thinner which leads to a reduction in total bone density and strength. The disease eventually leads to fracture of bones especially in the hip, wrist, knee, and spine. At present, when osteoporotic fracture occurs in knees and hips, joint replacement is often required. Millions of orthopedic prostheses made of bioinert materials have been implanted, an example of which is the Charnley total hip replacement, which is heralded as one of the most successful surgical inventions.

Long-term monitoring of 20000 Charnley joints has revealed that it has a survivability of 76% after 25 years implantation, that is, 24% of hip operations required revision surgery. Improved metal alloys, special polymers, and medical-grade ceramics are the basis for this success, which has enhanced the quality of life for millions of patients. Reasons for failure tend to be aseptic loosening of the femoral stem, where bone resorption occurred due to a mismatch in the Young's modulus of the bone and the metal stem. Many modifications and variations of the Charnley joint have been developed over the years, including coating the metal stem with a synthetic HA layer that can bond to the bone mineral in the bone; however, survivability studies are so far only medium term and have shown similar results to that of the Charnley prosthesis.

A New Direction

All present day orthopedic implants lack three of the most critical characteristics of living tissues: (1) the ability to self-repair; (2) the ability to maintain a blood supply; and (3) the ability to modify their structure and properties in response to environmental factors such as mechanical load. All implants have a limited lifespan and as life expectancy is continually increasing, it is proposed that a shift in emphasis from "replacement" of tissues to "regeneration" of tissues is required to satisfy this growing need for very long-term orthopedic repair.

One way to restore diseased or damaged tissue to its original state and function would be the successful engineering of the replacement tissue in the laboratory. In a typical tissue engineering application, cells would be harvested from the patient (i.e., osteogenic cells in the case of bone) and seeded on a synthetic scaffold that acts as a guide and stimulus for tissue growth in three dimensions creating a tissue engineering construct or living biocomposite. The biocomposite would then be implanted back into the patient. Over time, the synthetic scaffold should be resorbed into the body as nontoxic degradation products at the same rate that the cells produce their own extracellular matrix.

In this article, the development of scaffold technology is discussed, focusing primarily on porous glass scaffolds that bond to bone and the growth of bone and cartilage in the laboratory on such scaffolds. The biophysics techniques that are now being used to monitor cell behavior as the cells grow are also discussed.

Biomedical Materials

Any material that is implanted into the body should be biocompatible, that is, not cytotoxic (not toxic to cells). There are three classes of noncytotoxic materials; bioinert, bioactive, and bioresorbable. No material is completely inert on implantation, but the only response to the implantation of bioinert materials is encapsulation of the implant by the fibrous tissue. Examples of bioinert materials are medical-grade alumina, stainless steels, and high-density polyethylene that are used in the total hip replacements.

Resorbable materials are those that dissolve on contact with body fluids and the dissolution products can be secreted via the kidneys. The most common biomedical resorbable materials are polymers that degrade by chain scission such as polyglycolic (PGA) and polylactic acids (PLLA) and their co-polymers, which are commonly used as sutures.

Bioactive Materials

Bioactive materials stimulate a biological response from the body such as bonding to tissue. Bone is a natural composite of bone mineral (HA) and collagen and other proteins. Therefore, synthetic HA (with $Ca/P=1.667$) and other calcium phosphate ceramics, including coral, have gained much attention as a bone mineral substitute.

There are two classes of bioactive materials; class B bioactive materials bond to hard tissue (bone) and stimulate bone growth along the surface of the bioactive material (osteoconduction). Examples of class B bioactive materials are synthetic HA and tricalcium phosphate ceramics. Synthetic HA has been used in several clinical applications such as a bone defect filler and is used to coat the stainless steel or titanium alloy shaft of the total hip prosthesis so that it bonds to the thigh bone (femur). Tricalcium phosphate (β-TCP, with $Ca/P=1.5$) is an osteoconductive material that is also resorbable in the body. β-TCP is usually used in conjunction with synthetic HA to improve the resorbability of HA in applications such as the filling of bone defects left by cysts, sinus floor augmentation, and bone cements.

Class A bioactive materials not only bond to bone and are osteoconductive but they are also osteoproductive, that is, they stimulate the growth of new bone on the material away from the bone/implant interface and can bond to soft tissue such as gingival (gum) and cartilage. Examples of class A bioactive materials are bioactive glasses. A certain composition of melt-derived bioactive glass (46.1% SiO_2, 24.4% Na_2O, 26.9% CaO, and 2.6% P_2O_5, in mol), called Bioglass® is used in the clinic as a treatment for periodontal disease (Perioglas®) and as a bone-filling material (Novabone®). Bioglass® implants have also been used to replace damaged middle ear bones, restoring hearing to thousands of patients.

The mechanism of bone bonding to bioactive materials is thought to be due to the formation of an HA layer on the surface of the materials after immersion in body fluid. This layer is similar to the apatite layer in bone and therefore a strong bond can form. The layer forms quickest on class A bioactive materials. The mechanism of formation of the HA layer on bioactive glasses is shown in Figure 1. Stage 1 involves release of cations. Stage 2 is the break up of the silica-based glass network. These two stages are dissolution processes; therefore, these glasses are not only bioactive but are also resorbable in the body. β-TCP ceramics are also resorbable.

Figure 2 shows suggested mechanisms for osteoproduction, where new bone grows on bioactive glasses away from the glass–-host bone interface. The sequence follows on from the events in Figure 1 but concentrates on the effects of the glass on the cells within the bone and bone marrow, however it does not fully explain osteoproduction. Recent findings by Professor Dame Julia Polak's team at the Tissue Engineering and Regenerative Medicine Centre at Imperial College, London, have shown that the dissolution products of bioactive glasses up-regulate seven families of genes that regulate osteogenesis and the production of growth factors.

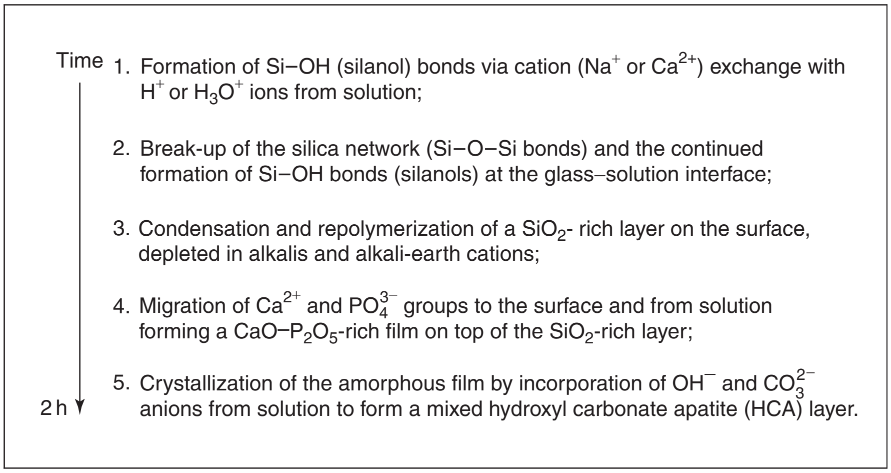

1. Formation of Si–OH (silanol) bonds via cation (Na^+ or Ca^{2+}) exchange with H^+ or H_3O^+ ions from solution;
2. Break-up of the silica network (Si–O–Si bonds) and the continued formation of Si–OH bonds (silanols) at the glass–solution interface;
3. Condensation and repolymerization of a SiO_2- rich layer on the surface, depleted in alkalis and alkali-earth cations;
4. Migration of Ca^{2+} and PO_4^{3-} groups to the surface and from solution forming a $CaO–P_2O_5$-rich film on top of the SiO_2-rich layer;
5. Crystallization of the amorphous film by incorporation of OH^- and CO_3^{2-} anions from solution to form a mixed hydroxyl carbonate apatite (HCA) layer.

Figure 1 Mechanism of formation of the HCA layer on the surface of bioactive glasses in solution.

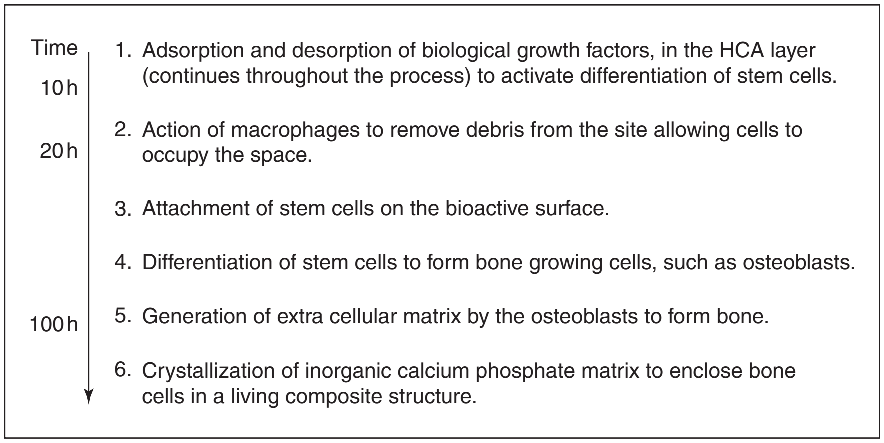

1. Adsorption and desorption of biological growth factors, in the HCA layer (continues throughout the process) to activate differentiation of stem cells.
2. Action of macrophages to remove debris from the site allowing cells to occupy the space.
3. Attachment of stem cells on the bioactive surface.
4. Differentiation of stem cells to form bone growing cells, such as osteoblasts.
5. Generation of extra cellular matrix by the osteoblasts to form bone.
6. Crystallization of inorganic calcium phosphate matrix to enclose bone cells in a living composite structure.

Figure 2 Suggested mechanism of cellular interactions between cells and bioactive glasses after implantation, after the formation of the HCA layer.

Composites

To overcome the low toughness of HA, a polyethylene–HA composite was developed by Professor William Bonfield and colleagues at the University of London. It is clinically available under the name HAPEX™ and has been used as middle ear implants and orbital floor replacements. The polymer provides toughness strength and the HA increases the compressive strength and provides bioactivity so that implants are not encapsulated by scar tissues. The composite is class B bioactive and is easily shaped with a scalpel by the surgeon and so is now routinely used to replace the bones of the middle ear.

Scaffolds for Bone Repair

The Criteria for an Ideal Scaffold

To be able to regenerate the trabecular bone, a construct is required that will mimic the structure and mechanical properties of the trabecular bone and stimulate new bone growth in the shape dictated by the scaffold. Therefore, the scaffold should have a structure that acts as a template for tissue growth in three dimensions. The template must be an interconnected macroporous network containing pores with diameters in excess of 100 μm to promote cell migration, tissue ingrowth and vascularization, and nutrient delivery to the center of the regenerating tissue on implantation. The scaffold material should be able to bond to the host bone without the formation of scar tissue, that is, it should be made from an osteoconductive material. If the bone is to be restored to its original state, the scaffold should be resorbable so that eventually there is no trace of the scaffold's presence. The degradation rate of the scaffold must be controllable so that it can be tailored to match the rate of bone growth. The dissolution products would ideally influence the genes in the bone generating stem cells to stimulate efficient cell differentiation and proliferation. Importantly, the mechanical properties of the scaffold should match that of the host bone and not decrease too rapidly during degradation so that bone regeneration occurs at load-bearing sites.

If the scaffold is to be mass produced so that surgeons can use it in the clinic, it must be made from a processing technique that can produce irregular shapes to match that of the defect in the bone of the patient. It must have the potential to be producible to the required ISO (International Standards Organization) or FDA (Food and Drug Administration) standards and be easily sterilized.

The need for implant materials to pass the FDA standards may be necessary for the safety of patients, but it places a large financial obstacle in the path of new scaffold developments. Many researchers use materials that have already been passed by the FDA so that they are sure their scaffold will be safe for use in the clinic. They are unwilling to risk using materials that have not undergone FDA testing because of the time and financial commitment required for fulfilling the extensive tests.

Polymer Scaffolds

Resorbable polymeric scaffolds have been developed with porous structures similar to the trabecular bone. There are three reasons why much effort has been put into using polymers as scaffolds. First, polymers are easy to process in the shape of a 3D scaffold with a pore morphology suitable for a tissue engineering application with techniques such as phase separation, gas foaming, freeze drying, combined solvent leaching and extrusion, and computer-controlled rapid prototyping techniques. Polymer fibers can be woven together using textile processing techniques.

Second, polymers can have high tensile properties and high toughness. The mechanical properties of polymers can be controlled very easily by changing the molecular weight (chain length) of the polymer. Third, bioresorbable polymers have been successfully used as dissolving sutures for many years. Therefore, these degradable polymers, such as the esters PGA and PLLA, have passed FDA regulations and can be implanted into the body.

There are however some problems with using biodegradable polymers as scaffolds for bone regeneration. First, while a degradable scaffold is desired, sutures dissolve within 2 weeks of implantation, which is too rapid for bone regeneration applications.

Second, although resorbable polymers can be made with high tensile strength and toughness and their mechanical properties can be matched with collagen, their Young's modulus is much lower than that of bone, therefore these polymers cannot be used in load-bearing sites where they undergo compressive forces.

A third problem is that the mechanical strength of polymers decreases rapidly as they degrade. High tensile strength polymers have long chains (high molecular weight), which entangle with each other. As a tensile force is applied to the entangled chains, the chains begin to unravel until they become straight. The maximum tensile strength of polymers is reached when the chains are fully extended. Therefore, for a polymer to be tough, it must have a molecular weight over the entanglement value. The mechanism for degradation of biodegradable polymers is chain scission. The polymers undergo hydrolysis and the chains are cut in two. The average molecular weight of the polymer is therefore approximately halved with every chain scission event. The mechanical properties of the polymer are proportionate to the square root of the molecular weight and therefore decrease very rapidly as the polymer degrades. Biodegradable polymers have also been found to produce an inflammatory response due to the acidic by-products of the degradation.

Bioactive Ceramic Scaffolds

Ceramics are crystalline materials and tend to have high compressive strength and Young's modulus but low toughness, that is, they are brittle materials. Alumina and synthetic HA are ceramics that are most commonly used in biomedical applications. Alumina is a bioinert ceramic that is very hard and resistant to wear. It is therefore commonly used as a replacement to the ball of the femur in total hip replacement. Bioactive ceramics that have been used as bone regeneration materials are synthetic HA and β-TCA. Synthetic HA has been used most regularly because of its similarity to bone mineral; it has a similar structure and Young's modulus. β-TCP is similar to bone mineral in that they are both calcium phosphate ceramics, however β-TCP is resorbable.

In a porous form, HA and β-TCP ceramics can be colonized by bone tissue. A problem with introducing pores into a ceramic is that the compressive strength of the material decreases dramatically. The strength of the scaffold depends on the thickness and strength of the struts or pore walls. Generally, for the brittle compression of a foam

$$\sigma_{\mathrm{cr}} \propto \rho_{\mathrm{r}}^{3/2} \qquad [1]$$

where σ_{cr} is the critical strength of the pore walls and ρ_{r} is the relative density, expressed as

$$\rho_{\mathrm{r}} = \rho_{\mathrm{b}}/\rho_{\mathrm{s}} \qquad [2]$$

where ρ_{b} is the bulk density of the scaffold and ρ_{s} is the skeletal (true) density of the material.

The simplest way to generate porous scaffolds from ceramics such as HA, is to sinter particles, preferably spheres of equal size. The scaffolds can then be pressed using cold isostatic pressing. As the sintering temperature increases, the pore diameter decreases, and mechanical properties increase as the packing of the spheres increases. Mechanical properties can be increased further by hot isostatic pressing (HIPing). High mechanical strengths can be achieved but the pore diameter is not high enough. Porosity can be increased by adding fillers such as sucrose, gelatine, and polymethyl methacrylate (PMMA) microbeads to the powder slurry, which burnout on sintering. However, this technique decreases the compressive strength to below that of the trabecular bone.

The majority of methods that are used to produce polymer foams cannot be applied to ceramic systems. However, a popular method for producing highly porous ceramics is to produce a polyurethane foam template that can be immersed in ceramic slurries under vacuum to allow the slurry to penetrate into the pores of the foam. The organic components are burnt out and the ceramic foams sintered (1350°C) producing a scaffold with interconnected pore diameters of up to 300 μm.

The ceramic slurries can also be foamed to obtain pores in the range of 20 μm up to 1–2 mm. The incorporation of bubbles is achieved by injection of gases through the fluid medium, mechanical agitation, blowing agents, evaporation of compounds, or by evolution of gas by *in situ* chemical reaction. A surfactant is generally used to stabilize bubbles formed in the liquid phase by reducing the surface tension of the gas–liquid interface. Surfactants are macromolecules composed of two parts, one hydrophobic and one hydrophilic. Owing to this configuration, surfactants tend to adsorb onto gas–liquid interfaces with the hydrophobic part being expelled from the solvent and a hydrophilic part remaining in contact with the liquid. This behavior lowers the surface tension of the gas–liquid interfaces, making the foam films thermodynamically stable, which would otherwise collapse in the absence of the surfactant.

The gel-casting method has been the most successful method used to produce macroporous bioactive HA ceramics with interconnected pores of greater than 100 μm in diameter. Suspensions of HA particles and organic monomers are foamed by agitation with the addition of a surfactant under a nitrogen atmosphere. *In situ* polymerization (cross-linking) of the monomers, which is initiated by a catalyst, creates a 3D polymeric network (gel). The porous gels are sintered to provide mechanical strength and to burnout the organic solvents. HA foams have been made with compressive strengths in excess of 10 MPa, which is similar to that of trabecular bone. When the foams were implanted into the tibia of rabbits, bone partially filled the pores after 8 weeks and there was no inflammatory response. The compressive strength of the scaffolds that were colonized by bone trebled.

Hydrated silicon ($SiOH_4$) has been found to be a major contributor to the mineralization of bone and gene activation, which has lead to the substitution of silica (SiO_2) for calcia (CaO) into synthetic HA. *In vivo* results showed that bone ingrowth in silica-substituted HA granules was significantly greater than that into phase pure HA granules.

The disadvantages of an HA scaffold over a bioactive glass scaffold with similar morphology are that HA resorbs only very slowly, the dissolution products do not stimulate the genes in the osteogenic cells and HA is only osteoconductive as it generates bone at a slower rate than bioactive glasses. HA is still a bone replacement material rather than a regenerative material.

Bioactive Glass Scaffolds

Theoretically, gel-casting could be applied to melt-derived bioactive glass powders. However, bioactive glasses undergo surface reactions on contact with solutions to produce an HCA surface layer and it is desirable to have control over the reaction before a scaffold is ready for clinical use.

Sacrificial porogens and foaming agents have also been used to create melt-derived bioactive glass (Bioglass®) scaffolds. Large pores with diameters in the region of 200–300 μm were created but the total porosity was just 21% and there were large distances between pores, so this process failed to mimic the interconnectivity of the trabecular bone.

The most successful method for the production of bioactive glass scaffolds of similar structure to trabecular bone mineral is the foaming of sol–gel derived bioactive glasses. The sol–gel process involves polymer reactions of the glass precursors in a solution (sol). The sol is a solution of silica species that forms a gel by cross-linking together into a silica network. Sol–gel derived bioactive glasses tend to be more bioactive and resorb quicker than melt-derived glasses of similar compositions. The compositions of gel-glasses can also contain fewer components while maintaining bioactivity. This is due to them having a textural nano-sized porosity that is inherent to the sol–gel process, which provides a specific surface area of 150–600 $m^2\,g^{-1}$, which is two orders of magnitude higher than melt-derived glasses. Along this surface there are many silanol groups that act as nucleation sites for HCA layer formation (Figure 1).

During the foaming process, air is entrapped in the sol under vigorous agitation as viscosity increases and the silica (–Si–O–Si–) network forms. A surfactant is added to stabilize the bubbles at short times. As the porous foam becomes a gel, the bubbles are permanently stabilized. The gel is then subjected to controlled thermal processes of aging (60°C) to strengthen it, drying (130°C), and thermal stabilization/sintering to remove organic species from the surface of the material (500–800°C). Bioactive glass foam scaffolds can contain macropores up to 600 μm in diameter, connected by pore windows with modal diameters in excess of 100 μm and compressive strengths up to 2.5 MPa. Figure 3 shows a scanning electron microscopy (SEM) micrograph of a pore network of a typical bioactive glass foam. *In vitro* cell studies using primary human osteoblasts have shown the foams stimulate formation and mineralization of bone nodules within 2 weeks of culture (Figure 4). Figure 4 shows osteoblasts that have attached to the concave surface of the pore. The cells have proliferated, coating the pore in an organic layer, and have released extracellular matrix, which has mineralized to form bone mineral. *In vivo* studies have shown that foam scaffolds implanted on rabbit crania stimulated new bone growth at a similar rate to that of the melt-derived bioactive glass powder available commercially.

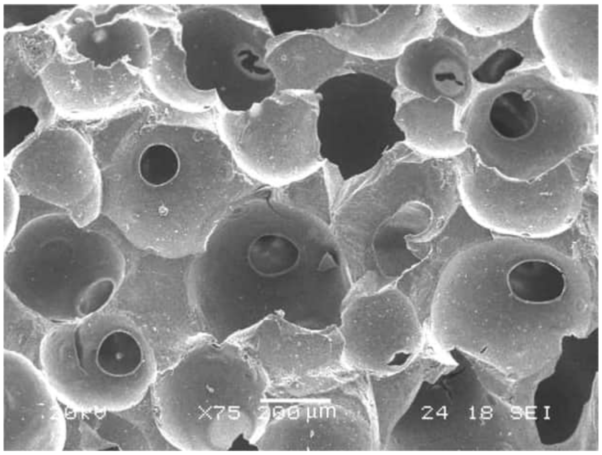

Figure 3 Scanning electron micrograph of a bioactive glass foam scaffold.

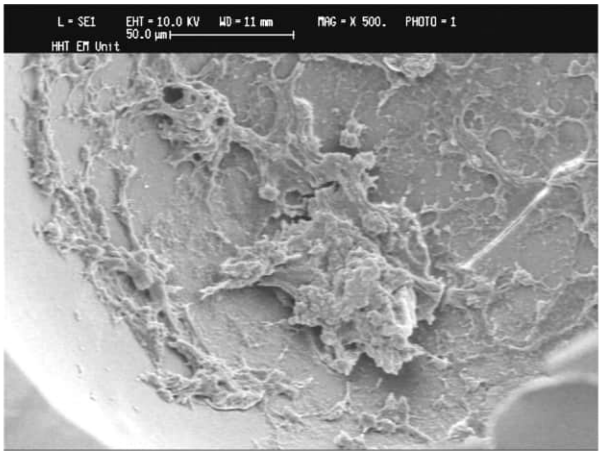

Figure 4 Scanning electron micrograph bone cells and mineralized bone extracellular matrix in a pore of a bioactive glass foam scaffold. (Courtesy of J Gough.)

Spectroscopy and Biophotonics

Vibrational spectroscopy is one of the most common techniques to study the surface reactions of bioactive materials. It is nondestructive, rapid, and can be used to analyze small areas of a sample surface. The two most commonly used vibrational spectroscopy techniques are Fourier transform infrared spectroscopy (FTIR) and Raman spectroscopy.

Fourier Transform Infrared Spectroscopy

FTIR spectra have been used to determine the rate of formation of the HCA layer on bioactive glasses and the technique is used as a quality assurance (QA) test for bioactivity. FTIR spectra of the glass surface area usually taken after a glass sample has been reacted in simulated body fluid (SBF) and dried. The crystalline HCA layer is characterized by the P–O bending vibration bands at 560 and 604 cm^{-1} (infrared wave number). Stretching and bending vibration bands for the amorphous silica network are also present in the spectra. The relative intensity of the bands can be used to monitor growth of the layer as a function of time. Figure 5 shows FTIR spectra of three forms of the sol–gel derived bioactive glasses of the 58S composition (60 mol.% SiO_2, 36 mol.% CaO, 4 mol.% P_2O_5) that were soaked in SBF for 2 h. The spectra show that the HCA layer thickness was thicker for the powders and foams with respect to the monolith. Although FTIR can be used for the characterization of dried materials after soaking or after implantation and removal, *in situ* measurements are hindered by the strong adsorption of water in the infrared region.

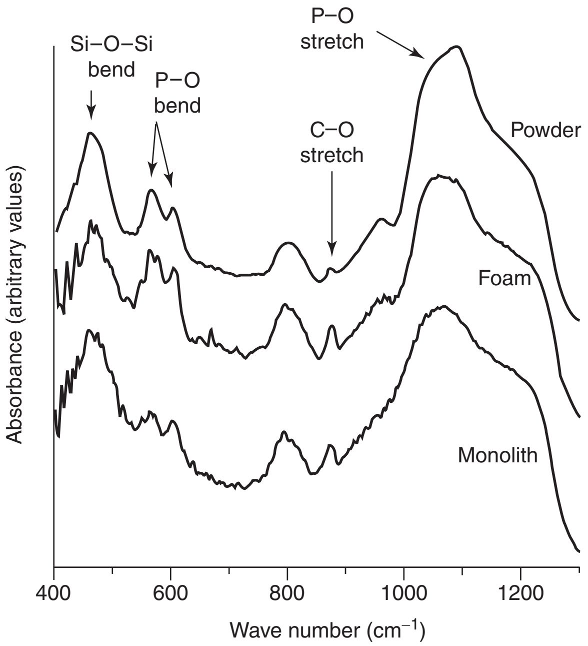

Figure 5 FTIR spectra for 58S glass powder, foam, and monolith after 2 h immersion in SBF at 37°C and 175 rpm agitation.

Bio-Raman Spectroscopy and Biophotonics

Raman spectra are fingerprints of the chemical composition of the material. Raman spectra are obtained by collecting electromagnetic radiation that has been scattered by molecules (Raman effect). The spectral shifts depend on the vibrational frequencies of the molecules. The low Raman signal and low Raman scattering of water, and the combination of Raman spectroscopy with optical microscopy (water immersion objectives) has allowed noninvasive *in situ* monitoring of cells in cell culture. This technique is called micro-Raman spectroscopy. The optical objective provides high spatial resolution and is used to locate the cell or part of the cell, such as the cytoplasm or the nucleus, from which a spectrum will be collected. A laser is then fired at the identified area and the scattered photons are collected by a detector.

Low scattering efficiency of the cells makes the measurement of Raman shifts difficult. Raman signals can be enhanced using UV lasers; however, high-powered lasers can denature the cells and change cell phenotype. Decreasing the laser power decreases the Raman signal, but reduces the risk of changes to the cell. A laser wavelength of 785 nm has been found to produce optimal *in situ* spectra of living cells. A single spectrum obtained from the nucleus of a cell can contain information about the protein and DNA content of the cell. Figure 6 shows a Raman spectrum of a cultured lung cell containing vibrational bands corresponding to DNA (A, G, T, C adenine, guanine, thymine, cytosine), BK: backbone, RP: ribose-phosphate and the proteins phenylalanine (Phe) and tyrosine (Tyr). Raman spectroscopy using 785 nm lasers can be used to monitor the biochemical changes taking place in a cell. During cell death, for example, the degradation of proteins, DNA breakdown, and the formation of lipid vesicles can be detected in real time.

Cells cultured on bioactive materials can also be monitored by *in situ* Raman spectroscopy. A background spectrum for the unreacted material can be subtracted from the spectrum of a cell on the material. The resultant spectrum will then also contain vibrational bands corresponding to the formation of any calcium phosphate layer on the surface of the bioactive material as a function of time.

Raman spectroscopy may hold the key for the *in situ* monitoring of bone cells growing on scaffolds. When acquisition techniques and interpretation of the spectra are perfected, the micro-Raman spectrometers can be linked to bioreactors and the effect of flow rates, growth factors, and dissolution products on cell behavior can be monitored in real time.

Conclusion

Numerous materials have been developed to replace living tissues. They are bioinert (stainless steel, alumina), bioresorbable (polyglycolic acid), or bioactive (synthetic HA and bioactive glasses). New biocomposites have been made that combine bioinert and bioactive properties. The latest generation of materials are used in combination with cells. Many techniques have been employed to produce porous scaffolds. The scaffold that most closely matches the criteria for an ideal scaffold and that most closely mimics the structure of the trabecular bone is the bioactive glass foam. However, these scaffolds do not yet have the

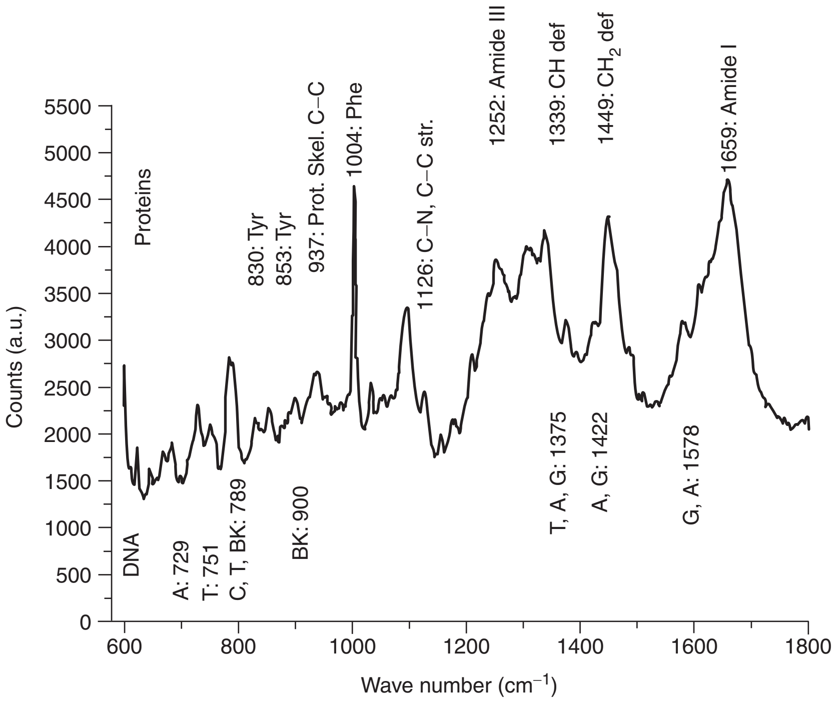

Figure 6 Raman spectrum of a cultured living lung cell. (Courtesy of I Notingher.)

mechanical properties to be directly implanted into load-bearing sites. Ideally, a bioactive glass/polymer foam composite would be developed with improved toughness. The properties of a scaffold must be optimized with respect to the cell response to the scaffold. Biophotonics techniques such as Raman spectroscopy have the potential to be able to monitor cell activity and intracellular processes of living cells in real time noninvasively.

Acknowledgments

Lloyds Tercentenary Foundation, EPSRC and MRC (UK), Dr. Julie Gough, Dr. Ioan Notingher.

Further Reading

Brinker CJ and Scherer GW (1990) *Sol–Gel ScienceThe Physics and Chemistry of the Sol–Gel Process*. Boston: Academic Press.

Chalmers J and Griffiths PR (2001) *Handbook of Vibrational Spectroscopy Volume 5Applications in Life, Pharmaceutical and Natural Sciences*. New York: Wiley.

Davies JE (2000) *Bone Engineering*. Toronto: EM^2.

Gibson LJ and Ashby MF (1988) *Cellular Solids Structure and Properties*. Oxford: Pergamon.

Hastings GW and Williams DF (1980) *Mechanical Properties of Biomaterials*. New York: Wiley.

Hench LL, Jones JR, Lenza RFS, and Vasconcelos WL (2003) Tissue engineering. In: Banner N, Polak JM, and Yacoub M (eds.) *Lung Transplantation*, pp. 367–373. Cambridge: Cambridge University Press.

Hench LL and Polak JM (2002) Third generation biomaterials. *Science* 295(5557): 1014–1020.

Hench LL and Wilson J (1993) *An Introduction to Bioceramics*. Singapore: World Scientific.

Jones JR, Sepulveda P, and Hench LL (2002) Bioactive materials for tissue engineering scaffolds. In: Polak JM, Hench LL, and Kemp P (eds.) *Future Strategies for Tissue and Organ Replacement*, pp. 3–19. London: Imperial College Press.

Notingher I, Verrier S, Haque S, Polak JM, and Hench LL (2003) Spectroscopic study of human lung epithelial cells (A549) in cultureliving cells versus dead cells. *Biopolymers (Biospectroscopy)* 72: 230–240.

Park J and Lakes RS (1992) *BiomaterialsAn Introduction*, 2nd edn. New York: Plenum.

Thomson RC, Yaszemski MJ, and Mikos AG (1997) Polymer scaffold processing. In: Lanza RP, Langer R, and Chick WL (eds.) *Principles of Tissue Engineering*, pp. 263–271. Austin, TX: Landes.

Wise DL (2000) *The Biomaterials and Bioengineering Handbook*. New York: Dekker.

Encyclopedia of Condensed Matter Physics

Second Edition

EDITOR-IN-CHIEF:
Tapash Chakraborty
University of Manitoba, Winnipeg, Manitoba, Canada

SECTION EDITORS:
Ana M. Sanchez
Department of Physics, University of Warwick, Coventry, United Kingdom

Hideo Aoki
Department of Physics, University of Tokyo, Tokyo, Japan

Robert H. Blick
Center for Hybrid Nanostructures, University of Hamburg & DESY, Hamburg, Germany

Roberto Raimondi
Mathematics and Physics Department, Roma Tre University, Rome, Italy

Rudolf A. Roemer
Department of Physics, University of Warwick, Coventry, United Kingdom

Vladimir Mihajlovic Fomin
Leibniz Institute for Solid State and Materials Research (IFW), Dresden, Germany

ELSEVIER
ACADEMIC PRESS
An imprint of Elsevier
elsevier.com/books-and-journals

Volume ISBN
ISBN 978-0-443-21826-2
9 780443 218262

Set ISBN
ISBN 978-0-323-90800-9
9 780323 908009

ENCYCLOPEDIA OF CONDENSED MATTER PHYSICS

SECOND EDITION

This page intentionally left blank

ENCYCLOPEDIA OF CONDENSED MATTER PHYSICS

SECOND EDITION

EDITOR-IN-CHIEF

Tapash Chakraborty*

Professor, Tier-I Canada Research Chair, University of Manitoba, Winnipeg, MB, Canada

VOLUME 5

ELSEVIER

---

*Retired.

Elsevier
Radarweg 29, PO Box 211, 1000 AE Amsterdam, Netherlands
The Boulevard, Langford Lane, Kidlington, Oxford OX5 1GB, United Kingdom
50 Hampshire Street, 5th Floor, Cambridge MA 02139, United States

Copyright © 2024 Elsevier Ltd. All rights reserved

No part of this publication may be reproduced or transmitted in any form or by any means, electronic or mechanical, including photocopying, recording, or any information storage and retrieval system, without permission in writing from the publisher. Details on how to seek permission, further information about the Publisher's permissions policies and our arrangements with organizations such as the Copyright Clearance Center and the Copyright Licensing Agency, can be found at our website: www.elsevier.com/permissions.

This book and the individual contributions contained in it are protected under copyright by the Publisher (other than as may be noted herein).

Notices
Knowledge and best practice in this field are constantly changing. As new research and experience broaden our understanding, changes in research methods, professional practices, or medical treatment may become necessary.

Practitioners and researchers may always rely on their own experience and knowledge in evaluating and using any information, methods, compounds, or experiments described herein. In using such information or methods they should be mindful of their own safety and the safety of others, including parties for whom they have a professional responsibility.

To the fullest extent of the law, neither the Publisher nor the authors, contributors, or editors, assume any liability for any injury and/or damage to persons or property as a matter of products liability, negligence or otherwise, or from any use or operation of any methods, products, instructions, or ideas contained in the material herein.

Library of Congress Cataloging-in-Publication Data
A catalog record for this book is available from the Library of Congress

British Library Cataloguing-in-Publication Data
A catalogue record for this book is available from the British Library

ISBN 978-0-32-390800-9

For information on all publications visit our website at http://store.elsevier.com

ELSEVIER Book Aid International
Working together to grow libraries in developing countries
www.elsevier.com • www.bookaid.org

Publisher: Oliver Walter
Acquisitions Editor: Oliver Walter
Content Project Manager: Naman Negi
Associate Content Project Manager: Nandhini Mahendran
Designer: Mark Rogers

EDITOR-IN-CHIEF BIOGRAPHY

Tapash Chakraborty is a retired professor of physics from the University of Manitoba, Canada, where he was also the Canada Research Chair in Nanoscale Physics (2003–17). His research focus has been on many-body theories of various quantum materials, such as nuclear matter, helium liquids, and electron-hole liquids, that he studied under the tutelage of late Professor Manfred Ristig, at the University of Köln (1979–81). Just a year after the discovery of the fractional quantum Hall effect, he (working with his coworkers) demonstrated that electron–electron interactions could actually lead to quantum Hall states with nontrivial spin configurations, and that the low-lying excitations could be described as "spin-reversed quasiparticles." This prediction motivated much experimental work from laboratories around the world, as a result of which the concept of spin-reversed quasi-particles was established.

Similarly, his work on the quantum Hall states in double layer systems has received much attention from the community. Furthermore, Dr. Chakraborty (working with Dr. P. Maksym and others) made pioneering contributions to the many-electron theory of quantum dots. Dr. Chakraborty has also contributed to the theory of electronic properties of various nanoscale systems, such as spin-orbit coupled quantum dots, quantum rings, and single- and double-layer graphene (primarily with Dr. V. Apalkov). He has authored many books and reviews: the book with Dr. Pietiläinen on the quantum Hall effect and the single-authored book on quantum dots have become standard references in their respective fields.

This page intentionally left blank

EDITORIAL ADVISORY BOARD

Ana M. Sanchez
Department of Physics, University of Warwick, Coventry, United Kingdom

Hideo Aoki
Department of Physics, University of Tokyo, Tokyo, Japan

Robert H. Blick
Center for Hybrid Nanostructures, University of Hamburg & DESY, Hamburg, Germany

Roberto Raimondi
Mathematics and Physics Department, Roma Tre University, Rome, Italy

Rudolf A. Roemer
Department of Physics, University of Warwick, Coventry, United Kingdom

Vladimir Mihajlovic Fomin
Leibniz Institute for Solid State and Materials Research (IFW), Dresden, Germany

This page intentionally left blank

INTRODUCTION

> Electrons in orbits contained by the quantum,
> And atoms conjoined by the dipolar force,
> Gravity balanced by pressure
> And flap of a wing.
> Here, I remember the angles and curves,
> Calculus, I learned it all –
> Each bird bit and moon fracture
> Fixed by the symmetries,
> Airborne and airless, aloft.
>
> – Alan Lightman: *Song of Two Worlds*

Condensed matter physics (CMP) is the largest discipline in physics, involving a wide variety of interesting concepts and challenges. To quote Leggett (1992), CMP embraces topics “as diverse as traditional solid-state physics, neutron stars and the physics of biological matter.” He further added that, by a liberal definition “just about all of physics outside atomic, nuclear and particle physics and cosmology” fall in this vast enterprise[1]. One of the primary goals of CMP is to explore the fundamental properties of matter—solids, liquids or gasses—comprising a large number of *interacting* constituent particles (Laughlin and Pines, 2000). The quantum-mechanical nature of these many-body systems makes condensed-matter highly nontrivial, sometimes counterintuitive and even astonishing. Superconductivity and the fractional quantum Hall effect (FQHE) naturally fall within that category. In fact, for the past four decades, the quantum Hall effects (QHEs) have been the epitome of elegant CMP (von Klitzing et al., 2020). Our fundamental system of units has been redefined following the discovery of the QHE when the “von Klitzing constant” $R_K = 25,\ 812.8074593045\ \Omega$ came into being (von Klitzing, 2019; Nawrocki, 2019). Observation of the QHE in graphene[2] was crucial in determining the Dirac nature of charge carriers there (see for example, Jiang et al., 2007).

Another effect that outwardly resembles the QHE but is conceptually quite different is the FQHE, which is a quintessential manifestation of electron correlations governed by the Coulomb interaction (Störmer, 1992; Eisenstein and Stormer, 1990). To explain this fascinating effect, Laughlin (1983) introduced his eponymous wave function that not only provided the foundation for understanding the effect but also triggered a new wave of ideas with impact far beyond the realm of CMP[3]. Who would have imagined that a large collection of interacting electrons confined on a plane in a perpendicular magnetic field would result in elementary excitations (quasiholes and quasiparticles) (Chakraborty and Pietiläinen, 1988, 1995; Halperin, 1983; Clark and Maksym, 1989) carrying fractional electron charge and obeying the exotic exchange statistics of anyons (Halperin, 1984; Arovas et al., 1984)? These quasiparticles and quasiholes of the Laughlin state still remain an enigma (Laughlin, 1984; Chakraborty, 1985; Morf and Halperin, 1986). Fractional statistics is a truly path-breaking concept in CMP that was introduced by Leinaas and Myrheim (1977), and has been recently confirmed experimentally (Bartolomei et al., 2020; Nakamura et al., 2020).

Much of the history of CMP can be viewed as a series of paradigm shifts[4]. The field evolved rapidly through frequent ground-breaking discoveries that challenged existing paradigms and opened up new applications, and this evolution is expected to continue (Leggett, 2018; Cohen, 2008). For example, our current understanding of

the FQHE required deep mathematical analysis and a wide range of experimental exploration, which revealed a treasure trove of unique phenomena that are yet to be fully understood or explained. Other studies of electron correlations in low spatial dimensions have ushered in many groundbreaking notions, such as Pfaffian states, Majorana fermions in condensed matter, Chern insulators, and topological quantum materials that promise a fault tolerant means to perform quantum computation. The presence of incompressible FQHE states in monolayer graphene (Apalkov and Chakraborty, 2006), bilayer graphene (Apalkov and Chakraborty, 2010, 2011), and double-layer graphene (Liu et al., 2019) has demonstrated the robustness of the effect, and provides invaluable insight into the nature of this effect.

---

[1] Interestingly, some similarities do exist between the mathematical frameworks that describe low-temperature CMP and early-universe cosmology. See Kibble and Srivastava (2013).

[2] An isolated single layer of graphite consisting of carbon atoms bonded together in a hexagonal structure. See, e.g., Abergel et al. (2010).

[3] For example, an important aspect of Laughlin's theory is its seamless concinnity of classical plasma physics and the planar electron gas that has inspired others to use a similar approach to quark-gluon plasma (Lu, 2022).

[4] A detailed exposition of the meaning and examples of “paradigm shifts” (Kuhn-type) can be found in Leggett (2018).

The dynamics of an electron in a periodic potential subjected to a perpendicular magnetic field has been an intriguing problem for more than half a century (Obermair and Wannier, 1976; Osadchy and Avron, 2001)[5]. Within the nearest neighbor tight-binding description of the periodic potential the electron energy spectrum is described by the Harper equation (Harper, 1955). Numerical solution of this equation (Hofstadter, 1976) has revealed that the applied field splits the Bloch bands into subbands and gaps. As the field is varied, the splitting of band continues indefinitely, leading to bands within bands within bands. When plotted as a function of the magnetic flux per lattice cell, the energy spectrum depicts a *fractal* pattern (a self-similar pattern that repeats at every scale) and is known in the literature as Hofstadter's butterfly because of the resemblance of the pattern to butterflies[6]. Observation of the butterfly spectra in real systems is an arduous task. For example, in ordinary crystalline lattices, the required magnetic field to see the butterflies exceeds 1000 Tesla, which is far beyond the reach of present-day technology. Graphene seems to be the ideal system in the quest of those fractal butterflies (Weiss, 2013). It is interesting to note that a mathematical solution of the Harper equation, in contrast to the numerical solution mentioned above, remained a challenging problem (the so-called Ten Martini Problem) for mathematicians until it was solved (Avila and Jitomirskaya, 2006) in 2006.

Magnetism has been known to mankind since ancient times, and it remains a major topic in CMP. The road to understanding magnetism has been long and tortuous. At various times in history, magnets were claimed to have the healing power to cure a myriad of ailments that included epilepsy, arthritis, gout, and baldness. Magnets were the prime ingredients for the "elixir of life" by Paracelsus (1493–1541). Then there was the healing process of "animal magnetism" proposed by Franz Anton Mesmer (1734–1815) (mesmerism)[7], which was famously mocked in Mozart's *Così fan tutte* (Steptoe, 1986). Our current understanding of magnetism is deeply rooted in quantum mechanics as Van Vleck explained (Van Vleck, 1978): "Quantum mechanics is the key to understand magnetism. When one enters the first room with this key there are unexpected rooms beyond, but it is always the master key that unlocks each door." For centuries, the magnetism of certain rocks and metallic iron was only used for the practical purposes of direction finding, particularly navigation with a compass. Motors, generators, and electrical distribution networks appeared only in the 19th century after the discovery of the deep connection between electricity and magnetism. Magnetic order is a collective phenomenon akin to superconductivity and superfluidity that involves a very large number of particles. The rich variety of magnetically ordered states in solids, not only ferromagnetism but also antiferromagnetism, ferrimagnetism, and a range of noncollinear structures, was confirmed only in the middle of the 20th century, with the availability of neutron beams in research reactors. A range of new magnetic materials are taking their place as active layers in thin film sensors and memory devices (Baltz et al., 2018). Besides information storage (Blundell, 2001), important technical applications include magnetic resonance imaging (MRI) and the use of magnetic nanoparticles in medicine.

Many outstanding discoveries in magnetism and magnetic materials have resulted in rapid advances in information storage technology. Over the last two decades spintronics has emerged as an important field of research both from the point of view of fundamental science and advanced technological applications (Yamaguchi et al., 2021; Pinarbasi and Kent, 2022). The giant magnetoresistance (GMR) effect, the spin Hall effect, and the spin galvanic effects are typical examples of developments in the field. Spintronics aims at understanding how the spin degree of freedom of the electrical carriers can be controlled in order to obtain devices with new functionalities and better performance. This endeavor often combines concepts from different aspects of condensed matter systems, giving the topic a fascinating interdisciplinary flavor. Spintronic phenomena are now being studied in an impressive range of different materials ranging from metals to half-metals to semiconductors, graphene and other two-dimensional systems such as transition metal dichalcogenides.

---

[5] For a recent review on butterflies in graphene, see for example Chakraborty and Apalkov (2015).

[6] However, as one of the authors of this Encyclopedia has (somewhat humorously) pointed out, this butterfly has Lebesgue measure zero, that is, it cannot fly!.

[7] A wonderful account of the use of magnetism in medicine since ancient times can be found in Mourino (1991).

The GMR effect and the related tunnel magnetoresistance effect (TMR) found their first commercial use in magnetic field sensors for hard-disk read-heads, before broadening their field of application to include magnetic sensors for the automobile industry, solid-state compasses, biosensors, and nonvolatile magnetic memory (Hartmann, 2000). The ability to manipulate the magnetic state of ferromagnetic structures led to initial developments in spintronics, where the spin direction was controlled by externally applied magnetic fields. However, the push for downscaling and faster timescales has prompted research advances in the past decade where the manipulation of magnetic configurations is achieved by local electric currents (the spin torque effect) (Brataas et al., 2012; Locatelli et al., 2014). In recent years, various novel concepts, such as chiral spintronics, skyrmionic spin textures, and magnetic domain walls in spintronics, have been actively pursued. The rate of progress in spintronics is truly astounding (Editorial, 2022).

In the past century, superconductivity has raised many theoretical challenges and triggered numerous technical developments. Discovered in mercury in 1911, this unique phenomenon occurs when the electrical resistance of many metals and alloys drops to zero when cooled below about 4 K, the temperature of liquid helium. More significantly, the material expels magnetic flux and becomes perfectly diamagnetic. Superconductivity has been adopted or evaluated for a wide range of technical applications (Rogalla and Kes, 2012). These include electric power generation, electric power transmission, high-speed maglev transportation, and ultra-strong magnetic field generation in high-resolution MRI and other nuclear magnetic resonance (NMR) systems. Interestingly, it took almost 50 years after the original discovery for the phenomena to be explained by the BCS theory (Tinkham, 2004) of reciprocal-space electron pairing, via the electron–phonon interaction. This electron–phonon mediated superconductivity became known as "conventional superconductivity" after the discovery of "high-temperature superconductivity" (Müller and Bednorz, 1987) at liquid nitrogen temperatures in tetragonal copper oxides in 1986. This threw open a new challenge to explain the properties of strongly correlated *anisotropic* electronic systems. Further new classes of superconductors that remain to be properly understood include the iron-based pnictides discovered in 2008 (Hosono et al., 2018). Recently, a two-dimensional superlattice made from a twisted bilayer of "magic angle" graphene was found to exhibit unconventional superconductivity (Cao et al., 2018), driven by electron–electron interactions.

The phenomenon of spontaneous symmetry breaking (SSB) is ubiquitous in physics, and plays a fundamental role in CMP, particle physics, and even in cosmology. A classic illustration of SSB being Heisenberg's 1928 paper on ferromagnetism (Heisenberg, 1928). It is responsible for various collective modes, such as the famous Nambu-Goldstone (NG) and Higgs modes. Named by Baker and Glashow (Baker and Glashow, 1962), SSB corresponds to the case where the ground or lowest-energy state does not have the symmetry of the underlying dynamics. Instead, multiple degenerate ground states are available and the symmetry breaking is *spontaneous* because it is not clear, a priori, which one of those ground states will be chosen. In this well-trodden territory a simple analogy of this abstruse concept given by A. Salam is illuminating (CERN, 1977): "Imagine a banquet where guests sit at round tables. A bird's eye view of the scene presents total symmetry, with serviettes alternating with people around each table. A person could equally well take a serviette from his right or from his left. The symmetry is spontaneously broken when one guest decides to pick up from his left and everyone else follows suit." Over the years, development of the concept of SSB has taken a circuitous route (Gaudenzi, 2022): "from the land of particle physics to the physics of many bodies (solids and nuclei), from there to the province of superconductivity, and from the latter back to particle physics … ." SSB's significance extends beyond the physics of the Higgs boson to the study of low-energy phenomena such as superconductivity, superfluidity, magnetism, and others. Historically, the particle physics community has been guided by this exploration in their quest to understand and discover particles like the Higgs boson. More to the point, when a continuous symmetry is spontaneously broken, a gapless mode, the NG mode, appears which governs the low-energy behavior of the system. As an example, in a solid, the acoustic phonon is the NG mode associated with translational symmetry breaking and determines the behavior of the specific heat at low temperature (the Debye T^3 law). Recently, signatures of Higgs and Goldstone modes have been proposed to exist in a perovskite oxide (Marthinsen et al., 2018), in other crystalline structures (Vallone, 2019), and also in various other quantum systems (Léonard et al., 2017). On a lighter note, it is the symmetry breaking that is claimed to have prevented the fabled donkey (Weintraub, 2012) in the parable by Jean Buridan (1300–50) from dying of starvation (Fubini, 1974).

Common to the theoretical descriptions of these phenomena across CMP and high-energy physics is Quantum field theory (QFT). QFT was originally developed to describe the fundamental processes in high-energy physics, but has now become a valuable tool to address problems across physics, in particular, in CMP (Fradkin, 2013; see also, Mustafa, 2023), statistical physics, modern quantum chemistry, and even in

pure mathematics (Folland, 2008). Advances in our understanding of strongly correlated electron systems in CMP such as high-temperature superconductivity and the FQHE have been aided by the QFT. It has facilitated the treatment of spontaneous symmetry broken states, such as superfluids. Interestingly, many of the conceptual developments in CMP have, in return, had a reciprocal impact in QFT. A spectacular example being Nambu's work in dynamical symmetry breaking (Weinberg, 1986; Nambu, 2009) in particle physics, based on the BCS theory of superconductivity.

A glass is a noncrystalline solid obtained by quenching a liquid. It has a liquid-like structure, but a transition from liquid to solid behavior occurs on cooling. It may have one of a continuum of possible ground states that exhibit frozen-in liquid-like disorder. The term "spin glass" was coined by B.R. Coles (Mydosh, 1993) in 1970 for a diluted magnetic material with frozen-in paramagnetic-like spin disorder where the magnetic moments interact with randomly varying positive or negative exchange interactions leading to a multitude of possible ground states with different, random orientations of the spins. As in a normal glass, the energy barriers between the continuum of metastable states prevent it from ever reaching equilibrium. This phase of condensed matter has been an important and productive area of research. Spin-glass models are conceptually simple, but embody sophisticated physics. These models have become a paradigm for the solution of complex optimization problems (Mézard, 2022): much like the undulating flight patterns of starlings around the skies over Rome (Parisi, 2023). After cooling from the paramagnetic phase, the spin glass remains out of equilibrium, and it slowly evolves. This aging phenomenon corresponds to the growth of a "spin-glass order" parameter, whose correlation length can be measured (Joh et al., 1999). A cooling temperature step during aging causes a partial "rejuvenation," while the "memory" of previous aging is stored and can be retrieved (Refregier et al., 1987; Bouchaud et al., 2001). Many glassy materials present aging, and rejuvenation and memory effects can be found in other cases, but they are usually less pronounced. Numerical simulations of these phenomena are under active investigation using custom-built computers (Baity-Jesi et al., 2023; Vincent, 2023). A general understanding of glassy systems, to which spin glasses bring some special insight, is being pursued. It was realized decades ago that the physics of spin glasses has deep connections with the behavior of complex biological systems. In fact, spin-glass type states in neural network models offer interesting insights into states of high and low brain activity, as observed in mammals (Recio and Torres, 2016). These analogies are potentially useful for applications in fields such as robotics and artificial intelligence (AI) (Andriuschenko et al., 2022).

One of the most spectacular phenomena in CMP, discovered in the last century, was Bose-Einstein condensation (BEC). This macroscopic quantum phenomenon had its genesis in the work of Satyendra Nath Bose (Bose, 1924; Blanpied, 1972; Tomczyk, 2022) (whose name is forever associated with bosons), and has fascinated physicists for decades, ever since the first observation of this exotic state of matter in an ultracold gas of rubidium atoms (Georgescu, 2020). Among the advances made in this field, we highlight only a few: simulation of correlated electron states, such as the FQHE state and a bosonic analog of the Laughlin state, and the famous BEC-BCS crossover from a BEC to a BCS superfluid of weakly bound Cooper pairs, as the interparticle interaction strength is varied. Noteworthy is the recent measurement of the dynamic structure factor in an ultracold Fermi gas of lithium-6 atoms in the "unitary" limit, where a linear phonon mode for low momentum transfer can be clearly discerned (Biss et al., 2022). Perhaps such a method might one day shed light on the Laughlin quasiparticle gap and the collective modes that are still largely unresolved (Chakraborty and Pietiläinen, 1988, 1995; Halperin, 1983; Clark and Maksym, 1989).

Liquid helium, ^{4}He, and the less common isotope ^{3}He are unique quantum systems (Volovik, 2009). They remain liquid even at absolute zero temperature, a direct manifestation of Heisenberg's uncertainty principle and zero-point energy. The light mass of helium atoms and their weak interatomic attraction leads to a substantial zero-point kinetic energy and the system remains in the liquid state at ambient pressure. Solidification occurs when a pressure of about 25 MPa is applied. The different quantum statistics of the two helium isotopes (^{4}He is a boson while ^{3}He is a fermion) are responsible for the different physical characteristics of the two systems. Microscopic approaches to understand the ground state and low-energy excitations of the liquid state have occupied researchers for many decades (see for example, Ristig and Clark, 1976; Lam et al., 1977). These highly correlated quantum fluids have been established as systems where the efficacies of different many-body theories can be tested (Kallio and Smith, 1977; Lantto et al., 1977). These systems have been described as Ariadne's thread in this Encyclopedia, where the strongly interacting constituent particles are treated by a variety of ingenious theoretical and experimental approaches. Interestingly, liquid helium has been proposed to be a medium to design multiexcitation detectors to probe *dark matter* (Schutz and Zurek, 2016) in the keV mass limit. Although this looks far afield from CMP, the interface between CMP and high-energy particle physics could inspire new horizons in CMP, as discussed earlier.

CMP also has an enormous impact on our daily lives with unceasing technological innovation stemming directly from the advances in CMP research. It is also closely associated with the progress of our understanding of materials science and mechanical, chemical, and electrical engineering that deals with properties of novel materials and devices. As some authors have very aptly pointed out (Chaikin and Lubensky, 1995): The use and understanding of matter in its condensed (liquid or solid) state have gone hand in hand with the advances of civilization and technology since the first use of primitive tools. So important has the control of condensed matter been to man that prehistoric ages—the Stone Age, the Bronze Age, the Iron Age—are named after the material dominating the technology of the time. In fact, modern civilization is entirely dependent on our deep understanding and practical use of materials, old and new: Steel, glass, and concrete have shaped our modern living with comfort, health, longevity, and material wealth. All around us, from a tiny paper clip to giant skyscrapers, from jet planes to modern medicines, and the ubiquitous plastics that are integrated into nearly all aspects of human life, are testaments to our control over the myriad behavior of materials (Miodownik, 2014). Today, a large number of materials are designed by using principles of quantum mechanics (Freeman, 2002).

The Silicon chip that launched the information age is a great example of the effect of CMP on our daily lives. The scaling of transistors down to the nanometer range has enabled them to be embedded in greater numbers in the all-pervasive electronic devices that have transformed every facet of life all around the world. The transition from room-size to pocket-size computers with ever increasing computational power and memory, that occurred in only a few decades, epitomizes the unrelenting progress made in this direction. Advances in nanoscale research have opened the door to exploration of the natural world at the ultra-small scale (Chakraborty, 2022), with the potential to shape our future world.

Quantum dots (QDs), the quasi-zero-dimensional electron systems, are one of the most extensively studied nanostructures in the past three decades. They represent the ultimate reduction in dimensionality of a semiconductor device. Here the electrons are confined (either electrostatically or structurally) in all three directions and occupy spectrally sharp energy levels similar to those found in atoms (Chakraborty, 1999), hence the popular moniker *artificial atoms* (Maksym and Chakraborty, 1990). QDs and other similar nanostructures (Chakraborty, 2003) offer a rich variety of fundamental phenomena that result from manipulation of single electrons (single electronics) or single spins at the nanoscale. The study of interacting electrons in a QD requires large-scale numerical computations involving matrices of dimensions in the millions ("monster matrices") (Chakraborty and Pietiläinen, 2005; Pietiläinen and Chakraborty, 2006). QDs are also thought to have vast potential for future technological applications. One prominent example being quantum cryptography where the QDs are used in single photon emitters (Nowak et al., 2014), and in single photon detectors (Shields et al., 2000). Quantum cryptography, in turn, forms the basis of the *quantum Internet* (Liao et al., 2018). Other applications include lasers, and spintronics in quantum computing, entertainment industry (Bourzac, 2013), and even in biology (Bruchez and Holz, 2007).

Research in recent years has increasingly revealed that quantum phenomena are also ubiquitous in the natural world (Ball, 2011). They govern how birds are able to navigate around the globe using Earth's magnetic field or how plants use photosynthesis to harvest sunlight for conversion to chemical energy. All depend on subtle quantum effects that are now coming to light, thereby ushering the topic of quantum biology into CMP. Deoxyribonucleic acid (DNA), the molecule responsible for storage of genetic information in the cells of all living organism, is entrusted with the task of preserving, copying, and transmitting information that are necessary for living beings to grow and function. It is often referred to as the body's hereditary material as DNA is replicated and transmitted from parents to their offspring. This "molecule of life" was discovered in 1869 by Friedrich Miescher in Tübingen, Germany, who called it "nuclein," as it was isolated from the nucleus of white blood cells (Dahm, 2005; Thess et al., 2021). It took more than eighty years from that momentous event, to discover that DNA has a right-handed double-helix structure with appropriate base pairing (Watson and Crick, 1953; Klug, 2004). That discovery was so important that it has been compared with the discovery of the atomic nucleus in physics (Frank-Khamenetskii, 1997). Understanding the structure of the atom heralded quantum physics, while understanding of the structure of DNA brought forth the field of molecular biology.

DNA has several remarkable properties that make this molecule a prime candidate for nano-electronic materials (Chakraborty, 2007). These include molecular recognition and the ability to self-assemble via the complementarity of the base sequences on the two strands, which means that DNA can be integrated error-free in current semiconductor technology. DNA can also detect information about its own integrity that can trigger its eventual repair mechanism. All these properties are perfectly suitable for developing nanoscale electronics involving DNA

(Taniguchi and Kawai, 2006). Despite the promise of harnessing biology to realize integrated molecular electronics remains fascinating, much work remains to be done to make it a reality (Braun and Keren, 2004).

Protein molecules play a vital role in all living organisms. They are described as Nature's robots (Tanford and Reynolds, 2001) because for every imaginable task required in a living organism, and for every step of that task, there is a protein designed to carry it out. These proteins are even programmed to know when to turn on or off. Just as the twenty-six letters in the alphabet can spell out hundreds of thousands of words, there are twenty different naturally occurring amino acids that can be combined into many more different proteins than there are atoms in the known universe! Protein's biological function is determined by its unique and native three-dimensional structures that are characteristic of individual proteins (Gomes and Faísca, 2019; Echenique, 2007). The question of how proteins fold to their unique, compact, and highly organized functional states has remained an enduring challenge ("The protein-folding problem") (Chan and Dill, 1993; Dill and MacCallum, 2012; Wolynes and Eaton, 1999). Recently, there has been a tremendous development in this area of research. In November 2020, an AI program called AlphaFold, designed to tackle the problem of protein folding, predicted the three-dimensional structures of almost every protein known to science—about 200 millions in all (Jumper et al., 2021). AlphaFold uses a machine learning methodology to bring together information from preexisting knowledge of protein structures, and other geometric and physical constraints to predict protein structures. While this has been heralded a watershed moment in structural biology (Perrakis and Sixma, 2021), there are many key questions that AlphaFold cannot address yet. These include aspects of protein behavior that cannot be understood from a static structure, such as how proteins respond to their environment or how intrinsically disordered proteins actually are organized. Some authors (Nasser et al., 2021) have likened it to solving a crime story: while AlphaFold presents a snapshot in time, the question about how we get there remains unanswered. Biological systems have developed elaborate mechanisms to ensure that proteins fold correctly, or otherwise, they are detected and degraded before any serious harm can result to the host organism. However, protein misfolding does happen and that misfolding in the cell is linked to an array of diseases, including cancers, cardiovascular disease, type II diabetes, and numerous neurodegenerative diseases, such as Alzheimer's, Parkinson's, and Huntington's disease. NMR spectroscopy has been an important technique to study protein folding where valuable insights are gained into many aspects of the folding process (Jane Dyson and Wright, 1996).

In this Encyclopedia, we strive to present a taste of all the developments in CMP described above (and much more), written by experts in the field. We are keenly aware that many important and interesting topics are not covered here. However, that is not for want of trying. As some authors had rightly pointed out (Hoddeson, 1992): The field is huge and varied and lacks the unifying features beloved of historians, neither a single hypothesis or set of basic equations underpin the field, as in quantum mechanics or relativity theory, nor a single spectacular and fundamental discovery such as uranium fission for nuclear technology or the structure of DNA for molecular biology. CMP owes what unity it has simply to a common concern with solid and liquid materials. This encompasses such a large range of theories and methods that the field resembles a confederation of interest groups rather than a single entity. Clearly, the task of collecting everything in one place is a monumental endeavor, but we do hope that our compilation of a large number of chapters in this five-volume work, covering a broad range of in-depth descriptions of varied phenomena in CMP will be a treasured source of facts and ideas for the community.

It is undeniably true that there would have been no Encyclopedia without the extraordinary contributions of the large number of authors whose valuable time and efforts brought this project to fruition. My sincere thanks to all of them. I also wish to extend my deep appreciation to the staff at Elsevier for their skillful handling of this huge project. The cover image was created by Hong-Yi Chen from National Taiwan Normal University. The image below was created by Elisabetta Collini, one of the authors. My deepest appreciation to them for taking the time to do this work. Finally, my sincere thanks to the Section editors, Vladimir Fomin, Ana Sanchez, Roberto Raimondi, Hideo Aoki, Rudolf Römer, and Robert Blick for the effort they all expended, that has contributed to the success of this venture. Special thanks go to Vladimir Fomin and Ana Sanchez for securing a large share of the chapters and for their enduring help in providing valuable advice and support to bring the project to fruition. Thanks are also due to many of my friends and colleagues, in particular, Michael Coey, Jürg Fröhlich, Sinéad Griffin, Peter Maksym, Eric Vincent, and Jakob Yngvason for their careful and critical reading of the introduction.

Tapash Chakraborty
St. Catharines
Ontario, Canada

References

Abergel DSL, Apalkov V, Berashevich J, Ziegler K, and Chakraborty T (2010) Properties of graphene: A theoretical perspective. *Advances in Physics* 59: 261. https://doi.org/10.1080/00018732.2010.487978.

Andriuschenko P, Kapitan D, and Kapitan V (2022) A new look at the spin glass problem from a deep learning perspective. *Entropy* 24: 697. https://doi.org/10.3390/e24050697.

Apalkov VM and Chakraborty T (2006) Fractional quantum Hall states of Dirac electrons in graphene. *Physical Review Letters* 97: 126801. https://doi.org/10.1103/PhysRevLett.97.126801.

Apalkov VM and Chakraborty T (2010) Controllable driven phase transitions in fractional quantum Hall states in bilayer graphene. *Physical Review Letters* 105: 036801. https://doi.org/10.1103/PhysRevLett.105.036801.

Apalkov VM and Chakraborty T (2011) Stable pfaffian state in bilayer graphene. *Physical Review Letters* 107: 186803. https://doi.org/10.1103/PhysRevLett.107.186803.

Arovas D, Schrieffer JR, and Wilczek F (1984) Fractional statistics and the quantum Hall effect. *Physical Review Letters* 53: 722. https://doi.org/10.1103/PhysRevLett.53.722.

Avila A and Jitomirskaya S (2006) Solving the ten martini problem. *Lecture Notes in Physics* 690: 5. https://doi.org/10.1007/3-540-34273-7_2.

Baity-Jesi M, et al. (2023) Memory and rejuvenation effects in spin glasses are governed by more than one length scale. *Nature Physics* 19: 978–985. https://doi.org/10.1038/s41567-023-02014-6.

Baker M and Glashow SL (1962) Spontaneous breakdown of elementary particle symmetries. *Physics Review* 128: 2462. https://doi.org/10.1103/PhysRev.128.2462.

Ball P (2011) Physics of life: The dawn of quantum biology. *Nature* 474: 272. https://doi.org/10.1038/474272a.

Baltz V, et al. (2018) Antiferromagnetic spintronics. *Reviews of Modern Physics* 90: 015005. https://doi.org/10.1103/RevModPhys.90.015005.

Bartolomei H, et al. (2020) Fractional statistics in anyon collisions. *Science* 368: 173. https://doi.org/10.1126/science.aaz5601.

Biss H, et al. (2022) Excitation spectrum and superfluid gap of an ultracold Fermi gas. *Physical Review Letters* 128: 100401. https://doi.org/10.1103/PhysRevLett.128.100401.

Blanpied WA (1972) Satyendranath Bose: Co-founder of quantum statistics. *American Journal of Physics* 40: 1212. https://doi.org/10.1119/1.1986805.

Blundell S (2001) *Magnetism in Condensed Matter*. New York: Oxford U.P.

Bose SN (1924) Plancks gesetz und lichtquantenhypothese. *Zeitschrift für Physik* 26: 178. https://doi.org/10.1007/BF01327326.

Bouchaud J-P, Dupuis V, Hammann J, and Vincent E (2001) Separation of time and length scales in spin glasses: Temperature as a microscope. *Physical Review B* 65: 024439. https://doi.org/10.1103/PhysRevB.65.024439.

Bourzac K (2013) Quantum dots go on display. *Nature* 493: 283. https://doi.org/10.1038/493283a.

Brataas A, Kent AD, and Ono H (2012) Current-induced torques in magnetic materials. *Nature Materials* 11: 372. https://doi.org/10.1038/nmat3311.

Braun E and Keren K (2004) From DNA to transistors. *Advances in Physics* 53: 441. https://doi.org/10.1080/00018730412331294688.

Bruchez MP and Holz CZ (2007) *Quantum Dots: Applications in Biology*. New Jersey: Humana Press. https://doi.org/10.1385/1597453692.

Cao Y, et al. (2018) Unconventional superconductivity in magic-angle graphene superlattices. *Nature* 556: 43. https://doi.org/10.1038/nature26160.

CERN. (1977) Gauge theories with the lid, partially, off. *CERN Courier* 17: 271. https://cds.cern.ch/record/1730245/files/vol17-issue9-p271-e.pdf.

Chaikin PM and Lubensky TC (1995) *Principles of Condensed Matter Physics*. Cambridge University Press. https://doi.org/10.1017/CBO9780511813467.

Chakraborty T (1985) Elementary excitations in the fractional quantum Hall effect. *Physical Review B* 31: 4026. https://doi.org/10.1103/PhysRevB.31.4026.

Chakraborty T (1999) *Quantum Dots: A Survey of the Properties of Artificial Atoms*. Amsterdam: North-Holland. https://doi.org/10.1016/B978-0-444-50258-2.X5000-7.

Chakraborty T (2003) Nanoscopic quantum rings: A new perspective. *Advances in Solid State Physics* 43: 79. https://doi.org/10.1007/978-3-540-44838-9_6.

Chakraborty T (ed.) (2007) *Charge Migration in DNA*. Springer. https://doi.org/10.1007/978-3-540-72494-0.

Chakraborty T (2022) *Nanoscale Quantum Materials: Musings on the Ultra-Small World*. CRC Press. https://doi.org/10.1201/9781003090908.

Chakraborty T and Apalkov VM (2015) Fractal butterflies of Dirac fermions in monolayer and bilayer graphene. *IET Circuits, Devices and Systems* 9: 19. https://doi.org/10.1049/iet-cds.2014.0275.

Chakraborty T and Pietiläinen P (1988) *The Fractional Quantum Hall Effect*. Springer Verlag. https://doi.org/10.1007/978-3-642-97101-3.

Chakraborty T and Pietiläinen P (1995) *The Quantum Hall Effects*, 2nd. Springer. https://doi.org/10.1007/978-3-642-79319-6.

Chakraborty T and Pietiläinen P (2005) Optical signatures of spin-orbit interaction effects in a parabolic quantum dot. *Physical Review Letters* 95: 136603. https://doi.org/10.1103/PhysRevLett.95.136603.

Chan HS and Dill KA (1993) The protein folding problem. *Physics Today* 46: 24. https://doi.org/10.1063/1.881371.

Clark R and Maksym P (1989) Fractional quantum Hall effect in a spin. *Physics World* 2: 39. https://doi.org/10.1088/2058-7058/2/9/23.

Cohen ML (2008) Fifty years of condensed matter physics. *Physical Review Letters* 101: 250001. https://doi.org/10.1103/PhysRevLett.101.250001.

Dahm R (2005) Friedrich miescher and the discovery of DNA. *Developmental Biology* 278: 274. https://doi.org/10.1016/j.ydbio.2004.11.028.

Dill KA and MacCallum JL (2012) The protein-folding problem, 50 years on. *Science* 338: 1042. https://doi.org/10.1126/science.1219021.

Echenique P (2007) Introduction to protein folding for physicists. *Contemporary Physics* 48: 81. https://doi.org/10.1080/00107510701520843.

Editorial (2022) New horizons in spintronics. Nature Materials 21: 1. https://doi.org/10.1038/s41563-021-01184-z.

Eisenstein JP and Stormer HL (1990) The fractional quantum Hall effect. *Science* 248: 1510. https://doi.org/10.1126/science.248.4962.1510.

Folland GB (2008) *Quantum Field Theory: A tourist guide for Mathematicians*. American Mathematical Society. https://doi.org/10.1090/surv/149.

Fradkin E (2013) *Field Theories of Condensed Matter Physics*. Cambridge University Press. https://doi.org/10.1017/CBO9781139015509.

Frank-Khamenetskii MD (1997) *Unraveling DNA: The Most Important Molecule of life*. Basic Books.

Freeman AJ (2002) Materials by design and the exciting role of quantum computation/simulation. *Journal of Computational and Applied Mathematics* 149: 27. https://doi.org/10.1016/S0377-0427(02)00519-8.

Fubini S (1974) Present trends in particle physics. In: *Proc. Intl. Conf. on High Energy Physics*. Didcot, England: Rutherford Laboratory. https://cds.cern.ch/record/417271/files/CM-P00060491.pdf.

Gaudenzi R (2022) *Historical Roots of Spontaneous Symmetry Breaking: Steps Towards an Analogy*. Springer. https://doi.org/10.1007/978-3-030-99895-0.

Georgescu I (2020) 25 Years of BEC. *Nature Reviews Physics* 2: 396. https://doi.org/10.1038/s42254-020-0211-7.

Gomes CM and Faísca PFN (2019) *Protein Folding: An Introduction*. Springer. https://doi.org/10.1007/978-3-319-00882-0_1.

Halperin BI (1983) Theory of the quantized Hall conductance. *Helvetica Physica Acta* 56: 75. https://doi.org/10.5169/seals-115362.

Halperin BI (1984) Statistics of quasiparticles and the hierarchy of fractional quantized Hall states. *Physical Review Letters* 52: 1583. https://doi.org/10.1103/PhysRevLett.52.1583.

Harper PG (1955) Single band motion of conduction electrons in a uniform magnetic field. *Proceedings of the Physical Society. Section A* 68: 874. https://doi.org/10.1088/0370-1298/68/10/304.

Hartmann U (2000) *Magnetic Multilayers and Giant Magnetoresistance: Fundamentals and Industrial Applications*. Berlin: Springer Verlag. https://doi.org/10.1007/978-3-662-04121-5.

Heisenberg W (1928) Zur theorie des ferromagnetismus. *Zeitschrift für Physik* 49: 619. https://doi.org/10.1007/BF01328601.

Hoddeson L (1992) *Out of the Crystal Maze: Chapters From the History of Solid-State Physics*. N.Y.: Oxford University Press.

Hofstadter D (1976) Energy levels and wave functions of Bloch electrons in rational and irrational magnetic fields. *Physical Review B* 14: 2239. https://doi.org/10.1103/PhysRevB.14.2239.

Hosono H, et al. (2018) Recent advances in iron-based superconductors toward applications. *Materials Today* 21: 278. https://doi.org/10.1016/j.mattod.2017.09.006.

Jane Dyson H and Wright PE (1996) Insights into protein folding from NMR. *Annual Review of Physical Chemistry* 47: 369. https://doi.org/10.1146/annurev.physchem.47.1.369.

Jiang Z, et al. (2007) Quantum Hall effect in graphene. *Solid State Communications* 143: 14. https://doi.org/10.1016/j.ssc.2007.02.046.

Joh YG, Orbach R, Wood JJ, Hammann J, and Vincent E (1999) Extraction of the spin glass correlation length. *Physical Review Letters* 82: 438. https://doi.org/10.1103/PhysRevLett.82.438.

Jumper J, et al. (2021) Highly accurate protein structure prediction with alphafold. *Nature* 596: 583. https://doi.org/10.1038/s41586-021-03819-2.

Kallio A and Smith RA (1977) How simple can HNC be and still be right? *Physics Letters B* 68: 315. https://doi.org/10.1016/0370-2693(77)90483-X.

Kibble T and Srivastava A (2013) Condensed matter analogues of cosmology. *Journal of Physics. Condensed Matter* 25: 400301. https://doi.org/10.1088/0953-8984/25/40/400301.

Klug A (2004) The discovery of the DNA double helix. *Journal of Molecular Biology* 335: 3. https://doi.org/10.1016/j.jmb.2003.11.015.

Lam PM, Clark JW, and Ristig ML (1977) Density matrix and momentum distribution of helium liquids and nuclear matter. *Physical Review B* 16: 222. https://doi.org/10.1103/PhysRevB.16.222.

Lantto LJ, Jackson AD, and Siemens PJ (1977) HNC variational calculations of boson matter. *Physics Letters B* 68: 311. https://doi.org/10.1016/0370-2693(77)90482-8.

Laughlin RB (1983) Anomalous quantum Hall effect: An incompressible quantum fluid with fractionally charged excitations. *Physical Review Letters* 50: 1395. https://doi.org/10.1103/PhysRevLett.50.1395.

Laughlin RB (1984) Primitive and composite ground states in the fractional quantum Hall effect. *Surface Science* 142: 163. https://doi.org/10.1016/0039-6028(84)90301-7.

Laughlin RB and Pines D (2000) The theory of everything. *Proceedings of the National Academy of Sciences of the United States of America* 97: 28. https://doi.org/10.1073/pnas.97.1.28.

Leggett A (1992) On the nature of research in condensed-state physics. *Foundations of Physics* 22: 221. https://doi.org/10.1007/BF01893613.

Leggett A (2018) Reflections on the past, present and future of condensed matter physics. *Science Bulletin* 63: 1019. https://doi.org/10.1016/j.scib.2018.07.004.

Leinaas JM and Myrheim J (1977) On the theory of identical particles. *Il Nuovo Cimento B* 37: 1. https://doi.org/10.1007/BF02727953.

Léonard J, et al. (2017) Monitoring and manipulating higgs and goldstone modes in a supersolid quantum gas. *Science* 358: 1415. https://doi.org/10.1126/science.aan2608.

Liao S-K, et al. (2018) Satellite-relayed intercontinental quantum network. *Physical Review Letters* 120: 030501. https://doi.org/10.1103/PhysRevLett.120.030501.

Liu X, Hao Z, Watanabe K, Taniguchi T, Halperin BI, and Kim P (2019) Interlayer fractional quantum Hall effect in a coupled graphene double layer. *Nature Physics* 15: 893. https://doi.org/10.1038/s41567-019-0546-0.

Locatelli N, Cros V, and Grollier J (2014) Spin-torque building blocks. *Nature Materials* 13: 11. https://doi.org/10.1038/nmat3823.

Lu W (2022) Quark-gluon plasma and nucleons à la Laughlin. *International Journal of Geometric Methods in Modern Physics* 19: 2250061. https://doi.org/10.1142/S021988782250061X.

Maksym P and Chakraborty T (1990) Quantum dots in a magnetic field: Role of electron-electron interactions. *Physical Review Letters* 65: 108. https://doi.org/10.1103/PhysRevLett.65.108.

Marthinsen A, et al. (2018) Goldstone-like phonon modes in a (111)-strained perovskite. *Physical Review Materials* 2: 014404. https://doi.org/10.1103/PhysRevMaterials.2.014404.

Mézard M (2022) Spin glasses and optimization in complex systems. *Europhysics News* 53: 15. https://doi.org/10.1051/epn/2022105.

Miodownik M (2014) *Stuff Matters: Exploring the Marvelous Materials That Shape Our Man-Made World*. N.Y.: Houghton Mifflin Harcourt.

Morf R and Halperin BI (1986) Monte Carlo evaluation of trial wave functions for the fractional quantized Hall effect: Disk geometry. *Physical Review B* 33: 2221. https://doi.org/10.1103/PhysRevB.33.2221.

Mourino MR (1991) From thales to lauterbur, or from the loadstone to MR imaging: Magnetism and medicine. *Radiology* 180: 593. https://doi.org/10.1148/radiology.180.3.1871268.

Müller KA and Bednorz JG (1987) The discovery of a class of high-temperature superconductors. *Science* 237: 1133. https://doi.org/10.1126/science.237.4819.1133

Mustafa MG (2023) An introduction to thermal field theory and some of its application. *The European Physical Journal Special Topics* 232: 1369–1457. https://doi.org/10.1140/epjs/s11734-023-00868-8.

Mydosh JA (1993) *Spin Glasses: An Experimental Introduction*. CRC Press.

Nakamura J, et al. (2020) Direct observation of anyonic braiding statistics. *Nature Physics* 16: 931. https://doi.org/10.1038/s41567-020-1019-1.

Nambu Y (2009) Nobel lecture: Spontaneous symmetry breaking in particle physics: A case of cross fertilization. *Reviews of Modern Physics* 81: 1015. https://doi.org/10.1103/RevModPhys.81.1015.

Nasser R, Dignon GL, Razban RM, and Dill KA (2021) The protein folding problem: The role of theory. *Journal of Molecular Biology* 433: 167126. https://doi.org/10.1016/j.jmb.2021.167126.

Nawrocki W (2019) *Introduction to Quantum Metrology*, 2nd. Springer. https://doi.org/10.1007/978-3-030-19677-6.

Nowak AL, et al. (2014) Deterministic and electrically tunable bright single-photon source. *Nature Communications* 5: 3240. https://doi.org/10.1038/ncomms4240.

Obermair GM and Wannier GH (1976) Bloch electrons in magnetic fields: Rationality, irrationality, degeneracy. *Physica Status Solidi (B)* 76: 217. https://doi.org/10.1002/pssb.2220760122.

Osadchy D and Avron JE (2001) Hofstadter butterfly as quantum phase diagram. *Journal of Mathematical Physics* 42: 5665. https://doi.org/10.1063/1.1412464.

Parisi G (2023) *In a Flight of Starlings: The Wonders of Complex Systems*. Penguin Press.

Perrakis A and Sixma TK (2021) Ai revolutions in biology. *EMBO Reports* 22: e54046. https://doi.org/10.15252/embr.202154046.

Pietiläinen P and Chakraborty T (2006) Energy levels and magneto-optical transitions in parabolic quantum dots with spin-orbit coupling. *Physical Review B* 73: 155315. https://doi.org/10.1103/PhysRevB.73.155315.

Pinarbasi M and Kent AD (2022) Perspectives on spintronics technology: Giant magnetoresistance to spin transfer torque magnetic random access memory. *APL Materials* 10: 020901. https://doi.org/10.1063/5.0075945.

Recio I and Torres JJ (2016) Emergence of low noise frustrated states in E/I balanced neural networks. *Neural Networks* 84: 91. https://doi.org/10.1016/j.neunet.2016.08.010.

Refregier P, Vincent E, Hammann J, and Ocio M (1987) Ageing phenomena in a spin-glass: Effect of temperature changes below Tg. *Journal of Physics (France)* 48: 1533. https://doi.org/10.1051/jphys:019870048090153300.

Ristig ML and Clark JW (1976) Density matrix of quantum fluids. *Physical Review B* 14: 2875. https://doi.org/10.1103/PhysRevB.14.2875.

Rogalla H and Kes PH (2012) *100 Years of Superconductivity*. Boca Raton: Taylor & Francis Group. https://doi.org/10.1201/b11312.

Schutz K and Zurek KM (2016) Detectability of light dark matter with superfluid helium. *Physical Review Letters* 117: 121302. https://doi.org/10.1103/PhysRevLett.117.121302.

Shields AJ, et al. (2000) Detection of single photons using a field-effect transistor gated by a layer of quantum dots. *Applied Physics Letters* 103: 3673. https://doi.org/10.1063/1.126745.

Steptoe A (1986) Mozart, mesmer and ‘cosi fan tutte’. *Musics and Letters* 67: 248. https://doi.org/10.1093/ml/67.3.248.

Störmer HL (1992) Two-dimensional electron correlation in high magnetic fields. *Physica B: Condensed Matter* 177: 401. https://doi.org/10.1016/0921-4526(92)90138-I.

Tanford C and Reynolds J (2001) *Nature's Robots: A History of Proteins*. Oxford University Press.

Taniguchi M and Kawai T (2006) Dna electronics. *Physica E: Low-dimensional Systems and Nanostructures* 33: 1. https://doi.org/10.1016/j.physe.2006.01.005.

Thess A, et al. (2021) Historic nucleic acids isolated by Friedrich Miescher contain RNA beside DNA. *Biological Chemistry* 402: 1179. https://doi.org/10.1515/hsz-2021-0226.

Tinkham M (2004) *Introduction to Superconductivity*. N.Y.: Dover.

Tomczyk H (2022) Did Einstein predict Bose-Einstein condensation? *Studies in History and Philosophy of Science* 93: 30. https://doi.org/10.1016/j.shpsa.2022.02.014.

Vallone M (2019) Higgs and goldstone modes in crystalline solids. *Physica Status Solidi* 257: 1900443. https://doi.org/10.1002/pssb.201900443.

Van Vleck JH (1978) Quantum mechanics—The key to understanding magnetism. *Reviews of Modern Physics* 50: 181. https://doi.org/10.1103/RevModPhys.50.181.

Vincent E (2023) Rejuvenated but remembering. *Nature Physics* 19: 926–927. https://doi.org/10.1038/s41567-023-02097-1.

Volovik GE (2009) *The Universe in a Helium Droplet*. Oxford University Press. https://doi.org/10.1093/acprof:oso/9780199564842.001.0001.

von Klitzing K (2019) Essay: Quantum Hall effect and the new international system of units. *Physical Review Letters* 122: 200001. https://doi.org/10.1103/PhysRevLett.122.200001.

von Klitzing K, Chakraborty T, Kim P, Madhavan V, Dai X, McIver J, Tokura Y, Savary L, Smirnova D, Rey AM, Felser C, Gooth J, and Qi X (2020) 40 years of the quantum Hall effect. *Nature Reviews Physics* 2: 397. https://doi.org/10.1038/s42254-020-0209-1.

Watson JD and Crick FHC (1953) Molecular structure of nucleic acids. *Nature* 171: 737. https://doi.org/10.1038/171737a0.

Weinberg S (1986) Superconductivity for particular theorists. *Progress of Theoretical Physics Supplement* 86: 43. https://doi.org/10.1143/PTPS.86.43.

Weintraub R (2012) What can we learn from Buridan's ass? *Canadian Journal of Philosophy* 42: 281. https://doi.org/10.1353/cjp.2012.0013.

Weiss D (2013) The butterfly emerges. *Nature Physics* 9: 395. https://doi.org/10.1038/nphys2680.

Wolynes PG and Eaton WA (1999) The physics of protein folding. *Physics World* 12: 39. https://doi.org/10.1088/2058-7058/12/9/24.

Yamaguchi A, Hirohata A, and Stadler BJH (2021) *Nanomagnetic Materials: Fabrication, Characterization and Application*. Elsevier. (Chapter 5). https://doi.org/10.1016/C2018-0-05445-6.

This page intentionally left blank

LIST OF CONTRIBUTORS FOR VOLUME 5

P Ambs
Université de Haute Alsace, ENSISA, Mulhouse, France

Vadym Apalkov
Department of Physics and Astronomy, Georgia State University, Atlanta, GA, United States

Maurizio Artoni
European Laboratory for Nonlinear Spectroscopy (LENS), Sesto Fiorentino, Firenze, Italy; Department of Engineering and Information Technology, Brescia University, Brescia, Italy; Istituto Nazionale di Ottica (INO-CNR), Firenze, Italy

SP Baker
Cornell University, Ithaca, NY, USA

Marcello Baricco
Department of Chemistry and NIS-INSTM, University of Turin, Turin, Italy

Franco Bassani[†]

WA Bassett
Cornell University, Ithaca, NY, USA

Jean Bellissard
School of Mathematics, Georgia Institute of Technology, Atlanta, GA, United States

TR Bieler
Michigan State University, East Lansing, MI, USA

K Binder
Johannes Gutenberg Universität Mainz, Mainz, Germany

C Brezinski
Université des Sciences et Technologies de Lille, Villeneuve d'Ascq, France

Jaehee Cho
Chonbuk National University, Jeonju, South Korea

Katerina A Christofidou
Department of Materials Science and Engineering, University of Sheffield, Sheffield, United Kingdom

TW Clyne
University of Cambridge, Cambridge, UK

MM Coleman
The Pennsylvania State University, University Park, PA, USA

P Colombo
University of Bologna, Bologna, Italy

KP Constant
Iowa State University, Ames, IA, USA

I Cristiani
Università di Pavia, Pavia, Italy

N Daldossoh
Università di Trento, Povo (Trento), Italy

M de Boissieu
Université Grenoble Alpes, CNRS, Grenoble INP-UGA, SIMaP, Grenoble, France

V Degiorgio
Università di Pavia, Pavia, Italy

Natasha Dropka
Leibniz-Institut für Kristallzüchtung (IKZ), Berlin, Germany

EN Economou
University of Crete, Heraklion, Greece

S Elsheikhi
University of Benghazi, Benghazi, Libya; University of Tokyo, Tokyo, Japan

DG Eskin
Brunel University London, Uxbridge, United Kingdom

C Ewels
Nantes Université, CNRS, Institut des Matériaux de Nantes Jean Rouxel, IMN, Nantes, France

JS Faulkner
Center for Biological and Materials Physics, Department of Physics, Florida Atlantic University, Boca Raton, FL, United States

---

[†] Deceased.

Michael Ferry
School of Materials Science and Engineering, The University of New South Wales, Sydney, NSW, Australia

Mike W Finnis
Department of Materials and Department of Physics, The Thomas Young Centre, Imperial College London, London, United Kingdom

W Beall Fowler
Lehigh University, Bethlehem, PA, United States

J Freudenberger
Leibniz IFW Dresden, Department of Metal Physics, Institute for Complex Materials, Dresden, Germany; TU Bergakademie Freiberg, Institute of Materials Science, Freiberg, Germany

J Friedrich
Fraunhofer Institute IISB, Erlangen, Germany

H Fujita
University of Tokyo, Tokyo, Japan

Z Gaburro
Università di Trento, Povo (Trento), Italy

Nathaniel P Gallop
Department of Physics, University of Warwick, Coventry, United Kingdom

AM Glazer
University of Oxford, Oxford, United Kingdom

JB Goodenough
University of Texas at Austin, Austin, TX, USA

O Gourdon
lowa State University, Ames, IA, USA

D Gout
lowa State University, Ames, IA, USA

Kevin-Peter Gradwohl
Leibniz-Institut für Kristallzüchtung (IKZ), Berlin, Germany

Uwe Grimm
Department of Mathematics and Statisics, The Open University, Walton Hall, Milton Keynes, United Kingdom

Giorgio Guizzetti
Dipartimento di Fisica, Università degli Studi di Pavia, Pavia, Italy

Th Hahn
Institut fur Kristallographie, RWTH Aachen, Aachen, Germany

A Harju
Aalto University, Espoo, Finland

Naoki Haruta
Fukui Institute for Fundamental Chemistry, Kyoto University, Kyoto, Japan

WF Hosford[†]

J-P Huignard
Thales Research & Technology, Palaiseau, France

Stuart JC Irvine
Swansea University, Wales, United Kingdom

T Janssen
University of Nijmegen, Nijmegen, The Netherlands

Shin-Woong Kang
Department of Nano Convergence Engineering, Jeonbuk National University, Jeonju, Korea

MI Katsnelson
Radboud University Nijmegen, Nijmegen, The Netherlands

James R Kermode
Warwick Centre for Predictive Modelling, School of Engineering, University of Warwick, Coventry, United Kingdom

Jong Kyu Kim
Pohang University of Science and Technology, Pohang, South Korea

H Klapper
Mineralogisch-Petrologisches Institut, Universität Bonn, Bonn, Germany

Robert Kudrawiec
Department of Semiconductor Materials Engineering, Faculty of Fundamental Problems of Technology, Wroclaw University of Science and Technology, Wrocław, Poland

Satyendra Kumar
Division for Research and Economic Development, and Department of Physics, University at Albany, Albany, NY, United States

GC La Rocca
NEST, Scuola Normale Superiore, Pisa, Italy

S Latil
CEA, IRAMIS, SPEC, GMT, Gif-sur-Yvette, France

Ron Lifshitz
Raymond and Beverly Sackler School of Physics & Astronomy, Tel Aviv University, Tel Aviv, Israel; School of Mathematics, University of Leeds, Leeds, United Kingdom

B Loiseaux
Thales Research & Technology, Palaiseau, France

[†] Deceased.

DA Lyashenko
Department of Physics and Mathematics, University of Eastern Finland, Joensuu, Finland

AE Markaki
University of Cambridge, Cambridge, UK

Paolo Mataloni
Physics Department, Sapienza University of Rome, Rome, Italy

F Mezei
Hahn-Meitner-Institut, Berlin, Germany

GJ Miller
Iowa State University, Ames, IA, USA

Rebecca L Milot
Department of Physics, University of Warwick, Coventry, United Kingdom

Eduard V Monaico
National Center for Materials Study and Testing, Technical University of Moldova, Chisinau, Republic of Moldova

Uwe Mueller
Macromolecular Crystallography, Helmholtz-Zentrum Berlin für Materialien und Energie GmbH, Berlin, Germany

Jian-Feng Nie
Monash University, Melbourne, VIC, Australia

PC Painter
The Pennsylvania State University, University Park, PA, USA

Lukas Palatinus
Institute of Physics of the CAS, Prague, Czechia

Maddalena Patrini
Dipartimento di Fisica, Università degli Studi di Pavia, Pavia, Italy

L Pavesi
Università di Trento, Povo (Trento), Italy

Jun Peng
Center for Hybrid Nanostructures, Universität Hamburg, Hamburg, Germany

B Raveau
Laboratoire de Cristallographie, ISMRA, Caen, France

Giancarlo Ruocco
Center for Life Nano Science @Sapienza, Istituto Italiano di Tecnologia, Roma, Italy; Dipartimento di Fisica, Universita' di Roma "La Sapienza", Roma, Italy

JS Rutherford
National University of Science and Technology, Bulawayo, Zimbabwe

Federico Scaglione
Department of Chemistry and NIS-INSTM, University of Turin, Turin, Italy

Walter Schirmacher
Institut für Physik, Universität Mainz, Mainz, Germany; Center for Life Nano Science @Sapienza, Istituto Italiano di Tecnologia, Roma, Italy

Michael Schreiber
Institut für Physik, Technische Universität Chemnitz, Chemnitz, Germany

E Fred Schubert
Rensselaer Polytechnic Institute, Troy, NY, USA

Caspar Schwalbe
MTU Aero Engines AG, Munich, Germany

Gautam Singh
Department of Applied Physics, Amity Institute of Applied Sciences, Amity University Uttar Pradesh, Noida, India

CM Soukoulis
Iowa State University, Ames, IA, USA

Riccardo Spagna
Institute of Crystallography—CNR, Montelibretti, Italy

EA Starke Jr.
University of Virginia, Charlottesville, VA, United States

M Strangwood
University of Warwick, Coventry, West Midlands, United Kingdom

J-B Suck
Chemnitz University of Technology, Chemnitz, Germany

Yu P Svirko
Department of Physics and Mathematics, University of Eastern Finland, Joensuu, Finland

Ion M Tiginyanu
Academy of Sciences of Moldova, Chisinau, Republic of Moldova; National Center for Materials Study and Testing, Technical University of Moldova, Chisinau, Republic of Moldova

L Tikana
Deutsches Kupferinstitut Berufsverband e.V., Düsseldorf, Germany

Y Toyozawa
University of Tokyo, Tokyo, Japan

RM Trevino
Michigan State University, East Lansing, MI, USA

V Vitek
University of Pennsylvania, Philadelphia, PA, USA

DA Walko
Argonne National Laboratory, Argonne, IL, USA

Manfred S Weiss
Macromolecular Crystallography, Helmholtz-Zentrum Berlin für Materialien und Energie GmbH, Berlin, Germany

DJ Willock
Cardiff Catalysis Institute, School of Chemistry, Cardiff University, Cardiff, United Kingdom

Kimihisa Yamamoto
Institute of Innovative Research, Tokyo Institute of Technology, Tokyo, Japan

I Yasui
University of Tokyo, Tokyo, Japan

An-Chou Yeh
Department of Materials Science and Engineering, National Tsing Hua University, Hsinchu, Taiwan, ROC; High Entropy Materials Center, National Tsing Hua University, Hsinchu, Taiwan, ROC

Jien-Wei Yeh
Department of Materials Science and Engineering, National Tsing Hua University, Hsinchu, Taiwan, ROC; High Entropy Materials Center, National Tsing Hua University, Hsinchu, Taiwan, ROC

Hung Yen
Department of Materials Science and Engineering, National Tsing Hua University, Hsinchu, Taiwan, ROC; High Entropy Materials Center, National Tsing Hua University, Hsinchu, Taiwan, ROC

AB Yu
ARC Research Hub for Computational Particle Technology, Department of Chemical and Biological Engineering, Monash University, Clayton, VIC, Australia

L Zeng
Michigan State University, East Lansing, MI, USA

Sen Zhang
Department of Chemistry, University of Virginia, Charlottesville, VA, United States

Weijie Zhang
Department of Chemistry, University of Virginia, Charlottesville, VA, United States

J-S Zhou
University of Texas at Austin, Austin, TX, USA

Robert Zierold
Center for Hybrid Nanostructures, Universität Hamburg, Hamburg, Germany

C Zweben
Zweben Consulting, Newtown Square, PA, United States

CONTENTS OF VOLUME 5

Magnetic point groups and space groups 1
Ron Lifshitz

Crystal structure 11
AM Glazer

Periodicity and lattices 17
JS Rutherford and AM Glazer

Crystal structure determination 29
Lukas Palatinus and Riccardo Spagna

Macromolecular crystallography 41
Uwe Mueller and Manfred S Weiss

Point groups 49
H Klapper and Th Hahn

Space Groups 61
T Janssen

Crystal Symmetry 69
Th Hahn and H Klapper

Crystal optics 80
DA Lyashenko and Yu P Svirko

Holography 88
P Ambs, J-P Huignard, and B Loiseaux

Sum rules and Kramers-Kronig relations in linear and nonlinear optics 105
Franco Bassani

Semiconductor optics 118
GC La Rocca

Ultrafast optics of topological materials 128
Vadym Apalkov

Electromagnetically induced transparency 138
Maurizio Artoni

Optical properties of materials 150
Giorgio Guizzetti and Maddalena Patrini

Photon statistics and coherence theory 167
Paolo Mataloni

Point defects 184
W Beall Fowler

Methods for bulk growth of inorganic crystals 190
J Friedrich

Crystal binding (interatomic forces): Ionic bonding and crystals 208
Mike W Finnis and James R Kermode

Crystal binding (interatomic forces): Metallic bonding and crystals 217
DJ Willock

Crystal growth, bulk: Theory and models 231
Natasha Dropka and Kevin-Peter Gradwohl

Film growth and epitaxy methods 248
Stuart JC Irvine

Thin Films, Mechanical Behavior of 261
SP Baker

Electronic and transport properties of aperiodic media 269
Jean Bellissard

Lattice dynamics: Aperiodic crystals 278
J-B Suck

Electronic structure of quasicrystals 290
Uwe Grimm and Michael Schreiber

Vibrational excitations in disordered solids 298
Walter Schirmacher and Giancarlo Ruocco

Atomic structure of quasicrystals 318
M de Boissieu

Materials: Composites 333
C Zweben

Self-organized porous semiconductor compounds 350
Ion M Tiginyanu and Eduard V Monaico

Structures: Liquid crystals 375
Gautam Singh, Shin-Woong Kang, and Satyendra Kumar

Highly Porous Metals and Ceramics 390
AE Markaki, P Colombo, and TW Clyne

Dislocations 404
V Vitek

Lattice Dynamics: Anharmonic Effects 411
MI Katsnelson

Ceramic Materials 416
KP Constant

Polymers, History of 424
MM Coleman and PC Painter

Neutrons and Neutron Scattering, History of 429
F Mezei

Ceramics, History of 437
I Yasui

Porous Silicon 442
Z Gaburro, N Daldossoh, and L Pavesi

Electronic states of semiconductor compounds and alloys 453
Robert Kudrawiec

Intermetallic Compounds, Electronic States of 469
O Gourdon, D Gout, and GJ Miller

Transition-Metal Compounds, Electronic and Magnetic Properties of 485
JB Goodenough

Micromechanical Devices and Systems 504
H Fujita and S Elsheikhi

Alloys: Overview 511
Federico Scaglione and Marcello Baricco

Alloys: Iron 522
Michael Ferry

Alloys: Steel 533
M Strangwood

Alloys: Magnesium 549
Jian-Feng Nie

Electronic structure: Impurity and defect states in metals and alloys 565
JS Faulkner

Alloys: Aluminum 573
EA Starke Jr. and DG Eskin

Alloys: The superalloys 583
Katerina A Christofidou and Caspar Schwalbe

Alloys: Copper 601
J Freudenberger, L Tikana, and WF Hosford

Alloys: Titanium 635
TR Bieler, RM Trevino, and L Zeng

High-entropy alloys: An overview on the fundamentals, development, and future perspective 647
Hung Yen, An-Chou Yeh, and Jien-Wei Yeh

Halide perovskites: Properties, synthesis, and applications 659
Nathaniel P Gallop and Rebecca L Milot

Powder processing—Models and simulations 679
AB Yu

Molecular clusters 694
Naoki Haruta and Kimihisa Yamamoto

Electronic states of carbon materials 702
S Latil and C Ewels

Atomic layer deposition of materials 716
Jun Peng and Robert Zierold

Catalysts: Combinatorial heterogeneous catalysis 729
Weijie Zhang and Sen Zhang

Catalysts: Materials 738
Weijie Zhang and Sen Zhang

Numerical Approximation and Analysis 750
C Brezinski

Computer Simulation Techniques in Condensed Matter Physics 754
K Binder

Multicircle Diffractometry Methods 761
DA Walko

Disorder and Localization Theory 771
A Harju, EN Economou, and CM Soukoulis

Optical Properties of Insulators 779
Y Toyozawa and S Elsheikhi

Rutheenates 786
J-S Zhou, JB Goodenough, and B Raveau

Optical Fibers 807
V Degiorgio and I Cristiani

Light Emitting Diodes 815
E Fred Schubert, Jaehee Cho, and Jong Kyu Kim

Diamond Anvil Cells 828
WA Bassett

Index *841*

Magnetic point groups and space groups☆

Ron Lifshitz[a,b], [a]Raymond and Beverly Sackler School of Physics & Astronomy, Tel Aviv University, Tel Aviv, Israel; [b]School of Mathematics, University of Leeds, Leeds, United Kingdom

© 2024 Elsevier Ltd. All rights reserved.

This is an update of R. Lifshitz, Magnetic Point Groups and Space Groups, Editor(s): Franco Bassani, Gerald L. Liedl, Peter Wyder, Encyclopedia of Condensed Matter Physics, Elsevier, 2005, Pages 219–226, ISBN 9780123694010, https://doi.org/10.1016/B0-12-369401-9/00748-8.

Introduction 2
Two-valued properties 2
Magnetic point groups 3
Magnetic point groups of finite objects 4
Magnetic point groups of crystals 4
Magnetic space groups 5
Magnetic symmetry of periodic crystals 6
Magnetic symmetry of quasiperiodic crystals 7
Lattices and Bravais classes 7
Phase functions and space-group types 8
Extinctions in neutron diffraction of antiferromagnetic crystals 9
Conclusion: Generalizations of magnetic groups 10
Acknowledgments 10
References 10

Abstract

The spatial symmetry of matter—including finite objects like molecules or atomic clusters, and extended objects like periodic or aperiodic crystals—is described using point groups and space groups. Magnetic point groups and space groups are the simplest extension of this description, to matter whose atomic constituents possess a property that can take one of two possible values, like the "up" or "down" orientations of a magnetic moment, or a spin. Magnetic groups—also known as antisymmetry groups, Shubnikov groups, Heesch groups, Opechowski-Guccione groups, as well as dichromatic, 2-color, or simply black-and-white groups—are here defined, and their structure and notation explained, while providing some pedagogical examples of their enumeration. The resulting magnetic selection rules, or extinctions, in neutron diffraction experiments are discussed. Further extensions to color groups and spin groups are briefly described.

Key points

- The spatial symmetry of matter is described using point groups and space groups. Magnetic point groups and space groups are the simplest extension of this description to matter whose atomic constituents possess a property that can take one of two possible values.
- Magnetic point groups are used to describe the point symmetry of magnetically ordered objects—whether these objects are finite, like molecules or clusters, or extended, like periodic or aperiodic crystals. They are defined below, and their structure and notation explained, while providing some pedagogical examples of their enumeration.
- Magnetic space groups are used to describe the full magnetic symmetry of extended magnetically ordered, periodic or aperiodic, crystals. They are also defined below, and their structure and different notations explained, while providing some pedagogical examples of their enumeration.
- Magnetic groups are also known in the literature as antisymmetry groups, Shubnikov groups, Heesch groups, Opechowski-Guccione groups, as well as dichromatic, 2-color, or simply black-and-white groups.
- One of the most direct physical consequences of having magnetic symmetry in crystals, is the systematic extinction of magnetic Bragg peaks in neutron diffraction patterns. These can be calculated directly from the magnetic space group.
- Magnetic groups are naturally generalized to cases where the property of interest is not limited to having one of only two possible values. The common extensions are to color groups with more than just two distinct colors, or to spin groups, where the orientation of the magnetic moments can vary continuously.

☆*Change History:* September 2022. R Lifshitz updated the chapter.

[1] The symmetry of nonmagnetic periodic crystals is discussed in numerous crystallography textbooks. For a nice informal introduction see Senechal (1990). For a detailed overview of the symmetry of nonmagnetic quasiperiodic crystals see Mermin (1992); for a more elementary introduction see Lifshitz (1996).

Introduction

Magnetic groups—also known as antisymmetry groups, Shubnikov groups, Heesch groups, Opechowski-Guccione groups, as well as dichromatic, 2-color, or simply black-and-white groups— are the simplest extension to standard point group and space group theory.[1] They allow directly to describe, classify, and study the physical consequences of the symmetry of materials, characterized by having a certain added property that locally can take one of two possible values. These may include finite objects like molecules or atomic clusters, as well as extended periodic or aperiodic crystals. To do so, one introduces a single additional symmetry operation of order two that interchanges the two possible values everywhere. This operation can be applied to the material along with any of the standard point group or space group operations, and is commonly denoted by adding a prime to the original operation. Thus, any rotation g followed by this external operation is denoted by g'.

We begin in Section "Two-valued properties" with a few typical examples of this two-valued property, some of which are illustrated in Fig. 1. In Section "Magnetic point groups" we discuss the notion of a magnetic point group, followed by a discussion on magnetic space groups in Section "Magnetic space groups." In Section "Extinctions in neutron diffraction of antiferromagnetic crystals" we describe one of the most direct physical consequences of having magnetic symmetry in crystals, which is the systematic extinction of magnetic Bragg peaks in neutron diffraction patterns. We finish in Section "Conclusion: Generalizations of magnetic groups" by briefly describing the generalization of magnetic point groups and space groups to cases where the property of interest is not limited to having one of only two possible values.

Two-valued properties

Let us begin by considering the structure of crystals of the cesium chloride (CsCl) type. In these periodic crystals the atoms are located on the sites of a body-centered cubic (bcc) lattice. Atoms of one type are located on the simple cubic lattice formed by the corners of the cubic cells, and atoms of the other type are located on the simple cubic lattice formed by the body centers of the cubic cells. The parent bcc lattice is bipartitioned in this way into two identical sublattices, related by a half body-diagonal translation. One may describe the symmetry of the cesium chloride structure as having a simple cubic lattice of ordinary translations, with a basis containing one cesium and one chlorine atom. Alternatively, one may describe the symmetry of the crystal as having twice as many translations per unit volume, forming a bcc lattice, half of which are primed to indicate that they are followed by an operation that exchanges the chemical identities of the two types of atoms. A similar situation occurs in crystals whose structure is of the sodium chloride (NaCl) type in which a simple cubic lattice is bipartitioned into two identical face-centered cubic (fcc) sublattices.

Another typical example is the orientational ordering of magnetic moments or spins, electric dipole moments, or any other tensorial property associated with each site in a crystal. Adopting the language of spins, if these can take only one of two possible orientations—"up" and "down"—as in simple Ising antiferromagnets, we have the same situation as above, with the two spin orientations replacing the two chemical species of atoms. In the case of spins, the external prime operation is a so-called antisymmetry operation that reverses the directions of the spins. Physically, one may think of using the operation of time inversion to reverse the directions of all the spins without affecting anything else in the crystal.

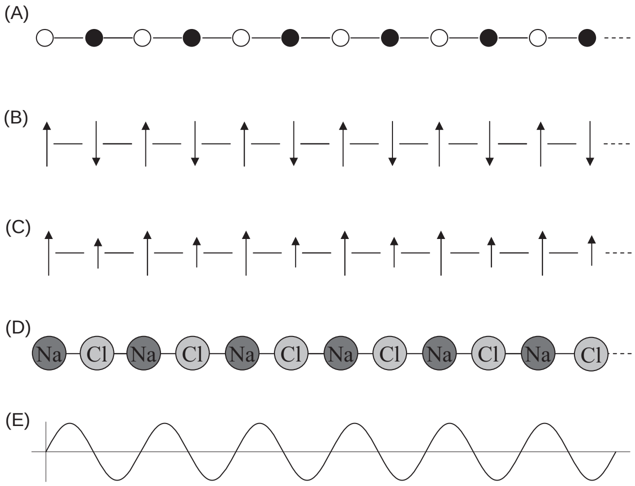

Fig. 1 Several realizations of the simple one-dimensional magnetic space group $p_p\bar{1}$ (or p_pm). Note that the number of symmetry translations is doubled if one introduces an operation e' that interchanges the two possible values of the property, associated with each crystal site. Also note that spatial inversion $\bar{1}$ (or mirror reflection m) can be performed without a prime on each crystal site, and with a prime ($\bar{1}'$or m') between every two sites. (a) An abstract representation of the two possible values as the two colors—black and white. The operation e' is the nontrivial permutation of the two colors. (b) A simple antiferromagnetic arrangement of spins. The operation e' is time inversion which reverses the directions of the spins. (c) A ferromagnetic arrangement of two types of spins, where e' exchanges them as in the case of two colors. (d) A 1-dimensional version of salt, where e' exchanges the chemical identities of the two atomic species. (e) A function $S(x)$ whose overall sign changes by the application of the operation e'. Enc. of Cond. Mat. Phys. (Elsevier, 2005), p. 219.

As a final example, consider a periodic or quasiperiodic scalar function of space, $f(\mathbf{r})$, as in Fig. 1(e), whose mean value is zero. One can often extend the point group or space group, describing the symmetry of such functions, by introducing an external prime operation that flips the sign of $f(\mathbf{r})$, by multiplying it by -1.

For the sake of clarity we shall adopt the picture of up-and-down spins, and the use of time inversion to exchange them, for the remaining of our discussion, but some terminology from the color description will be used when helpful. It should be emphasized, though, that most of what we say here—perhaps excluding the discussion of extinctions in Section "Extinctions in neutron diffraction of antiferromagnetic crystals"—applies equally to any other two-valued property. We describe the magnetic crystal using a scalar spin-density field $S(\mathbf{r})$ whose magnitude gives the magnitude of an atomic magnetic moment, or some coarse-grained value of the magnetic moment, at position $\mathbf{r}$. The sign of $S(\mathbf{r})$ gives the direction of the spin—a positive sign for "up" spins and a negative sign for "down" spins. The function $S(\mathbf{r})$ can be a discrete set of positive or negative delta functions, defined on the crystal sites as in Fig. 1(b), or a continuous spin-density field as in Fig. 1(e).

Magnetic point groups

A d-dimensional *magnetic point group* G_M is a subgroup of $O(d) \times 1'$, where $O(d)$ is the orthogonal group of d-dimensional rotations, and $1' = \{e, e'\}$ is the time inversion group containing the identity e and the time inversion operation e'. Note that we use the term "rotation" to refer to proper as well as improper rotations, such as mirrors and the spatial inversion.

Three types of subgroups exist: (1) The most trivial subgroups are simply the ordinary nonmagnetic point groups, containing rotations alone, with no use of the time-inversion operation; (2) Slightly less trivial subgroups are those in which all rotations appear both with and without time-inversion; and (3) Nontrivial subgroups are those where exactly half of the rotations are followed by time inversion and the other half are not. In the context of color symmetry, these three types of subgroups are often called *colorless*, *gray*, and *black-and-white* groups, respectively, a terminology which will become clear shortly.

More formally, if G is any ordinary nonmagnetic point group, namely, any subgroup of $O(d)$, it can be used to construct at most three types of magnetic point groups G_M, forming its so-called *magnetic superfamily*, as follows:

1. $G_M = G$, so that no rotation is followed by time inversion. It is an ordinary nonmagnetic point group.
2. $G_M = G \times 1'$, so that each rotation in G appears in G_M once by itself and once followed by time inversion. Note that in this case $e' \in G_M$.
3. $G_M = H + g'H$, where H is a subgroup of index 2 in G, and g is a particular element of G which is not in H, so that $G = H + gH$. Thus, exactly half of the rotations in G, which belong to its subgroup H, appear in G_M by themselves, and the other half, belonging to the coset $gH = \{gh \mid h \in H\}$, are followed by time inversion. Note that in this case $e' \notin G_M$.

Enumeration of magnetic point groups is thus straightforward. Any ordinary point group G—that is, any subgroup, usually finite, of $O(d)$—is trivially a colorless magnetic point group of type 1, and along with the time inversion operation generates a gray magnetic point group of type 2, denoted as $G1'$. One then lists all distinct subgroups H of index 2 in G, if there are any, to construct nontrivial black-and-white magnetic point groups of type 3. These are denoted either by the group-subgroup pair $G(H)$, or as we shall do here, by using the International (Hermann-Mauguin) symbol for G, while adding a prime to those elements in the symbol that do not belong to the subgroup H and are therefore followed by time inversion.

A simple way of finding all the subgroups H of index 2 in G is to pick a set of generators for G, and consider all combinations in which each generator of *even* order is either primed or unprimed. The resulting black-and-white point groups then need to be checked for equivalence as conjugate subgroups of $O(d) \times 1'$ and grouped into so-called *magnetic geometric crystal classes*. As an example, we enumerate in Table 1 the distinct classes of magnetic point groups in the orthorhombic crystal system. Tables of all

Table 1 Orthorhombic magnetic point groups.

Colorless	*Gray*	*Black & White*
222	$2221'$	$2'2'2$
$mm2$	$mm21'$	$m'm2'$; $m'm'2$
mmm	$mmm1'$	mmm'; $m'm'm$; $m'm'm'$

Magnetic point groups in the orthorhombic crystal system. Each row lists the magnetic superfamily of one of the ordinary, or colorless, orthorhombic point groups G, listed in the first column. The second column lists the trivial gray groups $G1'$. To enumerate the black-and-white point groups—listed in the third column by their International (Hermann-Mauguin) symbol—one considers all distinct subgroups H of index 2 in G. For example, the orthorhombic point group $G = 222 = \{e; 2_x; 2_y; 2_z\}$ has three subgroups of index 2, $H_1 = \{e; 2_x\}$, $H_2 = \{e; 2_y\}$, and $H_3 = \{e; 2_z\}$. This gives three corresponding black-and-white point groups—$22'2'$, $2'22'$, and $2'2'2$—in which two twofold rotations are primed and the third is not. As these groups are all equivalent as conjugate subgroups of $O(3) \times 1'$, they are merely different settings of just a single geometric crystal class of black-and-white point groups. On the other hand, taking the two mirrors as generators of the orthorhombic point group $G = mm2 = \{e, m_x, m_y; 2_z\}$, one can associate time inversion with just a single one of them (in which case the twofold rotation is also primed), or with both. This gives three black-and-white point groups—$m'm2'$, $mm'2'$, and $m'm'2$—of which only the first two are equivalent, yielding two geometric crystal classes of black-and-white point groups. In total there are $3 + 3 + 6 = 12$ types of orthorhombic magnetic point groups in three dimensions.

magnetic point groups that are compatible with periodic crystals—and therefore restricted to rotational axes of order 1, 2, 3, 4, and 6—appear in the original work by Shubnikov (1964) and in the more recent book by Litvin (2013), while Lifshitz (1997) provides the extension of these tables to all magnetic point groups in 2- and in 3-dimensions with rotational axes of arbitrary order.

Black-and-white magnetic point groups (type 3) can be used to describe the point symmetry of finite objects, as described in Section "Magnetic point groups of finite objects", as well as that of infinite crystals, as described in Section "Magnetic point groups of crystals." Trivial, or colorless, magnetic point groups (type 1), equivalent to ordinary nonmagnetic point groups, are usually mentioned only for the sake of completeness. Strictly speaking, they can be said to describe the symmetry of ferromagnetic materials with no spin-orbit coupling. Gray magnetic point groups (type 2) can be used to describe the point symmetry of infinite crystals, but because they include e' as a symmetry element they cannot, strictly speaking, be used to describe the symmetry of finite magnetic or two-colored objects, as explained below.

Magnetic point groups of finite objects

The magnetic symmetry of a finite object, such as a molecule or a cluster containing an equal number of two types of spins, can be described by a magnetic point group. We say that a primed or unprimed rotation from $O(d) \times 1'$ is in the magnetic point group G_M of a finite object in d dimensions, if it leaves the object invariant. Clearly, only black-and-white magnetic point groups (type 3 in the list above), can describe the symmetry of finite magnetically ordered structures. This is because time inversion e' changes the orientations of all the spins, and therefore cannot leave the object invariant unless it is accompanied by a nontrivial rotation. For this reason, point groups of type 2 are often called "gray" groups, as they describe the symmetry of "gray" objects which remain invariant under the exchange of black and white. For a comprehensive discussion on the magnetic symmetry of finite objects, see the original work by Shubnikov (1964).

Magnetic point groups of crystals

The magnetic point group of a d-dimensional magnetically ordered *periodic crystal*, containing an equal number of up and down spins, is defined as the set of primed or unprimed rotations from $O(d) \times 1'$ that leave the crystal *invariant to within a translation*. The magnetic point group of a crystal can be either of the first or of the second types listed above. It is a gray group (of type 2) if time inversion by itself leaves the crystal invariant to within a translation. In this case, any rotation in the magnetic point group can be performed either with or without time inversion. If time inversion cannot be combined with a translation to leave the crystal invariant, the magnetic point group is black and white (of type 3), in which case half of the rotations are performed without time inversion and the other half with time inversion.

Fig. 2(a) shows an example of a magnetically ordered periodic crystal, with tetragonal symmetry, given by the magnetic point group $G_M = 4\,mm1'$, which is of type 2. Here, time inversion can be followed by a translation to leave the crystal invariant. Fig. 2

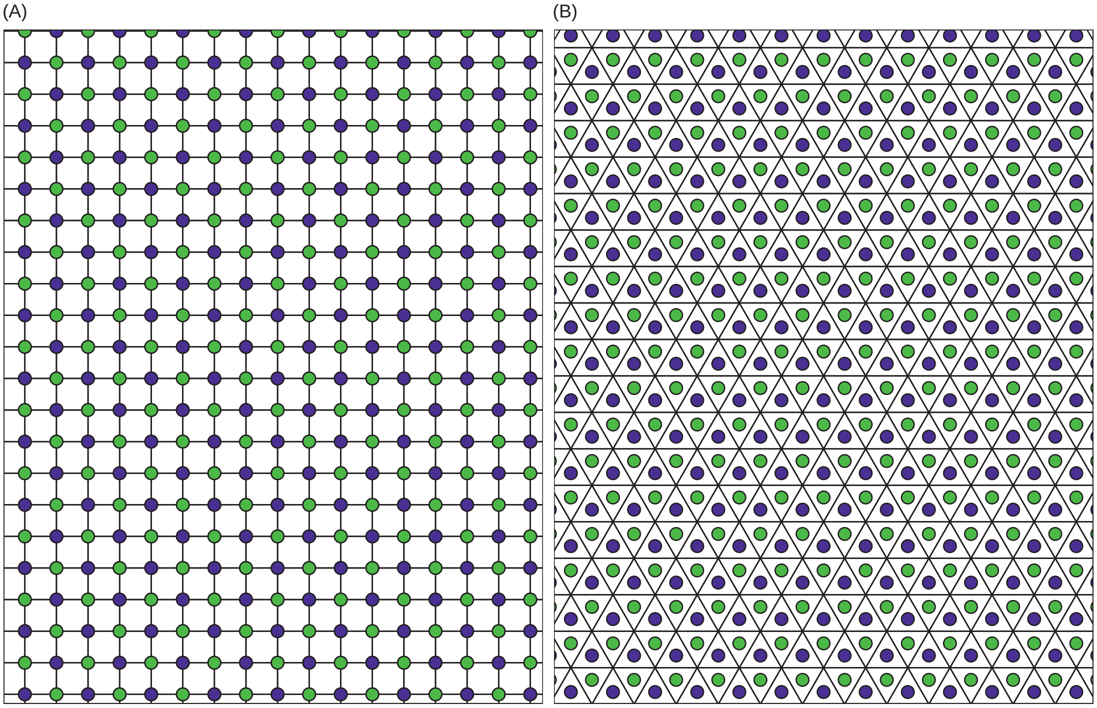

Fig. 2 Periodic antiferromagnets. (a) Tetragonal crystal with a gray magnetic point group $G_M = 4\,mm1'$, and a class-equivalent magnetic space group p_p4mm (also denoted p_c4mm). Time inversion leaves this tetragonal antiferromagnetic periodic crystal invariant to within a translation. (b) Hexagonal crystal with a black-and-white magnetic point group $G_M = 6'mm'$, and a lattice-equivalent magnetic space group $p6'mm'$. Time inversion does not leave this hexagonal antiferromagnetic periodic crystal invariant to within a translation. Enc. of Cond. Mat. Phys. (Elsevier, 2005), p. 222.

(b) shows an example of a periodic crystal with hexagonal symmetry, given by the magnetic point group $G_M = 6'mm'$, which is of type 3. Note that all right-side-up triangles contain a blue circle (spin up) and all up-side-down triangles contain a green circle (spin down). Time inversion, exchanging the two types of spins, cannot be combined with a translation to recover the original crystal. Time inversion must be combined with a nontrivial operation—such as mirrors of the horizontal type or odd powers of the sixfold rotation—that interchanges the two types of triangles to recover the original crystal. Note that mirrors of the vertical type (the first m in the International symbol) leave the crystal invariant without requiring time inversion, and are therefore unprimed in the symbol.

More generally, the magnetic point group of a d-dimensional magnetically ordered crystal—whether periodic or not[2]—is defined as the set of primed or unprimed rotations from $O(d) \times 1'$ that leave the crystal *indistinguishable*. This means that the rotated and unrotated crystals contain the same spatial distributions of finite clusters of spins of arbitrary size. The two crystals are thus statistically the same, though not necessarily identical to within a translation. Only for the special case of periodic crystals does the notion of *indistinguishability* reduce to invariance to within a translation.

Fig. 3 shows two aperiodic examples, analogous to the two periodic examples of Fig. 2. Fig. 3(a) shows an octagonal crystal with magnetic point group $G_M = 8\,mm1'$. One can see that time inversion rearranges the spin clusters in the crystal but they all still appear in the crystal with the same spatial distribution. This is because any finite spin cluster and its time-reversed image appear in the crystal with the same spatial distribution. Fig. 3(b) shows a decagonal crystal with magnetic point group $G_M = 10'm'm$. In this case, time inversion does not leave the crystal indistinguishable. It must be combined either with odd powers of the 10-fold rotation, or with mirrors of the vertical type, to produce a crystal with the same spatial distributions of finite spin clusters as in the original one.

Magnetic space groups

The full symmetry of a magnetically ordered crystal, described by a set of "up" and "down" spins, or a coarse-grained scalar spin-density field $S(\mathbf{r})$, is given by its magnetic space group $\mathcal{G}_M$. We said that the magnetic point group G_M is the set of primed or unprimed rotations that leave a periodic crystal invariant to within a translation, or more generally, leave a quasiperiodic crystal indistinguishable. We still need to specify the distinct sets of translations $\mathbf{t}_g$ or $\mathbf{t}_{g'}$ that can accompany the rotations g or g' in a periodic crystal to leave it invariant, or provide the more general characterization of the nature of the indistinguishability in the case of quasicrystals, as explained below.

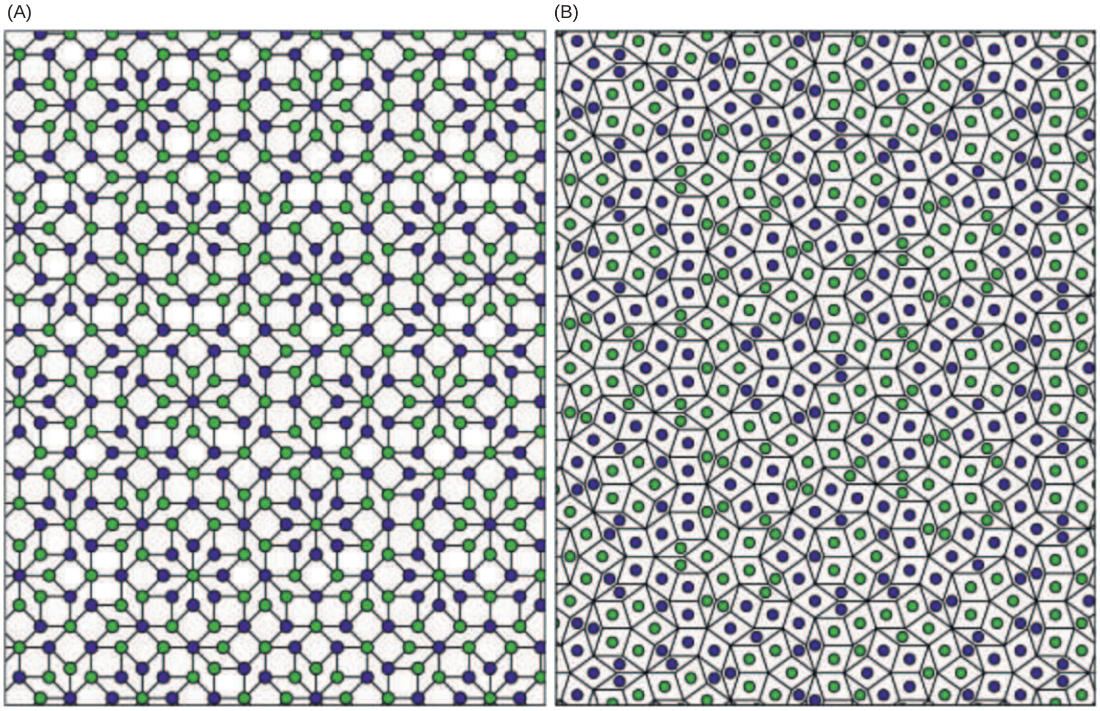

Fig. 3 Antiferromagnetic quasicrystals. (a) Octagonal quasicrystal with a gray magnetic point group $G_M = 8\,mm1'$, and a class-equivalent magnetic space group p_p8mm. Time inversion leaves this octagonal antiferromagnetic quasicrystal indistinguishable. (b) Decagonal quasicrystal with a black-and-white magnetic point group $G_M = 10'\,m'm$, and a lattice-equivalent magnetic space group $p10'm'm$. Time inversion does not leave this decagonal antiferromagnetic quasicrystal indistinguishable. Enc. of Cond. Mat. Phys. (Elsevier, 2005), p. 223.

---

[2] Of particular relevance is the generalization from periodic crystals to the wider category of *quasiperiodic crystals*. Quasiperiodic crystals that are explicitly aperiodic are called *quasicrystals*. For proper definitions and detailed terminology, see, for example Lifshitz (2003, 2007, 2011).

Magnetic symmetry of periodic crystals

One can take any ordinary nonmagnetic space group $\mathcal{G}$ of a periodic crystal, also called a Fedorov-Schönflies space group, and form its *magnetic superfamily*. As in the case of magnetic point groups, there are two trivial magnetic space-group types:

I. *Colorless magnetic space groups*: These are ordinary nonmagnetic Fedorov-Schönflies space groups, where $\mathcal{G}_M = \mathcal{G}$.
II. *Gray magnetic space groups*: Here $\mathcal{G}_M = \mathcal{G} \times 1'$ (denoted simply as $\mathcal{G}1'$), implying that every operation in $\mathcal{G}$ can be applied with or without being followed by time inversion.

Nontrivial black-and-white magnetic space groups take the form

$$\mathcal{G}_M = \mathcal{H} + (g'|\mathbf{t}_{g'})\mathcal{H}, \tag{1}$$

where $\mathcal{H}$ is a subgroup of index 2 in $\mathcal{G}$, and $(g'|\mathbf{t}_{g'})$ denotes a primed rotation g', possibly followed by a translation $\mathbf{t}_{g'}$. They are divided into two types, depending on their magnetic point groups G_M:

III. *Lattice-equivalent magnetic space groups*: If the magnetic point group G_M is black and white (of type 3), the point group H of $\mathcal{H}$ is a subgroup of index 2 of the point group G of $\mathcal{G}$, and the Bravais lattices of $\mathcal{G}$ and $\mathcal{H}$ are the same. Rotations in G that are not in H must be combined with time inversion to leave the magnetic crystal invariant to within a translation.
IV. *Class-equivalent magnetic space groups*: If the magnetic point group G_M is gray (of type 2), with all rotations in G appearing with and without time inversion, the point groups of $\mathcal{G}$ and $\mathcal{H}$ are the same, and the Bravais lattice T of $\mathcal{H}$ is a sublattice of index 2 of the Bravais lattice T_0 of $\mathcal{G}$. Translations in T_0 that are not in T must be combined with time inversion to leave the magnetic crystal invariant.

Enumeration of lattice-equivalent magnetic space-group types is straightforward. Given an ordinary nonmagnetic space group $\mathcal{G}$, simply consider all distinct subgroups H of index 2 of the point group G of $\mathcal{G}$, as explained in Section "Magnetic point groups." The only additional consideration is that there may be more than one way to orient the subgroup H relative to the Bravais lattice of translations that leave the periodic crystal invariant. Take, for example, the magnetic point group $m'm2'$, which as explained in Table 1, is equivalent to $mm'2'$. Consequently, on a primitive orthorhombic lattice, $Pm'm2'$ and $Pmm'2'$ are two different settings of the same magnetic space-group type. But, on an A-centered orthorhombic lattice, where the x- and y-axes are no longer equivalent, one needs to consider both options as distinct groups. We say that the two distinct magnetic space-group types $Am'm2'$ and $Amm'2'$ belong to the same magnetic *geometric crystal* class (i.e., have the same type of magnetic point group), but to two distinct magnetic *arithmetic crystal* classes. Lattice-equivalent magnetic space groups, also called translation-equivalent when the crystal is periodic, are denoted by taking the International symbol for $\mathcal{G}$, and adding a prime to those elements in the symbol that do not belong to $\mathcal{H}$ and must be followed by time inversion.

Enumeration of class-equivalent magnetic space-group types proceeds by considering all distinct pairs of lattices T_0 and T in a given crystal system, where T is a sublattice of index 2 in T_0. Translations in the sublattice T, making up the Bravais lattice of $\mathcal{H}$, leave the periodic magnetic crystal invariant, while translations in T_0 that are not in T must be combined with time inversion to leave it invariant. Like a color-blind person, an X-ray diffraction experiment, which is insensitive to the magnetic ordering, will exhibit the reciprocal lattice L_0 of T_0, while neutron diffraction will expose the additional Bragg peaks, contained in the reciprocal lattice L of T, encoding the magnetic order. Correspondingly, the lattice T_0, and its reciprocal L_0, are often called the colorless or colorblind lattices, as well as the paramagnetic or disordered lattices, while the sublattice T, and its reciprocal L, are often called the magnetic or ordered lattices.[3] Note that while T is a sublattice of T_0 of index 2, their reciprocal lattices in Fourier space play opposite roles, whereby L_0 is a sublattice L of index 2.

Different settings and notations are used to describe class-equivalent magnetic space groups, depending on which of the two lattices—the magnetic or the paramagnetic—and which of the two spaces—real space or Fourier space—are considered as primary. In the Opechowski and Guccione (1965), or OG setting, the paramagnetic lattice of translations T_0 is considered primary, lending its symbol to the magnetic space group, while the magnetic lattice T is denoted as a subscript. In the OG setting the class-equivalent magnetic space group is considered a member of the magnetic superfamily of the space group $\mathcal{G}$. In the Belov, Neronova, and Smirnova (1964), or BNS setting, the magnetic lattice of translations T is considered primary, lending its symbol to the magnetic space group, while the paramagnetic lattice T_0 is indicated as a subscript. In the BNS setting the class-equivalent magnetic space group is considered a member of the magnetic superfamily of the space group $\mathcal{H}$. Finally, if one follows the Rokhsar, Wright, and Mermin (1988), or RWM formalism, in which the nonmagnetic space groups are viewed primarily in Fourier-space, and which generalizes most easily to aperiodic magnetic crystals (Lifshitz, 1997, Section V), the magnetic reciprocal lattice L is considered primary, lending its symbol to the magnetic space group, while the paramagnetic reciprocal lattice L_0 appears as a subscript. As in the BNS setting, the class-equivalent magnetic space group is considered a member of the magnetic superfamily of the space group H, but it is the subscript that denotes a sublattice of the main symbol as in the OG notation.

In the cubic system, for example, there are two lattice-sublattice pairs of index 2—the simple cubic lattice P has a face-centered sublattice F of index 2; and the body-centered cubic lattice I has a simple cubic sublattice P of index 2. The first pair is denoted P_F in the OG notation; F_S (S for simple) in the BNS notation; and $I^*{}_P$ in the RWM notation, with the asterisk indicating that the lattice is specified in Fourier space. Recall that the reciprocal of an fcc lattice is a bcc lattice and vice versa. The second pair is denoted I_P in the OG notation; P_I in the BNS notation; and $P_F{}^*$ in the RWM notation.

---

[3] The reference to order-disorder is motivated by transitions like the one that occurs the in the β phase of brass (Madsen et al., 2016).

In the top part of Table 2 we enumerate all the cubic magnetic space group types with point group 432. Note that in addition to the different settings, there is a discrepancy in the different notations, which is due to the fact that when $e' \in G_M$, ordinary mirrors or rotations when unprimed may become glide planes or screw axes when primed, and vice versa. The only consistent way to avoid such confusion is to use only unprimed elements for the symbols of class-equivalent magnetic space-group types. This is the approach adopted by both the BNS and the RWM notations, but unfortunately not by the OG notation. Also note that there is no $1'$ at the end of the symbol, as it is clear from the existence of a subscript on the lattice symbol that the magnetic point group G_M contains e'. Comparisons between the OG and the BNS notions, and discussions regarding the advantages and disadvantages of each approach, are still ongoing, with new notations being proposed to this day (Campbell et al., 2022; Grimmer, 2009, 2010; Litvin, 2016).

Tables of periodic magnetic space-group types in two and in three dimensions are given in the early work by Belov and Tarkhova (1964, Table 11), Belov et al. (1964, Table 10), Opechowski and Guccione (1965), Koptsik (1966), and Opechowski (1986, Tables 11.2 and 17.3); and more recently have also been made available online by Litvin (2013), Stokes and Campbell (2022) and by the Bilbao Crystallographic Server (2022), accompanied by the review of Perez-Mato et al. (2015). Let us only summarize some statistics. Starting from the 17 space-group types in 2 dimensions, also known as the 17 plane groups, one can form a total of 80 magnetic space-group types as follows: 17 colorless groups, 17 gray groups, and 46 black-and-white groups of which 20 are class-equivalent and 26 are lattice-equivalent. Starting from the 230 space-group types in 3 dimensions, one can form a total of 1651 magnetic space-group types as follows: 230 colorless groups, 230 gray groups, and 1191 black-and-white groups of which 517 are class-equivalent and 674 are lattice-equivalent. These numbers have no particular significance other than the fact that they may seem surprisingly large.

Magnetic symmetry of quasiperiodic crystals

Lattices and Bravais classes

Magnetically ordered quasiperiodic crystals, in general, possess no lattices of real space translations that leave them invariant, but they do have reciprocal lattices (or Fourier modules) L that can be inferred directly from their neutron diffraction diagrams. To be more concrete, consider a scalar spin-density field with a well defined Fourier transform

Table 2 Magnetic space-group types with point groups 432 and 532.

I.	*II.*	*III.*	*IV.*		
#			BNS	RWM	OG
$P432$ (*207*)	$P4321'$	$P4'32'$	P_I432	P^*_F432	I_P432
$P4_132$ (*213*)	$P4_1321'$	$P4'_132'$	P_I4_132	$P^*_F4_132$	$I_P4'_132'$
$P4_232$ (*208*)	$P4_2321'$	$P4'_232'$	P_I4_232	$P^*_F4_232$	$I_P4'32'$
$P4_332$ (*212*)	$P4_3321'$	$P4'_332'$	P_I4_332	$P^*_F4_332$	I_P4_132
$F432$ (*209*)	$F4321'$	$F4'32'$	F_S432	$I^*_P\,432$	P_F432
$F4_132$ (*210*)	$F4_1321'$	$F4'_132'$	F_S4_132	$I^*_P\,4_132$	P_F4_232
$I432$ (*211*)	$I4321'$	$I4'32'$	–	–	–
$I4_132$ (*214*)	$I4_1321'$	$I4'_132'$	–	–	–
$P532$	$P5321'$	–	P_I532	P^*_F532	–
$P5_132$	$P5_1321'$	–	P_15_132	$P^*_F5_132$	–
$F532$	$F5321'$	–	F_S532	$I^*_P\,532$	–
$F5_132$	$F5_1321'$	–	F_S5_132	$I^*_P\,5_132$	–
$I532$	$I5321'$	–	–	–	–
$I5_132$	$I\,5_1321'$	–	–	–	–

Each row lists the magnetic superfamily of one non-magnetic space groups G, listed in Column I by its International (Hermann-Mauguin) symbol and by its number from the International Tables in italics. Column II lists the trivial gray groups $G1'$. Column III lists the lattice-equivalent space groups. Point group 432 has a single subgroup of index 2—the tetrahedral group 23—obtained by associating a prime with the twofold rotation axes (and consequently with the fourfold axes as well). This gives a single lattice-equivalent magnetic space-group for each nonmagnetic space group G. Point group 532 has no subgroup of index 2, and therefore no lattice-equivalent magnetic space-groups. Finally, there are two lattice-sublattice pairs in the cubic and the icosahedral systems. In both cases the simple or primitive lattice P has a face-centered sublattice F of index 2, and the body-centered lattice I has a simple or primitive sublattice P of index 2. Consequently, in the BNS setting, each non-magnetic fcc or fci space group gives rise to a single class-equivalent magnetic space group with an fcc or fci magnetic lattice and a primitive paramagnetic lattice, and each primitive space group gives rise to a single class-equivalent magnetic space group with a primitive magnetic lattice and a bcc or bci paramagnetic lattice. There are no class-equivalent magnetic space groups with a bcc or a bci magnetic lattice. These are listed in column IV in three different notations for the cubic groups and in the BNS and RWM notations for the icosahedral groups. For the RWM notation, recall that the reciprocal of a face-centered lattice F is a body-centered lattice in Fourier space, denoted by I^*, and vice versa. In total there are $8 + 8 + 8 + 6 = 30$ types of magnetic space groups with point group 432 and $6 + 6 + 4 = 16$ with point group 532.

$$S(\mathbf{r}) = \sum_{\mathbf{k}\in L} S(\mathbf{k})e^{i\mathbf{k}\cdot\mathbf{r}}, \tag{2}$$

in which the set L contains at most a countable infinity of wave vectors. In fact, the *magnetic reciprocal lattice L* of a magnetic crystal can be defined as the set of all integral linear combinations of wave vectors **k**, determined from its neutron diffraction diagram. Indeed, we expect to see a magnetic Bragg peak at every **k** in the closure of those that are experimentally observed, unless it is forbidden by symmetry, as explained in Section "Extinctions in neutron diffraction of antiferromagnetic crystals" below, or unless it is too weak to be detected experimentally.

The *rank* D of L is the smallest number of vectors needed to generate L by integral linear combinations. If D is finite the crystal is quasiperiodic. If, in particular, D is equal to the number d of spatial dimensions, and L extends in all d directions, the crystal is periodic. In this special case the magnetic lattice L is reciprocal to a lattice T of translations in real space that leave the magnetic crystal invariant, without applying time inversion. If $D > d$ the crystal is aperiodic, and the field $S(\mathbf{r})$ describes a magnetic quasicrystal. The reciprocal lattices L of magnetic crystals are classified into Bravais classes, just like those of non-magnetic crystals.

Phase functions and space-group types

We proceed by following the Rokhsar, Wright, and Mermin (1988, RWM) formalism and their notion of *indistinguishability*, used earlier to define the magnetic point group. The precise mathematical statement of this notion in the case of magnetic symmetry (Lifshitz, 1997, 1998) is the requirement that any symmetry operation of the magnetic crystal leave invariant all spatially averaged nth-order autocorrelation functions of its spin-density field,

$$C^{(n)}(\mathbf{r}_1, \cdots, \mathbf{r}_n) = \lim_{V\to\infty} \frac{1}{V}\int_V d\mathbf{r}S(\mathbf{r}_1 - \mathbf{r})\cdots S(\mathbf{r}_n - \mathbf{r}). \tag{3}$$

One can prove (Lifshitz, 1997, in the Appendix) that two quasiperiodic spin-density fields $S(\mathbf{r})$ and $\hat{S}(\mathbf{r})$ are indistinguishable in this way, if their Fourier coefficients, defined in Eq. (2), are related by

$$\hat{S}(\mathbf{k}) = e^{2\pi i\chi(\mathbf{k})}S(\mathbf{k}) \tag{4}$$

where χ is a real-valued linear function (modulo integers) on L, called a *gauge function*. By this we mean that for every pair of wave vectors $\mathbf{k}_1$ and $\mathbf{k}_2$ in the magnetic lattice L,

$$\chi(\mathbf{k}_1 + \mathbf{k}_2) \equiv \chi(\mathbf{k}_1) + \chi(\mathbf{k}_2), \tag{5}$$

where "≡" means equal to within adding an integer. Thus, for each element g or g' in the magnetic point group G_M of the crystal, which by definition leaves the crystal indistinguishable, there exists a corresponding gauge function $\Phi_g(\mathbf{k})$ or $\Phi_{g'}(\mathbf{k})$, called a *phase function*, satisfying

$$S(g\mathbf{k}) = \begin{cases} e^{2\pi i\Phi_g(\mathbf{k})}S(\mathbf{k}) & g \in G_M, \\ -e^{2\pi i\Phi_{g'}(\mathbf{k})}S(\mathbf{k}) & g' \in G_M. \end{cases} \tag{6}$$

Since for any $g, h \in G$, $S([gh]\mathbf{k}) = S(g[h\mathbf{k}])$, the corresponding phase functions for elements in G_M, whether primed or not, must satisfy a *group compatibility condition*,

$$\Phi_{g^*h^\dagger}(\mathbf{k}) \equiv \Phi_{g^*}(h\mathbf{k}) + \Phi_{h^\dagger}(\mathbf{k}), \tag{7}$$

where the asterisk and the dagger denote optional primes. A *magnetic space group*, describing the symmetry of a magnetic crystal, whether periodic or aperiodic, is thus given by a magnetic (reciprocal) lattice L, a magnetic point group G_M, and a set of phase functions $\Phi_g(\mathbf{k})$ and $\Phi_{g'}(\mathbf{k})$, satisfying the group compatibility condition (7).

In particular, if the point group is gray, the phase function $\Phi_{e'}(\mathbf{k})$ encodes all the information regarding the sublattice L_0, earlier referred to as the paramagnetic or color-blind lattice. To see this, note that the relation $(e')^2 = e$ implies—through the group compatibility condition (7) and the fact that $\Phi_e(\mathbf{k}) \equiv 0$—that $\Phi_{e'}(\mathbf{k}) \equiv 0$ or $1/2$. It then follows from the linearity of the phase function (5) that on exactly half of the wave vectors in L, $\Phi_{e'}(\mathbf{k}) \equiv 1/2$, and on the remaining half, $\Phi_{e'}(\mathbf{k}) \equiv 0$. The latter half form the sublattice L_0, which is of index 2 in L.

Magnetic space groups are classified in this formalism into *magnetic space-group types* by organizing sets of phase functions satisfying the group compatibility condition (7) into equivalence classes. Two such sets Φ and $\widehat{\Phi}$ are equivalent if: (I) they describe indistinguishable spin-density fields related as in (4) by a gauge function χ; or (II) they correspond to alternative descriptions of the same crystal that differ by their choices of absolute length scales and spatial orientations. In case (I) Φ and $\widehat{\Phi}$ are related by a *gauge transformation*,

$$\widehat{\Phi}_{g^*}(\mathbf{k}) \equiv \Phi_{g^*}(\mathbf{k}) + \chi(g\mathbf{k} - \mathbf{k}), \tag{8}$$

where, again, the asterisk denotes an optional prime.

In the special case that the crystal is periodic ($D = d$) it is possible to replace each gauge function by a corresponding d-dimensional translation **t**, satisfying $2\pi\chi(\mathbf{k}) = \mathbf{k}\cdot\mathbf{t}$, thereby reducing the requirement of indistinguishability to that of invariance to within a translation. Only then does the point group condition (6) become

$$S(g\mathbf{r}) = \begin{cases} S(\mathbf{r} - \mathbf{t}_g), & g \in G_M, \\ -S(\mathbf{r} - \mathbf{t}_{g'}), & g' \in G_M, \end{cases} \tag{9}$$

the gauge transformations (8) turn into the so-called Frobenius congruences (Senechal, 1990, page 69), which are related to simple shifts of the origin, and the whole description reduces to that given in Section "Magnetic symmetry of periodic crystals" for periodic crystals.

As an example, we enumerate in Table 2 the icosahedral magnetic space group types with point group 532, contrasting them with those of the cubic point group 432. Tables of magnetic space-group types on standard[4] axial quasicrystals in two and three dimensions with arbitrary rotational symmetry, as well as magnetic space-group types in the icosahedral crystal system in three dimensions, are given by Lifshitz (1997, Section V).

Extinctions in neutron diffraction of antiferromagnetic crystals

We said earlier that every wave vector $\mathbf{k}$ in the lattice L of a magnetic crystal is a candidate for a diffraction peak unless symmetry forbids it. We are now in a position to understand exactly how this happens. Given a wave vector $\mathbf{k} \in L$ we examine all magnetic point-group operations g or g' for which $g\mathbf{k} = \mathbf{k}$. For such elements, the point-group condition (6) reduces to

$$S(\mathbf{k}) = \begin{cases} e^{2\pi i \Phi_g(\mathbf{k})} S(\mathbf{k}) & g \in G_M, \\ -e^{2\pi i \Phi_{g'}(\mathbf{k})} S(\mathbf{k}), & g' \in G_M, \end{cases} \tag{10}$$

requiring $S(\mathbf{k})$ to vanish unless $\Phi_g(\mathbf{k}) \equiv 0$ if $g \in G_M$, and $\Phi_{g'}(\mathbf{k}) \equiv 1/2$ if $g' \in G_M$. It should be noted that the phase values in Eq. (10), determining the extinction of $S(\mathbf{k})$, are independent of the choice of gauge (8), and are therefore uniquely determined by the magnetic space-group type of the crystal, regardless of the choice of gauge.

Particularly striking are the extinctions when the magnetic space group $\mathcal{G}$ is class-equivalent (type IV), implying that the magnetic point group G_M is gray (type 2), containing time inversion e'. Equation (10) requires $S(\mathbf{k})$ to vanish on the whole paramagnetic sublattice L_0, where $\Phi_{e'}(\mathbf{k}) \equiv 0$. Thus, in magnetic crystals with class-equivalent space groups (type IV), at least half of the diffraction peaks are missing. Fig. 4 shows the positions of the expected magnetic Bragg peaks corresponding to the tetragonal and octagonal magnetic structures shown in Figs. 2(a) and 3(a), illustrating this phenomenon. Further details on magnetic extinctions including tabulated results are given by Even-Dar Mandel and Lifshitz, 2004; Lifshitz (1998, 2000); Lifshitz and Even-Dar Mandel (2004).

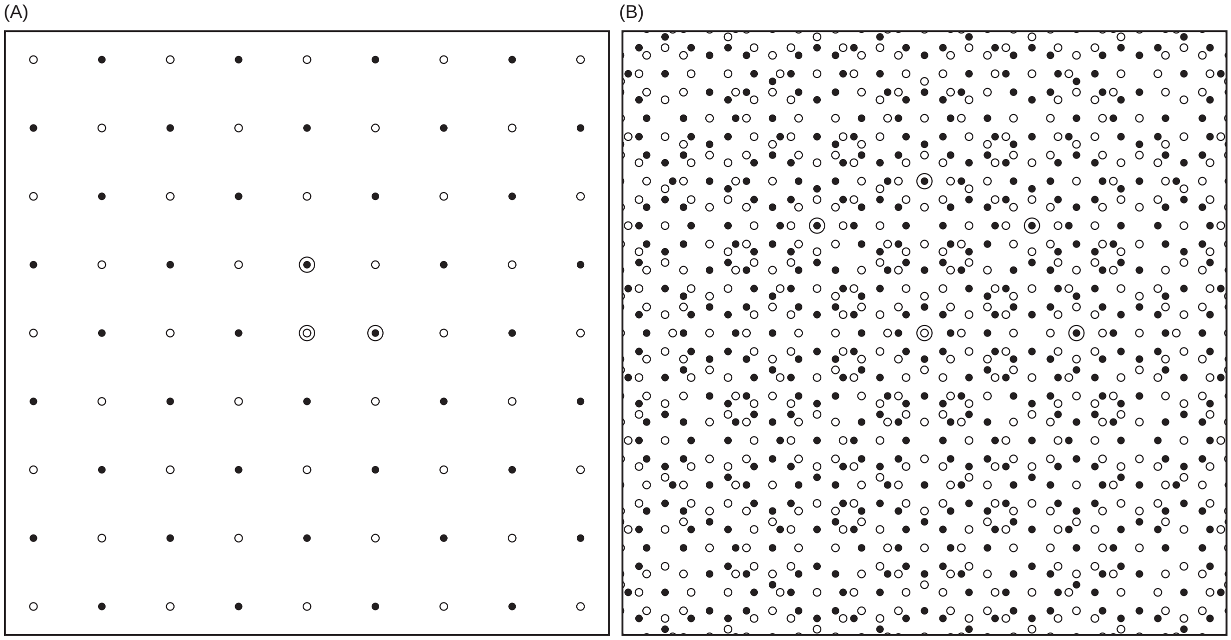

Fig. 4 Extinctions of magnetic Bragg peaks in crystals with class-equivalent magnetic space groups (type IV). Both figures show the positions of expected magnetic Bragg peaks indexed by integers ranging from −4 to 4. Filled circles indicate observed peaks and open circles indicate positions of extinct peaks. The origin and the D vectors used to generate the patterns are indicated by an additional large circle. (a) corresponds to the tetragonal crystal in Fig. 2(a) with magnetic space group p_p4mm and (b) corresponds to the octagonal crystal in Fig. 3(a) with magnetic space group p_p8mm. Enc. of Cond. Mat. Phys. (Elsevier, 2005), p. 225.

---

[4] See Lifshitz (1997, footnote 8) for the meaning of "standard" in this context.

Conclusion: Generalizations of magnetic groups

There are two natural generalizations of magnetic groups, going beyond what is discussed here. One is to color groups (Lifshitz, 1997; Schwarzenberger, 1984; Senechal, 1988) with more than two distinct colors, and the other is to spin groups (Even-Dar Mandel and Lifshitz, 2004; Lifshitz, 1998, 2000; Lifshitz and Even-Dar Mandel, 2004; Litvin, 1973, 1977; Litvin and Opechowski, 1974) where the spins are viewed as classical axial vectors free to rotate continuously in any direction.

An n-color point group G_C is a subgroup of $O(d) \times S_n$, where S_n is the permutation group of n colors. Elements of the color point group are pairs (g, γ) where g is a d-dimensional (proper or improper) rotation and γ is a permutation of the n colors. As before, for (g,γ) to be in the color point group of a finite object it must leave it invariant, and for (g, γ) to be in the color point group of a crystal it must leave it indistinguishable, which in the special case of a periodic crystal reduces to invariance to within a translation. To each element $(g, \gamma) \in G_C$ corresponds a phase function $\Phi_g^{\gamma}(\mathbf{k})$, satisfying a generalized version of the group compatibility condition (7). The color point group contains an important subgroup of elements of the form (e, γ) containing all the color permutations that leave the crystal indistinguishable without requiring any rotation g.

A spin point group G_S is a subgroup of $O(d) \times SO(d_s) \times 1'$, where $SO(d_s)$ is the group of d_s-dimensional proper rotations operating on the spins, and $1'$ is the time inversion group as before. Note that the dimension of the spins need not be equal to the dimension of space (e.g., one may consider a planar arrangement of 3-dimensional spins). Also note that because the spins are axial vectors there is no loss of generality by restricting their rotations to being proper. Elements of the spin point group are pairs (g, γ) where g is a d-dimensional (proper or improper) rotation and γ is a spin-space rotation possibly followed by time inversion. Here as well, elements of the form (e, γ) play a central role in the theory, especially in determining the symmetry constraints imposed by the corresponding phase functions $\Phi_e^{\gamma}(\mathbf{k})$ on the patterns of magnetic Bragg peaks, observed in elastic neutron-diffraction experiments.

Acknowledgments

I would like to thank David Mermin for teaching me how to think about crystals and their symmetry, and Shahar Even-Dar Mandel for joining me in my investigation of the magnetic symmetry in quasicrystals. I also thank Alastair Rucklidge for his kind hospitality at the School of Mathematics at the University of Leeds, where this manuscript was prepared, as well as the Cheney Foundation for their support of my visit. My research in these matters is funded by the Israel Science Foundation, most recently through grant No. 1667/16.

References

Belov NV, Neronova NN, and Smirnova TS (1964) The 1651 Shubnikov groups (Dichromatic space groups). In: Holser WT (ed.) *Colored Symmetry*, pp. 175–210. Oxford: Pergamon Press.
Belov NV and Tarkhova TN (1964) Dichromatic plane groups. In: Holser WT (ed.) *Colored Symmetry*, pp. 211–219. Pergamon Press.
Bilbao Crystallographic Server (2022) *Mag-Netic Space Groups List*. Last checked 2022.
Campbell BJ, Stokes HT, Manuel Perez-Mato J, and Rodríguez-Carvajal J (2022) Introducing a unified magnetic space-group symbol. *Acta Crystallographica. Section A* 78: 99–106.
Even-Dar Mandel S and Lifshitz R (2004) Sym-metry of magnetically ordered three-dimensional octagonal quasicrystals. *Acta Crystallographica. Section A* 60: 179–194.
Grimmer H (2009) Comments on tables of magnetic space groups. *Acta Crystallographica. Section A* 65: 145–155.
Grimmer H (2010) Opechowski-Guccione-like symbols labelling magnetic space groups independent of tabulated (0,0,0)+ sets. *Acta Crystallographica. Section A* 66: 284–291.
Koptsik VA (1966) *Shubnikov Groups*. Moscow: Izd. M. U.
Lifshitz R (1996) The symmetry of quasiperiodic crystals. *Physica A: Statistical Mechanics and its Applications* 232: 633–647.
Lifshitz R (1997) Theory of color symmetry for periodic and quasiperiodic crystals. *Reviews of Modern Physics* 69: 1181–1218.
Lifshitz R (1998) Symmetry of magnetically ordered quasicrystals. *Physical Review Letters* 80: 2717–2720.
Lifshitz R (2000) Magnetic quasicrystals: What can we expect to see in their neutron diffraction data? *Materials Science and Engineering A* 294–296: 508–511.
Lifshitz R (2003) Quasicrystals: A matter of definition. *Foundations of Physics* 33: 1703–1711.
Lifshitz R (2007) What is a crystal? *Zeitschrift für Kristallographie* 222: 313–317.
Lifshitz R (2011) Symmetry breaking and order in the age of quasicrystals. *Israel Journal of Chemistry* 51: 1156–1167.
Lifshitz R and Even-Dar Mandel SE-D (2004) Magnetically ordered quasicrystals: Enumeration of spin groups and calculation of magnetic selection rules. *Acta Crystallographica. Section A* 60: 167–178.
Litvin DB (1973) Spin translation groups and neutron diffraction analysis. *Acta Crystallographica. Section A* 29: 651–660.
Litvin DB (1977) Spin point groups. *Acta Crystallographica. Section A* 33: 279–287.
Litvin DB (2013) *Magnetic Group Tables*. IUCr.
Litvin DB (2016) Comparison of OG and BNS magnetic group type symbols. In: Aroyo MI (ed.) *International Tables for Crystallography*. vol. A, p. 863. Chester: IUCr. Chap. 3.6.4.
Litvin DB and Opechowski W (1974) Spin groups. *Physica* 76: 538–554.
Madsen A, Als-Nielsen J, Hallmann TR, and Lu W (2016) Critical behavior of the order-disorder phase transition in β-brass investigated by x-ray scattering. *Physical Review B* 94: 014111.
Mermin ND (1992) The space groups of icosahedral quasicrystals and cubic, orthorhombic, monoclinic, and triclinic crystals. *Reviews of Modern Physics* 64: 3–49.
Opechowski W (1986) *Crystallographic and Metacrystallo-Graphic Groups*. Amsterdam: North-Holland.
Opechowski W and Guccione R (1965) Magnetic symmetry. In: Rado GT and Suhl H (eds.) *Magnetism*. vol. 2A. New York: Academic Press. Chap. 3.
Perez-Mato JM, Gallego SV, Tasci ES, Elcoro L, de la Flor G, and Aroyo MI (2015) Symmetry-based computational tools for magnetic crystallography. *Annual Review of Materials Research* 45: 217–248.
Rokhsar DS, Wright DC, and David Mermin N (1988) Scale equivalence of quasicrystallographic space groups. *Physical Review B* 37: 8145–8149.
Schwarzenberger RLE (1984) Colour symmetry. *The Bulletin of the London Mathematical Society* 16: 209–240.
Senechal M (1988) Color symmetry. *Computers & Mathematcs with Applications* 16(5): 545–553.
Senechal M (1990) *Crystalline Symmetries: An Informal Mathematical Introduction*. Bristol: Adam Hilger.
Shubnikov AV (1964) Antisymmetry of finite figures. In: Holser WT (ed.) *Colored Symmetry*, pp. 88–172. Oxford: Pergamon Press.
Stokes HT and Campbell BJ (2022) ISOSPACEGROUP, ISOTROPY Software Suite. iso.byu.edu.

Crystal structure[☆]

AM Glazer, University of Oxford, Oxford, United Kingdom

© 2024 Elsevier Ltd. All rights reserved.

This is an update of J.S. Rutherford, Crystal Structure, Editor(s): Franco Bassani, Gerald L. Liedl, Peter Wyder, Encyclopedia of Condensed Matter Physics, Elsevier, 2005, Pages 289–294, ISBN 9780123694010, https://doi.org/10.1016/B0-12-369401-9/00686-0.

Introduction 11
Crystal symmetry 11
Unit cell contents 13
Crystallographic databases 14
The refinement model 14
Measures of quality 14
Derived geometric parameters 15
Further reading 16

Abstract

The description of crystal structures is given starting with some fundamental notions of crystal symmetry. The topics of lattices and space groups are briefly introduced and how these can be used with unit cell contents to describe the crystal structure. This leads to crystallographic databases where information on crystal structures is stored and can be searched. A brief discussion on refinement of diffraction information is given, together with the resulting geometric parameters.

Introduction

The bulk of our experimental knowledge of chemical structure, the arrangement of atoms in space, comes from the study of crystalline solids. This article intends to explain the nature of this chemical information, and how it may be extracted from the experimental results, given the form of the theoretical model used to describe the crystal structure.

This article first discusses some relevant elements of crystal symmetry and explains how the crystal structure is coded in a typical theoretical model. The information available from experimental techniques are used to establish crystal structures, especially X-ray diffraction and also diffraction of neutrons and electrons. A very large number of crystal structures have now been determined by these methods, and the resulting information is held in various crystallographic databases; these will therefore be described, focusing on the information they contain on individual determinations, which will typically include lattice parameters and space group, as well as the details of the unit cell contents as described by the refinement model used.

It is important to be able to evaluate the reliability of geometric descriptors derived from such a model, so refinement models and the published measures of the quality of the experimental structures determined are discussed. This is followed by a review of derived parameters, that is, those geometric descriptors of chemical interest.

Crystal symmetry

Ignoring defects, the crystal is a regular arrangement of identical building blocks, the unit cells, in three dimensions. The set of points equivalent to each other by the translation from one unit cell to another form a quasi-infinite three-dimensional geometric lattice, and, in order to describe a crystal structure, it is sufficient to define both this lattice and the structure or contents of an individual unit cell.

Crystal structures are characterized by their space group symmetry, that is, each structure falls into one of the 230 space group types detailed in International Tables for Crystallography. Each of these space groups falls into one of each of the broader categories of crystal system, Bravais lattice and crystal point group as shown below, that is, it will belong to a Bravais lattice type and a crystal point group within its crystal system.

[☆] *Change History*: October 2022. AM Glazer updated the whole article.

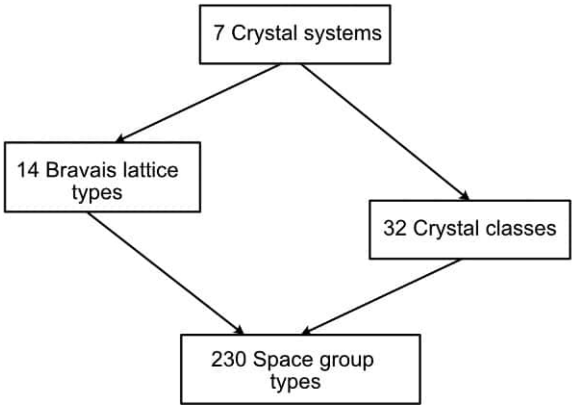

In general, a space group symmetry operation consists of a matrix ***R*** and a vector ***t***, which generate from a position vector x an equivalent point x' as

$$x' = Rx + t$$

where ***R*** is an operation of the corresponding crystal point group. When ***R*** is the identity operation (100/010/001) the overall operation is a lattice translation, and t will be integral unless the lattice is centered in some way. Other point symmetry operations ***R*** may be combined with fractional translations ***t*** to form alternate space group operations (screw axes and glide planes). When the possible combinations of Bravais lattices and crystal point groups are considered, and include the cases where screw axes and glide planes replace the pure rotation axes or mirror planes of the point group, the 230 space group types result. Table 1 gives the crystal classes, along with, for each class, the lattice parameters required to define the unit cell, the possible centerings and the point groups, classified according to the presence of polarity and chirality. The equivalent points in the various centered lattices are shown in Table 2.

Table 1 Some properties of the crystal systems.

Crystal system	*Restrictions on lattice parameters*	*Possible lattices*	*Point groups and their orders (in parentheses)*			
			Nonpolar nonchiral	*Polar nonchiral*	*Nonpolar chiral*	*Polar chiral*
Cubic	$\mathbf{a}(=\mathbf{b}=\mathbf{c})$ $(\alpha=\beta=\gamma=90^\circ)$	P,I,F	$m\bar{3}m$ (*48*) $\bar{4}3m$ (*24*), $m\bar{3}$ (*24*)		432(*24*), 23(*12*)	
Hexagonal	$\mathbf{a}(=\mathbf{b})\neq c$ $(\alpha=\beta=90^\circ,\ \gamma=120^\circ)$	P	6/*mmm*(*24*),$\bar{6}$ m2(*12*), 6/m(*12*), $\bar{6}$ (*12*)	6*mm*(*12*)	622(*12*)	6(*6*)
Trigonal	$\mathbf{a}(=\mathbf{b})\neq\mathbf{c}$ $(\alpha=\beta=90^\circ,\ \gamma=120^\circ)$	P,R	$\bar{3}m$(*12*), $\bar{3}$(*6*)	3 *m*(*6*)	32(*6*)	3(*3*)
Tetragonal	$\mathbf{a}(=\mathbf{b})\neq\mathbf{c}$ $(\alpha=\beta=\gamma=90^\circ)$	P,I	4/*mmm*(*16*), $\bar{4}$ 2*m*(*16*), 4/ *m*(*8*), $\bar{4}$ (*8*)	4 *mm*(*8*)	422(*8*)	4(*4*)
Orthorhombic	$\mathbf{a}\neq\mathbf{b}\neq\mathbf{c}$ $(\alpha=\beta=\gamma=90^\circ)$	P,I,C,F	*mmm*(*8*)	*mm*2(*4*)	222(*4*)	
Monoclinic	$\mathbf{a}\neq\mathbf{b}\neq c$ $(\beta\neq(\alpha=\gamma=90^\circ)$	P,C	2/*m*(*4*)	*m*(*2*)		2(*2*)
Triclinic	$\mathbf{a}\neq\mathbf{b}\neq\mathbf{c}\ \alpha\neq\beta\neq\gamma$	P	$\bar{1}$ (*2*)			1(*1*)

Table 2 Lattice types and their equivalent points under translation.

Lattice type	*No. of points*	*Equivalent points under translation are (x,y,z) +*
P	1	(0,0,0)
C	2	(0, 0, 0) (1/2, 1/2, 0)
I	2	(0, 0, 0) (1/2, 1/2, 1/2)
R	3	(0, 0, 0) (2/3, 1/3, 1/3) (1/3, 2/3, 2/3)
F	4	(0, 0, 0) (1/2, 1/2, 0) (1/2, 0, 1/2) (0, 1/2, 1/2)

Unit cell contents

The unit cell of the crystal will normally contain a number of formula units of the constituent substance. Although the chemical formula may be easy to define in the case of elements and synthetic compounds, it may be problematic in the case of biological materials because of their complexity, and also for many minerals. Assuming that the formula mass, M, can be reasonably estimated, the number, z, of formula units per unit cell can be calculated from its dimensions, provided the density of the crystal, ρ, is known, since

$$z = \rho N_A U / M$$

where N_A is Avogadro's number and U the cell volume.

For macromolecular crystals such as proteins, this process is complicated by the large and uncertain amount of solvent generally present in the crystal and so contributing to M, and by the difficulties in obtaining accurate density measurements.

Once the number of each type of atom is known, the next stage is to describe how the mean atomic positions are distributed within the unit cell. In a simple case, this merely means describing the contents of that normally smaller volume which may be used to generate the complete unit cell through the space group operations. This volume, in mathematical terms the fundamental domain of the space group, is referred to as the asymmetric unit. The asymmetric unit is not normally uniquely defined; however, when rotation or inversion axes are present, they must lie at the borders of the asymmetric unit. (Centers of symmetry $\bar{1}$ and mirror planes $m = \bar{2}$, are special cases of inversion axes.)

The volume of the asymmetric unit may be calculated using data from Tables 1 and 2. The number of equivalent points generated by each crystal point group is given in parentheses against it in Table 1. The number of points equivalent by translation is given in Table 2 for each lattice type. Multiplying these two numbers together will give the factor by which the asymmetric unit is smaller than the unit cell. For example, the trigonal space group $R3c$ has a rho-mbohedral lattice (triply primitive = 3) and belongs to point group $3m$ (order 6). The unit cell is therefore 18 times larger than the asymmetric unit. This number is termed the multiplicity of the general position of the space group; the explanation of this follows.

We can define another number z', the number of formula units in the asymmetric unit. For many structures $z' = 1$, and each of the atoms of the formula unit occupies a so-called general position within the asymmetric unit. In such a case, each atom's position is described by three arbitrary fractional coordinates (x_i, y_i, z_i). However, various exceptions exist. The most common is that $z' < 1$; this normally means that the positions of at least some of the atoms must coincide with one or more point symmetry elements (in addition to the identity), so that when the corresponding transformations are applied, their coordinates are unchanged. These atoms will lie on the boundaries of the asymmetric unit, and their coordinates will be restricted in some way. Such atoms are said to lie on special positions of the space group.

The various possible special or "Wyckoff" positions are listed, together with their multiplicities and local site symmetries, in International Tables for Crystallography. Where one or two coordinates are constricted, that special position type may be occupied by more than one type of atom (obviously with different free coordinates), whereas only one atom may occupy a special position comprising a set of points.

An example which illustrates many of these points, and where all the possible Wyckoff positions of the space group are used, is that of the isostructural crystals $M_3As_2O_8$ (M = Mg, Co). These have $z = 6$ in space group $I\bar{4}2d$. The Wyckoff positions for this space group are shown in Table 3; the general position with symbol e has multiplicity 16. This makes $z' = 3/8$ on the basis of the formula, and it immediately follows that elements M and As at least must lie on special positions or be disordered. The number of As atoms in the unit cell (12) cannot be satisfied by the multiplicity of one special position alone, and that of M (18) cannot even be satisfied by any combination of the special positions, which only have multiplicities of 8 or 4, unless some disorder is also present. The way in which these restrictions are resolved in the structure is also shown in Table 3, where all five Wyckoff position types are used. The As atoms are tetrahedrally coordinated (site symmetries 2 and $\bar{4}$ are subgroups of the tetrahedral group $\bar{4}3m$), and most of the M atoms are octahedrally coordinated (2 is a subgroup of $m\bar{3}m$), with one-ninth of the M atoms disordered among eight coordinate sites of symmetry $\bar{4}$.

Table 3 Distribution of the atoms over the Wyckoff positions of $I\bar{4}2d$ in the tetragonal $M_3AS_2O_8$ phases.

Site multiplicity	*Wyckoff symbol*	*Oriented site symmetry*	*Representative coordinates*	*Atoms*	*Occupancy*	*Contribution to cell contents*		
						M	*As*	*O*
16	e	1	(*x*,*y*,*z*)	O(1)	1			16
				O(2)	1			16
				O(3)	1			16
8	d	•2•	(*x*, 1/4, 1/8)	M(1)	1	8		
				As(1)	1		8	
8	c	2••	(0, 0, z)	M(2)	1	8		
4	b	$\bar{4}$	(0, 0, 1/2)	M(3)	0.5	2		
4	a	$\bar{4}$	(0, 0, 0)	As(2)	1		4	
					Totals	18	12	48

On the other hand, for molecular crystals, it is possible for the molecule (formula unit) to itself have some internal symmetry, and that $z' < 1$ indicates that some point symmetry elements of the molecule coincide with the site symmetry of a special position. Depending on the situation, this might not require any individual atoms to lie in special positions. Also, for molecular crystals, cases where $z' > 1$ are not uncommon, and rare cases exist where $z' = 1$ does not correspond to one molecule in a general position, but more than one in distinct special positions.

Crystallographic databases

The information on an individual structure will be held as a record on a crystallographic database. The main databases are CRYSTMET for metals and minerals, the Inorganic Crystal Structure Database (ICSD) for inorganic structures, the Cambridge Structural Database (CSD) for organic and organometallic structures, and the Protein Data Bank (PDB) for macromolecular structures. These are augmented by the Powder Diffraction File, the Surface Structure Database, and the Nucleic Acid Database for special purposes.

The information held in a database record (individual crystal structure) will include composition, lattice parameters, and space group, as well as basic details of the experiment and refinement. Typically, the databases as a whole are relational, or are otherwise structured to facilitate a wide range of possible searches. They are regularly updated with new crystal structures, but only after each submission has undergone an extensive validation procedure to ensure consistency and completeness, and to identify duplicate or related entries. Specialized software for search, retrieval, and visualization is made available to subscribers, along with regular updates to the databases themselves.

Applications of the databases fall into two main categories. First, there are searches for a single record or a limited group of records, as an aid in identification, structure description, property prediction, or possibly even structure determination through structure type. However, increasingly the databases are resources for "data mining," the discovery of new information through statistical analysis of the entire database.

The refinement model

How to construct the standard refinement model of an inorganic or "small molecule" crystal structure is discussed here. The least-squares refinement, the predominant method, is assumed here. The mean positions of the nuclei are defined by their fractional coordinates—some of which may be constrained for atoms in special positions—and, for X-ray and electron diffraction, their surrounding electron density is assumed to be spherical, and is described by its Fourier transform, the scattering factor. The distribution of the instantaneous nuclear position about its mean is described by the Debye–Waller or temperature factor, either isotropic or anisotropic. The latter form requires six components for an atom in a general position or on a center of symmetry, but will be constrained for other types of special positions.

There will be an overall scale factor (sometimes more, depending on the details of the data collection), in addition to the parameters mentioned above. Atomic site occupancies may be varied to take account of disorder or substitution. Modern refinements may also vary the relative contributions from the various twin orientations which may be present, or the Flack parameter that describes the absolute structure (chirality) of a chiral crystal structure.

However, in evaluating the results of a crystal structure determination, it is important to distinguish those quantities which are determined in an unbiased way by the refinement, and those for which presumed chemical information was applied. In many cases, any attempt to refine all possible parameters is doomed to failure; but this does invalidate the results of a more cautious refinement. In practice, the parameters to be refined must be chosen in such a way as to maintain a well-behaved refinement process. The inclusion of parameters with little impact on the agreement between calculation and observation will produce near-singular least-squares matrices and hence excessive parameter shifts. For this reason chemical information is frequently included in the form of geometric constraints or, increasingly often these days, restraints. A typical constraint is to refine a molecule or group as a rigid body. In the case of restraints, the assumed dimensions of the molecule or group are treated as additional observations with appropriate estimated errors.

In X-ray diffraction, the weakly-scattering hydrogen atoms are normally constrained or restrained in some way, and their precise positions are usually unreliable.

Because of the limited quality of diffraction data from macromolecular crystals, it is not possible to refine such structures using the same sort of least-squares model as for small molecules, and so constraints or restraints are invariably necessary.

An alternative approach to crystal structure determination that is growing in popularity and reliability is that of Rietveld analysis of powder diffraction data.

Measures of quality

The quality of a structure refinement is generally reported as the conventional R-factor

$$R = \frac{\sum_i |\Delta F_i|}{\sum_i |F_i^o|}$$

This quantity is related to the actual measure normally minimized, the weighted R-factor based on $|F|^2$

$$ {}_2R_w = \frac{\sum_i w_i|\Delta F_i|^2}{\sum_i w_i|F_i^o|^2} $$

typically being about half. Another measure which may be reported is the goodness-of-fit S,

$$ S = \frac{\sum_i w_i|\Delta F_i|^2}{n - m} $$

which should be about unity if the standard errors of the observations are correctly estimated, and the model used is adequate to fit the observations (i.e., the errors in the model are negligible).

The conventional R-factor is a good rough guide to the quality of a structure determination, but has shortcomings in terms of comparing refinements on different crystal structures, because it does not take account of the distribution of structure factors in each particular data set. Data sets of high variance (hypercentric distributions, superlattices, and other pseudosymmetric structures), tend to refine to higher values of the R-factor, both because the higher proportion of very strong and very weak diffraction peaks that cannot be measured with the same precision as the others, and because such data sets are more sensitive to limitations in the model.

Typically, the databases allow some screening of the quality of the individual structure determinations in the search process. The CSD, for example, allows a cut-off maximum to be applied to the conventional R-factor, as well as the elimination of structures where disorder is present. It also allows the comparison of structures based on the quality of the derived geometric descriptors (see next section), in its case the average standard error in C—C bond lengths.

Derived geometric parameters

Much of the importance of crystal structure determination lies in the information available on bond lengths (i.e., internuclear distances), bond angles, and other geometric descriptors. These may be calculated by standard methods; either the fractional coordinates may be transformed to orthogonal distance coordinates,

$$ \begin{gathered} X = ax \\ Y = ax\cos\gamma + by\sin\gamma \\ Z = ax\cos\beta + by\sin\beta\cos\alpha^* + cz\sin\beta\sin\alpha^* \end{gathered} $$

where α^* is an angle of the reciprocal lattice, or the calculations may be made using the metric tensor for the crystal,

$$ G = \begin{pmatrix} a\cdot a & a\cdot b & a\cdot c \\ b\cdot a & b\cdot b & b\cdot c \\ c\cdot a & c\cdot b & c\cdot c \end{pmatrix} $$

The first approach would be more appropriate for simple hand calculations, whereas the second is that used in molecular geometry programs.

It is also worthwhile to examine the validity of the anisotropic temperature factors determined by least-squares. These parameters may be visualized as ellipsoids using the ORTEP program (see Fig. 1). Very large or distorted thermal ellipsoids on individual atoms may indicate large amplitude internal motion or even short-range static disorder. The TLS (T—translation, L—libration, S—screw correlation) matrix formalism may be used to test whether individual atomic displacements within a molecule or group are consistent with rigid-body motion.

In addition to bond lengths and angles, metal and inorganic structures are frequently described in terms of coordination polyhedra. For organic and organometallic structures, additional descriptors are required to describe the molecular or group conformation; these include torsion angles and the deviation from planarity of a group of atoms.

The description of protein crystal structures is somewhat different. Precise bond lengths and angles are not experimentally accessible, but the various levels of organization are, these being:

1. primary structure, the sequence of amino acids present in each chain,
2. secondary structure, the local hydrogen-bonding patterns and chain torsion angles, which result in turn in the typical regular structures (helices and sheets),
3. tertiary structure, the three-dimensional relationships between the secondary structure elements, and
4. quaternary structure, the combination of protein chains to form the overall protein molecule.

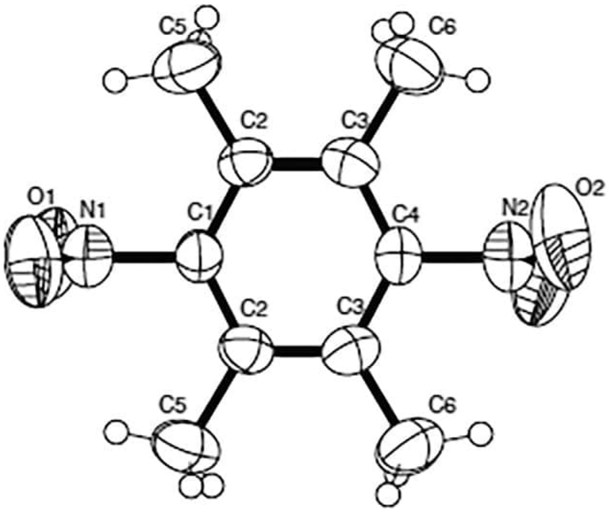

Fig. 1 ORTEP drawing of an organic molecule in its crystal structure, showing hydrogen atoms as small spheres and nonhydrogen atoms as 50% probability ellipsoids. The elongation of the oxygen (labeled "O") ellipsoids indicates large amplitude librations about the C—N bonds.

Further reading

Allen FH (2002) The Cambridge Structural Database: A quarter of a million crystal structures and rising. *Acta Crystallographica* B58: 380–388. International Union of Crystallography, Chester.

Belsky A, Hellenbrandt M, Karen VL, and Luksch P (2002) New developments in the Inorganic Crystal Structure Database (ICSD): accessibility in support of materials research and design. *Acta Crystallographica. Section B* 58: 364–369. International Union of Crystallography, Chester.

Berman HM, Battituz T, Bhat TN, Bluhm WF, Bourne PE, et al. (2002) The protein data bank. *Acta Crystallographica Section D* 58: 899–907. International Union of Crystallography, Chester.

Dunitz JD (1995) *X-Ray Analysis and the Structure of Organic Molecules*. Basel: Verlag Helvetica Chimica Acta.

Giacovazzo C (1992) Crystallographic computing. In: Giacovazzo C (ed.) *Fundamentals of Crystallography*, pp. 61–140. Oxford: Oxford University Press.

Giacovazzo C (1992) Symmetry in crystals. In: Giacovazzo C (ed.) *Fundamentals of Crystallography*, pp. 1–60. Oxford: Oxford University Press.

Müller U (1993) *Inorganic Structural Chemistry*. Chichester: Wiley.

Sands DE (1982) Molecular geometry. In: Sayre D (ed.) *Computational Crystallography*, pp. 421–429. Oxford: Clarendon Press.

Stout GH and Jensen LH (1989) *X-Ray Structure Determination: A Practical Guide*, 2nd edn. New York: Wiley.

Wells AF (1982) *Structural Inorganic Chemistry*, 5th edn. Oxford: Clarendon Press.

White PS, Rodgers JR, and Le Page Y (2002) CRYSTMET: a database of the structures and powder patterns of metals and intermetallics. *Acta Crystallographica. Section B* 58: 343–348. International Union of Crystallography, Chester.

Zanotti G (1992) Protein crystallography. In: Giacovazzo C (ed.) *Fundamentals of Crystallography*, pp. 535–597. Oxford: Oxford University Press.

Periodicity and lattices☆

JS Rutherford[a] **and AM Glazer**[b], [a]National University of Science and Technology, Bulawayo, Zimbabwe; [b]University of Oxford, Oxford, United Kingdom

© 2024 Elsevier Ltd. All rights reserved.

This is an update of F.J. Lamelas, Periodicity and Lattices, Editor(s): Franco Bassani, Gerald L. Liedl, Peter Wyder, Encyclopedia of Condensed Matter Physics, Elsevier, 2005, Pages 238–246, ISBN 9780123694010, https://doi.org/10.1016/B0-12-369401-9/00419-8.

Lattices in two and three dimensions 17
The reciprocal lattice, diffraction, and electronic band structure 22
Variations of periodicity: Superstructures and aperiodicity 25
Reference 28
Further reading 28

Abstract

The notion of periodicity in crystals is examined and how this can be varied in practice. In particular, the article discusses first of all the concept of superstructures, in which some sort of alternating motif occurs thus changing the repeat distance in a lattice. Crystals of this type are often incorrectly called in the literature superlattices: first of all they cannot be called lattices at all as they consist of atoms (a lattice must only consist of points). In any case such a superstructure is formed from a sublattice rather than a superlattice. In addition, some crystals do not have normal periodicity within a three-dimensional space, and are known as aperiodic crystals. Despite being aperiodic, they are still ordered. In mathematical terms they can by described with respect to a higher-dimension space and then projected back onto three dimensions. This generalizes our notion of what is meant by a crystal.

Lattices in two and three dimensions

A lattice is a periodic array of points generated by translation vectors (quasiperiodic lattices are discussed separately later). As an example, consider a two-dimensional rectangular lattice generated by the orthogonal vectors $\boldsymbol{a}_1$ and $\boldsymbol{a}_2$ (Fig. 1).

The lattice is assumed to be infinite in extent. Points on this lattice have position vectors

$$\boldsymbol{R} = n_1\boldsymbol{a}_1 + n_2\boldsymbol{a}_2 \tag{1}$$

where n_1 and n_2 are integers.

Lattices can be classified according to their symmetry properties. For example, the rectangular lattice in Fig. 1 has reflection lines which pass through the vertical and horizontal rows of points, and twofold rotation points coincident with the lattice points. Additional symmetry elements occur between the lattice points, as shown in Fig. 2.

According to the lattice condition, all points of the lattice must have the same environment; therefore, not all regular arrays of points are lattices. For example, in one dimension there is only one possible lattice type: an array of equally spaced points, as shown in Fig. 3.

If one classifies all two-dimensional lattices according to their symmetry elements, it is possible to show that there are only five distinct types, as shown in as Fig. 4.

The translation vectors define the edges of unit cells which are building blocks of the lattice. In two dimensions, the shape of the unit cell is specified by three lattice parameters: the magnitudes a and b of the translation vectors, and γ, the angle between the vectors (the magnitudes of the translation vectors are typically defined as $a = |\boldsymbol{a}_1|$, $b = |\boldsymbol{a}_2|$, and, in three dimensions, $c = |\boldsymbol{a}_3|$).

The choice of the unit cell is by no means unique. One could, for example, double the unit cells of Fig. 4 and generate the same lattice types. Unit cells containing only one lattice point are primitive; in this case, the positions of all lattice points can be written as integer sums of the translation vectors, as in Eq. (1). For the centered unit cell of Fig. 4c, the lattice points at the centers are given by half-integer sums of the translation vectors:

$$\boldsymbol{R}_{\text{center}} = (n_1 + 1/2)\boldsymbol{a}_1 + (n_2 + 1/2)\boldsymbol{a}_2 \tag{2}$$

Even primitive cells are not unique, since one could, for example, define an oblique primitive cell for the square lattice, as shown in Fig. 5.

In general, the conventional unit cell is chosen so as to be as small as possible, consistent with the underlying symmetry of the lattice. For example, the centered rectangular lattice (Fig. 4c) could be generated by an oblique primitive cell, but its symmetry elements are more obviously related to a rectangular unit cell (the symmetry elements of the centered rectangular lattice are identical to those of Fig. 2, with additional twofold rotation points along the cell diagonal). In other words, symmetry considerations can lead one to choose a conventional cell that is larger than a primitive cell.

The two-dimensional lattice types of Fig. 4 can be grouped within four systems based on the relative magnitudes of the translation vectors and the angle between them, as shown in Table 1.

☆*Change History*: September 2022. AM Glazer wrote section on 'Variations of periodicity: Superstructures and aperiodicity'.

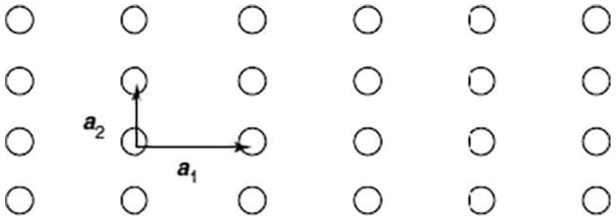

Fig. 1 Rectangular lattice with translation vectors $\boldsymbol{a}_1$ and $\boldsymbol{a}_2$.

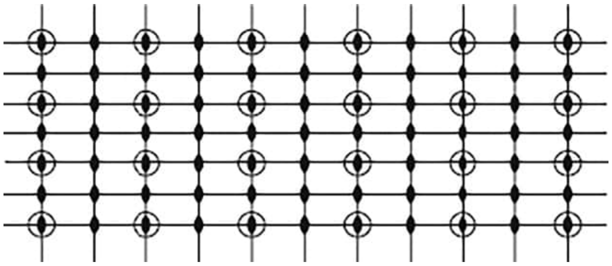

Fig. 2 Symmetry elements of the rectangular lattice. The points of the lattice are indicated by open circles, reflection lines by solid lines, and twofold rotation points by lens-shaped symbols.

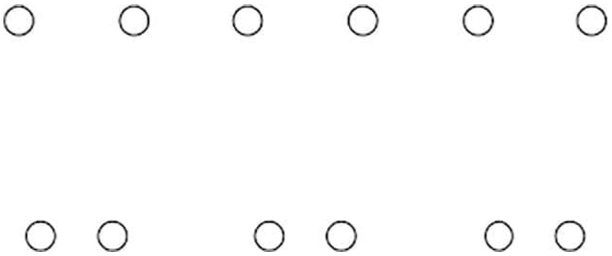

Fig. 3 Two periodic one-dimensional arrays of points. The lower example does not satisfy the lattice condition since some points have their nearest neighbor on the right, and some on the left.

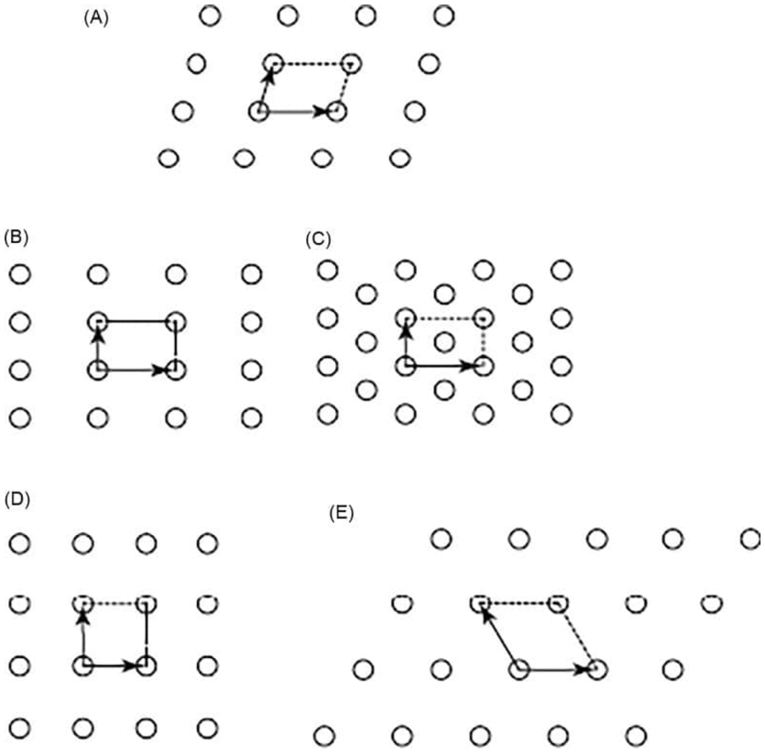

Fig. 4 The five two-dimensional lattice types: (a) oblique, (b) rectangular, (c) centered rectangular, (d) square, and (e) hexagonal. Outlines of unit cells are shown by the dashed lines. Except for (c), all of the unit cells shown here are primitive.

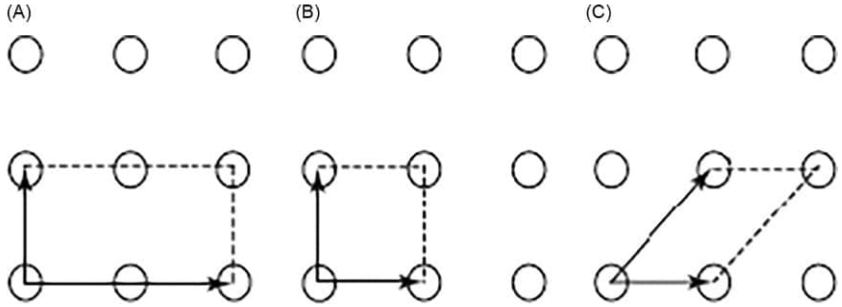

Fig. 5 Several unit cells which can generate a square lattice type, including (a) a nonprimitive cell containing two lattice points, (b) a conventional primitive cell, and (c) an oblique primitive cell. In counting the number of lattice points assigned to a cell, points at corners, on sides, and within the cell are given weights of 1/4, 1/2, and 1.

Table 1 The four two-dimensional systems.

System	*Lengths*	*Angle (°)*
Oblique	$a \neq b$	$\gamma \neq 90$
Rectangular	$a \neq b$	$\gamma = 90$
Square	$a = b$	$\gamma = 90$
Hexagonal	$a = b$	$\gamma = 120$

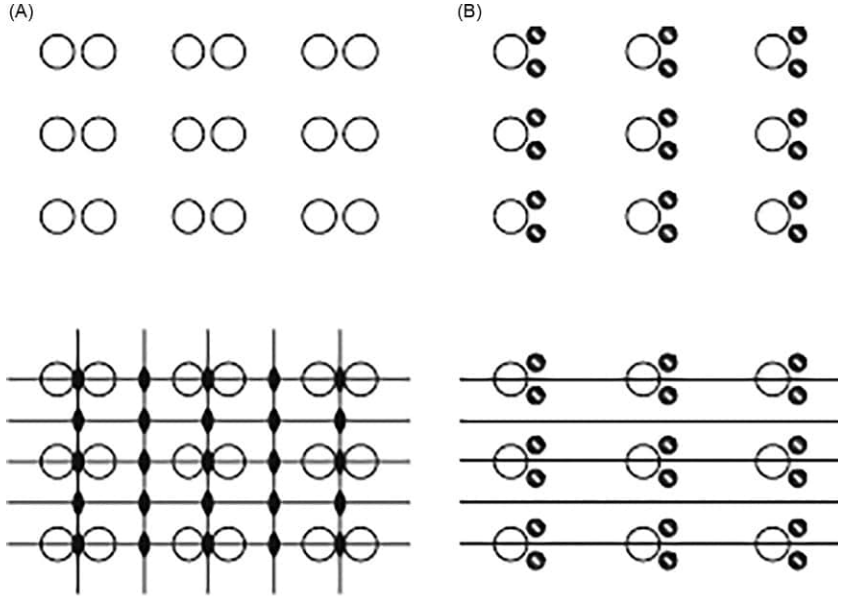

Fig. 6 Upper drawings: two structures with identical rectangular lattice types but different bases. Lower: the same structures repeated with symmetry elements superimposed. (a) Space group *p2mm*, indicating a primitive lattice (*p*) with twofold rotation points (2), and two sets of mirror lines (*mm*), (b) space group *pm*, indicating a primitive lattice with a single set of mirror lines.

Note that the number of lattice types (five) is not equal to the number of systems (four), since there are two rectangular lattice types (primitive and centered).

A periodic physical system such as a naturally occurring crystal can be described as a lattice with repeating units known as a basis attached to each lattice point. The basis may consist of a single atom, a molecule, or a larger assembly. The space group that characterizes the entire structure results from the combined symmetries of the lattice and the basis. Since bases with different symmetries can be attached to a given lattice, one expects a greater number of space groups than lattices. In two dimensions, there are 4 systems, 5 lattice types, and 17 space group types. An example of two structures with the same lattice but different space groups is given in Fig. 6.

Different space groups also arise according to the arrangement of asymmetric molecules on similar lattices. For example, if every other molecule is flipped after displacement along a lattice translation vector, then a glide-reflection symmetry element is produced. (In the glide-symmetry operation, the structure is translated along the glide line and then reflected across the line.) Examples of two space groups with and without glide symmetry are shown in Fig. 7.

In three dimensions, lattices are generated by three translation vectors: $\boldsymbol{a}_1$, $\boldsymbol{a}_2$, and $\boldsymbol{a}_3$. It can be shown that there are 14 symmetrically distinct lattices which satisfy the lattice condition. These are the Bravais lattices; the conventional unit cells are shown in Fig. 8. The shapes of the unit cells are characterized by six lattice parameters: the magnitudes a, b, and c of the translation vectors, and the angles α, β, and γ, shown in Fig. 9.

The 14 Bravais lattices are distributed among seven crystal systems, with relative lattice parameters given in Table 2.

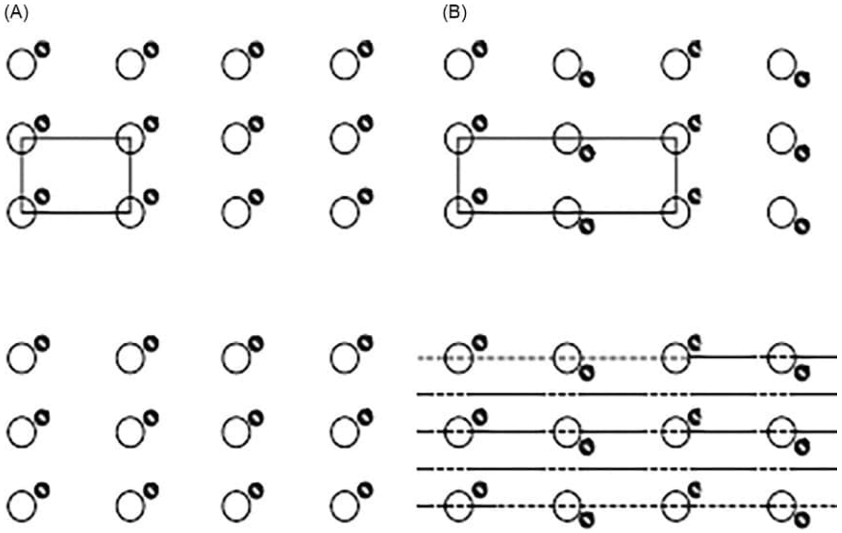

Fig. 7 Upper drawings: arrangements of identical molecules with and without glide-line symmetry. Unit cells are shown by the solid rectangles. Lower: the same structures with symmetry elements superimposed. (a) Space group *p*1: primitive lattice with no rotational, mirror, or glide symmetry. (b) Space group *pg*: primitive lattice with glide-line symmetry. (Note: the unit cell contains two molecules but only one lattice point, and is therefore primitive.)

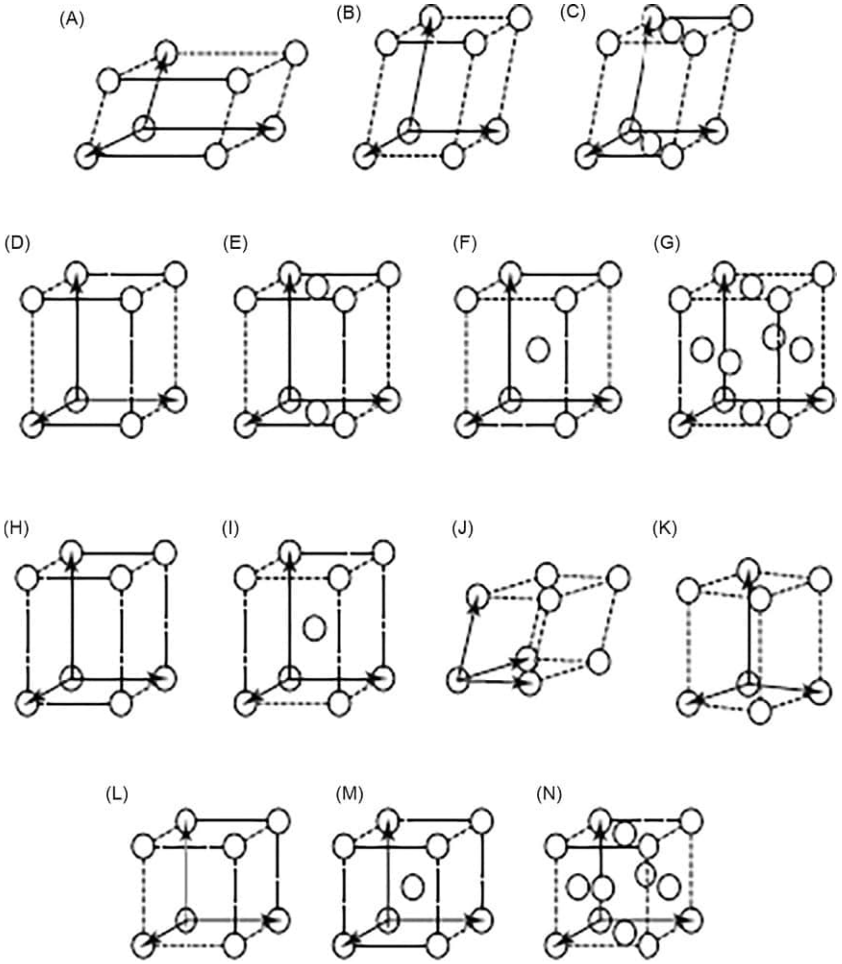

Fig. 8 The 14 Bravais lattice types, with lattice translation vectors shown as solid arrows. (a) triclinic, (b) monoclinic, (c) base-centered monoclinic, (d) orthorhombic, (e) base-centered orthorhombic, (f) body-centered orthorhombic, (g) face-centered orthorhombic, (h) tetragonal, (i) body-centered tetragonal, (j) rhombohedral, (k) hexagonal, (l) cubic, (m) body-centered cubic, and (n) face-centered cubic.

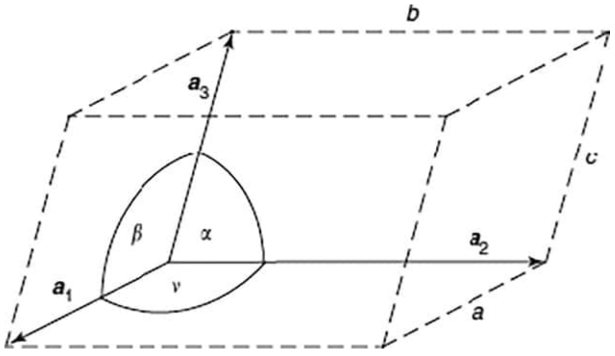

Fig. 9 Three-dimensional lattice parameters. The lengths of the cell edges are the magnitudes of the translation vectors *a*, *b*, and *c*. The interaxial angles a_1 ⊠ a_3, a_2 ⊠ a_3, and a_1 ⊠ a_2 are given by α, β, and γ.

Table 2 The seven three-dimensional crystal systems.

System	*Lengths*	*Angles*
Triclinic	$a \neq b \neq c$	$\alpha \neq \beta \neq \gamma$
Monoclinic	$a \neq b \neq c$	$\alpha = \beta = 90^\circ \neq \gamma$
Orthorhombic	$a \neq b \neq c$	$\alpha = \beta = \gamma = 90^\circ$
Tetragonal	$a = b \neq c$	$\alpha = \beta = \gamma = 90^\circ$
Trigonal	$a = b = c$	$\alpha = \beta = 90^\circ$, $\gamma = 120^\circ$
Hexagonal	$a = b \neq c$	$\alpha = \beta = 90^\circ$, $\gamma = 120^\circ$
Cubic	$a = b = c$	$\alpha = \beta = \gamma = 90^\circ$

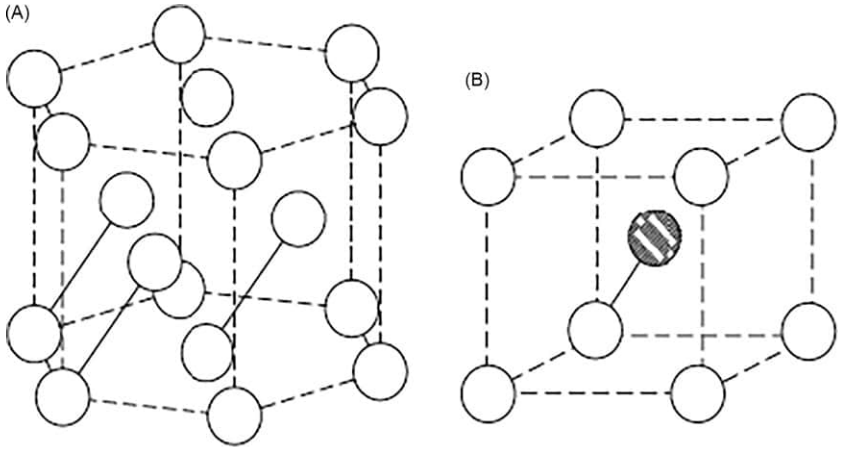

Fig. 10 Examples of structures produced by adding a basis to a Bravais lattice. (a) h.c.p cobalt. Pairs of atoms in the basis are connected by solid lines. The dashed lines show the edges of a hexagonal repeating structure with three times the volume of the conventional unit cell of Fig. 8k. (b) Cesium chloride. Open and filled circles represent oppositely-charged ions. The primitive cubic unit cell (also known as a simple cubic unit cell) is identical to that of Fig. 8l.

The combined symmetries of the 14 Bravais lattices and all possible bases lead to 230 space groups in three dimensions, first enumerated late in the nineteenth century and described explicitly in the International Tables for X-ray Crystallography. The classification of periodic structures as members of specific space groups is important in predicting properties, such as allowed reflections in X-ray diffraction, and allowed vibrational modes in optical spectroscopy.

A three-dimensional crystal can be "constructed" by placing a specific basis at each of the points of one of the 14 Bravais lattices. In the simplest case, the basis consists of a single atom and the full structure is simply that of the Bravais lattice. An example is face-centered cubic (f.c.c.) aluminum, which has the unit cell shown in Fig. 8n. As the complexity is increased, the basis can include more than one atom of the same element, as in hexagonal close-packed (h.c.p.) cobalt. In this structure, a basis consisting of two cobalt atoms is attached to the hexagonal lattice points, as shown in Fig. 10a. In the case of compounds, the basis contains two or more elements, as in cesium chloride, where the two-ion basis is attached to a primitive cubic lattice, as in Fig. 10b.

In all cases, it is the Bravais lattice (rather than the details of the basis) which determines the translational symmetry of the structure. That is, the crystal is invariant after a translation by a Bravais lattice vector, no matter what the basis is. This spatial periodicity results in the great utility of Fourier methods, as shown in the next section.

The reciprocal lattice, diffraction, and electronic band structure

A signal which is periodic in time can be conveniently described in terms of the strength of its harmonics. The signal can be defined completely in either the time or the frequency domain, using variables which have dimensions of time or inverse time. Similarly, a property such as the electron density of a spatially periodic structure can be described directly, in a space which has dimensions of length, or by a Fourier expansion in reciprocal lattice vectors, which have dimensions of inverse length. Many of the properties of a solid, such as its electronic band structure, are formulated most easily in reciprocal space (rather than direct space). Even from a purely structural standpoint, the reciprocal-space description is essential in the diffraction techniques which are used to solve crystal structures.

If one wishes to use the reciprocal lattice in order to describe physical properties, it is useful to define the reciprocal lattice as follows (in crystallography, the definition of the reciprocal lattice may differ slightly from that given here, for example, by the omission of the factors of 2π). Consider a solid with lattice translation vectors $\boldsymbol{a}_1$, $\boldsymbol{a}_2$, and $\boldsymbol{a}_3$. The reciprocal lattice vectors are defined by

$$\begin{gathered} b_1 = 2\pi \frac{a_2 \times a_3}{a_1 \cdot a_2 \times a_3}, \quad b_2 = 2\pi \frac{a_3 \times a_1}{a_1 \cdot a_2 \times a_3}, \\ b_3 = 2\pi \frac{a_1 \times a_2}{a_1 \cdot a_2 \times a_3} \end{gathered} \tag{3}$$

The denominator of these expressions ($a_1 \cdot a_2 \times a_3$) is the volume of the unit cell in direct space. The vectors b_1, b_2, and b_3 are the translation vectors which define the reciprocal lattice, just as a_1, a_2, and a_3 define the Bravais lattice in direct space. An arbitrary translation vector, which connects two points of the Bravais lattice, has the form

$$\boldsymbol{R} = n_1 a_1 + n_2 a_2 + n_3 a_3 \tag{4}$$

where n_1, n_2, and n_3 are integers. Similarly, an arbitrary reciprocal lattice vector can be written as

$$\boldsymbol{G} = m_1 b_1 + m_2 b_2 + m_3 b_3 \tag{5}$$

The form of the numerators in Eq. (3) leads to a compact expression for dot products between direct-space and reciprocal-space translation vectors. Note, for example, that $a_2 \cdot b_1 = a_3 \cdot b_1 = 0$ and $a_1 \cdot b_1 = 2\pi$. In general,

$$b_i \cdot a_j = 2\pi\delta_{ij} \tag{6}$$

This implies that any function of the form e^{iGr} will have the translational symmetry of the Bravais lattice, because, for an arbitrary lattice translation vector $\boldsymbol{R}$,

$$\begin{aligned} e^{iG\cdot(\boldsymbol{r}+\boldsymbol{R})} &= e^{iG\cdot \boldsymbol{r}} e^{iG\cdot \boldsymbol{R}} \\ &= e^{iG\cdot \boldsymbol{r}} e^{i(m_1 b_1 + m_2 b_2 + m_3 b_3)\cdot(n_1 a_1 + n_2 a_2 + n_3 a_3)} \\ &= e^{iG\cdot \boldsymbol{r}} e^{2\pi i(m_1 n_1 + m_2 n_2 + m_3 n_3)} = e^{iG\cdot \boldsymbol{r}} \end{aligned} \tag{7}$$

For a Bravais lattice where the translation vectors a_1, a_2, and a_3 are all perpendicular (these are the orthorhombic, tetragonal, and cubic cases), the corresponding reciprocal lattice can be immediately determined by inspection of Eq. (3). In this case, $b_1 \| a_1$ and $b_1 = 2\pi/a_1$. Similar relations hold for $\boldsymbol{b}_2$ and $\boldsymbol{b}_3$, that is, the reciprocal-space translation vectors are parallel to those in direct space, with magnitudes which are inversely proportional.

If the direct-space lattice vectors are not all perpendicular, then the reciprocal lattice vectors are not, in general, parallel to them, because, for example, $a_2 \times a_3$ may not be parallel to $\boldsymbol{a}_1$. Nonetheless, the reciprocal lattice vectors still have a straightforward interpretation in terms of lattice planes.

Lattice planes are labeled using Miller indices, which are assigned by taking the reciprocal of the intersection of the plane with each of the direct-space axes, as shown in Fig. 11.

In Fig. 11a, the first (100) plane which does not contain the origin, intersects the x-axis at a distance a from the origin. The plane is also parallel to the y and z axes; intersections with those axes are at infinity. Taking the reciprocal of these distances in lattice-parameter units, one obtains the Miller indices $(hkl) = (100)$ for these planes. Similarly, in Fig. 11b the intersections at (a, a, ∞) give $(hkl) = (110)$. In Fig. 11c, the intersections are $(\infty, a, a/2)$, giving Miller indices $(hkl) = (012)$.

If h, k, and l are integers, it can be shown that in any of the crystal systems a reciprocal lattice vector of the form

$$G_{hkl} = hb_1 + kb_2 + lb_3 \tag{8}$$

will be normal to the lattice planes with indices (hkl). The magnitude will be inversely proportional to the spacing of the planes, specifically,

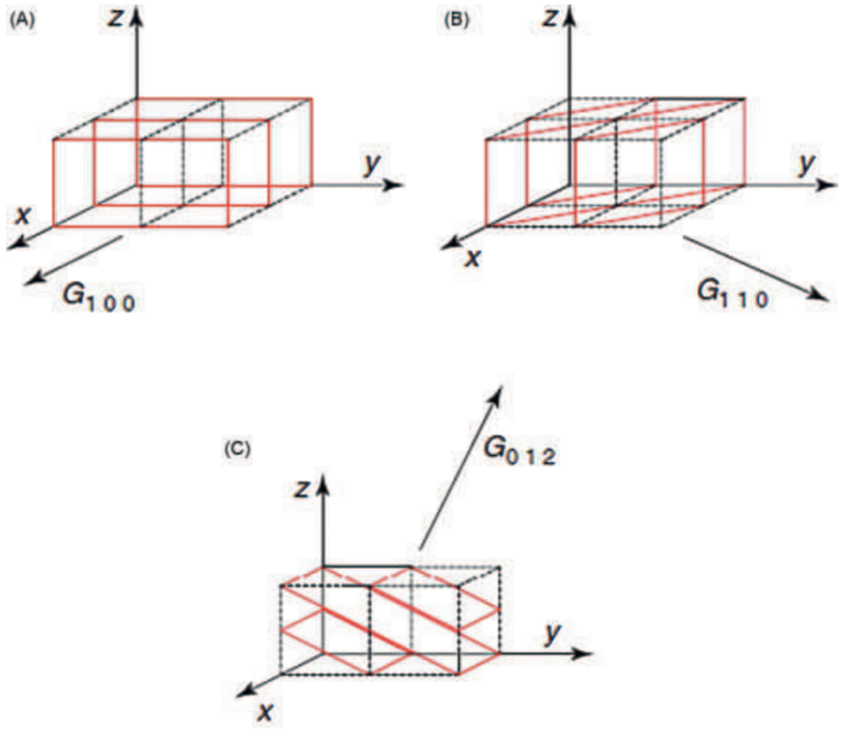

Fig. 11 Several examples of sets of planes in a cubic crystal, including (a) (1 0 0) planes, (b) (110) planes, and (c) (012) planes. Unit cells are shown with dashed lines and the sets of planes are in red. The corresponding reciprocal lattice vectors are normal to the planes and have magnitudes inversely proportional to the plane spacing.

$$G_{hkl} = \frac{2\pi}{\mathrm{d}_{hkl}} \tag{9}$$

where d_{hkl} is the spacing of the (hkl) planes.

The relationship between G_{hkl} and the (hkl) planes leads to an important formulation of the diffraction condition in the reciprocal space of the crystal. Fig. 12 shows the geometry of the Bragg diffraction. The incident beam has wavelength λ and propagates along the direction given by the wave vector $\boldsymbol{k}_{\mathrm{inc}}$. The magnitude of the wave vector is defined by

$$k_{\mathrm{inc}} = k_{\mathrm{sc}} \equiv k = \frac{2\pi}{\lambda} \tag{10}$$

where the first equality indicates that the scattering is elastic. By setting the phase shift between waves scattered from neighboring planes equal to 2π, one obtains the Bragg condition for constructive interference (or diffraction) from the hkl planes:

$$\lambda = 2\ \mathrm{d}_{hkl} \sin\theta \tag{11}$$

By inspection of Fig. 12, and using Eqs. (10), (11), and (9), one obtains.

$$q = 2k\sin\theta = 2\pi\frac{2\sin\theta}{\lambda} = \frac{2\pi}{\mathrm{d}_{hkl}} = G_{hkl} \tag{12}$$

In other words, Bragg's law (Eq. (11)) can be reformulated as Eq. (12), which indicates that if constructive scattering from the (hkl) planes is to occur, then the magnitude of the scattering vector is equal to the magnitude of the corresponding reciprocal lattice vector. Since both $\boldsymbol{q}$ and $\mathbf{G}_{hkl}$ are normal to the scattering planes, Eq. (12) holds for the vector quantities as well:

$$\boldsymbol{q} = \mathbf{G}_{hkl} \tag{13}$$

Eq. (13) is the basis of the Ewald sphere representation of the diffraction condition, shown in Fig. 13. In an X-ray, electron, or neutron diffraction measurement, one maps out intensities associated with specific reciprocal lattice points. In essence, a diffraction measurement yields an image or a projection of the reciprocal lattice, and indirectly, information on the actual atomic ordering in the direct-space lattice.

The motion of an electron in a crystal is strongly affected by the periodic nature of the lattice. A nearly free valence electron interacts with relatively-fixed ion cores and experiences a potential, which can be written as an expansion in reciprocal-lattice vectors:

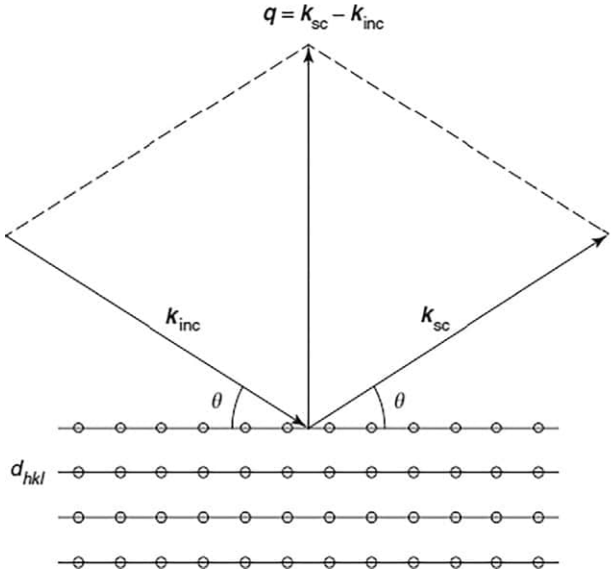

Fig. 12 Bragg scattering geometry. A beam with wave vector $\boldsymbol{k}_{\text{inc}}$ is incident with angle θ upon a set of atomic planes with spacing d_{hkl}. The scattered wave vector is $\boldsymbol{k}_{\text{sc}}$ and the scattering vector is $\boldsymbol{q}$. The small circles represent atoms or lattice points in direct space.

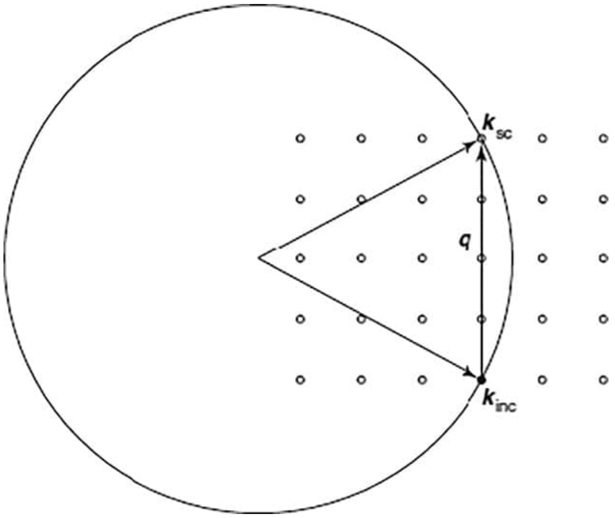

Fig. 13 The Ewald sphere construction of the diffraction condition $\boldsymbol{q} = \boldsymbol{G}_{hkl}$. This figure is drawn in reciprocal space; the small circles represent reciprocal lattice points, not atoms. The tip of the incident wave vector is placed at the origin, shown as a filled circle. The surface of the sphere gives the possible locations of the tip of an elastically scattered wave vector. When the diffraction condition is met, the scattered wave vector coincides with a reciprocal lattice point. In the example shown here, if the *z*-axis is assumed to be vertical, the Bragg condition for the (0 0 4) reflection is met, that is, $\boldsymbol{q} = \boldsymbol{G}_{004}$.

$$U(r) = \sum_j c_j e^{\mathrm{i}G_j r} \tag{14}$$

As shown by Eq. (7), a potential-energy function written in this form will have the periodicity of the Bravais lattice:

$$U(\boldsymbol{r} + \boldsymbol{R}) = U(\boldsymbol{r}) \tag{15}$$

for any lattice vector $\boldsymbol{R}$. One might expect that the electron would be scattered erratically during its interaction with the ions; however, this is not the case. It can be shown that solutions of the Schrödinger equation in a periodic potential, such as that of Eq. (14), are Bloch functions:

$$\Psi(r) = u_k(r)e^{\mathrm{i}k\cdot r} \tag{16}$$

where $\hbar\boldsymbol{k}$ is the momentum of the electron, e^{ikr} is a plane wave propagating in the direction of $\boldsymbol{k}$, and $u_k(r)$ is a function which has the periodicity of the Bravais lattice, that is,

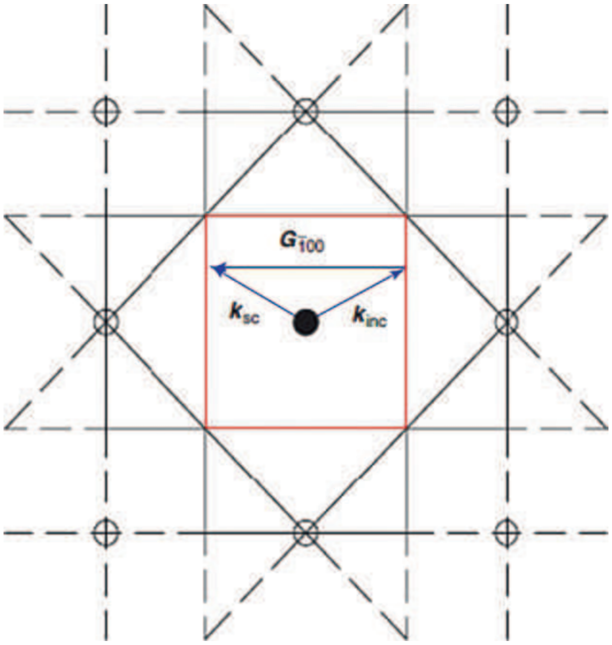

Fig. 14 Construction of Wigner–Seitz cells by drawing perpendicular bisectors of reciprocal lattice vectors. The first Brillouin zone is shown in red. Electron wave vectors and a scattering vector are shown in blue. The notation $G_{\bar{1}00}$ indicates that the scattering vector runs from the origin to the first point to the left of the origin.

$$u_k(r + \mathbf{R}) = u_k(r) \tag{17}$$

Eq. (16) indicates that electrons can propagate freely through the c as plane waves modulated by the lattice. The energy $\varepsilon(\boldsymbol{k})$ of an electron in a particular momentum state will have a specific form that depends on the potential energy function $U(r)$. (For a free electron (when $U = 0$), $\varepsilon \propto k^2$.)

The effect of the periodic structure on the electron becomes very strong when the wave vector $\boldsymbol{k}$ takes on particular values. In order to see how this comes about, consider the region of reciprocal space near the origin. Then draw a series of lines which bisect the reciprocal-lattice vectors, starting with the shortest ones, as shown in Fig. 14. This construction divides the reciprocal space into Wigner-Seitz cells. In reciprocal space, the central cell which surrounds the origin is known as the first Brillouin zone (Wigner-Seitz cells can also be drawn in direct space. As an example, a primitive unit cell can always be constructed by generating such a cell about a Bravais lattice point).

Electrons with wave vectors within the Brillouin zone have propagating Bloch wave functions and can move through the crystal. However, if the wave vector $\boldsymbol{k}_{\text{inc}}$ terminates anywhere on the zone boundary, the electron can undergo Bragg diffraction to a new state $\boldsymbol{k}_{\text{sc}}$, since the difference between these wave vectors is equal to a reciprocal lattice vector. One can see the that $\boldsymbol{k}_{\text{inc}}$ satisfies the condition for Bragg diffraction by comparing Fig. 14 to the Ewald sphere construction of Fig. 13.

When the Schrödinger equation is solved in a periodic potential (one of the simplest examples being the one-dimensional Kronig-Penney model), one finds that diffraction at the Brillouin zone boundary is accompanied by a discontinuity in the energy $\varepsilon(\boldsymbol{k})$, which is otherwise continuous within the zone. That is, a fundamental property of electrons in solids—the bandgap—follows directly from the periodicity of the Bravais lattice.

Variations of periodicity: Superstructures and aperiodicity

So far, we have assumed that lattices and crystal structures are infinite in extent and periodic. In this section, we shall look at some variations on this concept.

To begin with, we shall consider what is meant by a superlattice. Unfortunately, the condensed matter community consistently misuses this term. This is mainly because of a failure to distinguish between what is meant by a lattice and what is meant by a structure. As a reminder, a lattice is a periodic array of points (and therefore has no physical meaning but acts merely as a mathematical device for representing periodic symmetry). In contrast, a structure (or better an ideal crystal structure) is a periodic array of atoms or molecules.

Consider, for simplicity, some one-dimensional examples, as illustrated in Fig. 15. In (a), a series of points denotes a one-dimensional lattice with a unit cell repeat distance **a**. The translation vectors for this lattice are therefore given by

$$\mathbf{t}_n = n\mathbf{a}$$

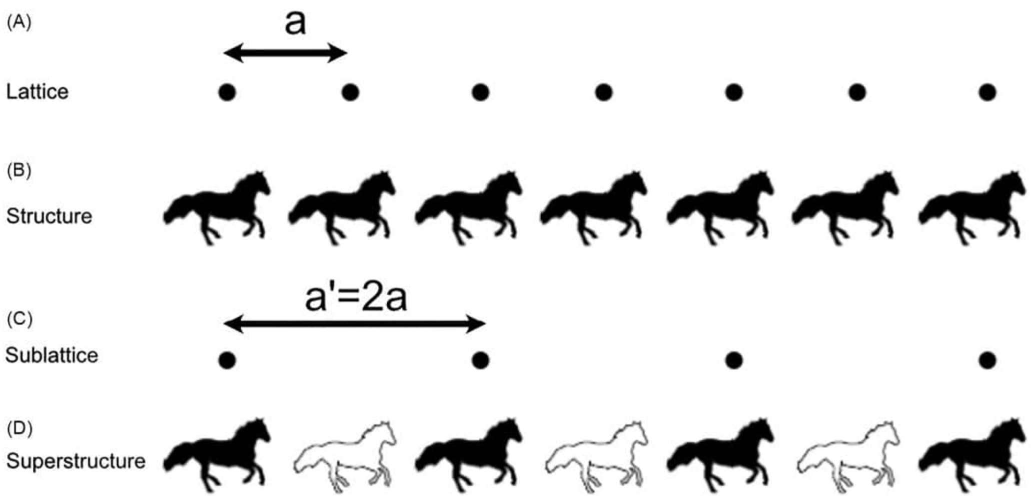

Fig. 15 Examples of one-dimensional lattices and structures.

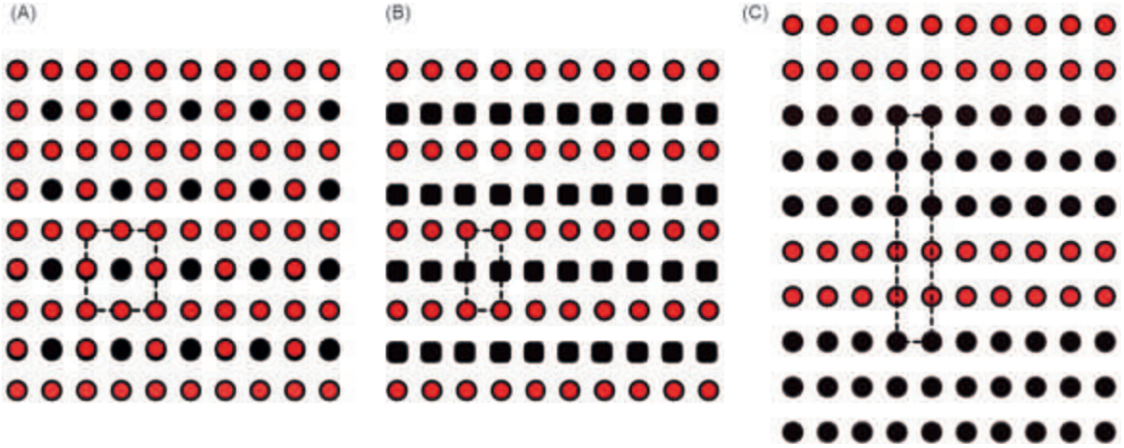

Fig. 16 Examples of superstructures in two dimensions, including (a) an ordered alloy, (b) an intercalated layered structure, and (c) a superstructure (heterostructure) prepared by the sequential deposition of two compounds. In all cases, the unit cell is marked by dashed lines.

In (b), a black horse is used to denote a molecule (i.e., consisting of either a single atom or many atoms) which is repeated in accordance with the translational symmetry of the lattice to form a one-dimensional crystal structure. Note that the unit cell of this structure is the same as for the lattice. In (c), every other lattice point has been removed so that now

$$\mathbf{t}'_n = n\mathbf{a}' \quad = 2n\mathbf{a}$$

The corresponding structure in our example is shown in (d), where every other molecule has been replaced, in this case, by a white horse. Now, the lattice in (c) contains half the number of lattice points (a), so this is a SUBLATTICE, not a superlattice! On the other hand, the structure in (d) has a doubled unit cell and so it consists of supercells. Therefore, it can be described as a SUPERSTRUCTURE! We see therefore see the source of the confusion in the literature. The first mistake is to refer to the structure (d) as a superlattice, when in fact, it is not a lattice but a crystal structure. The second error is in using the term superlattice, when in fact, the corresponding lattice is a sublattice.

In diffraction, the structure in (a) gives rise to reflections periodically spaced in proportion to $1/\mathbf{a}$, whereas for (d), extra reflections appear halfway between the main reflections (generally weaker in intensity than the main reflections). Such extra peaks are often called in the literature superlattice peaks, but this again causes confusion between the fundamental notions of lattice and structure. Better terminology is probably to call the extra peaks superstructure peaks, as they arise from the occurrence of a superstructure.

These concepts can be generalized to higher dimensions (Fig. 16).

In (a), two types of atoms are shown in an alternating array in all directions, typical of what is observed in an ordered metal alloy, for example, in β-brass (CuZn) at low temperature. In (b), layers of a foreign substance are intercalated between atomic layers to form a layered structure, typically found in clay minerals or when graphite has foreign atoms between the carbon layers. As with the ordered alloy, the enlargement of the unit cell, relative to that of the pure host, leads to additional superstructure reflections. As in the alloys, the increase in cell size often occurs in more than one direction, and so the array of new reflections can be one-, two-, or three-dimensional.

It is also possible to produce artificial, so-called heterostructures by sequential deposition of thin layers of dissimilar materials onto a substrate (c). Such structures are well known in semiconductor quantum-well systems or in magnetic multilayers. Here, the unit cell is enlarged only in one direction, and so the corresponding diffraction pattern consists of rows of new features normal to the layers.

Layers of atoms can often form on the surfaces of clean metals and semiconductors, a process often known as surface reconstruction. Although the reconstruction occurs on a bulk solid, its structure and reciprocal lattice can, to a certain extent, be considered as that from a very thin isolated layer whose symmetry is that of a subperiodic group known as a layer group. In this case, the Bragg reflections become elongated to form rods of scattering perpendicular to the surface.

So far, crystal structures have been described as being periodic and conforming to seven crystal systems and fourteen Bravais lattice types. In 1984, a rapidly-cooled metallic Al_4Mn alloy was observed by the Israeli-born materials scientist Daniel Shechtman to exhibit 10-fold symmetry in its electron diffraction pattern. This seemed to show that these materials, in some way, violated the rule that crystals could not show 5 or 10-fold symmetry. At first, Shechtman was disbelieved, and he initially found it difficult to be taken seriously. He was eventually proved correct and was awarded the Nobel Prize in 2011 for his discovery. Such materials have become known as quasiperiodic crystals or quasicrystals, and they clearly could not be explained by conventional crystal-symmetry arguments. Other examples appeared after this initial discovery, including naturally formed icosahedrite, a mineral with the composition $Al_{63}Cu_{24}Fe_{13}$. It is possible even to grow crystals with observable faces exhibiting fivefold symmetries.

Two types of quasicrystals are known. The first type, polygonal (dihedral) quasicrystals, have an axis of 8, 10, or 12-fold local symmetry (octagonal, decagonal, or dodecagonal quasicrystals, respectively). They are periodic along this axis and quasiperiodic in planes perpendicular to it. The second type, icosahedral quasicrystals, is aperiodic in all directions. The term aperiodic applies to those cases where long-range periodicity is not a feature of the solid, such as in amorphous materials like glass. The term aperiodic crystal is used to describe crystals where translational periodicity does not apply. Nonetheless, the atoms or molecules are arranged in some sort of order generated by different rules from the usual periodic rules.

One way to envisage quasi-periodicity is in considering the tiling of a floor without leaving gaps. In the conventional approach, a set of identical regular tiles of two-, three-, four-, and sixfold symmetry ends up with periodicity, but this is not possible with tiles having five or sevenfold symmetry. However, if one is prepared to use differently-shaped tiles, one can obtain many arrangements with local five or sevenfold symmetries. Perhaps the most famous example is that due to Roger Penrose, where two different shapes are used. In this case, with appropriate rules for stacking, fat and thin rhomb shapes can be placed together to fill two-dimensional space. Such an arrangement never repeats although it does show local orientational symmetry of a fivefold kind. Interestingly, if one superimposes a series of lines (Fig. 17), due to Robert Ammann (1946–94), as shown, the sets of lines together show evidence of fivefold symmetries! Furthermore, the lines are spaced by long (L) and short (S) distances in the sequence L S L L. . .. This sequence has an interesting property. If you replace every L by L S and every S by L, you find the series L S L L S L S. . ... This is simply a copy of the original sequence. This type of sequence is found in many places in nature and is known as a Fibonacci sequence. It is interesting

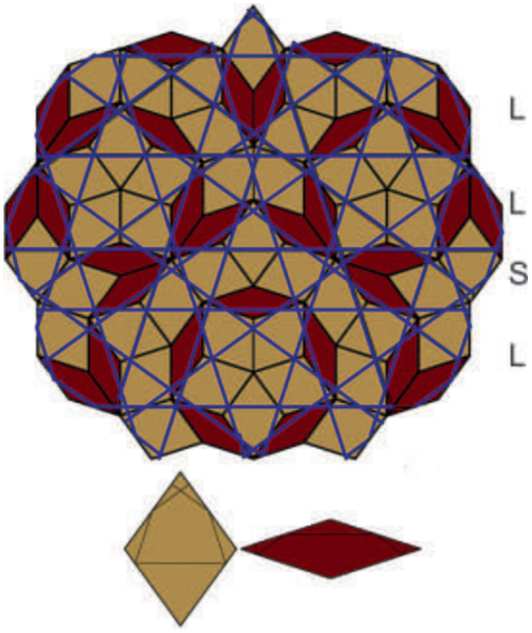

Fig. 17 Penrose tiling and lines due to Ammann.

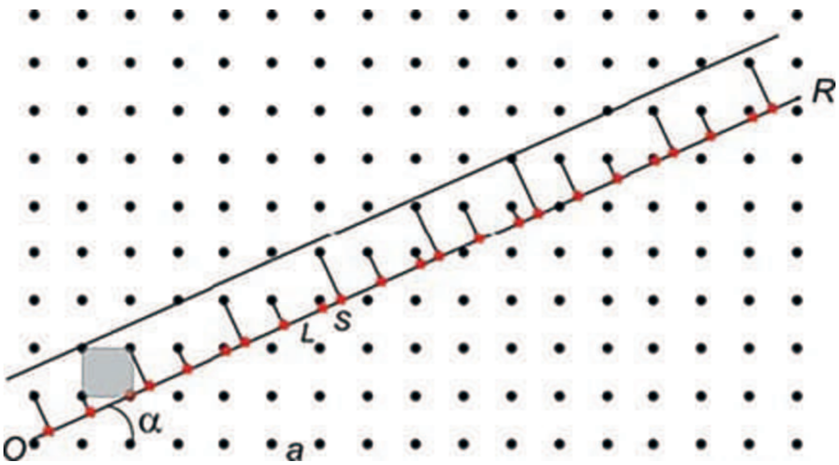

Fig. 18 The strip/projection method from two dimensions to one dimension.

to note that the ratio L/S is the 'golden mean' $\tau = (1 + \sqrt{5})/2 = 1.61803\ldots$... This arrangement is not random, nor is it periodic. It is not obvious what the overall symmetry is of an aperiodic arrangement in direct space, such as in the Penrose tiling example, where the fivefold symmetries are local. However, in reciprocal space, as seen through diffraction, the symmetry is revealed.

As a consequence of Shechtman's discovery, in 1992, the International Union of Crystallography revised the definition of a crystal in terms of reciprocal space, and more recently this has been revised yet again to include direct space. The definition is now as follows:

Direct-space definition: A solid is a crystal if its atoms, ions and/or molecules form, on average, a long-range ordered arrangement. In most crystals the arrangement is a periodic array that is governed by the rules of translational symmetry. In aperiodic crystals (incommensurate and quasicrystals) the arrangement is not periodic in three dimensions but is nevertheless still fully ordered, where the ordering follows particular mathematical rules.

Reciprocal-space definition: A solid is a crystal if it has essentially a sharp diffraction pattern. The word essentially means that most of the intensity of the diffraction is concentrated in relatively sharp Bragg peaks, besides the always present diffuse scattering. In all known cases, the positions of the diffraction peaks can be expressed by

$$\mathbf{H} = \sum h_i \mathbf{a}_i^* \quad (n \geq 3)$$

Here $\mathbf{a}_i^*$ and h_i are the basis vectors of the reciprocal lattice and integer coefficients, respectively, and the number n is the minimum for which the positions of the peaks can be described with integer coefficient h_i. The conventional crystals are a special class, though very large, for which $n = 3$ (The adjective 'known' reflects the fact that it is possible to envisage mathematically-based models that lie outside these definitions. See e.g., Grimm (2015)].

One important consequence of this definition is that an aperiodic crystal becomes periodic in a higher dimensionality n.

This can be illustrated by reference to Fig. 18. Starting with a simple square regular lattice, a slice is taken from O to R. Lattice points within this strip are then projected onto the line OR. This one-dimensional array of points, marked in red, forms a quasilattice, in which the spacings between them are either long (L) or short(S). With a suitable choice of the angle α the arrangement of long and short spaces can form a Fibonacci series. We see, therefore, that starting with a 1-d quasilattice, one can find a perfect lattice in a higher-dimensional space. This idea can be generalized to quasi-arrays in 2 and 3 dimensions.

Reference

Grimm U (2015) *Acta Crystallographica* B71: 258–274.

Further reading

Als-Nielsen J and McMorrow D (2001) *Elements of Modern X-Ray Physics*. New York: Wiley.
Ashcroft NW and Mermin ND (1976) *Solid State Physics*. Philadelphia: Saunders College.
Burns G and Glazer AM (2013) *Space Groups for Solid State Scientists*, 3rd ed. Academic Press.
Hammond C (1997) *The Basics of Crystallography and Diffraction*. Oxford: Oxford University Press.
International tables for X-ray crystallography. Henry NFM and Lonsdale K (eds.) (1965) *Symmetry Groups*. 2nd edn In: vol. 1. Birmingham: The Kynoch Press.
Jaric MV (ed.) (1988) *Introduction to Quasicrystals*. Boston: Academic Press.
Kittel C (1996) *Introduction to Solid State Physics*, 7th edn New York: Wiley.

Crystal structure determination☆

Lukas Palatinus[a] **and Riccardo Spagna**[b],*, [a]Institute of Physics of the CAS, Prague, Czechia; [b]Institute of Crystallography—CNR, Montelibretti, Italy

© 2024 Elsevier Ltd. All rights reserved.

This is an update of R. Spagna, Crystal Structure Determination, Editor(s): Franco Bassani, Gerald L. Liedl, Peter Wyder, Encyclopedia of Condensed Matter Physics, Elsevier, 2005, Pages 294-304, ISBN 9780123694010, https://doi.org/10.1016/B0-12-369401-9/00425-3.

Introduction 30
Types of input data 30
Structure factor normalization 31
Reflection statistics 32
Classification of phasing methods 32
Ab initio phasing methods 33
Patterson function 33
Direct methods 34
Structure Invariants 34
Probability methods 35
Phase determination in practice 36
Phasing of large structures through direct methods with density modification 36
Dual space iterative algorithms 36
Direct space methods 38
Genetic algorithms 38
Simulated annealing 39
Phasing methods for low-resolution diffraction data 39
Conclusion 39
References 40
Further reading 40

Abstract

Determination of crystal structures from diffraction requires first the solution of the crystallographic phase problem. Solving the phase problem is equivalent to the determination of atomic positions in the crystal structure and, as such, it is an essential part of the structure determination. Numerous methods have been developed for this purpose. They can be classified into several classes: ab initio methods include Patterson method, direct methods and dual space iterative algorithms. These methods do not require much more information than the diffraction data. Direct space methods like simulated annealing and genetic algorithms are used mostly for structure solution from powder diffraction data. They can handle lower data quality, but they require additional information, typically molecular connectivity.

Key points

- Crystal structure determination requires the solution of the phase problem
- Phase problem means unknown phases need to be assigned to Fourier coefficients of the scattering density, of which only amplitudes are known

---

☆*Change History*: March 2023. L Palatinus updated all changes, R Spagna approved the changes. The chapter was thoroughly updated and extended. Only specific sections from the previous versions were reused. These include Statistical analysis, Normalized structure factors and Probability distribution, which form sections Structure factor normalization and Reflection statistics in the new version. Patterson function, Direct methods (shortened). Other sections are newly written.

*Retired.

- Two main classes of methods for the solution of the phase problem exist in the field of small-molecule and inorganic crystallography: ab initio methods, direct space methods
- Ab initio methods include the Patterson method, direct methods, and dual space iterative algorithms
- Direct-space methods involve simulated annealing and genetic algorithms.

Introduction

Diffraction of X-rays by a crystal can be described in terms of a complex quantity called the structure factor, which is the Fourier transform of the electron density in the unit cell of the crystal (Mueller and Weiss, 2023). The diffraction occurs in discrete directions, which are determined by the orientation of the crystal with respect to the incident beam, and the *reciprocal lattice*, which is a dual lattice to the lattice of the crystal. Each diffracted beam can thus be assigned the three indices of the reciprocal lattice node it belongs to, typically denoted as $\mathbf{h} = (h,k,l)$. The amplitude and phase of the wave diffracted into the node $\mathbf{h}$ is the structure factor, and it can be computed as

$$F_{\boldsymbol{h}} = |F_{\boldsymbol{h}}|\, exp\,(i\phi_{\boldsymbol{h}}) = \sum_{j=1}^{N} f_j(\boldsymbol{h}).DWF.\exp\left(2\pi i\boldsymbol{h}\cdot\boldsymbol{x}_j\right)$$

The summation runs over al atoms in the unit cell of the crystal, f_j is the scattering power of the atom j in the direction given by $\mathbf{h}$, x_j is the vector of fractional atomic coordinates of atom j and DWF is the Debye-Waller factor, which accounts for the effects of the thermal motion and other random displacements of the atoms on their scattering power, and usually takes the form $\mathrm{DWF} = \exp(-Bh^2/4)$ with B being the displacement parameter characterizing the extent of the displacement. If f_j is considered a general function of $\mathbf{h}$, then the above expression can be considered exact. In practice, however, the structure is almost always considered to be composed of independent, non-interacting atoms, whose electron density is not deformed by interatomic interactions. In such case the atoms are spherical and f_j is a function of only the length of $\mathbf{h}$, it can be tabulated for each atomic type, and the structure factor can then be easily, and to a very good accuracy, calculated only from the knowledge of atomic types and their coordinates in the unit cell.

Once the structure factors are known, the electron density, $\rho(\mathbf{x})$ can be calculated:

$$\rho(\boldsymbol{x}) = V^{-1}\sum_{\boldsymbol{h}=-\infty}^{\infty} F_{\boldsymbol{h}}\, exp\,(-2\pi i\boldsymbol{h}\cdot\boldsymbol{x}) = V^{-1}\sum_{\boldsymbol{h}=-\infty}^{\infty} |F_{\boldsymbol{h}}|\, exp\,(i\phi_{\boldsymbol{h}})\, exp\,(-2\pi i\boldsymbol{h}\cdot\boldsymbol{x})$$

To obtain the exact electron density, a complete (infinite) set of structure factors is needed. However, a finite set of the most important structure factors (those with low $|\mathbf{h}|$) is needed in practice to obtain a good representation of $\rho(\boldsymbol{x})$.

In a diffraction experiment, the intensities of diffracted beams are detected on a detector. Under suitable approximations (kinematical diffraction, or the first Born approximation), the intensity is proportional to the amplitude-squared of the structure factor:

$$I \propto |F_{\boldsymbol{h}}|^2$$

Thus, the phase $\phi_{\boldsymbol{h}}$ of the structure factor is lost in the experiment and is not available. As a consequence, it is not possible to calculate the electron density directly from the quantities obtained in a diffraction experiment. The phases need to be recovered by other means. This problem is known as the *crystallographic phase problem*, and a lot of effort was dedicated to solving this problem. This text reviews the most important methods used to solve the crystallographic phase problem in several scenarios.

Types of input data

Several approaches to the solutions to the phase problem have been devised. Their use is to a large extent governed by the type of diffraction data available. The two key types of data with very different properties and thus information contents are single-crystal and powder diffraction data. As the name indicates, single-crystal data are obtained by performing the experiment on a single, monocrystalline piece of material. In such a case, individual intensities of all structure factors up to the maximum obtainable resolution (i.e., the maximum length of the vector $\mathbf{h}$) can be determined. If the resolution is sufficient, ab initio methods can usually be used. The limit for "sufficient" resolution is not strict, but generally the value for $d_{\min} = 1/|\mathbf{h}| = 1.2$ Å is considered border-case, especially for organic compounds. Most inorganic and small-molecule crystal structures, and even some macromolecular crystals provide data with sufficient resolution and are thus suitable of the application of ab initio methods (Fig. 1a). However, most crystals of macromolecules do not allow collecting measurable intensities up to sufficient resolution. In this case, special approaches are needed.

The second major type of diffraction data are powder diffraction data, which are obtained by diffraction on a large assembly of very small crystals. The diffraction pattern is then composed of a very large number of randomly oriented diffraction patterns.

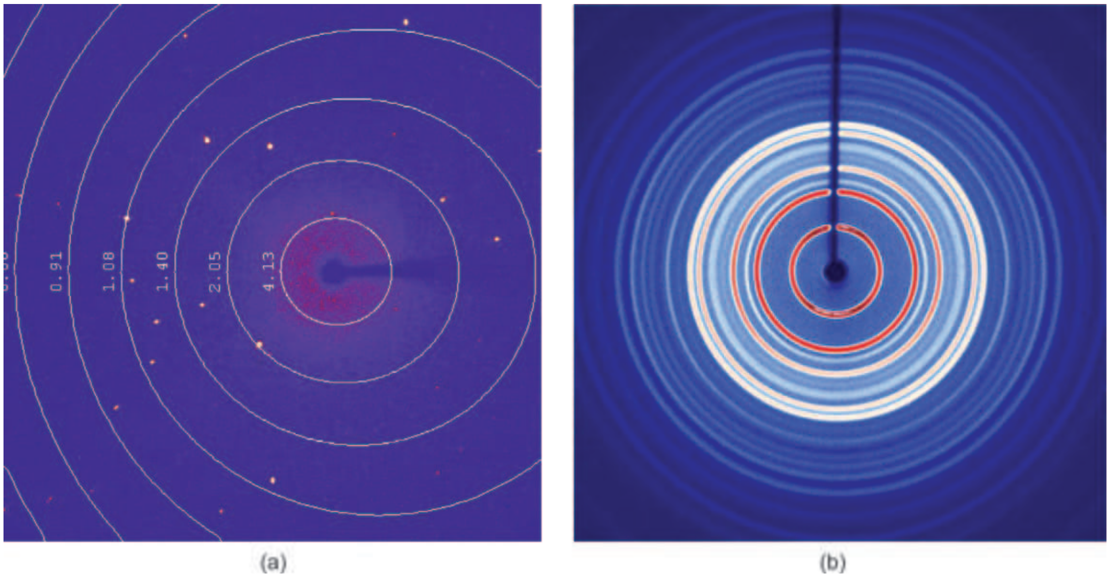

Fig. 1 (a) a diffraction pattern collected on a single crystal. Rings show the resolution in d = 1/|**h**| (b) a diffraction pattern collected on a powder sample.

Each reflection is thus distributed over a ring on the detector, and the diffraction can be represented as a one-dimensional pattern of intensity vs. diffraction angle (Fig. 1b). Due to the compression of the information from three dimensions to one, these data suffer from reflection overlap, especially at higher diffraction angles. Therefore, the individual reflection intensities cannot be extracted. Although ab initio methods can also be sometimes applied, the most common approach to the structure solution from powder diffraction data are the direct space methods.

Structure factor normalization

Before discussing individual approaches to the solution of the phase problem, it is useful to discuss the treatment of the intensities that makes them more suitable for the application of the phasing methods. The intensities are proportional to the structure-factor amplitude squared, but the proportionality constant is not known. Moreover, the Debye-Waller factor, which characterizes the effect of thermal vibrations on the intensities, is also not known.

Wilson (1942) proposed a simple method to put the observed amplitudes $|F_{\mathbf{h}}|_{obs}$ on an absolute scale, based on statistical analysis. He showed that the average of the squared structure amplitudes should be:

$$\langle |F_h|^2 \rangle = \sum_{j=1}^{N} f_j^2 = \sigma^{2\cdot}$$

assuming that thermal motion is isotropic and equal for all the atoms:

$$\langle |F_h|^2 \rangle_{obs} = K \langle |F_h|^2 \rangle \, exp\left(-\frac{Bh^2}{4} \right)$$

where K is the scale factor. A plot of the logarithm of the function vs. h^2 at some average value of h^2 would derive the values of K and B. The intensities can then be rescaled to bring them on absolute scale and remove approximately the effect of atomic displacement.

Such corrected intensities are still dependent on the atomic type, through the atomic scattering factors f_j. However, once the intensities have been corrected for thermal motion and placed on an absolute scale, it is simple to remove this dependence, too, and obtain the normalized structure magnitudes $|E_{\mathbf{h}}|$ from

$$|E_h|^2 = \frac{|F_h|^2}{\varepsilon \sigma^2}$$

where ε are numbers that vary with space group and type of reflections. These quantities are independent of the scattering angle and correspond to idealized point atom structures:

$$E_h = \sum_{j=1}^{N} \exp(2\pi i \boldsymbol{h} \cdot \boldsymbol{x})$$

These quantities depend solely on the positions of the atoms in the unit cell. Owing to this peculiarity, the values $E_{\mathbf{h}}$ play a key role in ab initio phasing methods, especially direct methods.

Reflection statistics

Hughes (1949) empirically, and Wilson (1949) by taking the analogy with the random-walk problem found that the diffracted intensities of a centrosymmetric crystal obey a Gaussian distribution. Expressed in terms of $|E|$, the centric distribution is (Fig. 2a):

$$P_{\bar{1}}(|E|) = \sqrt{\frac{2}{\pi}} exp\left(-\frac{|E|^2}{2}\right)$$

In further studies, the acentric distribution, i.e., the distribution of intensities of a non-centrosymmetric crystal, was obtained (Fig. 2b):

$$P_1(|E|) = 2|E|\, exp\left(-|E|^2\right)$$

These distributions are independent of the structure complexity. Theoretical values of the moments of higher order and the cumulative probability functions of $|E|$ can be calculated from the distributions. These values can be compared with the corresponding experimental values to argue about the presence or absence of a center of symmetry, which is otherwise very difficult or impossible to determine from diffraction data alone. The centric and acentric distribution were, however, derived under the assumption of a random distribution of essentially equal atoms in the unit cell of the crystal and as such are just an approximation. Distributions derived from experimental data may differ from the theoretical ones due to the special features in the structure like a combination of heavy and light atoms, atoms in special high-symmetry positions, pseudosymmetry or twinning.

Classification of phasing methods

It was made clear in the previous section that various types of data require various approaches to phasing. The most general methods, from the point of view of external information needed for phasing, are so called ab initio phasing methods. These methods require solely the diffraction data as an input. No other information about the crystal structure, sometimes not even the chemical composition, is needed. The three main methods in this family are the Patterson method, direct methods and dual space iterative algorithms.

If individual structure factor amplitudes are not known, like in powder diffraction, or if they are not sufficiently accurate for application of direct methods, then direct space methods can be used. These methods, most of then genetic algorithms or simulated annealing, also in principle do not require much more than the diffraction data and chemical composition. However, the complexity (and thus computation time) of the solution grows exponentially with the number of free parameters, and it is therefore necessary to provide additional information, typically molecular connectivity, to solve all but the simplest problems.

When diffraction data are collected to low resolution only, and the number of atoms in the structure is large (sometimes many thousands), typically from crystals of proteins, then ab initio methods fail, and the problem is too complex for direct space methods. Then, special methods developed for macromolecules are needed. These are either so called molecular replacement, where the initial structure model is obtained by locating a known fragment from a similar molecule, or experimental phasing methods, which exploit the differences in diffraction from very similar, yet slightly different structures, or the differences between diffraction at various wavelengths of the radiation.

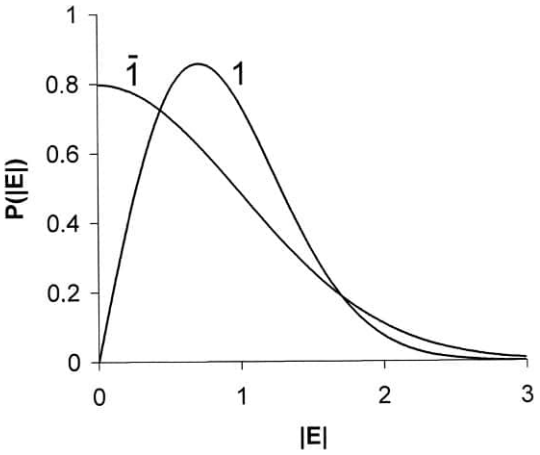

Fig. 2 The centric and acentric distributions of normalized amplitudes.

Ab initio phasing methods

Patterson function

Patterson (1934) introduced a function which is the convolution of electron density ρ(x) with itself:

$$P(\boldsymbol{u}) = \int_v \rho(\boldsymbol{x}) \cdot \rho(\boldsymbol{u} + \boldsymbol{x}) d\boldsymbol{x}$$

The Patterson function can be directly calculated from the set of squared but not phased reflection amplitudes $|F_\mathbf{h}|^2$

$$\boldsymbol{P(u) = \frac{1}{V}\sum_h |F_h|^2 \cos 2\pi h.u}$$

where V is the volume of the unit cell. The map computed gives a vectorial representation of the scattering objects (Fig. 3). This depends upon the fact that while $F_\mathbf{h}$ is related to the distribution of the atoms in the crystal, $|F_\mathbf{h}|^2$ depends on the distribution of interatomic distances. In fact,

$$|F_h|^2 = F_h \cdot F_h^* = \sum_{j=1}^{N} f_j^2 + \sum_{i \neq j=1}^{N} f_i f_j \cos\left[2\pi \boldsymbol{h} \cdot \left(\boldsymbol{x}_i - \boldsymbol{x}_j\right)\right]$$

depends on the distances ($\mathbf{x}_\mathrm{i}$—$\mathbf{x}_\mathrm{j}$) between the *i* and *j* atoms.

N atoms in the structure thus generate $N(N$-1) peaks in the Patterson function. This higher density of peaks with respect to the electron density makes the Patterson map difficult to interpret even with a moderate number of atoms.

Because the density in the Patterson map goes as squares of the numbers of electrons of the scattering atoms, Patterson maps of crystals that contain heavy atoms are dominated by the vectors between them.

Harker noticed that the symmetry of a crystal might provide particular vectors that would lead to a direct determination of the coordinates of individual atoms. For example, if the crystal's symmetry included an inversion center, there would be equivalent atoms at positions (x,y,z) and $(-x,-y,-z)$. The vector between these atoms would be found at $(2x,2y,2z)$ in the Patterson map, indicating the original atomic positions. This procedure greatly simplifies the interpretation of the Patterson map and allows one to obtain a good initial model; in fact, the structure factors $F^c_\mathbf{h}$ calculated with the heaviest atoms, f_1 and f_2, represent the predominant contribution to the structure factors $F_\mathbf{h}$ (Fig. 4).

The phase $\varphi^\mathrm{c}_\mathbf{h}$ is a good approximation of the true phase of $F_\mathbf{h}$ and an electron density map using as coefficients the observed structure factors and the calculated phases $\varphi^c_\mathbf{h}$ can be computed. The remaining atoms will be found following the so-called method of Fourier synthesis recycling, which is described later. This application of the Patterson function is called the heavy atom method.

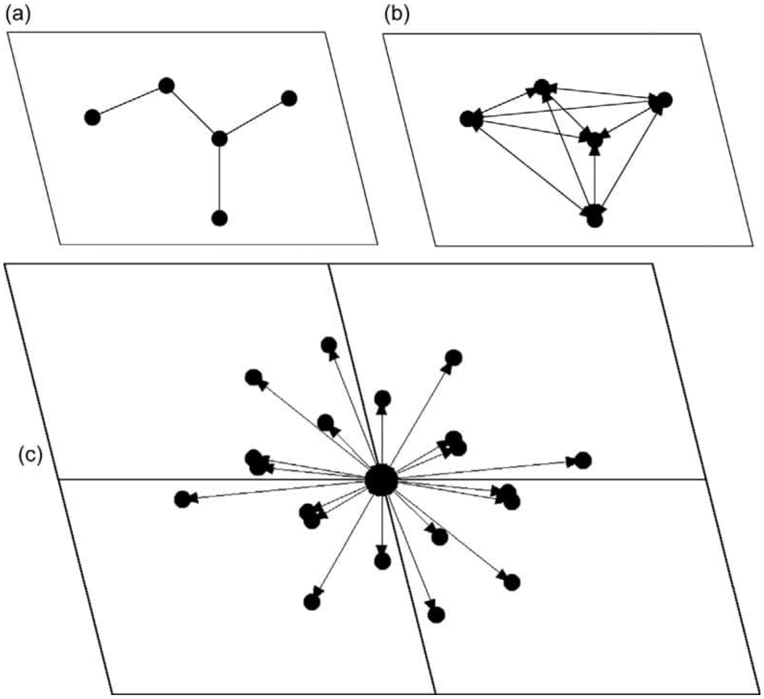

Fig. 3 (a) a planar structure of *5* atoms. (b) the corresponding interatomic vectors. (c) Patterson map with all interatomic vectors translated to the origin.

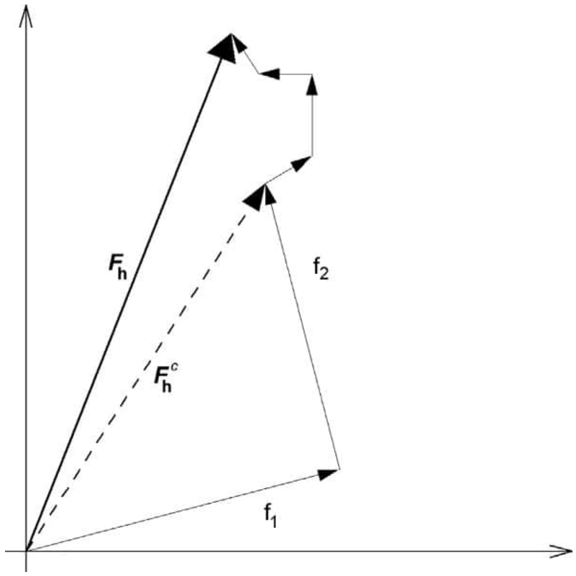

Fig. 4 Visualization of the heavy atom method in an Argand diagram. f_1 and f_2 are the contributions of the heavy atoms, forming partial structure factor $F^c_{\mathbf{h}}$, which is a good approximation to the total structure factor $F_{\mathbf{h}}$, because the remaining contributions are small.

Direct methods

Direct methods are those methods that exploit relationships among the intensities to determine the crystal structure directly.

In general, the phase, φ, and the amplitude, $|F|$, of a wave are independent quantities and only the amplitudes are obtainable from experiment. However, in diffraction from crystal structures these two sets of quantities are not independent and they can be related thanks to two properties of the electron density: (1) it is positive everywhere and (2) it is composed of discrete atoms.

Experimentally, a large number, M, of amplitudes can be measured and then a system of simultaneous equations formed by the definition of crystal structure factors can be written. The unknown quantities are the phases $\varphi_{\mathbf{h}}$ and the atomic positions $\mathbf{x}_j$, the known quantities are the $|F_{\mathbf{h}}|$ obtained from the measured intensities. Since the equation involves complex quantities, two equations, one for real and one for the imaginary part, can be considered. Therefore, there are $2M$ equations to determine $(M + 3N)$ unknown quantities and since the number of equations exceeds, by far, the number of unknowns, the problem to determine the phases is in principle over-determined.

Sayre (1952) derived a basic relationship between structure factors. Considering the structure composed of fully resolved and identical atoms, the two functions $\rho(x)$ and $\rho^2(x)$ must be very similar and show maxima at the same position.

Using this similarity, the following relationship, called Sayre's equation, can be derived:

$$F_{\mathbf{h}} = \frac{\theta_{\mathbf{h}}}{V} \sum_{\mathbf{k}} F_{\mathbf{k}} F_{\mathbf{h}-\mathbf{k}}$$

Here $\mathbf{V}$ is the volume of the unit cell and $\theta_{\mathbf{h}} = \frac{f_{\mathbf{h}}}{g_{\mathbf{h}}}$ is the ratio between the scattering factors of $\rho(x)$ and $\rho^2(x)$. Multiplying both sides by F-h:

$$|F_{\mathbf{h}}|^2 = \frac{\theta_{\mathbf{h}}}{V} \sum_{\mathbf{k}} |F_{\mathbf{h}} F_{\mathbf{k}} F_{\mathbf{h}-\mathbf{k}}| \exp[i(\phi_{-\mathbf{h}} + \phi_{\mathbf{k}} + \phi_{\mathbf{h}-\mathbf{k}})]$$

For large values of $|F_h|$, the left-hand side will be large, real and positive. It is therefore likely that the largest terms in the sum on the right-hand side will also be real and positive. It follows that, if F_k and F_{h-k} also have large moduli, the phases are linked by the relationship:

$$\Phi_{hk} = \phi_{-\mathbf{h}} + \phi_{\mathbf{k}} + \phi_{\mathbf{h}-\mathbf{k}} \cong 0 (mod\ 2\pi)$$

This probabilistic condition for three reflections with large structure factors has proved to be the most important original approach for the practical use of direct methods.

Structure Invariants

A structure invariant (s.i.) is a quantity which remains unchanged when the origin is arbitrary shifted. The intensities are, of course the simplest example of structure invariants, while the phases are, in general, dependent on the choice of the origin. Under certain conditions, phase relationships between structure factors are independent of this choice and are thus also s.i. The most general structure invariant relationship is represented by:

$$F_{h_1} F_{h_2} \cdots F_{h_m} = |F_{h_1} F_{h_2} \cdots F_{h_m}| \, exp\left[i\left(\phi_{h_1} + \phi_{h_2} + \cdots + \phi_{h_m}\right)\right]$$

where

$$\mathbf{h}_1 + \mathbf{h}_2 + \ldots + \mathbf{h}_\mathbf{m} = 0$$

Since the moduli of the structure factors are invariants themselves, the angular part:

$$\Phi_m = \phi_{h_1} + \phi_{h_2} + \cdots + \phi_{h_m}$$

is also a s.i. The most important of these general relationships is the case of three structure factors. The corresponding invariant is called the triplet invariant.

Probability methods

Probability methods were introduced by Hauptman and Karle (1953) and led to the joint probability distributions of a set of normalized structure factors. The distribution associated with triplet invariants for a non-centrosymmetric structure is given by:

$$P(\Phi_{hk}) = \frac{1}{L}\exp(G_{hk}cos\Phi_{hk})$$

And

$$G_{hk} = \frac{2}{\sqrt{N}}|E_{\boldsymbol{h}}E_{\boldsymbol{k}}E_{-\boldsymbol{h}-\boldsymbol{k}}|$$

where N is the number of atoms in the unit cell and L is a normalization constant.

In Fig. 5, the probability distributions for different values of the parameter G_{hk} are shown to have a maximum at Φ_{hk} equal to zero and the variance decreases as G_{hk} increases.

In centrosymmetric crystals, structure factors are real numbers with phases equal to 0 (for positive) or π (for negative structure factors), and the probabilistic relationship for the triplet can be expressed as the relationship between the signs of the structure factors:

$$S(-\boldsymbol{h})S(\boldsymbol{k})S(\boldsymbol{h}-\boldsymbol{k}) \cong +$$

where $S(\mathbf{h})$ stands for the sign of the reflection **h**. In this case, the basic conditional formula for sign determination is given by Cochran & Woolfson:

$$P_+ = \frac{1}{2} + \frac{1}{2}\tanh\left(\frac{1}{\sqrt{N}}|E_{-\boldsymbol{h}}E_{\boldsymbol{k}}E_{\boldsymbol{h}-\boldsymbol{k}}|\right)$$

The larger the absolute value of the argument of tanh, the more reliable the sign indication.

For fixed **h**, let the vector **k** range over the set of known values $E_\mathbf{k}E_{-\mathbf{h}-\mathbf{k}}$, then the total probability distribution for $\varphi_\mathbf{h}$ is given by the product of the single distributions, increasing the reliability of the estimate, in mathematical terms.

Calculation of the conditional joint probability distributions for $\varphi_\mathbf{h}$, under the condition that several phases $\varphi_\mathbf{k}$ and $\varphi_{\mathbf{h}-\mathbf{k}}$ are known, leads to the tangent formula, which expresses the most likely value of the phase $\phi_{\boldsymbol{h}}$given a set of known phases of triplet invariants containing the structure factor E_h:

$$\tan\phi_{\boldsymbol{h}} = \frac{\sum_{\boldsymbol{k}}|E_{\boldsymbol{k}}E_{\boldsymbol{h}-\boldsymbol{k}}|\sin(\phi_{\boldsymbol{k}} + \phi_{\boldsymbol{h}-\boldsymbol{k}})}{\sum_{\boldsymbol{k}}|E_{\boldsymbol{k}}E_{\boldsymbol{h}-\boldsymbol{k}}|\cos(\phi_{\boldsymbol{k}} + \phi_{\boldsymbol{h}-\boldsymbol{k}})}$$

This formula or its modifications and generalizations are used in almost all computer programs for phase determination by direct methods.

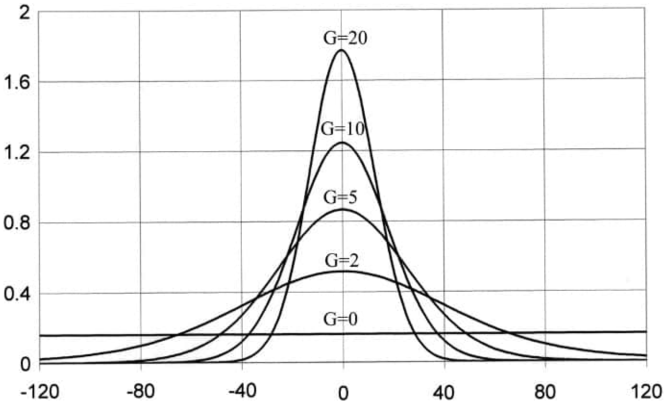

Fig. 5 The probability distributions for the phases of triplet invariants as a function of the parameter G.

Phase determination in practice

A typical procedure for phase determination uses a multisolution approach and for each trial, the following steps are performed:

1. Select suitable normalized structure factors and assign random values to their phases.
2. cyclically apply the tangent formula. Since this formula contains information on the positivity of the electronic density, the phases may converge to the correct values.
3. for each trial, compute a figure of merit, to estimate its quality.
4. Select the best solution out of all trials.

Phasing of large structures through direct methods with density modification

Procedures based on direct methods more or less similar to those described above are able to solve the crystal structure for small and medium size molecules (up to 200 atoms in the asymmetric unit) in a routine way, but fail for bigger molecular structures. Intuitively, it is seen that the reliability of the probability distributions for s.i.'s is an inverse function of N and as this number increases, the reliability of the relationships decreases whatever the value of the triple product of $|E|$s. The result is that the tangent formula is inadequate for macromolecules.

In spite of these considerations, it is possible to enlarge the size of crystal structures solvable by direct methods. The key to this improvement is based on the following:

1. the cyclical use, in both real and reciprocal space, of the refinement of atomic parameters or phases;
2. electron density modification and data extrapolation;
3. methods utilizing the properties of the Fourier transform; and
4. procedure for moving a well-oriented, but misplaced structural model to the correct position.

Small proteins (up to more than 2000 non-H atoms in the asymmetric unit and with data at atomic level resolution) have been solved ab initio by these algorithms.

Dual space iterative algorithms

Dual-space iterative algorithms approach the phasing problem as a constraint satisfaction problem. When solving a structure from X-ray diffraction data, the experiment provides us a constraint on the electron density: the correct electron density must have the property that the amplitudes of its Fourier transform match the experimentally determined ones. This constraint is called *the amplitude constraint*. This constraint alone is not sufficient to solve the phase problem, and therefore a second constraint needs to be added. The weakest and most general constraint is the requirement for the positivity of the electron density (*positivity constraint*). Another obvious constraint follows from the fact that crystals consist of individual atoms. We could thus require that the electron density contains only a limited number of significant peaks, and the rest of the unit cell is filled by almost zero density. A weaker variant of this constraint it the mere requirement that only a small part of the unit cell has significant density, with the rest being zero. In this weaker formulation there is no explicit assumption that the significant density is grouped into separated point-like peaks (*sparseness constraint)*. All these constraints are defined on the electron density rather than on its Fourier coefficients, and they are therefore direct-space constraints in contrast to the amplitude constraint, which is defined in reciprocal (Fourier) space. The fact that constraints in both spaces are used with equal importance distinguishes dual space algorithms from direct methods, which work predominantly in Fourier space. Once the constraints are defined, we may reformulate the phasing problem as follows: In the space of all possible electron densities, find the subset of densities that fulfil both the amplitude constraint and some of the direct space constraints. This subset is an intersection of the subsets fitting the amplitude constraint and the direct-space constraint.

The problem of finding an element from the intersection of two (or more) constraint sets is a well-known and thoroughly studied general problem. In the special case of convex constraint sets, well-defined iterative procedures exist, with proven convergence properties. For instance, the intersection between two convex constraint sets is always reached simply by alternating projections onto the first and the second set (Fig. 6a), where projection is a mapping from an arbitrary point ρ in the image space onto the nearest point of the constraint set C:

$$P : P(\rho) \in C \text{ and } ||P(\rho) - \rho|| = \min$$

The simplest iterative algorithm based on alternating two projections P_1 and P_2 can then be written as

$$\rho^{n+1} = P_2(P_1(\rho^n)) \equiv P_2 P_1 \rho^n$$

Where the last expression as a shorthand symbolic notation of applying first the projection P_1 and the P_2 to ρ^n.

In crystallography, the set associated with the amplitude constraint is unfortunately non-convex. In such case the algorithms developed for convex sets are not guaranteed to work, because they can get trapped in local minima (Fig. 6b). This drawback can be overcome by replacing simple projections by relaxed projections (overprojections), or combining these relaxed projections in more elaborate schemes. A relaxed projection R is defined as:

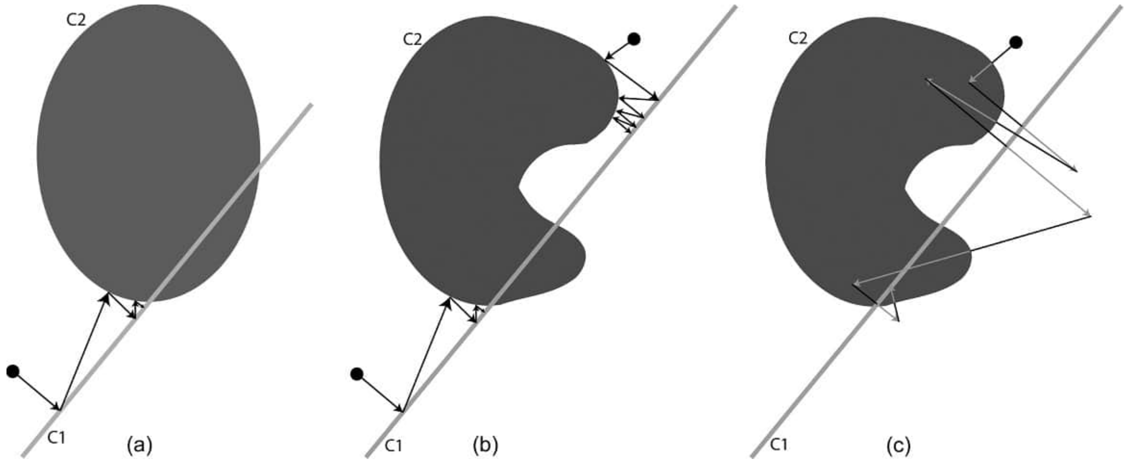

Fig. 6 Finding the intersection of two constraint sets. (a) Convex constraint sets and repeated projections. (b) Non-convex constraint sets and repeated projections starting from two different starting points. (c) Non-convex constraint sets and repeated overprojections.

$$R^{\gamma} = P + \gamma(P - I)$$

Where $\gamma = 1$, the superscript is usually omitted.

Fig. 6c illustrates that using relaxed projections may allow the iteration to escape from a local minimum.

Due to the non-convex nature of constraints in crystallography, no iterative algorithm has been found so far that would be guaranteed to solve the problem in finite time. Various dual space algorithms were proposed for use in crystallography (see Palatinus (2013) and Millane and Lo (2013) for review), which differ by the details of the iteration scheme as well as the details of the definition of the projections or projection-like operations used in the iteration.

Probably the best known of them is the charge flipping algorithm (Oszlányi and Sütő, 2004). Although it was not first proposed dual-space algorithm, it was the one that sparked the wide interest of the crystallographic community in this class of algorithms. The iteration scheme of the charge flipping algorithm is very simple:

$$\rho^{n+1} = P_r R_d \rho^n$$

The subscript d refers to the operation in direct space, and subscript r refers to the reciprocal space. In reciprocal space, a simple projection is used, i.e., in every iteration, the Fourier amplitudes of the current iterate are replaced by the experimental amplitudes. The constraint in the direct space is the positivity constraint with the additional modification that regions of the density that are small, but positive, are also set to zero. As the operation in direct space is a reflection, the actual operation is a multiplication of all density values below a given threshold by –1, i.e., "flipping" the values, which gave the algorithm its name (Fig. 7).

Other important algorithms used in crystallography include:

Elser's difference map (DM): $\rho^{n+1} = (I + \beta(P_d R_r^{\gamma_r} - P_r R_d^{\gamma_d})\rho^n$

Alternating averaged reflections (AAR): $\rho^{n+1} = \frac{1}{2}(I + R_r R_d)\rho^n$

Relaxed alternating averaged reflections (RAAR): $\rho^{n+1} = \left[\frac{1}{2}\beta(I + R_r R_d) + (1-\beta)\right]\rho^n$

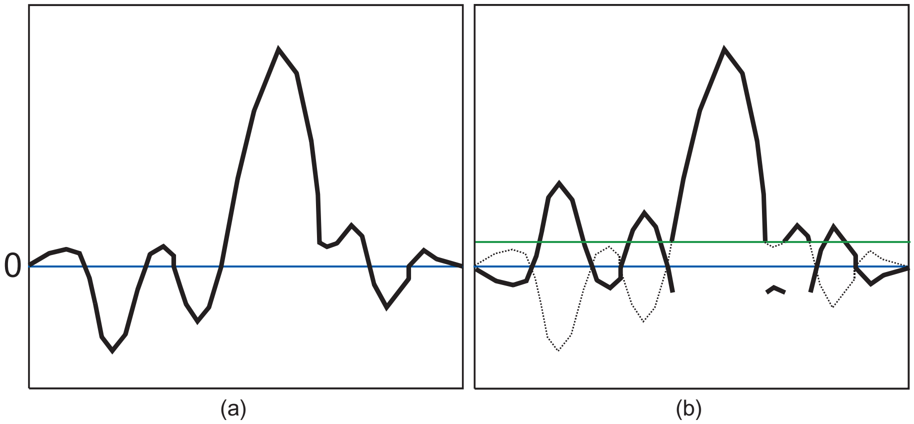

Fig. 7 (a) a simple one-dimensional density with positive and negative regions. (b) The same density after performing the charge-flipping operation, when all values below the threshold (green line) were multiplied by –1 (flipped).

A dual space algorithm dubbed *intrinsic* phasing (Sheldrick, 2015), with an iteration scheme somewhat similar to the charge flipping algorithm, but with the reflector in the reciprocal-space part, and with a very different real-space operation, is implemented in the very popular structure solution program SHELXT.

Direct space methods

Solving the phase problem directly (ab initio), i.e., obtaining the phases or scattering density from structure factor amplitudes, may be a difficult problem. If, however, not enough amplitudes are known, of if not individual amplitudes, but only some of their combinations are known, the problem is essentially impossible to solve. It is, however, a relatively easy task to verify, if a proposed solution fits the experimental data, and to compare, which of two proposed solutions fits the data better. This is the basis of the direct space methods, called sometimes also global optimization methods. They are being used mostly in connection with powder diffraction data, where the whole three-dimensional diffraction pattern is projected into a one-dimensional profile of intensity against the diffraction angle (cf. Fig. 1b), and thus reflections may overlap and individual intensity information is lost. However, the same technique may be applied also to any other diffraction data in case of need.

The basic principle of all direct space methods is generating trial crystal structures and comparing the data calculated from them with experimental data. The best trials are retained and, using the information about the past trials, new set of trials is generated in the next iteration.

The complexity of the task grows exponentially with the number of free parameters (degrees of freedom) of the structure. A structure with N atoms has, in general, 3N degrees of freedom—one for each coordinate of each atom in the structure. This number quickly becomes prohibitively large even for moderately large structures. The situation becomes more tractable, if the structure contains known and well-defined chemical motifs, such as a molecule with known connectivity. In case of a single molecule in the asymmetric unit of the crystal, the number of degrees of freedom is $6 + idf$, where the six degrees of freedom come from the three translations and three rotations of the molecule, and *idf* stands for internal degrees of freedom, which are typically only the molecular torsion angles, as the bond lengths and bond angles are usually well known for organic molecules (Fig. 8).

The key to the success of the structure solution by direct space methods is the algorithm for generating the trials. The algorithm must be able to sample the search space effectively, while converging quickly to the best solution once a trial in its vicinity is found. The two most studied and most used approaches to the problem are simulated annealing (with its variant parallel tempering) and genetic algorithms.

Genetic algorithms

As the name implies, genetic (or evolutionary) algorithms are inspired by natural processes occurring during evolution. Genetic algorithm is a global optimization algorithm based on generating a set of trial structures (parents) and using their quality (fitness) to generate a new, more fit generation (offspring).

The basic steps of genetic algorithms adapted to crystallographic problems are the following (Shankland et al., 1997; Kariuki et al., 2001):

(1) generate a random set of N_p trial structures—the parent generation
(2) use "mating algorithm" to generate a set of N_o offspring. The mating procedure combines the parameters of two parents generating the offspring, like the position of the molecule, its orientation and values of the degrees of freedom.

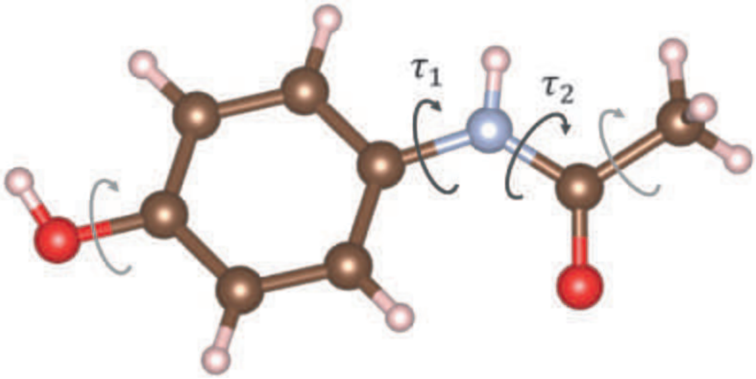

Fig. 8 Molecule of paracetamol with torsion angles outlined. Although the molecule has 10 non-hydrogen atoms, only two torsion angles need to be determined in the structure solution process. Note that the additional two torsion angles (gray without labels) are irrelevant for the solution process, because hydrogen atoms are weak scatterers, and they can be usually ignored in the structure solution step.

(3) Use "mutation algorithm" to generate N_m mutants, either only from the offspring or from both the parents and offspring. In a mutation one or a larger number of parameters are changed. The change may be to a completely random new value, or a random change of the previous value may be used.
(4) Select the $(N_p - N_m)$ trials from the set of $N_p + N_o$ trials using a suitable cost function that evaluates the match of these trials to the experimental data. The best trials should be selected, but not only the best ones. With some probability, less good trials are also selected to maintain the diversity of the population.
(5) Combine the $(N_p - N_m)$ selected trials with N_m mutants to obtain a new generation of parents. Note that copying some of the parents into a new generation is not following the natural evolution process. However, this procedure, called elitism, proved to be essential for the success of the algorithm.

Typically, the size of the population in one generation (N_p) is a few hundred, and it can take a few thousand generations to converge to the solution. Many variants of genetic algorithms can be created and have been tested, which differ by the way offspring is generated, mutations are computed and the next generation of trials is generated.

Simulated annealing

Like genetic algorithms, simulated annealing is a general algorithm for global optimization problems. It is inspired by the process of physical annealing, where the temperature is elevated first and then it is progressively lowered and in the process the system has the possibility to explore the energy landscape and find global energy minimum.

In the structure solution process, the role of temperature is to increase or decrease the probability of a less optimal trial to be accepted in the next set of trials. The basic algorithm of simulated annealing can be outlined as follows (David et al., 1998):

(1) Generate a set of random trials that sample the global parameter space effectively.
(2) Set a starting temperature T.
(3) Apply a random change to the parameters of each trial structure.
(4) Evaluate the cost function C for each trial. The cost function may include not only the match to the experimental data, but also other criteria, e.g., chemical or geometric, like connectivity, coordination numbers, bond angles…
(5) If the cost function is lowered after the random move, accept the new trial structure and reject the old one. If the cost function increases, accept the new trial with the probability proportional to $\exp\left(-\frac{\Delta C}{T}\right)$, where ΔC is the difference between the cost function values after and before the modification.
(6) Repeat the procedure, while progressively lowering T, until convergence.

We can see that the higher the temperature, the larger the probability that a change with positive ΔC will be accepted. This ensures that the system can escape local minima and explore the parameter landscape. As the temperature lowers, the system tends to settle into broad minima and progressively converge to the best structure inside these minima. In simulated annealing, the number of trials in one iteration cycle can reach many thousands. Here again, many variants and improvements of the basic simulated annealing procedure have been proposed and used. The one worth a special mention is *parallel tempering*, which differs from the standard algorithm by running the calculation at several temperatures at the same time and exchanging the trials between the temperatures rather than lowering the temperature for the whole set of trials.

Phasing methods for low-resolution diffraction data

Ab initio phasing methods are all based on the assumption of existence of discrete maxima in the scattering density. As the maximum spatial frequency of the available Fourier amplitudes decreases, the Fourier transform becomes more and more "blurry," until it is not composed of discrete maxima anymore. In such case, ab initio methods cannot be used, and if the size of the structure is large, direct space methods are also not feasible. This is frequently the case in macromolecular crystallography, especially in the structure determination of proteins. In these cases, the structures can be either solved by experimental approaches like single/multiple isomorphous replacement or single/multiple anomalous dispersion, or by a technique called molecular replacement, where a starting model is obtained by placing a known (or estimated) fragment of the molecule in the unit cell. See Mueller and Weiss (2023) for details on these techniques.

Conclusion

Numerous algorithms have been devised to solve the key step in crystal structure analysis—the assignment of the phases to the structure factors, and, as a consequence, the determination of positions of atoms in the crystal structure. The availability of these algorithms is one of the corner stones of the immense success of crystallography in the past century, with well over a million determined and published crystal structures. The constant development of the algorithms turned the solution of the phase problem in many cases to a routine and fast procedure performed automatically by specialized software. However, there are still problems that are hard to tackle and that require substantial effort. Further improvements of the structure solution algorithms are thus desirable. The next revolution in this utterly practical and important field may be around the corner thanks to the quickly developing field of machine learning/artificial intelligence.

References

David WIF, Shankland K, and Shankland N (1998) Routine determination of molecular crystal structures from powder diffraction data. *Chemical Communications* 8: 931–932.
Hauptman HA and Karle J (1953) *Solution of the Phase Problem. I. The Centrosymmetric Crystal. ACA Monograph, no.3*. Ohio: Polycrystal Book Service.
Hughes EW (1949) Limitations on the determination of phases by means of inequalities. *Acta Cryst* 2: 34.
Kariuki BM, Harris KDM, and Johnston RL (2001) Solving crystal structures from powder diffraction data using genetic algorithms, molecular crystals and liquid crystals science and technology. *Section A Molecular Crystals and Liquid Crystals* 469–481: 356.
Millane RP and Lo VL (2013) Iterative projection algorithms in protein crystallography. I. Theory. *Acta Crystallographica. Section A* 69: 517–527.
Mueller U and Weiss MS (2023) Macromolecular crystallography. In: *Reference Module in Materials Science and Materials Engineering*. Elsevier, ISBN: 9780128035818. https://doi.org/10.1016/978-0-323-90800-9.00086-X.
Oszlányi G and Sütő A (2004) Ab initio structure solution by charge flipping. *Acta Crystallographica. Section A* 60: 134–141.
Palatinus L (2013) The charge flipping algorithm in crystallography. *Acta Crystallographica. Section A* 69: 1–16.
Patterson AL (1934) A Fourier series method for the determination of the components of interatomic distances in crystals. *Physical Review* 46: 372–376.
Sayre D (1952) The squaring method: A new method for phase determination. *Acta Crystallographica* 5: 60–65.
Shankland K, David WIF, and Csoka T (1997) Crystal structure determination from powder diffraction data by the application of a genetic algorithm. *Zeitschrift für Kristallographie* 212: 550–555.
Sheldrick GM (2015) SHELXT—Integrated space-group and crystal-structure determination. *Acta Crystallographica. Section A* 71: 3–8.
Wilson AJC (1942) Determination of absolute from relative X-ray intensities data. *Nature* 150: 151–152.
Wilson AJC (1949) The probability distribution of X-ray intensities. *Acta Cryst* 2: 318–321.

Further reading

Clegg W, Blake AJ, Cole JM, Evans JSO, Main P, Parsons S, and Watkin DJ (2009) Crystals structure analysis. In: Clegg W (ed.) *Principles and Practice*. Oxford: Oxford University Press.
Cruickshank DWJ (1965) *Computing Methods in Crystallography*. Oxford: Pergamon.
Giacovazzo C, Monaco HL, Artioli G, Viterbo D, Milanesio M, Gilli G, Zanotti G, Ferraris G, and Catti M (2011) *Fundamentals of Crystallography*. C. Giacovazzo, 3rd edn. Oxford: Oxford University Press.
Giacovazzo C (2013) *Phasing in Crystallography*. A modern Perspective: Oxford University Pressl Oxford.
Rollett JS (1965) *Computing Methods in Crystallography*. Oxford: Pergamon.

Macromolecular crystallography[☆]

Uwe Mueller and Manfred S Weiss, Macromolecular Crystallography, Helmholtz-Zentrum Berlin für Materialien und Energie GmbH, Berlin, Germany

© 2024 Elsevier Ltd. All rights reserved.

This is an update of M. Wilmanns, M.S. Weiss, Molecular Crystallography, Editor(s): Franco Bassani, Gerald L. Liedl, Peter Wyder, Encyclopedia of Condensed Matter Physics, Elsevier, 2005, Pages 453–458, ISBN 9780123694010, https://doi.org/10.1016/B0-12-369401-9/00424-1.

Introduction 42
Text 42
Part 1. From objects to diffraction patterns 42
The scattering equation 42
Scattering by atoms and molecules 43
Scattering by a crystal 43
The diffraction experiment 44
Part 2. From the diffraction pattern to the structure 45
The electron density equation 45
The phase problem 45
Crystallographic phase determination 45
Model building and refinement 48
Conclusion 48
References 48

Abstract

Despite recent advances in other structure determination methods, such as for instance cryo-electron microscopy, macromolecular X-ray crystallography is still by far the most popular experimental method for determining the three-dimensional structure of biological macromolecules. More than 80% of all macromolecular structures determined to date, have been determined by crystallography. The physical principle behind X-ray crystallography is the elastic scattering of electromagnetic waves by the crystalline sample. The resulting three-dimensional diffraction pattern is recorded and analyzed. It contains the information on the spatial structure of the crystallized molecule, although the structure itself is not directly available from the diffraction pattern. The fact that only the amplitudes but not the phases of the X-ray reflections can be measured is also known as the crystallographic phase problem, which has to be solved before the structure can be determined.

Key points

- Despite recent advances in other structure determination methods, such as for instance cryo-electron microscopy, macromolecular X-ray crystallography is still by far the most popular experimental method for determining the three-dimensional structure of biological macromolecules.
- More than 80% of all macromolecular structures determined to date, have been determined by crystallography.
- The physical principle behind X-ray crystallography is the elastic scattering of electromagnetic waves by the crystalline sample.
- The resulting three-dimensional diffraction pattern is recorded and analyzed. It contains the information on the spatial structure of the crystallized molecule, although the structure itself is not directly available from the diffraction pattern.
- The fact that only the amplitudes but not the phases of the X-ray reflections can be measured is also known as the crystallographic phase problem, which has to be solved before the structure can be determined.

Nomenclature

$\vec{f}(\vec{s})$	Atomic form factor
$\vec{F}(hkl)$	Structure factor for reflection (hkl)
$\lvert\vec{F}(hkl)\rvert$	Structure factor amplitude for reflection (hkl)
$\boldsymbol{\alpha}(\mathbf{hkl})$	Phase for reflection (hkl)
$\mathbf{I(hkl)}$	Intensity of reflection (hkl)

[☆] *Change History*: September 2022. U Mueller and MS Weiss updated all sections.

https://doi.org/10.1016/B978-0-323-90800-9.00086-X

$\rho(x,y,z)$	Electron density at the point (x,y,z) in the unit cell; x, y and z are fractional coordinates and the unit of ρ is $e/\text{Å}^3$ ($1\ \text{Å} = 10^{-10}$ m).
P(uvw)	Patterson function value at position (u,v,w)

Introduction

Since its advent in 1914 when W. L. Bragg and W. H. Bragg managed to determine the three-dimensional structure of table salt based on the observed X-ray reflection intensities, X-ray crystallography or crystal structure determination by means of X-ray diffraction has become one of the fastest growing fields in chemistry, biochemistry and material science. Nearly everything that is known today with respect to how atoms arrange themselves into molecules has its origin in crystal structures. At the time of writing this chapter in the beginning of 2022, more than 250,000 inorganic crystal structures had been deposited in the Inorganic Crystal Structure Data Base (ICSD), nearly 1,200,000 molecular structures in the Cambridge Structural Data Base (CSD), and almost 200,000 structures of biological macromolecules in the Protein Data Bank (PDB) (Bruno et al., 2017). In present days, research fields ranging from physics to chemistry, mineralogy, geology, material science, metallurgy all the way to biology, pharmacy, and medicine embrace crystal structure determination as one of their most essential and relevant techniques. In this chapter, a brief introduction into crystal structure analysis will be given with a focus on biological macromolecules. The chapter will describe the principles of the technique rather than the more practical aspects. It should give the interested reader sufficient detail and background, so that more elaborate and more comprehensive texts (Blundell and Johnson, 1976; Drenth, 1994; Giaccovazzo et al., 1992; Glusker and Trueblood, 1985; Ladd and Palmer, 1994; Rhodes, 1993; Rupp, 2009; Stout and Jensen, 1968) can be read and understood.

Text

A complete description of X-ray crystallography as an experimental structure determination technique requires an in-depth discussion of the two main parts of the crystallographic experiment. At first, the relationship between the object to be studied and its corresponding diffraction pattern must be derived and understood. Then, the way back from the diffraction pattern to the structure has to be outlined and described.

Part 1. From objects to diffraction patterns

The scattering equation

Electromagnetic waves interact with matter. Their electric components force charged particles to oscillate with the same frequency as the incident wave. Oscillating electrons constitute moving charges, and moving charges emit electromagnetic radiation of the same frequency into all directions of space. This phenomenon is called *elastic scattering, Thomson scattering* or *scattering without loss of energy*. Atomic nuclei interact with electromagnetic waves in the very same way as electrons, but since a proton is about 2000 times heavier than an electron, and thus much less prone to be moved, the scattering by nuclei can be neglected for the purposes of X-ray crystallography. The mathematical description of the phenomenon of scattering is illustrated in Fig. 1.

The incoming X-ray wave (from the left) is represented by the vector $\vec{s}_{in}$ with $|\vec{s}_{in}| = 1/\lambda$ where λ is the wavelength of the incoming X-ray wave. The wave impinges upon the object and is then scattered by the whole object, in all directions of space. For simplicity, only the scattering at the points O and P is considered now, and only the scattering in the direction described by $\vec{s}_{out}$. $\vec{s}_{out}$ is a vector representing the scattered wave ($|\vec{s}_{out}| = 1/\lambda$). The difference vector between $\vec{s}_{out}$ and $\vec{s}_{in}$ ($\vec{s}_{out} - \vec{s}_{in}$) is called the scattering vector $\vec{s}$. The scattering vector describes the change in direction the X-ray wave undergoes upon scattering. The size of the object, i.e., the distance between points O and P in the example given here leads to a path difference $\Delta x = \vec{r}(\vec{s}_{out} - \vec{s}_{in})\,\lambda = \vec{r}\vec{s}\,\lambda$ between the two scattered waves shown in Fig. 1. This path difference results in a phase difference $\Delta\alpha = \Delta x \cdot 2\pi/\lambda = 2\pi\vec{r}\vec{s}$ between the two scattered waves. The wave scattered at point P has an amplitude proportional to the electron density $\rho(P)$ at point P and a phase of $2\pi\vec{r}\vec{s}$ relative to the wave scattered at point O. In order to compute the total wave $\vec{f}_T$ scattered by the object depicted in Fig. 1, an integration over all volume elements (V) of the scattering object has to be performed. This leads to the general scattering

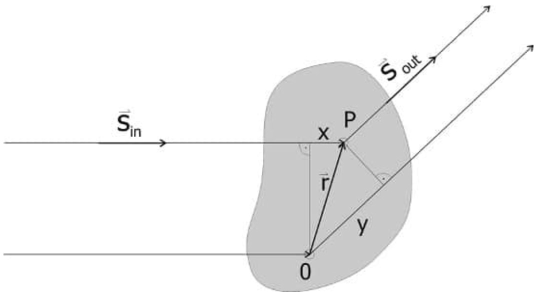

Fig. 1 Scattering of electromagnetic waves by an object.

equation (Eq. 1). $\vec{f}_T(\vec{s})$ describes the scattering by every conceivable object, which can be described by $\vec{r}$, $\rho(\vec{r})$, and V, into the direction defined by the vector $\vec{s}$.

$$\vec{f}_T\left(\vec{s}\right) = \int_{\text{Vol}} \rho\left(\vec{r}\right)\, e^{2\pi i \vec{r}\vec{s}}\, dV \quad \text{Scattering Equation} \tag{1}$$

Eq. (1) can also be regarded as a *Fourier Analysis* of the object to be studied by the X-rays.

Scattering by atoms and molecules

The description of the scattering of real atoms starts from the general scattering equation (Eq. 1). The integration over the whole volume V of the atom implies that the function $\vec{f}(\vec{s})$ is dependent on the form of the electron cloud of the atom. It is therefore also called the *Atomic Form Factor*. The atomic form factor is an intrinsic property of an atom or ion, which depends on the exact architecture of the electron cloud of the atom or the ion. Atomic form factors can be calculated using quantum mechanical approximations from the electron distribution of the atoms or ions, but they can also be measured very accurately for instance by X-ray scattering.

The scattering by a molecule can now simply be calculated based on the scattering of the atoms belonging to the molecule (Fig. 2a). The total scattered wave is the sum of the individually scattered waves in any given direction (Fig. 2b). Using the example of a three-atom molecule, the contributions by the three atoms have to be considered: $\vec{F}_1 = \vec{f}_1(\vec{s})\, e^{2\pi i \vec{r}_1 \vec{s}}$ for atom 1, $\vec{F}_2 = \vec{f}_2(\vec{s})\, e^{2\pi i \vec{r}_2 \vec{s}}$ for atom 2 and $\vec{F}_3 = \vec{f}_3(\vec{s})\, e^{2\pi i \vec{r}_3 \vec{s}}$ for atom 3. The result is shown in Eq. (2). It is also called the *Molecular Transform*.

$$\vec{F}_m\left(\vec{s}\right) = \sum_{j=1}^{3} \vec{f}_j\left(\vec{s}\right) e^{2\pi i \vec{r}_j \vec{s}} \quad \text{Molecular Transform} \tag{2}$$

$\vec{f}_j(\vec{s})$ are the atomic form factors and $\vec{r}_j$ the coordinates of the corresponding atoms j.

Scattering by a crystal

A crystal is defined as a solid object, which is periodic in three dimensions. In order to build up a crystal from its smallest unit, the unit cell, one just needs to know the contents of the unit cell and the so-called lattice translations $\vec{a}$, $\vec{b}$ and $\vec{c}$. For describing the scattering of one single unit cell of a crystal, $\vec{F}_{\text{unit cell}}(\vec{s})$, the contributions of all N atoms in the unit cell have to be added up (Eq. 3).

$$\vec{F}_{\text{unit cell}}\left(\vec{s}\right) = \sum_{j=1}^{N} \vec{f}_j\left(\vec{s}\right) e^{2\pi i \vec{r}_j \vec{s}} \tag{3}$$

Further on, in order to consider the scattering by the whole crystal now, the contributions of all unit cells of the crystal and all atoms in each unit cell have to be taken into account. Let $\vec{F}_{\text{unit cell}}(\vec{s})$ be the scattering of the first unit cell, and $\vec{F}'_{\text{unit cell}}(\vec{s})$ the scattering of a second unit cell shifted by $\vec{r} = u\vec{a} + v\vec{b} + w\vec{c}$ relative to the first unit cell (u, v, and w are integer values, and $\vec{a}$, $\vec{b}$, and $\vec{c}$ are the lattice translations) (Fig. 3a). It can be shown that the contribution of the second unit cell can be expressed as the scattering of the first unit cell and the vector that relates the two unit cells.

$$\vec{F}'_{\text{unit cell}}\left(\vec{s}\right) = \vec{F}_{\text{unit cell}}\left(\vec{s}\right) e^{2\pi i u \vec{a}\vec{s}}\; e^{2\pi i v \vec{b}\vec{s}}\; e^{2\pi i w \vec{c}\vec{s}} \tag{4}$$

To arrive at the scattering equation for the whole crystal, the sum over all unit cells has to be calculated. This can be reduced to summing over all combinations of u, v, and w.

$$\vec{F}_{\text{Crystal}}\left(\vec{s}\right) = \vec{F}_{\text{unit cell}}\left(\vec{s}\right) \sum_{u=0}^{n_1} e^{2\pi i u \vec{a}\vec{s}} \sum_{v=0}^{n_2} e^{2\pi i v \vec{b}\vec{s}} \sum_{w=0}^{n_3} e^{2\pi i w \vec{c}\vec{s}} \tag{5}$$

n_1, n_2 and n_3 are the numbers of the unit cells in the respective $\vec{a}$-, $\vec{b}$- and $\vec{c}$-directions. These numbers are large for typical crystals in the µm- to mm-size range. This means that the sums $\sum_{u=0}^{n_1} e^{2\pi i u \vec{a}\vec{s}}$, $\sum_{v=0}^{n_2} e^{2\pi i v \vec{b}\vec{s}}$, and $\sum_{w=0}^{n_3} e^{2\pi i w \vec{c}\vec{s}}$ will be zero unless $\vec{a}\cdot\vec{s}$, $\vec{b}\cdot\vec{s}$, and $\vec{c}\cdot\vec{s}$ are

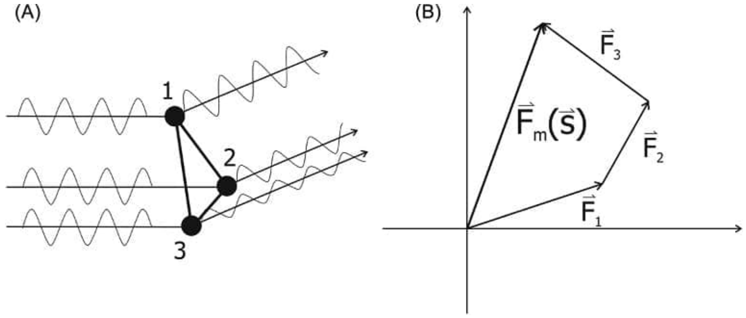

Fig. 2 (a) Scattering by a schematic three-atom molecule. Each of the three atoms contains a different number of electrons, (b) Argand diagram with the vector addition of the three individually scattered waves yielding the Molecular Transform.

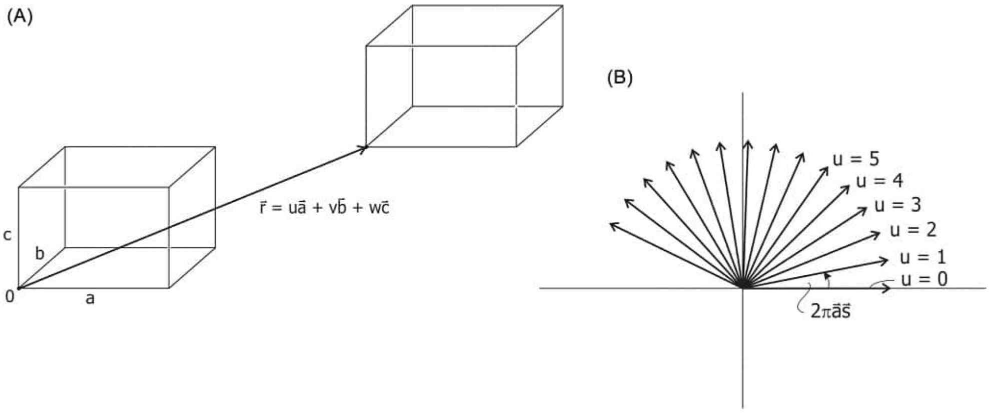

Fig. 3 (a) Two unit cells of a crystal, (b) Graphical representation of the Laue conditions in one dimension. In the case shown, the scalar product $\vec{a}\cdot\vec{s} \neq h$. As a result of this, the waves with different values of u exhibit phase differences $\neq 2\pi$. Due to the large number of waves to be considered (one for each unit cell of the crystal), the overall sum will be zero.

integral numbers. These conditions are also known as the *Laue Conditions* and they are illustrated in Fig. 3b as vector additions in an Argand diagram. In the case of the Laue conditions being fulfilled, the product of the three sums is equal to the total number of unit cells in a given crystal.

This derivation bears two important consequences. First, the scattering of a crystal is proportional to the scattering of just one unit cell and the total number of unit cells in the crystal. Consequently, in order to describe the scattering by the whole crystal, it is sufficient to consider the scattering by just one unit cell. Second, the scattering of a crystal leads to a discrete diffraction pattern. Only in those directions $\vec{s}$, in which the Laue conditions are obeyed, scattering will be observed. In all other directions the sum of all scattered waves will be zero. This leads to the observation of a diffraction pattern consisting of discrete maxima, the so-called X-ray reflections. Each reflection is identified by a unique combination of the three numbers h, k, and l, the Miller indices.

$$\vec{F}_{\text{Crystal}}\left(\vec{s}\right) = n\,\vec{F}_{\text{unit cell}}\left(\vec{s}\right) = n\sum_{j=1}^{N}\vec{f}_j\left(\vec{s}\right)e^{2\pi i\vec{r}_j\vec{s}} \quad (\text{n : number of unit cells}) \tag{6}$$

With $\vec{r}_j = x_j\vec{a} + y_j\vec{b} + z_j\vec{c}$ (x_j, y_j, and z_j are the fractional coordinates of atom j), and with the Laue conditions $\vec{a}\cdot\vec{s} = h$, $\vec{b}\cdot\vec{s} = k$, and $\vec{c}\cdot\vec{s} = l$, Eq. (6) can be transformed into Eq. (7).

$$\vec{F}\left(\vec{s}\right) = \vec{F}(hkl) = \sum_{j=1}^{N}\vec{f}_j\,e^{2\pi i\left(hx_j+ky_j+lz_j\right)} \tag{7}$$

Eq. (7) is also called the *Structure Factor Equation*. It constitutes the first of the two central equations in X-ray crystallography, the second one being the *Electron Density Equation* (see below). The Structure Factor Equation describes the scattering of a crystal defined by the unit cell vectors $\vec{a}$, $\vec{b}$, and $\vec{c}$, and by the atoms inside the unit cells of this crystal as defined by their atomic form factors (f_j) and their fractional coordinates (x_j, y_j, and z_j).

The diffraction experiment

A schematic representation of an X-ray experiment is shown in Fig. 4. The experiment itself involves the production or generation of X-rays, the selection of the X-rays for the experiment, the preparation of the crystal for the experiment, the actual data collection step and the processing and validation of the resulting data. Of course, if one is just interested in using X-rays to determine a crystal structure one may not be overly concerned with the way X-rays are produced and prepared for the measurement, but there are some

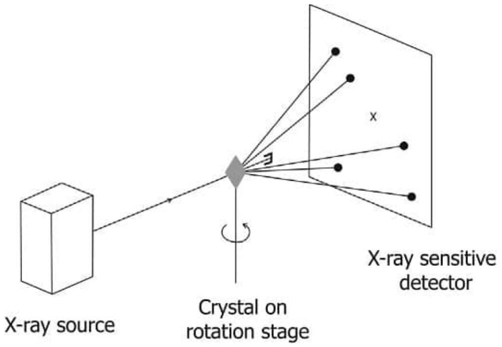

Fig. 4 Schematic representation of the diffraction experiment. Depicted are the X-ray source, the object (crystalline sample) mounted on a rotatable device and the detector for detecting the scattered waves.

important aspects that can potentially have a great impact on the quality of the obtained diffraction data and consequently on various stages of structure determination and certainly on the information content of the resulting structure. One should always keep in mind that the quality or the information content of a crystal structure is directly determined by the quality or the information content of the diffraction data that are the basis for the determination of the structure. Furthermore, the collection of diffraction data is the last real experimental step to be carried out in the course of a crystal structure analysis. Everything after that is merely a computer-based interpretation of the collected diffraction data.

Part 2. From the diffraction pattern to the structure

The electron density equation

The Fourier transformation of the general scattering equation (Eq. 1) leads to the electron density equation (Eq. 8), the second central equation in X-ray crystallography. Instead of integrating over the volume of the scattering object V, the integration proceeds now over diffraction space V*, which is sometimes also called reciprocal space, because of the reciprocal relationship to the real space with respect to its geometric parameters.

$$\rho\left(\vec{r}\right) = \int_{Vol^*}^{f_T}\left(\vec{s}\right) e^{-2\pi i \vec{r}\,\vec{s}}\, dV^* \text{ Electron Density Equation} \tag{8}$$

Similar to regarding Eq. (1) as a *Fourier Analysis* of the object, Eq. (8) can be regarded as a *Fourier Synthesis*. The object can be reconstructed from its diffraction pattern by taking into account all scattered waves. A simpler version of the electron density equation (Eq. 9) can be derived considering that the diffraction pattern of a crystal is discrete (see above), and that instead of integrating over the whole volume of diffraction space, we only need to sum over the observed X-ray reflections.

$$\rho(x, y, z) = \sum_{\mathrm{h,k,l}} |\vec{\mathrm{F}}(\mathrm{hkl})|\, \mathrm{e}^{-2\pi \mathrm{i}(\mathrm{hx+ky+lz})+\mathrm{i}\alpha(\mathrm{hkl})} \tag{9}$$

Eq. (9) demonstrates two points. First, in order to calculate the value for the electron density ρ at any given point (x,y,z) in the unit cell, all reflections have to be taken into account. Second, the summation can only be carried out if both the structure factor amplitude $|\vec{\mathrm{F}}|$ and the phase α are known for each reflection (hkl).

The phase problem

The data which are obtained from a diffraction experiment are the intensities I of the reflections (hkl). The intensity I(hkl) can be calculated by multiplying the structure factor $\vec{\mathrm{F}}(\mathrm{hkl})$ with its conjugated complex structure factor $\vec{\mathrm{F}}^*(\mathrm{hkl})$. The net result is that I(hkl) is proportional to the square of the structure factor amplitude $|\vec{\mathrm{F}}(\mathrm{hkl})|$ (Eq. 10).

$$\mathrm{I(hkl)} \propto |\vec{\mathrm{F}}(\mathrm{hkl})|\ |\vec{\mathrm{F}}^*(\mathrm{hkl})| = |\vec{\mathrm{F}}(\mathrm{hkl})|\ \mathrm{e}^{\mathrm{i}\alpha(\mathrm{hkl})} |\vec{\mathrm{F}}(\mathrm{hkl})|\ \mathrm{e}^{-\mathrm{i}\alpha(\mathrm{hkl})} = \left|\vec{\mathrm{F}}(\mathrm{hkl})\right|^2 \tag{10}$$

As a consequence, by having measured the X-ray intensities, we are only able to back-calculate the amplitudes $|\vec{\mathrm{F}}(\mathrm{hkl})|$ of the waves. The information about the phases α(hkl) is lost. This is known as the so-called *phase problem* in crystallography. The phase problem is the reason why an image of the molecule to be studied cannot be calculated directly from the diffraction data. Approaches to overcome the problem will be briefly discussed in the next chapter.

Crystallographic phase determination

Over time several methods have been developed to address the crystallographic phase problem. The decision as to which method to use is more or less governed by both the size of the molecules to be studied and the diffraction power of the corresponding crystals. For the crystallography of small molecules, i.e., molecules of up to a few hundred atoms, where the crystals typically exhibit very good diffraction properties, the so-called *direct methods* are the method of choice. These have nowadays been mostly automated and thus also made available to the non-expert user so that crystal structure determination of small molecules can be considered a routine feat. In macromolecular crystallography where the molecules are much larger and where the corresponding crystals typically exhibit limited diffraction properties, the method of choice nowadays is the so-called *molecular replacement* method. While up to a few years ago, methods based on *isomorphous replacement* or on the exploitation of *anomalous scattering* have been the most important methods for *de novo* structure determination of biological macromolecules, the advent of the structure prediction program AlphaFold2 has completely shifted the focus from those methods toward molecular replacement. For the sake of completeness, all of the mentioned approaches will be discussed in brief.

Molecular replacement

The method of molecular replacement relies on the availability of a molecular structure, which is similar to the unknown structure to be solved. The known structure can be computationally placed into the unknown structure's unit cell, and initial structure factors $\vec{\mathrm{F}}_\mathrm{P}$ can be calculated. Although these first calculated amplitudes $|\vec{\mathrm{F}}_\mathrm{P}|$ and phases α_P will not be correct, they may be used as starting values for further refinement.

In 2020, DeepMind researchers announced and published the solution to a 50-years old grand challenge in biochemical structural science: the sequence-structure relationship. By designing a deep learning algorithm into the neural network AlphaFold2, the three-dimensional structure of any given protein can be determined, using just its amino acid sequence as input (Jumper et al., 2021). Consequently, a fairly accurate and reliable computational model for nearly any protein's three-dimensional structure can be

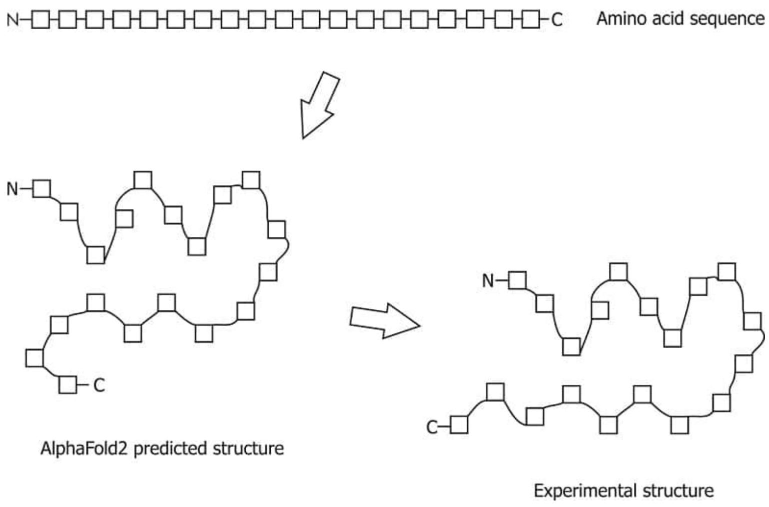

Fig. 5 Schematic view of a structure determination by molecular replacement using an AlphaFold2 predicted structure.

derived. This can then be used in a molecular replacement approach to determine the crystallographic structure from experimental data (McCoy et al., 2022).

Although the experimental structure may differ in some aspects from the model structure, the structural models derived from AlphaFold2 are usually similar enough to the final experimental structures, so that they can successfully be used as starting models for molecular replacement (Fig. 5).

A structure determination by molecular replacement is a six-dimensional problem. The known structure (referred to as the *search model*) needs to be properly oriented and placed in the unit cell of the crystal structure to be determined (referred to as the *target structure*). This requires three rotational and three translational parameters to be determined. This six-dimensional problem can be conveniently broken down into two three-dimensional problems.

Molecular replacement relies on the properties of the Patterson function (Eq. 11), which is essentially a Fourier Transform of the diffraction intensities. It can be calculated directly from the intensity data I(hkl) (or the square of structure factor amplitudes), without the need of the X-ray reflection phases α(hkl)

$$P(uvw) = 1/V\sum_{h,k,l}\left|\vec{F}(hkl)\right|^2 e^{-2\pi i(hu+kv+lw)} \quad \text{Patterson Function} \tag{11}$$

Here, u, v, and w the are coordinates in Patterson space. Since the Patterson Function P(uvw) is equivalent to a convolution of the electron density ρ(x,y,z) (Eq. 9) with itself (Eq. 12), maxima in P(uvw) correspond to vectors between peaks in ρ(x,y,z). Similarly, a Patterson map derived from a structure with N atoms, exhibits N(N-1) peaks. These peaks represent all interatomic vectors between atoms of the structure.

$$P(uvw) = \int_{x,y,z} \rho(x, y, z) * \rho(u + x, v + y, w + z)\, dx\, dy\, dz \tag{12}$$

In the first step of the molecular replacement procedure, the Patterson map of the search model is compared in all different orientations with the Patterson map derived from the experimental diffraction data. A maximum in the so-called rotation function determines the correct orientation of the search model. In a second step, the correctly oriented search model is translated through the entire unit cell, and the position is sought at which the discrepancy between model-derived data and experimental data is minimal. This so-called translation function determines the correct position of the search model in the unit cell of the target structure.

Isomorphous replacement

Historically the most relevant phase determination method in macromolecular crystallography is isomorphous replacement. In this method, diffraction data sets of two isomorphous crystals are compared with each other reflection by reflection. The first crystal may be the one of a native macromolecule, the second crystal may be one of a heavy atom derivative of the same macromolecule. This latter one can be prepared by either co-crystallization or soaking a native macromolecule crystal in a heavy atom containing solution. A detailed comparison of the two diffraction data sets will then in a first step yield the differences between the data sets, which are due to the heavy atom substructure. From these differences, the substructure can be determined. With the substructure at hand, one can then calculate the structure factor amplitude and the phase of just the substructure, and then use this heavy atom phase as a reference to calculate the phases of the reflections of the macromolecule crystal. An easy way to visualize this is a vector diagram (Fig. 6). The vector addition of the structure factor of the macromolecule alone $\vec{F}_P$ and the structure factor of the heavy atoms alone $\vec{F}_H$ will yield the structure factor of the heavy atom derivative $\vec{F}_{PH}$. If we know now the magnitude of both $\vec{F}_P$ and $\vec{F}_{PH}$ (these are the structure factor amplitudes which have been measured in the two diffraction experiments) and the magnitude and

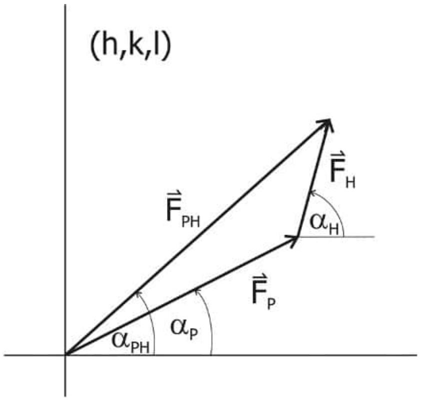

Fig. 6 Vector addition of the structure factors for the native macromolecule $\vec{F}_P$, the heavy atom substructure $\vec{F}_H$ and the heavy atom derivative of the macromolecule $\vec{F}_{PH}$.

direction of $\vec{F}_H$ (this can be calculated once the heavy atom substructure is known), all other parameters of the triangle in Fig. 6 can be calculated as well.

However, this vector addition is not unambiguous. The result of this calculation will not be a unique phase α(hkl) for a given reflection, but two possible solutions, which are symmetrical about the vector $\vec{F}_H$. This situation can be made unambiguous, for instance by including a second heavy atom derivative or by including anomalous scattering information.

Anomalous diffraction

Anomalous scattering occurs when the energy of the X-rays used for the diffraction experiment is close to an elemental X-ray absorption edge. If the structure to be determined contains such anomalous scatterers, a diffraction experiment can be carried out at two (or more) different X-ray energies. The differences between the diffraction patterns can then again be attributed to the anomalously scattering substructure, and in the same way as above, the substructure can be determined, and the substructure phase be used as a reference to determine the phase α_P. Important realizations of this approach haven been the so-called MAD (multiple wavelength anomalous diffraction) or SAD (single wavelength anomalous diffraction) methods.

Direct methods

The direct methods rely on the principle that the phase information is somehow included in the measured structure factor amplitudes. The underlying rationale is that structure factors are not independent of each other but that they are related through the structure. With the additional constraints that *(i)* the electron density can never be negative and that *(ii)* the structure to be determined consists of discrete atoms, phase sets can be constructed randomly and examined with respect to their validity.

The credibility of a given set of phases can be examined by considering probabilistic relationships between the phases of certain reflections, e.g., the *triplet invariants* (Eq. 13). It can be derived, that the phases of the three reflections (h_1, k_1, l_1), (h_2, k_2, l_2) and ($-h_1-h_2$, $-k_1-k_2$, $-l_1-l_2$) are related by the following equation:

$$\alpha(h_1, k_1, l_1) + \alpha(h_2, k_2, l_2) + \alpha(-h_1-h_2, -k_1-k_2, -l_1-l_2) \approx 0 \tag{13}$$

This equation is not absolutely but only approximately valid, and it is usually formulated as a probability. The stronger the three reflections (h_1, k_1, l_1), (h_2, k_2, l_2) and ($-h_1-h_2$, $-k_1-k_2$, $-l_1-l_2$) are, the higher the probability that the three phase values sum up to zero or an integral multiple of 2π.

Various measures to evaluate the quality of a given phase set have been introduced over time. The most widely known formula for this purpose is the *tangent formula* (Eq. 14). In this formula, the most probable value of the phase of one reflection $\alpha(h_1, k_1, l_1)$ is given as a function of the values of the phases of all other reflections (h_m, k_m, l_m) and ($-h_1-h_m$, $-k_1-k_m$, $-l_1-l_m$), which share a triplet invariant with (h_1, k_1, l_1). The reliability of the formula depends on the magnitude of the structure factor amplitudes of the reflections considered.

$$\tan[\alpha(h_1, k_1, l_1)] = \frac{\sum_i W_m \sin[-\alpha(h_m, k_m, l_m) - \alpha(-h_1-h_m, -k_1-k_m, -l_1-l_m)]}{\sum_i W_m \cos[-\alpha(h_m, k_m, l_m) - \alpha(-h_1-h_m, -k_1-k_m, -l_1-l_m)]} \tag{14}$$

Tangent Formula

The two sums in the enumerator and the denominator run over all possible triplet invariants i, in which the reflection (h_1, k_1, l_1) is involved, and the numbers W_m describe the weighted product of the normalized structure factor amplitudes of reflections (h_m, k_m, l_m) and ($-h_1-h_m$, $-k_1-k_m$, $-l_1-l_m$).

Relationships such as the triplet invariants and the tangent formula help to reduce the complexity of the phase set. Nevertheless, because of the large number of possible phase sets, direct methods for phase determination are typically only applicable to small structures.

Model building and refinement

Once initial phases have been determined by one of the methods described above, the electron density distribution can be calculated according to Eq. (9). The electron density is nothing but an image of the structure to be determined. It shows where in the unit cell the electrons (hence the atoms) are. Since molecular structures are usually described by the position of all of its atoms, the electron density has to be interpreted in terms of atomic positions and identities. Finally, the so obtained model can be subjected to a mathematical optimization procedure called refinement, in order to optimize the fit between the structure factors that can be calculated from the model and the ones that have been observed experimentally. This constant feedback between model and experimental data is one of the greatest strengths of the X-ray crystallography.

Conclusion

The aim of this chapter was to provide a basic and concise introduction into the method and the principles of X-ray crystallography of biological macromolecules. While we realize that other structure determination methods exist and continue to be developed further, we are convinced that X-ray crystallography will remain the dominant method for structure determination for many years to come. This is owed first and foremost to its capacity to result in structures to atomic resolution or sometimes even better, and second to its high degree of development, both on the instrumental and on the computational side, which lends itself to automation. This in turn makes the method accessible to experts and non-experts alike. Last but not least, due to the high information content of each individual structure, X-ray crystallography will continue to be used by many researchers in many different research fields.

References

Blundell TL and Johnson LN (1976) *Protein Crystallography*. Academic Press.
Bruno I, Gražulis S, Helliwell JR, Kabekkodu SN, McMahon B, and Westbrook J (2017) Crystallography and databases. *Data Science Journal* 16: 38ff.
Drenth J (1994) *Principles of Protein X-ray Crystallography*. Springer Verlag.
Giaccovazzo C, Monaco HL, Viterbo D, Scordari F, Gilli G, Zanotti G, and Catti M (1992) *Fundamentals of Crystallography*, 2nd edn. Oxford University Press.
Glusker JP and Trueblood KN (1985) *Crystal Structure Analysis*. Oxford University Press.
Jumper J, Evans R, Pritzel A, et al. (2021) Highly accurate protein structure prediction with AlphaFold. *Nature* 596: 583–589.
Ladd MFC and Palmer RA (1994) *Structure Determination by X-ray Crystallography*. New York and London: Plenum Press.
McCoy A, Sammito MD, and Read R (2022) Implications of AlphaFold2 for crystallographic phasing by molecular replacement. *Acta Crystallographica Section D* 78: 1–13.
Rhodes G (1993) *Crystallography Made Crystal Clear*. Academic Press.
Rupp B (2009) *Biomolecular Crystallography: Principles, Practice, and Applications to Structural Biology*. New York: Garland Science.
Stout GH and Jensen LH (1968) *X-ray Structure Determination*. Macmillan Publishing Co., Inc.

Point groups

H Klapper[a] **and Th Hahn**[b], [a]Mineralogisch-Petrologisches Institut, Universität Bonn, Bonn, Germany; [b]Institut fur Kristallographie, RWTH Aachen, Aachen, Germany

© 2024 Elsevier Ltd. All rights reserved.

This is an update of H. Klapper, Th. Hahn, Point Groups, Editor(s): Franco Bassani, Gerald L. Liedl, Peter Wyder, Encyclopedia of Condensed Matter Physics, Elsevier, 2005, Pages 323–334, ISBN 9780123694010, https://doi.org/10.1016/B0-12-369401-9/00422-8.

Brief review of groups **50**
Introduction to point groups **50**
General and crystallographic point groups **51**
General point groups 51
Crystallographic point groups 51
Symbols of the 32 crystallographic point groups **52**
Description of point groups **52**
Subgroups of the crystallographic point groups **55**
Examples 56
Symmetry of physical properties **56**
Definition of tensor symmetry 56
Neumann's principle 57
Tensors of odd rank **57**
Pyroelectricity and ferroelectricity 57
Piezoelectricity 58
Enantiomorphism and optical activity (optical gyration) **58**
Curie's principle **59**
Further reading **60**

Abstract

Definition: A group G is a set of N elements $\mathrm{g_i}$ with a composition law ("multiplication" $g_i \circ g_j$) of any two elements g_i and $g_j \in \mathcal{G}$ obeying the following four group axioms:

1. The "product" of any two group elements g_i and $g_j \in \mathcal{G}$ is again an element of the group: $\left(g_i \circ g_j\right) = g_k \in \mathcal{G}$ (axiom of closure).
2. There exists always a neutral element (identity) e, such that $(e \circ g_i) = (g_i \circ e) = g_i$ for any $g_i \in \mathcal{G}$.
3. For every $g_i \in \mathcal{G}$, there exists an inverse element $g_i^{-1} \in \mathcal{G}$ such that $(g_i \circ g_i^{-1}) = (g_i^{-1} \circ g_i) = e$.
4. For any three elements $g_i, g_j, g_k \in \mathcal{G}$, the associative law holds: $(g_i \circ g_j) \circ g_k = g_i \circ (g_j \circ g_k)$.

Nomenclature

$-\boldsymbol{\sigma}$	Hydrostatic pressure
$N(\mathcal{G}) = \lvert\mathcal{G}\rvert$	Order of group $\mathcal{G}$
$\mathcal{G}$	Point group of a crystal
$\mathcal{H}$	Subgroup
$\mathcal{P}$	Symmetry group of the property P
$[\boldsymbol{i}]$	Index of a subgroup or supergroup; number of orientation states of domains
$\boldsymbol{e}$	Neutral element, identity
$\boldsymbol{F}$	External physical influence (external field) on a crystal
$\boldsymbol{g_i}$	Element of $\mathcal{G}$
$\boldsymbol{p}$	Electric polarization vector, pyroelectric vector
$\boldsymbol{P}$	Physical (tensor) property of a crystal
$\boldsymbol{W}$	(3×3) matrix of a point-group operation
$\boldsymbol{\sigma_{ii}}, \boldsymbol{\sigma_{ij}}$	Uniaxial stress, shear stress

Brief review of groups

Definition: A group G is a set of N elements $\mathrm{g_i}$ with a composition law ("multiplication" $g_i \circ g_j$) of any two elements g_i and $g_j \in \mathcal{G}$ obeying the following four group axioms:

1. The "product" of any two group elements g_i and $g_j \in \mathcal{G}$ is again an element of the group: $\left(g_i \circ g_j\right) = g_k \in \mathcal{G}$ (axiom of closure).
2. There exists always a neutral element (identity) e, such that $(e \circ g_i) = (g_i \circ e) = g_i$ for any $g_i \in \mathcal{G}$.
3. For every $g_i \in \mathcal{G}$, there exists an inverse element $g_i^{-1} \in \mathcal{G}$ such that $(g_i \circ g_i^{-1}) = (g_i^{-1} \circ g_i) = e$.
4. For any three elements $g_i, g_j, g_k \in \mathcal{G}$, the associative law holds: $(g_i \circ g_j) \circ g_k = g_i \circ (g_j \circ g_k)$.

The finite number N of (different) elements of a group is the order of the group (finite groups). If the group contains infinitely many (different) elements, the group is said to be of infinite order (infinite group).

A finite group G is called cyclic, if it can be generated by one element $g : g^1 = g, g^2, g^3, \ldots, g^N = e$ and is of order N.

If the relation $(g_i \circ g_k) = (g_k \circ g_i)$ holds for all pairs $g_i, \; g_k \in \mathcal{G}$, the group is called commutative or Abelian. All groups containing only binary elements g_i (i.e., $g_i \circ g_i = g_i^2 = e$, or equivalently, $g_i = g_i^{-1}$) and all cyclic groups are commutative.

A subset H of a group $\mathcal{G}$, $\mathcal{H} \subset \mathcal{G}$, is called a subgroup of G, if H obeys the group axioms. In this case, G is a supergroup of H. For finite groups, the ratio of the orders of group and subgroup, $N(\mathcal{G})$ and $N(\mathcal{H})$, is the index $[i]$ of H in G: $[i] = N(\mathcal{G})/N(\mathcal{H}) = |\mathcal{G}|/|\mathcal{H}|$. According to the theorem of Lagrange, for finite groups the index $[i]$ is always an integer.

An illustrative representation of a finite group G of order N is the multiplication table or group table of $\mathcal{G} = \{e, g_2, g_3, g_4, \ldots, g_N\}$. It is an $(N \times N)$ square array of all products according to the abstract scheme of Table 1. Note that in each of the N rows and N columns of the table, each group element appears exactly once.

Groups of the same order and with the same structure of the group table, that is, with strict correspondence of their ordered elements and their products (irrespective of the names and symbols of the group elements), are isomorphic. If the group table is symmetric with respect to the main diagonal, the group is commutative.

In crystallographic groups, the group elements are symmetry operations (motions, isometries). The "multiplication" is the successive application of two operations. As an example, the group tables of the two crystallographic point groups 4 (fourfold 90° rotations, tetragonal) of order 4 (Table 2) and $2_x/m_x\ 2_y/m_y\ 2_z/m_z$ (short mmm, orthorhombic) of order 8 (Table 3) are discussed. Table 3 illustrates the various group-subgroup relations within this group: there are seven subgroups of order $N = 4$ and index $[i] = 2$. One of these subgroups, $2_y = m_y$, is displayed in the upper left (4×4) array in Table 3. The full (8×8) group table of $2_x/m_x 2_y/m_y 2_z/m_z$ is obtained from this $2_y/m_y$ subtable by adding any of the operations 2_x, m_x, 2_z, or m_z. From Table 3, it is easily derived that the seven subgroups of order 4 are $2_x/m_x$, $2_y/m_y$, $2_z/m_z$, $2_x2_y2_z$, $2_xm_ym_z$, $m_x2_ym_z$, and $m_xm_y2_z$, which are all isomorphic. There are seven further isomorphic subgroups of order 2 and index 4.

Introduction to point groups

Three kinds of three-dimensional groups are fundamental to the study of crystals: point groups, translation groups, and space groups. This article deals with the first type of groups, the point groups. These groups describe and govern the symmetry of finite (nonperiodic, i.e., not containing translations) objects, such as molecules, crystals, flowers, and objects of art, as well as the local symmetries ("site symmetries") of points in a periodic pattern (ornament, wallpaper, crystal structure).

Table 1 Multiplication table of a group $G = \{e, g_2, g_3, g_4, \ldots, g_N\}$ of order N.

	e	g_2	g_3	$\cdots$	g_N
e	e	g_2	g_3	$\cdots$	g_N
g_2	g_2	g_2^2	g_2g_3	$\cdots$	g_2g_N
g_3	g_3	g_3g_2	g_3^2	$\cdots$	g_3g_N
$\vdots$	$\vdots$	$\vdots$	$\vdots$	$\vdots$	$\vdots$
g_N	g_N	g_Ng_2	g_Ng_3	$\cdots$	g_N^2

Table 2 Group table (4×4) of the tetragonal crystallographic point group 4: successive 90° rotations forming a cyclic group of order 4, i.e., $4^4 = 1$ (this group is commutative).

	1	4^1	$4^2 = 2$	$4^3 = 4^{-1}$
1	1	4^1	2	4^3
4^1	4^1	2	4^3	1
$4^2 = 2$	2	4^3	1	4^1
$4^3 = 4^{-1}$	4^3	1	4^1	2

There is one subgroup of order $N = 2$ and index $[i] = 2$ with elements {1,2} (180° rotation).

Table 3 Group table (8 × 8) of the orthorhombic crystallographic point group $2_{\times}/m_x2_y/m_y2_z/m_z$ (short *mmm*) of order $N = 8$.

	1	2_y	m_y	$\bar{1}$	⋮	$2_{\times}$	m_x	2_z	m_z
1	1	2_y	m_y	$\bar{1}$	⋮	$2_{\times}$	m_x	2_z	m_z
2_y	$2y$	1	$\bar{1}$	m_y	⋮	2_z	m_z	$2_{\times}$	m_x
m_y	my	$\bar{1}$	1	2_y	⋮	m_z	2_z	m_x	$2_{\times}$
$\bar{1}$	$\bar{1}$	m_y	2_y	1	⋮	m_x	$2_{\times}$	m_z	2_z
…	…	…	…	…					
$2_{\times}$	$2_{\times}$	2_z	m_z	m_x		1	$\bar{1}$	2_y	m_y
m_x	m_x	m_z	2_z	$2_{\times}$		$\bar{1}$	1	m_y	2_y
2_z	2_z	$2_{\times}$	m_x	m_z		2_y	m_y	1	$\bar{1}$
m_z	m_z	m_x	$2_{\times}$	2_z		m_y	2_y	$\bar{1}$	1

The top left (4 × 4) array (separated by dotted lines) is the group table of the subgroup $2_y/m_y$ of order $N = 4$ and index $[i] = 2$. The group mmm can be obtained from the subgroup $2_y/m_y$ by "extension" of its (4 × 4) group table by any of the additional operations $2_{\times}$, m_x, 2_z, or m_z (here by $2_{\times}$ as the fifth element), each leading to the same supergroup *mmm* of index $[i] = 2$. Both, group and supergroup, are commutative, because all group elements g_i are binary.

In a more subtle fashion, one can distinguish two kinds of point-group symmetries:

1. Symmetry in "vector space": symmetry of a set of vectors, for example, of the face normals of a crystal ("crystal form"), of the translation vectors of a crystal lattice, and of the interatomic vectors of a crystal structure (Patterson vectors). These symmetries are visualized best as vector bushels originating from a common origin.
2. Symmetry in "point space": symmetry of any finite polyhedron, of a molecule, or of an atomic group; symmetry around an arbitrary point in an infinite crystal structure ("site symmetry") or around a lattice node in an infinite point lattice ("lattice point group").

It should be noted that in many textbooks on crystals, two terms are in general use: "point group" as the symmetry of a particular crystal and "crystal class" as the set of all crystals with the same point- group symmetry. Both receive the same symbol. It is of interest that the 32 three-dimensional crystallographic point groups were derived already around 1830.

General and crystallographic point groups

Point groups can be subdivided into crystallographic and noncrystallographic point groups. Both together are called general point groups.

General point groups

A "general point group" is a group of rigid motions (symmetry operations, isometries) which all leave at least one point of space invariant.

This definition leads to infinitely many mono-axial point groups, because it admits infinitely many rotation groups with rotation angles $\varphi = 360°/n$ for all integer values of n. All these rotation groups are of finite order $N = n$. Furthermore, there are some point groups of order $N = \infty$, because they contain rotations (or rotoinversions) of order infinity, that is, rotations with all possible (including arbitrarily small) rotation angles. These rotation groups of infinite order are symbolized as ∞ and $\overline{\infty} = \infty/m$ in Hermann-Mauguin notation and as C_∞ and $C_{\infty h} = C_{\infty i} = S_\infty$ in Schoenflies notation. They appear as symmetry elements of cones, cylinders, circles, and spheres. For details see the "Further reading" section, especially Vol. A of the *International Tables*.

The condition "leave at least one point of space invariant" means that all symmetry elements of the group (axes, planes, and point) intersect at this one point, thus excluding any translations among the symmetry operations. Invariance of more than one point is of course possible, but always leads to infinitely many invariant points. Examples are all "monoaxial" groups n (one rotation axis only), which have an invariant line, and the reflection group m, which has an invariant plane. The intersection of several rotation axes in one point or the presence of a center of symmetry $\bar{1}$, leads to only one invariant point which represents the center of the object.

Crystallographic point groups

A "crystallographic point group" is a group of rigid motions which all leave at least one point of space invariant and, in addition, map a point lattice onto itself ("crystallographic restriction").

As described elsewhere in this encyclopedia, the crystallographic restriction (lattice condition) restricts the permissible rotation angles to multiples of 180°, 120°, 90°, and 60° (two-, three-, four-, and sixfold axes). This reduces the infinitely many point groups to 10 for two dimensions and to 32 for three dimensions. The highest group orders are $N = 12$ for two and $N = 48$ for three dimensions.

Among the 32 three-dimensional crystallographic point groups, there are 11 centrosymmetric groups (so-called Laue groups), which are important in X-ray diffraction, and seven lattice point symmetries (holohedries), defining the seven crystal systems. It should be noted that the 32 three-dimensional crystallographic point groups discussed below can be attributed to 18 isomorphism classes (abstract point groups). A classification of the crystallographic point groups with respect to physical properties is given in Table 5.

Among the three-dimensional noncrystallographic point groups there are the two icosahedral point groups, which contain 6 fivefold, 10 threefold, and 15 twofold rotation axes. They have recently received particular attention due to their occurrence in quasicrystals and fullerenes.

In modern crystallography, point groups in four, five, and six dimensions have been derived and are used for the treatment of incommensurate and quasicrystals. There are 271 point groups in four, 955 in five, and 7104 in six dimensions, with highest orders $N = 1152$, 3840, and 51,840, respectively.

Symbols of the 32 crystallographic point groups

The two systems of symbols for the crystallographic point groups are briefly reviewed here:

1. Schoenflies symbols, first presented in 1891 in Schoenflies' classical book, are based on capital letters for rotation groups C, D, S, T, O with subscripts s, h, v, d for mirror planes in various orientations, and subscript i for an inversion center. The noncrystallographic icosahedral and sphere groups are denoted by letters I_h and K_h (for German "Kugelgruppe").
2. The Hermann-Mauguin or international symbols are based on the "blickrichtungen" (symmetry directions) of the various lattices (holohedries), with specific numbers 2, 3, 4, 6 for symmetry axes, m for a mirror plane, and $\bar{1}$ for an inversion center. The Hermann-Mauguin symbols for the icosahedral and the sphere groups are $2/m\bar{3}\bar{5}$ (often written as $\bar{5}\bar{3}2/m$) and $2/m\bar{\infty}$ (often written as $\infty\infty m$).

Symbols and groups orders of the 32 three-dimensional crystallographic point groups, both in Schoenflies and Hermann-Mauguin notation, are illustrated in Fig. 1.

Description of point groups

A formal description of point groups is already given by their group tables, in the section "Brief review of groups" and in Tables 1–3 of this article.

Algebraically, the point groups are usually represented by matrix groups, that is, by the set of (3×3) matrices W of their point group operations (motions, isometries) with determinants +1 and −1 or, in a more condensed form, by either the N (contravariant) coordinates x, y, z, of the symmetrically equivalent points, or the N (covariant) Miller indices $\{hkl\}$ of the symmetrically equivalent faces of the "general face form" (crystal form). N is the order of the point group.

Example: point group $2_y/m_y$ (cf. subgroup in Table 3), consisting of $N = 4$ group elements 1, 2_y, m_y, $\bar{1}$:

1. coordinates of equivalent general points: x, y, z (1), $-x, y, -z$ (2_y), $x, -y, z$ (m_y), $-x, -y, -z$ $(\bar{1})$;
2. Miller indices of equivalent general faces: (hkl) (1), $((\bar{b}, k, \bar{l})$ (2_y), $(b\bar{k}l)$ (m_y), $(\bar{b}\bar{k}\bar{l})$ $(\bar{1})$.

A complete algebraic representation of the 10 two- and the 32 three-dimensional crystallographic point groups, as well as of the two icosahedral groups is given in Vol. A of the International Tables (cf. "Further reading" section).

Geometrically, a point group is normally represented by means of the stereographic projection of its "framework of symmetry," that is, the spatial assemblage of its symmetry elements (rotation axes, mirror planes, and center of symmetry).

Fig. 1 shows the stereographic projections of the symmetry frameworks of the 32 three-dimensional crystallographic point groups, as well as the two icosahedral groups. The graphical symbols of rotation and rotoinversion axes, mirror planes, and inversion centers are explained elsewhere in this encyclopedia.

The most frequent use of these stereographic projections in mineralogy and crystallography is the characterization of the crystal morphology by the normals of the crystal faces (face poles), leading to the face forms (crystal forms), that is, sets of symmetrically equivalent faces. Each point group (order N) has a "general" face form $\{hkl\}$ with N faces, each one of "face symmetry" 1, and up to six "special" face forms with N/q faces with "face symmetry" >1 of order q, for example, $\{hk0\}$, $\{111\}$, $\{100\}$. Example: the face form cube $\{1\ 0\ 0\}$ has six faces with "face symmetry" $4\,mm$ (order 8) in point group $4/m\,\bar{3}2/m$ (order $6 \times 8 = 48$).

Complete listings of all general and special face forms of the crystallographic point groups and the icosahedral groups are presented in Vol. A of the *International Tables* (see the "Further reading" section).

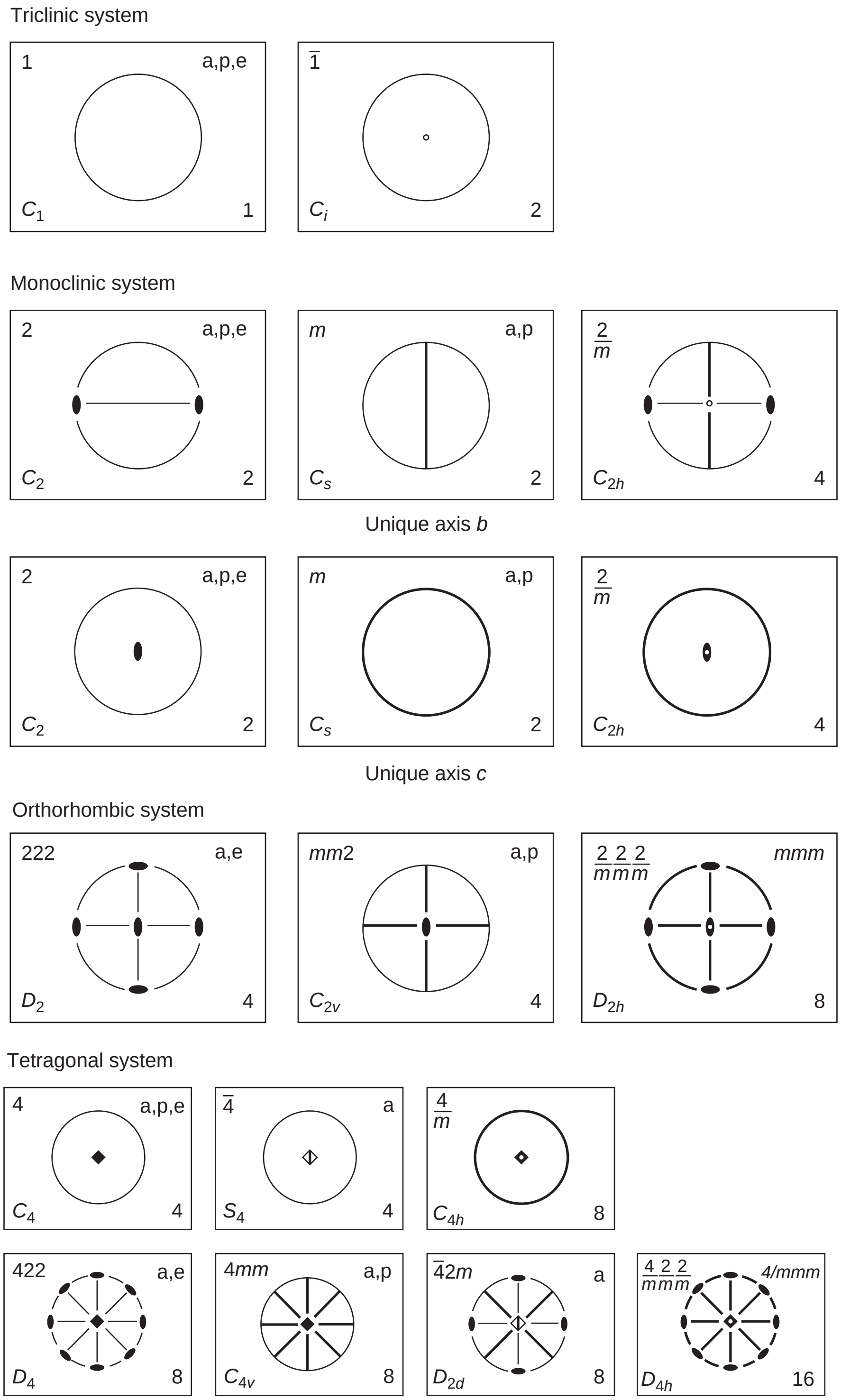
Triclinic system
1
a,p,e
C_1
1
$\bar{1}$
C_i
2
Monoclinic system
2
a,p,e
C_2
2
m
a,p
C_s
2
$\frac{2}{m}$
C_{2h}
4
Unique axis b
2
a,p,e
C_2
2
m
a,p
C_s
2
$\frac{2}{m}$
C_{2h}
4
Unique axis c
Orthorhombic system
222
a,e
D_2
4
mm2
a,p
C_{2v}
4
$\frac{2}{m}\frac{2}{m}\frac{2}{m}$
mmm
D_{2h}
8
Tetragonal system
4
a,p,e
C_4
4
$\bar{4}$
a
S_4
4
$\frac{4}{m}$
C_{4h}
8
422
a,e
D_4
8
4mm
a,p
C_{4v}
8
$\bar{4}2m$
a
D_{2d}
8
$\frac{4}{m}\frac{2}{m}\frac{2}{m}$
4/mmm
D_{4h}
16

Fig. 1 Stereographic projections of the symmetry elements of the 32 crystallographic point groups and the two icosahedral groups. Heavy solid lines or circles indicate mirror planes, thin lines are used for the projection circle and for auxiliary lines. Around each projection, the full (top left) and short (top right, if different) Hermann-Mauguin symbols, the Schoenflies symbol (bottom left) and the group order *N* (bottom right) are given. In the top right position the letters “a”, “p”, and “e” indicate that the point group is acentric (noncentrosymmetric), polar (pyroelectric) and enantiomorphic, respectively (cf. Table 5). No letter indicates a centrosymmetric point group. Reproduced with permission from Hahn Th and Klapper H (2002) *International Tables for Crystallography*, vol. A, *Space-Group Symmetry*, 5th edn. Dordrecht: Kluwer Academic; © International Union of Crystallography.

(Continued)

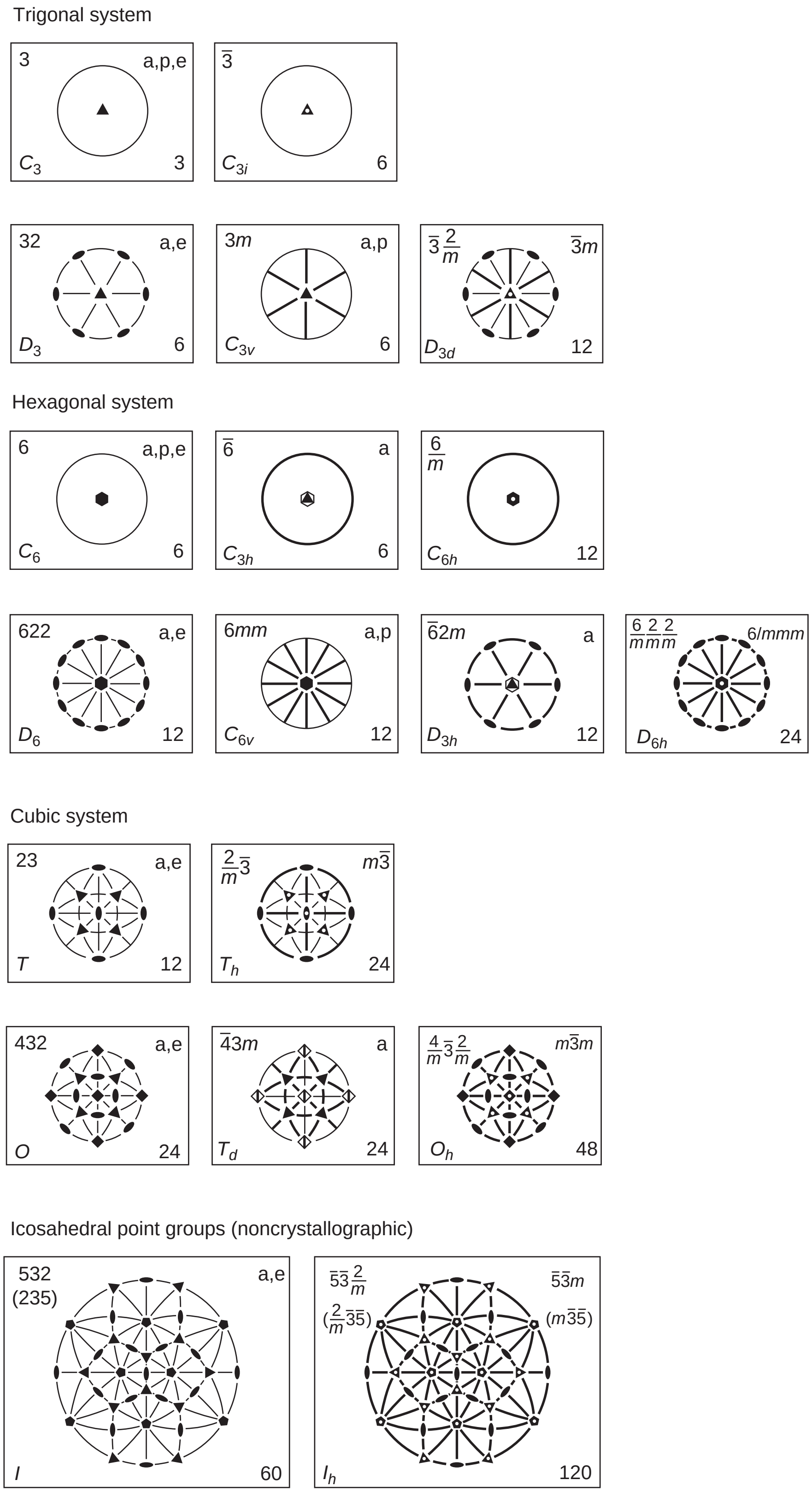
Trigonal system
3 a,p,e C_3 3
$\bar{3}$ C_{3i} 6
32 a,e D_3 6
3*m* a,p C_{3v} 6
$\bar{3}\frac{2}{m}$ $\bar{3}m$ D_{3d} 12
Hexagonal system
6 a,p,e C_6 6
$\bar{6}$ a C_{3h} 6
$\frac{6}{m}$ C_{6h} 12
622 a,e D_6 12
6*mm* a,p C_{6v} 12
$\bar{6}2m$ a D_{3h} 12
$\frac{6}{m}\frac{2}{m}\frac{2}{m}$ 6/*mmm* D_{6h} 24
Cubic system
23 a,e T 12
$\frac{2}{m}\bar{3}$ $m\bar{3}$ T_h 24
432 a,e O 24
$\bar{4}3m$ a T_d 24
$\frac{4}{m}\bar{3}\frac{2}{m}$ $m\bar{3}m$ O_h 48
Icosahedral point groups (noncrystallographic)
532 (235) a,e I 60
$\bar{5}\bar{3}\frac{2}{m}$ $(\frac{2}{m}\bar{3}\bar{5})$ $\bar{5}\bar{3}m$ $(m\bar{3}\bar{5})$ I_h 120

Fig. 1—cont'd

Subgroups of the crystallographic point groups

Group-subgroup relations, as defined in the first section, are of particular importance for physical phenomena such as phase transitions (symmetry breaking in the Landau theory), twinning, and domain structures. In solid-state chemistry, they are widely used for the classification of structural relations in families of related compounds (structure types).

Fig. 2 displays the sub- and supergroups of the two- and three-dimensional crystallographic point groups in the form of two "family trees." Each tree has two "summits": for two dimensions (Fig. 2A) the hexagonal holohedry 6 *mm* (order $N = 12$) and the

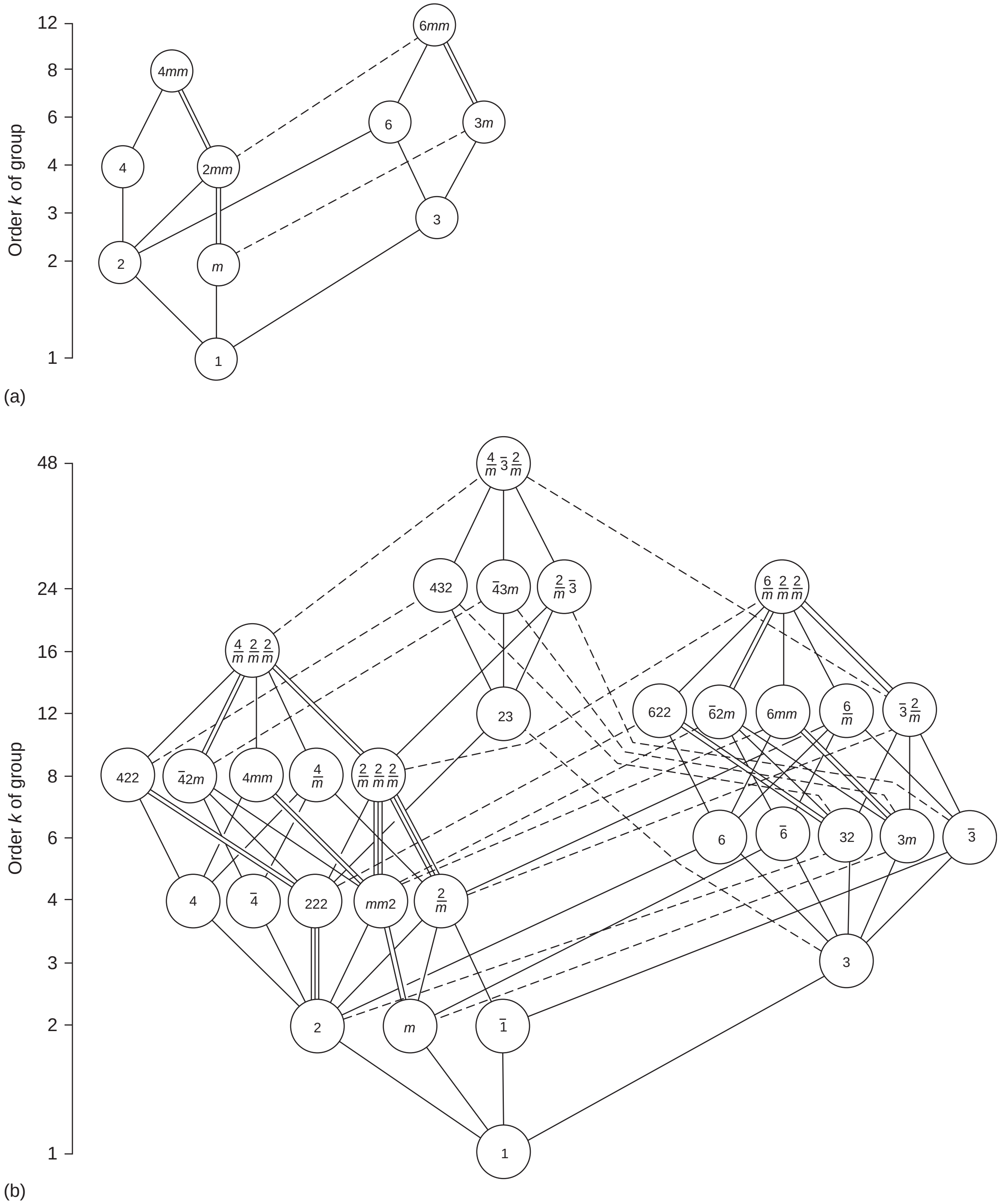
Order k of group
12
8
6
4
3
2
1
6mm
4mm
6
3m
4
2mm
3
2
m
1
(a)
Order k of group
48
24
16
12
8
6
4
3
2
1
$\frac{4}{m}\bar{3}\frac{2}{m}$
432
$\bar{4}3m$
$\frac{2}{m}\bar{3}$
$\frac{6}{m}\frac{2}{m}\frac{2}{m}$
$\frac{4}{m}\frac{2}{m}\frac{2}{m}$
23
622
$\bar{6}2m$
6mm
$\frac{6}{m}$
$\bar{3}\frac{2}{m}$
422
$\bar{4}2m$
4mm
$\frac{4}{m}$
$\frac{2}{m}\frac{2}{m}\frac{2}{m}$
6
$\bar{6}$
32
3m
$\bar{3}$
4
$\bar{4}$
222
mm2
$\frac{2}{m}$
3
2
m
$\bar{1}$
1
(b)

Fig. 2 Sub- and supergroup relations of the crystallographic point groups for (A) two and (B) three dimensions. The group orders *N* are given at the left margin of the diagrams. Solid lines refer to normal subgroups, dashed lines to sets of conjugate subgroups. Reproduced with permission from Hahn Th and Klapper H (2002) *International Tables for Crystallography*, vol. A, *Space-Group Symmetry*, 5th edn. Dordrecht: Kluwer Academic; International Union of Crystallography.

tetragonal holohedry $4\ mm$ ($N = 8$), for three dimensions (Fig. 2B) the cubic holohedry $4/m\bar{3}\,2/m$ ($N = 48$) and the hexagonal holohedry $6/m\ 2/m\ 2/m$ ($N = 24$). Their subgroups "mix" on the levels $N = 4$ (Fig. 2A) and $N = 12$ (Fig. 2B), where common subgroups of both branches appear first. Reading the diagrams downward, solid and dashed lines connect a point group G with all its maximal subgroups H. The subgroup index $[i]$ is given by the ratio of the group orders of G and $\mathcal{H} : [i] = N(\mathcal{G})/N(\mathcal{H})$. If the diagrams are read upward, the lines connect a point group H with all its minimal supergroups G, with supergroup index $[i] = N(\mathcal{G})/N(\mathcal{H})$. The index [i] is always an integer, according to the theorem of Lagrange.

In the diagrams, solid lines refer to normal subgroups, dashed lines to sets of conjugate subgroups. Two subgroups $\mathcal{H}_1$ and $\mathcal{H}_2$ are conjugate in G, if (at least) one symmetry operation g_j of G exists which maps $\mathcal{H}_1$ onto $\mathcal{H}_2 : g_j^{-1} \circ \mathcal{H}_\infty \circ g_j = \mathcal{H}_2$. Conjugate subgroups are "symmetrically equivalent" in G. If a subgroup H is equivalent only to itself (self-conjugate) and to no other subgroup, H is a normal (invariant) subgroup of G.

Example: the cubic point group $2/m\bar{3}$ (short: $m\bar{3}$) has six maximal subgroups. They are:

- two normal subgroups, one 23 (cubic) of index [2], and one $2/m2/m2/m$ (short: mmm, orthorhombic) of index [3];
- one set of four conjugate subgroups $\bar{3}$ (trigonal) of index [4]. They are symmetrically equivalent (conjugate) under the "lost" twofold rotations of $2/m\bar{3}$.

In three dimensions, [4] is the largest index of a maximal subgroup of a crystallographic point group. In two dimensions, it is [3]. Note that orthorhombic $2/m2/m2/m$ has three normal (nonconjugate) subgroups of the same type, $mm2$, $m2m$, and $2\ mm$, whereas the cubic point group 23 has four conjugate (symmetrically equivalent) subgroups of type 3.

When a crystal of symmetry G undergoes a (displacive) phase transition to a lower point group symmetry H, it splits into (twin) domains which are related by the lost symmetry operations of G. The number of domain states (orientation states) equals the subgroup index $[i] = N(\mathcal{G})/N(\mathcal{H})$.

Examples

1. Quartz (SiO_2) possesses the point group 32 of order $N = 6$ at room temperature. Upon heating above $T_c = 573\ °C$, it transforms into "high-quartz" with point group 622 and order 12. Upon cooling back below T_c, it loses the twofold axis 2 (contained in the hexagonal axis 6) and returns to "low-quartz" with symmetry 32, whereby it splits into domains of $[i] = 2$ orientation states ("Dauphine twin"). This is an example of a nonferroelastic transition and merohedral twinning.
2. Barium titanate ($BaTiO_3$) (and other perovskite compounds) undergoes, by cooling below 1251C, a ferroelastic and ferroelectric cubic-to-tetragonal phase transition from point group $4/m\bar{3}\,2/m$ (order 48) to $4\ mm$ (order 8) of index $[i] = 6$. This one-step transformation can be rationalized as a succession of two maximal-subgroup steps:
   (a) Reduction from $4/m\bar{3}\,2/m$ to $4/m2/m2/m$ (order 16), both centrosymmetric, with subgroup index [3]. This leads to a set of three conjugate tetragonal subgroups with their tetragonal axes oriented along the former three fourfold cube axes as well as to three ferroelastic 90° domain states.
   (b) Further reduction of each of the three conjugate $4/m2/m2/m$ subgroups to its normal subgroup $4\ mm$ of index [2], leading to two antiparallel ferroelectric domain states (180° domains).

The total index of both transition steps is $[3] \times [2] = [6]$. As a result, six different "orientation states" (domain states) are generated: three ferroelastic 90° domain states (pseudo-merohedral twins) [due to step (1)], each one being further split into two ferroelectric 180° domain states (merohedral inversion twins) [result of step (2)].

Symmetry of physical properties

Definition of tensor symmetry

Physical properties of crystals are strongly governed by symmetry. This holds in particular for the (nonscalar) anisotropic properties described by tensors, and for nontensorial properties such as cleavage and plasticity for which a comprehensive mathematical treatment does not exist. The components of the tensors describing crystal properties are usually referred to a Cartesian coordinate system, that is, three orthogonal axes X_1, X_2, X_3 with equal unit lengths.

Whereas the anisotropic properties themselves are independent of the choice of the coordinate system, their representation by tensors is not, that is, the tensor components change if the coordinate system is transformed. As a consequence, the symmetry of a physical property can be defined in two alternative, but equivalent ways:

1. a rigid motion (rotation, reflection, and inversion), represented by a unitary matrix W ($\det W = \pm 1$), is applied to the crystal, whereby the coordinate system is kept stationary. All motions, for which the tensor components of the transformed crystal are unchanged, are symmetry operations of the tensor property P;
2. alternatively, an arbitrary motion W is applied to the coordinate system with the crystal kept stationary. All motions, for which the tensor components are unchanged under the coordinate transformations W, are symmetry operations of the tensor property P. In both cases the rotation matrices are inverse to each other.

As a consequence of this invariance, some of the tensor components are equal or even zero. The number of independent components is decreased when the symmetry of the crystal increases. Thus, an increase of the point-group symmetry from 1 (triclinic) to $4/m\bar{3}\,2/m$ (cubic) or to the sphere group $\infty\infty m$ (i.e., isotropy) reduces the number of tensor components for symmetrical second-rank tensors from 6 to 1, and for double-symmetrical fourth-rank tensors (e.g., elasticity) from 21 to 3 (cubic) and 2 (isotropy). Even more drastic is this reduction for all tensors of odd rank (such as pyroelectricity and piezoelectricity): all components are zero if an inversion center is present, that is, properties described by odd-rank tensors do not exist in centrosymmetric crystals. This is further elucidated below.

Neumann's principle

A useful group-subgroup relation between physical and crystallographic symmetries is provided by "Neumann's principle" (first stated in 1833). It states that the symmetry of all physical properties of a crystal is higher than (or at least equal to) its crystallographic point-group symmetry, or in the language of groups: the crystallographic symmetry G is a proper or improper subgroup of any physical symmetry $\mathcal{P}, \mathcal{G} \subseteq \mathcal{P}$. This is illustrated in Table 4 for second-rank tensors which are, as all even-rank tensors, centrosymmetric. Their symmetries can be recognized by their representation surfaces, which are always ellipsoids or hyperboloids. The symmetry of a general ellipsoid or hyperboloid is $2/m\ 2/m\ 2/m$, but it degenerates to cylindrical and spherical symmetries with point groups $\infty/m\ 2/m$ ($\overline{\infty}\ 2/m$) and $\infty\ \infty\ m$ ($2/m\ \overline{\infty}$) for uniaxial (i.e., tetragonal, trigonal, hexagonal) and cubic crystals. It is obvious that in all cases the crystallographic symmetry is a proper subgroup of the "physical symmetry," except for the orthorhombic holohedry, for which they are identical. Note that all point groups within the same crystal system (e.g., orthorhombic 222, $mm2$, $2/m2/m2/m$) exhibit the same second-rank tensor symmetry.

In column 5 the terms "biaxial" and "uniaxial" refer to the number of "optical axes", i e., of circular sections through the index ellipsoid. For uniaxial crystals, the rotation axis of the tensor surface coincides with the main crystallographic symmetry axis. For orthorhombic crystals, the three principal tensor axes and the crystallographic symmetry axes are parallel. For monoclinic crystals, one principal tensor axis is fixed by symmetry; it is parallel to the monoclinic symmetry axis. For triclinic crystals, none of the principal tensor axes is fixed by symmetry, allowing their "orientation dispersion", e.g., with temperature.

The more the physical symmetry approximates the crystallographic symmetry, the higher the rank of its tensor. For example, in cubic crystals tensor properties of second rank are isotropic, whereas fourth rank tensors (e.g., linear elasticity) are not isotropic; they exhibit cubic crystallographic symmetry. For hexagonal crystals, on the other hand, the sixfold axis is still a continuous rotation axis also for fourth rank tensors.

Tensors of odd rank

Physical properties represented by odd-rank tensors are of particular importance for technological applications. Pyroelectricity and piezoelectricity under hydrostatic pressure are properties of first rank, represented by maximally three independent coefficients (i.e., by a vector). Important third-rank properties are piezoelectricity (under general stress), optical second-harmonic generation, and linear electrooptics. Odd-rank tensors are subject to strong constraints by symmetry, in particular by an inversion center which renders all tensor components zero, that is, properties of odd rank do not exist in centrosymmetric crystals.

Pyroelectricity and ferroelectricity

Pyroelectricity originates from a permanent electric dipole moment of the unit cell of the crystal structure or, in macroscopic terms, from an intrinsic ("spontaneous") electrical polarization. This polarization is changed by heating and cooling, thus giving rise to electric charges on certain crystal faces.

In a crystal, a spontaneous polarization can be present only along a polar direction which has no symmetrically equivalent directions. (In the literature, the condition for the occurrence of pyroelectricity is frequently expressed as "a unique (or singular) polar axis." This term, however, is misleading for point groups m and 1.) Such polar directions occur in the following

Table 4 Symmetry of second-rank polar tensor properties and optical birefringence (refractive-index ellipsoids) in the seven crystal systems.

Crystal system	*Holohedry*	*Type of ellipsoid or hyperboloid*	*Symmetry of tensor property*	*Optical birefringence (index ellipsoid)*
Triclinic	$\bar{1}$	General	$2/m\ 2/m\ 2/m$	Biaxial
Monoclinic	$2/m$	General	$2/m\ 2/m\ 2/m$	Biaxial
Orthorhombic	$2/m\ 2/m\ 2/m$	General	$2/m\ 2/m\ 2/m$	Biaxial
Tetragonal	$4/m\ 2/m\ 2/m$	Rotational	$N/m\ 2/m$	Uniaxial
Trigonal	$\bar{3}\ 2/m$	Rotational	$N/m\ 2/m$	Uniaxial
Hexagonal	$6/m\ 2/m\ 2/m$	Rotational	$N/m\ 2/m$	Uniaxial
Cubic	$4/m\ \bar{3}\ 2/m$	Spherical	$\infty\infty m\ (2/m\overline{\infty})$	Isotropic

Table 5 The 21 noncentrosymmetric crystallographic point groups (crystal classes) and the occurrence (+) of specific crystal properties.

Crystal system	*Noncentrosymmetric point group*	*First-rank tensor (e.g., pyroelectricity)*	*Third-rank tensor (e.g., piezoelectricity)*	*Enantiomorphism*	*Optical activity (opt. gyration)*
Triclinic	1	+ (3) [*uvw*]	+ (18)	+	+ (6)
Monoclinic	2	+ (1) [010][a]	+ (8)	+	+ (4)
	m	+ (2) [*u*0*w*][a]	+ (10)	–	+ (2)
Orthorhombic	222	–	+ (3)	+	+ (3)
	*mm*2	+ (1) [001]	+ (5)	–	+ (1)
Tetragonal	4	+ (1) [0 0 1]	+ (4)	+	+ (2)
	$\bar{4}$	–	+ (4)	–	+ (2)
	422	–	+ (1)	+	+ (2)
	4 *mm*	+ (1) [0 0 1]	+ (3)	–	–
	$\bar{4}\,2\,m$	–	+ (2)	–	+ (1)
Trigonal	3	+ (1) [0 0 1][b]	+ (6)	+	+ (2)
	32	–	+ (2)	+	+ (2)
	3 *m*	+ (1) [0 0 1][b]	+ (4)	–	–
Hexagonal	6	+ (1) [0 0 1]	+ (4)	+	+ (2)
	$\bar{6}$	–	+ (2)	–	–
	622	–	+ (1)	+	+ (2)
	6 *mm*	+ (1) [0 0 1]	+ (3)	–	–
	$\bar{6}\,2\,m$	–	+ (1)	–	–
Cubic	23	–	+ (1)	+	+ (1)
	432	–	–	+	+ (1)
	$\bar{4}\,3\,m$	–	+ (1)	–	–
Icosahedral	532 (235)	–	–	+	+ (1)
Spherical	∞ ∞ (2 ∞)	–	–	+	+ (1)

The number of nonzero independent tensor components is given in parentheses. For comparison, the noncentrosymmetric icosahedral and the sphere group (isotropy) are added. For first-rank tensors the direction [*uvw*] of the property vector is given. There are 10 pyroelectric, 20 piezoelectric, 11 enantiomorphic and 15 optically active crystal classes.

[a] Unique axis *b*.

[b] Hexagonal axis.

10 (“pyroelectric”) point groups: 6, 4, 3, 2, 1, and their combination with a “parallel” mirror plane: 6 *mm*, 4 *mm*, 3 *m*, *mm*2, *m* (Table 5). In point groups with a rotation axis, the electric polarization (“pyroelectric vector” p) is fixed parallel to this polar axis. For point group *m*, the pyroelectric vector p is oriented parallel to the mirror plane, and for point group 1 any direction of p is possible.

A polar crystal is ferroelectric if the direction of the spontaneous polarization can be reversed (“switched”) by an electric field, leading to a hysteresis behavior. Thus, ferroelectricity can only occur in the 10 pyroelectric point groups.

Piezoelectricity

Among the third-rank property tensors, piezoelectricity and its converse effect, the piezoelectric strain (“linear electrostriction”), are the most important properties for technological applications (pressure sensors, resonators, etc.). Well-known examples are single crystals of quartz (SiO_2) and textured (“poled”) ceramics of barium titanate ($BaTiO_3$). Of similar significance are, nowadays, the third-rank tensors of optical second-harmonic generation (for optical frequency doubling, for example, potassium dihydrogen phosphate, KDP) and of linear electrooptics (Pockels effect) (for light modulation, e.g., KDP).

Third-rank properties occur in all noncentrosy-metric crystal classes, except for the cubic class 432, where the combination of three perpendicular equivalent fourfold axes causes all tensor components to vanish. The combination of three equivalent twofold axes, present in the two cubic classes 23 and $\bar{4}3m$, however, still admits one independent nonzero component. The tensor is the same for both classes and exhibits the symmetry $\bar{4}3m$ (Table 5).

Piezoelectricity under hydrostatic pressure is possible only in the 10 pyroelectric crystal classes (see Table 5). An example for use of this effect for pressure sensors (e.g., formerly for submarines) is provided by $Li_2SO_4 \cdot H_2O$ (point group 2) single crystals.

Enantiomorphism and optical activity (optical gyration)

Enantiomorphism is a qualitative property stating that an object (molecule, crystal) may have a right- and a left-handed (“mirror image”) form or structure. This feature requires the absence of any “hand-changing” operation ($\det W = -1$), such as a reflection or roto-inversion (including the inversion 1). Thus, only the 11 non-centrosymmetric crystal classes containing only proper rotations

($\det W = +1$) allow enantiomorphism (Table 5). Enantiomorphism, of course, is also possible in noncrystallographic symmetry groups without mirror planes and rotoinversion axes.

Optical gyration is described by a second-rank tensor, but in contrast to the polar tensors of second rank shown in Table 4, it has an axial character, that is, it exhibits the features of a screw. Thus, the components of the axial gyration tensor change their signs if the handedness of the coordinate system is changed from right to left, and vice versa. Consequently, the invariance condition for tensor components g_{ij} under symmetry transformations, as described in the section "Definition of tensor symmetry" for polar tensors, has to be modified as follows: for all "hand-changing" symmetry operations W (i.e., $\det W = -1$), the transformed components $\tilde{g}_{ij}$ must equal their negative counterparts: $\tilde{g}_{ij} = (-1)g_{ij}$. From this, it follows directly that optical activity is forbidden in all centro-symmetric crystal classes. For proper rotations which preserve the handedness, a change of sign does not occur. Thus, all symmetry groups allowing enantiomorphism also permit optical activity. Crystals belonging to one of the enantiomorphic crystal classes may occur in two forms, either left- or right-handed, which exhibit opposite senses of rotation of the plane of polarization. A well-known example is provided by quartz SiO_2 (enantiomorphic crystal class 32), which crystallizes in a right- and a left-hand form with opposite senses of optical activity.

In addition to the 11 enantiomorphic crystal classes, there are four nonenantiomorphic classes exhibiting optical activity: m, $mm2$, $\bar{4}$, $\bar{4}2m$. In these cases, optical activity does not occur for all directions of light propagation, viz. not those parallel to the $\bar{4}$ axis and parallel or normal to the mirror plane m. All other propagation directions exhibit activity, whereby directions symmetrical with respect to $\bar{4}$ and m show opposite rotation senses. Thus, the four symmetry groups above show both (right and left) rotation senses in one and the same crystal.

The optical activity is isotropic in cubic crystals, as it is in optically active liquids (e.g., in solutions of dextro- or levo-sugar). In this case, the symmetry of the optical activity is described by the noncentro- symmetric sphere group $\infty\,\infty$ ($2\,\infty$). Geometrically, this symmetry group can be represented by a (right- or left-hand) rotating sphere or by a sphere which is densely covered with either right- or left-hand swirls.

Curie's principle

Until now the symmetry group G_P of physical properties of a "free" macroscopic crystal C with point group G_C was discussed. Now, the symmetry G_{CF} of a crystal C which is subject to an external influence F, for example, to an electric field, to uniaxial stress, to temperature changes, etc., is considered. For this treatment, point-group symmetries G_F of the external influences (Curie groups) are defined as follows:

1. Homogeneous electric field $\boldsymbol{E}$: ∞m (polar continuous rotation axis with "parallel" mirror planes, that is, symmetry of a stationary cone). Note that a rotating cone (left- or right-hand) represents geometrically the polar enantiomorphous group ∞; a stationary cone represents the polar group ∞m with "vertical" mirror planes.
2. Homogeneous magnetic field $\boldsymbol{H}$: ∞/m (symmetry of a rotating cylinder).
3. Uniaxial stress σ_{ii}: $\infty/m\ 2/m$ (symmetry of a stationary centrosymmetric cylinder).
4. Temperature change $\boldsymbol{\Delta}T$ or hydrostatic pressure $-\sigma$ (scalars): $\infty\,\infty\,m$ (symmetry of a stationary centrosymmetric sphere).
5. Shear stress σ_{ii}: $2/m\ 2/m\ 2/m$ (orthorhombic).

According to Curie's principle of 1894, the point- group symmetry G_{CF} of the crystal under the external field is the intersection symmetry of the symmetry G_C of the crystal without field and the symmetry G_F of the field without crystal: $\mathcal{G}_{CF} = \mathcal{G}_C \cap \mathcal{G}_F$; that is, G_{CF} is a (proper or improper) subgroup of both groups G_C and G_F.

As examples, consider the effect of an electric field ($\mathcal{G}_F = \infty$m) and a uniaxial stress ($\mathcal{G}_F = \infty/m\ 2/m$) along one of the (four) threefold rotoinversion axes 3 of cubic crystals with point groups $\mathcal{G}_C = 2/m\bar{3}$ and $\mathcal{G}_C = 4/m\bar{3}\ 2/m$

- Electric field parallel [1 1 1]:

$$2/m\bar{3} \cap \infty m:$$

$\mathcal{G}_{CF} = 3$ along [1 1 1]
(pyroelectric; optically active)

$$4/m\bar{3}\ 2/m \cap \infty m:$$

$\mathcal{G}_{CF} = 3m$ along [1 1 1]
(pyroelectric)

- Uniaxial stress parallel [1 1 1]:

$$2/m\overline{3} \cap \infty/m\ 2/m:$$

$\mathcal{G}_{CF} = \overline{3}$ along [1 1 1]

$$4/m\overline{3}\ 2/m \cap \infty/m\ 2/m:$$

$\mathcal{G}_{CF} = \overline{3}2/m$ along [1 1 1]

Note that, in contrast to uniaxial stress, the electric field destroys centrosymmetry, leading to pyroelectricity and even optical gyration. The polarity and the gyration sense are reversed upon reversal of the electric field. If the electric field and the uniaxial stress were applied to an arbitrary (nonsymmetry) direction of the above cubic crystals, point groups 1 and $\overline{1}$ would result in the two cases.

If a scalar influence, which is represented by the centrosymmetric sphere group G_E, for example, a temperature change $\mathbf{\Delta}T$, is applied to a crystal, its symmetry is not changed, $G_{CF} = G_C$, provided that no phase transition is induced. For further reading on the symmetry of physical properties, refer to the "Further reading" section.

Further reading

Authier A (ed.) (2003) International Tables for Crystallography. In: *Physical Properties of Crystals*, vol. D. Dordrecht: Kluwer Academic.

Bloss ED (1971) *Crystallography and Crystal Chemistry*. New York: Holt, Rinehart and Winston.

Buerger MJ (1965) *Elementary Crystallography*. New York: Wiley.

Buerger MJ (1971) *Introduction to Crystal Geometry*. New York: McGraw-Hill.

Hahn T and Klapper H (2002) Point groups and crystal classes. In: Th H (ed.) *International Tables for Crystallography. Space-Group Symmetry*, 5th edn, vol. A. Dordrecht: Kluwer Academic.

Kleber W, Bautsch HJ, Bohm J, and Kleber I (1990) *Einführung in die Kristallographie*, 17th, 18th edn, p. 1998. Berlin: Verlag Technik. now München: Oldenbourg.

Ledermann W (1976) *Introduction to Group Theory*. London: Longman.

McKie D and McKie C (1986) *Essentials of Crystallography*. Oxford: Blackwell.

Nye JF (1957) *Physical Properties of Crystals. Their Representation by Tensors and Matrices*, 1st edn. Oxford: Clarendon Press. Revised Edition 1985.

Paufler P (1986) *Physikalische Kristallographie*. Berlin: Akademie-Verlag and Weinheim: Verlag Chemie (VCH).

Philips FC (1971) *An Introduction to Crystallography*, 4th edn. London: Longman.

Schwarzenbach D (1996) *Crystallography*. Chicester: Wiley (original French edition 1996, German edition 2001).

Shuvalov LA (ed.) (1988) Modern Crystallography. In: *Physical Properties of Crystals*, vol. 4. Berlin: Springer.

Vainstein BK (1994) Modern Crystallography. *Fundamentals of Crystals. Symmetry and Methods of Structural Crystallography*, 2nd edn, vol. 1. Berlin: Springer.

Space Groups

T Janssen, University of Nijmegen, Nijmegen, The Netherlands

© 2005 Elsevier Ltd. All rights reserved.

This is an update of T. Janssen, Space Groups, Editor(s): Franco Bassani, Gerald L. Liedl, Peter Wyder, Encyclopedia of Condensed Matter Physics, Elsevier, 2005, Pages 1–8, ISBN 9780123694010, https://doi.org/10.1016/B0-12-369401-9/00423-X.

Introduction 61
Lattice Periodicity 61
Distance-Preserving Transformations 62
Space Groups, Plane Groups, Higher Dimensions 63
The Structure of a Space Group 63
Space Group Elements 64
Classification 64
Notation 65
Reciprocal Lattice, Invariant Functions, Extinction Rules 66
Representations of Space Groups 67
Aperiodic Crystals 68
Further Reading 68

Nomenclature

$\boldsymbol{a}, \boldsymbol{b}, \boldsymbol{c}$	lattice basis vectors
$\mathbf{a}^*\mathbf{b}^*\mathbf{c}^*$	reciprocal lattice basis vectors
A	translation subgroup of a space group
$D(R)$	matrix representation
$\exp(-i\boldsymbol{k}\cdot\boldsymbol{r})U(\boldsymbol{r})$	Bloch form of a wave function
$E(3)$	Euclidean group
$F(\boldsymbol{k})$	structure factor
G	space group
K	point group
$\boldsymbol{n}$	lattice translation vector
$O(3)$	orthogonal group in three dimensions
$\boldsymbol{r}_j$	position of an atom in the unit cell
R	orthogonal transformation
$\{R\|\boldsymbol{t}\}$	space group element
T_g	linear operator for group element g:
$\hat{\boldsymbol{\rho}}(\boldsymbol{k})$	Fourier component of $\rho(\boldsymbol{r})$
$\boldsymbol{\rho}(\boldsymbol{r})$	density function
$\boldsymbol{\psi}_i$	basis of a state space
$\boldsymbol{\psi}(\boldsymbol{r})$	wave function

Introduction

For the description or the study of properties of physical systems, symmetry is of paramount importance. The symmetry groups of crystals are the so-called space groups. Other symmetry operations, such as time reversal, are sometimes also relevant, but the most important operations are the elements of the space groups. Space group symmetry is a generalization of the property that crystals are, usually, periodic in three dimensions. This article deals with the periodicity, the other symmetry operations of crystals, the classification of the space groups, and, what is of greater relevance for the physical properties, their representations.

Lattice Periodicity

Ideally, the most common crystals consist of a periodic array of identical building blocks repeated in all three directions. There are other types of crystals also, but a discussion of these will be taken up at the end of this section. Real crystals always have shortcomings in their periodic order; they are finite, which implies that there is a limit to the periodicity. Repetition means that one may go from one block into another by a translation. Such a translation is given by a vector $\boldsymbol{n}$. All vectors of the translations form a lattice. That means there are three fundamental translations, with vectors $\boldsymbol{a}$, $\boldsymbol{b}$, and $\boldsymbol{c}$, such that each lattice translation $\boldsymbol{n}$ is a linear combination of these three with integer coefficients, and each such combination transforms a building block into another:

$$\boldsymbol{n} = n_1\boldsymbol{a} + n_2\boldsymbol{b} + n_3\boldsymbol{c}, \text{with integers} \quad n_1, n_2, n_3 \tag{1}$$

The building blocks do not have an overlap, and there are no gaps between them. Each building block consists of an arrangement of atoms or molecules. It is called a unit cell. The whole structure then remains the same if it is shifted by any of the translations of the lattice. Suppose that there are N atoms in the building block at positions $\boldsymbol{r}_1, \ldots, \boldsymbol{r}_N$. Then the position of an arbitrary atom of the crystal is given by the expression

$$\boldsymbol{r}_{\boldsymbol{n},j} = \boldsymbol{r}_j + n_1\boldsymbol{a} + n_2\boldsymbol{b} + n_3\boldsymbol{c} \tag{2}$$

for specific values of j, n_1, n_2, and n_3. The vectors $\boldsymbol{r}_j$ may be chosen inside the unit cell. The vectors $\boldsymbol{a}$, $\boldsymbol{b}$, and $\boldsymbol{c}$ are the basis vectors.

Because the building blocks are repeated in all directions, the three fundamental vectors are independent, which also means that every point in space can be reached from a fixed point by a linear combination, not necessarily with integer coefficients. In general, the coefficients are real numbers. In particular, the position of an arbitrary atom with respect to a chosen origin can be written as

$$\boldsymbol{r}_{\boldsymbol{n},j} = (n_1 + \xi_1)\boldsymbol{a} + (n_2 + \xi_2)\boldsymbol{b} + (n_3 + \xi_3)\boldsymbol{c} \tag{3}$$

Here $(n_1+\xi_1)$, etc., are real numbers. For example, for CsCl, the three basis vectors are in Cartesian coordinates $(a, 0, 0)$, $(0, a, 0)$, and $(0, 0, a)$. There is a Cs atom at $\boldsymbol{r}_1=(0, 0, 0)$ and a Cl atom at $\boldsymbol{r}_2=(a/2, a/2, a/2)$. With respect to the lattice basis, the Cl coordinates are $\xi_1 = \xi_2 = \xi_3 = 1/2$. The unit cell is a cube.

Distance-Preserving Transformations

Physical laws remain the same if positions are transformed into newer positions with the same distances. Therefore, such distance-preserving transformations are important for physics. Among them are translations, where all positions are shifted by the same translation vector. In addition, rotations around an arbitrary point and the full reflection of all points through an arbitrary point leave the distances invariant. Let O be an arbitrary point in space. Then the orthogonal group consists of all rotations leaving this point invariant and all products of such a rotation with the reflection through O. The group of three-dimensional orthogonal transformations is denoted by $O(3)_O$. Choosing O as origin and a basis of space consisting of three basis vectors $\boldsymbol{e}_1$, $\boldsymbol{e}_2$, $\boldsymbol{e}_3$, an orthogonal transformation R corresponds to a matrix via

$$R\boldsymbol{e}_i = \sum_{j=1}^{3} R_{ji}\boldsymbol{e}_j \ (i = 1, 2, 3) \tag{4}$$

For a special choice of the basis, namely, with three mutually perpendicular vectors of the same length, the matrices satisfy $\sum j R_{ij}R_{kj}=\delta_{ik}$ or $RR^{\mathrm{T}} = E$, where T indicates the transpose, and E the unit matrix. Such matrices are called orthogonal. Their determinant is either +1 (for rotations) or −1. If one chooses another origin, the orthogonal group around that point gives the same group of matrices, which can then be indicated by $O(3)$.

All distance-preserving transformations can be obtained as a combination of a translation and an orthogonal transformation around an origin O. The effect on a point $\boldsymbol{r}$ of an orthogonal transformation R together with a translation $\boldsymbol{t}$ is

$$\{R|\boldsymbol{t}\}\boldsymbol{r} = R\boldsymbol{r} + \boldsymbol{t} \tag{5}$$

All these transformations again form a group, the Euclidean group $E(3)$. Its elements are called Euclidean transformations. The product of two such transformations then is the subsequent execution of the two:

$$\begin{aligned}\{R_1|\boldsymbol{t}_1\}\{R_2|\boldsymbol{t}_2\}\boldsymbol{r} &= \{R_1|\boldsymbol{t}_1\}(R_2\boldsymbol{r} + \boldsymbol{t}_2) \\ &= R_1R_2\boldsymbol{r} + R_1\boldsymbol{t}_2 + \boldsymbol{t}_1\end{aligned} \tag{6}$$

from which it follows that

$$\{R_1|\boldsymbol{t}_1\}\{R_2|\boldsymbol{t}_2\} = \{R_1R_2|\boldsymbol{t}_1 + R_1\boldsymbol{t}_2\} \tag{7}$$

In particular, $\{R|\boldsymbol{t}\}=\{E|\boldsymbol{t}\}\{R|\boldsymbol{0}\}$ and $\{R|\boldsymbol{t}\}^{-1}=\{R^{-1}|-R^{-1}\boldsymbol{t}\}$.

A rotation R from $O(3)_O$ leaves the point O invariant. A translation $\boldsymbol{u}$ transfers O to $O+\boldsymbol{u}$ and this point is left invariant by $\{E|\boldsymbol{u}\}\{R|\boldsymbol{0}\}\{E|-\boldsymbol{u}\}$. This means that, the product $\{R|\boldsymbol{u}-R\boldsymbol{u}\}$ belongs to the orthogonal group $O(3)_{O+\boldsymbol{u}}$. In other words, the translation part $\boldsymbol{t}$ of a space group element $\{R|\boldsymbol{t}\}$ may be changed by an origin shift $\boldsymbol{u}$ according to

$$\boldsymbol{t} = \boldsymbol{t} + (E - R)\boldsymbol{u} \tag{8}$$

The combination of a translation and a rotation around O is then the same as a combination of another translation and a rotation around $O+\boldsymbol{u}$ (see Figure 1).

There is a simple matrix formulation for the action of a Euclidean transformation on a point $\boldsymbol{r}$ with coordinates x, y, and z:

$$\{R|\boldsymbol{t}\}\begin{pmatrix} x \\ y \\ z \\ 1 \end{pmatrix} = \begin{pmatrix} R_{11} & R_{12} & R_{13} & t_1 \\ R_{21} & R_{22} & R_{23} & t_2 \\ R_{31} & R_{32} & R_{33} & t_3 \\ 0 & 0 & 0 & 1 \end{pmatrix}\begin{pmatrix} x \\ y \\ z \\ 1 \end{pmatrix} \tag{9}$$

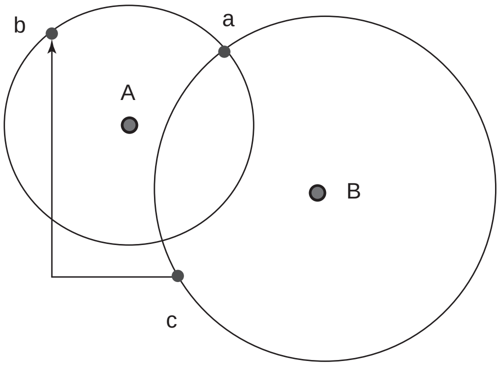

Figure 1 The 90° rotation around A brings a to b, a 90° rotation around B plus a translation brings a via c to b.

Space Groups, Plane Groups, Higher Dimensions

A collection of atoms which is invariant under the translations of a three-dimensional lattice is, in general, invariant under still more Euclidean transformations. A space group is a group of Euclidean transformations that has a translation subgroup as a lattice group, with three linearly independent basis vectors. If $\{E|\boldsymbol{a}\}$ is a translation from the translation subgroup, and $\{R|\boldsymbol{t}\}$ an arbitrary element of the space group, then the following relation holds:

$$\{R|\boldsymbol{t}\}\{E|\boldsymbol{a}\}\{R|\boldsymbol{t}\}^{-1} = \{E|R\boldsymbol{a}\} \qquad [10]$$

The first consequence is that the translation subgroup is an invariant subgroup. (A subgroup A of a group G is invariant if, for each element a of A and each g from G, the element gag^{-1} is an element of A.) Because $\{E|R\boldsymbol{a}\}$ is a translation, and therefore an element of the translation subgroup, $R\boldsymbol{a}$ belongs to the lattice. Consequently, the lattice is invariant under R, and because all R's form a subgroup of $O(3)$, this is a crystallographic point group, one of the 32 point groups. The Euclidean transformations leaving the CsCl structure invariant are the 48 elements of the cubic point group, combined with the lattice translations of the cubic lattice.

A plane group is a subgroup of the Euclidean group in two dimensions having as translation subgroup a two-dimensional lattice group. The elements R now form one of the 10 two-dimensional crystallographic point groups. The generalization to space groups in arbitrary dimensions then is straightforward. Such a group in arbitrary dimensions (including two) is also called a space group.

The Structure of a Space Group

The translation subgroup A of a space group G is invariant. (It is also called a normal subgroup.) The orthogonal transformations R appearing in the elements $\{R|\boldsymbol{t}\}$ form a three-dimensional crystallographic point group K. All the elements of K can now be numbered: $R_1{=}E, R_2,\ldots, R_N$. All elements $\{R_i|\boldsymbol{t}\}$ in G form a set S_i for fixed i. One can multiply two such sets: the product S_iS_j is the set S_k if $R_iR_j{=}R_k$. In this way, the sets S_i form a group, which is in fact identical to the group of all elements R_i, that is, the point group K. The group of sets S_i is called the factor group, and it is identical to (more precisely isomorphic to) the point group K. So, the space group G has an invariant subgroup A and the factor group G/A is isomorphic to the point group K.

From each set S_i, one may choose an element $\{R_i|\boldsymbol{t}_i\}$. Then, every other element from S_i may be written as the product of the representative $\{R_i|\boldsymbol{t}_i\}$ and a lattice translation $\{E|\boldsymbol{a}\}$. Of course, one could have chosen another representative element $\{R_i|\boldsymbol{t'}_i\}$. Then the two translations $\boldsymbol{t}_i$ and $\boldsymbol{t}_i'$ differ by a translation $\boldsymbol{a}$ from the lattice. The translations $\boldsymbol{t}_i$ are not necessarily lattice vectors, and they are determined by R_i only up to a lattice vector. If the representatives can be chosen such that their translation part is zero, that is, when all translations $\boldsymbol{t}_i$ are lattice vectors, the group has a simple structure: each element is a product of an element of the translation subgroup and an element of the point group. Then the space group is called symmorphic.

Consider as examples the plane groups of the two-dimensional structures for which the unit cell is given in Figure 2. The unit cells are rectangles, the lattices have bases vectors $(a, 0)$ and $(0, b)$. The example of Figure 2a has two different atoms in (0,0) and $(1/2, 1/2)$. The point group symmetry of the lattice consists of the identity E, the two mirrors m_x and m_y, and the inversion $-E$. All four elements transform the position of an atom to a position that is related to the original position by a lattice vector. Thus, the plane group has a point group ($2mm$) with four elements. The example of Figure 2b has one molecule at the position $(0, 0)$. There are only two point group elements leaving the molecule invariant, and the point group is 2 with elements E and $-E$, although the

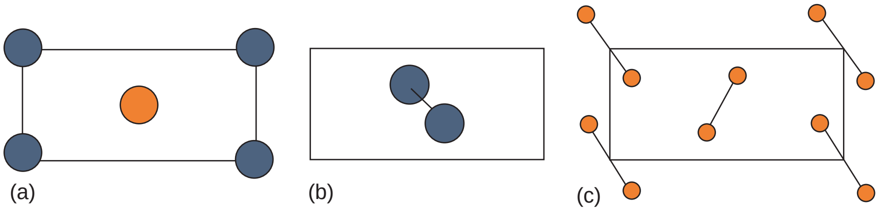

Figure 2 Three unit cells for the space groups (a) *pmm*, and (b) *p*2, (c) *pgg*.

lattice is the same. In example (c), there are molecules at (0, 0) and (1/2, 1/2). The subgroup leaving each molecule invariant has two elements: $\pm E$. The transformation m_x does not leave a molecule invariant, but the Euclidean transformation $\{m_x|(1/2, 1/2)\}$ does. The space group elements are the elements of the translation subgroup A and the cosets $\{-E|0\}A$, $\{m_x|(1/2, 1/2)\}A$, and $\{m_y|(1/2, 1/2)\}A$. The point group is again $2mm$.

Space Group Elements

Each element of a space group is a product of an orthogonal transformation (an element of the point group K) and a translation $\boldsymbol{t}$, the latter not always a lattice translation. The translations $\boldsymbol{t}_i$ form a vector system for the space group. The translations satisfy

$$\begin{aligned} &\boldsymbol{t}_i + R_i\boldsymbol{t}_j = \boldsymbol{t}_k \quad \text{up to a lattice vector } \boldsymbol{a} \\ &\text{if} \quad R_iR_j = R_k \end{aligned} \qquad [11]$$

The translations $\boldsymbol{t}_i$, however, depend on the choice of the origin. According to eqn [8] they change to $\boldsymbol{t}_i+(E-R_i)\boldsymbol{u}$, if the origin is shifted by a translation $\boldsymbol{u}$. This makes it necessary to review the concept of a symmorphic space group. A space group is called symmorphic if there is an origin such that all representatives $\{R_i|\boldsymbol{t}_i\}$ may be chosen with $\boldsymbol{t}_i=\boldsymbol{0}$. Then each element of G is the product of a point group element and a lattice translation. If the group is not symmorphic, then it is called nonsymmorphic.

A three-dimensional rotation has an axis and a rotation angle. If one chooses an orthonormal coordinate system and the rotation angle along the z-axis, then the rotation is given by a matrix

$$\begin{pmatrix} \cos\varphi & -\sin\varphi & 0 \\ \sin\varphi & \cos\varphi & 0 \\ 0 & 0 & 1 \end{pmatrix}$$

When an orthogonal transformation has a determinant equal to −1, it has the same form but with an overall minus sign. Consider the case that the orthogonal transformation is combined with a translation $\boldsymbol{t}$ with coordinates a, b, and c in the same reference system. By a shift of origin over the vector $\boldsymbol{u}$ with components x, y, and z, the translation is transformed into the translation $\boldsymbol{t}+(1-R)\boldsymbol{u}$, with components

$$a + x(1 - \cos\varphi) + y\sin\varphi,\ b - x\sin\varphi + y(1 - \cos\varphi),\ c$$

By a proper choice of $\boldsymbol{u}$, the first two components can be eliminated, but not the third. It is the case of a screw axis, a rotation combined with a translation along the rotation axis. If the rotation is over an angle $\varphi=2\pi m/n$, with n=2,3,4, or 6, the translation is always $1/n$ of a lattice vector. When the determinant is −1, the origin can always be shifted such that the translation vanishes, except for the case $n=2$. Then the orthogonal transformation is

$$\begin{pmatrix} 1 & 0 & 0 \\ 0 & 1 & 0 \\ 0 & 0 & -1 \end{pmatrix}$$

and the first two components cannot be changed. It is a mirror operation with a translation in the mirror plane, and is called a glide operation. The plane of the mirror is the glide plane (Figure 3).

In two dimensions, the only plane group elements with intrinsic nonzero translation components are glide operations. For a rotation with a translation, the latter can always be eliminated by a shift of the origin.

Classification

Because the orientation and the lattice constants may vary continuously, the number of space groups is infinite. However, there is good reason to identify space groups under certain conditions, for example, if they are just different orientations of the same group

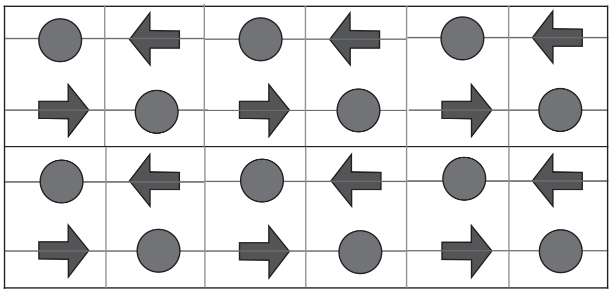

Figure 3 A two-dimensional pattern with *pgm* symmetry: rectangular lattice, horizontal mirrors, and vertical glides.

in space. In principle, which groups may be identified depends on the physics of the problem one wants to study by symmetry. Space groups are subgroups of the inhomogeneous affine group as well, the group of pairs of nonsingular linear transformations and translations. If a group G_1 may be transformed into group G_2 by a change of origin (translation) and a linear transformation of the lattice (homogeneous affine transformation), the two may be identified, or in other words considered as equivalent, because the choice of origin and basis does not change the physics. This is a definition inspired by physics. In mathematical language, the two groups are conjugated subgroups of the inhomogeneous affine group. This means that the groups G_1 and G_2 are considered to be equivalent if there is a nonsingular linear transformation S and a translation $\{E|\boldsymbol{t}\}$ such that

$$G_1 = \{S|\boldsymbol{t}\}G_2\{S|\boldsymbol{t}\}^{-1} \qquad [12]$$

With this relation, there are 219 equivalence classes of three-dimensional space groups. If the handedness of the basis is relevant, for instance, in the case of helical structures, there is a finer definition, which calls the groups equivalent if the conjugation is by an element $\{S|\boldsymbol{t}\}$ such that $\det(S)>0$. Then there are 230 equivalence classes of space groups in three dimensions. With both definitions, there are 17 different plane groups in two dimensions. A theorem by Bieberbach states that conjugation in the affine group is equivalent to isomorphism.

The space groups can also be grouped into larger classes. A coarser classification uses arithmetic equivalence. Choosing an origin and a lattice basis, the point group K of a space group corresponds to a group of integer matrices $D_1(K)$. After a basis transformation, corresponding to an integer nonsingular matrix S, the same group is represented by an integer matrix group $D_2(K)=SD_1(K)S^{-1}$. Two such groups are called arithmetically equivalent. Then a space group determines an arithmetic crystal class. If one drops the condition that the conjugation matrix S has integer entries and allows real matrices, two groups conjugated by S are said to be geometrically equivalent. Arithmetic equivalence implies geometric equivalence. Space groups may be grouped into affine equivalence classes, and further into arithmetic and geometric crystal classes. In three dimensions, there are 219 affine classes, 73 arithmetic classes, and 32 geometric classes. The latter two classifications can, of course, be used for point groups as well. For each arithmetic class there is exactly one symmorphic space group. Finally, there are seven systems (triclinic, monoclinic, orthorhombic, tetragonal, rhombohedral, hexagonal, and cubic) and six families (each three-dimensional system is a family, except the rhombohedral and hexagonal, which belong to the same family). The reader is referred to more specialized works on crystallography for a definition.

Notation

Because the full explanation of the notation and nomenclature for crystallographic groups requires much more space, only a brief discussion is presented here. There are two systems, the Hermann–Mauguin symbols, recommended by the International Union for Crystallography (IUCr), and the Schoenflies symbols. The latter are based on the symbols for the 32 point groups arranged in geometric classes. For each class there is a numbering of the corresponding space groups. An example is C_2^2 with point group C_2 consisting of an identity and a two-fold rotation. It is the second group with this point group. The Hermann–Mauguin symbols tend to have more information. They are based on the IUCr symbols for point groups. A second ingredient are the lattices. Lattices are considered to be equivalent if the point groups that leave them invariant (which on a lattice basis may be given by groups of integer matrices) may be represented by a change of lattice basis by the same groups of matrices. These classes are the Bravais classes. In three dimensions, there are 14 Bravais classes (Table 1). For lattices with the same point group symmetry, there is a common conventional basis on which the point group elements are simple, but one needs additional lattice vectors. For example, there are three Bravais classes for which the symmetry is the symmetry group of the cube, with 48 elements. The lattices of one Bravais class have a basis with three mutually perpendicular basis vectors of the same lengths. For the other two, the face-centered cubic (f.c.c.) and body-centered cubic (b.c.c.), there is a sublattice of this kind, but not all lattice vectors belong to that. One needs additional vectors to obtain all the lattice translations: $(0, 1/2, 1/2)$, $(1/2, 0, 1/2)$, and $(1/2, 1/2, 0)$ for f.c.c. and $(1/2, 1/2, 1/2)$ for b.c.c (Figure 4). These additional vectors are given by capital letters in three dimensions, and lower case letters in two dimensions.

Table 1 The 14 Bravais classes in three dimensions and their maximal symmorphic space groups

System	*Centering translations*	*Maximal symmorphic space group*	*Basis*
Triclinic	None	*P* –1	No relations
Monoclinic	None	*P*2/*m*	$a.c=\mathbf{b}.\mathbf{c}=0$
	(1/2,0,1/2)	*B*2/*m*	
Orthorhombic	None	*Pmmm*	Three axes perpendicular
	(1/2,1/2,1/2)	*Immm*	
	(0,1/2,1/2),(1/2,0,1/2),(1/2,1/2,0)	*Fmmm*	
	(1/2,1/2,0)	*Cmmm*	
Tetragonal	None	*P*4/*mmm*	Three axes perpendicular
	(1/2,1/2,1/2)	*I*4/*mmm*	$\lvert\mathbf{a}\rvert=\lvert\mathbf{b}\rvert$
Rhombohedral	None	*R* –3*m*	$\lvert\mathbf{a}\rvert=\lvert\mathbf{b}\rvert=\lvert\mathbf{c}\rvert$ $\angle(\mathbf{a},\mathbf{b})=\angle(\mathbf{b},\mathbf{c})=\angle(\mathbf{c},\mathbf{a})$
Hexagonal	None	*P*6/*mmm*	$\lvert\mathbf{a}\rvert=\lvert\mathbf{b}\rvert$, $\mathbf{c}\perp\mathbf{a}$, $\mathbf{c}\perp\mathbf{b}$ $\angle(\mathbf{a},\mathbf{b})=2\pi/3$
Cubic	None	*Pm* –3*m*	All basis vectors mutually perpendicular and equal in length
	(0,1/2, 1/2), (1/2,0,1/2) (1/2,1/2,0)	*Fm* –3*m*	
	(1/2,1/2,1/2)	*Im* –3*m*	

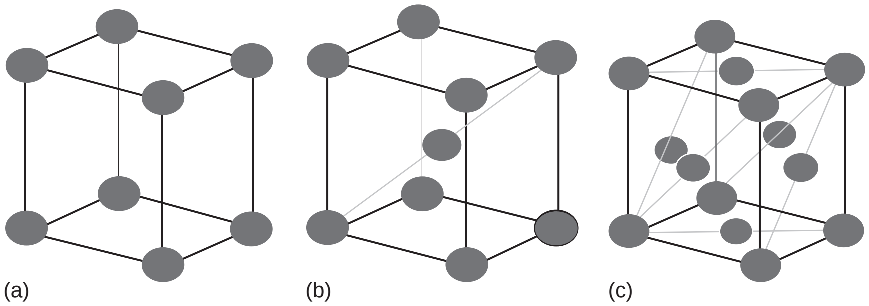

Figure 4 Unit cells for lattices from each of the three cubic Bravais classes. (a) Primitive, (b) b.c.c. with additional basis vector (1/2, 1/2, 1/2), and (c) f.c.c. with additional (0, 1/2, 1/2), (1/2, 0, 1/2), and (1/2, 1/2, 0).

The symbols of the symmetry groups of the three cubic lattices are $Pm\ -3m$,$Fm\ -3m$, and $Im\ -3m$. These are the Hermann–Mauguin symbols for the space groups of the primitive cubic, f.c.c., and b.c.c. lattices, respectively. For each of the 73 arithmetic crystal classes, and thus for all symmorphic space groups there is such a symbol, consisting of the symbol for the point group preceded by a letter indicating the additional lattice vectors (the centering).

Finally, for nonsymmorphic space groups, the nonlattice translations for the elements appearing in the symbol for the symmorphic space group are indicated by either a change of the letter or by a subindex. The symbol for a symmorphic space group with point group m may be Pm. If the mirror m becomes a glide with nonlattice translation in the third direction, the symbol is Pc. The symbol $P2$ gives a symmorphic space group with point group 2, $P2_1$ indicates a nonsymmorphic group with a screw axis. All space groups, their symbols and their elements can be found in the *International Tables for Crystallography, vol. A*.

Reciprocal Lattice, Invariant Functions, Extinction Rules

A function that is invariant under translations has special properties for its Fourier transform. Suppose $\rho(\boldsymbol{r})$ is such a function (e.g., a density function of a crystal). It has the property that $\rho(\boldsymbol{r})$ and $\rho(\boldsymbol{r}+\boldsymbol{a})$ are equal for every translation $\boldsymbol{a}$ from the lattice. Writing down the Fourier decomposition yields

$$\begin{aligned} \rho(\boldsymbol{r}) &= \int \hat{\rho}(\boldsymbol{k})\exp(\mathrm{i}\boldsymbol{k}\cdot\boldsymbol{r})\mathrm{d}\boldsymbol{k} \\ \rho(\boldsymbol{r}\ +\boldsymbol{a}) &= \int \hat{\rho}(\boldsymbol{k})\exp(\mathrm{i}\boldsymbol{k}\cdot(\boldsymbol{r}\ +\boldsymbol{a}))\mathrm{d}\boldsymbol{k} \end{aligned} \qquad [13]$$

from which it follows that $\boldsymbol{k}{\cdot}\boldsymbol{a}{=}0\ (\mathrm{mod}\ 2\pi)$ for each translation vector $\boldsymbol{a}$. Therefore, for each wave vector $\boldsymbol{k}$ occurring in the Fourier expansion, one has this relation. All vectors $\boldsymbol{k}$ satisfying this relation form a lattice, as is easily checked. This lattice is called the reciprocal lattice for the so-called direct lattice of the vectors $\boldsymbol{a}$.

If $\boldsymbol{a}$, $\boldsymbol{b}$, and $\boldsymbol{c}$ span the direct lattice, a basis for the reciprocal lattice is givenby a^*b^* c^*defined by

$$\boldsymbol{a}^* = 2\pi(\boldsymbol{b}\times\boldsymbol{c})/V, \boldsymbol{b}^* = 2\pi(\boldsymbol{c}\times\boldsymbol{a})/V, \boldsymbol{c}^* = 2\pi(\boldsymbol{a}\times\boldsymbol{b})/V \qquad [14]$$

where $V{=}\boldsymbol{a}{\cdot}(\boldsymbol{b}{\times}\boldsymbol{c})$ is the volume of the unit cell. Then the Fourier decomposition is

$$\rho(\boldsymbol{r}) = \sum_{\boldsymbol{k}\in\Lambda^*}\hat{\rho}(\boldsymbol{k})\exp(i\boldsymbol{k}\cdot\boldsymbol{r}) \qquad [15]$$

where Λ^* is the reciprocal lattice. Each vector of the reciprocal lattice can be expressed in terms of the basis of the lattice

$$\boldsymbol{k} = h\boldsymbol{a}^*\ +k\boldsymbol{b}^*\ +l\boldsymbol{c}^* \in \Lambda^* \qquad [16]$$

The reciprocal lattice is left invariant by the point group K as well.

Apart from translations, a lattice periodic function is generally left invariant by other distance-preserving transformations as well. Suppose $g{=}\{R|\boldsymbol{t}\}$ is an element of the space group that leaves a function $\rho(\boldsymbol{r})$ invariant. This means that $\rho(\boldsymbol{r})$ and $\rho(g^{-1}\boldsymbol{r})$ are the same (the exponent −1 is just for convenience). Then one has the relation

$$\rho(\boldsymbol{r}) = \rho\left(\{R|t\}^{-1}\boldsymbol{r}\right) \qquad [17]$$

For the Fourier components $\hat{\rho}(\boldsymbol{k})$, this implies

$$\hat{\rho}(\boldsymbol{k}) = \hat{\rho}(R\boldsymbol{k})\exp(\mathrm{i}R\boldsymbol{k}{\cdot}t) \qquad [18]$$

This is a very interesting formula. It is known that the wave vectors occurring in the Fourier decomposition belong to the reciprocal lattice. Now, consider a reciprocal lattice vector $\boldsymbol{k}$ that is invariant under orthogonal transformation R. Then the expression becomes

$\rho(\boldsymbol{k})=\rho(\boldsymbol{k})\exp(\mathrm{i}\boldsymbol{k}\cdot\boldsymbol{t})$. This is only possible if $\rho(\boldsymbol{k})=0$ or if $\boldsymbol{k}\cdot\boldsymbol{t}=0 \pmod{2\pi}$. If $\boldsymbol{t}$ is a translation from the lattice, this relation is trivially fulfilled. But if there is a $\boldsymbol{t}$ such that the second relation is not satisfied, this means that the corresponding Fourier component $\hat{\rho}(\boldsymbol{k})$ vanishes. This is an extinction rule.

An important example is the diffraction intensity. A crystal diffracts and the diffraction pattern consists of sharp Bragg peaks at the positions $\boldsymbol{k}$. The intensity of the peaks is given by the square of the absolute value of the static structure factor:

$$I(\boldsymbol{k}) = |F(\boldsymbol{k})|^2 = \left|\frac{1}{N}\sum_{j=1}^{N}\exp(\mathrm{i}\boldsymbol{k}\cdot\boldsymbol{r}_j)\right|^2 \qquad [19]$$

Here j runs over the N particles in the unit cell. It is the Fourier transform of the autocorrelation function, which is invariant under space group elements. Hence, the positions of the Bragg peaks are on the reciprocal lattice, and the extinction rules apply: the intensity is zero at $\boldsymbol{k}$ if there is a space group element $\{R|\boldsymbol{t}\}$ with $R\boldsymbol{k}=\boldsymbol{k}$ and $\boldsymbol{k}\cdot\boldsymbol{t}\neq 0 \pmod{2\pi}$. Additionally, one has for arbitrary $\boldsymbol{k}$ that $I(R\boldsymbol{k})=I(\boldsymbol{k})$. Consequently, the diffraction has the point group in its symmetry group.

Representations of Space Groups

Euclidean transformations act on positions in space. A quantum mechanical system in such a space has states on which the Euclidean transformations act as linear operators. For example, if the state is given by a wave function $\psi(\boldsymbol{r})$, the effect of a Euclidean transformation $\{R|\boldsymbol{t}\}$ gives a new wave function $\psi'(\boldsymbol{r})=\psi(R^{-1}(\boldsymbol{r}-\boldsymbol{t}))$. This is the action of a linear operator T_g, with $g=\{R|\boldsymbol{t}\}$. Choosing a basis $\psi(\boldsymbol{r})$ in the space of states, such a linear operator corresponds to a matrix $D(g)$:

$$T_g\psi_i(\boldsymbol{r}) = \sum_{j=1}^{N} D(g)_{ji}\psi_j(\boldsymbol{r}) \qquad [20]$$

(n is the dimension of the state space.) Now the matrices satisfy $D(g_1)D(g_2)=D(g_1g_2)$. This is called a (matrix) representation. If the dimension of the space is n, then the representation is said to be n-dimensional, and the matrices are $n\times n$. These representations are important for characterizing energy levels and other properties. Clearly, the space is mapped onto itself and, therefore, it is invariant under the group of transformations G. If there is no subspace (different from the origin or the whole space) that is invariant, the representation is said to be irreducible. In general, an energy level space carries an irreducible representation of the symmetry group, the dimension of the space is the level degeneracy, and there are orthogonality relations between states from the state space.

This gives a short argument why one should look at the irreducible representations of the space groups. The simplest space group is just a translation group, with three basis translations. Because the order in which translations are applied is not relevant, it is a commutative group, and according to the results of group theory the irreducible representations of commutative groups are one-dimensional, that is the matrices are just numbers. They satisfy $D(\{E|\boldsymbol{a}\})D(\{E|\boldsymbol{b}\})=D(\{E|\boldsymbol{a}+\boldsymbol{b}\})$. The solution is $D(\{E|\boldsymbol{a}\})=\exp(\mathrm{i}\boldsymbol{k}\cdot\boldsymbol{a})$ for some vector $\boldsymbol{k}$. Two vectors $\boldsymbol{k}$ and $\boldsymbol{k}'$ give the same representation if $\boldsymbol{k}-\boldsymbol{k}'$ belongs to the reciprocal lattice, because then $\boldsymbol{k}\cdot\boldsymbol{a}=\boldsymbol{k}'\cdot\boldsymbol{a} \pmod{2\pi}$ for all lattice vectors $\boldsymbol{a}$. Therefore, the irreducible representations are characterized by a vector from the unit cell of the reciprocal lattice. A special choice of this unit cell is the Brillouin zone. It is the unit cell of the reciprocal lattice consisting of all points in reciprocal space which are closer to the origin than to any other point of the reciprocal lattice. Of course, the unit cell of a lattice is not uniquely defined. However, the choice of the Brillouin zone is very convenient when studying electrons or elementary excitations in crystals.

A wave function $\psi(\boldsymbol{r})$ in a lattice periodic crystal which belongs to an irreducible representation of the lattice subgroup has a special form, the Bloch form, as follows from a group-theoretical argument. Under a translation $\boldsymbol{a}$, the function transforms to $\psi(\boldsymbol{r}-\boldsymbol{a})$ which should be equal to $\exp(\mathrm{i}\boldsymbol{k}\cdot\boldsymbol{a})\psi(\boldsymbol{r})$ for some $\boldsymbol{k}$. Then define $U(\boldsymbol{r})=\exp(\mathrm{i}\boldsymbol{k}\cdot\boldsymbol{r})\psi(\boldsymbol{r})$. It follows that

$$\begin{aligned} U(\boldsymbol{r}+\boldsymbol{a}) &= \exp(i\boldsymbol{k}\cdot(\boldsymbol{r}+\boldsymbol{a}))\psi(\boldsymbol{r}+\boldsymbol{a}) \\ &= \exp(i\boldsymbol{k}\cdot(\boldsymbol{r}+\boldsymbol{a}))\exp(-i\boldsymbol{k}\cdot\boldsymbol{a})\psi(\boldsymbol{r}) \\ &= U(\boldsymbol{r}) \end{aligned}$$

which proves that $\psi(\boldsymbol{r})$ is the product of a plane wave, $\exp(-\mathrm{i}\boldsymbol{k}\cdot\boldsymbol{r})$ and a lattice periodic function $U(\boldsymbol{r})$. This constitutes the well-known Bloch's theorem.

Consider a state space that is invariant under a space group acting on the space by operators T_g for each element g of the space group G. Suppose, furthermore, that the representation is irreducible. The translation subgroup A is a subgroup of G. So, there is a basis formed by functions ψ_i for the space consisting of the eigenvectors of the commuting operators T_a. One has

$$T_a\psi_j = \exp(\mathrm{i}\boldsymbol{k}_j\cdot\boldsymbol{a})\psi_j \qquad [21]$$

A subspace of the space is that belonging to one particular wave vector $\boldsymbol{k}$. For each state, ψ from this space it holds that $T_a\psi=\exp(\mathrm{i}\boldsymbol{k}\cdot\boldsymbol{a})\psi$. Applying T_g to any state from this space, ψ transforms to $T_g\psi$. How does this transform under the translations? Applying a translation $\{E|\boldsymbol{a}\}$ to the transformed vector:

$$\begin{aligned} T_a T_g \psi &= T_g (T_{g^{-1}} T_a T_g)\psi = T_g T_b \psi \\ &= \exp(\,-i\boldsymbol{k}\cdot\boldsymbol{b}) T_g \psi \end{aligned}$$

Here $\boldsymbol{b}=R^{-1}\boldsymbol{a}$ if $g=\{R|\boldsymbol{t}\}$. The state $T_g\psi$, therefore, acquires a phase factor $\exp(iR\boldsymbol{k}\cdot\boldsymbol{a})$ and belongs to the subspace of states transforming with a wave vector $R\boldsymbol{k}$. This means that, if there are states transforming under translations with a wave vector $\boldsymbol{k}$, then there are, in the irreducible space, states transforming with the wave vector $R\boldsymbol{k}$ for every point group element. One can write the whole space as a sum of spaces each belonging to a specific $R\boldsymbol{k}$. One of these spaces is that of states transforming with $\boldsymbol{k}$.

Now define the subgroup of G consisting of all elements $\{R|\boldsymbol{t}\}$ for which $R\boldsymbol{k}=\boldsymbol{k}$ (modulo the reciprocal lattice because $\boldsymbol{k}$ and $k+\boldsymbol{K}$ give the same representation if $\boldsymbol{K}$ belongs to the reciprocal lattice). This group is called the group of $\boldsymbol{k}$: $G_{\boldsymbol{k}}$. The subspace of states transforming with $\boldsymbol{k}$ under translations is invariant under the group of $\boldsymbol{k}$. Then for an element g from the group of $\boldsymbol{k}$:

$$T_g = \exp(i\boldsymbol{k}\cdot\boldsymbol{t})D_R \quad (g = \{R|\boldsymbol{t}\})$$

The operators form an irreducible representation of the group of $\boldsymbol{k}$. For a symmorphic group of $\boldsymbol{k}$ the elements g can be written as a product $\{E|\boldsymbol{t}\}\{R|0\}$ of a lattice translation and a point group element. In this case, the operators D_R form an irreducible representation of the point group of the group of $\boldsymbol{k}$, denoted by $K_{\boldsymbol{k}}$. These are known, and can be labeled by a label ν. Then a basis of the space of $G_{\boldsymbol{k}}$ transforms under g as

$$T_g\psi_j = \exp(i\boldsymbol{k}\cdot\boldsymbol{t})D_{kj}(R)\psi_k \tag{22}$$

The basis carries an irreducible representation ν of the point group K (simply take $\boldsymbol{t}=0$ in the last formula). Here the matrices $D(R)$ are the irreducible representation ν of the point group $K_{\boldsymbol{k}}$. For nonsymmorphic groups, the procedure is somewhat more complicated, because not only standard representations but projective representations also occur.

Finally, a basis for the full state space can be constructed as follows. The group of $\boldsymbol{k}$ is a subgroup of the space group G. G can be decomposed according to

$$G = G_{\boldsymbol{k}} + g_2 G_{\boldsymbol{k}} + \ldots + g_s G_{\boldsymbol{k}}$$

where the space group elements g_i have homogeneous parts R_i for which $R_i\boldsymbol{k}=\boldsymbol{k}_i$. Then the basis is defined as

$$\Psi_{ij} = T_{gi}\psi_j \tag{23}$$

The dimension of the representation is sd, where s is the number of points $\boldsymbol{k}_i$, and d the dimension of the point group representation $D(K_{\boldsymbol{k}})$. The irreducible representation carried by the state space then is characterised by the so-called "star" of $\boldsymbol{k}$ (all vectors $\boldsymbol{k}_i$), and an irreducible representation of the point group $K_{\boldsymbol{k}}$. This means that electronic states and phonons can be characterized by $\boldsymbol{k}$, ν. Their transformation properties under space group transformations follows from this characterization.

Aperiodic Crystals

Apart from crystals with three-dimensional lattice periodicity, there are materials with a diffraction pattern with sharp Bragg peaks on positions

$$\boldsymbol{k} = \sum_{i=1}^{n} h_i \boldsymbol{a}_i^{*} \quad (\text{integer } h_i) \tag{24}$$

When $n=3$, the structure is periodic. If $n3$, the structure is aperiodic, but it is still considered as crystal, because there is long-range order. Examples are modulated phases and quasicrystals. They may be described as intersections of physical space with a higher-dimensional lattice periodic structure. The symmetry of such structures is a space group in n dimensions, and in this case the theory of space groups in arbitrary dimensions can be used.

Further Reading

Cornwell JF (1997) *Group Theory in Physics.* San Diego: Academic Press.

Hahn Th. (ed.) (1992) *Space-Group Symmetry.* In: International Tables for Crystallography. vol. A, Dordrecht: Kluwer.

Hahn T and Wondratschek H (1994) *Symmetry of Crystals: Introduction to International Tables for Crystallography. vol. A.* Sofia, Bulgaria: Heron Press.

Janssen T (1973) *Crystallographic Groups.* North-Holland: Amsterdam.

Janssen T, Janner A, Looijenga-Vos A, and de Wolff PM (1999) Incommensurate and commensurate modulated structures. In: Wilson AJC and Prince E (eds.) *International Tables for Crystallography*, vol. C. Dordrecht: Kluwer *Mathematical, physical and chemical tables.* ch. 9.8.

Crystal Symmetry

Th Hahn[a] **and H Klapper**[b], [a]Institut fur Kristallographie, RWTH Aachen, Aachen, Germany; [b]Mineralogisch-Petrologisches Institut, Universität Bonn, Bonn, Germany

© 2005 Elsevier Ltd. All rights reserved.

This is an update of Th. Hahn, H. Klapper, Crystal Symmetry, Editor(s): Franco Bassani, Gerald L. Liedl, Peter Wyder, Encyclopedia of Condensed Matter Physics, Elsevier, 2005, Pages 312–323, ISBN 9780123694010, https://doi.org/10.1016/B0-12-369401-9/00421-6.

Introduction 70
Lattices and Their Symmetries 70
Crystallographic Coordinate Systems 71
"Primitive" Crystallographic Coordinate Systems 71
Conventional Crystallographic Coordinate Systems 71
Crystallographic Symmetry Operations and Symmetry Elements 72
Symmetry Operations 72
Symmetry Elements 72
Matrix Representation of Symmetry Operations 74
General Relations 74
Geometric Interpretation of (Crystallographic) Symmetry Matrices 76
Symbols for Point Groups and Space Groups 78
Schoenflies Symbols 78
Hermann–Mauguin (International) Symbols 78
Acknowledgments 79
Further Reading 79

Nomenclature

$\boldsymbol{a}, b, c$	Basis vectors of a lattice
$\boldsymbol{a}, \boldsymbol{b}, \boldsymbol{c}, \boldsymbol{\alpha}, \boldsymbol{\beta}, \boldsymbol{\gamma}$	Lattice parameters
$\boldsymbol{t}; t$	Translation; translation vector
$\boldsymbol{P}, \boldsymbol{A}, \boldsymbol{B}, \boldsymbol{C}, \boldsymbol{I}, \boldsymbol{F}, \boldsymbol{R}$	Centering types of lattices
$\boldsymbol{X}; \bar{X}$	Point; transformed point
$\boldsymbol{x}, \boldsymbol{y}, \boldsymbol{z}; \tilde{\boldsymbol{x}}, \tilde{\boldsymbol{y}}, \tilde{\boldsymbol{z}}$	Coordinates of points X and $\tilde{X}$
$\boldsymbol{r}; \tilde{r}$	Location vector; transformed location vector
$\boldsymbol{W}$	(3×3) matrix, rotation part of a symmetry operation
$\boldsymbol{w}$	(3×1) column, translation part of a symmetry operation
$\boldsymbol{W}_{ij}; \boldsymbol{w}_k$	Elements of W and $\boldsymbol{w}$
$\mathbb{W}, \mathbb{T}, \mathbb{r}$	(4×4) augmented matrix; (4×4) augmented matrix of pure translation; (4×1) augmented vector
$(\boldsymbol{hkl})$	Miller indices of a crystal face (lattice plane)
$[\boldsymbol{uvw}]$	Direction indices of a crystal edge (lattice direction)

Schoenflies Symbols

$C_n = C_1, C_2, C_3, C_4, C_6$	Cyclic group of order $n = 1,2,3,4,6$
$C_s; C_i$	Reflection group; inversion group (order 2)
S_4	Rotoinversion (rotoreflection) group of order 4
$D_n = D_2, D_3, D_4, D_6$	Dihedral group of order $m = 2n = 4,6,8,12$
T	Tetrahedral group (order 12)
O	Octahedral group (order 24)

Hermann–Mauguin (International) Symbols

$n=1, 2, 3, 4, 6$	n-fold rotation axes (order n)
$\bar{n}, \bar{1}, \bar{2}\equiv m,$	n-fold rotoinversion axes
$\bar{4},\bar{3},\bar{6}\equiv 3/m$	(orders 2, 2, 4, 6, 6, resp.)
$n_p=2_1, 3_1, 3_2, 4_1, 4_2, 4_3, 6_1, 6_2, 6_3, 6_4, 6_5$	n-fold screw axes (order ∞)
$m(\equiv\bar{2})$	reflection (mirror) plane (order 2)
a, b, c, n, d	glide reflection planes (order ∞)
g	glide line (two dimensions, order ∞)

Introduction

Among the various states of condensed matter, the crystalline state is governed by symmetry more than any other state (e.g., liquids, glasses). This is because all atoms of one type in a solid compound display the same structural behavior and adopt, as far as possible, the same atomic environment around them. This applies to all kinds of atoms in the compound and results from the tendency of any system to minimize its free energy. As a first consequence, this leads to three-dimensional periodicity (translational symmetry) of the atoms (ions, molecules) in a crystal structure. As a second consequence, further symmetries, such as rotations, reflections, and inversions (through a point), may occur.

As a rule, symmetry in science is described mathematically in terms of the "group theory." For crystals, the main symmetry groups are point groups, translation groups, and space groups (these are discussed elsewhere in this encyclopedia). Group elements are the symmetry operations discussed in the section "Crystallographic symmetry operations and symmetry elements." Fundamentals of crystallography and of crystallographic symmetry groups can be found in text books of crystallography and in *ITA* (2002) (cf. section "Further reading").

Two levels of crystalline symmetry must be distinguished:

1. "Microscopic" symmetry of the crystal structure: this implies a three-dimensional periodicity which is described by translation groups and their lattices. Furthermore, all permissible combinations of translations with reflections, rotations and inversions, including screw rotations and glide reflections, can occur as elements of space groups.
2. "Macroscopic" symmetry of the single (bulk) crystal: it is derived from the microscopic symmetry (space group) of the crystal structure by the suppression of all translations, both lattice translations and translation components of screw rotations and glide reflections. This leads to the point group of the crystal, which represents its morphological symmetry as manifested by the general face form, which may develop under ideal conditions during crystal growth. Furthermore, the symmetry of physical properties of crystals, in particular of tensor properties, is also described by point groups. Note that in this description, the macroscopic crystal is considered as an anisotropic homogeneous continuum.

Lattices and Their Symmetries

The symmetry operations of a crystal are "isometries" or "rigid motions", that is, mappings which preserve distances and, hence, angles and volumes also. The simplest motion is a translation which is a parallel displacement of an object by a translation vector $\boldsymbol{t}$. The three-dimensional periodicity (translation symmetry) of the (infinitely extended) crystal structure is described by the infinite set $\{\boldsymbol{t}\}$ of all translation vectors $\boldsymbol{t}$ mapping the structure onto itself, that is, by the lattice. It is represented by the equation

$$\{t\} = \{m \cdot \boldsymbol{a} + n \cdot \boldsymbol{b} + p \cdot \boldsymbol{c}\}(-\infty < m, n, p < +\infty) \qquad [1]$$

with $\boldsymbol{a}$, $\boldsymbol{b}$, $\boldsymbol{c}$ three linearly independent basis vectors spanning a three-dimensional parallelepiped called unit cell. Each translation t maps the crystal structure onto itself and is, hence, a symmetry operation of the crystal.

Equation [1] implies that for a given basis vector set $\boldsymbol{a}$, $\boldsymbol{b}$, $\boldsymbol{c}$, one unique lattice $\{t\}$ is defined. On the other hand, one and the same lattice can be generated by infinitely many different triplets $\boldsymbol{a}'$, $\boldsymbol{b}'$, $\boldsymbol{c}'$ of linearly independent lattice vectors, each triplet spanning a "primitive" (smallest) unit cell (this triplet is called "primitive basis" here). All these triplets are equally correct lattice bases. As will be shown below, one (or at most two) particularly symmetry-adapted basis vector sets are conventionally accepted by all scientists.

There exist four different types of lattice symmetries in two dimensions and seven in three dimensions. These so-called "lattice point symmetries" are defined as the symmetries of the infinite surrounding of each lattice point by the other lattice points. These lattice symmetries are also called "holohedries" (holohedral point groups), a term which stems from the old morphological classification, meaning "full face form." These holohedries determine the seven three-dimensional crystal systems and crystallographic coordinate systems: triclinic (anorthic), monoclinic, orthorhombic, tetragonal, trigonal/rhombohedral, hexagonal, cubic (see Table 1, see footnote there about trigonal/rhombohedral). Geometrically, these holohedral lattice symmetries are brought out directly in the so-called "Wigner–Seitz cells" or "Dirichlet domains" (see *ITA* (2002)).

Table 1 Crystal systems, lattice point symmetries, conventional crystallographic coordinate systems and Bravais lattice types in two and three dimensions. The lattice point symmetries (column 2) are given in Hermann–Mauguin (left) and in Schoenflies symbols (right); see Section "Symbols for point groups and space groups"

Crystal system	Lattice point symmetry (holohedry)		Conventional coordinate system (restrictions on cell parameters $a,b,c,\alpha,\beta,\gamma$)	Bravais lattices[a]
Two dimensions				
Oblique (monoclinic)	2		None	*mp*
Rectangular (orthorhombic)	2*mm*		$\gamma=90^\circ$	*op*, *oc*
Square (tetragonal)	4*mm*		$a=b, \gamma=90^\circ$	*tp*
Hexagonal	6*mm*		$a=b, \gamma=120^\circ$	*hp*
Three dimensions				
Triclinic (anorthic)	$\bar{1}$	C_i	None	a*P*
Monoclinic	2/*m*	C_{2h}	$\alpha=\gamma=90^\circ$ (unique axis b)	*mP*, *mC* *mA*, *mI*
			$\alpha=\beta=90^\circ$ (unique axis c)	*mP*, *mA* *mB*, *mI*
Orthorhombic	2/*m* 2/*m* 2/*m*	D_{2h}	$\alpha=\beta=\gamma=90^\circ$	*oP*, *oI*, *oF* *oA*, *oB*, *oC*
Tetragonal	4/*m* 2/*m* 2/*m*	D_{4h}	$a=b, \alpha=\beta=\gamma=90^\circ$	*tP*, *tI*
Trigonal[b]				
Rhombohedral lattice	$\bar{3}2/m$	D_{3d}	$a=b=c, \alpha=\beta=\gamma\neq 90^\circ$	*hR*
Hexagonal lattice	6/*m* 2/*m* 2/*m*	D_{6h}	$a=b, \alpha=\beta=90^\circ, \gamma=120^\circ$	*hP*
Hexagonal	6/*m* 2/*m* 2/*m*	D_{6h}	$a=b, \alpha=\beta=90^\circ, \gamma=120^\circ$	*hP*
Cubic	$4/m\bar{3}2/m$	O_h	$a=b=c, \alpha=\beta=\gamma=90^\circ$	*cP*, *cI*, *cF*

[a] Bravais lattices (column 4): The lower-case first letter of the symbol identifies the crystal system. Note that the trigonal and the hexagonal system both receive the letter *h*. Second letter of the symbol: *p*, *c* in two dimensions: primitive and centered cell. Three dimensions: *P* = primitive cell; A,B,C = one-face centered cell on(*b*,*c*), (*a*,*c*) or (*a*,*b*) face; I = body centered cell; F = all-face centered cell; R = rhombohedral centering of the hexagonal cell.

[b] In the trigonal crystal system two Bravais lattices, *hR* and *hP*, with different holohedries, $\bar{3}$ 2/*m* and 6/*m* 2/*m* 2/*m*, occur. Both are normally described by "hexagonal axes."

Crystallographic Coordinate Systems

"Primitive" Crystallographic Coordinate Systems

Whereas in physics and chemistry normally Cartesian coordinate systems are used, in crystallography quite different systems are applied. Here it is customary that every crystal receives its own specific crystallographic coordinate system, based on the symmetry of the crystal and characterized as follows:

1. Basis vectors are three linearly independent, shortest ("primitive") translation vectors of the crystal lattice (see eqn [1]). This implies six lattice parameters: three axial lengths a, b, c, and three interaxial angles α, β, γ. ("Primitive" means that the unit cell spanned by the three basis vectors contains only one lattice point, in contrast to "centered cells," see the next section.)
2. The origin of the coordinate system is free in principle, but for convenience in computation, it is usually chosen in a center of symmetry (inversion center), if present, otherwise in a point of high site symmetry of the space group (e.g., in an intersection of two or more symmetry axes).

The advantage of such a crystal-specific coordinate system is that all lattice points receive integer coordinates, and this applies to all choices of a primitive coordinate system for a given crystal. Note that the lattice parameters of a crystal vary with temperature and pressure.

Conventional Crystallographic Coordinate Systems

In order to define a unique crystallographic coordinate system for each crystal, special conventions have to be devised. It turns out, however, that the use of a special primitive coordinate system, as described in the preceding section, would indeed always characterize the crystal lattice uniquely, but in many cases would not bring out the symmetry of the crystal. This, however, is a universally accepted objective for the definition of the conventional crystallographic coordinate system in the form of a symmetrical parallelepiped as unit cell.

For this reason, the 14 Bravais types of lattices are considered, with the provision that all Bravais lattices with the same holohedry should have the same conventional coordinate system. A consequence of this procedure is that only for primitive Bravais lattices, all lattice points receive integer coordinates, whereas for centered lattices of the same lattice, symmetry points with fractional coordinates 1/2, 1/3, and 2/3 (and no others) appear. In this way, seven conventional coordinate systems result, which apply to the crystals of all 14 Bravais lattice types. As a typical example, the cubic crystal system is considered: for the primitive cubic lattice *cP*, the conventional coordinate system employs the three shortest lattice vectors with right interaxial angles $\alpha = \beta = \gamma = 90^\circ$. In this case, the conventional coordinate system is at the same time a primitive crystallographic basis. For the body-centered and all-face-centered cubic Bravais lattices *cI* and *cF*, however, only a fraction of the lattice points (1/2 for *cI* and 1/4 for *cF*) have integer coordinates represented by 0,0,0, whereas the remaining centering lattice points have fractional coordinates: 1/2, 1/2, 1/2 for *cI*, and 1/2, 1/2, 0 & 0, 1/2, 1/2 & 1/2, 0, 1/2 for *cF*. If only primitive cells were used, the coordinate system for *cP* would remain the same (cube = 90° rhombohedron), whereas for *cI* and *cF* rhombohedral cells with $\alpha = 109.47^\circ$ and $\alpha = 60^\circ$, respectively would result which would not display the cubic symmetry.

The conventional crystallographic coordinate systems are collected in Table 1, which lists the four plane and the seven spatial lattice symmetries with their point-group symbols and the restrictions on the general lattice parameters $a,b,c,\alpha,\beta,\gamma$ imposed by the lattice symmetry. The symbols of the Bravais lattices which belong to a given coordinate system are listed too. These symmetry criteria uniquely determine five of the seven three-dimensional coordinate systems because these five exhibit three or more symmetry directions ("blickrichtungen"): orthorhombic, tetragonal, rhombohedral, hexagonal, cubic. For the two exceptions, triclinic and monoclinic, no or only one symmetry direction exists. In these cases, metrical criteria, such as reduced bases (i.e., choice of the three (triclinic) or two (monoclinic) shortest lattice translations as basis vectors), have to be applied. It should be noted that for historical reasons, in the monoclinic system two different "settings" are in use, which are distinguished by the labeling of the unique symmetry axis: "unique axis *b*" and "unique axis *c*" settings. The *b*-axis setting is the more frequently used one (see Part 2 of *ITA* (2002)).

There is one case in which not one but two different conventional coordinate systems are in use, for trigonal crystals with a rhombohedral *hR* lattice. These crystals are alternatively described by "rhombohedral axes" or, more frequently, by "hexagonal axes," whereby the first case corresponds to a primitive rhombohedral unit cell, the second to the triple R-centered hexagonal unit cell. In contrast, crystals with a hexagonal *hP* lattice are always described by "hexagonal axes."

Detailed descriptions of the conventional crystallographic coordinate systems and reduced bases can be found in sections 1.2, 2.1, 8.3.1, 9.1 and 9.2 of *ITA* (2002).

Crystallographic Symmetry Operations and Symmetry Elements

Symmetry Operations

The following types of symmetry operations exist in crystals and are elements of crystallographic symmetry groups:

1. Translations (already treated in the section "Lattices and their symmetries").
2. Rotations around an axis, reflections across a plane and inversions in a point, as well as their combinations, that is, rotoinversions and rotoreflections. These operations constitute the so-called point-group operations, which leave at least one point of space invariant.
3. Combinations between point-group operations and translations, leading to screw rotations and glide reflections. Both types occur only in space groups, not in point groups. Screw rotations are rotations by an angle $\varphi 360^\circ/n$, followed by a translation (screw component) parallel to the rotation axis. Glide reflections are reflections across a plane, followed by a translation (glide component) parallel to the plane. The screw and glide components are rational fractions of a lattice translation.

An important fact of crystallographic symmetry is the restriction of the rotation angles φ by the translation lattice to $\varphi = 180^\circ, 120^\circ, 90^\circ, 60^\circ$, defining twofold, threefold, fourfold, and sixfold rotations and screw rotations. This is the consequence of the three-dimensional periodicity of crystals. Apart from a simple mathematical proof (see section "Matrix representation of symmetry operations"), this result is immediately obvious from the fact that a plane can be covered without gaps and overlaps only by parallelograms and their special forms (rectangles, rhombuses, squares), and by triangles and hexagons, but not by pentagons (corresponding to a rotation angle of 72°), heptagons, octagons, etc. Hence, rotation axes other than two-, three-, four-, and sixfold axes are not possible in crystals.

Symmetry Elements

In addition to symmetry operations (which represent "action" on an object), symmetry can also be described in (static) geometrical terms, known as symmetry elements. They form the geometric locus (geometric element), oriented in space, at which a symmetry operation or a cyclic group of operations is performed (plane for a reflection, line for a rotation, point for an inversion), together with a description of these operations. In other words, the symmetry element is the "invariant subspace" of a given operation, that is, the set of fixed points which are invariant under the operation.

Symmetry elements are reflection (mirror) planes, glide planes, rotation axes, screw axes and centers of symmetry. For rotoinversions and rotoreflections, the symmetry element consists of two items: axis and inversion point on the axis, or axis and mirror plane normal to the axis. For screw rotations and glide reflections, the screw and glide components have to be removed first in order to obtain the "fixed points" for screw axes and glide reflections.

Note that the group elements of a symmetry group are the symmetry operations, not the symmetry elements. This discrepancy of nomenclature has historical reasons and is the source of frequent misunderstandings.

The crystallographic symmetry elements (reflection and glide plane, rotation and screw axes, and rotoinversion axes) are illustrated in Figures 1–3. Printed and graphical symbols of all symmetry elements are collected in Table 2. Further details are given in Parts 1 and 8.1 of *ITA* (2002) and the references quoted therein. Complete "frameworks of symmetry elements" for the 17 plane groups, the 230 space groups, and the 32 crystallographic point groups are presented in Parts 6, 7 and 10.1 (and explained in section 2.2.6) of *ITA* (2002).

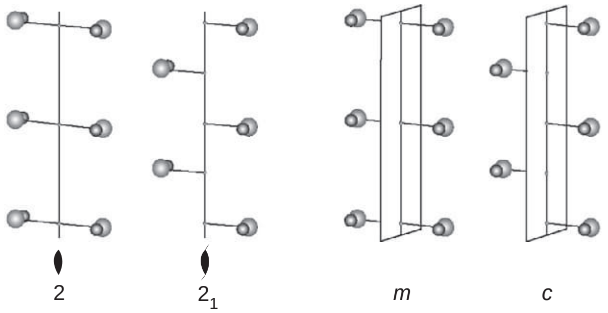

Figure 1 Symmetry elements in crystals: twofold rotation and screw axes 2 and 2_1 (left pair), and reflection and glide planes *m* and *c* (right pair). The "objects" are polar two-atomic molecules, in order to bring out the orientational differences between rotations and reflections. Note that each diagram extends over two translation periods along *c*. The graphical symbols underneath the diagrams are explained in Table 2.

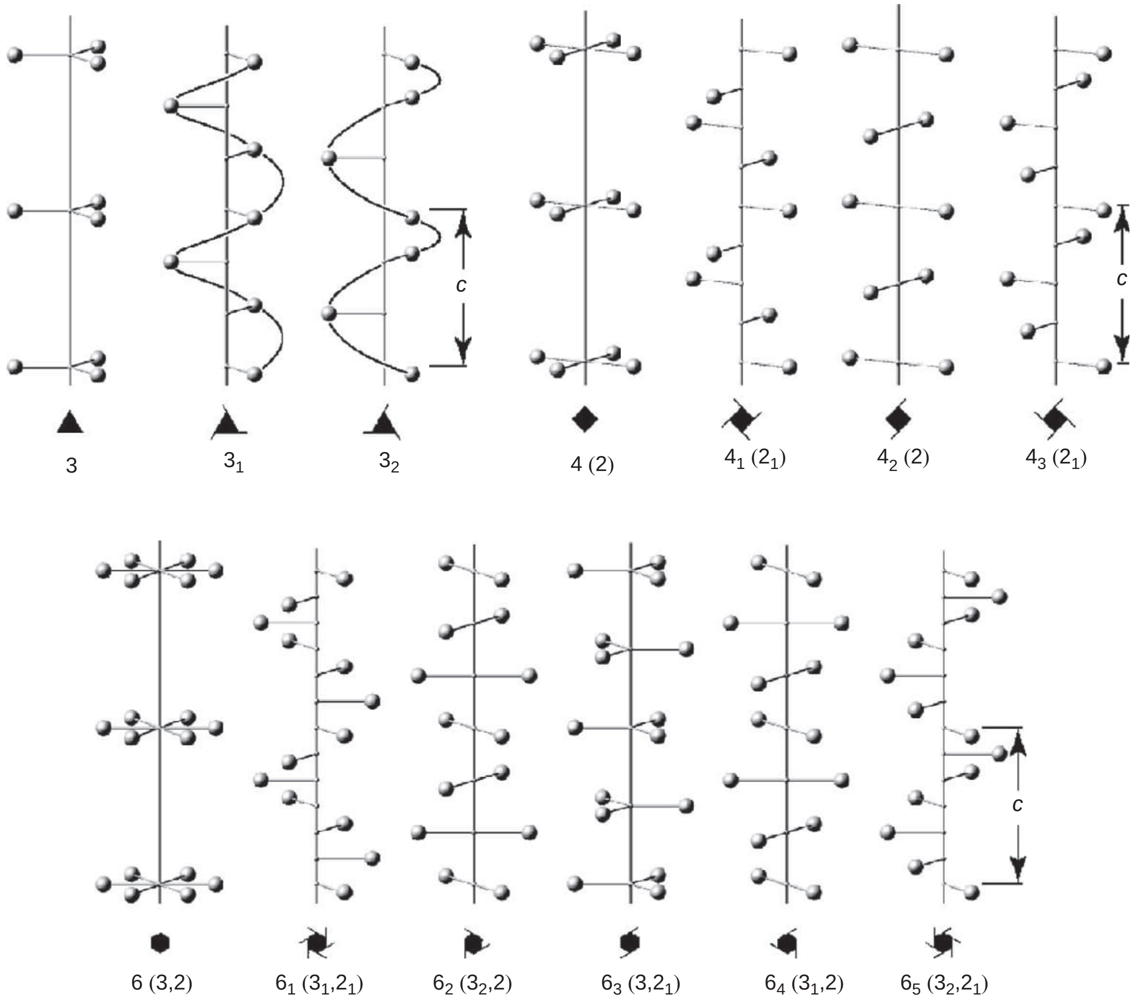

Figure 2 Symmetry elements in crystals: threefold rotation and screw axes (top row), fourfold rotation and screw axes (top row), and sixfold rotation and screw axes (bottom row). Each diagram extends over two translation periods along *c*. For the screw axes 3_1 and 3_2, the course of the screws (helices) is indicated in order to show the enantiomorphism (mirror images) of the two screw axes. The subelements (subgroups) of each symmetry element (cyclic group) are given in parentheses. The graphical symbols are explained in Table 2.

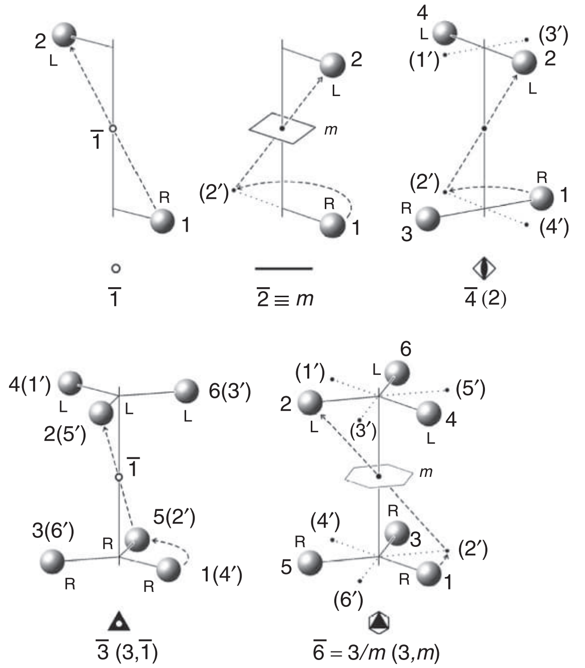

Figure 3 Symmetry elements in crystals: the five crystallographic rotoinversion axes $\bar{1}\bar{2}\bar{4}\bar{3}\bar{6}$ (orders 2, 2, 4, 6, 6, resp.), and their action on a spherical object. Starting from object 1, objects 2, 3, . . . are successively generated. The intermediate positions of the object (between the rotation and the inversion part of the operation) are labeled by numbers in parentheses. For all groups the first operation 1⟶(2′)⟶2 is indicated by dashed arrows. The labels R and L denote the handedness (right or left), if the object is chiral (starting object 1: R). All odd powers of rotoinversions are hand-changing (R↔L), even powers hand-preserving (R⟶R, L⟶L). Note that for axes $\bar{n}$ with n odd (i.e., for $\bar{1}$ and $\bar{3}$), the inversion point is a center of symmetry $\bar{1}$ (i.e., a subelement). For axes $\bar{n}$ with $n = 4k + 2$ (i.e., $\bar{2}$ and $\bar{6}$), a mirror plane m normal to the axis and intersecting the inversion point is a subelement, whereas for $n=4k$ (i.e., $\bar{4}$) neither $\bar{1}$ nor m occur as subelements. The subelements of the rotoinversion axes are noted in parentheses.

Matrix Representation of Symmetry Operations

General Relations

In the mathematical treatment of symmetry operations, normally the coordinate system, that is, the set of basis vectors ***a***, ***b***, ***c*** and the origin, is considered to be at rest, whereas the object is mapped onto itself (special affine mapping). (Equivalently, it is equally correct to transform the coordinate system, whereby the object is considered to be at rest.) A general symmetry operation transforms a point X with coordinates x, y, z into a symmetrically equivalent point $\tilde{X}$, with coordinates $\tilde{x}$, $\tilde{y}$, $\tilde{z}$ according to

$$\begin{aligned} \tilde{x} &= W_{11}x + W_{12}y + W_{13}z + w_1 \\ \tilde{y} &= W_{21}x + W_{22}y + W_{23}z + w_2 \\ \tilde{z} &= W_{31}x + W_{32}y + W_{33}z + w_3 \end{aligned} \qquad [2]$$

or, in matrix notation:

$$\begin{gathered} \begin{pmatrix} \tilde{x} \\ \tilde{y} \\ \tilde{z} \end{pmatrix} = \begin{pmatrix} W_{11} & W_{12} & W_{13} \\ W_{21} & W_{22} & W_{23} \\ W_{31} & W_{32} & W_{33} \end{pmatrix} \cdot \begin{pmatrix} x \\ y \\ z \end{pmatrix} + \begin{pmatrix} w_1 \\ w_2 \\ w_3 \end{pmatrix} \\ \tilde{r} = W \cdot r + w = (W, w) \cdot r \end{gathered} \qquad [3]$$

The (3×3) matrix W is the rotation part, and the (3×1) column matrix $\boldsymbol{w}$, the translation part of the symmetry operation. The matrices W represent all point-group operations, rotations, reflections, inversions, and rotoinversions. The two parts W and $\boldsymbol{w}$ can be assembled into an (augmented) (4×4) matrix $\mathbb{W}$ according to

Table 2 Printed and graphical symbols for symmetry elements in two and three dimensions. For glide planes only a few selected examples are given

Printed symbol	*Symmetry element and its orientation, glide and screw vectors* ***t***	*Graphical symbol normal to plane of projection*
m	Reflection (mirror) plane (three dimensions) Reflection (mirror) line (two-dimensions)	———————
a, *b*, or *c*	"Axial" glide plane	
a	⊥[0 1 0] or ⊥[0 0 1] $\boldsymbol{t} = 1/2\boldsymbol{a}$	– – – – – –
b	⊥[1 0 0] or ⊥[0 0 1] $\boldsymbol{t} = 1/2\boldsymbol{b}$	
c	⊥[1 0 0] or ⊥[0 1 0] $\boldsymbol{t} = 1/2\boldsymbol{c}$	······················
g	Glide line (two dimensions) ⊥[0 1]; ⊥[1 0]; $\boldsymbol{t} = 1/2\boldsymbol{a}$; $1/2\boldsymbol{b}$ (resp.)	– – – – – –
n	"Diagonal" glide plane ⊥[0 0 1]; ⊥[1 0 0]; ⊥[0 1 0]; $\boldsymbol{t} = 1/2(\boldsymbol{a}+\boldsymbol{b})$; $1/2(\boldsymbol{b}+\boldsymbol{c})$; $1/2(\boldsymbol{a}+\boldsymbol{c})$ (resp.)	–·–·–·–·–
d	"Diamond" glide plane (pair of planes) Orthorhombic: ⊥[0 0 1]; ⊥[1 0 0]; ⊥[0 1 0]; $\boldsymbol{t} = 1/4(\boldsymbol{a}\pm\boldsymbol{b})$; $1/4(\boldsymbol{b}\pm\boldsymbol{c})$; $1/4(\boldsymbol{c}\pm\boldsymbol{a})$ (resp.) Cubic (examples): ⊥[1 1 0]; ⊥[0 1 1]; ⊥[1 0 1]; $\boldsymbol{t} = 1/4(-\boldsymbol{a}+\boldsymbol{b}\pm\boldsymbol{c})$; $1/4(\pm\boldsymbol{a}-\boldsymbol{b}+\boldsymbol{c})$; $1/4(\boldsymbol{a}\pm\boldsymbol{b}-\boldsymbol{c})$ (resp.)	–·–·◂·–·– –·–·▸·–·–
1	None (identity)	
2, 3, 4, 6	*n*-fold rotation axis, *n* (three dimensions) *n*-fold rotation point, *n* (two dimensions)	⬮ ▲ ◆ ⬢
$\bar{1}$	Center of symmetry, inversion center	○
$\bar{2} = m, \bar{3}, \bar{4}, \bar{6}$	Rotoinversion axis, $\bar{n}$, with inversion point on the axis[a]	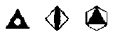
2_1		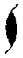
3_1, 3_2	*n*-fold screw axis, n_p	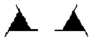
4_1, 4_2, 4_3	The screw component is the fraction *p*/*n* ***t*** of the shortest lattice translation ***t*** parallel to the axis	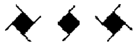
6_1, 6_2, 6_3, 6_4, 6_5		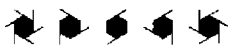

[a] The inversion point is a center of symmetry (inversion center) if ***n*** is odd.

Notes: 1. The graphical symbols (column 3) refer to planes and axes oriented normal to the plane of projection.

2. Diamond glide planes *d* occur only in orthorhombic *F* space groups, in tetragonal *I* space groups, and in cubic *I* and *F* space groups. They always occur in pairs with alternating vectors, for instance, $1/4\ (\boldsymbol{a}+\boldsymbol{b})$ and $1/4\ (\boldsymbol{a}-\boldsymbol{b})$. The second power of a glide reflection *d* (i.e., the result of two successive applications) is a lattice centering vector. The name "diamond glide" is due to its pronounced occurrence in the diamond structure.

3. Rotoreflections are not listed here, because they correspond to rotoinversions according to the following scheme: two-, three-, four-, and sixfold rotoreflections are identical with the rotoinversions $\bar{1}$ (inversion), $\bar{6}$, $\bar{4}$ and $\bar{3}$, respectively. Note that the even two- and sixfold rotoreflections (corresponding to the odd rotoinversions $\bar{1}$ and $\bar{3}$) contain a symmetry (inversion) center.

4. The following pairs of screw axes are "enantiomorphic," i.e. each pair consists of a right- and a left-handed screw axis: (3_1, 3_2), (4_1, 4_3), (6_1, 6_5) and (6_2, 6_4). The screw axes 2_1, 4_2, 6_3 are "neutral." Note that all rotation and screw axes may accommodate enantiomorphic structures, whenever the building units (atomic groups, molecules) of the structure are "chiral," i.e., either all right- or all left-handed.

5. A right-handed screw rotation is customarily defined as a counter-clockwise rotation with the screw vector pointing toward the observer.

$$\begin{pmatrix}\tilde{x}\\ \tilde{y}\\ \tilde{z}\\ \hdashline 1\end{pmatrix} = \left(\begin{array}{ccc:c} \mathbb{W}_{11} & \mathbb{W}_{12} & \mathbb{W}_{13} & w_1\\ \mathbb{W}_{21} & \mathbb{W}_{22} & \mathbb{W}_{23} & w_2\\ \mathbb{W}_{31} & \mathbb{W}_{32} & \mathbb{W}_{33} & w_3\\ \hdashline 0 & 0 & 0 & 1\end{array}\right)\cdot\begin{pmatrix}x\\ y\\ z\\ \hdashline 1\end{pmatrix}$$

$$= \left(\begin{array}{ccc:c} & W & & w\\ \hdashline 0 & 0 & 0 & 1\end{array}\right)\cdot\begin{pmatrix}x\\ y\\ z\\ \hdashline 1\end{pmatrix} = \mathbb{W}\cdot\mathbb{r}$$

[4]

Since every symmetry transformation is a "rigid-body motion," the determinant of the matrices W and $\mathbb{W}$ is

$$\det W = \det\mathbb{W} = 1 \qquad [5]$$

The sequence of two symmetry operations (successive application) is given by the product of their (4×4) matrices $\mathbb{W}_1$ and $\mathbb{W}_2$:

$$\mathbb{W}_3 = \mathbb{W}_2\cdot\mathbb{W}_1 \qquad [6]$$

whereby, $\mathbb{W}_3$ is again a symmetry operation.

The inverse operation $\mathbb{W}^{-1}$ is defined by $\mathbb{W}\cdot\mathbb{W}^{-1} = \mathbb{I}$, whereby $\mathbb{W}$ is the (4×4) unit matrix representing the identity operation:

$$\mathbb{W}^{\;1} = \left(\begin{array}{ccc:c} & W^{-1} & & -W^{-1}\cdot w\\ \hdashline 0 & 0 & 0 & 1\end{array}\right)$$

[7]

Finally, the augmented matrix for a translation ***t*** is

$$\mathbb{T} = \left(\begin{array}{ccc:c} & \boldsymbol{I} & & \boldsymbol{t}\\ \hdashline 0 & 0 & 0 & 1\end{array}\right),$$

$$\boldsymbol{t} = \begin{pmatrix}t_1\\ t_2\\ t_3\end{pmatrix}$$

[8]

and I the (3×3) unit matrix.

Note on the matrices W and $\theta\cdot k$ of eqns [3] and [4]: The rotation parts W of these matrices leave an atom located in the origin of the coordinate system invariant, that is, the symmetry element of W intersects the origin. The translation parts $\boldsymbol{w}$ consist of two components, first the (intrinsic) "screw or glide component" of a screw rotation or glide reflection (if present), second the "location parameter," which depends on the location of the symmetry element with respect to the origin. Thus, for a pure rotation or reflection through the origin, $\mathbf{w}=w_1,w_2,w_3 = (0,0,0)$.

Geometric Interpretation of (Crystallographic) Symmetry Matrices

A (3×3) matrix W of a rigid motion has two essential invariants, that is, two quantities which do not change under a transformation of the coordinate system and, hence, can serve to identify the "nature" of the motion. These quantities are the determinant, detW, and the trace, trW$W_{11}+W_{22}+W_{33}$. Their properties are as follows:

1. A rotation by an angle φ and its representation in a Cartesian coordinate system x_1, x_2, x_3 are assumed, whereby the rotation axis intersects the origin and is parallel to x_3. The rotation matrix is

$$W = \begin{pmatrix}\cos\phi & \sin\phi & 0\\ -\sin\phi & \cos\phi & 0\\ 0 & 0 & 1\end{pmatrix}$$

The trace is tr W = 1 +2 cos φ, valid for any coordinate system. Since this rotation maps a lattice point with integer coordinates onto another lattice point, all elements of the matrix, if referred to a crystallographic coordinate system, must be integers, hence tr W = 1 +2cosφ = m, and cosφ = 1/2(m −1) = 1/2p (m, p integers). Since cos φ is restricted to the range −1 to +1, only the following values of cos φ are compatible with lattice symmetry: cosφ = +1, +1/2, 0, −1/2, −1, corresponding to rotation angles of 0° ≡ 360°, 60°, 90°, 120°, and 180°. This is the famous "crystallographic restriction," which filters out the five permissible φ-angles (and their multiples) from the infinity of "n-fold rotations" with φ=360/n.

2. Since symmetry operations are rigid motions which preserve distances, angles, and volumes, the determinant of their matrices must be +1 or −1:

$$\det \mathrm{W} = \ +1\ :\ \text{rotation; handedness (left or right) of object retained;}$$

$$\det \mathrm{W} = \ -1\ :\ \text{reflection, inversion, rotoinversion : handedness of object reversed;}$$

3. By combining the possible values of detW and tr W, the "nature" of a symmetry operation by means of its (3×3) symmetry matrix W is identified, as shown in Table 3.
4. By more detailed analysis of the (3×3) "point-group" matrices W and the augmented (4×4) "space-group" matrices $\mathbb{W}$, further characteristics of symmetry operations can be derived, that is, the orientation of the axis or of the plane in the given coordinate system, as well as the location of the symmetry element (plane, axis, point) in the unit cell relative to the chosen origin (see *ITA* (2002), Part 11).
5. In order to illustrate the previous somewhat abstract considerations, some examples of (4×4) matrices for (glide) reflections and (screw) rotations, together with their geometric elements, are given in Table 4. A list of all (3×3) matrices occurring in crystallographic point and space groups is available in Part 11 of *ITA* (2002).

Table 3 Crystallographic symmetry operations as derived from their traces tr W and determinants det$W$ = +1 and −1

	det $\boldsymbol{W}$ = −1					det $\boldsymbol{W}$ = −1				
tr $\boldsymbol{W}$	+1	+1/2	0	−1/2	−1	+1	+1/2	0	−1/2	−1
H.-Mauguin symbol of operation	1	6	4	3	2	$\bar{1}$	$\bar{6} \equiv 3/m$	$\bar{4}$	$\bar{3}$	$\bar{2} \equiv m$
Schoenflies symbol of operation	C_1	C_6	C_4	C_3	C_2	C_i	C_{3h}	S_4	C_{3i}	C_s
Order n of operation[a]	1	6	4	3	2	2	6	4	6	2

[a] The "order" n of the operation $\boldsymbol{W}$ is the order of the cyclic group generated by $\boldsymbol{W}$, i.e., the power n of $\boldsymbol{W}$ for which the identity 1 is reached: $\boldsymbol{W}^n = 1$.

Table 4 Examples of augmented (4×4) matrices of symmetry operations (referred to the appropriate conventional coordinate system)[a]

Inversion with center in x_0, y_0, z_0 $\left(\begin{array}{ccc:c} -1 & 0 & 0 & 2x_0 \\ 0 & -1 & 0 & 2y_0 \\ 0 & 0 & -1 & 2z_0 \\ \hdashline 0 & 0 & 0 & 1 \end{array}\right)$	Twofold rotation along z in x_0, y_0, z $\left(\begin{array}{ccc:c} -1 & 0 & 0 & 2x_0 \\ 0 & -1 & 0 & 2y_0 \\ 0 & 0 & 1 & 0 \\ \hdashline 0 & 0 & 0 & 1 \end{array}\right)$	Twofold screw rotation along z in x_0, y_0, z $\left(\begin{array}{ccc:c} -1 & 0 & 0 & 2x_0 \\ 0 & -1 & 0 & 2y_0 \\ 0 & 0 & 1 & 1/2 \\ \hdashline 0 & 0 & 0 & 1 \end{array}\right)$
Glide reflection n with plane $\perp x$ in x_0, y, z $\left(\begin{array}{ccc:c} -1 & 0 & 0 & 2x_0 \\ 0 & 1 & 0 & 1/2 \\ 0 & 0 & 1 & 1/2 \\ \hdashline 0 & 0 & 0 & 1 \end{array}\right)$	Fourfold (screw) rotation 4_p with $p = 0, 1, 2, 3$ along z in 0, 0, z (§) $\left(\begin{array}{ccc:c} 0 & -1 & 0 & 0 \\ 1 & 0 & 0 & 0 \\ 0 & 0 & 1 & p/4 \\ \hdashline 0 & 0 & 0 & 1 \end{array}\right)$	Fourfold rotoinversion $\bar{4}$ along z in 0, 0, z $\left(\begin{array}{ccc:c} 0 & 1 & 0 & 0 \\ 1 & 0 & 0 & 0 \\ 0 & 0 & -1 & 0 \\ \hdashline 0 & 0 & 0 & 1 \end{array}\right)$
Threefold (screw) rotation 3_p with $p - 0, 1, 2$ along z in 0, 0, z (§) $\left(\begin{array}{ccc:c} 0 & -1 & 0 & 0 \\ 1 & -1 & 0 & 0 \\ 0 & 0 & 1 & p/3 \\ \hdashline 0 & 0 & 0 & 1 \end{array}\right)$	Sixfold (screw) rotation 6_p with $p - 0, 1, 2, 3, 4, 5$ along z in 0, 0, z (§) $\left(\begin{array}{ccc:c} 1 & -1 & 0 & 0 \\ 1 & 0 & 0 & 0 \\ 0 & 0 & 1 & p/6 \\ \hdashline 0 & 0 & 0 & 1 \end{array}\right)$	Threefold rotation 3 around body diagonal x, x, x (cubic system) (#) $\left(\begin{array}{ccc:c} 0 & 0 & 1 & 0 \\ 1 & 0 & 0 & 0 \\ 0 & 1 & 0 & 0 \\ \hdashline 0 & 0 & 0 & 1 \end{array}\right)$

(§) Note that $p = 0$ stands for a normal (nonscrew) rotation.

(#) Cyclic permutation of the coordinates. This matrix also represents the one threefold rotation around x, x, x in the rhombohedral coordinate system. There are four equivalent cubic body diagonals x, x, x; $-x, x, x$; $x, -x, x$ and $x, x, -x$ with different cyclic permutations of +1 and −1.

[a] The matrices in this table represent the "first powers" of the operations. Higher powers are obtained by repeated multiplication of the matrix. For point-group operations of order 2 ("binary" operations: inversions, twofold rotations, reflections), the second power is the identity, i.e., binary operations are their own inverses.

6. It should be noted that in quasicrystals (i.e., forms of solid matter not based on exact three-dimensional periodicity but rather on "quasiperiodicity"), symmetries may occur which go beyond the "crystallographic restriction" discussed above under point 1. For instance, quasicrystals with icosahedral symmetry (containing fivefold rotations), as well as with tenfold and twelvefold rotations have been found.

Symbols for Point Groups and Space Groups

So far, "individual" symmetry operations and symmetry elements have been treated with their printed and graphical symbols, see Table 2. In order to combine these into symbols for crystallographic point and space groups, rules for the combination have to be specified. There are two types of group symbols in use: the oldest are the Schoenflies symbols contained in Schoenflies' classic work of 1891. The second are the Hermann-Mauguin symbols, derived around 1928 in several papers by Hermann and Mauguin. The latter are now predominantly used in crystallography and crystal-structure analysis, and are customarily called "international symbols." Schoenflies symbols are often preferred in spectroscopy and in studies of molecules.

Schoenflies Symbols

These symbols are based on group theory and use capital letters to indicate the major types of symmetry groups.

C: Cyclic groups C_1, C_2, C_3, C_4, C_6 of order $C_1 = 1$, 2, 3, 4 and 6;

C_s=reflection group (s=*Spiegel*symmetry) of order 2;
C_i = inversion group of order 2;
D: Dihedral groups D_2, D_3, D_4, D_6, that is, a cyclic group C with additional twofold rotation axes normal to the main symmetry axis. The order m of these groups is twice that of the corresponding C_n group: $m = 2n$.
T: Tetrahedral group (order $n = 12$);
O: Octahedral group (order $n = 24$).

Subscripts h, v, and d indicate the presence of mirror planes perpendicular h = horizontal and parallel (v = vertical, d = diagonal) to the main symmetry axis, which is considered to be vertical, for example, C_{2h}, D_{4h}, T_h, O_{2v}, C_{6v}, D_{3d}. The Schoenflies symbols are independent of any coordinate system.

These symbols apply to three-dimensional crystallographic point groups. Space groups are indicated by superscripts added to the corresponding point-group symbols, for example, C_{2h}^5, D_2^4, D_{2h}^{16}, T_h^7, O_h^9. This implies that the Schoenflies symbols carry no information about the nature of the space group. No Schoenflies symbols exist for two-dimensional groups.

Hermann–Mauguin (International) Symbols

These symbols have, as their basis, the seven different point symmetries of the Bravais lattices. Every lattice, if viewed along a general direction, exhibits only inversion symmetry $\bar{1}$. There are, however, between zero (triclinic) and 13 (cubic) specific directions, along which symmetries above $\bar{1}$ are seen. These so-called "lattice symmetry directions" (blickrichtungen) and the symmetries seen along them are characteristic for the seven types of lattice symmetries (holohedries), see Table 1. They can be grouped into none (triclinic), one (monoclinic), two (rhombohedral), and three (all other lattices) classes of equivalent symmetry directions (e.g., the fourfold cubic rotation axes [1 0 0], [0 1 0], [0 0 1] form one class). These classes are arranged in a well-defined sequence (called "positions"), which is again characteristic for each crystal system. They form, thus, the basis of the Hermann–Mauguin (international) point-group and space-group symbols.

The representative lattice symmetry directions for these classes are presented in Table 5, both for two- and three-dimensional lattices. The three columns define the "position" of an entry in a Hermann–Mauguin group symbol (primary, secondary, and tertiary position). The entries in an actual symbol are those symmetry axes and symmetry planes, which are "observed" for the corresponding blickrichtung. A slash indicates the occurrence of a mirror (glide) plane perpendicular to an axis (e.g., $4/m$, $2_1/c$). In this way, the international point-group symbols are obtained. This process is illustrated, first for "point groups," by the following examples:

1, $\bar{1}$	triclinic; no symmetry direction, since {{\={1}}} is a point (Schoenflies symbols C_1, C_i);
2, m, $2/m$	monoclinic; only one symmetry direction along which is "seen" a twofold axis, the normal to a mirror plane or the combination of both (Schoenflies symbols C_2, C_s, C_2h);
$mm2$	orthorhombic; three perpendicular symmetry directions, two of which carry normals to mirror planes, the third a twofold axis (Schoenflies symbol C_{2v});
$4/m$	tetragonal, short for $4/m11$, since only the primary blickrichtung carries symmetry (Schoenflies symbol C_4h);
$6/m2/m2/m$ (short: $6/mmm$)	hexagonal holohedry; three classes of symmetry directions, the primary single direction is populated by a sixfold rotation axis and a perpendicular mirror plane: $6/m$. The three equivalent secondary and three equivalent tertiary directions are populated by twofold axes with perpendicular mirror planes, leading to a total of seven "occupied" blickrichtungen (Schoenflies symbol $D_{6/}h$);
$4/m\bar{3}2/m$ (short: $m\bar{3}\ m$)	cubic holohedry; point group of highest crystallographic symmetry; along the three cube edges of the cubic unit cell, symmetry axes/planes $4/m$ occur, the four body-diagonal directions of the cube are populated by {{\={3}}} inversion axes, and the six face diagonals carry $2/m$ symmetries. In total, there are 13 symmetry directions with 48 symmetry operations (=group order) (Schoenflies symbol O_h).

Table 5 Representative lattice symmetry directions for two and three dimensions. The number in parentheses refers to the number of equivalent symmetry directions of the given set, e.g., cubic [1 0 0] (3) refers to the three equivalent directions [1 0 0], [0 1 0], [0 0 1]

Lattice	*Symmetry direction (position in Hermann–Mauguin symbol)*		
	Primary	*Secondary*	*Tertiary*
Two dimensions			
Oblique (monoclinic)	Rotation	- - - - - -	- - - - - -
Rectangular (orthorhombic)	point	[1 0] (1)	[0 1] (1)
Square (tetragonal)	In	[1 0] (2)	[1 $\bar{1}$] (2)
Hexagonal	plane (1)	[1 0] (3)	[1 $\bar{1}$] (3)
Three dimensions			
Triclinic (anorthic)	None		
Monoclinic	[0 1 0] (1) (unique axis *b*) [0 0 1] (1) (unique axis *c*)	- - - - - -	- - - - - -
Orthorhombic	[1 0 0] (1)	[0 1 0] (1)	[0 0 1] (1)
Tetragonal	[0 0 1] (1)	[1 0 0] (2)	[1 $\bar{1}$ 0] (2)
Hexagonal	[0 0 1] (1)	[1 0 0] (3)	[1 $\bar{1}$ 0](3)
Rhombohedral (hexagonal axes)	[0 0 1] (1)	[1 0 0] (3)	- - - - - -
Rhombohedral (rhombohedral axes)	[1 1 1] (1)	[1 $\bar{1}$ 0] (3)	- - - - - -
Cubic	[1 0 0] (3)	[1 1 1] (4)	[1 $\bar{1}$ 0] (6)

The space-group symbols are modifications of the point-group symbols in two ways: first, the letter with the centering type of the appropriate Bravais lattice, P, A, B, C, I, F, R is added in front of the symbol. Second, as appropriate, the symbols for rotation axes are substituted by those of screw axes, and the symbols of reflection planes by those of glide planes. Lattice symmetry directions, which do not carry any symmetry, are represented by the symbol "1", as in $P31m$ and $P3m1$, or are left empty as in $P6_3/m$, short for $P6_3/m11$.

This procedure leads to the following full (and short) symbols, given as examples:

Monoclinic: $P2_1/c$, $C2/c$ (two of the frequently encountered space groups);

Orthorhombic: $P2_12_12_1$, $P2_1/n\,2_1/m\,2_1/a$ ($Pnma$), $C2/m\,2/c\,2_1/m$ ($Cmcm$), $I2_1/b\,2_1/c\,2_1/a$ ($Ibca$);

Trigonal: $P31m$, $P3m1$, $R3m$;

Hexagonal: $P6_3/m$, $P6_522$,$P\bar{6}2m$, $P6_3/m\,2/c\,2/m$ ($P6_3/mcm$);

Cubic: $I2_13$, $I2_1/a\bar{3}(Ia\bar{3})$, $P4_332$, $F\bar{4}3c$, $F4/m\bar{3}\,2/m$ ($Fm\bar{3}m$), $I4_1/a\bar{3}\,2/d$ ($Ia\bar{3}d$).

It is not possible to treat here the details of the derivation and the nomenclature of space groups. This topic requires a certain amount of practical acquaintance. The *International Tables*, Vol. A [*ITA* (2002)], contain complete listings and explanations of the 17 plane (two-dimensional) groups, the 230 space groups and the 32 crystallographic point groups. The so-called "subperiodic groups" (number of periodic dimensions lower than the total number of dimensions of the group), i.e., frieze, layer and rod groups, are presented in Vol. E (2002) of the *International Tables*. For textbooks, please see "Further reading" below.

Acknowledgments

The authors thank R A Becker, H Schmidt, and J Simons (Aachen) for the preparation of the diagrams.

Further Reading

Bloss ED (1971) *Crystallography and Crystal Chemistry*. New York: Holt, Rinehart and Winston.

Buerger MJ (1965) *Elementary Crystallography*. New York: Wiley.

Buerger MJ (1971) *Introduction to Crystal Geometry*. New York: McGraw-Hill.

Burns G and Glaser AM (1990) *Space Groups for Solid State Scientists*. New York: Academic Press.

Giacovazzo C (ed.) (1992) *Fundamentals of Crystallography*. Oxford: Oxford University Press.

Hahn Th and Wondratschek H (1994) *Symmetry of Crystals. Introduction to International Tables for Crystallography*, vol. A. Sofia: Heron Press.

International Tables for Crystallography. 5. Edition Hahn Th (ed.) (2002) *Space-group Symmetry*, 5. Edition, vol. A. Dordrecht: Kluwer Academic Publishers [1. Edition 1983, 5. Edition 2002, abbreviated as *ITA* (2002)].

International Tables for Crystallography. 1. Edition Kopsky V and Litvin DB (eds.) (2002) *Subperiodic Groups*, 1. Edition, vol. E. Dordrecht: Kluwer Academic Publishers.

Ledermann W (1976) *Introduction to Group Theory*. London: Longman.

McKie D and McKie Ch (1986) *Essentials of Crystallography*. Oxford: Blackwell.

Nye JF (1957) *Physical Properties of Crystals. Their Representation by Tensors and Matrices*. Oxford: Clarendon Press [1. Edition 1957, Revised Edition 1985].

O'Keefe M and Hyde BG (1996) *Crystal Structures I. Patterns and Symmetry*. Washington, DC: Mineralogical Society of America.

Schwarzenbach D (1996) *Crystallography*. Chichester: Wiley [Original French edition 1996, German edition 2001].

Shubnikov AV and Koptsik VA (1974) *Symmetry in Science and Art*. New York: Plenum Press.

Vainstein BK (1994) *Modern Crystallography, Vol. 1, Fundamentals of Crystals. Symmetry and Methods of Structural Crystallography*, 2. Edition. Berlin: Springer.

Wondratschek H and Neubüser J (1967) *Acta Crystallographica* 23: 349–352.

Crystal optics

DA Lyashenko and Yu P Svirko, Department of Physics and Mathematics, University of Eastern Finland, Joensuu, Finland

© 2024 Elsevier Ltd. All rights reserved.

This is an update of D.A. Lyashenko, Yu.P. Svirko, Crystal Optics, Editor(s): Franco Bassani, Gerald L. Liedl, Peter Wyder, Encyclopedia of Condensed Matter Physics, Elsevier, 2005, Pages 283–289, ISBN 9780123694010, https://doi.org/10.1016/B0-12-369401-9/00607-0.

Introduction 80
Maxwell equations 80
Constitutive equation in anisotropic medium 81
Fresnel equation, wave vector surface, and ray surface 83
Optical properties of uniaxial crystals 83
Optical properties of biaxial crystals 85
Polarization devices based on the crystal optics 86
Conclusion 87
References 87

Abstract

Crystal optics describes the light in anisotropic media when the optical response depends on the direction of propagation and polarization of the light beam, i.e. the refractive index may vary with direction. The optical anisotropy leads to the fundamental phenomenon of double refraction (birefringence) that has found a numerous applications optical engineering. In this chapter, we briefly discuss how the optical anisotropy can manifest itself in the light propagation and introduce basic devices to control light polarization.

Key points

- Causality principle and response function
- Constitutive equation and dielectric tensor
- Light wave propagation in anisotropic transparent medium
- Wave surface and ray surface in uniaxial and bi-axial crystals
- Wave plates and other devices to control polarization of the light beam

Introduction

Crystal optics describes the optical phenomena in anisotropic media when light waves may behave differently depending on direction propagation and polarization. This branch of optics is named after natural crystals that are used in optical devices for many years. The crystal optics techniques and approaches can also be employed to describe light propagation in non-crystalline bulk media (e.g., in an isotropic liquid) when static external fields induce optical anisotropy or in artificial structures, which can be created by recent advances in material science.

Conventionally, the crystal optics refers the light propagation in the transparent dielectric crystals leaving behind the dramatic enrichment of the propagation phenomena in the vicinity of the absorption resonances where the frequency and spatial dispersion may play decisive roles. Also, the crystal optics usually addresses the linear optical phenomena, which are governed by the second-rank tensor of the linear optical susceptibility. However, it is worth noting that the nonlinear optical phenomena, which arise due to dependence of the light propagation effects on the light wave amplitude and are governed by the higher-rank tensors of nonlinear susceptibility, are much more sensitive to the crystal symmetry. Nevertheless, the core part of the crystal optics has “crystallized” in pre-laser era and these intensity-dependent effects are studied in the framework of nonlinear rather than crystal optics. In this article, major effects in light propagation in anisotropic nonmagnetic media are discussed.

Maxwell equations

If the relative magnetic permeability of the medium is equal to 1 and no free electric charges and currents are present, the spatial and temporal evolution of the electric field $\mathcal{E}$, magnetic induction $\mathcal{B}$ and electric displacement $\mathcal{D}$ is determined by the Maxwell equations:

$$\operatorname{div} \mathcal{D} = 0$$

https://doi.org/10.1016/B978-0-323-90800-9.00143-8

$$\operatorname{div}\mathcal{B} = 0$$

$$\operatorname{curl}\mathcal{E} = -\frac{1}{c}\frac{\partial\mathcal{B}}{\partial t}$$

$$\operatorname{curl}\mathcal{B} = \frac{1}{c}\frac{\partial\mathcal{D}}{\partial t} \tag{1}$$

In the plane monochromatic wave with frequency ω and wave vector $\boldsymbol{k}$ that propagates in such a medium,

$$\mathcal{E}(t, \boldsymbol{r}) = \boldsymbol{E}e^{-i\omega t+i\boldsymbol{kr}} + \boldsymbol{E}^*e^{i\omega t-i\boldsymbol{kr}}$$

$$\mathcal{B}(t,\boldsymbol{r}) = \boldsymbol{B}e^{-i\omega t+ikr} + \boldsymbol{B}^*e^{i\omega t-ikr}$$

$$\mathcal{D}(t, \boldsymbol{r}) = \boldsymbol{D}e^{-i\omega t+i\boldsymbol{kr}} + \boldsymbol{D}^*e^{i\omega t-i\boldsymbol{kr}} \tag{2}$$

where the vectors ***E***, ***B***, ***D***, and ***k*** are perpendicular to one another:

$$\boldsymbol{k}\cdot\boldsymbol{D} = 0$$

$$\boldsymbol{k}\cdot\boldsymbol{B} = 0$$

$$\boldsymbol{k}\times\boldsymbol{E} = \frac{\omega}{c}\boldsymbol{B}$$

$$\boldsymbol{k}\times\boldsymbol{B} = -\frac{\omega}{c}\boldsymbol{D} \tag{3}$$

However, vectors ***E*** and ***D*** are not necessarily collinear. The plane containing vectors ***D*** and ***B*** (and perpendicular to the wave vector ***k***) is called the wave front plane, while those containing pair ***k***, ***B*** and ***k***, ***D*** are called the polarization plane and vibration plane, respectively. The plane containing orthogonal vectors ***E*** and ***B*** is perpendicular to the energy flux vector $\boldsymbol{S} = (c/4\pi) < [\mathcal{E}\times\mathcal{B}] >$, where angular brackets stand for averaging over the wave period $T = 2\pi/\omega$, the direction of the ray propagation in the medium (see Fig. 1). It is worth noting that ***S*** is not necessarily parallel to the wave vector ***k***.

One can observe from (1) that the number of variables in Maxwell's equations is greater than the number of equations, an additional relationship (constitutive equation) is needed between electric displacement $\mathcal{D}$ and the wave fields. However, since $\mathcal{E}$ and $\mathcal{B}$ in nonmagnetic media are related by the third Maxwell equation in (1), this constitutive equation, which should account for the material properties of the medium, can be reduced down to functional relationship between electric displacement $\mathcal{D}$ and electric field strength $\mathcal{E}$.

It is worth noting that deriving the constitutive equation, i.e. finding the relationship between $\mathcal{D}$ and $\mathcal{E}$ in particular medium, is beyond the scope electrodynamic and implies solving the light-matter interaction problem in the microscale (Landau and Lifshitz, 1984). Convectional approach involves quantum mechanical techniques that allow one to describe interaction of the electronic ensemble of particular medium with electromagnetic field. However, in order to solve the macroscopic problem of the propagation of the light wave it is often sufficient to consider restrictions that properties of the medium (e.g. its spatial symmetry) impose on the constitutive equation. We will see below that in crystal optics, such an approach enables transparent and consistent description of the light propagation by introducing uniaxial and bi-axial crystals.

Constitutive equation in anisotropic medium

Constitutive equation of the medium must obey the causality principle that ensures retrospective relationship between $\mathcal{D}$ and $\mathcal{E}$ is determined by the preceding electric field, but not by the future one. Similarly, the displacement is not necessarily local, that is, it could depend on the electric field not only at the point of observation, but also in some vicinity around it. With account for the causality and nonlocality, the constitutive equation for linear optics can be presented in the following form (Landau and Lifshitz, 1984):

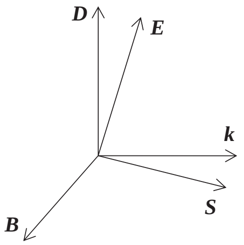

Fig. 1 Mutual orientation of vectors ***E, B, D, k***, and ***S*** in the anisotropic medium. Reproduced from Lyashenko DA and Svirko YuP (2005) Crystal optics. In: Encyclopedia of Condensed Matter Physics, 1st edn. Elsevier, 283–289.

$$\mathcal{D}_i(t,\boldsymbol{r}) = \sum\nolimits_{j=x,y,z}\int_{-\infty}^{t} dt_1 \int_V d\boldsymbol{r}_1 \psi_{\mathrm{ij}}(t - t_1,\boldsymbol{r} - \boldsymbol{r}_1)\mathcal{E}_j(t_1\boldsymbol{r}_1) \tag{4}$$

Here, the subscripts label the Cartesian axes x, y, z of the laboratory frame, $\psi_{\mathrm{ij}}(t - t_1, \boldsymbol{r} - \boldsymbol{r}_1)$ is the response function that describes the contribution into displacement at point $\boldsymbol{r}$ and time t resulting from the finite electric field at point $\boldsymbol{r}_1$ at time t_1. Since $\boldsymbol{\mathcal{D}}$ and $\boldsymbol{\mathcal{E}}$ are vector quantities, the response function is tensorial by nature and relates projections of the displacement and electric filed in the laboratory Cartesian frame. The properties of the response function are determined by the mechanism of the optical response in the medium and the medium symmetry. If the optical response is instantaneous, $\psi_{ij}(t - t_1, \boldsymbol{r} - \boldsymbol{r}_1) \propto \delta(t - t_1)$, the displacement at the moment t is given by the electric field at the same moment of time. If the displacement in a particular point $\boldsymbol{r}$ only depends on electric filed strength at this location, $\psi_{ij}(t - t_1, \boldsymbol{r} - \boldsymbol{r}_1) \propto \delta(\boldsymbol{r} - \boldsymbol{r}_1)$. Since the optical properties originate from the response of the electron ensemble on the light filed, the response function would normally have a maximum at $\boldsymbol{r} = \boldsymbol{r}_1$ and diminish for $|\boldsymbol{r} - \boldsymbol{r}_1| > a$, where a is the typical size of the atom or molecule. In crystals, the effects of the spatial dispersion are often associated with excitation of quasiparticles such as excitons, which may have effective radii of up to hundreds of angstroms.

The constitutive equation can be reduced to more familiar form if one considers propagation of a monochromatic wave with frequency ω and wave vector $\boldsymbol{k}$ (2):

$$D_i = \sum\nolimits_{j=x,y,z}\varepsilon_{ij}(\omega,\boldsymbol{k})E_j \tag{5}$$

where

$$\varepsilon_{ij}(\omega,\, \boldsymbol{k}) = \int_0^{\infty} d\tau \int_V d\boldsymbol{\rho}\psi_{\mathrm{ij}}(\tau,\, \boldsymbol{\rho})e^{i\omega\tau\, -\, \mathrm{i}\mathbf{k}\boldsymbol{\rho}} \tag{6}$$

is the dielectric tensor that governs the propagation of the electromagnetic waves in the medium.

In the following, the spatial dispersion effects (Agranovich and Ginzburg, 1984) (i.e., the dependence of the dielectric tensor on the wave vector), which in the most cases result in a minor correction in the wave propagation in anisotropic media, are ignored. However, if the spatial dispersion is the only source of the optical anisotropy (e.g., circular birefringence in chiral liquids), it should be taken into account to describe phenomena of the optical activity and circular dichroism.

Dielectric tensor is symmetric with respect to permutation of its indices, $\varepsilon_{ij}(\omega,\boldsymbol{k}) = \varepsilon_{ji}(\omega,-\boldsymbol{k})$. This fundamental symmetry relation arises from the Onsager principle of symmetry of kinetic coefficients (Landau and Lifshitz, 1984) and holds in nonmagnetic media at thermal equilibrium. Another important property of the dielectric tensor is its Hermicity that is, $\varepsilon_{ij}(\omega,\boldsymbol{k}) = \varepsilon^*_{ji}(\omega,\boldsymbol{k})$ in the frequency region where the absorption losses are negligible. Correspondingly, the energy dissipation rate when a light wave at frequency ω and wave vector $\boldsymbol{k}$ propagates in the medium is given by non-Hermitian part of the dielectric tensor:

$$Q = \frac{i\omega}{16c}\sum_{i,j=x,y,z}\left(\varepsilon^*_{ij}(\omega,\, \boldsymbol{k}) - \varepsilon_{ji}(\omega,\, \boldsymbol{k})\right)E_iE^*_j \tag{7}$$

In the transparent medium without spatial dispersion the dielectric tensor is real, $\varepsilon_{ij}(\omega) = \varepsilon^*_{ij}(\omega)$ (Landau and Lifshitz, 1984), and, therefore, there exists a Cartesian frame in which it can be presented in the diagonal form:

$$\varepsilon_{ij} = \begin{pmatrix} \varepsilon_1 & 0 & 0 \\ 0 & \varepsilon_2 & 0 \\ 0 & 0 & \varepsilon_3 \end{pmatrix} \tag{8}$$

ε_1, ε_2 and ε_3 are called the principal dielectric constants. The coordinate axes of this system are called principal dielectric axes of the crystal. In this coordinate frame, the constitutive Eq. (5) reduces down to $D_x = \varepsilon_1 E_x$, $D_y = \varepsilon_2 E_y$, $D_z = \varepsilon_3 E_z$, that is, displacement and electric field are not parallel one another unless $\boldsymbol{E}$ coincides with one of the principal axes or principal dielectric constants are equal.

If the optical response is not instantaneous, the dielectric tensor depends on the frequency, and, therefore, both orientation of the principal axes and magnitude of the principal dielectric constants may vary with frequency (Patrini and Guizzetti, 2022). On the other hand, crystal symmetry imposes restrictions on the structure of the dielectric tensor and, therefore, on the number of nonequal principal dielectric constants (Ivchenko, 2022; La Rocca, 2022). The competition between symmetry restrictions and frequency (also referred to as color) dispersion allows one to introduce three distinct groups in the optical classification of the crystals (Lovett, 2017).

In cubic crystals, three crystallographically equivalent, mutually orthogonal directions may be chosen. In crystals of cubic system, principal dielectric constants are equal, $\varepsilon_1 = \varepsilon_2 = \varepsilon_3 = \varepsilon$. Therefore, the constitutive equation in cubic crystals is the same as that in isotropic medium, $\boldsymbol{D} = \varepsilon\boldsymbol{E}$, that is, cubic crystals are optically isotropic. In these crystals, the frequency dispersion may change only the magnitude of the dielectric constant.

In crystals of trigonal, tetragonal, and hexagonal systems, the plain containing two equivalent perpendicular directions is perpendicular to the three-, four-, or sixfold rotation axis, respectively. Conventionally, this direction is chosen along the third principal axis. In these crystals, which are called uniaxial, relationship $\varepsilon_1 = \varepsilon_2 \neq \varepsilon_3$ holds at all frequencies.

In crystals of orthorhombic, monoclinic, and triclinic systems, no two equivalent directions can be chosen. These crystals in which $\varepsilon_1 \neq \varepsilon_2 \neq \varepsilon_3$, are called biaxial. In the crystals belonging to the orthorhombic system, the directions of the principal axes are fixed and coincide with twofold rotation axes and/or symmetry planes. This ensures their independence from the wave frequency. This situation changes for crystals of monoclinic system, in which the only twofold rotation axis exists, and correspondingly, orientation of just one principal axis does not show color dispersion. In the crystals of the triclinic system, both directions of principal axes and magnitudes of the principal dielectric indices may change with frequency.

Fresnel equation, wave vector surface, and ray surface

Maxwell Eqs. (3) allow one to arrive at the following equation for the amplitude of the displacement $\boldsymbol{D}$ when the light wave with frequency ω and wave vector $\boldsymbol{k}$ that propagates in the medium:

$$\frac{\omega^2}{c^2}\boldsymbol{D} = [\boldsymbol{k} \times [\boldsymbol{E} \times \boldsymbol{k}]] = \boldsymbol{k}^2\boldsymbol{E} - (\boldsymbol{k} \cdot \boldsymbol{E})\boldsymbol{k} \tag{9}$$

By using constitutive Eq. (5) one can arrive at three linear homogeneous equations for the Cartesian components of electric field in the principal crystal frame:

$$\begin{aligned}
&\left(k_y^2 + k_z^2 - \frac{\omega^2}{c^2}\varepsilon_1\right)E_x - k_x k_y E_y - k_x k_z E_z = 0\\
&-k_y k_x E_x + \left(k_x^2 + k_y^2 - \frac{\omega^2}{c^2}\varepsilon_2\right)E_y - k_y k_z E_z = 0\\
&-k_z k_x E_x - k_z k_y E_y + \left(k_x^2 + k_y^2 - \frac{\omega^2}{c^2}\varepsilon_3\right)E_z = 0
\end{aligned} \tag{10}$$

The compatibility condition for these equations is that the relevant determinant should vanish. This condition gives the so-called Fresnel's equation that defines the frequency dependence of the wave vector (or dispersion relation). By introducing vector $\boldsymbol{n} = (c/\omega)\boldsymbol{k}$ along direction of propagation and effective refraction index $n = \sqrt{n_x^2 + n_y^2 + n_z^2}$, the Fresnel equation is conventionally presented in the following form:

$$n^2\left(\varepsilon_1 n_1^2 + \varepsilon_2 n_2^2 + \varepsilon_3 n_3^2\right) - \left[n_1^2\varepsilon_1(\varepsilon_2 + \varepsilon_3) + n_2^2\varepsilon_2(\varepsilon_1 + \varepsilon_3) + n_3^2\varepsilon_3(\varepsilon_1 + \varepsilon_2)\right] + \varepsilon_1\varepsilon_2\varepsilon_3 = 0 \tag{11}$$

When the direction of propagation is given, solution of the Eq. (11) gives two different magnitudes of the effective refractive index. Fresnel's equation in coordinates $\{n_1, n_2, n_3\}$ defines the so-called wave vector surface.

Normal to the wave vector surface gives the direction of the energy propagation (Poynting vector) in the medium. Usually, it is described by so-called ray vector $\boldsymbol{s}$, which is introduced by condition $(\boldsymbol{ns}) = 1$. Since the Poynting vector is perpendicular to $\boldsymbol{E}$ and $\boldsymbol{B}$, one can readily arrive at

$$\begin{aligned}
\boldsymbol{s} \times \boldsymbol{B} &= -\boldsymbol{E}\\
\boldsymbol{s} \times \boldsymbol{D} &= \boldsymbol{B}
\end{aligned} \tag{12}$$

By replacing $\boldsymbol{E}$ with $\boldsymbol{D}$ and $\boldsymbol{k}$ with $-(\omega/c)\boldsymbol{s}$ and vice versa in (3) one may arrive at (12). This corresponds to the rule of duality in the crystal optics. According to this rule, an equation valid for vectors $\boldsymbol{E}$, $\boldsymbol{n}$, and tensor ε_{ij} is also valid if these variables are replaced with $\boldsymbol{D}$, $\boldsymbol{s}$, and tensor ε_{ij}^{-1}, respectively. For example, from Fresnel's equation (11) one can obtain the equation which defines the ray vector surface:

$$s^2\left(\varepsilon_3\varepsilon_2 s_1^2 + \varepsilon_1\varepsilon_3 s_2^2 + \varepsilon_1\varepsilon_2 s_3^2\right) - \left[s_1^2(\varepsilon_2 + \varepsilon_3) + s_2^2(\varepsilon_1 + \varepsilon_3) + s_3^2(\varepsilon_1 + \varepsilon_2)\right] + 1 = 0 \tag{13}$$

One can observe that when the direction of $\boldsymbol{s}$ is given, two rays with two different wave vectors can propagate in the crystal.

The above analysis can be visualized by means of simple geometrical constructions. One may draw the ellipsoid that corresponds to the tensor ε_{ij}^{-1} with semiaxes equal to the square roots of the principal dielectric constants. This equation is called ellipsoid of wave normals (also known as the index ellipsoid), and in the Cartesian frame with principal dielectric axes, it is described by the following equation:

$$\frac{x^2}{\varepsilon_1} + \frac{y^2}{\varepsilon_2} + \frac{z^2}{\varepsilon_3} = 1 \tag{14}$$

If the ellipsoid is cut by a plane which is orthogonal to the vector $\boldsymbol{n}$, the intersection of the plane with the ellipsoid will be an ellipse (see Fig. 2). The length of its axes determines the two values of the effective refractive index, while the axes determine the directions of the relevant vector $\boldsymbol{D}$. It is necessary to notice that unit vectors in these two directions and unite vector along n form Cartesian basis.

In order to find orientation of the electric field in the medium, the ellipsoid that corresponds to the tensor (8) with semiaxes equal to the square roots of the inverse principal dielectric constants (the Fresnel or ray ellipsoid) is considered:

$$\varepsilon_1 x^2 + \varepsilon_2 y^2 + \varepsilon_3 z^2 = 1 \tag{15}$$

If the ellipsoid is cut by a plane with normal $\boldsymbol{s}$, the intersection of the plane with ellipsoid will be an ellipse, whose axes determine the two values of effective refractive index and orientation of the relevant vector $\boldsymbol{E}$.

Optical properties of uniaxial crystals

In the uniaxial crystals, two principal dielectric constants are equal to one another ($\varepsilon_1 = \varepsilon_2 = \varepsilon_\perp$, $\varepsilon_3 = \varepsilon_\parallel$). This reduces the Fresnel equation (11) down to the product of two factors:

$$\left(n^2 - \varepsilon_\perp\right)\left[\varepsilon_\parallel n_3^2 + \varepsilon_\perp\left(n_1^2 + n_2^2\right) - \varepsilon_\parallel\varepsilon_\perp\right] = 0 \tag{16}$$

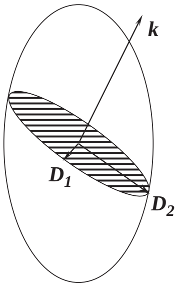

Fig. 2 Ellipsoid of wave normals. The normal to the wave vector section of the ellipsoid is ellipse (shaded). The lengths of its semi-axes determine the values of refractive index, while the directions of these orthogonal axes give the directions of oscillations, i.e. transverse components $\boldsymbol{D_1}$ and $\boldsymbol{D_2}$ of electric displacement vector. Reproduced from Lyashenko DA and Svirko YuP (2005) Crystal optics. In: Encyclopedia of Condensed Matter Physics, 1st edn. Elsevier, 283–289.

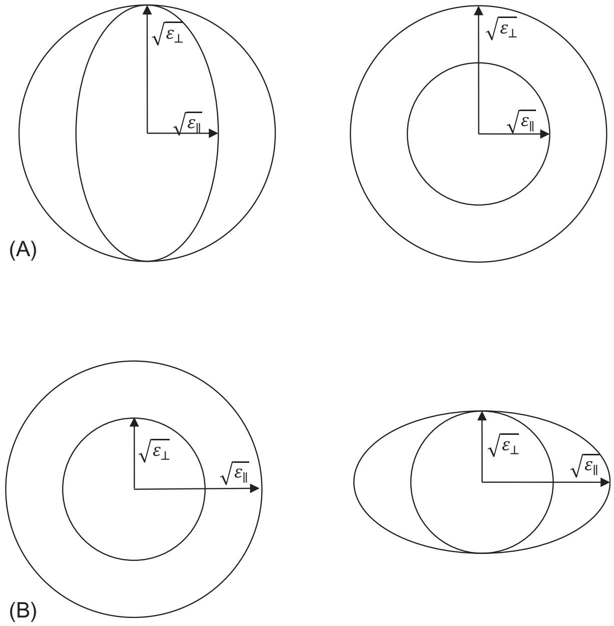
$\sqrt{\varepsilon_\perp}$
$\sqrt{\varepsilon_\parallel}$
(A)
$\sqrt{\varepsilon_\perp}$
$\sqrt{\varepsilon_\parallel}$
(B)

Fig. 3 Orthogonal sections of normal surfaces for uniaxial crystals: (A) negative crystal. The sphere with radius equal to $\varepsilon_\perp$ lies outside the spheroid with main semiaxes $\sqrt{\varepsilon_\perp}$ and $\sqrt{\varepsilon_\parallel}$. (B) positive crystal. The sphere with radius equal to $\sqrt{\varepsilon_\perp}$ lies inside the spheroid with main semi-axes $\sqrt{\varepsilon_\perp}$ and $\sqrt{\varepsilon_\parallel}$. Reproduced from Lyashenko DA and Svirko YuP (2005) Crystal optics. In: Encyclopedia of Condensed Matter Physics, 1st edn. Elsevier, 283–289.

This implies that the wave vector surface for uniaxial crystals consists of two separate surfaces, a sphere and spheroid, which touch one another at opposite poles on the n_3-axis. Depending on the sign of $\varepsilon_\perp - \varepsilon_\parallel$ the crystal is said to be a negative or a positive uniaxial crystal (the sphere lies outside or inside the spheroid, respectively; see Fig. 3).

Correspondingly, there may exist two types of waves that propagate along a given direction in a uniaxial crystal. These waves are called ordinary and extraordinary waves having the following refractive indices, respectively:

$$n_o = \sqrt{\varepsilon_\perp}$$

$$n_e = \sqrt{\frac{\varepsilon_\perp \varepsilon_\parallel}{\varepsilon_\perp \sin^2\theta + \varepsilon_\parallel \cos^2\theta}} \tag{17}$$

where θ is the angle between the optical axis (the principal axis "3") and the wave normal. Two refractive indices are equal only at $\theta = 0$ when the wave normal coincides with the optical axis.

The ray surface can be found by replacing $\boldsymbol{n}$ with $\boldsymbol{s}$ and $\varepsilon_\perp$, $\varepsilon_\parallel$ with $\varepsilon_\perp^{-1}$, $\varepsilon_\parallel^{-1}$ in (16). For the ordinary wave, the directions of the wave vector and ray vector are the same, that is, with respect of ordinary waves the crystal behaves like an isotropic medium. For the extraordinary wave, the directions of the ray vector and wave vector do not coincide; however, they lie in the plane containing the wave vector and optical axis. This plane is called the principal plane. The angle θ' between the ray vector of the extraordinary wave and the crystal axes is given by the following equation: $\tan\theta' = (\varepsilon_\perp/\varepsilon_\parallel)\tan\theta$.

Since the four vectors ***E***, ***D***, ***s***, and ***n*** always lie in the same plane, the extraordinary wave is polarized so that vector ***E*** lies in the principal plane. Therefore, in the ordinary wave, vector ***E*** lies in the plane, which is perpendicular to the principal one.

Optical properties of biaxial crystals

In biaxial crystals, the three principal values of the tensor are all different, that is, wave normally becomes ellipsoid rather than spheroid as in uniaxial crystals. The direction of principal axes may, in biaxial crystals, depend on frequency. The Fresnel surface can be obtained by solving Eq. (11). In the case of $\varepsilon_1 < \varepsilon_2 < \varepsilon_3$, the shape of one octant of the wave vector surface is shown in Fig. 4.

The singular point of self-intersection (there are four such points, one in each quadrant) gives the direction of the optical axes (referred as binormals) of the crystal. The dashed line in Fig. 4 passes through two opposite singular points and is at the following angle to the "3"-axis:

$$\tan\beta = \sqrt{\frac{\varepsilon_3(\varepsilon_2 - \varepsilon_1)}{\varepsilon_1(\varepsilon_3 - \varepsilon_2)}} \tag{18}$$

The directions of the optical axes are evidently the only ones for which the wave vector has only one magnitude.

The properties of the ray surface are entirely similar to those of the wave surface. The directions of optical ray axes (referred to as bi-radials) can be derived from (19) by replacing $\varepsilon_{1,2,3}$ with $\varepsilon_{1,2,3}^{-1}$:

$$\tan\gamma = \sqrt{\frac{\varepsilon_2 - \varepsilon_1}{\varepsilon_3 - \varepsilon_2}} \tag{19}$$

The directions of the wave vector and the ray vector are the same only for light propagating along one of the principal axes.

Near a singular point, the inner and outer parts of the wave vector surface are cones with a common vertex and, therefore, the direction of the normal to the surface becomes indeterminate. This implies that the wave vector along the binormal corresponds to an infinity of ray vectors, whose directions occupy a certain conical surface, called the cone of internal conical refraction. Similar results hold for the wave vectors corresponding to a given ray vector. The ray vectors along the biradial correspond to infinite number of wave vectors, whose directions occupy the cone of external conical refraction (Landau and Lifshitz, 1984).

In observations of the internal conical refraction, one can use a crystal plate cut perpendicular to the binormal. When monochromatic light wave incidents normally on one of the crystal faces, the wave vector of the transmitted wave is parallel to the binormal and so the rays are on the cone of internal refraction. Therefore, a collimated light beam that enters the crystal spreads out into a hollow cone emerging from the crystal as a hollow light cylinder.

In order to observe the external conical refraction, the crystal plate must be cut perpendicular to the biradial, and small apertures should be placed in exactly opposite positions on both crystal facets. When the first aperture is illuminated by a focused beam, only rays that propagate along the biradial can reach the second aperture. Therefore, the relevant wave vectors occupy the cone of the external conical refraction. It is worth noting, however, that the cone of light emerging from the crystal does not exactly coincide with the cone of external refraction because of the refraction on the crystal-vacuum interface.

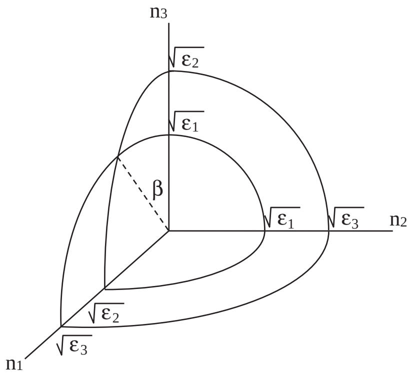

Fig. 4 One octant of the Fresnel surface of a biaxial crystal with $\varepsilon_1 < \varepsilon_2 < \varepsilon_3$. Dash line shows the optical axis (binormal) of the crystal. One can observe that section of the Fresnel surface by the plane normal to one of the coordinate axes consists of ellipse and circle. In the plane {***n***$_1$, ***n***$_2$}, ellipse with semi-axes $\sqrt{\varepsilon_1}$ and $\sqrt{\varepsilon_2}$ lies inside the circle with radius $\sqrt{\varepsilon_3}$, while in the plane {***n***$_2$, ***n***$_3$}, the circle with radius $\sqrt{\varepsilon_1}$ lies inside the ellipse with semi-axes $\sqrt{\varepsilon_2}$ and $\sqrt{\varepsilon_3}$. In the plane {***n***$_1$, ***n***$_3$}, the ellipse with semi-axes $\sqrt{\varepsilon_1}$ and $\sqrt{\varepsilon_3}$ and crosses the circle with radius $\sqrt{\varepsilon_2}$. Reproduced from Lyashenko DA and Svirko YuP (2005) Crystal optics. In: Encyclopedia of Condensed Matter Physics, 1st edn. Elsevier, 283–289.

Polarization devices based on the crystal optics

Since in the crystal two linear polarized waves with different wave vectors are allowed along a given direction, one can observe double refraction or birefringence at the vacuum–crystal interface. That is, an arbitrary polarized light beam entering an anisotropic crystal is divided into two beams with orthogonal linear polarizations. The direction of propagation of the beams is determined by the orientation of the incident wave vector with respect to the principal crystal axes and does not necessarily lie in the incident plane. These properties of the vacuum–crystal interface have enabled one to develop various devices to control and to investigate the polarization properties of the light. The polarization devices belonging to two most common types are discussed below. These are polarizers that produce linearly polarized light by splitting an elliptically polarized beam into two linearly polarized ones, and retarders that control the ellipticity of the light beam by changing the phase difference between its orthogonally polarized components (Bain, 2019).

The Nicol prism was invented in the nineteenth century and consists of a natural rhombic crystal of calcite, which is cut into two parts along a diagonal plane, and joined together again with Canada balsam (see Fig. 5). For a given angle of incidence, at the vacuum–crystal interface a light beam splits into ordinary and extraordinary rays with effective refractive indices $n_o = 1.6584$ and $n_e = 1.4864$, respectively. Since the refractive index of the Canada balsam $n_{balsam} = 1.5260$ satisfies the condition $n_e < n_{balsam} < n_o$, the ordinary ray undergoes total reflection at the Canada balsam joint while the extraordinary ray passes through. Therefore, the Nicol prism allows one to achieve linear polarization with practically no lateral displacement of the incident light beam. It is necessary to notice that a number of polarizing prisms (e.g., Glan–Foucault polarizer that employs total internal reflection similar to the Nicol prism and Wollaston prism that produce two orthogonally polarized output beams) have been devised.

The difference in the phase velocity of the ordinary and extraordinary waves in the birefringent crystal enables one to achieve a desired phase difference between them by changing the crystal thickness and/or the relevant refractive indices. Since the directions of vibrations in these waves are mutually orthogonal, the total phase difference accumulated between them determines polarization of the transmitted light. Such devices are called compensators because they enable to compensate the phase difference between orthogonal components of the elliptically polarized light wave. It is noticed here that these devices may also be referred to as retarders, because they introduce a finite retardation of one component with respect to another.

A compensator is usually made from a parallel plate of birefringent crystal that is cut so that the optic plate. At the vacuum–crystal interface ($z = 0$), the input wave at normal incidence divides into ordinary and extraordinary ones that propagate with phase velocities $v_o = c/n_o$ and $v_e = c/n_e$, respectively, and linearly orthogonally polarized. If the amplitudes of the orthogonal components of the light field in Eq. (1) at $z = 0$ are equal to E_x and E_y, respectively, those of the light waves emerging from the plate are given by $E_x \exp\{2\pi i n_o d/\lambda\}$ and $E_y \exp\{2\pi i n_e d/\lambda\}$, where λ is the wavelength in the vacuum. Therefore, the phase difference, which plate introduces between ordinary and extraordinary waves, is given by the following equation:

$$\Delta\varphi = \frac{2\pi d}{\lambda}(n_o - n_e) \tag{20}$$

The quarter-wave plate has a thickness of $d = \lambda/4 \mid n_o - n_e|$ and introduces a phase difference $\Delta\phi = \pm\pi/2$ to the transmitted wave. This wave plate transforms linearly polarized wave into circularly polarized one and vice versa. In order to obtain circularly polarized wave from linearly polarized, the optical axis of the plate is oriented at 45° to the incident polarization azimuth so that $E_x(z = 0) = E_y(z = 0)$.In such a case, the amplitudes of the transmitted ordinary and extraordinary polarized waves remain equal in magnitude. However, they acquire the $\pm\pi/2$ phase shift, that is, $E_x(z = 0) = E_y(z = 0)$ and $E_x(z = d) = \pm iE_y(z = d)$. This implies that the wave becomes left- or right-circular polarized depending on the relationship between n_o and n_e.

The wave plate with thickness of $d = \lambda/2 \mid n_o - n_e|$ is called the half-wave-plate, which allows one to rotate the polarization azimuth by 90°. If the optical axis of the plate is oriented at 45° to the incident polarization azimuth (that is, $E_x(z = 0) = E_y(z = 0)$), in the transmitted wave, the extraordinary polarized components acquire the π phase shift, that is, $E_x(z = d) = E_x(z = d)$ while $E_y(z = d) = -E_y(z = 0)$ One can readily find that this corresponds to the rotation of the polarization azimuth by 90° or to the transformation of the left circular polarized beam to the right circular polarized one.

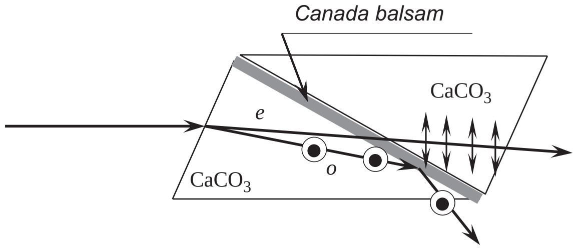

Fig. 5 The Nicol prism produces the light beam polarized in the plane of the picture (e-beam). The orthogonally polarized o-beam undergoes total internal reflection on the calcite-Canada balsam interface. Reproduced from Lyashenko DA and Svirko YuP (2005) Crystal optics. In: Encyclopedia of Condensed Matter Physics, 1st edn. Elsevier, 283–289.

The frequency dispersion results in color sensitivity of the wave plates. In order to achieve compensation of the phase shift for any wavelength, devices based on the combination of edges are used. The most common examples are the Babinet and Soleil compensators (Bain, 2019).

Conclusion

Crystal optics is a well documented discipline describing materials having optical properties depending on the direction in which the light is propagating. These are anisotropic crystals in the first instance. The term crystal optics has been coined in pre-laser era, i.e. it studies only linear optical phenomena in crystalline media including birefringence and its application to control the polarization of light. However, the nonlinear-optical, electro-optical and magneto-optical phenomena, which are widely used to control light beams, are essentially rely on the fundamental laws of crystal optics. In this article, we address the optical properties of bulk materials leaving behind rapidly developing optics of nanostructures that may also possess properties attractive for both fundamental principles and applications.

Starting from Maxwell's equations that describe the evolution of the electromagnetic field in the medium, we introduce phenomenological constitutive equation, which allows one to introduce the dielectric tensor and to address the propagation of light in uniaxial and bi-axial crystals. We introduce the general approach to the description of the light propagation in crystals using the wave and ray normals, and consider how the birefringent crystals can be employed to control the polarization of light.

References

Agranovich VM and Ginzburg V (1984) *Crystal Optics with Spatial Dispersion, and Excitons*. Berlin Heidelberg: Springer-Verlag.

Bain AK (2019) *Crystal Optics: Properties and Applications*. Weinheim: Wiley-VCH.

Ivchenko E (2022) Optical properties of dielectrics and semiconductors. In: *Encyclopedia of Condensed Matter Physics*, 2nd edn Elsevier. Chapter 00173.

La Rocca G (2022) Semiconductor optics. In: *Encyclopedia of Condensed Matter Physics*, 2nd edn Elsevier. Chapter 00032.

Landau LD and Lifshitz EM (1984) *Electrodynamics of Continuous Media*. Oxford: Pergamon.

Lovett DR (2017) *Tensor Properties of Crystals*. Boca Raton: CRC Press.

Patrini M and Guizzetti G (2022) Optical properties of materials. In: *Encyclopedia of Condensed Matter Physics*, 2nd edn Elsevier. Chapter 00029.

Holography☆

P Ambs[a], **J-P Huignard**[b,*], **and B Loiseaux**[b], [a]Université de Haute Alsace, ENSISA, Mulhouse, France; [b]Thales Research & Technology, Palaiseau, France

© 2024 Elsevier Ltd. All rights reserved.

This is an update of P. Ambs, J.-P. Huignard, B. Loiseaux, Holography, Editor(s): Franco Bassani, Gerald L. Liedl, Peter Wyder, Encyclopedia of Condensed Matter Physics, Elsevier, 2005, Pages 332–341, ISBN 9780123694010, https://doi.org/10.1016/B0-12-369401-9/00610-0

Introduction 88
Principle of holography 89
Principal holographic setups 89
The in-line hologram 89
Application of the Gabor holograms 90
The off-axis hologram 90
The Fourier hologram 91
Speckle noise in holographic imaging 93
Hologram characteristics and recording procedure 93
Applications of optical holography 95
Computer-generated holograms and diffractive optics 96
Analytical-type DOEs 96
Numerical-type DOEs 96
Digital holography 99
Artificial surfaces 100
Conclusion 102
References 102

Abstract

Holography was discovered in 1948 by Denis Gabor and its development started in the beginning of the 1960s with the invention of the laser. This article presents the basis of the holographic principles, and then the most commonly used optical setup to record and reconstruct holograms. A short review of the different recording materials and the applications follows. The computer-generated holograms and the diffractive optical elements with their computation algorithms and their applications are then described.

The last sections are dedicated to two recent fields of holography: the digital holography and the artificial surfaces.

Key points

- Optical holography: principle, optical recording set-up, application
- Computer generated holograms, diffractive optical elements: algorithms and applications
- Digital holography: principle and applications
- Artificial surfaces

Introduction

Holography was discovered in 1948 by Denis Gabor who proposed to use this technique to improve the resolution in electron microscopy (Gabor, 1948). Denis Gabor received the Nobel prize for this work in 1971. The word holography comes from Greek words meaning "total recording," and it is a technique for "wave front reconstruction" where both amplitude and phase of a wave front are recorded. The development of holography started in the beginning of the 1960s when coherent light sources became available with the invention of the laser. In 1962, E. Leith and J. Upatnieks made a major breakthrough with the invention of the off-axis reference beam optical holography (Leith and Upatnieks, 1962). A few years later, in 1967, A. Lohmann presented the first computer-generated hologram (Lohmann and Paris, 1967). The most spectacular application is the three-dimensional (3D)

☆*Change History*: July 2022. Ambs P, Huignard JP, and Loiseaux B are involved in the updated version. Numerous references have been added: 15 references in the 2016 version, 100 references in the updated version. Several parts of the text and figures were updated.

[*] Retired.

imaging, but there are now numerous applications where holography is even more useful and important for nondestructive testing, security, data storage, coherent wavefront shaping or for new optical elements for image display and projection in augmented reality, etc.

This article presents the basis of the holographic principles, and then the most commonly used optical setup to record and reconstruct holograms. A short review of the different recording materials and the applications follows. The following sections are dedicated to computer-generated holography and diffractive optics and finally the sections are devoted to the recent fields of digital holography and of artificial surfaces.

Principle of holography

The purpose of holography is a wave front reconstruction (Collier et al., 1971; Hariharan, 1984; Hecht, 2002; IIzuka, 1987; Saxby, 1988). It is a two-step process, which involves first, the recording of the amplitude and phase of the wave front, and second, its reconstruction. All the available recording materials (photographic plates, photopolymers, photorefractive crystals, etc.) or recording devices (CCD or CMOS cameras) are only sensitive to the intensity of the wave front, and therefore all the phase information is lost. Since the interferences between two coherent waves reflect their phase differences, the idea of recording the whole wave is to record the intensity of the interferences between the desired wave front (object beam) and a known reference wave (reference beam). This can be easily illustrated by the following equation when the O and R beams interfere with the same linear polarization:

$O(x,y)$ called the object beam, is the wave to be recorded:

$$O(x,y) = |O(x,y)| \exp\ j\Phi(x,y)$$

$R(x,y)$called the reference beam is a known wave that interferes with the object beam:

$$R(x,y) = |R(x,y)\ | \exp\ j\Psi(x,y)$$

$I(x,y)$ is the intensity of the interference pattern between the object and reference beams (* indicates the complex conjugate), and using the simplified notations O and R, one obtains:

$$I(x,y) = |O+R|^2$$

$$I(x,y) = |O|^2 + |R|^2 + OR^* + O^*R$$

It is assumed that the recording medium is an ideal holographic material in which the amplitude transmittance $t(x,y)$is proportional to the recorded intensity $I(x,y)$. To reconstruct the wave front, the hologram is illuminated by a wave identical to the reference beam and this is given by the following equation:

$$R(x,y)t(x,y) = |O|^2R + |R|^2R + O|R|^2 + O^*R^2$$

These last two terms of this development show that 3D imaging is possible since the complete amplitude and phase of the original wave front $O(x,y)$ is reconstructed. It can also be noted that due to the recording process, each point of the object contributes to the whole surface of the hologram. Therefore, even a partially illuminated hologram reconstructs the image of the whole object, but the quality of the image is affected due to a reduction of the spatial resolution and contribution of coherent speckle noise in the image plane.

Principal holographic setups

In the previous section, the basic principle of holography was presented and, in this section, the three principal setups that are used for optically recording and reconstructing holograms are detailed (Hariharan, 1984).

The in-line hologram

The in-line configuration shown in Fig. 1 is also named the Gabor hologram since D. Gabor first proposed this optical setup to demonstrate holography. The object is mostly transparent and may contain opaque particles. It is illuminated by a uniform coherent parallel beam and the transmitted wave is composed of two parts:

1. The wave directly transmitted by the object, noted as R, is constant and forms the reference.
2. The wave scattered by the particles, noted as O, and forms the object beam.

It is assumed that the intensity distribution $I(x,y)$ due to interference of O and R wave amplitudes is recorded on a photographic plate in early experiments, but now most commonly on 2D electronic sensors, whose transmittance $t(x,y)$ is proportional to the intensity and exhibits a constant offset t_0. Then, one has the following relation:

$$t(x,y) = t_0 + kI(x,y)$$

where k is a constant including the exposure time and the slope of the recording material.

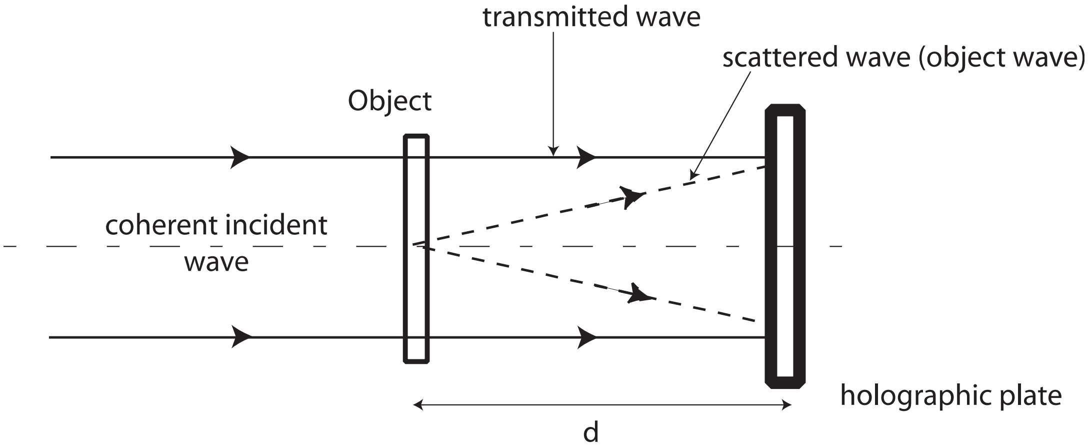

Fig. 1 Recording a Gabor hologram. From Ambs P, Huignard JP, and Loiseaux B (2016) *Holography, Reference Module in Materials Science and Materials Engineering*. Elsevier.

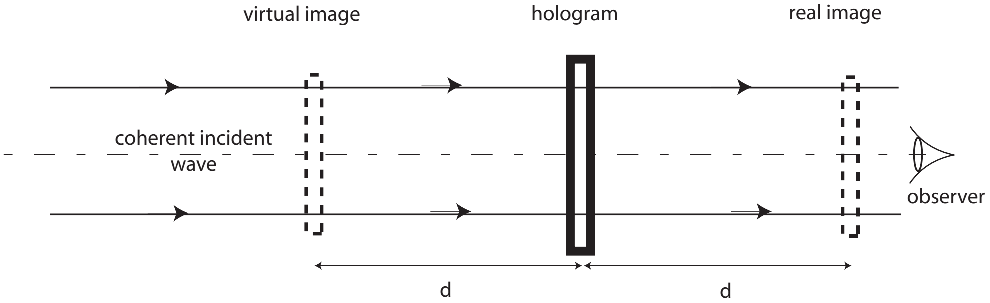

Fig. 2 Reconstructing a Gabor hologram. From Ambs P, Huignard JP, and Loiseaux B (2016) *Holography, Reference Module in Materials Science and Materials Engineering*. Elsevier.

To reconstruct the Gabor hologram, it is illuminated with a coherent parallel plane wave R (see Fig. 2), and the wave transmitted by the hologram is given by

$$Rt(x,y) = R\ \left(t_0 + k|R|^2\right) + kR|O|^2 + k|R|^2O + kR^2O^*$$

The three terms of the reconstruction are presented in Fig. 2. (1) $R(t_0 + k|R|^2 + k|O|^2)$ is the transmitted beam. (2) $k|R|^2O$ is the original object wave multiplied by a constant. It generates a reconstruction of the object located at its original position behind the hologram. It is a virtual image. (3) kR^2O^* is the complex conjugate of the original object. It generates a real image of the object in front of the hologram.

Application of the Gabor holograms

The main application of the Gabor holograms is in the particle analysis. In conventional imaging systems, the combination of a large depth of field with a high resolution is not possible. This bottleneck can be solved using a holographic recording that can store a high-resolution 3D image. The in-line hologram of the volume of moving particles is recorded using a triggered pulsed laser and the real 3D image can be analyzed by a conventional camera, which images the different planes of the volume. As an example of application, this setup was used to analyze the size and shape of droplets generated by injectors. Today, the in-line holography is typically an application of digital holography where the recording media, i.e. the holographic plate, is replaced by a high-resolution electronic camera. The reconstruction of the recorded hologram is then digitally computed through the calculation of the spatial 2D Fresnel or Fourier transform of the interferogram.

The off-axis hologram

With the Gabor hologram, the three reconstructed wave fronts are on the same axis and they cannot be spatially separated. To solve this problem, E. Leith and J. Upatnieks proposed in 1962 the off-axis recording setup (Leith and Upatnieks, 1962). In this case, the reference beam $R(x,y)$ and the object beam $O(x,y)$ are separated and interfering on the holographic plate under an angle α (see Fig. 3). The object beam and the off-axis plane wave reference beam are respectively expressed by

$$O(x,y) = |O(x,y)|\exp j\Phi(x,y)$$

$$R(x,y) = |R(x,y)|\exp j2\pi\xi x$$

where $\xi = \frac{\sin\alpha}{\lambda}$

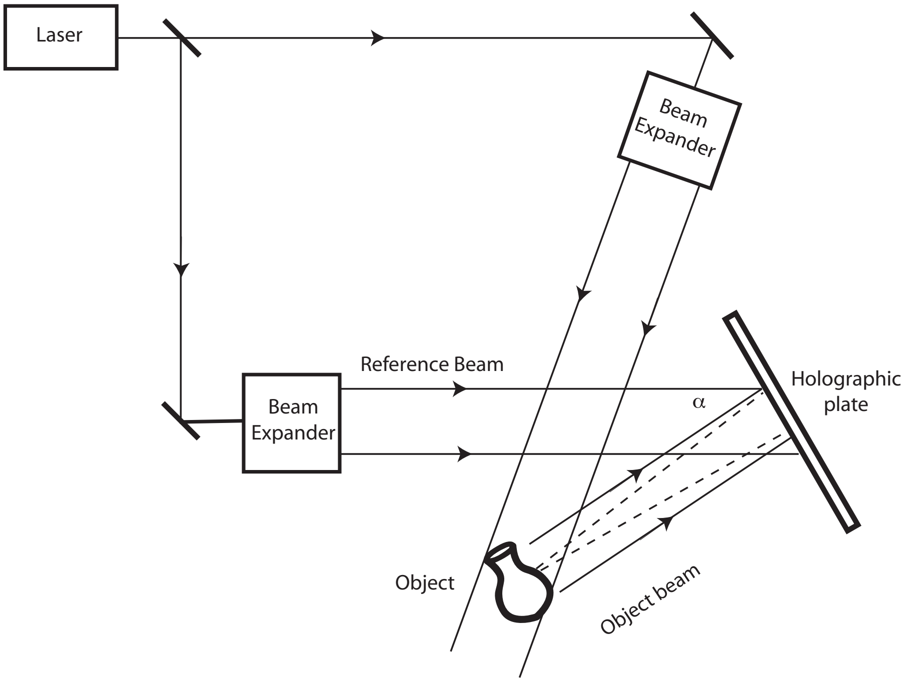

Fig. 3 Recording an off-axis hologram. From Ambs P, Huignard JP, and Loiseaux B (2016) *Holography, Reference Module in Materials Science and Materials Engineering*. Elsevier.

As in previous relations $I(x,y) = |R + O|^2$ is the intensity of the interference fringes.

Following the above formalism, it is clear that when reconstructing this type of hologram with the off-axis reference beam as shown in Fig. 4, it generates two spatially separated waves $W_1(x,y)$ and $W_2(x,y)$, respectively expressed by

$$W_1(x,y) = k|R|^2 O$$

where $W_1(x,y)$ is the original object wave multiplied by a constant factor and generates a virtual image of the object and $W_2(x,y) = kR^2O^* \exp(j4\pi\xi x)$ is the complex conjugate of the original object wave and generates a conjugate real image.

The three waves R, W_1, and W_2 are separated angularly and do not overlap as shown in the Gabor holograms. The off-axis setup is now the most common holographic recording configuration and it is used for reconstructing 3D images.

The Fourier hologram

In this case, the object is planar and the purpose is to record the amplitude and the phase of its Fourier transform (FT) (Goodman, 1968). The holographic technique is used to record this complex wave front. The hologram is formed by the interference pattern between the FT of the object $O(u,v)$ and a tilted wave that is the reference beam $R(u,v)$ (see Fig. 5)

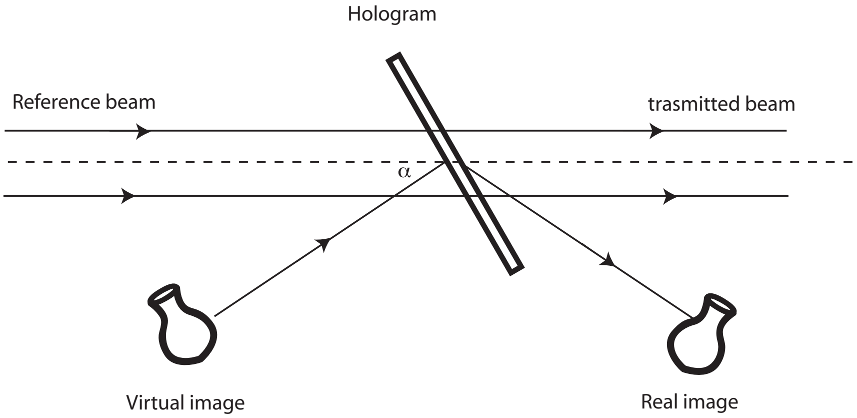

Fig. 4 Reconstructing an off-axis hologram. From Ambs P, Huignard JP, and Loiseaux B (2016) *Holography, Reference Module in Materials Science and Materials Engineering*. Elsevier.

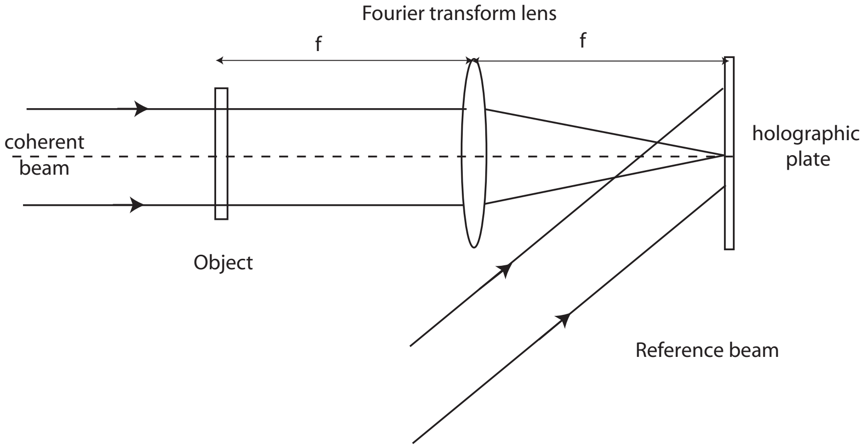
Fourier transform lens
f
f
coherent beam
holographic plate
Object
Reference beam

Fig. 5 Recording a Fourier hologram. From Ambs P, Huignard JP, and Loiseaux B (2016) *Holography, Reference Module in Materials Science and Materials Engineering*. Elsevier.

$$O(u,v) = FT[O(x,y)]$$

$$R(u,v) = \exp\ (\mathrm{j}2\pi ua)$$

where a is a constant.

$I(u,v)$ is the intensity of the interferences between the object and the reference beams

$$I(u,v) = I + |O(u,v)|^2 + O(u,v)\exp\ (\text{-j}2\pi ua) + O^*(u,v)\exp\ (j2\pi ua)$$

For the reconstruction, the hologram is illuminated by a parallel plane wave (of amplitude unity to simplify) and the wave transmitted by the hologram is

$$U(u,v) = t_0 + kI(u,v)$$

The hologram is placed in the front focal plane of a lens (see Fig. 6) and therefore the wave in the focal plane is the FT of $U(u,v)$ where

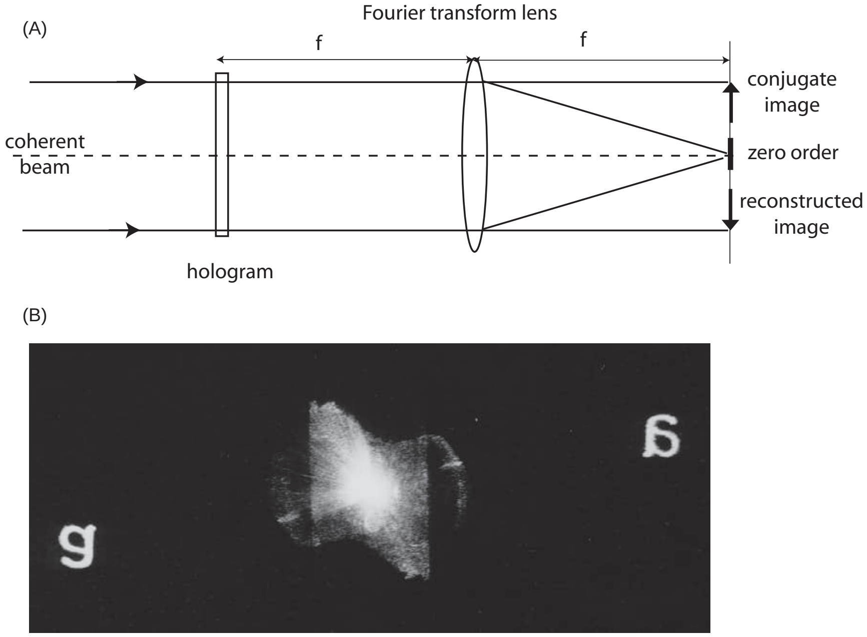
(A)
Fourier transform lens
f
f
coherent beam
hologram
conjugate image
zero order
reconstructed image
(B)

Fig. 6 Reconstructing a Fourier hologram (A) the optical setup, and (B) the optical reconstruction of a Fourier hologram. From Ambs P, Huignard JP, and Loiseaux B (2016) *Holography, Reference Module in Materials Science and Materials Engineering*. Elsevier.

$$U(x,y) = FT[U(u,v)] = (t_0 + k)\delta(x,y) + kO(x,y) \otimes O(x,y) + kO(x-a,y) + kO^*(-x+a,\ -y)$$

where $\otimes$, represents the correlation operator. This diffraction pattern is composed by a central order plus two terms:

1. $kO(x-a,y)$ is the +1 diffraction order that represents the original object beam separated by a distance a from the central order, and
2. $kO^*(-x+a,-y)$ is the −1 diffraction order that represents the complex conjugate of the original object beam separated by a distance $-a$ from the central order.

These two images of the object transparency are real.

Fourier holograms are not designed for 3D imaging; they have more specific applications such as optical correlation for pattern recognition, high-capacity holographic data storage, 2D imaging, diffractive optical elements, and optical interconnections.

Speckle noise in holographic imaging

The image reconstruction from a hologram illuminated by a highly coherent laser source will suffer from noise, named speckle noise, which limits the image quality. The speckle arises from the coherent illumination from any scattering object surface. Its origin is due to the diffraction of the object surface micro reliefs making up the coherent complex addition and interference of elementary waves with random phases. From this process it thus results an apparent image granularity of high contrast on the image which degrades the image signal-to-noise ratio. This effect is specific to any coherent imaging technique with a lens or hologram, it does not happen in conventional incoherent light source imaging. The statistic of the speckle pattern has been firstly analyzed in detail by J. Goodman in reference (Goodman, 2015) thus leading to estimation of image quality through the calculation of the image variance intensity. In the case of image formation by a hologram, it is shown that the size of the elementary speckle grain is of the order of the diffraction spot of the image formation system, which in the case of hologram is of the order of $\delta = \lambda \frac{F}{H}$ where λ is the laser wavelength, F is the distance from hologram to image and H the size of the hologram aperture. This effect must be carefully considered in any applications of coherent imaging and detection.

Hologram characteristics and recording procedure

An important parameter of the holographic reconstruction is the diffraction efficiency. It is defined as the ratio between the light beam intensity of the desired reconstructed image and the intensity of the incident beam illuminated on the hologram during the reconstruction.

Depending on the recording material, the hologram can introduce an amplitude or a phase modulation. A spatial phase modulation is often preferred since the diffraction efficiency is higher and can reach hundred percent. If the recording material thickness is small compared to the fringe spacing, a thin grating is recorded and the Raman–Nath diffraction regime applies. The reconstruction produces several diffraction orders and the efficiency gets reduced. On the other hand, a thick volume hologram is recorded if the thickness of the recording material is large compared to the fringe spacing. In such a case, a 3D grating is obtained and the Bragg diffraction regime applies. The fundamental properties of these thin-thick amplitude or phase volume holograms are well described by the coupled wave model firstly published by H Kogelnik in the reference (Kogelnik, 1969; Brotherton-Ratcliffe, 2013). Phase volume holograms have two very attractive properties (Moharam and Gaylord, 1981): (1) when illuminated by the reference beam, it reconstructs only one beam due to perfect spatial phase matching, and a diffraction efficiency of 100% can be theoretically reached, and (2) angular multiplexing of holograms is possible due to spatial selectivity. In this case, the angle of incidence of the reference beam is different for each of these holograms, which are recorded in the same volume.

Each hologram is then addressed and reconstructed when illuminated by the reference beam with the corresponding incidence angle. It is also possible to multiplex holograms using different wavelengths. Holograms, which can be sequentially stored in the same volume location by varying the reference beam angle at each recording step, provide the capability of high-capacity data storage of digital pages of information (Coufal et al., 2000; Curtis et al., 2011).

Also, holograms recorded with the optical setup of Fig. 3 are of the transmission type. However, if a hologram can be recorded by two waves traveling in opposite directions and illuminating respectively the front face and the rear face of the recording medium, the fringes inside the recording medium will be parallel to its faces; this is a reflective type of hologram. In these conditions the reflective hologram also exhibits very interesting properties, in particular its Bragg spectral selectivity which is now commonly used in wavelength filtering applications reference (Kogelnik, 1969).

The requirements for optically recording holograms are imposed by the contrast and stability of the interference fringes. The illuminating laser source must be coherent with an adequate coherence length, and the optical setup is stable and isolated from the vibrations. Note that the coherence length of the laser source, given by the classical formula $l_c = \frac{\lambda^2}{\Delta\lambda}$ with λ the wavelength and $\Delta\lambda$ the wavelength bandwidth is an important parameter since it limits the optical path length difference between the Signal and reference wavefronts interfering on the detector. Ideally, the recording media must not only have a high spatial resolution, typically higher than 1000 lines per mm, but also a linear response, a sensitivity range which can match the available laser wavelengths and a low noise.

Most of the hologram recording materials are nonerasable, such as the commonly used materials listed below:

1. Silver halide emulsions have been used since the beginning of holography. After processing, the light intensity is then transformed into an amplitude modulation. However, it is possible to change this modulation into a phase modulation by bleaching the plate thus allowing a higher diffraction efficiency to be reached. The use of photographic emulsions implies a chemical wet processing. Silver halide emulsions fulfill most of the requirements for holographic recording media – they are relatively sensitive, have a large spectral response, and a high spatial resolution. Holographic emulsions were easily commercially available until all the large photographic material companies stopped their production several years ago. Now, only a few small companies are still producing very high resolution holographic plates.
2. Dichromated gelatin is sensitized by ammonium dichromate imbedded into the gelatin, and it produces large area phase holograms. It is a very good material for holography with high resolution (>10,000 lines per mm), a controlled large modulation of the refractive index ($\Delta n > 0.1$), low absorption, and scattering. The use of dichromated gelatin is mastered at the industrial level with well-controlled processes to achieve $\sim 100\%$ diffraction efficiency.
3. Photopolymers films are organic materials that transform the light intensity into a refractive index modulation through a photopolymerization process. This is a self-processing photochemical reaction and the hologram is recorded and fixed by illuminating the photopolymer, and no further processing is required. Of late, several companies have been selling their photopolymers which exhibit excellent characteristics for high-efficiency holographic components ($\Delta n > 5 \times 10^{-2}$) as suitable for several applications (Curtis and Psaltis, 1994; Loiseaux et al., 1996; Weitzel et al., 1997; Joubert et al., 2002).
4. Organic materials such as photoresists thin films on glass substrate which are well developed for microelectronic technologies can be used for holographic recording. The illuminating coherent light gives a relief modulation after wet development and thus records a thin transmission type relief hologram. Photoresists are now very well-established materials used for the fabrication of the masters and for replicating the holograms by embossing. This is a largely developed technology for security applications (Bjelkhagen, 2005).
5. Photopolymers like polymethyl methacrylate - PMMA are an interesting phase volume holographic recording material, in particular the materials including photoinitiators like Irgacure or phenathrenequinone (PQ) doped PMMA. It is shown that Irgacure PMMA materials exhibit low shrinkage, very good stability and attractive potential qualities for high storage density by hologram multiplexing. Photochemical mechanisms in these types of photopolymers are now well analyzed and controlled. Meanwhile, the holographic characteristics with continuous wave or pulse exposure with visible green lasers have been published with efficiencies of 50% in mm thick materials. Irgacure PMMA also operate both in conventional or in polarization holography and thus benefit from the diffraction of an orthogonal direction of polarization. These materials now permit efficient phase volume holographic gratings and other types of diffractive components whose characteristics are well suited in laser and photonic applications (Steckman et al., 1998; Lin et al., 2009; Liu et al., 2017, 2019; Laux et al., 2007).
6. Holographic grating in glass: very efficient phase volume holographic gratings are also recorded in silicate glass doped with Cerium, Silver, and Fluorine. Grating recording is done in the UV, typically at a wavelength of 325 nm. UV exposure and thermal treatments photoinduce a localized index modulation due to material structural transformations and to local stresses in the glass volume (Photo Thermal Refractive Process). It thus results in the realization of several mm thick components of high optical quality, very good mechanical stability and very well suited for applications like spectral filtering, spectral combining of lasers, laser cavities mirrors, short pulse manipulation... (Mach et al., 2022; Glebov et al., 2002, 2014; Lumeau et al., 2009; Moser et al., 2008).
7. Erasable holographic materials are required for dynamic holography.
   a. The most commonly used materials in this category are photorefractive crystals. In this class of materials, the phase volume holographic grating is due to a photoinduced space charge field which modulates the crystal refractive index through the electrooptic effect (Yeh, 1993; Günter and Huignard, 2007). The index modulation can be erased by illuminating the crystal with a uniform beam intensity. Most of the photorefractive crystals also exhibit a dark storage time constant. A significant effort of research is still being done to investigate the phenomena involved in efficient hologram recording in the visible and near infrared spectral range. Photorefractive crystals permit the recording of dynamic holograms with time constants varying from nanoseconds to several seconds, and consequently, the diffracted wave front is probed in real time. Moreover, due to the nonlinear optical behavior of the material, there is an energy redistribution between the two recording beams. In other words, a low-intensity object beam can be amplified through an energy transfer from the reference beam. This unique property of the photorefractive crystals, due to self-diffraction mechanisms, opens up its applications like parametric image amplification. Many other attractive applications can be realized based on the specific characteristics of photorefractive effects in a variety of crystals. Presently, the most important materials used in experiments are: $LiNbO_3$ iron doped; $BaTiO_3$; $KnbO_3$; $Bi_{12}(Si, Ge, Ti)O_{20}$; for visible and GaAs; InP or CdTe for the near IR. Besides the spectral sensitivity, they differ in terms of speed, dark storage time, diffraction efficiency, and a two-wave mixing gain coefficient.
   b. Several other types of nonlinear optical effects have also been used in experiments of dynamic holography, in particular:
      - The nonlinear two beam interaction (2WM) creating a dynamic phase hologram in the materials. The reference beam which interferes with a low intensity signal beam acts as a pump which transfers its amplitude to the signal which is then amplified. It thus results an exponential gain coefficient on the signal beam intensity. In another important configuration, the dynamic hologram is readout with a beam which is antiparallel to the reference beam (4WM) and in these conditions generates an amplified phase conjugate wave of the incident signal wave (phase conjugate mirror with gain). These

mechanisms are at the origin of attractive properties like coherent image amplification, amplified phase conjugation and self-induced multimode cavities. (Rajbenbach et al., 1984). Demonstrations and applications of these remarkable properties will require the choice of the most efficient type of nonlinear interaction among the above list of materials and physical mechanisms, also as function of the requirements on the material response time, laser wavelength and its operating mode CW or pulsed (Fisher, 1983)

- The optical Kerr effect in transparent media, Stimulated Brillouin Scattering, photorefraction in doped liquid crystal or polymers, thermal gratings, or free carriers holographic gratings in semiconductor crystals. . . Also the hybrid structure like the optically addressed liquid crystal light valve is of great interest in holographic experiments (Residori et al., 2009). It consists of a 5-50 μm thick liquid crystal film sandwiched between a photoconductive crystal $Bi_{12}(Si, Ge, Ti)O_{20}$ or GaAs and a glass substrate with transparent electrodes. Under low applied voltage and low intensity incident fringe grating illumination, the device generates an efficient thin phase hologram due to a periodic reorientation of the liquid crystal molecules having a large birefringence. Another type of hybrid structure operating at video frame rate is in reference (Bortolozzo et al., 2015) using a CMOS detector, and an electrically addressed Liquid crystal SLM. CMOS camera and the SLM are symmetrically placed at 45 degrees from a 50% beam splitter and precisely imaged one onto each other. The holographic fringes are detected on the CMOS and video signal is transferred onto the Liquid crystal SLM which diffracts the holographic signal. Applications to dynamic interferometry of vibrating structures are demonstrated in ref. (Bortolozzo et al., 2015).

Applications of optical holography

Holography has a large range of applications although it is not as commonly used as it was expected to be in its early stages in the 1960s. Several applications are listed below:

1. Display is the most spectacular and public-oriented application of holography. Large transmissive and reflective holograms have been recorded, and 3D images with a large depth of field have been reconstructed. Different varieties have been developed, particularly in hologram reconstruction with white light, such as the rainbow or color holograms. For color imaging, three holograms of the object are recorded successively on the same plate by three lasers emitting blue, red, and green light respectively. The recording media must have a high resolution and a broad spectral sensitivity range. Such color reflective holograms reconstruct a 3D color object when illuminated by white light (Saxby, 1988).
2. Holography also has industrial applications in nondestructive testing, thanks to holographic interferometry (Smigielski, 1994). The purpose of classical interferometry is to compare two wave fronts, though most of the time one wave front is tested with a reference one. The principle of the double exposure holographic interferometry is, first, to record holographically the wave front coming from an object at rest. Second, some constraints or stress (mechanical, thermal, etc.) are applied to the object and the new wave front coming from the object is also recorded on the same support. When the resultant hologram is illuminated, it reconstructs the two wave fronts that interfere together and the resultant fringe pattern reveals the modifications of the object with a slight change in its shape. In particular, dynamic holography in photorefractive crystals is very well suited for these applications. As an example, the crystals permit realizing double exposure interferometry and when the object structure is vibrating at a given frequency, the photorefractive 2WM interaction operating in the time average recording mode, display in real time the vibration modes of the structures (Günter and Huignard, 2007; de Montmorillon et al., 1997; Kamshilin et al., 2009). These experiments based on dynamic holography are used in a diversity of industrial applications for metrology, non-destructive testing and vibrometry of structures. The functions of holographic interferometry are also performed most frequently with digital holographic techniques due to the availability of high-performance detector matrix and digital data processing (Schnars et al., 2015).
3. Holographic optical elements (HOEs) are also becoming an important industrial application. These elements are recorded optically, mainly on dichromated gelatin or in photopolymer and their purpose is to convert one wave front into another. One of the first industrial applications of HOEs is the head-up display that is used in airplanes and recently in cars (Teich et al., 2022). Holographic solutions are also one of the technologies used for waveguide combiners of smart glassed for augmented reality (AR), virtual reality (VR) or extended reality (XR) headsets (Kress and Chatterjee, 2021; Chang et al., 2020). HOEs can implement, even simultaneously, complex optical functions such as focusing, deflecting, multiplexing, spectral filtering, and active beam shaping (Mestre et al., 2007). Also, they are used in spectral pulse stretching and compression of lasers delivering ultrashort femto-second pulses (Loiseaux et al., 1996; Treacy, 1969; Maine et al., 1988; Mourou et al., 2015).
4. Holographic memories were studied in research laboratories, and an attempt to develop systems were considered by a few companies. The data pages are written as holograms into a thick layer of photopolymer coated onto a rotating disk (Coufal et al., 2000). The digital data can be recovered in parallel by reconstructing the holograms page-by-page. Therefore, a high data rate could be achieved and the recording medium would allow a very long archival lifetime. Few prototypes of holographic data storage systems were realized but actually impressive progress on the performances of electronic digital semiconductors memories surpass for the moment any other technological approach.
5. Since holograms are difficult to reproduce, they were used early as a security feature, on banknotes, for example. In this case, the original hologram is recorded optically on a photoresist and used to fabricate a master. The embossing of a sheet of a reflective

material produces the final hologram. Holographic solutions have been widely investigated for introducing anti-counterfeiting items both for biometric, banknotes or credit card document verification or for high-value product protection. For such applications both diffractive optical element (DOE) relief embossing and volume holography have been developed and are now commonly used. There are still ongoing research projects on this domain and the introduction of new technologies such as optical 3D printing by multi-photon polymerization (http://www.phenomenonproject.eu/) (Fagan, 1990; Bjelkhagen, 2005; Hilbert et al., 2020; Song et al., 2019).

6. Fiber Bragg Gratings (FBG) for telecommunications: UV illumination of silica glass around 244 nm permit to induce significant refractive index changes provided that appropriate methods of glass photosensitization are used. It was early recognized the important role of hydrogen treatments for enhancing the photosensitive response of silica-based glass, thus inducing index changes with high stability and as large as 10^{-3}. Research is still concerned to understand and to optimize the UV-induced index modulation, to minimize the sensitivity to changes of the environment, in particular when writing the gratings in a planar waveguide or in the core of a fiber. The Bragg grating photoinduced in low loss silica fibers is now a packaged technology fully developed in industry for applications in telecommunications and fiber sensors. They are a basic component for spectral filtering in dense wavelength optical communications networks (Kashyap, 2009; Poumellec, 1998; Niay et al., 1994; Chen et al., 2002; Brambilla et al., 1999; Groothoff et al., 2003).
7. The holographic techniques also apply in other domains than optical frequencies and are now proposed as essential to shape and process microwaves for radar systems and for analog or digital data transmissions in free space or over fiber links. High frequency microwave modulation of the optical laser carrier permit to attain very large bandwidth signal processing. The demonstrated optoelectronic architectures benefit from the use of holographic components and of the advanced concepts of optical holography transposed in the microwave spectral regions. (Iezekiel, 2009; Zhu et al., 2021; Vandelle et al., 2022).

Computer-generated holograms and diffractive optics

The purpose here is the same as for optically recorded holography. It is to reconstruct a desired wave front, but the process is different since no physical recording process is involved. The wave front is entirely computed and this brings flexibility and versatility.

Initially, the word computer-generated hologram (CGH) was used, but presently, it is often referred to as a diffractive optical element (DOE). A. Lohmann proposed the first CGH in 1967, and since then computation algorithms and fabrication methods have evolved following the progress of computers as well as the development of new fabrication technologies based on microlithography techniques. Presently, the DOEs can be classified into two classes (Kress and Meyrueis, 2009): analytical-type DOEs and numerical-type DOEs.

Analytical-type DOEs

The data composing such a DOE are in an analytical form and this is the case for diffractive lenses or gratings. These DOEs are pure phase elements and are fabricated accordingly. There are different approaches for the design of analytical-type DOEs, the direct DOE computation, the interferogram approach, and also the use of optical-design software.

Numerical-type DOEs

For this type of DOEs, the wave front to be reconstructed cannot be described by an analytical equation but must be computed using the propagation law. If the CGH illuminated by a plane wave reconstructs the desired wave front in the focal plane of a converging lens, the CGH will contain the inverse FT of the desired construction. If the CGH reconstructs without a lens at a given distance, then it will contain the inverse Fresnel transform of the desired reconstruction. The result of the Fourier or Fresnel transform is a 2D array of complex values. As for optically recorded holograms, the recording media are pure amplitude (mostly binary) or pure phase media, and therefore the complex data must be encoded to satisfy the requirements of the fabrication techniques. There are two types of encoding: first one is the cell-oriented encoding, and the second is the point-oriented encoding.

The first CGH presented by A. Lohmann used a cell-oriented encoding that he called phase-detour encoding (Lohmann and Paris, 1967). The hologram is a 2D array of cells representing the array of complex values, and an aperture in each cell represents each complex value. The surface of this aperture is proportional to the amplitude of the complex value to be encoded and its position in relation to the center of the cell is proportional to the phase. An adequate ratio between the aperture width and the cell size introduces the right carrier frequency that allows the separation of the central order from the two reconstructed orders (see Fig. 7). This encoding, known now as Lohmann's encoding, has given rise to several variations such as the encoding presented by W. H. Lee with two apertures per cell (Lee, 1970). The computation of these CGHs does not require powerful computers and is not time-consuming since only one Fourier or Fresnel transform is calculated. Originally, these CGHs were first drawn on a sheet of paper with a computer-controlled pen plotter and then photoreduced on a high-resolution photographic film.

In the 1980s, thanks to the progress of computers in terms of power and memory capacity, several point-oriented encoding methods were developed. The principle of the three main methods is described below. For these algorithms, the desired reconstruction window is placed into a larger 2D array, therefore the hologram and also the reconstruction plane is larger than the

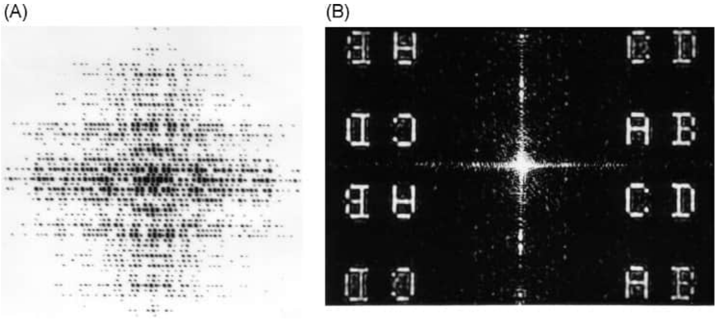

Fig. 7 Lohmann hologram: (A) the negative of the hologram and (B) optical reconstruction. From Ambs P, Huignard JP, and Loiseaux B (2016) *Holography, Reference Module in Materials Science and Materials Engineering.* Elsevier.

reconstruction window. This extra space allows a better convergence of the computation algorithm due to the phase and amplitude freedom outside the reconstruction window. Amplitude CGHs construct the desired reconstruction, its complex conjugate, and a zero order. In order to separate these terms, the reconstruction window should be placed at some distance from the center of the reconstruction plane. For phase CGHs with more than three-phase levels, only the desired reconstruction window appears in the reconstruction plane with no zero and no complex conjugate orders. However, this happens only if the computed phase levels are perfectly reproduced by the CGH.

The error diffusion algorithm consists of using a pulse width modulation technique for binarizing the hologram (Hauck and Bryngdahl, 1984). In the case of binary amplitude CGHs, the real part of the Fourier or Fresnel transform is made positive by adding an offset, and then normalized. Each of these sampled real values is binarized and the error, that is, the difference between the binary value and the analog value, is divided and distributed with a weight to the unprocessed neighbors before proceeding to the next point. By choosing the weight and the direction of the error diffusion carefully, it is possible to separate the quantization noise from the desired reconstruction. This algorithm has given rise to a lot of related algorithms, such as the complex error diffusion algorithm (see Fig. 8).

The next two encoding methods that are presented are iterative methods, they give better results in terms of signal-to-noise ratio (SNR) but their computation is more time-consuming.

The direct binary search (DBS) algorithm presented by Seldowitz and co-workers in 1987 (Seldowitz et al., 1987) is based on the optimization of an error criterion by the use of a Monte Carlo technique. To begin with, a random hologram is generated, and the error criterion between the desired image and the reconstruction of this hologram is computed. The random CGH is then scanned, and a new error is computed after inversion of a new pixel. Pixel modification is retained only if the error decreases, and the error criterion is thereby minimized. This cycle is stopped when the error stops decreasing. The error criterion can be defined for amplitude, intensity, or a complex image, depending on the application using the CGH. For some applications, the CGH must reconstruct a wave front with a specified amplitude and phase, and the error must then be based on a complex-amplitude error criterion. However, in many other applications (display, memory, interconnect, etc.) the CGH reconstruction is detected by a quadratic detector, leaving the phase as a free parameter, and the error criterion can be based on amplitude or intensity errors. Since

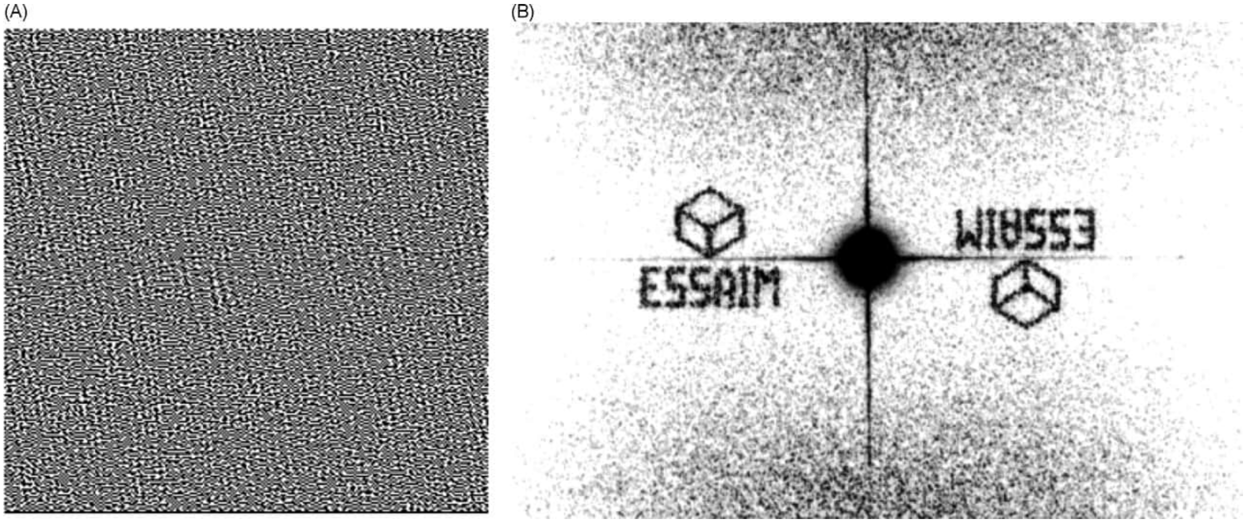

Fig. 8 Error diffusion encoding (A) the CGH and (B) the optical reconstruction. From Ambs P, Huignard JP, and Loiseaux B (2016) *Holography, Reference Module in Materials Science and Materials Engineering.* Elsevier.

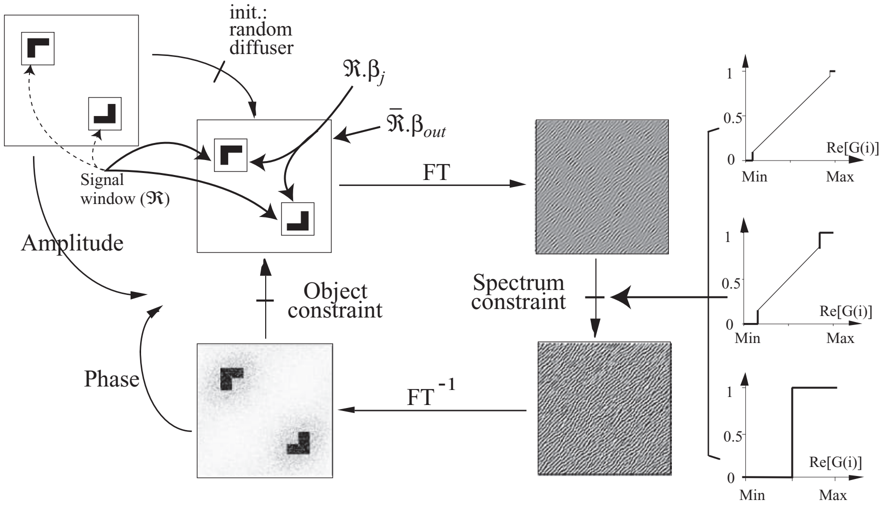

Fig. 9 IFTA for computing a binary amplitude CGH (After Wyrowski and Bryngdahl, 1988). From Ambs P, Huignard JP, and Loiseaux B (2016) *Holography, Reference Module in Materials Science and Materials Engineering*. Elsevier.

these errors use the phase freedom, the optimization algorithms converge better in this case. The original DBS algorithm was designed for binary CGHs; however, it can be extended to multilevel amplitude or phase CGHs at the expense of the computation time, since for each pixel, all levels must be tested.

The iterative Fourier transform algorithm (IFTA) presented in 1988 by F. Wyrowski (Wyrowski and Bryngdahl, 1988), is an iterative technique based on the Gerchberg–Saxton algorithm (Gerchberg and Saxton, 1972). Schematically, the principle of this method consists in going successively from the object plane to the spectrum plane by the application of constraints on the CGH (see Fig. 9). To be recorded, the CGHs must be quantized and often binarized, but IFTA can also be used to compute multilevel amplitude or phase CGHs. In the Fourier domain, the spectrum of the object is thus constrained to be a binary function. The object constraint must correct the quantization noise by injection of the desired image intensity in the signal windows. The inverse FT of this spectrum gives back an object plane in which the object constraint is thus applied to match the desired image intensity in the signal windows. However, to avoid stagnation of the algorithm the quantization of the spectral plane must be progressive, as is illustrated in Fig. 9, where three different steps of the binarization process are shown. In order to make its spectrum as uniform as possible, an equalizer can be applied to the desired signal. The simplest equalizer adds a random diffuser to the object plane.

For multilevel amplitude or phase CGHs, a multilevel progressive quantification is applied to the amplitude or the phase of the spectrum. Excellent quality phase CGHs can be fabricated using an IFTA method, they exhibit a high diffraction and a reconstruction with a high signal-to-noise ratio (see Fig. 10).

Today, most of the CGHs are computed using IFTA based methods. Compared to the other algorithms for computing CGHs, the CGHs computed with IFTA have the best tradeoff between the computing time and the quality of the reconstruction. Moreover, IFTA can be adjusted to fit the desired application. CGHs design software products are now commercially available.

Quality DOEs imply a very precise manufacturing with a perfect match between the computed phase and the actual phase of the component. To achieve these requirements, microlithography techniques are used to etch very precisely, in shape and depth, the chosen optical substrate such as quartz. Embossing techniques make cheaper DOEs, but the quality of their reconstruction is lower, particularly as the phase mismatch generates a zero order. Dynamic DOEs can also be implemented by displaying the DOE on a spatial light modulator (SLM). Liquid crystal on silicon (LCoS) SLMs with zero-twist nematic liquid crystal are particularly well suited for dynamic DOEs since they are pure phase modulators of the illuminating light and therefore allow a high diffraction

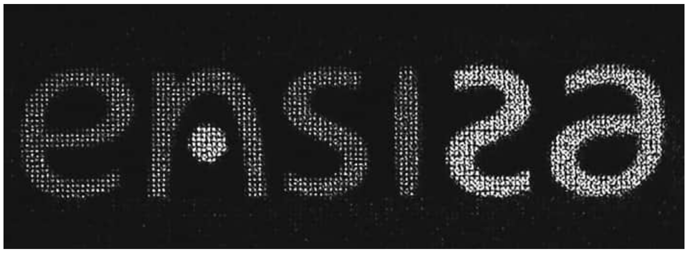

Fig. 10 The optical reconstruction of an IFTA encoded 8-level phase dynamic CGH displayed on a pure phase SLM. The reconstructed image is 128 × 26 pixels, and a 512 × 512 pixel hologram was computed and replicated to be displayed on the 792 × 600 pixels SLM. Due to a perfect phase matching, no complex conjugated order is appearing in the reconstruction.

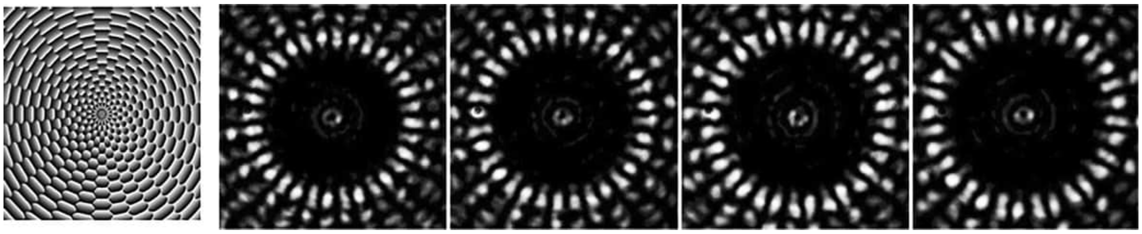

Fig. 11 Generation of a non-diffracting beam with a computed analytical DOE. Experimental results: (A) Phase DOE displayed on a pure phase LCoS SLM. (B–E) beam intensity measured at different distances from the SLM. (B) at 0.70 m, (C) at 0.90 m, (D) at 1 m, (E) at 1.2 m.

efficiency reconstruction of the DOE without the complex conjugated term. Following this approach CGH displayed on a very high-resolution LC-SLM were demonstrated for automotive head-up display of 3D images. (Skirnewskaja et al., 2021).

DOEs have a broad range of applications sectors such as industrial, defense, optical telecommunications, biotechnology, entertainment, and consumer electronics (Turunen and Wyrowski, 1997). The number of applications is expanding and includes for example laser beam shaping, Fourier filtering for optical image processing, 2D display (Fig. 10) and 3D display, structured light illumination for 3-D sensing, optical interconnects, hybrid lens, illumination of photovoltaic solar cells, diffractive encoders, optical tweezers, endoscopic imaging, complex optical functions generation.

DOEs can be used for beam shaping and generation of complex wavefront (Davis et al., 1996; Dudley et al., 2013; Li and Wang, 2017; Mestre et al., 2007). For example, an analytical DOE was computed for the creation of a higher order nondiffracting Bessel beam. Fig. 11A shows this DOE displayed on a pure phase LCoS SLM. Figs. 11B–E show the experimental results when the SLM is illuminated by a plane wave. The intensity of the beam at different distances from the SLM demonstrates that the wavefront remains constant over this range.

Digital holography

In digital holography (DH), the recording media is replaced by a high-resolution electronic camera. Using data from the recorded interference pattern, the object is reconstructed by a digital computer. Digital holography is a fast-growing field, because it suppresses all the difficulties related to the processing of the traditional holographic recording media and brings in a lot of versatility and flexibility and thus stimulated a lot of research and development works relevant to the theory and applications of the digitally restored images from interferograms detected on a CCD detector matrix (Schnars et al., 2015).

Digital holography is now used in industrial applications requiring a quantitative measurement of a wave front where it is successfully replacing the classical setups (Schnars et al., 2015). Fig. 12 shows the measurement of deformations using digital holography.

Therefore, digital holography is becoming a technique now widely used in applications to metrology, microscopy, polarization, Doppler and phase imaging… (Javidi et al., 2021). Also encrypted DH permits to realize novel applications for information security, in particular when using optical or digital correlation methods for object recognition (Javidi, 2005). DH allows obtaining the amplitude and phase of incident optical fields by phase shifting digital holography: a technique that consists of recording several holograms of the incident field with different known values of the phase on the reference wave. For each application both on axis and off axis configurations are implemented according to the spatial resolution of the pixels of the detection matrix and also in

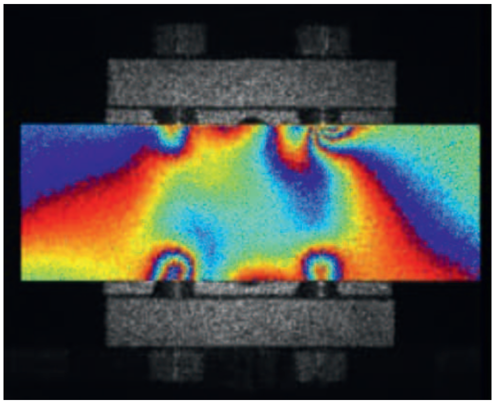

Fig. 12 Applications of digital holography; electronic speckle pattern interferometry for the measurement of the deformation of a rubber piece. *Source*: Thales RT. From Ambs P, Huignard JP, and Loiseaux B (2016) *Holography, Reference Module in Materials Science and Materials Engineering*. Elsevier.

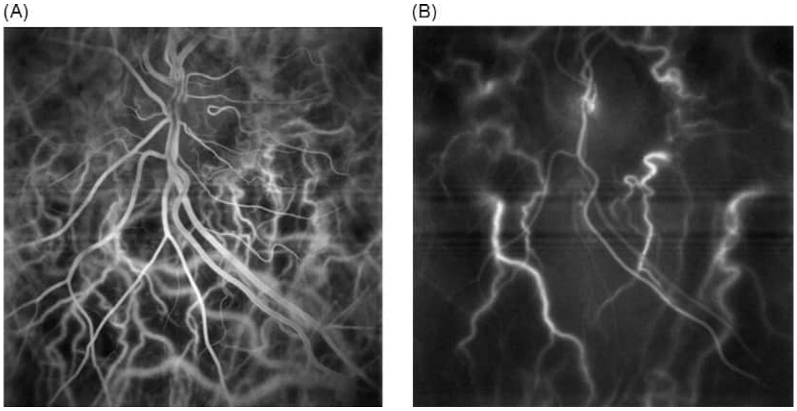

Figs. 13 Digital Doppler holographic images of the arteries and veins of the eye retina and choroid. Courtesy of Michael Atlan (CNRS-PSL Uni-ESPCI).

theory, the noise of the detected interferogram is limited by the shot noise of the reference wave (Gross and Atlan, 2007; Verpillat et al., 2010). Another important advantage in favor of using digital holography is the development of high-performance several megapixels CCD – CMOS technologies in terms of the number of pixels, very small pixel size, low noise, and readout speed. When also considering the most recent advances in digital processing of the detected interferograms on video signals, it appears clearly that digital holography will continue to expand applications in a large diversity of fields and thus demonstrates very interesting performances.

A rapidly expanding field of application concerns the digital holographic microscopy (DHM) that allows a subnanometer vertical resolution (Cuche et al., 1999; Emery et al., 2021). Digital holographic microscopes are now commercially available.

Another important application is in the field of biophotonics where DH can perform both the imaging of the eye retina and the Doppler image of blood cells flowing in the vessels. Note that to operate in real time, this application requires the development of algorithms to stabilize the image and to compensate for the aberrations introduced by the eye. In this experiment, the temporal resolution permits observing the changes of blood flow with the cardiac cycles and confirm interest for medical diagnostics of eye diseases. The Fig. 13 illustrates such full-field images of the retina vessels under very low laser illumination and are obtained by laser Doppler holography at a wavelength of 852 nm (Puyo et al., 2018).

DH still continues to evolve and to demonstrate original experiments issued of the advanced technics of very high precision optical metrology and spectroscopy and based on interferometers with two laser frequency combs. As an example, this is demonstrated in the recently published work (Vicentini et al., 2021) which develop a novel and powerful method of dual comb hyperspectral digital holography providing both 3D spatial and spectral imaging.

Artificial surfaces

1. Birefringing optical materials based on holographic techniques

Artificial optical materials exhibiting birefringence can be obtained by volume holographic recording technics in high resolution photosensitive materials. Artificial birefringence is achieved with a thick sinusoidally index grating if the grating period of the index modulation is small compared to the operating wavelength range (about a factor of 10). Under such conditions, all non-zero diffraction orders are evanescent and the grating is equivalent to a negative uniaxial birefringent material of optical axis normal to the index layers.

The ordinary and extraordinary index can be calculated (Campbell and Kostuk, 1995) for a volume holographic grating with a sinusoidal index modulation so that the holographic film behaves as a negative uniaxial medium. This has been experimentally demonstrated by Kim et al. (1995) with dichromated gelatin as holographic material and by Yang and Yeh (1996, 1997) in DuPont photopolymer films. As an example of applications, it was applied in reference (Joubert et al., 2002) to TN-LCD for widening their viewing angle.

2. Optical metasurface

The recent progress in nano-fabrication opened the route to new solutions for optical holography based on sub-wavelength elements, more generally called metasurfaces. Such optical metasurfaces have been recently identified as a future game changer to simplify bulky optical systems. They are generally described by light propagation methods based on either coherent scattering from each optical nano-antenna composing the optical surface or holographic synthesis. A wide range of applications based on new optical components offering efficient wavefront construction, polarization control are already proposed (Lalanne and Chavel, 2017; Spägele et al., 2021; Chen and Capasso, 2021; Huang et al., 2016; Wu et al., 2018).

3. Metasurface holography

The first demonstration of metasurface holography, was proposed in the infrared (Larouche et al., 2012) consisting of multilayers of metamaterials based on I-shape nanostructures, as reported by Linling Huang in its review of Nanophotonics (Huang et al., 2018; Lee et al., 2017; Malek et al., 2017).

4. Active metasurface

Active metasurfaces have been foreseen by N.L. Zheludev (Zheludev and Kivshar, 2012), during the first decade of the 21st century as opening new application fields with the introduction of new active elements in various nanophotonic systems. More recently, active metasurfaces integrating various functional materials or effects have been reported, among others: active devices based on phase change materials (Minovich et al., 2015; Chaudhary et al., 2019) (germanium antimony tellurium alloy Ge_2 Sb_2 Te5, vanadium dioxide VO_2), 2D materials (Xu et al., 2013) (graphene, borophene), thermal effect phased arrays (Sun et al., 2013), electro-optical modulations (Smalley et al., 2013), liquid crystals (Kobashi et al., 2016) and programmable gate arrays (Li et al., 2017).

Fig. 14 as an example of application from Li et al. (Li et al., 2015) illustrates the extension of multilevel phase holography with a pixel-level independent control of active elements based on reduced graphene-oxide (rGO) materials. Such materials pave the way to new design of active phased array optical antennas for which efficiency, field of view, signal-to-noise ratio have to be improved.

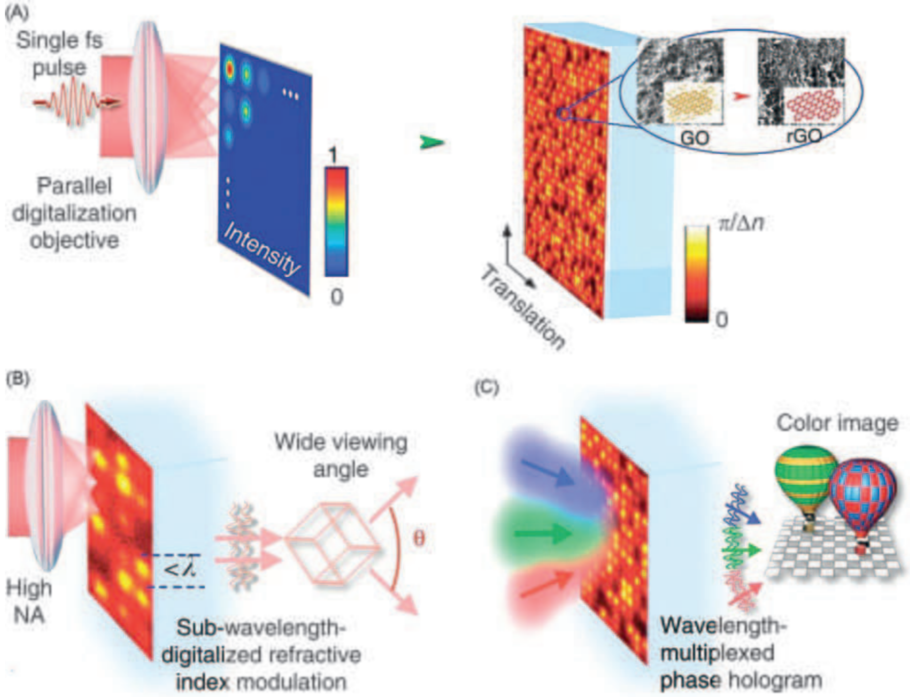
(A)
Single fs pulse
Parallel digitalization objective
Intensity
1
0
GO
rGO
Translation
π/Δn
0
(B)
High NA
<λ
Wide viewing angle
θ
Sub-wavelength-digitalized refractive index modulation
(C)
Color image
Wavelength-multiplexed phase hologram

Fig. 14 Reprogrammable multi-level phase holography based on reduced graphene-oxide (rGO) controlled by fs laser pulse. (A) Schematic illustration of the optical digitalization of refractive-index/phase modulation by the athermal photoreduction using a single fs pulse. The subwavelength-scale phase modulation from 0 to π is finely tuned by the intensity of a fs beam. The area-by-area parallel digitalization is achieved through an objective capable of generating MMAs with variant intensities in each focal spot corresponding to the phase correlation. (B) Scheme of wide-angle 3D images by confining the photoreduction at a subwavelength scale through increasing the NA of the parallel digitalization objective. (C) Reconstruction of color objects through the wavelength-multiplexed phase hologram recorded in GO polymers. With permission from Li X, Ren H, Chen X, Liu J, Li Q, Li C, Xue G, Jia J, Cao L, Sahu A, Hu B, Wang Y, Jin G, and Gu M (2015) Athermally photoreduced graphene oxides for three-dimensional holographic images. *Nature Communications* 6, 6984 under the terms of the CC-BY license. Copyright 2015, The Authors, published by Springer Nature.

Conclusion

Even if holography was invented in 1948 by Denis Gabor, it is only in the beginning of the 1960s that it expanded rapidly with the availability of a coherent light source, the laser. Until today, holography continues its development benefiting from the scientific and technical progress of the last 60 years.

Optical holography has a broad range of applications initially driven by 3D display and security holograms up to the more recent fields of AR, VR and XR. A new branch of optical holography has emerged thanks to the impressive progress of CMOS cameras and of the power of computers, it is digital holography, where the hologram is recorded by a camera and reconstructed by a digital computer. Digital holography brings in a lot of versatility and flexibility enabling numerous applications such as in industrial metrology, digital holographic microscopy, biophotonics imaging, and laser manufacturing.

Computer generated holography, taking advantage of the progress in the fabrication technologies coming from the semiconductor industry, has given rise to the field of DOEs. DOEs have a broad and expanding range of applications going from industry to consumer electronics through sectors such as defense, security, optical telecommunications, biotechnology.

Also, the holography has extended its concepts in the fields of nonlinear optics and in microwave optics. Here the coherent wave mixing of signal and pump beams in a nonlinear media induces a dynamic hologram enabling to amplify and to control amplitude and phase of complex signal waves carrying spatial and temporal information.

Nanotechnology and recent research in artificial surfaces and metamaterials show that holography always continue to stimulate novel ideas and progress of the technology thus leading to a bright future for innovative fields of applications.

References

Bjelkhagen HI (2005) New OVDs for personalized document based on color holography and Lippmann photography. In: Javidi B (ed.) *Optical and Digital Techniques for Information Security*, pp. 17–35. New York, NY, USA: Springer.

Bortolozzo U, Dolfi D, Huignard J-P, Molin S, Peigné A, and Residori S (2015) Self-adaptive vibrometry with CMOS-LCOS digital holography. *Optics Letters* 40: 1302–1305.

Brambilla G, Pruneri V, Reekie L, and Payne DN (1999) Enhanced photosensitivity in germanosilicate fibers exposed to CO_2 laser radiation. *Optics Letters* 24: 1023–1025.

Brotherton-Ratcliffe D (2013) Understanding diffraction in volume gratings and holograms. In: Mihaylova E (ed.) *Holography*. Rijeka: IntechOpen.

Campbell G and Kostuk RK (1995) Effective-medium theory of sinusoidally modulated volume holograms. *Journal of the Optical Society of America A* 12: 1113–1117.

Chang C, Bang K, Wetzstein G, Lee B, and Gao L (2020) Toward the next-generation VR/AR optics: A review of holographic near-eye displays from a human-centric perspective. *Optica* 7: 1563–1578.

Chaudhary K, Tamagnone M, Yin X, Spägele CM, Oscurato SL, Li J, Persch C, Li R, Rubin NA, Jauregui LA, Watanabe K, Taniguchi T, Kim P, Wuttig M, Edgar JH, Ambrosio A, and Capasso F (2019) Polariton nanophotonics using phase-change materials. *Nature Communications* 10: 4487.

Chen WT and Capasso F (2021) Will flat optics appear in everyday life anytime soon? *Applied Physics Letters* 118: 100503.

Chen KP, Herman PR, and Tam R (2002) Strong fiber Bragg grating fabrication by hybrid 157- and 248-nm laser exposure. *IEEE Photonics Technology Letters* 14: 170–172.

Collier RJ, Burckhardt CB, and Lin LH (1971) *Optical Holography*. New York: Academic Press.

Coufal HJ, Psaltis D, and Sincerbox GT (2000) *Holographic Data Storage*. Berlin: Springer.

Cuche E, Marquet P, and Depeursinge C (1999) Simultaneous amplitude-contrast and quantitative phase-contrast microscopy by numerical reconstruction of Fresnel off-axis holograms. *Applied Optics* 38: 6994–7001.

Curtis K and Psaltis D (1994) Characterization of the DuPont photopolymer for three-dimensional holographic storage. *Applied Optics* 33: 5396–5399.

Curtis K, Dhar L, Hill A, Wilson W, and Ayres M (2011) *Holographic Data Storage: From Theory to Practical Systems*. Chichester: Wiley.

Davis JA, Carcole E, and Cottrell DM (1996) Nondiffracting interference patterns generated with programmable spatial light modulators. *Applied Optics* 35: 599–602.

de Montmorillon L-A, Delaye P, Launay J-C, and Roosen G (1997) Novel theoretical aspects on photorefractive ultrasonic detection and implementation of a sensor with an optimum sensitivity. *Journal of Applied Physics* 82: 5913–5922.

Dudley A, Lavery M, Padgett M, and Forbes A (2013) Unraveling Bessel Beams. *Optics & Photonics News* 24: 22–29.

Emery Y, Colomb T, and Cuche E (2021) Metrology applications using off-axis digital holography microscopy. *Journal of Physics: Photonics* 3: 034016.

Fagan W (1990) Holographic optical security systems. SPIE Institutes for Advanced Optical Technologies 8, Tatabánya, Hungary. *SPIE* 10308: 381–386.

Fisher RA (1983) *Optical Phase Conjugation*. New York: Academic Press Inc.

Gabor D (1948) A new microscopic principle. *Nature* 161: 777–778.

Gerchberg RW and Saxton WO (1972) A practical algorithm for the determination of phase from image and diffraction plane pictures. *Optik* 35: 237–246.

Glebov L, Smirnov V, Stickley CM, and Ciapurin I (2002) New approach to robust optics for HEL systems. In: *AeroSense 2002, Orlando, FL, Merrit; P.H. ed., Proc. SPIE 4724, Laser Weapons Technology III* 101–109.

Glebov L, Smirnov V, Rotari E, Cohanoschi I, Glebova L, Smolski O, Lumeau J, Lantigua C, and Glebov A (2014) Volume-chirped Bragg gratings: Monolithic components for stretching and compression of ultrashort laser pulses. *Optical Engineering* 53: 051514.

Goodman JW (1968) *Introduction to Fourier optics*. San Francisco: McGraw-Hill.

Goodman JW (2015) *Statistical Optics*, 2nd edn Hoboken: John Wiley & Sons.

Groothoff N, Canning J, Buckley E, Lyttikainen K, and Zagari J (2003) Bragg gratings in air–silica structured fibers. *Optics Letters* 28: 233–235.

Gross M and Atlan M (2007) Digital holography with ultimate sensitivity. *Optics Letters* 32: 909–911.

Günter P and Huignard J-P (2007) *Photorefractive Materials and their Applications*. vols. 1-2-3. New York: Springer.

Hariharan P (1984) *Optical Holograhy, Principles, Techniques, Applications*. Cambridge: Cambridge University Press.

Hauck R and Bryngdahl O (1984) Computer-generated holograms with pulse-density modulation. *Journal of the Optical Society of America A* 1: 5–10.

Hecht E (2002) *Optics*, 4th edn San Francisco: Addison Wesley.

Hilbert F, Wiedenmann J, Stender B, Mantei W, Houbertz R, Carlier Q, Perez Covarrubias L, Heggarty K, Arnoux C, Monnereau C, and Baldeck P (2020) Impact of massive parallelization on two-photon absorption micro-and nanofabrication. *SPIE LASE, San Francisco, SPIE* 11271: 1127105.

Huang K, Dong Z, Mei S, Zhang L, Liu Y, Liu H, Zhu H, Teng J, Luk'yanchuk B, Yang JKW, and Qiu C-W (2016) Silicon multi-meta-holograms for the broadband visible light. *Laser & Photonics Reviews* 10: 500–509.

Huang L, Zhang S, and Zentgraf T (2018) Metasurface holography: from fundamentals to applications. *Nanophotonics* 7: 1169–1190.

Iezekiel S (2009) *Microwave Photonics: Devices and Applications*. Wiley-IEEE Press.

Iizuka K (1987) *Engineering Optics*. Berlin: Springer Verlag.

Javidi B (2005) *Optical and Digital Techniques for Information Security*. New York: Springer.

Javidi B, Carnicer A, Anand A, Barbastathis G, Chen W, Ferraro P, Goodman JW, Horisaki R, Khare K, Kujawinska M, Leitgeb RA, Marquet P, Nomura T, Ozcan A, Park Y, Pedrini G, Picart P, Rosen J, Saavedra G, Shaked NT, Stern A, Tajahuerce E, Tian L, Wetzstein G, and Yamaguchi M (2021) Roadmap on digital holography [Invited]. *Optics Express* 29: 35078–35118.

Joubert C, Laude V, Lee M-SL, and Plouin J (2002) Volume index gratings in the intermediate and form-birefringence regimes. *Applied Optics* 41: 6751–6762.

Kamshilin AA, Romashko RV, and Kulchin YN (2009) Adaptive interferometry with photorefractive crystals. *Journal of Applied Physics* 105: 031101.

Kashyap R (2009) *Fiber Bragg Gratings*, 2nd edn San Diego, London: Academic Press.

Kim TJ, Campbell G, and Kostuk RK (1995) Volume holographic phase-retardation elements. *Optics Letters* 20: 2030–2032.

Kobashi J, Yoshida H, and Ozaki M (2016) Planar optics with patterned chiral liquid crystals. *Nature Photonics* 10: 389–392.

Kogelnik H (1969) Coupled wave theory for thick hologram gratings. *Bell System Technical Journal* 48: 2909–2947.

Kress BC and Chatterjee I (2021) Waveguide combiners for mixed reality headsets: a nanophotonics design perspective. *Nanophotonics* 10: 41–74.

Kress BC and Meyrueis P (2009) *Applied Digital Optics: From Micro-optics to Nanophotonics*. Chichester: Wiley.

Lalanne P and Chavel P (2017) Metalenses at visible wavelengths: past, present, perspectives. *Laser & Photonics Reviews* 11: 1600295.

Larouche S, Tsai Y-J, Tyler T, Jokerst NM, and Smith DR (2012) Infrared metamaterial phase holograms. *Nature Materials* 11: 450–454.

Laux S, Cheriaux G, Merano M, Rachet V, Loiseaux B, and Huignard J-P (2007) Holographic bulk grating in a photopolymer for pulse stretching in a CPA laser. In: *CLEO/Europe and IQEC 2007 Conference Digest. Optical Society of America, Munich* CF_18.

Lee WH (1970) Sampled Fourier transform hologram generated by computer. *Applied Optics* 9: 639–643.

Lee S-Y, Kim Y-H, Cho S-M, Kim GH, Kim T-Y, Ryu H, Kim HN, Kang HB, Hwang C-Y, and Hwang C-S (2017) Holographic image generation with a thin-film resonance caused by chalcogenide phase-change material. *Scientific Reports* 7: 41152.

Leith EN and Upatnieks J (1962) Reconstructed wavefronts and communication theory. *Journal of the Optical Society of America* 52: 1123–1130.

Li S and Wang J (2017) Adaptive free-space optical communications through turbulence using self-healing Bessel beams. *Scientific Reports* 7: 43233.

Li X, Ren H, Chen X, Liu J, Li Q, Li C, Xue G, Jia J, Cao L, Sahu A, Hu B, Wang Y, Jin G, and Gu M (2015) Athermally photoreduced graphene oxides for three-dimensional holographic images. *Nature Communications* 6: 6984.

Li L, Cui TJ, Ji W, Liu S, Ding J, Wan X, Li YB, Jiang M, Qiu C-W, and Zhang S (2017) Electromagnetic reprogrammable coding-metasurface holograms. *Nature Communications* 8: 197.

Lin SH, Hsiao YN, and Hsu KY (2009) Preparation and characterization of Irgacure 784 doped photopolymers for holographic data storage at 532 nm. *Journal of Optics A: Pure and Applied Optics* 11: 024012.

Liu Y, Fan F, Hong Y, Zang J, Kang G, and Tan X (2017) Volume holographic recording in Irgacure 784-doped PMMA photopolymer. *Optics Express* 25: 20654–20662.

Liu P, Sun X, Zhao Y, and Li Z (2019) Ultrafast volume holographic recording with exposure reciprocity matching for TI/PMMAs application. *Optics Express* 27: 19583–19595.

Lohmann AW and Paris DP (1967) Binary Fraunhofer holograms, generated by computer. *Applied Optics* 6: 1739–1748.

Loiseaux B, Delboulbé A, Huignard JP, Tournois P, Cheriaux G, and Salin F (1996) Characterization of perpendicular chirped phase volume grating pairs for laser pulse stretching. *Optics Letters* 21: 806–808.

Lumeau J, Glebova L, Golubkov V, Zanotto ED, and Glebov LB (2009) Origin of crystallization-induced refractive index changes in photo-thermo-refractive glass. *Optical Materials* 32: 139–146.

Mach L, Mohammadian N, Mhibik O, Glebov L, and Divliansky I (2022) Intracavity spatial mode conversion by holographic phase masks. *Optics Express* 30: 4988–4998.

Maine P, Strickland D, Bado P, Pessot M, and Mourou G (1988) Generation of ultrahigh peak power pulses by chirped pulse amplification. *IEEE Journal of Quantum Electronics* 24: 398–403.

Malek SC, Ee H-S, and Agarwal R (2017) Strain Multiplexed Metasurface Holograms on a Stretchable Substrate. *Nano Letters* 17: 3641–3645.

Mestre M, Viaris de Lesegno B, Farcy R, Pruvost L, Bourderionnet J, Delboulbé A, Loiseaux B, and Dolfi D (2007) Fast reconfigurable and transient-less holographic beam-shaping realized by a AOM-SLM device. *The European Physical Journal - Applied Physics* 40: 269–274.

Minovich AE, Miroshnichenko AE, Bykov AY, Murzina TV, Neshev DN, and Kivshar YS (2015) Functional and nonlinear optical metasurfaces. *Laser & Photonics Reviews* 9: 195–213.

Moharam MG and Gaylord TK (1981) Rigorous coupled-wave analysis of planar-grating diffraction. *Journal of the Optical Society of America* 71: 811–818.

Moser C, Ho L, and Havermeyer F (2008) Self-aligned non-dispersive external cavity tunable laser. *Optics Express* 16: 16691–16696.

Mourou G, Wheeler JA, and Tajima T (2015) Extreme light. *Europhysics News* 46: 31–35.

Niay P, Bernage P, Douay M, Fertein E, Lahoreau F, Bayon JF, Georges T, Monerie M, Ferdinand P, Rougeault S, and Cetier P (1994) Behavior of Bragg gratings, written in germanosilicate fibers, against/spl gamma/–ray exposure at low dose rate. *IEEE Photonics Technology Letters* 6: 1350–1352.

Poumellec B (1998) Links between writing and erasure (or stability) of Bragg gratings in disordered media. *Journal of Non-Crystalline Solids* 239: 108–115.

Puyo L, Paques M, Fink M, Sahel JA, and Atlan M (2018) In vivo laser Doppler holography of the human retina. *Biomedical Optics Express* 9: 4113–4129.

Rajbenbach H, Huignard JP, and Refrégier P (1984) Amplified phase-conjugate beam reflection by four-wave mixing with photorefractive Bi12SiO20 crystals. *Optics Letters* 9: 558–560.

Residori S, Bortolozzo U, and Huignard JP (2009) Slow light using wave mixing in liquid crystal light valve. *Applied Physics B* 95: 551–557.

Saxby G (1988) *Practical Holography*. New York: Prentice Hall International (UK) Ltd.

Schnars U, Falldorf C, Watson J, and Jueptner W (2015) *Digital Holography and Wavefront Sensing*, 2nd edn Berlin Heidelberg: Springer.

Seldowitz MA, Allebach JP, and Sweeney DW (1987) Synthesis of digital holograms by direct binary search. *Applied Optics* 26: 2788–2798.

Skirnewskaja J, Montelongo Y, Wilkes P, and Wilkinson TD (2021) LiDAR-derived digital holograms for automotive head-up displays. *Optics Express* 29: 13681–13695.

Smalley DE, Smithwick QYJ, Bove VM, Barabas J, and Jolly S (2013) Anisotropic leaky-mode modulator for holographic video displays. *Nature* 498: 313–317.

Smigielski P (1994) *Holographie Industrielle*. Toulouse: Teknea.

Song Q, Pigeon YE, and Heggarty K (2019) Faceted Fresnel DOEs creating the perception of a floating 3D virtual object under divergent illumination. *Optics Communications* 451: 231–239.

Spägele C, Tamagnone M, Kazakov D, Ossiander M, Piccardo M, and Capasso F (2021) Multifunctional wide-angle optics and lasing based on supercell metasurfaces. *Nature Communications* 12: 3787.

Steckman GJ, Solomatine I, Zhou G, and Psaltis D (1998) Characterization of phenanthrenequinone-doped poly(methyl methacrylate) for holographic memory. *Optics Letters* 23: 1310–1312.

Sun J, Timurdogan E, Yaacobi A, Hosseini ES, and Watts MR (2013) Large-scale nanophotonic phased array. *Nature* 493: 195–199.

Teich M, Schuster T, Leister N, Zozgornik S, Fugal J, Wagner T, Zschau E, Häussler R, and Stolle H (2022) Real-time, large-depth holographic 3D head-up display: selected aspects. *Applied Optics* 61: B156–B163.

Treacy E (1969) Optical pulse compression with diffraction gratings. *IEEE Journal of Quantum Electronics* 5: 454–458.

Turunen J and Wyrowski F (1997) *Diffractive Optics for Industrial and Commercial Applications*. Berlin: Akademie Verlag.

Vandelle E, Bertrand M, Hoang TQV, and Loiseaux B (2022) Experimental demonstration of anomalous refraction with a 3D-printed binary grating. In: *EuCAP 2022 IEEE proceedings, #1570770295 (Madrid, Spain, 27 March to 1 April 2022)*.

Verpillat F, Joud F, Atlan M, and Gross M (2010) Digital holography at shot noise level. *Journal of Display Technology* 6: 455–464.

Vicentini E, Wang Z, Van Gasse K, Hänsch TW, and Picqué N (2021) Dual-comb hyperspectral digital holography. *Nature Photonics* 15: 890–894.

Weitzel KT, Wild UP, Mikhailov VN, and Krylov VN (1997) Hologram recording in DuPont photopolymer films by use of pulse exposure. *Optics Letters* 22: 1899–1901.

Wu K, Coquet P, Wang QJ, and Genevet P (2018) Modelling of free-form conformal metasurfaces. *Nature Communications* 9: 3494.
Wyrowski F and Bryngdahl O (1988) Iterative Fourier-transform algorithm applied to computer holography. *Journal of the Optical Society of America A* 5: 1058–1065.
Xu M, Liang T, Shi M, and Chen H (2013) Graphene-like two-dimensional materials. *Chemical Reviews* 113: 3766–3798.
Yang C and Yeh P (1996) Form birefringence of volume gratings in photopolymers. *Applied Physics Letters* 69: 3468–3470.
Yang C and Yeh P (1997) Artificial uniaxial and biaxial dielectrics with the use of photoinduced gratings. *Journal of Applied Physics* 81: 23–29.
Yeh P (1993) *Introduction to Photorefractive Nonlinear Optics*. New York: Wiley.
Zheludev NI and Kivshar YS (2012) From metamaterials to metadevices. *Nature Materials* 11: 917–924.
Zhu J, Yang Y, McGloin D, Liao S, and Xue Q (2021) 3-D printed all-dielectric dual-band broadband reflectarray with a large frequency ratio. *IEEE Transactions on Antennas and Propagation* 69: 7035–7040.

Sum rules and Kramers-Kronig relations in linear and nonlinear optics

Franco Bassani*, Scuola Normale Superiore, Pisa, Italy

© 2024 Elsevier Ltd. All rights reserved.

This is an update of F. Bassani, Optical Sum Rules and Kramers–Kronig Relations, Editor(s): Franco Bassani, Gerald L. Liedl, Peter Wyder, Encyclopedia of Condensed Matter Physics, Elsevier, 2005, Pages 200–206, ISBN 9780123694010, https://doi.org/10.1016/B0-12-369401-9/00615-X

Introduction **105**
Elementary description of sum rules **106**
Kramers-Kronig dispersion relations **107**
Kramers-Kronig relations and linear sum rules **108**
Relativistic and spatial dependent corrections **110**
General description of nonlinear optical functions **111**
Kramers-Kronig relations and sum rules in non-linear optics **113**
Harmonic generation 113
Pump and probe 114
Examples and applications to nonlinear processes **114**
The anharmonic oscillator 114
Second-harmonic generation 115
Data analysis 116
Conclusion **116**
References **116**

Abstract

Causality implies the Kramers-Kronig (KK) relations linking the real and imaginary parts of any response function. They have a fundamental importance in optics allowing, for instance, a determination of the absorption at any frequency from the measurement of the reflectivity on the entire spectrum. Most importantly, the KK dispersion relations also lead to a large number of sum rules, among which the Thomas-Reiche-Kuhn (TRK) sum rule for the absorption coefficient and the Altarelli-Dexter-Nussenzweig-Smith (ADNS) sum rule for the refractive index. These important results have long being known in linear optics, but they have also been generalized to non-linear optics.

Key points

- linear response
- non-linear response
- causality
- Kramers-Kronig dispersion relations
- sum rules
- dielectric function
- non-linear susceptibilities

Introduction

The optical properties of atoms, molecules, and solid materials have been an active field of research for the past two centuries and have given the most precise information on the microscopic structure of matter (Greenway and Harbeke, 1968; Bassani and Pastori-Parravicini, 1975; Bassani and Altarelli, 1983). Since the early 19th century it was known that absorption peaks occur at specific frequencies and that a corresponding dispersion shows up in the frequency dependence of the dielectric function $\varepsilon(\omega)$ (or in the refractive index $n(\omega)$).

We recall that in any medium all the optical functions (dispersion, absorption, reflection, …) depend on the frequency ω and on the momentum of the photon $\hbar\vec{k} = \hbar\frac{2\pi}{\lambda}$,$\hbar$ being the reduced Planck constant. They can all be expressed in terms of the complex dielectric function $\tilde{\varepsilon}\left(\vec{k},\omega\right)$. In crystalline materials the optical constants are tensors (second-rank tensors in the linear approximation), but this aspect may be neglected for our purposes. For electromagnetic waves the magnetic susceptibility is considered unitary and one can also use the dipolar approximation $\left(\hbar\vec{k} \simeq 0\right)$ because of the very small light momentum (neglect of spatial dependence).

---

*Deceased.

From Maxwell equations it can be seen that the imaginary part of the dielectric function can be expressed in terms of the conductivity σ, so that

$$\tilde{\varepsilon}(\omega) = \varepsilon_1(\omega) + i\varepsilon_2(\omega) = 1 + 4\pi\chi(\omega) + \frac{4\pi\sigma(\omega)}{\omega}i, \tag{1}$$

where the subscripts 1 and 2 denote real and imaginary part, respectively, and the real susceptibility χ is defined in terms of the polarization $\vec{P}$ (dipole moment per unit volume) and of the electric field $\vec{E}$ by

$$\vec{P}(\omega) = \chi(\omega)\vec{E}(\omega). \tag{2}$$

If the susceptibility is also extended to include the conductivity, so that

$$\tilde{\chi}(\omega) = \chi(\omega) + \frac{i\sigma(\omega)}{\omega} = \chi_1 + i\chi_2, \tag{3}$$

the usual expression for the complex dielectric function follows $\tilde{\varepsilon}(\omega) = 1 + 4\pi\tilde{\chi}(\omega)$. The complex refractive index is defined as

$$\tilde{n}(\omega) = \sqrt{\tilde{\varepsilon}(\omega)} = n(\omega) + i\kappa(\omega). \tag{4}$$

The absorption of radiation can be related to the conductivity induced by the electric field by considering the energy lost per unit time per unit volume

$$\frac{\mathrm{d}W}{\mathrm{d}t} = \vec{J}\cdot\vec{E} = \frac{\mathrm{d}\vec{P}}{\mathrm{d}t}\cdot\vec{E} = \sigma E^2, \tag{5}$$

so that the absorption coefficient $\eta(\omega)$, defined as $\frac{\mathrm{d}W}{\mathrm{d}x} = -\eta W = \frac{\mathrm{d}W}{\mathrm{d}t}\frac{n}{c}$, is given by

$$\eta = \left|\frac{\mathrm{d}W}{\mathrm{d}t}\right|\frac{n}{Wc} = \frac{4\pi\sigma}{nc} = \frac{\omega\varepsilon_2}{nc} = \frac{2\omega\kappa}{c}. \tag{6}$$

Also the reflection and transmission amplitudes can be obtained from the dielectric function through Fresnel relations, which in the case of normal incidence from vacuum to a medium are

$$\frac{E_r}{E_0} = r = \frac{\tilde{n} - 1}{\tilde{n} + 1}, \quad \frac{E_t}{E_0} = t = \frac{2}{\tilde{n} + 1}, \tag{7}$$

$R = |r|^2$ and $T = n|t|^2$ being the reflectivity and the transmittance, respectively.

The above described optical functions give the electromagnetic properties of matter. Their detailed dependence on frequency is related to the microscopic structure of the material considered and to its interaction with the radiation field (Greenway and Harbeke, 1968; Bassani and Pastori-Parravicini, 1975; Bassani and Altarelli, 1983). We will here consider general properties of the linear (Bassani, 2005a) and nonlinear (Bassani, 2005b) optical functions which only depend on time causality.

Elementary description of sum rules

The traditional phenomenological model for the optical constants is the Lorentz oscillator model, where the equation of motion of a specific electron with oscillator frequency ω_j and damping γ_j is given by

$$\frac{\mathrm{d}^2 x}{\mathrm{d}t^2} + \omega_j^2 x + \gamma_j\frac{\mathrm{d}x}{\mathrm{d}t} = \frac{eE}{m}. \tag{8}$$

From this one obtains for the complex dielectric function in a volume **V** for a number of resonance frequencies ω_j

$$\tilde{\varepsilon}(\omega) = 1 + \frac{4\pi e^2}{mV}\cdot\left(\sum_j \frac{f_j}{\left(\omega_j^2 - \omega^2\right) - i\gamma_j\omega}\right), \tag{9}$$

where the oscillator strength f_j gives the intensity of the resonance at frequency ω_j with damping constant γ_j. The conservation of the electron number and the asymptotic behavior ($\omega \to \infty$) of (9), made to coincide with that of free electrons ($f_j = 1, \omega_j = 0, \gamma_j = 0$) gives immediately the f-sum rule, first demonstrated in 1925 by W. Thomas, F. Reiche and W. Kuhn, and called the TRK sum rule:

$$\sum_j f_j = N. \tag{10}$$

This states that the sum of the oscillator strengths of all optical transitions is equal to the total number of electrons N.

Although the TRK sum rule was derived with classical mechanics it is worth mentioning that the quantum description of the oscillator strength implies that, for the sum rule to hold, also the commutation relation between momentum and position operator must hold, as pointed out by Heisenberg. In fact one can see, by expressing the optical functions in terms of the transition probability rates, observing that electrons are excited from state i to state f, with a probability rate given by the Fermi golden rule

$$P_{if} = \frac{2\pi}{\hbar}|f|eEx|i|^2\delta\left(E_f - E_i - \hbar\omega\right), \tag{11}$$

that the quantum mechanical expression for the imaginary part of the dielectric function is

$$\varepsilon_2(\omega) = \frac{4\pi^2}{V}\sum_{ij}|f|ex|i|^2\delta\left(E_f - E_i - \hbar\omega\right). \tag{12}$$

Considering in expression (9) that

$$\lim_{\gamma\to 0}\frac{\gamma}{\left(\omega_j - \omega\right)^2 + \left(\frac{\gamma}{2}\right)^2} = 2\pi\delta\left(\omega_j - \omega\right), \tag{13}$$

one obtains the quantum-mechanical expression of the oscillator strength

$$f_{fi} = \frac{2m}{\hbar^2}|\langle f|x|i\rangle|^2\left(E_f - E_i\right). \tag{14}$$

Taking into account the general Heisenberg expression for the time dependence of the displacement x

$$m\dot{x} = \frac{m}{i\hbar}[x, H], \tag{15}$$

where the square brackets denote commutators, and considering the eigenstates expression

$$H|j\rangle = E_j|j\rangle, \tag{16}$$

one obtains for the oscillator strength

$$f_{fi} = \frac{2m}{\hbar^2}\langle i|x|f\rangle\langle f|x|i\rangle\left(E_f - E_i\right) = \frac{1}{i\hbar}\left(\langle i|x|f\rangle\langle f|p_x|i\rangle - \langle i|p_x|f\rangle\langle f|x|i\rangle\right), \tag{17}$$

which, summing over the final states, gives

$$\sum_f f_{fi} = \frac{1}{i\hbar}\langle i|[x, p_x]|i\rangle = 1, \tag{18}$$

because of Heisenberg commutation rules $[x, p_x] = i\hbar$. Summing over all occupied initial states, one obtains immediately the TRK sum rule (10).

In general the oscillator strength, depends continuously on the frequency, so that the TRK sum rule can be expressed in terms of the imaginary part of the dielectric function as

$$\int_0^\infty \omega\varepsilon_2(\omega)\mathrm{d}\omega = \frac{2\pi^2e^2}{m}\varrho, \tag{19}$$

which relates the total radiation absorbed to the total electron density $\varrho = N/V$.

This is a very important property, because it gives a general constraint which the absorption of the medium must obey. When the sum rule (19) is saturated at a given frequency no further absorption can occur at higher frequencies. This explains why in light elements (low electron density) hard X-rays are not absorbed and hard γ-rays pass through all materials. The sum rule (19) is also useful to check the results of approximate calculations or experiments. It must always be obeyed by the exact optical functions.

Kramers-Kronig dispersion relations

A connection between sum rules and the causality principle was established on the basis of the relation between the real and the imaginary part of the susceptibility $\tilde{\chi}(\omega)$. This can be obtained by considering the complex ω plane and observing that the susceptibility does not have poles on the upper plane because the polarization can be expressed from the time dependent response operator $G(\tau)$ as

$$P(t) = \int_{-\infty}^{+\infty} G(\tau)E(t - \tau)\mathrm{d}\tau, \tag{20}$$

with the condition $G(\tau) = 0$ for $\tau < 0$ due to time causality. Then, taking the Fourier transform, one obtains

$$P(\omega) = \tilde{\chi}(\omega)E(\omega), \tag{21}$$

with

$$\tilde{\chi}(\omega) = \int_0^\infty G(\tau)\exp[i\omega\tau]\mathrm{d}\tau. \tag{22}$$

The fact that $\tilde{\chi}(\omega)$ is analytic in the upper complex plane gives, using Cauchy theorem on a contour closed to infinity where $\tilde{\chi}(\omega)$ goes to zero (see Fig. 1)

$$\tilde{\chi}(\omega) = \frac{1}{\pi i}\int_{-\infty}^{+\infty}\frac{\tilde{\chi}(\omega')}{\omega' - \omega}\mathrm{d}\omega', \tag{23}$$

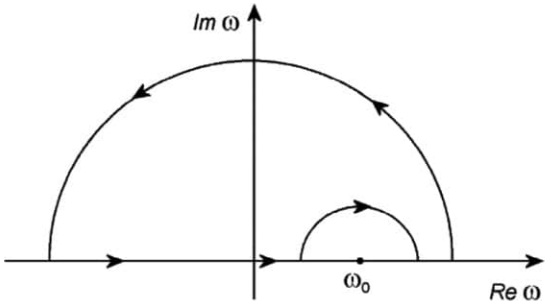

Fig. 1 Indication of the contour on the complex plane where the integral of the function $\chi(\omega')/(\omega' - \omega_0)$ by Cauchy theorem is equal to $i\pi\chi(\omega_0)$. From Bassani F (2005a) Optical Sum Rules and Kramers-Kronig Relations. ECMP 1st edn.

where the line on the integral denotes that the principal part must be considered. Since $\chi(-\omega) = \chi^*(\omega)$, one obtains the standard form of Kramers-Kronig (KK) relations

$$\chi_1(\omega) = \frac{2}{\pi}\int_0^\infty \frac{\omega'\chi_2(\omega')}{\omega'^2 - \omega^2}\,\mathrm{d}\omega', \tag{24}$$

$$\chi_2(\omega) = -\frac{2\omega}{\pi}\int_0^\infty \frac{\chi_1(\omega')}{\omega'^2 - \omega^2}\,\mathrm{d}\omega'. \tag{25}$$

In the case of metals, besides the pole at ω, the function $\frac{\tilde{\chi}(\omega')}{\omega' - \omega}$ has an additional pole at $\omega' = 0$ because $\sigma(0) \neq 0$. This can be taken into account by considering the function $\tilde{\chi} - \frac{\sigma(0)}{\omega} i$, which does not have such a pole and is analytic on the upper plane. Then dispersion relations (23) and (24, 25) apply, provided the term $\frac{\sigma(0)}{\omega}$ is added to the imaginary part of $\tilde{\chi}(\omega)$ and the principal part of the integrals is considered along all the real axis, including the point at $\omega = 0$, were $\tilde{\chi}_2(\omega')$ has a pole.

The above KK relations are very useful because they relate the dispersion to the absorption. Similar relations can be obtained for the other optical constants $\tilde{\sigma}$,$\tilde{n}(\omega)$,r, and $\mathrm{Im}\left(\frac{1}{\varepsilon}\right)$.

They can be all connected to specific sum rules by considering the asymptotic behavior which can be obtained from the KK relations, and comparing it to that which follows from a specific model of the material system. Since the asymptotic behaviors must coincide, sum rules are obtained. We can see immediately that the TRK sum rule (10) or (19) can be obtained when we consider the asymptotic behavior from (24) by using the so called superconvergence theorem, which amounts to letting $\omega' \to 0$ in the denominator, and comparing it with the asymptotic behavior from expression (9) ($\omega_j \to 0$ in the denominator).

As a consequence of the above discussion, we can conclude that sum rules and KK dispersion relations derive from the causality principle only, and from the knowledge of the short-time (or high frequency) behavior of the system. Complicated properties due to electron-electron interaction or external potentials are not relevant for sum rules and Kramers-Kronig relations. Also not essential is the quantum-mechanical approach.

A revival of the field of sum rules started in the early 1970s after the discovery of the refractive index sum rule by Altarelli, Dexter, Nussezveig and Smith (ADNS) which states for the real part of the refracting index

$$\int_0^\infty (n(\omega) - 1)\mathrm{d}\omega = 0. \tag{26}$$

After that new sum rules and more KK-type relations where derived for all optical functions and are now being used to interpret a variety of effects. New K·K relations and sum rules have also been found in nonlinear optics. Sum rules can be now explored in the entire frequency range using the properties of synchrotron radiation. They are also being used as stringent tests for approximate theories.

Kramers-Kronig relations and linear sum rules

We have derived KK relations (24), (25) for the complex susceptibility function by direct integration, but causality and KK relations have more direct implications; they can be summarized in what is known as a Titchmarsh theorem which states the following (Titchmarsh, 1968). Any square integrable function $f(\omega)$ which fulfills one of the three conditions below fulfills all three of them:

(i) the inverse Fourier transform $F(t)$ of $f(\omega)$ vanishes for $t < 0$,

(ii) $f(\omega)$ is the limit for $\varepsilon \to 0^+$ of a functions $\tilde{f}(\omega + i\varepsilon)$ that is analytic in the upper half plane and square integrable on the real axis and on any line parallel to it,

(iii) $\tilde{f}(\omega)$ verifies the KK identity

$$\tilde{f}(\omega) = \frac{1}{\pi i}\int_{-\infty}^{\infty} \frac{\tilde{f}(\omega')}{\omega' - \omega}\mathrm{d}\omega', \tag{27}$$

or equivalently for $F(t)$ real,

$$\begin{aligned} f_1(\omega) &= \frac{2}{\pi}\int_0^{\infty} \frac{\omega' f_2(\omega')}{\omega'^2 - \omega^2}\,\mathrm{d}\omega', \\ f_2(\omega) &= -\frac{2\omega}{\pi}\int_0^{\infty} \frac{f_1(\omega')}{\omega'^2 - \omega^2}\,\mathrm{d}\omega'. \end{aligned} \tag{28}$$

The above theorem proves that KK relations are a direct consequence of causality, but it also implies that any combinations of analytic functions satisfies KK relations if they are square integrable. For establishing KK relations one does not need to know the explicit form of the causal response function, which is determined by the specific operator being considered, by the Hamiltonian, and by the time-dependent perturbing potential. One only needs to know its asymptotic behavior which can be obtained in the classical approximation from the Lorentz oscillator model, or in the quantum theory from the quantum expression of the response function at zero-time. The same holds for the sum rules, which are obtained by comparing the above described asymptotic behavior with that obtained from KK relations.

Let us consider the optical case in the dipole approximation. The interaction Hamiltonian can then be written as

$$H' = -\vec{P}\cdot\vec{E}(t), \tag{29}$$

where $\vec{P} = \sum_i e\vec{r}_i$ is the polarization (it can be used as an operator in quantum mechanics) and $\vec{E}(t)$ is the electric field, which is taken as a sinusoidal function. While in the classical approximation one considers directly the time dependence of the polarization (Lorentz oscillator model), in the quantum mechanical approach the response function can be obtained from the trace of the density matrix operator ϱ_0 on the ground state of the system, and to first order is given by

$$\mathrm{G}(\tau) = \mathrm{Tr}\left\{\frac{1}{i\hbar}[P(-\tau),\ \varrho_0]P\right\}, \tag{30}$$

where $P(\tau)$ is defined in the interaction representation. This gives for the susceptibility the expression

$$\chi(\omega) = \frac{1}{\hbar}\sum_n |0|P|n|^2\left\{\frac{1}{\omega + \omega_{n0} + i\varepsilon} - \frac{1}{\omega - \omega_{n0} + i\varepsilon}\right\}, \tag{31}$$

where ε is an arbitrarily small frequency which accounts for the adiabatic switching on of the perturbation.

The sum rules can now be obtained from the two expressions of the asymptotic behavior, which must coincide. The first is given by the zero-time response function and its derivatives, and can be obtained integrating by part the Fourier transform of $\mathrm{G}(\tau)$, with $\mathrm{G}(\infty) = 0$. One obtains

$$\begin{aligned} \underset{\omega\to\infty}{\chi}(\omega) &= \int_0^{\infty} \mathrm{G}(\tau)\exp[-i\omega\tau]\mathrm{d}\tau = \\ &= \frac{\mathrm{G}(0^+)}{-i\omega} + \frac{\mathrm{G}'(0^+)}{-\omega^2} + \frac{\mathrm{G}''(0^+)}{-i\omega^3} + \frac{\mathrm{G}'''(0^+)}{\omega^4} + \dots, \end{aligned} \tag{32}$$

where the time derivatives are denoted with the apex. The second is obtained from the KK relations (24) with the superconvergence theorem,

$$\underset{\omega\to\infty}{\chi_1} = -\frac{2}{\pi\omega^2}\int \omega'\chi_2(\omega')\mathrm{d}\omega' + O(\omega^{-2}), \tag{33}$$

$$\underset{\omega\to\infty}{\chi_2} = \frac{2}{\pi\omega}\int \chi_1(\omega')\mathrm{d}\omega' + O(\omega^{-1}). \tag{34}$$

By computing the limits of expression (32) it can be seen that $G(0^+) = 0$, $G'(0^+) = \omega_p{}^2/4\pi$, etc. Then, two sum rules are immediately obtained: The first from the asymptotic behavior of the real part is the TRK sum rule

$$\int_0^\infty \omega' \chi_2(\omega')\mathrm{d}\omega' = \frac{\pi}{2}\frac{\mathrm{d}}{\mathrm{d}t}G(t)\bigg|_{t=0^+} = \frac{1}{8}\omega_\mathrm{p}^2, \tag{35}$$

where $\omega_\mathrm{p}^2 = \frac{4\pi e^2 \varrho}{m}$. The second refers to the asymptotic behavior of the imaginary part of the susceptibility which, by comparing with (32) is

$$\int_0^\infty \chi_1(\omega')\mathrm{d}\omega' = \frac{\pi}{2}G(t)\bigg|_{t=0^+} = 0, \tag{36}$$

where the second equality can be obtained from the quantum-mechanical expression of $\boldsymbol{G}(t)$ or from the Lorentz oscillator model.

In the case of metals the imaginary part of $\chi(\omega)$ has a pole $\omega = 0$ due to the fact that the conductivity $\sigma(\omega)$ is different from zero at zero frequency. As shown for the KK relations, this can be handled by adding to $\tilde{\chi}(\omega)$ the term $\left(-\frac{\sigma(0)}{\omega}i\right)$ which cancels the pole, preserving the properties of the function. This is the dominant term in the asymptotic behavior for $\omega \to \infty$, so that, by comparing with (34) one obtains the sum rule for metals:

$$\int_0^\infty \chi_1(\omega')\mathrm{d}\omega' = \frac{\pi}{2}\sigma(0). \tag{37}$$

Other similar sum rules can be obtained for all optical constants (conductivity σ, refractive index $\tilde{n}$,$\varepsilon^{-1}(\omega)$) in the same way, above described, because they are all related to the real and imaginary part of the susceptibility. Analogously to eq. (36) is the ADNS sum rule for the real part of the index of refraction which can be obtained immediately from the observation that the dispersion relations (28) apply to $\tilde{n}(\omega)-1$ for both the metallic and nonmetallic media and that the asymptotic behavior of the complex refractive index is

$$\underset{\omega\to\infty}{\tilde{n}}(\omega) \simeq 1 - \frac{\omega_\mathrm{p}^2}{2\omega^2} + O\left(\omega^{-2}\right). \tag{38}$$

As a consequence one obtains the ADNS sum rule (26) for both metallic and nonmetallic media.

Applications of the above described sum rules and KK relations are innumerable and have been of great help in understanding the basic properties of optics in condensed matter. They explain immediately why above a given frequency all materials are transparent to the electromagnetic radiation.

They show immediately the strict connection between the absorption edge in solids and the value of the static dielectric constant.

The KK dispersion relations have allowed the determination of the optical constants from the measurements of only one of them on the entire optical spectrum (for instance the reflectivity in semiconductors, where the transmittance cannot be measured because it is too small). In that case dispersion relations can be derived for the reflectivity amplitude $r = |r| e^{i\theta}$. They connect the measured reflectivity $\boldsymbol{R}$ to the phase θ through the function

$$\ln r = \ln|r| + i\theta = \frac{1}{2}\ln R(\omega) + i\theta(\omega), \tag{39}$$

which has been proven to have the required analytic behavior in the upper half of the complex ω plane. One can then obtain the phase, and from eq. (7) the complex refractive index and all optical constants. This has extended the knowledge of the optical transitions in solids, and consequently of the electronic band structure over an extended energy range.

The availability of synchrotron radiation over a very extended frequency range has furthermore allowed the direct verification of the sum rules. The results obtained on the metal Al are reported in Fig. 2 (Shiles et al., 1980).

Relativistic and spatial dependent corrections

One can extend the sum rules beyond the dipole approximation, by considering spatial dispersion and the relativistic definition of the current from Dirac equation. One must consider the fact that $\vec{k}$ is related to ω by the expression $\varepsilon(k,\omega)\omega^2 = k^2(\omega)c^2$ so that one must take this into account when performing the integration over frequency.

One can be limited to first-order contributions in k^2 because of the small value of $|\vec{k}|$ in optics. The lowest-order contribution is of order k^2 because the linear term vanishes due to time reversal. Following Ginzburg and Meiman a Taylor expansion about $k = 0$ can obtained as

$$\varepsilon\left(\frac{\omega\sqrt{\varepsilon}}{c},\omega\right) \simeq \varepsilon(0\omega) + \frac{\omega^2}{2c^2}\varepsilon\left(\frac{\omega\sqrt{\varepsilon}}{c},\omega\right)\frac{\partial^2\varepsilon}{\partial k^2}\bigg|_{t=0}, \tag{40}$$

which gives

$$\varepsilon\left(\frac{\omega\sqrt{\varepsilon}}{c},\omega\right) \simeq \frac{\varepsilon(0,\omega)}{1 - \frac{\omega^2}{2c^2}\frac{\partial^2\varepsilon}{\partial k^2}\Big|_{k=0}}. \tag{41}$$

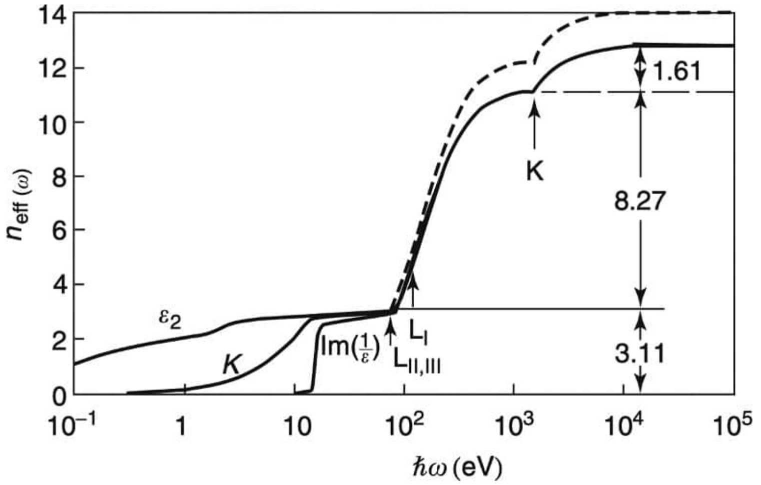

Fig. 2 Sum rule for ε_2, κ and $-\text{Im}\ (\varepsilon_l^{-1})$: in Al the solid line shows the saturation at $n = 13$. Reproduced with permission from Shiles E, Sasaki T, Inokuti M, and Smith DY (1980) Self-consistency and sum-rule tests in the Kramers-Kronig analysis of optical data: Applications to aluminum. *Physical Review B* 22: 1612.

The calculation of the second derivative of the dielectric function with inclusion of relativistic corrections has been carried out by Scandolo, Bassani and Lucarini; it is rather complex and will not be reported here (see Scandolo et al. (2001)). When the result is substituted in the frequency dependence (41) its asymptotic behavior is obtained, and the sum rules can be derived in the usual way with spatial dispersion and relativistic corrections. The sum rule on the real part of the susceptibility is unchanged, and gives zero. That on the imaginary part is modified by a contribution which depends on the expectation value of the kinetic energy of the electrons on the total ground state of the system $T_0 = \langle 0|\frac{1}{2}mv^2|0\rangle$. The result is

$$\int_0^\infty \omega'\varepsilon_2(\omega')\mathrm{d}\omega' = \frac{\pi}{2}\omega_{\mathrm{p}}^2\left(1 - \frac{2}{3}\frac{T_0}{mc^2}\right). \tag{42}$$

This correction is very small, of the order of $\approx 10^{-3}$ in Al, where tests of sum rule have been made, but it may be easily detected in heavy materials using synchrotron radiation up to very high frequencies.

General description of nonlinear optical functions

Nonlinear optics includes a number of phenomena which are of great interest and have become of very common use with the availability of intense laser radiation (Blombergen, 1965; Shen, 1980; Boyd, 1992). Among them multiple-frequency generation, dynamic Stark effect, two-photon absorption, stimulated Raman absorption, electromagnetically induced transparency. All these phenomena must obey the causality principle, and consequently Kramers-Kronig (KK) relations and optical sum rules may be obtained for nonlinear optical phenomena in a way totally analogous to that used in linear optics as described above (Bassani and Scandolo, 1991; Lucarini et al., 2003, 2005).

One may start with the definition of the n-th order polarization of a medium, expressed in terms of the external electric fields as

$$P^{(n)}(t) = \int_{-\infty}^{+\infty} \mathrm{d}t_1 \ldots \mathrm{d}t_n G^{(n)}(t_1, \ldots, t_n)E_1(t - t_1)\ldots E_n(t - t_n), \tag{43}$$

where the response function is symmetric under an exchange of variables, and satisfies the time causality condition

$$G^{(n)}(t_1, t_2, \ldots, t_n) = 0 \quad \text{if any} \quad t_i < 0. \tag{44}$$

The electric fields are taken to be sinusoidal with given frequencies, of the form

$$\vec{E}_n(\tau) = E_n(\omega_n)\exp[-i\omega_n\tau] + E_n^*(\omega_n)\exp[i\omega_n\tau], \tag{45}$$

where by convention the first term gives contributions to the susceptibility of argument ω_n and the second of argument $-\omega_n$.

Taking the Fourier transform of the polarization, one obtains the expression for the frequency component of the polarizability at any order

$$P^{(n)}(\omega) = \chi^{(n)}(\omega_1, \ldots, \omega_n)E_1(\omega_1)\ldots E_n(\omega_n)\delta[\omega - (\omega_1 + \ldots + \omega_n)], \tag{46}$$

where $\chi^{(n)}(\omega_1, \ldots, \omega_n)$ is defined as the Fourier transform of $G^{(n)}(t_1, \ldots, t_n)$,

$$\chi^{(n)}(\omega_1,\dots,\omega_n)=\int_0^\infty \mathrm{d}t_1\dots\int_0^\infty \mathrm{d}t_n \exp\left[i(\omega_1 t_1+\,\dots\,+\omega_n t_n)\right]G^{(n)}(t_1,\dots,t_n), \tag{47}$$

and the symmetry in time implies that it is symmetric for the exchange of frequencies. The reality of $G_n^{(n)}(t_1,\dots,t_n)$, implies also

$$\chi^{(n)}(-\omega_1,\dots,-\omega_n)=\chi^{(n)*}(\omega_1,\dots,\omega_n). \tag{48}$$

If the fields are not sinusoidal one can expand them in their Fourier components of type (45) and the sum over the frequencies ω_1, ..., ω_n must be considered, with the appropriate field amplitudes.

It can be observed that in the nonlinear case the polarization is obtained by multiplying the n-th order susceptibility by all the field amplitudes, so that its dimensionality depends on the order considered. The susceptibilities $\chi^{(n)}(\omega_1,\dots,\omega_n)$ contain all the optical properties of the system to all orders, in the presence of a number of radiation beams.

The various terms of the susceptibilities to any order correspond to particular phenomena, and specific expressions can be obtained in each case, but, since one is interested in the general properties, only the asymptotic behavior for $\omega\to\infty$, or $t\to 0^+$ is relevant. A simple way to obtain it in the classical model is to extend the Lorentz oscillator scheme described in the linear case by adding to the harmonic contribution a potential with all the anharmonic terms, and solving the resulting equations of motion by iteration. A more precise quantum-mechanical expression can be used, which is an extension of equation (30) given above for the linear case

$$G^{(n)}(t_1,\,\dots,t_n)=\frac{1}{n!(i\hbar)^n}\sum T(1,\,\dots,n)\{\mathrm{Tr}[P(-t_1),\,\dots[P(-t_n),\varrho_0]]P\}, \tag{49}$$

where $\boldsymbol{T}$ denotes the time ordering operator, and $\boldsymbol{P}$ is the dipole moment operator, whose time dependence is expressed in the interaction representation in terms of the Hamiltonian H_0.

Since dissipation is proportional to the time average

$$\left\langle\frac{\mathrm{d}P(t)}{\mathrm{d}t}E(t)\right\rangle, \tag{50}$$

it vanishes when the fields and the polarization oscillate at different frequencies.

At different orders, different effects appear considering all possible frequencies of the external electromagnetic fields. It is convenient to indicate the frequency of $P(\omega)$ and those of the external fields explicitly in the susceptibilities.

In second order one has with a single very intense beam the second-harmonic generation from $\chi^{(2)}(2\omega_1;\omega_1,\omega_1)$ and optical rectification from $\chi^{(2)}(0;\omega_1,-\omega_1)$; at higher orders we have higher-harmonic generation $\chi^{(n)}(n\omega_1;\omega_1,..,\omega_1)$. With different beams, in second order one has the sum and difference frequency generation $\chi^{(2)}(\omega_1+\omega_2;\omega_1,\omega_2)$ and $\chi^{(2)}(\omega_1-\omega_2,\omega_1,-\omega_2)$ and at higher order all possible sums and differences. These do not give any absorption because the polarization frequency and the field frequency are different; the real and imaginary parts define in this case the phases of the susceptibility amplitudes.

In third order and at higher odd orders an important contribution to the susceptibility corresponds to the so-called pump and probe experiments, where one detects the dispersion and the absorption of a weak probe beam of frequency ω, in the presence of an intense beam of frequency ω_2. The nonlinear susceptibility $\chi^{(2n+1)}$ is proportional to the intensity of the pump beam at the n-th power. The susceptibility $\chi^{(3)}(\omega;\omega,\omega_2,-\omega_2)$ and more generally $\chi^{(2n+1)}(\omega;\omega,\omega_2,-\omega_2,\dots)$ contains a dynamical Stark effect when ω is close to a first-order resonance, a two-photon absorption when $\omega+\omega_2$ is close to a possible transition frequency, the stimulated Raman effect when $\omega-\omega_2$ is close to a transition frequency. In the pump and probe case, with a three-level system one also obtains, under particular conditions, a coherent interference effect which produces electromagnetically induced transparency (EIT) inside the first-order absorption line.

To consider the general properties related to pump and probe nonlinear dispersive-dissipative effects, one can study the dielectric function which is the sum of the linear contribution and all odd nonlinear contributions with final frequency ω of the probe field

$$\varepsilon_{\mathrm{tot}}(\omega;\omega_2,E_2(\omega_2))=\varepsilon^{\mathrm{L}}(\omega)+\varepsilon^{\mathrm{NL}}(\omega;\omega_2,E(\omega_2))==1+4\pi\sum_{n\ \mathrm{odd}}a_n\chi^{(n)}(\omega;\omega,\omega_2,\ -\omega_2\dots\omega_2,\ -\omega_2)E^{n-1}(\omega_2), \tag{51}$$

where

$$a_n=\frac{1}{2^{n-1}}\frac{(n-1)!}{\left(\frac{n-1}{2}\right)!\left(\frac{n-1}{2}\right)!}, \tag{52}$$

The nonlinear contribution is given by the sum of the terms with $n>1$, and the numerical factor is given by the invariance of the susceptibility for permutation of the frequencies. The most important nonlinear term is clearly $\chi^{(3)}(\omega;\omega,\omega_2,-\omega_2)$.

Kramers-Kronig relations and sum rules in non-linear optics

The analytic properties of the nonlinear optical susceptibilities can be examined in increasing order, and a number of sum rules can be obtained easily, when KK relations hold, by extending the procedure given for the linear case.

A first property follows immediately from causality due to Titchmarsh theorem: the susceptibility is holomorphic in the upper half of the complex plane associated with one of the frequency variables when all the others are kept fixed. A second more general theorem due to causality was derived by Scandolo; the nonlinear susceptibility is holomorphic in the upper half-plane of any straight line with positive slope in the frequency space of all the ω_i. This holds of course also by taking the line with zero slope along a given axis, provided the other values can be kept fixed.

From the above results one can see immediately that KK relations can be established in most cases previously described, in second and higher harmonic generation along ω_1, as well as in pump and probe experiment along ω, keeping ω_2 fixed. They do not apply in optical rectification, because any straight line in the space ω, $\omega_2 = -\omega$ cannot have positive slope; they do not apply also for $\chi^{(3)}(\omega_1;\omega_1,-\omega_1,\omega_1)$, when only one beam is present. The asymptotic behavior of the nonlinear susceptibilities is in general much faster than in the linear case, so that one may consider all integrable products of the type $\omega^k\chi^{(n)}(\omega)$, along the line of positive slope which is considered, and thus obtain a number of KK relations. From them, (using the superconvergence theorem as shown in the linear case) the asymptotic behavior of the real and the imaginary part of the susceptibility can be obtained in terms of their moments (integral of powers of the frequency times the susceptibility), up to a given value, above which the integral does not converge. Comparison of such asymptotic behavior of the susceptibility with the behavior obtained from specific calculations gives a number of new sum rules for the nonlinear susceptibilities considered.

Harmonic generation

As a first example let us consider the second-harmonic generation. The asymptotic behavior of $\chi^{(2)}(2\omega,\omega,\omega)$ as $\omega \to \infty$ can be obtained easily from the anharmonic oscillator model or equivalently from quantum theory. They give similar results, provided the appropriate third-order derivative $\frac{\partial^3 V(x)}{\partial x^3}$ for x-polarized radiation is substituted in the quantum theory by its expectation value on the ground-state wave function. The following second-harmonic asymptotic behavior obtains

$$\underset{\omega\to\infty}{\chi^{(2)}}(2\omega;\omega,\omega) = +\frac{1}{2!}\frac{e^3}{m^2}\left[\frac{\partial^3 V(x)}{\partial x^3}\right]_0 \frac{1}{4}\frac{1}{\omega^6} + o\left(\omega^{-6}\right), \tag{53}$$

where the potential term is given by the anharmonic coefficient in the extended Lorentz model, and by its expectation value on the ground state in the quantum mechanical approach. In the presence of the polarized beams of the same frequency the derivatives can refer to the polarization directions of the fields and to the polarizations directions of $\vec{P}$, so that a third-order tensor component is defined. As a consequence of the asymptotic behavior (53) one obtains three independent KK relations, one for $\chi^{(2)}(2\omega;\omega,\omega)$, one for $\omega^2\chi^{(2)}$, and another one for $\omega^4\chi^{(2)}$. They can be summarized as follows in terms of their real and imaginary part χ_1, χ_2:

$$\begin{aligned}\omega^{2\alpha}\chi_1^{(2)}(2\omega;\omega,\omega) &= \frac{2}{\pi}\int_0^\infty \frac{\omega'^{2\alpha+1}\chi_2^{(2)}(2\omega';\omega',\omega')}{\omega'^2-\omega^2}\,\mathrm{d}\omega',\\ \omega^{2\alpha-1}\chi_2^{(2)}(2\omega;\omega,\omega) &= -\frac{2}{\pi}\int_0^\infty \frac{\omega'^{2\alpha}\chi_1^{(2)}(2\omega';\omega',\omega')}{\omega'^2-\omega^2}\,\mathrm{d}\omega',\end{aligned} \tag{54}$$

with $0 \le \alpha \le 2$. By comparing the asymptotic behavior obtained from the above KK relations, via the superconvergence theorem, which amounts to neglecting ω'^2 in the denominator of (54), with the one given above, (53), one obtains six sum rules which can be summarized as follows:

$$\begin{aligned}&\int_0^\infty \omega^{2\alpha}\chi_1^{(2)}(2\omega;\omega,\omega)\mathrm{d}\omega = 0, \quad \text{for} \quad \alpha = 0,1,2,\\ &\int_0^\infty \omega^{2\alpha+1}\chi_2^{(2)}(2\omega;\omega,\omega)\mathrm{d}\omega = 0, \quad \text{for} \quad \alpha = 0,1,\\ &\int_0^\infty \omega^5\chi_2^{(2)}(2\omega;\omega,\omega) = -\frac{\pi}{2}\cdot\frac{e^3}{8}m^{-2}\varrho\left[\frac{\partial^3 V}{\partial x^3}\right]_0.\end{aligned} \tag{55}$$

The procedure given has been extended to higher harmonics and gives a large number of sum rules. All integrals of even moments of the real part of the susceptibility vanish up to the $2n$ moment, and all odd moments of the imaginary part of the susceptibility vanish, with the exception of the $2n + 1$ moment.

Pump and probe

Now, consider the pump and probe experiments, where the response to a beam of frequency ω is studied in the presence of an intense beam of frequency ω_2. The nonlinear contributions due to the probe beam alone are neglected, and the nonlinear susceptibility $\chi^{(3)}(\omega;\omega,\omega_2,-\omega_2)$, or more generally $\chi^{(2l+1)}(\omega;\omega,\omega_2,-\omega_2\ldots-\omega_2)$ for a very intense pump beam is considered. The asymptotic behavior can be obtained also in this case from the anharmonic oscillator model, or from the quantum-mechanical approach by using the Fourier transform (47) of the response function (49) for $t_1 \to 0^+$. One can show that the asymptotic behavior of the nonlinear susceptibility is

$$\tilde{\chi}^{\mathrm{NL}} = -\frac{C}{\omega^4} + o\left(\omega^{-4}\right), \tag{56}$$

with

$$\begin{aligned} C = &-\sum_{n\ \mathrm{odd}>1} \frac{a_n e^2}{n!(-i\hbar)^{n-1} m^2} E_2^{n-1}(\omega_2) \int \mathrm{d}t_2 \ldots \int \mathrm{d}t_n \cdot \\ &\cdot \exp\left[-i(\omega_2 t_2 - \omega_2 t_n)\right] \mathrm{Tr}\left\{ \frac{\partial^2 V}{\partial x^2} \sum_{P'} T(2\ldots n)\left[P(-t_2)\cdot\left[\ldots P(-t_n), \varrho_0\right]\right] \right\} \end{aligned} \tag{57}$$

and

$$a_n = \frac{1}{2^{n-1}} \frac{(n-1)!}{\left(\frac{n-1}{2}\right)!\left(\frac{n-1}{2}\right)!}.$$

From this it can be seen that two KK relations follow. One is the same as the linear KK relations and applies to $\chi^{\mathrm{NL}}(\omega;\omega_2,E_2)$. The other typical of nonlinear contribution for the probe-pump situation applies to $\omega^2\chi^{\mathrm{NL}}(\omega;\omega_2,E_2)$

$$\begin{aligned} \omega^2\chi_1^{\mathrm{NL}}(\omega;\omega_2,E_2) &= \frac{2}{\pi} \fint \mathrm{d}\omega' \frac{\omega'^3 \chi_2^{\mathrm{NL}}(\omega';\omega_2,E_2)}{\omega'^2 - \omega^2}, \\ \omega^2\chi_2^{\mathrm{NL}}(\omega;\omega_2,E_2) &= \frac{2\omega}{\pi} \fint \mathrm{d}\omega' \frac{\omega'^2 \chi_1^{\mathrm{NL}}(\omega';\omega_2,E_2)}{\omega'^2 - \omega^2}. \end{aligned} \tag{58}$$

This relation, appropriate to the nonlinear contribution, can be used to relate dispersive to dissipative nonlinear phenomena, as well as the original KK relation.

From the asymptotic expansion (56) and the two KK relations obtained, one can derive four sum rules for the nonlinear susceptibility, by following the usual procedure of imposing that their asymptotic behaviors coincide. They are the following:

$$\begin{aligned} &\int_0^\infty \chi_1^{\mathrm{NL}}(\omega;\omega_2,\,E(\omega_2))\mathrm{d}\omega = 0, \\ &\int_0^\infty \omega_2^{\mathrm{NL}}(\omega;\omega_2,\,E(\omega_2))\mathrm{d}\omega = 0, \\ &\int_0^\infty \omega^2\chi_1^{\mathrm{NL}}(\omega;\omega_2,\,E(\omega_2))\mathrm{d}\omega = 0, \\ &\int_0^\infty \omega^3\chi_2^{\mathrm{NL}}(\omega;\omega_2,\,E(\omega_2))\mathrm{d}\omega = C\frac{\pi}{2}, \end{aligned} \tag{59}$$

where $\boldsymbol{C}$ is given by (57). The first two are analogous to the linear sum rules whose validity is thus extended to the optical response to all orders in the presence of a pump beam. The last two are typical of the nonlinear susceptibility. The last one in particular gives a measure of the strength of the nonlinear response through the value of the constant $\boldsymbol{C}$.

Another simple sum rule gives immediately the nonlinear contribution of the pump field to the static susceptibility (limit $\omega \to 0$ in the KK dispersion relations)

$$\varepsilon^{\mathrm{NL}}(0;\omega_2,E(\omega_2)) = \frac{2}{\pi}\int_0^\infty \mathrm{d}\omega' \frac{\chi_2^{\mathrm{NL}}(\omega';\omega_2,E(\omega_2))}{\omega'}. \tag{60}$$

Analogous sum rules can be obtained for all the nonlinear optical functions related to the susceptibility, as in the linear case.

Examples and applications to nonlinear processes

The anharmonic oscillator

One can display the relevance of the above-described sum rules by considering the simple, but physically significant anharmonic-oscillator case.

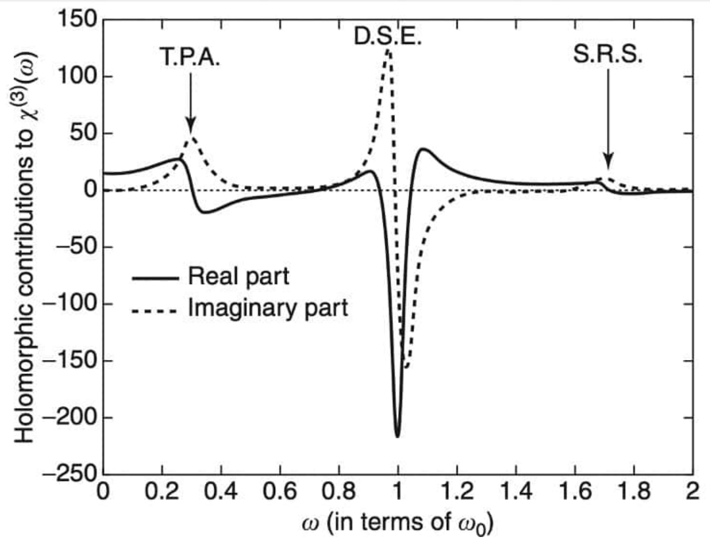

Fig. 3 Anharmonic part of the optical response of the nonlinear oscillator. From Bassani F (2005b) Sum Rules and Kramers-Kronig Relations in Nonlinear Optics. ECMP 1st edn.

By solving the equation of motion with the probe frequency ω and the pump ω_2 one obtains in third order the anharmonic contribution $\chi^{(3)}(\omega;\omega,\omega_2,-\omega_2)$. The result is displayed in Fig. 3 as a function of the frequency of the probe beam ω.

One can observe the modification of the absorption near the resonance ω_0 which is a dynamic Stark effect with a positive and a negative contribution; also a peak is present in correspondence to a two-photon absorption at $\omega_0 - \omega_2$ and another peak due to stimulated Raman absorption at $\omega = \omega_0 + \omega_2$. The sum rules (59) are all verified, but include contributions from all these effects and cannot be referred to a particular phenomenon on its own.

Analogous results are obtained from a quantum-mechanical study of the oscillator, where however differences are found from the classical model in the nonlinear optical functions.

Second-harmonic generation

A further example of how the sum rules can be used to verify detailed theories, and to implement useful simplified models can be seen as an application to second-harmonic generation.

The quantum-mechanical calculation of $\chi^{(2)}(2\omega;\omega,\omega)$ is very complicated, because a knowledge of all excited states and a double summation involving all dipole matrix elements between them is required. One can set up a simple model by considering an expansion about the main poles at ω_0 and $\omega_0/2$, ω_0 being the average frequency of the direct interband transitions in the semiconductors, which is also responsible for the static linear dielectric constant. Thus one writes

$$\begin{aligned}\chi^{(2)}(2\omega;\omega,\omega) = {} & \frac{f_1}{\omega-\omega_0+i\boldsymbol{\varepsilon}^+} + \frac{f_2}{(2\omega-\omega_0)+i\boldsymbol{\varepsilon}^+} + \\ & + \frac{f_3}{(\omega-\omega_0+i\boldsymbol{\varepsilon}^+)^2} + \mathrm{c.c}(\omega \to -\omega),\end{aligned} \tag{61}$$

where $\boldsymbol{\varepsilon}^+$ is a positive infinitesimal which can be set to zero. The coefficients f_i give the strength of the poles and substitute the detailed double sum of dipole matrix elements. Imposing the sum rules, one can obtain expressions for all the coefficient f_i, in terms of the quantity C which appears in the 5th moment sum rule (see eq. (59)).

Taking the limit $\boldsymbol{\varepsilon}^+ \to 0$, and expressing the first-order susceptibility in terms of the average transition frequency to the conduction band as

$$\chi = \frac{\varrho e_1^2}{m(\omega_0^2-\omega^2)}, \tag{62}$$

one obtains Miller's empirical rule

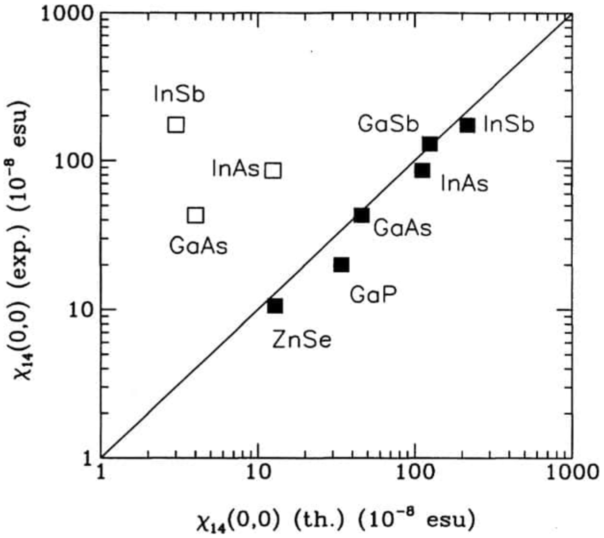

Fig. 4 Second order static susceptibility for some semiconductors. Abscissae: theoretical calculations in units of 10^{-8} esu; ordinate: experimental data squares in units of 10^{-8} esu. Reproduced with permission from Scandolo S and Bassani F (1995) Miller's rules and the static limit for second harmonic generation. *Physical Review B* 51: 6928.

$$\chi^{(2)}_{ijk}(2\omega;\omega,\omega) = \Delta_{ijk}\chi^{(1)}_{ii}(2\omega)\chi^{(1)}_{jj}(\omega)\chi^{(1)}_{kk}(\omega), \tag{63}$$

where Miller's empirical constant $\mathbf{\Delta}$ is given by

$$\Delta_{ijk} = -\frac{1}{2e^3\varrho^2}\left\langle \frac{\partial^3 V}{\partial r_i \partial r_j \partial r_k} \right\rangle_0. \tag{64}$$

This can be easily computed for crystals from pseudopotential theory, by means of the values of the pseudopotential parameters used in the energy band calculations. One can thus compute the static limit in a number of semiconductors and obtain values of $\chi^{(2)}(0,0)$ in good agreement with experiment, as shown in Fig. 4 (Scandolo and Bassani, 1995).

Similar result can be obtained for third- and higher-order harmonic generation processes.

Data analysis

The above described sum rules and KK relations can be also used to complete the experimental data available by imposing that they verify such general properties. This is particularly useful in nonlinear optics, where results on a limited frequency range are experimentally available, and only at a few fixed frequencies both real and imaginary nonlinear susceptibilities are measured. For this, refer to the detailed analysis by Lucarini et al. (Lucarini et al., 2003, 2005).

Conclusion

It has been shown that the principle of time causality implies a number of Kramers-Krönig relations between the real and the imaginary part of the linear and nonlinear susceptibilities and of all optical response functions. From them a variety of sum rules can be obtained for the frequency moments of the real and the imaginary parts of the linear and nonlinear susceptibilities.

The dispersion relations and the sum rules are shown to be useful to interpret experimental data and to verify the accuracy of theoretical models.

References

Bassani F (2005a) *Optical Sum Rules and Kramers-Kronig Relations*, ECMP, 1st edn.
Bassani F (2005b) *Sum Rules and Kramers-Kronig Relations in Nonlinear Optics*, ECMP, 1st edn.
Bassani F and Altarelli M (1983) Interaction of radiation with condensed matter. In: Kock EE (ed.) *Handbook on Synchrotron Radiation*, 463–606. North Holland, Amsterdam.
Bassani F and Pastori-Parravicini G (1975) *Electronic Properties and Optical Transitions in Solids*. Oxford: Pergamon Press.
Bassani F and Scandolo S (1991) Dispersion relation and sum rules in nonlinear optics. *Physical Review B* 44: 8446.
Blombergen N (1965) *Nonlinear Optics*. N. Y.: Benjamin.

Boyd RW (1992) *Nonlinear Optics*. New York, Amsterdam: Academic Press.

Greenway DL and Harbeke G (1968) *Optical Properties and Band Structure of Semiconductors*. Oxford: Pergamon Press.

Lucarini V, Bassani F, Peiponen K-E, and Saarinen JJ (2003) Dispersion theory and sum rules in linear and nonlinear optics. *Rivista del Nuovo Cimento* 26: 120.

Lucarini V, Saarinen JJ, Peiponen K-E, and Vartiainem EM (2005) *Kramers-Kronig Relations in Optical Materials Research*. Heidelberg: Springer.

Scandolo S and Bassani F (1995) Miller's rules and the static limit for second harmonic generation. *Physical Review B* 51: 6928.

Scandolo S, Bassani F, and Lucarini V (2001) Spatial-dispersion and relativistic effects in the optical sum rules. *European Physical Journal B* 23: 319.

Shen YR (1980) *The Principles of Nonlinear Optics*. New York: Wiley.

Shiles E, Sasaki T, Inokuti M, and Smith DY (1980) Self-consistency and sum-rule tests in the Kramers-Kronig analysis of optical data: Applications to aluminum. *Physical Review B* 22: 1612.

Titchmarsh EC (1968) *The Theory of Functions*. Oxford: Oxford University Press.

Semiconductor optics

GC La Rocca, NEST, Scuola Normale Superiore, Pisa, Italy

© 2024 Elsevier Ltd. All rights reserved.

This is an update of G.C. La Rocca, Semiconductor Optics, Editor(s): Franco Bassani, Gerald L. Liedl, Peter Wyder, Encyclopedia of Condensed Matter Physics, Elsevier, 2005, Pages 297–303, ISBN 9780123694010, https://doi.org/10.1016/B0-12-369401-9/00734-8.

Introduction 118
The dielectric function 118
Interband transitions 120
Phonon-assisted transitions 122
Excitons and polaritons 123
Modulation spectroscopy 125
Novel light emitting materials 126
Conclusion 127
References 127

Abstract

An overview of the optical spectra of semiconductors is presented illustrating their relation to the critical points of the electronic band structure and the direct vs indirect character of the fundamental gap. The basic properties of the dielectric function are described. Direct interband transitions, including exciton and polariton features, are considered as well as indirect phonon assisted transitions. Illustrative absorption and reflectivity spectra along with modulation spectroscopy results are presented. A few examples of novel light-emitting semiconducting materials are finally discussed.

Key points

- The role of the dielectric function in the theoretical interpretation of the optical properties is discussed.
- Semiconductor spectroscopy is related to the electronic band structure.
- Modulation spectroscopy is discussed as a tool to determine the critical points in the Brillouin zone.
- Direct and indirect interband transitions are considered.
- Exciton and polaritons are introduced.

Introduction

Even though the paramount role of semiconductors, and of silicon above all, in modern technology is mainly due to their use in electronic microdevices, the optical properties of these materials are also of great interest. In particular, many applications of semiconductors are based on optoelectronic effects: the transformation of light in electrical current (photovoltaic devices), and the transformation of electrical current in light (semiconductor light emitting diodes and lasers), the choice of device architectures being greatly expanded by the band engineering capabilities offered by heterostructures. Of course, the spectroscopy of semiconductors has been, and continues to be, a subject of crucial relevance also from the point of view of basic science as it allows a detailed study of the electronic structure of these materials (Bassani and Pastori Parravicini, 1975; Agranovich and Ginzburg, 1984; Cohen and Chelikowsky, 1988; Yu and Cardona, 1995).

In the following, we will concentrate mainly on bulk properties rather than on heterostructures, and focus on the optical part of the spectrum due to interband electronic excitations, possibly assisted by phonon participation (La Rocca, 2005). After discussing general concepts related to the linear optical response functions, the corresponding absorption spectra will be considered as they are much less sensitive than luminescence to extrinsic effects. Excitonic and polaritonic phenomena will also be touched upon and the role of external perturbations on the optical properties will be discussed (modulation spectroscopy). Finally, emerging light-emitting semiconductor materials will be considered.

The dielectric function

Semiconductors are characterized by an energy gap of the order of the electronvolt (see Table 1), and correspondingly by an absorption edge in the near infrared or in the visible below which they are nearly transparent and above which they are almost opaque. Actually, a direct measurement of the absorption is rather difficult as it is so strong when the frequency is higher than the

Table 1 Energy gap values (in eV) of cubic semiconductors at room temperature

	AlSb (i)	*CdTe (d)*	*GaAs (d)*	*GaP (i)*	*GaSb (d)*
E_g	1.52	1.45	1.43	2.26	0.71
	Ge (i)	InAs (d)	InP (d)	InSb (d)	Si (i)
E_g	0.67	0.35	1.35	0.18	1.14

(d) = direct gap; (i) = indirect gap.

Reproduced from La Rocca G (2005) *Semiconductor Optics*, 1st edn. ECMP.

threshold frequency that no radiation goes through the semiconductor, but for extremely thin layers. This difficulty can be overcome when the optical quality of the surfaces makes it possible to measure by ellipsometry both the real and the imaginary part of the dielectric function as a function of the light frequency. Alternatively, a measurement of the reflectivity over a large frequency range with sufficient accuracy and the application of the Kramers-Kronig relations allow to determine the real and the imaginary part of the reflection coefficient. From this the dispersion and the absorption can be obtained, establishing the bases for the experimental determination of the optical response of semiconductors and of its theoretical interpretation in terms of the electronic band structure.

We recall that the normal incidence reflection coefficient, defined as the ratio between the electric field of reflected and incident wave, is related to the complex index of refraction $\tilde{n}$ by the Fresnel relation

$$r = \frac{E_r}{E_i} = \frac{\tilde{n} - 1}{\tilde{n} + 1} = |r|e^{i\theta}, \tag{1}$$

and taking the logarithm:

$$\log r = \log|r| + i\theta. \tag{2}$$

Since this is an analytic function of the frequency ω in the upper complex plane $\omega + i\eta$, the following Kramers-Kronig relation holds true

$$\theta(\omega) = -\frac{2\omega}{\pi}\mathscr{P}\int_0^\infty \frac{\log|r(\omega')|}{\omega'^2 - \omega^2}d\omega', \tag{3}$$

and from the measured reflectivity $|r(\omega')|^2$, $\theta(\omega)$ can be obtained, and consequently the real and imaginary parts of $\tilde{n} = n + ik$ can be derived from (1).

This amounts to the knowledge of dispersion and absorption since the complex dielectric function is related to $\tilde{n}$ by

$$\tilde{\varepsilon} = \varepsilon_1 + i\varepsilon_2 = \tilde{n}^2. \tag{4}$$

The dissipation is related to the imaginary parts, since the absorption coefficient is given by

$$\alpha(\omega) = \frac{2k\omega}{c} = \frac{\varepsilon_2\omega}{nc}, \tag{5}$$

while the real part $n(\omega)$ gives the dispersion.

To relate the measured optical constants to the electronic structure, we must consider the interaction between the electromagnetic radiation and the electrons which can be expressed in the Coulomb gauge by the minimal coupling Hamiltonian as

$$H' = \frac{|e|}{mc}\vec{A}\cdot\vec{p}, \tag{6}$$

where $\vec{A} = \vec{A}_0 e^{-i\omega t} + \vec{A}_0^{\star} e^{i\omega t}$ denotes the vector potential (the contribution to H' proportional to A^2 being neglected) and the momentum operator $\vec{p}$ induces the transition between different electronic states. We recall that the transition probability per unit time between an occupied lower initial state $|i>$ and an empty higher final state $|f>$ is given by the Fermi golden rule

$$P^{(1)}_{i\to f} = \frac{2\pi}{\hbar}|\langle f|H'|i\rangle|^2\delta\left(E_f - E_i - \hbar\omega\right). \tag{7}$$

In the case of semiconductors we must sum over all occupied initial states (valence bands) and empty final states (conduction bands) in the unit volume to compute the electromagnetic power dissipated at a given frequency

$$W(\omega) = \frac{1}{V}\sum_{i,f}\hbar\omega P^{(1)}_{i\to f}, \tag{8}$$

where V is the crystal volume. The absorption coefficient is by definition

$$\alpha(\omega) = \frac{\text{dissipated power per unit volume}}{\text{incoming flux}} = \frac{W(\omega)}{\left(\frac{cnE^2}{2\pi}\right)}. \tag{9}$$

The imaginary part of the dielectric function, rather than the absorption coefficient, can be directly calculated as it does not depend on the real part of the index of refraction. From the above expressions, we obtain for the dissipative function

$$\varepsilon_2(\omega) = \left(\frac{2\pi e}{m\omega}\right)^2 \sum_{c,v} \int \frac{2d\vec{k}}{(2\pi)^3} \left| < \psi_{c\vec{k}} \middle| \vec{p} \middle| \psi_{v\vec{k}} > \right|^2 \delta\left(E_c\left(\vec{k}\right) - E_v\left(\vec{k}\right) - \hbar\omega\right), \tag{10}$$

where the wavefunctions and their energies are given by a band structure calculation, the integration is over the first Brillouin zone and a factor of two assuming spin degeneracy has been included. Here, as the wavevector of light $2\pi/\lambda$ is much smaller than the size of the Brillouin zone π/l, being l the lattice constant, only allowed "vertical" transitions between electronic states having the same $\vec{k}$ have been considered.

The real part $\varepsilon_1(\omega)$ is then obtained from the Kramers-Kronig dispersion relation

$$\varepsilon_1(\omega) = 1 + \frac{2}{\pi} \mathscr{P} \int_0^\infty \frac{\omega' \varepsilon_2(\omega')}{\omega'^2 - \omega^2} d\omega' \tag{11}$$

and from the complex dielectric function the optical dispersion and absorption properties follow. We finally recall that since most semiconductors of interest (e.g., those in Table 1) are cubic their optical response is isotropic as assumed here.

Interband transitions

The optical absorption in crystals is mostly due to interband transitions, i.e. to the promotion of electrons from occupied valence bands to empty conduction bands. Because of the energy conserving δ-function in (10), a singular behavior of the response functions is obtained in the vicinity of the critical points of the Brillouin zone (Van Hove singularities), where for a given couple of conduction and valence bands

$$\vec{\nabla}_k \left(E_c\left(\vec{k}\right) - E_v\left(\vec{k}\right)\right) = 0. \tag{12}$$

In fact, near a critical point it is often a good approximation to consider the transition matrix element as a constant. Then, the integral in (10) is simply proportional to the joint density of states $J(\omega)$:

$$J(\omega) = \int \frac{2d^3k}{(2\pi)^3} \delta\left(E_c\left(\vec{k}\right) - E_v\left(\vec{k}\right) - \hbar\omega\right) = \frac{2}{(2\pi)^3} \int_{S(\omega)} \frac{d^2k}{\left|\nabla_{\vec{k}}\left(E_c\left(\vec{k}\right) - E_v\left(\vec{k}\right)\right)\right|}, \tag{13}$$

where the two-dimensional integral is over a surface $S(\omega)$ in $\vec{k}$-space for which $E_c\left(\vec{k}\right) - E_v\left(\vec{k}\right) = \hbar\omega$.

The location of critical points in the Brillouin zone is mainly (but not completely) determined by symmetry considerations. For cubic semiconductors, the points Γ, X, L and W in the Brillouin zone (see Fig. 1) are always critical points; other critical points usually occur along lines or planes of symmetry, but critical points at a generic wavevector $\vec{k}$ cannot be excluded. Van Hove

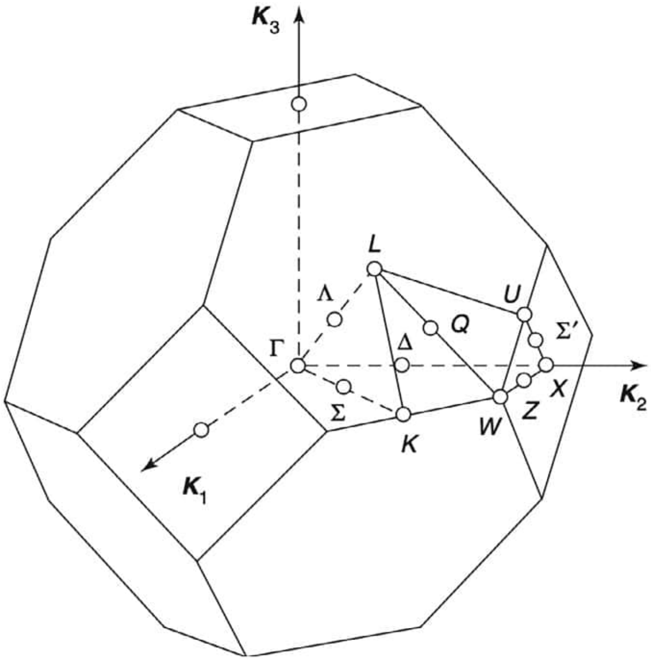

Fig. 1 Brillouin zone of cubic semiconductors (FCC lattice); lines and points of high symmetry are indicated. Reproduced from La Rocca G (2005) *Semiconductor Optics*. 1st edn. ECMP.

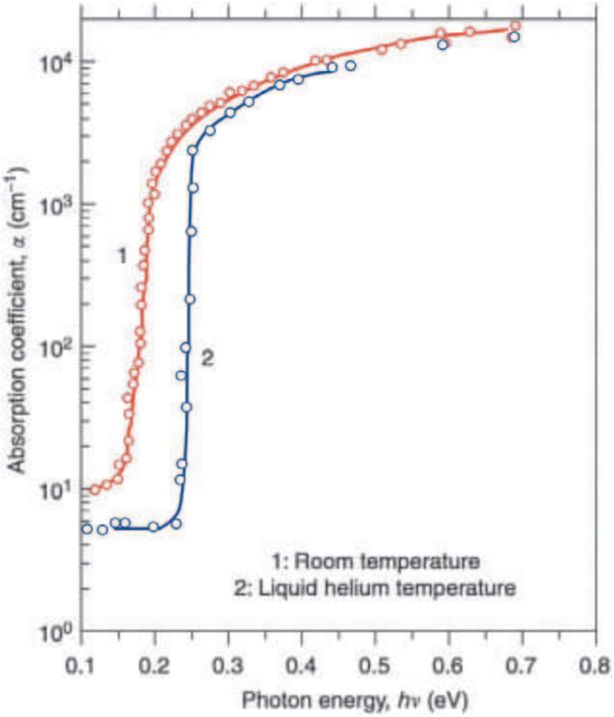

Fig. 2 Absorption edge of InSb. Based on NSM NSM Archive (2001) http://www.ioffe.ru/SVA/NSM/Semicond/http://www.ioffe.ru/SVA/NSM/Semicond/.

singularities have been found in the optical spectra of all semiconductors, and this has allowed the identification of the critical point transition peaks and the verification of the band structure.

A direct gap semiconductor is characterized by having both the conduction band minimum and the valence band maximum at the same wavevector $\vec{k}$ (typically the Γ point at $\vec{k} = 0$). When the optical transition between them is allowed, the absorption edge at a frequency corresponding to the band gap E_g is due to the fact that the joint density of states vanishes for $\hbar\omega < E_g$ and increases sharply for $\hbar\omega \simeq E_g$. In particular, assuming a parabolic dispersion of the conduction and valence band states for $\hbar\omega \geq E_g$

$$J(\omega) \propto \sqrt{\hbar\omega - E_g}. \tag{14}$$

This result correctly describes the gross features of the absorption edge for allowed interband transitions in direct gap semiconductors. As an example, the absorption spectrum of InSb near its direct gap is shown in Fig. 2 (NSM Archive, 2001) exhibiting a well pronounced absorption edge and becoming opaque at frequencies $\hbar\omega > E_g$ with an absorption coefficient $\alpha \approx 10^4$ cm^{-1}.

In Fig. 3 the entire experimental excitation spectrum of Ge (the lowest gap of which is indirect, see below) is compared to that computed as described above from a pioneering band structure calculation based on empirical pseudopotentials (Brust et al., 1962). In this classical example, not only have the critical points been identified, but also the full band structure has been put to test obtaining a satisfactory agreement with the measured data. From the calculation of the dipole matrix elements at all points of the Brillouin zone and for all possible transitions to higher conduction bands, it can be concluded that most of the absorption is due to transitions to the lowest empty conduction bands. This fact can also be proved by verifying the *f*-sum rule in the optical range

$$\int_0^{\omega_M} \omega \varepsilon_2(\omega) d\omega \simeq \frac{2\pi^2 e^2 n_{\text{eff}}}{m}, \tag{15}$$

where in this case the frequency ω_M is just above the spectrum in the visible region, and n_{eff} is about equal to the number of valence electrons which take part in the optical transitions (8 per unit cell in elemental semiconductors such as Ge).

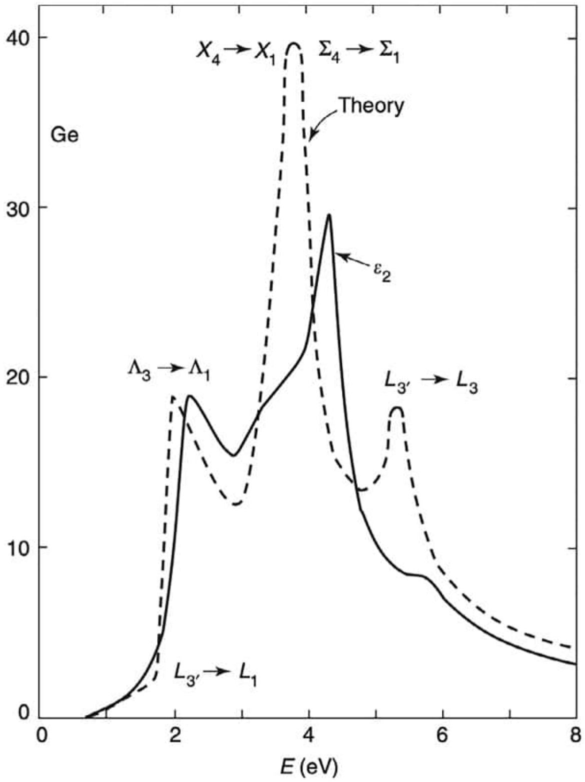

Fig. 3 Imaginary part of the dielectric function of Ge: the solid line is experimental, the dashed one theoretical; optical transitions at critical points are identified. Reproduced with permission from Brust D, Phillips JC, Bassani F (1962) *Physical Review Letters* 9: 94.

Phonon-assisted transitions

Differently from the case of direct gap semiconductors such as GaAs and InSb, for Si and Ge while the top of the valence band is still at the center of the Brillouin zone (Γ point), the minimum of the conduction band occurs away from Γ (close to the *X* point along the Δ line in Si, at the *L* point in Ge). This has been clearly observed by cyclotron resonance experiments, but it also shows in the optical properties, because the electron-phonon interaction makes possible an optical transition between different points of the Brillouin zone, the missing (pseudo)momentum being provided by the phonon emitted or absorbed.

The probability of an indirect transition can be calculated in second order perturbation theory taking the perturbation interaction to be the sum of (6) and the electron-phonon interaction. Assuming constant matrix elements involving the states near the extrema which give the strongest contribution, one obtains

$$\varepsilon_2(\omega) \propto \left(n_{\overleftarrow{q}_o v_o} + \frac{1}{2} \pm \frac{1}{2}\right) \iint \frac{2d\overleftarrow{k}_1 d\overleftarrow{k}_2}{(2\pi)^6} \delta\left(E_c\left(\overleftarrow{k_1}\right) - E_v\left(\overleftarrow{k_2}\right) \pm \hbar\omega_{v_o}\left(\overleftarrow{q_o}\right) - \hbar\omega\right), \tag{16}$$

where +(−) refers to creation (destruction) of a phonon of mode v_o with the wavevector $\overleftarrow{q_o}$ which connects the valence band maximum and the conduction band minimum.

The summation over the final electronic states above the edge ($\hbar\omega_o$) gives an energy dependence which is different from that of direct transitions, and precisely

$$\varepsilon_2(\omega) = 0 \quad \text{when } \omega < \omega_o,$$
$$\varepsilon_2(\omega) \propto (\omega - \omega_o)^2 \quad \text{when } \omega > \omega_o.$$

Furthermore, different edges occur in correspondence to each phonon, and their values depend on the fact that the phonons are absorbed or emitted. At low temperature we can only create phonons, and consequently the edge occurs at higher energy

$$\hbar\omega_o = E_g + \hbar\omega_{v_o}\left(\overleftarrow{q_o}\right). \tag{18}$$

At higher temperature we can also absorb phonons, with a temperature dependent probability given by the Bose-Einstein factor, and the edge is shifted to lower energy

$$\hbar\omega_o = E_g - \hbar\omega_{v_o}\left(\overleftarrow{q_o}\right). \tag{19}$$

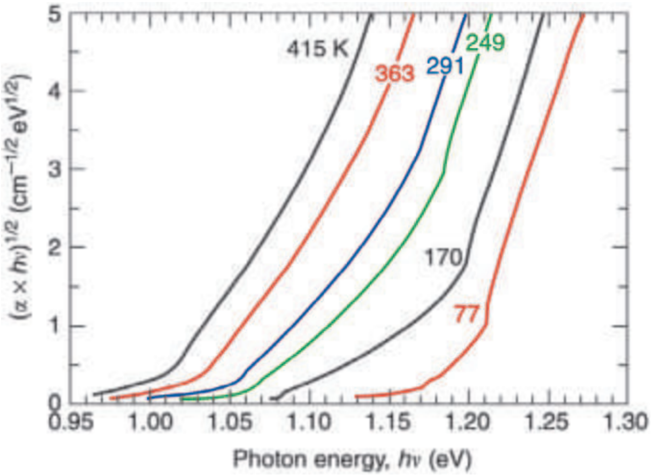

Fig. 4 Indirect absorption edge of Si at various temperatures. Based on NSM NSM Archive (2001) http://www.ioffe.ru/SVA/NSM/Semicond/http://www.ioffe.ru/SVA/NSM/Semicond/.

Indirect transitions are responsible for the weak absorption tail in Si and Ge, which reflects their conduction band structures. We show in Fig. 4 the absorption tail of Si; a fit to the profile of the indirect edge gives the frequency of the phonons which make the transition possible. At higher energies, when allowed direct transitions set in, the contribution of phonon-assisted indirect transitions to the absorption is negligible.

Excitons and polaritons

The discussion above neglects the attractive interaction between the electron promoted into the conduction band and the hole left behind in the valence band. However, their motion is correlated and, in particular, they can be bound into Wannier-Mott excitonic states with an energy below that of the single particle energy gap. Due to the large dielectric constant ($\varepsilon_o \approx 10$) and the small reduced mass ($\mu = (m_e m_h)/(m_e + m_h) \approx 0.1 m_o$) typical of semiconductors, the exciton radius a_o is much larger than the lattice constant and the binding energy correspondingly small. In first approximation, an exciton turns out to be a "rescaled hydrogen atom" with binding energies depending only on the principal quantum number n

$$E_n = E_g - \frac{R^*}{n^2}; \quad R^* = \frac{\mu e^4}{2\varepsilon_o^2 \hbar^2} = \frac{\hbar^2}{2\mu a_o^2} = \frac{e^2}{2\varepsilon_o a_o}, \tag{20}$$

the exciton Bohr radius a_o being larger than 1 nm and the effective Rydberg R^* being typically of the order of 10 meV. Thus, the exciton absorption lines are typically prominent only at low temperatures, as shown for GaAs in Fig. 5.

The optical resonances below the band gap corresponding to the excitonic bound states can be described by the following complex dielectric constant

$$\varepsilon(\omega) = \varepsilon_b + \sum_n \frac{f_n}{(E_n/\hbar)^2 - \omega^2 - i\gamma_n \omega}, \tag{21}$$

where ε_b is a background dielectric constant, γ_n a phenomenological linewidth (e.g., due to phonon scattering), and the oscillator strength f_n is proportional to the square of the dipole matrix element between valence and conduction band extrema and inversely proportional to the exciton volume ($f_n \propto (n a_o)^{-3}$).

Recently, Rydberg excitons levels with a very high principal quantum number n, akin to the Rydberg states of alkali atoms, have been observed: in Fig. 6 high resolution spectra of the yellow P exciton series in C_2O are shown exhibiting levels with n larger than 20 (Kazimierczuk et al. (2014)). These excitons are truly *giant* extending over distances of the order of micrometers (much larger than the wavelength of the resonating light).

In correspondence to the excitonic resonances, when damping processes are small compared to the exciton-photon coupling, the electromagnetic waves propagating in the crystal hybridize with the exciton polarization giving rise to polariton states, i.e. the proper modes of Maxwell's equations with the dielectric function given in (21). Their dispersion law is obtained from

$$\omega^2 = \frac{c^2}{\varepsilon(\omega)} k^2, \tag{22}$$

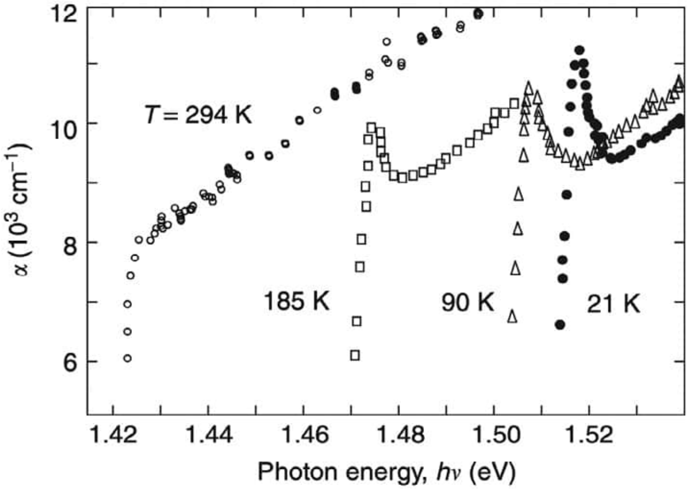

Fig. 5 Excitonic absorption in GaAs, at room temperature the exciton peak is no longer observed. Based on NSM NSM Archive (2001) http://www.ioffe.ru/SVA/NSM/Semicond/http://www.ioffe.ru/SVA/NSM/Semicond/.

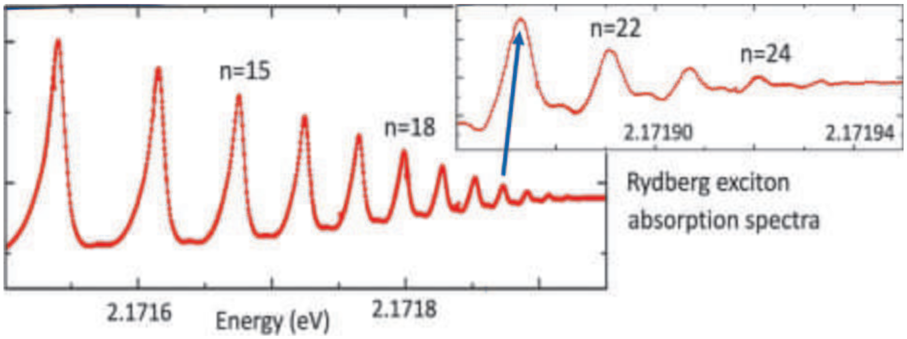

Fig. 6 Absorption spectra of a natural cuprous oxide crystal at 1.2 K: the inset shows Rydberg exciton levels up to $n = 25$. Data from Kazimierczuk T et al. (2014) *Nature* 514: 343.

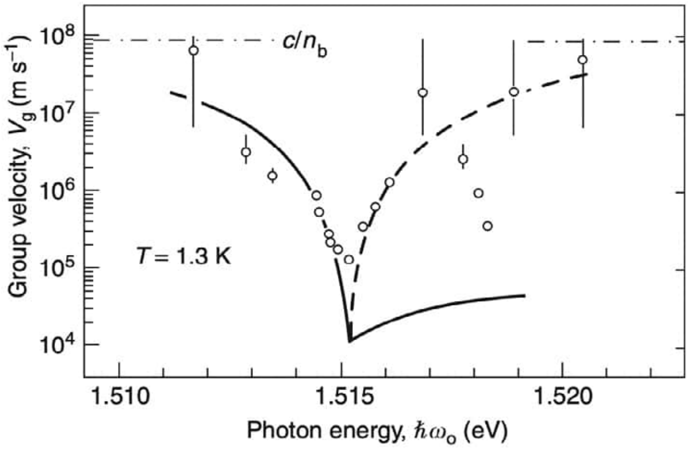

Fig. 7 Exciton-polariton group velocity in GaAs, the solid and dashed lines are the theoretical values for the lower and upper polariton branch, respectively. Reproduced with permission from Ulbrich RG, Fehrenbach GW (1979) *Physical Review Letters* 43: 963.

giving for each excitonic resonance two branches (upper and lower polaritons) accompanied by a region of anomalous dispersion with a strongly reduced group velocity, as shown for GaAs in Fig. 7 (Ulbrich and Fehrenbach, 1979). In polar semiconductors, having strong infrared absorption lines due to optical phonons, phonon-polariton states are similarly formed.

Recently, the light-matter interaction in the strong coupling regime, particularly in planar semiconductor microcavities, have been extensively studied and the physics of interacting polaritons has revealed a number of fundamental many-body phenomena related to Bose-Einstein condensation and superfluidity (Carusotto and Ciuti (2013)).

Modulation spectroscopy

In an experimental spectrum, e.g., of the reflectivity, the van Hove singularities such as those shown in Fig. 3 might be difficult to identify. As an example, the optical reflectivity of Si in Fig. 8 exhibit quite a smooth behavior as a function of frequency. However, the possibility of employing a phase-sensitive detection technique in conjunction with a periodic modulation of an external perturbation improves, on the one hand, the signal to noise ratio by several orders of magnitude and, on the other hand, allows to enhance the sharp features of a spectrum with respect to a smoothly varying background. Modulation spectroscopy allows to directly measure derivative spectra showing very clearly the stronger singularities in the first (and higher order) derivatives of, say, the reflectivity as a function of frequency.

Thus, from the experimental point of view, much information on the properties of semiconductors can been obtained by measuring changes induced by externally applied perturbations. The latter can preserve the symmetry of the crystal (as for hydrostatic pressure or temperature changes) or lower it (as for uniaxial stress or electric and magnetic fields), in which case detailed information on the symmetry properties of the critical points of the electronic bands can be obtained. For instance, the reflectivity of Ge around 2.2 eV is dominated by interband transitions involving states along the Λ line in the Brillouin zone: uniaxial stress along the [001] direction does not split the degeneracy among the eight [111] valleys, whereas uniaxial stress along the [111] direction induces a difference between the two of them along the stress axis and the other six; in the latter case a polarization dependence of the reflectivity is observed.

One of the most common techniques of modulation spectroscopy is electroreflectance, in which the reflectivity is measured while applying an AC electric field parallel or perpendicular to the sample surface. The changes in optical constants measured by electroreflectance modulation spectroscopy have a very simple interpretation in the regime of low applied fields. In this case, as shown in Fig. 9 (Aspnes, 1972), the spectra are simply proportional to the third derivative of the respective optical constant with respect to frequency according to

$$\Delta\varepsilon(\omega) \propto \frac{e^2F^2}{\mu\hbar}\frac{1}{\omega^2}\frac{d^3}{d\omega^3}\left(\omega^2\varepsilon(\omega)\right), \tag{23}$$

where F is the electric field and μ the reduced mass of the relevant interband transition. The electroreflectance spectra (Fig. 9a) show much sharper features than those obtained by ellipsometry (Fig. 9c).

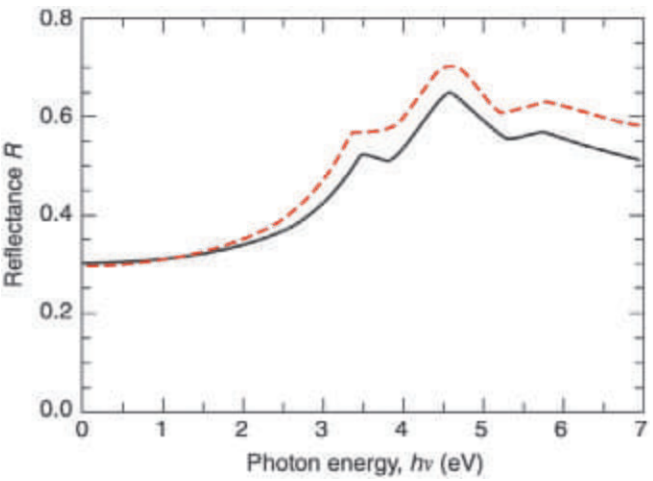

Fig. 8 Reflectivity spectrum of Si: dashed line is experiment, solid line is theory, based on an empirical pseudopotential band structure calculation. Based on NSM NSM Archive (2001) http://www.ioffe.ru/SVA/NSM/Semicond/http://www.ioffe.ru/SVA/NSM/Semicond/.

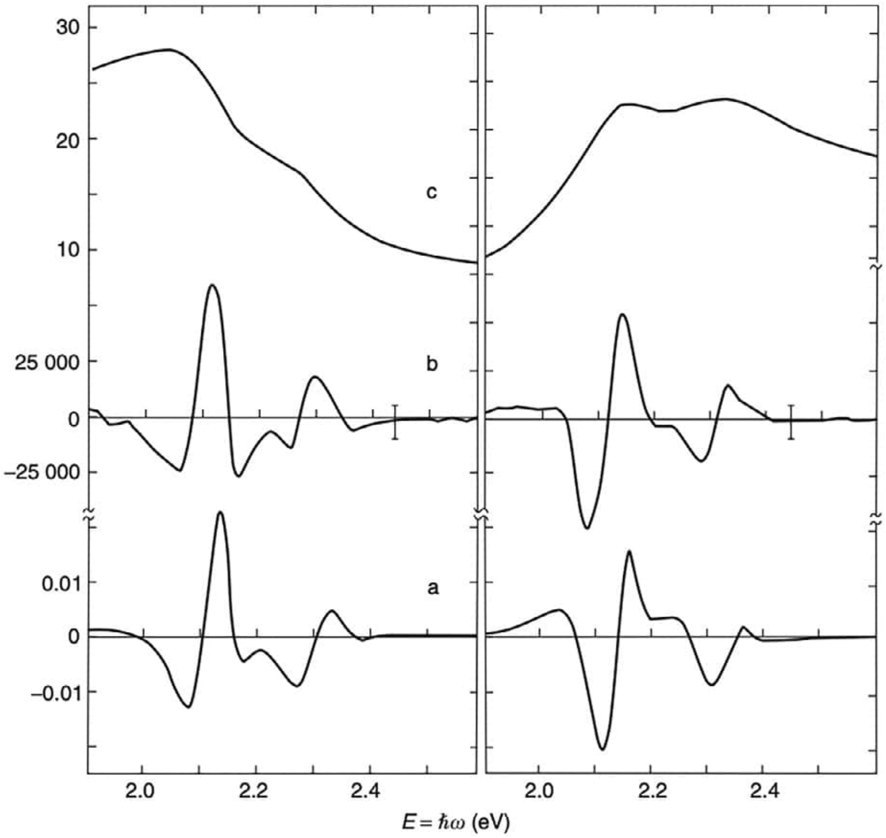

Fig. 9 Real part (left panels) and imaginary part (right panels)of the dielectric function of Ge at the E_1 and $E_1 + \Delta_1$ gaps from low-field electroreflectance (a), compared to the third-order derivatives as in Eq. (23) (b) calculated from ellipsometric data (c). Reproduced with permission from Aspnes DE (1972) *Physical Review Letters* 28: 168.

Novel light emitting materials

Semiconductors are a key class of materials from the technological viewpoint, with silicon playing a paramount role in the electronic industry. However, for optoelectronic applications and lasing in particular, silicon is hampered by the fact that its fundamental gap is indirect. Thus, a long standing goal in this research field is finding a good light-emitting material to be integrated on silicon. Substantial progress has been made with on-chip materials based on porous Si, Ge and SiGe alloys or also III–V semiconductors (Zhou et al., 2015). More recently, a strategy based on hexagonal Ge (2H—Ge) has been successfully pursued. Differently from the ordinary cubic Ge (c-Ge), 2H—Ge has a direct gap which can be seen as the result of folding the L point conduction band minimum of c-Ge to the Γ point. Most importantly, Si can be alloyed into 2H—Ge to form 2H - $Si_\gamma Ge_{(1-\gamma)}$ which for $\gamma < 0.35$ maintains a direct gap tunable within the energy 0.3–0.7 eV. This has been experimentally observed (Fadaly et al., 2020) in quantum wires of 2H - $Si_\gamma Ge_{(1-\gamma)}$ as shown in Fig. 10.

Following the discovery of graphene, which is gapless, many monolayer thick materials have been studied including elemental semiconductor ones with direct gaps in the optical range such as phosphorene ($E_g \sim 2$ eV), i.e. a single layer of black phosphorous which in the bulk has a small band gap ($E_g \sim 0.3$ eV). A particularly interesting family of 2D semiconducting compounds is that of transition metal dichalcogenides (TMD) in which the character of the gap changes from indirect to direct going from a multilayer down to a monolayer thickness. In the monolayer limit, their direct gaps cover a range of energies: $MoTe_2$ ($E_g \sim 1.1$ eV), $MoSe_2$ ($E_g \sim 1.6$ eV), WSe_2 ($E_g \sim 1.7$ eV), MoS_2 ($E_g \sim 1.9$ eV), WS_2 ($E_g \sim 2.0$ eV). Their absorption spectra at the fundamental gap show pronounced exciton resonances as shown in Fig. 11 for MoS_2 (Mak et al., 2010) where the A and B exciton peaks correspond to transitions from the spin-orbit split valence band to the conduction band.

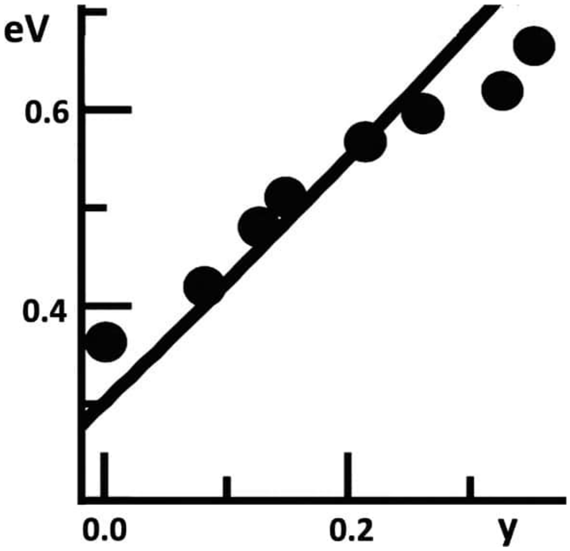

Fig. 10 Tunable direct gap in hexagonal $Si_yGe_{(1-y)}$ alloys, the line showing the calculated Γ point band gap. Based on Fadaly EMT et al. (2020) *Nature* 580: 205.

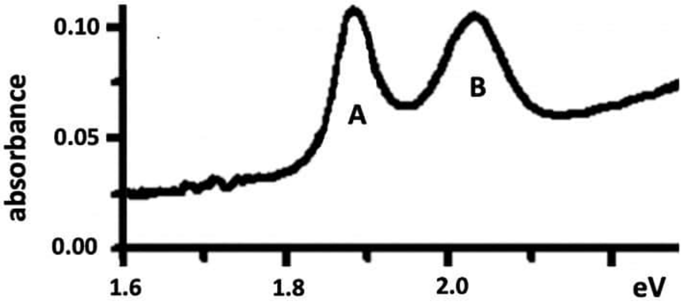

Fig. 11 Absorption spectrum at the direct gap of a monolayer of MoS_2 showing the prominent *A* and *B* exciton peaks. Based on Mak KF et al. (2010) *Physical Review Letters* 105: 136805.

Conclusion

An overview of semiconductor optics has been presented focusing on the basic principles of the field and illustrating them via a variety of examples mainly based on traditional bulk materials. The study of their optical properties has played a crucial role in the understanding of the electronic structure of this important class of solids. While the optical properties of the main bulk semiconductors have been established for long, the current research in the field is mainly driven by the fundamental interest in complex physical phenomena as well as by the technological need for new materials and architectures for optoelectronic applications.

References

Agranovich VM and Ginzburg VL (1984) *Crystal Optics with Spatial Dispersion and Excitons*. Berlin: Springer-Verlag.
Aspnes DE (1972) *Physical Review Letters* 28: 168.
Bassani F and Pastori Parravicini G (1975) *Electronic States and Optical Transitions in Solids*. Oxford: Pergamon Press.
Brust D, Phillips JC, and Bassani F (1962) *Physical Review Letters* 9: 94.
Carusotto I and Ciuti C (2013) *Reviews of Modern Physics* 85: 299.
Cohen ML and Chelikowsky JR (1988) *Electronic Structure and Optical Properties of Semiconductors*. Berlin: Springer-Verlag.
Fadaly EMT, et al. (2020) *Nature* 580: 205.
Kazimierczuk T, et al. (2014) *Nature* 514: 343.
La Rocca G (2005) *Semiconductor optics*, 1st edn. ECMP.
Mak KF, et al. (2010) *Physical Review Letters* 105: 136805.
NSM Archive (2001) http://www.ioffe.ru/SVA/NSM/Semicond/http://www.ioffe.ru/SVA/NSM/Semicond/
Ulbrich RG and Fehrenbach GW (1979) *Physical Review Letters* 43: 963.
Yu PY and Cardona M (1995) *Fundamentals of Semiconductors*. Berlin: Springer-Verlag.
Zhou Z, Yin B, and Michel J (2015) *Light Science and Applications* 4: e358.

Ultrafast optics of topological materials

Vadym Apalkov, Department of Physics and Astronomy, Georgia State University, Atlanta, GA, United States

© 2024 Elsevier Ltd. All rights reserved.

Introduction 128
Solids in a field of an optical pulse 129
Topological properties of graphene-like materials 131
Ultrafast electron dynamics: Interference effects 133
Ultrafast electron dynamics: Topological resonance 135
Conclusion 136
References 136

Abstract

Two-dimensional graphene-like materials with honeycomb crystal structure have non-trivial topological properties, which are characterized in terms of accumulation of topological phase of the Bloch wave functions and the phase of the interband dipole matrix elements when an electron is transferred in the reciprocal space. One of the natural ways to probe these topological properties is to apply a strong and short optical pulse, which induces the transfer of electrons in the reciprocal space over a large distance. In such pulses, the nontrivial topology of the graphene-like systems results in two phenomena. One is due to the interference effect in the interband electron dynamics, which results in appearance of interference fringes in the conduction band population distribution in the reciprocal space. This effect is realized in the graphene-like systems with small bandgap. Another phenomenon is related to the effect of topological resonance, which is the cancellation of the dynamic phase by the accumulated topological phase. The topological resonance is realized only in graphene-like systems with broken inversion symmetry and results in ultrafast valley polarization if a circular pulse is applied to the system.

Key points

- Two dimensional graphene-like materials, for example, pristine graphene and transition-metal dichalcogenide monolayers have honeycomb crystal structure with nontrivial topological properties.
- The topology is characterized in terms of intraband and interband Berry connections.
- Topological properties can be probed by femtosecond long and ultrastrong optical pulses.
- For semimetal graphene-like materials, which have an inversion symmetry, the optical pulse results in interference pattern in the conduction band population distribution in the reciprocal space.
- For semiconductor graphene-like materials, for which the inversion symmetry is broken, the topological resonance can be observed in the ultrafast electron dynamics
- The topological resonance occurs due to cancellation of the dynamic phase by the accumulated topological phase.
- For a circularly polarized pulse, the topological resonance results in ultrafast valley polarization of graphene-like semiconductor systems.

Introduction

Short and strong optical pulses with the duration of a few femtoseconds and the amplitude of around 1 $V/\text{Å}$ can strongly modify both optical and transport properties of solids and have extensively used to probe and control the electron systems in solids (Apalkov and Stockman, 2012; Gruber et al., 2016; Heide et al., 2018, 2019; Higuchi et al., 2017; Kaiser et al., 2000; Liu et al., 2017; Mashiko et al., 2018; Motlagh et al., 2017, 2018; Nematollahi et al., 2019; Schiffrin et al., 2012; Shin et al., 2018; Sun et al., 2012; You et al., 2017). Such pulses produce strong interband mixing, which results highly non-perturbative electron dynamics. Such nonlinear dynamics results, for example, in metallization of dielectrics when the conductance of a dialectic solid increases by 18 orders of magnitude during a femtosecond-long pulse (Schiffrin et al., 2012). If the band gap of a solid is larger than the frequency of the pulse then such strongly nonlinear electron dynamics is also highly reversible, i.e., the electron system returns to its initial state after the pulse.

In addition to strong interband mixing, an ultrastrong optical pulse also results in long electron excursion in the reciprocal space. During the pulse an electron can propagate through almost the entire Brillouin zone. In topological materials, during such transfer the electron accumulates a topological phase, which can interfere with optically-induced interband dynamics and can affect both the transport and optical properties of topological materials (Oliaei Motlagh et al., 2018, 2019a). In this relation, the interaction of topological materials with strong optical pulses opens unique possibility to probe nontrivial topologically induced effects in solids.

https://doi.org/10.1016/B978-0-323-90800-9.00003-2

In solids, there is a natural way to define nontrivial topological properties through accumulation of the phase of the Bloch wavefunctions when an electron is transferred through the reciprocal space. This phase which is called the geometric or Berry phase, determines both the local topological properties and the global topological charge of solid systems (Xiao et al., 2010). Two-dimensional topological systems that are based on the honeycomb crystal structure include such materials as pristine graphene, silicene, germanene, and transition metal dichalcogenide (TMDC) monolayers. The honeycomb crystal structure has two sublattices, *A* and *B*, while in the reciprocal space there are two valleys, *K* and *K*′, connected by the time reversal symmetry. The valleys are also called the Dirac points. For pristine graphene, which has an inversion symmetry, two sublattices *A* and *B* are equivalent and graphene is a semimetal with zero bandgap. In this case, near the Dirac points, the electrons are described by an effective massless Dirac Hamiltonian. If the inversion symmetry of graphene-like materials is broken, i.e., the sublattices *A* and *B* are not equivalent, then the system becomes a semiconductor with a finite bandgap. Among such gapped materials, TMDC monolayers with the bandgap of 1.1–2.1 eV (Conley et al., 2013; Jiang, 2015; Mak et al., 2010; Novoselov et al., 2016; Wang et al., 2012; Xiao et al., 2012) play a special role.

The TMDCs are composed of transition metals such as Mo, W, Ta, Re, Nb, or Zr, and chalcogens such as S, Se, or Te. They are usually denoted as $MX_2$where M and X stand for the transition metal and the chalcogen, respectively. TMDCs are layered crystals with in-plane strong covalent bond and out-of-plane weak Van der Waals coupling that allows to isolate monolayers (Novoselov et al., 2016). TMDC monolayers are stable, and unlike the corresponding bulk solids, which are indirect semiconductors, these are direct semiconductors. This property has been proved to be tremendously useful in optoelectronics applications.

Similar to graphene, TMDC monolayers have honeycomb crystal structure with two triangular sublattices *A* and *B* (Geim and Novoselov, 2007), where each site of sublattice *A* is occupied by one metal atom, while each site of sublattice *B* is occupied by two chalcogen atoms per site (Liu et al., 2013). Thus, the inversion symmetry is intrinsically broken, which opens a finite bandgap at the Dirac points, i.e., at the two valleys *K* and *K*′. The degeneracy of the K- and K′-valleys is still protected by the time reversal symmetry (Geim and Novoselov, 2007).

The topological properties of solids are defined in terms of accumulation of the phase of the Bloch wave functions while an electron is transferred in the reciprocal space (Xiao et al., 2010). Mathematically, the topology of solids can be also described in terms of intraband and interband Berry connections. Introducing the lattice-periodic Bloch functions $\Psi_{\mathbf{k}}^{(\alpha)}$, where α is the corresponding energy band, i.e., the conduction and valence bands, one can define the intraband

$$\mathscr{A}^{\alpha\alpha}(\mathbf{k}) = \left\langle \Psi_{\mathbf{k}}^{(\alpha)} \middle| i\frac{\partial}{\partial \mathbf{k}} \middle| \Psi_{\mathbf{k}}^{(\alpha)} \right\rangle \tag{1}$$

and interband

$$\mathscr{A}^{\alpha\alpha_1}(\mathbf{k}) = \left\langle \Psi_{\mathbf{k}}^{(\alpha)} \middle| i\frac{\partial}{\partial \mathbf{k}} \middle| \Psi_{\mathbf{k}}^{(\alpha)} \right\rangle \tag{2}$$

Berry connections. Here $\alpha_1 \neq \alpha$. While the intraband Berry connection, $\mathscr{A}^{\alpha\alpha}$, determines the accumulation of the phase of an electron that is transferred through the band α, the interband Berry connection $\mathscr{A}^{\alpha\alpha_1}$ is proportional to the interband dipole matrix element.

Solids in a field of an optical pulse

First, we describe the general theory of the interaction of ultrastrong and ultrashort optical pulses with topological materials. The amplitude of the electric field in such pulses is around IV/Å and the duration of the pulses is ~10 fs. The pulse should be short enough so it strongly affects the electron dynamics but does not damage the solid itself. At the same time for such a short pulse, less than 10 fs, the scattering processes do not affect the electron dynamics and the dynamics can be considered as a coherent one. The coherent electron dynamics in the time-dependent field of the optical pulse is described by the time dependent Schrödinger equation (TDSE)

$$i\hbar\frac{d\Psi}{dt} = H(t)\Psi, \quad H(t) = H_0 - e\mathbf{F}(t)\cdot\mathbf{r}, \tag{3}$$

where $H(\mathrm{t})$ is the Hamiltonian of an electron system, which consists of the field-free Hamiltonian, H_0, and the part, which describes the interaction of electrons with the field of the pulse, $-e\mathbf{F}(t)\mathbf{r}$. Here, $\mathbf{F}(t)$ is the pulse's electric field, e is the electron charge, and we used the length gage to describe the interaction of the optical pulse with the solid.

In solids, which have a multi-band structure, the electric field of the pulse generates two types of electron dynamics. The first one is the intraband adiabatic dynamics, which is determined by the Bloch acceleration theorem (Bloch, 1929). This theorem determines the time evolution of the wave vector, $\mathbf{k}(t)$, in the time-dependent electric field, $\mathbf{F}(t)$

$$\mathbf{k}(\mathbf{q}, t) = \mathbf{q} + \frac{e}{\hbar}\int_{-\infty}^{t} \mathbf{F}(t')dt', \tag{4}$$

where $\mathbf{k}$ is the electron crystal wave vector and $\mathbf{q}$ is its initial value, i.e., before the pulse, $\mathbf{q} = \mathbf{k}\ (\mathbf{q}, -\infty)$. The intraband electron dynamics is adiabatic, i.e., after the pulse, an electron returns to its initial state with initial wave vector, $\mathbf{q}$, while the electron wave function can get an extra phase, the Berry phase.

The adiabatic solutions of the Schrödinger equation (3), which are the solutions within a single band α, i.e., without an interband coupling, are the well-known Houston functions (Houston, 1940)

$$\Phi_{\alpha\mathbf{q}}^{(\mathrm{H})}(\mathbf{r},t) = \Psi_{\mathbf{k}(\mathbf{q},\mathbf{t})}^{(\alpha)}(\mathbf{r}) \exp\left(i\phi_{\alpha}^{(\mathrm{D})}(\mathbf{q},t) + i\phi_{\alpha}^{(\mathrm{B})}(\mathbf{q},t)\right), \tag{5}$$

where $\alpha = 1, \ldots, N$ is the band index and N is the number of bands. Here the dynamic phase, $\phi_{\alpha}^{(\mathrm{D})}$, and the geometric phase, $\phi_{\alpha}^{(\mathrm{B})}$, are defined as

$$\phi_{\alpha}^{(\mathrm{D})}(\mathbf{q},t) = \frac{-1}{\hbar}\int_{-\infty}^{t} dt'(E_{\alpha}[\mathbf{k}(\mathbf{q},t')]), \tag{6}$$

$$\phi_{\alpha}^{(\mathrm{B})}(\mathbf{q},t) = \frac{e}{\hbar}\int_{-\infty}^{t} dt'\mathbf{F}(t') \cdot \mathscr{A}^{\alpha\alpha}[\mathbf{k}(\mathbf{q},t')]. \tag{7}$$

The geometric phase or the topological phase is determined by the nontrivial topological properties of the solid. After the pulse, this phase can result in an extra nontrivial phase to the wave function, $\phi_{\alpha}^{(\mathrm{B})}(\mathbf{q}, t = \infty)$, that can be expresses as

$$\begin{aligned}\phi_{\alpha}^{(\mathrm{B})}(\mathbf{q},t=\infty) &= \frac{e}{\hbar}\int_{-\infty}^{\infty} dt'\mathbf{F}(t') \cdot \mathscr{A}^{\alpha\alpha}[\mathbf{k}(\mathbf{q},t')] \\ &= \oint_{C_{\mathbf{q}}} d\mathbf{k} \cdot \mathscr{A}^{\alpha\alpha}(\mathbf{k}),\end{aligned} \tag{8}$$

where the Bloch acceleration theorem has been used and the last integral is calculated over a closed electron trajectory in the reciprocal space. For such a trajectory, $\mathbf{q}$ is the initial wave vector and the trajectory is determined by the field of the pulse. The nontrivial topological phase can be accumulated only for a circularly (elliptically) polarized pulse, for which an electron trajectory is of a circular (elliptical) shape.

The interband electron dynamics results in redistribution of electrons between the bands. This dynamics is determined by solutions of TDSE (3). The solutions can be parameterized by the initial wave vector $\mathbf{q}$ and can be expanded in the basis of Houston functions ${\Phi_{\alpha\mathbf{q}}}^{(H)}(\mathbf{r}, t)$ as

$$\Psi_{\mathbf{q}}(\mathbf{r},t) = \sum_{\alpha=1}^{N} \beta_{\alpha\mathbf{q}}(t)\Phi_{\alpha\mathbf{q}}^{(H)}(\mathbf{r},t), \tag{9}$$

where $\beta_{\alpha\mathbf{q}}(t)$ are the expansion coefficients, which satisfy the following system of equations

$$i\hbar\frac{\partial\beta_{\alpha\mathbf{q}}(t)}{\partial t} = -\sum_{\alpha_1\neq\alpha} e\mathbf{F}(t)\mathscr{A}^{\alpha\alpha_1}(\mathbf{q},t)e^{i\left(\phi_{\alpha\alpha_1}^{(\mathrm{D})}(\mathbf{q},t)+\phi_{\alpha\alpha_1}^{(\mathrm{B})}(\mathbf{q},t)\right)}\beta_{\alpha_1\mathbf{q}}(t) \tag{10}$$

Here

$$\phi_{\alpha\alpha_1}^{(\mathrm{D})}(\mathbf{q},t) = \phi_{\alpha_1}^{(\mathrm{D})}(\mathbf{q},t) - \phi_{\alpha}^{(\mathrm{D})}(\mathbf{q},t) \tag{11}$$

$$\phi_{\alpha\alpha_1}^{(\mathrm{B})}(\mathbf{q},t) = \phi_{\alpha_1}^{(\mathrm{B})}(\mathbf{q},t) - \phi_{\alpha}^{(\mathrm{B})}(\mathbf{q},t) \tag{12}$$

$$\mathscr{A}^{\alpha\alpha_1}(\mathbf{q}) = \left\langle \Psi_{\mathbf{q}}^{(\alpha)} \middle| i\frac{\partial}{\partial\mathbf{q}} \middle| \Psi_{\mathbf{q}}^{(\alpha_1)} \right\rangle, \tag{13}$$

and $\mathscr{A}^{\alpha\alpha_1}(\mathbf{q})$ is the interband (non-Abelian) Berry connection (Wilczek and Zee, 1984; Xiao et al., 2010; Yang and Liu, 2014), which is proportional to the interband dipole matrix elements, ${\phi_{\alpha\alpha_1}}^{(\mathrm{D})}(\mathbf{q}, t)$is the transition dynamic phase, and ${\phi_{\alpha\alpha_1}}^{(\mathrm{B})}(\mathbf{q}, t)$ is the transition Berry phase.

The interband transitions between the bands α and α_1 are determined by the effective dipole matrix element

$$\begin{aligned}\mathbf{D}_{\alpha\alpha_1}^{(eff)} &= \mathscr{A}^{\alpha\alpha_1}(\mathbf{q},t)e^{i\left(\phi_{\alpha\alpha_1}^{(\mathrm{D})}(\mathbf{q},t)+\phi_{\alpha\alpha_1}^{(\mathrm{B})}(\mathbf{q},t)\right)} \\ &= |\mathscr{A}^{\alpha\alpha_1}(\mathbf{q},t)|e^{i\left(\phi_{\alpha\alpha_1}^{(\mathrm{D})}(\mathbf{q},t)+\phi_{\alpha\alpha_1}^{(\mathrm{B})}(\mathbf{q},t)+\phi_{\alpha\alpha_1}^{(\mathrm{A})}(\mathbf{q},t)\right)},\end{aligned} \tag{14}$$

where ${\phi_{\alpha\alpha_1}}^{(\mathrm{A})}$ is the phase of the interband Berry connection.

The solution of the system (10) determines the different characteristics of the interaction of optical pulses with solids. Namely, the pulse-induced population of the conduction band both during the pulse and after the pulse, the electric current generated during the pulse and the corresponding transferred charge through the system, absorbance of the optical pulse, and generation of high optical harmonics during the pulse. The residual conduction band population, i.e., the conduction band population after the pulse, also characterizes the level of irreversibility of the electron dynamics during the pulse.

The electron dynamics in the field of the pulse is completely determined by the properties of the effective dipole matrix element, ${\mathbf{D}_{\alpha\alpha1}}^{(eff)}$ [see Eq. 14]. In the graphene-like topological materials, the topology affects both the amplitude of ${\mathbf{D}_{\alpha\alpha_1}}^{(ef)}$ and its phase, i.e., the topological phase, resulting in some nontrivial features in the ultrafast electron dynamics. Below we discuss some specific properties of such dynamics in graphene-like materials.

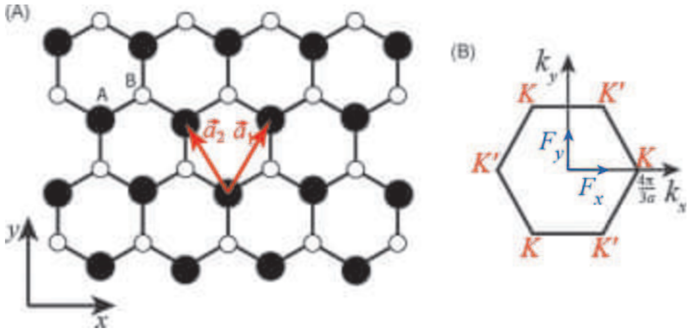

Fig. 1 (A) Honeycomb crystal structure of graphene-like materials. It consists of two sublattices, A and B. For a system with inversion symmetry, like pristine graphene, two sublattices are equivalent and the system has zero bandgap at two valleys *K* and *K*′ (Dirac points) in the reciprocal space, which are shown in panel (B). For a system with broken inversion symmetry, just as the TMDC monolayer, the sublattices are not equivalent and the system has a finite bandgap. Panel (B) shows the first Brillouin zone of graphene-like materials. Points *K* and *K*′ correspond to two valleys of the low-energy spectrum. The blue arrows illustrate the *x* and *y* components of the applied field due to an external optical pulse.

Topological properties of graphene-like materials

Graphene-like materials have hexagonal lattice structure, which is shown schematically in Fig. 1A. The lattice has two sublattices, "A" and "B". Pristine graphene, which is a monolayer of carbon atoms, has inversion symmetry and two sublattices are equivalent. The lattice structure is determined by the lattice vectors $\mathrm{a}_1 = a/2\left(\sqrt{3},\ 1\right)$ and $\mathrm{a}_2 = a/2\left(\sqrt{3},\ -1\right)$. Here a is the lattice constant, which for graphene is 2.46 Å. The first Brillouin zone of graphene-like materials is a hexagon, see Fig. 1B, with the vertices at the $\mathbf{K} = (2\pi/a)\left(1/3,\ 1/\sqrt{3}\right)$ and $\mathbf{K}' = (2\pi/a)\left(-1/3,\ 1/\sqrt{3}\right)$ points. These points are called the Dirac points. For graphene, the low energy dispersion near these points are described by the Dirac gapless relativistic equation. The points K and K' are connected by the time-reversal symmetry and are two valleys of graphene-like materials.

The simplest model of graphene, which captures its essential properties, is a nearest-neighbor tight-binding model, which describes coupling between the two sublattices A and B with the coupling constant $\gamma = 3.03$ eV (see Fig. 1). In the reciprocal space the corresponding Hamiltonian H_0 is a 2×2 matrix, which has the following form

$$H_0 = \begin{pmatrix} 0 & \gamma f(\mathbf{k}) \\ \gamma f^*(\mathbf{k}) & 0 \end{pmatrix} \tag{15}$$

where

$$f(\mathbf{k}) = \exp\left(i\frac{ak_x}{\sqrt{3}}\right) + 2\exp\left(-i\frac{ak_x}{2\sqrt{3}}\right)\cos\left(\frac{ak_x}{2}\right). \tag{16}$$

The energy spectrum of the Hamiltonian H_0 consists of the conduction and valence bands with the corresponding energy dispersions $E_c(\mathbf{k}) = -\gamma\,|f(\mathbf{k})|$ and $E_v(\mathbf{k}) = \gamma\,|f(\mathbf{k})|$ with the wave functions of the form

$$\Psi_{\mathbf{k}}^{(c)} = \frac{e^{i\mathbf{k}\cdot\mathbf{r}}}{\sqrt{2}}\begin{pmatrix} 1 \\ e^{-i\phi_{\mathbf{k}}} \end{pmatrix} \tag{17}$$

and

$$\Psi_{\mathbf{k}}^{(v)} = \frac{e^{i\mathbf{k}\cdot\mathbf{r}}}{\sqrt{2}}\begin{pmatrix} -1 \\ e^{-i\phi_{\mathbf{k}}} \end{pmatrix}. \tag{18}$$

Here the subscripts "c" and "v" stand for the conduction band and the valence band, respectively. The parts of the wave functions without $e^{i\mathbf{k}\cdot\mathbf{r}}$ are the Bloch functions, which are used to calculate the intraband and interband Berry connections. The Berry connections are singular or have maximum at the Dirac points, i.e. at the K and K' points. To understand their properties we consider a low energy effective model of graphene, which is described by the Dirac massless Hamiltonian.

The Hamiltonian H_0 describes the pristine graphene, which has an inversion symmetry and the corresponding energy dispersion is gapless. For graphene placed on a substrate or for other graphene-like materials, such as TMDC monolayers, the inversion symmetry is broken and two sublattices A and B becomes inequivalent, which can be described by an extra mass term of the form

$$H_\Delta = \begin{pmatrix} \Delta/2 & 0 \\ 0 & -\Delta/2 \end{pmatrix}. \tag{19}$$

The extra term which breaks the inversion symmetry of the system, opens a bandgap Δ at the Dirac points.

To understand the topological properties of two-dimensional (2D) graphene-like materials we first consider the low energy effective model of gapped graphene. This model covers both graphene with broken inversion symmetry due to, for example, a substrate, and also other graphene-like materials, such as TMDCs, black phosphorus, silicene, germanene, and so on. The model is described by the following Hamiltonian

$$H_D = \begin{pmatrix} \Delta/2 & \hbar\tau v_F\left(k_x - ik_y\right) \\ \hbar\tau v_F\left(k_x + ik_y\right) & -\Delta/2 \end{pmatrix}, \tag{20}$$

where $v_F \sim 10^6$ m/s is the Fermi velocity and τ is the valley index, which is 1 for the K valley and -1 for the K' valley. The energy spectrum of the low energy Hamiltonian H_D is given by the following expressions

$$E_c(\mathbf{k}) = \sqrt{\left(\frac{\Delta}{2}\right)^2 + \hbar^2 v_F^2 k^2} \tag{21}$$

for the conduction band and

$$E_v(\mathbf{k}) = -\sqrt{\left(\frac{\Delta}{2}\right)^2 + \hbar^2 v_F^2 k^2} \tag{22}$$

for the valence band.

With the known wavefunctions, the Berry connections, both intraband and interband, can be found. The effective dipole matrix element, which determines the coupling between the valence and the conduction bands, depends on the transition Berry phase, $\phi_{vc}^{(B)}(\mathbf{q}, t)$, which is proportional to the difference $\mathscr{A}^{vv} - \mathscr{A}^{cc}$. For the effective model, this difference is

$$\mathscr{A}^{vv} - \mathscr{A}^{cc} = \frac{\tau\Delta}{2E_c(\mathbf{k})}\,\frac{[\hat{\mathbf{z}} \times \mathbf{k}]}{k^2}. \tag{23}$$

This expression shows that if a graphene-like system is gapless, $\Delta = 0$, i.e., the system has inversion symmetry, then $\mathscr{A}^{vv} - \mathscr{A}^{cc} = 0$ and the effective coupling of the valence and conduction bands does not depends on the intraband Berry connection. Thus, for such systems, even for the topologically nontrivial materials like pristine graphene the topology does affect ultrafast electron dynamics in a sense that it does not bring an extra topological phase into the problem.

For graphene-like systems with broken inversion symmetry, i.e., $\Delta \neq 0$, the difference $\mathscr{A}^{vv} - \mathscr{A}^{cc}$ is nonzero and the intraband Berry connection brings an extra topological phase into the effective coupling, which results, as we will see below, in the effect of topological resonance, when the topological phase cancels the dynamic phase and enhances the interband electron transfer.

Another manifestation of the topology comes from the interband Berry connection, which is proportional to the interband dipole matrix element. For the low energy model, the interband Berry connection takes the following form

$$\mathbf{A}^{cv} = \frac{v_F}{2kE_c(\mathbf{k})}\left\{\tau[\hat{\mathbf{z}} \times \mathbf{k}] + i\frac{\Delta}{2E_c(\mathbf{k})}\mathbf{k}\right\}. \tag{24}$$

There are two effects of the inter band Berry connection on the electron dynamics. The first one is due to an extra contribution, $\phi_{cv}^{(A)}$, to the topological phase of the effective inter band coupling, and the second effect is related to the amplitude of $\mathscr{A}^{cv}$.

We can see from Eq. (24) that phase $\phi_{cv}^{(A)}$ is zero for the systems with inversion symmetry, i.e., for $\Delta = 0$. Thus for topological systems without the band gap, the total topological phase, which includes both intraband and interband contributions, in the effective interband coupling is zero and does not affect the ultrafast electron dynamics.

We can understand the properties of the amplitude of $\mathscr{A}^{cv}$, i.e., the magnitude of the interband coupling, by considering the case of $\Delta = 0$. Then from Eq. (24) we can find the following expression

$$\left|\mathscr{A}_x^{cv}\right| = \frac{|k_y|}{2\hbar\left(k_x^2 + k_y^2\right)}, \tag{25}$$

$$\left|\mathscr{A}_y^{cv}\right| = \frac{|k_x|}{2\hbar\left(k_x^2 + k_y^2\right)} \tag{26}$$

The magnitude of the interband coupling is singular at the $\mathbf{k} = 0$ point. For example, at $k_x = 0, \left|\mathscr{A}_x^{cv}\right|$ behaves as $1/|k_y|$, which shows that the interband coupling is the strongest at the Dirac points, i.e., the $\mathbf{k} = 0$ points. For $\Delta \neq 0$, the singularly of the interband coupling becomes less pronounced but still the coupling has the maxima at the Dirac points.

The ultrafast electron dynamics in the field of the pulse is therefore characterized by the following properties of the effective interband dipole coupling: (i) The magnitude of the interband coupling has well pronounced maxima at the Dirac points. This property results in the interference effects (Kelardeh et al., 2015, 2016), which will be discussed below. They are visible as bright spots in the conduction band population distribution in the reciprocal space and can be observed in graphene-like systems with zero or small bandgap, Δ. (ii) The effective interband coupling has a topological phase, which is accumulated during the pulse and compete with the dynamic phase resulting in topological resonance (Oliaei Motlagh et al., 2018, 2019a). The topological resonance produces large valley polarization in graphene-like materials placed in the field of a circularly polarized pulse. Since the topological phase is nonzero only in the systems with broken inversion symmetry, the topological resonance can be observed only if $\Delta \neq 0$.

Ultrafast electron dynamics: Interference effects

For strong optical pulses, an electron is transferred during the pulse through almost the entire Brillouin zone. In this case, to have a realistic description of ultrafast electron dynamics, the tight-binding model should be considered, for which the system of differential equations (10) has to be solved at all points in the first Brillouin zone. The main characteristics of the electron dynamics is the residual conduction band population, i.e., the population after the pulse. To observe the interference effects in the CB population distribution in the reciprocal space, a short linearly polarized pulse can be considered. The simplest profile of such a pulse with just a single oscillation of electric field is given by the following expression

$$F_x = F_0 e^{-u^2}\left(1-2u^2\right), \tag{27}$$

where $u = t/\tau$, $\tau = 1$ fs, and F_0 is the amplitude of the pulse. The pulse satisfies the condition that the area under the pulse is zero, $\int_{-\infty}^{\infty} F_x(t)dt = 0$.

For such a pulse, an electron twice passes the region near the Dirac point, where the interband coupling is the strongest, resulting in the interference of the two pathways (Kelardeh et al., 2015; Koochaki Kelardeh et al., 2017). The origin of the interfering pathways can be understood from Fig. 2. Here the first path, shown by the red line in the left panel, describes the following process: during the first passage of the Dirac point an electron is transferred from the valence band to the conduction band and during the second passage it remains in the conduction band. The second path is shown by the blue line in the right panel. It describes the following process: during the first passage of the Dirac point the electron remains in the valence band, but during the second passage it is transferred to the conduction band. The dynamic phases accumulated along these paths determine if the interference corresponding to two pathways constructive or destructive.

First, we consider the case of pristine graphene, i.e., $\Delta = 0$, for which the interband coupling has well pronounced maxima at the Dirac points. The residual CB population distribution is shown in Fig. 3 for different field amplitudes. The distribution clearly illustrates the interference patterns with bright and dark spots corresponding to the constructive and destructive interference, respectively. Such interference occurs only for electrons, which, during the pulse, can reach the Dirac points. With increasing pulse amplitude the electrons from the farther regions in the reciprocal space can pass the Dirac points. As a result, with increasing F_0 the interference region becomes larger, which is clearly visible in Fig. 3. For instance, while for $F_0 = 0.4$ V/Å the interference fringes are realized only near the Dirac points, at $F_0 = 2.25$ V/Å, the interference pattern occupies the whole Brillouin zone. Therefore, the number of observable bright spots is proportional to the magnitude of the optical pulse. At the same time the distance between the bright spots depends only on the frequency of the pulse but not on its amplitude.

The origin of the interference effects in the coherent electron dynamics is the highly localized nature of the interband coupling at the Dirac points. Such localization is well pronounced in pristine graphene, which has zero bandgap, $\Delta = 0$. As it was shown in the previous section, for graphene-like materials with broken inversion symmetry, i.e., $\Delta > 0$, with increasing bandgap the interband coupling as a function of the reciprocal vector becomes broadened. As a result the interference pattern in the conduction band population distribution becomes less pronounced and with less contrast (Oliaei Motlagh et al., 2019b). This property is illustrated in Fig. 4 where the numerical data are shown for gapped graphene with different bandgaps.

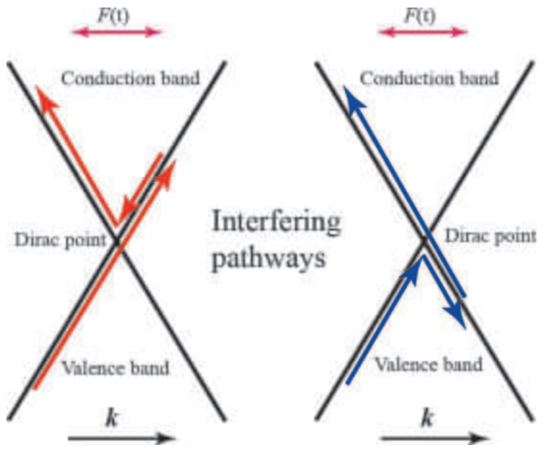

Fig. 2 Two interfering pathways, which result in the interference effects in coherent electron dynamics in graphene-like materials. Each pathway corresponds to two passages of the Dirac point during intraband electron dynamics. The interband coupling is the strongest near the Dirac point. An electron, which is initially in the valence band, while passing the Dirac point in the reciprocal space, can be transferred to the conduction band or remains in the valence band. Similarly, if an electron is initially in the conduction band then, while passing the Dirac point, it can be transferred to the valence band or remain in the conduction band. Then, the left panel shows the first interfering path, when an electron during the first passage of the Dirac point is transferred to the conduction band and then stays in the conduction band, while the right panel show the second interfering pathway, when an electron is transferred to the conduction band during the second passage of the Dirac point.

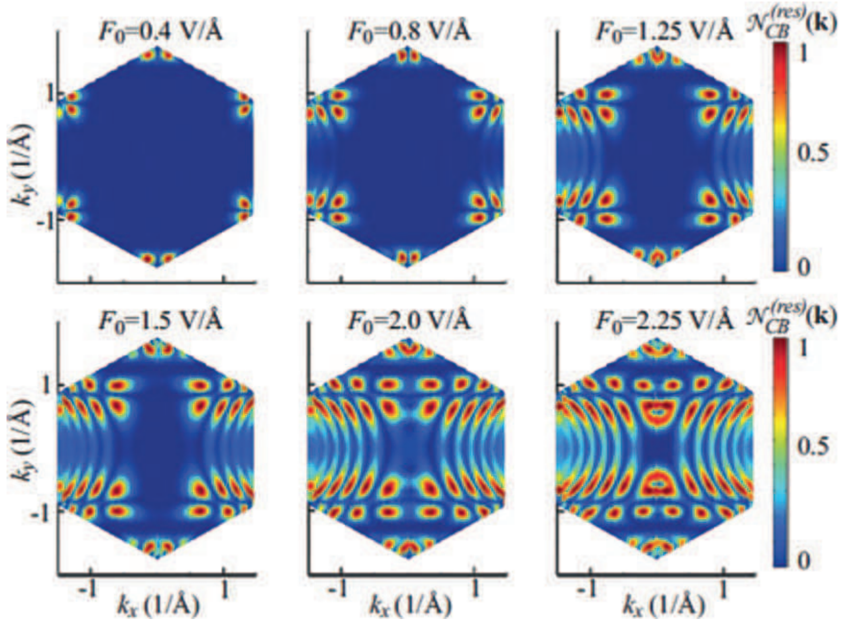

Fig. 3 Conduction band population distribution in the reciprocal space for pristine graphene placed in linearly polarized optical pulse. The pulse is polarized in the x direction. Different panels correspond to different field amplitudes F_0. The data illustrate the interference effects in the coherent electron dynamics induced by a strong and short optical pulse. With increasing field amplitude the number of visible dark and bright fringes increase, while the distance between the bright spots is determined by the frequency of the pulse but not its amplitude. Reproduced with permission from Kelardeh HK, Apalkov V, and Stockman MI (2015) *Physical Review B* 91(4): 045439, doi: 10.1103/PhysRevB.91.045439.

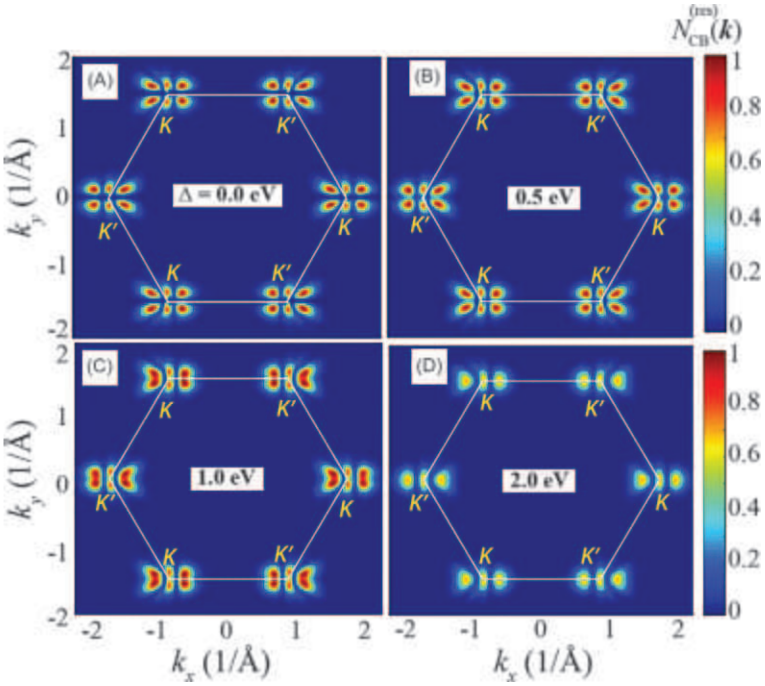

Fig. 4 Conduction band population distribution for gapped graphene-like material in the field of the linearly polarized optical pulse. The pulse is polarized in the x direction. Different panels correspond to different values of the bandgap, Δ, as marked in the figure. At small bandgaps, the interference pattern has large contrast, while the contrast becomes much less pronounced with increasing bandgap. This is due to the properties of the interband dipole matrix element, which has sharp maxima at the Dirac points only in the systems with small bandgap. Reproduced with permission from Oliaei Motlagh SA, Nematollahi F, Mitra A, Zafar AJ, Apalkov V, and Stockman MI (2019b) *Journal of Physics: Condensed Matter* 32(6): 065305, ISSN 0953-8984 1361-648X, doi:10.1088/1361-648X/ab4fc7.

The interference fringes are formed only if an electron passes the Dirac point at least twice during the field-induced transfer in the reciprocal space. It happens for a linearly polarized pulse as shown in Figs. 3 and 4 and can also occur for a circularly polarized pulse with at least two oscillations (Kelardeh et al., 2016).

Ultrafast electron dynamics: Topological resonance

The interference effects discussed in the previous section are realized in the systems with relatively small bandgap, Δ, so that the magnitude of the effective interband coupling has sharp maxima at the Dirac points. At the same time, if the bandgap is small, then the topological phase of the effective interband coupling is almost zero. That means the phase is proportional to the bandgap of the graphene-like system. At large bandgap, the phase of the interband coupling is nonzero and in this case another effect in topological materials can be observed (Oliaei Motlagh et al., 2018, 2019a). It is called the topological resonance and is realized when the accumulated topological phase cancels the dynamic phase. The condition of the topological resonance between the two bands α and α_1 can be expressed through the following relation

$$\frac{d}{dt}\left[\phi^{(\mathrm{D})}_{\alpha\alpha_1}(\mathbf{q},t) + \phi^{(\mathrm{B})}_{\alpha\alpha_1}(\mathbf{q},t) + \phi^{(\mathrm{A})}_{\alpha\alpha_1}(\mathbf{q},t)\right] = 0 \tag{28}$$

If this condition is satisfied then, assuming that the time variations of the magnitude of the interband coupling and the field itself are small, the mixing of the bands α and α_1 is strong. For example, if the two bands are the valence and conduction bands, then under the condition of the topological resonance there is a strong transfer of electrons from the valence band to the conduction band. The most important property of expression (28) is that the condition of the topological resonance depends on the valley index, τ. This is because the topological phase has opposite signs at the K and K' valleys (see Eqs. (23), (24)). As a result, if the topological resonance is observed in one of the valley then it cannot be realized in another valley. Due to this property, after a specially designed pulse, the residual conduction band populations of the two valleys can be different, resulting in valley polarization. The graphene-like systems, even with the finite bandgap, have time reversal symmetry. In this case to observe the residual, i.e., after the pulse, valley polarization, a circularly polarized pulse, which breaks the time reversal symmetry, should be applied. The valley polarization produced by an ultrashort circular pulse is shown in Fig. 5. It is realized only in gapped graphene

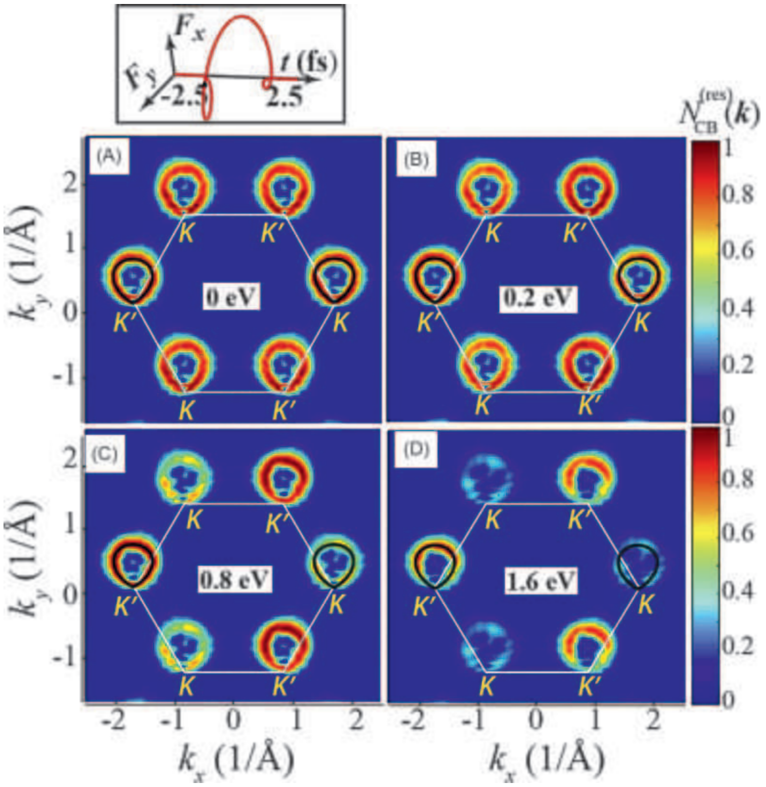

Fig. 5 Conduction band population distribution in the reciprocal space for gapped graphene-like material placed in a single oscillation circularly polarized pulse. The profile of the pulse is shown in the inset. The amplitude of the pulse is 0.5 V/Å Different panels correspond to different values of the bandgap as marked in the figure. Large valley polarization induced by optical pulse is visible only for systems with large bandgap, while for zero bandgap materials, such as pristine graphene, the valley polarization is exactly zero. The origin of the valley polarization in graphene-like materials is the topological resonance, which occurs only in systems with broken inversion symmetry, i.e., with the finite bandgap. Reproduced with permission from Oliaei Motlagh SA, Nematollahi F, Apalkov V, and Stockman MI (2019a) *Physical Review B* 100(11): 115431, doi: 10.1103/PhysRevB.100.115431.

systems, while no valley polarization is visible in pristine graphene, i.e., at $\Delta = 0$. The origin of the valley polarization after a femtosecond-long pulse is the topological resonance, when the topological phase cancels the dynamic phase. The valley polarization in gapped graphene systems can be also produced by a continuous-wave circularly polarized pulse. In this case the pulse is long and weak and the origin of the valley polarization is an intrinsic chiral property of the interband dipole matrix element, i.e., $\mathscr{A}_x^{cv} \pm i\mathscr{A}_y^{cv} \propto (1 \pm \tau)$. Thus, the left circular polarized pulse excites electrons in the K valley only, while the right circularly polarized pulse excites the K' valley. The topological resonance, which can happen only in a strong and short pulse, can not be realized in a continuous-wave pulse, for which the electron excursion in the reciprocal space is very small and no topological phase can be accumulated during the pulse.

The topological resonance, which is due to compensation of the dynamic phase by the topological phase, is similar to the regular resonance, when the dynamic phase is compensated by the time dependent phase of the field of the pulse, i.e., exp. $(i\omega t)$, where ω is the frequency of the pulse. The fundamental difference between these two resonances is that the regular resonance depends on the frequency of the pulse but not on its amplitude, while the topological resonance depends on the amplitude of the pulse but not on its frequency.

The valley polarization induced by an ultrashort optical pulse is the fundamentally fastest possible induction of the valley polarization in graphene-like systems. The examples of the gapped graphene systems are TMDC monolayers. The minimal tight binding model of TMDC materials consists of three bands, which come from the coupling of the nearest neighbor metal d orbitals (Liu et al., 2013). The TMDC materials also have strong spin-orbit interaction compared to graphene. Since the low energy physics in TMDC monolayers can be described within the effective model of gapped graphene, interaction of TMDC monolayers with femtosecond long circularly polarized pulse also results in finite residual valley polarization (Motlagh et al., 2018).

The valley polarization induced by a circularly polarized pulse in gapped graphene like materials can be probed by a linearly polarized pulse. Such a linearly polarized pulse produces anomalous all optical Hall current (Motlagh and Apalkov, 2021). The Hall current is due a preferable population of one of the valleys.

In 2D graphene-like materials with broken inversion symmetry, topological resonance results in finite residual valley polarization when such materials are placed in circularly polarized optical pulse. Topological resonance can be also observed in 3D topological materials, such Weyls semimetals (Nematollahi et al., 2019). In this case, the topological resonance does not preferably populate a specific Dirac point, but results in asymmetric conduction band population distribution around the Dirac points.

Conclusion

Ultrastrong optical pulses can induce not only strong interband mixing in solids, resulting, for example, in ultrashort metallization of a dielectric, but also adiabatically mix the states within a single band, which can be understood as an electron transfer within a band. In topological materials, during such transfer an electron can accumulate a topological phase. Such a phase can modify the interband electron transfer resulting in topologically related effects in ultrafast electron dynamics. The examples of solids with nontrivial topological properties are graphene-like materials. Although globally these materials do not have any net topological charge, locally, they have nontrivial topological properties, which are characterized in terms of the Berry connection or the Berry curvature. The graphene-like materials also have two valleys, which are related by the time reversal symmetry and have opposite topological charges.

The topologically-induced effects that can be observed in graphene-like materials are determined by another symmetry, which can be present in honeycomb crystal systems. This is the inversion symmetry. If the graphene-like system has the inversion symmetry, like in pristine graphene, then the system is gapless, but if the inversion symmetry is broken then the system is semiconductor with a finite bandgap, like TMDC monolayers.

In graphene-like materials with inversion symmetry or weakly broken inversion symmetry, i.e., with small bandgap, the interference effects in the interband electron dynamics can be observed. These effects are visible as bright and dark spots in the conduction band population distribution in the reciprocal space. Experimentally, such highly nonuniform distribution can be measured by angle-resolved photoemission spectroscopy technique. With increasing the bandgap, the interference effects become strongly suppressed. In this case, the effect of topological resonance can be observed if graphene-like materials are placed in the field of ultrashort and ultrastrong optical pulses. This effect is purely topological and is due to cancellation of the dynamic phase by the topological phase, where the topological phase is accumulated during an electron transfer in the reciprocal space. The topological resonance results in ultrafast valley polarization in gapped graphene-like materials placed in the field of a circularly polarized pulse.

References

Apalkov V and Stockman MI (2012) *Physical Review B* 86: 165118.

Bloch F (1929) *Zeitschrift für Physik A* 52: 555.

Conley HJ, Wang B, Ziegler JI, Haglund RF, Pantelides ST, and Bolotin KI (2013) *Nano Letters* 1530-6984, 13(8): 3626. https://doi.org/10.1021/nl4014748.

Geim AK and Novoselov KS (2007) *Nature Materials* 6(3): 183.

Gruber E, Wilhelm RA, Pétuya R, Smejkal V, Kozubek R, Hierzenberger A, Bayer BC, Aldazabal I, Kazansky AK, Libisch F, Krasheninnikov AV, Schleberger M, et al. (2016) *Nature Communications* 7: 13948. https://doi.org/10.1038/ncomms13948.

Heide C, Boolakee T, Higuchi T, Weber HB, and Hommelhoff P (2019) *New Journal of Physics* 21: 045003.

Heide C, Higuchi T, Weber HB, and Hommelhoff P (2018) *Physical Review Letters* 121: 207401.

Higuchi T, Heide C, Ullmann K, Weber HB, and Hommelhoff P (2017) *Nature* 550: 224.

Houston WV (1940) *Physics Review* 57: 184.

Jiang JW (2015) *Frontiers of Physics* 10: 287. https://doi.org/10.1007/s 11467-015-0459-z.

Kaiser A, Rethfeld B, Vicanek M, and Simon G (2000) *Physical Review B* 61: 11437.

Kelardeh HK, Apalkov V, and Stockman MI (2015) *Physical Review B* 91(4): 045439. https://doi.org/10.1103/PhysRevB.91.045439.

Kelardeh HK, Apalkov V, and Stockman MI (2016) *Physical Review B* 93(15): 155434.

Koochaki Kelardeh H, Apalkov V, and Stockman MI (2017) *Physical Review B* 96(7): 075409. https://doi.org/10.1103/PhysRevB.96.075409.

Liu G-B, Shan W-Y, Yao Y, Yao W, and Xiao D (2013) *Physical Review B* 88(8): 085433. https://doi.org/10.1103/PhysRevB.88.085433.

Liu HZ, Li YL, You YS, Ghimire S, Heinz TF, and Reis DA (2017) *Nature Physics* 13: 262.

Mak KF, Lee C, Hone J, Shan J, and Heinz TF (2010) *Physical Review Letters* 105: 136805.

Mashiko H, Chisuga Y, Katayama I, Oguri K, Masuda H, Takeda J, and Gotoh H (2018) *Nature Communications* 9(1): 1468. ISSN 2041-1723. https://doi.org/10.1038/s41467-018-03885-7.

Motlagh SAO and Apalkov V (2021) *Nanophotonics* 10(14): 3677. https://doi.org/10.1515/nanoph-2021-0227.

Motlagh SAO, Apalkov V, and Stockman MI (2017) *Physical Review B* 95: 085438.

Motlagh SAO, Wu JS, Apalkov V, and Stockman MI (2018) *Physical Review B* 98(12): 125410. ISSN 2469-9950.

Nematollahi F, Oliaei Motlagh SA, Apalkov V, and Stockman MI (2019) *Physical Review B* 99(24): 245409. https://doi.org/10.1103/PhysRevB.99.245409.

Novoselov KS, Mishchenko A, Carvalho A, and Castro Neto AH (2016) *Science* 353(6298): aac9439. http://science.sciencemag.org/content/sci/353/6298/aac9439.full.pdf.

Oliaei Motlagh SA, Wu J-S, Apalkov V, and Stockman MI (2018) *Physical Review B* 98(8): 081406. https://doi.org/10.1103/PhysRevB.98.081406.

Oliaei Motlagh SA, Nematollahi F, Apalkov V, and Stockman MI (2019a) *Physical Review B* 100(11): 115431. https://doi.org/10.1103/PhysRevB.100.115431.

Oliaei Motlagh SA, Nematollahi F, Mitra A, Zafar AJ, Apalkov V, and Stockman MI (2019b) *Journal of Physics: Condensed Matter* 32(6): 065305. ISSN 0953-8984 1361-648X. https://doi.org/10.1088/1361-648X/ab4fc7.

Schiffrin A, Paasch-Colberg T, Karpowicz N, Apalkov V, Gerster D, Muhlbrandt S, Korbman M, Reichert J, Schultze M, Holzner S, Barth JV, Kienberger R, et al. (2012) *Nature* 493: 70.

Shin HJ, Nguyen VL, Lim SC, and Son J-H (2018) *Journal of Physics B: Atomic, Molecular and Optical Physics* 51(14): 144003. https://doi.org/10.1088/F1361-6455/Faac59a.

Sun D, Aivazian G, Jones AM, Ross JS, Yao W, Cobden D, and Xu X (2012) *Nature Nanotechnology* 7(114). https://doi.org/10.1038/nnano.2011.243.

Wang O, Kalantar-Zadeh K, Kis A, Coleman JN, and Strano MS (2012) *Nature Nanotechnology* 7: 699.

Wilczek F and Zee A (1984) *Physical Review Letters* 52: 2111.

Xiao D, Chang M-C, and Niu Q (2010) *Reviews of Modern Physics* 82(3): 1959. https://doi.org/10.1103/RevModPhys.82.1959.

Xiao D, Liu GB, Feng W, Xu XD, and Yao W (2012) *Physical Review Letters* 108: 196802.

Yang F and Liu RB (2014) *Physical Review B* 90: 245205.

You YS, Yin Y, Wu Y, Chew A, Ren X, Zhuang F, Gholam-Mirzaei S, Chini M, Chang Z, and Ghimire S (2017) *Nature Communications* 8(1): 724. ISSN 2041-1723. https://doi.org/10.1038/s41467-017-00989-4.

Electromagnetically induced transparency☆

Maurizio Artoni[a,b,c], [a]European Laboratory for Nonlinear Spectroscopy (LENS), Sesto Fiorentino, Firenze, Italy; [b]Department of Engineering and Information Technology, Brescia University, Brescia, Italy; [c]Istituto Nazionale di Ottica (INO-CNR), Firenze, Italy

© 2024 Elsevier Ltd. All rights reserved.

This is an update of M. Artoni, Electromagnetically Induced Transparency, Editor(s): Franco Bassani, Gerald L. Liedl, Peter Wyder, Encyclopedia of Condensed Matter Physics, Elsevier, 2005, Pages 36–42, ISBN 9780123694010, https://doi.org/10.1016/B0-12-369401-9/00613-6.

Introduction 138
Coherence and population trapping 139
Electromagnetic induced transparency 140
Fast and slow light 142
Light storage 145
EIT analogs 145
Conclusion 147
References 148

Abstract

Electromagnetically induced transparency (EIT) is an important effect which renders an otherwise optically opaque medium transparent to light over a narrow spectral region. The effect has been observed in atomic gases, molecules and solids when subject to external laser irradiation. The article focuses on the necessary background tools to understand the underlying physics while overviewing some of the most relevant prospects.

Key points

- Electromagnetically induced transparency (EIT) describes a phenomenon by which an opaque optical medium becomes transparent due to quantum interference effects.
- EIT has been observed in atomic, molecular and solids media.
- EIT has been widely employed to control light wave propagation, including control of the refractive index and enhancement of optical nonlinearities.
- EIT is crucial for the development of next generation optical memories, quantum communications and modern quantum sensing as well as for the control of single-photons devices.

Introduction

Electromagnetically induced transparency effects are rather subtle (Harris, 1997; Marangos, 1998) and rely on states quantum coherence and interference. Three-level atomic and molecular systems coupled to two laser fields are archetype setups where the effect occurs as a result of the cancellation of absorption at a resonance transition frequency. The transparency resulting from such an absorption quenching is deliberately induced by one of the two laser fields upon modifying the medium optical response to the other field. The large degrees of transparency observed in a medium where strong absorption would normally be expected has then been termed *electromagnetically induced transparency* (*EIT*).

Such a phenomenon has been exploited to either control or eliminate the hampering effects that certain materials have on a propagating light beam and, in particular, to control the group velocity of light pulses. Most celebrated is the achievement of two extreme regimes for ultrafast and ultraslow light propagation where a light pulse may travel faster than *c*, the speed of light in vacuum, or may rather slow down at the a bike's pace of a few meters per second. It has also been used to bring light to a full stop inside a medium hence laying the ground for photon storage techniques to be exploited in modern quantum memories. From the outset, *EIT* has also stimulated a considerable amount of work on fundamental issues: nonlinear optics at low-light levels, photon entanglement and entanglement of atomic ensembles, quantum information processing and storage as well as enhanced acousto-optical effects, just to mention a few. Some of these have been observed over the past decades or so while others continue to spur interest in the quest for all-optical lightwave control for the next generation integrated photonic devices.

☆*Change History*: October 2022. M Artoni has updated the introduction section, added 22 recent references, Figure 7-8, and refined the diction of all figures captions. The Section "EIT Analogue" was added and the section "Conclusions and prospects" has been thoroughly rewritten and extended to include for recent applications as well as new directions in the field.

https://doi.org/10.1016/B978-0-323-90800-9.00121-9

We will start with a preliminary brief discussion on coherent population trapping, a closely related effect whose observation first raised interest in induced transparency phenomena. The core of the article will then provide the necessary understanding of the physics underlying the phenomenon of electromagnetically induced transparency while a brief outline of some topical challenges and opportunities will be given in the concluding sections.

Coherence and population trapping

Cancellation of absorption due to the coherence between a pair of atomic states and subsequent trapping of the population is perhaps one of the earliest examples of transparency induced in an otherwise absorbing medium. Specifically, the coherent superposition of two atomic states leads under certain conditions to trapping of the population and hence to transparency. This typically occurs in three level atomic systems, or at least systems that can be adequately reduced to a three levels configuration when interaction with two electromagnetic fields is considered. A basic configuration leading to effects of coherent population trapping (CPT) is reported in Fig. 1.

The phenomenon has been first observed in Gozzini's group in Pisa (Alzetta et al., 1976) and later in Stroud's group in Rochester (Whitley and Stroud, 1976). The Pisa group performed experiments that established coherence between the Zeeman split lower levels of sodium atoms using a multimode laser. They employed a spatially varying magnetic field and observed a series of spatially separated dark lines, originally called *dark resonances*, corresponding to the locations where the Zeeman splitting matched the frequency difference between modes of the coupling laser. The other experiment involved instead the hyperfine lower levels of atomic sodium and similar findings were observed. These early observations were explained using the notion of coherent population trapping in a dark-eigenstate of a three-level lambda medium (Arimondo and Orriols, 1976; Gray et al., 1978).

The usual atomic dipole selection rules normally require that two pairs of levels are dipole coupled whilst the transition between the third pair is dipole forbidden. The basic scheme in Fig. 1 comprises the states $|1\rangle$, $|2\rangle$ and $|3\rangle$ coupled by two near-resonance laser fields whose strengths are defined in terms of the Rabi frequencies $\Omega_1 = \mu_{12}\mathcal{E}_1/\hbar$ and $\Omega_2 = \mu_{23}\mathcal{E}_2/\hbar$, respectively. Defining the frequency of transitions between states as $\omega_{21} = (E_2 - E_1)/\hbar$, $\omega_{23} = (E_2 - E_3)/\hbar$ and $\omega_{31} = (E_3 - E_1)/\hbar$ one can further introduce the *one-photon* frequency detuning $\delta_{21} = \omega_{21} - \omega_1$ and $\delta_{23} = \omega_{23} - \omega_2$ as well as the *two-photon* (Raman) detuning $\delta \equiv \delta_{21} - \delta_{23} = (\omega_{21} - \omega_{23}) - (\omega_1 - \omega_2)$.

In a simple treatment the bare atom Hamiltonian $H_o = \sum_{i=1,2,3} \hbar\omega_i |i\rangle\langle i|$ should be modified to include the interactions due to the two atom-field couplings to obtain in the dipole approximation a total Hamiltonian H of the form (Loudon, 2000).

$$H = H_o + H_I \equiv H_o - \frac{\hbar\Omega_1}{2} |2\rangle\langle 1| - \frac{\hbar\Omega_2}{2} |2\rangle\langle 3| + h.c. \tag{1}$$

In general, the eigenstates of H turns out to be linear superpositions of the bare atomic states $|1\rangle$, $|2\rangle$ and $|3\rangle$. At exact resonance ($\delta_{21} = \delta_{23} = 0$) two of the eigenstates of H turn out to be symmetric and antisymmetric *coherent superpositions* of the two lower states of the bare-atom basis (Scully and Zubairy, 1997) namely,

$$\begin{aligned} |C\rangle &= \frac{\Omega_1}{\Omega} |1\rangle + \frac{\Omega_2}{\Omega} |3\rangle \\ |NC\rangle &= \frac{\Omega_2}{\Omega} |1\rangle - \frac{\Omega_1}{\Omega} |3\rangle \end{aligned} \tag{2}$$

where $\Omega = (\Omega_1^2 + \Omega_2^2)^{1/2}$. Note that no component of the bare state $|2\rangle$ appears in these superpositions and that state $|C\rangle$ is coupled to the upper state $|2\rangle$ via the electric-dipole interaction whilst the state $|NC\rangle$ is not. This can easily be seen by evaluating the (dipole) transition matrix element $\langle 2| H_I |NC\rangle$. The two probability amplitudes that are summed to give the whole transition amplitude between $|NC\rangle$ and the atom's upper state $|2\rangle$ have in fact equal and opposite magnitudes. In the present lambda configuration, coherent trapping occurs as due to the destructive quantum interference between the probability amplitudes associated with two

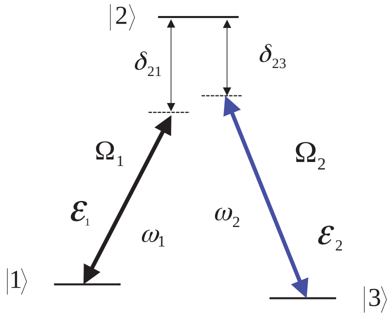

Fig. 1 Lambda (Λ) scheme leading to coherent population trapping (CPT). The applied fields of amplitude $\mathcal{E}_1$ and $\mathcal{E}_2$ with frequencies ω_1 and ω_2 need not be in single-photon resonance, but the two-photon resonance condition ($\delta_{21} \simeq \delta_{23}$) should be met and the field strengths should be of comparable magnitude ($\Omega_1 \approx \Omega_2$). The states $|1\rangle$ and $|3\rangle$ are typically Zeeman or hyperfine sub-levels of the ground state and are initially populated.

(dipole) transitions. Conversely, the transition amplitude $\langle 2|\ H_I\ |C\rangle$ does not cancel to zero and $|C\rangle$ remains coupled to the upper state $|2\rangle$.

When the steady-state regime has been reached, the state $|NC\rangle$ will acquire all the atom's population under the (combined) effects of optical pumping from $|C\rangle$ to $|2\rangle$ and spontaneous emission from $|2\rangle$ to $|NC\rangle$. At last, no absorption process will depopulate the state $|NC\rangle$ where all population will remain *trapped.* The non-coupled state $|NC\rangle$ is often referred to as *dark* state whilst the other state $|C\rangle$, which remains coupled to the fields, is instead referred to as *bright* state.

Electromagnetic induced transparency

A highly opaque medium may be rendered almost transparent also through electromagnetic induced transparency (EIT). Even in this case, as for coherent population trapping, cancellation of absorption relies on a process involving laser-induced coherence and quantum interference between the atomic coherences excited by the electromagnetic fields.

Formally coherences are identified with the off-diagonal elements of the density matrix ρ. Off-diagonal elements of the density matrix play a critical role in the evolution of an atom coupled to electromagnetic fields (Loudon, 2000) and many EIT effects in three-level systems have been investigated in terms of the density matrix (Marangos, 1998; Scully and Zubairy, 1997). Besides, this approach naturally lends itself to the inclusion of dampings that cause the decay of populations and coherences such as, e.g. radiative decay and collisions.

Characteristic configurations for which electromagnetically induced transparency takes place in three-level atoms interacting with two near-resonance electromagnetic fields are shown in Fig. 2. The usual atomic dipole selection rules normally require that $|g\rangle - |e\rangle$ and $|e\rangle - |m\rangle$ transitions be dipole allowed *but* not the $|g\rangle - |m\rangle$ transition. Often $|m\rangle$ is a metastable state. In the Λ or ladder scheme, $|g\rangle$ is normally the ground state of the atom and is where the largest part of the population initially resides while states $|e\rangle$ and $|m\rangle$, which remain essentially unpopulated throughout the process, need not be ground state(s).

To understand how EIT works to reduce absorption when two laser fields interact with a three-level atom we here examine, for definiteness, the Λ configuration in Fig. 2. The states $|g\rangle$ and $|e\rangle$ are coupled by a *probe* field of amplitude $\mathcal{E}_p$ and frequency ω_p while the excited state $|e\rangle$ is coupled to $|m\rangle$ by a *coupling* field of amplitude $\mathcal{E}_c$ and frequency ω_c. The Rabi frequencies of these two fields, proportional to their intensities, are respectively Ω_p and Ω_c. The one-photon detunings δ_p and δ_c as well as the two-photon (Raman) detuning δ are here defined as in the previous section. The off-diagonal decay rates for the coherences ρ_{eg}, ρ_{em} and ρ_{gm} are denoted by γ_1, γ_2 and γ_3, respectively. The explicit form of the total hamiltonian H is in this case,

$$H = H_o + H_1 + H_2 = \sum_{i=g,m,e} \hbar\omega_i\ |i\rangle\ \langle i| + H_1 + H_2 \tag{3}$$

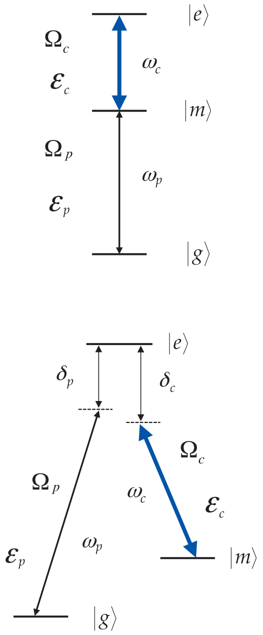

Fig. 2 Basic EIT level configurations, with a ladder (or cascade) scheme (upper) and a Λ scheme (lower). State $|m\rangle$ in the Λ scheme need not be a ground state. As for coherent population trapping (CPT) the two-photon (Raman) resonance condition should be met ($\delta_p \simeq \delta_c$), yet the strength of one of the two applied fields could be appreciably larger than the that of the other ($\Omega_p \ll \Omega_c$).

where the atom-field coupling terms are

$$H_1 = -\frac{\mu_{eg}\,\mathcal{E}_p}{2} e^{-i\omega_p t}\,|e\rangle\,\langle g| + h.c.$$

$$H_2 = -\frac{\hbar\Omega_c}{2} e^{-\omega_c t}\,|e\rangle\,\langle m| + h.c.$$

From the Liouville equation for the density matrix ρ one obtains a set of coupled equations connecting the density matrix elements and their temporal derivatives. These equations are usually solved by numerical methods. If a steady-state limit is sought for, however, all time derivatives in the density matrix elements vanish. Under the additional assumption that the coupling field is much stronger than the probe, the former is the only field that must be retained to all orders. Within these two limits one arrives at a simplified form of the coupled density matrix equations and an exact solution can be attained. If initially the atoms are in the ground state $|g\rangle$, i.e.,

$$\rho_{gg}(0) \simeq 1,\ \rho_{ee}(0) \simeq 0,\ \rho_{mm}(0) \simeq 0,\ \rho_{em}(0) \simeq 0, \tag{4}$$

the simplified set of coupled equations for a resonant coupling beam ($\delta_c = 0$) reads as,

$$\begin{aligned} \dot{\tilde{\rho}}_{eg}(t) &= -\left(\gamma_1 + i\delta_p\right)\tilde{\rho}_{eg}(t) + \frac{i\mu_{eg}\,\mathcal{E}_p}{2\hbar} + \frac{i\Omega_c}{2}\tilde{\rho}_{mg}(t) \\ \dot{\tilde{\rho}}_{mg}(t) &= -\left(\gamma_3 + i\delta_p\right)\tilde{\rho}_{mg}(t) + \frac{i\Omega_c}{2}\tilde{\rho}_{eg}(t), \end{aligned} \tag{5}$$

where $\delta_p = \omega_{eg} - \omega_p$ denotes the probe field detuning while the new variables $\tilde{\rho}_{eg} = \rho_{eg}\,e^{i\omega_p t}$ and $\tilde{\rho}_{mg} = \rho_{mg}\,e^{i\left(\omega_p + \omega_{me}\right)t}$ have been introduced. In the steady–state limit one has from Eq. (5),

$$\tilde{\rho}_{eg} = \frac{\mu_{eg}\,\mathcal{E}_{\mathrm{p}}\,\left(\delta_p - i\gamma_3\right)}{\left(\delta_p - i\gamma_3\right)\left(\delta_p - i\gamma_1\right) - \Omega_c^2/4}. \tag{6}$$

The steady-state coherence (6) is directly proportional to the probe susceptibility χ_p (Loudon, 2000; Scully and Zubairy, 1997) and hence the density matrix off-diagonal element ρ_{eg} describes the medium optical response to the incident probe ω_p and, in particular, its absorption or transparency properties.

The expression for ρ_{eg} contains a number of terms in the various parameters that will lead to cancellation of its value, both real and imaginary parts, when two-photon resonance takes place. In this case, in fact, the real part of (6) is always zero while for appropriately strong coupling beams, or when $\Omega_c^2 \gtrsim \gamma_1\gamma_3$, the imaginary part of (6) is seen to become several orders of magnitude smaller than the value it acquires when the coupling beam is absent, making the medium essentially transparent. It is likewise seen that the lorentzian-like absorption dip obtained by expanding (6) around resonance exhibits a width given approximately by Ω_c^2/γ_1. Because there exists an upper bound to the coupling beam Rabi frequency Ω_c for EIT to take place, namely $\Omega_c \lesssim \gamma_1$, it then follows that quenching of absorption only takes place over a small bundle of probe frequencies which is appreciably narrower than the natural linewidth γ_1. Thus under the two-photon resonance condition and in the presence of a coupling whose Rabi frequency Ω_c's such that (Scully and Zubairy, 1997; Marangos, 1998; Harris, 1997),

$$\sqrt{\gamma_1\gamma_3} \lesssim \Omega_{\mathrm{c}} \lesssim \gamma_1 \tag{7}$$

a probe field can propagate without being absorbed within a small *sub-natural* transparency frequency window, even though it would be strongly absorbed in the absence of the coupling beam.

Within a density matrix formulation the interference that leads to induced transparency manifests itself in the vanishing of the imaginary part of the coherence $\tilde{\rho}_{eg}$.

The real and imaginary parts of the susceptibility exhibited by a probe of frequency ω_p are obtained from the macroscopic polarization $\mathcal{P}\left(\omega_p\right) = \epsilon_o\chi\left(\omega_p\right)\mathcal{E}_p$ which can be related, in fact, to the microscopic coherence $\rho_{eg}(\omega_p)$ at ω_p via the expression $\mathcal{P}\left(\omega_p\right) = (N/V)\mu_{eg}\rho_{eg}\left(\omega_p\right)$ (Loudon, 2000). Here N/V is the atoms density in the medium while μ_{eg} is the dipole matrix element associated with the atomic transition. This relation holds for a medium sufficiently dilute that dipole-dipole coupling between atoms can be ignored. Besides, for the relatively large fields used in most EIT experiments a semiclassical treatment where the fields are treated classically, i.e. in terms of Maxwell's equations and susceptibilities, and the coherences are treated quantum mechanically with spontaneous decay added as a phenomenological damping proves adequate. Only when atoms are coupled to cavities modes or when the statistical properties of light (Artoni and Loudon, 1998) are important a fully quantum approach is indeed required. In the *semi-classical* limit the complex probe susceptibility for a resonant coupling beam ($\delta_c = 0$) can be written as (Artoni et al., 2001a, 2001b)

$$\chi_p = 3\pi\mathcal{N}_p\frac{\Gamma_1\left(\delta_p - i\gamma_3\right)}{\left(\delta_p - i\gamma_3\right)\left(\delta_p - i\gamma_1\right) - \Omega_c^2/4}, \tag{8}$$

where $\mathcal{N}_p$ is the scaled sample average density $N\lambda\!\!\!^{-}{}_p^3/V$ and $\lambda\!\!\!^{-}_p = \lambda_p/2\pi$ is the resonant probe reduced wavelength. The expression (8) depends upon parameters, namely detunings and laser intensities, that can all be directly controlled within an experiment.

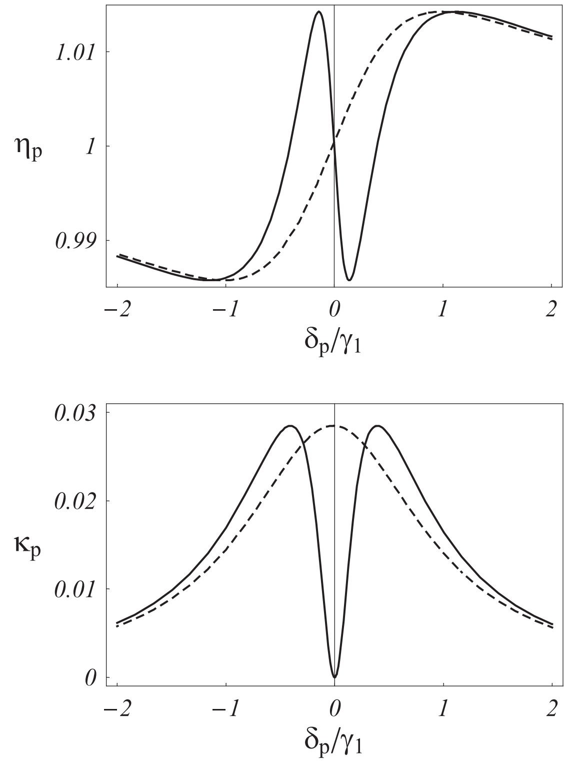

Fig. 3 Real (upper) and imaginary (lower) part of the probe refractive index n_p as a function of the probe detuning in the absence (dashed) and in the presence (solid) of a resonant coupling beam. The detuning δ_p is in units of γ_1 and the Rabi frequency is $\Omega_c = 0.8 \times \gamma_1$. Due to destructive interference the imaginary part κ_p, associated with medium absorption, vanishes at exact resonance when the coupling field is on. The real part η_p, which determines the medium dispersion, is likewise modified in the presence of the coupling field and acquires a rather steep slope around resonance.

The optical response of a medium is described by its index of refraction that is proportional, in turn, to the susceptibility and hence the optical response of an EIT-medium will in general depend on the (external) coupling beam. The real and imaginary parts of the probe refractive index $n_p \equiv \eta_p + i\kappa_p = \sqrt{1 + \chi_p}$ associated with the medium dispersion and absorption, respectively, are plotted in Fig. 3 as a function of the probe detuning δ_p. The absorption vanishes at exact resonance and this is a striking result when compared with the situation in which the coupling field is absent ($\Omega_c = 0$). Most EIT experiments have carried out on ensembles of atoms. In these experiments one measures the transmission of a *weak* probe in the presence of a *strong* coupling field through an otherwise optically opaque medium. The first demonstration was performed by Harris group at Stanford in two atomic systems, namely strontium (Boller et al., 1991) and lead (Field et al., 1991) vapors. In both experiments narrow-band pulsed laser radiation was used.

In the *Sr* experiment, the first to be reported and whose results are here shown in Fig. 4, the atoms are pumped into the $4d5d\ ^1D_2$ *autoionizing* state starting from the $5s5p\ ^1D_2$ state via a pulsed *probe* laser (337.1 nm) spanning the transition that was to be rendered transparent. A *coupling* laser (570.3 nm) was instead applied between this autoionizing state and the metastable bound state $4d5p\ ^1D_2$. In the absence of the coupling beam, the probe field excited the system to the state $|2\rangle$ exhibiting strong absorption which made the *Sr* vapor completely opaque. Transmission, measured as the ratio of the transmitted to the incident intensity, was estimated to be e^{-20} at resonance. When the coupling laser was applied, instead, the resonant transmission increased dramatically to be nearly 40%.

In the *Pb* experiment, on the other hand, transparency was demonstrated using bound states of a *collisionally* broadened medium. Here a ladder configuration was adopted where probe and coupling beams coupled the $6s^26p7s\ ^3P_1$ excited state respectively to the $6s^26p^2\ ^3P_0$ ground state and the state $6s^26p7p\ ^3D_1$. These two experiments serve to demonstrate the principle of EIT in three levels systems. They also indicate how electromagnetically induced transparency can take place when the excited states are either autoionizing or collisionally broadened.

Fast and slow light

Along with induced transparency there is a concomitant modification of the refractive properties of the medium. These are characterized by a very steep variation of the real part η of the medium complex refractive index n with frequency as shown, e.g., in Fig. 3. Here, for comparison, η is plotted both in the absence and in the presence of the coupling beam that causes the transparency.

Since in an ideal EIT regime atoms are decoupled from the light fields, the atoms susceptibility vanishes at resonance and the complex index n remains close to unity throughout the EIT transparency window. The propagation speed c/n of a monochromatic beam of light is then essentially unchanged from its speed c in vacuum. This means that the propagation velocity of the beam phase

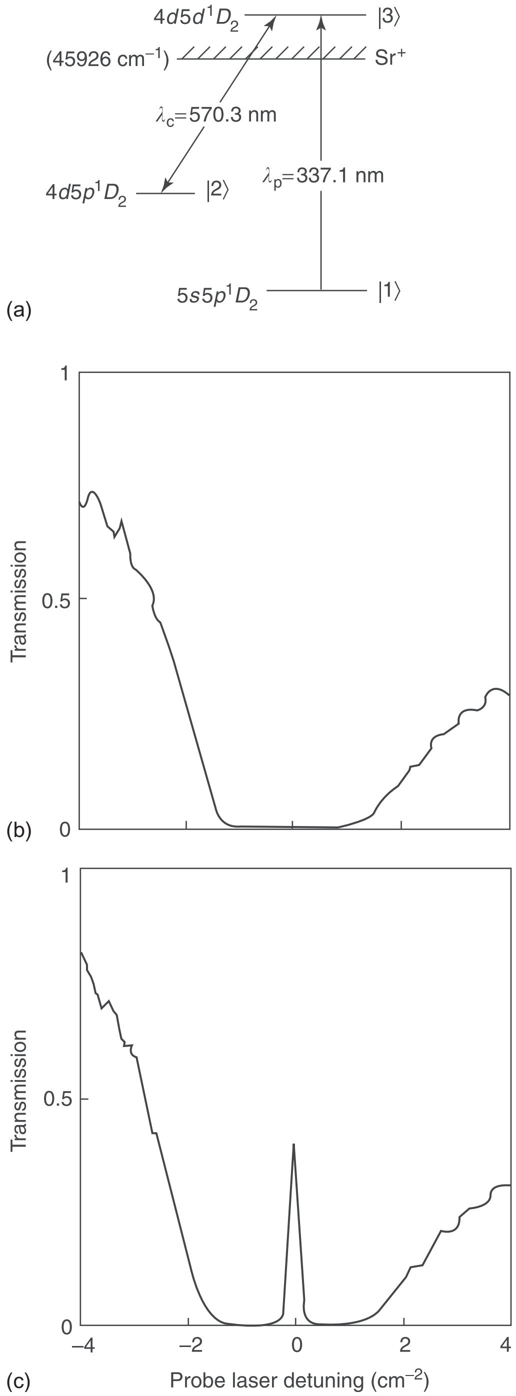

Fig. 4 EIT in Strontium (Sr) vapors (a) Sr energy levels and Λ configuration with coupling and probe beam of wavelength λ_c and λ_p respectively. Transmission vs. probe laser detuning in the absence (b) and in the presence (c) of a coupling beam. Under the conditions of this experiment transmission goes from zero to about 40%. (Reproduced with permission from Harris S (1997) Electromagnetically induced transparency. *Physics Today* 50: 36).

front in the medium, i.e. its *phase velocity*, is basically *c*. Yet for a light pulse, which contains instead several Fourier components at different frequencies, the small variations in the phase velocity that each component experiences in the medium can add up to make an appreciable effect. Components with slightly different speeds get in fact out of phase with each other, with the net result that the velocity of the pulse envelope, i.e. its *group velocity*, is different from *c* (Artoni and Loudon, 1997).

Consider, for instance, the superposition of two monochromatic plane waves of the form $\cos[(\omega_o \pm \delta\omega)t - (k_o \pm \delta k)z]$. Addition gives $2\cos[\delta\omega(t - (\delta k/\delta\omega)z)]\ \cos(\omega_o t - k_o z)$, which is a wave with an amplitude that retains its shape as it propagates with the velocity $\delta\omega/\delta k$. More generally, if we superpose many waves whose frequencies and wave numbers are distributed in a small range about the center values ω_o and k_o, we obtain a wave of the form $A(t - z/v_g)\ \cos(\omega_o t - k_o z)$. The intensity, averaged over a few optical periods, is proportional to $A^2(t - z/v_g)$, which describes a light pulse propagating without change of shape at a group velocity v_g defined as $d\omega/dk$.

Using the relation $k = \omega n/c$ with $n = \eta + i\kappa$, one can for very small absorptions ($\kappa \ll 1$) express v_g in terms of the real part η of the refractive index and its derivative $d\eta/d\omega$, so that for a given frequency ω one has (Matsko et al., 2001; Milonni, 2002),

$$v_g(\omega) \equiv \frac{d\omega}{dk(\omega)} = \frac{c}{\eta(\omega) + \omega\, d\eta(\omega)/d\omega}. \tag{9}$$

In the presence of electromagnetically induced transparency $d\eta(\omega)/d\omega$ is large and positive around resonance as one can see from Fig. 3 and according to (9) very small group velocities can be attained. By substituting the expression (8) into (9) one has indeed at the resonance frequency ω_o,

$$\frac{v_g^o}{c} \simeq \frac{\Omega_c^2}{6\pi \mathcal{N}_p \gamma_1 \omega_o}. \tag{10}$$

Note that v_g^o depends on the control field intensity, proportional to Ω_c^2, and on the atomic density N/V. Decreasing of the control beam power or increasing of the atomic density can make v_g^o orders of magnitude smaller than the speed of light c in vacuum.

Evidence for ultraslow light is typically provided by measuring the time delay between a pulse propagating in a medium of given length L and a twin pulse that has instead propagated in vacuum. The leading edge of a pulse that enters the medium is in fact rapidly decelerated while its tail outside the medium still propagates at the speed c. As a result, upon entering the medium, the spatial extent of the pulse is compressed (by the ratio c/v_g) and its energy decreased as photons are being expended to establish the coherence between the states $|g\rangle$ and $|m\rangle$, or, in other words, to change atomic state, with any excess energy carried away by the control field. As the pulse exits the medium its spatial extent increases again and the atoms return to their original ground state. The pulse as a whole, however, has experienced a peak-shift Δx given approximately by

$$\Delta x \simeq L\left(1 - \frac{c}{v_g^o}\right) \tag{11}$$

with a concomitant pulse delay τ given by $\Delta x/c$.

The possibility of manipulating the group velocity in EIT media was first pointed out by Harris (1997). The subject, however, was truly brought to focus by a remarkable experiment of Hau et al. (1999) in which an ultracold gas of Na atoms was used to reduce the speed of light pulses at a minimum of 17 m/s! The large and negative pulse delay τ measured in this experiment is reported in Fig. 4 for different experimental conditions. Although the first demonstration of ultraslow light used ultracold gases, shortly thereafter two groups reported ultraslow light propagation in hot Rb gases (Kash et al., 1999; Anon, 1999). This work was a milestone on the way to making ultraslow light "on the cheap", i.e., without expensive atomic traps (Fig. 5).

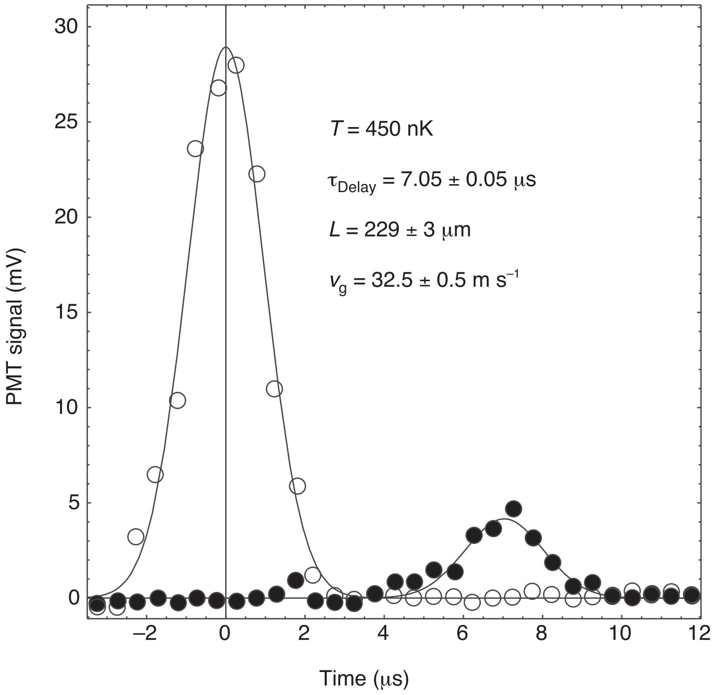

Fig. 5 Pulse delay. The front pulse (open circles) is a reference pulse that has propagated in vacuum. The other pulse (filled circles) is delayed by 7.05 μs in a 229-μm-long atom cloud. The corresponding light speed is 32.5 m/s. The curves represent gaussian fits to the measured pulses. (Reproduced with permission from Hau LV et al. (1999) Light speed reduction to 17 metres per second in an ultracold atomic gas. *Nature* 397: 594).

Furthermore, it follows from (9), that group velocities can become infinite or even negative when $d\eta(\omega)/d\omega$ is sufficiently negative, i.e., when the real part of the refractive index decreases with frequency. Because in the visible $\eta(\omega)$ normally increases with frequency the case $d\eta/(\omega)/d\omega < 0$, for historical reasons, is called *anomalous dispersion.* Directly from Fig. 3 one sees that in EIT media $\eta(\omega)$ acquires negative slopes just slightly off-resonance. A negative group velocity means that the peak of the pulse emerging from the medium moves faster than the pulse peak that has propagated in vacuum at speed *c*. This, according to (11), leads to a *positive* peak shift Δx rather than negative ones as obtained in ultraslow light experiments. Such anomalous group velocities can occur without significant pulse distortion. An infinite group velocity, on the other hand, means that the peak of the pulse emerging from the medium occurs at the same time as the peak of the pulse entering the medium as seen again from (11). The pulse, in other words, appears to cross the medium instantaneously. Superluminal peak velocities have been observed, though with substantial pulse attenuation and pulse compression. Such a superluminal behavior does not contradict relativity as the pulse peak velocity is not in general the velocity at which a signal can be transmitted.

Unlike the pioneering experiments that demonstrated anomalous group velocities of single-photons wavepackets carried out nearly a decade ago by Raymond Chiao at Berkeley, the anomalous dispersion regime attained by using electromagnetically induced transparency have been shown to lead to a much larger superluminal effect. Again, these experiments in no way contradict the principle of Einstein causality, i.e., the principle that no *signal* can propagate faster than *c* because the superluminal peak pulse velocity is not a signal velocity.

Light storage

Recent advances in quantum information science have led to many interesting new concepts such as quantum communications and, in particular, quantum memories (Simon, 2010). The practical implementation of these concepts involves storing, retrieval and transport of quantum states between different nodes of a network. Methods for manipulating photons and their quantum information in EIT atomic media have been extensively investigated (Lukin, 2003; Lvovsky et al., 2009; Ma et al., 2017). Photons are indeed most promising carriers of quantum information: they are fast, robust, and readily available. Atoms, on the other hand, represent reliable and long-lived storage units. These methods essentially consist in trapping single-photon pulses in atomic media by adiabatically reducing their group velocity to zero and subsequently releasing them after a suitable interval of time. Recalling (11) it follows that upon adiabatically ramping down the coupling beam while the probe pulse is inside the atomic sample, its group velocity can actually be brought to zero. The probe pulse, spatially compressed, remains inside the atomic cloud until the coupling beam is switched on again as the storage sequence in Fig. 6 (Liu et al., 2001) clearly shows. This method has been used for coherent storage of a single-photon into a single-atom (Holger et al., 2011), opening the way to implement a single-atom quantum memory, where "write" and "read" operations of states of light "in" and "out" of a single-atom trapped inside an optical cavity can be achieved. This clearly realizes reversible coherent transfer of quantum information carried by light pulses *to* atoms and vice versa (Lukin, 2003). Although during these early attempts storage times on the order of a second were hard to attain, light pulses can today be coherently stored for up to 1 min and even within solid-state devices (de Riedmatten, 2013).

EIT analogs

Long since its first observation in atomic gases (Harris et al., 1990; Boller et al., 1991), *EIT* effects have been observed also in solid and molecular compounds. At variance with atoms, solid media exhibit a number of hampering factors (Artoni and Birman, 1994)

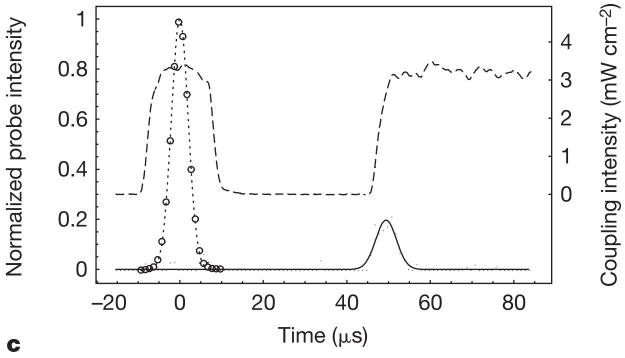

Fig. 6 Light storage. The reference pulse (open circles) enters the atomic sample while the coupling beam (dashed curve) is switched on. After the coupling beam is adiabatically switched off at around 18 μs the probe pulse is compressed and entirely enclosed within the atomic sample. Revival of the probe pulse takes place after the coupling field is turned off at around 45 μs. During the time interval when the coupling laser is off, coherent information imprinted in the probe pulse, is stored in the atomic medium. (Reproduced with permission from Liu C et al. (2001) Observation of coherent optical information storage in an atomic medium using halted light pulses. *Nature (London)* 409: 490).

as e.g. faster coherence dephasing rates, whereas molecular structures suffer from many decay pathways to lower levels. Much work on EIT effects in a variety of solids and molecules has nevertheless appeared starting with early demonstrations e.g. in quantum wells (Serapiglia et al., 2000) and molecular lithium (Lazoudis et al., 2010).

There exists, in addition, a plethora of *EIT*-like effects that manifest themselves in altogether different systems such as e.g. in superconductors (Anisimov et al., 2011), metasurfaces (Tassin et al., 2012), nanostructures (Hsu et al., 2014), optomechanical (Dong et al., 2012; Lu et al., 2018) and plasmonics devices (Dyer et al., 2013) as well as in optical resonators (Limonov et al., 2017; Liu et al., 2017) and linearly coupled RLC circuits (Garrido Alzar et al., 2002), just to mention a few. Among them, the latter have been extensively explored in the form of coupled-mode optical platforms where different modes can be simultaneously excited in different micro-cavity resonators (Peng et al., 2014) or even within the same resonator (Xiao et al., 2009; Zhao et al., 2017). Transparency through interference, in fact, can be attained in such otherwise opaque solid micro-cavities. These are ideal platforms for highly tunable all-optical control of transparency owing to the ultrahigh quality factors, on-chip integrability and room temperature operations.

Primarily for the purpose of illustrating an example of *EIT*-like effects, we briefly review here the basic phenomenology of *EIT*-like transmission in a single microcavity (Xiao et al., 2009). A tapered fiber with a micrometer size waist is used to evanescently excite two whispering gallery modes (WGM) in a silica coated microtoroid (resonator) stand on a silicon wafer at room temperature (See Fig. 7a, inset). Although it is well known that bringing the two WGM modes (1) and (2) simultaneously on-resonance within a single micro-cavity is difficult, yet one may harness their different thermal responses, viz different modes experience different wavelength shifts when subject the *same* temperature variation. It is this special feature that enables thermal tuning of the spectral distance between the two (far) detuned modes (7a) into resonance as the microcavity surrounding temperature changes. The black solid lines in Fig. 7b through Fig. 7d depict three typical *EIT*-like transmission spectra corresponding to three different modes detunings that are obtained by gradually increasing the temperature. Notice that mode (2) experiences an appreciable blueshift, at variance with the other mode (1) which shifts very little with temperature. In particular, when the two modes are tuned to overlap (Fig. 7c) the field (1) creates a sharp transparency window within the broad resonant absorption profile of the other field (2); the two fields can then be regarded respectively as "coupling" and "probe" just as in a familiar Λ-configuration of three atomic levels. The transparency window that opens around the control field position may be envisaged as a direct analog of the *EIT* transparency

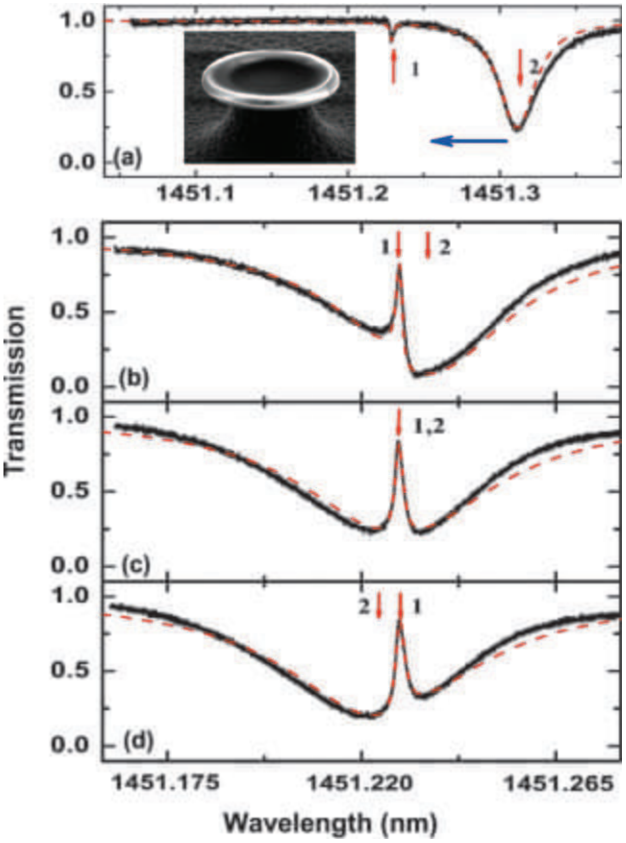

Fig. 7 Transmission spectra (*solid*) from a PDMS-coated silica microtoroid where two largely detuned (a) whispering-gallery modes (1) and (2) are brought to overlap (Reproduced with permission from Xiao YF et al. (2009) Electromagnetically induced, transparency-like effect in a single polydimethylsiloxane-coated silica microtoroid. *Applied Physics Letters* 94: 231115). Red and blue arrows denote respectively the modes resonant wavelengths and the shift direction of mode (2) as the surrounding temperature gradually increases from (b–d) *Inset*: A scanning electron microscopy (SEM) image of the microtoroid.

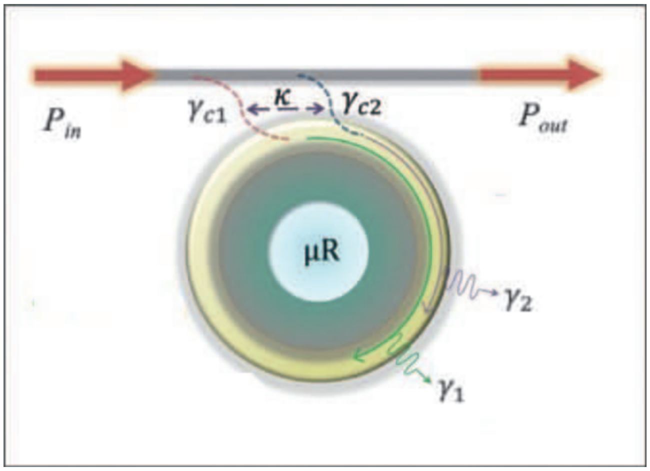

Fig. 8 Light coupling into a two-mode microcavity resonator (μR) through a tapered fiber (P_{in}) at near-critical coupling conditions. The interference between the two optical pathways associated with the resonant modes (1) and (2) simultaneously excited in the resonator can lead to *EIT*-like transparency in the transmission spectrum (P_{out}). Here γ_{c1} and γ_{c2} denote the fiber's coupling strength with the two modes (1) and (2), κ represents the direct coupling strength between mode (1) and (2), while γ_1 and γ_2 are the modes intrinsic losses (resonator quality factors).

phenomenon in atomic vapors. Within this context the transparency observed in the transmission spectra at the fiber's exit port (See Fig. 8) can be thought of as due the interference between the two optical pathways simultaneously spun inside the micro-resonator.

The actual transmission line-shapes of Fig. 7b–d are determined by a number of conditions and mainly the coupling strength between the two resonating modes (κ), the coupling between each mode and the fiber (γ_{c1}, γ_{c2}), the modes intrinsic losses as well as the polarizations mismatch (See Fig. 8). The optimization of these conditions remains an important challenge for any realistic implementation of *EIT*-like schemes in solid coupled-mode microcavity platforms.

Conclusion

As of today, we are some 32 years on from the first EIT experiments in atomic vapors (Harris et al., 1990; Boller et al., 1991) and nearly 46 since the earliest demonstrations of coherence effects between pairs of (quantum) atomic states (Alzetta et al., 1976; Whitley and Stroud, 1976), along with their interpretation (Arimondo and Orriols, 1976; Gray et al., 1978) through the introduction of the notion of coherent population trapping (Section "Coherence and population trapping").

The intense research activity undertaken since then, its various implications and the extensive efforts to harness applications, has made the field to grow, remaining an active subject over so many years and still fostering proposals for novel applications and interesting insights. For such reasons *EIT* has earned quite a significant place in optics, with a profound impact upon far reaching photonics technologies.

The article is meant to illustrate the basic physics behind *EIT*, by which one can eliminate the effect of a medium on a propagating light beam by changing e.g. its absorption or refraction or group velocity. Although basic physics concepts are crucial to understand the phenomenology of EIT (Section "Electromagnetic induced transparency"), we have tried to connect also with experiments. Much literature clearly exists, yet we found it instructive to illustrate early pioneering demonstrations (Sections "Fast and slow light" and "Light storage") as well as more recent developments of *EIT*-like effects (Section "EIT analogs") observed in metamaterials. The latter turn out to have great functionalities in the areas of sensing, slow-light, electromagnetic induced absorption, etc. When turning to the future, on the other hand, predictions are as usual risky, nevertheless we offer here below some thoughts on mainstream applications that are likely to spur new and emerging ones, hopefully stimulating further insights.

First, since the pioneering work on ultraslow light in atomic clouds as e.g. Hau et al. (1999) there has been substantial interest in its potential extension to solids. Slow and even stopped light can now be routinely attained in solid materials easing important steps toward the integration and scalability needed for many potential applications while in turn substantiating early important attempts as, e.g., in semiconductors (Artoni et al., 2000; Serapiglia et al., 2000) and in Ruby crystals either at cryogenic (Turukhin et al., 2002) or at room temperature (Bigelow et al., 2003).

Over the years more sophisticated solid media settings, with similar three-level *EIT* interaction configurations, ranging from hybrid prototypes as e.g. cold-atom photonic crystal-fiber waveguides (Venkataraman et al., 2011; Bajcsy et al., 2011), cold-atom dynamic waveguides (Wu et al., 2009a, 2009b; Wu et al., 2010; Moiseev et al., 2014), miniaturized atomic vapor cells

(Baluktsian et al., 2010; Rost, 2010) to full-solid interfaces as e.g. whispering-gallery (Peng et al., 2014) and semiconductors (Bassani et al., 2004) microcavities, moving layered semiconductor structures (Artoni et al., 2001b), light-dragging effect in semiconductors (Artoni et al., 2001a, 2001b), color centers in diamond (Doherty et al., 2013; Ovartchaiyapong et al., 2014; MacQuarrie et al., 2013), bulk CuCl (single) semiconductor crystals exhibiting biexcitonic transitions (Chesi et al., 2003), crystals doped with rare-earth-metal ions or with nitrogen-vacancy color centers (Simon, 2010; Childress et al., 2014; Hausmann et al., 2014; He et al., 2006), tunable metamaterials (Wu et al., 2009a, 2009b) have laid a substantial ground for today's range of potential *EIT* applications in solids.

Second, recent advances in quantum information science have led to the introduction of interesting new concepts such as quantum memories, whose practical implementation involves storing, retrieval and transporting quantum information viz. "quantum states" between different nodes of a network. Photons, as a matter of fact, are promising carriers of quantum information: they are fast, robust and readily available. Atoms, on the other hand, represent reliable and long-lived storage units. Methods for manipulating photons and their quantum information in atomic media subject to *EIT*, as means to attain atomic quantum memories, have long been suggested (Lukin, 2003) and realized (Tsai et al., 2020; Bao et al., 2012). They essentially rely on trapping single photon Gaussian pulses in cold atomic samples by adiabatically reducing their group velocity to zero and subsequently releasing them after a suitable interval of time (*storage time*). This represents a reversible technique for coherent transfer of quantum information carried by light pulses *to* atoms and vice versa (Lukin, 2003). In the past few years EIT-based quantum memories have been realized also in warm atomic ensembles (Hosseini et al., 2011.) as well as in solid systems (Zhou et al., 2012). High-quality *EIT*-based atomic quantum memories can find interesting applications such as distributed quantum gates (Daiss et al., 2021), a building block of quantum networks, and can advance more in general high-fidelity quantum information processing. High performance *EIT*-based quantum memories can also be employed in quantum metrology to enhance atomic magnetometry (Bao et al., 2020), to implement distributed quantum computation (Awschalom et al., 2021), to attain color-entanglement (Viscor et al., 2012), etc.

Third, as photon-photon interaction strengths are typically very weak, powerful lasers tightly focused on nonlinear materials ought to be employed in conventional nonlinear optics to attain the required efficiency; this is a long-standing goal of technological relevance. Ultraslow light pulses in EIT media, however, may experience (Milonni, 2002) exceedingly large nonlinearities so that nonlinear optical processes may become efficient even at energy densities as low as a photon per atomic cross section (Yan et al., 2006; Wu et al., 2013). Because strong photon-photon interactions enable a number of important applications, including quantum-by-quantum control of light fields (García-Maraver et al., 2004), single-photon switches and transistors (Sun et al., 2018), all-optical deterministic quantum logic (Ottaviani et al., 2003; Rebić et al., 2004) and the realization of strongly correlated states of light and matter, *EIT* enabled low-light-level nonlinear optics (Chang et al., 2014) has become over the years quite a relevant and fruitful direction of investigation.

Finally, it is worth recalling that *EIT* can also be observed in a mechanical field, where a superconducting artificial atom is coupled to a 1D-transmission line (surface acoustic waves), which opens the possibility that superconducting circuits can be engineered to interact with acoustic fields in parameter regimes not readily accessible to purely electromagnetic systems (Andersson et al., 2020).

Analog forms of induced transparency (Section "EIT analogs") could also be observed e.g. in optomechanical devices, where resonators are coupled to radiation pressure (Safavi-Naeini et al., 2011), or in superconducting quantum circuit architectures in the microwave regime (Gu et al., 2016; Long et al., 2018). Applications in quantum nonlinear optics as e.g., signal routing through cross-phase modulation (Schmidt and Imamoglu, 1996; Słowik et al., 2011), in reflectionless (Wu et al., 2016; Horsley et al., 2013) and anisotropic (anomalous Cherenkov emission) media (Carusotto et al., 2001) or more recently in the quantum thermodynamics of *EIT* heat engines (Harris, 2016; Zou et al., 2017; Zhang et al., 2021) further witness the wide-reaching perspective of the field.

References

Alzetta G, et al. (1976) An experimental method for the observation of r.f. transitions and laser beat resonances in oriented Na vapour. *Nuovo Cimento della Societa Italiana di Fisica B* 36: 5.

Andersson G, et al. (2020) Electromagnetically induced acoustic transparency with a superconducting circuit. *Physical Review Letters* 124: 240402.

Anisimov PM, et al. (2011) Objectively discerning Autler-Townes splitting from electromagnetically induced transparency. *Physical Review Letters* 107: 163604.

Anon (1999) Slow light for the rest of Us. *Physical Review Focus* 3: 37.

Arimondo E and Orriols G (1976) Nonabsorbing atomic coherences by coherent two-photon transitions in a three-level optical pumping. *Lettere al Nuovo Cimento della Societa Italiana di Fisica* 17: 333.

Artoni M and Birman JL (1994) Non-classical states in solids and detection. *Optics Communications* 104: 319.

Artoni M and Loudon R (1997) Quantum theory of optical pulse propagation through an absorbing and dispersive slab. *Physical Review A* 55: 1347.

Artoni M and Loudon R (1998) Quantum theory of optical-pulse propagation through an amplifying slab. *Physical Review A* 57: 622.

Artoni M, et al. (2000) Electromagnetic-induced transparency of Wannier-Mott excitons. *Europhysics Letters* 49: 445.

Artoni M, et al. (2001a) Highly anomalous group velocity of light in ultracold rubidium gases. *Physical Review A* 63: 023805.

Artoni M, et al. (2001b) Fresnel light drag in a coherently driven moving medium. *Physical Review Letters* 86: 2549.

Awschalom D, et al. (2021) Roadmap: Development of Quantum Interconnects (QuICs) for Next-Generation Information Technologies. *PRX Quantum* 2: 017002.

Bajcsy M, et al. (2011) Laser-cooled atoms inside a hollow-core photonic-crystal fiber. *Physical Review A* 83: 063830.

Baluktsian T, et al. (2010) Fabrication method for microscopic vapor cells for alkali atoms. *Optics Letters* 35: 1950.

Bao XH, et al. (2012) Efficient and long-lived quantum memory with cold atoms inside a ring cavity. *Nature Physics* 8: 517.

Bao H, et al. (2020) Spin squeezing of 10–11 atoms by prediction and retrodiction measurements. *Nature* 581: 159.

Bassani F, et al. (2004) Electromagnetically induced transparency in bulk and microcavity semiconductors. *Journal of Luminescence* 110: 174.

Bigelow M, et al. (2003) Observation of ultraslow light propagation in a ruby crystal at room temperature. *Physical Review Letters* 90: 113903.
Boller KJ, et al. (1991) Observation of electromagnetically induced transparency. *Physical Review Letters* 66: 2593.
Carusotto I, et al. (2001) Slow group velocity and Cherenkov radiation. *Physical Review Letters* 87: 064801.
Chang DE, et al. (2014) Quantum nonlinear optics-photon by photon. *Nature Photonics* 8: 685.
Chesi S, et al. (2003) Polaritonic stop-band transparency via exciton-biexciton coupling in CuCl. *Physical Review Letters* 91: 057402.
Childress L, et al. (2014) Atom-like crystal defects: From quantum computers to biological sensors. *Physics Today* 67: 38.
Daiss S, et al. (2021) A quantum-logic gate between distant quantum-network modules. *Science* 371: 614.
de Riedmatten H (2013) A long-term memory for light. *Physics* 6: 80.
Doherty MW, et al. (2013) The nitrogen-vacancy colour centre in diamond. *Physics Reports* 528: 1.
Dong C, et al. (2012) Optomechanical dark mode. *Science* 338: 1609.
Dyer GC, et al. (2013) Induced transparency by coupling of Tamm and defect states in tunable terahertz plasmonic crystals. *Nature Photonics* 7: 925.
Field JE, et al. (1991) Observation of electromagnetically induced transparency in collisionally broadened lead vapor. *Physical Review Letters* 67: 3062.
García-Maraver R, et al. (2004) Cavity QED quantum phase gates for a single longitudinal mode of the intracavity field. *Physical Review A* 70: 062324.
Garrido Alzar C, et al. (2002) Classical analog of electromagnetically induced transparency. *American Journal of Physics* 70: 37.
Gray HR, et al. (1978) Coherent trapping of atomic populations. *Optics Letters* 3: 218.
Gu X, et al. (2016) Polariton states in circuit QED for electromagnetically induced transparency. *Physical Review A* 93: 063827.
Harris S (1997) Electromagnetically induced transparency. *Physics Today* 50: 36.
Harris S (2016) Electromagnetically induced transparency and quantum heat engines. *Physical Review A* 94: 053859.
Harris S, et al. (1990) Nonlinear optical processes using electromagnetically induced transparency. *Physical Review Letters* 64: 1107.
Hau LV, et al. (1999) Light speed reduction to 17 metres per second in an ultracold atomic gas. *Nature* 397: 594.
Hausmann BJ, et al. (2014) Diamond nonlinear photonics. *Nature Photonics* 8: 369.
He QY, et al. (2006) Coherently induced stop-bands in resonantly absorbing and inhomogeneously broadened doped crystals. *Physical Review B* 73: 195124.
Holger P, et al. (2011) A single-atom quantum memory. *Nature* 473: 190.
Horsley S, et al. (2013) Optical nonreciprocity of cold atom Bragg mirrors in motion. *Physical Review Letters* 110: 223602.
Hosseini M, et al. (2011) High efficiency coherent optical memory with warm rubidium vapour. *Nature Communications* 2: 1.
Hsu CW, et al. (2014) Theoretical criteria for scattering dark states in nanostructured particles. *Nano Letters* 14: 2783.
Kash MM, et al. (1999) Ultraslow group velocity and enhanced nonlinear optical effects in a coherently driven hot atomic gas. *Physical Review Letters* 82: 5229.
Lazoudis A, et al. (2010) Electromagnetically induced transparency in an open Λ-type molecular lithium system. *Physical Review A* 82: 023812.
Limonov MF, et al. (2017) Fano resonances in photonics. *Nature Photonics* 11: 543.
Liu C, et al. (2001) Observation of coherent optical information storage in an atomic medium using halted light pulses. *Nature (London)* 409: 490.
Liu YC, et al. (2017) Electromagnetically induced, transparency in optical microcavities. *Nano* 6: 789.
Long J, et al. (2018) Electromagnetically induced transparency in circuit quantum electrodynamics with nested polariton states. *Physical Review Letters* 120: 083602.
Loudon R (2000) *The Quantum Theory of Light*, 3rd edn Oxford: Clarendon Press.
Lu H, et al. (2018) Optomechanically induced transparency at exceptional points. *Physical Review Applied* 10: 014006.
Lukin M (2003) Trapping and manipulating photon states in atomic ensembles. *Review of Modern Phyiscs* 75: 457.
Lvovsky AI, et al. (2009) Optical quantum memory. *Nature Photonics* 3: 706.
Ma L, et al. (2017) Optical quantum memory based on electromagnetically induced transparency. *Journal of Optics* 19: 043001.
MacQuarrie ER, et al. (2013) Mechanical spin control of nitrogen-vacancy centers in diamond. *Physical Review Letters* 111: 227602.
Marangos JP (1998) Electromagnetic induced transparency. *Journal of Modern Optics* 45: 471.
Matsko A, et al. (2001) Slow, ultraslow, stored and frozen light. *Advances in Atomic, Molecular, and Optical Physics* 46: 191.
Milonni PW (2002) Controlling the speed of light pulses. *Journal of Physics B* 35: 471.
Moiseev SA, et al. (2014) Stationary and quasistationary light pulses in three-level cold atomic systems. *Physical Review A* 89: 043802.
Ottaviani C, et al. (2003) Polarization qubit phase gate in driven atomic media. *Physical Review Letters* 90: 197902.
Ovartchaiyapong P, et al. (2014) Dynamic strain-mediated coupling of a single diamond spin to a mechanical resonator. *Nature Communications* 5: 4429.
Peng B, et al. (2014) What is and what is not electromagnetically induced transparency in whispering-gallery microcavities. *Nature Communications* 5: 5082.
Rebić S, et al. (2004) Polarization phase gate with a tripod atomic system. *Physical Review A* 70: 032317.
Rost JM (2010) Tubes for quantum electronics. *Nature Photonics* 4: 74.
Safavi-Naeini AH, et al. (2011) Electromagnetically induced transparency and slow light with optomechanics. *Nature* 472: 69.
Schmidt H and Imamoglu A (1996) Giant Kerr nonlinearities obtained by electromagnetically induced transparency. *Optics Letters* 21: 1936.
Scully M and Zubairy M (1997) *Quantum Optics*. Cambridge: Cambridge University Press.
Serapiglia GB, et al. (2000) Laser induced quantum coherence in a semiconductor quantum well. *Physical Review Letters* 84: 1019.
Simon C (2010) Quantum memories. *European Physical Journal D: Atomic, Molecular, Optical and Plasma Physics* 58: 1.
Słowik K, et al. (2011) Cross-Kerr nonlinearities in an optically dressed periodic medium. *Physica Scripta* 2011: 014022.
Sun S, et al. (2018) A single-photon switch and transistor enabled by a solid-state quantum memory. *Science* 361: 57.
Tassin P, et al. (2012) Electromagnetically induced, transparency and absorption in metamaterials: The radiating two-oscillator model and its experimental confirmation. *Physical Review Letters* 109: 187401.
Tsai PJ, et al. (2020) Quantum storage and manipulation of heralded single photons in atomic quantum memories. *Physical Review Research* 2: 033155.
Turukhin AV, et al. (2002) Observation of ultraslow and stored light pulses in a solid. *Physical Review Letters* 88: 023602.
Venkataraman V, et al. (2011) Few-photon all-optical modulation in a photonic band-gap fiber. *Physical Review Letters* 107: 193902.
Viscor D, et al. (2012) Two-color quantum memory in double- media. *Physical Review A* 86: 053827.
Whitley RM and Stroud CR (1976) Double optical resonance. *Physical Review A* 14: 1498.
Wu JH, et al. (2009a) All-optical light confinement in dynamic cavities in cold atoms. *Physical Review Letters* 103: 133601.
Wu JH, et al. (2009b) Tunable photonic metamaterials. *Journal of Modern Optics* 56: 768.
Wu JH, et al. (2010) Stationary light pulses in cold thermal atomic clouds. *Physical Review A* 82: 013807.
Wu JH, et al. (2013) Radiation damping optical enhancement in cold atoms. *Light: Science & Applications* 2: e54.
Wu JH, et al. (2016) Coherent perfect absorption in one-sided reflectionless media. *Scientific Reports* 6: 1.
Xiao YF, et al. (2009) Electromagnetically induced, transparency-like effect in a single polydimethylsiloxane-coated silica microtoroid. *Applied Physics Letters* 94: 231115.
Yan X, et al. (2006) Dynamic control of four-wave-mixing enhancement in coherently driven four-level atoms. *Physical Review A* 73: 013816.
Zhang XJ, et al. (2021) Doppler-broadened quantum electromagnetically-induced-transparency heat engines. *Physical Review A* 103: 062205.
Zhao G, et al. (2017) Raman lasing and Fano lineshapes in a packaged fiber-coupled whispering-gallery-mode microresonator. *Scientific Bulletin* 62: 875.
Zhou ZQ, et al. (2012) Realization of reliable solid-state quantum memory for photonic polarization qubit. *Physical Review Letters* 108: 190505.
Zou Y, et al. (2017) Quantum heat engine using electromagnetically induced transparency. *Physical Review Letters* 119: 050602.

Optical properties of materials

Giorgio Guizzetti and Maddalena Patrini, Dipartimento di Fisica, Università degli Studi di Pavia, Pavia, Italy

© 2024 Elsevier Ltd. All rights reserved.

This is an update of G. Guizzetti, M. Patrini, Optical Properties of Materials, Editor(s): Franco Bassani, Gerald L. Liedl, Peter Wyder, Encyclopedia of Condensed Matter Physics, Elsevier, 2005, Pages 183–191, ISBN 9780123694010, https://doi.org/10.1016/B0-12-369401-9/00614-8.

Introduction **151**
Maxwell's equations in a medium **151**
The complex dielectric function **152**
Complex refractive index **154**
Reflection and transmission properties **155**
Unpolarized light 155
Polarized light 156
Ellipsometric functions 157
Optical spectra and theoretical models: Selected examples **159**
Optical spectra 159
Theoretical models 160
Conclusion **165**
References **165**

Abstract

Starting from Maxwell equations and constitutive equations of a medium we consider the linear macroscopic optical response for homogeneous, isotropic, non-magnetic materials. The complex dielectric function and complex refractive index are derived with their connections with optical reflectance, transmittance and absorptance, for both unpolarized and polarized light. A few selected examples of optical response for solids (metals, semiconductors and insulators) are presented, together with the simplest classical and quantum models producing analytical expressions for the optical structures observed in experimental spectra. Analytical models give insights into optical response of materials and heterostructures, and should be used both to fit experimental data and simulate performances of electronic and photonic devices.

Key points

- Complex dielectric function.
- Complex refractive index.
- Electromagnetic waves reflection and transmission.
- Ellipsometry.
- Optical response of materials with polarized light.
- Optical spectra features and modeling.

Nomenclature

$\mathcal{A}$ (dimensionless)	Absorptance
B **(T)**	Magnetic induction
D **($\mathbf{C\ m^{-2}}$)**	Electric displacement
E **($\mathbf{V\ m^{-1}}$)**	Electric field
h **($\mathbf{J\ s^{-1}}$)**	Planck constant
H **($\mathbf{A\ m^{-1}}$)**	Magnetic field
j **($\mathbf{A\ m^{-2}}$)**	Current density
j_{cond} **($\mathbf{A\ m^{-2}}$)**	Internal current density
j_{ext} **($\mathbf{A\ m^{-2}}$)**	External current density
k **(dimensionless)**	Extinction coefficient
M **($\mathbf{A\ m^{-1}}$)**	Magnetization (magnetic moment per unit volume)
n **(dimensionless)**	Refractive index
$\tilde{n} = n + ik$ (dimensionless)	Complex refractive index

n_e (dimensionless)	Extraordinary refractive index
n_o (dimensionless)	Ordinary refractive index
$\mathrm{P}\ (\mathrm{C\ m^{-2}})$	Polarization (electric dipole moment per unit volume)
$\mathrm{q}\ (\mathrm{m^{-1}})$	Wavevector
$\tilde{\mathbf{q}} = \mathbf{q}_1 + i\mathbf{q}_2$	Complex wavevector
$\tilde{r}$ (dimensionless)	Reflection Fresnel coefficient
R (dimensionless)	Reflectivity
$\mathcal{R}$ (dimensionless)	Reflectance
$\tilde{t}$ (dimensionless)	Transmission Fresnel coefficient
T (dimensionless)	Transmittivity
$\mathcal{T}$ (dimensionless)	Transmittance
$v\ (\mathrm{m\ s^{-1}})$	Phase velocity
$\nu\ (\mathrm{s^{-1}})$	Frequency
$\alpha\ (\mathrm{cm^{-1}})$	Absorption coefficient
αd (dimensionless)	Optical density
δ (nm)	Classical skin depth
$\varepsilon\ (\mathrm{C^2\ N^{-1}\ m^{-2}})$	Dielectric function
$\tilde{\varepsilon} = \varepsilon_1 + i\varepsilon_2$	Complex dielectric function
$\varepsilon_0 = 8.859 \times 10^{-12}\ \mathrm{C^2N^{-1}\ m^{-2}}$	Vacuum permittivity
ε_r (dimensionless)	Relative dielectric function
λ (nm)	Wavelength
$\mu_0 = 4\pi \times 10^{-7}\ \mathrm{T\ m\ A^{-1}}$	Vacuum magnetic permeability
$\rho\ (\mathrm{C\ m^{-3}})$	External introduced charge density
$\sigma\ (\Omega^{-1}\ \mathrm{cm^{-1}})$	Optical conductivity
$\tilde{\sigma} = \sigma_1 + i\sigma_2$	Complex conductivity
ϕ_B (°)	Brewster angle
χ (dimensionless)	Electrical susceptibility
$\omega = 2\pi\nu\ (\mathrm{s^{-1}})$	Angular frequency
$\tilde{\chi}$ (dimensionless)	Polarization state
$\tan\psi$, $\cos\Delta$ (dimensionless)	Ellipsometric functions

Introduction

The optical properties of materials are of major interest from both the applicative and the fundamental points of view. They are indeed quantified by macroscopic functions, such as the refractive index, the absorption coefficient and reflectivity, the knowledge of which is necessary in designing and implementing optic or optoelectronic components and devices. They give reasons of the nature of the material (e.g. allowing the distinction between metals, semiconductors and insulators), and of the material homogeneity, crystal structure and composition. Moreover, the macroscopic optical response should be related to microscopic properties, such as the electronic and vibrational structures, by means of classical models (e.g. Drude Lorentz model) and quantum treatments (e.g. for interband and intraband optical transitions).

In this article, the optical properties of macroscopic materials are described, basing only on classical arguments. Starting from Maxwell's equations in a medium, the propagation of electromagnetic (em) waves in isotropic, linear and homogeneous materials is treated. To this aim, complex macroscopic quantities as the dielectric function, the optical conductivity, the refractive index and the absorption coefficient are introduced, together with the dispersion relations which they obey. Some hints at their extensions to anisotropic and nonlinear materials are given.

The reflection and transmission properties of em waves are then analyzed at the interface between different materials, and the appropriate functions are defined for unpolarized light waves. Their extension for polarized waves follows, with the addition of the ellipsometric functions which are particularly interesting from the application point of view. Links between the different optical functions and brief hints at their measurement techniques are given. Finally, selected examples of optical spectra from the far infrared to vacuum ultraviolet are reported, together with some reliable theoretical models; these last allow best-fit of analytical expressions to the experimental spectra, determining the optical functions in terms of free-variable independent parameters.

Maxwell's equations in a medium

The theoretical framework for the optical properties of a material is given by Maxwell's equations which describe the propagation of an electromagnetic wave in a medium and which in SI units are:

$$\nabla \cdot \mathbf{D} = \rho \qquad \nabla \cdot \mathbf{B} = 0$$

$$\nabla \times \mathbf{E} = -\frac{\partial \mathbf{B}}{\partial t} \quad \nabla \times \mathbf{H} = \mathbf{j} + \frac{\partial \mathbf{D}}{\partial t} \tag{1}$$

where **E** and **H** are the electric and magnetic fields, **D** the electric displacement, **B** the magnetic induction, ρ the external introduced charge density, **j** the current density.

The relations between the electric and magnetic fields are:

$$\mathbf{D} = \varepsilon_0 \mathbf{E} + \mathbf{P} \quad \mathbf{H} = \frac{\mathbf{B}}{\mu_0} - \mathbf{M} \tag{2}$$

where **P** is the polarization (electric dipole moment per unit volume) and **M** the magnetization (magnetic moment per unit volume), ε_0 and μ_0 the vacuum permittivity and magnetic permeability.

The current density **j** in the more general case contains two terms:

$$\mathbf{j} = \mathbf{j}_{ext} + \mathbf{j}_{cond} \tag{3}$$

where $\mathbf{j}_{ext}$ is the current density introduced into the medium from an external source and $\mathbf{j}_{cond}$ is the conduction current which is induced by a driving em field and which arises from the motion of charges in phase with the field (Stern, 1963; Wooten, 1972).

All these quantities are macroscopic, i.e. the average of their microscopic counterparts over a volume ΔV with small linear dimensions compared to the wavelength λ of the em wave, but large enough to contain many atoms. Then the medium can be treated as continuous from the view point of optical properties, although an ideally perfect crystal is not rigorously homogeneous on a microscopic scale. For instance, the internal charge density has crystal periodicity and varies sharply in the unit cell.

In the following, we treat with homogeneous, isotropic, non-magnetic ($\mathbf{B} = \mu_0 \mathbf{H}$) materials, and in the absence of external charges ($\rho = 0$) and currents ($\mathbf{j}_{ext} = 0$). Moreover, we consider the linear response regime, i.e. the variations in the internal charge density and in the current density induced by a driving em field of small intensity are proportional to the field. In these assumptions, the appropriate constitutive equations of the medium are:

$$\mathbf{P} = \varepsilon_0 \chi \mathbf{E} \, \mathbf{j}_{cond} = \sigma \mathbf{E} \tag{4}$$

where χ is the electric susceptibility and σ is the conductivity. The susceptibility χ and the conductivity σ contain the response of the medium to the em field E. They both appear at the right-hand side of the last of Maxwell's Eq. (1) and represent two different currents, the conduction current $\mathbf{j}_{cond}$ and the polarization current $\mathbf{j}_{pol} = \frac{\partial \mathbf{P}}{\partial t} = \varepsilon_0 \chi \frac{\partial \mathbf{E}}{\partial t}$. Since we will consider periodic solutions of Maxwell's equations, $\mathbf{j}_{cond}$ and $\mathbf{j}_{pol}$ are $\pi/2$ out of phase: $\mathbf{j}_{cond}$ is in phase with **E** and gives a time-average power absorption per unit volume $P_a = \langle \mathbf{j} \cdot \mathbf{E} \rangle = \sigma \langle \mathbf{E}^2 \rangle$; j_{pol}, instead, is $\pi/2$ out of phase with **E** and does not provide any absorption. We stress that j_{cond} and j_{pol}, and thus χ and σ, are not independent quantities because they have the same origin: the motion of charges (free or bound) induced by the em field. As it will be shown below, the real quantities χ and σ should be better represented by the real and imaginary parts of a single complex quantity. Moreover, the conductivity σ which appears in Eq. (4) is sometimes called optical conductivity, which in the limit of zero-frequency equals the usual dc electrical conductivity: for a static field **E** $\sigma \neq 0$ only in conductors, whereas for time-variable fields **E**(t) $\sigma \neq 0$ for both conductors and insulators.

An alternative parameter which characterizes a material is defined through Eq. (2) by:

$$\mathbf{D} = \varepsilon_0 \mathbf{E} + \mathbf{P} = \varepsilon_0 \mathbf{E} + \varepsilon_0 \chi \mathbf{E} = \varepsilon \mathbf{E} \tag{5}$$

where the quantity $\varepsilon = \varepsilon_0 (1 + \chi)$ is termed the dielectric constant or dielectric function (as it will be evident below, the second nomenclature is more appropriate when dealing with time-dependent fields). The dimensionless quantity $\varepsilon_r = \varepsilon/\varepsilon_0 = (1 + \chi)$ is the relative dielectric function.

ε and σ are the parameters which allow to completely characterize the optical response of the material: they describe the velocity of the wave in the medium and its spatial attenuation, i.e. the energy absorbed by the medium, respectively. ε and σ are functions of frequency (this property is called time dispersion) and wavevector (spatial dispersion) of the em wave. Moreover, they depend also on internal/external physical parameters, such as temperature, pressure, static magnetic or electric fields.

In the aforementioned hypotheses and from Maxwell's equations, the following wave equation can be derived:

$$\nabla^2 \mathbf{E} = \varepsilon_r \varepsilon_0 \mu_0 \frac{\partial^2 \mathbf{E}}{\partial t^2} + \sigma \mu_0 \frac{\partial \mathbf{E}}{\partial t} \tag{6}$$

This is the so-called d'Alembert equation for a wave propagating in a generic absorbing medium. Solutions of Eq. (6) are necessarily restricted to transverse waves because $\nabla \cdot \mathbf{E} = 0$ in the absence of a net charge density ρ. In vacuum ($\varepsilon_r = 1$, $\sigma = 0$) the wave velocity coincides with the velocity of light $c = \left(\sqrt{\varepsilon_0 \mu_0}\right)^{-1}$, while in a non-absorbing medium ($\sigma = 0$) the phase velocity is $v = \left(\sqrt{\varepsilon_r \varepsilon_0 \mu_0}\right)^{-1} = c/\sqrt{\varepsilon_r} = c/n$, where $n = \sqrt{\varepsilon_r} = c/v$ is the refractive index of the medium. The wave amplitude attenuation is described by the second term on the right of Eq. (6).

The complex dielectric function

It must be emphasized that, in the case of time-dependent em fields, there will generally be a phase shift between the motion of the charge carriers and the electric field **E** (similarly to what happens in ac circuits). In such cases the complex formalism is particularly convenient to describe phase shifts, and in addition to describe dispersion and absorption effects at the same time (Stern, 1963). Complex fields are usually defined, the real parts of which have physical meaning and are the ones involved in Maxwell's equations. For instance, $\mathbf{E}(\mathbf{r}, t) = \mathrm{Re}\left[\tilde{\mathbf{E}}(\mathbf{r}, t)\right]$, where the tilde distinguishes the complex quantity from its real counterpart.

Since the experimental measurements of the optical properties of solids are usually conducted with monochromatic light, we will consider a solution of Eq. (6) in the form of a monochromatic plane wave:

$$\tilde{\mathbf{E}}(\mathbf{r}, t) = \tilde{\mathbf{E}}_0 \exp\left[i(\tilde{\mathbf{q}}\cdot\mathbf{r} - \omega t)\right] \tag{7}$$

where $\tilde{\mathbf{E}}$ is the complex electric field, $\tilde{\mathbf{E}}_0 = \mathbf{E}_0 e^{i\varphi_0}$ is the polarization vector with arbitrary phase φ_0, $\mathbf{r}$ is the position vector with respect to an arbitrary coordinate system, $\omega = 2\pi\nu$ is the angular frequency, and $\tilde{\mathbf{q}} = \mathbf{q}_1 + i\mathbf{q}_2$ is the complex wavevector of the em wave in the medium. The absolute value of the wavevector in vacuum is $q = 2\pi/\lambda = \omega/c$. In fact, $\tilde{\mathbf{q}}$ describes the phase and spatial attenuation of the em wave, its explicit form being written as:

$$\begin{aligned} \mathbf{E}(\mathbf{r}, t) = \mathrm{Re}\ \tilde{\mathbf{E}}(\mathbf{r}, t) &= \mathrm{Re}\left[\tilde{\mathbf{E}}_0 \exp\left[i(\tilde{\mathbf{q}}\cdot\mathbf{r} - \omega t)\right]\right] = \\ &= \mathrm{Re}\left[\tilde{\mathbf{E}}_0 \exp\left[i(\mathbf{q}_1\cdot\mathbf{r} - \omega t)\right]\right] \exp(-\mathbf{q}_2\cdot\mathbf{r}) \\ &= \mathbf{E}_0 \cos(\mathbf{q}_1\cdot\mathbf{r} - \omega t + \varphi_0) \exp(-\mathbf{q}_2\cdot\mathbf{r}) \end{aligned} \tag{8}$$

In fact, $\mathbf{q}_1$ and $\mathbf{q}_2$ are perpendicular to the constant phase planes and to the constant amplitude planes, respectively. If $\mathbf{q}_1 // \mathbf{q}_2$, the wave is homogeneous, otherwise it is referred as inhomogeneous (Born and Wolf, 1980).

By inserting the monochromatic plane wave expression Eq. (7) in Eq. (6) the wave dispersion relation is obtained:

$$\tilde{\mathbf{q}}\cdot\tilde{\mathbf{q}} = \mu_0\left(\varepsilon + i\frac{\sigma}{\omega}\right)\omega^2 = \mu_0\tilde{\varepsilon}\omega^2 \tag{9}$$

where a complex dielectric function $\tilde{\varepsilon}$ has been introduced as:

$$\tilde{\varepsilon} \equiv \varepsilon_1 + i\varepsilon_2 = \varepsilon + i\frac{\sigma}{\omega} \tag{10}$$

The real part $\varepsilon_1 = \varepsilon$ describes the wave dispersion whereas the imaginary part $\varepsilon_2 = \sigma/\omega$ accounts for the dissipation of energy by the material. Alternatively, the complex conductivity $\tilde{\sigma} \equiv \sigma_1 + i\sigma_2 = -i\omega\tilde{\varepsilon} = \sigma - i\omega\varepsilon$ is sometimes used instead of $\tilde{\varepsilon}$.

The possibility of a phase shift between $\tilde{\mathbf{D}}$ (or $\tilde{\mathbf{j}}$) and $\tilde{\mathbf{E}}$ is now easily included by defining $\tilde{\mathbf{D}} = \tilde{\varepsilon}\,\tilde{\mathbf{E}}$ (or $\tilde{\mathbf{j}} = \tilde{\sigma}\,\tilde{\mathbf{E}}$). Moreover, when considering an em field given by Eq. (7), the displacement current $\partial\mathbf{D}/\partial t$ and the conduction current $\mathbf{j}_{cond}$ which appear in Maxwell's equations can be combined as follows:

$$\mathbf{j}_{cond} + \frac{\partial\mathbf{D}}{\partial t} = \sigma\mathbf{E} + \varepsilon\frac{\partial\mathbf{E}}{\partial t} = \mathrm{Re}\left[(\sigma - i\omega\varepsilon)\tilde{\mathbf{E}}\right] = \mathrm{Re}\left[\tilde{\sigma}\tilde{\mathbf{E}}\right] = \mathrm{Re}\left[-i\omega\tilde{\varepsilon}\tilde{\mathbf{E}}\right] \tag{11}$$

Thus the response function $\tilde{\varepsilon}$ accounts not only for the displacement current $\partial\mathbf{D}/\partial t$, which is $\pi/2$ out-of-phase with $\mathbf{E}$ and does not dissipate energy, but also, in its imaginary part, for the conduction current $\mathbf{j}_{cond}$, which is in phase with $\mathbf{E}$ and dissipates energy. The same holds for $\tilde{\sigma}$. When the optical response of a medium is calculated according to a specific model, either $\tilde{\varepsilon}$ or $\tilde{\sigma}$ must be introduced (but not both), since each one already includes both the in-phase and out–of-phase components.

In a general treatment, ε and σ are functions of space and time since the space-time representation of Maxwell's equations has been adopted. They are response functions or linear integral operators that connect the fields $\mathbf{D}(\mathbf{r}, t)$ and $\mathbf{j}(\mathbf{r}, t)$ with the electric field $\mathbf{E}(\mathbf{r}', t')$ at all other positions and all earlier times. Thus, in general, (Wooten, 1972):

$$\mathbf{D}(\mathbf{r}, t) = \int d\mathbf{r}' \int_{-\infty}^{t} \varepsilon(\mathbf{r}, \mathbf{r}', t, t')\ \mathbf{E}(\mathbf{r}', t')\,dt' \tag{12}$$

i.e. $\mathbf{D}(\mathbf{r}, t)$ and $\mathbf{E}(\mathbf{r}, t)$ are not proportional each to other, whereas this is true for their Fourier components. In fact, fields and sources should be decomposed into a complete set of monochromatic plane waves, for example:

$$\mathbf{E}(\mathbf{r}, t) = \int d\mathbf{q} \int_{-\infty}^{+\infty} \tilde{\mathbf{E}}(\mathbf{q}, \omega) \exp\left[i(\mathbf{q}\cdot\mathbf{r} - \omega t)\right] d\omega \tag{13}$$

where $\tilde{\mathbf{E}}(\mathbf{q}, \omega)$ is the Fourier transform of $\mathbf{E}(\mathbf{r}, t)$, with:

$$\tilde{\mathbf{E}}(\mathbf{q}, \omega) = \left(\frac{1}{2\pi}\right)^4 \int d\mathbf{r} \int_{-\infty}^{+\infty} \mathbf{E}(\mathbf{r}, t) \exp\left[-i(\mathbf{q}\cdot\mathbf{r} - \omega t)\right] dt \tag{14}$$

Operating the Fourier transform of Eq. (12) and utilizing the convolution theorem, one obtains:

$$\tilde{\mathbf{D}}(\omega, \mathbf{q}) = \tilde{\varepsilon}(\omega, \mathbf{q})\ \tilde{\mathbf{E}}(\omega, \mathbf{q}) \tag{15}$$

where the complex dielectric function $\tilde{\varepsilon}(\omega, \mathbf{q})$, Fourier transform of $\varepsilon(\mathbf{r}, t)$, shows up as the proportionality constant between the complex field components. An analogous relation $\tilde{\mathbf{j}}(\omega, \mathbf{q}) = \tilde{\sigma}(\omega, \mathbf{q})\ \tilde{\mathbf{E}}(\omega, \mathbf{q})$ can be obtained.

The frequency and wavevector dependence of $\tilde{\varepsilon}(\omega, \mathbf{q})$ and $\tilde{\sigma}(\omega, \mathbf{q})$ describe the time and the spatial dispersion of the material, respectively (Melrose and Mc Phedran, 1991). The spatial dispersion is associated to the presence of natural lengths in the medium, such as the dimension of atoms and inter-atomic spacings; its effect is weak for wavelengths which are long as compared to the natural lengths. In the optical spectral range the spatial dispersion should be neglected and $\tilde{\varepsilon}(\omega, \mathbf{q}) = \tilde{\varepsilon}(\omega)$; this is not possible at X-ray wavelengths. Moreover, we note that the wave dispersion relation (Eq. 9), which bounds ω and $\tilde{\mathbf{q}}$, does not imply in general a connection between time dispersion and spatial dispersion. In principle, it is possible to investigate separately the temporal response of a medium (and hence the time dispersion in ω) by subjecting it to a spatially uniform field that oscillates in time, or the spatial response (and hence the spatial dispersion in $\tilde{\mathbf{q}}$) with a static field that is spatially periodic.

In an anisotropic medium the polarization **P** and $\mathbf{j}_{cond}$ generally lie in a direction different from that of **E** (Wooten, 1972). This situation can be handled by representing the complex dielectric function as a tensor $\tilde{\varepsilon}_{ij}$. The real and imaginary parts of $\tilde{\varepsilon}_{ij}$ are symmetric also for an anisotropic medium, thus it is possible to put each of them into diagonal form in an appropriate set of coordinate axes (principal axes). The two sets do not coincide in general, until the crystal has symmetry at least as high as orthorhombic. In the particular case of cubic crystal symmetry, $\tilde{\varepsilon}_{ij}$ reduces to a scalar quantity.

In a nonlinear dielectric medium, it is possible to expand the relation between **P** and **E** in a Taylor series about $\mathbf{E} = 0$. Thus $\mathbf{P} = \varepsilon_0 (\chi\, \mathbf{E} + \chi^{(2)}\, \mathbf{E}^2 + \chi^{(3)}\, \mathbf{E}^3 + \ldots)$ where the $\chi^{(n)}$ coefficient describes the n-th order nonlinear effect. Eq. (6) is not applicable to em waves in nonlinear media. However, Maxwell's equations can be used to derive a nonlinear partial differential equation that these waves obey.

Finally, the real and imaginary parts of $\tilde{\varepsilon}$ are not independent quantities, being related one to other by the integral relations, the so called Kramers-Kronig relations (Smith, 1985). These relations follow rigorously from the requirement of causality (i.e., there can be no effect before the cause) and apply to the real and imaginary part of whatever linear response function. Thus, the complex dielectric function $\tilde{\varepsilon}(\omega)$ obeys the following relations:

$$\begin{aligned} \varepsilon_1(\omega) &= \varepsilon_0 + \frac{2}{\pi} P \int_0^{\infty} \frac{\omega' \varepsilon_2(\omega')}{\omega'^2 - \omega^2}\, d\omega' \\ \varepsilon_2(\omega) &= -\frac{2\omega}{\pi} P \int_0^{\infty} \frac{\varepsilon_1(\omega') - \varepsilon_0}{\omega'^2 - \omega^2}\, d\omega' \end{aligned} \tag{16}$$

where P stands for the principal value of the integral.

We remind that $\tilde{\varepsilon}$ and $\tilde{\sigma}$ describe macroscopic properties of materials, but they can be related to polarizabilities on the atomic scale and give reasons of microscopic properties of condensed matter, e.g. electronic and vibrational structures.

Complex refractive index

In analogy with the statement $n^2(\omega) = \varepsilon_r(\omega)$ valid in non-absorbing media, where n is the refractive index, it is useful to define a complex quantity, the so called complex refractive index $\tilde{n}(\omega)$ that is related to the relative complex dielectric function $\tilde{\varepsilon}_r(\omega) = \tilde{\varepsilon}(\omega)/\varepsilon_0$ by the relation:

$$\tilde{n}^2(\omega) = \tilde{\varepsilon}_r(\omega) \tag{17}$$

The real part of $\tilde{n}(\omega)$ coincides with the usual refractive index whereas the imaginary part is the extinction coefficient of the medium (Christy, 1972; Wooten, 1972). Thus:

$$\tilde{n}(\omega) = n(\omega) + i k(\omega) \tag{18}$$

and then the real and imaginary part of $\tilde{\varepsilon}_r$, including absorption contribution, should be written as:

$$\varepsilon_{r1} = n^2 - k^2 \qquad \varepsilon_{r2} = 2\, n\, k \tag{19}$$

Also, the inverse relations should be derived:

$$n = \left\{ \frac{1}{2} \left[\varepsilon_{r1} + \left(\varepsilon_{r1}^2 + \varepsilon_{r2}^2 \right)^{\frac{1}{2}} \right] \right\}^{1/2} \qquad k = \frac{\varepsilon_{r2}}{2n} \tag{20}$$

The dispersion relation of Eq. (9) assumes the following expression:

$$\tilde{\mathbf{q}} \cdot \tilde{\mathbf{q}} = \mu_0\, \tilde{\varepsilon}\, \omega^2 = \mu_0\, \varepsilon_0\, \tilde{\varepsilon}_r\, \omega^2 = \frac{\omega^2}{c^2}\, \tilde{n}^2 \tag{21}$$

If the wave is homogeneous, i.e. $\mathbf{q}_1 \,//\, \mathbf{q}_2$, it holds $\tilde{\mathbf{q}} = \frac{\omega}{c}\, \tilde{n}\, \mathbf{u}_q$, where $\mathbf{u}_q$ is the unit vector parallel to $\tilde{\mathbf{q}}$, and then $\mathbf{q}_1 = \frac{\omega}{c}\, n\, \mathbf{u}_q$, $\mathbf{q}_2 = \frac{\omega}{c}\, k\, \mathbf{u}_q$. Thus Eq. (7) should be written as:

$$\tilde{\mathbf{E}}(\mathbf{r}t) = \tilde{\mathbf{E}}_0 \exp\left[-\frac{\omega}{c}\, k\, \mathbf{u}_q \cdot \mathbf{r} \right] \cdot \exp\left[i \left(\frac{\omega}{c}\, n\, \mathbf{u}_q \cdot \mathbf{r} - \omega\, t \right) \right] \tag{22}$$

The extinction coefficient k measures the attenuation of the wave amplitude with the propagation distance inside the medium, while n determines is the phase velocity c/n in the medium. The penetration depth δ or classical skin depth, defined as the distance at which the field amplitude drops of $1/e$, is $\delta = c/(\omega k)$.

In anisotropic material, $\tilde{n}(\omega)$ is no more a scalar quantity, and as it is stated for $\tilde{\varepsilon}$, it should be a tensor. For example, in a uniaxial crystal (i.e. $\tilde{\varepsilon}_{xx} = \tilde{\varepsilon}_{yy} \neq \tilde{\varepsilon}_{zz}$) ordinary ($n_o$) and extraordinary ($n_e$) refractive indexes are defined, for light propagation in the *xy* plane and along the z direction, respectively.

Just as ε_1 and ε_2, also n and k satisfy Kramers-Kronig relations.

An additional important macroscopic quantity of the medium is the absorption coefficient α, which describes the relative decrease in the wave intensity I with unit distance (in the propagation direction, i.e. $u_q // d\mathbf{r}$). Since the wave intensity (i.e. the power which is incident on the unit area perpendicular to u_q) is $I = n\, c\, \varepsilon_0\, E^2 / 2$, from Eq. (22) it follows:

$$\alpha(\omega) = \frac{2\, k\, \omega}{c} = \frac{4\, \pi\, k}{\lambda} = \frac{\omega \;\; \varepsilon_{r2}}{n \;\; c} \tag{23}$$

The exponential attenuation of I after a propagating distance d accounts for the phenomenological Lambert-Beer law:

$$I = I_0\, e^{-\alpha \mathrm{d}} \tag{24}$$

where I_0 is the incident wave intensity. Differently from n and k, α is a dimensional quantity usually measured in cm^{-1}. The αd coefficient that reflects both the physical chemical properties and the geometry of the medium is referred to as optical density.

Reflection and transmission properties

Unpolarized light

While the refractive index n is measurable with a high degree of accuracy through experimental techniques that do not require absolute intensity measurements, such as minimum deviation, Brewster angle and interferometric techniques, the complete determination of n and k (or α) of a medium generally requires the measurement of the intensity reflected I_r, transmitted I_t and/or absorbed I_a with respect to the intensity I_0 of an em wave incident on the material surface. From the energy conservation law it follows:

$$I_0 = I_r + I_t + I_a \tag{25}$$

Dividing both sides by I_0, one obtains:

$$\mathcal{R} + \mathcal{T} + \mathcal{A} = 1 \tag{26}$$

where $\mathcal{R}$, $\mathcal{T}$ and $\mathcal{A}$ are the reflectance, the transmittance and the absorbance of the medium, respectively. The connection between these quantities and the optical functions of the medium can be obtained by Maxwell's equations with appropriate surface boundary conditions, i.e. the tangential components of **E** and **H** and the normal components of **D** and **B** at the surface of the material are continuous.

Hereafter, we only deal with specularly reflected light: this condition is well matched when surface irregularities and roughness have length scales much smaller than the light wavelength λ. In this case diffuse reflection losses are negligible.

Consider the simplest case of a plane monochromatic wave, propagating in a medium with refractive index $\tilde{n}_0$, which is normally incident on the surface of a semi-infinite medium with refractive index $\tilde{n}$ giving rise to the phenomena of reflection and refraction. Applying the boundary conditions both to the electric field **E** and to the magnetic field **H** (with $\mathbf{E} = \mu_0\, \mathbf{H} \times \mathbf{v}$ in a transverse electromagnetic wave), the tangential components of the incident (*0*), reflected (*r*) and refracted (i.e. transmitted, *t*) fields must obey (Hecht, 2014):

$$\begin{aligned} \tilde{E}_t &= \tilde{E}_0 + \tilde{E}_r \\ \tilde{n}\tilde{E}_t &= \tilde{n}_0\tilde{E}_0 - \tilde{n}_0\tilde{E}_r \end{aligned} \tag{27}$$

By solving for $\tilde{E}_r$ and $\tilde{E}_t$, one has:

$$\tilde{r} = \frac{\tilde{E}_r}{\tilde{E}_0} = \frac{\tilde{n}_0 - \tilde{n}}{\tilde{n}_0 + \tilde{n}} \qquad \tilde{t} = \frac{\tilde{E}_t}{\tilde{E}_0} = \frac{2\tilde{n}_0}{\tilde{n}_0 + \tilde{n}} \tag{28}$$

where $\tilde{r}$ and $\tilde{t}$ are complex quantities in the more general case, and are named reflection and transmission Fresnel coefficients, respectively. Then, the reflected and transmitted waves change in amplitude and phase with respect to the incident one, and while $\tilde{r}$ changes only in sign inverting the propagation direction, $\tilde{t}$ changes the absolute value. We note that $\tilde{t} = 1 + \tilde{r}$ and $\tilde{t}$ value should exceed unity. Moreover, in transparent media (n_0 and n real) the phase change in reflection is π when $n_0 < n$.

At the interface of the two media, the reflected and transmitted intensity relative to the incident one are called reflectivity R and transmittivity T, and are given by:

$$\begin{aligned} R &= \frac{I_r}{I_0} = |\tilde{r}|^2 = \left|\frac{\tilde{n}_0 - \tilde{n}}{\tilde{n}_0 + \tilde{n}}\right|^2 = \frac{(n - n_0)^2 + (k - k_0)^2}{(n + n_0)^2 + (k + k_0)^2} \\ T &= \frac{I_t}{I_0} = \mathrm{Re}\left(\frac{\tilde{n}}{\tilde{n}_0}\right) |\tilde{t}|^2 = \mathrm{Re}\left(\frac{\tilde{n}}{\tilde{n}_0}\right) \left|\frac{2\tilde{n}_0}{\tilde{n}_0 + \tilde{n}}\right|^2 \end{aligned} \tag{29}$$

We note that R and T are ≤ 1 with $R + T = 1$, as expected by the energy conservation at the interface between different media.

When considering the reflection, absorption, and transmission properties of optical materials, care must be taken to differentiate between reflectivity and reflectance, transmittivity and transmittance. To make the distinction between these terms clear, let us consider a sample of material with $\tilde{n}$ and thickness d, immersed in air ($\tilde{n}_0 = 1$), as shown in Fig. 1. Coming from air, the

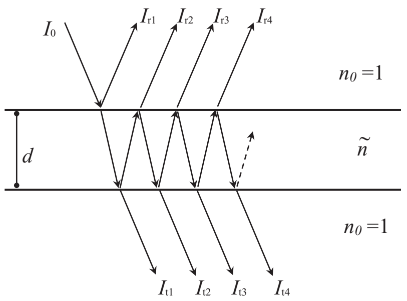

Fig. 1 Reflected and transmitted beams generated by an em wave with intensity I_0 near-normally incident on a layer with complex refractive index $\tilde{n}$ immersed in air. Refracted and reflected angles are exaggerated for clearness.

near-normally incident beam is split into reflected and transmitted fractions (as determined by R and T) at each interface, giving rise to secondary beams: reflectance and transmittance are obtained by summing up all the multiple-reflected and multiple-transmitted elements, which account also for light absorption along the thickness d. The total intensity reflected from the front surface is

$$I_r = I_{r1} + I_{r2} + \ldots + I_{rn} + \ldots == \left(R + RT^2 e^{-2\alpha d} + R^3 T^2 e^{-4\alpha d} + \ldots.\right) I_0 \tag{30}$$

Then, since $T = 1 - R$, the reflectance R is

$$\mathcal{R} = \frac{I_r}{I_0} = R + \frac{(1 - R)^2 R e^{-2\alpha d}}{1 - R^2 e^{-2\alpha d}} \tag{31}$$

Similarly the transmittance $\mathcal{T}$ results

$$\mathcal{T} = \frac{(1 - R)^2 \; e^{-\alpha d}}{1 - R^2 e^{-2\alpha d}} \tag{32}$$

and the absorptance $\mathcal{A} = 1\text{-}\mathcal{R} - \mathcal{T}$ is equal to:

$$\mathcal{A} = \frac{(1 - R)\;\left(1 - e^{-\alpha d}\right)}{1 - R\, e^{-\alpha d}} \tag{33}$$

In the only case that the optical density $\alpha d >> 1$, the reflectance $\mathcal{R}$ has only the first term in Eq. (31) and coincides with the reflectivity R of the material; there is no more intensity transmitted. If the thickness of the sample is sufficiently low to allow transmittance, $\mathcal{T}$ depends on α, d and R.

Polarized light

In order to evaluate the Fresnel coefficients in the general case of a plane wave propagating in a medium with refractive index $\tilde{n}_0$ and incident at an angle ϕ_0 on a semi-infinite medium with refractive index $\tilde{n}$, it is convenient to consider separate cases with the electric vector polarized perpendicular to and parallel to the plane of incidence (Azzam and Bashara, 1977 and Aspnes, 1985). There is no loss of generality in doing so, since any electric or magnetic vector may be resolved into components normal to- and parallel to- this plane. The subscripts s and p are usually refer to the normal and parallel component, respectively.

The electric field $\tilde{\mathbf{E}}_0\ (\mathbf{r}, t)$ associated to an incident plane wave propagating in the z direction of a local coordinate system xyz (Fig. 2) can be represented as:

$$\tilde{\mathbf{E}}_0\ (\mathbf{r}, t) = \mathrm{Re}\left\{\left(\mathbf{i}\ \tilde{E}_{0p} + \mathbf{j}\ \tilde{E}_{0s}\right)\ \exp\ \left[i\left(\tilde{\mathbf{q}}\cdot\mathbf{r} - \omega\, t\right)\right]\right\} \tag{34}$$

where $\tilde{E}_{0p}$ and $\tilde{E}_{0s}$ are the complex field components of $\tilde{\mathrm{E}}_0$ that describe both amplitude and phase dependence along the x (p direction) and y (s direction) axes of the system. The electric field of the reflected wave can be represented in another local coordinate system as:

$$\tilde{\mathbf{E}}_r\,(\mathbf{r}', t) = \mathrm{Re}\ \left\{\left(\mathbf{i}'\ \tilde{r}_p \tilde{E}_{rp} + \mathbf{j}'\ \tilde{r}_s \tilde{E}_{rs}\right)\ \exp\ \left[i\left(\tilde{\mathbf{q}}'\cdot\mathbf{r}' - \omega t\right)\right]\right\}. \tag{35}$$

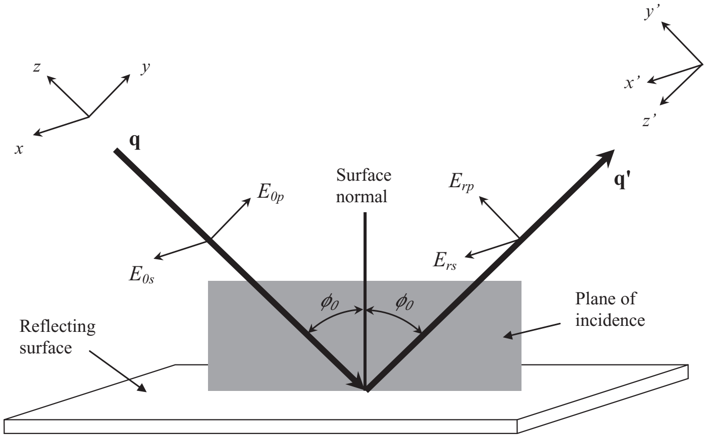

Fig. 2 Reflection of an em wave from a surface. The field components E_s and E_p are shown, together with the coordinate axes for the incident and reflected waves. The plane of incidence contains the incoming wavevector **q** and the specularly outgoing **q'**, as well as the surface normal.

An analogous expression holds for the transmitted electric field. As in the previous case, by imposing the surface boundary conditions for the electric and magnetic fields at the interface, the complex Fresnel coefficients in reflection ($\tilde{r}_p$ and $\tilde{r}_s$) and transmission ($\tilde{t}_p$ and $\tilde{t}_s$) are obtained:

$$\tilde{r}_p = \frac{\tilde{E}_{rp}}{\tilde{E}_{0p}} = \frac{\tilde{n}_0\, cos\ \tilde{\varphi} - \tilde{n}\ cos\ \tilde{\varphi}_0}{\tilde{n}_0\, cos\ \tilde{\varphi} + \tilde{n}\ cos\ \tilde{\varphi}_0} \qquad \tilde{t}_p = \frac{\tilde{E}_{tp}}{\tilde{E}_{0p}} = \left(1 + \tilde{r}_p\right) \frac{cos\ \tilde{\varphi}_0}{cos\ \tilde{\varphi}}$$

$$\tilde{r}_s = \frac{\tilde{E}_{rs}}{\tilde{E}_{0s}} = \frac{\tilde{n}_0\ cos\ \tilde{\varphi}_0 - \tilde{n}\ cos\ \tilde{\varphi}}{\tilde{n}_0\ cos\ \tilde{\varphi}_0 + \tilde{n} cos\ \tilde{\varphi}} \qquad \tilde{t}_s = \frac{\tilde{E}_{ts}}{\tilde{E}_{0s}} = 1 + \tilde{r}_s \tag{36}$$

where $\tilde{\phi}_0$ and $\tilde{\phi}$ are the incident and refraction complex angles which are no more purely geometrical quantities. The refracted em wave is generally inhomogeneous, i.e. it is characterized by different directions for planes of constant amplitude (parallel to the interface and perpendicular to $\mathbf{q}_2$) and for planes of constant phase (perpendicular to $\mathbf{q}_1$). In particular, the generalized Snell law at the interface between two absorbing media is written as:

$$\tilde{n}_0\ sen\ \tilde{\phi}_0 = \tilde{n}\ sen\ \tilde{\phi} \tag{37}$$

If the ambient medium is transparent, such as vacuum or air, the quantity $n_0\ sen\ \phi_0 = \tilde{n}\ sen\ \tilde{\phi}$ is real, and then $\tilde{\varphi}$ is determined starting from $\tilde{n}$ and $\tilde{\phi}_0$. At normal incidence the distinction between parallel and perpendicular components disappears and $\tilde{r}_s = \tilde{r}_p = \tilde{r}$ and $\tilde{t}_s = \tilde{t}_p = \tilde{t}$, i.e. Eq. (36) reduce to Eq. (28).

From the Fresnel coefficients in Eq. (36) and the energy conservation at the interface, reflectivity R_j and transmittivity T_j ($j = s, p$) are derived as:

$$R_j = \left|\tilde{r}_j\right|^2 \qquad T_j = \text{Re}\left(\frac{\tilde{n}\ \cos\tilde{\phi}}{\tilde{n}_0 \cos\tilde{\phi}_0}\right)\left|\tilde{t}_j\right|^2 \tag{38}$$

Again it is verified that $R_s + T_s = 1$ and $R_\text{p} + T_\text{p} = 1$. At normal incidence Eq. (38) reduce to Eq. (29). In case of unpolarized waves, it holds:

$$R = \frac{1}{2}\left(R_p + R_s\right)\ T = \frac{1}{2}\left(T_p + T_s\right) \tag{39}$$

At any angle of incidence ϕ_0 (except for $\phi_0 = 0$ o $\phi_0 = \pi/2$) it is $R_s > R_p$. Moreover, when both materials are transparent ($k_0 = k = 0$), and when $\phi_0 + \phi_0 = \pi/2$ (*i.e.* the reflected and refracted waves are perpendicular) it follows that $R_p = 0$. The p component is refracted without losses, while the s component is only partially refracted. This particular value of ϕ_0 is called Brewster angle ϕ_B and from the Snell law it follows $\tan\phi_B = n/n_0$. In Fig. 3 R_p and R_s components vs the angle of incidence for bulk silicon immersed in air and in the transparent wavelength region ($\text{n} \cong 3.42$) are reported. The Brewster angle value is $\phi_B \cong 73.7°$. If $k \neq 0$ R_p goes through a non-zero minimum in correspondence of a different value of $\phi > \phi_B$ which is called pseudo-Brewster angle.

Ellipsometric functions

An alternative way to describe the optical response of a material is based on the variation of the state of polarization of an em wave produced by reflection on the surface. The polarization state of an em wave is expressed by $\tilde{\chi}$, defined as (Azzam and Bashara, 1977 and Aspnes, 1985):

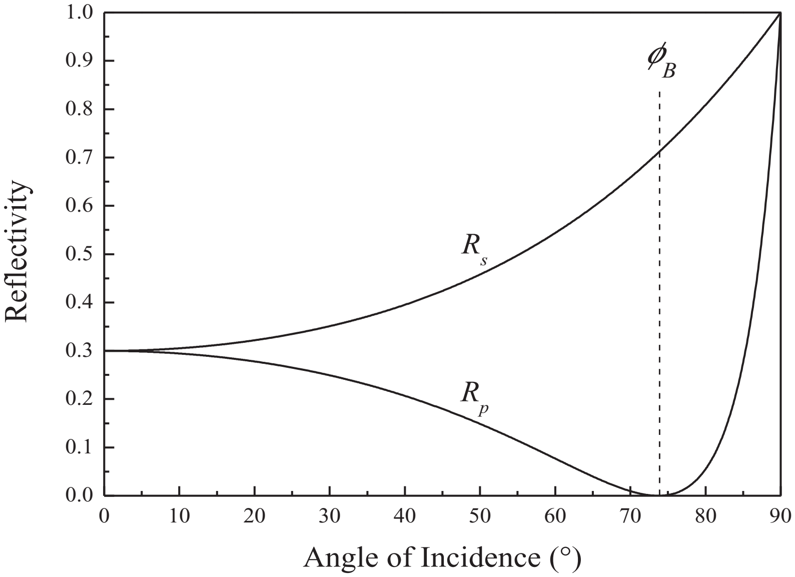

Fig. 3 Polarized reflectivities R_s and R_p as a function of the angle of incidence for Silicon in the subgap transparency spectral region ($n = 3.42$). R_p reaches zero value at the Brewster angle $\phi_B = 73.7°$.

$$\tilde{\chi} = \frac{\tilde{E}_p}{\tilde{E}_s} \tag{40}$$

Since $\tilde{E}_p$ and $\tilde{E}_s$ are complex, $\tilde{\chi}$ is in general a complex quantity: if $\tilde{E}_p$ and $\tilde{E}_s$ are in phase, $\tilde{\chi}$ is real and the em wave is linearly polarized. In the case of $\tilde{E}_p$ and $\tilde{E}_s$ are $\pi/2$ out of phase, $\tilde{\chi}$ is purely imaginary; if, in addition, $|\tilde{E}_p| = |\tilde{E}_s|$ then $\tilde{\chi} = \pm i$ and the wave is circularly polarized. Elliptical polarization is obtained when $\tilde{E}_p$ and $\tilde{E}_s$ are out of phase by $\pi/2$ and have different amplitudes, or in the more general case when the phase angle has any value different from 0 and $\pi/2$.

The incident and reflected waves are characterized by the polarization states $\tilde{\chi}_0$ and $\tilde{\chi}_r$, respectively, that are connected by the following relationship:

$$\tilde{\chi}_r = \frac{\tilde{E}_{rp}}{\tilde{E}_{rs}} = \frac{\tilde{r}_p\,\tilde{E}_{0p}}{\tilde{r}_s\,\tilde{E}_{0s}} = \frac{\tilde{r}_p}{\tilde{r}_s}\,\tilde{\chi}_0 \tag{41}$$

where $\tilde{r}_p$ and $\tilde{r}_s$ are defined by Eq. (36). Since $\tilde{r}_p$ and $\tilde{r}_s$ are complex quantities (i.e. $\tilde{r} = |\tilde{r}|\ e^{i\theta}$), it is evident that the reflected wave has a different polarization state with respect to the incident one.

When linearly polarized light impinges on a material surface, the reflected light is generally elliptically polarized. This ellipse of polarization is completely characterized by the ratio of the two axes and by the orientation of the major axis. From this fact the name ellipsometry is given to the experimental technique which allows to determine the variation in polarization state by reflection on a sample surface.

In ellipsometry the crucial quantity is the ratio $\tilde{\rho}$, defined as the ratio between $\tilde{\chi}_r$ and $\tilde{\chi}_0$:

$$\begin{aligned} \tilde{\rho} &= \frac{\tilde{\chi}_r}{\tilde{\chi}_0} = \frac{\tilde{r}_p}{\tilde{r}_s} = \\ &= \left(\frac{E_{rp}}{E_{rs}}\right)\left(\frac{E_{0s}}{E_{0p}}\right) \exp\left\{ i\left[\left(\beta_p - \beta_s\right)_r - \left(\beta_p - \beta_s\right)_0\right]\right\} \end{aligned} \tag{42}$$

Here $(\beta_p - \beta_s)$ is the phase difference between p and s field components. The absolute value of $\tilde{\rho}$ gives information on the amplitude ratio of reflected to incident E_p and E_s, whereas the phase of $\tilde{\rho}$ is given by the variation of the phase difference caused by reflection. The quantity $\tilde{\rho}$ is usually written in the compact form:

$$\tilde{\rho} = \tan\psi e^{i\Delta} \tag{43}$$

where

$$\tan\psi = \rho = \frac{|\tilde{r}_p|}{|\tilde{r}_s|} = \frac{r_p}{r_s} \quad \Delta = \left(\beta_p - \beta_s\right)_r - \left(\beta_p - \beta_s\right)_0 \tag{44}$$

A single ellipsometric measurement gives $\tilde{\rho}$, i.e. the ellipsometric functions $\tan\psi$ and $\cos\Delta$, which allow to determine the optical properties of a material. As an example, in the case of a semi-infinite material with complex dielectric function $\tilde{\varepsilon}$, assuming that the ambient medium is void ($\tilde{\varepsilon}_o = 1$) and ϕ_0 is the angle of incidence, it is possible to obtain a simple relation which bounds $\tilde{\rho}$ and $\tilde{\varepsilon}$:

$$\tilde{\varepsilon} = \mathrm{sen}^2\,\phi_0 + \mathrm{sen}^2\,\phi_0\ \ \tan^2\phi_0 \left| \frac{1-\tilde{\rho}}{1+\tilde{\rho}} \right|^2 \tag{45}$$

It is then immediate to derive the real and imaginary part of $\tilde{\varepsilon} = \varepsilon_1 + i\varepsilon_2$. In addition, in transparent media, ellipsometry is widely used to determine the refractive index and the thickness of a thin film layer deposited on a substrate with known optical properties.

We note that the reflection/absorption/transmission properties of a medium are of major interest from the application point of view. Moreover, they allow a complete optical characterization of a homogeneous, isotropic medium, i.e. the determination of ε_1 and ε_2 or n and k. Since there are two unknown parameters, at least two independent measurements are needed. In transparent materials, R and T should be used, or R measurements at different angles of incidence. In semi-infinite media (or with finite thickness but opaque) only reflection and ellipsometric measurements should be performed.

Moreover, the Fresnel coefficient $\tilde{r} = |\tilde{r}|\, e^{i\theta}$ expresses the linear relation between incident and reflected electric field amplitudes which obey causality. As stated above, it follows that a dispersion relation exists which connects its real and imaginary parts. Using the normal incidence reflectivity $R = |\tilde{r}|^2$, the dispersion relation between the absolute value R and the phase angle θ should be written as (Smith, 1985):

$$\theta(\omega) = -\frac{\omega}{\pi} P \int_0^{\infty} \frac{\ln R(\omega')}{\omega'^2 - \omega^2}\, d\omega' \tag{46}$$

Then θ should be determined, in principle, at whatever frequency if $R(\omega)$ is known over the whole spectral interval. In practice, $R(\omega)$ is measured over a finite spectral range and some means of extrapolating experimental results over inaccessible spectral ranges are necessary. Finally, n and k are calculated on the basis of Eqs. (28) and (29).

Optical spectra and theoretical models: Selected examples

Optical spectra

A lot of optical spectra articles and data collections have been published by different authors, regarding different spectral intervals and material samples. The "Handbook of Optical Constant of Solids" (Palik, 1985) has been the first systematic and critical database which tabulated n and k values over the widest spectral range (ideally from X-rays to microwaves), depending on literature availability, for a large number of materials of technological and physical interest: 37 materials have been examined by several authors, and the critiques for each materials have been preceded by 11 chapter articles that discuss various aspects of optical response, with some emphasis on experimental techniques and sample preparation. This handbook has been followed by a second volume (Palik, 1991), including 43 new materials, and by the handbook of Adachi (1999).

In the following we report on a few examples of the optical response, most of all on semiconductor materials for these reasons:

(a) semiconductor materials present characteristics intermediate between metals and insulators: in the case of heavily doping they may reach an optical conductivity approaching that of metals, on the contrary they behave like an insulator when fundamental energy gap is very large (above 3 eV);

(b) they are the most important materials for technological applications, in particular being the main components not only of micro/nanoelectronics devices, but also of photonic devices such as lasers, LED, photodetectors and imaging, solar cells, optical computers;

(c) the optical functions of semiconductors considerably change in controlled way—and are precisely tunable—as a function of: order/disorder in the crystal structure (monocrystals, polycrystals, amorphous); doping; external perturbations (temperature, electric or magnetic fields, pressure, strain, electromagnetic radiations); surface conditions (specular, rough, with oxides or overlayers).

Here we will focus on the optical response of materials as obtained with linear spectroscopic techniques and on the simpler interpretative models, both classical and quantum. An advanced discussion on the optical properties of dielectrics and semiconductors (including magneto- and electro-optical effects, metamaterials, photoluminescence, quasi-particles and non-linear optics) is presented elsewhere (Ivchenko, 2023).

The determination of the optical functions of semiconductors at and beyond the fundamental absorption edge is a powerful tool in studying their electronic band structure, whereas at lower energies it gives information on the vibrational structure and free carriers concentration. To this purpose, reliable physical models with analytical expressions for the optical functions in terms of free-variable parameters are adopted in the fit by least-square regression to experimental data on limited spectral intervals. As a result, physically significant parameter values are a direct outcome of the analysis, including e.g.: (a) parameters that describe the optical functions, the most important being the energies of the optical gap E_g, of interband optical transitions and of the vibrational modes (phonons); (b) thickness of films, and (c) parameter confidence limits and correlation coefficients. Moreover, the analytical expressions allow researchers to perform simulations of the optical response of an heterostructure or optoelectronic devices, such as solar cells. In this application, the device designer with a commercial or home-made software should specify the analytical model and its input parameters to calculate the optical functions of each layer material component, which in turn are applied in multilayer optical simulations to predict the transmittance (if any), reflectance, absorbance, and optical quantum efficiency spectra for the specific device.

Fig. 4 shows a pictorial sketch of the ε_1 and ε_2 spectra of crystalline GaAs as a function of photon energy from the far infrared to the vacuum ultraviolet (Blakemore, 1982). These trends are typical for heteropolar semiconductors (III–V, II–VI and their mixed compounds) with crystal structure of diamond or zincblende and for insulators The strong optical structures around 0.03 eV (the so called reststrahlen region) are due to resonant excitation of transverse lattice vibrational modes of crystal (phonons) promoting absorption of the incident radiation: this absorption is high for semiconductors with ionic component of atom bonding (e.g. Ga^+ and As^-) and weak or absent for purely covalent bonding in homopolar Si and Ge (Yu and Cardona, 1996).

Below the reststrahlen range ε_1 asymptotically approaches the static dielectric constant ε_s, while ε_2 becomes negligibly small. Above the reststrahlen there is a large energy interval where ε_1 and ε_2 are quasi constant, up to ~ 1.4 eV, corresponding to the energy gap E_g of GaAs, where the absorption increases abruptly (fundamental absorption edge). From that energy on, the behavior is due to the electronic interband transitions, that is each electron should be promoted from an occupied valence band state to empty conduction band state through absorption of one incident photon. The sharp structures in ε_2 correspond to the main critical points in the electronic band structure of the crystal (Bassani and Pastori Parravicini, 1974).

These typical dielectric function trends could be importantly influenced by the actual sample material conditions, i.e. free carrier concentration, crystalline phases, and sample temperature of operation, just to cite a few of them.

In the first case the phonon resonances can be screened by increasingly high free-carrier concentration in metals and semiconductors. The so called doping of semiconductors mainly affects the optical response at and below the reststrahlen region, as it is evident in Fig. 5, that reproduces the reflectivity (R) spectrum of bulk GaAs as a function of free electron concentration for n-doping. The strong resonant structure due to the transverse optical phonon is screened progressively with increasing doping; in additional lower photon energies a large plateau with high R values is growing and enlarging, quasi reaching the Dingle plateau (R about unity) typical of metals.

Optical spectra of materials strongly depend also on the order/disorder amount in their crystalline structure. As it is evident for the case of Silicon (Fig. 6), a semiconductor substantially changes in optical response from the monocrystal (prefix: c) to the micro/nano-crystalline ($\mu c - nc$) or amorphous phase (a). The strong and sharp dispersion and absorption peaks of c-Si smear out and reduce to an unique large structure in a-Si. Moreover an elemental or compound material should crystallize in different structures (allotropy), characterized by completely different physical properties, such as the optical functions. A striking and well known example is given by Carbon: it is an insulator within the diamond structure, a semimetal with hexagonal layered structure (graphite), a semiconductor with fullerene structure, an amorphous material with carbon black.

Among the external perturbations which affect the optical properties of solids, material temperature is certainly the most important, both from the fundamental and application point of view. As an example, in Fig. 7 the absorption coefficient of Silicon at the fundamental indirect edge at different temperatures is shown. The two segments of a straight line drawn through the experimental points represent the two contributions due to phonon absorption and emission (see below) (Yu and Cardona, 1996).

Theoretical models

The most important feature characterizing semiconductors and insulators is the energy gap value E_g, which is given by the difference between the minimum energy E_c in the conduction band and the maximum energy E_v of the valence band. The energy E of an electronic state in a band diagram is a function of the electron wavevector $\boldsymbol{k}$, and if the minimum and the maximum have the

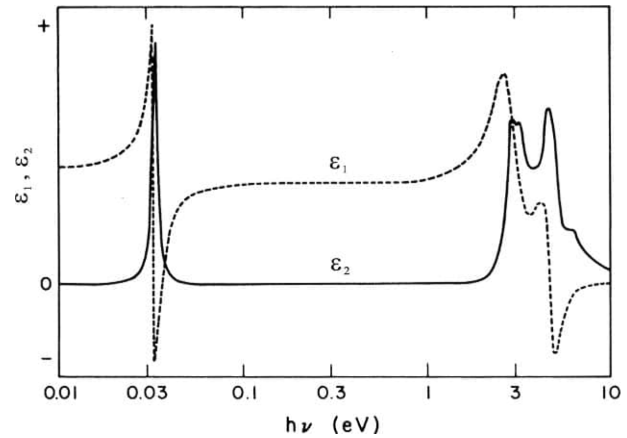

Fig. 4 Schematic representation of the real part ε_1 and imaginary part ε_2 of the complex dielectric function for crystalline GaAs vs photon energy $h\nu$, from the far infrared to vacuum ultraviolet. From Blakemore JS (1982) Semiconducting and other major properties of gallium arsenide. *Journal of Applied Physics* 53, R123.

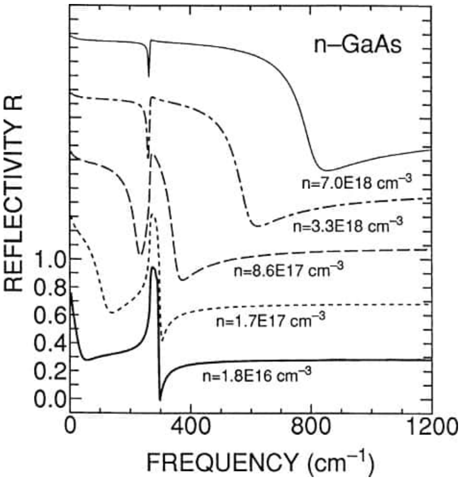

Fig. 5 Infrared reflectivity spectrum as a function of carrier concentration for *n*-type GaAs. Note that photon energy is expressed in wavenumber units (cm^{-1}). From Adachi S (1999) *Optical Properties of Crystalline and Amorphous Semiconductors.* Boston: Kluwer Academic Publications.

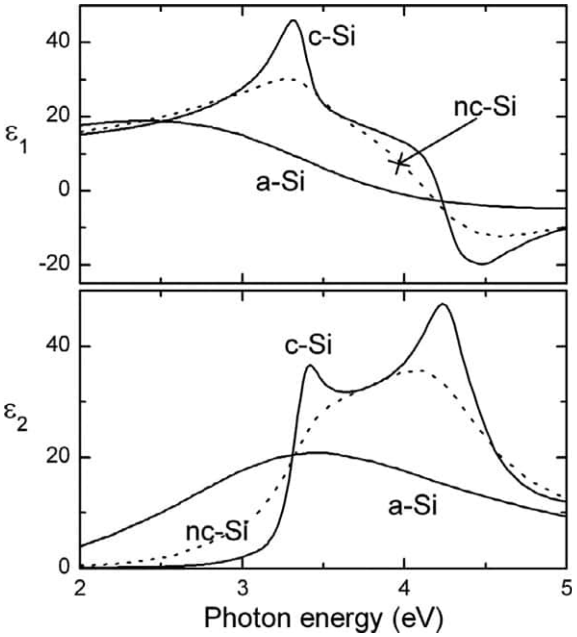

Fig. 6 Optical spectra of real ε_{r1} and imaginary ε_{r2} part of the complex dielectric function in the interband region for crystalline (c), nanocrystalline (n) and amorphous (a) Silicon. From Petrik P (2012) Characterization of nanocrystals using spectroscopic ellipsometry. In: Neralla S (ed.) *Nanocrystals.* London: IntechOpen Limited.

same ***k***, the gap is called direct, otherwise it is called indirect. Most semiconductors and insulators have a direct energy gap, but several technologically important semiconductors such as Si, Ge and GaP have an indirect gap, which limits their use in light emitting devices (LED and lasers).

A simple quantum model (Bassani and Pastori Parravicini, 1974; Yu and Cardona, 1996) for a direct optical transitions at the fundamental absorption edge gives in the parabolic band approximation the following α dependence:

$$\alpha \propto \left(h\nu - E_g\right)^{1/2} \text{ for } h\nu \geq E_g \tag{47}$$

$$\alpha = 0 \ \text{ for } \ h\nu < E_g$$

Then a plot of the square absorption coefficient α as a function of $h\nu$ should be a straight line, whose intercept with the abscissa gives E_g. In the case the gap is indirect, the momentum conservation in the interband optical transition involves the assistance of a phonon of energy E_p, which can be absorbed or emitted (this last only feasible at $T > 0$). The resulting α dependence in the indirect case is:

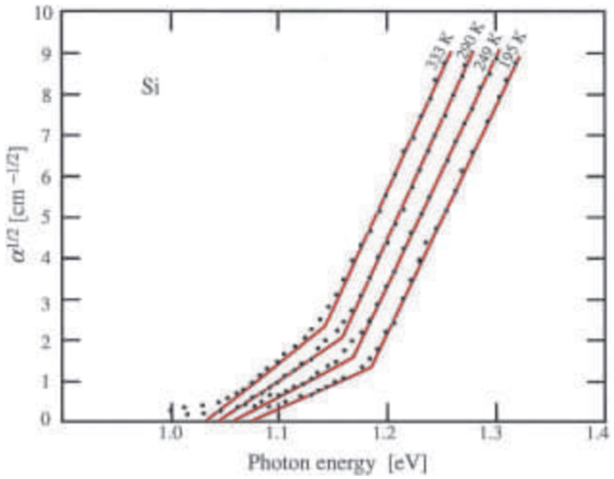

Fig. 7 Square root of the absorption coefficients of Si vs photon energy at different temperatures. From Yu PY and Cardona M (1996) *Fundamentals of Semiconductors*. Berlin: Springer-Verlag.

$$\alpha \propto \left(h\nu \mp E_p - E_g\right)^2 \text{ for } h\nu \geq E_g \pm E_p \tag{48}$$

$$\alpha = 0 \text{ otherwise,}$$

where + sign refers to one phonon absorption and – sign to emission. We note that the different shape of absorption spectrum makes the experimental distinction between a direct and indirect gap relatively straightforward. Moreover the indirect gap is more sensitive to material temperature, as due to the temperature dependent population of phonons which mediate the optical transitions. In Fig. 7 the two segments of a straight line drawn through the experimental points represent the two contributions due to phonon absorption and emission in accordance with Eq. (48).

Noticeably, Eq. (47) is deduced for perfectly crystalline semiconductors and insulators. Actually, for the majority of samples, dopant impurities, defect levels and other imperfections introduce structural disorder, which is maximum in amorphous materials. Disorder leads to additional energy level tails in valence and conduction bands so that fundamental absorption edge is no more a sharp transition; moreover broad bands of defect levels form in the gap, through which hopping conduction may occur (Adachi, 1999). As a consequence, the absorption coefficient α under the gap Eg shows a near universal exponential tail (the so called Urbach tail) (Urbach, 1953):

$$\alpha\,(E) = \alpha_0\ \exp\ \left[(E - E_0)/E_u\right] \tag{49}$$

where E is the photon energy, E_0 is an energy close to E_g and E_u determines the spectral width of the tail. Above the band edge Tauc and co-workers (Tauc et al., 1966) published for the absorption coefficient the following expression:

$$\alpha(E) = A_T\ \left(E - E_g\right)^2/E \tag{50}$$

where A_T value and the optical gap energy E_g should be determined by a fit to experimental spectra.

Later on, several models have been proposed, which are extensions of the Urbach and Tauc ones (someone including also Lorentz model), to obtain better fits to experimental spectra above and under E_g, without discontinuities, and to ensure the Kramers-Kronig consistency of ε_1 and ε_2 (see the reviews of Adachi, 1999, Rodriguez-DeMarcos and Larruquert, 2016).

The optical structures due to interband transitions, lattice vibrations and free-carrier absorption are well fitted by the phenomenological models due to Lorentz and Drude, that highlight the relevant optical fingerprints, allowing an initial feeling for optical properties (Christy, 1972; Wooten, 1972). Moreover, these classical models have quantum mechanical counterparts which are easily understood as generalization of their classical analogs.

The Lorentz model (also called Harmonic Oscillator Approximation, HOA) describes the motion of elementary bound charges in presence of an external electromagnetic field oscillating with frequency ω; the motion is analogue to a damped harmonic oscillator subject to a periodic external force. The stationary solution for the charge displacement $\mathbf{r}$ is:

$$\tilde{\mathbf{r}} = \frac{q\,\tilde{\mathbf{E}}_{loc}}{m}\ \frac{1}{\left(\omega_0^2 - \omega^2\right) - \mathrm{i}\,\Gamma\,\omega} \tag{51}$$

where: q is the charge and m the mass of the oscillator bound by an elastic restoring force $m\ \omega_0\ \mathbf{r}$; ω_0 is the frequency of energy resonance for the oscillator, Γ the coefficient of viscous damping (radiation damping, scattering in a solid); $\mathbf{E}_{loc}$ the local electric field.

For N electrons per unit volume elastically bound to the nucleus with resonance frequency ω_0, from (51) the dipole moment $\mathbf{p} = -e\mathbf{r}$ follows, then the polarization $\mathbf{P}$ and finally the relative complex dielectric function $\tilde{\varepsilon}_r$ (cfr. Eqs. (4), (5) and (10)), with the following expression:

$$\tilde{\varepsilon}_r = 1 + \frac{N\,e^2}{\varepsilon_0\,m}\,\frac{1}{(\omega_0^2 - \omega^2) - \mathrm{i}\,\Gamma\,\omega} \tag{52}$$

Separating the real ε_{r1} and the imaginary ε_{r2} parts of $\tilde{\varepsilon}_r$ we have:

$$\begin{aligned} \tilde{\boldsymbol{\varepsilon}}_{r1} &= n^2 - k^2 = 1 + \frac{Ne^2}{\varepsilon_0 m}\,\frac{(\omega_0^2 - \omega^2)}{(\omega_0^2 - \omega^2)^2 + \Gamma^2\omega^2} \\ \tilde{\boldsymbol{\varepsilon}}_{r2} &= 2nk = 1 + \frac{Ne^2}{\varepsilon_0 m}\,\frac{\Gamma\omega}{(\omega_0^2 - \omega^2)^2 + \Gamma^2\omega^2} \end{aligned} \tag{53}$$

The frequency dependence of ε_{r1} and ε_{r2} at each energy resonance is illustrated in Fig. 8: the shape of ε_{r1} is termed dispersive, whereas that of ε_{r2}, typical of an absorption structure, is called Lorentzian curve. We note that Eq. (52) automatically meets causality, linearity and Kramers- Kronig requirements.

In this classical oscillator model if the considered atom has different types of bound electrons, each with a resonance frequency $\omega_{j,}$ broadening Γ_j and density N_j, as due to additive property of dielectric functions (whereas n and k are not), Eq. (52) should be extended giving:

$$\tilde{\boldsymbol{\varepsilon}}_r = 1 + \frac{e^2}{\varepsilon_0\,m}\sum_j \frac{N_j}{\left(\omega_j^2 - \omega^2\right) - i\Gamma_j\omega} \quad with \sum N_j = N \tag{54}$$

s an example, the ε_{r1} and ε_{r2} experimental spectra of GaAs are well fitted with 7 Lorentz oscillators as shown in Fig. 9. We underline that these oscillators have no physical origin, i.e. the parameters ω_j of the fit do not necessarily correspond to frequencies of real interband optical transitions.

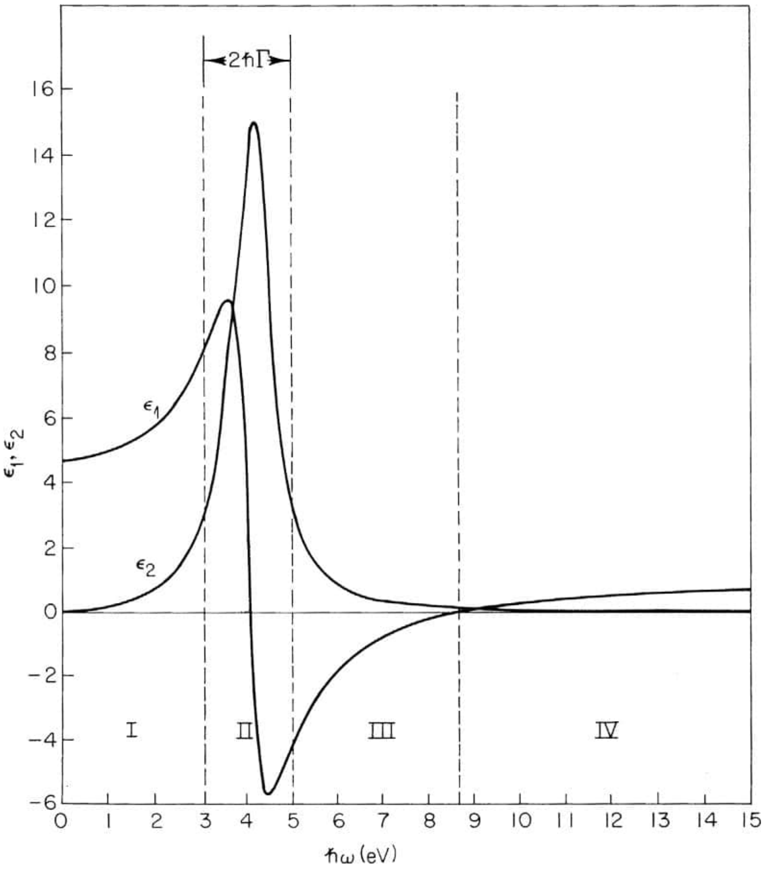

Fig. 8 Typical spectra of ε_{r1} and ε_{r2} obtained by the harmonic oscillator model with charge $-e$, resonance frequency $\omega_0 = 4$ eV, damping $\Gamma = 1$ eV. In the region I, II, III and IV the material is primarily transmitting, absorbing, reflecting and transmitting, respectively. From Wooten F (1972) *Optical Properties of Solids*. New York: Academic Press.

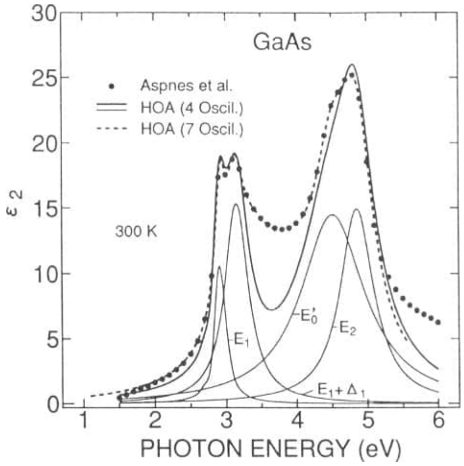

Fig. 9 Fit results of harmonic oscillator approximation (HOA) to the experimental ε_{r2} spectrum (dots) of GaAs. Individual contribution to ε_{r2} of four harmonic oscillators are shown by light solid lines. A better result for seven oscillators is plotted by dashed line. From Adachi S (1999) *Optical Properties of Crystalline and Amorphous Semiconductors*. Boston: Kluwer Academic Publications.

The Lorentz model perform a best-fit also to the lineshape of the absorption and reflectance spectra of infrared active optical phonons, since phonons are quantized simple harmonic oscillators. Then in Eq. (51) q and m are charge and reduced mass of the oscillating ions and $\omega_0 \equiv \omega_T$ is its resonance frequency (T stays for transverse vibration). In Yu and Cardona (1996) several experimental phonon reflectivity spectra of zinc-blende-type semiconductors are reported: they all should be fitted reasonably well with Eq. (51) and the values of the only adjustable parameters ω_0 and Γ are there listed.

A more realistic model for the dielectric function $\tilde{\varepsilon}$ (ω) in the interband region is based on a quantum approach giving a sum (on a continuous background) of lineshape functions, opportunely weighted and centered at the energy of the critical points (CP) in the electronic band structure (Bassani and Pastori Parravicini, 1974, Wooten, 1972). The resulting $\tilde{\varepsilon}$ (ω) expression is:

$$\tilde{\boldsymbol{\varepsilon}}_r = 1 + \frac{e^2}{\varepsilon_0\, m} \sum_j \frac{N f_j}{\left(\omega_j^2 - \omega^2\right) - i\Gamma_j \omega} \tag{55}$$

which is formally similar to Eq. (54), but some terms have quite different meaning. In Eq. (55) ω_j is the transition frequency of an electron between two quantum states (respectively in valence and in conduction band), separated by an energy gap of $\hbar\omega_j$. The parameter f_j, called oscillator strength, is the probability of the transition, subjected to the condition $\sum f_j = 1$, which corresponds to the sum rule $\sum N_j = N$ in Eq. (54).

Morevoer, the free-carrier optical contribution in doped semiconductors and metals is well reproduced by the Drude model (Christy, 1972; Wooten, 1972), that can be directly derived by Lorentz model nulling the elastic restoring force, that is setting $\omega_0 = 0$ in Eq. (52). In this case the factor $Ne^2/\varepsilon_0\, m$ coincides with ω_p^2, where ω_p is the so-called optical plasma frequency of quasi-free electrons, and $\Gamma = 1/\tau$, where τ is the mean free time between collisions. For photon energies $\hbar\omega$ small compared with $k_B T$ (k_B Boltzmann constant and T the absolute temperature) the Drude formulation coincides con quantum result for intraband transitions. As an example, the reflectivity spectra in Fig. 5 were reproduced with Drude-Lorentz models, using parameter values determined by best-fit to experimental spectra.

Finally, the refractive index n values, their dispersion and temperature dependence in the transparency ($k \approx 0$) spectral interval between the fundamental absorption edge and phonon absorption are basic parameters of semiconductors and insulators. They are useful for a lot of applications in optical instruments (e.g. optical crystals and glasses) and photonic devices for multimedia communication systems (optical fibers, focusing, coupling, and modulation of radiation). In Fig. 10 several spectra of refractive index dispersions vs wavelength for various semiconductors and insulators are collected. A few empirical formulae are currently used to simulate the refractive index dispersion, but the most accurate to fit the experimental data, is the following two-pole Sellmeier dispersion model:

$$n^2 = A + \frac{B\,\lambda^2}{\left(\lambda^2 - C\right)} + \frac{D\,\lambda^2}{\left(\lambda^2 - E\right)} \tag{56}$$

where λ is the radiation wavelength (Ghosh, 1998). The term A represents the contribution of the optical transitions at the gaps higher than E_g, whereas the second term represents the contribute at E_g; the last term, accounting for decrease of n at higher wavelengths, is due to lattice absorption. The values of the coefficients A, B, C, D and E, deduced by best-fit to experimental data of Fig. 10 are also reported. Note that the Sellmeier dispersion model is not Kramers-Kronig consistent, thus is to be considered a valid approximation only on a restrict spectral interval.

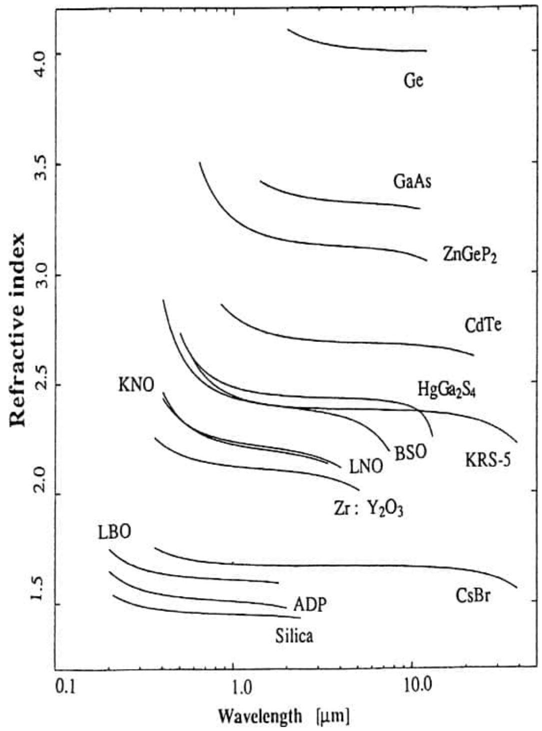

Fig. 10 Refractive index spectra vs wavelength for several optical materials in the transparency region between the fundamental absorption edge and the reststrahlen region. From Ghosh G (1998) *Handbook of Thermo-Optic Coefficients of Optical Materials With Applications*. New York: Academic Press. Chapter 2.

Conclusion

In the framework of classical physics, the fundamental quantity describing the optical properties of materials, that is the complex dielectric function $\tilde{\varepsilon}$, has been introduced and discussed. The treatment has been limited to the linear response and to homogenous, isotropic, non-magnetic materials. Then the macroscopic quantities related to $\tilde{\varepsilon}$, such as the complex refractive index, reflectance, transmittance, absorption, have been introduced. Particular emphasis has been given to the reflection of polarized light and ellipsometry, which is the experimental technique allowing to directly measure both the real ε_1 (dispersive) and the imaginary ε_2 (dissipative) parts of $\tilde{\varepsilon}$.

A few experimental optical spectra are reported, which are selected to describe the main features of the optical response of solids from the far-infrared to vacuum ultraviolet, with their dependence on crystalline order, doping and temperature. Moreover, simple theoretical models, both phenomenological and derived from quantum treatments, with the analytical expressions for the optical functions are recalled. Their best-fits to experimental data allow the determination of some fundamental parameters which, in the usual theory-experiment feedback loop, enable to refine the calculated electronic and vibrational structures, and to simulate and design multilayered photonic devices.

During the last 40 years the impressive progress in epitaxial techniques allowed to growth micro/nano-structures and related devices exhibiting new optical features which extend and deepen the understanding of the optical properties of materials, while substantially respecting the above considerations. A more recent striking case is represented by optical metamaterials, designed to obtain artificial structures with properties not found in nature. Their unique optical properties, such as negative refractive index (which do not break the laws of physics), can be extended from GHz all the way to optical frequencies. After 20 years of research, today the metamaterials move out of the lab, promising enhanced performance in applications, from optical accessories to photonics devices.

References

Adachi S (1999) *Optical Properties of Crystalline and Amorphous Semiconductors*. Boston: Kluwer Academic Publications.

Aspnes DE (1985) The accurate determination of optical properties by ellipsometry. In: Palik ED (ed.) *Handbook of Optical Constants of Solids*. Orlando: Academic Press Inc. Chapter 5.

Azzam RMA and Bashara NM (1977) *Ellipsometry and Polarized Light*. Amsterdam: North-Holland Publ. Comp.

Bassani F and Pastori Parravicini G (1974) *Electronic States and Optical Transitions in Solids*. Oxford: Pergamon.

Blakemore JS (1982) Semiconducting and other major properties of gallium arsenide. *Journal of Applied Physics* 53: R123.

Born M and Wolf E (1980) *Principles of Optics*. Cambridge: Cambridge University Press.
Christy RW (1972) Classical theory of optical dispersion. *American Journal of Physics* 40: 1403.
Ghosh G (1998) *Handbook of Thermo-Optic Coefficients of Optical Materials with Applications*. New York: Academic Press. Chapter 2.
Hecht E (2014) *Optics*. Edinburgh: Pearson Education Limited. Chapter 4.
Ivchenko EL (2023) *Optical Properties of Dielectrics and Semiconductors, Encyclopedia of Condensed Matter Physics*. Amsterdam: Elsevier.
Melrose DB and Mc Phedran RC (1991) *Electromagnetic Process in Dispersive Media*. Cambridge: Cambridge University Press. Chapter 6.
Palik ED (ed.) (1985) *Handbook of Optical Constants of Solids*. Orlando: Academic Press Inc.
Palik ED (ed.) (1991) *Handbook of Optical Constants of Solids II*. Orlando: Academic Press Inc.
Rodriguez-DeMarcos LV and Larruquert JI (2016) Analytic optical-constant model derived from Tauc-Lorentz and Urbach tail. *Optic Express* 24: 28561–28572.
Smith DY (1985) Dispersion theory. In: Palik ED (ed.) *Handbook of Optical Constants of Solids*. Orlando: Academic Press Inc. Chapter 3.
Stern F (1963) Elementary theory of the optical properties of solids. *Solid State Physics* 15: 299–408.
Tauc J, et al. (1966) Optical properties and electronic structure of amorphous germanium. *Physica Status Solidi* 15: 627.
Urbach F (1953) The long-wavelength edge of photographic sensitivity and of the electronic absorption of solids. *Physical Review Journals Archive* 92: 1324.
Yu PY and Cardona M (1996) *Fundamentals of Semiconductors*. Berlin: Springer-Verlag.
Wooten F (1972) *Optical Properties of Solids*. New York: Academic Press.

Photon statistics and coherence theory[☆]

Paolo Mataloni, Physics Department, Sapienza University of Rome, Rome, Italy

© 2024 Elsevier Ltd. All rights reserved.

This is an update of P. Mataloni, Photon Statistics and Coherence Theory, Editor(s): Franco Bassani, Gerald L. Liedl, Peter Wyder, Encyclopedia of Condensed Matter Physics, Elsevier, 2005, Pages 280–286, ISBN 9780123694010, https://doi.org/10.1016/B0-12-369401-9/00611-2.

Introduction 167
Coherent light – Poissonian statistics 168
Thermal and chaotic light – Super Poissonian statistics 169
Nonclassical light – Sub Poissonian statistics and role of quantum detection efficiency 171
First order coherence 172
Second order coherence 175
Brown-Twiss correlations – Photon bunching and photon antibunching 178
Basic photon statistics at beam splitters 179
Conclusion 183
References 183
Further reading 183

Abstract

The statistical properties of light are discussed in the classical and quantum optics context, looking at the different features of the two approaches. Optical fluctuations are characterized according to the three statistical distributions in which they can occur, Poissonian, super Poissonian and sub Poissonian, respectively. The corresponding behaviors are discussed by studying first the expressions of the variances, then by looking at the respective correlation functions and coherence degrees, at the first and second order. This leads to demonstrate that only an analysis performed at the second order degree of coherence allows to distinguish among the three statistical behaviors and between classical and nonclassical light. The study of the peculiar properties of nonclassical light allows also to discuss the role played by photodetector efficiency within the different photon statistics. According to the values of the degree of second order coherence, a further way to identify the behavior of light, namely coherent, bunched and antibunched, is introduced. Finally, the peculiar role played by the beam splitter on the output state statistics, for some experimental condition, is discussed.

Key points

- Poissonian, super Poissonian and sub Poissonian statistical distributions of light
- Correlation functions
- First and second order coherence degrees
- Optical Beam Splitter
- Classical and nonclassical light
- Photon bunching and antibunching

Introduction

The study of optical fluctuations gives us the possibility to understand the statistical properties of light. There are different kinds of light, each one characterized by a particular statistical distribution (Mandel and Wolf, 1965). Depending on the size of fluctuations, three different photon statistics can be considered, namely *Poissonian*, *super-Poissonian* and *sub-Poissonian*. We will describe the main characteristics of these kinds of light in Sections "Coherent light – Poissonian statistics," "Thermal and chaotic light – Super Poissonian statistics," "Nonclassical light – Sub Poissonian statistics and role of quantum detection efficiency," where the main properties of the corresponding photon statistical distribution are discussed.

A deep knowledge of the different kinds of light cannot be separated from the role played by *photodetection*. This aspect will be briefly examined in paragraph 3 regarding its consequences on quantum light detection.

The statistical properties of Poissonian, super-Poissonian and sub-Poissonian light is studied by performing *correlation measurements* between different parts of the light beam, each one associated to a particular set of space-time coordinates. By *first-order*

[☆] *Change History*: July 2022. P Mataloni updated the chapter.

correlation measurements it is not possible to distinguish between the various photon statistics, an objective that can be achieved by performing *second-order* correlation measurements, e.g. by measuring *intensity/photon* correlations. We will first discuss this aspect in Section "First order coherence" by examining first-order coherence phenomena.

Depending on its nature, light can show either *classical* or *nonclassical* behaviors. While the Poissonian and super Poissonian light properties are described in an equivalent way either in the classical or in the *quantum* frame, the peculiar features of sub Poissonian light can be explained only by a fully quantum approach. Indeed, it is only through second-order correlation measurements that it is possible to distinguish between classical and nonclassical behaviors, as said. Second-order coherence degree will be introduced in Sections "Second order coherence" and, "Brown-Twiss correlations – Photon bunching and photon antibunching" for the three models of photon statistics, using either a classical or a quantum description and it will be used also to describe the phenomena of *photon bunching* and *antibunching*. Section "Basic photon statistics at beam splitters" describes the consequences on photon statistics related to a few physical situations in which single and two photon states impinge on a beam splitter.

Coherent light – Poissonian statistics

It is well known that the intimate nature of optical phenomena can be explained by considering light not only in terms of waves but also of particles. Referring to these concepts the theoretical study of optical phenomena has developed over the years following both classical and quantum theory. Among the various characteristics of light, a full comprehension of its statistical properties can be achieved by considering light as a photon stream rather than as an electromagnetic wave. It is in particular this granular picture that allows us to justify the unavoidable presence of optical fluctuations both in the classical and quantum approach.

To understand the statistical phenomena of a photonic stream we need to consider that a photon counting measurement is affected not only by the intrinsic instabilities of the light beam but also by those typical of a photon counter, deriving from the non-perfect quantum efficiency of detector. We may disregard this effect for the moment by implicitly assuming a 100% photo-detector quantum efficiency.

To have an idea of the photon fluctuations associated to a photonic stream, let's consider the model of a continuous wave (cw) single-mode laser beam operating above threshold, a situation implying a stable output power. This kind of light represents the best approximation of a classical monochromatic beam, perfectly coherent, since amplitude, frequency and phase are constant.

The number of photons per second of a laser is extremely high, even in the case of a low output power. Nearly 3×10^{15} photons/sec are generated by a Helium-Neon (He—Ne) laser with an output power of 1 mW, hence, in the example we are going to discuss, it's more simple to consider a laser beam attenuated of at least a factor 10^6.

By dividing the light beam into gradually shorter temporal segments and sampling photons in each of them, statistical fluctuations become more and more evident because of the random temporal distribution of photons. At a certain point, for short enough time intervals, the main part of them will be empty while the segments containing one photon become rare and with a negligible number of segments containing two or more photons. This feature is peculiar of a Poissonian photon distribution. This can be demonstrated by considering a beam of finite length containing an average number of photons $\overline{n}$ and divided in N equal subsegments. It comes out that the probability of finding n subsegments with one photon and $(N - n)$ with zero photons, equivalent to the probability of counting n photons in the beam, is given by the binomial distribution: $P(n) = \frac{N!}{n!(N-n)!} p^n (1 - p)^{N-n}$, where $p = \frac{\overline{n}}{N}$. It is possible to demonstrate that, in the limit N→∞, this probability corresponds exactly to the Poisson distribution:

$$P(n) = \frac{\overline{n}^n}{n!} e^{-n} \ (n = 0, 1, 2 \ldots) \tag{1}$$

whose characteristic parameters are the mean value:

$$\overline{n} \equiv < n > = \sum_{n=0}^{\infty} nP(n) \tag{2}$$

and the variance:

$$Var(n) \equiv (\Delta n)^2 = \sum_{n=0}^{\infty} (n - \overline{n})^2 P(n) = \overline{n} \tag{3}$$

the second one indicating the amount of spread of the distribution.

The standard deviation of the photon counting measurements is, accordingly, $\Delta n = \sqrt{\overline{n}}$ and the fractional uncertainty in the number of photons of the coherent beam is expressed as:

$$\frac{\Delta n}{\overline{n}} = \frac{1}{\sqrt{\overline{n}}} \tag{4}$$

with $\frac{\Delta n}{\overline{n}} \rightarrow 0$ for increasing $\overline{n}$. This result approaches the behavior of a classical wave for a large photon number.

The Poisson distribution applies to a coherent cw laser beam which is, as said, the best approximation of a classical stable wave, with the relevant difference that, in the case of a classical wave, the variance, expressed in terms of the intensity, vanishes: $(\Delta I)^2 = 0$.

The nonvanishing value of Δn is the consequence of the particle-like nature of light in the quantum approach. According to (4) this aspect becomes less and less relevant with increasing $\overline{n}$, a condition in which the Poisson distribution approaches a Gaussian distribution.

We may adopt the Poissonian coherent light as a term of comparison with other kinds of light, considering for each of them the variance of the corresponding statistical distribution.

Thermal and chaotic light – Super Poissonian statistics

To understand the typical features of super-Poissonian statistics we refer to the case of *thermal light*, the radiation emitted by an ideal object known as a black body, a perfect emitter and absorber of radiation. A black body can be modeled as a cavity containing radiation at thermal equilibrium with its walls. Within the continuum spectrum of modes oscillating in the cavity we consider a single mode field with quantized energy $E_n = \left(n + \frac{1}{2}\right)\hbar\omega$. A good example of thermal light source is given by a filament lamp, where photon number fluctuations derive from the random presence of the absorption and emission processes occurring therein with a characteristic time depending on the operation parameters of the source, such as the temperature.

According to statistical mechanics the probability that the mode is thermally excited to its nth excited state, a situation corresponding to having n photons in the mode, is given by the Boltzmann factor:

$P(n) = \frac{exp\left(-n\hbar\omega/k_BT\right)}{\sum_n exp\left(-n\hbar\omega/k_BT\right)}$, where k_B is the Boltzmann constant.

Adopting the notation $x = exp\left(-\hbar\omega/k_BT\right)$ the thermal probability is expressed as

$$P(n) = \frac{x^n}{\sum_{n=0}^{\infty} x^n} \tag{5}$$

and the average number of photons excited in the mode at temperature T is:

$$\overline{n} = \sum_n nP(n) = \frac{x}{1-x} = \frac{1}{exp\left(\hbar\omega/k_BT\right)-1} \tag{6}$$

Starting from (5), we define $x = \frac{\overline{n}}{(1+\overline{n})}$ and arrive to an alternative expression of the probability given in (2.1), namely the *Bose-Einstein distribution*,

$$P(n) = \frac{\overline{n}^n}{(1+\overline{n})^{1+n}} \tag{7}$$

It is significantly broader than the Poissonian distribution for any value of $\overline{n}$, as shown in Fig. 1. A coherent and a thermal source having the same average number $\overline{n}$ of photons, the same frequency and bandwidth, are expected to have completely different photon statistics because of their different photon distributions.

An indication of the size of fluctuations related to the number of photons is given by the variance, expressed as: $(\Delta n)^2 = \sum_{n=0}^{\infty} (n-\overline{n})^2 P(n) = \overline{n^2} - \overline{n}^2$. It is possible to demonstrate that in the case of a thermal distribution the variance is given by the sum of two contributions, related respectively to the wave-like and the particle-like nature of the photon:

$$(\Delta n)^2 = \overline{n}^2 + \overline{n} > \overline{n} \tag{8}$$

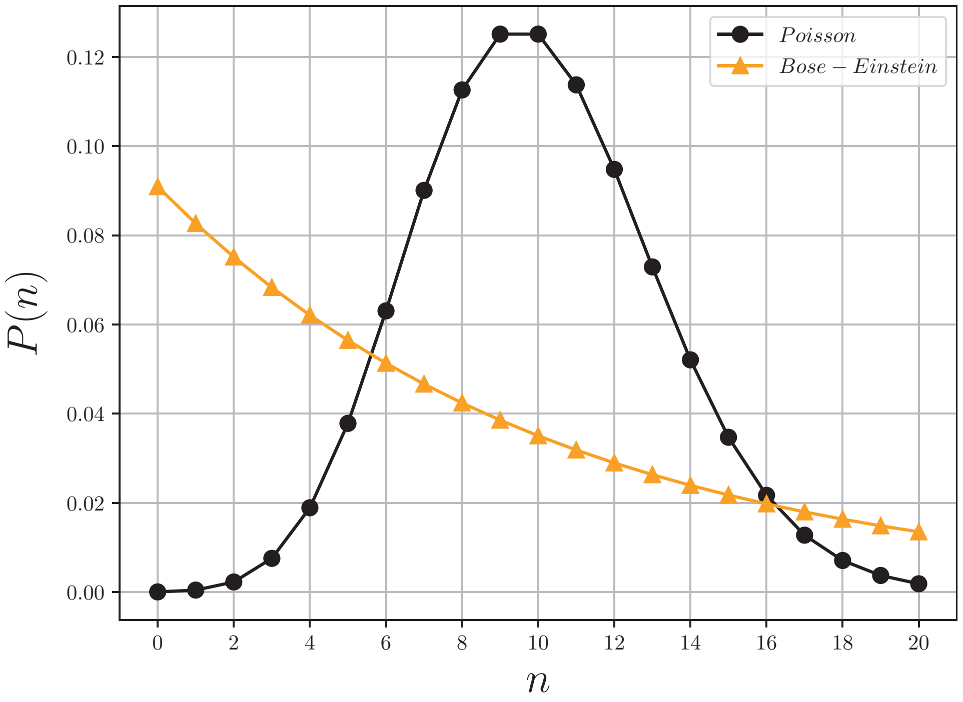

Fig. 1 Poisson and Bose-Einstein distributions ($\overline{n} = 10$).

This result gives direct evidence of the super-Poissonian nature of thermal light. Regarding the standard deviation, $\Delta n \to \overline{n}$ for $\overline{n} \gg 1$, moreover the fractional uncertainty in the number of photons, $\frac{\Delta n}{\overline{n}} = \sqrt{1 + \frac{1}{\overline{n}}} \to 1$ for increasing $\overline{n}$. Compared with the fractional uncertainty of a Poissonian light, these results clearly demonstrate the different behavior of super Poissonian light for many photons.

Chaotic light, produced by a common spectroscopic source, such as a gas discharge lamp, is a further example of super Poissonian light. The gas atoms present in the source are randomly excited by an electrical discharge and emit radiation on a single spectral line independently of one another.

The behavior of chaotic light can be investigated by looking at the time dependence of the amplitude or intensity of the light beam. It is known from spectroscopy that line broadening processes present in a source are responsible of the intensity fluctuations occurring around an average value on a timescale which is inversely proportional to the bandwidth of the spectrum. The temporal fluctuations and the frequency spectrum of light are complementary manifestations of the same physical properties of the light source. In the present case, the superposition of the emission of many independent atoms radiating with different phases and frequencies, is precisely responsible for the generation of the chaotic light.

We consider the classical model of a N-excited-atom source with emission linewidth broadened by collisions occurring at a rate $\gamma_{coll}[\sec^{-1}]$, e.g. with a coherence time $\tau_c = 1/\gamma_{coll}$. An example of the wave trains radiated by a single atom after each collision is shown in Fig. 2, where the electric field amplitude is schematically represented as a function of time.

The total electric field radiated by N identical atoms is expressed as:

$$E(t) = \sum E_i(t) = E_0\, exp\,(-i\omega_0 t)[\,exp\,(i\varphi_1(t)) + \,exp\,(i\varphi_2(t)) + \,\ldots + exp\,(i\varphi_N(t))] \tag{9}$$

where E_0 and ω_0 are the amplitude and the frequency of the field radiated by a single atom. Similarly, $\varphi_i(t)$, for $i = (1, 2, \ldots, N)$, corresponds to the random phase associated to the wave emitted by each atom. The average frequency spectrum (in the present case atom collisions determine a Lorentzian spectrum centered at ω_0) is obtained by the Fourier decomposition of $E(t)$. It is worth noting that collisions are not the only effect responsible of line broadening. A further mechanism is given by the Doppler effect which determines a Gaussian frequency broadening.

The beam intensity is proportional to $|E(t)|^2$. It is a random function of time, varying on a timescale of the order of the coherence time τ_c. The cycle-averaged intensity $I(t)$ is defined as the average of the intensity over an oscillation cycle at frequency ω_0. In many cases the corresponding fluctuations are too rapid to be detected, so that one can measure the average of the fluctuations over the response time of the detector. Fig. 3 shows the computer simulation of a typical temporal evolution of the cycle-averaged intensity for a chaotic light beam.

The average intensity $\overline{I}$ is the result of the ensemble average over many values of $I(t)$, measured over a period much longer than τ_c:

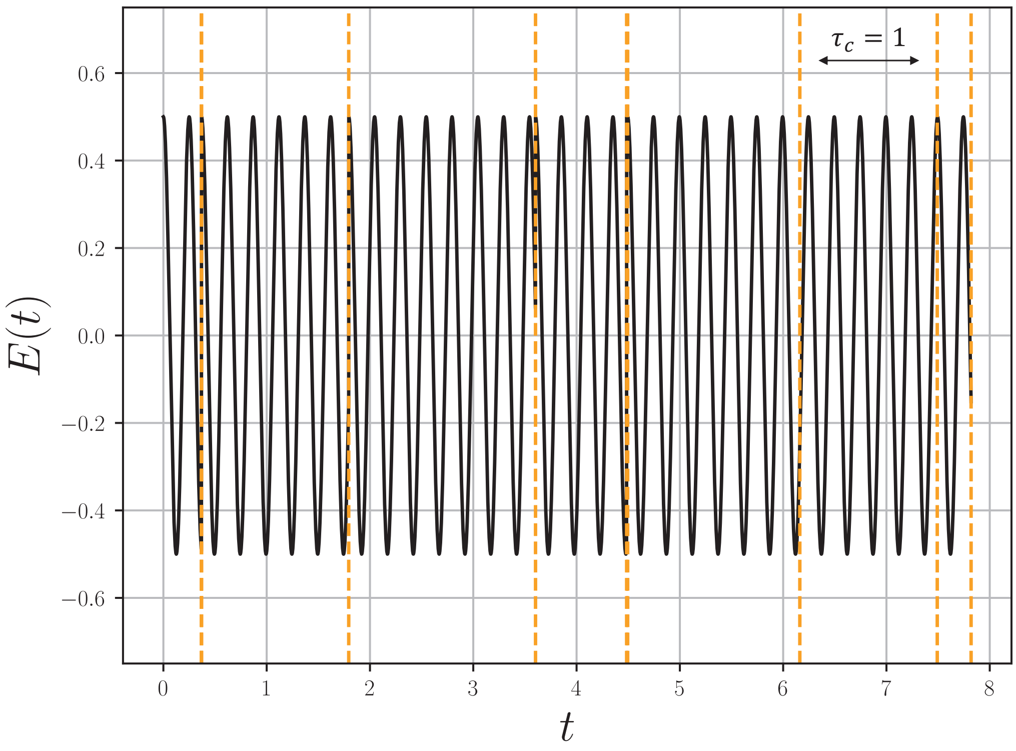

Fig. 2 Sequence of wave trains emitted for chaotic light.

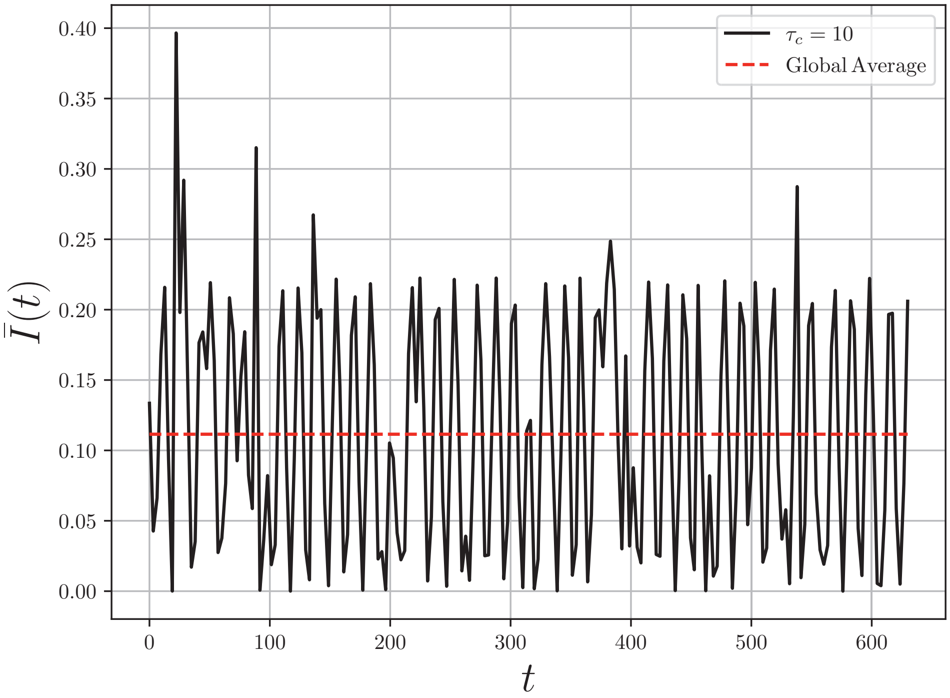

Fig. 3 Temporal evolution of chaotic light.

$$\bar{I} = \overline{I(t)} \propto \overline{|E(t)|^2} = E_0^2 \overline{|\, exp\,(i\varphi_1(t)) + \,\ldots + exp\,(i\varphi_N(t))|^2} = NE_0^2 \tag{10}$$

This result is a consequence of the zero average contribution of the cross-terms between the phase factors of different radiating atoms. The dashed line in Fig. 3 indicates the value of $\bar{I}$ corresponding to the fluctuating intensity.

We can calculate the mean value of $I(t)^2$ by the same procedure:

$$\overline{I(t)^2} \propto E_0^4 \overline{|\, exp\,(i\varphi_1(t)) + \,\ldots + exp\,(i\varphi_N(t))|^4} = E_0^4[N + 2N(N-1)] = \left(2 - \frac{1}{N}\right)\bar{I}^2 \tag{11}$$

Since the number N is very large ($N \gg 1$), we obtain: $\overline{I(t)^2} = 2\bar{I}^2$. It comes out the important result regarding the variance:

$$(\Delta I)^2 = \overline{I(t)^2} - \overline{I(t)}^2 = \bar{I}^2 \tag{12}$$

According to what we have found in the case of thermally excited photons within a single cavity mode for $\bar{n} \gg 1$, the size of fluctuations, given by the standard deviation ΔI, is equal to $\bar{I}$, confirming in this way the super-Poissonian behavior of the chaotic source.

Other examples of (quasi)thermal/(quasi)chaotic light have been studied in the years. As an example, we remember the source realized by passing a single mode cw laser light beam through a rotating ground-glass. The intensity fluctuation properties of this source are similar as the ones of true thermal light except for the large number of photons involved (much larger than 1) and for the coherence time that can be varied between 10^{-5}sec and 1 sec (Martienssen and Spiller, 1964).

A single-mode laser operating below threshold or a multi-mode laser exhibit in suitable conditions the characteristic behavior of a chaotic light.

It is worth underlining that the results described above in the case of chaotic light are valid only if the integration time of the intensity measurement is much shorter than the coherence time. If this is not the case, the measurement corresponds to an average operation performed over more than one fluctuation and the measured statistical behavior appears as a Poissonian one.

Nonclassical light – Sub Poissonian statistics and role of quantum detection efficiency

Entering in the region defined by the relation $\Delta n < \sqrt{n}$ i.e., going below the Poissonian statistics limit, corresponds to enter in the region of nonclassical photon states. Sub Poissonian statistics is indeed one of the signatures of the quantum nature of light.

A pure nonclassical state is given by a *photon number state* $|n>$ $(n = 1, 2, \ldots)$,provided by a stream of periodically spaced identical photons. The corresponding photon number distribution is:

$$P(n) = \delta(n, \overline{n}) \tag{13}$$

where $\delta = 1$ *for* $n = \overline{n}$ and $\overline{n}$ is an integer. In this peculiar condition the standard deviation vanishes, $\Delta n = 0$, since the number of photons is perfectly defined. Besides the pure state limit represented by (13), the sub Poissonian requirement $\Delta n < \sqrt{n}$ is satisfied even in the case of a non-constant time interval between photons, provided that the photon sequence is not completely random as for Poissonian light.

Quantum light has great importance in modern quantum optics because of its applications whenever transmission of signals through single photons is required, as in quantum communications and quantum computing. One could think to attain the single-photon regime by strongly attenuating a laser beam to ensure that the probability of having more than one photon becomes negligible. It is worth to point out that this method is poorly efficient because of the intrinsic Poissonian statistics that obliges to strongly increase the attenuation of the coherent beam to make negligible the events with 2 or more photons.

Heralded single photon sources based on spontaneous parametric down-conversion (Harris et al., 1967; U'Ren et al., 2005) have been so far widely adopted to generate single photons, however their main limitation resides on the probabilistic nature of the spontaneous emission process. More recently, a new generation of single photon sources, built on single quantum dots excited by a perfect sequence of femtosecond laser pulses and operating within optical microscopic cavities, have been demonstrated to generate single photons at high repetition rate, approaching in this way the model of a single-photon deterministic source (Senellart et al., 2017).

Other approaches to single photon generation have been demonstrated, among the others we remember the possibility of storing excitation in an atomic ensemble falling neutral atoms (Chou et al., 2004) and the use of defects in diamond nanocrystals (Kurtsiefer et al., 2000).

Single photon states are very fragile. Indeed, in the actual experimental conditions sub Poissonian statistics suffers both the optical losses of the experimental setup and the imperfect quantum efficiency of detectors. The two processes determine a random sampling of the photons; therefore, the quantum photon statistics tends to be degraded to the Poissonian one.

We have not considered up to now the quantum efficiency η of the detectors since we implicitly assumed to work with $\eta = 1$. We conclude this section by briefly examining the role played by photodetection statistics when $\eta = \frac{\overline{m}}{\overline{n}} \leq 1$, with $\overline{n}$ and $\overline{m}$ corresponding respectively to the average number of photons and of photoelectrons ejected by the photodetector.

The granular nature of light is also reflected in photon counting in optical devices, causing the presence of the so-called *shot noise* of the electric charges emitted by the detector. Shot noise is also called Poisson noise, since it can be modeled by a Poisson process. According to the semiclassical theory of optical photodetection, it is immediate to see that, in the case of a Poissonian coherent light the photocount statistical distribution is still Poissonian.

A Poissonian photocount distribution holds also for a light beam in which the intensity varies in time such as for chaotic light, provided that the integration time Δt of detection is much longer than the coherence time τ_c of the light. In this case the photocount variance is Poissonian, $(\Delta m)^2 = \overline{m}$. On the other hand, when $\Delta t \ll \tau_c$, the photocount distribution reproduces the one of a super Poissonian light, $(\Delta m)^2 = \overline{m} + \overline{m}^2$.

The semiclassical theory is not adequate to describe quantum light detection, thus a full quantum treatment of photodetection is necessary to understand how a detector operates with sub-Poissonian light and how much it is important to work with high efficiency photodetectors.

According to the quantum treatment of photodetection the relationship existing between $(\Delta m)^2$ and $(\Delta n)^2$ is given by:

$$(\Delta m)^2 = \eta^2 (\Delta n)^2 + \eta(1-\eta)\overline{n} \tag{14}$$

The analysis of (14) suggests the following conclusions:

1) For $\eta = 1$ it comes out that $\Delta m = \Delta n$, hence photon fluctuations are automatically transferred to photocount fluctuations.
2) In the case of a Poissonian light, $(\Delta n)^2 = \overline{n} \rightarrow (\Delta m)^2 = \eta\overline{n} \equiv \overline{m}$, for any value of η. We have in this case a Poissonian photocount statistics regardless the value of η.
3) For $\eta \ll 1 \Rightarrow (\Delta m)^2 = \eta\overline{n} \equiv \overline{m}$, regardless the incoming photon statistics.

We conclude that only a large value of quantum efficiency ($\eta \Rightarrow 1$) guarantees a faithful measurement of a sub-Poissonian photon statistic. An imperfect detector will randomize more and more the photoelectron stream and the measured statistics will fatally become Poissonian.

First order coherence

To deepen our understanding of optical fluctuations we need to introduce the concept of coherence in its various meanings both in classical and quantum optics. On the one hand the concept of coherence has been always associated with interference optical phenomena, on the other hand it is involved in the entire field of statistical optics and, more in general, in the quantum description of photon states. In its broadest sense, optical coherence theory deals with the statistical description of fluctuations, thus it can be said that optical coherence phenomena are manifestations of the correlations existing within them (Mandel and Wolf, 1965).

The first-order correlation function of the electric field at times t and $t + \tau$ is defined as

$$G^{(1)}(\tau) = \overline{E^*(t)E(t+\tau)} \tag{15}$$

It expresses how the value of the electric field at time $t+\tau$ is affected by the value at time t. It comes out that $G^{(1)}(0) = \overline{|E^*(t)E(t)|}^2 = \overline{I(t)} = I$ for $\tau = 0$. Furthermore, $G^{(1)}(-\tau) = G^{(1)*}(\tau)$, because of its Hermitian symmetry.

The degree of first-order temporal coherence, defined as

$$g^{(1)}(\tau) = \frac{G^{(1)}(\tau)}{G^{(1)}(0)} = \frac{\overline{E^*(t)E(t+\tau)}}{\overline{E^*(t)E(t)}} \tag{16}$$

is a complex function, independent of the intensity, with the properties: $g^{(1)}(-\tau) = g^{(1)*}(\tau)$ and $0 \leq |g^{(1)}(\tau)| \leq 1$. The value of $|g^{(1)}(\tau)|$ gives us a measure of the amount of correlation existing between $E(t)$ and $E(t+\tau)$.

In the ideal case of a monochromatic plane wave of amplitude E_0, $E(t) = E_0\, exp\,(-i\omega_0 t)$ the degree of first-order temporal coherence becomes

$$g^{(1)}(\tau) = exp\,(-i\omega_0 t) \tag{17}$$

and $|g^{(1)}(\tau)| = 1$, meaning that $E(t)$ and $E(t+\tau)$ are fully correlated whatever the value of τ. In the real case of a single mode coherent laser beam this result can be valid for large values of τ (up to nearly 3 msec for a single mode solid state laser).

For a chaotic collision-broadened light the correlation function of the whole light beam is obtained from the single-atom contribution,

$$\overline{E^*(t)E(t+\tau)} = NE_0^2\; exp\left(-i\omega_0 t - \frac{\tau}{\tau_c}\right) \tag{18}$$

Thus, the first-order coherence degree is:

$$g^{(1)}(\tau) = exp\left(-i\omega_0 t - \frac{|\tau|}{\tau_c}\right), \text{with modulus } |g^{(1)}(\tau)| = exp\left(-\frac{|\tau|}{\tau_c}\right) \tag{19}$$

Note that the exponential shape of $|g^{(1)}(\tau)|$ is consistent with the characteristic Lorentzian frequency spectrum holding for a line shape broadening due to collisions.

Insofar as other broadening effects are concerned, one can consider the case of chaotic light generated by atoms in a gas characterized by a spread in their velocities. The consequent Doppler broadening effect leads to a Gaussian distribution of the emission frequencies. In this case the degree of first-order coherence is

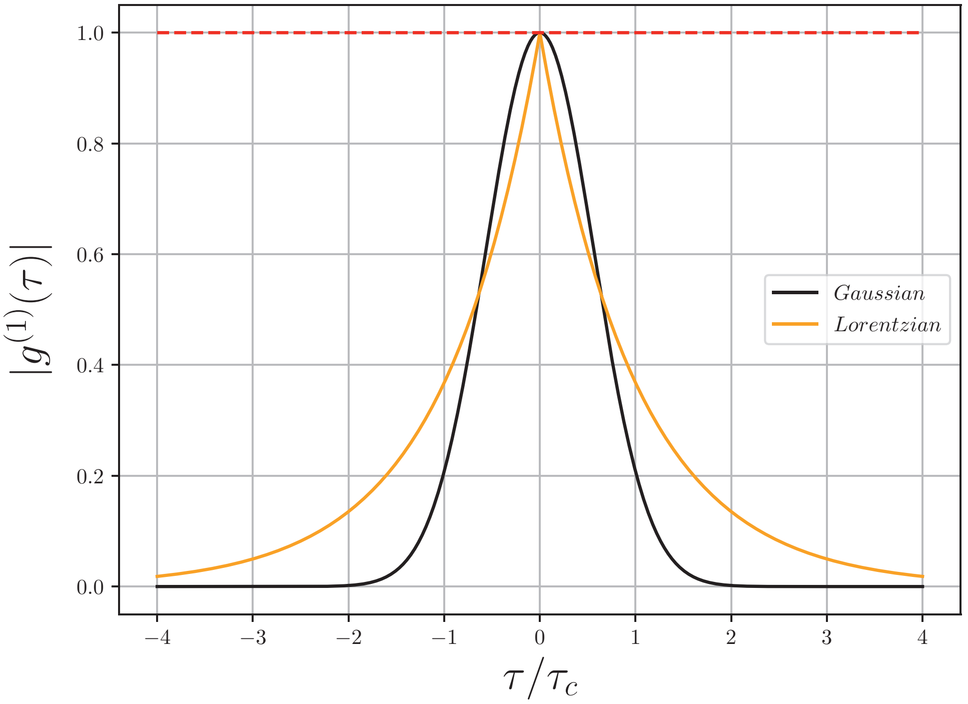

Fig. 4 Modulus of the first-order coherence degree expressed in function of the normalized time delay τ/τ_c for collision-broadened and Doppler-broadened chaotic light. The red dashed line corresponds to the case of coherent light.

$$g^{(1)}(\tau) = exp\left[-i\omega_0 t - \frac{\pi}{2}\left(\frac{\tau}{\tau_c}\right)^2\right], \text{with modulus } \left|g^{(1)}(\tau)\right| = exp\left[-\frac{\pi}{2}\left(\frac{\tau}{\tau_c}\right)^2\right] \tag{20}$$

where $\tau_c = \frac{\sqrt{\pi}}{\Delta}$ and Δ^2 corresponds to the variance of the Gaussian distribution.

Fig. 4 shows how $|g^{(1)}(\tau)|$ varies with τ for a partially coherent light in the two cases of collision and Doppler broadening. The dashed line $|g^{(1)}(\tau)| = 1$ corresponds to the case of a monochromatic coherent wave.

Light emitted from a partially coherent source is modeled as a sequence of random, uncorrelated wave packets, each one with a characteristic longitudinal coherence length $l_c = c\tau_c$. The values of the coherence times and the corresponding values of l_c are shown in Table 1 for different kinds of light sources. The case of a single-mode laser, whose coherence length is of the order of several hundreds of meters, represents the best approximation of a monochromatic plane wave with $l_c = \infty$, as said.

The same formalism adopted for temporal correlation can be used to investigate $g^{(1)}(r_1, r_2)$ in the case of two spatial points of the wavefront with coordinates $\boldsymbol{r}_1$ and $\boldsymbol{r}_2$,

$$g^{(1)}(r_1, r_2) = \frac{G^{(1)}(\boldsymbol{r}_1, \boldsymbol{r}_2)}{\sqrt{[I(\boldsymbol{r}_1)I(\boldsymbol{r}_2)]}} \tag{21}$$

By this expression, knowing $|g^{(1)}(r_1, r_2)|$ $(0 \leq |g^{(1)}(r_1, r_2)| \leq 1)$ it is possible to determine the radius of the transverse coherence area. In the ideal case of a coherent plane wave, $|g^{(1)}(\boldsymbol{r}_1, \boldsymbol{r}_2)| = 1$ whatever the distance $\boldsymbol{r}_1 - \boldsymbol{r}_2$. This is equivalent to say that the coherence area of a plane wave is infinitely large. In the general case, the first order coherence degree $g^{(1)}(\boldsymbol{r}_1 t_1, \boldsymbol{r}_2 t_2)$ is defined for any pair of space–time points.

The beam splitter (BS) is an essential tool, in classical and quantum optics, for the understanding of interference phenomena and for its profound implications with photon statistics. In the last section an overview on the fundamental role of BS in quantum optics is presented. For the moment it is sufficient to consider the BS as a semitransparent mirror with the following characteristics:

- reflection coefficient $r = |r|e^{i\varphi}$
- transmission coefficient $t = |t|e^{i\theta}$

We will consider in general a symmetric BS, having equal probability to reflect or transmit the light, $R = T = \frac{1}{2}$, being $R = |r|^2$ and $T = |t|^2$ the reflectivity and the transmittivity of the BS.

A Mach–Zehnder interferometer (MZI), composed of two symmetric BSs and two total reflecting mirrors (M), operating at 45 deg., is sketched in Fig. 5.

The light beam is incident on one of the two input ports of the first BS and is divided into two equal beams, with electric field $E_1(t)$ and $E_2(t)$, traveling through the two optical paths 1 and 2. The two beams meet in the second BS, where superposition and interference of the two electric fields occur, depending on the relative phase ϕ.

Table 1 Coherence times and coherence lengths of different light sources.

Source	*Coherence time* τ_c	*Coherence length* l_c
White light (400–700 nm)	3.6 fsec	1.08 μm
LED ($\lambda = 800$ nm, $\Delta\lambda = 50$ mn)	43 fsec	0.01 mm
Spectral lamp (Hg)	10 psec	3 mm
Multimode cw He—Ne laser ($\lambda = 633$ nm)	0.67 nsec	20 cm
Single mode Nd: YAG laser ($\lambda = 1064$ nm)	3 msec	900 m

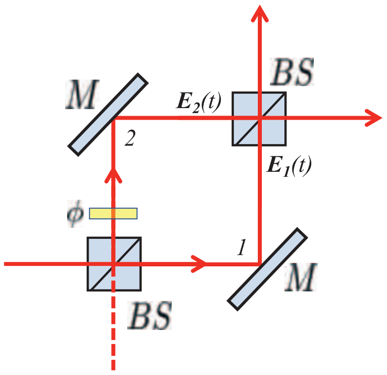

Fig. 5 The Mach Zehnder interferometer

By the above assumptions, one has $g_{12}^{(1)} = \frac{\overline{E_1^* E_2}}{\sqrt{I_1 I_2}}$. The average intensity corresponding to the two-wave superposition is:

$$I = \overline{|E_1 + E_2|^2} = I_1 + I_2 + 2\sqrt{I_1 I_2}\left|g_{12}^{(1)}\right| \cos\phi \tag{22}$$

Where ϕ is the phase of $g_{12}^{(1)}$. It can be suitably adjusted by varying, within half of the wavelength $\lambda = \frac{2\pi c}{\omega}$, the delay between the two optical paths. Optical interference arises exactly from the third term of the above expression, thus, from the value of the mutual correlation degree, $g_{12}^{(1)}$. Two important cases are considered, depending on the limit values of $g_{12}^{(1)}$:

$$\left|g_{12}^{(1)}\right| = 1 \text{ (coherent waves)} \Rightarrow I = I_1 + I_2 + 2\sqrt{I_1 I_2}\cos\phi \tag{23}$$

$$\left|g_{12}^{(1)}\right| = 0 \text{ (incoherent waves)} \Rightarrow I = I_1 + I_2 \tag{24}$$

In the general case of partially coherent waves, $0 \leq |g_{12}^{(1)}| \leq 1$, the intensity I is a sinusoidal function of ϕ; the larger the $|g_{12}^{(1)}|$, the larger the amplitude of the oscillation. In this case, measuring the interference strength as a function of the optical path delay, all the necessary information about the temporal or spatial behavior of the correlation degree, such as the temporal coherence length or the transverse coherence radius of the light beam, are obtained. One can express the modulation depth by the visibility parameter

$$V = \frac{I_M - I_m}{I_M + I_m} = 2\frac{\sqrt{I_1 I_2}}{I_1 + I_2}\left|g_{12}^{(1)}\right| \tag{25}$$

where I_M and I_m are the maximum and the minimum of light intensity corresponding to $\phi = 0$ and $\phi = \pi$, respectively. In a symmetric interferometer ($I_1 = I_2$), $V = |g_{12}^{(1)}|$. For $|g_{12}^{(1)}| = 1$ we have $I_M = 4I$ and $I_m = 0$. It is worth to remember once more that the results given from (22) to (25) holds for both Poissonian and single-mode super Poissonian light. Regarding first-order coherence phenomena, there is no way to distinguish between the different statistical distributions of a single mode laser and a chaotic light source.

The description of first order coherence given so far, based on classical wave theory, allows to explain any kind of interference phenomena. In fact, there is no way to recognize different behaviors between classical and nonclassical light at the level of first-order interference phenomena. In quantum optics, where a single mode quantum photon state is equivalent to a n-level quantum harmonic oscillator, the general expression of a single mode scalar electric field operator is:

$$\widehat{E}(\chi) = \widehat{E}^{+}(\chi) + \widehat{E}^{-}(\chi) = \frac{1}{2}\widehat{a}e^{-i\chi} + \frac{1}{2}\widehat{a}^{\dagger}e^{i\chi} \tag{26}$$

where $\widehat{E}^{+}(\chi)$ and $\widehat{E}^{-}(\chi)$ are the positive and negative frequency parts of the electric field operator and $\chi = \omega_0 t - kz - \frac{\pi}{2}$ corresponds to the phase angle of the optical field propagating with wavevector $\boldsymbol{k}$ along the direction z. In (26) $\widehat{a}^{\dagger}$ and $\widehat{a}$ are the creation and destruction operators for the harmonic oscillator. Writing the expression of the first order correlation function for two fields $\widehat{E}(\chi_1)$ and $\widehat{E}(\chi_2)$, having different phase angles, e.g. with $|\chi_1 - \chi_2| = \omega_0\tau$, it is immediate to verify that $g^{(1)}(\chi_1;\chi_2) = g^{(1)}(\tau) = \exp(i\omega_0\tau)$ (Glauber, 1963).

These simple passages demonstrate that the quantum description of first order coherence returns the same results obtained by classical theory, therefore no difference exists between classical and quantum predictions at the level of first order interference phenomena.

In the next paragraph, we will see that this is possible within the context of second order coherence.

Second order coherence

As done for first-order coherence, consider two temporal measurements in which many pairs of samples of the cycle-averaged intensity are measured at a fixed delay τ. The classical definition of the intensity correlation function, valid either for chaotic or coherent light, corresponds to the average of the products of each pair of samples:

$$G^{(2)}(\tau) = \overline{I(t)I(t+\tau)} = \overline{E^*(t)E^*(t+\tau)E(t+\tau)E(t)} \tag{27}$$

The correlation function $G^{(2)}(\tau)$ can be normalized to the square of the long-time-averaged intensity $\overline{I(t)}$ given in (10) to obtain the degree of second-order temporal coherence:

$$g^{(2)}(\tau) = \frac{\overline{I(t)I(t+\tau)}}{\overline{I(t)}^2} = \frac{\overline{E^*(t)E^*(t+\tau)E(t+\tau)E(t)}}{\overline{E^*(t)E(t)}^2} \tag{28}$$

Because of symmetry properties, $g^{(2)}(\tau) = g^{(2)}(-\tau)$. Furthermore, the following inequalities can be demonstrated:

$$1 \leq g^{(2)}(0) \leq \infty 0 \leq g^{(2)}(\tau) \leq \infty g^{(2)}(\tau) \leq g^{(2)}(0) \tag{29}$$

For a large number N of radiating atoms, it is possible to obtain $g^{(2)}(\tau) = 1 + |g^{(1)}(\tau)|^2$. Thus, in the two cases of collision and Doppler broadening, we can write, respectively:

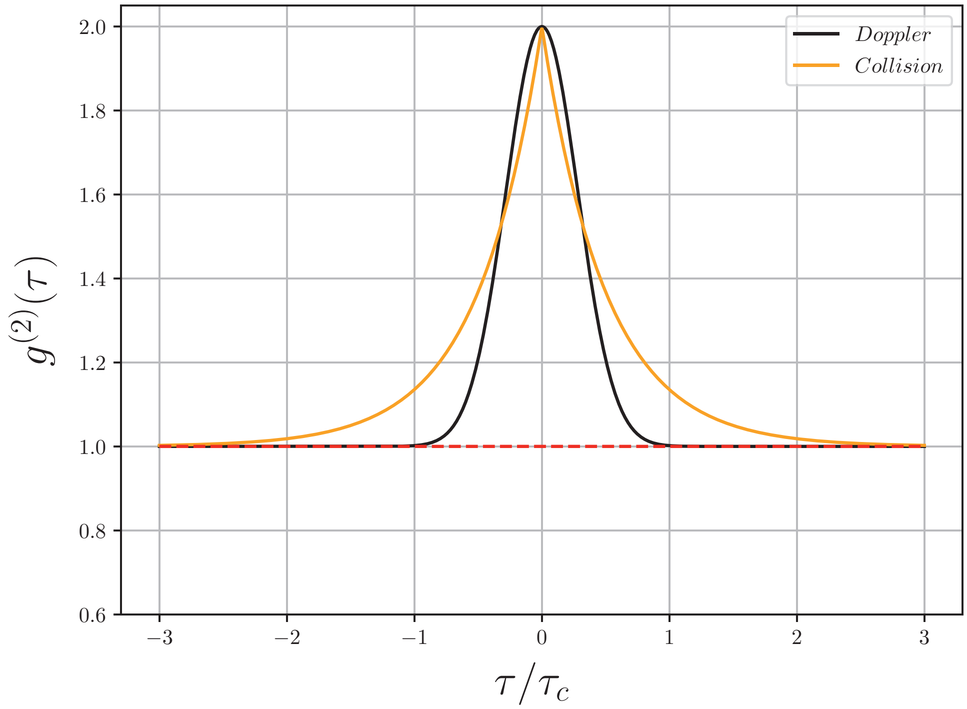

Fig. 6 Second-order coherence degree expressed in function of the normalized time delay τ/τ_c for collision-broadened and Doppler-broadened chaotic light. The red dashed line corresponds to the case of coherent light.

$$g^{(2)}(\tau) = 1 + exp\left(-2\frac{|\tau|}{\tau_c}\right) g^{(2)}(\tau) = 1 + exp\left[-2\pi\left(\frac{\tau}{\tau_c}\right)^2\right] \tag{30}$$

It comes out that, for both cases, $g^{(2)}(0) = 2$ and $g^{(2)}(\tau \gg \tau_c) = 1$.

Fig. 6 shows the behavior of $g^{(2)}(\tau)$ of both the models of chaotic light having Lorentzian and Gaussian frequency distribution. Starting from $g^{(2)}(0) = 2$ at zero-time delay, the intensities $I(t)$ and $I(t+\tau)$ become more and more uncorrelated by increasing τ, therefore $g^{(2)}(\tau) \to 1$. At variance with chaotic light, for a classical stable wave, $g^{(2)}(\tau) = 1$ for any value of τ. This case is represented by the horizontal dashed line in the same Figure (Arecchi, 1965).

Similarly with the case of first-order coherence, the definition of the second-order coherence degree can be generalized to the spatial case,

$$g^{(2)}(\mathbf{r}_1, \mathbf{r}_2) = \frac{\overline{E^*(\mathbf{r}_1)E^*(\mathbf{r}_2)E(\mathbf{r}_2)E(\mathbf{r}_1)}}{\overline{|E(\mathbf{r}_1)|^2}\ \overline{|E(\mathbf{r}_2)|^2}} \tag{31}$$

and more in general, $g^{(2)}(\mathbf{r}_1, t_1; \mathbf{r}_2, t_2)$ can be defined for any pair of space–time points.

One of the main features of the degree of second-order coherence measurement consists of the possibility of distinguishing between classical and nonclassical radiation. So far, the main aspects of optical coherence have been analyzed in terms of the classical wave theory of light. The particle aspect of light is considered whenever it is possible to count photons (or rather, the photoelectrons ejected from a photoemissive surface by the absorption of photons).

Let's consider a single mode nonclassical photon state $|n>$, equivalent to a n-level quantum harmonic oscillator. For the creation and destruction operators $\hat{a}^\dagger$ and $\hat{a}$ the following equations hold:

$$\hat{a}^\dagger\Big|n > \sqrt{n+1}\Big|n+1 > \hat{a}\big|n >= \sqrt{n}\big|n - 1 > \tag{32}$$

where n is the number of photons belonging to the state $|n>$ with $\hat{n}|n >= n|n >$. According to the expression of a single mode electric field given in (26), we can express the mutual degree of second order coherence of two fields, $\hat{E}(\chi_1)$ and $\hat{E}(\chi_2)$ in terms of the operators $\hat{a}^\dagger$ and $\hat{a}$

$$g^{(2)}(\tau) = g^{(2)}(\chi_1; \chi_2) = \frac{\overline{\hat{a}^\dagger\hat{a}^\dagger\hat{a}\hat{a}}}{\overline{\hat{a}^\dagger\hat{a}}^2} \tag{33}$$

It is worth noting that, similarly with the first order coherence function, the expression of $g^{(2)}(\tau)$ doesn't depend on the spatial and temporal coordinates. On the other hand, we have seen for classical light that, at variance with $g^{(1)}(\tau)$, $g^{(2)}(\tau)$ is strictly dependent on the nature of light. With $\hat{a}^\dagger\hat{a} = \hat{n}$ corresponding to the photon number operator and considering that the commutator of the creation and destruction operators is $\left[\hat{a}, \hat{a}^\dagger\right] = \hat{a}\hat{a}^\dagger - \hat{a}^\dagger\hat{a} = 1$, we are able to obtain a new expression of $g^{(2)}(\tau)$ in terms of the average and average square number of photons of the field:

$$g^{(2)}(\tau) = \frac{\overline{n(n-1)}}{\bar{n}^2} = \frac{\overline{n^2} - \bar{n}}{\bar{n}^2} \tag{34}$$

This expression of $g^{(2)}(\tau)$ can be explained as follows: the probability of counting a photon is proportional to the number of photons n in the field. Since the number of photons available in a second measurement is reduced by one unit, the probability of counting a second photon is proportional to $n - 1$, therefore the two-photon counting probability is proportional to $\overline{n(n-1)} = \overline{n^2} - \bar{n}$. Note that this expression of $g^{(2)}(\tau)$ is completely independent of τ, thus we can write $g^{(2)}(\tau) = g^{(2)}(0)$.

Considering the general expression of the photon number variance $(\Delta n)^2 = \overline{n^2} - \bar{n}^2$, we may express the second order coherence degree in terms of the photon number variance:

$$g^{(2)}(0) = \frac{(\Delta n)^2 + \bar{n}^2 - \bar{n}}{\bar{n}^2} = 1 + \frac{(\Delta n)^2 - \bar{n}}{\bar{n}^2} \tag{35}$$

We already know that the variance of a pure $|n>$ state, $(n = \bar{n} = 1, 2, \ldots)$ vanishes, therefore

$$g^{(2)}(0) = 1 - \frac{\bar{n}}{\bar{n}^2} = 1 - \frac{1}{\bar{n}} \tag{36}$$

obtaining $g^{(2)}(0) = 0$ in the case $n = \bar{n} = 1$.

More in general, since $(\Delta n)^2 \geq 0$, it must be $\overline{n^2} \geq \bar{n}^2$ and the following inequality holds for photon number states:

$$g^{(2)}(0) \geq 1 - \frac{1}{\bar{n}} \ (\bar{n} \geq 1) \tag{37}$$

The approach based on the particle aspect of light accounts for the occurrence of the same values of the degrees of second order coherence of the other photon number distributions, already examined in the frame of classical wave theory. By referring to (35) the corresponding results are the following:

- Chaotic light (super-Poissonian statistics): $\Delta n^2 = \bar{n}^2 + \bar{n} \Rightarrow g^{(2)}(0) = 2$; $g^{(2)}(\infty) = 1$ (either collision or Doppler broadened)
- Coherent light (Poissonian statistics): $\Delta n^2 = \bar{n} \Rightarrow g^{(2)}(\tau) = 1$ (whatever the value of τ)
- Nonclassical light (sub Poissonian statistics): $\Delta n^2 \leq \bar{n} \Rightarrow 1 - \frac{1}{\bar{n}} \leq g^{(2)}(0) \leq 1$

These results are summarized in Fig. 7, where the degree of second order coherence, expressed as a function of $\bar{n}$ is reported for chaotic, coherent and photon number nonclassical light. Nonclassical states corresponding to the inequality: $1 - \frac{1}{\bar{n}} \leq g^{(2)}(0) < 1$ are identified by the gray region in Fig. 7 and the pure number states $|n>$ are given by the yellow dots in the same Figure.

In the same figure we also show the behavior of the degree of second order coherence $g^{(2)}(0) = 3 + \frac{1}{\bar{n}}$ of the *squeezed vacuum state* whose variance is $(\Delta n)^2 = 2\bar{n}(\bar{n} + 1)$. Squeezed states of light are another example of light which noise can be below the limits set by quantum mechanics. The photon-number fluctuations in squeezed vacuum state light are thus classified as super Poissonian.

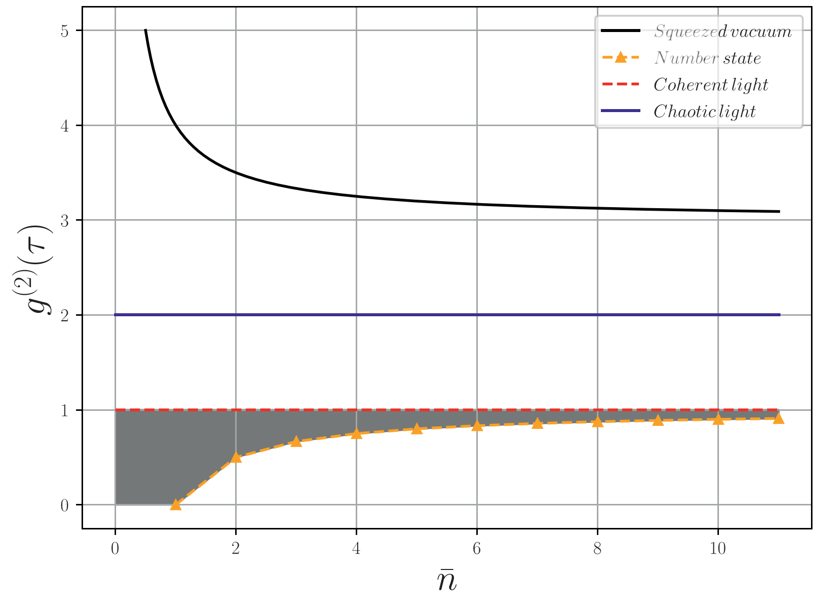

Fig. 7 Degree of second-order coherence expressed as a function of $\bar{n}$ for different kinds of light states.

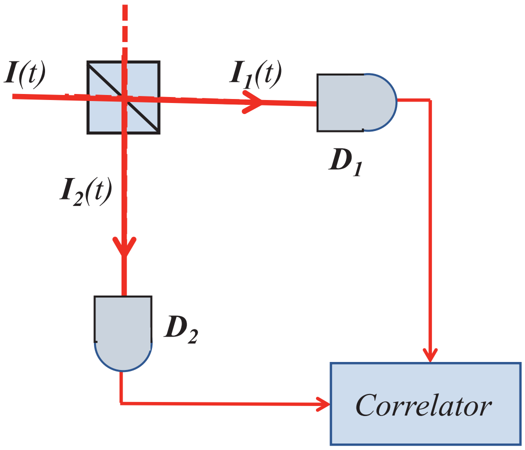

Fig. 8 Hanbury Brown-Twiss apparatus.

Brown-Twiss correlations – Photon bunching and photon antibunching

The measurements of the second order coherence degree are based on the original experimental apparatus invented by Hanbury Brown and Twiss (HBT) for stellar interferometry purposes. Indeed, the original HBT experiment (Hanbury Brown and Twiss, 1956) was carried out to measure the angular diameter of stars by the observation of spatial coherence effects. The corresponding setup is schematically illustrated in Fig. 8.

Quasi-monochromatic radiation, properly selected in the single spatial mode, is impinging on a symmetric BS, so that half of the original intensity $I_1(t)$, is directed toward detector D_1, the other half, $I_2(t)$, goes toward detector D_2. The two output currents, i_1 and i_2, are directly proportional to the intensities $I_1(t)$ and $I_2(t)$,replicating the fluctuations of the optical signal. The output detector signals are used to determine, by means of a correlator, the average of the product of $I_1(t)$ and $I_2(t+\tau)$, with the variable delay τ setted through an electronic time delay generator. This operation allows to measure the correlation of intensity fluctuations. By assuming a stationary field, $\overline{I_1(t)} = \overline{I_2(t+\tau)}$, and detectors with instantaneous response time, in the hypothesis for both detectors of a null optical delay with respect the BS, we have:

$$g_{12}^{(2)}(\tau) = \frac{\overline{I_1(t) I_2(t+\tau)}}{\overline{I_1(t)}\,\overline{I_2(t)}} = \frac{\overline{I(t) I(t+\tau)}}{\overline{I(t)}^2} \tag{38}$$

By this scheme, any measurement affected by temporal or spatial coherence of the light can be performed since the correlation measurements between $i_1$and i_2 allow to evaluate in general the second order coherence function $g_{12}^{(2)}(\mathbf{r}_1, t_1; \mathbf{r}_2, t_2)$.

By considering the light beam impinging on the BS as a stream of photons $g_{12}^{(2)}(\tau)$ is expressed in terms of the number of counts registered in D_1 and D_2, namely $m_1$and m_2:

$$g_{12}^{(2)}(\tau) = \frac{\overline{m_1(t) m_2(t+\tau)}}{\overline{m_1(t)}\,\overline{m_2(t)}} \tag{39}$$

This expression corresponds to the number of simultaneous counts registered as a function of τ in a certain temporal window, normalized to the product of the average number of counts in the two detectors. Thus, in the photon interpretation of light the average number of the measured coincidences becomes relevant rather than the correlation of the intensities.

An alternative way to measure the second order statistical properties of a light is also used, namely the Mandel Q-parameter:

$$Q = \frac{(\Delta n)^2 - \bar{n}}{\bar{n}} = \frac{\overline{n(n-1)} - \bar{n}^2}{\bar{n}} = \bar{n}\left[g^{(2)}(0) - 1\right] \tag{40}$$

It comes out that nonclassical states lie within the region $-1 \leq Q < 0$, coherent light and chaotic light are identified by the values $Q = 0$ and $Q = \bar{n}$, respectively.

We are now able to understand what happens when a stream of photons impinges on the BS. While in the intensity classical picture given in (27) the intensity splits in half on the BS whatever its value, in the particle picture there is a 50% probability that each photon is reflected or transmitted by the BS and goes toward a detector or the other (Grangier et al., 1986). In case it is separated in time from the other photons the probability of simultaneous coincidences at $\tau = 0$ vanishes and grows for $|\tau| \neq 0$. This result, a signature of the quantum nature of light, corresponds to the so-called *photon antibunching*.

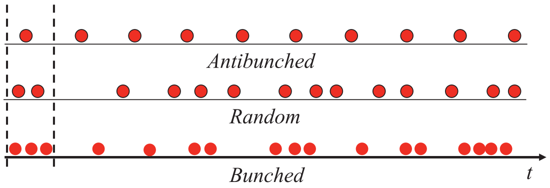

Fig. 9 Sequence of photons for: antibunched, random and bunched light.

Let's now consider the case of bunches of photons in the photonic stream. This determines a higher probability of coincidences at short delays with respect to what happens for larger values of τ. This case, corresponding to the so-called *photon bunching*, is just the translation into quantum language of the kind of intensity fluctuations occurring in the classical description of chaotic light.

Coherent light corresponds to the case of a *random* temporal sequence of photons. In the classical picture it has no intensity fluctuations, thus no photon bunches are expected in the quantum picture. The average number of coincidences is constant with τ.

The three cases are shown in Fig. 9.

Photon bunching and photon antibunching represent a further way to classify the different kinds of light. Sub-Poissonian photon statistics and photon antibunching are genuine quantum feature with no classical analog. They appear frequently together in nonclassical light and could be interpreted as different manifestations of the same quantum phenomenon. This is not the case; in fact, it has been demonstrated that sub Poissonian statistics doesn't necessarily imply photon antibunching but can be accompanied in some case by photon bunching (Zou and Mandel, 1990). In general, they must be considered as distinct phenomena.

Basic photon statistics at beam splitters

The optical beam splitter is an essential tool present in many experiments in which the ambivalent nature of light, wave, or stream of particles, is manifested.

In this section a few examples are discussed, regarding situations in which one or more photons are incident in the input ports of a BS or a combination of more BSs. Depending on the initial conditions the output solutions are classical or genuinely quantum.

In the classical wave description of first order interference, the meaning of BS is very simple, while things are expected to be more complex when the quantum statistical behavior of photons is considered. In the language of quantum optics, the lossless BS is treated as a *unitary operator* in which the phases of the transmission and reflection coefficients are $\theta = 0$ and $\varphi = \frac{\pi}{2}$. A few situations are below examined (Weihs and Zeilinger, 2001).

a) Stream of equally spaced single photons incident on a beam splitter from the same input port

Let's consider a sequence of equally spaced identical photons shining on the input mode *a* of a symmetric and lossless BS, while no photon is impinging on the other input arm *b* (see Fig. 10). In the quantum language, we may write:

$$\hat{a}^{\dagger}|0>_a = |1>_a \rightarrow \frac{1}{\sqrt{2}}[|1>_c|0>_d + i|0>_c|1>_d] \tag{41}$$

where the factor i accounts for the phase shift $\frac{\pi}{2}$ gained by the field from the reflection on the BS. The expression given in (41) is equivalent to say that the output state is a *superposition state* of the single photon in modes *c* and *d*, similarly the vacuum state $|0>$ in the input mode *b* is divided with equal probability in modes *c* and *d*. Since for each photon the probability of being transmitted or reflected is 50% two random sequences of photons can be registered in the two BS output modes. The noise introduced by the beam splitter in the output modes *c* and *d* is called *partition noise*. As an equivalent point of view the added noise is coming from the vacuum state $|0>$ incoming in the input mode *b* of the BS.

b) Stream of single photons incident on an input port of a Mach-Zehnder interferometer

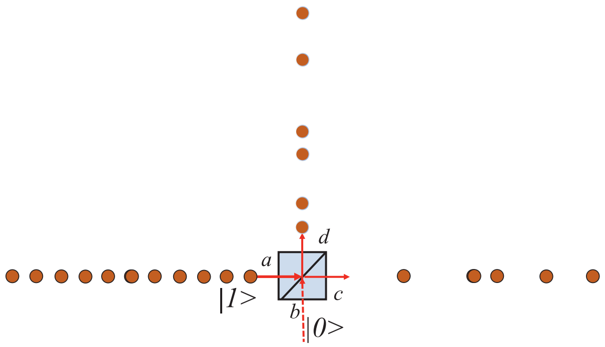

Fig. 10 Single photon partition due to the BS introduces random noise in the output photon streams.

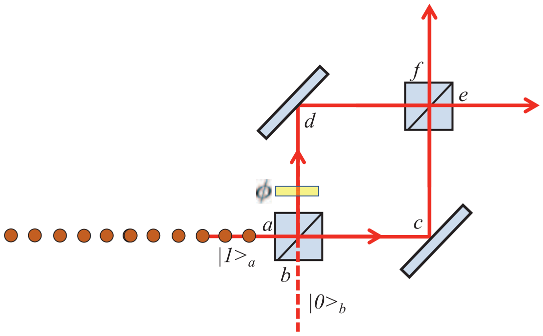

Fig. 11 Single photons incident on a Mach Zehnder interferometer.

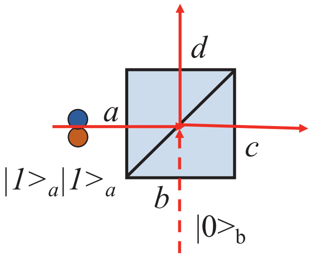

Fig. 12 Two photons shining a BS from the same input port.

Regarding this case (see Fig. 11), we have:

$$\hat{a}^{\dagger}|0>_a = |1>_a \rightarrow \frac{1}{\sqrt{2}}\left[|1>_c|0>_d + ie^{i\phi}|0>_c|1>_d\right] \rightarrow \frac{1}{2}\left[0>_e|1>_f| + i|1>_e|0>_f + ie^{i\phi}|1>_e|0>_f - e^{i\phi}|0>_e|1>_f\right]$$
$$= \frac{1}{2}\left[|0>_e|1>_f\left(1 - e^{i\phi}\right) + i|1>_e|0>_f\left(1 + e^{i\phi}\right)\right] \tag{42}$$

It's easy to obtain that the probabilities to find the photon in the output modes *e* or *f* are:

$$p_e = cos^2\frac{\phi}{2}\ p_f = sin^2\frac{\phi}{2} \tag{43}$$

This result demonstrates once more the presence of interference fringes in the output modes 5 e 6 even at the single photon level, as with a classical light beam.

The number of photons is maximized in either one of the two output modes for $\phi = n\pi$ $(n = 0, 1, 2\ldots)$, depending on the parity of n. In these cases, the noise introduced by the MZI vanishes while it is maximized in both the output modes *e* and *f* for $\phi = (2n+1)\frac{\pi}{2}, (n = 0, 1, 2\ldots)$.

c) Two independent photons incident on a beam splitter from the same input port

The case of two independent particles, shining the same input port of a BS (see Fig. 12), is quite simple to study. Considering the input state and its evolution through the BS we find:

$$|1>_a|1>_b \rightarrow \frac{1}{2}(|1>_c|0>_d + i|0>_c|1>_d)(|1>_c|0>_d + i|0>_c|1>_d) \tag{44}$$

It's easy to find from (44) that the partition probabilities of the two particles at the output of the BS follow the rules of the classical binomial distribution:

both photons on mode 3: $p = 0.25$.
both photons on mode 4: $p = 0.25$
one photon each in modes 3 and 4: $p = 0.50$

Even in this case the BS adds new random noise to the system.

d) Two independent photons incident on a beam splitter in a superposition of input ports

In this case (depicted in Fig. 13) the input state is expressed as a coherent superposition of two possible events:

$$\frac{1}{\sqrt{2}}\left(|1>_a|1>_a + e^{i2\phi}|1>_b|1>_b\right) \tag{45}$$

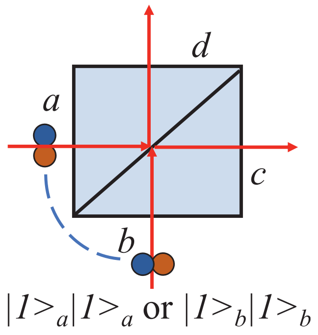

Fig. 13 Two photons enter together in either one of the input ports of BS.

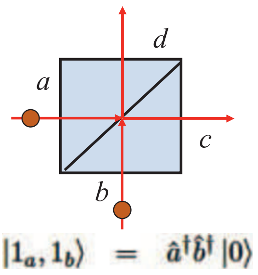

Fig. 14 two indistinguishable photons, one in each input port of the BS.

Considering the evolution for each photon entering through mode *a* or *b* toward the output modes *c* and *d*, it is easy to find that the output state is a function of the global phase, thus the following possibilities are expected:

- two photons in the same output mode *c*, or *d*. In this case the noise is the same that they have in the input mode, *a* or *b*.
- one photon in mode *c* and the other in mode *d*, or viceversa, with suppression of noise in both cases.

e) Two indistinguishable photons incident on the BS, one from port a and one from port b

In the case of Fig. 14 two *indistinguishable* particles are incident on a symmetric BS ($r = t$) from the ports *a* and *b*.

The concept of indistinguishability means that, *in principle*, it is *impossible* to know where each particle is coming from when they arrive on the BS. This condition is guaranteed if the two photons are *identical* in terms of frequency, bandwidth, $\boldsymbol{k}$ vector, polarization, and arrival time. The transformation of the input field in the BS is expressed as:

$$\widehat{a}^{\dagger}\widehat{b}^{\dagger}\Big|0>=\Big|1_{a},1_{b}>\rightarrow\frac{1}{2}\left(c^{\dagger}+id^{\dagger}\right)\left(ic^{\dagger}+d^{\dagger}\right)\Big|0>=\frac{i}{2}\left[\left(c^{\dagger}\right)^{2}+\left(d^{\dagger}\right)^{2}\right]\Big|0>=\frac{1}{2}\left[|2_{c}>|0_{d}>+|0_{c}>|2_{d}>\right] \tag{46}$$

The output state given in (46) is the result of a cancelation of the $c^{\dagger}d^{\dagger}$ and the $-d^{\dagger}c^{\dagger}$ terms and can be considered as an entangled state, corresponding to a coherent superposition of having 2 photons in the output port *c* and 0 photon in the output port *d*, or 0 photons in *c* and 2 photons in *d*. The state given in (46) has great relevance for *quantum metrology*.

The complete absence of photon coincidences between *c* and *d* is the signature of a radical change of the BS partition, from the classical binomial to the quantum Bose-Einstein statistics. This is the essence of the fundamental Hong-Ou-Mandel experiment (Hong et al., 1987), an effect without any classical analog.

Since the photons are not perfectly monochromatic, the temporal region in which a coincidence dip is registered corresponds to the photon wave-packet, as shown In Fig. 15. In ideal conditions, coincidences vanish, with a consequent visibility of 100% for a temporal delay $\Delta t = 0$, i.e. when the two photon wave-packets are coincident. Note that, due to the Poissonian distribution, the theoretical limit for the Hong-Ou-Mandel visibility is 50% for indistinguishable weak coherent photon states (Kim et al., 2020).

More in general, considering the BS as a device able to perform a symmetric partition of two indistinguishable input particles, the input state can be expressed in terms of a superposition of the equally possible events $|1_a, 1_b>$ and $|1_b, 1_a>$. It has the form of a symmetric state in the case of two incident bosons:

$$\frac{1}{\sqrt{2}}\left[|1_{a},1_{b}>+|1_{b},1_{a}>\right] \tag{47}$$

or of an antisymmetric state in the case of two incident fermions

$$\frac{1}{\sqrt{2}}\left[|1_{a},1_{b}>-|1_{b},1_{a}>\right] \tag{48}$$

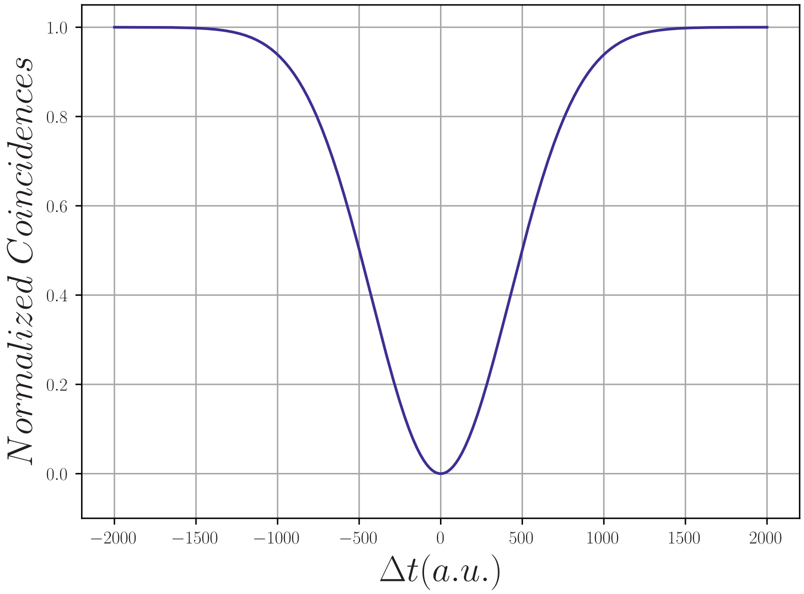

Fig. 15 Coincidence dip registered in a Hong-Ou-Mandel experiment.

Here we use the (+) or the (−) sign depending on the symmetric or antisymmetric nature of the state upon interchange of the particles.

The states corresponding to the output ports of the BS are:

$$\frac{1}{\sqrt{2}}[|1_c, 1_c > + |1_d, 1_d >] \tag{49}$$

for two incident bosons, and:

$$\frac{1}{\sqrt{2}}[|1_c, 1_d > -|1_d, 1_c >] \tag{50}$$

which is equivalent to the case of two incident fermions.

The result shown in (49) is equivalent to the one given in (46). Photons are bosons, therefore in the Hong-Ou-Mandel experiment the two input photons occupy the same output port, c or d (*bosonic coalescence*). The opposite would happen in the case of two fermions, that, following the Fermi-Dirac statistics, occupy separately the output ports c and d in agreement with the Pauli exclusion principle. In this case, as shown in (50), we expect a peak of coincidences instead of a dip. This effect can be simulated by a polarization entangled state of two photons, expressed as:

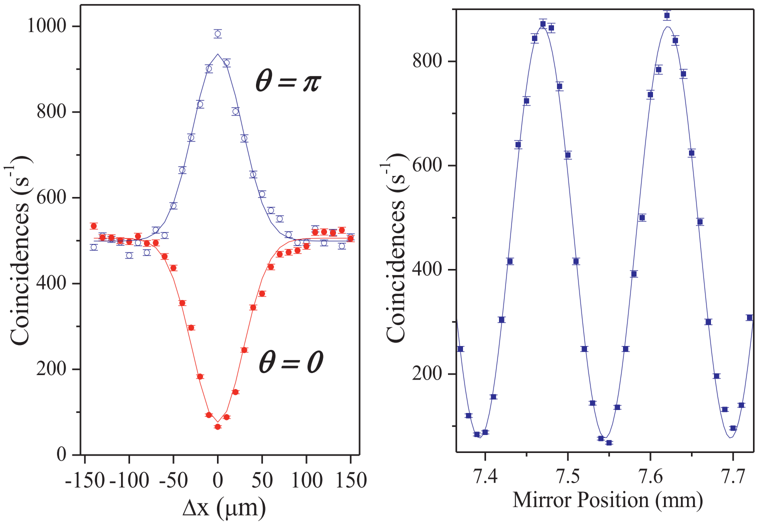

Fig. 16 Dip-peak (triplet-singlet) transition occurring in a 2-photon polarization entangled state.

$$\psi = \frac{1}{\sqrt{2}}\left[\left(\left|H_a, V_b > +e^{i\theta}\right|H_b, V_a >\right)\right] \tag{51}$$

This state allows to simulate the behavior of two bosons for $\theta = 0$ (symmetric triplet state) or two fermions for $\theta = \pi$ (antisymmetric singlet state). An experimental example of this simulation is shown in Fig. 16 where the dip-peak transition ($\theta = 0 \rightarrow \theta = \pi$) for the entangled state (51) is reported (Barbieri et al., 2005).

In this section we have presented some of the possible examples that can occur when one or more particles are incident on a beam splitter. Some of these results open the way to the understanding of some of the modern quantum information protocols.

Conclusion

Aim of this chapter was to investigate optical fluctuations to understand the intimal properties of light in its various manifestations, both classical and quantum. We have carried out this study by analyzing first the different statistical distributions governing the behavior of light and discussing how a non-perfect detection of photons may affect the statistics of the photonic beam.

To quantify the statistical properties of the different kinds of light we have introduced the basic elements of the coherence theory, at the first and second order, examined both in the classical and quantum contexts.

The behavior of light has been also classified in terms of the concept of bunching and antibunching. The properties of the beam splitter and its fundamental role in the statistics of photonic beams have been finally discussed.

References

Arecchi FT (1965) Measurement of the statistical distribution of Gaussian and laser sources. *Physical Review Letters* 15: 912–915.

Barbieri M, Cinelli C, Mataloni P, and De Martini F (2005) Polarization-momentum hyperentangled states: Realization and characterization. *Physical Review A* 72: 0521101–0521108.

Chou CW, Polyakov SV, Kuzmich A, and Kimble HJ (2004) Single photon generation from stored excitation in an atomic ensemble. *Physical Review Letters* 92: 2136011–2136014.

Glauber RJ (1963) The quantum theory of optical coherence. *Physics Review* 130: 2523–2539.

Grangier P, Roger G, and Aspect A (1986) Experimental evidence for a photon anticorrelation effect on a beam splitter. A new light on single photon interference. *Europhysics Letters* 1: 173–179.

Hanbury Brown R and Twiss RQ (1956) Correlation between photons in two coherent beams of light. *Nature* 177: 27–29.

Harris SE, Oshman MK, and Byer RL (1967) Observation of tunable optical parametric fluorescence. *Physical Review Letters* 18: 732–734.

Hong CK, Ou ZY, and Mandel L (1987) Measurement of subpicosecond time intervals between two photons by interference. *Physical Review Letters* 59: 2044–2046.

Kim H, Kim D, Park J, and Moon HS (2020) Hong-Ou-Mandel interference of two independent continuous-wave coherent photons. *Photonics Research* 8: 1491–1495.

Kurtsiefer C, Mayer S, Zarda P, and Weinfurter H (2000) Stable solid-state source of single photons. *Physical Review Letters* 85: 290–293.

Mandel L and Wolf E (1965) Coherence properties of optical fields. *Reviews of Modern Physics* 37: 231–287.

Martienssen W and Spiller E (1964) Coherence and fluctuations in light beams. *American Journal of Physics* 32: 919–926.

Senellart P, Solomon G, and White A (2017) High performance semiconductor quantum-dot single photon sources, 12. *Nature Nanotechnology* 1026–1039.

U'Ren AB, Silberhorn C, Ball JL, Banaszek K, and Walmsley IA (2005) Characterization of the nonclassical nature of conditionally prepared single photons. *Physical Review A Rapid Communications* 72: 0218021–0218024.

Weihs G and Zeilinger A (2001) Photon statistics at beam splitters: An essential tool in quantum information and teleportation. https://www.semanticscholar.org/paper/Photon-statistics-at-beam-splitters%3A-an-essential-Weihs-Zeilinger/745401e6f033f4d617aaf6dabb40259440d3da78.

Zou XT and Mandel L (1990) Photon-antibunching and sub-Poissonian photon statistics. *Physical Review A* 475–476.

Further reading

Fox M (2006) *Quantum Optics An Introduction*, 2nd edn. New York: Oxford University Press.

Loudon R (2000) *The Quantum Theory of Light*, 3rd edn. New York: Oxford University Press.

Mandel L and Wolf E (1995) *Optical Coherence and Quantum Optics*. New York: Cambridge University Press.

Milonni PW and Eberly JR (1988) *Lasers*. New York: Wiley.

Saleh BEA and Teich MC (1991) *Fundamentals of Photonics*. New York: Wiley.

Wolf E (2007) *Introduction to the Theory of Coherence and Polarization of Light*. New York: Cambridge University Press.

Point defects

W Beall Fowler, Lehigh University, Bethlehem, PA, United States

© 2024 Elsevier Ltd. All rights reserved.

This is an update of W.B. Fowler, Point Defects, Editor(s): Franco Bassani, Gerald L. Liedl, Peter Wyder, Encyclopedia of Condensed Matter Physics, Elsevier, 2005, Pages 318–323, ISBN 9780123694010, https://doi.org/10.1016/B0-12-369401-9/00412-5.

Introduction: Types of point defects 185
Control of point defects 185
Point defect diffusion 186
Point defects in normal metals and superconductors 186
Point defects in semiconductors 187
Point defects in insulators 187
Semiconducting oxides 188
Point defects for quantum computing 189
Conclusion 189
References 189

Abstract

A "point defect" is an atomic-scale imperfection in an otherwise perfect crystal. It thus may be contrasted with an "extended defect" which involves a large portion of the crystal and which is important in determining its mechanical properties. Much of solid-state technology is associated with point defects, and indeed this topic is central to many of the articles in this compilation. Hence, this article will address general properties of point defects in condensed matter, while other articles delve into more specific properties and applications. Kaxiras (2003) and Kittel (2004) are two general texts on condensed-matter physics that include basic elements of this article, while Tilley (2018) treats a wide array of topics related to point defects, including applications.

Glossary

Antisite defect An atom on the "wrong" site in a crystal that contains more than one type of chemical constituent.

Atomic diffusion The motion of an atom over a macroscopic distance as the result of a series of individual microscopic motions which are statistical in nature.

Chemical impurity An atom, ion, or (small) molecule that is chemically different from the perfect-crystal constituents.

Color centers Point defects in insulators that generate optical activity in the visible.

Configuration coordinate diagram Plot of energy vs. atomic position for a molecule or defect.

Deep defects Defects in semiconductors or insulators in which the electron or hole is strongly bound and is not likely to be unbound at room temperature.

Doping The introduction of chemical impurities into a crystal.

Extended defect An imperfection that extends through a large portion of a crystal.

F center An electron trapped at a halogen-ion vacancy in an alkali halide crystal.

Fermi energy The chemical potential of a solid.

Frenkel defect A vacancy-interstitial pair.

Hydrogen passivation The change of the nature of the electrical properties of defects by the incorporation of hydrogen into the defect.

Interstitial An atom or ion at a position other than a perfect-crystal site.

n-type A semiconductor with an excess of donors.

Negative-U A situation in which the "effective" Coulomb interaction between electrons or holes is negative

p-type A semiconductor with an excess of acceptors.

Perfect crystal A periodically repeated array of identical building blocks such as atoms or arrays of atoms.

Perovskite oxides Compounds of the type ABO_3, where "A" and "B" represent different cations.

Point defect An imperfection in a perfect crystal that is of the order of atomic size.

Schottky defect An isolated vacancy in an otherwise perfect non-ionic crystal.

Shallow donors and acceptors Defects in semiconductors in which the electron (donor) or hole (acceptor) is weakly bound and is likely to be unbound at room temperature.

Stokes shift The energy difference between absorption and emission bands.

Substitutional defect A defect that occurs on a perfect-crystal -atom site.

Vacancy The absence of an atom or ion from its perfect-crystal site.
Zero-phonon transition An optical transition from the zero-point vibrational level of one electronic state to the zero-point level of another state.

Key points

- Atomic-scale defects, such as impurities and missing or displaced atoms, are called "point defects" and are commonplace in otherwise regular, perfect crystals and glassy materials.
- Such defects are responsible for most of the properties that have made materials useful in both ancient and modern technologies.
- These defects may introduce both desirable and undesirable properties, depending on the applications.
- Understanding the nature, the effects, and the control of these defects is therefore of great importance.

Introduction: Types of point defects

In a solid that contains no chemical impurities, the fundamental intrinsic point defects are vacancies, interstitials, and antisites. A "vacancy" (also called a "Schottky defect") is a missing atom from a normally occupied site, while an "interstitial" is an extra atom in a normally unoccupied site. A "Frenkel defect" results when an atom is moved from a normal site to an interstitial site. In compound solids (e.g., GaAs), an "antisite" defect exists when an atom of one of the constituent elements is located at a site normally occupied by that of a different element.

A compound solid has another degree of freedom that can lead to vacancies and interstitials, namely chemical stoichiometry. A slight abundance of one of the components can lead to interstitials of that component, vacancies of another component, or antisites. This issue is particularly relevant in complex oxides such as perovskites, in which standard preparations or heat treatments often yield non-stoichiometric crystals.

Chemical impurities may be present substitutionally (placed on a normal atomic position in the crystal) or interstitially. Furthermore, the presence of certain chemical impurities may induce the existence of vacancies or interstitials. For example, if a second-column impurity ion such as Ca^{2+} substitutes for Na^+ (a first-column ion) in an insulating ionic solid such as NaCl, it is likely that there will be a Na^+ vacancy nearby, in order for overall charge neutrality to be satisfied.

Particularly in semiconductors, but also in insulators, specific point defects may exist in different charge states. The charge states will clearly influence the electrical and optical properties of the solid. Charge states may be changed by varying the chemical potential (Fermi energy) of the solid, by various photoionization processes, or by charge injection.

While the simplest notion of atoms in solids is that of spheres of different sizes, an understanding of point defects (especially in nonmetals), in fact, relies heavily on chemical bonding ideas. For example, interstitials in semiconductors almost never simply sit at empty sites, interacting weakly with their neighbors. Rather, the interstitial atom and its neighbors reorganize their bonding and their positions, often forming the so-called split interstitial whose structure is governed by chemical bonding concepts. Similarly, a cation atom next to a cation vacancy in certain oxides (e.g., Ga_2O_3) may shift position to yield a cation interstitial between two cation half-vacancies (Varley et al., 2011; Kyrtsos et al., 2017).

Control of point defects

The control of point defects in solids is a central role of materials physics, and it is often the ultimate source of success or failure in a particular application.

The first step in point defect control is in the crystal growth process. It is at this point that desired impurities may be introduced and undesired impurities may be avoided. The outcome depends on the purity of the starting material, the detailed growth process, and the growth environment. In general, the growth environment, including chemicals used in the process, will lead to some incorporation of impurities, whose concentration in most cases can be made small enough to not interfere with the applications of the material.

Even an elemental solid such as silicon, prepared with care, will contain intrinsic defects as a consequence of thermal equilibrium. Although a perfect crystal structure represents the most stable arrangement energetically, in thermal equilibrium a number of defects will exist as determined by Boltzmann statistics:

$$N_D = BN\exp\left(-AE/kT\right). \tag{1}$$

Here N_D is the number of defects, N the number of atomic sites, and A and B are dimensionless factors of order 1. E is the energy required to create the defect, k is Boltzmann's constant, and T is the Kelvin temperature. If, for example, the creation energy is 0.35 eV, the room-temperature equilibrium fraction of defects can be $\sim 10^{-6}$, large enough to have noticeable effects. Commonly, the creation energy is larger, but even then, exposure of the solid to high temperatures during growth or processing can lead to a significant fraction of intrinsic defects, which can be "frozen in" at concentrations appropriate to the higher temperature if cooling occurs faster than thermal equilibrium can be established.

In some cases, additional thermal processes may reduce the defect concentration through annealing. On the other hand, thermal treatments that are necessary for the construction of complex semiconductor devices may yield unwanted outcomes relative to the point defects in portions of the device, such as thermally stimulated diffusion of impurity atoms from one region of the device to another.

In thin films, such as those that occur in semiconductor devices, applied electric fields may also lead to changes in the location or configuration of point defects. Electric-field-induced diffusion of atoms or ions may occur. Or, trapping of mobile charges may lead to changes in defect configurations.

Point defects may be created or modified by external ionizing irradiation, either by photons or by high-energy particles. A number of different processes may take place, depending on the material and the properties of the radiation. Heavy particles (such as neutrons or α-particles) of sufficient energy can displace atoms in the crystal by momentum-and-energy-conserving "billiard-ball" collisions. For lighter particles such as electrons or γ-rays, the requirements of both energy and momentum conservation in this process require very high energies for the incoming particle.

In some non-metallic crystals, irradiation can introduce point defects by simply ionizing atoms or ions, in which case the energy required is much more modest, namely the band gap, of order several electron volts. In such cases, the defect creation occurs via a chemical reaction between the ionized atom, or the atom in an excited state, and one or more other atoms in its vicinity.

Point defect diffusion

Point defect diffusion is a process in which a defect moves a macroscopic distance as the result of a series of short-range, statistical motions. Many specific mechanisms of defect diffusion may exist, depending on the defect or defects, the host, and other conditions such as temperature and external fields. The interaction of point and extended defects may lead to large enhancements of point defect diffusion. Detailed treatments of diffusion may be found in Borg and Dienes (1988), Flynn (1972), and Murch and Nowick (1984).

An impurity at an interstitial site is considered, for example. Thermally activated motion over a potential barrier will be required for the impurity to move to an equivalent nearest-neighbor site. If there is just one impurity and there are no additional fields, its net motion will be a "random walk"; its long-range displacement will be hampered by its tendency to jump back toward, in addition to away from, the initial site, and neither direction will be favored. Calculations using statistical methods show that the net distance traveled by the impurity will vary as the square root of time.

If, however, an external field yields a net force in one direction, then the probability of jumps in that direction will be greater than the probability of jumps in the reverse direction, so there will be a net motion of the impurity in the direction of the net force.

Furthermore, diffusion can take place in the absence of external fields if there is a concentration gradient of impurity atoms. An impurity will tend to jump from a region of higher concentration to a region of lower concentration, since in a direction of higher concentration the neighboring interstitial sites are more likely to be already occupied. This effect is described by Fick's first law:

$$J(x) = -D\frac{\partial C(x)}{\partial x} \tag{2}$$

Here $J(x)$ is the impurity flux in the x-direction, $C(x)$ is the impurity concentration, and D is the diffusion coefficient. The diffusion coefficient D contains all the material properties, and it is also a function of temperature. Since the diffusion process involves thermal motion over a barrier, the diffusion coefficient D often varies with temperature, T, in a way similar to Eq. (1):

$$D = D_0 \exp(-\Delta E/kT) \tag{3}$$

Here, ΔE is the height of the potential barrier and k is Boltzmann's constant.

In crystals of low symmetry, such as rutile or monoclinic oxides, the diffusion coefficient for certain point defects will generally show a strong dependence on crystal direction (Johnson et al., 1975).

Point defects in normal metals and superconductors

Because metals contain nearly-free electrons, charge neutrality in the region of a point defect will automatically be satisfied. Hence issues such as charge-compensating defects or charge-state effects, which are of major importance in nonmetals, are not relevant in metals. Nevertheless, point defects are still of importance in affecting the properties of metals. Two examples are mentioned here: electrical properties and magnetic properties (Kaxiras, 2003; Kittel, 2004; Tilley, 2018).

Even though charge neutrality in the region of point defects in metals exists, point defects still scatter conduction electrons. This is particularly important at low temperatures, where phonon scattering in the perfect crystal is reduced while impurity scattering remains.

Magnetic impurities can be important in both magnetic and nonmagnetic metals. In the latter case the magnetic moment of the impurity is partially, but not completely, screened by the conduction electrons. In the former case, interactions between the magnetic atoms are important and will help determine the magnetic properties of the defective material.

In most cases, point defects have negative effects on superconductivity, since superconductivity involves coherent effects between charged particles. In high-T_c superconductors, however, impurities can increase the number of mobile charges. Furthermore, impurities have been of some use in studying the mechanisms for superconductivity.

Point defects in semiconductors

Semiconductors are useful in electronics because it is possible to add impurities in a way that leads to specified concentrations of mobile charges that, in turn, can carry current. Useful background material on semiconductors may be found in Jackson and Schröter (2008), McCluskey and Haller (2012), and Yu and Cardona (2010).

The deliberate addition of impurities is called "doping." In the simplest elemental semiconductors, such as silicon (a group IVb element), each atom has four valence electrons and forms bonds to four neighbors. If a phosphorous (a group Vb element) atom replaces a silicon atom, four of the phosphorous valence electrons form bonds, and the fifth is only weakly bound to the phosphorous atom. This weakly bound electron can be thermally ionized at normal temperatures, yielding a conduction electron. The result is called n-type conduction.

If, on the other hand, a boron (a group IIIb element) atom replaces a silicon atom, a valence electron is needed to form bonds with the four neighbors, leaving a missing electron—a "hole"—in the valence band, weakly bound to the boron. This hole can be thermally ionized at normal temperatures, yielding a positively charged conducting "particle." The result is called p-type conduction.

This simple picture does not always hold. For example, nitrogen is also a group Vb element, but a nitrogen atom substituting for a silicon atom does not yield a weakly bound electron. Rather, the nitrogen relaxes from the center of the substitutional site and forms bonds with the neighboring silicons in which all the electrons are involved and none are left to be weakly bound. This example shows that in general, localized ("deep") and delocalized ("shallow") defect states may coexist, and which configuration is more stable depends on details.

In some cases, doping in compound semiconductors (such as GaAs) follows similar logic. For example, silicon in GaAs is amphoteric; if Si replaces Ga the system is n-type, whereas if it replaces As the system is p-type.

It has been found difficult to achieve p-type doping in a number of compound semiconductors. For example, most divalent impurities substituting for the cation in the nitrides lead to hole states that are too deep in energy to be ionized at room temperature. In some cases p-type doping may be overcompensated by unintentional n-type defects.

Along with deliberately introduced dopants, many other kinds of defects may occur in semiconductors. Some are relatively benign; for example, substitutional C in Si does not trap electrons or holes; so it may occur in a relatively large concentration and have little effect on the electronic properties of Si. Others may themselves trap electrons or holes, or they may combine with dopants in a way that "passivates" the electrical activity of the defect. For example, substitutional B in Si may combine with a H atom, resulting in a B-H pair in which the H is bond-centered (i.e., located within a B-Si bond) in the positive or the neutral charge state. In this configuration, the H atom supplies the fourth bonding electron, so there is a no weakly-bound hole and p-type conduction is suppressed.

Hydrogen is a common and significant impurity in semiconductors (Stavola and Fowler, 2018; Van de Walle, 2007). There is considerable evidence that in a number of oxide semiconductors (such as SnO_2), interstitial H or H at an anion vacancy may lead to n-type conduction. Semiconductor processing involves compounds that contain hydrogen, so it is commonly present. Hydrogen is also amphoteric; it may passivate both donors and acceptors. In fact, hydrogen is, in many cases, a "negative-U" defect. This means that it will never occur as a neutral atom in thermal equilibrium; for any pair of hydrogen atoms (in general, well-separated), the sum of the energies of H^+ and H^- is lower that the energy of two neutral H's, and the charge state (plus or minus) will depend on the location of the Fermi level. If in fact the H's are mobile, it is possible that interstitial H_2 molecules will form, whose energy is still lower and thus represents the most stable state.

Defect motion is of great importance in semiconductor technology, and it has been widely studied. As noted earlier, atomic diffusion may occur during high-temperature processing, and in semiconductors this may yield deleterious effects on resulting devices. Processes that involve impurities coupled with intrinsic defects are common. For example, a substitutional Au atom in Si can switch places with an interstitial Si, forming an interstitial Au, which in turn has a very high diffusivity.

An important phenomenon in optical and some electrical applications is recombination-enhanced diffusion. In some situations, the energy gained from the recombination of an electron and a hole is sufficient to allow atomic motion over potential barriers. For example, optical excitation in ZnSe can induce a diffusion jump of an interstitial Zn atom.

Diffusion of impurity atoms in semiconductors may be enhanced by electric fields. For example, N and B may be induced to diffuse in SiC under high temperature conditions in the presence of a field associated with a built-in p-n junction in the material.

Another important issue is the effect of charge states on diffusion. Because the structure and energetics of defects may be strongly dependent on charge states, so may the diffusion coefficient. Hence, atomic diffusion phenomena observed in n-type and in p-type semiconductors may be quite different.

Point defects in insulators

Insulating solids share with semiconductors the existence of a bandgap, a region of forbidden energy between filled and empty electronic states. They also share some physics, such as the possible existence of defect states of different charge. Topics related to this section are treated by Fowler (1968), Hayes and Stoneham (1985), Pajot (2010), and Pajot and Clerjaud (2013).

A fundamental distinction between insulators and semiconductors is that defect states in insulators are almost never sufficiently shallow in energy to provide charge carriers at normal temperatures. Hence, defects in insulators are almost always "deep."

There are many distinctions between insulators and semiconductors concerning important properties and applications. For example, the bandgaps of insulators span the energy range of visible photons, so defects in insulators may have important optical properties (Fowler, 1968). Indeed, in the early German literature on defects in alkali halides (e.g., NaCl), such defects were called "farbzentren" (or "color centers"). Many precious gems have significant colors because of naturally occurring point defects in an insulating host. One result of these properties was the invention of the ruby laser, and insulator hosts have proven useful in connection with other optical devices and lasers as well.

Point defects in nonmetallic crystals will, if they have energy levels within the gap between the valence and conduction bands, lead to characteristic optical absorptions that involve the excitation of electrons or holes from a ground state to an excited state. In many cases, there is also luminescence as the excited defect returns to the ground state.

The general theory of optical absorption, as well as some aspects of luminescence, is similar for deep semiconductor and insulator defects. In both cases, the electron-phonon interaction is involved. The defect in its ground electronic state has neighboring atoms that vibrate about sites whose equilibrium positions are determined, in part, by the defect wave function. When the defect is electronically excited, the neighboring atoms, responding to a new defect wave function, relax to new equilibrium positions. This process may be represented by a configuration coordinate diagram (Fig. 1) of energy, E, vs. an average position of the neighboring atoms, R. This idealized case consists of two displaced parabolas representing the harmonic energy of the vibrating atoms in ground (m) and excited (k) states. η and γ denote the quantized vibrational levels associated with the parabolas. An optical transition, in general, involves a change of both electronic and vibrational quantum numbers.

In the weak-coupling limit, where the excited-state parabola is nearly above that of the ground state, the strongest transitions involve no change in vibrational quantum number. In this case, at low temperature, if only the zero-point vibrational level of the ground state is occupied, the strongest transition will be a sharp "zero-phonon" transition from A to C to the zero-point level of the excited state.

In the strong-coupling limit shown in Fig. 1, with both horizontal and vertical displacements of the parabolas, the zero- and few-phonon transitions are weak because the vibrational wave functions of the low-lying displaced oscillators do not overlap strongly, and the optical absorption is characterized by a broad multi-phonon transition A to B which is approximately vertical in the configuration coordinate R.

In the absence of nonradiative processes, the excited defect will luminesce, emitting a photon as it returns to the ground state. In general, the radiative lifetime is at least several orders of magnitude longer than the vibrational relaxation rates, so the excited defect will relax to its lowest vibrational state; for example, at low temperature it will relax to the zero-point state C before the defect radiates. In the weak-coupling limit the zero-phonon line C to A will be identical to that for absorption, while few-phonon lines will lie at lower photon energy (in contrast to absorption, where they lie at higher energies). In the strong-coupling limit the broad multi-phonon emission C to D will be "Stokes-shifted" to lower photon energy from that for absorption, as shown in Fig. 1.

In the strong-coupling limit, then, the electron-phonon coupling has substantial effects. For example, for an electron trapped at a Cl^- vacancy in KCl (an F center), the optical absorption peak at low temperature is at 2.3 eV with a width at half-maximum of 0.16 eV, while the luminescence peak is at 1.2 eV with a width of 0.26 eV.

Semiconducting oxides

Semiconducting oxides represent an important class of materials that combine properties of insulators and semiconductors. While the energy difference between valence and conduction bands is large, typical for an insulator, n-type doping is nevertheless possible by defects that do not lead to optical absorption in the visible range. These transparent conducting oxides have many applications, such as touch screens on cell phones. Materials having these properties include ZnO, In_2O_3, SnO_2, and Ga_2O_3 (He, 2020; Yu and Cardona, 2010).

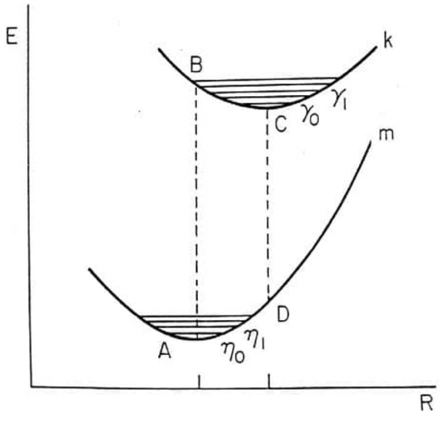

Fig. 1 Configuration coordinate diagram for a model system.

Point defects for quantum computing

Point defects, one in particular, are in serious consideration as vehicles for quantum computing. The leading candidate which has been widely studied is a complex in diamond that consists of a carbon vacancy adjacent to a nitrogen impurity, the so-called diamond NV center. This defect combines optical and spin properties in a particular way to make it a very attractive prospect. Details of these processes and prospects may be found, for example, in Childress and Hanson (2013).

Conclusion

Point defects in solids are of great importance and can have a wide variety of properties and applications. Other articles in this compilation delve more deeply into these topics. Internet searches under "crystal point defect" will provide up-to-date connections, as well.

References

Borg RJ and Dienes GJ (1988) *An Introduction to Solid-State Diffusion*. San Diego: Academic Press. 2012.

Childress L and Hanson R (2013) Diamond NV centers for quantum computing and quantum networks. *MRS Bulletin* 38: 134–138.

Flynn CP (1972) *Point Defects and Diffusion*. Oxford: Clarendon Press.

Fowler WB (1968) *Physics of Color Centers*. New York: Academic Press.

Hayes W and Stoneham AM (1985) *Defects and Defect Processes in Nonmetallic Solids*. New York: Wiley. reprinted by Dover, New York, 2012.

He H (2020) Metal oxide semiconductors and conductors. In: Cui Z and Korotcenkov G (eds.) *Solution Processed Metal Oxide Thin Films for Electronic Applications*, pp. 7–30. Amsterdam: Elsevier B. V.

Jackson KA and Schröter W (eds.) (2008) *Handbook of Semiconductor Technology*. In: vol. 1 and 2. Weinheim: Wiley-VCH.

Johnson OW, Paek SH, and DeFord JW (1975) Diffusion of H and D in TiO_2: Suppression of internal fields by isotope exchange. *Journal of Applied Physics* 46: 1026–1033.

Kaxiras E (2003) *Atomic and Electronic Structure of Solids*. Cambridge: Cambridge University Press. 2010.

Kittel C (2004) *Introduction to Solid State Physics*, 8th edn. New York: Wiley.

Kyrtsos A, Matsubara M, and Bellotti E (2017) Migration mechanisms and diffusion barriers of vacancies in Ga_2O_3. *Physical Review B* 95: 245202.

McCluskey MD and Haller EE (2012) *Dopants and Defects in Semiconductors*. Boca Raton, Florida: CRC Press.

Murch GE and Nowick AS (eds.) (1984) *Diffusion in Crystalline Solids*. New York: Academic Press.

Pajot B (2010) *Optical Absorption of Impurities and Defects in Semiconducting Crystals I. Hydrogen-like Centres*. Berlin: Springer-Verlag.

Pajot B and Clerjaud B (2013) *Optical Absorption of Impurities and Defects in Semiconducting Crystals II. Electronic Absorption of Deep Centres and Vibrational Spectra*. Berlin: Springer-Verlag.

Stavola M and Fowler WB (2018) Tutorial: Novel properties of defects in semiconductors revealed by their vibrational spectra. *Journal of Applied Physics* 123: 161561.

Tilley RJD (2018) *Principles and Applications of Chemical Defects*. Oxon and New York: Routledge.

Van de Walle CG (2007) Hydrogen in semiconductors and insulators. *Journal of Alloys and Compounds* 446–447: 48–51.

Varley JB, Peelaers H, Janotti A, and Van de Walle CG (2011) Hydrogenated cation vacancies in semiconducting oxides. *Journal of Physics. Condensed Matter* 23: 334212.

Yu PY and Cardona M (2010) *Fundamentals of Semiconductors*, 4th edn. Berlin: Springer-Verlag.

Methods for bulk growth of inorganic crystals☆

J Friedrich, Fraunhofer Institute IISB, Erlangen, Germany

© 2024 Elsevier Ltd. All rights reserved.

This is an update of G. Müller, J. Friedrich, Crystal Growth, Bulk: Methods, Editor(s): Franco Bassani, Gerald L. Liedl, Peter Wyder, Encyclopedia of Condensed Matter Physics, Elsevier, 2005, Pages 262–274, ISBN 9780123694010, https://doi.org/10.1016/B0-12-369401-9/00416-2.

Introduction **190**
Melt growth **191**
Crystal pulling 191
Czochralski technique 191
Nacken Kyropulous method 194
Shaped crystal growth 194
Directional solidification 196
Gradient freeze and Bridgman-Stockbarger techniques 196
Zone melting in crucibles 198
Floating zone (crucible-free zone melting) 199
Verneuil technique 200
Solution growth **200**
Principle of solution growth 202
Low temperature solution growth 202
High temperature solution growth 202
Hydrothermal growth 203
Growth under extreme high pressure 204
Vapor growth **204**
Sublimation technique (physical vapor transport) 205
Chemical vapor transport and chemical vapor deposition 205
Conclusion **206**
References **207**

Abstract

Many modern technological systems would not exist without synthetic single crystals. Therefore, the technology to prepare and to produce bulk single crystals—which is called "crystal growth"—is one of the current key technologies. This article gives an overview about the techniques which are used to grow bulk single crystals of inorganic materials. This includes melt, solution and vapor growth techniques.

Key points

- Overview of melt growth techniques including principles and typical crystal materials
- Overview of solution growth techniques including principles and typical crystal materials
- Overview of vapor growth techniques including principles and typical crystal materials

Introduction

Synthetic single crystals are enabler for many modern technological systems. The production of bulk single crystals is called "crystal growth."

This article gives a brief overview about the techniques which are used to grow bulk single crystals of inorganic materials. More detailed information on the different technologies and materials can be found in Rudolph (2015). The fundamental physical and physicochemical mechanisms which govern the crystal growth processes are treated by Nishinaga (2015). The basics and the methods for growing epitaxial films are described by Kuech (2015). The status of the growth of organic materials can be found, e.g., in Nishinaga (2015).

The structure of the article is sketched in Fig. 1.

☆*Change History*: October 2022. J Friedrich updated the chapter. Figs. 24 and 26 are new and Figs. 1, 23, and 25 are replaced by new one.

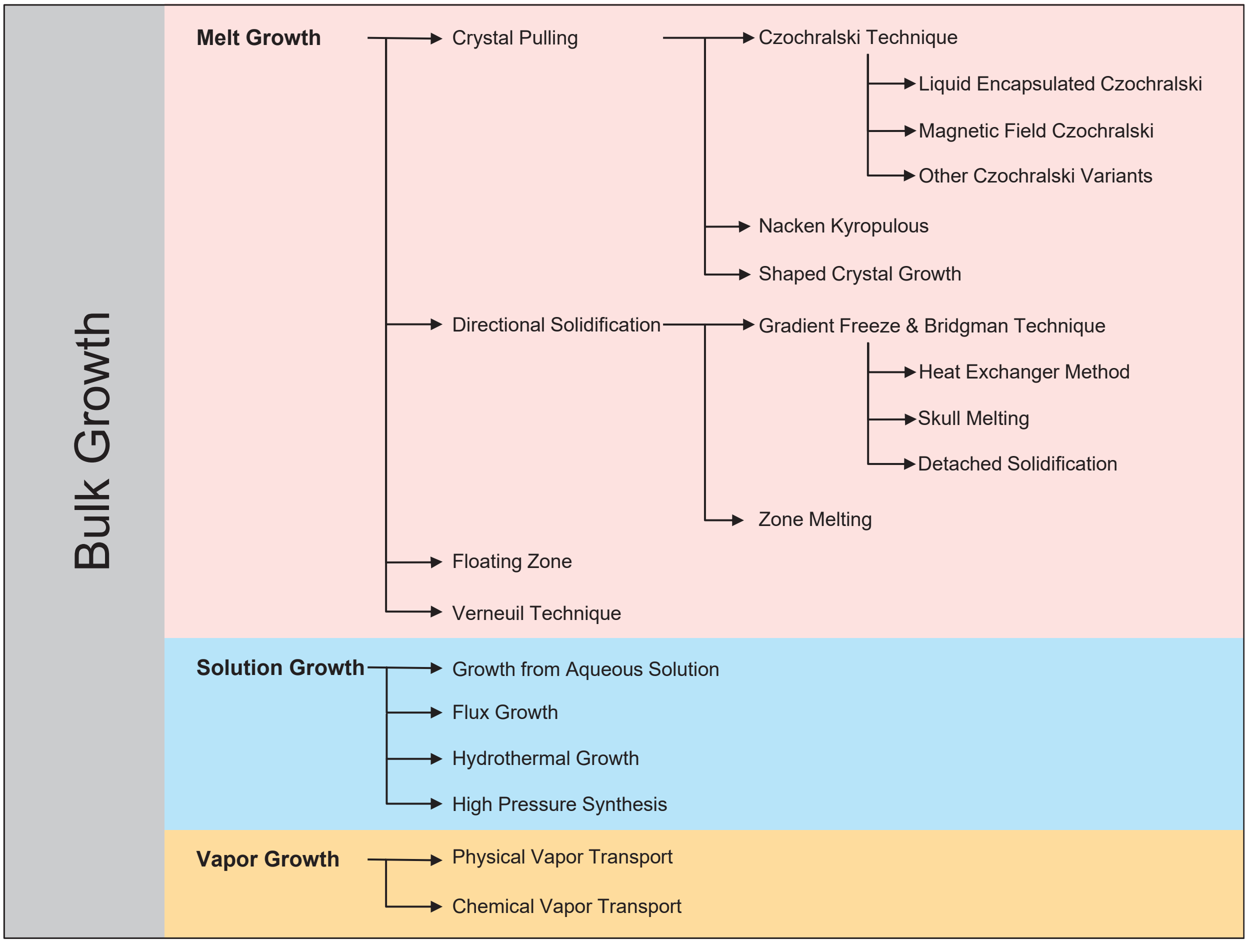
Bulk Growth
Melt Growth
Crystal Pulling
Czochralski Technique
Liquid Encapsulated Czochralski
Magnetic Field Czochralski
Other Czochralski Variants
Nacken Kyropulous
Shaped Crystal Growth
Directional Solidification
Gradient Freeze & Bridgman Technique
Heat Exchanger Method
Skull Melting
Detached Solidification
Zone Melting
Floating Zone
Verneuil Technique
Solution Growth
Growth from Aqueous Solution
Flux Growth
Hydrothermal Growth
High Pressure Synthesis
Vapor Growth
Physical Vapor Transport
Chemical Vapor Transport

Fig. 1 Overview of methods for bulk crystal growth.

Melt growth

The most frequently used and most important method of producing bulk single crystals is by solidifying the material from its melt (melt growth). In a few cases melt growth is not feasible for certain reasons, e.g., if the crystal to be grown has no congruent melting point or if the melting point or vapor pressure are too high. In these cases the crystals have to be grown either from solutions or from the vapor phase.

Crystal pulling

Czochralski technique

The Czochralski method (Cz) is the most important method for the production of bulk single crystals of a wide range of electronic and optical materials (Fig. 2). At the beginning of the process, the feed material is put into a cylindrically shaped crucible and melted by resistance or radio-frequency heaters. After the feed material is completely molten a seed crystal with a diameter of typically a few mm is dipped from top into the free melt surface and a small portion of the dipped seed is melted. A melt meniscus is formed at the contact interface between seed and melt. Then, the seed is slowly withdrawn from the melt (often under rotation) and the melt crystallizes at the interface by forming a new crystal portion. During the further growth process, the shape of the crystal, especially the diameter, is controlled by carefully adjusting the heating power, the pulling rate and the rotation rate of the crystal. Usually an automatic diameter control is applied. This diameter control is based, either on the control of the meniscus shape (e.g., for silicon) or on the weighing of the crystal (e.g., for GaAs, InP) or of the melt (e.g., for oxides).

In order to control the convective heat and species transport in the melt including the shape of the solid-liquid interface, which is playing one of the most dominant roles in terms of the crystal quality, a proper combination of crystal and crucible rotation is used during the whole process.

The most important technical application of the Cz method is the growth of dislocation—free silicon crystals with diameters up to 300 mm and a weight up to 400 kg in industrial production (see Fig. 3). Silicon crystals with diameters of 450 mm and a weight exceeding 400 kg were already demonstrated (von Ammon et al., 2015). The silicon crystals are used in microelectronics as well as in

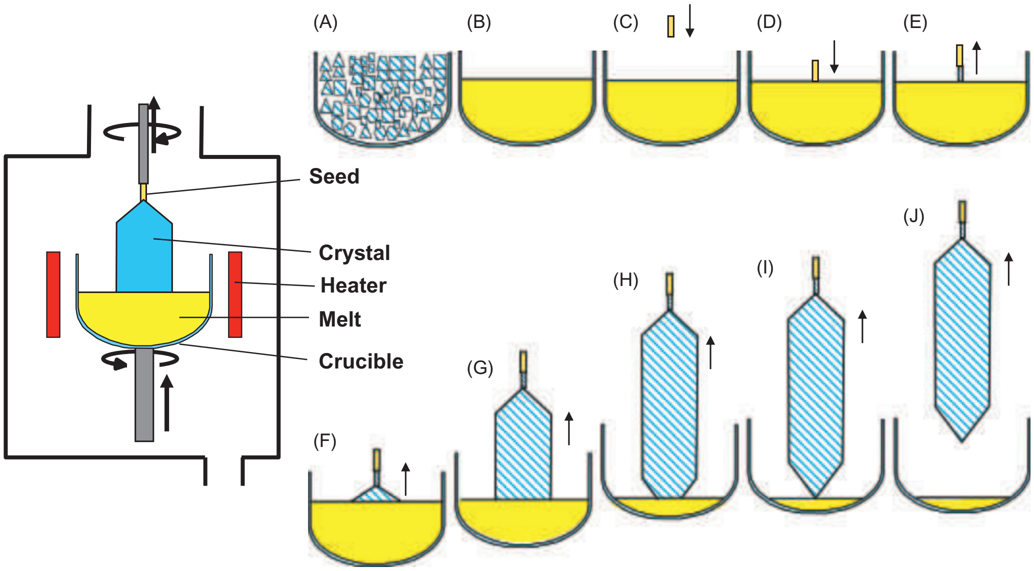

Fig. 2 Schematic of the principle of the Czochralski method (left) and illustration of the different steps (a–j) of the Cz process for growing a Si crystal. (a) The polycrystalline feedstock is melted (b) in a crucible. (c, d) Seeding procedure: The seed crystal is dipped into the melt, followed by Dash necking (e), shouldering (f), cylindrical growth (g), growth of end cone (h), lift off (i), cooling down and removing of the crystal (j). After von Ammon W, Friedrich J, and Müller G (2015) Czochralski growth of silicon crystals. In: Nishinaga T, Rudolph P, and Kuech TF (eds.) *Handbook of Crystal Growth*, 2nd ed., pp. 45–104. Amsterdam: Elsevier/ North-Holland.

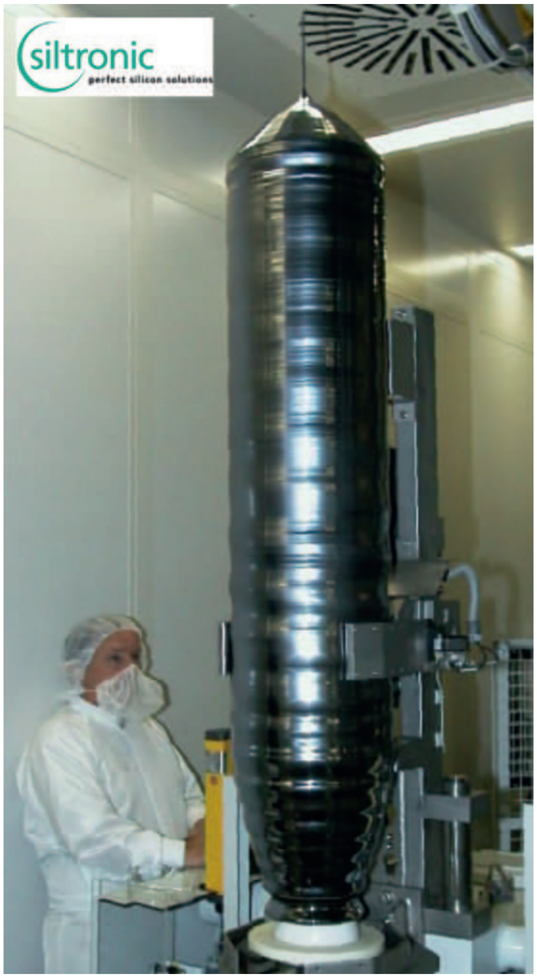

Fig. 3 Silicon crystal with a diameter of 300 mm and a weight exceeding 250 kg, grown by the Cz method. By courtesy of Siltronic AG.

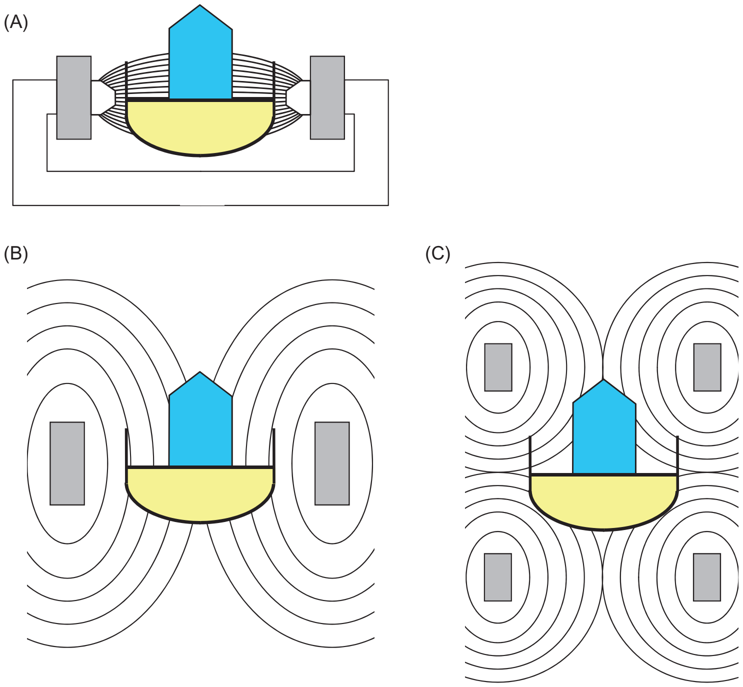

Fig. 4 Examples of typical configurations for magnetic field in the MCz method. (a) transversal; (b) axial; (c) cusp. Gray areas are sections of magnetic coils, the curved lines denote the magnetic field lines.

photovoltaics. The Cz method is also applied to grow on an industrial scale germanium crystal with diameters of typically 150 mm to be used as substrates for III–V multi junction solar cells (Rudolph, 2015), IR optics and gamma ray detectors. Furthermore, several technically important oxide and fluoride crystals like garnets, niobates, tantalates, silicates, vanadates, aluminates, germanates are grown by the Cz method.

The heat and species transport in the melt has a very strong influence on the crystal properties as they are responsible for the uniformity of dopants on the micro- and macro-scale as well as for the shape of the solid-liquid interface and, therefore, for the thermal stress generated in the crystal. During crystal growth the use of stationary or time dependent electromagnetic fields enables the control of the flow in electrically conducting melts (e.g., semiconductors). A Lorentz force is generated in the melt which depends on the magnetic field configuration and leads either to a damping of the flow or to a stimulation of a certain flow pattern. Today, magnetic fields (Fig. 4) are quite common in the industrial production of silicon crystals with 300 mm diameter. More details on the usage of magnetic fields in crystal growth can be found, e.g., in Friedrich (2007).

In order to improve the axial uniformity of the dopant distribution in the grown crystal, the crystal can be grown in such way that the melt volume is kept constant by supplying the solidified portion from a source. Such a source can be realized either by continuously supplying the melt with a feed (Continuous Czochralski method (CCz)) or by placing an inner crucible with holes in a larger outer crucible (Double Crucible Czochralski technique). Although the feasibility of these methods was demonstrated, its use for production of electronic silicon is limited owing to technical and material problems preventing a high yield. Another Cz variant is the so-called "multiple pulling" technique (see Fig. 5). In the multiple pulling Cz method the crucible is kept at melting

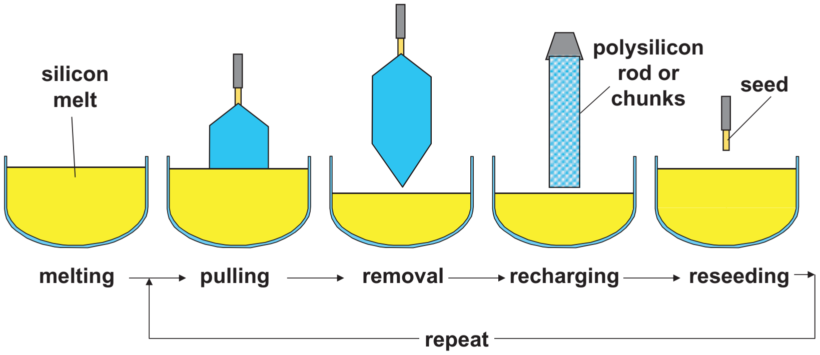

Fig. 5 Sketch of a Cz process with repeated use of the crucible by recharging and without cooling down the crucible between growth runs. From Müller G and Friedrich J (2010) Optimization and modeling of photovoltaic silicon crystallization processes, 14th international summer school on crystal growth. *AIP Conference Proceedings* 1270: 255–281.

temperature after the growth process and filled again with silicon after removal of the grown crystal (Müller and Friedrich, 2010). The advantage of this method is cost saving by multiple using of the crucible and saving the time period for cooling down and heating up periods. Today the multiple pulling Cz technique is used in industrial production for solar as well as electronic silicon crystals. More details about Cz growth of silicon crystals can be found in von Ammon et al. (2015).

If the material to be grown has a high partial pressure of one or more components at the melting point, a modified Cz-set-up can be used which is called the Liquid Encapsulated Czochralski method (LEC). In this LEC-set-up a liquid, usually boric oxide, is applied to encapsulate the melt and the crystal in order to prevent the evaporation of a volatile component from the melt and crystal. In this case the pressure of the inertial gas in the growth chamber must exceed the partial pressures of the volatile components. The LEC-technique was historically the industrial production technique for the growth of the compound semiconductors GaAs, GaP, InP, PbSe and PbTe.

However, the low thermal conductivity of the liquid encapsulant causes large temperature gradients and large temperature non-linearities in the growing crystal. This is unfavorable with respect to the crystal quality as a relatively large number of structural defects (dislocations) are generated in the crystal. LEC has therefore often been replaced by the Vertical Gradient Freeze (VGF) technique (see below).

Nacken Kyropulous method

The Kyropulous (or Nacken-Kyropulous) method is rather similar to the Cz method. The main difference is that the crystal is not growing at the top of the melt as in the Cz method but is partly immersed in the melt. In order to extract efficiently the heat from the growing crystal usually a seed with a large diameter is used. Growth is achieved by either lowering continuously the heating power or by pulling out the growing crystal carefully from the melt.

This method is especially used to produce sapphire boules with a weight of 100 kg and more. From the sapphire boules substrates are manufactured on which GaN based LEDs are epitaxially deposited on an industrial scale. Also, alkali halide crystals for optical components (NaCl, KBr) and alkali iodides for scintillators (NaI, CsI) are grown by the Kyropulous technique. Crystals with dimensions over 500 mm have been achieved.

Shaped crystal growth

For a variety of technological applications, crystals of specified size and shape like plates, rods, tubes, fibers are required. Often it is more cost efficient to grow shaped crystals instead of preparing the needed shape from cylindrical boules as they are grown by, e.g., the Cz method.

The diameter of a crystal in the Cz pulling techniques is controlled by the shape and position of the melt meniscus at the triple contour crystal-melt-gas (or encapsulant). This control can be improved by using a die which is in contact to the melt. The melt raises in a narrow channel within the die due to capillary effects. When the seed crystal is dipped onto the melt portion at the top of the die, the meniscus is formed and liquid solidifies at the seed while the seed is pulled away (Fig. 6). This causes new liquid to raise up in the die. The heat of crystallization is removed from the solid-liquid interface very efficiently by conduction and by radiation.

The method for growing shaped crystals as described above is commonly known as Stepanov method (non wetting die-melt system) or Edge-defined Film-fed Growth (EFG) (wetting die-melt system). In the case of fiber crystals the method is also called

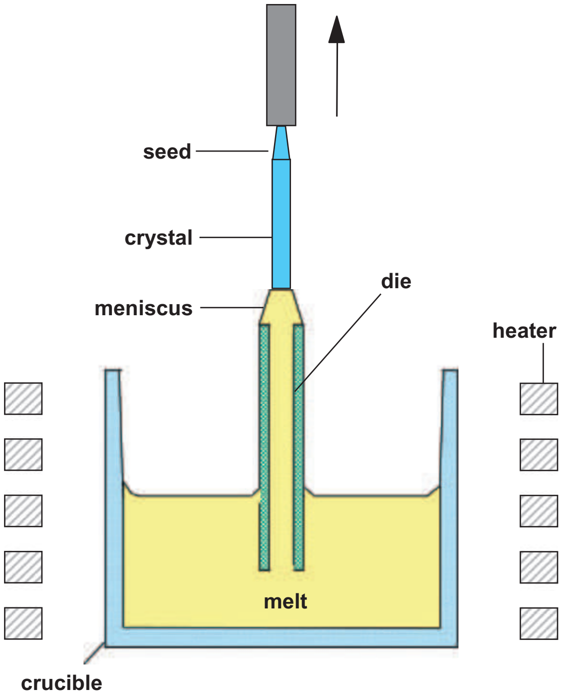

Fig. 6 Schematic of the principle of the Edge defined Film fed Growth (EFG) method.

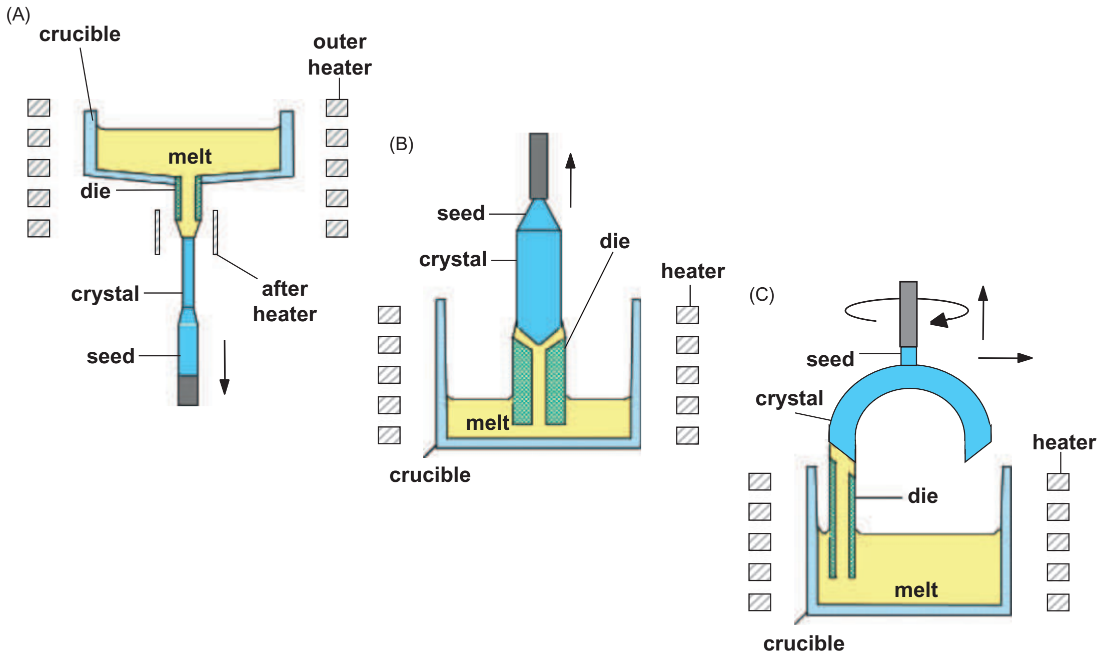

Fig. 7 Schematic of the principle of the μPD (a), NCS (b), GES (c) methods.

Micro Pulling Down method (μPD) because a crystal fiber with a diameter of only some hundred microns can be grown from a die by pulling the crystal downwards (Fig. 7a). Variants of the EFG method are the Non-capillary Shaping (NCS) method where the diameter of the die channel is greater than the value of the capillary constant (Fig. 7b). The NCS method offers advantages in order to avoid the generation of bulk micro defects in the growing crystal caused by gaseous or solid inclusions.

Applying a continuous displacement to the growing crystal or the die allows one to grow crystals with more complex shapes (Fig. 7c), like for example domes or hollow cones. This method is named Growth from an Element of Shape (GES).

Nowadays, shaped crystal growth is mainly used for industrial production of sapphire. Sapphire crystals in form of ribbons up to 150 mm in width, tubes up to 85 mm in diameter, fibers, near-net-shaped domes (up to 80 mm in diameter), rods of various cross-sections, rods with capillary channels, etc., are grown by the shaped growth techniques described above (Kurlov (2001), see Fig. 8). For photovoltaic applications thin silicon ribbons or thin wall (octagonal) tubes have been industrially produced by EFG

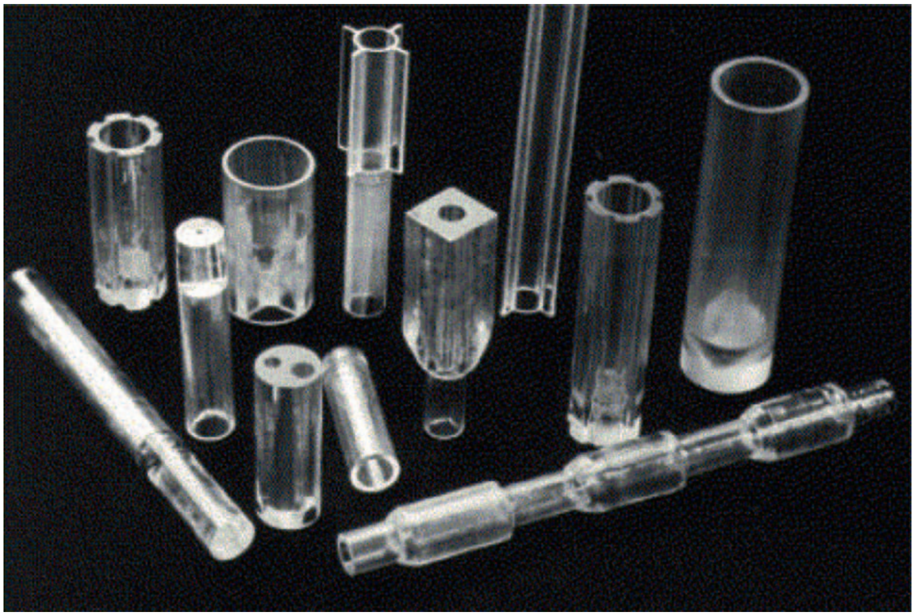

Fig. 8 Shaped sapphire crystals grown by the EFG, NCS, and GES techniques. From Kurlov VN (2001) Sapphire: Properties, growth, and applications. In: Buschow KHJ, Cahn RW, Flemings MC, Ilschner B, Kramer EJ, Mahajan S, and Veyssière P (eds.) *Encyclopedia of Materials: Science and Technology*, pp. 8259–8265. Amsterdam: Elsevier/North-Holland.

like methods. But, most of these technologies were stopped due to cost and productivity reasons a few years ago. The EFG technique is nowadays also used for the industrial production of Ga_2O_3 crystals, a novel ultra-wide-band-gap semiconductor material for power electronic and optoelectronic applications.

Directional solidification

Opposite to crystal pulling, the growth of single crystals in directional solidification is achieved by melting a charge in a crucible and controlled freezing of the melt inside this crucible from one end (seed) to the other (tail). Directional solidification is the basic principle of controlled solidification of a melt. It has been used for many materials for a long time and has its origin and greatest importance in the field of metallurgical casting.

Directional solidification has several advantages compared to the Cz methods. It operates usually under stable hydrodynamic conditions, it is well suited for computer modeling and for automatic process control, the crystal solidifies under low thermal stress conditions, cylindrical or square shaped crystals are grown without any diameter control, and the equipment is less expensive.

However, a crucial limitation of directional solidification is that a strong interaction between the growing crystal and the crucible material might occur, resulting in crystal imperfections which limits the yield and hence the industrial applicability. Furthermore, the failures generated in the crystal during growth, e.g., by twinning or polycrystal formation cannot be observed in situ during growth. A correction by re-melting as it is done in the Cz methods is, therefore, not possible.

Gradient freeze and Bridgman-Stockbarger techniques

The crystal growth configuration consists typically of a tube furnace which provides a temperature profile with a negative gradient parallel to the growth direction (Fig. 9). The method can be carried out by moving the growth interface in horizontal or vertical direction. The single-crystal seed is positioned at one end of the horizontal boat or the lower end of the vertical crucible. Then, the crystal is grown by a controlled shifting of the temperature profile relatively to the solid-liquid interface. Three possibilities exist: moving the crucible relatively to the fixed furnace (Bridgman-Stockbarger method); moving the furnace relatively to the fixed crucible; and without any mechanical movement, only by shifting the temperature profile by a controlled change of the heating powers of the furnace (Tamann-Stoeber or Gradient Freeze Method).

Based on one of these principles one calls the technique the horizontal Bridgman (HB) or the vertical Bridgman (VB) or the Vertical Gradient Freeze (VGF) method. From an industrial point of view, the vertical configurations (VGF, VB) are preferred because they result in a higher yield of appropriate shapes of the wafers compared to the HB method.

The increasing interest in the use of directional solidification results from the fact that it uses the simplest principle of melt growth and that the structural perfection of the single crystals with respect to thermal stress and dislocation formation is better than of crystals produced by Cz methods.

Nowadays, the VGF or VB method is mainly used for the production of compound semiconductors like high quality GaAs (Fig. 10) and InP single crystals or CdZnTe crystals for infrared detectors. A variety of oxide and fluoride crystals are grown by VGF/VB methods for high value applications, too. As one example might serve CaF_2 crystals (Fig. 11) utilized as lenses for the deep ultra violet wavelength in the semiconductor lithography technology. In the field of metallurgy, directional solidification is used to grow single crystalline turbine blades made from nickel-based superalloys (Fig. 12).

In the last two decades the directional solidification (DS) method has gained much attention for the industrial production of silicon ingots for photovoltaic applications. The DS method is usually a combination of the classical VB and VGF method (Fig. 13). In this case the crucibles have square cross sections with dimensions of multiple the dimensions of solar cell wafers (today

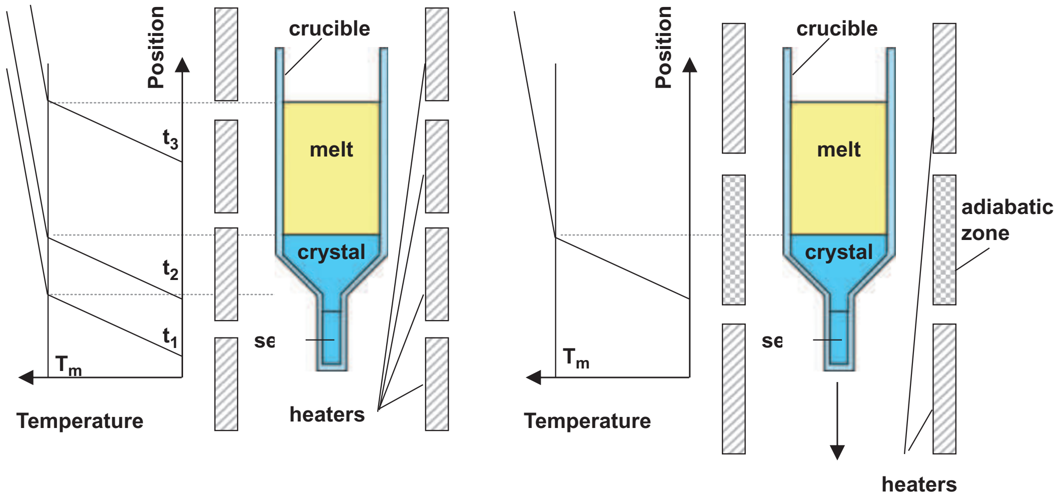

Fig. 9 Schematic of the principle of directional solidification methods; (a) Vertical Gradient Freeze Method; (b) Vertical Bridgman Method.

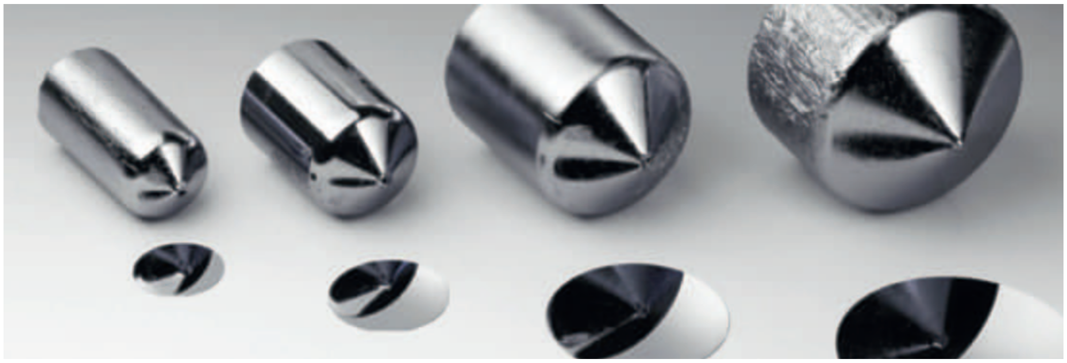

Fig. 10 GaAs crystals and wafers grown by the VGF-technique with 2″, 3″, 4″, and 6″ diameter. By courtesy of Freiberger Compound Materials.

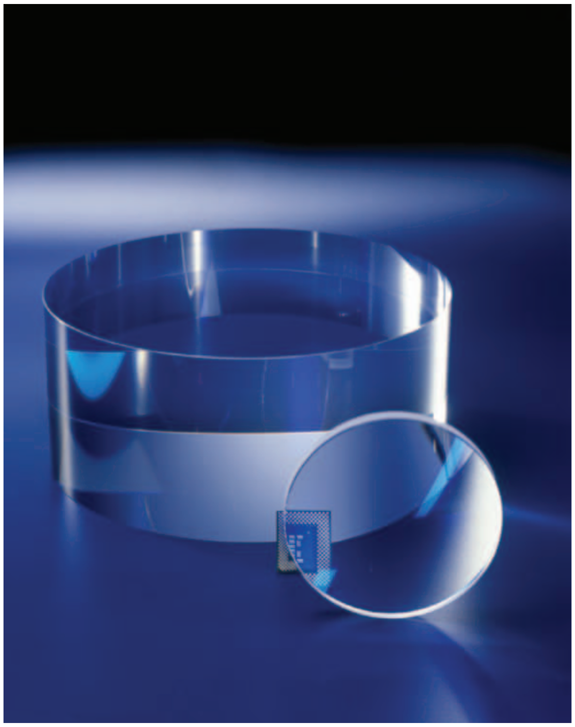

Fig. 11 CaF_2 crystals as lense material for the microlithography are grown by modified Bridgman-Stockbarger methods. By courtesy of Hellma Materials.

156 mm × 156 mm). Three DS variants are in use. DS without seed crystals resulting in standard "multi-crystalline" ingots (see Fig. 14a), DS with small sized silicon particles at the flat bottom resulting in so-called "high performance multi" silicon ingots (Fig. 14b), and DS with single crystalline seed plates at the flat bottom resulting in "quasi-mono-crystalline" ingots (Fig. 14c). In the past up to 70% of the solar silicon ingots were grown by DS. But, the market share of DS silicon has dropped already and will drop further in favor of Cz silicon because of the potential to achieve a higher solar cell efficiencies at lower production cost than DS.

Today, often an active cooling below the crucible bottom is used during DS of solar silicon to extract the heat more efficiently. Originally, a gas-cooled heat exchanger was applied. Therefore, this special variant of the DS technique is also named Heat Exchanger Method (HEM). HEM was developed mainly for the growth of large sapphire crystals with diameters up to 500 mm. Today, large BGO (Bismuth Germanate) crystals are also grown industrially by HEM in addition to sapphire and silicon.

For refractory materials with high chemical reactivity and melting points above 2000 °C often no suitable crucible material exists. This problem can be overcome by using the Skull Melting technique, where the material to be grown serves as an inner cover of a cooled crucible. Radio-frequency heating is used to melt the charge contained in a water cooled crucible (e.g., copper). As a result of the water cooling, a skull of sintered material is formed and acts as a non-contaminating inner crucible wall for the melt. Crystals are typically grown by directional solidification of the molten charge without a seed crystal. The method is used, for example, to grow several hundreds of tons of cubic ZrO_2 per year for gemstones. Sometimes this technique is also named Cold Crucible Technology especially when the melt is levitated by a RF field in such way that no contact exists between the molten charge and the water cooled crucible.

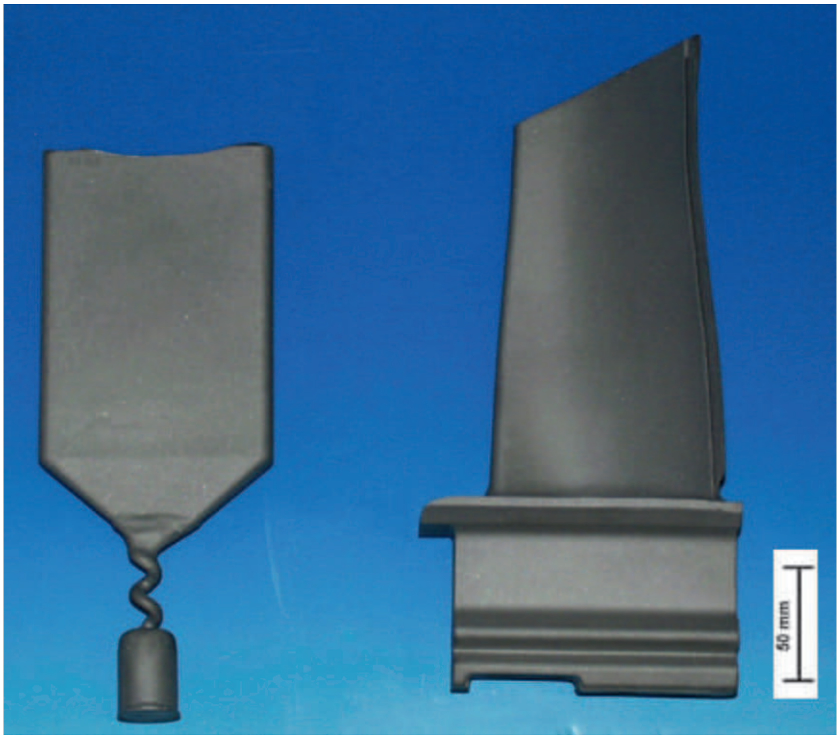

Fig. 12 Single crystalline turbine blades made by directional solidification of nickel-based superalloys. By courtesy of Institute of Science and Technology of Metals, University Erlangen-Nuremberg.

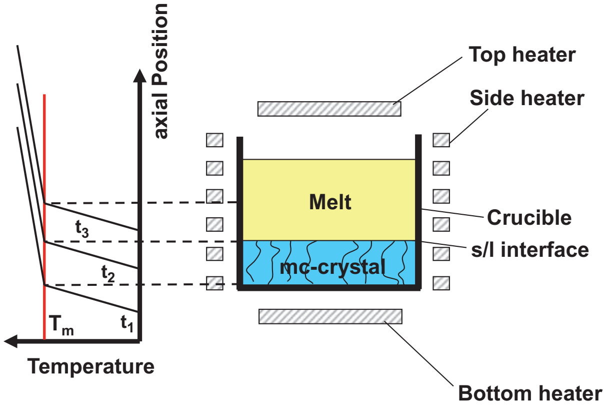

Fig. 13 Schematic sketch of a DS set-up (right) for the crystallization of mc-Si. The sketched axial temperature profiles (left) are related to different time steps (t_1, t_2, t_3) of the process; t_1 affiliates the beginning of crystallization, t_2 and t_3 intermediate steps. T_m denotes the melting temperature. The dashed horizontal lines mark the position of the s-l interface at the corresponding time steps (t_1, t_2, t_3). After Müller G and Friedrich J (2010) Optimization and modeling of photovoltaic silicon crystallization processes, 14th international summer school on crystal growth. *AIP Conference Proceedings* 1270: 255–281.

One interesting variant of the directional solidification method is the so-called detached solidification. In detached solidification, which is also called de-wetting growth process, a small gap between the growing crystal and the crucible wall exists. The formation and stability of such a gap depends on the wetting behavior between the melt and the crucible material, the contact angle, the growth angle and external forces (especially a certain gas pressure difference between the gap and the top of the melt). The experimental results achieved so far for CdTe, Ge, GeSi and GaSb on a laboratory scale on earth and also under microgravity conditions demonstrate that the structural perfection of the crystals is generally improved when the de-wetting effect occurred. However, a transfer to industrial production did not take place so far.

Zone melting in crucibles

In zone melting only a part of the solid is molten in a crucible or a boat by using a resistance or RF zone heater; Fig. 15 shows the horizontal arrangement of zone melting. Growth is achieved by moving the heat source relatively to the axis of the container.

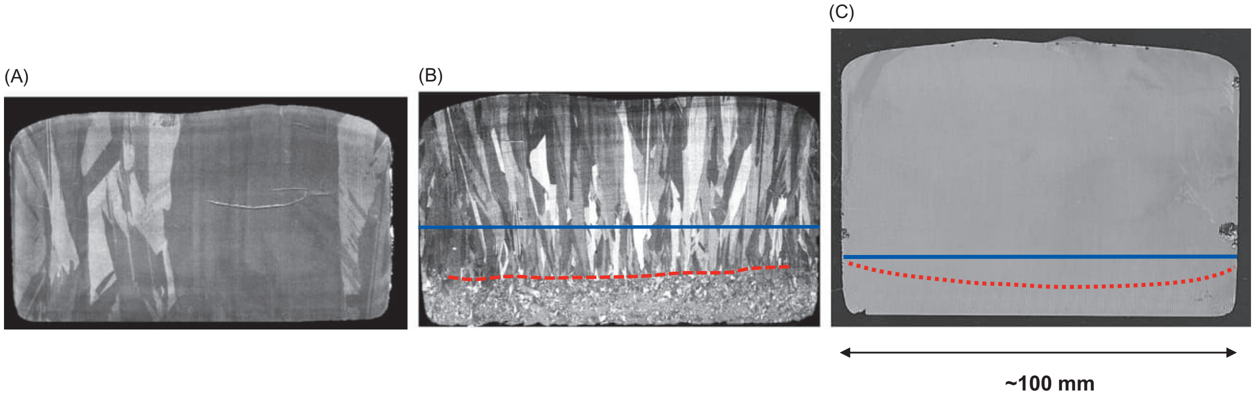

Fig. 14 Scan images revealing different grain orientations of vertical cuts (parallel to the growth direction) of silicon crystals grown without seeding (a: standard multi), with polycrystalline silicon particles as seeds (b: high performance multi), and with single crystalline seed (c: quasi-mono). The blue lines mark the seed surface before the melting process. The dotted lines mark the shape and position of the interface at beginning of growth. By courtesy of Fraunhofer IISB, Erlangen.

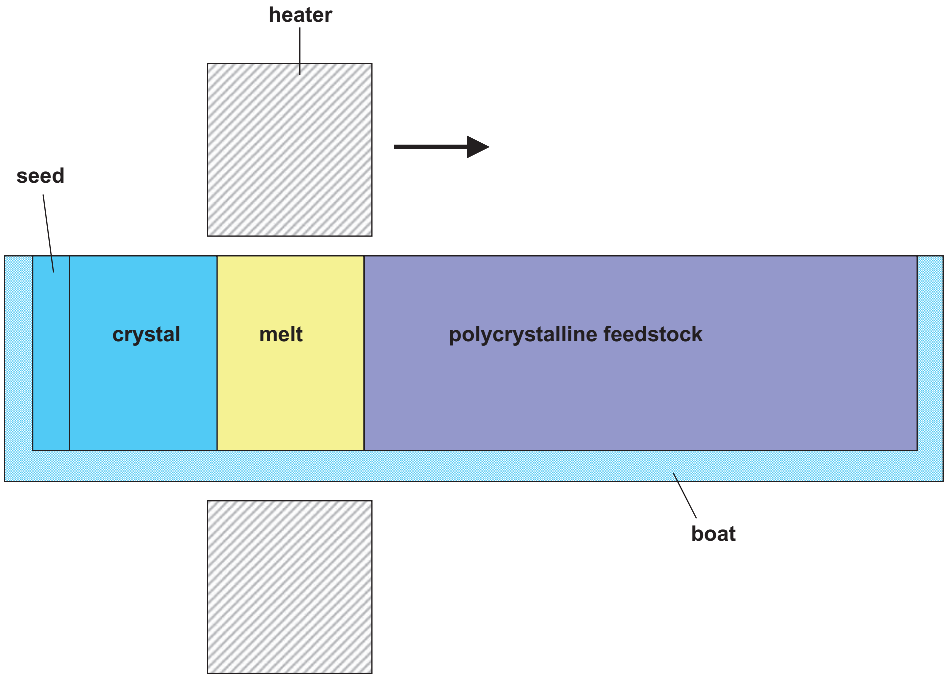

Fig. 15 Schematic of the principle of zone melting.

Nowadays, the importance of zone melting for bulk crystal growth is mainly limited to its use for purification of the feed material. Impurities with a segregation coefficient $k_0 < 1$ can be accumulated very efficiently by multiple passes of melt zones toward the end of the ingot. Therefore, zone melting is still the industrial standard technology for purification of metals and, e.g., germanium feedstock.

Floating zone (crucible-free zone melting)

The floating zone (FZ) technique is a crucible-free crystal growth method. In FZ growth, the molten zone is kept between two vertical solid rods by its own surface tension (Fig. 16). The FZ process is started by dipping a seed crystal into one end of the molten zone. Then the molten zone is moved toward the feed rod and at the other zone end the crystal is growing.

The main advantage of the FZ technique is the absence of a container which avoids any contamination by the crucible material. Furthermore, the generation of crystal defects caused by an interaction between the growing crystal and the container is avoided. Therefore, the technique is especially useful for growth of highly reactive materials, intermetallic compounds, and refractory materials. The heating of the molten zone can be achieved by several methods including RF, optical, electron beam, laser and resistance heating.

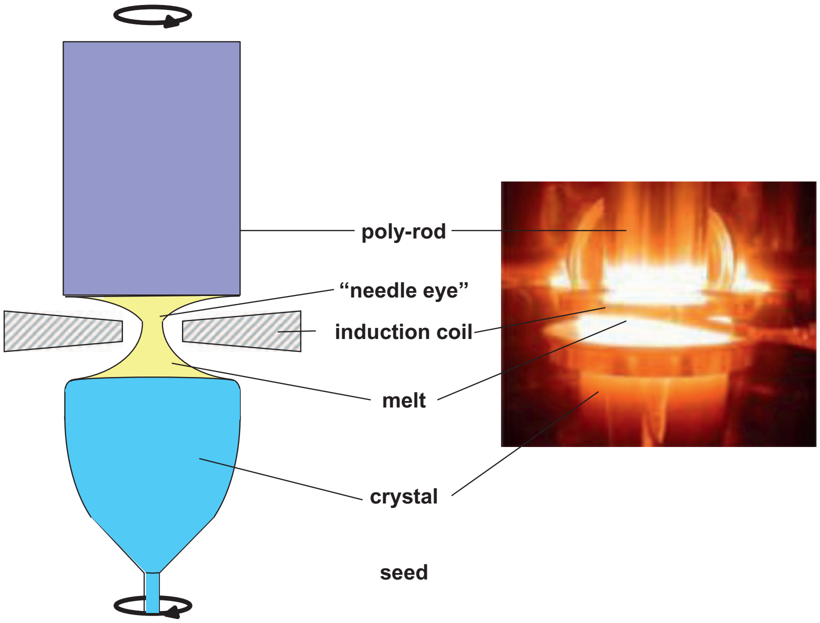

Fig. 16 Schematic principle (left) and photography (right) of the Floating Zone method for growing Si crystals.

The industrial application of the FZ technique is rather limited because the maximum sample diameter is relatively small due to the difficulties to maintain a stable molten zone. Usually the maximum height of the molten zone is only a few mm. It depends mainly on the ratio between the surface tension and the density of the melt.

In the industrial FZ growth of silicon the so-called needle-eye technique is used to stabilize the shape of the molten zone by an electromagnetic pressure field generated with a specially shaped rf-induction coil. This enables the production of silicon crystals with diameters up to 200 mm and extremely low oxygen contamination ($<10^{16}$ cm^{-3}). Such pure silicon crystals are needed especially for the fabrication of power electronic devices.

Crystals of other materials with higher density and lower surface tension like, e.g., GaAs or GaSb can only be grown with larger diameters under microgravity conditions (Fig. 17).

Verneuil technique

The Verneuil technique (Fig. 18), also called the flame fusion technique, is one of the oldest methods for growing refractory oxide crystals. The feed consists of a fine powder of the crystal material which is transported into the flame of an oxygen-hydrogen burner. The fused particles are falling down on top of the growing crystal and form a thin melt film on top of it. A continuous growth process is achieved by slowly pulling down the crystal. It is important to balance the rate of powder feed and the rate of pulling to maintain a constant growth rate and crystal diameter. Otherwise, the thermal field in the vicinity of the solid-liquid interface is changed which results in poor crystal quality.

The advantage of this process is the low equipment costs. The main disadvantage is the extremely large temperature gradient causing a high density of stress-induced crystal defects. Therefore, often an after heater is used in order to prevent the crystal from cracking.

Nowadays, the Verneuil technique is exploited for the economic mass production of, e.g., sapphire and ruby crystals for jewelry and precision bearings (several hundreds of tons per year). Most high-melting oxide compounds can be grown using this technique.

Solution growth

Growth of a crystal from a solution is an option for cases where melt growth is not possible for reasons like extremely high melting temperature, extremely high vapor pressure, non-congruent melting or destructive structure transformations during cooling of the crystal (e.g., quartz). In solution growth the elements or compounds of the material to be crystallized are dissolved in a suitable solvent. Crystal growth is achieved by supersaturation of the solution and deposition of the crystal material on a seed crystal.

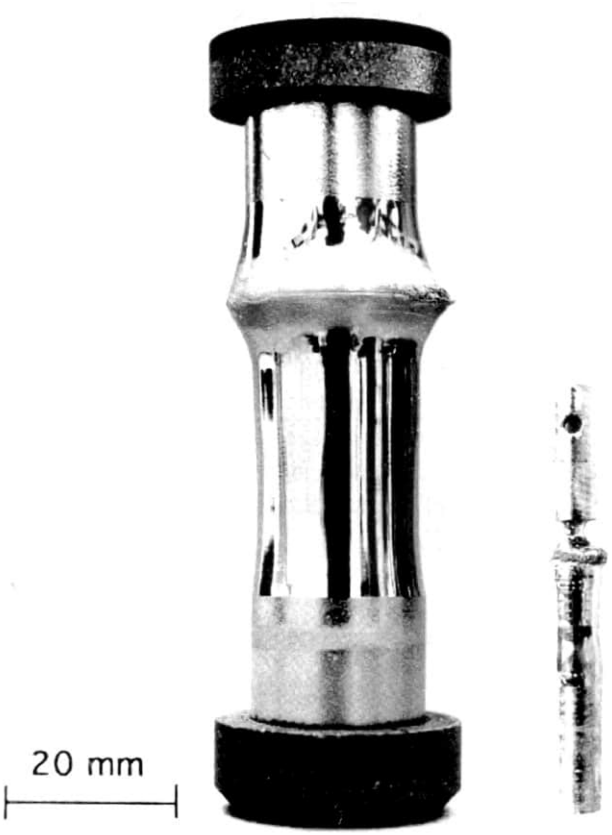

Fig. 17 GaAs crystals grown by the Floating Zone technique; left: sample grown in space under microgravity during the German Spacelab mission D2, right: sample grown on earth with maximum size. By courtesy of Fraunhofer IISB, Erlangen.

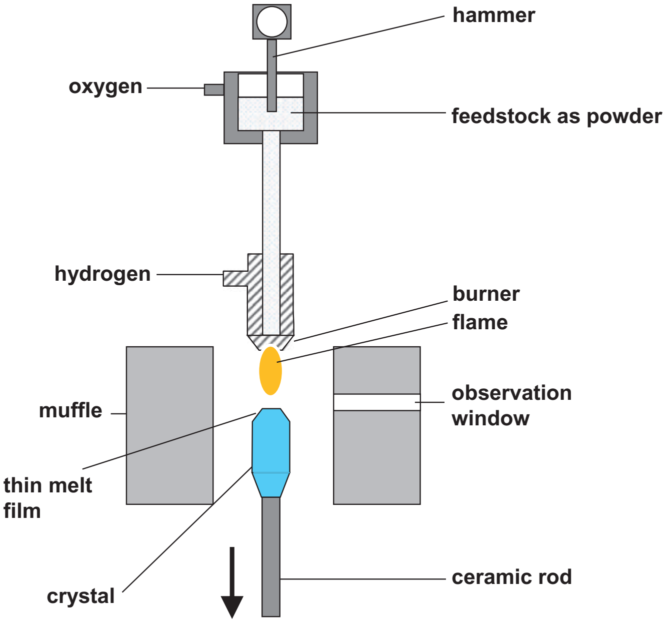
hammer
oxygen
feedstock as powder
hydrogen
burner
flame
muffle
observation
window
thin melt
film
crystal
ceramic rod

Fig. 18 Schematic principle of the Verneuil method.

Principle of solution growth

Firstly a solvent must be found which dissolves the crystal material and is not incorporated into the growing crystal. Then, the solution has to be supersaturated which can be achieved by different means:

(a) In the temperature changing technique, the solution is supersaturated by slow cooling as the solubility is usually decreasing with decreasing temperature (supersaturation is achieved by slow heating, if the solubility decreases with increased temperature)
(b) In the evaporation technique, the supersaturation is obtained by controlled evaporating of the solvent at a constant temperature.
(c) In the temperature gradient technique, two regions of different temperatures T1 and T2 (<T1) are established. In the region with temperature T1 the feed material is dissolved, while crystal growth takes place in the region with temperature T2.

In solution growth, the growth rate is mostly limited by the transport rate of the solute to the growth interface. Therefore, an active mixing, e.g., by stirring and crucible rotation techniques are in use (e.g., Sangwal (2001), see Fig. 19).

An important issue in solution growth is the selection of a suitable solvent. At the growth temperature the solvent should generally have a sufficient solubility of the material to be grown and also a low vapor pressure and a low viscosity.

Low temperature solution growth

Low temperature solution growth is one of the simplest methods to grow single crystals especially if aqueous solutions are used (Fig. 19). Industrially important crystals grown by low temperature solution growth are potassium dihydrogen phosphate (KDP, Fig. 20), ammonium dihydrogen phosphate (ADP), both for electro-optic applications.

High temperature solution growth

Practically any material can be grown by high-temperature solution growth (often also called flux growth). Mainly low melting temperature solvents (fluxes), often molten salts and oxides, are used as solution.

For a variety of technical important materials like $Sr_{1-x}Ba_xNb_2O_6$ (SBN), $Pb_{1-x}Ba_xNb_2O_6$ (PBN), $LiNbO_3$, $BaTiO_3$ (BTO), BaB_2O_4 (BBO), the so-called Top Seeded Solution Growth method (TSSG) is used (Fig. 21). TSSG corresponds to the Cz method the only difference is that a solution is used instead of the melt.

A special industrial application case for solution growth is the production of CdTe crystals respectively CdZnTe for X-ray detectors. They are grown by the so-called Traveling Heater Method (THM). THM is a variant of zone melting, but the "melt"

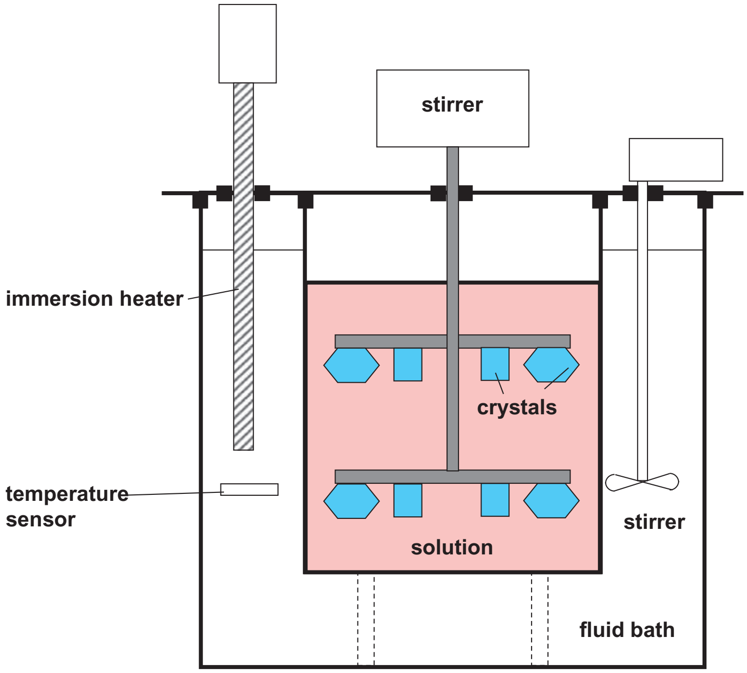

Fig. 19 Apparatus for crystal growth by the temperature changing method using a fluid bath. After Sangwal K (2001) Growth from solutions. In: Buschow KHJ, Cahn RW, Flemings MC, Ilschner B, Kramer EJ, Mahajan S, and Veyssière P (eds.) *Encyclopedia of Materials: Science and Technology*, pp. 3671–3680. Amsterdam: Elsevier/North-Holland.

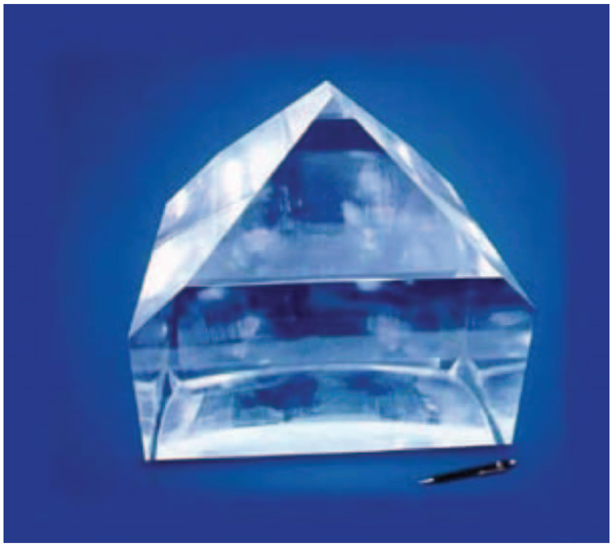

Fig. 20 Potassium dihydrogen phosphate (KDP) single crystal grown from aqueous solution. By courtesy of CEA.

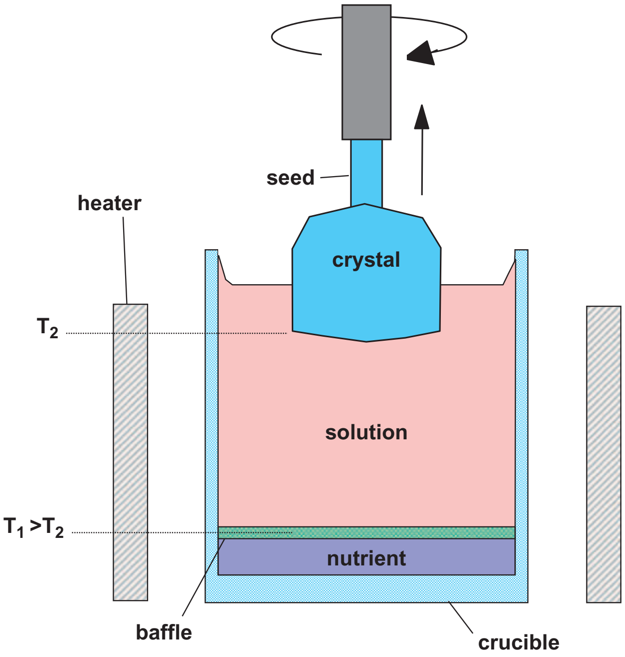

Fig. 21 Typical set up for the temperature gradient solution growth technique with top seeding (TSSG).

zone is replaced by a solution (e.g., Te in the case of CdTe). The movement of the “traveling” heater causes the dissolution of the feed at the high temperature end of the zone and growth at the low temperature end. For other semiconductor crystals like SiC or GaN the use of solution growth is limited to research.

The principle of solution growth allows also to grow thin layers epitaxially on substrates. This technique, which is called Liquid Phase Epitaxy (LPE) is used, e.g., for growth of HgCdTe layers on CdZnTe substrates for infrared applications.

In summary one can state that crystals grown from solution have less structural defects than crystals grown from melts due to the lower growth temperature. However, the growth rates are small compared to melt growth techniques and sometimes the solvent contaminates the crystal.

Hydrothermal growth

Hydrothermal growth is a special variant of solution growth from aqueous solution at temperatures above 100 °C. The increased temperatures (up to about 400 °C) are necessary to enhance the solubility of the solute in the aqueous solvent. But this causes an

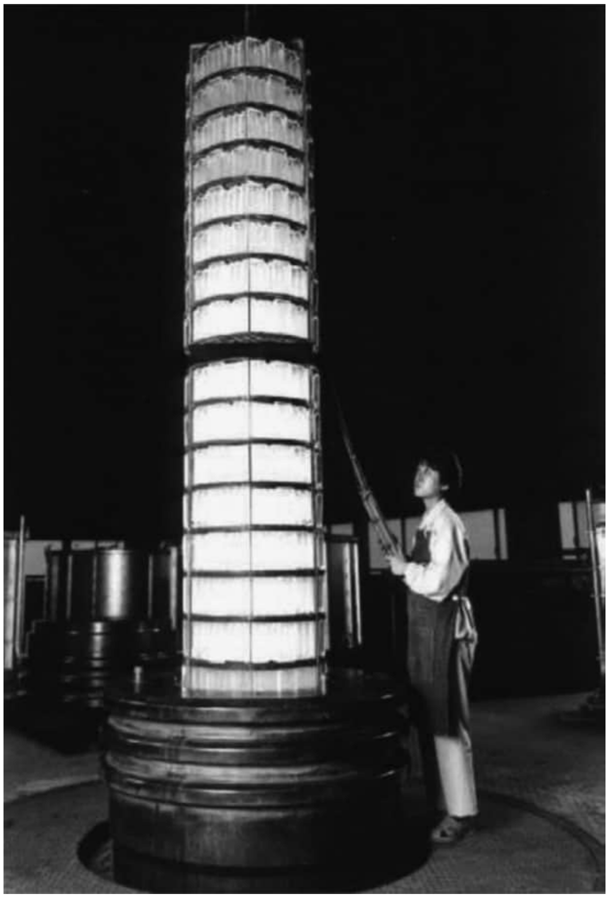

Fig. 22 Production of quartz crystals in the world's largest autoclave. From Rudolph P (2015) *Handbook of Crystal Growth*, Vol. II, 2nd ed., Amsterdam: Elsevier/North-Holland.

extremely high pressure (several kbars) of the supercritical aqueous solvent. The growth process includes typically heterogeneous reactions and is supported by mineralizers. A precisely controlled temperature gradient is used to achieve the crystallization at the seed location (principle c in section "Principle of solution growth").

The most important application of the hydrothermal method is the industrial growth of synthetic quartz (SiO_2) crystals (Fig. 22). It is carried out in special vessels called autoclave or bomb under pressures of typically 170 MPa and temperatures around 400 °C. This technique is also used in industry to grow berlinite ($AlPO_4$), calcite ($CaCO_3$), gallium phosphate ($GaPO_4$), triglycine sulfate (TGS) and zincite (ZnO) crystals. In addition, another variant of the hydrothermal method, called "ammono"-thermal method, was developed which uses supercritical ammonia (instead of water). GaN bulk crystals are grown by this ammono method even on an industrial scale. Also other nitrides can be synthesized by this technique.

Growth under extreme high pressure

High pressure synthesis refers to the growth of diamond crystals. Diamond can be grown from graphite at a temperature around 1300–1500 °C under a pressure of around 60 kbar. These conditions are provided by a set up with special anvils generating the high pressure in the heated growth cell. The growth cell contains graphite mixed with a metal or alloy that serves as a solvent/catalyst. At around 1300–1500 °C diamond is the stable modification whereas graphite becomes meta-stable and is partially dissolved in the solvent. The solubility difference acts as driving force for the conversion of carbon from graphite to diamond crystals.

Vapor growth

Vapor growth is like solution growth usually applied when melt growth is impractical. Due to the lower temperatures as compared to melt growth, many thermally activated processes like impurity incorporation, compositional uniformity, structural imperfection, are usually decelerated. Therefore, the crystal quality can be enhanced. However, in vapor growth the growth rates are usually also considerably decreased due to the small density of crystal material in the gas-phase, the low transport rate in the vapor to the growth interface and the decreased interface kinetics with decreasing temperature. It is therefore mainly used in cases where melt and solution growth are not applicable or has severe disadvantages.

Sublimation technique (physical vapor transport)

In physical vapor transport (PVT) often called as sublimation growth, a source material held at a temperature T1 sublimates, and its vapor is transported by diffusion and convection to the seed crystal held at a lower temperature T2 where it can crystallize. The supersaturation at the crystallization front depends on the difference of the partial pressures of the sublimated material in the source and equilibrium pressure in the growth region as well as on the total vapor pressure in the system. The supersaturation has to be precisely controlled in order to avoid parasitic nucleation.

The sublimation technique is industrially used to produce silicon carbide crystals (Fig. 23) with diameters of up to 150 mm and even 200 mm for electronic applications. The growth takes place in an inductively heated graphite crucible at elevated temperatures (2100–2400 °C). The transport of gaseous Si, Si_2C and SiC_2 species is established from the SiC source to the growing SiC single crystal in an Argon atmosphere (10–100 mbar).

Also aluminum nitride (Fig. 24) is grown in industry by the PVT method at temperatures far above 2000 °C. The PVT method is also used for II-VI compounds.

Chemical vapor transport and chemical vapor deposition

In the crystal growth methods by chemical vapor transport (CVT) or deposition (CVD), respectively, a reactive gas is used which reacts with the source material or gaseous chemical compounds (called precursor) containing the crystal components. These chemical species containing the source material are transported in the gas phase to the growth zone of a reactor. Here, the reactions take place by forming the crystal components which are then deposited at the growth interface.

Both methods CVT/CVD have nearly no importance in bulk crystal growth. Only thick free-standing gallium nitride wafers, respectively gallium nitride boules (Fig. 25) are presently grown by a hydride CVD called HVPE (Hydride Vapor Phase Epitaxy).

But CVD is the dominant industrial method for producing thin films including epitaxially grown layers, especially by using metal organic precursors, called metal organic vapor deposition MOCVD.

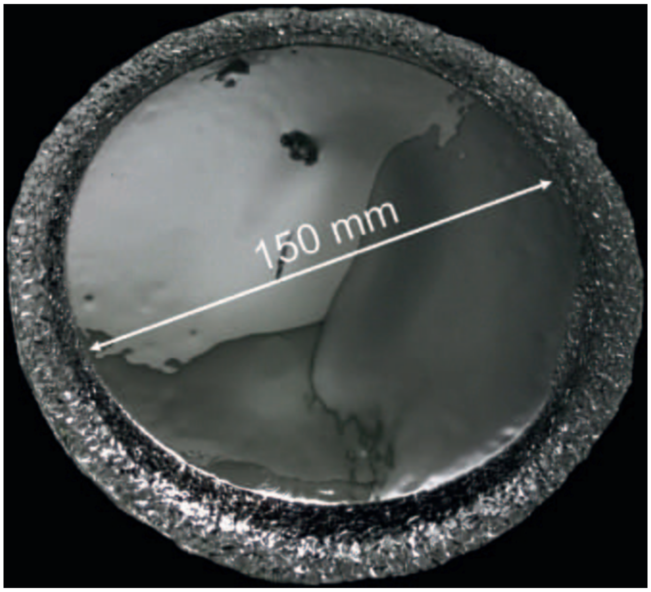

Fig. 23 SiC crystal with 150 mm diameter grown by the PVT method. By courtesy of Crystal Growth Lab, Materials Department 6, Friedrich-Alexander Universität Erlangen-Nürnberg.

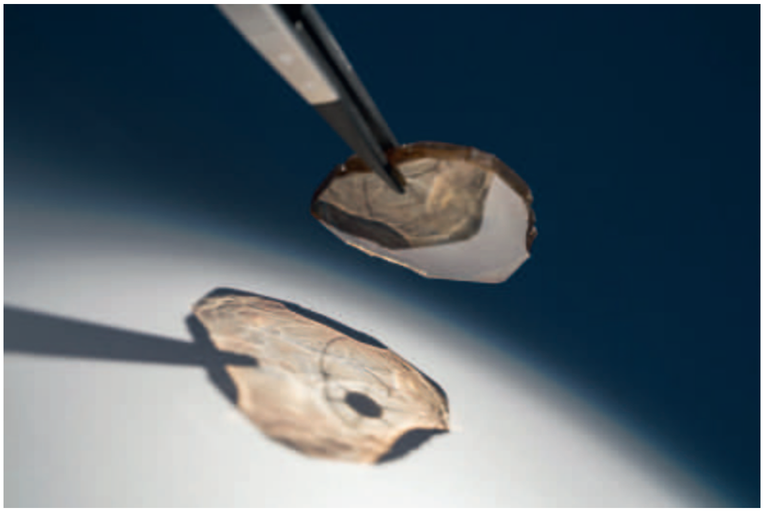

Fig. 24 AlN crystal with 35 mm "diameter" grown by the PVT method. By courtesy of Fraunhofer IISB, Erlangen.

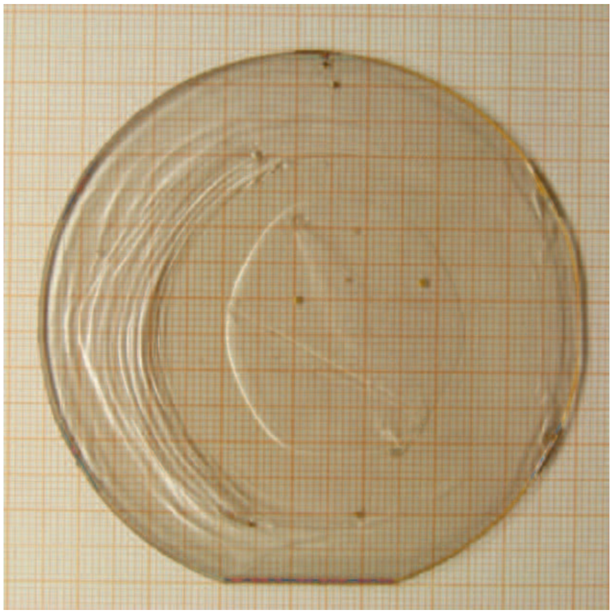

Fig. 25 1.5 mm thick free-standing GaN crystal with 3″ diameter grown by the HVPE method after separation from the sapphire seed wafer. By courtesy of Fraunhofer IISB, Erlangen.

Conclusion

Bulk growth of inorganic crystals is an important industrial key technology. Fig. 26 gives an overview about the development of the annually produced wafer area of different semiconductor crystals and sapphire based on the data of different market surveys.

The mainly industrially used crystal materials are grown by solidification of their melt like Si, sapphire, GaAs, InP, Ge, CZT. Only a few materials are grown from solution or vapor phase. This is true especially for the class of wide band gap semiconductor materials like SiC, GaN, AlN and Diamond.

The growth techniques are well established and suitable to grow in principle any inorganic crystal material. Nevertheless continuous R&D efforts are still necessary for a further development of the crystal growth processes to fulfill the demands on special crystal properties coming from the various fields of applications. Among the most important R&D tasks are

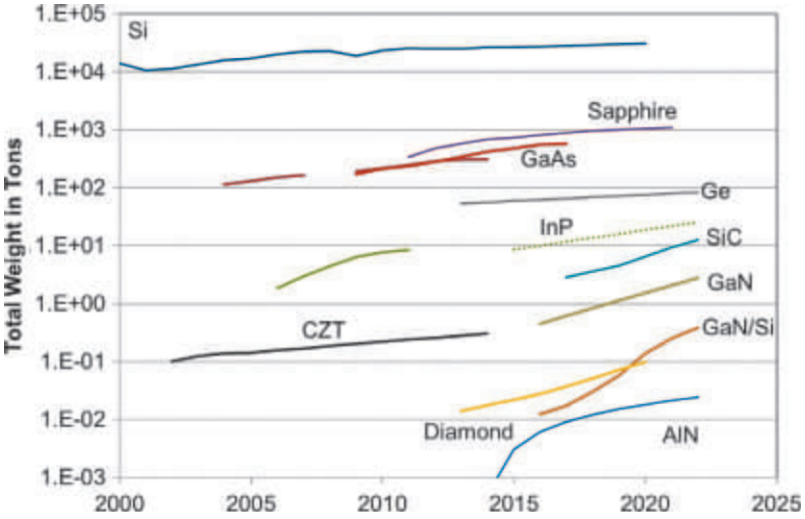

Fig. 26 Development of the annually produced wafer area of different semiconductor crystals (Si, Ge, GaAs, InP, SiC, GaN, CdZnTe (CZT), Diamond) and sapphire based on the data of different market surveys (http://www.yole.fr, https://ihsmarkit.com). In case of silicon only silicon for electronics is considered, but not silicon for photovoltaics. By courtesy of Fraunhofer IISB, Erlangen.

- avoiding of crystal defects which are deleterious for the performance of devices made from the crystals,
- better control of crucial processing parameters in order to tailor the physico-chemical properties of the crystals according to the needs of their applications,
- an increased uniformity of the relevant crystal properties in the micro- and macro-scale and finally
- up-scaling of the growth systems in order to grow crystals of larger dimension for higher productivity and yield.

References

Friedrich J (2007) Control of melt convection in VGF and CZ crystal growth configurations by using magnetic fields: Theory and examples. In: Dost S and Okano Y (eds.) *Crystal Growth Under Applied Fields, Transworld Research Network 37/661(2)*, 31–59.

Kuech TF (2015) *Handbook of Crystal Growth*, 2nd ed. vol. III. Amsterdam: Elsevier/North-Holland.

Kurlov VN (2001) Sapphire: Properties, growth, and applications. In: Buschow KHJ, Cahn RW, Flemings MC, Ilschner B, Kramer EJ, Mahajan S, and Veyssière P (eds.) *Encyclopedia of Materials: Science and Technology*, pp. 8259–8265. Amsterdam: Elsevier/North-Holland.

Müller G and Friedrich J (2010) Optimization and modeling of photovoltaic silicon crystallization processes, 14th international summer school on crystal growth. *AIP Conference Proceedings* 1270: 255–281.

Nishinaga T (2015) *Handbook of Crystal Growth*, 2nd ed. vol. I. Amsterdam: Elsevier/North-Holland.

Rudolph P (2015) *Handbook of Crystal Growth*, 2nd ed. vol. II. Amsterdam: Elsevier/North-Holland.

Sangwal K (2001) Growth from solutions. In: Buschow KHJ, Cahn RW, Flemings MC, Ilschner B, Kramer EJ, Mahajan S, and Veyssière P (eds.) *Encyclopedia of Materials: Science and Technology*, pp. 3671–3680. Amsterdam: Elsevier/North-Holland.

von Ammon W, Friedrich J, and Müller G (2015) Czochralski growth of silicon crystals. In: Nishinaga T, Rudolph P, and Kuech TF (eds.) *Handbook of Crystal Growth*, 2nd ed., pp. 45–104. Amsterdam: Elsevier/North-Holland.

Relevant websites

http://www.siltronic.com—Siltronic AG.
http://www.freiberger.com—Freiberger Compound Materials.
http://www.hellma-materials.com—Hellma Materials.
http://www.wtm.uni-erlangen.de—Friedrich-Alexander-University Erlangen - Nuremberg.
http://www.iisb.fraunhofer.de—Fraunhofer IISB.
http://www.cea.fr—Commissariat à l’énergie atomique et aux énergies alternatives.
https://www.crystals.tf.fau.eu—Friedrich-Alexander-University Erlangen - Nuremberg.
http://www.yole.fr—Yole Developpement.
https://ihsmarkit.com—IHS Markit Technology.

Crystal binding (interatomic forces): Ionic bonding and crystals

Mike W Finnis[a] **and James R Kermode**[b], [a]Department of Materials and Department of Physics, The Thomas Young Centre, Imperial College London, London, United Kingdom; [b]Warwick Centre for Predictive Modelling, School of Engineering, University of Warwick, Coventry, United Kingdom

© 2024 Elsevier Ltd. All rights reserved.

This is an update of M.W. Finnis, Ionic Bonding and Crystals, Editor(s): Franco Bassani, Gerald L. Liedl, Peter Wyder, Encyclopedia of Condensed Matter Physics, Elsevier, 2005, Pages 21–28, ISBN 9780123694010, https://doi.org/10.1016/B0-12-369401-9/00408-3.

Introduction 208
The rigid ion model 209
Beyond the rigid ion model 212
The basic second-order model 212
Modeling deformable ions 213
Variable charge transfer models 214
Machine-learned potentials 214
Conclusion 215
References 215

Abstract

We discuss in general terms the models that are appropriate for describing interatomic forces and performing atomistic simulations in ionic materials. In particular we show how the framework of density functional theory (DFT) and second-order perturbation theory provides a unified way of deriving ionic models, including the Born model and shell models, besides variable charge-transfer models, such as charge equilibration models, and the self-consistent tight-binding model. We also discuss progress in the direct numerical fitting of functions to calculated data, which has made significant progress in recent years with the development of machine learning interatomic potentials and other data-driven approaches.

Key points

- Models of bonding and interatomic forces in ionic materials
- Explanation of most classes of model by deriving them from density-functional theory (DFT)
- Examples from rigid-ion models to deformable ion models and charge-transfer models
- Brief introduction to machine-learning approaches

Introduction

We can distinguish the models of ionic materials by their increasing degrees of sophistication, which are described briefly below. All contain parameters of one sort or another that have to be fitted either to experimental data or to the data from best available calculations. These are usually calculations using Kohn–Sham density functional theory (DFT), which has proved to be a reliable method in very many cases, especially if the system only involves light and nonmagnetic elements. To provide data of so-called chemical accuracy (better than 1 meV/atom) and to deal with the more difficult elements, higher quality first-principles methods are required, which are much more computationally expensive, and impractical for the routine generation of large quantities of data. Following this introduction, there is a more detailed discussion of how ionic models in general can all be related to DFT within second-order perturbation theory.

The simplest ionic model is the *rigid ion model*. It is sometimes called the *Born model* after its pioneer Max Born and his coworkers in Edinburgh, who over 50 years ago developed most of the mathematical description of the ionic model that we still use; see for example the book by Born and Huang (1954). Within the context of density functional perturbation theory, we can think of it as a first-order model, as we shall see in the following section. The ions interact by the Coulomb interaction, in addition to which there is a short-range pairwise repulsion.

Ions are not rigid, and the *shell model* was first developed by Dick and Overhauser (1958) to include their polarizability. In its simplest version, a spherical shell of charge $-q^s$ surrounds an ion of reduced charge $\Delta Z + q^s$ and is attached to it by a harmonic spring. The nominal ionic charge is ΔZ. The repulsion between ions is now modeled as a repulsion between the centers of these shells.

The compressible ion model is an extension of the shell model in which the radius of the shells is a variable. The energy of a compressible ion is a function of this radius, which adjusts according to the environment of the ion. This model is most strongly motivated by the case of oxygen, as discussed further below. The traditional models were mainly constructed by fitting their parameters to experimental data. This provides a disincentive to making them too sophisticated since the number of parameters would become so large that they could fit anything without any guarantee of being physically sound. The compressible ion model was held back for this reason, since in its early days, the parameters were determined by fitting them to experimental phonon dispersion curves. The work of Madden, Wilson, Pyper, and others (see for example, Wilson et al., 1996 and references therein) attempted to reduce the empirical nature of the parameters by fitting them individually, rather than altogether. They were fitted to total energy data obtained by first-principles calculation on molecules and crystals at chosen interatomic distances. This approach also made it feasible to introduce independent parameters to describe quadrupolar polarization. Further developments of the polarizable ion approach include the fitting of model parameters to a large number of forces as a function of atomic configurations (Tangney and Scandolo, 2002), This approach, which uses the data generated by molecular dynamics performed with a densify-functional code, is discussed further below. Even so, the most sophisticated ionic models take no explicit account of covalent effects, and this may be a significant shortcoming.

None of the aforementioned ionic models allow for the fact that the charge associated with an ion also depends on its environment. This has been treated in an empirical way by the model introduced by Streitz and Mintmire (1994). A more recent approach is to use self-consistent tight binding, which in principle can be regarded as an ionic model with a degree of covalency included, as described in Finnis (2003a). Covalency is represented in the tight-binding model by the nonvanishing elements of a Hamiltonian matrix linking atomic-like orbitals. In fact most other models can be derived from a tight-binding description by making specific approximations, perhaps the most drastic being the complete neglect of interatomic Hamiltonian matrix elements as in the variable charge transfer, or charge equilibration model, or the neglect of *all* covalent effects, as in the rigid ion model.

This article is an update of the original, which was entirely based on Chapter 9 of the book by Finnis (2003a). We focus here on key methodological developments rather than aiming to provide a comprehensive review of applications; for the latter, see for example, Pedone et al. (2022). Since Finnis (2003b) was published, a key trend in the construction of interatomic potentials has been the increased use of data-driven and machine learning techniques to automatically construct nonparametric models from reference data, typically at the DFT level. Initially such approaches were mainly applied to covalent materials where interactions are short-ranged, but recently they are seeing increased adoption also for ionic systems.

The rigid ion model

To derive ionic models, like other models, we start with an input charge density $\rho^{\text{in}}(\mathbf{r})$. It is constructed, at least notionally, by superimposing spherical "atomic" charge densities. The atomic charge density in the sense used here is not necessarily the same as the charge density of free atoms. A judicious choice of atomic charge density could make the input charge ρ^{in} closer to the exact, self-consistent charge density ρ^{ex}, improving the accuracy of a first-order model . The usual picture of the charge in an ionic crystal is of course a superposition of *ions* rather than of atoms, and we might expect that these would be a better starting point. Whether ionic or atomic-like charge densities are superimposed, the variational principle tells us that the error we make in the energy is only second order in the error we make in the charge density, provided that the energy is formulated as a functional of the charge density.

A neat general recipe for the "atomic charge density" is to take the electron density of the nearest noble gas in the same row of the periodic table (see Fig. 1 and Harrison, 1980). Thus oxygen, fluorine, sodium, magnesium, and aluminum would all be represented by the charge density of neon atoms, chlorine and potassium by argon, and so forth.

This leads us to construct a first-order model for the total energy as follows: First, superimpose the noble gas atoms at the positions required in the material, keeping their charge densities rigid. Let us denote the superimposed charge density by $\rho_{\text{ng}}^{\text{in}}$, where the individual noble gas atom on site I has a density ρ_{ng}^{I}. Thus

$$\rho_{\text{ng}}^{\text{in}}(\mathbf{r}) = \sum_{I} \rho_{\text{ng}}^{I}(\mathbf{r} - \mathbf{R}_I). \tag{1}$$

Let us denote by $E^{\text{HKS}}[\rho_{\text{ng}}^{\text{in}}, V_{\text{ext}}]$ the first-order energy of this system, where

$$E^{\text{HKS}}[\rho_{\text{ng}}^{\text{in}}, V_{\text{ext}}] = T_s[\rho_{\text{ng}}^{\text{in}}] + \int \rho_{\text{ng}}^{\text{in}}(\mathbf{r})V_{\text{ext}}(\mathbf{r})d\mathbf{r} + E_{\text{xc}}[\rho_{\text{ng}}^{\text{in}}] - \int \rho_{\text{ng}}^{\text{in}}(\mathbf{r})V_{\text{xc}}^{\text{in}}(\mathbf{r})d\mathbf{r} + E_{ZZ}. \tag{2}$$

The notation introduced here is as follows: E^{HKS} is a density functional that describes the total energy (Hohenberg and Kohn, 1964; Kohn and Sham, 1965); $T_s[\rho]$ is the kinetic energy of noninteracting electrons with density ρ, V_{ext} is the potential felt by the electrons from the atomic nuclei, $E_{\text{xc}}[\rho]$ is the exchange and correlation energy of the electrons with density ρ, $V_{\text{xc}}^{\text{in}}$ is the exchange and correlation potential, and E_{ZZ} is the nucleus–nucleus Coulomb repulsion. The energy of this system is strongly repulsive because the equilibrium spacing of noble gas atoms is considerably larger than that of the cations and anions in ionic materials. Indeed, because we are dealing with closed shell atoms, we expect the first-order charge density and energy to be rather good approximations to the exact, self-consistent quantities we denote ρ_{ng} and E_{ng}. We now "switch on" the integer charge differences ΔZ_I on the nuclei which

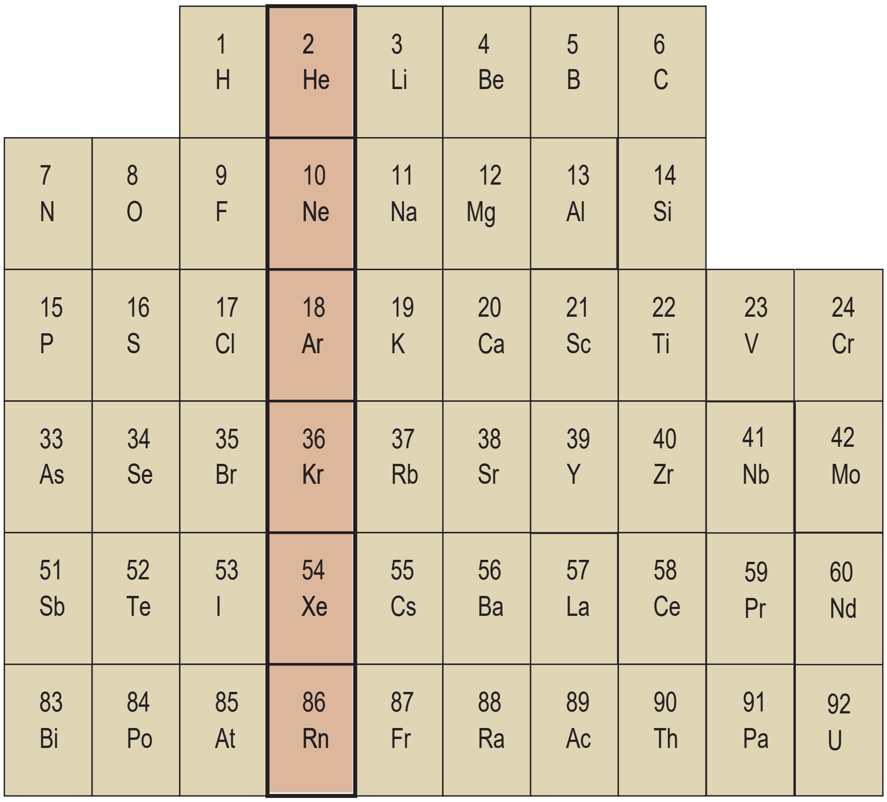

		1 H	2 He	3 Li	4 Be	5 B	6 C		
7 N	8 O	9 F	10 Ne	11 Na	12 Mg	13 Al	14 Si		
15 P	16 S	17 Cl	18 Ar	19 K	20 Ca	21 Sc	22 Ti	23 V	24 Cr
33 As	34 Se	35 Br	36 Kr	37 Rb	38 Sr	39 Y	40 Zr	41 Nb	42 Mo
51 Sb	52 Te	53 I	54 Xe	55 Cs	56 Ba	57 La	58 Ce	59 Pr	60 Nd
83 Bi	84 Po	85 At	86 Rn	87 Fr	88 Ra	89 Ac	90 Th	91 Pa	92 U

Fig. 1 The periodic table centered on the noble gases.

are required to create the nuclei of the actual cations and anions. We regard this as a perturbing external potential to the electrons, given by

$$\Delta V_{\text{ext}}(\mathbf{r}) = -\sum_I \frac{\Delta Z_I}{|\mathbf{r} - \mathbf{R}_I|}. \tag{3}$$

To first order this does not disturb the charge density but it introduces a strong electrostatic cohesive energy, due to the attraction between the unlike charges, which, because of their alternating arrangement in space, more than compensates for the repulsion of like charges. We'll now examine how this works. The total change in the electrostatic interactions of the nuclei introduced by our "transmutation" is

$$\Delta E_{ZZ} = \sum_{I \neq J} \frac{Z_I \Delta Z_J}{|\mathbf{R}_I - \mathbf{R}_J|} + \frac{1}{2} \sum_{I \neq J} \frac{\Delta Z_I \Delta Z_J}{|\mathbf{R}_I - \mathbf{R}_J|}. \tag{4}$$

The second term is called the total *Madelung energy* of the particular structure, and we denote it here as $N_a E_{\text{M}}$, where N_a is the total number of atoms and E_{M} is the Madelung energy per atom:

$$E_{\text{M}} = \frac{1}{2N_a} \sum_{I \neq J} \frac{\Delta Z_I \Delta Z_J}{|\mathbf{R}_I - \mathbf{R}_J|}. \tag{5}$$

Let us consider in more detail the example of a simple binary crystal structure, in which a formula unit consists of n^C cations of charge ΔZ^C and n^A anions of charge ΔZ^A. These charges derived according to the above definition are sometimes called *formal* charges, to distinguish them from actual electronic charge transfers. Generally, for any material, summing over all sites, charge neutrality requires that

$$\sum_I \Delta Z_I = 0. \tag{6}$$

For our binary crystal, the charge neutrality condition holds for each formula unit

$$n^C \Delta Z^C + n^A \Delta Z^A = 0. \tag{7}$$

Table 1 Madelung constants for ionic crystals, after Johnson and Templeton (1961).

Structure	α_M
NaCl	1.75
CsCl	1.76
α-Al_2O_3	1.68
V_2O_5	1.49

In this case the Madelung energy per atom can be written as

$$E_{\mathrm{M}} = \alpha_M \frac{\Delta Z^C \Delta Z^A}{2R_{CA}}, \tag{8}$$

where R_{CA} is the nearest-neighbor cation–anion distance and α_M is the Madelung constant, which is tabulated in the literature for a number of crystal structures, for example, Johnson and Templeton (1961) and Ashcroft and Mermin (1976, Table 20.4). Examples are given in Table 1. For an arbitrary arrangement of ions, for example, within a supercell, which may comprise thousands of atoms, or without periodic boundary conditions, there are special strategies for calculating $N_a E_{\mathrm{M}}$, such as the Ewald method for periodic systems, which are well described in the textbooks, for example, Ziman (1972, p. 39). Our first-order model for the total energy omits the second-order effects, which arise from the deviation of both ρ_{ng} and of the final exact charge density ρ^{ex} from $\rho_{\mathrm{ng}}^{\mathrm{in}}$:

$$\begin{aligned} E^{(1)} &= E^{\mathrm{HKS}}[\rho_{\mathrm{ng}}^{\mathrm{in}}, V_{\mathrm{ext}}] + \int \rho_{\mathrm{ng}}^{\mathrm{in}}(\mathbf{r})\Delta V_{\mathrm{ext}}(\mathbf{r})d\mathbf{r} + \Delta E_{ZZ} \\ &= E^{\mathrm{HKS}}[\rho_{\mathrm{ng}}^{\mathrm{in}}, V_{\mathrm{ext}}] + N_a E_{\mathrm{M}} - \sum_{I \neq J} \int \rho_{\mathrm{ng}}^{I}(\mathbf{r} - \mathbf{R}_I) \frac{\Delta Z_J}{|\mathbf{r} - \mathbf{R}_J|} d\mathbf{r} \\ &+ \sum_{I \neq J} \frac{Z_I \Delta Z_J}{|\mathbf{R}_I - \mathbf{R}_J|} - \sum_{I} \int \rho_{\mathrm{ng}}^{I}(\mathbf{r} - \mathbf{R}_I) \frac{\Delta Z_I}{|\mathbf{r} - \mathbf{R}_I|} d\mathbf{r}. \end{aligned} \tag{9}$$

The interaction of the atomic charge density with the perturbation on its own site has been separated out as the final term. This expression is dominated by the first two terms, namely, $E^{\mathrm{HKS}}[\rho_{\mathrm{ng}}^{\mathrm{in}}, V_{\mathrm{ext}}]$ and the Madelung energy. It is a reasonable approximation to write $E^{\mathrm{HKS}}[\rho_{\mathrm{ng}}^{\mathrm{in}}, V_{\mathrm{ext}}]$ as a sum of pairwise interactions V_{IJ} since we are dealing with closed-shell atoms. With this assumption we obtain the simplest form of the rigid ion model

$$E_{\mathrm{rim}} = \frac{1}{2} \sum_{I \neq J} V_{IJ} + N_a E_{\mathrm{M}}. \tag{10}$$

The remaining first-order terms will be much smaller, as discussed in Finnis (2003a). Now compare these terms with the pairwise electrostatic contributions to $E^{\mathrm{HKS}}[\rho_{\mathrm{ng}}^{\mathrm{in}}, V_{\mathrm{ext}}]$:

$$\iint \frac{\rho_{\mathrm{ng}}^{I}(\mathbf{r})\rho_{\mathrm{ng}}^{J}(\mathbf{r}')}{|\mathbf{r} - \mathbf{r}'|} d\mathbf{r}d\mathbf{r}' + \frac{Z_I Z_J}{R_{IJ}} - \int \left\{ \frac{\rho_{\mathrm{ng}}^{I}(\mathbf{r}) Z_J}{|\mathbf{r} - \mathbf{R}_J|} + \frac{\rho_{\mathrm{ng}}^{J}(\mathbf{r}) Z_I}{|\mathbf{r} - \mathbf{R}_I|} \right\} d\mathbf{r}. \tag{11}$$

This interaction will generally be much bigger. Notice that it involves the full nuclear charges Z rather than ΔZ; second, it is always repulsive, because it comprises the direct Coulomb interaction between nuclei partially screened by the electron distributions; and third, it is of longer range, being nonzero when ρ_{ng}^{I} overlaps ρ_{ng}^{J}, not merely Z_J. The terms we are considering are all strictly pairwise, and so can be exactly accounted for by a relatively small correction to the V_{IJ} we have introduced to represent $E^{\mathrm{HKS}}[\rho_{\mathrm{ng}}^{\mathrm{in}}, V_{\mathrm{ext}}]$. Since the form of V_{IJ} in practical applications has been parameterized, the extra terms could be absorbed without explicitly evaluating them.

Let us now return to the rigid ion model in the form (10) and consider its virtues, the chief of which is simplicity, and its shortcomings, which can be defined in terms of polarization of the ions and covalency. It was first derived on the basis of overlapping noble gas atomic charge densities by Gordon and Kim (1972) and Kim and Gordon (1974). They used a completely local DFT (including the local kinetic energy functional) to evaluate the pair potential between noble gas atoms, with atomic charge densities overlapped but unrelaxed, and they discovered that this could account fairly well for the lattice parameters and bulk moduli of ionic crystals. Their $E^{\mathrm{HKS}}[\rho_{\mathrm{ng}}^{\mathrm{in}}, V_{\mathrm{ext}}]$ could also be fairly well fitted by the Lennard-Jones potential (Gordon and Kim, 1972), the parameters of which we have used, together with the appropriate Madelung energy, to calculate bond lengths in a number of compounds, as illustrated in Fig. 2, where the results are compared with experimental bond lengths. Because some of the crystal structures are a bit complicated, we have made convenient simplifications so that the bond length can be predicted by minimizing the energy analytically with respect to R_{CA}. For example, we have only included nearest neighbor interactions in the Lennard-Jones potential. Then for Al_2O_3, we took as the "experimental" bond length the sum of ionic radii for Al^{3+} and O^{2-}, namely, 0.191nm (Kittel, 1976), which is also the mean of the two close neighbor bond lengths observed in the actual corundum structure. Such ionic radii incidentally reproduce the experimental bond lengths of the other common oxides to an accuracy of 0.002nm. Notice that in some cases a mixture of rare gases is involved, for example, Nb_2O_5 has to be built out of Kr and Ne because Nb in the 5+ state of ionization resembles Kr. Since a value for the Madelung constant was not listed in this case by Johnson and Templeton,

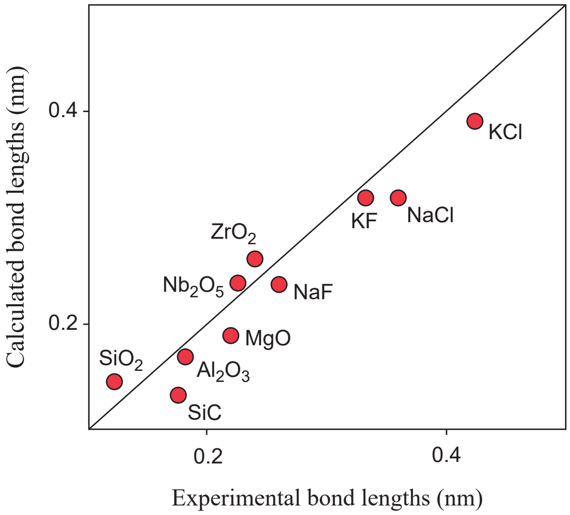

Fig. 2 Bond lengths calculated from Lennard-Jones and Madelung energies.

we assumed their V_2O_5 value would do for Nb_2O_5. The agreement of calculated and observed bond lengths in such diverse materials as ZrO_2 and KCl, with no fitting of parameters to any experimental data, is quite striking. Not surprisingly the worst candidate tested here is SiC, which is a classic covalent compound, but even in this case the crude ionic model does better than we might have expected since the perturbations ΔZ_I are by no means small. Such is the power of the variational principle. We should add that the relatively good agreement of this model breaks down when it comes to calculating the second derivative of the energy, the bulk modulus. Superficially, that is easily repaired if one allows the pair potential to be empirically fitted. Predictions of phonon frequencies and the properties of defects nevertheless generally require a higher quality model than rigid ions can provide even when some degree of empirical fitting is allowed.

Beyond the rigid ion model

The basic second-order model

Several other models can be derived within the broad framework of a second-order functional, which can be written in terms of the reference density from the noble gas atoms as

$$\begin{aligned} E^{(2)}[\rho] = {} & E^{\mathrm{HKS}}[\rho^{\mathrm{in}}_{\mathrm{ng}}, V_{\mathrm{ext}}] + \int \rho^{\mathrm{in}}_{\mathrm{ng}}(\mathbf{r})\Delta V_{\mathrm{ext}}(\mathbf{r})d\mathbf{r} + \Delta E_{ZZ} + \int [\rho(\mathbf{r}) - \rho^{\mathrm{in}}_{\mathrm{ng}}(\mathbf{r})]\Delta V_{\mathrm{ext}}(\mathbf{r})d\mathbf{r} \\ & - \frac{1}{2}\int\int [\rho(\mathbf{r}) - \rho^{\mathrm{in}}_{\mathrm{ng}}(\mathbf{r})]\chi_{e1}^{-1}(\mathbf{r}, \mathbf{r}')[\rho(\mathbf{r}') - \rho^{\mathrm{in}}_{\mathrm{ng}}(\mathbf{r}')]d\mathbf{r}d\mathbf{r}'. \end{aligned} \tag{12}$$

The linear response function $\chi_{e1}(\mathbf{r}, \mathbf{r}')$, of which the inverse operator $\chi_{e1}^{-1}(\mathbf{r}, \mathbf{r}')$ appears here, measures the density induced at $\mathbf{r}$ by a delta function of external potential at $\mathbf{r}'$. Recall that the first term represents the energy of the noble gas solid to first order, and the idea is that the above rigid ion model has taken care of this and the next two terms, that is all terms of first order in ΔV_{ext}. The task is then to approximate the two remaining terms that depend on $[\rho - \rho^{\mathrm{in}}_{\mathrm{ng}}]$ and that are both of second order in ΔV_{ext}. The second-order energy functional in this picture is therefore

$$\begin{aligned} E^{(2)}[\rho] = {} & \frac{1}{2}\sum_{I \neq J} V_{IJ} + N_a E_{\mathrm{M}} + \int [\rho(\mathbf{r}) - \rho^{\mathrm{in}}_{\mathrm{ng}}(\mathbf{r})]\Delta V_{\mathrm{ext}}(\mathbf{r})d\mathbf{r} \\ & - \frac{1}{2}\int\int [\rho(\mathbf{r}) - \rho^{\mathrm{in}}_{\mathrm{ng}}(\mathbf{r})]\chi_{e1}^{-1}(\mathbf{r}, \mathbf{r}')[\rho(\mathbf{r}') - \rho^{\mathrm{in}}_{\mathrm{ng}}(\mathbf{r}')]d\mathbf{r}d\mathbf{r}'. \end{aligned} \tag{13}$$

The difference between this second-order functional and a general second-order functional is that the one-electron energies are here subsumed into the classical pairwise potential, an approximation that is only at all justified by the closed-shell electronic structure of noble gas atoms. By this maneuver, we have shifted the entire responsibility for the description of any covalent bonding effects, which are of second order in $[\rho - \rho^{\mathrm{in}}_{\mathrm{ng}}]$, onto χ_{e1}. The response function χ_{e1} refers to an electron density distribution $\rho^{\mathrm{in}}_{\mathrm{ng}}$, and we can only model it in rather crude ways. Whatever way we do this, and an example is given below, the model so generated is entirely classical in form, and requires $E^{(2)}[\rho]$ to be minimized directly with respect to ρ, without the solution of any Schrödinger equation. The resulting density will then satisfy

$$\rho(\mathbf{r}) - \rho^{\mathrm{in}}_{\mathrm{ng}}(\mathbf{r}) = \int \chi_{e1}(\mathbf{r}, \mathbf{r}')\Delta V_{\mathrm{ext}}(\mathbf{r}')d\mathbf{r}'. \tag{14}$$

Modeling deformable ions

The above formalism is a way to derive the shell model , and its many variations, in order to extend the rigid ion model to introduce deformable ions. Originally this model was entirely empirical, providing sufficient disposable parameters to fit phonon spectra much better than previous models. Now from the previous analysis, we are in a better position to see how its parameters can be related to real physical quantities. The shell model is in effect a representation of the terms in $\rho - \rho_{\mathrm{ng}}^{\mathrm{in}}$:

$$\begin{aligned}\Delta E^{(2)}[\rho] = & \int [\rho(\mathbf{r}) - \rho_{\mathrm{ng}}^{\mathrm{in}}(\mathbf{r})]\Delta V_{\mathrm{ext}}(\mathbf{r})\mathrm{d}\mathbf{r} \\ & -\frac{1}{2}\int\int [\rho(\mathbf{r}) - \rho_{\mathrm{ng}}^{\mathrm{in}}(\mathbf{r})]\chi_{e1}^{-1}(\mathbf{r},\mathbf{r}')[\rho(\mathbf{r}') - \rho_{\mathrm{ng}}^{\mathrm{in}}(\mathbf{r}')]\mathrm{d}\mathbf{r}\mathrm{d}\mathbf{r}'.\end{aligned} \tag{15}$$

In this case the density $\rho - \rho_{\mathrm{ng}}^{\mathrm{in}}$ of Eq. (13) is modeled by the sum of displacements by $\mathbf{u}_I^s$ of rigid, spherical shells of negative charge $-\Delta q_I^s$ originally centered about each atom. Each shell is tethered to its nucleus by a spring. At equilibrium in a perfect crystal an undisturbed shell can be thought of as representing part of the density $\rho_{\mathrm{ng}}^{\mathrm{in}}$. The shells are assumed to be massless since the inertia of electrons does not enter the dynamics of the system in the Born–Oppenheimer approximation , which is the framework for all the models. When the atoms are not in their equilibrium positions, the shells are subject to three kinds of forces, corresponding to three terms in the total energy. First, they are pulled toward their nuclei by the tethering spring; second, they are pulled toward other nuclei by the Coulomb attraction; and third, the shells repel each other. The first two kinds of forces are a representation of the term $\int(\rho - \rho_{\mathrm{ng}}^{\mathrm{in}})\Delta V_{\mathrm{ext}}$ in Eq. (13). In the harmonic approximation, the change in energy when the shells are displaced by $\mathbf{u}_I^s$ from their nuclei has the form

$$\begin{aligned}\Delta E^{(2)} = & \frac{1}{2}ku_I^{s2} + \sum_{J\neq I}\left\{-q_I^s\Delta Z_J\left[\frac{1}{|\mathbf{R}_I + \mathbf{u}_I^s - \mathbf{R}_J|} - \frac{1}{|\mathbf{R}_I - \mathbf{R}_J|}\right]\right. \\ & \left. + \frac{1}{2}q_I^s q_J^s\left[\frac{1}{|\mathbf{R}_I + \mathbf{u}_I^s - \mathbf{R}_J - \mathbf{u}_J^s|} - \frac{1}{|\mathbf{R}_I - \mathbf{R}_J|}\right]\right\}.\end{aligned} \tag{16}$$

A number of points can be made about this model. First, it captures the long-ranged Coulomb interactions between induced dipoles. The on-site elements of χ_{e1}^{-1} are represented within the first term $\frac{1}{2}ku_I^{s2}$ while the last term in the braces represents its intersite elements. The Coulomb interactions in (16) could be expanded to first order in $\mathbf{u}_I^s$ to display the dipole–dipole interactions explicitly, and indeed the model could be formulated in terms of variable dipoles on the sites instead of explicit shell charges and displacements. These Coulomb interactions are an important part of the inverse response function we are trying to model. However, they are certainly not the whole story since the true inverse response function contains terms in the kinetic energy and the exchange and correlation energy. A short-ranged empirical potential between the ls can be introduced to model these contributions.

In a more realistic model, the shells should be allowed to change their radius in response to their environment. Such an effect might be accomplished by including a kind of compressibility of the ion as a further parameter, which adds a functional dependence on $(r^s - r_0^s)$ to the potential energy, where r^s and r_0^s are the current and relaxed values of the shell radius. This was the idea behind the "breathing shell" model , and subsequently the "compressible ion" model, see for example Marks et al. (2001) and references therein. The compressibility of an ion has a significant effect on properties, and is most noticeable in the case of oxygen because the size of the O^{2-} ion is particularly sensitive to its environment. Indeed, in free space the O^{2-} ion is unstable, which can be thought of as the limiting case of the radius of the ion going to infinity as its coordination is reduced to zero. A noteworthy example of the importance of compressible oxygen is one of the simplest of ionic oxides, MgO. Within the rigid ion model, the Cauchy relation between elastic constants, $C_{12} = C_{44}$, holds since the potential energy is purely pairwise, yet experimentally C_{12} and C_{44} differ by more than 50%. The shell model does not help here because by symmetry, the elastic strains do not displace the shells from their lattice sites, and the Cauchy relation still holds. The difference between C_{12} and C_{44} is only obtained when compressible oxygen ions are introduced. This is because the elastic constant C_{12} is associated with a change in volume, which induces compression or expansion of the ions if the model allows them this degree of freedom. It may help to appreciate this if you think of C_{12} as a linear combination of the bulk modulus $B = \frac{1}{3}(C_{11} + 2C_{12})$ and the shear modulus $C' = \frac{1}{2}(C_{11} - C_{12})$, that is, $C_{12} = \frac{1}{3}(3B - 2C')$.

There are now more sophisticated models with polarizable ions, going beyond the notion of spherical shells and harmonic springs. Closer in spirit to the density functional framework is the approach of Ivanov and Maksimov (1996). These authors represent $(\rho - \rho_{\mathrm{ng}}^{\mathrm{in}})$ as a superposition of atomic charge densities ρ_{ng}^I, each of which is allowed to shift rigidly with respect to its nucleus, thereby modeling the dipole moments. They calculated the associated changes in energy with a completely local density functional along the lines of Gordon and Kim (1972). A natural extension also considered by Ivanov and Maksimov is to include parameters that describe distortions of the atomic charge densities, such as expansion and contraction or quadrupolar distortion. Besides the local density approximations for kinetic, exchange, and correlation energies, the only limitation of this approach is the number of free parameters one is prepared to include to characterize the charge density.

Another line of attack starts as before with the assumption that the ions are polarizable as dipoles and quadrupoles , and that they are compressible. The strategy is then as far as possible to obtain the many parameters such a model requires as independently as possible, by fitting functions to an extensive set of first-principles calculations on ions in specially chosen potential wells or in clusters. It is a great improvement on the simple shell model, and can reproduce a range of strain energy data and phonon spectra. However, in spite of the extensive use of first-principles calculations, it is impossible to eliminate some arbitrary choices regarding the functional forms used, and some pairwise approximations. A detailed example of this approach is given by Marks et al. (2001).

Tangney and Scandolo (TS) extended the polarizable ion approach using the "force matching" idea of Ercolessi and Adams (1994) to determine the potential parameters which best reproduce the DFT energies, forces, and stresses on a database of reference configurations. The approach has been applied to a range of oxides including SiO_2 (Tangney and Scandolo, 2002), TiO_2 (Han et al., 2010), and Al_2O_3 (Sarsam et al., 2013). Reformulations of the TS potential to replace the long-range Coulomb interactions with either Yukawa truncation (Kermode et al., 2010) or Wolf summation (Brommer et al., 2010) dramatically reduces the computational cost with negligible loss of accuracy because of physical screening processes which limit the true interaction range.

Variable charge transfer models

In the models described so far in this article, a fixed charge transfer between ions is defined. The net charges on ions are fixed at the formal charges, which are specified by the electronic structure of noble gases. In reality, the occupancy of atomic orbitals varies with the local atomic environment, so it is worth thinking about how this effect can be modeled. In fact a model of ionic crystals that includes covalency, polarisable ions (dipoles and quadrupoles), and variable charge transfer was introduced by Finnis et al. (1998) under the heading of self-consistent tight binding. Self-consistent tight binding offers a way to treat pure metal atoms as well as their oxides since, at least for *sd*-bonded metals, it models the nature of chemical bonding from the metallic to the ionic state.

Conceptually the application of self-consistent tight binding to an ionic material is no different to its application to metals. However, an alternative input charge density might be considered. In the tight-binding models discussed previously, atomic charge densities were superimposed to create the notional input charge density so that all the long-ranged electrostatic interactions appeared in the second-order term. However, one could also formulate the tight-binding model starting from the superimposed atomic charge densities of noble gases, in which case the Coulomb interactions would appear in the pair potential, exactly as they do in the rigid ion model. A systematic study of the consequences of one or the other starting point has not yet been made.

In spite of advantages of self-consistent tight binding in comparison to the models introduced earlier in this chapter, it has certain disadvantages that should be mentioned. These include the obvious one of greater computation time, but there may be others. For example, in current implementations the second-order term is represented by Coulomb interactions between point multipoles. This appears to take no account of the effect that the *compressible ion model* is trying to capture. The logical way to describe a compressible oxygen ion within tight binding would be to include more orbitals of *s* and *p* characters in the basis set so that the spread of the charge density on an anion could vary by transfer of electrons between the orbitals on a site. The price to pay would be more parameters to determine and more computation time. The benefits over a first-principles tight-binding method would be diminished or eliminated.

On the other hand, notions of compressible ions and charge transfer are not absolute; a transfer of electrons from cations to anions might be rather well described in terms of the charge density by a contraction of anion densities accompanied by an expansion of cation charge densities, and vice versa. The tight-binding model predicts a violation of the Cauchy relations because of its noncentral forces and covalency, and possibly charge transfer, whereas the compressible ion model predicts the Cauchy violation from the form of its classical nonpairwise potential energy. A one-to-one mapping of these properties such as charge transfer between the compressible ion model and the tight-binding model is not unique, so it would be unfair to dismiss one or the other description as wrong; they may both be grasping at the same physics from different points of view.

The classical variable charge model (13) is also the basis of an empirical model that includes charge transfers (Streitz and Mintmire, 1994). These authors considered the determination of ρ as a variational problem for which the solution equalizes a classical chemical potential of the electrons everywhere. The result is a model that has some similarities to that of Ivanov and Maksimov (1996). We can think of it as a second-order ionic model with charge transfer, or as a tight-binding model in which the effect of covalency (intersite matrix elements of the Hamiltonian) is neglected. It is a model which enables large-scale molecular dynamics simulations to be carried out, giving a broad-brush description that may be adequate if details such as the relative energies of different structures are not of interest. A prominent example of an empirical variable charge framework, which has been widely applied to ionic materials, is the ReaxFF reactive force field of van Duin et al. (2001); however, due to the large number of terms, parametrization of these models for multicomponent-systems remains challenging.

Machine-learned potentials

In the 2020s, we are witnessing a gradual paradigm shift in the use of DFT calculations, from fitting simple physical models of interatomic potentials, including empirical tight-binding models, to fitting models with the help of machine-learning algorithms. The aim as always is to simulate very large systems and perform the sampling required to obtain dynamic and thermodynamic properties at high temperature, but the ambition has become higher: we now want to retain the accuracy of DFT or better, but still at a small fraction of its computational cost.

With a successful machine-learned potential, we can compute the energy and forces on an arbitrary configuration of ions, although the price may be to lose any explicit representation of the distinct physical effects that 20th-century models tried to capture (Behler and Csányi, 2021; Unke et al., 2021). The most successful current schemes (Behler and Parrinello, 2007; Bartók et al., 2010;

Drautz, 2019) require the total energy to be expressed as a sum over atoms of atom-centered short-ranged functions of the atomic coordinates within some cut-off radius. The functions should ideally form a complete basis to describe uniquely *all* possible arrangement of ions within the cut-off while respecting the symmetries of rotational invariance and permutations of identical elements (Bartók et al., 2013; Dusson et al., 2022). This is typically done using local per-atom *descriptors* (local, per-atom) which are combined in global structural *representations* to provide invariant or equivariant features over the relevant symmetry groups.

An alternative to manually constructing representations, which satisfy the required symmetries, is to learn the representation together with the mapping from atomic positions to energies and forces. This approach has seen considerable recent success through equivariant (Batzner et al., 2022) and message-passing (Batatia et al., 2022a, b) neural networks, which have been shown to provide improved accuracy and transferability over the descriptor-based approaches discussed above.

Although dramatic progress has been made for elemental metals and insulators, and to an increasing extent multicomponent materials (Byggmästar et al., 2021; Darby et al., 2022), the evident long-ranged interactions that we have discussed for ionic materials pose a challenge to this approach. While charge transfer among ions may be described by short-ranged functions, their Coulomb interactions are long-ranged, and alter the electron distribution and energy associated with every ion in a way that cannot be captured by a mapping of the configuration of its near neighbors. This is a nuanced matter, however, since the restricted functional forms used in empirical potentials can drastically limit their predictive accuracy even when full electrostatics are taken into account: for example, a recent machine learning potential for silica (Erhard et al., 2022) nonetheless achieves higher accuracy than empirical potentials on a range of structural and thermodynamic properties despite using a radial cut-off of just 5 Å.

To make further progress, the local energy idea has to be augmented in some way to account for long-ranged and self-consistent Coulomb interactions, as we discussed for tight-binding models, and some significant progress has been made in this direction, notably in the *PhysNet* approach of Unke and Meuwly (2019), which includes long-range interactions using partial charges learned from DFT at the same time as the energies, and through charge-equilibration schemes, which combine environment-dependent atomic electronegativities with accurate atomic energies (Ko et al., 2021; Staacke et al., 2022). The rapid progress and high level of research activity in the field are grounds for optimism.

Conclusion

The nature of the bonding in ionic crystals is fundamental to the way the computer simulation of them is carried out. This article has focussed on reviewing how the interatomic forces can be modeled. We have presented a unified view of a hierarchy of well-known, classical models by showing how they can all be derived from Kohn–Sham DFT, a standard quantum-mechanical description of the bonding. This physics-based approach to the functional form of a model employs perturbation theory and a sequence of judicious approximations. Although DFT itself is a very accurate and widely used model for calculating interatomic forces in a range of materials, with simplified models much larger systems can be simulated for longer times, and this enables new data and insights to be gained about processes in materials, and facilitates the calculation of thermophysical properties. The earliest and best-known model is the simple rigid-ion model, in which the ions carry fixed charges, interacting at a separations r via the long-ranged $1/r$ Coulomb potential, combined with short-ranged, repulsive pairwise interactions. Increasing levels of sophistication and accuracy require the ions to be deformable, typified by the shell model and, for consistency with known elastic constants, they should also be compressible. To go beyond this and acknowledge that there are no *purely* ionic materials requires the introduction of charge transfer between the ions, such as the ReaxFF model. All these models can be derived as simplified versions of tight-binding models which themselves are derived from DFT, but the choice usually involves a trade-off between the requirements of speed and accuracy. Finally, we have described alternative approaches to constructing models of interatomic forces that are becoming more prominent because they promise near-DFT accuracy at a fraction of the cost. Such models rely on DFT as the engine for generating a large database of energies, forces, and structures, to which very flexibly expressed potentials and forces are fitted or machine-learned. They have already proved to be a powerful tool in the realm of metallic elements, but there are still major challenges posed by the long-ranged interactions and charge-transfers in ionic materials, which require special treatment. Nevertheless, progress in the field is evident, and we are optimistic that such potentials will make an impact in the near future.

References

Ashcroft NW and Mermin ND (1976) *Solid State Physics*. Orlando: Harcourt Brace.

Bartók AP, Payne MC, Kondor R, and Csányi G (2010) Gaussian approximation potentials: The accuracy of quantum mechanics, without the electrons. *Physical Review Letters* 104 (13): 136403. ISSN: 0031-9007, 1079-7114. https://doi.org/10.1103/PhysRevLett.104.136403.

Bartók AP, Kondor R, and Csányi G (2013) On representing chemical environments. *Physical Review B: Condensed Matter* ISSN: 0163-1829. 87(18): 184115. https://doi.org/10.1103/PhysRevB.87.184115.

Batatia I, Batzner S, Kovács DP, Musaelian A, Simm GNC, Drautz R, Ortner C, Kozinsky B, and Csányi G (2022a) The design space of E(3)-equivariant atom-centered interatomic potentials. *arXiv:2205.06643*.

Batatia I, Kovács DP, Simm GNC, Ortner C, and Csányi G (2022b) MACE: Higher order equivariant message passing neural networks for fast and accurate force fields. *arXiv:2206.07697*.

Batzner S, Musaelian A, Sun L, Geiger M, Mailoa JP, Kornbluth M, Molinari N, Smidt TE, and Kozinsky B (2022) E(3)-Equivariant graph neural networks for data-efficient and accurate interatomic potentials. *Nature Communications* 13(1): 2453. ISSN: 2041-1723. https://doi.org/10.1038/s41467-022-29939-5.

Behler J and Csányi G (2021) Machine learning potentials for extended systems: a perspective. *The European Physical Journal B* 94(7): 142. https://doi.org/10.1140/epjb/s10051-021-00156-1. 1434-6028, 1434-6036.

Behler J and Parrinello M (2007) Generalized neural-network representation of high-dimensional potential-energy surfaces. *Physical Review Letters* ISSN: 0031-9007. 98(14): 146401. https://doi.org/10.1103/PhysRevLett.98.146401.

Born M and Huang K (1954) *Dynamical Theory of Crystal Lattices*. Oxford: Clarendon Press.

Brommer P, Beck P, Chatzopoulos A, Gahler F, Roth J, and Trebin H-R (2010) Direct Wolf summation of a polarizable force field for silica. *The Journal of Chemical Physics* 132(19): 194109. ISSN: 0021-9606. https://doi.org/10.1063/1.3396084.

Byggmästar J, Nordlund K, and Djurabekova F (2021) Modeling refractory high-entropy alloys with efficient machine-learned interatomic potentials: Defects and segregation. *Physical Review B: Condensed Matter* 104(10): 104101. ISSN: 0163-1829. https://doi.org/10.1103/PhysRevB.104.104101.

Darby JP, Kermode JR, and Csányi G (2022) Compressing local atomic neighbourhood descriptors. *npj Computational Materials* 8: 166. ISSN: 2057-3960, 2057-3960. https://doi.org/10.1038/s41524-022-00847-y.

Dick BG and Overhauser AW (1958) Theory of the dielectric constants of alkali halide crystals. *Physical Review* 112: 90–103.

Drautz R (2019) Atomic cluster expansion for accurate and transferable interatomic potentials. *Physical Review B: Condensed Matter* 99(1): 014104. ISSN: 0163-1829. https://doi.org/10.1103/PhysRevB.99.014104.

Dusson G, Bachmayr M, Csányi G, Drautz R, Etter S, van der Oord C, and Ortner C (2022) Atomic cluster expansion: Completeness, efficiency and stability. *Journal of Computational Physics* 454: 110946. ISSN: 0021-9991. https://doi.org/10.1016/j.jcp.2022.110946.

Ercolessi F and Adams JB (1994) Interatomic potentials from first-principles calculations: The force-matching method. *EPL* 26(8): 583–588.

Erhard LC, Rohrer J, Albe K, and Deringer VL (2022) A machine-learned interatomic potential for silica and its relation to empirical models. *npj Computational Materials* 8(1): 1–12. ISSN: 2057-3960, 2057-3960. https://doi.org/10.1038/s41524-022-00768-w.

Finnis M (2003a) *Interatomic Forces in Condensed Matter*. Oxford: OUP.

Finnis M (2003b) Interatomic forces in materials. *Progress in Materials Science* 49: 1–18.

Finnis MW, Paxton AT, Methfessel M, and van Schilfgaarde M (1998) The crystal structure of Zirconia from first principles and self consistent tight binding. *Physical Review Letters* 81: 5149–5152.

Gordon RG and Kim YS (1972) Theory for the forces between closed-shell atoms and molecules. *Journal of Chemical Physics* 56: 3122–3133.

Han XJ, Bergqvist L, Dederichs PH, Müller Krumbhaar H, Christie JK, Scandolo S, and Tangney P (2010) A polarizable interatomic force field for TiO_2 parameterized using density functional theory. *Physical Review B* 81: 134108.

Harrison WA (1980) *Electronic Structure and the Properties of Solids*. San Francisco: W. H. Freeman.

Hohenberg P and Kohn W (1964) Inhomogeneous electron gas. *Physical Review* 136: B864–B871.

Ivanov OV and Maksimov EG (1996) Generalized variational approach to Kim-Gordon electron gas theory for ionic crystals. *Solid State Communications* 97: 163–167.

Johnson QC and Templeton DH (1961) Madelung constants for several structures. *Journal of Chemical Physics* 34: 2004–2007.

Kermode JR, Cereda S, Tangney P, and De Vita A (2010) A first principles based polarizable O(N) interatomic force field for bulk silica. *The Journal of Chemical Physics* 133(9): 094102. ISSN: 0021-9606, 1089-7690. https://doi.org/10.1063/1.3475565.

Kim YS and Gordon RG (1974) Theory of binding of ionic crystals: Application to alkali-halide and alkali-earth-dihalide crystals. *Physical Review B* 9: 3548–3554.

Kittel C (1976) *Introduction to Solid State Physics*, fifth ed. New York: Wiley.

Ko TW, Finkler JA, Goedecker S, and Behler J (2021) A fourth-generation high-dimensional neural network potential with accurate electrostatics including non-local charge transfer. *Nature Communications* ISSN: 2041-1723. 12(1): 398. https://doi.org/10.1038/s41467-020-20427-2.

Kohn W and Sham LJ (1965) Self-consistent equations including exchange and correlation effects. *Physical Review* 140: A1133–A1138.

Marks NA, Finnis MW, Harding JH, and Pyper NC (2001) A physically transparent and transferable compressible ion model for oxides. *Journal of Chemical Physics* 114: 4406–4414.

Pedone A, Bertani M, Brugnoli L, and Pallini A (2022) Interatomic potentials for oxide glasses: Past, present, and future. *Journal of Non-Crystalline Solids: X* 15: 100115. ISSN: 2590-1591. https://doi.org/10.1016/j.nocx.2022.100115.

Sarsam J, Finnis MW, and Tangney P (2013) Atomistic force field for alumina fit to density functional theory. *The Journal of Chemical Physics* 139(20): 204704. https://doi.org/10.1063/1.4832695. 0021-9606, 1089-7690.

Staacke CG, Wengert S, Kunkel C, Csányi G, Reuter K, and Margraf JT (2022) Kernel charge equilibration: Efficient and accurate prediction of molecular dipole moments with a machine-learning enhanced electron density model. *Machine Learning: Science and Technology* 3(1): 015032. ISSN: 2632-2153. https://doi.org/10.1088/2632-2153/ac568d.

Streitz FH and Mintmire JW (1994) Electrostatic potentials for metal-oxide surfaces and interfaces. *Physical Review B* 50: 11996–12003.

Tangney P and Scandolo S (2002) An ab initio parametrized interatomic force field for silica. *The Journal of Chemical Physics* 117(19): 8898. ISSN: 0021-9606. https://doi.org/10.1063/1.1513312.

Unke OT and Meuwly M (2019) PhysNet: A neural network for predicting energies, forces, dipole moments, and partial charges. *Journal of Chemical Theory and Computation* 15(6): 3678–3693. ISSN: 1549-9618, 1549-9626. https://doi.org/10.1021/acs.jctc.9b00181.

Unke OT, Chmiela S, Sauceda HE, Gastegger M, Poltavsky I, Schütt KT, Tkatchenko A, and Müller K-R (2021) Machine learning force fields. *Chemical Reviews* 121(16): 10142–10186. ISSN: 0009-2665, 1520-6890. https://doi.org/10.1021/acs.chemrev.0c01111.

van Duin ACT, Dasgupta S, Lorant F, and Goddard WA (2001) ReaxFF: A reactive force field for hydrocarbons. *The Journal of Physical Chemistry. A* 105(41): 9396–9409. ISSN: 1089-5639. https://doi.org/10.1021/jp004368u.

Wilson M, Huang YM, Exner M, and Finnis MW (1996) Transferable model for the atomistic simulation of Al_2O_3. *Physical Review B* 54: 15683–15689.

Ziman JM (1972) *Principles of the Theory of Solids*, second ed. Cambridge: CUP.

Crystal binding (interatomic forces): Metallic bonding and crystals[☆]

DJ Willock, Cardiff Catalysis Institute, School of Chemistry, Cardiff University, Cardiff, United Kingdom

© 2024 Elsevier Ltd. All rights reserved.

This is an update of D.J. Willock, Metallic Bonding and Crystals, Editor(s): Franco Bassani, Gerald L. Liedl, Peter Wyder, Encyclopedia of Condensed Matter Physics, Elsevier, 2005, Pages 353–361, ISBN 9780123694010, https://doi.org/10.1016/B0-12-369401-9/00410-1.

Introduction 217
Band structure 218
Tight Binding approximation 218
Band filling and metallic behavior 222
Band structure in three dimensions 225
Dependence of metallic structure on the density of states 228
Conclusion 229
References 230

Abstract

Metal bonds differ from ionic and covalent bonds in the degree of delocalization of electrons between nuclei. In this chapter we will use the ideas of band theory to look at the way these delocalized electrons can be described mathematically. A tight binding approach helps identify electron states that stabilize the structure (bonding states) or destabilize the system if occupied (anti-bonding states). Density of states per energy unit is compared between bands formed from different atomic orbitals in 1-D examples. Band theory is then applied to understand the crystal structures taken on by the first row transition metals.

Key points

- Metal bonding is the result of a delocalization of electrons across many atoms.
- To understand metallic bonding, we must look into the band theory of electronic states in crystalline materials.
- Tight binding theory is one way to develop a band structure for a model based on a linear combination of atomic orbitals.
- The band structure gives a rational for the energies of electronic states which depends on the crystal structure.
- We can use the band structure and density of states to rationalize the crystal structures adopted by different metals.

Introduction

Metals form an important class of technological materials that are exploited widely for their ductility and high electrical and thermal conductivities. The general physical definition of the metallic state is based on these macroscopic properties. In this article the electronic structure of metals is considered based on a simple extension of the linear combination of atomic orbitals, that is used to describe bonding in molecules, but applied to the solid state. This makes it possible to define the metallic state precisely using the crystal orbitals responsible for bonding and so consider the importance of the metallic state in the cohesive energy of solids and its influence on structure.

The types of bonding discussed in this section of the *Encyclopedia* can be broadly divided into localized effects, involving only a few atoms in the vicinity of the chemical bond, and de-localized effects involving co-operative interactions between many atom centers. Localized interactions include covalent and hydrogen bonding while ionic and van der Waals interactions may be classed as de-localized. The concept of the Metallic bond is a little more difficult to define rigorously and has been the subject of much debate. Broadly speaking, the metallic bond can be considered as the sharing of electron density by multiple atomic centers in condensed phases. What allows us to distinguish Metallic bonding from other situations is the electronic character of the bond. The classic view of the metallic bond in solids is the “sea of electrons” concept which gives the impression of de-localization of the electrons in metallic systems. The metallic bond in this picture is an extreme example of the covalent bond and it has been suggested that the metallic bond as a concept can be subsumed into this class of bonding. However, the metallic state requires a combination of de-localized crystal orbitals and knowledge of their occupation and is a collective property of the entire electron density rather than a few specific states. In this article these ideas will be expanded and the influence of the metallic state of a solid on its stability and structure will be considered.

[☆] *Change History*: April 2023. D.J. Willock updated all sections and figures.

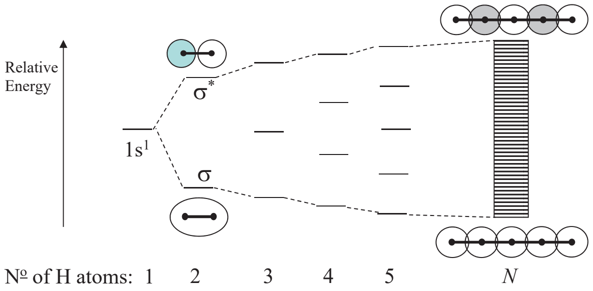

Fig. 1 Schematic illustration of the build-up of a band of states from the aggregation of H atoms. *N* is the number of atoms in a bulk sample and will be of the order of the Avagadro Constant (6.022×10^{23} mol^{-1}). Insets show the molecular orbitals for the H_2 molecule and for the top and bottom of the condensed phase band of states.

The limit of very weak interaction between the atomic cores and the valence electrons is usually employed to build a model of the electronic states in metals using the nearly free electron approximation (Kittel, 2018). In this contribution the opposite approach will be used in which crystal orbitals are built up from atomic orbitals. This gives better insight into the chemical bonding nature of the metallic state.

Band structure

The idea of a chemical bond as the sharing of electron density between atoms can be rationalized by the formation of molecular orbitals from atomic orbitals. For example, a hydrogen atom has a $1s^1$ configuration and when the orbitals from two atoms overlap in molecular H_2 they can combine in two ways. Firstly, overlap between the 1s orbitals can be constructive, leading to a build up of charge between the two nuclei and giving an interaction between the atoms that lowers the energy compared to the atomic state. This favors H_2 formation through the formation of a bonding orbital (σ in Fig. 1). The alternative is destructive interference between the atomic orbitals in the overlap region. This leads to a lowering of the electron density in the inter-atomic region compared to two non-interacting atoms at the same positions. If this molecular orbital is occupied a de-stabilizing contribution to the energy is obtained and the total energy is higher than that of the isolated atom states. This molecular orbital is, therefore, anti-bonding in nature (σ^* in Fig. 1). In molecular H_2 each atom supplies a single electron and so the bonding orbital is fully occupied (2 electrons) and the anti-bonding orbital is not occupied, so overall the bond is favored.

Fig. 1 also shows a schematic representation of the interactions of atomic orbitals in larger aggregations of H atoms. The difference in energy of the molecular orbitals and atomic orbitals are influenced by two main factors. Firstly, the degree of overlap between atomic orbitals; the more overlap the bigger the perturbation from the atomic state. Secondly, the energy of the two atomic orbitals; when these are well matched the difference between the energies of the molecular and atomic states is greater than when they are very different in energy. In the case of the H_2 molecule the orbital energies for the atomic states are identical and so this is optimal. If a third H atom is included the additional *s*-orbital will interact only weakly with the molecular orbitals of the H_2 molecule since the bonding and anti-bonding states are well separated in energy from the atomic state of the new atom. As more atoms are introduced to produce the 1-D solid the same number of molecular orbitals are formed as 1s orbitals that are supplied, but the energy range for the set of orbitals increases only slowly with the number of atoms. Making the leap to the 1-D solid with some large number of atoms (*N* in Fig. 1) there will be *N* crystal orbitals spread over an energy range not too dissimilar to the gap between the H_2 bonding and anti-bonding orbitals. There are now too many crystal orbitals to illustrate them all. Fig. 1 does show the extreme cases of the lowest energy crystal orbital with all bonding between neighboring atoms and the highest energy crystal orbital with all anti-bonding interactions between neighbors. In general, states at the bottom of the band will be stabilizing for crystal formation from gaseous atoms since they are lower in energy than the atomic 1 s states. The states above the band center in this situation are destabilizing since they have higher energies than the atomic 1s states. In this simple example a filled band has zero contribution to the lattice energy overall.

Tight Binding approximation

The approach of building up condensed phase crystal orbitals based on molecular orbital theory can be given some mathematical structure by defining the linear combinations of atomic orbitals that are present in the 1-D chain, (Hoffmann, 2002) (Fig. 2).

The appropriate linear combination of atomic orbitals will be:

$$\psi_p = \sum_n c_{pn}\chi_n$$

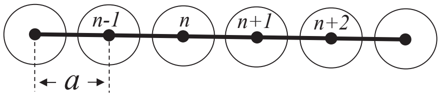

Fig. 2 An idealized one-dimensional array of atoms, each atom contributes a single s-orbital to the system, the lattice parameter, *a*, is shown as the separation between neighbors so the unit cell contains a single atom.

where c_{pn} is the coefficient for the p^{th} crystal orbital constructed from the local atomic functions, χ_n, at each site, n, in the lattice. From the discussion above, if there are N atomic orbitals in the crystal there must be N values of p. The possible values of p can be found by considering the effect of crystal translational symmetry on the electron density.

The density of electrons, $\rho(X)$, at any point, X, in the crystal is related to the crystal wavefunctions via:

$$\rho(X) = \sum_{p}^{Ne/2} \psi_p^*(X)\psi_p(X)$$

where N_e is the number of electrons to be accommodated in the crystal orbitals and "$*$" signifies the complex conjugate. The density of electrons can be observed experimentally using X-ray diffraction, whereas the crystal orbitals are not experimental observables. Translational symmetry implies that the density must be the same at all equivalent points in the crystal. In the one dimensional lattice with repeat unit, a, this means that the densities at a point x in one unit cell and at any point $X = x + na$ (where n is any integer) must be the same. The wavefunctions need not have the same property but this restriction on the density can be met if, for any crystal orbital:

$$\psi_p^*(x + na)\psi_p(x + na) = \psi_p^*(x)\psi_p(x)$$

This leads to the expression of the crystal wavefunctions as Bloch functions:

$$\psi_k(X) = u(X)\exp(i\,kX)$$

Here $i = \sqrt{-1}$. The term $u(X)$ describes a periodic array of the functions local to the unit cells of the crystal:

$$u(X) = \sum_{n} \chi_n(X - na)$$

Fig. 3A shows $u(X)$ for the example of a line of s-orbitals, this time drawn as the radial function for the orbital at each lattice site. Provided we think of the line of atoms as effectively infinite this sum over local site functions is periodic in the lattice vector because

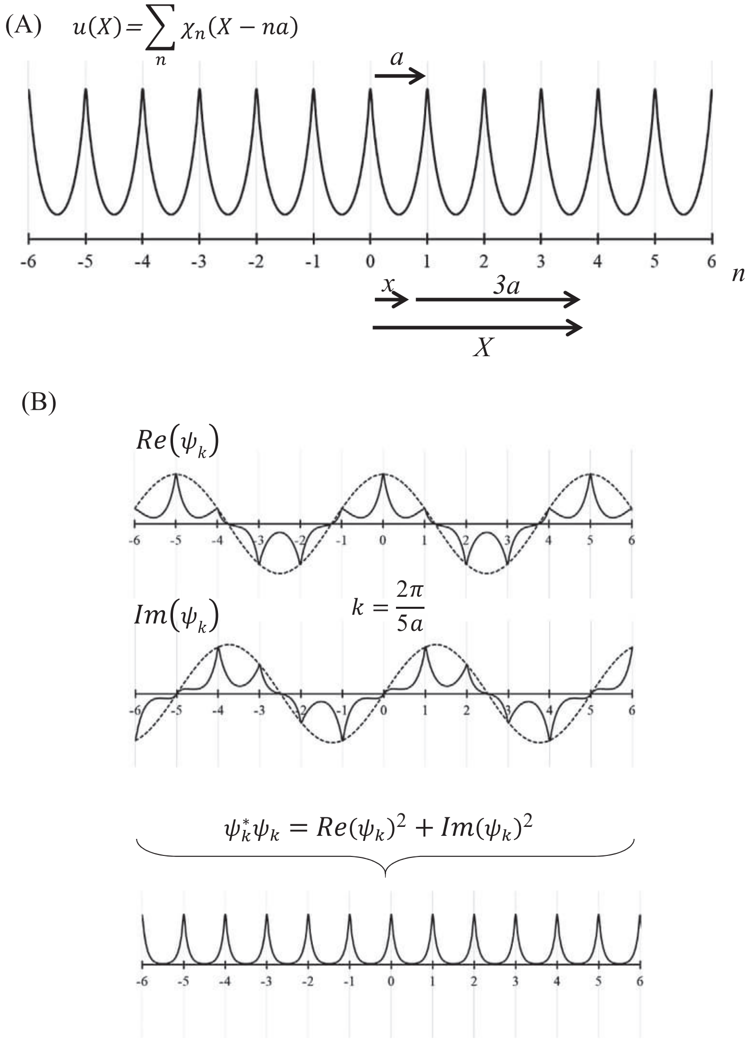

Fig. 3 Plots of the real part of a periodic wavefunction based on Bloch functions. The radial part of each local atomic function is modulated by the periodic function with the *k*-vector indicated. The atomic positions are numbered on the axes.

a shift by a whole number of lattice vectors would not change the function. This is equivalent to ignoring surface effects in real crystals when dealing with bulk properties.

The complex exponential term in the Bloch function is also periodic via the standard mathematical relation:

$$\exp(i\,kX) = \cos(kX) + i\,\sin(kX)$$

Then

$$\psi_k^*(x+na)\psi_k(x+na) = u(X)^2\exp(-ikX)\exp(ikX) = u(X)^2 = \psi_k^*(x)\psi_k(x)$$

As $u(X)$ has the periodicity of the lattice so does the density derived from crystal orbitals based on Bloch functions, as required. Fig. 3B shows an illustrative example for the case of $k = 2\pi/(5a)$ with the real and imaginary parts of the wavefunction plotted separately and then the product $\psi_k^*\psi_k$ to show graphically that the Bloch functions give contributions to the density with the same periodicity as the lattice. In Fig. 3B the real and imaginary parts of the $\exp(ikX)$ term for the state are shown as dashed lines. This demonstrates how the complex exponential term controls the periodicity of the phase pattern of the crystal orbital along the atomic row on a length scale greater than the cell vector. In this example, the wavefunction is periodic on a scale of $5a$.

Fig. 4 gives some further examples of the real part of periodic wavefunctions with different k-vector values. For this line of s-orbitals, $k = 0$ (Fig. 4A) corresponds to the all-bonding orbital that we identified earlier as the lowest energy crystal orbital. The $k = \pi/a$ Bloch function (Fig. 4D) corresponds to the all anti-bonding condition between neighbors that gives the highest energy crystal orbital for a line of s-orbitals. Fig. 4B and C also show the $k = \pi/(3a)$ and $k = 2\pi/(3a)$ solutions which repeat over $6a$ and $3a$ respectively. These orbitals have intermediate energies as they contain a mix of bonding and anti-bonding interactions between neighbors. Fig. 4 illustrates that the degree of anti-bonding in this example increases with the magnitude of the k-vector.

The wave-vector, k, is commonly used as the label for the crystal orbitals as has been done above, it is related to the integer p via:

$$\mathrm{k} = \frac{2\pi \mathrm{p}}{\mathrm{Na}},\quad \mathrm{p} = -\frac{\mathrm{N}}{2}\ldots.-1,0,1,\ldots..\frac{\mathrm{N}}{2},\quad \mathrm{k} = -\frac{\pi}{\mathrm{a}}\ldots.,0,\ldots..\frac{\pi}{\mathrm{a}}$$

The integer p has $N+1$ values, however the $p = -N/2$ and $p = N/2$ cases are equivalent, both would give solutions periodic on a length scale of $2a$ (see Fig. 4D). This means that the N atomic orbitals that are combined will form N crystal orbitals ($2N$ electronic states).

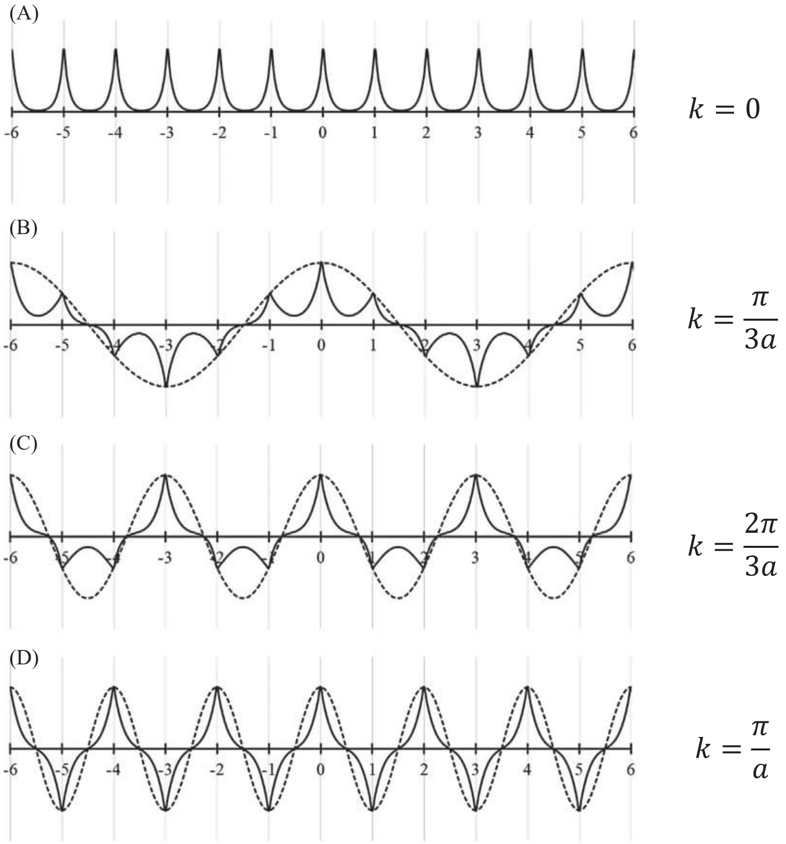

Fig. 4 Example plots for the real part of Bloch functions for the cases (A) $k = 0$, (B) $k = \pi/(3a)$, (C) $k = 2\pi/(3a)$ and (D) $k = \pi/a$. In each case the atomic positions are numbered on the x-axis and the real (cosine) part of the $\exp(i\,kX)$ term is shown as a dashed line.

The k-vectors have units of reciprocal length and allowed values ranging from $-\pi/a$ to π/a. Now another lattice or line of points can be constructed for the values of k that give valid Bloch functions for the lattice. This line is related to the real space row of atomic sites but the lattice points give the periodicities of waves with reciprocal length units, i.e. they are points in reciprocal space. The allowed values of k define the range in reciprocal space occupied by the unique Bloch states which is known as the Brillouin zone.

Using the crystal orbitals in the Schrödinger equation gives the orbital energy as a function of the wavevector k:

$$E_k = \frac{\int_{-\infty}^{\infty} \psi_k^* H \psi_k dx}{\int_{-\infty}^{\infty} \psi_k^* \psi_k dx}$$

Here, H, is the Hamiltonian describing the interaction of the electron in the crystal orbital with the line of atoms. The crystal orbitals in terms of Bloch states allow the numerator and denominator of this expression to be written as:

$$\int_{-\infty}^{\infty} \psi_k^* H \psi_k dx = \sum_n^N \sum_m^N \exp(ik(na - ma)) \int_{-\infty}^{\infty} \chi_n^*(X-na) H \chi_m(X-ma) dX$$

and

$$\int_{-\infty}^{\infty} \psi_k^* \psi_k dx = \sum_n^N \sum_m^N \exp(ik(na - ma)) \int_{-\infty}^{\infty} \chi_n^*(X-na) \chi_m(X-ma) dX$$

In which m and n are integers identifying sites along the row of atoms and now the integrals required are over the local atomic functions. To obtain a qualitative insight into the band structure the simplifying tight binding approximations can be used which give the integrals required for the numerator the values:

$$\int_{-\infty}^{\infty} \chi_n^*(X-na) H \chi_m(X-ma) dX = \alpha \qquad m = n$$
$$\int_{-\infty}^{\infty} \chi_n^*(X-na) H \chi_m(X-ma) dX = \beta \qquad m = n \pm 1$$
$$\int_{-\infty}^{\infty} \chi_n^*(X-na) H \chi_m(X-ma) dX = 0 \quad m < n - 1 \text{ or } m > n + 1$$

That is to say, the on-site term is given the parameter, α, the term for nearest neighbors the parameter, β, and all other terms are simply ignored. This concentration on local interactions is the reason the approximation itself is called "tight binding". Although the interaction contributions are considered in this way the crystal orbitals are still de-localized along the entire chain of atoms. For the denominator the tight binding approximation is even more severe:

$$\int_{-\infty}^{\infty} \chi_n^*(X-na) \chi_m(X-ma) dX = 1 \quad m = n$$
$$\int_{-\infty}^{\infty} \chi_n^*(X-na) \chi_m(X-ma) dX = 0 \quad m \neq n$$

So the overlap between an atomic orbital with itself is taken to be 1 and the overlap between neighboring sites and beyond is taken to be insignificant. Using these integral values in the energy expression gives the formula:

$$E_k = \alpha + 2\beta \cos(ka)$$

The factor of 2 occurs as each site has one neighbor to the left and one to the right in the chain. The energy of a particular crystal orbital depends on the local energy terms and the wave-vector of the orbital. For a given system the local interaction integrals are simply fixed parameters. In general the relationship between the energy, E_k and the wave-vector of the state, k, is termed the dispersion relation.

This model can now be applied to the band of states for the 1-D chain of hydrogen atoms for which the local functions are s-orbitals on each H atom. As we saw in Fig. 4, when $k = 0$ the exponential factor in the crystal orbital Bloch function is 1 and so all site orbitals are in phase giving a low energy contribution. In contrast, when $k = \pm \pi/a$ the complex exponential gives a wave that changes sign between neighboring unit cells of the crystal and so all neighboring orbitals have an anti-bonding interaction, a high energy contribution. The dispersion equation provides a way to calculate a numerical estimate of the energy of the crystal orbital for any k-value and so quantify the difference between bonding and anti-bonding. Fig. 5 shows the resulting dispersion relation for a line of s-orbitals from the tight binding approximation. The low energy states are around $k = 0$ while for k near its limiting values of $\pm \pi/a$ the energy of the states are higher than for the isolated atomic orbitals, implying that β is negative. The overall band width is 4β, so the strength of interaction between neighboring sites controls the band width. The energy of the band center ($k = \pi/(2a)$) from the dispersion relation is the α parameter value, as the cosine term is zero at this point. So the on-site orbital energy term controls the position of the band on the energy axis.

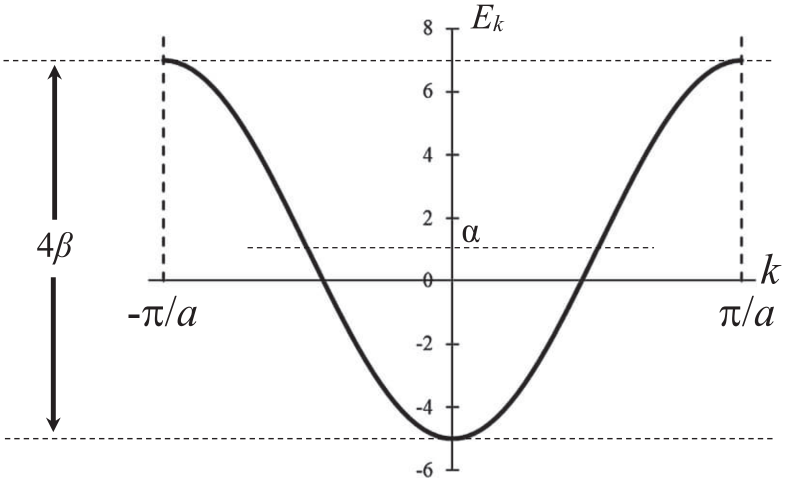

Fig. 5 The dispersion relation for a line of s-orbitals from the tight binding approximation. In this example we have taken $\alpha = 1$ and $\beta = -3$ with arbitrary energy units. The choice of negative β corresponds to bonding overlap between neighboring unit cells at $k = 0$.

The allowed values of k are defined with the quantum number p, are evenly spaced in reciprocal space at intervals of $2\pi/(Na)$. However, the relationship between the energy and the k-vector is not linear. In particular, near the Brillouin zone boundary the dispersion curve flattens, so that many k-vectors in this region have almost the same energy. In one dimension a similar effect is seen at the zone center. The density of states (DOS), $N(E)$, is defined as the number of energy levels within a small energy increment as a function of the state energy. In one dimension the regions in which the dispersion curve flattens out lead to a higher DOS than in regions in which the dispersion curve is steep.

Band filling and metallic behavior

The metallic state can now be defined based on the electron occupancy of the crystal orbitals. For the line of *s*-orbitals from hydrogen atoms there are N-crystal orbitals and the Pauli exclusion principle dictates that each orbital can contain a maximum of 2 electrons, one spin up and one spin down. The crystal orbitals, therefore, give rise to $2N$ electron states, each hydrogen atom delivers one electron and so the states are half filled. This assumes that states are simply filled from the lowest energy upwards until all electrons have been placed in crystal orbitals. However, since the energy separation of states within a band is extremely small, this strict ordering is only possible at zero Kelvin. At any finite temperature an electron at the top of the occupied levels can be promoted to the un-occupied states by thermal excitation. The probability of occupancy of a state, $f(E_k)$, is controlled by Fermi-Dirac statistics:

$$f(E_k) = \frac{1}{1 + \exp\left(\frac{E_k - E_F}{k_B T}\right)}$$

Here E_F is the Fermi energy which, in metals, corresponds to the energy of the highest occupied state at zero Kelvin, k_B is the Boltzmann constant and T the temperature. More generally E_F is defined from this formula as the energy at which the probability of occupancy is exactly one half.

Fig. 6 shows plots of the Fermi-Dirac probability function at different temperatures. At 0 K it can be seen that the low energy states are filled up to E_F but above E_F all states are empty. At higher temperatures, however, electrons from below the Fermi energy can be promoted to the higher states, leading to the tail feature. These promotions can only occur if there are states available to receive the electrons that are excited. In the one dimensional H example the band of $2N$ states is half filled and so there are states available for the thermally excited electrons to move into. This situation gives rise to the electrical and thermal conduction in metals, filled and empty states are so close together that the promotion of electrons at energies close to E_F can occur easily. These electrons at the interface between the occupied and un-occupied states are active in transport giving rise to the metallic behavior of the solid. Accordingly, condensed hydrogen is expected to be a metal.

The construction of the crystal orbitals also show that the occupied states are those which are largely bonding and so solid H is favored over separated gas phase H atoms. In the laboratory, the liquid state of H has been achieved at low temperature and very high pressure using shock wave pressure methods and is found to have metallic conductivity. However, under most circumstances, $N/2$ diatomic molecules is an even more stable situation and so the diatomic gas is the normal state.

There are a few less exotic examples of solids with 1-D aspects to their electronic structure. For example, the solid formed by salts of the $[Pt(CN)_4]^{2-}$ anion contain square planar complexes stacked in the crystallographic *c*-direction. In the simple $K_2[Pt(CN)_4]$ salt (Fig. 7A) neighboring Pt centers are 3.48 Å apart. Within each complex the Pt atom is in the 2+ oxidation state and so has a d^8 electron configuration. Fig. 8 shows each orbital type and their arrangement along the line of complexes for the

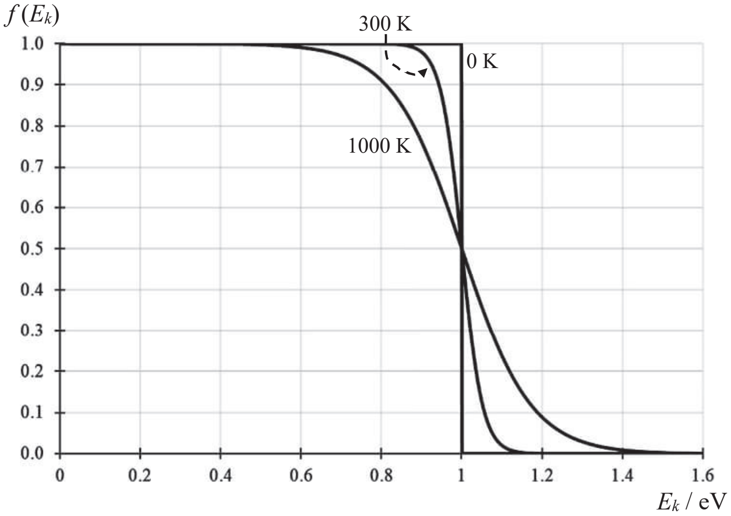

Fig. 6 Plots of the Fermi-Dirac statistics function for temperatures of 0 K, 300 K and 1000 K. This example has the value of E_F set to 1 eV.

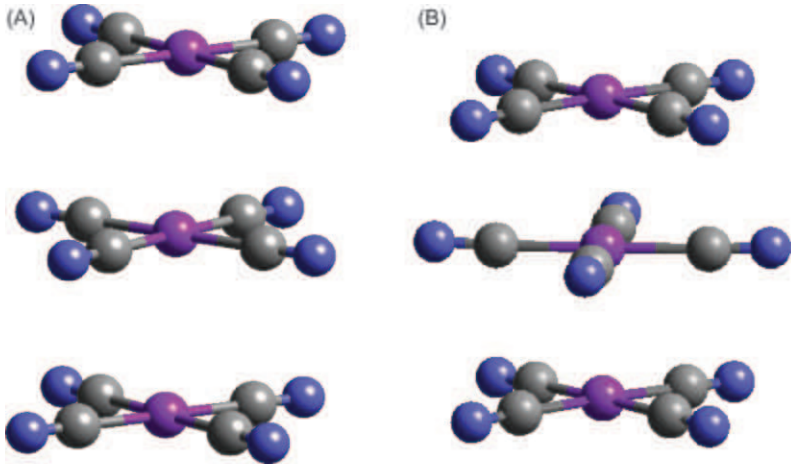

Fig. 7 Chain structures formed by $[Pt(CN)_4]^{2-}$ in the solid state. (A) From $K_2[Pt(CN)_4]$, (B) from $K_2[Pt(CN)_4]$. $Br_{0.3}$. For clarity cations, dopants and water of crystallization have been omitted. Atom colors: C: gray, N: blue and Pt: purple.

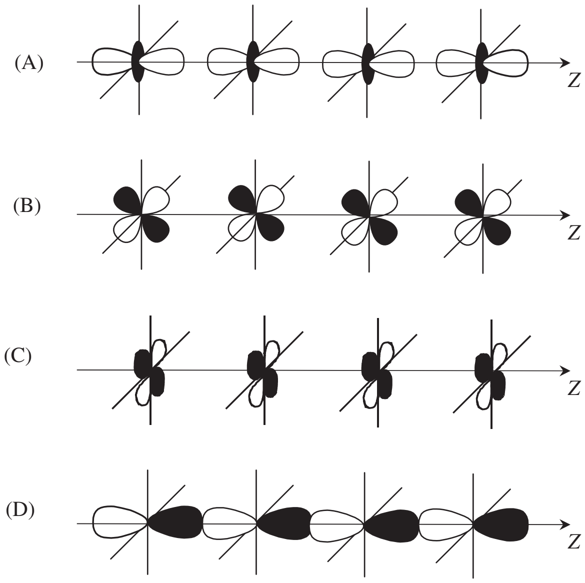

Fig. 8 The arrangement of orbitals for the $k = 0$ wave-vector case for a chain of atoms along the Z-axis. (A) d_{z2}, (B) d_{xz} or d_{yz}, (C) d_{xy}, d_{x2-y2} have the same bonding symmetry but with orbitals rotated 45° in the xy plane, (D) p_z.

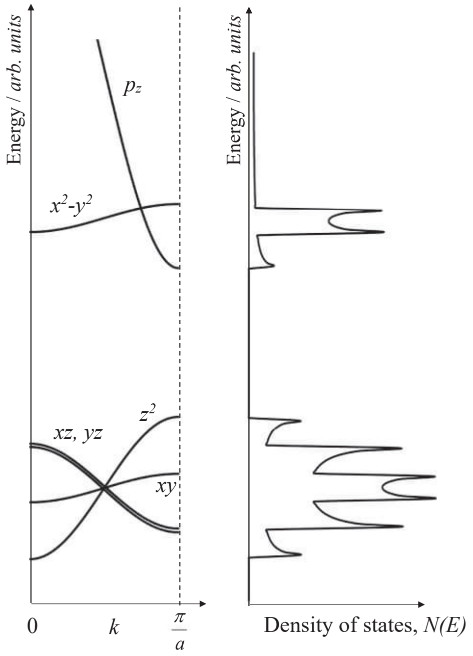

Fig. 9 The dispersion curves and density of states (DOS) for the bands formed along the stacking direction in $K_2[Pt(CN)_4]$ by the Pt centered orbitals.

$k = 0$ wave-vector. By convention the Z-direction for defining the orbital orientation is aligned with the stacking direction of the complexes. Fig. 9 shows the dispersion plots in the positive k-vector region for each of the bands formed. The interaction with the CN^- ligands puts the energy of the molecular anti-bonding orbital involving the $d_{x2\text{-}y2}$ atomic orbital above the other d-orbitals. In terms of tight binding theory this means that the α parameter is larger for $d_{x2\text{-}y2}$ than the other d-orbitals and so this is un-occupied. The dispersion curves of the bands formed between the metal centers depend on the symmetry of the orbitals with respect to the chain direction. At $k = 0$, the d_{z2} orbital has a bonding arrangement, similar to the s-orbitals used in the hydrogen example, and so the dispersion curve for this band is similar to Fig. 5. The d_{xz} and d_{yz} orbitals form a degenerate pair of bands in which the $k = 0$ orbital is anti-bonding, which means that the energy of the crystal orbitals decrease as k approaches π/a. The tight binding parameter, β, in this case is positive. These orbitals also have π-symmetry (Fig. 8B), rather than σ, which leads to a weaker overlap between neighbors and so a smaller magnitude for the tight binding β-parameter. Since the band width is 4β this results in a narrower range of energies in the band than for d_{z2}. The d_{xy} and $d_{x2\text{-}y2}$ orbitals both have δ-symmetry bonding interactions at $k = 0$ (Fig. 8C) so the bands are narrower still. The 6p orbitals of Pt are empty within the complex, however the molecular orbital involving the Pt p_z orbital is only just higher in energy than $d_{x2\text{-}y2}$. The symmetry of the p_z orbital gives σ anti-bonding at $k = 0$ (Fig. 8D) while at $k = \pm\pi/a$ each alternate p_z orbital is inverted, giving a bonding arrangement. For orbitals with this symmetry, states at the Brillouin zone boundary are lower in energy than at the center and so the dispersion relation appears inverted compared to orbitals with bonding at $k = 0$.

In the dispersion curves for these bands of the Pt complex stacks (Fig. 9) the four occupied complex orbitals involving d_{z2}, d_{xy}, d_{xz} and d_{yz} have similar energies and so have been assigned the same α-parameter, this means they cross at $k = \pi/(2a)$. All four orbitals form a continuous band of states. However, the strength of interaction between neighbors is not the same in them all and so they have different band widths as discussed above. The $d_{x2\text{-}y2}$ and p_z orbital form another overlapping set of bands. The p_z orbital states on the complexes are above the $d_{x2\text{-}y2}$ however the interaction between neighbors is stronger for the p-orbitals and so the p_z-band is wider, leading to the lowest un-occupied states being p_z in nature.

Just as the line of H orbitals gave the same number of crystal orbitals as the number of atomic orbitals in the line each of the d-orbitals in the Pt stack will have the same number of crystal orbitals in the corresponding bands. This means that when we look at the DOS in Fig. 9 the area under the contribution to the DOS from each band is the same and so bands with a narrow band width will have a relatively high density of states. We have seen that the band width is controlled by the β parameter in the tight binding theory and so the weaker the overlap between orbitals in neighboring unit cells the narrower the band and the higher the density of states per unit energy. Also, in Fig. 9 we can see that the degenerate d_{xz} and d_{yz} bands generate twice the DOS of contributions from single orbitals.

For $K_2[Pt(CN)_4]$ there is a band gap between the occupied and unoccupied states so the material is a semi-conductor in the chain direction. However, metallic behavior can be induced by the addition of halide dopant ions to give chemical formulae such as $K_2[Pt(CN)_4]$ $Br_{0.3}$. This is a level of "dopant" much greater than used in classical semi-conductors such as silicon and so the concentration of extrinsic carriers is correspondingly higher. The halide anions withdraw electrons from the Pt chains giving empty states in the top of the occupied band and placing the Fermi level at the interface between filled states and empty states in the band. Measurements confirm that the electrical conductivity is 10^4–10^5 times greater along the stack direction than perpendicular to it in the doped material. The crystal structure is also strongly affected by this change to a metallic form. The Pt-Pt distance in the doped material is 2.89 Å, not much greater than in Pt metal (2.78 Å). This reduction in Pt-Pt distance can be understood in terms of the bonding character for the chain states. In the $K_2[Pt(CN)_4]$ material there is a completely filled band of states and so both bonding and anti-bonding crystal orbitals are occupied. When the dopant is added charge is withdrawn from the high lying anti-bonding states and the free Fermi surface corresponds to an overall bonding character from the crystal orbitals. The increased bonding along the chain direction leads to the observed shortening of the Pt-Pt distance. To accommodate this there is also a rotation of alternate complexes to avoid steric clashes between CN ligands, as can be seen in Fig. 7B.

Band structure in three dimensions

It is more common for crystals to contain bonding between metal atoms in X, Y and Z directions. This is the case in elemental metal solids and metal alloys. In three dimensions (3-D) the unit cells of solids are described by a packing volume with sides defined by vectors, $\underline{a}$, $\underline{b}$ and $\underline{c}$. A position anywhere in the crystal, $\underline{R}$, can then be written based on the cell vector directions:

$$\underline{\mathrm{R}} = \underline{\mathrm{r}} + \underline{\mathrm{T}}$$

where the vector, $\underline{r}$, is a position in an arbitrary reference unit cell:

$$\underline{\mathrm{r}} = \mathrm{f_a}\underline{\mathrm{a}} + \mathrm{f_b}\underline{\mathrm{b}} + \mathrm{f_c}\underline{\mathrm{c}}$$

The f coefficients being the fraction of the cell vector in the direction indicated by the subscript defining the position of a point in the reference unit cell.

The vector, $\underline{T}$, is a translation vector between unit cells:

$$\underline{\mathrm{r}} = \mathrm{n_a}\underline{\mathrm{a}} + \mathrm{n_b}\underline{\mathrm{b}} + \mathrm{n_c}\underline{\mathrm{c}}$$

Where n is an integer for the number of unit cells in the direction indicated by the subscript from the arbitrary reference cell to the cell containing the position $\underline{R}$.

Correspondingly, the reciprocal wave-vectors have three components in reciprocal space. The reciprocal space unit cell has dimensions related to the real space unit cell by the relations:

$$\underline{\mathrm{a}}^* = \frac{2\pi}{\mathrm{V_c}}\,\underline{\mathrm{b}} \times \underline{\mathrm{c}} \quad \underline{\mathrm{b}}^* = \frac{2\pi}{\mathrm{V_c}}\,\underline{\mathrm{c}} \times \underline{\mathrm{a}} \quad \underline{\mathrm{c}}^* = \frac{2\pi}{\mathrm{V_c}}\,\underline{\mathrm{a}} \times \underline{\mathrm{b}}$$

Where V_c, is the volume of the unit cell, "×" means a vector cross-product and superscript "*" refers to the reciprocal lattice. As $V_c = \underline{a}\,.\,(\underline{b} \times \underline{c})$, these reciprocal space cell vectors have units of reciprocal length and an alternative way to write the reciprocal space vectors is:

$$\underline{\mathrm{a}}^* = \left(\frac{2\pi}{\mathrm{a}}, 0, 0\right) \underline{\mathrm{b}}^* = \left(0, \frac{2\pi}{\mathrm{b}}, 0\right) \underline{\mathrm{c}}^* = \left(0, 0, \frac{2\pi}{\mathrm{c}}\right)$$

Where the cell vector letter without the underline refers to the scalar length of the vector. The bracket notation has the components of the vectors in the order of the cross product directions. For orthogonal cells, $\underline{a}^*$ is aligned with $\underline{a}$, $\underline{b}^*$ with $\underline{b}$ and $\underline{c}^*$ with $\underline{c}$, but not all cells are orthogonal so the use of the cross products to define the directions keeps the discussion general for any crystal structure.

The k-vector in 3-D can now be expressed as a combination of reciprocal vectors:

$$\underline{\mathrm{k}} = \mathrm{f_{a*}}\underline{\mathrm{a}}^* + \mathrm{f_{b*}}\underline{\mathrm{b}}^* + \mathrm{f_{c*}}\underline{\mathrm{c}}^*$$

where the factors, f, are fractional values from $-\frac{1}{2}$ to $+\frac{1}{2}$ controlling the repeat of the wave vector in the direction indicated by the subscript.

This leads to straightforward generalization of the Bloch function to 3-D, (Ashcroft and Mermin, 1976):

$$\psi_{\underline{k}}(\underline{R}) = u(\underline{R})\exp(i\,\underline{k}.\underline{R})$$

For example, if we take the k-vector with $(f_{a*}, f_{b*}, f_{c*}) = \left(\frac{1}{2}, 0, 0\right)$, i.e., $\underline{k} = \frac{\underline{a}^*}{2} = \left(\frac{\pi}{a}, 0, 0\right)$,

$$\psi_{\underline{a}^*/2}(\underline{R}) = u(\underline{R})\exp\left(i\,\frac{\underline{a}^*}{2}.\underline{R}\right)$$

the argument of the complex exponential becomes,

$$\frac{\underline{\mathrm{a}}^*}{2}.\underline{\mathrm{R}} = \left(\frac{\pi}{\mathrm{a}}, 0, 0\right).((\mathrm{n_a} + \mathrm{f_a})\mathrm{a}, (\mathrm{n_b} + \mathrm{f_b})\mathrm{b}, (\mathrm{n_c} + \mathrm{f_c})\mathrm{c}) = \pi(\mathrm{n_a} + \mathrm{f_a})$$

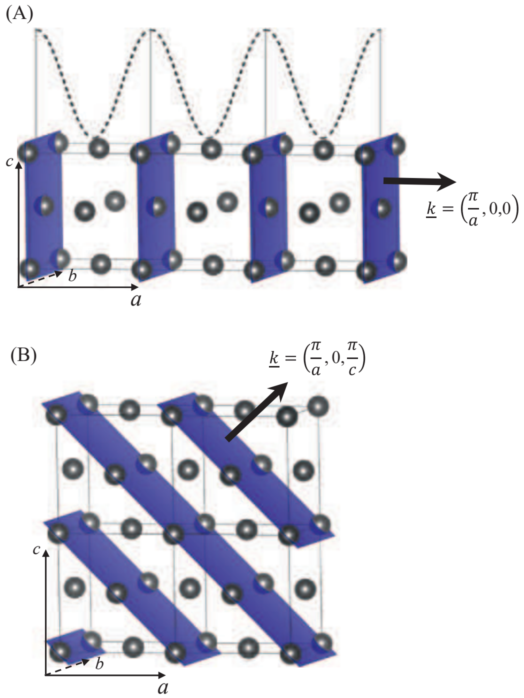
(A)
c
b
a
$\underline{k} = \left(\frac{\pi}{a}, 0, 0\right)$
(B)
$\underline{k} = \left(\frac{\pi}{a}, 0, \frac{\pi}{c}\right)$
c
b
a

Fig. 10 Illustration of Bloch functions using an fcc crystal structure example. (A) $\underline{k} = \left(\frac{\pi}{a}, 0, 0\right)$ the dashed curve shows the relation of the real part of the complex exponential to the unit cell and planes in the crystal are used to show the periodicity in the 3-D structure. (B) $\underline{k} = \left(\frac{\pi}{a}, 0, \frac{\pi}{c}\right)$. In both cases the cell vectors are slightly displaced from the unit cell boundaries for clarity and the bold arrow shows the crystal direction in which the function is periodic labeled with the $\underline{k}$-vector.

which means the crystal orbital is periodic on scale of $2a$ in the $\underline{a}^*$direction because the wavefunction value at any position with a fractional co-ordinate f_a would be the same as that at any equivalent position related by an even number of cell translations in the $\underline{a}$ direction. This is illustrated in Fig. 10A using a set of planes drawn over three unit cells of a face centered cubic (fcc) crystal structure to show the repeating pattern for the $\underline{k} = \left(\frac{\pi}{a}, 0, 0\right)$ Bloch function.

Fig. 10B, illustrates the $\underline{k} = \left(\frac{\pi}{a}, 0, \frac{\pi}{c}\right)$ orbital which is a phase pattern orientated to give a wave pointing diagonally at 45° in the *ac* plane for this cubic crystal.

These two examples show that the periodicity of the lattice will be different according to the direction considered. This in turn means that, rather than the Brillouin zone defining a single range for k, its extent will depend on the direction taken so that the Brillouin zone becomes a volume of the reciprocal space. The first Brillouin zone is the shape formed by the Wigner-Seitz cell in this lattice. This is the primitive cell constructed by taking the intersections of planes placed at the half way point between each reciprocal lattice point. At all points on the surface of this volume the k-vector will have a value of $\pm\pi/d$ (d now being the repeat distance in the corresponding direction in the real space lattice).

The shape of the Brillouin zone is linked to the structure adopted by the metal. Examples of the Brillouin zone for two common structures found in elemental metals, body centered cubic (bcc) and face centered cubic (fcc) are shown in Fig. 11.

The geometry of the crystal will also affect the band structure. Based on tight binding theory we should include a β term for each nearest neighbor. In 1-D this gives a factor of 2, for bcc the factor will be 8 and for fcc there are 12 nearest neighbors for each atom. So, the dispersion relation itself is dependent on the structure adopted by a particular metal.

The vector nature of $\underline{k}$ in 3-D also influences the number of states as a function of energy, which was introduced in 1-D as the density of states (DOS). The number of states at a particular energy will depend on the number of possible k-vectors that have equivalent state energies. For large values of k there are many k-vectors with the same magnitude but with different directions in reciprocal space, leading to a high degree of degeneracy. This, coupled with the flattening of the dispersion relation, leads to a high DOS at large k. In contrast with the 1-D situation, however, at the zone center there are only a few wave-vectors of the same length and so although the dispersion relation may flatten out there is no longer a significant increase in the DOS. Indeed, at the zone center, $\underline{k} = (0,0,0)$, all three components are zero and so there is only one state.

In this picture, when E_F is far from the Brillouin zone edge, the k-vectors of the states at the Fermi level define the surface of a sphere centered on the origin. An example is shown in Fig. 12A for the case of Na metal. Here one electron per atom is present but the band is formed from the atomic 3s and 3p orbitals with only the lowest lying crystal orbitals occupied. This leads to a near perfect sphere representing the boundary between occupied and unoccupied crystal orbitals. Fig. 12B the example of the Brillouin zone for the fcc metal Cu is shown with the Fermi surface included. Copper is a transition metal with a valence shell configuration of $4s^1 3d^{10}$ so the electron density is higher than for sodium. The directions in reciprocal space where the distance from the origin to the Brillouin zone edge is shortest is along the directions equivalent to $\underline{k} = (1,1,1)$, i.e. vectors in which all three components have the

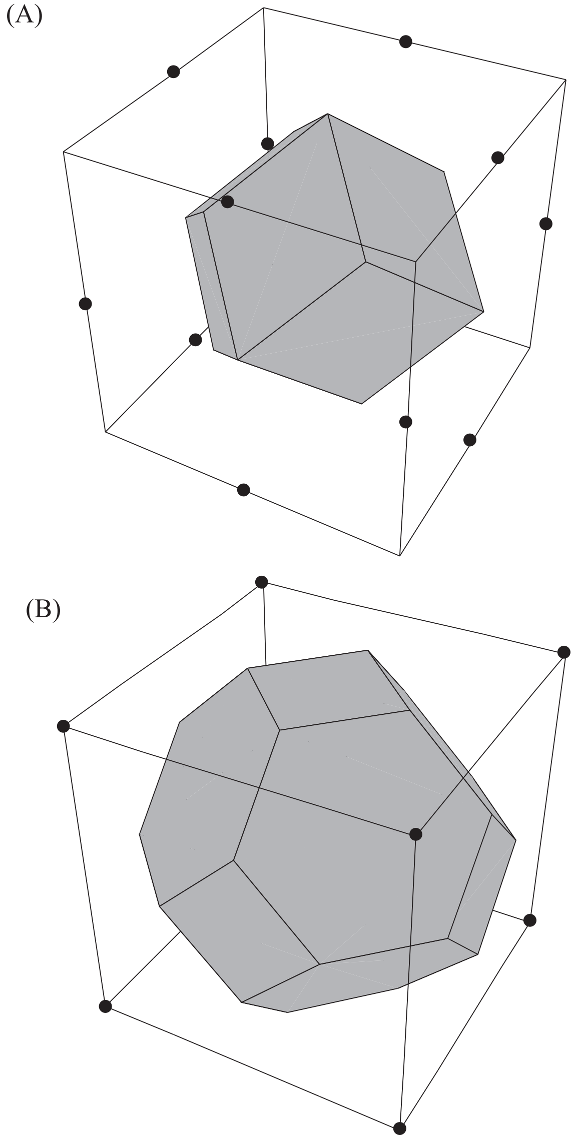

Fig. 11 The first Brillouin zone for the real space lattices of, (A) bcc structures and (*B*) fcc structures. Note that the reciprocal space lattice of the bcc lattice is actually fcc and *visa versa*.

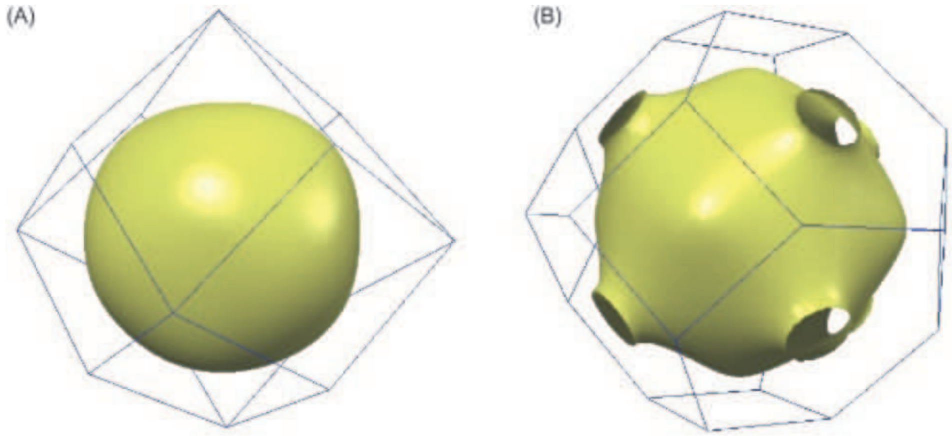

Fig. 12 The Fermi surface defining the extent of occupied states in the Brillouin zone for the examples of, (A) Na, which has the bcc structure and (B) Cu, which has the fcc structure.

same magnitude. For Cu crystal orbitals with *k*-vectors in these directions are fully occupied and as the dispersion relation flattens off near the zone edge round tube like features appear. In other directions the Fermi surface still falls short of the Brillouin zone boundary, so Cu still has a large area of free Fermi surface. This leads to the excellent electrical and thermal conductivity of copper metal.

Dependence of metallic structure on the density of states

The shape and volume of the Brillouin zone controls the electron density at which the Fermi surface touches the Brillouin zone boundary. Near the boundary the dispersion curve flattens off leading to an increased DOS. Differences in the reciprocal lattices between structures will affect the point at which this occurs and so different crystal lattices will have different total electronic energies at a given density.

For example, Fig. 11 shows the shape of the Brillouin zones for the fcc and bcc lattices. The points in the diagrams represent the points on the reciprocal space lattice at the spacing set by the reciprocal space vectors. In fact, the reciprocal space primitive vectors for the fcc lattice are the same as the real space bcc primitive vectors and *visa versa*.

Fig. 13 shows a sketch of the DOS for the fcc and bcc crystal structures. At low electron density all occupied states are well within the Brillouin zone boundary and so the DOS simply increases with the state energy as the number of degenerate *k*-vectors also increases. As the wave-vectors approach the Brillouin zone boundary the dispersion curve levels out and the degeneracy of states increases giving a greater DOS. However, if the energy is increased further the number of available states decreases again since only the sections of volume furthest from the center of the Wigner-Seitz cell are still available. We have seen this starting to happen for the case of Cu in Fig. 12B. At the Fermi level in Cu there are no further states available in directions like $\underline{k} = (1, 1, 1)$, but there are still empty states in the band in other directions. If we were to add more electrons, even though they would occupy higher *k*-states the density of states would decrease as the number of directions in reciprocal space still inside the Brillouin zone would reduce. In general, as shown in Fig. 13, this leads to a peak in the DOS in the vicinity of the Brillouin zone boundary. Because of the geometry of the reciprocal space lattices the peak occurs at lower energy for the fcc real space lattice than for the bcc case. For a metal with electron density at the fcc peak the fcc structure will be preferred because the Fermi energy will be lower than in the bcc lattice. However, if the density of electrons is near the bcc peak the fcc DOS has begun to fall dramatically and so a lower energy electron configuration is possible in the bcc structure.

The DOS of real metals is more complex than this illustration using a single band in fcc and bcc structures. However, the example does serve to show that the DOS will influence the relative total electronic energy of alternative metal lattices. Or, conversely, the electron density of a metal can have a dramatic influence on the optimal crystal structure.

This idea has been tested using higher level calculations on the first row transition metals to obtain the band structures and densities of states for the valence shells in bcc, fcc and hexagonal close packed (hcp) structural alternatives, as shown in Fig. 14, (Pettifor, 1970). The shape of the DOS for each structure is largely controlled by the interaction of the metal d-orbitals in the different crystallographic directions since the overlap of the spherical s-orbitals is less influenced by the lattice geometry. At low energies the calculated DOS are all very similar. However, at 0.35 eV, corresponding to 3 electrons per atom, the bcc plot shows a distinct dip and so at this point an increase in electron density with this structure must occupy higher energy states than are required in the close packed lattices.

In Fig. 14D, integration of the occupied state energies is used to compare the relative internal energies calculated for the different structures for each valence electron count. In this plot fcc is used as the reference. For example, if the bcc-fcc curve is positive a structure with that number of valence electrons will have a lower internal energy as an fcc lattice than it would as a bcc lattice and so the fcc structure is preferred. The hcp-fcc curve shows a much smaller range as both structures are close packed and so differences in binding energy are due to more long range effects.

As noted above the dip in the bcc DOS at 0.35 eV corresponds to around 3 electrons per atom. In Fig. 14D up to this point the bcc-fcc curve is positive and more positive than the hcp-fcc curve. So that in this regime the close packed lattices are indeed lower in energy than bcc and under standard conditions the early transition metals, Sc ($3d^1 4s^2$) and Ti ($3d^2 4s^2$) have the hcp structure. Just

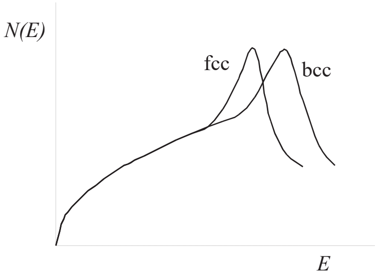

Fig. 13 Schematic diagram of the DOS for the fcc and bcc crystal systems. The peaks correspond to the point when the *k*-vector just touches the Brillouin zone boundary.

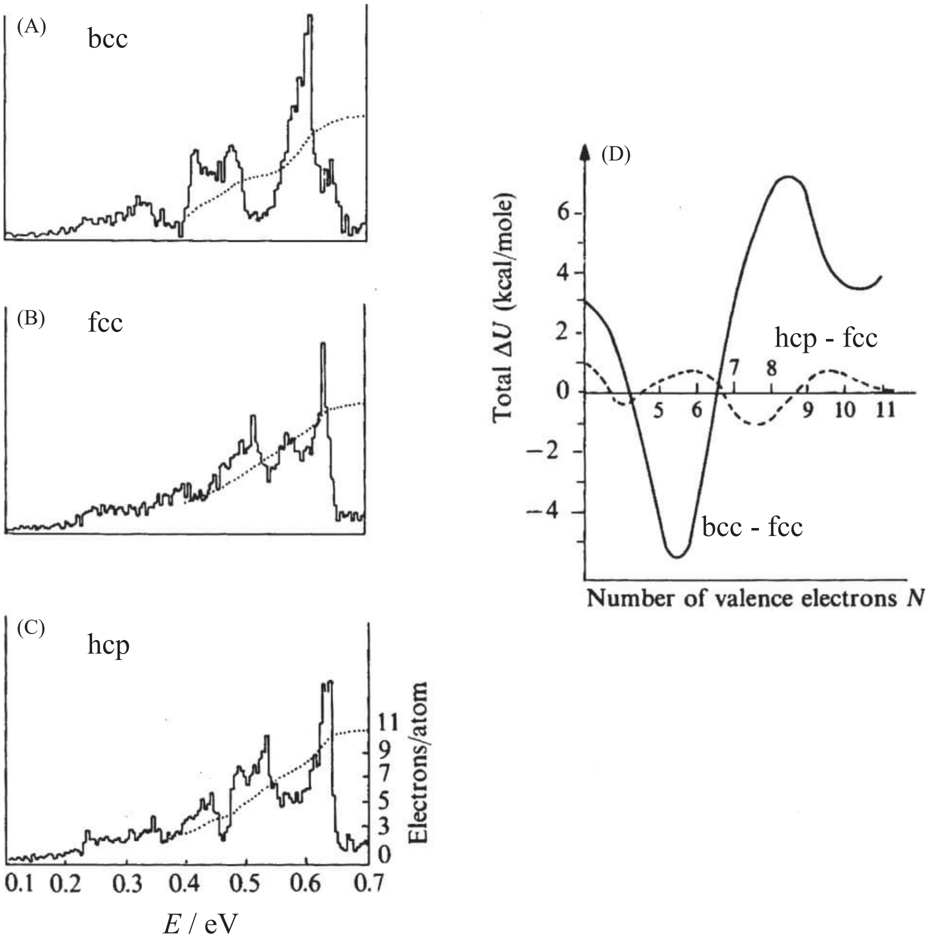

Fig. 14 The DOS for (A) bcc, (B) fcc and (C) hcp structures. The dotted line on each diagram is the integrated DOS and shows the level of the Fermi energy in the metal with the number of electrons per atom indicated on diagram (C). (D) The total electronic energy of the bcc and hcp structures relative to that of the fcc as a function of electron density taken from (Pettifor, 1970).

above 0.4 eV there is a peak in the bcc DOS and so the total energy at the corresponding electron densities favors the bcc structure (bcc-fcc negative, Fig. 14D). Vanadium and chromium with 5 and 6 valence electrons, respectively, both adopt this lattice. Manganese has a complex structure which has not been included in this study while Fe ($3d^6 4s^2$) has the bcc structure at room temperature against the predicted fcc lattice from Fig. 14D. However, magnetic effects seem to dominate this choice of structure for Fe since above the Curie temperature the fcc structure is observed. For higher electron densities the close packed structures are found again, with the choice of fcc or hcp finely balanced. Even so, the total electronic energies indicate that at 7 and 8 valence electrons hcp is more stable than fcc while the situation is reversed for 9 and 10 outer electrons. This trend is observed experimentally, with the structures of Co and Ni being hcp and Cu and Zn taking up the fcc structure.

Conclusion

We have seen how the concept of metals being formed from the interaction of ionic cores with a sea of electrons can be made more concrete through the development of band theory. Band theory leads to the classification of electronic states that are delocalized in the crystal using the k-vector that describes the periodicity of the state wavefunction on length scales longer than the unit cell. In tight bonding theory a band of states is then formed from each orbital of the unit cell. The metallic state is then easily defined as a material in which at least one of the electronic bands is only partially filled. In these materials electrons near to the top of the filled states, i.e. those at the Fermi energy, can easily move into the empty states just above. This gives rise to the high electronic and thermal conduction properties we associate with metals. The degree of bonding/antibonding for solids can also be understood by considering the wavefunction energy relative to that of the free atoms. In a tight binding approach this is the energy for the orbital forming the band represented by the site parameter, α, and so states with lower energy than this will be bonding and those with higher energy anti-bonding. The effect of the delocalization of the electrons is captured in the tight binding, β parameter which controls the band width. This parameter depends on the atomic arrangement in the crystal and so gives us a way to compare the stability of alternative crystal structures.

However, although the tight binding approach as described here gives conceptual insight, any two parameter model will be restricted in accuracy. Over the last 40 years increasingly sophisticated solutions to electronic structure problem have been developed, most notably through density functional theory (DFT) as reviewed by Jones (2015). Implementation of DFT for solids using computer simulations has allowed very accurate models of the electronic structure to be created bringing in not only the interaction of the valence electrons with the lattice site ions but also important electron-electron exchange and correlation energies. The crystal orbitals are still represented by Bloch functions, (Payne et al., 1992), but now the energies of the states compare accurately with experimental measurements of material properties. Indeed, by combining these methods with thermodynamic calculations of the effects of entropy on the stability of metals it is possible to predict the experimental melting and boiling points of metals, (Löffelsender et al., 2022).

Density functional theory is now a widely used practical tool helping us understand and design new approaches to thermal insulation, (Nielsen et al., 2013), energy storage, (Jain et al., 2016), catalysis, (Qi et al., 2022), and many other technologically important materials.

References

Ashcroft NW and Mermin ND (1976) *Solid State Physics*. New York: Holt, Rinehart and Winston.

Hoffmann R (2002) *Solids and Surfaces: a Chemist's View of Bonding in Extended Structures*. Print on demand der Ausg. 1988. ed New York, NY: Wiley-VCH.

Jain A, Shin Y, and Persson KA (2016) Computational predictions of energy materials using density functional theory. *Nature Reviews Materials* 1: 15004. https://doi.org/10.1038/natrevmats.2015.4.

Jones RO (2015) Density functional theory: Its origins, rise to prominence, and future. *Reviews of Modern Physics* 87: 897–923. https://doi.org/10.1103/RevModPhys.87.897.

Kittel C (2018) *Introduction to Solid State Physics*, Global edition, [9th edn] Hoboken, NJ: Wiley.

Löffelsender S, Schwerdtfeger P, Grimme S, and Mewes J-M (2022) It's complicated: On relativistic effects and periodic trends in the melting and boiling points of the Group 11 coinage metals. *Journal of the American Chemical Society* 144: 485–494. https://doi.org/10.1021/jacs.1c10881.

Nielsen MD, Ozolins V, and Heremans JP (2013) Lone pair electrons minimize lattice thermal conductivity. *Energy & Environmental Science* 6: 570–578. https://doi.org/10.1039/C2EE23391F.

Payne MC, Teter MP, Allan DC, Arias TA, and Joannopoulos JD (1992) Iterative minimization techniques for *ab initio* total-energy calculations: molecular dynamics and conjugate gradients. *Reviews of Modern Physics* 64: 1045–1097. https://doi.org/10.1103/RevModPhys.64.1045.

Pettifor DG (1970) Theory of the crystal structures of transition metals. *Journal of Physics C: Solid State Physics* 3: 367–377. https://doi.org/10.1088/0022-3719/3/2/018.

Qi G, Davies TE, Nasrallah A, Sainna MA, Howe AGR, Lewis RJ, Quesne M, Catlow CRA, Willock DJ, He Q, Bethell D, Howard MJ, Murrer BA, Harrison B, Kiely CJ, Zhao X, Deng F, Xu J, and Hutchings GJ (2022) Au-ZSM-5 catalyses the selective oxidation of CH_4 to CH_3OH and CH_3COOH using O_2. *Nature Catalysis* 5: 45–54. https://doi.org/10.1038/s41929-021-00725-8.

Crystal growth, bulk: Theory and models☆

Natasha Dropka and Kevin-Peter Gradwohl, Leibniz-Institut für Kristallzüchtung (IKZ), Berlin, Germany

© 2024 Elsevier Ltd. All rights reserved.

This is an update of J.J. Derby, Crystal Growth, Bulk: Theory and Models, Editor(s): Franco Bassani, Gerald L. Liedl, Peter Wyder, Encyclopedia of Condensed Matter Physics, Elsevier, 2005, Pages 274–282, ISBN 9780123694010, https://doi.org/10.1016/B0-12-369401-9/00415-0.

Introduction **231**
Overview and key issues **232**
Crystal growth theory 232
Thermodynamics 232
Kinetics 234
Crystal growth modeling 235
Continuum methods 235
Process engineering 239
Crystal growth analysis 241
Defects 241
Segregation 243
Morphological instability 244
Conclusion **245**
Acknowledgments **245**
References **246**

Abstract

Understanding the crystal properties that emerge during growth is crucial to further improve crystal quality and open the doors to novel, unprecedented applications. There is no single theory or approach that can describe the full complexity of crystal growth.

However, there are many different tools that are particularly powerful when trying to understand the underlying physical nature of related processes. This chapter attempts to provide an overview of the basic crystal growth theories, including thermodynamic concepts and kinetic considerations, emerging numerical modeling techniques such as CFD and machine learning, and crystal growth analysis involving crystal defects, morphological instabilities, and segregation.

Key points

- Introduction: This section highlights the role of theory and models in crystal growth.
- Overview and key issues: This section provides an overview of basic crystal growth theories, crystal growth modeling, and crystal growth analysis. The focus is on key issues related to thermodynamics, kinetics, continuum methods, process engineering, crystal defects, segregation and morphological instability.
- Summary and future directions: This section addresses the challenges in crystal growth theory and models, and the synergy potential of physics-based and data-driven approaches.

Introduction

Artificially grown crystals are used in a variety of technological applications such as microelectronics, photovoltaics, optics, lasers, light-emitting diodes, and telecommunication, and are therefore an essential pillar of our modern society (Scheel and Fukuda, 2003; Nishinaga, 2015). These industrially grown crystals are characterized by superior perfection compared to all crystals occurring in nature.

In the case of the economically most important semiconductor crystal, silicon, ingots are grown with weights up to 2000 kg and with defect concentrations of less than one in a billion atoms (Abrosimov et al., 2017) to meet the ever-increasing demands of the solar and electronics industry.

Our technological progress is therefore limited by the quality of such crystals, which have to be produced in complex, application-specific growth processes. Understanding the crystal properties that emerge during growth is crucial to further improving their quality and opening the doors to novel, unprecedented applications.

☆*Change History*: September 2022. N Dropka updated the chapter. He updated text, references, Figs. 3, 6, and 8.

There is no single theory or approach that can describe the full complexity of crystal growth, and many unanswered questions remain.

However, there are many different tools that are particularly powerful when trying to understand the underlying physical nature of related processes. This paper attempts to provide an overview of the basic crystal growth theories, emerging numerical modeling techniques, and crystal growth analysis.

Overview and key issues

Crystal growth theory

Crystallization is a phase transition from a disordered phase (vapors, solutions, and melts) into a highly-ordered solid phase, called a crystal. Crystal growth is the stage of crystallization, in which the crystal constituents (atoms, molecules) attach to the existing crystal surface, leading to the growth of the crystal. For relevant technological bulk crystal growth processes, this crystal surface is typically an existing seed crystal, where a crystal nucleus has to form before growth. The associated nucleation theory will not be discussed further here.

The crystal growth theory attempts to describe the mathematical framework of why and how crystals with certain properties grow. However, due to the wide range of materials, growth methods, and overall complexity of the process, there is no general theory describing this topic.

Important fundamental descriptions related to bulk crystal growth can be divided into thermodynamic and kinetic theories, which are discussed in sub-sections "Thermodynamics" and "Kinetics", respectively. The main difference between these theories lies in the fact that thermodynamics describes the general tendencies why phenomena can occur, while kinetics describes the rate at which a given process occurs and the pathway by which it occurs.

Thermodynamics

Thermodynamics is an essential tool to understand a wide range of aspects of crystal growth e.g. the driving force of crystallization, stability regions of materials, stoichiometry of compounds, optimal growth conditions, shape of crystals, defect concentrations, incorporation of foreign atoms into the crystal (segregation), etc. (Rudolph, 1998, 2003).

Classical thermodynamics deals with the description of states of many-particle systems at equilibrium with respect to macroscopic physical quantities, such as pressure p, temperature T, volume V and entropy S (Wallace, 1972; Lupis, 1983). These concepts can be utilized to describe crystal growth phenomena since they generally occur close to equilibrium and the related time scales are large compared to the kinetic time scale of atoms. A state of a system is at equilibrium if the free energy is minimized. The equilibrium related to the crystallization process (T, p = const.) is characterized by the minimization of the Gibbs free energy G of the system, which is defined as:

$$G = U + p \cdot V - T \cdot S = H - T \cdot S \tag{1}$$

where U is the internal energy and H is the enthalpy. The potential H is predominantly determined by the decrease in internal energy through the formations of atomic bonds in the crystal and is thus minimized ($H \rightarrow \min$) by the ordering process during crystallization. However, this ordering is inherent with a decrease in entropy $S \rightarrow \min$, which counteracts the minimization of G. Hence, disordering and the formation of defects ($S \rightarrow \max$) becomes more and more important with increasing temperature. In other words, there is a limit on how perfect a crystal can be, and a crystal at thermodynamic equilibrium has an associated point defect concentration, such as vacancies, self-interstitials, or impurity atoms (more on defects in sub-section "Defects").

As a simple model, we only consider the formation energy of a defect E_d (increases G) and a defect concentration n (decreases G, through the increase of entropy). One can approximate the equilibrium defect concentration by analytical methods (shown in detail in e.g. Gottstein, 2013):

$$n = N \exp\left(-\frac{E_d}{k_B T}\right) \tag{2}$$

where N is the concentration of atoms in the crystal lattice and k_B is the Boltzmann constant. The defect concentration as a function of temperature is shown in Fig. 1 for different formation energies (bold line). One can see that the defect concentrations at high temperatures (e.g. during crystal growth, close to the melting point of a material) are significant, and a diffusion-limited freeze-in of only a fraction of the equilibrium point defects has severe implications for the material quality (dashed line). The task is therefore not to grow perfect crystals, but to develop growth processes that control the defect formation to the extent necessary for the desired application.

Thermodynamics can also be employed to predict the existence and coexistence of phases under different conditions and possible phase transitions. Crystallization involves a first-order phase transition that is a discontinuous change in enthalpy, entropy, and volume. At the equilibrium point, the crystalline and the disordered phase are stable and coexist separated by a phase boundary (interface). It requires some kind of deviation from this equilibrium (temperature, pressure, concentration) to create a driving force of crystallization.

Considering a one-component system with a solid and a fluid phase close to the equilibrium point (the same is true for any two phases), one can approximate the temperature dependence of G in the solid and liquid as linear, as shown in Fig. 2.

The temperature dependence of G of the fluid phase is stronger than the one of the solid phase, which is mostly caused by the entropic term $T \cdot S$ of Eq. (1). Hence, there exists a point where these functions cut, which indicates the equilibrium temperature T_e at which both phases coexist. If there are deviations from the equilibrium temperature (supercooling by ΔT), the two phases can still exist, one being stable and the other metastable. The resulting difference in Gibbs free energy ΔG between the solid and the liquid

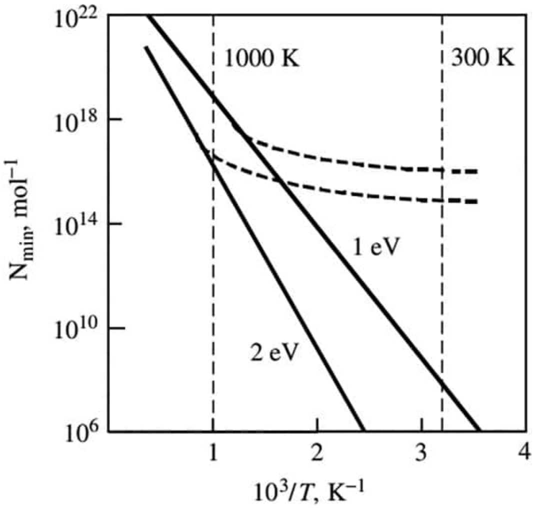

Fig. 1 Equilibrium point defect concentration N_{min} as a function of T for defect formation energies E_d of 1 eV and 2 eV (bold line) and a schematic freeze-in of the defect concentration due to diffusion limitations (dashed line) for $N = N_A = 6.022{\cdot}10^{23}$ mol^{-1}, the Avogadro constant. Based on Rudolph P (2003) Thermodynamic fundamentals of phase transitions applied to crystal growth processes, In: Scheel HJ and Fukuda T (Eds.), *Crystal Growth Technology*, Wiley, pp. 15–42, reprinted with permission of Elsevier.

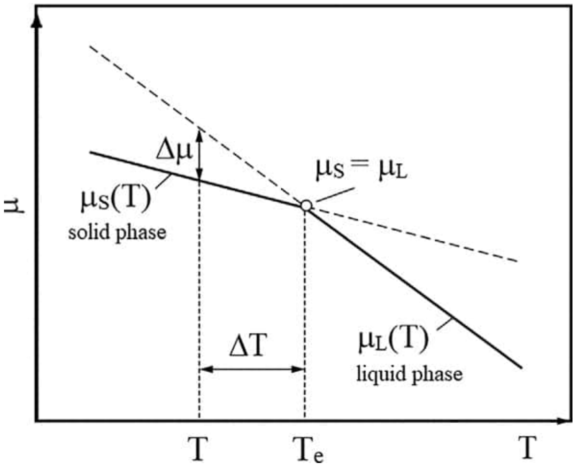

Fig. 2 Schematic temperature dependence of G (equivalent to chemical potential μ for one-component systems) for the solid S (crystal) and liquid phase L (melt) close to the equilibrium temperature T_e.

represents the driving force of crystallization. If a crystal seed is present, this leads directly to the propagation of the phase boundary into the metastable phase and subsequent crystallization. Other possible driving forces of crystallization can be changes in pressure or concentration (supersaturation). Similar considerations can be used to estimate the rate of crystal growth, as shown for example by Nishinaga (2016).

The coexistence of distinct phases ($\Delta G = 0$) can also be studied as a function of different physical quantities (T, p, concentrations, magnetic field, etc.) and the corresponding graphical representation is called a phase diagram. Phase diagrams of two-component systems at constant pressure (binary phase diagram) are particularly important for understanding crystal growth.

These are often determined experimentally, but can also be calculated/simulated from the Gibbs free enthalpies (further reading: Kaufman and Bernstein, 1970). As a simple example of a binary phase diagram, the Si/Ge system is shown in Fig. 3a, a system with complete miscibility in the solid and in the liquid. The bold solid lines represent the phase boundaries indicating where the liquid and the solid SiGe coexist. While the pure substances Si and Ge have a defined melting point, SiGe has a broad temperature region (A to B) where the solid and the liquid coexists. A melt with a certain SiGe composition—as indicated by the dashed line in Fig. 3a starts crystallizing at temperature T_A and composition A, enriches in Ge during cool down, and fully crystallizes at T_B with composition B (Zinkevich et al., 2006). This has severe implications for crystal growth. While pure Si and Ge crystals are grown by the Czochralski method (Cz) by keeping the melting point constant and temperature gradients small, growing SiGe is a big challenge. Cz-growth is only feasible close to the pure substances; other methods must be used for high concentrations, such as e.g. epitaxy method (far from equilibrium).

Generally, phase diagrams are more complex. As an example, the β-Ga_2O_3/La_2O_3 system is shown in Fig. 3b. Several congruently melting, intermediate, stable phases and eutectics can be observed. In view of this, finding a suitable crystal growth method for the desired crystal usually starts with studying phase diagrams.

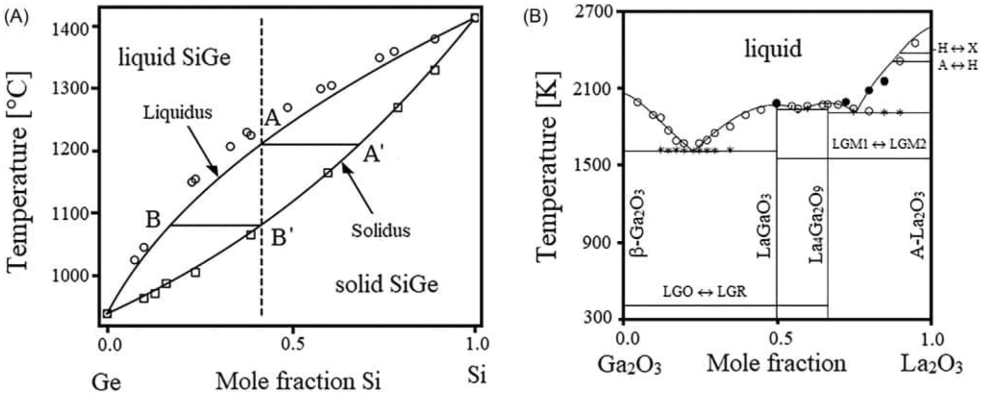

Fig. 3 Binary phase diagram of: (a) Si—Ge (courtesy of K. Böttcher, IKZ) and (b) Ga_2O_3-La_2O_3. Based on Zinkevich M, Geupel S, Aldinger F, Durygin A, Saxena SK, Yang M, Liu ZK (2006) Phase diagram and thermodynamics of the La_2O_3–Ga_2O_3 system revisited. *Journal of Physics and Chemistry of Solids* 67: 1901–1907; reprinted with permission of Elsevier.

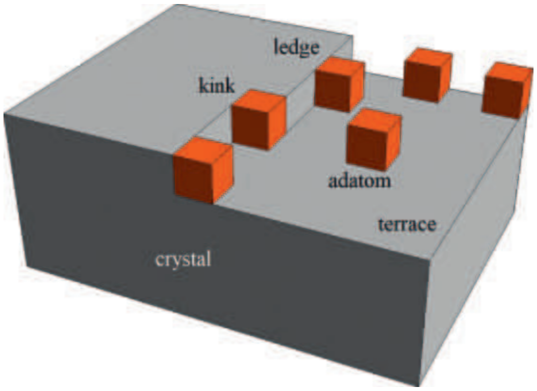

Fig. 4 Different lattice sites with different desorption energies as considered in the Kossel-Stranski model. Based on Derby JJ (2005) Crystal growth, bulk: Theory and models. *Encyclopedia of Condensed Matter Physics*. Elsevier Ltd.

Kinetics

Thermodynamic considerations are very powerful in describing which phases are stable, but they do not explain how these phase transitions occur. Certain mechanisms might be hindered or not given enough time to take place, and therefore metastable states might dominate in practical applications. Kinetic theories look at how a crystal actually grows atom by atom. Therefore, kinetic theories are essential for understanding crystal growth, and have to be considered for reliable insights (Nancollas and Purdie, 1964).

A simple kinetic theory of crystal growth was first described by Kossel (1927) and Stranski (1928). It is assumed that the crystal surface does not deviate significantly from bulk and that potential sites for crystal growth units arriving at the crystal surface to attach are the bulk lattice sites, which are the energetically favorable. Consequently, they describe the growth by giving different desorption energies to different types of lattice sites (see Fig. 4) (Derby, 2005). With the Kossel-Stranski model it was possible to predict the stability of facets in crystals.

The growth of a perfect crystal requires the nucleation of the crystal growth units on a perfect crystal surface (Gibbs, 1928). This monolayer nucleus would then laterally grow towards the edge of the crystal face. The nucleation process is generally slower than the lateral growth and transport mechanisms, and should therefore be the rate determining step. This picture would predict a critical supersaturation/supercooling below which no crystal growth can take place, which has not been observed in several systems (Volmer and Schultze, 1931). Frank (1949) could describe this discrepancy by considering imperfect, real crystals containing dislocations. He showed that, for example, a screw dislocation can serve as a source for perpetual steps and further on as nucleation sites for lateral monolayer growth, avoiding the need for nucleation, as shown in Fig. 5a and b. These growth spirals originating from dislocations could be observed in many substances as shown in Fig. 5c (Seiss et al., 2013; Shtukenberg et al., 2013; Fan et al., 2018). It has been shown on nearly-perfect crystals that both the nucleation mechanism and the dislocation mechanism proposed by Frank can occur, even on different crystal facets of the same single crystal (Sears, 1956).

Kinetic theories can also be applied to describe the growth habit that results from crystal growth.

When there are sufficient steps to nucleate on, growth is limited by the transport of crystal growth units to these steps. In this case, the fastest growing facet outgrows and the slowest growing facets dominants, resulting in a highly-faceted crystal habit. On the other hand, when nucleation of new layers on the surface dominates, which is the case when the crystallization driving force is high, then the surface tends to be atomically rough, referred to as kinetic roughening. It plays a key role in crystal growth from the vapor phase (e.g. molecular beam epitaxy) and is generally undesirable when atomically flat interfaces are desired (Wolf, 1991). In summary, all

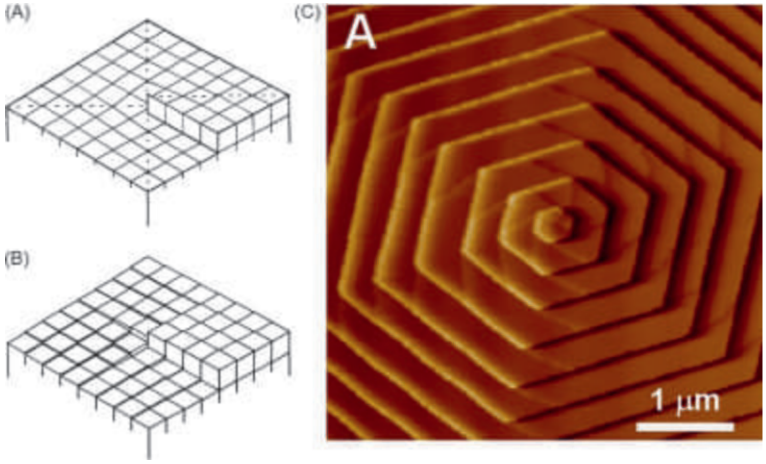

Fig. 5 Sketch of a screw dislocation emerging normal at the crystal surface as: (a) continuous deformation of the plane, (b) in a block model, and (c) an image of a real growth spiral arising from a screw dislocation. Based on Frank FC (1949) The influence of dislocations on crystal growth. *Discussions of the Faraday Society* **5**: 48–54.; Shtukenberg AG et al. (2013) Illusory spirals and loops in crystal growth. *Proceedings of the National Academy of Sciences* 110: 17195–17198; reprinted with permission of RCS.

these theories offer insights into the mechanism of crystal growth, but the actual crystal growth process is much more complex. Crystal growth is a field of active research and numerical modeling and simulation are becoming increasingly important.

Crystal growth modeling

The crystal growth processes involve a wide variety of physical and chemical phenomena taking place over a wide range of length and time scales, as shown in Fig. 6. At the lowest microscopic scale are ab initio molecular dynamics (MD) methods dealing with atomic behavior, while on the macroscopic scale are continuum methods. The latter provide a deeper insight into the various transport phenomena (e.g. momentum, heat, and mass transport) and thermoelastic stress occurring during the crystal growth and their relationships to crystal growth process parameters. The gained knowledge is essential for process development, scale up, optimization and control.

The pioneer attempt to model crystal growth processes on the macro scale goes back to the '70s and the work of Kobayashi and Arizumi (1970a, 1970b) and Kobayashi (1978). They used a simple steady state 2D axisymmetric model to describe the Czochralski growth of germanium and garnets (Yttrium Aluminium Garnet (YAG) and Gadolinium Gallium Garnet (GGG)). Within the last 5 decades, numerous studies have been devoted to the modeling of various crystal growth processes for various materials at the large-scale, as extensively reviewed in e.g., Derby and Yeckel (2004), Derby et al. (2007), Milller and Ostrogorsky (1994), Yeckel and Derby (2003), Polezhaev (2003), Szmyd and Suzuki (2000) and Rudolph (2010a, 2010b).

The models became more complex and closer to the real crystal growth setups, handling 3D geometries, transient processes, chemical reactions, magnetic and electric fields, etc.

Continuum methods

The transport of heat, mass, and momentum is especially important in bulk crystal growth processes in all solids (crystal and furnace parts) and fluids (melt, solution phase in the solution growth and gas atmosphere) present in the furnace.

For incompressible (density = constant), Newtonian fluids, flows are described by mass conservation equation:

$$\nabla\cdot\vec{u} = 0 \tag{3}$$

where u is the fluid velocity.

Governing equations for conservation of moment (Naver-Stokes equation) have the form:

$$\rho\frac{D\vec{u}}{Dt} = \rho\left(\frac{\partial\vec{u}}{\partial t} + \left(\vec{u}\cdot\nabla\right)\vec{u}\right) = -\nabla p + \mu\nabla^2\vec{u} - \rho_{ref}\vec{g}\left(\alpha\left(T - T_{ref}\right) + \alpha_c\left(c_i - c_{i,ref}\right)\right) + \vec{F} \tag{4}$$

The following notation was used: D/Dt is the substantial derivate, t is the time, ρ is the fluid density, p is the pressure, μ is the dynamic viscosity, g is the gravitational vector, T is the fluid temperature, c_i is the molar concentration of solute i, α is the coefficient of thermal volumetric expansion, α_c is the coefficient of concentrational volumetric expansion and F is the volumetric body force acting in the fluid. The notation ref. is used for the characteristic value in the domain.

If magnetic field is applied on the fluid, F will be equal Lorentz force density F_L, defined in:

$$\vec{F}_L = \vec{j}\times\vec{B} = \sigma_{el}\left(\vec{E} + \left(\vec{u}\times\vec{B}\right)\right)\times\vec{B} \tag{5}$$

where J is the current density, B is the magnetic induction, σ_{el} is the electrical conductivity and E is the electric field strength.

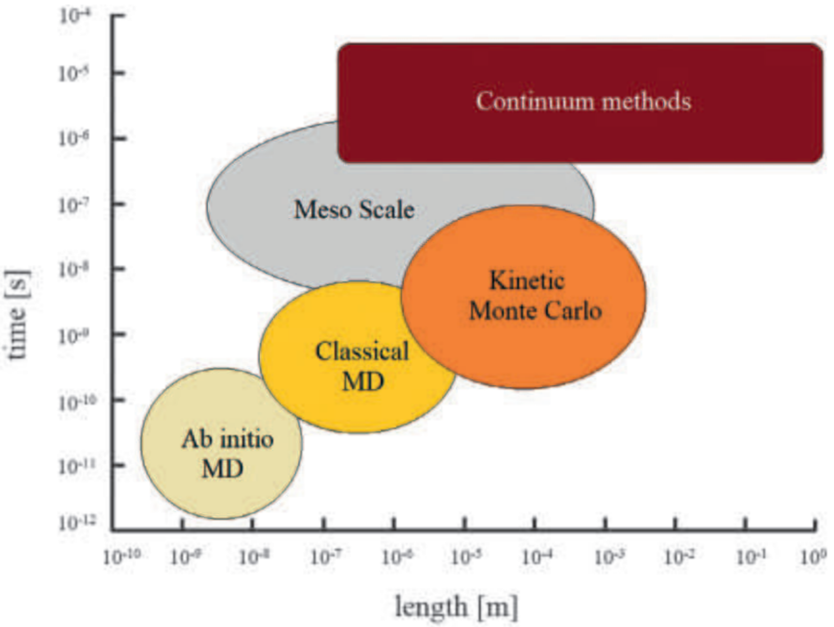

Fig. 6 Different modeling approaches in crystal growth for various time and length scales. Based on Derby JJ et al. (2007) Large-Scale Numerical Modeling of Melt and Solution Crystal Growth. in: Skowronski M, DeYoreo JJ, Wang CA (Eds.). *Perspectives on Inorganic, Organic, and Biological Crystal Growth: From Fundamentals to Applications, 13th International Summer School on Crystal Growth.*

The Lorentz force density can be derived from the solution of following equations: (i) Magnetic induction equation:

$$\frac{\partial \vec{B}}{\partial t} = \frac{1}{\mu_r \cdot \sigma_{el}}\left(\nabla^2 \vec{B}\right) + \left(\nabla \times \left(\vec{u} \times \vec{B}\right)\right) \tag{6}$$

where μ_r is the magnetic permeability; (ii) Gauss law for magnetism:

$$\nabla \cdot \vec{B} = 0 \tag{7}$$

$$\nabla \cdot \vec{E} = 0 \tag{8}$$

and (iii) Maxwell-Faraday equation:

$$\nabla \times \vec{E} = -\frac{\partial \vec{B}}{\partial t} \tag{9}$$

$$\nabla \times \vec{H} = \vec{j} \tag{10}$$

where H is the magnetic field strength.

Governing equation for conservation of energy has a form:

$$\rho c_p \frac{DT}{Dt} = \rho c_p \left(\frac{\partial T}{\partial t} + \left(\vec{u} \cdot \nabla\right) T\right) = \lambda \nabla^2 T + A \tag{11}$$

where c_p is the heat capacity, λ is the heat conductivity and A is the general heat source in the fluid. If heat is generated by a chemical reaction, the heat source A has the form:

$$A = \Delta H_i \cdot R_i \tag{12}$$

where ΔH_i is the reaction enthalpy and R_i is the chemical reaction rate for the component i.

For multicomponent systems, the species conservation equation is given in a form:

$$\frac{Dc}{Dt} = \frac{\partial c_i}{\partial t} + \left(\vec{u} \cdot \nabla\right) c_i = D_i \nabla^2 c_i + R_i \tag{13}$$

where D_i is the molar diffusion coefficient for the species i. In the simplest case, the chemical reaction rate R_i is directly proportional to the concentration of the component c_i aka the reaction rate is of the first order:

$$R_i = -k \cdot c_i = -k_0 e^{-\frac{E_A}{RT}} \cdot c_i \tag{14}$$

where k is the reaction rate constant defined via an Arrhenius equation and E_A is the activation energy for the chemical reaction.

In the crystal growth furnace, the field distribution in each body, i.e. in each domain, is governed by the differential equations described above. To be able to solve them, along the domain boundaries, boundary conditions must be imposed. In the case of transient simulations, also initial conditions for the whole domain must be defined. There are four types of boundary conditions (BC): (i) Dirichlet BC with specified variables u, T or c_i; (ii) Neumann BC with specified heat or mass fluxes; (iii) Robin BC with a weighted combination of Dirichlet and Neumann BCs and (iv) radiation BC (a kind of Neumann BC with non-linear temperature dependence T^4).

Along the moving boundary of the crystallization front, the Stefan and isothermal conditions have to be satisfied:

$$\left[(-\lambda_l \nabla T)_l + (\lambda_s \nabla T)_s\right]\cdot \vec{n}_{s,l} = \Delta H_s r_{growth} \qquad (15)$$

$$T = T_m$$

where ΔH_s is the latent heat of solidification, r_{growth} is the crystal growth rate, T_m is the melting temperature, and n is the vector orthogonal to the crystallization front.

Governing equations can be derived for any coordinate system (e.g. rectangular (Cartesian), cylindrical or spherical), although the most convenient form is usually assumed for the sake of simplicity, especially when defining the boundary conditions.

A cylindrical coordinate system is commonly used in the bulk crystal growth techniques with axisymmetric crystals, such as Czochralski (Cz), Floating Zone (Fz), and Vertical Gradient Freeze (VGF). In directional solidification (DS), where the crystal grows in a rectangular crucible, the Cartesian coordinate system is the better choice (Fig. 7).

Governing conservation equations can be transformed into a dimensionless form, which reveals the governing dimensionless groups, allows identification of significant and insignificant terms, and facilitates scaling of the process.

The dimensionless form of the conservation equations are given below:

$$\frac{D\overrightarrow{u^*}}{Dt^*} = -\nabla^* p^* + \frac{1}{Re}\nabla^{*2}\vec{u}^* + \frac{Gr}{Re^2}T^* + \frac{Gr_c}{Re^2}c_i^* + \frac{Ha^2}{Re}\left(\vec{j}^* \times \overrightarrow{B^*}\right) \qquad (16)$$

$$\frac{DT^*}{Dt^*} = \frac{1}{Re\cdot Pr}\nabla^2 T^* + A^* \qquad (17)$$

$$\frac{Dc^*}{Dt^*} = \frac{1}{Re\cdot Sc}\nabla^2 c^* + R^* \qquad (18)$$

$$\frac{D\vec{B}^*}{Dt^*} = \frac{1}{Re_m}\nabla^2 \vec{B}^* + \nabla \times \left(\vec{u}^* \times \vec{B}^*\right) \qquad (19)$$

Cartesian coordinates x,y,z can be made dimensionless (notation *) by dividing them with the characteristic length scale L of the geometry, e.g. diameter or height of the grown material:

$$x^* = \frac{x}{L}; y^* = \frac{y}{L}; z^* = \frac{z}{L} \qquad (20)$$

In the same way, other variables can be made dimensionless by using their characteristic value (notation ref), mean value (notation av) or their characteristic difference value (notation $\Delta_{T,ref}$ for temperature difference) in the domain, e.g.:

$$\vec{u}^* = \frac{\vec{u}}{u_{av}} \qquad (21)$$

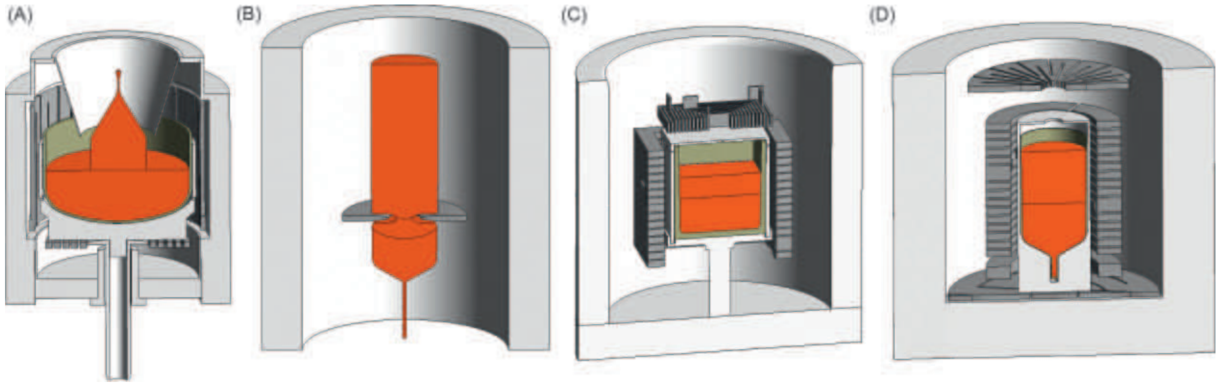

Fig. 7 The most popular bulk crystal growth techniques: (a) Czochralski, (b) Floating zone, (c) Directional Solidification and (d) Vertical Gradient Freeze.

$$T^* = \frac{T - T_{ref}}{\Delta_{T,ref}} \tag{22}$$

$$c_i^* = \frac{c_i}{c_{ref}} \tag{23}$$

$$t^* = \frac{t \cdot u_{av}}{L} \tag{24}$$

$$p^* = \frac{p}{\rho \cdot u_{av}} \tag{25}$$

$$\nabla^* = L \cdot \nabla \tag{26}$$

$$\nabla^{2*} = L^2 \cdot \nabla^2 \tag{27}$$

$$B^* = \frac{B}{B_{ref}} \tag{28}$$

$$H^* = \frac{H}{H_{ref}} \tag{29}$$

$$J^* = \frac{J}{J_{ref}} \tag{30}$$

The solutions of non-dimensional equations depend on the coefficients that appear in them, known as dimensionless numbers. Their definitions and detailed descriptions are given in Table 1.

The material properties and *Pr* number of several important melts for electronic industry are summarized in Table 2. The data show the difference in *Pr* numbers of 4 orders of magnitude.

Small values of the *Pr* number, i.e. $Pr \ll 1$, means the thermal diffusivity dominates, whereas with $Pr \gg 1$, the momentum diffusivity dominates. In other words, Pr number provides information on the relative thicknesses of the momentum and thermal boundary layers. Similarly, the Schmidt *Sc* number provides information on the relative thickness of the momentum and concentration boundary layers.

In buoyancy driven flows that are common in crystal growth, the values of Gr and Pr numbers (and derived Ra numbers) determine the flow regime, as shown in Fig. 8. Knowing the onset of turbulence is of particular importance for process stability and control.

Table 1 The most important dimensionless numbers in crystal growth.

Reynolds	Ratio of inertia to viscous forces	$Re = \frac{u_{av} \cdot L \cdot \rho}{\mu}$
Reynolds (magnetic)	Ratio of convection to diffusion in magnetic field	$Re_m = u_{av} \cdot L \cdot \sigma_{el} \cdot \mu_0$
Prandtl	Ratio of molecular momentum and thermal diffusivities	$Pr = \frac{\mu \cdot c_p}{\lambda}$
Grashof	Ratio of buoyancy to viscous forces	$Gr = \frac{\alpha \cdot g \cdot \Delta_{T,ref} \cdot L^3}{\nu^2}$
Schmidt	Ratio of molecular momentum and mass diffusivities	$Sc = \frac{\nu}{D}$
Hartmann	Ratio of electromagnetic force to the viscous force	$Ha = B \cdot L \cdot \left(\frac{\sigma}{\mu}\right)^{0.5}$
Rayleigh	A measure of the vigor of convection	$Ra = Gr \cdot Pr$
Péclet	Ratio of heat transfer by convection to conduction	$Pe = Re \cdot Pr$
Péclet (mass transfer)	Ratio of bulk mass transfer to diffusive mass transfer	$Pe_D = Re \cdot Sc$

Notation: ν is the kinematic viscosity ($\nu = \mu\ \rho^{-1}$); μ_0 is the magnetic permeability of the free space.

Table 2 Properties of the relevant melts for electronic and solar industry (Milller and Ostrogorsky, 1994; Rudolph and Mühlberg, 1993; Miller et al., 2017; Dobrovinskaya et al., 2008).

Melt	T_m [K]	ρ [kg m^{-3}]	μ [Pas]	λ [W m^{-1} K^{-1}]	c_p [J kg^{-1} K^{-1}]	α [K^{-1}]	*Pr*
Si	1683	2530	8.855×10^{-4}	67	1037	1.32×10^{-4}	0.014
Ge	1209	5510	7.439×10^{-4}	39	404	1.11×10^{-4}	0.008
GaAs	1511	5720	2.791×10^{-3}	17.8	434	1.87×10^{-4}	0.068
InP	1335	5050	8.18×10^{-4}	22.8	424	4.4×10^{-4}	0.015
InSb	798	6480	2.138×10^{-3}	9.23	263	1.0×10^{-4}	0.055
Ga_2O_3	2170	6000	0.1	20	800	1.8×10^{-5}	4
CdTe	1365	5670	$2.36e \times 10^{-3}$	1	187	5.0×10^{-4}	0.413
Al_2O_3	2323	3030	0.00545	2.05	1260	3.56×10^{-4}	33.5

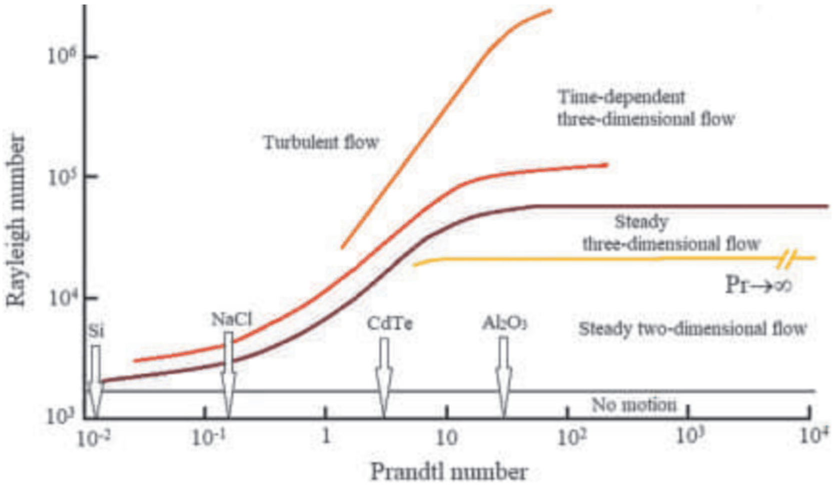

Fig. 8 Rayleigh-Prandtl regime diagram for steady, transitional, time-dependent and turbulent buoyancy driven flows. Based on Krishnamurti R (1973) Some further studies on the transition to turbulent convection. *Journal of Fluid Mechanics* 60: 285–303.

In the case of Cz-Si growth, for melt height $L = 0.2$ m and axial $\Delta T = 50$ K, the key dimensionless numbers have values $Gr = 4.2 \times 10^9$, $Pr = 0.014$ and $Ra = 5.9 \times 10^7$. According to the Rayleigh-Prandtl diagram (Fig. 8), the flow regime is turbulent. In the pure buoyancy regime, the Gr number of order 1×10^9 is the universal criterion for the transition to turbulence (Bejan and Lage, 1990; Krishnamurti, 1973).

Relative importance of buoyancy with respect to forced convection is determined by the ratio of Gr and Re^2 numbers.

Buoyancy convection is negligible if the following criterion is met:

$$\frac{Gr}{Re^2} < 0.1 \tag{31}$$

Forced convection is negligible if:

$$\frac{Gr}{Re^2} > 10 \tag{32}$$

Both convection types (buoyancy and forced) are important in the range:

$$0.1 < \frac{Gr}{Re^2} < 10 \tag{33}$$

Again, in case of previously mentioned Cz-Si growth with $Gr \sim 1 \times 10^9$, transition between solely buoyancy to mixed regime (Eq. 31) occurs at $Re = 1 \times 10^4$, while transition from mixed to pure forced convection regime (Eq. 32) occurs at $Re = 1 \times 10^5$.

Besides aiding in understanding the growth phenomena, dimensionless numbers can also strongly facilitate the scale up of the process and equipment. The importance of the latter is directly related with the common challenge in the crystal growth to improve process economy while preserving the crystal quality. For reaching that goal, higher crystallization yields and upscaled crystal sizes are beneficial. The fundamental approach to scale up is achieved by applying the principle of similitude (Marphy, 1950; Kline, 1986) between the small scale and the commercial equipment. That means keeping the characteristic dimensionless groups that characterize the process phenomena constant during scale up. To achieve similitude between two crystal growth processes and equipment, all criteria must be fulfilled: geometric, kinematic and dynamic similarity.

Process engineering

Computational fluid dynamics (CFD) is a traditional tool for solving the governing differential equations by replacing them with approximate algebraic equations at discrete points of the solution domain. Obtained velocity, concentration, pressure and temperature fields help understanding the key process steps and process parameters determining the complex, highly interrelated physical phenomena in crystal growth. The bottleneck of this approach is the fact that CFD simulations, especially in 3D and with transient character are laborious, expensive and time consuming, without the ability to generalize. The prediction accuracy of CFD simulations is highly dependent on the availability and accuracy of material data over a wide temperature range, especially when anisotropy and radiation are present in solids. Oversimplified domain geometry (e.g. choosing the 2D model for non-axisymmetric geometry), neglecting turbulence and the transient process nature lead to poor quality predictions, especially at industrial scale and for the growth of novel crystalline materials.

One of the most exciting novel tools that has recently appeared in the field of crystal growth is machine learning (ML). This collection of statistical methods has a great potential in acceleration of fundamental and applied research, particularly with respect of process and equipment multi-objective optimization, process control, generalization and interpretability of the results. Also, ML methods have one important advantage to CFD models, as they can be trained on both experimental and numerical data pools. They don’t require explicitly described knowledge of physical laws underlying the data nor the material data of the species present in the growth equipment, that knowledge is implicitly contained in the training data.

In the last few years, ML applications are mushrooming in all fields of crystal growth and on all scales, from bulk to epitaxial growth, from numerical simulations to experiments and from atomic to macro scale (Kutsukake et al., 2020, 2022; Dropka and Holena, 2017; Dropka et al., 2021a; Dropka et al., 2021b; Chou et al., 2022; Qi et al., 2020; Tsunooka et al., 2018; Dang et al., 2019, 2021; Asadian et al., 2009; Yu et al., 2021; Schimmel et al., 2021; Takehara et al., 2020; Boucetta et al., 2019; Osada et al., 2020).

The first measurable success is mirrored in the fact that enlargement of SiC wafer size from 1 in. to 6 in. was reached in less than 3 years with a support of machine learning, while it took 40 years to enlarge Si wafers diameter from 1 in. to 12 in. by common numerical and experimental approaches (Dold, 2015).

There are many available ML algorithms e.g., artificial neural network (ANN), Decision Trees (DTs), Random Forest etc. The guiding principles of choice depend mainly on the volume and quality of input data, type of output, targeted prediction accuracy, and required interpretability of results.

The ANN method is the most widely used ML technique in general and also in crystal growth. Therefore, the basic principles will be shortly explained.

This method resembles a simple concept of human brain and is particularly powerful when correlating a very large number of variables with highly non-linear dependences (Rojas, 1996). ANNs are capable pointwise to approximate smooth functions to any degree of accuracy.

An ANN is defined principally by its architecture, i.e. a set of artificial neurons and connections between them. The simplest kind of neural network is a multi-layer perceptron network (Fig. 9). The neurons are usually organized into layers: an input layer, one or more hidden layers and an output layer. Each neuron performs as a computational unit that receives inputs x_i, multiplies them by weights w_i and then uses the sum of such weighted inputs as the argument for a nonlinear function (a common choice is a logistic sigmoidal function $f(x,w)$ (Eq. 34)), which activates neuron and yields the final output y_j.The whole ANN receives inputs by neurons in the first layer, and obtains output by the neurons in the last layer, i.e. the neurons are interconnected in a feed-forward way.

$$y_j = f(x, w) = \frac{1}{1 + e^{-\left(\sum_{i=1}^{n} \left(w_{j,\,i} \cdot x_i + b_i\right)\right)}} \tag{34}$$

By adjusting the weights $\Delta w_{j,\,i}$ of connections and biases b_i of artificial neurons (aka ANN training), the targeted output y_j can be obtained for a specific combination of inputs x_i. The aim of ANN training is to adjust the weights and biases to minimize some kind of error E (e.g. the sum of squared differences between the outputs y_j of the network and the desired output o_j over all the neurons in the output layer) measured on the network.

$$E(x,\, w,\, o) = \sum_j \left(y_j - o_j\right)^2 \tag{35}$$

The weights can be adjusted using various methods, e.g. the method of gradient descendent with constant learning rate:

$$\Delta w_{j,i} = -\eta \frac{\partial E}{\partial w_{j,i}} \tag{36}$$

Before ANN training, it is necessary to choose the ANN architecture, the activation function and the training method. A comparison of different ANN architectures is usually estimated by the k-fold cross validation method (Rojas, 1996). It starts by dividing the training set into k subsets. For each ANN architecture, the training is performed k times, each time using one of the subsets as the

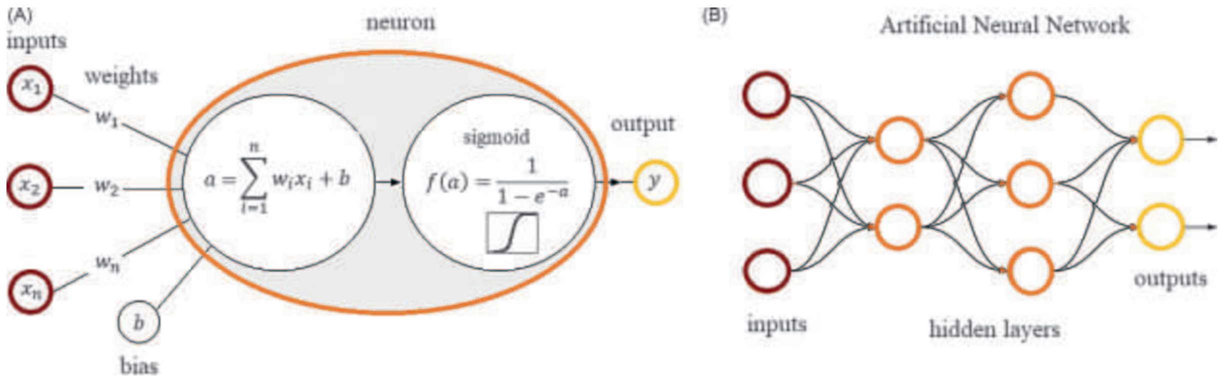

Fig. 9 Example of a feed forward multi-layer perceptron artificial neural network: (a) neuron, (b) architecture.

validation set and the remaining subsets as the training set. In the next step, the architecture is selected that had the smallest error averaged over the validation sets from the k runs. Finally, the ANN model with this architecture is used to train on all the data. After being trained, the ANN model reflects the relationship between the input and output of the system.

An example of ANN-based real-time prediction of interstitial oxygen in Cz-Si growth as a function of process parameters, age of hot-zone parts, monitored temperature, and crystal diameter is given in (Kutsukake et al., 2020) (Fig. 10). ANN was trained on industrial experimental crystal growth data. Accurate, real-time prediction of various key process parameters and finally their optimization was the topic of many studies.

If the understanding of how some crystal growth parameters contribute to the optimization goal, aka the interpretability of the results, DT is a better choice. Once "sensitive parameters" have been identified, an optimization is easy and straightforward.

The DT method works in the following way: each node in the tree represents a variable x_i from the input datasets, each branch a decision and each leaf at the end of a branch the corresponding output value y_i. The decision process aka splitting starts from the top root node downwards through the tree until a bottom leaf is reached which contains the result. The splits are made in such a way that the sum of squared errors with respect to the average values of the y_i in the above subsets is minimal.

An example of Classification Tree (type of DT) analysis of the process parameters influencing interface deflection in VGF-GaAs growth is given in Fig. 11 (Dropka et al., 2021a, 2021b). Orange branches correspond to the growth recipes where leaf nodes have a convex shape of s/l interface ($y2 \leq 0$, denoted as "-"). The results revealed x4 (the power of the upper side heater), followed by x5 (the power of the lower side heater) and x1 (the growth rate) as the most decisive inputs and the range of their values for the favorable interface shape. Their significance decreases in the order mentioned above.

In this chapter, we presented the different approaches to solve macroscale continuum models from CFD simulations, dimensional analysis based on dimensionless numbers to machine learning techniques. In our opinion, the latter are capable of significantly accelerating both fundamental and applied research and will certainly shape crystal growth in the future.

Crystal growth analysis

Defects

Crystal defects are unavoidable imperfections in the periodic crystal lattice in real crystalline solids (Rudolph, 2007; Rudolph, 2010a, 2010b; Klapper and Rudolph, 2015; Hurle and Rudolph, 2004).

Crystal defects are traditionally classified after their dimensionality that may vary from 0 to 3 (Fig. 12). The 0-dimensional are point defects which include vacancies, interstitial atoms, substitutional atoms, and antisites (in compounds). If substitutional atoms are incorporated intentionally, they are called dopants. If they enter the crystal structure by accident, they are building residual impurities. The 1-dimensional are line defects that include all kinds of dislocations, i.e. screw and edge dislocations, mixed dislocations, partial dislocations, and dislocation loops. The 2-dimensional planar defects are, e.g. grain boundaries, phase boundaries, facets, stacking faults and twins. The 3-dimensional are bulk defects, such as precipitates (second phase particles), inclusions (foreign particles at the crystallization front) and microvoids (intrinsic vacancy conglomerates).

Alternatively, the crystal defects can be classified according to their origin. For example, they can come from: the feedstock, the substrate, and/or during different process steps: furnace heating up, stationary growth, transient growth, cooling down and further crystal processing.

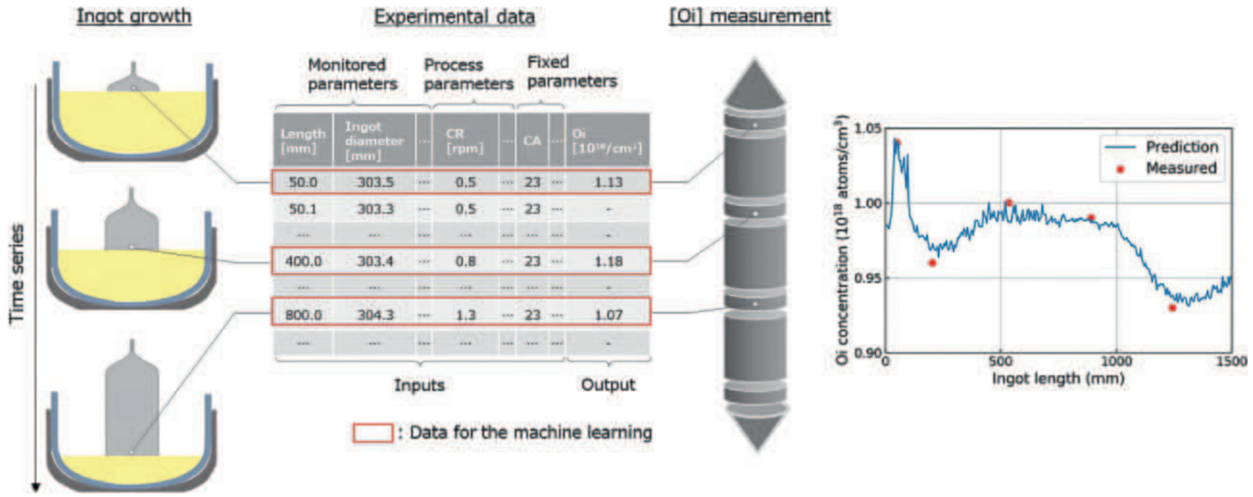

Length [mm]	Ingot diameter [mm]	···	CR [rpm]	···	CA	···	Oi [10^{18}/cm^3]
50.0	303.5	···	0.5	···	23	···	1.13
50.1	303.3	···	0.5	···	23	···	-
···	···	···	···	···	···	···	-
400.0	303.4	···	0.8	···	23	···	1.18
···	···	···	···	···	···	···	-
800.0	304.3	···	1.3	···	23	···	1.07
···	···	···	···	···	···	···	-

Fig. 10 Example of prediction of oxygen concentration in Cz-Si ingot as a function of process parameters using ANN model trained on experimental crystal growth data. The derived ANN architecture includes 3 layers with 47 neurons, 43 inputs and 1 output. Based on Kutsukake K et al. (2020) Real-time prediction of interstitial oxygen concentration in Czochralski silicon using machine learning. *Applied Physics Express* 13: 125502.

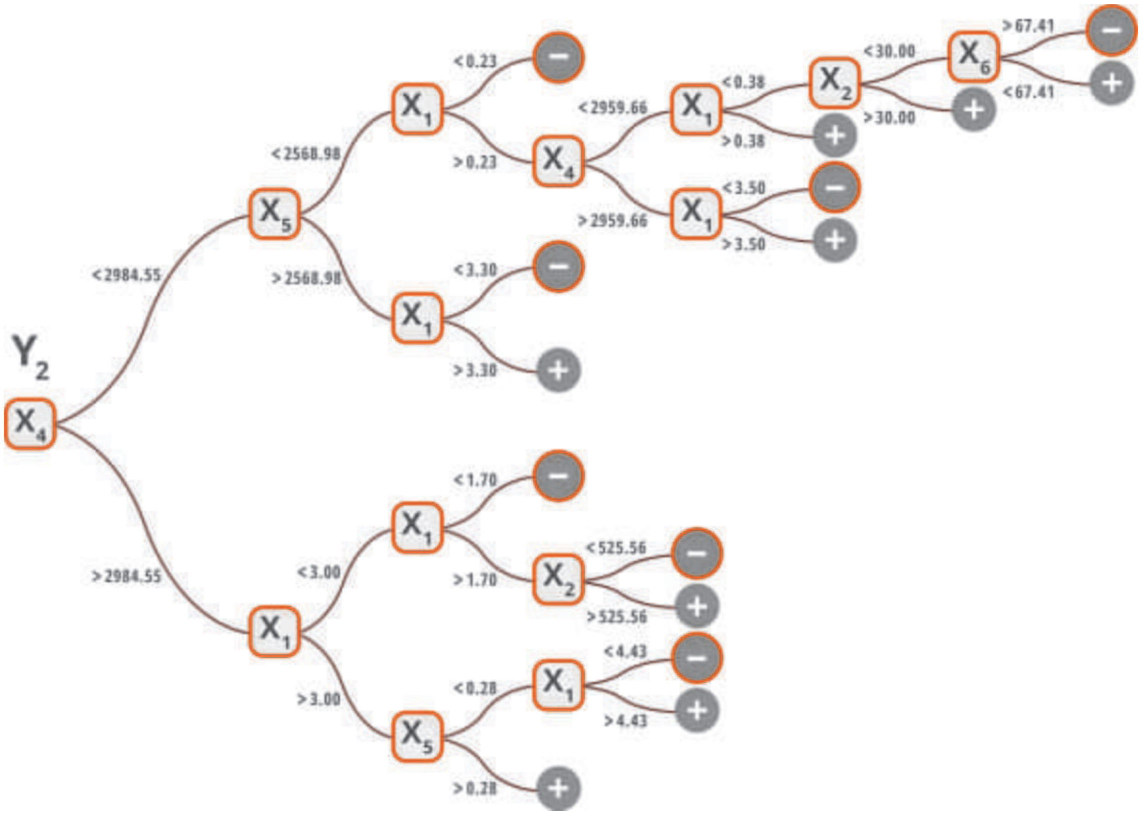
Y_2
X_4
<2984.55
>2984.55
X_5
<2568.98
>2568.98
X_1
<0.23
>0.23
−
X_4
<2959.66
>2959.66
X_1
<0.38
>0.38
+
X_2
<30.00
>30.00
+
X_6
>67.41
<67.41
−
+
X_1
<3.50
>3.50
−
+
X_1
<3.30
>3.30
−
+
X_1
<3.00
>3.00
X_1
<1.70
>1.70
−
X_2
<525.56
>525.56
−
+
X_5
<0.28
>0.28
+
X_1
<4.43
>4.43
−
+

Fig. 11 Example of Classification Tree analysis of the dependence of the solid-liquid interface deflection on the growth rate and power of heaters in VGF-GaAs growth (Dropka et al., 2021a, 2021b). Notation: x1-crystal growth rate [mm h^{-1}], x2-power in inner top heater [W], x4-power in upper side heater [W], x5-power in lower side heater [W], x6-power in bottom heater [W], y2-interface deflection [m], + concave interface deflection, – convex interface deflection. Courtesy of Anne Riemann, IKZ.

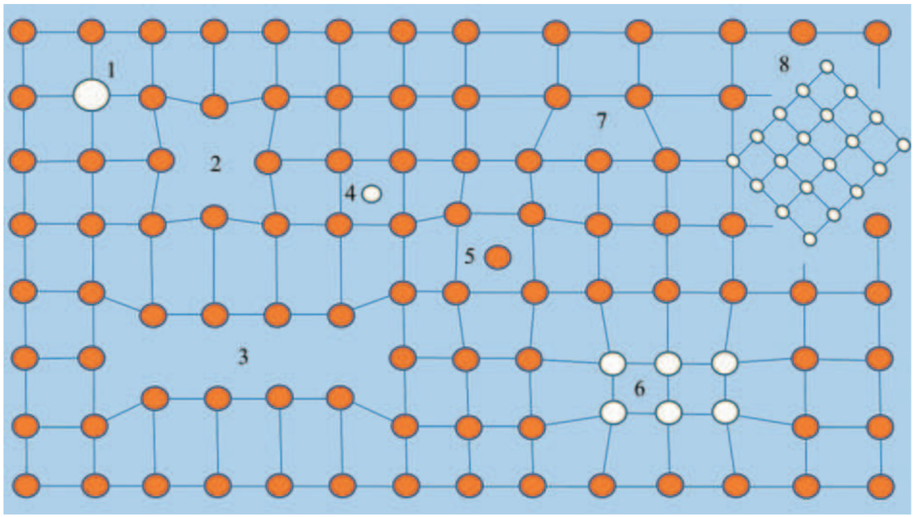

Fig. 12 Scheme of crystal lattice with defects: (1) substitutional impurity atom, (2) vacancy, (3) vacancy type dislocation loop, (4) interstitial impurity atom, (5) self-interstitial atom, (6) precipitate of impurity atoms, (7) edge dislocation, (8) incongruous inclusion. Based on Rudolph P (2010) Transport phenomena of crystal growth-heat and mass transfer. *AIP Conference Proceedings* 107: 1270.

In addition, the defects can be classified according to their influence on the structural, chemical, electronic and radiation properties of the crystal.

In the case of Si, which is the predominant semiconductor material for the photovoltaics and electronic industry, common defects are: (i) self-interstitial point defects, which can act as carrier traps, (ii) dislocation and dislocation-loop line defects, which can reduce the minority carrier lifetime in solar cells and lead to eddy circuits and shorts in microelectronics, (iii) grain boundaries planar defects that may cause impurity gettering and consequently reduction in solar cell efficiency, and finally (iv) microvoid bulk defects in metal-oxide-semiconductor (MOS) transistors can lead to degradation of the gate oxide.

In order to ensure high quality of the grown crystals and to meet different application requirements, controlling the formation of crystal defects aka crystal defects engineering is crucial. There are two feasible approaches to tackle this topic: (i) in situ control of the crystal growth process and (ii) post-annealing of the bulk crystals or their wafers. The first approach can be achieved by growing crystal within "defect-free regime" defined by Voronkov criteria (Voronkov, 1982):

$$1 \times 10^{-3} < \frac{r_{growth}}{gradT} < 2 \times 10^{-3}\ \frac{cm^2}{K \cdot min} \tag{37}$$

using very low puling velocities of about 0.5 mm/min and low cooling rates. The second approach is coupled with: (i) growing crystal with high puling and high cooling rates followed by annealing of wafer and (ii) high pulling and high cooling rates with annealing of wafers and deposition of epi-layers as proposed by Dornberger et al. (2001). The latter approach is the most cost-effective.

In the growth of crystal compounds, defect control can also be achieved by coupling with compositional control via a fixed temperature vapor source of the volatile component. The vapor-pressure controlled Czochralski growth of GaAs crystals is a typical example of this approach (Neubert et al., 2008).

Segregation

Solutes generally have a different equilibrium solubility in the crystal and the melt. Segregation arises from this difference. Segregation describes the enrichment of solute atoms in the crystal or the melt during crystallization. These solute atoms can be intentional, as in the case of doping semiconductors, or unintentional, in the form of impurities. Understanding the distribution of solute atoms, and hence segregation arising from crystal growth is essential for achieving homogenous doping or crystal purification.

A key concept for studying segregation is the segregation coefficient k, which is defined as the ratio of the solute concentration in the crystal and the melt. Its equilibrium value k_0 can be determined from an equilibrium phase diagram. A sketch of a phase diagram of a melting point reducing solute in a crystal/melt system can be seen in Fig. 13a. The melting temperature of the pure crystal is indicated by T_m, and the equilibrium solute concentration in the crystal and the melt is indicated by C_S and C_L, respectively. The liquidus and solidus line can be approximated by lines, since relevant solute concentrations are generally small (compare to the left side of the phase diagram in Fig. 3a). In this case, the k_0 is a constant and determined by $k_0 = C_S/C_L$. For deviations from this linear approximation (for instance for higher solute concentrations), k_0 is temperature-dependent. In the case of a melting point reducing solute, k_0 is <1 (as in Fig. 13a), in the case of a melting point increasing solute it is >1, and no segregation occurs in the case of $k_0 = 1$. For most solutes, the segregation coefficient is <1, which can be qualitatively understood by the fact that it is energetically less favorable for solute atoms to be incorporated in a crystal (resulting in a crystal defect) than being dissolved in a melt. For instance, segregation coefficients of most transition metals in Si are $<10^{-3}$, and the segregation coefficients

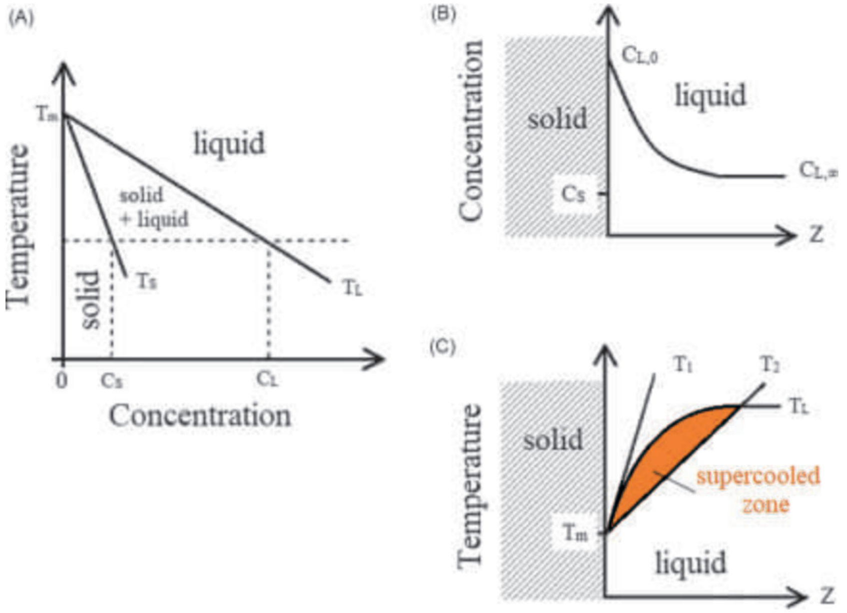

Fig. 13 The solidification of the melt with low concentration of solute: (a) simplified part of the phase diagram, (b) axial segregation of solute, (c) constitutional supercooling conditions in temperature-distance-from-the-interface diagram. Notation: T_L,T_S,T_m,T_1,T_2 are liquidus, solidus, melting and two different cases of actual temperatures in the melt; C_L,C_S are solute concentrations at liquidus and solidus curves.

for typical dopants such as P or As are around 10^{-1} (Johnston et al., 2012). Hence, from here on in this section it is assumed that $k < 1$, but all statements can be translated to the $k > 1$ case.

For real crystal growth applications, deviations from the equilibrium segregation coefficient can be observed. The impact of the crystallization conditions on the segregation coefficient was first described in Burton et al. (1953) within the BPS model (named after Burton, Prim, and Slichter). Deviations from equilibrium lead to reduced segregation and hence their effective segregation coefficient k_{eff} is closer to unity than k_0. In the BPS model one assumes that the solute atoms get rejected after at the propagating crystal/melt interface that they can diffuse into the melt. Consequently, a boundary layer with increased solute concentration builds up, which results in:

$$k_{eff} = \frac{k_0}{k_0 + (1 - k_0)\exp\left(-\frac{r_{growth}\cdot\delta}{D}\right)} \tag{38}$$

where r_{growth} is the propagation velocity of the crystal/melt interface (growth velocity), δ is the thickness of the boundary layer, and D is the diffusion coefficient of the solute atoms in the melt. For a small $\frac{r_{growth}\cdot\delta}{D}$ the effective segregation coefficient approaches k_0, which is achieved by a small growth velocity, a narrow boundary layer thickness (e.g. by stirring), and a high diffusivity. For a large $\frac{r_{growth}\cdot\delta}{D}$, the effective segregation coefficient converges to 1. For homogenous doping of a crystal, one wants achieve a low segregation ($k_{eff} \rightarrow 1$), while for crystal purification (as for instance in zone refining) a high segregation ($k_{eff} \rightarrow k_0$) is preferred.

The solute distribution of a growing crystal can be understood by the concept of normal freezing (Pfann, 1952). Here, the crystal grows directionally into the melt, as depicted in Fig. 14. In this model transport of solute atom (e.g. via diffusion) in the melt is instantaneous, while neglected in the crystal. This is a good approximation for crystal growth, since transport mechanisms in the melt are fast, and diffusion mechanisms in the crystal are slow relative to growth time scales. The resulting solute concentration as a function of solidified fraction m is called the Scheil equation (Scheil, 1942) and is:

$$C_S = k\cdot C_0\,(1-m)^{k-1} \tag{39}$$

where C_0 is initial solute concentration in the melt.

The presented models represent a starting point to study segregation in crystal growth. The theories here had several short comings, as the treatment of transport phenomena in the crystal and the melt was simplified, only one-dimensional problems were considered, and most importantly the systems were closed systems (no solute atoms from or to the environment). In real growth processes more complicated considerations often have to be taken into account and numerical methods are required.

Morphological instability

Under certain crystal growth conditions, when the solutes (e.g. impurities or low concentration dopants) are not homogeneously mixed in the melt and when the solute boundary layer is well developed, the solid-liquid interface can become morphologically unstable due to the constitutional supercooling effect (Fig. 13) (Wenzl et al., 1993).

Supercooled zones in melts are observed when the liquidus temperature gradient at the solid-liquid interface is higher than the actual temperature gradient in the melt. The region where the melt is constitutionally supercooled is marked by the shaded area in Fig. 13c. In this situation the interface becomes morphologically unstable because any fluctuation forms a protuberance of the interface. Depending on the intensity of supercooling, interface shape may become wavy, cellular and even dendritic (Fig. 15) (Warren and Langer, 1993).

The constitutional supercooling is an adverse phenomenon that leads to polycrystallinity and limits crystal growth applications.

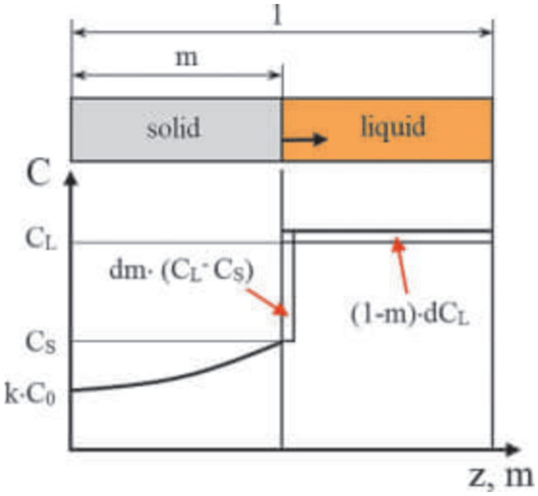

Fig. 14 Schematic solute concentration distribution of normal freezing of a melt.

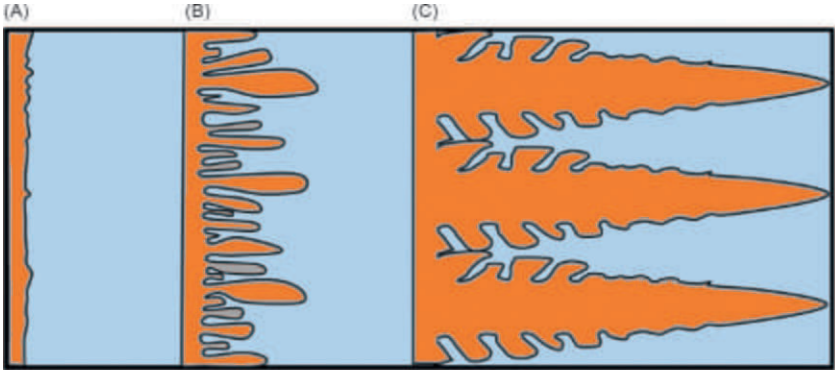

Fig. 15 Interface shapes for different intensity of constitutional supercooling: (a) wavy for a weak, (b) cellular for moderate and (c) dendritic interface for a strong supercooling. Based on Warren JA, Langer J (1993) Prediction of dendritic spacings in a directional-solidification experiment. *Physical Review E* 47: 2702; reprinted with permission of APS.

The first theoretical studies of constitutional supercooling were published by Tiller et al. (1953) and Hurle (1961). They derived theoretically the condition for the preservation of morphological stability of the interface, i.e. a prevention of constitutional supercooling.

The onset of the constitutional supercooling is determined by Mullins-Sekerka criterion (Mullins and Sekerka, 1964):

$$\frac{dT_L}{dz} < \frac{mc_0(1 - k)\cdot r_{growth}}{k\cdot D} \tag{40}$$

where m is a slope of liquidus curve on the phase diagram (Fig. 13a) and k is a segregation coefficient (a ratio of solute concentration in the solid to solute concentration in the melt). The slope m can be estimated from the equation of Thurmond and Kowalchik (1960):

$$m = \frac{T_m^2\cdot R}{\Delta H_S} \tag{41}$$

$$k = \frac{C_S}{C_L} \tag{42}$$

where R is a gas constant ($R = 8.314$ J mol^{-1} K^{-1}).

From this equation it is obvious that the tendency for supercooling increases as: (i) temperature gradients decrease, (ii) diffusion coefficients increase, (iii) crystal growth rates increase and (iv) solidus/liquidus lines become steeper. Against this background, the following measures can be beneficial to morphological stability: (i) optimization of the hot zone in the furnace by adding heat shields to increase the temperature gradients, (ii) slowing down the growth process and (iii) increase the melt convection by external forces (e.g. Lorentz force, vibrational force, etc.).

Conclusion

The crystal growth processes with their complex physical and chemical phenomena, which extend over large length and time scales, can still not be described with a single theory, despite remarkable progress.

In the coming years, ML techniques are expected to significantly accelerate basic research in bulk crystal growth to achieve this goal. The main benefit lies in the prompt and precise ML predictive power, which is a stepping stone to explaining new theories and hypotheses when no convincing theory is available.

ML enables quantitative comparison of theoretical models based on their predictive success, which could reveal key factors relevant to their success and thus contribute to theory development. Moreover, ML can serve as a final trusted criterion for explaining novel theoretical models, free from human errors.

The clear game-changer in these endeavors will be the generation of open-source research data infrastructure in the future.

Acknowledgments

The authors thank K. Böttcher (IKZ) for assistance in proofreading the article and providing Fig. 3a, and A. Riemann (IKZ) for providing Fig. 11.

References

Abrosimov NV, et al. (2017) A new generation of 99.999% enriched 28Si single crystals for the determination of Avogadro's constant. *Metrologia* 54: 599–609.

Asadian M, et al. (2009) Optimization of the parameters affecting the shape and position of crystal–melt interface in YAG single crystal growth. *Journal of Crystal Growth* 311: 342–348.

Bejan A and Lage JL (1990) The Prandtl number effect on the transition in natural convection along a vertical surface. *The Journal of Heat Transfer* 112: 787–790.

Boucetta A, Kutsukake K, Kojima T, Kudo H, Matsumoto T, and Usami N (2019) Application of artificial neural network to optimize sensor positions for accurate monitoring: an example with thermocouples in a crystal growth furnace. *Applied Physics Express* 12: 125503.

Burton JA, Prim RC, and Slichter WP (1953) The distribution of solute in crystals grown from the melt. Part I. Theoretical. *The Journal of Chemical Physics* 21: 1987–1991.

Chou T, Anooz SB, Grüneberg R, Irmscher K, Dropka N, Rehm J, Tran TV, Miller W, Seyidov P, Albrecht M, and Popp A (2022) Toward precise n-type doping control in MOVPE grown β-Ga_2O_3 thin films by deep learning approach. *Crystals* 12: 8–19.

Dang Y, Liu L, and Li Z (2019) Optimization of the controlling recipe in quasi-single crystalline silicon growth using artificial neural network and genetic algorithm. *Journal of Crystal Growth* 522: 195–203.

Dang Y, Zhu C, Ikumi M, Takaishi M, Yu W, Huang W, Liu X, Kutsukake K, Harada S, Tagawa M, and Ujihara T (2021) Adaptive process control for crystal growth using machine learning for high-speed prediction: application to SiC solution growth. *CrystEngComm* 23: 1982–1990.

Derby JJ (2005) Crystal growth, bulk: Theory and models. In: *Encyclopedia of Condensed Matter Physics*. Elsevier Ltd.

Derby JJ and Yeckel A (2004) Modeling of crystal growth processes. In: Müller G, Metois JJ, and Rudolph P (eds.) *Crystal Growth—From Fundamentals to Technology*, pp. 143–168. Amsterdam: Elsevier.

Derby JJ, et al. (2007) Large-Scale Numerical Modeling of Melt and Solution Crystal Growth. In: Skowronski M, DeYoreo JJ, and Wang CA (eds.) *Perspectives on Inorganic, Organic, and Biological Crystal Growth: From Fundamentals to Applications, 13th International Summer School on Crystal Growth*.

Dobrovinskaya ER, Lytvynov LA, and Pishchik V (2008) *Sapphire: Material, Manufacturing, Applications*. Springer Verlag.

Dold P (2015) Silicon Crystallization Technologies. *Semiconductors and Semimetals* 92: 1–61.

Dornberger E, Virbulis J, Hanna B, Hoelzl R, Daub E, and von Ammon W (2001) Silicon crystals for future requirements of 300mm wafers. *Journal of Crystal Growth* 229: 11–16.

Dropka N and Holena M (2017) Optimization of magnetically driven directional solidification of silicon using artificial neural networks and Gaussian process models. *Journal of Crystal Growth* 471: 53–61.

Dropka N, Böttcher K, and Holena M (2021a) Development and optimization of VGF-GaAs crystal growth process using data mining and machine learning techniques. *Crystals* 11: 1218.

Dropka N, Ecklebe S, and Holena M (2021b) Real time predictions of VGF-GaAs growth dynamics by LSTM Neural Networks. *Crystals* 11: 138.

Fan X, et al. (2018) Controllable growth and formation mechanisms of dislocated WS2 spirals. *Nano Letters* 18: 3885–3892.

Frank FC (1949) The influence of dislocations on crystal growth. *Discussions of the Faraday Society* 5: 48–54.

Gibbs JW (1928) The collected Works of J. Willard Gibbs, Longmans, Green and Co., New York.

Gottstein G (2013) *Physical Foundations of Materials Science*. Springer Science & Business Media. pp. 71–79.

Hurle DTJ (1961) Constitutional supercooling during crystal growth from stirred melts-I: Theoretical. *Solid State Electronics* 3: 37–44.

Hurle DTJ and Rudolph P (2004) A brief history of defect formation, segregation, faceting, and twinning in melt-grown semiconductors. *Journal of Crystal Growth* 264: 550–564.

Johnston MD, et al. (2012) High-temperature refining of metallurgical-grade silicon: A review. *JOM* 64: 935–945.

Kaufman L and Bernstein H (1970) *Computer Calculation of Phase Diagrams*. New York: Academic Press. ISBN 0-12-402050-X.

Klapper H and Rudolph P (2015) Defect generation and interaction during crystal growth. In: Rudolph P (ed.) *Handbook of Crystal Growth*, pp. 1093–1141. Elsevier.

Kline SJ (1986) *Similitude and Approximation Theory*. New York: Springer-Verlag.

Kobayashi N (1978) Computational simulation of the melt flow during Czochralski growth. *Journal of Crystal Growth* 43: 357–363.

Kobayashi N and Arizumi T (1970a) The numerical analysis of the solid-liquid interface shapes during the crystal growth by the Czochralski method. *Japanese Journal of Applied Physics* 9: 361–367.

Kobayashi N and Arizumi T (1970b) The numerical analysis of the solid-liquid interface shapes during the crystal growth by the Czochralski method. Part II. Effect of the crucible rotation. *Japanese Journal of Applied Physics* 9: 1255–1259.

Kossel W (1927) Nachrichten von der Gesellschaft der Wissenschaften zu Göttingen, Mathematisch-Physikalische Klasse. *Zur Theorie des Kristall Wachstums* 1927: 135–143.

Krishnamurti R (1973) Some further studies on the transition to turbulent convection. *Journal of Fluid Mechanics* 60: 285–303.

Kutsukake K, et al. (2020) Real-time prediction of interstitial oxygen concentration in Czochralski silicon using machine learning. *Applied Physics Express* 13: 125502.

Kutsukake K, Nagai Y, and Banba H (2022) Virtual experiments of Czochralski growth of silicon using machine learning: Influence of processing parameters on interstitial oxygen concentration. *Journal of Crystal Growth* 584: 126580.

Lupis CHP (1983) *Chemical Thermodynamics of Materials*. Amsterdam: Elsevier Science Publishing Co., Inc.

Marphy G (1950) *Similitude in Engineering*. New York: The Roland Press Company.

Miller W, Böttcher K, Galazka Z, and Schreuer J (2017) Numerical modelling of the czochralski growth of β-Ga_2O_3. *Crystals* 7: 26–41.

Milller G and Ostrogorsky A (1994) Convection in melt growth. In: Hurle DTJ (ed.) *Bulk Crystal Growth, Growth Mechanisms and Dynamics, Handbook of Crystal Growth*. vol. 2b, pp. 709–819. North-Holland, Amsterdam: Elsevier.

Mullins WW and Sekerka RF (1964) Stability of a Planar Interface during Solidification of a Dilute Binary Alloy. *Journal of Applied Physics* 35: 444–451.

Nancollas GH and Purdie N (1964) The kinetics of crystal growth. *Quarterly Reviews, Chemical Society* 18: 1–20.

Neubert M, Rudolph P, Frank-Rotsch C, Czupalla M, Trompa K, Pietsch M, Jurisch M, Eichler S, Weinert B, and Scheffer-Czygan M (2008) Crystal growth by a modified vapor pressure-controlled Czochralski (VCz) technique. *Journal of Crystal Growth* 310: 2120–2125.

Nishinaga T (2015) Progress in art and science of crystal growth and its impacts on modern society. *Japanese Journal of Applied Physics* 54: 050101.

Nishinaga T (2016) Thermodynamics-for understanding crystal growth. *Progress in Crystal Growth and Characterization of Materials* 62: 43–57.

Osada K, Kutsukake K, Yamamoto J, Yamashita S, Kodera T, Nagai Y, Horikawa T, Matsui K, Takeuchi I, and Ujihara T (2020) Adaptive Bayesian optimization for epitaxial growth of Si thin Films under various constraints. *Materials Today Communications* 25: 101538.

Pfann WG (1952) Segregation of two solutes, with particular reference to semiconductors. *JOM* 4: 861–865.

Polezhaev VI (2003) Modeling of technologically important hydrodynamics and heat/mass transfer processes during crystal growth. In: Scheel HJ and Fukuda T (eds.) *Crystal Growth Technology, chapter 8*. West Sussex, UK: John Wiley & Sons.

Qi X, et al. (2020) Optimization of the melt/crystal interface shape and oxygen concentration during the Czochralski silicon crystal growth process using an artificial neural network and a genetic algorithm. *Journal of Crystal Growth* 548: 125828.

Rojas R (1996) *Neural Networks: A Systematic Introduction*. Berlin: Springer.

Rudolph P (1998) Elements of thermodynamics for the understanding and design of crystal growth processes. *Materials Science Forum* 276: 1–26.

Rudolph P (2003) Thermodynamic fundamentals of phase transitions applied to crystal growth processes. In: Scheel HJ and Fukuda T (eds.) *Crystal Growth Technology*, pp. 15–42. Wiley.

Rudolph P (2007) Fundamentals of defects in crystals. *AIP Conference Proceedings* 916: 69–92.

Rudolph P (2010a) Transport phenomena of crystal growth-heat and mass transfer. *AIP Conference Proceedings* 107: 1270.

Rudolph P (2010b) Defect formation during crystal growth from the melt. In: Dhanaraj G, Byrappa K, Prasad V, and Dudley M (eds.) *Springer Handbook of Crystal Growth*, pp. 159–201. Springer, Berlin, Heidelberg: Springer Handbooks.

Rudolph P and Mühlberg M (1993) Basic problems of vertical Bridgman growth of CdTe. *Materials Science and Engineering B* 16: 8–17.

Scheel HJ and Fukuda T (2003) *Crystal Growth Technology*. New York: Wiley.

Scheil E (1942) Bemerkungen zur Schichtkristallbildung. *International Journal of Materials Research* 34: 70–72.

Schimmel S, et al. (2021) Boundary conditions for simulations of fluid flow and temperature field during ammonothermal crystal growth-a machine-learning assisted study of autoclave wall temperature distribution. *Crystals* 11: 254.

Sears GW (1956) Evaporation of perfect crystals. *The Journal of Chemical Physics* 24: 868–873.

Seiss M, Ouisse T, and Chaussende D (2013) Comparison of the spiral growth modes of silicon-face and carbon-face silicon carbide crystals. *Journal of Crystal Growth* 384: 129–134.

Shtukenberg AG, et al. (2013) Illusory spirals and loops in crystal growth. *Proceedings of the National Academy of Sciences* 110: 17195–17198.

Stranski IN (1928) Zur Theorie des Kristallwachstums. *Zeitschrift für Physikalische Chemie* 136: 259–278.

Szmyd JS and Suzuki K (2000) *Modelling of Transport Phenomena in Crystal Growth. Volume 6 of Developments in Heat Transfer*. Southampton, England: WIT Press.

Takehara Y, Sekimoto A, Okano Y, Ujihara T, and Dost S (2020) Bayesian optimization for a high and uniform-crystal growth rate in the top-seeded solution growth process of silicon carbide under applied magnetic field and seed rotation. *Journal of Crystal Growth* 532: 125437.

Thurmond CD and Kowalchik M (1960) Germanium and silicon liquidus curves. *Bell System Technical Journal* 39: 169–204.

Tiller WA, Jackson KA, Rutter JW, and Chalmers B (1953) The redistribution of solute atoms during the solidification of metals. *Acta Metallurgica* 1: 428–437.

Tsunooka Y, Kokubo N, Hatasa G, Harada S, Tagawa M, and Ujihara T (2018) High-speed prediction of computational fluid dynamics simulation in crystal growth. *CrystEngComm* 20: 6546–6550.

Volmer M and Schultze W (1931) Condensation of crystals. *Zeitschrift Für Physikalische Chemie-Abteilung a-Chemische Thermodynamik Kinetik Elektrochemie Eigenschaftslehre* 156: 1–22.

Voronkov VV (1982) The mechanism of swirl defects formation in silicon. *Journal of Crystal Growth* 59: 625–643.

Wallace DC (1972) Thermodynamics of crystals. *American Journal of Physics* 40: 1718–1719.

Warren JA and Langer J (1993) Prediction of dendritic spacings in a directional-solidification experiment. *Physical Review E* 47: 2702.

Wenzl H, Oates WA, and Mika K (1993) Defect thermodynamics and phase diagrams in compound crystal growth process. In: Hurle DTJ (ed.) *Handbook of Crystal Growth*. vol. 1A, pp. 103–186. Elsevier.

Wolf DE (1991) Kinetic roughening of vicinal surfaces. *Physical Review Letters* 67: 1783–1786.

Yeckel A and Derby JJ (2003) Computational simulations of the growth of crystals from liquids. In: Scheel HJ and Fukuda T (eds.) *Crystal Growth Technology*. West Sussex, UK: John Wiley & Sons. ch. 6.

Yu W, et al. (2021) Geometrical design of a crystal growth system guided by a machine learning algorithm. *CrystEngComm* 23: 2695–2702.

Zinkevich M, Geupel S, Aldinger F, Durygin A, Saxena SK, Yang M, and Liu Z-K (2006) Phase diagram and thermodynamics of the La_2O_3–Ga_2O_3 system revisited. *Journal of Physics and Chemistry of Solids* 67: 1901–1907.

Film growth and epitaxy methods[☆]

Stuart JC Irvine, Swansea University, Wales, United Kingdom

© 2024 Elsevier Ltd. All rights reserved.

This is an update of F. Lévy, Film Growth and Epitaxy: Methods, Editor(s): Franco Bassani, Gerald L. Liedl, Peter Wyder, Encyclopedia of Condensed Matter Physics, Elsevier, 2005, Pages 210–222, ISBN 9780123694010, https://doi.org/10.1016/B0-12-369401-9/00418-6.

Introduction **249**
Physical vapor deposition **249**
Evaporation 250
Sputtering 250
Ion plating 252
Thermal-spraying 252
Molecular beam epitaxy (MBE) **252**
Chemical vapor deposition (CVD) **254**
Graphene CVD and other 2D materials 255
Metal organic vapor phase epitaxy (MOVPE) **255**
Atomic layer deposition **256**
Energy-assisted chemical vapor deposition **256**
Plasma-assisted CVD 256
UV-assisted and photo-assisted CVD 256
Film growth by condensed-phase reaction **257**
Sol-gel deposition 257
Chemical bath deposition (CBD) 257
Langmuir-Blodgett deposition 257
Electrodeposition 257
Liquid phase epitaxy **258**
Conclusion **259**
Acknowledgments **259**
References **259**

Abstract

Film and epitaxy growth form an essential part of engineering components, electronic and photonic devices. This chapter provides a summary of commonly used techniques both in research and for production scale. Examples of materials and applications are given for each of the techniques described. The chapter is broadly divided into two sections depending on the method to deliver elements onto the deposition surface. Vapor phase deposition includes evaporation techniques, chemical vapor deposition and energy assisted processes, covering a range of vapor pressures from atmospheric down to ultra-high vacuum. Solution based methods can be aqueous or solvent based and will normally entail a heterogeneous reaction to yield the required material onto the substrate. This includes chemical bath deposition, sol-gel and electrodeposition. Epitaxial growth is covered with descriptions of the commonly used techniques of molecular beam epitaxy (MBE), metal organic vapor phase epitaxy (MOVPE) and liquid phase epitaxy (LPE).

Key points

- Thin film deposition from the vapor using solid sources and chemical precursors.
- Background vapor pressure of the deposition chamber and significance of mean free path.
- The process of evaporation of solid sources by heating with electron beam, sputtering with plasma or laser ablation.
- The use of chemical precursors in the vapor in the form of organometallics and halides.
- The range of materials deposited as thin film coatings covers hard coatings, optical coatings and functional compound semiconductor films. 2D coatings such as graphene are also covered.

[☆] *Change History*: March 2023. SJC Irvine updated the text and added new Figures 1–11.

- Deposition from the liquid phase from chemical bath deposition, electrodeposition, sol-gel and liquid phase melts.
- 2D organic coatings using the Langmuir Blodgett deposition process.
- Epitaxial growth of compound semiconductors using either MBE, MOVPE or LPE.

Introduction

The growth of thin films covers an enormous range of applications from hard coatings on machine tool surfaces to semiconductor thin films for electronic and photonic devices. This chapter describes many of the commonly used thin film deposition methods and gives the reader an introduction to the different methods depending on the material being deposited and the application.

By way of introduction, the considerations for all deposition methods are as follows and shown schematically in Fig. 1.

- Substrate or surface to be coated.
- Environment for deposition, e.g. vacuum, chemical vapor, liquid etc.
- Source material.
- Transport of source material to the coating surface.
- Effluent, to include treatment of exhaust gases, removal of deposition material from deposition chamber.

These factors will be considered for each of the deposition methods, as appropriate. The next consideration is the crystalline form of the coating. Depending on the application, this can be amorphous, polycrystalline or single crystal. The latter is achieved through epitaxial growth where the substrate is a polished single crystal with the alignment of the lattice spacing between the substrate and the epitaxial film.

For each deposition method it is necessary to consider what drives the deposition process? Under equilibrium conditions there will be no film growth, so supersaturation needs to be created through a difference in chemical composition from the source to the film surface, or through changing parameters such as temperature or pressure. A combination of these deposition drivers is also possible. Alternatively, the loss of material from the surface can occur due to sublimation or chemical reaction, sometimes referred to as etch-back. Etch-back can sometimes be useful to present a clean surface prior to deposition. Again, this can be achieved through either chemical non-equilibrium or through changing physical parameters such as temperature and pressure.

The structural, morphology, electrical or optical properties of interest of a thin film depend on the application but in general, considerations will include: adhesion to the substrate, film thickness, film composition and film morphology. The latter is important since depending on the application a smooth or a rough surface is required. These can be controlled by the deposition process.

Physical vapor deposition

The process of physical vapor deposition (PVD) entails the evaporation of a solid source in a vacuum chamber and subsequent condensation onto a substrate surface. The quality of the vacuum depends on the material being deposited and the desired film properties but in general the aim is to minimize scattering from the ambient gas and avoid film contamination. This typically will require a vacuum of $<10^{-2}$ Pa (Haque et al., 2021). For very high purity applications such as for the deposition of semiconductor thin films in Molecular Beam Epitaxy (MBE) an Ultra-High Vacuum (UHV) is required ($<10^{-6}$ Pa). The choice of vacuum also determines the extent of molecular scattering between the source and substrate. For a molecular beam process the mean free path (MFP) needs to be much larger than the source to substrate distance. The MFP is determined by the following equation.

$$MFP = \frac{k_B T}{\sqrt{2}\pi d^2 p} \tag{1}$$

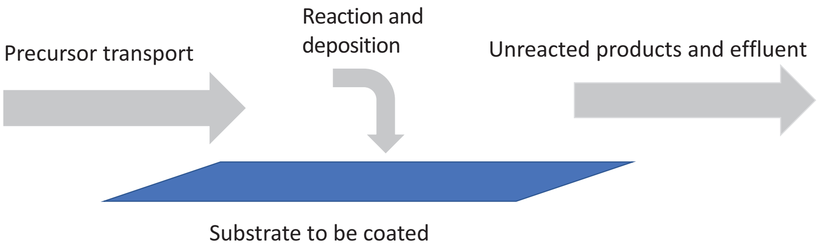

Fig. 1 Generic representation of thin film deposition.

Where k_B is Boltzman's constant, T is temperature of the gas in Kelvin, d is diameter of the molecule and p is the pressure of the gas. For example, 10^{-2} Pa will have a MFP of 50 cm and for 10^{-6} Pa it extends to 5 km. Differences between PVD methods are mostly associated with the method for evaporating the source material. Materials that are more volatile can be heated in a crucible while less volatile materials will require ion sputtering.

Evaporation

Thermal evaporation of elemental sources or compounds can be achieved, in the simplest case, by an electrically heated tungsten wire surrounding the source material. Examples of this approach would be in metallization of gold or silver for electrical contacts. Further refinements could entail the use of a crucible that is resistively heated. For crucible evaporation, the source (normally a metal) will need to be above its melting point. Compounds can also be evaporated from a melt or sublimed from the solid but can be more complex as the components will normally evaporate at a different rate, requiring an adjustment to the source composition or an additional elemental source of the less volatile component. In general, these approaches apply to relatively low melting point sources and most appropriate to single element evaporation. For higher melting point elements and compounds an electron beam source can be used (as illustrated in Fig. 2) which has the advantage of directly heating the source material without heating the crucible which can be water cooled to prevent damage. This method is commonly used for the deposition of optical coating materials where excellent uniformity of deposition can be achieved over multiple substrates. An example is the deposition of Ag/Al-doped ZnO reported by Sahu et al. (2007) which demonstrates the ability of e-beam evaporation to produce very controlled and uniform thicknesses of multiple optical layers. Other examples of e-beam evaporation are for anti-reflection coatings and optical filters (Sharma et al., 2018).

Sputtering

Sputtering is one of the most versatile thin film deposition techniques and can be used to deposit a very wide range of materials either as elements or compounds. The target material, instead of being heated, as with evaporation technique, is bombarded with ions from an inert gas discharge. The kinetic energy transfer causes the release of atomic species from the target surface. The target forms the cathode of a DC or AC plasma discharge. DC sputtering requires a conducting target whereas for AC sputtering the target can be conducting or insulating. The DC sputter process is also called "DC sputter diode discharge." This is the simplest form of sputter deposition and is shown schematically in Fig. 3. Characteristics of the operating conditions of a DC diode sputtering system are as follows.

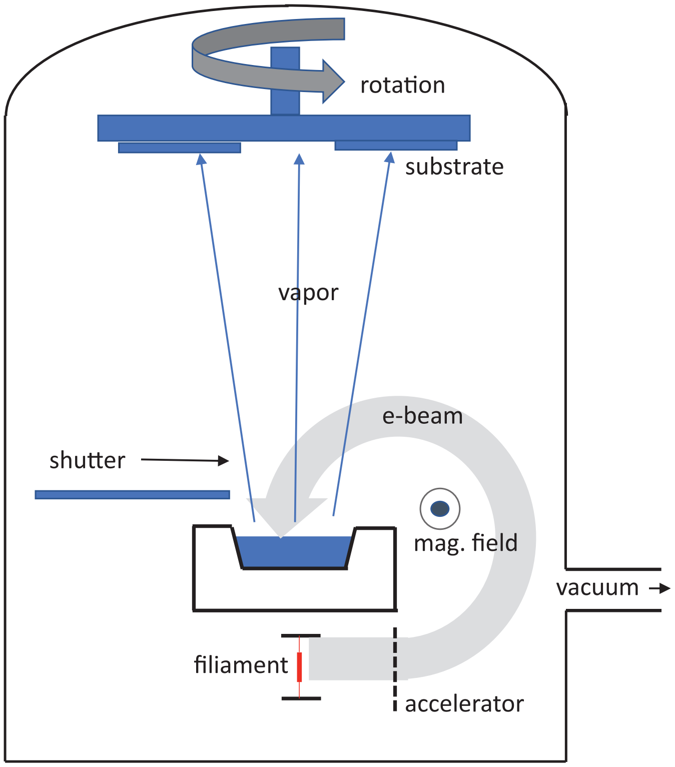

Fig. 2 Schematic of electron beam heated evaporation source.

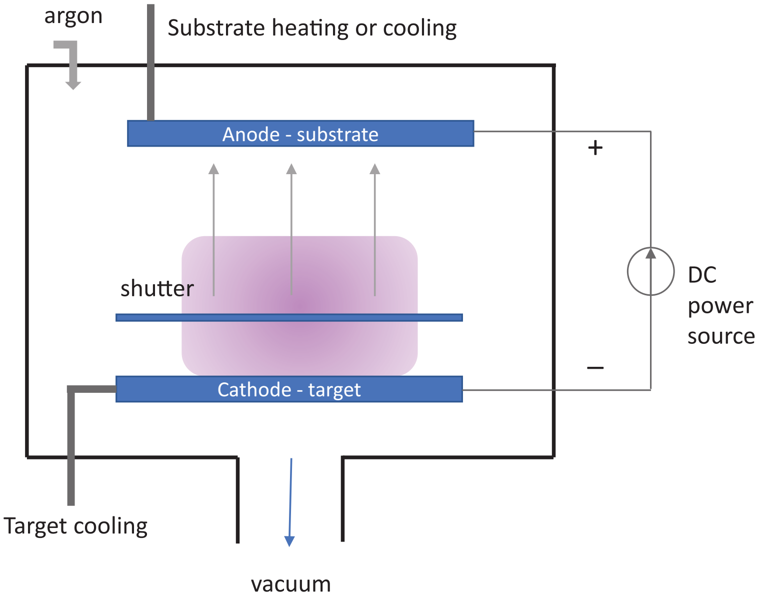

Fig. 3 Schematic of DC sputter discharge.

1. High operating voltages 2000–5000 V.
2. Narrow pressure range for the working gas pressure 2–4 Pa
3. Short ion mean free path (<1 cm)
4. Low mean energy for ions bombarding the cathode target (few eV)

The diode sputtering system can be adapted to sputter insulating targets by going to an AC field at RF frequencies.

The deposition rate in sputter deposition depends on the beam current density onto the target. Low-pressure glow discharge will typically have low current giving low deposition rates. It is also desirable to keep the ion current low near the substrate to avoid ion damage and sputtering of deposited material.

A magnetic field can be used to confine the ion current close to the cathode target yielding higher target current and keeping the ion density low near the substrate. This is achieved with magnetic coils or permanent magnets in the target holder as shown in Fig. 4. This is called magnetron sputtering. An example of radiofrequency (RF) magnetron sputtering is given by Yang et al. (2009) to deposit Al doped ZnO at room temperature for uniform transparent conducting oxides (TCOs). This is an example of the versatility of magnetron sputtering in depositing functional coating with good composition control, good optical transparency and control of electrical properties. The sputter targets were ZnO and Al_2O_3. Having separate targets enables independent control of the flux from each target. The base pressure was 4×10^{-4} Pa. Under operating conditions the chamber pressure is increased to 0.1–1 Pa with the admittance of argon gas. Uniformity of the film can be optimized by a combination of adjusting the distance between sputter target and the substrate and then rotating the substrate.

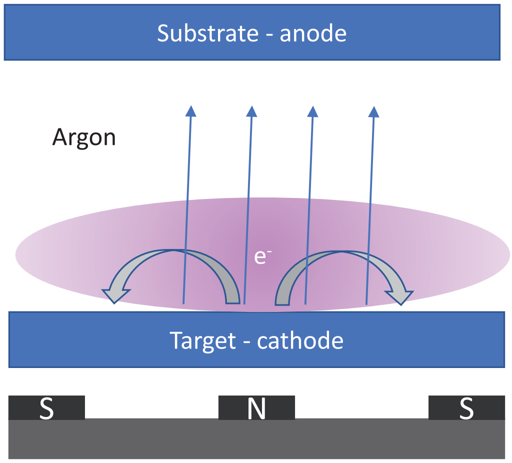

Fig. 4 Schematic of magnetron sputtering.

Characteristics of magnetron sputtering systems are given by Gudmundsson (2020).

1. Secondary electrons confined by the magnetic field to sustain plasma close to the cathode.
2. High sputtering rates.
3. Operating pressure range 0.2–4 Pa.
4. Cathode voltage in range 300–700 V.
5. Discharge current density 4–60 mA cm^{-2}.
6. Deposition rate 20–200 nm min^{-1}.

Both DC and AC or pulsed electric fields can be used with magnetron sputtering. As with diode sputtering, the DC configuration is used for conducting targets and RF can be used for insulating targets such as the example given for ZnO deposition. A further variant on magnetron sputtering is to replace the argon gas with a reactive gas such as O_2, N_2 or CH_4 to enable "reactive magnetron sputtering." The reactive gas species provides the sputtering ions and enables reaction both on the sputter target and at the substrate. This can be used to deposit compound films containing the reactive species such as oxides and nitrides. Further details reactive magnetron sputtering can be found in the review by Gudmundsson (2020).

Ion plating

Ion plating is a variant on physical vapor deposition processes where an ion beam is added to energize the surface. This has the advantages of sputter removal of impurities from the surface and providing heating to the surface to improve atom surface mobility. The sputter removal of surface impurities has the benefit of improving surface adhesion. However, the ion energies are sufficient that surface defects can be formed that may need to be subsequently annealed out. In an example given by Matthews and Teer (1980), ion assisted deposition of TiN, at temperatures below 600 °C, was used to prevent powder formation and enabled a high film density. Ion plating has been extensively used for producing hard, adherent coatings to steel. Kim et al. (2002) used a combination of DC magnetron sputtering and ion plating to produce "superhard" Ti-Si-N films onto steel. An arc cathode gun was used for the Ti source and a DC magnetron gun for the Si. Nitrogen was introduced as N_2 near the substrate. In this example we can see combinations of techniques being used to achieve the desired film composition and properties.

Thermal-spraying

The previous described PVD processes entail transport of atomic or molecular species to a substrate. Thermal spraying entails the transport of droplets. This can be used for rapid deposition of thick films, with high density, a number of micron thick. When the droplets hit the substrate, they spread out to form a coherent film. This implies that some kinetic energy is needed in the transport process. A variety of different sources can be used to achieve these conditions (Cinca and Guilemany, 2012).

1. High Velocity Oxygen Fuel (HVOF): an oxygen combustion flame heats specimen to high temperature which expands and sprays droplets onto the substrate.
2. Detonation gun: the oxygen – fuel gas supply is pulsed to give "explosive" bursts of sprayed droplets at higher velocity than for HVOF.
3. Flame spray: the powdered metal is melted in a combustion flame which expands and sprays the droplets.
4. Plasma spray: the source powder is injected into a low-voltage, high-current plasma that melts the powder. This is particularly advantages with refractory materials.
5. Cold gas spray: The metal powder is sprayed onto the target with high pressure gas and the film is subsequently annealed to form an alloy coating. For example, Ti-Al powder can be sprayed and then annealed at 630 °C to form $TiAl_3$/Al composite coating for aircraft components (Cinca and Guilemany, 2012).

Molecular beam epitaxy (MBE)

Molecular Beam Epitaxy entails producing very pure beams of atoms or molecules, directed at a single crystal substrate in ultra-high vacuum (10^{-8}–10^{-9} Pa). In this method, the MFP is much greater than the chamber dimensions resulting in very low probability of molecular collisions between the source and substrate and low background contamination. Epitaxy is the process of growing a single crystal thin film where the crystal structure of the growing film is templated by a highly polished single crystal substrate. The simplest epitaxial approach is to use the same material for the substrate and the layer such as GaAs on GaAs. This ensures lattice matching but the electrical properties of the layer can be changed in the epitaxial film. Alternatively, a different composition film can be grown but maintaining lattice matching between the layer and the substrate as is the case with $Al_xGa_{1-x}As$ on GaAs.

An MBE chamber is shown schematically in Fig. 5. The source materials are contained in accurately heated cells with a small hole for the vaporized molecules to escape. These cells are called Knudsen cells or K-cells. In front of each cell is a shutter so each beam can be turned on and off. Epitaxial films of precise thickness and composition can be grown by control of the sequencing of the K-cell shutters. MBE is suitable for high crystalline quality compound semiconductor multi-layer devices for high-speed electronics

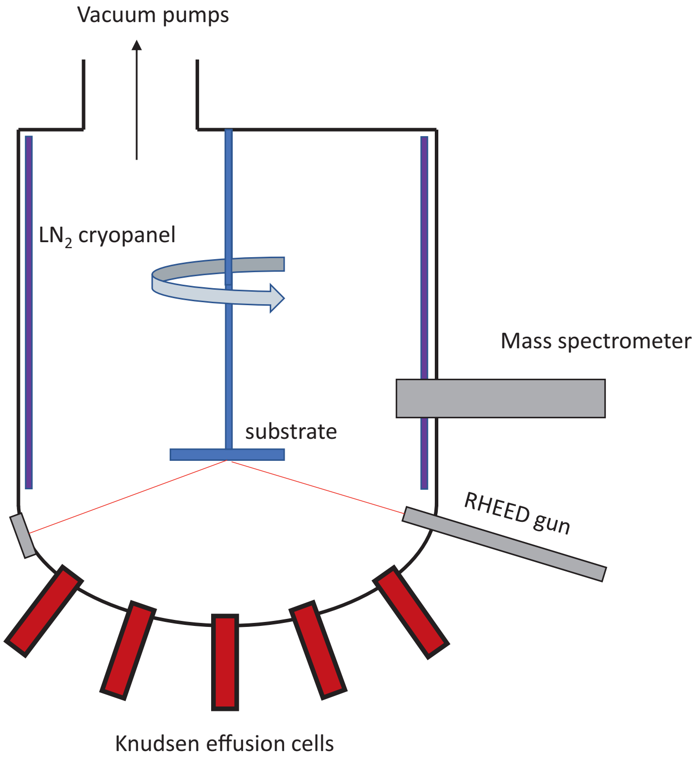

Fig. 5 Schematic of an MBE chamber showing Knudsen effusion cells for the elemental sources, beamed onto the heated substrate.

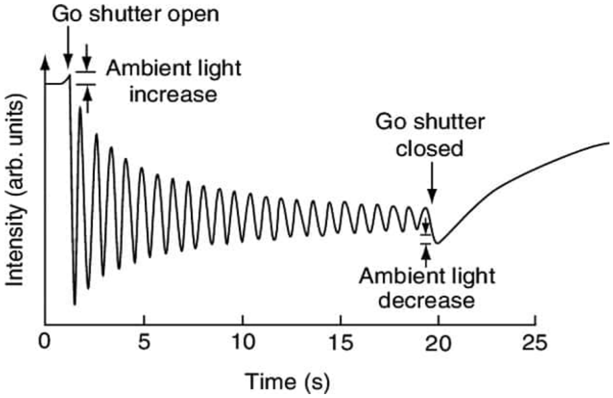

Fig. 6 Reflection high-energy electron diffraction (RHEED) oscillations for GaAs (100) MBE where each oscillation corresponds exactly to one Ga + As monolayer (Neave et al., 1983). From Neave JH, Joyce BA, Dobson PJ, and Norton N (1983) Dynamics of film growth of GaAs by MBE from Rheed observations. *Applied Physics A* 31: 1–8.

and opto-electronic applications. The UHV chamber environment allows for in situ monitoring of the growth process using techniques such as RHEED (Reflection High Energy Electron Diffraction), AES (Auger Electron Spectroscopy) and XPS (X-ray Photo-electron Spectroscopy). For example, in pioneering work by Neave et al. (1983) the now familiar RHEED oscillation method was used to show that GaAs epitaxial films grew by a layer-by-layer process (Fig. 6). This is now a routine tool in research and production MBE systems to establish epitaxial growth and measure film thickness.

An example of recent MBE is the growth of InAs/GaAs quantum dot laser structures on silicon substrates (Kwoen et al., 2018). This illustrates a number of key advances including the hetero-epitaxy of $Al_xGa_{1-x}As$ on silicon where there is a large lattice mismatch but the single crystal film is templated by the silicon substrate. This work also illustrates the formation of InAs quantum dots within the film, driven by a strain field. MBE is now a well-established research and production process for a wide range of compound semiconductor materials.

Chemical vapor deposition (CVD)

In PVD techniques the source is located inside the growth chamber and a vacuum is required to prevent reaction of the components in the vapor. Chemical Vapor Deposition (CVD) has the advantage of having the source materials outside of the reaction chamber and are carried in a gas flow to the growth chamber. The chemical precursors need to be stable at the temperature of delivery. This is either around ambient temperature or above ambient temperature in the case of less volatile precursors. The precursors must be stable at the storage temperature and preferably, liquids but solids can be sublimed or dissolved into a suitable solvent. The method of transport is to bubble a fixed flow rate of a carrier gas such as nitrogen through the precursor and then mix with other precursors and a dilution gas flow through a network of pipes. For example, to deposit a film of SiO_2 precursors for Si such as $SiCl_4$ and for the oxidant, O_2 or H_2O could be selected. For some precursor combinations, the mixing process can occur at the entrance to the growth chamber. This may be necessary if there is a reaction between the precursors at ambient temperature.

The reaction chambers can take many different forms, depending on the application but in general can be classified as horizontal or vertical depending on how the gas stream impinges on the substrate. The reaction chamber pressure is typically in the range of 10^3–10^5 Pa. Schematics of vertical and horizontal reactor configurations are shown in Fig. 7. The heated substrate is kept at a temperature significantly higher than the impinging gas or the chamber walls. The chamber walls can be water cooled or just radiate to the surroundings. A pyrolysis reaction will occur between the precursors at or just above the substrate surface. CVD can be used for volume production as a continuous process using a vertical injection of the precursors onto a moving substrate as illustrated in Fig. 7C. This type of configuration is described, by Yates et al. (2012), for deposition of fluorine doped tin oxide for transparent conductors used in thin film photovoltaic production.

Examples of the CVD reactions are given as follows.

$$\text{Oxides}: SiCl_2H_2 + 2N_2O \rightarrow SiO_2 + 2N_2 + 2HCl$$

$$\text{or } SiH_4 + O_2 \rightarrow SiO_2 + 2H_2$$

$$\text{Nitrides}: 3SiH_4 + 4NH_3 \rightarrow Si_3N_4 + 12H_2$$

$$\text{or } TiCl_4 + N_2 + 4H_2 + Ar \rightarrow 2TiN + 8HCl + Ar$$

$$\text{Carbides}: TiCl_4 + CCl_4 + Ar \rightarrow TiC + 8HCl + Ar$$

These reactions deposit a film onto the heated substrate that must be at a high enough temperature for pyrolysis to occur. With very reactive combinations of precursors such as SiH_4 and O_2 this can considerably suppress the pyrolysis temperature. Volatile reaction products and unreacted precursors are carried out of the reactor in the gas stream and are taken through wet or dry effluent treatment to avoid toxic gases from entering the environment. A recent review of CVD methods is given by Sun et al. (2021) where further details can be found of CVD reactor types, operating conditions and applications.

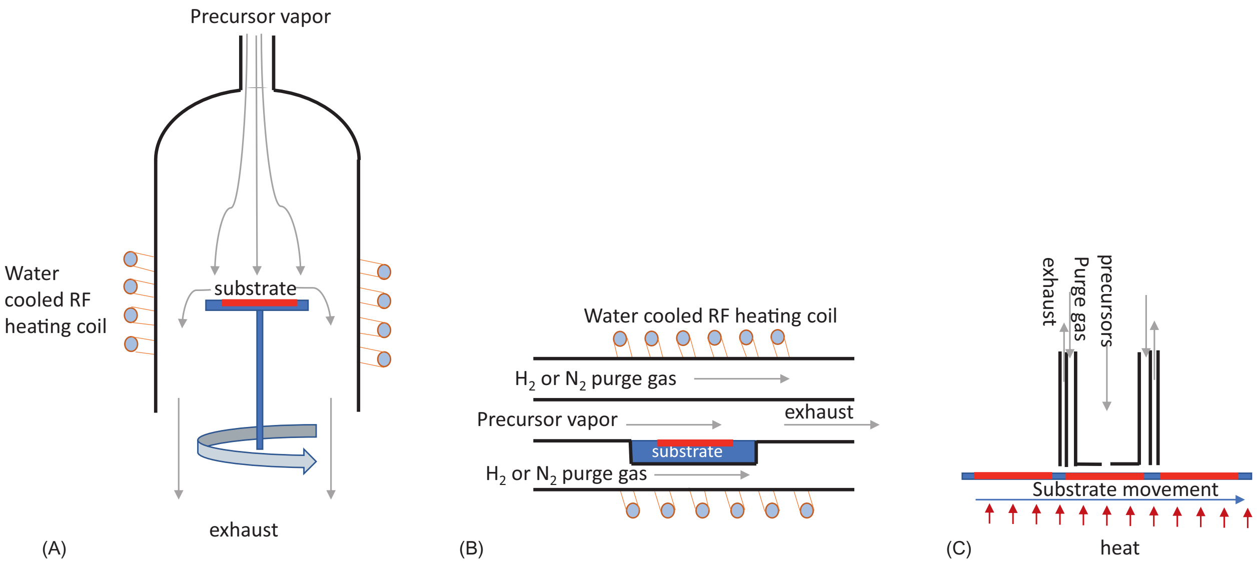

Fig. 7 Schematics of commonly used CVD reactor configurations, (A) vertical reactor, (B) horizontal reactor, (C) in-line CVD coating.

Graphene CVD and other 2D materials

One of the most common methods for producing graphene 2D films is by a CVD process. The process is catalytic onto a metal surface such as copper. Copper is a good choice as the solubility of copper in graphene is low so has minimal effect on the film properties (Munoz and Gomez-Aleixandre (2013)) it also is self-limiting at one monolayer. Nickel promotes a different kinetic process that can lead to multiple graphene layers. The catalytic process starts with the dissociation of hydrogen to produce hydrogen radicals, which react with the hydrocarbon. The precursors are typically methane in hydrogen but any simple alkane can be used and more complex organics (Saeed et al., 2020). The application of CVD has been extended to the rapidly growing topic of 2D transition metal dichalcogenides such as MoS_2 and WS_2. The precursors are typically chlorides for the transition metal source and hydrides for S (Tang et al., 2020).

Metal organic vapor phase epitaxy (MOVPE)

Metal Organic Vapor Phase Epitaxy (MOVPE) can be viewed as a sub-set of CVD but one that has become pre-eminent in producing high quality epitaxial films of compound semiconductors for applications such as solid state lasers, detectors, high frequency devices and white light LEDs (Irvine and Capper, 2019). A more general term covering epitaxial and polycrystalline thin films is Metal Organic Chemical Vapor Deposition (MOCVD). This was the preferred description by the inventor of this process Hal Manasevit (Manasevit, 1981) and includes polycrystalline thin films in addition to epitaxial films. This differs from CVD in the use of metal-organic precursors for the metal component. For example, GaAs can be deposited from trimethyl gallium (TMG) and arsine (AsH_3). All organometallic sources have also been used for compounds where hydrides are not suitable or to create different kinetic conditions such as for the compounds CdTe (Kartopu and Irvine, 2019) and GaSb (Aardvark et al., 1997). The reactions between the precursors occur within the gas phase boundary layer or at the surface and is a pyrolysis reaction. Some examples of reactions in MOVPE to yield compound semiconductor epitaxial films are given here.

$$(CH_3)_3Ga + AsH_3 \rightarrow GaAs + 3CH_4$$

$$(CH_3)_2Cd + (C_3H_7)_2Te + 2H_2 \rightarrow CdTe + 2CH_4 + 2C_3H_6$$

$$(CH_3)_3Ga + (CH_3)_3Sb + 3H_2 \rightarrow GaSb + 6CH_4$$

$$(CH_3)_3Ga + NH_3 \rightarrow GaN + 3CH_4$$

Ternary and quaternary alloys can be grown by adding the appropriate precursors to the gas stream. In the case of all organometallic precursor sources some addition of hydrogen is normally required to produce the stable alkane leaving groups. This would normally be provided with a hydrogen carrier stream. The carrier gas for nitrides is nitrogen. Argon can also be used as an inert carrier gas which can be useful for oxides such as the wide bandgap semiconductor Ga_2O_3, (Zhou et al., 2019).

The reactors for MOVPE are similar to those for CVD and for production scale will be capable of growing uniformly over multiple wafers. There are two main types of MOVPE reactor chamber, horizontal and vertical (Lundin and Talalaev, 2019). Horizontal reactors direct flow horizontally across the substrate and vertical reactors direct the flow normal to the surface of the substrate. In both cases a boundary layer of flow is formed close to the substrate surface and for multi-wafer reactors some form of substrate rotation is used to ensure good uniformity. A picture of the Aixtron AIX 2800G4 15 × 4 inch horizontal planetary reactor is shown in Fig. 8. The organometallic precursors are contained in electropolished stainless steel bubblers and are required to be of

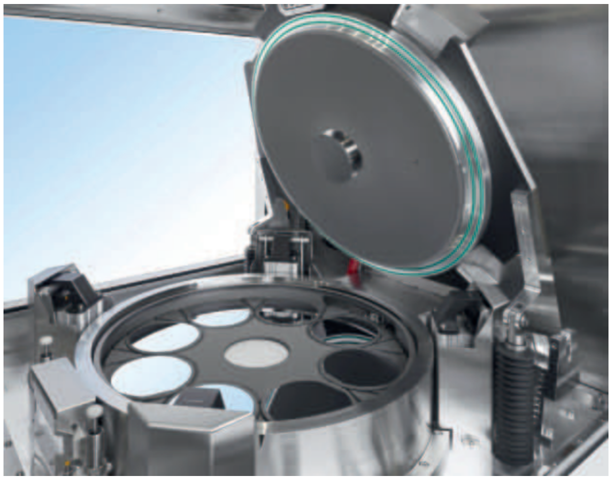

Fig. 8 An example of a production MOVPE reactor chamber. This is the AIX 2800G4 reactor chamber in the 8 × 6 inch configuration for growth of III-V compound semiconductors. Courtesy of Vincent Meric, Aixtron GMBH.

very high purity for epitaxial growth. The carrier gas, which also must be very high purity and low moisture level, is bubbled through the precursor to entrain a saturated vapor of the precursor. Further mixing and dilution with other precursors and the carrier gas will occur prior to introduction into the reactor chamber.

Atomic layer deposition

Atomic layer deposition (ALD) is also referred to as Atomic Layer Epitaxy (ALE) for the epitaxial process and is a variant of the CVD process. The distinct difference between ALD and CVD is in the sequence for feeding the precursors into the reaction chamber. For CVD the precursors are mixed before they reach the substrate but for ALD they are kept separate so the surface is seeing only one precursor at a time. Each precursor saturates the surface in turn and reacts to yield an atomic layer. The sequence for ALD is as follows.

1. The first reactant (A) is introduced into the reactor and saturates the surface.
2. The excess of reactant A and its gaseous products are purged or pumped from the reactor.
3. The second reactant (B) is introduced into the reactor and saturates the surface.
4. The excess of reactant B and gaseous products are purged or pumped from the reactor.

An advantage of ALD over more conventional CVD methods is the ability for conformal coverage over non-planar surfaces (Cremers et al., 2019) with applications in micro-electronics and in nanotechnology. For example, the oxide Al_2O_3 can be used as a passivating layer in semiconducting devices and can be grown with excellent conformal coverage over complex surfaces with the thickness of a few nanometers. Al_2O_3 can be grown by ALD from the precursors trimethylaluminium (TMA) and water vapor (Arts et al., 2019).

Energy-assisted chemical vapor deposition

The CVD processes discussed so far have relied on pyrolysis driven reactions to deposit a thin film. Depending on the material being deposited and the precursors used this can sometimes require a surface temperature of over 1000 °C. Lower temperature deposition can often be achieved by using less stable precursors but this is not always the case. The term energy-assisted″ is used generically when additional, non-thermal energy, is used to promote the reaction process at a lower temperature than could be achieved by pyrolysis.

Plasma-assisted CVD

Plasma-assisted CVD can be used to produce materials that are difficult to produce by conventional CVD or where low temperature deposition is required (<400 °C). An example is the plasma-assisted CVD of diamond for high power electronics, requiring very high purity, low defect concentration and a fast growth rate (Silva et al., 2009). These conditions are satisfied by microwave plasma assisted deposition that can supply a high rate of hydrogen radicals to drive the process. The process gasses are hydrogen and methane. Both H radicals and CH_3 radicals are produced by electron bombardment from the plasma. CH_3 attaches to the diamond surface and the H radicals will strip off the H ligands on the surface to leave vacant surface sites for more CH_3 radicals to adsorb. Different kinetic processes occur at different chamber pressures. At low pressure the process is dominated by electron bombardment. At high pressure it is dominated by H radical collisions with CH_4 to yield CH_3 plus H_2. In either case the key to a successful diamond growing process is the high generation rate of H radicals. More recent developments have enabled plasma assisted CVD of 2D materials such as graphene, MoS_2 and WS_2 (Han et al., 2018).

UV-assisted and photo-assisted CVD

UV-assisted or UV photo-assisted CVD has its origins in the 1980s with a drive to produce high quality semiconductor materials at low temperatures. This was particularly important for II-VI semiconductors where it was necessary to grow at low temperature for a CVD or MOCVD process in order to reduce concentrations of point defects. In a review by Irvine (1987) a number of examples are given of growth temperatures below the pyrolysis temperature for the precursors used. The process of UV-assisted CVD relies on organometallic precursors having strong absorption bands in the UV (<300 nm). These absorption bands result in photolysis of the organic ligands from the metal atom, resulting in deposition of the metal species. The same was also true of the chalcogenide component in the II-VI compound. A disadvantage of UV-assisted CVD is the need for high quality quartz windows that must be kept free of deposit. Longer wavelength stimulation has proved to be easier to manage where surface reactions are stimulated by either a laser or halogen lamp source. This also includes categories of photo-assisted catalytic growth where the photon absorption in the growing film releases charge back to the surface to assist the release of organic ligands. Surface irradiation with a broad band lamp source can stimulate both photo-catalytic and surface pyrolysis type reactions. An example of Photo-assisted MOCVD (PA MOCVD) is using a tungsten-halogen lamp inside the reaction chamber and illuminating the substrate surface. An example of PA MOCVD is given by Li et al. (2008) for the growth of ZnO.

Film growth by condensed-phase reaction

Sol-gel deposition

Sol-gel is a thin film growth technique using a solution of the precursors to deposit, for example, thin films of oxides. It is a low-cost method that can produce high quality polycrystalline films with controlled nanoparticle size. The sol-gel method is multi-step, shown schematically in Fig. 9, as follows (Parashar et al., 2020).

1. Hydrolysis of the precursor in water or alcohols for the synthesis of metal-oxide nanoparticles.
2. Condensation of adjacent molecules to form polymeric networks leading to a colloid. This is the gel phase.
3. Aging process. Changes the structure of the gel to reduce porosity.
4. Drying process. This can take one of three different forms, supercritical drying, thermal drying and freeze drying. Each of these methods will affect the pore density.
5. Thermal treatment/calcination to drive off the residues and water molecules to leave a nanoparticle metal oxide film.

The sol-gel method is finding a diverse range of applications with recent research in antibacterial polymer coatings and marine antifouling coatings (Lelo et al., 2022). Inorganic coatings such as ZnO have applications as optical coatings and in semiconductor devices (Arya et al., 2021).

Chemical bath deposition (CBD)

Chemical Bath Deposition is a solution method commonly used for oxide and chalcogenide thin films (Hone and Abza, 2019) and has advantages of being low cost and deposition low temperature. Ionic salts are dissolved in an aqueous solution to achieve a supersaturation to drive precipitation and film nucleation on a suitable substrate. The solubility of the ionic salts can be adjusted by changing the composition of the solvent using, for example, an alcohol. A complexing agent is used as a catalyst to avoid spontaneous precipitation. This controls the release of the ions into solution affecting deposition rate, film roughness and adhesion. Examples of complexing agents are hydrazine and ammonia. The pH of the solution will control the OH^- ion content which in turn will affect porosity and morphology of the film.

Langmuir-Blodgett deposition

This method entails the transfer of a floating monolayer on the surface of a water bath onto a substrate, slowly withdrawn from the surface. A schematic of the Langmuir-Blodgett method is shown in Fig. 10. The organic molecules need a hydrophilic head group and a hydrophobic tail. The hydrophobic head will bond to the water surface but not dissolve due to the hydrophobic tail. The molecules will spread across the surface but to make a continuous film it is necessary to form a dense packing of the molecules. Isotherms of the surface pressure (π) and the surface area can be plotted to determine the required surface pressure for a dense film. In practice this is achieved using a boom to compress the surface, as shown in Fig. 9. Multiple monolayers can be formed by repeating the passage of the substrate through the surface film. Further details of the Langmuir-Blodgett method and its applications can be found in the review by Rocha Rodrigues et al. (2020).

Electrodeposition

This method relies on an electric current being passed through an ionic solution between an anode and cathode where the cathode is the surface to be deposited. In the example of Cu plating, the anode is made of copper and as the electric current is passed through the $CuSO_4.5H_2O$ electrolyte, Cu^+ cations dissolved from the anode and passes to the cathode, plating it with a copper film. The rate of film deposition is simply controlled by the current and film thickness by the total charge transfer. The process is readily scaled for industrial scale coating, normally of metal films such as electrogalvanizing to deposit a protective zinc film. Anodizing is another electrodeposition technique used to protect metal surfaces such as aluminium. In anodization the part to be coated forms the anode where oxygen ions react with the aluminium surface to form a stable film of Al_2O_3.

$$2Al + 3O^{2-} \rightarrow 6e^- + Al_2O_3$$

Semiconductor compounds such as CdTe can also be grown by electrodeposition and is particularly attractive for large area coatings for photovoltaic applications (Dharmadasa and Haigh, 2006). The cell potential needs to be carefully controlled to enable simultaneous deposition of both components. A review of deposition conditions and reaction mechanisms is given by Manivannan and Noyel Victoria (2018).

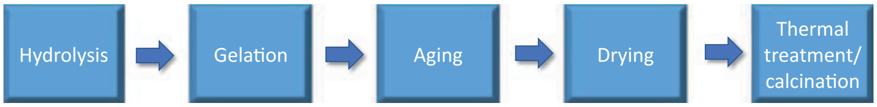

Fig. 9 Schematic of the steps in a sol-gel process.

It is also possible to deposit films by electroless deposition where an electric current is not necessary. In this process, the ion concentration in the electrolyte needs to be sufficiently high to allow deposition. Electroless deposition has an advantage over electrodeposition in that it does not require a conducting substrate. This has made it popular in the electronics industry for depositing Cu conducting tracks and has also proved to be very effective for conformal coverage over non-planar surfaces (Ghosh, 2019).

Liquid phase epitaxy

Liquid Phase Epitaxy is an established technique for producing very high purity epitaxial films of compound semiconductors such as GaAs, AlGaAs, InP and GaP (Kuphal, 1991). Various techniques have been deployed to bring the melt into contact with a substrate but the most versatile is the sliding boat technique, which is illustrated in Fig. 10. This technique has the advantage of allowing multiple layers to be grown to produce detector and laser device structures. The melt composition and temperature must be carefully controlled to create supersaturation for growth. If the substrate is too hot then melt back can occur. This can sometimes be used intentionally to create a clean surface. The growth temperature is typically well below the congruent melting point of the epitaxial layer. A melt is maintained by using a metal solvent such as Ga in the case of GaAs. The composition must be controlled to give growth at the desired temperature following an initial homogenization step at a slightly higher temperature. A small decrease in temperature creates the supersaturation condition for epitaxial growth to occur. Once growth is commenced, a compositional gradient will be established in the melt which will control the growth rate (Fig. 11).

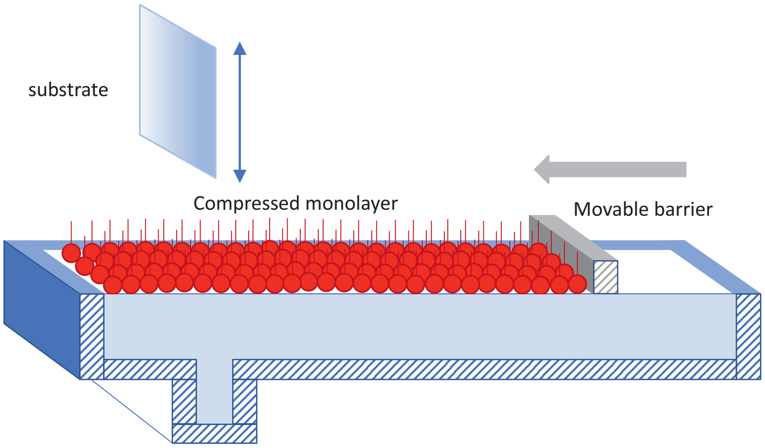

Fig. 10 Schematic of a Langmuir-Blodgett trough showing how the movable boom creates a compressed monolayer.

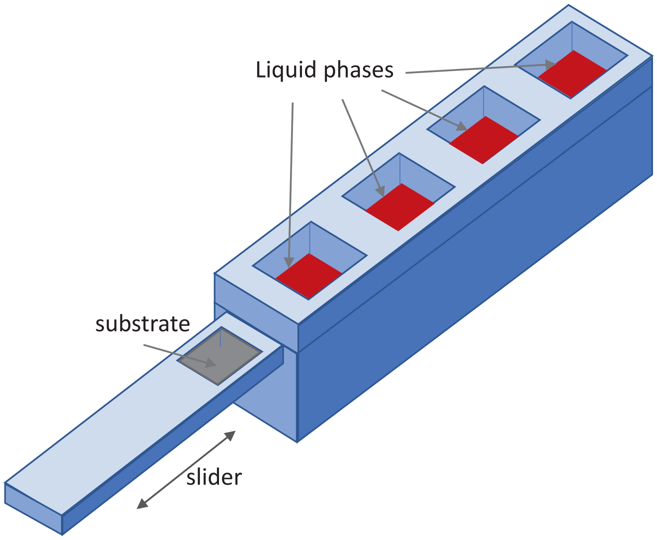

Fig. 11 Schematic of sliding boat LPE.

Conclusion

This chapter has covered a broad range of the most commonly used thin film deposition methods and examples of the range of materials deposited. The precursor for deposition can be either from the vapor or from a liquid. The first section of this chapter has concentrated on the vapor deposition methods from simple evaporation through to chemical vapor deposition. An attempt has been made to draw out common themes such as the gas vapor pressure and mean free path. These factors determine the degree of interaction between the gas phase molecules that dictate the degree of pre-reaction and transport mechanism to the growth interface. The choice of method depends on factors such as the volatility of the elements to be deposited, deposition temperature and application. Many of the vapor phase deposition methods have reached large scale industrial production for a range of applications including ion assisted deposition for high temperature and hard coatings, sputter deposition for a wide range of optoelectronic and electronic functional coatings, CVD for coating of glass and MOCVD for compound semiconductor devices.

Future directions in coating technology for protective coatings will face the challenge of higher temperature operation and more aggressive environments. For example, ceramic matrix composites for gas turbine engines operating at gas inlet temperatures of $>1700\ ^\circ\text{C}$. At the other end of the scale, environmental barrier coatings for the marine environment will be required for anti-fouling without causing pollution. Sol-gel has proved to be a versatile and easily scalable process that could provide the means for large-scale protective coatings.

The rapid growth in electronic and opto-electronic devices from computer chips to infrared lasers for fiber-optic communications has heavily depended on developments in thin film coatings. Production scale MOCVD has driven the revolution in high efficiency lighting based on GaN LEDs. Future prospects are for new materials such as gallium oxide and 2D transition metal dichalcogenides to provide a new generation of electronic devices. Graphene produced by CVD is another rapidly growing application where integration with silicon could revolutionize computer chips.

Another rapidly growing industry is photovoltaics (PV) for solar energy conversion. The industry is currently dominated by silicon but still depends on thin film coating for surface passivation and conductors. Second generation thin film PV is now reaching large scale production with Cadmium telluride and copper indium gallium diselenide (CIGS). Large scale thin film deposition uses physical vapor deposition. Future prospects exist for the perovskite solar cells with MAPI (methyl ammonium lead iodide) being the most successful to date but with a wide range of alternative compositions that can be explored to achieve high efficiency, low-cost materials supply and good environmental compatibility. The materials can be deposited by CVD methods or by solution based methods where, in the latter case, the films can be printed onto a suitable substrate such as glass or sheet steel in a continuous process.

Future development of thin film growth, whether they be solution or gas phase deposition will be driven by demands for new materials for higher performance, durability and at lower cost. The latter will depend on market prices for materials where lower cost alternatives with the same or better performance might be achieved. The cost of thin films will also be driven by the efficiency of utilization of the precursor materials. This becomes an increasing concern as the processes go to larger scale. The design of an RF sputtering system to achieve high utilization of the targets or for CVD a high reaction rate to minimize the amount of unreacted precursor passing to the exhaust effluent treatment. Finally, I would like to mention conformal coverage of coatings. For protective coatings the existence of pin-holes will be a point of failure but the surface being coated could be microscopically rough. For electronic devices there is a demand for thinner coatings that nevertheless have to be conformal. For example, a thin dielectric layer could produce shunt paths if the coating is not continuous. For example, ALD has proved to be a technique with exceptional surface coverage for very thin films. The ultimate challenge will be conformal coverage of monolayer 2D materials that will stretch the limits of thin film deposition technology.

Acknowledgments

The author acknowledges financial support from the European Regional Development Fund (ERDF) for funding the 2nd Solar Photovoltaic Academic Research Consortium (SPARC II).

References

Aardvark A, Mason NJ, and Walker PJ (1997) The growth of antimonides by MOVPE. *Progress in Crystal Growth and Characterization of Materials* 35(2–4): 207–241.

Arts K, Vandalon V, Puurunen RL, Utriainen M, Gao F, Kessels WMM, and Knoops HCM (2019) Sticking probabilities of H_2O and $Al(CH_3)_3$ during atomic layer deposition of Al_2O_3 extracted from their impact on film conformality. *Journal of Vacuum Science & Technology A* 37: 030908.

Arya S, Mahajan S, Khosla A, Datt R, Gupta V, Young S-J, and Oruganti SK (2021) Review—Influence of processing parameters to control morphology and optical properties of Sol-Gel synthesized ZnO nanoparticles. *ECS Journal of Solid State Science and Technology* 10: 023002.

Cinca N and Guilemany JM (2012) Thermal spraying of transition metal aluminides: An overview. *Intermetallics* 24: 60–72.

Cremers V, Puurunen R, and Dendooven J (2019) Conformality in atomic layer deposition: Current status overview of analysis and modelling. *Applied Physics Reviews* 6: 021302.

Dharmadasa IM and Haigh J (2006) Strengths and advantages of electrodeposition as a semiconductor growth technique for applications in macroelectronic devices. *Journal of the Electrochemical Society* 153(1): G47–G52.

Ghosh S (2019) Electroless copper deposition: A critical review. *Thin Solid Films* 669: 641–658.

Gudmundsson JT (2020) Physics and technology of magnetron sputtering discharges. *Plasma Sources Science and Technology* 29: 113001.

Han ZJ, Murdock AT, Seo DH, and Bendavid A (2018) Recent progress in plasma-assisted synthesis and modification of 2D materials. *2D Materials* 5: 032002.

Haque SM, De R, Prathap C, Srivastava SK, and Rao KD (2021) E-Beam evaporation of silicon: Native oxidation and quasicontinuous tailoring of optical properties. *Physica Status Solidi A: Applications and Materials Science* 218: 2100299.

Hone FG and Abza T (2019) Short review of factors affecting chemical bath deposition method for metal chalcogenide thin films. *International Journal of Thin Film Science and Technology* 8(2): 43–53.

Irvine SJC (1987) UV photo-assisted crystal growth of II-VI compounds. *Critical Review in Materials and Solid State Science* 13(4): 279–309.

Irvine S and Capper P (2019) *Metalorganic Vapor Phase Epitaxy (MOVPE): Growth, Materials Properties, and Applications*. Wiley.

Kartopu G and Irvine SJC (2019) Chapter 10, Cadmium telluride and related II-VI materials. In: Irvine S and Capper P (eds.) *Metalorganic Vapor Phase Epitaxy (MOVPE): Growth, Materials Properties, and Applications*. Wiley.

Kim KH, Choi S-r, and Yoon S-y (2002) Superhard Ti–Si–N coatings by a hybrid system of arc ion plating and sputtering techniques. *Surface and Coatings Technology* 298: 243–248.

Kuphal E (1991) Liquid phase epitaxy. *Applied Physics A: Materials Science & Processing* 52: 380–409.

Kwoen J, Jang B, Lee J, Kageyama T, Watanabe K, and Arakawa Y (2018) All MBE grown InAs/GaAs quantum dot lasers on on-axis Si (001). *Optics Express* 26(9): 11568–11576.

Lelo I, Giacobello F, Castellano A, Sfameni S, Rando G, and Plutino MR (2022) *Development of antibacterial and antifouling innovative and eco-sustainable sol–gel based materials: from marine areas protection to healthcare applications, Gels* 8: 26–55.

Li X, Zhang B, Zhu H, Dong X, Xia X, Cui Y, Huang K, and Du G (2008) Properties of ZnO thin films grown on Si substrates by photo-assisted MOCVD. *Applied Surface Science* 254: 2081–2084.

Lundin W and Talalaev R (2019) Chapter 12, Epitaxial systems for III-V and III-nitride MOVPE. In: Irvine S and Capper P (eds.) *Metalorganic Vapor Phase Epitaxy (MOVPE): Growth, Materials Properties, and Applications*. Wiley.

Manasevit HM (1981) Recollections and reflections of MO-CVD. *Journal of Crystal Growth* 55: 1–9.

Manivannan R and Noyel Victoria S (2018) Preparation of chalcogenide thin films using electrodeposition method for solar cell applications – A review. *Solar Energy* 173: 1144–1157.

Matthews A and Teer DG (1980) Deposition of Ti-N compounds by thermionically assisted triode reactive ion plating. *Thin Solid Films* 72(3): 541–549.

Munoz R and Gomez-Aleixandre C (2013) Review of CVD synthesis of graphene. *Chemical Vapour Deposition* 19: 297–322.

Neave JH, Joyce BA, Dobson PJ, and Norton N (1983) Dynamics of film growth of GaAs by MBE from Rheed observations. *Applied Physics A* 31: 1–8.

Parashar M, Shukla VK, and Singh R (2020) Metal oxides nanoparticles via sol–gel method: a review on synthesis, characterization and applications. *Journal of Materials Science: Materials in Electronics* 31: 3729–3749.

Rocha Rodrigues R, Silva RLCG, Caseli L, and Peres LO (2020) Conjugated polymers as Langmuir and Langmuir-Blodgett films: Challenges and applications in nanostructured devices. *Advances in Colloid and Interface Science* 285: 102277.

Saeed M, Alshammari Y, Majeed SA, and Al-Nasrallah E (2020) Chemical vapour deposition of graphene—Synthesis, characterisation, and applications: A review. *Molecules* 25: 3856.

Sahu DR, Lin S-Y, and Huang J-L (2007) Study on the electrical and optical properties of Ag/Al-doped ZnO coatings deposited by electron beam evaporation. *Applied Surface Science* 253: 4886–4890.

Sharma N, Kumar M, Kumari N, Vinod K, and Sharma AL (2018) Design and deposition of single and multilayer antireflection coatings of glass substrate using electron beam deposition. *Materials Today: Proceedings* 5: 6421–6425.

Silva F, Hassouni K, Bonnon X, and Gicquel A (2009) Microwave engineering of plasma-assisted CVD reactors for diamond deposition. *Journal of Physics: Condensed Matter* 21: 364202.

Sun L, Yuan G, Gao L, Yang J, Chhowalla M, Gharahcheshmeh MH, Gleason KK, Choi YS, Hong BH, and Liu Z (2021) Chemical vapour deposition. *Nature Reviews Methods Primers* 1: 5.

Tang L, Li T, Luo Y, Feng S, Cai Z, Zhang H, Liu B, and Cheng H-M (2020) Vertical chemical vapor deposition growth of highly uniform 2D transition metal dichalcogenides. *ACS Nano* 14: 4646–4653.

Yang W, Zhuguang L, Peng D-L, Zhang F, Huang H, Xie Y, and Wu Z (2009) Room-temperature deposition of transparent conducting Al-doped ZnO films by RF magnetron sputtering method. *Applied Surface Science* 255(11): 5669–5673.

Yates HM, Evans P, Sheel DW, Nicolay S, Ding L, and Ballif C (2012) The development of high performance SnO_2: F as TCOs for thin film silicon solar cells. *Surface & Coatings Technology* 213: 167–174.

Zhou H, Zhang C, Feng Q, Zhao S, Ma P, and Hao Y (2019) A review of the most recent progresses of state-of-art gallium oxide power devices. *Journal of Semiconductors* 40: 011803.

Thin Films, Mechanical Behavior of

SP Baker, Cornell University, Ithaca, NY, USA

© 2005 Elsevier Ltd. All rights reserved.

TThis is an update of S.P. Baker, Thin Films, Mechanical Behavior of, Editor(s): Franco Bassani, Gerald L. Liedl, Peter Wyder, Encyclopedia of Condensed Matter Physics, Elsevier, 2005, Pages 187–194, ISBN 9780123694010, https://doi.org/10.1016/B0-12-369401-9/00571-4.

Introduction 261
Thin Film Stresses 261
Measurements of Thin Film Deformation 263
Plastic Behavior 263
Dislocation Mediated Plasticity 264
Diffusion Mediated Plasticity 265
Elastic and Anelastic Behavior 265
Fracture and Delamination 266
Conclusion 267
Further Reading 268

Introduction

Materials in the form of thin films (layers having thicknesses of a few micrometers or less) are the basic building blocks of microfabricated or nanofabricated devices such as integrated microelectronic circuits. They are used as electrical conductors and insulators, magnetic layers, optical reflectors and absorbers, chemical passivations and catalysts, and as structural elements. Although often intended for nonmechanical functions, the mechanical properties of thin films are very important. Thin films are typically found attached to much more massive substrates, and the constraint of the substrate can lead to very high stresses in the film. These stresses may, in turn, lead to failure by a variety of mechanisms, including excessive elastic or plastic deformation, void formation, fracture, or delamination. Understanding the stress states in, and the mechanical response of, thin films is thus a prerequisite to optimizing reliability in microfabricated and nanofabricated devices.

Achieving this goal is complicated by the fact that the mechanical behavior of thin films often does not follow the scaling laws developed for bulk materials. Thus, the mechanical properties of thin films must be measured directly. In this article, the sources of stress in thin films, common mechanical property measurements, and some factors that determine non-bulk-like mechanical response in thin films are briefly reviewed.

Thin Film Stresses

While thin films may experience stresses due to externally applied loads, the largest source of stress in a film typically arises from an interaction between the film and substrate. The origins of these stresses can be understood by the simple thought experiment shown in Figure 1. In Figure 1a, a stress-free film is shown attached to a substrate. Because the film is stress free, one can imagine that it is removed from its substrate without changing dimensions as shown in Figure 1b. One can then imagine that some process occurs that changes the in-plane dimensions of the film relative to the substrate. For example, suppose the film shrinks relative to the substrate as shown in Figure 1c. Since there is no interaction between the film and the substrate, each attains its equilibrium dimension and remains stress free. The film can then be returned to the substrate by imposing a biaxial stress on the detached film in order to elastically deform it, until it again has the same dimension as the substrate, as shown in Figure 1d, and reattaching the film to the substrate, as shown in Figure 1e. To complete the thought experiment, the externally applied forces are removed. The final configuration is shown in Figure 1f. The film continues to support biaxial stresses, and the substrate distorts elastically due to the forces transmitted across the film/substrate interface.

Any process that changes the equilibrium dimensions of the film and the substrate, relative to each other after the film has been deposited on the substrate, will lead to substrate interaction stresses. These dimensional changes can arise from four different sources: (1) Thermal strains arise due to differential thermal expansion. If the elastic strain in the film is zero at some temperature, T_0, then the elastic strain required in the film to accommodate the thermal strains at any other temperature, T, is

$$\varepsilon_{\mathrm{th}} = \int_{T_0}^{T} (\alpha_{\mathrm{s}}(T) - \alpha_{\mathrm{f}}(T))\mathrm{d}T \qquad [1]$$

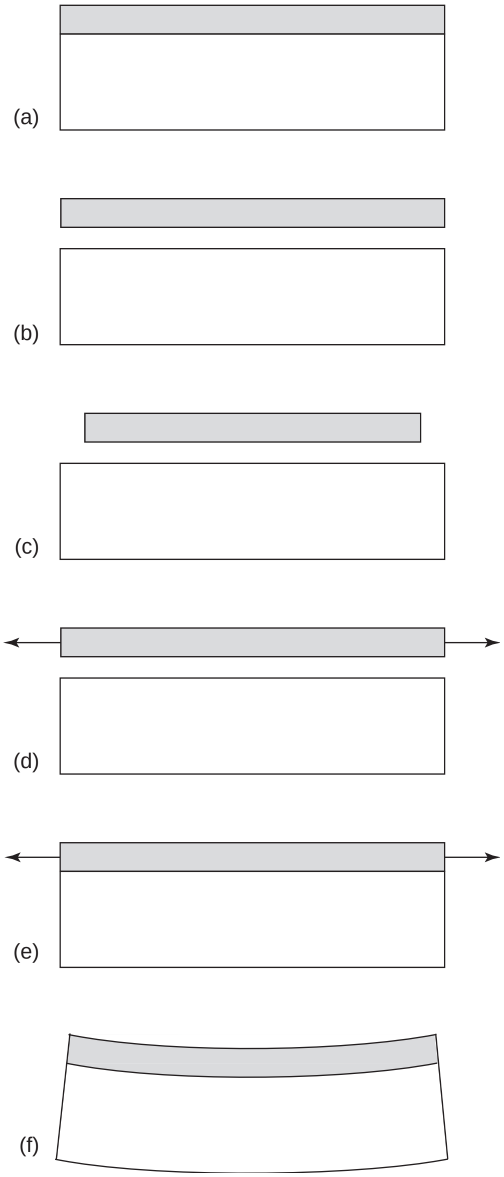

Figure 1 Thought experiment showing how an interaction between a film and substrate leads to high stresses in the film (description in text). Any process that changes the equilibrium in-plane dimension of the film relative to the substrate after the film is attached to the substrate leads to high stresses in the film.

where $\alpha_f(T)$ and $\alpha_s(T)$ are the (temperature dependent) thermal expansion coefficients of the film and substrate, respectively. (2) Structure evolution strains arise from structural changes that change the density of the film. Grain growth, densification, ion implantation, chemical reactions, and phase changes are common sources. The accommodation strain in such cases is given by

$$\varepsilon_{\text{evol}} = \frac{-e_T}{3} \qquad [2]$$

where e_T is the dilatational strain associated with the structure evolution. (3) Epitaxial strains arise when the film is deposited in such a way that there is some crystallographic registry between the film and substrate. If the pertinent in-plane lattice parameters, a_s and a_f, of the film and substrate, respectively, are not the same, then the elastic strain required in the film is

$$\varepsilon_{\text{epi}} = \frac{a_s - a_f}{a_f} \qquad [3]$$

(4) Surface (interface) stresses arise from the change in bonding at free surfaces and interfaces compared to that in the bulk. While the forces arising from a single interface are small, surface stresses can be significant in multilayer films where the interface density is high. For a multilayer consisting of alternating layers of materials A and B having thicknesses t_A and t_B, respectively, the total stress exerted on the substrate is

$$\sigma_{\text{int}} = \frac{2\left(f_{A/B} + f_{B/A}\right)}{t_A + t_B} \qquad [4]$$

where $f_{A/B}$ is the interface force per unit width of A at an A/B interface, and $f_{B/A}$ is the interface force per unit width of B at a B/A interface.

Substrate interaction stresses, particularly those arising from structure evolution strains, are often referred to as "intrinsic," but this terminology should be avoided since the stresses are not intrinsic to either the film or the substrate but rather always arise from an interaction between the two. Because the structure in films can be inhomogeneous, the stresses in films can be inhomogeneous as well.

Measurements of Thin Film Deformation

Measuring mechanical properties in thin films is challenging because of the difficulty in manipulating such a thin object. This problem has been overcome by testing films while they are still attached to their substrates or by using microfabrication or nanofabrication methods to prepare samples without the need to handle the film.

The most common tests are nanoindentation and substrate curvature methods, in which the film is tested while still supported by the substrate. Commercial equipment is available for both of these tests. In nanoindentation, the load and displacement are recorded as a hard tip of a known shape is pressed into the sample surface and removed. By the use of an appropriate analysis model, a measure of elastic stiffness, hardness, and time-dependent behavior can be obtained. Nanoindentation tests are simple to perform, and quantitative information can be obtained from very small (tens of nanometers in diameter), well-located (within some tens of nanometers) volumes of materials. However, the primary disadvantage of nanoindentation lies in distinguishing film properties from substrate influences, which arise as indentations become large and surface influences (mainly due to roughness, surface layers, or particles), which become large as indentations become small.

Substrate curvature tests make use of the curvature shown in Figure 1f. If the film is thin and/or compliant relative to the substrate, then the stress in the film is related to the curvature induced via

$$\sigma = Y_s \frac{t_s^2}{6t_f}\left(\frac{1}{R} - \frac{1}{R_0}\right) \qquad [5]$$

where R_0 and R are the radii of curvature of the substrate before and after the film is attached, respectively, t_f and t_s are the thicknesses of the film and substrate, respectively, and $Y_s = E_s/\left(1 - \nu_s^2\right)$ is the biaxial modulus of the substrate, assumed to be isotropic with Young's modulus, E_s, and Poisson's ratio, ν_s. Equation [5] is known as the Stoney equation and applies when the product of ratios t_sY_s/t_fY_f is large, typically greater than ~100. R_0 and R are typically measured either by scanning a laser across the sample and observing the position of the reflected beam, or using optical interferometry. The substrate curvature method is very accurate and repeatable, as well as relatively simple and flexible. It is often used *in situ* to measure the stresses that arise in films during deposition or thermal cycling. The main disadvantage is that it is not possible to control the strain without changing the conditions that give rise to that strain (e.g., change in temperature).

Results from substrate curvature measurements conducted *in situ* during thermal cycling of 1 μm thick Cu films are shown in Figure 2, and provide an introduction to several unique features of thin film deformation behavior. Such tests are often used because they mimic the thermal cycles that films undergo during manufacture and use. Three sets of data are shown. The solid line indicates data obtained from a computer simulation based on steady-state deformation mechanisms for bulk Cu, including the microstructural length scales of the film. The open and filled circles are data from substrate curvature measurements. The Cu films were prepared identically except that a thin passivation layer was deposited on one, while the other was left with the Cu-free surface exposed. The shapes of the experimental stress–temperature hystereses in Figure 2 show that the stresses can be much higher in thin films than in comparable bulk materials, particularly at high temperatures.

In recent years, a number of tests have been developed to test free-standing films or parts of films. The two most common examples are bulge tests and microtensile tests. In bulge tests, microfabrication methods are used to remove a section of the substrate from behind a film, and pressure is applied to cause the film to bulge out. With an appropriate analysis model, pressure–deflection data can be converted to stress–strain data. For microtensile tests, free-standing tensile test samples are prepared by first removing the adjacent film material and then removing the substrate from behind the sample, leaving a substrate frame to which the sample remains attached at both ends. Loads are applied to these substrate sections to distort the film. Microfabricated test structures are of great interest for the study of free-standing thin film structures.

Plastic Behavior

As is the case in bulk materials, the plastic behavior of thin films depends on the microstructure. Unlike bulk materials, however, the plastic behavior of thin films is often found to depend on the sample size. In addition, the plastic behavior of thin films is extremely sensitive to conditions at thin film interfaces.

The microstructures of crystalline thin films may be categorized into three groups: Single-crystal films arise primarily when films are deposited epitaxially. Nonepitaxial films are often nanocrystalline (grain sizes ~10 nm) in their as-deposited state. The mechanical behavior of such films is similar to that of "bulk" nanocrystalline materials and is not considered here. If a

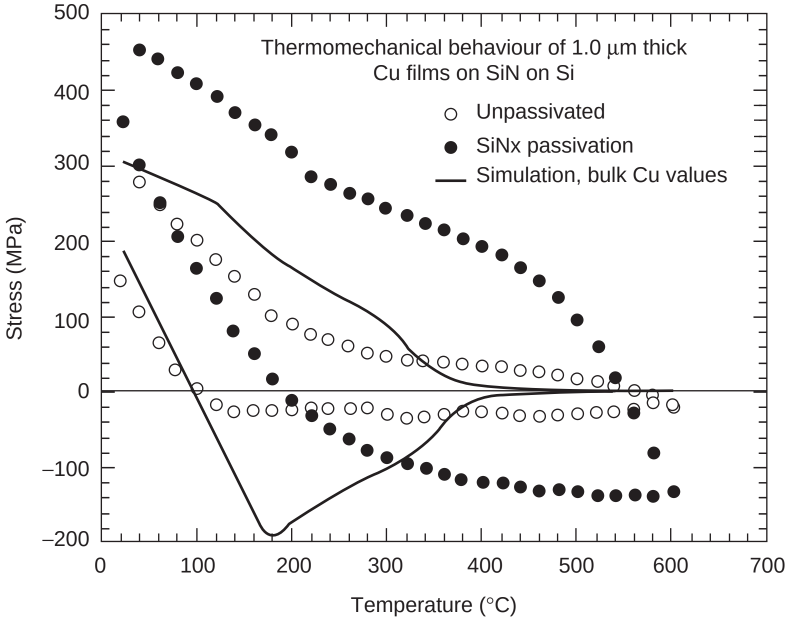

Figure 2 Stresses induced by thermal cycling in Cu films on Si substrates. The films were prepared identically except that a thin SiNx passivation layer was deposited on one. The solid line is a simulation showing the behavior expected based on scaling laws derived for bulk Cu.

fine-grained film is annealed, the mean final grain size is often found to be of the same order as the film thickness. Such films typically have "columnar" grain structure (all grain boundaries perpendicular to the plane of the film), in which certain orientations are strongly preferred. For example, in f.c.c. metal films, grains with (1 1 1) and (1 0 0) planes parallel to the plane of the film are most common as they minimize interface and strain energy, respectively.

Dislocation Mediated Plasticity

The high strength of crystalline thin films at low temperatures (Figure 2) is due to constraints on dislocation motion. An epitaxial thin film on a substrate provides a simple example of how the constraint of the substrate affects the mechanical behavior of thin films. A film with a capping layer is illustrated in Figure 3. A threading dislocation (a dislocation that runs from the top to the bottom of the film) is shown at "**a**" of Figure 3 in an unstressed film. When a stress is applied, the threading dislocation can relax the applied strain by moving on its glide plane. However, because the film is encapsulated between the substrate and cap layer, the threading dislocation can only move ahead by leaving misfit dislocations behind at the interfaces (indicated by "**b**" in Figure 3). The threading dislocation moves forward only when the elastic strain energy relieved by its motion is sufficient to provide the energy required to form the misfit dislocation. Thus, there is a threshold stress (critical stress) for dislocation motion. Since the total strain energy in the film depends linearly on the film thickness and the energy per unit length of the misfit dislocation is approximately constant, the critical stress varies with reciprocal film thickness. A widely used derivation gives

$$\sigma_c = \frac{\sin\phi}{\sin\phi\cos\lambda}\,\frac{b}{2\pi(1-\nu)t_f} \times \left[\frac{\mu_f\mu_s}{(\mu_f+\mu_s)}\ln\left(\frac{\beta_s t}{b}\right) + \frac{\mu_f\mu_p}{\left(\mu_f+\mu_p\right)}\ln\left(\frac{\beta_p t_p}{b}\right)\right] \qquad [6]$$

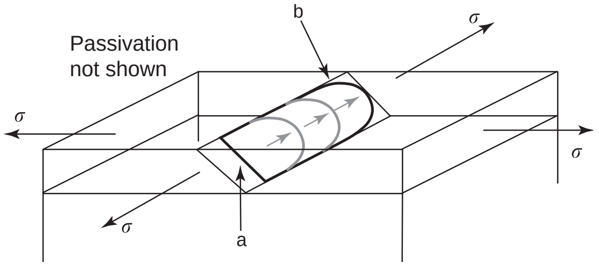

Figure 3 A dislocation gliding on its slip plane in the channel created by a thin film between a substrate and a passivation layer. (a) A threading dislocation extends from the top of the film to the bottom at zero stress. (b) In order to move through the film, the dislocation must leave misfit dislocations at the film/substrate and film/passivation interfaces.

where b is the magnitude of the Burgers vector, φ and λ are the angles between the film normal and the glide plane normal, respectively, μ the shear modulus, and β a constant. The subscripts f, s, and p refer to the substrate, film, and passivation layers, respectively.

The concept of critical strain is particularly important in microelectronic devices containing epitaxial semiconductor layers, as the misfit dislocations that form when the critical strain is exceeded can spoil the electronic function of the device. The reciprocal dependence of critical stress on the film thickness predicted by eqn [6] has been observed in epitaxial semiconductor films. However, higher values have also been reported. This may be due to experimental difficulties associated with observing the formation of the first misfit dislocations, or to a lack of appropriate dislocation sources. From a reliability perspective, eqn [6] provides an accurate measure of the minimum thickness at which misfit dislocations may appear in an epitaxial film.

Interestingly, an inverse dependence of strength on thickness is also seen in polycrystalline metal films, although at stress levels much higher than those predicted by eqn [6]. One can obtain such data, for example, by recording the stress at room temperature at the end of thermal cycles as in Figure 2 for films of various thicknesses. Neither the fact that the yield stress increases as t_f decreases, nor that eqn [6] underpredicts the result, is surprising. As strain increases, a threading dislocation moving through the film must interact with misfit dislocations in its path as well as other threading dislocations and is constrained from long-range motion by grain boundaries, just as in bulk materials. That these events occur in the narrow channel of the film leads to very high stresses indeed. However, while a number of models have been presented, the precise origin of the t_f^{-1} dependence is not yet clear.

The arguments above are based on the assumption that dislocations are preserved at the interfaces. If dislocations are not preserved, then the behavior will be very different. The limiting case is that of a free-standing film, which has no critical strain threshold for dislocation motion and no misfit dislocations to block the threading dislocation motion. A film with one free surface (e.g., Figure 2) represents an intermediate case. However, a free surface is not needed to eliminate misfit dislocations. If the resistance to interface sliding is sufficiently low, then the cores of misfit dislocations can spread into the interface. The consequence is that the mechanical behavior of certain film systems (e.g., copper on nitride or oxide layers, as is commonly used in microelectronics) is very sensitive to any variation in interface chemistry that affects interface strength. Stress levels in fully encapsulated films can be varied over a wide range in this manner.

Another example of interface control of properties is multilayer films, in which manipulation of interface strength and density can be used to create exceptionally strong films. For example, by deposition of alternating thin layers with well-bonded, dislocation blocking interfaces, films with strengths approaching the theoretical strength can be generated.

Diffusion Mediated Plasticity

At high temperatures, the high strength of thin films is due to constraints on diffusion, and the difference between thin film behavior and that expected on the basis of bulk scaling laws is even more dramatic. For example, at the low strain rates imposed for the data in Figure 2, the simulation predicts that the stress would be relaxed to near zero at temperatures above 400°C, while the real films support significant stresses at these temperatures.

This discrepancy can be understood as follows: Figure 4 shows a schematic cross section of a film on the substrate with a capping layer. A stress applied in the plane of the film can be relaxed if the material diffuses between the grain boundaries and the interfaces as shown in Figure 4a. The simulation in Figure 2 was obtained by assuming that the interface diffusivity is the same as the grain boundary diffusivity. In order to achieve the stresses seen in the real capped film at high temperatures, interface diffusion must be turned completely off in the simulation and relaxation allowed to occur by other mechanisms, such as thermally activated dislocation glide. While high stresses due to limited interface diffusivity might be expected in tightly bound interfaces such as Al/SiO_2, similar high stresses are often seen in films with interfaces known to have poor adhesion and high diffusivity such as Cu/SiN_x. The reasons for this are presently unknown.

An uncapped film provides an interesting case, as shown in Figure 4b. Here diffusion is allowed between the grain boundaries and the free surface, but not between the grain boundaries and the interface with the substrate. Tensile stresses, for example, are relaxed by diffusion of material from the free surface into the grain boundaries. Each grain boundary is filled with a wedge of material and the stresses are relaxed near the film surface, but not near the interface. This provides an inhomogeneous stress state with high shear stresses on the interface.

Elastic and Anelastic Behavior

Elastic strain is deformation that is fully recovered upon removal of the applied load. This definition encompasses both elastic deformation that arises from bond stretching and twisting, and anelastic deformation that arises from atomic reconfigurations (e.g., defect motions). Elastic deformation occurs at short timescales (transmitted at phonon velocities) while anelastic deformation is time dependent on a much longer scale.

Elastic deformation depends on the type and density of interatomic bonds in the material. One does not expect radically new types of interatomic bonds in a film just because it is thin. Indeed, the changes that can be expected in elastic constants should be of the order of N_{defect}/N_{bulk}, the ratio of atoms in nonbulk environments to the number in bulk environments. For example, consider a film comprised of cubic grains with side d having boundaries of width δ. The ratio of grain boundary to interior volume is $3\delta/d$.

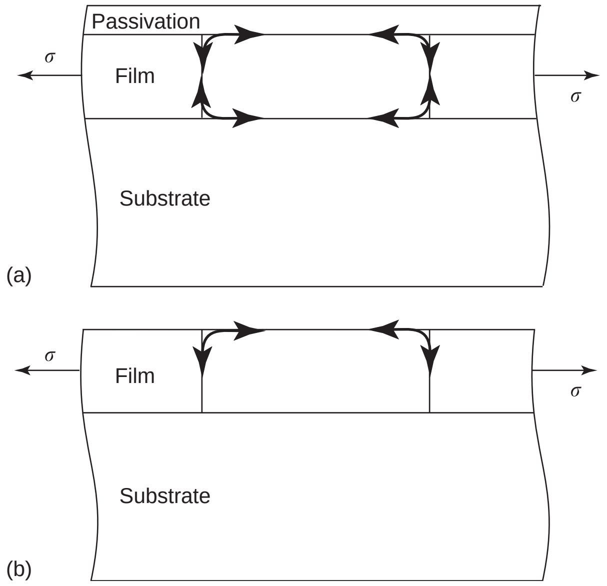

Figure 4 (a) Stresses can be relaxed in a passivated film only if diffusion is allowed along the interfaces. (b) In an unpassivated film, stresses can be relaxed by diffusion between the grain boundaries and the free surface.

If the grain interiors have modulus E_{grain} and the boundaries have a modulus of zero (an extreme example!), then the isostrain composite modulus of the film is

$$E = (1 - 3\delta/d)E_{\text{grain}} \tag{7}$$

For $\delta = 0.2$ nm, one would need $d = 6$ nm$(= t_f)$ to achieve a modulus reduction of only 10%. Given this expectation, a great deal of excitement has accompanied reports of much larger deviations. However, it now appears that all such reports can be attributed to experimental errors.

Anelastic behavior, on the other hand, can be much more prominent in thin films than in bulk. An example can be seen in Figure 2. Upon initial heating, the experimental data initially follow the predicted thermoelastic slope. At some point, the data deviate from this slope, indicating the onset of inelastic deformation. Careful inspection reveals that the inelastic strain is compressive, while the applied stress is still tensile. This "negative yielding" is similar to the well-known Bauschinger effect in bulk metals, but is much larger. As is the case with plastic deformation by both dislocation and diffusion mediated plasticity, anelastic recovery is also very sensitive to interface conditions. For example, quite spectacular anelastic recoveries of up to several tenths of a percent strain can be achieved by adjusting interface adhesion.

Two mechanisms, dislocation motion and boundary sliding, that are often used to explain anelastic behavior in bulk metals, probably also account for anelastic behavior in films. For example, consider a film that has been plastically deformed so that loops having the form shown in Figure 3 have been generated at stress levels above σ_{ch} (eqn [6]). If the applied stress is then reduced below σ_{ch}, it becomes energetically favorable for the dislocation loops to run out of the film, increasing the strain energy (and stress) in the film, but reducing the total energy by reducing misfit dislocation line length. The quasi-2D structure of films can promote grain boundary sliding by allowing grain rotations in the plane of the film. In addition, shear stresses along the film/substrate interface generated by anisotropy or diffusional mechanisms can be relaxed by sliding along the interface, which can also lead to anelastic behavior.

The highly textured nature of films also leads to non-bulk-like scaling behavior. For example, a film composed of a cubic material has lower stiffness, but higher surface energy when (1 0 0) planes are parallel to the plane of the film compared to the case where (1 1 1) planes are parallel to the film plane. Thus, a transition from (1 1 1) to (1 0 0) orientation (stiff to compliant) with film thickness has been predicted and experimentally verified. For Cu, Ag, and Au, for example, the difference is more than a factor 2. For a given elastic strain, the stresses are then much higher in the (1 1 1) orientations, leading to very inhomogeneous stress states and high shear stresses on the interfaces near (1 1 1)/(1 0 0) grain boundaries.

Fracture and Delamination

Brittle films with sufficiently weak interfaces may fail by delamination from the substrate (Figure 5a) or by fracture (Figure 5b). The driving force, G, for delamination can be found by comparing the elastic strain energy per unit area of the film far ahead of the delamination crack with that which is far behind the crack. For a straight crack front,

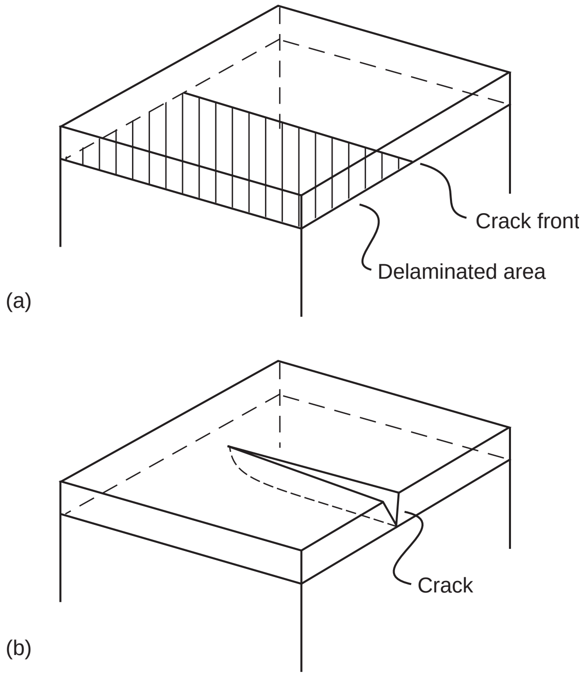

Figure 5 (a) Delamination of, and (b) through thickness (channeling) cracks in a thin film.

$$G = \frac{1 - \nu_{\mathrm{f}}^2}{2E_{\mathrm{f}}}\sigma^2 t_{\mathrm{f}} \qquad [8]$$

where σ is the stress in the film before delamination.

Several tests have been developed for quantitative assessment of the interfacial fracture toughness, Γ, or the value of G at delamination. If the stress in the film is well known, the thickness at which it delaminates can be used to determine Γ from eqn [8]. In many cases, a highly stressed "superlayer" is added on top of the target film of interest to accelerate the process. While the solution is more complicated, it is straightforward to find Γ for the target interface if the stresses in the layers and their thicknesses are known. In addition, several tests of film adhesion have been developed, which do not require a detailed knowledge of film stress states. In these tests, the film is bonded between two massive substrates and external loads are applied to the substrates to drive a delamination crack. These tests include the four-point bend test, the double-cantilever beam test, and several others.

Because thin films are normally under stress, subcritical delamination is an important failure mode and topic of study. Subcritical delamination occurs when chemical processes assist crack propagation so that films delaminate under conditions where G is less than the value required for rapid or "critical" crack propagation in the absence of chemical assistance. Under constant stress, subcritical delamination may occur very slowly over very long durations and is a particularly insidious failure mode. Recent work suggests that subcritical delamination of thin films is similar to subcritical cracking in glass with a region where crack velocity v depends exponentially on G when the chemical reaction rate is controlling, and a region at higher G where v is independent of G when diffusion of the chemical species to the crack tip is controlling.

Cracks that extend through the film thickness (Figure 5b), also known as channeling cracks, are similar to channeling dislocations (Figure 3) in that there is a critical stress needed for channeling crack propagation, established by the requirement that the strain energy released by the crack propagation must be sufficient to produce the new surface area and other energy costs associated with the crack. Channeling cracks, such as channeling dislocations, can also form arrays to relax strains and form configurations that depend on both interactions and sources. The mechanics of film cracking are well developed.

Conclusion

Films on substrates normally support very high stresses due to the constraint of the substrate, but do not exhibit the mechanical behavior of chemically equivalent bulk materials, and thus must be separately studied. While a number of dislocation- and diffusion-based mechanistic models for film deformation have been proposed, a complete model capable of predicting the plastic and anelastic behavior of a film based on its microstructure remains elusive. A significant factor in this is that the microstructural configurations that are assumed in such models have not been sufficiently well verified experimentally. In general, thin films follow the rule that “smaller is stronger.” This is an area of ongoing development, and new experimental methods and models are expected to extend a detailed knowledge to smaller length scales and both shorter and longer timescales.

Further Reading

Arzt E (1998) Size effects in materials due to microstructural and dimensional constraintsa comparative review. *Acta Materialia* 46: 5611–5626.
Baker SP (2001) Plastic deformation and strength of materials in small dimensions. *Materials Science and Engineering A* A319–321: 16–23.
Freund LB and Suresh S (2003) *Thin Film MaterialsStress, Defect Formation and Surface Evolution*. Cambridge: Cambridge University Press.
Nix WD (1989) Mechanical properties of thin films. *Metallurgical Transactions* 20A: 2217–2245.
Ohring M (1992) *The Materials Science of Thin Films*. San Diego, CA: Academic Press.
Suo Z (2003) Reliability of interconnect structures. In: Gerberich WW and Yang W (eds.) *Interfacial and Nanoscale Fracture*. Amsterdam: Elsevier.
Vinci RP and Baker SP (eds.) (2002) *Mechanical Properties in Small Dimensions*, MRS Bulletin, vol. 27, no. 1. Warrendale, PA: Materials Research Society.
Vinci RP and Vlassak JJ (1996) Mechanical behavior of thin films. *Annual Review of Materials Science* 2: 431–462.

Electronic and transport properties of aperiodic media

Jean Bellissard, School of Mathematics, Georgia Institute of Technology, Atlanta, GA, United States

© 2024 Elsevier Ltd. All rights reserved.

This is an update of J. Bellissard, Deterministic Aperiodic Solids, Electronic Properties of, Editor(s): Franco Bassani, Gerald L. Liedl, Peter Wyder, Encyclopedia of Condensed Matter Physics, Elsevier, 2005, Pages 402–408, ISBN 9780123694010, https://doi.org/10.1016/B0-12-369401-9/01134-7.

Aperiodic media 269
Transport mechanisms 269
The Hull 270
Noncommutative Brillouin zone 272
Exponents 274
Conductivity 275
References 276
Further reading 277

Abstract

This article provides a review of methods and results concerning the electronic and transport properties of aperiodic solids.

Key points

- Aperiodic materials, examples
- Conductivity properties of aperiodic materials
- Delone sets and construction of the hull, examples from quasicrystals
- Observable algebra, how to deal with lack of periodicity, the Brillouin zone as a noncommutative manifold
- The integrated density of states, local density of states, Green–Kubo formula for conductivity, numerical calculations and examples
- Characteristic exponents for the density of states, the local density of states, the transport exponents, Guarneri's inequalities
- Qualitative behavior of the conductivity, the anomalous Drude formula

Aperiodic media

Several classes of aperiodic solids have been the focus of attention in Material Sciences, Condensed Matter Physics, from the point of view of experiments or theory. Examples of such materials are the following:

1. Electrons in a uniform magnetic field are sensitive to the vector potential, which cannot be constant in space at non vanishing magnetic field, thus breaking the translation symmetry (Landau, 1930; Peierls, 1933; Shoenberg, 1984).
2. Randomly distributed impurities or defects break the translation invariance in crystal-like normal metals or doped semiconductors (Anderson, 1958; Shklovskii and Efros, 1984; Akkermans et al., 1995). However, electrons feel them only at low temperature. Similarly only phonons of short wavelength are sensitive to disorder.
3. Amorphous materials, such as glass, silicon (in its amorphous phase) (DiVincenzo et al., 1984), and even liquid at short time scale, have been considered in the literature (Bernal, 1964; Johnson, 1999; Inoue, 2000; Langer J, 2006).
4. Artificial structures, like *superlattices* or arrays of quantum dots, are technologically available and can be designed to break the translation symmetry.
5. Quasicrystals, such as $Al_{62.5}Cu_{25}Fe_{12.5}$ or $Al_{70.5}Pd_{22}Mn_{7.5}$, have a point-like diffraction spectrum with symmetries (like the 5-fold or 10-fold symmetries) incompatible with spatial periodicity (Shechtman et al., 1984; Hippert and Gratias, 1994; Kremer, 1996).

In view of the growing importance of aperiodic materials, there is a need for mathematical and numerical methods to study them, since the usual Bloch theory (Jones, 1975; Ashcroft and Mermin, 1976) cannot be used, due to the lack of translation symmetry. To avoid complexity, as a first approximation, the degrees of freedom (electrons, holes, phonons, and lacunae) will be considered as independent and moving in an infinite volume limit ideal solid.

Transport mechanisms

Various mechanisms of electronic transport can be observed experimentally in aperiodic materials.

(i) For metals, the conductivity increases as the temperature decreases. Moreover, the Fermi liquid theory (Landau) predicts (Pines and Nozières, 2018; Mahan, 2000)

$$\sigma(T) \overset{T\downarrow 0}{\sim} T^{-2}.$$

(ii) Thermally activated processes (if a gap arises at the Fermi level), give (Ashcroft and Mermin, 1976)

$$\sigma(T) \overset{T\downarrow 0}{\sim} e^{-\Delta/T}.$$

(iii) For weakly disordered systems (strongly doped semiconductors and normal metals), there is a residual conductivity at low temperature, due to *quantum interferences* (Bergmann, 1984)

$$\sigma(T) \overset{T\downarrow 0}{\sim} \sigma_0 > 0.$$

(iv) In strongly disordered systems (lightly doped semiconductors) with small density of states (DOS) at the Fermi level, *Mott variable range hopping* predicts in dimension d (Mott, 1968; Shklovskii and Efros, 1984)

$$\sigma(T) \overset{T\downarrow 0}{\sim} e^{-(T_0/T)^{1/(d+1)}}.$$

(v) High-quality quasicrystals are metallic alloys but their conductivity decreases with the temperature (see Fig. 1) and exhibits a scaling behavior (Berger et al., 1991; Berger, 1994)

$$\sigma(T) \overset{T\downarrow 0}{\sim} \sigma_0 + aT^{\gamma}, \qquad 1 < \gamma < 1.5$$

on a large range of temperatures (from 50 mK to 1000 K in some cases). In most cases, $\sigma_0 > 0$ (residual conductivity) but there are examples for which $\sigma_0 \approx 0$ (cf. Fig. 1).

The Hull

The *Hull* of an aperiodic solid and its canonical transversal (Bellissard, 1986), or *atomic surface*, is the main construction (as the Brillouin zone for a crystal). It represents in a compactified way all possible samples of the material that can be ideally produced.

As a good approximation, atomic nuclei are supposed to be frozen at their ideal equilibrium position at zero temperature. The set $\mathcal{L}$ of atomic positions is thus a discrete subset of the space $\mathbb{R}^d$ (d is the dimension of the material). $\mathcal{L}$ is called *uniformly discrete* whenever the minimum distance between any two distinct points of $\mathcal{L}$ is positive. $\mathcal{L}$ is called *relatively dense* whenever there is a radius R large enough so that any ball of radius R meets $\mathcal{L}$ on at least one point. A set is *Delone* if it is both uniformly discrete and relatively dense. A Delone set is *repetitive* if, given any finite patch p (namely a finite set of the form $p = \mathcal{L} \cap B$ where B is some open ball), and any small length $\varepsilon > 0$, there is a radius $R_p > 0$ such that any ball of radius R_p contains a translated copy of p modulo an error smaller than ε. A Delone set has *finite type* if the set of vectors joining two of its points is itself discrete (this latter set is denoted by $\mathcal{L} - \mathcal{L}$). At last, a *Meyer set* is a Delone set such that the family $\mathcal{L} - \mathcal{L}$ of vectors joining two of its points is itself a Delone set (Lagarias, 1996, 1999; Lagarias and Pleasants, 2003).

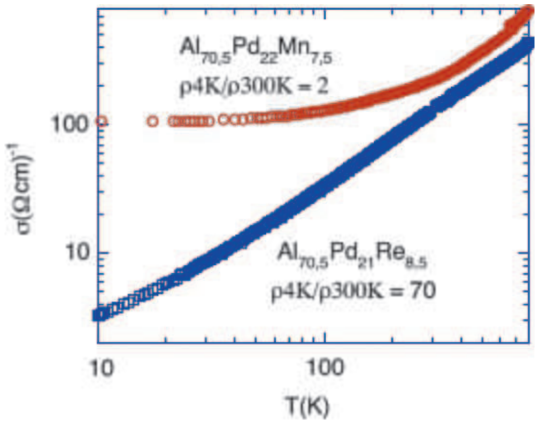

Fig. 1 Conductivity of two examples of quasicrystals.

Examples:

(i) Throwing point randomly in space with fixed density (Poisson's law) gives a discrete set which, with probability one, is neither uniformly discrete nor relatively dense.
(ii) Throwing randomly impurities on sites of a silicon perfect diamond lattice gives a uniformly discrete which, with probability one, is not relatively dense.
(iii) In the ideal limit of zero temperature, most solids have their atoms distributed on a Delone set (Bellissard et al., 2010). But amorphous ones, like glass or silicon, have not finite type and are not repetitive because their two-point correlation function falls off quickly at large distance. Perfect crystals and quasicrystals are described by a finite type repetitive Delone set (Lagarias, 1999).
(iv) Typical examples of Meyer sets are provided by crystals and quasicrystals (see Fig. 2). These are the sets with point-like diffraction pattern and no diffuse part.

The solid is *homogeneous* whenever $\mathcal{L}$ and $\mathcal{L} + a$ have similar global physical properties. However, an observer sees only a finite sample in practice, namely, he sees only what happens in a *bounded window* $\Lambda \subset \mathbb{R}^d$. A sequence $\mathcal{L}_n = \mathcal{L} + a_n$ of translated is said to *converge to* the discrete set $\mathcal{L}_\infty$ if and only if, for any bounded window Λ the family $\mathcal{L}_n \cap \Lambda$ of points of $\mathcal{L}_n$ contained in Λ converges to $\mathcal{L}_\infty \cap \Lambda$. The *Hull* Ω of $\mathcal{L}$ is defined as the family of limit points of translated of $\mathcal{L}$. By construction, any point $\omega \in \Omega$ corresponds to a set $\mathcal{L}_\omega$ obtained as the limit of a subsequence of translated of $\mathcal{L}$. It can be proved that, as soon as $\mathcal{L}$ is uniformly discrete, Ω is a *compact* and *metrizable* set (Bellissard et al., 2000).

- Metrizability means that the topology defined above can be described through a metric. An example of such metric (it is not the only one) is the following: the distance $d(\omega, \omega')$ between the points ω, ω' of the Hull is the smallest number $\varepsilon > 0$ such that $\mathcal{L}_\omega$ and $\mathcal{L}_{\omega'}$ coincide in the ball centered at the origin of radius $1/\varepsilon$ modulo an error of ε.
- Compactness means that the set can be approximated by a finite one. Namely, given any $\varepsilon > 0$, there is a finite set $\{a_1, \ldots, a_d\}$ of vectors $\mathbb{R}^d$ such that any ω is within the distance ε of at least one of the $\mathcal{L} + a_i$'s. Hence in a ball of radius $1/\varepsilon$, $\mathcal{L}_\omega$ looks like $\mathcal{L} + a_i$ modulo an error smaller than ε.

In other words compactness of the Hull is a way of expressing that $\mathcal{L}$ describes an homogeneous solid. In particular the minimum distance between distinct points in $\mathcal{L}_\omega$ is at least equal to the one in $\mathcal{L}$. Moreover the properties of being Delone, finite type, repetitive, and Meyer are inherited by all the $\mathcal{L}_\omega$s.

In addition, if $a \in \mathbb{R}^d$ is a vector in space, then $\mathcal{L}_\omega + a$ also belongs to the Hull, thus defining point denoted by $\tau^a\omega$. It can be shown that the map $(a, \omega) \mapsto \tau^a\omega$ is continuous and satisfies $\tau^{a+a'}\omega = \tau^a(\tau^{a'}\omega)$ while $\tau^0\omega = \omega$, hence giving a *topological action* of the translation group on the Hull. Therefore $(\Omega, \mathbb{R}^d, \mathrm{t})$ is a *topological dynamical system*.

To build the Hull, it is convenient to use the *canonical transversal* also called the *atomic surface* Ξ, defined as the set of points ω in the Hull such that the set $\mathcal{L}_\omega$ contains the origin $0 \in \mathbb{R}^d$ (see Fig. 3). Starting from a point in Ξ and translating it, it takes a minimum distance between two points in $\mathcal{L}$ at least to have $0 \in \mathcal{L}_\omega + a$ again. So $\mathcal{L}_\omega$ can be seen as the trace of Ξ in the *orbit* of ω. Since such an

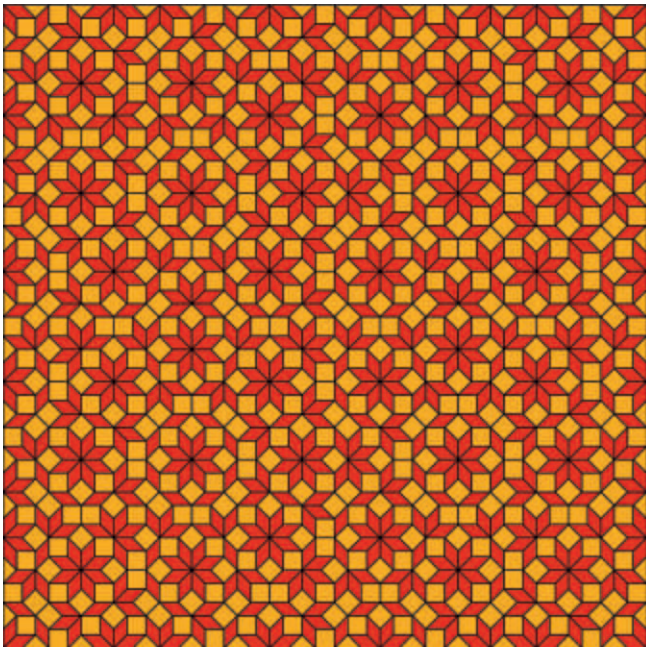

Fig. 2 A Meyer set: the Ammann–Beenker tiling.

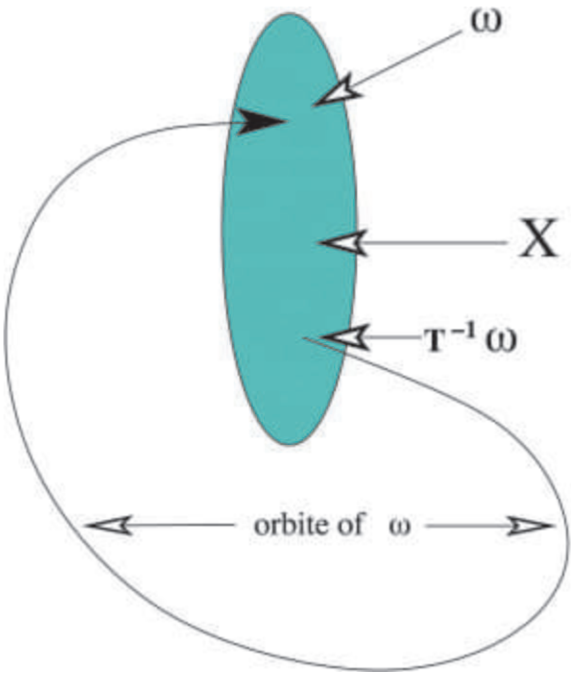

Fig. 3 Schematic view of the atomic surface (canonical transversal).

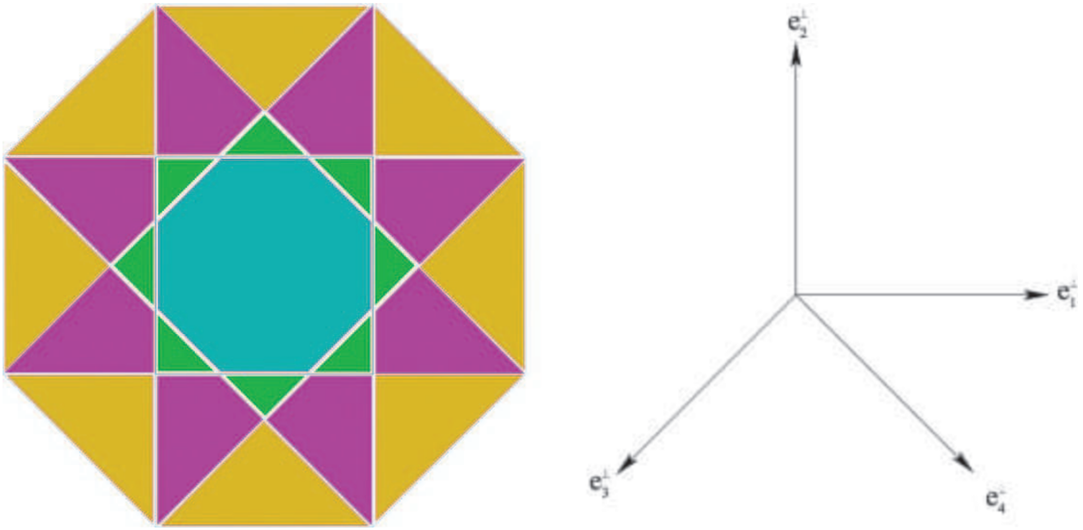

Fig. 4 The atomic surface (canonical transversal) of the Ammann–Beenker tiling (Its topology, inherited from the construction, is discontinuous along any line boarding the colored areas as well as all their translated along the directions of the four vectors $e_i^\perp$, $i = 1, 2, 3, 4$).

orbit can be seen as the space $\mathbb{R}^d$ in which the solid is living and since the points of $\mathcal{L}_\omega$ are the positions of atoms, Ξ represents where the atom is in the Hull. This is why Ξ is also called (especially in quasicrystallography) the *atomic surface*.

For periodic materials, the Hull is the d-torus obtained by identifying points in spaces that differ by a vector of the period group (the Bravais lattice). The transversal is the (finite) set of atoms of the unit cell. For quasicrystals, the Hull is a torus of higher dimension in which the physical space $\mathbb{R}^d$ has irrational slopes. Moreover, the Hull has the topology of a Cantor set in the direction perpendicular to the physical space (see Fig. 4).

Noncommutative Brillouin zone

The description of dynamical degrees of freedom (electrons, holes, and phonons) cannot be done through Bloch theory since the translation invariance is broken. However any observable describing them can be given by a *covariant operator* namely a family $A = (A_\omega)_{\omega\in\Omega}$ of self-adjoint bounded operators acting on the Hilbert space $\mathcal{H}$ of quantum states such that (i) $T(a)A_\omega T(a)^{-1} = A_{T^a\omega}$

if $T(a)$ is the translation operator by $a \in \mathbb{R}^d$ acting on $\mathcal{H}$ and (ii) for any quantum state $|\psi\rangle$ the map $\omega \mapsto A_\omega|\psi\rangle$ is continuous (*strong continuity*). If the material is periodic, all such observables are matrix valued functions over the Brillouin zone. Hence the algebra of observable is the noncommutative analog of the space of continuous functions on Brillouin zone, leading to the notion of *Noncommutative Brillouin Zone* (NCBZ). Such functions can be integrated: if $\mathbb{P}$ is an $\mathbb{R}^d$ invariant probability measure on the Hull, then $\mathcal{T}_{\mathbb{P}}(A)$ is defined as the average of the diagonal matrix elements of A_ω and is equal to the *trace per unit volume* of A. The map $A \mapsto \mathcal{T}_{\mathbb{P}}(\mathsf{A})$ is linear, positive (namely $\mathcal{T}_{\mathbb{P}}(A^*A) \geq 0$), and *tracial* namely $\mathcal{T}_{\mathbb{P}}(AB) = \mathcal{T}_{\mathbb{P}}(BA)$. It is the noncommutative analog of the integral over the NCBZ. In addition, if $\vec{R} = (R_1, \dots, R_d)$ is the *position operator*, then $\vec{\nabla} A = \imath[\vec{R}, A]$ gives a family of d commuting derivations (namely, $\vec{\nabla} = (\partial_1, \dots, \partial_d)$ is linear and obeys the *Leibniz rule* $\vec{\nabla}(AB) = \vec{\nabla}(A)B + A\vec{\nabla}(B)$ generalizing the derivatives *w.r.t.* the quasimomentum in the NCBZ. Depending upon the degrees of freedom (electrons, holes with spin or spinless, or phonons) this algebra of observable will be represented in various Hilbert spaces. Most formulae found in textbooks, valid for periodic crystals, extend in a similar way to aperiodic materials provided the integral over quasi-momenta is replaced by $\mathcal{T}_{\mathbb{P}}$ and the derivatives $\vec{\nabla}_k$ by $\vec{\nabla}$.

In the independent particle approximation, the electron or holes will be described by a Hamiltonian $H = (H_\omega)_{\omega \in \Omega}$ coming from a Schrödinger operator. The simplest example, for spinless electrons, acts on $\mathcal{H} = L^2(\mathbb{R}^d)$ and is given by

$$H_\omega = -\frac{\hbar^2}{2m}\,\Delta + \sum_{a \in \mathfrak{A}} \sum_{\vec{r} \in \mathcal{L}_\omega^a} v_a(\vec{R} - \vec{r}),$$

where $\mathfrak{A}$ is a finite set labeling various species of atoms, $\mathcal{L}_\omega^a$ represents the set of positions for the atoms of species $a \in \mathfrak{A}$, and v_a is the atomic pseudo-potential created by atoms of species a acting on the charge carrier. In the *tight binding representation*, the Hamiltonian becomes a matrix indexed by the atomic sites and the corresponding atomic species, acting on $\mathcal{H}_\omega = \ell^2(\mathcal{L}_\omega)$, of the form

$$\langle x, a|H_\omega|y, b\rangle = h_{ab}(\mathrm{t}^{-x}\omega, y - x), \qquad a, b \in \mathfrak{A},\ x \in \mathcal{L}_\omega^a\ y \in \mathcal{L}_\omega^b,$$

where h is some continuous matrix-valued function on the set Γ of pairs (ω, x) such that ω belongs to the transversal and $x \in \mathcal{L}_\omega$.

In the harmonic approximation, phonons are described by bosons creations and annihilation operators attached to each atomic site with a polarization index, $a_{\omega,x;a}$, $a^\dagger_{\omega,x;a}$ such that $[a_{\omega,x;a}, a^\dagger_{\omega,y;b}] = \delta_{ab}\delta_{xy}\mathbf{1}$ whenever $(\omega, x) \in\Gamma$ and a and b are the polarization index (usually varying from 1 to d, if d is the dimension). Then the phonon Hamiltonian, restricted to a finite volume Λ, acts on the boson Fock space of $\ell^2(\mathcal{L}_\omega)$ and is given by

$$H^{(ph)}_{\omega;\Lambda} = \sum_{x,\, y \in \mathcal{L}_\omega \cap \Lambda} \hbar\, \kappa_{ab}(\mathrm{t}^{-x}\omega, y - x)\ a^\dagger_{\omega,x;a} a_{\omega,y;b} + W_{\omega;\Lambda},$$

where W represents the anharmonic contributions. Here κ can be seen as the matrix elements of a covariant operator $K = (K_\omega)_{\omega \in \Omega}$. The eigenvalues of K are the square of the vibrational mode frequencies allowed to propagate through the solid.

The charge carrier DoS $\mathcal{N}(\Delta)$, in an energy interval Δ, is defined as the number of eigenstates of the charge carrier Hamiltonian describing the charge carrier motions per unit volume with energy within Δ. Similarly, the vibrational density of states (VDoS) in some frequency interval Δ is the number of phonon modes with frequency within Δ. The *Shubin formula* (Bellissard, 1986, 1989, 1992) shows that they are given by

$$\mathcal{N}_{\mathbb{P}}(\Delta) = \mathcal{T}_{\mathbb{P}}(\chi_\Delta(H)) \ \ (\textbf{charge carriers}), \qquad \mathcal{N}_{\mathbb{P}}(\Delta) = \mathcal{T}_{\mathbb{P}}\Big(\chi_\Delta(K^{1/2})\Big) \ \ (\textbf{phonons}),$$

where $\chi_\Delta(E) = 1$ if $E \in \Delta$ and 0 otherwise. A useful example of formula expressed with this formalism is the Kubo formula for the electric conductivity in the *relaxation time approximation* (RTA) given by

$$\sigma_{ij} = \frac{e^2}{\hbar}\, \mathcal{T}_{\mathbb{P}}\left(\partial_j\left(\frac{1}{1 + e^{\beta(H-\mu)}}\right) \frac{1}{\hbar/\tau_{rel} + \mathfrak{L}_H - \imath\hbar\widetilde{\omega}}(\partial_i H)\right), \qquad \textbf{Kubo's formula} \qquad (1)$$

where H is the one-particle Hamiltonian, $\mathfrak{L}_H = \imath[H, \cdot]$, $\beta = 1/k_B T$ is the inverse temperature (k_B is Boltzmann's constant), $\widetilde{\omega}$ is the current frequency, τ_{rel} is the inelastic collision time, μ is the chemical potential fixed by the charge carrier density n_{el} as

$$n_{el} = \mathcal{T}_{\mathbb{P}}\left(\frac{1}{1 + e^{\beta(H-\mu)}}\right) = \int_{-\infty}^{+\infty} d\mathcal{N}_{\mathbb{P}}(E)\, \frac{1}{1 + e^{\beta(E-\mu)}},$$

Prodan (2017) has developed a computational program based on the principles of noncommutative geometry, showcasing several applications to quantum Hall effect and topological insulators. It allows to numerically compute correlation functions, to estimate the errors due to various approximation schemes. These algorithms converge extremely fast to the thermodynamic limit.

To illustrate this method, an application to the integer quantum Hall effect is provided by Roche et al. (1997) and Prodan (2017), which was probably the first example of accurate numerical calculation of the Hall conductivity from a realistic model of electron in magnetic field, in a disordered medium at various temperatures. In Fig. 5, σ_{xx} and σ_{xy} denote, respectively, the direct conductivity and the transverse conductivity with respect to the current flow in a Hall sample. This figure describes the transition from Chern number 0 to Chern number 1, corresponding to a insulator-metal transition. As can be seen from Fig. 5, there is a fix point seen in the transverse conductivity as temperature varies. This property was later understood through a singularity in the current–current correlation function (Prodan and Bellissard, 2016; Prodan, 2017).

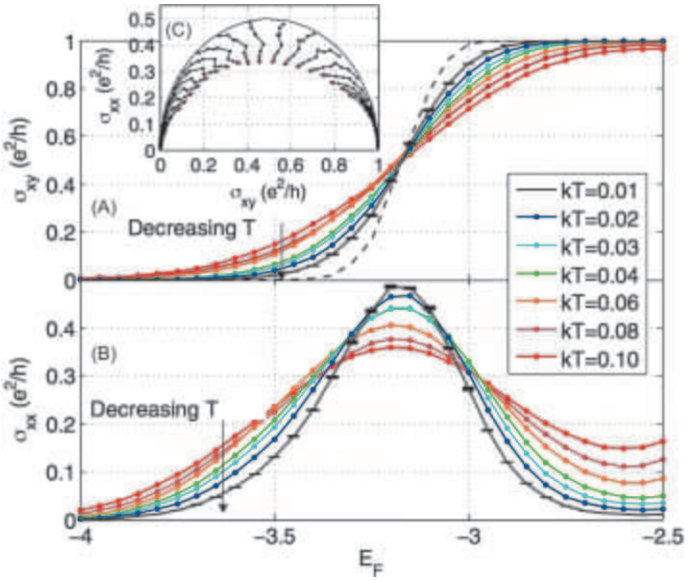

Fig. 5 The simulated (A) σ_{xy} and (B) σ_{xy}, as function of the Fermi level E_F at different temperatures T. The *dashed line* in panel (A) represents the Chern number. The marker sizes (*black rectangle*) corresponding to $k_BT = 0.01$ reflect the actual statistical errors. The inset (C) shows the flow of σ with T (extracted from Roche et al. (1997)).

Exponents

The main reference here is Bellissard (2002). The main difference between periodic and aperiodic solids can be seen in the electron energy spectrum or in the phonon vibrational spectrum (at least for short wavelength). The band spectrum can be a Cantor set, at least in 1D or near the ground state if the dimension is higher. The electrons can be localized (Anderson localization) or can have exotic long distance behavior. The phonon spectrum is likely to have a large low energy optical band exhibiting quantum chaos. Various scaling exponents classify such a behavior. The *spectral exponents* are associated with the DoS, VDoS, or the *local density of states* (LDoS). The *diffusion exponents* are associated with the motion of a typical wave packet in space.

The DoS (or VDoS) regularity is characterized by its behavior as the size $|\Delta|$ of the energy or frequency interval goes to zero, namely, $\mathcal{N}(\Delta) \sim |\Delta|^d$. Such a definition is ambiguous and, even in computer simulations, difficulties in interpreting results can be overwhelming. The symbol $\sim$ should then be defined as follows: if $f(\varepsilon)$ is a positive decreasing function of $0 < \varepsilon < 1$ (or $1 < \varepsilon < \infty$) then

$$\alpha^\star = \lim_{\varepsilon\downarrow 0}{}^\star \frac{\ln f(\varepsilon)}{\ln \varepsilon}, \quad \text{denoted by} \quad f \overset{\varepsilon\downarrow 0}{\sim} \varepsilon^{\alpha^\star},$$

where $\star$ stands for *sup* (or +) or *inf* (or −) and similarly if $\varepsilon \uparrow\infty$. Therefore the DoS exponent (and similarly for the VDoS) is defined by

$$\mathcal{N}_{\mathbb{P}}([E-\varepsilon, E+\varepsilon]) \overset{\varepsilon\downarrow 0}{\sim} \varepsilon^{d^\star_{DOS}(E)}.$$

The LDoS, also called the *spectral measure*, is defined as follows: if $H = (H_\omega)_{\omega\in\Omega}$ is the one-particle Hamiltonian for the charge carriers, the LDoS $\mu_{\omega,\phi}$ relative to the quantum state $|\phi\rangle$ and its *spectral exponent* $d^\pm_{\omega,\phi}(E)$ are defined by

$$\begin{aligned}\mu_{\omega,\phi}([E-\delta, E+\delta]) &:= \int_{E-\delta}^{E+\delta} d\mu_{\omega,\phi} = \frac{1}{\pi}\Im m \int_{E-\delta}^{E+\delta} dE' \langle\phi|(E' - \imath 0^+ - H_\omega)^{-1}|\phi\rangle \\ &\overset{\delta\downarrow 0}{\sim} \delta^{d^\star_{\omega,\phi}(E)}.\end{aligned}$$

Whenever Δ is an interval of energy and if $\star = \sup$ (*resp.* $\inf$), $d^\star_{\omega,\phi}(\Delta)$ will be infimum (*resp.* supremum) over $\Delta' \subset \Delta$ of the supremum (*resp.* infimum) over $E \notin \Delta'$ of $d^\star_{\omega,\phi}(E)$'s, where $\int_{\Delta'} d\mu_{\omega,\phi} = 0$. Then $d^{\star,\pm}_\omega(\Delta)$ will be the supremum (*resp.* infimum) over the state $|\phi\rangle$ of the $d^\star_{\omega,\phi}(\Delta)$'s. It turns out that $d^{\star,\pm}_\omega(\Delta)$ is independent of ω with probability one and the common value is called $d^{\star,\pm}_{LDOS}(\Delta)$. In all cases

$$d^{-,\pm}_{LDOS}(\Delta) \leq d^-_{DOS}(\Delta)$$

The LDoS is *absolutely continuous* (*ac*) on an interval Δ whenever for almost all $E \in \Delta$, there is $0 < C(E) < \infty$ such that $\mu_{\omega,\phi}([E-\delta, E+\delta]) \leq C(E)\delta$. The Radon–Nykodym theorem implies the existence of an integrable function F such that $\mu_{\omega,\phi}(dE) = F(E)dE$. (Here dE is called the Lebesgue measure.) In such a case, $d^\star_{\omega,\phi}(E) = 1$ on Δ so that $d^\star_{\omega,\phi}(\Delta) = 1$. The LDoS is *pure point* (*pp*) on Δ if it can be written as a sum of Dirac measures $\mu_{\omega,\phi}(dE) = \sum_i \delta(E - E_i)dE$. In such a case, the E_i are eigenvalues and $d^{\star}_{\omega,\phi}(E_i) = 0$ on Δ, implying $d^{\star}_{\omega,\phi}(\Delta) = 0$. The LDoS is *singular continuous* (*sc*) if $\mu_{\omega,\phi}([E - \delta, E + \delta]) \downarrow 0$ as $\delta \downarrow 0$ for all $E \in \Delta$ and if there is almost no $E \in \Delta$ for which $\mu_{\omega,\phi}([E - \delta, E + \delta]) \leq C(E)\delta$ with $0 < C(E) < \infty$. In particular, if $0 < d^{\star}_{\omega,\phi}(\Delta) < 1$, then the LDoS is *sc* on Δ.

A charge carrier moving in the solid is a quantum wave interfering with itself after colliding with atomic nuclei. The resulting effect of too many reflections is a slowing down of its motion so that the distance it goes after time t behaves like

$$r(t) \overset{t\uparrow+\infty}{\sim} t^{\bar{\beta}},$$

where $\bar{\beta}$ is called a *diffusion exponent*. Like for the case of spectral exponents, there are many ways of defining $\bar{\beta}$. If $\vec{R}$ is the position operator for the charge carriers, then $\vec{R}(t) = e^{\imath tH/\hbar}\vec{R}e^{-\imath tH/\hbar}$ denotes the position after time t, and $|\vec{R}(t) - \vec{R}|$ is the distance that the particle goes during this time. To measure it, it is convenient to select particles having energy in some interval Δ and prepared in the quantum state located at the origin of space, denoted by $|0\rangle$. Since the system is not translation invariant, it is better to average over the choice of the origin (using $\mathbb{P}$). To avoid meaningless time oscillations, it is also convenient to average over time too, leading to the following formula

$$(L_{\Delta,\,q}(t))^q \;=\; \int_{-t}^{+t} \frac{ds}{2t} \int_X d\mathbb{P}_{tr}(\omega)\langle 0|\Pi_{\omega,\Delta}\,|\vec{R}_\omega(s) - \vec{R}|^q\,\Pi_{\omega,\Delta}|0\rangle \;\overset{t\uparrow\infty}{\sim}\; t^{q\,\bar{\beta}^{\star}_q(\Delta)}.$$

where $\Pi_{\omega,\,\Delta}$ projects on eigenvalues of H_ω located in Δ. The extra parameter q gives information about the distribution of distances in the initial state.

The diffusion exponents permit to classify the motion of the charge carriers (or of the phonon modes) according to their values. In a periodic crystal, it is known that $\bar{\beta}^{\star}_q(\Delta) = 1$ for all q's because the motion is *ballistic*. On the opposite side, in an Anderson insulator, where all states are localized, $\bar{\beta}^{\star}_q(\Delta) = 0$. In general $0 \leq \bar{\beta}^{\star}_q(\Delta) \leq 1$ and $\bar{\beta}^{\star}_q(\Delta)$ increases with q. The value $q = 2$ is special and is amenable to experimental measurements. There are situations for which $\bar{\beta}_2 = 1/2$ in particular in weakly disordered systems or if *quantum chaos* occurs: this is *quantum diffusion*. It is important to notice that such a diffusion is not due to some loss of information, but the net result of quantum interferences in a complex environment. The motion is called *subballistic* if $1/2 < \bar{\beta}_2 < 1$ and *subdiffusive* if $0 < \bar{\beta}_2 < 1/2$.

These exponents are related by the *Guarneri inequality* (here, d is the space dimension)

$$\beta^{\star}_q(\Delta)\,d \;\geq\; d^{\star}_{LDOS}(\Delta). \qquad \textbf{Guarneri's bound} \tag{2}$$

Thus, in dimension $d = 1$, *ac* spectrum implies (quasi) ballistic motion. In higher dimension, for any $\varepsilon > 0$, it is possible to find models of Hamiltonians with *ac* spectrum and diffusion exponent smaller than $1/d + \varepsilon$. In particular *ac* spectrum is compatible with quantum diffusion for $d \geq 2$.

Conductivity

For the results here see Bellissard (2002). One of the most striking consequence of the previous scaling analysis is the behavior of the conductivity at low temperature. The classical *Drude formula* asserts that the conductivity of a metal is given by

$$\sigma = \frac{e^2 n_{el}\tau_{rel}}{m^*} \overset{\tau_{rel}\uparrow\infty}{\sim} \tau_{rel}, \qquad \textbf{Drude formula}$$

where m^* is the effective mass of the charge carriers and τ_{rel} is the typical relaxation time for collisions. In view of the RTA Kubo formula (1), the scaling analysis leads to

$$\sigma \overset{\tau_{rel}\uparrow\infty}{\sim} \tau_{rel}^{2\beta_F - 1}, \qquad \textbf{anomalous Drude formula} \tag{3}$$

where $\beta_F = \bar{\beta}_2^{\star}(E_F)$ is the diffusion exponent for $q = 2$ at the Fermi level E_F. The inelastic relaxation time increases as the temperature goes to zero so that (i) if the motion is ballistic or subballistic, then the solid behaves like a conductor; (ii) if the motion is diffusive, then there is a *residual conductivity* at zero temperature; and (iii) if the motion is subdiffusive, the solid behaves like an insulator. In the former case (metallic), the addition laws for conductivity show that if several relaxation mechanisms coexists, the one with the shortest relaxation time will dominate (Matthiessen rules). On the contrary in the latter case (insulating), the one with the longer relaxation time will dominate. In most situations, the dominant dissipative mechanisms come from the phonon–electron collisions in two possible forms: (i) direct collisions leading to the Bloch law $\tau_{rel} \sim T^{-5}$ as $T \downarrow 0$ (ii) electron–electron interactions through the lattice (BCS term) leading to the Landau Fermi liquid theory with $\tau_{rel} \sim T^{-2}$. While in the metallic case the Fermi liquid theory applies, the Bloch law dominates in the insulating case leading to $\sigma \sim T^{5(1-2\beta_F))}$. If, as computer simulation suggests for $3D$-quasicrystals, $.35 < \beta_F < .40$, it provides a mechanism for the results shown in Fig. 1 (*AlPdRe*-compound).

Another striking numerical observation is that at *small energy scale* and for *finite volume*, the level spacing distribution of eigenvalues for quasicrystalline lattices follows the Wigner–Dyson law: some *quantum chaos* occurs, namely, the effective Hamiltonian behaves like a *random matrix*. Such a feature is likely to be *universal* in aperiodic media. If so, analysis provided for weakly disordered systems should apply then leading to a quantum diffusive regime at small energy or a long time scales and, consequently, producing a residual conductivity at low temperature as shown for the *AlPdMn* compound in Fig. 1. But it might be an artifact of the finite volume. However, following an argument by Thouless, used in disordered systems, it follows that (i) the time it takes for the particle with diffusion exponent $\bar{\beta}$ to reach the boundary of a sample of size L is $t_{Th} \sim L^{1/\bar{\beta}}$ (called the *Thouless time*), and (ii) the time it takes for the particle to realize that the spectrum is actually discrete due too the finite volume is given by the Heisenberg principle $t_H \Delta E \approx \hbar$ where $\Delta E \sim L^{-d}$ is the average level spacing so that $t_H \sim L^d$ (called the *Heisenberg time*). If $\bar{\beta} > d$ then, the particle reaches the boundary too fast and therefore it will dominantly see the effect of the finite volume, namely, of the Wigner–Dyson level spacing distribution. If, on the other hand $\bar{\beta} < 1/d$, the particle has never the time to reach the boundary so that it behaves like if only the subdiffusion was allowed. Hence

$$\beta_F < \frac{1}{d} \Rightarrow \sigma \overset{T\downarrow 0}{\sim} T^{\gamma}, \qquad \beta_F > \frac{1}{d} \Rightarrow \sigma \overset{T\downarrow 0}{\sim} \sigma_0 > 0.$$

The Guarneri inequality (2) predicts a *sc* spectrum near the Fermi level in the former case while the latter is compatible with *ac* spectrum if $d > 2$. It is reasonable to expect that a slight change in the hopping parameters of the effective tight-binding Hamiltonian between atomic sites due to chemical constraints (e.g., by changing *Mn* into *Re*) might produce such a drastic change in behavior in Fig. 1.

References

Akkermans E, Montambaux G, Pichard J-L, and Zinn-Justin J (1995) *Les Houches 1994: Physique Quantique mésoscopique*. Elsevier.

Anderson PW (1958) Absence of diffusion in certain random lattices. *Phys. Rev.* 109: 1492–1505. http://prola.aps.org/abstract/PR/v109/i5/p1492_1.

Ashcroft NW and Mermin ND (1976) *Solid State Physics*. New York: Saunders College, ISBN: 978-0030839931.

Bellissard J (1986) K-theory of C*—Algebras in solid state physics. *Statistical Mechanics and Field Theory: Mathematical Aspects*: 99–156. https://doi.org/10.1007/3-540-16777-3_74.

Bellissard J (1989) C*-algebras in solid state physics: 2D electrons in uniform magnetic field. *Operator Algebras and Applications*: 49–76. https://doi.org/10.1017/CBO9780511662287.005. https://www.cambridge.org/core/books/operator-algebras-and-applications/calgebras-in-solid-state-physics-2d-electrons-in-uniform-magnetic-field/F9B71622C7F1568DC38916E8978ACFC0.

Bellissard J (1992) Gap labelling theorems for Schrödinger operators. In: Waldschmidt M, Moussa P, Luck JM, and Itzykson C (eds.) *From Number Theory to Physics*, pp. 538–630. Berlin, Heidelberg: Springer Berlin Heidelberg.

Bellissard J (2002) Coherent and dissipative transport in aperiodic solids: An overview. In: Garbaczewski P and Olkiewicz R (eds.) *Dynamics of Dissipation*, pp. 413–485. Springer.

Bellissard J, Hermmann D, and Zarrouati M (2000) Hull of aperiodic solids and gap labelling theorems. In: Moody MB and Baake RV (eds.) *Directions in Mathematical Quasicrystals*, pp. 207–259. Providence: AMS.

Bellissard J, Radin C, and Shlosman S (2010) The characterization of ground states. *Journal of Physics A: Mathematical and Theoretical* ISSN: 1751-8113. 43(30): 305001. https://doi.org/10.1088/1751-8113/43/30/305001.

Berger C (1994) Electronic properties of quasicrystals experimental. In: Hippert F and Gratias D (eds.) *Lectures on Quasicrystals*. Editions de Physique.

Berger C, Gozlan A, Lasjaunias JC, Fourcaudot G, and Cyrot-Lackmann F (1991) Electronic properties of quasicrystals. *Physica Scripta* ISSN: 1402-4896. 1991(T35): 90. https://doi.org/10.1088/0031-8949/1991/T35/020.

Bergmann G (1984) Weak localization in thin films: a time-of-flight experiment with conduction electrons. *Physics Reports* ISSN: 0370-1573. 107(1): 1–58. https://doi.org/10.1016/0370-1573(84)90103-0.

Bernal JD (1964) The Bakerian lecture, 1962 the structure of liquids. *Proceedings of the Royal Society of London. Series A. Mathematical and Physical Sciences* ISSN: 0080-4630. 280(1382): 299–322. https://doi.org/10.1098/rspa.1964.0147.

DiVincenzo DP, Mosseri R, Brodsky MH, and Sadoc JF (1984) Long-range structural and electronic coherence in amorphous semiconductors. *Physical Review B* ISSN: 01631829. 29(10): 5934–5936. https://doi.org/10.1103/PhysRevB.29.5934.

Hippert F and Gratias D (1994) *Lectures on Quasicrystals*. Les Ulis: Editions de Physique.

Inoue A (2000) Stabilization of metallic supercooled liquid and bulk amorphous alloys. *Acta Materialia* ISSN: 13596454. 48(1): 279–306. https://doi.org/10.1016/S1359-6454(99)00300-6.

Johnson WL (1999) Bulk glass-forming metallic alloys: Science and technology. *MRS Bulletin* ISSN: 08837694. 24(10): 42–56. https://doi.org/10.1557/S0883769400053252/METRICS.

Jones H (1975) *The Theory of Brillouin Zones and Electronic States in Crystals*, 2nd edn. North Holland: Amsterdam. https://books.google.co.uk/books?id=2D1RAAAAMAAJ&redir_esc=y&hl=en&pli=1.

Kremer F (1996) Beyond quasicrystals. *Zeitschrift für Physikalische Chemie* ISSN: 2196-7156. 194(2): 277–278. https://doi.org/10.1524/zpch.1996.194.Part_2.277a.

Lagarias JC (1996) Meyer's concept of quasicrystal and quasiregular sets. *Communications in Mathematical Physics* ISSN: 00103616. 179(2): 365–376. https://doi.org/10.1007/BF02102593.

Lagarias JC (1999) Geometric models for quasicrystals I. Delone sets of finite type. *Discrete & Computational Geometry* ISSN: 0179-5376. 21(2): 161–191. https://doi.org/10.1007/PL00009413.

Lagarias JC and Pleasants PA (2003) Repetitive Delone sets and quasicrystals. *Ergodic Theory and Dynamical Systems* ISSN: 01433857. 23(3): 831–867. https://doi.org/10.1017/S0143385702001566.

Landau L (1930) Diamagnetismus der Metalle. *Zeitschrift für Physik* ISSN: 14346001. 64(9–10): 629–637. https://doi.org/10.1007/BF01397213.

Langer J (2006) Shear-transformation-zone theory of deformation in metallic glasses. *Scripta Materialia* ISSN: 13596462. 54(3): 375–379. https://doi.org/10.1016/j.scriptamat.2005.10.005.

Mahan GD (2000) *Many-Particle Physics*. Boston, MA: Springer US, ISBN: 978-1-4419-3339-3. https://doi.org/10.1007/978-1-4757-5714-9.

Mott NF (1968) Conduction in glasses containing transition metal ions. *Journal of Non-Crystalline Solids* ISSN: 0022-3093. 1(1): 1–17. https://doi.org/10.1016/0022-3093(68)90002-1.

Peierls R (1933) Zur Theorie des Diamagnetismus von Leitungselektronen. *Zeitschrift fur Physik* ISSN: 1434-6001. 80(11–12): 763–791. https://doi.org/10.1007/BF01342591.

Pines D and Nozières P (2018) *The Theory of Quantum Liquids*. CRC Press, ISBN: 9780429492662. https://doi.org/10.4324/9780429492662. https://www.taylorfrancis.com/books/9780429961212.

Prodan E (2017) A Computational Non-commutative Geometry Program for Disordered Topological Insulators. *SpringerBriefs in Mathematical Physics.* , vol. 23. Cham: Springer International Publishing, ISBN: 978-3-319-55022-0. https://doi.org/10.1007/978-3-319-55023-7.

Prodan E and Bellissard J (2016) Mapping the current-current correlation function near a quantum critical point. *Annals of Physics* ISSN: 0003-4916. 368: 1–15. https://doi.org/10.1016/J.AOP.2016.01.022.

Roche S, Trambly de Laissardière G, and Mayou D (1997) Electronic transport properties of quasicrystals. *Journal of Mathematical Physics* ISSN: 0022-2488. 38(4): 1794–1822. https://doi.org/10.1063/1.531914.

Shechtman D, Blech I, Gratias D, and Cahn JW (1984) Metallic phase with long-range orientational order and no translational symmetry. *Physical Review Letters* ISSN: 0031-9007. 53(20): 1951–1953. https://doi.org/10.1103/PhysRevLett.53.1951.

Shklovskii BI and Efros AL (1984) Electronic Properties of Doped Semiconductors. *Springer Series in Solid-State Sciences.* , vol. 45. Berlin, Heidelberg: Springer Berlin Heidelberg, ISBN: 978-3-662-02405-8. https://doi.org/10.1007/978-3-662-02403-4.

Shoenberg D (1984) *Magnetic oscillations in metals*. Cambridge University Press, ISBN: 9780521224802. https://doi.org/10.1017/CBO9780511897870. https://www.cambridge.org/core/books/magnetic-oscillations-in-metals/56C41223B4CDE32E43BD3109BFD74722.

Further reading

Solid State Physics

Ashcroft NW and Mermin ND (1976) *Solid State Physics*. New York: Holt, Rinehart and Winston.

Jones H (1960) *The Theory of Brillouin Zones and Electronic States in Crystals*. Amsterdam: North Holland.

Mahan G (1990) *Many Particles Physics, 2nd Printing*. Plenum.

Disordered Systems

Akkermans E, Montambaux G, Pichard J-L, and Zinn-Justin J (1995) *Les Houches 1994: Physique Quantique Mésoscopique.* Elsevier.

Shklovskii BI and Efros AL (1984) *Electronic Properties of Doped Semiconductors.* Springer, Berlin.

Ziman JM (1979) *Models of Disorder. The Theoretical Physics of Homogeneously Disordered Systems.* Cambridge University Press.

Random Matrices

Beenaker CWJ (1997) Random matrix theory of quantum transport. *Reviews of Modern Physics* 69: 731–808.

Hiai F and Petz D (2000) *The Semicircle Law, Free Random Variables and Entropy.* American Mathematical Society.

Mehta M (1990) *Random Matrices*, 2nd edn. Academic Press.

Voiculescu D, Dykema K, and Nica A (1992) *Free Random Variables.* Providence, Rhode Island: AMS.

Quasicrystals and Aperiodic Order

Axel F and Gratias D (1995) *Beyond Quasicrystals.* Berlin: Springer.

Baake MB and Moody RV (2000) Directions in Mathematical Quasicrystals. *CRM Monograph Series.* , vol. 13. Providence: AMS.

Hippert F and Gratias D (1994) *Lectures on Quasicrystals.* Les Ulis: Les Editions de Physique.

Moody RV (1997) The Mathematics of Long-Range Aperiodic Order. *NATO ASI Series C.* , vol. 489. Dordrecht: Kluwer.

Patera J (1998) Quasicrystals and discrete geometry. *Fields Institute Monographs.* , vol. 10. Providence, RI: American Mathematical Society.

Takeuchi S and Fujiwara T (1998) *Quasicrystals.* Singapore: World Scientific.

Electronic Properties of Quasicrystals

Bellissard J (2003a) Coherent and dissipative transport in aperiodic solids. In: Garbaczewski P and Olkiewicz R (eds.) *Dynamics of Dissipation. Lecture Notes in Physics*, vol. 597, pp. 413–486. Springer.

Roche S, Mayou D, and de Laissardière GT (1997) Electronic transport properties of quasicrystals. *Journal of Mathematical Physics* 38: 1794–1822.

Functional Analysis

Reed M and Simon B (1972) *Methods of Modern Mathematical Physics. I. Functional Analysis.* New York-London: Academic Press. 1975. II. Fourier Analysis, Self-Adjointness. New York-London: Academic Press [Harcourt Brace Jovanovich, Publishers].

Simon B (1978) *Methods of Modern Mathematical Physics. IV. Analysis of Operators.* Academic Press.

Noncommutative Geometry

Bellissard J (2003b) Noncommutative geometry of aperiodic solids. In: *Geometric and Topological Methods for Quantum Field Theory, (Villa de Leyva, 2001)*, pp. 86–156. River Edge, NJ: World Sci. Publishing.

Connes A (1994) *Noncommutative Geometry.* San Diego: Academic Press.

Varilly JC, Figueroa H, and Gracia-Bondia JM (2000) *Elements of Noncommutative Geometry.* Boston: Birkhauser.

Dynamical Systems

Cornfeld I, Fomin S, and Sinai YG (1982) *Ergodic Theory.* New York: Springer-Verlag.

Gottschalk W and Hedlund GA (1955) *Topological Dynamics.* Providence, RI: American Mathematical Society.

Katok A and Hasselblatt B (1995) *Introduction to the Modern Theory of Dynamical Systems.* Cambridge: Cambridge University Press.

Numerical Noncommutative Geometry

Prodan E (2017) *A Computational Non-Commutative Geometry Program for Disordered Topological Insulators.* Springer, Science.

Lattice dynamics: Aperiodic crystals

J-B Suck, Chemnitz University of Technology, Chemnitz, Germany

© 2024 Elsevier Ltd. All rights reserved.

This is an update of J.-B. Suck, Lattice Dynamics: Aperiodic Crystals, Editor(s): Franco Bassani, Gerald L. Liedl, Peter Wyder, Encyclopedia of Condensed Matter Physics, Elsevier, 2005, Pages 82-93, ISBN 9780123694010, https://doi.org/10.1016/B0-12-369401-9/00513-1.

Introduction	278
Incommensurate modulated structures	280
Incommensurate composites	281
Quasicrystals	282
Phonon dispersions	282
Generalized vibrational density-of-states	284
Atomic dynamics and cluster structure	285
Quasicrystals and their rational approximants	285
Low-energy modes in quasicrystals	286
Temperature dependence of the atomic dynamics	286
Phason flips	288
Phason fluctuation in quasicrystals	288
Conclusion	289
References	289

Abstract

After a brief introduction into aperiodic crystals and one of the most often used experimental methods to investigate their dynamics (inelastic neutron scattering (INS)) the phonon and phason dynamics of the three most often met aperiodic crystals, incommensurate modulated structures, incommensurate composites and quasicrystals are discussed separately.

Key points

Incommensurate modulated structures: dispersion: of amplitudon and phason branches. Incommensurate composites: Phonon dispersion a phason diffusion. Quasicrystals: Phonon dispersion, generalized density of states, phason flips and long wavelength phason diffusion.

Introduction

Crystals with aperiodic structure are solids with long-range order (LRO) in the atomic positions but no translational invariance of a unit cell position. Their Fourier module consists of sharp diffraction spots, proving their LRO, which includes a long-range bond orientational order (BOO). The wave vectors Q of these diffraction spots can be represented by the sum over integer multiples of a number of rationally independent basis vectors, k, which span the Fourier module of the aperiodic crystal

$$Q = \sum_{i=1}^{n} m_i k_i. \tag{1}$$

In contrast to periodic crystals, where the number of rationally independent basis vectors is equal to the dimension of the crystal (and of its periodic reciprocal lattice), for aperiodic crystals n exceeds the dimension of the space, in which the crystal is embedded. The minimal necessary number of independent basis vectors defines the "rank" of the Fourier module, which is finite in the quasiperiodic case. In a space of dimension n (the n-dim space), the crystal structure, aperiodic in three-dimensional (3D) Euclidean space, can be presented as a "periodic" structure with a unit cell, which usually has a relatively simple structure. Generally, the aperiodic structure can be obtained by an appropriate intersection of the n-dim periodic structure with the physical space, in which the aperiodic structure is observed. For quasicrystals (QCs), this intersection involves the intersection of the n-dim lattice with the physical space, which has an "irrational" slope relative to the orientation of the n-dim lattice. After a small change of this slope to a

https://doi.org/10.1016/B978-0-323-90800-9.00196-7

rational value, this intersection will lead to a crystal in physical space, which is periodic, but locally has a structure similar to the QCs. Such crystals are called "approximants" (to the corresponding QCs), the dynamics of which are discussed below as well.

Incommensurably modulated crystals, incommensurate composites, and QCs all belong to the aperiodic crystals. However, in some of their fundamental properties, they are different from each other. Therefore, the restriction to one or the other of them is mentioned explicitly as has just been done for QCs. Assuming that the physical (direct, external, or parallel) space, by which the *n*-dim space is intersected, is 3D, the remaining ($n-3$)-dimensional subspace is the "internal" or "perpendicular" (perp) space, which in the case of an incommensurably modulated crystal can be viewed as containing the information on the phase of the modulation function with respect to the original commensurate lattice, out of which the incommensurate phase developed. In view of the atomic dynamics, it is important to realize that the additional dimensions belonging to the internal space can be interpreted as additional degrees of freedom not present in periodic crystals.

In *n*-dim space, the information about the atomic positions (density distribution) in the aperiodic structure in physical space is "stored" in $n-3$ dimensional hypersurfaces, for QCs called "atomic surfaces." The aperiodic structure is the intersection of the physical space with this periodic array of hypersurfaces. It depends on the shape of these atomic surfaces, and the consequences a shift of the physical space in the direction of the internal space will have on the aperiodic structure after the intersection: for continuous surfaces, it just results in a phase change of an incommensurate modulation. For disjunct atomic surfaces, as, for example, in the case of QCs, it leads to sudden changes of the atomic distribution, all of which, however, have the same energy. Thus, the ground state is infinitely degenerated. Likewise, a slow change of the modulation phase does not cost energy.

The Fourier module of the *n*-dim lattice is a periodic reciprocal *n*-dim lattice with sharp diffraction spots. This is the space in which inelastic scattering experiments are done to investigate the atomic dynamics. For incommensurate crystals, the 3D reciprocal space can be constructed on the basis of three reciprocal basis vectors. For QCs, which also contain rotation axes other than two-, three-, four-, and sixfold, one obtains the physical reciprocal space by a projection of the *n*-dim reciprocal space on the physical reciprocal space. Again, $n-3$ reciprocal lattice components belong to the reciprocal perpendicular space, and are usually called Q_{perp}. As the 3D projection plane in the *n*-dim reciprocal lattice has to have the same irrational slope with respect to the *n*-dim reciprocal lattice as the intersection in the *n*-dim real space had, all Bragg peaks of the *n*-dim reciprocal lattice will be projected into this hyperplane, as there is no mutual "shading" of different reflections because of the irrational slope. Thus, the Fourier module in this case consists of a dense set of Bragg reflections. In principle, this leads to infinitely many overlapping Brillouin zones and correspondingly to infinitely many gaps in the dispersion curves. Fortunately however, most of the Bragg peaks have an immeasurably small intensity and can therefore be neglected, leading to a diffraction pattern with a finite number of intense Bragg (for fssingle crystals) or Debye–Scherrer peaks (for polycrystals), the intensity of which is highest for peaks stemming from Bragg peaks in the *n*-dim Fourier module with smallest Q_{perp}. This fact enables the definition of pseudo-Brillouin zones (PBZs) next to reciprocal lattice points with highest Bragg peak intensity and dispersion relations for phonon and phase modes.

The dynamics of aperiodic phases has been studied most often by neutron inelastic scattering (NIS). Special questions such as the amplitudon mode and the central peak have been investigated by light scattering, and some experiments have also been done by X-ray inelastic scattering (XIS).

As aperiodic crystals usually contain more than one type of scatterer and different scatterers couple differently to the used probe, in all cases the total dynamic structure factor, $S(Q,\omega)$, was determined. For samples with *n* elements this is the weighted sum of the $n(n+1)/2$ partial dynamic structure factors, $S_{i,\,j}(Q,\omega)$, where the weights are given by the coupling strength to the probe (here NIS is used as an example in the following equation and consequently the scattering length *b*) and the atomic concentration *c* of each of the *n* elements

$$\begin{aligned}\sigma S(Q,\omega) = 4\pi \sum\sum b_i b_j c_i c_j S_{i,j}(Q,\omega) \\ + \sum \sigma_i^{\text{inc}} c_i S_i^{\text{S}}(Q,\omega) \ \ (i,j=1,\ldots,n),\end{aligned} \tag{2}$$

where σ are σ^{inc} are the total and the incoherent scattering cross sections and S_i^{S} is the self part of the dynamic structure factor of the element *i*. Alternatively, the single-particle motions can be investigated via the generalized vibrational density-of-states (GVDOS), which again is the weighted sum of the partial density-of-states of each element in the sample, weighted by the strength of the coupling of this element to the scattered probe (here for neutrons again)

$$G(\omega) = \frac{\sum w_i c_i g_i(\omega)}{\sum w_i c_i}, \tag{3}$$

$$w_i = \frac{e^{-2W_i}\sigma_{\text{sc}}^i}{M_i}. \tag{4}$$

Here, e^{-2W_i} is the Debye–Waller factor and M_i is the mass of the scatterer *i*. The density-of-states (DOS), as always, contains the information on the single-particle dynamics of the system, while the dynamic structure factor reflects also the collective atomic dynamics for coherent neutron scatterers, as is needed for measurements of dispersion relations.

In what follows, the vibrational modes (propagation and displacements in external space in the *n*-dim representation) and the phason modes (propagation in external space, displacements in internal space) of the three most often met aperiodic crystals, incommensurate modulated structures, incommensurate composites, and QCs are discussed separately.

Incommensurate modulated structures

Incommensurate modulated structures (Currat and Janssen, 1988) are crystal structures in which the atoms in the originally periodic lattice in the normal (N) phase have been displaced by a periodic (static) modulation function in the transition from the N to the incommensurate (I) phase, the period of this modulation being incommensurate with the periodicity of the original lattice. For a 3D crystal, Eq. (1) can therefore be rewritten as

$$Q = ba^{*} + kb^{*} + lc^{*} + \sum_{i=4}^{n} m_i k_i, \tag{5}$$

where the first three terms describe the reciprocal lattice of the 3D basic (periodic) average structure, and a^*, b^*, c^*, and k_i are rationally independent. In reciprocal space, these structures (and with this also their dynamics) are characterized by a reciprocal lattice which contains the Bragg peaks of the original periodic lattice plus satellites from the incommensurate modulation. Due to the fact that incommensurate structures often form as a consequence of frustration caused by competing interactions, the incommensurate phase normally exists only within a certain temperature (and pressure) range, which is bounded by two transition temperatures, T_I and T_c. $\Delta T = T_\mathrm{I} - T_\mathrm{c}$ is, in some cases, only a few degrees wide, can, however, also extend down to $T_\mathrm{c} = 0$ K. If $T_\mathrm{c} > 0$ K, the wavelength of the modulation locks-in at T_c onto a rational fraction of the underlying (the main) lattice periodicity, either in a strongly discontinuous manner or by disappearance of phase defects. In contrast to this, the transition into the incommensurate phase at T_I is a second-order phase transition with a well-defined order parameter. From the viewpoint of the atomic dynamics, this transition from the periodic basis structure to the aperiodic modulation is normally associated with the softening of a phonon branch and the appearance of a Lorentzian shaped central peak at zero energy, part of which is most likely of dynamical origin also. The softening (additional (broad) minimum in the dispersion branches (see Fig. 2)) of the dispersion occurs at a wave vector, which will become the modulation wave vector of the incommensurate phase as is shown in Fig. 1.

For continuous modulation functions, theory (excluding the influence of defects) predicts a softening down to a zero-frequency mode, with a finite phason gap for interruptions of the continuity of the modulation function by defects. Experimentally, the soft mode branch finishes at T_I with a finite frequency, which however, because of the strong overdamping of the soft mode, often cannot be resolved in NIS experiments. In the I-phase, this branch will then split up into two branches, the "amplitudon" (acoustic like) and the "phason" branches, the latter being related to a continuous shift of the modulation function with respect to the lattice. Near T_c, discommensurations (see below) develop which always lead to a finite gap for the phason mode, called "phason gap." The intensity of the acoustic modes is proportional to the intensity of the Bragg peak or satellite reflection at the Γ-point. This enables the identification of the phason mode, which is too intense for being an acoustic mode at the (weak) satellite reflection. In addition, the slope of the phason dispersion is lower than that of the lowest acoustic mode. The corresponding dispersion relations are shown in Fig. 2.

While the amplitudon branch will increase with decreasing temperature (normal hardening of the acoustic phonons on temperature decrease), the phason energy may be temperature independent, as has been demonstrated for $(\mathrm{ClC_6D_4})_2\mathrm{SO_2}$, for

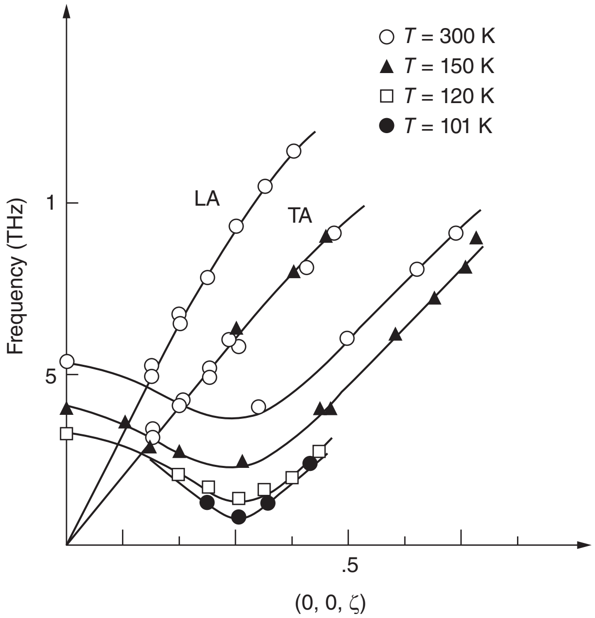

Fig. 1 Mode softening in ThBr above the transition into the incommensurate modulated phase at T_I. Approaching T_I from higher T, the modes show a frequency decrease next to the modulation wave vector $q_\mathrm{s} = 3.1\ \mathrm{nm}^{-1}$, which arrives close to $\omega = 0$ in the I-phase.

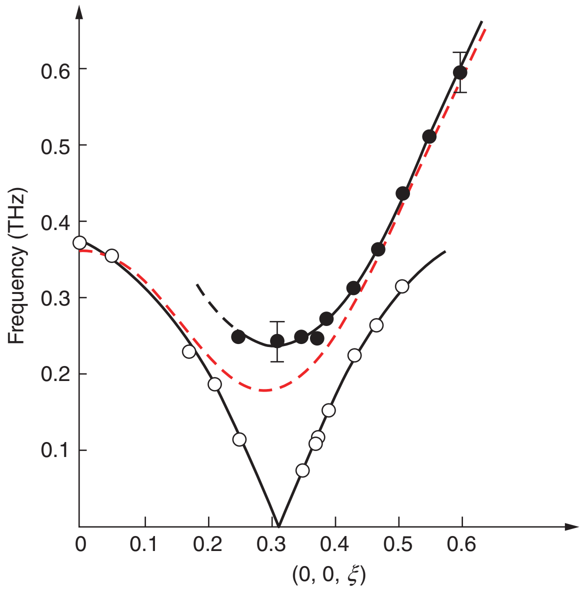

Fig. 2 Phason and amplitudon branches next to the incommensurate modulation vector at 3.1 nm^{-1} in ThBr below T_I.

which the phason gap (~80 GHz) could be resolved. The temperature dependence of the width of the modes $\Gamma(T)$ is expected to be approximately the same for all three modes, which meet at the incommensurate modulation wave vector q_s.

The theoretical description of the atomic dynamics of the incommensurate phases often makes use of the periodicity of the corresponding crystals when lifted into n-dim space or applies models for the incommensurate structure in real space. Most of the experimental results for incommensurate modulated crystals have been modeled very successfully using the discrete frustrated Φ^4 (DIFFOUR) model near the phase transition, where the modulation amplitude is still small. At temperatures well below T_I, the modulation amplitude may become rather large. As a consequence of this, a transition from a continuous to a discontinuous modulation function takes place, which means that the atomic surfaces are no longer continuous and smooth. This is always the case for QCs, where the atomic surfaces are generally discrete bounded objects. In the other two aperiodic crystals, modulated and composite, however, such a transition, a "discommensuration transition," may take place, resulting in domains with a structure close to a commensurate superstructure, separated by strongly incommensurate domain walls, sometimes called solitons. In this case, the description of the atomic dynamics has to also take into account a harmonic and nonlinear contributions. This situation was successfully described using the incommensurate version of the Frenkel–Kontorova model.

The transition occurs in metals and insulators for different reasons: in metals, an incommensurability of the Fermi wave vector with the basis lattice periodicity leads to a Peierls instability, which gives rise to the lattice dynamical precursor effects (local softening of the longitudinal acoustic branch) near the ordering vector, $2k_\text{F}$. In insulators, the incommensurate structure either results from an intrinsic lattice instability, which corresponds to the "displacive" limit, or from a collective ordering mode in the "order–disorder limit." In these cases, the corresponding modulation wave vector is not predictable beforehand. Thus, the lattice dynamics is at the origin of these modulated phases.

Incommensurate composites

Different from the crystals with incommensurate modulation, which is the only aperiodic structure, where a dominant "parent" periodic structure persists, incommensurate composites can be imagined to be made up of two (or more) interpenetrating periodic sublattices (Currat and Janssen, 1988), the unit cell parameters of which are mutually incommensurate. Each of these sublattices, modeled by the incommensurate double chain model (DCM), pertain, to a large extent, to their dynamical characteristics as far as phonons are concerned. Thus, for example, two longitudinal acoustic branches have been found in $Bi_2Sr_2CaCu_2O_{8+\delta}$, which consists of two sublattices, one for each subsystem. However, as all aperiodic lattices, they also have phason degrees of freedom, which in this case concerns the phase between the two sublattices, which changes when one sublattice slides against the other, leading to "sliding modes," as predicted by the DCM. Whether or not these sliding modes have been observed experimentally is still under debate. As in the case of modulated crystals, these simplified descriptions are only valid as long as the interaction between the mutually incommensurate systems is not too strong. It is very likely that phasons are primarily "diffusive" in incommensurate composites, but considerably less experimental information exists on these systems than on the incommensurably modulated phases discussed above.

Quasicrystals

1D, 2D, and 3D QCs have been found, of which the 1D QCs consist of an aperiodic stacking (e.g., in a Fibonacci sequence) of periodic lattice planes. 2D QCs are made up of lattice planes with a quasiperiodic structure with pentagonal, octagonal, decagonal, or dodecagonal point symmetry, which are stacked periodically (El Hor et al., 2003). Finally, 3D quasiperiodic structures have aperiodic lattices with icosahedral point symmetry.

The atomic structure of 2D and 3D QCs is based on "atomic clusters" of 1–2 nm diameter. In 2D QCs, these are cylindrical clusters made up of a stacking of the quasiperiodic lattice planes, neighboring planes often being rotated against one another, often with some "filling" atoms between the clusters. The atomic structure is dense. 3D QCs, the icosahedral ones, can be roughly divided into three classes on the basis of the dominant type of cluster characteristic of their structure: Mackay clusters, Bergman clusters and Tsai clusters (De Boissieu, 2012), where the Bergman clusters are also characteristic of the Frank–Kasper type of periodic crystals with many atoms per unit cell. As 2D QCs are often "relatives" of the icosahedral phases, here these QCs are put in the same category as their icosahedral neighbors. Because the atomic dynamics is dominated by the type of atomic interaction (interaction potential) and the "local" structure, one expects that the type of cluster, which dominates the local environment of the vibrating atom, will influence the phonon dynamics.

Concerning the phasonic motions (displacements in internal space), one distinguishes two possible phasonic modes (apart from the static-phason strain): "phason flips," which only cause a local change in the phase of the aperiodic lattice by a (mostly collective) jump of a few neighboring atoms, leading to a "violation" of the matching rules of the perfect quasiperiodic lattice. These have to be distinguished from "phasons," which are collective diffusive modes. These are different from the incommensurate modulated phases due to the fact that QCs always have discontinuous aperiodic modulation because of the discrete bounded atomic surfaces, which cause jumps or discontinuities in the modulation function, when moving in internal space.

Of these structures, up to now, the atomic dynamics of mainly icosahedral (i-) and decagonal (d-) QCs has been investigated using NIS, XIS, and X-ray intensity correlation techniques. On single crystals, using crystal spectrometers, dispersion curves for acoustic phonons and some low-lying optic branches have been measured. On polycrystalline samples, bands at intermediate energies and the GVDOS have been determined by time-of-flight (TOF) spectroscopy for several metastable and nearly all stable quasicrystalline samples from the total dynamic structure factor, which one measures in all these cases. For i-AlCuFe also, the Fe partial density-of-state was measured using XIS and ^{57}Fe substitution. Quasielastic neutron scattering (QENS) was used on polycrystalline samples and an AlPdMn single crystal to measure phason flips and X-ray diffraction, and correlation techniques to investigate diffusing phasons in QCs. In the following, results from these four types of investigations will be discussed starting with the vibrational degrees of freedom in physical space.

Phonon dispersions

Very characteristic for all phonon branches investigated so far is the important width of the phonon peaks in the measured spectra as soon as the modulus q of the wave vector $\boldsymbol{q}$ of the measured excitation exceeds a certain critical value, which essentially in all cases is $\sim$3–4 nm^{-1} (Quilichini, 1997). The broadening of the peaks is of such an importance that the rapidly increasing width prevented measurements of excitations above energies of ~6–8 THz, even though the vibrational density-of-states (VDOS) often extends to twice that energy.

As an example, Fig. 3 shows some of the transverse acoustic branches measured with an AlPdMn single crystal along the twofold direction, the Γ point ($q = 0$, starting point of the dispersion) being one of the strongest Bragg peaks in this crystallographic direction. As the intensity of the inelastic structure factor is proportional to the intensity of the Bragg peak at the Γ point, and only next to a strong Bragg peak the PBZ is well defined, this choice is essential for the result of the experiment.

Fig. 3 already demonstrates this very characteristic property of the lattice dynamics of QCs: the rapid damping of the lattice vibrations as soon as the wavelength of the excitation is smaller than ~2 nm, which in several cases is just the approximate diameter of the building unit. Corresponding results have also been obtained by computer simulations of icosahedral QCs, which show above the acoustic dispersion branches, rather dispersionless broadbands of optic modes, as they have also been found experimentally in some cases, and at even higher energies quasicontinuous spectra, which cannot be resolved in single excitations any more. This fact has limited so far the investigation of single excitations to energies below 8 THz, that is, to about half the upper energy limit of all vibrational excitations.

As is shown in Fig. 4, for icosahedral QCs one finds "isotropic" dispersion branches for longitudinal and for transverse phonons, as these crystals, due to the high symmetry of the icosahedral structure, have—in the hydrodynamic limit—only two phonon elastic constants (plus two phason elastic constants and a phonon–phason one). This has also been proven experimentally for the sound velocity. In contrast, the sound "absorption" is anisotropic because of phonon–phason coupling.

For 2D QCs, computer simulations had predicted some anisotropies concerning lattice modes with polarization vectors in the aperiodic plane and in the periodic direction, respectively. However, experimentally the differences observed for d-AlCoNi (Mackay-type) single crystals using NIS are much less important and not far outside the error limits of the experimental results. Likewise, the gap structure of the dispersions, predicted for aperiodic lattices especially in low dimensions, has not clearly been confirmed experimentally up to now.

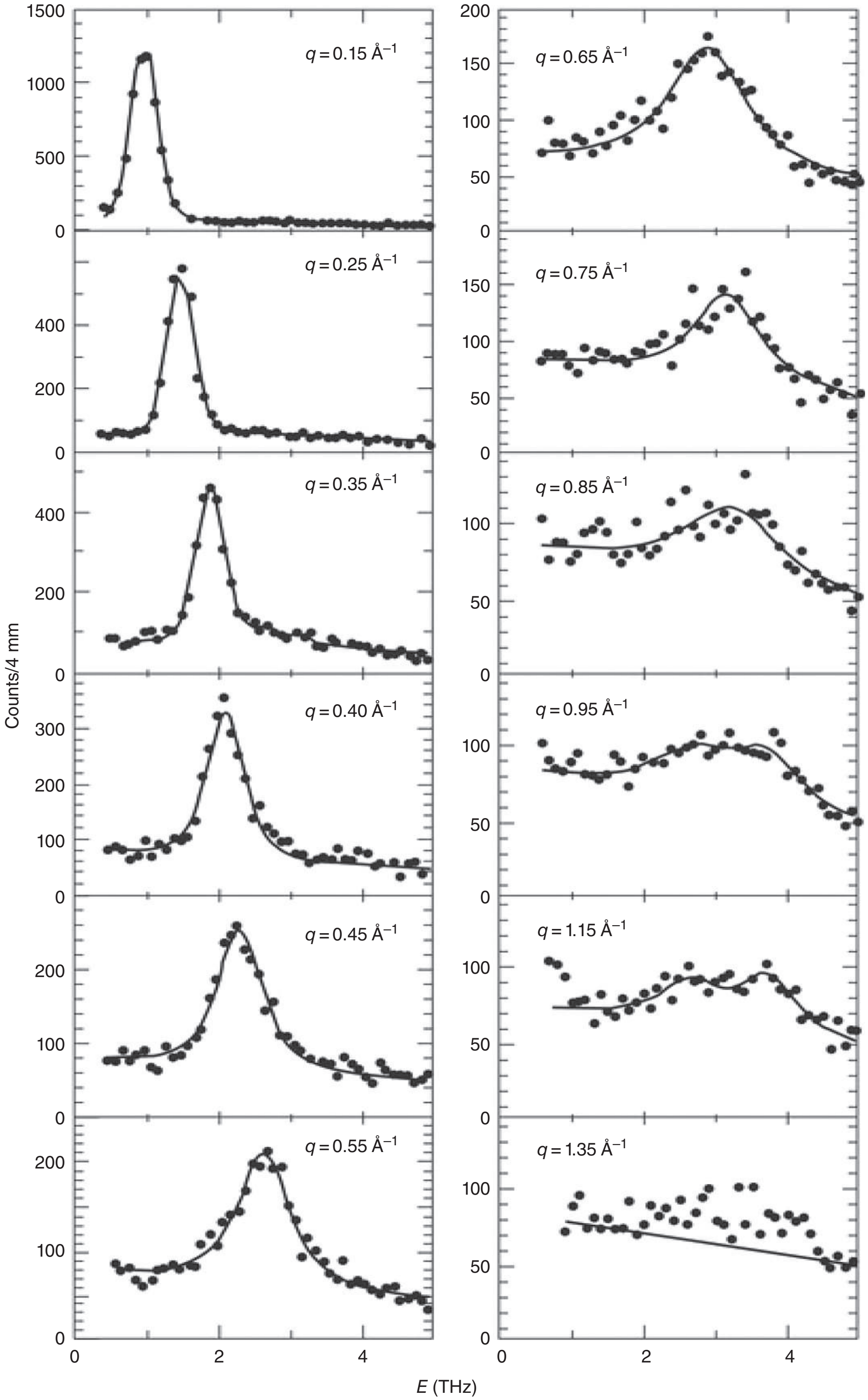

Fig. 3 Spectra of transverse phonons measured by NIS at a strong Bragg peak in the twofold direction of an i-AlPdMn single crystal (Mackay type). The rapid increase of the phonon line width for $q > 4$ nm^{-1} is obvious. The line width increases roughly proportional to q^2.

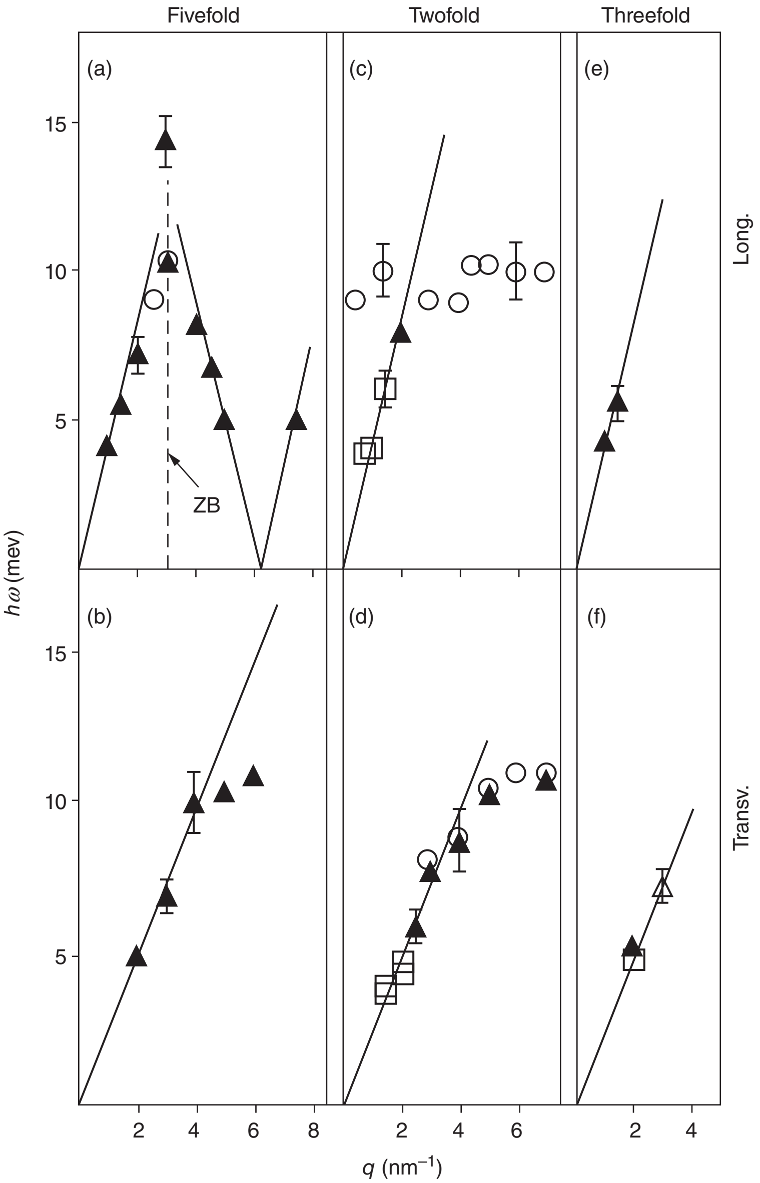

Fig. 4 Dispersion of longitudinal and transverse phonons in i-AlLiCu (Frank–Kasper type) proving the isotropy of each of these excitations with respect to the three different crystallographic axes (twofold, threefold, and fivefold).

Above the acoustic branches, very few dispersionless branches of very broad excitations have been measured by NIS on single crystals by triple axis spectrometry (TAS) and extracted from $S(Q, \omega)$ measured on TOF spectrometers. Both results are in good agreement. These excitations have been suggested to have the character of optic modes.

The phonon dispersions of QCs have been investigated in the accessible energy range (up to 4 THz in all cases, up to 6 THz for few examples, and up to 8 THz in one case) for most of the thermodynamically stable QCs using single crystals and mostly NIS and, in some cases, also XIS.

Generalized vibrational density-of-states

The energy range above 8 THz could be accessed by NIS up to now using only polycrystalline samples and TOF spectroscopy. In this case, one obtains angular-averaged (in reciprocal space) dispersion relations from the shape of the total dynamic structure factor and the GVDOS from its intensity averaged in a reasonably large region of reciprocal space. In order to cover the full energy range, in what follows, the discussion will therefore concentrate more on the GVDOS, which have been determined for most of the thermodynamically stable and several metastable QCs. The GVDOS normally contains several energy bands, the position (energy of the center of gravity of the band) and intensity of which are usually different for different samples. Thus, it is mainly the shape (and the energy range and the slope at lowest energy (if resolved)) of the GVDOS, which can be used to characterize the atomic dynamics of a sample via the GVDOS.

One obtains considerably more detailed information, if the experimental results are combined with results from computer simulations (CSs). These simulations are based on interactions, which are either calculated directly during the simulation, as is done in the method due to Car and Parrinello, or they are modeled in a more or less realistic manner. The second basic input is a model for the atomic structure, which in the case of QCs is always a structural model for a rational approximant, because of the finite size of the computer model, and it is of similar uncertainty as is the complicated interaction. Because of these inherent uncertainties, the comparison of the results of CSs with those of experiments is "essential" for a judgment on the quality of the simulation results, that is, how realistic these results are. If they are in fairly good agreement, nothing is proved; however, it seems reasonable to use them for the interpretation of the measured results, as they provide very detailed information, which otherwise is possible only with great effort and extensive cost of experiments. In what follows, therefore, the experimental results will be confronted with those from realistic CSs as far as they exist.

Atomic dynamics and cluster structure

As mentioned above, QCs are built from different types of clusters, the structure of which should influence the dynamics as it is the local structure which has the strongest influence on the dynamics. In fact, one finds a difference in the shape of the corresponding GVDOS for the two types of QCs. QCs dominated by more or less complete Mackay icosahedra, such as i-AlPdMn, i-AlCuFe, and d-AlCoNi, seem to have very smooth, nearly structureless one- or two-band spectra, whereas QCs of the Frank–Kasper type, such as i-AlLiCu, i-ZnMGRE (RE = Ho, Er, . . ., and also Y), and d-ZnMgY have more structured spectra with several energy subbands. This is easily seen in a comparison of Fig. 5 with Fig. 7.

CSs suggest that this stronger band structure is due to a stronger grouping of the local vibrational density-of-states (LVDOS), that is, the vibrational spectra of all atoms on different Wyckoff positions in this computer-approximant to the Frank–Kasper type of QCs. This is different in the case of the Mackay type of QCs, where the LVDOS are more different from one another and result in a broad smooth spectrum after summation.

Quasicrystals and their rational approximants

Because one of the basic input parameters for CSs, the structural model, is based on considerable approximations in the case of QCs, quite a few simulations have also been done on periodic crystals with similar chemical compositions as the QCs have, but with a well-known structure. Compared to the atomic dynamics of QCs, the dynamics of these periodic crystals is rather similar to that of the corresponding aperiodic phase if the periodic crystal is an approximant to the QCs. For example, the GVDOS of AlLiCu in the i-(Fank–Kasper type) and the periodic R-phase (built up of the same kind of clusters) are very similar to each other, having energy bands at essentially the same energies, but with slightly different intensities. The same results have been obtained in the

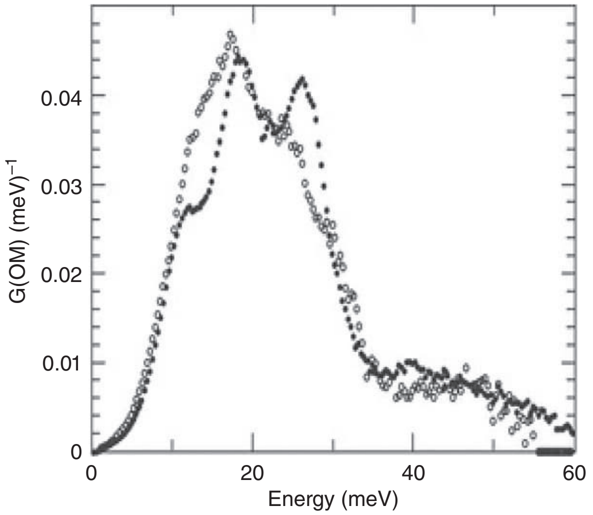

Fig. 5 GVDOS of i-$Zn_{63}Mg_{26}.3gY_{10.7}$ and d-$Zn_{58}Mg_{40}Y_2$ (both Frank–Kasper type) showing the highly structured distributions with several energy bands and subbands.

measurement of the phonon dispersions of the same alloy system, where also hardly any difference could be detected except for a dispersionless branch at the upper energy limit of this investigation in the case of the i-phase seen in the center of Fig. 4. Likewise, CSs of this alloy system, providing the information on the partial (element specific) dynamical properties, showed a small difference in peak intensity but not in peak position in the calculated GVDOS of the i- and R-phase, respectively. Even more identical results have been obtained for the Mackay type of QCs d-$Al_{71.5}Co_{13.5}Ni_{15}$ and its modulated approximant $Al_{71.5}Co_{15.5}Ni_{13}$. In fact, phonon dispersion measurements done on both types of QCs suggest slightly narrower phonon groups for the rational approximant compared with the QCs in the case of the Frank–Kasper type but not in the case of QCs of the Mackay type. These nearly identical results can be understood from the fact that the atomic dynamics is most strongly determined by the local (cluster) structure and potential, which seem to be sufficiently similar for the QCs and their approximants, while their structure differs on the long-range scale. For the 2D QCs just mentioned, this striking similarity of the atomic dynamics was even found at 1000 K, which also means that the thermal expansion (see below) of the QC and its rational approximant are nearly identical. All these conclusions do not apply to periodic crystals of similar chemical composition as the QCs have, but to those which are (structurally) not approximants.

Low-energy modes in quasicrystals

Within the harmonic approximation, which should also apply to QCs at not too high temperatures, at low energies, one expects to find the linear dispersions $\omega = vq$, of transverse (TA) and longitudinal (LA) acoustic phonons, which join the linear dispersions of transverse and longitudinal ultrasound near $q = 0$. Here v is the sound velocity of the mode under consideration ($v = v_T or\ v_L$) and q is the corresponding wave vector of the mode. On the basis of the Debye approximation, one therefore expects the phonon density-of-states (PDOS) to start at the lowest energies proportional to $\omega^{(d-1)}$, where d is the dimension of the sample under consideration. For a 3D system with particle density n and a weighted mean value of the sound velocity v, one therefore expects the PDOS to start at the lowest energies proportional to the Debye DOS

$$G_{\text{Deb}}(\omega) = \frac{\omega^2}{2\pi n v^3}, \tag{6}$$

$$\frac{3}{v^3} = \frac{1}{v_L^3} + \frac{2}{v_T^3}. \tag{7}$$

For several—but not all—QCs (and some of their rational approximants), this general rule does not apply either for the measured GVDOS or for the CSs calculated PDOS. One finds a considerably higher intensity in the low-energy region compared to the intensity calculated by using the known sound velocities. Corresponding higher values for these QCs have also been found for the low-temperature specific heat by different groups. Likewise, the temperature dependence of the sound velocity of these QCs shows an unexpected behavior. Investigations of this kind are only possible with thermodynamically stable QCs as normal production defects have to be annealed out before.

Metastable QCs obtained by annealing of a metallic glass show additional low-energy modes stemming from the large grain boundary volume in these samples, as annealing here leads to nanocrystalline samples as has been shown for i-PdSiU and AlCuV. In this case, the intensity of the low-energy modes reaches nearly the level of a well-relaxed metallic glass.

Temperature dependence of the atomic dynamics

The temperature dependence of the dynamics outside the quasielastic region has been investigated most extensively for i- and d-QCs of the Macky type. In all cases, one finds a considerable shift of the GVDOS to lower energies, that is, an anharmonic behavior of the DOS. However, on quantifying this shift with temperature, for example, with the "integrated" amount of modes shifted (e.g., integration from 0 to 16 or 25 meV) into the low-energy region, one finds a linear dependence of this transfer of modes with temperature up to 1000 K in all investigations, for d-AlCoNi even in the full range of temperatures investigated (up to 1100 K). This linear increase of the shifted intensity is parallel to the shift of the Debye–Scherrer lines in the diffraction diagrams to lower momentum transfers with increasing temperature, caused by the expansion of the lattice. Investigating the shift of lines having contributions only from the periodic axis or only from the aperiodic lattice planes, one observes, for example, in the case of d–$Al_{71.5}Co_{13.5}Ni_{15}$ that at temperatures above 750 K, the thermal expansion of the QCs in the periodic direction is stronger with increasing T than in the aperiodic plane.

Investigations of the energy dependence of the shifted intensity (by how much has one to shift the intensity of the calculated PDOS to arrive at the experimentally determined GVDOS) show a nearly constant energy shift of $\delta\omega/\omega$ of ~6–10% at all temperatures analyzed from the upper limit of the GVDOS down to ~12 meV. After this, one finds a strong increase of the shifted intensity, becoming more important with increasing temperature and reaching a relative shift of 20% and more. The participation ratio P ($P(\omega) = 1$ if all atoms of the model take part in the mode at frequency ω) shows, in the case of a QC or its approximant, that the smallest participation, that is, the strongest localization of the vibrations takes place at the smallest and highest frequencies.

This is shown in Fig. 6. Correlating this relative frequency shift $\delta\omega/\omega$ with the participation ratio P for the modes at these energies, CSs show that the strongest shifts correlate with the lowest participation ratio. Thus, one has to conclude that a large part of the shifted modes are most likely localized modes. The same CSs clearly demonstrate that the Al atoms contribute more strongly to these shifts than do the TM atoms, as one would expect from the structure, where the TM atoms form a rigid network in the clusters.

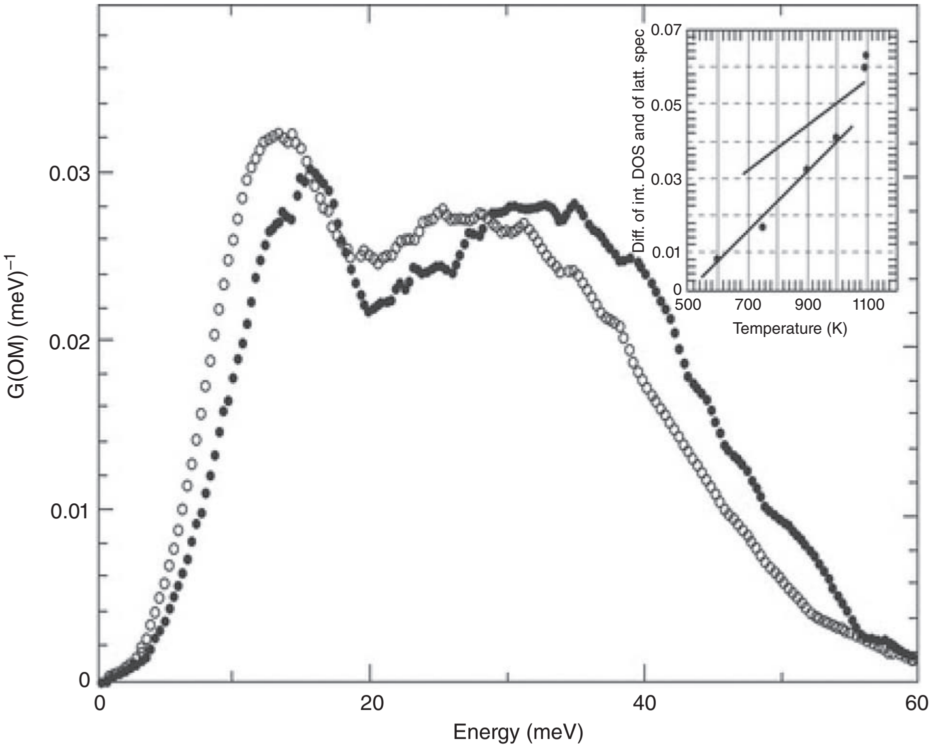

Fig. 6 Participation ratio as a function of the energy of the vibrations for the orthorhombic approximant o-$Al_{13}Co_4$ to quasicrystalline d-$Al_{71.5}Co_{13.5}Ni_{15}$ in comparison with the chemically comparable but nonapproximant Al_3Ni. The strong decrease of the participation (=localization) of the modes with $\omega < 12$ meV in the case of the approximant is clearly seen.

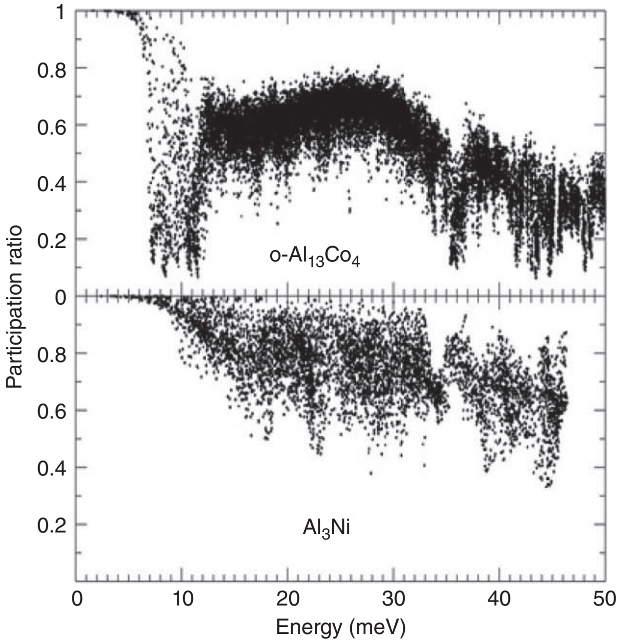

Fig. 7 GVDOS of i-$Al_{63}Pd_{26.3}Mn_{10}$ (Mackay type) showing the important shift of the GVDOS to lower energies with increasing temperature. The insert demonstrates that the integrated shifted intensity has a linear behavior nearly parallel to the linear shift of the Debye–Scherrer lines in the diffraction diagrams (expansion of the alloy), except for temperatures higher than 1000 K.

For i-AlPdMn, a new phenomenon comes in at temperatures above 1000 K. While one finds essentially the same linear behavior for the integrated intensity and shift of the Debye–Scherrer peaks, as for d-AlCoNi up to 1000 K, the integrated intensity suddenly increases well above this linear continuation (see Fig. 7).

A careful investigation of the total dynamic structure factor of i-AlPdMn in the low-energy region shows that this additional intensity is due to quasielastic scattering being caused most likely by phason flips (see below), that is, a new degree of freedom in addition to the phonon degrees of freedom. As this quasielastic intensity gets considerably broader with increasing wave vector transfers Q, it overlaps with the inelastic region of the spectra and thus contributes to the intensity used to determine the GVDOS.

Phason flips

As the n-dim space corresponding to the structure of the QCs is a "periodic lattice" decorated by disconnected atomic surfaces, any movement of the physical space, with which the n-dim space is intersected, orthogonal to itself will lead to sudden jumps in the atomic positions instead of a continuous change as in the case of a continuous modulation function such as in perfect incommensurably modulated systems. Phason degrees of freedom will, therefore, always concern either flips of atoms in the aperiodic structure, corresponding to a local deviation of the intersection or by a diffusion kind of motion on a much longer timescale.

On the basis of calculations, one expects the phason dynamics to be frozen-in at lower temperatures even in random tilings, where phasons are principally in an unlocked state—in contrast to the locked state in energetically stabilized QCs below the unlocking transition. Only at temperatures well above room temperature, one could expect unlocking and with this, any sign from phason dynamics. Starting from a perfect (decorated) tiling at lower temperatures, phason flips will violate the matching rules and lead to a random tiling, which will be stabilized by its configurational entropy. The reverse mechanism will most likely be incomplete due to kinematic constraints. This process has been studied in several CSs, and at least in one of these investigations, correlated flips of several atoms have been observed.

Experimentally, quasielastic scattering has been found for most of the thermodynamically stable QCs by different groups at temperatures near the upper limit of the existence region of the QCs using polycrystalline samples and TOF spectroscopy. In the case of i-AlCuFe, for example, one obtains a nearly Q-independent width Γ of the Lorentzian fitted to the quasielastic spectrum, Γ being $\sim$0.1 meV. This width of the spectrum would then correspond to jumps in the region of $h/\Gamma \approx 7$ ps. The Q-dependence of the integrated intensity of this quasielastic signal with a maximum at 10 nm^{-1} suggests a process localized within a jump distance of 0.4 nm. The most detailed investigation was done at 1073 K using a single crystal of i-AlPdMn on a cold neutron TAS. While the Q-dependence of the quasielastic scattering from polycrystalline samples only allows one to determine the jump distances of the scattering atoms, experiments on single crystals allow, in addition, one to determine the orientation of the jumps. The variation of the measured intensity with the rotational angle in reciprocal space can be best fitted by a model for quasielastic scattering from simultaneous correlated jumps of several atoms in the phason flips. The quasielastic spectra can be fitted with one broad Lorentzian with $\Gamma = 0.7$ meV or (better) with two Lorentzians with $\Gamma = 0.2$ and 0.7 meV. Measurements on the twofold axis now show a maximum of the intensity near 27 nm^{-1}, which corresponds to considerably shorter jump distances than found in the less detailed investigation of i-AlCuFe.

Phason fluctuation in quasicrystals

For reasons mentioned in the previous section, one does not expect to find propagating phason modes as in the case of modulated phases. However, phasons do play a role in the elastic and dynamic properties of QCs. The elastic-free energy of a QC is given by three different terms

$$F = F_{\text{phon}}(\lambda, \mu) + F_{\text{phas}}(K_1, K_2) + F_{\text{cross}}(K_3). \tag{8}$$

Here λ and μ are the Lame coefficients, K_1 and K_2 the phason elastic constants, and K_3 the phonon–phason coupling term. From investigations of the diffuse scattering, assuming $K_3 = 0$, one can obtain the ratio of K_2/K_1, which at 300 K was found to be near −0.5 for i-AlPdMn. At temperatures in the range of 1000 K, a diffusive relaxation of phason strain or "phason walls" (left behind a moving dislocation in a QC) can lead to a collective diffusive phasonic excitation or long wavelength phason fluctuations. According to different theoretical investigations performed by several authors, these fluctuations will contribute to the Debye–Waller factor and to the diffuse scattering in a similar way as do phonons and defects, with the exception that the timescales of phonon and phason fluctuations differ by many orders of magnitude, lattice vibrations being in the picosecond range, while the characteristic times for long wavelength phason fluctuations is more between 0.1 and 100 s. Correspondingly, phonons can follow a lowering of the temperature instantaneously, whereas phason fluctuations fall out of equilibrium as a consequence of fast T-changes.

Experimentally, phason diffusion has been investigated in reciprocal space using high-resolution X-ray diffraction to study the phonon and the phason contribution to the Debye–Waller factor in a single crystal of i-AlCuFe in the temperature range between 300 and 1023 K, and to study diffuse scattering from a single crystal of i-AlPdMn as a function of temperature between 300 and 1043 K. Finally, X-ray intensity fluctuation spectroscopy (XIFS) has been used to investigate the time and temperature dependence of the diffuse scattering from a single crystal of i-AlPdMn at 923 K (Janssen et al., 2002; Francoual et al., 2003). In real space, in situ HRTEM was used to investigate the time-dependent structural changes in d-AlCoCu at 1123 K.

The X-ray diffraction experiment demonstrates a very strong temperature dependence of the phason contribution to the Debye–Waller factor (change by a factor of 9 between 750 and 650 K) and to the diffuse scattering, which decreases with increasing T while the intensity of large Q_{perp} reflections increases. Freezing of the phason dynamics was observed just below 900 K already. The most detailed results were obtained using highly coherent synchrotron radiation in the XIFS experiment. Here, the time evolution of the speckle pattern from diffuse scattering could be directly resolved and a time-dependent intensity correlation $g(Q, t)$ could be determined from the time dependence of the measured intensity

$$F_{\mathrm{cor}}(Q, t) = [1 - \beta g(Q, t)], \tag{9}$$

where β corrects for the partial coherence of the beam. Above 923 K, the expected exponential decay $g(Q,t) = \exp(-t/\tau(Q))$ was found with $\tau(Q)$ proportional to $1/Q^2$, that is, D_{phas} proportional to λ^2, which proves the diffusive character of the long wavelength phason fluctuation observed, as the width Γ of the spectrum should be $\Gamma = DQ^2 = D4\pi^2/\tau$ for diffusive dynamics. D_{phas} was found to be $1.5 \times 10^{-16}\ \mathrm{m}^2\ \mathrm{s}^{-1}$ with the phason excitation wavelength λ between 50 and 100 nm. Again, a very strong temperature dependence was found, τ varying between 60 and 300 s when lowering the temperature from 923 K to 873 K.

A comparable slow phason dynamics was found in the in situ HRTEM investigations of single crystals of d-AlCoCu at 1123 K. The duration for a change of the position of one of the columnar clusters of the decagonal structure was smaller than 10 s, the time between jumps was between 0.1 s and 10 min.

Conclusion

After discussing the phonon and phason dynamics in incommensurate modulated structures and incommensurate composites, phonon dispersions and the generalized vibrational density of states are discussed in more details including the temperature dependence of the atomic dynamics and the strong temperature dependence of the phason dynamics.

References

Currat R and Janssen T (1988) Excitations in incommensurate crystal phases. *Solid State Physics—Advances in Research and Applications* 41(C): 201–302. https://doi.org/10.1016/S0081-1947(08)60380-X.

De Boissieu M (2012) Phonons, phasons and atomic dynamics in quasicrystals. *Chemical Society Reviews* 41(20): 6778–6786. https://doi.org/10.1039/C2CS35212E.

El Hor H, et al. (2003) *Dynamical Properties of Quasicrystalline Alloys Investigated by Neutron Inelastic Scattering and Computer Simulations based on Realistic Potentials*, pp. 382–413. Springer.

Francoual S, et al. (2003) Dynamics of phason fluctuations in the [formula presented] quasicrystal. *Physical Review Letters* 91(22): 1–4. https://doi.org/10.1103/PhysRevLett.91.225501.

Janssen T, Radulescu O, and Rubtsov AN (2002) Phasons, sliding modes and friction. *The European Physical Journal B—Condensed Matter and Complex Systems* 29(1): 85–95. https://doi.org/10.1140/EPJB/E2002-00265-Y.

Quilichini M (1997) Phonon excitations in quasicrystals. *Reviews of Modern Physics* 69(1): 277–314. https://doi.org/10.1103/RevModPhys.69.277.

Electronic structure of quasicrystals☆

Uwe Grimm[a,*] **and Michael Schreiber**[b], [a]Department of Mathematics and Statisics, The Open University, Walton Hall, Milton Keynes, United Kingdom; [b]Institut für Physik, Technische Universität Chemnitz, Chemnitz, Germany

© 2024 Elsevier Ltd. All rights reserved.

This is an update of U. Grimm, M. Schreiber, Quasicrystals, Electronic Structure of, Editor(s): Franco Bassani, Gerald L. Liedl, Peter Wyder, Encyclopedia of Condensed Matter Physics, Elsevier, 2005, Pages 95–100, ISBN 9780123694010, https://doi.org/10.1016/B0-12-369401-9/00467-8.

Introduction 290
Aperiodically ordered solids 291
Quasicrystal surfaces 291
Transport properties 291
Magnetic properties 292
Electronic density of states 293
The nature of the electronic states 295
The role of clusters 296
Conclusion 296
References 296
Further reading 297

Abstract

The unusual electronic transport properties and magnetic properties of quasicrystals are described in terms of the electronic structure of these aperiodically ordered systems. Experimental results for thermopower and conductivity as well as the Hall coefficient are discussed. The electronic density of states is analyzed. Critical electronic states with a multifractal probability distribution are shown.

Key points

- Quasicrystals are aperiodically ordered solids
- Quasicrystal surfaces are themselves quasicrystalline
- Quasicrystals, often composed of elements which are good conductors, show very low electric conductivity
- Thermoelectric powers and Hall coefficients depend crucially on the composition and show anomalies
- Quasicrystals have interesting magnetic properties
- One can interpret quasicrystals as Hume–Rothery solids
- A deep pseudo-gap in the electronic density of states appears at the Fermi level, yielding a strong tendency towards localization
- Electronic states are so-called ‘critical’ states that show a multifractal probability distribution
- The energy spectra of many one-dimensional quasiperiodic systems have neither a continuous part nor a point part but are purely singular continuous
- A hierarchical sequence of clusters of atoms can help to explain the electronic properties

Introduction

Quasicrystals are aperiodically ordered solids (Barber, 2009). Their unusual transport properties, especially the low electric conductivity, are indications of the particular electronic structure of these materials. There are several approaches towards understanding the electronic structure of these systems. Whereas a complete understanding is still lacking, quasicrystals can heuristically be described as Hume–Rothery alloys, which qualitatively accounts for the experimentally observed properties. Other approaches that have been followed are based on the investigation of electrons in aperiodic potentials and on a hierarchical cluster picture of quasicrystals.

☆*Change History*: March 2022. M Schreiber updated the article to reflect recent results. All chapters except Introduction and Summary were changed, in particular by adding citations.

*Uwe Grimm passed away during the preparation of this manuscript.

https://doi.org/10.1016/B978-0-323-90800-9.00023-8

Aperiodically ordered solids

Quasicrystals were first discovered in a rapidly quenched AlMn alloy in the early 1980s (Shechtman et al., 1984). For his discovery, Dan Shechtman was awarded the Nobel Prize in Chemistry 2011. Today, many quasicrystalline compounds have been identified, mostly in aluminum or zinc-magnesium based ternary alloys, some of which can be grown to form nicely faceted single crystals of macroscopic size.

The fingerprint of a quasicrystal is a diffraction which consists of Bragg peaks, like for a periodic crystal, but which displays a symmetry that is incompatible with lattice periodicity in three-dimensional space. So far, non-crystallographic symmetries that have been experimentally observed in quasicrystals comprise icosahedral symmetry, featuring axes of two-, three- and five-fold rotational symmetry, as well as dodecagonal, decagonal and octagonal symmetry with a single axis of 15-, 10- or 8-fold rotational symmetry, respectively. Dodecagonal, decagonal and octagonal quasicrystals are periodically ordered along the distinguished axis. In contrast to the icosahedral quasicrystals, such phases show anisotropic physical properties.

The apparent paradox of a Bragg-like diffraction with crystallographically forbidden symmetry can be resolved by interpreting quasicrystals as aperiodically ordered solids (Grimm and Scheffer, 2001; Grimm, 2015). The definition of a crystal has been adapted to include quasicrystals, alongside incommensurate structures, as aperiodic crystals. Their structure is usually described in terms of quasiperiodic tilings (or coverings) of space, which play the role of the lattice in conventional crystals. Quasiperiodic tilings can, for instance, be derived as projections of sections through higher-dimensional periodic lattices. This approach can accommodate the symmetries that are observed in quasicrystals. Structure models consist of decorating the basic building blocks of such tilings with atoms, very much in line with the unit-cell picture of a conventional periodic crystal. For icosahedral quasicrystals, this yields a six-dimensional description of the structure, for the quasicrystalline phases with one periodic axis the analogous description of a quasiperiodic plane requires at least four space dimensions, and the positions of the Bragg peaks can be indexed accordingly. Direct evidence for the structure is furthermore obtained by high-resolution electron microscopy and atomic force microscopy. While there exist sophisticated structure models for various quasicrystals, many important questions remain unanswered, for instance concerning inherent disorder in the structure such as stochastic occupancy of atomic sites, or how the quasicrystalline structure actually grows (Häussler et al., 2003). A detailed discussion of the structure of quasicrystalline alloys is given by De Boissieu (2005).

Due to the aperiodic structure of these materials, important concepts used in conventional crystals, such as the notion of a Brillouin zone, do not strictly apply for quasicrystals. However, in many cases there are, albeit often less precisely defined, analogues of these concepts, such as the pseudo-Brillouin or Jones zone. This zone is constructed from the main structural peaks, it is nearly isotropic in quasicrystals and, in contrast to the case for amorphous alloys, is a sharply defined polyhedron.

Quasicrystal surfaces

Many of the experimental techniques used to probe electronic properties of quasicrystals, such as photoemission experiments, are surface sensitive, because the escape depth for elastic electrons is of the order of a few nanometers. Therefore, it is important to know something about the surface structure in order to interpret the experimental results of such measurements.

There has been a long discussion about quasicrystal surfaces, with results depending on the preparation of the surface. However, as a result of progress in experimental techniques, both concerning the preparation of quasicrystalline samples and the image resolution of electron microscopy, it appears to have been established that quasicrystal surfaces, prepared by sputtering in ultra-high vacuum and suitable annealing, are themselves quasicrystalline and can be understood as a termination of the bulk structure.

Evidence for this is presented in Fig. 1, which shows a high-resolution scanning tunneling microscopy image of a flat terrace of the fivefold surface of an icosahedral quasicrystal (Papadopolos et al., 2002). This technique measures corrugations in the electronic density at the surface arising from the positions of the surface atoms. As shown in Fig. 1, the pattern obtained for the particular terrace is in good correspondence with a patch of a perfect quasiperiodic Penrose tiling. The matching of the surface structure for this terrace and other terraces with a bulk model of the icosahedral quasicrystal corroborates that the surfaces in this case are consistent terminations of the bulk structure, so there should be no artefacts in experimental measurements due to surface reconstructions.

Transport properties

The particular, nearly isotropic order in quasicrystals, which in a sense is intermediate between that of conventional periodic crystals and amorphous systems, is reflected in unusual electronic properties (Berger, 1994). Quasicrystals, despite being composed of elements which in their pure form are good conductors, show very low electric conductivity which decreases with temperature and also with the structural perfection of the quasicrystal. So their behavior is not at all metallic; it is rather reminiscent of a system at a metal-insulator transition, with no energy gap but zero conductivity at zero temperature.

An example is the icosahedral phase in the Al-Pd-Re system, which shows extremely high resistivity at low temperatures, up to $10^6 \mu\Omega$ cm, with a very strong temperature dependence — the resistivity at a temperature of 0.3 K being about 100 times as large as that at 300 K.

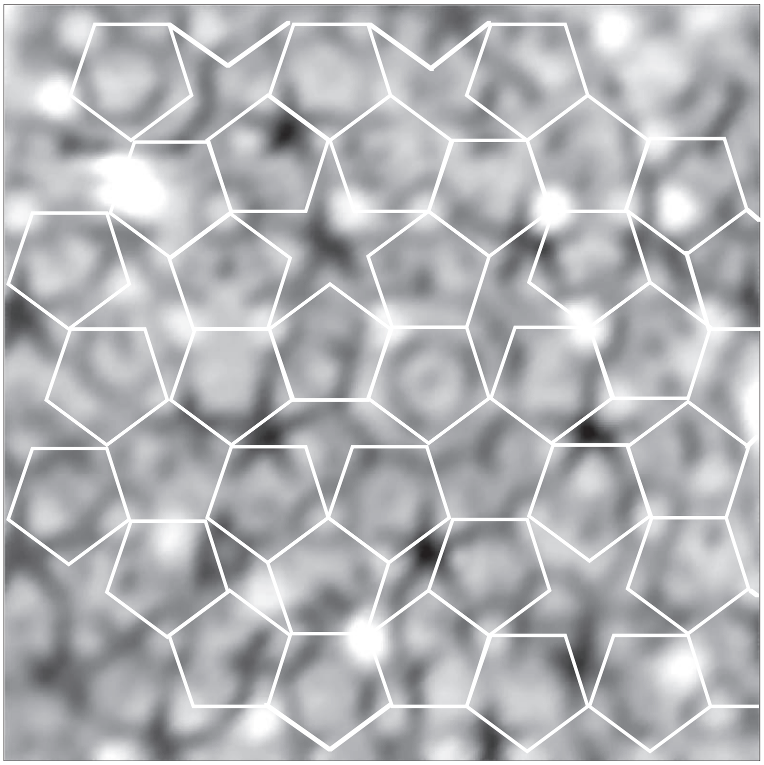

Fig. 1 75 Å × 75 Å segment of a scanning tunneling microscopy image of a terrace of an icosahedral Al-Pd-Mn quasicrystal surface with a superimposed patch of a perfect Penrose tiling of edge length 7.8 Å. Reprinted with permission from Papadopolos Z, Kasner G, Diehl RD et al. (2002) Bulk termination of the quasicrystalline five-fold surface of $Al_{70}Pd_{21}Mn_9$. *Physical Review B* 66(184207): 1–13. Copyright 2002 American Physical Society.

Other transport properties also show interesting phenomena (Poon, 1992). Examples are large thermoelectric powers and Hall coefficients that depend crucially on the composition, and may even undergo sign changes as the temperature is changed. Though these transport properties partly resemble those of amorphous phases and crystalline complex metal alloy phases of similar composition, the anomalies appear to be particularly pronounced in quasicrystals. For instance, the residual conductivity appears to be the lowest and the thermopower the largest for the 'optimal' quasicrystal composition, to an extent that such properties, alongside diffraction, are often used as an indicator for the structural perfection of quasicrystals.

An example of an in-situ measurement on a thin film is presented in Fig. 2. It shows that, while the temperature dependence of the conductivity is similar in the amorphous and icosahedral phase, the transition to the quasicrystal is accompanied by a strong decrease in conductivity and increase in thermopower, and the low-temperature conductivity in the quasicrystal is nearly zero after several hours of heat treatment (Haberkern, 2002).

Experimental values of the conductivity σ_{4K} at a temperature of 4 K are in the range of a few tens to a few hundred $(\Omega\ \text{cm})^{-1}$. The increase in conductivity with temperature is well described by a relationship of the form $\sigma_{4K} = A(\sigma_{300K} - \sigma_M)$, which shows that the low-temperature conductivity could vanish even for a finite conductivity at temperature 300 K. Experimentally, σ_M turns out to be around 150 $(\Omega\ \text{cm})^{-1}$ for high-quality icosahedral quasicrystals. Given that the actual values for σ_{300K} are in the range of 200–500 $(\Omega\ \text{cm})^{-1}$, this indicates that these materials are not far from a metal-insulator transition.

For the Hall effect, the temperature dependence can reasonably well be reproduced by a description of the Fermi sphere with electron and hole pockets. In a simple two-band model of free electrons, a change in composition can affect the balance between electrons and holes, and thus account for changes in the sign of the Hall coefficient. Within this picture, the Hall coefficient provides information about the matching between the Fermi surface and the pseudo-Brillouin zone. Similar comments apply to the strong variations and sign changes observed in the temperature dependence of the thermopower, which appear to be correlated to changes in the Hall coefficients and hence might also reflect the sign of majority carriers in the alloy.

Magnetic properties

One might expect quasicrystals to show interesting magnetic properties. The reason is that most aluminum-based quasicrystals contain a fair amount of transition metals, and there is a class of magnesium-zinc-based quasicrystals containing rare earth atoms, which provide strong localized magnetic moments. However, no long-range magnetic order has been observed in these quasicrystals to date.

In aluminum-based quasicrystals, it appears that only a low fraction of the transition metal atoms in the quasicrystal actually have magnetic moments. One often finds rather small paramagnetic susceptibilities; structurally perfect quasicrystals tend to show

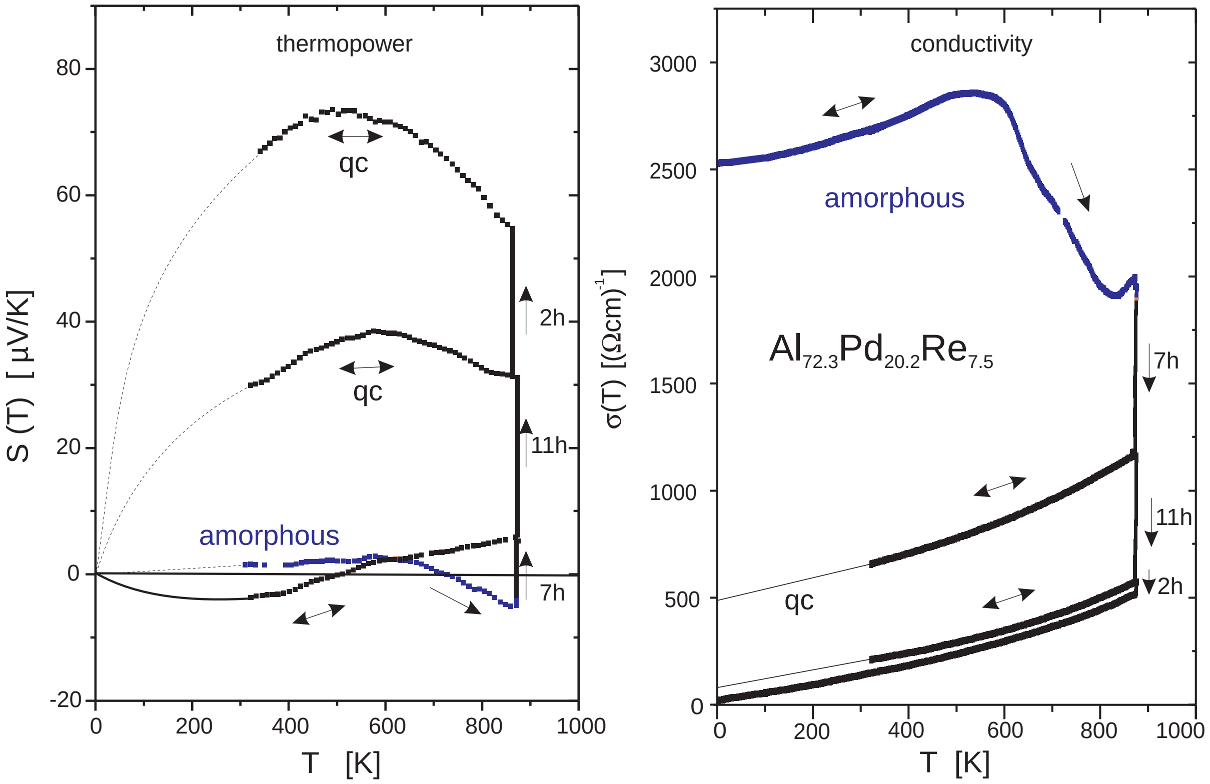

Fig. 2 In situ measurements of the thermopower (left) and conductivity (right) of an initially amorphous AlPdRe thin film during heat treatment and formation of the quasicrystalline (qc) phase. Arrows indicate reversible and irreversible branches. Reprinted with permission from Haberkern R (2002) Electronic transport properties of quasicrystalline thin films. In: Suck J-B, Schreiber M, and Häussler P (Eds.), *Quasicrystals—An Introduction to Structure, Physical Properties, and Applications*. Berlin: Springer, pp. 364–378. Copyright Springer 2002.

diamagnetic behavior, and there appears to be a correlation between diamagnetism and high resistance in the samples. The situation is somewhat different in quasicrystals containing rare earth elements. Though there had been early reports on an antiferromagnetic ordering in these quasicrystals, these results could not be confirmed and have presumably been caused by the presence of conventional crystalline phases in the samples. However, spin-glass freezing transitions have been observed at relatively low temperatures.

The recent discovery of stable binary icosahedral quasicrystals in rare earth and cadmium compounds (Goldman et al., 2013) provides quasicrystalline materials with localized magnetic moments, and hence a new model system for attaining a deeper understanding of the nature of magnetic interactions in aperiodic structures. So far no long-range order has been found in these systems (Kong et al., 2014). However, both ferromagnetic (Hiroto et al., 2013) and antiferromagnetic (Kim et al., 2012) order have now been observed in low-order approximant phases.

The theory of magnetic point and space groups of quasicrystals is discussed by Ron Lifshitz in this Encyclopedia.

Electronic density of states

To date, the transport properties and the electronic structure of quasicrystals have not been completely understood. Experimental results for aluminum-based quasicrystals such as AlPdMn, which is unique in that is has both icosahedral and decagonal phases, clearly indicate that hybridization between the aluminum sp states and the transition-metal d electrons plays an important role, which is sensitive to details of the local atomic environments.

There is a rather general heuristic picture that interprets quasicrystals as Hume–Rothery solids (Mizutani, 2011). The idea behind this is that there exists a strong interaction between the structure and the electrons, and that quasicrystals occur precisely when the number of electrons available to the system is such that the Fermi surface in momentum space closely matches the pseudo-Brillouin zone. The matching gives rise to a resonant scattering between the conduction electrons and the static structure, leading to a deep pseudo-gap in the electronic density of states and a stronger tendency towards localization at the Fermi level. Thus it offers an explanation why the above-mentioned anomalies of the transport properties are more pronounced in quasicrystals.

This heuristic argument, in combination with the hybridization effects mentioned above, can account for the qualitative behavior of transport properties and their dependency on the composition of the alloy, and has also been supported by experimental and theoretical investigations. It also provides an explanation for the stability of quasicrystals and their existence at

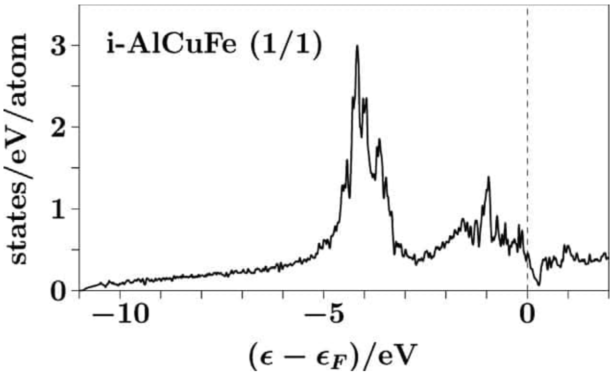

Fig. 3 Ab initio electronic density of states for the 1/1 cubic approximant of the icosahedral AlCuFe quasicrystal, as obtained by the atomic-sphere approximation to the linear muffin-tin orbital method (ASA-LMTO). The Fermi energy ε_F is indicated by a dashed line. Figure courtesy of H. Solbrig (Chemnitz).

certain compositions, because the pseudo-gap formation reduces the energy of the occupied states close to the Fermi energy, and thus lowers the total energy (Krajčí and Hafner, 2002).

An example of an ab initio calculation of the electronic density of states for aperiodic approximant of an icosahedral quasicrystal, i.e. a cubic system with very similar short-range ordering as the quasicrystal, is presented in Fig. 3. It clearly shows a pronounced pseudo-gap feature close to the Fermi energy (Solbrig and Landauro, 2003).

Experimentally, the electronic density of states has been investigated by X-ray emission (XES) and absorption (XAS) spectroscopy (Fournee et al., 2002). Fig. 4 shows an example of experimental results for the aluminum partial density of states in pure face-centered cubic (fcc) aluminum and in icosahedral AlCuFe quasicrystals. Clearly, the aluminum valence band is shifted towards higher binding energies, an effect caused by the strong sp-d hybridization in the alloy. In addition, the observed conduction band is much flatter in the quasicrystalline alloy than in pure aluminum. Together, this leads to a depletion of available states at the Fermi

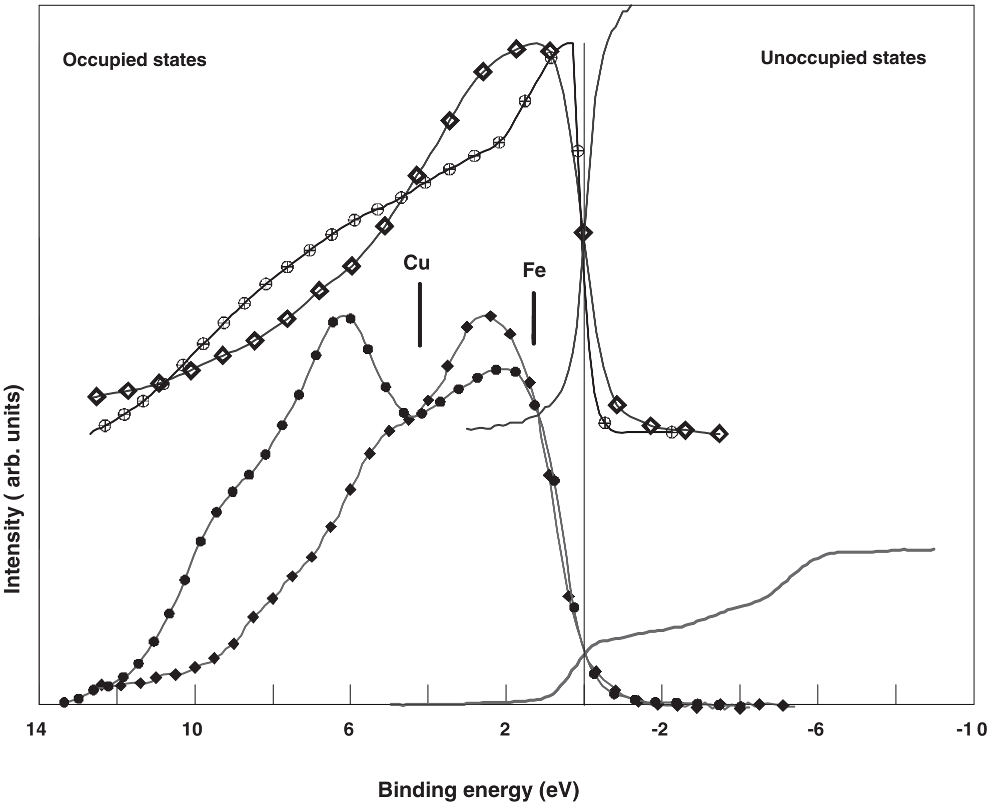

Fig. 4 Occupied Al 3p and Al 3s, d (left side of the figure) and unoccupied Al p (right side of the figure) spectral distributions in fcc Al (upper set of curves) and icosahedral Al-Cu-Fe (lower set of curves). Changes in the shapes of the spectral curves from fcc Al to the icosahedral compound emphasize that the quasicrystal is no longer a free electron system. The vertical bars show the maxima of the Cu 3d and Fe 3d distributions in the quasicrystal, respectively. Figure courtesy of E. Belin-Fer􏰀e (Paris).

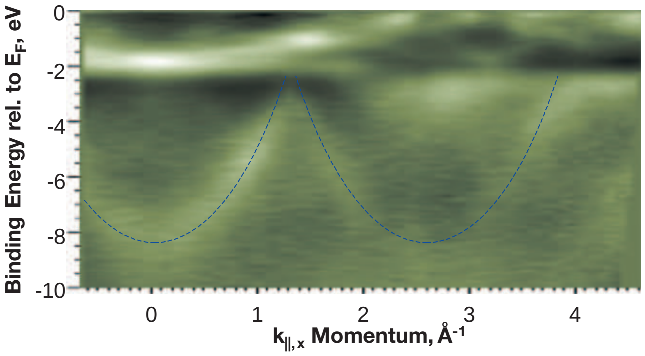

Fig. 5 Intensity plot of angle-resolved photoemission spectra for AlNiCo valence electrons for photon energy 95 eV, obtained after mapping the angle into momentum $k_{\|,}x$. The dashed line indicates the parabolic band-like character of the sp-derived states. Reproduced with permission from Rotenberg E, Theis W, Horn K, Gille P (2000) Quasicrystalline valence bands in decagonal AlNiCo. *Nature* 406: 602–605. Copyright 2000, Macmillan Magazines Ltd.

energy, as seen in Fig. 4, and thus an experimental verification of a pronounced pseudogap at the Fermi energy, in accordance with the majority of experimental results (Belin-Ferré, 2002).

However, as shown in Fig. 5, angle-resolved photoemission experiments on decagonal AlCoNi revealed free-electron-like behavior of the sp and d bands, with d bands crossing the Fermi energy (Rotenberg et al., 2000). This indicates that, even though the density of electronic states may still be very low at the Fermi energy, there might be quasi-free electronic states that can contribute to electronic transport.

While these results point to a well-defined sharp Fermi surface, previous experimental attempts to investigate the Fermi surface using the de Haas-van Alphen effect have not been very successful. There has been one published report on de Haas-van Alphen oscillations in quasicrystals, but these results have so far remained unreproduced. In other investigations, quantum oscillations have not been found. However, this does not rule out that they exist, but the effects may be small due to a rather short mean free path of the electrons.

Photoemission experiments (Chiang et al., 2019) of an oxide quasicrystal, which is not a Hume-Rothery alloy, also revealed metallic behavior.

The nature of the electronic states

From a theoretical point of view, the particular aperiodic order present in quasicrystals should affect the nature of electronic states in such systems (Sire, 1994). On the one hand, in a conventional, periodic crystal, there are extended Bloch states, and conduction electrons can move freely through an idealized perfect crystal. This allows for electronic transport, so the system is a conductor, as long as the Fermi energy lies within a band of electronic states and not in a gap. In a three-dimensional system, this property is not destroyed by weak disorder. In a strongly disordered system, on the other hand, one expects the electrons to be localized at energetically favorable positions, and the system behaves as an insulator.

In quasicrystals, apart from the periodic direction in dodecagonal, decagonal and octagonal phases, there are no extended Bloch waves due to the aperiodicity. Waves do not propagate easily, the diffusion of wave packets in neither ballistic nor diffusive (Mayou, 1994). There exists a competition between the aperiodicity, which tends to localize the electron, and the repetitivity of the structure (the same structural motives appearing over and over again), which tends to have a delocalizing effect because electrons can tunnel between identical local environments. The result is that in simple model Hamiltonians one usually observes electronic states that are neither extended over the entire system nor exponentially localized, but are so-called 'critical' states that show a multifractal probability distribution (Grimm and Schreiber, 2003). Fig. 6 shows an example of such a probability distribution which was obtained for a model of an electron moving on the Penrose tiling, which is a planar aperiodic tiling of decagonal symmetry (Repetowicz et al., 1998).

A recent investigation (Grimm and Römer, 2021) of the level-spacing statistics showed that the spectral properties can be described by the Gaussian orthogonal ensemble typical for metallic behavior, but no criticality.

For large classes of one-dimensional quasiperiodic systems, it can be shown in a mathematically rigorous way that the corresponding energy spectra have the unusual property that they contain neither a continuous part nor a point part, but are purely singular continuous (Damanik, 2000). Roughly, this means that the density of states is a fractal structure, such as a Cantor set, and the integrated density of states is a 'devil's staircase'. These rather strange spectral properties of discrete aperiodic Schrödinger operators provide another hint at the origin behind the particular behavior of quasicrystals.

However, the angle-resolved photoemission results mentioned above indicate the presence of quasi-free electronic states. The data, however, cannot rule out that these eigenstates are critical which might explain the weakness of the band-like emission observed in the quasicrystal when compared to that for periodic crystalline materials.

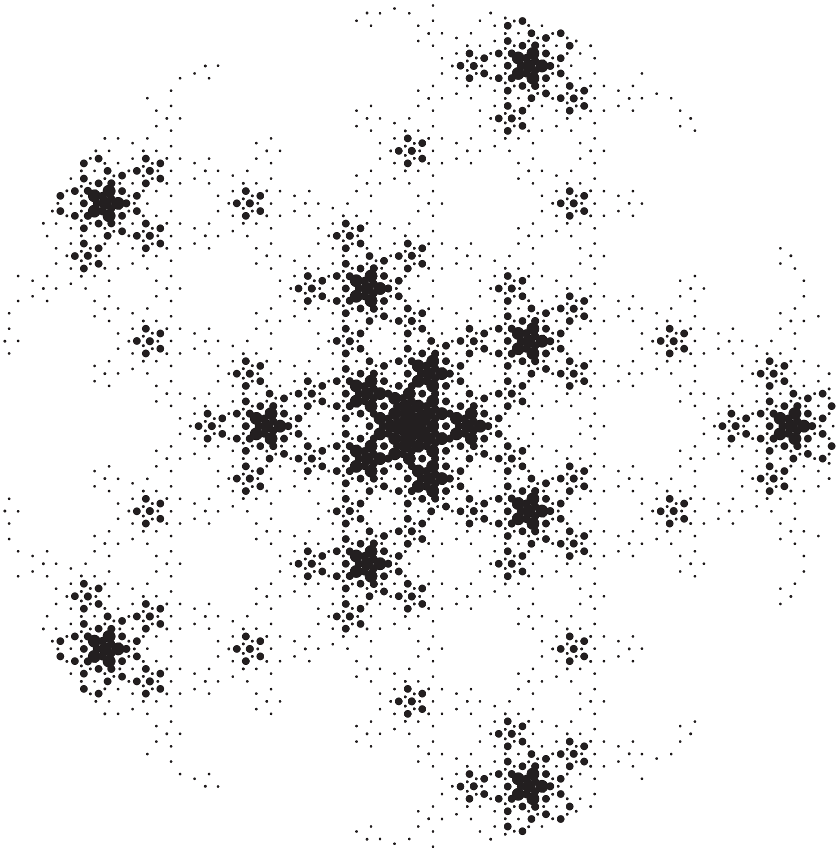

Fig. 6 Sketch of the probability distribution for a multifractal wave function of a simple tight-binding model Hamiltonian on the Penrose tiling. Reprinted with permission from Repetowicz P, Grimm U, and Schreiber, M (1998) Exact eigenstates of tight-binding Hamiltonians on the Penrose tiling. *Physical Review B* 58: 13482–13490. Copyright 1998, American Physical Society.

The role of clusters

Finally, there has been an attempt to explain the electronic properties by using a cluster-based picture of quasicrystals. This acknowledges the arguably important role of local clusters of atoms in quasicrystals. According to this approach, the quasicrystal structure is described in terms of a hierarchical sequence of clusters of atoms making up larger superclusters of clusters and so on. Such a hierarchical structure leads to a density of states that has spiky, self-similar features.

Whereas clusters are definitely important features of the local structure of quasicrystals, the assumption of a hierarchical cluster structure appears somewhat artificial, however, and leads to strange consequences, such as the presence of holes in the structure. Therefore, the validity of this approach appears limited, though it does predict an asymmetry of the density of states at the Fermi energy, which is in accordance with the experimental results.

Conclusion

The electronic structure of quasicrystals continues to be an active and controversially discussed topic of current research. While we now have a reasonable qualitative picture of some important aspects, the electronic structure is still not completely understood. Any progress is intimately linked to a better understanding of the structure formation and growth of quasicrystals, and of the theory of electronic transport in aperiodically ordered solids.

However, current experiments lead to an improved knowledge of the actual structure and the amount and type of inherent disorder, and it is conceivable that a more coherent picture of the electronic structure of these fascinating materials will emerge in the near future.

References

Barber EM (2009) *Aperiodic Structures in Condensed Matter: Fundamentals and Applications.* Boca Raton, FL: CRC Press.

Belin-Ferré E (2002) Electron densities of states in quasicrystals and approximants. In: Suck J-B, Schreiber M, and Häussler P (eds.) *Quasicrystals—An Introduction to Structure, Physical Properties, and Applications*, pp. 338–363. Berlin: Springer.

Berger C (1994) Electronic properties of quasicrystals: Experimental. In: Hippert F and Gratias D (eds.) *Lectures on Quasicrystals*, pp. 463–504. Les Ulis: Les Editions de Physique.

Chiang C-T, Ellguth M, Schumann FO, et al. (2019) Electronic band structure of a two-dimensional oxide quasicrystal. *Physical Review B* 100: 125149.
Damanik D (2000) Gordon-type arguments in the spectral theory of one-dimensional quasicrystals. In: Baake M and Moody RV (eds.) *Directions in Mathematical Quasicrystals*, pp. 277–305. Providence, RI: American Mathematical Society.
De Boissieu M (2005) Quasicrystals. In: Bassani F, Liedl GL, and Wyder P (eds.) *Encyclopedia of Condensed Matter Physics*, pp. 86–95. Amsterdam: Elsevier.
Fournee V, Belin-Ferré E, Pecheur P, et al. (2002) Electronic structure of Al-Pd-Mn crystalline and quasicrystalline alloys. *Journal of Physics: Condensed Matter* 14: 87–102.
Goldman AI, Kong T, Kreyssig A, et al. (2013) A family of binary magnetic icosahedral quasicrystals based on rare earths and cadmium. *Nature Materials* 12: 714–718.
Grimm U (2015) Aperiodic crystals and beyond. *Acta Crystallographica* B71: 258–274.
Grimm U and Römer RA (2021) Gaussian orthogonal ensemble for quasiperiodic tilings without unfolding: R-value statistics. *Physical Review B* 104: L060201.
Grimm U and Scheffer M (2001) Incommensurate crystals and quasicrystals. In: Meyers RA (ed.) *Encyclopedia of Physical Science and Technology*. 3rd edn, vol. 7, pp. 731–750. San Diego: Academic Press.
Grimm U and Schreiber M (2003) Energy spectra and eigenstates of quasiperiodic tight-binding Hamiltonians. In: Trebin H-R (ed.) *Quasicrystals—Structure and Physical Properties*, pp. 210–235. Weinheim: Wiley-VCH.
Haberkern R (2002) Electronic transport properties of quasicrystalline thin films. In: Suck J-B, Schreiber M, and Häussler P (eds.) *Quasicrystals—An Introduction to Structure, Physical Properties, and Applications*, pp. 364–378. Berlin: Springer.
Häussler P, Barzola-Quiquia J, Haberkern R, et al. (2003) On fundamental structure forming processes—Disordered and quasicrystalline systems. In: Trebin H-R (ed.) *Quasicrystals—Structure and Physical Properties*, pp. 289–310. Weinheim: Wiley-VCH.
Hiroto T, Gebresenbut GH, Pay Gómez C, et al. (2013) Ferromagnetism and re-entrant spin-glass transition in quasicrystal approximants Au–SM–Gd (SM = Si, Ge). *Journal of Physics: Condensed Matter* 25: 426004.
Kim MG, Beutier G, Kreyssig A, et al. (2012) Antiferromagnetic order in the quasicrystal approximant Cd_6Tb studied by x-ray resonant magnetic scattering. *Physical Review B* 85: 134442.
Kong T, Bud'ko SL, Jesche A, et al. (2014) Magnetic and transport properties of i–R–Cd icosahedral quasicrystals (R = Y, Gd–Tm). *Physical Review B* 90: 014424.
Krajčí M and Hafner J (2002) Phonons and electrons in quasicrystals. In: Suck J-B, Schreiber M, and Häussler P (eds.) *Quasicrystals—An Introduction to Structure, Physical Properties, and Applications*, pp. 393–420. Berlin: Springer.
Mayou D (1994) Introduction to the theory of electronic properties of quasicrystals. In: Hippert F and Gratias D (eds.) *Lectures on Quasicrystals*, pp. 417–462. Les Ulis: Les Editions de Physique.
Mizutani U (2011) *Hume–Rothery Rules for Structurally Complex Alloy Phases*. Boca Raton, FL: CRC Press.
Papadopolos Z, Kasner G, Diehl RD, et al. (2002) Bulk termination of the quasicrystalline five-fold surface of $Al_{70}Pd_{21}Mn_9$. *Physical Review B* 66(184207): 1–13.
Poon SJ (1992) Electronic properties of quasicrystals: An experimental review. *Advances in Physics* 41: 303–363.
Repetowicz P, Grimm U, and Schreiber M (1998) Exact eigenstates of tight-binding Hamiltonians on the Penrose tiling. *Physical Review B* 58: 13482–13490.
Rotenberg E, Theis W, Horn K, and Gille P (2000) Quasicrystalline valence bands in decagonal AlNiCo. *Nature* 406: 602–605.
Shechtman D, Blech I, Gratias D, and Cahn JW (1984) Metallic phase with long-range orientational order and no translational symmetry. *Physical Review Letters* 53: 1951–1953.
Sire C (1994) Properties of quasiperiodic Hamiltonians: Spectra, wavefunctions and transport. In: Hippert F and Gratias D (eds.) *Lectures on Quasicrystals*, pp. 505–533. Les Ulis: Les Editions de Physique.
Solbrig H and Landauro CV (2003) Electronic transport parameters and spectral fine structure: From approximants to quasicrystals. In: Trebin H-R (ed.) *Quasicrystals—Structure and Physical Properties*, pp. 254–271. Weinheim: Wiley-VCH.

Further reading

Baake M and Grimm U (2013) *Aperiodic Order. Volume 1: A Mathematical Invitation*. Cambridge: Cambridge University Press.
Dubois J-M (2005) *Useful Quasicrystals*. Singapore: World Scientific.
Kellendonk J, Lenz D, and Savinien J (eds.) (2015) *Mathematics of Aperiodic Order*. Basel: Birkhäuser.
Stadnik ZM (ed.) (1999) *Physical Properties of Quasicrystals*. Berlin: Springer.
Steurer W and Deloudi S (2009) *Crystallography of Quasicrystals: Concepts, Methods and Structures*. Berlin: Springer.
Thiel PA (ed.) (2011) *Quasicrystals*, In: *Special Issue Israel Journal of Chemistry* 51: 1133–1354.

Vibrational excitations in disordered solids

Walter Schirmacher[a,b] **and Giancarlo Ruocco**[b,c], [a]Institut für Physik, Universität Mainz, Mainz, Germany; [b]Center for Life Nano Science @Sapienza, Istituto Italiano di Tecnologia, Roma, Italy; [c]Dipartimento di Fisica, Universita' di Roma "La Sapienza", Roma, Italy

© 2024 Elsevier Ltd. All rights reserved.

Introduction **298**
Density of states (DOS) 299
The boson peak 299
Models and suggestions for explaining the BP anomalies **301**
Experimental investigations **305**
Specific heat and thermal conductivity 305
Spectroscopic methods 306
Early investigations 306
Inelastic Neutron and Raman scattering 307
Nuclear inelastic scattering 308
Inelastic X-ray scattering 309
Simulations **312**
Discussion **314**
References **315**

Abstract

The vibrational excitations of disordered solids differ appreciably from those of crystals. The reason for this anomalous behavior can be traced to the absence of the lattice symmetry, i.e., to the structural disorder. We review the experimental findings and simulational results of the vibrational spectrum of disordered solids, in particular of glasses. We further give an overview of the existent pertinent models and theoretical treatments for explaining the vibrational anomalies, in particular the enhancement of the vibrational density of states with respect to the Debye law ("boson peak").

Key points

- Glasses, and in general disordered materials, are defined by the lack of long range structural order that gives rise to a complex phenomenology in their vibrational properties.
- The thermal motion of atoms and molecules in glasses cannot be simply described in terms of the wave-like oscillations known to solid-state physicists as phonons.
- From a macroscopic point of view, this complexity is reflected in anomalies that appear in the thermal and transport properties of glasses as well as in their density of states, all of which distinguish amorphous materials from their crystalline counterparts.
- Aims of the present chapter are
  - presenting the macroscopic phenomenology peculiar of the glassy materials;
  - summarize the main techniques for the microscopic determination of the vibrational properties in disordered materials;
  - discuss the main theories capable of explain the experimental findings.

Introduction

The vibrational excitations of disordered solids, in particular of glasses, have attracted the attention of experimental (Baldi et al., 2011; Buchenau et al., 1984, 1986; Chumakov et al., 2004; Foret et al., 1997; Leadbetter, 1969; Monaco and Giordano, 2009; Pan et al., 2021; Sette et al., 1998; Wuttke et al., 1995; Zeller and Pohl, 1971) and theoretical work (Buchenau et al., 1991; Derlet et al., 2012; Franz et al., 2015; Ganter and Schirmacher, 2010; Götze and Mayr, 1999; Gurevich et al., 2003; Jäckle, 1981; Karpov et al., 1983; Laird and Schober, 1991; Léonforte et al., 2006; Marruzzo et al., 2013a; Maurer and Schirmacher, 2004; Mayr, 2009; Mizuno et al., 2013a; Monaco and Mossa, 2009; Parisi, 2003; Schirmacher, 2006; Schirmacher et al., 1998, 2007; Schirmacher and Ruocco, 2022; Shintani and Tanaka, 2008) (to cite only a few at the beginning) in the last three-quarter century. In crystals the

https://doi.org/10.1016/B978-0-323-90800-9.00166-9

harmonic vibrational excitations – the phonons – can be satisfactorily described by the symmetry properties of the lattice (Ashcroft and Mermin, 1976). In modern crystalline-lattice dynamics investigations (Monacelli and Mauri, 2021), therefore, the emphasis is on anharmonic effects. On the other hand, in disordered solids, due to the absence of the lattice symmetries, even the theoretical descriptions of the harmonic vibrational excitations poses a challenge. Scientific efforts facing this challenge are still a very active part of condensed-matter research.

Density of states (DOS)

In a solid the harmonic part of the potential energy, i.e. the part, which is bilinear in the displacements $\mathbf{u}_i(\mathbf{r}, t)$ (where i denotes the center of mass of a molecule) can be written as $E_{pot} = \sum_{ij} \frac{1}{2} \mathbf{u}_i \overleftrightarrow{D}_{ij} \mathbf{u}_j$ with the dynamical (or Hessian) matrix

$$D_{ij}^{\alpha\beta} = \frac{\partial}{\partial r_i^{\alpha}} \frac{\partial}{\partial r_j^{\beta}} E_{pot}(\mathbf{r}_1, \ldots, \ \mathbf{r}_N). \tag{1}$$

The DOS is then given by

$$g(\omega) = \frac{1}{3N} \left\langle \sum_{\mu=1}^{3N} \delta(\omega - \omega_\mu) \right\rangle, \tag{2}$$

where the eigenfrequencies ω_μ are the square-roots of the eigenvalues $\lambda_\mu = \omega_\mu^2$ of the dynamical matrix, and N is the number of atoms/molecules.

We have started our review of vibrational excitations in disordered solids by introducing the dynamical matrix and the corresponding DOS, because this concept remains valid going from crystalline to amorphous solids. Concepts like Bloch's theorem, leading to dispersion relations in reciprocal space are not valid in the absence of crystalline order, but the DOS, the normalized histogram of eigenfrequencies, can be considered for any type of arrangements of the atomic or molecular sites $\mathbf{r}_i$. This is the reason, why most of the experimental and simulational efforts dedicated to the vibrational spectra of glasses[1] are aimed at finding out the DOS, i.e. the vibrational spectrum of the material.

The boson peak

A paradigm for the anomalous vibrational features of glasses is the so-called boson peak (BP), which is an enhancement of the DOS with respect to Debye'$g(\omega) \propto \omega^2$ law. The latter transforms to a T^3 law for the temperature dependence of the specific heat $C(T)$ (Ashcroft and Mermin, 1976). In contrast to Debye's $C(T) \propto T^3$ prediction, in glasses at low temperatures, $C(T)$ behaves completely in a different way. At very low temperatures, in the range around ~ 1 K, $C(T)$ varies almost linearly with temperature (Lasjaunias et al., 1975; Zeller and Pohl, 1971), and the thermal conductivity (which is orders of magnitude smaller than that of crystals) quadratically (Beekman and Cahill, 2017; Cahill and Pohl, 1989; Lasjaunias et al., 1975; Zeller and Pohl, 1971). This behavior has been successfully ascribed to bistable states in the amorphous structure, between which quantum-mechanical tunneling becomes possible (tunneling states, two-level systems (Anderson et al., 1972; Phillips, 1972, 1987; Yu and Leggett, 1988)). At slightly higher temperatures, the specific heat of glasses still does not follow Debye's T^3 law. If plotted as $C_V(T)/T^3$ one observes a broad maximum around 10 K, see the upper panel of Fig. 1. In the same temperature regime, the temperature variation of the thermal conductivity exhibits a pronounced shoulder, as is shown in the lower panel of Fig. 1. It seems likely that this deviation from Debye's $C(T) \propto T^3$ law must be due to a deviation of Debye's $g(\omega) \propto \omega^2$ law for the DOS. Indeed, in Raman spectra, which – in some way (see below) – represent the DOS, a broad continuum in the ~ 50 cm^{-1} ($\widehat{=}$ 1.3 THz) range[2] was found, in a frequency region, where there is no intensity in the corresponding crystal, see Fig. 2. It was further found that the anomalous Raman spectrum of glasses in the frequency range below 100 cm^{-1} precisely follows the temperature dependence of the boson occupation factor $n(\omega) + 1 = [1 - e^{-\hbar\omega/k_B T}]^{-1}$. For this reason the low-frequency spectral anomaly in the 1 THz range was called "boson peak" (Jäckle, 1981). Shuker and Gammon (1970) argued, that in disordered solids the selection rules for Raman scattering (Berne and Pecora, 2005) do not apply and came up with a formula for the (depolarized = VH) Raman spectrum.

$$I_{VH}(\omega) \propto C(\omega)[n(\omega) + 1] \frac{g(\omega)}{\omega}. \tag{3}$$

Here $C(\omega)$ is the so-called light-vibration coupling coefficient (Jäckle, 1981; Schmid and Schirmacher, 2008, 2009; Viliani et al., 1995; Mazzacurati et al., 1992), which Shuker and Gammon (1970) assumed to be frequency-independent. Now, if the temperature dependence of the Raman intensity is due to the boson occupation factor, the conclusion is that the spectrum $g(\omega)/\omega$ must be *temperature independent*, and that, consequently, the BP anomaly in the DOS must be a *harmonic* effect. This means that the boson peak must be a feature of the harmonic degrees of freedom.[3]

---

[1] We take "glasses" and "amorphous solids" as synonyms, independent of the preparation process.

[2] The Raman intensity is usually reported as a function of $\nu/c = \omega/2\pi c$, which has the unit of an inverse length. 32 cm^{-1} (in the Raman slang "32 wavenumbers") correspond to $\nu = 1$ THz and to $h\nu = \hbar\omega = 4$ meV.

[3] Recent theoretical efforts, claiming that the BP anomaly would be of anharmonic origin (Baggioli and Zaccone, 2019), turned out to be mathematically in error (Shvaika et al., 2021).

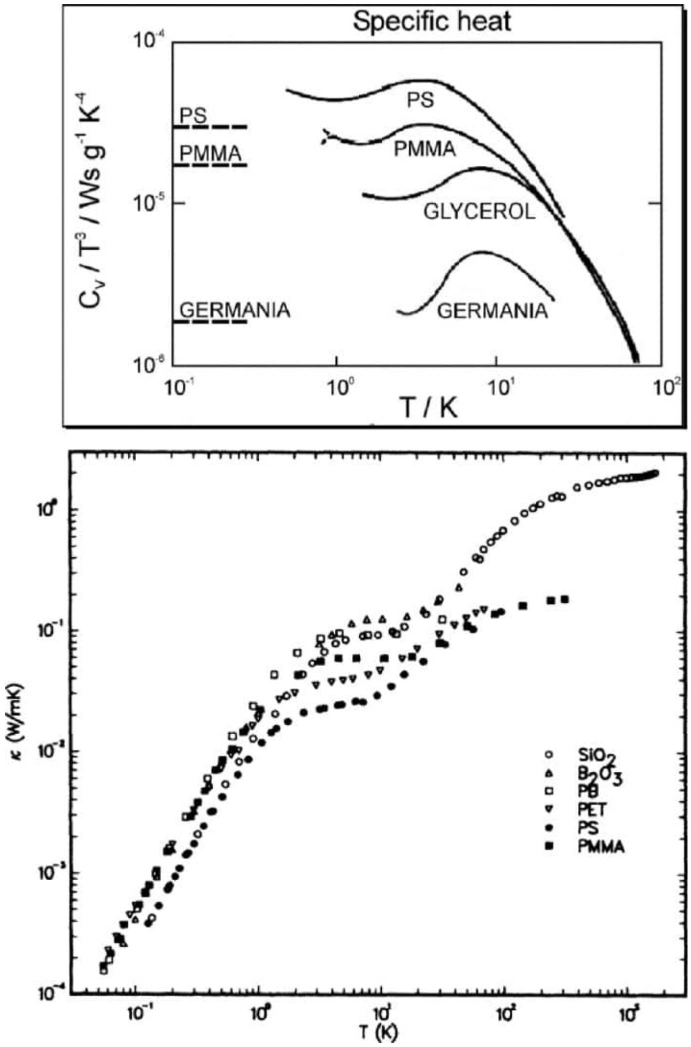

Fig. 1 Top: Specific heat, divided by T^3 of several materials against temperature T. Bottom: Thermal conductivity of several glassy materials against temperature. Note that, compared to glassy SiO_2, at $T = 10$ K, the thermal conductivity of α-quartz is 4 orders of magnitude larger (Beekman and Cahill, 2017; Cahill and Pohl, 1989). Top: From Yu CC and Leggett AJ (1988) *Comm. Condens. Matter Phys.* 14: 231. Bottom: From Freeman JJ and Anderson AC (1986) *Phys. Rev. B* 34: 5684.

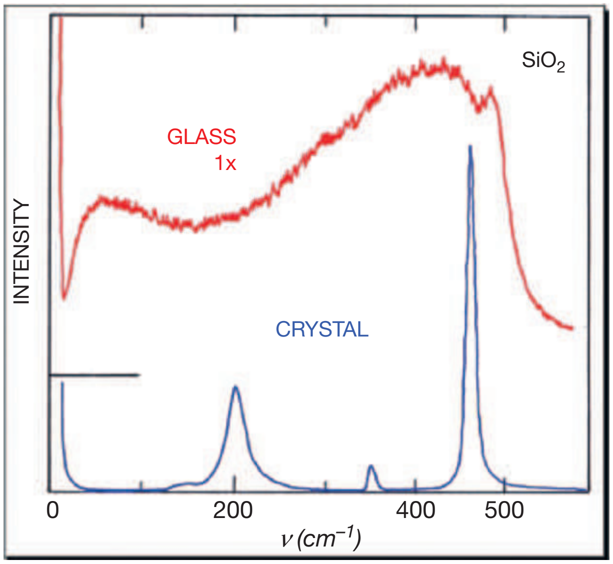

Fig. 2 Raman spectrum of glassy and crystalline SiO_2. From Shuker R and Gammon R (1970) *Phys. Rev. Lett.* 25: 222.

Further, in a seminal paper Buchenau et al. (1984), using inelastic neutron scattering, showed a strong deviation of the DOS of SiO_2 glass from the ω^2 law, which, if represented as $g(\omega)/\omega^2$ shows up as a maximum. They identified this with the Raman boson peak, although the Raman (would-be) DOS did not agree to that extracted from the neutron spectra. In order to cope with this discrepancy, one introduced the frequency dependence of the coefficient $C(\omega)$ (Jäckle, 1981; Schmid and Schirmacher, 2008, 2009; Viliani et al., 1995; Mazzacurati et al., 1992), into the Shuker-Gammon formula (3). Because the deviation of the specific heat of glasses from the T^3 law is due to the boson peak in the DOS, the maximum in the temperature variation of $C(T)/T^3$ of glasses is also called boson peak (Ramos, 2020).

The boson peak and related vibrational anomalies are observed in most glassy or disordered materials, and almost the entire scientific work on vibrational excitations in glasses has been devoted to uncover the nature of the (harmonic) vibrational wave functions associated with the BP. The present review simply cannot cover the overwhelmingly large amount of literature published on this subject. We just select some key results, indicating in some way or another the origin of the anomaly. In fact, as we shall state in the conclusion, the matter is still highly controversial.

We start (section "Models and suggestions for explaining the BP anomalies") by enumerating (most of) the suggestions put forward in the past for explaining the boson peak. In sections "Experimental investigations" and "Simulations." we try to give an overview over the vast amount of experimental and simulational work on the present topic. In the final section "Discussion." we discuss the present status of the interpretation of the boson-peak-related vibrational anomalies of glasses.

Models and suggestions for explaining the BP anomalies

In contrast to the rather convincing explanation of the linear-T behavior of the specific heat and the T^2 behavior of the thermal conductivity in the ~ 1 K range in terms of bistable tunneling defects (Anderson et al., 1972; Phillips, 1972) the boson peak (BP) was from the beginning subject to rather diverse modelling, which continues until now. We here give a brief historical overview and refer to the quoted original literature for more details.

- Karpov, Klinger and Ignat'ev (Karpov et al., 1983) tried to formulate a classical version of the tunneling model, the soft-potential model. This model features a set of structural defects with anharmonic potentials with very small positive and negative quadratic (stiffness) terms. The (renormalized) density of states of such defects can be shown (Buchenau et al., 1991, 1992; Gurarie and Chalker, 2003; Gurevich et al., 2005; Karpov et al., 1983) to vary as ω^4, due to a swallow-tail singularity in the classification of catastrophe theory (Arnold, 1992; Thom, 1989).
- Orbach (Orbach, 1986) conjectured that glasses (in particular network glasses) might exhibit a self-similar (fractal) structure. Such structures, imbedded in a homogeneous medium at larger scales were known to exhibit a transition from a Debye-type spectrum $g(\omega) \propto \omega^2$ waves (phonons) at low frequencies (large wavelengths) to fractal-type behavior $g(\omega) \propto \omega^{1/3}$ at higher frequencies ("phonon-fracton crossover," Alexander and Orbach, 1982; Nakayama et al., 1994). Simulations of percolating networks, which are examples of such imbedded fractal structures (Nakayama et al., 1994; Yakubo and Nakayama, 1989) indeed showed such a crossover, but, unfortunately, no boson-peak-type enhancement. Furthermore, no traces of self-similar structure were found experimentally in glasses, except in loose structures such as aerogels (Vacher et al., 2007) or biopolymers (Mori et al., 2020).
- According to an argument of Ioffe and Regel (Ioffe and Regel, 1960), (electronic) waves with a scattering mean-free path ℓ smaller than its wavelength cannot exist. This lead Mott (Mott, 1990) to the conclusion that waves in the presence of disorder, which would produce an attenuation with a mean-free path shorter than the wavelength, become localized by disorder (Anderson-localization, (Abrahams et al., 1979; Anderson, 1958)). This argument was taken over in papers discussing BP-related anomalies (Akkermans and Maynard, 1985; Elliott, 1992; Foret et al., 1996; Graebner et al., 1986), in which it was conjectured that the anomalies are due to phonon localization (John et al., 1983; Kirkpatrick, 1985).
- A step forward in the understanding of the BP anomalies was the investigation of disordered-force constant models by making contact with hopping transport in disordered systems. It was noted by Alexander et al. (1981) that the excitation dynamics of a harmonic system of masses m connected with force constants K_{ij}, which obeys an equation of motion

$$m\frac{d^2}{dt^2}u_i = -\sum_j K_{ij}(u_i - u_j) \tag{4}$$

with scalar "displacements" $u_i = u(\mathbf{r}_i)$ can be mapped to a disordered random-walk (hopping) problem by replacing the double time derivative with a single one. Schirmacher and Wagener (1989) noted that the cross-over of the AC conductivity $\sigma(\omega)$ from being frequency-independent to a strong disorder-induced frequency dependence (Dyre and Schrøder, 2000) corresponds in the analogous harmonic force constant system to a cross-over from a frequency independent to a frequency dependent (squared) sound velocity (elastic constant). They realized that this crossover produces a boson peak and corroborated it with calculations by the coherent-potential approximation (CPA) (Schirmacher and Wagener, 1992, 1993). Using the self-consistent localization theory (Economou et al., 1984; Vollhardt and Wölfle, 1980), Schirmacher and Wagener (1993) predicted phonon Anderson localization to happen much above the boson peak, near the upper band edge.

- A pathfinding paper on the boson-peak anomaly was published 1992 by S. R. Elliott (Elliott, 1992). He argued that in an amorphous structure there exists a length scale at which the atomic structure is no more distinct. This length scale is the

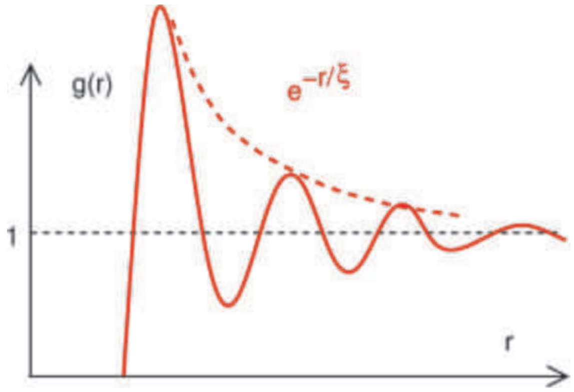

Fig. 3 Sketch of a typical radial distribution function $g(r)$ of an amorphous (monatomic) structure, which approaches the decorrelated value $g(r) \to 1$.

correlation length and describes the decay of the radial distribution function[4] $g(r)$ toward its decorrelated value 1 (s. Fig. 3). On a scale larger than ξ the material looks homogeneous and isotropic, therefore, so the argument of Elliott, waves with wavelength λ larger than ξ can be supported by the material. Waves with smaller λ become rather strongly scattered, and, with increasing frequency, the vibrational excitation loses gradually its wave character, as formulated by Ioffe and Regel (1960). Converting length scales to frequency scales by the transverse velocity v_T, which is roughly equal to the Debye velocity $v_D = \omega_D/k_D$ (Debye frequency ω_D, divided by the Debye wavenumber $k_D = \sqrt[3]{6\pi^2 N/V} = \sqrt[3]{6\pi^2}/a$, where a is an intermolecular spacing) Elliott (1992) conjectured that the frequency at which disorder-induced deviations from the Debye wave physics should occur near $\omega_B = v_T/\xi \sim \omega_D a/\xi$, i.e. roughly 1/10 of the Debye frequency. This is precisely the frequency range of ~1 THz, around which the boson peak is observed in most materials (Pan et al., 2021). A correlation between the boson-peak position and v_T/ξ is indeed observed in many glasses (Duval et al., 1990a; Elliott, 1992; Pan et al., 2021).

- In a model calculation on a 3-dimensional lattice with randomly distribution of force constants Schirmacher et al. (1998) considered a mass-spring system of the type (4) on a simple-cubic lattice with Gaussian force-constant disorder, truncated from below. The model was treated both by CPA and by numerical diagonalization. In Fig. 4 we show their result for the reduced DOS $g(\omega)/\omega^2$. First, the agreement of the CPA with the numerical data showed that the CPA is a reliable mean-field theory for disorder. In both calculations a pronounced BP is visible (Fig. 4). The inclusion of negative force constants demonstrated that the BP is strongly enhanced by the presence of negative force constants and is a precursor of an instability, which occurs in the presence of too many negative force constants. The authors further evaluated the mean-free path $\ell(\omega)$, and found by comparison with the wavelength $\lambda(\omega)$ that the BP position is near the Ioffe-Regel limit, where $\ell(\omega) \sim \lambda(\omega)$. The authors also evaluated the level-distance statistics of the eigenvalues and demonstrated that the vibrational states near and above the BP are *delocalized*, because the statistics follows that of the Gaussian Orthogonal Ensemble (GOU) of random matrices (Mehta, 1991; Stöckmann, 1999). A mobility edge, above which the states are localized, appears only very near the upper end of the band, thus corroborating the predictions of Schirmacher and Wagener (1993). It was proved later in numerical investigations of a similar force-constant model (Pinski et al., 2012a, b) that these states obey the Porter-Thomas statistics (Porter, 1965), i.e., are of the same type as random-matrix eigenstates.

- That in a disordered harmonic system an extended frequency region exists, in which the vibrational states are neither propagating nor localized had already been found by Allen et al. (Allen and Feldman, 1993; Allen et al., 1999; Feldman et al., 1993) in a simulation of amorphous Si. Allen et al. (1999) called the corresponding excitations "diffusons," because the intensity of such waves obey a diffusion equation like light in milky glass (Ishimaru, 1978). They called the Debye waves below the Ioffe-Regel crossover "propagons" and the localized states near the Debye frequency "locons." They deliberately avoided the term "phonons," because phonons are by definition the eigenstates of a crystal.
- A model calculation similar to that of Schirmacher et al. (1998) (a crystal with force-constant disorder) was presented later by Taraskin et al. (2002), but with a somewhat different interpretation. They observed - similar to the findings in (Schirmacher et al., 1998) that - with increasing disorder - the lowest van-Hove singularity[5] of the lattice broadens, moves down in frequency, and then smoothly goes over to the low-frequency BP. They concluded that the BP is essentially due to the leveling off of the transverse phonon branch and not so much due to disorder. This view was corroborated later by experimentalists who compared silicate glassses with their crystalline counterparts (Chumakov et al., 2011, 2014; Zorn, 2011) (see below).

- Grigera et al. (2003) investigated a disordered mass-spring model (Euclidean random-matrix model, ERM) by a diagrammatic procedure. Inspired by the behavior of a mean-field theory obtained from a class of diagrams, they obtained a BP-type anomaly,

---

[4] $g(r) - 1$ is the Fourier transform of the structure factor $S(k)$ minus 1 (Elliott, 1984; Hansen and McDonald, 1986) of the amorphous material, which can be measured by elastic X-ray or neutron diffraction. $4\pi r^2 g(r) N/V$ (particle number N volume V) gives the probability density for the presence of other atoms/molecules with distance r from a given one at the origin.

[5] A Van-Hove singularity occurs in the DOS of a crystal at a frequency, at which the phonon dispersion $\omega(k)$ becomes constant at the Brillouin-zone boundary.

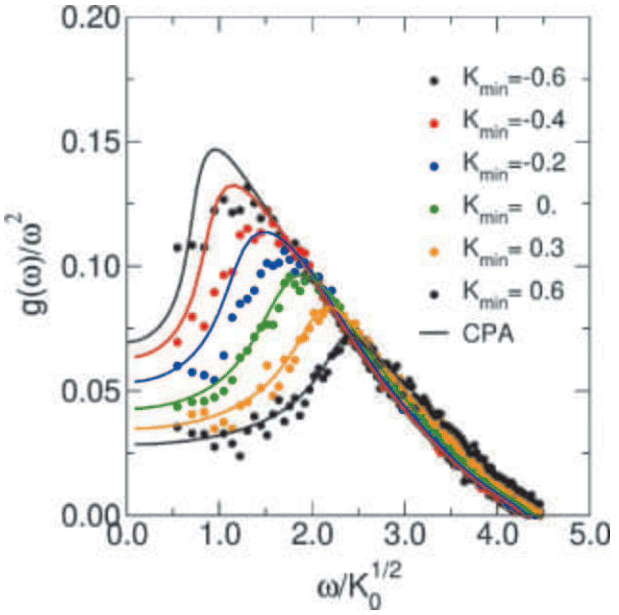

Fig. 4 Reduced DOS $g(\omega)/\omega^2$ 2 versus frequency for Gaussian force-constant distributions with $\sigma/K_0 = 1$ and several lower cutoffs (in units of K_0). The symbols represent the numerical diagonalization, the full lines the CPA results. The agreement is achieved without any adjustable parameters. From Schirmacher W, Diezemann G, and Ganter C (1998) *Phys. Rev. Lett.* 81: 136.

which – with increasing disorder – leads to an instability like the CPA of Schirmacher et al. (1998) with too many negative force constants. This instability was interpreted as a transition from a minima-dominated potential-energy surface (PES) to a saddle-dominated PES. The ERM model was shown to imply Rayleigh scattering, i.e. a sound attenuation $\Gamma(\omega) \propto \omega^4$ (Ganter and Schirmacher, 2010; Grigera et al., 2011; Schirmacher et al., 2019), in agreement to the disordered-lattice calculations (Schirmacher et al., 1998; Taraskin et al., 2002) and the HET theory (see below).

- Schirmacher (2006) formulated a heterogeneous-elasticity theory (HET), which is a theory of elasticity, in which the shear modulus G exhibits spatial fluctuations. This theory was solved for the averaged DOS by field-theoretical techniques for a mean-field theory (Self-consistent Born approximation, SCBA), which predicts.
  - a disorder-induced boson peak independent of an underlying lattice;
  - a disorder-induced Rayleigh-like sound attenuation $\Gamma(\omega) \propto \omega^4$;.
  - a minimum of the transverse phase velocity $v_T(\omega)$ near the BP. This theory conforms with the previous conclusions that the BP is a phenomenon produced by the structural disorder of the glass. Within the same theoretical framework a theory for the thermal diffusivity was formulated. Combined with the inelastic scattering from two-level system, he found an explanation for the characteristic shoulder in the temperature dependence of the thermal conductivity: It is an *upside-down boson peak* (see Fig. 5).

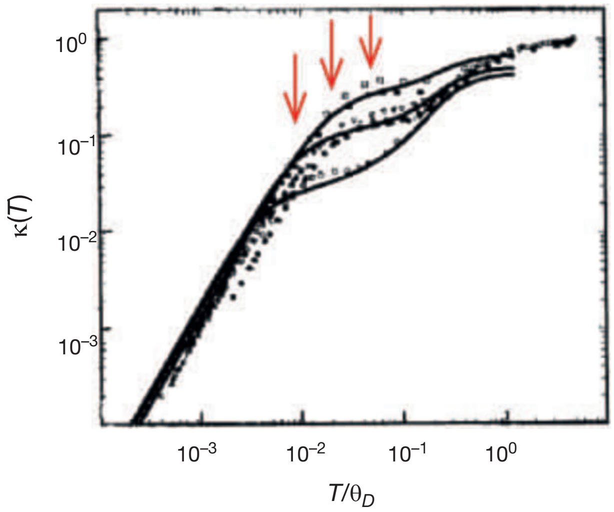

Fig. 5 Thermal conductivity calculated in self-consistent Born approximation (SCBA) (Schirmacher, 2006) for three values of the disorder parameter $\gamma \propto \langle(\Delta G)^2\rangle$, compared with the data of Fig. 1 (Freeman and Anderson, 1986), scaled with the Debye temperature Θ_D. The red arrows correspond both to the boson peak positions of the specific heat, calculated in SCBA as those of the experiments. From Schirmacher W (2006) *Europhys. Lett.* 73: 892.

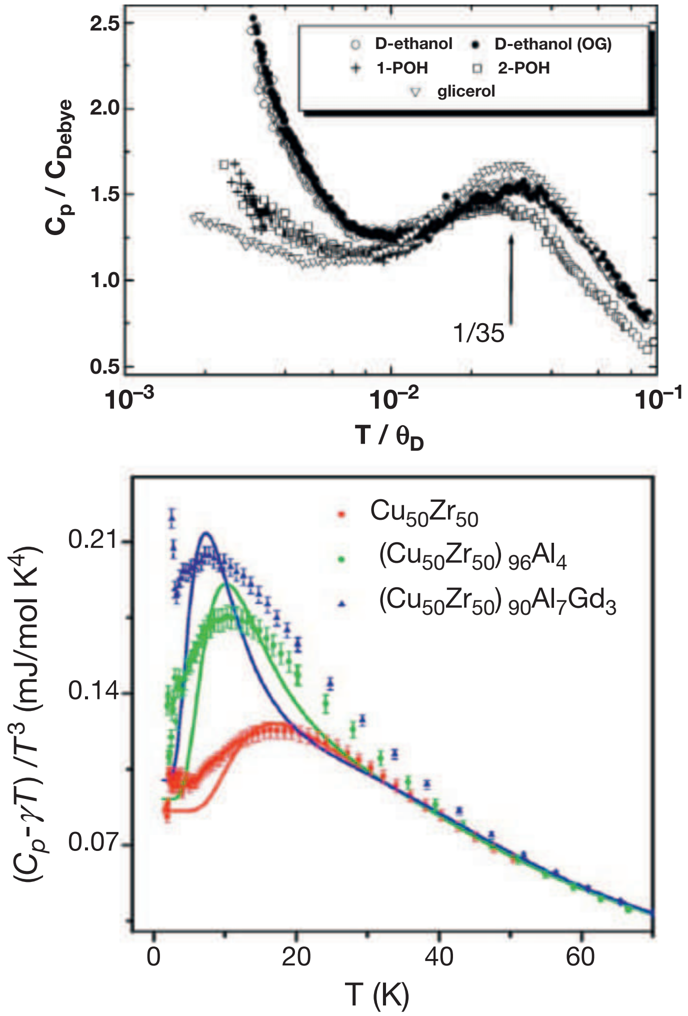

Fig. 6 Top: $C(T)/C_D(T) \propto C(T)/T^3$ against T/Θ_D for four different (glassy) alcohols, compared with glassy glycerol. Bottom: $[C(T)-\gamma T]/T^3$ for three metallic glasses. γT is the Sommerfeld contribution of the electrons. Top: From Ramos MA, Talón C, and Vieira S (2002) *J. Non-Cryst. Sol.* 307: 80. Bottom: From Li Y, Bai HY, Wang WH, and Samwer K (2006) *Phys. Rev. B* 74: 052201.

The anomalous increase of the DOS above the Debye DOS was subsequently shown (Schirmacher et al., 2007) to be related to the Rayleigh ω^4 behavior of the sound attenuation: It was shown that the excess DOS is just proportional to the sound attenuation $\Gamma(\omega)$.

The SCBA version of HET, which only applies to Gaussian distributions of elastic moduli and moderate disorder was generalized by means of an off-lattice version of the CPA, again by field-theoretical techniques (Köhler et al., 2013). This version served recently to obtain a disorder classification of glasses (Pan et al., 2021) (Fig. 6).

- An important aspect in the discussion about the boson peak has been contributed by the theoretical investigation of the jamming transition (DeGiuli et al., 2014a, b; Franz et al., 2015; Liu et al., 2011; O'Hern et al., 2003; Wyart, 2005, 2010, 2012; Wyart et al., 2005). The disordered solid is considered as a random packing of soft spheres with a finite range of interactions. The latter induce a number of constraints, which lead to a finite shear elasticity. The instability of the solid – where the shear stiffness becomes zero – is reached at the isostatic point, where the number of constraints equal the number of degrees of freedom (Maxwell, 1864). It was shown by simulations and effective-medium calculations that in such random packings near the jamming instability a boson peak appears in the vibrational spectrum. This was rationalized by a rather simple mean-field jamming model, the so-called perceptron (Franz and Parisi, 2016; Franz et al., 2015), which was introduced in connection with neural networks. The generic frequency dependence in the mean-field limit (dimension $d \to \infty$) is given by a modification of the Marchenko-Pastur law of rectangular random matrices (Marchenko and Pastur, 1967)

$$g(\omega) \propto \omega \frac{\sqrt{\left(\omega^2 - \omega_0^2\right)\left(\omega_{\max}^2 - \omega^2\right)}}{\omega^2 + \omega_*^2}. \tag{5}$$

In finite dimensions the gap below ω_0 is filled with Debye-type waves, so that one has in general (DeGiuli et al., 2014a; Franz et al., 2015)

$$g(\omega) \propto \begin{cases} \omega^{d-1} & \omega \ll \omega_0 \\ \omega^2/\omega_0^2 & \omega_0 \ll \omega \ll \omega_* \\ \text{const.} & \omega_* \ll \omega \ll \omega_{\max}. \end{cases} \tag{6}$$

The resulting boson peak at ω_0 marks – as in the heterogeneous-elasticity theory – the crossover between the Debye wave regime and the random-matrix regime. The eigenvectors of random matrices (Mehta, 1991) are known to be delocalized.

Experimental investigations

Specific heat and thermal conductivity

The specific-heat BP, i.e. a maximum in the temperature variation of $C(T)/T^3$, see the top panel of Fig. 1, is observed in practically all glassy materials. As further examples we display in Fig. 6 boson peaks of a number of alcohols (Ramos et al., 2002) and metallic glasses (Li et al., 2006). In the latter the Sommerfeld contribution due to the free electrons γT, with $\gamma = \frac{1}{3}\pi^2 k_B^2 N(E_F)$ ($N(E_F)$ is the electronic DOS at the Fermi level), must be subtracted, in order to obtain the vibrational contribution. It is interesting to note that in many cases the BP temperature $T_{\max}$ is proportional to the Debye temperature Θ_D.

We mentioned in the introduction (bottom panel of Fig. 1), that in the temperature variation of the thermal conductivity a characteristic shoulder (plateau) is observed near $T_{\max}$. Similar features are observed in other complex solids like oriental glasses (Yoreo et al., 1986), and other disordered crystalline materials (Ackerman et al., 1981; Avila et al., 2006; Cohn et al., 1999; Suekuni et al., 2015; Tachibana, 2015; Tachibana et al., 2008). In all cases the temperature in the middle of the plateau of the thermal conductivity coincides with $T_{\max}$ of the boson peak (Krivchikov and Jeżowski, 2020), as displayed in Fig. 7, where thermal-conductivity data are displayed with a temperature scale normalized with $T_{\max}$.

As mentioned also in the introduction, there is a correspondence between of the vibrational part of the specific heat and the vibrational DOS $g(\omega)$. This relationship is given by (Ashcroft and Mermin, 1976)

$$C(T) = \frac{\hbar^2\omega^2}{k_B T^2}\int_0^\infty d\omega g(\omega)\frac{e^{\hbar\omega/k_B T}}{\left[e^{\hbar\omega/k_B T} - 1\right]^2}. \tag{7}$$

Buchenau et al. (1986) showed for the example of glassy SiO_2, by comparing with inelastic neutron-scattering data, that the DOS obtaining from the neutrons reproduces the temperature variation of the specific heat using (7).

Inverting Eq. (7) for $g(\omega)$ is a mathematically ill-posed problem, but, using methods explained in Tikhonov and Arsenin (2005) (Tikhonov regularization) it can be still achieved, for obtaining the DOS, as shown by Surovtsev (2001). This has been widely used in the meantime (Ando et al., 2018; Pan et al., 2021).

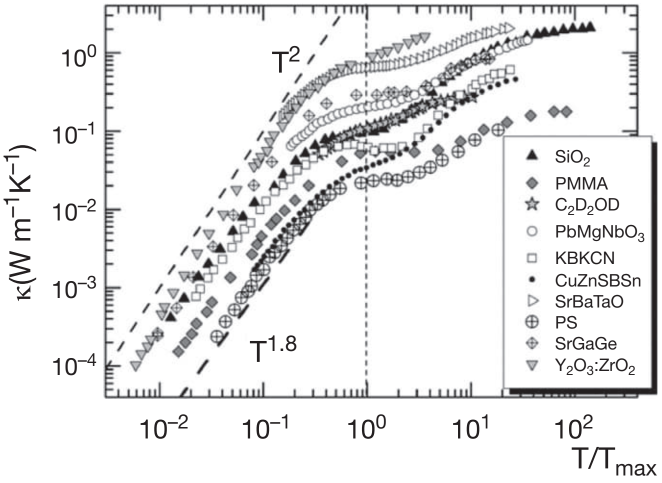

Fig. 7 Temperature dependence of the thermal conductivity of several materials plotted vs. $T/T_{\max}$, where $T_{\max}$ is the maximum of the reduced specific heat $C(T)/T^3$: SiO_2 (Cahill and Pohl, 1987; Damon, 1973), PMMA and PS (Stephens, 1973), glassy C_2D_2OD (Krivchikov et al., 2011), oriental glass $(KBr)_{0.75}(CN)_{0.25}$ (Yoreo et al., 1986), disordered ferroelectric perovskite crystals (Tachibana, 2015; Tachibana et al., 2008), clathrate semiconductors (Avila et al., 2006; Cohn et al., 1999; Suekuni et al., 2015) and disordered $Y_2O_3ZrO_2$ (Ackerman et al., 1981). The dashed line indicated the (boson) peak of $C(T)/T^3$. From Krivchikov AI and Jeżowski A (2020) *arXiv:2011.14728*.

Spectroscopic methods

Early investigations

Other than by the temperature dependence of the specific heat, information about the vibrational DOS of a solid can be obtained by several spectroscopic methods: Raman spectroscopy (Berne and Pecora, 2005; Jäckle, 1981), neutron (Schober, 2014), X-ray (Sette et al., 1998), and nuclear (Chumakov and Rüffer, 1998) inelastic scattering as well as Terahertz spectroscopy (Ohsaka and Ihara, 1994; Schmuttenmaer, 2004; Taraskin et al., 2006). In the early times vibrational spectroscopy in glasses was focussed on comparing the obtained spectra with those of their crystalline counterparts. In Fig. 8 we show an investigation the paradigmal glass silica (SiO_2). The Raman and neutron spectrum of glassy silica is compared with the spectrum of polycrystalline quartz. It is observed that in the regime above ~300 cm^{-1}–10 THz the spectra exhibit essentially the same features, which correspond to the typical vibrational excitations of a covalent network (Galeener et al., 1983).

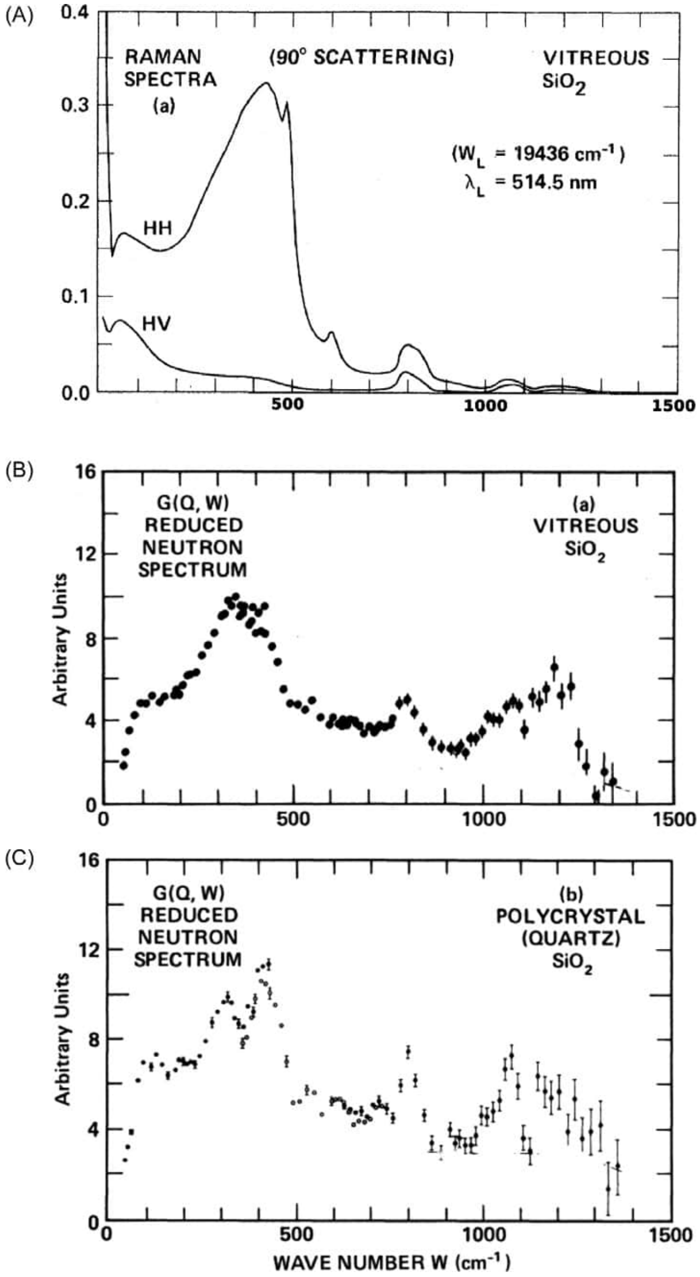

Fig. 8 (A) HH and VH Raman intensity of vitreous silica, (B) vibrational density of states $g(\omega)$ of vitreous silica, and (C) $g(\omega)$ of polycrystalline silica, both obtained by inelastic neutron scattering. From Galeener FL, Leadbetter AJ, and Stringfellow MW (1983) *Phys. Rev. B* 27: 1052.

Inelastic Neutron and Raman scattering

For incoherent neutron scattering the scattering intensity is given by the incoherent one-phonon neutron scattering law (Schober, 2014)

$$S_{\text{incoh}}(k,\ \omega) \propto k^2[n(\omega,\ T)+1]\frac{g(\omega)}{\omega}. \tag{8}$$

Here $\hbar\mathbf{k}$ is the momentum transfer and $\hbar\omega$ the energy transfer experienced by the neutrons during the scattering process.

The thermal prefactor $n(\omega, T)$ is due to the condition of detailed balance $S(k,-\omega)=S(k,\omega)e^{-\hbar\omega/k_BT}$. In principle, (8) applies only to *incoherent* neutron scattering, which would limit the investigations mainly to hydrogen-containing materials like glycerol (Wuttke et al., 1995) or water (Mallamace et al., 2015). However, it was demonstrated, that expression (8) may be used for coherent spectra, averaged over all experimentally available momenta $\hbar\mathbf{k}$ ("incoherent approximation" (Carpenter and Price, 1985; Fabiani et al., 2008; Oskotskii, 1967; Schober, 2014)).

Let us have a look at the DOS of glassy glycerol and silica, obtained (Wischnewski et al., 1998; Wuttke et al., 1995) by inelastic neutron scattering, shown in Fig. 9. The DOS is plotted as $g(\omega)/\omega^2$, which should be frequency independent if Debye's law would apply. We see that the strong enhancement with respect to the Debye expectation (boson peak) is temperature independent in the low-temperature regime 50 to 150 K. This is again an indication that in this low-temperature regime the boson peak is likely to be of

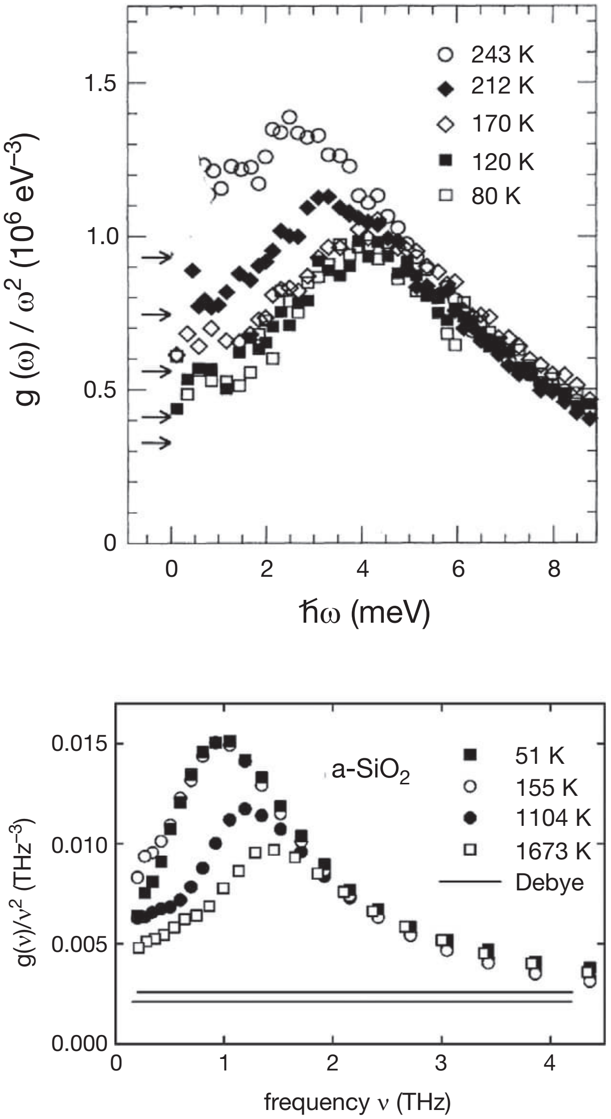

Fig. 9 Density of states of glasses as evaluated by inelastic neutron scattering. Top: Glycerol, Bottom: SiO_2. It can be seen that in both cases in the low-temperature region (below ~170 K) the boson-peak spectrum is temperature independent. The arrows (top panel) and straight lines (bottom panel) correspond to the Debye $g(\omega) \propto \omega^2$ prediction (Ashcroft and Mermin, 1976). Top: From Wuttke J, Petry W, Coddens G, and Fujara F (1995) *Phys. Rev. E* 53: 4026; Bottom: From Wischnewski A, Buchenau U, Dianoux AJ, Kamitakahara WA, and Zarestky JL (1998) *Phys. Rev. B* 57: 2663.

harmonic origin. The temperature dependence at higher T (or smaller frequency) due to the anharmonic interaction may come about – like in crystalline solids (Götze and Michel, 1974; Horner, 1974; Monacelli and Mauri, 2021) – in two different ways: (*i*) indirectly via a change of the elastic constants, (viz. the sound velocities) with T (quasi-harmonic effect), or (*ii*) via a direct change of the excitation spectrum.

Among the many subsequently reported neutron-scattering results on the vibrational spectrum of glasses (Arai et al., 1999; Buchenau et al., 1984, 1986, 1988; Inamura et al., 2001; Reichenauer et al., 1989; Vacher et al., 1989; Wright and Sinclair, 1985; Zanatta et al., 2013; Zorn, 2003) many investigations focussed on the extraction of the Raman-coupling function $C(\omega)$ by comparing the neutron spectra with the Raman spectra (Achibat et al., 1993; Benassi et al., 1991; Duval et al., 1990b, 1993, 1999; Hehlen et al., 2000a; Ivanda et al., 2001; Lannin, 1977; Saviot et al., 1999; Sokolov et al., 1993; Surovtsev, 2001, 2004; Surovtsev et al., 2003, 2004; Surovtsev and Sokolov, 2002a, b; Zemlyanov et al., 1992). All of these showed that $C(\omega) \propto \omega$ in the BP frequency regime is linearly proportional to the frequency ω. This was used subsequently to study the DOS by Raman spectroscopy (Caponi et al., 2009; Corezzi et al., 2013; Deschamps et al., 2012; Hehlen et al., 2000b; Hehlen and Neuville, 2015; Kalampounias et al., 2006; Moriya et al., 2008; Parshin et al., 2006; Rossi et al., 2012; Schulte et al., 2008).

In 2008 Schmid and Schirmacher (2008) published a theory of Raman scattering, which makes it possible to describe Raman spectra and other spectra containing information on the DOS in a unified way. This was used subsequently, in combination with heterogeneous-elasticity theory (Schirmacher, 2006; Schirmacher et al., 2007, 2014; Schirmacher and Ruocco, 2022) to describe and reconcile Raman, neutron-scattering and specific-heat data in a unified way (Benzine et al., 2021; Pan et al., 2021; Schulte et al., 2011; Unruh et al., 2008).

Nuclear inelastic scattering

A powerful method for measuring the vibrational DOS is nuclear inelastic scattering (NIA) (Seto et al., 1995; Sturhahn et al., 1995). It had already been pointed out as early as 1960 by Singwi and Sjölander (1960) that the resonance fluorescence spectrum of Mössbauer impurities essentially gives the same information as the incoherent neutron scattering law. But in conventional Mössbauer experiments or by applying conventional X-Ray sources the frequency range was not extended enough to observe phonon spectra. This situation changed with the advent of high-brilliance ***synchrotron sources, and it was shown (Seto et al., 1995; Sturhahn et al., 1995) that the NIA method can successfully be used to extract phonon spectra of solids. A severe drawback of this method is that there are only a few Mössbauer isotopes available with resonance energies accessible by synchrotron radiation, namely ^{57}Fe ($E_0 = 14.4$ keV), ^{119}Sn ($E_0 = 23.9$ keV), ^{151}Eu ($E_0 = 21.6$ keV). Chumakov et al. (2004) imbedded ferrocene molecules with ^{57}Fe as central atom into several glassy hosts in order to successfully extract the vibrational DOS of the hosts. The authors made sure that the ferrocene molecules were tightly bound into the hosts, so that the spectra are not due to an extra motion of the impurity, but represent the host spectra. In Fig. 10 the results for the vibrational DOS of four glass-forming materials are shown

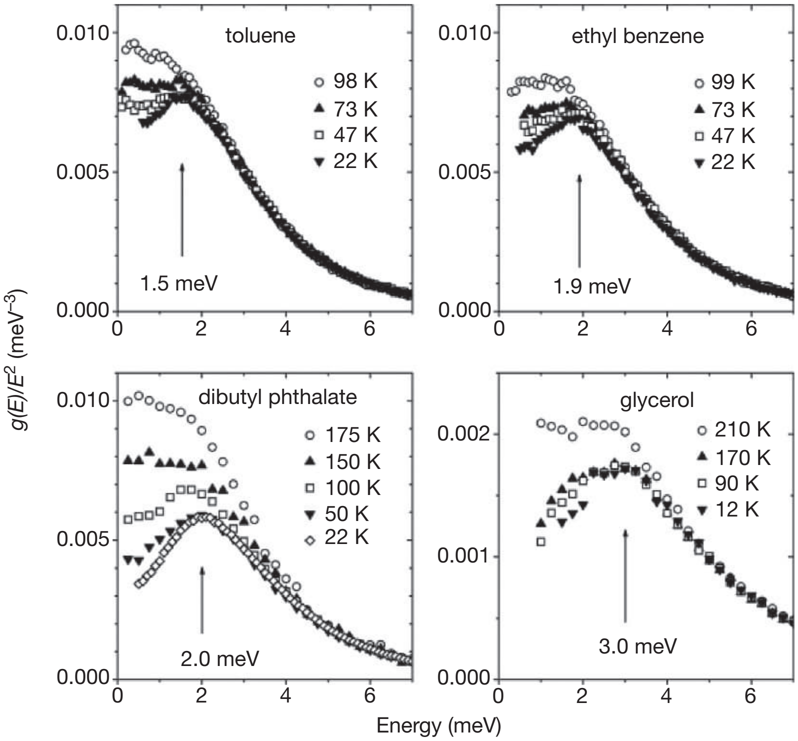

Fig. 10 Reduced DOS of collective motions in toluene, ethylbenzene dibutylphthalate, and glycerol glasses. Arrows indicate the energy of the boson peak estimated from the data at lowest temperature From Chumakov AI, Sergueev I, van Bürck U, Schirmacher W, Asthalter T, Rüffer R, Leupold O, and Petry W (2004) *Phys. Rev. Lett.* 92: 245508.

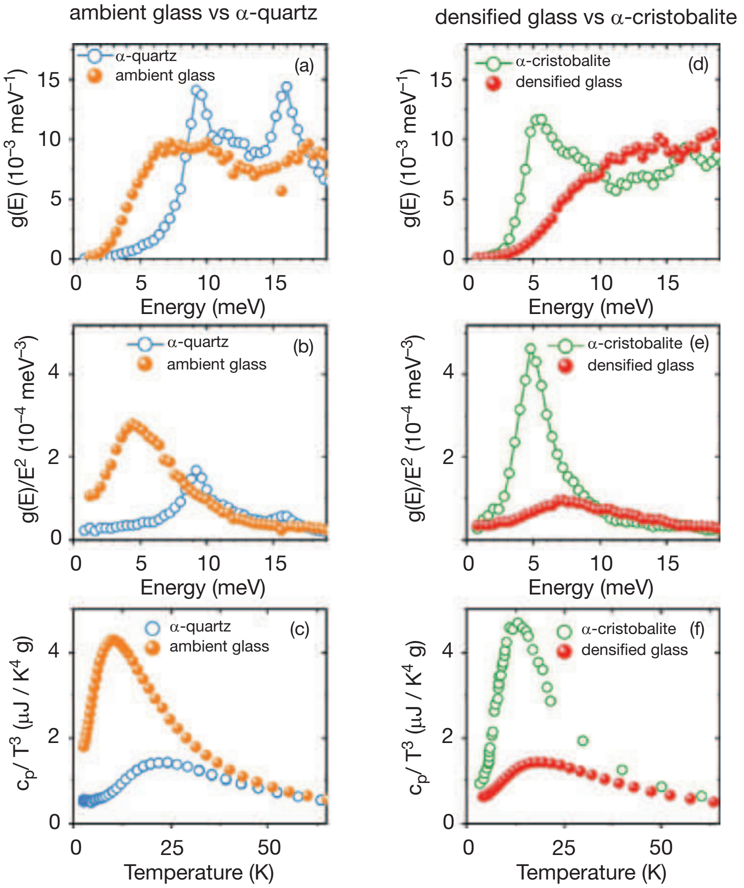

Fig. 11 Comparison of the density of states (A), (D) and the reduced density of states (B), (E) obtained with the nuclear inelastic scattering technique, and of the specific heat (C), (F) for ambient silica glass and α-quartz (A)–(C), and for densified silica glass and α-cristobalite (D)–(F). From Chumakov AI et al. (2014) *Phys. Rev. Lett.* 112: 025502.

(Chumakov et al., 2004). The authors found that all spectra (and further spectra from the literature) exhibited an exponential decrease of the DOS beyond the boson peak. It has been shown recently (Tomaras and Schirmacher, 2013), by applying instanton techniques (Cardy, 1978), that this exponential decrease is a disorder-induced phenomenon like the band tails observed in the electron spectra of disordered materials (Cohen et al., 1988).

Later the NIA method was used to compare the spectra of glassy silicates with the DOS, obtained from the phonon dispersions of the corresponding crystals (Chumakov et al., 2011, 2014; Zorn, 2011). Following the conclusions of the model calculations of Taraskin et al. (2002) the authors substantiated the point of view that the boson peak is a broadened version of the lowest (transverse-acoustic) van-Hove singularity of the corresponding crystal. They explained the fact that in crystals in the low-frequency regime of ~1 THz no such singularity occurs by pointing out that glasses usually have a lower density than the corresponding crystals. In the case of SiO_2 they compared the DOS of the ambient SiO_2 glass with that of crystalline α quartz and that of densified SiO_2 glass with that of cristobalite, which has a higher density. In both cases the glassy boson peak is observed near the corresponding van-Hove singularity. The boson peaks in the specific heat of these materials corroborate these findings (see Fig. 11). The authors state the opinion that quite generally in all glassy materials the boson peak would be due to the leveling-off of the transverse acoustic sound dispersion near the quasi-Brillouin zone (quasi-van-Hove singularity), i.e. the BP would in general *not* be caused by the structural disorder. We will comment on this in the discussion section.

Inelastic X-ray scattering

A breakthrough in the vibrational spectroscopy of glasses was the development of inelastic-X-ray spectrometers at synchrotron sources with extremely narrow resolution (Sette et al., 1995, 1998). Due to the very high brilliance of the synchrotron radiation it was possible to devise monochromators and analyzers (using very-high-order reflections) with resolution of ~1 meV, comparable to that of thermal neutron scattering. In contrast to the latter for the X-rays there is no upper kinematic limit in energy. For the neutron investigations it was not possible to investigate acoustical waves above the ~1 Thz or 4 meV regime. Similar to neutrons, the X-rays are sensitive to the *longitudinal* degrees of freedom.

Instead of averaging over the momenta, as done in the incoherent approximation, the observation of the **k** dependence of the spectra can provide useful information on the nature of the vibrational wavefunctions, which underly the observations. The spectra are given by the *coherent* scattering law

$$S_{\mathrm{coh}}(k,\omega) \propto [n(\omega)+1]\chi''(k,\omega) \tag{9}$$

where $\chi(k,\omega)=\chi'(k,\omega)+i\chi''(k,\omega)$ is the complex dynamical susceptibility, which is usually parametrized as a damped harmonic oscillator (DHO) with resonance frequency $\Omega(k)$ and sound attenuation (damping) coefficient $\Gamma(k)$

$$\chi(k,z)=\frac{k^2}{-\omega^2+\Omega(k)^2-i\omega\Gamma(k)} \tag{10}$$

Inelastic scattering experiments featuring a resonance $\Omega(k)$ are usually referred to as Brillouin spectra and $\Gamma(k)$ is then the Brillouin line width (full width at half maximum, FWHM for $\Gamma \ll \Omega$).

Indeed the first inelastic X-ray scattering (IXS) experiments on glassy glycerol (Masciovecchio et al., 1996; Sette et al., 1998), LiCl:6H_2O (Masciovecchio et al., 1996) and SiO_2 (Benassi et al., 1996) revealed a pronounced propagating longitudinal sound excitation, i.e. $\Omega(k) \propto k$ which extends into the $k \sim 5\ \mathrm{nm}^{-1}$ range, which corresponds to a wavelength of ~1 nm. Interestingly, in all cases the propagating wave-like excitations extended beyond the boson-peak energy $E_{BP}=\hbar\omega_{BP}$, as indicated in the top panel of Fig. 12 for the case of glycerol (Sette et al., 1998). Similar features were found in glassy SiO_2 (Benassi et al., 1996).

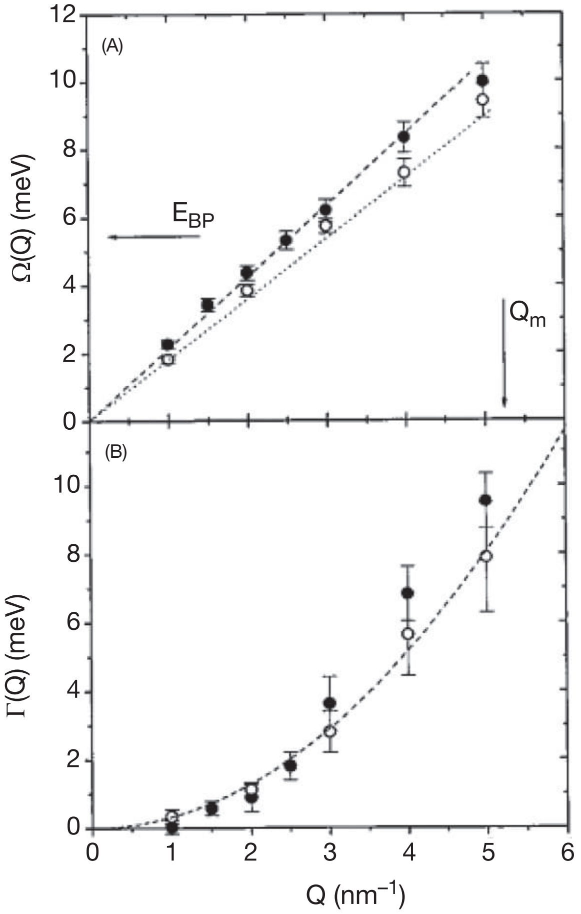

Fig. 12 Momentum (Q) dependence of the DHO resonance frequency parameter $\Omega(Q)$ and $\Gamma(Q)$, Eqs. (9) and (10), for glassy glycerol. From Sette F, Krisch MH, Masciovecchio C, Ruocco G, and Monaco G (1998) *Science* 280: 1550.

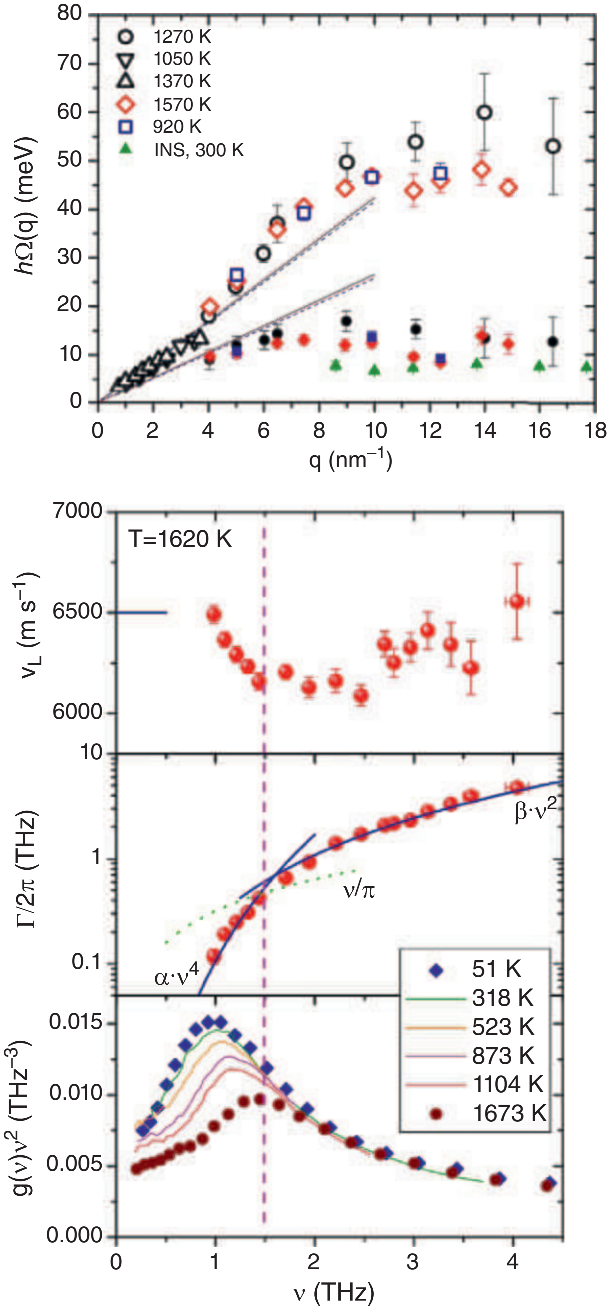

Fig. 13 Upper panel: Dispersions of maxima of the dynamical structure factors obtained by inelastic X-ray and neutron scattering experiments (Baldi et al., 2008 and citations quoted therein). Lower panel, top: Frequency-dependent sound velocity $v_L(\nu) = \Omega_L(q)/q$ vs. $\nu = \Omega(q)/2\pi$, middle: Brillouin line width (sound attenuation) $\Gamma(\nu)$, bottom: reduced DOS $g(\nu)/\nu^2$ obtained by neutron scattering, using the incoherent approximation. From Baldi G, Giordano VM, Monaco G, and Ruta B (2010) *Phys. Rev. Lett.* 104: 195501.

Some authors were astonished that ab*ove* the boson peak and the Ioffe-Regel frequency propagating modes would exist (Foret et al., 1997; Vacher et al., 1998), but later experiments confirmed the presence of these modes, which proved to be of longitudinal character.

In subsequent times the resolution of the X-ray beam-lines was increased and further details about the vibrational excitations of glasses were revealed. Here, we focus on the example of glassy SiO_2. In the top panel of Fig. 13 the dispersion $\Omega(q)$ is shown together with the maxima of inelastic neutron scattering (INS) data obtained by the same authors. The latter show the boson peak near $\hbar\omega = 6$ meV as a wavenumber independent feature. Two years later Baldi et al. (Baldi et al., 2010, 2011) found a crossover in the sound attenuation (Brillouin line width) from a Rayleigh-like behavior $\Gamma(\omega) \propto \omega^4$ to ω^2, as predicted by heterogeneous-elasticity theory (HET) (Marruzzo et al., 2013a; Schirmacher, 2006; Schirmacher et al., 2007, 2014; Schirmacher and Ruocco, 2022) near the boson-peak frequency 1.5 THZ $\widehat{=}$ 6 meV.This crossover is accompanied by a kink in the frequency-dependent longitudinal sound velocity $v(\omega)$, where $v(\omega) = \Omega(q)/q|_{\omega=\Omega(q)}$, predicted as well by HET theory. Similar findings were obtained as well for glassy glycerol (Monaco and Giordano, 2009) and sorbitol (Ruta et al., 2010). In the latter materials, as remarked by Baldi et al. (2011) the connection between $\Gamma(\omega)$ and $v(\omega)$, as given by HET theory is sufficient to explain the boson peak in the INS data, whereas in glassy SiO_2 it is not. The missing boson-peak intensity could then be additionally due to optic-like or van-Hove-singularity like modes (Baldi et al., 2012, 2016, 2017; Chumakov et al., 2011, 2014, 2016).

Simulations

Since the first molecular-dynamics (MD) simulation of a Lennard-Jones glass[6] of Rahman et al. (1976), in which the DOS was calculated and was shown to agree to the Fourier transform of the velocity autocorrelation function (Hansen and McDonald, 1986; Schirmacher et al., 2014), a very large number of MD simulations has been published, and, again, we can only mention a few, which – to our opinion – contributed most to the understanding the low-frequency anomalies of glasses.

In the 1970–80 years only limited computer power and storage capacity was available, so the simulated systems could have only particle numbers of $N = 500$ to 2000. In simulations of such small systems Laird and Schober (Laird and Schober, 1991; Schober and Laird, 1991) found low-frequency modes, which, by analyzing the participation ratio appeared to be localized.

The participation ratio p is defined by (Dean and Bell, 1970)

$$p = \left[N \sum_i (\mathrm{e}_i \cdot \mathrm{e}_i)^2 \right]^{-1} \tag{11}$$

of the eigenvectors e_i of the dynamical matrix (1) normalized as $\sum_i (\mathrm{e}_i \cdot \mathrm{e}_i) = 1$. p takes values of the order unity for extended states and small values of order $1/N$ for localized ones. In macroscopic large disordered materials, as stated above, the low-frequency vibrational excitations are acoustical waves, because the material on a large scale is homogeneous and isotropic. In the systems of only $\sim$1000 particles, the low-frequency acoustic waves do not exist, because their wavelengths would be much larger than the sample size. Therefore Laird and Schober (1991) argued that the localized excitations, which they observed at small frequencies, would – in a larger system – hybridize with the acoustical waves (like heavy-mass impurities in crystals (Economou, 1979)), and called these excitations "quasi-localized." Quite recently a revival of the investigation of such small systems took place in the literature (Angelani et al., 2018; Baity-Jesi et al., 2015; Lerner and Bouchbinder, 2021; Lerner et al., 2016; Mizuno et al., 2017; Paoluzzi et al., 2019; Parisi et al., 2020; Wang et al., 2020). It was found that the DOS of the quasi-localized modes of small systems follows a scaling $g(\omega) \propto \omega^{\alpha}$, where in many investigated systems $\alpha \approx 4$ (Lerner and Bouchbinder, 2021). In other systems the observed exponent α ranged between 2 and 4, dependent on the preparation protocol (Angelani et al., 2018; Paoluzzi et al., 2019; Parisi et al., 2020).

In the 2000er years the advancement of machine power and storage, in particular the advent of parallel computing (Patterson and Hennessy, 2009) made it possible to treat systems with 10^5 to 10^7 particles, enabling to disentangle the boson peak from the finite-size resonances of the acoustic waves. One of the first of such studies treated a Lennard-Jones system (Léonforte et al., 2005) and glassy SiO_2 (Léonforte et al., 2006). It was shown, confirming other similar findings (Lemaître and Maloney, 2006; Wittmer et al., 2002) that the overwhelming part of the vibrational displacements in a glass do not follow an external strain in an affine way. Instead, these displacements display *non-affine* patterns, as shown in Fig. 14. Léonforte et al. (2006) found that the correlation length ξ of these patterns is as large as $\sim$10 interatomic spacings both in the Lennard-Jones and SiO_2 glass. In a representation against $\omega\xi/v_T$ – in accord with the empirical law of Elliott (1992) and Duval et al. (1990a) – the observed boson peaks coincide, as displayed in Fig. 14. Further studies of model glasses focussed on evaluating the local spatial fluctuations of elastic constants. As shown in the two seminal papers of Lutsko (Lutsko, 1988, 1989) local elastic constants – including the non-affine contributions – can be evaluated by a coarse-graining procedure. Such a procedure was applied in a number of papers (Derlet et al., 2012; Marruzzo et al., 2013a; Mizuno et al., 2013a, b). These studies confirmed the presence of spatial fluctuations of elastic constants in glasses, which is the basic assumption of heterogeneous-elasticity theory, HET (Schirmacher, 2006; Schirmacher and Ruocco, 2022; Schirmacher et al., 2014). In fact, using the example of a simulated soft-sphere glass, i.e. a quenched system of $N = 10^7$ particles with interparticle potential varying as $\phi(r) \propto r^{-12}$ Marruzzo et al. (2013a) showed that the observed boson peak is due to the spatially fluctuating elastic constants and can be perfectly described by HET using exactly the observed statistics. The data were evaluated for the DOS $g(\omega)$ from the velocity autocorrelation function and the longitudinal (L) and transverse (T) current correlation functions (Hansen and McDonald, 1986; Schirmacher et al., 2014) $C_{L,T}(k,\omega) = (\omega/k^2)\mathrm{Im}\{\chi_{L,T}(k,\omega)\}$ with the longitudinal and transverse dynamic susceptibility given by the DHO formula (10). The quantities $\Omega_{L,T}(k)$ and $\Gamma_{L,T}$ were converted to complex frequency-dependent elastic constants $G(\omega)$ (shear modulus) and $M(\omega) = K + \frac{4}{3}G(\omega)$ (longitudinal modulus) as

---

[6] A Lennard-Jones glass is a liquid, in which particles interact via a Lennard-Jones potential $\phi(r) \propto Ar^{-12} - Br^{-6}$, quenched to a very low temperature.

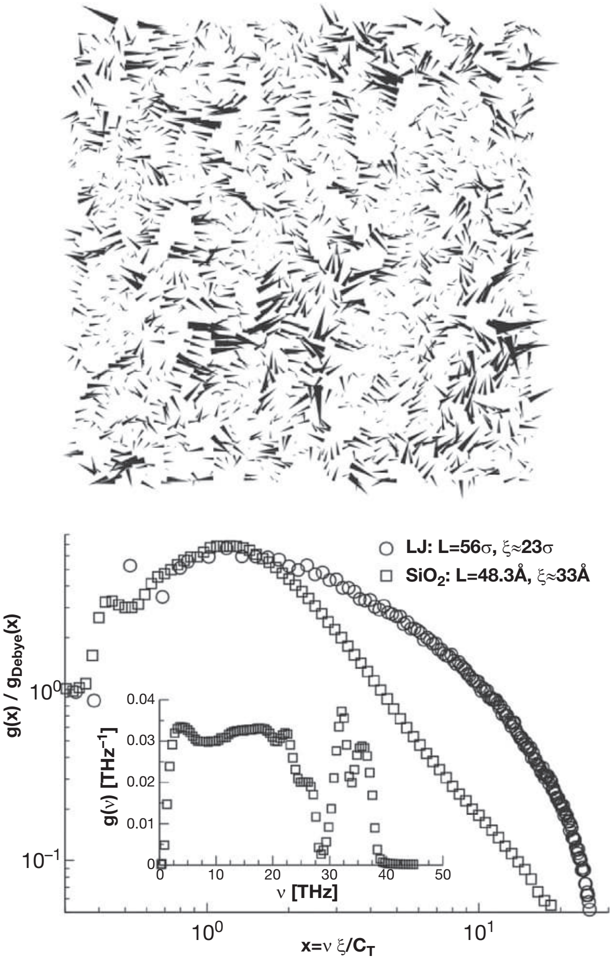

Fig. 14 Top: Non-affine displacements in a computer SiO$_2$ glass subject to a global shear; bottom: reduced DOS $g(\nu)/\nu^2$ scaled with the transverse sound velocity and the correlation length ξ for the SiO$_2$ glass and a Lennard-Jones-glass (Léonforte et al., 2005). From Léonforte F, Tanguy A, Wittmer J-P, and Barrat J-L (2006) *Phys. Rev. Lett.* 97: 055501.

$$\begin{aligned} G(\omega) &= \frac{\rho m}{k^2}\left[\Omega_T(k)^2 - i\omega\Gamma_T(k)\right]_{\omega=\Omega_L(k)} \\ M(\omega) &= \frac{\rho m}{k^2}\left[\Omega_L(k)^2 - i\omega\Gamma_L(k)\right]_{\omega=\Omega_L(k)} \\ &= K + \frac{4}{3}G(\omega). \end{aligned} \tag{12}$$

Here ρ_m is the mass density. The transverse and longitudinal data sets could be reconciled by taking the bulk modulus K frequency-independent and real, as demonstrated in the bottom panel of Fig. 15, i.e. it was found that $\Gamma_L(\omega) = \frac{4}{3}\Gamma_T(\omega)$ and, indeed, $M'(\omega) = K + \frac{4}{3}G'(\omega)$. *Furthermore, the prediction of heterogeneous-elasticity theory, HET (*Marruzzo et al., *2013a*; Schirmacher, *2006*; Schirmacher et al., *2007) (blue lines) lie on top of the simulated frequency dependent spectral quantities.* This holds for three very different temperatures. It is remarkable that the spatial distribution of the fluctuating local shear moduli, extracted from the simulation, agrees with the distribution used in the theory. The temperature dependence at very low frequencies could be traced to anharmonic effects (Marruzzo et al., 2013b). The downward kink of the real parts of the elastic coefficients at the BP frequency, which correspond to the downward kink of the k dependent sound velocity (Baldi et al., 2011; Monaco and Giordano, 2009), which is predicted by HET, arises as a consequence of the Kramers-Kronig relation between the real and imaginary parts of the complex moduli. Similar features had also been observed in an earlier simulation of a Lennard-Jones glass (Monaco and Mossa, 2009).

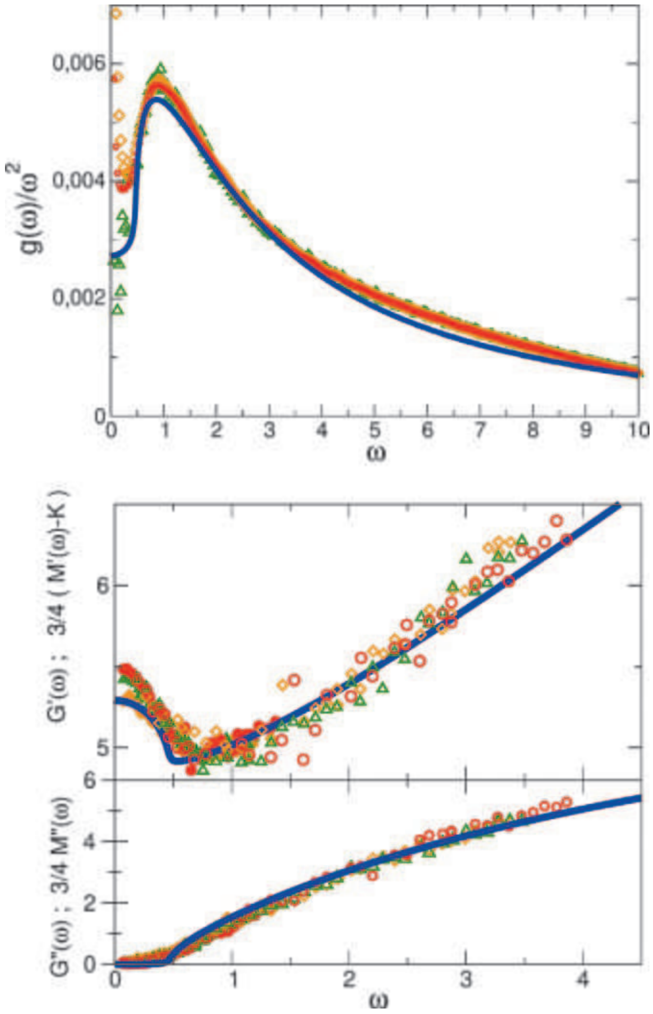

Fig. 15 Comparison of the results of a soft-sphere glass simulation (symbols) for three different temperatures $T = 5{\cdot}10^{-5}$, $T = 5 \cdot 10^{-4}$, $T = 5 \cdot 10^{-3}$ (in Lennard-Jones units), with the prediction of heterogeneous-elasticity theory (HET) (Schirmacher, 2006; Schirmacher et al., 2007) (blue lines). Top panel: reduced DOS $g(\omega)/\omega^2$. Bottom panels: Real and imaginary part of the complex shear modulus, obtained from both, the complex transverse and longitudinal sound velocities, see text. From Marruzzo A, Schirmacher W, Fratalocchi A, and Ruocco G (2013a) *Scientific Reports* 3: 1.

Discussion

Let us try to summarize, what has been found in the last half century about the origin of the boson-peak related vibrational anomalies of glasses. Beside that – on the theoretical side – the subject is highly controversial, we find that – on the experimental (and computer-experimental) side – the evidence is that the boson peak is *not universal*, i.e. in different materials the spectral features leading to an enhanced reduced DOS in the THz regime are caused by different physical mechanisms. For the prototypical glass SiO_2 there is clear evidence for the presence of local oscillators in the THz regime, which are most probably librations[7] of SiO_2 tetrahedra (Buchenau et al., 1984), giving rise to optical modes and van-Hove peaks in the corresponding crystal (Chumakov et al., 2014). On the other hand, in non-network glasses like metallic glasses or the computer models, it has become clear that the structural disorder is responsible for the boson peak. In such materials the BP marks the transition from sound-like vibrational excitations to random-matrix like excitations. It has been demonstrated by investigating the vibrational spectrum of a macroscopic model glass that both features, the disorder-induced boson peak and a smeared van-Hove singularity coexist at different frequencies (Wang et al., 2018). In fact, as remarked by Baldi et al. (2011) both mechanisms might be present in glassy SiO_2. For a simulated metallic glass Brink et al. (2016) recently demonstrated that the BP clearly comes from the disorder and not from a smeared van-Hove singularity. Particularly difficult in this respect is the interpretation of specific heat data. As stated above, a BP in the specific heat is observed not only in glasses but in in an extended number of (complex) crystalline materials (Krivchikov and Jeżowski, 2020). In the latter, they are most probably due to low-frequency "rattlers," i.e. loosely bound heavy-mass molecules or residues.

---

[7] The term "libration" denotes the rotational oscillation of a tetrahedron around its center of mass.

References

Abrahams E, Anderson PW, Licciardello DC, and Ramakrishnan TV (1979) *Phys. Rev. Lett.* 42: 673.
Achibat T, Boukenter A, and Duval E (1993) *J. Chem. Phys.* 99: 2046.
Ackerman DA, Moy D, Potter RC, Anderson AC, and Lawless WN (1981) *Phys. Rev. B* 23: 3386.
Akkermans E and Maynard R (1985) *Phys. Rev. B* 32: 7850.
Alexander S, Bernasconi J, Schneider WR, and Orbach R (1981) *Rev. Mod. Phys.* 53: 175.
Alexander S and Orbach R (1982) *J. Physique (Paris)* 43: 625.
Allen PB and Feldman JL (1993) *Phys. Rev. B* 48: 12581.
Allen PB, Feldman JL, and Fabian J (1999) *Philos. Magazine* 79: 1715.
Anderson PW (1958) *Phys. Rev.* 109: 1492.
Anderson PW, Halperin B, and Varma CM (1972) *Philosophical Magazine* 25: 1.
Ando MF, Benzine O, Pan Z, Garden J-L, Wondraczek K, Grimm S, Schuster K, and Wondraczek L (2018) *Sci. Rep.* 8: 5394.
Angelani L, Paoluzzi M, Parisi G, and Ruocco G (2018) *Proc. Nat. Acad. Sci.* 115: 8700.
Arai M, Inamura Y, Otomo T, Kitamura N, Bennington SM, and Hannon A (1999) *Physica B* 263-264: 268.
Arnold VI (1992) *Catastrophe Theory*. Berlin: Springer-Verlag.
Ashcroft NW and Mermin ND (1976) *Solid State Physics*. Rinehart and Winston, Austin: Holt.
Avila MA, Suekuni K, Umeo K, Fukuoka H, Yamanaka S, and Takabatake T (2006) *Phys. Rev. B* 74: 125109.
Baggioli M and Zaccone A (2019) *Phys. Rev. Lett.* 122: 145501.
Baity-Jesi M, Martín-Mayor V, Parisi G, and Perez-Gaviro S (2015) *Phys. Rev. Lett.* 115: 267205.
Baldi G, Benassi P, Fontana A, Giugni A, Monaco G, Nardone M, and Rossi F (2017) *J. Chem. Phys.* 147: 164501.
Baldi G, Carini G, Carini G, Chumakov A, Maschio RD, D'Angelo G, Fontana A, Gilioli E, Monaco G, Orsingher L, Rossi B, and Zanatta M (2016) *Philos. Magazine* 96: 754.
Baldi G, Giordano VM, and Monaco G (2011) *Phys. Rev. B* 83: 174203.
Baldi G, Giordano VM, Monaco G, and Ruta B (2010) *Phys. Rev. Lett.* 104: 195501.
Baldi G, Giordano VM, Monaco G, Sette F, Fabiani E, Fontana A, and Ruocco G (2008) *Phys. Rev. B* 77: 214309.
Baldi G, Zanatta M, Gilioli E, Milman V, Refson K, Wehinger B, Winkler B, Fontana A, and Monaco G (2012) *J. Chem. Phys.* 137: 214502.
Beekman M and Cahill D (2017) *Cryst. Res. Technol.* 52: 1700114.
Benassi P, Krisch M, Masciovecchio C, Mazzacurati V, Monaco G, Ruocco G, Sette F, and Verbeni R (1996) *Phys. Rev. Lett* 77: 3835.
Benassi P, Pilla O, Mazzacurati V, Montagna M, Ruocco G, and Signorelli G (1991) *Phys. Rev. B* 44: 11734.
Benzine O, Pan Z, Calahoo C, Bockowski M, Smedskaer MM, Schirmacher W, and Wondraczek L (2021) *Sci. Reports* 11: 24454.
Berne BJ and Pecora R (2005) *Dynamic Light Scattering*. New York: Wiley.
Brink T, Koch L, and Albe K (2016) *Phys. Rev. B* 94: 224203.
Buchenau U, Galperin YM, Gurevich VL, Parshin DA, Ramos MA, and Schober HR (1992) *Phys. Rev. B* 46: 2798.
Buchenau U, Galperin YM, Gurevich VL, and Schober HR (1991) *Phys. Rev. B* 43: 5039.
Buchenau U, Nücker N, and Dianoux AJ (1984) *Phys. Rev. Lett.* 53: 2316.
Buchenau U, Prager M, Kamitakahara WA, Shanks HR, and Nücker N (1988) *Europhys. Lett.* 6: 695.
Buchenau U, Prager M, Nücker N, Dianoux AJ, Ahmad N, and Phillips WA (1986) *Phys. Rev. B* 34: 5665.
Cahill D and Pohl RO (1989) *Sol. State Comm.* 70: 927.
Cahill DG and Pohl RO (1987) *Phys. Rev. B* 35: 4067.
Caponi S, Corezzi S, Fioretto D, Fontana A, Monaco G, and Rossi F (2009) *Phys. Rev. Lett.* 102: 027402.
Cardy JL (1978) *J. Phys. C* 11: L321.
Carpenter JM and Price DL (1985) *Phys. Rev. Lett.* 54: 441.
Chumakov A, Monaco G, Han X, Xi L, Bosak A, Paolasini L, Chernyshov D, and Dyadkin V (2016) *Philos. Magazine* 96: 743.
Chumakov AI, Sergueev I, van Bürck U, Schirmacher W, Asthalter T, Rüffer R, Leupold O, and Petry W (2004) *Phys. Rev. Lett.* 92: 245508.
Chumakov AI and Rüffer R (1998) *Hyperfine Int.* 113: 59.
Chumakov AI, et al. (2011) *Phys. Rev. Lett.* 106: 225501.
Chumakov AI, et al. (2014) *Phys. Rev. Lett.* 112: 025502.
Cohen MH, Chou M-Y, Economou EN, John S, and Soukoulis CM (1988) *IBM J. Res. Dev.* 32: 82.
Cohn JL, Nolas GS, Fessatidis V, Metcalf TH, and Slack GA (1999) *Phys. Rev. Lett.* 82: 779.
Corezzi S, Caponi S, Rossi F, and Fioretto D (2013) *J. Phys. Chem. B* 117: 14477.
Damon DH (1973) *Phys. Rev. B* 8: 5860.
Dean P and Bell RJ (1970) *Discuss. Faraday Soc.* 50: 55.
DeGiuli E, Laversanne-Finot A, Düring G, Lerner E, and Wyart M (2014a) *Soft Matter* 10: 5628.
DeGiuli E, Lerner E, Brito C, and Wyart M (2014b) *Proc. Nat. Acad. Sci.* 111: 17054.
Derlet PM, Maass R, and Löffler JF (2012) *Eur. Phys. J. B* 85: 148.
Deschamps T, Martinet C, de Ligny D, Bruneel J, and Champagnon B (2012) *J. Non-Cryst. Sol.* 358: 3156.
Duval E, Boukenter A, and Achibat T (1990a) *J. Phys. Condens. Matter* 2: 10227.
Duval E, Boukenter A, and Achibat T (1990b) *J. Phys. Condens. Matter* 2: 10227.
Duval E, Novikov VN, and Boukenter A (1993) *Phys. Rev. B* 48: 16785.
Duval E, Saviot L, Surovtsev N, Wiedersich J, and Dianoux AJ (1999) *Philos. Mag.* 79: 2051.
Dyre J and Schrøder B (2000) *Rev. Mod. Phys.* 72: 873.
Economou EN (1979) *Green's Functions in Quantum Physics*. Heidelberg: Springer-Verlag.
Economou EN, Soukoulis CM, and Zdetsis AD (1984) *Phys. Rev. B* 30: 1686.
Elliott SR (1984) *The Physics of Amorphous Materials*. New York: Longman.
Elliott SR (1992) *Europhys. Lett.* 19: 201.
Fabiani E, Fontana A, and Buchenau U (2008) *J. Chem. Phys.* 128: 244507.
Feldman JL, Kluge MD, Allen PB, and Wooten F (1993) *Phys. Rev. B* 48: 12589.
Foret M, Courtens E, Vacher R, and Suck J-B (1996) *Phys. Rev. Lett.* 77: 3831.
Foret M, Courtens E, Vacher R, and Suck J-B (1997) *Phys. Rev. Lett.* 78: 4669.
Franz S and Parisi G (2016) *J. Phys. Math. Theor.* 49: 145001.
Franz S, Parisi G, Urbani P, and Zamponi F (2015) *Proc. Nat. Acad. Sci.* 112: 14539.
Freeman JJ and Anderson AC (1986) *Phys. Rev. B* 34: 5684.
Galeener FL, Leadbetter AJ, and Stringfellow MW (1983) *Phys. Rev. B* 27: 1052.
Ganter C and Schirmacher W (2010) *Phys. Rev. B* 82: 094205.
Götze W and Mayr MR (1999) *Phys. Rev. E* 61: 578.
Götze W and Michel KH (1974) In: Horton GK and Maradudin AA (eds.) *Dynamical Properties of Solids*, vol. I. Amsterdam: North Holland. ch. 9.

Graebner JE, Golding B, and Allen LC (1986) *Phys. Rev. B* 34: 5696.
Grigera TS, Martín-Mayor V, Parisi G, Urbani P, and Verrocchio P (2011) *J. Statist. Mech.* 2011. P02015.
Grigera TS, Martín-Mayor V, Parisi G, and Verrocchio P (2003) *Nature* 422: 289.
Gurarie V and Chalker JT (2003) *Phys. Rev. B* 68: 134207.
Gurevich VL, Parshin DA, and Schober HR (2003) *Phys. Rev. B* 67: 094203.
Gurevich VL, Parshin DA, and Schober HR (2005) *Phys. Rev. B* 71: 014209.
Hansen J-P and McDonald I (1986) *Theory of Simple Liquids.* New York: Academic Press.
Hehlen B, Courtens E, Vacher R, Yamanaka A, Kataoka M, and Inoue K (2000a) *Phys. Rev. Lett.* 84: 5355.
Hehlen B, Courtens E, Vacher R, Yamanaka A, Kataoka M, and Inoue K (2000b) *Phys. Rev. Lett.* 84: 5355.
Hehlen B and Neuville DR (2015) *J. Phys. Chem. B* 119: 4093.
Horner H (1974) In: Horton GK and Maradudin AA (eds.) *Dynamical Properties of Solids*, Vol. I. Amsterdam: North Holland. ch. 9.
Inamura Y, Arai A, Nakamura M, Otomo T, Kitamura N, Bennington SM, Hannon AC, and Buchenau U (2001) *J. Non-Cryst. Sol.* 293-295: 389.
Ioffe AF and Regel AR (1960) *Prog. Semicond.* 4: 237.
Ishimaru A (1978) *Wave Propagation and Scattering in Random Media.* New York: Academic Press.
Ivanda M, Kiefer W, and Mariotto G (2001) *Sol. State Comm.* 117: 423.
Jäckle J (1981) In: Phillips WA (ed.) *Amorphous Solids: Low-Temperature Properties*, p. 135. Berlin: Springer-Verlag.
John S, Sompolinky H, and Stephen MJ (1983) *Phys. Rev. B* 28: 5592.
Kalampounias AG, Yannopoulos AN, and Papatheodorou GN (2006) *J. Non-Cryst. Sol.* 352: 4619.
Karpov VG, Klinger MI, and Ignat'ev FN (1983) *Z. Eksp. Teor. Fiz* 84: 760. english translation in *Sov. Phys. JETP* 57:439.
Kirkpatrick TR (1985) *Phys. Rev. B* 31: 5746.
Köhler S, Ruocco R, and Schirmacher W (2013) *Phys. Rev. B* 88: 064203.
Krivchikov AI and Jeżowski A (2020) *arXiv:2011.14728.*
Krivchikov AI, Bermejo FJ, Sharapova IV, Korolyuk OA, and Romantsova OO (2011) *Low Temp. Phys.* 37: 517.
Laird BB and Schober HR (1991) *Phys. Rev. Lett.* 66: 636.
Lannin JS (1977) *Phys. Rev. B* 15: 3863.
Lasjaunias J, Ravex A, Vandorpe M, and Hunklinger S (1975) *Sol. State Comm.* 17: 1045.
Leadbetter AJ (1969) *J. Chem. Phys.* 51: 779.
Lemaître A and Maloney C (2006) *J. Statist. Phys.* 123: 415.
Léonforte F, Boissière R, Tanguy A, Wittmer J-P, and Barrat J-L (2005) *Phys. Rev. B* 72: 224206.
Léonforte F, Tanguy A, Wittmer J-P, and Barrat J-L (2006) *Phys. Rev. Lett.* 97: 055501.
Lerner E and Bouchbinder E (2021) *J. Chem. Phys.* 155: 200901.
Lerner E, Düring G, and Bouchbinder E (2016) *Physical review Letters* 117(3): 035501.
Li Y, Bai HY, Wang WH, and Samwer K (2006) *Phys. Rev. B* 74: 052201.
Liu A, Nagel SR, van Saarlos W, and Wyart M (2011) In: Berthier L, Biroli G, Bouchaud J-P, Cipeletti L, and van Saarlos W (eds.) *Dynamical Heterogeneities in Glasses, Colloids and Granular Media.* Oxford, UK: Oxford University Press.
Lutsko JF (1988) *J. Appl. Phys.* 64: 1152.
Lutsko JF (1989) *J. Appl. Phys.* 65: 2991.
Mallamace F, Corsaro C, Mallamace D, Wang Z, and Chen S-H (2015) *Front. Phys.* 10: 106103.
Marchenko VA and Pastur LA (1967) *Matematicheskii Sbornik* 114: 507.
Marruzzo A, Schirmacher W, Fratalocchi A, and Ruocco G (2013a) *Scientific Reports* 3: 1.
Marruzzo A, Schirmacher W, Köhler S, Fratalocchi A, and Ruocco G (2013b) *Eur. Phys. J. spec. Topics* 216: 83.
Masciovecchio C, Ruocco G, Sette F, Krisch M, Verbeni R, Bergmann U, and Soltwisch M (1996) *Phys. Rev. Lett* 76: 3356.
Maurer E and Schirmacher W (2004) *J. Low Temp. Phys.* 137: 453.
Maxwell JC (1864) *Philos. Mag.* 27: 250.
Mayr SG (2009) *Phys. Rev. B* 79: 060201.
Mehta ML (1991) *Random Matrices.* London: Academic Press.
Mizuno H, Mossa H, and Barrat J-L (2013a) *Europhys. Lett.* 104: 56001.
Mizuno H, Mossa H, and Barrat J-L (2013b) *Phys. Rev. E* 87: 042306.
Mizuno H, Shiba H, and Ikeda A (2017) *Proceedings of the National Academy of Sciences* 114(46): E9767. http://www.pnas.org/content/114/46/E9767.full.pdf.
Monacelli L and Mauri F (2021) *Phys. Rev. B* 103: 104305.
Monaco G and Giordano VM (2009) *Proc. Nat. Acad. Sci.* 106: 3659.
Monaco G and Mossa S (2009) *Proc. Nat. Acad. Sci.* 106: 16907.
Mori T, et al. (2020) *Phys. Rev. E* 102: 022502.
Moriya Y, Yoshida T, Kawaji H, Atake T, Fukuhara M, Kimura H, and Inoue A (2008) *Mat. Sci. Eng. B* 148: 207.
Mott NF (1990) *Metal-Insulator Transitions*, 2nd edn. London: Taylor & Francis.
Nakayama T, Yakubo K, and Orbach RL (1994) *Rev. Mod. Phys.* 66: 381.
O'Hern CS, Silbert LE, Liu AJ, and Nagel SR (2003) *Phys. Rev. E* 68: 011306.
Ohsaka T and Ihara T (1994) *Phys. Rev. B* 50: 9569.
Orbach R (1986) *Science* 231: 814.
Oskotskii VS (1967) *Sov. Phys. Solid State* 9: 420.
Pan Z, Benzine O, Sawamura S, Limbach R, Koike A, Bennett TD, Wilde G, Schirmacher W, and Wondraczek L (2021) *Phys. Rev. B* 104: 134106.
Paoluzzi M, Angelani L, Parisi G, and Ruocco G (2019) *Phys. Rev. Lett* 123: 155502.
Parisi G (2003) *J. Phys. Condens. Matter* 15: S765.
Parisi G, Urbani P, and Zamponi F (2020) *Theory of Simple Glasses.* Cambridge, UK: Cambridge University Press.
Parshin MA, Laermans C, and Melehin VG (2006) *Eur. Phys. J. B* 49: 47.
Patterson DA and Hennessy JL (2009) *Computer Organization and Design.* Amsterdam: Morgan Kaufmann Elsevier.
Phillips WA (1972) *J. Low-Temp. Phys.* 7: 351.
Phillips WA (1987) *Rep. Prog. Phys.* 50: 1657.
Pinski S, Schirmacher W, and Römer RA (2012a) *Europhys. Lett.* 97: 16007.
Pinski S, Schirmacher W, Whall T, and Römer RA (2012b) *J. Condens. Matt.* 24: 405401.
Porter CE (1965) *Statistical Theories of Spectra: Fluctuations.* Berlin: Springer-Verlag.
Rahman A, Mandell MJ, and McTague JP (1976) *J. Chem. Phys.* 64: 1564.
Ramos MA (2020) *Low-Temp. Phys.* 46: 104.
Ramos MA, Talón C, and Vieira S (2002) *J. Non-Cryst. Sol.* 307: 80.
Reichenauer G, Fricke J, and Buchenau U (1989) *Europhys. Lett.* 8: 415.
Rossi B, Caponi S, Castiglione F, Corezzi S, Fontana A, Giarola M, Mariotto G, Mele A, Petrillo C, Trotta F, and Viliani G (2012) *J. Phys. Chem. B* 116: 5253.

Ruta B, Baldi G, Giordano VM, Orsingher L, Rols S, Scarponi F, and Monaco G (2010) *J. Chem. Phys.* 133: 041101.
Saviot L, Duval E, Surovtsev N, Jal JF, and Dianoux AJ (1999) *Phys. Rev. B* 60: 18.
Schirmacher W (2006) *Europhys. Lett.* 73: 892.
Schirmacher W, Diezemann G, and Ganter C (1998) *Phys. Rev. Lett.* 81: 136.
Schirmacher W, Folli V, Ganter C, and Ruocco G (2019) *J. Phys. A: Math. Theor.* 52: 464002.
Schirmacher W, Ruocco G, and Scopigno T (2007) *Phys. Rev. Lett.* 98: 025501.
Schirmacher W and Ruocco G (2022) In: Ramos RA (ed.) *Low-Temperature Thermal and Vibrational Properties of Disoredered Solids; A Half-Century of Universal "Anomalies" of Glasses*, p. 331. New Jersey: World Scientific.
Schirmacher W, Scopigno T, and Ruocco G (2014) *J. Noncryst. Sol.* 407: 133.
Schirmacher W and Wagener M (1989) In: Dianoux AJ, Petry W, and Teixeira J (eds.) *Dynamics of Disordered Materials*, p. 231. Heidelberg: Springer.
Schirmacher W and Wagener M (1992) *Philos. Mag. B* 65: 861.
Schirmacher W and Wagener M (1993) *Sol. State Comm.* 86: 597.
Schmid B and Schirmacher W (2008) *Phys. Rev. Lett.* 100: 137402.
Schmid B and Schirmacher W (2009) *Phys. Rev. Lett.* 103: 169702.
Schmuttenmaer CA (2004) *Chem. Rev.* 104: 1759.
Schober H (2014) *J. Neutron Res.* 17: 109.
Schober HR and Laird BB (1991) *Phys. Rev. B* 44: 6746.
Schulte A, Guo Y, Schirmacher W, Unruh T, and Cardinal T (2008) *Vibr. Spectrosc.* 48: 12.
Schulte A, Schirmacher W, Schmid B, and Unruh T (2011) *J. Phys. Condens. Matter* 23: 254212.
Seto M, Yoda Y, Kikuta S, Zhang XW, and Ando M (1995) *Phys. Rev. Lett.* 74: 3828.
Sette F, Krisch MH, Masciovecchio C, Ruocco G, and Monaco G (1998) *Science* 280: 1550.
Sette F, Ruocco G, Krisch MH, Bergmann U, Masciovecchio C, Mazzacurati V, Signorelli G, and Verbeni R (1995) *Phys. Rev. Lett.* 75: 850.
Shintani H and Tanaka H (2008) *Nature Materials* 7: 870.
Shuker R and Gammon R (1970) *Phys. Rev. Lett.* 25: 222.
Shvaika A, Shpot M, Schirmacher W, Bryk T, and Ruocco G (2021) *Phys. Rev. Lett.* 127: 179601.
Singwi KS and Sjölander A (1960) *Phys. Rev.* 120: 1093.
Sokolov AP, Kisliuk A, Quitmann D, and Duval E (1993) *Phys. Rev. B* 48: 7692.
Stephens RB (1973) *Phys. Rev. B* 8: 2996.
Stöckmann H-J (1999) *Quantum Chaos.* Cambridge, UK: Cambridge University Press.
Sturhahn W, Toellner TS, Alp EE, Zhang X, Ando M, Yoda Y, Kikuta S, Seto M, Kimball CW, and Dabrowski B (1995) *Phys. Rev. Lett.* 74: 3832.
Suekuni K, Tanaka HI, Kim FS, Umeo K, and Takabatake T (2015) *J. Phys. Soc. Japan* 84: 103601.
Surovtsev NV (2001) *Phys. Rev. E* 64: 061102.
Surovtsev NV (2004) *Phys. Stat. Sol. C* **1**: 2867.
Surovtsev NV, Adichtev SV, Rössler E, and Ramos MA (2004) *J. Phys. Condens. Matter* 16: 223.
Surovtsev NV, Shebanin AP, and Ramos MA (2003) *Phys. Rev. B* 67: 094203.
Surovtsev NV and Sokolov AP (2002a) *Phys. Rev. B* 66: 054205.
Surovtsev NV and Sokolov AP (2002b) *Phys. Rev. B* 66: 054205.
Tachibana M (2015) *Sol. St. Comm.* 211: 1.
Tachibana M, Kolodiazhnyi T, and Takayama-Muromachi E (2008) *Appl. Phys. Lett.* 93: 092902.
Taraskin S, Simdyankin S, Elliott S, Neilson J, and Lo T (2006) *Phys. Rev. Lett.* 97: 055504.
Taraskin SN, Loh YL, Natarajan G, and Elliott SR (2002) *Phys. Rev. Lett.* 86: 1255.
Thom R (1989) *Structural Stability and Morphogenesis: An Outline of a General Theory of Models*. Reading, MA: Addison-Wesley.
Tikhonov AN and Arsenin VY (2005) *Methods of Solitions of Ill-Posed Problems.* Moscow: Nauka. in Russian.
Tomaras C and Schirmacher W (2013) *J. Phys. Condens. Matter* 25: 495402.
Unruh T, Schulte A, Guo Y, Schirmacher W, and Schmid B (2008) *Vibr. Spectrosc.* 48: 12.
Vacher R, Foret M, Courtens E, and Pelous J (1998) *Philos. Mag.* 77: 523.
Vacher R, Woignier T, Pelous J, Coddens G, and Courtens E (1989) *Europhys. Lett.* 8: 161.
Vacher R, Woignier T, Pelous J, Coddens G, and Courtens E (2007) *Europhys. Lett.* 8: 161.
Viliani G, Dell'Anna R, Pilla O, Montagna M, Ruocco G, Signorelli G, and Mazzacurati V (1995) *Phys. Rev. B* 52: 3346.
Mazzacurati V, Montagna M, Pilla O, Viliani G, Ruocco G, and Signorelli G (1992) *Phys. Rev. B* 45: 2126.
Vollhardt D and Wölfle P (1980) *Phys. Rev. Lett.* 45: 482.
Wang L., Ninarello A., Guan P., Berthier L., Szamel G. and Flenner E., *Nat. Commun.* **10** (1), 2019, 26, https://doi.org/10.1038/s41467-018-07978-1.
Wang Y, Hong L, Wang Y, Schirmacher W, and Zhang J (2018) *Phys. Rev. B* 98: 174207.
Wischnewski A, Buchenau U, Dianoux AJ, Kamitakahara WA, and Zarestky JL (1998) *Phys. Rev. B* 57: 2663.
Wittmer JP, Tanguy A, Barrat J-L, and Lewis L (2002) *Europhys. Lett.* 57: 423.
Wright AC and Sinclair RN (1985) *J. Non-Cryst. Sol.* 76: 351.
Wuttke J, Petry W, Coddens G, and Fujara F (1995) *Phys. Rev. E* 53: 4026.
Wyart M (2005) *Annales de Physique (Paris)* 30: 1.
Wyart M (2010) *Europhys. Lett.* 89: 64001.
Wyart M (2012) *Phys. Rev. Lett.* 109: 125502.
Wyart M, Silbert M, Nagel SR, and Witten TA (2005) *Phys. Rev. E* 72: 051306.
Yakubo K and Nakayama T (1989) *Phys Rev. B* 40: 517.
Yoreo JJD, Knaak W, Meissner M, and Pohl RO (1986) *Phys. Rev. B* 34: 8828.
Yu CC and Leggett AJ (1988) *Comm. Condens. Matter Phys.* 14: 231.
Zanatta M, Fontana A, Orecchini A, Petrillo C, and Sacchetti F (2013) *J. Phys. Chem. Lett.* 4: 1143.
Zeller RC and Pohl RO (1971) *Phys. Rev. B* 4: 2029.
Zemlyanov MG, Malinovskii VK, Novikov VN, Parshin PP, and Sokolov AP (1992) *Sov. Phys. JETP* 74: 151.
Zorn R (2003) *J. Phys Condens. Matter* 15: R1025.
Zorn R (2011) *Physics* 4: 44.

Atomic structure of quasicrystals[☆]

M de Boissieu, Université Grenoble Alpes, CNRS, Grenoble INP-UGA, SIMaP, Grenoble, France

© 2024 Elsevier Ltd. All rights reserved.

This is an update of M. de Boissieu, Quasicrystals, Editor(s): Franco Bassani, Gerald L. Liedl, Peter Wyder, Encyclopedia of Condensed Matter Physics, Elsevier, 2005, Pages 86–95, ISBN 9780123694010, https://doi.org/10.1016/B0-12-369401-9/00693-8

Introduction 318
Which system forms quasicrystal? 319
Superspace crystallography and quasicrystals 321
Structural quality of quasicrystal 323
From diffraction data to a quasicrystal model: The case of the CdYb icosahedral quasicrystalline phase 324
General structure determination principles and periodic approximant 324
Phasing the data 324
Modeling and refining the quasicrystal atomic structure 326
Other examples 328
Icosahedral quasicrystals 328
Decagonal phase 329
Beyond the ideal quasicrystalline model and phason modes 329
Conclusion 331
Acknowledgments 331
References 331

Abstract

The structure determination of quasicrystals is presented. After an introduction on quasicrystals, the principles of the superspace crystallography are briefly introduced. This is then illustrated on the structure determination of the CdYb quasicrystal going from data collection to the final models. Other examples are briefly presented. Phason diffuse scattering is introduced in the last section.

Key points

- Introduction to aperiodic crystals
- Quasicrystal a special class of aperiodic crystals
- Presentation of the superspace crystallography for a non-specialist
- Quasicrystals are found in many different systems
- Structure of the binary CdYb icosahedral quasicrystal
- Phason fluctuations, phason elastic constants and diffuse scattering.

Introduction

The atomic structure of condensed matter materials has for long time been described by the ideal periodic crystal model: a unit cell, which repeats periodically towards infinity, is 'decorated' by a motif describing the atomic positions within the unit cell. The atomic structure is completely determined by the unit cell symmetry and size, and by its 'decoration'. Only particular symmetries are compatible with periodicity, leading to the 14 Bravais lattices and 230 different space groups (see 'Periodicity and lattices' and 'Space groups' articles). For instance, only two-, three-, four- and sixfold rotation axes are allowed, the fivefold rotational symmetry being incompatible with periodicity.

Extremely powerful tools have been developed for solving periodic atomic structures by means of the analysis of the intensity distribution in the X-ray, neutron or electron diffraction pattern and complex structures such as proteins, which contain several thousands of atoms in the unit cell, are now almost routinely determined (see 'diffraction', 'structure determination' articles). Indeed, if an X-ray (or neutron or electron) beam is sent on a periodic crystal, it is diffracted in specific directions and forms the so-called diffraction pattern. The diffraction pattern of a crystal is best understood through the use of Fourier transforms. The periodic crystal is described as the convolution between a periodic lattice (set of delta peaks) and a motif which describes the atomic

---

[☆] *Change History:* June 2023. M. de Boissieu replaced Figures 4, 7 to 14, and 16.

positions within the unit cell. Its Fourier transform (FT), which corresponds to the observed diffraction pattern, is the product of the FT of the lattice and the FT of the motif. The FT of the periodic lattice is also a periodic lattice, the reciprocal lattice. Positions of reciprocal lattice points, indicate the directions for which there is diffraction and are directly related to the Bragg law which relates the lattice plane d-spacing, the reciprocal lattice vectors and the incoming radiation wavelength. The reciprocal lattice has the same point group symmetry as the crystal under study, i.e., if a crystal has a threefold rotation axis the reciprocal space also has threefold symmetry. It follows from this that a fivefold diffraction pattern is 'forbidden,' or more precisely is incompatible with periodic lattice translation. The intensity distribution of the Bragg peaks depends on the atomic decoration of the unit cell and is given by the square of the FT of the 'decoration' or motif. All the structural information is contained in this intensity distribution but cannot be used directly because the phase of the Fourier transform is unknown. Direct methods or phasing algorithms such as the charge flipping, or low-density elimination allow to overcome this 'phase problem.' Phases are determined for the strongest Fourier amplitudes, and Fourier transformed. This allows to derive a starting model which is further refined against the observed Bragg peak intensity distribution.

In most materials departure from this ideal model is present in term of disorder which can be positional disorder, chemical disorder, partially occupied sites, vacancies, dislocations distribution, etc. This disorder gives rise to a supplementary contribution in the diffraction pattern which is smoothly varying in reciprocal space and is named diffuse scattering (Krivoglaz, 1969). When the disorder is not too large (bounded correlation-correlation) the resulting diffraction pattern is the superposition of Bragg peaks with the diffuse scattering. The later gives information on how the defects are distributed in the materials, with possible short range chemical order, distortion or changes in local interatomic distances, etc.

At the extreme, if too much disorder is present, material is described by the glass model in which only short-range order exists: it is characterized by a diffraction pattern in which Bragg reflections no longer exist and presents a smooth variation as a function of the scattering angle.

It is fair to say that most of the physical properties of materials are relying on their periodic description. The Bloch theorem and Brillouin zone boundaries are for instance key 'ingredients' in elaborating the theory of physical properties of condensed matter materials and both rely on the underlying periodicity. When disorder is present it is most of the time treated as a perturbation.

Quasicrystals belong to the large family of aperiodic crystals which encompasses incommensurately modulated phases, incommensurate composites and quasicrystals. All aperiodic crystals are characterized by the presence of long-range order, with Bragg peaks in their diffraction pattern and the absence of periodicity at least in one direction (Janssen et al., 2018). Incommensurately modulated crystals were observed soon after the discovery of the Bragg Laue, first in metallic alloys (Dehlinger, 1927) (Daniel and Lipson, 1942). In this case an ideal periodic structure is modulated by a wave (distortion or chemical) whose wavelength is incommensurate with the ideal structure periodicity. Composite structures are characterized by two interacting subsystems, with two periodicities whose ratio is irrational. They were first identified in the fool's gold $Hg_{3-\delta}AsF_6$ where mercury 1D chains ordered below 120 K (Hastings et al., 1977; Pouget et al., 1978) and in the compound TTF (Johnson and Watson, 1976) where ions form guest chain along the c axis of the TTF host lattice.

Both incommensurate modulated phases and incommensurate composites structures are best understood using the superspace theory developed by P.M. de Wolf, A. Janner and T. Janssen. In this theory the periodicity is recovered in a space of higher dimension than our 3D space (Janssen and Janner, 2014).

In 1984, Shechtman et al. published the electron diffraction pattern of a rapidly cooled AlMn alloy which displayed Bragg reflections and fivefold symmetry axes (Shechtman et al., 1984). This brought a lot of excitement, since two characteristic features of the diffraction pattern, believed to be incompatible, were present: long range order, as evidenced by the Bragg peaks, and fivefold symmetry. An example of the Laue diffraction pattern of a high-quality Al—Pd—Mn icosahedral quasicrystal is shown Fig. 1: Bragg peaks are sharp and the fivefold symmetry, characteristic of the icosahedron, is clearly visible. The discovery of Shechtman was named quasicrystal and is a new kind of long range ordered matter belonging to the aperiodic crystals' family. Soon after this discovery single grain quasicrystals have been obtained from slow cooling from the melt, establishing quasicrystals as a third class of aperiodic crystals. Besides the icosahedral symmetry, quasicrystals have been obtained in systems which are a periodic stacking of quasiperiodic planes with 8-fold, 12-fold and 10-fold symmetry.

Which system forms quasicrystal?

The first quasicrystalline samples were obtained by rapid quench from the melt and were metastable. As a consequence, only small single grains (less than 1 μm) could be synthesized and the only tool to pinpoint the quasicrystalline character was electron diffraction. Since then a large number of quasicrystalline phases have been discovered, in various systems (Janssen et al., 2018).

A large number of quasicrystals are made of intermetallic alloys Al, Zn or Cd based, such as AlMn, AlPdMn, AlCuFe, AlNiCo, ZnMgSc, ZnMgY, CdYb, AuGeSi . . .. (Tsai, 2013). Some of them are stable at room temperature and can be obtained by slow cooling from the melt, or usual growth process such as Bridgman or Czochralski, leading to mm or even cm sized single grain quasicrystals. Their composition range is in general very limited, almost as a line compound. The stabilizing mechanism of intermetallic quasicrystal is far from being understood, but size effects and Hume-Rothery electronic stabilization are believed to play a crucial

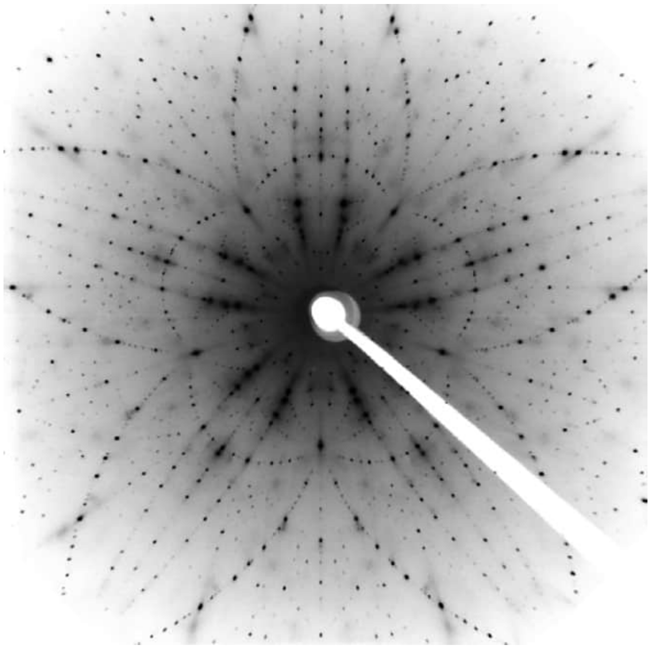

Fig. 1 Fivefold axis Laue X-ray diffraction pattern of the i-AlPdMn phase. Courtesy of W. Steurer, ETH Zürich, Switzerland.

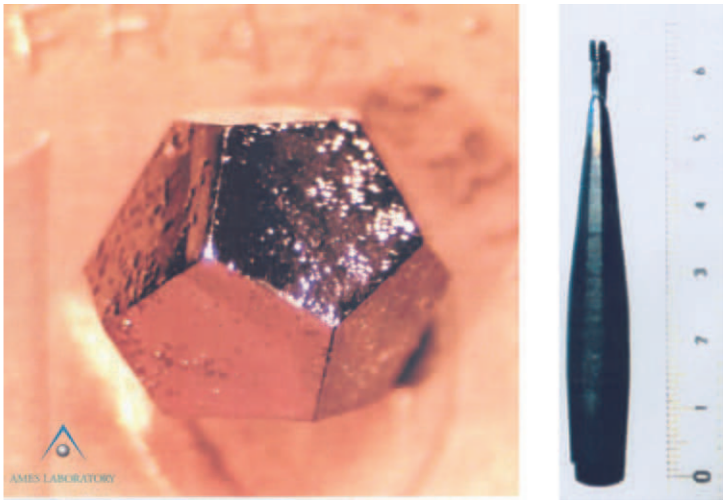

Fig. 2 Left panel: Single grain of the ZnMgY phase obtained by slow cooling from the melt (Courtesy of P. Canfield, Ames laboratory, United States). Right panel: single grain of the i-AlPdMn quasicrystal obtained bt Czochralski growth. From Boudard M, Bourgeat-Lami E, de Boissieu M, Janot C, Durand-Charre M, Klein H, Audier M and Hennion B (1995) Czokralski growth of AlPdMn quasicrystal. *Philosophical Magazine Letters* **71**: 11–16.

role (Janssen et al., 2018; Tsai, 2013). The Fig. 2 displays an example of a single grain of the ZnMgY icosahedral phase obtained by slow cooling from the melt whose facets form a dodecahedron, nicely illustrating the icosahedral symmetry at a macroscopic scale (Inaba et al., 2000). Also shown is a centimeter single crystal of the icosahedral AlPdMn phase obtained by Czochralski growth (Boudard et al., 1995).

The recent discovery of a layer 2D dodecagonal quasicrystal in the Ba—Ti—O system grown on a metallic substrate, has opened the route to possible discovery of oxide quasicrystals (Förster et al., 2013) and demonstrating that intermetallic quasicrystals are not the only possible quasicrystals.

Another large family of quasicrystals, most of them with dodecagonal symmetry, has been synthetized in soft condensed matter such as supramolecular dendrimer liquid crystals, surfactant-coated metallic nanoparticles, mesoporous silica, colloidal copolymer micelles in solution, and ABC star terpolymers and two kinds of linear block copolymers in condensed (Dotera, 2011). In this case the length scale at play is much larger than interatomic distances and is rather of the order of the interparticle distances i.e., 1 nm or larger.

Superspace crystallography and quasicrystals

The understanding of the structure of incommensurately modulated structures has been munch improved by the introduction of superspace crystallography by P.M. de Wolf, A. Janner and T. Janssen (Janssen and Janner, 2014). The same approach can be applied to quasicrystals where periodicity is recovered in a space of dimension larger than three. For icosahedral quasicrystals, a six-dimensional space is necessary to recover periodicity. It is beyond the scope of this article to give the details of this approach and we refer to (Janssen et al., 2018) for an introduction.

As an illustration of this procedure, we elaborate in the following on a simple 1-D example: the Fibonacci chain. It is built up with two tiles whose length is in the ratio $\tau/1$, τ being the golden mean (1.618...). The Fibonacci chain can be constructed by a substitution rule L- >LS and S- >L, where L and S stand for the long and short segment. The resulting 1-D structure is quasiperiodic and has the form LSLLSLSLLSLLS.... A compact description of this structure is achieved in a 2-D periodic space, briefly described hereafter. Let us start with a square lattice in a 2-D space. The latter is decomposed in two orthogonal subspaces: the physical space, also called parallel space (E_{par}), and a complementary space called perpendicular space (E_{per}, Fig. 3). The slope of the physical space with respect to the lattice is irrational and is equal to $1/\tau$. The square lattice is decorated with segment lines, elongated along the perpendicular direction, and whose length is equal to the projection of the square onto the perpendicular space. The 1-D quasicrystal is obtained as a section of the decorated periodic lattice by E_{par}: each time the E_{par} line intercepts a segment line, an atomic position is generated. The final result is the Fibonacci chain. The advantage of the high dimensional description is that, since periodicity is recovered, the relationship between direct and reciprocal space can be computed using FT. The indexing of the diffraction pattern can be carried out, and structural modeling and refinement against observed data can be handled. Moreover, all the information on the structure (local environment, interatomic distances, etc.) is now contained in a very compact form with the decorated square unit cell. More complex structures can be generated: for instance, the segment line can be given a longer length: this will generate additional positions in the 1-D quasicrystal. It is also possible to add other segment lines in the square unit cell, which could mimic another atomic species.

This procedure generalizes to the case of 3-D quasicrystals such as icosahedral phases. In this case the higher-dimensional space is six-dimensional and the 6D lattice is hyper-cubic. Segment lines are now 3-D objects called occupation domains or atomic surfaces. The problem of structure determination is that of finding the location and the detailed shape of the occupation domains. Although it might seem a simple task, it is a complex problem, for which only recently satisfactory solutions have been proposed. Indeed, specifying the shape of a 3-D occupation domain requires an infinite number of parameters, and guidelines have to be found for the modeling.

Let us return to the 1-D case and look for the diffraction pattern of the Fibonacci chain. The diffraction pattern can be computed from the FT of the 2-D decorated lattice: this is the product of the FT of the lattice with the FT of the segment line. The 2D reciprocal space is also decomposed into the parallel (physical) reciprocal space and the perpendicular one. As a result of the FT of the decoration which are segment lines, intensities are stronger when the perpendicular component of the reciprocal vector is small as illustrated in Fig. 4. Remembering that the section becomes a projection by FT, the 1D diffraction pattern is obtained by projecting all the points in 2D onto the parallel 1D physical reciprocal space. The 2D diffraction pattern can be indexed by two integer indices, and each reciprocal lattice vector has a component in the parallel space and one in the 'perpendicular' space. This is kept after the projection scheme, and the 1D diffraction pattern is also indexed by two integers. Since the slope is irrational, there is a dense set of Bragg reflections, but only a finite number of them are larger than a given threshold. The procedure is illustrated in Fig. 4.

In the case of the icosahedral phase, six integer indices are necessary for indexing the diffraction pattern: they correspond to the six directions pointing towards the vertices of an icosahedron. The Fig. 5 display the X-ray diffraction pattern measured along a fivefold axis for the icosahedral AlPdMn quasicrystal. Indexing is carried out with two indices along this specific axis, following a procedure analogous to the Fibonacci chain, but this corresponds to a summarized notation of the real six indices. All Bragg peaks can be indexed un-ambiguously at a position that can be exactly computed and from which a lattice parameter a_{6D} can be derived and is equal to 0.6451 nm in this case. Note the two length scale at play 1 and τ, where τ is the golden mean and which are characteristic of the icosahedral quasicrystal. These two length scales have a ratio that is irrational. There is also along this particular twofold axis an inflation property that is characteristic of the quasicrystalline long range order: if a reflexion is found at a position 1, there will be also reflexions at any power of τ, as illustrated by the red lines.

Within this scheme of superspace crystallography, the route from diffraction data to the atomic structure is in some sense similar to what is achieved in standard crystallography: the point group and space group of the quasicrystal is determined from the

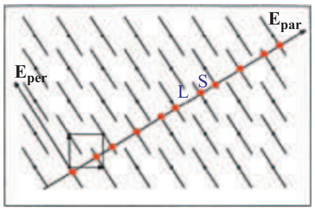

Fig. 3 Illustration of the 2-D description of a 1-D quasicrystal, here the Fibonacci chain (see text).

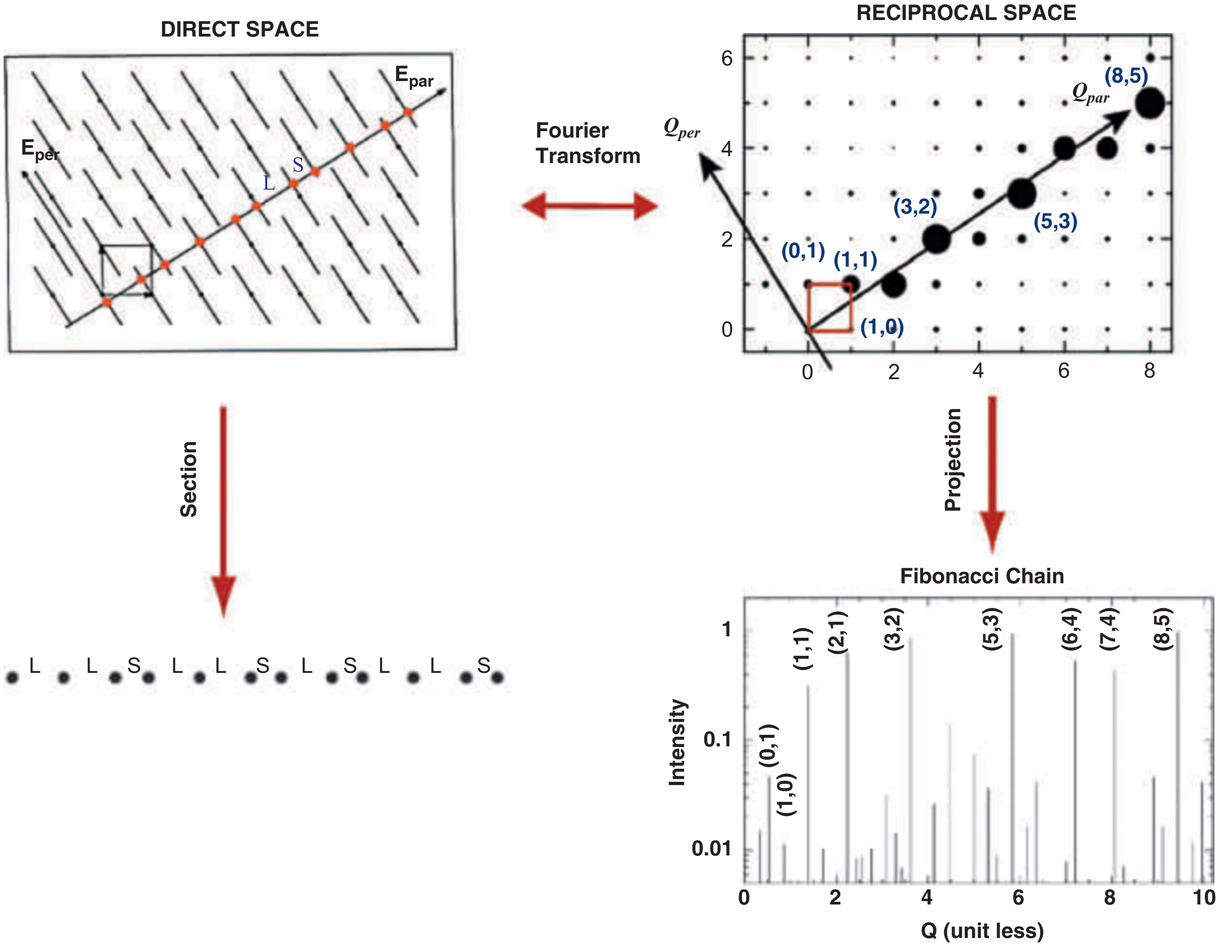
DIRECT SPACE
E_par
E_per
L
S
Section
L L S L L S L S L L S
Fourier Transform
RECIPROCAL SPACE
Q_per
Q_par
(8,5)
(3,2)
(5,3)
(0,1)
(1,1)
(1,0)
0
2
4
6
8
Projection
Fibonacci Chain
(1,1)
(2,1)
(3,2)
(5,3)
(6,4)
(7,4)
(8,5)
(0,1)
(1,0)
Intensity
1
0.1
0.01
0
2
4
6
8
10
Q (unit less)

Fig. 4 Illustration of the super-space crystallography principle (see text) in the case of the 1D Fibonacci quasicrystal. Starting from 2D lattice with segment lines as 'decoration' in direct space, its Fourier transform gives the 2D diffraction pattern. It can be indexed by two integer indices. The 1D diffraction pattern is obtained from a projection of the 2D diffraction. For the direct space the 1D structure is obtained as a section of the 2D periodic space.

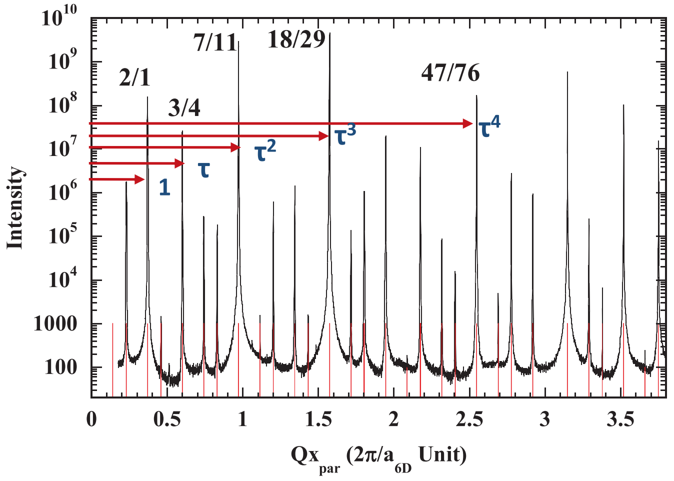

Fig. 5 X-ray diffraction pattern taken along a fivefold axis in the i-AlPdMn phase. The two number indices is a short-hand notation for the six indices scheme. Note that the position of the indexed Bragg reflections scales with τ, the golden mean.

diffraction spectrum (see Fig. 3). Then reciprocal space data phasing allows in general to specify approximately the position and shape of the atomic surface, from this a model is proposed which is then compared to available diffraction data. We will follow these steps in the following, but first we give a brief outline of the high degree of structural quality obtained in quasicrystals.

Structural quality of quasicrystal

As for any materials, quasicrystals contain defects (vacancies, dislocations, strain, etc.), which will result in either a Bragg peak broadening or diffuse scattering. Because of the quasiperiodic arrangement, the effect of defects on the diffraction will depend on both the parallel and the perpendicular component of the reciprocal lattice vector. In the theory of QC, a distortion or a fluctuation associated with the perpendicular component has been named phason (we will come back later on this notion) and leads to changes in the diffraction pattern associated with the perpendicular component of the scattering wave-vector (Q_{per}). For instance, we can imagine that the slope of the parallel space in Fig. 3 is changing: if the slope becomes rational this will lead to a periodic structure. Such a change is equivalent to a shear strain in the perpendicular direction and has been named 'phason strain'. A distribution of phason strain will result in a broadening of the Bragg reflection (which are no longer delta peaks), in very much the same way that a distribution of elastic strain in a periodic crystal leads to a Bragg peak broadening. In the early days of quasicrystal studies, most of the obtained quasicrystals displayed distorted diffraction patterns, or Bragg peak broadening, so that the notion of long-range quasiperiodic order had been even questioned. Quasicrystals obtained most recently display a high degree of quasiperiodic long-range order, demonstrated by Bragg peaks which are almost resolution limited.

In some cases, the structural quality is such that dynamical X-ray diffraction has been evidenced. The Fig. 6 shows 2-D images of Bragg peaks obtained in a high-resolution setting. The left part shows Bragg peaks in an i-AlPdMn sample obtained by the Czochralski method, whereas the right part correspond to the same Bragg reflections, once the single quasicrystal has been annealed (Letoublon et al., 2001). As it is evident, Bragg reflections are almost resolution limited after annealing of the sample, with a coherent length which is of the order 10 μm. Of course, quasicrystals still contain some defects and are not as 'perfect' as silicon for instance, but their quality is comparable to the best inter-metallic alloys and the notion of long-range quasiperiodic order is now strongly supported by experimental results.

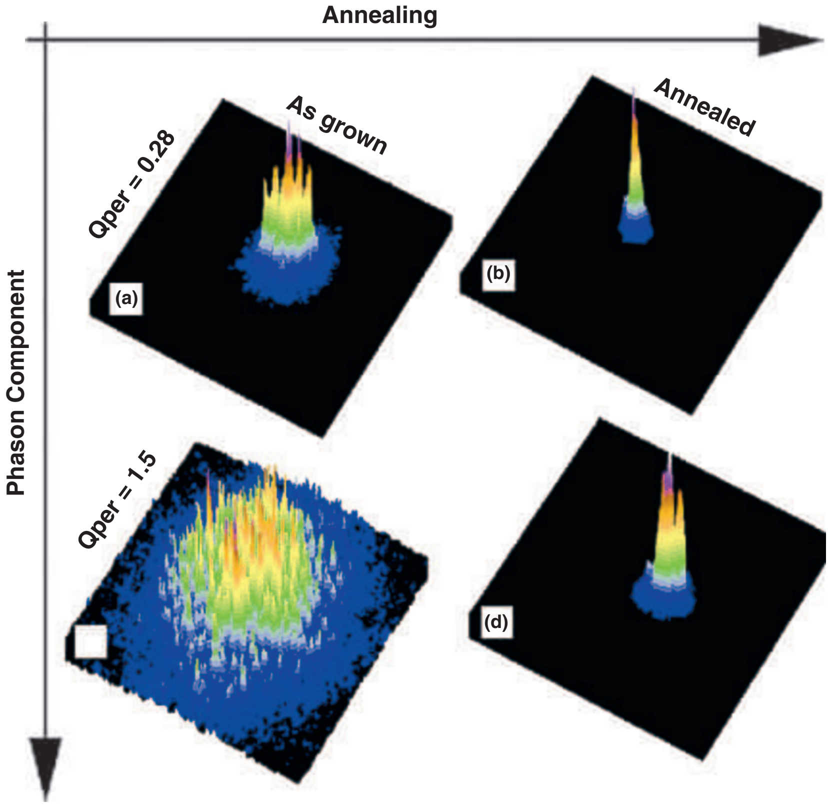

Fig. 6 2-D images of the Bragg reflections obtained in the i-AlPdMn phase for an as grown single grain quasicrystal (left) and the same sample after annealing (right). Whereas Bragg reflections are broadened (with a broadening proportional to Qper) in the as cast sample, they are almost resolution limited in the annealed sample. From Letoublon A, Yakhou F, Livet F, Bley F, de Boissieu M, Mancini L, Caudron R, Vettier C and Gastaldi J (2001) Coherent X-ray diffraction and phason fluctuations in quasicrystals. *Europhysics Letters* **54**: 753–759.

From diffraction data to a quasicrystal model: The case of the CdYb icosahedral quasicrystalline phase

General structure determination principles and periodic approximant

The understanding of the atomic structure of quasicrystals made tremendous progresses in recent years. It can be said that in a few systems the understanding of the quasicrystal atomic structure together with its crystal chemistry is analogous to what is achieved for periodic intermetallic with relatively large unit cells. This means that not only the atomic positions have been determined, but also and very importantly the chemical nature of each atom and the way it is connected to other chemical species is well understood.

The general method used for the structure determination of quasicrystals will be exemplified with the case of the icosahedral $Cd_{5.7}Yb$ quasicrystal known as a 'Tsai' type quasicrystal, in the recognition of professor An-Pang Tsai's (1958–2019) exceptional series of new intermetallic quasicrystal discoveries (Tsai et al., 2000). The i-CdYb quasicrystal discovery is particularly interesting because this was the first binary quasicrystal, that could be obtained by slow cooling from the melt as large single grain quasicrystal. Moreover, there is a very good 'contrast' between the Cd with $Z = 48$ electrons and the Yb with $Z = 70$ electrons when X-ray diffraction is used. This means that Cd and Yb atoms can be easily distinguished by X-ray diffraction.

Finally in the same system and for a small composition change, it is possible to synthetize periodic approximants. In the high dimensional picture, a crystalline approximant can be obtained by changing the slope of the cut space which becomes rational. For instance, in the case of the 2D Fibonacci chain description if τ the golden mean is replaced by 1/1 the resulting sequence will be LSLSLS. . .. We say that in this case a 1/1 approximant has been generated. Depending on the symmetry of the periodic approximant, there is a relation between the unit cell of the 6D periodic structure and the cell parameter of the crystalline approximant. In the case of the CdYb system a 1/1 and 2/1 periodic approximant can be synthetized. The Cd_6Yb phase is a cubic 1/1 approximant with a lattice parameter equal to 1.56 nm and a Im3 space group. The $Cd_{5.8}Yb$ is a cubic 2/1 approximant with a lattice parameter τ times larger and equal to 2.52 nm (τ is the golden mean). The structure determination of these two periodic approximants gives key information for the modeling of the structure of the quasicrystal (Pay Gómez and Lidin, 2001; Pay Gómez and Lidin, 2003). Indeed, when comparing the diffraction pattern of the 1/1 approximant and the quasicrystal, it is striking to notice that the positions of the most intense Bragg peaks are located almost (although not exactly) at the same position in reciprocal space. This is exemplified in the Fig. 7 which displays a twofold section of the reciprocal lattice of the 1/1 approximant and the quasicrystal, the Bragg peak intensity being proportional to the area of each circle.

The main cluster which is used for the structure description of the 1/1 and 2/1 approximant and the quasicrystal is shown in Fig. 8. It is a series of atomic shells with an overall icosahedral symmetry except for the first shell. The first shell is a Cd tetrahedron, that occurs in several orientations and is thus disordered. The second shell is a Cd dodecahedron, the third shell is a Yb icosahedron, the fourth shell is a Cd icosidodecahedron and finally the last shell is a large triacontahedron containing 156 atoms. It is important to stress that this cluster is markedly different from what is encountered in organic chemistry with, for instance, fullerenes. Here the Cd—Yb system is an intermetallic system, with an almost close packing of a small (Cd) and a large (Yb) atom as is exemplified in the bottom row of the Fig. 8. This is very much like the case of Franck-Kasper phases. The large cluster is connected along twofold axis, sharing a face, and along threefold axis where there is an overlap as exemplified in Fig. 9. Moreover, in the 2/1 approximant an extra 'building block' is necessary to describe the structure: a prolate rhombohedra with Cd atoms on vertices and mid-edges, together with Yb atoms along the long diagonal. All the different units that constitute the necessary 'ingredients' for the icosahedral quasicrystal modeling are displayed in Fig. 9.

Phasing the data

Solving the atomic structure of the icosahedral i-CdYb quasicrystal was achieved thanks to a large data collection of Bragg peak intensities using synchrotron radiation and a sophisticated modeling achieved in the 6-D periodic space (Takakura et al., 2007).

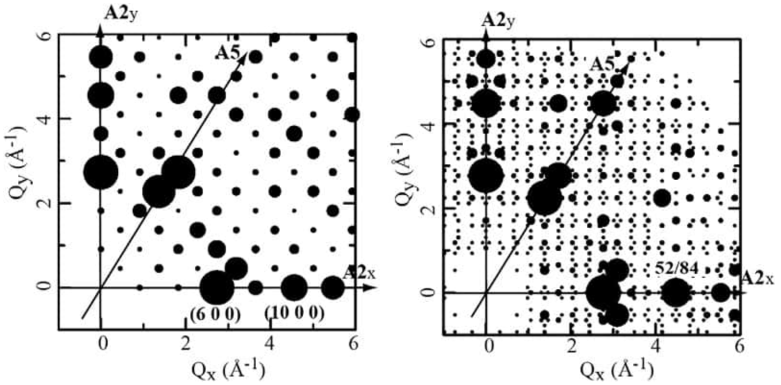

Fig. 7 Comparison of the twofold section of reciprocal space for the Cd_6Yb 1/1 approximant (left) and the $Cd_{5.7}Yb$ icosahedral quasicrystal (right). The area of the disks are proportional to the Bragg peak intensities. The intensity distribution of the strongest Bragg peaks is similar. This is a signature of similar local environments.

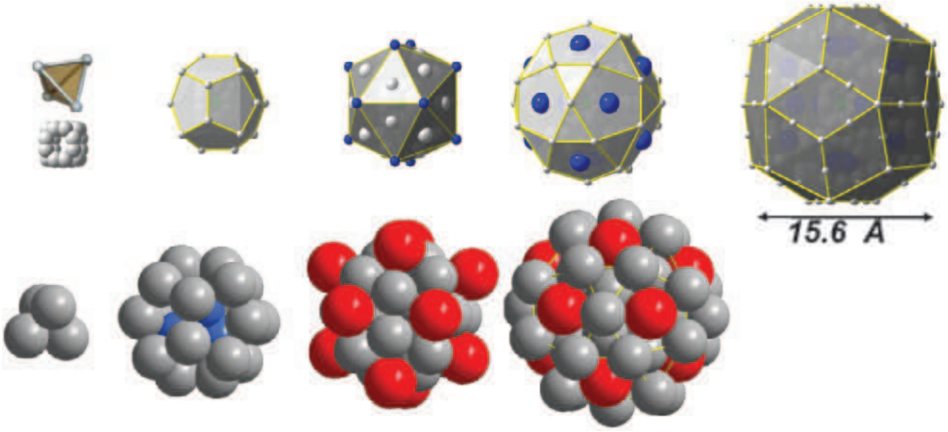

Fig. 8 The principal cluster which can be used for the description of both the 1/1 and 2/1 approximant and the icosahedral quasicrystal in the CdYb system. Gray spheres stand for Cd atoms. Blue (respectively red) spheres stand for Yb atoms. The upper row describes the successive shells starting from a Cd disordered tetrahedron, a Cd dodecahedron, an Yb icosahedron, a Cd icosidodecahedron and a final Cd triacontahedron that contains 156 atoms. The 1/1 approximant is a BCC packing of this large cluster, which interpenetrates along the threefold axis. The bottom row is the same description in sphere packing model that emphasizes that the cluster is a close-packing of a large (Yb) and a small (Cd) atom, quite similarly to so called Franck and Kasper phases.

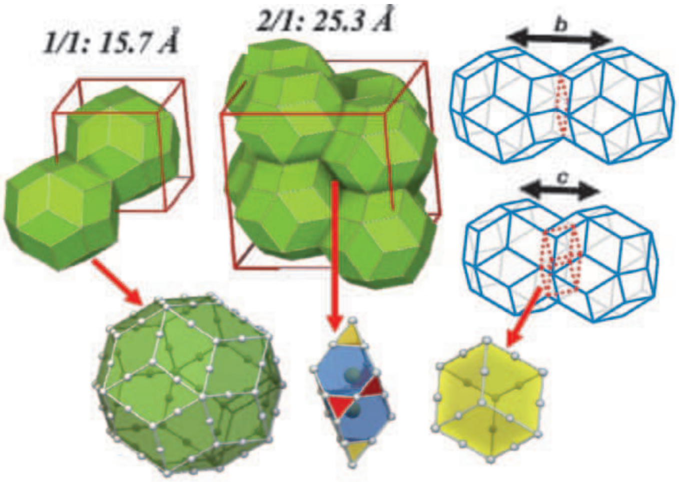

Fig. 9 Description of the cubic 1/1 and 2/1 approximant using the three elementary building blocks: a large triacontahedron, a prolate and oblate rhombus shown on the bottom part of the figure. The 1/1 approximant is shown on the left, the 2/1 on the central panel. The right panel shows the connection of the large triacontahedron along a twofold (b) or threefold (c) axis. From Takakura H, Gomez CP, Yamamoto A, de Boissieu M and Tsai AP (2007) Atomic structure of the binary icosahedral Yb-Cd quasicrystal. *Nature Materials* **6**: 58–63.

More than 5000 independent integrated Bragg peak intensities have been measured, from which the structure factor moduli can be extracted (square root of the Bragg peak intensities). The first step in the structure determination is to provide a first density map. As for a periodic crystal, one major problem is the so-called phase problem, since only the amplitude of the Fourier components is measured by diffraction. New phasing tools such as the low-density elimination or the charge flipping methods developed for periodic crystals, have been shown to be valid for the case of aperiodic crystals including quasicrystals. This has been a major step in the field, since before only Patterson analysis was feasible. Using these new phasing methods, which provide at least 60% of correct phases, the measured structure factors can be phased and a first 6D density map computed by Fourier transform. This is a crucial step that already leads to detailed information on the structure. An example of a section of the 6-D electron density map obtained by Fourier transform of the phased amplitudes of the CdYb quasicrystal is given in Fig. 10. The section shows the 6D periodicity and is built up by a linear combination of two 6D lattice vectors with indices [100000] and [011111]. The segment lines, elongated in the perpendicular direction, are the traces of the 3D atomic surfaces, which lie in the perpendicular space. This is completely analogous to what was presented in the introduction. As can be seen on this figure, only three different positions in the 6D cube are occupied, labeled V (for vertex), E (for mid-edge, 0.500000) and B (for body-center, ½(111,111)). The traces have different length in perpendicular spaces: the largest one is at the B position, then at O and finally at E. This is indicating that the atomic surfaces to be considered have significantly different sizes. We can also notice that the electron density is higher on the B site, which means that this site is likely occupied by Yb atoms for they have a larger number of electrons (70) than Cd one's (48). A complete analysis of the

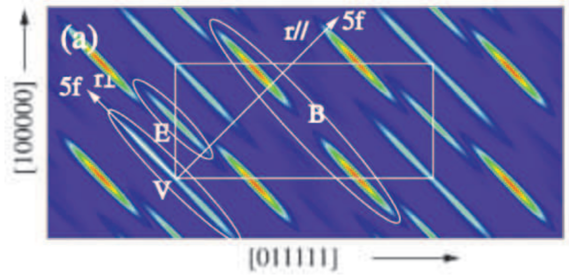

Fig. 10 Section of the 6D CdYb electron density obtained by Fourier transform of the phased structure factors. The section contains a fivefold axis both in physical, parallel space and in the perpendicular space. V, E and B stand for vertex, mid-edge and body-center sites respectively. The elongated density encircled in white ellipsoids, are the traces of the 3D atomic surfaces lying in the perpendicular direction. Note that the electron density is higher at the B position, indicating this site is occupied by Yb atoms.

6D Fourier map allows one determining what are the most likely clusters in the resulting 3D quasicrystalline structure. As was already anticipated, the large Tsai-type cluster is observed, with the same chemical decoration as the one observed in periodic approximant, i.e., the icosahedron is made of Yb atoms whereas the rest of the cluster is built up with Cd atoms.

Although the previous density maps already give some information on the resulting atomic structure, it is obviously necessary to go beyond if any detailed information has to be predicted. Indeed, some phases are wrongly assigned on one hand, and on the other hand the density maps suffer from severe Fourier termination effects, which leads to unreasonable short interatomic distances. Therefore, and similarly to what is done for periodic crystals, a modeling of the structure is a necessary following step, allowing a refinement against measured data. It has to be pointed out that the comparison with diffraction data remains a powerful test, especially for weak Bragg reflections which are very sensitive to the details of the atomic structure (details of the atomic surface shape for instance).

Modeling and refining the quasicrystal atomic structure

Modeling of the atomic structure of quasicrystals requires in principle an infinite number of parameters since it is an infinite structure. Although the high dimensional description simplifies the quasicrystal picture, the number of parameters remains much larger than the one which can be refined using the diffraction data. This is why a certain number of constraints or hypothesis have been proposed to restrict models within a reasonable number of parameters.

First the chemical composition and atomic density should be close to the experimental one's. Then short distances should be avoided, and finally the crystal-chemistry should be similar to what is known with periodic approximants. All those constraints are particularly important for any atomic scale simulation of physical properties of quasicrystals. Although these constraints are 'simple' they are already difficult to fulfill, but not enough to restrict fully the modeling.

A second set of hypothesis comes with the knowledge (when feasible) of the atomic structure of periodic approximants. We have already seen that for the CdYb case the 'building blocks' to be used for the modeling of the quasicrystal structure could be determined from the 1/1 and 2/1 approximant. This is validated by the first density map calculation.

Using these set of constraints and hypothesis, a model with a restricted number of parameters (about 250) can be used for comparison with experimental data. The large overlapping triacontahedron cluster is placed on the vertices of the so-called 12-fold packing quasicrystalline network proposed by C. Henley. Indeed, this icosahedral quasicrystal networks allows to place a large triacontahedron cluster on each node of this network with cluster-cluster connections along two- and threefold axis, as this is observed in the periodic approximants. The remaining gaps in between the clusters are filled with the decorated prolate. This modeling is in fact very much compatible with the initially observed electron density (Takakura et al., 2007). Finally, the atomic positions are allowed to be moved from their 'ideal' position. This parameter is sometime called a 'parallel' shift and allows the clusters to depart from their ideal position as was identified in early modeling of quasicrystals (de Boissieu et al., 1990). This is an extremely important parameter that allows describing the crystal chemistry of the quasicrystal.

Using this approach, a full 6D model could be proposed and refined against the experimental data containing 5000 independent Bragg peak intensities. The agreement between the model and the experiment is very good with an R factor of 0.09. The 6D model can then be used to understand the corresponding 3D structure.

As expected from the model many large triacontahedron clusters can be found and are connected along 2- and threefold axis. This is illustrated in the Fig. 11 which displays the cluster distribution in the resulting 3D structure. The left part shows a 3D view of the atomic structure highlighting the large triacontahedron cluster in green and the decorated prolate in blue. This prolate is sometime isolated as observed in the 2/1 approximant, but most of the time it appears grouped in portions of the so-called Bergman cluster which is illustrated on the right part. What also results from the structure is a very strong distortion of the icosahedral symmetry of the clusters. This is illustrated in the right panel of the Fig. 11 and is the result of the orientation of the central tetrahedron. This is in fact very similar to what is observed in the 1/1 approximant in the Zn—Sc systems which is isostructural. Whereas the central tetrahedron appears as disordered at high temperature, it orders below 190 K leading to a doubling of the cell

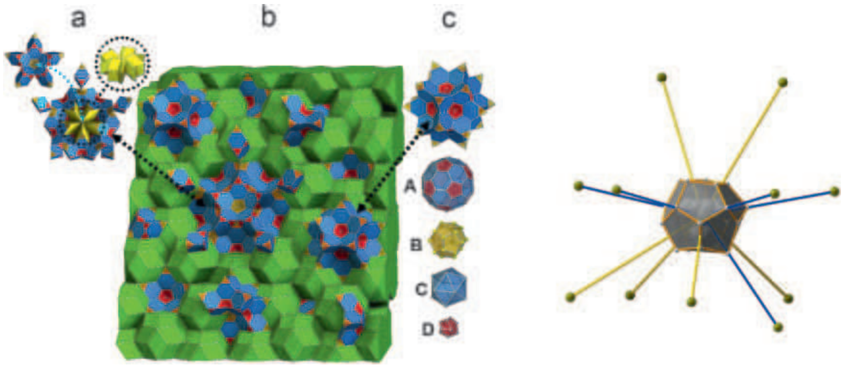

Fig. 11 Resulting 3D quasicrystalline model as obtained from a section of the 6D model. Left panel: distribution of the large triacontahedron cluster (in green) and the decorated prolate (in blue). Some clusters formed by the prolate are highlighted. In particular the large Bergman cluster whose decomposition is shown on the right of the panel. Left panel: zoom on the first shell of the cluster, the Cd dodecahedron, as obtained after the refinement. The central tetrahedron produces a significant distortion that is clearly visible on the figure. From Takakura H, Gomez CP, Yamamoto A, de Boissieu M and Tsai AP (2007) Atomic structure of the binary icosahedral Yb-Cd quasicrystal. *Nature Materials* **6**: 58–63.

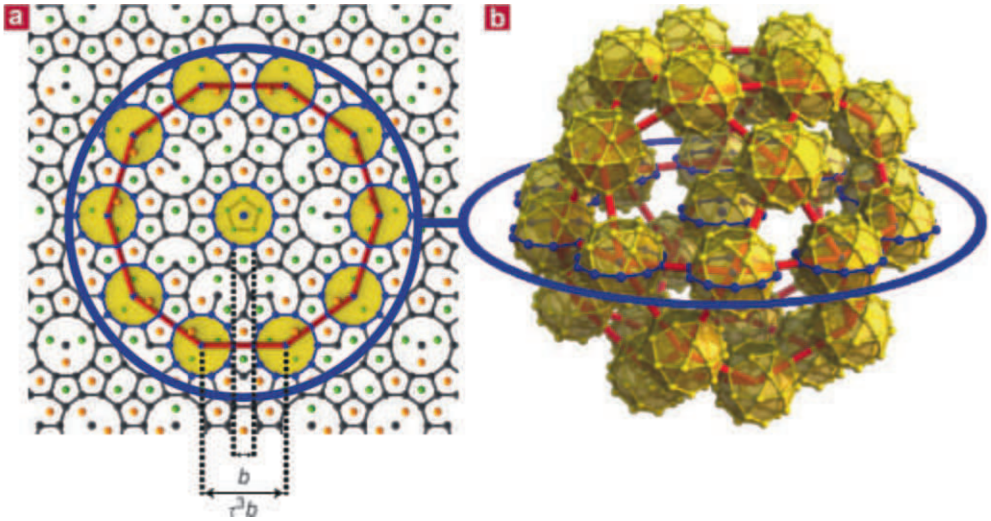

Fig. 12 Hierarchical distribution of the clusters. The position of the large triacontahedron cluster is shown by colored circles. The left panel is a fivefold section whereas the right one is a 3D view. The clusters are arranged in a cluster of clusters, here an icosidodecahedron shown ad a yellow disk (10 cluster in the plane) or a yellow cluster. At a larger scale this cluster of cluster also arrange in a bigger cluster, again an icosidodecahedron shown with red link. The scale change in this hierarchical packing is τ^3, where τ is the golden mean. From Takakura H, Gomez CP, Yamamoto A, de Boissieu M and Tsai AP (2007) Atomic structure of the binary icosahedral Yb-Cd quasicrystal. *Nature Materials* **6**: 58–63.

along 110 together with a monoclinic distortion. The ordering of the central tetrahedron induces a severe departure from icosahedral symmetry of the shells (Ishimasa et al., 2007). The very same is observed in the icosahedral phase, which might seem surprising at first sight. This distortion is clearly visible on the Fig. 11 right panel. In fact, although the icosahedral symmetry of each cluster is broken, the overall icosahedral symmetry of the structure is recovered as a result of the different orientations of the cluster upon icosahedral symmetry.

Another interesting feature of the quasicrystal structure concerns its hierarchical nature. This is exemplified with the 3D triacontahedron cluster distribution. The Fig. 12 displays the spatial distribution of the triacontahedron cluster centers. The left part is a fivefold section whereas the right part is a 3D view. When looking at the central part of the left panel, one clearly observes a ring of 10 dots, i.e., an arrangement of 10 clusters. In fact, this is a 'cluster of clusters' whose shape is an icosidodecahedron as shown by the yellow color clusters on the right panel. At a larger scale this yellow 'clusters of clusters' arrange themselves in an even larger cluster as illustrated by the red connections. This 'inflated' large cluster is again an icosidodecahedron. The length scale change is each time τ^3, where τ is the golden mean. This hierarchical packing goes to infinity in the ideal quasicrystal model and is a signature of the quasiperiodic long-range order.

Finally, it is also interesting to look at the projected electron density. Because there is a long-range quasiperiodic order, the projected electron density displays clear maxima, from which dense atomic planes can be defined. An illustration is given on the Fig. 13 that displays the twofold projection of the electron density of the CdYb icosahedral quasicrystal. The gray color scale

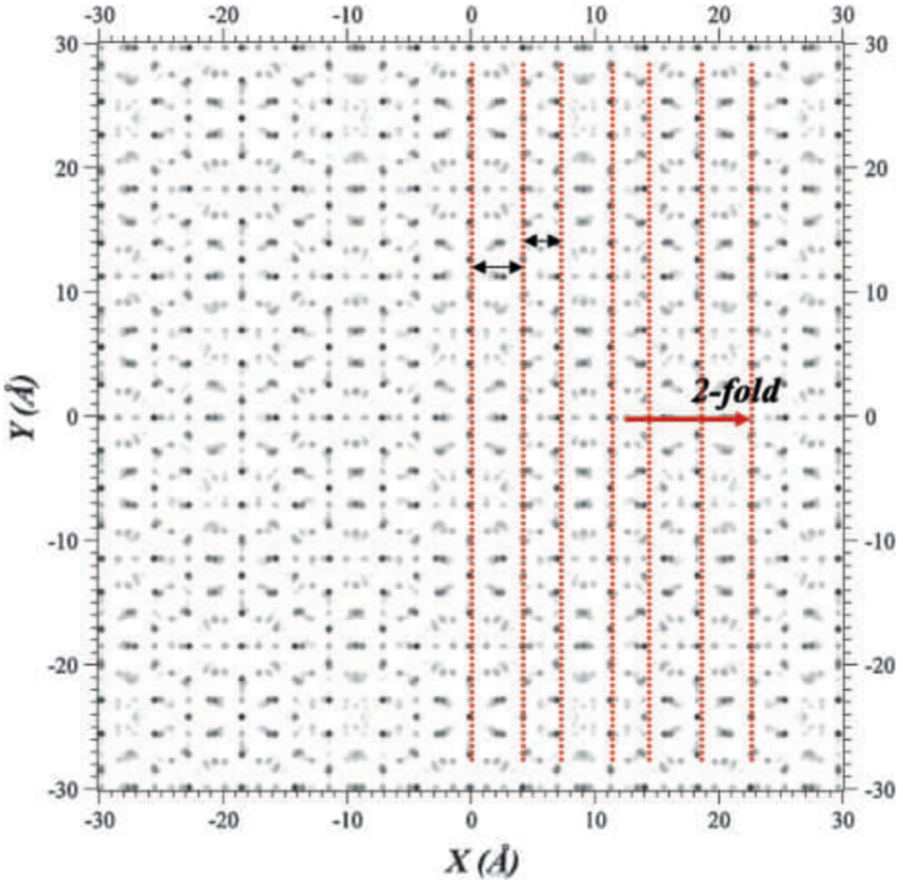

Fig. 13 Projected atomic density of the CdYb quasicrystal on a twofold plane. The gray scale indicates the scale of the density. High density points correspond to atomic column. They are arranged in relatively dense planes, highlighted by the red dashed lines, separated by two length scale in the ratio 1/τ.

indicates the value of the projected density, the highest value being black. First, one clearly sees black spots, which are the signature of atomic columns. Second, it is possible to define dense atomic planes, for which the density of these columns is rather high: they are highlighted by red dashed vertical line on Fig. 13. Finally, this set of dense atomic planes are quasiperiodically distributed with two characteristic length scales related by the golden mean. Already observed in the first models proposed for the i-AlPdMn quasicrystal (Boudard et al., 1992), this description is very useful to understand the faceting or the surfaces of quasicrystals.

Other examples

Icosahedral quasicrystals

It is not possible to review all the quasicrystalline structures which have been solved since the discovery of quasicrystals in 1984. After a period of exploration of the superspace crystallography, first employed for rapidly quenched sample in the icosahedral Al—Mn systems (Cahn et al., 1988a, 1988b, 1988c), various modeling strategies have been tested. The main problem, as explained in the previous chapter, being the determination of the exact shape of the so-called atomic surface. When there are no high order periodic approximants at hand, other strategies have to be defined. They were proposed for so-called Mackay type quasicrystals, for which the main cluster is believed to be a Mackay cluster as observed in i-AlCuFe and i-AlPdMn (Boudard et al., 1992; Gratias et al., 2001; Quiquandon and Gratias, 2006) but for which a complementary Bergman cluster is of importance (Gratias et al., 2001).

For intermetallic compounds, all icosahedral structure discovered so far fall in three categories: Mackay-type, Bergman-Type and Tsai-type as a reference to the main constituting atomic cluster. Again, as emphasized in the previous paragraph, those cluster have to be viewed as rather dense sphere packing and are markedly different to what is encountered in oxide or organic compounds.

The procedure described in section "From diffraction data to a quasicrystal model: The case of the CdYb icosahedral quasicrystalline phase" is now mature and has been applied to various system. The chemical disorder, with site occupancy mixing could even been solved in a few systems such as the Zn—Sc binary quasicrystal. This structure is isomorphic to the one of the CdYb quasicrystal Zn playing the role of Cd and Sc the one of Yb. However, its chemical composition indicates that some Zn/Sc disorder should occur, unlike what is observed in the Cd—Yb case. All the tools for structure determination are mature so that this kind of chemical disorder can be delt with, in a way that is completely similar to what is achieved for complex periodic intermetallic compounds

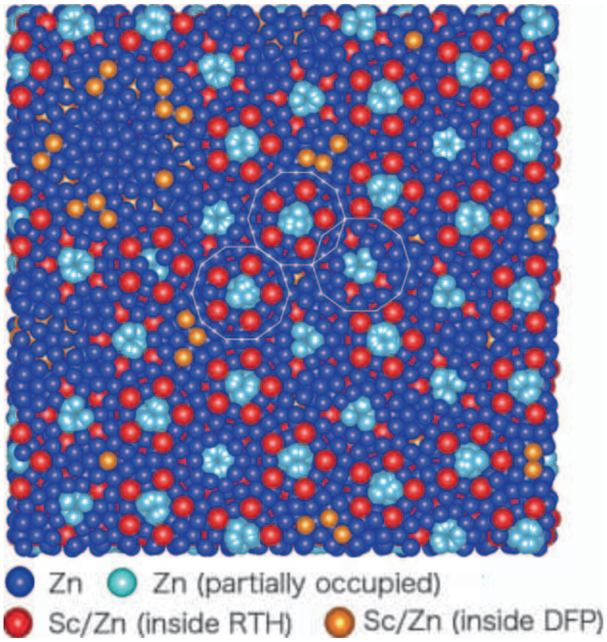

Fig. 14 Zn—Sc icosahedral quasicrystal structure. A fivefold section of the quasicrystal model is displayed. Zn and Sc atoms are show as blue and red spheres respectively. Position with a mixed Zn/Sc occupation are show as orange spheres. They are located on specific local environment. The white lines are the traces of the large triacontahedron cluster. From Yamada T, Takakura H, Euchner H, Pay Gomez C, Bosak A, Fertey P and de Boissieu M (2016) Atomic structure and phason modes of the Sc-Zn icosahedral quasicrystal. *IUCrJ* **3**(4): 247–258.

(Yamada et al., 2016). An illustration of the resulting structure is given in the Fig. 14: fully occupied sites (Zn or Sc) but also mixed occupied site are highlighted on this figure illustrating the high quality of structure determination which can be achieved now.

Such a detailed understanding of the quasicrystal structure allowed detailed studies on physical properties as for instance phonons (de Boissieu et al., 2007).

Decagonal phase

The decagonal phase is a periodic stacking of quasiperiodic planes. A large number of studies have been performed on such systems. Because of the periodic axis, if viewed along the 10-fold symmetry axis, interpretation of high-resolution transmission electron microscopy images is possible. Indeed, many models have been proposed from similar images analysis. One should keep in mind however, that the observed images are projections of the structure. In the ‘simple’ decagonal phases, where the periodicity is of the order 4 Å, there are only two different atomic layers, and the interpretation is relatively easy. This is not the case however for other decagonal phases.

The direct interpretation of images is appealing, since one can directly see the structure, although atomic resolution is difficult to achieve. The first step is to find the underlying quasiperiodic lattice, in the form of a tiling (Penrose tiling or equivalent). Note that it is not obvious, a priori, that a quasicrystal can be described by a decorated tiling. Various types of tilings have been used in the d-AlNiCo, most of them being a variant of the Penrose tiling which is made of two tiles. The second step is to find a decoration for the proposed tiling. This is achieved most of the time by super-imposing the tiling on the images (Hiraga et al., 1994). Since atoms are not visible, atom positions are inferred from the known approximant phases. An image is then simulated and compared to the experimental image. One interesting modeling has been proposed with the so-called quasi-unit cell approach. Instead of using two tiles, a single atomic cluster configuration is used to map the structure: specific overlap rules are used to generate a complete covering. Fig. 15 shows the electron diffraction pattern together with the corresponding high-resolution images. The single cluster covering is superimposed on the figure, and the decoration is shown in the enlarged part. Agreement between the simulated image and the experimental one is satisfactory (Steinhardt et al., 1998).

The same procedure as the one described for the i-CdYb quasicrystal has also been used using X-ray diffraction. In the case of decagonal quasicrystals, the atomic surfaces are 2D objects. Refinement of the occupation parameters and of the parallel shift is carried out in a similar way. The resulting structure is close to the one obtained by HREM images analysis, although a description in terms of a single cluster is probably a too crude approximation (Steurer, 2004; Steurer and Deloudi, 2009).

Beyond the ideal quasicrystalline model and phason modes

The idealized description of periodic crystals is known to be an approximation. In fact very few real materials can be described as perfectly ordered structure corresponding to the ideally infinite periodic crystal. In periodic crystals, fluctuations

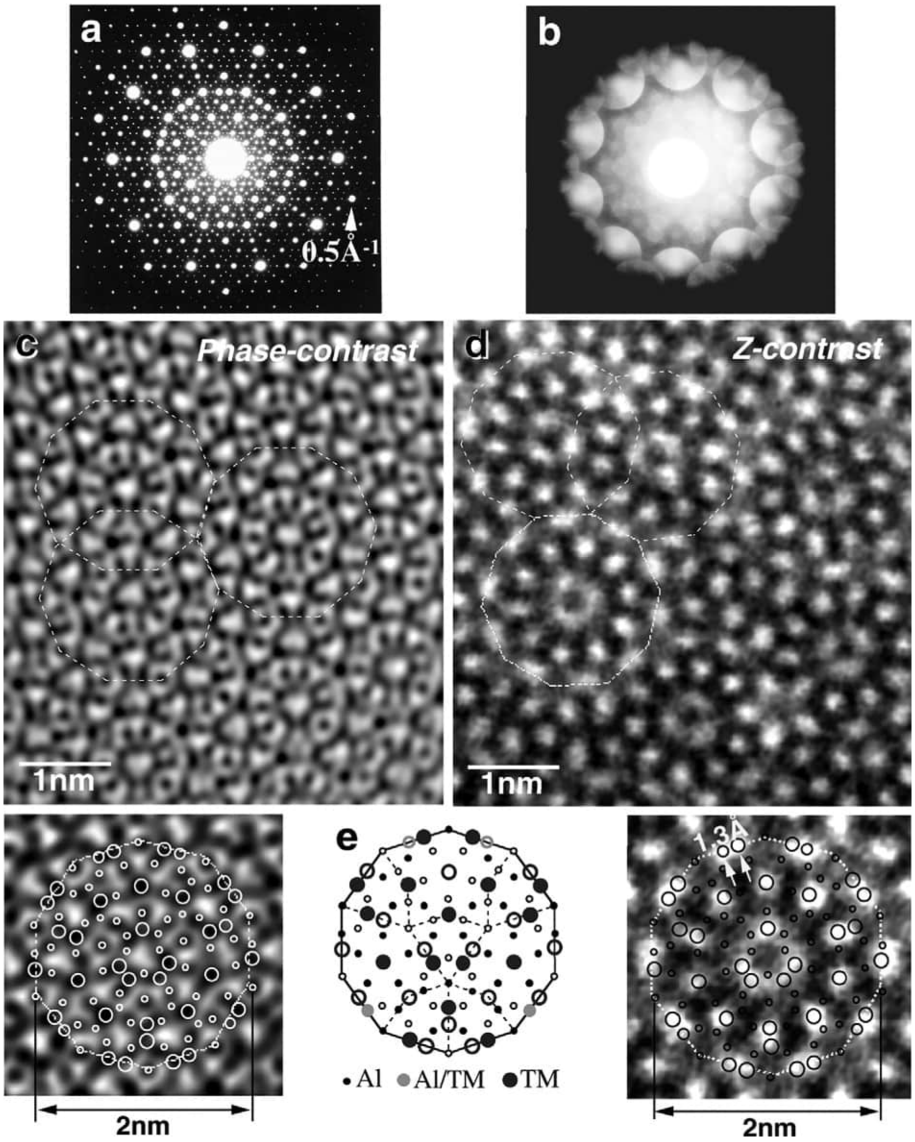

Fig. 15 (a) and (b) electron diffraction pattern of the AlNiCo decagonal phase. (c) Corresponding phase contrast image. The quasi-unit cell is outlined. (d) corresponding *Z*-contrast images. (e), (f) and (g) quasi-unit cell decoration compared to the experimental images. Courtesy of E. Abe, NIMS, Tsukuba, Japan.

(phonons, pre-transitional phonon soft modes, etc.), defects and in general disorder are present with various degrees of strength. Understanding the disorder, its correlations, its influence on physical properties is thus known to be a key challenge in solid state physics and material science. This disorder most often shows up as so-called diffuse scattering which occurs near or in between the Bragg peaks which is one of the key tools to study defects.

The same is of course true for quasicrystals. However, because of the aperiodic long-range order there are new excitations named phason modes (cp. section "Structural quality of quasicrystal"). Phason modes are a consequence of the degeneracy of the free energy with respect to a translation of the cut space, in the high dimensional description of aperiodic crystals. A detailed introduction to phason is beyond the scope of this article and can be found in (Janssen et al., 2018). The main point to be emphasized is that phason fluctuations, exactly as phonon fluctuations, will give rise to diffuse scattering with a characteristic signature in the diffraction pattern: the phason diffuse scattering is located 'beneath' the Bragg peaks, with a $1/q^2$ decay (q is the distance from the Bragg peak position) and a shape anisotropy that is determined by only two phason elastic constants in the case of icosahedral quasicrystals (Janssen et al., 2018). Such phason diffuse scattering has been observed in all icosahedral quasicrystals even those with an extremely high degree of perfection as shown by their Bragg width resolution limited. This is in particular the case for the i-AlPdMn quasicrystal (de Boissieu et al., 1995), whose phason fluctuations become dynamics at high temperature (Francoual et al., 2003). The Fig. 16 illustrates the presence of phason diffuse scattering in the case of the icosahedral ZnSc quasicrystal. The left panel of the figure displays a 2D slice of the reciprocal space as detected on a synchrotron radiation beam line using hybrid pixel detectors. A clear anisotropic distribution of diffuse scattering is observed around the Bragg peaks.

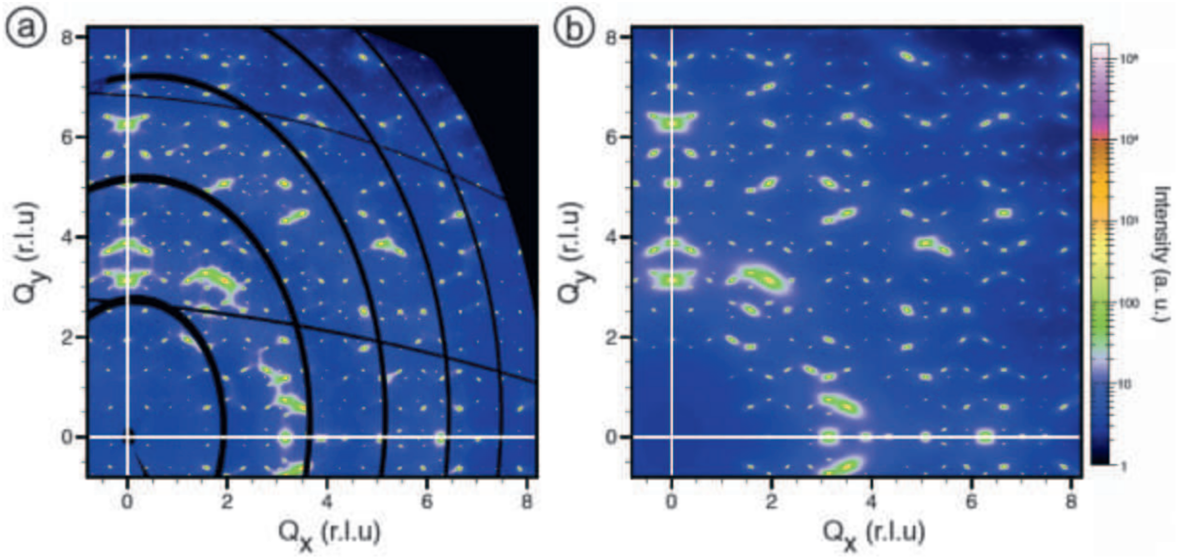

Fig. 16 Phason diffuse scattering as observed in the Zn—Sc icosahedral quasicrystal. Left panel: Reconstructed twofold section of reciprocal space as measured by X-ray synchrotron using a Zn—Sc single grain quasicrystal. Anisotropic distribution of diffuse scattering is well visible around the Bragg peaks. Right panel: simulation of the diffuse scattering using the two phason elastic constant K1 and K2. The agreement with experiment is excellent. From Yamada T, Takakura H, Euchner H, Pay Gomez C, Bosak A, Fertey P and de Boissieu M (2016) Atomic structure and phason modes of the Sc-Zn icosahedral quasicrystal. *IUCrJ* 3(4): 247–258.

This distribution of diffuse scattering is perfectly reproduced on the right panel, using only two phason elastic constants as parameters. This is a very nice illustration of the specific phason fluctuation (here most likely quenched in) occurring in most quasicrystals.

Conclusion

In conclusion the atomic structure of quasicrystals is now rather well understood. The high dimensional approach is a very powerful tool for analyzing diffraction data and a detailed analysis and modeling is now possible. The resulting structure can be analyzed in term of clusters, local environment, and dense atomic planes. The crystal chemistry can also be well understood, in a way very similar to what is achieved for complex periodic crystals. Phason fluctuations are also important to understand the disorder of quasicrystals. It is thus fair to say that the understanding of the atomic structure of quasicrystal is now very well advanced and sufficient for the purpose of detailed atomic scale simulation for the understanding of their physical properties.

Acknowledgments

This overview is dedicated to the memory of Ted Janssen and An-Pang Tsai, two major scientists in the field of aperiodic crystals, with whom I had the chance to share many results and discussions.

References

Boudard M, de Boissieu M, Janot C, Heger G, Beeli C, Nissen H, Vincent H, Ibberson R, Audier M, and Dubois JM (1992) Neutron and X-ray single crystal study of the AlPdMn icosahedral phase. *Journal of Physics. Condensed Matter* 4: 10149–10168.

Boudard M, Bourgeat-Lami E, de Boissieu M, Janot C, Durand-Charre M, Klein H, Audier M, and Hennion B (1995) Czokralski growth of AlPdMn quasicrystal. *Philosophical Magazine Letters* 71: 11–16.

Cahn JW, Gratias D, and Mozer B (1988a) A 6-D structural model for the icosahedral (Al, Si)—Mn quasicrystal. *Journal de Physique Archives* 49: 1225–1233.

Cahn JW, Gratias D, and Mozer B (1988b) Patterson Fourier analysis of the icosahedral (Al, Si)—Mn alloys. *Physical Review B* 38: 1638–1642.

Cahn JW, Gratias D, and Mozer B (1988c) Six dimensional Fourier analysis of the icosahedral $Al_{73}Mn_{21}Si_6$ alloy. *Physical Review B* 38: 1643–1647.

Daniel V and Lipson H (1942) An X-ray study of the dissociation of an alloy of copper, iron and nickel. *Proceedings of the Royal Society A* 181: 368–378.

de Boissieu M, Janot C, and Dubois JM (1990) Quasicrystal structure: Cold water on the Penrose tiling scheme. *Journal of Physics. Condensed Matter* 2: 2499–2517.

de Boissieu M, Boudard M, Hennion B, Bellissent R, Kycia S, Goldman AI, Janot C, and Audier M (1995) Diffuse scattering and phason elasticity in the AlPdMn icosahedral phase. *Physical Review Letters* 75(1): 89.

de Boissieu M, Francoual S, Mihalkovic M, Shibata K, Baron AQR, Sidis Y, Ishimasa T, Wu D, Lograsso T, Regnault LP, Gähler F, Tsutsui S, Hennion B, Bastie P, Sato TJ, Takakura H, Currat R, and Tsai AP (2007) Lattice dynamics of the Zn–Mg–Sc icosahedral quasicrystal and its Zn–Sc periodic 1/1 approximant. *Nature Materials* 6: 977–984.

Dehlinger U (1927) Über die Verbreiterung der Debyelinien bei kaltbearbeiteten Metallen. *Zeitschrift für Kristallographie* 65: 615–631.

Dotera T (2011) Quasicrystals in soft matter. *Israel Journal of Chemistry* 51(11–12): 1197–1205.

Förster S, Meinel K, Hammer R, Trautmann M, and Widdra W (2013) Quasicrystalline structure formation in a classical crystalline thin-film system. *Nature* 502(7470): 215–218.

Francoual S, Livet F, de Boissieu M, Yakhou F, Bley F, Letoublon A, Caudron R, and Gastaldi J (2003) Dynamics of phason fluctuations in the i-AlPdMn quasicrystal. *Physical Review Letters* 91: 225501. 1–4.

Gratias D, Puyraimond F, Quiquandon M, and Katz A (2001) Atomic clusters in icosahedral F-type quasicrystals. *Physical Review B* 63: 024202. 1–16.

Hastings JM, Pouget JP, Shirane G, Heeger AJ, Miro ND, and MacDiarmid AG (1977) One-Dimensional Phonons and "Phase-Ordering" Phase Transition in $Hg_{3-\delta}AsF_6$. *Physical Review Letters* 39(23): 1484–1487.

Hiraga K, Abe E, and Matsuo Y (1994) The structure of an Al-Pd decagonal quasicrystal studied by high-resolution electron microscopy. *Philosophical Magazine Letters* 70(3): 163–168.

Inaba A, Takakura H, An PT, Fisher IR, and Canfield PC (2000) Heat capacities of icosahedral and hexagonal phases of Zn-Mg-Y system. *Materials Science and Engineering A* 294–296: 723–726.

Ishimasa T, Kasano Y, Tachibana A, Kashimoto S, and Osaka K (2007) Low temperature phase of the Zn-Sc approximant. *Philosophical Magazine* 87: 2887–2897.

Janssen T and Janner A (2014) Aperiodic crystals and superspace concepts. *Acta Crystallographica. Section B* 70(4): 617–651.

Janssen T, Chapuis G, and de Boissieu M (2018) *Aperiodic Crystals. From Modulated Phases to Quasicrystals*, 2nd edn. p. 20. Oxford: Oxford University Press.

Johnson CK and Watson CR (1976) Superstructure and modulation wave analysis for the unidimensional conductor hepta- (tetrathiafulvalene) pentaiodide. *The Journal of Chemical Physics* 64(6): 2271–2286.

Krivoglaz M (1969) *Theory of X-Ray and Thermal-Neutron Scattering by Real Crystals*. New York: Plenum Press.

Letoublon A, Yakhou F, Livet F, Bley F, de Boissieu M, Mancini L, Caudron R, Vettier C, and Gastaldi J (2001) Coherent X-ray diffraction and phason fluctuations in quasicrystals. *Europhysics Letters* 54: 753–759.

Pay Gómez C and Lidin S (2001) Structure of Ca13Cd76: A novel approximant to the MCd5.7 quasicrystals (M.Ca, Yb). *Angewandte Chemie* 40: 4037–4039.

Pay Gómez C and Lidin S (2003) Comparative structural study of the disordered MCd/sub 6/quasicrystal approximants. *Physical Review B* 68: 024203.

Pouget JP, Shirane G, Hastings JM, Heeger AJ, Miro ND, and MacDiarmid AG (1978) Elastic neutron scattering of the "phase ordering" phase transition in $Hg_{3-\delta}AsF_6$. *Physical Review B* 18(7): 3645–3656.

Quiquandon M and Gratias D (2006) An unique ideal structure model for AlPdMn and AlCuFe icosahedral phases. *Physical Review B* 74: 214205.

Shechtman D, Blech I, Gratias D, and Cahn JW (1984) Metallic phase with long-range orientational order and no translational symmetry. *Physical Review Letters* 53: 1951–1953.

Steinhardt PJ, Jeong H-C, Saitoh K, Tanaka M, Abe E, and Tsai AP (1998) Experimental verification of the quasi-unit-cell model of quasicrystal structure. *Nature* 365: 55–57.

Steurer W (2004) Twenty years of structure research on quasicrystals. Part I. Pentagonal, octagonal, decagonal and dodecagonal quasicrystals. *Zeitschrift fuer Kristallographie* 219: 391–446.

Steurer W and Deloudi S (2009) *Crystallography of Quasicrystals*. Springer.

Takakura H, Gomez CP, Yamamoto A, de Boissieu M, and Tsai AP (2007) Atomic structure of the binary icosahedral Yb-Cd quasicrystal. *Nature Materials* 6: 58–63.

Tsai AP (2013) Discovery of stable icosahedral quasicrystals: Progress in understanding structure and properties. *Chemical Society Reviews* 42: 5352–5365.

Tsai AP, Guo JQ, Abe E, Takakura H, and Sato TJ (2000) A stable binary quasicrtystal. *Nature* 408: 537–538.

Yamada T, Takakura H, Euchner H, Pay Gomez C, Bosak A, Fertey P, and de Boissieu M (2016) Atomic structure and phason modes of the Sc-Zn icosahedral quasicrystal. *IUCrJ* 3(4): 247–258.

Materials: Composites

C Zweben, Zweben Consulting, Newtown Square, PA, United States

© 2024 Elsevier Ltd. All rights reserved.

This is an update of C.H. Zweben, Composites: Overview, Editor(s): Franco Bassani, Gerald L. Liedl, Peter Wyder, Encyclopedia of Condensed Matter Physics, Elsevier, 2005, Pages 192–208, ISBN 9780123694010, https://doi.org/10.1016/B0-12-369401-9/00545-3.

Introduction 333
Overview of composite materials and applications 334
Reinforcements 336
Glass fibers 336
Carbon (graphite) fibers 337
Boron fibers 337
Fibers based on silicon carbide 338
Fibers based on alumina 338
Aramid fibers 338
High-density polyethylene fibers 338
PBO fibers 338
Characteristics and properties of composite materials 338
Overview of mechanical and physical properties 339
Overview of manufacturing processes 340
Polymer matrix composites 340
Metal matrix composites 344
Carbon matrix composites 345
Ceramic matrix composites 346
Thermal management materials 347
Conclusion 347
Acknowledgments 348
References 349

Abstract

Composite materials, which we define as two or more materials bonded together, have revolutionary properties compared to traditional monolithic materials. As a result, they have had dramatic effects on an increasing number of applications. We divide them into four key classes: polymer matrix, metal matrix, carbon matrix and ceramic matrix. At this time, polymer matrix composites (PMCs) are the most widely used. In this article, we examine the four classes of composites, including reinforcements, matrix materials, manufacturing process, applications, and future developments.

Key points

- What is a composite material?
- What are the four classes of composite materials?
- What are the types of reinforcement materials?
- What are the key reinforcing fibers?
- How are composites made?
- What are the key applications of composite materials?
- What are the likely future developments?

Introduction

A composite material is two or more materials bonded together (Kelly, 1994). This definition distinguishes composite materials (composites) from materials like alloys. The most important composites consist of matrices reinforced with various types of fibers, whiskers or particles. Using composites technology, it is possible to design new, multifunctional materials with unique properties and combinations of properties that cannot be obtained with any monolithic material.

Many widely used materials are composites, but not generally recognized as such. For example, what are typically called tungsten carbide cutting tools are actually composites consisting of tungsten carbide particles bound together with a cobalt matrix, rather than monolithic tungsten carbide (Zweben, 1994, 1998). The reason for using the composite is that it has much higher fracture toughness than monolithic tungsten carbide, a brittle ceramic.

Composites are material systems. Their properties depend on those of the constituents (reinforcement and matrix), reinforcement coating, if any, and the process by which the composite is made. All of these have pronounced effects, and altering any can greatly affect properties.

The development of composites and the related design and manufacturing technologies is one of the most important advances in the history of materials. Composites are widely used, and are enabling materials in many applications. For example, Voyager, which was in effect an all-composite aircraft, was the first to fly around the world without refueling. However, we emphasize that modern composites technology is only about five decades old. In the history of materials, this is hardly the blink of an eye. However, the basic technologies required to design and manufacture reliable structures are well developed (Gdoutos, 2018; Crane, 2018; Talreja, 2018; Johnson, 2018; Zweben, 1998).

It is common to think of composite materials primarily as structural materials. However, there are numerous examples of applications for which nonmechanical properties, such as thermal, electrical, magnetic and piezoelectric, for example, are of primary interest. Important applications based on nonmechanical properties include glass-fiber-reinforced polymer printed circuit boards, magnetic-particle-reinforced polymer audio and video recording tape and ceramic-particle-reinforced polymer sensors.

Another unique characteristic of composites is that many are made with processes that have advantages over those used for monolithic materials (Pourtarsip, 2018). To cite one example, manufacturing methods for fiber-reinforced polymers allow fabrication of aircraft structures having shapes that are aerodynamically superior to those made from metals. Another illustration is magnetic-particle-reinforced polymer permanent magnets that easily can be made into complex shapes by process like injection molding.

Composites are usually categorized by the type of material used for the matrix. The primary classes are polymer matrix composites (PMCs), metal matrix composites (MMCs), intermetallic matrix composites (IMCs), ceramic matrix composites (CMCs), and carbon matrix composites (CAMCs). The last category, CAMCs, includes carbon/carbon composites (CCCs), which consist of carbon matrices reinforced with carbon fibers (Savage, 1993). At this time, PMCs are the most widely used.

We note that biological structural materials occurring in nature are typically composites. Common examples are wood, bamboo, bone, teeth, and shell. Further, use of artificial composite materials is not new. Bricks made from straw-reinforced mud were employed in biblical times. This material also has been widely used in the American Southwest for centuries, where it is known as adobe. In current terminology, it would be described as an organic-fiber-reinforced ceramic matrix composite.

As discussed earlier, there are many types of composites. This article concentrates on those that are used primarily because of their mechanical and thermal properties.

Overview of composite materials and applications

For the purposes of this article, we divide solid materials into four categories: polymers, metals, ceramics and carbon. We consider carbon to be a separate class because of its many unique forms and characteristics. There are reinforcements and matrix materials in all four categories of solids. This results in the potential for a limitless number of new material systems having unique properties that cannot be obtained with any single monolithic material. As Table 1 shows, composites consisting of all possible combinations of matrix materials and reinforcements have been produced.

For decades, CCCs were the only significant type of CAMC (Savage, 1993). However, there are now other types of composites utilizing a carbon matrix. Notable among these is silicon carbide fiber-reinforced carbon, which is being used in military aircraft gas turbine engine components (Gonczy, 2015; Ruggles-Wrenn, 2018; Steibel, 2019).

As Table 2 shows, the characteristics of the four classes of matrix materials used in composites differ radically. This is reflected in the properties of the resulting composites.

Composites are now important commercial and aerospace materials. At this time, PMCs are the most widely used (Pourtarsip, 2018). MMCs are employed in a significant and increasing number of commercial and aerospace applications, such as automobile engines, electronic packaging, cutting tools, circuit breaker contact pads, high-speed and precision machinery, and aircraft structures (Clyne, 2018). CCCs are used in high temperature, lightly loaded applications, such as aircraft brakes, rocket nozzles, glass processing equipment and heat treatment furnaces (Ruggles-Wrenn, 2018). The Space Shuttle Orbiter has CCC leading edges.

Table 1 Classes of composite materials.

	Reinforcement			
Matrix	*Polymer*	*Metal*	*Ceramic*	*Carbon*
Polymer	X	X	X	X
Metal	X	X	X	X
Ceramic	X	X	X	X
Carbon	X	X	X	X

Table 2 Properties of selected matrix materials.

Material	*Class*	*Density (g/cm^3)*	*Modulus (GPa)*	*Tensile Strength (MPa)*	*Tensile Failure Strain (%)*	*Thermal Conductivity (W m^{-1} K^{-1})*	*CTE (10^{-6} K^{-1})*
Epoxy	Polymer	1.8	3.5	70	3	0.1	60
Aluminum (6061)	Metal	2.7	69	300	10	180	23
Titanium (6Al-4 V)	Metal	4.4	105	1100	10	16	9.5
Silicon Carbide	Ceramic	2.9	520	–	< 0.1	81	4.9
Alumina	Ceramic	3.9	380	–	< 0.1	20	6.7
Glass (borosilicate)	Ceramic	2.2	63	–	<0.1	2	5
Amorphous Carbon	Carbon	1.8	20	–	< 0.1	5–90	2

Although CMCs are not as widely used as the other classes of composites at this time, there recently have been significant applications in aircraft gas turbine engines that are indicative of their potential (Ruggles-Wrenn, 2018).

Composites technology makes possible the use of an entire class of solid materials, ceramics, in applications for which monolithic versions are unsuited because of their great strength scatter and poor resistance to mechanical and thermal shock (Ruggles-Wrenn, 2018). Further, some manufacturing processes for CAMCs are well adapted to the fabrication of large, complex structures. This allows consolidation of parts, which can reduce manufacturing costs.

In addition to their excellent structural properties, composites have unique physical properties that make them of great interest for applications such as thermal management and packaging of microelectronic, optoelectronic and microelectromechanical (MEMS) devices (Zweben, 2001, 2002a, b, 2018a, b). For example, carbon fibers with thermal conductivities much greater than that of copper are now commercially available. These reinforcements are being used in polymer, metal, and carbon matrices to create composites with high thermal conductivities that are being used in applications for which thermal management is important. Discontinuous versions of these fibers are also being incorporated in thermoplastic injection molding compounds, improving their thermal conductivity by as much as two orders of magnitude or more. This greatly expands the range of products for which injection molded polymers can be used. In addition, there are an increasing number of composites reinforced with diamond particles, which impart very high thermal conductivities and low CTEs. Thermal management materials are covered in a section near the end of the article.

Composites are now used in a wide and increasing range of important commercial and aerospace applications (Clyne, 2018; Pourtarsip, 2018; Ruggles-Wrenn, 2018; Rawal et al., 1990), including

- Internal combustion engines
- Machine components
- Thermal management
- Electronic, optoelectronic and microelectromechanical system (MEMS) packaging
- Automobile, train, ship, spacecraft, launch vehicle and aircraft structures
- Aircraft and commercial gas turbine engines
- Spacecraft structures
- Mechanical components, such as brakes, drive shafts and flywheels
- Tanks and pressure vessels
- Dimensionally stable components
- Process industries equipment requiring resistance to high-temperature corrosion, oxidation and wear
- Offshore and onshore oil exploration and production
- Sports and leisure equipment
- Biomedical devices
- Prosthetics and orthotics
- Dental restoration materials
- Civil engineering structures
- Instrument structures
- Antennas

Over the years, increasing production volumes have helped to reduce material prices, increasing their attractiveness in cost-sensitive applications.

As mentioned earlier, composites technology is in its infancy. We anticipate that new and greatly improved materials are likely to emerge. We also expect that new concepts will emerge, such as “smart materials’ that incorporate greater functionality, including integration of electronics, sensors, and actuators (Peijs, 2018).

Reinforcements

The main types of reinforcements used in composite materials include continuous fibers, discontinuous fibers, whiskers (elongated single crystals), particles (including flakes) and numerous forms of fibrous architectures produced by textile technology, such as fabrics and braids (Gdoutos, 2018; Ko, 1993). In addition, there is increasing interest in composites reinforced with various types of nanoparticles, such as carbon nanotubes, graphite nanoplatelets and silica (clay) nanoparticles.

As mentioned earlier, use of natural-fiber reinforcement is far from a new idea. However, in recent years there has been considerable work on composites reinforced with a variety of naturally occurring fibrous materials, including wood fiber, kenaf, hemp, flax, jute, sisal, banana leaf, China reed and rice hulls. Matrices include thermoplastic and thermoset polymers and Portland cement. A number of material systems have been used in production applications, such as construction and automobile parts.

Increasingly, designers are using hybrid composites that combine different types of reinforcements and reinforcement forms to achieve greater efficiency and reduce cost. For example, fabrics and unidirectional tapes are often used together in structural components. In addition, carbon fibers are combined with glass or aramid to improve impact resistance. Laminates combining composites and metals, such as “Glare,” which consists of layers of aluminum and glass fiber-reinforced epoxy, are being used in aircraft structures to improve fatigue resistance. There are also examples of composites reinforced with combinations of fibers and particles.

The great importance of composites and the revolutionary improvements in properties that they offer derive to a great extent from the development of synthetic fibers with unprecedented properties (Gdoutos, 2018). The key synthetic fibers are made from glass, carbon (sometimes called graphite), ceramics and high-modulus organics, such as aramids. Most fibers are produced in the form of multifilament bundles called strands or ends in their untwisted forms, and yarns when twisted. Some fibers are produced as monofilaments, which generally have much larger diameters than strand filaments. Table 3 presents typical properties of key fibers, which we discuss in the following subsections.

Fiber strength requires some discussion. Most of the key fibrous reinforcements are made of brittle ceramics or carbon. It is well known that the strengths of monolithic ceramics decrease with increasing material volume because of the increasing probability of finding strength-limiting flaws. This is called size effect. As a result of size effect, fiber strength typically decreases monotonically with increasing gage length (and diameter). Flaw sensitivity also results in considerable strength scatter at a fixed test length. Consequently, there is no single value that characterizes fiber strength. This is also true of key organic reinforcements, such as aramid fibers. Consequently, the values presented in Table 3 should be considered approximate values and are useful primarily for comparative purposes. Note that because unsupported fibers buckle under very low stresses, it is very difficult to measure their inherent compression strength, and these properties are almost never reported. Instead, composite compression strength is measured directly.

Glass fibers

Glass fibers are used primarily to reinforce polymers. The leading types of glass fibers are E-glass, high-strength (HS) glass and corrosion resistant (CR). E-glass fibers, the first major synthetic composite reinforcement, originally was developed for electrical insulation applications (that is the origin of the “E”). E-glass fibers are, by many orders of magnitude, the most widely used of all

Table 3 Properties of key reinforcing fibers.

Fiber	*Density (G/cm^3)*	*Axial Modulus (GPa)*	*Axial Tensile Strength (MPa)*	*Axial CTE (10^{-6} K^{-1})*	*Axial Thermal Conductivity (W m^{-1} K^{-1})*
E-glass	2.6	70	2000	5	0.9
HS glass	2.5	83	4200	4.1	0.9
Aramid	1.4	124	3200	−5.2	0.04
Boron	2.6	400	3600	4.5	–
SM carbon (PAN)	1.7	235	3200	−0.5	9
UHM carbon (PAN)	1.9	590	3800	−1	18
UHS (IM) carbon (PAN)	1.8	290	7000	−1.5	160
UHM carbon (pitch)	2.2	895	2200	−1.6	640
UHK carbon (pitch)	2.2	830	2200	−1.6	1100
SiC monofilament	3.0	400	3600	4.9	–
SiC multifilament	3.0	400	3100	–	–
Si-C-O	2.6	190	2900	3.9	1.4
Si-Ti-C-O	2.4	190	3300	3.1	–
Aluminum oxide	3.9	370	1900	7.9	–
High Density Polyethylene	0.97	172	3000	–	–
High Modulus PBO	1.58	270	5800	−6.0	–

fibrous reinforcements. The primary reasons for this are their low cost and early development compared to other fibers. Glass fibers are produced as multifilament bundles. Filament diameters range from 3 to 20 μm. Table 3 presents representative properties of E-glass and HS glass fibers.

E-glass fibers have relatively low elastic moduli compared to other reinforcements. In addition, E-glass fibers are susceptible to creep and creep (stress) rupture. HS glass is stiffer and stronger than E-glass and has better resistance to fatigue and creep.

The thermal and electrical conductivities of glass fibers are low, and glass fiber-reinforced PMCs are often used as thermal and electrical insulators. The CTE of glass fibers is also low compared to most metals.

Carbon (graphite) fibers

Carbon fibers, often called graphite fibers in the United States, are used to reinforce polymer-, metal-, ceramic-, and carbon matrices. There are dozens of commercial carbon fibers, with a wide range of strengths and moduli. As a class of reinforcements, carbon fibers are characterized by high stiffness and strength and low density and coefficient of thermal expansion (CTE). Fibers with nominal tensile moduli as high as 895 GPa and with tensile strengths of 7000 MPa are commercially available. Carbon fibers have excellent resistance to creep, stress rupture, fatigue and corrosive environments, although they oxidize at high temperatures. Some types of carbon fibers also have extremely high thermal conductivities - many times that of copper. This characteristic is of considerable interest in electronic packaging and other applications where temperature control is important. Carbon fibers are the workhorse reinforcements in high performance aerospace and commercial PMCs and some CMCs. Of course, as the name suggests, carbon fibers are also the reinforcements in carbon/carbon composites.

Most carbon fibers are highly anisotropic. Axial modulus, tension and compression strength and thermal conductivity are typically much greater than the corresponding properties in the radial direction. Carbon fibers generally have small, negative axial CTEs (which means that they get shorter when heated) and positive radial CTEs. Diameters of common reinforcing fibers, which are produced in the form of multifilament bundles, range from 4 to 10 μm. Carbon fiber stress-strain curves tend to be nonlinear. Modulus increases with increasing tensile strain and decreases with increasing compressive strain.

The three key precursor materials for carbon fibers are polyacrylonitrile (PAN), petroleum pitch and coal tar pitch. Rayon-based fibers, once the primary CCC reinforcement, are far less common in new applications. Another type of carbon fiber, referred to as "vapor grown" by their manufacturer are made by a chemical vapor deposition type of process. Some of the latter have reported axial thermal conductivities as high as 2000 W m^{-1} K^{-1}, five times that of copper.

Carbon fibers made from PAN are the most widely used. There are dozens on the market. Fiber axial moduli range from about 235 GPa to 590 GPa. They generally provide composites with excellent tensile and compressive strengths, although strength properties tend to drop off as modulus increases. Fibers having nominal tensile strengths as high as 7 GPa are available. Table 3 presents properties of three types of PAN-based carbon fibers and two types of pitch-based carbon fibers. The PAN-based fibers are standard modulus (SM), ultrahigh strength (UHS) and ultrahigh modulus (UHM). SM PAN fibers are the most widely used type of carbon fiber reinforcement. They are one of the first types commercialized and tend to be the least expensive. UHS PAN carbon fibers are the strongest type of another widely used class of carbon fiber called intermediate modulus (IM), because their axial modulus falls between those of SM and UHM carbon fibers. IM fibers are also widely used in aircraft and other aerospace structural applications. PAN fibers have relatively low thermal axial and transverse thermal conductivities.

A key advantage of pitch-based fibers is that they can be produced with much higher axial moduli and thermal conductivities than those made from PAN precursors. For example, UHM pitch fibers with nominal moduli as high as 895 GPa are available. In addition, some pitch fibers, which we designate UHK, have extremely high axial thermal conductivities. For example, there are commercial UHK fibers with a nominal axial thermal conductivity of 1100 W m^{-1} K^{-1}, almost three times that of copper. However, composites made from pitch-based carbon fibers generally are somewhat weaker in tension and shear, and much weaker in compression, than those using PAN-based reinforcements.

As mentioned earlier, carbon fibers display nonlinear stress-strain behavior, making the method of calculating modulus critical. Various tangent and secant definitions are used throughout the industry, contributing to the confusion in reported properties. The moduli presented in Table 3 are based on tangents to the stress-strain curves at the origin.

Boron fibers

Boron fibers primarily are used to reinforce PMCs and, to a lesser extent, MMCs. Boron fibers are produced as monofilaments (single filaments) by chemical vapor deposition of boron on a tungsten wire or carbon filament, the former being the most widely used. They have relatively large diameters (100–140 μm) compared to most other reinforcements. Table 3 presents representative properties of boron fibers having a tungsten core and diameter of 140 μm. The ratio of overall fiber diameter to that of the tungsten core influences effective fiber properties. For example, fiber specific gravity is 2.57 for 100-μm fibers and 2.49 for 140-μm fibers. Because boron fibers are more expensive than many types of carbon fibers, their use is much more restricted.

Fibers based on silicon carbide

Silicon carbide-based fibers are used primarily to reinforce metals and ceramics. There are a number of commercial fibers based on silicon carbide. One type, a monofilament, is produced by chemical vapor deposition of high purity silicon carbide on a carbon monofilament core. Some versions use a carbon-rich surface layer that serves as a reaction barrier in MMCs and CMCs.

There are a number of multifilament silicon-carbide-based fibers made by pyrolysis of polymers. Some of these contain varying amounts of silicon, carbon and oxygen, titanium, nitrogen, zirconium and hydrogen. Table 3 presents properties of selected silicon-carbide-based fibers.

Fibers based on alumina

Alumina-based fibers are used primarily to reinforce metals and ceramics. As for silicon-carbide-based fibers, they have a number of different chemical formulations. The primary constituents, in addition to alumina, are boria, silica and zirconia. Table 3 presents properties of high-purity alumina fibers.

Aramid fibers

Aramid, or aromatic polyamide fibers are high modulus organic reinforcements primarily used in PMCs and for ballistic protection. There are a number of commercial aramid fibers produced by several manufacturers. As for other reinforcements, they are proprietary materials with differing properties. Table 3 presents properties of one widely used aramid fiber, "Kevlar" 49. As for carbon fibers, aramid fibers have nonlinear stress-strain curves.

High-density polyethylene fibers

High-density polyethylene fibers primarily are used to reinforce polymers and for ballistic protection. Table 3 presents properties of one type. The properties of high-density polyethylene tend to decrease significantly with increasing temperature, and they are susceptible to creep deformation (time-dependent deformation under constant stress), even at low temperatures.

PBO fibers

Many polymeric fibers have been developed over the years. One that appears to be making successful inroads is poly(p-phenylenebenzobisoxazole (PBO). There are two version, regular and high modulus (HM). Table 3 presents properties of the latter, which has the highest modulus of any commercial organic fiber.

Applications include aerospace components, sports equipment and audio speaker cones.

Characteristics and properties of composite materials

Composites are strongly heterogeneous materials. That is, the properties of a composite material vary considerably from point to point in the material. For example, the properties of a point located in the matrix are typically very different from one in the reinforcement phase. Most monolithic polymers, ceramics, metallic alloys, and intermetallic compounds are usually considered homogeneous materials, to a first approximation. The analytical theories that define the relationships between the properties of the constituent materials making up the composite and the properties of the resulting composite are called micromechanics (Gdoutos, 2018).

Many artificial composites, especially those reinforced with fibers, are anisotropic, which means that their properties vary with direction (the properties of isotropic materials are the same in every direction). They share this characteristic with a widely used natural fibrous composite, wood. As for wood, when structures made from artificial fibrous composites are required to carry load in more than one direction, they are typically used in laminated form. The laminated form of wood is known as plywood. We note that the strength properties of some metals also vary with direction. This is typically related to the manufacturing process, such as rolling. In addition, all single crystals are anisotropic.

With the exception of MMCs, composites do not display plastic behavior as monolithic metals do, which makes composites more sensitive to stress concentrations. However, the absence of plastic deformation does not mean that composites should be considered brittle materials like monolithic ceramics. The heterogeneous nature of composites results in complex failure mechanisms that impart an effective toughness. Fiber-reinforced materials have been found to produce durable, reliable structural components in countless applications. For example, PMCs have been used in production boats, electrical equipment, and solid rocket motors since the 1950s and extensively in aircraft since the early 1970s. The technology has progressed to the point where the entire empennages (tail sections) of commercial aircraft are made of carbon/epoxy. Passenger planes under development are scheduled to have virtually all-composite structures, including wings and fuselages.

There are a large and increasing number of materials that fall in each of the four types of composites, so that generalization is difficult. However, as a class of materials, composites tend to have the following characteristics: tailorable mechanical and physical properties; high strength; high modulus; low density: low CTE; excellent resistance to fatigue, creep, creep rupture, corrosion and wear. Composites are available with tailorable thermal and electrical conductivities that range from very low to very high.

As for monolithic materials, each of the four classes of composites has its own particular attributes. For example, CMCs tend to have particularly good resistance to corrosion, oxidation, and wear, along with high temperature capability.

The outstanding mechanical properties of composite materials has been a key reason for their extensive use in structures. However, composites also have important physical properties, especially low, tailorable coefficient of thermal expansion (CTE) and high thermal conductivity, resulting in use in an increasing number of applications. Key examples are electronic packaging and thermal management, as discussed later.

Many composites, such as PMCs reinforced with carbon and aramid fibers, and silicon carbide particle-reinforced aluminum, have low CTEs, which are advantageous in applications requiring dimensional stability. Examples include spacecraft structures, instrument structures, optical benches and optoelectronic packaging. By appropriate selection of reinforcements and matrix materials, it is possible to produce composites with near-zero CTEs.

Coefficient of thermal expansion tailorability provides a way to minimize thermal stresses and distortions that often arise when dissimilar materials are joined. For example, the CTE of silicon carbide particle-reinforced aluminum depends on particle content. By varying the amount of reinforcement, it is possible to match the CTEs of a variety of key engineering materials, such as steel, titanium, and alumina (aluminum oxide). This characteristic of composites has particular value in electronic packaging, because thermal stresses can cause failure of ceramic substrates, semiconductors, and solder joints.

There are a large and increasing number of thermally conductive PMCs, MMCs, and CAMCs. One of the most important types of reinforcements for these materials is pitch fibers. As discussed earlier, PAN-based fibers have relatively low thermal conductivities. However, pitch-based fibers with thermal conductivities more than twice that of copper are commercially available. These ultrahigh-thermal-conductivity (UHK) reinforcements also have very high stiffnesses and low densities. Fibers made by chemical vapor deposition (CVD), also called vapor-grown fibers have reported thermal conductivities as high as 2000 W m^{-1} K^{-1}, about five times that of copper. Fibers made from another form of carbon, diamond, also have the potential for thermal conductivities in this range. PMCs and CCCs reinforced with UHK carbon fibers are being used in a wide range of applications, including spacecraft radiators, battery sleeves, electronic packaging and motor enclosures. MMCs reinforced with diamond particles have reported thermal conductivities as high as 1200 W m^{-1} K^{-1}, three times that of copper. The latter materials are of great interest in electronic and optoelectronic packaging.

Overview of mechanical and physical properties

As discussed earlier, initially, the excellent mechanical properties of composites were the main reason for their use. However, there are an increasing number of applications for which the unique and tailorable physical properties of composites are key considerations. For example, the extremely high thermal conductivity and tailorable CTE of some composite material systems are leading to their increasing use in electronic packaging. Similarly, the extremely high stiffness, near-zero CTE, and low density of carbon fiber-reinforced polymers have made these composites the materials of choice in a variety of applications, including spacecraft structures, antennas and optomechanical system components such as telescope metering structures and optical benches.

As discussed, composites are complex, heterogeneous, and often anisotropic material systems. Their properties are affected by many variables, including in-situ constituent properties; reinforcement form, volume fraction and geometry; properties of the interphase, the region where the reinforcement and matrix are joined (also called the interface); and void content. The process by which the composite is made affects many of these variables. Composites containing the same matrix material and reinforcements, when combined by different processes, may have very different properties.

It is important to keep in mind several other important things when considering composite properties. First, most composites are proprietary material systems made by proprietary processes. There are few industry or government standards for composites and reinforcements, as there are for many structural metals. However, this limitation also applies to many monolithic ceramics and polymers, which are widely used engineering materials. Despite their inherently proprietary nature, there are some widely used composite materials made by a number of manufacturers that have similar properties. Notable examples are standard-modulus- and intermediate-modulus-carbon-fiber-reinforced epoxy.

Another critical issue is that properties are sensitive to the test methods by which they are measured, and there are many different test methods used throughout the industry. Further, test results are very sensitive to the skill of the technician performing them. As a consequence of these factors, it is very common to find significant differences in reported properties of what is nominally the same composite material. Because of these considerations, the properties of composite materials in this article should be considered approximate values. As for all materials, composite properties depend on temperature. We present room temperature values.

There is often a great deal of confusion among those unfamiliar with composites, about the effect of reinforcement form. The properties of composites are very sensitive to reinforcement form, reinforcement volume fraction and internal reinforcement geometry.

It is important to keep in mind that a key problem with discontinuous-fiber reinforcement is that it is often difficult to control fiber orientation. For example, material flow during processing can significantly align fibers in some regions. This affects all mechanical and physical properties, including modulus, strength, CTE, thermal conductivity, etc. This has been a frequent source of failures.

Traditional fabric reinforcements have fibers oriented at 0 and 90 degrees. For the sake of completeness, we note that triaxial fabrics, which have fibers at 0, +60 and −60 degrees, are now commercially available. Composites using a single layer of this type of reinforcement are approximately quasi-isotropic, which means that they have the same inplane elastic (but not strength) properties in every direction. Their thermal conductivity and CTE are also approximately isotropic in the plane of the fabric. "Perfect" fabrics would have exactly isotropic thermal properties.

Overview of manufacturing processes

Manufacturing processes for some composites have significant advantages over those used for monolithic metals and ceramics. For example, fiber-reinforced polymers and ceramics can be fabricated in large, complex shapes that would be difficult or impossible to make with other materials. The ability to fabricate complex shapes allows consolidation of parts, which reduces machining and assembly costs. For example, one-piece PMC grill opening panels are widely used in automobiles, replacing as many as 12 metal parts that have to be joined by welding or bolting.

Some processes allow fabrication of parts in their final shape (net shape) or close to their final shape (near-net shape), which also can reduce manufacturing costs. The relative ease with which smooth shapes can be made is a significant factor in the use of composites in boats, aircraft, and other applications for which fluid dynamic and aerodynamic considerations are important. We discuss manufacturing methods in the respective sections for the key composites.

Polymer matrix composites

Polymer matrix composites (PMCs) are the most efficient structural materials that have ever been developed for moderate temperature applications (Gdoutos, 2018; Pourtarsip, 2018; Zweben, 1998). As a result, they are now baseline materials in numerous applications, including aircraft, spacecraft, boats, solid-fuel launch vehicles, industrial equipment and sports equipment. At this time, thermosetting polymers are the key matrix materials for structural applications, but use of thermoplastics is gradually increasing.

There are now many reliable processes for making PMCs (Pourtarsip, 2018).

The high thermal conductivities of some PMCs has led to their increasing use in applications like spacecraft structures and electronic packaging components, such as printed circuit board heat sinks, heat spreaders and heat sinks used to cool microprocessors. The addition of discontinuous thermally conductive carbon fibers and ceramic particles to thermoplastics significantly increases thermal conductivity, opening the door to use of injection molded parts in an increasing number of applications, such as heat sinks and motor covers.

Polymers are relatively weak, low-stiffness, viscoelastic materials with low thermal conductivities and high coefficients of thermal expansion. In order to obtain materials with mechanical properties that are acceptable for structural applications, it is necessary to reinforce them with continuous or discontinuous fibers.

The addition of ceramic or metallic particles to polymers results in materials that have increased modulus. However, as a rule, strength typically does not increase significantly, and may actually decrease.

There are many particle-reinforced polymers used in electronic packaging, primarily because of their physical properties. For these applications, ceramic particles, such as alumina, aluminum nitride, boron nitride and even diamond are added to obtain electrically insulating materials with higher thermal conductivities and lower CTEs than those of the base polymer.

Metallic particles such as silver, copper, and aluminum are added to create materials that are both electrically and thermally conductive. These materials have replaced solders in some applications. Magnetic composites are made by incorporating ferrous or magnetic ceramic particles in various polymers.

As discussed, for a wide range of applications, composites reinforced with continuous fibers are the most efficient structural materials at low to moderate temperatures. Consequently, we focus on them. Table 4 presents room temperature mechanical properties of unidirectional polymer matrix composites reinforced with key fibers: E-glass, aramid, boron, standard modulus (SM) PAN (polyacrylonitrile) carbon, intermediate modulus (IM) PAN carbon, ultrahigh modulus (UHM) PAN carbon, ultrahigh modulus (UHM) pitch carbon and ultrahigh thermal conductivity (UHK) pitch carbon. The fiber volume fraction is 60%, a typical value.

The properties presented in Table 4 are representative of what can be obtained with a well-made PMC employing an epoxy matrix. Epoxies are widely used, provide good mechanical properties, and can be considered a reference matrix material. Properties of composites using other resins may differ from these.

The properties of PMCs, especially strengths, depend strongly on temperature. The temperature dependence of polymer properties differs considerably. This is also true for different epoxy formulations, which have various glass transition temperatures.

The properties shown in Table 4 are axial, transverse and shear moduli, Poisson's ratio, tensile and compressive strengths in the axial and transverse directions, and inplane shear strength. The Poisson's ratio presented is called the major Poisson's ratio. It is defined as the ratio of the magnitude of transverse strain divided by the magnitude of axial strain when the composite is loaded in

Table 4 Representative mechanical properties of selected unidirectional polymer matrix composites.

Fiber	*Axial Modulus (GPa)*	*Transverse Modulus (GPa)*	*Inplane Shear Modulus (GPa)*	*Poisson's Ratio*	*Axial Tensile Strength (MPa)*	*Transverse Tensile Strength (MPa)*	*Axial Compressive Strength (MPa)*	*Transverse Compressive Strength (MPa)*	*Inplane Shear Strength (MPa)*
E-glass	45	12	5.5	0.28	1020	40	620	140	70
Aramid	76	5.5	2.1	0.34	1240	30	280	140	60
Boron	210	19	4.8	0.25	1240	70	3310	280	90
SM Carbon (PAN)	145	10	4.1	0.25	1520	41	1380	170	80
UHM (PAN)	310	9	4.1	0.20	1380	41	760	170	80
UHM (Pitch)	480	9	4.1	0.25	900	20	280	100	41

Nominal Fiber Volume Fraction = 60%.

the axial direction. Note that transverse moduli and strengths are much lower than corresponding axial values. Unidirectional composites share this characteristic with wood, which is stronger and stiffer along the grain than perpendicular to it.

Elastic moduli are based on tangents to the stress-strain curves at the origin. Using this definition, tensile and compressive moduli are usually very similar. However, this is not the case for moduli computed using various secants. These typically produce compression moduli that are significantly lower than tensile moduli, because the stress-strain curves are nonlinear.

As a result of the low transverse strengths of unidirectional laminates, they are rarely used in structural applications. The design engineer selects laminates with layers in several directions to meet requirements for strength, stiffness, buckling, etc. There are an infinite number of laminate geometries that can be selected. For comparative purposes, it is useful to consider quasi-isotropic laminates, which have the same elastic properties in all directions in the plane of the fibers. We note that through-thickness properties of quasi-isotropic laminates are somewhat similar to the transverse properties of unidirectional composites.

Laminates have quasi-isotropic elastic properties when they have the same percentage of layers every 180/n degrees, where n is greater than or equal to three. The most common quasi-isotropic laminates have layers that repeat every 60, 45, or 30 degrees. We note, however, that strength properties in the plane are not isotropic for these laminates, although they tend to become more uniform as the angle of repetition becomes smaller. Laminates have quasi-isotropic CTEs and coefficients of thermal expansion when they have the same percentage of layers in every 180/m degrees, where m is greater than or equal to 2. For example, laminates with equal numbers of layers at 0 degrees and 90 degrees have quasi-isotropic thermal properties.

Table 5 presents the mechanical properties of quasi-isotropic laminates having equal numbers of layers at 0, +45, −45 and 90 degrees. The elastic moduli of all quasi-isotropic laminates are the same for a given material. Note that the moduli and strengths are much lower than the axial properties of unidirectional laminates made of the same material. In many applications, laminate geometry is such that the maximum axial modulus and tensile and compressive strengths fall somewhere between axial unidirectional and quasi-isotropic values.

Table 6 presents physical properties of selected unidirectional composite materials having a typical fiber volume fraction of 60%. The densities of all of the materials are considerably lower than that of aluminum, and some are lower than that of magnesium. This reflects the low densities of both fibers and matrix materials. The low densities of most polymers give PMCs a significant advantage over most MMCs and CMC at low-to-moderate temperatures, all other things being equal.

As Table 6 shows, all of the composites have relatively low axial CTEs. This results from the combination of low fiber axial CTE, high fiber stiffness and low matrix stiffness. The CTE of most polymers is very high. Note that the axial CTEs of PMCs reinforced with aramid fibers and some carbon fibers are negative. This means that, contrary to the general behavior of most monolithic materials, they contract in the axial direction when heated.

The transverse CTEs of the composites are all positive, and their magnitudes are much larger than the magnitudes of the corresponding axial CTEs. This results from the high CTE of the matrix and a Poisson effect caused by constraint of the matrix in the axial direction and lack of constraint in the transverse direction. The transverse CTE of aramid composites is particularly high, in part, because the fibers have a relatively high positive radial CTE.

We note that PMCs also undergo dimensional changes due to moisture absorption and desorption. These changes are usually described by coefficients of moisture expansion, which are analogous to CTEs. This subject is beyond the scope of the current article.

The axial thermal conductivities of composites reinforced with glass, aramid, boron, and a number of the carbon fibers are relatively low. In fact, E-glass and aramid PMCs are often used as thermal insulators. As Table 6 shows, most PMCs have low thermal conductivities in the transverse direction, as a result of the low thermal conductivities of the matrix and the fibers in the radial direction. Through-thickness conductivities of laminates tend to be similar to the transverse thermal conductivities of unidirectional composites.

Table 7 presents the inplane thermal conductivities and CTEs of quasi-isotropic laminates made from the same materials as in Table 6. Here again, a fiber volume fraction of 60% is assumed.

Note that the CTEs of the quasi-isotropic composites are higher than the axial values of corresponding unidirectional composites. However, the CTEs of quasi-isotropic composites reinforced with aramid and carbon fibers are still very small. By appropriate selection of fiber, matrix, and fiber volume fraction, it is possible to obtain quasi-isotropic materials with CTEs very close to zero. The through-thickness CTEs of these laminates are positive and relatively large. However, this is not a significant issue for most applications. One exception is optical mirrors, for which through-thickness CTE can be an important issue.

The inplane thermal conductivity of quasi-isotropic laminates reinforced with UHM pitch carbon fibers is similar to that of aluminum alloys, while UHK pitch carbon fibers provide laminates with a conductivity over 50% higher. Both materials have densities about 35% lower than aluminum.

As mentioned earlier, through-thickness thermal conductivities of laminates tend to be similar to the transverse thermal conductivities of unidirectional composites, which are relatively low. If laminate thickness is small, this may not be a severe limitation. However, low through-thickness thermal conductivity can be a significant issue for thick laminates and for very high thermal loads. Through-thickness conductivity can be increased by addition of thermally conductive reinforcements such as discontinuous carbon fibers, ceramic particles like boron nitride or carbon nanotubes.

Fiber-reinforced thermoset PMCs are made by a wide variety of processes, many of which are highly automated, including hand lay-up, filament winding, tape placement, fiber placement, and various types of resin transfer molding.

A significant recent advance in PMC technology is the development of injection moldable carbon-fiber-reinforced thermoplastics with much higher thermal conductivities than those available in the past. Unreinforced polymers have thermal conductivities in the range of 0.2 W m^{-1} K^{-1}. A number of commercially available PMCs consisting of thermoplastic matrices reinforced with

Table 5 Mechanical properties of selected quasi-isotropic polymer matrix composites.

Fiber	*Axial Modulus (GPa)*	*Transverse Modulus (GPa)*	*Inplane Shear Modulus (GPa)*	*Poisson's Ratio*	*Axial Tensile Strength (MPa)*	*Transverse Tensile Strength (MPa)*	*Axial Compressive Strength (MPa)*	*Transverse Compressive Strength (MPa)*	*Inplane Shear Strength (MPa)*
E-Glass	23	23	9.0	0.28	550	550	330	330	250
Aramid	29	29	11	0.32	460	460	190	190	65
Boron	80	80	30	0.33	480	480	1100	1100	360
SM Carbon (PAN)	54	54	21	0.31	580	580	580	580	410
IM Carbon (PAN)	63	63	21	0.31	1350	1350	580	580	410
UHM Carbon (PAN)	110	110	41	0.32	490	490	270	270	205
UHM Carbon (Pitch)	165	165	63	0.32	310	310	96	96	73
UHK Carbon (Pitch)	165	165	63	0.32	310	310	96	96	73

Fiber Volume Fraction = 60%.

Table 6 Physical properties of selected unidirectional polymer matrix composites.

Fiber	*Density (g/cm^3)*	*Axial CTE (10^{-6} K^{-1})*	*Transverse CTE (10^{-6} K^{-1})*	*Axial Thermal Conductivity (W m^{-1} K^{-1})*	*Transverse Thermal Conductivity (W m^{-1} K^{-1})*
E-Glass	2.1	6.3	22	1.2	0.6
Aramid	1.38	−4.0	58	1.7	0.1
Boron	2.0	4.5	23	2.2	0.7
SM Carbon (PAN)	1.58	0.9	27	5	0.5
IM Carbon (PAN)	1.61	0.5	27	10	0.5
UHM Carbon (PAN)	1.66	−0.9	40	45	0.5
UHM Carbon (Pitch)	1.80	−1.1	27	380	10
UHK Carbon (Pitch)	1.80	−1.1	27	660	10

Fiber volume fraction = 60%.

Table 7 Physical properties of selected quasi-isotropic polymer matrix composites.

Fiber	*Density (G/cm^3)*	*Axial CTE (10^{-6} K^{-1})*	*Transverse CTE (10^{-6} K^{-1})*	*Axial Thermal Conductivity (W m^{-1} K^{-1})*	*Transverse Thermal Conductivity (W m^{-1} K^{-1})*
E-Glass	2.1	10	10	0.9	0.9
Aramid	1.38	1.4	1.4	0.9	0.9
Boron	2.0	6.5	6.5	1.4	1.4
SM carbon (PAN)	1.58	3.1	3.1	2.8	2.8
IM carbon (PAN)	1.61	2.3	2.3	6	6
UHM Carbon (PAN)	1.66	0.4	0.4	23	23
UHM Carbon (Pitch)	1.80	−0.4	−0.4	195	195
UHK Carbon (Pitch)	1.80	−0.4	−0.4	335	335

Fiber volume fraction = 60%.

discontinuous carbon fibers have reported thermal conductivities ranging from 2 W m^{-1} K^{-1} to as high as 100 W m^{-1} K^{-1}. Matrices include PPS, nylon 6, polycarbonate and liquid crystal polymers. These composites are also electrically conductive. Electrically insulating PMCs reinforced with thermally conductive discontinuous ceramic particles, such as boron nitride, have reported thermal conductivities of up to 15 W m^{-1} K^{-1}.

Metal matrix composites

MMCs consist of metals reinforced with a variety of ceramic fibers, carbon fibers, whiskers, and particles (Zweben, 1998; Clyne, 2018). There are wide ranges of materials that fall in this category. An important example cited earlier is a material consisting of tungsten carbide particles embedded in a cobalt matrix, which is used extensively in cutting tools and dies. This composite, often referred to as a cermet, cemented carbide or simply, but incorrectly as "tungsten carbide," has much better fracture toughness than monolithic tungsten carbide, which is a brittle ceramic material.

Another interesting MMC, tungsten carbide particle-reinforced silver, is a key circuit breaker contact pad material. Here, the composite provides good electrical conductivity and much greater hardness and wear resistance than monolithic silver, which is too soft to be used in this application. Ferrous alloys reinforced with titanium carbide particles have been used for many years in numerous aerospace and commercial production applications, including dies, engine valves, and aircraft fuel pumps. Compared to the monolithic base metals, they offer better wear resistance, higher stiffness, and lower density.

MMCs are also have been used in automobile engine blocks. In one design, the cylinder walls of an aluminum engine block are reinforced with a combination of discontinuous aluminum oxide (alumina) and carbon fibers, enabling elimination of cast iron cylinder liners (Hayashi et al., 1989). MMCs also have been used in high-speed electronics manufacturing equipment and in equipment used for production of microprocessor chips, such as photolithography tables. Other applications include diesel engine pistons, aircraft structures, aircraft engine fan exit guide vanes, actuators, and automobile and train brake rotors.

One of the most important uses for MMCs is in electronic packaging and thermal management (Zweben, 2001, 2002b, 2018b). For example, silicon carbide particle-reinforced aluminum, often called Al/SiC in the electronics industry, is being used in high volume production parts such as microprocessor lids and power modules for hybrid electric vehicles. Other MMCs used in packaging are carbon fiber reinforced-aluminum, beryllium oxide (beryllia) particle-reinforced beryllium and silicon/aluminum. Here, the advantages are high stiffness, high thermal conductivity and low density and CTE. Two traditional packaging materials, copper/tungsten and copper/molybdenum, are also MMCs. The CTEs of all of these composites can be tailored by varying the ratio of the two constituents. Another major advantage of the newer composites is that they have relatively low densities.

Monolithic metallic alloys are among the most widely used structural materials. By reinforcing them with continuous fibers, discontinuous fibers, whiskers and particles, new materials are created with enhanced or modified properties, such as higher strength and stiffness, better wear resistance, lower CTE, etc. In some cases, the improvements are dramatic.

The greatest increases in strength and modulus are achieved with continuous fibers, at least in the direction parallel to the fibers, called the axial or longitudinal direction. As for PMCs, transverse properties are dominated by the properties of the matrix and interface. However, because the metal matrices are in themselves structural materials, transverse strength properties are frequently great enough to permit use of unidirectional MMCs in some structural applications. This is usually not possible for PMCs. The boron fiber-reinforced aluminum struts used on the Space Shuttle Orbiter are a good example. Other key MMCs reinforced with continuous fibers include silicon-carbide-reinforced titanium and carbon-fiber-reinforced aluminum.

The key particle-reinforced MMCs, include titanium-carbide-reinforced steel, aluminum reinforced with silicon carbide and with alumina particles, titanium-carbide-particle-reinforced titanium and titanium boride-reinforced titanium.

Aluminum reinforced with silicon carbide particles is arguably the most important of the newer types of structural MMCs. The low cost of the aluminum matrix and silicon carbide particles makes these composites of particular interest. There are wide ranges of materials falling in this category. They are made by a variety of processes. Properties depend on the type of particle, particle volume fraction, matrix alloy, and the process used to make them. Table 8 presents representative composite properties for three particle volume fractions, 25%, 55%, and 70%. Properties of common steel, aluminum and titanium alloys are shown for comparison.

We see that as particle volume fraction increases, modulus and yield strength increase, and fracture toughness, tensile ultimate strain and CTE of particle-reinforced composites decrease. Particulate reinforcement also improves elevated temperature strength properties and, perhaps surprisingly, fatigue resistance. The ability to tailor CTE by varying particle volume fraction is a key attribute of these materials.

There are a variety of processes to make silicon carbide particle-reinforced aluminum, including powder metallurgy, stir casting and pressure and pressureless infiltration. The last two, as well as remelt casting can make net shape or near-net shape parts. Fiber-reinforced MMCs are made by a variety of process, including pressure infiltration and diffusion bonding.

Carbon matrix composites

Carbon matrix composites (CAMCs) consist of a carbon matrix reinforced with any combination of fibers, whiskers, or particles (Savage, 1993; Zweben, 1998; Ruggles-Wrenn, 2018). For many years, the only significant CAMCs were carbon/carbon composites (CCCs), in which the reinforcements are discontinuous or continuous carbon fibers. In the last few years, a new proprietary carbon matrix material system was developed which has a silicon carbide fiber reinforcement. This material is now being used for engine flaps on a military aircraft engine. One of the key reported advantages of this new material is that it has a higher CTE than CCCs, reducing the tendency of protective ceramic coatings to crack. The focus of this section is on CCCs.

CCCs are used in a variety of applications, including electronic packaging, spacecraft radiator panels, rocket nozzles, reentry vehicle nose tips, the Space Shuttle Orbiter leading edges and nose cap, aircraft brakes, heat treating furnaces and glass making equipment.

As for PMCs, there are many different CCC materials having widely different mechanical and physical properties. The primary advantages of CCCs are: high strength compared to competing materials at very high temperatures, high stiffness, ablation resistance, high thermal conductivity (some systems), low CTEs, low density and absence of outgassing. In addition, CCCs are less brittle than monolithic carbon.

The primary disadvantages are: susceptibility to oxidation at temperatures above about 370C to 500C (700F to 930F), low interlaminar (through-thickness) tensile and shear strengths for materials with 2D reinforcement; microcracking at low stresses in

Table 8 Properties of silicon-carbide-particle-reinforced aluminum, aluminum, titanium and steel.

Property	*Aluminum 6061-T6*	*Titanium 6Al-4 V*	*Steel 4340*	*Composite Particle Volume Fraction (%)*		
				25	*55*	*70*
Modulus, GPa	69	113	200	114	186	265
Tensile Yield Strength, MPa	275	1000	1480	400	495	–
Tensile Ultimate Strength, MPa	310	1100	1790	485	530	225
Elongation (%)	15	5	10	3.8	0.6	0.1
Specific Modulus, GPa	5	26	26	40	63	88
CTE, 10^{-6} K^{-1}	23	9.5	12	16.4	10.4	6.2
Density, g/cm^3	2.77	4.43	7.76	2.88	2.96	
3.00						

some directions for 3D composites; and high cost of many systems. Because of the low interlaminar strength properties of CCCs, many applications, particularly those with thick walls often use three-dimensional reinforcement.

As mentioned earlier, one of the most significant limitations of CCCs is oxidation. Addition of oxidation inhibitors to the matrix and protective coatings raises the threshold substantially. In inert atmospheres, CCCs retain their properties to temperatures as high as 2400C (4300F).

The combination of high thermal conductivity and low density makes CCCs attractive candidates for thermal management and electronic packaging. In addition, CCCs have very low CTEs, leading to their use as thermal doublers with carbon fiber-reinforced PMC structures. The unique combination of properties possessed by CCCs, combined with a lack of outgassing, also makes them attractive for optical systems.

The two leading types of processes used to make CAMCs. The first is chemical vapor infiltration (CVI). CVI is a process in which gaseous chemicals are reacted or decomposed, depositing a solid material on a fibrous preform. In the case of CAMCs, hydrocarbon gases like methane and propane are broken down, and the material deposited is the carbon matrix. The second class of processes involves infiltration of a preform with polymers or pitches, which are then converted to carbon by pyrolysis (heating in an inert atmosphere). After pyrolysis, the composite is sometimes heated to high temperatures to graphitize the matrix. To minimize porosity, the process is repeated until a satisfactory density is achieved. This is called densification. Common matrix precursors are phenolic and furan resins, and pitches derived from coal tar and petroleum.

Ceramic matrix composites

As a class of materials, monolithic ceramics are characterized by high stiffness and hardness, resistance to wear, corrosion and oxidation, and high temperature operational capability. However, they also have serious deficiencies, which have severely limited their use in applications that are subjected to significant tensile stresses (Zweben, 1998; Ruggles-Wrenn, 2018).

A fundamental problem is that ceramics have very low fracture toughnesses, which makes them very sensitive to the presence of small flaws. This results in great strength scatter and poor resistance to thermal and mechanical shock. Civil engineers recognized this deficiency long ago, and do not use ceramic materials like stone and concrete to carry tensile loads. In the latter, this function has been relegated to reinforcing bars or prestressing cables made of steel or, more recently, PMCs. An important exception has been in lightly loaded structures where dispersed reinforcing fibers of asbestos, steel, glass, and carbon allow modest tensile stresses to be supported.

Ceramic matrix composites (CMCs) can be thought of as an improved form of carbon matrix composite in which the carbon matrix is replaced with ceramics that are stronger and much more resistant to oxidation. CMCs employ a variety of reinforcements including continuous fibers, discontinuous fibers, whiskers, and particles. Continuous fibers provide the best properties. There are many different types of CMCs, and they are at various stages of development. As discussed earlier, straw-reinforced mud is an ancient CMC, as is concrete, which consists of a cement matrix reinforced with stone and sand.

The key advantage of ceramic matrix composites is that, when properly designed and manufactured, they have many of the advantages of monolithic ceramics, such as much lower density than high-temperature metals, but are much more durable. That is, CMCs have higher effective fracture toughnesses, so that they are less susceptible to failure when subjected to mechanical and thermal shock. As a consequence, it is possible to consider CMCs for applications where they are subjected to moderate tensile loads. However, CMCs are the most complex of all types of composites, and CMC technology is less developed than that of PMCs, MMCs and CAMCs.

CMCs are being used in a number of commercial production applications. One of the most successful is silicon-carbide-whisker-reinforced alumina cutting tool inserts, which have greater fracture toughness, and are therefore more durable than monolithic alumina. Another application is silicon-carbide-whisker-reinforced aluminum nitride crucibles, which are used for casting molten aluminum. In this application, the key advantage of the CMC over monolithic ceramics is thermal shock resistance. Silicon-carbide particle-reinforced alumina is being used in slurry pumps because of the good durability and wear resistance of this material. In this application, the process makes it possible to fabricate reliable, complex parts that would be hard to make out of monolithic ceramics. Other potential high temperature CMC applications include coal fired power plant candle filters used for particulate removal, natural gas burner elements, and U-tubes. In addition, there are a wide variety of candidate applications including stationary gas turbine combustor liners and shrouds, abradable rim seals, reverberatory screens, particle separators, tube shields, recuperators, turbine tip shoes, pipe hangers, heat treating furnace fans, hot gas filters and natural gas burner elements.

Aerospace applications of ceramic matrix composites were limited until recently, when they have begun to make significant penetration in aircraft engines. The key CMCs are silicon carbide fiber reinforced silicon carbide (SiC/SiC) and oxide fiber reinforced oxide (Ox/Ox). SiC/SiC produced by an infiltration process is being used in turbine engine shrouds. Oxide-Oxide CMCs are being used on Mixers, Center Bodies and Engine Core Cowls.

One of the most significant earlier applications are fighter aircraft engine flaps. There are two types. Both use silicon carbide matrices. One is reinforced with carbon fibers, and the other a multifilament silicon carbide fiber. Another application is a missile diverter thruster made of carbon-fiber-reinforced silicon carbide. Again, the process used to make this part is CVI. The Space Shuttle Orbiter thermal protection system (TPS) made extensive use of tiles composed of a three-dimensional network of discontinuous oxide fibers with silicate surface layers. While there is no continuous matrix for most of the tile, the surface region is a form of CMC. In a sense, this can be considered at type of functionally graded material.

The addition of continuous fibers to a ceramic matrix can significantly change failure modes. Monolithic ceramics have linear stress-strain curves and fail catastrophically at low strain levels. However, well designed and fabricated CMCs display nonlinear stress-strain behavior with much more area under the curve, indicating that more energy is absorbed during failure, and that the material has a less catastrophic failure mode.

Reinforcements that have been used for CMCs include continuous fibers, discontinuous fibers, whiskers, and particles. Key continuous fibers used in CMCs include carbon, silicon carbide-based, alumina-based, alumina-boria-silica, quartz, and alkali-resistant glass. Steel wires are also have been used. Discontinuous CMC fibers are primarily silica-based. Silicon carbide is the key whisker reinforcement. Particulate reinforcements include silicon carbide, zirconium carbide, hafnium carbide, hafnium diboride, and zirconium diboride.

A large number of ceramics have been considered for matrix materials, including alumina, glass, glass-ceramic, mullite (aluminum silicate), cordierite (magnesium aluminosilicate), Yttrium alumina garnet (YAG), barium aluminosilicate (BAS), barium magnesium aluminosilicate (BMAS), calcium aluminosilicate (CAS), barium and strontium aluminosilicate (BSAS, or celsian), "Blackglas" (silicon oxycarbide or Si—O—C), silicon nitride, silicon carbide, silicon nitride-bonded silicon carbide, silicon carbide and silicon, hafnium carbide, tantalum carbide, zirconium carbide, hafnium diboride, zirconium diboride and molybdenum disilicide.

The most mature CMCs consist of silicon carbide matrices reinforced with silicon carbide-based fibers (SiC/SiC) and silicon carbide reinforced with carbon fibers (C/SiC).

As for other classes of composite materials, there are many processes that can be used to make CMCs. Key considerations in process selection are porosity and reactions between reinforcements, reinforcement coatings, and matrices. The most important processes for making CMCs at this time are chemical vapor infiltration, melt infiltration, preceramic polymer infiltration and pyrolysis (PIP), slurry infiltration, sol-gel, hot pressing and hot isostatic pressing. In addition, there are a number of reaction-based processes, which include reaction bonding and direct metal oxidation ("Dimox").

Thermal management materials

One of the most significant new areas for composites is in thermal management (Zweben, 2001, 2002b, 2018a, b). There are many engineering uses of these materials, but perhaps the most important is in packaging of microelectronics, optoelectronics and microelectromechanical systems (MEMS). Packaging provides support and protection to semiconductors and ceramics, which typically have low coefficients of thermal expansion (CTEs) and removes heat by conduction. The material requirements for these applications are high thermal conductivity, low CTE to minimize thermal stresses, and low density to minimize weight. Composites offer advantages in all three areas.

Table 9 presents properties of traditional packaging materials, including thermal conductivity, CTE, density and specific thermal conductivity, which we define as density divided by specific gravity. Specific thermal conductivity is a useful figure of merit where both thermal conductivity and weight are important. We see that, aside from CVD diamond (diamond produced by chemical vapor deposition), the maximum thermal conductivity is for copper, which has a high CTE. The materials with low CTEs all have thermal conductivities that are no better than that of aluminum. In addition, they all have relatively high densities. These are all significant deficiencies. Increasing heat fluxes has resulted in a need for improved materials.

Table 10 shows properties of some of the increasing number of new monolithic and composite packaging materials that have been developed in response to the universally recognized thermal management problems. A number are being used in production applications. Reinforcements include continuous (Cont.) and discontinuous (Disc.) thermally conductive carbon fibers, and a variety of particles, including diamond, silicon carbide and beryllia. Monolithic materials, all of which are carbonaceous, include carbon foam, natural graphite and highly oriented pyrolytic graphite (HOPG). We see that these materials offer great advantages over traditional packaging materials.

Conclusion

Composites are now baseline materials in countless applications. However, the technology, which is only several decades old, is still in its infancy. In the future, we are likely to see significant improvements in properties of existing fibers, matrices and processes, and development of new ones. So far, composites have been used primarily for their excellent mechanical properties, environmental resistance and durability. This is likely to continue. In addition, we foresee increasing use in applications for which non-mechanical properties, such as thermal conductivity and coefficient of thermal expansion are important. Among these are packaging of microelectronics, optoelectronics and microelectromechanical systems. These are extremely large and growing markets.

Development is under way on multifunctional and smart composites, which incorporate electronics, sensors, actuators and microprocessors. Potential applications include everything from spacecraft to cell phones.

Nanotechnology is one of the most exciting and challenging areas for composites. Polymers reinforced with low-cost silicate (clay) nanoparticles are already being used in commercial production applications. Carbon nanotubes and graphite nanoplatelets have impressive mechanical, thermal and electrical properties that make them attractive candidate reinforcements.

In addition to these trends, it is likely that important new materials and applications will emerge.

Table 9 Properties of traditional packaging materials.

Reinforcement	*Matrix*	*Thermal Cond. (W/m-K)*	*CTE (ppm/K)*	*Specific Gravity*	*Specific Thermal Cond. (W/m-K)*
–	Aluminum	218	23	2.7	81
–	Copper	400	17	8.9	45
–	CVD Diamond	1100–1800	1–2	3.52	310–510
–	Invar	11	1.3	8.1	1.4
–	Kovar	17	5.9	8.3	2.0
	C-I-C	164	8.4	8.4	20
	C-Mo-C	182	6.0	9.9	18
	Titanium	7.2	9.5	4.4	1.6
Copper	Tungsten	157–190	5.7–8.3	15–17	9–13
Copper	Molybdenum	184–197	7.0–7.1	9.9–10.0	18–20
	Solder – Sn63/Pb37	50	25	8.4	6.0
–	Epoxy	1.7	54	1.2	1.4
E-glass Fibers	Epoxy	0.16–0.26	11–20	2.1	0.1

Table 10 Properties of advanced packaging materials.

Reinforcement	*Matrix*	*Thermal Cond. (W/m-K)*	*CTE (ppm/K)*	*Specific Gravity*	*Specific Thermal Cond. (W/m-K)*
–	Carbon Foam	135–245	−1	0.6–0.9	220–270
–	HOPG	1300–1700	−1.0	2.3	740–850
–	Natural Graphite	150–500	–	–	–
Invar	Silver	153	6.5	8.8	17
Cont. Carbon Fibers	Aluminum	218–290	−1 – +16	2.3–2.6	84–126
Disc. Carbon Fibers	Aluminum	185	6.0	2.5	74
Disc. Carbon Fibers	Polymer	20–290	4–7	1.6–1.8	12–160
Silicon	Aluminum	126–160	6.5–17	2.5–2.6	49–63
SiC Particles	Aluminum	170–220	6.2–16.2	3.0	57–73
Beryllia Particles	Beryllium	240	6.1	2.6	92
Natural Graphite	Epoxy	370	−2.4	1.94	190
Cont. Carbon Fibers	Polymer	330	−1	1.8	183
Disc. Carbon Fibers	Copper	300	6.5–9.5	6.8	44
SiC Particles	Copper	320	7–10.9	6.6	48
Cont. Carbon Fibers	SiC	370	2.5	2.2	170
Cont. Carbon Fibers	Copper	400–420	0.5–16	5.3–8.2	49–79
Cont. Carbon Fibers	Carbon	400	−1.0	1.9	210
Cont. Carbon Fibers	SiC	370	2.5	2.2	170
Graphite Flake	Aluminum	400–600	4.5–5.0	2.3	174–260
Diamond Particles	Aluminum	550–600	7.0–7.5	3.1	177–194
Diamond & SiC Particles	Aluminum	575	5.5	–	–
Diamond Particles	Copper	600–1200	5.8	5.9	330–670
Diamond Particles	Cobalt	>600	3.0	4.12	>145
Diamond Particles	Magnesium	550	8	–	–
Diamond Particles	Silicon	525	4.5	–	–
Diamond Particles	SiC	600	1.8	3.3	182

Acknowledgments

Portions of this article were taken from: Zweben C (1998) Composite Materials and Mechanical Design". In: Kutz M (ed) *Mechanical Engineers' Handbook*, 2nd edn. John Wiley & Sons, New York. and Zweben C (2002) Metal Matrix Composites, Ceramic Matrix Composites, Carbon Matrix Composites and Thermally Conductive Polymer Matrix Composites. In: J Harper (ed) *Handbook of Plastics, Elastomers and Composites*, 4th edn, pp. 321-344. McGraw-Hill, New York. They appear courtesy of the publishers.

References

Clyne TW (2018) Volume 4: Metal matrix composites. In: Beaumont PWR and Zweben CH (eds.) *Comprehensive Composite Materials II*. Oxford: Academic Press.

Crane R (2018) Volume 7: Testing, nondestructive evaluation and structural health monitoring. In: Beaumont PWR and Zweben CH (eds.) *Comprehensive Composite Materials II*. Oxford: Academic Press.

Gdoutos E (2018) Volume 1: Reinforcements and general theories of composites. In: Beaumont PWR and Zweben CH (eds.) *Comprehensive Composite Materials II*. Oxford: Academic Press.

Gonczy ST (2015) Federal Aviation Administration (FAA) airworthiness certification for ceramic matrix composite components in civil aircraft systems. In: *MATEC Web of Conferences 29*, p. 00002.

Hayashi T, et al. (1989) *The Properties of Hybrid Fiber Reinforced Metal and Its Application for Engine Block*. SAE Technical Paper No. 890557, Warrendale, Pennsylvania, USA: Society of Automotive Engineers.

Johnson A (2018) Volume 8: Design and analysis of composite structures. In: Beaumont PWR and Zweben CH (eds.) *Comprehensive Composite Materials II*. Oxford: Academic Press.

Kelly A (1994) Introduction. In: Kelly A (ed.) *Concise encyclopedia of composite materials*, Revised edn. Oxford: Pergamon Press.

Ko FK (1993) Advanced textile structural composites. In: Moran-Lopez IJ and Sanchez JM (eds.) *Advanced Topics in Materials Science and Engineering*. New York: Plenum Press.

Peijs T (2018) Volume 6: Nanocomposites and multifunctional materials. In: Beaumont PWR and Zweben CH (eds.) *Comprehensive Composite Materials II*. Oxford: Academic Press.

Pourtarsip A (2018) Volume 3: Polymer matrix composites: manufacture and applications. In: Beaumont PWR and Zweben CH (eds.) *Comprehensive Composite Materials II*. Oxford: Academic Press.

Rawal SP, et al. (1990) *Composite Materials for Space Applications. NASA CR-187472*. Hampton, Virginia: National Aeronautics and Space Administration.

Ruggles-Wrenn M (2018) Volume 5: Ceramic and carbon matrix composites. In: Beaumont PWR and Zweben CH (eds.) *Comprehensive Composite Materials II*. Oxford: Academic Press.

Savage G (1993) *Carbon-Carbon Composites*. London: Chapman & Hall.

Steibel J (2019) Ceramic matrix composites taking flight at GE Aviation. *American Ceramic Society Bulletin* 98(330).

Talreja R (2018) Volume 2: Polymer matrix composites: Fundamentals. In: Beaumont PWR and Zweben CH (eds.) *Comprehensive Composite Materials II*. Oxford: Academic Press.

Zweben C (1994) Metal matrix composites: Aerospace applications. In: Flemings MC, et al. (eds.) *Encyclopedia of Advanced Materials*. Pergamon Press.

Zweben C (1998) Composite materials and mechanical design. In: Kutz M (ed.) *Mechanical Engineers' Handbook*, 2nd edn. New York: John Wiley & Sons.

Zweben C (2001) Heat sink materials for electronic packaging (eds.-in-chief). In: Buschow KH, et al. (eds.) *The Encyclopedia of Materials: Science and Technology*. Cambridge: Elsevier Science.

Zweben C (2002a) Metal matrix composites, ceramic matrix composites, carbon matrix composites and thermally conductive polymer matrix composites. In: Harper J (ed.) *Handbook of Plastics, Elastomers and Composites*, 4th edn, pp. 321–344. New York: McGraw-Hill.

Zweben C (2002b) Thermal management and electronic packaging applications. *ASM Handbook, Volume 21, Composites*. Materials Park, Ohio: ASM International.

Zweben C (2018a) Metal matrix composite thermal management materials. In: Beaumont PWR and Zweben CH (eds.) *Comprehensive Composite Materials II*, vol. 4, pp. 386–396. Oxford: Academic Press.

Zweben C (2018b) Polymer matrix composite thermal materials. In: Beaumont PWR and Zweben CH (eds.) *Comprehensive Composite Materials II*, vol. 3, pp. 592–612. Oxford: Academic Press.

Self-organized porous semiconductor compounds

Ion M Tiginyanu[a,b] **and Eduard V Monaico**[b], [a]Academy of Sciences of Moldova, Chisinau, Republic of Moldova; [b]National Center for Materials Study and Testing, Technical University of Moldova, Chisinau, Republic of Moldova

© 2024 Elsevier Ltd. All rights reserved.

Introduction **350**
Formation, morphology and physical properties of self-organized arrays of pores in semiconductor compounds **351**
Self-organized ordered arrays of TiO_2 nanotubes 351
Self-ordered distribution of pores in nanotemplates based on II-VI and III-V semiconductor compounds 354
Self-organized pores perpendicular to the crystal surface 354
Self-organized pores parallel to the crystal surface 356
Three-dimensional modulation of the porous layer 360
Hopping electrodeposition: The deposition of self-organized monolayer of Au nanodots on porous structures **363**
Applications of self-organized ordered arrays **365**
Conclusion **369**
Acknowledgments **370**
References **370**

Abstract

This chapter provides a review of self-organization of pores in semiconductor compounds when subjected to electrochemical etching. The influence of key factors upon self-organization is elucidated under anodization of semiconductor compounds at high applied potentials or current densities implying growth of current line-oriented pores. A comparative analysis of the morphologies of pores in III-V and II-VI compounds is performed. It is shown that the direction of pore propagation can be efficiently controlled using photolithographic masks deposited prior the anodization. Besides, the formation of quasi-ordered nanotubular structures of titania via anodization of titanium foils is reviewed. The possibility for the deposition of self-organized size-saturated monolayer of metal nanodots using pulsed electroplating on porous semiconductor templates is highlighted. The prospects of application of described porous structures in light-driven micro-engines as well as in photocatalytic, photonic, electronic and ferromagnetic device structures are discussed.

Key points

- Electrochemistry as cost-effective approach for porosification of semiconductor compounds in a controlled fashion;
- Types of pores in semiconductor compounds;
- Self-ordering of pores in semiconductor compounds;
- Multilayer porous structures with modulation of the degree of porosity;
- Uniform deposition of self-assembled monolayer of metal dots via pulsed electroplating according to the proposed "hopping electrodeposition";
- Applications of self-organized arrays of pores including those functionalized by metal.

Introduction

Starting with the rapid development of nanotechnology in the 1990s, a variety of porous materials has been reported. A considerable interest has been triggered by the discovery of macroporous Si more than three decades ago by Lehmann and Föll (1990). Nowadays, there are several well studied self-ordered porous materials finding applications in many fields: (i) porous alumina introduced by Masuda and Fukuda (1995); (ii) TiO_2 nanotubes by Macak et al. (2007); and (iii) self-ordered porous III-V semiconductor compounds (see the works of Christophersen et al., 2003; Föll et al., 2003a,b, 2009; Langa et al., 2003).

However, besides the versatility of porous alumina oxide for introducing self-ordering, its applicability is limited as a porous template to be filled in by other materials, with subsequent its removal due to the dielectric behavior leading to a passive role in the nanofabrication processes. In comparison with porous alumina, TiO_2-based nanomaterial has attracted a lot of attention in research and is considered a semiconductor nanoarchitecture with potential for a variety of applications due to its unique structural, optical and electronic properties, non-toxicity, corrosion resistance, etc. Compared to porous alumina, the templates from titanium dioxide have a number of advantages such as accessibility, biocompatibility, high photocatalytic characteristics, photostability, etc. TiO_2 nanotubes (NTs) can be fabricated via facile hydrothermal method, solvothermal method, template-mediated techniques and electrochemical anodic oxidation, the last one representing a cost-effective approach. The fabrication of TiO_2 nanotubes was

https://doi.org/10.1016/B978-0-323-90800-9.00105-0

first demonstrated back in 1984 and nowadays, 4 generations of such nanostructures are known. First and second generations used aqueous solutions containing HF acid or fluorine salts and allowed fabrication of nanotubes with length up to 5 μm. However, in the latest generations, organic solutions containing fluoride salts are used which allows the fabrication of NTs up to 1000 μm long (see Paulose et al., 2007; Rani et al., 2010).

Despite the fact that TiO_2 is considered a semiconductor material, its electrical conductivity is relatively low. In connection with this, semiconductor porous structures with controlled conductivity are of major interest. Porous materials from III-V group are perfect candidates able to fill this gap. An essential contribution to the controlled nanostructuring of these materials was made by the groups of H. Föll, I. Tiginyanu, and P. Schmuki. The systematization of technological parameters, morphologies, pore geometries, etc., allowed one to elucidate the regularities of self-ordering during the pore growth (see Christophersen et al., 2003; Föll et al., 2003b, 2010). Besides the optimum electrochemical parameters (electrolyte nature and its concentration, applied anodization potential, temperature, etc.), an important factor leading to self-ordering proved to be the presence of the crystallographically oriented pores.

On the other hand, the absence of crystallographically oriented pores in II–VI semiconductors is somewhat unexpected since, for instance, ZnSe has the same zinc-blend crystal structure as GaAs, GaP and InP. This feature was explained taking into account the nature of chemical bonds between constituent atoms and electronegativity difference (Langa et al., 2011; Monaico et al., 2020a).

It is worth to mention that self-ordering in porous materials is introduced without any lithographic means. Lithographic masks are used solely to control the direction of pore growth in the restricted space under the fotorezist leading to spectacular porous architectures (Monaico et al., 2019b). Moreover, using holes in the photoresist mask leads to the formation of non-connected pore networks in a semiconductor wafer for microfluidic applications.

This chapter represents a review of the literature data and of some unpublished recent results related to self-ordering in TiO_2 nanotubular arrays as well as in III-V and II-VI porous semiconductor compounds. We present technological routes enabling one to reach self-ordering of pores aligned perpendicular or parallel to the crystal surface or even 3D modulation of the porous architecture. Along with these, promising applications of the porous materials under consideration are discussed with respect to light-driven micro-engines, photocatalytic, photonic, electronic, and ferromagnetic device structures.

Formation, morphology and physical properties of self-organized arrays of pores in semiconductor compounds

Self-organized ordered arrays of TiO_2 nanotubes

The self-organization in electrochemical technologies is a complex process that depends on many factors such as solution concentration, temperature, pH value, applied potential, etc.

An impressive hexagonal self-ordering of TiO_2 nanotubes exhibiting an increase in the internal diameter was reported by Macak et al. (2007) who studied formation of hexagonally ordered and close-packed nanotube layers by repeated anodization of Ti substrates in ethylene glycol/NH_4F electrolytes. The authors demonstrated that among the mentioned above factors, the purity of the used Ti foil is also important for highly ordering of TiO_2 nanotubes. Besides, two step anodization similar to that used for preparing highly ordered porous alumina was applied. The nanotubes obtained during the first step were removed, and the remaining dimples served as initial sites for the formation of ordered nanotubes during the second anodization. Note that a strong variation of the nanotube wall thickness from 65 to 12 nm at the bottom and top respectively was reported. This feature was explained by chemical dissolution of TiO_2 wall in fluoride containing electrolytes.

The fabrication of TiO_2 nanotubes with V-shape profile of walls by changing the electrolyte temperature was proposed by Enachi et al. (2010b). The authors demonstrated that electrochemical etching of the Ti foil in an electrolyte containing ethylene glycol and HF allows the preparation of nanotubes with controllable inner diameter in the range from 10 nm to over 250 nm by changing the electrolyte temperature from −20 °C to +50 °C. As can be seen from Fig. 1a, the electrochemical etching at applied potential of 120 V in the electrolyte containing 100 mL ethylene glycol, 10 ml H_3PO_4 and 1 mL HF at temperature 0 °C leads to the fabrication of closely packed TiO_2 nanotubes with hexagonal shape. It was established that the shape of nanotubes can be changed to circular at elevated temperatures, as shown in Fig. 1b and c. An interesting peculiarity observed is that the change of the temperature leads to the increase in the inner diameter of the TiO_2 nanotubes, while the outer diameter remains unchanged, as can be seen in Fig. 1d. Based on this statement, it is possible to prepare TiO_2 nanotubes with modulated inner diameter by changing in a controlled fashion the electrolyte temperature during the electrochemical etching.

Along with this, the anodized Ti foil at low temperatures showed the initiation of a self-arranged ordered porous structure confirmed also by two-dimensional Fourier transform taken from the SEM image. The obtained porous structures demonstrated intriguing cathodoluminescence properties. Formation of resonator modes from isolated individual nanotubes as well as from cluster on TiO_2 nanotubes which are separated from each other by around 200 meV were observed from the spectral distribution of cathodoluminescence by Enachi et al. (2010a, 2012).

The obtained TiO_2 nanotubes have closed ends at the interface with the titanium foil, as a result of the formation of a barrier oxide layer. Over the time, efforts have been undertaken to develop techniques for obtaining open-ended nanotubes, which allow flow-through with increase of photocatalytic activity as well as broad applications. Albu et al. (2007) proposed and demonstrated an approach in two steps consisting of selective dissolution of titanium metal in Br_2/CH_3OH electrolyte at the first step, allowing one to fabricate free-standing TiO_2 nanotubular membrane, followed by etching in HF vapors of the back side of the oxide nanotubes. Thereafter, several other approaches were reported: evaporation of Al film on Ti foil followed by anodization through Ti,

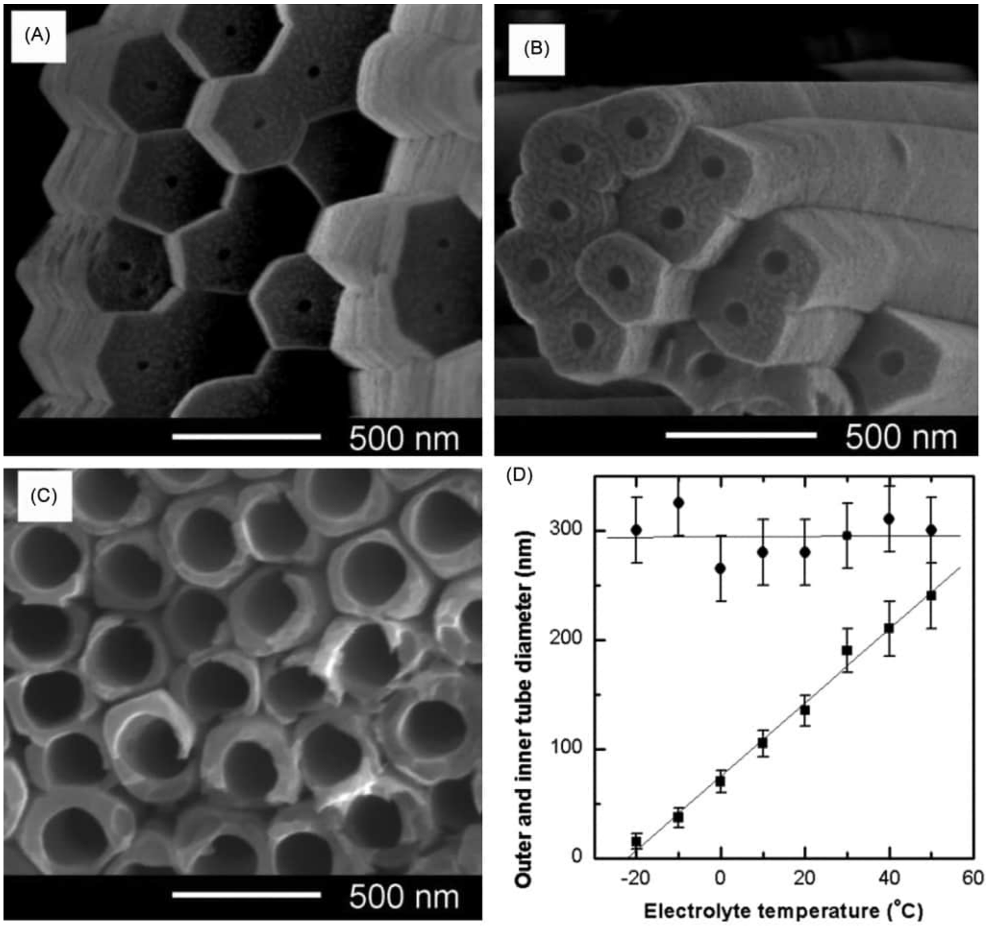

Fig. 1 SEM images of TiO_2 nanotubes obtained via electrochemical etching of Ti sheets at different electrolyte temperatures: −10 °C (a); 0 °C (b); and +30 °C (c). (d) Dependence of the inner (squares) and outer (circles) nanotube diameters upon the electrolyte temperature. Reprinted from Enachi M., Tiginyanu I., Sprincean V., Ursaki V. (2010b) Self-organized nucleation layer for the formation of ordered arrays of double-walled TiO_2 nanotubes with temperature controlled inner diameter. *Physica Status Solidi (RRL)—Rapid Research Letters* 4: 100–102. https://doi.org/10.1002/pssr.201004069. Copyright © 2010 with permission from John Wiley and Sons.

till the penetration of pores in Al due to the use of fluoride electrolyte and finally selective dissolution of Al; two-step anodization (Yip et al., 2012); double-sided anodization reported by Wong et al. (2016); applying higher anodization voltage for 5 min at the end of electrochemical etching resulting in release of free-standing membrane with open-sided TiO_2 nanotubes (Liao et al., 2012); reduction of the applied anodization voltage at the end of electrochemical etching followed by chemical dissolution of Ti foil (Kant and Losic, 2009); plasma etching using a mix of Ar and SF_6 with ratio 5:1 as reactive gas for 5 min (Ciobanu and Plesco, 2021).

Titanium dioxide can be found in three phases of crystallization: anatase, brookite and rutile. Among all the phases, the rutile phase is thermodynamically stable for titanium dioxide. The mentioned crystalline phases of titanium dioxide exhibit different properties, including density, refractive index and catalytic properties.

Enachi et al. (2009) investigated the influence of heat treatment on the structural properties of TiO_2 nanotubes by means of X-ray diffraction and Raman scattering. Raman spectrum analysis showed that the initially prepared samples are amorphous. As the annealing temperature increases to 300 °C, an anatase structure is formed. After annealing at 500 °C the rutile structure was observed, which coexisted with the anatase structure. Note that a complete phase transition to the rutile structure at 800 °C was reported by Hummel (1984). Notwithstanding this, the performed thermal annealing in the temperature range from 450 °C to 850 °C for 2 h by Enachi et al. (2016), showed the presence of the peaks related to the anatase phase in the case of the sample treated at 850 °C. As can be seen from Fig. 2, the maxima assigned to the rutile phase are more pronounced, but also the maxima of the anatase phase are observed which demonstrates mixed phases also for this heat treatment regime. The data are in good agreement with the review study of (Roy et al., 2011) and (Tsuchiya and Schmuki, 2020) mentioning that the complete phase transformation into rutile occurs at temperatures as high as 900 °C.

The transformation process depends mainly on the structure dimensions, shape, crystallographic orientations, but also on the calcination conditions like atmosphere or calcination time (Li et al., 2016; Winardi et al., 2010; Zhao et al., 2014).

Complimentarily, the SEM and TEM analysis presented in Fig. 3 demonstrated that as-grown nanotubes possess very smooth surface without any crystal planes. However, it is clearly seen that by thermal annealing at 850 °C some porosity is introduced in

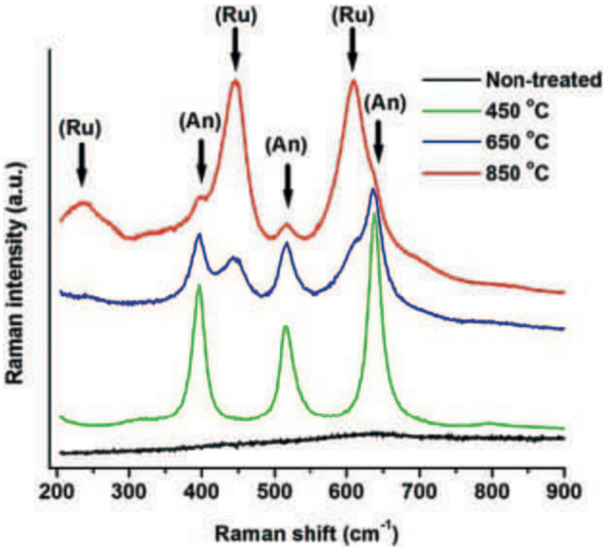

Fig. 2 Raman spectrum of as-grown TiO_2 nanotubes and heat treated at 450 °C, 650 °C, 850 °C. Reprinted from Enachi M., Guix M., Postolache V., Ciobanu V., Fomin V.M., Schmidt O.G., Tiginyanu I. (2016). Light-induced motion of microengines based on microarrays of TiO_2 nanotubes. *Small* 12: 5497–5505. https://doi.org/10.1002/smll.201601680. Copyright © 2016 with permission from John Wiley and Sons.

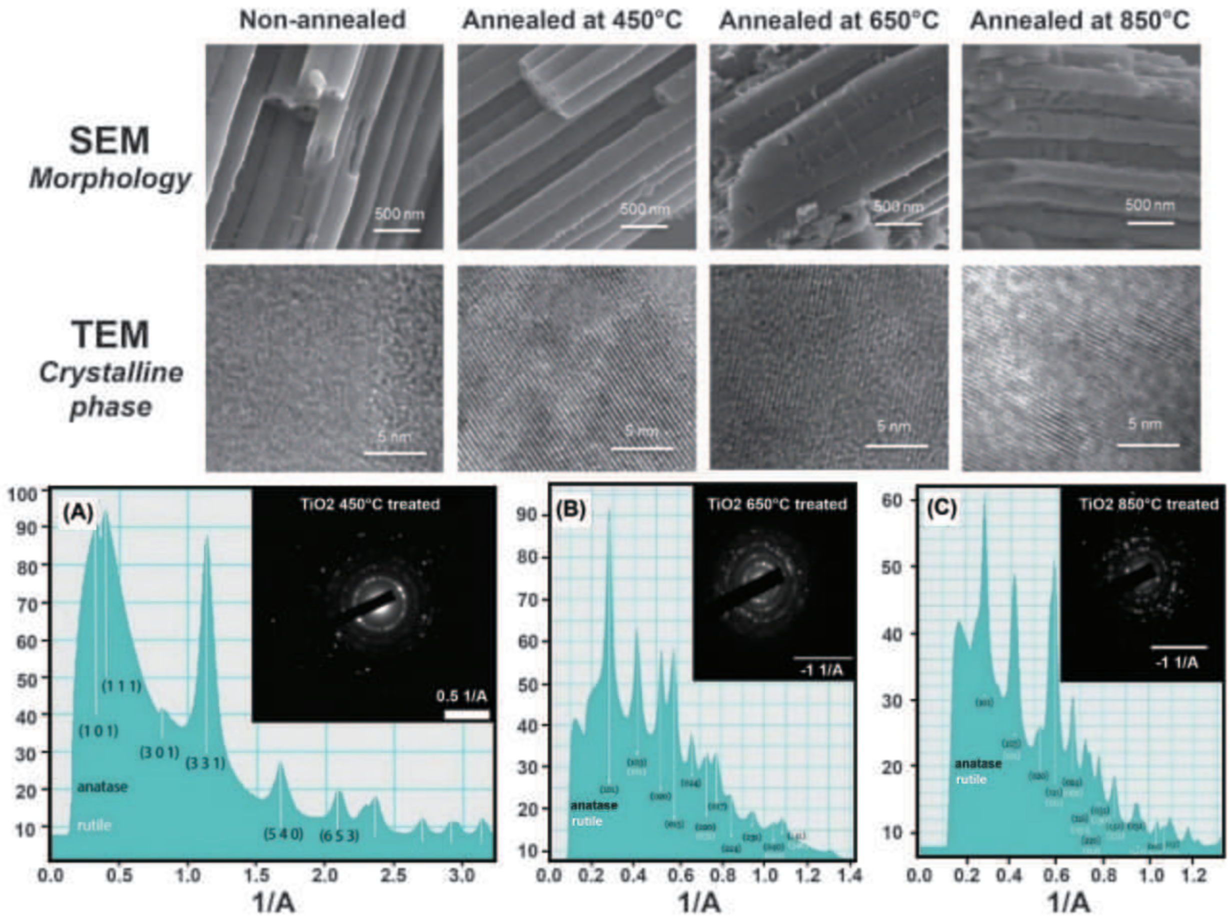
Non-annealed
Annealed at 450°C
Annealed at 650°C
Annealed at 850°C
SEM
Morphology
TEM
Crystalline phase
500 nm
5 nm
(A)
TiO2 450°C treated
0.5 1/A
(1 1 1)
(1 0 1)
(3 0 1)
(3 3 1)
(5 4 0)
(6 5 3)
anatase
rutile
100
90
80
70
60
50
40
30
20
10
0.0
0.5
1.0
1.5
2.0
2.5
3.0
1/A
(B)
TiO2 650°C treated
-1 1/A
anatase
rutile
0.0
0.2
0.4
0.6
0.8
1.0
1.2
1.4
1/A
(C)
TiO2 850°C treated
-1 1/A
anatase
rutile
60
50
40
30
20
10
0.0
0.2
0.4
0.6
0.8
1.0
1.2
1/A

Fig. 3 SEM and TEM images study of the morphology and crystallinity of as-grown and annealed at different temperatures TiO_2 nanotubes. The upper line indicates the annealing temperature. The electron diffractogram and average rotational diagram of samples treated at (a) 450 °C, (b) 650 °C and (c) 850 °C. Reprinted from Ciobanu V., Plesco I. (2021) TiO_2 nanotubes for photocatalytic degradation of methylene blue. *Journal of Engineering Sciences* 28: 23–30. https://doi.org/10.52326/jes.utm.2021.28(1).01. This work is licensed under a Creative Commons Attribution 4.0 International License, https://creativecommons.org/licenses/by/4.0/.

nanotube walls. The detailed study of the crystallinity of the material with different phases was analyzed by Rotational Average method which calculates a medium intensity of the electron reflection at certain distance from the ED central spot (Ciobanu and Plesco, 2021). To each reflection there was assigned the corresponding crystallographic planes, which reflect the values of the lattice constant *d* and the intensity of the maxima. It was established that the samples treated at 450 °C show only one phase and the material is nanocrystalline, while in the samples annealed at higher temperatures all reflections can be attributed to the anatase and rutile phases, corroborating well with previously published data by Enachi et al. (2015b).

An alternative possibility to control the crystallographic structure by direct writing using a focused laser beam was proposed and demonstrated by Enachi et al. (2013). TiO_2 nanotubes with an outer diameter of about 200 nm and a wall thickness of 70–80 nm obtained by anodization in a mixture of hydrogen fluoride (1 mL) and H_3PO_4 (10 mL) in ethylene glycol (100 mL) under 100 V during 2 h were used for this purpose. The obtained samples were subjected to a thermal treatment in a nitrogen atmosphere for 30 min at temperatures between 400 °C and 900 °C in the furnace, another set of samples was heated locally with a diode pumped solid state (DPSS) laser, with a wavelength of 532 nm and a power of 7–20 mW focused on area of 20 μm^2. As a result of focused laser beam treatment of as-grown TiO_2 nanotubes array exhibiting amorphous phase, the anatase phase or a combination of rutile and anatase structures can be obtained in a controlled fashion. The micro-cathodoluminescence image showed a green light emission (500 nm) from the periphery of the region marked with a laser spot with a power of 13 mW, while no emission was observed inside the marking. A similar emission, but with a lower intensity, was observed at 650 nm. Besides, the panchromatic image of CL suggests that, unlike the periphery of the region marked with a laser spot, there was no emission at any wavelength inside the marked region. When the laser beam power was increased to 20 mW the CL image was different (see Fig. 4). Although the green emission comes from the periphery of the region marked with the laser spot similar to the previous case (laser beam power 13 mW), an IR emission at 800 nm is observed from inside the region marked by the laser beam (Fig. 4b), which comes from Ti^{3+} interstitial ions in the rutile phase. CL with different wavelengths emitted from different regions after laser beam marking is well illustrated in the two-color image (Fig. 4c). The Raman spectra from Fig. 4e, measured along the surface treated by the laser spot, convincingly confirms that the region of the laser spot has a rutile structure, while the periphery has an anatase structure. These results are in full agreement with the CL data. Note that transition from amorphous phase to anatase one is performed at laser beam power density lower than 0.4×10^5 W cm^{-2}, while the rutile phase can be obtained at higher laser beam power densities. It is to be noticed that no changes in morphology were observed in samples treatment by laser beam at power density under 1×10^5 W cm^{-2}.

Self-ordered distribution of pores in nanotemplates based on II-VI and III-V semiconductor compounds

Self-organized pores perpendicular to the crystal surface

The field of solid-state-based porous materials encompasses dielectric and semiconductor nanotemplates. Among dielectric nanotemplates, porous anodic aluminum oxide (AAO) gained interest due to the pioneer works of Martin (1994) and Masuda and Fukuda (1995). Later on, researchers (Ali et al., 2010; Ali and Maqbool, 2013) succeeded to fabricate self-organized porous

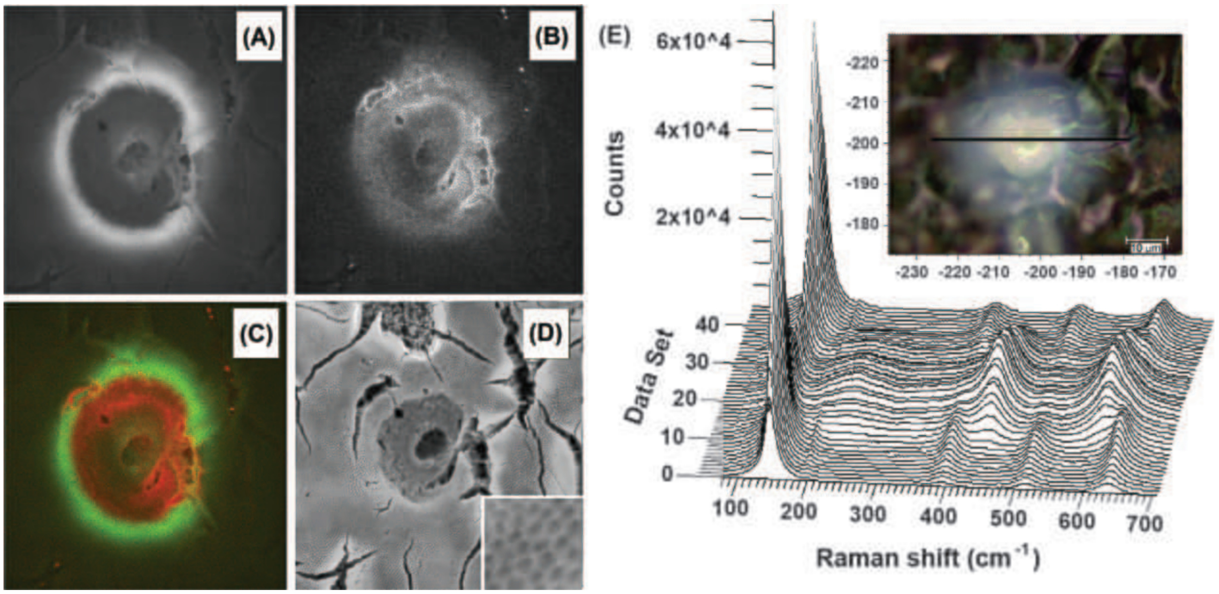

Fig. 4 Micro-CL image measured at 550 nm (a) and 800 nm (b), two-color composite image (c) and SEM image (d) taken from a TiO_2 NTs matrix treated by 20 mW power laser beam. The field of view of the image is 30.0 µm. (e) Scanning measurements of Raman spectra across a laser beam treated area and nearby regions. The laser beam with the power of 20 mW was focused on a spot with the diameter of 3 µm. Inset is the optical microscope image with the black line indicating the Raman scan. Reprinted from Enachi M., Stevens-Kalceff M.A., Sarua A., Ursaki V., Tiginyanu I. (2013) Design of titania nanotube structures by focused laser beam direct writing. *Journal of Applied Physics* 114: 234302. https://doi.org/10.1063/1.4849836. Copyright © 2013 with permission of AIP Publishing.

AAO via one step anodization process and to use the fabricated AAO template in nanofabrication process of highly ordered binary nanowires via electrodeposition. However, despite the high self-organization and self-ordering, AAO templates usually play a passive role in the nanofabrication due to limitations in electrical conductivity. It should be noted that the titanium oxide obtained by anodization possesses relatively low electrical conductivity. In connection with this, elaboration of conductive semiconductor nanotemplates whose properties can be adjusted by external electric fields, illumination, temperature, etc., has become an important topic of study. Good candidates suitable for nanotemplate fabrication via anodization proved to be III-V and II-VI semiconductor compounds. The versatility of morphologies and the application of porous semiconductor compounds have been described in detail in a recent review paper by Monaico et al. (2020a). First of all, it should be mentioned that in semiconductor compounds three types of pores were reported up to now: crystallographically oriented pores or "crysto pores"; current line-oriented pores or "curro pores"; and fractal pores. The fractal pores will not be taken into consideration in the present study due to the random distribution of pores which is far away from self-ordering and reported morphologies cannot be repeated in a controlled fashion. As it was established by Langa et al. (2002), the cross-sectional shape of pores, growth rate, etc., strongly depend on the applied electrochemical parameters during anodization. Moreover, the shape of nanopores can be tuned in *n*-GaP substrates with different crystallographic orientations by anodization in HBr electrolyte, as it was demonstrated by Wloka et al. (2005) and Müller et al. (2009) regarding rectangular and triangular shapes.

The authors of Föll et al. (2003b) focused on the formation of pores in III-V semiconductors, highlighting the main properties of the crystallographically oriented pores and current-line oriented pores. The main characteristics of the crystallographically oriented pores are the following: (i) triangular cross-sectional shape; (ii) they tend to grow along ⟨111⟩B crystallographic direction independent of the initial surface orientation; (iii) are obtained at low current densities; (iv) can intersect each other leading to new ultra-porous three-dimensional architectures. Among properties inherent to current line-oriented pores one can mention the following ones: (i) round cross-sectional shape; (ii) their formation requires higher applied current densities; and the last but not least (iii) they cannot intersect each other, probably the most important one from the point of view of self-ordering process.

Examples of current line-oriented pores and crystallographically oriented pores produced in an InP anodized substrate are presented in Fig. 5a. It should be noted that self-organization of pores during their growth leads to hexagonal packing of pores with the formation of highly ordered templates, as can be seen in the inset from Fig. 5a. The self-ordering of current line-oriented pores can be explained by the schematic illustration from Fig. 5b. The process of anodization starts at some root nucleus followed by branching of crysto pores. After a certain time of anodization, usually from 10 to 20 s, when the formed nucleation layer is fully filled with pores, the branching is stopped and the second phase begins, i.e., the transition from crysto pores to curro pores occurs. Taking into account that around each pore a depletion layer (W) is formed and the fact that curro pores cannot intersect, they start to push each other to maintain the two depletion layers 2 W between them. In this way, the process of self-ordering occurs without any lithographic means.

Recent systematization of the literature data demonstrated that curro pores are inherent to both III-V (except for GaAs) and II-VI semiconductor compounds, while crysto pores have been reported just in III-V semiconductor compounds (see Monaico et al., 2020a). Despite the intensive study of the GaAs material, the attempts to obtain current line-oriented pores were unsuccessful.

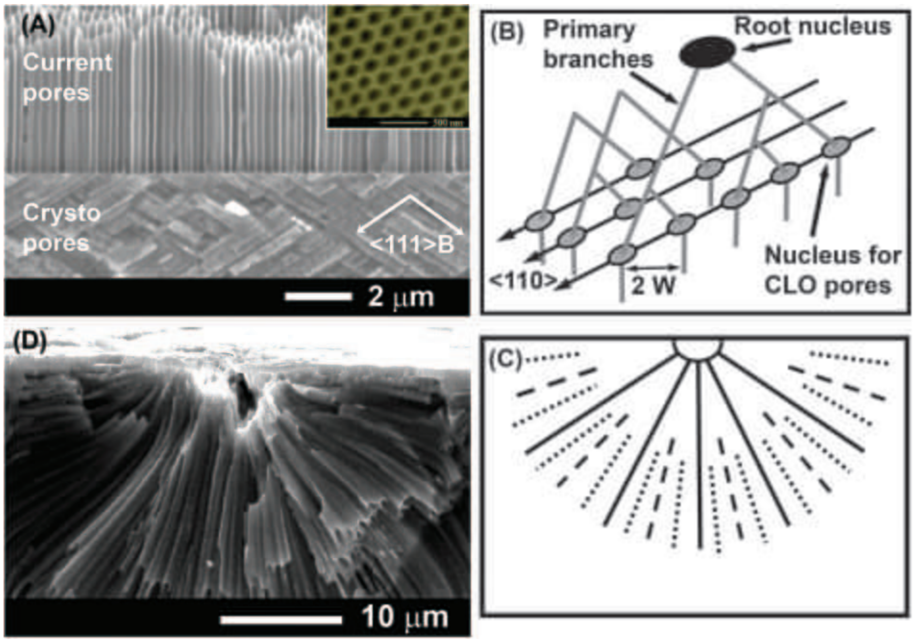

Fig. 5 (a) SEM image of porous InP layers anodized with changing the applied potential from 7 to 1 V resulting in formation of curro pores and crysto pores respectively. The inset represents top view of porous layer exhibiting hexagonal ordering. Schematic representation of the development of the porous structure in III-V (b) and II-VI (c) during anodic etching. (d) SEM image with experimental demonstration of the pore formation in *n*-CdSe, according to the model proposed in (c). Panel (a): Reprinted from Föll H., Langa S., Carstensen J., Christophersen M., Tiginyanu I. M. (2003b). Pores in III–V semiconductors. *Advanced Materials* 15: 183–198. https://doi.org/10.1002/adma.200390043. Copyright © 2003 with permission from John Wiley and Sons.

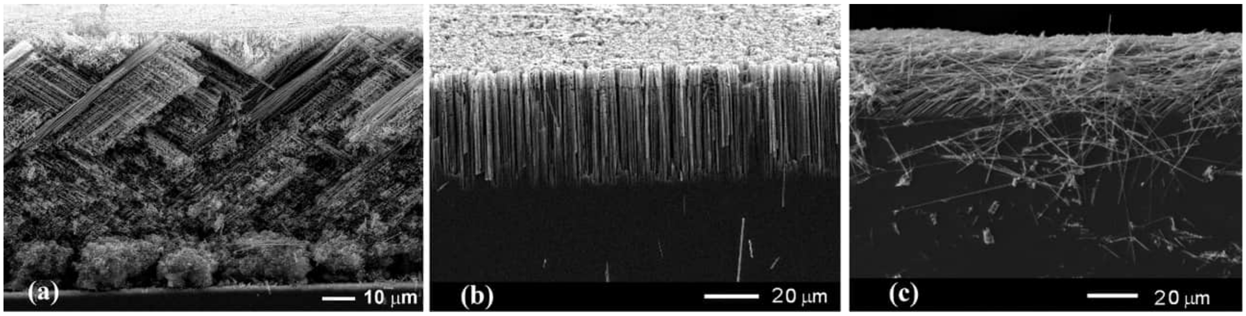

Fig. 6 Cross-sectional view of SEM images taken from GaAs nanowires produced on n-GaAs substrates with (100) (a), (111)B (b) and (001) (c) crystallographic orientations in 1 M HNO_3 electrolyte at applied potential of 4 V. Panels (b and c): Reprinted from Monaico E.V., Morari V., Ursaki V.V., Nielsch K., Tiginyanu I.M. (2022b) Core–shell GaAs-Fe nanowire arrays: Fabrication using electrochemical etching and deposition and study of their magnetic properties. *Nanomaterials* 12: 1506. https://doi.org/10.3390/nano12091506. This work is licensed under a Creative Commons Attribution 4.0 International License, https://creativecommons.org/licenses/by/4.0/.

Using n-GaAs substrates with different crystallographic orientations subjected to anodization in different electrolytes HCl, NaCl, HNO_3, HBr, etc., showed that the crystallographic orientation influences just the direction of propagation of pores in depth, the pores being tilted to the surface for (100) and (111)A orientations; perpendicular for (111)B orientation, and preponderant parallel to the surface for (001) orientations, as is illustrated in Fig. 6. The nature of the electrolyte determines the growth speed of pores, their density, as well as the possibilities of obtaining GaAs nanowires via one step anodization in HNO_3, as was reported by Monaico et al. (2020b, 2022b). However, some complex pores consisting of three circular pores were observed in the dynamic transitory regime of electrochemical etching during the switching of the applied voltage from a high value to a lower one or vice-versa (see Monaico et al., 2021). In spite of their circular shape, it was suggested that they are crystallographically oriented pores, round shape being explained by isotropic etching of a primary triangular pore wall formed during stationary anodization, which occurs in the subsequent dynamic regime of anodizing determined by the derivative of the current.

In contrast to III-V semiconductor compounds, the lack of crysto pores in II-VI semiconductor compounds denotes the not so high ordering of pores. In this case, the anodization starts at some imperfections at the surface and the pores grow radially away from the root nuclei, as is illustrated in Fig. 5c. During the development of the porous structure, when the condition is fulfilled that the space between two neighboring pores is bigger than 2 W, their branching takes place. The experimental demonstration of this model by Monaico et al. (2004) is presented in Fig. 5d based on anodized *n*-type CdSe single crystals with a concentration of free electrons of 3×10^{17} cm^{-3} at 300 K. When the radial porous domain meets another porous domain, the pores are forced to change their direction of propagation, and after some time of anodization, a porous network with pores parallel to each other is obtained.

Later on, using similar crystals Tiginyanu et al. (2005) showed that anodization under UV illumination results in a uniform nucleation of pore thus providing conditions for the growth of parallel pores with the diameter about 200 nm, stretching perpendicularly to the initial surface of the sample. It is worth to mention, that the width of the depletion layer strongly depends upon the concentration of free electrons and anodization voltage (see Table 1). The decrease in the thickness of pore walls down to 10–20 nm in the prepared nanotemplates based on as-grown samples with a free electron concentration of 2×10^{18} cm^{-3} leads to a blueshift of the excitonic emission lines by around 10 meV.

The formation of arrays of parallel pores starting with nucleation layer through radial ramification was reported in other II-VI semiconductor compounds, for instance in ZnSe (Irmer et al., 2009; Langa et al., 2011; Monaico et al., 2009b) and ZnCdS solid solutions (Colibaba et al., 2014b; Monaico et al., 2014a).

Let us discuss the issue of ZnO porosification. Due to the low chemical stability, the electrochemical nanostructuring of ZnO has been less investigated. In a recent study, Zalamai et al. (2021) reported nano-micro-nanostructuring rather than porosification. As a result of anodization, formation of nano-micro-structures with pyramidal shape on the O-face and inverted pyramids or tunnels on the Zn-face was evidenced. The applied potential during anodization allows one to tune the transverse dimensions of the produced structures. To our knowledge, up to now, porous layers with parallel pores have not been reported in the literature. Notwithstanding this, a simple technological approach of porous ZnSe matrix transformation into porous ZnO template via thermal annealing was demonstrated by Ursaki et al. (2009).

Self-organized pores parallel to the crystal surface

To make use of industrial approaches of planar semiconductor technologies, it is important to develop methods for the preparation of templates with pores oriented parallel to the top surface of the substrate. In continuation we will focus on the technological approaches of pore self-organization and technological tricks aiming at controlling the growth and direction of propagation of pores. Tiginyanu et al. (2011) demonstrated cost-effective approach for obtaining pores parallel to the InP and ZnSe crystal surface. In this study, the sample surface was covered with strips of photoresist (FR), acting as a shield against electrochemical nanostructuring of the surface underneath FR, while anodization is performed through the open windows between strips, as is illustrated in the schematic representation from Fig. 7a. According to the proposed approach, the pores start to nucleate on the surface unprotected by FR, and during the growth, the pores at the edge are forced to deflect into space under FR. The thickness of the walls of the porous

Table 1 Systematized data of porous III-V and II-VI semiconductor compounds.

Semiconductor compound	*Band-gap, eV*	*Electron concentration, cm^{-3}*	*Diameter of pores (nm), required applied voltage (V)*	*Typical electrolyte*	*References*
GaAs	1.42	1–3 $\times 10^{18}$	50–200 nm, 4 V, 25–250 mA cm^{-2}	HCl, HNO_3, NaCl	Schmuki et al. (1996); Ono et al. (2013); Tiginyanu et al. (2007b); Monaico et al. (2021)
		1×10^{18}, 2×10^{18} (111)B and (001) oriented	100–400 nm triangular cross-sectional shape nanowires, 4 V	HNO_3, HCl:H_2SO_4	Monaico et al. (2020b, 2022b); Asoh et al. (2014)
InAs	0.36	3×10^{18}	100–200 nm rod-like micro- and nanostructures, pulses with the amplitude of 6 V and the duration of 1 ms at a pulse repetition frequency of 1 Hz	H_3PO_4:HNO_3	Litovchenko et al. (2007)
		3×10^{18}	150 nm at 35 V. Hard to obtain thick porous layers.	KOH	Monaico et al. (2014a)
InP	1.35	1.3×10^{18}	70–140 nm at 5 V in 1.75 M and 3.5 M NaCl	NaCl	Tiginyanu et al. (2008)
		1.7–3 $\times 10^{18}$	100–150 nm; 3D porous structures at 100–350 mA cm^{-2}	NaCl, HCl	Chai et al. (2015); Weng et al. (2017); Langa et al. (2005)
		1.3×10^{18}	Nanowires—50 nm; 10 nm thick nanowalls; nanobelts with thickness about several nm at 15 V for 3 s	HCl	Monaico et al. (2014b)
		5×10^{18}	66 nm at 3.3 V	KCl	Quill et al. (2013)
GaP	2.26	2–8 $\times 10^{17}$	300–500 nm, 25 V	H_2SO_4	Tiginyanu et al. (2012, 2015b)
		2–8 $\times 10^{17}$ (100) oriented	Rectangular shape 233 $\times$ 327 nm at decrease of applied potential from 30 V to 15 V with a scan rate 5 mV s^{-1}	HBr	Wloka et al. (2005)
		3×10^{17} (111) oriented	Triangular shape 100 nm at 15 V	HBr	Müller et al. (2009)
		4×10^{17} (111) oriented	Triangular shape 200–300 nm at current density 0.9 A for 8 $\times$ 8 cm^2	HBr + oxalic acid	Zhu et al. (2014)
GaN	3.4	MOCVD 2.5×10^{18}	50–100 nm, 15–25 V	HNO_3	Yang et al. (2017)
		HVPE	Porous concentric pyramidal structures, <50 nm, 25 V	HNO_3	Tiginyanu et al. (2016)
		HVPE $>5 \times 10^{17}$	Uniform pores, 50 nm at 70 V on Ga-face; 10 nm at 15 V on N-face	HNO_3, HCl, NaCl	Monaico et al. (2019a)
		HVPE $>5 \times 10^{17}$	Multilayer porous structures, 25 V	HNO_3	Braniste et al. (2017a,b)
CdSe	1.74	3×10^{17}	200–400 nm, in the dark, 25 V 30 nm, UV assisted, 15 V	HCl	Monaico et al. (2004); Tiginyanu et al. (2005)
		2×10^{18}	50 nm, 15 V 10–20 nm, 5 V	HCl	Monaico et al. (2006)
		1×10^{18}	120 nm, 18 V	NaCl	Tiginyanu et al. (2007b)

(*Continued*)

Table 1 (Continued)

Semiconductor compound	*Band-gap, eV*	*Electron concentration, cm^{-3}*	*Diameter of pores (nm), required applied voltage (V)*	*Typical electrolyte*	*References*
ZnSe	2.7	4.4×10^{16} 7.2×10^{16} 3.0×10^{17} 2.1×10^{18}	600–900 nm at 50 V; 400–500 nm at 30 V; 100 nm at 9 V; 40 nm at 6 V;	$K_2Cr_2O_7$:H_2SO_4:H_2O	Monaico et al. (2007a,b); Irmer et al. (2009)
ZnTe	2.3	3×10^{18}	p-type, nanowires, 50 nm, pulsed 5 V	HNO_3:HCl:H_2O	Monaico et al. (2009a)
ZnO	3.37	3×10^{18}	pyramids on the O-face, 1–5 μm at 5 V; 10–50 μm at 10 V inverted pyramids or tunnels on Zn-face	HCl	Zalamai et al. (2021)
		1×10^{17} ZnSe templates	via thermal treatment of porous ZnSe at 800 °C during 1 h	–	Ursaki et al. (2009)
ZnCdS	2.9 3.0 3.3	2×10^{18}	30 nm $Zn_{0.4}Cd_{0.6}S$—16 V; $Zn_{0.5}Cd_{0.5}S$—40 V; $Zn_{0.67}Cd_{0.33}S$—70 V	HCl, HNO_3	Colibaba et al. (2014a,b, 2016)

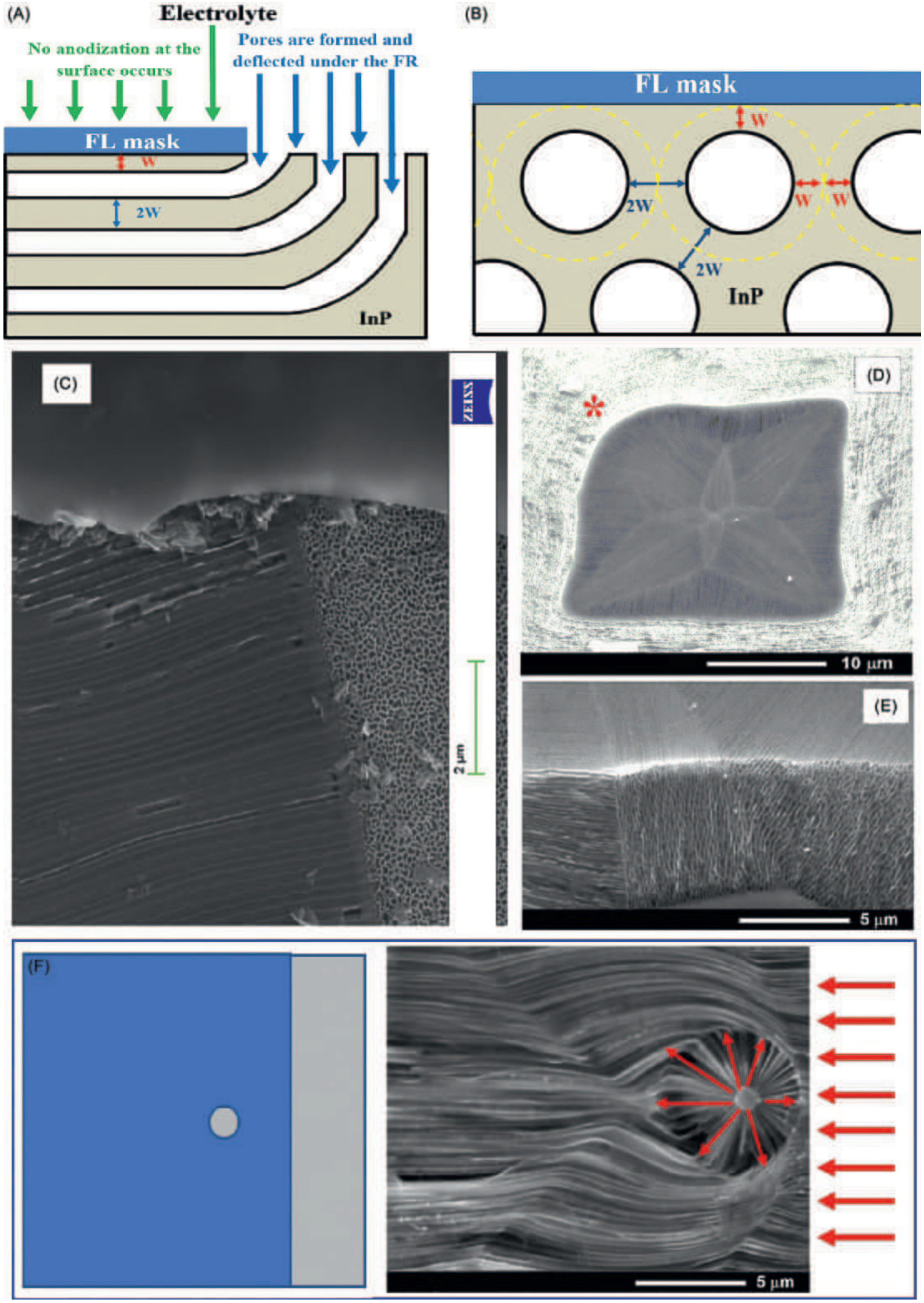
(A)
Electrolyte
No anodization at the surface occurs
Pores are formed and deflected under the FR
FL mask
W
2W
InP
(B)
FL mask
W
2W
W
W
2W
InP
(C)
ZEISS
2 μm
(D)
10 μm
(E)
5 μm
(F)
5 μm

Fig. 7 Schematic presentation of surface depletion regions during anodization under approach with pores parallel with the top surface (a) and lateral view in (b). (c) SEM image of porous InP after electrochemical etching according to schematic presentation from (a). SEM images of porous InP after anodization through open windows in the photoresist, (d) top view under the photoresist, (e) cross-sectional tilted view of (d). (f) SEM image of anodized InP using approach from (a) but with an open hole in the FR (see left side image in f). Panel (e): Reprinted from Monaico Ed., Monaico E.I., Ursaki V.V., Tiginyanu I.M., Nielsch K. (2019b) Electrochemical deposition by design of metal nanostructures. *Surface Engineering and Applied Electrochemistry* 55: 367–372. https://doi.org/10.3103/S1068375519040070. Copyright © Allerton Press, Inc. 2019 with permission from Pleiades Publishing, Ltd.

skeleton is equal to two depletion layers (2 W) due to the existence of two semiconductor-electrolyte junctions, while the thickness of the thin layer under the FR is two times smaller, implying just one semiconductor-electrolyte junction as is depicted in Fig. 7b. The experimental demonstration of the parallel pores is presented in Fig. 7c. Buried pores aligned parallel to the sample surface can be seen under the thin surface layer after the removal of the FR. Yang et al. (2017) proposed to use laser scribing process in GaN epilayers to perform lateral etching to obtain pores parallel to the top surface.

Moreover, spectacular porous architectures were obtained by applying specially designed masks on the sample surface subjected to anodization, as is illustrated in Fig. 7d. Instead of FR strips, Monaico et al. (2019b) used FL mask in the form of squares. In this case, the pores are forced to develop by the self-ordering process in the restricted space under the FR. Taking into account that the curro pores cannot intersect each other, keeping at least 2 W between them, a complicated self-organization of pores occurs. During the anodization, some pores stop to grow, while other ones are forced to change their direction of propagation in the remaining unetched space. Note that a spectacular morphology is obtained also in cross-section (see Fig. 7e). A special attention has to be paid to the left upper corner in the Fig. 7d marked with asterisk. It is clearly seen that if the corner of the used FL mask is not so sharp, the influence of the neighboring pores is not so pronounced. Taking into consideration the "competition" between pores in occupying the space under the FR, recently we investigated the evolution of self-ordering of pores through FL mask with an open window with round shape, as is illustrated in the Fig. 7f. From the SEM image after anodization of *n*-InP wafer one can see the formation of the primary pores under the photoresist and at the same time the formation of the porous domain through the open window with the formation of the secondary pores. When anodizing from the right side, the primary pores grow, avoiding the porous domain. It can certainly be concluded that anodization in combination with photolithographic means opens a new avenue for controlling the self-organization of the pores leading to new morphologies obtained by design.

Three-dimensional modulation of the porous layer

Anodization of semiconductor compounds proves to be a cost-effective tool for use in nanotechnologies due to the possibility to fabricate ordered structures such as two-dimensional (2D) single crystals of nanopores, the porous skeleton being characterized by good electrical conductivity. The results from Fig. 7 described above demonstrated that under optimum anodization conditions (at the optimum applied voltage for the formation of curro pores) the pores can be deflected to grow parallel to the crystal surface. Moreover, using FL mask with a special design, the pores grow in the restricted space under the FR, leading to a spectacular morphology due to the self-organization processes. Note, that the final morphology strongly depends on the used shape (triangle, square, octahedral shape, etc.) of the FL mask and on its transverse dimensions.

Over the last years, a considerable research activity has been focused at the fabrication of three-dimensional (3D) ordered porous structures possessing electrical conductivity. Langa et al. (2005) demonstrated formation of 3D structures by external modulation of the current density representing smooth Bragg-like structure. The anodization in 5% HCl electrolyte of (100) *n*-type InP crystals with a free carrier concentration of 3×10^{18} cm^{-3} was realized in galvanostatic mode at 600 mA cm^{-2} for 0.1 min in the first phase and 0 mA/cm^2 for 0.5 min in the second phase. Our subsequent research has shown that the sequence of applied current is not very important. It was mentioned above that after beginning of anodization usually 20 s are required for the crysto pores to ramify in the so-called nucleation layer (at mentioned free electron concentration the thickness is about 2 μm) followed by self-ordering process of curro pores. An example of multilayer porous structures is presented in Fig. 8a. In the first phase, the sample was anodized in 3.5 M NaCl electrolyte at 100 mA cm^{-2} followed by anodization at consecutively changed low/high current densities (50 mA cm^{-2}/ 500 mA cm^{-2}) resulting in the formation of parallel porous layers with different degrees of porosity. Recent comparative study of *n*-InP anodization in HCl and NaCl electrolytes performed by Monaico et al. (2020c), revealed no significant influence of the nature of the electrolyte upon the velocity of the pore's growth.

Tiginyanu et al. (2007a) demonstrated for the first time that pulsed potentiostatic anodization (2 V, 4 V, and 6 V) of *n*-InP substrates in an environmentally friendly electrolyte based on aqueous solution of NaCl leads to spatial nanostructuring of the material through modulation of the degree of porosity and changes in the morphology of the porous layers. As illustrated in Fig. 8b, the morphology changes considerably due to the induced self-organization of pores governed by transition from crystallographically oriented to current-line oriented pores.

The absence of the crysto pores in II-VI semiconductor compounds stands out again. The formation of flat porous layers with different degrees of porosity at successive anodization in potentiostatic regime of *n*-ZnSe crystals with a free carrier concentration of 1.5×10^{17} cm^{-3} was reported by Monaico et al. (2007b) (see Fig. 8c). It was found that the CL emission intensity strongly depends upon the diameters of the pores which determine the thickness of the porous skeleton walls. An interesting finding was established during the successive anodization at higher voltage followed by lower applied voltage (15 V and 8 V). The morphology reported by Monaico et al. (2009b) evidenced layer porosification at different length scales as is shown in the image from Fig. 8d. This feature can be explained by the creation of thicker or thinner space-charge-region W at different applied potentials. In accordance with the Eq. (1), the space-charge-region equals

$$W = \sqrt{\frac{2 * \varepsilon * \varepsilon_0 (V_{bi} - V_{dc})}{q * N_D}}, \tag{1}$$

where: ε—dielectric constant; ε_0—free space permittivity; V_{bi}—built in voltage; q—elementary charge; N_D—free carrier concentration; and V_{dc} represents the applied voltage.

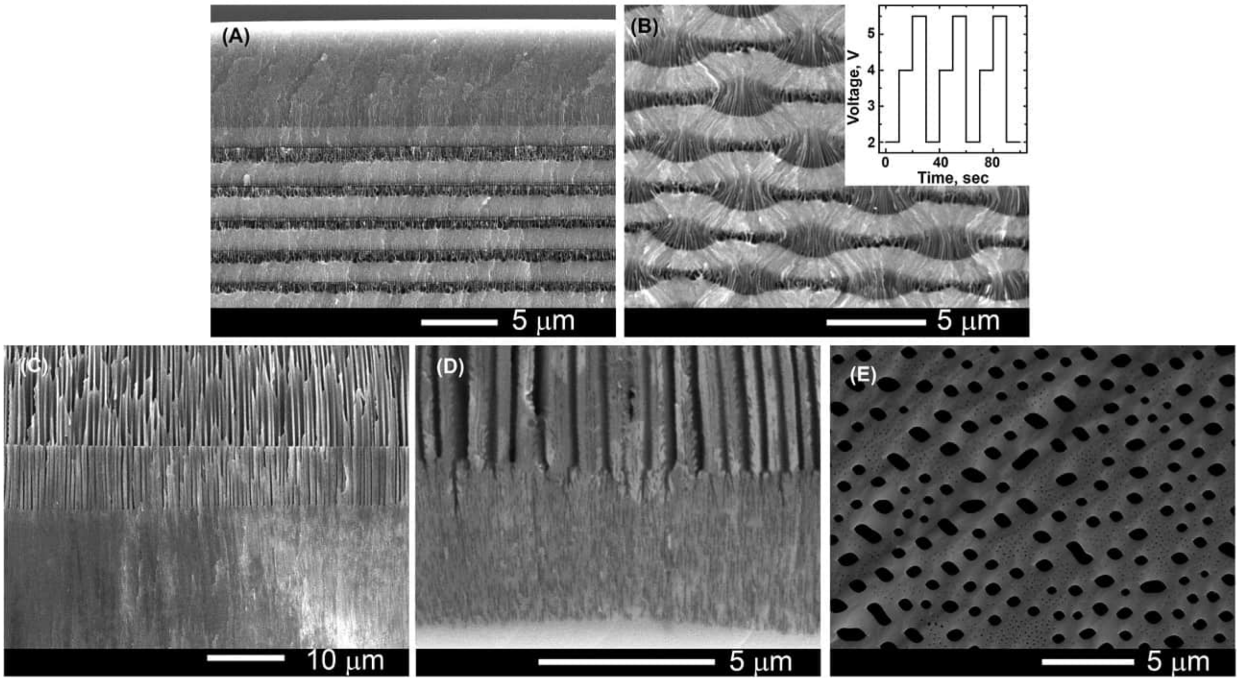

Fig. 8 SEM images of anodized InP crystal in 3.5 M NaCl electrolyte (a) in galvanostatic mode at 100 mA cm^{-2} followed by anodization at consecutively changed low/high current densities (50 mA cm^{-2}/500 mA cm^{-2}) resulting in multilayer porous structures with different degrees of porosity; (b) in potentiostatic mode at consecutively changed anodization potential 2 V, 4 V, and 6 V demonstrating modulation of porous layer due to the transition from crysto to curro pores. (c) SEM image of multilayer porous structures with different degrees of porosity as well as successive anodization leading to the perforation of primary pore walls in cross-section (d) and top view (e). Panel (c and d): Reprinted from Monaico E., Tighineanu P., Langa S., Hartnagel H.L., Tiginyanu I. (2009b) ZnSe-based conductive nanotemplates for nanofabrication. *Physica Status Solidi (RRL) Rapid Research Letters* 3: 97–99. https://doi.org/10.1002/pssr.200903026. Copyright © 2009 with permission from John Wiley and Sons.

Experimental demonstration of the formation of a porous layer with two different diameters of pores in the same plane is presented in Fig. 8e. During the first anodization of *n*-ZnSe at 15 V a porous layer with the pore's diameter about 500 nm and thick skeleton walls is formed (see the upper porous layer in Fig. 8d). As the applied voltage is reduced to 8 V, a new porous layer is created with diameter of pores as low as 50 nm and much thinner pore walls in comparison with previous anodization (see the bottom porous layer in Fig. 8d). At the same time, these 50-nm narrow pores grow in the skeleton walls of the first porous layer. The observed successive porosification of the same layer at two different length scales opens new possibilities for the design and fabrication of device structures based on porous semiconductor compounds.

Let us pass to the issue of porosification of GaN which represents a class of wide-bandgap III-N semiconductor compounds. Almost all reported porous morphologies were obtained on GaN grown by metal organic chemical vapor deposition (MOCVD). Using light assisted wet etching, nanowires or pyramidal structures consisting of nanowires, representing threading dislocations, were reported by Youtsey et al. (1999), Díaz-Guerra et al. (2005), Radzali et al. (2014), Zhang et al. (2018), while porous layers with parallel pores obtained by anodic etching were reported in the works of Tseng et al. (2014), Kim et al. (2016), Yang et al. (2017), Li et al. (2021). It is to be noted, however, that MOCVD-grown layers suffer from internal strains and defects related to mismatches of crystal lattices and thermal expansion coefficients with the substrate, and are usually limited to thickness of 2–3 µm.

Among other growth methods, Hydride Vapor Phase Epitaxy (HVPE) has proven to be one of the most relevant techniques allowing one to obtain thick free-standing GaN substrates at growth rates up to 500 µm/h, as was reported by Bockowski et al. (2016). Applying photoelectrochemical and electrochemical etching on Ga-face and N-face of (0001) HVPE grown 300 µm thick GaN free-standing substrates acquired from SAINT-GOBAIN Crystals, Tiginyanu et al. (2016) reported three-dimensional self-organized nanostructured architectures which were assigned to spatial modulation of electrical conductivity during the HVPE growth. Fig. 9a and b illustrate the atomic force microscope (AFM) images of the surface topography recorded on the as-grown HVPE GaN substrate. Well-defined circular regions are observed, which form structures similar to concentric rings.

Taking into account that electrochemical and photoelectrochemical (PEC) etching is extremely sensitive to the local doping, electrical properties of the sample along the surface were investigated using Kelvin Probe Force Microscopy (KPFM), also known as surface potential microscopy (Fig. 9c). Self-organized 3D nanostructured architectures have been revealed, including quasi-ordered concentric hexagonal structures on both Ga-face and N-face, as shown in Fig. 9d and e. Note that KPFM is able to investigate just the sample surface, while anodization allows to study the uniformity of doping along the depth. A detailed investigation of the

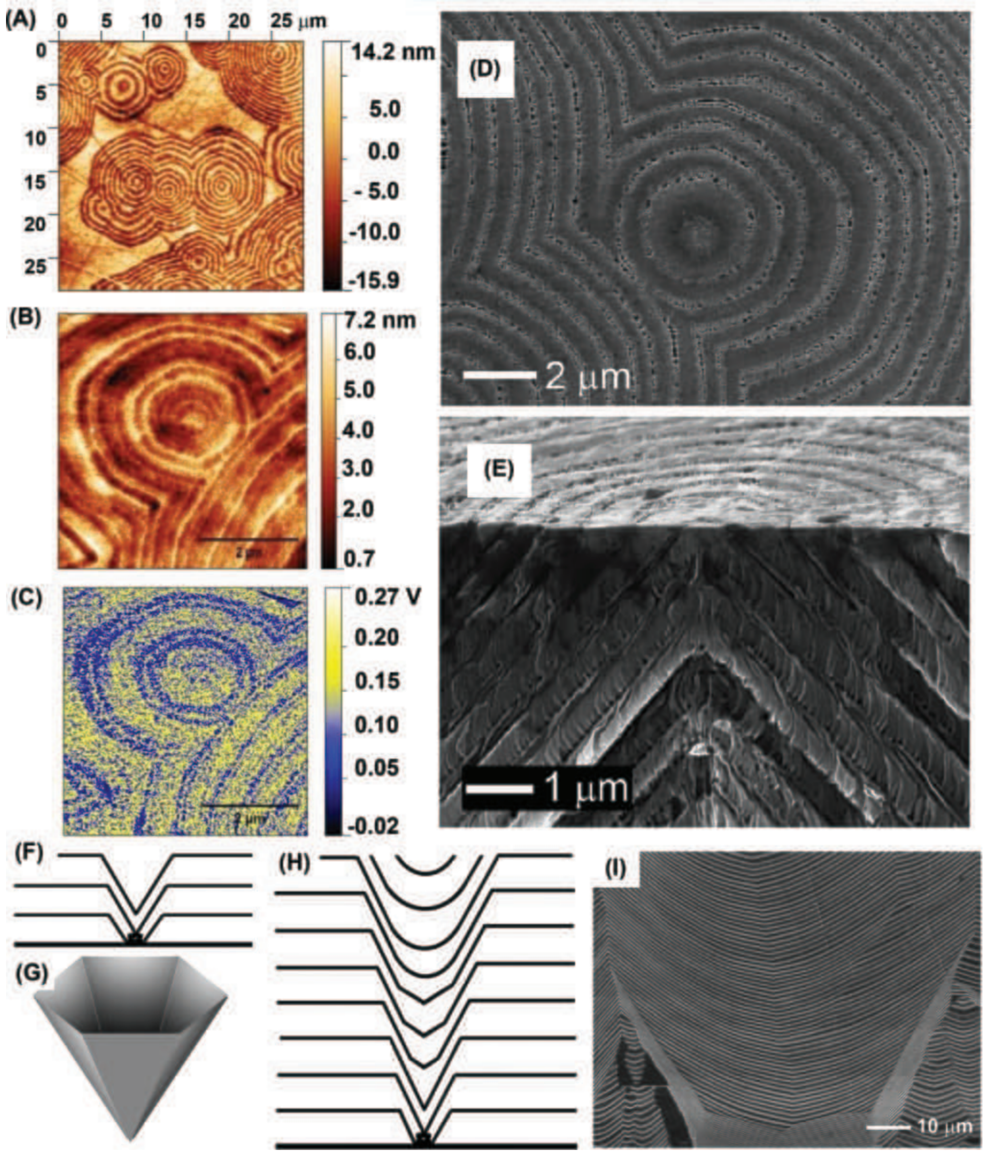

Fig. 9 (a, b) AFM images taken from the surface of an HVPE grown GaN substrate. (c) The image of the KPFM taken from the surface shown in (b). SEM images of the GaN sample subjected to electrochemical etching: top view (d) and cross-sectional view (e). Schematic of the pit formation over an imperfection reducing locally the growth rate (f), 3D drawing of the emerging V-pit (g), schematic representation of the V-pit formation, growth and annihilation (h), and cross-sectional SEM image taken from an overgrown V-pit (the cleavage was subjected to PEC-etching) (i). Reprinted from Tiginyanu I., Stevens-Kalceff M.A., Sarua A., Braniste T., Monaico E., Popa V., Andrade H.D., Thomas J.O., Raevschi S., Schulte K., Adelung R. (2016) Self-organized three-dimensional nanostructured architectures in bulk GaN generated by spatial modulation of doping. *ECS Journal of Solid State Science and Technology* 5: P218–P227. https://doi.org/10.1149/2.0091605jss. Copyright © 2016 The Electrochemical Society. Reproduced by permission of IOP Publishing Ltd. All rights reserved.

modulation of electrical conductivity and lattice distortions in the as-grown and PEC etched HVPE GaN substrates was realized by Wolff et al. (2019).

According to the proposed model for the growth of bulk HVPE-grown GaN (see Tiginyanu et al., 2016) based on the obtained results and literature data, the growth process of bulk GaN via HVPE techniques is governed by the formation and subsequent overgrowth of the so-called V-type defects or pits on the film surface, as is illustrated in the schematic overview in Fig. 9f. It is expected, that on Ga-face representing growth surface, the V-type defects will be not definitely but in the huge part annihilated. Later on, different porous morphologies produced by anodization in the depth of a 300 µm thick HVPE-grown GaN substrates (MTI-corporation, USA) with respect to the N- or Ga-face were reported by Monaico et al. (2019a). On the N-face a porous structure in the form of pyramids was formed, while homogenous porous matrices with pores oriented perpendicular to the wafer surface were generated at a depth of up to 50 µm at the Ga-face.

Hopping electrodeposition: The deposition of self-organized monolayer of Au nanodots on porous structures

Electrochemical deposition of metal nanodots has been proven to be one of the most cost-efficient and effective methods, especially when deposition is carried out on semiconductor substrates or matrices possessing electrical conductivity. Using pulsed electroplating, (Sato et al., 1999) demonstrated self-organized deposition of Pt dots on bulk n-GaAs and n-InP substrates with free electron concentration about 10^{16} cm^{-3}, while control of the dots positioning was realized by electroplating in combination with electron beam lithography. Later on, Hasegawa and Sato (2005) found the Fermi-level pinning at the metal-semiconductor interface to be greatly reduced, resulting in a strong dependency of the Schottky barrier height on the metal work function.

The possibility to cover a huge surface inherent to porous n-GaP and n-InP with free electron concentration of 2×10^{17} and 1.3×10^{18} cm^{-3}, respectively, by a self-assembled monolayer of gold nanodots (see Fig. 10a and b) was in premiere reported by Tiginyanu et al. (2015a). Using pulsed electrochemical deposition, the authors found that after nucleation each dot increases in size up to a critical transverse dimension of about 20 nm, the process of electrodeposition of gold being continuously supported by the

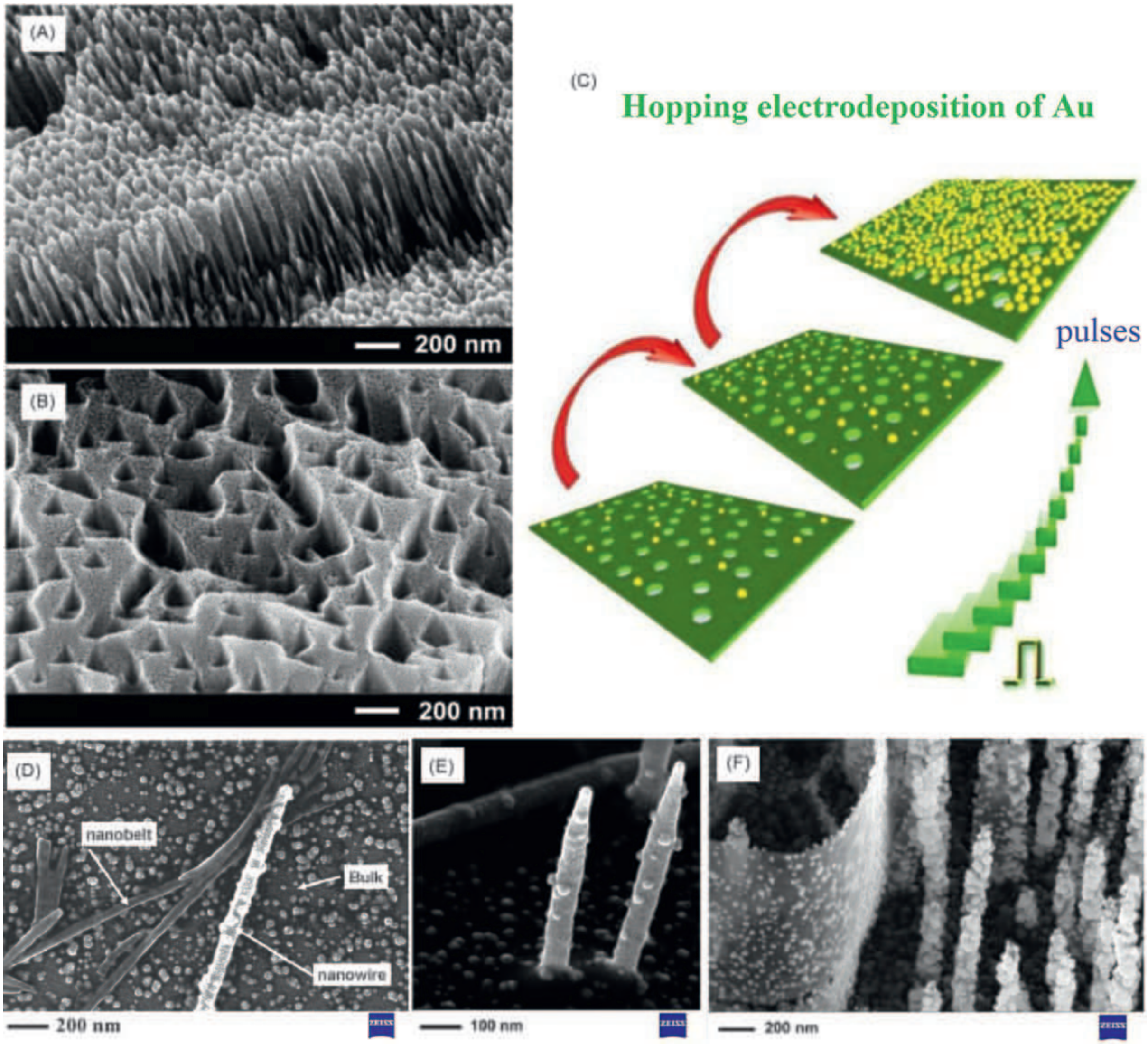

Fig. 10 SEM images taken from fragments of porous GaP after electrochemical deposition of Au dots for 5 s (a) and 100 s (b). Schematic illustration of the "hopping electrodeposition" mechanism is presented in (c). SEM images of one *n*-InP nanowire and several nanobelts on bulk InP substrate (d) and magnified SEM image of a few nanowires (e) after pulsed electrochemical deposition for 120 s. (f) SEM image of a nanowall and several nanowires after electrochemical deposition for 300 s. The estimated thickness of the nanostructures: nanowire—50 nm; nanowall—10 nm; nanobelt—about a few nanometers. Panels (a and b): Reprinted from Tiginyanu I., Monaico E., Nielsch K. (2015a) Self-assembled monolayer of Au nanodots deposited on porous semiconductor structures. *ECS Electrochemistry Letters* 4: D8–D10. https://doi.org/10.1149/2.0041504eel. Copyright © 2015 The Electrochemical Society. Reproduced by permission of IOP Publishing Ltd. All rights reserved. Panel (f): Reprinted from Monaico E.V., Tiginyanu I.M., Ursaki V.V., Nielsch K., Balan D., Prodana M., Enachescu M. (2017) Gold electroplating as a tool for assessing the conductivity of InP nanostructures fabricated by anodic etching of crystalline substrates. *Journal of the Electrochemical Society* 164: D179–D183. https://doi.org/10.1149/2.1071704jes. Copyright © The Electrochemical Society 2017. Reproduced by permission of IOP Publishing Ltd. All rights reserved.

formation of new nanodots. Schematic illustration of the "hopping electrodeposition" mechanism is depicted in Fig. 10c. To explain the new findings, the authors took into account the emergence of a Schottky barrier at the metal-semiconductor interface as soon as the transverse dimension of the dot reaches the threshold value. Note that the barrier potential is oriented in the opposite direction relative to the applied cathodic voltage. Under these conditions, one can imagine electrodeposition as a hopping process: gold deposition jumps to other local areas as soon as one or more dots reach the threshold value of the diameter. The process of hopping electrodeposition continues until the entire surface inherent to the porous template is covered by a monolayer of gold nanodots. It is interesting to note that after the self-assembled monolayer is formed, further electroplating of gold is spatially non-uniform and leads to the deposition of particles with relatively large diameters.

The hopping electrodeposition via pulsed electrochemical deposition of metal nanodots proved to be an original approach and effective tool for estimation of the electrical conductivity in 1D and 2D nanostructures as was demonstrated by Monaico et al. (2017). It is known that a good electrical conductivity of semiconductor surfaces is required for electrochemical deposition. It has been mentioned above that the electrical conductivity of the walls of the porous semiconductor skeleton is higher compared to that of the walls of porous TiO_2 or dielectric nanotemplates (like porous alumina), which ensures good conditions for the deposition of nanotubes on the inner surface of the pores. Another proof of a good electrical conductivity demonstrated by Tiginyanu et al. (2012) is the uniform deposition of Pt on the surface of the pores, regardless of their shape (such as, for example, circular and triangular-shaped pores).

The essence of the proposed approach for the estimation of the conductivity of semiconductor nanostructures according to their transversal geometric dimensions is the mechanism of "hopping electrodeposition" discussed above. Fig. 10d shows the SEM image of an n-InP nanowire and several nanobelts on a massive InP substrate obtained by "fast electrochemical etching" (the term introduced by Monaico et al. (2014b)), followed by pulsed electrochemical deposition of Au for 120 s. It is clearly seen that the surface of the nanowire, after the electrochemical deposition of Au, is covered by a uniform monolayer of gold nanodots and some larger gold conglomerates at higher magnification in Fig. 10e. Several larger Au conglomerates are formed because the deposition time is longer than the time required to deposit a monolayer of 20 nm size-saturated Au dots. Unlike nanowires, the surface of nanobelts remains intact, meaning that no electrochemical deposition occurs on them.

As concern 10 nm thick *n*-InP nanowalls, possessing an intermediate thickness between nanowires and nanobelts, a comparative Au electroplating is presented in Fig. 10f. It should be mentioned that all nanostructures (nanowires, nanobelts and nanowalls) are produced simultaneously at the same bulk *n*-InP substrate, and the electroplating is performed on them in the same process. Comparing Au deposition on nanowires (SEM images in Fig. 10e and f), it can be stated that few larger Au nanoparticles are deposited on the monolayer of Au nanodots within 120 s (Fig. 10e), while the number of large nanoparticles deposited on nanowires increases significantly after deposition for 300 s (Fig. 10f). Also, in Fig. 10e it can be seen that the density of large Au nanoparticles on nanowires and on the massive InP substrate is almost the same, which suggests that the electrical conductivity of nanowires is comparable to that of massive semiconductor crystals. In contrast, the surface of the nanowall in Fig. 10f is only partially covered by Au nanodots, which means that 20 nm Au nanodots monolayer is not completely formed on the surface of the nanowall. One can conclude that the nanowall has an intermediate conductivity value between those of the nanowire and the nanobelt.

Nowadays, metal nanostructures play an important role in many applications, for instance in nanoelectronics, plasmonics and nanophotonics. Traditionally, metal nanoparticles are obtained in solutions, and positioning them on a chip remains a challenge.

A method for controlled deposition of metallic nanodots along predetermined directions by using cost-effective and accessible techniques was proposed and demonstrated by Monaico et al. (2019b). The proposed approach can be explained by Fig. 7a and b. During the anodization using FL-based process, a thin surface layer with the thickness of one SCR is formed under the FL mask, in contrast to the thickness of the porous skeleton walls. Taking into consideration that the electrochemical deposition occurs selectively on semiconductor nanostructures, depending on their geometric parameters, especially thickness, the electrodeposition takes place along the walls of the first row of pores (having thickness 2 W) under this thin layer (with the thickness 1 W).

The mechanism of hopping electrodeposition was used for the fabrication of free-standing large-area nanoperforated gold membranes in the work of Monaico et al. (2020d). In this approach, at the beginning a thin film consisting of gold nanodots is deposited on GaAs surface, the perforation of this layer being controlled by the width of the deposition pulse. The procedure is followed by electrochemical etching of GaAs substrate through deposited Au film. As was demonstrated, during the porosification of GaAs, the reaction gazes contribute to the detachment of the Au layer, resulting in free-standing perforated Au membrane that can be transferred to other substrates, inclusive flexible ones due to the excellent flexibility of the membrane.

The modulation of the electrical conductivity of GaN crystals during the HVPE growth was also highlighted by the study of the electrochemical deposition of gold governed by the mechanism of "hopping electrodeposition." During the electrochemical deposition of Au, as in the case of electrochemical etching, the current passes through the electrical path with the lowest resistance. Thus, experimentally optimizing the parameters of electrochemical deposition, especially the value of the amplitude of the deposition pulse, predominant deposition of gold on regions with higher conductivity was realized, forming concentric structures similar to those in Fig. 11b. It should be noted that regions with different conductivities can also be identified with the help of an electron microscope, by evidencing different contrast in SEM images, as is presented in Fig. 11a.

Thus, the combination of electrochemical nanostructuring of semiconductor substrates and electrochemical deposition of metals is a powerful tool for the manufacture of new hybrid metal-semiconductor nanoarchitectures for various electronic, photonic and plasmonic applications.

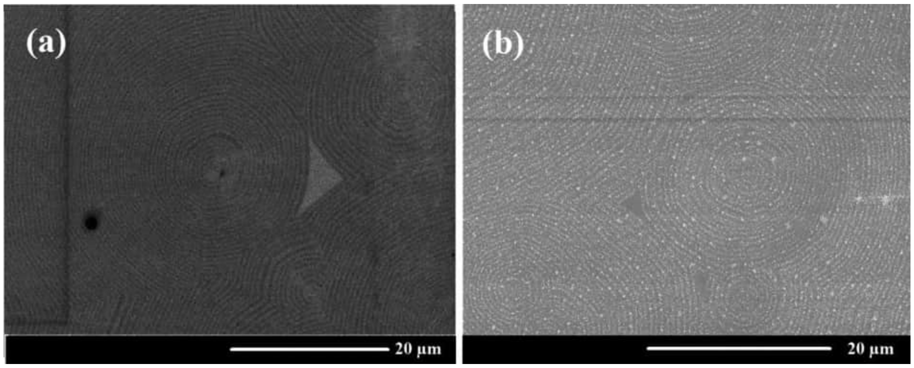

Fig. 11 (a) SEM image of the as-grown HVPE GaN substrate with back-scattered electron detector (BSE). (b) SEM image with secondary electron detector (SE) of the sample from (a) after pulsed electrochemical deposition demonstrating gold deposition on regions with higher conductivity forming concentric structures.

Applications of self-organized ordered arrays

At present, low-dimensional materials are in the attention of both scientists and manufacturers of electronic and photonic devices. The widespread implementation of nanometer-sized devices has already revolutionized information and communication technologies, and is currently working intensively in various fields vital to civilization, such as medicine, the environment, renewable energy sources, etc. The most enigmatic phenomena are hidden in the labyrinth of nano-object interactions. In this context, in continuation we will focus on some applications of elaborated and described above nanostructures: micro-submarines consisting of networks of TiO_2 nanotubes with capabilities to transport micro- and nano-capsules in a fluid environment, photonic and photocatalytic applications as well as a micro-nano-device with a record capacitance per square micrometer based on self-organized porous GaP/Pt nanocomposites. It is worth to mention also the perspective for using self-organized porous architectures for nonlinear optical applications (see the works of Reid et al., 2005a,b; Radhanpura et al., 2010), although we will not address this issue here.

a. Light-driven micromotors

The term "nanobots" attracted attention after the famous essay given by the Nobel laureate Prof. Richard Feynman in 1959 and published later in 1992 (Feynman, 1992), mentioning the potential to "swallow the surgeon" of machines small enough for us to ingest. Nowadays, researchers intensively work on creation of micro-nano-robots, able to transform chemical energy or the energy of the external field into motion, with the aims to perform certain complex tasks, for instance drug-delivery systems as it was described in review work of Medina-Sánchez et al. (2018) as well as in the Chapter by Mariana Medina-Sánchez, Microrobots. In general, micromotors are classified according to the energy source for the propulsion of the micromotor. Four sources of energy are known to propel the micromotors: light; ultrasound; magnetic and electric fields (Dong et al., 2016; Leal-Estrada et al., 2021; Cao et al., 2021; Niedert et al., 2020; Rajabasadi et al., 2021).

Light is one of the most attractive fuels for micro- and nanomotors, because it is a renewable energy source that can be easily controlled, does not require physical connections to micromotors, and usually does not lead to the formation of impurities. Two major advantages should be mentioned for light-driven micromotors: the speed of the motors can be controlled by the intensity of the light and the on/off switching mechanism is fast. To date, most light-driven micro- and nanomotors use ultraviolet or visible light. Up to now different low-dimensional objects were used as self-propelled micromotors, for instance tubular structures by Wrede et al. (2021), nanowires by Karaca et al. (2021), nanoparticles by Hu et al. (2022).

It is worth mentioning that most of the studies have been focused on the development of micromotors based on individual nanostructures. A self-propelled light-driven micromotors, named by authors micro-submarines, based on TiO_2 self-organized arrays of nanotubes, with the inner cone-shaped cavity, capable to pick-up and release the micro-particles was reported by Enachi et al. (2016) (see Fig. 12). The cargo capability takes place due to the distribution of tasks in the network of nanotubes, where some nanotubes are responsible for the cargo while transportation is provided by other nanotubes under UV illumination. Propulsion is generated by the ejection, through the wide ends of the nanotubes, of the oxygen bubbles formed inside of nanotubes due to the photocatalytic properties of titanium dioxide. The first demonstration of light-controlled bubble-propelled single-component metal oxide tubular TiO_2 microengines has been realized by Mou et al. (2015). In the process of moving, the micro-submarine captures micro- or nano-particles in its path and keeps them attached to the narrow ends of some nanotubes, while other nanotubes in the network continue to work as nano-motors, thus contributing to the propulsion of the submarine. The release of taken on board micro- or nano-particles is realized by interrupting the UV light.

b. The prospect of using metallized TiO_2 nanotubes as photonic lenses

Numerical calculations using the multiple-scattering approach showed that the focusing properties of flat and concave lenses assembled from TiO_2 nanotubes with metallized inner and outer surfaces are comparable to those of lenses made of nanorods with a negative refractive index $n = -1$. Negative Index Materials (NIM) introduced by Veselago (1968) are synthetic materials that

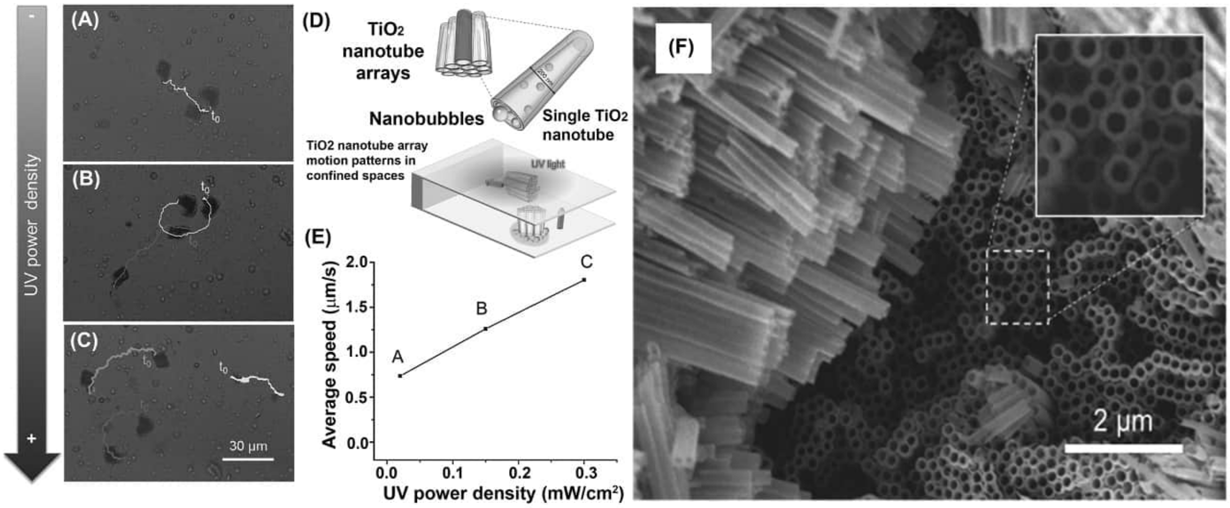

Fig. 12 (a, b, c) Optical images and corresponding tracking of a microarray of TiO_2 nanotubes during (a) 61 s, (b) 85 s, and (c) 55 s, moving under the UV illumination (d), along with the corresponding tracking (starting point is labeled by t_0). The average speed associated with the aforementioned tracks is represented in panel (e). The power density of the UV irradiation constitutes (a) 0.02 mW cm^{-2}, (b) 0.15 mW cm^{-2}, and (c) 0.3 mW cm^{-2}. (f) SEM image of a cluster of titanium oxide nanotubes. Reprinted from Enachi M., Guix M., Postolache V., Ciobanu V., Fomin V.M., Schmidt O.G., Tiginyanu I. (2016) Light-induced motion of microengines based on microarrays of TiO2 nanotubes. *Small* 12: 5497–5505. https://doi.org/10.1002/smll.201601680. Copyright © 2016 with permission from John Wiley and Sons.

exhibit amazing optical properties and enable one to develop new optical elements. Note that Veselago's work did not arouse the interest of researchers for a relatively long period of time. Only several decades later, due to the development of nanotechnologies and low dimensional materials, a great effort was focused at exploration of lenses with different configurations and composition capable to operate especially in the visible region of the spectrum, as it was reported by Pendry (2000); Foca et al. (2005, 2009); Sergentu et al. (2004, 2006, 2007); Tiginyanu et al. (2009); VanbéSien and Centeno (2014); Fan et al. (2017), etc.

Sergentu et al. (2008) proposed to assemble NIM from TiO_2 nanotubes with inner and outer surfaces covered with a thin film of metal. Although both flat and concave lenses showed focusing properties, the focusing characteristics of concave lenses proved to be better. Moreover, according to the results of simulations, introducing a disorder in the arrangement of TiO_2 nanotubes contributes to the improvement of the focal spot.

The high resistivity of the TiO_2 nanotubes implies application of costly and sophisticated deposition techniques for metallization, Atomic Layer Deposition (ALD) providing uniform deposition along the whole nanotube's depth (Dvorak et al., 2019). It was mentioned above, that templates based on semiconductor compounds from III-V and II-VI groups can be easily decorated by metallic nanotubes, nanowires or nanodots via pulsed electrochemical deposition representing cost-effective technology for InP (Tiginyanu et al., 2008); GaAs (Monaico et al., 2022a,b); GaP (Tiginyanu et al., 2015b); ZnSe (Tiginyanu et al., 2011; Monaico et al., 2009b). For the development of photonic lenses working in the visible region of the spectrum, materials possessing wider bandgaps should be used, for instance GaP and ZnSe. The results of calculations demonstrated good focusing properties of flat photonic lenses assembled from metallized porous GaP slabs, especially at long wavelengths including the far infrared spectral range (see Tiginyanu et al., 2015b) as well as prospects of novel focusing elements and beam splitters based on metallized ZnSe porous structures for application in the visible region of the spectrum (Tiginyanu et al., 2011). It should be mentioned that focusing properties are determined by the morphology (geometry of nanotubes and their spatial distribution) of the structure and the material used.

c. Photocatalytic applications

Among other semiconductors, TiO_2 is considered as one of the most promising materials for photocatalytic applications due to the low-cost production, low toxicity among the possibilities to obtain a large active surface in a relatively small volume. The photocatalytic reactions on TiO_2 nanoparticles have been investigated for almost 50 years. In the last 10 years, however, the research interest was attracted by one-dimensional nanostructures, namely by the arrays TiO_2 nanotubes providing more control over morphology and charge-carrier separation mechanism. An important criterion to enhance the photocatalytic activity was found to be the crystalline phase as well as the relative percentages of anatase and rutile phases in the samples, as was reported by Zakir et al. (2022); Luo et al. (2015); Wang et al. (2020); Nie et al. (2021). According to the study of Enachi et al. (2015a), the anatase phase was found to be efficient for the photodegradation of Rhodamine B dye under UV light with enhancement of the percentage of degradation by samples doped with Ag. It should be mentioned that doping or covering with other noble metals like Au and Pt showed negative impact on photodegradation of Rhodamine B dye. On the other hand, functionalization of TiO_2 nanotube arrays with Au, Pt or Pd nanoparticles resulted in high-efficiency photocatalytic H_2 production from ethanol solutions, as was reported in the works of Lee et al. (2013); Hejazi et al. (2019); Wang et al. (2021); Yoo et al. (2018); and Kim et al. (2021). The impact of functionalization via different deposition techniques and structural engineering of TiO_2 nanotube arrays was reflected in review works of Lim et al. (2019) and Zhou et al. (2017).

Shaban et al. (2019) reported efficient photocatalytic degradation of methylene blue (MB) using Ni-doped TiO_2 nanotubes under visible light. Besides, Ciobanu and Plesco, 2021 performed a comparative study of the degradation of MB under UV or visible light using TiO_2 nanotubes annealed at different temperatures. The amount of 20 mg of TiO_2 nanotubes with crystalized anatase phase, as a result of annealing at 650 °C, demonstrated 85% photodegradation of MB under UV illumination for 25 min, while higher photocatalytic activity in the visible light demonstrated samples possessing predominant rutile phase (thermally treated at 850 °C). The anatase phase was found to be more efficient also for the degradation of acid orange, as was reported by Liu et al. (2012).

d. Variable capacitance micro-nano-device

Porous semiconductor nanotemplates due to their properties that can be engineered find wide applications in electronics, optics, biomedical applications, photonics, etc. Among advantages over other porous templates like porous anodic aluminum oxide or etched ion-track membranes one can mention the following ones: (i) the properties of semiconductor nanotemplates can be adjusted by application of external electric field, illumination, temperature, etc., and (ii) semiconductor nanotemplates possess higher electrical conductivity of porous skeleton, providing favorable conditions for metal nucleation (Tiginyanu et al., 2015a) and uniform deposition on the pores walls without any activation or sensibilization of the porous skeleton walls, avoiding contamination (Tiginyanu et al., 2008; Monaico et al., 2020a). Combining electrochemical etching and electroplating for the purpose of filling semiconductor nanotemplates with metal increases the area of their applications in nanoelectronics and optoelectronics.

In the work of Vanmaekelbergh et al. (1997) the formation of a semiconductor/metal Schottky barrier junction with a huge internal contact area is produced between interpenetrating GaP and gold nanometer-scale network systems. The huge surface of a Schottky contact implies an enormous capacitance, which has been exploited in a variable capacitance device developed by Tiginyanu et al. (2012) on two-dimensional metal-semiconductor networks prepared via pulsed electrochemical deposition of Pt on the walls of pores inside of self-organized porous GaP templates with parallel pores.

The morphology in cross-section of the developed micro-nano-device is presented in Fig. 13a. In the process of variable capacitance device elaboration, two important issues were taken into account, namely: (i) to assure the high value of the Schottky

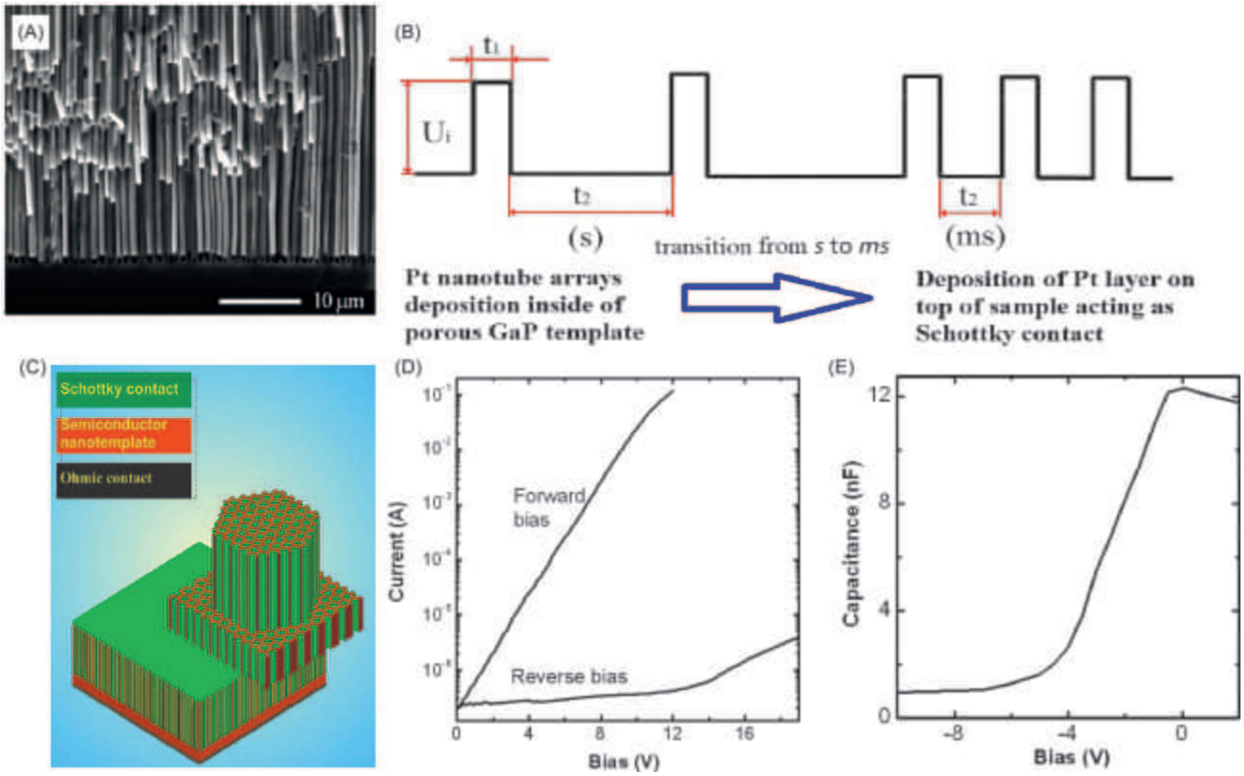

Fig. 13 (a) The morphology of deposited Pt nanotubes in porous GaP template used for the fabrication of a variable capacitance device. (b) The consequence of pulses and the duration between the pulses allowing the deposition of frontal contact connected to all nanotubes in the same process of the Pt deposition. (c) The schematics of the device: porous GaP template (red color); deposited Pt inside porous GaP template and frontal surface acting as Schottky contact (green color); Ohmic contact deposited on backside of bulk GaP substrate (black color). (d) Current-voltage characteristics. (e) Capacitance-voltage characteristics. Panels (a, d and e): Reprinted from Tiginyanu I., Monaico E., Ursaki V. (2012) Two-dimensional metallo-semiconductor networks for electronic and photonic applications. *ECS Transactions* 41: 67–74. https://doi.org/10.1149/1.4718392. Copyright © 2012 The Electrochemical Society. Reproduced by permission of IOP Publishing Ltd. All rights reserved.

barrier (about 1.1–1.3 eV for Pt on GaP), and (ii) the right choice of the width of the porous skeleton walls, to assure overlapping of the two depletion regions in the skeleton walls, starting from a certain applied potential. Therefore, the width of a wall between pores cannot be less than the double depletion region without applied potential. According to the work of Tiginyanu et al. (2012), the thickness of the porous GaP layer was 70 μm in 500-μm thick substrate. The Schottky contact was deposited by means of pulsed electroplating of Pt on the inner surface of the porous skeleton and on the top surface by switching the duration between the pulses (t_2) from 1 s to milliseconds (see Fig. 13b). The proposed approach of electrochemical deposition of the top contact in the same technological process assures the connection of each grown Pt nanotube to the formed Pt top contact. In this case the nanotubes are spliced with the deposited layer on the surface. The ohmic contact from the backside of the sample was realized by deposition of In. The schematic representation of the variable capacitance device based on Pt/porous GaP is presented in Fig. 13c.

The measured current-voltage and capacitance-voltage characteristics of the elaborated device is presented in Fig. 13d and e, respectively. One can see from this characteristic that the capacitance starts to decrease sharply from 12 to 2 nF under the applied negative potential in the range from 0.5 to 4 V, indicating that the device reaches a capacitance density variation of about 6×10^{-3} pF V^{-1} per 1 μm^2 of surface. This value is much higher in comparison with other 2D variable capacitance devices based on flat p-n junction or deposited two-dimensional thin film on the semiconductor surface. More recently, Monaico (2022) proposed and elaborated the technological route of pulsed electrochemical deposition in 300 μm deep porous GaP template with the aim to increase capacitance by 4–5 times. The optimization of parameters of pulsed electrochemical deposition showed that uniform deposition of Pt nanotubes inside 300-μm long pores occurs at pulse duration of 100 μs and the duration between pulses of 3 s during 15 h of electroplating.

e. Ferromagnetic core-shell coaxial GaAs/Fe nanostructures

Among noble metals, magnetic nanoparticles have been intensively studied over the last years due to their unique magnetic properties, along with other characteristics important for various applications. Moreover, apart from applications of individual magnetic nanoparticles, arrays of ferromagnetic nanostructures such as wires and tubes are of interest in the field of high-density data storage, microelectronics, spintronics, and microwave devices, as was reported by Piraux (2020); Mohammed et al. (2017); Staňo and Fruchart (2018). According to the works of Bran et al. (2021); Bran (2022); Streubel et al. (2016); Ruiz-Clavijo et al. (2019); Körber et al. (2022) the possibilities to tune the geometry of the magnetic nanotubes give rise to novel effects and functionalities. In particular, tubular arrays and coaxial core-shell structures offer advantages over nanowires, owing to the possibilities to vary the thickness of the tube wall or the shell in addition to the control of the length and diameter (García et al., 2021; Proenca et al., 2020).

An important peculiarity of anodization of GaAs is the absence of current line-oriented pores in this material as was discussed in section "Self-organized pores perpendicular to the crystal surface." Thus, anodization of GaAs substrates leads to the formation of crysto pores having triangular cross-sectional shape (Föll et al., 2003b), and at optimized applied potential the transition from pores to nanowires occurs as was reported by Li et al. (2011); Asoh et al. (2014); and Monaico et al. (2020b). As a result of electrochemical deposition of Fe, Monaico et al. (2022b) reported recently the possibilities to produce magnetic nanotube arrays with triangular cross-sectional shape (see Fig. 14a) oriented both in-plane and out-of-plane with the substrate surface. The results illustrated in the inset from Fig. 14a correspond to Fe electroplating at a short time of electrodeposition to disclose the triangular shape of nanowires. An important finding is that nanowires are oriented perpendicularly to or preponderantly parallel with the GaAs surface in the case of used (111)B or (001) crystallographic orientation of GaAs wafer, respectively. It was found that the coercivity and the remanence ratio of polycrystalline Fe nanotubes deposited on GaAs nanowires increase with increasing their coverage with Fe nanoparticles. The produced structures exhibited also some magnetic anisotropy with respect to the coercivity and the remanence ratio.

Going back to the shape control of the nanostructures, it should be mentioned that based on our preliminary results, nanowires with round cross-sectional shape (see Fig. 14b) were obtained under anodization of (001) oriented GaAs substrates at applied potential between the nanowires formation and electropolishing. Further, along with pores with triangular shape and absence of curro pores in GaAs, pores with circular shape were fabricated by Monaico et al. (2021) under stationary and dynamic regimes of anodization. The unusual circular shape for crysto pores was explained by isotropic etching of the walls of a primary triangular pore formed during stationary anodization, which occurs in the subsequent dynamic regime of anodization determined by the derivative of the current.

Keeping in mind the fascinating property of crysto pores to intersect each other, diameter modulated GaAs nanowires can be easily produced by cost-effective electrochemical etching techniques. According to features of galvanostatic and potenţiostatic anodization of (111)B oriented GaAs substrates reported in details by Monaico et al. (2020b), at certain values of anodization current or voltages, a combination of crysto pores aligned perpendicularly to the sample surface and tilted pores intersecting them was evidenced. This finding enables one to fabricate nanowires with modulated diameter or perforated nanowires at optimized anodization parameters (potential, electrolyte, temperature, etc.), as illustrated in Fig. 14c and d.

The impact of the shape and alignment of GaAs nanowires upon magnetic properties of core-shell GaAs/Fe nanostructures is the subject of our further investigations.

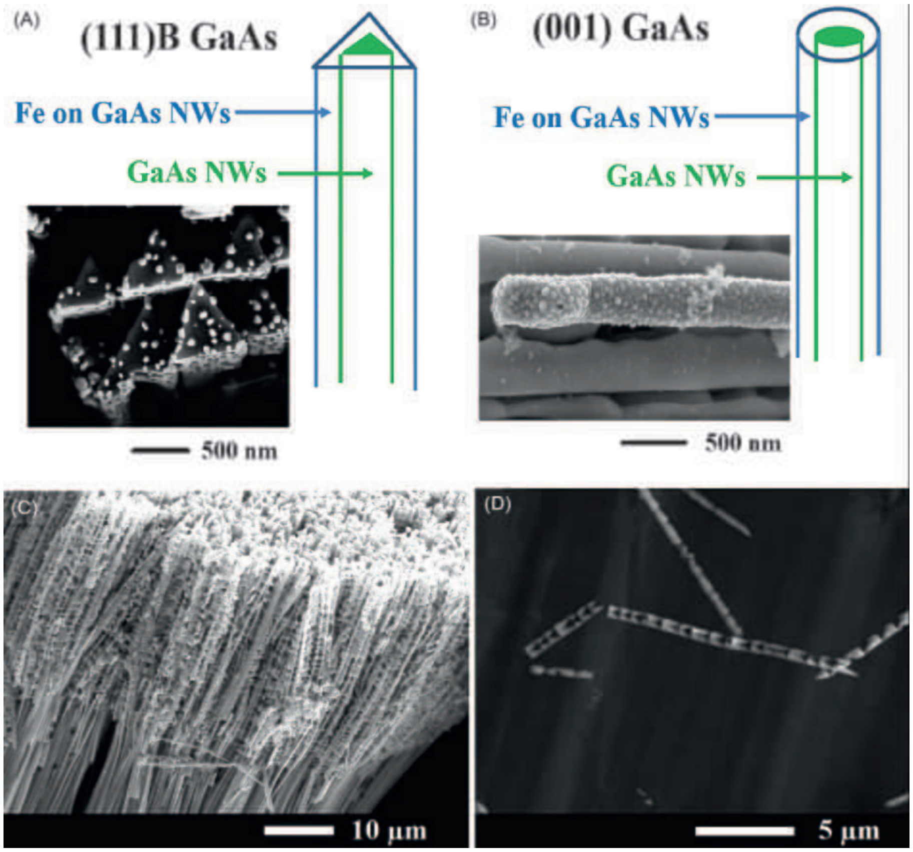

Fig. 14 Schematic representation of core-shell GaAs/Fe nanostructures with triangular (a) and circular cross-sectional shapes in (b). The inset represents SEM images of GaAs nanowires after Fe electroplating. SEM image of diameter modulated GaAs nanowires at anodization potential of 4.5 V in 1 M HNO_3 of (111)B oriented GaAs crystals for a short time, leading to self-induced oscillations in nanowires diameter, followed by anodization at 4 V resulting in smooth side walls of nanowires (c). SEM image of dispersed nanowires on substrate demonstrating perforation of nanowires due to the crysto pores (d).

Conclusion

Self-organization proved to be a powerful and cost-effective tool for developing a new class of semiconductor-based nanotemplates for nanofabrication. Anodic etching of semiconductor compounds under specific conditions enabled one to fabricate two-dimensional single crystals of nanopores which seemed impossible without application of lithography. Successful combination of electrochemical etching and electroplating resulted in an important technological breakthrough: nonlithographic fabrication of two-dimensional metal-dielectric periodic structures for micro-opto-electronic and photonic applications, an important prerequisite for this achievement being the elaboration of the so-called "jumping electrodeposition."

Porosification of semiconductor compounds combined with the application of special masks brought to light a variety of fascinating morphologies, including formation of networks of pores oriented parallel to the top surface of the semiconductor substrate and of porous domains excluding pore percolation between them. These findings are very important for nanofabrication. Semiconductor nanotemplates whose properties can be controlled by illumination, temperature, applied electric or magnetic fields provide more possibilities for developing hybrid nanoarchitectures by filling in the pores with other materials. In particular, no passivation or activation, leading to contamination of the porous skeleton, is required for uniform deposition along the pore's depth of metal nanotubes or nanodots.

Since the year of 2000, electrochemical etching of III-V (InP, GaAs, and GaP) compounds has been most intensively studied. Later on, II-VI compounds and GaN started to be more actively investigated and an explosion in publications devoted to porous GaN occurred over the last years. Taking into account the fascinating properties of GaN, including biocompatibility, its wide implementation in lighting technologies and high frequency/high power electronics, increasing attention should be paid in the coming years to the exploration of porosification of GaN and related nitride alloys for concrete applications.

Special attention should continue to be paid to the exploration of TiO_2 nanotube arrays finding many applications due to their high photocatalytic activity and biocompatibility. Light-driven micro-engines based on self-organized arrays of TiO_2 nanotubes, capable to pick-up, transport and release micro/nano-particles in a controlled fashion is a promising example for broadening the areas of applications of titania nanotubular structures.

Though the analysis in the present Chapter was restricted to electrochemical etching, it is not the only approach to produce porous materials. The combination of electrochemical technologies with other techniques, particularly with thermal deformation of pores and selective area sublimation, which gained momentum over the last years, could be an interesting approach for enlarging the technological tools for the preparation of nanostructured semiconductor compounds. Besides, new technological approaches have been proposed recently for the manufacture of the so-called aero-materials exhibiting a very high degree of porosity, such as aero-GaN, aero-Ga_2O_3 and aero-ZnS with broad prospects for practical applications (see Tiginyanu et al., 2019; Dragoman et al., 2019a,b; Braniste et al., 2019, 2020, 2021; Plesco et al., 2020, 2021).

Acknowledgments

The authors acknowledge support from the National Agency for Research and Development of Moldova under the Grants #20.80009.5007.20, #21.00208.5007.15/PD. The authors would like to acknowledge the contribution of the COST Action "CONFINED MOLECULAR SYSTEMS: FROM A NEW GENERATION OF MATERIALS TO THE STARS" (COSY) CA21101.

References

Albu SP, Ghicov A, Macak JM, Hahn R, and Schmuki P (2007) Self-organized, free-standing TiO_2 nanotube membrane for flow-through photocatalytic applications. *Nano Letters* 7: 1286–1289. https://doi.org/10.1021/nl070264k.

Ali G and Maqbool M (2013) Fabrication of cobalt-nickel binary nanowires in a highly ordered alumina template via AC electrodeposition. *Nanoscale Research Letters* 8: 352. https://doi.org/10.1186/1556-276X-8-352.

Ali G, Ahmad M, Akhter JI, Maqbool M, and Cho SO (2010) Novel structure formation at the bottom surface of porous anodic alumina fabricated by single step anodization process. *Micron* 41: 560–564. https://doi.org/10.1016/j.micron.2010.04.010.

Asoh H, Kotaka S, and Ono S (2014) High-aspect-ratio vertically aligned GaAs nanowires fabricated by anodic etching. *Materials Research Express* 1: 045002. https://doi.org/10.1088/2053-1591/1/4/045002.

Bockowski M, Iwinska M, Amilusik M, Fijalkowski M, Lucznik B, and Sochacki T (2016) Challenges and future perspectives in HVPE-GaN growth on ammonothermal GaN seeds. *Semiconductor Science and Technology* 31: 093002. https://doi.org/10.1088/0268-1242/31/9/093002.

Bran C (2022) Novel magnetic properties in curved geometries. *Nanomaterials* 12: 1175. https://doi.org/10.3390/nano12071175.

Bran C, Fernandez-Roldan JA, del Real RP, Asenjo A, Chubykalo-Fesenko O, and Vazquez M (2021) Magnetic configurations in modulated cylindrical nanowires. *Nanomaterials* 11: 600. https://doi.org/10.3390/nano11030600.

Braniste T, Ciers J, Monaico E, Martin D, Carlin J-F, Ursaki VV, Sergentu VV, Tiginyanu IM, and Grandjean N (2017a) Multilayer porous structures of HVPE and MOCVD grown GaN for photonic applications. *Superlattices and Microstructures* 102: 221–234. https://doi.org/10.1016/j.spmi.2016.12.041.

Braniste T, Monaico E, Martin D, Carlin J-F, Popa V, Ursaki VV, Grandjean N, and Tiginyanu IM (2017b) Multilayer porous structures on GaN for the fabrication of Bragg reflectors. In: *Nanotechnology VIII*, pp. 83–89. SPIE. https://doi.org/10.1117/12.2266280.

Braniste T, Zhukov S, Dragoman M, Alyabyeva L, Ciobanu V, Aldrigo M, Dragoman D, Iordanescu S, Shree S, Raevschi S, Adelung R, Gorshunov B, and Tiginyanu I (2019) Terahertz shielding properties of aero-GaN. *Semiconductor Science and Technology* 34: 12LT02. https://doi.org/10.1088/1361-6641/ab4e58.

Braniste T, Dragoman M, Zhukov S, Aldrigo M, Ciobanu V, Iordanescu S, Alyabyeva L, Fumagalli F, Ceccone G, Raevschi S, Schütt F, Adelung R, Colpo P, Gorshunov B, and Tiginyanu I (2020) Aero-Ga_2O_3 nanomaterial electromagnetically transparent from microwaves to terahertz for internet of things applications. *Nanomaterials* 10: 1047. https://doi.org/10.3390/nano10061047.

Braniste T, Ciobanu V, Schütt F, Mimura H, Raevschi S, Adelung R, Pugno NM, and Tiginyanu I (2021) Self-propelled aero-GaN based liquid marbles exhibiting pulsed rotation on the water surface. *Materials* 14: 5086. https://doi.org/10.3390/ma14175086.

Cao HX, Jung D, Lee H-S, Go G, Nan M, Choi E, Kim C-S, Park J-O, and Kang B (2021) Micromotor manipulation using ultrasonic active traveling waves. *Micromachines* 12: 192. https://doi.org/10.3390/mi12020192.

Chai X, Weng Z, Xu L, and Wang Z (2015) Tunable electrochemical oscillation and regular 3D nanopore arrays of InP. *Journal of the Electrochemical Society* 162: E129. https://doi.org/10.1149/2.0341509jes.

Christophersen M, Langa S, Carstensen J, Tiginyanu IM, and Föll H (2003) A comparison of pores in silicon and pores in III–V compound materials. *Physica Status Solidi A: Applications and Materials Science* 197: 197–203. https://doi.org/10.1002/pssa.200306499.

Ciobanu V and Plesco I (2021) TiO_2 nanotubes for photocatalytic degradation of methylene blue. *Journal of Engineering Sciences* 28. https://doi.org/10.52326/jes.utm.2021.28(1).01.

Colibaba G, Goncearenco E, Nedeoglo D, Nedeoglo N, Monaico E, and Tiginyanu I (2014a) Obtaining of II-VI compound substrates with controlled electrical parameters and prospects of their application for nanoporous structures. *Physica Status Solidi C: Current Topics in Solid State Physics* 11: 1404–1407. https://doi.org/10.1002/pssc.201300590.

Colibaba GV, Monaico EV, Goncearenco EP, Nedeoglo DD, Tiginyanu IM, and Nielsch K (2014b) Growth of ZnCdS single crystals and prospects of their application as nanoporous structures. *Semiconductor Science and Technology* 29: 125003. https://doi.org/10.1088/0268-1242/29/12/125003.

Colibaba GV, Monaico EV, Goncearenco EP, Inculet I, and Tiginyanu IM (2016) Features of nanotemplates manufacturing on the II-VI compound substrates. In: Sontea V and Tiginyanu I (eds.) *3rd International Conference on Nanotechnologies and Biomedical Engineering, IFMBE Proceedings*, pp. 188–191. Singapore: Springer. https://doi.org/10.1007/978-981-287-736-9_47.

Díaz-Guerra C, Piqueras J, Popa V, Cojocaru A, and Tiginyanu IM (2005) Spatially resolved cathodoluminescence of GaN nanostructures fabricated by photoelectrochemical etching. *Applied Physics Letters* 86: 223103. https://doi.org/10.1063/1.1940734.

Dong R, Zhang Q, Gao W, Pei A, and Ren B (2016) Highly efficient light-driven TiO_2–Au Janus micromotors. *ACS Nano* 10: 839–844. https://doi.org/10.1021/acsnano.5b05940.

Dragoman M, Braniste T, Iordanescu S, Aldrigo M, Raevschi S, Shree S, Adelung R, and Tiginyanu I (2019a) Electromagnetic interference shielding in X-band with aero-GaN. *Nanotechnology* 30: 34LT01. https://doi.org/10.1088/1361-6528/ab2023.

Dragoman M, Ciobanu V, Shree S, Dragoman D, Braniste T, Raevschi S, Dinescu A, Sarua A, Mishra YK, Pugno N, Adelung R, and Tiginyanu I (2019b) Sensing up to 40 atm using pressure-sensitive aero-GaN. *Physica Status Solidi RRL: Rapid Research Letters* 13: 1900012. https://doi.org/10.1002/pssr.201900012.

Dvorak F, Zazpe R, Krbal M, Sopha H, Prikryl J, Ng S, Hromadko L, Bures F, and Macak JM (2019) One-dimensional anodic TiO_2 nanotubes coated by atomic layer deposition: Towards advanced applications. *Applied Materials Today* 14: 1–20. https://doi.org/10.1016/j.apmt.2018.11.005.

Enachi M, Trofim V, Coseac V, Tiginyanu IM, and Ursaki VV (2009) Characterization of structure and luminescence of titania nanotubes. *Moldavian Journal of the Physical Sciences* 8: 214–220.

Enachi M, Stevens-Kalceff M, Tiginyanu I, and Ursaki V (2010a) Cathodoluminescence of TiO_2 nanotubes prepared by low-temperature anodization of Ti foils. *Materials Letters* 64: 2155–2158. https://doi.org/10.1016/j.matlet.2010.07.028.

Enachi M, Tiginyanu I, Sprincean V, and Ursaki V (2010b) Self-organized nucleation layer for the formation of ordered arrays of double-walled TiO_2 nanotubes with temperature controlled inner diameter. *Physica Status Solidi (RRL)—Rapid Research Letters* 4: 100–102. https://doi.org/10.1002/pssr.201004069.

Enachi M, Stevens-Kalceff M, Burlacu A, Tiginyanu I, and Ursaki V (2012) Processing-induced modification of photo- and cathodoluminescence spectra of TiO_2 nanotubes. *ECS Transactions* 45: 167. https://doi.org/10.1149/1.3700424.

Enachi M, Stevens-Kalceff MA, Sarua A, Ursaki V, and Tiginyanu I (2013) Design of titania nanotube structures by focused laser beam direct writing. *Journal of Applied Physics* 114: 234302. https://doi.org/10.1063/1.4849836.

Enachi M, Guix M, Braniste T, Postolache V, Ciobanu V, Ursaki V, Schmidt OG, and Tiginyanu I (2015a) Photocatalytic properties of TiO_2 nanotubes doped with Ag, Au and Pt or covered by Ag, Au and Pt nanodots. *Surface Engineering and Applied Electrochemistry* 51: 3–8. https://doi.org/10.3103/S1068375515010044.

Enachi M, Lupan O, Braniste T, Sarua A, Chow L, Mishra YK, Gedamu D, Adelung R, and Tiginyanu I (2015b) Integration of individual TiO_2 nanotube on the chip: Nanodevice for hydrogen sensing. *Physica Status Solidi (RRL)—Rapid Research Letters* 9: 171–174. https://doi.org/10.1002/pssr.201409562.

Enachi M, Guix M, Postolache V, Ciobanu V, Fomin VM, Schmidt OG, and Tiginyanu I (2016) Light-induced motion of microengines based on microarrays of TiO_2 nanotubes. *Small* 12: 5497–5505. https://doi.org/10.1002/smll.201601680.

Fan Q, Huo P, Wang D, Liang Y, Yan F, and Xu T (2017) Visible light focusing flat lenses based on hybrid dielectric-metal metasurface reflector-arrays. *Scientific Reports* 7: 45044. https://doi.org/10.1038/srep45044.

Feynman RP (1992) There's plenty of room at the bottom. *Journal of Microelectromechanical Systems* 1: 60–66. https://doi.org/10.1109/84.128057.

Foca E, Föll H, Daschner F, Sergentu VV, Carstensen J, Frey S, Knöchel R, and Tiginyanu IM (2005) Efficient focusing with a concave lens based on a photonic crystal with an unusual effective index of refraction. *Physica Status Solidi A: Applications and Materials Science* 202: R35–R37. https://doi.org/10.1002/pssa.200510003.

Foca E, Sergentu VV, Daschner F, Tiginynau IM, Ursaki VV, Knöchel R, and Föll H (2009) Superlensing with plane plates consisting of dielectric cylinders in glass envelopes. *Physica Status Solidi A: Applications and Materials Science* 206: 140–146. https://doi.org/10.1002/pssa.200824209.

Föll H, Carstensen J, Langa S, Christophersen M, and Tiginyanu IM (2003a) Porous III–V compound semiconductors: Formation, properties, and comparison to silicon. *Physica Status Solidi A: Applications and Materials Science* 197: 61–70. https://doi.org/10.1002/pssa.200306469.

Föll H, Langa S, Carstensen J, Christophersen M, and Tiginyanu IM (2003b) Pores in III–V semiconductors. *Advanced Materials* 15: 183–198. https://doi.org/10.1002/adma.200390043.

Föll H, Leisner M, Cojocaru A, and Carstensen J (2009) Self-organization phenomena at semiconductor electrodes. *Electrochimica Acta* 55: 327–339. https://doi.org/10.1016/j.electacta.2009.03.076.

Föll H, Leisner M, Cojocaru A, and Carstensen J (2010) Macroporous semiconductors. *Materials* 3: 3006–3076. https://doi.org/10.3390/ma3053006.

García J, Manterola AM, Méndez M, Fernández-Roldán JA, Vega V, González S, and Prida VM (2021) Magnetization reversal process and magnetostatic interactions in $Fe_{56}Co_{44}/SiO_2/Fe_3O_4$ core/shell ferromagnetic nanowires with non-magnetic interlayer. *Nanomaterials* 11: 2282. https://doi.org/10.3390/nano11092282.

Hasegawa H and Sato T (2005) Electrochemical processes for formation, processing and gate control of III–V semiconductor nanostructures. *Electrochimica Acta* 50: 3015–3027. https://doi.org/10.1016/j.electacta.2004.11.066.

Hejazi S, Altomare M, Mohajernia S, and Schmuki P (2019) Composition gradients in sputtered Ti–Au alloys: Site-selective Au decoration of anodic TiO_2 nanotubes for photocatalytic H_2 evolution. *ACS Applied Nano Materials* 2: 4018–4025. https://doi.org/10.1021/acsanm.9b01022.

Hu Y, Liu W, and Sun Y (2022) Self-propelled micro-/nanomotors as "on-the-move" platforms: Cleaners, sensors, and reactors. *Advanced Functional Materials* 32: 2109181. https://doi.org/10.1002/adfm.202109181.

Hummel FA (1984) *Introduction to Phase Equilibria in Ceramic Systems*. New York: Routledge. https://doi.org/10.1201/9780203749944.

Irmer G, Monaico E, Tiginyanu IM, Gärtner G, Ursaki VV, Kolibaba GV, and Nedeoglo DD (2009) Fröhlich vibrational modes in porous ZnSe studied by Raman scattering and Fourier transform infrared reflectance. *Journal of Physics D Applied Physics* 42: 045405. https://doi.org/10.1088/0022-3727/42/4/045405.

Kant K and Losic D (2009) A simple approach for synthesis of TiO_2 nanotubes with through-hole morphology. *Physica Status Solidi (RRL) Rapid Research Letters* 3: 139–141. https://doi.org/10.1002/pssr.200903087.

Karaca GY, Kuralay F, Uygun E, Ozaltin K, Demirbuken SE, Garipcan B, Oksuz L, and Oksuz AU (2021) Gold–nickel nanowires as nanomotors for cancer marker biodetection and chemotherapeutic drug delivery. *ACS Applied Nano Materials* 4: 3377–3388. https://doi.org/10.1021/acsanm.0c03145.

Kim HJ, Park J, Ye BU, Yoo CJ, Lee J-L, Ryu S-W, Lee H, Choi KJ, and Baik JM (2016) Parallel aligned mesopore arrays in pyramidal-shaped gallium nitride and their photocatalytic applications. *ACS Applied Materials & Interfaces* 8: 18201–18207. https://doi.org/10.1021/acsami.6b05500.

Kim M, Lee J, Je M, Heo B, Yoo H, Choi H, Choi J, and Lee K (2021) Electric field-driven one-step formation of vertical p–n junction TiO_2 nanotubes exhibiting strong photocatalytic hydrogen production. *Journal of Materials Chemistry A* 9: 2239–2247. https://doi.org/10.1039/D0TA10062E.

Körber L, Kézsmárki I, and Kákay A (2022) *Mode Splitting of Spin Waves in Magnetic Nanotubes With Discrete Symmetries*. https://doi.org/10.48550/arXiv.2202.06601.

Langa S, Carstensen J, Tiginyanu IM, Christophersen M, and Föll H (2002) Formation of tetrahedron-like pores during anodic etching of (100) oriented n-GaAs. *Electrochemical and Solid-State Letters* 5: C14. https://doi.org/10.1149/1.1423803.

Langa S, Tiginyanu IM, Carstensen J, Christophersen M, and Föll H (2003) Self-organized growth of single crystals of nanopores. *Applied Physics Letters* 82: 278–280. https://doi.org/10.1063/1.1537868.

Langa S, Sirbu L, Monaico E, Carstensen J, Föll H, and Tiginyanu IM (2005) Morphology and chemical composition microanalysis of 2D and 3D ordered structures on porous InP. *Physica Status Solidi A: Applications and Materials Science* 202: 1411–1416. https://doi.org/10.1002/pssa.200461117.

Langa S, Tiginyanu IM, Monaico E, and Föll H (2011) Porous II-VI vs. porous III-V semiconductors. *Physica Status Solidi C: Current Topics in Solid State Physics* 8: 1792–1796. https://doi.org/10.1002/pssc.201000102.

Leal-Estrada M, Valdez-Garduño M, Soto F, and Garcia-Gradilla V (2021) Engineering ultrasound fields to power medical micro/nanorobots. *Current Robotics Reports* 2: 21–32. https://doi.org/10.1007/s43154-020-00033-2.

Lee K, Hahn R, Altomare M, Selli E, and Schmuki P (2013) Intrinsic Au decoration of growing TiO_2 nanotubes and formation of a high-efficiency photocatalyst for H_2 production. *Advanced Materials* 25: 6133–6137. https://doi.org/10.1002/adma.201302581.

Lehmann V and Föll H (1990) Formation mechanism and properties of electrochemically etched trenches in n-type silicon. *Journal of the Electrochemical Society* 137: 653. https://doi.org/10.1149/1.2086525.

Li X, Guo Z, Xiao Y, Um H-D, and Lee J-H (2011) Electrochemically etched pores and wires on smooth and textured GaAs surfaces. *Electrochimica Acta* 56: 5071–5079. https://doi.org/10.1016/j.electacta.2011.03.084.

Li J, Wang Z, Wang J, and Sham T-K (2016) Unfolding the anatase-to-rutile phase transition in TiO_2 nanotubes using X-ray spectroscopy and spectromicroscopy. *Journal of Physical Chemistry C* 120: 22079–22087. https://doi.org/10.1021/acs.jpcc.6b07613.

Li X, Hu T, Lin S, Ma Z, Wang J, and Zhao L (2021) Fabrication of layer-ordered porous GaN for photocatalytic water splitting. *International Journal of Hydrogen Energy* 46: 7878–7884. https://doi.org/10.1016/j.ijhydene.2020.11.277.

Liao J, Lin S, Pan N, Li D, Li S, and Li J (2012) Free-standing open-ended TiO_2 nanotube membranes and their promising through-hole applications. *Chemical Engineering Journal* 211–212: 343–352. https://doi.org/10.1016/j.cej.2012.09.070.

Lim SY, Law CS, Liu L, Markovic M, Hedrich C, Blick RH, Abell AD, Zierold R, and Santos A (2019) Electrochemical engineering of nanoporous materials for photocatalysis: Fundamentals, advances, and perspectives. *Catalysts* 9: 988. https://doi.org/10.3390/catal9120988.

Litovchenko V, Evtukh A, Semenenko M, Grygoriev A, Yilmazoglu O, Hartnagel HL, Sirbu L, Tiginyanu IM, and Ursaki VV (2007) Electron field emission from narrow band gap semiconductors (InAs). *Semiconductor Science and Technology* 22: 1092–1096. https://doi.org/10.1088/0268-1242/22/10/003.

Liu N, Paramasivam I, Yang M, and Schmuki P (2012) Some critical factors for photocatalysis on self-organized TiO_2 nanotubes. *Journal of Solid State Electrochemistry* 16: 3499–3504. https://doi.org/10.1007/s10008-012-1799-z.

Luo Z, Poyraz AS, Kuo C-H, Miao R, Meng Y, Chen S-Y, Jiang T, Wenos C, and Suib SL (2015) Crystalline mixed phase (anatase/rutile) mesoporous titanium dioxides for visible light photocatalytic activity. *Chemistry of Materials* 27: 6–17. https://doi.org/10.1021/cm5035112.

Macak JM, Albu SP, and Schmuki P (2007) Towards ideal hexagonal self-ordering of TiO_2 nanotubes. *Physica Status Solidi (RRL) Rapid Research Letters* 1: 181–183. https://doi.org/10.1002/pssr.200701148.

Martin CR (1994) Nanomaterials: A membrane-based synthetic approach. *Science* 266: 1961–1966. https://doi.org/10.1126/science.266.5193.1961.

Masuda H and Fukuda K (1995) Ordered metal nanohole arrays made by a two-step replication of honeycomb structures of anodic alumina. *Science* 268: 1466–1468. https://doi.org/10.1126/science.268.5216.1466.

Medina-Sánchez M, Xu H, and Schmidt OG (2018) Micro- and nano-motors: The new generation of drug carriers. *Therapeutic Delivery* 9: 303–316. https://doi.org/10.4155/tde-2017-0113.

Mohammed H, Moreno JA, and Kosel J (2017) *Advanced Fabrication and Characterization of Magnetic Nanowires, Magnetism and Magnetic Materials*. IntechOpen. https://doi.org/10.5772/intechopen.71077.

Monaico EV (2022) Engineering of semiconductor compounds via electrochemical technologies for nano-microelectronic applications. *Journal of Engineering Sciences* 29: 8–16. https://doi.org/10.52326/jes.utm.2022.29(1).01.

Monaico E, Ursaki VV, Urbieta A, Fernández P, Piqueras J, Boyd RW, and Tiginyanu IM (2004) Porosity-induced gain of luminescence in CdSe. *Semiconductor Science and Technology* 19: L121–L123. https://doi.org/10.1088/0268-1242/19/12/L04.

Monaico E, Ursaki VV, Tiginyanu IM, Dashevsky Z, Kasiyan V, and Boyd RW (2006) Porosity-induced blueshift of photoluminescence in CdSe. *Journal of Applied Physics* 100: 053517. https://doi.org/10.1063/1.2338833.

Monaico E, Tiginyanu IM, Ursaki VV, Sarua A, Kuball M, Nedeoglo DD, and Sirkeli VP (2007a) Photoluminescence and vibrational properties of nanostructured ZnSe templates. *Semiconductor Science and Technology* 22: 1115–1121. https://doi.org/10.1088/0268-1242/22/10/007.

Monaico E, Ubrieta A, Fernandez P, Piqueras J, Tiginyanu IM, Ursaki VV, and Boyd RW (2007b) Intense luminescence from porous ZnSe layers. *Moldavian Journal of the Physical Sciences* 6: 129–134.

Monaico E, Coseac V, Ursaki VV, Syrbu NN, and Tiginyanu IM (2009a) In: Tiginyanu IM and Balmus I (eds.) *Photoluminescence of ZnTe nanowires prepared by electrochemical etching of bulk ZnTe*. Proceedings of the 6th International Conference on Microelectronics and Computer Science (ICMCS 2009), October 1–3, 2009, pp. 150–153. Chisinau, Moldova: Technical University of Moldova.

Monaico E, Tighineanu P, Langa S, Hartnagel HL, and Tiginyanu I (2009b) ZnSe-based conductive nanotemplates for nanofabrication. *Physica Status Solidi (RRL) Rapid Research Letters* 3: 97–99. https://doi.org/10.1002/pssr.200903026.

Monaico E, Colibaba G, Nedeoglo D, and Nielsch K (2014a) Porosification of III–V and II–VI semiconductor compounds. *Journal of Nanoelectronics and Optoelectronics* 9: 307–311. https://doi.org/10.1166/jno.2014.1581.

Monaico E, Tiginyanu I, Volciuc O, Mehrtens T, Rosenauer A, Gutowski J, and Nielsch K (2014b) Formation of InP nanomembranes and nanowires under fast anodic etching of bulk substrates. *Electrochemistry Communications* 47: 29–32. https://doi.org/10.1016/j.elecom.2014.07.015.

Monaico EV, Tiginyanu IM, Ursaki VV, Nielsch K, Balan D, Prodana M, and Enachescu M (2017) Gold electroplating as a tool for assessing the conductivity of InP nanostructures fabricated by anodic etching of crystalline substrates. *Journal of the Electrochemical Society* 164: D179. https://doi.org/10.1149/2.1071704jes.

Monaico E, Moise C, Mihai G, Ursaki VV, Leistner K, Tiginyanu IM, Enachescu M, and Nielsch K (2019a) Towards uniform electrochemical porosification of bulk HVPE-grown GaN. *Journal of the Electrochemical Society* 166: H3159. https://doi.org/10.1149/2.0251905jes.

Monaico E, Monaico EI, Ursaki VV, Tiginyanu IM, and Nielsch K (2019b) Electrochemical deposition by design of metal nanostructures. *Surface Engineering and Applied Electrochemistry* 55: 367–372. https://doi.org/10.3103/S1068375519040070.

Monaico E, Tiginyanu I, and Ursaki V (2020a) Porous semiconductor compounds. *Semiconductor Science and Technology* 35: 103001. https://doi.org/10.1088/1361-6641/ab9477.

Monaico EI, Monaico EV, Ursaki VV, Honnali S, Postolache V, Leistner K, Nielsch K, and Tiginyanu IM (2020b) Electrochemical nanostructuring of (111) oriented GaAs crystals: From porous structures to nanowires. *Beilstein Journal of Nanotechnology* 11: 966–975. https://doi.org/10.3762/bjnano.11.81.

Monaico EI, Trifan C, Monaico EV, and Tiginyanu I (2020c) Elaboration of the platform for flexoelectric investigation of GaN microtubes. *Journal of Engineering Sciences* XXVII(4): 45–54. https://doi.org/10.5281/zenodo.4288263.

Monaico EV, Monaico EI, Ursaki VV, and Tiginyanu IM (2020d) Free-standing large-area nanoperforated gold membranes fabricated by hopping electrodeposition. *ECS Journal of Solid State Science and Technology* 9: 064010. https://doi.org/10.1149/2162-8777/aba6a2.

Monaico EI, Monaico EV, Ursaki VV, and Tiginyanu IM (2021) Evolution of pore growth in GaAs in transitory anodization regime from one applied voltage to another. *Surface Engineering and Applied Electrochemistry* 57: 165–172. https://doi.org/10.3103/S106837552102006X.

Monaico EV, Busuioc S, and Tiginyanu IM (2022a) Controlling the degree of hydrophilicity/hydrophobicity of semiconductor surfaces via porosification and metal deposition. In: Tiginyanu I, Sontea V, and Railean S (eds.) *5th International Conference on Nanotechnologies and Biomedical Engineering, IFMBE Proceedings*, pp. 62–69. Cham: Springer International Publishing. https://doi.org/10.1007/978-3-030-92328-0_9.

Monaico EV, Morari V, Ursaki VV, Nielsch K, and Tiginyanu IM (2022b) Core–shell GaAs-Fe nanowire arrays: Fabrication using electrochemical etching and deposition and study of their magnetic properties. *Nanomaterials* 12: 1506. https://doi.org/10.3390/nano12091506.

Mou F, Li Y, Chen C, Li W, Yin Y, Ma H, and Guan J (2015) Single-component TiO_2 tubular microengines with motion controlled by light-induced bubbles. *Small* 11: 2564–2570. https://doi.org/10.1002/smll.201403372.

Müller K, Wloka J, and Schmuki P (2009) Novel pore shape and self-organization effects in n-GaP(111). *Journal of Solid State Electrochemistry* 13: 807–812. https://doi.org/10.1007/s10008-008-0771-4.

Nie X, Wang J, Duan W, Zhao Z, Li L, and Zhang Z (2021) Effects of different crystallization methods on photocatalytic performance of TiO_2 nanotubes. *Applied Physics A: Materials Science & Processing* 127: 879. https://doi.org/10.1007/s00339-021-05041-3.

Niedert EE, Bi C, Adam G, Lambert E, Solorio L, Goergen CJ, and Cappelleri DJ (2020) A tumbling magnetic microrobot system for biomedical applications. *Micromachines* 11: 861. https://doi.org/10.3390/mi11090861.

Ono S, Kotaka S, and Asoh H (2013) Fabrication and structure modulation of high-aspect-ratio porous GaAs through anisotropic chemical etching, anodic etching, and anodic oxidation. *Electrochimica Acta* 110: 393–401. https://doi.org/10.1016/j.electacta.2013.06.025.

Paulose M, Prakasam HE, Varghese OK, Peng L, Popat KC, Mor GK, Desai TA, and Grimes CA (2007) TiO_2 nanotube arrays of 1000 μm length by anodization of titanium foil: Phenol red diffusion. *Journal of Physical Chemistry C* 111: 14992–14997. https://doi.org/10.1021/jp075258r.

Pendry JB (2000) Negative refraction makes a perfect lens. *Physical Review Letters* 85: 3966–3969. https://doi.org/10.1103/PhysRevLett.85.3966.

Piraux L (2020) Magnetic nanowires. *Applied Sciences* 10: 1832. https://doi.org/10.3390/app10051832.

Plesco I, Braniste T, Wolff N, Gorceac L, Duppel V, Cinic B, Mishra YK, Sarua A, Adelung R, Kienle L, and Tiginyanu I (2020) Aero-ZnS architectures with dual hydrophilic–hydrophobic properties for microfluidic applications. *APL Materials* 8: 061105. https://doi.org/10.1063/5.0010222.

Plesco I, Ciobanu V, Braniste T, Ursaki V, Rasch F, Sarua A, Raevschi S, Adelung R, Dutta J, and Tiginyanu I (2021) Highly porous and ultra-lightweight aero-Ga_2O_3: Enhancement of photocatalytic activity by noble metals. *Materials* 14: 1985. https://doi.org/10.3390/ma14081985.

Proenca MP, Sousa CT, Ventura J, and Araújo JP (2020) 6—Cylindrical magnetic nanotubes: Synthesis, magnetism and applications. In: Vázquez M (ed.) *Magnetic Nano- and Microwires (Second Edition), Woodhead Publishing Series in Electronic and Optical Materials*, pp. 135–184. Woodhead Publishing. https://doi.org/10.1016/B978-0-08-102832-2.00006-2.

Quill N, Lynch RP, O'Dwyer C, and Buckley DN (2013) Electrochemical formation of ordered pore arrays in InP in KCl. *ECS Transactions* 50: 377. https://doi.org/10.1149/05006.0377ecst.

Radhanpura K, Hargreaves S, Lewis RA, Sirbu L, and Tiginyanu IM (2010) Heavy noble gas (Kr, Xe) irradiated (111) InP nanoporous honeycomb membranes with enhanced ultrafast all-optical terahertz emission. *Applied Physics Letters* 97: 181921. https://doi.org/10.1063/1.3509404.

Radzali R, Zainal N, Yam FK, and Hassan Z (2014) Characteristics of porous GaN prepared by KOH photoelectrochemical etching. *Materials Research Innovations* 18. https://doi.org/10.1179/1432891714Z.000000000989. S6-412-S6-416.

Rajabasadi F, Schwarz L, Medina-Sánchez M, and Schmidt OG (2021) 3D and 4D lithography of untethered microrobots. *Progress in Materials Science* 120: 100808. https://doi.org/10.1016/j.pmatsci.2021.100808.

Rani S, Roy SC, Paulose M, Varghese OK, Mor GK, Kim S, Yoriya S, LaTempa TJ, and Grimes CA (2010) Synthesis and applications of electrochemically self-assembled titania nanotube arrays. *Physical Chemistry Chemical Physics* 12: 2780–2800. https://doi.org/10.1039/B924125F.

Reid M, Cravetchi I, Fedosejevs R, Tiginyanu IM, Sirbu L, and Boyd RW (2005a) Enhanced nonlinear optical response of InP(100) membranes. *Physical Review B* 71: 081306. https://doi.org/10.1103/PhysRevB.71.081306.

Reid M, Cravetchi IV, Fedosejevs R, Tiginyanu IM, and Sirbu L (2005b) Enhanced terahertz emission from porous InP (111) membranes. *Applied Physics Letters* 86: 021904. https://doi.org/10.1063/1.1849813.

Roy P, Berger S, and Schmuki P (2011) TiO_2 nanotubes: Synthesis and applications. *Angewandte Chemie, International Edition* 50: 2904–2939. https://doi.org/10.1002/anie.201001374.

Ruiz-Clavijo A, Ruiz-Gomez S, Caballero-Calero O, Perez L, and Martin-Gonzalez M (2019) Tailoring magnetic anisotropy at will in 3D interconnected nanowire networks. *Physica Status Solidi RRL: Rapid Research Letters* 13: 1900263. https://doi.org/10.1002/pssr.201900263.

Sato T, Kaneshiro C, and Hasegawa H (1999) Formation of size- and position-controlled nanometer size Pt dots on GaAs and InP substrates by pulsed electrochemical deposition. *Japanese Journal of Applied Physics* 38: 2448. https://doi.org/10.1143/JJAP.38.2448.

Schmuki P, Lockwood DJ, Fraser JW, Graham MJ, and Isaacs HS (1996) Formation and properties of porous GaAs. *MRS Online Proceedings Library* 431: 439–447. https://doi.org/10.1557/PROC-431-439.

Sergentu VV, Foca E, Langa S, Carstensen J, Föll H, and Tiginyanu IM (2004) Focusing effect of photonic crystal concave lenses made from porous dielectrics. *Physica Status Solidi A: Applications and Materials Science* 201: R31–R33. https://doi.org/10.1002/pssa.200409035.

Sergentu VV, Ursaki VV, Tiginyanu IM, Foca E, Föll H, and Boyd RW (2006) Focusing slabs made of negative index materials based on inhomogeneous dielectric rods. *Physica Status Solidi A: Applications and Materials Science* 203: R48–R50. https://doi.org/10.1002/pssa.200622120.

Sergentu VV, Ursaki VV, Tiginyanu IM, Foca F, Föll H, and Boyd RW (2007) Design of negative-refractive-index materials on the basis of rods with a gradient of the dielectric constant. *Applied Physics Letters* 91: 081103. https://doi.org/10.1063/1.2770964.

Sergentu VV, Tiginyanu IM, Ursaki VV, Enachi M, Albu SP, and Schmuki P (2008) Prediction of negative index material lenses based on metallo-dielectric nanotubes. *Physica Status Solidi (RRL) Rapid Research Letters* 2: 242–244. https://doi.org/10.1002/pssr.200802130.

Shaban M, Ahmed AM, Shehata N, Betiha MA, and Rabie AM (2019) Ni-doped and Ni/Cr co-doped TiO_2 nanotubes for enhancement of photocatalytic degradation of methylene blue. *Journal of Colloid and Interface Science* 555: 31–41. https://doi.org/10.1016/j.jcis.2019.07.070.

Staňo M and Fruchart O (2018) Chapter 3—Magnetic nanowires and nanotubes. In: Brück E (ed.) *Handbook of Magnetic Materials*, pp. 155–267. Elsevier. https://doi.org/10.1016/bs.hmm.2018.08.002.

Streubel R, Fischer P, Kronast F, Kravchuk VP, Sheka DD, Gaididei Y, Schmidt OG, and Makarov D (2016) Magnetism in curved geometries. *Journal of Physics D: Applied Physics* 49: 363001. https://doi.org/10.1088/0022-3727/49/36/363001.

Tiginyanu IM, Monaico E, Ursaki VV, Tezlevan VE, and Boyd RW (2005) Fabrication and photoluminescence properties of porous CdSe. *Applied Physics Letters* 86: 063115. https://doi.org/10.1063/1.1864240.

Tiginyanu IM, Monaico E, Albu S, and Ursaki VV (2007a) Environmentally friendly approach for nonlithographic nanostructuring of materials. *Physica Status Solidi (RRL) Rapid Research Letters* 1: 98–100. https://doi.org/10.1002/pssr.200701007.

Tiginyanu IM, Ursaki VV, Monaico E, Foca E, and Föll H (2007b) Pore etching in III-V and II-VI semiconductor compounds in neutral electrolyte. *Electrochemical and Solid-State Letters* 10: D127. https://doi.org/10.1149/1.2771076.

Tiginyanu I, Monaico E, and Monaico E (2008) Ordered arrays of metal nanotubes in semiconductor envelope. *Electrochemistry Communications* 10: 731–734. https://doi.org/10.1016/j.elecom.2008.02.029.

Tiginyanu IM, Foca E, Sergentu VV, Ursaki VV, Daschner F, Knöchel R, and Föll H (2009) Design and characterization of novel focusing elements based on photonic metamaterials. *Journal of Nanoelectronics and Optoelectronics* 4: 20–39. https://doi.org/10.1166/jno.2009.1003.

Tiginyanu IM, Ursaki VV, Monaico E, Enachi M, Sergentu VV, Colibaba G, Nedeoglo DD, Cojocaru A, and Föll H (2011) Quasi-ordered networks of metal nanotubes embedded in semiconductor matrices for photonic applications. *Journal of Nanoelectronics and Optoelectronics* 6: 463–472. https://doi.org/10.1166/jno.2011.1197.

Tiginyanu I, Monaico E, and Ursaki V (2012) Two-dimensional metallo-semiconductor networks for electronic and photonic applications. *ECS Transactions* 41: 67. https://doi.org/10.1149/1.4718392.

Tiginyanu I, Monaico E, and Nielsch K (2015a) Self-assembled monolayer of Au nanodots deposited on porous semiconductor structures. *ECS Electrochemistry Letters* 4: D8. https://doi.org/10.1149/2.0041504eel.

Tiginyanu I, Monaico E, Sergentu V, Tiron A, and Ursaki V (2015b) Metallized porous GaP templates for electronic and photonic applications. *ECS Journal of Solid State Science and Technology* 4: P57. https://doi.org/10.1149/2.0011503jss.

Tiginyanu I, Stevens-Kalceff MA, Sarua A, Braniste T, Monaico E, Popa V, Andrade HD, Thomas JO, Raevschi S, Schulte K, and Adelung R (2016) Self-organized three-dimensional nanostructured architectures in bulk GaN generated by spatial modulation of doping. *ECS Journal of Solid State Science and Technology* 5: P218. https://doi.org/10.1149/2.0091605jss.

Tiginyanu I, Braniste T, Smazna D, Deng M, Schütt F, Schuchardt A, Stevens-Kalceff MA, Raevschi S, Schürmann U, Kienle L, Pugno NM, Mishra YK, and Adelung R (2019) Self-organized and self-propelled aero-GaN with dual hydrophilic-hydrophobic behaviour. *Nano Energy* 56: 759–769. https://doi.org/10.1016/j.nanoen.2018.11.049.

Tseng WJ, van Dorp DH, Lieten RR, Vereecken PM, and Borghs G (2014) Anodic etching of n-GaN epilayer intoporous GaN and its photoelectrochemical properties. *Journal of Physical Chemistry C* 118: 29492–29498. https://doi.org/10.1021/jp508314q.

Tsuchiya H and Schmuki P (2020) Less known facts and findings about TiO_2 nanotubes. *Nanoscale* 12: 8119–8132. https://doi.org/10.1039/D0NR00367K.

Ursaki VV, Zalamai VV, Burlacu A, Klingshirn C, Monaico E, and Tiginyanu IM (2009) Random lasing in nanostructured ZnO produced from bulk ZnSe. *Semiconductor Science and Technology* 24: 085017. https://doi.org/10.1088/0268-1242/24/8/085017.

VanbéSien O and Centeno E (2014) Flat lenses. In: *Dispersion Engineering for Integrated Nanophotonics*, pp. 37–62. John Wiley & Sons, Ltd. https://doi.org/10.1002/9781118649398.ch2.

Vanmaekelbergh D, Koster A, and Marín FI (1997) A schottky barrier junction based on nanometer-scale interpenetrating GaP/Gold networks. *Advanced Materials* 9: 575–578. https://doi.org/10.1002/adma.19970090713.

Veselago VG (1968) The electrodynamics of substances with simultaneously negative values of e and μ. *Soviet Physics Uspekhi* 10: 509. https://doi.org/10.1070/PU1968v010n04ABEH003699.

Wang K, Zhuo Y, Chen J, Gao D, Ren Y, Wang C, and Qi Z (2020) Crystalline phase regulation of anatase–rutile TiO_2 for the enhancement of photocatalytic activity. *RSC Advances* 10: 43592–43598. https://doi.org/10.1039/D0RA09421H.

Wang K, Yu R, Wang L, Guan S, and Ji L (2021) 3D Burr-like Pt nanoparticles as co-catalyst decorated on TiO_2 nanotubes: An effective hydrogen production photoanode with enhanced photoelectrochemical performance. *Journal of Materials Science: Materials in Electronics* 32: 11737–11750. https://doi.org/10.1007/s10854-021-05800-1.

Weng Z, Chai X, Liu L, Li L, Xu H, Song Z, Wang Z, Wu C, Mi W, and Liang K (2017) Effects of temperature and current density on the porous structure of InP. *Journal of Solid State Electrochemistry* 21: 545–553. https://doi.org/10.1007/s10008-016-3387-0.

Winardi S, Mukti RR, Kumar K-NP, Wang J, Wunderlich W, and Okubo T (2010) Critical nuclei size, initial particle size and packing effect on the phase stability of sol-peptization-gel-derived nanostructured titania. *Langmuir* 26: 4567–4571. https://doi.org/10.1021/la904619x.

Wloka J, Mueller K, and Schmuki P (2005) Pore morphology and self-organization effects during etching of n-type GaP(100) in bromide solutions. *Electrochemical and Solid-State Letters* 8: B72. https://doi.org/10.1149/1.2103507.

Wolff N, Jordt P, Braniste T, Popa V, Monaico E, Ursaki V, Petraru A, Adelung R, Murphy BM, Kienle L, and Tiginyanu I (2019) Modulation of electrical conductivity and lattice distortions in bulk HVPE-grown GaN. *ECS Journal of Solid State Science and Technology* 8: Q141. https://doi.org/10.1149/2.0041908jss.

Wong RJ, Liu S, Ng YH, and Amal R (2016) Fabrication of high aspect ratio and open-ended TiO_2 nanotube photocatalytic arrays through electrochemical anodization. *AICHE Journal* 62: 415–420. https://doi.org/10.1002/aic.15117.

Wrede P, Medina-Sánchez M, Fomin VM, and Schmidt OG (2021) Switching propulsion mechanisms of tubular catalytic micromotors. *Small* 17: 2006449. https://doi.org/10.1002/smll.202006449.

Yang C, Liu L, Zhu S, Yu Z, Xi X, Wu S, Cao H, Li J, and Zhao L (2017) GaN with laterally aligned nanopores to enhance the water splitting. *Journal of Physical Chemistry C* 121: 7331–7336. https://doi.org/10.1021/acs.jpcc.7b00748.

Yip C-T, Guo M, Huang H, Zhou L, Wang Y, and Huang C (2012) Open-ended TiO_2 nanotubes formed by two-step anodization and their application in dye-sensitized solar cells. *Nanoscale* 4: 448–450. https://doi.org/10.1039/C2NR11317A.

Yoo J, Zazpe R, Cha G, Prikryl J, Hwang I, Macak JM, and Schmuki P (2018) Uniform ALD deposition of Pt nanoparticles within 1D anodic TiO_2 nanotubes for photocatalytic H_2 generation. *Electrochemistry Communications* 86: 6–11. https://doi.org/10.1016/j.elecom.2017.10.017.

Youtsey C, Romano LT, Molnar RJ, and Adesida I (1999) Rapid evaluation of dislocation densities in n-type GaN films using photoenhanced wet etching. *Applied Physics Letters* 74: 3537–3539. https://doi.org/10.1063/1.124153.

Zakir O, Mountassir EM, Elyaagoubi M, Lekbira M, Idouhli R, Aityoub A, Eddine Khadiri M, Rafqah S, Abouelfida A, and Outzourhit A (2022) Anodic TiO_2 nanotube: Influence of annealing temperature on the photocatalytic degradation of carbamazepine. *Journal of the Australian Ceramic Society*. https://doi.org/10.1007/s41779-022-00752-z.

Zalamai VV, Colibaba GV, Monaico EI, and Monaico EV (2021) Enhanced emission properties of anodized polar ZnO crystals. *Surface Engineering and Applied Electrochemistry* 57: 117–123. https://doi.org/10.3103/S1068375521010166.

Zhang M-R, Jiang Q-M, Hou F, Wang Z-G, and Pan G-B (2018) Fabrication of high aspect ratio gallium nitride nanostructures by photochemical etching for enhanced photocurrent and photoluminescence property. *Scripta Materialia* 146: 115–118. https://doi.org/10.1016/j.scriptamat.2017.11.022.

Zhao Y, Zhang Y, Liu H, Ji H, Ma W, Chen C, Zhu H, and Zhao J (2014) Control of exposed facet and morphology of anatase crystals through TiO_xF_y precursor synthesis and impact of the facet on crystal phase transition. *Chemistry of Materials* 26: 1014–1018. https://doi.org/10.1021/cm403054w.

Zhou X, Liu N, and Schmuki P (2017) Photocatalysis with TiO_2 nanotubes: “Colorful” reactivity and designing site-specific photocatalytic centers into TiO_2 nanotubes. *ACS Catalysis* 7: 3210–3235. https://doi.org/10.1021/acscatal.6b03709.

Zhu C, Zheng M, Xiong Z, Li H, and Shen W (2014) Electrochemically etched triangular pore arrays on GaP and their photoelectrochemical properties from water oxidation. *International Journal of Hydrogen Energy* 39: 10861–10869. https://doi.org/10.1016/j.ijhydene.2014.05.022.

Structures: Liquid crystals

Gautam Singh[a], **Shin-Woong Kang**[b], **and Satyendra Kumar**[c], [a]Department of Applied Physics, Amity Institute of Applied Sciences, Amity University Uttar Pradesh, Noida, India; [b]Department of Nano Convergence Engineering, Jeonbuk National University, Jeonju, Korea; [c]Division for Research and Economic Development, and Department of Physics, University at Albany, Albany, NY, United States

© 2024 Elsevier Ltd. All rights reserved.

This is an update of S. Kumar, S.-W. Kang, Liquid Crystals, Editor(s): Franco Bassani, Gerald L. Liedl, Peter Wyder, Encyclopedia of Condensed Matter Physics, Elsevier, 2005, Pages 111–120, ISBN 9780123694010, https://doi.org/10.1016/B0-12-369401-9/00690-2.

Introduction **375**
Nematic phases **375**
Blue phases 378
Twist-bend nematic phase 378
Ferroelectric nematic phase 379
Calamitic mesophases **380**
Discotic or columnar mesophases **382**
Bent-core mesophases **383**
Conclusion **388**
References **388**

Abstract

Liquid crystal systems continue to reveal new and unique manifestations of varying symmetry, dimensionality, and order in different phases. These phases serve as testing grounds for scientific concepts and predictions from theoretical considerations. This article provides an overview of the liquid crystal phases and phase transitions that have engendered significant scientific interest and investigations over the past two decades. In addition to the conventional nematic phase, general descriptions of the twist-bend, ferroelectric nematic, biaxial nematic, and blue phases are presented. Calamitic phases formed by mesogens having a molecular dipole and a chiral center, mesophases (B1-B7) arising from a bent shape of the molecular core, and discotic phases of oblate-core molecules are described.

Introduction

Liquid crystal (LC) is a state of matter intermediate between crystalline solids characterized by a regular periodic arrangement of atoms or molecules and isotropic liquids lacking any order. They exhibit varying degrees of orientational, bond orientational, and translational order in specific spatial directions. For example, molecules are arranged in stacked layers in the liquid crystal phase, known as the smectic-A (SmA) phase. It possesses one-dimensional translational order in the stacking direction, similar to a *crystal*. However, within the layers, the molecular arrangement is *liquid*-like. Such a phase that is "liquid" in two in-plane directions and "crystal" in the third direction is one example of a large number of liquid crystal phases.

Liquid crystal phases are formed by materials made of anisotropic molecules or other entities, such as nonspherical aggregates of molecules in surfactant solutions known as micelles. The simplest of the LC phases, the nematic (N) phase, is formed when the molecules are oriented on average parallel to a common direction represented by an apolar unit vector, $\boldsymbol{n}$, and referred to as the *director*. The structure of the phases with degrees of order higher than the N phase is different for different molecular shapes and intermolecular interactions. We will introduce different nomenclatures used to describe them. In this chapter, we shall first describe the N phase (s) and then other phases exhibited by rod-like, disk-like, and then bent-core (banana) shaped molecules. Although more than 50 LC phases are known, we will focus only on those that are of fundamental scientific interest, commonly encountered, and or have the potential for technological applications. Classification of the various phases is usually based on the concepts of symmetry (Kumar, 2000), dimensionality, and the types of order relevant to liquid crystals, such as orientational order, translational order, bond-orientational order, chirality, and dipolar ordering.

Nematic phases

In the simplest of LC phases, the nematic phase, rod-like molecules are oriented with their long axis on average parallel to the director, $\boldsymbol{n}$. The degree of order is described (de Gennes and Prost, 1993) by a symmetric, diagonal, traceless, and real tensor order parameter $\mathbf{Q}$:

$$\tilde{Q} = \begin{bmatrix} -\frac{S+\eta}{2} & 0 & 0 \\ 0 & -\frac{S-\eta}{2} & 0 \\ 0 & 0 & S \end{bmatrix}$$

When the scalar parameter η is zero, it describes the **uniaxial N phase**, Fig. 1, which may comprise rod-like, disk-like, or bent-core molecules. In the uniaxial N phase, orientational order exists only along ***n*****,** and the two directions orthogonal to ***n*** are degenerate. The parameter S then measures how well the molecules' symmetry axes are aligned. If we assume that the long axes of individual molecules make an angle θ with respect to ***n***, then S reduces to.

$$S = \tfrac{1}{2} < 3\ \cos^2\theta - 1 >,$$

where <...> specifies thermal average. Optically, such phases are described by two indices of extraordinary and ordinary refraction, n_e and n_o, respectively, and the optic axis is parallel to ***n***.

Almost all flat-panel liquid crystal displays used in commercial products, such as laptop computers, handheld devices, and flat-panel televisions, employ the N phase. In these devices, the ability to control the spatial orientation of the optic axis of this phase with the application of an electric field permits required changes in the optical path length and the state of polarization of the transmitted light beam and forms the basis of their operation.

If the parameter η is not zero, then $\tilde{Q}$ represents a phase with additional orientational order along a secondary director, ***m***, in the plane orthogonal to the primary director, ***n***. Such a phase, shown in Fig. 2, is known as the **biaxial nematic phase**, N_{bx} phase, and it has three different indices of refraction along the three spatial directions. The parameter η measures the degree of biaxial order along the secondary director, ***m***.

The biaxial nematic phase was predicted (Freiser, 1970) based on symmetry arguments, followed by a flurry of activity in theoretical and experimental areas. The biaxial nematic phase was discovered (Yu and Saupe, 1980) in lyotropic liquid crystals that had remained the only type of system to exhibit this phase. However, in monomeric (or molecular) systems, there were several

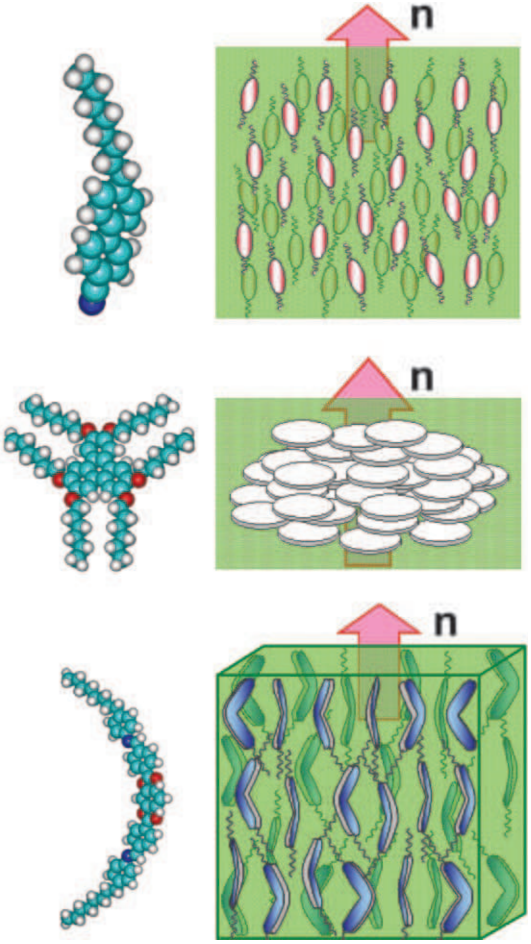

Fig. 1 Schematic representation of the molecular arrangement of rod-like, discotic, and bent-core molecules (top to bottom) in the uniaxial N phase.

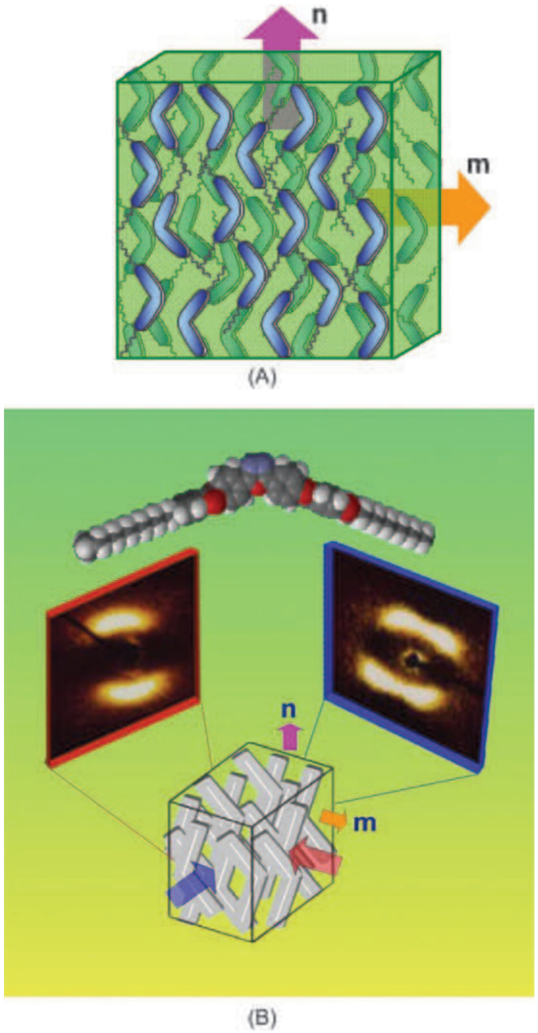

Fig. 2 (A) Arrangement of bent-core molecules in the N_{bx} phase. (B): X-ray diffraction patterns for the incidence directions (*red* and *blue arrows*) of X-rays with respect to the unit directions $\boldsymbol{n}$ and $\boldsymbol{m}$. Rubbed substrates we used to define $\boldsymbol{n}$ while an applied electric field controlled the orientation of $\boldsymbol{m}$.

(false) reports of its discovery. According to a group of experts who analyzed (Praefcke et al., 1998) all prior reports of the existence of the N_{bx} phase until 1998, the presence of this phase had yet to be substantiated. It is only very recently that its existence has been confirmed (Acharya et al., 2004, 2003) in the bent-core mesogens with X-ray diffraction on samples in which surface treatment and electric field were used to align the primary and secondary directors, respectively. The structure of this phase and experimental situations that confirmed the biaxiality are schematically shown in Fig. 2. After this discovery, more careful studies of the N phases formed by new bent-core materials revealed (Southern et al., 2008; Lee et al., 2009) the existence of both uniaxial and biaxial nematic phases at different temperatures in several single component systems. It should be pointed out that the results (Van Le et al., 2009) of different investigations contradicted those in Acharya et al. (Acharya et al., 2004, 2003). However, reexamination of the results in Van Le et al. (2009) using the same technique and samples revealed (Yoon et al., 2010) that differences lie in the sample and data quality and the interpretation of results in Van Le et al. (2009).

A particular case of the uniaxial N phase arises when it is constituted of chiral (lacking mirror symmetry) molecules or when a small amount of chiral agent is dissolved in the N phase. This phase, known as the **cholesteric phase,** was first observed in the cholesterol derivatives. In the cholesteric phase, the local unit vector $\boldsymbol{n}$ describes a helical trajectory of a well-defined pitch, Fig. 3. Since there is no directionality to the vector $\boldsymbol{n}$, the molecular orientation repeats after every ½ pitch length (or π–rotation). The pitch is generally strongly temperature dependent and often comparable to the wavelength of visible light. Cholesteric phases exhibit brilliant colors due to Bragg reflection of light at the corresponding pitch. Thus, they reflect the different color of light at different temperatures. This property forms the basis of the "mood rings." The director for the cholesteric phase, in its component form, is written as $\boldsymbol{n} = [\cos(q_o z + \phi), \sin(q_o z + \phi), 0]$.

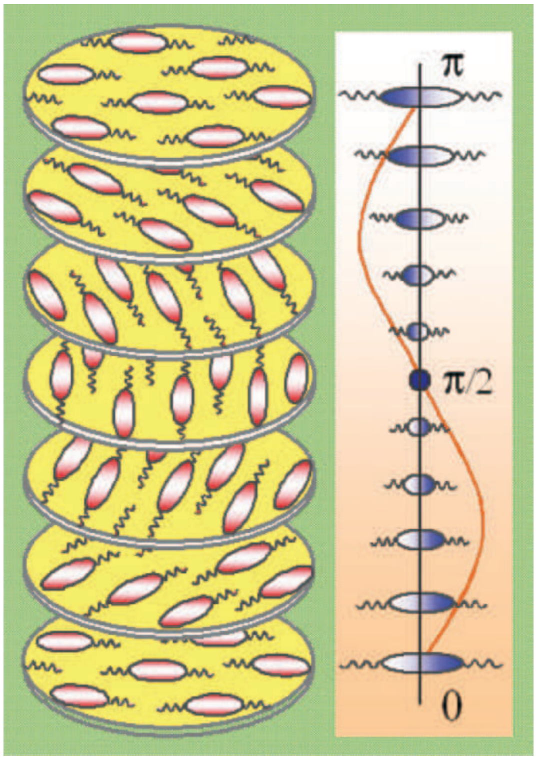

Fig. 3 The orientation of molecules describes a helical trajectory in a cholesteric phase. Bragg reflections in the optical regime occur for wavelengths equal to 1/2 of the pitch length.

Blue phases

Blue phases are formed by chiral compounds and appear over a very narrow temperature range between the isotropic liquid and the cholesteric phases. The term "blue phase" was coined based on their blue fog-like appearance in cholesteryl-benzoate and -nonanoate (Reinitzer, 1888; Coates and Gray, 1973). The blue phases are further classified as blue phase-I (BP-I), blue phase-II (BP-II), and blue phase-III (BP-III) based on their structure. Both BP-I and BP-II possess cubic symmetry, whereas the BP III phase is isotropic and is also known as the *amorphous* or *fog* phase. Their structures are comprised of double-twist *cylinders*, schematically shown in Fig. 4A. In a double-twist cylinder, the director rotates spatially about a radius of the cylinder (only two are shown) and becomes parallel to the cylinder axis at the center. The organization of such cylinders determines the type of BP that is obtained. For instance, when double-twist cylinders are loosely and randomly oriented in a spaghetti-like network, they form the isotropic BP-III phase (Fig. 4B). Cylinders order into a three-dimensional simple cubic structure in the BP-II phase and a body-centered cubic lattice in the BP-I phase (Fig. 4C and D). Blue phases are optically isotropic because of their cubic symmetry; however, colorful textures are usually observed due to the defects at the intersections of double-twist cylinders. Such defects self-assemble into cubic lattices and stabilize the BPs.

For a long time, the study of BPs has been limited by the very small temperature range over which they exist. However, the recent advents of wide temperature range BPs achieved via polymer stabilization or bimesogens and nanoparticle doping have engendered much research activity (Kikuchi et al., 2002; Coles and Pivnenko, 2005; Yoshida et al., 2009) involving these phases. The possibility of alignment-layer-free devices, submillisecond response, high optical contrast, wide viewing angle, and polarization-independent birefringence are some of their characteristics that are vital for their use in novel photonics and display applications.

Twist-bend nematic phase

The twist-bend nematic (N_{tb}) phase is a relatively recently discovered phase formed by achiral bent-shape molecules in which the local director traces an oblique helicoid of nanoscale pitch (Dozov, 2001; Panov et al., 2010; Chen et al., 2013, 2014; Wang et al., 2015). The local director $\boldsymbol{n}$ is tilted with respect to the helical axis $\widehat{\mathrm{N}}$ at a constant tilt angle $\theta < \pi/2$, unlike the cholesteric phase in which the tilt angle is $\pi/2$ (Fig. 5A). A negative value of the bend elastic constant is the prerequisite for the N_{tb} phase formation. One of the striking features of this phase is that it is chiral even though the constituting molecules are achiral. Consequently, the phase shows coexisting right- and left-handed helical domains (i.e., doubly degenerate chirality) (Fig. 5B). The spontaneous chirality, layer-free helical ordering with nanoscale pitch, ultrafast electro-optical response, and tunable periodic stripes are the characteristic properties of the N_{tb} phase. So far, this phase has been observed in two different systems: achiral dimeric mesogens with an odd

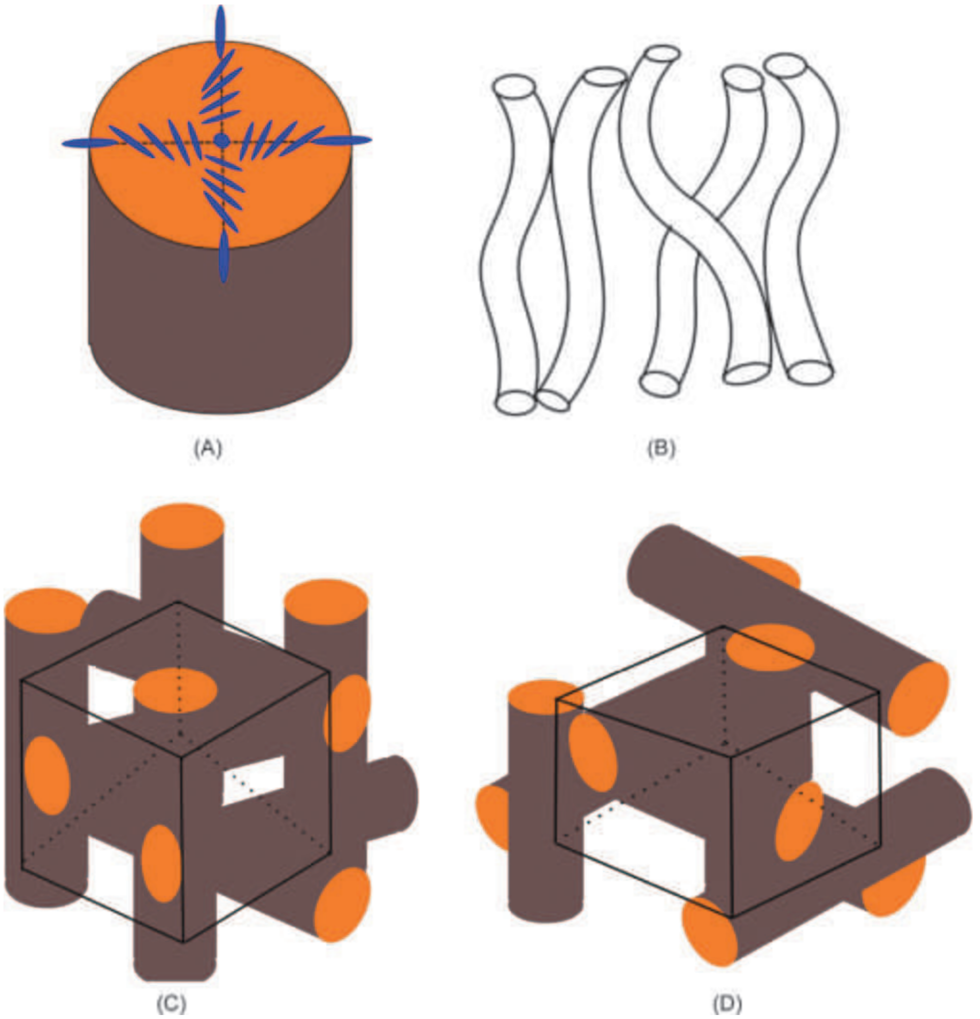

Fig. 4 (A) Schematic representation of a double twist cylinder (top view), wherein director can spatially rotate along a radius of the cylinder (only two are shown) and become parallel to cylinder axis at the center. The ordering of double twist cylinders in isotropic liquid leads to the formation of blue phases. The cylinders are disordered in the BPIII phase (B) but have long-range simple cubic order in the BPII phase (C), and body centered cubic order in the BPI phase (D).

number of carbon–carbon bonds in the alkyl linkage segment (e.g., two cyanobiphenyls linked with flexible heptyl chain) (Panov et al., 2010; Chen et al., 2013, 2014) and in rigid bent-core mesogens (Chen et al., 2013, 2014). Moreover, the N_{tb} phase at room temperature was recently reported in achiral rigid bent-core trimer (i.e., hybrid dimer) mesogens (Wang et al., 2015).

The unusual features of the N_{tb} phase render them very interesting for fundamental research and technological applications in fast-switching photonic devices, sensors, etc.

Ferroelectric nematic phase

The ferroelectric nematic (N_F) phase, theoretically envisioned by M. Born (Born, 1916), is a three-dimensional ordered phase possessing macroscopic spontaneous polarization density ($\mathbf{P_s}$). The much-awaited experimental discovery of the N_F phase underlying the conventional N phase is very recent and is being investigated in a thermotropic calamitic mesogenic compound, namely, 4-[(4-nitrophenoxy) carbonyl] phenyl 2,4-dimethoxybenzoate (RM734) (Chen et al., 2020). These molecules possess a longitudinal dipole moment.

In the conventional N phase (Fig. 6A), the polar mesogens are oriented on average parallel to the director but antiparallel to each other, that is, in the up and down directions with equal probability eliminating the possibility of a macroscopic $\mathbf{P_s}$. However, in the N_F phase (Fig. 6B), the mesogenic dipoles align nearly parallel to each other along a preferred direction with the loss of the up–down symmetry of the director orientation (i.e., $\boldsymbol{n} \neq -\boldsymbol{n}$). Consequently, the N_F phase develops a nonzero macroscopic polarization density, $\mathbf{P_s}$, which is temperature dependent. It is predicted that highly polar and slightly wedge-shaped mesogens are essential for forming the N_F phase. The direct optical textural observation of macroscopic domains of opposite polarization in

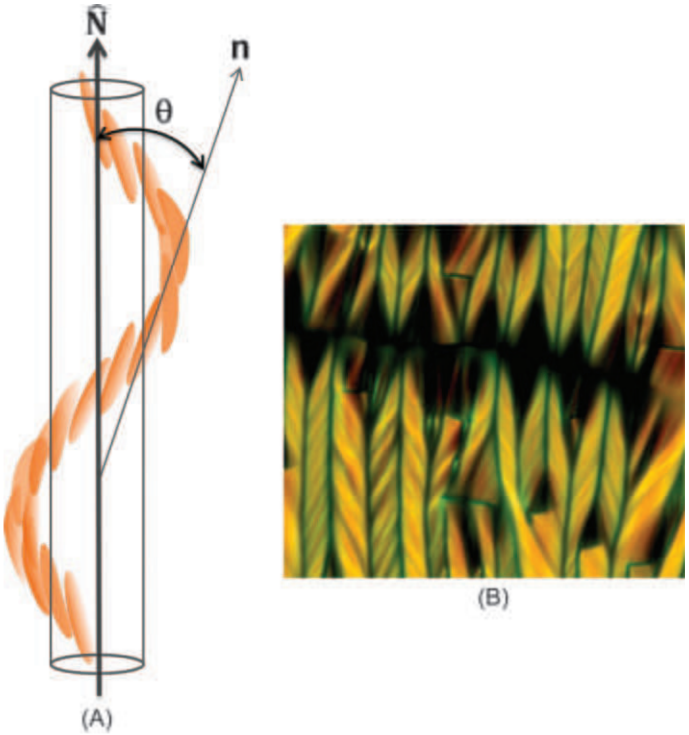

Fig. 5 (A) Schematic of the N_{tb} phase of achiral bent shape molecule. The local director ***n***, helical axis $\hat{\mathbf{N}}$, and heliconical tilt θ are shown in the right-handed N_{tb} region. (B) Rope-like texture showing doubly degenerate helical structure in N_{tb} phase of achiral bent shape dimer CB7CB.

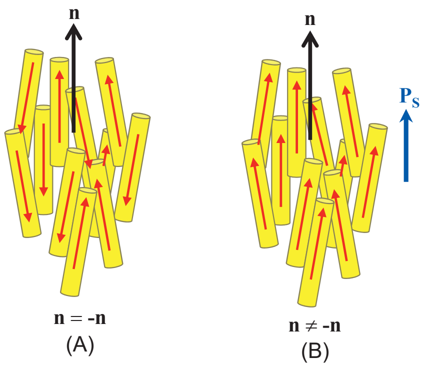

Fig. 6 Schematic representations of (A) the conventional N and (B) the ferroelectric nematic N_F phases of a thermotropic calamitic mesogen. Here, ***n*** denotes the director, the *black* and *red arrows* indicate the direction of the director and molecular dipoles, respectively; and $\mathbf{P_S}$ represents the spontaneous polarization density.

the absence of an external applied electric field is considered a hallmark of the N_F phase (Chen et al., 2020). Moreover, the unique characteristic features of the N_F phase, such as (i) the giant dielectric permittivity, (ii) a strong nonlinear optical response, (iii) a very fast electro-optical response (~100 to 1000 times faster than the conventional N phase), and (iv) having high fluidity eventually make it ideal for much anticipated advanced optical and electro-optical LC devices (Nishikawa et al., 2017; Mertelj et al., 2018; Sebastián et al., 2020; Li et al., 2021; Chen et al., 2021). Besides such exciting features of the N_F phase, specific concerns like (i) exact phase structure, (ii) structure–property relationship, (iii) nature of N-N_F phase transition, (iv) obtaining a room temperature phase with a wide temperature range, (v) direct transition to the N_F phase from the isotropic phase, and (vi) realization of the phase at room temperature essential for practical commercial devices remain to be investigated. It is worth pointing out that much has to be done to completely explore this intriguing N_F phase's fundamental and applied aspects (Larventovich, 2020).

Calamitic mesophases

Molecules with cylindrical shapes can form, in addition to the N and cholesteric phases, another class of phases that are layered structures known as the *smectic* mesophases. They all possess the translational order in the direction perpendicular to the layers.

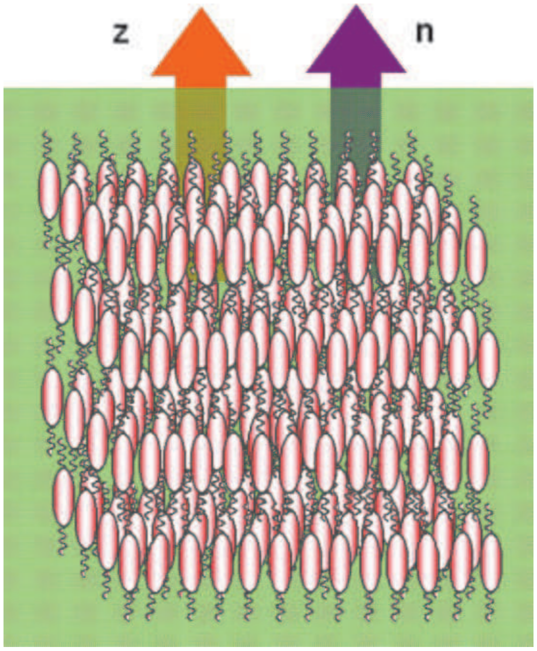

Fig. 7 In the smectic-A phase, molecules are almost perfectly parallel to each other, ***n***, and the layer normal **z**. Within a smectic layer, they have to particular positional or bond-orientational order.

In the two in-layer directions, the molecules also may have varying degrees of translational and bond-orientational orders to form a variety of smectic phases. These phases are denoted with a different letter in the order of their discovery.

A liquid-like order of molecules characterizes the smectic-A (SmA) phase in the directions parallel to the smectic layers. As illustrated in Fig. 7, the centers of mass of molecules lie in parallel layers, and the mass density of the phase is expected to vary in a sinusoidal manner along the z-direction. A two-component order parameter Ψ(r) describes the SmA phase

$$\Psi(r) = \Psi_0 \exp[i(q \cdot r + \phi)]$$

where Ψ_0 is the amplitude, ϕ is a phase factor, and the wave vector $\boldsymbol{q}$ is taken to be parallel to the *z*-direction. The molecules are oriented approximately parallel to each other within the layers, defining a director ***n*** that is coincident with the layer normal, **z**.

The **smectic-C (SmC) phase**, Fig. 8, is very similar to the SmA phase and has layers with liquid-like molecular order. The major difference is that the molecules are tilted with respect to the layer normal. The molecular tilt, or the angle between ***n*** and the layer normal **z**, in the SmC phase, is a strong function of temperature, as shown (Kumar, 1981) for the compound terephthal-bis-butylaniline in Fig. 9.

Other more ordered phases possess different degrees of bond-orientational and positional orders within the smectic layers. A good description of these so-called *hexatic* and *crystal* smectic phases can be found in Kumar (2000). Other exotic calamitic phases with long-range bond-orientational and positional order are known to exist with and without molecular tilt. Such phases, also known as exotic smectics, will not be discussed in this article.

Ferroelectric and **antiferroelectric smectic phases** are formed by molecules lacking reflection symmetry and having a permanent molecular dipole moment directed nearly perpendicular to the long molecular axis. These phases are very similar to the SmC phase with added chirality along the direction parallel to the layer normal. Molecular dipoles within a smectic layer of this phase are all oriented in the same direction, that is, in a *ferroelectric* manner. This chiral ferroelectric smectic phase is denoted as the SmC* phase (Fig. 10A); here, "*" implies the chiral nature. The SmC* phase possesses macroscopic spontaneous polarization density **P**, the orientation of which can be manipulated with the help of a torque exerted on molecular dipoles by an applied electric field. Electro-optical devices based on the SmC* phase have been shown to respond with a time constant of a few microseconds, about a thousand times faster than nematic devices.

When the dipole ordering in two adjacent smectic layers is antiparallel, as shown in Fig. 10B for E = 0, the phase is known as the antiferroelectric SmC* phase or SmC_A^* phase. The structure is still helical, but here azimuthal orientation of molecules in two layers with oppositely directed **P** describes the helical trajectory. The direction of molecular dipoles in these phases can be controlled with an applied electric field giving rise to different optical states. Two possible scenarios for the applied electric field, **E**, larger than a threshold field $\mathbf{E}_{\mathbf{th}}$ but in applied opposite directions are also shown in Fig. 10B. Other versions of the ferroelectric phases, such as ferrielectric, are also known and can be found in the literature.

The **twist-grain boundary (TGB) phase** is an analog of the Abrikosov phase in a type-II superconductor and is made of blocks of smectic layers, with no in-plane order, permeated by regions of twist deformation, Fig. 11. Depending on the absence (or SmA) or presence (or SmC) of molecular tilt with respect to the layer normal, one obtains the $\mathrm{TGB_A}$ or $\mathrm{TGB_C}$ phases. In these phases, a twist axis exists parallel to the smectic planes. Consequently, the phase appears to be a string of smectic-like slabs of a fixed dimension

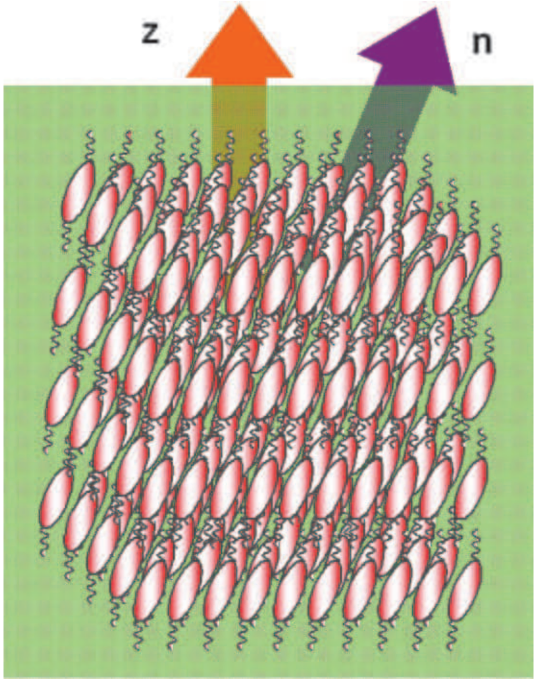

Fig. 8 In the smectic-C phase, the director ***n*** along which the molecules are oriented, is oblique relative to the layer normal **z**. Within a layer, the arrangement of molecules is liquid-like.

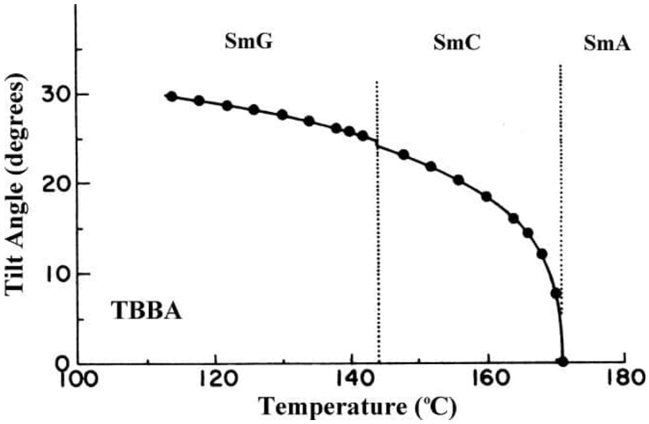

Fig. 9 Temperature dependence of molecular tilt angle in the SmC and SmG phases of TBBA. The tilt continuously goes to zero as the SmA phase is approached.

l_s and arranged adjacent to each other with a narrow (of length l_d) region of twist defect. When the angle of twist, δ, between neighboring slabs is such that $2\pi/\delta$ is an integer (or a rational) number, it is referred to as the *commensurate* TGB phase, and X-ray diffraction pattern of an oriented sample features a discrete set of reflections at the same magnitude of momentum transfer vector. However, if $2\pi/\delta$ is an irrational number, then the X-ray pattern consists of a continuous diffraction ring and is referred to as the *incommensurate TGB* phase.

Discotic or columnar mesophases

Somewhat larger molecules that have nearly flat disk-like cores exhibit discotic mesophases. These molecules like to naturally pack by forming stacks (or columns) of cores, as illustrated in Fig. 12. Here, the alkyl chains are not shown for clarity. The columns of molecules form two-dimensional lattices depending on the details of molecular shape and intermolecular interactions. There is no long-range positional order in the direction of the column axis. They are *crystal* in two dimensions and *liquid* in one, in contrast to the calamitic mesophases.

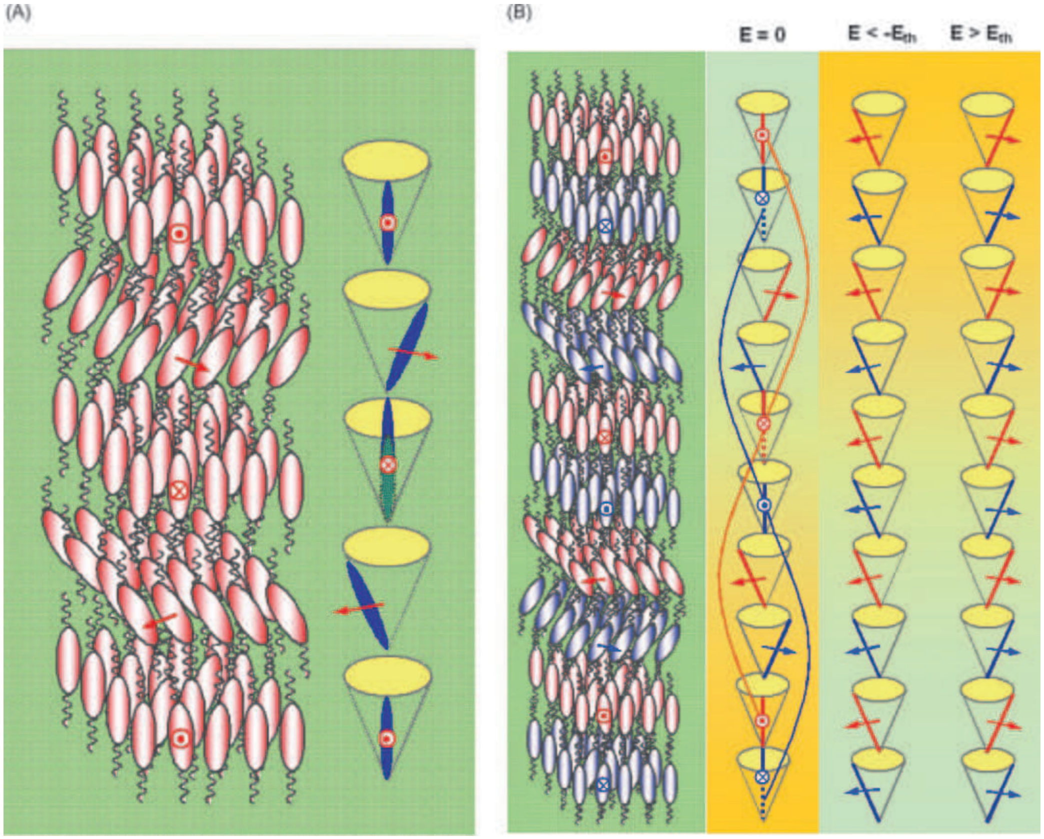

Fig. 10 (A) Ferroelectric SmC* phase; (B) Antiferroelectric SmC_A^* phase in which oppositely tilted molecules describe a double helical trajectory. *Red* and *blue arrows* represent molecular dipoles. The antiferroelectric phase reverts to the ferroelectric phase when a field higher than a threshold is applied. The orientation of the molecular dipoles depends on the direction of the field.

Depending on the 2D space group corresponding to the arrangement of columns, these are given different names. In the **hexagonal (D_h) phase**, the disks are arranged in a close-packed hexagonal manner, and the plane of the molecular cores is perpendicular to the column axis. The cores can also be tilted with respect to the column axis and permit the formation of the **rectangular (D_r)** or the **rectangular face-centered** molecular arrangement. In the D_r phase, the planes of the core are tilted with respect to molecules in neighboring columns, forming a herringbone arrangement. The tilted cores are shown as ellipses in Fig. 12B.

Bent-core mesophases

As the name suggests, the bent-core (or banana) mesophases are formed by molecules resembling a boomerang (see Figs. 1 and 13). In recent years, the discovery (Niori et al., 1996; Link et al., 1997) of several novel mesophases formed by bent-core molecules has engendered much scientific interest. The phases exhibited by bent-core molecules are denoted as B_i, where $i = 1, 2, \ldots, 8$, etc. The progression of the index i does not imply a systematic evolution of the structure of such phases. The structure of some of the phases has been determined while it remains uncertain for others. In the following, we will summarize what is reasonably well known at this time. We will discuss the structure of different phases in order to minimize confusion. This is an active area of research, and our understanding of some of these phases will likely undergo revision or refinements. Their names and notations are likely to change in the near future as we learn more about them and streamline the nomenclature based on symmetry.

Owing to their unique geometrical shape of molecules, the phases have revealed surprising structures and properties. For example, the formation of polar and chiral structures by *achiral* molecules is unexpected. Bent core materials show the largest electronic second-order susceptibility $\chi^{(2)}$ of all known LCs. Until now, the formation of ferroelectric phases with macroscopic electric polarization was limited to chiral molecules. Also, some bent-core mesophases exhibit interesting ferroelectric and antiferroelectric properties.

In the **B_1 phase**, the molecules partially overlap along their overall long axis, and they are arranged in smectic layers. Additionally, in a plane perpendicular to the smectic layers, molecules are organized in a 2D centered rectangular lattice, Fig. 13. Based on the studies of single domain samples, there are no indications of long-range positional correlations in the direction perpendicular to the plane containing the 2D lattice. From a symmetry point of view, this phase resembles the columnar D_r phase.

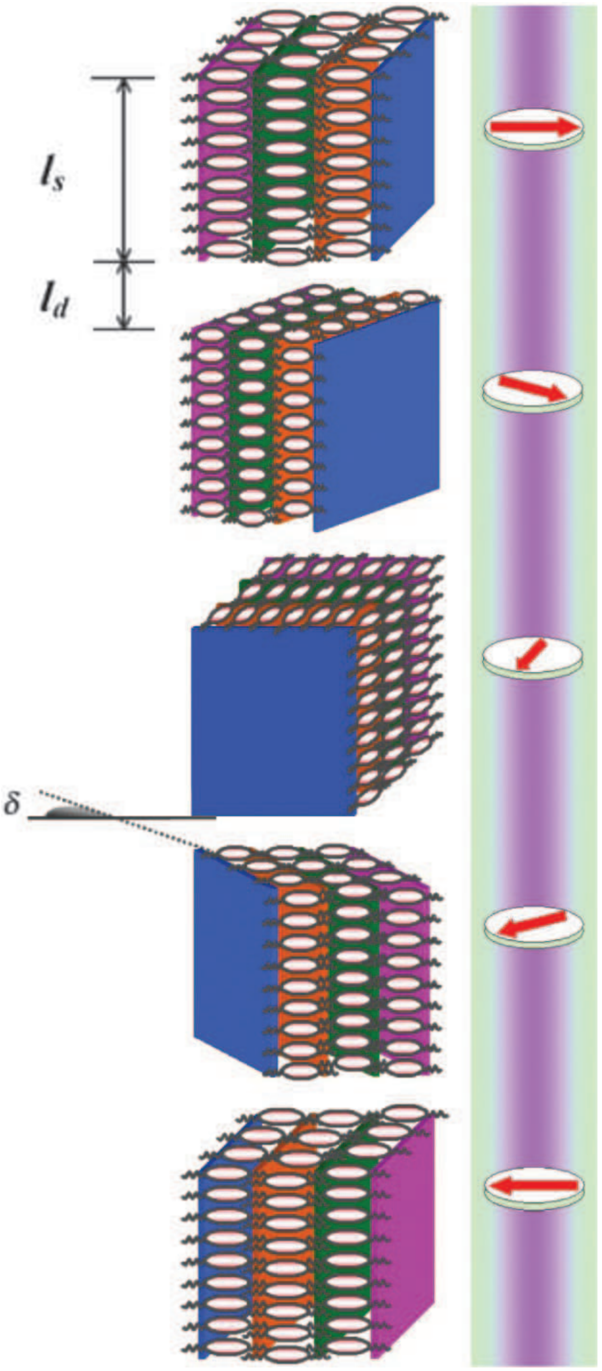

Fig. 11 Schematic drawing of TGB$_A$ phase with pitch axis vertical. The *red arrows* mark the direction of the layer normal.

The unit cell dimensions, as expected, are related to the molecular size. For example, in the case of a series of bent-core azo compounds (Prasad et al., 2004), the rectangular cell dimensions were $a = 36.4 \pm 0.2$ Å and $c = 30.4 \pm 0.2$ Å. Two forms of the B$_1$ phase have been reported; in one of the forms, the molecules are orthogonal to the smectic layers while in the second form, they are tilted like the SmC phase. These have been assigned the names B$_{1o}$ and B$_{1t}$ for the orthogonal and tilted phases, respectively.

A group of four phases that consist of stacked layers (or smectic) are known as the **B$_2$ phase**(s). Here, the molecules are tilted, and the phase resembles the tilted chiral phases (SmC*, SmC$_A^*$) of calamitic mesogens. The molecules forming these phases may possess a dipole moment **p** directed along their apex. Furthermore, the tilt in adjacent layers may be in the same azimuthal direction (synclinic) or opposite directions (anticlinic). The direction of molecular dipoles in one smectic layer may be parallel to that in adjacent layers (ferroelectric) or antiparallel (antiferroelectric). These four possibilities (Walba et al., 2000) are schematically shown in Fig. 14 and denoted as SmC$_A$P$_F$, SmC$_S$P$_F$*, SmC$_S$P$_A$, and SmC$_A$P$_A$*. It should be noted that the SmC$_S$P$_F^*$ and SmC$_A$P$_A$*

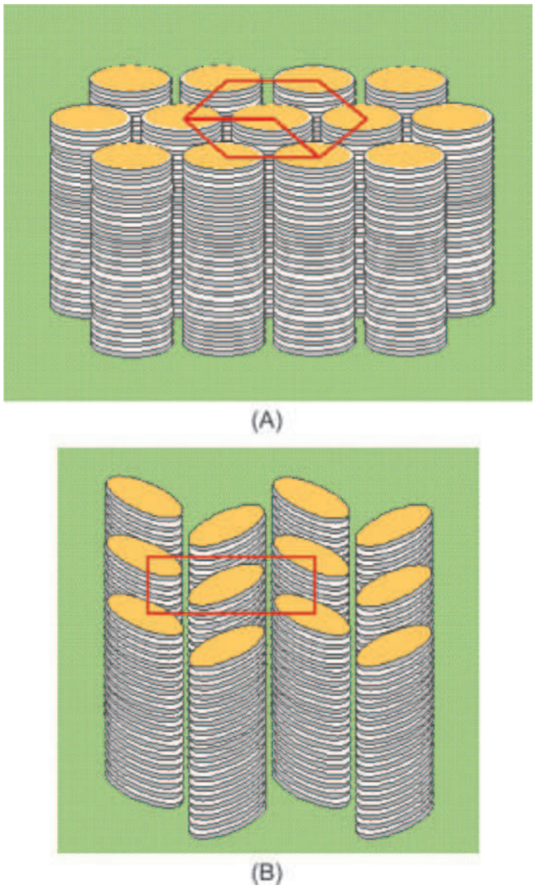

Fig. 12 (A) Hexagonal D_h and (B) rectangular D_r columnar mesophases. Discotic mesophases lack positional order in the direction of the column axis.

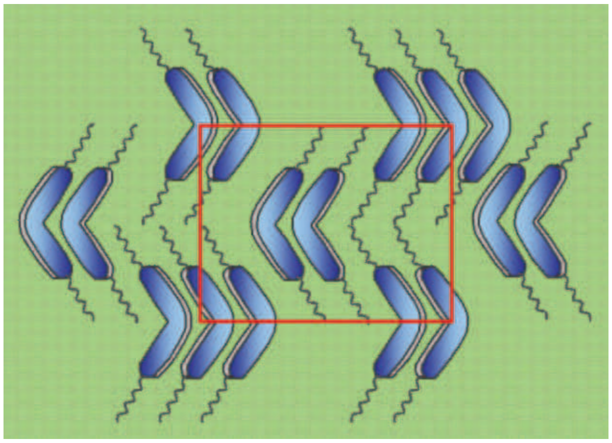

Fig. 13 Molecules in the B_1 phase occupy a rectangular lattice across smectic layer interfaces—no long range-positional correlations exit in the direction perpendicular to the rectangle.

phases essentially possess the same symmetry as the calamitic ferroelectric SmC* phase and antiferroelectric SmC_A^* phases, respectively, and they may exist in both left- and right-handed chiral states. The other two phases, SmC_SP_A and SmC_AP_F, are antiferroelectric and ferroelectric racemates, respectively.

The **B_3 and B_4 phases** are crystalline phases. The B4 phase is also called the blue crystal phase in literature. This phase is chiral and exhibits circular dichroism. Only preliminary details about the structure of the B_3 and B_4 phases are available at this time. We will not discuss the details of these phases here.

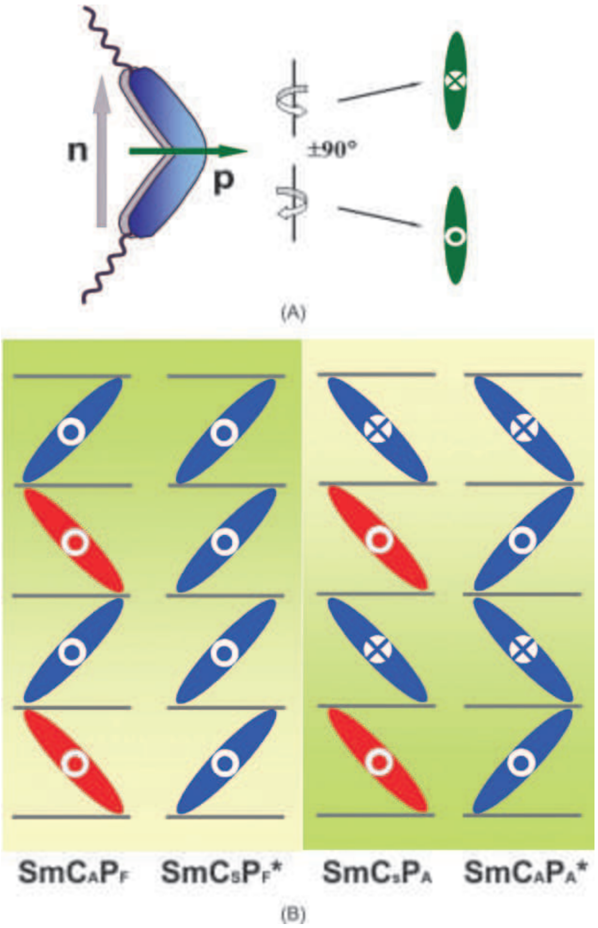

Fig. 14 (A) Different views of bent-core molecules and (B) the four structures formed in the B_2 phase. In some materials, more than one structure may be simultaneously present.

The **B_6 and B_8 mesophases** possess smectic stacked layer organization with no in-plane order. The B_6 and B_8 phases differ from the regular smectic phases in an important way. The smectic layer spacing is different from molecular length because, in the B_6 phase, the molecules have partial lengthwise overlap at the smectic layer interface. However, unlike the B_1 phase, there is no other order present in the B_6 and B_8 phases, Fig. 15, apart from the smectic layering. The primary layer thickness is less than the molecular length. Such phases exhibit additional peaks in X-ray diffraction patterns corresponding to a length less than twice the molecular length. A tilted analog phase of the B_6 phase has also been reported (Pelz et al., 2003). In the B_8 phase, the molecules in the neighboring layers form weak antiparallel associations with molecules in the adjacent layers and act as dimers with no overlap of the cores. The smectic layer spacing in this phase is close to twice the molecular length. The B_6 and B_8 phases can be considered analogs of the SmA_d and SmA_2 phases in the *frustrated* (or polar) smectics (Prost, 1984). The B_8 phase possesses an antiferroelectric arrangement of molecular dipoles. Tilted and chiral variants of the B_6 and B_8 phases are also likely to exist but have not yet been reported.

The **B_7 phase** exhibits chiral textures of both right- and left-handedness under a polarizing microscope. There are some reports of this phase responding to an applied electric field in both ferro- and antiferroelectric manner. The B_7 phase has a layered structure with either the same or different tilts in adjacent layers, which are either ferroelectric or antiferroelectric. They exhibit twisted helical filaments of high- and low-birefringence focal conics striped patterns parallel or normal to the smectic layers. Unraveling the structure of this phase has been the most challenging of all bent-core mesophases. Optical, freeze-fracture, and high-quality synchrotron x-ray diffraction studies of thin (Coleman et al., 2003) and bulk (Kang et al., 2004) samples are beginning to reveal a complex three-dimensional structure. In the B_7 phase, SmC^*-type layers are subdivided into stripes with splay deformation and defect lines shown as red and blue vertical lines in Fig. 16. Splay deformations naturally cause smectic layer (thickness) undulations because the disorder of **P** and molecular tilt produces a smaller molecular tilt and thus higher layer spacing. For a specific sign of splay, there are four possible combinations of handedness and orientations of **P** across smectic layers. These four combinations are the same as already discussed for the B_2 phase (Fig. 16). The essential features of layer undulations and molecular arrangement are illustrated in Fig. 16. The uniformity of the pitch in the layer-normal direction on a macroscopic scale requires thinner layer regions between the defect (vertical blue and red) lines to tilt and become thicker. This results in a polarization-modulated structure with a

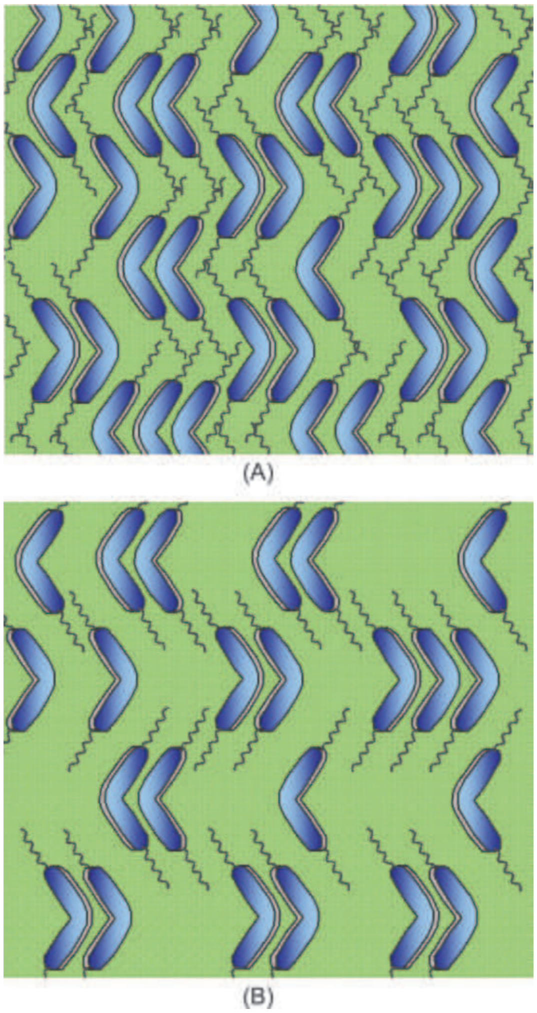

Fig. 15 (A) Partial bilayer structure of the B_6 and (B) bilayer structure of the B_8 phase.

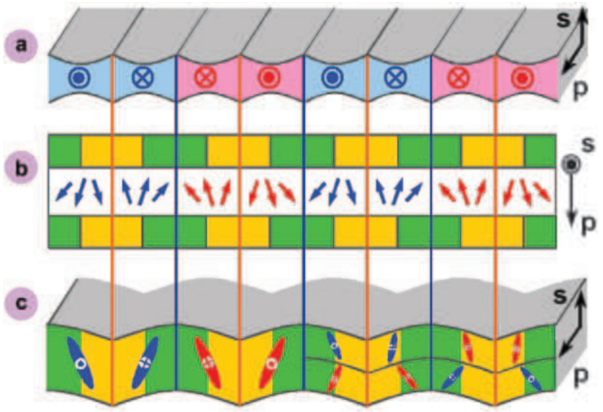

Fig. 16 (A) Variation of the layer spacing due to polarization modulation induced by the formation of splay stripes shown in (B). (C) Different regions separated by defect lines possess local structures similar to the SmC_SP_F and SmC_AP_F structures of the B_2 phase. Vectors **P** and **S** represent the spontaneous polarization density and average layer normal directions, respectively. *Arrows* in (B) and vector directions in (A) and (C) represent the molecular dipoles and their splay organization.

pitch much larger than the smectic layer spacing. X-ray studies reveal that the period of modulations of the smectic layers is very well-defined, giving rise to sharp Bragg peaks in the transverse direction. The undulations have a temperature and material-dependent period ranging from approximately 150 to 350 Å. The length over which the undulations are correlated is the same as the dimension over which the smectic layers prevail, that is, undulations are long-range deformations and an integral feature of the B_7 phase.

The likelihood of helical polarization-modulated filaments and twisted grain boundary (TGB) structures with polarization modulation gives rise to the possibility of forming several unique defect structures and hence the large variety of textures exhibited by the B_7 phase.

The **B_5 phase** (Eremin et al., 2002) is generally obtained upon cooling from the B_2 phase. Molecular arrangement in the B_5 phase is similar to the B_2 phase. The liquid-like X-ray diffraction peaks at large angles arising from the in-plane structure of the smectic layers are quite sharp. However, they remain reasonably wide to suggest that the in-plane structural order is short range. This phase is likely to be an analog of the orthogonal hexatic smectic (SmB_{hex}) phase of calamitic liquid crystals. The B_5 phase responds, albeit sluggishly, to the applied field confirming increased order and viscosity.

Many soft condensed matter systems and biological materials are liquid crystalline. For example, rod-like objects, such as tobacco mosaic virus on one hand and carbon nanotubes on the other are known to form LC phases. With our ever-expanding knowledge of naturally occurring phenomena and efforts to synthesize new molecular shapes, the list of liquid crystal phases is bound to keep growing, revealing new structures and novel scientific phenomena.

Conclusion

The field of liquid crystals is truly interdisciplinary. Organic synthesis of new molecules with different architectures has yielded new phases propelling this field in new directions. We have seen the discovery of new and unexpected phases and the phases that have been theoretically predicted. The couplings between their structure, physical properties, and responsiveness to external stimuli continue to open the doors to new opportunities for technological innovations. This trend shows no sign of slowing down, and we anticipate new research directions to arise in the coming years.

References

Acharya BR, et al. (2003) The elusive thermotropic biaxial nematic phase in rigid bent-core molecules. *Pramana* 61(2): 231–237.

Acharya BR, Primak A, and Kumar S (2004) Biaxial nematic phase in bent-core thermotropic mesogens. *Physical Review Letters* 92(14): 145506.

Born M (1916) Über anisotrope Flüssigkeiten. Versuch einer Theorie der flüssigen Kristalle und des elektrischen Kerr-Effekts in Flüssigkeiten. *Sitzungsber. Preuss. Akad. Wiss.* 30: 614–650.

Chen D, et al. (2013) Chiral heliconical ground state of nanoscale pitch in a nematic liquid crystal of achiral molecular dimers. *Proceedings of National Academy of Sciences USA* 110(40): 15931–15936.

Chen D, et al. (2014) Twist-bend heliconical chiral nematic liquid crystal phase of an achiral rigid bent-core mesogen. *Physical Review E* 89(2): 022506.

Chen X, et al. (2020) First-principles experimental demonstration of ferroelectricity in a thermotropic nematic liquid crystal: Polar domains and striking electro-optics. *Proceedings of National Academy of Sciences USA* 117(25): 14021–14031.

Chen X, et al. (2021) Polar in-plane surface orientation of a ferroelectric nematic liquid crystal: Polar monodomains and twisted state electro-optics. *Proceedings of National Academy of Sciences USA* 118(22): e2104092118.

Coates D and Gray GW (1973) Optical studies of the amorphous liquid-cholesteric liquid crystal transition: The “blue phase”. *Physics Letters A* 45(2): 115–116.

Coleman DA, et al. (2003) Polarization-modulated smectic liquid crystal phases. *Science* 301(5637): 1204–1211.

Coles HJ and Pivnenko MN (2005) Liquid crystal ‘blue phases’ with a wide temperature range. *Nature* 436: 997–1000.

de Gennes PG and Prost J (1993) *The Physics of Liquid Crystals.* New York: Oxford University Press.

Dozov I (2001) On the spontaneous symmetry breaking in the mesophases of achiral banana-shaped molecules. *Europhysics Letters* 56(2): 247.

Eremin A, et al. (2002) Structural characterization of the new polymorphic mesophases formed by bent-core molecules. *Liquid Crystals* 29(6): 775–782.

Freiser MJ (1970) Ordered state of a nematic liquid. *Physical Review Letters* 24(19): 1041.

Kang S-W, Reddy RA, Sadashiva BK, and Kumar S (2004) *Proceedings of the 20th International Liquid Crystal Conference, paper SYN-P141, July 5, Ljubljana, Slovenia.*

Kikuchi H, et al. (2002) Polymer-stabilized liquid crystal blue phases. *Nature Materials* 1(1): 64–68.

Kumar S (1981) High-resolution x-ray measurements of the smectic phases of terephthal-bis-(4n)-alkylanilines. *Physical Review A* 23(6): 3207.

Kumar S (2000) *Liquid Crystals – Experimental Study of Physical Properties and Phase Transitions*. Cambridge: Cambridge University Press.

Larventovich OD (2020) Ferroelectric nematic liquid crystal, a century in waiting. *Proceedings of National Academy of Sciences USA* 117(26): 14629–14631.

Lee GS, et al. (2009) Direct confirmation of biaxiality in a bent-core mesogen through the measurement of electro-optic characteristics. *Journal of Applied Physics* 105(9): 094509.

Li J, Nishikawa, et al. (2021) Development of ferroelectric nematic fluids with giant-ε dielectricity and nonlinear optical properties. *Science Advances* 7(17): eabf5047.

Link DR, et al. (1997) Spontaneous formation of macroscopic chiral domains in a fluid smectic phase of achiral molecules. *Science* 278(5345): 1924–1927.

Mertelj A, et al. (2018) Splay nematic phase. *Physical Review X* 8(4): 041025.

Niori T, et al. (1996) Distinct ferroelectric smectic liquid crystals consisting of banana shaped achiral molecules. *Journal of Materials Chemistry* 6(7): 1231–1233.

Nishikawa H, et al. (2017) A fluid liquid-crystal material with highly polar order. *Advanced Materials* 29(43): 1702354.

Panov VP, et al. (2010) Spontaneous periodic deformations in nonchiral planar-aligned bimesogens with a nematic-nematic transition and a negative elastic constant. *Physical Review Letters* 105(16): 167801.

Pelz K, Weissflog W, Baumeister U, and Diele S (2003) Various columnar phases formed by bent-core mesogens. *Liquid Crystals* 30(10): 1151–1158.

Praefcke K, et al. (1998) Design of low-molar mass thermomesogens in the search for biaxial nematic liquid crystals. *Molecular Crystals and Liquid Crystals* 323(1): 231–259.

Prasad V, Kang SW, Qi X, and Kumar S (2004) Photo-responsive and electrically switchable mesophases in a novel class of achiral bent-core azo compounds. *Journal of Materials Chemistry* 14(9): 1495–1502.

Prost J (1984) The smectic state. *Advances in Physics* 33(1): 1–46.

Reinitzer F (1888) Beiträge zur Kenntnis des Cholesterins. *Monatshefte für Chemie* 9(1): 421–441.

Sebastián N, et al. (2020) Ferroelectric-ferroelastic phase transition in a nematic liquid crystal. *Physical Review Letters* 124(3): 037801, 1–6.

Southern CD, et al. (2008) Thermotropic biaxial nematic order parameters and phase transitions deduced by Raman scattering. *Europhysics Letters* 82(5): 56001.

Van Le K, et al. (2009) Electro-optic technique to study biaxiality of liquid crystals with positive dielectric anisotropy: The case of a bent-core material. *Physical Review E* 79(3): 030701.

Walba DM, et al. (2000) A ferroelectric liquid crystal conglomerate composed of racemic molecules. *Science* 288(5474): 2181–2184.

Wang Y, et al. (2015) Room temperature heliconical twist-bend nematic liquid crystal. *CrystEngComm* 17(14): 2778–2782.

Yoon HG, et al. (2010) Nematic biaxiality in a bent-core material. *Physical Review E* 81(5): 051706.

Yoshida H, et al. (2009) Nanoparticle-stabilized cholesteric blue phases. *Applied Physics Express* 2(12): 121501.

Yu LJ and Saupe A (1980) Observation of a biaxial nematic phase in Potassium Laurate-1-Decanol-Water mixtures. *Physical Review Letters* 45(12): 1000.

Highly Porous Metals and Ceramics

AE Markaki[a], **P Colombo**[b], **and TW Clyne**[a], [a]University of Cambridge, Cambridge, UK; [b]University of Bologna, Bologna, Italy

© 2005 Elsevier Ltd. All rights reserved.

This is an update of A.E. Markaki, P. Colombo, T.W. Clyne, Highly Porous Metals and Ceramics, Editor(s): Franco Bassani, Gerald L. Liedl, Peter Wyder, Encyclopedia of Condensed Matter Physics, Elsevier, 2005, Pages 318–332, ISBN 9780123694010, https://doi.org/10.1016/B0-12-369401-9/01121-9.

Introduction 390
Mechanical Properties and Performance Requirements 392
Elastic Constants and Stiffness-Critical Lightweight Structures 392
Strength, Fracture Mechanics, and Energy-Absorbing Structures 394
Transport Properties and Multifunctional Applications 396
Electrical and Thermal Insulation Characteristics 396
Fluid Permeability and Specific Surface Area 399
Magnetic Actuation and Magnetomechanical Devices 401
Further Reading 403

Introduction

Porous cellular metals and ceramics are now being intensively studied. This has arisen partly from a growing appreciation that biomaterials must be thoroughly understood, not only to exploit them effectively, but also to develop biomimetic materials with attractive properties and biocompatible materials and structures. Since many natural and biological materials are cellular, often with relatively high-porosity levels (although sometimes these pores are, at least, partly filled with a fluid or a soft and compliant solid in the natural state), study of manufactured porous materials has become an important branch of materials science. In fact, various types of porous materials, quite different from any biological system, are also being heavily investigated. Furthermore, certain well-established areas of porous material usage, such as filters, catalyst supports, and heat exchangers, are being subjected to renewed scrutiny, as novel porous materials and structures are developed.

Interest extends to both processing developments and to relationships between microstructure and properties. The concept of microstructure should be defined with care in highly porous materials, since it is sometimes used to refer only to the cell structure (i.e., the size, volume fraction, shape, etc. of the pores), whereas in practice, the microstructure of material constituting the cell wall may also be important. Distinctions can be drawn between different types of porous materials, based on their cell structure. The most significant classification is that between open-cell and closed-cell materials. An obvious difference is that open-cell foams are permeable to fluids, which has various implications, but there are also some rather systematic differences between the two types of materials, relating to various thermophysical and mechanical properties, and also to the applications for which they might be suitable.

However, further classification is probably needed. Some porous materials exhibit distinct, separate cells, but with some connectivity – as, for example, might result from rupturing of some cell walls. Such configurations differ noticeably from open structures having such high connectivity that it is difficult to delineate any individual cells. It might be argued that the latter should be termed "open-network materials," rather than "cellular materials." Open-network materials can, for example, be produced by assembling a set of fibers or fine wires. Such assemblies can be isotropic or they may be highly oriented – commonly either in-plane or uniaxially aligned – and hence exhibit pronounced anisotropy in both structures and properties. Ropes, cables, braided wires, etc. are effectively open-network materials of this type, as are various types of insulation blankets, filters, etc. There are many such products in commercial use, based on metallic, ceramic, or polymeric fibers, with or without strong interfiber bonding.

Classifying ropes, or bonded assemblies of short struts, as (open-network) materials brings into sharp focus the issue of whether such things should really be termed materials or structures. In fact, many highly porous materials should probably be treated as "quasimaterials," since they are in many ways genuinely intermediate between the two. An important feature of quasimaterials, and of highly porous materials in general, is that the "pore architecture" introduces extra degrees of freedom into microstructural design. In thinking about terminology and classification, it is instructive to consider the combinations of pore content, connectivity, and anisotropy exhibited by various actual and putative materials and quasimaterials. This is illustrated graphically in Figure 1, which presents data for a number of well-known products and natural materials. Void content is simply evaluated, while anisotropy can be characterized via observed variations with direction of a suitable property, such as Young's modulus E (see the section "Elastic constants and stiffness-critical lightweight structures"). Intercell connectivity is more difficult to quantify. In constructing Figure 1, the ease of permeation of fluids through the material (see the section "Fluid permeability and specific surface area") has been used as the indicator, represented by the specific permeability κ (in m^2), which is independent of the fluid used in the measurement. Good intercell connectivity leads to high permeability. However, the permeability drops as the scale of the structure becomes finer,

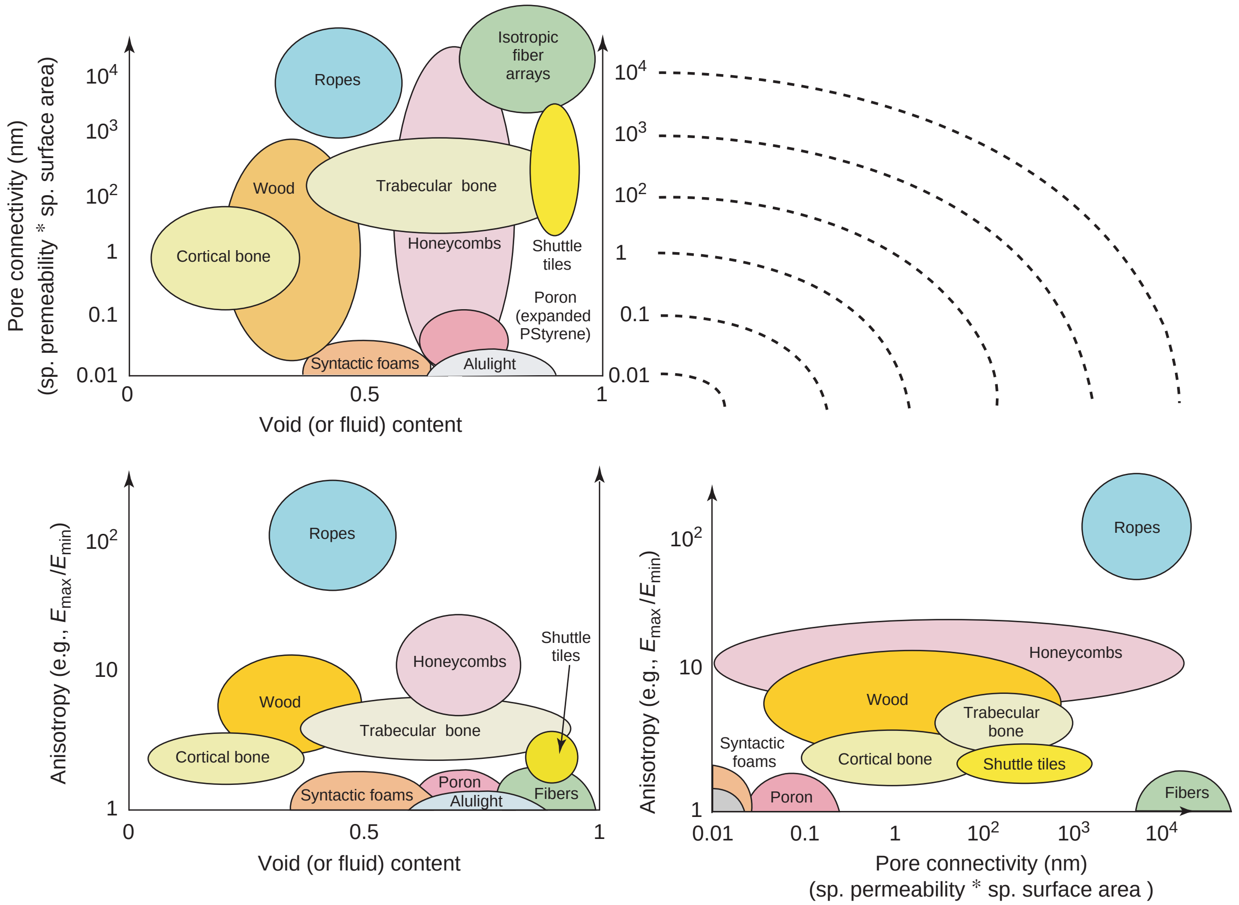

Figure 1 Semiquantitative map designed to aid classification according to pore architecture, showing the combinations of void content, anisotropy, and pore connectivity exhibited by a variety of highly porous materials. (“Alulight” is a closed-cell aluminum foam made via a gas generation route.)

so κ has been multiplied by the specific surface area (in m^{-1}), which rises as this occurs, to give a connectivity parameter designed to be scale independent, at least to a first approximation. Figure 1 highlights the wide range of cell architectures obtainable. Of course, the scale of the structure is a further important variable.

Highly porous materials are also sometimes classified according to whether their cell structures are regular or stochastic (i.e., exhibiting random variations in cell size, shape, and distribution). This can affect certain characteristics, particularly mechanical properties, since it influences stress concentration effects and crack propagation paths. The distinction is not, however, a very rigid one, since porous materials which do not, strictly speaking, have regular or periodic cell structures may nevertheless exhibit a relatively narrow distribution of cell size and shape. Finally, some porous materials tend to exhibit bimodal distributions of pore size, so that, for example, the cell walls might themselves be porous. This can influence a wide range of properties. An illustration is presented in Figure 2 of cell structures in four different types of highly porous materials, exhibiting a wide range of regularity, anisotropy, connectivity, and scale.

In this article, a brief outline is given of how various properties of highly porous materials are predicted and controlled. It is sometimes possible to apply conventional composite theory, with one of the constituents taken as having zero stiffness or strength or conductivity, etc. However, models of this type often breakdown for high porosity levels, particularly as the pores become contiguous (open-celled), and, in general, rather different approaches are needed in this regime, taking proper account of the cell architecture. Furthermore, porous materials may have interesting transport properties or potential for actuation characteristics and these often require rather specialized analysis. In outlining these structure–property relationships, reference is periodically made to the applications for which particular properties are most relevant. Of course, minimization of weight is a common motivation for using porous materials, and this is a key objective for many applications, but transport properties such as permeability and

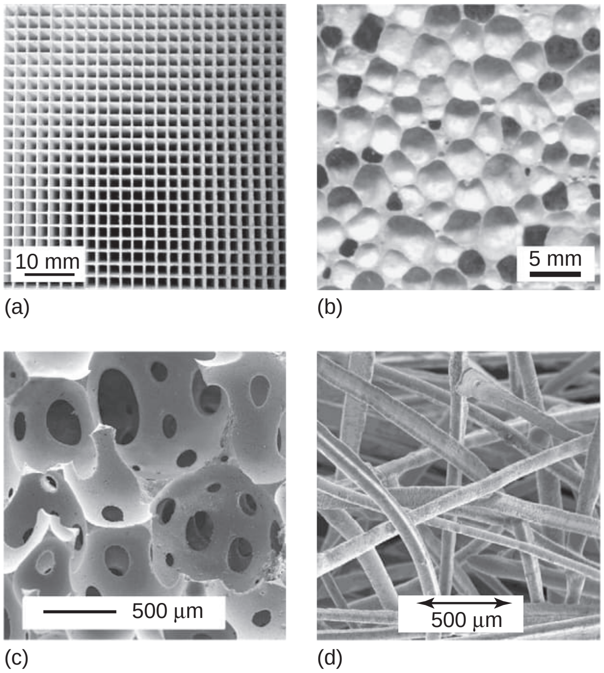

Figure 2 Microstructures of (a) a ceramic honeycomb, (b) a closed-cell metallic foam, (c) an open-cell SiOC foam, and (d) an open-network structure made by bonding metallic fibers together.

conductivity may also be of critical importance. Overall, the coverage is of necessity highly abbreviated and the bibliography provided will need to be consulted for any detailed information.

Mechanical Properties and Performance Requirements

Elastic Constants and Stiffness-Critical Lightweight Structures

The elastic constants of porous materials can be predicted using conventional composite theory models, with the "reinforcement"-ascribed zero stiffness (and zero Poisson ratio). For example, Figure 3 shows how axial and transverse Young's modulus and Poisson ratio are predicted to vary with void content, and with void aspect ratio, according to the Eshelby method, which is based on assuming that ellipsoid-shaped inclusions (pores) are dispersed throughout the matrix. The following equation gives the elastic constants

$$\mathbf{C} = \left[\mathbf{C}_{\mathrm{m}}^{-1} - f\{(\mathbf{C}_{\mathrm{i}} - \mathbf{C}_{\mathrm{m}})[\mathbf{S} - f(\mathbf{S} - \mathbf{I})] + \mathbf{C}_{\mathrm{m}}\}^{-1}(\mathbf{C}_{\mathrm{i}} - \mathbf{C}_{\mathrm{m}})\mathbf{C}_{\mathrm{m}}^{-1}\right]^{-1} \quad [1]$$

where C is the stiffness tensor, the subscripts m and i refer to matrix and inclusions (pores), S is the Eshelby tensor (dependent on inclusion aspect ratio s), I is the identity tensor and f is the volume fraction of inclusions (pores). The model is known to be unreliable for high inclusion contents, but it, nevertheless, serves to illustrate a few simple points.

First, the specific stiffness of porous materials differs little from that of the matrix, since the Young's modulus falls off in a broadly similar way to the density (rule of mixtures line). In fact, apart from the axial stiffness of a material with aligned, highly elongated pores, which approximates closely to the rule of mixtures line, the stiffness falls off more sharply than the density, so the specific stiffness of porous materials is, in general, lower than that of corresponding monolithic materials.

Second, porous materials can be quite significantly anisotropic in stiffness, if the pores are aligned and elongated. This is the case in many natural cellular materials. In fact, it is clear from the plot that the pores do not need to be highly elongated for this to be the case, since the $s = 3$ curves are fairly close to those for infinite aspect ratio. However, it is also worth noting that the plot suggests that elastic anisotropy is unlikely to be dramatic (greater than a factor of 2 or so). Some assumptions, such as those of the equal stress model, lead to much greater predicted anisotropy, but these are known to be very unreliable, at least for cylindrical inclusions (pores). On the other hand, experimental data for transverse stiffness often suggest that it is much lower than in the axial direction. For example, typical woods (with a void content of ~20–40%) are often quoted as having an axial (parallel to grain) stiffness of

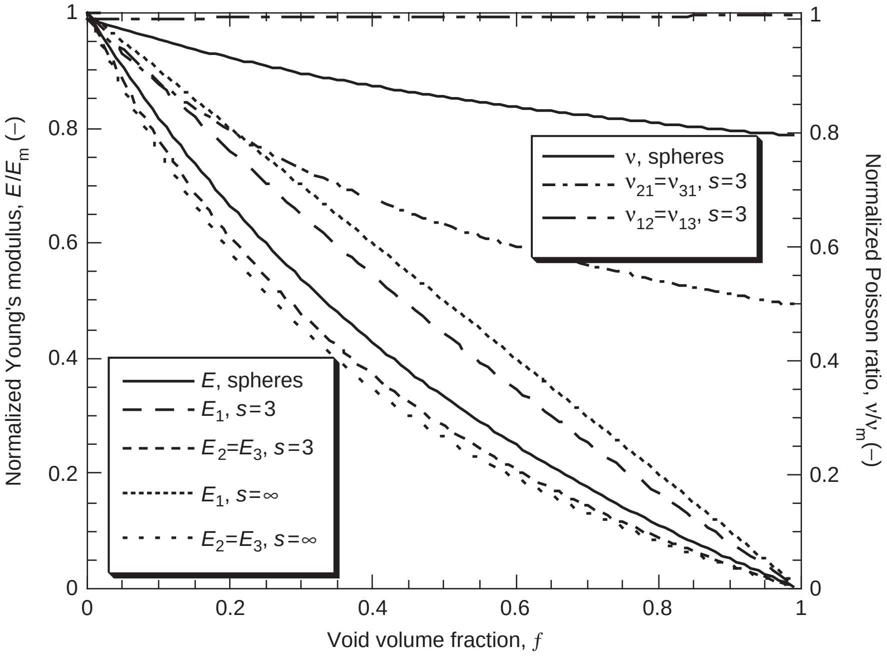

Figure 3 Predicted dependence on void content *f*, and void aspect ratio *s*, of the Young's modulus and Poisson ratio, obtained using the Eshelby method (eqn [1]).

~10 GPa, but a transverse value of only ~1 GPa. For bone, the quoted anisotropy is usually lower, but is still substantial in some cases. Partial explanation for such discrepancies is often related to difficulties in measuring a true transverse stiffness. The strength (and creep resistance) is often dramatically lower under transverse loading (see below), so that inelastic straining commonly occurs at low applied loads during stiffness measurement. However, it should also be recognized that this type of model, which takes no account of the distribution of voids, and assumes that they have no contiguity (i.e., that the cells are all closed), may be very unreliable for high-void contents and for open-cell materials. Finally, it must be noted that these models assume the base material to be isotropic. For many natural materials, such as wood, the cell walls themselves exhibit high degrees of structural alignment, and hence are highly anisotropic, both elastically and in terms of strength. Obviously, such effects should be taken into account when predicting the effect of the presence of pores.

It can also be seen in Figure 3 that the Poisson ratio may vary significantly when voids are introduced, although the relative changes are predicted to be smaller than those for stiffness. However, it should again be emphasized that, particularly at high-void contents, and with open-cell structures, geometrical aspects can assume much greater importance, and the "mean field" approach of the Eshelby method is certainly not well-suited for prediction of elastic constants at high-void contents. For highly porous materials of this type, geometrically specific models may be more appropriate. For example, consider the plots shown in Figure 4. These relate to porous materials composed of an isotropic (random) array of slender cylindrical fibers, bonded together at junction points – see Figure 2d. A model has been developed for such material, based on assuming that deformation arises solely from elastic-bending deflections of the fiber segments between junctions. The following simple equation is derived for the normalized Young's modulus

$$\frac{E}{E_m} = \frac{9(1-f)}{32(L/D)^2} \qquad [2]$$

where L/D is the aspect ratio of fiber segments between joints. These stiffnesses, both measured and predicted, are well below those predicted by the Eshelby method for the void contents concerned. In general, open-cell materials are less stiff than closed-cell ones with similar void contents, while open-network materials are the least stiff. These discrepancies highlight some of the limitations of applying conventional composite theory approaches to highly porous materials, particularly if they have open-cell or open-network structures. It might also be noted that the model used to produce the plots in Figure 4 predicts a Poisson ratio value of ~0.32, independent of void-content and fiber segment aspect ratio.

Finally, it should be emphasized that, while porous materials do not have superior specific stiffness to monolithic materials under uniaxial loading, they can exhibit dramatic advantages when subjected to bending moments or torques. The reason for this is that "bending stiffness" and "torsional stiffness" are raised, not only by the material having a higher Young's modulus, but also by it

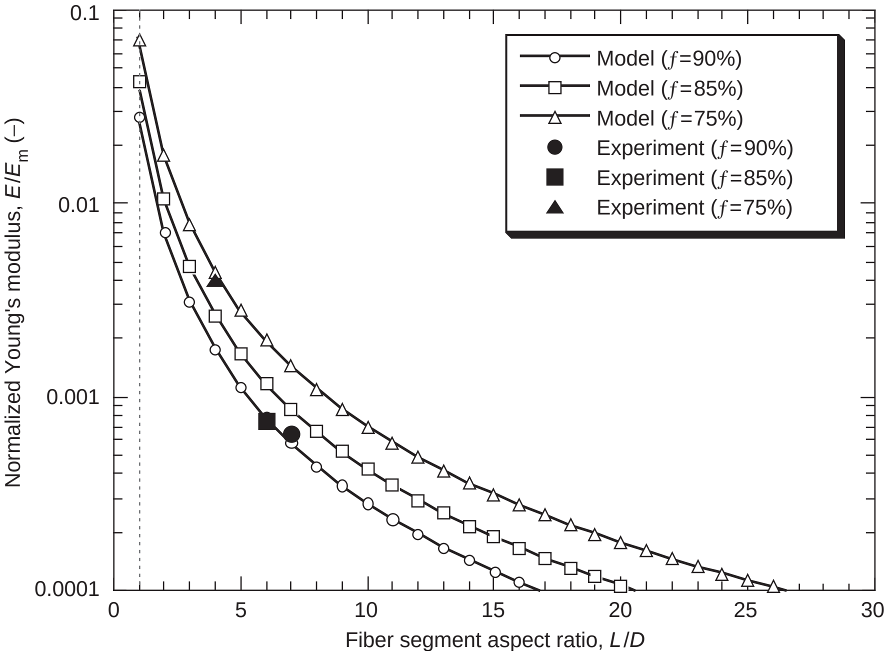

Figure 4 Predicted Young's modulus of an open-network porous material comprising an isotropic array of bonded fibers, as a function of the aspect ratio L/D, of fiber segments between junctions, according to eqn [2]. Curves are plotted for several void contents (f) and some corresponding experimental data are also shown.

being located further from the neutral axis or neutral plane. Depending on the exact boundary conditions, the appropriate figure of merit for stiffness-critical weight minimization (E/ρ for uniaxial loading) is commonly $E^{1/2}/\rho$ or $E^{1/3}/\rho$ for bending, which can make highly porous materials attractive for construction of many types of stiff, lightweight structures. A simple example of this is sandwich panels, for which optimizing the design of highly porous core material is an important issue.

Strength, Fracture Mechanics, and Energy-Absorbing Structures

In general, pores are expected to cause both stress concentration effects and easier crack paths, leading to reductions in strength. In principle, a conventional fracture mechanics calculation should allow estimation of the effect of a dispersed set of (closed cell) pores on the strength and toughness. The passage of a crack through pores reduces the need for material to be fractured and hence reduces the fracture energy. Neglecting any effects of preferential crack paths or reductions in constraint near pores, the fracture energy should thus be proportional to the relative density (1–f), with no dependence on pore size. The stiffness falls off with increasing void content in a broadly similar manner (see the section "Elastic constants and stiffness-critical lightweight structures"). Pores will also act as crack-initiating flaws, reducing the stress required for the onset of fast fracture. In this role, the pore size is significant. To a zeroth approximation, the strength of a porous material could thus be written as a conventional fracture mechanics strength

$$\sigma_* = \left(\frac{G_c E}{\pi c}\right)^{1/2} \approx (1 - f)\left(\frac{G_{cm} E_m}{\pi R}\right)^{1/2} \qquad [3]$$

where c is the flaw size, G_{cm} is the fracture energy of the base material and R is the radius of the crack-initiating (largest) pore, assumed to be spherical. This equation is plotted in Figure 5, which illustrates how high-porosity contents and large pores lead to low-fracture strengths. However, it should be recognized that experimental strengths (and fracture energies) tend to be very low for most highly porous metals and ceramics, even if the pores are relatively fine, and, in general, these predictions are over-estimates, particularly for metals. This is thought to be largely due to a tendency for cracks to preferentially follow high-porosity paths and for ductile tearing of ligaments between pores to occur readily as stress concentration effects operate. This can substantially reduce the effective toughness. While tensile strengths are higher if the pore (cell) structure is fine and regular, most experimentally measured values for highly porous materials are no higher than a few MPa, although some reported values for materials based on metal fibers are in the range of several tens of MPa.

Where highly porous materials are used in load-bearing situations, attempts are often made to ensure that they experience predominantly compressive loads (although it may be noted that this is not possible under bending and twisting moments, which is when their elastic properties can be most effectively exploited – see the section "Elastic constants and stiffness-critical lightweight

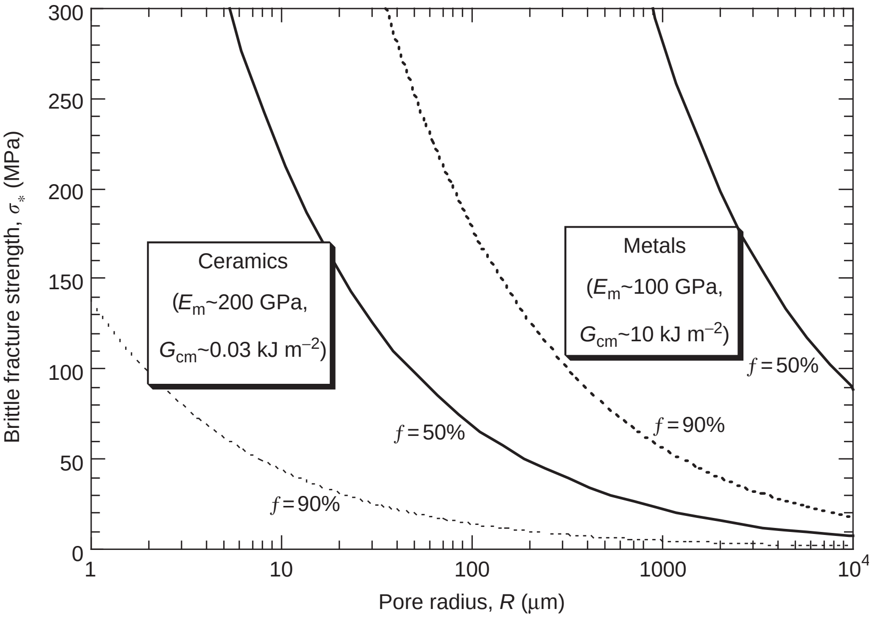

Figure 5 Predicted dependence of the fracture strength of porous metals and ceramics on void content and size, according to eqn [3].

structures"). Under uniaxial compression, highly porous materials tend to yield at relatively low stresses (from a few MPa up to a few tens of MPa) and then undergo quite large strains without the stress level rising much. This strain is associated with local plastic deformation and/or fracture and crushing events. Such deformation can be useful when substantial energy absorption is required without high stresses being generated, as in cushioning of impact events or redistribution of static or dynamic loading configurations. Of course, polymeric foams have long been used for such purposes, but they do not have high energy-absorbing potential and they also suffer from other drawbacks, such as susceptibility to fire. Metals offer particular promise in this regard, since very high local plastic strains can, in principle, be generated, due to the reduced constraint on individual cell walls or network members. This potential has not yet been fully exploited and further work is required on optimization of the energy-absorbing characteristics of highly porous metals. Some such material incorporates significant levels of ceramic in the cell walls (introduced to facilitate the processing) and this certainly impairs plasticity and energy absorption. On the other hand, there may be some situations in which predominance of brittle crushing processes over plastic deformation may be advantageous, since it will tend to result in reduced stress transfer to the component being protected.

Strength can be markedly anisotropic in porous materials. In highly aligned cellular materials, such as wood, factors of 10 between axial and transverse strengths are commonly observed. In materials such as wood and bone, this is partly attributable to the alignment of microstructural constituents (cellulose microfibrils, collagen, etc.) within the cell walls, as well as to the anisotropic cell geometry. However, even in the absence of such effects, strength anisotropy from cell or network geometry can be dramatic, with ropes providing a graphic example. The nature of the bonding in transverse directions is clearly relevant to the magnitude of the anisotropy and in some cases this can be very weak indeed.

Finally, it should be emphasized that the toughness and strength of highly porous materials is not a simple topic. While the presence of pores tends, in general, to promote premature yielding and fracture, there are situations in which the compressibility of porous materials represents a substantial advantage. For example, while the outstanding toughness and damage tolerance of wood arises partly from specific energy-absorbing mechanisms, notably fiber pullout, it is also partly due to the compressibility conferred by the presence of pores. This allows intrusive events, such as the introduction of screws, to take place without the large stress buildup and consequent macroscopic distortion or crack propagation which would tend to result with most fully dense materials, even those with relatively high toughness. Bone is also able to withstand screwing and similar fixation operations quite well, although they can sometimes cause cracking. It might also be argued that the damage tolerance and general mechanical versatility of ropes arises largely from their compressibility, or, at least, from the relative independence of individual strands, which is clearly associated with the presence of the free space. Unfortunately, most manufactured porous materials do not exhibit toughening mechanisms analogous to those operating in wood and bone, which are attributable to their complex, multiscaled microstructures. Furthermore, the damage tolerance and flexibility of rope-like materials is achieved at the cost of very high compliance and low strength in transverse directions. The degree to which most manufactured porous materials benefit mechanically from their high compressibility has thus been rather limited, although it has been noted in some cases that they are suitable for screwing etc. Nevertheless, open-network quasimaterials of various types have excellent potential for offering attractive combinations of mechanical properties and their further development seems likely.

Transport Properties and Multifunctional Applications

Electrical and Thermal Insulation Characteristics

Since there is substantial resistance to the passage of both heat and electrical charge through pores (gaseous or vacuum), porous materials have long been of interest as insulators. However, there are important differences between the two cases for porous materials. In particular, pore connectivity is often an important issue for heat flow. The main reason for this is that convective heat transfer can be significant. There is a scale effect here, since natural thermal convection within closed cells tends to be significant only when the cells are relatively large (typically, $>\sim 10$ mm). However, in open-cell materials natural convection can occur even with finer structures and forced convection can be an important heat transfer mechanism (to such an extent that open-pore materials are often used as heat exchangers – see the section "Fluid permeability and specific surface area"). In the electrical case, on the other hand, the focus is entirely on current paths through the matrix, assuming that the breakdown field for ionization of gas in the pores is not reached. In this section, attention is concentrated on conductive transfer.

From a mathematical point of view, conduction of heat and of electrical charge are indistinguishable. The basic equations of unidirectional heat and current flow may be written as

$$q = -K\frac{\partial T}{\partial x} \tag{4}$$

$$j = -\sigma\frac{\partial V}{\partial x} \tag{5}$$

where q is the heat flux (W m^{-2}) arising from a thermal gradient $\partial T/\partial x$ (K m^{-1}) in a material of thermal conductivity K (W m^{-1} K^{-1}), while j is the current density (A m^{-2}), σ is the electrical conductivity (Ω^{-1} m^{-1} or S m^{-1}) and $\partial V/\partial x$ is the electric field (V m^{-1}). It is common to use the resistivity ρ (Ω m), which is the reciprocal of the electrical conductivity. Both conductivities are proportional to the concentration of carriers, and to their mobility. For thermal conduction, either electrons or phonons can be effective carriers. Good thermal conduction is conferred by the presence of free electrons (metals) or by high phonon velocities (light, stiff materials) and large phonon mean free paths (few scattering centers, i.e., low levels of defects, grain boundaries, etc.). In contrast to this, only electrons or ions can act as carriers of electric charge. Since electrons are much more mobile than ions, materials with free electrons (metals) have vastly greater electrical conductivities than all other materials. Differences in thermal conductivity between different types of material are much less dramatic.

It therefore follows that, if the objective is electrical insulation, then most ceramics are effective anyway and there is little incentive to make them porous, unless a large volume is beneficial – for example, in increasing the thickness of a ceramic insulating layer while keeping its mass low. The electrical resistance of such a porous ceramic layer would probably be similar to a dense ceramic layer of the same thickness, although other electrical properties, such as dielectric characteristics, will often be substantially different. For metals, on the other hand, electrical conductivity will fall as the porosity is increased, but even highly porous metals are unlikely to be suitable for electrical insulation purposes. In addition, there may be interest in maximizing the electrical conductivity of porous metals, so as to facilitate electrical connections or allow resistance welding.

For thermal insulation purposes, however, there is interest in quantifying the conductivity of both ceramics and metals, as a function of porosity level and pore architecture. If the pores are treated as isolated ellipsoids, then the Eshelby method can again be employed, leading to the following equation for the conductivity (electrical or thermal)

$$K = \left[K_{\mathrm{m}}^{-1} + f\{(K_{\mathrm{m}} - K_{\mathrm{I}})[S - f(S - I)] - K_{\mathrm{m}}\}^{-1}(K_{\mathrm{i}} - K_{\mathrm{m}})K_{\mathrm{m}}^{-1}\right]^{-1} \tag{6}$$

which reduces for the case of spheres to the familiar Maxwell equation

$$\frac{K}{K_{\mathrm{m}}} = \frac{2(1 - f) + (K_{\mathrm{I}}/K_{\mathrm{m}})(1 + 2f)}{(2 + f) + (K_{\mathrm{I}}/K_{\mathrm{m}})(1 - f)} \tag{7}$$

This Eshelby expression is very similar to that for the elastic constants (eqn [1]), but these are now second-rank tensors, rather than fourth rank. Predictions from eqn [6] are shown in Figure 6a, with the void conductivity taken as zero ($K_{\mathrm{air}} \sim 0.025$ W m^{-1} K^{-1}, compared with typical values of $\sim$10–200 for metals and 1–150 for ceramics). As with the elastic constants, the reliability is rather poor at high-void contents ($>\sim 50\%$), when the structure will not in most cases approximate well to a matrix containing a set of isolated ellipsoidal voids and the pore architecture should be taken into account. In general, conductivities fall significantly below the Eshelby-predicted levels at high-void contents, as the conduction paths through the matrix become longer and more convoluted, particularly if the pore connectivity is high. This is illustrated by Figure 6b, which presents a normalized plot of thermal conductivity data for various porous metals and ceramics, with structures ranging from a set of layered splats to open three-dimensional fibrous networks. These include the silica fiber-based space shuttle tiles and plasma-sprayed zirconia thermal barrier coatings (TBCs). The latter exhibit normalized conductivities well below the Eshelby predictions, even though the void content is relatively low. This is a consequence of their layered structure, with many poorly bonded interfaces normal to the heat flow direction. (Note that the blown metallic foams have closed-cell structures, while the infiltrated and fibrous ones are open cell.)

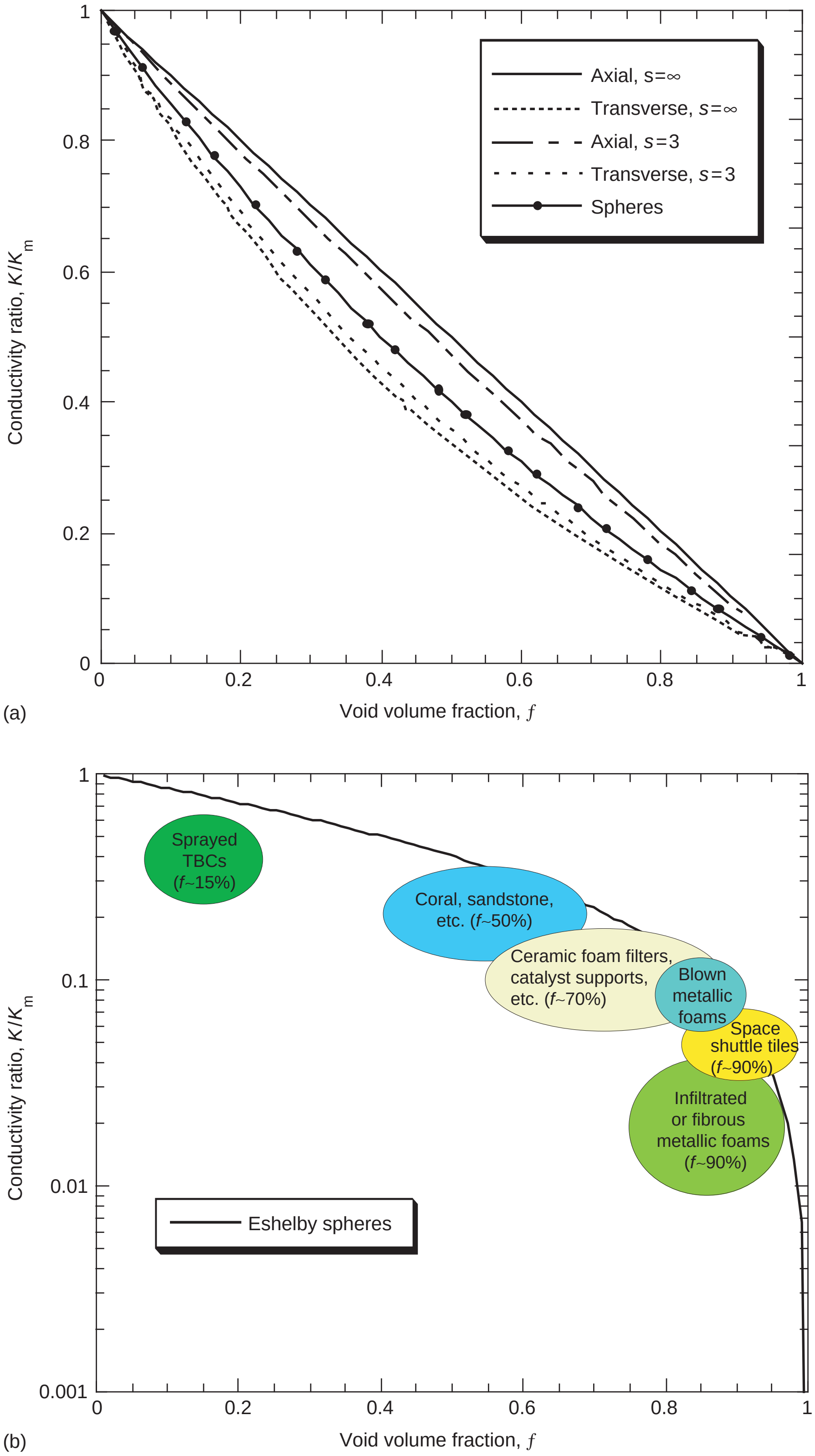

Figure 6 (a) Predicted dependence of the conductivity ratio on void content, *f*, and aspect ratio, *s*, obtained using the Eshelby method (eqn [6]), and (b) typical experimental ranges for the thermal conductivity ratio of various porous metallic and ceramic materials, with the Eshelby prediction for spheres included for reference purposes.

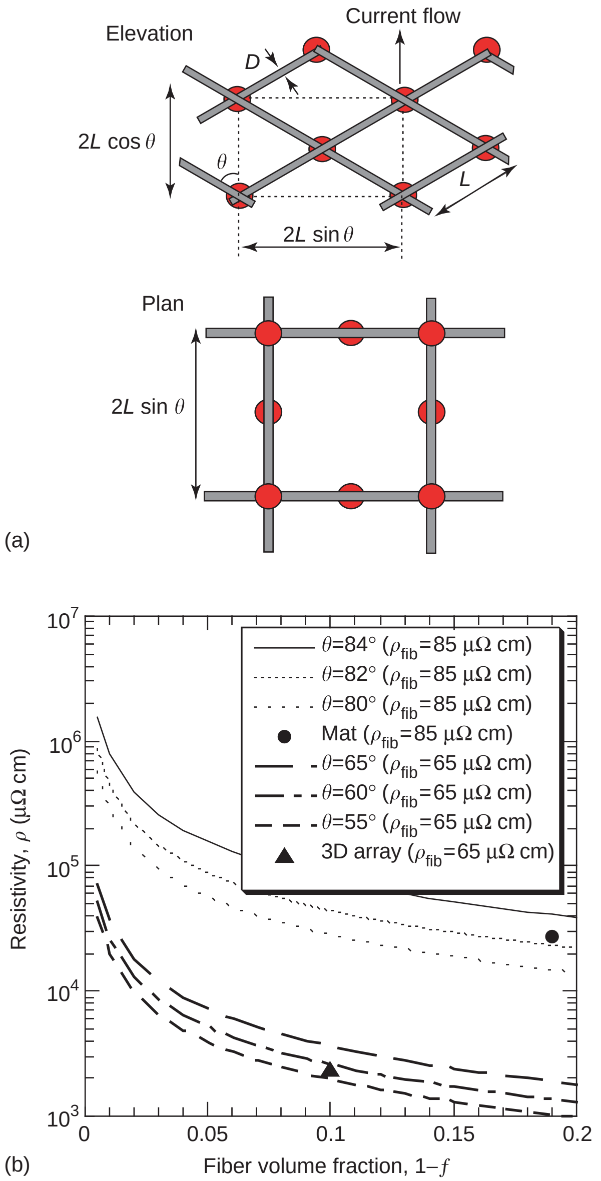

Figure 7 (a) Unit cell for a simple geometrical model of a bonded fiber array and (b) predicted resistivities compared with experimental data for two brazed materials – a mat made from long austenitic fibers (85 μΩ cm) and a 3D array material made from short ferritic fibers (65 μΩ cm).

With particular pore architectures, the behavior can often be predicted quite reliably using simple geometrical models. For example, electrical conduction through a bonded metallic-fiber array has been represented using the model shown in Figure 7a, assuming symmetry about the current flow axis, with all fibers equally inclined to it. It is easily shown that the resistivity of such material is related to that of the fibers by

$$\rho = \frac{\rho_{\text{fib}}}{(1-f)\cos^2\theta} \qquad [8]$$

where θ is the inclination angle. A comparison is presented in Figure 7b between predictions from this equation and some experimental data. The resistivity of such material tends be much higher than that of pore-free metal, by several orders of magnitude, even when the porosity content is only ~80%, and it can be seen that the model captures this effect. That the internal architecture is important in this case is clear from the predicted sensitivity to the fiber inclination angle.

However, it is important to recognize that such simple models are only expected to be reliable if the transport process is dominated by conventional conduction through an isotropic matrix. This is quite likely for electrical current flow through a porous metal, but for heat flow through metals or ceramics there may also be significant convective and/or radiative contributions, while heat conduction through gas in the pores can be relevant and may be affected by pore dimensions, gas pressure, etc. Prediction of the thermal conductivity values exhibited by the materials represented in Figure 6b thus requires modeling that takes into account both structural architecture and details of the heat transfer conditions.

Fluid Permeability and Specific Surface Area

The permeability of an open-celled porous material is an important property for several types of application. Permeation of fluids through such materials is a key issue for heat exchangers, filters, fuel cells, batteries, catalyst platforms, fuel tank baffles, fluid diffusers/mixers, and various types of textiles, as well as in many natural systems such as soils and rocks. The permeation process is clearly facilitated by high cell connectivity. The scale of the structure, which can be characterized by the specific surface area

$$S = \frac{A_{\text{sur}}}{V_{\text{tot}}} \qquad [9]$$

is also of importance. The resistance to fluid flow increases as the scale is refined, but a high surface area may be beneficial in some applications, including many electrochemical devices and combustion-related systems, such as solid fuel rocket propellants. For heat exchangers, there is expected to be an optimal specific surface area, allowing both rapid fluid permeation and efficient local heat exchange. This will also be true for filters, since the scale needs to be sufficiently fine to entrap the target bodies in the fluid stream, but not so fine that the entrapped bodies rapidly cause the permeability to fall as clogging occurs. Finally, it may be noted that encouragement of permeation is desirable in certain biomedical applications, such as porous surfaces of prosthetic implants into which bone growth is to be promoted. Clearly, the permeation velocities of interest may cover a very wide range. Some example materials, designed for particular applications in which permeation and surface area are relevant, are shown in Figure 8.

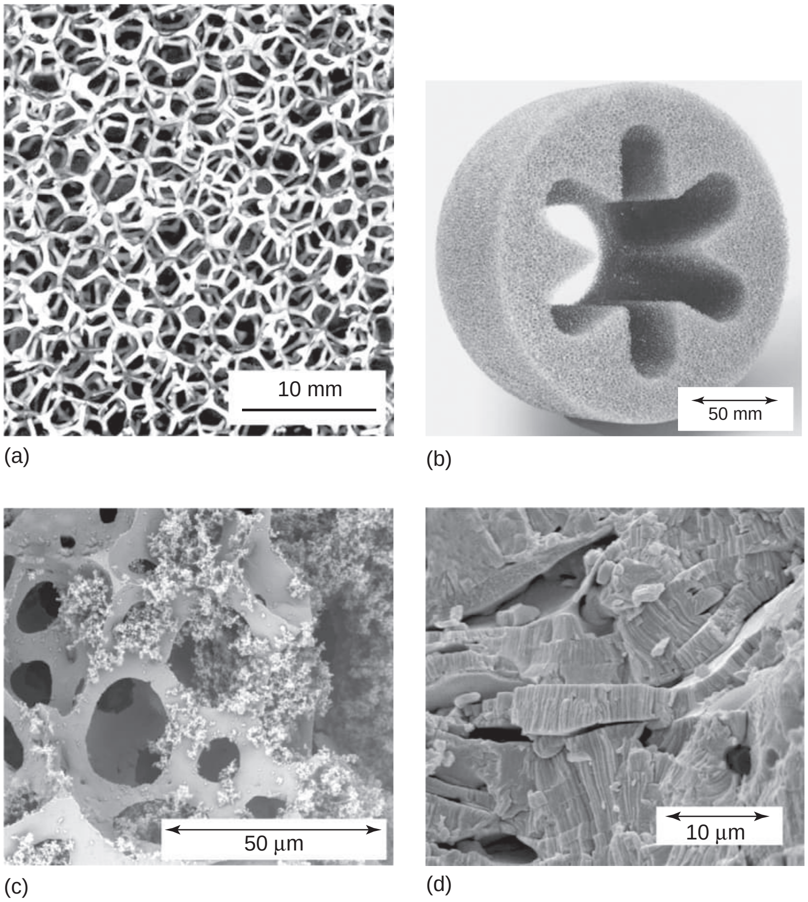

Figure 8 Examples of porous materials for specific applications: (a) microstructure of "Duocel" Al foam ($f\sim90\%$), (b) rocket propellant component made of Duocel, (c) alumina filter ($f\sim90\%$) with entrapped soot particles, and (d) plasma-sprayed zirconia thermal barrier coating (TBC), used in gas turbine engines ($f\sim15\%$). ((c) From Green DJ and Colombo P (2003) Cellular ceramics: intriguing structures, novel properties, and innovative applications. *MRS Bulletin* 28(4): 296–300. Reproduced by permission of MRS Bulletin.)

Laminar flow of a fluid through a porous medium commonly conforms to Darcy's law, which may be written as

$$\frac{Q}{A} = \frac{\kappa}{\eta}\frac{\partial P}{\partial x} \qquad [10]$$

where Q is the volumetric flow rate ($\mathrm{m^3\,s^{-1}}$), A is the sectional area ($\mathrm{m^2}$), $\partial P/\partial x$ is the pressure gradient ($\mathrm{Pa\,m^{-1}}$), η is the dynamic viscosity of the fluid (Pa s) and κ is the specific permeability ($\mathrm{m^2}$). Permeability can thus be measured experimentally by recording the flow rate under a known pressure gradient. It should have the same value for all fluids.

Accurate prediction of permeability as a function of pore architecture is a relatively complex problem, but some simple models have been developed. The value of $\sqrt{\kappa}$ has dimensions of length and one approach involves equating this to some appropriate distance, such as the pore diameter or the hydraulic radius of the structure, defined as

$$R_\mathrm{h} = \frac{f}{S} \qquad [11]$$

Such a rationale leads to the so-called Kozeny equations, of which the best known is probably the Blake–Kozeny equation. This is based on semi-empirical correlations for flow through packed beds and may be written as

$$\kappa \approx \frac{f^3}{4.2\,S^2} \qquad [12]$$

The specific surface area S, can be measured directly or can be estimated via a suitable geometrical model for the pore architecture, giving relationships such as the following

$$S \approx \frac{3.84}{D} \quad (f \approx 0.36) \quad \text{dense random packing of solid spheres (diameter } D\text{)} \qquad [13]$$

$$S = \frac{3\pi}{D(L/D)^2} \quad \left(f = 1 - \frac{3\pi}{4(L/D)^2}\right) \quad \text{cubic array of cylinders (diameter } D,\ \text{length } L\text{)} \qquad [14]$$

Relationships can also be derived for fiber bundles, planar random fiber arrays, woven fabrics, overlapping (poorly bonded) pancakes, etc. Predictions from the Blake–Kozeny equation, for the geometries of eqns [13] and [14], are shown in Figure 9, together with representative ranges of experimental data for various types of porous material. It can be seen that these data are, at least, broadly consistent with this simple model, with the permeability falling as the structural scale is refined, and as the void content is

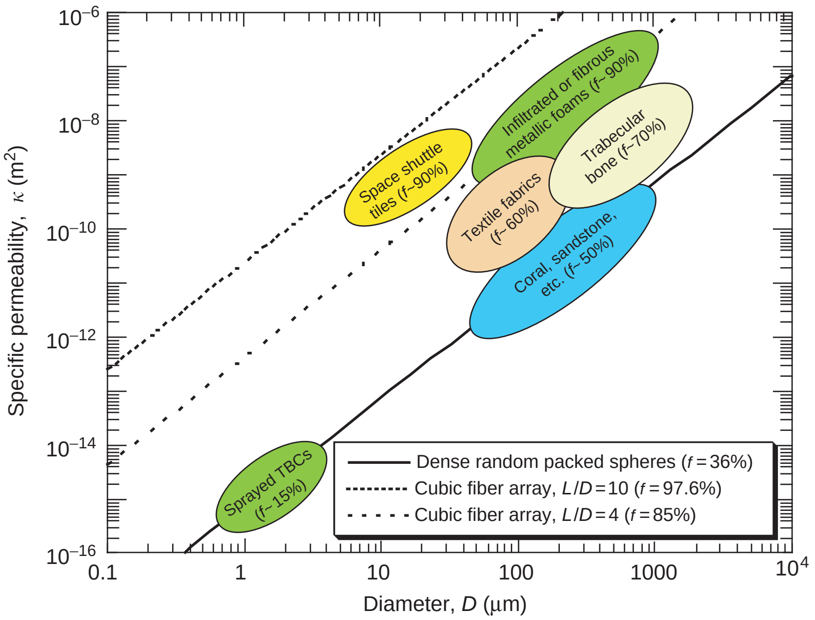

Figure 9 Plot of specific permeability against the structural length scale showing predictions from the Blake–Kozeny equation (eqn [12]), for a packed bed of spheres (eqn [13]) and for a cubic array of cylindrical fibers (eqn [14]), with two different aspect ratios between the joints. Also shown are the approximate ranges of experimental data obtained with various types of porous material.

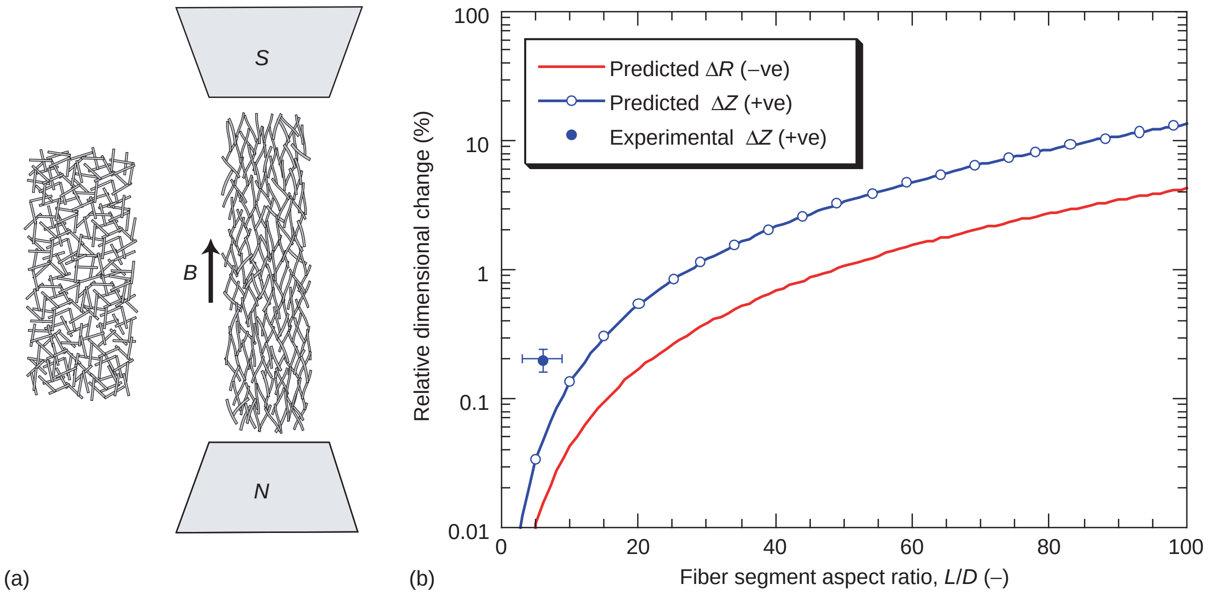

Figure 10 (a) Schematic depiction of how an isotropic porous material made by bonding of ferromagnetic fibers will tend to deform elastically in an applied magnetic field and (b) predicted (eqns [15] and [16]) and measured shape changes (M_s=1.6 MJ T^{-1} m^{-3}; E_f=210 GPa; B=1 T).

reduced. The product of permeability and specific surface area can be taken as a measure of pore connectivity, as plotted in Figure 1, but it may be noted that all of the materials represented in Figure 9 have a relatively high connectivity.

Correlations can be established between permeability and the efficiency of convective heat transfer, but such treatments are beyond the scope of the present article. However, it is worth noting that, in practice, the choice of materials and the design of pore architecture, for applications such as heat exchangers and fuel cell elements are often driven, not solely by transport phenomena optimization, but also by mechanical performance and high temperature stability requirements.

Magnetic Actuation and Magnetomechanical Devices

Porous materials have high potential for usage in various types of actuators, partly because of their relatively low stiffness. A high permeability may also be beneficial in some circumstances – for example, it might facilitate rapid temperature change, perhaps leading to shape changes via differential thermal contraction or the shape memory effect. There is also scope for magnetic actuation with certain types of pore architecture, particularly those containing slender members of ferromagnetic materials, which tend to align with an applied magnetic field. This concept is illustrated in Figure 10a, which shows how a material composed of bonded magnetic fibers would deform in such a field. Deformation of this type has recently been analyzed. The shape changes illustrated in Figure 10a are predicted to conform to the following equations

$$\frac{\Delta Z}{Z} = \left(\frac{16\ M_s B}{9\ E_f}\right)\left(\frac{L}{D}\right)^2 \qquad [15]$$

$$\frac{\Delta R}{R} = \left(\frac{-16\ M_s B}{9\pi E_f}\right)\left(\frac{L}{D}\right)^2 \qquad [16]$$

where M_s is the saturation magnetization of the fiber material, B is the applied magnetic field, E_f is the Young's modulus of the fiber, and L/D is the aspect ratio of the fiber segments between joints. Predictions are compared with experiment in Figure 10b. It can be seen that quite substantial macroscopic strains could be generated, particularly with relatively high fiber segment aspect ratios.

Estimates have also been made of the peak strains that could be induced in this way in a surrounding matrix, such as an embryonic network of bone cells growing into the fiber array. The analysis leads to the following equation for such strains

$$\varepsilon_{\max} \approx \frac{12\pi M_s B \sin\theta (L/D)^2}{\left(9\pi E_f \tan\theta + 28 E_e (L/D)^3\right)} \qquad [17]$$

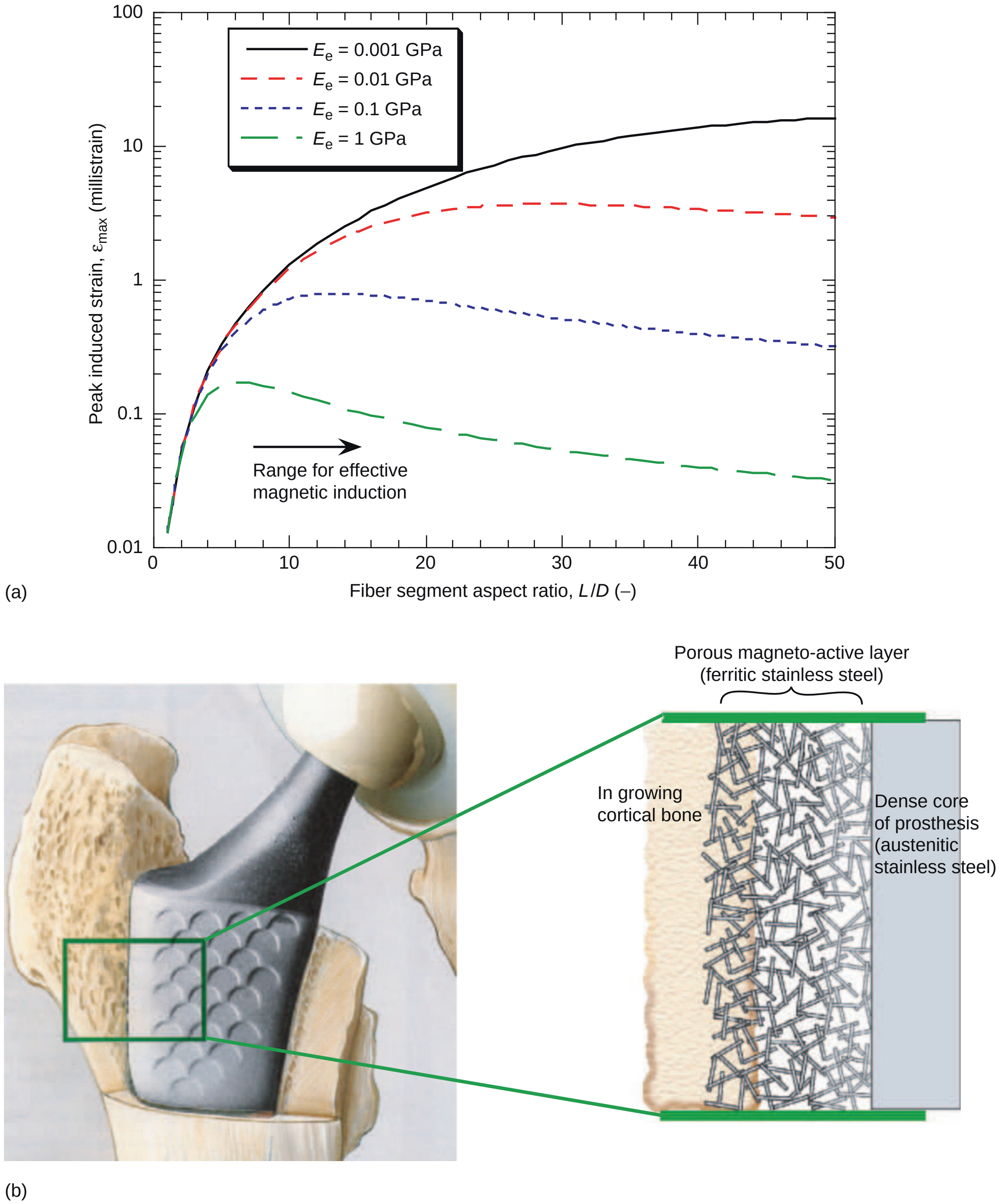

Figure 11 Estimated dependence (eqn [17]) on fiber segment aspect ratio, of the maximum strains induced in a compliant surrounding matrix when a ferromagnetic fiber array is subjected to an applied magnetic field and (b) an integrated prosthesis design, incorporating a porous surface layer in which mechanical straining could be induced in this way (B=1.5 T; M_s=1.6 MJ T^{-1} m^{-3}; θ=30°; E_f=210 GPa).

Predictions are shown in Figure 11a for several matrix stiffness levels. Since such a bone network would have a stiffness of the order of 0.01–0.1 GPa, and since strains of at least around 1 millistrain are known to be required for effective mechanical stimulation of bone growth, it can be seen that this model suggests that such stimulation could be generated with a suitable external magnetic field (B~1.5 T), provided the fiber segment aspect ratio was at least ~5–10. A possible prosthesis design allowing such an effect to be exploited is shown in Figure 11b.

Further Reading

Ashby MF, Evans AG, Fleck NA, Gibson LJ, Hutchinson JW, and Wadley HNG (2000) *Metal Foams: A Design Guide.* Boston: Butterworth-Heinemann.
Banhart J (2001) Manufacture, characterisation and application of cellular metals and metal foams. *Progress in Materials Science* 46: 559–632.
Bardhan P (1997) Ceramic honeycomb filters and catalysts. *Current Opinion in Solid State & Materials Science* 2: 577–583.
Buckley JD, Strouhal G, and Gangler JJ (1981) Early development of ceramic fiber insulation for the space shuttle. *American Ceramic Society Bulletin* 60: 1196–1200.
Fox AC and Clyne TW (2004) Oxygen transport through the zirconia layer in plasma sprayed thermal barrier coatings. *Surface & Coatings Technology* 184: 311–321.
Freyman TM, Yannas IV, and Gibson LJ (2001) Cellular materials as porous scaffolds for tissue engineering. *Progress in Materials Science* 46: 273–282.
Gauckler LJ, Waeber MM, Conti C, and Jacob-Duliere M (1985) Industrial application of open pore ceramic foam for molten metal filtration. *Light Metals* 1261–1283.
Gibson LJ (2000) Properties and applications of metallic foams. In: Clyne TW (ed.) *Comprehensive Composite Materials*, vol. 3, pp. 821–832. Amsterdam: Elsevier.
Gibson LJ and Ashby MF (1999) *Cellular Solids, Structure and Properties.* Cambridge: Cambridge University Press.
Hull D and Clyne TW (1996) *Introduction to Composite Materials.* Cambridge: Cambridge University Press.
Markaki AE and Clyne TW (2001) The effect of cell wall microstructure on the deformation and fracture of aluminium-based foams. *Acta Materialia* 49: 1677–1686.
Markaki AE and Clyne TW (2004) Magneto-mechanical stimulation of bone growth in a bonded array of ferromagnetic fibres. *Biomaterials* 25: 4805–4815.
Richardson JT, Remue D, and Hung J-K (2003) Properties of ceramic foam catalyst supports: mass and heat transfer. *Applied Catalysis A* 250: 319–329.
Saracco G and Specchia V (1998) Catalytic filters for flue-gas cleaning. In: Cybulski A and Moulijn JA (eds.) *Structured Catalysts and Reactors*, pp. 417–434. New York: Dekker.
Scheffler M and Colombo P (eds.) (2005) *Cellular Ceramics. Structure, Manufacturing, Properties and Applications.* Weinheim: Wiley-VCH.
Scheidegger AE (1974) *The Physics of Flow through Porous Media.* Toronto: University of Toronto Press.
Vandeperre LJ, Wang J, and Clegg WJ (2004) Effects of porosity on the measured fracture energy of brittle materials. *Philosophical Magazine* 84: 3689–3704.

Dislocations

V Vitek, University of Pennsylvania, Philadelphia, PA, USA

© 2005 Elsevier Ltd. All rights reserved.

This is an update of V. Vitek, Dislocations, Editor(s): Franco Bassani, Gerald L. Liedl, Peter Wyder, Encyclopedia of Condensed Matter Physics, Elsevier, 2005, Pages 437–444, ISBN 9780123694010, https://doi.org/10.1016/B0-12-369401-9/00413-7.

Introduction 404
Principal Characteristics of Dislocations 404
Elastic Fields and Energy Associated with Dislocations 405
Forces on Dislocations and Interaction between Dislocations 405
Dislocation Multiplication 406
Dislocation Dissociation and Stacking Faults 407
Dislocation Cores 408
Further Reading 410

Introduction

Dislocations are the line defects found in all crystalline materials. They are important in many branches of condensed matter physics, but most significantly they are defects, the motion of which produces plastic flow. The notion of dislocations has two starting points. First, the dislocation was introduced as an elastic singularity by considering the deformation of a body occupying a multiply connected region of space. Second, dislocations were introduced into crystal physics by Taylor, Orowan, and Polanyi in the context of analysis of the large discrepancy between the theoretical and experimental strength of crystals. These two approaches became almost immediately intertwined since the crystal dislocations are sources of long-ranged elastic stresses and strains that can be examined in the continuum framework. In fact, the bulk of the dislocation theory employs the continuum elasticity when analyzing a broad variety of dislocation phenomena encountered in plastically deforming crystals. The most comprehensive monographs devoted to the dislocation theory are books of Friedel, Nabarro, and Hirth and Lothe. An excellent simple introduction to this topic is the book by Hull and Bacon.

In this article, the crystallographic concept of dislocations is explained, the relation between dislocation movement and plastic strain is shown, the concept of the force acting on a dislocation due to externally applied stress is introduced, and the most important aspects of dislocation energetics and properties related to the long-ranged elastic fields are summarized. Then the dislocation nucleation and multiplication which is the most important ingredient in understanding of the plastic deformation, and brittle-to-ductile transition is discussed. Finally, the properties that relate to the atomic structure of materials are paid attention to; in particular, the significance of dislocation dissociation and the dislocation core structure is elucidated.

Principal Characteristics of Dislocations

A dislocation line in a continuum is obtained by cutting the material along any surface that terminates on this line, giving the two cut surfaces a relative displacement and joining them again together. Suppose the cut is made along a planar surface terminating in a straight line, and that this line and the normal to the surface define an orthonormal coordinate system. Fixed vector translations of the cut surfaces parallel, respectively, to the three axes of this system define the three basic types of dislocation. When the displacement is parallel to the line, the result is a screw dislocation. The other two translations, both perpendicular to the line, produce (equivalent) edge dislocations; if the displacement is perpendicular to the cut, a material needs to be removed or added to rejoin the two surfaces. (Three more types of "dislocation," in which the two parts of the continuum on each side of the cut are given a relative rotation before rejoining, can be introduced. The line singularities of this type are called disclinations. These line defects play important role, for example, in liquid crystals but they are not the subjects of this article.) A straight dislocation of general mixed character is obtained when the fixed translation of the cut surfaces has components both parallel and perpendicular to the line. A curved dislocation in a plane or in three dimensions may be introduced in the same way with the surface of the cut (generally nonplanar) terminating on the curve. Since the dislocation line has been introduced as the edge of a surface, it can either terminate on external surfaces or internally by closing on itself and forming a loop. Alternatively, it may meet other dislocation lines at points where at least three dislocations meet and total sum of their Burgers vectors is zero; such points are called dislocation nodes. However, the dislocation line can never end abruptly inside the body.

The principal characteristics of a dislocation are the relative displacement of the two cut surfaces and the line terminating the cut. The former defines the Burgers vector of the dislocation and the latter the dislocation direction, the surface over which the cut has been made has no significance. In the continuum, the dislocation is defined mathematically by the relation $\oint \mathrm{d}u = b$, where $\boldsymbol{u}$ is the displacement vector, $\boldsymbol{b}$ the Burgers vector, and the integral is along any circuit encompassing the dislocation line; for circuits not encircling the dislocation $\oint \mathrm{d}u = 0$. This relation is then the main boundary condition when determining within the elasticity theory, the displacement, strain, and stress fields associated with a dislocation.

Dislocations defined in the continuum have exact analogs in crystals. If the same virtual process of introducing a dislocation is employed in crystals then if the cut surfaces are to rejoin without introducing a fault along the cut, the translation vector, that is, the Burgers vector, must be a repeat vector of the Bravais lattice. A formal definition of the Burgers vector, analogous to the above path integral, invokes the concept of corresponding paths in the real crystal and a defect-free reference crystal. If a closed circuit, consisting of the same number of equivalent atoms to atom steps, is made either in the real or the reference crystal, the corresponding path in the other crystal will not, in general, be closed, and the closure failure is defined as the net Burgers vector of the dislocation lines that thread through the circuit in the real crystal.

The density of dislocations present in a body of material, ρ, is defined as the total length of dislocations per unit volume (dimension m^{-2}). The plastic strain, ε^{pl}, which is produced if these dislocations move, on average, a distance $-d$, is $\varepsilon^{pl} = \rho b -d$, where $b$is the magnitude of the Burgers vector of the dislocations.

Elastic Fields and Energy Associated with Dislocations

In a continuum the dislocation defined above is a line singularity invoking a long-ranged elastic field. The details of the evaluation of the strain and stress fields in the framework of linear isotropic and anisotropic elasticity can be found, for example, in the books by Nabanna and co-workers. In the case of straight dislocations their stress and strain fields decrease as d^{-1}, where d is the distance from the dislocation line. These fields have a complex angular dependence for a fixed distance from the dislocation line. Formally, both the stress and strain diverge at the dislocation line but physically this means that there is a region, centered at the dislocation line, in which the linear elasticity does not apply. This region, the dimensions of which are of the order of the lattice spacing in crystalline materials, is called the dislocation core and it can only be fully accounted for within atomic level models of dislocations. This is discussed in more detail later in this article. The stress and strain fields of a dislocation loop decrease far away from its center as d^{-2}, similarly as the field of a dislocation dipole formed by two dislocations of opposite Burgers vectors.

The elastic energy associated with the long-range stress and strain fields of a straight dislocation is

$$E_{el}^{sl} = \frac{Kb^2}{4\pi}\ln\left(\frac{R}{r_o}\right)$$

where R is the radius of a cylinder centered on the dislocation line and r_o is the core radius. K is a constant depending on the elastic moduli and orientation of the dislocation line. (In the isotropic case, $K = [\mu/(1 -v)](1 -v\cos^2\theta)$ where μ is the shear modulus, v is the Poisson ratio, and θ is the angle between the dislocation line and the Burgers vector.) This energy diverges as $R \rightarrow \infty$ and thus depends on the size of the crystal, but it is generally assumed that when a material contains many dislocations of opposite signs, their stress fields cancel at about half of the average dislocation separation and R is identified with this distance. The elastic energy of dislocation loops is always finite and depends logarithmically on their size. For example, in an elastically isotropic medium, the energy of a glissile planar circular loop of radius r (the Burgers vector lies in the plane of the loop) is

$$\mathrm{E}_{el}^{loop} = 2\pi r\frac{\mu b^2}{4\pi(1 -\upsilon)}\left[\ln\left(\frac{8r}{r_o}\right) -1\right]$$

It is noteworthy that this energy can be interpreted as the energy per unit length of the dislocation times the length of the dislocation loop $2\pi r$. This suggests that the increase of the energy of a dislocation ΔE, associated with an increase of its length Δl, can be written as $\Delta E=\tau\Delta l$, where τ is the energy of the dislocation per unit length. In general, τ will be different for different dislocation shapes, but when the curvature of the dislocation line is small, and this concept is usually restricted to this situation, τ is well approximated as the energy per unit length of a straight dislocation. It is generally dependent on the orientation of the dislocation line, but in many analyses it has been approximated by a constant of the order of $\mu b^2/2$. Since $\tau=\Delta E/\Delta l$, it also has the meaning of a line tension, in analogy with the behavior of a taut string, and this approach to evaluation of the energy change with the change in dislocation length is called the line tension approximation. (Since the energy of the dislocation depends on the angle θ between the dislocation line and its Burgers vector, a more rigorous expression for the line tension is $\tau = \mathrm{E} +\partial^2\mathrm{E}/\partial\theta^2$, analogously as in the case of anisotropic surface tension. This is not essential when using isotropic elasticity when τ is always positive and $\tau\approx\mathrm{E}$ is a good approximation. However, in highly anisotropic crystals the more rigorously determined line tension may even become negative for certain orientations. In this case, the dislocations decrease their energy by increasing their length and changing orientation. This has been observed, for example, in β-brass.)

Forces on Dislocations and Interaction between Dislocations

According to the Colonnetti principle there is no elastic interaction between internal and external stresses, that is, the response of a medium to external loading is the same whether it is self-stressed or not. However, if the source of internal stresses is displaced, the external stress may be doing work. This is what happens in the case of a dislocation. Its motion induces the relative displacement of two parts of the body by the Burgers vector within the region swept by the dislocation. One may consider an element of the dislocation line $\boldsymbol{\Delta l}$ that is displaced by a vector $\boldsymbol{\Delta r}$ in a body subject to an external stress σ_{ij}^{e}. The area within which the material has been displaced by the Burgers vector is $\Delta S = |\Delta r\Delta l|$ and the unit vector normal to this surface has components $n_j = \varepsilon_{jlk}\Delta r_l\Delta l_k/\Delta S$

(Einstein summation convention is used). When displacing the material the external stress produced work $\Delta W = -\sigma^{e}_{ij} n_j b_i \Delta S = -\sigma^{e}_{ij} b_i \varepsilon_{jlk} \Delta r_l \Delta l_k$. This can be expressed alternatively as $\Delta W = F_l \Delta r_l |\Delta l|$ with

$$F_l = \varepsilon_{ljk} \sigma^{e}_{ij} b_i \varsigma_k$$

where ς_k is the k component of the unit vector parallel to the dislocation line. This expression can be interpreted such that F_l is the l component of the force, called the Peach–Koehler force, by which the stress σ^{e}_{ij} acts on the dislocation per unit length. The physical meaning of this force is that $F_l \Delta r_l$ is the work done when the dislocation of unit length is displaced by $\Delta \boldsymbol{r}$, produced by the stress σ^{e}_{ij} that is doing work when the material is being displaced by the Burgers vector in the area swept by the dislocation. For example, in the case of an edge dislocation parallel to the axis x_3 and the Burgers vector b parallel to the axis x_1, $F_1 = \sigma^{e}_{12} b$ and $F_2 = -\sigma^{e}_{11} b$. The component F_1 and thus the shear stress σ^{e}_{12} drive the glide in the slip plane $x_1 x_3$, and the component F_2 and thus the tensile stress σ^{e}_{11} drive the climb perpendicular to the slip plane.

When using the Peach–Koehler formula, it is immaterial whether σ^{e}_{ij} is an externally imposed stress field or the stress arising from another internal source of stresses. Thus, if σ^{e}_{ij} is identified with the stress associated with another dislocation, this formula determines the force between the two dislocations. The interaction energy between two dislocations marked, respectively (1) and (2), separated by a distance r, can then be evaluated as the work done when the dislocation (2) is brought in from a distance R, against the force $F^{(1-2)}$ exerted on dislocation (2) by the dislocation (1). This force obviously decreases as $1/r$. The interaction energy per unit length of the dislocations is then $E^{int}_{(1-2)} = -\int_{R}^{r} F^{(1-2)} dr$.This interaction energy, proportional to $\ln(R/r)$, could also be evaluated as the part of the elastic energy corresponding to the cross terms between the stress and strain fields of dislocations (1) and (2), respectively. Similarly, elastic interaction between dislocations and other defects inducing internal stresses, such as inclusions, cracks, stress inducing point defects, is determined.

Dislocation Multiplication

Consider first the homogeneous nucleation of a circular glissile dislocation loop. The energy of such loop as a function of its radius is given above. The work done by the shear stress σ parallel to the Burgers vector acting in the plane of the loop during the growth of the loop is $\sigma b \pi r^2$. If the loop is to form and grow spontaneously, this work has to exceed its elastic energy already at the stage when the loop radius is only slightly larger than the radius of the core. Consider, for example, that this has to occur when $r{=}2r_o$. The condition for spontaneous formation of the loops is then $\sigma = \mu b / (4\pi(1-\upsilon) r_o)(\ln 16 - 1)$. Since $r_o \approx b$, the stress needed for the dislocation nucleation is (taking $v = 1/3$) $\sigma \approx 0.2\mu$, which is of the same order of magnitude as the ideal shear strength of materials. This is a very high stress, and in most metallic, covalent, and even in ionic materials the plastic flow and intensive dislocation multiplication occur at stresses three to five orders of magnitude lower. Thus, homogeneous nucleation of individual dislocation loops cannot be the usual mechanism of dislocation nucleation. However, a collective homogeneous nucleation at finite temperatures by the mechanism akin to the Kosterlitz–Thouless transition is a possibility albeit not yet unequivocally proven.

An alternative heterogeneous mechanism, known as the Frank–Read source, requires stresses much lower than the ideal shear strength of the material. This process of generation of dislocations is shown schematically in Figure 1. A dislocation lying in a glide plane is pinned at two points (marked by bold dots), for example owing to intersection with dislocations in different glide planes.

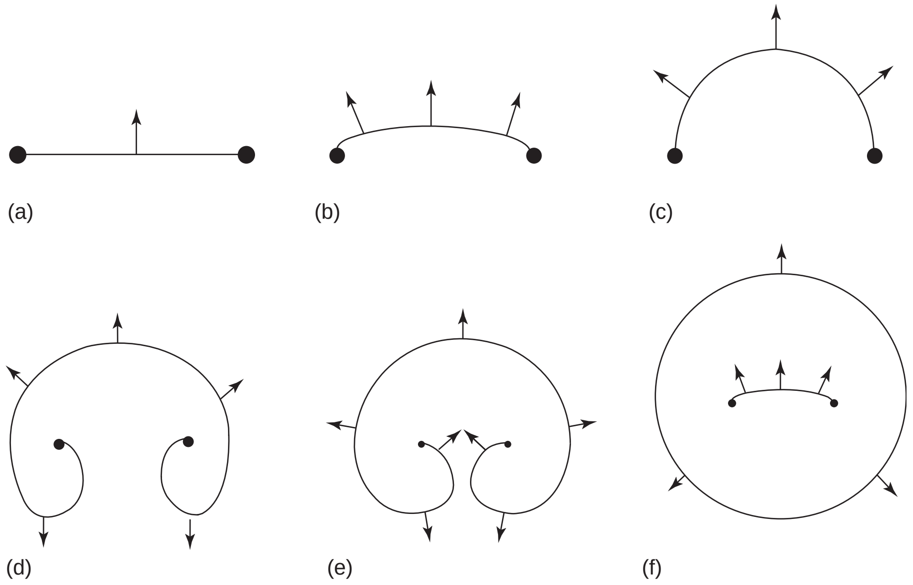

Figure 1 Successive stages in the operation of a double-needed Frank–Read dislocation source.

If these points are fixed, the dislocation can bow out under the action of a shear stress and adopt the successive configurations shown in (Figure 1b–1f). Eventually the two segments of opposite sign meet (Figure 1e), mutually annihilate, and a closed dislocation loop is produced (Figure 1f). A line segment between the pinning points remains available to repeat the whole process. The bowing out of the dislocation is opposed by the line tension of the dislocation that pulls the dislocation back by the force (per unit length) equal to $\tau\kappa$, where κ is the curvature of the line. In the isotropic case, the curvature is the largest when the dislocation forms the half-circle of radius d, where $2d$ is the separation of the pinning points (Figure 1c). Thus, the condition for the onset of the operation of the Frank–Read source is $\sigma b = \tau/d$. Taking $\tau = \mu b^2/2$, the stress needed for the operation of the source is $\sigma = \mu b/2d$. Since d may be three or four orders of magnitude larger than b, this leads to a stress that is several orders of magnitude lower than the ideal shear strength of the material, in agreement with experimental observations. Hence, Frank–Read-type dislocation sources, the geometrical configurations of which may be more complex than that in Figure 1, represent the principal mechanism of dislocation multiplication during deformation. Nevertheless, homogeneous dislocation nucleation may still occur in the case where no sources are available. However, the stresses then reach the level of the ideal shear strength. This occurs, for example, in nanoindentation.

Dislocation Dissociation and Stacking Faults

A vital characteristic of dislocations in crystalline materials is their possible dissociation into partial dislocations with Burgers vectors smaller than the lattice vector. Such dislocation splitting can occur if the displacements corresponding to the Burgers vectors of the partials lead to the formation of metastable planar faults which then connect the partials. The reason for the splitting is, of course, the decrease of the dislocation energy when it is divided into dislocations with smaller Burgers vectors. For example, if the dislocation with the Burgers vector $\boldsymbol{b}$ splits into two partials with Burgers vectors b_1 and b_2, such that $\mathrm{b} = \mathrm{b}_1 + \mathrm{b}_2$ and the angle between the vectors b_1 and b_2 is acute, then $b^2 > b_1^2 + b_2^2$. Since the elastic energy of a dislocation is proportional to the square of its Burgers vector, the self-energy of the total dislocation is larger than that of two partials. This is the basis of the so-called b^2 criterion for estimation whether a dissociation is energetically favorable. However, to determine the energy balance precisely, one has to consider also the interaction energy between partials and the energy of the planar fault formed between them. A simple example is splitting of $1/2\langle 1\,1\,0\rangle$ dislocations into two Shockley partials with the Burgers vectors $1/6\langle 1\,1\,2\rangle$ on $\{111\}$ planes. The planar fault formed by the $1/6\langle 1\,1\,2\rangle$ displacement is an intrinsic stacking fault. The stacking of $\{111\}$ planes in an ideal face-centered cubic (f.c.c.) lattice can be described as a repeat sequence …ABCABCABC… and the $1/6\langle 1\,1\,2\rangle$ displacement between layers B and C produces the stacking sequence …ABCAB | ABCABC…; this corresponds to the stacking fault marked by |.

In general, stacking-fault-like defects can be very conveniently analyzed using the notion of γ-surfaces (Stacking-fault-like defects include not only stacking faults but also other planar defects such as antiphase domain boundaries and complex stacking faults encountered in ordered alloys and compounds). To introduce the idea of γ-surfaces, a generalized stacking fault is defined first: imagine that the crystal is cut along a given crystallographic plane and the upper part displaced with respect to the lower part by a vector $\boldsymbol{u}$, parallel to the plane of the cut, as shown in Figure 2. The fault created in this way is called the "generalized stacking fault" and it is not, in general, metastable. The energy of such fault, $\gamma(u)$, can be evaluated using atomistic methods and/or density-functional theory based approaches; relaxation perpendicular to the fault has to be carried in such calculations. Repeating this procedure for various vectors $\boldsymbol{u}$ within the repeat cell of the given crystal plane, an energy–displacement surface can be constructed, commonly called the γ-surface. The local minima on this surface determine the displacement vectors of all possible metastable stacking-fault-like defects, and the values of γ at these minima are the energies of these faults.

Symmetry arguments can be utilized to assess the general shape of these surfaces. If a mirror plane of the perfect lattice perpendicular to the plane of the generalized stacking fault passes through the point corresponding to a displacement $\boldsymbol{u}$, the first

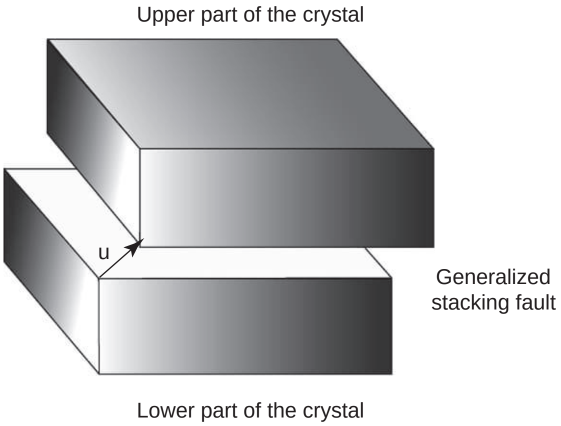
Upper part of the crystal
u
Generalized stacking fault
Lower part of the crystal

Figure 2 Formation of the generalized stacking fault.

derivative of the γ-surface along the normal to this mirror plane vanishes owing to the mirror symmetry. This implies that the γ-surface will possess extrema (minima, maxima, or inflexions) for those displacements, for which there are at least two nonparallel mirror planes of the perfect lattice perpendicular to the fault. Whether any of these extrema corresponds to minima, and thus to metastable faults, can often be ascertained by considering the change in the nearest neighbor configuration produced by the corresponding displacement. Hence, the symmetry-dictated metastable stacking-fault-like defects can be ascertained on a crystal plane by analyzing its symmetry. Such faults are then common to all materials with a given crystal structure. The intrinsic stacking faults in f.c.c. crystals are symmetry-dictated since three mirror planes of the $\{101\}$ type pass through the points that correspond to the displacements $1/6\langle 1\,1\,2\rangle$. However, other minima than those associated with symmetry-dictated extrema may exist in any particular material. These cannot be anticipated on crystallographic grounds, and their existence depends on the details of atomic interactions and can only be revealed by calculations of the γ-surface.

The primary significance of the dislocation dissociation is that it determines uniquely the slip planes, identified with the planes of splitting and corresponding stacking-fault-like defects, and, consequently, the operative slip systems. The fact that $\{111\}$ planes are the slip planes in f.c.c. materials is a typical example. As discussed above, metastable stacking faults always exist on these planes and since their energy is in many cases relatively low, dislocations split in $\{111\}$ planes and are confined to them.

Dislocation Cores

It has already been mentioned above that every crystal dislocation possesses a core region in which the linear elasticity does not apply and the structure and properties of the core can only be fully understood when the atomic structure is adequately accounted for. When a dislocation glides, its core undergoes changes that are the source of an intrinsic lattice friction. This friction is periodic with the period of the crystallographic direction in which the dislocation moves. The applied stress needed to overcome this friction at 0 K temperature is called the Peierls stress and the corresponding periodic energy barrier is called the Peierls barrier.

In general, the dislocation core structure can be described in terms of the relative displacements of atoms in the core region. These displacements are usually not distributed isotropically but are confined to certain crystallographic planes. Two distinct types of dislocation cores have been found, depending on the mode of the distribution of significant atomic displacements. When the core displacements are confined to a single crystallographic plane, the core is planar (a more complex planar core, called zonal, may be spread into several parallel crystallographic planes of the same type). Dislocations with such cores usually glide easily in the planes of the core spreading and their Peierls stress is commonly low. In contrast, if the core displacements spread into several nonparallel planes of the zone of the dislocation line, the core is nonplanar, extended spatially. The glide planes of dislocations with such cores are often not defined uniquely, their Peierls stress is high, and their glide well below the melting temperature is enabled by thermal activation over the Peierls barriers.

A planar dislocation core can be regarded as a continuous distribution of dislocations in the plane of the core spreading. The reason for the core extension is the decrease of the dislocation energy when it is redistributed into dislocations with smaller Burgers vectors. Such approach to the analysis of the dislocation core is the basis of the Peierls–Nabarro model. If the coordinate system in the plane of the core spreading is chosen such that the axes x_1 and x_2 are parallel and perpendicular to the dislocation line, respectively, the corresponding density of continuous distribution of dislocations has two components: $\rho_\alpha = \partial u_\alpha / \partial x_2$ $(\alpha = 1, 2)$, where u_α is the α-component of the displacement vector $\boldsymbol{u}$ in the x_1, x_2 plane. Owing to the dislocation distribution, the displacement $\boldsymbol{u}$ increases gradually in the direction x_2 from zero to the Burgers vector so that $\int_{-\alpha}^{+\alpha} \rho_\alpha \mathrm{d}x_2 = b_\alpha$, where b_α is the corresponding component of the Burgers vector. In the continuum approximation, the elastic energy of such dislocation distribution can be expressed as the interaction energy of the dislocation distribution with itself:

$$\mathrm{E}_{\mathrm{el}} = \sum_{\alpha,\beta=1}^{2} \int_{-\alpha}^{+\alpha} \int_{-\alpha}^{+\alpha} K\alpha\beta \rho_\alpha \rho_\beta \ln(|\mathrm{x}_2 - \mathrm{x}_2'|)\mathrm{dx}_2 \mathrm{dx}_2'$$

where $K_{\alpha\beta}$ are constants depending on the elastic moduli and orientation of the dislocation line. On the atomic scale, the displacement across the plane of the core spreading causes a disregistry that leads to an energy increase. The displacement $\boldsymbol{u}$ produces locally a generalized stacking fault, and in the local approximation the energy associated with the disregistry can be approximated as

$$\mathrm{E}_\gamma = \int_{-\alpha}^{+\alpha} \gamma(u)\mathrm{dx}_2$$

where $\gamma(u)$ is the energy of the γ-surface for the displacement $\boldsymbol{u}$. The continuous distribution of dislocations describing the core structure is then found by the functional minimization of the total energy $\mathrm{E}_{\mathrm{tot}} = \mathrm{E}_{\mathrm{el}} + \mathrm{E}_\gamma$ with respect to the displacement $\boldsymbol{u}$. When the displacement vector is always parallel to the Burgers vector, the Euler equation corresponding to the condition $\delta \mathrm{E}_{\mathrm{tot}} = 0$ leads to the well-known Peierls equation

$$\mathrm{K} \int_{-\alpha}^{+\alpha} \frac{1}{\mathrm{x}_2 - \mathrm{x}_2'} \frac{\mathrm{d}u}{\mathrm{d}x_2'} \mathrm{d}x_2' = -\frac{\partial \gamma}{\partial u}$$

where u is the displacement in the direction of the Burgers vector and K is a constant depending on the elastic moduli and orientation of the dislocation line; in the isotropic elasticity K is given earlier. In the original Peierls–Nabarro model, $\partial\gamma/\partial u$ was taken as a sinusoidal function and the Peierls equation then has an analytical solution

$$u = \frac{b}{2\pi} \tan^{-1}\left(\frac{x_2}{\zeta}\right)$$

where 2ζ measures the width of the core (for $-\zeta > x_2 > \zeta$, the disregistry is greater than half its maximum value) and it is proportional to the separation of the crystal planes into which the core spreads. The Peierls stress evaluated in the framework of this model is

$$\tau_{\mathrm{P}} = \frac{2\mu}{\alpha}\exp(-4\pi\zeta/b)$$

where μ is the shear modulus and α a constant of the order of 1. This stress is very small even when the core is very narrow; for example, if $\zeta = b$, $\tau_{\mathrm{P}} \approx 10^{-5}\mu$. This is a general characteristic of the planar cores and this is the reason why in f.c.c. metals, in which dislocations possess planar cores, the Peierls stress is practically negligible.

The nonplanar cores can be divided into two classes: crosslip and climb cores. In the former case, the core displacements lie in the planes of core spreading, whereas in the latter case, they possess components perpendicular to the planes of spreading. Climb cores are less common and are usually formed at high temperatures by a climb process. The best-known example of the crosslip core is the core of the $1/2\langle 1\,1\,1\rangle$ screw dislocations in body-centered cubic (b.c.c.) metals that is spread into three $\{110\}$ planes intersecting along the $\langle 1\,1\,1\rangle$ direction. Figure 3 shows two alternate structures of such core. The core shown in Figure 3a is spread asymmetrically into the $(\bar{1}\ 0\ 1)$,$(0,\ \bar{1}, 1)$, and $(\bar{1}\ 1\ 0)$ planes that belong to the $[1\,1\,1]$ zone and is not invariant with respect to the $[1\ 0\ \bar{1}]$ diad and another energetically equivalent configuration, related by this symmetry, operation exists. The core in Figure 3b is invariant with respect to the $[1\ 0\ \bar{1}]$ diad. These core structures were found by atomistic calculations employing (1) central-force many-body potentials and (2) a tight binding and/or density-functional theory based approach, respectively. Atomistic calculations employing appropriate descriptions of atomic interactions are the principal tool for investigations of such cores since direct observations are often outside the limits of experimental techniques. The example presented here shows that the structure of such cores is not determined solely by the crystal structure but may vary from material to material even when they crystallize in the same structure. The Peierls stress of dislocations with these cores is commonly several orders of magnitude higher than that of dislocations with planar cores. Furthermore, the movement of the dislocations is frequently affected not just by the shear stress parallel to the Burgers vector in the slip plane but by other stress components. Thus, the deformation behavior of materials with nonplanar dislocation cores may be very complex, often displaying unusual orientation dependencies and breakdown of the Schmid law. The nonplanar dislocation cores are the more common the more complex is the crystal structure, and thus these cores are more prevalent than planar cores. In this respect, f.c.c. materials (and also some hexagonal close-packed (h.c.p.) materials with basal slip) in which the dislocations possess planar cores and, consequently, the Peierls stress is very low, are a special case rather than a prototype for more complex structures.

Additional complex features of the dislocation core structures arise in covalent crystals where the breaking and/or readjustment of the bonds in the core region may be responsible for a high lattice friction stress, and in ionic solids where the cores can be charged which then strongly affects the dislocation mobility. Such dislocation cores affect not only the plastic behavior but also electronic and/or optical properties of covalently bonded semiconductors and ionically bonded ceramic materials.

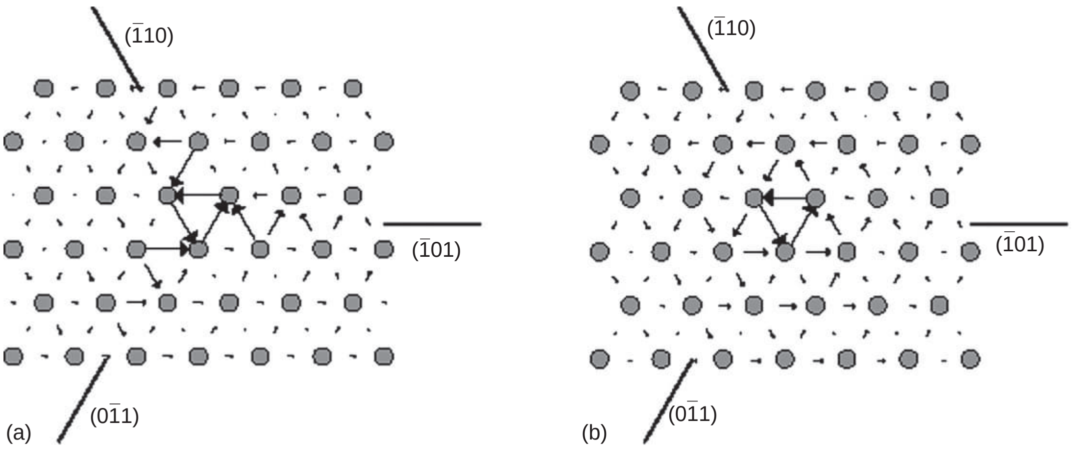

Figure 3 Two alternate core structures of the 1/2 [1 1 1] screw dislocation depicted using differential displacement maps. The atomic arrangement is shown in the projection perpendicular to the direction of the dislocation line ([1 1 1]) and circles represent atoms within one period. The [1 1 1] (screw) component of the relative displacement of the neighboring atoms produced by the dislocation is represented by an arrow between them. The length of the arrows is proportional to the magnitude of these components. The arrows, which indicate out-of-plane displacements, are always drawn along the line connecting neighboring atoms and their length is normalized such that it is equal to the separation of these atoms in the projection when the magnitude of their relative displacement is equal to |1/6 [1 1 1]|.

Further Reading

Colonnetti G (1915) *Accadutti. Licwinaz R. C.* 24: 404.
Eshelby JD (1956) In: Seitz F and Turnbull D (eds.) *Solid State Physics*, vol. 3, p. 79. New York: Academic Press.
Friedel J (1964) *Dislocations*. Oxford: Pergamon.
Hirth JP and Lothe J (1982) *Theory of Dislocations*, 2nd edn New York: Wiley.
Hull D and Bacon DJ (2001) *Introduction to Dislocations*. Oxford: Butterworth-Heinemann.
Khantha M, Pope DP, and Vitek V (1994) *Physical Review Letters* 73: 684.
Kléman M and Lavrentovich OD (2003) *Soft Matter PhysicsAn Introduction*. New York: Springer.
Kosterlitz JM and Thouless DJ (1973) *Journal of Physics C: Solid State Physics* 6: 1181.
Lardner RW (1974) *Mathematical Theory of Dislocations and Fracture*. Toronto: University of Toronto Press.
Nabarro FRN (1967) *Theory of Crystal Dislocations*. Oxford: Clarendon Press.
Orowaon E (1934) *Zeitschrift für Physik* 89: 634.
Paidar V and Vitek V (2002) In: Westbrook JH and Fleisher RL (eds.) *Intermetallic Compounds: Principles and Practice*, vol. 3, p. 437. New York: Wiley.
Peach MO and Koehler JS (1950) *Physical Review* 80: 436.
Polanyi M (1934) *Zeitschrift für Physik* 89: 660.
Taylor GI (1934) *Proceedings of Royal Society London A* 145: 362.
Vitek V (2004) *Philosophical Magazine* 84: 415.
Volterra V (1907) *Ann. Sci. Ec. Norm. Sup. Paris* 24: 401.

Lattice Dynamics: Anharmonic Effects

MI Katsnelson, Radboud University Nijmegen, Nijmegen, The Netherlands

© 2005 Elsevier Ltd. All rights reserved.

This is an update of M.I. Katsnelson, Lattice Dynamics: Anharmonic Effects, Editor(s): Franco Bassani, Gerald L. Liedl, Peter Wyder, Encyclopedia of Condensed Matter Physics, Elsevier, 2005, Pages 77–82, ISBN 9780123694010, https://doi.org/10.1016/B0-12-369401-9/00512-X.

Introduction 411
Formulation of the Problem 411
Thermodynamics 412
Thermal Expansion 412
Temperature Dependence of Elastic Moduli 413
Lattice Heat Capacity at High Temperatures 413
Phonon Spectra and Damping 413
Temperature Dependences of Phonon Frequencies 413
Phonon Damping 414
Transport Properties 415
Further Reading 415

Introduction

Crystal lattice dynamics is based on the concept of phonons, that is, weakly interacting waves of atomic (or ionic) vibrations and corresponding quasiparticles (according to a corpuscular-wave dualism of the quantum physics, any excitation wave in a system can also be described as a particle). Due to the smallness of typical atomic displacements, $\bar{u}$ in crystals in comparison with interatomic distances d, one can pass rigorously from a problem of strongly interacting "particles" forming the crystal (atoms, ions, or molecules) to a problem of weakly interacting "quasiparticles" (phonons). In the leading order in the smallness parameter $\eta = \bar{u}/d$, the crystal lattice dynamics and thermodynamics can be described in terms of an ideal phonon gas (harmonic approximation). For the ground state, the harmonic approximation can be justified rigorously on the basis of the adiabatic (Born–Oppenheimer) approximation of quantum mechanics due to the smallness of the ratio of the electron mass, m to the atomic (or ionic) mass M. With the increase in temperature T, the parameter η increases as well; however, due to a semi-empirical Lindemann criterion $\eta \simeq 0.1$ at the melting point $T = T_{\mathrm{m}}$, higher-order contributions to thermodynamic properties are usually small up to the melting temperature. This statement is true for most of the average characteristics. At the same time, for some peculiar modes, the harmonic approximation can be completely inadequate, especially in the vicinity of some structural transformations, such as ferroelectric phase transitions or martensitic transformations in metals (soft modes). It is not sufficient also for quantum crystals, such as solid He^3 and He^4. Even in a generic case, some phenomena can be understood only beyond the picture of the ideal phonon gas, which means beyond the harmonic approximation. All these phenomena are called anharmonic. There are anharmonic effects in the crystal lattice thermodynamics (thermal expansion, temperature dependences of elastic moduli, etc.), kinetics (phononphonon scattering processes which are responsible for the thermal conductivity of insulators), and dynamics (phonon damping and temperature dependences of the phonon frequencies measured by the inelastic neutron scattering method).

Formulation of the Problem

In the adiabatic approximation, one can split the quantum-mechanical problem of the crystal into an electronic (a solution of the Schrödinger equation for fixed coordinates of nuclei $\{\boldsymbol{r}_j\}$) and a nuclear one which is the base of the theory of crystal lattice properties. Keeping in mind the smallness of the atomic displacements $\eta<1$, one can expand the energy of the nuclei $V(\{\boldsymbol{r}_j\})$ into the displacement vectors $\boldsymbol{u}_j = \boldsymbol{r}_j - \boldsymbol{R}_j$, $\boldsymbol{R}_j$ being the equilibrium lattice positions:

$$V(\{\boldsymbol{r}_j\}) = V_0 + \frac{1}{2}\sum_{j_1 j_2 \alpha_1 \alpha_2} V_{j_1 j_2}^{\alpha_1 \alpha_2} \boldsymbol{u}_{j_1}^{\alpha_1} \boldsymbol{u}_{j_2}^{\alpha_2} + \frac{1}{6}\sum_{j_1 j_2 \alpha_1 \alpha_2} V_{j_1 j_2 j_3}^{\alpha_1 \alpha_2 \alpha_3} \boldsymbol{u}_{j_1}^{\alpha_1} \boldsymbol{u}_{j_2}^{\alpha_2} \boldsymbol{u}_{j_3}^{\alpha_3} + \ldots, V_{j_1 \ldots j_n}^{\alpha_1 \ldots \alpha_n} = \left(\frac{\partial^n V}{\partial \boldsymbol{u}_{j_1}^{\alpha_1} \ldots \boldsymbol{u}_{j_n}^{\alpha_n}} \right)_{\boldsymbol{u}=0} \qquad [1]$$

where α_j are Cartesian indices and the linear term is absent due to the equilibrium conditions. The harmonic approximation corresponds to taking into account only the quadratic term in the expansion [1]. Then the nuclear Hamiltonian, which is the sum of the potential energy V and the kinetic energy of nuclei, can be represented as a sum of the Hamiltonians of independent oscillators (phonons) by the transformation

$$\boldsymbol{u}_j = \sum_{\lambda} \sqrt{\frac{\hbar}{2 M_j N_0 \omega_\lambda}} \mathrm{A}_\lambda \boldsymbol{e}_\lambda \exp\left(\mathrm{i}\boldsymbol{q}\boldsymbol{R}_j\right), \mathrm{A}_\lambda = b_\lambda + b_{-\lambda}^{\dagger} \qquad [2]$$

where N_0 is the number of unit cells in the crystal, M_j is the mass of the jth nucleus, $\lambda \equiv \boldsymbol{q}\xi$ are the phonon quantum numbers ($\boldsymbol{q}$ is the wave vector running the Brillouin zone and ξ is the polarization index, $-\lambda \equiv -\boldsymbol{q}\xi$), $\boldsymbol{e}_\lambda$ is the polarization vector, b_λ and $b_\lambda^\dagger$ are the annihilation and creation phonon operators. In the phonon representation, the total Hamiltonian of the crystal lattice has the form

$$H = V_0 + H_0 + \sum_{k=3}^{\infty} H^{(k)}, H_0 = \sum_\lambda \hbar\omega_\lambda \left(b_\lambda^\dagger b_\lambda + \frac{1}{2}\right), H^{(k)} = \sum_{\lambda_1 \ldots \lambda_k} \frac{\Phi^{(k)}_{\lambda_1 \ldots \lambda_k}}{k!} A_{\lambda_1} \ldots A_{\lambda_k} \qquad [3]$$

where H_0 is the Hamiltonian of the ideal phonon gas (the harmonic approximation) and the multiphonon scattering matrix elements $\Phi^{(k)}_{\lambda_1 \ldots \lambda_k}$ are proportional to the *kth* derivatives of the potential energy and the factors $\sqrt{\hbar/2M_j\omega_{\lambda_i}}$. These matrix elements describe the processes of phonon–phonon interaction, such as a merging of two phonons into one or, vice versa, a decay of a phonon into two (k=3), scattering of two phonons into two new states (k=4), etc. The anharmonic effects connected with these interactions are called self-anharmonic. There is also another kind of anharmonic effect which is connected to the dependence of the phonon frequencies ω_λ on the interatomic distances in the Hamiltonian H_0. These effects are called quasiharmonic. They are characterized by the microscopic Grüneisen parameters

$$\gamma_\lambda = -\frac{\partial \ln \omega_\lambda}{\partial \ln \Omega} \qquad [4]$$

where Ω is the crystal volume. For noncubic crystals, the dependence of ω_λ on shear deformations should also be considered. The point is that for harmonic oscillators described by the quadratic potential energy and, correspondingly, by linear interatomic forces, the frequencies are not dependent either on the amplitudes of oscillations or on the equilibrium positions. Due to nonlinear (anharmonic) effects, there are renormalizations of the frequencies. Up to the lowest order η^2, one should take into account the quasiharmonic effects and the self-anharmonic effects with k=3 and 4.

Thermodynamics

Thermal Expansion

Thermal expansion, characterized by the coefficient,

$$\alpha_p = \frac{1}{\Omega}\left(\frac{\partial \Omega}{\partial T}\right)_p \qquad [5]$$

(T is the temperature and p is the pressure) equals to zero in harmonic approximation. This can be easily proved from the Gibbs distribution for the potential energy V, which is quadratic in the atomic displacements $\boldsymbol{u}_j$ (and, moreover, if it is just an arbitrary even function of $\boldsymbol{u}_j$). It can be calculated by using the known thermodynamic identity

$$\left(\frac{\partial \Omega}{\partial T}\right)_p = -\left(\frac{\partial S}{\partial p}\right)_T \qquad [6]$$

where S is the entropy; as a consequence, due to the third law of thermodynamics, the thermal expansion coefficient should vanish at $T \to 0$. If one calculates the entropy in harmonic approximation but with the phonon frequencies dependent on the volume (quasiharmonic approximation), one can derive the Grüneisen law

$$\alpha_p = \frac{\gamma(T) C_V(T)}{\Omega B_T} \qquad [7]$$

where $B_T = -\Omega(\partial p/\partial \Omega)_T$ is the isothermal bulk modulus,

$$\gamma(T) = \frac{\sum_\lambda \gamma_\lambda C_\lambda}{\sum_\lambda C_\lambda}, C_\lambda = \left(\frac{\hbar\omega_\lambda}{k_B T}\right)^2 \frac{\exp(\hbar\omega_\lambda/k_B T)}{[\exp(\hbar\omega_\lambda/k_B T) - 1]^2} \qquad [8]$$

is the macroscopic Grüneisen parameter (which is temperature independent assuming that γ_λ=const and $C_V(T) = k_B \sum_\lambda C_\lambda$ is the constant-volume lattice heat capacity. It follows from eqn [7] that the temperature dependence of the thermal expansion coefficient at low and high temperatures is the same as for the heat capacity: $\alpha_p \sim T^3$ at $T \ll \theta_D$ (θ_D is the Debye temperature) and $\alpha_p \simeq$ const at $T \geqslant \theta_D$.

For noncubic crystals, one should introduce parameters characterizing the anisotropy of the thermal expansion $\alpha_i = \partial u_i/\partial T$, where u_i are different deformations, for example, for uniaxial crystals with c-axis different from a- and b-axes, one can introduce $du_1 = d\ln\Omega$ and $du_2 = d\ln(c/a)$. As a generalization of eqn [6], one can prove from the equilibrium conditions at finite temperatures

$$\alpha_i = \sum_j (B^{-1})_{ij} \left(\frac{\partial S}{\partial u_j}\right)_T \qquad [9]$$

where $B_{ij} = (1/\Omega)\left(\partial^2 F/\partial u_i \partial u_j\right)$ is the matrix of isothermal elastic moduli and F is the free energy. In particular, for the uniaxial crystals

$$\begin{aligned}\left(\frac{\partial \ln c}{\partial T}\right) &= \frac{1}{3BB_{22}}\left[(B_{22}-2B_{12})\frac{\partial S}{\partial u_1}+(2B_{11}-B_{12})\frac{\partial S}{\partial u_2}\right]\\ \left(\frac{\partial \ln a}{\partial T}\right) &= \frac{1}{3BB_{22}}\left[(B_{22}+2B_{12})\frac{\partial S}{\partial u_1}-(B_{11}+B_{12})\frac{\partial S}{\partial u_2}\right]\end{aligned} \qquad [10]$$

where $B = B_{11} - B_{12}^2/B_{22}$ is the bulk modulus of the uniaxial crystal.

Temperature Dependence of Elastic Moduli

Temperature dependence of the elastic moduli B_{ij} is another important anharmonic effect. This temperature dependence in quasiharmonic approximation results from the ideal phonon gas contribution to the free energy, $F_{\mathrm{ph}} = -k_{\mathrm{B}}T\sum_{\lambda}\ln[2\sinh(\hbar\omega_{\lambda}/2k_{\mathrm{B}}T)]$, and from the volume dependence of the electronic contributions to the moduli. As a result, both terms behave as $\delta B_{ij} \propto -T^4$ at $T \ll \theta_{\mathrm{D}}$ and $\delta B_{ij} \propto -T$ at $T \gg \theta_{\mathrm{D}}$. Normally, this contribution is negative (elastic moduli decrease with the temperature increase), but for some shear moduli in peculiar cases an opposite behavior sometimes takes place (acoustic soft modes), usually near the structural phase transitions. Empirically, for many cubic crystals the trigonal shear modulus B_{44} at the melting point is 55% of its value at zero temperature (Varshni melting criterion).

Lattice Heat Capacity at High Temperatures

In harmonic approximation, the molar constant-volume heat capacity at $T \gtrsim \theta_{\mathrm{D}}$ is independent of both the temperature and the chemical composition of the crystal: $C_V = 3R$ (Dulong–Petit law, $R \simeq 8.3144\,\mathrm{J\ mol^{-1}K^{-1}}$ is the gas constant). Self-anharmonic effects lead to linear temperature dependence of the heat capacity, $\delta C_{\mathrm{V}} \sim R\eta^2 \sim R(k_{\mathrm{B}}T/E_{\mathrm{coh}})$ where E_{coh} is a typical energy of the chemical bonding. These terms arise from both three-phonon and four-phonon processes (the second-order perturbation effect in $H^{(3)}$ and the first-order one in $H^{(4)}$, see eqn [3]):

$$C_V^{(3)} = \frac{4k_{\mathrm{B}}^2T}{3}\sum_{\boldsymbol{kq}\xi\eta\varsigma}\frac{\left|\Phi^{(3)}_{\xi\boldsymbol{k};\,\eta\boldsymbol{q};\,\varsigma,-\boldsymbol{k}-\boldsymbol{q}}\right|^2}{\hbar^3\omega_{\xi\boldsymbol{k}}\omega_{\eta\boldsymbol{q}}\omega_{\varsigma,-\boldsymbol{k}-\boldsymbol{q}}} \qquad [11]$$

$$C_V^{(4)} = -k_B^2T\sum_{\boldsymbol{kq}\xi\eta\varsigma}\frac{\Phi^{(4)}_{\xi\boldsymbol{k};\,\xi,-\boldsymbol{k};\,\eta\boldsymbol{q};\,\eta,-\boldsymbol{q}}}{\hbar^2\omega_{\xi\boldsymbol{k}}\omega_{\eta\boldsymbol{q}}} \qquad [12]$$

The three-phonon contribution [11] is always positive (the growth of C_{V} with the increase in the temperature), whereas the four-phonon one [12] can be, in principle, of arbitrary sign. Experimental separation of the self-anharmonic contribution to the lattice heat capacity is a difficult problem since it has, in general, the same order of magnitude and temperature dependence as the difference

$$C_P - C_V = T\Omega B_T\alpha_p^2 \qquad [13]$$

(C_P is the experimentally measurable heat capacity at a constant pressure) and, in metals, as the electron heat capacity.

Phonon Spectra and Damping

Temperature Dependences of Phonon Frequencies

According to classical mechanics, for a generic nonlinear system, the oscillation frequencies are dependent on the oscillation amplitudes. Therefore, one can expect that anharmonic effects lead to the temperature-dependent phonon spectra, due to growth of average oscillation amplitudes with the increase in temperature. In quantum terms, the same effect can be described as an appearance of the phonon self-energy due to the phonon–phonon interaction processes. Up to the second order in the smallness parameter η, the temperature shift of the phonon frequency ω_{λ} is determined by the following expression:

$$\Delta\omega_{\lambda} = \Delta_{\lambda}^{(\mathrm{qh})} + \Delta_{\lambda}^{(3)} + \Delta_{\lambda}^{(4)} \qquad [14]$$

where $\Delta_{\lambda}^{(\mathrm{qh})} = -\gamma_{\lambda}\Delta\Omega(T)/\Omega$ is the quasiharmonic contribution due to the temperature dependence of the crystal volume $\Omega(T)$, and $\Delta_{\lambda}^{(3)}$ and $\Delta_{\lambda}^{(4)}$ are the contributions of the three-phonon and four-phonon processes, correspondingly:

$$\Delta^{(3)}_{\xi\boldsymbol{k}} = -\frac{1}{2\hbar^2}\mathscr{P}\sum_{\boldsymbol{q}\eta\varsigma}\left|\Phi^{(3)}_{\xi\boldsymbol{k};\eta\boldsymbol{q};\varsigma,-\boldsymbol{k}-\boldsymbol{q}}\right|^2 \times \left(\frac{1+N_{\eta q}+N_{\varsigma,\boldsymbol{k}+\boldsymbol{q}}}{\omega_{\eta q}+\omega_{\varsigma,\boldsymbol{k}+\boldsymbol{q}}+\omega_{\xi k}} + \frac{1+N_{\eta q}+N_{\varsigma,\boldsymbol{k}+\boldsymbol{q}}}{\omega_{\eta q}+\omega_{\varsigma,\boldsymbol{k}+\boldsymbol{q}}+\omega_{\xi k}} + \frac{N_{\eta q}-N_{\varsigma,\boldsymbol{k}+\boldsymbol{q}}}{\omega_{\varsigma,\boldsymbol{k}+\boldsymbol{q}}-\omega_{\eta q}-\omega_{\xi k}} - \frac{N_{\eta q}-N_{\varsigma,\boldsymbol{k}+\boldsymbol{q}}}{\omega_{\eta q}-\omega_{\varsigma,\boldsymbol{k}+\boldsymbol{q}}-\omega_{\xi k}}\right) \qquad [15]$$

$$\Delta^{(4)}_{\xi\boldsymbol{k}} = \frac{1}{2\hbar}\sum_{\boldsymbol{q}\eta}\Phi^{(4)}_{\xi\boldsymbol{k};\,\xi,-\boldsymbol{k};\,\eta\boldsymbol{q};\,\eta,-\boldsymbol{q}}(1+2N_{\eta\boldsymbol{q}}) \qquad [16]$$

where $\mathscr{P}$ is the principal value symbol and $N_{\lambda} = (\exp\hbar\omega_{\lambda}/k_{\mathrm{B}}T-1)^{-1}$ is the Planck function. At high temperatures $T \gtrsim \theta_{\mathrm{D}}$, one can use the classical asymptotic $N_{\lambda} \simeq k_{\mathrm{B}}T/\hbar\omega_{\lambda}$ and see that all three contributions in eqn [14] are linear in temperature. Usually, the

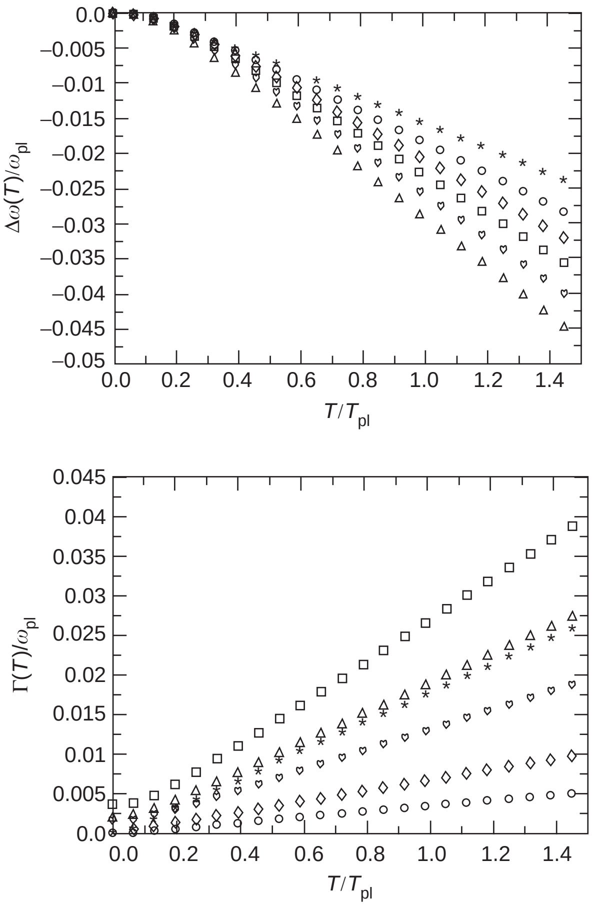

Figure 1 Temperature dependences of the frequency shifts (upper panel) and phonon damping (lower panel) for different phonon modes at the symmetric points of the Brillouin zone for face-centered cubic (f.c.c) phase of calcium. $\omega_{\text{pl}} = \left(4\pi Ze^2/M\Omega_0\right)^{1/2}$ is ionic plasma frequency, Z, M, and Ω_0 are the valency, ionic mass, and atomic volume, respectively, $T_{\text{pl}} = \hbar\omega_{\text{pl}}/k_B = 476\text{K}$ is the corresponding temperature. Asterisks and hearts label different phonon modes for *L* point, circles and triangles for *W* point, and squares and diamonds for *X* point. (From Katsnelson MI, Trefilov AV, Khlopkin MN, and Khromov KYu (2001) *Philosophical Magazine B* 81: 1893.)

phonon frequencies decrease with the temperature increase; a typical behavior is shown in Figure 1 (upper panel). However, for the soft modes, $\mathrm{d}\omega_\lambda/\mathrm{d}T > 0$, as it is illustrated by Figure 2. In the framework of the perturbation theory, this behavior is connected with the contribution $\Delta_\lambda^{(4)}$.

Phonon Damping

Beyond the harmonic approximation, the phonons cannot be considered as stable quasiparticles; for example, due to the three-phonon processes, they can decay into couples of other phonons. As a result, the phonon damping arises (which can be measured experimentally as a half-width of phonon peaks in inelastic neutron scattering spectra). In the lowest-order perturbation theory, the damping, or the inverse phonon lifetime, is equal to

$$\Gamma_{\xi k} = \frac{\pi}{2\hbar^2}\sum_{q\eta\varsigma}\left|\Phi^{(3)}_{\xi\boldsymbol{k};\eta\boldsymbol{q};\varsigma,-\boldsymbol{k}-\boldsymbol{q}}\right|^2 \left\{\left(1+N_{\eta\boldsymbol{q}}+N_{\varsigma,\boldsymbol{k}+\boldsymbol{q}}\right)\times\delta\left(\omega_{\eta\boldsymbol{q}}+\omega_{\varsigma,\boldsymbol{k}+\boldsymbol{q}}-\omega_{\xi\boldsymbol{k}}\right)+\left(N_{\eta\boldsymbol{q}}-N_{\varsigma,\boldsymbol{k}+\boldsymbol{q}}\right)\times\left[\delta\left(\omega_{\varsigma,\boldsymbol{k}+\boldsymbol{q}}-\omega_{\eta\boldsymbol{q}}-\omega_{\xi\boldsymbol{k}}\right)-\delta\left(\omega_{\eta\boldsymbol{q}}-\omega_{\varsigma,\boldsymbol{k}+\boldsymbol{q}}-\omega_{\xi\boldsymbol{k}}\right)\right]\right\} \qquad [17]$$

The delta functions in eqn [17] correspond to the energy and momentum conservation laws for the decay processes. At high temperatures $T \gtrsim \theta_D$, the damping is linear in T (see Figure 1, lower panel). Note that, both the damping and the frequency shift do not vanish at T=0 where all $N_\lambda = 0$. These residual effects are due to quantum zero-point oscillations; they are of the order of $\sqrt{m/M}$ and small, in general (with the exception of the quantum crystals). For acoustic phonons with $q \to 0$, the damping [17] is linear in q, as well as in the phonon frequency; however, this is not true for the case $ql \ll 1$, where l is the phonon mean free path. For this regime, according to general hydrodynamics consideration, the damping behaves like q^2l.

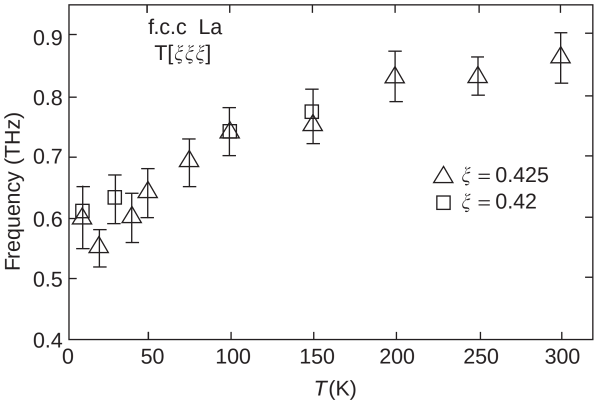

Figure 2 Temperature dependence of the phonon frequencies of the $T[\xi\xi\xi]$ phonon branch in (f.c.c) lanthanum in the soft mode region. (From Stassis C, Smith GS, Harmon BN, Ho KM, and Chen Y (1985) *Physical Review B* 31: 6298.)

For strongly anharmonic modes, the phonon damping can be comparable with the frequency; phonons are not well-defined in such a situation (high-temperature body-centered cubic (b.c.c) phases of Ti and Zr can be considered as examples). The perturbation theory reviewed here can also be insufficient under resonance conditions, where the frequency ratio for different phonons with the same wave vector is close to 1:2, 1:3, etc.

Transport Properties

If one neglects phonon–phonon interactions as well as phonon scattering by any defects (impurities, different isotopes, crystal surface, etc.) and by other quasiparticles (conduction electrons in metals, spin waves in magnetic crystals, etc.), the mean free path $l=\infty$ which means, in particular, infinitely large thermal conductivity κ (any nonequilibrium distribution of the phonon momenta and energies conserves for an ideal phonon gas). This means that for the case of perfect, isotopically homogeneous, large enough insulating crystals, the anharmonic effects should determine the values and temperature dependences of both l and κ; they are connected by a simple relation:

$$k = \frac{1}{3}\frac{C_V \bar{v} l}{\Omega} \qquad [18]$$

where $\bar{v}$ is a characteristic sound velocity. In principle, the same processes of phonon decay which are responsible for $\Gamma_{\xi \boldsymbol{k}}$ contribute to the mean free path. However, for a continuum medium theory, any process of phonon–phonon interaction cannot lead to a finite thermal conductivity, since the momentum is conserved at any individual interaction act and any redistribution of the momenta among the phonons cannot change the energy current of the phonon gas as a whole. In crystals, Umklapp processes are possible when the momentum is conserved with the accuracy of some nonzero reciprocal lattice vector $\boldsymbol{g}$, and only these processes lead to the relaxation of the energy current and to finite κ. The energy conservation law for the Umklapp processes results in the appearance of some finite activation energy so that $l \propto \exp(\text{const} \times \theta_D/T)$ at $T \to 0$. For the very small temperatures, when the phonon mean free path is larger than the crystal size L, one should replace $l \to L$ in eqn [18] and thus $\kappa \propto C_V \propto T^3$. For high temperatures $T \geqslant \theta_D$, one has $\kappa \propto l \propto 1/T$.

Further Reading

Aksenov VL, Plakida NM, and Stamenkovic S (1989) *Neutron Scattering by Ferroelectrics*. Singapore: World Scientific.
Bötger H (1983) *Principles of the Theory of Lattice Dynamics*. Berlin: Academic–Verlag.
Cowley RA (1963) The lattice dynamics of an anharmonic crystal. *Advances in Physics* 12: 421.
Cowley RA (1968) Anharmonic crystals. *Reports on Progress in Physics* 31: 123.
Kaldis E, Mihailovic D, Müller KA, and Ruani G (eds.) (1995) *Anharmonic Properties of High-T_c Cuprates*. Singapore: World Scientific.
Katsnelson MI and Trefilov AV (2002) *Crystal Lattice Dynamics and Thermodynamics*. Moscow: Atomizdat.
Katsnelson MI and Trefilov AV (2004) Nonperturbative anharmonic phenomena in crystal lattice dynamics. In: Tokuyama M and Oppenheim I (eds.) *Slow Dynamics in Complex SystemsThird International Symposium*, vol. 708, 727. AIP Conference Proceedings Series.
Leibfried G and Ludwig W (1961) Theory of anharmonic effects in crystals. In: Seitz F and Turnbull D (eds.) *Solid State Physics*, vol. 12, p. 275. New York: Academic Press.
Peierls R (2001) *Quantum Theory of Solids*. Oxford: Oxford University Press.
Vaks VG, Kravchuk SP, and Trefilov AV (1988) Microscopic theory of anharmonic effects in alkali and alkaline earth metals. *Soviet Physics – Uspekhi* 31: 474.
Varshni YP (1970) Temperature dependence of the elastic constants. *Physical Review B* 2: 3952.
Ziman JM (2001) *Electrons and PhononsThe Theory of Transport Phenomena in Solids*. Oxford: Oxford University Press.

Ceramic Materials[☆]

KP Constant, Iowa State University, Ames, IA, USA

© 2016 Elsevier Inc. All rights reserved.

This is an update of K.P. Constant, Ceramic Materials, Reference Module in Materials Science and Materials Engineering, Elsevier, 2016, ISBN 9780128035818, https://doi.org/10.1016/B978-0-12-803581-8.01122-X.

Introduction **416**
Properties **417**
Mechanical/Structural **417**
Toughened, Scratch Resistant Glass for Screens 417
Electrical **417**
Fuel Cells 418
Optical **418**
Translucent Concrete 418
Processing **419**
Additive Manufacturing of Ceramics **419**
Architectural Installations 419
Thin Film Techniques **420**
Diamond Coatings 420
Sustainable Processing **420**
Eco-Ceramics 421
Trends in Ceramic Materials **422**
Nanotechnology/MEMS 422
Bioceramics 422
Conclusion **423**
Further Reading **423**

Introduction

Although some of the earliest artifacts from ancient civilizations bear witness to man's long history of utilization of ceramic materials, modern ceramic science is advancing at an unprecedented pace. Ceramics remained an art (often with closely guarded secrets) for the majority of recorded history, and has only in the past century become the science it is today. With the pressures of increasingly demanding high-tech applications, whether smaller, larger, hotter, tougher, cleaner, brighter, or smarter, ceramics are often the material of choice.

State-of-the-art characterization and fabrication techniques allow one to achieve a new level of understanding of atomic-scale processes and capability for manipulation of atomic structure. In effect, ceramics can often be built atom-by-atom, layer-by-layer.

That said, what are ceramics? The definition is becoming increasingly more difficult to articulate. For a significant fraction of society, the definition relates to the art of making and decorating pottery, or other items of 'baked' clay. However, from the viewpoint of the scientist or engineer, ceramics are often defined by the chemistry, behavior, and/or processing methods used to create them. For example, a definition might be: an artifact made of hard, brittle, electrically insulating material produced from nonmetallic minerals by firing at high temperatures. This definition specifies chemistry, properties, and processing. While this definition is accurate for a large fraction of ceramics, it is not all-inclusive, and examples of ceramics that do not conform to one or more parts of this definition are becoming increasingly common. There are examples of ceramics (some discussed here) that are not brittle and electrically insulating, or are not made from nonmetallic minerals, or not fired at high temperatures. As an example, ceramic superconductors are among the most conductive materials known. An acceptable, but not complete, definition might be a refractory, inorganic, and nonmetallic material. Even this attempt at description is flawed, as the boundaries between biology and ceramics blur.

The field of ceramics (and all materials) is often represented as the four corners of a tetrahedron labeled structure, properties, processing, and performance. In this article, an overview of current ceramic science and engineering is presented through discussion of properties, novel processing, and general trends, with examples of the applications that demonstrate these advancements. Structure and performance are addressed within the context of both the properties and processing of these advanced ceramics.

[☆] *Change History*: May 2015. K.P. Constant. In the 'Properties' section, the portion on transparent ceramics for ballistic protection was changed to a discussion on toughened glass for touch screens. The section on photonic bandgap materials was changed to a description of light transmitting concrete. In 'Processing' – '3D rapid prototyping' was changed to 'Additive Manufacturing.' In 'Trends,' computational materials was added. Table I, Figure 1 and Figure 3 were deleted. New figures 1 and 2 were added. Figure 3 and Figure 5 are old figures.

Properties

Ceramics have long been associated with characteristic properties such as high hardness, high stiffness, resistance to high temperatures, and chemical inertness, but today's ceramics stretch conventional applications of ceramics beyond what in the past were considered their fundamental limitations. A huge body of work has been generated in the past quarter of a century, some of which is highlighted here with examples in which mechanical, electrical, and optical properties are critical. Although not represented in the examples below, ceramics are also often used in thermal and magnetic applications in which there are many examples of exciting and novel advances.

Mechanical/Structural

Ceramics are often used where high hardness is required but are usually limited by their lack of toughness. A number of innovations have improved upon this mechanical deficiency including those demonstrated in the development of high hardness, scratch resistant cover glass in handheld electronic devices. Toughness can also be improved by the use of hard coatings on tough substrates. Although carbide coatings have long been used for grinding and for cutting tools, even harder diamond coatings are becoming increasingly popular. Because the processing techniques required are the most novel aspect of that field, thin film diamond coatings are discussed in the 'processing' section.

Toughened, Scratch Resistant Glass for Screens

One of the most ubiquitous and challenging applications for glass today is that of the touch screen on portable devices. As these devices are often carried in pockets with coins and keys and often dropped, the demands on the performance of the glass are high. The primary mechanical requirements for such an application include that they be thin and light, have high transparency and scratch and impact resistance. The combination of these properties eliminates plastics because of the mechanical requirements, especially scratch resistance. The concept of toughening glass has been understood for many centuries. In fact, Prince Rupert's Drops, made by the thermal tempering of a drop of molten glass through rapid quenching in cold water, were first reported in the 17th century, though the underlying mechanism was not known. We now understand that the extreme rapid cooling places the surface of the glass in a state of mechanical compression, while the interior, cooling more slowly, is in tension. This compressive state is much stronger than unstressed glass and can also be induced chemically by ion exchange on the surface. Likewise, tempered sheet glass, made either by thermal quenching or by ion exchange has also been employed for well over a century, however significant advances continue to be made in both the development of the chemistry and the processing for the toughening of sheet glass. Current specialized glass can be produced with a hardness close to sapphire, which is 9 on the Mohs scale of hardness (compared to 7 for standard glass). A number of companies are manufacturing specialized toughened glasses, with the most well known being Gorilla Glass™, by Corning, which, according to their own literature, has been included in more than 3 billion devices. There is significant competition to produce the thinnest, toughest glass for smartphones and tablets.

While the specifics of the chemistry and processing remain a closely guarded industrial secret, in general, toughening is achieved through ion exchange. The initial glass is an aluminosilicate and is fabricated in sheets that are under a millimeter thick. The compressive stress is induced through the introduction of large ions into the surface of the glass by placing the glass in a molten potassium salt bath to replace sodium at approximately 400 °C. Other advances include antimicrobial and anti-smudge screens. Additionally, the materials must be compatible with the electrical requirements of touch screen functioning and optical transparency required for imaging. Emerging technologies promise a thin, strong, and flexible glass that can be wrapped around a device or structure. It has been reported that the chemistry and processing of some of these advanced glasses has been aided by computational modeling, a topic that will be addressed in 'Trends in Ceramic Materials'.

Beyond handheld devices but not yet available commercially, the super tough glass is also being investigated for other uses requiring larger pieces of glass, for example, in an automobile windshield. Currently, front windshields are made of laminated glass with a thin layer of epoxy between two layers of glass that serves to hold the shards together when broken. If glass toughened in the manner of that in current handheld devices, safer and better performing windshields are possible.

Electrical

Ceramics have long been used in the electronics industry as passive devices such as capacitors and insulators, and continue to be critical in those functions; however, in a variety of other electrical applications ceramics have become increasingly important. These include applications such as sensors (gas and chemical), conductive oxides (mixed conductors), and high-power/high-temperature electronic materials.

Fuel Cells

The exponential growth of portable electronic devices, cellular phones, computers, etc., provides strong motivation for the development of fuel cells and high-energy-density batteries. Fuel cells can provide clean energy for a variety of portable energy needs. Ceramic materials play a large role in the development of commercially viable products. Solid oxide, proton exchange membranes, and direct methanol fuel cells, lithium ion batteries, oxide-ion electrolytes, proton conductors, and mixed ionic/electronic conductors are all ceramic-based technologies. Solid oxide fuel cells (SOFC) are electrochemical energy conversion devices based on ion-conducting oxide electrolytes and are used in a broad spectrum of power-generation applications from small lightweight compact devices to large SOFC/turbine hybrid systems. The cells are solid-state devices operating at high temperatures. Because of this, there is great design flexibility (no liquid management required as in other 'batteries'). There are a variety of designs and geometries currently under investigation. The most common electrolyte materials include yttria (Y_2O_3) stabilized zirconia (ZrO_2), often called 8YSZ as it contains 8% yttria. This ceramic is ion conducting in both oxidizing and reducing environments. The most common anode material is a cermet (ceramic-metal composite) composed of Ni and 8YSZ. Nickel provides the electronic conductivity and catalytic activity while the 8YSZ supports the Ni particles and improves the anode thermal expansion match. The most common cathode material is a strontium-doped lanthanum manganite (Sr-doped $LaMnO_3$) – called LSM. The interconnect materials is usually doped $LaMnO_3$ or a metal that is stable in both oxidizing and reducing environments, however, metal interconnects require lower operating temperatures. The cost of these fuel cells is still a limiting factor in terms of broad applications and ways to reduce the costs are being aggressively sought, including reducing operating temperatures to allow the use of metallic interconnects and increasing the power density. Much effort has focused on the techniques to make dense ceramic coatings using the techniques of the semiconductor industry including chemical vapor deposition (CVD), electrochemical vapor deposition (EVD), physical vapor deposition (PVD), and screen printing as well as more traditional techniques such as sol–gel, tape casting, slurry casting, and centrifugal casting. The former techniques often have film quality and performance advantages, but also have low deposition rates (they are slow) and are costly. The latter techniques are efficient and economical but often result in lower-quality films. Increasingly important to the development on new fuel cell technologies is the advancement of modeling and simulation to achieve higher efficiency and energy conversion.

Optical

Although glass has long been used as an optically transparent material, and in fibers for communication and laser surgery, crystalline ceramics are gaining in importance in a variety of optical applications, including wireless technologies, microwave dielectrics, luminescent materials, and nonlinear optical materials. A novel blend of traditional and modern optical ceramics is that of light transmitting concrete. This application is a reminder that ceramics remain one of the most commonly used structural materials and that there is potential for advancement in this area as well as in more technology-based uses.

Translucent Concrete

While concrete has long been the workhorse for building infrastructure in cities and roads, it is not typically employed for its aesthetic appeal. Recently, a translucent concrete has been developed by combining traditional concrete with transparent components, usually fibers, to form an attractive, sustainable structural materials and design elements (**Figure 1**). Concrete has been used since the Roman times, and its basic components of sand or aggregate, cement and water are basically the same, although there are numerous modifications possible to effect structure and properties. In translucent concrete, optically transmitting fibers, typically

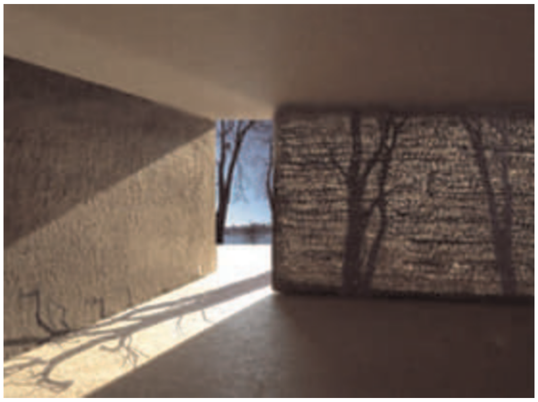

Figure 1 Architectural wall made concrete made translucent by the incorporation of glass fibers spanning the width of the wall (http://dornob.com/see-through-light-transmitting-concrete-material/#axzz2v1i4eRSM).

made from glass, but can also be made from polymers are embedded in the concrete during forming. If aligned across the thickness of the concrete, the fiber can transmit light.

Fabrication of translucent concrete can be accomplished in a number of ways. Although initially the fibers were placed manually, the process is now usually automated, reducing the cost of the product. The concrete used typically has a finer aggregate compared to traditional concrete and the fibers typically make up less than 5 vol% of the structure. The density, about 2200 kg m^{-3}, and compressive strength, 50 MPa are comparable to that standard concrete. The insulation value is slightly compromised by the presence of the fibers.

There are numerous functional advantages to this material, in addition to aesthetic appeal. Daylight could be used in building interiors without compromising privacy or energy efficiency as is usually the case with traditional windows. Additionally, as design elements, concrete and glass are considered sustainable materials as compared to wood.

Processing

The processing of advanced ceramics can be divided into two general classes with respect to the starting material – those that involve powders (powder processing) obtained by a variety of methods, and those that do not. In this section, recent advances in each method are presented through a specific example of each.

Additive Manufacturing of Ceramics

A recent advance in the forming stage of ceramic processing is that of additive manufacturing – also called 3D printing. There are a number of techniques that fall into this general category. The concept is to translate a 3D computer-generated design (CAD model) to a physical structure without the traditional step of making a mold in which to shape the product or the time and cost associated with machining a ceramic to desired dimensions. These methods can often make very complex geometries in a variety of shapes, sizes, surface finishes, and materials compositions. Most of these techniques rely on cutting 2D 'slices' from the 3D model and building them one on top of the other. These techniques usually begin with a bed of fine ceramic powder. Some techniques deposit binder into specific areas of the powder to 'select' the shape that remains after the entire shape is formed.

Other techniques use a laser or directed light to cure a polymer component added to the ceramic powder for that purpose. Layer upon layer of powder is added to the bed, each layer representing a subsequent 2D slice of the desired product. Regardless of technique, the result is that some ceramic powder is held in place as part of the shape to be made, while the remainder can be removed from the part, often by shaking. The powder is then further consolidated through heat treatment and sintering to form a monolithic ceramic part. These techniques have a variety of applications including those that are obvious – prototyping parts for testing before investing in tooling for mass production, but also less obvious, such as one-of-a- kind designs like prosthetic devices for biomedical uses.

Architectural Installations

In a recent demonstration of the power of 3-D printing for architectural applications, a number of powder 3-D printers were used to manufacture cement composite blocks that were individually labeled in the process to designate the block's position in the final structure (Figure 2). Additionally, this technique can be used to fabricate very small components as discussed in the section on MEMS.

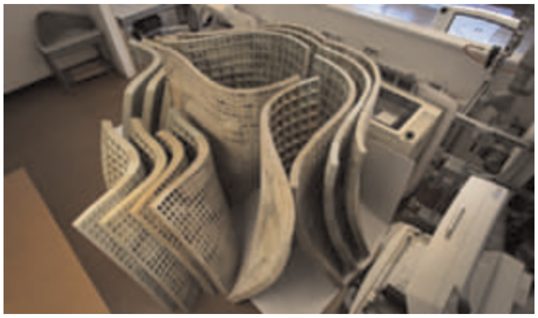

Figure 2 3D printed cement structure comprising 840 custom made blocks 9 ft high by 12 ft by 12 ft structure. (http://ceramics.org/ceramic-tech-today/first-and-largest-3-d-printed-cement-structure-blooms-at-uc-berkeley-campus (Published April 9, 2015))

Thin Film Techniques

A variety of thin film techniques have emerged from the semiconductor industry many involving ceramic materials including oxides, nitrides, and carbides. Most of them rely on liquid or gas-phase precursors and sophisticated control of chemistry, temperature, and pressures. These techniques often result in the growth of thin films of chemistries and morphologies not achievable in bulk form through traditional powder processing in similar temperature or pressure regimes (or sometimes in any temperature or pressure regime). One example of such techniques is presented here: CVD (chemical vapor deposition) of diamond thin films.

Diamond Coatings

Diamonds are truly an extreme material, having several properties that can only be described in superlatives: the hardest, the stiffest, the highest thermal conductor, highest sound propagation velocity, etc. Additionally, diamonds are very resistant to chemical corrosion, are biologically compatible, are optically transparent over a huge range of frequencies, and are excellent electrical insulators. However, their scarcity and availability only in single-crystal form have prevented widespread exploitation of most of these properties. With the exception of industrial diamonds created for cutting and grinding, the use of synthetic diamonds has been very limited. Rather than attempting to recreate nature's approach to diamond making (extreme temperatures and pressures), an alternative method has been discovered which has two significant advantages to nature's approach – easier processing resulting in a more convenient form. This method, which induces diamond growth by adding carbon atoms one-at-a-time to template, can be achieved without high temperature and pressure, and results in a thin film coating rather than isolated single crystals. Although this idea was conceived half a century ago (in the 1950s), it was not until the mid-1980s that good-quality films were grown. The concept, while relatively simple, presents numerous engineering challenges. At the heart of the technique is CVD. In this technique, a gas-phase chemical reaction occurs above a solid surface (often called a substrate as it forms the mechanical support for the resulting film). For the case of diamond films, a method of activating the gas-phase carbon-containing precursors is required. These include a hot filament or electrical discharge, or a combustion flame.

The most common method of diamond thin film growth uses methane, CH_4, as a precursor gas. The gas concentration (usually diluted with H_2) and temperature of the substrate must be controlled to suppress the deposition of graphite or amorphous carbon. The method used is normally tailored to the desired application. For example, hot-filament techniques, which use a refractory metal (such as tungsten or tantalum), can be used to make good-quality diamond films for mechanical application, but they are not suitable for electronic applications because they contain metallic impurities from the filament that degrade the electrical properties.

Although requiring more expensive equipment than hot-filament growth, microwave plasma CVD reactors are currently the most widely used technique for diamond growth as they produce high-quality, chemically pure films. The substrate requirements for this process are significant. Among them, the substrate must be able to withstand the thermal and chemical conditions of the reactor, which precludes a large number of materials including all polymers, most metals, and many electronic materials. Also, because diamond has such a low thermal expansion coefficient, α, it is susceptible to delamination or flaking off a substrate which contracts more on cooling from the reaction temperature (usually about 700 °C, so a substrate with a low α is required). In addition, the substrate must be able to form a carbide to some extent, as it has been suggested that the diamond films actually grow off an initial carbide interfacial layer. Currently silicon wafers are the most commonly used substrate material.

The chemical and physical processes that occur during thin-film growth are complex, but a very simplified model can be described by the schematic in **Figure 3**. Not all reactions result in diamond; the process is slow and requires very careful control of both the chemical and physical conditions of the system. Much effort has been expended to understand the gas-phase chemistry of this system, and progress continues to date, resulting in improved, more efficient methods and higher-quality thin films.

Widespread application of diamond thin films is still limited by economic restrictions, but they are beginning to be used for cutting tools, thermal management where rapid heat dissipation is required, IR windows, and electronic devices. Recently, work has been reported which uses diamond thin films as an ideal substrate for integrating microelectronics with biological sensing functions. More on this topic is discussed later in the section Trends in Ceramic Materials.

A related recent development is that of diamond-like-carbon (DLC), a material that displays some, but not all, of the properties of a typical diamond. DLC is amorphous, but has hardness similar to crystalline diamond. This material is typically made in a high pressure diamond anvil cell, not by the thin film techniques described above.

Sustainable Processing

Increasingly strict legislative controls and escalating public concern for the local and global environment have affected most manufacturers of goods including those of ceramics as is testified to by the recent creation of ISO 14000 – a family of standards that is focused on certifying manufacturers and organizations in environmental management systems.

The environmental impact of any class of materials can be considered to have many aspects including: the source of raw materials, the energy and by-products associated with all stages of manufacture, and the disposal of the product when it is no longer useful. Ceramics are typically inert, and do not generally produce environmental hazards when disposed of, however, acquiring raw

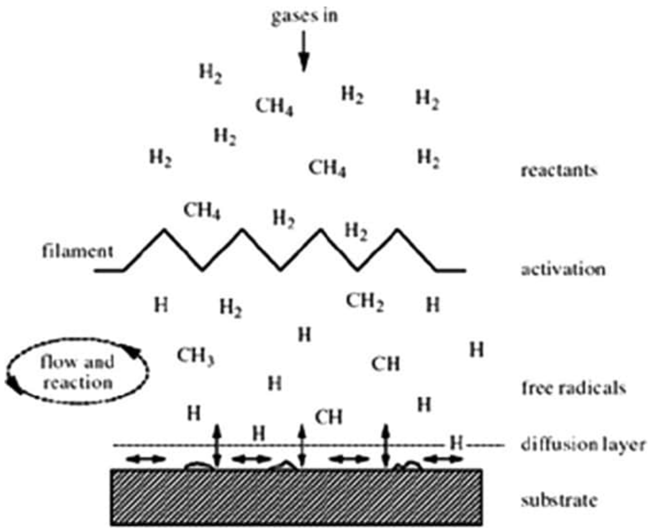

Figure 3 Schematic of the physical and chemical processes occurring during diamond CVD. Reproduced with permission from May, P.W., 2000. Philosophical Transactions of the Royal Society of London. Series A 358, 473–495.

materials and refining and processing them can negatively impact the environment. Alternatively, ceramics can also be considered in terms of their use in remediation of the environmental impact of energy production. There has been increased awareness of each of these aspects in the manufacture of ceramics as well as in other materials. One such environmental application of ceramics has already been discussed in SOFC for clean energy storage solutions.

Eco-Ceramics

Environmentally friendly ceramics usually refer to those that undergo processing using environmentally benign solvents or resulting in harmless by-products. NASA reported the development of a method to make a SiC ceramic using wood as the preform to supply both the structure and the carbon for the process. In this technique, wood is pyrolyzed to form a carbon structure that is then infiltrated with silicon or silicon alloy. The result is a SiC-based ceramic with a microstructure imposed by the original wood and a shape that duplicates that of the pyrolyzed form (it is biomorphic). The structure (and therefore, properties) is tailorable by the choice of wood and can be further adjusted by laminating wood layers in various arrangements. This technique has been used to produce porous and nonporous structures of various compositions based on SiC. Since the initial work by NASA, other researchers have used this biomorphic approach to develop ultra high temperature ceramics composites of C/SiC–ZrC (Figure 4).

Concrete, as the most used construction material has a significant carbon ‘footprint’ – contributing 5% of global greenhouse gas emissions in the manufacture of Portland cement, a process typically fueled by coal. A recent report suggests that a reformulation could simultaneously improve the strength of concrete and reduce the energy costs of its production. The approach to reformulation utilizes a computationally derived database, revealing an emerging trend as cited in the next section.

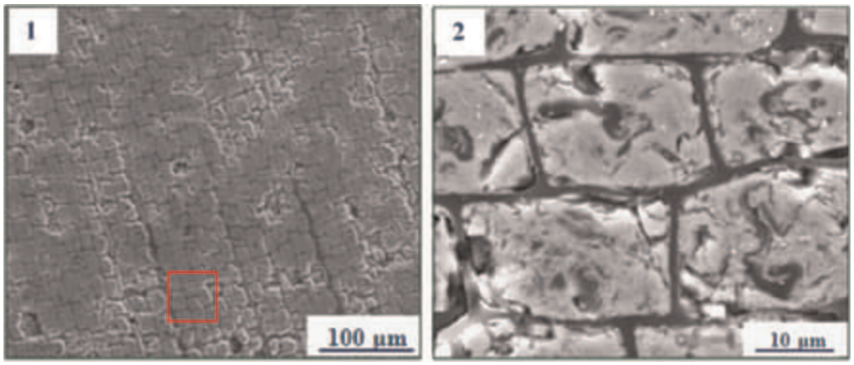

Figure 4 Wood used as a template to form high-tech ceramics. Microstructure of pine infiltrated with PZC/PCS precursor. (Fabrication and characterization of biomorphic cellular C/SiC–ZrC composite ceramics from wood. Reproduced from Jiewen, L., Shouquan, Y., Min, G., *et al.*, 2015. Ceramics International 41 (6), 7853–7859.)

Trends in Ceramic Materials

The most notable general trends in ceramics are those of the entire materials industry, and perhaps science and engineering as a whole, some of which have already been reflected in the examples given above. The first includes an ever-aggressive shrinking scale of our technological devices – requiring a more complete understanding of how material properties vary for very thin films and small grains (sometimes comprising fewer than 100 atoms). The second includes a focus on biological systems both from perspective of using natural systems to inspire and inform ceramic structure and processing, but also employing ceramics in biological systems (as prosthetic devices or drug delivery). Third, is the application of ever more powerful computing resources to apply to computational efforts to derive properties from first principles and model material behavior. Additionally computing power can enhance our ability to use combinatorial approaches and databases to explore novel formulations and manage and process enormous quantities of disparate data, as the example in the section on eco-ceramics describes. This trend that significantly impacts ceramics as well as all of materials science.

Nanotechnology/MEMS

As the scale of electronic devices shrinks, so has the scale of both the starting materials and the components of such devices. The trend toward nanoscale control has impacted ceramics as it has most fields of engineering and science. In a like manner, mechanical devices have continued to shrink to smaller and smaller dimensions, resulting in what is termed MEMS (micro-electromechanical systems). Ceramics are particularly well suited for MEMS applications in biological and chemical sensing systems (they tend to be chemically inert, even at high temperatures and severe environments). The advantages they bring to full-scale mechanical devices (e.g., engines) are also present at the microscale. Low density and high temperature capability make ceramics an attractive choice for high-speed devices such as nanoturbines. Ceramic MEMS have been made by microcasting a liquid ceramic precursor (e.g., polysilazanes) in a mold produced from photoresist by conventional lithographic methods (Figure 5). The resulting form is then pyrolyzed to convert to a Si–C–N amorphous ceramic. A second method of producing MEMS involves photopolymerization, a technique becoming increasingly widespread in the rapid prototyping industry. The technique involves adding a photo- initiator to a liquid ceramic precursor that will promote polymerization upon exposure to light of a specific wavelength. Shapes are constructed by exposing a layer of the precursor through a mask that has the desired shape. 3D structures are made by successive exposure to another layer, which has either the same, or a different geometry depending upon the desired result. Exposure can also be accomplished through the 'writing' of a directed laser beam. The exposed material polymerizes, and solidifies, allowing the remaining unexposed liquid to be washed away. In this way, a 3D structure can be created. The resolution achievable by such efforts is related to several factors both of the chemistry of precursor and photoinitiator and the physical characteristics of the mask or direct-write system. A similar approach to direct writing of structures is found in computer-controlled ink-jet printing of ceramic parts that is limited only by the length scale of the droplet. This technique relies on a colloidal, gel-based ink that forms a self-supporting structure. This technique, called robocasting has produced features as small as 100 mm, and has been made out of silica, alumina, lead-zirconate-titanate, and hydroxyapatite.

Bioceramics

Perhaps one of the most transformational trends in ceramics is that of bioceramics. Biology can take a variety of roles in the development of advanced ceramics from serving as the inspiration (or more directly, the template) for novel structures as discussed in the previous section on eco-ceramics to providing the motivation for the development of materials to be used in biomedical applications. Biomimicry is really nothing new – ancient people observed animals to learn the best methods to stalk prey, to identify safe foods to eat, and to predict weather changes, but until we developed the tools to examine nature at the microscopic (and now, atomic) level, we have made few efforts to copy nature at these length scales. Today, however, many scientists and engineers are again carefully studying natural materials striving to glean their secrets. Examples include the study of fracture toughness and interfacial design of the fiber-matrix ceramic composite that constitutes sea-urchin teeth and the self-assembled opal structure used as a template for photonic bandgap materials. Ceramics for biomedical applications have also become increasingly important in improving the quality of life for many of the worlds aging. Ceramics can be bioinert (such as alumina or zirconia) or can be

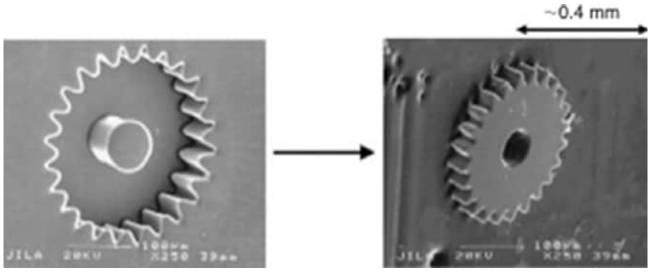

Figure 5 Left: Photoresist mold about 200 μm across. Right: The fired ceramic gear. (Am. Cer. Soc. Bull., 80 (5) 25, (2001).

bioactive (including hydroxyapatite and bioactive glass and glass ceramics). Ceramics have been used or are being developed for use in replacement joints for hips and knees, replacements for diseased or damaged bone, and reconstruction of teeth and jawbones. Ceramic and carbon coatings are also used in a variety of biomedical devices including prosthetic heart valves. The bonding between hard and soft tissue is being studied to improve such applications. Ceramics are also being used for controlled drug delivery. For example, therapeutic treatment of cancer has been achieved using glass beads doped with radioactive isotopes. In addition, in the drug-delivery arena, rapid prototyping, or 3D printing techniques have been used to fabricate specialized drug-delivery devices. These ceramics are functionally graded structures that can yield complex release profiles in which there is control time, dosage, and even the chemistry of the drug. Ceramics can also be employed as biosensors. Diamond, because of its electrical and chemical properties is a good candidate for integrated sensing materials, and recently, selective biological modification and adsorption has been achieved. In this work, DNA oligonucleotides were covalently bonded to nanocrystalline diamond thin films resulting in an extremely stable, highly selective platform for sub- sequent surface hybridization processes. This integration of DNA and other biological materials with microelectronics has broad-ranging implications for the development of completely integrated bioelectronic sensing systems.

Conclusion

While these examples testify to the extent and breadth of the research and development in advanced ceramics, there remains much to be understood and accomplished. The ever-expanding variety of analytical tools will provide the technology to further probe the structure and properties of ceramic materials, often at the nanoscale. The blurring of lines between ceramics, biology, and other fields of engineering will most certainly persist requiring that tomorrow's ceramists be cognizant of a broad range of fields and have command of a variety of analytical tools and techniques. Although continually evolving, ceramics will continue to have a large role in the shaping of our society.

Further Reading

Abdolhosseini Qomi MJ, Krakowiak KJ, Bauchy M, et al. (2014) Combinatorial molecular optimization of cement hydrates. Nature. *Communications* 5.

Adams TA, Nease J, Tucker D, and Barton P (2013) Energy conversion with solid oxide fuel cell systems: a review of concepts and outlooks for the short and long term. *Industrial & Engineering Chemistry Research* 52: 3089–3111.

Barsoum MB (1997) *Fundamentals of Ceramics.* McGraw-Hill.

Hench LL (1998) Bioceramics. *Journal of American Ceramics Society* 81(7): 1705–1728.

Jiewen L, Shouquan Y, Min G, et al. (2015) Fabrication and characterization of biomorphic cellular C/SiC–ZrC composite ceramics from wood. *Ceramics International* 41(6): 7853–7859.

Liew L, Zhang W, An L, et al. (2001) Ceramic MEMS. *American Ceramic Society Bulletin* 80(5): 25.

May PW (2000) Diamond thin films: A 21st-century material. *Philosophical Transactions of the Royal Society of London Series A* 358: 473–495.

Minh N (2003) *Recent advances in solid oxide fuel cell technology – SOFCs for power generation applications*. Bulletin, July: American Ceramic Society, 2003.

Miodownik M (2014) *Stuff Matters*. Boston: Houghton Mifflin Harcourt.

Rahaman MN (2003) *Ceramic Processing and Sintering*, second ed. Dekker.

Rice RW (2003) *Ceramic Fabrication Technology*. New York: Dekker.

Singh M, Martinez-Fernandez J, and deArellano-Lopez AR (2003) Environmentally conscious ceramics (eco-ceramics) from natural wood precursors. *Current Opinion in Solid State and Materials Science* 7(3): 247–254.

Wang R (1998) Fracture toughness and interfacial design of a biological fiber-matrix ceramic composite in sea urchin teeth. *Journal of the American Ceramic Society* 81(4): 1037–1077.

Yand W, Auciello O, Butler JE, et al. (2002) DNA-modified nanocrystalline diamond thin-films as stable, biologically active substrates. *Nature Materials* 1: 253–257.

Polymers, History of

MM Coleman and PC Painter, The Pennsylvania State University, University Park, PA, USA

© 2005 Elsevier Ltd. All rights reserved.

This is an update of M.M. Coleman, P.C. Painter, Polymers, History of, Editor(s): Franco Bassani, Gerald L. Liedl, Peter Wyder, Encyclopedia of Condensed Matter Physics, Elsevier, 2005, Pages 386–391, ISBN 9780123694010, https://doi.org/10.1016/B0-12-369401-9/00482-4.

Introduction 424
Early History: Developments in the Nineteenth Century 424
The First Synthetic Plastic 425
The Dawn of Understanding 426
The Post 1930s 427
Final Words 427
Further Reading 428

Introduction

Although this article presents only a very brief history of polymers, it would be remiss if it did not open by acknowledging that without polymers this encyclopedia would not have been written! Mother Nature, with ingenious dexterity, used "natural" organic polymers such as proteins, polypeptides, carbohydrates, and DNA, to build the structural elements of life itself. Long before there was any fundamental understanding of the macromolecular nature of materials such as cotton, silk, wool, wood, leather, bone, and ivory, humankind found ways to use and modify these materials to produce articles for clothing, utensils, and shelter. One could write books on this subject alone, so in this short history the focus is on how the foundations of our understanding of the nature of polymer materials were laid. In doing so, a lot of important and interesting things have been left out. Accordingly, the focus is on the history of semisynthetic and synthetic polymers, mentioning natural rubber only in passing. (Rubber actually deserves a history of its own and the interested reader is encouraged to consult the sources listed at the end of this review.)

To many people, the birth of polymer science as a discipline starts with Hermann Staudinger and his assertion that materials such as natural rubber are covalently bonded long-chain molecules, as opposed to some sort of colloidal aggregate. Jumps such as this in our understanding of nature do not occur in a vacuum, however. Staudinger was building on a wealth of work by nineteenth-century chemists and entrepreneurs, whose goal was to produce substitutes for various types of increasingly expensive or difficult to obtain natural materials such as ivory and silk.

Early History: Developments in the Nineteenth Century

Perhaps the most enduring images of the industrial revolution of the nineteenth century are those provided by the ironmasters and engineers. One thinks of a world of railways, "dark, satanic mills," and the social and political consequences of the division of labor and the creation of an urban working class. It is the world according to Charles Dickens, built on iron, steel, coal, and the power of steam. Natural polymers, such as cotton and wool, were, of course, key materials and after Charles Goodyear's discovery of vulcanization, natural rubber would join them. But, from about the middle to the end of the nineteenth century onward, various synthetic and semisynthetic polymer materials were also introduced and these were to have a profound social and economic impact.

In 1845, common household items such as combs and toothbrushes were often laboriously fashioned from bone or ivory and were thus expensive and unavailable (except in crude wooden forms) to most people. This was to change, although not immediately, with the work of the Swiss chemist, Christian Schönbein. The story (perhaps apocryphal) has it that he used his wife's apron to wipe up some spilled concentrated nitric and sulfuric acid while conducting experiments in his home. After washing the apron, he put it in front of the fire to dry, upon which it immediately flared brightly and disappeared. Schönbein had discovered guncotton, formed by nitrating the cellulose in the apron. Not only did guncotton have more explosive power than gunpowder, it gave off far less smoke. This was considered a major advance, because it lessened the confusion of the battlefield and generals could now see the people they were slaughtering. Advances in military technology were often spin-off materials and processes that are useful in everyday life, however, and this was to be no exception. Cellulose in its native form is both insoluble and infusible and cannot be cast from solution or molded to make useful objects. However, a French doctor, Louis Menard, found that nitrated cellulose would dissolve in a mixed solvent of alcohol and ether and cast to form a transparent film, called collodion. This was used to dress cuts and wounds. Crucially, it was also found that at levels of nitration of ~13% or less, nitrated cellulose is no longer explosive, although still highly flammable.

Alexander Parkes, a prolific English inventor and true material scientist, had already achieved considerable fame as a metallurgist when he found that the addition of castor oil and camphor to nitrated cellulose lowered its softening temperature. The resulting material, which he modestly called Parkesine, could then be molded. Various objects made from this new material were displayed at the Great Exhibition at the Crystal Palace in 1862, where it won a medal for excellence of product. Parkes seems to have been unaware of the special role of camphor as a plasticizer, however. In some of his publications he omitted reference to it completely and the commercial exploitation of Parkesine was ultimately a failure. Nevertheless, it marked the beginning of the plastics industry.

This history now shifts across the Atlantic, where the next development came as a direct consequence of a shortage of elephants and rhinoceroses. It is a classic case of a short supply of one material, in this case ivory, providing the impetus for the development of another. The American billiard ball manufacturing company, Phelan and Callendar, offered a prize of $10 000 (a very large sum in those days) to anyone who could invent a substitute for ivory billiard balls. John Hyatt took up the challenge and chose to experiment with Parkesine. One can speculate that Hyatt might have misspent his youth in pool halls, because he was intrigued by the problem and spent several years of his life working toward a solution. He did not win the prize, but did establish the Albany Billiard Ball Company, which used a mixture of gum shellac and wood pulp to make the bulk of the ball. This was coated with nitrocellulose, which gave this new ball some interesting properties. Hyatt later reported, "We had a letter from a billiard saloon proprietor in Colorado mentioning that occasionally the violent contact of the balls would produce a mild explosion and saying that he did not care so much about it, but that instantly every man in the room pulled a gun." It seems that controlling the degree of nitration remained a problem.

This experience with nitrocellulose prompted Hyatt to investigate its properties in more detail. He eliminated castor oil from his formulations, using only camphor, and, with good old-fashioned Yankee ingenuity, solved the manufacturing problems that had plagued Parkes. He produced a hard material that could be softened by heating to 90°C and called it celluloid. Celluloid was an enormous success. Many common objects that were previously expensive could now be mass-produced cheaply. These ranged from knife handles to false teeth, from combs to that symbol of Victorian rectitude, the stiff celluloid collar. It also provided film for the fledgling movie industry, whose stars became known as the "celluloid kings and queens."

Celluloid was not a true synthetic polymer, of course, but a chemically modified natural polymer. Its central significance to the development of the field was not so much the nature of the objects produced, although these had an important social and economic impact, but the engineering techniques and machines developed to produce these goods. An example is the artificial silk fiber produced by Count Hilaire de Chardonnet, who developed an extrusion process in which a nitrocellulose solution was forced through a small orifice producing a lustrous thread. Unfortunately, nitrocellulose lost none of its incendiary qualities in this process. The workers in Chardonnet's factory quickly dubbed the product "mother-in-law silk" (buy your mother-in-law this nice blouse and stand her in front of the fire), thus revealing an interesting, though morbid, sense of humor. Chardonnet overcame this problem by "denitrating" the fibers by passing them through a solution of aqueous ammonium hydrogen sulfide and, in effect, regenerating cellulose.

There are easier ways to make regenerated cellulose and in the early 1890s Cross, Bevan, and Beadle discovered that cellulose could be rendered soluble by sodium hydroxide and carbon disulfide. A basic solution of cellulose xanthate is formed, which regenerates cellulose upon acidification. Fibers from regenerated cellulose were called rayon, while films were known as cellophane. By the 1930s cellophane was being used to wrap an enormous range of goods, not only to protect them from spoilage, but also because they had customer appeal. A grocery chain reported an increase in sales of an astonishing 2100% in two weeks once their doughnuts were wrapped in cellophane. In a mid-twentieth century poll by the *New York Times*, cellophane was considered to be one of the key discoveries of the century to that date and was even included in a Cole Porter song (You're the Top). The impact of these materials was enormous, but cheaper synthetic polymers have now largely replaced them.

The First Synthetic Plastic

The first truly synthetic polymer materials are the "phenolic resins," originally synthesized by reacting phenol (or, as it was called at the time, carbolic acid, a compound that was, and still is, commonly used as a disinfectant) and formaldehyde (an aqueous solution of which, formalin, had been used in the embalming business for thousands of years). It was actually an Englishman, Arthur Smith, who in 1899 was awarded the first patent for the application of phenol/formaldehyde resins as electrical insulators. But it was Dr. Leo Hendrik Baekeland, a Belgium chemist born in Gent and living in the US, who made the big breakthrough.

Baekeland was an interesting man. He graduated with a Ph.D. degree, "maxima cum laude" and then taught at the University of Gent until 1889. He then left for the US, where he quickly invented Velox, a photographic paper superior to anything else then available. George Eastman, who in 1888 introduced the Kodak camera with the slogan "you press the button, we do the rest," made up his mind to buy Velox and invited Baekeland to Rochester. Baekeland had decided to ask for what was then the very large sum of $50000, but had it in the back of his mind that he would settle for $25000. Eastman offered him a million, allowing Baekeland to retire to his laboratory in Yonkers, New York, and look for new chemical worlds to conquer.

Baekeland decided to try and develop a less flammable replacement for shellac, a natural coating derived from the resinous secretions of tiny lac beetles. According to one source, his immediate goal was to develop a wood varnish for bowling alleys, all the rage at that time. Other sources state that Baekeland perceived the growing impact of electricity on everyday life and his goal was to produce a new synthetic insulator. It took roughly 150000 beetles ~6 months to produce enough resin to make one pound of shellac and the demands of the fledgling electrical industry had created a shellac shortage.

Although Baekeland is given the credit for the discovery of phenolic resins, there were significant contributions from many others including Adolf Baeyer, Arthur Smith, Adolf Luft, and James Swinburne. Baekeland's key discovery (made in 1907), one that set him apart from the competition, was that phenolic resins could be made in two parts. In essence, he developed a process where a polycondensation reaction was carried out at an elevated temperature. He then stopped the reaction at an intermediate point by cooling to ambient temperature, where the partially reacted resin solidified. In the second stage, this reasonably stable intermediate material was placed into a mold and heated under enormous pressure. This transformed the material (by continued polymerization and cross-linking reactions) into a hard, shiny, intractable, relatively brittle solid. Bakelite, as Baekeland called his new material, could be molded and machined; it was hard, relatively strong, lightweight, and resistant to heat. It was the first true synthetic polymer and there was nothing else like it on the face of the planet. It found use not only in electrical fixtures, but also in knife handles, buttons, cameras, radio, and telephone equipment, essentially anything that required a molded part. It was advertised as the "Material of a Thousand Uses." And it was.

The Dawn of Understanding

The polymeric materials discussed so far were developed in a largely "Edisonian" fashion, by trial and error, and in the absence of any fundamental understanding of the macromolecular nature of polymers. In fact, the prevailing view at that time was that materials like silk, cellulose, and natural rubber were colloidal aggregates of small molecules. Not only that, the chemistry of what were then called "high molecular compounds," which could not be purified by crystallization or distillation, was regarded with disdain by the academic chemical community and referred to as "grease chemistry."

It was therefore an act of considerable courage for Hermann Staudinger to decide to devote the bulk of his efforts to these "high molecular compounds." He asserted in lectures and papers (published in the period 1917–1920) that these materials were covalently bonded long-chain molecules. Although Staudinger, at the ripe old age of 39, was a distinguished chemist, holding academic positions at prestigious universities in Karlsruhe, Zurich, and Freiburg, convincing his colleagues was to be no easy matter. For example, Staudinger recollects in *Arbeitserinnerungen* (Working Memoirs) that he was advised in the 1920s by a famous organic chemist of the day, H Wieland, "My dear chap, give up your ideas on big molecules. There are no organic molecules with a molecular weight of more than 5000. Just clean up your products and they will crystallize and reveal themselves as low molecular weight compounds." In 1925, after giving a lecture at the Zurich Chemical Society, he was attacked by a number of leading scientists and in frustration quoted Martin Luther, "Here I stand and can do no other."

Staudinger could not accept that the physical properties of rubber, proteins, cellulose, and the like could be explained by the idea that they consisted of associations of small molecules held together by some unknown force. (It was speculated at the time that some undiscovered "vital" or life force could be involved.) Staudinger maintained that the atoms in these molecules were connected by covalent chemical bonds, as in low molecular weight materials like benzene, but these molecules just happened to be incredibly large! Despite the apparent reasonableness of this position, the dispute became almost theological in its intensity. Von Baeyer had it right when he pronounced his "Three Stages of a Triumphant Theory": First it is dismissed as untrue; second it is rejected as contrary to religion; and third it is accepted as dogma and every scientist claims to have long appreciated its truth! Staudinger was, of course, correct, and he was belatedly recognized for his achievements in 1953, when he was awarded the Nobel Prize in chemistry. Sometimes you have to outlive your enemies!

Numerous experiments performed by the late 1920s and early 1930s provided accumulating evidence in favor of the existence of macromolecules. Particularly important were Staudinger's work on polyoxymethylenes, where he systematically studied changes in the physical and chemical properties of this polymer and a homologous series of its oligomers; the X-ray diffraction studies of Meyer and Mark, establishing the chain structure of cellulose; and the molecular weight measurement made possible by Svedberg's development of the ultracentrifuge. However, it was the brilliant experimental studies of Wallace Hume Carothers, which were to remove any lingering doubt about the macromolecular, long-chain nature of polymers.

Carothers obtained his doctorate from the University of Illinois, and then took up a teaching position at Harvard. In 1928, Charles Stine persuaded Carothers to leave his teaching post and join the DuPont Company to head a newly formed fundamental research laboratory. He was given wide discretion and he clearly stated at the outset that his goal was to tackle the problem of macromolecules from a chemical approach, by synthesizing compounds of high molecular weight and known constitution. Carothers is best known for the discoveries of nylon and neoprene, but his general contributions to polymer synthesis and polymer structure/property relationships were truly seminal.

Wallace Carothers was probably the first to appreciate the enormous importance of monomer functionality in the production of condensation or step-growth polymers. Amongst many other things Carothers is also credited with categorizing the two major classes of polymerization: condensation or step-growth (which he referred to as "C" type polymerization) and addition (called "A" type). Carothers' crowning glory, one of the major outcomes from his fundamental studies of polymerization, was the discovery of polyamides, or as they are now known universally, nylons. The first major market was ladies' stockings, introduced in the early 1940s. There was a huge demand for this product, which in these days of less formal wear is hard to imagine. Nylon production was co-opted for the war effort after Pearl Harbor was bombed (replacing silk in parachutes and so on), but when nylon stocking production was resumed in 1945 there were actually so-called nylon riots among people lining up to purchase the limited supply. This is a great story, one that would take more space than available here, but it is also a tragic one. Carothers never lived to see the extraordinary success of nylon. The bouts of depression, to which he had long been subject, became increasingly frequent after 1935 and he began to believe he was a failure as a scientist. He left his home in Wilmington, Delaware, on April 28, 1937 and checked into a Philadelphia hotel room, where he swallowed lemon juice laced with potassium cyanide.

The Post 1930s

Following Staudinger and Carothers, the synthesis of polymer materials would become based on chemical principles, rather than empirical trial and error. It was now understood what types of functional groups could react to form polymers and chemists set about making them. Nevertheless, it took years of effort by many scientists to achieve a firm understanding of the details of reaction mechanisms and their kinetics. For example, industrial scale polymerization of vinyl monomers in Germany by what became recognized as a free radical mechanism was in early work (late 1920s) initiated by exposure to sunlight. Initiation also played a crucial role in the development of a high-pressure process for the polymerization of ethylene by Fawcett and Gibson at ICI (Imperial Chemical Industries) in England in the 1930s. While trying to react benzaldehyde with ethylene at high pressure, a waxy solid was formed which they recognized to be a polymer of ethylene. A subsequent experiment blew up the apparatus and ICI banned high-pressure studies until stronger reaction vessels could be constructed. Fawcett left to join Carothers' group in America, but Perrin continued work in secret after normal working hours, risking both his life and his job. By 1936, it was recognized that small amounts of oxygen could initiate the reaction and by 1939, production of significant quantities was achieved. This turned out to be crucial for the war effort. Because polyethylene turned out to have an extremely low dielectric loss, it was ideal for radar cable insulation. As Robert Wattson Watts, the British inventor of radar, stated, "The availability of polyethylene transformed the design, production, installation and maintenance of airborne radar from the most insoluble to the comfortably manageable. And so, polyethylene played an indispensable part in the long series of victories in the air, on the sea and the land, which were made possible by radar."

By 1950, significant advances in understanding free radical polymerization, the nature of copolymerization, emulsion polymerization, etc., had been achieved. At the same time, the period between the first and second World Wars had seen the introduction of a number of important condensation polymers, which included not only nylon, but also the polyurethanes. Otto Bayer, who just happened to have the same name as the large German company for whom he worked, became head of the Central Scientific Laboratory at the ripe old age of 31. He was aware of the work of Staudinger and Carothers and reasoned that a superior "condensation" polymerization would be one where a small molecule (such as water) was not split off. He had worked on isocyanate chemistry and perceived that diisocyanates might form the basis for making such polymers. Synthesizing diisocyanates is hard and dangerous chemistry and one of Bayer's closest colleagues remarked, "If you had ever tried to make a monoisocyanate, you would not have come up with the mad idea of trying to produce diisocyanates. The reaction of phosgene on diamines would result in almost anything except diisocyanate, and would probably be thoroughly unstable, anyway." Others added, "It will explode!" This is another great story, which too cannot be told properly for want of space, but needless to say, Bayer succeeded.

Although some addition polymerizations involving catalysts and ionic initiators were performed between the two World Wars, it was not until the early 1950s that things really took off, when catalysts for the low pressure polymerization of ethylene were discovered, independently and almost simultaneously in the early 1950s, by Karl Ziegler in Germany and Robert Banks and Paul Hogan at the Phillips Petroleum company in the USA. These were not the only scientists involved, as workers at Standard Oil of Indiana were pursuing similar goals, while Giulio Natta, a Professor at the Politecnico di Milano, had become interested in the field after he heard a lecture given by Ziegler. Natta had sent some of his collaborators to work in Ziegler's laboratory to learn the art and craft of the technique and upon their return, Natta set out to synthesize polypropylene, which could not be made free radically. They succeeded and filed for a patent just days before Ziegler's group, who by then had also succeeded in polymerizing propylene. Although Ziegler and Natta were jointly awarded the 1963 Nobel Prize in chemistry, they were no longer speaking to one another. Polypropylene also became the subject of one of the longest patent cases in history.

There is much more to this story, and the history of the development of many other major polymers and classes of polymers is equally fascinating. But although a history of polymer materials naturally focuses on how these materials were discovered and synthesized, an understanding of the physics and physical chemistry of these materials was equally important. It was Carothers, looking for a physical chemist to join his group, who hired the newly graduated Paul Flory in 1934. Carothers encouraged Flory to carry out mathematical investigations of polymerization and the subsequent impact that Flory was to have on the field of polymer science is difficult to overstate. Flory's book, *Principles of Polymer Chemistry*, is still a classic 50 years after publication and essential reading for anyone starting out in this field. In 1974, he was awarded the Nobel Prize in chemistry for his fundamental achievements, both theoretical and experimental, in the physical chemistry of macromolecules. While many other notable scientists have contributed to the theory of polymers, Pierre-Gilles de Gennes has a knack for seeing commonalities in wildly different physical systems and then reducing these observations to simple scaling arguments. His book, *Scaling Concepts in Polymer Physics*, is also a required reading for aspiring polymer physicists. In 1991, his peers recognized de Gennes' accomplishments and he was awarded the Nobel Prize in physics.

Final Words

There is much that has been omitted and many great scientists have been slighted by these omissions. The authors can only suggest that if they have sparked any interest in the reader that he or she refers to the references cited below.

Further Reading

Furukawa Y (1998) *Inventing Polymer ScienceStaudinger, Carothers, and the Emergence of Macromolecular Science*. Philadelphia, PA: University of Pennsylvania Press.
Kaufman M (1963) *The First Century of Plastics*. London: The Plastics Institute.
Mark HF (1993) *From Small Organic Molecules to Large*. Washington, DC: American Chemical Society.
Morawetz H (1985) *PolymersThe Origin and Growth of a Science*. New York: Wiley.
Mossman STI and Morris PJT (eds.) (1994) *The Development of Plastics*. Cambridge: The Royal Institute of Chemistry.
Painter PC and Coleman MM (2003) *Painter and Coleman on Polymers*, 2-CD-ROM Set. Disk One: *Polymer Science and Engineering*. Disk Two: *The Incredible World of Polymers: Tales of Innovation, Serendipity and Perseverance*. Lancaster, PA DesTech Publications.

Neutrons and Neutron Scattering, History of

F Mezei, Hahn-Meitner-Institut, Berlin, Germany

© 2005 Elsevier Ltd. All rights reserved.

This is an update of F. Mezei, Neutrons and Neutron Scattering, History of, Editor(s): Franco Bassani, Gerald L. Liedl, Peter Wyder, Encyclopedia of Condensed Matter Physics, Elsevier, 2005, Pages 76–83, ISBN 9780123694010, https://doi.org/10.1016/B0-12-369401-9/00756-7.

Introduction 429
Establishing the Conceptual Foundations 429
Neutron Diffraction 430
Inelastic Scattering 431
Polarized Neutrons 432
Polarization Analysis 433
Neutron Spin Echo 434
Steady-State and Pulsed Neutron Sources 434
Neutron Optics 435
Further Reading 436

Introduction

The expression “neutron scattering” commonly refers to the study of condensed or gaseous matter by observing the scattering of a neutron beam from a sample of the material in question. If the energy of the neutrons in the beam is much higher than the typical energy of the interactions of the atoms in the sample matter (e.g., the energy of chemical binding within constituent molecules), the collision of neutrons with the nuclei of the atoms depends only on the properties of the individual nuclei and carries no information on the properties of the material. Thus, the subject matter of this article is the history of using low-energy (typically less then 1 eV) neutron radiation for exploring what happens inside common materials.

The idea that neutrons can reveal precious information about the structure of such materials – solids, liquids, and to some extent also gases – was born shortly after neutrons were discovered by Chadwick in 1932. Practical neutron scattering started as a parasitic activity on research reactors built in the 1940s for developing nuclear energy. Since the 1960s, several facilities around the world have been specifically designed, built, and dedicated primarily for neutron scattering research to serve by the end of the twentieth century a worldwide community of about 7000 users of neutrons as one of their tools in the study of a vast variety of topics in condensed matter research, including physics, chemistry, biology, geology, archeology, and engineering. In 1994, Shull and Brockhouse, the two outstanding pioneers of neutron scattering in the 1950s, were awarded the Nobel prize in physics for discovering how the neutrons show “where the atoms are and what they do.”

Establishing the Conceptual Foundations

As early as in 1936, Elsasser suggested that neutrons move as waves through matter and as these waves scatter on the nuclei of individual atoms, interference may occur between the partial waves scattered from different atoms, as was known since the 1910s for X-rays. This was demonstrated in the same year by observing the strong reflection of neutrons on large magnesium oxide single crystals. In this respect, the fundamental difference that neutrons scatter on the nuclei and X-rays on the electron cloud surrounding these nuclei in the atoms was of no principal consequence.

In 1936, Bloch also made a visionary proposition, which in contrast had no analogy in X-rays. Due to the fact that the neutron possesses a magnetic moment, Bloch realized that they could also feel the magnetic fields inside magnetic materials. The magnitude of the neutron magnetic moment is $\mu_n = 1.04 \times 10^{-3}\,\mu_B$, where the Bohr magneton μ_B essentially equals the magnetic moment of a free electron. The internal average magnetic field (induction) inside ferromagnetic iron is $B = 2.2\,\mathrm{T}$ and the energy of the Zeeman interaction in this field $E = -\mu_n B = 1.32 \times 10^{-7}\,\mathrm{eV}$ acts as a potential on the neutron (attractive if the neutron magnetic moment is parallel to the field B, and repulsive for antiparallel direction), which can measurably deflect a neutron beam. Bloch pointed out that, since the internal magnetic field distribution in a magnetic material is not homogeneous but shows strong maxima centered around the position of the nuclei, the internal magnetic field distribution shows a periodic structure in crystalline magnets and therefore with neutrons, not only the atomic structure determines the Bragg diffraction peaks well known for X-rays, but there is also a contribution from the magnetism of the atoms.

It is of particular historical interest that while Bloch’s visionary recognition of the great potential of neutron scattering in the study of magnetic materials proved to be of outstanding importance in the investigation of magnetic phenomena, for example, the study of high-temperature superconductors in recent decades, he proposed a mathematical expression, which was debated for nearly 15 years and finally proved to be wrong. This controversy reflected a fundamental ambiguity of electromagnetic theory, which could finally be settled by the neutron reflectivity experiments of Hughes and Burgy (1951). In electromagnetic theory, two fields are associated with magnetic materials: the so-called magnetic field H and magnetic induction B. These two are equal outside the magnetized matter, the only place where one could place a measuring device. This was going to change with the neutrons: as neutral particles, neutrons interact weakly with most materials and can penetrate deep inside heavy objects (e.g., many centimeters in steel), and as a quantum mechanical particle wave, they can theoretically spread over an unlimited volume of the sample. So magnetism could, for the first time, be observed inside magnetic materials, with the measuring probe, the neutron occupying the same space as the sample magnetic material. Although the details did not appear to be so clear at that time, Bloch's 1936 theory implied that the interaction between the neutron magnetic moment and magnetism corresponds everywhere, including the inside of matter, to the energy

$$E = -\mu_n H \qquad [1]$$

whereas the different formulas proposed by Schwinger in 1937 were shown to correspond to the general assumption

$$E = -\mu_n B \qquad [2]$$

The experiments of Hughes and Burgy, which could only be done when a few years after World War II intense neutron beams became available for research at nuclear reactors, settled the ambiguity in favor of eqn [2]. To overcome a repulsive energy barrier of $\sim$100 meV corresponding to the magnetic induction B inside iron for the neutrons with magnetic moment opposite to the magnetization of the sample, the neutrons needed to have at least 5 m s^{-1} velocity perpendicular to the surface. Below this value, the neutron beam is totally reflected. Thus for typical velocities of the neutron beams available from reactors in the range of 2000 m s^{-1}, the range of total reflection will extend up to grazing incident angles of $\sim$0.1° (the so-called critical angle). Hughes and Burgy determined the potential energy by the observation of the critical angle in magnetized Fe films. Their conclusion that $E = -\mu_n B$ was shown to imply that the magnetic moment of the neutron should be considered as a microscopic Amperian current loop, and not as a dipole built by opposing charges.

Actually, the total potential energy at a surface is the sum of the magnetic and nuclear contributions, where the latter designates the average potential presented by the interaction between the neutrons and the nuclei of the atoms in the sample, and the detailed shape of the reflectivity curve above the critical angle of total reflection depends on the detailed profile of the potential, which can show considerable structure, for example, in surfaces consisting of a number of thin layers. Decades after the pioneering work of Hughes and Burgy, neutron reflectivity became a widely-used tool for the study of surfaces and thin film structures, in particular following Felcher's important study of the penetration depth of magnetic fields at the surface of superconductors in 1979.

Neutron Diffraction

Practical neutron scattering work started more than 10 years after the theoretical suggestions by Elsasser and Bloch, when nuclear fission reactors became available for research. The energy of fission neutrons is very high ($\sim$MeV), and they first need to be slowed down before they can be used in neutron scattering work. This was achieved by the thermalization process, in which neutrons are made to collide randomly with light, small absorbing nuclei (originally C in graphite) whereby after a few collisions a neutron gas with a temperature close to the temperature of the moderator is produced. The energy of the neutron emerging from a moderator

$$E = mv^2/2 \qquad [3]$$

(where m is the neutron mass, $m=1.67\times10^{-24}$ g) is on average close to the thermal energy $k_B T$ at the temperature of the moderator, that is, 25 meV at room temperature. The corresponding neutron velocity $v=2200$ m s^{-1} is equivalent in quantum wave mechanics to a wavelength of $\lambda=0.18$ nm, as given by the de Broglie relation

$$h/\lambda = mv \qquad [4]$$

where h is Planck's constant. This wavelength is comparable to the 0.154 nm of the Kα X-ray radiation of copper, mostly used for crystallographic studies at that time. However, the wavelength distribution in the neutron beam extracted from the moderator was very broad and to build the first neutron diffractometer in 1948, Shull and Wollan at Oak Ridge used a monochromator single crystal to obtain a neutron beam with a well-defined wavelength. The next step was to measure the neutron scattering power for a large number of atomic nuclei by studying the neutron diffraction pattern for many well-known crystals. It turned out that this power changes rather randomly from one nucleus to the other, and, in particular, in neutron diffraction one can see the contributions of light elements (e.g., hydrogen) also in the presence of much heavier ones. This is an important contrast of great practical utility to X-ray diffraction, where heavy elements in the crystals tend to mask the lighter ones.

The first decisive discovery by using neutron scattering was made by Shull and Smart in 1949 at Oak Ridge: they found a new Bragg peak in the neutron diffraction pattern of MnO at low temperatures, which could not be seen in X-ray studies (Figure 1). It was the first experimental evidence for antiferromagnetism, showing that the magnetic moments of the Mn atoms are aligned parallel for every second atom in certain lines and antiparallel for the atoms in-between. This breakthrough established neutron scattering as the preferred tool for the study of magnetism on the atomic scale. It is worth noting that this seminal discovery was made before the controversy on the coupling between neutron and magnetism had been settled. However, the existence of Bragg peaks in a sample without preferred magnetic orientation did not depend on the exact form of the interaction.

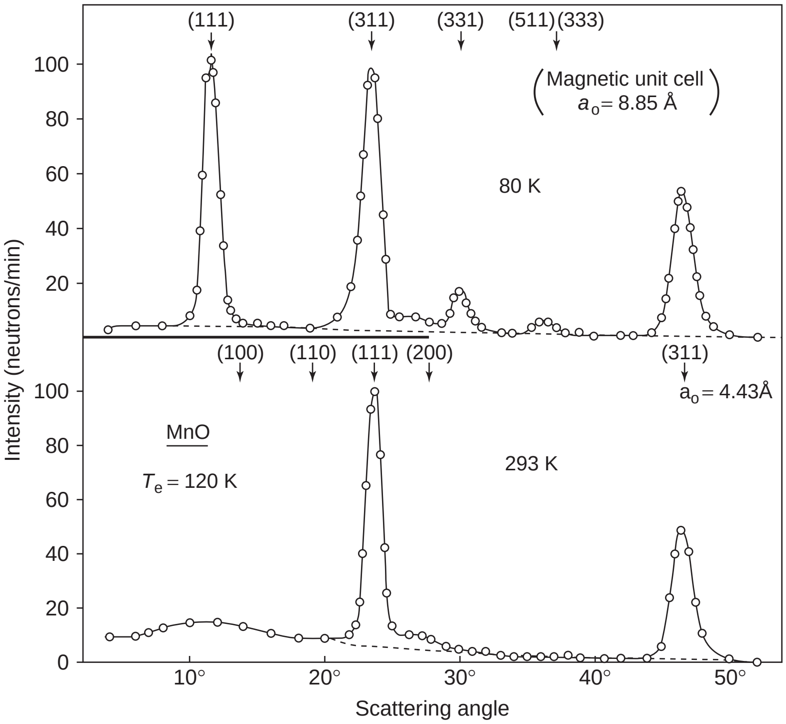

Figure 1 The first experimental evidence for antiferromagnetism by neutron diffraction. (Shull CG and Smart JS (1949) *Physical Review* 76: 1256.)

Neutron diffraction experiments can not only reveal crystalline long-range order, but also much less regular arrangements of atoms. In such cases the Bragg peaks are replaced by broad "diffuse scattering" structures in the scattering diagram (such as in the lower curve in Figure 1 arround 11° scattering angle), which carry information on a large variety of phenomena, such as the way in which one atom is surrounded by neighbors in a liquid or the size and arrangement of precipitates in an alloy. Information on larger structures shows up at smaller scattering angles, which gradually led (from the late 1950s) to the development of small angle neutron scattering (SANS) as a very special form of neutron diffraction.

Inelastic Scattering

The atoms and molecules inside condensed matter move around locally with energies comparable to k_BT. This leads to the appearance of the so-called inelastic scattering processes, in which the energy of the scattered particle is changed by an exchange with the kinetic energy of the atoms. Since for ordinary temperatures, the energy of the thermal motion of atoms in the sample is comparable to the energy of the neutrons from ambient moderators, the energy change of the neutron in the corresponding inelastic scattering processes can be quite substantial, and therefore readily measurable. In contrast, the quanta of X-rays with wavelength convenient for scattering work on condensed matter (i.e., in the range of atomic distances in the sample) are very high, and inelastic processes due to motion of atoms are difficult to observe. For example, the energy of the above-mentioned Kα X-ray radiation is 7.8 keV, ~300000 times higher than energy of neutrons with similar wavelength. Since the early 1950s, several research groups have demonstrated the existence of such inelastic processes in neutron scattering. The decisive breakthrough came from Brockhouse at Chalk River by the introduction of triple-axis-spectroscopy in 1958, a technique to put these studies on firm grounds adequate for theoretical interpretation.

In 1954 van Hove developed a general theoretical framework for neutron (and other) scattering experiments in condensed matter. The particular significance of the van Hove theory for neutrons was that since the neutron interaction with most condensed matter sample is weak (again a very important difference from X-rays), this theory applies with great precision in most cases. The theory allows us to calculate the probability for the neutron to scatter from an initial state with velocity $\boldsymbol{v}_i$ to a final state with velocity $\boldsymbol{v}_f$ for any complete model of the behavior of the sample, including both the arrangement of the atoms in space and their motion, for example, vibrations around steady equilibrium positions in solids, or the microscopic motion leading to fluidity in liquids. The van Hove scattering function $S(\boldsymbol{q}, E)$ is a function of two parameters, the momentum transfer vector $\boldsymbol{q}$ and the energy transfer E, which are defined in terms of the initial and final neutron velocities as follows:

$$q = mv_f/\hbar - mv_i/\hbar \quad \text{and} \quad E = mv_f^2/2 - mv_i^2/2 \qquad [5]$$

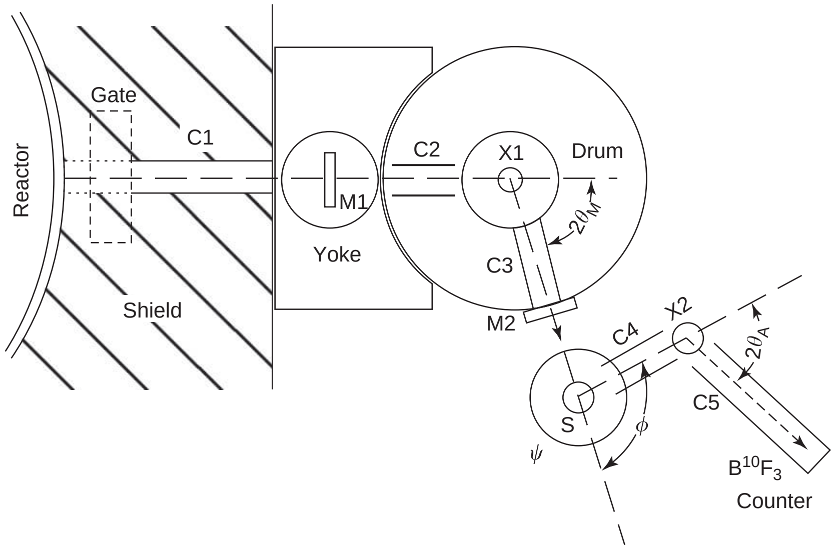

Figure 2 The basic layout of triple-axis spectrometers. The single crystals X1 and X2 are the monochromator and analyzer, respectively, and S is the sample. (Brockhouse BN and Stewart AT (1958) *Reviews of Modern Physics* 30: 236.)

where $\hbar = h/2\pi$ and v_f and v_i are the absolute values of the velocity vectors $\boldsymbol{v}_f$ and $\boldsymbol{v}_i$. The triple-axis technique of Brockhouse allows us to select a well-defined pair of values $\boldsymbol{q}$ and E. This was a real breakthrough, since the computing power in theoretical calculations was rather limited at that time and model calculations such as the energy dispersion relation of a phonon or magnon excitation branch α in single crystals, $E_\alpha(\boldsymbol{q})$, could only be calculated for special momentum transfer vectors $\boldsymbol{q}$ in highly symmetric directions in the crystals.

The principle of triple-axis spectroscopy is very simple (Figure 2): both the initial and final neutron velocities can be selected with great flexibility, by a monochromator and an analyzer crystal, in order to fulfill both the equations in [5] for a wide range of desired values of the four parameters represented by the vector $\boldsymbol{q}$ and the scalar E. This requires calculating the three scattering angles for the monochromator, sample and analyzer, and automatically setting the spectrometer and the orientation of these three crystals in the right configuration. This was the key technical innovation behind the introduction of triple-axis spectroscopy. The most common mode of operation is to design scans of one of the above-mentioned four parameters, for example, in "constant $\boldsymbol{q}$" scans a set of data points are taken at different E values, while the vector $\boldsymbol{q}$ is kept constant with respect to the sample. The diffractometer, or "two-axis" spectrometer, used by Shull and collaborators differs from the one in Figure 2 only by the lack of the analyzer crystal: the detector only records the distribution of the scattered neutrons as a function of the scattering angle, without analyzing the magnitude of their velocity. This is done under the tacit and frequently valid assumption that the inelastic scattering is weak compared to the elastic one with $v_f = v_i$, and therefore it can be neglected.

An alternative approach to inelastic scattering is to produce pulses of neutrons with a constant initial velocity $\boldsymbol{v}_i$ and determine the final velocity vector $\boldsymbol{v}_f$ by recording the time of arrival of the neutrons at the immobile detector banks surrounding the sample, where the position of each detector corresponds to a given scattering angle. A 2–4 m flight path between the sample and the detectors is sufficient to determine the final neutron velocities with a reasonable precision. This "time-of-flight" (TOF) method was developed at several places in incremental steps parallel to the triple-axis technique, including early work with mechanical choppers to produce neutron pulses by Jacrot at Saclay. TOF techniques are most often used for isotropic samples, for example, liquids, where only the absolute value of $\boldsymbol{q}$ matters, not its direction compared to the orientation of the sample. Figure 3 shows the elementary excitation spectrum of superfluid ^{4}He below 2.17 K. The observation of the minimum in the $E(q)$ dispersion relation at $q = 19.3\,\text{nm}^{-1}$ provided direct evidence for the theories of Landau and Feynman.

Polarized Neutrons

The van Hove scattering function as given above applies to the simplified situation of neglecting the neutron magnetic moment. While the initial and final states of the neutrons are only fully characterized by not only keeping track of the velocity but also of the direction of the magnetic moment vector $\boldsymbol{\mu}$ (or that of the associated neutron spin with $s = 1/2$), only the velocity has been considered so far. This corresponds to the real experimental situation in "unpolarized neutron scattering," where $\boldsymbol{\mu}$ is randomly oriented in the incoming beam and its orientation is not determined in the scattered beam. In the most general case, one needs to define both the initial and final states by the five parameters ($\boldsymbol{v}_i$, $\boldsymbol{\mu}_i$) and ($\boldsymbol{v}_f$, $\boldsymbol{\mu}_f$), respectively (vector $\boldsymbol{\mu}$ represents only two free parameters, since its magnitude is given). Thus, the van Hove scattering function will take the form $S_{\alpha,\beta}(\boldsymbol{q}, E)$, describing the

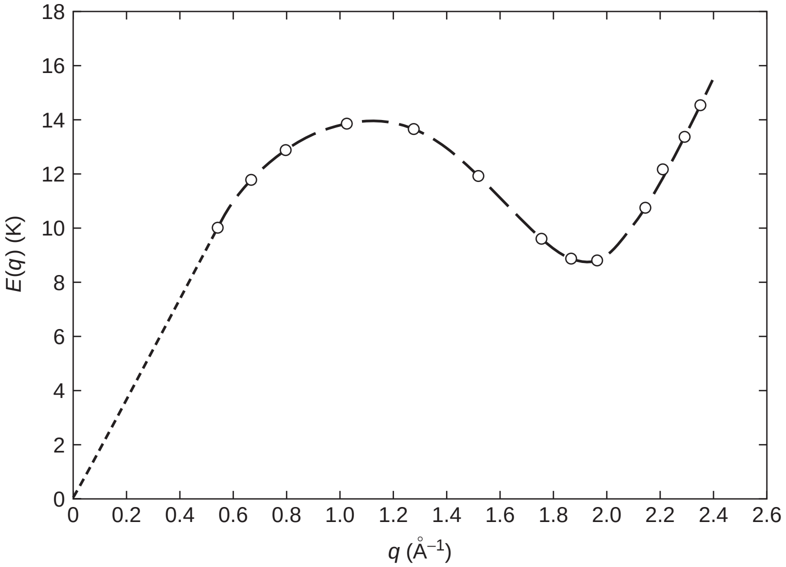

Figure 3 The dispersion relation of elementary excitations in superfluid ^{4}He observed by inelastic neutron scattering. (Yarnell JL, Arnold GA, Bendt PJ, and Kerr EC (1958) *Physical Review Letters* 1: 9.)

scattering probability from an initial neutron state with magnetic moment direction α to a final one with magnetic moment direction β.

The two basic methods used nearly exclusively until now to produce polarized neutron beams were also discovered early on, in 1951. One of them is essentially the reflection of neutrons on magnetized mirrors used by Hughes and Burgy to identify the interaction of neutrons with magnetic fields, as discussed above. The potential in eqn [2] for the internal B field in the ferromagnetic mirror (Fe or Co or their alloys) makes the critical angle of total reflection different for neutrons with magnetic moment oriented parallel or antiparallel to the direction of the field magnetizing the mirror. Thus, in the angular range between these two critical angles (referred to as "spin up" and "spin down" critical angles), the reflectivity will be substantially larger for one direction of the neutron magnetic moment, and the mirror selects from the originally unpolarized beam a preferred magnetic moment (or spin) direction. This technique is simple and inexpensive; it has the disadvantage though that the difference between the "up" and "down" critical angles is rather small, and therefore it can only select a rather limited fraction of the neutrons emerging from the reactor in all directions. In 1976 Mezei introduced the "supermirrors" to enhance the angular range of efficient polarizing neutron mirrors by complementing the range of total reflection by a range of nearly total reflection by interference on a stack of up to ~500 thin layers of alternating magnetic and nonmagnetic layers with carefully designed sequence of thicknesses between ~3 and 50 nm. Most mirror-based neutron polarizers in operation today use supermirrors.

The other basic method of polarizing neutrons is to use an adequate Bragg reflection from a single crystal. In ferromagnetic materials, unlike the case of antiferromagnets shown in Figure 1, the magnetism of the atoms leads to a magnetic contribution to the Bragg peaks corresponding to the atomic crystal structure. This makes the intensity of the reflection dependent on the relative direction of the neutron magnetic moment with respect to the magnetic field polarizing the sample. For a few special Bragg peaks in various materials, the intensity of the reflection can be two orders of magnitude different for neutron spins parallel or antiparallel to the crystal magnetization. This was first observed by Shull in 1950 for a reflection in magnetite, Fe_3O_4. He also pointed out that by observing the effect of the beam polarization on the scattered beam intensity in a magnetized sample one can increase the sensitivity of neutron scattering experiments in the study of weak signals from magnetic samples by orders of magnitude, for example, for detecting ordered magnetic moments in the range of $10^{-3}\,\mu_B$ per atom.

Polarization Analysis

For the unambiguous identification of the magnetic signals in complex magnets or inelastic scattering, in particular in paramagnetic or antiferromagnetic samples which cannot be magnetized in moderate fields, one needs to resort to polarization analysis. Here the scattered beam intensity might not depend on the initial beam polarization; instead, the scattered beam polarization needs to be determined. Experimentally this can be achieved by replacing both the monochromator and analyzer crystals on a triple-axis spectrometer by a crystal with a polarizing reflection and control the beam polarization between the polarizer and analyzer crystals, for example, by maintaining it in a given direction or "flipping" it. Several researchers have made important steps in this direction, in particular, Drabkin and collaborators at Gatchina. In 1969, Koehler, Moon, and Riste established the first experimental evidence for the characteristic polarization behavior of different scattering processes. In the approach, they established (what is now called "one-dimensional polarization analysis") that both the initial and final beam polarization can be either parallel (+ or "up") or antiparallel (– or "down") to the field direction on the sample. Thus, the choice of α and β directions in the above general form of the van Hove scattering function reduces to the combinations: "+ +" for the probability of scattering from the + neutron spin direction to the same one, $S_{++}(\boldsymbol{q}, E)$, and similarly "– –," "+ –," and "– +." The first two processes are without change of spin direction ("non-spin flip") and the last two ones involve the reversal of the neutron spin ("spin flip"). Later developments (primarily at Delft, Gatchina, and ILL, Grenoble) led to generalized or vectorial (3D) polarization analysis (or polarimetry), where α and β can be arbitrary directions. A historically important example of complex vectorial behavior of the scattered beam polarization is the early prediction by Halpern and Johnson in 1942 for the magnetic scattering in paramagnetic samples, giving the direction of the scattered beam polarization $\boldsymbol{P}_\mathrm{f}$ (which is defined as the average of the individual neutron magnetic moment directions in the beam) as a function of the initial one $\boldsymbol{P}_\mathrm{i}$ and the unit vector parallel to the momentum transfer $\hat{\boldsymbol{u}}=\boldsymbol{q}/\mathrm{q}$ as

$$\boldsymbol{P}_\mathrm{f} = -\hat{\boldsymbol{u}}(\boldsymbol{P}_\mathrm{i}\hat{\mathbf{u}})$$

Special cases of this relation (when $\boldsymbol{P}_\mathrm{i}$ and $\hat{\boldsymbol{u}}$ are either parallel or perpendicular) have been demonstrated in 1969 by Koehler, Moon, and Riste, while the full vectorial relation could only be verified later.

Neutron Spin Echo

The generic scheme of neutron scattering experiments consisting of preparation of an initial beam with more or less well-defined $\boldsymbol{v}_\mathrm{i}$ and analysis of the final distribution of $\boldsymbol{v}_\mathrm{f}$, as it is common, for example, for triple axis (Figure 2), TOF, and other techniques. It implies that for the observation of small changes, the initial and final velocities must be very well defined, that is, very few neutrons will be selected from a broad distribution in direction and absolute velocity. The neutron spin echo method, invented by Mezei in Budapest (1972) uses a drastically different paradigm. It consists in making each neutron effectively carry its own stopwatch and, using this, compare a selected component of $\boldsymbol{v}_\mathrm{i}$ with another component of $\boldsymbol{v}_\mathrm{f}$. Thus, the determination of minute relative changes of the neutron energy in the 10^{-6} range can be measured at a rough monochromaticity of 10–20%. The Larmor precession of the magnetic moment of each neutron in well-defined magnetic fields serves as the clock attached to each neutron (Figure 4). Neutron spin echo thus allows to extend the upper limit of time domain 10^{-14}–10^{-9} s where atomic motions can be studied by methods of inelastic neutron scattering up to 10^{-6} s, making accessible many processes in macromolecular systems.

Steady-State and Pulsed Neutron Sources

The most recent revolution in neutron scattering is driven by the evolution of the methods of producing neutron beams. As we have seen, the need to select neutron beams with a more or less well-defined initial velocity $\boldsymbol{v}_\mathrm{i}$ by some monochromator implies that one should throw away the vast majority of the neutrons produced with a broad velocity distribution and emitted in all directions by the

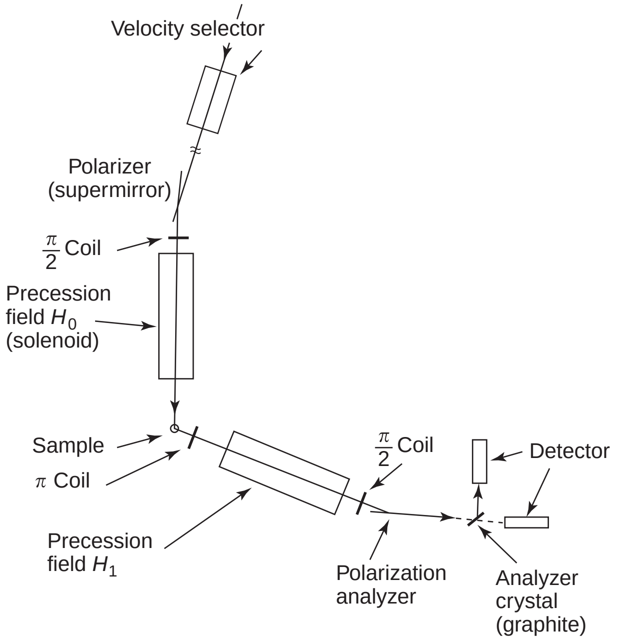

Figure 4 The layout of a neutron spin echo spectrometer. (Mezei F (ed.) (1980) *Neutron Spin Echo*. Berlin: Springer.)

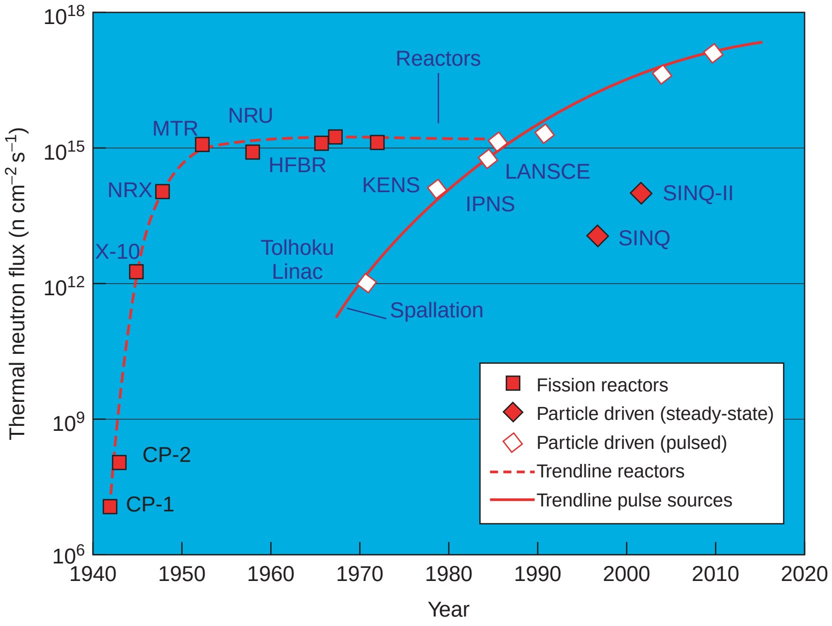

Figure 5 Evolution of the flux of neutron sources available for neutron scattering over the past decades at different facilities. The flux is defined here as the number of neutrons crossing unit area of the surface of the ambient temperature moderator in unit time. It is measured in units of cm^{-2} s^{-1}. For pulsed sources, the flux at the peak of the pulses is shown.

moderators. Cutting out pulses of the beam by a mechanical chopper was found early on as an efficient way to select their velocity, for example, 0.2 ms pulses every 10 ms provide a suitable monochromatic beam for TOF spectroscopy over a typical flight path of 20 m. Such a monochromator only needs neutrons for a short time every 10 ms; for the rest the source could be switched off to save costs and heat production, the latter being the ultimate technical limitation. It is difficult but not impossible to operate reactors in a pulsed fashion, and this approach has been pioneered at Dubna near Moscow since the 1960s. The IBR-2 pulsed reactor source at Dubna today achieves 1500 MW instantaneous power (heat production) when switched on for about 0.3 ms, while steady-state reactors cannot practically surpass 100 MW.

Neutrons can also be produced by accelerators, that can easily operate in a pulsed mode. This approach was first pioneered by Tohuku University in the 1960s using electrons. The most efficient accelerator-based neutron production technique, the so-called "spallation," was established in Argonne near Chicago by Carpenter and collaborators in the 1970s. Here a pulsed proton beam is accelerated to typically 1 GeV energy, and each proton absorbed in a heavy-metal target sets free ~30 neutrons in a series of collisions with the nuclei. Thus, the energy needed per neutron produced (~30 MeV) is much less than the ~190 MeV heat accompanying the birth of a recoverable neutron in the fission process in reactors. The great new potential offered by high-power spallation sources, as illustrated in Figure 5 by the peak instantaneous neutron flux they can produce during the pulse, is based on this double gain of efficiency: less heat is produced per usable neutron and the source is switched off for much of the time when no neutrons are needed. Although, by itself, the peak flux of a pulsed source compared to the time average flux of a steady-state reactor does not fully characterize its performance in all applications, the great potential of progress with future multi-MW spallation sources is well illustrated in Figure 5.

Neutron Optics

While source performance has not improved much since the 1950s in terms of number of neutrons produced, the intensity of neutron beams available in scattering experiments has steadily increased over the same period of time, in particular by the advent of Institut-Laue-Langevin (ILL) in Grenoble, the most powerful neutron scattering facility in the world operated through a European collaboration. At the 58 MW fission reactor at ILL three different moderator temperatures 25, 300, and 2000 K are available in order to provide the best-adapted neutron spectrum for the various instruments, and that has become a standard for more recent research reactors. The art of "neutron optics," the development of increasingly efficient components for transporting, shaping, monochromatizing, and analyzing neutron beams has also steadily progressed. One of the key inventions was the introduction of neutron guides by Maier-Leibniz in München in the early 1960s. Neutron guides are rectangular tubes with cross-section up to 100--200 cm^2 with the internal walls made of totally reflecting mirrors (usually highly polished glass coated with an adequate metallic layer). These guides can transport intense neutron beams over large distances with minimal losses with a beam divergence limited by the critical angle of total reflection (typically a few tenths of a degree). More recently, the divergence, and hence the intensity of the beam transported in the guides, is enhanced by using supermirror coating. The early single crystal monochromators are replaced by arrays of single crystals focusing the beam on the sample, and an increasingly larger fraction of the scattered neutrons is captured by using large position-sensitive area detectors. The combination of continuously advancing neutron optics with the enhanced neutron flux of the next-generation neutron sources means that the power of neutron scattering methods is increasing much faster than indicated by the trendline in Figure 5 for spallation sources.

Further Reading

Bacon GE (1975) *Neutron Diffraction*. Oxford: Clarendon Press.
Mezei F (1986) La Nouvelle Vague in polarized neutron scattering. *Physica* 137B: 295–308.
Schofield P (ed.) (1983) *The Neutron and its Applications*. Bristol and London: The Institute of Physics.
Squires GL (1978) *Introduction to the Theory of Thermal Neutron Scattering*. Cambridge: Cambridge University Press.

Ceramics, History of

I Yasui, University of Tokyo, Tokyo, Japan

© 2005 Elsevier Ltd. All rights reserved.

This is an update of I. Yasui, Ceramics, History of, Editor(s): Franco Bassani, Gerald L. Liedl, Peter Wyder, Encyclopedia of Condensed Matter Physics, Elsevier, 2005, Pages 173–177, ISBN 9780123694010, https://doi.org/10.1016/B0-12-369401-9/00481-2.

Introduction **437**
History of Development of Ceramics **438**
Large-sized Insulator and Ceramic Carrier 438
Alumina (Aluminum Oxide) and Substrate Material 438
Development of Ceramic Capacitors 439
History of Piezoelectric Ceramics 439
Ion Conductivity Ceramics 439
Development of Ceramic Sensors 440
Ferrite Materials and Magnetic Recording 440
Ceramic Turbocharger and Ceramic Turbine 440
Superconducting Ceramic Materials 440
Optical Fibers 440
Conclusion **441**
Further Reading **441**

Introduction

A ceramic is defined as a nonmetallic inorganic solid, but in a narrow sense it is a massive solid obtained by the heat treatment process of inorganic powders.

Ceramics have a long history. One of the first materials used by humans was a stone implement. Obsidian in composition, such a material can be classified as being glassy. Similarly, porcelain and earthenware also have a long history. The same can be said of glass too; human beings produced glassy solids in 3000 BC. Ceramic powder was also used as an adhesive at the time of the construction of the pyramids.

Ceramics are classified, from the viewpoint of structure, as: (1) single crystal, (2) sintering object, (3) glass, and (4) powder.

1. The technology to produce single crystals artificially is difficult; moreover, it is not suitable for mass production. Commercial ceramic products in the form of single crystals are, therefore, rather new historically. At present, some of the single crystals such as a quartz oscillation unit and an optical crystal are of much importance, because it is impossible to obtain the desired properties by using materials other than single crystals.
2. Sintered bodies are obtained by a forming process where starting powders are pressurized and the massive solid is obtained by subsequent heat treatment. Although earthenware was the origin of this technique, ceramics with various functionalities were developed.
3. Glass is a material obtained through a melting state by heating starting raw powders at a high enough temperature. Since the composition of common glasses was similar to that of earth, it was made artificially as early as in 3000 BC. However, these early glasses were not transparent. Although glass as a transparent material was developed later, it was only in the twentieth century that the technology of manufacturing sheets of glass with larger area became available.
4. Powders have been used from the BC period by grinding natural ores. The history of pigments also goes back a long way. Powder today means such materials as can be used in making high-performance sintered ceramic bodies. Original materials for ceramics were natural minerals, especially silicates. Clay, which is a natural silica mineral and very suitable for the production of porcelains, was the primary raw material for a long time. It is, therefore, understandable that the industry which used clay emerged first. The ceramic industry showed a marked progress after materials other than silicates came into use. Alumina is the first example and titanium oxide as a dielectric followed in industrial use. These simple oxides offered an easy control of the properties of their powders, suggesting that substances with easy handling became raw materials for practical use.

Silicate industries have also undergone constant development. The wall thickness of ordinary china used for tableware is ~1 mm; ~50 μm thick silicate ceramics are manufactured in large quantities as catalyst carriers for cars (in the absence of this technology, automobiles would perhaps be contributing to air pollution at levels even higher than they do now).

As a next step, complex oxides constituted the mainstream of the practical use of ceramics. The first generation of complex oxide ceramics are barium titanates and ferrites. These substances came to be used, due to a great deal of development in the management of purity, fine-tuning of composition, surface modification, etc. For example, the control of grain boundaries is one of the most important parameters that determines the total characteristics of a ceramic material. New types of ceramic heaters, which are capable of self-control of temperature with a composition of barium titanates, were developed and used. These are characterized by controlled grain boundaries and the so-called positive temperature coefficient (PTC).

Most industrial applications of ceramics exploit the characteristics of the substrates on the one hand and the electronic or ionic properties of their constituents on the other.

Nowadays, the most useful example of functional ceramics are lead zirconium titanates (PZTs). For instance, cellular phone designs are materialized by using these piezoelectric ceramics. Barium titanates and ferrites, sometimes called electronic ceramics, are extensively used in the electronics industry. This is because the electronic properties play a crucial role in determining the function of these ceramics.

Simultaneously, materials using the ionic properties of ceramics have also emerged and are used practically. The purification of the exhaust gas of a car is attained due to the use of zirconium oxide ceramics as an oxygen sensor, thus utilizing the ionic conductivity of oxide ions. It is called a solid electrolyte because the substance has conductivity due to an ionic motion within a solid. One of the notable examples is beta alumina, which is now used as an electrolyte for an Na–S battery, a large-sized rechargeable battery for load leveling of electric power.

A compositional survey of the possible properties of oxides containing two or three metals has already been conducted. Although additive agents are used to promote sintering or optimization of properties, compounds which principally contain more than four kinds of metals are seldom examined. In this unexplored area, a new category of ceramic materials has emerged, that is, superconducting ceramics.

It is to be noted that the most important characteristic of ceramics is their tolerance to high temperature. For many years, oxides have been used as refractory materials. It is quite clear that “refraction” supports the basic technology in the metal-refining industry. By extending the function of an oxide as a high-temperature material to the extreme, its application in the area of energy production etc., can be expected. However, it was not oxides, but nitrides and carbides, which attracted attention as such materials in the 1980s. As a result, a ceramic turbocharger was developed for automobiles. Although non-water-cooled engines made from ceramics were proposed to be used, this has not yet been realized.

The glass industry at present is very large in scale. This is one of the several reasons for natural silica to be the major raw material in the industry. An example of the application of glass, which uses transparency to its extreme, is the optical fiber. An optical fiber is made from very high purity silica although it includes a very small quantity of additives to control the contour of refractivity.

The composition of the often used glasses resembles that of sheet glass or bottles. The insulated film used in semiconductor devices is also glassy. Although only glassy material with a simple composition can be used in device processes, one can expect new compositions to find future applications.

Cement is a material which has been used in large quantities for a long time. Of course, it is also a product of the silicate industries. The use of a material in such large quantities is bound to pose a problem of depletion of resources, sooner or later.

History of Development of Ceramics

In the preceding section, an outline of ceramics was given from the historical point of view. The present section selects some ceramics as examples to consider the development process in more detail.

Large-sized Insulator and Ceramic Carrier

The largest ceramic (1.2 m $\varnothing \times 12$ m length) ever made was the insulator for 1000 kV power transmission. In consideration of it being corrosion-proof and earthquake-resistant, it had a special form of a bamboo hat and was made of large-sized porcelain with a thick wall.

The catalyst system was established as a primary means of automobile exhaust gas purification. Although started in the form of pellets, the monolithic honeycomb-type catalyst carrier was developed in 1976. This type of catalyst opened up the possibility of stricter emission control of automobiles.

Cordierite, with a composition of $2MgO{\cdot}Al_2O_3{\cdot}5SiO_2$, was used because of excellent heat resistance due to a low expansion coefficient. In the initial stage, the number of cells was ~200/square inches (1 inch=2.54 cm) but later reached 900 square inches, and the wall thickness decreased from 12 mil (1 mil=0.0254 mm) to 2 mil.

Alumina (Aluminum Oxide) and Substrate Material

Some aluminum oxides have been used for many years as refractory materials. Examples range from highly pure alumina crucibles to low-purity alumina pipes or plates for low-heat-resistance applications. Their application as an insulator for spark plugs was developed in 1931, and alumina started being used in automobile and electronics industries.

The decisive extensive use of ceramic materials in electronic industries occurs in the form of substrate materials used as a part of large-scale integrated circuits. Alumina substrates for electronic circuits cover a wide range of products, such as those made by the thick-film process, the thin-film process, and multilayer-type circuit boards. Alumina powders with purity higher than 99.5%, with 0.2% of magnesium oxide as additives, are generally used to give a flat and smooth surface, which is excellent for use as substrates.

The multilayer aluminum circuit board was first developed by IBM for the CPU used in the 308 X series mainframe computers. The CPU was $90 \times 90\ mm^2$ in size and the number of layers was 33. It was evaluated that this circuit board had superior properties both in the delay time of signal propagation and heat dissipation. Silver, gold, copper, etc., were used as conductive materials for wiring.

Because of the success of the alumina circuit board for the CPU, other substrate materials with higher heat dissipation capability, such as in the AlN and SiC boards, were investigated. Since AlN and SiC have simple crystal structures, both materials have excellent thermal conductivity, provided the grain boundaries are controlled. Since AlN is an insulator, it is only necessary to control the grain boundaries to obtain a high heat conduction, but since SiC has electronic conductivity, it is inevitable to control the grain boundaries so that it is electrically insulating. It was found that the addition of BeO as a sintering agent changed ceramics to insulating substrates.

Although ceramic substrates for large-scale integrated circuits were excellent in performance, the production cost was a prohibitive factor for use of this product. The semiconductor packaging process was changed, and it was found that even plastic could be used as a substrate. If ceramic substrates continue to be used in the electronics industries, they will be limited to high-performance type of products, such as single crystals or diamond.

Development of Ceramic Capacitors

Natural materials such as mica have historically been used in capacitors for a long time. Electrolyte capacitors use an aluminum oxide thin film as a dielectric. Several other oxides have been used as capacitor materials for many years.

It is well-known that barium titanate has a high dielectric constant (several 1000 or more). This ceramic was independently developed and studied in USA, Japan, and the Soviet Union. The abnormalities of the dielectric constant of barium titanate were discovered by Wainer and Salomon in 1942, which was an important breakthrough in the application of ceramics after World War II. Subsequently, Vul and co-workers, von Hippel, and Ogawa and Waku studied the ferroelectric properties of barium titanate.

However, from the point of its practical use, it is important to note that it took a remarkably long time from the discovery of barium titanate as a substance to its development as a ceramic capacitor. It was actually in the 1990s that the ceramic capacitor with a multilayer-type structure using barium titanate came to be loaded into almost all electric devices. This is because it took time to develop the process of manufacturing multilayer ceramic capacitors on a large scale. A process using the doctor blade method is first used to form thick films, and it is necessary to carry out the lamination of films. The technical developments, other than that of a ceramic layer, were also important. The development of conductive layers using nickel for an internal electrode was also a key factor in the development of the technology.

History of Piezoelectric Ceramics

The piezoelectric effect was discovered by Jack and Pierre Curie in 1880. Materials that display the piezoelectric effect need to be in the form of single crystals. Therefore, in order to use this effect for practical purposes, single crystals of appropriate materials were produced industrially. In Japan, Toyo Communication Equipment industrialized the production of quartz by the hydrothermal method in 1959.

Other materials were also studied for use as piezoelectric ceramics. Since it was reported by Bell Laboratories in 1963 that the thin film of CdS worked as a piezoelectric transducer, development of piezoelectric thin films and thick films started. The development of the thick-film process and materials that were more suitable for mass production attracted much attention. PZT, that is, $Pb(Zr, Ti)O_3$, discovered in the late 1950s, became the primary candidate for practical applications. A phase transition occurs when the Zr/Ti ratio is 53/47. In the vicinity of the phase boundary with this composition, the dielectric constant and the piezoelectric constant become the maximum.

In order to make a piezoelectric body of this composition, materials with random orientation cannot be used. Therefore, polarization processing was indispensable during sintering and the related process itself had to be developed. A number of sheets must be laminated as a layer, especially in the case of an actuator; thus, the manufacturing technology acquires key importance.

In Europe, a restriction in the use of lead in electronic products will be in effect from the year 2006. PZT, of course, contains lead. It does not necessarily mean that this material will be prohibited from use in Europe soon, but it is also possible, that if a new material for replacement is developed, PZT will then be forbidden. Therefore, development of piezoelectric materials which do not contain lead is now in severe competition.

Ion Conductivity Ceramics

It has been known for many years that glass and other ceramics show an alkali ion conduction. For example, a group of substances called beta alumina, containing Na as a component (in spite of being known as alumina), have been known as Na ionic conductors for many years. Their crystal structures were analyzed in the 1950s.

The Na–S battery, which uses beta alumina as an electrolyte, was proposed as a large-sized rechargeable battery for load leveling after the oil crisis of the 1970s. The Na–S battery attained the level of practical use at last by a joint development of NGK Insulators and the Tokyo Electric Power Co., (the delivery track record in 2002 was set at 5000 kW).

Although historically, ZrO_2 has been used due to its very high chemical durability at very high temperature, it was already known at the end of the nineteenth century that ZrO_2, with the addition of CaO or Y_2O_3, has oxygen ion conductivity. This material attracted attention after its use as an oxygen sensor for automobile exhaust gas purification was proposed. As an oxygen sensor,

ZrO_2 plays the role of a solid electrolyte similar to that in fuel cells. A solid electrolyte-type fuel cell, on the other hand, has not yet reached a stage where it can be used in practical applications.

Development of Ceramic Sensors

It must be noted that a ceramic material used as a chemical sensor brings about an improvement in the performance of various electrical appliances. The range of home electrical appliances which were originally apparatuses that could only detect temperature, now also include appliances (such as air conditioners, microwave ovens, or refrigerators) which can detect humidity, carbon dioxide, infrared radiation, etc. This development has been required from the viewpoint of increasing energy efficiency in relation to global warming and other environmental issues. In addition, detection of flammable gas, such as hydrogen, methane, and a liquefied petroleum gas, is indispensable because of concerns of safety. A gas sensor that made use of SnO_2 was developed. The principle of a gas sensor itself is rather conventional. The ZrO_2 sensor already mentioned is the so-called concentration cell type, and the principle is also classic.

The SnO_2-type gas sensor utilizes the characteristics of compounds as semiconductors, along with the capability of gas adsorption. It has, therefore, been an important target in its development as to how the most suitable textures and microstructures could be formed in ceramics to enhance the properties of adsorption of thick-film materials.

There are several ways for a modified usage of ion-conducting ceramics to detect a certain gas. One is to use ion-conducting ceramics together with the auxiliary electrode, which consists of the conduction ion and detection gas components. For example, in the case of the carbon dioxide sensor using beta alumina, $NaCO_3$ (containing Na^+, the conduction ion of beta alumina) and the carbon dioxide of the detection gas will be used as the auxiliary electrode. Many approaches for development range between such theoretical understanding and the practical design of a sensor (see section "Further reading").

Ferrite Materials and Magnetic Recording

A ferrite, which is a magnetic oxide body, was invented by Takei and Kato in the 1930s. Ferrites are widely used as a core material for a transformer or magnetic heads. The oxide permanent magnet was also invented during almost the same period, and after that, it has been used as a low-cost permanent magnet material. Iron oxide ceramic powder is used as a magnetic recording material in videotapes such as VHS. A record system may change to a perpendicular type and oxide powder may be used again, although currently metallic materials are used for the purpose of high-density recording.

Ceramic Turbocharger and Ceramic Turbine

Silicon nitride and silicon carbide, which are the main components of nonoxide ceramics, are artificial compounds. Since these compounds have a strong covalent bond in nature, till 1960 it was accepted that they could not be sintered.

The first oil shock pushed the development of efficient energy devices, and the use of ceramic materials, which can be employed at much higher temperatures, was pursued. It was proposed in the 1980s that nonoxide ceramics could be used as parts of a gas turbine. The ceramic gas turbine project (CGT) was actually undertaken from 1988 to 1999 in Japan. A CGT with 300 kW power for co-generation and a 100 kW CGT for automobile use were developed. However, it has not reached the stage of commercial production, mainly because of production costs.

Ceramic turbocharger turbine blades made of silicon nitride are an example of a practical application of a nonoxide. Ironically, the material originally developed for raising energy efficiency was used in the automobile industry, which aimed at producing fuel-inefficient cars. However, the ripple effect was large. Nonoxide ceramics now have several applications, which are growing steadily.

Superconducting Ceramic Materials

In 1986, an oxide superconductor of the lanthanum–barium–copper system was first announced by Bednorz and Muller of the IBM Zurich Research Institute and its critical temperature T_c was 35 K, which exceeded the historical T_c 23 K of the NbGe. The Y–Ba–Cu system oxide was discovered in the following year and the critical temperature exceeded 77 K, which is the temperature of liquid nitrogen. Then, various new compound oxides, such as the Hg system, the TI system, and the Bi system, were announced.

A F Hebard and others have reported that the powder of C_{60} with doped potassium ($K_3 C_{60}$) shows a superconducting nature at a critical temperature of $T_c = 18$ K, and the same thin film of $K_3 C_{60}$ shows the superconducting nature at a critical temperature of T_c=16 K. MgB_2 has recently been reported to become superconducting at 39 K (for further details, see section "Further reading"). Thus, superconductivity is serving as a frontier of the science of new compounds in the ceramics system.

Optical Fibers

In 1964, Nishizawa succeeded in developing graded-index-type optical fibers for communications.

In 1966, Kao found that if heavy metals contained in glass were removed, the absorption loss of light in glass decreased dramatically. This epoch-making discovery was the key to utilizing an optical fiber and one that enabled the material development of low-loss fibers. Kao also had the foresight of proposing the structure of today's optical fibers consisting of a clad with a low refractive index and a core with a high a refractive index glass.

Following the basic work of Nishizawa and Kao, Corning Inc. succeeded in making low-loss (20 dB km^{-1}) fibers. Subsequently, the basic technology of the present-day information technology grew through a stiff competition in the development of optical fibers.

Conclusion

Ceramics are practically useful materials. From their discovery, through application development and testing (the so-called seed-driven route), ceramics have come a long way. However, new materials with superior properties continue to be desired in a variety of application areas. Given the limitations of the global environment, exploring new ceramic materials is a real challenge for further sustainability.

Further Reading

Bednorz JG and Muller KA (1986) *Zeitschrift fur Physik B* 64: 189.
Burger WG and Weigei CW (1982) *IBM Journal of Research and Development* 297.
Hebard AF, et al. (1991) *Nature* 350: 600.
Nagamatsu J, Nakagawa N, Muranaka T, Zenitani Y, and Akimitsu J (2001) Superconductivity at 39 K in MgB_2. *Nature* 410: 63.
Ogawa T (1947) Physical-properties theory research. No. 6, 1.
Tsuji S, Mizuishi K, Nakayama Y, Shimaoka M, and Hirao M (1983) *Japanese Journal of Applied Physics* 22: 239–242.
von Hippel, Breckenridge RG, Chesley FG, and Tisza L (1946) *Ind. Eng. Chem.* 38: 1097.
Vul M and Goldman LM (1945) *C. R. USSR* 46: 139.
Wainer and Salomon AN (1942) *Electronic Reports 8* – Titanium Alloy Mfg. Co.
Wu MK, Ashuburn JR, Torng CJ, Hor PH, Meng RL, et al. (1987) *Physical Review Letters* 58: 908.
Yamazoe N and Miura N (1994) *Sensors and Actuators B* 20: 95–102.

Porous Silicon[☆]

Z Gaburro, N Daldossoh, and L Pavesi, Università di Trento, Povo (Trento), Italy

© 2016 Elsevier Inc. All rights reserved.

This is an update of Z. Gaburro, N. Daldossoh, L. Pavesi, Porous Silicon, Reference Module in Materials Science and Materials Engineering, Elsevier, 2016, ISBN 9780128035818, https://doi.org/10.1016/B978-0-12-803581-8.01134-6.

Generalities and Definitions **442**
Fabrication Procedures **442**
Anodization 442
Anodization Mechanisms 443
Drying Techniques 445
Oxidation Techniques 446
Structural Properties 447
Chemical Properties 447
Electronic Properties 447
Electrical Properties 448
Optical Properties **448**
Light Diffusion and Scattering 448
PL **448**
S-Band 449
Other Bands **450**
Absorption 450
Applications **451**
LEDs 451
Sensors, Biosensors, Medical Applications 452
Further Reading **452**

This article deals with generalities and definitions of porous silicon (PSi): fabrication techniques, structural properties, chemical properties, electronic properties, electrical properties, optical properties, and actual or potential applications of PSi. Optical properties include light transport, photoluminescence (PL), and electroluminescence (EL).

Generalities and Definitions

PSi was discovered by Uhlir in 1956 while performing electrochemical etching of silicon. In 1990, Canham showed that certain PSi materials can have large PL efficiency at room temperature in the visible: a surprising result, since the PL efficiency of bulk silicon (Si) is very low, due to its indirect energy bandgap and short nonradiative lifetime. The reason for this was the partial dissolution of silicon, which causes (1) the formation of small silicon nanocrystals in the PSi material; (2) the reduction of the effective refractive index of PSi with respect to silicon, and hence an increased light extraction efficiency from PSi; and (3) the spatial confinement of the excited carriers in small silicon regions where nonradiative recombination centers are mostly absent. In general, PSi is an interconnected network of air holes (pores) in Si. PSi is classified according to the pore diameter, which can vary from a few nanometers to a few micrometers depending on the formation parameters (**Figure 1**). According to the general classification of porous materials, three size regimes are defined as in **Table 1**.

The word 'nanoporous' is sometimes used for the smallest-pore regime to emphasize the nanometric dimension. The volumetric fraction of air of the material is called porosity (P). The internal surface of PSi per unit volume can be very large, of the order of 500 $m^2\ cm^{-3}$. The enhanced PL efficiency of Psi–compared to Si–has motivated research toward other porous semiconductor materials. For example, highly porous SiC, GaP, $Si_{1-x}Ge_x$, and Ge structures have been investigated.

Fabrication Procedures

Anodization

PSi is mostly fabricated by electrochemical anodization–often referred to as electrochemical etching–of bulk Si wafers in diluted aqueous or ethanoic hydrofluoric acid (HF). Ethanol is often added to facilitate evacuation of H_2 bubbles, which develop during the process. Typical anodization arrangements are schematically shown in **Figure 2**. Another much less common technique is stain etching, or chemical etching (with no current flow), performed with HF– HNO_3 solution.

[☆] *Change History*: June 2015. Z. Gaburro, N. Daldossoh, and L. Pavesi updated the reference list.

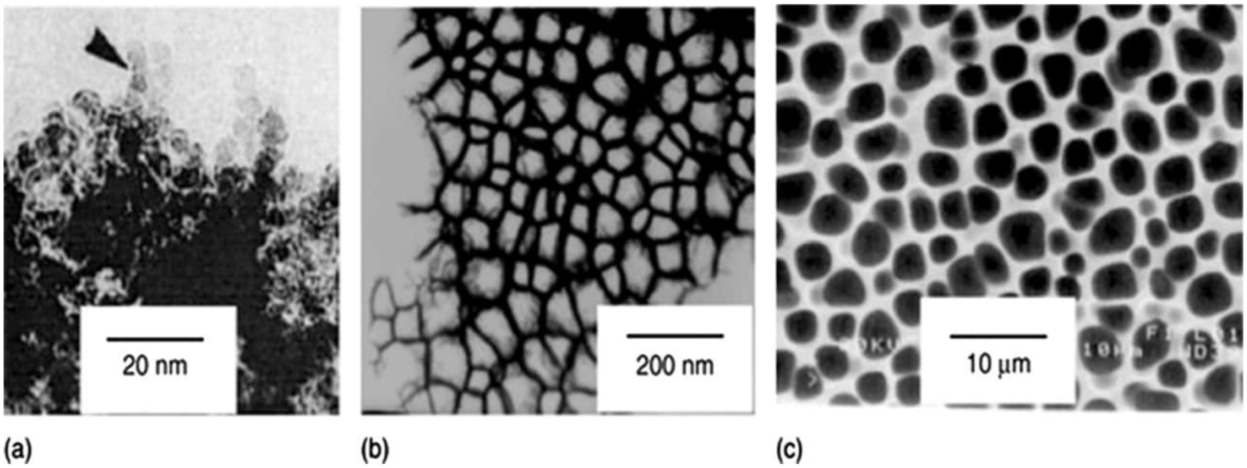

Figure 1 Examples of PSi structures: (a) microporous, (b) mesoporous, and (c) macroporous. (a) Reproduced with permission from Cullis, A.G., Canham, L.T., 1991. Visible light emission due to quantum size effects in highly porous crystalline silicon. Nature 353, 335–337; © Nature Publishing Group.

Table 1 IUPAC classification of porous materials

Dominant pore width (nm)	*Type of material*
≤ 2	Microporous
2–50	Mesoporous
>50	Macroporous

The anodization can be performed either in potentiostatic (voltage-controlled) or in galvanostatic (current-controlled) mode. The latter is normally preferred, because it supplies the required charge for the reaction at constant rate, regardless of any evolution – during anodization – of the cell electrical impedance, ultimately leading to more homogeneous and reproducible material. The typical values of the most important anodization parameters, along with their impact on the anodization process, are reported in Tables 2 and 3. Three sample setups for fabrication of different PSi structures are shown in Table 4. The anodization can be modulated. The modulation is most easily achieved by varying the applied current density. Modulation results in controlled changes of the microstructure and the porosity of PSi along the growth direction. For example, PSi multilayer films can be simply created by varying the current density in time.

The position of pore nucleation can be controlled by etch pits, defined by a lithographic step before the anodization (Figure 3). This option is in practice limited to macroporous PSi, since present lowest lithographic resolution limits are in the range of a hundred nanometers. For example, ordered two-dimensional periodical matrices of pores can be formed, leading to materials with remarkable optical transport properties (2D photonic crystals, see Figure 4). PSi singlelayers or multilayers can be fabricated as free-standing samples. The detachment from the substrate can be achieved by applying a short pulse of high current density, that is, exceeding the electropolishing threshold, typically some hundreds of mA cm^{-2}.

Anodization Mechanisms

Typical current–voltage (I–V) characteristics of the electrochemical cell are shown in Figure 5. It should be stressed that the quantity having physical meaning is the current density J (at the Si/electrolyte interface), rather than the absolute current I. J and I scale with a fixed constant for a given cell, provided that the area of the Si sample exposed to the electrolyte is well defined and fixed.

In order to form PSi, the current at the Si side of the Si/electrolyte interface must be carried by holes, injected from the bulk toward the interface. The current must be kept between zero and the electropolishing threshold, which can be identified as the value of the first maximum of the anodic regime in the I–V curve. Useful regimes are included in the hashed region of Figure 5, where the electropolishing threshold voltage (for the curve marked with open circles) is $V \sim 1.3$ V. In order to achieve significant hole current in n-type Si, external illumination of the sample is required, depending on the doping level. If the current exceeds the electropolishing threshold, the anodization results in a progressive, complete removal of Si. The wafer then has a mirror-like appearance.

A hypothesized chemical reaction which could describe the anodization is .

$$Si + 6HF \rightarrow H_2SiF_6 + H_2 + 2H^+ + 2e^- \qquad [1]$$

The last term – a negative charge at the interface, to be neutralized by the current flow – would explain the need of hole injection from the substrate toward the Si/electrolyte interface. Similar to most semiconductor junctions, at the Si/electrolyte interface a

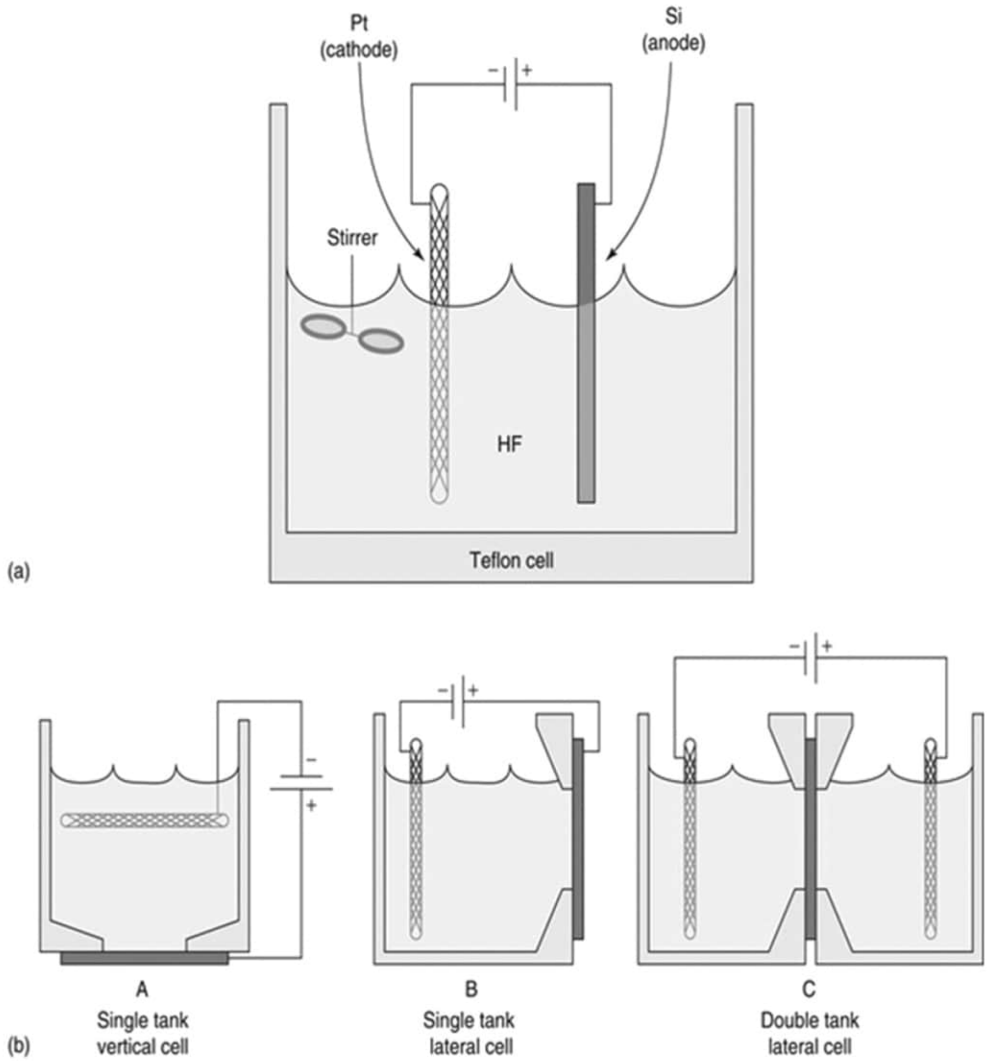

Figure 2 Schematic anodization arrangements: (a) principle and (b) practical examples (A, B, and C). Platinum and Teflon are mostly used because of their chemical resistance to HF. In the practical arrangements A, B, and C, the Si area exposed to the solution–typically ~1 cm^2, circular–is well defined by the Teflon cell. Rubber gaskets between Si and Teflon can easily avoid spills. Type A is easier to design, type B is convenient when Si illumination is desirable (e.g., for *n*-type Si, see section 'Fabrication procedures'), and type C does not require electrical contacts on Si. An optional stirrer is sometimes used to improve diffusion of HF during the anodization and H bubbles removal.

Table 2 Critical parameters of the anodization procedure

Parameter	*Typical range*	*Unit*
HF concentration	2–40	% (in weight)
Current density	0.5–150	mA cm^{-2}
Anodization time	5–1800	s
Temperature	250–300	K
Wafer resistivity (*p*-type)	0.001–100	Ω cm
Wafer resistivity (*n*-type)	0.001–100	Ω cm

Source: A typical electrochemical solution can include, for example, water (H_2O) in an approximately equal amount of HF, the rest being ethanol.

depletion zone is formed. The width of this depletion zone depends on the doping and may explain the different pore sizes found in p^--and p^+-type doped silicon. In addition, the depletion layer width depends on the surface curvature: the anodization preferentially occurs at the pore tips where the curvature is largest. Moreover, when the depletion zones of adjacent pores meet each other, the current flow is suddenly pinched off. Further Si etching is blocked, and pore collapsing is prevented. For this reason, the reaction is self-limited in the hashed anodization regimes of Figure 5, and leads to a porous structure rather than to electropolishing. As further

Table 3 Effect of anodization parameters on PSi formation

An increase of	*Porosity*	*Etching rate*	*Electropolishing threshold*
HF concentration	Decrease	Decrease	Increase
Current density	Increase	Increase	
Anodization time	Increase	Almost constant	Increase
Temperature			Increase
Wafer doping (*p*-type)	Decrease	Increase	
Wafer doping (*n*-type)	Increase	Increase	

Source: As an approximate rule of thumb, the etch rate is of the order of 1 nm s^{-1} for each mA cm^{-2} of the anodization current density.

Table 4 Three sample sets of anodization parameters, for p-type Si substrates, resulting in the three different structural regimes described in **Table 1**

HF concentration (%)	15	15	2
Current density(mA cm^{-2})	50	50	5
Wafer resistivity (Ω cm)	5	0.01	10
Resulting structure	Microporous	Mesoporous	Macroporous

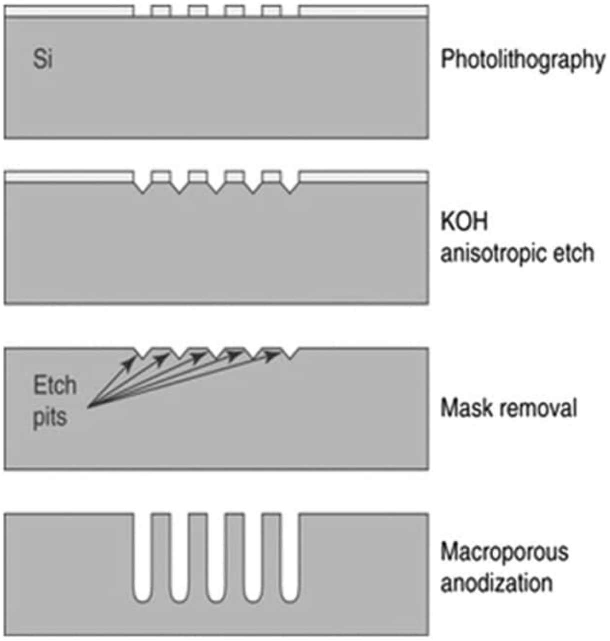

Figure 3 Schematic lithographic procedure resulting in the definition of pore-starting etch pits.

practical consequence, in stationary conditions, the porosity remains approximately constant, whereas the overall thickness of the PSi layer grows essentially linearly in time.

Back-side illumination (most conveniently achieved using cells of type B, Figure 2) in potentiostatic regime, with *n*-type Si, allows a useful, further control on the hole injection, both in terms of carrier flux (which is proportional to illumination intensity) and of localization of the injection, which is concentrated in the region of the pore tips, acting as hole collectors. The etching process leads to a very regular pore growth, which is most effectively exploited to fabricate macroporous photonic crystal devices (Figure 4).

Drying Techniques

Due to large capillary stress, drying of samples is a critical step and can result in extended cracking if special procedures are not followed. Methods to reduce or eliminate the capillary stress include pentane drying, supercritical drying, freeze drying, and slow evaporation rates. Pentane drying is the easiest to implement. Pentane has a very low surface tension, and shows no chemical interaction with PSi (unlike ethanol). Using pentane as drying liquid enables to strongly reduce the capillary tension, but since water and pentane are nonmiscible liquids, ethanol or methanol have to be used as intermediate liquids. Using this drying technique, PSi layers with porosity values up to 90% and thickness up to 5 μm exhibit no cracking pattern after drying. Super-critical drying

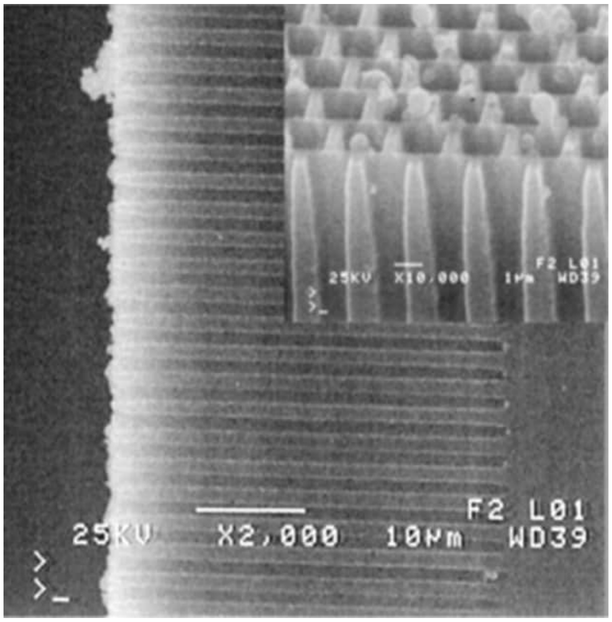

Figure 4 Example of a photonic crystal (cross section and top-view images of the same sample) realized with ordered macroporous PSi in a *p*-type doped silicon substrate. This photonic crystal has a photonic bandgap at 3.5 μm.

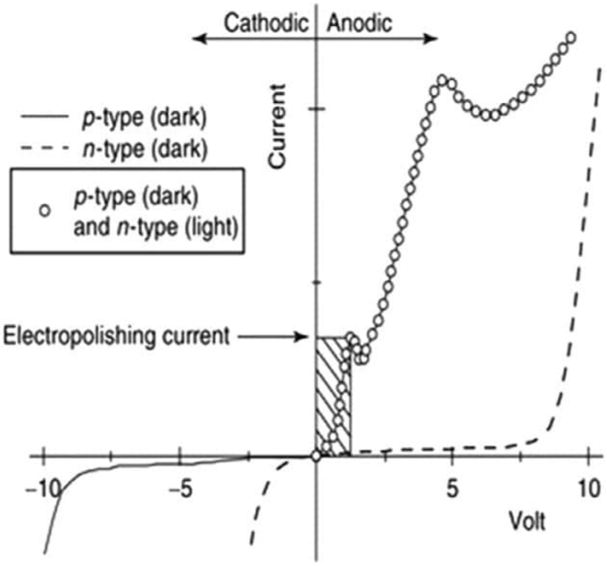

Figure 5 Typical *I*–*V* characteristics of an electrochemical cell for PSi fabrication (**Figure 2**). The hashed region corresponds to the useful regime where PSi can be achieved, assuming the *I*–*V* characteristic marked with hollow circles. In the anodic regime, the characteristics of a cell with *n*-type Si will lie in the region bounded by the characteristic in dark (dashed line) and in full light (hollow circles).

requires a specific apparatus but is more effective in preventing cracking of the film so that PSi layers of porosity values up to 95% were demonstrated.

Oxidation Techniques

As soon as PSi samples are dried, hydrogen surface passivation is gradually replaced by native oxide. This chemical change affects most PSi properties, for example, PL and electrical conductivity. Since the characteristics of the native oxide strongly depend on many factors such as the storage conditions, evolution of sample properties is often poorly characterizable. To stabilize PSi properties, oxidation is often used. Oxidation implies the formation of a layer containing the original Si atoms. Therefore, it also reduces the nanocrystallite size, with remarkable impact on PL emission energy (blue-shift). The employment of controlled oxidation procedures is therefore a valuable post-anodization option toward a better control of PSi properties and stabilization.

Tested oxidation procedures on PSi include anodic oxidation, chemical oxidation, thermal oxidation, plasma-assisted oxidation, and irradiation-enhanced oxidation. Anodic oxidation is an electrochemical process, in which oxide layers are formed with current injection. As such, the technique is structurally selective: more conductive paths get more oxidized. This selectivity is particularly interesting for light-emitting diode (LED) applications, where more conductive paths are usually associated to large injection channels, which are poorly luminescent, and their oxidation results in enhanced EL quantum efficiency. Another application of controlled oxidation – mostly thermal – is the fabrication of small, blue-luminescent PSi nanocrystallites.

Structural Properties

Structural properties of PSi have been investigated by electron microscopy, scanning probe microscopy, X-ray scattering techniques, X-ray absorption techniques, and Raman spectroscopy. In particular, X-ray absorption spectroscopy can be performed not only by extended X-ray absorption fine structure (EXAFS) analysis, but also by X-ray excitation of optical luminescence (XEOL), a convenient tool for luminescent samples, in which absorption is probed via the measurement of the corresponding optical emission. A general feature resulting from the comparison of these techniques is that highly luminescent PSi is a composition of extensively connected Si crystals of nanometric dimensions (typically, 1–5 nm in radius). Sizes smaller than Si Bohr radius (~ 4.9 nm), imply significant quantum confinement effects. Raman measurements are also often used to demonstrate crystallinity in PSi skeleton and infer information on the size of Si nanocrystals.

Accurate determination of pore size distribution in mesoporous Si is usually given by the analysis of adsorption isotherms of gases at low temperature (Brunauer–Emmett–Teller, or BET, method). The physical adsorption by a porous surface is increased relative to a nonporous one because of capillary condensation in pores. This increase in adsorption starts when the gas pressure is high enough to fill the smallest pores.

Chemical Properties

Surface chemical composition of PSi is best probed with Fourier transform infrared (FTIR) spectroscopy. FTIR signal in PSi is larger and easier to measure than in bulk Si due to much larger specific area. Chemical bonds and their IR resonance positions detected in PSi are shown in Table 5. In fresh, as-prepared samples, oxygen is normally absent, the dominant bonds being Si–H_x groups ($x = 1$, 2, or 3). Aging is observed as a slow replacement of H by O bonds in PSi. Also, luminescence fatigue is explained by photochemical reactions occurring on the surface of the Si nanocrystals.

Electronic Properties

The first and most favorable explanation for the visible emission in PSi is the quantum confinement of excitons in nanometer-sized silicon. An empirical law, based on the effective mass approximation, links the energy gap E_g of silicon nanocrystals with their sizes $\ell : E_g(\ell) + E_g^{Si} + 88.34/(\ell)^{1.37}$(eV), when ℓ is given in Å. The energy gap opening is given by an equal energy shift of the bottom of the conduction band to high energy and of the top of the valence band to low energy. The nature of the energygap is still indirect even though a quasidirect bandgap can be formed in ultrasmall Si nanocrystals.

Table 5 Wave number positions and attributions of the absorption peaks observed in several PSi samples by Fourier transform infrared absorption FTIR measurements

Peak position (cm^{-1})	*Attribution*	*Peak position* (cm^{-1})	*Attribution*
3610	OH stretch (SiOH)	1463	CH_3 asymmetric deformed
3452	OH stretch (H_2O)	1230	$SiCH_3$ bending
2958	CH stretch (CH_3)	1056–1160	SiO stretching in O–SiO and C–SiO
2927	CH stretch (CH_2)		
2856	CH stretch (CH)	979	SiH bending in SI_2– H– SiH
2248	SiH stretch (O_3– SiH)	948	SiH bending in Si_2– H– SiH
2197	SiH stretch (SiO_2– SiH)	906	SiH_2 scissor
2136	SiH stretch (Si_2O– SiH)	856	SiH_2 wagging
2116	SiH stretch (Si_2H– SiH)	827	SiO bending in O–Si–O
2087	SiH stretch (Si_3– SiH)	661	SiH wagging
1720	CO	624	SiH bending in (Si_3SiH)

Electrical Properties

Electrical resistivity in PSi is five orders of magnitude higher than in intrinsic Si, because PSi is depleted of free carriers. Depletion can occur either because of the energy gap widening from quantum confinement which reduces the thermal generation of free carriers, or because of trapping of free carriers. Trapping can occur during the preparation of PSi either because the binding energy of dopant impurities are increased or because of the formation of surface states. It has been demonstrated that the dopants are still present in essentially unchanged concentration after the etching, but are in a neutral state.

The electrical transport is mainly affected by the disordered structure of the Si skeleton which restricts the conductive paths to a highly constrained geometry, which for certain porosities forms a percolated or fractal geometry. As a consequence, conductivity is thermally activated, strongly frequency dependent, and highly dispersive. Several models have been proposed to explain the electrical transport properties. They differ on the transport paths and mechanisms. The proposed transport paths range from transport in the Si nanocrystals (with diffusion or tunneling between the Si nanocrystals or at their surface) to transport in the amorphous and disordered matrix surrounding the nanocrystals, or through both. The suggested mechanisms are band transport, activated hopping in band tail, trap-controlled hopping through nanocrystals, activated deep states hopping, Pool–Frenkle processes, and activated hopping in fractal networks.

Given the large specific area per unit volume, the electrical transport is strongly influenced by external factors such as residual electrolyte and ambient atmosphere. The latter property is very interesting for sensor applications. Certain gases – for example, NO_2 – have the capability of modifying the free carrier population. Changes in the electrical conductivity in the presence of sub-ppm concentrations of such gases can be detected at room temperature operation. Other gaseous species (e.g., polar liquid vapors) also affect electrical transport via electric field interactions with charge carriers.

Optical Properties

Light Diffusion and Scattering

The dimension l of the PSi structures (i.e., the pore size and the porous layer thickness), compared to the optical wavelengths λ, can range from $l \ll \lambda$ all the way to $l \approx \lambda$. There are accordingly two different regimes of light propagation and interaction with PSi.

The first regime is $l \ll \lambda$. The radiation fields cannot resolve the PSi structures, and the interaction can be conveniently described by means of an 'effective medium approximation,' where a macroscopic dielectric constant (or a refractive index) is evaluated as a suitable combination of the dielectric constants of Si and air. The result is, in general, a complex dielectric function of space. Effective medium theories, which are routinely used for PSi, are enumerated in **Table 6**. Refractive index values are reported in **Figure 6**.

The second regime is $l \sim \lambda$. These kinds of structures are called mesoscopic: the structural size is small compared to the wave coherence length, that is, the maximum length along which phase memory and coherent phenomena are observable. The porous geometrical structure strongly influences light transport and interaction. Useful mathematical models take advantage either of the Bloch theorem (in the case of periodical structures (photonic crystals)), or of statistical and Green's function methods (in the case of aperiodic or random structures).

Mixed regimes are also possible in PSi. The most important case is the one-dimensional (1D) mesoscopic structure: the anodization parameters are set to achieve microporous PSi (size of pores $\ll \lambda$, first regime), but the anodizing current density is modulated to obtain periodical or aperiodical thin layer structures (thickness $\sim \lambda$, second regime along the PSi growth direction). Each layer is different from adjacent layers in terms of porosity and thus of effective dielectric constant (and effective refractive index). Compared to other thin-film growth techniques, PSi has the advantage of allowing a continuous tuning of the refractive index over a wide range ($1.4 \ll n_{\mathrm{eff}} \ll 1.4$), and of being a fast and cheap technique that can lead to structures of several hundreds of layers, with typical fabrication times ranging from few minutes to few hours.

In the presence of high-index liquids (and/or their vapors), the refractive index of the porous layer changes, affecting light transport properties. The effect can be exploited for gas sensors and biosensors applications.

PL

Microporous PSi structures have been reported to luminesce efficiently in the near infrared (IR) (0.8 eV), in the whole visible range, and in the near ultraviolet (UV) (**Figure 7**).

Table 6 Useful effective medium approximation for the dielectric function of PSi

Theory	*Formula*
Bruggeman	$P\frac{\varepsilon_M - \varepsilon_{\mathrm{eff}}}{\varepsilon_M + 2\varepsilon_{\mathrm{eff}}} + (1 - P)\frac{\varepsilon - \varepsilon_{\mathrm{eff}}}{\varepsilon + 2\varepsilon_{\mathrm{eff}}} = 0$
Maxwell Garnett	$\frac{\varepsilon_{\mathrm{eff}} - \varepsilon_M}{\varepsilon_{\mathrm{eff}} + 2\varepsilon_M} = (1 - P)\frac{\varepsilon - \varepsilon_M}{\varepsilon + 2\varepsilon_M} = 0$
Looyenga	$\varepsilon_{\mathrm{eff}}^{1/3} = (1 - P)\varepsilon^{1/3} + P\varepsilon_M^{1/3}$

Source: ε, dielectric function of Si; ε_M, dielectric function of host material (normally: air); $\varepsilon_{\mathrm{eff}}$, calculated effective dielectric function; P, porosity.

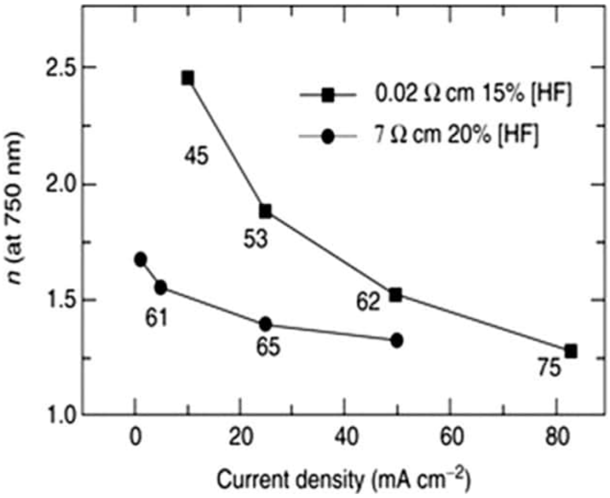

Figure 6 Refractive index as a function of current density and porosity for two different substrate doping levels.

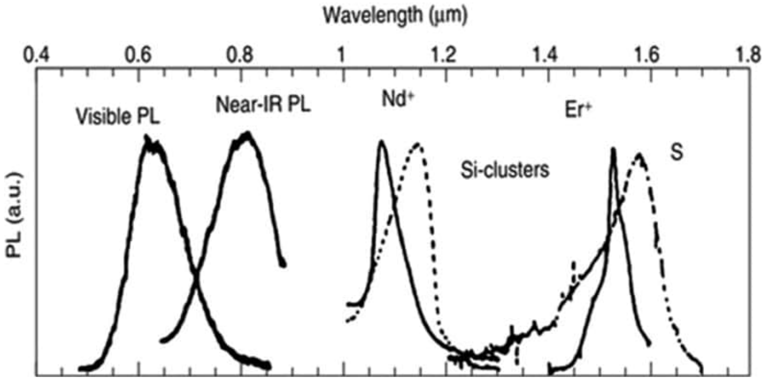

Figure 7 Room temperature photoluminescence spectra for various PSi structures which have been oxidized or implanted with some selected impurities. Reproduced from Fauchet, P.M., Tsybeskov, L., Duttagupta, S.P., Hirschman, K.D., 1997. Stable photoluminescence and electroluminescence from porous silicon. Thin Solid Films 297(1–2), 254–260, with permission from Elsevier.

Such a broad range of emission energies arises from a number of clearly distinct luminescent bands, which are listed in Tables 7–9. In addition, PSi has been used as an active host for rare-earth impurities, for example, Nd or Er, or dye solutions. Direct energy transfer between PSi and the impurity or dye is demonstrated. The most efficient and studied emission is the slow (S) band because it can be excited by electrical injection. The most popular model for the PL – especially for the S-band – is excitonic radiative recombination subject to quantum confinement. Other models are surface states models, the siloxene model, defect models, the surface hydrides model, and the hydrogenated amorphous silicon model. Coexistence of more than one mechanism is likely.

S-Band

It can be tuned from close to the bulk silicon bandgap through the whole visible range. The large spectral width comes from inhomogeneous broadening and vibronic coupling of the radiative transitions. The S-band efficiency is not proportional to the

Table 7 PSi luminescence bands

Spectral range	*Peak wavelength (nm)*	*Label*
UV	~350	UV band
Blue-green	~470	Fast (F) band
Blue-red	400–800	Slow (S) band
Near IR	1100–1500	IR band

Table 8 Some spectral characteristics of the S-band

Property	*Typical values*	*Comments*
Peak wavelength	1100–400 nm	At 300 K, depends on porosity
PL external quantum efficiency	$\geq 5\%$	At 300 K, depends on porosity
FWHM	0.3 eV	At 300 K (8 meV in PSi microcavities)
PL decay times	$\simeq 10\ \mu s$	Strongly dependent on wavelengths, temperature and aging condition
Polarizability ratio	$P \leq 0.2$	
Fine structure under resonant excitation	Phonon replica at 56 and 19 meV	Heavily aged PSi, energies consistent with Si phonons

Table 9 Some spectral characteristics of the F-band

Property	*Typical values*	*Comments*
Peak wavelength	480 nm	UV excitation at 300 K
PL efficiency	$\geq 0.1\%$	External quantum efficiency UV excitation at 300 K
FWHM	0.4 eV	UV excitation at 300 K
PL decay times	1ns	Independent on wavelength and excitation conditions

inner surface area: a 'threshold' porosity has to be exceeded to achieve an efficient luminescence. Postanodization chemical etching in HF, corresponding to a porosity increase, results in a strong rise in PL efficiency and a blue shift of the visible band. External quantum efficiencies higher than 0.1% are obtainable from high-porosity PSi layers of all types, but efficiency normally decreases in the order n^--type, p^--type, n^+-type, and p^+-type doped PSi. High porosity is essential for high visible PL efficiency. The inefficient luminescence observed from inhomogeneous material of low porosity originates from microscopic areas of high porosity. Isolated nanocrystals, produced by dispersing a colloidal suspension of PSi fragments on a glass coverslip, show external quantum efficiencies □88%, with a number of bright-to-dark nanocrystals in the suspension of only 2.8%. Thus, the average quantum efficiency of a PSi layer of 1% results from a statistical distribution of high and low quantum efficiency nanocrystals.

Phonon-assisted luminescence (vibronic-coupled transitions) is demonstrated by fine structure in resonantly excited PL at low temperature. Thus, the electronic and the vibronic structure of the luminescence of PSi are similar to crystalline Si, with an energy shift consistent with quantum confinement. At large confinement energies(>0.7 eV), no-phonon quasidirect transitions dominate, because of the breakdown of k-conservation under strong confinement.

The luminescence is polarized parallel to the exciting light. This is measured by recording the polarization ratio $\rho = (I_{\parallel} - I_{\perp})/(I_{\parallel} + I_{\perp})$. ρ is zero on the IR band and nonzero on the S-band (tending to zero as the energy approaches that of the Si bandgap). The interpretation is that PSi is an ensemble of randomly oriented aspherical nanocrystals, preferentially aligned along the $\langle 100 \rangle$ direction. Recombining carriers have bulk-like wave functions which are sensitive to the shape of the nanocrystals.

Aging effects include a blue shift in the S-band and changes in the PL efficiency (both increasing and decreasing have been observed), which can be explained in terms of surface oxidation. Anticorrelation exists between the dangling bond density and the luminescence efficiency; thus, the effect of the oxidation depends on its passivation properties.

Other Bands

The F-band is observed only in oxidized PSi, and it is probably originated from contaminated or defective Si oxide. Annealing in water vapor activated the blue emission indicating a possible major role of adsorbed hydroxyls in the emission process. The IR band is weak at room temperature, and becomes much stronger at cryogenic temperatures. Its origin seems to be related to dangling bonds, although no direct correlation has been demonstrated.

Absorption

The absorption coefficient has been measured in PSi by optical transmission, photoluminescence excitation (PLE), and photo-thermal deflection spectroscopy (PDL). Transmission spectra are shifted toward higher energy compared to bulk Si with a shift, which increases with increasing porosity. This observation is consistent with quantum confinement model. The line shape analysis of the absorption coefficient shows that its energy dependence follows a trend like that of an indirect gap semiconductor similar to Si, but displaced to higher energy.

A characteristic feature of PSi is the large displacement (Stokes shift) between the absorption edge and the emission peak energy (see Figure 8). The existence of localized states that can account for the observed shift has been demonstrated. Such states can lead to self-trapped excitons at some surface bonds of Si crystallites, such as Si–Si dimers and Si–O double bonds, giving reduced

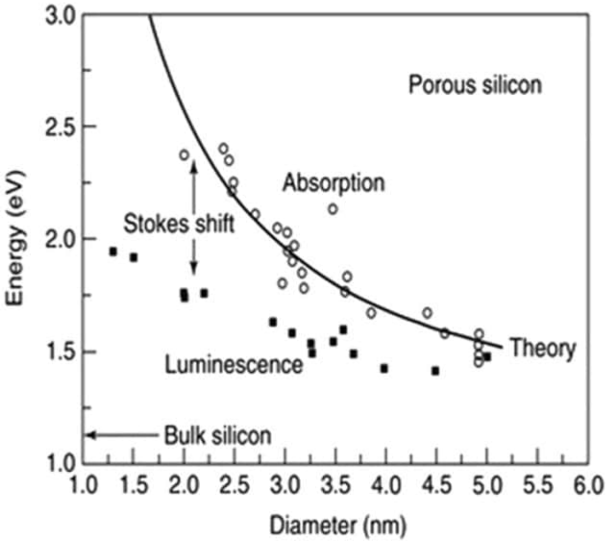

Figure 8 Compilation of optical bandgaps of PSi samples obtained from optical absorption (unfilled symbols) and luminescence (filled symbols). The lines represent calculated values with the empirical law reported in the text.

dependence of the luminescence energy on size, and a very large Stokes shift. Other models for the Stokes shift are based on Si quantum dot relaxation from distorted configurations, giving rise to new transitions involving localized states that lower the emission threshold with respect to the absorption.

Applications

Important actual or perspective applications of PSi are shown in Table 10.

LEDs

Si *p*/*n* junction emits light both in forward and in reverse bias conditions. Power efficiency is $\sim 10^{-4}(10^{-8})$ at 1.1 μm wavelength in forward (reverse) bias. Also in PSi based devices, EL is observed both in the IR and in the visible. Efficiency is higher than in bulk Si diodes, depending on the diode structure and on the PSi contact method. Initially, EL was observed with wet contacts and later with solid contacts. Major achievements in terms of quantum efficiency are summarized in Figure 9.

Table 10 Potential application areas of PSi

Application area	*Role of PS*	*Key property*
Optoelectronics	LED	Efficient electroluminescence
	Waveguide	Tunability of refractive index
	Field emitter	Hot carrier emission
	Optical memory	Nonlinear properties
Micro-optics	Fabry-Perot filters	Refractive index modulation
	Photonic bandgap structures	Regular macropore array
	All optical switching	Highly nonlinear properties
Energy conversion	Antireflection coatings	Low refractive index
	Photo-electrochemical cells	Photocorrosion cells
	Solar cells	
Environmental monitoring	Gas sensing	Ambient sensitive properties
Microelectronics	Micro-capacitor	High specific surface area
	Insulator layer	High resistance
	Low-k material	Electrical properties
Wafer technology	Buffer layer in heteroepitaxy	Variable lattice parameter
	SOI wafers	High etch selectivity
Micromachining	Thick sacrificial layer	Highly controllable Etching parameters
Biotechnology	Tissue bonding	Tunable chemical reactivity
	Biosensors	Enzyme immobilization

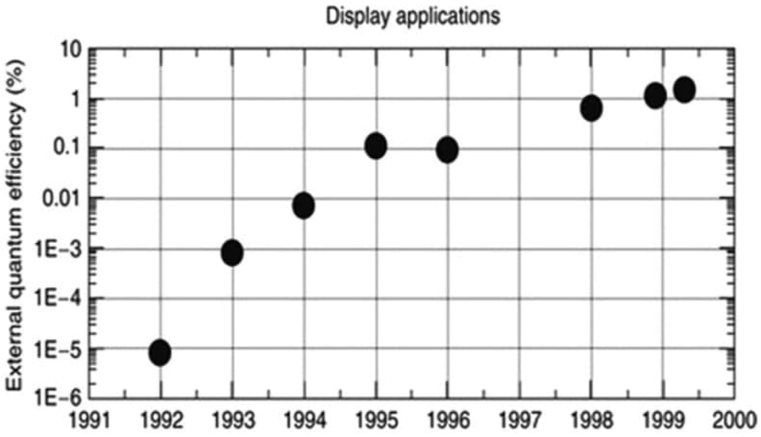

Figure 9 Time evolution of the external quantum efficiency of porous silicon-based LEDs for display applications.

Sensors, Biosensors, Medical Applications

PSi is a twofold promising material for sensor applications. On one side, its electrical and optical properties strongly depend on the environment, because of its large specific area. Useful sensing parameters include, for example, the electrical conductivity and photoluminescence. Most sensing parameters can effectively work at room temperature. On the other side, it supplies a handy template to hold chemical and biological species. Target species can be immobilized in the PSi matrix, a practice which is especially useful for biological samples–such as oligonucleotides, biotin, or antibodies. Techniques for immobilization range from physical adsorption to the replacement of hydride bonds with Si alkyls, and to antibody bonding at functionalized PSi surface with subsequent antibody–antigen interactions. Species identification can be performed by probing optical, electrical, or chemical properties. Examples include, respectively, reflectivity or wave-guiding measurements (which depend on the dielectric constant of the species, as already discussed), conductance measurements, and pH measurements. Biocompatibility of PSi has suggested medical applications, such as *in vivo* slow release of drugs, *in vivo* diagnostic tests, and template for bone growth.

Further Reading

Amato G, Delerue C, and von Bardeleben HJ (1997) Optical and structural properties of porous silicon nanostructures. In: Manasreh MO (ed.) *Opto-Electronic Properties of Semiconductors and Superlattices*. series ed., 5: pp. 1–644. Newark: Gordon and Breach.

Bisi O, Ossicini S, and Pavesi L (2000) Porous silicon a quantum sponge structure for silicon based optoelectronics. *Surface Science Report* 38(1–3): 5–126.

Brus L (1996) Semiconductor colloids individual nanocrystals, opals and porous silicon. *Current Opinion Colloid and Interface Science* 1(2): 197–201.

Buriak JM (2002) Organometallic chemistry on silicon and germanium surfaces. *Chemical Review* 102(5): 1272–1308.

Canham L (ed.) (2014) *Handbook of Porous Silicon*. Springer Reference ISBN: 978–3–319–04508–5 (Online).

Canham LT (1990) Silicon quantum wire fabrication by electrochemical and chemical dissolution of wafers. *Applied Physics Letters* 57(10): 1046–1048.

Cullis AG, Canham LT, and Calcott PDJ (1997) The structural and luminescence properties of porous silicon. *Journal of Applied Physics* 82(3): 909–965.

Filler MA and Bent SF (2003) The surface as molecular reagent organic chemistry at the semiconductor interface. *Progress in Surface Science* 73: 1–56.

Föll H, Christophersen M, Carstensen J, and Hasse G (2002) Formation and application of porous silicon. *Material Science and Engineering R* 39(4): 93–141.

Gautier G and Kouassi S (2015) Integration of porous silicon in microfuel cells: A review. *International Journal of Energy Research* 39: 1–25. https://doi.org/10.1002/er.3206.

Gelloz B and Koshida N (2003) Electroluminescence of nanocrystalline porous silicon devices. In: Nalwa HS and Rohwer LS (eds.) *Handbook of Luminescence, Display Materials, and Devices*, pp. 127–156. Stevenson Ranch, CA: American Scientific Publisher.

Gösele U and Lehmann V (1995) Light-emitting porous silicon, matter. *Chemical Physics* 40(4): 253–259.

Granitzer P and Rumpf K (2010) Porous Silicon – A Versatile Host. *Material in Materials* 3: 943–998. https://doi.org/10.3390/ma3020943.

Harraza Farid A (2014) Porous silicon chemical sensors and biosensors. *A review in Sensors and Actuators B: Chemical* 202: 897–912. https://doi.org/10.1016/j.snb.2014.06.048.

Kochergin V and Föll H (2009) *Porous Semiconductors-Optical Properties and Applications, Springer Series: Engineering Materials and Processes*. Springer.

Martin-Palma Raul J and Manso-Silvan Miguel (2010) *Vicente Torres-Costa Biomedical applications of nanostructured porous silicon: a review in Journal of Nanophotonics* 4(1). , 042502https://doi.org/10.1117/1.3496303.

Monouk de Plessis A (2014) Decade of Porous Silicon as Nano-Explosive Material. *Propellants, Explosives, Pyrotechnics* 39: 348–364. https://doi.org/10.1002/prep.201300053.

Ossicini S, Pavesi L, and Priolo F (2003) *Light Emitting Silicon for Microphotonics. Springer Tracts in Modern Physics*. 194: Berlin: Springer.

Sailor MJ (2011) *Porous Silicon in Practice: Preparation, Characterization and Applications. Porous Silicon in Practice: Preparation, Characterization and Applications*. Weinheim: Wiley-VCH ISBN: 978–3–527–31378–5.

Sailor MJ, Heinrich JL, and Lauerhaas JM (1997) Luminescent porous silicon synthesis, chemistry, and applications. *Studies in Surface Science and Catalysis* 103: 209–235.

Santos H (ed.) (2014) *Porous Silicon for Biomedical Applications*, p. 558. Woodhead Publishing. ISBN :9780857097118.

Smith RL and Collins SD (1992) Porous silicon formation mechanisms. *Journal of Applied Physics* 71(8): R1–R22.

Stewart MP and Buriak JM (2000) Chemical and biological applications of porous silicon technology. *Advanced Materials* 12(12): 859–869.

Yerokhov VY and Melnyk II (1999) Porous silicon in solar cell structures a review of achievements and modern directions of further use. *Renewable and Sustainable Energy Reviews* 3(4): 291–322.

Electronic states of semiconductor compounds and alloys☆

Robert Kudrawiec, Department of Semiconductor Materials Engineering, Faculty of Fundamental Problems of Technology, Wroclaw University of Science and Technology, Wrocław, Poland

© 2024 Elsevier Ltd. All rights reserved.

This is an update of J.C. Phillips, Semiconductor Compounds and Alloys, Electronic States of, Editor(s): Franco Bassani, Gerald L. Liedl, Peter Wyder, Encyclopedia of Condensed Matter Physics, Elsevier, 2005, Pages 256-264, ISBN 9780123694010, https://doi.org/10.1016/B0-12-369401-9/00460-5.

Introduction **453**
Overview **454**
Chemical bonding in tetrahedrally coordinated crystals 454
Electronegativity and ionicity 454
Electronic band structure 455
Group IV and chemical trends 455
III-V semiconductors and chemical trends 457
II-VI semiconductors and chemical trends 458
Alloys 459
Polymorphism and ordering 460
Key issues **460**
Highly mismatched alloys 460
Band anticrossing model 463
Strain and band gap engineering 464
Van der Waals semiconductors and their alloys 465
Perovskites and their alloys 466
Conclusion **467**
References **467**
Further reading **468**

Abstract

Semiconductor alloys enable the band gap engineering in heterostructures widely used in optoelectronic devices. This article discusses the electronic properties of tetrahedrally coordinated crystals (group IV, III-V and II-VI semiconductors), and then uses these semiconductors as a model system to discuss chemical trends in semiconductor alloys and band gap engineering. Both the regular alloys and the highly mismatched alloys are described and compared for the three material groups. Additionally, the discussion of chemical trends in semiconductor compounds and alloys is extended to van der Waals crystals and perovskites, which are the next generation of semiconductors for optoelectronic devices.

Key points

- crystal lattice constant vs valence radius in the same group of semiconductors.
- band gap vs crystal lattice constant in regular semiconductor alloys.
- band gap vs crystal lattice constant in highly mismatched alloys.
- strain engineering in regular and highly mismatched alloys.
- chemical trends in the electronic band structure in van der Waals crystals and perovskites.

Introduction

As a result of arranging atoms in a periodic crystal lattice, we obtain a crystal that is characterized by a given symmetry and has specific mechanical, electrical and optical properties. These properties depend on the atoms and the symmetry of the crystal, i.e., the arrangement of the atoms. The same atoms arranged differently lead to crystals with different properties, and this is called polymorphism. The presence of stable crystalline compounds depends on the atoms and their arrangement as well as external conditions such as hydrostatic pressure or temperature. Among the semiconductors, the simplest and most studied system are those made of tetravalent elements, i.e., Si and Ge, which crystallize in the diamond structure. Another group that is equally well

---

☆*Change History*: April 2023. R. Kudrawiec rewritten the chapter and replaced figures.

researched, understood and widely used in the semiconductor industry is III-V compounds (GaAs, InP, GaSb, GaN, . . .). Like Si and Ge, most of them exist in a cubic structure (mainly Zinc-Blende (ZB) structure) and share eight valence electrons per anion/cation pair. However, some of them (III-Nitrides: InN, GaN, AlN) prefer hexagonal structure but retain tetragonal coordination of atoms. Tetragonal coordination is also realized in the II-VI compounds, but many of them prefer an octahedral coordinated rock salt structure. This article discusses the electronic properties of tetrahedrally coordinated semiconductor crystals, and then uses these compounds as a model system to discuss chemical trends in the alloying of semiconductor compounds. A lot of attention has been devoted to semiconductor alloys, which enable the band gap engineering in semiconductor heterostructures widely used in various optoelectronic devices. In this case, both the regular alloys and the highly mismatched alloys are described and compared for the three material groups (IV, III-V and II-VI semiconductors). Additionally, the discussion of chemical trends in semiconductor alloys is extended to van der Waals crystals and perovskites, which are the next generation of semiconductors recently intensively explored.

Overview

Chemical bonding in tetrahedrally coordinated crystals

In tetrahedrally coordinated crystals such as C, Si or Ge the electronic states can be described approximately as superpositions of Pauling's sp^3 hybrid atomic orbitals, see Fig. 1. The same description can be applied to diatomic compounds such as GaAs or InP, but in this case we are dealing with two types of hybrids, those pointing toward and away from the nearest neighbors. They correspond to bonding and antibonding band states, i.e., the valence and conduction band, respectively. When two atoms in a unit cell differ slightly in electronegativity (case of GaAs or InP) then the bonds are covalent, as in Si or Ge. However, as the difference in electronegativity and valence radius increases, the nature of these bonds becomes more and more ionic.

Electronegativity and ionicity

In general, electronegativity is the tendency for an atom to attract electron density when forming a chemical bond in a given chemical element. The higher the electronegativity, the more an atom attracts electrons. The first precise electronegativity scale was proposed by Linus Pauling and was based on the energy of bonds as an extension of the theory of valence bonds (Pauling, 1932). This scale starts at 0.79 and ends at 3.98 and is known as the electronegativity in Pauling units (dimensionless quantity). Both the atomic number of an element and the distance at which its valence electrons are on the charged nucleus affect the electronegativity of the atom.

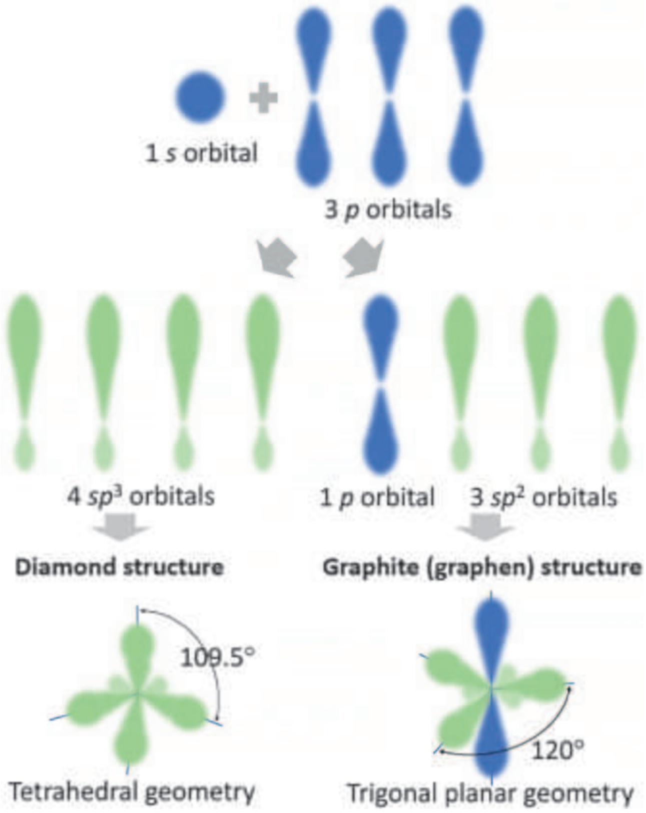

Fig. 1 Schematic illustration of the process of hybridization of *s* and *p* orbitals for carbon in the cubic diamond structure (left panel) and graphite (graphene) structure (right panel).

The ionicity of chemical bonds (polarity) characterizes a bond on a continuous scale from covalent to ionic bond, and electronegativity serves as a simple way to estimate bond ionicity. Usually, bonding is considered ionic where the ionic character is greater than the covalent character, but of course, a strict division into the nature of the bonds can be difficult in many cases and may not really be needed. Unlike covalent bonding, purely ionic bonding cannot exist because the close proximity of the atoms involved in the bond always allows some degree of sharing of the electron density between them. Therefore, all ionic bonding has some covalent character. Very often bonds with partially ionic and partially covalent character are called polar covalent bonds.

Very often electronegativity is a very good reference point for tracking changes in the band structure for semiconductor alloys as will be shown later in this chapter.

Electronic band structure

The electronic band structure (or simply band structure) of a given crystal is unique, as is the electronic structure of an atom. The band structure is obtained in the framework of the band theory, which is only an approximation to the quantum state of a solid, and applies to solids consisting of many identical atoms bonded together. Two factors determine the band structure of a perfect infinite crystal, i.e., the atoms and their arrangement. External factors such as pressure or temperature also influence the band structure, but this is a secondary effect.

In general, the band structure of a crystal describes the range of energy levels that electrons may have within it and the ranges of energy that they may not have (called band gaps). Imperfections in the crystal (point defect, impurities, dislocations) and the surface introduce additional energy states for electrons that are not discussed in this chapter.

To describe electronic states in solid state, the reciprocal lattice is introduced. This lattice exists in the space of spatial frequencies known as reciprocal space and represents the Fourier transform of a periodic spatial function in real space known as the direct lattice in which the arrangement of the atoms can be described (cubic, hexagonal lattice, etc.). While the direct lattice is the lattice of a crystal, the reciprocal lattice exists in the space of spatial frequencies known as $\boldsymbol{k}$-space, where $\boldsymbol{k}$ refers to the wavevector of plane waves of the Fourier transform. In solid state physics, $\boldsymbol{k}$-space is closely related to momentum space according to the proportionality $\boldsymbol{p} = h\boldsymbol{k}/2\pi$, where $\boldsymbol{p}$ is the momentum vector and h is the Planck constant. In this way $\boldsymbol{k}$-space provides a way to visualize the results of the Fourier transform of a spatial distribution of atoms in crystal lattice and enables the assigning of energy states to the electron. The first Brillouin zone ($\boldsymbol{k}$-space defined by the crystal symmetry) is used to represent the electron band structure for semiconductor compounds and alloys.

Thus, to describe the electronic states in a semiconductor crystal, we need to know the Brillouin zone for a given crystal structure (the Brillouin zone for the diamond structure and the zinc blend structure is shown in Fig. 2) and the dependence of the electron's energy on its wavevector in this space, i.e., $\boldsymbol{k}$-vector. These relationships can be obtained under various models, including the $\boldsymbol{kp}$ model or the density-functional theory (DFT), which is a computational quantum mechanical modeling method used in solid state physics to investigate the electronic structure of many-body systems in condensed phases. Today, DFT is one of the most powerful and versatile methods available in condensed matter physics for studying electronic band structure. This method also makes it possible to test the stability of a given compound in a given crystal structure, which makes it very useful in band gap engineering.

The electronic band structure obtained within DFT method for Si is shown in Fig. 2. The most important information that can be extracted from the electron band structure presented in this form is the value of the energy gap, i.e., the energy distance between the top of the valence band and the minimum in the conduction band. In such a band model, the energy gap separates the energy states occupied by electrons (valence band) from the unoccupied states (conduction band) and determines the electrical and optical properties of a given crystal. An electron must appear in the conduction band or a hole in the valence band (i.e., a quasiparticle that describes the lack of an electron in the valence band) for such material to conduct electricity. It depends on doping, but for undoped semiconductors it depends on the width of the energy gap. Therefore, narrow-gap semiconductors show conductivity even in the absence of doping, while wide-gap semiconductors without doping and without defects and impurities are insulators. This means that a simple analysis of the band gap width gives an indication of the conductivity potential of a given crystal. In the case of optoelectronic devices such as light emitting diodes or laser diodes, the character of the energy gap (direct vs indirect) is a key issue. For Si the minimum of conduction band is close to the X point of Brillouin zone while the maximum of the valence band is in the center of Brillouin zone at the Γ point, see Fig. 2. In such a situation, for an electron from the conduction band to recombine radiatively with a hole from the valence band, phonons (lattice vibrations) are needed to fulfill the principle of conservation of momentum and energy. This is at least a three-particle process, which is much less likely than a two-particle process, i.e., the electron-hole recombination. Therefore, direct gap semiconductors, in which the conduction band minimum and the valence band maximum are at the same point in the Brillouin zone, are used for light emitters. In addition to the width of the band gap and its nature (indirect vs direct), many other parameters that are important for the engineering of bands in semiconductor devices, e.g., effective masses for electrons and holes, can be derived from the band structure. In this chapter only the band gap is analyzed because it is the most important parameter of the band structure that determines the electrical and optical properties of semiconductor compounds and alloys.

Group IV and chemical trends

Fig. 3 shows the band gap as a function of the crystal lattice constant for group IV (elemental) semiconductors: diamond, silicon, germanium, gray tin (α-Sn) in the diamond structure. As the atomic number for these atoms increases, the valence radius increases

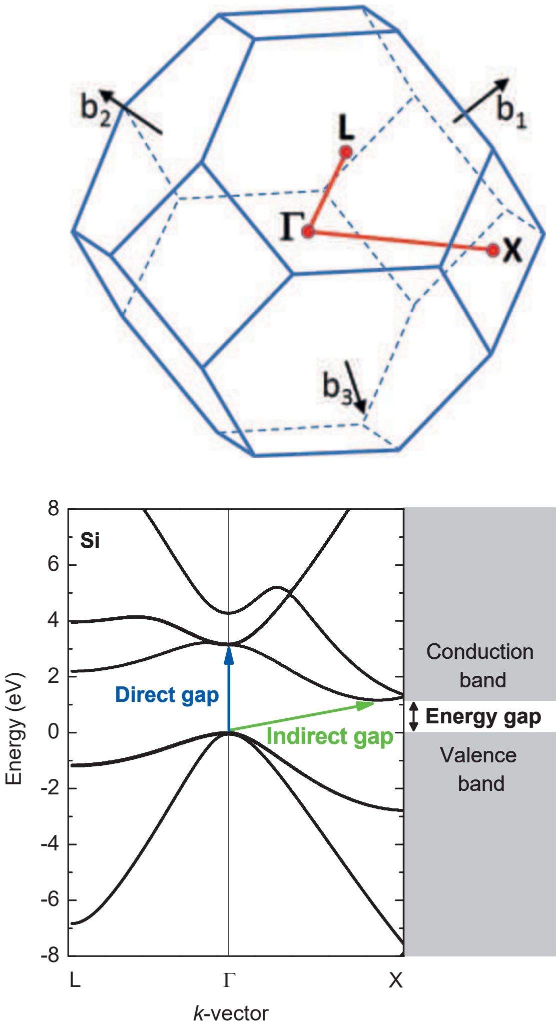

Fig. 2 The Brillouin zone for the diamond structure and the zinc blend structure (upper panel). The electronic band structure of Si along the Γ-L and Γ-X path together with the marked direct and indirect energy gap (bottom panel).

(C—0.70 Å; Si—1.10 Å; Ge—1.25 Å; Sn—1.45 Å) and leads to a larger lattice constant of the crystal, see Fig. 3 (a). This is the expected trend, but when it comes to lead, the preferred structure is no longer that of a diamond. Lead exists in a face-centered cubic (FCC) structure and forms metallic bonds in which only the *p*-electrons are delocalized and shared between the Pb^{2+} ions. Note that the lightest element in this group, carbon, forms other stable allotropes including graphite, but with the tetrahedrally coordinated and covalently bonded cubic structure of the diamond, it is the most stable crystal. The series of these four elemental semiconductors (C, Si, Ge and Sn) makes it possible to follow the chemical trends in the band structure of tetrahedrally coordinated semiconductor crystals.

Going from light element to heavy, the band structure changes from wide-gap semiconductor (C) through typical semiconductor (Si), narrow-gap semiconductor (Ge) and reaching semimetal (Sn), see Fig. 3 (b) and (c). The valence orbitals that participate in the formation of the valence and conduction bands in these semiconductors have the same symmetry (*s* and *p*) but they originate from other period and this is the reason for the observed very significant changes in the electronic band structure. These changes can be correlated with the crystal lattice constant as a narrowing of the band gap with an increase in the crystal lattice constant, which appears to be a very general chemical trend in semiconductors when the crystallographic structure is preserved. This trend is intuitively understandable also from the point of view of simple models in quantum mechanics. By bringing the same atoms together in place of degenerate energy levels (the case of separated atoms), bonding (valence band) and anti-bonding (conduction band) states are created, separated from each other by an energy gap, which will be larger if the distance between the atoms (crystal lattice constant) is smaller. However, it should be remembered that as the atomic number increases, subsequent shells are filled and electrons from these shells affect the dispersion of the valence and conduction bands including the band gap. This, among other factors, makes α-Sn a semi-metal and Pb loses tetrahedral coordination and is present in the FCC structure. In addition, many other parameters (elastic constants or band gap) describing elemental semiconductors (C, Si, Ge, Sn) show similar chemical trends, i.e., a regular change with the increase of the crystal lattice constant.

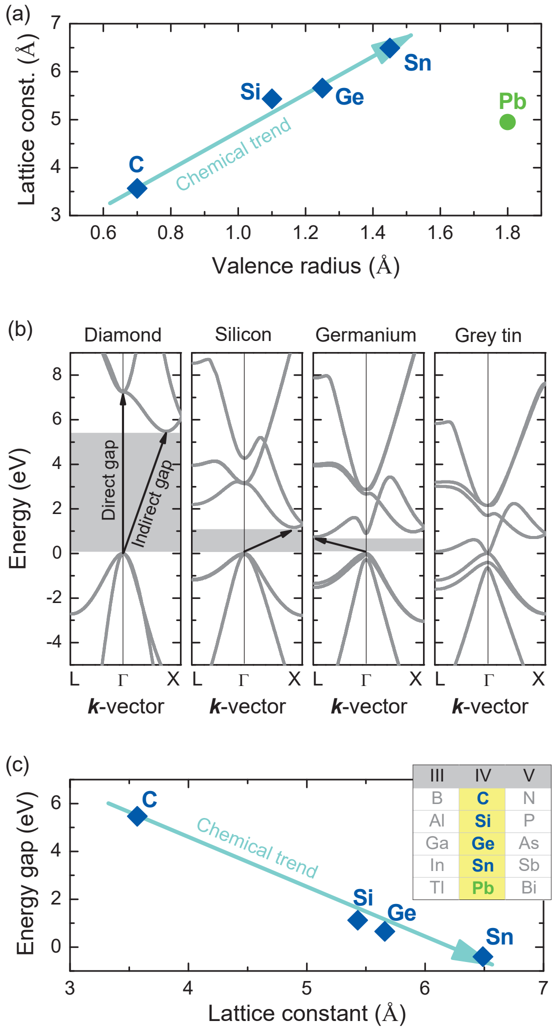

Fig. 3 (a) Relationship between the crystal lattice constant and the valence radius for elemental IV semiconductors in diamond structure (blue diamonds) and lead in FCC structure (green square). (b) Electronic band structure for diamond, silicon, germanium and gray tin. (c) Relationship between the energy gap and the crystal lattice constant for group IV materials (diamond, silicon, germanium, and gray tin) in the diamond cubic structure.

III-V semiconductors and chemical trends

In III-V semiconductors, the cation (group III atom) is surrounded by four anions (group V atom) and vice versa. The valence electrons from the cation (two *s* electrons and one *p* electron) and the valence electrons from the anions (two *s* electrons and three *p* electrons) form bonding and anti-bonding sp^3 hybrid atomic orbitals. Unlike Si, they are not the same due to the different electronegativities of the two atoms. Therefore, the nature of the bonds changes from covalent to ionic. In this case, the bond ionicity can also be a measure for studying changes in the electronic band structure. However, the lattice constant is of great technological importance and is therefore used in these considerations.

When the atomic number for group III (or group V) atoms increases, the valence radius of the atom increases and the lattice constant of the ZB III-V semiconductor increases as well. In analogy to group IV semiconductors, one can expect chemical trends for group III-V semiconductors, and this is exactly the case, but the number of semiconductor compounds is much greater here, and chemical trends must be analyzed in appropriate subgroups.

Fig. 4 shows the band gap as a function of the lattice constant for III-V semiconductors in the ZB structure. To observe chemical trends, these compounds have been grouped as wurtzite III-nitrides (black hexagons), Al-V (blue squares), Ga-V (green squares), and In-V (red squares) compounds. The energy gap for many B-V compounds has not yet been investigated experimentally and therefore they are not shown in this figure. Nitrides are also present in ZB structure and therefore they are plotted in this figure together with Al-V, Ga-V, and In-V compounds. For all these groups it is clearly visible that the band gap narrows with the increase in the crystal lattice constant (going from N through P and As to Sb). Bismides, which are not plotted in this figure, are narrow gap semiconductors (AlBi) and semimetals (GaBi and InBi) that additionally confirm this trend.

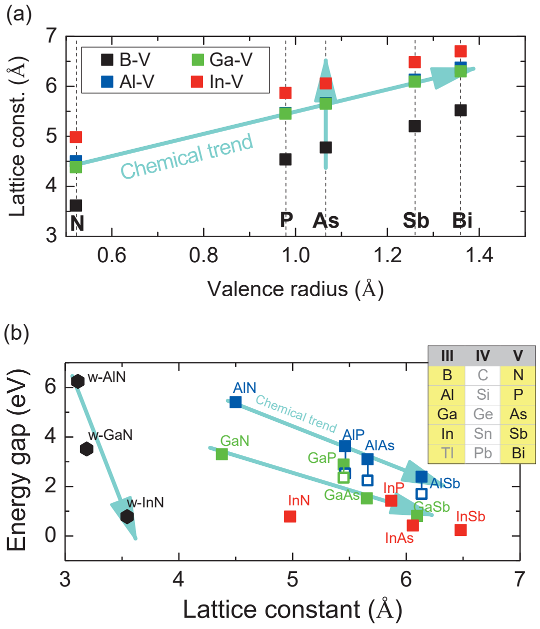

Fig. 4 (a) Relationship between the crystal lattice constant and the valence radius for III-V semiconductors in zinc-blende structure. (b) Relationship between the energy gap and the crystal lattice constant for III-V semiconductors: solid points—direct band gap, open points—indirect band gap.

The same trend is observed looking for these compounds grouped with the fixed group V atom, i.e., nitrides, phosphides, arsenides, and antimonides going from Ga to In, i.e., the band gap narrows with the increase in the crystal lattice constant. Al-V compounds (AlN, AlP, AlAs and AlSb) are a little bit out of this trend due to a little bit smaller lattice constant going from Al to Ga. B-V compounds are not plotted in this figure as some of them (BP and BSb) are not well studied experimentally. However, it is worth emphasizing here that both Al-V and B-V compounds are indirect gap semiconductors.

Summarizing this analysis, clear and systematic changes are observed going from light elements to heavy elements: the material varies from a wide gap semiconductor through a semiconductor and a narrow gap semiconductor to a semi-metallic one.

II-VI semiconductors and chemical trends

In this group of semiconductors the tetragonal coordination of atoms is also realized, but many compounds from this group (MgO, MgS, MgSe, CdO) prefer an octahedral coordinated rock salt structure. In the ZB structure the cation (group II atom) is surrounded by four anions (group VI atom) and vice versa. Like Si and Ge, the valence electrons in ZB structure of II-VI semiconductors form bonding and anti-bonding sp^3 hybrid atomic orbitals sharing eight valence electrons per anion/cation pair, but only two electrons are from the cation (two *s* electrons) and as many as six electrons are from the anion (two *s* electrons and four *p* electrons). Therefore, some of tetrahedrally coordinated crystals prefer wurtzite (W) structure (BeO, ZnO, HgO) and many others like MgO, MgS, MgSe, CdO, HgS, prefer an octahedral coordinated rock salt (RS) structure.

The relation between the band gap and the lattice constant for II-VI semiconductors is shown in Fig. 5 with a clear distinction of the crystallographic structure (squares—ZB; hexagons—W; diamonds—RS). As seen most of the semiconductors in this family of

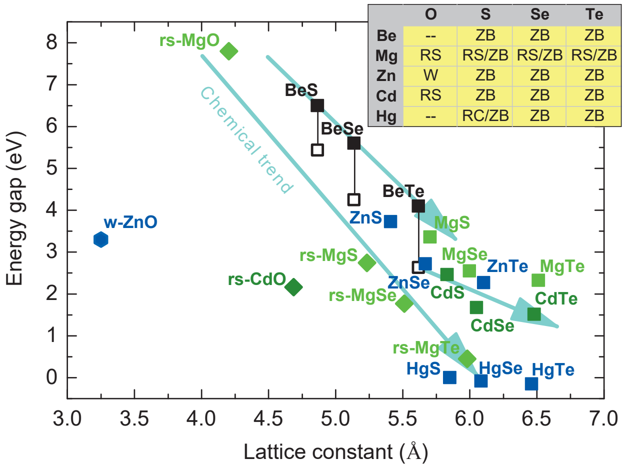

Fig. 5 Relationship between the energy gap and the crystal lattice constant for II-VI semiconductors: solid points—direct band gap, open points—indirect band gap.

compounds are ZB crystals, which exhibit chemical trends similar to those observed in group IV and III-V semiconductors, i.e., the band gap narrows with the increase in the crystal lattice constant (going from S through Se to Te). The same trend is observed looking for these compounds grouped with the fixed group VI atom, i.e., for sulfides, selenides, and tellurides.

It is also worth noting that changes in the preferred crystallographic structure are also correlated with chemical trends. Going to compounds with oxygen, i.e., the lightest atom in group VI, which has the smallest radius and the greatest electronegativity, the compounds occur in the wurtzite or rock salt structure. In the case of group II atoms, the heaviest atom is Hg, which, when bonding to S, prefers a structure other than ZB (i.e., RC—red cinnabar), while for bonding to the heaviest group VI atoms (Se or Te, which are similar in terms of electronegativity and valence radii), the preferred crystal structure for HgSe and HgTe is the ZB structure. Cadmium is very similar in this respect: CdTe, CdSe and CdS prefer the ZB structure, but CdO occurs in the RS structure. The Mg-VI compounds are less explored experimentally than the Cd-VI compounds, but they seem to prefer the RS structure especially the MgO compound.

Alloys

An alloy semiconductor is a combination of two or more semiconductors, i.e., elemental semiconductors (Si with Ge) or semiconductor compound from the same group (GaAs with InAs or ZnS with ZnSe). An alloy crystal is often called a mixed crystal or a solid solution. Note that the alloy is formed from a physical mixture of two or more compounds, while a compound is formed from a chemical reaction. For example, GaAs (or InAs) is not an alloy, it is a compound consisting of Ga (In) atoms bonded to As atoms. $Ga_{1-x}In_xAs$ is an alloy compound consisting of GaAs and InAs with a mole ratio of (1−x):x. The bonds in GaAs and InAs have characteristics intermediate character between the covalent and ionic terms.

Like $Ga_{1-x}In_xAs$, $Si_{1-x}Ge_{x-}$ is an alloy semiconductor composed of elemental semiconductors where the bonds Si-Ge, Si-Si and Ge-Ge can still be described by the covalent term. However, silicon carbide (SiC with a mole ratio of 0.5:0.5) is a compound, not an alloy, even though it is composed of elemental semiconductors (Si and C). This is that the chemical bonds in SiC cannot be described only by the covalent term present in the diamond structure. They have characteristics intermediate to those associated with the covalent and ionic terms, because of the large difference in electronegativity of the atoms (1.90 (Si) vs 2.55 (C) in contrast to 2.01 (Ge) in $Si_{1-x}Ge_x$). Therefore, SiC is the case of a compound with only Si-C bonds, where Si-Si and C-C bonds are treated as imperfections in the periodic lattice.

An alloy with two components is called a binary alloy; one with three is a ternary alloy; one with four is a quaternary alloy; one with five is a quinary (or a pentanary) alloy. The resulting alloy has properties, including the band structure, different from those of its components, i.e., elemental semiconductors or semiconductor compounds. Electronic band parameters of semiconductor alloys and their dependence on the composition of the alloy are very important in the engineering of semiconductor heterostructures. Therefore, a lot of attention has been paid to these problems in the past, and they are still being intensively explored for new alloys. So far, it has been observed that parameters such as crystal lattice constant, elastic constants or other parameters related to mechanical properties can be described by linear interpolation, while parameters related to the band structure (band gap, splitting of spin-orbit band, etc.) show deviations from such interpolation. The greater the difference in electronegativity of isovalent elements in the alloy, the greater the deviations from linearity. Alloys consisting of similar elements can usually be obtained with a full range of compositions and are called regular semiconductor alloys. $Si_{1-x}Ge_x$ and $Ga_{1-x}In_xAs$ are good examples of regular alloys.

The crystal lattice constant for $Ga_{1-x}In_xAs$ (a^{GaInAs}) can be calculated from linear interpolation:

$$a^{GaInAs} = (1-x)a^{GaAs} + xa^{InAs} \tag{1}$$

where a^{GaAs} and a^{InAs} is the crystal lattice constant for GaAs and InAs, respectively, and x is the mole fraction of InAs in $Ga_{1-x}In_xAs$ alloy.

The band gap for $Ga_{1-x}In_xAs$ (E_g^{GaInAs}) at the Γ point of Brillouin zone can be calculated by interpolation:

$$E_{\mathrm{g}}^{GaInAs} = (1-x)E_{\mathrm{g}}^{GaAs} + xE_{\mathrm{g}}^{InAs} - bx(1-x) \tag{2}$$

with the bowing parameter (b) describing the deviation from linearity. For this alloy the bowing parameter equals 0.47 eV. E_g^{GaAs} and E_g^{InAs} is the band gap at the Γ point of Brillouin zone for GaAs and InAs, respectively.

Fig. 6 shows the dependence of the direct energy gap in this alloy on the composition (panel a), the dependence of the crystal lattice constant of the $Ga_{1-x}In_xAs$ alloy on the composition (panel b) as well as the change of the energy gap as a function of the crystal lattice constant (panel c), which results from these two dependencies shown on the panel (a) and (b). Analogous relationships can be plotted for those alloys of groups IV, III-V, and II-VI, in which the semiconductors are present in the same crystal structure. However, within the same crystal structure, semiconductors can differ significantly in terms of the valence radii of the anions (cations) and their electronegativity. Alloys of such semiconductors were distinguished by Walukiewicz and named Highly Mismatched Alloys (HMAs) (Walukiewicz and Zide, 2020). Examples of HMAs are $C_{1-x}Ge_x$, $GaN_{1-x}As_x$, and $ZnO_{1-x}Se_x$ for group IV, III-V, and II-VI semiconductors, respectively, and they are discussed in a separated section.

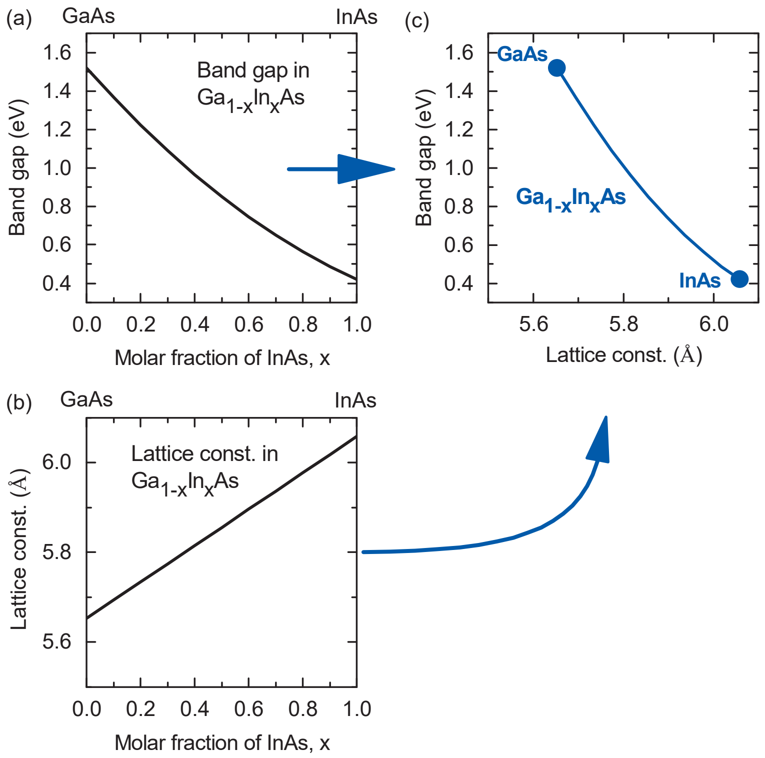

Fig. 6 Dependence of the direct energy gap (a) and the crystal lattice constant (b) of the $Ga_{1-x}In_xAs$ alloy on the molar fraction of InAs. Changes in the direct energy gap of the $Ga_{1-x}In_xAs$ alloy as a function of its crystal lattice constant (c).

Polymorphism and ordering

Polymorphism means the existence of a solid material in more than one crystal structure. In general, many compounds exhibit polymorphism. In this case, a good example to illustrate this phenomenon is SiC, which was previously discussed. In this material Si is tetrahedrally coordinated by C and vice versa. Various types of SiC differ one from another only by the order in which successive planes of Si (or C) atoms are stacked along the *c* axis, see Fig. 7. One polytype is the zinc-blende structure (3C) while the reminder, including two of the more frequently occurring forms, 4H and 6H (hexagonal), and 15R (rhombohedral), possess uniaxial symmetry (Wu et al., 2015). Each of these polytypes has a different band gap, and different Bruillen zones must be used to describe the electronic band structure for these crystals, and these zones result from the lattice system in which the crystal is described. In this case, SiC is a good example where the same atoms arranged differently lead to crystals with different electronic structure and different optical, electronic and mechanical properties.

Note that SiC is a compound but can be considered as an ordered alloy in which each Si atom is surrounded by four C atoms. In general, the same situation can be present in $Si_{1-x}Ge_x$ at $x = 0.5$, but the differences in the electronegativity of Si and Ge atoms are smaller, the bonds are more covalent than SiC, and therefore not every Si atom is surrounded by four Ge atoms, and not every Ge atom is surrounded by four Si atoms (Jager, 1995). This phase exhibits long-range order rather than random arrangement typical for alloys. An ordered alloy phase has been found not only in $Si_{1-x}Ge_x$, but also in many III–V and II–VI semiconductor alloys (Mascarenhas, 2002). In general, polymorphism and ordering are features of crystals that are not desirable in materials used in semiconductor devices because they make it difficult to control the homogeneity of the material properties. Therefore, random alloys are the ones that are desirable in band engineering in semiconductor heterostructures.

Key issues

Highly mismatched alloys

Semiconductor alloys consisting of anions (cations) that differ significantly in electronegativity or the valence radius of atoms are usually difficult to achieve and therefore very often they are not studied in the full range of compositions. HMAs contain elements with very different properties. These alloys are not well described by virtual crystal approximations or bowing parameter modified model. The parameters describing the band structure (e.g., energy gap) show very large deviations from the interpolation with a small square term (small bowing parameter) introduced to Eq. (2) as a correction to linear interpolation. Therefore, HMAs can be

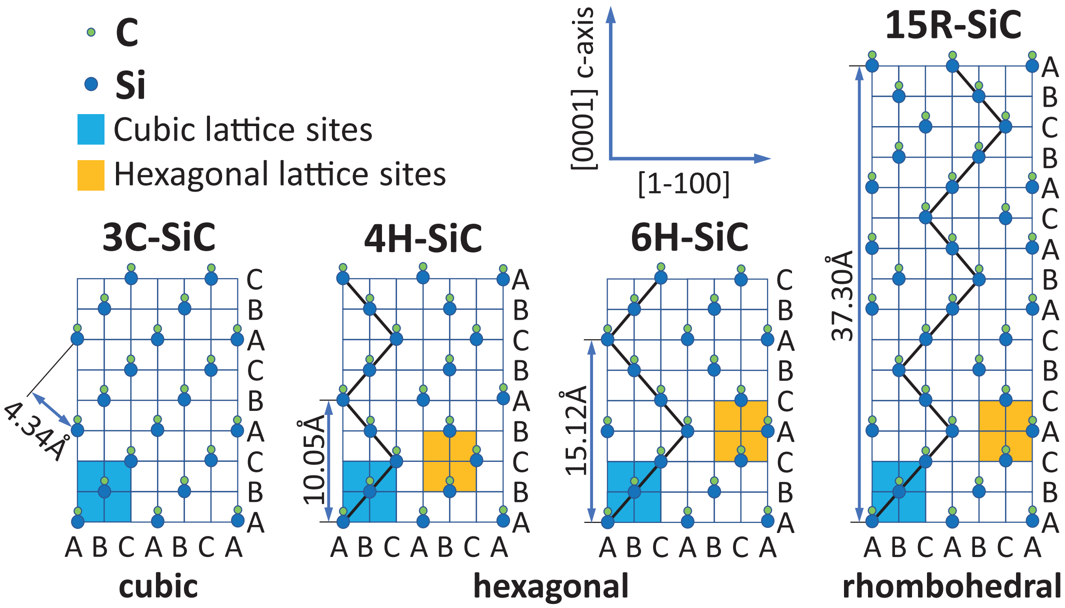

Fig. 7 Stacking sequences for different SiC polytypes (3C-, 4H-, 6H- and 15R-SiC) in the [11–20] plane. Blue color box—the cubic lattice site with the stacking sequence of ABCABC; Orange color box—the hexagonal lattice sites with the stacking sequence of BCB (CAC, CBC, BAB, ACA, ABA).

treated as a separate class of materials. It is also worth emphasizing here that this high mismatch does not apply to epitaxy on a foreign substrate with a very different lattice constant, such as GaN epitaxy on silicon. It concerns the alloy itself in terms of the isovalent elements that compose it and which differ greatly in electronegativity and/or valence radii.

Within the framework of elemental semiconductors (C, Si, Ge and Sn), a binary alloy with a full range of compositions can be easily obtained for $Si_{1-x}Ge_x$. The other five alloys ($C_{1-x}Si_x$, $C_{1-x}Ge_x$, $C_{1-x}Sn_x$, $Si_{1-x}Sn_x$, and $Ge_{1-x}Sn_x$) can be classified as HMAs. Compared to regular alloys, they are distinguished by a larger mismatch in terms of electronegativity of atoms and/or their valence radii.

In general, HMAs are much more difficult to synthesize due to the large mismatch in the valence radii of the alloying atoms and the significantly different bond energies in the elemental crystals. The bond energies in a crystal determine its melting point and for the lightest and heaviest elements of group IV they are very different: 3550 °C (diamond) vs 232 °C (tin). Therefore, alloying these two crystals is a challenge and a lot of the group IV HMAs are within the scope of theoretical considerations, but one of them ($Ge_{1-x}Sn_x$) has been synthesized, intensively studied and used in lasers (Wirths et al., 2015; Wirths et al., 2016; Zhou et al., 2020). This is the case when the mismatch in electronegativity of Ge and Sn atoms is small (2.01 (Ge) vs 1.96 (Sn)) and the difference in their valence radii is significantly smaller than in the case of C and remaining group IV atoms, see valence radii in Fig. 3(a).

The electronic band structure for selected compositions of $Ge_{1-x}Sn_x$ alloy and elemental crystals (Ge and Sn) is shown in Fig. 8 (Polak et al., 2017). Fig. 9 shows the change of the energy gap (direct $\Gamma_7 - \Gamma_8$ and indirect $L - \Gamma_8$) as a function of composition. These results clearly show that the changes in the electronic band structure of the $Ge_{1-x}Sn_x$ alloy are highly nonlinear with composition. So far $Ge_{1-x}Sn_x$ alloys with x up to 0.25 were obtained (Oehme et al., 2014) and the observed band gap for this alloy is consistent with theoretical predictions shown in Fig. 9 (Polak et al., 2017).

For III-V semiconductors, alloying in the full range of compositions is obtained for nitrides (AlN, GaN, and InN), phosphides (AlP, GaP, and InP, but AlP is still unexplored), arsenides (AlAs, GaAs, and InAs), and antimonides (AlSb, GaSb, and InSb). Moreover, phosphides mix with arsenides (III-$P_{1-x}As_x$) and arsenides mix with antimodines (III-$As_{1-x}Sb_x$) in the full range of composition. These alloys can be treated as regular alloys because the energy gap for ternary alloys can be described by Eq. (2) with a small bowing parameter. So far, most of the heterostructures for emitters are produced on the basis of this type of alloys.

Mixing phosphides with antimonides (III-$P_{1-x}Sb_x$) is more challenging and less explored. These alloys can already be considered as HMAs, but of course there is no clear distinction between regular alloys and HMAs.

III-V alloys diluted with bismides (dilute bismides) are a good example, where the character of these alloys is changing from HMAs ($GaAs_{1-x}Bi_x$) to a regular alloy ($InSb_{1-x}Bi_x$) mixing III-V with III-Bi (Polak et al., 2015). This family of materials is technologically important because it allows to close the energy gap in III-V materials and make them competitive with II-VI semiconductor alloys in the area of mid- and far-infrared detectors.

Typical examples of HMAs in group III-V are nitrogen-diluted III-V semiconductors (dilute nitrides) and III-N diluted with group V atoms. They are the same alloys but are divided into two subgroups because they do not mix in the full range of compositions in the crystalline form, and the extreme compositions occur in different crystallographic structures, i.e., III-N prefer the wurtzite structure. In general, the alloying of GaN with GaAs was achieved in the whole range of compositions by lowering the growth temperature in the epitaxial process, but it was an amorphous material when the growth temperature was too low and the composition was far from binary compounds (Yu et al., 2009).

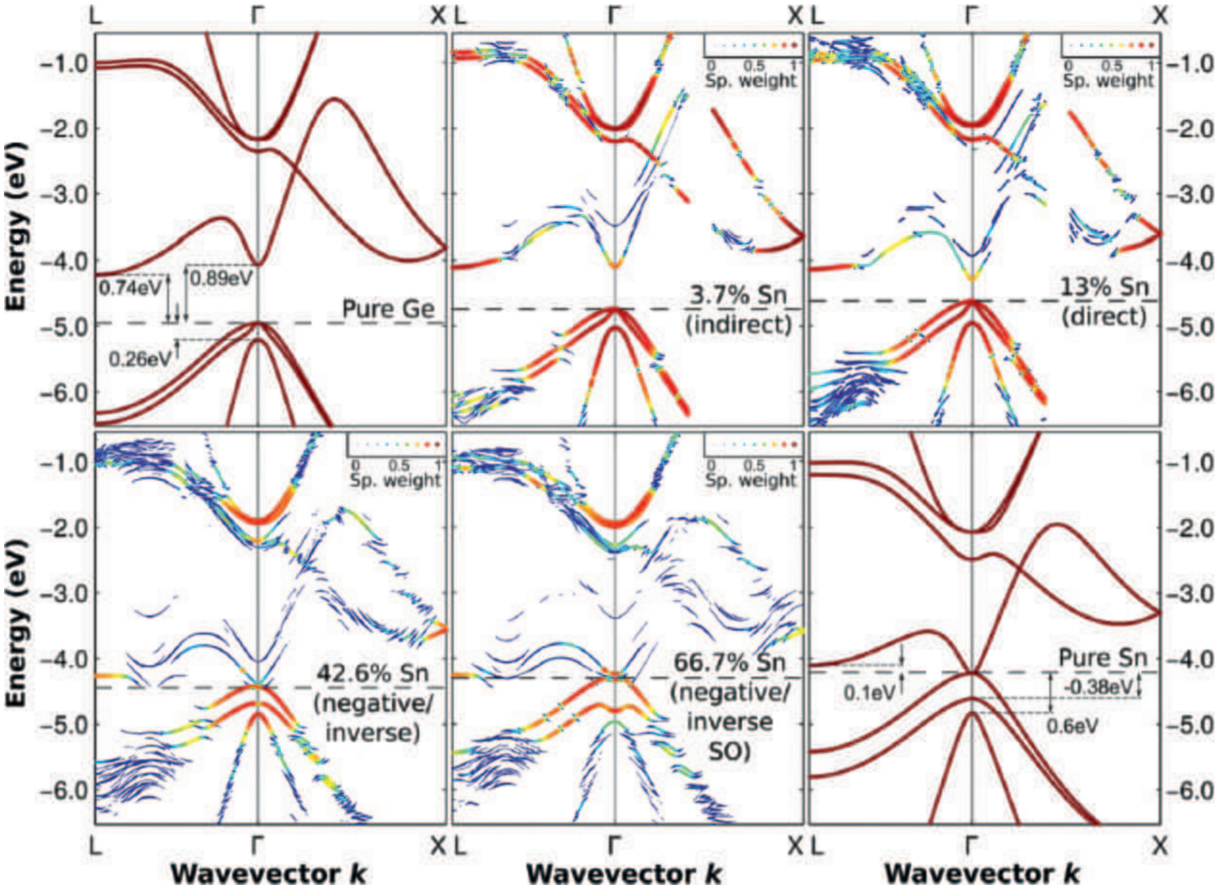

Fig. 8 (a) The band structure of parent compounds: Ge and α-Sn (first and last picture respectively) and examples of unfolded band structures for the four distinct regions (direct, indirect, inverse (negative) and inverse with inverse spin-orbit). The color and point size represents the Bloch spectral weight; points with weight lower than 0.05 have not been shown. Reproduced with permission from Polak et al., J. Phys. D: Appl. Phys. 50, 195,103 (2017). Copyright 2017 IOP Publishing.

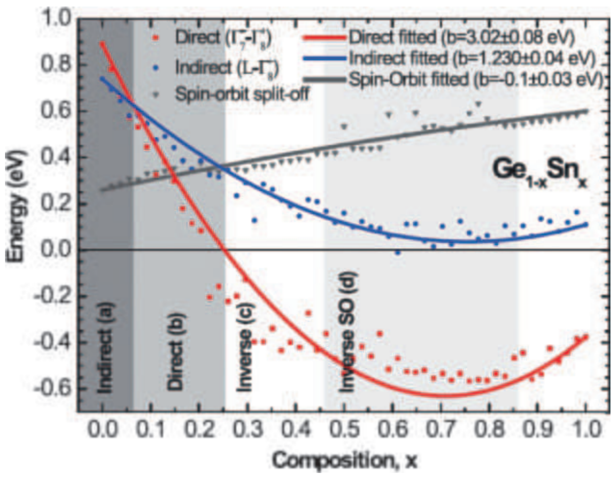

Fig. 9 The indirect, direct and spin-orbit energy gaps in $Ge_{1-x}Sn_x$ as a function of Sn concentration. Reproduced with permission from Polak et al., J. Phys. D: Appl. Phys. 50, 195,103 (2017). Copyright 2017 IOP Publishing.

II-VI alloys have been less extensively studied than III-V alloys mainly due to the toxicity of Cd and Hg, which limits their application. Due to the high ionicity of the bonds in II-VI alloys many of them are considered unstable in semiconductor devices and this is another reason why III-V alloys dominate in optoelectronic devices. However, it should be remembered that mid-infrared detectors are still manufactured based on $Hg_{1-x}Cd_xTe$ alloy. Most of II-VI alloys obtained so far ($Zn_{1-x}Cd_xS$, $Zn_{1-x}Cd_xSe$,

$Zn_{1-x}Cd_xTe$, $ZnS_{1-x}Se_x$, $ZnSe_{1-x}Te_x$, $Cd_{1-x}Hg_xSe$, $Cd_{1-x}Hg_xTe$, . . .) can be treated as regular alloys, but II-VI compounds (ZnS, ZnSe, ZnTe) diluted with oxygen (dilute oxides) and ZnO diluted with S (or Se) should be treated as HMAs (Welna et al., 2014; Welna et al., 2015). The group of II-VI alloys also includes those that have not been synthesized so far and that can be treated as HMAs by looking at the differences in electronegativity of atoms and their valence radii ($Be_{1-x}Hg_xS$ or $Be_{1-x}Hg_xSe$).

Band anticrossing model

For HMAs, the electronic band structure cannot be described in terms of the virtual crystal approximation, and the changes in the band gap as a function of composition are difficult to approximate by Eq.(2), because the bowing parameter reaches large values and the dependence deviates from the parabolic one. Therefore, the band anticrossing (BAC) model (Shan et al., 1999; Wu et al., 2002), is often used to describe the electronic band structure of HMAs including the band gap. Originally, this model was proposed by Walukiewicz and coworkers to explain the pressure dependence of optical transitions observed for Ga(In)NAs alloys (Shan et al., 1999). Subsequently, it was extended to explain the electronic band structure in other HMAs, including III-N diluted with group V atoms (Wu et al., 2004; Alberi et al., 2007a; Alberi et al., 2007b; Levander et al., 2010), dilute bismides (Alberi et al., 2007a; Alberi et al., 2007b; Polak et al., 2015), II-VI diluted with O (Welna et al., 2014; Welna et al., 2015; Yu et al., 2002; Yu et al., 2003), and ZnO diluted with group VI atoms (Ting et al., 2015; Welna et al., 2017). $GaN_{1-x}As_x$ is best suited for presenting the BAC model, because on the same material the anticrossing effect can be shown in the conduction band (CB) as well as in the valence band (VB). Moreover, it was the most extensively studied material in the context of BAC model.

Fig. 10 shows the electronic band structure of $GaN_{1-x}As_x$ obtained within the BAC model for $GaN_{1-x}As_x$ diluted with N (left panel) and As (right panel). In the regime of $GaN_{1-x}As_x$ diluted with N (i.e., $1-x < 0.05$), a resonant level corresponding to N atoms is located above the CB minimum of the GaAs host. The interaction between N-related and CB states is modeled using the perturbation theory described by the following Hamiltonian:

$$H_{\mathrm{BAC}} = \begin{pmatrix} E_{\mathrm{CB}}(k) & C_{\mathrm{NCB}}\sqrt{1-x} \\ C_{\mathrm{NCB}}\sqrt{1-x} & E_{\mathrm{N}} \end{pmatrix}, \tag{3}$$

where x is the mole fraction of substitutional N atoms. E_{N} is the energy of N-related states (s-like in this case) and $E_{\mathrm{CB}}(k)$ is the energy dispersion of the CB of the GaAs host, both with respect to the top of the valence band of the host, and C_{NCB} is a constant that describes the interaction between N-related and CB states. For dilute-N $GaN_{1-x}As_x$ alloy, these parameters are: $C_{\mathrm{NCB}} = 2.7$ eV and $E_{\mathrm{N}} = 1.65$ eV (Shan et al., 1999; Wu et al., 2002).

Two highly non-parabolic subbands, $E_-(k)$ and $E_+(k)$, are formed due to the band anticrossing interaction between N-related and CB states. The k-vector dispersion of these subbands is given by Eq. (4):

$$E_{\pm}(k) = \frac{1}{2}\left[E_{\mathrm{N}} + E_{\mathrm{CB}}(k) \pm \sqrt{[E_{\mathrm{N}} - E_{\mathrm{CB}}(k)]^2 + 4C_{\mathrm{NCB}}^2(1-x)}\right]. \tag{4}$$

In the regime of $GaN_{1-x}As_x$ diluted with As (i.e., $x < 0.05$), a resonant level corresponding to As atoms is located above the VB of the GaN host. The interaction between As-related (p-like states in this case) and VB states is modeled using a Hamiltonian analogous to the previous one:

$$H_{\mathrm{simplified}}^{\mathrm{N-rich}} = \begin{pmatrix} E_{\mathrm{VB}}(\mathrm{k}) & C_{\mathrm{AsVB}}\sqrt{x} \\ C_{\mathrm{AsVB}}\sqrt{x} & E_{\mathrm{As}} \end{pmatrix}, \tag{5}$$

where x is the mole fraction of substitutional As atoms, E_{As} is the energy of As-related states, $E_{\mathrm{VB}}(k)$ is the energy dispersion of the VB of the GaN host, and C_{AsVB} is a constant describing the interaction between the As-related and VB states. For dilute-As

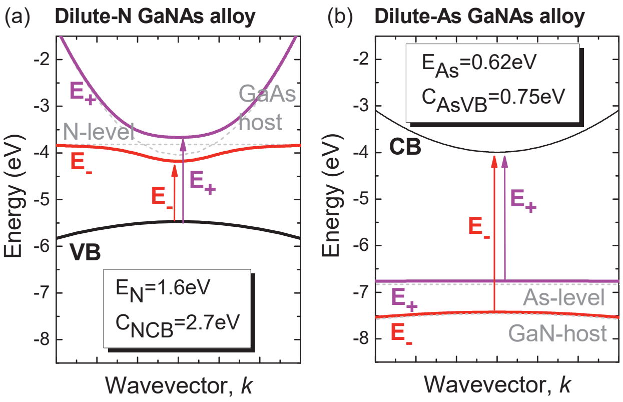

Fig. 10 Repulsive anticrossing interaction of (a) localized N-states (2% N) with the extended GaAs conduction-band (CB) states, and (b) localized As-states (2% As) with the extended GaN valence-band (VB) states. Bands are plotted vs the vacuum level.

$GaN_{1-x}As_x$ alloy, these parameters are: $C_{AsVB} = 0.75$ eV and $E_{As} = 0.62$ eV (Wu et al., 2004). In this case, highly non-parabolic subbands are formed in the VB and they are given by Eq. (6):

$$E_{\pm}(k) = \frac{1}{2}\left[E_{As} + E_{VB}(k) \pm \sqrt{\left[E_{As} - E_{VB}(k)\right]^2 + 4C_{AsVB}^2 x}\right]. \tag{6}$$

In general, the band anticrossing interaction in the VB is more complex because of complexity of the VB. In the case of $GaN_{1-x}As_x$ diluted with As, the full Hamiltonian for the band anticrossing interaction in the VB should be composed of three subbands typical of host material (WZ GaN in this case) and three states associated with the isovalent dopant (As in this case) with the p_x, p_y, and p_z symmetry. A Hamiltonian with three valence subbands and one As-related level (all states with spin up and spin down) was developed and subsequently applied to study of the electronic band structure for $GaN_{1-x}As_x$ (Alberi et al., 2007a; Alberi et al., 2007b). Also, the full-valence BAC Hamiltonian with three host subbands and three resonant levels has been developed for dilute bismides, i.e., ZB III-V alloys with a few percent of Bi atoms with the band anticrossing interaction between the Bi-related and VB states (Gladysiewicz et al., 2015).

BAC parameters (the position of resonant level relative to the CB (or VB) states and the interaction constant between the resonant level and CB (or VB) states) are needed to describe the electronic band structure within the BAC model. These parameters were quite intensively studied for dilute nitrides, dilute oxides, and dilute bismides. It was observed that the interaction constant is smaller for alloys in which the difference in electronegativity of isovalent atoms is smaller, which is consistent with the assumptions of the model (Polak et al., 2015; Shan et al., 1999; Wu et al., 2002). The position of the resonant level relative to the VB changes according to the position of the host VB to the vacuum level.

Strain and band gap engineering

In optoelectronic devices, band gap engineering is necessary to obtain the desired semiconductor heterostructure. As shown, it can be obtained by alloying semiconductors, but an equally important element is the strain engineering, which is an indispensable element of the deposition of layers on a given substrate. The lattice constant of the deposited layer usually has a different crystal lattice constant than the substrate, which in this case determines the lattice constant in the plane of the heterostructure and generates strains in the deposited layers. These strains modify the electronic band structure including the energy gap.

Considerable limitations in band engineering exist for elemental semiconductors (i.e., group IV) due to a few materials (in fact Si, Ge, and Sn) and the small number of possible alloys. In addition, these materials, without $Ge_{1-x}Sn_x$, have an indirect energy gap, which limits their use in optoelectronics. Therefore, III-V compounds are key materials in such semiconductor devices as light emitting diodes and lasers. Due to alloying different III-V compounds it is possible to tune the band gap and grow low dimensional heterostructures with a desired quantum confinement for electrons and holes, but their band gap tuneability is also quite strongly limited because of earlier mentioned strain. It comes from the fact that all III-V heterostructures have to be grown on a given substrate with a given crystal lattice constant (GaN, GaAs, InP or GaSb).

With a few exceptions (e.g., AlSb, GaSb and InAs, which are known as 6.1 Å family compound) the different crystal lattice constant of binary compounds limits the content of III-V alloys, which can be deposited on a given substrate with the thickness below the critical thickness. In addition, the built-in compressive (or tensile) strain strongly influences the electronic band structure and thereby limits the band gap tuning. The problem of strain engineering is illustrated in the sketch in Fig. 11. For a given alloy the band gap narrows with the increase in the crystal lattice constant according to previously discussed chemical trend for III-V alloys, which can be realized by mixing group III (or group V) atoms for regular alloys. Such a layer can be deposited on the X substrate with the lattice constant a_X greater than the lattice constant of the AC compound (a_{AC}) and smaller than the lattice constant of the BC compound (a_{BC}). Then, the layer with a lattice constant lower than a_X is under tensile strain, and the layer with a lattice constant greater than a_X is under compressive strain, as long as the thicknesses of these layers are below the critical thickness. Exceeding the critical thickness is not desirable because it generates dislocations and leads to deterioration of optical/electrical properties of the deposited layers. Therefore, strains significantly limit the range of alloy compositions of a given layer that can be deposited on a given substrate. Moreover, the strains narrow the range of the energy gap change due to its modification, compare the thin and thick lines in Fig. 11: compressive strains open the energy gap, while tensile strains narrow the energy gap.

The introduction of additional semiconductor compounds (AD and BD) for alloying allows to obtain a quaternary alloy that can be lattice matched to a specific substrate, see Fig. 11 (b). Such layers play a very important role in semiconductor devices. For substrates that are crucial in the optoelectronic devices (GaAs, InP and GaSb), it is possible to obtain quaternary layers lattice matched to the GaAs, InP and GaSb substrate within regular alloys: GaInPAs/GaAs, GaInPAs/InP, AlGaInAs/InP and GaInAsSb/GaSb.

Quaternary alloys allow for a more independent tuning of the band gap and the strain than the ternary alloys in which these two quantities are related. Apart from the energy gap and strain, the band gap discontinuity is an another parameter that needs to be tuned in quantum heterostructures. This is especially important for quantum wells where the quantum confinement must be precisely matched to the desired emission or other requirements. Such engineering is possible with quinary alloys but is still challenging in terms of control of the alloy composition.

In general, the band gap engineering is easier if we have more compounds with different energy gaps and band gap discontinuities that can be alloyed together. Therefore, III-V semiconductors have great potential in this area. In addition to regular alloys,

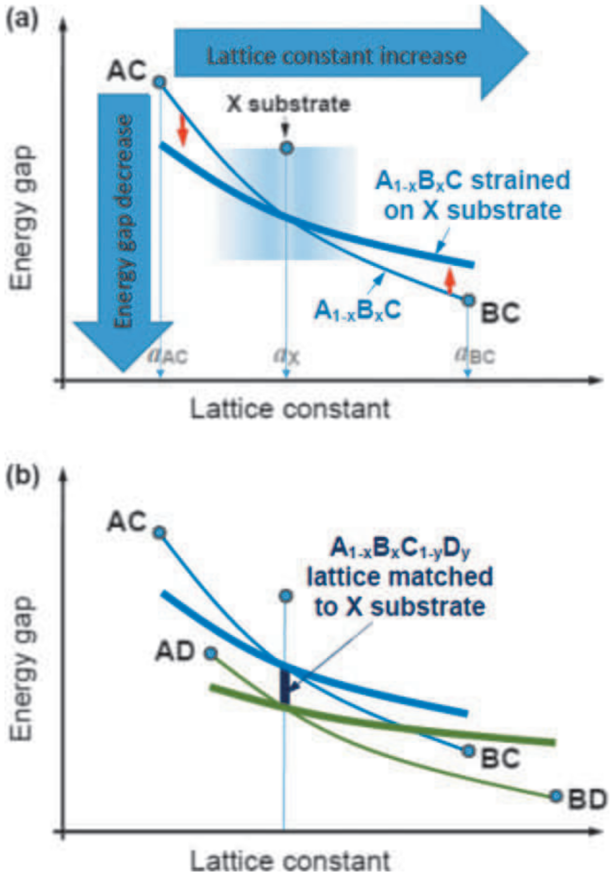

Fig. 11 (a) Sketch of energy gap dependence on the crystal lattice constant for unstrained ternary $A_{1-x}B_xC$ alloy (thin blue line) and a layer of $A_{1-x}B_xC$ alloy deposited on X substrate (thick blue line). (b) Unstrained (thin lines) and strained (thick lines) ternary $A_{1-x}B_xC$ (blue lines) and $A_{1-x}B_xD$ (green lines) alloys and $A_{1-x}B_xC_{1-y}D_y$ alloy lattice matched to X substrate.

HMAs also have great advantages as some of them offer new features in band gap engineering. One of them, related to strain, is a different relationship between the energy gap and the crystal lattice constant as shown in Fig. 12. For a regular alloy (in this case $GaP_{1-y}As_y$ or $Ga_{1-x}In_xAs$) reducing the crystal lattice constant leads to the opening of the energy gap (this is a well-known chemical trend discussed earlier). For HMAs ($GaN_{1-y}As_y$ in this case), the narrowing of the energy gap along with the reduction of the crystal lattice constant can be achieved, see Fig. 12. Such a relation between the energy gap and the crystal lattice constant is not observed for regular alloys and, therefore HMAs offer new possibilities in band gap engineering. In this case, it is possible to obtain $Ga_{1-x}In_xN_{1-y}As_y$ lattice matched to GaAs with an energy gap much narrower than the GaAs energy gap, see Fig. 12.

Van der Waals semiconductors and their alloys

The best known representative of van der Waals crystals is graphite, which can be exfoliated into a single layer (graphene layer). It is worth emphasizing here that graphite is an allotropic form of carbon, which was previously discussed in the diamond form and where the carbon is tetrahedrally coordinated with sp^3 hybrid atomic orbitals. In graphite, carbon is trigonally coordinated and covalently bounded with sp^2 hybrid atomic orbitals in the plane, see Fig. 1. In each plane (layer), the carbon atoms are arranged in a honeycomb lattice and the individual layers are called graphene. The *p*-orbitals that do not hybridize between atoms from adjacent layers are oriented perpendicular to these planes. Therefore, bonding between layers is relatively weak van der Waals bonds, which allows the layers to be easily separated by mechanical exfoliation. Silicon or germanium in the graphite structure is not stable, but graphene equivalents realized by silicon (silicene) or germanium (germanene) atoms are more and more often considered and studied (Liu et al., 2019; Acun et al., 2015; Molle et al., 2018).

Another quite well explored van der Waals crystals are transition-metal dichalcogenides (TMDs) with MX_2 formula, where M is a transition-metal atom (Mo or W) and X is a chalcogen atom (S, Se, or Te), see Fig. 13. They are layered crystals in a hexagonal structure consisting of sixfold-bonded metal atoms sandwiched between two threefold-bonded chalcogenide atoms with a covalent interaction between atoms within a layer and a van der Walls interaction between layers.

The relation between the band gap and the crystal lattice constant for MoS_2, $MoSe_2$, $MoTe_2$, WS_2, and WSe_2 compounds is shown in Fig. 13 with energy gaps taken from Kopaczek et al., 2022. In this case the chemical trends previously discussed for tetrahedrally

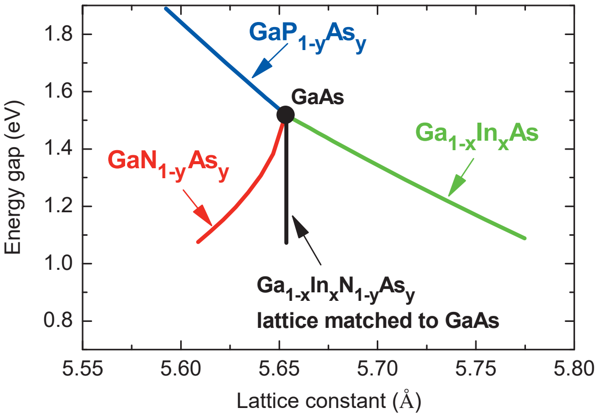

Fig. 12 The relation between the energy gap and the crystal lattice constant for regular alloys (GaP$_{1-y}$As$_y$ and Ga$_{1-x}$In$_x$As) and GaN$_{1-y}$As$_y$, which is a HMA, together with the lattice matched Ga$_{1-x}$In$_x$N$_{1-y}$As$_y$ HMA.

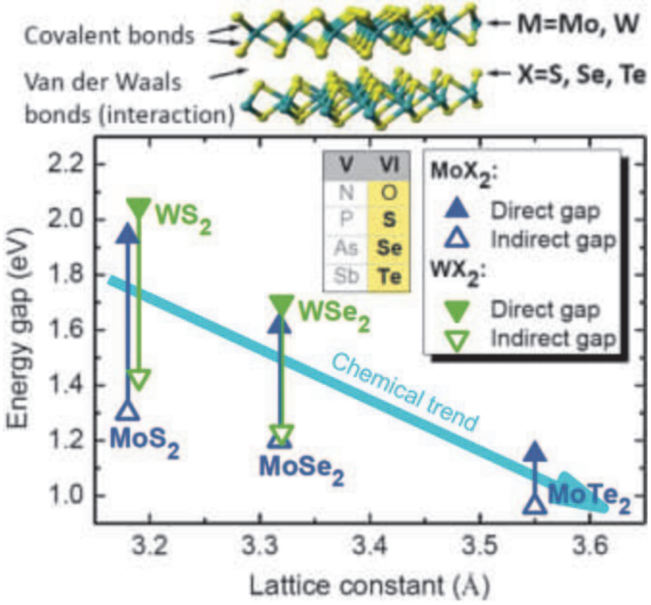

Fig. 13 Arrangement of atoms and relationship between the energy gap and the crystal lattice constant for MoX$_2$ and WX$_2$ compound semiconductors.

coordinated semiconductor crystals can be easily recognized, i.e., the band gap narrows with the increase in the crystal lattice constant. In addition, it has been observed that the preferred crystallographic structure changes from 2H to 1T going to heavier atoms: MoTe$_2$ occurs in 2H and 1T structure, while WTe$_2$ prefer 1T structure (Zhou et al., 2022) is semi-metal and is not shown in Fig. 13. The dependence of the energy gap on the composition for Mo$_{1-x}$W$_x$X$_2$ and MoS$_{2(1-x)}$Se$_{2x}$ alloys can be described by Eq.(2) as for regular III-V alloys (Wu et al., 2014; Kopaczek et al., 2021). This issue is currently being researched for both bulk crystals and single layers.

Perovskites and their alloys

Organic-inorganic hybrid perovskites adopt crystal structure with general formula of ABX$_3$, where A is organic cation, B is the metal element, and X is the halide element. The hybrid perovskite methylammonium lead halides (MAPbX$_3$) is composed of corner-sharing PbX$_6$ octahedrons with the organic cation MA$^+$ occupying the voids in the three-dimensional inorganic framework, see Fig. 14. The energy gap of MAPbX$_3$ compounds is dominated by the PbX$_6$ octahedrons, while the MA$^+$ cation contribution is little. This means that the electronic band structure of MAPbX$_3$ can be tuned by changing the Pb-X bond length and Pb-X-Pb angle in the inorganic framework. This can be achieved by changing X from Cl through Br to I. By replacing atoms with a small valence radius with atoms with a large valence radius, the crystal lattice constant increases and the energy gap decreases as shown in Fig. 14. This relationship is a well-known chemical trend observed for tetrahedrally coordinated crystals, i.e., IV, III-V and II-VI semiconductors. The dependence of the energy gap on the composition for MAPbCl$_{3(1-x)}$Br$_{3x}$, MAPbCl$_{3(1-x)}$I$_{3x}$, and

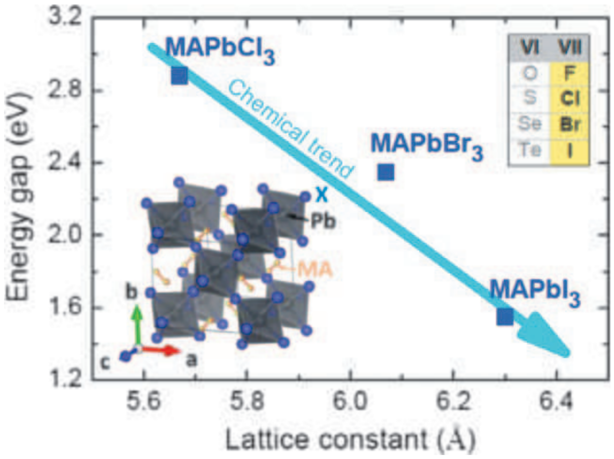

Fig. 14 Arrangement of atoms and relationship between the energy gap and the crystal lattice constant for MAPbX$_3$ compound semiconductors.

MAPbBr$_{3(1-x)}$I$_{3x}$ alloys can be described by Eq.(2) as for regular III-V alloys, but is still being investigated. In addition, it is worth emphasizing here that these compounds and their alloys occur in different crystallographic structures depending on the temperature (orthorhombic, tetragonal and cubic).

Conclusion

In summary, the electronic band structure for group IV semiconductors as well as III-V and II-VI semiconductors have been well studied and understood so far. The same chemical trends, i.e., the narrowing of the energy gap with the increase of the crystal lattice constant, can be observed for the groups of semiconductor materials occurring in the same crystallographic structure. Semiconductor alloying is essential to obtain materials with the desired performance, and this topic has also been extensively researched over the past decades and is quite well understood at the moment, but many alloys are still unexplored, especially HMAs. In general, alloying is easily achieved for similar crystals, i.e., crystals that crystallize in the same structure and are composed of isovalent atoms of similar electronegativity and valence radius. Then, the crystal lattice constant of such an alloy and many parameters related to mechanical properties can be linearly interpolated, and the parameters related to the band structure, including the energy gap, can be described by a quadratic interpolation with a bowing parameter describing deviations from linearity. For regular alloys, the bowing parameter is relatively small in relation to the energy gap value and increases for HMAs. However, for many HMAs, the band gap can no longer be described in terms of the quadratic approximation with a reasonable bowing parameter (i.e., smaller value of bowing than the energy gap), and in this case the BAC model is very useful for estimating the energy gap. The chemical trends that have been observed for tetrahedrally coordinated semiconductors are also present for van der Waals crystals and perovskites, which have been known for a long time but which should rather be classified as a new generation of materials for use in semiconductor devices. In this case, it can also be expected that some of these alloys will behave like regular alloys and some like HMAs. According to the chemical trends and in analogy to dilute oxides (II-VI HMAs), MX$_2$ (M = Mo or W; X = S, Se, or Te) diluted with oxygen can be HMAs within van der Waals crystals. Within perovskites, MAPbX$_3$ diluted with fluorine can be HMAs. But first, such crystals must be obtained, and this can be a challenge. In general, the synthesis of homogeneous HMAs with a low defect concentration is challenging and was not discussed in this chapter. The further development of semiconductor alloys (both known and new) will be driven by their demand in specific semiconductor devices and may largely focus on improving their homogeneity and controlling their electrical conductivity through appropriate doping, i.e., issues that were not addressed in this chapter. Next emerging directions in semiconductor heterostructures go beyond the mixing of semiconductor compounds from the same family and are associated with the growth of III-V materials on silicon and combining different groups of materials, i.e., depositing van der Waals crystals on III-V materials or combining van der Waals crystals with perovskites. In these types of directions, strain engineering does not play a significant role, and among the promising materials for applications, there are those that are tolerant to defects. Unlike III-V semiconductors, the defect tolerant semiconductor compounds and alloys can be produced using cheaper methods than molecular beam epitaxy or metalorganic vapor-phase epitaxy, which are required for the growth of III-V (or II-VI) heterostructures for optoelectronic devices. Therefore, the next generation of cheaper semiconductor devices can be based on these types of compounds and alloys. The chemical trends presented and discussed in this chapter should also work for semiconductor compounds and alloys with non-tetragonal atom coordination as shown for van der Waals crystals and perovskites.

References

Acun A, Zhang L, Bampoulis P, Farmanbar M, van Houselt A, Rudenko AN, Lingenfelder M, Brocks G, Poelsema B, Katsnelson MI, and Zandvliet HJW (2015) Germanene: The germanium analogue of graphene. *Journal of Physics: Condensed Matter* 27: 443002.

Alberi K, Dubon OD, Walukiewicz W, Yu KM, Bertulis K, and Krotkus A (2007a) Valence band anticrossing in GaBi$_x$As$_{1-x}$. *Applied Physics Letters* 91: 051909.

Alberi K, Wu J, Walukiewicz W, Yu KM, Dubon OD, Watkins SP, Wang CX, Liu X, Cho Y-J, and Furdyna J (2007b) Valence-band anticrossing in mismatched III-V semiconductor alloys. *Physical Review B* 75: 045203.

Gladysiewicz M, Kudrawiec R, and Wartak MS (2015) 8-band and 14-band kp modeling of electronic band structure and material gain in Ga(In)AsBi quantum wells grown on GaAs and InP substrates. *Journal of Applied Physics* 118: 055702.

Jager W (1995) In: Kasper E (ed.) *Properties of Strained and Relaxed Silicon Germanium, EMIS Data reviews Series No.* vol. 12, p. 53. London: INSPEC.

Kopaczek J, Woźniak T, Tamulewicz-Szwajkowska M, Zelewski SJ, Serafińczuk J, Scharoch P, and Kudrawiec R (2021) Experimental and theoretical studies of the electronic band structure of bulk and atomically thin $Mo_{1-x}W_x$Se2 alloys. *ACS Omega* 6(30): 19893–19900.

Kopaczek J, Zelewski S, Yumigeta K, Sailus R, Tongay S, and Kudrawiec R (2022) Temperature dependence of the indirect gap and the direct optical transitions at the high-symmetry point of the Brillouin zone and band nesting in MoS_2, $MoSe_2$, $MoTe_2$, WS_2, and WSe_2 crystals. *Journal of Physical Chemistry C* 126: 5665–5674.

Levander AX, Yu KM, Novikov SV, Tseng A, Foxon CT, Dubon OD, Wu J, and Walukiewicz W (2010) $GaN_{1-x}Bi_x$: Extremely mismatched semiconductor alloys. *Applied Physics Letters* 97: 141919.

Liu N, Bo G, Liu Y, Xu X, Du Y, and Dou SX (2019) Recent progress on germanene and functionalized germanene: Preparation, characterizations, applications, and challenges. *Small* 1805147.

Mascarenhas A (2002) *Spontaneous Ordering in Semiconductor Alloys*. New York: Kluwer Academic.

Molle A, Grazianetti C, Tao L, Taneja D, Alam H, and Akinwand D (2018) Silicene, silicene derivatives, and their device applications. *Chemical Society Reviews* 47: 6370–6387.

Oehme M, Kostecki K, Schmid M, Oliveira F, Kasper E, and Schulze J (2014) Epitaxial growth of strained and unstrained GeSn alloys up to 25% Sn. *Thin Solid Films* 557: 169–172.

Pauling L (1932) The nature of the chemical bond. IV. The energy of single bonds and the relative electronegativity of atoms. *Journal of the American Chemical Society* 54(9): 3570–3582.

Polak MP, Scharoch P, and Kudrawiec R (2015) First-principles calculations of bismuth induced changes in the band structure of dilute Ga–V–Bi and In–V–Bi alloys: Chemical trends versus experimental data. *Semiconductor Science and Technology* 30: 094001.

Polak MP, Scharoch P, and Kudrawiec R (2017) The electronic band structure of $Ge_{1-x}Sn_x$ in the full composition range: Indirect, direct, and inverted gaps regimes, band offsets, and the Burstein–Moss effect. *Journal of Physics D: Applied Physics* 50: 195103.

Shan W, Walukiewicz W, Ager JW, Haller EE, Geisz JF, Friedman DJ, Olson JM, and Kurtz SR (1999) Band anticrossing in GaInNAs alloys. *Physical Review Letters* 82: 1221.

Ting M, dos Reis R, Jaquez M, Dubon OD, Mao SS, Yu KM, and Walukiewicz W (2015) Electronic band structure of ZnO-rich highly mismatched $ZnO_{1-x}Te_x$ alloys. *Applied Physics Letters* 106: 092101.

Walukiewicz W and Zide JMO (2020) Highly mismatched semiconductor alloys: From atoms to devices. *Journal of Applied Physics* 127: 010401.

Welna M, Kudrawiec R, Nabetani Y, and Walukiewicz W (2014) Band anticrossing in ZnOSe highly mismatched alloy. *Applied Physics Express* 7: 071202.

Welna M, Kudrawiec R, Nabetani Y, Tanaka T, Jaquez M, Dubon OD, Yu KM, and Walukiewicz W (2015) Effects of a semiconductor matrix on the band anticrossing in dilute group II-VI oxides. *Semiconductor Science and Technology* 30: 085018.

Welna M, Baranowski M, Linhart WM, Kudrawiec R, Yu KM, Mayer M, and Walukiewicz W (2017) Multicolor emission from intermediate band semiconductor $ZnO_{1-x}Se_x$. *Scientific Reports* 7: 44214.

Wirths S, Geiger R, von den Driesch N, Mussler G, Stoica T, Mantl S, Ikonic Z, Luysberg M, Chiussi S, Hartmann JM, Sigg H, Faist J, Buca D, and Grützmacher D (2015) Lasing in direct-bandgap GeSn alloy grown on Si. *Nature Photonics* 9: 88–92.

Wirths S, Buca D, and Mantl S (2016) Si–Ge–Sn alloys: From growth to applications. *Progress in Crystal Growth and Characterization of Materials* 62: 1–39.

Wu J, Shan W, and Walukiewicz W (2002) Band anticrossing in highly mismatched III–V semiconductor alloys. *Semiconductor Science and Technology* 17: 860.

Wu J, Walukiewicz W, Yu KM, Denlinger JD, Shan W, Ager JW III, Kimura A, Tang HF, and Kuech TF (2004) Valence band hybridization in N-rich $GaN_{1-x}As_x$ alloys. *Physical Review B* 70: 115214.

Wu YJ, Wu PH, Jadczak J, Huang YS, Ho CH, Hsu HP, and Tiong KK (2014) Piezoreflectance study of near band edge excitonic-transitions of mixed-layered crystal $Mo(S_xSe_{1-x})_2$ solid solutions. *Journal of Applied Physics* 115: 223508.

Wu R, Zhou K, Yue CY, Wei J, and Pan Y (2015) Recent progress in synthesis, properties and potential applications of SiC nanomaterials. *Progress in Materials Science* 72: 1–60.

Yu KM, Walukiewicz W, Wu J, Beeman JW, Ager JW III, and Haller EE (2002) Band anticrossing in group $II\text{-}O_xVI_{1-x}$ highly mismatched alloys: $Cd_{1-x}Mn_yO_xTe_{1-x}$ quaternaries synthesized by O ion implantation. *Applied Physics Letters* 80: 1571.

Yu KM, Walukiewicz W, Wu J, Shan W, Beeman JW, Scarpulla MA, Dubon OD, and Becla P (2003) Diluted II-VI oxide semiconductors with multiple band gaps. *Physical Review Letters* 91: 246403.

Yu KM, Novikov SV, Broesler R, Demchenko IN, Denlinger JD, Liliental-Weber Z, Luckert F, Martin RW, Walukiewicz W, and Foxon CT (2009) Highly mismatched crystalline and amorphous $GaN_{1-x}As_x$ alloys in the whole composition range. *Journal of Applied Physics* 106: 103709.

Zhou Y, Miao Y, Ojo S, Tran H, Abernathy G, Grant JM, Amoah S, Salamo G, Du W, Liu J, Margetis J, Tolle J, Zhang Y-H, Sun G, Soref RA, Li B, and Yu S-Q (2020) Electrically injected GeSn lasers on Si operating up to 100 K. *Optica* 7: 924.

Zhou R, Wu J, Chen Y, and Xie L (2022) Polymorph structures, rich physical properties and potential applications of two-dimensional $MoTe_2$, WTe_2 and their alloys. *Chinese Journal of Chemistry* 40(8): 989–1004.

Further reading

Adachi S (2009) *Properties of Semiconductor Alloys: Group-IV, III–V and II–VI Semiconductors*. John Wiley & Sons.

Henini M (ed.) (2005) *Dilute Nitride Semiconductors*. Elsevier Ltd.

Kudrawiec R and Hommel D (2020) Bandgap engineering in III-nitrides with boron and group V elements: Toward applications in ultraviolet emitters. *Applied Physics Reviews* 7(4), 041314.

Vurgaftman I, Meyer JR, and Ram-Mohan LR (2000) Band parameters for III–V compound semiconductors and their alloys. *Journal of Applied Physics* 89: 5815.

Vurgaftman I and Meyer IR (2003) Band parameters for nitrogen-containing semiconductors. *Journal of Applied Physics* 94: 3676.

Relevant websites

https://www.angelo.edu/faculty/kboudrea/periodic/trends_atomicradius.htm.
https://www.angelo.edu/faculty/kboudrea/periodic/trends_electronegativity.htm.
https://www.webelements.com.
https://materialsproject.org.
http://www.crystallography.net.
https://materials.springer.com.

Intermetallic Compounds, Electronic States of[☆]

O Gourdon, D Gout, and GJ Miller, Iowa State University, Ames, IA, USA

© 2016 Elsevier Inc. All rights reserved.

This is an update of O. Gourdon, D. Gout, G.J. Miller, Intermetallic Compounds, Electronic States of, Reference Module in Materials Science and Materials Engineering, Elsevier, 2016, ISBN 9780128035818, https://doi.org/10.1016/B978-0-12-803581-8.01049-3.

Introduction 469
What are Intermetallic Compounds? 469
Classifying Electronic States in Intermetallic Compounds 472
Electronic Interactions Between Different Metallic Types 473
d–*d* Interactions 473
***d*–(*s*)*p* Interactions** 477
sp–*sp* Interactions 479
Conclusion 483
Further Reading 484

Introduction

Intermetallic compounds provide a rich and diverse resource to study the relationships among chemical composition, atomic structure, electronic structure, and physical properties. Since the majority of chemical elements are 'metals,' even with thermodynamic constraints, the numbers, types, and complexity of intermetallic compounds are immense, which is readily apparent in *Pearson's Handbook of Intermetallic Phases*. An understanding of the electronic states of an intermetallic compound can provide insights into the chemical bonding factors influencing composition and structure as well as the electronic underpinnings of its electrical and magnetic behavior. Experimental determination of electronic states, largely through photoelectron spectroscopy, demands pure samples, which can be a challenge to obtain because most metals react readily with oxygen. On the other hand, there is a great deal of effort on quantum mechanical calculations of the electronic structure. This article provides an overview of a comprehensive general picture of electronic states in intermetallic compounds, including brief descriptions of specific examples.

What are Intermetallic Compounds?

At first glance, the answer seems obvious: intermetallic compounds are chemical substances formed when two or more metallic elements combine with a definite composition. They typically have small heats of formation (ca. – 50 to −10 kJ mol^{-1}) when compared to salts and polymeric compounds (ca. – 500 to −100 kJ mol^{-1}), but frequently show finite ranges in composition for a single phase, called homogeneity widths. Some melt congruently without decomposition into different phases, while many decompose peritectically into a liquid phase and another solid with a different composition. Concerning their structures, the various metal constituents are usually ordered in different sublattices, each with its own distinct population of atoms. In this way, elements of differing sizes or electronegativities can combine to give new compounds. Often, the corresponding structures are distinct from those of the component elements, but this is not necessary.

One important aspect of the definition is the combination of 'metallic' elements. Chemical substances are classified as either metals or nonmetals, and many periodic tables of the elements include a zigzag line, with metals on the left and nonmetals on the right. A closer examination of the elements near this line reveals numerous unusual trends in structural and physical properties, such that in addition to the classification as normal metals, semiconductors and insulators, there are also 'metametals' and 'semimetals.' The different classification schemes for 'metals' show the following characteristics.

1. Normal metals (alkali, alkaline earth, noble (Cu, Ag, Au) and many 'transition metals'):
   (a) Ductile materials based on close-packed structures with high coordination numbers (12, 8 + 6) and high symmetry (cubic or hexagonal).
   (b) Typically electropositive elements with low first ionization potentials and low electron affinities.
   (c) Increasing electrical resistivities with increasing temperature; values ~1 μΩ cm.
   (d) Temperature-independent paramagnetism. Examples include the alkali, alkaline earth, noble (Cu, Ag, Au), and many 'transition metals.'
2. Metametals (Zn, Cd, Hg, Ga, In, Tl, Pb, and *β*-Sn as assigned by W. Klemm in the 1950s):
   (a) Ductile materials based on nearly close-packed structures with moderately high symmetry (hexagonal and orthorhombic) and coordination numbers (6 + 6; 4 + 8).
   (b) Higher electronegativities than normal metals (except Pt and Au).

[☆] *Change History*: February 2015. G.J. Miller, added one additional current reference.

  - (c) Increasing electrical resistivities with increasing temperature; values ~10 – 100 μΩ cm.
  - (d) Temperature-independent diamagnetism. W. Klemm in the 1950 s assigned Zn, Cd, Hg, Ga, In, Tl, Pb, and β-Sn to this category.

3. Semimetals (Sb, Bi, Te, Po):
   - (a) Brittle materials based on network structures with low densities.
   - (b) Larger electronegativities than most normal metals and metametals.
   - (c) Decreasing electrical resistivities with increasing temperature; values ~mΩ cm.
   - (d) Temperature-independent diamagnetism.

These classifications depend largely on their electrical properties and, therefore, are linked closely with their electronic states, which are depicted by their positions in the periodic table, shown in Figure 1. The electronic behavior of an element is related to the valence atomic orbitals, which are utilized for chemical bonding, and leads to three primary categories of metallic elements ($P\sharp =$ *Pettifor number*, see below):

1. A (*s or sd*): alkali and alkaline-earth elements, excluding Be and Mg ($P\sharp$: 7–16), and A$'$ (*fsd*): rare-earth and actinide metals ($P\sharp$: 17–48);
2. T (*ds*): early half of the transition metal series ($P\sharp$: 49– ~ 60), and T′ (*dsp*): late half of the transition metal series ($P\sharp$: ~ 58–72); and
3. M(*sp* or *spd*) : post-transition elements including Be, Mg, and Al ($P\sharp$: 73–83), and M′ (*sp* or *spd*): semimetals ($P\sharp$: 84–92).

Periodic trends are especially important – whether the focus is on the main group (*sp*) or transition (*ds*) elements, the valence energy levels (E_{ns}, E_{np}, E_{nd}) drop linearly with the atomic number across a horizontal series. Among the main group elements, the valence *s* and *p* orbitals become less tightly bound as the valence period increases (except between 4*s* and 3*s* due to the presence of 3*d* orbitals). Furthermore, from left to right across a horizontal series, $E_{np} - E_{ns}$ increases so that *sp* hybridization is more important for lower nuclear charges. Within the transition series, the valence $(n+1)s$ orbital is less tightly bound than the *nd* orbitals, while the energies of 4*d* are lower than those of 3*d* orbitals. Thus, $E_{(n+1)s} - E_{nd}$ increases from 3*d* to 4*d* elements, but then drops going to 5*d* elements due to relativistic effects. These variations in valence state energies affect numerous properties, for example, the colors of Cu, Ag, and Au; the onset of semiconducting behavior at high pressures in Ca and Sr; as well as the distortion of the hexagonal close-packed structures of Zn and Cd. To represent the general as well as subtle changes in atomic electronic structure, Pettifor developed a phenomenological numerical coordinate by placing the chemical elements in an order representative of their atomic

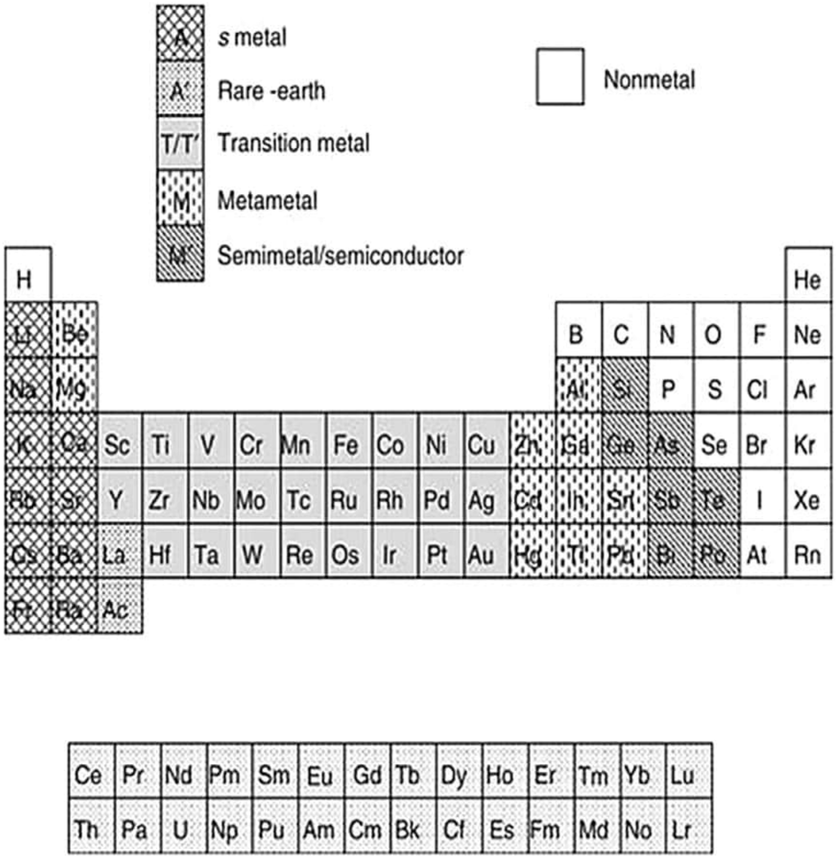
A
s metal
A′
Rare -earth
T/T′
Transition metal
M
Metametal
M′
Semimetal/semiconductor
Nonmetal
H He
Li Be B C N O F Ne
Na Mg Al Si P S Cl Ar
K Ca Sc Ti V Cr Mn Fe Co Ni Cu Zn Ga Ge As Se Br Kr
Rb Sr Y Zr Nb Mo Tc Ru Rh Pd Ag Cd In Sn Sb Te I Xe
Cs Ba La Hf Ta W Re Os Ir Pt Au Hg Tl Pb Bi Po At Rn
Fr Ra Ac
Ce Pr Nd Pm Sm Eu Gd Tb Dy Ho Er Tm Yb Lu
Th Pa U Np Pu Am Cm Bk Cf Es Fm Md No Lr

Figure 1 The periodic table of elements showing the different categories of metals based on the nature of the valence orbitals.

properties and giving each element the number in the sequence – the Pettifor number (*P*♯). This scheme has proved quite useful in separating different structural classes – in the periodic table, it nicely separates the different classifications of metals.

Furthermore, the term 'intermetallic compound' is occasionally used interchangeably with 'alloys,' but they do differ from conventional metal alloys in a number of important ways. Conventional alloys consist basically of a disordered solid solution of two or more metallic elements with similar sizes and chemical characteristics. They do not have any particular chemical formula, and are best described as consisting of a base material to which certain percentages of other elements have been added. For example, type 304, a popular grade of stainless steel, has the composition Fe–18%Cr–8%Ni. An intermetallic compound, on the other hand, is based upon a definite atomic ratio, with a fixed or narrow range of chemical composition. Figure 2 shows the Al–Ni phase diagram as an example of a binary system showing solid solutions and intermetallic compounds.

Elements such as B, Si, Ge, P, As, and Se, themselves nonmetals, as well as C, when combined with metallic elements are considered to form 'intermetallic compounds' because their structures resemble those of other intermetallics, and they form with definite compositions. The elements H, N, O, S, and halogens are not considered to give intermetallic compounds, although numerous sulfides and some halides show a metallic character. The smaller elements, for example, H, B, C, N, and O can often occupy interstitial sites in intermetallic compounds, which greatly affect their mechanical, chemical, and physical properties.

The atoms in conventional alloys are linked through relatively weak interatomic interactions, often called 'metallic bonds,' with the atomic nuclei placed in a 'gas' of valence electrons that are able to move relatively freely, which explains their ductility, electrical conductivity, and temperature-independent paramagnetism. In contrast, chemical bonding in intermetallic compounds may show significant polar covalent character, which can produce strong interatomic interactions, brittle mechanical behavior, transport properties ranging from semiconducting to superconducting, and various magnetic interactions leading to complex magnetic structures. However, in intermetallic compounds whose mechanical and electronic properties resemble those of alloys, the individual elements tend to occupy different positions within the crystal lattice. This condition, which is referred to as 'ordering,' often leads to abrupt changes in the physical properties of the material.

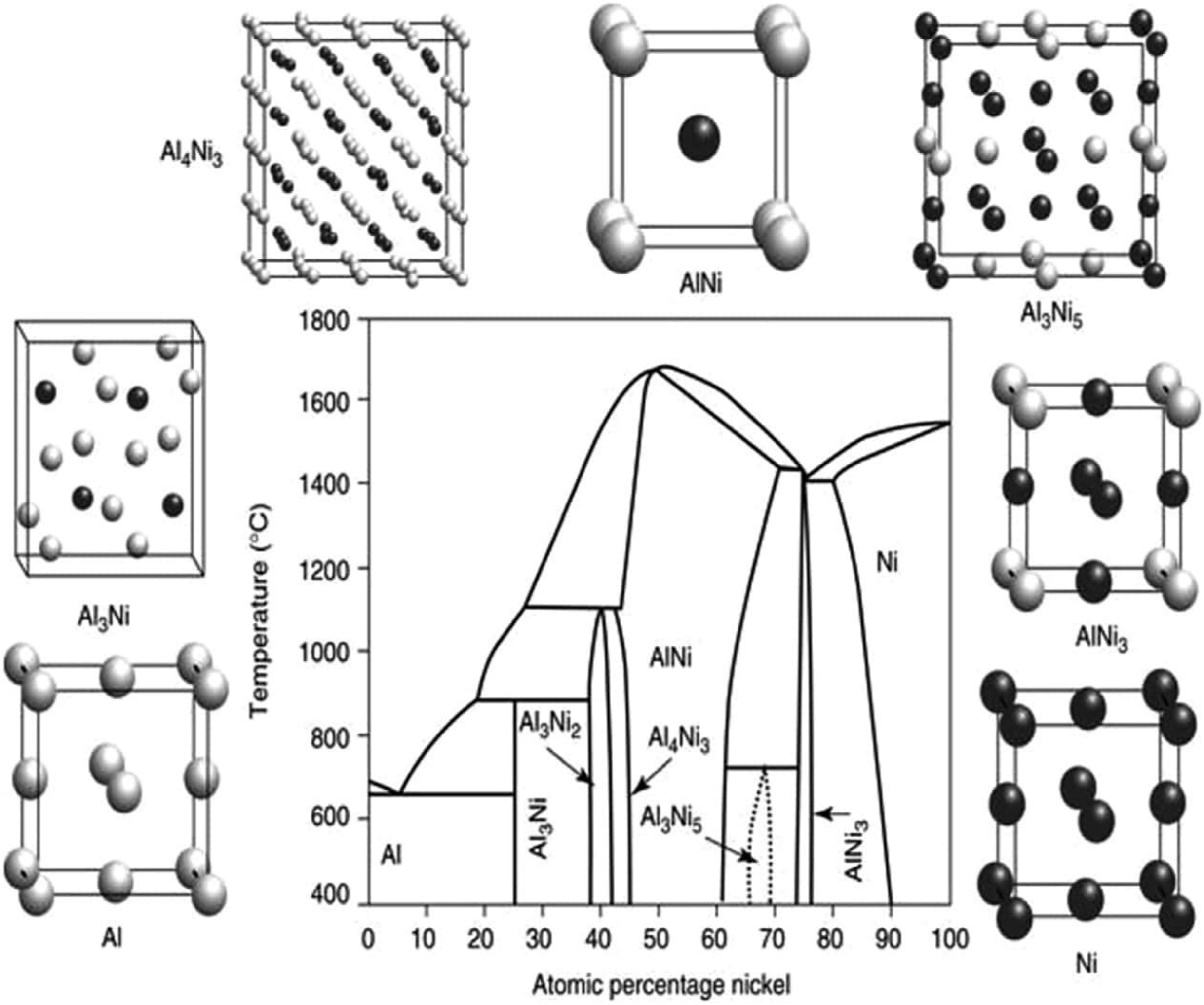

Figure 2 Al–Ni phase diagram and structures of various intermetallic compounds in this binary system. Light-colored spheres are Al; dark-colored spheres are Ni.

Classifying Electronic States in Intermetallic Compounds

One useful tool for assigning compounds into different categories is a van Arkel–Ketelaar triangle, which maps compounds according to two related chemical coordinates using an electronegativity scale based upon the average one-electron valence shell energy of the ground-state free atom, called the configuration energy (CE). In this map, shown in Figure 3, the horizontal coordinate is the average CE of the constituents, while the vertical coordinate is the difference, so that metallic substances lie to the left. The transition from metallic to nonmetallic behavior involves either increasing electronegativity in general, or increasing electronegativity difference between constituents. Since CE represents the average energy of a valence electron, CE correlates with the separation between the energies of the valence *s* and *p* orbitals, and so influences the way atoms will interact with one another. Low CE values give small $E_{np}-E_{ns}$ values and broad, frequently overlapping energy bands. In many cases, the electronic states for these systems behave like nearly free electron states. Moreover, valence *d* orbitals are important for the properties of transition elements and valence *f* orbitals for the rare-earth and actinides – changes in the band filling of these orbitals affect the structure, cohesive energies, thermodynamic properties, and magnetic character. Unlike valence *s* and *p* orbitals, the valence *d* and *f* orbitals give narrower energy bands, and have more atomic-like character in compounds. The 4*f* orbitals in rare-earth elements and their compounds are generally localized, while the 5*f* orbitals in actinides have a greater role in chemical bonding.

This qualitative picture implies a variation in the description of states from a nearly free electron (NFE) model to a tight-binding (TB) model. In NFE, the electronic states are treated as linear combinations of plane waves (the eigenstates for a free electron gas). The arrangement of positively charged atomic nuclei creates a potential that perturbs the free electron states. The extension of this approach is toward pseudopotentials, which makes the valence states orthogonal to the core atomic states. In TB, the electronic states are treated as linear combinations of atomic orbitals (the one-electron eigenstates of free atoms). Pseudo-potential methods as well as TB methods have been used to study metals and semiconductors – the TB methods lead to useful chemical insights by virtue of starting from atoms, and have provided valuable understanding even for systems in which NFE would be entirely appropriate.

To calculate the electronic densities of states (DOS), multi-electron terms in the total electronic energy may be treated either in the local density approximation (LDA) or in the local spin density approximation (LSDA) and the one-electron terms can be treated scalar relativistically. For the heavier elements, spin–orbit coupling should also be considered. For many ground-state properties (structure, cohesive energy, magnetism, and electronic transport), the LDA is quite effective. Numerous recipes exist for calculating the exchange and correlation terms. An especially valuable analysis of the DOS is through the crystal orbital Hamilton population (COHP) analysis, which allows states to be identified according to the bonding, nonbonding, or antibonding character of the interatomic interactions (COHP values are, respectively, less than, equal to, or greater than zero).

Experimental determination of electronic states can be carried out by photoelectron spectroscopy, which is a surface-sensitive technique. de Haas–van Alphen effect gives information about the Fermi surface in reciprocal space, but demands quite pure

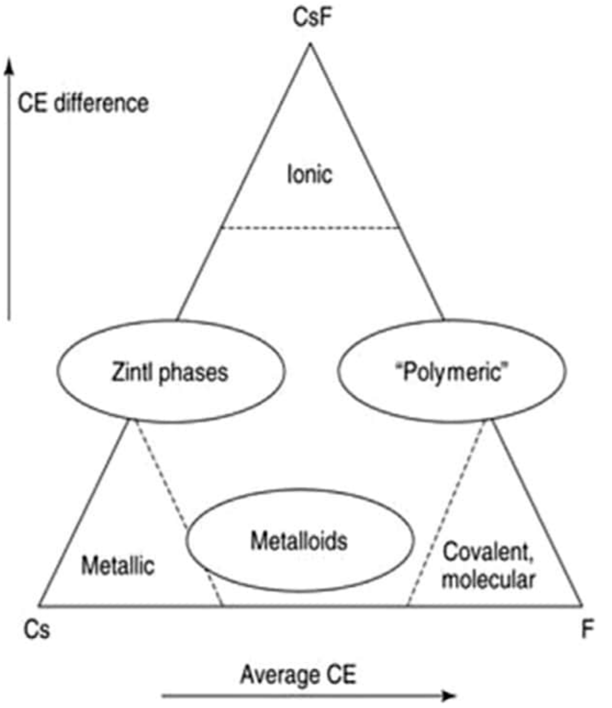

Figure 3 The van Arkel–Ketelaar triangle based on configuration energies of the atomic components.

samples. Hall effect measurements provide information about the charge carriers. Other methods, such as specific heat and magnetic susceptibility studies on metals, can give values of the DOS at the Fermi level.

Electronic Interactions Between Different Metallic Types

An examination of Pearson's *Handbook of Intermetallic Phases* shows that the predominant classes of intermetallic compounds involve the following combinations of metallic elements using the designations in Figure 1: (1) $A'-T'$; (2) A–M and $A-M'$; (3) $T-T'$; (4) $(T,T')-(M,M')$; and (5) $(A,A')-(T,T')-(M,M')$. Very few examples exist for $(A,A')-(A,A')$, $(M,M')-(M,M')$, $(A,A')-T$, $T-T$, and $T'-T'$. This observation guides our emphasis to the important electronic interactions: (1) *d–d*; (2) *d–sp*; and (3) *sp–sp*.

The two most important factors influencing the electronic DOS are the relative energies of the atomic orbitals of the different constituents and the strengths of the interatomic orbital interactions leading to bandwidths, that is, band dispersion. Energy gaps, pseudogaps, and peaks in the DOS arise from these two fundamental characteristics. Since the majority of intermetallic compounds show metallic properties, the 'perfect' screening of conduction electrons means that there is essentially no charge transfer between different elements. Therefore, the 'common band' model is most appropriate for analyzing the DOS. Additional factors include composition and the coordination environments surrounding each element in a structure.

d–d Interactions

Intermetallic compounds involving just transition metals are technologically important due to their mechanical, chemical, and physical properties. Some of the strongest chemical bonds in condensed phases are found among these compounds, as measured by their cohesive energies. The electronic states of transition metals exhibit a partially occupied, narrow valence *d* band that lies near the bottom of a broad valence *s* or *sp* band. Since the valence *d* electrons remain relatively tightly bound to their parent atoms, the appropriate method to treat the *d–d* electronic interactions is the TB model. When different transition metals combine to give an intermetallic compound, the primary effect is the way the different *d* orbitals interact – the valence *s* or *sp* band remains broad, and contributes to the chemistry and physics of these materials by adjusting the extent of filling of the *d* bands. The *d–d* orbital interactions break down into σ, π, and δ types of orbital overlap, with σ overlap the greatest and δ overlap the lowest (Scheme 1).

The *d–d* π interactions are important for the structural variation of the transition metals in the 4*d* and 5*d* periods (h.c.p.–b.c.c.–h.c.p.–f.c.c.) (b.c.c. – body-centered cubic; f.c.c. – face-centered cubic; h.c.p. – hexagonal close-packed). These overlaps affect the shape of the *d*-band DOS – see Figure 4, which compares the DOS curves for a b.c.c. and f.c.c. 4*d* transition metal. The local environments in the two structures both have cubic symmetry, and the local *d* orbitals are split into e_g and t_{2g} levels. The local coordination environment of the b.c.c. structure creates a region of low, nonzero DOS values close to six valence *s* and *d* electrons between two regions of high DOS values. This region of low DOS is called 'quasigap' or 'pseudogap.' COHP analysis of the DOS shows that *d–d* bonding states are below the pseudogap while antibonding states lie above. On either side of six valence *s* and *d* electrons, close-packed (h.c.p., f.c.c.) structures are preferred. Trends in effective nuclear charge and occupation of bonding versus antibonding states help explain the trend that across a period of transition metals, the *d* bandwidth slightly increases and then sharply decreases while the *d* band center steadily decreases. These trends have profound influences on the states of transition metal intermetallics.

When two different transition metals form an intermetallic compound, the shape of the DOS will depend on both the structure and the electronic characteristics of the component elements. In the case of disordered alloys AB, the 'common band' model is appropriate for understanding heats of formation and trends in cohesive energies with respect to metals A and B (see Scheme 2). In this model, the valence *d* band of each transition metal is characterized by an energetic center ($\varepsilon_{\mathrm{M}}^0$; $\mathrm{M}=A,\mathrm{B}$) a bandwidth (W_{M}^0; $\mathrm{M}=A,\mathrm{B}$), and band filling (N_{M} electrons; $0 \le N_{\mathrm{M}} \le 10$; A, B; indicated by the shaded regions in Scheme 2). The resulting *d* band for the disordered alloy AB has a bandwidth given by $W_{\mathrm{AB}} = \overline{W}\left[1 + 3\left(\Delta\varepsilon/\overline{W}\right)^2\right]^{1/2}\left(\overline{W} = \left(W_{\mathrm{A}}^{\mathrm{AB}} + \overline{W}_{\mathrm{A}}^{\mathrm{AB}}\right)/2\right)$; $\Delta\varepsilon = \varepsilon_{\mathrm{A}} - \varepsilon_{\mathrm{B}}\left\langle\varepsilon_{\mathrm{A}}^0 - \varepsilon_{\mathrm{B}}^0\right\rangle$, band filling of $\overline{N} = (N_A + N_B)/2$. To construct this *d* band for the alloy AB, there is 'renormalization' of the average band energies ($\varepsilon_{\mathrm{M}}^0 \to \varepsilon_{\mathrm{M}}$; $\mathrm{M}=\mathrm{A},\mathrm{B}$) to keep local charge neutrality (i.e., no effective charge transfer) and the bandwidths ($W_{\mathrm{M}}^0 \to W_{\mathrm{M}}^{\mathrm{AB}}$; $M=A,\mathrm{B}$) due to changes in atomic volumes from the element to the alloy. In this *d* band, states below the band center $\overline{\varepsilon}$ are mostly from metal *B*, while those above $\overline{\varepsilon}$ are mostly from metal A (as indicated by the dashed line for the AB band). Therefore, electrons flow from A to B because B is more electronegative than A($\varepsilon_{\mathrm{A}}^0 < \varepsilon_{\mathrm{A}}^0$), but also flow back from B to A through orbital overlap in alloy AB.

The common band model predicts that the most stable intermetallic compounds and alloys would arise from combinations of transition metals at opposite ends of the transition metal series and that the highest cohesive energies exist for AB systems with

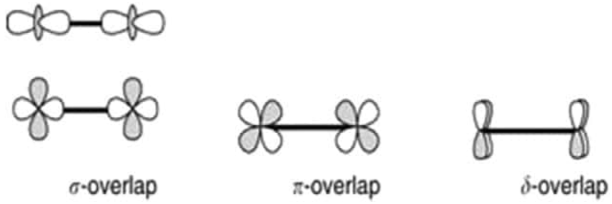

Scheme 1

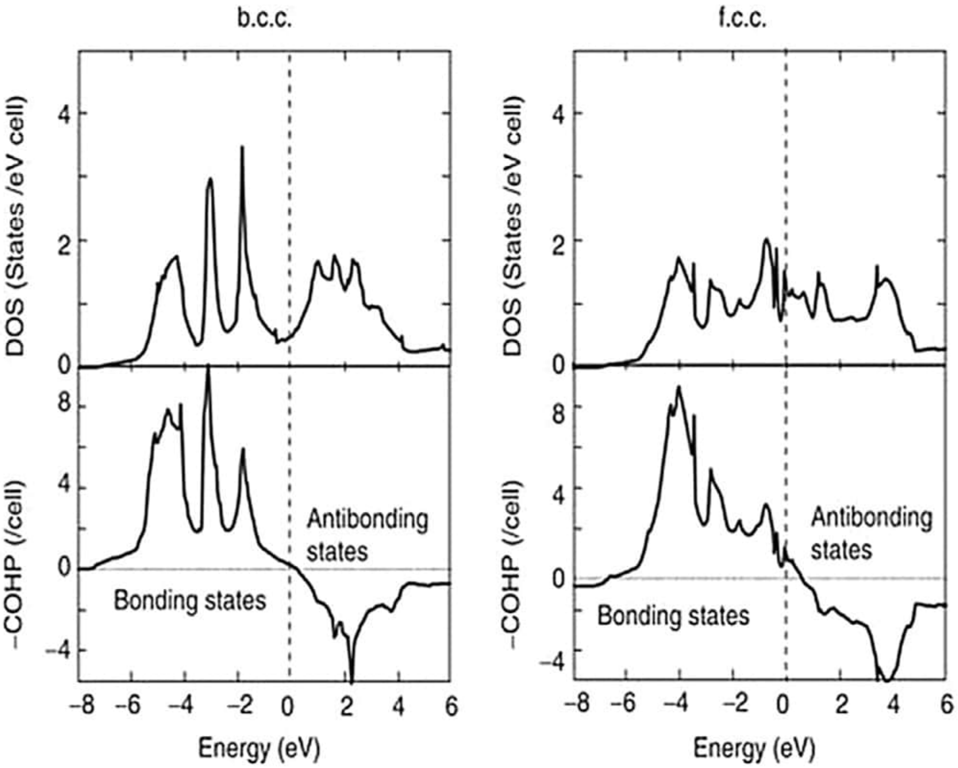

Figure 4 DOS and nearest-neighbor COHP analysis for the b.c.c. and f.c.c. structures of a typical 4*d* transition metal. The energy zero corresponds to six valence *s* and *d* electrons. In the COHP curves, metal–metal bonding states occur for –COHP $>$ 0; antibonding states for –COHP $<$ 0.

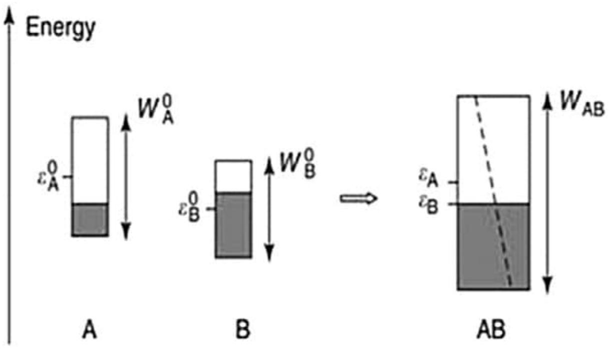

Scheme 2

$\overline{N}$: 5. Specifically, the cohesive energy for AB, U^{AB} : $-k\overline{N}(10-\overline{N})W_{AB}+cW_{AB}^2$ (k, c are positive constants) has an attractive part related to band filling and a repulsive part related to the number of nearest neighbors, which is proportional to the square of the bandwidth. The expression for the heat of formation of AB is more complicated, but takes the form ΔH_f^{AB} : $f(\overline{N}(10-\overline{N}))(\Delta N)^2$ where $\Delta N = N_B - N_A$. Negative heats of formation occur for $\overline{N}$ between 3.33 and 6.67 electrons per atom. For an intermetallic compound AB, with an ordering of A and B atoms, this model is appropriate for adjacent elements (small $\Delta\varepsilon$ values), but is less appropriate as this energy difference increases. For larger $\Delta\varepsilon$ values, a pseudogap can open in the DOS, as seen in Figure 5 for TiFe, which adopts the CsCl-structure type. The DOS curves of Ti and nonmagnetic Fe show features as expected – a lower band center and a narrower bandwidth for Fe. In TiFe, the *d* bandwidth is wider than that for either element, but the shape shows a pseudogap at the center of the *d*-band and the Fermi level falls in this pseudogap. States below this pseudogap are mostly Fe-orbitals, while those above are mostly Ti-orbitals. Nevertheless, TiFe is not held together by ‘ionic’ forces because the perfect screening of the valence electrons negates any charge transfer – there is a ‘renormalization’ of the energies of each transition metal. The DOS shows aspects of the local coordination, but the principal factor creating the pseudogap in TiFe is the energy difference between the band centers of Ti and Fe. COHP analysis of the DOS of TiFe shows that states below the Fermi level are Ti–Fe bonding; those above are Ti–Fe antibonding. The homonuclear Fe–Fe and Ti–Ti interactions are weaker (longer distances) and bonding below the Fermi level, but

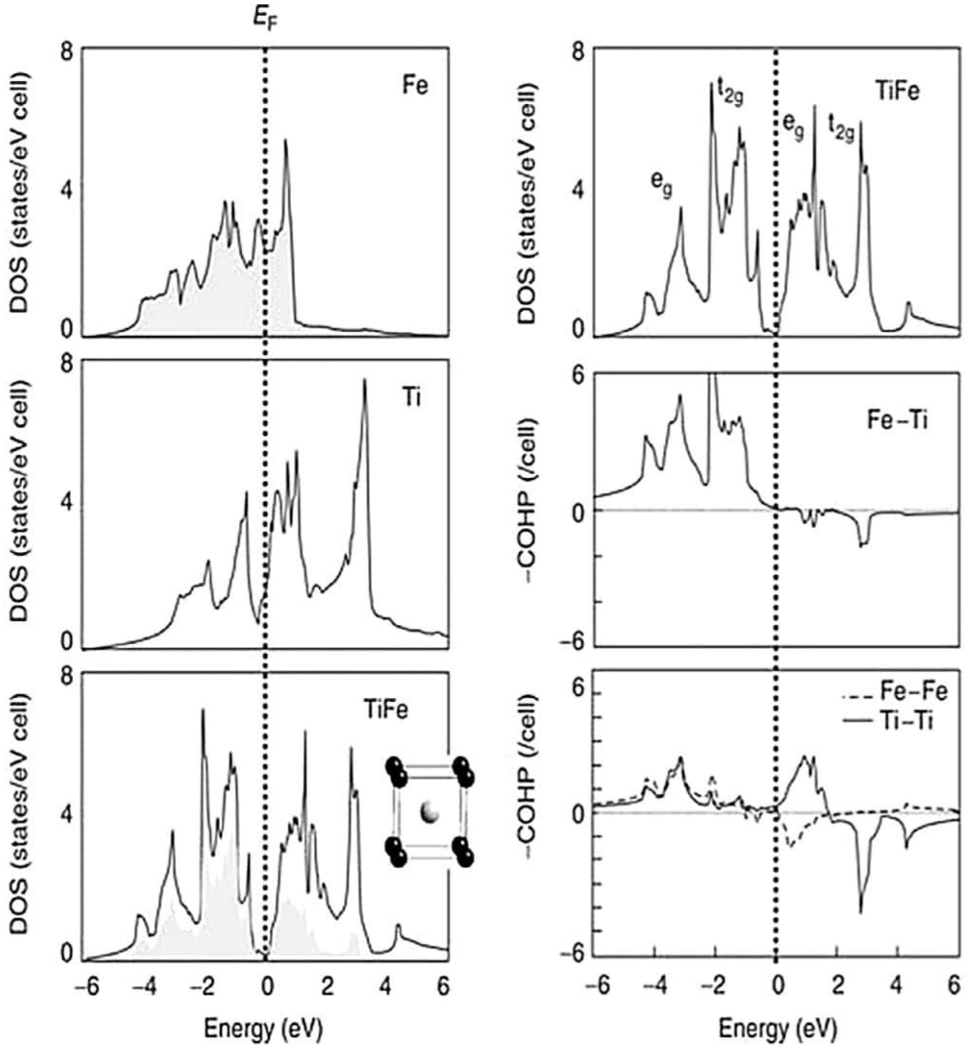

Figure 5 Left: DOS curves of nonmagnetic Fe, Ti, and TiFe. The shaded regions in the DOS of TiFe are Fe states. Right: Assignment of the peaks in the DOS of TiFe into local e_g and t_{2g} levels as well as COHP analyses for Ti–Fe, Ti–Ti, and Fe–Fe near-neighbor interactions.

the crossover from bonding to antibonding interactions does not occur at the pseudogap. Therefore, another aspect of the pseudogap in intermetallic compounds is the creation of bonding states below the gap and antibonding states above. Therefore, many stable intermetallic compounds show low DOS values at the Fermi level, which can be accounted for by certain metal-metal interactions through a COHP analysis of the DOS.

Trends in the features of DOS curves depend on the types of interactions, the relative magnitudes of orbital overlaps and atomic electronegativities. Figure 6 shows the trends in DOS and COHP curves for TiRu, TiRh, and TiPd, which follows the structural trend b.c.c.–f.c.c.–h.c.p., but with ordered arrangements of metals. A pseudogap is noticeable in all cases for six states per formula, although it is less clear in the TiRh and TiPd cases. TiRu adopts the CsCl structure with eight nearest-neighbor Ti–Ru interactions and 12 s nearest-neighbor homonuclear (Ti–Ti and Ru–Ru) contacts. In TiRh and TiPd, there are six heteroatomic (Ti–Rh or Ti–Pd) and six homoatomic (Ti–Ti, Rh–Rh, Pd–Pd) nearest-neighbor contacts, which interferes with the pseudogap. Additionally, the band-widths become narrower as the 4*d* metal becomes more electronegative. Again, there is no charge transfer between Ti and the 4*d* metal, in accordance with the common band model.

If the DOS value at the Fermi level is sufficiently high, then the structure is susceptible to an electronic distortion, which will perturb the electronic states near the Fermi level and lower the total electronic energy. This effect can happen in one of two ways: (1) a structural distortion, as in VIr (which distorts away from the cubic CsCl-structure type); or (2) ferromagnetism. For ferromagnetism to occur, the local exchange energy must also be sufficiently large, and this occurs for some of the 3*d* elements, which have the smallest spatial extent. The Stoner criterion states that ferromagnetism is preferred when $IN(E_F) > 1$, where I is the intra-atomic exchange energy (chemists will think about the so-called ‘pairing energy’ – the energy penalty in putting two electrons

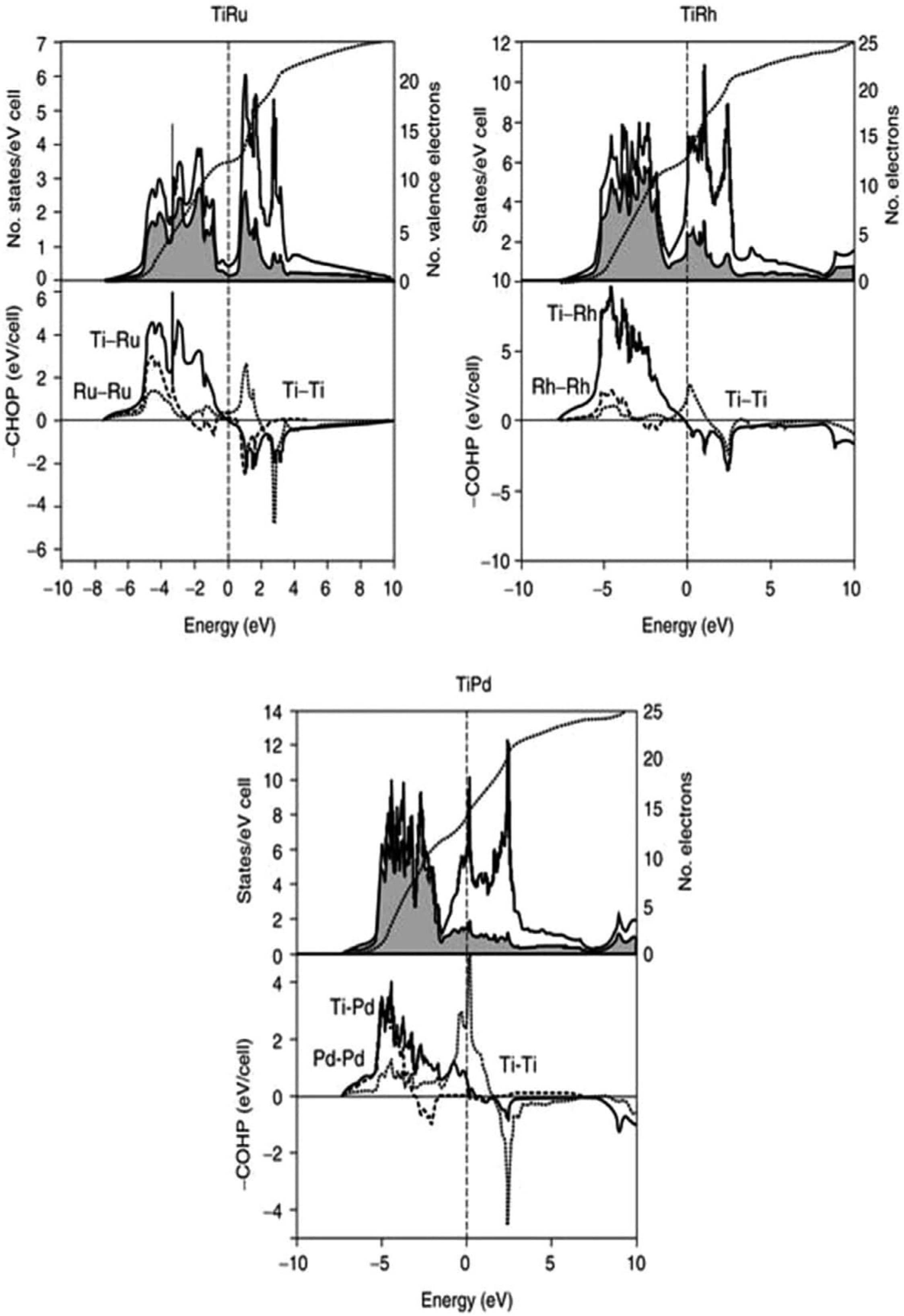

Figure 6 DOS and COHP analyses of the 3*d*–4*d* intermetallic compounds, TiRu, TiRh, and TiPd. Shaded regions of the DOS are states from the electronegative metal (Ru, Rh, Pd). Fermi levels are indicated by the dashed lines.

into the same atomic orbital) and $N(E_F)$ is the value of the DOS at the Fermi level. Since $N(E)$ is typically inversely proportional to the bandwidth W, when either intra-atomic or inter-atomic interactions lead to narrow bands, and the local exchange is sufficiently large, ferromagnetism frequently occurs – the 3*d* elements Fe, Co, and Ni as well as compounds involving Mn are especially susceptible.

d–(*s*)*p* Interactions

Intermetallic compounds between transition metals and main group metals display interesting magnetic, superconducting, mechanical, and structural properties. In most cases, the electronic states near the Fermi level of these compounds are dominated by the *d* orbitals of the transition metal component. Their electronic structures arise from two dominant factors: (1) the expansion of the transition metal lattice due to the insertion of the main group (*sp*) element; and (2) the interaction between the valence *d* bands on the transition metal with the *sp* bands of the main group element. Three categories occur (see Figure 7): (1) where the *d* levels lie much deeper in energy than the main group atom (e.g., PdLi); (2) where the opposite is true (e.g., 'PdF'); and (3) the intermediate case where the two are of similar energy (e.g., PdB). In the first two cases, there is a rather weak interaction between the two sets of orbitals. The transition metal *d* band is narrower than in the pure metal, as a result of stretching the metal lattice to accommodate the nonmetal. These two cases do differ, however: (a) PdF is quite 'ionic,' involving charge transfer from metal *d* states to the low-lying fluorine-located bands - note that the Fermi level drops from the top of the *d* band; (b) PdLi utilizes the common band

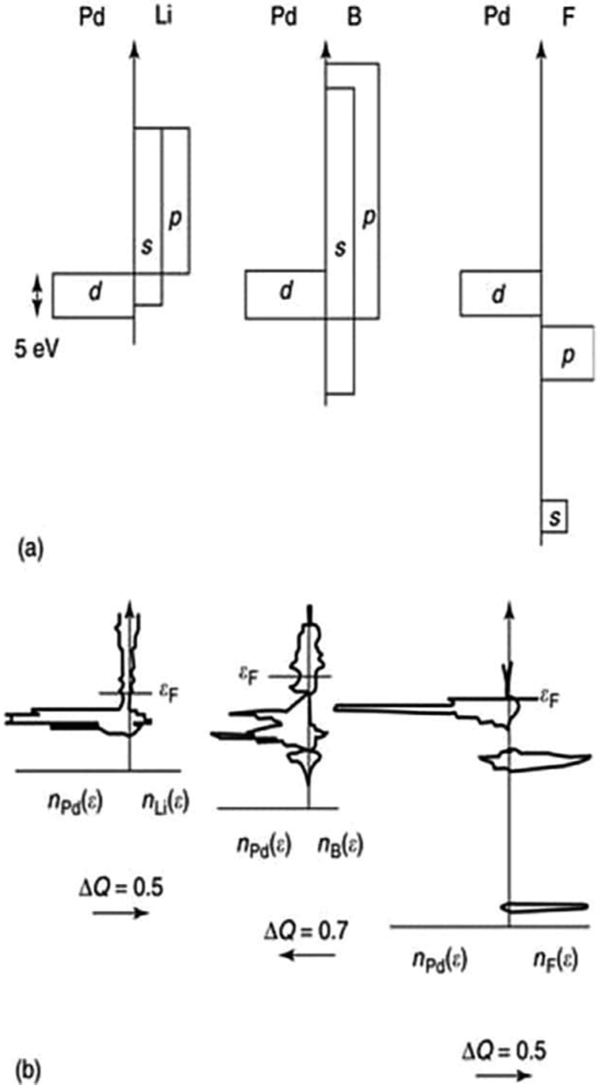

Figure 7 Schematic (a) and calculated (b) partial densities of states for the atomic components in the three examples: PdLi, PdB, and PdF. Reprinted with permission from Gelatt Jr., C.D., Williams, A.R., Moruzzi, V.L., 1983. Theory of bonding of transition metals to nontransition metals. Physical Review B 27, 2005–2013. © American Physical Society.

picture, but the Fermi level rises above the top of the Pd 4*d* band – note the significant contribution from Li valence states in the region of the Pd 4*d* band. A similar example is the case of CsAu, which is an unusual example of a red, transparent, semiconducting intermetallic compound – its photoelectron spectrum shows a band gap of 2.6 eV. The case of PdB is most interesting because strong mixing occurs between the two sets of orbitals. These bands can be separated into bonding, non-bonding, and antibonding regions between the metal and nonmetal. Changes to the DOS will occur on composition – the strongest interactions will typically involve transition metal–main group metal, but the DOS will depend on the concentration of different orbitals. In transition metal-rich compounds, the metal *d* band will dominate and be broadened by T–T interactions; in main group metal-rich compounds, the metal *sp* bands may now become apparent.

One factor governing the atomic arrangements in intermetallic compounds is the relative strengths and concentrations of heteroatomic (between different elements) and homoatomic (between identical elements) interactions. As the molar concentration of the transition metal increases, the *d* band will become wider and may adjust its position depending on the relative electronegativity of the main group metal. For example, in the Ni–Al system, one can see the influence of composition on the DOS in Figure 8 for three different examples. As there is an increased dilution of Ni in Al, the Ni 3*d* bands become narrower and pull away below the Fermi level.

Main group elements show extensive structural diversity as the number of valence *s* and *p* electrons changes. For less than the half-filled band situation, for example, among group 13 elements like Al and Ga, clusters based on octahedra, square pyramids, and tetrahedra are common. Such clusters can be used to visualize structures through condensation of vertices, edges, or faces and create new understanding of electronic and bonding characteristics, as in transition metal trialuminides, MAl_3 (M = rare-earth element, Ti, Zr, Hf, V, Nb, Ta). As the number of valence electrons increases in this family, the network of Al-based polyhedra changes from octahedra to square pyramids. The DOS shows a pseudogap at the Fermi level (see Figure 9 for $TaAl_3$ as an example), which is largely influenced by the bonding states of the Al polyhedra. Nevertheless, M–Al orbital interactions also split the 5 M *d* levels into two sets (e_g below t_{2g}), which also contributes to the observed pseudogaps in the DOS curves as well as the preferred structures and electronic properties. In fact, such compounds are called *d–p* covalent intermetallics – COHP analysis of the DOS in $TaAl_3$ shows maximum bonding character for both Al–Al and Ta–Al interactions.

Pseudogaps occur in intermetallics for reasons based on structure and atomic electronegativities. Another important growing class of compounds is the set of half-metallic ferromagnets, of which the 'semi-Heusler alloys' represent significant examples ('semi-Heusler' alloys, ABX, consist of cubic closest packed X atoms with B atoms in all octahedral holes and A atoms ordered in one-half of the tetrahedral holes of the close-packed array of X 'Heusler' alloys, A_2BX, have all tetrahedral holes filled). These compounds are cubic intermetallic phases combining main group metals (Sn and Sb) with two different transition metals (one early T – Ti, Zr, Hf, V, Nb; one late T′ – Fe, Co, Ir, Ni, Pt). Their electronic properties, and therefore, their electronic states, depend strongly on the number

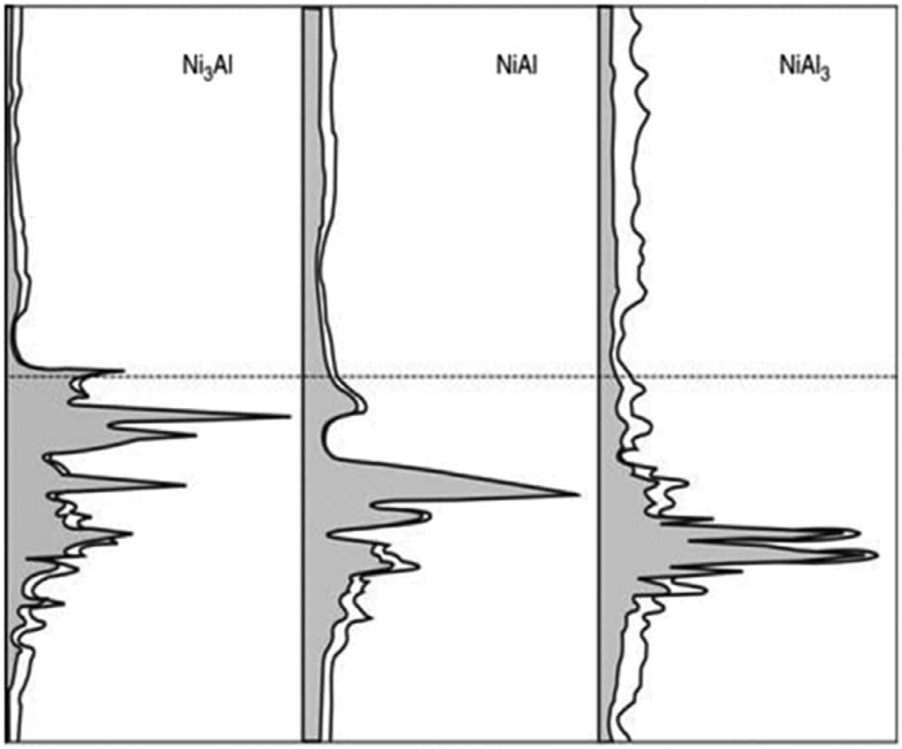

Figure 8 DOS curves for Ni_3Al, NiAl, and $NiAl_3$ presented with the Fermi level set as the energy reference. The shaded regions indicate the Ni 3*d* and 4*s* components to the DOS and Ni 3*d* states are labeled.

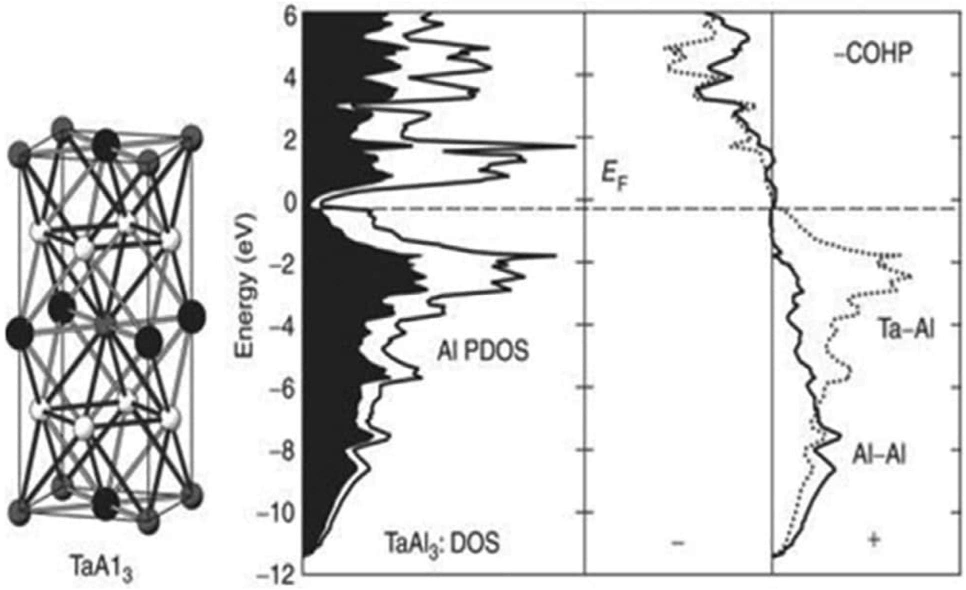

Figure 9 Structure, DOS, and COHP analysis for TaAl$_3$. Large, dark spheres are Ta; small shaded spheres are Al. The shaded regions in the DOS are Al states, and the Fermi level is marked by a dashed line. In the COHP curves, the solid line shows Al–Al interactions; the dotted line shows Ta–Al interactions.

of valence electrons: 18-electron examples such as TiCoSb are diamagnetic semiconductors, 17-electron examples are metallic and Pauli paramagnetic, whereas 19- or 22-electron examples show half-metallic ferromagnetic behavior. Half-metallic ferromagnetism originates when the nonmagnetic electronic structure is susceptible to splitting of the majority and minority spin DOS, and the Fermi level falls in an energy gap for either spin, as seen in the LSDA DOS for VCoSb, a 19-electron example, in Figure 10 (VCoSb is a weak ferromagnet because there is an energy gap at nine states for both spin states; a half-metallic ferromagnet shows an energy gap just in the minority spin band, as seen in NiMnSb). The nonmagnetic DOS at the Fermi level for 19 electrons (VCoSb) is large, and is susceptible to ferromagnetism within the Stoner criterion. The lowest energy valence orbitals are from Sb, then from Co, finally from V since the atomic electronegativities increase from V to Co to Sb. The gap in the DOS at 18 valence electrons originates from these valence orbitals, the symmetry of the local coordination environments and metal–metal interactions: (1) Sb has four valence orbitals and the five Co 3*d* orbitals make nine low-lying orbitals to be filled for 18 electrons; (2) the tetrahedral coordination of Sb around Co and octahedral coordination around V keep the Co 3*d* levels low and split by a small amount; and (3) V–Co orbital interactions help to keep a band gap at 18 electrons, which accounts for the properties of TiCoSb. In these examples, the gap opens through *d*–*d* interactions between the two different transition metals – note the strength of early-late *d*–*d* interactions, just as mentioned in an earlier section.

sp–*sp* Interactions

Due to the widely different electronegativities of these elements, theoretical determinations of their electronic states range from NFE through pseudopotentials to TB models. There are three principle types of interactions (see Figure 1): A–A, A–M, and M–M. A–A interactions are best modeled by the NFE because the active metals have the lowest $E_{np}-E_{ns}$ values and diffuse valence atomic orbitals. The more electronegative main group metals (M) require pseudopotential or TB models because $E_{np}-E_{ns}$ increases and the valence atomic orbitals become contracted. In intermetallic structures, coordination environments surrounding A-type elements involve several atoms and often resemble densely packed structures, whereas those around M-type elements show lower coordination numbers and some directional bonding character. As the electronegativity difference between main group elements increases, the DOS develops a structure, that is, peaks and pseudogaps (or gaps), as seen for the three hypothetical compounds: ‘NaMg,’ ‘NaAl,’ and ‘MgAl’ in Figure 11. A–M compounds constitute an important class of compounds called ‘polar intermetallics,’ in which orbital interactions within the network of electronegative M atoms typically maximizes bonding interactions. If the local structure around the M atoms obey classical valence rules, then these compounds are called ‘Zintl phases.’ Subtle electronic effects can arise from valence *d* orbitals: for alkaline-earth elements, there can be contributions of $(n-1)d$ orbitals to *ns* bands, especially under pressure, whereas for Cu, Ag, Au, Zn, Cd, and Hg, $(n-1)d$ orbitals can hybridize with the valence *ns* and *np* bands.

Hume–Rothery ‘electron compounds’ are formed between noble metals and *sp* metals – in these systems, the noble metal *d* band is filled, so that the dominant orbital interactions will be *sp*–*sp* interactions. There are five phases that Hume–Rothery identified as controlled by electron count: (1) h.c.p. (three subcategories: ζ ($c/a=1.633$), ε ($c/a=1.55-1.58$), and η ($c/a=1.77-1.78$)); (2) f.c.c.; (3) b.c.c./CsCl-type (β-brass); (4) β-manganese; and (5) γ-brass. TB models account for the structural variations very well, which attests to the importance of orbital interactions influencing these structures. Analysis of the DOS and band structure for CuZn reveal, however, that optimized metal-metal bonding is not the driving force here (Figure 12). As Pettifor and co-workers have shown, the

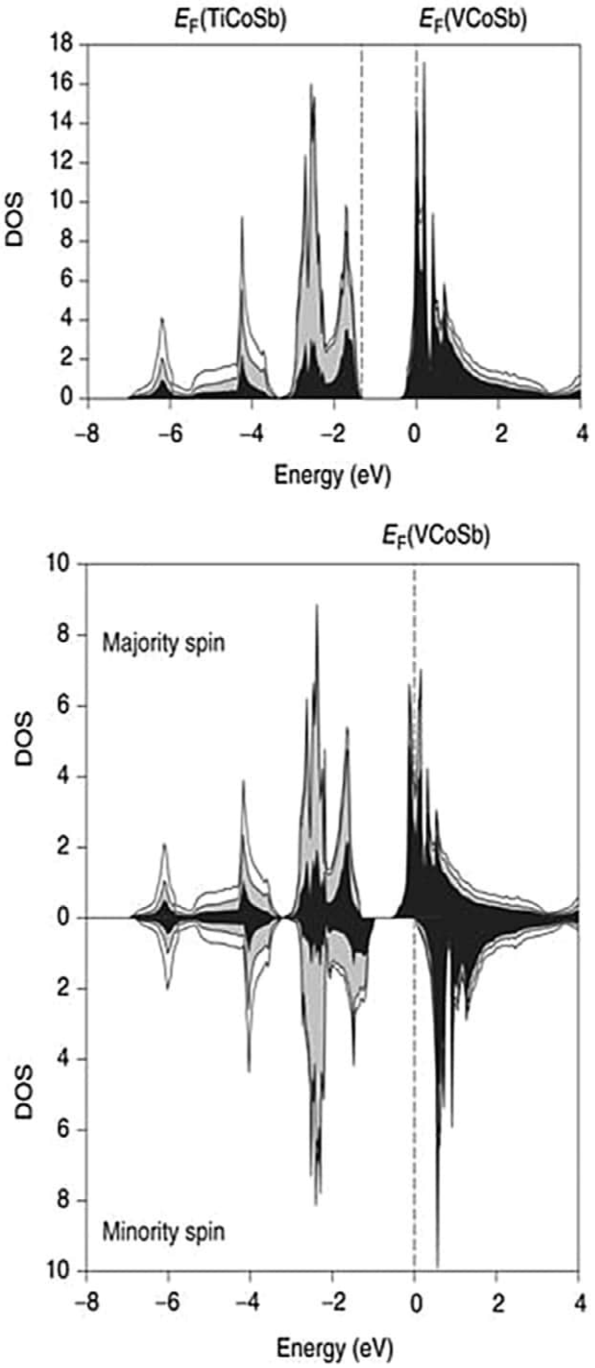

Figure 10 Nonmagnetic (top) and LSDA (bottom) DOS for VCoSb, a semi-Heusler alloy. The dashed line indicates the Fermi level – note the bandgap in the minority spin states. Black regions are V orbitals; gray regions are Co orbitals; white regions are Sb orbitals.

structural trend is driven by van Hove singularities in the DOS (places where the band structure has zero slope, which occur at the bottom or top of energy gaps at Brillouin zone boundaries). The band structure shows that the valence *d* bands are well below the Fermi level, but, nevertheless, hybridize with the NFE-like *sp* bands. Numerous quasicrystalline and approximant systems (Li–Cu–Al, Mg–Zn–Al) have been interpreted as similar 'electron compounds,' but the NFE gives little structural chemical information.

Zintl phases involve combinations of electropositive and electronegative main group metals, for example, LiAl, in which the electronegative element forms a structure based on the octet rule if one assumes that the electropositive element donates all of its valence electrons. The octet rule demands that eight bonding or nonbonding valence electrons surround main group (*sp*) elements

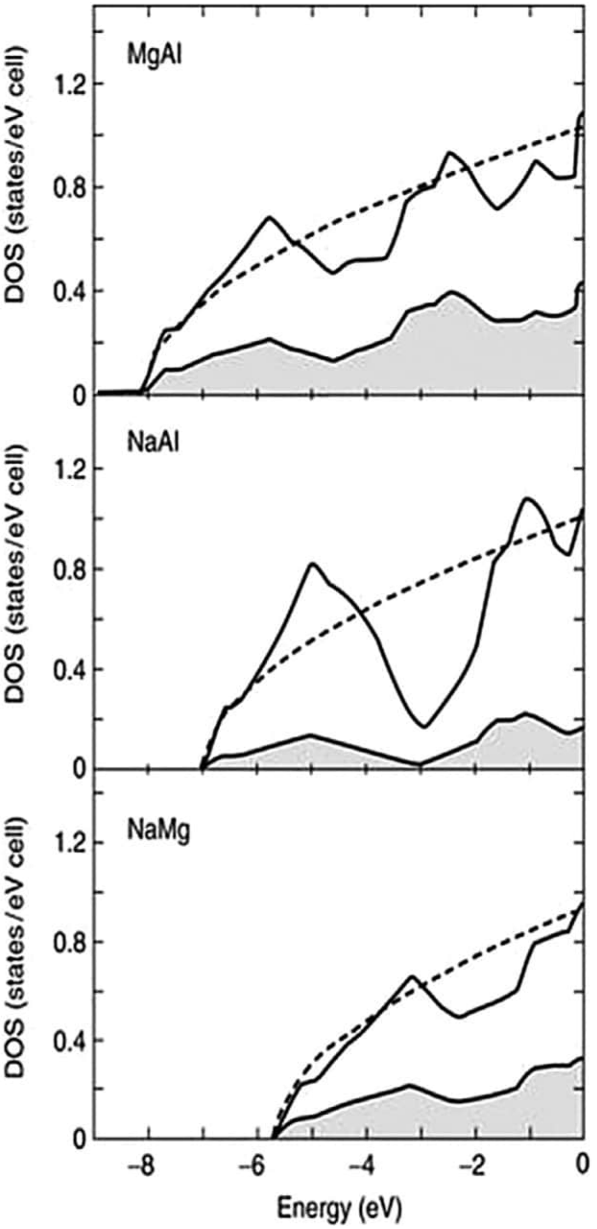

Figure 11 DOS curves for NaMg, NaAl, and MgAl, and the shaded regions are states from the more electropositive element. The dashed line shows a free electron type DOS.

in stable structures. Thus, the structure of LiAl has a diamond network of four-bonded Al atoms, which is formulated as 'Al$^-$,' isoelectronic with Si. The DOS of Zintl phases show either a gap or pseudogap at the Fermi level with bonding states within the electronegative metal network fully occupied (Figure 13). So, 'classical' Zintl phases are defined as follows: They are compounds that (1) contain an alkali or alkaline-earth metal and an electronegative main group element that is a metal, semimetal, or smallgap semiconductor; (2) are electronically balanced or close-shell compounds, that is, the number of valence electrons provided by the constituents equals the number of electrons needed for two-center, two-electron covalent bonds in the structure; (3) are semiconductors or poor conductors; (4) are either diamagnetic or show a very weak temperature-independent paramagnetism; and (5) are typically brittle.

Among the *sp* class of intermetallic compounds, the Hume–Rothery phases behave as normal metals while Zintl phases are typically semiconductors. 'Polar intermetallics' represent an intermediate class of compounds, formed between active metals with electronegative metals, but the DOS shows a pseudogap near the Fermi level. COHP analysis of the DOS indicates optimized bonding in the electronegative component and the active metal behaves like a cation, but typically does not donate its full

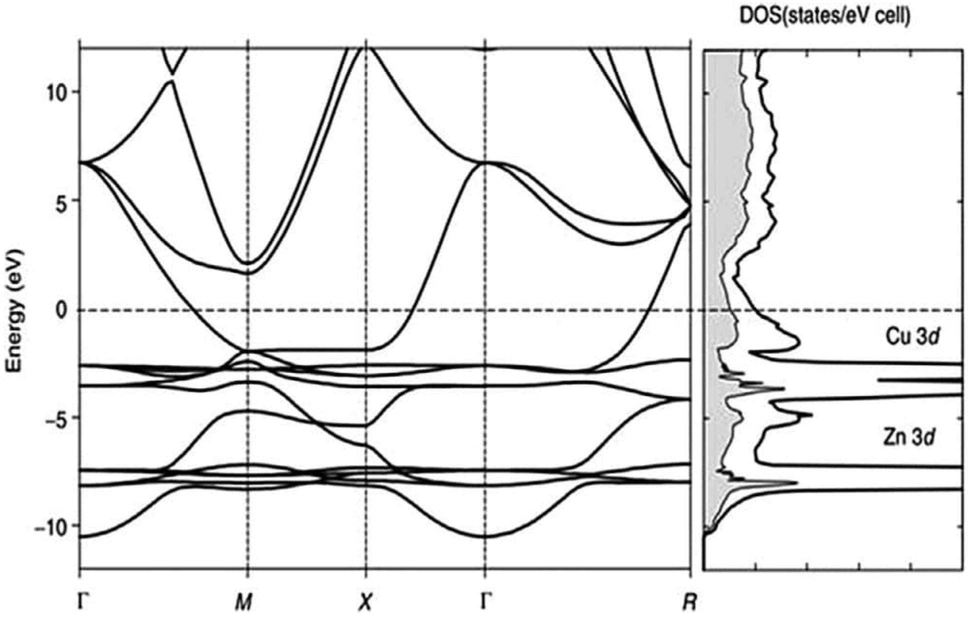

Figure 12 Energy bands and DOS for CuZn (β-brass structure). Shaded region in the DOS comes from valence *s* and *p* orbitals of Cu.

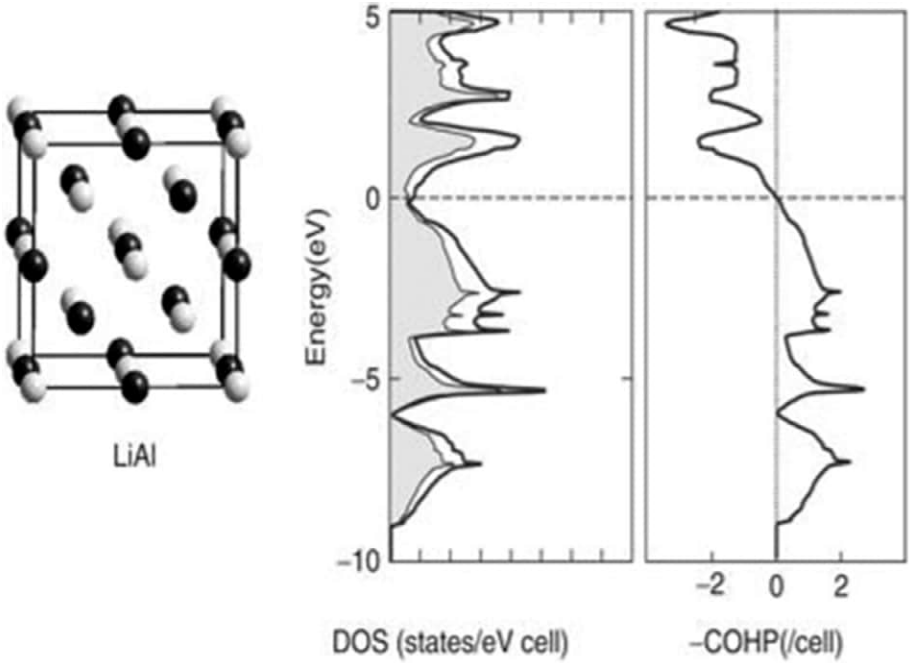

Figure 13 Structure, DOS, and Al–Al COHP analysis for LiAl. Shaded region is Al orbitals.

complement of valence electrons. The structure of the electronegative component, however, cannot be explained by the octet rule – there is substantial delocalized bonding. The most prolific example of this structural class is the $BaAl_4$-type, whose structure is adopted by hundreds of examples involving transition metals as well (Figure 14). There are numerous subcategories based on how different elements are arranged: $ThCr_2Si_2$, $CaBe_2Ge_2$, $BaNiSn_3$ are three common examples.

In polar intermetallics where the active metal is among the rare-earth elements, the predominant interatomic interactions involve 6*s* and 5*d* valence orbitals of the rare-earth with the valence *s* and *p* orbitals of the main group element. If there is significant hybridization between the valence 4*f* orbitals and the *sp* orbitals of the main group metals, then interesting properties may arise, for example, 'heavy fermion' behavior. Valence fluctuations in the rare-earth element are also important for this situation, while a

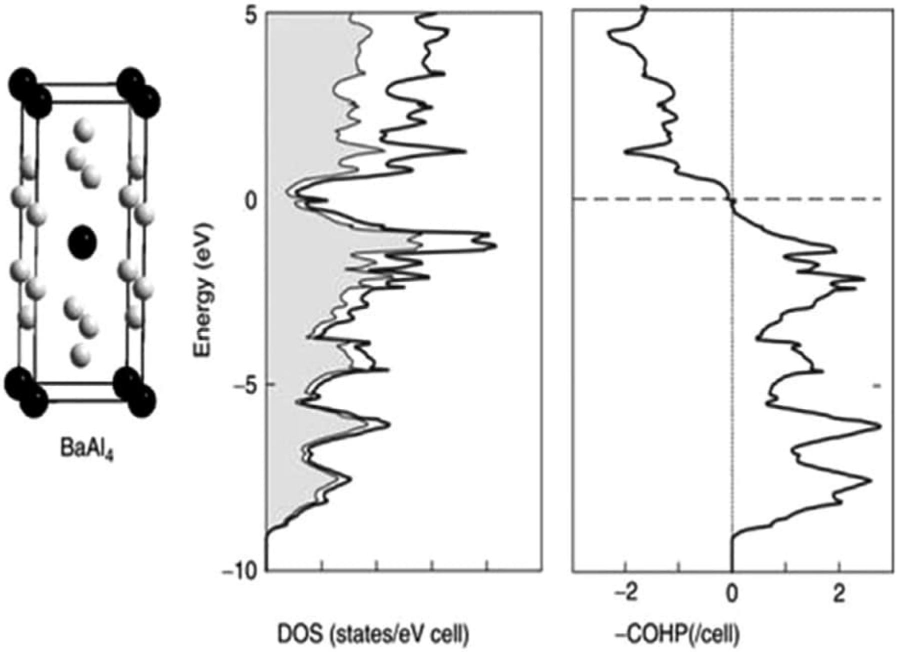

Figure 14 Structure, DOS, and Al–Al COHP analysis for $BaAl_4$. Shaded region is Al orbitals.

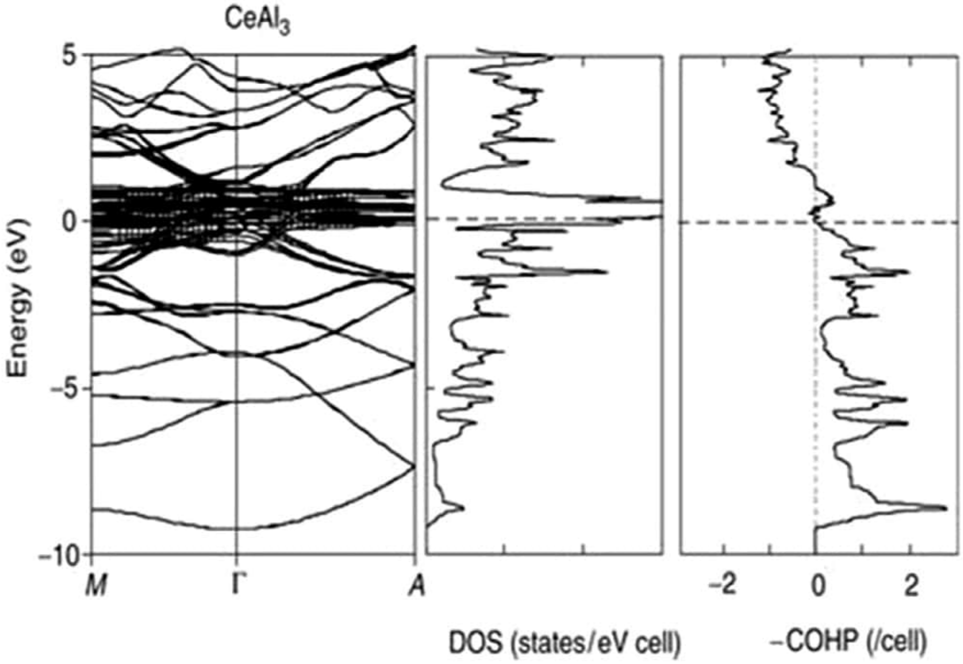

Figure 15 Band structure, DOS, and Al–Al COHP analysis for $CeAl_3$.

COHP analysis of the *sp*–*sp* interactions shows nearly maximum bonding within the main group framework. This is frequently observed for Ce, but is also possible with Yb, with an *f* band that mixes with states near the crossover from bonding to antibonding characteristics (Figure 15).

Conclusion

Describing the electronic states of intermetallic compounds requires an understanding of the distinct electronic structures of the various types of metallic elements. These elements combine in many different ways, and the nature of these interactions can be addressed using different quantum mechanical approximations, varying from the NFE model to the TB theory. Fundamental factors controlling the electronic states include: (1) composition, (2) relative electronegativities of elements, which control the relative valence orbital energies, and (3) coordination environments (structure and atomic arrangements). Depending on the nature of these interactions, conducting properties can vary from metallic to semiconducting while magnetic properties can range from itinerant ferromagnetism to diamagnetic. Valence fluctuations and heavy fermion behavior are possible for rare-earth compounds, and 5*f* orbitals contribute to the chemical bonding interactions in actinide compounds.

Further Reading

Burdett JK (1995) *Chemical Bonding in Solids*. New York, NY: Oxford University Press.
Pettifor D (1995) *Bonding and Structure of Molecules and Solids*. New York, NY: Oxford University Press.
Pöttgen R and Johrendt D (2014) *Intermetallics*. Berlin: De Gruyter.
Westbrook JH and Fleischer RL (1995) *Intermetallic Compounds Principle and Practice*. New York, NY: Wiley.

Transition-Metal Compounds, Electronic and Magnetic Properties of ☆

JB Goodenough, University of Texas at Austin, Austin, TX, USA

© 2017 Elsevier Inc. All rights reserved.

This is an update of J.B. Goodenough, Transition-Metal Compounds, Electronic and Magnetic Properties of, Reference Module in Materials Science and Materials Engineering, Elsevier, 2017, ISBN 9780128035818, https://doi.org/10.1016/B978-0-12-803581-8.10138-9.

Introduction **485**
Metal–Ligand Interactions **486**
Redox couples f^n or d^n 486
Rare-Earth $4f^n$ Configurations 487
The *d*-Block d^n Configurations **487**
Metal–Metal Interactions **490**
Additional Illustrative Examples **497**
Spinels 497
Rutiles **497**
Energy Bands and Redox Couples **498**
Electron Energies 498
Rare-Earth Compounds **499**
Transition-Metal *d*-Block Compounds **500**
Further Reading **502**

Introduction

The electronic and magnetic properties of transition-metal compounds are imparted by the d and/or $4f$ electrons of the transition-metal compounds. (This article does not cover the actinides.) The outer s and p electrons of these compounds, which are primarily responsible for the chemical bonding, are split by an energy gap E_g between filled anionic bonding bands and empty cationic antibonding bands. The s and p states contribute to the electronic and magnetic properties of the transition-metal compounds through covalent mixing with the d and/or $4f$ orbitals.

The $4f$ electrons always form localized $4f^n$ configurations as on a free atom unless a $4f^n/4f^{n+1}$ redox couple is overlapped by the Fermi energy (the electrochemical potential) ε_F of a partially filled broadband of itinerant-electron states, in which case hybridization of the $4f$ and itinerant electron states creates massive itinerant electrons called heavy fermions. The d electrons, on the other hand, may be localized, itinerant, or vibronic depending on the relative strengths of the intra-atomic and the inter-atomic interactions and how the competition between these two is modulated by disturbances of the periodic potential of a crystalline array of the like atoms or by elastic and thermal energies.

The intra-atomic energies are those of the free transition-metal atom as modified by covalent mixing with the ligand orbitals. The Hamiltonian for the electrons of a free atom has three components of descending magnitude:

$$H = H_o + U + \lambda \mathbf{L}\cdot\mathbf{S} \quad [1]$$

where H_o corresponds to the energy of a single electron moving in the field of a nucleus of effective charge $+(Z-\sigma_l)e$. The atomic number Z is reduced by a screening σ_l of the other atomic electrons; σ_l depends on the orbital angular momentum quantum number l of the electron being screened from the nuclear charge $+Ze$. The energy U is the electrostatic energy required to add an electron to a configuration of d or $4f$ electrons and is a measure of the separation of successive ionization energies; $U=J_c-J_{ex}$ has two components, a Coulombic repulsion J_c and a quantum-mechanical correction J_{ex} that keeps electrons of parallel spin in different orbitals by the Pauli exclusion principle. The last term in eqn [1] gives rise to the multiplet splitting of a ${}^{2S+1}L_J$ term, where Russell–Saunders coupling applies to the d^n and $4f^n$ configurations of total angular momentum quantum number $\mathbf{J} = \mathbf{L} + \mathbf{S}$; $\mathbf{L}$ and $\mathbf{S}$ are the total orbital and spin angular-momentum quantum numbers. The atomic magnetic moment is

$$\boldsymbol{\mu}_A = -g_L \mathbf{J} \mu_B \quad [2]$$

where g_L is the Landé spectroscopic splitting factor and μ_B is the Bohr magneton.

In a solid, the 'interatomic interactions' depend on the expectation value for an electron to transfer to a neighboring atom without a change of energy as a result of the perturbation H' of the free-atom potentials by their proximity to one another:

$$b_{ij} \equiv \left(\psi_i, H'\psi_j\right) \approx \varepsilon_b\left(\psi_i, \psi_j\right) \quad [3]$$

☆*Change History*: July 2015. J. Goodenough made changes throughout the text.

where ε_b is a one-electron energy and (ψ_i, ψ_j) is the overlap integral of the initial and final atomic orbitals occupied by the electron. The subscripts refer to atoms at $\boldsymbol{R}_i$ and $\boldsymbol{R}_j$ in the crystal. Electron transfers between states of the same energy are treated in the firstorder theory ($\Delta E \sim b$) and between states separated by an energy Δ or U in the second-order theory ($\Delta E \sim b^2/\Delta$ or b^2/U). The tight-binding bandwidth for electrons transferring between like atoms of a periodic array of crystallographically equivalent sites with $U = 0$ is given by

$$W_b \approx 2zb \qquad [4]$$

where z is the number of like nearest neighbors and b is the b_{ij} for these nearest neighbors. The crossover from localized-electron behavior (intra-atomic interactions dominant) to itinerant-electron behavior (interatomic interactions dominant) occurs where

$$W_b \approx U \qquad [5]$$

This crossover is known as the 'Mott-Hubbard transition.'

The localized electrons occupy an n-electron configuration d^n or f^n located at a single transition-metal atom and having an energy corresponding to that of a redox couple d^{n-1}/d^n or f^{n-1}/f^n. Successive redox couples are separated by an energy U. The itinerant electrons, on the other hand, belong equally to all the like atoms of a periodic array on crystallographically equivalent sites; they are described by a band of single-electron energies of width W_b that is occupied by electrons in accordance with the Pauli exclusion principle and the Fermi–Dirac distribution function. In this limit, a $U < W_b$ is assumed to be screened by the other electrons so as to make $U = 0$. For narrower bandwidths W_b, this 'electronic Fermi-gas model' must be modified by the introduction of a finite $U < W_b$. This problem can be treated by mass-renormalization techniques that transform the electrons into a 'quasiparticle Fermi liquid.'

Impurities, lattice defects, and substitutional dopants all disturb the periodic potential of an array of transition-metal atoms in a solid. These disturbances narrow the effective width of W_b by introducing localized states (Anderson localized states) at the top and bottom of a band of itinerant-electron states above and below, respectively, a 'mobility edge.' If the Fermi energy ε_F lies in the energy range of localized states, the conductivity is described as 'variable-range hopping' between these localized states.

The Mott–Hubbard transition may not be smooth as originally assumed; it is a first order transition that gives an abrupt volume change where the electrons transform from itinerant to localized character; the localized electrons give a larger equilibrium M–O bond length than itinerant electrons. The first-order character of this transition generally introduces the coexistence of two different equilibrium bond lengths at crossover. In the latter case, the resulting bond-length fluctuations at high temperatures order at lower temperatures so as to give long-range-ordered atomic clusters, a charge-density wave (CDW), or a charge-ordered (CO) state in order to minimize the elastic energy. The elastic energies associated with local site deformations are also minimized by cooperative ordering. Examples of local site distortions are displacements of a cation from the center of symmetry of its interstice, cation clustering, valence disproportionation, and an orbital ordering that either lowers the local site symmetry or increases its deformation from cubic symmetry.

The electronic and magnetic properties of the d electrons of transition-metal compounds are strongly influenced not only by whether they occupy states with $W_b < U$, $W_b \approx U$, or $W_b > U$ but also by order–disorder transitions. Order–disorder transitions are driven by the heat $T\Delta S$ associated with disorder. Heat also drives disordering of long-range magnetic order, which removes magnetostrictive and/or exchange-strictive deformations of the crystal symmetry; and by increasing the crystal volume, it may induce changes from antiferromagnetic to ferromagnetic coupling, that is, 'exchange inversion,' below a long-range magneticordering temperature.

In mixed-valent compounds, the transport properties also depend critically on whether the time $\tau_h \approx \hbar/W_b$ for an electron to hop from one atom to a like nearest neighbor is $\tau_h > \omega_R{}^{-1}$, $\tau_h \approx \omega_R{}^{-1}$, or $\tau_h < \omega_R{}^{-1}$, where $\omega_R{}^{-1}$ is the period of an optical-mode vibration that would trap the charge carrier at a single site as a 'small dielectric polaron.'

In the following sections, the metal–ligand interactions are first introduced to construct ligand-field orbitals having the same symmetries as the atomic d orbitals. The interactions between the ligand-field orbitals of neighboring metal atoms are then discussed for $W_b < U$, $W_b \approx U$, and $W_b > U$. Next, the significance of the radial extension of the ligand-field orbitals and the location of the Fermi energy relative to the edges of the broad filled and empty bands is presented in the context of illustrative examples of the varied phenomena that are encountered in these materials.

Metal–Ligand Interactions

Redox couples f^n or d^n

The description of the outer electrons of a primarily ionic transition-metal compound begins with a point-charge model; the electrostatic Madelung energy E_M of that model generally lowers the most energetic ligand (anion) p orbitals an energy ΔE_p below the lowest unoccupied redox energy of the transition-metal atom. A $\Delta E_p \leqslant 0$ may pin the antibonding redox couple at the top of the bonding ligand-p band; in this case, the redox couple can commonly be treated by the molecular-orbital or band theory. However, back electron transfer from the anion across an energy $\Delta E_p > 0$ to an empty d or f orbital on the cation is treated in the second-order perturbation theory to give a stabilization energy $\Delta E \sim (b^{ca})^2/\Delta E_p$ of occupied bonding states that tends to compensate for the loss in electrostatic Madelung energy E_M of the point-charge model; the empty antibonding d or f orbitals of the d^n or f^n configuration are correspondingly destabilized by an energy ΔE. As noted in eqn [3], the expectation value for a back electron transfer depends on the cation–anion overlap integral in b^{ca} and, therefore, on the relative symmetries of the interacting orbitals. Consequently, symmetry arguments are used to develop a parametrized second-order description of the 'ligand-field orbitals'; these orbitals take account of the interactions between the d or f electrons and the anions. Next, the metal–metal, metal–anion–metal, and/or metal–anion–anion–metal interactions are introduced; the ligand-field orbitals either remain localized or become itinerant depending on the relative strengths of these inter-atomic interactions and the intra-atomic energy U_{eff} for the atomic ligand-field orbitals.

Rare-Earth $4f^n$ Configurations

The rare-earth 4f electrons are tightly bound to their atomic nucleus and are largely buried within a $5s^2 5p^6$ core-electron cloud that prevents strong overlap of the 4f orbitals with the orbitals of the neighboring ligands. Consequently, the $4f^n$ configurations remain localized with a $U_{\mathrm{eff}} \gg W$, and any splitting of the individual f-orbital energies by interaction with the ligands is smaller than the intra-atomic multiplet splittings by $\lambda \boldsymbol{L} \cdot \boldsymbol{S}$. Therefore, the localized $4f^n$ configurations in a compound retain their atomic magnetic moment $\boldsymbol{\mu}_{\mathrm{A}} = g_{\mathrm{J}} \boldsymbol{J} \mu_{\mathrm{B}}$ of eqn [2]. Nevertheless, the interactions with the ligands contribute, along with the 'magnetic dipole–dipole $4f^n$ interactions,' to the weak 'spin–spin interatomic exchange' interactions between $4f^n$ configurations that are responsible for long-range magnetic order at low temperatures and also to the 'magnetocrystalline anisotropy' that introduces a preferred orientation of $\boldsymbol{\mu}_{\mathrm{A}}$ relative to the crystallographic axes and an associated 'magnetostriction' below the magnetic-ordering temperature. Long-range ordering of the spins $\boldsymbol{S}$ induces long-range ordering of the orbital angular momenta $\boldsymbol{L}$ by the spin–orbit coupling $\lambda \boldsymbol{L} \cdot \boldsymbol{S}$; and interactions with the ligands order the orbitals responsible for $\boldsymbol{L}$, and therefore $\boldsymbol{J}$, relative to the crystallographic axes and also induce the anion displacements responsible for the magnetostriction. Magnetostriction reflects the orientation of the atomic moments; 'exchange striction' reflects changes in the binding energy due to magnetic order and, therefore, reflects the symmetry of the long-range magnetic order.

The d-Block d^n Configurations

The five d orbitals of a free atom are degenerate, but with more than one electron or hole in a d^n manifold, the spin degeneracy is removed by the ferromagnetic direct-exchange interactions between electron spins in orthogonal atomic orbitals. The Pauli exclusion principle keeps electrons of the same spin in different d orbitals, which reduces the energy $U = J_{\mathrm{c}} - J_{\mathrm{ex}}$ by the intra-atomic exchange energy J_{ex}. These spin–spin exchange interactions produce the 'Hund intra-atomic exchange field $\mathrm{H}'_{\mathrm{ex}}$ responsible for the Hund highest multiplicity rule for the free atom. The splitting between states of different spin for a given orbital will be designated Δ_{ex}.

The atomic orbitals f_m with azimuthal orbital angular momentum operator L_z, where $L_z f_m = -i\hbar\, \partial f_m / \partial \phi = \pm m\hbar\, f_m$ with $m = -l, \ldots, +l$, have the angular dependencies for $l = 2$:

$$\begin{aligned} f_0 &\sim \left(\cos^2\theta - 1\right) \sim \left[\left(z^2 - x^{\mathrm{L}}\right) + \left(z^2 - y^2\right)\right]/r^2 \\ f_{\pm 1} &\sim \sin^2\theta \exp(\pm \mathrm{i}\phi) \sim [yz \pm izx]/r^2 \\ f_{\pm 2} &\sim \sin^2\theta \exp(\pm \mathrm{i}2\phi) \sim \left[\left(x^2 - y^2\right) \pm \mathrm{i}2xy\right]/r^2 \end{aligned} \qquad [6]$$

In an isolated octahedral site, the xy and $(yz \pm \mathrm{i}zx)$ orbitals only overlap the neighboring O – $2p_\pi$ orbitals while the $[(z^2 - x^2) + (z^2 - y^2)]/r^2$ and $(x^2 - y^2)/r^2$ orbitals only overlap the O–2s and O – $2\mathrm{p}_\alpha$ orbitals. These two groupings of orbitals are distinguished by symmetry as a twofold-degenerate set of e orbitals and a threefold-degenerate set of t orbitals (Figure 1). The electron-transfer (resonance) energy integrals $b^{\mathrm{ca}} \equiv (f_m, H'\phi_{\mathrm{o}}) \approx \varepsilon_{\mathrm{mo}}(f_m, \phi_{\mathrm{o}})$ describing the expectation of a virtual charge transfer to an empty cation-d orbital from a same-symmetry sum of near-neighbor oxygen orbitals ϕ_{o} contain both an overlap integral (f_m, ϕ_{o}) and a one-electron energy $\varepsilon_{\mathrm{mo}}$ that are larger for σ-bonding than for π-bonding, that is, $b_\sigma{}^{\mathrm{ca}} > b_\pi{}^{\mathrm{ca}}$. Therefore, the antibonding e states of a σ-bond are raised higher by the energy $\Delta E \equiv (b^{\mathrm{ca}})^2 / \Delta E_p$ than are the antibonding t states of a π-bond. The resulting cubic-field splitting is

$$\Delta_{\mathrm{c}} = \Delta E_\sigma - \Delta E_\pi = \Delta_{\mathrm{M}} + \left(\lambda_\sigma^2 - \lambda_\pi^2\right)\Delta E_p + \lambda_s^2 \Delta E_s \qquad [7]$$

where Δ_{M} is a purely electrostatic energy that is small and of uncertain sign due to the penetration of the ligand-p^6 electron cloud by the cation-d wave function. The dimensionless covalent-mixing parameters are seen to be

$$\begin{gathered} \lambda_\sigma = b_\sigma^{\mathrm{ca}} / \Delta E_p, \quad \lambda_\pi = b_\pi^{\mathrm{ca}} / \Delta E_p \\ \lambda_s = b_s^{\mathrm{ca}} / \Delta E_s \end{gathered} \qquad [8]$$

in which ΔE_p and ΔE_s are the point-charge energy gaps between the degenerate atomic d orbitals and the ligand p and s orbitals, respectively. The second-order ligand-field wave functions are

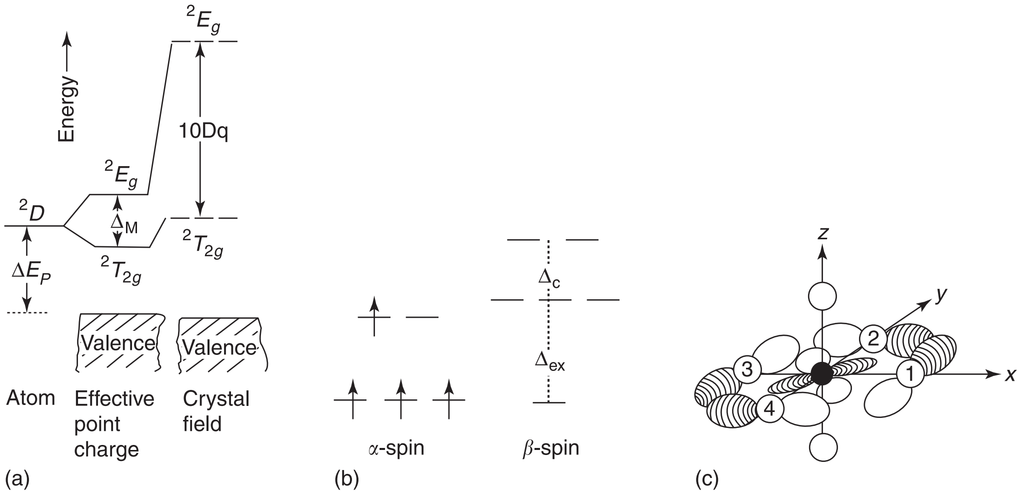

Figure 1 Schematic crystal-field splitting of the *d*-state manifold of a transition-metal atom M in an octahedral site: (a) the one-electron d^1 configuration ($\Delta_{ex}=0$); (b) the high-spin d^4 configuration, and (c) $\phi_{xy}=p_y^{(1)}+p_x^{(2)}-p_y^{(3)}-p_x^{(4)}$ that hybridizes with a d_{xy} orbital.

$$\begin{aligned} \psi_t &= N_\pi(f_t - \lambda_\pi\phi_\pi) \\ \psi_\sigma &= N_\sigma(f_e - \lambda_\sigma\phi_\sigma - \lambda_s\phi_s) \end{aligned} \qquad [9]$$

where N_π and N_σ are normalization constants that constrain a one-electron state to contain a single electron.

Covalent mixing extends the ligand-field wave functions out over the anions, thereby reducing the electron–electron Coulomb energy U from its atomic value. For an octahedral-site cation, the ligand-field U is larger for electrons in the π-bonding t-manifold than for those in the σ-bonding e-manifold, that is, $U_t > U_e$.

As an aside, attention is drawn to the earlier crystal-field model in which the covalent component to the orbitals is neglected and the cubic-field splitting is simply parametrized as $\Delta_c = 10$ Dq. In this model also, the symmetry arguments distinguish the e and t manifolds in a cubic field or other splittings in lower symmetry, but the energy of the atomic d-state manifold is conserved and the crystal-field wave functions are simply the atomic wave functions f_m. Although this parametrized model allows interpretation of spectroscopies that measure the energy splittings, it fails completely to account for a lowered ligand-field U and for the interatomic interactions between like atoms that are responsible for long-range magnetic order where a $W_b < U_{\mathrm{eff}}$ is found or for metallic conductivity where a $W_b > U_{\mathrm{eff}}$ occurs.

If a d-block transition-metal ion occupies a tetrahedral site, similar considerations apply, but in this case the t orbitals have a larger orbital overlap and are raised higher in energy than the e orbitals by the cubic-field splitting Δ_c. Early crystal-field calculations give the relative values of Δ_c for the two cases as

$$\Delta_c(\text{terahedral}) \approx (4/9)\Delta_c(\text{octahedral}) \qquad [10]$$

The d-electron Hamiltonian that includes the interactions with the ligand p and s orbitals is

$$H = H_o + J_c + (\Delta_c - J_{ex}) + (\lambda \boldsymbol{L}\cdot\boldsymbol{S} + \Delta_{nc}) \qquad [11]$$

where Δ_{nc} is a noncubic component of the ligand-field splitting arising from a distortion of the site symmetry. Since the octahedral-site Δ_c is the same order of magnitude as the intra-atomic exchange energy Δ_{ex}, the $d^4 - d^7$ octahedral-site configurations may be either high-spin t^3e^1, t^3e^2, t^4d^2, t^5e^2 where $\Delta_{ex} > \Delta_c$ or low-spin t^4e^0, t^5e^0, t^6e^0, t^6e^1 where $\Delta_c > \Delta_{ex}$. Moreover, lowering of the site symmetry to tetragonal or orthorhombic may stabilize an intermediate-spin d^5 or d^6 configuration t^4e^1 or t^5e^1, respectively. The larger the covalent mixing parameters $\lambda_\sigma > \lambda_\pi$, the smaller is Δ_{ex} and the larger is Δ_c. Moreover, the effective energy U_{eff} required to add an electron to a d^n manifold to make it d^{n+1} must take into account Δ_c as well as Δ_{ex}. For an octahedral-site cation, the U_{eff} for $n = 3$ and $n = 8$ is increased by Δ_c; for $n = 5$ it is increased by Δ_{ex} if $\Delta_c < \Delta_{ex}$, and for $n = 6$ by Δ_c if $\Delta_c > \Delta_{ex}$.

By splitting the $m = \pm 2$ energies of eqn [6] into real $(x^2 - y^2)$ and xy components, the operator $L_z = -i\hbar\partial/\partial\phi$ makes the azimuthal component of the orbital angular momentum imaginary, which means that the two e orbitals have $m = 0$ and the t manifold has orbitals with $m = 0, \pm 1$. It follows that configurations with zero, three, or six t electrons have their orbital angular momentum completely quenched (i.e., $L = 0$) to first order, and a spin-only atomic moment $\boldsymbol{\mu}_A = gS\mu_B$ with $g \approx 2$ is a fair approximation.

The octahedral-site splitting may leave an orbital degeneracy, as occurs with high-spin Mn(III) : t^3e^1 or Cu(II) : t^6e^3, for example, or with high-spin Fe(II) : t^4e^2 or Co(II) : t^5e^2. In this case, the cubic site symmetry is unstable relative to a site distortion that removes the orbital degeneracy. This instability is known as a 'Jahn–Teller distortion.' In a crystal, a long-range-cooperative site distortion, that is, orbital ordering, minimizes the elastic energy that resists the distortion and lowers the space-group symmetry of the crystal. Cooperative Jahn–Teller distortions may transform isotropic 3D interatomic spin–spin interactions into a ferromagnetic interaction

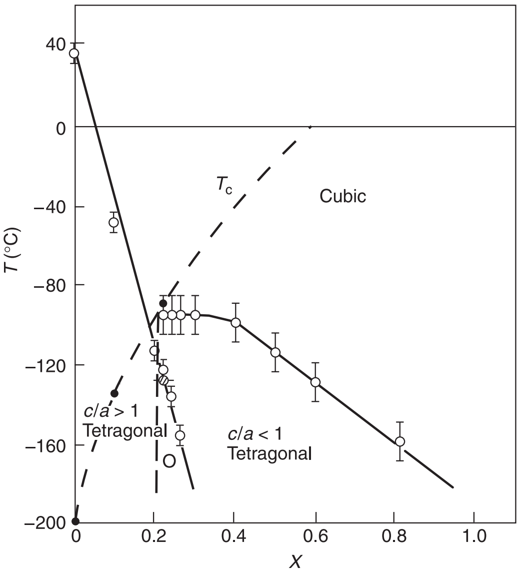

Figure 2 Phase diagram of the spinel system $Ni_{1-x}Fe_x[Ni_xCr_{2-x}]O_4$. Solid lines are tetragonal-cubic transition temperatures T_t. The O-orthorhombic phase may be a coexistence of tetragonal $c/a > 1$ and $c/a < 1$ phases. After Arnott, R.J., Wold, A, Rogers, D.B., 1964. Journal of the Physics and Chemistry of Solids 25, 161.

in one crystallographic direction and an antiferromagnetic interaction in another as is illustrated by $LaMnO_3$ (*vide supra*). Removal of a t^n-orbital degeneracy ($n = 1, 2, 4$, or 5) may either quench the orbital angular momentum or enhance it so as to gain a further splitting by the spin–orbit coupling $\lambda \boldsymbol{L} \cdot \boldsymbol{S}$; where σ-bonding electrons determine the magnetic order, a long-range collinear-spin configuration below a magnetic-ordering temperature introduces long-range order of the orbital angular momenta through $\lambda \boldsymbol{L} \cdot \boldsymbol{S}$ even where the concentration of orbitally degenerate cations is not large. Therefore, below a long-range magnetic-ordering temperature, distortions that enhance $\boldsymbol{L}$ and introduce a large magnetostrictive component scale with the concentration of cations with the t-orbital degeneracy. On the other hand, spin–orbit coupling prevents a cooperative ordering of the orbital momenta in the paramagnetic state of disordered spins; so cooperative distortions setting in above a magnetic-ordering temperature quench the orbital angular momenta. The two types of distortion can be distinguished as they have opposite sign. This situation is beautifully illustrated in Figure 2 by the spinel system $Ni_{1-x}Fe_x[Ni_xCr_{2-x}]O_4$ in which the tetrahedral-site Ni(II):e^4t^4 are the Jahn–Teller ions.

The $A[B_2]X_4$ spinel structure consists of a close-packed-cubic array of anions X; the electrostatic Madelung energy is minimized by an ordering of the B cations on half of the octahedral sites and the A cations on tetrahedral sites of the interstitial space of the $[B_2]X_4$ array. The $Ni_{1-x}Fe_x[Ni_xCr_{2-x}]O_4$ spinel also illustrates how the crystal-field splittings influence the site-preference energies of transition-metal cations. Sites that leave the higher-energy d orbitals empty are stabilized relative to those that leave them occupied. The Cr(III) ion has the configuration t^3e° in an octahedral site and e^2t^1 in a tetrahedral site, which gives it a strong octahedral-site preference. The high-spin Fe(III) ion with configurations t^3e^2 or e^2t^3 has little site preference. The Ni(II) ion, on the other hand, has an octahedral-site configuration t^6e^2 as against e^4t^4 in a tetrahedral site, which gives it a definite octahedral-site preference; but it is forced into the tetrahedral sites of the spinel by the Cr(III) ions, which have a stronger octahedral-site preference.

Ionic size also determines site preference. Smaller cations prefer tetrahedral sites; the d-block transition-metal cations of intermediate size, with the exception of Mn(II) and Cu(I), prefer octahedral sites, and the larger rare-earth ions prefer a greater oxygen coordination. Where a smaller cation is forced by electrostatic Coulomb energies into an octahedral site, it may be unstable relative to a cooperative displacement from the center of symmetry of its interstice. Such a displacement introduces a local electric-dipole moment, and a cooperative parallel displacement gives a 'ferroelectric polarization' analogous to a 'ferromagnetic magnetization.' Therefore, such a displacement is referred to as a ferroelectric-type displacement even though the cooperativity may involve antiparallel displacements to give an antiferroelectric analogous to an antiferromagnet in which neighboring spins are aligned antiparallel. Lighter transition-metal cations of a given d-block can be stabilized in octahedral sites in their highest valence states, that is, with a d^0 configuration, but as the cation size decreases with increasing atomic number and formal valence state, the site preference changes from octahedral to tetrahedral. It is the ions with sizes at crossover to a tetrahedral-site preference that undergo ferroelectric displacements. In the 3d row, the T(IV) has an octahedral-site preference, but if the structure forces the Ti–O bond length to be greater than its equilibrium value, as occurs in the perovskite $BaTiO_3$, the Ti(IV) ions may undergo a cooperative ferroelectric displacement. In $BaTiO_3$, there are three successive cooperative displacements; on lowering the temperature, the Ti(IV) ions are displaced first toward one near-neighbor O^{2-} ion, then toward two, and finally toward three. The smaller V(V) cation, on the other hand, has a definite tetrahedral site preference, but when forced into an octahedral site as in V_2O_5, it forms a short double bond V=O indicating molecular-orbital formation with both p_σ and the two p_π orbitals. The V(IV) may also form a $(V{=}O)^{2+}$ vanadyl ion with an occupied d_{xy} orbital in the plane perpendicular to the d_{yz} and d_{zx} orbitals involved in the π molecular orbitals. In the 4d block, it is the Nb(V) ion that corresponds to the Ti(IV) and the Mo(VI) that corresponds to the V(V). In the 5d series, the

W(VI) corresponds to the Ti(IV), and WO_3 is an antiferroelectric without a stretching of the W–O bond length by a counter cation as in $BaTiO_3$.

Finally, it is noteworthy that where a transition-metal cation is deprived of its stable oxygen coordination, as occurs in the oxygen-deficient perovskite $BaZr_{1-x}In_xO_{3-0.5x}$, water may enter the oxygen vacancies at lower temperatures ($T \leqslant 400\,^\circ C$) to introduce OH^- anions and protonic conduction; the Zr(IV) ion is stable in eightfold oxygen coordination and definitely prefers a sixfold over the fivefold oxygen coordination just as the large Ba^{2+} ion prefers a 12-fold over the 11-fold coordination.

Metal–Metal Interactions

A measure of the strength of the interatomic cation–cation interactions is also the energy integral b_{ij} of eqn [3]. Direct cation–cation electron transfers b^{cc} between cations sharing a common site edge or face are distinguished from cation–anion–cation transfers b^{cac} that occur across an anion. The latter interactions are possible because the shared anion-p component (neglecting the smaller anion-s component for simplicity) of the ligand-field wave functions provides a significant overlap of the wave functions on neighboring cations. For a $(180^\circ - \phi)$ cation–anion–cation interaction, the electron transfer integrals b_σ^{cac} across a common anion-p_σ orbital must be distinguished from the smaller b_π^{cac} across a common anion-p_π orbital; in a 90° cation–anion–cation interaction, the electron transfer integral is $b_{\pi\sigma}^{cac}$ as it occurs across an anion-p orbital that σ-bonds with the d orbital on one cation and π-bonds with the d orbital on the other cation. With the ligand-field wave functions of eqn [9], these integrals become

$$b^{cc} = \varepsilon_{cc}\left(\psi_i, \psi_j\right) \tag*{[12]}$$

which varies sensitively with the interatomic separation R,

$$\begin{aligned} b_\pi^{cac} &\approx \varepsilon_\pi \lambda_\pi^2 \\ b_\sigma^{cac} &\approx \varepsilon_\sigma \lambda_\sigma^2 \cos\,\phi \\ b_{\pi\sigma}^{cac} &\approx \varepsilon_{\pi\sigma} \lambda_\pi \lambda_\sigma \end{aligned} \tag*{[13]}$$

for a $(180^\circ - \phi)$ M-anion-M interaction. Two general conclusions follow. First, there is a critical cation–cation separation R_c below which the tight-binding bandwidth of eqn [4] is $W_b \approx 2zb^{cc} > U_{eff}$ and suppresses the localized-electron behavior to introduce the d electrons into either itinerant-electron states or cation-cluster molecular orbitals. Second, it is possible to have itinerant and localized electrons coexisting on the same atom. For example, $(180^\circ - \phi)$ cation–anion–cation interactions dominate in an AMO_3 perovskite, which has a simple cubic array of corner-sharing $MO_{6/2}$ octahedra with a larger A-site cation in the body center. A $b_\sigma > b_\pi$ and a $U_e < U_t$ allow a $W_\sigma > U_e$ or a mixed-valent $\tau_h < \omega_R^{-1}$ of e electrons in the presence of $W_\pi < U_t$ as is illustrated by metallic and magnetic $SrFeO_3$ and the metallic ferromagnet $La_{0.7}Sr_{0.3}MnO_3$.

The criterion for itinerant versus localized behavior in a mixed-valent compound is somewhat different from that in a single-valent compound. In a mixed-valent compound, electron transfer between atoms of a redox couple does not require overcoming an energy gap U_{eff}. However, the time $\tau_h \approx \hbar/W$ for an electron to transfer from one atom to another must be compared to the period $\omega_R^{-1} \approx 10^{-12}$ s of an optical-mode local vibration that traps a charge carrier. If the ligands have time to relax to an equilibrium position that distinguishes the smaller size of a cation of higher charge, then the stronger covalent bonding at the smaller site raises the energy of the empty antibonding orbitals above those of the occupied orbitals by ε_p as occurs with a redox couple in solution. The atomic relaxations thus self-trap a charge carrier, localizing it to a single site by introducing a small energy barrier between occupied and empty states. The self-trapped carriers are called 'dielectric small polarons'; they move diffusively with a small activated mobility

$$\mu = (eD_o/kT)\,\exp\,(-\Delta G_m/hT) \tag*{[14]}$$

in which $\Delta G_m = \Delta H_m - T\Delta S_m$ is the free energy required to equalize the energies of the orbitals on neighboring sites. This mobility contrasts with that for an itinerant electron:

$$\mu = e\tau_s/m^* \tag*{[15]}$$

where τ_s is the mean free time between scatterings of the electronic charge carrier from aperiodicities in its periodic potential and m^* is the effective carrier mass. The crossover from polaronic to itinerant electronic behavior occurs where $\tau_h \approx \omega_R^{-1}$ or the polaron bandwidth is $W \approx \hbar\omega_R$. The polaronic bandwidth is reduced from the tight-binding bandwidth W_b of eqn [5] as

$$W = W_b\,\exp\,\left(-\lambda\varepsilon_p/\hbar\omega_R\right) \tag*{[16]}$$

where $\lambda \sim \varepsilon_p/W_b$ is a measure of the strength of the electron–lattice coupling. The transition from polaronic to itinerant electronic behavior in a mixed-valent compound would generally occur where U_{eff} remains a little larger than W_b, but Coulomb interactions between the charge carriers may slow τ_h and induce charge ordering at higher charge concentrations. Moreover, local site distortions at Jahn–Teller ions increase ε_p, which stabilizes polaronic behavior to larger values of W_b. Moreover, the virial theorem favors a first-order transition from localized to itinerant-electronic behavior, and the conditions under which the two types of crossover are found appear to be similar.

A first-order transition at $W_b \approx U_{\mathrm{eff}}$ leads to bond-length instabilities; the two coexisting equilibrium bond lengths order at lower temperatures in a variety of ways to give such unusual phenomena as high-temperature superconductivity in copper oxides or a colossal magnetoresistance in manganese and cobalt oxides with a perovskite structure. At higher temperatures, bad-metal behavior with an unusual temperature dependence of the resistivity is found. As the temperature is increased, the bandwidth narrows and a smooth transition from itinerant to vibronic to polaronic behavior may be encountered.

The interatomic interactions of interest in the localized-electron regime $W_b < U_{\mathrm{eff}}$ are the spin–spin interactions. The origin of the spin–spin interactions is in the quantum-mechanical exchange term J_{ex} entering U, so the spin–spin interactions are referred to as 'exchange interactions.'

The most general form of the bilinear interatomic spin–spin coupling between localized spins at $\boldsymbol{R}_i$ and $\boldsymbol{R}_j$ is

$$V_{ij} = S_i \cdot \boldsymbol{K}_{\mathrm{S}} \cdot \boldsymbol{S}_j + \boldsymbol{S}_i \cdot \boldsymbol{K}_{\mathrm{A}} \cdot \boldsymbol{S}_j \qquad [17]$$

where $\boldsymbol{K}_{\mathrm{S}}$ and $\boldsymbol{K}_{\mathrm{A}}$ are symmetric and antisymmetric tensors. The first term reduces to an isotropic and an anisotropic component, $-2J_{ij}\boldsymbol{S}_i \cdot \boldsymbol{S}_j - 2\boldsymbol{S}_i \cdot \Gamma \cdot \boldsymbol{S}_j$, where $\Gamma \sim (\Delta g/g)^2$ represents a symmetric tensor and Δg is the deviation of the spectroscopic splitting factor from $g = 2$. The antisymmetric term can be reduced to $-2\boldsymbol{D}_{ij} \cdot \boldsymbol{S}_i \times \boldsymbol{S}_j$, where the Dzialoshinskii vector $\boldsymbol{D}_{ij} \sim (\Delta g/g)$ has its axis determined by the crystal symmetry. A quantitative description of the magnetization $M(T)$ of a ferromagnetically aligned subarray may require inclusion of a biquadratic term $-2\gamma_{ij}(\boldsymbol{S}_i \cdot \boldsymbol{S}_j)^2$ where the magnitude of a cation–cation interaction varies sensitively with the cation separation R. In addition, the coexistence of localized and itinerant electrons (or molecular-orbital electrons) adds an additional term H_{ex}^D, so the full phenomenological expression for the spin–spin interactions becomes

$$H_{\mathrm{ex}} = H_{\mathrm{ex}}^D - \sum_{ij}{}' \left\{ J_{ij}\boldsymbol{S}_i \cdot \boldsymbol{S}_j + \gamma_{ij}\left(\boldsymbol{S}_i \cdot \boldsymbol{S}_j\right)^2 + \boldsymbol{D}_{ij} \cdot \boldsymbol{S}_i \times \boldsymbol{S}_j + \boldsymbol{S}_i \cdot \Gamma \cdot \boldsymbol{S}_j \right\} \qquad [18]$$

Measurement of the magnetic susceptibility $\chi_{\mathrm{m}} \equiv M(T)/H_{\mathrm{a}}$, where H_{a} is an applied magnetic field, reveals whether localized spins are present in a compound and the character of the dominant spin–spin interactions, which may be ferromagnetic ($J_{ij} > 0$) or antiferromagnetic ($J_{ij} < 0$). In the absence of localized spins, a compound may be diamagnetic ($\chi_{\mathrm{m}} < 0$) or paramagnetic ($\chi_{\mathrm{m}} > 0$), but χ_{m} is normally small and temperature independent in this case. However, superconductors exhibit a transition below their critical temperature from a $\chi_{\mathrm{m}} > 0$ in the normal-metal state to a $\chi_{\mathrm{m}} < 0$ in the superconductive state. Localized spins, on the other hand, give a temperature-dependent paramagnetic susceptibility $\chi_{\mathrm{m}}(T) > 0$ that reflects not only the magnitudes of the atomic magnetic moments, but also the character of the spin–spin interactions. Moreover, the spin–spin interactions stabilize long-range magnetic order below a ferromagnetic Curie temperature T_{c} or an antiferromagnetic Néel temperature T_{N}. Several types of magnetic order are found.

'Ferromagnetism' refers to a parallel alignment of spins that gives a saturation magnetization $M_{\mathrm{s}}(0) = \sum_i N_i \mu_{\mathrm{A}i}$ at $T = 0$ K, where N_i is the number per unit volume of a transition-metal cation with moment $\mu_{\mathrm{A}i}$ and the sum is over all the different kinds of transition-metal cations that are present. The zero-field saturation magnetization $M_{\mathrm{s}}(T)$ decreases with increasing temperature T, falling sharply to zero at $T = T_{\mathrm{c}}$. In this case, the paramagnetic susceptibility obeys a Curie–Weiss law

$$\chi_{\mathrm{m}} = C/(T - \theta) \qquad [19]$$

where the Curie constant for a single spin species is

$$C = Ng^2 J(J + 1)\mu_{\mathrm{B}}^2/3k \qquad [20]$$

and the Weiss constant $\theta = CW$ reflects the strength of the ferromagnetic interactions through the W of the internal Weiss molecular field WM that aligns the spins. Critical fluctuations above T_{c} makes the $\chi_{\mathrm{m}}{}^{-1}(T)$ plot bend from linear as $\chi_{\mathrm{m}}{}^{-1}$ approaches zero, which makes $T_{\mathrm{c}} \leqslant \theta$.

'Antiferromagnetism' refers to a magnetic order that leaves the zero-field saturation magnetization $M(T) = 0$ at all temperatures below a Néel temperature T_{N}. Néel antiferromagnetism consists of two like ferromagnetic subarrays aligned antiparallel to one another to give $M_{\mathrm{s}}(T) = M_1(T) - M_2(T) = 0$. In this case, a $W < 0$ makes the Weiss constant of the Curie–Weiss law $\theta < 0$, and $\chi_{\mathrm{m}}{}^{-1}$ is finite at $T_{\mathrm{N}} > 0$. The antisymmetric term $\boldsymbol{D}_{ij} \cdot \boldsymbol{S}_i \times \boldsymbol{S}_j$ of eqn [18] may cant the spins of an antiferromagnet to give a weak ferromagnetism. That this weak ferromagnetic component is not due to an impurity is beautifully illustrated by α-$\mathrm{Fe_2O_3}$, which has the crystallographic and magnetic structure shown in Figure 3 at room temperature. The weak ferromagnetic component has been used in magnetic recording. In this structure, the Dzialoshinskii vector $\boldsymbol{D}_{ij}$ is oriented parallel to the c-axis, so spin canting occurs if the spins lie in the basal plane. Dipole–dipole interactions orient the spins in the basal plane of α-$\mathrm{Fe_2O_3}$ in the temperature interval $250\ \mathrm{K} < T < T_{\mathrm{N}} = 953$ K; but below the Morin temperature $T_{\mathrm{M}} = 250$ K, the spin orientation switches to the c-axis and the weak ferromagnetic component disappears abruptly.

'Ferrimagnetism' refers to an antiferromagnetic coupling of two ferromagnetic subarrays with magnetizations $M_1(T)$ and $M_2(T)$ where $M_{\mathrm{s}}(T) = M_1(T) - M_2(T) \neq 0$ at all temperatures. Normally, $M_{\mathrm{s}}(0) \neq 0$ in a ferrimagnet, but $\mathrm{Fe_2(SO_4)_3}$ is an example where the

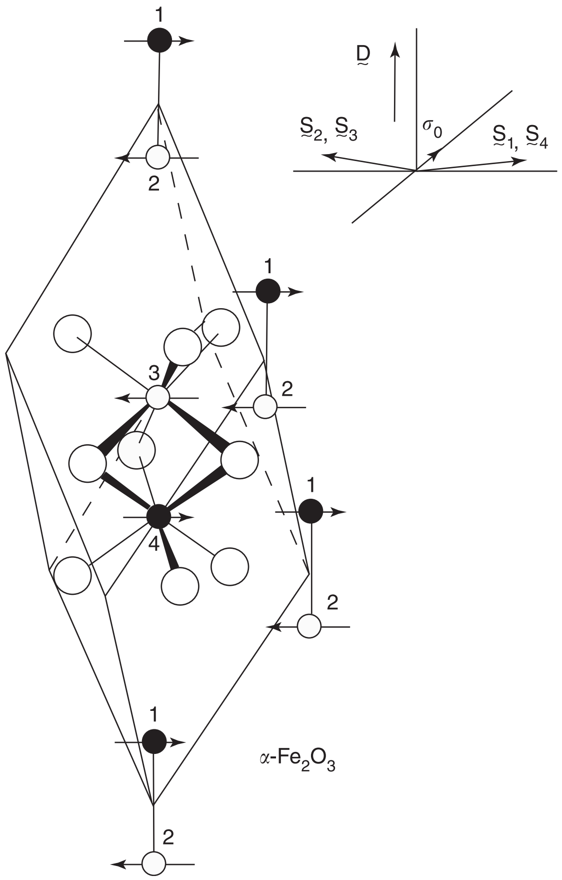

Figure 3 Antiferromagnetic spin configurations found in α-Fe_2O_3 in the temperature interval 250 K $< T <$ 953 K and the spin canting responsible for a weak ferromagnetic component σ_0. After Shull, C.G., Strauser, W.A., Wollan, E.O., 1951. Physical Review 83, 333.

Fe(III) atoms of the two subarrays are in sites that are crystallographically inequivalent, so $M_s(T) \neq 0$ although $M_s(0) = 0$. The inverse paramagnetic susceptibility of a ferrimagnet is hyperbolic, approaching a Curie–Weiss law with $\theta < 0$ at high temperatures, but falling to zero at a Curie temperature $T_c > 0$. The most celebrated ferrimagnets are the ferrospinels, which have an antiferromagnetic coupling of tetrahedral-site and octahedral-site cations. Figure 4 illustrates the magnetic order in Fe[NiFe]O_3, where the octahedral-site cations are bracketed in the formula. In this case, the Fe(III) moments cancel one another and the net magnetization per formula unit is due to the nickel with $\mu_{Ni} \approx 2\mu_B$. Interestingly, substitution of Ni(II) by a nonmagnetic Zn(II) ion increases the magnetization because the Zn atoms prefer tetrahedral sites: $Zn_xFe_{1-x}[Ni_{1-x}Fe_{1+x}]O_4$ has a magnetization per formula unit for small x of $\mu_{mol} = (2+8x)\mu_B$. A rhombohedral component of the ligand field at an octahedral site of the spinel structure splits the t manifold into a nondegenerate a_1 orbital ($m = 0$) of lower energy and a twofold degenerate e_π-orbital manifold with $m = \pm 1$. Consequently, substitution of an Fe(II) for Ni(II) on the octahedral sites introduces mobile spins associated with the mixed iron valence, but it has little effect on the magnetocrystalline anisotropy. On the other hand, substitution of Co(II) for Ni(II) leaves the

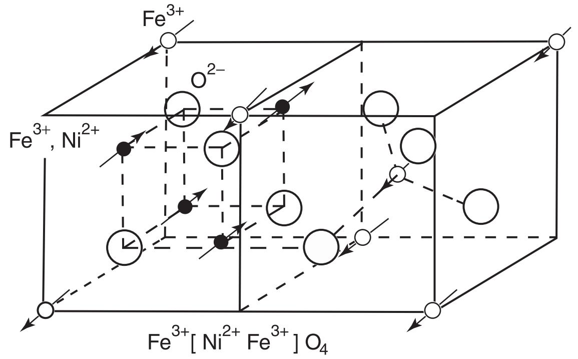

Figure 4 Ferrimagnetic order of Fe[NiFe]O_4. After Hastings, J.M., Corliss, L.M., 1953. Reviews of Modern Physics 25, 114.

spinel an insulator but introduces a large magnetocrystalline anisotropy that increases linearly with the cobalt concentration as a result of splitting of the e_π-orbital degeneracy by $\lambda \boldsymbol{L} \cdot \boldsymbol{S}$.

'Spin-density wave (SDW)' refers to a noncollinear spin configuration that has a propagation vector q with a wavelength that may be either commensurate or incommensurate with a lattice period. Parallel alignment of near-neighbor spins in a ferromagnet or within a subarray of a Néel antiferromagnet or ferrimagnet may oppose weaker antiferromagnetic interactions between next-near-neighbor spins of the array. In this case, the crystal compensates either by changing its structure so as to weaken the antiferromagnetic interactions or by forcing the spins to become canted or, more commonly, to form an SDW. An SDW has an $M_s(T) = 0$ below T_N and is, therefore, antiferromagnetic. Figure 5 illustrates a simple spiral-spin (helical) configuration found in the rutile structure of MnO_2. Canting of the octahedral-site spins is found in the tetragonal spinel $Cu[Cr_2]O_4$. Figure 6 illustrates the spiraling of this canted-octahedral-site configuration observed in $Co[Cr_2]O_4$.

'Metamagnetism' refers to the transformation of antiferromagnetic order to ferromagnetic order in a moderate applied magnetic field. For example, an SDW having ferromagnetic nearest-neighbor interactions is transformed at 50 K in MnP to a ferromagnet on which a weak SDW component is superimposed.

An analogous, but not strictly metamagnetic, situation is found in some double perovskites $La_2M_aM_bO_6$ where ordering of the M_a and M_b cations introduces ferromagnetic M_a-O-M_b interactions within slabs, but leaves antiferromagnetic M_a-O-M_a and M_b-O-M_b interactions across antiphase boundaries. The ferromagnetic slabs are oriented antiparallel to one another in zero magnetic field, but the large magnetization of a slab allows a modest applied magnetic field to create a parallel orientation of the slabs except for spiral-spin interfaces centered at the antiphase boundaries.

'Frustrated systems' are those where strong antiferromagnetic interactions are unable to align all near-neighbor spins antiparallel to one another. This situation occurs, for example, in a close-packed plane or among the octahedral sites of a spinel. Frustration lowers the temperatures below which long-range magnetic order is found and leads to compromise spin configurations. In a close-packed plane with antiferromagnetic interactions between nearest neighbors, for example, the spins order at 120° rather than 180° with respect to one another.

'Spin glasses' are compounds containing ferromagnetic clusters in an antiferromagnetic matrix. Since the clusters are randomly distributed, the coupling between the clusters is frustrated, and the ferromagnetic regions assume random orientations below a spin-glass freezing temperature T_g. A 'cluster glass' consists of antiferromagnetic clusters in a ferromagnetic matrix.

Several processes contribute to the microscopic origins of the spin–spin interactions.

'Direct exchange' between spins in orthogonal orbitals is ferromagnetic; it is a 'potential exchange' as it does not involve electron transfer. The intra-atomic exchange splitting Δ_{ex} responsible for Hund's highest multiplicity rule for the free atom is a direct exchange.

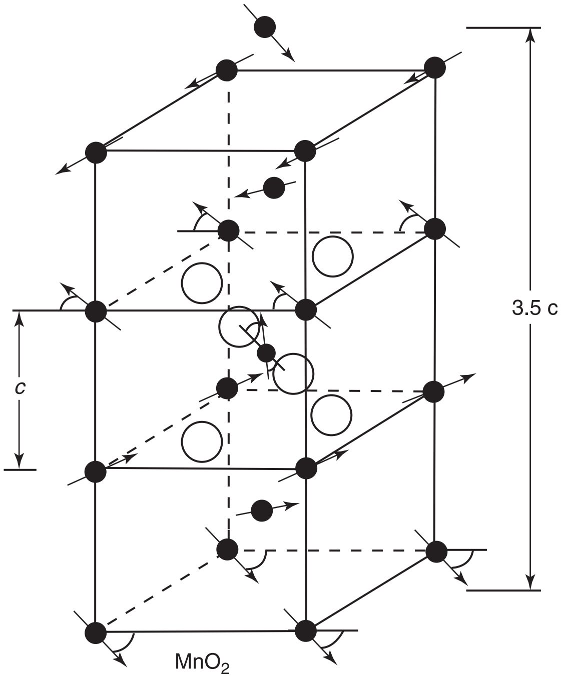

Figure 5 Spiral-spin configuration propagating parallel to the *c*-axis of MnO_2 (oxygen coordination shown for only one cation; cf., **Figure 9** for rutile structure). Turn angle between spins in successive (0 0 1) planes is $2\pi/7$. After Erickson, R.A., 1953. Physical Review 90, 779; Yoshimori, A., 1959. Journal of the Physical Society of Japan 14, 807.

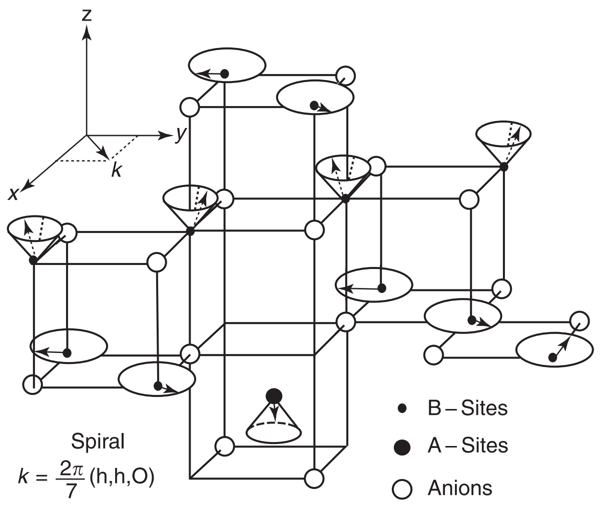

Figure 6 Complex spiral-spin configuration found in the spinel Co[Cr$_2$]O$_4$. Spiral propagates along the [1 1 0] direction. After Dwight, K., Manyuk, N., 1969. Journal of Applied Physics 40, 1156.

Interactions between spins on two atoms with overlapping orbitals is a 'kinetic exchange.' Two features are controlling, conservation of the spin angular momentum in the transfer and an angular dependence for electron spins having only the two directions α and β:

$$\alpha = \alpha' \cos(\theta/2) + \beta \sin(\theta/2) \qquad [21]$$

where θ is the angle between localized spins on the two neighboring atoms. Therefore, the spin-independent electron-transfer integral b_{ij} of eqn [3] is replaced by a spin-dependent integral

$$t_{ij}^{\uparrow\uparrow} = b_{ij} \cos(\theta/2) \quad \text{or} \quad t_{ij}^{\uparrow\downarrow} = b_{ij} \sin(\theta/2) \qquad [22]$$

'Superexchange' refers to interactions that require overcoming an energy barrier ΔE; in this case, the electron transfer is virtual and is treated in a second- or higher-order perturbation theory. Two cases must be distinguished:

1. If the overlapping orbitals are each half-filled, electron transfer is constrained by the Pauli exclusion principle to be antiferromagnetic and

$$\Delta E_{\text{ex}}^{S} \approx -\left|t_{ij}^{\uparrow\downarrow}\right|^2 / U_{\text{eff}} = \text{const} + J_{ij} \boldsymbol{S}_i \cdot \boldsymbol{S}_j \qquad [23]$$

where $\Delta E = U_{\text{eff}}$ corresponds to the interaction in a single-valent compound; the $J_{ij} \sim \left(2b_{ij}{}^2\right)/4S^2U_{\text{eff}}$ reduces to $2b^2/U_{\text{eff}}$ for nearest neighbors with $S = 1/2$.

2. If the overlapping orbitals are 'half-filled and empty' or 'filled and half-filled,' ΔE_{ex} favors a ferromagnetic charge transfer and

$$\Delta E_{\text{ex}}^{S} = \text{const} - J_{ij} \boldsymbol{S}_i \cdot \boldsymbol{S}_j \qquad [24]$$

with $J_{ij} \approx (2b_{ij}\Delta_{\text{ex}}/4S^2U_{\text{eff}}^2)$ follows from a third-order perturbation theory.

With half-filled t^3 configurations, the $(180° - \phi)\, t^3e^0 - \text{O} - t^3e^0$ interactions of the RCrO$_3$ (R = rare-earth) and Sr$_{1-x}$Ca$_x$MnO$_3$ perovskites are all antiferromagnetic as are the $t^3e^2 - \text{O} - t^3e^2$ interactions in the RFeO$_3$ perovskites. An antisymmetric $\boldsymbol{D}_{ij} \cdot \boldsymbol{S}_i \times \boldsymbol{S}_j$ exchange term and/or cooperative rotations of the octahedral sites may cant the antiparallel spins by a few degrees to give a weak ferromagnetic moment. On the other hand, the double perovskite La$_2$NiMnO$_6$ with ordered Ni(II) and Mn(IV) exhibits ferromagnetic Ni(II) : t^6e^2 – O – Mn(IV) : t^3e^0 superexchange interactions. In the perovskite LaMnO$_3$, the cooperative Mn(III)-site distortions of Figure 7 remove the e-orbital degeneracy of the t^3e^1 configuration and introduce $(180° - \phi)$ Mn(III)–O–Mn(III) superexchange interactions that are ferromagnetic in (0 0 1) planes ($\lambda_\sigma > \lambda_\pi$) and antiferromagnetic between basal planes. Here also, a spin canting gives a weak ferromagnetic component. However, dilution of the Mn(III) ions in LaMn$_{1-x}$Ga$_x$O$_3$ introduces regions of orbital disorder at lower temperatures that are ferromagnetic in three dimensions because local site distortions induced by cooperative site rotations introduce an orbital mixing associated with tetragonal and orthorhombic site distortions. Where the ferromagnetic Curie temperature T_c of the orbitally disordered regions is higher than the Néel temperature

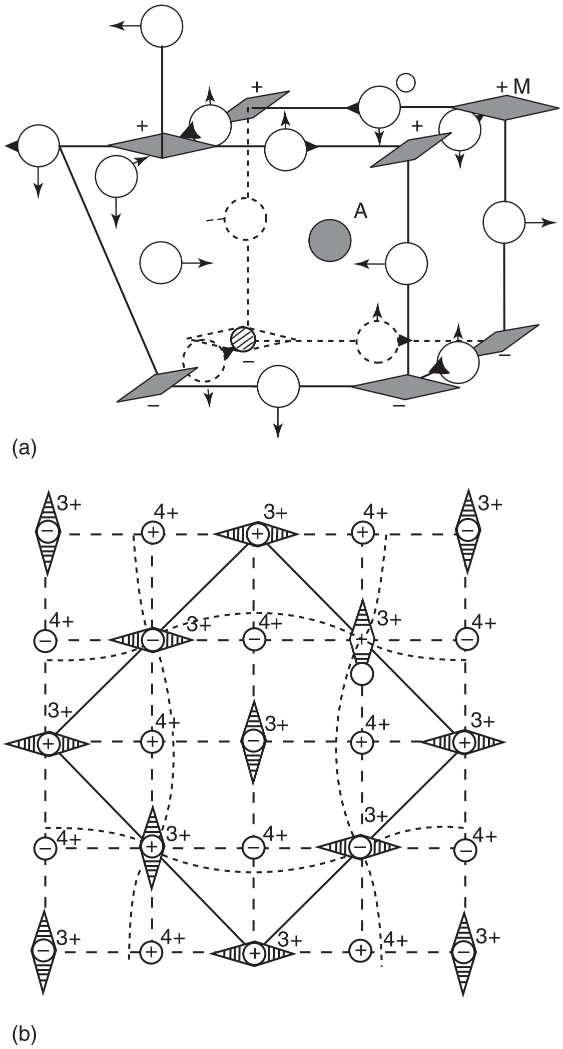

Figure 7 (a) Ordering of occupied *e* orbitals into (0 0 1) planes of $LaMnO_3$ and associated oxygen displacements. This cooperative orbital ordering is superimposed on a cooperative rotation of the $MnO_{6/2}$ octahedra (shown by arrows). Cooperative rotations bend the $(180° - \phi)$ B–O–B bond angle in ABO_3 perovskites when the geometric tolerance factor $t \equiv (A-O)/\sqrt{2}(B-O) < 1$; (A – O) and (B–O) are the equilibrium (A–O) and (B–O) bond lengths. (b) Charge, orbital, and spin [up (+), down (−)] ordering in $La_{0.5}Ca_{0.5}MnO_3$.

T_N of long-range antiferromagnetic order in the orbitally ordered matrix, an applied magnetic field stabilizes the orbitally disordered phase relative to the orbitally ordered phase to convert a spin glass into a ferromagnet.

'Semicovalent exchange' involves a two-electron transfer from a single anion-*p* orbital, one to each of the two cations on opposite sides in a $(180° - \phi)$ cation–anion–cation interaction. Since the two transferred electrons have opposite spins, the rules for ferromagnetic versus antiferromagnetic coupling are the same as those for superexchange. A $U_{eff} \approx 0$ for the itinerant O–2*p* electrons gives semicovalent exchange the form $-J_{ij}\boldsymbol{S}_i \cdot \boldsymbol{S}_j$ with $J_{ij} \approx \left(2b_{ij}{}^2/8S^2\Delta\right)$, where $\Delta = \Delta E_p$ is the 'charge-transfer energy gap.' To illustrate the significance of the semicovalent-exchange component to the total exchange, consider again the $(180° - \phi)$ t^3e^0–O–t^3e^0 interactions in the $RCrO_3$ and $Ca_{1-x}Sr_xMnO_3$ perovskites

$$\Delta E_{ex}^{S} \approx \sum_{ij}{}' \left(2b_{ij}^2/4S^2\right)\left[1/U_{eff}) + (1/2\Delta)\right] \qquad [25]$$

Whereas the superexchange interactions treat only the π-bonding t^3 – O – t^3 interactions, semicovalent exchange also includes the σ-bonding interactions if a $(\Delta_{ex}/\Delta)^2$ multiplier is added. A $\Delta \leqslant U_{eff}$ in $RCrO_3$ and $Ca_{1-x}Sr_xMnO_3$ makes the semicovalent-exchange component dominant to give a total exchange-energy parameter $J_{ex} \sim \langle \cos^2\phi > \rangle$ (cf., eqn [13]). A $T_N \sim \langle \cos^2\phi \rangle$ in an RMO_3 perovskite family signals localized-electron antiferromagnetism.

'Double exchange' occurs in mixed-valent transition-metal compounds in which a mobile spin has a $\tau_h < \omega_R{}^{-1}$ in the presence of localized spins. The mobile spin couples to the localized spin by the Hund intra-atomic exchange field to give a ferromagnetic interaction with a spin-dependent $t_{ij}^{\uparrow\uparrow} = b_{ij}\cos(\theta/2)$ in the tight-binding formula of eqn [4], so

$$H_{\text{ex}}^{D} \approx -Nc(1-c)zb_{ij}\cos(\theta/2) \qquad [26]$$

where Nc is the concentration of mobile charge carriers and $(1-c)z$ is the fraction of near-neighbor sites that are empty. Polaronic charge carriers do not introduce a double-exchange coupling as their τ_h is long compared to the time for a spin to relax to a disordered orientation. Equation [26] is the de Gennes formulation that he applied to the metallic ferromagnetic compositions of the system $La_{1-x}Sr_xMnO_3$; it assumes the coexistence of conductive ($\tau_h < \omega_R{}^{-1}$) σ-bond electrons in the presence of localized spins $S = 3/2$ from the π-bond t^3 manifold. The original Zener formulation for double exchange in this system constrained the $\tau_h < \omega_R{}^{-1}$ to a $Mn^{3+}-O-Mn^{4+}$ two-manganese polaron that he assumed to move diffusively, but with no motional enthalpy ($\Delta H_m = 0$). In fact, the electrons of e-orbital parentage undergo a crossover with increasing x from polaronic to itinerant-electronic behavior in this system. **Figure 8** shows a small compositional and temperature range where the Zener model was thought to be applicable; it also reveals a discontinuous change in T_c at the transition from Zener to de Gennes double-exchange as predicted from the virial theorem for a transition from polaronic to itinerant-electron conduction. In fact, the ferromagnetism in the FV phase of **Figure 8** has been shown to be the result of superexchange and orbital mixing as in the $LaMn_{1-x}Ga_xO_3$. An orbital ordering that lifts the degeneracy of the σ^* band of e-orbital parentage stabilizes the AFM phase of **Figure 8**; metallic, ferromagnetic (0 0 1) planes are coupled antiparallel to one another along the c-axis by t^3-O-t^3 superexchange. However, charge and orbital ordering in $La_{0.5}\,Ca_{0.5}\,MnO_3$ traps the mobile charge carriers to give zigzag ferromagnetic chains coupled antiparallel to one another in the (0 0 1) planes, see **Figure 7(b)**. The Mn^{3+} ions are confined to stripes of zigzag chains, as shown in the CO phase in **Figure 8**.

The spinel Fe_3O_4 has mixed Fe(II) and Fe(III) valence states on the octahedral sites, and an antiferromagnetic Fe–O–Fe superexchange interaction couples antiparallel the tetrahedral-site and octahedral-site spins to give a ferrimagnetic moment per Fe_3O_4 molecule of $\sim 4\,\mu_B$; the spins of the two Fe(III) ions cancel one another, and the ferromagnetic alignment of the octahedral-site spins reduces the spin-disorder scattering for motion of the minority-spin electrons in the presence of the localized majority-spin electrons to give a $\tau_h \approx \omega_R{}^{-1}$ between room temperature and a charge-order Verwey transition temperature $T_V \approx 120$ K. The mobile electrons give a ferromagnetic double-exchange interaction between the octahedral-site cations below room temperature. Fe_3O_4 represents another situation where itinerant and localized spins can coexist on the same atom. However, at higher temperatures spin-disorder scattering converts a $\tau_h \approx \omega_R{}^{-1}$ to a $\tau_h > \omega_R{}^{-1}$, and the mobile electrons become polaronic.

'Indirect exchange,' also known as Yaffet–Kittel–Kasuya–Yosida (YKKY) exchange, is a coupling of localized spins by a partially filled band of itinerant electrons; it is an extension of the de Gennes double exchange to a broad itinerant-electron band. Intra-atomic exchange stabilizes an itinerant-electron spin density parallel to the localized spin in the vicinity of the transition-metal atom, but this itinerant-electron spin density decreases at larger distances, reversing sign in a series of oscillations. If a neighboring localized spin is close enough to be overlapped by the parallel spin density, then the localized spins are coupled ferromagnetically; but if the antiparallel spin density overlaps the neighboring spins, they couple antiferromagnetically. The

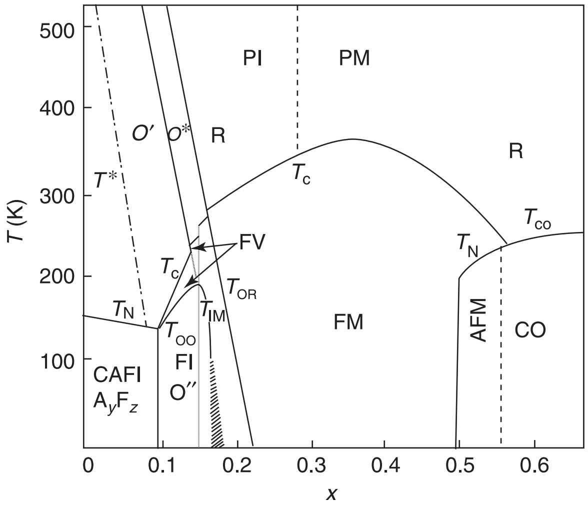

Figure 8 Phase diagram of the system $La_{1-x}Sr_xMnO_3$. CAFI = canted-spin type-A antiferromagnetic insulator (ferromagnetic (0 0 1) planes coupled antiparallel with orbital ordering of **Figure 7(a)**). FI, FV, and FM = ferromagnetic insulator, vibronic conductor (Zener polarons), and de Gennes metal, respectively. AFM = type-A antiferromagnetic metal. CO = charge-ordered phase. O′ and O″ refer to different orbitally ordered orthorhombic phases, O^* to an orbitally disordered orthorhombic phase, and R to a rhombohedral phase. PI and PM are, respectively, paramagnetic-insulator and paramagnetic-metal phases. After Goodenough, J.B., Zhou, J.-S., 2001. Structure and Bonding 98, 87.

extension of the parallel spin-density domain increases as the concentration of itinerant electrons decreases and their effective mass increases.

Additional Illustrative Examples

Spinels

The dominant interaction in the ferrospinel Fe[NiFe]O_4 is the antiferromagnetic 135° $t^3-\mathrm{O}-e^2$ interaction between half-filled σ-bonding orbitals on the tetrahedral-site Fe(III)$:e^2t^3$ and the octahedral-site Ni(II)$:t^6e^2$ and Fe(III)$:t^3e^2$ ions.

In an A[M_2]O_4 spinel in which the tetrahedral-site A cation has no spin, the only spin–spin interactions are those between octahedral-site transition-metal atoms M. The octahedral-site cations in the spinel structure of Figure 4 share only octahedral-site edges; they interact with one another by M–M and 90° M – X – M interactions. The octahedral-site Cr(III)$:t^3e^0$ cations in Zn[Cr_2]O_4, Zn[Cr_2]S_4, and Cd[Cr_2]S_4 all have ferromagnetic 90° Cr – X – Cr interactions by direct exchange and $t^3-p_{\pi\sigma}-e^0$ superexchange whereas the t^3-t^3 interactions are antiferromagnetic by superexchange. The antiferromagnetic t^3-t^3 interactions decrease exponentially with increasing Cr–Cr separation, that is, with increasing lattice parameter on going from Zn[Cr_2]O_4 to Zn[Cr_2]S_4 to Cd [Cr_2] S_4. The 90° Cr – X – Cr interactions, on the other hand, increase significantly on going from an oxide to a more covalent sulfide. Experimentally, Cd[Cr_2]S_4 is a ferromagnetic insulator, the Cr–Cr interactions in Zn[Cr_2]S_4 are just strong enough to convert the ferromagnetic coupling into an SDW, and in Zn[Cr_2]O_4 stronger antiferromagnetic Cr–Cr interactions are frustrated to give a low T_N.

As pointed out above, Fe_3O_4 is a good electronic conductor because of mixed Fe(III) and Fe(II) valence states on the octahedral sites. On the other hand, Mn_3O_4 and Co_3O_4 are insulators because the Mn(II) and Co(II) ions occupy tetrahedral sites having a different potential energy for the M(II)/M(III) couple than that at the octahedral sites. With Mn(III)$:t^3e^1$ on octahedral sites, Mn_3O_4 undergoes a cooperative Jahn–Teller orbital ordering that distorts the spinel from cubic to tetragonal symmetry; the room temperature axial ratio is $c/a = 1.16$. Fe_3O_4 is a Néel ferrimagnet with ferromagnetic double-exchange coupling among the octahedral sites whereas antiferromagnetic t^3-t^3 interactions between octahedral-site Mn(III) lead to a complex magnetic order. Co_3O_4 is a Néel antiferromagnet because the octahedral-site *Co*(III)$:t^6e^0$ ions are in their low-spin state with $S = 0$ and the tetrahedral sites consist of two interpenetrating face-centered-cubic arrays as in the diamond structure with antiferromagnetic $t^3-\mathrm{O}-t^3$ superexchange interactions between the Co(II)$:e^4t^3$ ions.

Rutiles

Most MX_2 compounds with X = F or O crystallize in the rutile structure of Figure 9. This structure has a body-centered-tetragonal array of octahedral-site cations that share edges along the *c*-axis; these *c*-axis chains share octahedral-site corners. The anions form $sp^2\sigma$-bonds with three cation neighbors and π-bond with two quasidegenerate *t* orbitals, e_π; the other *t* orbital, $d_\parallel$, is directed along the *c*-axis where it overlaps with the corresponding $d_\parallel$ orbitals of two next-near-neighbor cations. The MO_2 oxides illustrate several features discussed above.

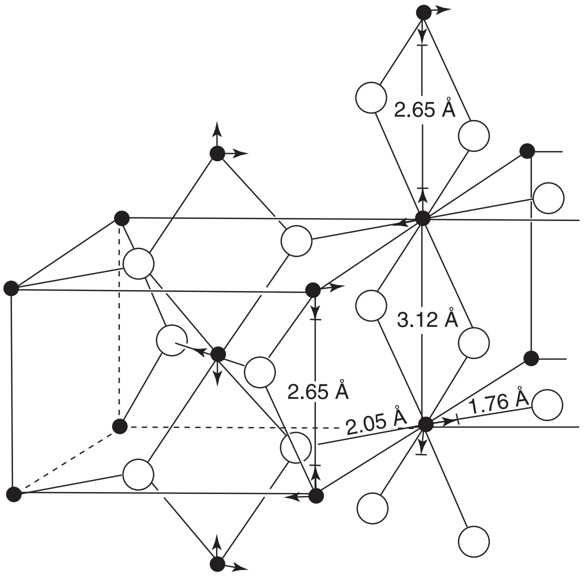

Figure 9 The tetragonal rutile structure and the cation displacements (arrows) found in VO_2 at $T < 67\,°\mathrm{C}$.

The bottom of the empty 3*d* bands of TiO_2 lies ~ 3 eV above the top of the filled O–2*p* bands, which makes TiO_2 an insulator and a crystal transparent. However, the Ti(IV) are not displaced from the center of their octahedra as in $BaTiO_3$ and $PbTiO_3$ which are ferroelectrics. In TiO_2, there is no spontaneous displacement, but displacements in an electric field give TiO_2 a large dielectric constant, which makes TiO_2 a white pigment widely used in paint and the finishing of paper. The itinerant-electron 3*d* bands can be doped *n*-type, in which case *n*-TiO_2 can be used for photoelectrolysis. Removal of oxygen is accommodated by an ordering of the oxygen vacancies into 'shear planes' that separate slabs, *n* rutile cells wide, in a Ti_nO_{2n-1} family of shear structures. Ti(IV) octahedra share common faces across a shear plane, and electrostatic forces displace the cations toward opposite site faces; itinerant electrons reside on the Ti cations within the rutile slabs. The formation of shear planes allows cooperative displacements of the Ti(IV) cations, which reduces the cost in elastic energy. The shear-plane phenomena are associated with cations that also exhibit ferroelectric displacements in other contexts. At low temperatures, the itinerant electrons within the 3*d* bands of a slab condense into $d_{\|}-d_{\|}$ homopolar bonds to form pairs of Ti(III) displaced toward one another. In Ti_4O_7, these two-electron bonds are mobile and disordered in a small temperature interval above the long-range ordering temperature $T_t \approx 160$ K. The mobile electron pairs represent bipolarons.

Above 67 °C, the single 3*d* electron of a V(IV) cation occupies overlapping itinerant-electron bands of $d_{\|}$ and e_π parentage; the metallic conductivity is nearly isotropic. The $d_{\|}$ band is formed by strong V–V interactions along the *c*-axis: the π^* bands by strong $e_\pi - \mathrm{O}:2p_\pi - e_\pi$ interactions with nearest and next-nearest neighbors. Below 67 °C, these itinerant electrons condense into $d_{\|}-d_{\|}$ homopolar bonds and the smaller V(IV) cations are also displaced toward a corner-sharing oxygen by a rocking of the pairs to form molecular clusters consisting of two vanadyl $(\mathrm{V{=}O})^{2+}$ cations bonded by a homopolar V–V bond. The oxygen atoms that bridge a V–V bond each belong to another such cluster. The resulting monoclinic-tetragonal first-order transition at $T_t = 67\,°\mathrm{C}$ produces an insulator–metal transition across which the formation of the V=O vanadyls lifts the π^* bands above the Fermi energy, leaving the $d_{\|}$ band half-filled, and V–V pairing introduces a gap in the narrow $d_{\|}$ band that localizes the electrons in homopolar bonds. This localization of electrons to a molecular cluster is to be distinguished from formation of a 1D CDW as envisioned by a 'Peierls distortion' in which the electrons of the pairs remain itinerant.

In CrO_2, the Cr–Cr separation along a *c*-axis chain is too large ($R > R_c$) for the $d_{\|}$ electrons to form a band of itinerant-electron states; they form localized $d_{\|}{}^1$ states separated from a $d_{\|}{}^2$ configuration by a finite energy gap $(U - W_{\|})$. The remaining single e_π electron occupies a π^* band of itinerant-electron states. This band is one-quarter filled, and extrapolation of the superexchange rules to band magnetism would predict ferromagnetic correlations among the e_π electrons; and CrO_2 is a ferromagnetic metal. Below the Curie temperature T_c, the *c*-axis expands as a result of 'exchange striction'; the half-filled $d_{\|}{}^1$ orbitals would be stabilized by antiferromagnetic superexchange, but their parallel alignment removes the *c*-axis bonding by the $d_{\|}$ electrons because the Pauli exclusion principle prevents $d_{\|}$-electron transfer if the spins are parallel.

In MnO_2, both the $d_{\|}$ and the e_π electrons are localized and a $d_{\|}{}^1 e_\pi^2$ manifold means that both sets of orbitals are half-filled, which leads to antiferromagnetic interactions between nearest and next-nearest neighbors by superexchange. Since both nearest and next-nearest neighbors share a common $\mathrm{O}-2p_\pi$ orbital, the antiferromagnetic interactions along the *c*-axis are stronger than those between nearest neighbors, and the competition leads to the antiferromagnetic spiral-spin configuration propagating along the *c*-axis that is illustrated in **Figure 5**.

The 4*d* electrons have a greater radial extension than the 3*d* electrons, so they have larger overlap integrals with neighboring atoms than do the 3*d* orbitals. Consequently, NbO_2 and MoO_2 do not have localized 4*d* electrons; they both form *c*-axis M–M pairs, but without the rocking of the pairs that occurs in VO_2. The homopolar-bond states of NbO_2 lie below the bottom of the π^* band of e_π-orbital parentage, and NbO_2 is a semiconductor below $T_t \approx 800\,°\mathrm{C}$. With one additional 4*d* electron, MoO_2 has one electron per formula unit in the π^* bands and is a metal. Low-spin Ru(IV) and Rh(IV) are also accessible in octahedral sites of an oxide, but they contain too many 4*d* electrons to allow stabilization of homopolar bonds in M–M pairs. With two and one hole per formula unit, respectively, in the $d_{\|}$ and π^* bands, these oxides are metallic and retain the rutile structure to lowest temperatures.

Energy Bands and Redox Couples

Electron Energies

In an ionic model of a compound, which is illustrated in **Figure 10** for MnO, the energy E_I required to remove the last electron from the cation and place it on an O^- ion at infinite separation is more than compensated by the electrostatic Madelung energy $E_M > E_I$ that is gained by assembling the point charges in a crystalline array. Conservation of energy raises the cation energy levels and lowers the anion energies. The crystalline electric field at the octahedral-site Mn^{2+} of MnO raises the $\mathrm{Mn}:3d^5$ level into the energy gap $E_g \approx 6$ eV between the filled $\mathrm{O}^{2-}:2p^6$ and empty $\mathrm{Mn}^{2+}:4s^0$ bands. Covalent back transfer of electrons from the O^{2-} to the Mn^{2+} ions reduces E_M, but it introduces a compensating quantum-mechanical repulsion between the bonding O-2*p* and antibonding Mn-4*s* orbitals to retain a large E_g. The covalent mixing and the like-atom interactions broaden the bonding and antibonding *s* and *p* states into bands of one-electron itinerant-electron states, and it is convenient to label the upper bonding bands as $\mathrm{O}^{2-}:2p^6$ bands and the lower antibonding bands as $\mathrm{Mn}:4s^0$.

Where a d^n or $4f^n$ manifold falls in the energy gap E_g, as occurs in MnO, further oxidation of the cation is possible. Similarly, where an empty d^{n+1} manifold lies in the gap, reduction of the cation is possible if this manifold is not too close in energy to the bottom of the broad *s* and *p* antibonding bands. In the case of octahedral-site manganese, three valence states are stable: Mn(II), Mn(III), and Mn(IV) corresponding to Mn(III)/Mn(II) and Mn(IV)/Mn(III) redox couples lying in the gap. The splitting $U_{\mathrm{eff}} - U_\sigma$

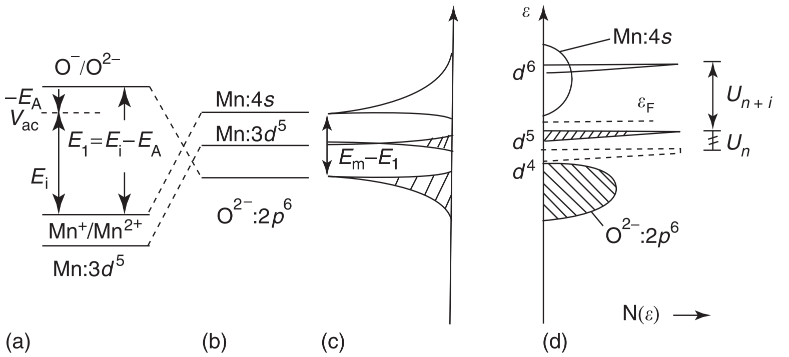

Figure 10 Schematic construction of electronic energies from the point-charge model, (a) and (b), to energy bands for $Mn:4s^0$ and $O^{2-}:2p^6$ in (c) and (d).

between the $Mn(II):t^3e^2$ and $Mn(III):t^3e^1$ energies is small; in fact, W_σ approaches U_σ in the perovskites $LaMnO_3$ and $SrMnO_3$ containing Mn(III) and Mn(IV), respectively, and a $\tau_h < \omega_R{}^{-1}$ for the σ^* electrons makes $La_{0.7}Sr_{0.3}MnO_3$ a ferromagnetic metal.

Since $E_M - E_I$ decreases on going from the halides (group VII) to the oxides and chalcogenides (group VI) to the pnictides (group V) and down any column of the periodic table to heavier anions, the energy gap E_g between bonding and antibonding *s* and *p* bands decreases accordingly. Consequently, the higher cation valence states accessible in an oxide may not be available in a sulfide or selenide. For example, the $Mn^{2+}:d^5$ manifold lies below the $S^{2-}:3p^6$ energy in the point-charge model, so the Mn(IV) state is not accessible in the chalcogenides. MnS_2 is $Mn^{2+}(S_2)^{2-}$, for example, in contrast to $Mn^{4+}(O^{2-})_2$ in MnO_2. However, where a d^n manifold lies close to the top of the bonding anion-*p* bands, covalent mixing raises antibonding states of *d*-orbital symmetry to the top of the broad bonding bands; the redox couple becomes pinned at the top of the bonding bands and changes from primarily *d* to primarily anion-*p* character as the d^n manifold falls below the anion-p^6 energy in the point-charge model. Where the anion component becomes dominant, the electronic states of the redox couple are itinerant; and where both the hole concentration and the anion character in these itinerant antibonding states are large enough for a cooperative condensation of the holes into purely anion antibonding states of anion–anion pairs, diatom anions are formed.

Rare-Earth Compounds

An energy $U > E_g \gg W$ separates the $4f^n$ and $4f^{n+1}$ localized-electron manifolds of the rare-earth ions. Therefore, they have a single R^{3+} valence state unless a $4f^n$ configuration falls within E_g, as occurs for the $Ce^{3+}:4f^1$ and $Pr^{3+}:4f^2$ or the $Eu^{2+}:4f^7$ in an oxide. However, the R-5*d* orbitals are itinerant, and covalent bonding pushes the antibonding 6*s* and 6*p* states above the bottom of the 5*d* band. Normally the 5*d* band is empty, but it can accept electrons. Doping EuO with Gd substitution for Eu, for example, creates shallow one-electron donor states below the bottom of the 5*d* conduction band just as substitution of P for Si creates *n*-type silicon. In EuO, the $Eu:4f^7$ level lies ~ 1.1 eV below the bottom of the 5*d* band; the $4f^7-O-5d^0$ superexchange interactions are ferromagnetic and stronger than the antiferromagnetic $4f^7-O-4f^7$ interaction because of the large U_{eff} between $4f^7$ and $4f^8$ as well as the smaller overlap integrals. In the $Eu_{1-x}Gd_xO$ system, the YKKY indirect exchange by itinerant 5*d* electrons initially increases the ferromagnetic Curie temperature T_c with *x*; but as *x* increases, the extension of the ferromagnetic 5*d* volume about a rare-earth atom decreases to below a nearest-neighbor separation; the YKKY interaction becomes antiferromagnetic, and T_c decreases with a further increase of *x*. $Eu_{1-\delta}O$ contains polaronic $\tau_h > \omega_R{}^{-1}$ holes in the Eu(III)/Eu(II) redox couple. On the other hand, annealing in a Eu atmosphere creates $EuO_{1-\delta}$, and the oxygen vacancies trap two electrons. On cooling $EuO_{1-\delta}$ below the Curie temperature T_c, the 5*d* electrons with spin parallel to the $4f^7$ spin $S = 7/2$ are stabilized relative to the 5*d* electrons of antiparallel spin by direct intra-atomic exchange. The spin degeneracy of the two-electron trap state is also removed, the energy of the antiparallel trapped electron is raised above the bottom of the parallel-spin 5*d* conduction band. As a result, $EuO_{1-\delta}$ transforms from a semiconductor to a metal on cooling through T_c as is illustrated in Figure 11. Just above T_c, the carriers thermally excited into the 5*d* band stabilize regions of short-range ferromagnetic order by double-exchange electron transfer; ferromagnetic alignment reduces the spin-disorder scattering of the mobile electrons, and their stabilization by the intra-atomic exchange interaction confines the mobile electrons to the region of short-range ferromagnetic order. A mobile electron confined to clusters of short-range ferromagnetic order is called a 'magnetic polaron.' In an external magnetic field, the size of the ferromagnetic clusters grows; at a percolation threshold, the compound undergoes a drop in electrical resistance. This magnetoresistance is large in EuO.

The valence state of a rare-earth ion is defined by its occupied $4f^n$ configuration. $Eu_{1-\delta}O$ is in a mixed Eu^{3+}/Eu^{2+} valence state since the holes occupy the $Eu^{3+}/Eu^{2+}\,4f^6/4f^7$ couple. GdS, on the other hand, has the Gd configuration $4f^7 5d^1$, and the itinerant 5*d* electrons that make GdS a metal are valence electrons. Therefore, the Gd of GdS is considered to be in the trivalent state corresponding to a localized $4f^7$ configuration. SmS has its $4f^6$ level just below the bottom of the 5*d* band; pressure increases the width of the 5*d* band, and above 6.5 kbar the 5*d* band overlaps the $4f^7$ level. A first-order contraction of the rocksalt structure at

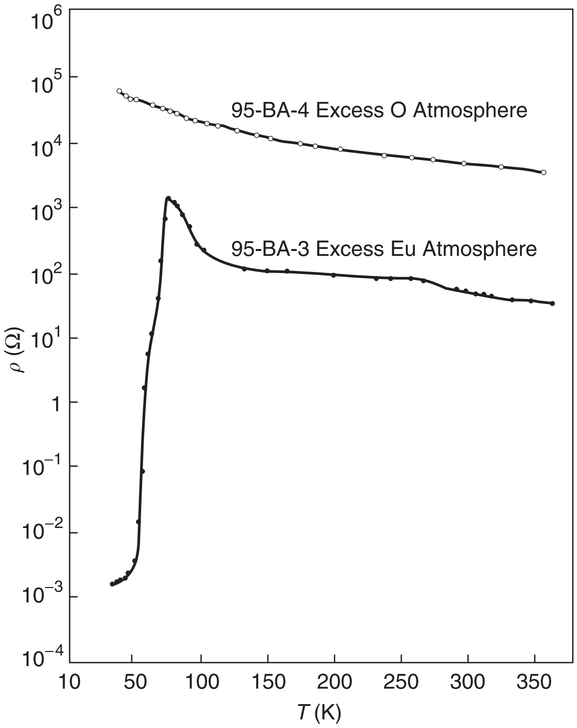

Figure 11 Resistivity vs. temperature for EuO annealed in a europium-rich atmosphere ($EuO_{1-\delta}$) and an oxygen-rich atmosphere ($Eu_{1-\delta}O$). After Oliver, M.R., Dimmock, J.O., McWhorter, A.L., Reed, T.B., 1972. Physical Review B 5, 1078.

crossover raises the $4f^6$ level into the 5d band to where 0.5 electrons per Sm are donated to the 5d band. Hybridization of 5d and 4f states creates 'heavy fermions' at the Fermi energy and the compound is said to be in an intermediate-valence state.

Transition-Metal *d*-Block Compounds

The smaller U_{eff} of the d-block transition-metal compounds makes localized 4d and 5d spins relatively rare; localized spins associated with 3d electrons are common, but they may also be itinerant as discussed above for oxides with a rutile structure. The existence of four valence states for vanadium in V_2O_5, VO_2, V_2O_3, and VO shows that the $U_{\text{eff}}=U_\pi$ separating octahedral-site t^1, t^2, and t^3 configurations is in the neighborhood of 2 eV, which makes $W \approx U_{\text{eff}}$ in these compounds. Both VO_2 and V_2O_3 exhibit insulator–metal transitions due to cation clustering, V_2O_5 contains short V=O bonds due to displacement of the V(V) from the center of symmetry of its interstice, and VO is a semimetal exhibiting V–V bond-length fluctuations. On the other hand, the Ti–Ti interactions in metallic TiO make $W > U_\pi$; it becomes a conventional superconductor below $T_{\text{cs}} = 1$ K.

For a given valence state, the effective nuclear charge seen by the d electrons increases on going to heavier atoms of a given d-block and the redox energy is correspondingly stabilized. However, in an octahedral site, the splitting U_{eff} between a Cr(III): t^3e^0 and a Cr(II): t^3e^1 configuration is increased by the cubic-field splitting Δ_c, which is why CrO has not been prepared; the Cr(III)/Cr(II) level lies close to the bottom of the 4s band. However, CrS has been prepared; it has hexagonal rather than cubic close-packing of the anions (NiAs rather than NaCl structure) with a cooperative Jahn–Teller orbital ordering that distorts the structure from hexagonal symmetry. The d^5 configuration of MnO is more stable than the d^6 configuration of $Fe_{1-\delta}O$ because a $U_{\text{eff}} = U_\pi + \Delta_{\text{ex}}$ separates the Fe(III): t^3e^2 and Fe(II): t^4e^2 octahedral-site states. Since the majority-spin electrons occupy different d orbitals, they are more tightly bound to the nucleus than the minority-spin electron, which is why the minority-spin electron of Fe_3O_4 can have a $\tau_h \approx \omega_R^{-1}$.

The antiferromagnetic order in MnO is illustrated in Figure 12. The dominant interactions are 180° Mn(II)–O–Mn(II) antiferromagnetic superexchange interactions between half-filled t^3 and e^2 configurations; these interactions order parallel the spins of a (1 1 1) plane, whereas the t^3-t^3 superexchange interactions across shared octahedral-site edges within these planes are antiferromagnetic. Parallel spin alignment makes these t^3-t^3 interactions nonbonding, whereas those between neighboring, antiparallel (1 1 1) planes are bonding. Consequently, MnO distorts from cubic to rhombohedral ($\alpha > 60°$) symmetry on cooling through T_N as a result of exchange striction. Similar antiferromagnetic $180° \, e^2-O-e^2$ superexchange interactions are dominant in $Fe_{1-\delta}O$ and CoO, but these compounds exhibit a distortion below T_N that is due to a large magnetostriction; the orbital degeneracies

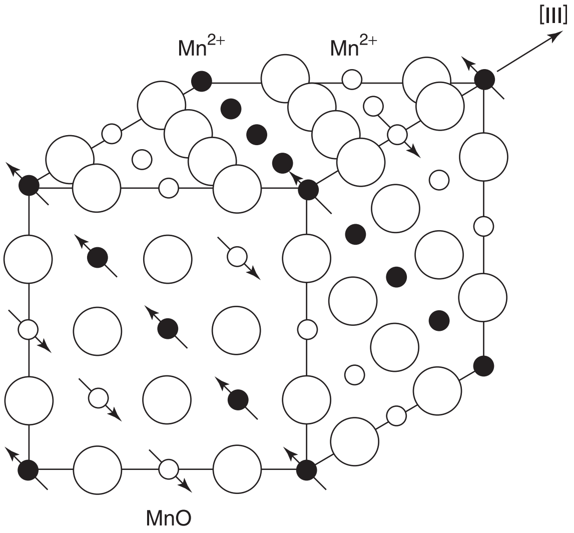

Figure 12 Spin configurations of antiferromagnetic MnO. After Shull, C.G., Strauser, W.A., Wollan, E.O., 1951. Physical Review 83, 333.

of the Fe(II)$:t^4e^2$ and Co(II)$:t^5e^2$ configurations are removed by an enhancement of the orbital angular momentum once long-range collinear ordering of the spins allows ordering of the orbital angular momentum through the spin–orbit coupling $\lambda \boldsymbol{L}\cdot\boldsymbol{S}$. $Fe_{1-\delta}O$ becomes rhombohedral ($\alpha < 60°$) below T_N with spins oriented parallel to the [1 1 1] axis in opposition to the dipole–dipole forces; CoO becomes tetragonal ($c/a < 1$) and the dipole–dipole interactions force the spins a little away from the tetragonal c-axis.

Pinning of a redox couple at the top of an anion-p band replaces the gap U_{eff} with a charge-transfer gap $\Delta = \Delta E_p$. The Ni(II)$:t^6e^2$ configuration of NiO is pinned at the top of the O–2p bands, and a $\Delta < U_{\text{eff}} = U_\sigma + \Delta_{\text{ex}}$ adds a semicovalent exchange comparable to the superexchange antiferromagnetic Ni(II)$:e^2$ – O – Ni(II)$:e^2$ interaction provide a high Néel temperature. In NiS, the Ni(I)$:t^6e^3$ configuration is at the top of the S–3p bands. At temperatures $T > 350\,°$C, NiS has the NiAs structure, but it transforms into the peculiar millerite structure at lower temperatures. It is possible to retain the NiAs structure at low temperatures by quenching from above 650 °C. This metastable phase undergoes a first-order insulator–metal transition at a Néel temperature $T_N = 264$ K. On lowering the temperature through T_N, there is an abrupt increase in volume with only a small distortion of the structure as the width of the σ^* band of e-orbital parentage changes from $W_\sigma \approx U_{\text{eff}} = U_G + \Delta_{\text{ex}}$ to $W_\sigma < U_{\text{eff}}$; the Mott–Hubbard transition is not smooth.

The lattice instabilities occurring where $W \approx U_{\text{eff}}$ are more commonly expressed by either stabilization of a CDW or, in a mixed-valent compound, by a dynamic spinodal phase separation. For example, the low-spin Ni(III)$:t^6e^1$ configuration in the $RNiO_3$ family of **Figure 13** is pinned at the top of the O–2p bands; this single-valent family undergoes a transition from an antiferromagnetic insulator with $W < U_\sigma$ to metallic $LaNiO_3$ with $W > U_\sigma$ as the $(180° - \phi)$ Ni–O–Ni bond angle increases with increasing size of the rare-earth R^{3+} ion. The samples in the shaded area of **Figure 13** exhibit bond-length fluctuations and stabilization of a CDW below a $T_t = T_N$ that are characteristic of the lattice instabilities encountered at crossover. Below the insulator–metal transition T_{MI}, a distortion to monoclinic $P2_1/n$ symmetry reflects bond-length fluctuations that become static for $R = H_O$, . . ., Lu, Y with long-range ordering of Ni(III) ions distinguished by alternating covalent and ionic Ni–O bond lengths. Moreover, applying pressure to $PrNiO_3$ lowers $T_{MI} = T_N$ until it terminates at a first-order transition to a quantum-critical-point phase.

Pinning of a redox couple at the top of the O–2p bands may also be revealed by oxidation of the transition-metal array. For example, the $x = 0$ composition of the layered $Li_{1-x}CoO_2$ cathode material contains low-spin Co(III)$:t^6e^0$ and is a charge-transfer-gap semiconductor. However, the t^5/t^4 Co(IV)/Co(III) redox couple is pinned at the top of the O–2p bands, and removal of Li from between adjacent CoO_2 layers of edge-shared octahedra creates a two-phase region $0.1 < x < 0.4$ in which a semiconductive phase and a metallic phase of smaller Co–Co separation coexist as a result of a strong intra-atomic Δ_{ex} in isolated high-spin Co(IV): t^3e^2. At $x > 0.6$, peroxide formation at the surface leads to the loss of oxygen as gaseous O_2.

The high-temperature copper-oxide superconductors provide an example where strong electron–lattice interactions in a mixed-valent system at the $\tau_h \approx \omega_R{}^{-1}$ crossover leads to a remarkable physical phenomenon. In these layered oxides, the $x^2 - y^2$ orbital of the Cu(III)/Cu(II) couple is pinned at the top of the O–2p bands of a CuO_2 sheet. The $(CuO_2)^{2-}$ planes of the single-valent parent compounds are antiferromagnetic insulators, but removal of electrons from these sheets induces a transition from the antiferromagnetic phase to a metallic phase that is not superconductive. Superconductivity appears in an intermediate $\tau_h \approx \omega_R{}^{-1}$ crossover phase where there is a strong electron coupling to bond-length fluctuations that order into a traveling CDW (or stripes) phase at low temperatures as is illustrated in **Figure 14** for the $La_{2-x}Sr_xCuO_4$ system.

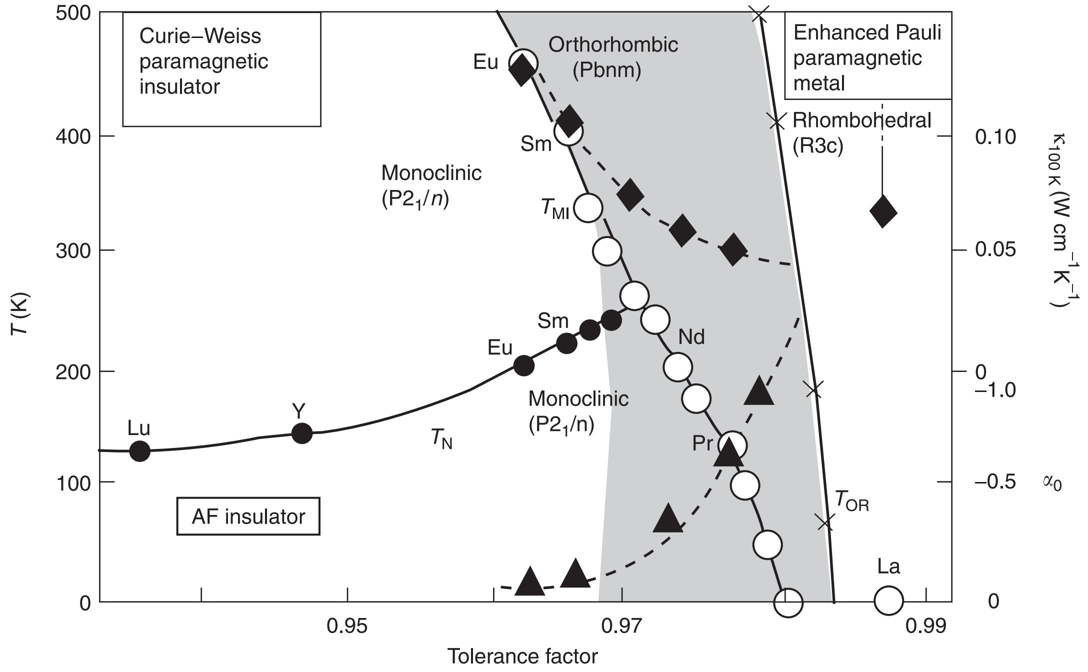

Figure 13 Schematic phase diagram of the $RNiO_3$ (R = rare-earth) family. The triangle symbol is for the $^{18}O/^{16}O$ isotope effect, the diamond is for the lattice contribution to the thermal conductivity at 100 K; both of these signal bond-length fluctuations in the shaded region. In the nonshaded region, a $T_N \sim \langle \cos^2\phi \rangle$ indicates localized-electron antiferromagnetism; $LaNiO_3$ is metallic. Reproduced with permission from Zhou, J.-S., Goodenough, J.B., Dabrowski, B., 2003. Physical Review B 67, 020404.

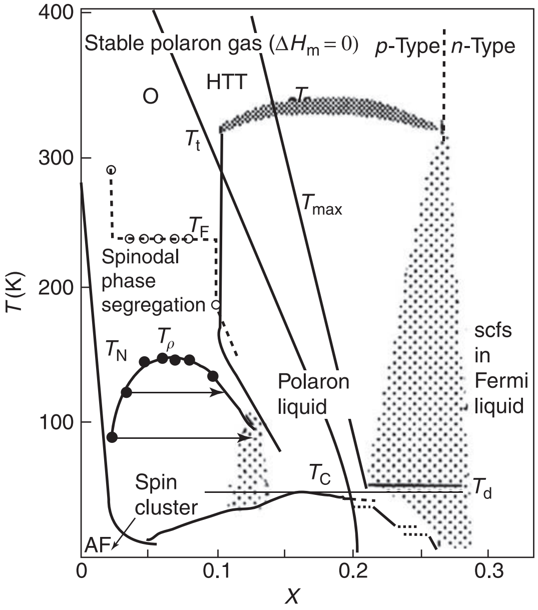

Figure 14 Phase diagram for the superconductive system $La_{2-x}Sr_xCuO_4$. After Goodenough, J.B., Zhou, J.-S., 2001. Structure and Bonding 98, 95.

Further Reading

Bertaut EF (1966) Spin configuration of ionic structures. In: Rado GT and Suhl H (eds.) *Magnetism: A Treatise on Modern Theory and Materials.* 3: pp. 149–209. New York, NY: Academic Press. (Chapter 4).

Gleitzer C and Goodenough JB (1985) Mixed-valence iron oxides. In: Clarke MJ, et al. (ed.) *Structure and Bonding.* 98: pp. 1–76. Berlin: Springer. (Chapter 1).

Goodenough JB (1963) *Magnetism and the Chemical Bond.* New York, NY: Wiley and Interscience.

Goodenough JB (1966) Magnetism and crystal structure in non-metals. In: Rado GT and Suhl H (eds.) *Magnetism: A Treatise on Modern Theory and Meterials*. 3: pp. 1–62. New York, NY: Academic Press. (Chapter 1).

Goodenough JB (1972) Theory of antiferromagnetism and ferrimagnetism. In: Hench LL and Dove DB (eds.) *Physics of Electronic Ceramics*, pp. 777–831. New York, NY: Dekker. (Chapter 24).

Goodenough JB (1974) Some comparisons of fluorides, oxides, and sulfides containing divalent transition metal atoms. In: Rao CNR (ed.) *Soild State Chemistry*, pp. 215–364. New York, NY: Dekker. (Chapter 4).

Goodenough JB (2001) *Structure and Bonding*. 98: Berlin: Springer.

Hench LL and Dove DB (1972) *Physics of Electronic Ceramics*. New York, NY: Dekker.

Jona F and Shirane G (1962) *Ferroelectric Crystals.* Oxford: Pergamon.

Kanamori J (1966) Anisotropy and magnetostriction of ferromagnetic and antiferromagnetic materials. In: Rado GT and Suhl H (eds.) *Magnetism: A Treatise on Modern Theory and Materials*. 1: pp. 127–199. New York, NY: Academic Press. (Chapter 4).

Lax B and Button KJ (1962) *Microwave Ferrites and Ferrimagnets*. New York, NY: McGraw-Hill.

Morrish AH (1965) *The Physical Properties of Magnetism*. New York, NY: Wiley.

Mott NF (1974) *Metal-Insulator Transitions*. London: Taylor and Francis.

Rado GT and Suhl H (1966) *Magnetism: A Treatise on Modern Theory and Materials*. 1–4: New York, NY: Academic Press.

Rao CNR (1974) *Solid State Chemistry*. New York, NY: Dekker.

Rao CNR and Rao KJ (1978) *Phase Transitions in Solids*. New York, NY: McGraw-Hill.

Reiss H (1972) *Progress in Solid State Chemistry*. 5: Oxford: Pergamon.

Smith J and Wijn HPJ (1959) *Ferrites*. New York, NY: Wiley.

Micromechanical Devices and Systems[☆]

H Fujita[a] **and S Elsheikhi**[b], [a]University of Tokyo, Tokyo, Japan; [b]University of Benghazi, Benghazi, Libya

© 2017 Elsevier Inc. All rights reserved.

This is an update of H. Fujita, S. Elsheikhi, Micromechanical Devices and Systems, Reference Module in Materials Science and Materials Engineering, Elsevier, 2017, ISBN 9780128035818, https://doi.org/10.1016/B978-0-12-803581-8.10162-6.

Introduction 504
Micromachining 504
Materials for MEMS 505
Microactuators 506
Applications 507
Sensors 507
Printers 508
Optical Devices 508
Chemistry and Biomedical Applications 509
Future Development of MEMS 510
References 510
Further Reading 510

Introduction

The successful extension of semiconductor technology to fabricate mechanical parts of the sizes from 10–100 μm opened wide ranges of possibilities for micromechanical devices and systems. The fabrication technique is called micromachining. Micromachining processes are based on silicon integrated circuits (IC) technology and used to build three-dimensional (3D) structures and movable parts by the combination of lithography, etching, film deposition, and wafer bonding. The same technology base that enabled miniaturization and large-scale integration of electronics offers three distinctive features defining micromachined devices and systems: miniaturization, multiplicity, and microsystem integration. Miniaturization is clearly essential. Small parts respond fast, constitute miniature machines that work in extremely shallow spaces, add functionality to portable or wearable devices, and realize tools to investigate the nanometric world. Millions of such parts can work cooperatively to do things impossible for a single device alone. Thus, multiplicity is one key to successful micromechanical systems. The coordination of these parts is accomplished by integrating them with electrical circuits. Furthermore, optical, sensing, fluidic, and biological elements are to be integrated in multi-functional microsystems in a cost-effective manner. The research field concerning micro-mechanical devices is referred to as MEMS (microelectromechanical systems) in USA, Micromachine in Japan, and MST (micro-system technology) in Europe.

The root of MEMS research can be found in the research of silicon sensors. A noticeable turning point from sensor research toward MEMS research was the demonstration of micromachined gears and turbines made on a silicon chip in 1987. Since then, development has continued in micromachining processes, material varieties, microactuators, and the application of MEMS.

Micromachining

MEMS generally requires complex microstructures that are thick, 3D, and movable. Therefore, many technologies have been developed on the basis of semiconductor microfabrication processes including lithography, etching, and deposition. Pre-designed patterns are transferred by exposure to resists that have sensitivity to light, X-ray, or electron beam and those that are coated on substrates. Photo-lithograph through a glass-chromium mask is most commonly used. Parts of the resist remain on the substrate according to the exposed patterns by development. Using the resist pattern as a masking layer, one can selectively etch the substrate or the film on it. In another process, the resist mold pattern can be replicated by deposition. After resist removal, the next material is deposited on the patterned substrate. The material is, then, patterned by lithography and etching. These sequences are very similar to the IC fabrication.

There are special processes for micromachining to obtain 3D structures and movable parts (**Table 1**). To construct 3D microstructures, researchers have used anisotropic wet etching, deep reactive ion etching, and replication of deep lithography patterns. Another 3D fabrication technique is capable of folding micromachined plates out from the substrate by removing either a thin film under it or the substrate itself. The removal process is called sacrificial layer etching. Selective etching of the 'sacrificial' material should be performed without damaging microstructures. **Table 2** shows the choice of etching solution or gas, the structural material and the sacrificial material. Even after release etching, microstructures tend to stick to the substrate. Sublimation drying,

---

[☆] *Change History*: July 2015. S. Elsheikhi added abstract and keywords, expanded text with additional review materials, updated the list of reference, and provided an Change History.

Table 1 Micromachining processes

Process (material)	*Feature*	*Application*
Wet anisotropic etching (single-crystal silicon)	Precise structures defined by crystal facets	Pressure sensor membrane, V-groove (channel, fiber alignment), Optical flat mirror surface
Dry anisotropic etching (silicon)	3D structure defined by mask patterns	High aspect ratio microstructure, through hole
Sacrificial layer etching (various thin films)	Integrated circuits compatible fabrication of micromovable structures	Integrated sensor, Arrayed MEMS (e.g., digital micromirror device)
Wafer bonding (Si or glass substrate)	Closed cavity formation, 3D assembly of devices on substrates	Hybrid integration of multifunctional system, Packaging, and encapsulation
Electroforming (metal)	Replication of resist patterns by electroplating through the resist mask	Metallic 3D structures, Mater for injection molding
Injection molding and thermal embossing (polymer)	Low cost replication from precise master	3D microstrutures for fiber alignment or microchannels

Table 2 Selectivity of etching

Etching liquid/gas	*Etched material*	*Resistant material*
HF(+NH_4 F)	SiO_2	Si
KOH	Si	SiO_2, Si_3 N_4
Hot H_3PO_4	Si_3 N_4	SiO_2, Si
XeF_2 (gas)	Si	SiO_2, Si_3 N_4
SF_6 (plasma)	Si	Ni, Al
O_2 (plasma)	Polymer	Al

supercritical drying, release etching by plasma or gas, and surface coating are typical methods to prevent sticking. Wafer bonding is also essential to micromachining. 3D stacking of structures, sealing of cavities and channels, hermetic or vacuum encapsulation of sensing/actuation elements and combination of devices made of different materials and processes are accomplished by bonding wafers together. Glass and silicon substrates are bonded by applying 400–500 V at 600–800 K; this is called anodic bonding. Two silicon substrates can be fusion bonded at ~1370 K after careful cleaning of the surfaces to CO_2bonded. Replication of micro molds is the inexpensive way of fabricating many microstructures. Molds can be made by deep lithography or deep etching. Electroplating of metals, chemical vapor deposition (CVD) of polysiliconfilms, and injection molding of polymers are commonly used for replication. Finally, direct fabrication of microstructures may be possible by beam assisted deposition or solidification by laser beam, electron beam assisted deposition, and focused ion beam (FIB) etching.

In recent years some multifunctional machine tools have been developed to implement several mechanical machining operations on one machine in order to rapidly and economically fabricate those components/products. Research has also focused on the development of hybrid machines that can integrate conventional and non-conventional machining processes in a single platform. Hybrid micro-machining processes have been significantly improved in terms of machinability of hard-to-machine materials, tool life, geometrical accuracy, surface integrity and machining efficiency (Chavoshi and Luo, 2015). In 2014, the College International Pour la Recherche en Productique (CIRP) collaborative working group on hybrid processes proposed the following definition for 'hybrid machining processes': *hybrid machining processes are based on the simultaneous and controlled interaction of machining mechanisms and/or energy sources/tools having a significant effect on the process performance*. The wording 'simultaneous and controlled interaction' means that the processes/energy sources should interact more or less in the same processing zone and at the same time (Lauwers *et al.*, 2014). Accordingly, these hybrid micro-machining processes are classified as *assisted* (vibration-assisted, laser-assisted, fluid-assisted, magnetic field-assisted and external electric field-assisted) and combined hybrid micromachining processes (ECDM: micro-electrochemical discharge machining, SEDCM: simultaneous micro-EDM and micro-ECM, JECM-LD: Laser drilling assisted with jet electrochemical machining, ECM-Grinding: electrochemical machining for grinding and EDM-ER: Micro-electrodischarge machining and electrorheological fluid-assisted polishing) (Chavoshi and Luo, 2015).

Materials for MEMS

Silicon is the most common material in micromachining because (1) the fabrication processes are well established, (2) it has excellent mechanical properties, and (3) integration with electronic circuits and sensors is possible. It also has piezoresistive properties used for strain detection. SiO_2 and SiN films serve as electrical and thermal insulators. They are also excellent masking layers for anisotropic wet etching by TMAH and KOH. Optical waveguides may be made of SiO_2. SiN and other nitride films, for example, TiN and A1N, are very hard and used for low friction and antiwear coating.

Other materials that may not be common for IC fabrication are also useful in MEMS. Actuator materials produce force and displacement. They include piezoelectric materials (PZT, ZnO, quartz), magnetostrictive material (TbFe), shape memory alloy

(TiNi), and some conductive polymers. Compound semiconductors such as GaAs, GaN, and InGaAs can be micromachined in a way similar to silicon, and offer optically active and passive components. MEMS devices can be made from polymers by processes such as injection moulding, embossing orstereolithography and are especially well suited to microfluidic applications such as disposable blood testing cartridges (Mamilla and Chakradhar, 2014).

Metals can also be used to create MEMS elements. While metals do not have some of the advantages displayed by silicon in terms of mechanical properties, when used within their limitations, metals can exhibit excellent reliability. Metals can be deposited by electroplating, evaporation, and sputtering processes. Commonly used metals include gold, nickel, aluminum, copper, chromium, titanium, tungsten, platinum, and silver (Mamilla and Chakradhar, 2014).

Researchers have developed batch fabrication processes for all of those materials achieving the features of MEMS mentioned above.

Microactuators

Microactuators are key devices allowing MEMS to perform physical functions. Many types of microactuators have been successfully operated. Some of them are driven by force associated with physical fields. Force can be generated in the space between stationary and moving parts using electric, magnetic, and flow fields. Some others utilize actuator materials introduced before. Thermal expansion and phase transformations, such as the shape-memory effect and bubble formation, cause shape or volume changes. Micromachining technology allows one to make structures in which a well-controlled field is generated or to deposit and pattern actuator materials. Typical sizes of microactuators are from 10 μm to 1 mm. Although the physical principle that describes the motion of macroscopic objects is still applicable to microactuators, the relative importance of various forces changes in small dimensions. It is called a scaling effect. Table 3 shows the dependence of some physical parameters and forces on the characteristic dimension of an object. The scaling effect and the compatibility with micromachining process are important issues when a microactuator is designed.

One of the most significant scaling effects is that friction dominates over inertia forces in the micro world. Researchers have tried many ways of minimizing friction by suspending movable parts with flexures, applying smooth coatings, using rotational contacts, levitating objects, and using friction drive mechanism.

Each actuation principle has its own advantages and disadvantages (Table 4). The choice and optimization of an approach should be made according to the requirements of a particular application. Generally speaking, the electrostatic actuator is more suitable for performing tasks that can be completed within a chip (e.g., positioning of devices/heads/probes, sensors with servo feedback for self-test or readout, light deflection and modulation) since it is easily integrated on a chip, easily controlled, and consumes little power. On the contrary, the other types of actuators are more robust, more capable of producing larger forces, and more suitable for performing external tasks (propulsion, manipulation of objects, etc.).

Table 3 Scaling effect (L: characteristic dimension)

Parameter	*Formula*	*Scaling*	*Comment*
Gravity, f_g	Mg	L^3	g: gravity const., m: mass
Inertial force, f_i	Ma	L^4	a: acceleration
Elasticity, f_e	$eS\Delta L/L$	L^2	e: Yang's modulus
Surface tension, F_s	$L\gamma$	L	γ: surface wetting constant
Resonant frequency, ω	$\sqrt{K/m}$	L^{-1}	M: spring constant ($\propto L$)
Moment of inertia, I	αmr^2	L^5	α: shape constant, r: radius of rotor
Reinors number, R_e	f_i/f_f	L^2	Ratio between inertia and viscosity ($\propto L^2$)
Heat conduction, Q_c	$\lambda\delta\ TA/d$	L	δT: temperature difference, λ: heat conductivity, A: cross-section area ($\propto L^2$)
Thermal expansion, F_r	$eS\Delta L(T)/L$	L^2	Valid for piezoelectric deformation ($\Delta L(E)$)
Magnetic force, F_m	$\mu SH^2/2$	L^4	μ: permittivity, H: magnetic field ($\propto L$)
Electrostatic force, F_e	$\varepsilon SE^2/2$	L^2	ϵ: permittivity, E: electric field (constant)

Table 4 Comparison of driving principles

	Electrostatic	*Magnetic*	*Piezoelectric*	*Shape memory alloy*	*Thermal*
Speed	Excellent	Good	Good	Fair	Poor
Force	Poor	Good	Excellent	Excellent	Excellent
Integration with circuits	Excellent	Good	Fair	Good	Excellent
Power consumption	Excellent	Fair	Good	Fair	Poor
Robustness in harsh environments	Poor	Good	Good	Excellent	Excellent

Applications

Figure 1 maps the prospective applications in optics, transportation and aerospace, robotics, chemical analysis systems, bio-technologies, medical engineering, and microscopy using scanning microprobes. Most of these applications have a common feature in that only very lightweight objects such as mirrors, heads, valves, cells, and microprobes are driven, and very little physical interaction with the external environment is necessary.

Sensors

The first successful application of MEMS was pressure sensors for the precise control of an automobile engine combustion for clean exhaust in 1980s. MEMS accelerometers are currently used for air bag ignition sensors. MEMS gyroscopes, or angular rate sensors, are applied to navigation systems, active suspensions, and spin suppression systems. Precisely micromachined membranes serve as pressure sensing element; its deflection by applied pressure is detected by piezoresistive gauges made on the silicon membrane. In the accelerometer, a proof mass suspended by a flexible suspension is micromachined (Figure 2). When acceleration is applied to the proof mass, the initial force displaces the mass and the suspension; this motion is detected by either the strain gage, that is, an integrated piezoresistor, or the change in capacitance between the mass and a fixed electrode. Better linearity and stability can be

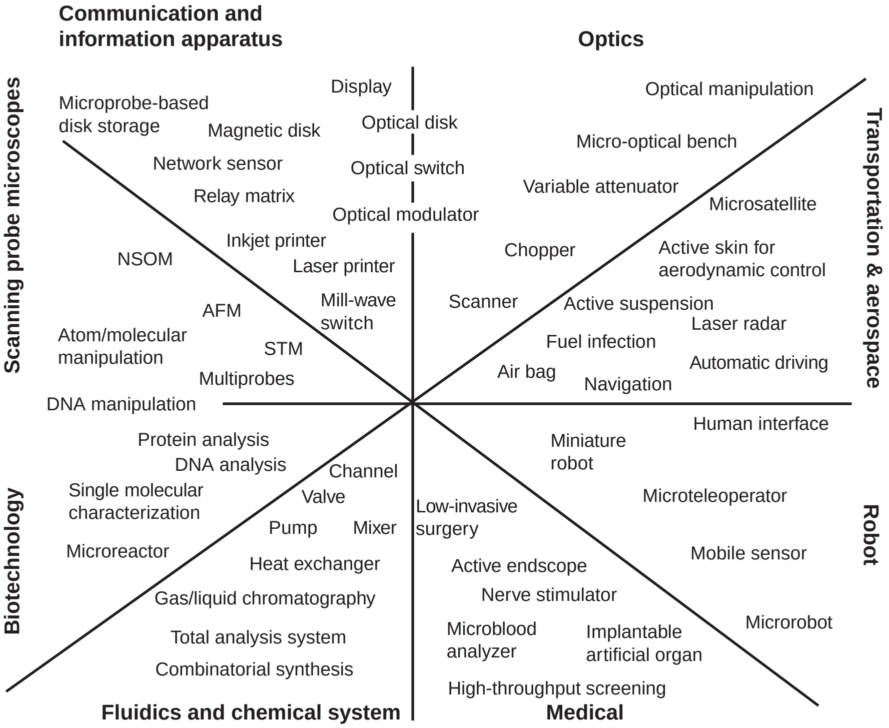
Communication and information apparatus
Optics
Scanning probe microscopes
Transportation & aerospace
Biotechnology
Robot
Fluidics and chemical system
Medical
Microprobe-based disk storage
Magnetic disk
Display
Optical disk
Optical switch
Optical modulator
Network sensor
Relay matrix
Inkjet printer
Laser printer
Mill-wave switch
NSOM
AFM
STM
Atom/molecular manipulation
Multiprobes
DNA manipulation
Optical manipulation
Micro-optical bench
Variable attenuator
Microsatellite
Chopper
Active skin for aerodynamic control
Scanner
Active suspension
Laser radar
Fuel infection
Air bag
Navigation
Automatic driving
Human interface
Miniature robot
Microteleoperator
Mobile sensor
Microrobot
Protein analysis
DNA analysis
Channel
Valve
Single molecular characterization
Pump
Mixer
Microreactor
Heat exchanger
Gas/liquid chromatography
Total analysis system
Combinatorial synthesis
Low-invasive surgery
Active endscope
Nerve stimulator
Microblood analyzer
Implantable artificial organ
High-throughput screening

Figure 1 A map of MEMS applications.

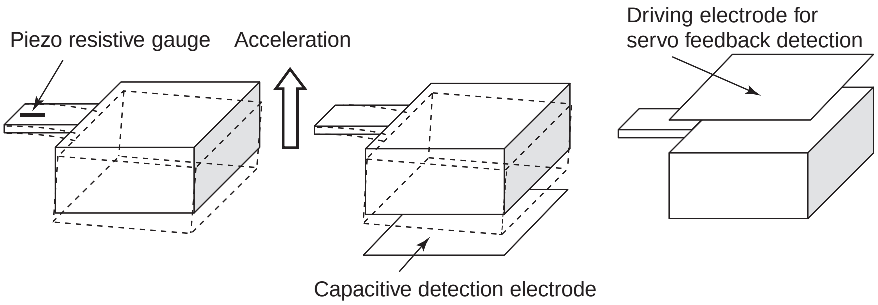
Piezo resistive gauge
Acceleration
Driving electrode for servo feedback detection
Capacitive detection electrode

Figure 2 Micromachined accelerometer.

achieved by feedback measurement in which the inertia force is canceled by electrostatic force; the magnitude of the force is proportional to the acceleration.

Another application of MEMS sensors relates to the tracking of rehabilitation progress of stroke patients by monitoring parameters such as range of motion. A useful description of the most common mistakes that may occur when such measurements are included in remote tele-rehabilitation regimes is provided in a recent article on the subject (KarchĖáka *et al.*, 2014).

Printers

The ink jet printer head is another example of successful MEMS products. Micro nozzles and channels of 10 – 20 μm in size are micromachined in an array. A microheater is attached to each channel. The heater generates a bubble in the channel when a current pulse flows through it. An ink droplet is ejected from the nozzle by the pressure pulse caused by the bubble. The amount of the droplet is in the order of a few pL now. A typical head has hundreds of nozzles and channels which operate as fast as 10 kHz. This device takes the advantage of the scaling effect, that is, the speed of heating and cooling increases with decrease in size. Thus, fine pictures and documents are printed on paper. Some heads use piezoactuators and electrostatic actuators to eject ink droplets.

Optical Devices

MEMS is very suitable to optical applications. Light beams can be controlled easily by moving mirrors, shutters, or gratings. MEMS with small feature sizes, precise motion, and arraying capability can realize wide varieties of micro optical MEMS devices and systems based on interference, diffraction and refraction. MEMS technology also enables precisely aligned integration of active and passive optical devices, micromechanical elements and optical fibers. Therefore, optical MEMS devices and systems are used for optical scanners, micro-optical benches, arrayed micromirror displays, optical switches, modulators and attenuators.

The most successful example is a display. An array of movable micromirrors corresponding to pixels reflects light and projects an image on the screen. Each mirror is randomly accessible and tilted either ±10° by electrostatic force. The pixel becomes bright or dark depending on the angle of the mirror. The mirror moves within 0.1 ms and controls the brightness by pulse-width-modulation of reflected light. The array is micromachined on top of the IC which allow the individual control of many mirrors within a short time.

MEMS based optical switches have been intensively studied. Optical switches, by means of mechanical movement, have favorable characteristics such as wave-length independence, polarization independence, large contrast, and small crosstalk. 2D MEMS optical switches change the optical path either straight or to a predetermined angle and connect it to one of the two output paths. The typical configuration of an N port 2D MEMS optical switch is shown in Figure 3. Light beams from input optical fibers are collimated by lenses. Micromirrors are inserted at appropriate positions to reflect beams and connect them to the output optical fibers. The alignment between fibers and mirrors is precisely determined by micromachined structures. Arrayed movable mirrors of several hundreds of micrometers in size are driven by microactuators. An on-off motion of the N^2 mirrors is necessary in the switch. The port count, N, is from 2 to 32. For port counts as large as a few hundreds, 3D MEMS switches are used. The schematic configuration is shown in Figure 4. Micromirrors have motion with two degrees of freedom, that is, rotation around two orthogonal axes. Two sets of arrays consisting of N such mirrors are used. Collimated input light beams hit one of the mirrors in the first array that direct the beam to one of the mirrors in the second array. The second mirror reflects the light straight into the output fiber. The

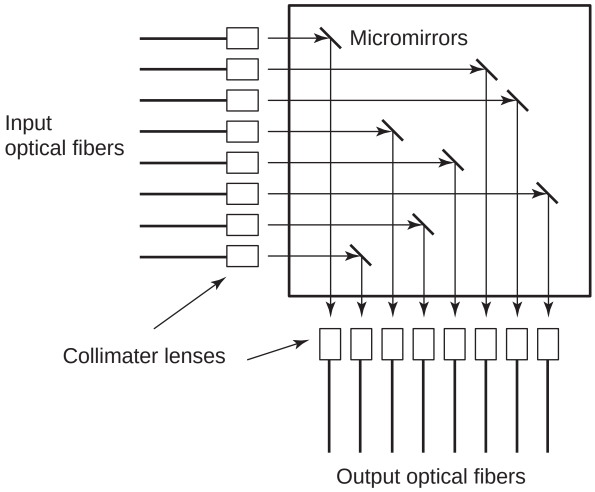

Figure 3 Principle of a 2D MEMS optical switch. Each micromirror is individually driven by a microactuator in the on-off fashion.

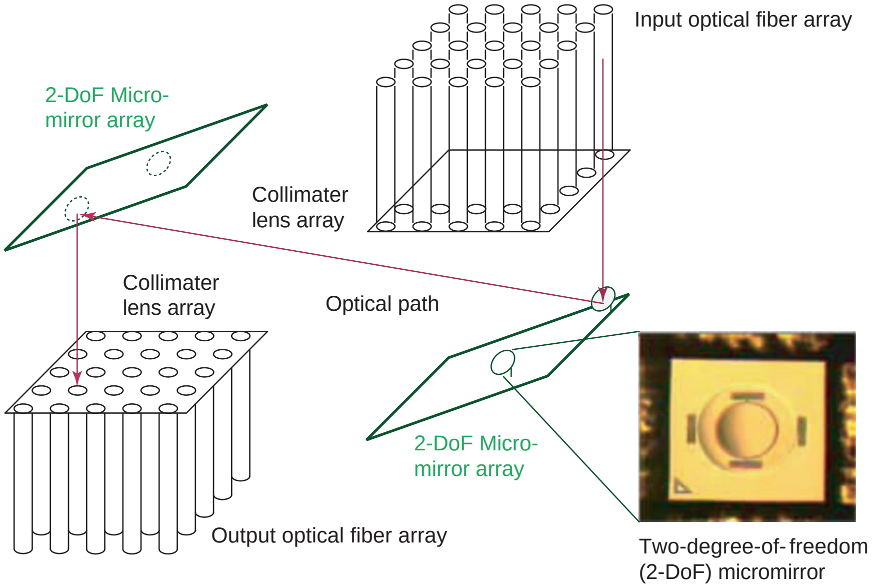
Input optical fiber array
2-DoF Micro-
mirror array
Collimater
lens array
Collimater
lens array
Optical path
2-DoF Micro-
mirror array
Output optical fiber array
Two-degree-of- freedom
(2-DoF) micromirror

Figure 4 Principle of 3D MEMS optical switch.

analog control of mirror angles allows cross connection of a large number of signals. Those switches have application to optical cross connects, add-drop switches for wavelength divided multiplexing networks, and back-up or inspection apparatuses.

Optical scanners based on movable MEMS mirrors have many applications including bar-code readers, laser range finders, scanning laser microscopes, variable optical attenuators, and laser projection display. Some of them are already introduced in the market.

Chemistry and Biomedical Applications

Handling fluid in micromachined channels offers benefits in chemistry and biotechnology because of the scaling effect. The chemical reaction is completed within a few seconds due to short diffusion time in micro-channels and reactors. Fast and precise temperature control is possible. Arrayed channels allow simultaneous chemical processing of a large variety of reactions. Only a small amount of samples or chemicals are required for chemical analysis and medical diagnosis. Even individual handling and observation of a cell or a molecule has been accomplished.

A typical microchemical chip is composed of one layer having grooves of 10 – 100 μm in dimension and another layer for sealing and connection to external pipes. Fluids flow in the channel to be mixed, heated, reacted, extracted, separated, and analyzed. Glass and PDMS (poly di-methyl siloxane) are two favored materials for the chip. Applications of microchemical chips include DNA analysis and amplification, blood analysis, environmental monitoring, combinatorial chemical synthesis, bioreactors and sensors, and production of fine chemicals.

The most successful product is the DNA electrophoresis in the micro channel. The device has two orthogonal channels (Figure 5). The sample solution containing DNA that is labeled by a fluorescent dye is introduced in the shorter channel by electro-osmotic effect. A small amount of the sample is injected into the long separation channel by introducing a buffer solution

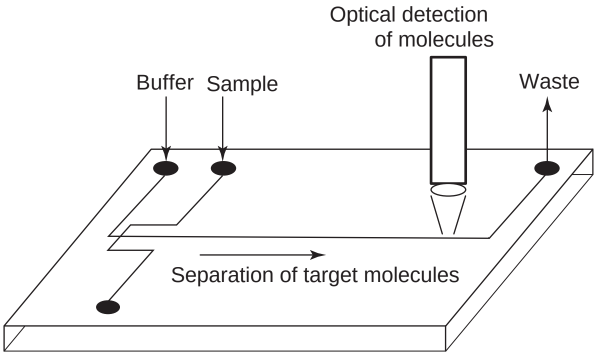
Optical detection
of molecules
Buffer
Sample
Waste
Separation of target molecules

Figure 5 Principle of a chemical analysis chip based on capillary electrophoresis.

from the end of the other channel. DNA fragments are driven by an electric field in the channel and separated due to the difference in migration speed depending on their length. Separation is completed within seconds and detected by fluorescence.

Future Development of MEMS

The future prospects of MEMS for making contributions to the future society are envisaged in three areas: (1) offering easier access to information for a wider public, (2) making human lifestyles more compatible with the environment, and (3) improving people's social welfare.

Breakthroughs to be accomplished by MEMS would be in five general areas: machine intelligence, downsizing and parallelism, biomimetics, informatics, and environment monitoring/preservation. Downsizing and parallelism will be the direct benefit from miniaturization and multiplicity. Machine intelligence and information networks can be very much improved by introducing MEMS integrated with microelectronics. These breakthroughs are likely to be realized by MEMS technologies within ten years. They may, for example, be used in healthcare for minimally invasive diagnosis and treatment.

References

Chavoshi SZ and Luo X (2015) Hybrid micro-machining processes: A review. *Precision Engineering* 41: 1–23.
KarchĖáka J, Šimšíka D, Jobbágya B, Galajdováa A, and Onofrejováb D (2014) MEMS sensors in evaluation of human biomechanical parameters. *Procedia Engineering* 96: 209–214.
Lauwers B, Klocke F, Klink A, et al. (2014) Hybrid processes in manufacturing. *CIRP Annals – Manufacturing Technology* 63: 561–583.
Mamilla VR and Chakradhar KS (2014) Micro machining for micro electro mechanical systems (MEMS). *Procedia Materials Science* 6: 1170–1177.

Further Reading

Elwenspoek M and Wiegerink R (2001) *Mechanical Microsensors*. Berlin: Springer.
Fujita H (2003) *Micromachines as Tools for Nanotechnology*. Berlin: Springer.
Kensall DW (1998) Special issue on integrated sensors, microactuators, and microsystems (MEMS). *Proceedings of the IEEE* 86(8): 1531–1787. August 21.
Nam-Trung N and Steven TW (2002) *Fundamentals and Applications of Microfluidics*. Boston, MA: Artech House Publishers.
Petersen KE (1982) Silicon as a mechanical material. *Proceedings of the IEEE* 70: 420.
Rai-Choudhury P (1997) *Handbook of Microlithography, Micromachining and Microfabrication*. vol. 2. Bellingham, WA: SPIE Optical Engineering Press.
Senturia SD (2001) *Microsystem Design*. Boston, MA: Kluwer Academic.

Alloys: Overview

Federico Scaglione and Marcello Baricco, Department of Chemistry and NIS-INSTM, University of Turin, Turin, Italy

© 2024 Elsevier Ltd. All rights reserved.

This is an update of M. Baricco, Alloys: Overview, Editor(s): Franco Bassani, Gerald L. Liedl, Peter Wyder, Encyclopedia of Condensed Matter Physics, Elsevier, 2005, Pages 57–64, ISBN 9780123694010, https://doi.org/10.1016/B0-12-369401-9/00531-3.

Introduction **511**
Crystal structures in metals and alloys **512**
Chemical bonds and crystal structures 512
Solid solutions 512
Intermediate phases 512
Phase stability and transformations in metallic alloys **512**
Thermodynamics and kinetics of phase transformations 512
Free energy and phase diagrams 513
Microstructure of metallic alloys 515
Properties of metallic alloys **516**
Mechanical properties 516
Electrical and magnetic properties 517
Chemical properties 518
Materials selection 518
Advanced metallic materials **518**
Amorphous alloys 518
Nanoporous gold 519
Conclusion **520**
References **521**

Abstract

The chapter titled *Alloys: overview* summarizes general information on metallic materials available in the market and it adds recent findings in new alloys, with a focus on metallic glasses and nanoporous gold, whose applications are of relevant importance in the recent cutting edge technologies.

Key points

- The structural and functional properties of Metallic Alloys are related to their electronic and crystalline structure, as well as to their microstructure.
- Phase Stability and Transformations in Metallic Alloys is ruled by thermodynamic and kinetic factors. The description of the equilibrium phases is reported at constant pressure as composition–temperature plots, known as phase diagrams.
- Depending on their composition, structure and microstructure, Metallic Alloys cover a wide range of properties. An excursus of the principal ones, i.e. mechanical, electrical, magnetic and chemical, are reported.
- Metallic glasses or amorphous alloys are advanced metallic materials characterized by a short-range order atomic arrangement. Usually obtained by rapid solidification of the liquid, they show increased properties compared with their crystalline counterpart.
- Nanoporous metals are promising materials constituted by a scaffold of metallic ligaments and nano-sized porosities; obtained by dealloying of a crystalline or amorphous precursor and thanks to their intriguing properties, they find applications in many technological fields such as catalysts, electro-catalysts, actuators, heat exchangers, energy storage, Raman and SERS substrates.

Introduction

Metallic alloys belong to a fundamental class of engineering materials, with structural and functional properties related to their electronic and crystalline structure, as well as to the microstructure. While structural properties have been usually associated to conventional metallurgy processes, functional properties take part when the alloy microstructure is properly tailored in a micro or nanoscale. In this article, the fundamental aspects of metallic alloys are described and recent findings in the fields of amorphous alloys and nanoporous gold, that might significantly contribute to the cutting edge technologies, are also reported.

Crystal structures in metals and alloys

Chemical bonds and crystal structures

The crystal structure, the chemistry of constituent atoms and the nature of the chemical bonds determine the properties of materials (Christian, 2002). In metals and alloys, atoms are linked by metallic bonds where valence electrons are delocalized over the whole crystal, even if some contributions from covalent and ionic bonds may be observed in special cases. Alkali metals are purely metallic bonded, whereas metals close to metalloids, such as zinc, have increasing covalent bond contributions.

The structure of metals may be described in terms of hard-sphere packing, where non-interpenetrating equal spheres are interconnected to fill the volume as much as possible. Considering a simple layered structure of spheres, hexagonal close-packed (h.c.p.) and face-centered cubic (f.c.c.) crystal structures may be easily built up. On the other hand, considering a slightly lower packing factor, a body-centered cubic (b.c.c.) structure is formed. Furthermore, the allotropy in the metal structure might occur on heating, as observed in iron, which shows a transition from b.c.c. to f.c.c. at 910 °C and a further transition from f.c.c. to b.c.c. at 1400 °C before melting at 1539 °C.

In metallic alloys, the constituent elements may be simply mixed in a solid solution or may form an intermediate phase. In the case of alloys, the difference in electronegativity between constituent atoms becomes the main factor in defining the nature of the chemical bond. In the case of a high difference in electronegativity, an ionic contribution to the chemical bond may be observed. As a consequence, rather complicated crystal structures may be formed. Crystallographic parameters relative to various alloys are available in structural databases.

Solid solutions

Solid solutions may be distinguished as substitutional, when the volume of constituent elements is similar, and interstitial, when a volume difference (size factor) higher than $\sim 15\%$ is observed. A typical example of substitutional solid solution of Zn in Cu is observed in brass, whereas an interstitial solid solution of C in f.c.c. Fe is observed in austenite. Complete solid solubility may be obtained only in alloys when components have the same crystal structure, and the size factor is lower than $\sim 8\%$. Au–Ni and Ag–Au–Pt are examples of systems showing complete solid solubility.

Sometimes the distribution of atoms in a solid solution deviate from randomness. When similar atoms group themselves preferentially, a clustering effect is observed. On the other hand, when an atom is preferentially surrounded by different atoms, the solid solution is said to show a short-range ordering.

Intermediate phases

When the limit of solid solubility is exceeded on alloying, a second phase is formed. It may be the primary solid solution of the alloying elements, such as in simple eutectic systems, but more often it appears as an intermediate phase. When only metallic components are present in the system, the intermediate phase is called an intermetallic compound.

The simplest intermediate phase is due to long-range ordering of components in the solid solution (ordered phases). In this case, crystallographic positions are preferentially occupied by a specific element, so that an ordering parameter may be defined. Different sub-lattices constituted by single components may be defined in the structure, as evidenced by diffraction techniques. The ordering parameter changes continuously in a limited temperature range, following a second-order thermodynamic transition. Ordering of phases is effective in improving mechanical properties and it is fundamental in superalloys.

When the atoms constituting the intermediate phase show a particular value of the valency electron concentration (e/a), electron phases are formed. For instance, *50%* of Zn atoms in a Cu matrix give an electron concentration of 1.50, where a b.c.c. β-phase appears. In the same Cu-Zn system, the complex cubic γ-phase and h.c.p. ε-phase are formed for electron concentrations equal to 1.62 and 1.75, respectively. The formation of electron phases is based on the empirical Hume–Rothery's observations, later explained in terms of density of states for valency electrons. Electron phases show a metallic behavior and exist over a range of compositions, such as in brasses and bronzes.

When the intermetallic phase contains a large number of vacant lattice sites, a defect phase may be formed in a limited composition range. Very common intermetallic compounds are known as Laves phases, where the radii of components have the ratio $r_A/r_B = 1.225$, so that a very high packing density is achieved. The interaction of transition metals (M) with small nonmetallic elements (X) generally leads to the formation of interstitial compounds, such as hydrides, borides, nitrides, and carbides. If the ratio between atomic radii r_X/r_M is lower than 0.59, simple compound structures are obtained, where the transition metal forms an f.c.c. or h.c.p. lattice.

In recent years, rather complex intermediate phases have been continuously discovered. Frank–Kasper phases show a huge number of atoms in the unary cell. Quasicrystalline phases show a fivefold symmetry, which was considered forbidden according to the classical crystallographic rules.

Phase stability and transformations in metallic alloys

Thermodynamics and kinetics of phase transformations

Phase stabilities and transformations in metallic alloys are ruled by thermodynamic and kinetic factors. As schematically shown in Fig. 1, in order to transform a phase (a) into a phase (b), a gain in free energy is necessary (Bassani et al., 2005). This free energy

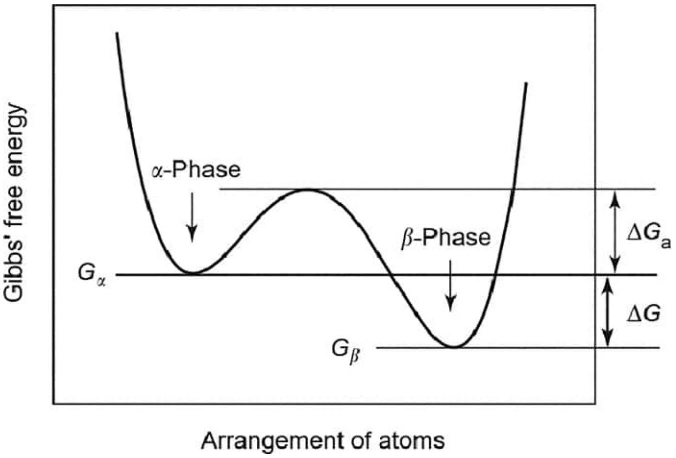

Fig. 1 Free energy as a function of the arrangement of atoms in a phase transformation. Reproduced with permission from Bassani, F., Liedl, G. L. and Wyder, P. (eds) (2005) *Encyclopedia* 1st ed., p. 59.

difference $\triangle G = G\text{-}G$ represents the driving force for the phase transformation. The phase transformation becomes possible if the activation barrier $\triangle G_a$ is overcome and the new phase is formed at a reasonable rate.

The kinetics of a phase transformation is strongly related to the mechanism. In fact, when the crystallography and/or the chemical composition of the two phases are significantly different, a reconstructive transformation occurs, and a motion of single atoms is necessary. The whole kinetics of phase transformation may be controlled either by the diffusivity or by interface migration. A typical example is given by perlite formation in eutectoidic steels. On the contrary, a cooperative movement of neighboring atoms occurs in displacive transformations, which are diffusionless and generally very fast, because no activation barrier is present. The formation of martensite in steel by quenching represents an example of such a kind of phase transformation.

The kinetics of phase transformation in metallic alloys is often described in terms of time–temperature–transformation curves (TTT), which are a graphical representation of the time necessary to start and to complete isothermally the phase transformation in a specific temperature range. In the case of cooling treatments, continuous-cooling-transformation curves (CCT) are more appropriate. In order to draw thermal treatments in steels, databases of TTT and CCT diagrams are available. The kinetics of phase transformations may be described in terms of the Avrami equation $y = 1 - e^{(-kt)^m}$, where y is the transformed fraction, t is the time, k is a temperature-dependent rate constant, and m is an empirical parameter ranging from 0.5 up to 4, which depends on the type of transformation.

Free energy and phase diagrams

The free energy of a phase depends on several factors, such as composition, temperature, pressure, strain, surfaces, and interfacial energy. In order to define the equilibrium conditions for a generic multicomponent system, the free energy of all phases must be known as a function of composition, temperature, and pressure. The thermodynamic equilibrium is reached when the chemical potential of all elements is the same in all phases (common tangent rule). The number of equilibrium phases is defined by the well-known Gibbs' phase rule and the amount of each phase can be calculated according to the lever rule. The description of the equilibrium phases is generally reported at constant pressure as composition–temperature plots, known as phase diagrams.

In the case of a simple binary metallic system, the equilibrium thermodynamics may be estimated by means of suitable models. For instance, the regular solution model considers only solution phases, where the free energy is described by means of an ideal entropy term and a temperature-independent term for the enthalpy of mixing. This term considers the chemical interactions between the constituent elements, and it turns out positive in the case of repulsion and negative in the case of attraction. When the enthalpy of mixing becomes zero, the solution is ideal. On the basis of the regular solution model, several binary phase diagrams may be calculated, giving solubility or immiscibility either in the liquid or in the solid phases. Examples of phase diagrams calculated with the regular solution model are reported in Fig. 2.

As an example, a full miscibility for the liquid and solid phases is shown in Cu–Ni, simple eutectics are observed in Cu–Ag and in Al–Si, and a single peritectic is observed in Ag–Pt. Intermediate phases are shown in the phase diagrams as single lines (line compounds) or as compounds with limited solubility, such as in bronze and brass.

The equilibrium conditions for a ternary system may be represented by the Gibbs' triangle, where isothermal sections of the phase diagrams are reported as a function of the composition of components. The method for plotting compositions in a ternary phase diagram is shown in Fig. 3. For multicomponent systems, only sections of the phase diagram are usually reported (pseudo-binary phase diagrams). Phase diagrams are generally determined experimentally. Physical properties of alloys with different compositions are followed as a function of temperature, giving an experimental evidence of transition temperatures and equilibrium points. Calorimetric techniques are used for the determination of thermophysical quantities.

Modern computing techniques allow the description of the thermodynamics of multicomponent systems of industrial interest. For instance, by means of the CALPHAD (CALculation of PHAse Diagrams) method, the free energy of all phases is described as a

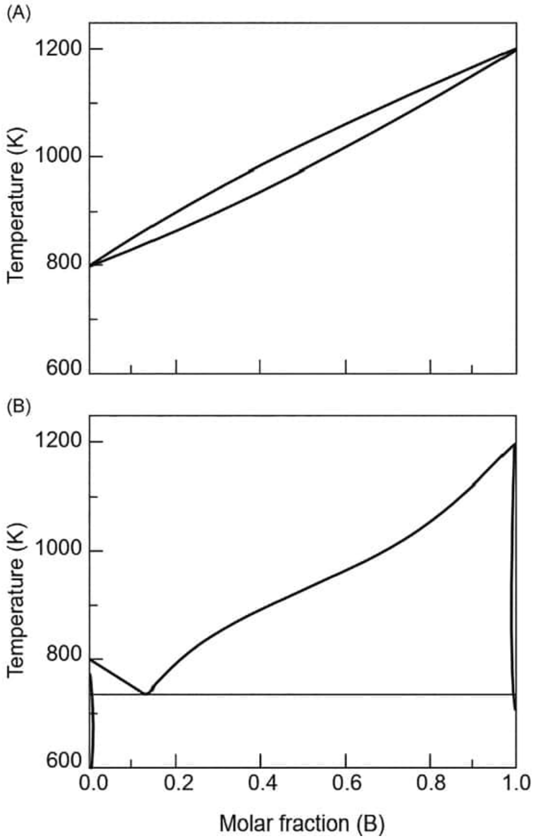

Fig. 2 Examples of binary phase diagrams calculated according to the regular solution model. (a) Ideal solution; (b) Interaction parameter equal to 10^4 J mol^{-1} and 3×10^4 J mol^{-1} for the liquid and solid phases, respectively. An entropy of melting of 10 J mol^{-1} K^{-1} has been considered for both pure elements. Reproduced with permission from Bassani, F., Liedl, G. L. and Wyder, P. (eds) (2005) *Encyclopedia*, 1st ed., p. 60.

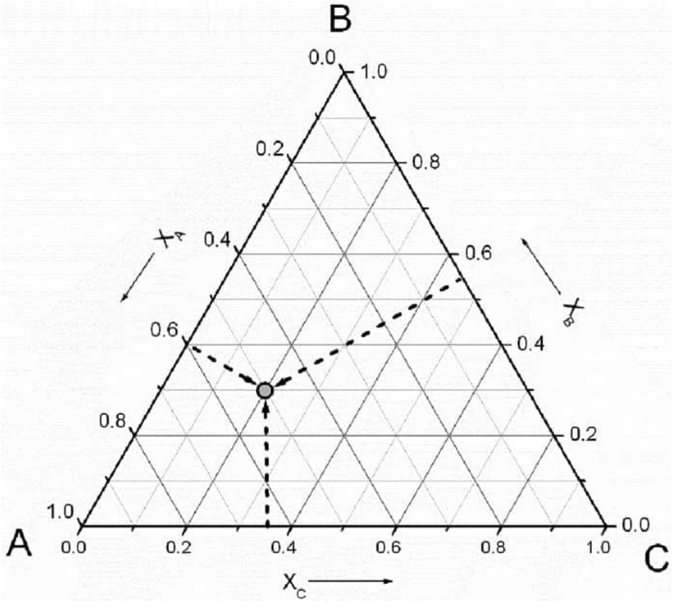

Fig. 3 Representation of compositions for ternary alloys. The vertices represent 100% of A, B, or C. The binary systems are represented in the boundaries of the triangle. Ternary alloys are reported in the middle of the triangle. The distances of the points from the boundaries represent the relative proportions of the components indicated in the opposite vertex of the triangle. The point indicated in the figure indicates the composition with 20% of C, 50% of A, and 30% of B. Reproduced with permission from Bassani, F., Liedl, G. L. and Wyder, P. (eds) (2005) *Encyclopedia*, 1st ed., p. 60.

function of temperature and composition through parameters obtained by an assessment of experimental data and *ab-initio* calculations (Saunders and Miodownik, 1998). Databases of parameters are available for metallic alloys of industrial interest, allowing the calculation of equilibrium conditions, phase diagrams, and thermodynamic quantities.

Microstructure of metallic alloys

Properties of metallic alloys are often related to the microstructure, which depends on phase transformations and mechanical treatments involved in the processing (Davis, 1998; Haasen, 1996). Examples of microstructures are shown in Fig. 4.

Reconstructive phase transformations usually proceed by nucleation and growth mechanisms. In the case of a single phase, the grain size determines the grain boundary area, which affects the strength through the Hall–Petch relationship. Grain size is ruled by solidification rate, plastic deformation, and recrystallization treatments. Eutectic and eutectoid transformations give a lamellar microstructure. The significant composition difference between the parent and the product phases needs atomic diffusion, so the interlamellar spacing is related to the temperature of the phase transformation. As an example, the temperature of thermal treatments in steels defines the final microstructure, ranging from coarse perlite to fine bainite. Similar fine microstructures may be also obtained by tempering of martensite, previously obtained by quenching. For light alloys, precipitation hardening is related

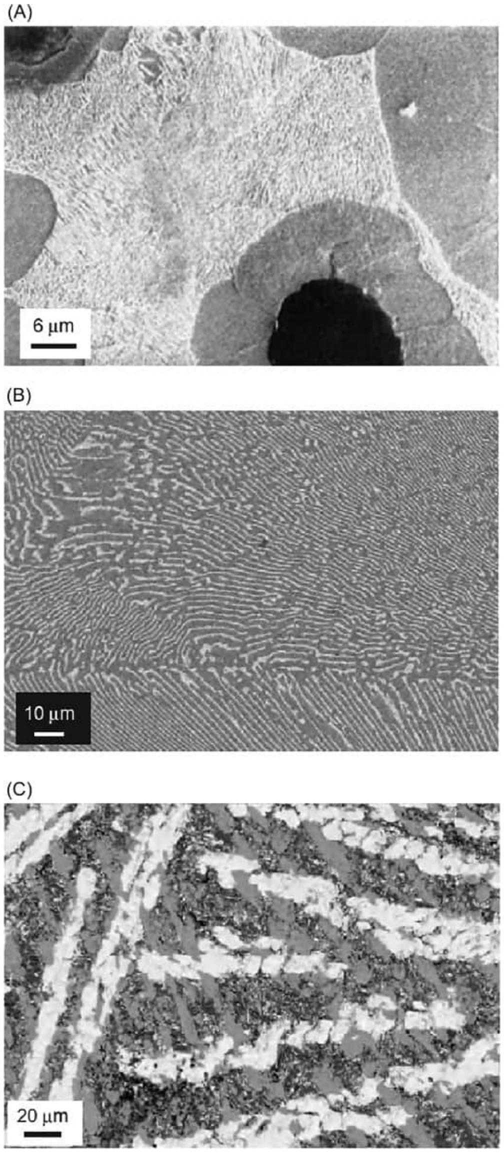

Fig. 4 Examples of microstructures. (a) Microstructure in spheroidal cast iron: black zone is the nodular graphite, surrounding gray area is ferrite, and the light area is perlite. (b) Microstructure in eutectic $Pb_{26}Sn_{74}$: white areas are Pb-rich solid solution and dark areas are the Sn-rich solid solution. (c) Microstructure in as-cast $Al_{87}Ni_7Ce_6$: white area is $Al_{11}Ce_3$; gray area is Al_3Ni; dark area is f.c.c. Al. (Courtesy of Rizzi P, University of Torino, Italy.) Reproduced with permission from Bassani, F., Liedl, G. L. and Wyder, P. (eds) (2005) *Encyclopedia*, 1st ed., p. 61.

to the microstructure. Metastable phases with interfaces coherent to the matrix may be produced by suitable aging treatments of supersaturated solid solutions obtained by quenching. Similar microstructural effects are observed in spinodal decompositions, where composition fluctuations occur up to the gradient of concentration (uphill diffusion). In recent years, very fine microstructures may be obtained by suitable processing, giving nanostructured alloys. As an example, ball milling of metallic powders, electrodeposition or severe plastic deformation of ingots, may give a grain size down to few tenths of nanometers, leading to improved properties with respect to coarse-grain materials.

Properties of metallic alloys

Mechanical properties

Synthesis and processing of metallic alloys is mainly aimed at mechanical applications. In fact, metallic materials show a very broad range of mechanical properties, which may be often modified by suitable thermomechanical treatments. Basic mechanical properties of metallic alloys are generally determined by standard tensile tests, leading to the classical stress–strain curves shown in Fig. 5.

Elastic properties are obtained from the elastic range of a tensile test, and they are mainly related to the composition of metallic alloys. The Young modulus (E) of alloys ranges from ~40 GPa for Mg-based compositions up to more than 400 GPa for W and Os. The Young modulus for Al-based alloys is ~70 GPa, for Cu based and Ti-based alloys is ~100 GPa, and for ferrous alloys is ~200 GPa. Metallic alloys have a shear modulus (G) ~3/8 of E and a Poisson ratio (ν) of 0.33. After thermomechanical treatments and changes of the microstructure, the elastic properties remain rather constant, so that they may be considered an intrinsic property of the alloys. The Young modulus of metallic alloys generally decreases as a function of temperature $\left(\frac{dE}{dT} < 0\right)$.

The strength and elongation properties may be obtained from the plastic range of the stress–strain curve. The yield stress σ_y represents the transition from the elastic to the plastic regime. It depends on the dislocations mobility, so it can be significantly modified by thermomechanical treatments. The strengthening mechanisms in metallic alloys are related to the hindering of dislocation movements. This goal may be obtained by alloying, because the presence of alloying atoms may generate a stress field. In work-hardening processes, the presence of a high dislocation density leads to an entanglement between crossing dislocations. For precipitation-hardening, widely used in light alloys, the presence of precipitates with interfaces coherent with the matrix produces efficient stress fields against dislocation movements. With the reduction of the grain size, a dislocation pile-up occurs at the grain boundaries and a strengthening in the alloy is observed. For superalloys, a precipitation of the ordered phase may be induced in the disordered matrix, so that dislocations may be blocked at the antiphase boundaries.

Often the yielding point cannot be identified easily, so the stress corresponding to a plastic deformation of 0.2% ($\sigma_{0.2\%y}$) is considered. In the case of annealed low-carbon steels, a nonuniform yield phenomenon may be observed, with the resulting production of Luder's lines at the surface. In this case, an upper-(σ_{uy}) and a lower-(σ_{ly}) yield stress are identified. As long as a uniform plastic deformation acts in the metallic alloys, a hardening effect is observed, according to the general equation $\sigma = Ke^n$ where σ is the true stress, ε is the true strain, K is the strength coefficient, and n is the strain-hardening exponent. The last parameter measures the tendency of an alloy to be strengthened as a result of plastic deformation. When the plastic deformation becomes nonuniform, a neck begins to form in the test specimen and an apparent maximum is observed in the nominal stress–strain curve. Necking phenomena are very dangerous for metallic alloys aimed at high-plastic deformation, such as in deep-drawing. Certain metallic materials, under special deformation conditions, behave as superplastic alloys, so they resist necking and show uniform elongations up to 1000 times the normal amount.

Fracture in metallic alloys may be ductile or fragile. In ductile fracture, a significant plastic deformation acts before rupture and a characteristic cup–cone fracture is observed at the surface of the test specimen. Brittle fracture is more dangerous because it happens

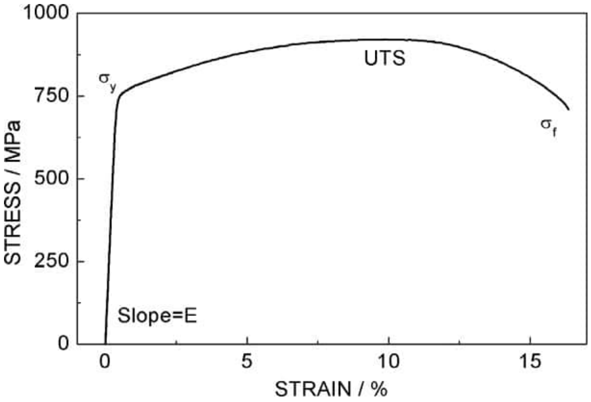

Fig. 5 Example of a stress–strain curve for steel (0.4% C, 4% Cr). Basic mechanical parameters are indicated: E, Young modulus; σ_y, yield stress, UTS, ultimate tensile stress, σ_f, fracture stress. Reproduced with permission from Bassani, F., Liedl, G. L. and Wyder, P. (eds) (2005) *Encyclopedia*, 1st ed., p. 62.

suddenly without prior evident plastic deformation. Fracture may be intergranular, when it follows the grain boundaries, or intragranular, when it crosses the interior of the grains. Fracture by cleavage is often observed instead of by shear. A ductile-to-brittle transition may be observed in a limited temperature range by standard impact tests (Charpy type). For instance, for ferritic steels it occurs below room temperature and may be crucial for low-temperature applications. The tendency for crack propagation is defined by the fracture toughness (Kc). It is obtained from a specific test, where increasing stresses are applied to a pre-cracked specimen. Depending on the mode of loading, different fracture toughness parameters are defined (I, II, and III).

Fracture is generally pictured as consisting of two stages: crack formation and growth. Crack formation may be due to processing or use of the alloy. It generally happens at the surfaces, and it is often related to repeated stresses in the elastic range, a phenomenon known as fatigue. Due to this reason, for metallic alloys it is necessary to define an endurance limit, which is about one half of the tensile strength: below this value, the alloy can withstand an unlimited number of stress cycles without fracture. Unfortunately, some alloys (e.g., Al-based alloys) do not show this limit, so that the fatigue strength must be defined for a given number of cycles.

Hardness of metallic alloys is determined by specific tests, which are based on the resistance to penetration. A commercial hardness tester forces a small sphere, pyramid, or cone into the body of the alloy by means of an applied load. Hardness numbers may be roughly related to tensile strength. When the applied load is small, the hardness may be determined for single phases evidenced in the microstructure of the alloy. For instance, a resolution down to 200 mm may be obtained by the microhardness Vickers test.

For applications at high temperature, the creep phenomena may occur in metallic alloys. They are due to the occurrence of a plastic strain when the alloy is stressed in the elastic regime. Creep is related to dislocations climbing induced by the high temperature. For moderate stresses, grain boundary sliding may even occur, because of atomic diffusion. Creep may be avoided in superalloys, where precipitates of ordered phases hinder the dislocation movements.

Electrical and magnetic properties

Electrical properties of metallic alloys are closely linked to the electronic structure, and the conduction of electrons depends on partially filled bands. According to Mathiessen's rule, the electrical resistivity of alloys increases linearly with temperature near room temperature and above, although the behavior at very low temperature is more complex. Electrical resistivity is strongly enhanced by the presence of foreign atoms in a solid solution in the metal matrix. As an example, the effect of the addition of 0.1 wt% of different atoms in Cu is shown in Fig. 6.

It is clear that the effect is strongly dependent on the electronic configuration of the foreign atom. Oxygen has a very big effect, and, to produce copper wires, oxygen-free material is necessary. Cold rolling increases resistivity only slightly and it is often used as a means for strengthening alloys for electrical conductors. Metallic alloys behave as superconductors only at very low temperatures and they have been fully replaced by high-temperature oxide superconductors for practical applications. Thermoelectric effects of metallic alloys are widely used for devices such as thermocouples, thermoresistors, and Peltier junctions.

The magnetic properties of metallic alloys are of fundamental interest, and they are linked to several industrial applications. The primary applications arise in ferromagnetic alloys, based on Fe, Ni, Co, and some rare-earth metals. On the basis of the values of magnetization induced in the material when subjected to a magnetizing field, represented graphically by the hysteresis loop, ferromagnetic metallic alloys are distinguished in soft and hard magnets.

Soft magnetic alloys are characterized by high magnetic permeability, low coercive field, and low core losses. For these materials, a high saturation magnetization is generally desirable. These materials are suitable for electrical motors, transformers, and relays, because of the fast response of magnetization to the applied magnetic field. In Fe, there is a strong relationship between permeability and crystallographic directions, so that the magnetic flux runs better along the (100) direction (i.e., the edge of the cubic unary cell), giving low-energy losses. For this reason, commercial steel containing 3% Si is processed so that a preferred

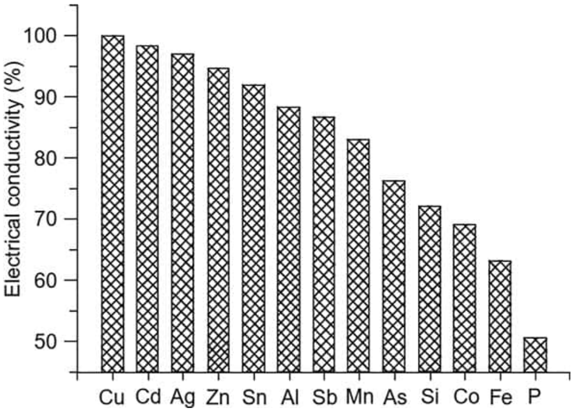

Fig. 6 Effect of the addition of 0.1 wt% of various elements in solid solution on the electrical conductivity of copper. Reproduced with permission from Bassani, F., Liedl, G. L. and Wyder, P. (eds) (2005) *Encyclopedia*, 1st ed., p. 62.

orientation of grains is obtained (Goss texture). Amorphous alloys show still lower power losses, and they find applications in small-sized transformers. Magnetic shields may be obtained using materials with very high magnetic permeability, such as Fe–Ni alloys.

On the contrary, hard magnets have a high coercive field and a high saturation magnetization. A parameter representative of the magnetic energy that can be stored per unit of mass is given by the maximum external energy, $(BH)_{max}$, which is calculated on the demagnetizing portion of the hysteresis loop. These materials are mainly used as permanent magnets, often used to convert electrical energy to mechanical motion (electrical engines) or to convert mechanical motion to electrical energy (microphones). Defects able to hinder the movements of dislocations are usually also able to hinder the movement of magnetic domains, increasing the magnetic hardness of the material. So, high carbon and alloyed steels are often used as permanent magnets. In recent years, new metallic alloys, characterized by a strong magnetic anisotropy in the unary cell, have been developed. These materials contain rare earths as alloying element, such as in $SmCo_5$ and in $Fe_{14}Nd_2B$.

Chemical properties

Metallic alloys are not chemically stable. In fact, metallurgical processes devoted to the production of metals from their oxides are often counter-balanced by corrosion and oxidation, which progressively transform the metallic alloys in more stable compounds. Corrosion is a wet phenomenon, which is possible only in the presence of humidity. The corrosion resistance of metallic alloys is generally related to the properties of parent elements, according to the electromotive series. A control of the microstructure of the alloys may change the mechanism of corrosion, which should not be localized but uniformly distributed on the whole surface. In several cases, the addition of elements prone to passivity (Cr, Al) is used to increase the corrosion resistance of alloys, such as in the case of stainless steel. Corrosion might be also avoided by deposition of thin layers of a metal on the surface of the alloy, such as in zinc coating and tinning of steel. Oxidation is a high-temperature process, due to the reaction of the metallic alloy with the atmosphere. At the very beginning of the reaction, a thin layer of the oxide is formed at the surface. If the volume of the oxide is at least as great as the volume of the metal from which it formed, the oxide is protective, and oxidation proceeds slowly. On the contrary, if the volume of oxide is less than this amount, the layer is not continuous and it is less effective in preventing the access of oxygen to the alloy surface, so that the reaction rate becomes high. Often the simultaneous formation of two or more oxide layers is observed, such as in steel, where a variable amount of FeO, Fe_3O_4, and Fe_2O_3 layers are formed at different temperatures.

Materials selection

For specific applications, it is a combination of material properties (material index) that characterizes the performance. Properties of alloys are available in databases, so that merit indices, combined with Ashby's charts (Ashby, 1992), allow optimization of the material selection process.

Advanced metallic materials

Amorphous alloys

The physical properties of metallic glasses or amorphous alloys are determined by a short-range order atomic arrangement. They are usually obtained by rapid solidification of the liquid, which is usually achieved by a melt-spinning apparatus (Fig. 7(a)). The molten alloy is ejected, by a gas overpressure, from a quartz or boron nitride crucible, onto a copper wheel rotating at high speed. The melting is induced by a water-cooled coil around the crucible. The atmosphere in the chamber can be purged and filled with argon, in order to avoid the oxidations during the melting of the alloy or kept in air, depending on the alloy. The copper wheel rapidly transfers and dissipates the heat of the melt that solidify in a ribbon shape.

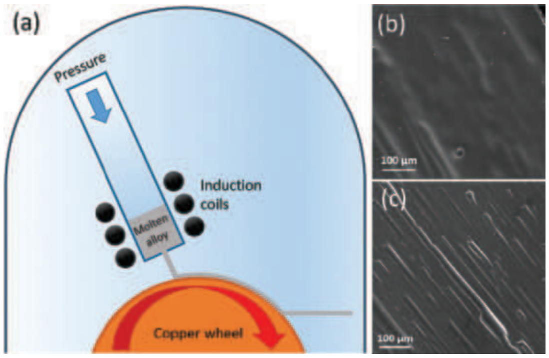

Fig. 7 (a) Scheme of a melt spinning apparatus. SE-SEM images of an Au-based melt-spun ribbon: (b) details of the air-side, (c) details of the wheel-side.

Process parameters affect the dimension of the ribbon: the size of the crucible nozzle determines the width of the ribbon, the speed of the wheel the thickness (i.e., the higher is the rate, the thinner is the ribbon) and the quantity of the molten alloy the lengths. The speed of the wheel is between 10 and 60 m/s and resulting in a cooling rate of 10^4–10^6 K/s. A melt-spun ribbon is characterized by a different finishing on the two sides: the surface that solidifies in contact with the atmosphere of the apparatus (named air-side) is usually wave and shiny, while the side that solidifies in contact with the copper wheel (named wheel-side) is dull and signed by longitudinal roughness due to the surface irregularities of the wheel and cavities when gas bubbles remain trapped during the quenching procedure (Fig. 7(b) and (c)).

During the rapid quenching of the melt, the competition between thermodynamics and kinetics of crystallization forces the system to avoid nucleation. In fact, below the liquidus equilibrium temperature, thermodynamics expects a lower free energy for the crystalline state, involving the movements of atoms into an ordered configuration. As the liquid is cooled down, an increasing of the melt viscosity and a decreasing of atoms mobility occur on undercooling, avoiding nucleation of crystals and promoting glass formation. Since faster is the cooling of the glass, the lower is its density, the melt-spinning process is a key step for metallic glass synthesis. Not all systems are good glass formers and not all compositions are suitable to solidify in the amorphous state. As described empirically by Inoue (Inoue, 2015a,b), multi-element alloys with negative heats of mixing, low temperature of melting from deep eutectics of the binaries, significant difference in atomic size (over ~12%) among constituents define the rules of thumb to obtain a metallic glass.

The easiness of a system to solidify in the amorphous state is generally defined as glass forming ability (GFA), and a criterion for its evaluation was proposed by Turnbull in the early 1980s (Wang et al., 2004) by the definition of the reduced glass transition temperature $T_{rg} = \frac{T_g}{T_m}$, where T_g is the glass transition temperature and T_m is the melting temperature of the alloy: if T_{rg} is greater than *2/3*, the alloys have a very slow nucleation and growth kinetics and can be undercooled down to T_g even at low speeds, obtaining a metallic glass. In some cases, a bulk metallic glass can be obtained, i.e., with a thickness of the amorphous material in a certain extent, i.e., from few millimeters to more than one centimeter. A high GFA is linked to a low critical cooling rate, and to a high thickness of the obtained glass.

The history of metallic glasses starts in the 60s of the last century but it still going on. The first metallic glass was synthesized in 1969 by Duwez et al. (Wang et al., 2004; Klement et al., 1960) by quenching an Au-Si molten alloy at very high rates of 10^5–10^6 K/s.

A huge number of alloy systems are able to solidify in the glassy state, named accordingly with the element that is in the major content. Formation and characterization of various Zr, La, Mg and Pd based metallic glasses have been reported and efforts are on-going to develop several amorphous systems based on transition metals and rare-earths. Technological importance of metallic glasses covers different field from aerospace to magnetic application, from corrosion resistance to biomedical, from jewelry to sport equipment (Davidson et al., 2013; Hofmann and Roberts, 2015; Khan et al., 2018; Fan et al., 2019; Greer, 2014). For instance, among the zirconium glassy alloys, the first to be marketed under the name of Vitreloy-1 was the quinary alloy $Zr_{41.2}Ti_{13.8}Cu_{12.5}Ni_{10}Be_{22.5}$, developed at Caltech. Exploiting the excellent mechanical properties, this alloy was applied for the production of golf and baseball clubs (Telford, 2004).

Au-based amorphous alloys have been explored firstly with the intent of finding new alloys for jewelry application due to the bright surface finishing. The Au-Si system is characterized by a deep eutectic and represents the base for all later Au-based metallic glasses. Remaining on this specific system, such composition has been then modified by adding a third element with different atomic size and crystalline symmetry, with the effect of reducing the melting temperature (Vega and Newman, 2014) and facilitating the glass formation. Increasing the complexity of the alloy, the Au-Cu-Si system has been widely explored to prepare amorphous alloys (Chao et al., 2017; Xu et al., 2018). Moving from the ternary to the quaternary system by adding Ti, the glass forming ability is further increased due to the strong negative heat of mixing with Si and Au. After rapid solidification, the resulting material may be not constituted by a fully homogeneous phase (Fiore et al., 2009; Fiore and Battezzati, 2008) and the matrix may contain quenched-in $Cu_{15}Si_4$ crystals (Scaglione et al., 2010). Literature (Schroers et al., 2005) reports a series of compositions with high glass forming ability (maximum sample thickness between 2 and 5 mm) with good processability, high hardness and a gold content of 49 at. %, hallmarked as 18 k gold alloys. The combination of these properties makes the alloys attractive for many electronic, medical and dental applications, as well as for surface coating. In 2009, quinary elements Au-based alloys with low Au concentration ($35 \leq x \leq 50\%$ at. Au) (Guo et al., 2009) were prepared with the aim of exploring the GFA of materials. Among them, $Au_{40}Cu_{28}Pd_5Ag_7Si_{20}$ was the one with the best GFA. This composition was further modified by decreasing the amount of gold of 10 and 20 atomic percent and increasing the copper of the same amount (Scaglione et al., 2015b; Xue et al., 2017), obtaining fully amorphous ribbons.

Nanoporous gold

Nanoporous metals are promising materials constituted by a scaffold of metallic ligaments and porosities ranging from nano-size to hundreds of microns. Among them, nanoporous gold (NPG) is certainly one of the most studied. Au-based amorphous alloys have been applied as precursors to synthesize, by selective etching, NPG. Dealloying is the route to obtain such a material. It can be chemical, when driven by the dissolution of the less noble element in a basic or acid solution according to standard potential of elements, or can be electrochemical, when the process is assisted by an applied external potential. During dealloying, the less-noble elements are oxidized as ions in the electrolyte, while the noble ones reorganize, by surface diffusion, in a porous structure made up of interconnected ligaments and porosities. The Fig. 8(a) shows a typical morphology of a sample after dealloying an Au-based amorphous ribbon. Fig. 8(b) reports the cross-section view of the ribbon, after dealloying. The line in the middle has been originated by the process occurred from the external surfaces to the inner of the ribbon when the two dealloying fronts are in touch.

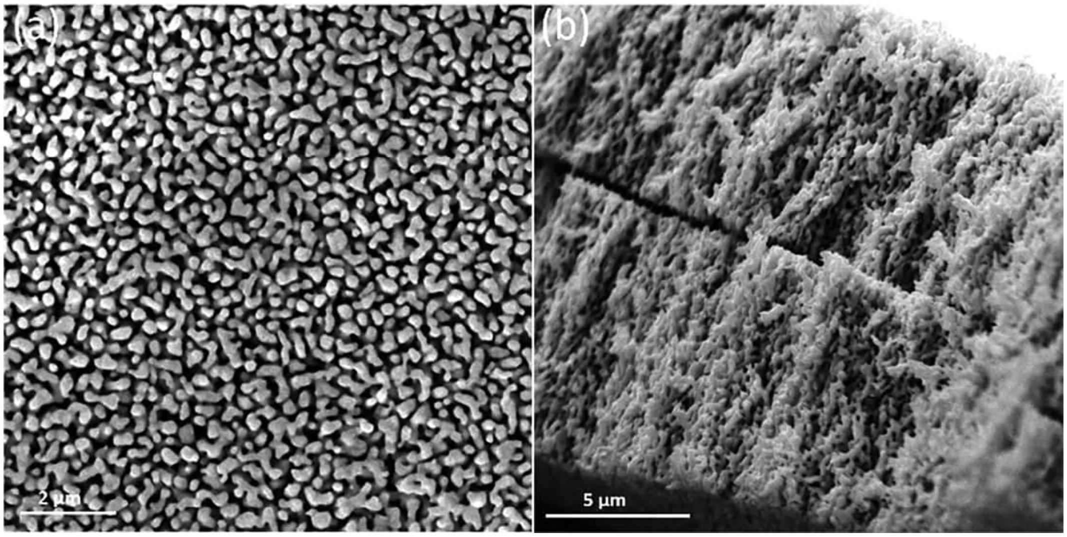

Fig. 8 SE-SEM image of a NPGs by de-alloying an Au based amorphous precursors; (a) top view, (b) cross-section view.

The first NPGs were achieved by dealloying simple binary systems, i.e., Au-Cu (Morrish et al., 2011), Au-Ag (Erlebacher et al., 2001). Aiming to define the basic concept of dealloying, the role of the composition, the critical potential and mechanism associated with the formation of a porous structure have been outlined. In particular, the concept of parting limit considers that the dealloying process is a combined mechanism of dissolution of the less noble elements and surface diffusion of the noble ones. The extent of the porosities inside the bulk of the alloy is limited by the percolation of the electrolyte inside the interconnected pores formed after the oxidation of less noble components in solution. If the less noble components exceed a certain limit concentration, called parting limit, the mechanism proceed gradually in the inner part of the alloy until the sample is fully nanostructured; vice versa below this threshold value, the noble metal is in excess and tends to passivate the surface and dealloying is stopped at the surface sample. For Au-Ag and Au-Cu alloys the parting limit has been evaluated in ~45 at. % Au (55 at. % Cu or Ag) and it was shown that this value was close to the percolation threshold for the lattice.

A further step was moving from dealloying amorphous alloys toward to two-component solid solutions, multi-component crystalline alloys, Ag-Au-Pt (Vega and Newman, 2014), Au-Cu-Mn-Zn (Scaglione et al., 2015a), or intermetallic compounds embedded in a solid solution, aimed to achieve a bimodal distribution of ligaments and pores (Zhang et al., 2009; Vukmirovic et al., 2002). Dealloying a crystalline alloy, the original grain is retained in terms of shape and orientation (Van Petegem et al., 2009); while the less noble elements are dissolved in a proper etching solution, the noble constituents, in each grain, reorganize in a structure formed by a network of ligaments of the remaining element. Associated to the dissolution of the less noble components in the alloy, the surface diffusion of the nobler element rules the mechanism of dealloying.

Recently, the advantages to prepare nanoporous metals from amorphous precursors, whose composition conform with the requirements related to the parting limit for dealloying, have been dealt in terms of mechanism of dealloying, morphology of samples and increasing properties compared to crystalline counterparts (Scaglione et al., 2015a). Enhances properties have been ascribed to trapped elements and the rough morphology of ligaments. Indeed, the dealloying of an amorphous precursor together with the dissolution of the less noble element and surface diffusion of gold adatoms involve the nucleation and growth of new crystals that are going to impinge forming multi-grained ligaments.

The scientific interest in these materials has rapidly increased in the recent decades, thanks not only to the versatile sizing of ligaments and pores (Xue et al., 2018) but also due to their intriguing properties addressed to potential applications in many technological fields. Literature reports NPG as a catalyst, electro-catalysts, actuators, heat exchangers, energy storage, Raman and SERS substrates. Such morphology, has been demonstrated, increases the electrocatalytic activities toward several reactions (i.e., hydrogen evolution reaction (Scaglione et al., 2018), methanol electro-oxidation (Xue et al., 2019a; Paschalidou et al., 2016)) and enhance Surface Enhanced Raman Spectroscopy (SERS) performances of substrates prepared with this material, achieving low detection limits of analyte with probe molecules (Xue et al., 2016). Furthermore, this versatile material lends well itself to be functionalized and applied as a platform for bio-sensing application (Scaglione et al., 2019; Xue et al., 2019b).

Conclusion

Main aspects of metallic alloys have been presented. Structural and functional properties related to electronic and crystalline structure of alloys have been highlighted, in connection with their microstructure. Recent findings in the field of amorphous alloys and nanoporous gold have been presented.

References

Ashby MF (1992) *Materials Selection in Mechanical Design*, 2nd edn. 3: 665. Elsevier, Available at http://www.knovel.com/web/portal/browse/display?_EXT_KNOVEL_DISPLAY_bookid=1472%5Cnhttp://video.yahoo.com/watch/111582/992708.

Bassani F, Liedl GL, and Wyder P (eds.) (2005) *Encyclopedia*, 1st ed. Elsevier.

Chao B-K, et al. (2017) Gold-rich ligament nanostructure by dealloying Au-based metallic glass ribbon for surface-enhanced Raman scattering. *Scientific Reports* 7(1): 7485. https://doi.org/10.1038/s41598-017-08033-7.

Christian JW (2002) In: Christian, J. W. B. T.-T. T. of T. in M. and A (ed.) *The Theory of Transformations in Metals and Alloys*. Oxford: Pergamon, https://doi.org/10.1016/B978-0-08-044019-4.X5000-4.

Davidson M, et al. (2013) Investigating amorphous metal composite architectures as spacecraft shielding. *Advanced Engineering Materials* 15(1–2): 27–33. https://doi.org/10.1002/adem.201200313.

Davis JR (ed.) (1998) *Metals Handbook Materials*, 2nd edn. Park: ASM International.

Erlebacher J, et al. (2001) Evolution of nanoporosity in dealloying. *Nature* 410(6827): 450–453. https://doi.org/10.1038/35068529.

Fan M, et al. (2019) Intrinsic dissipation mechanisms in metallic glass resonators. *Journal of Chemical Physics* 151(14). https://doi.org/10.1063/1.5116895. AIP Publishing, LLC.

Fiore G and Battezzati L (2008) Developing Au-based amorphous alloys. *Reviews on Advanced Materials Science* 18(2): 190–192. Bolshoj 61, Vas Ostrov, St Ptersburg, 199178, Russia: Inst Problems Mechanical Engineering-Russian Acad Sciences.

Fiore G, Ichim I, and Battezzati L (2009) Effect of minor elements addition on glass formation and properties of gold alloys. *Journal of Physics: Conference Series* 144: 12039. https://doi.org/10.1088/1742-6596/144/1/012039. IOP Publishing.

Greer AL (2014) Metallic glasses. *Physical Metallurgy: Fifth Edition* 1(March): 305–385. https://doi.org/10.1016/B978-0-444-53770-6.00004-6.

Guo H, et al. (2009) Glass-forming ability and properties of new Au-based glassy alloys with low Au concentrations. *Materials Transactions* 50(6): 1290–1293. https://doi.org/10.2320/matertrans.ME200809.

Haasen P (1996) *Physical Metallurgy*, 3rd edn. Cambridge: Cambridge University Press.

Hofmann DC and Roberts SN (2015) Microgravity metal processing: From undercooled liquids to bulk metallic glasses. *NPJ Microgravity* 1(January): 1–10. https://doi.org/10.1038/npjmgrav.2015.3.

Inoue A (2015a) Advanced materials and materials genome—Review bulk glassy alloys: Historical development and current research. *Engineering* 1(2): 185–191. https://doi.org/10.15302/J-ENG-2015038. THE AUTHORS.

Inoue A (2015b) Bulk glassy alloys: Historical development and current research. *Engineering* 1(2): 185–191. https://doi.org/10.15302/J-ENG-2015038.

Khan MM, et al. (2018) Recent advancements in bulk metallic glasses and their applications: A review. *Critical Reviews in Solid State and Materials Sciences* 43(3): 233–268. https://doi.org/10.1080/10408436.2017.1358149. Taylor & Francis.

Klement WK, Willens RH, and Duwez P (1960) Non-crystalline structure in solidified gold–silicon alloys. *Nature*. https://doi.org/10.1038/187869b0.

Morrish R, Dorame K, and Muscat AJ (2011) Formation of nanoporous Au by dealloying AuCu thin films in HNO3. *Scripta Materialia* 64(9): 856–859. https://doi.org/10.1016/j.scriptamat.2011.01.021. Acta Materialia Inc.

Paschalidou EM, et al. (2016) Partially and fully de-alloyed glassy ribbons based on Au: Application in methanol electro-oxidation studies. *Journal of Alloys and Compounds* 667: 302–309. https://doi.org/10.1016/j.jallcom.2016.01.181. Elsevier B.V.

Saunders N and Miodownik AP (1998) *CALPHAD: A Comprehensive Guide*. New York: Edited by Elsevier Science.

Scaglione F, Gebert A, and Battezzati L (2010) Dealloying of an Au-based amorphous alloy. *Intermetallics* 18(12). https://doi.org/10.1016/j.intermet.2010.08.005.

Scaglione F, Celegato F, et al. (2015a) A comparison of de-alloying crystalline and amorphous multicomponent Au alloys. *Intermetallics* 66. https://doi.org/10.1016/j.intermet.2015.06.022.

Scaglione F, Paschalidou EM, et al. (2015b) Nanoporous gold obtained from a metallic glass precursor used as substrate for surface-enhanced Raman scattering. *Philosophical Magazine Letters* 95(9): 474–482. https://doi.org/10.1080/09500839.2015.1093665.

Scaglione F, et al. (2018) Amorphous molybdenum sulphide @ nanoporous gold as catalyst for hydrogen evolution reaction in acidic environment. *Journal of Materials Science* 53(17): 12388–12398. https://doi.org/10.1007/s10853-018-2490-2. Springer US.

Scaglione F, et al. (2019) Functionalized nanoporous gold as a new biosensor platform for ultra-low quantitative detection of human serum albumin. *Sensors and Actuators, B: Chemical* 288(February): 460–468. https://doi.org/10.1016/j.snb.2019.03.005. Elsevier.

Schroers J, et al. (2005) Gold based bulk metallic glass. *Applied Physics Letters* 87(6): 1–4. https://doi.org/10.1063/1.2008374.

Telford M (2004) The case for bulk metallic glass. *Materials Today* 7(3): 36–43. https://doi.org/10.1016/S1369-7021(04)00124-5.

Van Petegem S, et al. (2009) On the microstructure of nanoporous gold: An X-ray diffraction study. *Nano Letters* 9(3): 1158–1163. https://doi.org/10.1021/nl803799q.

Vega AA and Newman RC (2014) Nanoporous metals fabricated through electrochemical dealloying of Ag-Au-Pt with systematic variation of Au:Pt ratio. *Journal of the Electrochemical Society* 161(1): C1–C10. https://doi.org/10.1149/2.003401jes. 65 south main street, pennington, nj 08534 usa: electrochemical soc inc.

Vukmirovic MB, Dimitrov N, and Sieradzki K (2002) Dealloying and corrosion of Al alloy 2024-T3. *Journal of the Electrochemical Society* 149(9): B428–B439. https://doi.org/10.1149/1.1498258. 65 South Main Street, Pennington, nj 08534 USA: Electrochemical Soc Inc.

Wang WH, Dong C, and Shek CH (2004) Bulk metallic glasses. *Materials Science & Engineering R: Reports* 44(2–3): 45–90. https://doi.org/10.1016/j.mser.2004.03.001.

Xu Y, et al. (2018) 3D nanoporous gold with very low parting limit derived from Au-based metallic glass and enhanced methanol electro-oxidation catalytic performance induced by metal migration. *ChemNanoMat* 4(1): 88–97. https://doi.org/10.1002/cnma.201700170. John Wiley & Sons, Ltd.

Xue Y, et al. (2016) Excellent surface enhanced Raman scattering obtained with nanoporous gold fabricated by chemical de-alloying. *Chemical Physics Letters* 665. https://doi.org/10.1016/j.cplett.2016.10.046.

Xue Y, et al. (2017) Improving the chemical de-alloying of amorphous Au alloys. *Corrosion Science* 127: 141–146. https://doi.org/10.1016/j.corsci.2017.08.026. Elsevier.

Xue Y, et al. (2018) Shape controlled gold nanostructures on de-alloyed nanoporous gold with excellent SERS performance. *Chemical Physics Letters* 709. https://doi.org/10.1016/j.cplett.2018.08.044.

Xue Y, Scaglione F, et al. (2019a) Electrodeposited platinum on de-alloyed nanoporous gold with enhanced electro-catalytic performance. *Applied Surface Science* 476. https://doi.org/10.1016/j.apsusc.2019.01.099.

Xue Y, Wang S, et al. (2019b) Nanoporous gold chemically de-alloyed from Au-based amorphous thin film for electrochemical nonenzymatic H<inf>2</inf>0<inf>2</inf> sensing. *Chemical Physics Letters* 723. https://doi.org/10.1016/j.cplett.2019.03.024.

Zhang Z, et al. (2009) Fabrication and characterization of nanoporous gold composites through chemical dealloying of two phase Al–Au alloys. *Journal of Materials Chemistry* 19(33): 6042. https://doi.org/10.1039/b904052h.

Alloys: Iron

Michael Ferry, School of Materials Science and Engineering, The University of New South Wales, Sydney, NSW, Australia

© 2024 Elsevier Ltd. All rights reserved.

This is an update of M. Ferry, Alloys: Iron, Editor(s): Franco Bassani, Gerald L. Liedl, Peter Wyder, Encyclopedia of Condensed Matter Physics, Elsevier, 2005, Pages 46–53, ISBN 9780123694010, https://doi.org/10.1016/B0-12-369401-9/00532-5.

Introduction 522
The production of iron alloys 523
Structure and properties of iron 524
Alloying elements in iron 524
Interstitial alloys 525
Substitutional alloys 526
Phase transformations in iron alloys 527
Thermomechanical behavior 528
Cold deformation 528
Hot deformation 528
Static annealing 529
Some recent developments in iron alloys 529
Magnetic alloys 529
Shape memory alloys 530
Intermetallic compounds 530
Direct strip cast alloys 530
Advanced high strength steels 531
Additive manufactured alloys 532
Conclusion 532
References 532

Abstract

Iron alloys are arguably the most important class of engineering materials as a huge number of types can be produced by controlling the type and quantity of alloying elements, casting method, thermal and mechanical processing, etc. Factors contributing to the attractiveness of iron as the principal component of many engineering alloys include (Gladman, 1997; Leslie, 1981): the ability to be produced relatively inexpensively; it has a high melting temperature (1538 °C) which allows thermally activated processes over a range of temperatures and it is allotropic thereby allowing its alloys to undergo several useful phase transformations to generate a wide variety of microstructures, and mechanical and physical properties.

Key points

- Iron is a vital base element for generating the most important class of engineering alloy.
- The structures, phase stability and thermophysical properties of iron are key factors in the creation of a vast array of iron alloys suitable for myriad engineering applications.
- Alloying elements in iron have a major impact on final microstructure, properties and applications
- The development of new types of iron alloys and processing routes continues unabated.

Introduction

Iron alloys are arguably the most important class of engineering materials as a huge number of types can be produced by controlling the type and quantity of alloying elements, casting method, thermal and mechanical processing, etc. Factors contributing to the attractiveness of iron as the principal component of many engineering alloys include (Gladman, 1997; Leslie, 1981): the ability to be produced relatively inexpensively; it has a high melting temperature (1538 °C) which allows thermally activated processes over a range of temperatures and it is allotropic thereby allowing its alloys to undergo several useful phase transformations to generate a wide variety of microstructures, and mechanical and physical properties.

Fig. 1 presents a subgroup of a much wider range of commercially available iron alloys (Ferry, 2005). The alloys given in this figure contain carbon, are generally classed as steels or cast irons, and are by far the most widely used iron alloys but it is pertinent to note that many others are also important. Depending on alloying additions and the complexity of the various processing stages,

https://doi.org/10.1016/B978-0-323-90800-9.00129-3

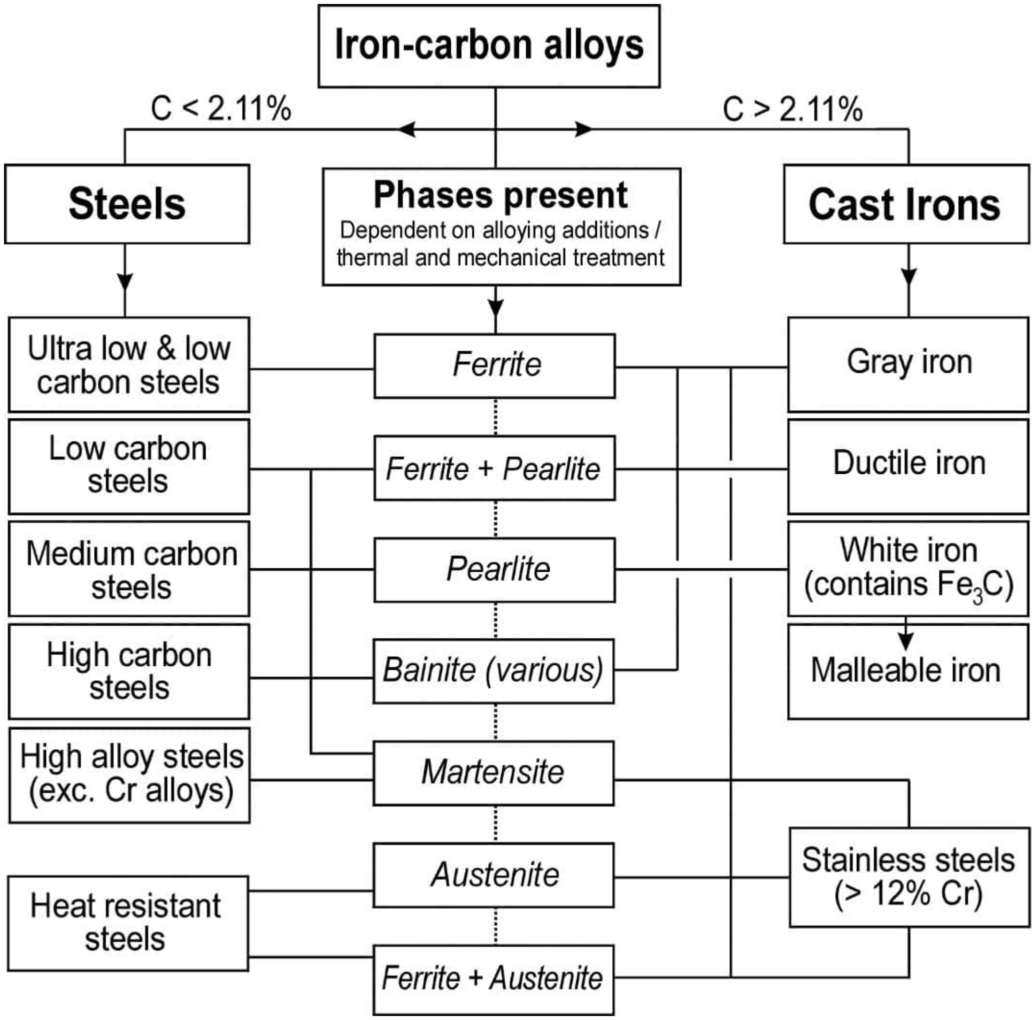
Iron-carbon alloys
C < 2.11%
C > 2.11%
Steels
Phases present
Dependent on alloying additions / thermal and mechanical treatment
Cast Irons
Ultra low & low carbon steels
Low carbon steels
Medium carbon steels
High carbon steels
High alloy steels (exc. Cr alloys)
Heat resistant steels
Ferrite
Ferrite + Pearlite
Pearlite
Bainite (various)
Martensite
Austenite
Ferrite + Austenite
Gray iron
Ductile iron
White iron (contains Fe_3C)
Malleable iron
Stainless steels (> 12% Cr)

Fig. 1 Classification scheme for iron–carbon alloys (range is not exhaustive). From Ferry M (2006) Direct Strip Casting of Metals and Alloys. Woodhead Publishing UK.

microstructures (and properties) of steels and cast irons vary dramatically, and include one or more of the following phases: ferrite, pearlite, bainite (range of structures), austenite, and martensite as well as second-phase dispersions such as cementite, graphite, intermetallic compounds, and precipitates. However, a detailed treatment of the structure and properties of Fe—C alloys is beyond the scope of this overview.

There are a range of essentially carbon-free iron alloys that also generate microstructures with attractive properties. Examples include Fe—Be and FePt that exploit the martensitic reaction to generate shape memory behavior (Dunne, 2000) and those alloys that exhibit important physical properties such as Fe—Ni invar alloys with very low thermal expansion coefficients and multi-component alloys such as $(Fe, Co)_{44}Zr_7Cu_1B_{15}$ (HITPERM) and $Nd_2Fe_{14}B$ with exceptional magnetic and magneto-mechanical properties (Jiles, 2003). The ability to generate iron alloys with such a large range of microstructures and properties has resulted in the use of these materials in an enormous number of applications.

The production of iron alloys

Iron alloy components have been produced from the liquid state for many centuries with mass production of steel commencing in the late nineteenth century. Molten steel was traditionally cast into standing molds, but continuous casting was developed in the 1950s which enabled the production of huge tonnages of steel. Most of the world's steel production is now obtained through this casting route. Following casting, as-cast slabs are thermal and mechanical processed to the desired final shape. In the last few decades, however, near-net-shape casting processes have been developed that are capable of producing near-final-shape products directly from liquid with secondary processing such as hot rolling reduced to an absolute minimum. On a reduced scale, there are various types of novel iron alloys produced in the amorphous, nanocrystalline, and intermetallic form. These materials are either manufactured by conventional casting or by rapid solidification processing, spray deposition, mechanical attrition, and sintering or physical and chemical vapor deposition, etc. Iron alloys produced by these more exotic techniques are generally restricted to specific applications. Recent advances in additive manufacturing technologies such as 3D printing have enabled conventional and more novel iron alloys to be directly net-shape fabricated into complex final shapes and intricate components.

Structure and properties of iron

The production of pure iron is not possible, but numerous studies have been carried out on the properties of high-purity iron. Iron is situated toward the end of the first transition series in the periodic table with an electron configuration $1s^2 2s^2 2p^6 3s^2 3p^6 3d^6 4s^2$. Iron lies at the left of the larger atomic species Co, Ni, and Cu which are known to crystallize with a close-packed structure. To the left of iron are the less-filled states of Ti, V, Cr, and Mn which subsequently crystallize with a body-centered cubic (b.c.c.) crystal structure. Iron lies between these groups of elements and, depending on temperature, may exist either as the b.c.c. structure ($1394\,^{\circ}\mathrm{C} > \mathrm{T}_{\alpha} < 912\,^{\circ}\mathrm{C}$) or the face-centered cubic (f.c.c.) structure ($912\,^{\circ}\mathrm{C} < \mathrm{T}_{\gamma} < 1394\,^{\circ}\mathrm{C}$). The high-temperature b.c.c. structure is not expected under normal circumstances but is a result of magnetic energy effects. The b.c.c. structure exists at standard temperature and pressure, but extreme pressures will generate a hexagonal close-packed (h.c.p.) structure (ε-iron).

An important difference between α-iron and γ-iron is the structure of their dislocations (Honeycombe, 1985): the Burgers vector of the minimum energy configuration in α-iron is $a/2\ \langle 111 \rangle$ and while dislocations can theoretically dissociate into segments of $a/2\ \langle 001 \rangle$, the stacking fault energy (SFE) is so high that substantial dissociation has not been observed. In contrast, γ-iron has a relatively low SFE (<80 mJ m^{-2}) and dislocations readily dissociate by the reaction $a/2\ \langle 011 \rangle \rightarrow a/6\ \langle 112 \rangle + a/6\ \langle 211 \rangle$, which generates a ribbon of stacking fault. The difference in both crystal structure and SFE of α-iron and γ-iron strongly influences the deformation and annealing behavior of these phases.

Due to the various allotropic transformations in iron ($\delta \leftrightarrow \gamma \leftrightarrow \alpha$), many physical properties, such as specific volume and electrical conductivity, change discontinuously through these critical temperatures. A notable consequence of the f.c.c. ↔ b.c.c. transformation is the change in magnitude of the self-diffusion coefficient, D, which follows an Arrhenius-type relationship:

$$D = D_{\mathrm{o}} \exp\left(Q/RT\right)$$

where D_{o} is a frequency factor that is virtually independent of absolute temperature (T) and Q is the activation energy for self-diffusion. Table 1 shows the values of D_{o} and Q for iron and other alloying elements. It is easily shown that the rate of self-diffusion of iron decreases by two orders of magnitude when f.c.c. iron transforms to the more open b.c.c. structure.

Alloying elements in iron

A number of elements are added to iron to produce a variety of alloys with a wide range of microstructures and properties (Fig. 1). Alloying elements have a strong influence on the stable temperature range of b.c.c. and f.c.c. phases. The classic Wever classification (Fig. 2) has shown that most alloying elements fall into four categories with each generating a particular phase diagram. This figure shows that a particular alloying element in iron may either expand the γ-field (austenite stabilizer) or contract this field (ferrite stabilizer). Elements may also form iron-rich compounds that reduce the extent of the γ-field. The overall behavior is a result of the different enthalpies of solution in both the crystal structures of iron which leads to either an increase or decrease of the temperature range in which austenite is stable. Alloying elements can also be grouped into three major classes: those that form interstitial and substitutional solid solutions, and those that are almost completely immiscible with the crystal lattices of iron.

Table 1 Approximate diffusivity of various interstitial and substitutional elements in iron.

Phase	*Element*	*Activation energy, Q (KJmol^{-1})*	*Frequency factor, D$_{\circ}$(mm^{2}s^{-1})*	*Temperature range (°C)*
α-Iron	Fe	240	200	700–750
	C	80	0.62	700–750
	N	76	0.3	700–750
	Co	226	20	700–790
	Ni	258	970	700–900
γ-Iron	Fe	284	49	900–1050
	C	135	15	900–1050
	Co	364	3000	1050–1250
	Ni	280	77	930–1050
δ-Iron	Fe	239	190	1400–450

After Ferry M (2005) Alloys: Iron. In: *Encyclopedia of Condensed Matter Physics*, Bassani F, Liedl G, and Wyder P (eds) UK: Elsevier, 46–53.

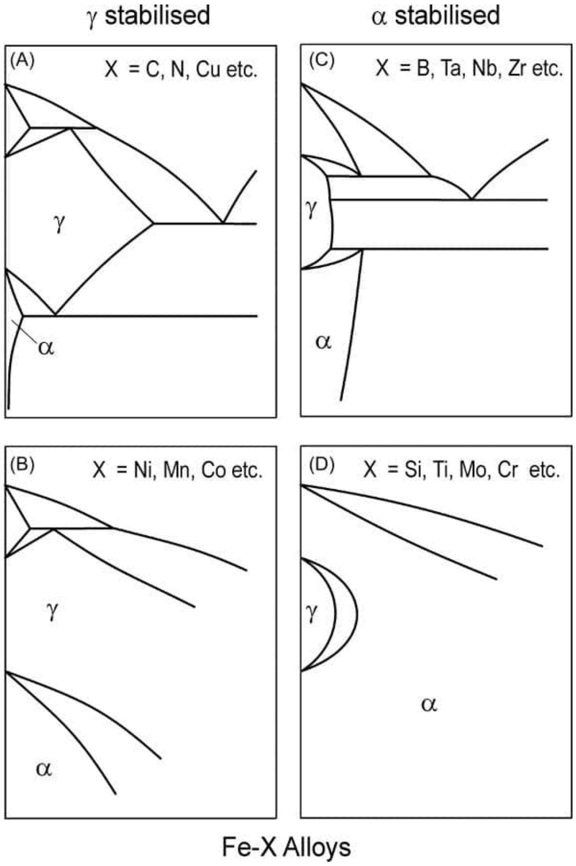

Fig. 2 Classification of iron alloy binary phase diagrams: (A) and (B) austenite stabilizers; (C) and (D) ferrite stabilizers. After Ferry M (2005) Alloys: Iron. In: *Encyclopedia of Condensed Matter Physics*, Bassani F, Liedl G, and Wyder P (eds) UK: Elsevier, 46–53.

Interstitial alloys

The elements H, C, N, and O are considerably smaller than Fe and, therefore, tend to occupy interstitial sites in both the lattices of iron. Fig. 2A shows how the γ-field is stabilized for alloys containing interstitial elements since the f.c.c. lattice provides sites of lower strain energy than does the b.c.c. lattice. These elements have a high rate of diffusion in both the crystal structures of iron, particularly in the less densely packed b.c.c. structure, and are considerably more mobile than substitutional elements (Fig. 3 and Table 1). Nevertheless, interstitial elements have low solubility, particularly in α-iron (ferrite), due to the less favorable geometry of the b.c.c. lattice. The solubility of interstitial elements decreases markedly with temperature and obeys a similar relation as diffusivity:

$$C_{\mathrm{Fe-X}}(T) = A\,\exp\,(B/T)$$

where A and B are constants and X is either an equilibrium or metastable phase such as graphite, Fe_2B, Fe_3C, and Fe_3N_4 in equilibrium with either ferrite or austenite. Table 2 gives values of the maximum solubility of various interstitial elements in ferrite and austenite which shows that hydrogen has the highest solubility in ferrite which is demonstrated by a small value of the constant, B (not shown). Table 2 also shows that the solubility of C and N in both forms of ferrite are considerably lower than in austenite.

In the Fe—C system, graphite does not usually form in either ferrite or austenite due to its high activation energy of nucleation. The cementite phase (Fe_3C) or other less stable carbides tend to form instead. The difference between the equilibrium Fe–graphite and metastable (constitutional) Fe–Fe_3C phase diagram is shown in Fig. 4, which illustrates the subtle differences in the phase boundaries. Fe–Fe_3C is probably the most important binary system with the following array of characteristics: (1) various types of invariant phase transformations are possible (peritectic, eutectic, and eutectoid) and (2) the solubility of C in α-iron at 727 °C is only 0.022 wt% whereas γ-iron can accommodate 0.77 wt% C at this temperature. Carbon levels below ~2.11 wt% are classified as steels while higher carbon alloys are classified as cast iron. Steels are classified further into hypoeutectoid ($C < 0.77$ wt%) or hypereutectoid ($C > 0.77$ wt%) while cast irons are classified as either hypoeutectic ($C < 4.30$ wt%) or hypereutectic.

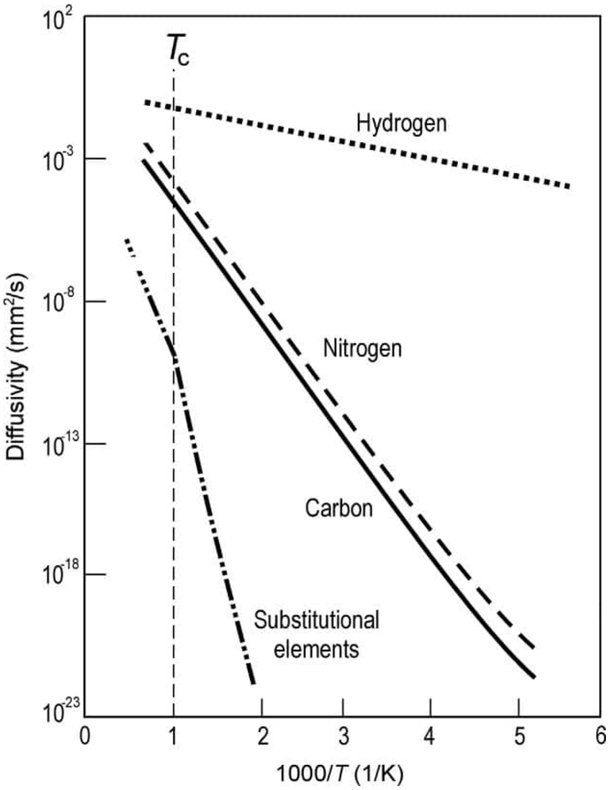

Fig. 3 Variation of average diffusivity with temperature for various substitutional and interstitial elements in α-iron. After Ferry M (2005) Alloys: Iron. In: *Encyclopedia of Condensed Matter Physics*, Bassani F, Liedl G, and Wyder P (eds) UK: Elsevier, 46–53.

Table 2 Solubility of various interstitial elements in iron.

Phase	*Element*	*Equilibrium phase*	*Temperature of maximum solubility (°C)*	*Maximum solubility (at.%)*
α-Iron	H	H_2	905	$1–2 \times 10^{-3}$
	B	Fe_2B	915	<0.02
	C	Fe_3C	727	0.095
	N	Fe_4N	590	0.4
γ-Iron	C	Fe_3C	1148	8.8
	N	Fe_4N	650	10.3
δ-Iron	C	Fe_3C	1495	0.09

After Ferry M (2005) Alloys: Iron. In: *Encyclopedia of Condensed Matter Physics*, Bassani F, Liedl G, and Wyder P (eds) UK: Elsevier, 46–53.

Substitutional alloys

There are many substitutional elements that are partially or completely soluble in both crystal structures of iron. Elements with the largest solubility fall close to Fe in the periodic table: Cr, Ni, Co, Mn, and V. A number of elements, such as Ti, Ca, and K, have almost no solubility in iron. For alloying elements with an f.c.c. or h.c.p. structure, the γ-field is stabilized (Fig. 2A and B) whereas the γ-field is reduced by elements that form Hume–Rothery phases with Cu, Ag, and Cu (Fig. 2C) or when iron is alloyed with the b.c.c. transition metals V, Ti, Mo, W, Cr, etc. (Fig. 2D). For those elements that restrict the γ-field completely, austenite cannot exist which eliminates the possibility of generating several important decomposition products (pearlite, bainite, or martensite). These alloys are non heat-treatable in the sense that phase transformations cannot be exploited to control the microstructure and properties. To achieve the desired mechanical properties such as yield strength, these alloys must either be work hardened (which can also recrystallize to produce a fine grain size) or elements are used to promote solid solution strengthening. The heat-treatable alloys are far more amenable to strengthening over a wide range by controlling the transformation products during austenite decomposition.

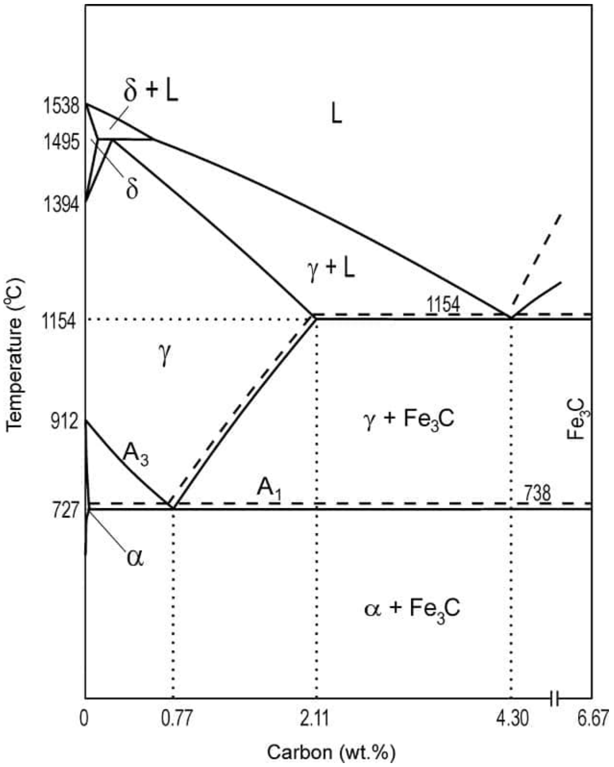

Fig. 4 Schematic diagram of the metastable (constitutional) Fe–Fe$_3$C and the stable (equilibrium) Fe–graphite diagram (dashed) showing important temperatures and compositions. After Ferry M (2005) Alloys: Iron. In: *Encyclopedia of Condensed Matter Physics*, Bassani F, Liedl G, and Wyder P (eds) UK: Elsevier, 46–53.

Most alloys of iron usually consist of a combination of interstitial and substitutional elements which results in various complex interactions involving atom species. For example, the rate of diffusional transformation is usually controlled by the more sluggish substitutional elements (as shown by the lower diffusivity of these elements, Fig. 3) which favors the formation of nonequilibrium microstructures following austenite decomposition. In addition, elements can combine to produce enhanced strengthening by the generation of atom complexes (Mn—C, etc.) in the lattice or from the formation of alloy carbides ([Fe$_a$X$_b$Y$_{c...}$]C$_j$).

Phase transformations in iron alloys

The allotropic transformations that occur in pure iron can result in a number of important phase transformations in its alloys (Zackay and Aaronson, 1962; Honeycombe and Bhadeshia, 1995). As indicated in Fig. 2, a given concentration of a ferrite stabilizer can eliminate the austenite phase field, whereas an austenite stabilizer will expand this field to allow the alloy to undergo several useful transformations. For example, Fig. 4 shows that a number of transformations are possible in the Fe—C system. The following brief discussion is devoted mainly to this system as carbon is the most important alloying addition to iron.

During solidification, the peritectic reaction can occur over a certain compositional range. For the peritectic composition (0.09 wt% C), the following invariant reaction can occur at 1495 °C: $L \rightarrow L + \delta \rightarrow \gamma$. In this reaction, liquid + δ-iron transforms isothermally to austenite and has several important consequences during continuous casting of steels.

At higher carbon levels, that is, 0.77 wt% C, the eutectoid reaction occurs at 727 °C: $\gamma \rightarrow \alpha + \mathrm{Fe_3C}$. For slow cooling rates, austenite (0.77 wt% C) decomposes via a diffusional transformation to produce pearlite which is a lamellar structure containing successive layers of ferrite (0.022 wt% C) and cementite (6.67 wt% C). With increasing cooling rate, the formation of diffusional products such as pearlite and ferrite are suppressed thereby generating nonequilibrium microstructures ranging from a series of bainitic structures to martensite.

At very high cooling rates, diffusional transformation products do not form since atomic diffusion is necessary for nucleation and growth of these phases. This results in the formation of martensite; a term not restricted to iron-base alloys but used to define the product of a non-diffusional phase transformation both in metals and ceramics. The martensitic transformation has the following important characteristics: each atom retains its original neighbors and there is no interchange among the atoms; the transformation does not involve individual atomic jumps characteristic of diffusion-controlled and interface-controlled transformations; the reaction is diffusionless which means the martensite product has the same composition as the parent phase. In Fe—C alloys, the martensite transformation generates a hard, brittle phase whereas, for essentially carbon-free alloys, the martensite is ductile.

For very low carbon levels (<0.022 wt%), Fe—C may undergo a series of precipitation reactions after cooling through the solvus where supersaturated carbon in ferrite decomposes at low temperatures to produce a series of precipitates. This can result in considerable hardening that may or may not be useful depending on the desired application of the alloy.

For carbon levels greater than ~2.11 wt%, Fe—C undergoes the eutectic reaction: $L \rightarrow \gamma + Fe_3C$. At the eutectic composition (4.3 wt% C), liquid iron transformations take place at 1147 °C to produce austenite and cementite with subsequent cooling to room temperature promoting additional phase changes. It is well-known that alloying additions such as Si promote the formation of graphite rather than cementite. Similar to steels, cast irons can generate a wide range of microstructures and properties depending on alloying additions, cooling behavior, etc.

It is clear that the transformation products that form during austenite decomposition in iron-base alloys are expected to be diverse and are influenced by a large number of processing and material-related variables. A particular transformation is achieved by the control of the type and quantity of alloying elements, the cooling rate through the transformation range, and thermomechanical treatments prior to or during transformation, etc. In addition to the classic phase transformations associated with Fe—C, several additional transformations are known to occur in iron alloys. The ability of the alloys of iron to undergo such a diverse range of phase transformations is a major factor contributing to their immense popularity as an engineering material.

Thermomechanical behavior

An understanding of deformation of ferrite and austenite is important as these phases undergo a significant amount of plastic deformation during thermomechanical processing, the most common method for producing useful final components (Manohar et al., 2001). During deformation, many microstructural changes occur: the original grains change shape and an internal substructure forms, texture changes take place, precipitation may occur, dynamic recovery (DRV) or dynamic recrystallization (DRX) processes are possible, and the constituent particles may fracture and redistribute. The most notable material factors that affect both the deformation microstructure of iron alloys include SFE, crystal structure, initial grain size and shape, and the size, shape, and volume fraction of a second phase.

Cold deformation

Cold deformation is restricted to low homologous temperatures ($T < 0.5T_m$), where T_m is the absolute melting temperature. During cold deformation of either ferrite or austenite, there is a marked increase in dislocation density resulting in considerable work hardening and grains subdivide in a complex manner to produce a range of features such as a cellular substructure, microbands, deformation twins, deformation bands, and larger-scale heterogeneities such as shear bands (Humphreys and Hatherly, 2004). In high SFE b.c.c. α-iron, slip is the principal deformation process and occurs in the close-packed <111>direction but the slip plane may be any of the planes {110}, {112}, or {123}. In contrast, γ-iron has a relatively low SFE (<80 mJ m^{-2}) which results in deformation by slip on $\{111\}\langle 011\rangle$ systems as well as by twinning. The different modes of deformation result in differences in the work-hardening rate of these phases as well as in the development of deformation textures.

Hot deformation

Hot deformation is carried out at $T > 0.5T_m$ and is distinguished from cold working by the absence or near absence of strain hardening and lower matrix dislocation content (Humphreys and Hatherly, 2004). Deformation becomes more homogeneous with increasing temperature with the frequency of microstructural inhomogeneities such as microbands, transition bands, and shear bands reduced considerably. The driving pressure for softening by recovery and recrystallization (either dynamic or static) is the stored energy of deformation. The process of recovery reduces the internal energy of the metal through mechanisms such as annihilation dislocations and their re-arrangement into low-angle grain boundaries.

The relatively low SFE of austenite does not allow for substantial DRV whereas DRV occurs extensively in ferrite since dislocation climb occurs readily and, for a given temperature, the rate of diffusion of iron atoms in ferrite is ~100× greater than in austenite (Manohar et al., 2001). In ferrite, a significant proportion of the stored energy is released by DRV which reduces the driving force for both dynamic and static recrystallization (SRX). Since the reorganization of dislocations is more difficult in austenite, DRX can occur readily. These differences in the dynamic restoration processes generate two distinctive stress–strain (flow) curves, Fig. 5. Deformation of austenite results in an increase in flow stress via work hardening but at a critical strain (ε_c), there is sufficient stored energy to initiate DRX which tends to eventually decrease the flow stress since the rate of work hardening is offset by the softening caused by recrystallization. In contrast, extensive DRV in ferrite leads to a balance between dislocation generation and annihilation which rapidly results in a steady-state flow stress. There is also insufficient stored energy to dynamically recrystallize this phase. During hot working, successive cycles of DRX in austenite have the capability of refining the grain size whereas grain refinement in ferrite can only be achieved by SRX.

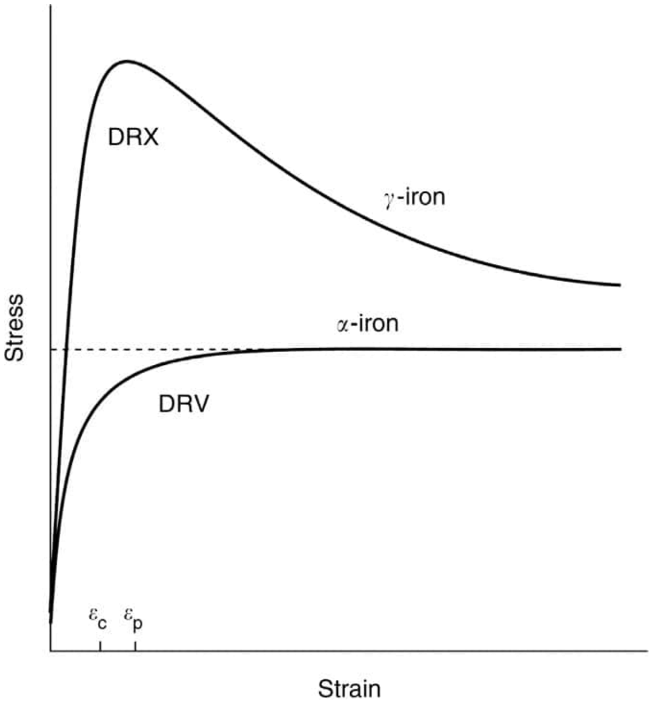

Fig. 5 Schematic diagram of typical flow curves associated with the hot deformation of ferrite (α-iron) and austenite (γ-iron). After Ferry M (2005) Alloys: Iron. In: *Encyclopedia of Condensed Matter Physics*, Bassani F, Liedl G, and Wyder P (eds) UK: Elsevier, 46–53.

Static annealing

The principal material factors influencing static annealing in iron alloys include composition, initial grain size, initial texture, and second-phase precipitates (Humphreys and Hatherly, 2004). Processing variables are also important and include the mode of deformation, strain, strain rate, and temperature of deformation. In general, both SRX and DRX are initiated by nucleation of strain-free grains at microstructural inhomogeneities such as transition bands, shear bands, and grain boundaries. Cold-deformation of fine-grained ferrite results in nucleation predominantly at prior grain boundaries but a coarse grain size results in substantial shear band nucleation, particularly in those iron alloys containing high levels of interstitial elements.

The most desirable nucleation sites in cold-rolled α-iron are grain boundaries as these nuclei often have orientations where $\langle 1\ 1\ 1\rangle$ is almost parallel to the normal direction (ND) of the sheet (Ray et al., 1994). This is significant since a strong $\langle 1\ 1\ 1\rangle \| \mathrm{ND}$ texture in cold-rolled and annealed steels results in superior sheet formability. Austenitic alloys recrystallize in a similar manner to ferritic alloys, that is, nucleation occurs mainly at grain boundaries, but other microstructural heterogeneities characteristic of deformed austenite also play an important role. Due to the physical processes associated with slip and twinning during cold rolling, austenitic alloys do not produce a high fraction of favorable $\langle 1\ 1\ 1\rangle \| \mathrm{ND}$ nuclei resulting in reduced formability.

Some recent developments in iron alloys

Magnetic alloys

Iron is ferromagnetic below the Curie temperature and these alloys exhibit a remarkably wide range of magnetic properties. Magnetic materials are broadly classified into two main groups with either soft or hard magnetic characteristics (McHenry and Laughlin, 2000; Jiles, 2003). Soft magnetic alloys have high permeability, low coercivity, and low hysteresis loss whereas hard magnetic (or permanent) magnetic alloys have a sufficiently large resistance to demagnetizing fields due to their high coercivity, remanence, and energy product.

Table 3 gives some properties of a select range of ferromagnetic alloys which includes some of the more recently developed alloys that possess either an amorphous, or a nanocrystalline phase embedded in an amorphous matrix. These materials are usually produced as ribbons or fibers by rapid solidification techniques and are often followed by a series of heat treatments. Soft magnetic alloys based on these structures are generally complex and contain elements such as Cr, Mo, and Al and varying amounts of metalloids (B, Si, C, and P) that help to form the glassy phase. These alloys have low anisotropy combined with high resistivity (which reduces eddy current losses) and have high permeability and low power losses. The most widely investigated alloys in this new class of soft magnetic materials are $Fe_{73.5}Si_{13.5}B_9Nb_3Cu_1$ (FINEMET), $Fe_{88}Zr_7B_4Cu_1$ (NANOPERM), and $Fe_{44}Co_{44}Zr_7B_4Cu_1$ (HITPERM)

Table 3 Some notable ferromagnetic iron alloys showing typical properties.

Material	*Initial relative permeability* (μ_e)	*Hysteresis loss per cycle* (Jm^{-3})	*Saturation induction* (Wbm^{-2})	$(BH)_{max}(KJm^{-3})$
Soft magnetic alloys				
Commercial iron ingot	1.5×10^2	270	2.14	
Non grain oriented (NGO) electrical steel (Fe-Si2.0-3.8%)		1.5–5	1.6–1.8	
Grain oriented (GO) electrical steel (Fe-3%Si)		1.32–1.46	1.7–2.0	
Fe-Ni70-80% (PERMALLOYS)	10^5	>90	0.75	
$Fe_{73.5}Cu_1Nb_3Si_{13.5}B_9$ (FINEMET)	10^5–1.1×10^5	35–38	1.2–1.25	
$Fe_{86\text{-}91}Zr_7B_{3\text{-}6}Cu_{<1}$ (NANOPERM)	22–48×10^3	76–116	1.5–1.65	
$Fe_{44}Co_{44}Zr_7B_4Cu_1$ (HITPERM)	1–2.5×10^3	<35	1.6–2	
$Fe_{76}Si_9B_{15}$ (2605)	1.06×10^4	0.68	1.49	
$Fe_{85}Si_{1\text{-}2}B_{8\text{-}9}P_4Cu_1$ (NANOMET)	27×10^3	0.25–0.28	1.8–1.9	
Hard magnetic alloys				
Fe-1Mn-0.9C (martensitic)				3.8
Fe-3.5Cr-0.9C-0.3Mn (martensitic)				5.0
Fe-24.5Co-13.5Ni-8Al-2Nb (Alnico-XII)				76.8
$Fe_{60}Pt_{40}$				120
$Nd_2Fe_{14}B$ (oriented)				320–400
$Nd_2Fe_{14}B$ (sintered nanophase)				450

After Ferry M (2005) Alloys: Iron. In: *Encyclopedia of Condensed Matter Physics*, Bassani F, Liedl G, and Wyder P (eds) UK: Elsevier, 46–53.

etc. which are produced by rapid solidification and crystallization annealing to produce a nanocrystalline structure. Compared with more conventional iron alloys, these materials have very high permeabilities and large inductions.

Permanent magnetic iron-base materials include a variety of alloys and intermetallic compounds. The most widely studied materials in recent years are neodymium–iron–boron ($Nd_2Fe_{14}B$) and iron–platinum alloys. For permanent magnets, a parameter that specifies its performance characteristic, that is, its resistance to demagnetization, is the maximum energy product $(BH)_{\text{max}}$ where B and H are the magnetic induction and magnetic field strength, respectively. To date, the highest values of $(BH)_{\text{max}}$ are obtained in oriented Nd–Fe–B alloys (320–400 kJ m^{-3}) and sintered fine-grained versions of these alloys (~450 kJ m^{-3}).

Shape memory alloys

Iron alloys can exploit the martensitic reaction to enable a component to be deformed at one temperature with subsequent recovery of the original shape upon heating (Dunne, 2000). This so-called shape memory effect (SME) is associated with the ability of some martensites to undergo thermal reversion on reheating which, on a macroscopic scale, corresponds to up to 15% strain recovery. There are various types of SME including pseudoelasticity, one- and two-way shape memory behavior and magnetic field-induced shape memory. Iron-base shape memory alloys are produced either by conventional casting and thermomechanical processing, or mechanical attrition and sintering, or rapid solidification processing. While the various types of shape memory phenomena occur in alloys of the type of Fe–Mn–Si–Cr, FeBe, FePt, and Fe–Pd–Pt, they are largely under development and more work is required to explore the potential of shape memory iron alloys.

Intermetallic compounds

Iron alloys in the form of an ordered b.c.c structure consisting of two simple cubic interpenetrating sublattices (CsCl or B2 structure) are intermetallic compounds based on the stoichiometric ratios, FeCo, FeAl, and Fe_3Al (Munroe, 2000). These materials have received considerable attention in high-temperature structural applications due to their low density, high electrical resistivity, high strength at temperature, and excellent resistance to oxidation and corrosion in various aggressive chemical environments (Munroe, 2000). Such materials are either thermomechanically processed in a manner similar to metals or produced by more novel processing routes. While binary iron-base intermetallics are inherently brittle and have low creep resistance, considerable work is being carried out to improve these critical properties both by alloy design and by carefully controlling the various processing stages.

Direct strip cast alloys

There have been substantial developments in the mass production of iron alloys by direct strip casting (DSC) which produces as-cast strip products of a thickness less than 2 mm (Ferry, 2006). DSC actually dates back to 1846 when Sir Henry Bessemer developed and

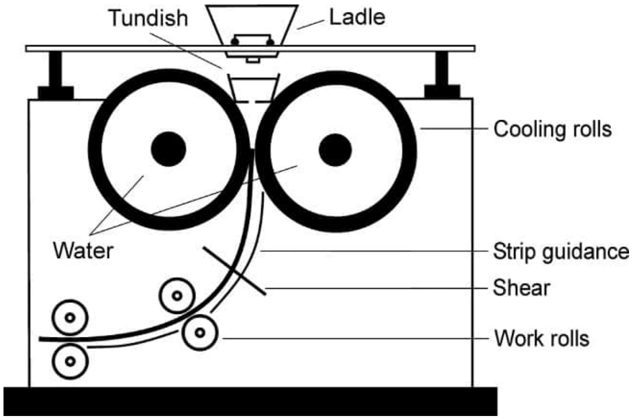

Fig. 6 Schematic diagram of Bessemer's twin roll strip caster. After Ferry M (2005) Alloys: Iron. In: *Encyclopedia of Condensed Matter Physics*, Bassani F, Liedl G, and Wyder P (eds) UK: Elsevier, 46–53.

patented a twin roll casting machine to produce tin and lead strip products (Fig. 6). However, the numerous challenges associated with strip casting steel on a commercial scale were not resolved until the beginning of the 21st century. Iron alloys produced by DSC include carbon and alloy steels, stainless steel, iron–silicon alloys, and cast iron (Ferry, 2006). DSC often produces a microstructure that is markedly different from the same material produced by conventional casting and thermomechanical processing (TMP). This is a result of the high solidification rates that tend to produce far-from-equilibrium microstructures. By a careful control of casting parameters and alloying additions, as-cast low carbon steel strip can be generated with a final microstructure consisting of one or more of the following phases: martensite, bainite, acicular ferrite, and polygonal ferrite (Ferry, 2006).

Advanced high strength steels

Driven largely by the automotive industry, a range of advanced high strength steels (AHSS) have been developed with unique combinations of high strength and elongation/formability (Matlock and Speer, 2009). These structural steels are designed for two main purposes: (i) improved first is passenger safety – structural components with higher strength and elongation can absorb greater energy with lower intrusion in the event of a crash, and (ii) 'light-weighting' – higher strength components allow thinner sheet to be used that reduces the automobile mass, which is a potent multiplier on the CO_2 emissions during service. When compared with conventional low and high strength steels, AHSS have superior mechanical properties due to their final structure generated by the control of steel composition and processing route. For example, excellent properties can be generated by controlled cooling from the austenite or austenite + ferrite phase fields after either hot rolling or during continuous annealing after cold rolling. Fig. 7 shows the three main types of AHSS. 1st generation AHSS are largely ferritic and include dual phase (DP), complex phase (CP) and transformation induced plasticity (TRIP) steels. 2nd generation AHSS are largely austenitic and include twinning induced

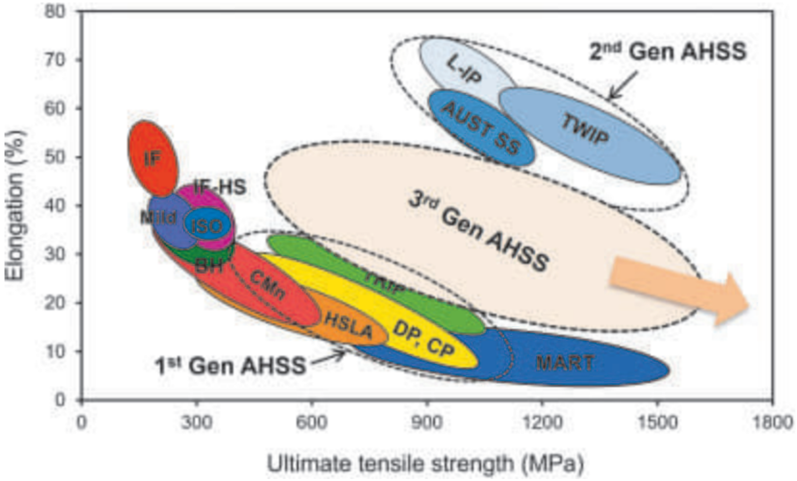

Fig. 7 Tensile strength and elongation combinations exhibited by existing and targeted Advanced High Strength Steels (AHSS): 1st Gen (DP, CP, TRIP); 2nd Gen (TWIP, AUST SS), and 3rd Gen (under constant development). Adapted from Matlock D and Speer J (2009) Third generation of AHSS: Microstructure design concepts. In: Haldar A, Suwas S, and Bhattacharjee D (eds) *Microstructure and Texture in Steels*. London: Springer.

plasticity (TWIP) steels and austenitic stainless steels (AUST SS) and exhibit superior strength/elongation combinations. However, they are expensive due to the large alloying additions (e.g. 20 wt% Mn) needed for stabilizing the austenite phase to room temperature. 3rd generation AHSS are under intense development and are targeted to have strength/elongation combinations significantly greater that the 1st generation but below that of the 2nd generation. The attractiveness lies in their lower cost due to the leaner alloying additions (typically 2–5 wt%).

Additive manufactured alloys

The recent advent and rapid development of additive manufacturing technologies, commonly called 3D printing, has demonstrated huge advantages in processing various metals and alloys, including various iron alloys, into complex net-shape components. Metal 3D printing is usually a layer-by-layer manufacturing process involving the melting of consecutive deposited layers of metal powder on a base (substrate) using either a laser or electron beam. Each melted surface layer usually solidifies rapidly to generate a built component exhibiting novel microstructures and properties. As such, additive manufacturing of iron alloys is a promising and versatile method for producing complex and intricate-shaped components with tailorable microstructures and properties (Haghdadi et al., 2021; Li et al., 2022). Indeed, manufacturing such intricate shaped components by the conventional processing routes described previously is almost impossible. There is currently a massive research and development effort underway on additive manufacturing of new and existing engineering alloys, including most of the iron alloys reported in Fig. 1. 3D printing generates a wide range of microstructures from near-equilibrium to far-from-equilibrium depending on the type of steel and processing parameters.

Conclusion

This brief overview highlights the importance of iron as a vital base element for generating a very broad suite of engineering alloys, often called steels and cast irons, that can be created with selective additions of a combination of certain alloying elements such as C, Mn, Ni, Cr, Mo, N etc. The allotropic transformation of pure iron, in addition to judicious selection of alloying elements, is sufficient to produce an incredibly large variety of microstructures and, hence, property profiles. The microstructures of these alloys were shown to be further modified by myriad secondary processes, such as casting, hot and cold working operations and various other thermomechanical treatments that enables this alloy class to be regarded as one of the most important for modern engineering applications. The future development of new types of alloys and processing methods will undoubtedly broaden the usage of these critical engineering materials.

References

Dunne DP (2000) Functional memory metals. *Materials Forum* 24(2000): 95–108.
Ferry M (2005) Alloys: Iron. In: Bassani F, Liedl G, and Wyder P (eds.) *Encyclopedia of Condensed Matter Physics*, pp. 46–53. UK: Elsevier.
Ferry M (2006) *Direct Strip Casting of Metals and Alloys*. UK: Woodhead Publishing.
Gladman T (1997) *The Physical Metallurgy of Microalloyed Steels*. London: Institute of Materials.
Haghdadi N, Laleh M, Moyle M, and Primig S (2021) Additive manufacturing of steels: A review of achievements and challenges. *Journal of Materials Science* 56: 64–107.
Honeycombe RWK (1985) *The Plastic Deformation of Metals*. London: Edward Arnold.
Honeycombe RWK and Bhadeshia HKDH (1995) *Steels – Microstructure and Properties*. London: Edward Arnold.
Humphreys FJ and Hatherly M (2004) *Recrystallization and Related Annealing Phenomena*, 2nd edn, Oxford: Elsevier Science.
Jiles DC (2003) Recent advances and future directions in magnetic materials. *Acta Materialia* 51: 5907–5939.
Leslie WC (1981) *The Physical Metallurgy of Steels*, 1st edn, London: McGraw Hill.
Li C, Ferry M, Kruzic JJ, and Li X (2022) Review: Multi-principal element alloys by additive manufacturing. *Journal of Materials Science* 57: 9903–9935.
Manohar PA, Ferry M, and Chandra T (2001) Recrystallization of ferrite and austenite. In: Buschow KHJ, et al. (ed.) *Encyclopedia of Materials Science and Technology*. vol. 4, pp. 3019–3024. Oxford: Elsevier.
Matlock D and Speer J (2009) Third generation of AHSS: Microstructure design concepts. In: Haldar A, Suwas S, and Bhattacharjee D (eds.) *Microstructure and Texture in Steels*. London: Springer.
McHenry ME and Laughlin DE (2000) Nano-scale materials development for future magnetic applications. *Acta Materialia* 48: 223–238.
Munroe PR (2000) Intermetallic compound development for the 21st century. *Materials Forum* 24: 5–18.
Ray RK, Jonas JJ, and Hook RE (1994) Cold rolling and annealing textures in low and extra low carbon steels. *International Materials Review* 39: 129–172.
Zackay VF and Aaronson HI (1962) *Decomposition of Austenite by Diffusional Processes*. USA: TMS-AIME.

Alloys: Steel

M Strangwood, University of Warwick, Coventry, West Midlands, United Kingdom

© 2024 Elsevier Ltd. All rights reserved.

Introduction 533
Iron 533
Alloying element behavior in iron 534
Interstitial alloying elements 534
Substitutional alloying elements 536
Phase transformations and microstructures 536
Categories of irons and steels 538
Processing 541
Mechanical properties 544
Chemical properties 547
Functional properties 547
Conclusion 548
References 548

Abstract

The main classes of iron-based alloys have been summarized in terms of their alloying elements, microstructures, processing routes and properties, concentrating on strength, toughness and magnetic properties. The governing metallurgical principles behind the behavior have also been covered to identify how and why commercial iron-based alloys have been developed and are being improved. Important terminology relating to iron-based alloys commonly used by metallurgists and which will be encountered in further study have been identified to provide a basis for future reading.

Objectives

- Summarize the main range of iron-based alloys (steels and cast irons) commercially available.
- Describe the main microstructural features observed in iron-based alloys.
- Indicate the principal alloying elements used in iron; their effects on phase stability and kinetics of phase transformations; and their influence on properties.
- Introduce the main processing routes used for iron-based alloys and their effects on structure and properties.
- Relate the main mechanical properties (strength and toughness/ductility) to composition, structure and processing; summarize the thermal and magnetic properties of iron-based alloys.

Introduction

Iron is the fourth most abundant element in the Earth's crust, which, combined with its relative ease of extraction and wide range of processing routes and property combinations make iron-based alloys (principally steels and cast irons) the most important class of engineering materials. The use of iron-based artifacts dates back to 1800 BCE and the 'iron age' followed the 'stone' and 'bronze' ages in the classical ages of man. The smelting of iron using coke instead of charcoal by Abraham Darby from the start of the 1700s is a key step in the Industrial Revolution that led to the current global production of nearly 2 billion tonnes of iron and steel annually, which dwarfs that of other metallic alloys (aluminum-based alloys are second with a global annual production of around 60 million tonnes). Although the use of coke to cheaply and efficiently produce iron and steel established the modern steel industry, it now presents a major problem to its future sustainability as the production of iron and steel contributes some 6–7% of the total global annual CO_2 emissions. However, the wide-range of properties available means that iron-based alloys will continue in use for the foreseeable future.

This summary of iron-based alloys aims to briefly introduce the main features and terminology of this class of alloys to act as a basis for further study.

https://doi.org/10.1016/B978-0-323-90800-9.00191-8

Iron

Iron, atomic number 26, is the central element of the first transition series in the periodic table and has an electronic configuration of $1s^2$, $2s^2$, $2p^6$, $3s^2$, $3p^6$, $3d^6$, $4s^2$. As an element under atmospheric pressure it is stable in the *bcc* (body centered cubic, ferrite) form up to 912 °C above which the *fcc* (face centered cubic, austenite) form is stable. Iron is unusual in that the *bcc* form becomes stable again at temperatures between 1394 °C and the melting temperature (1538 °C). Conventionally, the low temperature *bcc* form is referred to as α-ferrite (δ-ferrite is the high temperature form), while austenite is referred to as γ; at temperatures of a few hundred K and below the application of high pressures (around 10 GPa) can cause the *hcp* (hexagonal close packed, ε) form of iron to form. The atomic radius of iron is 0.126 nm, which allows significant amounts of other alloying elements to be taken into solid solution and so control over the structure and properties of iron-based alloys.

Alloying element behavior in iron

Apart from isolated examples, such as ARMCO® iron, which is ~99.85 wt% Fe, commercial iron-based materials are alloyed with a number of different elements, either deliberately added or as impurities from extraction and processing. The exact effects of individual alloying elements on the structure and properties of the iron-based alloy vary, but the types of alloying element and their effects can be grouped into a number of broad groups.

Interstitial alloying elements

Atoms treated as hard spheres in *bcc* and *fcc* arrangements only fill 68% and 74% of the available space leaving spaces or *interstices* between them. These interstices can be bounded by four (tetrahedral) or six (octahedral) iron atoms and contain a spherical space that could accommodate a solute atom provided its radius was small enough, Fig. 1 and Table 1. Atoms in the first and second row

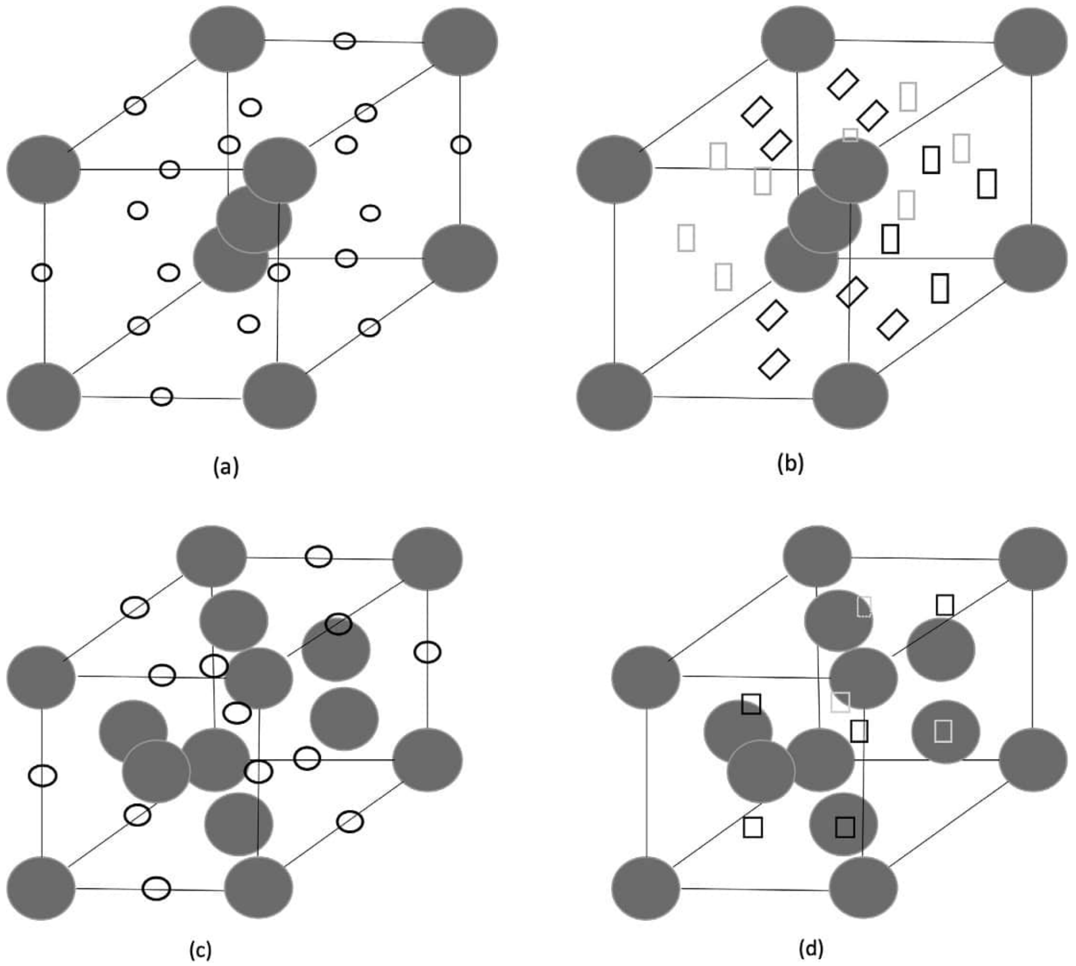

Fig. 1 Schematic diagrams of the *bcc* and *fcc* unit cells showing iron atoms (solid circles); octahedral interstices (open circles); and tetrahedral interstices (open rectangles); (a) octahedral interstices in *bcc*; (b) tetrahedral interstices in *bcc*; (c) octahedral interstices in *fcc*; and (d) tetrahedral interstices in *fcc*. For (b) and (d) the interstices located behind the atoms are outlined in light gray.

Table 1 Radius values of circle just fitting in interstices in iron unit cells along with atomic radii of interstitial atoms at room temperature.

	Octahedral interstice in bcc	*Tetrahedral interstice in* bcc	*Octahedral interstice in* fcc	*Tetrahedral interstice in* fcc
Ideal sphere radius (nm)	0.0196	0.0369	0.0522	0.0286
B atom radius (nm)	0.085	0.085	0.085	0.085
C atom radius (nm)	0.071	0.071	0.071	0.071
N atom radius (nm)	0.065	0.065	0.065	0.065

of the periodic table are of an appropriate (if somewhat too large) size to fit into these interstices. Of these elements B, C and N are the common alloying elements in iron that are taken into solution interstitially. Addition of these elements markedly reduces the alloy liquidus so that complete melting is achieved at much lower temperatures. The atomic radii of these alloying element atoms differ from that of the interstice sphere, Table 1, which causes strain in the surrounding lattice of iron atoms. The size mismatch between C or N and the interstices in austenite is less than in ferrite so that more of these elements can be taken into solution (higher solubility limit), e.g., the maximum solubility of C in ferrite is 0.02 wt%, whereas 2.0 wt% C can be dissolved in austenite in the binary Fe-C alloy system. Defects in the iron matrix have more open structures (grain boundaries) or strain fields associated with them (dislocations) which can offset some of the strain energy around a solute interstitial atom and so C and N concentrations are higher at boundaries and at dislocations (Cottrell atmospheres (Cottrell and Bilby, 1949)) than away from defects. The interaction between these interstitials and dislocations gives a large strengthening effect, which will be covered in more detail later.

In solution, Fe-X (X = B, C or N) bonds exist so that the greater solubility of interstitials in austenite stabilizes that phase relative to ferrite so that as the alloy contains more C or N, the temperature above which the equilibrium structure is 100% austenite (Ae3 temperature) decreases from 912 °C (pure iron) to 723 °C for Fe-0.8 wt% C. Carbon (and nitrogen) are therefore considered to be austenite-stabilizers. The boron atom is smaller than the interstitial space and the Fe-B bond energy is also relatively low so that B in iron-based alloys will lower the liquidus, but has negligible effect on the stability of ferrite and austenite as the effective Fe-B bond distances are relatively large. The more disordered structures in grain boundaries mean that the co-ordination of iron around B can be increased so that most B in solution in iron-based alloys is located at boundaries.

The number of interstitial sites in an *fcc* or *bcc* unit cell is large, Fig. 1, e.g. there are 4 octahedral and 8 tetrahedral interstices in an *fcc* unit cell, while the maximum amount of an interstitial alloying element in solution is around 1 atom per three unit cells. As such, there are always empty interstitial sites available for an atom to move into and the iron lattice distortion required for an interstitial atom to move from one site to an adjacent one is relatively small (a function of the migrating atom atomic radius) so that diffusion of interstitials is rapid with a lower temperature dependence than for non-interstitial (substitutional) alloying elements. The diffusivity (or diffusion coefficient), *D*, of an element can be used as a measure of its ease of motion in the solid state. This is usually represented as:

$$D = D_0 \; exp\left(\frac{-Q}{R\,T}\right)$$

Where Q is the activation energy (representing temperature-dependence) and D_0 is the pre-exponential factor; typical values are summarized in Table 2. The values are only strictly valid for binary Fe—X alloys, which is reasonable for substitutional alloying elements (see next section), but the presence of strong carbide- and nitride- formers, such as Cr and Nb, can reduce the movement of interstitial alloying elements in more highly alloyed systems.

Table 2 Typical diffusivity parameters for selected alloying elements in iron.

Phase	*Element*	*Activation energy,* Q *(kJ mol^{-1})*	*Pre-exponential factor,* D_0 *(mm^2 s^{-1})*	*Temperature range (°C)*
α-ferrite	Fe	240	200	700–750
	C	80	0.62	700–750
	N	76	0.3	700–750
	Cr	343	3×10^6	700–750
	Co	226	20	700–790
	Ni	258	970	700–790
γ-austenite	Fe	284	49	900–1050
	C	135	15	900–1050
	Cr	405	1.8×10^6	950–1050
	Co	364	3000	1050–1250
	Ni	280	190	930–1050

Substitutional alloying elements

As atomic number increases, the atomic radius of alloying elements increases so that, for alloying elements commonly taken into solution in iron, the strain energy involved for aluminum and later elements in the periodic table is too great for thermodynamic stability and they cannot be accommodated in interstices. An exception to this occurs for iron-based alloys under intense irradiation, e.g., high neutron fluxes in nuclear reactors, where the atoms are displaced into interstitial sites to give highly energetic and short-lived defects. Under less energetic conditions, these alloying elements are taken into solution by replacing, or substituting for, an iron atom on the *bcc* or *fcc* lattice. As such these are substitutional alloying elements. The solubility limit for these alloying elements depends on the size difference, valency and crystal structure of the alloying element compared with the host iron solvent (Hume-Rothery rules, (Hume-Rothery, 1967)). Thus, the first transition series elements, such as Cr, Mn, Co and Ni exhibit high solubilities, e.g. ASTM Grade HK contains 25 wt% Cr and 20 wt% Ni in solution, whereas the solubility of elements such as Al is limited ($\sim$1 wt% in austenite and 11 wt% in ferrite).

The ferrite- or austenite–stabilizing nature of substitutional alloying elements in iron is more varied than for the interstitials, partly because most iron-based alloys contain carbon, which is a strong austenite-stabilizer and elements having strong M-X bonds can precipitate carbo-nitrides at high temperatures (in the austenite field) removing carbon from solution and so de-stabilizing austenite. In this way strong carbo-nitride formers, e.g., Ti, V, Cr, Nb, Mo, Ta and W, are ferrite-stabilizers regardless of whether their stable crystal structure is *bcc*, *fcc* or *hcp*.

For non-carbo-nitride formers, then the situation is little clearer. Elements with a stable *fcc* structure, such as Co, Ni and Cu are austenite-stabilizers. However, Mn has a stable *bcc* structure and is an austenite-stabilizer while Si with a diamond structure (based on interlocking *fcc* unit cells) is a ferrite-stabilizer. The behavior of the alloying elements can be classified into four groupings based on their binary Fe-X phase diagram characteristics (Wever classification (Weber, 1928-1929)).

As for interstitial alloying elements, there are substitutional alloying elements that have limited solid solubility and show a marked tendency to concentrate into the liquid during solidification and to grain boundaries in the solid state. The largely detrimental effects of these elements on mechanical properties means that they are viewed as impurities; arising from coke (S), iron ore (P; this is added as a strengthener in some 're-phosphorized' sheet steels) or scrap (Sn).

As substitutional alloying element atoms occupy an iron atom site in the lattice, their migration can only occur if the iron (or substitutional alloying element) atom on the neighboring lattice site is missing. The absence of an atom on a lattice site is known as a vacancy, which is a thermally-activated defect. The need to generate these defects and the greater distortion of the iron lattice in transitioning the larger substitutional alloying element atom from one site to the neighboring one means that substitutional alloying element diffusion rates are much slower than those for interstitial alloying elements, while their temperature dependence is much greater, Table 2.

Phase transformations and microstructures

Most of the mechanical and some of the functional properties of iron-based alloys derive from the matrix microstructure (fine precipitates will be covered later). In pure iron, the room temperature microstructure will be composed of grains of α-ferrite, whose size would be controlled only by cold rolling and annealing cycles. The fixed point transformation temperatures and need only for iron atom re-arrangement leaves little control of or variation in the microstructure. Alloying to give cast irons or steels allows the microstructure (and, hence, properties) to be controlled and tailored to a much greater extent. This arises through:

(i) Introducing multiple phase fields on the phase diagram, e.g., in pure iron ferrite would form from austenite on cooling through 912 °C, whereas in alloy steels ferrite and austenite co-exist between Ae3 (temperature above which steel is 100% austenite at equilibrium) and Ae1 (temperature below which steel is 100% ferrite at equilibrium). The microstructure can be manipulated while cooling or holding in this two-phase region.

(ii) The transformation temperatures, e.g., Ae3 and Ae1, can be controlled by the balance of ferrite- and austenite-stabilizers in solution; an extreme example of this would be the Fe-30 wt% Ni steel, which remains as austenite down to liquid nitrogen temperatures. Alloying therefore opens up a much wider temperature range in which to process and modify the microstructure of iron-based alloys.

(iii) The presence of interstitial and, particularly, substitutional alloying elements can slow the rate of diffusional transformations, allowing other metastable structures, e.g., bainite and martensite, to form during processing, with transformation occurring below the Ae3—Ae1 temperature range.

(iv) Precipitates formed at high temperatures, e.g., Nb(C,N), can slow the movement of grain boundaries resulting in finer structures or slow growth of diffusional transformation products. Elements, such as B, that concentrate on grain boundaries can stop these acting as nucleation sites and further slow the formation of diffusional transformation products. Other precipitates can form at lower temperatures to provide strengthening.

The phases possible in iron-based alloys are thus expanded from ferrite and austenite to include pearlite (a mixture of ferrite and cementite (Fe_3C)), the various forms of bainite and the range of martensites (Pereloma and Edmonds, 2012). The conditions under which these matrix phases form are often represented on time-temperature-transformation (TTT) and continuous cooling transformation (CCT) diagrams, Fig. 2. These diagrams have traditionally been determined experimentally, but commercial software has developed to offer these as options.

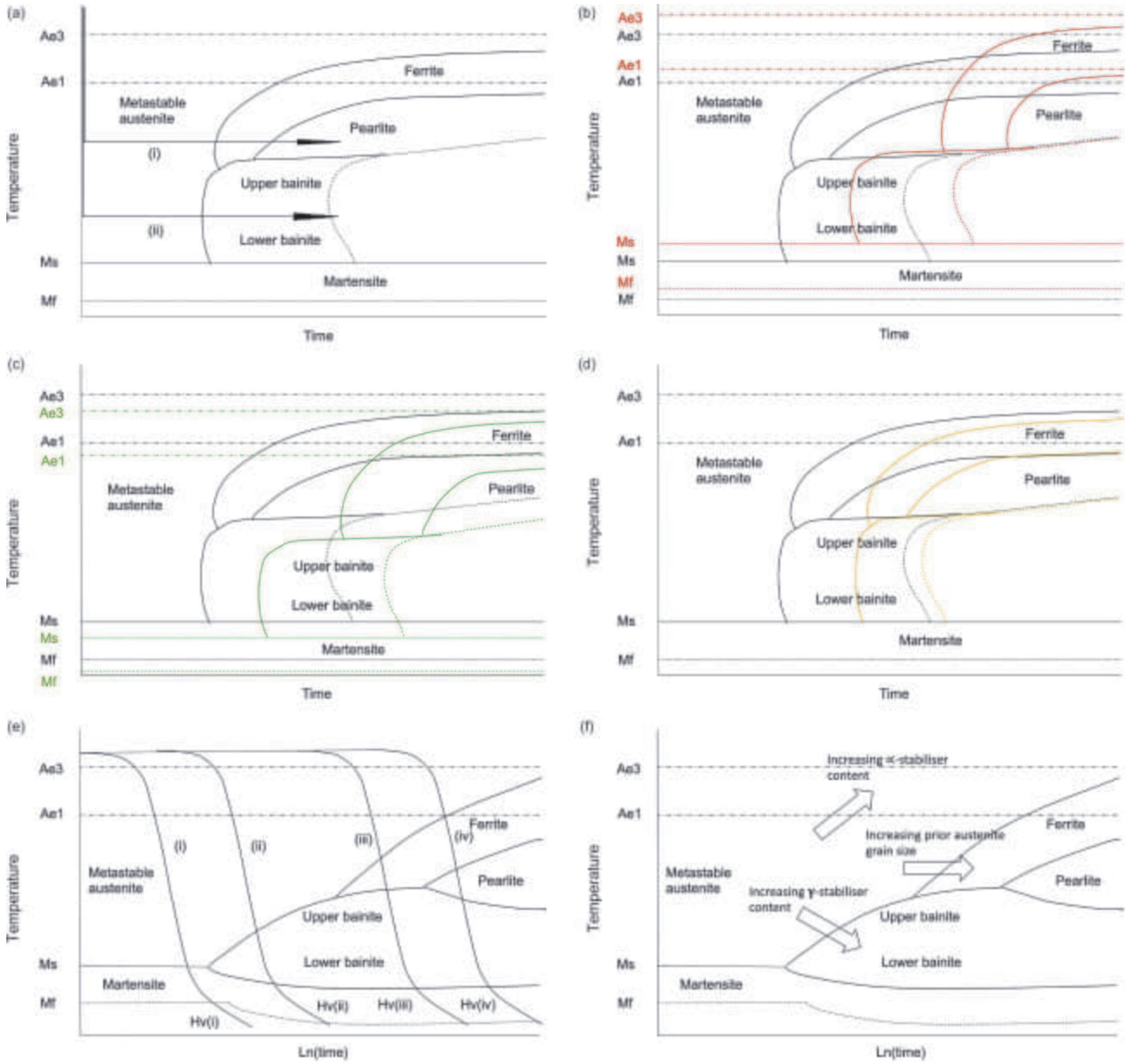
(a)
Ae3
Ae1
Metastable austenite
Ferrite
Pearlite
(i)
Upper bainite
(ii)
Lower bainite
Ms
Martensite
Mf
Temperature
Time
(b)
Ae3
Ae3
Ae1
Ae1
Metastable austenite
Ferrite
Pearlite
Upper bainite
Lower bainite
Ms
Ms
Mf
Mf
Martensite
Temperature
Time
(c)
Ae3
Ae3
Ae1
Ae1
Metastable austenite
Ferrite
Pearlite
Upper bainite
Lower bainite
Ms
Ms
Mf
Mf
Martensite
Temperature
Time
(d)
Ae3
Ae1
Metastable austenite
Ferrite
Pearlite
Upper bainite
Lower bainite
Ms
Mf
Martensite
Temperature
Time
(e)
Ae3
Ae1
Metastable austenite
(i)
(ii)
(iii)
(iv)
Ferrite
Pearlite
Upper bainite
Lower bainite
Ms
Martensite
Mf
Hv(i)
Hv(ii)
Hv(iii)
Hv(iv)
Temperature
Ln(time)
(f)
Ae3
Ae1
Increasing α-stabiliser content
Increasing prior austenite grain size
Ferrite
Metastable austenite
Increasing γ-stabiliser content
Pearlite
Upper bainite
Lower bainite
Ms
Martensite
Mf
Temperature
Ln(time)

Fig. 2 (a) Schematic TTT diagram showing transformation start (solid) and finish (dashed lines); the arrows show two examples of heat treatments covered by this type of diagram, i.e., quench to a given temperature followed by an isothermal hold. (b) The effects of alloying with an α-stabilizer, such as Cr or Mo are shown by the movement to red lines and text. (c) The effects of alloying with an γ-stabilizer, such as Ni or Mn are shown by the movement to green lines and text. (d) The effect of increasing prior austenite grain size is shown by the movement to yellow lines. (e) Schematic CCT diagram showing four example cooling curves ((i)—(iv)); CCT diagrams usually exhibit the final hardness values, which would decrease from Hv(i) to Hv(iv) as martensite is progressively replaced by bainite, ferrite and, finally, pearlite. (f) Arrows showing the effects of α-, γ-stabilizers and increasing prior austenite grain size on a CCT diagram.

Ferrite is generally the highest temperature transformation product, which forms initially on austenite grain boundaries by a diffusional mechanism that involves redistribution of carbon and substitutional alloying elements, e.g. Mn would be partitioned to the remaining austenite along with carbon, whereas Cr would be enriched in the growing ferrite. This phase is variously described as grain boundary, allotriomorphic and pro-eutectoid ferrite; if formed within the bulk of a prior austenite grain and not on the grain boundary, it can be termed idiomorphic ferrite.

Pearlite is the product of a eutectoid transformation which occurs by co-ordinated, simultaneous diffusional formation of ferrite and cementite (Fe_3C). Pearlite is a lamellar structure of alternating plates of ferrite and cementite which grow by carbon diffusion in austenite from ahead of a ferrite plate to a position ahead of the adjacent cementite plate.

As temperature decreases or cooling rate increases the driving force for decomposition of austenite increases so that the need for compositional equilibrium is relaxed leading to displacive + diffusional (bainite) and fully displacive (martensite) transformations. Diffusional transformations relieve strains in the parent phase and so interfacial energy dominates the shapes of the product phase regions, often leading to smoothly curved boundaries. Products of displacive transformations are constrained to lie within a single austenite grain so that they grow across that grain from one boundary in lenticular units as now a balance of strain and interfacial energies needs to be minimized. Displacive transformations are also referred to as shear transformations as the parent (*fcc*) lattice is sheared to form the product (*bcc*) lattice (some schemes refer to diffusional transformation as civilian and displacive as military to indicate the order involved). The shearing action means that the product contains a high dislocation density.

Bainite (Bhadeshia, 2015) forms initially as a displacive lenticular ferrite sub-unit with no diffusion involved so the ferrite has the same composition as the parent austenite including that of interstitial alloying elements. At the formation temperatures of bainite, interstitial alloying elements can diffuse distances of less than a micron during the transformation, although substitutional alloying elements remain frozen in place. The high strain energy associated with carbon trapped in ferrite provides a strong driving force for the sub-micron diffusion of carbon and its precipitation as iron carbide. Bainite that forms at higher temperatures, e.g., 500–550 °C, is termed upper bainite with carbon diffused to the edge of the ferrite sub-unit as well as formed nanometric-sized iron carbides in a single orientation in the sub-unit. Lower bainite forms at lower temperatures, e.g., 400–450 °C, with more restricted carbon diffusion so that the carbides within the sub-unit are still present, but not those at the sub-unit edge. The transition between the two forms is gradual over the transformation temperature range.

Martensite (Olson and Owen, 1992) is the product of a fully displacive transformation with no diffusion even that of interstitials over sub-micron distances; the martensite is therefore super-saturated with carbon. Lower carbon martensites (<0.5 wt% C depending on overall composition) have a lath sub-structure, but, with increasing carbon content (0.5–1.0 wt% C) the larger strain energy causes the sub-structure to change to twins; at carbon levels of 0.6 wt% C and above the lenticular twinned martensite regions will have some untransformed austenite between them at room temperature. From Fig. 2, different matrix phases and mixtures of phases can be generated from a single composition through the use of different heat treatment temperatures or different cooling rates. This is beneficial as the different phases possess different mechanical and functional properties allowing a range of properties to be tailored from a single composition. One downside of this is that thick sections would experience a variation in cooling rate from surface to center and, along with that, a potential spatial variation in structures and properties. Examples of steel microstructures are shown in Fig. 3.

Categories of irons and steels

Fig. 4 is a concise summary of the major types of commercially-available cast irons and steels. The categorization has arisen mainly from the industrial sector requirements for which the grades were developed (Llewellyn and Hudd, 1998; Honeycombe and Bhadeshia, 1995)). Thus, low carbon steels with a ferritic structure would possess relatively low strength (onset of plastic deformation and stress to cause fracture), but good ductility (uniform elongation and thinning when undergoing plastic deformation), which means that flat sheets can be readily be pressed / drawn into complex 3D shapes for automotive structures and packaging applications. Increasing the carbon content (without other alloying element increases) introduces pearlite into the structure, which increases strength, but at the expense of ductility.

As the carbon level approaches 0.4 wt% then joining components by fusion welding becomes increasingly difficult and so various substitutional alloying elements are used to continue increasing strength while maintaining ductility or toughness (energy absorbed in fracture) through grain size refinement and precipitate strengthening (see later). Thus, medium carbon steels tend to be more highly alloyed and would be rolled for plate, thicker sections, beams (long products) or forged; the higher alloy content allows bainite and martensite to be formed in the thicker sections if required.

High carbon steels (0.6–1.2 wt% C) tend to be used in applications where high strength is needed without particularly high toughness, such as railway and tram rails, which are based around 0.8 wt% C with a fully pearlitic structure, that offers good wear resistance. Steels used for drills and other machining bits operate at elevated temperatures (500–550 °C) with high strength, which requires stable precipitates and so these steels would be high carbon (up to 1.2 wt% C) with additions of strong carbide-forming elements (Cr, V and Mo for lower strengths and temperatures; Ti, Ta and W for higher strengths and operating temperatures). These would be shaped and heat treated in the single-phase austenite field before being quenched to a fully martensitic structure before being tempered to precipitate the alloy carbides in a fine ferrite matrix.

The steels summarized above would be shaped by thermo-mechanical methods, e.g. extrusion, rolling, drawing and forging, either hot ($T > 0.6$ of the melting temperature in K) or cold ($T < 0.3$ of the melting temperature in K). Few steels are produced with carbon contents above 1.2 wt% as the property mixes and processing routes offer few advantages until cast iron compositions at around 2 wt% C. The high carbon content means that the fully liquid temperature (liquidus) is between 1150 and 1400 °C so that melting and filling of complex mold shapes is achieved more easily. The high carbon content means that these irons cannot be mechanically shaped without cracking and so the component must be cast to final shape. As the liquid metal will lose heat to the mold as it flows into it, it must be cast at a temperature above the liquidus (superheat) so that it remains liquid until the mold is fully filled. The lower liquidus temperatures of cast irons allow greater superheats to be used without excessive oxidation and loss of material. In early cast irons the carbon was present as coarse (multi-micron) cementite particles in a matrix of pearlite, but the addition of >1 wt% Si converts the cementite into graphite in a connected flake-like form. This did not improve the toughness of the cast iron but the formation of graphite during solidification does involve an expansion that combats the liquid to solid contraction of the iron matrix so that the net volume change on casting is very small. Thus, the mold could be made to the final dimensions

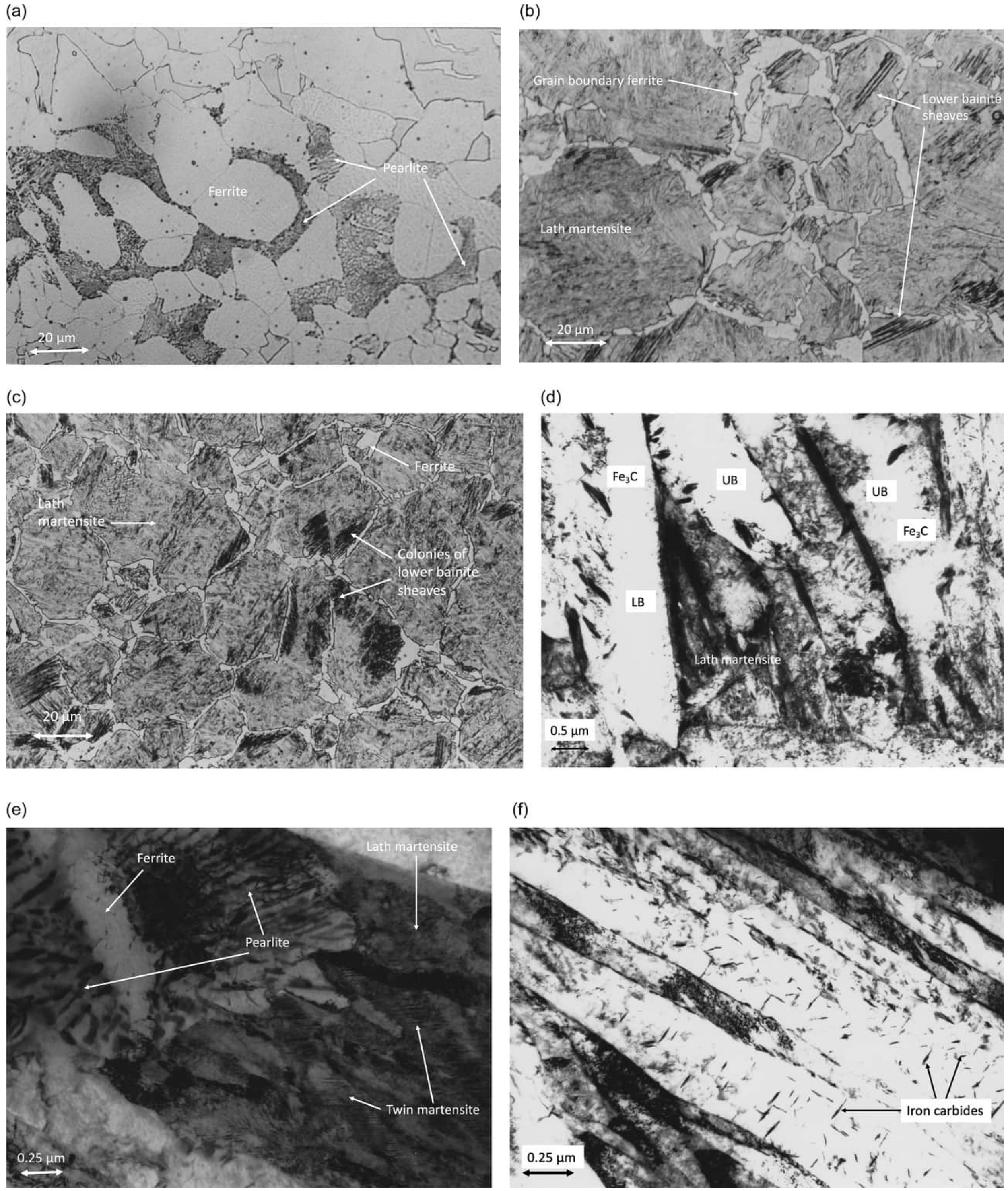
(a)
Ferrite
Pearlite
20 µm
(b)
Grain boundary ferrite
Lower bainite sheaves
Lath martensite
20 µm
(c)
Ferrite
Lath martensite
Colonies of lower bainite sheaves
20 µm
(d)
Fe_3C
UB
UB
Fe_3C
LB
Lath martensite
0.5 µm
(e)
Ferrite
Lath martensite
Pearlite
Twin martensite
0.25 µm
(f)
Iron carbides
0.25 µm

Fig. 3 Example steel microstructures. (a) Allotriomorphic ferrite grains and pearlite colonies (optical micrograph); these are coarse features and the separate lamellae in some pearlite colonies can be resolved, in other colonies the image plane cuts the lamellae at oblique angles so that the lamellae are not resolvable and the pearlite appears darker. (b) Grain boundary ferrite with lower bainite sheaves growing from their interfaces in a matrix of lath martensite; the internal lath structure of the martensite makes it gray and is faintly resolvable after nital etching whereas the finer internal carbide structure of lower bainite makes it appear black. (c) As for (b), but with a longer isothermal hold so that more adjacent lower bainite sheaves form to give colonies. (d) Transmission electron microscope (TEM) image of fine structure of lower bainite (LB) where fine cementite particles in the ferritic lath are in one orientation and upper bainite (UB) where the intra-lath carbides are complemented by carbides on the interface of the lath (inter-lath carbide). (e) TEM image showing fine structures of ferrite, pearlite, lath and twin martensite. (f) multi-oriented fine carbides in tempered lath martensite (Strangwood, 1987).

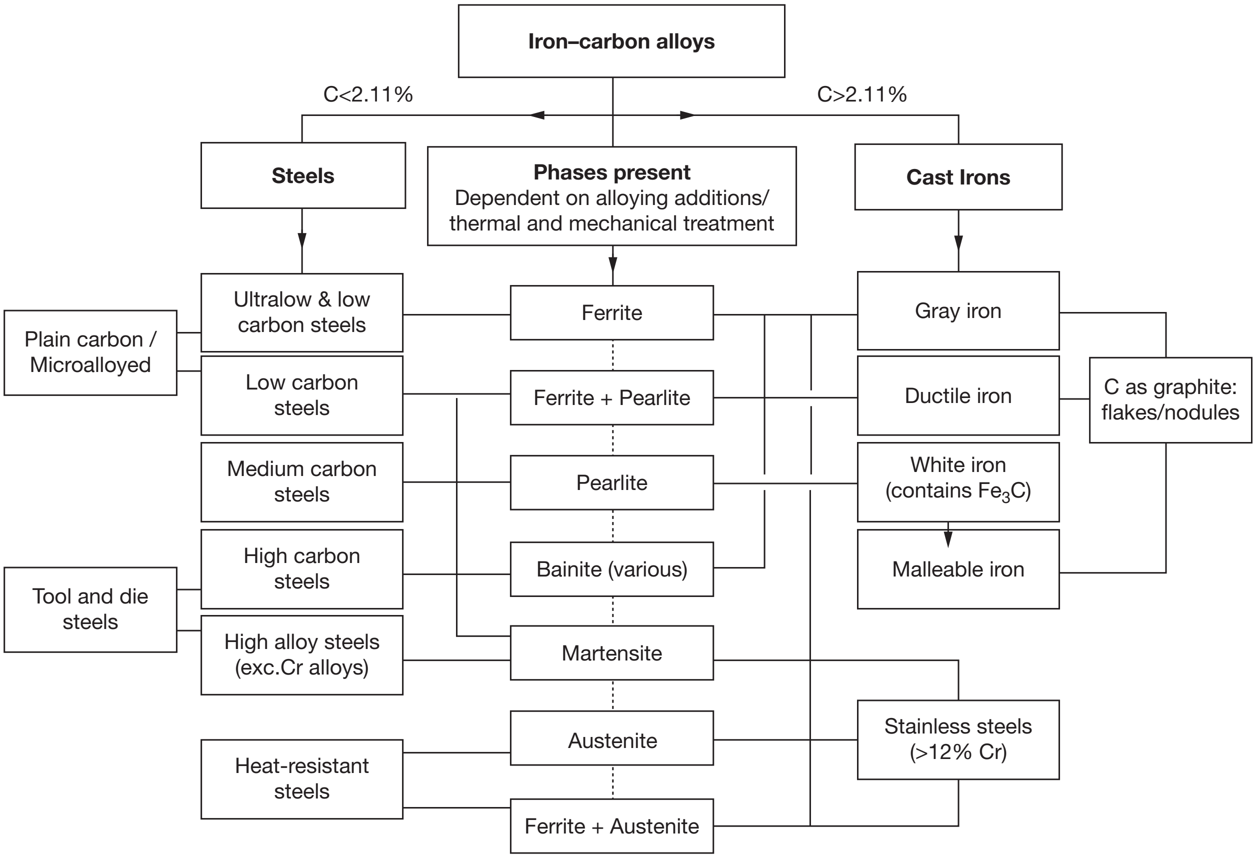
Iron–carbon alloys
C<2.11%
C>2.11%
Steels
Phases present
Dependent on alloying additions/ thermal and mechanical treatment
Cast Irons
Plain carbon / Microalloyed
Ultralow & low carbon steels
Low carbon steels
Medium carbon steels
High carbon steels
High alloy steels (exc.Cr alloys)
Tool and die steels
Heat-resistant steels
Ferrite
Ferrite + Pearlite
Pearlite
Bainite (various)
Martensite
Austenite
Ferrite + Austenite
Gray iron
Ductile iron
White iron (contains Fe3C)
Malleable iron
C as graphite: flakes/nodules
Stainless steels (>12% Cr)

Fig. 4 Classification scheme for the major iron-based alloys.

of the component. Subsequently small additions of Mg and Ce have been found to change the graphite morphology into spheres (SG iron), which has improved the toughness of these cast irons and formed the development of austempered ductile iron (ADI) along with increased alloying. ADI has lower density than wrought steels and improved vibration damping and so is being used for many gear box casings in wind turbines.

A wide range of stainless steels have been developed principally to develop oxidation-resistant alloys for a range of corrosive environments, e.g., saline solutions and various acids, and shapes, e.g., crevices. The basis for stainless steels is the replacement of a non-protective iron oxide surface layer with a self-healing protective chromia (Cr_2O_3) layer. The stoichiometric nature of chromia means that growth is so slow as to be effectively zero, although increased temperature does accelerate this and the chromia vaporizes at 1000–1100 °C. In order for the chromia layer to be self-healing so that scratches re-form chromia rather than any less-protective oxide, there needs to be a minimum of 12 wt% Cr in solution. This level of Cr would mean that the steel was ferrite from liquid to room temperature (ferritic stainless steel) providing medium strength, but poor ductility. Many applications, e.g., stainless steel knives and automotive trim, require thin sheet and so these are usually made in austenitic stainless steels, which contain sufficient nickel, e.g., 18 wt% Cr, 8 wt% Ni, to stabilize austenite down to room temperature. Carbon is not generally used as an austenite-stabilizer because of the strong carbide-forming nature of Cr as formation of Cr-rich carbides could locally deplete the matrix in Cr so that corrosive attack can take place. This corrosion, being localized, can lead to failure of the component, e.g., perforation of a pipe, for the loss of a small amount of material. The risk of carbide formation is highest in the heat affected zone (HAZ) around fusion welds (material from the component that has not been melted but has been heated up to the melting range) and so this is referred to as weld decay. Stainless steel grades that are weldable will either be L (low carbon) or stabilized where Ti or Nb has been added to combine with any carbon in preference to Cr. Austenitic stainless steels are low strength and so for greater load-bearing capability martensitic or duplex (ferrite + austenite) grades are used. Martensitic grades have reduced Ni content so that the austenite transforms to martensite on cooling to room temperature and an increased C content so that, on tempering, strengthening carbide precipitates form. Higher Cr content is needed to ensure that sufficient is retained in solution after carbide formation. These steels are not readily welded because of the potential for weld decay. Duplex stainless steels are very highly alloyed and are heat treated to give equal fractions of ferrite and austenite with the ferrite distributed as particles in the austenite. The isolated ferrite regions provide strength, while the continuous austenite provides toughness. Duplex stainless steels and the more highly alloyed superduplex stainless steels possess exceptional corrosion resistance particularly against localized corrosion (represented by the pitting resistance equivalence number PREN).

The final example class of steels is that of heat resisting power generation steel, which must combine a number of requirements. The need for higher efficiency is driving increases in steam operating temperatures and pressures which the components must withstand for decades and so both oxidation resistance and creep resistance are required. The steelwork must also retain sufficient toughness at room temperature during its operating lifetime to ensure that brittle fracture does not occur during shutdowns. The large amount of steel needed means that costly alloys, such as superduplex or nickel-based alloys are not economical, which has led to the development of the 9–12 Cr steel grades. These steels can be shaped by hot deformation and welded to assemble items such as heat exchangers, while being able to operate under ultra-supercritical (USC) conditions (566 °C at 24.1 MPa steam pressure to 621 °C at 7.2 MPa steam pressure). The steels are sufficiently alloyed that they form fully martensitic (lath as carbon level is around 0.1 wt%) structures that are tempered to form a fine array of Cr-rich carbides along with nitrides that help increase the creep strength of the steel. During service this structure will overage with the carbides and nitrides coarsening which reduces their strengthening contribution and allows the tempered martensite matrix to coarsen (further weakening it). The steels developed (grades 91, 92 and MarBN) are alloyed and heat treated to reduce these coarsening rates.

The text above and the examples in Table 3 is only a summary consideration of the 1000s of steel and iron grades available, but should provide a foundation for further study in the recommended reading.

Processing

The previous section has provided examples of steel and iron grades identifying some processing influences. Non-scrap iron (Moore and Marshall, 1991) is derived from the blast furnace which is a tower structure which reacts carbon in the form of coke with oxygen injected at the base to generate CO in an exothermic reaction that provides the heat needed to heat the rest of the charge (iron ore and limestone); the rising CO reduces the iron oxide to liquid iron by the overall reaction:

$$Fe_2O_3\ (s) + 3CO\ (g) \rightarrow 2Fe\ (l) + 3CO_2\ (g)$$

The blast furnace process produce pig iron, which is saturated with C (around 4 wt%) along with some Mn (manganese oxide is present in most iron ores) along with S from the coke and P from the iron ore. While Mn is beneficial, the high carbon content makes the iron unusable, while the S and P compromise the toughness of the alloy. Limestone additions remove most of the oxide impurities from the molten pig iron as a lower density liquid slag layer that floats above the liquid iron. The separation, however, is not perfect and some oxides are trapped in the iron as non-metallic inclusions, which also compromise toughness.

The desired steel and iron compositions summarized in the previous section are achieved by primary and secondary steelmaking processes, which reduce the C and P by blowing oxygen through the liquid iron in a basic converter under conditions that prevent large-scale re-oxidation of the iron. Additions are made to reduce S and to achieve the desired levels of elements such as Mn, Si and Ni in the molten steel, which is usually transferred to a 300–400 t capacity ladle. Elements that readily oxidize, such as Cr, are not effectively added in the converter and so their composition is adjusted in secondary steelmaking in the ladle. Alloying is carried out in the liquid phase, where fluid flow ensures full dissolution and mixing to give a uniform composition.

There is a drive to use more scrap (converters can contain up to 50% scrap which is mixed with molten pig iron) with electric arc furnaces (EAFs) able to melt a 100% scrap load, which should only need modification of the carbon and alloying levels without needing to reduce the very high levels of C from pig iron. The use of scrap should also not have the P and S levels associated with pig iron, but will pick up different impurities, such as Cu and Sn from scrap that can alter the resulting steel properties. Specialist (generally high value) steels such as the 9–12 Cr grades and bearing steels are formulated from melting their constituents in small batches (10s rather than 100 s of tonnes) in vacuum or inert gas furnaces (e.g. vacuum induction melting VIM) that are considered ‘clean’ melting, i.e., low non-metallic, S and P contents. The ingots resulting from solidification of these casts might be further refined by techniques such as vacuum arc remelting (VAR) or electro-slag refining (ESR). The use of these techniques improves the properties of these steels (not used for cast irons), but with the penalty of small tonnages and high costs (energy and monetary).

The bulk of the 1.6 billion tonnes of steel and iron processed annually comes via the blast furnace and converter or EAF routes and produces liquid of the correct composition that is solidified via continuous casting and (to a much lesser extent) ingot casting. Although the liquid can be considered compositionally uniform, solidification introduces composition variations through macro- and micro-segregation. The degree of segregation in continuous casting is much less than in ingot casting giving final product that has much less scatter in properties. Continuous casting uses a bottomless water-cooled copper mold that produces a continuous strand (that is removed steadily at around 5–8 km h^{-1}) with a square or rectangular cross-section up to 2.5 × 0.4 m in size); ingots typically taper with a base dimension up to 1 × 1 m and height of 2–3 m.

The strand/ingot sizes are suitable for solidification, but final products can be plates/sheets down to less than 1 mm in thickness or complex shapes such as rails so that post-casting processing (Llewellyn and Hudd, 1998) is needed, Fig. 5. Large reductions in thickness would be achieved by hot rolling when the yield stress of the steel is reduced along with the rolling load. Integrated plant would deliver the strand flame cut to slabs directly from the continuous caster to the hot rolling mill; otherwise, and for ingots, castings would cool for storage prior to reheating and then hot rolling. Slabs would only be heated prior to the hot rolling process and would be hot rolled to around 35 mm thickness in a series of rolling passes. During hot rolling, the austenite grains would be deformed and recrystallize, either during rolling (dynamic recrystallization) or between rolling passes (static recrystallization); recrystallization would refine the grain size with the recrystallized grain size being inversely related to the strain imposed, although a

Table 3 Selected mechanical properties of various commercial steels and cast irons.

Stel grade	*Composition (wt%)*	*Microstructure*	*Yield stress (MPa)*	*Tensile strength (MPa)*	*Elongation to failure (%)*	*Comments*
Ultralow carbon	0.0024–0.0028C, 0.031–0.069 Ti, 0.07 Mn, 0.007 Si, <0.002 N	Ferrite	100	270	55	Thin (~1 mm thick) strip (Kim et al., 2002)
Low carbon	0.1C, 1.7 Mn, 0.25 Si, 0.02 (Nb + Ti)	Ferrite + martensite	350	600	27	https://ahssinsights.org
Medium carbon	0.4C, 0.55 Mn, 1.0 Ni, 1.25 Cr, 0.3 Mo	Bainite + tempered martensite	1200	1600	12	Weidmann et al. (1990)
High carbon	0.8C, 0.8 Mn	Very fine pearlite	–	3000	1–2	Pearlitic steel wire—patented (Weidmann et al., 1990)
High alloy	18.8 Ni, 10.8 Co, 4.22 Mo, 1 Ti	C-free tempered martensite with intermetallic precipitates	937–2318	1053–2539	16.7–8.0	Properties vary with tempering time and temperature (Sha and Guo, 2009)
Heat resistant steel	0.12C, 8.16 Cr, 0.95 Mo, 0.54 Mn, 0.27 Si, 0.14 V, <0.02 N	Tempered martensite with fine alloy carbide precipitates	>450	600–850	>15	Designed for operation at up to 600 °C (Pandey et al., 2017)
Stainless steel	0.099C, 11.68 Cr, 0.37 Si, 0.4 Mn, 0.4 Ni, 0.0095 N	As-quenched and tempered martensite	303–1127	380–1427	7.0–18.0	Lim et al. (1993)
Stainless steel	0.027C, 17.53 Cr, 12.2 Ni, 2.49 Mo, 1.7 Mn, 0.22 Si, 0.07 N	Austenite	275	570	48	185 GPa Young's modulus (Ganesan et al., 2009)
Stainless steel	25 Cr, 7 Ni, 3.6 Mo, 0.25 N, 0.7 Cu, 0.7 W	Ferrite + austenite	650	840	30	185–205 GPa Young's modulus, superduplex stainless steel (Charles, 1991)
Cast iron (gray)	4.35C, 2.23 Si, 0.4 Mo, 0.079 P, 0.089 S, 0.13 Cr, 0.009 Mo	Flake graphite and pearlite	–	150	1.3	Lian et al. (2020)
Cast iron (ADI)	3.45C, 2.43 Si, 0.089 Mn, 0.06 Mg, 0.061 Cr, 0.024 Ni	Graphite nodules, upper bainite and austenite	640	950	6	60J Charpy impact energy (Refaey and Fatahalla, 2003)
Cast iron (white)	2.45C, 1.33 Si, 0.64 Mn, 0.08 P, 0.08 S	Primary Fe_3C in a pearlite matrix	–	572	1.2	8J Charpy impact energy (Hsu et al., 2007)
Cast iron (malleable)	2.45C, 1.33 Si, 0.64 Mn, 0.08 P, 0.08 S	Graphite in acicular ferrite (bainite) and austenite	–	1083	2.5	16J Charpy impact energy—heat treated white cast iron (Hsu et al., 2007)

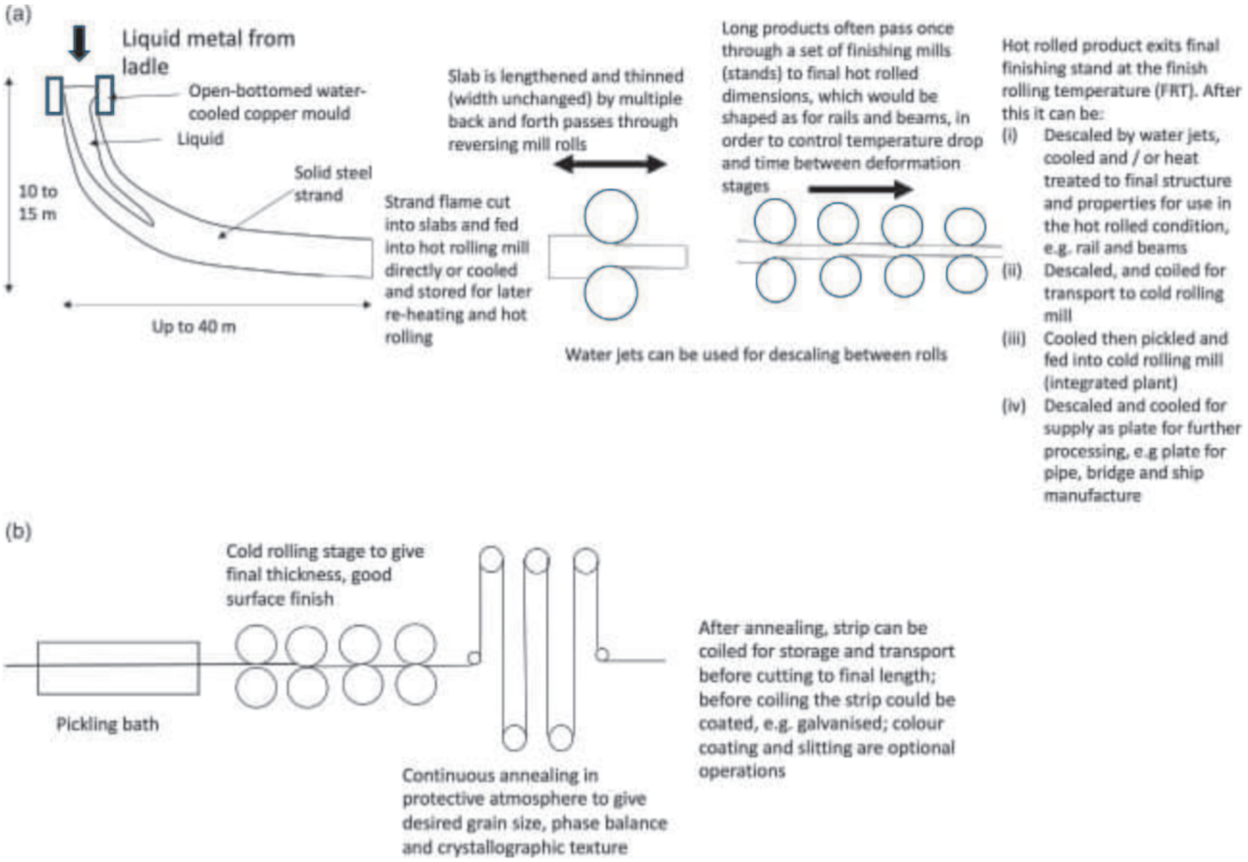
(a)
Liquid metal from ladle
Open-bottomed water-cooled copper mould
Liquid
Solid steel strand
10 to 15 m
Up to 40 m
Strand flame cut into slabs and fed into hot rolling mill directly or cooled and stored for later re-heating and hot rolling
Slab is lengthened and thinned (width unchanged) by multiple back and forth passes through reversing mill rolls
Long products often pass once through a set of finishing mills (stands) to final hot rolled dimensions, which would be shaped as for rails and beams, in order to control temperature drop and time between deformation stages
Water jets can be used for descaling between rolls
Hot rolled product exits final finishing stand at the finish rolling temperature (FRT). After this it can be:
(i) Descaled by water jets, cooled and / or heat treated to final structure and properties for use in the hot rolled condition, e.g. rail and beams
(ii) Descaled, and coiled for transport to cold rolling mill
(iii) Cooled then pickled and fed into cold rolling mill (integrated plant)
(iv) Descaled and cooled for supply as plate for further processing, e.g plate for pipe, bridge and ship manufacture
(b)
Cold rolling stage to give final thickness, good surface finish
Pickling bath
Continuous annealing in protective atmosphere to give desired grain size, phase balance and crystallographic texture
After annealing, strip can be coiled for storage and transport before cutting to final length; before coiling the strip could be coated, e.g. galvanised; colour coating and slitting are optional operations

Fig. 5 Schematic diagram of steel processing route; (a) casting and hot rolling, and (b) cold rolling.

limiting recrystallized austenite grain size can be approached toward the end of the hot rolling passes (Humphreys and Hatherly, 2004). High strength steel grades, i.e., those whose microstructures contain large amounts of pearlite, bainite and/or martensite, need to be shaped hot with any subsequent processing being heat treatment, e.g., quenching and tempering, as the low ductility of these grades prevents significant cold deformation. Hot deformation of steels is usually carried out in air rather than protective atmospheres and so significant oxide scale formation can occur, which produces a rough, dull surface and poor shape tolerance. The oxide scale can be removed by pickling in an HCl-based acid solution, while finish machining would be needed if tight dimensional tolerance and good surface finish is required.

Austenitic steels and steels with majority ferrite structures can be shaped by cold methods to give good tolerances and surface finishes (oxide scale from hot working would need to be removed prior to cold deformation). If the section size is large, then cold working would be difficult, due to the large deformation loads involved and strain variation through the section resulting in spatially varying structure and properties in the final component. Unlike hot deformation, recovery and recrystallization do not occur during cold deformation, so that the steel work hardens. This can be beneficial as it provides a low cost route to yield stress increase without extra alloying. Increased work hardening, however, does reduce ductility and so the cold deformed material is subjected to a controlled anneal to give the desired mix of strength and ductility (in the same way as copper would be supplied in quarter, half and three quarters hard conditions). Annealing would be carried out in a protective atmosphere in order to preserve the good surface finish from cold deformation (Humphreys and Hatherly, 2004). Annealing of cold rolled strip can also lead to improved later formability (Ray et al., 1994). Cold rolled materials (strip) can be annealed in continuous furnaces, which gives much more rapid heating rates (3–30 °C s^{-1}) and can also include a coating stage, e.g., molten zinc pot for galvanized strip material or polymer coating. Non-continuous product or smaller production runs would need to be batch annealed which is a much slower process as the furnace needs to be loaded cold, evacuated and re-filled with a protective atmosphere and then heated to the annealing temperature (600–800 °C) before holding for the required time and then cooled to room temperature. The greater thermal mass of the furnace and load compared to a strip of steel means that the heating rate is much less (~5 °C min^{-1}). The longer heating phase allows recovery to occur so that the rate of recrystallization is reduced and, for certain grades, the properties obtained are poorer compared with a continuous process.

Mechanical properties

As noted, steel grades have been developed to achieve required property mixes (Honeycombe and Bhadeshia, 1995) with much of the study of steel metallurgy associated with making that process more reliable and more rapid. Although the required properties may include chemical and functional ones, the majority of steels have been developed on the basis of mechanical properties with achieving higher yield stress and tensile strength without compromising ductility and toughness remaining a principal goal.

Elastic deformation of iron and steel components in service is important and generally should be minimized. The material property representing the resistance to elastic deformation is the Young's modulus, which, unlike titanium-based alloys, is relatively constant for most irons and steels at 210 GPa. The only real difference exists for highly alloyed austenitic stainless steels when the value decreases to around 170 GPa.

Many standards for steel grades are based on values for yield stress (onset of plastic deformation) and tensile strength (stress under which necking occurs leading to final fracture). Both of these values are dependent on the difficulty of dislocation motion (to different extents); in irons and steels there are five principal strengthening mechanisms.

Alloying element atoms, both interstitial and substitutional, differ in size from the sites that they occupy and so introduce elastic strain fields into the iron matrix around the atom in solution. These strain fields interact with the strain fields of the dislocations to provide strength increments that increase with the amount of alloying element in solution; this is solid solution strengthening. The matrix strain and, hence, the strengthening increases with atom size mismatch, but this is self-limiting as the greater the size difference the lower the solubility so, for substitutional alloying elements the extent of solid solution rarely exceeds 100 MPa. Interstitial alloying elements such as C and N have a much larger solid solution strengthening effect, because they are small and mobile enough to move to and occupy the compressive strain field region of dislocations leading to a net reduction in strain and so strain energy. These atmospheres effectively pin dislocations as dislocation movement away from the interstitial atom requires the separate strain fields to be re-established; the energy required is manifested in a higher external stress for yield. This is the basis of the yield point effect in ferritic steels, Fig. 6. Initially, dislocations are pinned by interstitial atmospheres (Cottrell atmospheres previously mentioned) and so require a high external stress to cause movement (as the full dislocation and interstitial strain fields need to be re-established once the dislocation moves away from the interstitial). Once freed from their interstitial atmospheres, however, the dislocations can move under a lower stress giving a plateau on the stress-strain curve until dislocation multiplication occurs to a level at which normal work hardening behavior (see below) is seen. The yield point effect can give unsightly thickness variations (Lüders bands/stretcher marks) when final shapes need low and variable cold deformation strains, e.g., curved car body panels. To avoid this, the strip is rolled to a strain beyond the yield point effect plateau, i.e., into the work hardening regime just prior to stamping or forming (Dieter, 1988).

Once the solubility limit is exceeded, precipitate particles are formed with a range of sizes and spacings. Very fine precipitates (up to ~10 nm) can be coherent with the matrix so that dislocations move through (cut) the precipitates, which have higher modulus than the matrix and create a strain field in the surrounding matrix. Both of these effects increase the resistance to dislocation motion. In irons and steels, fine (Nb,V)(C,N) precipitates tend to be coherent, but larger examples of these and most

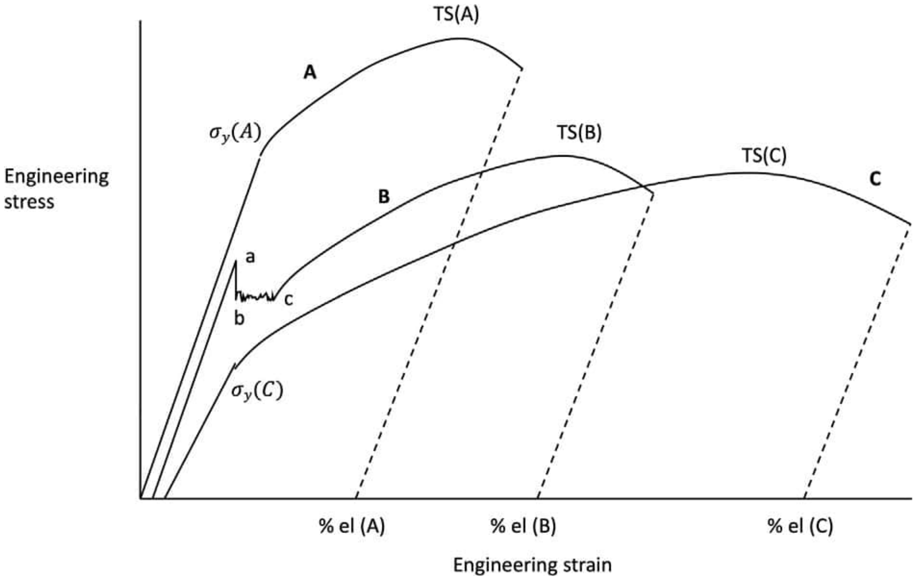

Fig. 6 Schematic engineering stress—engineering strain curves for (A) medium carbon engineering steel, (B) low carbon ferritic steel and (C) austenitic steel. The curves are slightly displaced along the x-axis to separate them. The onset of plasticity is shown by the yield stress (σ_y) for A and C, while B shows the yield point effect with an initial upper yield stress (a) followed by a lower yield stress (b), which holds until work hardening starts to dominate at (c). The onset of necking is shown by the tensile strength (TS) points and ductility differences are shown by the % elongation to failure values (% el).

other precipitate types, e.g., cementite and Cr-rich carbides, are incoherent. Dislocations cannot pass through incoherent particles and so must loop around them (Orowan bowing), when the strengthening is proportional to the volume fraction and inversely proportional to the precipitate size (radius). Many strengthening precipitates are used in steels with the most effective being precipitated at lower temperatures, such as VC, Mo_2C, $M_{23}C_6$ and Fe_3C, particularly from tempering of martensitic structures.

Increasing yield stress by solid solution and precipitate strengthening requires increased alloy additions, but the yield stress of grades with good ductility can be increased by cold deformation as for the yield point effect, Fig. 6. Plastic deformation increases the number density of dislocations in a given volume of metal proportionately with the plastic strain. Dislocations interact with each other impeding the movement of mobile dislocations so an increased dislocation density increases yield stress. However, there is little increase in the tensile strength and the ductility of the alloy decreases as work hardening increases.

Grains are regions of crystalline material in a given orientation and grain boundaries represent the area where these orientations change from one to the next. As dislocations are constrained to move along certain (slip) planes, then they cannot move from one grain to an adjacent one. Additionally, the different grain orientations mean that grains do not all start yielding under the same external stress, but softer orientations yield first and then increasing stress extends yield to other grains eventually giving macroscopic plastic deformation of the specimen/component. When dislocations in a deforming grain meet the boundary with a non-deforming grain they are stopped and pile-up. The pile-up projects a stress concentration into the adjacent (non-deforming) grain with the size of the stress concentration being proportional to the grain size. When the combination of stress concentration and external stress reach a critical value, yield is initiated in the adjacent grain. Thus, smaller grain sizes result in higher strength, described by the Hall-Petch relationship, Table 4.

The aim of many steel grades and processing is to maintain as fine a grain size as possible, which can arise mainly from nucleation of new grains, transformation of the matrix grains or recrystallization. In cast irons and cast steels, nucleation of solid grains from the liquid is often employed with nucleation being enhanced by (i) rapid solidification rates by placing 'chills' in the mold that extract heat more rapidly; (ii) adding inoculant particles (small particles that are solid while the iron and steel are molten) which provide a site from which the solid metal can grow; and (iii) vibrating the casting during solidification which transports solid fragments from the already solidified portion into the remaining liquid where they can grow into new solid grains. During hot deformation of wrought products single grains are deformed, e.g., becoming pancake-shaped during rolling, with a high dislocation density. However, at elevated temperatures the excessive dislocations and their associated strain energy can be removed by nucleation of new (recrystallized) grains—generally several new grains for each original grain, leading to refinement of grain size. As mentioned previously, this recrystallization occurs either during deformation (dynamic recrystallization) or after deformation

Table 4 Summary of strengthening contribution relationships used for iron-based alloys; yield stress and critical resolved shear stress can be related by the Taylor factor (m, generally between 2.24 and 3.06); $\sigma_y = \frac{\tau_{CRSS}}{m}$.

Mechanism	*Formula*	*Parameters*	*Comments*
Peierls-Nabarro stress in pure iron	–	σ_0 (tension) τ_0 (shear)	~50 MPa (Kimura, 1999) ~33 MPa (Caillard, 2010)
Solid solution strengthening	$\Delta\sigma_s = k_{si}\sqrt{c_i}$	k_{si} = solid solution strengthening coefficient for solute, *i* c_i = concentration of *i* in solution (at.%)	Assumed additive for multiple solutes (Soboyejo, 2003; Leslie, 1981)
Precipitate strengthening (coherent)	$\Delta\tau_{coh} = k_{coh}\sqrt{r\,f}$	k_{coh} = constant, dependent on precipitate, matrix and composition r = mean precipitate radius f = precipitate volume fraction	Often referred to as cutting or shearing of deformable particles (Martin, 1980)
Precipitate strengthening (incoherent)	$\Delta\tau_{ppt} = \frac{G\,b}{\lambda}$	G = shear modulus (~80 GPa for iron) b = Burger's vector ($\frac{a}{2} < 110 >$ for *fcc* and $\frac{a}{2}\langle 111\rangle$ for *bcc*; a = lattice parameter) λ = mean particle spacing (~)	Often referred to as Orowan looping (Martin, 1980)
Work hardening	$\Delta\sigma_{WH} = \alpha\,G\,b\,\sqrt{\rho_b}$	α = work hardening rate (function of composition and microstructure) ρ_b = dislocation density (length/unit volume or number per unit area)	Dislocation density often related to plastic strain, ε_p. (Martin, 1980)
Grain size refinement	$\Delta\sigma_{GB} = \frac{k_{HP}}{\sqrt{D}}$	k_{HP} = Hall-Petch constant (material-specific; ~0.74 MPa √m for low carbon steel) D = average grain diameter	Hall-Petch relationship, also termed grain boundary strengthening (Hall, 1951; Petch, 1953). Can be applied to different boundary types with different constants, e.g., lath and twin boundaries in martensite
Phase balance	$\sigma_y = \sum_j f_j\,\sigma_{yj}$	f_j = volume fraction of phase *j* σ_{yj} = yield stress of phase *j*	This is a rule of mixtures approach using the known yield stress or calculating it for each phase based on the equations above (Young and Bhadeshia, 1994; Goodall et al., 2018)

(static recrystallization). In hot rolling, the slab being reduced in thickness passes back and forth through a single set of 'reversing' rolls, where the time between forward and reverse passes, determines the time for static recrystallization. After repeated recrystallization during hot rolling the grain size tends to reach a limit for roughly spherical (equiaxed) austenite grains. Cooling on completion of hot rolling (often in a coil for ease of handling) causes decomposition of austenite into ferrite, pearlite, bainite and/or martensite. The limiting, equiaxed austenite grain size leads to a ferrite grain size of around 15–25 μm. Further refinement would require more ferrite grains to form on cooling. Ferrite grains form on austenite grain boundaries and so finer grains require more grain boundary area, which is achieved by not recrystallizing during the final few passes so that the austenite grains are 'pancaked' with a higher boundary area per unit volume than if they were spherical. This approach requires the temperature at which the austenite stops recrystallizing (various measures used such as non-recrystallization temperature—Tnr) to be raised into the single phase austenite phase field. Alloying with small amounts of strong carbo-nitride formers, of which Nb is the most potent, results in microalloyed or high strength low alloy (HSLA) steels (Gladman, 1997), which can be rolled to give a final ferrite grain size of 4–7 μm [https://steeluniversity.org]. HSLA steels have good strength values for low carbon levels, which means that they can be readily fusion welded.

The final strengthening mechanism is that of phase balance. The matrix phases of irons and steels increase in strength in the general order:

$$\text{Austenite} < \text{ferrite} < \text{pearlite} < \text{bainite} < \text{martensite}$$

Changing the phase balance, by heat treatment allied with composition, as summarized above, can be used to change the strength of the alloy, although higher alloy contents would be needed to achieve phases such as bainite and martensite in thicker sections. The strength of martensite is often too high, when combined with its low ductility and toughness, for service application and so steels with more than a few % of martensite in the structure will be tempered to remove the excess carbon from solution to leave a matrix of fine (sub-micron) ferrite (former martensite laths and twins) containing fine and closely spaced carbide precipitates. Tempering takes place below Ae1 (typically between 200 °C and 700 °C for a few hours). Tempering at 550 °C and above allows substitutional alloying elements to diffuse so that stronger alloy carbides precipitate (Fe_3C forms at lower temperatures), which gives an increase in strength, known as secondary hardening. Strength decreases and ductility increases with increasing tempering time and/or temperature. Tempering close to Ae1 can give coarsening of the fine matrix lath structure and is generally avoided if possible. Some lower tempering temperatures are also avoided, due to segregation and possible precipitation of solute atoms (such as S and P) to grain boundaries to give grain boundary failure (reversible and irreversible temper embrittlement).

Strength is usually not the only property needed with minimum toughness often being required as well. Toughness is measured either by a fracture energy (J) at a specified single temperature or over a range, as in the Charpy or Izod impact tests (Dieter, 1988) or by a critical stress concentration factor (MPa $m^{-0.5}$) to cause a crack to become self-propagating, as in fracture toughness (K_{Ic} testing) (Dieter, 1988). Impact tests are relatively quick and easy to perform whereas fracture toughness testing is more specialized and time-consuming, which makes it less common as a material qualification test. When fracture occurs, the creation of fresh surfaces requires surface energy to be provided and so work is done. The energy involved in creating surfaces is small compared with that associated with plastic deformation. Brittle failure only creates cleavage surfaces and so absorbs little energy, whereas ductile failure where the metal voids and the voids extend and coalesce by dislocation motion absorbs greater amounts of energy and so is much tougher. Increasing strength by restricting dislocation motion will generally come at the expense of toughness. Grain boundaries can divert cracks and so refinement of grain size is the only one of the five mechanisms that can increase strength and toughness.

Features that allow voids (or cracks) to form and propagate more readily, reduce the amount of dislocation motion required to fully separate the sample/component into two and so reduce toughness. In irons and steels, there are two main ways that this occurs. Firstly, as noted above, iron- and steel-making causes non-metallic inclusions, such as oxides, to be trapped in the metallic matrix. These inclusions, being ceramics, are harder and with higher modulus than the surrounding iron/steel. In addition, their lack of metallic bonding can cause the interface between the inclusion and the matrix to be weak. The inclusions generally form at high temperatures in the liquid, where fluid flow allows them to grow rapidly so they are multi-micron in size. On plastic deformation, or in the strain field ahead of a crack/defect, the inclusion does not deform as readily as the matrix and so can crack and decohere accompanied by stress concentration in and work hardening of the metallic matrix so that crack initiation and propagation is accelerated with less plastic strain, i.e., toughness is decreased. The greater the size and number density of inclusions then, generally, the lower the toughness. The second main feature is that of grain boundary embrittlement by elements, such as S and P, that segregate to grain boundaries and weaken the bonding across them. This means that the grain boundaries can separate with very little plastic deformation and the toughness is reduced to that corresponding to just the formation of new surfaces. The iron/steel is now brittle and the process a form of embrittlement (e.g., grain boundary embrittlement or temper embrittlement). Iron- and steel-making has developed to reduce the amount of the impurity or tramp elements (S, P, Sn) and reduce the size and number of inclusions present—the steels have become 'cleaner.' In the case of S, a compromise is made in that the full removal of S is achievable, but expensive and so the Mn levels in the steel are maintained to fully precipitate the S as MnS inclusions; these inclusions do contribute to ductile crack initiation and propagation, but this is far better than the brittle failure associated with S in solution on grain boundaries.

Some rough relationships exist between strength and toughness and other mechanical properties, e.g., increased strength delays the initiation of fatigue cracks on smooth samples while increased fracture toughness permits greater fatigue life in a cracked sample before final failure. A full description of the development of other mechanical properties, such as creep, wear and fatigue resistance, is beyond the scope of this overview, which has aimed to show the approaches generally adopted by the iron and steel industry along with their effects as a basis for further reading.

Chemical properties

The principal chemical property associated with irons and steels is corrosion resistance, such as in the stainless steels noted above. Many structures will be constructed of non-stainless steels and irons and require corrosion protection through:

Coatings—as noted above zinc, polymer and paint coatings can be applied to strip steel after cold rolling and annealing, while other structures would be painted after assembly. Small structures and components can be coated by plasma and electrochemical techniques with chromium to provide a protective chromia surface, although, unlike stainless steels, this not self-healing. Oil and gas pipelines can be coated with polymer-based protective coatings when produced as pipe sections or after assembly in the field.

Iron- and steel-based structures can be electrically connected to sacrificial anodes—metals that corrode in preference to iron—to protect the load-bearing structure. This approach is often used for maritime structure, e.g., oil rigs, where blocks of magnesium are attached to the steel structure. The sacrificial anodes will be consumed during service and so periodic replacement is required.

Large structures, such as pipelines, can also be protected by an impressed current, where the potential of the iron or steel structure is altered to lower the corrosion current. Corrosion rate is also pH-dependent and so pipelines might need differing levels of impressed current as they traverse different soil types with different pHs.

Corrosion behavior is very environment-dependent (e.g., temperature, pH, ion concentrations, partial pressure of oxygen and full or partial immersion) and so the assessment of corrosion resistance is generally made under a limited number of controlled conditions, e.g., seawater is often simulated by 3.5% aqueous NaCl solution, for comparison purposes.

Functional properties

In terms of thermal properties, then low alloy ferritic steels have similar thermal conductivity and expansivity values, Table 5. Highly alloyed steels and cast irons with a significant graphite content will possess different values, which can be further modified if the matrix structure changes from ferritic to austenitic. Thus, austenitic stainless steels have low thermal conductivity and high thermal expansivity, which makes machining more difficult and contributes to earlier thermal fatigue in high temperature plant operations. Alloying of Ni with Fe, however, can reduce thermal expansivity and is the basis of the Invar series of alloys.

The electronic structure of iron with its four un-paired 3d electrons means that it is one of only four ferromagnetic elements. Irons and steels are widely used for their magnetic properties either as metallic alloys, e.g., electrical steel, or compounds, e.g., ferrites and $Nd_2Fe_{14}B$ (Jiles, 2003). Iron-based alloys and compounds are unusual in the range of magnetic properties that can be generated. The formation of balanced magnetic domains means that iron and ferritic steels can show no net magnetic moment. However, in 'clean' steels, domain walls move readily under an external field to give a soft magnetic material with a narrow hysteresis loop (low coercivity). This behavior is sought for electrical steels, which are low carbon and low alloy, but contain 3.5 wt% Si, which enhances the magnetization as well as increasing resistivity so that eddy current losses are reduced. This steel finds widespread use as a core for windings in electric motors and transformers as laminates of thin sheet (0.3 mm) formed by cold rolling and annealing. More controlled processing produces Goss textured sheet, where grains are preferentially oriented with the *bcc* cell edge easy magnetization direction ($\langle 100 \rangle$) in the plane of the sheet. Less costly processing produces non-grain oriented (NGO) sheet at the cost of greater hysteresis losses. The drive to increased electrification of vehicles is driving the production of more electrical steel and for greater performance; 6 wt% Si would give better electrical and magnetic properties but the lack of ductility makes processing on an industrial scale too difficult currently.

Increased coercivity, i.e., harder magnetic materials, for iron-based alloys can be achieved by impeding domain wall motion, through finer grains size, dislocation density and, most effectively, by the presence of non-magnetic particles, such as carbo-nitrides. In this way increased mechanical strength (and hardness) is allied with increased magnetic hardness.

Metallic iron-based alloys show a limited maximum magnetic hardness and harder magnetic properties come from Fe-based compounds, such as oxide-based ferrites and one of the hardest magnetic materials, $Nd_2Fe_{14}B$, which require ceramic processing methods, such as powder processing. As for metallic iron-based alloys, refining the grain size of $Nd_2Fe_{14}B$ increases the magnetic moment. These materials are finding increasing use in high torque electric motors and in wind turbines. Table 6 summarizes the range of magnetic properties available in commercial iron-based alloys and compounds.

Table 5 Selected thermal properties of stainless steels (Charles, 1991).

Grade	*Coefficient of thermal expansivity (10^{-6} K^{-1})*	*Specific heat capacity (J kg^{-1} K^{-1})*	*Thermal conductivity (W m^{-1} K^{-1})*
Ferritic	10–12.5	450–480	21–60
Austenitic	16	520–544	15–16
Duplex	13.5–14.5	500–530	17–19

Table 6 Some notable ferromagnetic iron alloys showing typical properties.

Material	*Initial relative permeability* (μ_0)	*Hysteresis loss per cycle* (*J m*$^{-3}$)	*Saturation induction* (*Wb m*$^{-2}$)	(BH)$_{max}$ (*kJ m*$^{-3}$)
Soft magnetic alloys				
Commercial iron ingot	1.5×10^2	270	2.14	
Fe-3Si (oriented silicon iron)	1.5×10^3	40–140	2.0	
Fe-45Si (PERMALLOY 45)	2.7×10^3	120	1.60	
$Fe_{73.5}Si_{13.5}B_9Nb_3Cu_1$ (FINEMET)	5×10^3–2×10^5		1.0–1.2	
$Fe_{88}Zr_7B_4Cu_1$ (NANOPERM)	1×10^4–1×10^5		1.5–1.8	
$Fe_{44}Co_{44}Zr_7B_4Cu_1$ (HITPERM)	2×10^3–3×10^4		1.6–2.1	
Hard magnetic alloys				
Fe-1Mn-0.9C (martensitic)				3.8
Fe-3.5Cr-0.9C-0.3Mn (martensitic)				5.0
Fe-24.5Co-13.5Ni-8Al-2Nb (Alnico-XII)				76.8
$Fe_{60}Pt_{40}$				120
$Nd_2Fe_{14}B$ (oriented)				320–400
$Nd_2Fe_{14}B$ (sintered nanophase)				450

Conclusion

The structures, processing and properties of iron-based alloys have been briefly covered along with the main strategies used to achieve the property mixes offered by this class of alloys. This is not comprehensive or very detailed, but should provide a basis for more informed further study.

Alloy and process development of iron-based alloys continues to improve property mixes as well as improve efficiency. These traditional improvements are being modified by the need for more sustainable iron and steel production, i.e., reducing the carbon footprint of the iron and steel industry, while future electrification is providing more applications for iron-based materials with improved functional properties.

References

Bhadeshia HKDH (2015) *Bainite in Steels*. Boca Raton: CRC Press.

Caillard D (2010) Kinetics of dislocations in pure Fe. Part I. In situ straining experiments at room temperature. *Acta Materialia* 58: 3493–3503.

Charles J (1991) In: Charles J and Bernhardsson S (eds.) *'The Duplex Stainless Steels: Materials to Meet Your Needs', Duplex Stainless Steels '91*, 3–48. J. de Physique, Paris.

Cottrell AH and Bilby BA (1949) Dislocation theory of yielding and strain ageing of iron. *Proceedings of the Physical Society* 62(1): 49–62.

Dieter GE (1988) *Mechanical Metallurgy*. London: McGraw-Hill.

Ganesan V, Mathew MD, and Sankaro Rao KB (2009) Influence of nitrogen on tensile properties of 316LN SS. *Materials Science and Technology* 25(5): 614–618.

Gladman T (1997) *The Physical Metallurgy of Microalloyed Steels*. London: Institute of Materials.

Goodall A, Yulin J, Davis CL, and Strangwood M (2018) *'Effect of Tempering on Hardness of Q & T Steel Plate', THERMEC 2018, Materials Science Forum*.

Hall EO (1951) The deformation and aging of mild steel: III Discussion of results. *Proceedings. Royal Society of London* 64(9): 747–753. 941, 311–316.

Honeycombe RWK and Bhadeshia HKDH (1995) *Steels—Microstructure and Properties*. London: Edward Arnold.

Hsu C-H, Lu J-K, and Chen F-S (2007) Effects of copper and malleablizing time on mechanical properties of austempered malleable iron. *MMTA* 38A: 2419–2427.

Hume-Rothery W (1967) *The Structure of Alloys of Iron*. Oxford: Pergamon Press.

Humphreys FJ and Hatherly M (2004) *Recrystallisation and Related Annealing Phenomena*. Oxford: Elsevier Science.

Jiles DC (2003) Recent advances and future directions in magnetic materials. *Acta Materialia* 51: 5907–5939.

Kim S-Y, Kwak J-H, Chung J-H, and Cho K-M (2002) Effect of titanium on the formability of Ti IF steels. *Metals and Materials International* 8: 155–161.

Kimura H (1999) Mechanical properties of high purity iron and its dilute alloys. *Materials Transactions, JIM* 40(10): 1025–1031.

Leslie WC (1981) *The Physical Metallurgy of Steel*. London: McGraw-Hill.

Lian XT, Zhu JN, Dong H, Wang YM, and Liu JP (2020) Effects of micro-alloying elements on microstructure, element distribution and mechanical properties in gray irons. *International Journal of Metalcasting* 14(4): 1025–1032.

Lim LC, Lai MO, Ma J, Northwood DO, and Miao B (1993) Tempering of AISI 403 stainless steel. *Materials Science and Engineering* A171: 13–19.

Llewellyn D and Hudd R (1998) *Steels: Metallurgy and Applications*. London: Elsevier.

Martin JW (1980) *Micromechanisms in Particle-Hardened Alloys*. Cambridge: Cambridge University Press.

Moore C and Marshall RI (1991) *Steelmaking*. London: Institute of Metals.

Olson GB and Owen WS (1992) *Martensite*. Metals Park, OH: ASM International.

Pandey C, Mahaptra MM, Kumar P, and Saini N (2017) Effect of creep phenomena on room-temperature tensile properties of cast and forged P91. *Engineering Failure Analysis* 79: 385–396.

Pereloma E and Edmonds DV (2012) *Phase Transformations in Steels*. Cambridge: Woodhead Publishing.

Petch NJ (1953) The cleavage strength of polycrystals. *The Journal of the Iron and Steel Institute London* 173: 25–28.

Ray RK, Jonas JJ, and Hook RE (1994) Cold rolling and annealing textures in low and extra low carbon steels. *International Materials Review* 39: 129–172.

Refaey A and Fatahalla N (2003) Effect of microstructure on properties of ADI and low alloyed ductile iron. *Journal of Materials Science* 38: 351–362.

Sha W and Guo Z (2009) *Maraging steels: Modelling of Microstructure, Properties and Applications*. Cambridge: Woodhead Publishing.

Soboyejo WO (2003) *Mechanical Properties of Engineering Materials*. NY: Marcel Dekker.

Strangwood M (1987) *The Prediction and Assessment of Weldmetal Microstructures*. PhD thesis University of Cambridge.

Weber F (1928-1929) Archiv. *Eisenhüttenussen* 2: 193.

Weidmann G, Lewis P, and Reid N (1990) *Structural Materials*. London: Butterworths.

Young CH and Bhadeshia HKDH (1994) Strength of mixtures of bainite and martensite. *Materials Science and Technology* 10(3): 209–214.

Alloys: Magnesium☆

Jian-Feng Nie, Monash University, Melbourne, VIC, Australia

© 2024 Elsevier Ltd. All rights reserved.

This is an update of H. Jones, Alloys: Magnesium, Editor(s): Franco Bassani, Gerald L. Liedl, Peter Wyder, Encyclopedia of Condensed Matter Physics, Elsevier, 2005, Pages 54–57, ISBN 9780123694010, https://doi.org/10.1016/B0-12-369401-9/00535-0.

Introduction **550**
Overview **551**
Deformation mechanisms 551
Designations of alloys and tempers 552
Processing of magnesium alloys 553
Alloying 553
Casting 553
Thermomechanical processing 554
Continuous sheet casting 554
Machining 554
Welding and Joining 555
Additive manufacturing 555
High-pressure die cast magnesium alloys 555
Sand cast or permanent mold cast magnesium alloys 557
Magnesium extrusion alloys 558
Mg-Al based alloys 558
Mg-Zn based alloys 559
Mg-Mn-RE based alloys 560
Mg-RE based alloys 560
Magnesium plate/sheet alloys 560
Mg-Al based alloys 560
Mg-Zn based alloys 561
Mg-RE based alloys 561
Mg-Li based alloys 562
Applications of magnesium alloys 562
Key issues **562**
Conclusion **563**
References **563**
Further reading **564**

Abstract

Mg is an abundant and attractive metal, and it can be used for many energy-efficient and environmental-friendly applications in transportation, communication, hydrogen storage and biodegradable products sectors. Considerable efforts have been made in the past 20 years for wider applications of magnesium alloys, and a remarkable progress is achieved on the design and development of cost-effective alloys with improved properties. A significant achievement is also made for the fundamental understanding of alloy microstructures, deformation mechanisms, precipitation processes, alloying effects on formability, and processing-microstructure-property relationships.

Key points

- Metal production
- Deformation mechanisms
- Designation of alloys and tempers
- Alloy processing
- High-pressure die cast alloys
- Sand cast alloys
- Extrusion alloys

☆*Change History:* September 2022. J-F Nie is involved in the preparation of the update. The update is almost fully different from the previous one due to the rapid progress on this topic in the past 20 years.

- Sheet alloys
- Applications
- Key issues

Introduction

Magnesium is the lightest of all commonly used structural metals. It has a density of 1.74 g·cm^{-3} at 20 °C, approximately two-third that of aluminum and quarter that of steels. It is the eighth most abundant element in the earth's crust, the third most plentiful element dissolved in seawater, and the seventh most abundant element by mass in the human body. It is extracted from seawater, lake brines, dolomite, magnesite and other minerals, and commercially available with purity exceeding 99.8%, but is rarely used in engineering applications in unalloyed form. Magnesium has a relatively low melting temperature (650 °C) and high specific heat, Table 1. Therefore, magnesium can be cast readily to near-net shape by conventional casting methods, especially by pressure die casting. Magnesium can also be machined readily, with approximately 55% of the power required to machine aluminum and its alloys. Magnesium alloys have the highest specific stiffness and strength of all structural alloys, making them potentially suitable for automotive applications in which large components, presently fabricated from steel, can be advantageously replaced with this much lighter metal. Magnesium is the third most commonly used structural metal, after aluminum and iron.

Magnesium was first recognized by Joseph Black in 1755 as a new element whose oxide was magnesia (magnesium oxide, MgO). It was first isolated by Humphry Davy in 1808 by evaporating the mercury from a magnesium amalgam that he made by electrolyzing a mixture of wet magnesium oxide and mercuric oxide. Davy suggested a name magnium, but magnesium is the one used nowadays. This name come from Magnesia, a district in Thessaly of Greece where the magnesia was first found. In 1828

Table 1 Basic properties of magnesium

Property	*Value*
Atomic number	12
Atomic weight	24.305
Atomic radius	0.160 nm
Crystal structure	Hexagonal
Lattice parameters (25 °C)	$a = 0.321$ nm $c = 0.521$ nm
Density (20 °C)	1.738 g cm^{-3}
Melting point	650 °C
Boiling point	1090 °C
Latent heat of fusion	370 kJ kg^{-1}
Latent heat of evaporation	5250 kJ kg^{-1}
Heat of combustion	25,100 kJ kg^{-1}
Volume change on solidification	−4.2%
Volume change during cooling (650–20 °C)	−5%
Thermal conductivity (25 °C)	156 W m^{-1} K^{-1}
Thermal expansion coefficient	25.2×10^{-6} K^{-1}
Specific heat capacity (20 °C)	1025 J kg^{-1} K^{-1}
Self-diffusivity coefficient along [0001]	1.0×10^{-4} m^2 s^{-1}
Activation energy for self-diffusivity along [0001]	134.7 kJ mol^{-1}
Self-diffusivity coefficient perpendicular to [0001]	1.5×10^{-4} m^2 s^{-1}
Activation energy for self-diffusivity perpendicular to [0001]	136 kJ mol^{-1}
Elastic constants	
C_{11}	59.7 GPa
C_{12}	26.2 GPa
C_{13}	21.7 GPa
C_{33}	61.7 GPa
C_{44}	16.4 GPa
Young's modulus	45 GPa
Shear modulus	17 GPa
Poisson's ratio	0.35
Stacking fault energy (0 K)	
intrinsic fault I_1	18 mJ m^{-2}
intrinsic fault I_2	36 mJ m^{-2}
extrinsic fault E	54 mJ m^{-2}
twin-like fault T_2	42 mJ m^{-2}
Damping capacity (loss factor)	0.014–0.060
Standard electrode potential	−2.40 V

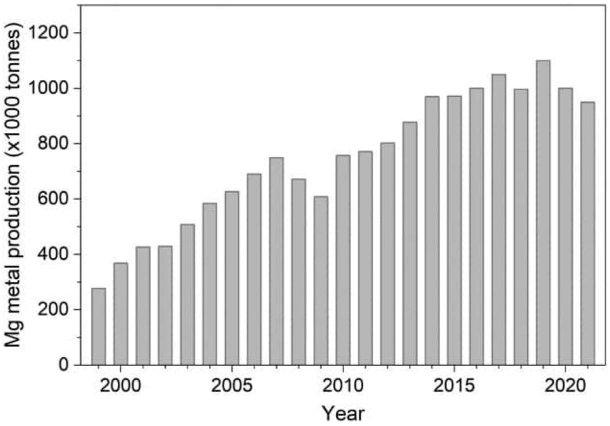

Fig. 1 World production of magnesium in the period 1999–2021.

Antoine Alexandre Brutus Bussy isolated the magnesium metal by fusing dehydrated magnesium chloride with metallic potassium at elevated temperatures. The first production of magnesium was made by Michael Faraday in 1833 through electrolytic reduction of dehydrated magnesium chloride. Robert Wilhelm Bunsen made a commercial quantity of pure magnesium in 1852 from molten dehydrated magnesium chloride. The commercial production of magnesium metal on a larger scale started in 1886, reached 10 t per annum in 1890. It was increased to about 3000 t per annum at the end of World War I, and 300,000 t late in World War II. The global commercial production of magnesium metal was around 250,000 t per annum between 1970 and 1999, approximately 368,000 t in 2000, but rose rapidly to around 757,000 t in 2010, reached about 1,000,000 t in 2020, Fig. 1. China now produces about 85% of the global production of magnesium metal.

Magnesium metal is currently produced by completely different processes. One is electrolysis of magnesium chloride the operates in the liquid state, the other is Pidgeon process which involves solid-state thermal reduction of magnesium oxide by ferrosilicon at high temperature. The electrolysis process, adopted by Norsk Hydro and Dow Chemical Company in the past, used to account for 75% of the global production of magnesium. It is environmentally friendly, but its energy consumption is costly. The Pidgeon process is less efficient than the electrolysis, but became dominate since 2000, when China became the major producer of magnesium, where the low cost of labor, energy and ferrosilicon allowed this process to be economically competitive.

In 2021, about 45% of the global magnesium was used to produce light weight magnesium products for applications in the automotive, electronic and aerospace industries, nearly 35% was consumed as an alloying element in aluminum, 16% was used to desulphurize steels, and 4% was used to refine titanium sponge and to produce nodular cast irons, Fig. 2.

Overview

Deformation mechanisms

Magnesium has a hexagonal crystal structure with a c/a ratio of 1.623 at 25 °C. Its close-packed plane is (0001), and its close-packed direction is $\langle 11\bar{2}0\rangle$. Perfect dislocations include those with Burgers vectors in the basal plane ($1/3 < 11\bar{2}0 >$, or $\langle a\rangle$ type), Burgers vectors perpendicular to the basal plane ([0001], or $\langle c\rangle$ type) and Burgers vectors in a pyramidal plane ($1/3\ \langle 11\bar{2}3\rangle$, or $\langle c+a\rangle$ type). Imperfect dislocations include those having a Shockley partial type Burgers vector ($1/3\ \langle 10\bar{1}0\rangle$) on the basal plane, a Burgers vector perpendicular to the basal plane (1/2[0001]), or a Burgers vector in a pyramidal plane ($1/6\ \langle 20\bar{2}3\rangle$). Stacking faults include intrinsic faults I_1 and I_2, extrinsic fault E and twin-like fault T_2 (Chetty and Weinert, 1997). Basal slip can be activated at very low stress at room temperature and is a major deformation mode. Non-basal slips, such as pyramidal I $\{10\bar{1}1\}\langle 11\bar{2}3\rangle$ and pyramidal II $\{11\bar{2}\bar{2}\}\langle 11\bar{2}3\rangle$ slip and prismatic slip can also occur at room temperature, but at much higher stress. The basal and non-basal slips

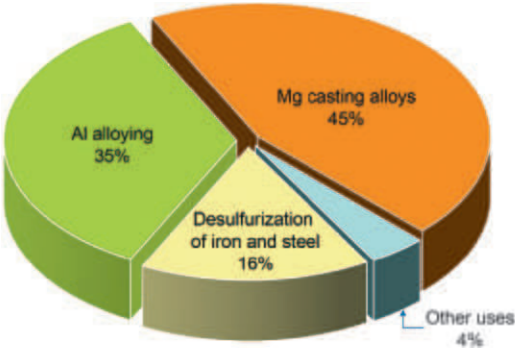

Fig. 2 Breakdown of global usage of magnesium in 2021.

often occur together in polycrystalline magnesium alloys to allow individual grains to plastically deform to meet the shape change imposed by their neighboring grains (Partridge, 1967; Agnew, 2012). Apart from dislocation slip, twinning is another important deformation mode. The twinning modes include those leading to twin formation on $\{10\bar{1}1\}$, $\{10\bar{1}2\}$, $\{10\bar{1}3\}$, $\{10\bar{1}4\}$, $\{10\bar{1}5\}$, $\{30\bar{3}4\}$, $\{11\bar{2}1\}$ and $\{11\bar{2}4\}$. The $\{10\bar{1}2\}$ extension twin occurs most frequently, and it forms under the stress condition that favors an extension along the *c*-axis. The formation and growth of $\{10\bar{1}1\}$ contraction twin cause a contraction along the *c*-axis.

Under an applied external stress σ, the resolved shear stress along the slip/twinning direction on the slip/twinning plane, τ, is given by $\tau = \sigma \cos \alpha \cos \beta$, where α is the angle between the applied stress axis and the slip/twinning direction, and β is the angle between the applied stress axis and the slip/twinning plane normal. The orientation factor, $\cos\alpha \cos \beta$, is also known as Schmid factor, and it is an important parameter for plastic deformation of highly textured polycrystalline magnesium alloys. The resolved shear stress must be larger than a critical value, the critical resolved shear stress (CRSS), in order to activate slip or twinning. The CRSS values for basal and non-basal slips and twinning modes in pure magnesium are provided in Fig. 3 (Nie et al., 2020). Pyramidal slip is more difficult to activate than basal slip, and the activation of contraction twinning needs a higher CRSS than that of extension twinning. CRSS values for basal slip and extension twinning are almost temperature independent, in comparison with others deformation modes whose CRSS values decrease significantly with increasing temperature. Since CRSS values for dislocation slip and twinning are all low, it is a common practice to thermomechanically process magnesium alloys at warm to high temperatures in order to maximize deformation modes to facilitate plastic deformation. Additions of alloying elements or solute atoms can increase or decrease CRSS values, and hence influence the plastic deformation process. Additions of specific alloying elements can also change the recrystallization texture of thermomechanically processed magnesium alloys.

In addition to intra-granular deformation modes of slip and twinning, inter-granular deformation such as grain boundary sliding can also occur, especially when the grain size of polycrystalline pure magnesium is reduced to the vicinity of 1 micron. Less studies have been made on grain boundary sliding in magnesium alloys, mainly because this deformation mode is thought unlikely to occur in wrought magnesium alloys produced by conventional processing methods in which the grain size is usually above 5–10 μm.

Dynamic recrystallization generally does not occur during plastic deformation of magnesium alloys at room temperature, but it plays a major role in texture formation during hot deformation of magnesium alloys. Factors influencing the size and orientation of fully recrystallized grains are temperature, strain, strain rate, solutes, and second-phase particles. While it is now well known that some specific alloying elements can change recrystallization behavior and texture, even at remarkably low concentrations, the precise role of such alloying elements in texture changing remain to be revealed.

Designations of alloys and tempers

Magnesium alloys are commonly designated by the American Society for Testing Materials. One or two letters are generally used in this designation system. The first letter indicates the major principal alloying element, and the second letter represents the next principal alloying element that is in less quantity. These two letters are listed alphabetically when the added two alloying elements are equal in quantity. The code used for alloying elements is the following: A—aluminum; B—bismuth; C—copper; D—cadmium; E—rare earths; F—iron; H—thorium; J—strontium; K—zirconium; L—lithium; M—manganese; N—nickel; P—lead; Q—silver; R—chromium; S—silicon; T—tin; V—gadolinium; W—yttrium; X—calcium; Y—antimony; Z—zinc. These two letters (or one letter) are followed by two (or one) numbers that indicate the weight percentages of these principal alloying elements, rounded off to the nearest whole number. For example, AZ91 represents the alloy Mg-9Al-1Zn-0.3Mn (wt%) in metallurgical notation. The composition of this alloy is (90Mg, 9Al, 1Zn, 0.3Mn, wt%) in which the actual concentration may vary in the range 8.3–9.7 for Al and 0.4–1.0 for Zn. More letters and numbers are added when the alloy contains more than two intentionally added elements. A suffix letter A, B, or C, etc. may also be used for some alloys, and they refer to variations in composition within the specified range. For example, the suffix letter E in higher-purity AZ91E indicates that the concentrations of impurity elements Fe, Ni and Cu, which

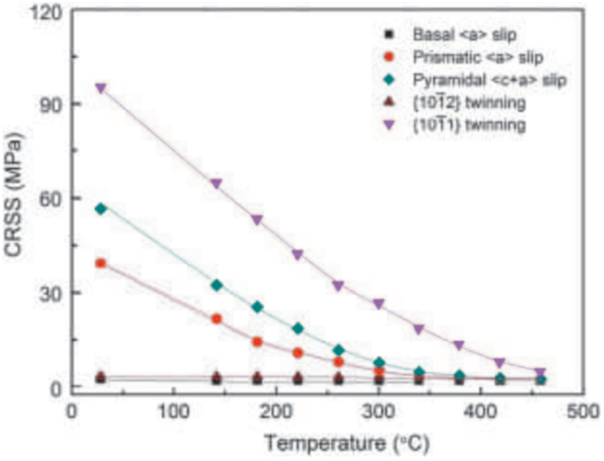

Fig. 3 Critical resolved shear stress (CRSS) values for different slip and twinning modes and their variation with temperature for pure Mg single crystals (Nie et al., 2020). From Nie JF, Shin KS, Zeng ZR (2020) Microstructure, deformation, and property of wrought magnesium alloys. *Metallurgical and Materials Transactions A: Physical Metallurgy and Materials Science* **51**: 6045–6109.

are detrimental to the alloy corrosion resistance, are lower (Fe 0.015 wt% max., Ni 0.001 wt% max. and Cu 0.015 wt% max.) than those in a less-pure alloy AZ91C. Some magnesium alloys may be used in the heat-treated or work-hardened conditions, i.e., tempers. The temper designations for magnesium alloys are specified in the same way that has been adopted for aluminum alloys. Commonly used tempers are T5 (alloys artificially aged after casting), and T6 (alloys solution treated, quenched and artificially aged).

Processing of magnesium alloys

Alloying

Alloying elements are added to molten magnesium in conventional productions. The intentionally added alloying elements are usually in the form of pure elements or master alloys, and most of them have appreciable solubilities in molten magnesium. One exception to this is beryllium that is usually added at a ppm level which, while being substantially low, is sufficient to reduce the oxidation rate of molten magnesium. The magnesium oxide layer that forms on the molten magnesium does not provide efficient barrier to further oxidation. Molten magnesium ignites and burns when it exposes to air. It is for this reason that the molten magnesium, which is associated with the melting operation in foundry, needs to be covered by a protective gas, which has been 0.2% SF_6, or 0.5–1% SO_2, in dry air. Sulphur hexafluoride was the commonly used component of the cover gas in the past, but the environmental legislations in many countries have eliminated the use of this gas because of its extremely high global warming potential. Sulphur dioxide has a zero green-house potential, but it is a toxic gas and has to be used at a low concentration in the foundry. An alternative cover gas, which uses a low concentration of HFC-134a in nitrogen, carbon dioxide, or air, has been commercially developed in recent years.

For the purpose of corrosion resistance, it is necessary to control the concentration of impurity elements iron, nickel and copper to the ppm level in the cast product. For magnesium alloys that are free of zirconium, manganese is often added to the molten alloy to react with iron to form intermetallic compounds that settle down to the crucible bottom before the molten alloy is cast. In this way, the concentration of iron in the cast alloy is usually less than 40–50 ppm. For magnesium alloys that contain additions of zirconium and/or rare-earth elements, the iron content can be reduced to the ppm level by these elements reacting with iron to form intermetallic particles that are excluded from the casting.

Casting

Magnesium alloy products can be readily produced by conventional casting processes such as high-pressure die casting (HPDC), sand casting, permanent mold casting and thixo-casting. HPDC includes both hot-chamber and cold-chamber processes. In each of these processes, molten alloy is injected into a near-net-shape and smoothly finished cavity within seconds under high pressure. Products with thin walls can be cast by these processes due to the excellent fluidity of molten magnesium alloy, and most HPDC magnesium products do not need to have any post-casting machining. Most automotive and electronic components made of magnesium alloys are produced by HPDC. The most commonly used magnesium alloy for this process is AZ91. This alloy is cast at a temperature in the range 620–640 °C for hot-chamber HPDC, and 650–680 °C for cold-chamber HPDC. Alloys containing less contents of aluminum, such as AM60 (93.7Mg, 6Al, 0.3Mn, wt%), are generally cast at slightly higher temperature. The HPDC magnesium alloys are generally not heat treatable. This is because the gas or air bubbles trapped inside the casting will cause surface blistering or even distortion of the casting if it is heat treated at high temperatures. The casting generally has adequate strength in the as-cast state due to the presence of finer grains and second-phase particles resulting from fast solidification rate of the HPDC processes. A key requirement for the major alloying elements in magnesium die cast alloys is that the addition of such elements should enhance the fluidity of the molten magnesium. Such elements do not need to have appreciable reduction in their equilibrium solid solubilities with temperature that is required for precipitation hardening that is needed for sand castings. Some recent studies demonstrate that it is possible to heat treat HPDC magnesium alloys for a relatively short duration at high temperatures without causing any problem of surface blistering.

Sand casting and permanent mold casting are used to produce magnesium products that are not suitable for HPDC or require mechanical properties for specific applications. As casting is made by pouring molten alloy from the top the mold or pushed from the bottom of the mold with a low-pressure, the solidification rate is much lower than that associated with HPDC. Consequently, the casting has a much coarser grain size and a relatively strong solute segregation (thus non-uniform distribution of the added alloying elements), and its mechanical properties are not sufficient for final applications in the as-cast state. The casting needs to be heat treated in the T6 condition in order to meet the application specifications. The purpose of the T6 temper is to generate a denser and uniform distribution of nano-scale precipitates to make the casting stronger. To avoid the formation of coarse dendrites in the casting, grain refiners are often added to the molten alloy before casting. The most effective grain refiner for magnesium alloys is zirconium, which is often added in the form of a Mg-Zr master alloy. The magnesium-rich side of the binary Mg-Zr phase diagram is peritectic, and at temperatures below 862 °C, the crystal structure and lattice dimensions of zirconium are very similar to those of magnesium. The remarkable grain refinement made by zirconium is mainly through heterogeneous nucleation of magnesium on undissolved Zr particles and stronger restriction to the growth of magnesium grains imposed by the dissolved Zr in the molten alloy (StJohn et al., 2005). While zirconium can provide significant grain refinement and lead to the formation of fine and equiaxed grains, its addition increases the alloy cost. Well-known magnesium alloys for sand casting are WE54 (90.55Mg, 5Y, 2Nd, 2HRE, 0.45Zr, wt%, where HRE represents heavy rare-earth) and WE43 (92.55Mg, 4Y, 2Nd, 1HRE, 0.45Zr, wt%) that were developed for elevated temperature applications. A key requirement for the major alloying elements in magnesium alloys for sand casting is that they should have significant reduction in their equilibrium solid solubilities with temperature that is necessary for precipitation hardening, in addition to their beneficial effects on the fluidity of the molten magnesium.

Thermomechanical processing

After melting, alloying, casting and homogenization, billets of magnesium alloys are hot extruded. The billets for extrusion are typically 150–550 mm in diameter, preheated to 300–450 °C, and extruded at a speed of 0.5–30 m min^{-1} into solid or hollow profiles of various shapes by direct extrusion that is commonly used by the industry. The profiles are straightened in the extrusion direction after the extrusion to remove the residual stress, to improve mechanical properties, and to meet the required straightness. For the profiles that are made of age hardenable magnesium alloys, they are usually cooled rapidly by forced air after exiting the die and subsequently aged at a temperature in the range 100–200 °C to further increase their strength. In general, magnesium alloys are more difficult to extrude than aluminum alloys. The extrusion speed commonly used for magnesium alloys is 5–10 times slower than those used for most aluminum alloys, and the extrusion needs to be carried out at a higher pressure or higher temperature, which inevitably increases the processing cost. Together with the higher cost of magnesium billets, extruded magnesium products are more expensive than aluminum products of similar profiles. The extrudability of a specific magnesium alloy is usually assessed by its extrusion limit diagram that specifies the range of speed and temperature over which this alloy can be extruded without any visible surface defects (Atwell and Barnett, 2007). Alloy composition is a crucial factor in controlling extrudability of magnesium alloys. In general, alloys having a lean composition have a larger processing window and therefore can be extruded at much higher speed. Within the extrusion limit diagram, faster extrusion leads to coarser grains and thus lower strength of the extruded product. The most common extrusion alloy is AZ31 (95.7Mg, 3Al, 1Zn, 0.3Mn, wt%). The contents of Al and Zn in this alloy are not sufficiently high for any precipitation hardening. The extrusions of this alloy are used in the as-extruded state. Extrusions of alloy AZ80 (90.88Mg, 8.5Al, 0.5Zn, 0.12Mn, wt%) and ZK60 (94.05Mg, 5.5Zn, 0.45Zr, wt%) are usually used in a T5 temper, and ZK60, WE43 and WE54 extrusions are normally given a T6 temper before their final applications.

Similar to the billets used for magnesium alloy extrusions, slabs for magnesium alloy sheets are produced by direct chill casting, and they need to be homogenized for up to 24 h at 300–500 °C, machined to certain sizes, before being repeatedly hot rolled in the temperature range 300–500 °C. The typical thickness reduction is 10% per pass in order to avoid any cracking of the rolled alloy plate. Intermediate reheats are often used due to the low volumetric heat content of magnesium and the relatively limited process window of hot rolling. Some alloys are also cold rolled, annealed or aged after hot rolling. The rollability of magnesium alloy is influenced by alloy composition and processing parameters such as hot rolling temperature, thickness reduction per pass, and rolling speed. Higher-temperature hot rolling gives rise to better rollability of magnesium alloy plate because of the activation and operation of more deformation modes such as non-basal slip and twinning and accelerated processes of dynamic recrystallization and grain growth. It may also lead to weaker basal texture and thus better stretch formability of the resultant sheet. A higher rolling speed usually leads to better rollability, which is attributable to more deformation modes activated at higher strain rates and the accelerated occurrence of dynamic recrystallization. Increased thickness reduction per pass can also lead to reduced sizes of recrystallized grains and more homogeneous microstructure. The original microstructure in the as-cast or homogenized state is usually fully replaced after repeated deformation and recrystallization. Nowadays, it is possible to commercially produce magnesium alloy sheet with a minimum thickness of 0.35 mm to a width of over 2 m. Most magnesium sheet is made of alloy AZ31 and is generally used in H24 temper which is a hard-rolled state.

Continuous sheet casting

Twin-roll casting (TRC) of magnesium strips emerged in the past two decades as an energy-efficient alternative process for producing magnesium sheet. In the TRC process, molten metal is poured between two large counter-rotating water-cooled rolls and solidifies as a thin shell against each of the two cold rolls. The two solid shells are compressed together at the so-called kissing point of the two rolls and exit as a single strip having a thickness of about 3–5 mm that can be further reduced down to 0.35 mm using a conventional finishing mill. The width of the strip and hence the sheet can be up to 2 m, depending on the size of the rollers. Compared with the conventional route for sheet production, the TRC process significantly reduces the energy and capital costs. A range of magnesium alloys, including AZ31, ZM61 (92.8Mg, 6Zn, 1.2Mn, wt%) and some new alloy compositions, have been successfully twin-roll cast into thin strips. Challenges to wider industry adoption of the TRC process are the tendency of the molten magnesium metal to oxidize during the operation, surface defects and internal segregation. A typical internal defect is centerline segregation that arises from the impingement of the two dendritic solidification fronts, which are enriched in alloying elements, in the center of the strip.

Machining

Magnesium alloys can be readily machined. For the machining of magnesium alloys, the amount of power required is approximately 55% of that for aluminum alloys and 10% of that for stainless steels; the drilling speed is generally about 50% higher than that for aluminum alloys and more than 20 times higher than that for stainless steels; and the rough turning speed is about 1.9 times faster than that for aluminum alloys and 21 times faster for stainless steels. While magnesium alloys can be machined in air, they are usually machined with a coolant such as mineral oils. This is because magnesium swarf or fine turnings may ignite in air and they may also chemically react water-based coolants. Magnesium alloys can also be chemically machined. Some of them are prone to contour etching and AZ31 is used for producing printing plates.

Welding and Joining

Manufactured products made of either cast and wrought magnesium alloys can be welded by inert gas shielded tungsten arc or consumable electrode processes. The to-be-welded products are often preheated to 250–300 °C to reduce weld cracking during solidification. While generally having the same composition as the to-be-welded product, filler rods having higher alloying contents and thus lower melting point and wider freezing range are also used in order to reduce or eliminate hot cracks in the weld. Since magnesium has low heat capacity and heat of fusion, the welding of magnesium products can be done with less energy and higher speed than those for aluminum products. However, the relatively high vapor pressure of molten magnesium can cause some evaporative loss during welding, and the relative low viscosity and low surface tension of liquid magnesium lead to increased sputter during welding and reduced surface quality of the welded region. In recent years, friction stir welding, in which heat is generated through mechanical friction between a rapidly rotating pin and two stationary products to plastically deform and to fuse the two pieces together, has been increasingly used to join products made of either similar or different magnesium alloys, or join magnesium products to products made of other metals such as aluminum alloys or steels. Since liquid phase is not formed in this technique, shielding gas is not required during the welding. Due to the severe plastic deformation involved in the friction stir welding (FSW) process, the weld has a much finer microstructure and thus better mechanical properties than the base alloy. A derived technique named friction stir processing is also increasingly used to modify the surface of magnesium plates and sheets for better mechanical properties and corrosion resistance.

Additive manufacturing

Additive manufacturing, also known as 3D printing, has emerged in recent years as a new technology to build parts of complex internal or external geometries layer by layer from powder or wire of metallic alloys. It offers an opportunity to manufacture components that cannot be made by conventional casting or thermomechanical processing routes. Many additive manufacturing technologies are available, but only selective laser melting, selective electron beam melting and direct metal deposition-based additive manufacturing processes have received more attention and wider industry applications. While a variety of metallic materials have been additively manufactured, including superalloys, stainless steels, and alloys of titanium, aluminum and magnesium, 3D printing of magnesium alloy products is still in its infancy. A key reason is that magnesium alloys are difficult to be additively manufactured. Magnesium alloys have low vaporization temperature, and their powders are highly combustible. Gas-atomized magnesium alloy powders such as Elektron 91, 43 and 21 have been specifically designed and optimized for additive manufacturing. Compared to powder-based additive manufacturing technologies, wire deposition-based processes have lower risk of combustion and a higher production rate, and they appear to be more promising for laboratory and industry production of magnesium parts.

High-pressure die cast magnesium alloys

Magnesium alloys based on the Mg-Al system represent the most widely used high-pressure die cast magnesium alloys. They have been used in automotive vehicles due to their excellent castability and the weight savings they provide. The notable alloy is AZ91, Table 2. The addition of zinc can generate some strengthening effect, but it has to be controlled to be less than 1 wt% over which

Table 2 Tensile and creep properties of commonly used high-pressure die-cast magnesium alloys.

Alloy	*Tensile Property 20 °C*			*Tensile Properly 150 °C*			*Tensile Property 175 °C*			*%Tensile Creep at 50 MPa, 200 h*		*Salt Spray Corrosion Rate*
	Y.S. MPa	*T.S. MPa*	*Elong. %*	*Y.S. MPa*	*T.S. MPa*	*Elong. %*	*Y.S. MPa*	*T.S. MPa*	*Elong. %*	*150 °C*	*175 °C*	*mg cm^{-2} day^{-1}*
AZ91D	150	222	3	105	160	18	89	138	21	2.7	–	0.10
AS21	121	210	6	87	120	27	78	110	23	0.19	1.27	–
AS41	138	206	5	94	154	20	85	127	22	0.05	2.48	0.16
AE42	137	225	11	100	160	22	86	135	23	0.06	0.33	0.21
AE44	132	252	12	105	153	32	96	137	34	< 0.05	< 0.1	–
AX51	128	192	7	102	161	7	–	–	–	–	–	–
AX52	161	228	13	–	–	–	133	171	23	–	–	–
AJ52	134	212	6	108	164	14	100	141	18	0.04	0.05	0.09
AJ62	143	240	7	116	166	27	103	143	19	0.05	0.05	0.11
MRI153M	170	250	6	135	190	17	112	139	4	0.18	–	0.09
MRI230D	180	235	5	150	205	16	–	–	–	–	–	0.10
A380	168	290	3	155	255	6	151	238	9	0.08	–	0.34

Y.S.: yield strength; T.S.: tensile strength; Elong.: elongation.

Commercial aluminium casting alloy 380 is also included for the purpose of comparison.

causes increased susceptibility to hot cracking during solidification. About 0.3 wt% manganese is also added to this alloy for the purpose of corrosion resistance. AZ91 has excellent die-castability, but its ductility and fracture toughness are moderate presumably because of the eutectic particles or discontinuous precipitates of the equilibrium β phase that has a composition of $Mg_{17}Al_{12}$. Alloys containing less aluminum have been developed, including AM60 and AM 50 (94.7Mg, 5Al, 0.3Mn, wt%), so that the amount of $Mg_{17}Al_{12}$ phase around grain boundaries is reduced. These aluminum-lean alloys have better ductility and fracture toughness, and they have been used to fabricate automotive parts such as steering wheels, seat frames and wheels.

While the AM series alloys exhibit good strengths at room and elevated temperatures, they are prone to substantial creep deformation when exposed to moderate loads at temperatures above 150 °C. The widely accepted interpretation attributes the inferior creep resistance of the AM series alloys to discontinuous precipitation of the equilibrium $Mg_{17}Al_{12}$ phase at grain boundaries or to softening of the $Mg_{17}Al_{12}$ phase during creep. In this interpretation, grain boundary sliding is assumed to be the major creep deformation mode and discontinuous precipitation of $Mg_{17}Al_{12}$ during creep is the key factor that limits the creep resistance of the AM series alloys. However, the reduced volume fraction of discontinuous precipitates of $Mg_{17}Al_{12}$ in AM60 and AM50 alloys leads to only moderate improvement in creep resistance. An alternative interpretation is that the excessive creep deformation of the AM series alloys is primarily due to the relatively high diffusivity, combined with relatively high concentrations, of aluminum in solution in the α-Mg matrix. This interpretation is supported by experimental observations that only limited improvements in creep resistance is obtained in alloys containing significant amounts of Al and yet free of discontinuous precipitation of the $Mg_{17}Al_{12}$ phase. According to this interpretation, further improvements in creep resistance of magnesium die casting alloys can be achieved by reducing the equilibrium solid solubility of aluminum in magnesium and/or adding alloying elements that have lower solid diffusivity and are yet soluble in magnesium.

Creep resistance of Mg-Al alloys is improved by adding a small amount of silicon which can reduce the amount of $Mg_{17}Al_{12}$. Two commercial alloys, namely AS41 (94.2Mg, 4.5Al, 1Si, 0.3Mn, wt%) and AS21 (96.5Mg, 2.2Al, 1Si, 0.3Mn, wt%), have been developed, Table 2. While alloy AS21 has better creep resistance than AS41, it is more difficult to die cast because of the reduced fluidity resulting from the lower aluminum content in this alloy. During the fast solidification in high-pressure die casting, the silicon combines with some of the magnesium to precipitate fine and relatively hard particles of Mg_2Si in grain boundaries.

The addition of rare-earth (RE) elements to Mg-Al alloys leads to the development of two commercial die-cast alloys, AE42 (93.7Mg, 4Al, 2RE, 0.3Mn, wt%) and AE44 (91.7Mg, 4Al, 4RE, 0.3Mn, wt%) (Bakke et al., 2007), that have superior creep resistance to the AS41 and AS21 alloys, Table 2. The alloy AE42 was developed first, but its creep properties deteriorate rapidly at temperatures higher than 175 °C, presumably because of the relatively high level of aluminum retained in the α-Mg matrix after die casting. The creep properties of this alloy are improved by adding more rare-earth elements, which led to the development of alloy AE44, which was intended for automotive powertrain applications where the operating temperature may go up to 200 °C. The improved creep resistance is attributed to increased content of RE-containing intermetallic phases and reduced aluminum content in the α-Mg matrix resulting from increased RE content. The addition of different RE elements leads to different intermetallic phases in the microstructure, but it does not strongly affect the creep resistance of die-cast AE44 alloys. It is for this reason that a lower-cost variant of the AE44 alloys, which uses cheaper RE element lanthanum, has received more research and attention. The dominant intermetallic phase is $(Al, Mg)_3La$ in the die-cast Mg-4Al-4La (92Mg, 4Al, 4La, wt.%) alloy, and $Al_{11}RE_3$ in the die-cast Mg-4Al-4Ce (92Mg, 4Al, 4Ce, wt%) alloy. The $(Al, Mg)_3La$ and $Al_{11}RE_3$ phases are thermally stable at temperatures up to 500 °C, and they are likely to be the equilibrium phase in their alloys. Each of these two phases forms as fine-scale lamellae in inter-dendritic regions of magnesium grains. The addition of a small amount (0.3 wt%) of manganese to die-cast alloy AE44 leads to remarkable enhancement in creep resistance. The improved creep resistance is due to dynamic precipitation of nano-scale Al-Mn particles during creep that reduces dislocation slip. Indeed, the manganese-containing AE44 alloys exhibit moderate age hardening response when they are isothermally aged at 200–300 °C after die casting. These alloys can be aged by a T5 temper without any ductility loss, as demonstrated (Zhu et al., 2021).

The addition of alkaline earth elements such as strontium and/or calcium to Mg-Al alloys leads to substantial enhancement in creep properties, Table 2. Both strontium and calcium have some adverse effect on alloy castability and increase the susceptibility to hot tearing, therefore they are usually added to alloys containing higher aluminum contents. Sr or Ca additions reduce the equilibrium solid solubility of Al in α-Mg grains, and the solid solution of Ca or Sr, which have a larger atomic size than Mg, in α-Mg can also reduce the overall diffusion rate of atoms in the alloy. The precise role of Sr and Ca in improving the creep resistance is still unclear due to the lack of data on the diffusivity of Ca in solid magnesium and detailed understanding of microstructures of these alloys. A few experimental alloys have been developed and found industrial applications (Pekguleryuz and Kaya, 2003), including AJ62 (91.7Mg, 6Al, 2.3Sr, wt%), AXE522 (91Mg, 5Al, 2Ca, 2RE, wt%), AX81 (91Mg, 8Al, 1Ca, wt%), and those that are known only by their proprietary designations such as MRI153M (90.7Mg, 8Al, 1Ca, 0.3Sr, wt%), and MRI230D (90.2Mg, 6.5Al, 2Ca, 1Sn, 0.3Sr, wt%). The alloy AJ62 has been used to die-cast around an aluminum alloy core to make a hybrid 6-cylinder engine for one model of BMW cars. Although substantial improvements in creep resistance are obtained in die-cast alloy AJ62 that does not have any precipitates of $Mg_{17}Al_{12}$, the creep resistance of this alloy is still significantly inferior to those of sand cast magnesium alloys based on the Mg-RE systems.

Mg-RE based alloys have been developed for high-pressure die casting and for elevated temperature applications. An alloy developed in early days is MEZ (96.65Mg, 2.5RE, 0.5Zn, 0.35Mn, wt%). It has better creep resistance than die-cast AE42 at temperatures above 150 °C, but its tensile yield strength and ductility at room temperature are both low Subsequently, a modified version that contains a larger amount of RE elements in different combinations was developed to address the inferior strength at room temperature. This alloy, designated EZ41 (95.83Mg, 1.63La, 0.97Ce, 0.96Nd, 0.11Y, 0.5Zn, wt%) and also known as AM-HP2, exhibits excellent creep resistance at temperatures 150–200 °C (Zhu et al., 2015).

Sand cast or permanent mold cast magnesium alloys

One of the key requirements for the alloying elements used in sand casting magnesium alloys is that their equilibrium solid solubility in magnesium decreases with temperature so that the resultant alloy is age hardenable. While the solid solubility of aluminum in magnesium decreases from a maximum of 12.7 wt% at 437 °C to around 2% at room temperature, the decomposition of the supersaturated solid solution of alloy AZ91 does not lead to any significant precipitation hardening. This is due to the absence of GP zones and intermediate precipitate phases. The equilibrium precipitate β forms directly from the supersaturated solid solution upon artificial ageing, in the form of continuous precipitates inside individual magnesium grains and discontinuous precipitates along grain boundaries. The coarse distribution of this precipitate phase is unable to generate any sufficient age hardening. Additions of trace elements to this alloy do not seem to be effective in refining the distribution of the β precipitate.

Adding larger amount of zinc to Mg-Al alloys leads to the development of Mg-Zn-Al alloys with the Zn:Al weight ratio in the range 3:1 to 1:1. Examples include Mg-12Zn-4Al (84Mg, 12Zn, 4Al, wt.%), Mg-8Zn-8Al (84Mg, 8Zn, 8Al, wt.%) and Mg-8Zn-4Al (88Mg, 8Zn, 4Al, wt%) alloys. Some of these alloys are also suitable for high-pressure die casting due to their excellent castability. These alloys contain large volume fractions of intermetallic particles of equilibrium ϕ phase and/or metastable icosahedral quasi-crystalline *i* phase. A fraction of these particles can be dissolved after heat treatment at temperatures close to 325 °C. When the alloy is water quenched after this relatively high temperature heat treatment, an appreciable level of supersaturation of Zn and Al atoms in magnesium can be obtained. Subsequent ageing at 150–200 °C leads to a remarkable age hardening response, which is due to the formation of a finely dispersed, diamond-shaped precipitates having a quasi-crystalline structure. Quaternary addition of a small amount of Ca to the Mg-Zn-Al alloy does not change the age hardening response, but it leads to an enhancement in creep resistance.

Most alloys based on the Mg-Zn system are age hardenable. Binary Mg-Zn alloys can be grain refined by zirconium, and two commercial alloys, ZK51 (94.8Mg, 4.5Zn, 0.7Zr, wt%) and higher strength ZK61 (93.3Mg, 6Zn, 0.7Zr, wt%) have been developed. However, these two alloys have reduced age hardening response, and they are susceptible to microporosity, prone to hot cracking, and not weldable. For this reason, the commercial use of these alloys is very limited. The addition of 3 wt% copper to binary Mg-6Zn (94Mg, 6Zn, wt%) alloy reduces the susceptibility of the binary alloy to microporosity and eliminates the tendency to hot cracking. In addition, the addition of copper to the binary Mg-Zn alloy raises the eutectic temperature and allows higher temperatures to be used for solution treatment so that higher concentrations of zinc and copper in solid solution can be obtained for stronger age hardening response. The resultant alloy ZC63 (90.5Mg, 6Zn, 3Cu, 0.5Mn, wt%) has been commercially produced by sand casting (Westengen and Aune, 2006), and the castings can be welded using the standard tungsten-inert gas technique. However, this alloy has not found applications in the automotive industry because of the corrosion problem. The most successful commercial alloy in this group of alloys is ZE41 (93.9Mg, 4.2Zn, 1.3Ce, 0.6Zr, wt%). In T5 temper condition, this alloy has moderate strength at temperatures up to 150 °C and has been used to cast transmission housings of helicopters.

Rare earth (RE) elements such as Nd, Y, and Gd have relatively large solid solubility in magnesium. They are effective in solid solution strengthening and resultant alloys respond well to age hardening even at relatively high ageing temperatures. A commercial alloy that has been developed based on the Mg-Y-Nd-Zr system is WE54 (Westengen and Aune, 2006). Since pure yttrium is expensive, difficult to alloy with magnesium and has strong affinity for oxygen, a cheaper yttrium-rich misch-metal containing around 75% of yttrium, together with heavy rare earth metals such as gadolinium and erbium, has been used for yttrium. The alloy WE54 has high strength at ambient and elevated temperatures and superior creep resistance at temperatures up to 300 °C, Table 3. In addition, its corrosion resistance is superior to that of other high-temperature magnesium casting alloys, and comparable with aluminum casting alloys A356 and A357. The strength of this alloy is achieved via precipitation of plate-shaped precipitates formed on prismatic planes of magnesium. The shape and orientation of such precipitates are quite effective in impeding dislocation glide and propagation of deformation twins. Precipitation process in this alloy is complex, and it involves the formation of short-range ordered solute clusters, GP zones and several intermediate precipitate phases (Nie et al., 2016).

The alloy WE54 is typically produced by sand casting and used in T6 temper. However, subsequent practical applications of this alloy indicated that the ductility of this alloy gradually decreased to unacceptable levels during prolonged exposure to temperatures around 150 °C. This reduction in ductility is due to secondary precipitation of GP zones that occurs slowly throughout the grains. Subsequently, an alternative composition WE43 was developed. The slightly reduced yttrium content and the slightly increased neodymium content in this alloy permits the originally adequate ductility to be retained during long-term exposure at elevated temperatures. Alloy WE43 is being used to sand cast transmission housings for helicopters and some components for racing car engines. Some Mg-Gd-Y-Zr experimental alloys that have superior strength to the WE alloys have been developed in recent years. These alloys contain larger amount of RE elements, typically in the range 10–16 wt%. Gadolinium is used in these alloys because its solid solubility in magnesium is several times higher than that of neodymium at the solution treatment temperature, therefore it is added in larger quantity to obtain larger volume fraction of precipitates. The Mg-Gd-Y-Zr alloys have stronger age hardening response than the WE alloys when they are aged at 200–250 °C. The precipitates formed in these alloys are similar to those observed in the WE alloys.

WE alloys and the Mg-Gd-Y-Zr alloys are expensive and thus they are only used for aerospace applications. Requirements for a cost-effective Mg-RE alloy for automotive cylinder blocks and crank cases led to the development of an alloy designated EZ30 (96.5Mg, 2.7RE, 0.3Zn, 0.5Zr, wt%, also known as AM-SC1 (Bettles et al., 2003)). The RE content in this alloy is much lower than those in the WE alloys and the Mg-Gd-Y-Zr alloys, but the dominant use of Nd and Ce led to sufficient age hardening response and thus strength. In a T6 temper, its overall mechanical properties such as tensile and compressive strengths, creep resistance and

Table 3 Mechanical and physical properties of commonly used sand cast or permanent mold cast magnesium alloys.

Alloy	*Tensile Property 20 °C*			*Tensile Property 200 °C*			*Creep Stress at 0.1% Strain, 100 h (MPa)*		*Fatigue Limit (unnotched) (MPa)*	*Thermal Conductivity (W m^{-1} K^{-1})*
	Y.S. MPa	*T.S. MPa*	*Elong. %*	*Y.S. MPa*	*T.S. MPa*	*Elong. %*	*150 °C*	*200 °C*	*20 °C*	*20 °C*
WE54 (T6)	205	280	6	185	242	10	–	160	95–100	52
WE43 (T6)	186	270	7	170	242	16	212	148	85	51
ZC63 (T6)	125	210	4	118	142	11	92	59	90	123
ZE41 (T5)	140	205	5	95	130	29	86	43	90–105	109
QE22 (T6)	195	260	3	166	193	24	140	75	100–110	113
EV31 (T6)	163	293	7	152	268	17	–	100	115–120	116
EZ30 (T6)	134	228	10	124	189	16	>110	>60	94	102

Y.S.: yield strength; T.S.: tensile strength; Elong.: elongation.

fatigue, and corrosion properties all meet the requirements for automotive engine blocks. A sand cast 3-cylinder diesel engine made of this alloy, weighs about 14 kg, and was road tested over 40,000 km in a Volkswagen Lupo car. The addition of a small amount of gadolinium to a Mg-Nd-Zn-Zr alloy led to the development of a proprietary alloy designated EV31 (95.1Mg, 3Nd, 1Gd, 0.4Zn, 0.5Zr, wt%, also known as Elektron 21). This alloy has mechanical and corrosion properties similar to WE43, and improved strength and creep resistance over the EZ30 alloy.

Mg-Gd alloys containing a few weight percent of gadolinium do not exhibit age hardening response when they are aged at 200–250 °C. The addition of small amount of zinc, silver, or in combination to Mg-Gd alloys can generate a significant age hardening response and an improved creep resistance. This remarkably improved tensile and creep strengths is due to the formation of a uniform and dense distribution of nano-scale precipitates that is absent in the Mg-6Gd-0.6Zr (93.4Mg, 6Gd, 0.6Zr, wt%) alloy. For example, the Mg-6Gd-2Ag-0.6Zr (91.4Mg, 6Gd, 2Ag, 0.6Zr, wt%) alloy exhibits the highest hardness increment during isothermal ageing at 200 °C (Gao and Nie, 2008). An increase in the Gd content led to the development of an experimental alloy, Mg-15Gd-2Ag-0.6Zr (82.4Mg, 15Gd, 2Ag, 0.6Zr, wt%) alloy, that has a 0.2% proof strength of 320 MPa when tested in a T6 temper at room temperature, which is the highest among the magnesium casting alloys (Nie, 2012). The Mg-6Gd-2Zn-0.6Zr (91.4Mg, 6Gd, 2Zn, 0.6Zr, wt%) alloy in a T6 temper has a tensile strength of 137 MPa at 25 °C and 124 MPa at 175 °C. Its creep resistance (stress to produce 0.1% strain at 100 h) is well above 90 MPa at 175 °C (Nie et al., 2005). The most notable commercial alloy in the silver-containing magnesium casting alloys is QE22 (94.8Mg, 2.5Ag, 2RE(Nd), 0.7Zr, wt%). The precipitation process in this alloy has not been well studied, even though the maximum age hardening response and the excellent creep resistance are associated with the presence of thermally stable nano-scale precipitates in the microstructure. Alloy QE22 has superior tensile properties at temperatures up to 250 °C and creep resistant up to 200 °C. This alloy has been used for sand casting aerospace components such as helicopter rotor fittings, gearbox housings and aircraft landing wheels.

Magnesium extrusion alloys

Mg-Al based alloys

Alloy AZ31 is commonly used for extruding solid and hollow profiles for general purpose applications. Depending on the extrusion profile and extrusion conditions, the extrusions of this alloy may have quite different textures. Cylindrical solid bars of this alloy extruded at temperatures below 400 °C and a relatively low speed usually have a strong basal texture, with basal planes and $\langle 10\bar{1}0\rangle$ directions of most grains lying nearly parallel to the extrusion direction (ED). The removal of Zn from this alloy does not change the texture. In general, an increase in extrusion temperature or extrusion speed causes more grains to have their $\langle 2\bar{1}\bar{1}0\rangle$ axes lying nearly parallel to the ED, in addition to the dominant presence of the $\langle 10\bar{1}0\rangle$ $\sim$// ED texture. Extrusions made at temperatures above 450 °C generally have a dominant $\langle 2\bar{1}\bar{1}0\rangle$ $\sim$// ED texture. These textures can all be classified as basal fibre textures (BF-1 and BF-2 in Fig. 4) (Nie et al., 2020). The $\langle 10\bar{1}0\rangle$ $\sim$// ED (BF-1) is commonly termed deformation texture, which is also seen in warm or cold extruded products of pure magnesium, Mg-Al, Mg-Mn, Mg-Li and Mg-RE alloys, and $\langle 2\bar{1}\bar{1}0\rangle$ $\sim$// ED (BF-2) is termed the recrystallisation texture.

Alloy AZ31 produced under commonly used extrusion conditions usually suffers from a problem of tension-compression yield asymmetry; its yield strength under compression is much lower than that under tension, Table 4. This problem is intimately related to the strong basal texture of the extrusion. The basal texture allows $\{10\bar{1}2\}$ deformation twins to form readily upon compressive

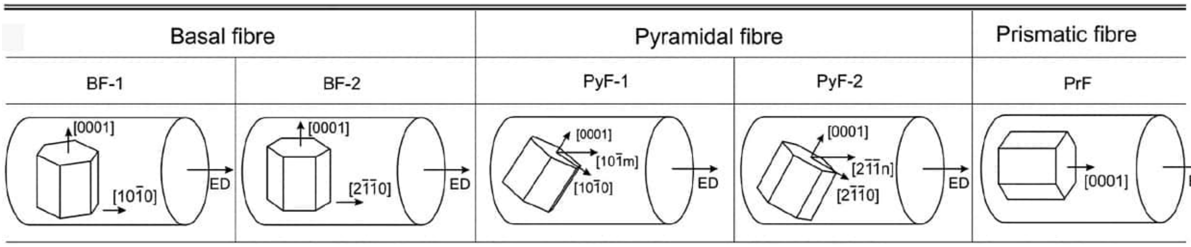

Fig. 4 Extrusion textures of magnesium and its alloys. Adapted from Nie JF, Shin KS, Zeng ZR (2020) Microstructure, deformation, and property of wrought magnesium alloys. *Metallurgical and Materials Transactions A: Physical Metallurgy and Materials Science* **51**: 6045–6109.

Table 4 Room temperature tensile and compressive properties of commonly used extruded solid bars of magnesium alloys.

Alloy	*Tensile Property*			*Compressive Yield Strength*
	Y.S. MPa	*T.S. MPa*	*Elong. %*	*MPa*
AZ31 (F)	200	255	12	97
AZ61 (F)	205	305	16	130
AZ80 (F)	240	340	10	145
AZ80 (T5)	275	380	7	240
ZK60 (T5)	285	350	11	250
M1 (F)	180	255	12	83
ME10 (F)	184	259	25	129
WE43 (T6)	170	260	12	165
VW76 (T5)	310	410	9	~310

Y.S.: yield strength; T.S.: tensile strength; Elong.: elongation.

loading along the extrusion direction—leading to occurrence of plastic deformation at lower stress. Decreasing extrusion temperature can reduce the tension-compression yield asymmetry problem. Extrusions made at temperatures around or below 175 °C have comparable tensile and compressive yield strengths, and the tension-compression yield asymmetry problem is thus fully eliminated due to the significantly reduced grain size, which makes deformation twinning difficult to occur upon compressive loading. Extrusions of ultra-high strength have been made based on a Mg-3.5Al-3.3Ca-0.4Mn (92.8Mg, 3.5Al, 3.3Ca, 0.4Mn, wt%) alloy that is extruded at 350 °C with a relatively low speed. They have a tensile strength of 410 MPa and a ductility of 5.6% when tested at room temperature. Their microstructure has a predominant $\langle 10\bar{1}0\rangle$ ~// ED texture, and it contains a mixed distribution of dynamic recrystallized grains of ~1 µm, elongated strips of deformed grains, intermetallic particles of ~0.5 µm, and nano-scale precipitates. Dilute alloys based on the Mg-Al-Ca-Mn system have also been experimentally developed for higher speed extrusion and thus lower processing cost. One example is a Mg-0.3Al-0.21Ca-0.47Mn (99.02Mg, 0.3Al, 0.21Ca, 0.47Mn, wt%) alloy that can be extruded at 500 °C with a remarkable speed of 60 m min^{-1} without any surface defects (Nakata et al., 2018). The as-extruded microstructure has fully recrystallized grains of ~27 µm and a weakened basal texture. This alloy is also age hardenable. When tested in a T5 temper, the fast extruded products of this alloy have a tensile yield strength of 207 MPa and a ductility to 13%.

Mg-Zn based alloys

Most alloys based on the Mg-Zn system are age hardenable and suffer less from the problem of tension-compression yield asymmetry, especially when the alloy has a higher alloying content and is in a T6 temper. The commercial alloys developed thus far include ZM21 (97Mg, 2Zn, 1Mn, wt%), ZK30 (96.55Mg, 3Zn, 0.45Zr, wt%), ZK60, ZM61 and ZMC711 (91Mg, 7Zn, 1Mn, 1Cu, wt%). The alloy ZM2l can be extruded at higher speeds. The as-extruded microstructure generally has a mixture of fine-scale equiaxed recrystallized grains and coarse elongated un-recrystallized grains. The size and area fraction of recrystallized grains increase with increased extrusion speed or temperature, which leads to decreased yield strength and increased elongation. A laboratory alloy developed in recent years is ZE20 (97.8Mg, 2Zn, 0.2Ce, wt%). This alloy can be extruded at a speed 25% higher than AZ31 for extrusions at 400 °C, and the extrusions have a tensile yield strength of 135 MPa and a ductility of 27% that are better than those of AZ31. An increase in the zinc content in Mg-Zn based alloys causes deterioration in extrudability. This undesirable effect is reduced by adding zirconium. Alloy ZK60 can be extruded at a speed that is an order of magnitude higher than that of Mg-6Zn (94Mg, 6Zn, wt%) alloy. This enhanced extrudability is due to the fine and uniform as-cast grain size of the billet and the increased solidus temperature of the alloy ZK60. Extrusions of alloy ZK60 respond well to age hardening and hence they are commonly used in a T5 temper. Extruded bars of ZM61 may exhibit a tensile yield strength of 340 MPa and a ductility of 8% when tested in a T6 temper. Alloy ZMC711 was developed as a weldable high strength extrusion alloy but finds little application nowadays due to its corrosion problem.

Mg-Mn-RE based alloys

A few Mg-Mn based alloys have been developed for higher speed extrusion. Binary Mg-1Mn (99Mg, 1Mn, wt%) alloy has extrudability superior to other magnesium extrusion alloys and its processing window is as large as that of wrought aluminum alloy AA6063. The addition of 0.4 wt% cerium-rich mischmetal to this alloy led to a commercial alloy designated ME10 (also known as AM-EX1 (Easton et al., 2008)). This alloy can be extruded at a speed two times faster than AZ31, and its tensile yield strength is compatible with those of AZ31 and T6 tempered AA6063. It also has better ductility and reduced tension-compression asymmetry, due to the finer grain size and the presence of pyramidal (non-basal) fiber texture (Fig. 4).

Mg-RE based alloys

Several commercial and experimental alloys have been developed based on the Mg-RE system, including WE54, WE43, EV31 and VW76 (86.5Mg, 7Gd, 6Y, 0.5Zr, wt%; also known as Elektron 675). These alloys all contain large amount of RE elements and hence they have to be extruded at very low speeds at higher temperatures. These alloys do not suffer from the problem of tension-compression yield asymmetry, and their tensile properties are also quite uniform when tested along the directions parallel and perpendicular to the extrusion direction. Due to the high cost of RE elements and processing, these alloys are mainly used for defense and specialized applications. A unique feature of extrusions of these alloys is the combination of high tensile strength and good creep resistance at elevated temperatures. Alloy VW76 has the highest elevated temperature tensile yield strength, in addition to its good fatigue strength and excellent resistance to corrosion and ignition. For example, extrusions of this alloy have 310 MPa tensile yield strength and 9% ductility when tested a T6 temper and at room temperature, and their tensile yield strength is still above 300 MPa when the testing temperature reaches 200 °C. Further increase in the RE and Zn contents led to the development of a remarkably stronger laboratory alloy VWZ1062 (82Mg, 10Gd, 5.7Y, 1.6Zn, 0.7Zr, wt%). In a T5 temper, extrusions of this alloy have 473 MPa tensile yield strength and 8% ductility, 524 MPa compressive yield strength and 6% plasticity. The T5 treatment generates a dense distribution of nano-scale precipitates inside magnesium grains, and hence an enhancement in strength. The presence of the precipitates and the small grain size suppress the activation of deformation twinning upon compressive loading, hence the tension-compression asymmetry is eliminated.

Extrusions of Mg-RE based alloys exhibit more and unique textures. The microstructure of WE43 alloy has a mixture of $\langle 10\bar{1}0\rangle$ // ED and $\langle 2\bar{1}\bar{1}1\rangle$ // ED textures in the as-extruded condition, but a dominant $\langle 2\bar{1}\bar{1}1\rangle$ // ED texture in the fully-annealed condition. The $\langle 2\bar{1}\bar{1}1\rangle$ // ED is a pyramidal fiber texture (Fig. 4) also known as RE-texture. It is also commonly observed in extrusions of magnesium alloys containing dilute RE contents (as low as 0.5–1.0 wt%) and some RE-free alloys such as Mg-Zn-Ca-Mn. Other pyramidal-fiber textures are also frequently observed in extruded Mg-RE alloys, including pyramidal plane//ED and $\langle 10\bar{1}m\rangle$ // ED (PyF-1), pyramidal plane // ED and $\langle 2\bar{1}\bar{1}n\rangle$ // ED (PyF-2), or pyramidal plane // ED and $\langle 2\bar{1}\bar{1}n\rangle$–$\langle 10\bar{1}m\rangle$ // ED, where m represents 2/3, 1, or 1.5, and n represents 1, 2, or 3. In addition, a prismatic texture in the form of prismatic plane // ED and [0001] // ED (PrF, Fig. 4) is also is found in a few alloys that are extruded under some particular conditions. Such alloys include Mg-Mn-RE, Elektron 675, Mg-RE-Zn and Mg-RE-Ag that contain higher amount of RE elements.

Magnesium plate/sheet alloys

Mg-Al based alloys

AZ31 is the most commonly used alloy for fabricating sheet for applications at room or slightly higher temperatures. Sheet of this alloy is strengthened mainly by strain hardening and it is weldable. Hot rolled sheet of AZ31 has a strong basal texture, with a preferred orientation of basal planes parallel to the sheet surface (SB-1 and SB-2 in Fig. 5). The strong basal texture causes unsatisfactory formability at or close to room temperature. Forming limit curves for annealed sheet of AZ31, together with that of aluminum alloy 5052 for the purpose of comparison, are shown in Fig. 6. The formability of AZ31 sheet is adequate when tested at 200 °C, but very poor at room temperature. The formability of AZ31 sheet can be improved by higher temperature hot rolling, reverse rolling (reversing the sheet direction after each rolling pass) or cross rolling.

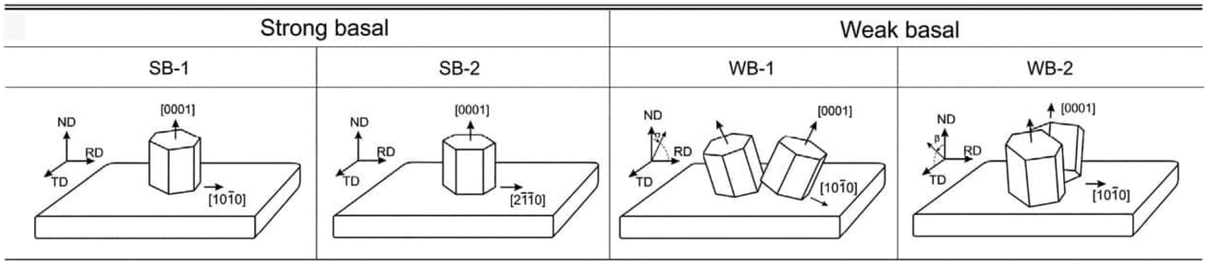

Fig. 5 Sheet textures of magnesium and its alloys. Adapted from Nie JF, Shin KS, Zeng ZR (2020) Microstructure, deformation, and property of wrought magnesium alloys. *Metallurgical and Materials Transactions A: Physical Metallurgy and Materials Science* **51**: 6045–6109.

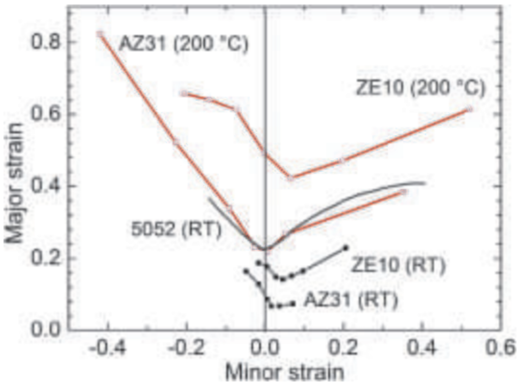

Fig. 6 Forming limit diagram for sheets of magnesium alloys AZ31 and ZE10 and aluminum alloy 5052. AZ31 and ZE10 are tested at room temperature (RT) and 200 °C. From Polmear IJ, StJohn D, Nie JF, Qian M (2017) *Light Alloys*, 5th edn. Elsevier: Oxford.

Table 5 Room temperature tensile properties of warm rolled and annealed ZEK100 sheet.

Alloy	*Orientation*	*Tensile Yield Strength (MPa)*	*Ultimate Tensile Strength (MPa)*	*Elongation (%)*
Ce-containing	RD	131	234	17
	45°	110	237	23
	TD	115	222	13
La-containing	RD	123	241	23
	45°	108	240	25
	TD	96	243	25
Nd-containing	RD	111	243	28
	45°	101	234	28
	TD	84	238	29
Gd-containing	RD	88	229	29
	45°	78	227	30
	TD	66	233	32
MM-containing	RD	131	233	19
	45°	108	243	25
	TD	99	247	25

Adapted from Al-Samman T, Li X (2011) Sheet texture modification in magnesium-based alloys by selective rare earth alloying. *Materials Science and Engineering A* **528**: 3809–3822.

Mg-Zn based alloys

Several Mg-Zn based sheet alloys have been commercially developed, including ZK31 (96.3Mg, 3Zn, 0.7Zr, wt%), ZM21, ZE10 (98.6Mg, 1.2Zn, 0.2RE, wt%), and ZEK100 (98.4Mg-1.4Zn-0.1RE-0.1Zr, wt%). ZK31 has limited weldability. While ZM21 sheet is weldable and does not require stress-relieving, it has a strong basal texture and hence its formability at room temperature is quite limited. Sheets of ZE10 and ZEK100 are weldable and formable. The addition of small amounts of RE elements to Mg-Zn alloys remarkably weakens the basal texture, with basal poles spreading along the sheet transverse direction (TD), as shown in WB-2 in Fig. 5, and thus improves sheet formability. Forming limit curves of annealed ZE10 sheet is shown in Fig. 6 (Polmear et al., 2017). The ZE10 sheet has better formability than AZ31 at both room temperature and 200 °C under conditions of plane strain and biaxial stretching. It also has better deep drawability than AZ31, but it has greater susceptibility to earing than AZ31. Similar to other magnesium alloy sheets, sheets of ZE10 and ZEK100 suffer from anisotropy of their mechanical properties. Different tensile properties are obtained when the sheet is tested along different directions such as rolling direction (RD), transverse direction (TD) and at 45 degrees to the RD (Al-Samman and Li, 2011), Table 5. Sheet anisotropy is strongly influenced by the type of RE additions and hence the intensity of the weakened basal texture. When tested along the TD, the highest ductility is achieved in the gadolinium-containing sheet, which has weaker basal texture than those in the sheets of alloys containing light RE elements such as cerium, lanthanum, neodymium or misch-metal.

Mg-RE based alloys

Commercial sheets made of Mg-RE based alloys are very limited. Magnesium alloys containing relatively high RE content are generally difficult to roll into thin sheet. Alloy WE43 can be hot rolled into plates and T5 tempered. Such plate may have a fully recrystallized microstructure that has a weakened basal texture. It generally does not have the tension-compression yield asymmetry problem along the rolling, normal and transverse directions of the plate. Reducing the RE content to 1–3 wt% and adding small amount of zinc led to the development of laboratory alloys VZ21 (97.21Mg, 1.68Gd, 1.11Zn, wt%) and VZ31 (96.2Mg-2.74Gd-1.06Zn, wt%) that can be hot rolled readily into thin sheet (Wu et al., 2011). In the annealed condition, the resultant sheet contains recrystallized grains with a significantly weakened basal texture. It has an excellent stretch formability, together with good tensile yield strength and ductility, when tested at room temperature.

Mg-Li based alloys

Lithium has an ultra-low density (0.53 g cm^{-3}) and substantially large solubility in solid magnesium. Adding more than 5.7 wt% Li to magnesium leads to the formation of a body-centered cubic β-phase, which is essentially a solid solution of magnesium in lithium. The microstructure becomes fully occupied by the β-phase when the lithium content is greater than 11 wt%. These unique features develop Mg-Li alloy sheet or plate that has extensive cold-formability and is attractive for some specific applications where weight-saving is critical. Commercial alloys developed so far include LA141 (85Mg, 14Li, 1Al, wt%), MA18 (85.95Mg, 10.8Li, 2.25Zn, 0.75Al, 0.25Ce, wt%), and MA21 (80.37Mg, 8.75Li, 4.8Al, 4.5Cd, 1.5Zn, 0.08Ce, wt%). All three alloys are weldable. The LA141 alloy has been used for fabricating armor plate and for aerospace components.

Applications of magnesium alloys

Magnesium alloys have been used in a broad range of applications, including automotive vehicles, military aircraft, electronic devices, biodegradable implants, superconductors, shape memory devices, and hydrogen storage. Massive use of magnesium alloys in the automotive industry began in 1930s when Volkswagen started to replace cast iron by magnesium alloys for engine crank case and transmission housing castings in the Beetle motor car, with a weight saving of about 50 kg. Large increases in magnesium price in the mid-1970s led to replacement of such magnesium products by aluminum alloy castings. Driven by environmental legislations and fuel consumption minimization, magnesium products received renewed application in the automotive industry in the first decade of 2000. Current applications of magnesium alloy components include steering wheels and steering column components, instrument panels, seat frames, small motor housings, engine valve cover and oil pan. Developments have also been made with die cast gearbox sand cast engine blocks, which can lead to further significant weight savings. Porsche has recently selected magnesium sheet for the roof of its new model of the 911 GT3. Renault Samsung Motors also decided in recently years to use magnesium sheet for the walls of VIP back seats and the trunks of upgraded SM7 vehicles.

Magnesium alloy castings have been used for engine and transmission housings of helicopters for many years. However, their use in passenger aircraft interiors is still limited due to flammability restrictions imposed by the US Federal Aviation Administration (FAA). FAA announced in 2013 that it would now allow magnesium in aircraft seats provided magnesium alloys are tested to and meet the flammability performance requirements in the FAA Fire Safety Branch document. Currently, WE43 and EV31 are the only two alloys that have passed extensive flammability tests conducted by the FAA, and WE43 is being used to produce 16G-compatible seats which will bring a significant weight reduction compared to commonly used aluminum alloys.

In the past two decades, magnesium alloy die castings have been widely used for thin-wall computer housings, mobile phone and video camera housings where lightness, surface finish and electromagnetic shielding are attractive consideration to customers. Magnesium alloys have also been increasingly used to manufacture frames and wheels of bicycles where light weight and vibration damping capacity are special considerations. In recent years, Magnesium Elektron Limited and BIOTRONIK developed the world's first clinically proven magnesium-based bioresorbable scaffold, SynerMag® 410 alloy system. The latest generation BIOTRONIK magnesium scaffold has been clinically trialed. Magnesium alloy MgB_2 was discovered in 2001 (Nagamatsu et al., 2001) to have superconductivity at approximately 40 K (−233 °C), which is nearly twice that of the traditional metallic superconductor Nb_3Sn. One very recent discovery is that polycrystalline Mg-Sc alloys containing more than 18 at % (29 wt%) scandium exhibit an interesting shape memory phenomenon (Ogawa et al., 2016). The density of these Mg-Sc alloys is only one-third of those of commonly used TiNi shape memory alloys.

Driven by demands for clean and renewable energies, there has been an increasing interest in developing magnesium-based alloys for solid-state hydrogen storage. Magnesium has an attractively large hydrogen storage capacity. It can store approximately 7.6 wt% hydrogen, more than any other metal or metallic alloy (Shang et al., 2021). However, the hydrides formed in magnesium are very stable, and it is necessary to use a relatively high temperature, ~280 °C, to release the hydrogen. The kinetic of the hydrogen absorption/desorption process is also slow. It is often necessary to use catalyst to accelerate the reaction. New alloy compositions and dopants and novel processes are currently being extensively explored to solve these problems.

Key issues

There are several issues that restrict wider applications of magnesium alloys. They include price, lack of alloying and manufacturing technologies that can lead to lower-cost and better-performing magnesium products. The magnesium price was about US$2300 per ton for the past 10 years but jumped over US$11000 per ton in September 2021, with an average of US$4700 per ton for the past 12 months. This high price, if sustained, would impose a large barrier to the more usage of magnesium for applications in transportation and electronic industries. In comparison to other commodity materials such as aluminum, the production and processing costs of magnesium products are relatively high, and there remain limited choices in the selection of magnesium alloys for specific applications. The critical technological issues include the lack of effective and low-cost grain refiners for aluminum-containing magnesium alloys, stronger precipitation hardening alloys for sand castings and wrought products, wrought alloys with higher formability that can lead to lower-processing cost, more corrosion-resistant or stainless alloys. Inevitably, further improvement in existing, or development of new, alloying and/or processing technologies requires better understanding of the complex processing-microstructure-property relationships, which in turn requires deeper understanding of some fundamental issues such as interactions between lattice defects of dislocations and deformation twins and solutes, solute clusters and second-phase particles and their impacts on mechanical properties and formability, the physical origin of the pyramidal-fiber texture in some magnesium extrusions can give rise to less tension-compression yield asymmetry, and whether dynamic recrystallization can be facilitated to occur massively, by adding some specific alloying elements or reducing magnesium grain to below some critical sizes, during room temperature sheet forming. One more recent progress in addressing some of these issues is the development of some compositionally lean magnesium alloys that are intrinsically suitable for higher-speed extrusion or rolling and hence lower processing cost. A strategy used in strengthening such relatively soft alloys is further refinement in magnesium grain size and introduction of nano-scale precipitates that are more effective in strengthening even at a substantially low volume fraction.

Conclusion

Magnesium is abundant and the lightest structural metal. Together with some attractive physical properties such as low melting point and high specific heat, magnesium and its alloys have received increasing attention, more extensive research and wider engineering applications in the past 20 years, especially for energy efficient and environmentally friendly applications in the transportation industry. The magnesium metal annual production has been increased by nearly three times since 2000. Majority of this production is made by the Pidgeon process. Currently, about 45% of the annually produced magnesium metal is used for making magnesium casting alloys, only a tiny fraction (~5%) is used for fabricating wrought products, in contrast to more extensively used steels and aluminum alloys where wrought products dominate. Magnesium itself is not strong enough for engineering applications. It deforms readily by dislocation slip and/or mechanical twinning. Additions of some specific alloying elements can impede or facilitate the deformation modes for better mechanical properties or formability. There are more commercial magnesium casting alloys than wrought alloys, even after extensive global research on wrought alloys in the past 20 years. Magnesium products are usually produced from magnesium alloys by high-pressure die casting, permanent mold casting or sand casting or thermomechanical processing such as hot extrusion or hot rolling. These manufactured products can be readily welded by conventional welding technologies. While a remarkable progress has been made in the development and application of magnesium alloys, the full potential of magnesium alloys, as an emerged class of materials for engineering, energy or biomedical applications, is still far from being fully explored. There remain some critical scientific and technological issues that require better understanding at fundamental and experimental levels. With the advent of new manufacturing and processing technologies, advanced facilities for microstructural characterization, and super-computing facilities for atomistic understanding of impacts of solute atoms of added alloying elements, it is foreseeable that properties and applications of magnesium alloys can be further enhanced and widened to the level currently enjoyed by aluminum alloys.

References

Agnew SR (2012) Deformation mechanisms of magnesium alloys. In: Bettles C and Barnett M (eds.) *Fundamentals of Processing, Properties and Applications*, pp. 63–104. Oxford: Woodhead Publishing.

Al-Samman T and Li X (2011) Sheet texture modification in magnesium-based alloys by selective rare earth alloying. *Materials Science and Engineering A* 528: 3809–3822.

Atwell DL and Barnett MR (2007) Extrusion limits of magnesium alloys. *Metallurgical and Materials Transactions A: Physical Metallurgy and Materials Science* 38: 3032–3041.

Bakke P, Bowles AL, and Westengen H (2007) Elevated temperature alloys—Paths for further performance gains in AE44. In: Kainer KU (ed.) *Proceedings of the 7th International Conference on Magnesium Alloys and their Applications*, pp. 55–66. Weinheim: Wiley-VCH.

Bettles CJ, Forwood CT, Jones DS, Griffths JR, Frost MT, StJohn DH, Qian M, Song GL, and Nie JF (2003) *AMC-SC1: A New Magnesium Alloy Suitable for Powertrain Applications*. The Society of Automotive Engineers. 2003-01-1365.

Chetty N and Weinert M (1997) Stacking faults in magnesium. *Physical Review B* 56: 10844–10851.

Easton M, Beer A, Barnett M, Davies C, Dunlop G, Durandet Y, Blacket S, Hilditch T, and Beggs P (2008) Magnesium alloy applications in automotive structures. *JOM* 60: 57–62.

Gao X and Nie JF (2008) Enhanced precipitation-hardening in Mg-Gd alloys containing Ag and Zn. *Scripta Materialia* 58: 619–622.

Nagamatsu J, Nakagawa N, Muranaka T, Zenitani Y, and Akimitsu J (2001) Superconductivity at 39 K in magnesium diboride. *Nature* 410: 63–64.

Nakata T, Xu C, Ajima R, Matsumoto Y, Shimizu K, Sasaki TT, Hono K, and Kamado S (2018) Improving mechanical properties and yield asymmetry in high-speed extrudable Mg-1.1Al-0.24Ca (wt%) alloy by high Mn addition. *Materials Science and Engineering A* 712: 12–19.

Nie JF (2012) Precipitation and hardening in magnesium alloys. *Metallurgical and Materials Transactions A: Physical Metallurgy and Materials Science* 43: 3891–3939.

Nie JF, Gao X, and Zhu SM (2005) Enhanced age hardening response and creep resistance of Mg-Gd alloys containing Zn. *Scripta Materialia* 53: 1049–1053.

Nie JF, Wilson NC, Zhu YM, and Xu Z (2016) Solute clusters and GP zones in binary Mg-RE alloys. *Acta Materialia* 106: 260–271.

Nie JF, Shin KS, and Zeng ZR (2020) Microstructure, deformation, and property of wrought magnesium alloys. *Metallurgical and Materials Transactions A: Physical Metallurgy and Materials Science* 51: 6045–6109.

Ogawa Y, Ando D, Sutou Y, and Koike J (2016) A lightweight shape-memory magnesium alloy. *Science* 353: 368–370.

Partridge PG (1967) The crystallography and deformation modes of hexagonal close-packed metals. *Metallurgical Reviews* 12: 169–194.

Pekguleryuz MO and Kaya AA (2003) Creep resistant magnesium alloys for powertrain applications. *Advanced Engineering Materials* 5: 866–878.

Polmear IJ, StJohn D, Nie JF, and Qian M (2017) *Light Alloys*, 5th edn Oxford: Elsevier.

Shang Y, Pistidda C, Gizer G, Klassen T, and Dornheim M (2021) Mg-based materials for hydrogen storage. *Journal of Magnesium and Alloys* 9: 1837–1860.

StJohn D, Qian M, Easton MA, Cao P, and Hildebrand Z (2005) Grain refinement of magnesium alloys. *Metallurgical and Materials Transactions A: Physical Metallurgy and Materials Science* 36: 1669–1679.
Westengen H and Aune TK (2006) Magnesium casting alloys. In: Friedrich HE and Mordike BL (eds.) *Magnesium Technology*, pp. 145–204. Berlin: Springer.
Wu D, Chen RS, and Han EH (2011) Excellent room-temperature ductility and formability of rolled Mg-Gd-Zn alloy sheets. *Journal of Alloys and Compounds* 509: 2856–2863.
Zhu S, Easton MA, Abbott TB, Nie JF, Dargusch MS, Hort N, and Gibson MA (2015) Evaluation of magnesium die-casting alloys for elevated temperature applications: Microstructure, tensile properties, and creep resistance. *Metallurgical and Materials Transactions A: Physical Metallurgy and Materials Science* 46: 3543–3554.
Zhu S, Abbott TB, Nie JF, Ang HQ, Qiu D, Nogita K, and Easton MA (2021) Re-evaluation of the mechanical properties and creep resistance of commercial magnesium die-casting alloy AE44. *Journal of Magnesium and Alloys* 9: 1537–1545.

Further reading

Avedesian MM and Baker H (eds.) (1999) *ASM Specialty Handbook: Magnesium and Magnesium Alloys*. Ohio: ASM International.
Friedrich HE and Mordike BL (eds.) (2006) *Magnesium Technology*. Berlin: Springer.
Nie JF (2014) Physical metallurgy of light alloys. In: Laughlin DE and Hono K (eds.) *Physical Metallurgy*, pp. 2009–2156. Oxford: Elsevier.
Pekguleryuz MO, Kainer KU, and Kaya AA (eds.) (2013) *Fundamentals of Magnesium Alloy Metallurgy*. Oxford: Woodhead Publishing.

Electronic structure: Impurity and defect states in metals and alloys

JS Faulkner, Center for Biological and Materials Physics, Department of Physics, Florida Atlantic University, Boca Raton, FL, United States

© 2024 Elsevier Ltd. All rights reserved.

This is an update of J.S. Faulkner, Metals and Alloys, Impurity and Defect States in, Editor(s): Franco Bassani, Gerald L. Liedl, Peter Wyder, Encyclopedia of Condensed Matter Physics, Elsevier, 2005, Pages 384–392, ISBN 9780123694010, https://doi.org/10.1016/B0-12-369401-9/00469-1.

Introduction 565
The Green's function from multiple scattering theory 566
Pure metals 567
Impurities in metals 567
Coherent potential approximation 569
Order-N methods 571
Extensions and approximations 572
Conclusion 572
References 572

Abstract

The most commonly used methods for treating the impurity and defect states in metals and alloys start with the calculation of the one-electron Green's function $G(E, \mathbf{r}, \mathbf{r}')$ (Faulkner and Stocks, 2019). The density functional theory (DFT) makes it possible to write a simple equation for this function. The local density approximation or the generalized gradient approximation are used to generate the effective one-electron potential $V(\mathbf{r})$. In any version of the DFT, $V(\mathbf{r})$ is a functional of the density of the electrons in the system, $\rho(\mathbf{r})$, which means that the one-electron equation must be solved self-consistently.

Introduction

The most commonly used methods for treating the impurity and defect states in metals and alloys start with the calculation of the one-electron Green's function $G(E, \mathbf{r}, \mathbf{r}')$ (Faulkner and Stocks, 2019). The density functional theory (DFT) makes it possible to write a simple equation for this function

$$\left[E + \frac{\hbar^2}{2m}\nabla^2 - V(\mathbf{r})\right] G(E, \mathbf{r}, \mathbf{r}') = \delta(\mathbf{r} - \mathbf{r}') \tag{1}$$

The local density approximation or the generalized gradient approximation are used to generate the effective one-electron potential $V(\mathbf{r})$. In any version of the DFT, $V(\mathbf{r})$ is a functional of the density of the electrons in the system, $\rho(\mathbf{r})$, which means that the one-electron equation must be solved self-consistently. The charge density is obtained from the Green's function by integration

$$\rho(\mathbf{r}) = -\frac{2}{\pi}\int_{-\infty}^{E_F} G(E, \mathbf{r}, \mathbf{r})dE, \tag{2}$$

where the Fermi energy E_F is defined by the requirement that the integral of $\rho(\mathbf{r})$ over all space is equal to the total number of electrons, and the 2 is required by the electron spins. The total energy is

$$E_{total} = \sum_{occ.} E_i - \frac{1}{2}\int \frac{\rho(\mathbf{r})\rho(\mathbf{r}')}{|\mathbf{r} - \mathbf{r}'|} d\mathbf{r}d\mathbf{r}' + E_{xc}[\rho] - \int \frac{\delta E_{xc}[\rho]}{\delta\rho(\mathbf{r})}\rho(\mathbf{r})d\mathbf{r}. \tag{3}$$

The sums are over all occupied states including spin, and the exchange correlation functional $E_{xc}[\rho]$ is determined by the particular method used to calculate the effective one-electron potential.

The one-electron potential for a metal or alloy can be written as a sum of potentials that describe the interaction of the electron with each of the atoms in the solid

$$V(\mathbf{r}) = \sum_{i=1}^{N} v_i(\mathbf{r} - \mathbf{R}_i). \tag{4}$$

In order to eliminate surface states, it is convenient to imagine the N atoms in the solid are in a supercell, and that the supercells are periodically reproduced to fill all space. The potential associated with the $i\underline{th}$ atom with its nucleus at $\mathbf{R}_i$, $v_i(\mathbf{r} - \mathbf{R}_i)$, is zero outside of the region Ω_i. The Ω_i fill the entire supercell and do not overlap. At some point, N will be allowed to approach infinity and the supercell to fill all space.

The Green's function from multiple scattering theory

The multiple scattering equations for wave functions are derived and discussed in the article Electronic Structure: Scattering methods (for electronic structure calculations). The version of these equations that deals with Green's functions starts from the operator equation (Faulkner and Stocks, 1980).

$$G(z) = (z - H_0 - V)^{-1} = G_0(z)[I + VG(z)] = G_0(z) + G_0(z)T(z)G_0(z), \tag{5}$$

where H_0 is the kinetic energy operator, z is a complex energy, and

$$G_0(z) = (z - H_0)^{-1}. \tag{6}$$

For the case that the potential is a sum of atomic potentials as in Eq. (4), the scattering matrix for the system,

$$T(z) = V[I + G_0(z)T(z)] \tag{7}$$

can be written

$$T = \sum_{i=1}^{N}\sum_{j=1}^{N}\tau^{ij}, \tag{8}$$

where the scattering path operator τ^{ij} is

$$\tau^{ij} = t^i\delta_{ij} + t^i G_0 \sum_{k\neq i}^{N}\tau^{kj}, \tag{9}$$

and $t^i = (1 - v_i G_0)^{-1} v_i$ is the t-matrix that describes the scattering from $v_i(\mathbf{r} - \mathbf{R}_i)$ embedded in a vacuum.

A function that is very useful in analyzing experiments is the density-of-states (DOS) $\rho(E)$, which is the number of energy levels between the energies E and $E + \mathrm{d}E$. The DOS associated with just the $i\underline{\text{th}}$ atom can be calculated from,

$$\rho_i(E) = -\frac{2}{\pi}\operatorname{Im}\lim_{z\downarrow E}\int_{\Omega_i} G(z, \mathbf{r}, \mathbf{r})d\mathbf{r}, \tag{10}$$

where $G(z, \mathbf{r}, \mathbf{r}') = \langle \mathbf{r}|G|\mathbf{r}'\rangle$. Of course, the DOS for the supercell is $\rho(E) = \sum_{i=1}^{N}\rho_i(E)$. The Green's functions and scattering operators that will be used henceforth are obtained from the above by letting z approach E from above the real axis.

When the position vectors $\mathbf{r}$and $\mathbf{r}'$ are in the region Ω_n, the Green's function in the position representation can be shown to take the form

$$G(E, \mathbf{r}_n, \mathbf{r}'_n) = \sum_{LL'} Z_L^n(E, \mathbf{r}_n)\tau_{LL'}^{nn}(E)Z_{L'}^{n*}(E, \mathbf{r}'_n) - \sum_{L} Z_L^n(E, \mathbf{r}_n)J_L^{n*}(E, \mathbf{r}'_n), \tag{11}$$

where

$$\tau_{LL'}^{nn} = t_{LL'}^n + \sum_{L_1, L_2, L_3, L_4} t_{LL_1}^n \sum_{i\neq n, j\neq n} g_{L_1L_2}^{ni}\tau_{L_2L_3}^{ij}g_{L_3L_4}^{jn}t_{L_4L'}^n = t_{LL'}^n + \sum_{L_1, L_2} t_{LL_1}^n \sum_{i\neq n} g_{L_1L_2}^{ni}\tau_{L_2L'}^{in}, \tag{12}$$

and $t_{LL'}^n(E)$ is the scattering matrix for the nth atom. The matrix $\boldsymbol{\tau}$ with elements $\tau_{LL'}^{mn}$ is is the inverse of the matrix $\mathbf{M}$ that has elements,

$$M_{LL'}^{mn} = m_{LL'}^n\delta_{mn} - g_{LL'}^{mn}(1 - \delta_{mn}). \tag{13}$$

The function $Z_L^n(E, \mathbf{r}_n)$ is the solution of the equation,

$$\left[-\frac{\hbar^2}{2m}\nabla^2 + v_n(\mathbf{r}_n) - E\right]Z_L^n(E, \mathbf{r}_n) = 0, \tag{14}$$

that is regular at the origin and joins smoothly to

$$Z_L^n(E, \mathbf{r}_n) \rightarrow \sum_{L'} Y_{L'}(\mathbf{r}_n)j_{l'}(\alpha r_n)m_{L'L}^n(E) - i\kappa Y_L(\mathbf{r}_n)h_l(\alpha r_n), \tag{15}$$

when $\mathbf{r}$ is outside of Ω_n. As usual, $j_l(\alpha r_n)$ and $h_l(\alpha r_n)$ are the spherical Bessel and Hankel functions, and $Y_L(\mathbf{r}) = Y_{l,\ m}(\vartheta, \phi)$ is the spherical harmonic. The matrix $\mathbf{m}^n$ with elements $m_{LL'}^n$ is the inverse of the scattering matrix $\mathbf{t}^n$ whose elements are

$$t^n_{LL'}(E) = \iint j_l(\alpha r) Y^*_L(\mathbf{r}) \langle \mathbf{r} | t(E) | \mathbf{r}' \rangle Y_{L'}(\mathbf{r}') j_l(\alpha r') d\mathbf{r} d\mathbf{r}'. \tag{16}$$

The function $J^n_L(E, \mathbf{r}_n)$ is a real solution of the differential equation (14) that joins smoothly to $Y_L(\mathbf{r}_n) j_l(\kappa r_n)$ when $\mathbf{r}$ is outside of Ω_n. The $g^{nm}_{LL'}$ in Eq. (12) can be pictured as propagators that take an electron from site n to m, and are given by

$$g^{nm}_{LL'} = -4\pi i\kappa i^{l-l'} \sum i^{-\lambda} C^{\Lambda}_{LL'} h_\lambda(\kappa R_{nm}) Y^*_\Lambda(\mathbf{R}_{nm}), \tag{17}$$

where $\mathbf{R}_{nm} = \mathbf{R}_m - \mathbf{R}_n$ and the Gaunt factors $C^{\Lambda}_{LL'} = \int Y_\Lambda Y^*_L Y_{L'} d\Omega$ are related to Clebsch-Gordon coefficients. This equation for the Green's function is correct for any kind of solid, but it is difficult to calculate except for pure metals, metals with impurities, and alloys using approximations.

Pure metals

The expression for the Green's function, Eq. (11), is greatly simplified for infinite periodic solids. The case of one atom per unit cell will be treated because the extension to more than one atom is straightforward. The atoms are on the sites $\mathbf{R}_i$ of a Bravais lattice. Bloch's theorem follows from the invariance of the crystal under translations,

$$\psi_{\mathbf{k}}(\mathbf{r} + \mathbf{R}_{ij}) = e^{i\mathbf{k}\cdot\mathbf{R}_{ij}} \psi_{\mathbf{k}}(\mathbf{r}). \tag{18}$$

There are only N Bloch vectors, $\mathbf{k}_i$, because of the periodic boundary conditions. It follows that the matrix $\mathbf{g}$ with elements $g^{ij}_{LL'}$ can be put into block diagonal form by transforming it with the matrix $\mathbf{U}$ with elements

$$U^{ij}_{LL'} = {}^1\!/\!_{\sqrt{N}} e^{-i\mathbf{R}_i\cdot\mathbf{k}_j} \delta_{LL'}. \tag{19}$$

$$\left[\mathbf{U}^\dagger \mathbf{g} \mathbf{U}\right]^{ij}_{LL'} = g_{LL'}(E, \mathbf{k}_i)\delta_{ij} = \sum_{m=1}^{N} e^{i\mathbf{k}_i\cdot\mathbf{R}_{0m}} g^{0m}_{LL'}(E), \tag{20}$$

Since the matrices $\mathbf{m}^i$ are the same for every cell, the transformed matrix $\mathbf{U}^\dagger\mathbf{M}\mathbf{U}$is easily inverted. When the $\mathbf{U}$ matrix is used to transform back and then N is allowed to go to infinity, the scattering path matrix for the periodic crystal is

$$\boldsymbol{\tau}^{mn}_0(E) = \frac{1}{N}\sum_{i=1}^{N} e^{-i\mathbf{k}_i\cdot\mathbf{R}_{mn}} [\mathbf{m}(E) - \mathbf{g}(E, \mathbf{k}_i)]^{-1} = \frac{\Omega}{(2\pi)^3} \int e^{-i\mathbf{k}\cdot\mathbf{R}_{mn}} [\mathbf{m}(E) - \mathbf{g}(E, \mathbf{k})]^{-1} d\mathbf{k}. \tag{21}$$

We suppress the angular momentum indices L and L' in this and succeeding equations by the use of block matrices.

The functions $\mathbf{g}(E, \mathbf{k})$ are called structure constants in Korringa-Kohn-Rostoker (KKR) band theory, and sophisticated methods have been developed for calculating them. The standard approximation in the application of this formula is that the elements of $\mathbf{m}(E)$ and $\mathbf{g}(E, \mathbf{k})$ that correspond to angular momenta such that $l > l_{\max}$ are ignored. Thus, the matrices that must be inverted in Eq. (21) have dimension $(l_{\max} + 1)^2$.

Impurities in metals

When an impurity atom replaces one of the atoms in a periodic metal, the scattering matrix $\mathbf{m}^i$ will obviously change on the impurity site. The scattering matrices on the adjoining sites will also change because of the effect that the impurity has on its neighboring atoms. Even the Green's functions $\mathbf{g}^{ij}$ that connect the atoms affected by the impurity will change, because the size difference between the impurity atom and the host atoms will cause displacements from the sites of the original periodic lattice. In metals, it is reasonable to assume that the influence of the impurity is screened beyond a certain number of nearest neighbor shells to the point that it has no noticeable effect on the rest of the lattice. It follows that the $N \times N$ matrix $\mathbf{M}$ for the metal with an impurity can be written $\mathbf{M} = \mathbf{M}_0 + \Delta\mathbf{M}$, where $\Delta\mathbf{M}$ is a matrix with elements

$$\Delta M^{mn}_{LL'} = \left(m^n_{LL'} - m^n_{0LL'}\right)\delta_{mn} - \left(g^{mn}_{LL'} - g^{mn}_{0LL'}\right)(1 - \delta_{mn}). \tag{22}$$

In this equation, $m^n_{0LL'}$ and $g^{mn}_{0LL'}$ are the matrix elements of the original periodic solid. All of the elements of $\Delta\mathbf{M}$ are zero except for those associated with the N_I sites of the atoms that are influenced by the impurity. Assuming that this is one or two nearest-neighbor shells, N_I is 13 or 19 for an fcc lattice and it is 9 or 15 for a bcc lattice.

Let us call the set of sites influenced by the impurity S_I. If $n \subset S_I$, the coefficients $\tau^{nn}_{LL'}$ that appear in the expression for the Green's function in Eq. (11) are elements of the matrix

$$\boldsymbol{\tau}^I = \left[\mathbf{I} - \boldsymbol{\tau}^I_0 \Delta\mathbf{M}^I\right]^{-1} \boldsymbol{\tau}^I_0. \tag{23}$$

The elements of $\boldsymbol{\tau}_0^I$ are the matrix elements of the scattering path operators for the host lattice $\boldsymbol{\tau}_0^{mn}$, where $m \subset S_I$ and $n \subset S_I$. The matrix $\Delta\mathbf{M}^I$ contains only the non-zero elements of $\Delta\mathbf{M}$. No angular momentum indices are included beyond $l_{\max}$, so the dimension of the matrices in Eq. (26) is $N_I(l_{\max}+1)^2$.

The best way to calculate the DOS and charge density associated with the sites influenced by the impurity is

$$\rho_n^I(E) = -\frac{1}{\pi}\mathrm{Im}\sum_{LL'}\tau_{LL'}^{I,nn}(E)\int_{\Omega_n} F_{L'L}^n(E,\mathbf{r},\mathbf{r})d\mathbf{r}, \tag{24}$$

and

$$\rho_n^I(\mathbf{r}) = -\frac{1}{\pi}\mathrm{Im}\sum_{LL'}\int_{-\infty}^{E_F}\tau_{LL'}^{I,nn}(E)F_{L'L}^n(E,\mathbf{r},\mathbf{r})dE, \tag{25}$$

where $F_{L'L}^n(E,\mathbf{r}_n{}',\mathbf{r}_n) = Z_{L'}^{n*}(E,\mathbf{r}_n{}')Z_L^n(E,\mathbf{r}_n)$. In summary, we assume a charge density for the host atoms and a crystal structure. We use the DFT to calculate the potential for the host atoms, $V_0(\mathbf{r})$, and hence the scattering matrix $\mathbf{t}_0(E)$. We obtain the coefficients $\tau_{0,\,LL'}^{nn}$ from Eq. (21) and then calculate the Green's function using Eq. (11) and the charge density using Eq. (2). This process is iterated until the charges are self-consistent. At this point we have the coefficients for all the sites of the host lattice, and we have the elements of the matrix $\boldsymbol{\tau}_0^I$. It is now necessary to guess charge densities for the impurity sites with $n \subset S_I$, calculate the potentials and scattering matrices, and construct the matrix $\Delta\mathbf{M}^I$. The coefficients and Green's functions for these sites are obtained from Eqs. (23) and (11). The Fermi energy is not changed, and the new charge densities at the impurity sites are obtained from Eq. (25). The potentials must be iterated to self-consistency. These formulas have been very successful in predicting resistivities, hyperfine energies, and energies of formation, but only if the relaxation of the atoms in the nearest-neighbor shells away from the periodic lattice sites is allowed to occur. The calculations are sensitive to approximations to the shape of the self-consistent potentials, and, where relevant, spin polarization must be included.

An interesting formula for the DOS can be obtained using a theorem from scattering theory derived by the Russian academician M. G. Krein. In operator language, Krein's theorem states that

$$Tr[G(z)-G_0(z)] = \frac{i}{2\pi}\lim_{\varepsilon\downarrow 0}\int_{-\infty}^{\infty}\frac{\ln\det\left(I-i2\sqrt{E'+i\varepsilon}\,T(E'+i\varepsilon)\right)}{(E'-z)^2}dE'. \tag{26}$$

Using the formula for the DOS in Eq. (10), this equation can, with some effort, be put into the form

$$\rho(E)-\rho_0(E) = -\frac{2}{\pi}\mathrm{Im}\frac{d\ln\det\mathbf{M}(E)}{dE}, \tag{27}$$

where $\rho(E)$ is the DOS for the system of scatterers, $\rho_0(E)$ is the DOS for free electrons, and $\mathbf{M}(E)$ is the matrix defined in Eq. (13). This is called Lloyd's formula because Lloyd derived it without the help of Krein's theorem. Krein's theorem can immediately be used for impurities by defining H_0 to be the Hamiltonian for the host lattice rather than just the kinetic energy, and a version of Lloyd's formula that gives the change in the total DOS caused by the impurity can be obtained.

The simplest theory for an impurity is to picture it as a single spherically-symmetric scatterer embedded in a free-electron gas. Then Krein's theorem leads to

$$\rho(E)-\rho_0(E) = -\frac{i}{\pi}\mathrm{Im}\sum_l(2l+1)\frac{d\ln[1--2\alpha t_l(E)]}{dE}. \tag{28}$$

For such a scatterer, the t-matrix defined in Eq. (16) becomes $t_{LL'} = t_l\delta_{ll'}\delta_{mm'}$ with

$$t_l = -\frac{1}{\alpha}e^{i\eta_l}\sin\eta_l, \tag{29}$$

where the η_l are scattering phase shifts. From this, we obtain the Friedel sum

$$\rho(E)-\rho_0(E) = \frac{2}{\pi}\sum_l(2l+1)\frac{d\eta_l}{dE}. \tag{30}$$

The Friedel formula appears in many text books on condensed matter physics, but the assumptions that go into its derivation are very limiting. Leaving aside the fact that the electronic spectrum of the host resembles a free electron gas for very few solids, the assumption that the change in the spectrum is confined to one site is internally inconsistent. It is typical that the impurity atom loses or gains charge from the host. The charge will be screened to make the system charge neutral, but the screening charge is typically distributed over one or two nearest-neighbor shells.

Coherent potential approximation

It should be clear that the impurity equations described in the preceding section can be generalized to deal with several interacting impurities in a metal. It is only necessary to increase the number of sites N_i influenced by the impurity atoms. However, when the concentration of impurities reaches the point at which most of the impurity atoms are within range of each other, the impurity equations are no longer useful. It is then necessary to treat the material as an alloy, and to develop a different class of theories. The problem of finding the solutions of Schroedinger's equation for a potential function that is not periodic is difficult because Bloch's theorem, Eq. (18), no longer holds. Progress has been made on substitutional solid-solution alloys that are made up of two or more species of atoms distributed randomly on the sites $\mathbf{R}_i$of a Bravais lattice. In the following, we concentrate on binary alloys, although the generalization to ternary, quaternary, etc. is straightforward.

The ensemble of all alloys that can be constructed out of $N_A = c_A N$ A atoms and $N_B = c_B N$ B atoms contains $M_c = N\,!\,/N_A\,!\,N_B!$ atomic arrangements. Experimentally, it is observed that all alloys with the concentrations c_A and c_B have the same electronic structure. It follows that, as $N \to \infty$, all of the arrangements have the same electronic structure with probability one, and it can be found by averaging over the ensemble. The ensemble average of a one-electron wave function has no meaning, but, because of the linear relation between the Green's function and the electronic properties, the ensemble average of the Green's function is useful.

The ensemble average of the function in Eq. (11) can be obtained if we make the assumption that the resulting alloy model is isomorphous. That is, we assume that the Green's function takes one of two forms, $G_A(E, \mathbf{r}_n, \mathbf{r}_n{}')$ if there is an A atom on site n and $G_B(E, \mathbf{r}_n, \mathbf{r}_n{}')$ if there is an B atom on that site. With this assumption, the ensemble averaged Green's function is

$$\langle G_n(E, \mathbf{r}_n, \mathbf{r}'_n)\rangle = c_A G_A(E, \mathbf{r}_n, \mathbf{r}'_n) + c_B G_B(E, \mathbf{r}_n, \mathbf{r}'_n), \tag{31}$$

where

$$G_A(E, \mathbf{r}_n, \mathbf{r}'_n) = \sum_{LL'} Z_L^A(E, \mathbf{r}_n)\langle \tau_{LL'}^{nn}\rangle_A Z_{L'}^{A*}(E, \mathbf{r}'_n) - \sum_{L} Z_L^A(E, \mathbf{r}_n) J_L^{A*}(E, \mathbf{r}'_n), \tag{32}$$

and

$$G_B(E, \mathbf{r}_n, \mathbf{r}'_n) = \sum_{LL'} Z_L^B(E, \mathbf{r}_n)\langle \tau_{LL'}^{nn}\rangle_B Z_{L'}^{B*}(E, \mathbf{r}'_n) - \sum_{L} Z_L^B(E, \mathbf{r}_n) J_L^{B*}(E, \mathbf{r}'_n). \tag{33}$$

The charge density for an A atom, $\rho_A(\mathbf{r}_n)$, is obtained by inserting $G_A(E, \mathbf{r}_n, \mathbf{r}_n)$ into Eq. (2), and similarly for the B atom. From these charge densities we calculate the potentials $v_A(\mathbf{r}_n)$ and $v_B(\mathbf{r}_n)$. The functions $Z_L^A(E, \mathbf{r}_n)$ and $J_L^A(E, \mathbf{r}_n)$ are obtained using $v_A(\mathbf{r}_n)$ in Eq. (13), and the functions $Z_L^B(E, \mathbf{r}_n)$ and $J_L^B(E, \mathbf{r}_n)$ are obtained using $v_B(\mathbf{r}_n)$.

The averages $\langle \tau_{LL'}^{nn}\rangle_A$ and $\langle \tau_{LL'}^{nn}\rangle_B$ are the ensemble averages of the scattering path operator subject to the condition that there is an A or B atom on site n. These averages are simplified considerably by making a mean field approximation. It is assumed that, on average, the scattering of the electrons from all the sites other than site n is described by replacing the actual potentials on those sites with a potential $v_c(\mathbf{r})$, called the coherent potential. The scattering from $v_c(\mathbf{r})$ is described by a t-matrix, $\mathbf{t}_c(E)$, which has an inverse $\mathbf{m}_c(E)$. It follows that, within the coherent potential approximation (CPA) (Faulkner, 1982), the ensemble averages $\langle \tau_{LL'}^{nn}\rangle_A$ and $\langle \tau_{LL'}^{nn}\rangle_B$ are the elements of the matrices obtained from Eq. (23)

$$\langle \boldsymbol{\tau}^{nn}\rangle_A = \left[\mathbf{I} - \boldsymbol{\tau}_c^{nn}(\mathbf{m}_A - \mathbf{m}_c)\right]^{-1}\boldsymbol{\tau}_c^{nn}, \tag{34}$$

and

$$\langle \boldsymbol{\tau}^{nn}\rangle_B = \left[\mathbf{I} - \boldsymbol{\tau}_c^{nn}(\mathbf{m}_B - \mathbf{m}_c)\right]^{-1}\boldsymbol{\tau}_c^{nn}. \tag{35}$$

The matrices $\mathbf{m}_A$ and $\mathbf{m}_B$ are the inverses of the t-matrices calculated from the potentials $v_A(\mathbf{r})$ and $v_B(\mathbf{r})$. From Eq. (24), it can be seen that the matrix $\boldsymbol{\tau}_c^{nn}$ is

$$\boldsymbol{\tau}_c^{nn}(E) = \frac{\Omega}{(2\pi)^3}\int \left[\mathbf{m}_c(E) - \mathbf{g}(E, \mathbf{k})\right]^{-1} d\mathbf{k}. \tag{36}$$

The number of impurity sites N_I is one, so the matrices in these equations have dimension $(l_{\max} + 1)^2$. As would be expected, none of these equations depend on the choice of a site n.

In the language of multiple-scattering theory used here, the condition originally put forward by P. Soven that defines the mean field t-matrix $\mathbf{t}_c(E)$ is

$$c_A\langle \boldsymbol{\tau}^{nn}\rangle_A + c_B\langle \boldsymbol{\tau}^{nn}\rangle_B = \boldsymbol{\tau}_c^{nn}. \tag{37}$$

In words, this is the condition that, on average, there is no scattering from A and B atoms embedded in the coherent potential host matrix. Space does not allow for descriptions of all the arguments put forward to justify this CPA condition. Perhaps the most convincing arguments come from the formulation of the problem of calculating the Green's function of an alloy in terms of infinite order perturbation theory. Diagrams are then used to analyze the contributions to the Green's functions in a manner analogous to field theory, quantum electrodynamics, or many-body theory. It has been argued that the CPA contains the maximum number of classes of diagrams that can be included and still retain a Green's function that is properly analytic. The criterion that is used to specify the diagrams included in the CPA is called the single-site approximation. It has been shown by R. Mills and P. Ratanavararaksa and also A. Mookerjee that it is possible to go beyond the single-site approximation and retain an analytic Green's function, but it is difficult.

The procedure for calculating the electronic states within the CPA is first to guess starting values for the charge densities $\rho_A(\mathbf{r})$ and $\rho_B(\mathbf{r})$ and from them calculate $v_A(\mathbf{r})$ and $v_B(\mathbf{r})$. The t-matrices $\mathbf{t}_A(E)$ and $\mathbf{t}_B(E)$ are calculated, and a first guess to $\mathbf{t}_c(E)$ is just the average of them $\mathbf{t}_c(E) \approx c_A\mathbf{t}_A(E) + c_B\mathbf{t}_B(E)$. Eqs. (32)–(35) are then iterated to self-consistency in the charge densities and also in the coherent potential t-matrix $\mathbf{t}_c(E)$.

Calculations with this version of the CPA have been carried out on many alloy systems. The predicted electronic densities of states agree well with the ones measured in ultraviolet photoemission spectroscopy experiments. The zero temperature resistivities of alloys have been accurately predicted. Even the propensity of a random alloy to transform into a superlattice structure or into an incommensurately ordered structure has been successfully predicted.

A problem that is endemic to this version of the CPA is that the Coulomb effects are not treated correctly. Integrating the charge densities $\rho_A(\mathbf{r})$ and $\rho_B(\mathbf{r})$ and subtracting the nuclear charges Z_A and Z_B leads to the net charges on the A and B sites, q_A and q_B. It would seem that there should be a Madelung contribution to the potentials $v_A(\mathbf{r})$ and $v_B(\mathbf{r})$ as in ordered alloys, but the only Madelung potentials that are commensurate with the assumption of an isomorphous alloy are zero. The isomorphous model of an alloy with the charge q_A on every A atom and q_B on every B atom is not realistic. Using order-N methods that will be described in the next section, it is possible today to calculate the electronic structure for supercells containing thousands of atoms with no approximation other than the DFT. In Fig. 1 we show the charges on 512 copper atoms and 512 zinc atoms distributed randomly on the sites of a supercell with the structure of a body centered cubic lattice. The distribution is broad, and upon reflection is what would be expected on the basis of physical intuition. It should be compared with the prediction of the isomorphous model that all the Cu atoms would take on exactly 0.09978 electron charges, and Zn atoms would lose the same amount.

A version of the CPA can be constructed that leads to a polymorphous model of the alloy in which each atom has a different charge, but it requires a different kind of averaging. Recall that we consider periodically reproduced supercells. In the binary alloy model, N_A A atoms and N_B B atoms are distributed over the $N = N_A + N_B$ sites. The green's function defined in Eq. (11) for the alloy is different for each of the $M_c = N!/N_A!\,N_B!$ possible atomic arrangements, and can be labeled $G_n^i(E, \mathbf{r}_n, \mathbf{r}_n')$ to emphasize that. Then, the ensemble average in Eq. (27) can more properly be written

$$\langle G_n(E, \mathbf{r}_n, \mathbf{r}_n') \rangle = \frac{1}{M_c} \sum_{i=1}^{M_c} G_n^i(E, \mathbf{r}_n, \mathbf{r}_n'). \tag{38}$$

It is also possible to consider one supercell with the atomic arrangement i, and average over the sites

$$\{G^i(E, \mathbf{r}, \mathbf{r}')\} = \frac{1}{N} \sum_{n=1}^{N} G_n^i(E, \mathbf{r}, \mathbf{r}'). \tag{39}$$

We have seen that, as $N \to \infty$, $\langle G_n(E, \mathbf{r}_n, \mathbf{r}_n') \rangle$ is independent of the site index n. It is equally clear that in the same limit, $\{G^i(E, \mathbf{r}, \mathbf{r}')\}$ is independent of the arrangement index i. The equivalence of the ensemble-average in Eq. (38) with the site average in Eq. (39) is

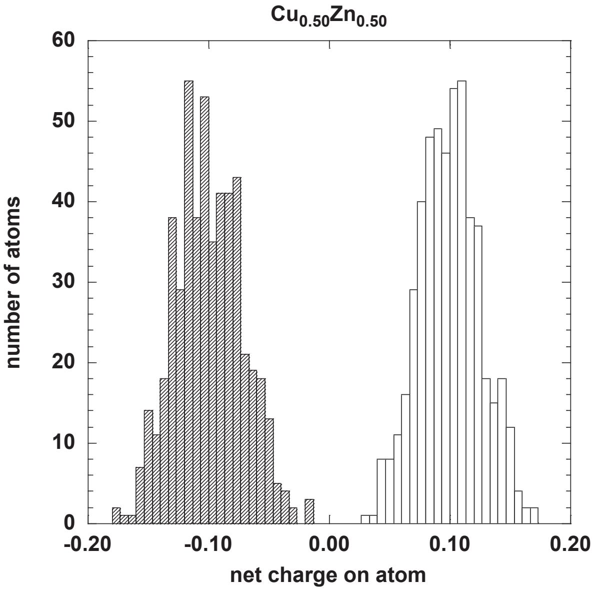

Fig. 1 The distribution of charges on the sites of a 50% copper-zinc alloy modeled with a supercell containing 1024 atoms. The charges on the copper sites are shown with the white histograms, and the charges on the zinc sites are cross-hatched. Created by the author using KaleidaGraph.

similar to the Ergodic theorem first proposed by Boltzmann, and can be proved by similar arguments. If the condition is imposed that the alloy must be isomorphous, the site average will lead to the same averaged potential as the ensemble average result shown in Eq. (27). However, the site average can lead to a polymorphous model.

Applying the CPA philosophy to the site averaged Green's function leads to

$$\{G(E,\mathbf{r},\mathbf{r}')\} = \frac{1}{N}\sum_{n=1}^{N}\{G_n(E,\mathbf{r},\mathbf{r}')\}, \tag{40}$$

where

$$\{G_n(E,\mathbf{r},\mathbf{r}')\} = \sum_{LL'} Z_L^n(E,\mathbf{r})\{\tau_{LL'}^{nn}(E)\}Z_{L'}^n(E,\mathbf{r}') - \sum_{L} Z_L^n(E,\mathbf{r})J_L^n(E,\mathbf{r}'), \tag{41}$$

and

$$\{\boldsymbol{\tau}^{nn}\} = \left[\mathbf{I} - \boldsymbol{\tau}_c^{nn}(\mathbf{m}_n - \mathbf{m}_c)\right]^{-1}\boldsymbol{\tau}_c^{nn}. \tag{42}$$

Inserting the Green's function for an index n into Eq. (2) produces a charge density, $\rho_n(\mathbf{r})$, and hence a one-electron potential, $v_n(\mathbf{r})$, for every site. From the potential, we calculate the t-matrix $\mathbf{t}_n$ and its inverse $\mathbf{m}_n$ which appears in Eq. (38). As in the isomorphous CPA, the scattering path for the coherent potential host lattice $\boldsymbol{\tau}_c^{nn}$ is calculated from Eq. (36). The condition that defines the coherent potential is

$$\frac{1}{N}\sum_{n=1}^{N}\{\tau^{nn}\} = \tau_c^{nn}, \tag{43}$$

instead of Eq. (37).

Since we are focusing on a specific supercell, the position $\mathbf{R}_n$of each atom is known and the Madelung potential for the nth site is

$$v_n^M = \sum_{m\neq n=1}^{N} M(|\mathbf{R}_n - \mathbf{R}_m|)q_n, \tag{44}$$

where

$$q_n = \int_{\Omega_n}\rho_n(\mathbf{r})d\mathbf{r} - Z_n, \tag{45}$$

and $M(|\mathbf{R}_n - \mathbf{R}_m|)$ is the Madelung matrix. The Madelung matrix is defined so that the sum in Eq. (44) gives the contribution to the Coulomb potential from all of the periodically reproduced supercells. A sophisticated method for calculating it was developed by P. P. Ewald, and it reduces to $1/|\mathbf{R}_n - \mathbf{R}_m|$ when $N \to \infty$. The potentials $v_n(\mathbf{r})$ contain the Madelung shift v_n^M.

The polymorphous version of the CPA has been applied to several alloy systems. For alloys that have a large amount of charge transfer, such as copper-gold or copper-palladium, it gives better results than the ones obtained with the isomorphous CPA, but the improvements are quite small for alloys like silver-palladium that have a small charge transfer. The polymorphous CPA has the disadvantage that it requires the use of a specific supercell. This is a small price to pay for the improvement in the treatment of the Coulomb energy. It is quite easy to apply because the charge densities $\rho_A(\mathbf{r})$ and$\rho_B(\mathbf{r})$ and the effective t-matrix $\mathbf{t}_c$ from the isomorphous CPA are used as the starting values in the self-consistent iterations.

Although the coherent potential $v_c(\mathbf{r})$ is introduced into the discussion, it is never calculated or used. The only potentials used in Eq. (14) to calculate wave functions are real potentials for real atoms, $v_n(\mathbf{r})$. From the analytic properties of $\mathbf{t}_c$ it follows that $v_c(\mathbf{r})$, if it existed, would be complex and energy-dependent.

Order-N methods

A brute force method for calculating the electronic states of a disordered solid is to simply model a portion of the solid in a supercell. The nuclei do not have to be placed on the sites of a Bravais lattice, and any combination of atomic species can be used. This makes it possible to approach a much wider range of problems than the CPA can deal with. Supercells containing a large number of atoms can be treated with the band-theory methods that have been developed to treat solids with N atoms per unit cell. All of these methods require an operation that is the equivalent of inverting or diagonalizing an $N \times N$ matrix, and these operations require an amount of computer time that scales as N^3. Even though computer speeds increase exponentially, this scaling always places a limit on the size of the supercell that can be used. For this reason, considerable effort has been devoted to the development of order-N methods for electronic structure calculations for which the computer times scale as N rather than N^3.

An order-N method called the locally self-consistent multiple-scattering (LSMS) method was developed by G. M. Stocks and his collaborators (Yang Wang et al., 1995). Each atom in the supercell is considered to be the center of a cluster of a local interaction zone (LIZ) that contains N_{LIZ} atoms. The matrix $\mathbf{M}^n$ with elements defined in Eq. (13) is truncated so that only the scatterers in the LIZ corresponding to site n are included. This is typically the nth site and its first seven or eight nearest neighbor shells. Truncating the angular momentum expansions at $l_{\max}$, the order of $\mathbf{M}^n$ is $(l_{\max}+1)^2 N_{LIZ}$ and $N_{LIZ} < 100$. After the inversion of $\mathbf{M}^n$, only the matrix elements $\tau_{LL'}^{nn}$ corresponding to the central atom are used. With these matrix elements, the Green's function $G_n(E, \mathbf{r}_n, \mathbf{r}_n{}')$ is calculated from Eq. (11), and hence the charge density $\rho_n(\mathbf{r}_n)$ and the net charge on the site q_n are obtained. The Madelung shift on the nth site is calculated using Eq. (44), and the next iteration for the potential $v_n(\mathbf{r})$ is acquired by adding that to the DFT potential calculated from the charge density. This procedure scales with N, although the prefactor is $(l_{\max}+1)^6 N_{LIZ3}$.

The LSMS puts nothing on the sites outside the LIZ. The locally self-consistent Green's function (LSGF) method proposed by I. A. Abrikosov and his collaborators puts coherent potentials on those sites. The LSGF makes use of the equations for an impurity cluster in a metal, Eqs. (22)–(25), with the coherent potential scattering matrix $\mathbf{m}_c$ replacing the host matrix $\mathbf{m}_0$. The matrix $\boldsymbol{\tau}^I$ in Eq. (23) contains the average scattering path operators for all the scatterers in the LIZ. Only the matrix for the central site, $\{\boldsymbol{\tau}^{nn}\}$, is used in the equation that defines $\mathbf{m}_c$, which is Eq. (43). The charge density $\rho_n(\mathbf{r}_n)$ is obtained by inserting the Green's function from Eq. (41) into Eq. (2). This charge density and the Madelung shift from Eq. (44) is used to calculate the new potential $v_n(\mathbf{r})$ in the self-consistent process.

The LSMS has the advantage that the atoms can be placed anywhere in the supercell, while the atoms should be on the sites of a Bravais lattice in the LSGF. The advantage of the LSGF is that the LIZ can be made much smaller. In fact, for $N_{LIZ} = 1$, which means that it contains only the central atom, the LSGF is identical to the site-averaged CPA described above. That level of approximation is adequate for many calculations on alloys.

The LSMS and LSGF are order-N because the propagation of electrons from one atom to another is treated properly only for atoms within the LIZ. It should be noted that the range of the Coulomb interactions is not assumed to be short. The Ewald sum in Eq. (44) includes the contributions from all the atoms in the supercell, and indeed from the atoms in the periodically reproduced supercells that fill all space. The calculation of the Madelung shifts takes very little time in comparison with the rest of the calculation, and experience has shown that it is not a good idea to truncate it.

Extensions and approximations

All of the equations in this article have been written in the non-relativistic form because they are easier to picture. They can easily be transformed to the Dirac form using the relativistic density functional theory (RDFT) of A. K. Rajagopal and others. The spin-polarized version of these equations has been used very successfully to explain the magnetism of metals and alloys. Instead of using the full multiple-scattering version of the equations depicted here, many authors choose to approximate them with a variational version called the linear combination of muffin-tin orbitals (LMTO). These approximations are discussed for wave functions (Faulkner, 2016).

The amount of computer time required for calculations with Green's functions can be significantly reduced with the help of sophisticated techniques derived from their properties. Using the analyticity of the Green's functions, it is frequently possible to carry out integrals over the energy, such as Eq. (2), by making the energy complex and integrating over a contour rather than along the real axis. It is also possible to use a finite-temperature version of the DFT that improves the convergence of some of the integrals. Finally, the range of the propagators $\mathbf{g}^{mn}$ that describe the motion of the electron from one site to another can be made short by shifting the zero of the potential between scatterers.

Of course, many properties of alloys are calculated using statistical methods such as Monte Carlo, molecular dynamics, and the cluster-variational method. The electronic structure appears in these calculations only in the calculation of the interatomic potentials. Different approaches to the calculation of these potentials are the embedded atom method, the generalized perturbation method, and the mixed-space cluster expansion method.

Conclusion

Modern computer suites such as the ones provided by the MuST group use the theory outlined above to study complex phenomena in the fields of condensed matter physics and materials science. They normally operate on highly parallel computers like the Summit 200 petaflop supercomputer at the Oak Ridge National.

References

Faulkner JS and Stocks GM (1980) *Physical Review B* 21(8).

Faulkner JS (1982) *Progress in Materials Science*, Vol. 27. In: Christian JW, Haasen P, and Massalski TB (eds.). England: Pergamon Press, Oxford.

Faulkner JS (2016) Electronic structure: Scattering methods (for electronic structure calculations). In: *Reference Module in Materials Science and Materials Engineering*. Elsevier, ISBN: 9780128035818. https://doi.org/10.1016/B978-0-12-803581-8.01041-9.

Faulkner JS and Stocks GM (2019) *and Yang Wang, Multiple Scattering Theory: Electronic structure of solids*. Temple Circus, Temple Way, Bristol, UK: IOP Publishing.

Yang Wang GM, Stocks WA, Shelton DMC, Nicholson ZS, and Temmerman WM (1995) *Physical Review Letters* Vol. 75(15).

Alloys: Aluminum☆

EA Starke Jr.[a] **and DG Eskin**[b], [a]University of Virginia, Charlottesville, VA, United States; [b]Brunel University London, Uxbridge, United Kingdom

© 2024 Elsevier Ltd. All rights reserved.

This is an update of E.A. Starke, Alloys: Aluminum, Editor(s): Franco Bassani, Gerald L. Liedl, Peter Wyder, Encyclopedia of Condensed Matter Physics, Elsevier, 2005, Pages 18–24, ISBN 9780123694010, https://doi.org/10.1016/B0-12-369401-9/00534-9.

Introduction 573
Main features and classification of aluminum alloys 574
Processing of aluminum alloys 576
Aluminum alloy design 578
Non-heat-treatable alloys 578
Heat-treatable alloys 579
Alloys for additive manufacturing 580
Microstructural features 581
Applications of aluminum alloys 581
Conclusion 582
References 582

Abstract

This chapter describes the origins and classification of aluminum alloys; main types of heat treatments regimes, basic types of processing and related microstructural features. The principles of aluminum alloys design as applicable to different types of aluminum alloys are discussed. Main applications of aluminum alloys are summarized.

Key points

- Importance of aluminum alloys for modern applications
- Heat treatable and not heat treatable aluminum alloys: limitations and advantages
- Main processing routes for aluminum alloys
- Microstructure evolution upon solidification and deformation; main microstructural features
- Alloy design and applications of aluminum alloys

Introduction

Aluminum (Al) is the third most abundant element and the most common metal (8% in mass) in the Earth crust; but because it is very reactive with oxygen and some other elements it is not found in the native state but mostly in a form of mixed oxides, hydroxides and aluminosilicates (Altenpohl, 1998). The most important ore containing aluminum is bauxite but nepheline, kaolin, and alunite are also used. Sir Humphrey Davy (England) in 1808 predicted that alumina is an oxide of a then unknown element that he called "aluminum" though he was not successful in extracting it. This name is still used in the USA and Canada though the rest of the world adopted the term "aluminium." Hans Christian Oersted (Denmark) in 1825 isolated aluminum in a pure form. 2 year later Friedrich Wohler (Germany) produced small amounts of aluminum and in 1845 tested some of physical and mechanical properties, demonstrating its light weight and high ductility. First production of aluminum started in 1855 by Henri Sainte-Claire Deville (France) using electrolytical reduction of aluminum chloride by potassium and sodium. The produced aluminum was more expensive than gold being used for jewelry and as expensive tableware. During the construction of the Washington Monument, the world's tallest structure of that period, a material was needed to top off the structure, serving as a lustrous apex and a lightning rod. A cast aluminum pyramid 2.83 kg in weight was produced by William Frishmuth in 1884 and mounted on the top. It was the largest aluminum casting for that time, cost a fortune and was the first architectural application of this metal. Two years later the price for Al went down due to the invention of a new production process. In the 1890s, aluminum was used by Alfred Gilbert to cast a famous statue of Anteros (a.k.a. Eros) in Piccadilly Circus in London, the first sculpture made of aluminum taking advantage of its lightness and corrosion resistance.

In 1886, Charles Martin Hall in the USA and Paul-Louis Toussaint Héroult in France independently developed an economically viable method of producing aluminum, which ultimately led to its widespread use throughout the world. Their invention replaced

---

☆*Change History:* August 2022. DG Eskin prepared the update. All sections of the articles were amended/updated with the following new items: Main features and classification of aluminum alloys; Alloys for additive manufacturing. Figs. 1A, B, and Tables 1, 2 are new. Significantly updated list of references.

the chemical reduction process with electrolytic reduction alumina using carbon anodes. In this energy-intensive process, a solution of alumina in a molten mixture of cryolite (Na_3AlF_6) with calcium fluoride is electrolyzed to produce metallic 99% pure aluminum. Austrian chemist Carl Joseph Bayer discovered a way of enriching bauxite to yield alumina, known as the Bayer process, in 1889. These two processes have lowered metal's cost from $15/pound in 1884 to $0.50/pound in 1890. Modern production of the aluminum is based on the Bayer and Hall–Héroult processes. Some novel developments include the use of inert anodes (e.g., NiO and SnO_2) to eliminate carbon emissions. The production of aluminum remains energy consuming and, therefore, it concentrated in the countries with abundant sources of cheap electricity such as hydro (China, India, Russia, Norway, Canada), natural gas (United Arab Emirates) and geothermal (Iceland). The versatility of aluminum has resulted in it replacing many older, more established materials, and it is now produced and consumed, on a volumetric basis, more than all other nonferrous metals combined, including copper, magnesium, lead, and zinc. High energy costs and environmental impact of primary aluminum production necessitate recycling. The production of aluminum from bauxite requires about 17,000 kWh/ton of electricity, while the same amount of recycled aluminum consumes approximately 750 kWh (Totten et al., 2019). Therefore, the recycled aluminum substitutes primary aluminum with an energy gain of 95%. Aluminum and its alloys are highly recyclable with almost 85% of all ever produced aluminum still in circulation. Current efforts are focused on increasing the proportion of recycled aluminum closer to 100%.

Main features and classification of aluminum alloys

Aluminum is silver in color, light and ductile metal with good electrical and thermal conductivity, and high corrosion resistance (Mondolfo, 1976; Davis, 1993; Polmear, 1995). It has a low density of 2.7 g cm^{-3} compared to that of iron (7.9 g cm^{-3}), copper (8.96 g cm^{-3}) and titanium (4.5 g cm^{-3}) due to its low atomic mass of 27. The high ductility and isotropic formability of aluminum are due to the high symmetry and thermodynamic stability of the face-centered cubic (f.c.c.) crystal lattice and its high stacking-fault energy (162 mJ/m^2). In the pure form, aluminum has a low stiffness (Young's modulus, E) of 70 GPa compared to 211 GPa for Fe or 116 GPa for Ti; and a low tensile strength of 90 MPa, compared to 280 MPa for Fe and 240 MPa for Ti. However, its specific modulus, i.e., modulus divided by density, is almost equal to that for iron, titanium, and magnesium. An advantageous chemical property of aluminum is its reactivity with oxygen, which leads to the formation of a strong thin film of Al_2O_3 on the surface, which shields the base metal from further environmental interactions. The electrical and thermal conductivity of solid aluminum are 26.5 nΩ m (at 20 °C) and 237 W $(m\ K)^{-1}$, respectively. This makes Al a light and cheap alternative to copper as an electric conductor (61% IACS). With taking into account the density, a wire of aluminum weighs half as much as a wire of copper that has the same electrical conductivity.

Pure aluminum is not, however, used commercially because of its low strength. The mechanical and functional properties of aluminum are improved by alloying. Alloying elements in aluminum can be classified by the type of solidification reactions with aluminum and the variation of solubility in the solid aluminum. Most common main alloying elements and impurities in Al alloys have a eutectic type of solidification in the Al-rich corner of the phase diagram; these are Si, Cu, Mg, Zn, Ni, Fe, Li, Ag, Ca, Sn, Sb (Mondolfo, 1976; Belov et al., 2005). Transition elements that are usually added to Al alloys for grain control during solidification and recrystallization through dispersoid formation have typically a peritectic reaction with Al during solidification (Ti, Zr, Nb, Cr, Ta, Hf, V, Mo) with notable exceptions of Mn and Sc that have a eutectic type of the phase diagram with Al (Mondolfo, 1976; Belov et al., 2005). Rare-earth metals that are sometimes added for dispersion hardening and structure control (Ce, Er, La, Ho, Nd, Re, Sm, Y, Yb) have a eutectic reaction with Al (Mondolfo, 1976; Belov et al., 2005). A small group of alloying elements form a miscibility gap in the liquid state and are used in free-machining and self-lubricating alloys, e.g., Bi, Cd, Pb, In (Mondolfo, 1976; Davis, 1993). Among the alloying elements that have large solubility in the solid aluminum (this solubility typically decreases with temperature making possible supersaturation, solution hardening and precipitation hardening) are Ag (55.6 wt%), Zn (31.6 wt%), Mg (17.4 wt %), Cu (5.7 wt%), Li (4.2 wt%), Si (1.6 wt%), Mn (1.8 wt%) (Mondolfo, 1976). Transition elements such as Zr, Ti, Sc tend to form supersaturated solid solutions in aluminum upon solidification with a sufficiently high cooling rate, opening way to dispersion hardening upon annealing (Toropova et al., 1998).

A major metallurgical development in alloy design occurred in 1906 when Alfred Wilm (Germany) accidently discovered the process of "age hardening" in Al-Cu alloys. He was conducting research directed toward improving the strength of aluminum alloys. He knew that steel could be strengthened if the right compositions were cooled fast enough from high temperatures, so following this recipe he heated some Al–(3.5–5.5) wt% Cu alloys, plus less than 1% magnesium and manganese, to a high temperature and quenched them in water. To his frustration, many of the alloys he tested were softer after quenching than after casting. However, after a few days he found that their hardness and tensile properties had increased considerably. One of the alloys, designated Duralumin, is still in use today. Later, in 1919, P.D. Merica, R.G. Waltenberg, and H. Scott (USA) explained the phenomenon of age hardening as a result of clustering and precipitation of solute atoms from the supersaturated solid solution in a form of phases. However, these nano-microstructural features were too small to be resolved by optical microscopy (not transmission electron microscopes were then available). Only in 1938 the X-ray diffraction studies of A. Guinier (France) and G.D. Preston (UK) allowed them to independently discover the formation of atomic clusters that distorted the crystal lattice and resulted in hardening. These clusters are now called Guinier–Preston zones. Direct proof of nano-scale precipitates was not obtained until the development of transmission electron microscopy in 1959. Since the 1930s the development of alloys that utilize precipitation hardening took off and resulted in the modern alloys of Al-Cu-Mg, Al-Zn-Mg-(Cu), Al-Mg-Si, and Al-Li-Mg-(Cu) groups (Vasudevan and Doherty, 1989; Davis, 1993; Polmear, 1995).

Not all of commercial aluminum alloys are hardened by precipitates. There are also alloys that are hardened by solution hardening, i.e., by solute atoms that are retained in the solid solution and induce strains due to the difference of atomic radii, the most notable are Al-Mg alloys (Sanders et al., 1986; Polmear, 1995).

Therefore, the aluminum alloys are classified as heat-treatable (age-hardenable) or non-heat-treatable (non-age-hardenable), depending on whether or not they undergo precipitation (age) hardening (Polmear, 1995; Totten et al., 2019). There are also two main different product forms of aluminum alloys; i.e., wrought alloys that have been worked or deformed into plates, sheets or profiles from cast billet and ingots (typically made by continuous or semi-continuous casting) and casting (or foundry) alloys that are produced and used in a near-shape "*as-cast*" condition. Wrought aluminum alloys are normally designated by a four-digit numerical system developed by the Aluminum Association (Davis, 1993; Aluminum Association, 1997). The nomenclature has now been accepted by most countries and is called the International Alloy Designation System (IADS). The system used for casting alloys (three digits) is slightly different from that used for wrought alloys; however, the first digit designates the alloy group (series) and is essentially the same for both wrought and cast alloys. Table 1 gives a summary of the alloying systems.

The 1XXX alloys contain a minimum of 99% aluminum, so this is mostly commercially pure aluminum. In this series, 10XX is used to designate unalloyed compositions that have natural impurity limits. The last two of the four digits in the designation indicate the minimum aluminum percentage, e.g., 1087 means 99.87% pure Al. Alloy grades having second digits other than zero indicate special control of one or more individual impurities. In the 2XXX through 8XXX alloy series, the second digit indicates alloy modification. If the second digit is zero, it indicates the original alloy; integers 1 through 9 indicate modifications of the original alloy, in many cases the purity with regard to Fe and Si. In casting alloys, the second two digits identify the specific aluminum alloy or, for the 1XX.X series, indicate purity. The last digit in casting alloy grades, which is separated from the others by a decimal point, indicates the product form, whether casting (0) or ingot (1). A modification of an original alloy or the impurity limits for unalloyed aluminum are indicated by a letter preceding the numerical designation. The letters are assigned in alphabetical sequence starting with A but omitting I, O, Q, and X, the X being reserved for experimental alloys.

Despite being widely adopted, the Aluminum Association system is not unique, there is also an ISO (The International Organization for Standardization) system accepted in some European countries as well as national alloy grades that are used in Russia, China, Japan, Germany, France etc.

The heat-treatment or temper-nomenclature system developed by the Aluminum Association has also been adopted as part of the IADS by most countries (Davis, 1993; Aluminum Association, 1997; Totten et al., 2019). It is used for all forms of wrought and cast aluminum alloys with the exception of ingots. The system is based on the treatments used to develop the various tempers and takes the form of letters added as suffixes to the alloy number. One or more digits following the letter indicate subdivisions of the tempers, when they significantly influence the characteristics of the alloy. Table 2 summarizes the heat treatment conditions of the alloys.

Alloys supplied in the as-fabricated condition (F) are shaped by cold working, hot working, or casting processes in which no special control over thermal conditions or strain hardening is employed. Annealed wrought products (O) are annealed to obtain lowest-strength temper and annealed cast products—to improve ductility and dimensional stability. Work hardened products (H) are strengthened by strain hardening, with or without supplementary thermal treatment to produce some reduction in strength. Those can be strain hardened only (H1X), strain hardened and annealed (H2X) or strain hardened and stabilized (H3X). Solution treated alloys (W) are unstable and change their properties due to natural aging. Thermally treated alloys (T) encompass: T1 (cooled and naturally aged); T2 (cooled, cold worked and naturally aged); T3 (solution heat treated, cold worked and naturally aged); T4 (solution heat treated and naturally aged); T5 (cooled and artificially aged); T6 (solution heat treated and artificially aged to the maximum hardness); T7 (solution heat treated and overaged or stabilized); T8 (solution heat treated, cold worked and artificially

Table 1 Alloying systems for aluminum alloys according to the Aluminum Association classification (Davis, 1993; Aluminum Association, 1997).

Alloying series of wrought alloys	*Main alloying elements*	*Alloying series of casting alloys*	*Main alloying elements*
1XXX	–	1XX.X	–
2XXX	Cu, Cu + Mg	2XX.X	Cu
3XXX	Mn, Mn + Mg	3XX.X	Si, Si + Mg, Si + Cu
4XXX	Si	4XX.X	Si
5XXX	Mg	5XX.X	Mg
6XXX	Mg + Si	6XX.X	Not in use
7XXX	Zn, Zn + Mg; Zn + Mg + Cu	7XX.X	Zn, Zn + Mg; Zn + Mg + Cu
8XXX	Other elements, e.g., Li, Bi	8XX.X	Sn, Sn + Cu, Sn + Cu + Si
9XXX	Reserved for future use	9XX.X	Not in use

Table 2 Temper designations for aluminum alloys (Aluminum Association, 1997).

Designation	*Condition*
F	As-fabricated
O	Annealed or recrystallized
H followed by 2 digits	Work hardened
W	Solution heat treated
T followed by 1 or more digits	Thermally treated

aged); T9 (solution heat treated, artificially aged and cold worked) and T10 (cooled, cold worked and artificially aged). Tempers that involve deformation are called thermo-mechanical treatment.

A new class of aluminum alloys is emerging, i.e., alloys for additive manufacturing (Aboulkhair et al., 2019). Those are specifically designed for high cooling rates, structure stability and specific casting properties. Most of them are currently proprietary alloys but maybe unified in a new internationally recognized grade system in the coming years.

Processing of aluminum alloys

The final product from an aluminum alloy can be obtained by a number of methods, i.e., by shape casting in a variety of molds; by deformation of cast billets or ingots; by additive manufacturing; and by compacting and sintering of powders (Polmear, 1995; Altenpohl, 1998; Totten et al., 2019). Only the last technology does not include the melting stage, though melting can be involved in powder making. Shape casting is typically done either in sand (clay) molds (low cooling rate, large and complex shapes) or in metallic molds-dies (higher cooling rate, smaller shapes). For the small and complexly shaped castings, high-pressure die casting or investment (lost wax, lost foam) casting are used. Alloys for subsequent deformation are cast in round billets (rods) or flat ingots (sheets) by a (semi-) continuous casting technology that involves indirect and direct cooling by water (direct-chill casting, Properzi, Hazelett, twin roll casting). Additive manufacturing uses powders or wire to build a complex shape layer-by-layer (hence, another name—3D printing). The rapid remelting of the feedstock is done typically by laser or electron-beam heating.

In fabricating any aluminum alloy products, the alloy composition is made by adding the alloying elements to molten aluminum, usually in the form of a concentrated master alloy (sometimes called hardener), with the requisite purity and composition (Hatch, 1984; Vasudevan and Doherty, 1989; Polmear, 1995). Two types of alloying elements are normally added: those for achieving strength through hardening mechanisms and those to control the grain structures during solidification (grain refiners) and deformation (anti-recrystallization agents), the former producing nucleating particles during solidification, the latter forming "*dispersoids*" upon annealing. During solidification of an ingot or a casting, some of the alloying elements and impurities may precipitate out of the melt, forming coarse "*constituent*" particles within the as-cast structure. These are usually formed through primary solidification, eutectic or peritectic reactions. For wrought products, additional precipitation of the alloying elements may occur as the ingot is annealed or worked down to the final product form (such as sheet or plate). These are usually much smaller dispersoids.

Some of constituent phases potentially impair the properties of the final product in several ways. (a) By tying up alloying elements that are added on purpose to develop the desired properties, these elements then become not available to contribute to strength and other beneficial properties of the aluminum alloy. (b) In addition, the constituent particles are typically more brittle than the surrounding aluminum and frequently possess elongated shape, hence, presenting stress concentrators in the structure and promoting the nucleation and growth of cracks, impairing the beneficial mechanical properties. One typical goal of aluminum alloy processing is to reduce the size and amount of the constituent particles in the aluminum alloy product, especially in wrought products. Note that in casting alloys, a significant portion of the alloys structure is occupied by the major eutectic structure constituent, e.g., Al-Si eutectics, that defines the casting properties of the alloys and, therefore, is an essential beneficial component of the structure (Glazoff et al., 2019). An example of such a structure is given in Fig. 1a that shows a modified Al-Si eutectic that defines the properties of these alloys.

Casting and especially wrought alloys are grain refined upon casting with the aim to achieve a uniform equiaxed grains (dendrites), which is important for the mechanical and technological properties upon casting and downstream processing, e.g., decreases hot and cold cracking, shortens homogenization, improves ductility upon hot deformation. A typical example of the grain refined structure of a DC cast billet from a 7075 alloy is shown in Fig. 1b. Casting is conventionally followed by a homogenization (or solution) treatment. This is the stage when nonequilibrium structure constituents (eutectics) dissolve and enrich the aluminum solid solutions with the alloying elements such as Cu, Si, Mg, Zn, Li whereas some of the elements (e.g., Zr, Ti, Mn, Cr, V, Sc) that have supersaturated aluminum during solidification precipitate as dispersoids (Hatch, 1984; Vasudevan and Doherty, 1989; Toropova et al., 1998). For alloys used in the as-cast condition and for non-age-hardenable alloys, homogenization may be the final heat treatment. But for age-hardenable alloys further heat treatments will be required. For wrought alloys, hot working follows the homogenization for ingot breakdown (rolling) and shape change (forging, extrusion) to the appropriate product form. Since aluminum and its alloys have high stacking-fault energy, sufficient dynamic recovery normally occurs during hot deformation to give rise to a stable polygonized substructure, an example of which is shown in Fig. 1c. The grains elongate in the direction of metal flow and do not recrystallize. The fine distribution of dispersoids associated with Cr, Mn, Zr, Sc additions delays or prevents static recrystallization by pinning down subgrain boundaries and stabilizing the polygonised structure, retaining the elongated or "*pancake-shaped*" grains during subsequent processing (Hatch, 1984; Vasudevan and Doherty, 1989; Davis, 1993). An example of the grain structure of a hot-worked aluminum-alloy plate is shown in Fig. 1d. The dispersoids, and any remaining constituents and primary phases that may be present, are strung out in the working direction; their spacing increases in the working direction and decreases normal to the working direction. In some cases, large constituent phases, if present, are broken up during the working operation. After the initial processing for shape change, non-age-hardenable alloys may then be cold worked and/or annealed to develop the desired strength, and age-hardenable or heat-treatable alloys may be solutionized (operation similar to homogenization but aimed at further increasing the concentration of useful alloying elements in the solid solution), quenched (fixation of the supersaturated solid solution at a lower temperature), in some cases stretched to remove residual stresses developed

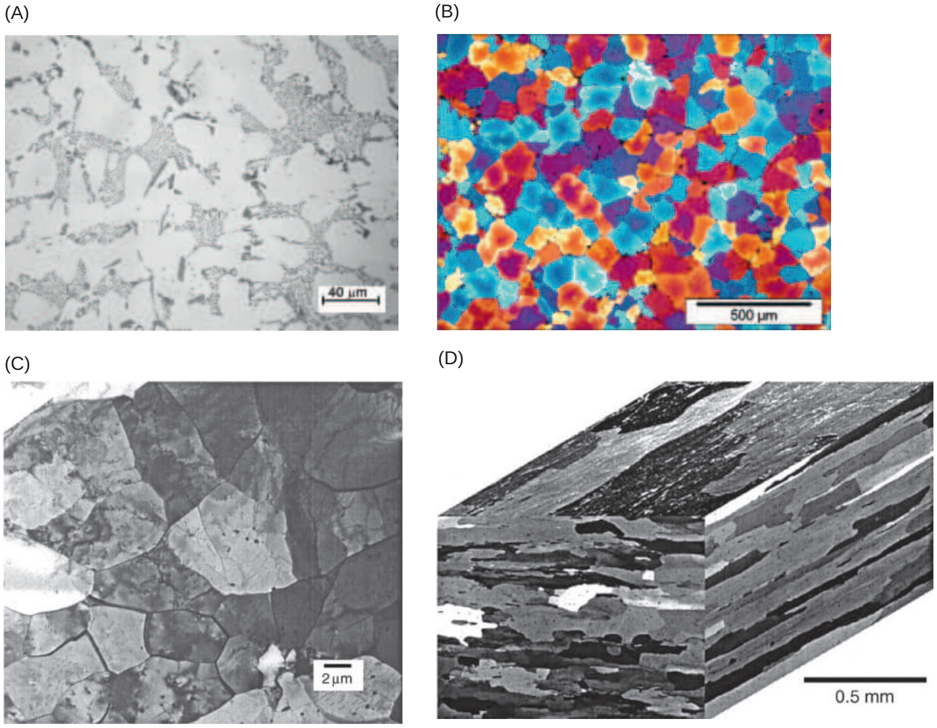

Fig. 1 Typical microstructures formed in aluminum alloys: (a) an as-cast A357 alloy showing modified Al-Si eutectics (optical microscopy, OM); (b) a grain refined structure of an as-cast 7075 billet (OM); (c) subgrain (polygonized) structure formed upon hot rolling of an Al–Cu–Mg–Li–Zr alloy (transmission electron microscopy, TEM); and (d) a "pancake" grain structure formed upon hot deformation in the same alloy as (c) (OM).

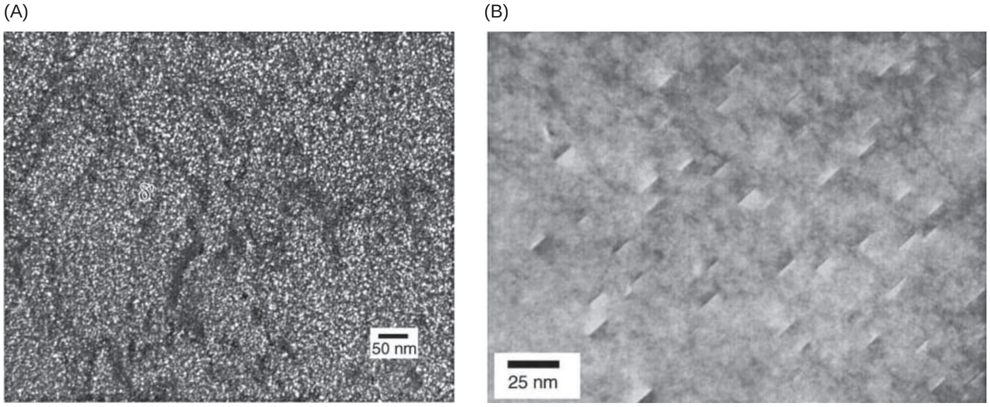

Fig. 2 (a) Dark-field TEM micrograph of an Al–2.7% Cu–1.8% Li–0.6% Zn–0.3% Mg–0.3% Mn–0.12% Zr alloy quenched and naturally aged for 7 days. The matrix precipitation is dominated by fine coherent δ′ (Al_2Li) spherical precipitates and (b) bright-field TEM micrograph of the same alloy quenched and artificially aged at 150 °C for 6 h (T6 temper). The matrix precipitation is dominated by fine θ″/θ′ (Al_2Cu) plates and δ′ spheres (not visible).

during quenching or for creating nucleation sites for precipitation, and either naturally aged at room temperature or artificially aged at some moderate temperatures (Hatch, 1984; Davis, 1993; Polmear, 1995). A structure of an Al–2.7% Cu– 1.8% Li–0.6% Zn–0.3% Mg–0.3% Mn–0.12% Zr alloy naturally aged at room temperature after a rapid quench from the solution heat-treatment temperature is shown in Fig. 2a and the same alloy artificially aged at 150 °C for 6 h after a rapid quench from the solution heat-treatment temperature is shown in Fig. 2b. The main purpose of aging treatments is to precipitate fine, coherent or semi-coherent particles from the supersaturated solid solution, which will hinder the dislocation movement and, thereby, increase the strength of the alloy (Hatch, 1984; Totten et al., 2019).

Alloys that are prone to corrosion in moist air may be clad with pure aluminum, which is not susceptible to corrosion and can offer protection in an aggressive environment, or they may be anodized (Vasudevan and Doherty, 1989; Polmear, 1995; Totten et al., 2019). Cladding is typically done by joint hot rolling of the main alloy ingot with thinner layers of pure aluminum on top and at the bottom. More recently a technology of joint direct-chill casting of clad ingot has been commercialized, making the bonding between the main alloy and the clad layer more reliable. Anodizing is a method for producing a very thick, protective oxide film on the surface of aluminum. The anodized film normally contains chemical compounds such as chromates, which are collected from the anodizing bath and render the film more corrosion resistant than films that form naturally in air.

Aluminum alloy design

After Wilm discovered age hardening of the Al– Cu–Mg–Mn alloy through serendipity, traditional aluminum alloy development primarily relied on a trial-and-error philosophy. The rapid acceleration of aluminum production in the first half of the 20th century was driven by the automotive and aircraft industries. If the former used aluminum in luxury cars, the latter utilized light weight and high specific strength of aluminum alloys for building mass produced airplanes, from engines to fuselage. At that time most aluminum alloys were developed by simply identifying a given alloying element that led to gains in a certain mechanical property, typically strength, and continuing to add that element until the property began to degrade. The amount of secondary element used would then be the percentage that corresponded with maximum performance. This process would then follow in ternary and higher-order systems in order to optimize a given mechanical property. Up until the 1940s only optical microscopes were available for structure examination, and phase diagrams availability and use were very limited. Therefore, the alloy design occurred with little knowledge of the corresponding microstructural components or appropriate thermodynamic understanding, for instance the phase diagram of the particular alloying system. Unfortunately, this practice led to the slow adoption of novel alloys into various applications creating a disparity with the design community. Yet main alloying systems used today, i.e., casting alloys of Al–Si–(Mg)–(Cu) system and wrought alloys of Al–Cu–(Mg), Al–Zn–(Cu)–Mg and Al–Mg–Si, have been developed prior to the 1940s (Mondolfo, 1976).

From the 1950s and progressively up to nowadays, the aluminum-based alloy development utilizes the knowledge of phase diagrams and the productive interplay between empirical research and theoretical science. Phase diagrams represent the phase state of an alloy as a function of temperature and alloy concentration (pressure is rarely an important factor in condensed systems) and are widely used for alloy design and process development (e.g., determining the temperatures of heat treatment). There are currently software programs (e.g., Thermocalc, Pandat, MTData) available that use thermodynamic functions and extensive databases for the calculation of multi-component phase diagrams and some physical properties. Such calculations reduce the effort required to determine equilibrium and nonequilibrium (these software packages allow one to take into account diffusion) conditions in a multicomponent system. Materials design can now be viewed as the best application of available models for the prediction and synthesis of alloys with desired properties. Nowadays, a combination of thermodynamic calculations, vast experimental data and artificial intelligence opens way for developing alloys that are far from traditional in composition, or for optimizing the existing grades for the best performance (Belov et al., 2005; Glazoff et al., 2019; Mishra and Thapliyal, 2021). Of course, all theoretical calculations must be verified experimentally, but these experiments can now be based on the sound theory and not on a trial-and-error approach.

The most general understanding of alloy design must derive itself from the metallurgical paradigm of processing–structure–-property relationships (Polmear, 1995; Glazoff et al., 2019). In order to optimize a given property, one must determine the necessary ideal microstructural components, which are dictated by the alloy composition and processing from solidification through final manufacture. Fundamentally, to properly determine the resulting microstructure for a given thermomechanical processing routine, the pertinent literature and (non)equilibrium phase diagrams must be consulted. The basic empirical structure–-property relationships found in aluminum alloys are summarized in Table 3. This table highlights the general structural features desired to optimize a given property.

Non-heat-treatable alloys

The 1XXX, 3XXX, 5XXX, and some of the 8XXX series alloys are non-heat-treatable, or rather non-age-hardenable (Mondolfo, 1976; Sanders et al., 1986; Davis, 1993). These alloys are primarily strengthened by the elements in solid solution, dispersoids and by deformation structures. One of the first non-heat-treatable alloys, other than the 1100 alloy that only contained 0.95 wt% Fe and Si as impurities, was an alloy containing 1.25 wt% Mn and 0.12 wt% Cu, now designated as 3003, that was introduced in 1906, the same year that Wilm discovered age hardening. Alloy 3003 can develop yield strength up to 400 MPa by special thermomechanical treatments that assure the non-recrystallized or fine recrystallized structure after deformation. Magnesium is added to non-heat--treatable alloys for its solid-solution strengthening effect. It also enhances work hardening and makes aluminum more anodic. In general, solid-solution alloys are more resistant to corrosion than two-phase alloys. Al–Mg alloys have a high resistance to corrosion, particularly in seawater and alkaline solutions. However, when the magnesium concentration exceeds the solid solubility in binary alloys, it precipitates at grain boundaries as Al_3Mg_2, which is anodic to the matrix and promotes intergranular attack.

Aluminum combines readily with transition metals, such as Ti, V, Cr, Mn, Fe, Co, Ni, Zr, and Sc to form intermetallic phases with little or no solubility in the aluminum matrix at room temperature (but with a considerable tendency to form supersaturated solid solutions upon solidification) (Toropova et al., 1998; Belov et al., 2005). This supersaturated solid solution decomposes upon technological anneals or homogenization to form intermetallic phases (dispersoids) that increase the strength by enhancing work

Table 3 Property–microstructure relationships in aluminum alloys.

Property	*Desired microstructural feature(s)*	*Function of feature(s)*
Good casting properties	Large amount of eutectics or pure solid solution Narrow solidification range Fine, uniform grains	Provides good fluidity and feeding, reduces cracking and porosity upon casting Less stress accumulation, less segregation and cracking
Strength	Fine grain size with a uniform dispersion of small, hard particles (dispersoids, precipitates)	Inhibits dislocation motion, pins subgrain boundaries
Ductility and toughness	Fine structure with clean grain boundaries and no large or shearable precipitates	Encourages plasticity and work hardening, inhibits void formation and growth
Creep resistance	Slow diffusing alloying elements Thermally stable particles within the matrix and on the grain boundaries	Slows-down diffusion processes Inhibits grain boundary sliding and coarse microstructure
Fatigue crack initiation resistance	Fine grain size with no shearable particles and no surface defects No brittle inclusions and intermetallics with elongated/sharp morphology	Prevents strain localization, stress concentration, and surface slip steps
Fatigue crack propagation resistance	Large grain size with shearable particles and no anodic phases or hydrogen traps	Encourages crack closure, branching, deflection, and slip reversibility
Pitting corrosion	No anodic phases	Prevents preferential dissolution of second-phase particles
Stress corrosion cracking and hydrogen embrittlement	Hard particles and no anodic phases or interconnected hydrogen traps	Homogenizes slip and prevents crack propagation due to anodic dissolution of phases

hardening during working operations, and by refining the grain structure. They increase the work hardening since they are usually incoherent with the matrix (metastable Al_3Zr, Al_3Ti and equilibrium Al_3Sc are notable exceptions), are nondeformable, and must be looped or bypassed by moving dislocations. This increases the dislocation density and blocks the dynamic recovery and recrystallization processes (the temperature of the recrystallization onset may go up to the solidus temperature in the case of Sc in Al-Mg alloys). During hot working, the subgrain structure that is developed can also increase the strength. Smaller (less than 0.6 μm) intermetallic dispersoids aid in the stabilization of the substructure. The intermetallic particles generally do not add a component of the dispersion strengthening because of their low volume fraction, relatively large size, and interparticle spacing. The famous exception is Sc that when added alone (up to 0.3 wt%) or in combination with Zr (0.15 wt% each) to Al-Mg alloys can provide dispersion hardening due to the precipitation of coherent spherical Al_3Sc particles that retain coherency and size stability to high temperatures (Toropova et al., 1998). Such Al-Mg-Sc alloys attract a lot of attention in aerospace and automotive industries, and become effectively age-hardenable, though the aging temperatures are above typical, being in the range 250 °C–350 °C.

It is customary to control both composition and cooling rates in order to prevent large primary phases from forming. For example, commercial Al–Mn alloys most often contain less than 1.25 wt% Mn, although as much as 1.82 wt% is soluble in pure aluminum. The 1.25 wt% limit is imposed because Fe, present in most aluminum alloys as an impurity, decreases the solubility of Mn in aluminum. This increases the probability of forming large primary particles of Al_6Mn, which can have a disastrous effect on ductility.

Silicon is a principal addition to most aluminum casting alloys because it forms an Al-Si eutectic that increases the fluidity of the melt (Glazoff et al., 2019). In the solid state, hard silicon particles are the major contributor to the strength of non-heat-treatable casting alloys. An additional improvement in strength can be obtained by minor additions of Mg or by trace alloy additions, for example, Na or Sr that modify the eutectics. The latter also minimizes porosity and increases ductility.

Heat-treatable alloys

The 2XXX, 4XXX, 6XXX, 7XXX, and some 8XXX series wrought alloys as well as 2XX.X, 3XX.X and 7XX.X series casting alloys are considered heat-treatable (age-hardenable) (Hatch, 1984; Vasudevan and Doherty, 1989; Davis, 1993; Starke and Staley, 1996; Gokhale et al., 2013; Ovsyannikov et al., 2016). These alloys contain elements whose solubility in solid aluminum is substantial at high temperature and decreases with temperature, e.g., Cu, Zn, Mg + Si, Li. The concentration of these elements significantly exceeds their equilibrium solid solubility at room and moderately higher temperatures. One or several of the transition elements Cr, Mn, Zr, and Sc are typically added to age-hardenable wrought alloys to control the grain structure upon and after deformation; however, the grain and deformation structures play only a secondary role in the strengthening of this class of materials.

A normal heat-treatment cycle after deformation processing for wrought alloys (or after casting for casting alloys) includes a soak at a high temperature to dissolve the soluble constituent particles and any other precipitates that may be soluble (dispersoids containing the elements Cr, Mn, or Zr have already precipitated at this point). After the aluminum alloy has been held at the solutionizing temperature for a sufficient time, the alloy is rapidly cooled or quenched to prevent precipitation of coarse phases and to obtain a solid solution supersaturated with both solute elements and vacancies. The next step involves aging at room temperature (natural aging) or at an intermediate temperature (artificial aging).

Quenching is accompanied by a change in free energy, which increases progressively as the difference between the solutionizing temperature and the final quenching temperature increases, which defines the difference in the equilibrium solubility and the supersaturation degree at the aging temperature (Hatch, 1984; Polmear, 1995). The volume free energy change representing this difference is the driving force for precipitation and is associated with the transfer of solute atoms to a more stable phase. However, when precipitation occurs there are other factors that increase the free energy, e.g., the formation of the interface between the matrix and the precipitate requires an increase in the surface free energy; and, if there is a volume change or interfacial strains associated with the precipitate (i.e., due to the coherent or semi-coherent nature of the interface), there is an increase in the elastic strain energy. The change in free energy when a precipitate forms, ΔG, is the sum of these free energy changes and can be expressed mathematically as

$$\Delta G = V\Delta G_v + A\gamma + V\Delta G_s \tag{1}$$

where V is the volume of the new phase; ΔG_V is the free energy decrease due to creation of a volume, V, of the precipitates and is therefore negative; A is the area of the interface between the matrix and the precipitate; γ the energy of the new surface formed; and $V\Delta G_s$ is the increase in elastic strain energy per unit volume of precipitate.

The critical increase in the free energy, ΔG^*, required for a nucleus to become an equilibrium or metastable precipitate is known as the activation energy barrier for nucleation and can be expressed as

$$\Delta G^* = \left(16\pi\gamma^3\right)/\left(3\left[\Delta G_v - \Delta G_s{}^2\right]\right) \tag{2}$$

The nucleation rate, N, can be expressed as

$$N = C\exp\left(-\frac{Q}{kT}\right)\exp\left(-\frac{\Delta G^*}{kT}\right) \tag{3}$$

where C is the number of nucleating sites per unit volume, Q is the activation energy for diffusion, k is the Boltzmann constant, and T the absolute temperature.

The precipitates typically go through a number of morphological transformations: starting with the formation of atomic clusters (GP zones), followed by the formation of a series of metastable phases that feature coherent and semi-coherent boundaries with the matrix, and eventually the formation of a stable phase. The GP zones and coherent precipitates are the main hardening agents upon natural aging, while coherent and semi-coherent precipitates harden alloys during artificial aging (Hatch, 1984; Totten et al., 2019).

There are a number of requirements for an effective age-hardenable alloy. First, there has to be a sufficient volume fraction of the hardening phase for the desired strength. An examination of aluminum binary diagrams suggests that the most attractive alloying additions would be, in decreasing volume fraction of the second phase, Ag, Mg, Li, Zn, and Cu. The required volume fraction will depend on the effectiveness of the second phase in impeding dislocation motion, that is, whether it is a "soft" or "hard" phase, and its size and spacing. Second, the aging potential must be adequate and the nucleation of the precipitates should be as close as possible to being homogeneous. This is generally accomplished by the addition of a second alloying element. The addition of the second alloying element may: (1) reduce the solubility of the first element, (2) increase the diffusion rates by trapping vacancies, (3) increase the driving force for nucleation, or (4) reduce the activation energy against nucleation. If the strain term in Eq. (1) is large, nucleation may be aided by defects, for example, dislocations. For this type of nucleation, the precipitate distribution depends on the distribution of the defects.

The stability of the aging effect depends on the stability (growth rate) of the hardening precipitates that is mainly dependent on the diffusion rate of the contributing elements.

Alloys for additive manufacturing

Specialized alloy development for additive manufacturing (AM) is still an young field with most of AM alloys being based on conventional casting or wrought alloys with small variations in chemical composition. Light alloys, especially Al-based, has attracted strong attention in additive manufacturing due to the promise of a high specific strength, yet this is hindered upon AM due to the high thermal expansion/contraction of aluminum alloys, which results in cracking, distortion and segregation, deteriorating the service performance. Alloy development is currently based on near-eutectic Al-Si-(Mg)-(Mn) alloys due to their good casting properties (but average strength) or alloys with transition metals stemming from rapidly-solidified alloys with good thermal stability (but poor casting performance) (Aboulkhair et al., 2019; Aversa et al., 2019; Martin et al., 2017; Mishra and Thapliyal, 2021; Thapliyal et al., 2021). Both groups have deficiencies that are partially mitigated through operating in a tiny processing window, which is often not transferrable between machines (even of the same model), requiring costly optimization. On the other hand, AM provides novel opportunities for alloy development that is currently guided by thermodynamic calculations to alter alloys through nano-additives or a combination of low-diffusing elements, achieving a new level or new combination of properties and quality. This requires targeted material development intimately linked to specific alloy characteristics, processing, and characterization.

The heating and cooling rates upon AM are up to five orders of magnitude faster than in conventional processing, causing AM components to have non-optimal microstructure, mechanical properties and dimension accuracy due to the formation of defects such as porosity, epitaxial columnar grains, distortion and cracking, lack of nucleation control, residual stresses and thermal contraction. This poor service performance imposes barriers for Al-10 wt% Si-based as well as 2XXX-, 6XXX- and 7XXX-series alloys to be suitable materials for AM. Recently, some Al-based alloys have been specifically designed for AM, mostly exploiting earlier developments in rapid solidification (RS) and dispersion hardening. This includes alloys with transition metals, e.g., Sc and Zr (Scalmalloy, Addalloy) with good service performance such as thermal stability and strength, though still inadequate process performance. Achieving high-quality AM parts with bespoke, thermally stable properties requires the control of composition, structure and processing on the nano- and micro-level. For example, small additions of Zr nanoparticles can help in avoiding cracking of AM 6XXX- and 7XXX-series alloys through grain refining, thereby achieving adequate mechanical properties (Martin et al., 2017). Completely new alloys with a high amount of transition metals (Al20Si5Fe3Cu, Al85Nd8Ni5Co2, Al7NiZnMg) are under development (Plotkowski et al., 2020).

Microstructural features

Chemical composition and processing regime control the microstructure and thus the physical, mechanical, and corrosion properties of aluminum alloy products. In general, microstructural features of importance for property control include the following (Hatch, 1984; Vasudevan and Doherty, 1989):

1. *Coherency, volume fraction, and distribution of strengthening precipitates*. These form intentionally during aging treatments and unintentionally during cooling, including quenching. The precipitates normally range in size from 1 to 10 nm.
2. *Size, distribution, and coherency of dispersoid particles*. These form during the ingot preheating or homogenization treatment by precipitation of the transition elements Cr, Mn, Ti, Zr, Sc. They are present by design to control the grain structure and degree of recrystallization. Dispersoids normally range in size from 10 to 200 nm.
3. *Degree of recrystallization*. This is determined by the thermomechanical history. During bulk metal deformation processing at elevated temperatures, the dislocations in aluminum alloy products arrange themselves into a structure of small-angle sub-boundaries by the process known as dynamic recovery. As temperature decreases and strain rate increases, the stored energy increases. This increase in stored energy is manifested by an increase in number and consequent decrease in the size of subgrains and an increase in the dislocation density in cell walls. During subsequent heat treatments, the stored energy of deformation may decrease by either static recovery or recrystallization. The final product may be completely unrecrystallized (cold worked), partially recrystallized (polygonised), or completely recrystallized.
4. *Grain size and shape*. In casting alloys, the grain size, dendrite arm spacing and fineness of eutectics are paramount factors for the performance and properties. In the wrought alloys, the grain size and shape are controlled by thermomechanical history and may be influenced by ingot grain refining practice.
5. *Crystallographic texture* (i.e., preferential crystallographic orientation of grains). The deformation process used to produce the product and the thermo-mechanical history determines this.
6. *Intermetallic constituent particles*. These form mostly by eutectic reactions during solidification, primarily from impurities, for example, iron and silicon. Because the low solubility of iron in pure aluminum is further reduced by alloying elements, constituent particles containing iron are virtually insoluble. Other constituent particles, e.g., Al_3Zr, can be primary intermetallics formed in peritectic systems. The amount, size and size distribution of insoluble constituent particles are controlled by the alloy composition (purity), cooling rate upon solidification, and the extent and nature of bulk deformation. Constituents generally range in size from 1 to 30 μm.
7. Porosity may be a factor in thick plates and, particularly, in castings. It is controlled by the amount of hydrogen that is retained in the liquid or solid aluminum. Individual pores can range up to and beyond 200 μm.

Applications of aluminum alloys

Aluminum alloys are lightweight, resistant to atmospheric corrosion, and have good mechanical properties (especially if their low density is taken into account), which makes them a popular material for use in a wide variety of applications. The first mass applications of aluminum alloys were in automobiles and airplanes (Altenpohl, 1998; Polmear, 1995; Starke and Staley, 1996). They remain materials of choice in aerospace applications and, increasingly, in modern personal and transport vehicles, driven by the need for light weight to limit the emissions, increase fuel efficiency, and enable longer range for electric cars. Other applications are also very important (Menzie et al., 2010): packaging, building structures, marine applications, electric conductors, to name a few. In total about 41% of global aluminum production is consumed by foil and packaging; 22% by transport; 11% by construction; 13% by electric engineering; 8% by machine engineering; and 5% by consumer goods.

The 1XXX alloys are strain-hardenable and not toxic, have high formability, corrosion resistance, and good electrical conductivity. They are often used for electrical applications and as foil and strip for packaging. The 2XXX alloys are heat-treatable, and possess excellent combinations of high strength and toughness even at elevated temperatures, but are not resistant to atmospheric corrosion; so, they are usually painted or clad in such exposures. They are primarily used for aircraft frames, truck body applications, and cryogenic propellant tanks. The 3XXX alloys have high formability, corrosion resistance, and can be joined by a variety of methods. They are widely used in cooking utensils, beverage cans, food containers, chemical equipment, roofing and siding, and in heat exchangers. The 4XXX alloys are heat-treatable and have good casting characteristics along with medium strength. They are primarily used in forging applications, for example, engine pistons, and for welding wires. The 5XXX alloys are strain-hardenable, tough and weldable, and have excellent corrosion resistance, even in salt water, along with moderate strength. They find wide application in highway bridges, storage tanks, marine and automotive structures, and pressure vessels. The 6XXX alloys are heat-treatable, have high corrosion resistance, excellent extrudability, and moderate strength. They are primarily used in building and construction, automotive, marine and aerospace applications. The 7XXX alloys are heat-treatable and can provide the highest strengths of all aluminum alloys. They are primarily used for automotive and aerospace applications. The 8XXX series is used for alloys that contain lesser-used alloying elements such as nickel and lithium. Some are used for electrical conductors and the lithium-containing alloys have found application in the aerospace industry due to the lithium effect in reducing density and increasing rigidity.

Aluminum casting alloys are used for engine blocks and pistons, heavy-duty structural parts in automotive and airplane applications, pumps, impellers, fittings etc.

Conclusion

Aluminum alloys possess a number of very attractive characteristics that, together with their light weight, make them extremely attractive for many applications. Since aluminum comprises 8% of the Earth crust by weight, the overall reserves are adequate to cope with anticipated demands for the foreseeable future. Cost differentials and carbon footprint with respect to competing materials will probably dictate the extent to which aluminum will be used. The cost includes the price of the electrical energy needed for the extraction of the metal from its minerals, and this may be greatly reduced in the future since aluminum can be fully recycled for many applications. In addition, aluminum often pays off when lifecycle costs, instead of acquisition costs, are considered.

References

Aboulkhair NT, Simonelli M, Parry L, Ashcroft I, Tuck C, and Hague R (2019) 3D printing of aluminium alloys: Additive manufacturing of aluminium alloys using selective laser melting. *Progress in Materials Science* 106: 100578.

Altenpohl DG (1998) *Aluminum: Technology, Applications, and Environment*. Washington, DC: The Aluminum Association.

Aluminum Association (1997) *Aluminum Standards and Data*. DC: The Aluminum Association Washington.

Aversa A, Marchese G, Saboori A, Bassini E, Manfredi D, Biamino S, Ugues D, Fino P, and Lombardi M (2019) New aluminum alloys specifically designed for laser powder bed fusion: A review. *Materials* 12: 1007.

Belov NA, Eskin DG, and Aksenov AA (2005) *Multicomponent Phase Diagrams. Application for Commercial Aluminum Alloys*. Oxford, UK: Elsevier.

Davis JR (ed.) (1993) *ASM Specialty Handbook: Aluminum and Aluminum Alloys*. Phoenix, AZ: ASM International.

Glazoff MV, Khvan AV, Zolotorevsky VS, Belov NA, and Dinsdale AT (2019) *Casting Aluminum Alloys. Their Physical and Mechanical Metallurgy*. Oxford, UK: Butterworth-Heinemann.

Gokhale AA, Prasad NE, and Wanhill RJH (2013) *Aluminum-Lithium Alloys: Processing, Properties, and Applications*. Oxford, UK: Butterworth-Heinemann.

Hatch JE (ed.) (1984) *Aluminum: Properties and Physical Metallurgy*. Metals Park, OH: American Society for Metals.

Martin JH, Yahata BD, Hundley JM, Mayer JA, Schaedler TA, and Pollock TM (2017) 3D printing of high-strength aluminum alloys. *Nature* 549: 365–369.

Menzie WD, Barry JJ, Bleiwas DI, Bray EL, Goonan TG, and Matos G (2010) *The Global Flow of Aluminum From 2006 Through 2025. Open-File Report 2010–1256*. U.S. Department of the Interior and U.S. Geological Survey.

Mishra RS and Thapliyal S (2021) Design approaches for printability-performance synergy in Al alloys for laser-powder bed additive manufacturing. *Materials & Design* 204: 109640.

Mondolfo LF (1976) *Aluminum Alloys. Structure and Properties*. London, UK: Butterworths.

Ovsyannikov B, Grushko O, and Ovchinnikov V (2016) *Aluminum-Lithium Alloys: Process Metallurgy, Physical Metallurgy, and Welding*. Boca Raton, FL: CRC Press.

Plotkowski A, Sisco K, Bahl S, Shyam A, Yang Y, Allard L, Nandwana P, Marquez Rossy A, and Dehoff RR (2020) Microstructure and properties of a high temperature Al–Ce–Mn alloy produced by additive manufacturing. *Acta Materialia* 196: 595–608.

Polmear IJ (1995) *Light Alloys, Metallurgy of the Light Metals*. London, UK: Arnold.

Sanders RE Jr., Baumann SF, and Stumpf HC (1986) Non-heat-treatable aluminum alloys. In: Starke EA and Sanders TH (eds.) *Aluminum Alloys: Their Physical and Mechanical Properties*. vol. III, pp. 1441–1484. West Midlands, UK: EMAS.

Starke EA Jr. and Staley JT (1996) Application of modern aluminum alloys to aircraft. *Progress in Aerospace Science* 32: 131–172.

Thapliyal S, Shukla S, Zhou L, Hyer H, Agrawal P, Agrawal P, Komarasamy M, Sohn Y, and Mishra RS (2021) Design of heterogeneous structured Al alloys with wide processing window for laser-powder bed fusion additive manufacturing. *Additive Manufacturing* 42: 102002.

Toropova LS, Eskin DG, Kharakterova ML, and Dobatkina TV (1998) *Advanced Aluminum Alloys Containing Scandium. Structure and Properties*. Amsterdam, NL: Gordon and Breach OPA.

Totten GR, Teryakioglu M, and Kessler O (eds.) (2019) *Encyclopedia of Aluminum and Its Alloys*. Boca Raton, FL: CRC Press.

Vasudevan AK and Doherty RD (eds.) (1989) *Aluminum Alloys—Contemporary Research and Applications*. London, UK: Academic Press.

Relevant websites

https://www.aluminiumleader.com/economics/world_market/.

https://www.european-aluminium.eu/activity-report-2020-2021/market-overview/.

Alloys: The superalloys

Katerina A Christofidou[a] **and Caspar Schwalbe**[b], [a]Department of Materials Science and Engineering, University of Sheffield, Sheffield, United Kingdom; [b]MTU Aero Engines AG, Munich, Germany

© 2024 Elsevier Ltd. All rights reserved.

Introduction 583
Classification and key phases in superalloys 585
Ni-Fe-based superalloys 585
Ni-based superalloys 587
Alloys for turbine blades 587
Alloys for turbine disks 588
Alloys for additive manufacture 590
Co-based superalloys 591
Physical metallurgy 592
Future industry demands and sustainability considerations 593
Future propulsion systems 594
Embodied carbon 595
Considerations around securing the supply of superalloys 596
Element cost 596
Element production rates 596
Conclusion 598
Acknowledgments 598
References 598

Abstract

Superalloys are the materials of choice for high temperature structural applications, particularly within the aerospace industry. In this chapter, a brief overview of superalloys, their development, applications, physical metallurgy, and future considerations is included. Short case studies are used to highlight the drivers of superalloy design and the synergistic development of the field with manufacturing practices to achieve the required balance of properties for high temperature service. The chapter concludes with a brief section on future considerations, particularly on decarbonization and sustainability factors.

Key points

This chapter aims to equip the reader with:

- A historical context and trends driving the development of superalloys for key applications.
- An understanding of the role of alloy composition in delivering a desirable property balance for specific industrial applications.
- A brief summary of how superalloys obtain their unique high temperature strength and the mechanisms that drive the plastic deformation of this alloy class.
- A basic understanding for future industry demands of superalloys and what key challenges are associated with delivering green aeroengine concepts.
- Insights into principal challenges surrounding the sustainability of superalloy component manufacturing and securing the necessary raw materials.

Introduction

Metallurgical and materials advances have come to define human history by enabling transformative technological developments. Superalloys are no exception, being synonymous with the jet age. While it is difficult to provide an exact definition of superalloys, Sims, Stoloff and Hagel (Sims et al., 1987) define superalloys as "…alloys based on Group VIIIA-base elements developed for elevated-temperature service, which demonstrate combined mechanical strength and surface stability." It is indeed their combination of properties, ranging from strength to fatigue and environmental resistance, and damage tolerance, derived from their unique microstructures, that has seen superalloys deployed widely in a number of applications across the aerospace and energy generation sectors. This is particularly the case where temperatures in excess of 700 °C are encountered in service, i.e. at a temperature beyond the stability of steels.

https://doi.org/10.1016/B978-0-323-90800-9.00192-X

Superalloys were first discovered in the late 1920s when small amounts of Al and Ti were added to the well-known 80/20 Ni-Cr alloy, resulting in significant strengthening, and marked improvements in creep performance compared to the ferritic steels used then in high strength - high temperature applications. Although not rationalized until years later in the 1950s, the additions of Al and Ti resulted in the precipitation of the γ' phase, from which superalloys derive their exceptional mechanical properties. The continuous development of jet engine technologies, coupled with the immediate need for strong but also cost efficient and reliable materials during World War II, led to a clear demand for new materials in jet engine applications. Consequently, over the 1950s and 1960s, superalloys experienced increased usage along with concentrated efforts on compositional design to advance the jet age. Since then, a continual drive for efficiency improvements within the power generation industries, and particularly within the aviation sector, has led to remarkable developments in manufacturing technologies, enabling ever more complicated alloy compositions and components to be realized.

Fig. 1 utilizes data presented by Sims in 1984 (Sims, 1984) and additional literature (refer to Tables 1 and 2 for reference list) to illustrate a timeline of superalloy chemistry development as charted through the primary companies and regions relevant to the

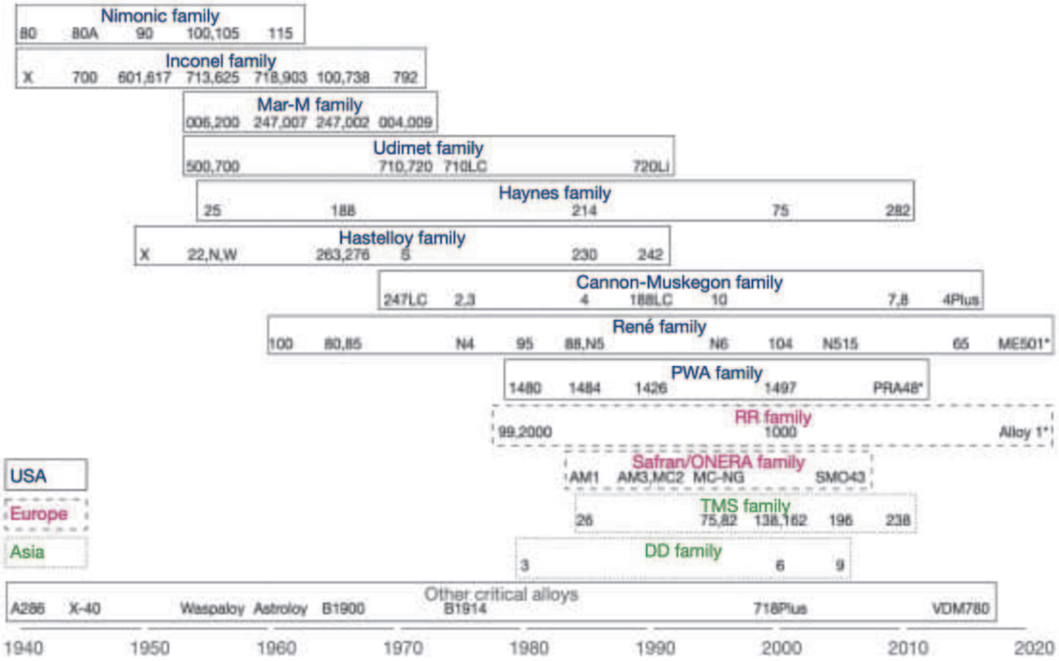

Fig. 1 Overview of key superalloy development ordered by time of development and sorted by alloy families and regions of development. Data taken from Sims (1984), Sims et al. (1987), Reed (2006), Naze et al. (2021), Keefe et al. (1992), Powell et al. (2016), Guédou et al. (1993), Guédou et al. (2008b), Hardy et al. (2004), Hardy et al. (2020), Ning et al. (2010), Radavich and Furrer (2004), Reynolds (2010), and Mourer and Bain (2013).

Table 1 Chemical composition of selected Nickel based blade alloys used in a turbine application industrial context. Data adapted from "The Superalloys. Fundamentals and Applications" (Reed, 2006) and through personal discussions with Prof. Jonathan Cormier.

Alloy (wt%)	*Ni*	*Cr*	*Co*	*Mo*	*W*	*Al*	*Nb*	*Ta*	*Ti*	*Re*	*Ru/Pt*	*Other*
Nimonic 80A	Bal.	19.5	–	–	–	1.4	–	–	2.4	–	–	0.06 C, 0.003 B and 0.06 Zr
U700	Bal.	15.0	17.0	5.0	–	4.0	–	–	3.5	–	–	0.06 C and 0.03 B
MAR-M002	Bal.	8.0	10.0	–	10.0	5.5	–	2.6	1.5	–	–	0.15C, 0.02 B, 0.03 Zr and 1.5 Hf
MAR-M247	Bal.	8.0	10.0	0.6	10.0	5.5	–	3.0	1.0	–	–	0.15 C, 0.02 B, 0.03 Zr and 1.5 Hf
PWA1480	Bal.	10.0	5.0	–	4.0	5.0	–	12.0	1.5	–	–	–
PWA1484	Bal.	5.0	10.0	2.0	6.0	5.6	–	9.0	–	3.0	–	0.1 Hf
SRR99	Bal.	8.0	5.0	–	10.0	5.5	–	3.0	2.2	–	–	–
RR2000	Bal.	10.0	15.0	3.0	–	5.5	–	–	4.0	–	–	–
René N4	Bal.	9.0	8.0	2.0	6.0	3.7	0.5	4.0	4.2	–	–	0.2 Hf
René N6	Bal.	4.2	12.5	1.4	6.0	5.8	–	7.2	–		–	0.2 Hf, 0.05 C, 0.04 B
CMSX-4	Bal.	6.5	9.6	0.6	6.4	5.6	–	6.5	1.0	3.0	–	0.1 Hf
CMSX-10	Bal.	2.0	3.0	0.4	5.0	5.7		8.0	0.2	6.0	–	0.03 Hf
TMS196	Bal.	4.6	5.6	2.4	5.0	5.6	–	5.6	–	6.4	5.0	0.1 Hf
TMS238	Bal.	4.6	6.5	1.1	4.0	5.9	–	7.6	–	6.4	5.0	0.1 Hf
AM1	Bal.	7.0	8.0	2.0	5.0	5.0	1.0	8.0	1.8	–	–	–
AM3	Bal.	8.0	5.5	2.3	5.0	6.0	–	3.5	2.0	–	–	–
TROPEA	Bal.	6.5	9.0	0.6	6.0	5.6	–	9.0	1.0	1.0	2.0 (Pt)	0.1 Hf
DD6	Bal.	4.3	9.0	2.0	8.0	5.6	0.5	7.5	–	2.0	–	0.1 Hf
DD9	Bal.	3.5	7.0	2.0	6.5	5.6	0.5	7.5	–	4.5	–	0.1 Hf

Table 2 Chemical composition of selected Nickel based disk alloys used in a turbine application industrial context. Data taken from Keefe et al. (1992), Powell et al. (2016), Guédou et al. (1993), Guédou et al. (2008b), Hardy et al. (2004), Hardy et al. (2020), Ning et al. (2010), Radavich and Furrer (2004), Mourer and Bain (2013), and Reynolds (2010).

Alloy (wt%)	*Ni*	*Cr*	*Co*	*Fe*	*Mo*	*W*	*Al*	*Nb*	*Ta*	*Ti*	*C*	*B*	*Zr*	*Other*
IN718	Bal.	19.0	–	18.5	3.0	–	0.5	5.1	–	0.9	0.04	–	–	–
Waspaloy	Bal.	19.5	13.5	–	4.3	–	1.3	–	–	3.0	0.08	0.01	0.05	–
U720Li	Bal.	16.0	15.0	–	3.0	1.3	2.5	–	–	5.0	0.03	0.02	0.05	–
Astroloy	Bal.	15.0	17.0	–	5.3	–	4.0	–	–	3.5	0.06	0.03	–	–
IN100	Bal.	10.0	15.0	–	3.0	–	5.5	–	–	4.7	0.18	0.02	0.06	–
René 95	Bal.	14.0	8.0	–	3.5	3.5	3.5	3.5	–	2.5	0.15	0.01	0.05	–
René 88DT	Bal.	16.0	13.0	–	4.0	4.0	2.1	0.7	–	3.7	0.03	0.02	0.03	–
René 104	Bal.	13.1	18.2	–	3.8	1.9	3.5	1.4	2.7	3.5	0.03	0.03	0.05	–
ME501	Bal.	12.0	18.0	–	2.9	3.0	3.0	1.5	4.8	3.0	0.06	0.03	0.06	0.4 Hf
N18	Bal.	11.2	15.6	–	6.5	–	4.4	–	–	4.4	0.02	0.02	0.03	0.5 Hf
SM043	Bal.	13.3	12.2	–	4.6	3.0	2.9	1.5	–	3.6	0.02	0.01	0.05	0.25 Hf
PRA48	Bal.	10.1	19.6	–	2.8	2.6	3.1	1.6	7.3	2.2	0.03	0.03	0.05	0.4 Hf
RR1000	Bal.	15.0	18.5	–	5.0	–	3.0	–	2.0	3.6	0.03	0.02	0.06	0.5 Hf
Alloy 1	Bal.	13.3	14.0	1.0	2.1	3.1	3.2	1.4	4.9	2.9	0.03	0.03	0.08	0.4 Si and 0.6 Mn
FGH96	Bal.	16.0	13.0	–	4.0	4.0	2.1	0.7	–	3.7	0.04	0.01	0.03	–
EP741NP	Bal.	9.0	15.8	–	3.9	5.5	5.1	2.6	–	1.8	0.04	0.02	0.02	–

field. It is clear that the need for improved gas turbine technologies has been the primary driver for the advancement of superalloy chemistry design. However, in addition to their remarkable combination of properties at high temperatures, superalloys also exhibit exceptional performance in oxidizing and corrosive environments. This has led to them becoming ubiquitous in applications within highly corrosive environments, particularly within the power generation industries.

Classification and key phases in superalloys

As the definition put forward by Sims et al. (1987) suggests, superalloys are based on Group VIIIA-base elements and can be classed in three categories: Ni-Fe-based, Co-based, and Ni-based, depending on the concentration of the base element in the material and the key strengthening mechanisms utilized. The following sections present a brief introduction into the three key classifications of superalloys along with details of the phases present, applicable strengthening mechanisms and discussion of their historical development. For a comprehensive list of superalloy compositions the reader is referred to the seminal book by Reed (2006) or to the work of Reed and Rae (2014).

Ni-Fe-based superalloys

Ni-Fe based superalloys represent a natural progression from austenitic stainless steels. Using significant concentrations of both Ni and Fe, they are classified as a distinct category of alloys strengthened either primarily through solid solution modifications or precipitation hardening derived from both ordered and carbide phases. Ni-Fe-based superalloys are the most widely used class of superalloys due to their versatility at an approachable cost level. They are used across a broad range of sectors where both mechanical and environmental performance (particularly corrosion resistance) are paramount but where the service temperature does not usually exceed 700 °C. As an example, the most popular superalloy of all time, Inconel 718 (IN718), finds uses in a variety of industries ranging from the aerospace, marine, automotive, nuclear and petrochemical sectors, to cryogenic tanks for superconducting magnets, while remaining of great significance in jet engines where its usage often continues to exceed 50% by weight (Schafrik and Sprague, 2008).

Solid solution strengthened Ni-Fe based alloys are characterized by additions of Cr, Mo and W. In a study by Roth et al. (1997), Mo and W were found to be particularly potent solid solution strengtheners, calculated to offer ~1015 and 977 MPa at.%$^{-1/2}$ strengthening improvements respectively. In addition to the solid solution strengthening afforded by additions of Mo and W, both elements are also known to have significantly lower diffusivities compared to most elements within the matrix, enabling improvements in the creep performance of the material. In contrast, while Cr additions enable improvements in oxidation and corrosion performance through the formation of protective and continuous Cr_2O_3 scales, the solid solution potency of the element is only 337 MPa at. %$^{-1/2}$. However, the increased solubility of Cr within the face centered cubic (FCC) γ matrix enables considerably higher additions of the element to be utilized. Furthermore, Cr, Mo and W are potent formers of topologically closed packed phases, such as the σ, μ and Laves phases, that cause the deterioration of the mechanical performance of the material, particularly under creep conditions (Wilson, 2016).

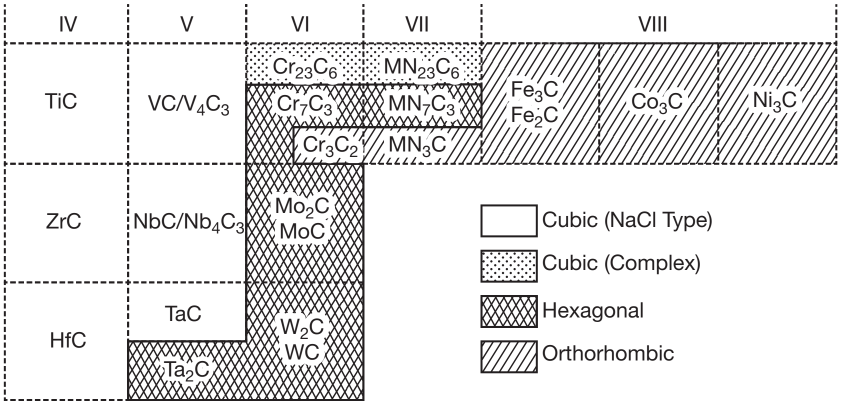

Fig. 2 Relationship between structures of carbides and the positions of metals in the Periodic Table (after Goldschmidt). Taken from Jena AK and Chaturvedi MC (1984) The role of alloying elements in the design of nickel-base superalloys. *Journal of Materials Science* 19: 3121–3139. https://doi.org/10.1007/BF00549796.

Carbide strengthening may further enhance the mechanical performance of Ni-Fe-based superalloys, via not only direct hardening, but also through the grain boundary pinning effects of carbide particles resulting in grain refinement and modifications to the recrystallisation behavior of the material. The most prominent carbide species observed in Ni-Fe-based superalloys are MC-type B1 (Strukturbericht notation) FCC monocarbides, where M may be Nb, Ti, Ta or Hf, or a mixture thereof, depending on the alloy composition - as shown in Fig. 2. Controlling the morphology of MC carbides to small globular particles at grain boundaries imparts the greatest benefits for strength and helps avoid grain boundary sliding during creep degradation as well as conveying damage tolerance. However, the formation of MC films along grain boundaries, often observed when inappropriate processing conditions have been chosen, results in embrittlement. Furthermore, destabilization of the MC carbides may occur, assisted by excessive additions of Mo and W, and leads to the formation of the non-cubic M_6C and $M_{23}C_6$ carbides, Fig. 2, with often deleterious effects on mechanical performance particularly if irregular morphologies are encountered.

In addition to solid solution and carbide strengthened Ni-Fe-based superalloys, intermetallic precipitation hardening is often utilized to further improve the mechanical properties of these materials. Additions of Al lead to the coherent formation of the ordered cubic Ni_3Al – $L1_2$ phase referred to as the γ' phase, Fig. 3. Where substantial concentrations of Nb are used at low Al:Nb ratios, the coherent and ordered tetragonal γ'' Ni_3Nb phase forms, Fig. 3. The coherent and ordered nature of the γ' and γ'' phases gives rise to appreciable strengthening within the alloys, which can be further tailored through control of the volume fraction, precipitate size, lattice misfit as well as fault energies of the precipitates. While both precipitates offer substantial strengthening benefits, the γ'' phase is by nature metastable and prolonged exposures at temperatures above 650 °C cause the transformation of the phase to the orthorhombic $D0_a$ δ–Ni_3Nb phase, which often tends to precipitate in a lath or needle like morphology, leading to embrittlement of the material. Consequently, particularly for applications where high temperature performance is critical, the γ' phase has been the dominant precipitation strengthening phase and is almost entirely utilized in the strengthening of Ni-based superalloys. Thus, the majority of the discussion within this review is focused on γ' strengthened superalloys.

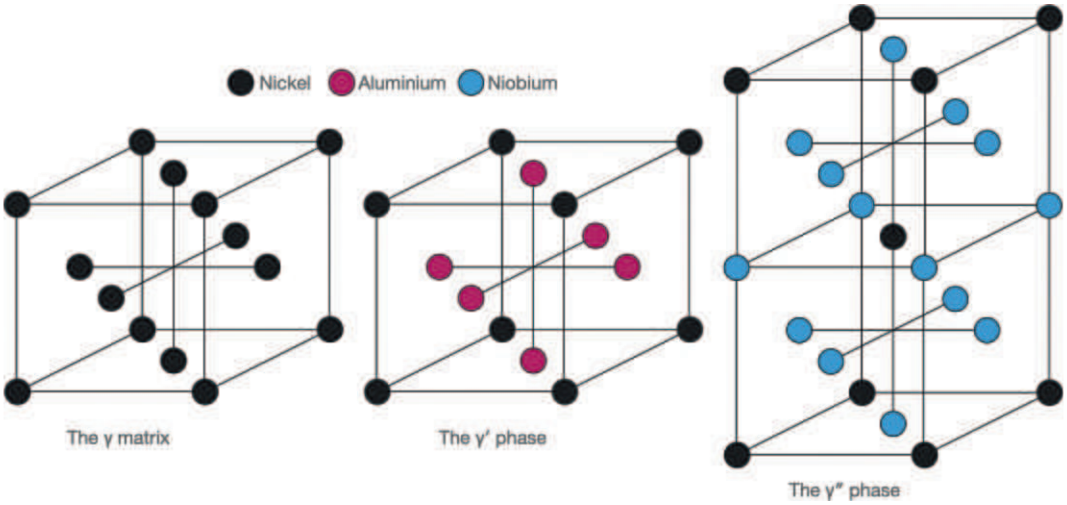

Fig. 3 Chemical element arrangement in the crystal structures of the gamma-matrix (FCC-A1), gamma-prime (L12) and gamma-double prime (D022) phases that are key for precipitate strength.

Ni-based superalloys

Before charting the key development phases in the design of Ni-based superalloys, it is worth highlighting the fundamental characteristics that make Ni a suitable element for high temperature applications.

High temperature service necessitates materials that exhibit a combination of high strength, creep, fatigue and environmental resistance, favorable thermal expansion coefficient, to avoid in-service geometrical incompatibilities; as well as reduced density and cost. In addition, due to the prolonged high temperature exposure of these materials, a further requirement of microstructural stability is required so that the mechanical performance can be maintained during service for prolonged periods at high temperatures. With these considerations in mind, Ni forms an ideal base for high-temperature alloys. Firstly, with the exception of Cu, it is the only non-platinum group metal that adopts an FCC crystal structure, which remains stable at all temperatures, thus providing an inherent toughness and ductility to materials derived from it. Secondly, Ni exhibits a remarkable tolerance for alloying due to the fact that its third electron shell is nearly filled, hence, forming fewer chemical compounds that lead to intermetallic phases, which may degrade mechanical performance. Thirdly, Ni intrinsically displays low rates of self-diffusion, providing improved resistance against creep degradation.

As previously stated, Ni-based superalloys derive their strength primarily through precipitation hardening from the formation of the coherent, ordered, γ'–Ni_3Al phase. The historical evolution of Ni-based superalloys has focused on the compositional development of the alloys to account for demanding environments, while also utilizing advances in manufacturing to create a holistic approach toward microstructural design. Building on cast and wrought Ni-Fe-based alloys and austenitic stainless steels, the mechanical performance of Ni-based superalloys was initially improved through a reduction in the concentration of Fe in favor of increased Ni and Co concentrations, coupled with an increase in the concentrations of Al and Ti to promote the formation of the γ' phase. Due to the tolerance that Ni has for alloying, ever increasing numbers of elements have been used to tailor the performance of Ni-based superalloys further. Solid solution strengthening using Mo and W, as with Ni-Fe-based superalloys, continues to be utilized in Ni-based superalloys. Cr and Co, albeit less potent solid solution strengtheners than Mo and W, also feature prominently. Cr and Co exhibit high solubilities within the FCC Ni-based matrix, while also providing alternative benefits e.g. improved environmental resistance through Cr_2O_3 formation for Cr additions, or a pronounced reduction in stacking fault energy from Co additions that reduce the dislocation cross-slip potential of the alloy thus allowing for improvements in the creep performance of the material. Elements such as Al, Ti, Ta, Nb and Hf are also commonly found in Ni-based superalloys for the optimization of the γ' phase. For example, increased concentrations of these elements lead to an increase in the γ' volume fraction, modification of the anti-phase boundary energy and thus the order strengthening of the phase, as well as modifications of the γ/γ' lattice misfit and therefore the morphology and coarsening kinetics of the γ' phase, which may further influence mechanical performance. Additions of C, B and Zr are also frequently included for polycrystalline compositions and have been tailored over the years to optimize grain boundary strengthening and carbide/boride formation potential.

While the themes that have dominated compositional development in superalloys commonly include mechanical performance at high temperatures, the competitive advantage that can be derived by original equipment manufacturers (OEMs) from utilizing their own alloy compositions and defined manufacturing processes has led to a number of alloy development programs over the years to create bespoke alloys for key gas turbine components. A brief outline of key case studies that highlight the evolution of superalloy compositions and manufacture, is included below.

Alloys for turbine blades

The design of alloys for turbine blades, presents an exceptional case study in the synergistic development of alloy composition and manufacturing technologies to facilitate the increased temperature capability of these components. Turbine blades were initially produced in a wrought form with alloys such as the Nimonic series (80, 80A, 90, 105 and 115), IN100, and Udimet 700, i.e. alloys utilizing few alloying elements and relatively modest γ' fractions. The improvements in casting technologies facilitated the development of alloys with increased γ' concentrations as well as the introduction of simple cooling channel architectures within turbine blade components. Consequently, the compositions of the alloys could be developed to include a higher number of alloying elements, in particular higher concentrations of segregation prone solid solution strengthening elements, γ' forming elements as well as higher levels of C, B and Zr. The development of investment casting to allow for cooling channels to be included in the blade design further served to moderately allow for turbine entry temperatures higher than the temperature capabilities of the material as the cooling employed could provide an effective reduction in the service temperature experienced by the component. Further developments in the manufacturing technologies led to the introduction of the Bridgman process that facilitated the casting of directionally solidified (DS) alloys, with a reduced susceptibility to Coble creep, resulting in overall improved creep performance. Following on from the success of the Bridgman process, the addition of a single crystal seed or grain selector with a diameter smaller than the grain size, led to the momentous ability to cast turbine blade components in single crystal configurations, thus eliminating grain boundaries and minimizing creep degradation.

Since the advent of single crystal castings in the 1980s, the compositions of turbine blade alloys have evolved to optimize their resistance to creep deformation. As a result, most single crystal turbine blade compositions now utilize $\sim$70% by volume of the γ' phase, with very high additions of Al and increased concentrations of Ta in favor of Ti. This allows for strengthening of the γ' phase, while also increasing the strength of the γ phase through solid solution strengthening and reducing the propensity to form freckle defects. Solid solution strengthening has also been of great interest due to both the strength benefits it offers, but more importantly the reduced diffusion through the γ matrix providing improved creep performance. Such is the importance of creep strengthening in turbine blade materials, that the use of increased levels of refractory elements is now widely implemented and Mo, W, Re and Ru are the key elements used in single crystal superalloys for creep strengthening. However, their concentrations need to be judicially reviewed as these elements also increase the propensity of the alloy toward TCP phase formation, particularly when increased levels of Cr are included, while simultaneously increasing the raw cost of the material. The addition of Cr may appear superfluous, given the propensity for turbine blade alloys to form a protective Al_2O_3 scale, but the addition of Cr is known to accelerate Al_2O_3 formation and so aid in environmental performance. It is thus a critical element within turbine blade compositions. Table 1, shows several of the relevant turbine blade alloys discussed herein, offering insights into compositional development.

In parallel to compositional modifications of single crystal alloys, advances in coating technologies also enabled further increases in the turbine entry temperature as sufficient insulation of turbine blade components could be achieved, while also providing improved environmental resistance for the material. As coatings became more common for turbine blades, it became a key design criterion to optimize for coating compatibility and cohesion with the blade substrate during service operation.

Exploring the development of turbine blade materials through the lens of the people and places that have contributed to their evolution provides interesting insights, Table 1. The early years of turbine blade alloys were dominated by material manufacturers, particularly Special Metals through their Nimonic and Udimet series, and INCO through the Inconel alloy family, Fig. 1. Through the 1960s and the equiaxed casting phase for turbine blade materials, Martin-Marietta Materials introduced the ever-popular Mar-M002, Mar-M200 and Mar-M247 alloys, whereas OEMs, starting with General Electric (GE), also entered the alloy design landscape. Pratt & Whitney (P&W) pioneered directional solidification but opted to use Mar-M200, which was later modified with Hf additions, leading to the derivative PWA 1422 alloy (Quigg, 1993). The advent of single crystal casting methodologies saw the increased involvement of OEMs in alloy design, with all major jet-engine manufacturers (GE, P&W and Rolls-Royce) investing in alloy development programs, resulting in the introduction of several René alloys from GE, SRR99 and RR2000 from Rolls-Royce (RR), and several PWA iterations from P&W (Quigg, 1993). In France, most key alloys were developed under the lead of ONERA, like the AM and MC alloy series, with a recent exception of the alloy Tropea developed by Safran and PPrime. However, more recently, the OEM boon in alloy design has receded, and the market leader to this day is Cannon-Muskegon (CM) a materials company that recognized a gap in the market for smaller OEMs not able to develop their own alloys (Wahl and Harris, n.d.). Responding to market demand, CM released a range of single crystal and DS alloys. CMSX-4, one of the flagship CM single crystal alloys, has seen increased adoption by a number of companies across industrial sectors utilizing gas turbines. Such is the dominance of CMSX-4, that it appears in nearly a third of all publications on single crystal superalloys since its introduction.

In recent years, increased efforts for the design of novel turbine blade materials, particularly single crystal alloys, have been prominent in Japan and China. Through the Japanese National Institute for Materials Science, the TMS alloy series was established, aimed at progressively improving the creep performance of single crystal alloys through judicious compositional design (Koizumi et al., 2004). Careful, systematic studies of the effect of several elements on the mechanical performance of these materials led to hundreds of compositions, and six "generations" of superalloys, culminating with the sixth generation TMS-238 alloy. TMS-238 was designed to have mechanical performance similar to TMS-196, but with notably improved oxidation and hot-corrosion resistance, recognizing the increased importance of environmental resistance in ensuring the longevity of single crystal components in service (Kawagishi et al., 2012). However, the cost of the TMS alloy series is markedly higher than any other single crystal superalloy family, owing to the increased utilization of refractory and platinum group metals to achieve the impressive levels of creep resistance observed in these compositions, Fig. 4. In contrast to Japan, where alloy design efforts were concentrated to a single research institution, Chinese interest in turbine blade superalloy compositions has been varied and widespread, with a steady increase in interest starting from c. 2009 with $\sim$60 documents with Chinese affiliations. This has culminated in nearly 600 documents in 2022 alone. While the majority of the work reported has focused on understanding existing alloys or ones with simple modifications (e.g. DD3), more recently, unique compositions have also been reported such as DD6 and DD9.

The critical relationships between strength, creep and cost for turbine blade alloys is highlighted in Fig. 4, where the tensile yield strength at 650 °C and creep rupture life at 1100 °C and 140 MPa are plotted for a number of key alloys mentioned above. The size of the bubble for each alloy corresponds to its average element price per tonne (specified in USD for averaged price data between 2016 and 2018). Looking at Fig. 4, the reader can find the superalloy CMSX-4 in the center of the graph, displaying an excellent trade-off between creep resistance, yield strength and price. Based on Fig. 4, the more recently developed superalloys, DD9 and Rene N6, provide a substantial improvement in creep life (noting that the x-axis is logarithmic) while maintaining comparable levels of yield strength and price. Meanwhile, the commercial alloys TMS-196 and TMS-238 offer a remarkable improvement in creep life, with a lower yield strength, but at a 12.5 fold increase in price per ton compared to CMSX-4. Provided the turbine gas temperature continues to rise in future engines, new alloys are expected to be developed to meet this demand, most likely occupying the development space highlighted in gray in the top right corner, while trying to minimize any further increases in price. Furthermore, the compatibility with coating technologies is expected to be an ever more important criterion, particularly with the changing temperature profiles and fuels expected of newer generation propulsion systems (Naze et al., 2021).

Alloys for turbine disks

Alloys developed for turbine disks offer a second case study that further demonstrates the synergistic development of compositional modifications, coupled with manufacturing improvements, to deliver critical components with enhanced service performance. The ever-increasing need for higher turbine entry temperatures, required for improved jet engine efficiency, sparked the boom in development for turbine blade materials. However, innovation in turbine blade technologies alone is inadequate if not complemented by developments in the turbine disks housing the blades. The design of materials for turbine disk technologies is further

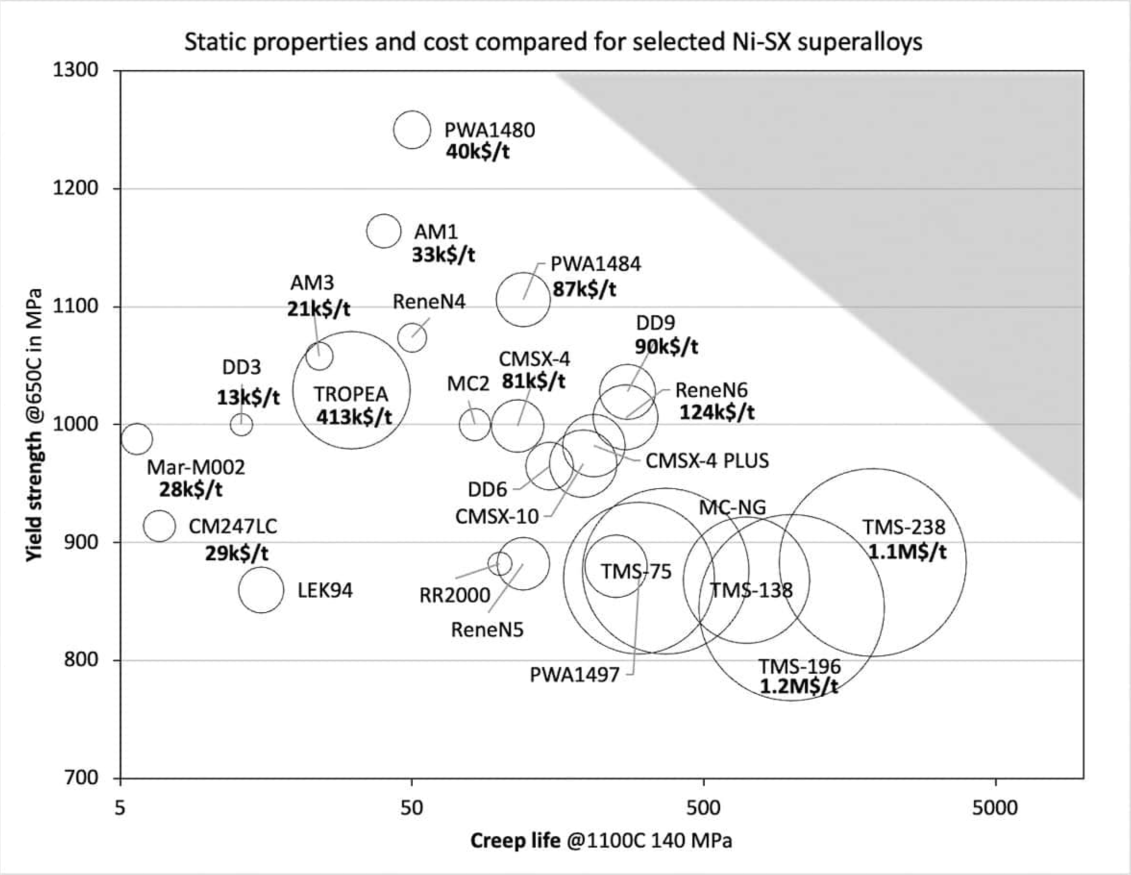

Fig. 4 Static properties (creep at 1100 °C and 140 MPa and yield strength at 650 °C in MPa) plotted for selected Ni-based single crystal superalloys. The size of the bubble of each alloy represents its specific alloy price in USD per ton. The element prices were extracted from the US National Mining Information Centre of the United States Geological Survey [see https://www.usgs.gov/centers/national-minerals-information-center]. Property data used in this figure courtesy of Mansoz B PhD thesis, Université de Toulouse, France, 2023, Florence Pettinari-Sturmel and Jonathan Cormier.

complicated by their size and operating environment, resulting in conflicting mechanical properties required at the bore and rim of the component, which a single material must be able to meet. For example, the rim of the component operates at a higher temperature compared to the bore, thus necessitating improved creep performance. In contrast, the bore of the component is much cooler, but experiences higher stresses due to both the rotational speed and combined weight of the turbine blades and the component itself, thus, necessitating good strength. Historically, the most popular alloys used for turbine disks have been the cast and wrought IN718, Waspaloy and Udimet 720Li alloys, utilizing increasing fractions of the γ' phase for improved mechanical performance, see compositions in Table 2. However, with Udimet 720Li, a γ' fraction and compositional complexity limit was reached for alloys to be able to be reliably manufactured using cast and wrought methods. Therefore, alternative manufacturing routes were sought to be able to deliver the balance of mechanical performance required for turbine disks, while simultaneously providing improved manufacturing quality. Thus, the emergence of powder metallurgy (P/M) in the 1960s provided a viable alternative for turbine disk component processing, enabling components from highly alloyed compositions to be manufactured with reduced segregation, due to the rapid solidification of powder particles, while retaining forgeability.

In stark difference to turbine blade compositional design, which has now come to be dominated by a materials manufacturer (Cannon–Muskegon) rather than OEMs, the development of powder metallurgy compositions for turbine disk applications has been, and continues to be, entirely driven by the OEMs. This highlights the enormous perceived competitive advantage that may be garnered from improved turbine disk service performance.

Investigations into P/M superalloys were initiated in the 1960s and progressed throughout the 1970s, focusing on the key parts of the manufacturing route development, from the production of "clean" pre-alloyed powders, to the powder consolidation steps and thermomechanical processing (Gessinger and Bomford, 1974). Initial interest in P/M superalloys was driven in part by gas turbine OEMs necessitating the manufacture of compositions with increased concentrations of Cr for hot corrosion resistance, as opposed to the Cr lean alloys, developed for turbine blades. In parallel, the demonstration of oxide dispersion strengthened (ODS) aluminium materials, further invigorated the possibility of ODS-Ni-based alloys that could only be manufactured using P/M methods. Despite these drivers, the advances in cleaner cast and wrought technologies, as well as the impressive levels of compositional development of Ni-based superalloys that rendered ODS-Ni-based alloys unnecessary, meant that progress in P/M superalloys did not gain momentum until much later in the 1970s and 1980s to address challenges in making carefully controlled polycrystalline Ni-based superalloys with γ' fractions in excess of 45%.

Alloys such as IN100, Waspaloy and Udimet 700 dominated the initial research on P/M development, aiming to understand the effect of the process on the alloy properties, in particular fatigue and crack growth (Gessinger and Bomford, 1974). By 1974, Pratt and Whitney and GE advanced to scale-up production of IN100 and Astroloy, and René 95 respectively. Using the lessons learned from introducing P/M superalloys into service, enabled the bespoke design of new alloy chemistries targeting damage tolerance. GE introduced René 88DT in 1988 (Krueger et al., 1990) and openly discussed the development program for the alloy in the Superalloys 1992 meeting (Krueger et al., 1992), emphasizing damage tolerance as a key criterion for the development of the material as well as using P/M René 95 properties to frame the design targets. It wasn't until nearly a decade later that Rolls-Royce introduced their first P/M superalloy, RR1000, owing to their continued successful use of Udimet 720Li. Notably, in a paper presented in the Superalloys 2004 meeting, the development program for RR1000 also highlighted the use of thermodynamic calculation software for the prediction of phase formation. Utilizing CALPHAD and New-PHACOMP methods limited the number of compositions experimentally tested, and hence the overall cost of the development program. The main aim in the design of RR1000 was to minimize the volume fraction of γ' required for strength so that the damage tolerance of the alloy could be maintained. The formation of carbides was considered vital for the alloy, which led to an increase in the concentration of Co and the introduction of Hf, compared to U720Li. Similarly, the formation of TCP phases was identified as an issue and was controlled through the concentrations of Al, Cr and Mo, informed by New-PHACOMP calculations (Hardy et al., 2004).

Following a very different approach for the development of their next iteration of turbine disk superalloys, GE and P&W, collaborated on the High Speed Civil Transport project initiated by NASA to develop their respective alloys (Huron et al., 2008; Mourer and Bain, 2013; Reynolds, 2010). Two iterations of the alloy matrix were performed, and the alloys produced for screening tests were manufactured following the conventional powder metallurgy route of powder consolidation, extrusion, isothermal forging and supersolvus heat treatment. The first stage of design was to optimize the concentrations of the grain boundary strengthening elements, B, C, Hf and Zr, before the bulk alloy composition could be defined (Huron et al., 2008). The initial design criteria for the alloy were improved creep resistance and time dependent crack growth resistance, for which the concentrations of Ta, Nb and W were varied in the first matrix of alloys, and a reduction in the γ' solvus temperature, which was reflected in changes in the Al:Ti ratio and the concentration of Co. Subsequently, two base compositions that reflected the results obtained from the screening tests were selected, and a further iteration of alloys was designed, aimed at optimizing the compositions of Nb, Ta, Ti and explored higher Co concentrations for lower γ' solvus temperatures (Huron et al., 2008). After the completion of the High Speed Civil Transport program, both GE and P&W independently continued their development efforts utilizing the knowledge acquired through the program. This led to the design of René 104 (also referred to as ME3) and ME501 (GE) and PRA48 (P&W) as referred to in the literature/patents. The compositions of these alloys are, as expected, remarkably similar, Table 2 (Huron et al., 2008; Reynolds, 2010; Mourer and Bain, 2013).

Similarly to most alloy development programs, Safran also opted for an iterative process, informed by prior knowledge from the existing alloy N18 and simple PHACOMP calculations. Their main approach was to develop a powder processed alloy with a γ' fraction between 40% and 50%. However, the major issue was the control of TCP phases, for which a lower Cr concentration was used compared to most wrought alloys. Alloy SMO43, or N19, was developed, but Guédou et al. (2008a) state that this is a base composition from which further iterations can be performed.

Following on from RR1000, the next iteration of P/M alloys from RR focused on achieving improved mechanical performance through the utilization of a higher number density of small γ' particles at a volume fraction up to 53%, while also maintaining a coarse grain size (i.e. not relying on grain refinement for strength) (Hardy et al., 2020). In order to achieve the γ' distribution specified, Al, Ti, Ta and Nb were controlled to be within the 12.65–13.15 at.% range. The trends observed in turbine disk alloy compositional development, Table 2, highlight an initial utilization of higher fractions of γ' forming elements (Al, Ti, Ta and Nb) that has now plateaued reflecting the emphasis on manufacturability as well as time dependent crack growth. Further to the optimization of the mechanical performance, careful control of Ti, Ta and Nb to achieve phase stability was also sought, particularly in avoiding the formation of the δ and η phases. Oxidation and corrosion resistance were also explicitly taken into consideration at the design stage, reflecting the more holistic approach toward alloy design for high temperature structural parts.

Away from the developments on P/M disk alloys in the US and Europe, China and Russia have also explored the use of P/M alloys. While little is known about the Russian P/M alloy development programs, the Russian P/M superalloy EP741NP has been investigated by Radavich and Furrer (2004) and is believed to have been designed for improved creep resistance and elevated temperature service rather than conventional yield strength. In contrast to the secrecy surrounding the Russian P/M programs, the Chinese FGH96 alloy developed in the 1990s (Tao et al., 2011) has been extensively studied and reported upon in the open literature, with a notable increase in reports starting in 2012 and peaking with 180 publications in 2022 alone, reflecting the sustained interest in the material, its manufacturability and properties.

Alloys for additive manufacture

The case studies on turbine blade and turbine disk materials serve to demonstrate the synergistic development of superalloy compositions and manufacturing methodologies. Manufacturing advancements have been of paramount importance in enabling superalloy components to be utilized in some of the most inimical environments known. Consequently, the advent of metal additive manufacturing (AM) has been of particular interest to the superalloys community, recognizing the potential that AM has to enable a step-change in efficiency improvements due to increased geometrical freedom as well as an improved "buy-to-fly" ratio reducing waste.

Several methodologies for metal AM are now available commercially. However, the three most prominent methodologies for Ni-based superalloys are laser powder bed fusion (L-PBF), electron beam melting (EBM) and laser directed energy deposition (L-DED). The first two methodologies are often referred to as "powder bed" techniques, as the component is built layer by layer using a thin layer of powder, over which the energy source traces the required geometry to melt it, before a second powder layer is spread. In contrast to the powder bed method, directed energy deposition relies on the deposition of molten material to the required surface, i.e. powder is blown into the path of the laser directly, hence the method is also often referred to as "blown powder." For further details on metal AM, the reader is referred to the book "Additive Manufacturing Technologies" by Gibson et al. (2021).

As with most developing manufacturing processes, the majority of the work on AM of superalloys involves the use of established and commercially available compositions. Owing to the complicated and very rapid solidification profiles encountered within AM, the most readily AM-amenable superalloys are those that are also highly weldable, i.e. mainly Ni-Fe-based solid solution strengthened alloys, alloys comprising γ' fractions below 30%, or indeed γ'' strengthened alloys, such as the most popular AM superalloys, IN718 and IN625. The majority of the work presented in the open literature revolves around optimization of process parameters as well as small compositional changes to achieve repeatable builds with desirable grain structures, unlocking the potential for localized microstructural control.

While some of the benefits of AM can be derived for components manufactured from readily weldable alloys, the impact of AM would be most pronounced for components operating at the highest temperatures, thus necessitating high γ' fraction alloys. Of the high γ' fraction superalloys, CM247LC has been the most widely studied in AM, albeit with limited success for L-PBF production routes due to the cracking susceptibility of the alloy, resulting in unacceptable mechanical performance. Though EBM of CM247LC and other high γ' superalloys is achievable, the technology has lagged behind in industrial uptake, due to difficulties in ensuring the integrity of internal cooling channels, as well as thermal management, that often results in undesirable microstructures. The acquisition of Arcam by GE Additive, however, has accelerated the innovation on EBM, stimulating the industrialization of the methodology (Ramsperger and Eichler, 2023).

Nevertheless, despite the promising results from EBM of high γ' fraction superalloys, L-PBF remains of great industrial importance. Thus, considerable research is underway to understand high γ' fraction superalloys and design alloys capable of operating at the highest temperatures with improved amenability to L-PBF. To date, the alloy design landscape has been dominated by OEMs, notably within the aerospace industry. However, little information has been shared in the open literature about the design methodologies and strategies utilized, although several patents can be readily accessed (Engeli et al., 2017). In addition to the efforts of OEMs, alloy manufacturers as well as academic institutions have also been actively involved in alloy design activities. Similarly to the later compositional iterations of alloys for turbine disk applications, the open literature suggests that the development of novel compositions amenable to L-PBF utilizes computational approaches to enable rapid screening and downselection of alloys for testing (Tang et al., 2021; Ghoussoub et al., 2022a; Conduit et al., 2019; Sun et al., 2022). Conduit et al. (2019) proposed a probabilistic neural network approach, coupled with thermodynamic calculations, that led to the development of Alloy DLD, which showed promising properties when compared to the CM247LC and C263 alloys manufactured using L-PBF. Comparably, using the "Alloys-by-design" approach, Tang et al. (2021) and Ghoussoub et al. (2022b) explored the composition space of Ni-based alloys to identify and screen superalloys for applications at temperatures in excess of 850 °C. As a result of the work by Oxford University in collaboration with Alloyed, the ABD-850 AM and ABD-900 AM alloys have been introduced as viable candidates and patented (Crudden and Nemeth, 2019). In addition, the commercial uptake of these compositions has been ensured through collaboration with Aubert and Duval for the manufacture and supply of metal powders. Continuing the trend of materials manufacturers, Carpenter Technology are also active in the development of bespoke alloys for additive manufacturing, both in terms of more traditional Ni-based compositions, as well as CoNi-based concepts (Zhou et al., 2020; Forsik et al., 2018). Further to the more traditional compositions explored for AM, the concepts of Co-based γ'-strengthened superalloys (see next section), high entropy superalloys (Yeh and Tsao, 2017), and oxide-dispersion-strengthened alloys (Smith et al., 2020) are also being considered as possible solutions to achieve high temperature performance, while simultaneously being amenable to L-PBF. Albeit still in its relative infancy, it is anticipated that over the next decade substantial compositional developments will be achieved to realize superalloys manufactured using AM methodologies, potentially ushering in a new era for superalloy design.

Co-based superalloys

Ni-based and Ni-Fe-based superalloys form the largest categories of superalloys by volume of consumption. However, the third family of superalloys, Co-based superalloys, is of historical importance, and the advent of γ'-strengthened Co-based superalloys offers considerable promise for the development of novel compositions, particularly with improved amenability to AM. The very first patents involving Co-based alloys, were filed in the early 1900s for alloys based on the Co-Cr binary and Co-Cr-W ternary systems. These systems formed the then popular Stellite alloys that were widely used in various applications, such as industrial machinery, hip replacements and cutlery (Sims et al., 1987). A variation of Stellite alloys based on the Co-Cr-Mo-C quaternary system, commonly referred to as Vitallium, was also used widely in dentures. Vitallium was soon identified as a suitable aerospace alloy with the slight modification of reduced C content. The modified Vitallium alloy formed the foundation of conventional

Co- based superalloys that flourished in turbine blade applications until the late 1950s. Strengthening in these conventional Co-based superalloys is derived primarily from the formation of carbides and through solid solution strengthening of the matrix. Elements such as Ta, W, Nb, Cr and Mo contribute to solid solution strengthening, but they can also combine with C to form complex carbides. Hence, the extent of the contributions of each of the mechanisms to the strength of the alloys depends on the alloying elements used and the carbon content of the alloy. In addition to the mechanisms utilized in Ni-Fe-based alloys, carbides in Co-based alloys may also form skeletal networks that support loads during mechanical stressing. The typical carbides that may form in Co-based alloys are the MC, M_6C, M_7C_3 and $M_{23}C_6$ species, in which M is the metallic conjugate of the compound. Generally, as with Ni-Fe-based superalloys, MC carbides are the most desirable due to their cubic structure that forms coherently with the A1 matrix and may offer increased stability to higher temperatures. Precipitation of M_7C_3 and $M_{23}C_6$ is considered deleterious, not only due to crystallographic instability issues, but also due to the high Cr content that is consumed in the formation of these carbides, which may lead to reduced environmental resistance.

While conventional Co-based superalloys continue to be used in a variety of applications, particularly where hot corrosion and weldability are a concern, it is γ' strengthened Co-Al-W-based superalloys that have dominated the literature and interest since 2006, when the stable formation of the ternary $L1_2$ $Co_3(Al,W)$ phase in the Co-Al-W system was identified by Sato et al. (2006). While the bulk of the work has been focused on model higher order systems deriving from the Co-Al-W ternary, key activities have also focused on developing alloys for specific jet engine applications. Pollock et al. (2010) and Tsunekane et al. (2011) identified the potential of single crystal castings and claimed a 150 °C advantage over conventional Ni-based single crystal alloys. Additionally, the low segregation of elements during solidification suggested that the alloys may not be prone to instabilities, hence, large castings of these alloys may be achieved. The manufacture of Co-Al-W in single crystal form also allowed the creep behavior of these alloys to be determined and compared against equivalent Ni-based single crystal alloys (Titus et al., 2012; Eggeler et al., 2014, Titus et al., 2015; Eggeler et al., 2016).

While the initial work on Co-Al-W-based alloys focused on their capabilities as cast, single-crystal turbine blade components, the latter developmental years have instead explored the potential of these materials for polycrystalline applications manufactured through cast and wrought, powder metallurgy as well as additive manufacturing methodologies. Building on extensive studies of fundamental systems and through robust experimental testing to establish the effects of differing alloying additions, Neumeier et al. (2015) reported the development of novel wrought Co-Al-W-based superalloys with improved mechanical and oxidation performance, compared to commonly used cast and wrought Ni-based alloys. More recently, Carpenter Technology Corp., utilizing computational design tools derived from the improved understanding of the thermodynamics of Co-based alloys, have also developed a viable cast and wrought CoNi-based superalloy that utilizes both Cr_2O_3 and Al_2O_3 scales for high temperature oxidation resistance, further demonstrating the commercial interest in materials from this family (Forsik et al., 2018; Forsik et al., 2020). In parallel to the activities exploring cast and wrought compositions, Knop et al. (2014) and Yan et al. (2014) have also explored polycrystalline Co-based superalloys for turbine disk applications, manufactured by powder metallurgy. Although these did not show significant improvements over Ni-based alloys, they did demonstrate the potential for continued development in the field (Hardy et al., 2018). With increased interest for high temperature capable alloys amenable to additive manufacture, research into Co-Al-W-based alloys has also been of interest in the last 5 years. Indeed, following on from the successful demonstration from Carpenter Technology Corp. of a cast and wrought alloy, a collaboration between the company and researchers at the University of California Santa Barbara and Oak Ridge National Laboratories reported on the development of a defect resistant CoNi-based superalloy for AM applications. The resultant composition contained ~70% by volume of γ' precipitates but crucially, was found to be amenable to both electron beam melting and laser powder bed fusion manufacturing methodologies and was able to achieve yield strengths in excess of 1GPa, while simultaneously retaining ductility levels of ~13% at room temperature (Murray et al., 2020; Pollock et al., 2020). The rapid development of commercially viable alloys from the Co-Al-W-system has highlighted the importance of accelerated alloy development methodologies that utilize both high throughput testing and advanced computational tools in realizing novel compositions, while enabling manufacturing compatibility to be integrated at the initial stages of compositional design.

However, despite the efforts of the community and several beneficial attributes of alloys based on the Co-Al-W system, several limitations still exist. The most notable limitation is the supply of Co, an element that is mined almost exclusively in the Democratic Republic of Congo (DRC) following often ethically questionable practices. Coupled with the increased usage of Co in batteries, the instability in the supply of the element is a critical concern and in the absence of appreciable and demonstrable benefits over Ni-based superalloys, the industrial use of Co-based alloys is likely to remain low.

Physical metallurgy

The performance of superalloys, primarily those strengthened by ordered γ'-$L1_2$ and γ''- $D0_{22}$ intermetallics, stems from the configurations of the dislocation structures as well as the interactions of the dislocations with the precipitate distributions, planar faults and line defects arising in the precipitates. Furthermore, the compositional and microstructural complexity of superalloys results in intricate deformation mechanisms that change considerably depending on the conditions applied.

For example, Fig. 5, highlights the relative deformation differences in tensile tests of the single-crystal Ni-based superalloy CMSX-4 performed at 750 °C with strain rates changing from 10^{-2} s^{-1} to 10^{-6} s^{-1}. The results demonstrate that the yield strength of the alloy is not significantly influenced by the strain rate applied, whereas the ultimate tensile strength is appreciably affected

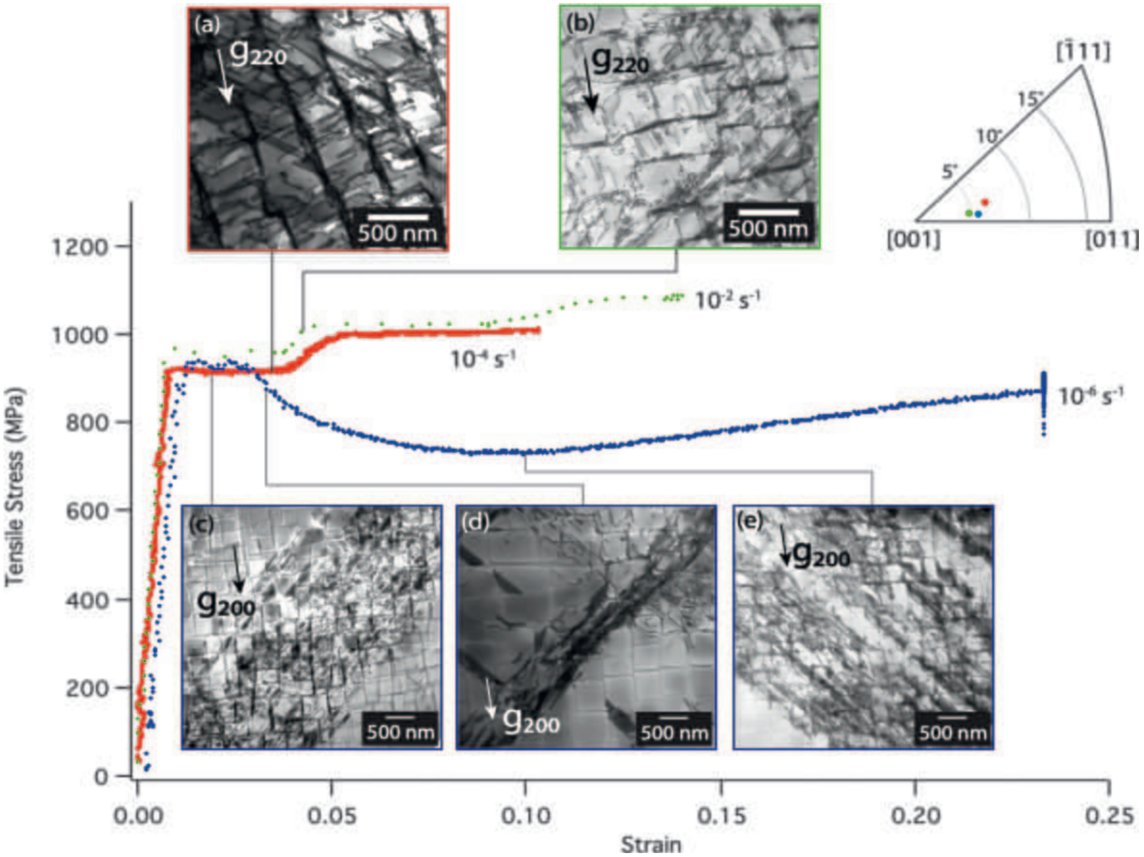

Fig. 5 Tensile stress-strain curves of CMSX-4 deformed at 750 °C at three different strain rates: 10^{-2} s^{-1} (the green curve), 10^{-4} s^{-1} (the red curve) and 10^{-6} s^{-1} (the blue curve). All samples were tested to failure, presented as stress vs. strain. (A) A TEM micrograph with two beam contrast, g = (220) from a tensile specimen tested at a strain rate 10^{-4} s^{-1}, interrupted at 3.3% strain. (B) TEM micrograph with two beam contrast, g = (220) from a tensile specimen tested at a strain rate 10^{-2} s^{-1} interrupted at 4.8% strain. (C–E) TEM micrographs with two beam contrast, g = (200) from a tensile specimen tested at a strain rate 10^{-6} s^{-1}. (C) The deformation structure interrupted at 1.2% strain. (D) The deformation structure interrupted at 2.7% strain. (E) The deformation structure interrupted at 10.2% strain. Inset: an inverse pole figure showing the orientations of the three specimens tested to failure in relation to the [001] tensile direction. Image and caption reproduced with permission from Wang-Koh YM, Messe OMDM, Schwalbe CWM, *et al.* (2023) The effect of strain rate on the tensile deformation behavior of single crystal, Ni-based superalloys. *Metallurgical and Materials Transactions A* 54: 1456–1468. https://doi.org/10.1007/s11661-023-07007-x.

(Wang-Koh, 2018). The corresponding TEM micrographs shown in Fig. 5, illustrate the dislocation response observed at selected key deformation stages, highlighting the differing deformation characteristics that result simply as a function of strain rate.

The tensile test example highlights that the use of these alloys for critical components requires extensive certification testing. Common test conditions and types are summarized in the Metallic Materials Properties Development and Standardization handbook and include physical properties, static properties like tensile, compression yield, shear and ultimate strength as well as fatigue and creep properties.

While the example included in Fig. 5 demonstrates the complicated deformation mechanisms active in superalloys, the principles of deformation in superalloys fall outside the scope of this introductory chapter and the reader is referred to the extensive review work of Reed (2006) and Reed and Rae (2014). Nevertheless, a summary of the key strengthening mechanisms that may be operational in γ'-strengthened superalloys is included in Table 3. The key strengthening mechanisms in superalloys can usually be grouped into the following: intrinsic strength (i.e. Peierls-Nabarro), dislocation hardening (i.e. forest hardening), grain size hardening (i.e. Hall-Petch), solid solution hardening, precipitate and coherency hardening (via antiphase boundaries, stacking faults and interfacial pinning). Depending on the deformation regime the components exposed to these mechanisms require a specific combination of mechanisms to deliver the desired strength. Thus, most alloys are tailored in composition and processing for the specific environments they operate in.

Future industry demands and sustainability considerations

While superalloys continue to serve the materials requirements of several sectors, in particular the aerospace and energy generation sectors, the continual drive toward decarbonization [European Commission, Directorate-General for Mobility and Transport,

Table 3 Summary of strengthening mechanisms in superalloys.

Mechanism	*Notes*	*Key elements*	*Further reading*
Grain size refinement and strengthening	Just as with any class of metallic materials, the grain size offers an effective method through which improvements in strength may be achieved. Care must be taken to ensure balance of mechanical performance, particularly due to notable deterioration of creep life with decreasing grain size. C, B and Zr are used for grain boundary control, often utilizing carbide/boride formation.	C, B and Zr	Hall, 1951; Petch, 1953; Jena and Chaturvedi, 1984
Solid solution strengthening of the γ phase	Utilizing elements with atomic radii that differ to that of the major element, i.e. Ni, Fe or Co, such that the lattice distorts around the substitutional solute atom, creating a strain field that interacts with dislocations and impedes dislocation motion, resulting in an increase in the strength of the material. Interactions occur due to both the lattice misfit and the elastic modulus mismatch.	Co, Cr, Mo, W, Re, Ru	Roth et al., 1997; Fleischer, 1961; Fleischer, 1963
γ' precipitate fraction	Increasing fractions of the γ' phase result in an increase in the strength of the material at higher temperatures. Care must be taken to ensure balance of properties and manufacturability is maintained.	Al, Ti, Ta, Nb, Hf	Beardmore, 1969
γ' precipitate size	γ' precipitate size and the overall distribution of γ' particles has a strong effect on the dislocation interactions observed, which is further complicated by the fault energies of the phase, resulting in plastic deformation regimes dominated by weakly coupled dislocations (for small precipitate sizes and large precipitate separation), strongly coupled dislocations (small precipitate separation, larger size) or Orowan looping (very large and/or incoherent precipitates).	Al, Ti, Ta, Nb, Hf	Raynor and Silcock, 1970; Balikci et al., 2000; Mignanelli et al., 2014; Hisazawa et al., 2017
Order strengthening	The ordered nature of the γ' phase, coupled with its coherency with the γ matrix, leads to complex faults forming within the γ' phase as a result of plastic deformation. These modify the energetics of the structures further affecting dislocation motion. Anti-phase boundaries, complex stacking faults, and, superlattice intrinsic and extrinsic stacking faults, all may form within the γ' phase. A summary of the deformation mechanisms active in the alloy CMSX-4 at different temperature and creep stresses can be found in the cited paper by Barba et al. The relative energies of the faults can be modified to further increase strength and modify mechanical performance. However, while their importance for the mechanical properties of superalloys is undisputed, experimental determination of these fault energies is complicated and an area of continued research.	Al, Ti, Ta, Nb, Hf	Raynor and Silcock, 1970; Barba et al., 2017
Coherency strengthening	Coherent precipitate interfaces can store a significant amount of energy in the form of misfit stress, and thus may act as energy sinks for dislocations, resulting in the formation of interfacial dislocation networks. Depending on the vector of the stored interfacial edge dislocations and glissile mixed dislocations a repulsive force might provide an additional barrier against precipitate shearing but on the other hand might provide the leading dislocation segment needed to form the superdislocation pair required to shear the precipitate phase.		Gerold and Haberkorn, 1966; Gerold and Pham, 1979; Goodfellow et al., 2019

Directorate-General for Research and Innovation, Flightpath 2050: Europe's vision for aviation: maintaining global leadership and serving society's needs, Publications Office, 2011 – see website list: 2] will result in a systemic transformation to the applications of superalloys, the environments in which they operate, as well as both the development of their chemistry and manufacturing. Considering the demands placed upon jet engines alone, several innovations are currently being evaluated to not only reduce greenhouse gas emissions, but also consider the embodied carbon emissions of engines. The discussion included below, albeit brief and non-exhaustive, provides a glimpse into the complexity of decarbonization, and thus the future of superalloys through the effects of the proposed solutions on superalloy design and manufacture.

Future propulsion systems

The aerospace industry is under tremendous pressure to explore ways through which carbon emissions can be reduced, focusing primarily on net-zero and true-zero propulsion concepts.

The leading net-zero technology currently being explored, particularly in the context of long-haul aviation, is the use of sustainable aviation fuels (SAF) in conventional engines. Critically, SAF usage is often also referred to as a "drop-in" solution, as it does not necessitate a fundamental change in the architecture of engines, enabling immediate reductions in emissions. Briefly, SAFs are made from organic waste products such as plant-based cooking oils and have the potential to reduce carbon emissions by

80% across their lifecycle [see website list: 3]. A number of engines from notable manufacturers are already certified to fly with a mixture of up to 50% of SAFs fuels. However, regulatory pressures further complicate the matter, particularly in terms of mandated mixture ratios, that are sought to be imposed on airlines refuelling, for example, in the European Union in the future. A further key challenge of SAFs is their low production rate, with only 100 million liters of SAFs produced in 2021, attracting severe criticism on the sustainability of SAFs as viable, longer-term solutions [see website list: 3]. From the perspective of the superalloys field, the usage of SAFs is a fairly uncomplicated solution due to their "drop-in" nature, as no dramatic changes are expected to the overall conditions encountered within the jet engine, with perhaps only a consideration to the corrosion behavior of the materials. While unambitious for the development of the superalloys field, the usage of SAFs would allow the exploration of embodied carbon considerations to be developed without the added pressures of changing design properties. Thus, this would build confidence within the supply chains, enabling developments in superalloys compositions and manufacture to be realized faster and be adapted quicker for novel true-zero propulsion systems.

A second, perhaps less widely discussed solution that targets both reductions in carbon dioxide as well as nitrogen oxide, is water rich combustion [see website list: 4]. First developed in a military context with engines like the F-402 to increase thrust at take-off, the concept is also able to reduce fuel consumption and nitrogen oxide emissions for water to fuel ratios below 1 in civil engines like the CFM 56-7B, in particular for short haul flights of up to 1000 km distance according to the study by Zahid (2022). Much like in the case of SAFs, water-rich combustion does not fundamentally alter the jet engine and the associated mechanical properties required of the superalloys within the turbine. However, little research is available that explores the effects of water-rich atmospheres on the properties of superalloys. Thus, while the design criteria are unchanged, the intrinsic performance of superalloys in water rich environments remains a critical limitation to the adoption of water-rich combustion.

In the exploration of other fuel alternatives, the use of hydrogen has dominated the discussion. Unlike SAFs and water-rich combustion, the use of hydrogen fuel is not a "drop-in" solution but would necessitate architectural changes to the turbine [see https://www.rolls-royce.com/media/press-releases/2022/18-07-2022-rr-announces-leading-edge-hydrogen-programme-and-developments-in-hybrid.aspx]. Several challenges persist with hydrogen fuels, particularly due to the low fuel energy density, leading to fuel storage considerations. Furthermore, before a hydrogen fuel solution can be considered true-zero, the more fundamental challenge of green hydrogen generation needs to be addressed. Despite these foundational challenges, hydrogen has emerged as the most likely zero-carbon fuel alternative for aviation, posing a considerable development consideration to the field of superalloys. Hydrogen-rich environments are known to lead to embrittlement in several classes of alloys, and γ'-superalloys are no exception, with some alloys being particularly prone to embrittlement at the expected operating temperatures (Dollar and Bernstein, 1988; Chen and Wilcox, 1990; Tarzimoghadam et al., 2017). To date fundamental questions remain, such as how hydrogen interacts with the defects and solutes contained in today's superalloys for cyclic test conditions. Crucially, the inadequate infrastructure for such testing and characterization in hydrogen-rich environments is impacting on the pace at which innovations can be realized in the field. However, new hydrogen research centers currently being planned and built, seek to close this gap within the decade.

While alternative fuel combustion concepts are dominating the discussion for long-haul aviation, technologies such as hydrogen fuel cells and electric propulsion are paving the way for short haul, regional aviation [see https://www.rolls-royce.com/media/press-releases/2022/19-07-2022-easyjet-and-rr-pioneer-hydrogen-engine-combustion-technology-in-h2zero-partnership.aspx, https://www.bayern.de/freistaat-macht-weg-frei-fr-das-wasserstoffzentrum-pfeffenhausen-umsetzungsphase-kann-beginnen/, https://www.mtu.de/technologies/clean-air-engine/flying-fuel-cell/]. These technologies are continuously gaining in interest and pose a range of technological challenges for the materials community, in particular for functional materials. However, the fundamental change in propulsion and the inherent reduction in the operational temperatures of the systems, means indeed that superalloys would no longer be necessary.

Embodied carbon

In addition to net-zero concepts, an area through which the aerospace propulsion industry is seeking to explore immediate impact in terms of emissions, is that of embodied carbon in existing propulsion products, e.g. through systemic changes to manufacturing practices, repair and recyclability technologies and/or usage of raw materials. The realization that the production of engine components today is particularly intensive in terms of emissions and environmental impact has led to several initiatives for the aerospace supply chains, such as the establishment of the International Aerospace Environmental Group (IAEG) [see website list: 9]. Efforts to reduce emissions along the production chain of engine manufacturers are quantifiable according to the emissions Life Cycle Assessment (LCA) outlined in ISO14014, allowing quantitative comparisons of engine parts at critical stages along the production chain [see https://www.iaeg.com]. Methods to reduce the negative environmental impact associated with production include: design for longevity, component repair, recyclability, manufacturing powered by green energy sources and reductions in the manufacturing waste.

One method to reduce part specific production waste is by introducing AM components. AM parts have the potential to save significant amounts of production energy, as the ability to produce near net shape components both decreases material waste, while also leading to a reduction in additional post-processing operations, such as machining, that further reduce the embodied carbon of the technology. In addition, AM offers the ability to build complex designs previously inaccessible with conventional subtractive manufacturing. Thus enabling, for example, complex cooling channels to be embedded within parts, leading to significantly enhanced component longevity. However, despite the numerous potential benefits of AM, a particular challenge that has limited its widespread industrial uptake for critical parts is quality assurance and repeatability. For example, it is critical that the mechanical properties of AM components can be correlated with local microstructures, particularly for complex parts where the process parameters can lead to spatially resolved microstructures, and thus properties. Nevertheless, the improved scientific understanding of microstructural control utilizing AM, coupled with the active integration of control systems, will usher substantial developments over the next decade and support the efforts on the establishment of standards and certification of an increasing number of components manufactured through AM methods.

Aside from the carbon emission reductions that may be realized through careful consideration of the manufacturing practices employed for superalloys and beyond, the stability of the supply of the raw materials needed for superalloys as well as ethical considerations for mining practices are also critical in substantially improving the sustainability of the field. Recycling of superalloys can be seen in light of its positive influence on reducing the environmental impact of mining and the energy intensive refining processes required for the key elements found in superalloys. While currently not widely utilized, recycling, and particularly alloy design with revert considerations in mind, are continuously expanding in interest and the industry is mindful of improving performance. To further understand why recycling practices might become increasingly more relevant in the field, the following section will examine the considerations and factors surrounding the supply of superalloy elements.

Considerations around securing the supply of superalloys

Leaving short term political measures aside, securing the long-term supply of superalloys can be expressed in terms of their element prices, element supply, and reserves. This section examines these three pressure factors briefly in their historical context on the use of the Pt-group metals Re and Ru, that are routinely used in turbine blade materials.

Element cost

Ni-based superalloys consist on average of nine alloying elements beside nickel. Most common are Co, Cr, W, Ta, Al, Mo, Ti, Re and Ru (a Pt-group element). Fig. 6 compares the historic average prices of a number of these key elements (from 1960 to 2019) and includes a red curve that charts the price of Kerosene for a full A380 fuel tank for comparison (note the y-axis is logarithmic). Three key observations can be made from Fig. 6.

Firstly, the price of Re dramatically spiked in the late 2000s and pressured engine manufacturers to develop a new group of alloys that were able to deliver good creep properties with a significantly reduced Re content. Successful alloys developed include the alloy CMSX-8 by Cannon-Muskegon (Wahl, 2012) and the alloy Rene N515 by General Electric (Schafrik, 2016).

Secondly, the prices of Platinum group elements show an upward trend. A number of recently patented nickel-based single crystal superalloys have additions of Ru (a Pt-group element), see alloys for turbine blades section (Koizumi et al., 2004). Despite their enhanced creep properties, see Fig. 4, the alloy prices of these alloys are principally driven by the addition of Ru.

Thirdly, the price of Kerosene for one long-haul flight is equivalent or higher than all element prices (per ton) plotted, with the notable exception of Re and Ru. The addition of about one kilogram of Re to a turbine blade cluster can result in significant net savings in emissions and money. Re-containing blades exhibit significantly higher creep lives (compare Fig. 4 and Table 1), and thus allow the manufacturers to raise the combustion temperature, which in turn results in an efficient fuel burn, thereby providing significant fuel savings [see https://ec.europa.eu/environment/ipp/lca.htm].

Element production rates

Generally, elemental costs are a combination of element production rates and industrial demand. Fig. 7 plots the production rates of key Ni-base superalloy element additions from 1960 to 2018. The following observations can be made.

On average, production rates for superalloy elements have increased gradually and seemingly in line with industrial demand, as production rates largely scale with element prices. Despite the energy intensive extraction methods, the average production rates and prices seem to not be impacted by the volatility and mid-term price dynamics in the energy market. Lastly, the production rates of the two elements, Re and Ru, associated with significant creep life improvements for turbine blades (see earlier section) are very low.

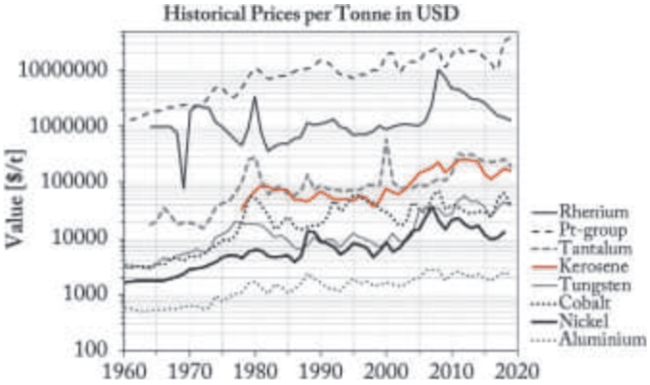

Fig. 6 Historical development of key superalloy element prices compared against the Kerosene price of a full A380 fuel tank. The element prices were extracted from the US National Mining Information Centre of the United States Geological Survey [see https://www.usgs.gov/centers/national-minerals-information-center].

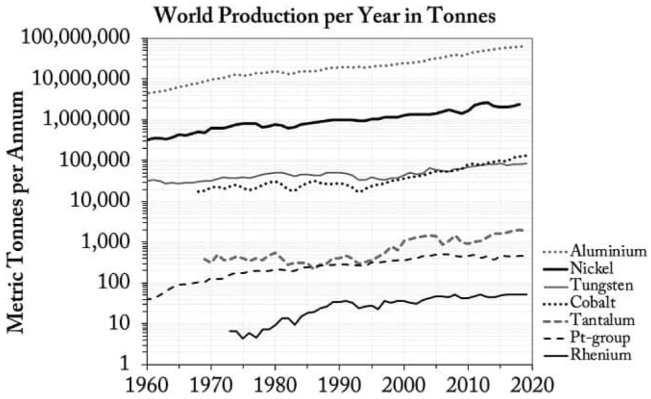

Fig. 7 Historical production rates of key superalloy elements. The element production rates were extracted from the US National Mining Information Centre of the United States Geological Survey [see https://www.usgs.gov/centers/national-minerals-information-center].

The production rate of Re is lower (48.6 t in 2018) than that of all platinum group elements (471 t in 2018). However, when considering only the Pt-group element Ru, an annual global production of 30.5 t was reported in 2018 (cite USGS).

The two alloying elements with highest impact on high temperature creep properties, Re and Ru do not only have low production rates but also originate from very few suppliers worldwide, Fig. 8.

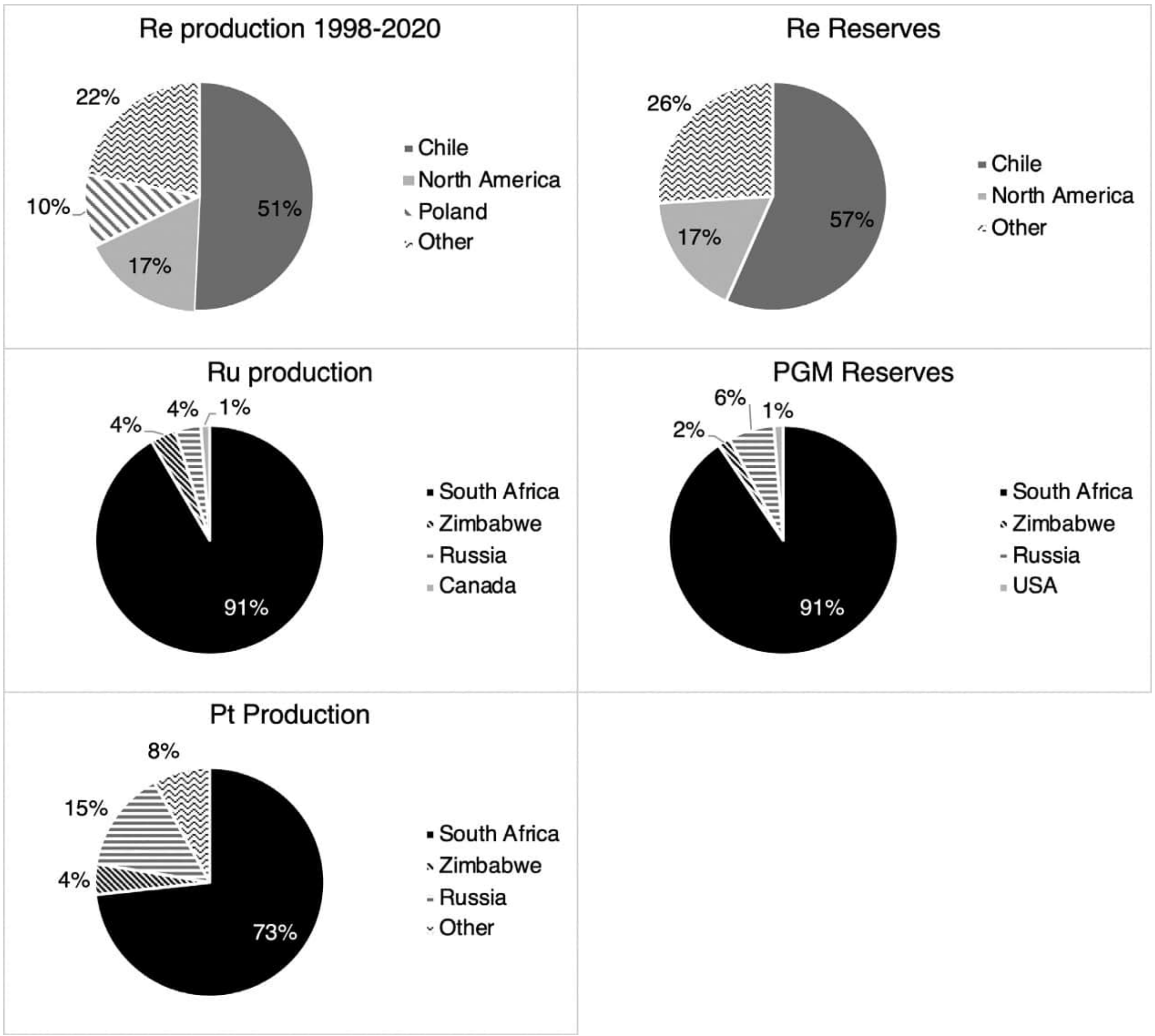

Fig. 8 Regional Re, Ru and Pt production shares as well as Re and Pt Group regional reserve shares. The data was extracted from the US National Mining Information Centre of the United States Geological Survey [see https://www.usgs.gov/centers/national-minerals-information-center].

More than half of all Re production and reserves come from Chile (see Fig. 8). For Ru, this dependence is even more pronounced, with 91% of all production and reserves originating from the UG2 orebody of the Bushveld Complex in the Republic of South Africa. Due to the low primary production rates the supply chain is quite consolidated from ore to refined product.

These dependencies point toward the necessity to efficiently recycle high Re and Ru containing superalloys to ensure their long-term availability to the industry.

Conclusion

This chapter has sought to provide a brief overview of superalloys, their development, applications, physical metallurgy, and future considerations. Much like the development of most materials, superalloys have been born out of necessity, and their study, to this day, is closely aligned to industrial need. Although superalloy development has been heavily influenced by the aerospace industry, the exceptional combination of mechanical performance and environmental stability at high temperatures, have seen superalloys become the material of choice for structural applications in high-temperature and/or highly corrosive environments, with increasing utilization within the energy sector.

The future of superalloys is a future tied closely to energy supply and regulation. Legislation centered around decarbonization is expected to spur a new wave of innovation, both in terms of carbon-free production processes as well as alloy compositions that can deliver carbon-free engines for transportation and energy production. Furthermore, the intricate challenges of sustainability and the stability of supply of key elements, are likely to feature prominently in the design and utilization of superalloys in the future. It remains to be seen where the field of superalloys is headed, particularly for aerospace applications, and what future superalloys may have in net-zero engines is yet unknown. Nevertheless, the unique property balance that superalloys exhibit makes them uniquely suited for applications in the most extreme of environments and most damage critical parts across a number of industries.

Acknowledgments

The authors would like to acknowledge the support of Paul M. Mignanelli, Jingyuan Ma, Cathie M. F. Rae and Jonathan Cormier.

References

Balikci E, Mirshams RA, and Raman A (2000) Tensile strengthening in nickel-base superalloy IN738LC. *Journal of Materials Engineering and Performance* 9.

Barba D, Alabort E, Pedrazzini S, Collins DM, Wilkinson AJ, Bagot PAJ, Moody MP, Atkinson C, Jérusalem A, and Reed RC (2017) On the microtwinning mechanism in a single crystal superalloy. *Acta Materialia* 135: 314–329.

Beardmore P (1969) On the temperature dependence of the flow stress of nickel-base alloys. *Transactions Aime* 245.

Chen PS and Wilcox RC (1990) *Hydrogen Induced Fracture Characteristics of Single Crystal Nickel-Based Superalloys*. NASA-CR 183992. NASA.

Conduit BD, Illston T, Baker S, Duggappa DV, Harding S, Stone HJ, and Conduit GJ (2019) Probabilistic neural network identification of an alloy for direct laser deposition. *Materials & Design* 168.

Crudden DJ and Nemeth A (2019) *A nickel-base alloy*. Patent No. WO 2019/021015 A1.

Dollar M and Bernstein IM (1988) The effect of hydrogen on deformation substructure, flow and fracture in a nickel-base single crystal superalloy. *Acta Metallurgica* 36: 2369–2376.

Eggeler YM, Titus MS, Suzuki A, and Pollock TM (2014) Creep deformation-induced antiphase boundaries in L1 2 -containing single-crystal cobalt-base superalloys. *Acta Materialia* 77: 352–359.

Eggeler YM, Müller J, Titus MS, Suzuki A, Pollock TM, and Spiecker E (2016) Planar defect formation in the γ' phase during high temperature creep in single crystal CoNi-base superalloys. *Acta Materialia* 113: 335–349.

Engeli R, Etter T, and Geiger F (2017) *Ni-base superalloy composition and method for SLM processing such Ni-base superalloy composition*. European Patent Office. Patent No. EP3257956A1.

Fleischer RL (1961) Solution hardening. *Acta Metallurgica* 9: 996–1000.

Fleischer RL (1963) Substitutional solution hardening. *Acta Metallurgica* 11.

Forsik SA, Polar-Rosas A, Wang T, Kernion S, Epler ME, and Zhou N (2018) *Precipitation hardenable cobalt-nickel base superalloy and article made therefrom*. United States patent office. Patent No. US2018/0305792A1.

Forsik SAJ, Zhou N, Wang T, Polar Rosas AO, Dicus AD, Colombo GA, Ricci A, and Epler ME (2020) Recent developments in the design of next generation γ'-strengthened cobalt–nickel superalloys. *Superalloys 2020. The Minerals, Metals & Materials Series*. Cham: Springer. https://doi.org/10.1007/978-3-030-51834-9_83.

Gerold V and Haberkorn H (1966) On the critical resolved shear stress of solid solutions containing coherent precipitates. *Physics of the Solid State* 16: 675–684.

Gerold V and Pham H-M (1979) Precipitation hardening by misfitiing particles and its comparison with experiments. *Scripta Metallurgica* 13: 895–898.

Gessinger GH and Bomford MJ (1974) Powder Metallurgy of Superalloys. *International Metallurgical Reviews* 19: 51–76.

Ghoussoub JN, Klupś P, Dick-Cleland WJB, Rankin KE, Utada S, Bagot PAJ, Mccartney DG, Tang YT, and Reed RC (2022a) A new class of alumina-forming superalloy for 3D printing. *Additive Manufacturing* 52.

Ghoussoub JN, Tang YT, Dick-Cleland WJB, Németh AAN, Gong Y, Mccartney DG, Cocks ACF, and Reed RC (2022b) On the influence of alloy composition on the additive manufacturability of Ni-based superalloys. *Metallurgical and Materials Transactions A* 53: 962–983.

Gibson I, Rosen D, Stucker B, and Khorarani M (2021) *Additive Manufacturing Technologies*. Springer Cham.

Goodfellow AJ, Kelleher J, Jones NG, Dye D, Hardy MC, and Stone HJ (2019) The effect of Mo on load partitioning and microstrain evolution during compression of a series of polycrystalline Ni-Based superalloys. *Acta Materialia* 176: 318–329.

Guédou J-Y, Lautridou JC, and Honnorat Y (1993) N18, Powder metallurgy superalloy for disks: Development and applications. *Journal of Materials Engineering and Performance* 2: 551–556.

Guédou J-Y, Augustins-Lecallier I, Nazé L, Caron P, and Locq D (2008a) Development of a new fatigue and creep resistant PM nickel-base superalloy for disk applications. In: Reed RC, Green KA, Caron P, Gabb TP, Fahrmann MG, Huron ES, and Woodard SA (eds.) *Superalloys 2008*.

Guédou J-Y, Augustins-Lecallier I, Nazé L, Caron P, and Locq D (2008b) Development of a new fatuge and creep resistant PM nickel-base superlaloy for disk applications. In: Reed RC, Green KA, Caron P, Gabb TP, Fahrmann MG, Huron ES, and Woodard SA (eds.) *Superalloys 2008*. TMS.

Hall EO (1951) The deformation and ageing of mild steel: III Discussion and results. *Proceedings of the Physical Scoeity. Section B* 64.

Hardy MC, Zirbel B, Shen G, and Shankar R (2004) Developing damage tolerance and creep resistance in a high strength nickel alloy for disc applications. In: Green KA, Pollock TM, Harada H, Howson TE, Reed RC, Schirra JJ, and Walston S (eds.) *Superalloys 2004*. TMS.

Hardy MC, Dye D, Stone HJ, and Yan HY (2018) *Alloy*. United States patent office. Patent No. US10094004B2.

Hardy MC, Argyrakis C, Kitaguchi HS, Wilson AS, Buckingham RC, Severs K, Yu S, Jackson C, Pickering EJ, Llewelyn SCH, Papadaki C, Christofidou KA, Mignanelli PM, Evans A, Child DJ, Li HY, Jones NG, Rae CMF, Bowen P, and Stone HJ (2020) Developing alloy compostiions for future high temperature disk rotors. In: Tin S, Hardy MC, Clews J, Cormier J, Feng Q, Marcin J, O'Brien C, and Suzuki A (eds.) *Superalloys 2020. The Minerals, Metals & Materials Series*. Cham: Springer. https://doi.org/10.1007/978-3-030-51834-9_2.

Hisazawa H, Terada Y, Adziman F, Crudden D, Collins D, Armstrong D, and Reed R (2017) The effect of Nb/Ti ratio on hardness in high-strength Ni-based superalloys. *Metals* 7.

Huron ES, Bain KR, Mourer DP, and Gabb TP (2008) Development of high temperature capability P/M disk superalloys. In: Reed RC, Green KA, Caron P, Gabb TP, Fahrmann MG, Huron ES, and Woodard SA (eds.) *Superalloys 2008. The Minerals, Metals & Materials Series*. Cham: Springer.

Jena AK and Chaturvedi MC (1984) The role of alloying elements in the design of nickel-base superalloys. *Journal of Materials Science* 19: 3121–3139.

Kawagishi K, Yeh AC, Yokokawa T, Kobayashi T, Koizumi Y, and Harada H (2012) Development of an oxidation-resistance high-strength sixth-generation single-crystal superalloy TMS-238. In: Huron ES, Reed RC, Hardy MC, Mills MJ, Montero RE, Portella PD, and Telesman J (eds.) *, Superalloys 2012: 12th International Symposium on Superalloys*.

Keefe PW, Mancuso SO, and Maurer GE (1992) Effects of heat treatment and chemistry on the long-term phase stability of a high strengthe nickel-based superalloy. In: Antolovich SD, Stusrud RW, Mackay RA, Anton DL, Khan T, Kissinger RD, and Klarstrom DL (eds.) *Superalloys 1992. The Minerals, Metals & Materials Series*. Cham: Springer.

Knop M, Mulvey P, Ismail F, Radecka A, Rahman KM, Lindley TC, Shollock BA, Hardy MC, Moody MP, Martin TL, Bagot PAJ, and Dye D (2014) A new polycrystalline Co-Ni superalloy. *JOM* 66: 2495–2501.

Koizumi Y, Kobayashi T, Yokokawa T, Zhang J, Osawa M, Harada H, Aoki Y, and Arai M (2004) Developmnet of next-generation Ni-base single crystal superalloys. In: Green KA, Pollock TM, Harada H, Howson TE, Reed RC, Schirra JJ, and Walston S (eds.) *Superalloys 2004*. TMS.

Krueger DD, Kissinger RD, Menzies RG, and Wukusick CS (1990) *Fatigue crack growth resistant nickel-base article and alloy and method for making*. United States patent application.

Krueger DD, Kissinger RD, and Menzies RG (1992) Development and introduction of a damage tolerant high temperature Nickel-base disk alloy, René 88DT. In: Antolovich S, Stusrud RW, Mackay RA, Anton DL, Khan T, Kissinger RD, and Klarstrom DL (eds.) *Superalloys 1992. The Minerals, Metals & Materials Series*. Cham: Springer.

Mignanelli PM, Jones NG, Hardy MC, and Stone HJ (2014) The influence of Al:Nb ratio on the microstructure and mechanical response of quaternary Ni–Cr–Al–Nb alloys. *Materials Science and Engineering A* 612: 179–186.

Mourer DP and Bain KR (2013) *Nickel-base alloy, processing therefor, and components formed thereof*. United States patent office. Patent No. US8613810B2.

Murray SP, Pusch KM, Polonsky AT, Torbet CJ, Seward GGE, Zhou N, Forsik SAJ, Nandwana P, Kirka MM, Dehoff RR, Slye WE, and Pollock TM (2020) A defect-resistant Co-Ni superalloy for 3D printing. *Nature Communications* 11: 4975.

Naze L, Maurel V, Eggeler G, Cormier J, and Cailletaud G (2021) *Nickel Base Single Crystals Across Length Scales*. Elsevier.

Neumeier S, Freund LP, and Göken M (2015) Novel wrought γ/γ' cobalt base superalloys with high strength and improved oxidation resistance. *Scripta Materialia* 109: 104–107.

Ning Y, Yao Z, Guo H, Fu MW, Li H, and Xie X (2010) Investigation on hot deformation behavior of P/M Ni-base superalloy FGH96 by using processing maps. *Materials Science and Engineering A* 527: 6794–6799.

Petch NJ (1953) The cleavage strength of polycrystals. *Journal of the Iron and Steel Institute* 174: 25–28.

Pollock TM, Dibbern J, Tsunekane M, Zhu J, and Suzuki A (2010) New Co-based γ-γ' high-temperature alloys. *JOM*: 58–63.

Pollock TM, Clarke AJ, and Babu SS (2020) Design and tailoring of alloys for additive manufacturing. *Metallurgical and Materials Transactions A* 51: 6000–6019.

Powell AM, Bain K, Wessman A, Wei D, Hanlon T, and Mourer D (2016) Advanced supersolves nickel powder disk alloy DOE: Chemistry, properties, phase formations and thermal stability. In: Hardy MC, Huron ES, Glatzel U, Griffin B, Lewis BE, Rae C, Seetharaman V, and Tin S (eds.) *, Superalloys 2016: Proceedings of the 13th International Symposium on Superalloys*.

Quigg RJ (1993) New alloy developments in single crystal and DS alloys. *High Temperature Materials and Processes* 11: 247–254.

Radavich JF and Furrer D (2004) Assessment of Russion P/M superalloy EP741NP. In: Green KA, Pollock TM, Harada H, Howson TE, Reed RC, Schirra JJ, and Walston S (eds.) *Superalloys 2004. The Minerals, Metals & Materials Series*. Cham: Springer.

Ramsperger M and Eichler S (2023) Electron beam based additive manufacturing of alloy 247 for turbine engine application: From research towards industrialisation. *Metallurgical and Materials Transactions A* 54: 1730–1743. https://doi.org/10.1007/s11661-022-06955-0.

Raynor D and Silcock JM (1970) Strengthening mechanisms in γ' -precipitating alloys. *Metal Science Journal* 4: 121–130.

Reed RC (2006) *The Superalloys. Fundamentals and Applications*. Cambridge: Cambridge University Press.

Reed RC and Rae CMF (2014) Physical Metallurgy of the Nickel-Based Superalloys. In: Laughlin DE and Hono K (eds.) *Physical Metallurgy*, Fifth Edition, pp. 2215–2290. Elsevier. ISBN: 9780444537706.

Reynolds PL (2010) *Superalloy compositions, articles, and methods of manufacture*. United States patent office. Patent No. US 2010/0158695 A1.

Roth HA, Davis CL, and Thomson RC (1997) Modeling solid solution strengthening in nickel alloys. *Metallurgical and Materials Transactions A* 28: 1329–1335.

Sato J, Omori T, Oikawa K, Ohnuma I, Kainuma R, and Ishida K (2006) Cobalt-base high-temperature alloys. *Science* 312: 90–91.

Schafrik RE (2016) Materials for a non-steady-state world. *Metallurgical and Materials Transactions A* 47: 2539–2549.

Schafrik R and Sprague R (2008) Superalloy technology - A perspective on critical innovations for turbine engines. *Key Engineering Materials* 380: 113–134.

Sims CT (1984) A history of superalloy metallurgy for superalloy metallurgists. *Superalloys 1984*. TMS.

Sims CT, Stoloff NS, and Hagel WC (1987) *Superalloys Ii*. John Wiley & Sons.

Smith TM, Thompson AC, Gabb TP, Bowman CL, and Kantzos CA (2020) Efficient production of a high-performance dispersion strengthened, multi-principal element alloy. *Scientific Reports* 10: 9663.

Sun Z, Ma Y, Ponge D, Zaefferer S, Jagle EA, Gault B, Rollett AD, and Raabe D (2022) Thermodynamics-guided alloy and process design for additive manufacturing. *Nature Communications* 13: 4361.

Tang YT, Panwisawas C, Ghoussoub JN, Gong Y, Clark JWG, Németh AAN, Mccartney DG, and Reed RC (2021) Alloys-by-design: Application to new superalloys for additive manufacturing. *Acta Materialia* 202: 417–436.

Tao Y, Liu JT, and Zhang YW (2011) Evaluation of mechanical properties of a superalloy disk with a dual microstructure. *Advanced Materials Research* 278: 381–386.

Tarzimoghadam Z, Ponge D, Klöwer J, and Raabe D (2017) Hydrogen-assisted failure in Ni-based superalloy 718 studied under in situ hydrogen charging: The role of localized deformation in crack propagation. *Acta Materialia* 128: 365–374.

Titus MS, Suzuki A, and Pollock TM (2012) Creep and directional coarsening in single crystals of new γ–γ' cobalt-base alloys. *Scripta Materialia* 66: 574–577.

Titus MS, Eggeler YM, Suzuki A, and Pollock TM (2015) Creep-induced planar defects in L1 2-containing Co- and CoNi-base single-crystal superalloys. *Acta Materialia* 82: 530–539.

Tsunekane M, Suzuki A, and Pollock TM (2011) Single-crystal solidification of new Co–Al–W-base alloys. *Intermetallics* 19: 636–643.

Wahl JB (2012) New single crystal superalloys, CMSX-7 and CMSX-8. In: Huron ES, Reed RC, Hardy MC, Mills MJ, Montero RE, Portella PD, and Telesman J (eds.) *, Superalloys 2012: 12th International Symposium on Superalloys*.

Wahl, J. B. & Harris, K. Improved 3rd Generation Single Crystal Superalloy CMSX-4® Plus (SLS) – A study of evolutionary alloy development. https://cannonmuskegon.com/wp-content/uploads/2018/08/Improved-3rd-Generation-Single-Crystal-Superalloy-CMSX-4%C2%AE-Plus-SLS.pdf Cannon Muskegon.

Wang-Koh MY (2018) *Understanding the yield behaviour of single crystal Ni-based superalloys*. Doctor of Philosophy, University of Cambridge.

Wilson AS (2016) Formation and effect of topologically close-packed phases in nickel-base superalloys. *Materials Science and Technology* 33: 1108–1118.

Yan HY, Vorontsov VA, and Dye D (2014) Alloying effects in polycrystalline γ' strengthened Co–Al–W base alloys. *Intermetallics* 48: 44–53.

Yeh AC and Tsao TK (2017) *High-entropy superalloy*. United States patent office. Patent No. US2017/0369970 A1.

Zahid SS (2022) *Impact of Water Injection on Emissions of Nitrogen Oxides from Aircraft Engines*. Master of Science in Aeronautics and Astronautics, Massachusetts Institute of Technology.

Zhou N, Dicus AD, Forsik SA, Wang T, Colombo GA, and Epler ME (2020) Development of a new alumina-forming crack-resistant high-γ' fraction Ni-base superalloy for additive manufacturing. *Superalloys 2020*. *The Minerals, Metals & Materials Series*. Cham: Springer. https://doi.org/10.1007/978-3-030-51834-9_102.

Relevant websites

https://www.usgs.gov/centers/national-minerals-information-center—USGS National Minerals Information Center.

https://data.europa.eu/doi/10.2777/50266—Publications Office of the European Union.

https://www.iata.org/en/programs/environment/sustainable-aviation-fuels/—International Air Transport Association.

https://www.mtu.de/technologies/clean-air-engine/water-enhanced-turbofan/—MTU Aeroengines.

https://www.rolls-royce.com/media/press-releases/2022/18-07-2022-rr-announces-leading-edge-hydrogen-programme-and-developments-in-hybrid.aspx—Rolls-Royce plc.

https://www.rolls-royce.com/media/press-releases/2022/19-07-2022-easyjet-and-rr-pioneer-hydrogen-engine-combustion-technology-in-h2zero-partnership.aspx—Rolls-Royce plc.

https://www.bayern.de/freistaat-macht-weg-frei-fr-das-wasserstoffzentrum-pfeffenhausen-umsetzungsphase-kann-beginnen/—Bayerische Staatsregierung – Bavarian State Government.

https://www.mtu.de/technologies/clean-air-engine/flying-fuel-cell/—MTU Aeroengines.

https://www.airbus.com/en/innovation/zero-emission/electric-flight—Airbus.

https://www.iaeg.com—International Aerospace Environmental Group.

https://ec.europa.eu/environment/ipp/lca.htm—European Commission.

https://www.thenakedscientists.com/articles/science-features/whats-rhenium-doing-jet-engine—The Naked Scientists.

Alloys: Copper☆

J Freudenberger[a,b], **L Tikana**[c], **and WF Hosford**[d], [a]Leibniz IFW Dresden, Department of Metal Physics, Institute for Complex Materials, Dresden, Germany; [b]TU Bergakademie Freiberg, Institute of Materials Science, Freiberg, Germany; [c]Deutsches Kupferinstitut Berufsverband e.V., Düsseldorf, Germany; [d]Deceased

© 2024 Published by Elsevier Ltd.

This is an update of W.F. Hosford, Alloys: Copper, Editor(s): Franco Bassani, Gerald L. Liedl, Peter Wyder, Encyclopedia of Condensed Matter Physics, Elsevier, 2005, Pages 24–45, ISBN 9780123694010, https://doi.org/10.1016/B0-12-369401-9/00533-7.

Introduction 602
Copper production 602
Properties of copper 603
Uses 603
Electrical properties 604
Color 604
Deformation mechanisms 605
Commercial grades of copper 606
Copper alloys 608
High copper alloys 610
Copper silver alloys 611
Beryllium copper 611
Chromium and zirconium copper 612
Copper nickel silicon alloys (nickel-silicon bronze) 612
Oxygen dispersion-strengthened (ODS) copper 613
Commercial alloys 614
Brass 614
Bronze 617
Aluminum bronze 618
Copper nickel alloys 620
Shape memory alloys 621
Property relationships 621
Manufacturing processes 622
Casting 622
Forming 622
Extrusion and forging 623
Powder processing 624
Additive manufacturing 624
Deformation textures 624
Thermal response 625
Recovery 625
Recrystallization 626
Grain growth 630
Annealing textures 630
Anisotropy 631
Corrosion 631
Hydrogen sickness 633
Conclusion 634
References 634
Further reading 634

Abstract

This chapter presents the key properties of copper and copper alloys. This presentation is based on structure-property relationships and comes alongside with insights into production and processing of copper and its alloys. The economically most important copper grades and alloys are presented, and specific measures and problems are highlighted.

☆*Change History*: October 2022. The update was made by J. Freudenberger and L. Tikana. The text of any section was updated, while many figures from the initial version are taken to the updated version. Some figured were deleted and also new figures and tables were added (i.e. Figs. 1, 2b, 4, 17, 18, 19, 23b, 24, 28, 32, 36, 43; Tabs. 3, 4, 6, 7, 9). New passages were added to the chapter (Cu-Ag alloys, Cr- and Zr-copper allyos, Cu-Ni-Si alloys, ODS alloys, property relationships, manufacturing processes, additive manufacturing).

Key points

- Copper is soft, malleable, ductile, and has an excellent conductor of heat and electricity, and it resists corrosion.
- The excellent conductivity of copper and most of its alloys is the key factor determining the area of application of the alloys.
- Brass and bronze are the most common copper alloys, though many more are in use.
- In terms of industrial use, copper ranks third, behind iron and aluminum, while copper is a 100% recyclable metal.
- The properties of copper and its alloys are driven by structural features being tuned by processing conditions.

Introduction

Copper is one of the first metals known to mankind. Besides natural materials, copper was the only metal used for more than 10.000 years to particularly make tools. The oldest water pipe made from copper with a length of approx. 400 m was dated back to 2500 BCE. Even before, objects were made from copper, particularly tools, household utensils, jewelry and weapons. After copper had been shaped by simple hammering at the beginning of its discovery, copper was already melted and cast into molds at this time. The trade in copper and objects made from it can be proven at this time by similar finds. All this makes copper the metal of mankind, since it is strongly bound to the intellectual and intercultural development of mankind as well as boosters the modern development of industry and society. Meanwhile the applications of copper and its alloys broadened, nevertheless, its use in the supply of water is still an important application due to its forming and anti-bacterial properties. In modern life copper is mainly used because of its excellent thermal and electrical conductivity in electronic and electrical devices. This chapter provides an introduction to the processing chain of copper from ore to metal alongside with the description of structure-property relationships of the most relevant copper alloys at presence.

Copper production

Copper is one of the few metals that are found in their native state. For this reason, Copper is known to ancient civilizations and is applied for over 10,000 years. This makes it the first and longest used metal, as even today copper is used in almost all areas of modern life. Even though copper occurs in nature, traces of copper can be found virtually in all rocks. In fact, the copper content in the earth's crust is about 0.006%, placing copper in 23rd place of the most frequent elements. Due to its high affinity for sulfur, copper is most often found in sulfidic form. Although the sulfide ores have a significantly lower copper content than the minerals, they are mainly used for copper production as they occur in larger deposits. Most copper ores contain 0.5% Cu or less, iron being the principal metallic impurity. The ores are ground to a fine powder and concentrated (normally by floatation) to 20–25% Cu. This concentrate is melted as a matte of mixed Cu and Fe sulfides containing up to 60% Cu. The matte is oxidized to remove the iron as an oxide and burn off the sulfur. The product is called blister copper which contains 98.5% Cu. Blister copper is fire refined to a tough-pitch (99.5% Cu). It is, then electrolytically refined to 99.99% Cu. Au, Ag, and Pt metals are recovered from slime.

In the period 2010–2020, 207 Mt. of copper have been mined, while reserves have grown to 870 Mt. In 2021 the global copper mine production reached 21 Mt. The largest producer of mined copper is Chile (5.6 Mt). Refinery production in 2021 reached 24 Mt., while China is the largest producer thereof (10 Mt). The total refined copper number encompasses presently, recycled copper from copper contained in end-of-life products contributes to about 1/3 of the total copper supply (ICSG, 2021). Fig. 1 shows the global distribution and major countries of copper production in 2021.

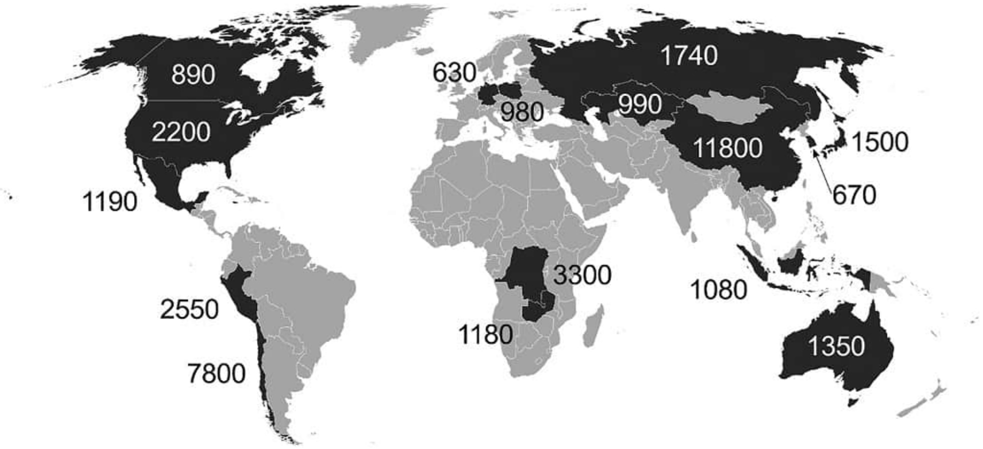

Fig. 1 Most relevant world mine and refinery production of copper, given in kt, in 2021 (USGS, 2022).

Properties of copper

Copper is used mainly because of its high thermal and electrical conductivity. In fact, it shows the second highest values upon all metals at room temperature, just silver has a slightly higher conductivity at a significant higher price. Accordingly, about 2/3 of pure and low alloyed copper is used in electrical industry. Besides this, copper has a high ductility easing forming processes and good corrosion resistance as well as anti-microbial effect. The reddish color is a unique feature of copper. With the exception of gold and copper other metals appear silvery in color.

The physical properties of copper are listed in Table 1.

Uses

Copper and copper-based alloys are used in a variety of applications that are necessary for a reasonable standard of living. Its continuous production and use are essential for society's development. How society exploits and uses its resources, while ensuring that tomorrow's needs are not compromised, is an important factor in ensuring society's sustainable development. Fig. 2a shows the principal uses of copper per properties. Its excellent electrical conductivity accounts for most of its use, principally as wire. Corrosion resistance, thermal conductivity, formability, and unique color account for almost the rest of the consumption of copper. Copper is

Table 1 Physical properties of copper.

Physical property	*Value*
Atomic number	29
Atomic mass	63.546 amu
Stable isotopes	^{63}Cu 69%, ^{65}Cu 31% All other isotopes have very short half-lives (<13 h)
Crystal structure	f.c.c.
Space group	225, $Fm\overline{3}m$
Lattice parameter (25 °C)	0.36149 nm
Density (20 °C)	8960 kg m^{-3}
Electrical conductivity	$59.77 \times 10^6\ \Omega^{-1}\ \text{m}^{-1} = 103.06$ IACS
Melting point	1357.77 K
Heat of fusion	206 J kg^{-1}
Volume change on solidification[a]	4.92%
Boiling point	2835 K
Heat of vaporization	4721 J kg^{-1}
Linear thermal expansion coefficient (20 °C)	16.5 µm mK^{-1}
Thermal conductivity (0 °C)	400 W mK^{-1}
Specific heat (20 °C)	384.4 J kg^{-1} K^{-1}
Elastic stiffness constant (20 °C)	
c_{11} [b]	169.1 GPa
c_{12} [b]	122.2 GPa
c_{44} [b]	75.42 GPa
Young's modulus (20 °C)	
Polycrystal	130 GPa
⟨1 1 1⟩ direction	191.2 GPa
⟨1 1 0⟩ direction	130.3 GPa
⟨1 0 0⟩ direction	66.6 GPa
Shear modulus (20 °C)	
Polycrystal	48 GPa
Poisson's ration	0.34
Energy of vacancies[c]	1944.3 J kg^{-1}
High-angle grain-boundary energy[d]	625 mJ m^{-2}
Stacking fault energy[e]	45 mJ m^{-2}

All data provided by Wolfram Research (2007), except where noted.

[a] ASM (1979).

[b] Ledbetter and Naimon (1974).

[c] Bourassa and Lengeler (1976).

[d] Murr (1975).

[e] Branicio et al. (2013).

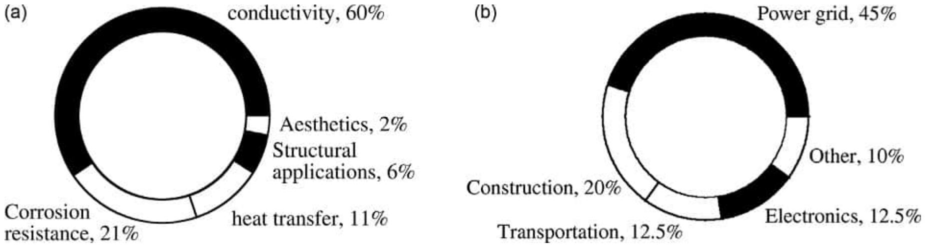

Fig. 2 (a) Uses of copper per key properties (data taken from ASM, 2001). (b) Uses of copper per market sector (Copperalliance, 2022).

used in computers, electrical appliances, gears, bearings turbine blades, cookware, generators, motors, transformers, locks and keys, just some of the none-exhaustive list of end-use products exploiting copper's advantages. Fig. 2b shows the share of copper uses per market sectors.

Electrical properties

In order to ease the comparison of the electrical conductivity, the International Annealed Copper Standard (IACS) was established in 1914 by the US Department of Commerce. The standard was empirically derived upon the electrical conductivity of commercially available copper. This conductivity is used as benchmark value of 100% IACS. As this definition was not made for copper of highest purity, it should not be surprising that these grades come up with an electrical conductivity of 104% according to the IACS standard. This shows that the electrical conductivity strongly depends on the impurities within the material.

These impurities depend on the refinery process. However, it appears not relevant to the applicant which process has been used, but the properties of the copper are. Therefore, copper is graded into oxygen-containing copper, deoxidized copper and oxygen-free copper. If oxygen remains in the copper, it is sensitive to hydrogen sickness. In consequence the metal must be deoxidized, which is commonly performed with the addition of phosphorous. The excess in phosphorous is incorporated into the matrix causing a severe drop in conductivity. The highest conductivity is observed in non-deoxidized oxygen-free copper.

All impurities raise the electrical resistivity of copper. At low concentrations, the increase is proportional to the concentration of the impurity. In general, the effect of solutes in raising the resistivity is greater for large differences between the atomic diameter of the solute and that of copper as shown in Fig. 3. Also solutes of high valency (P, Si, and As) have a greater effect on the resistivity than those of low valency such as Ag, Au, and Cd.

Color

One outstanding characteristic of copper is that the metal shows a distinctive red-orange color. This is since copper has poor reflectivity in the ultraviolet range of the spectrum, whereas the reflectance in the infrared range is very good. In contrast to this, the reflectance of silver is almost constant and very good in the whole range of visible light. The dependence of reflectivity on the

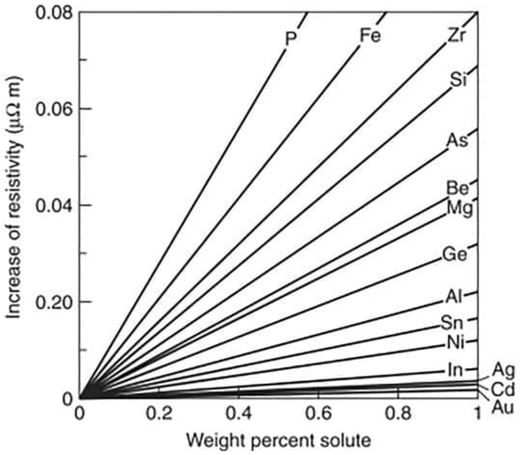

Fig. 3 All impurities increase the resistivity of copper (ASM, 2001).

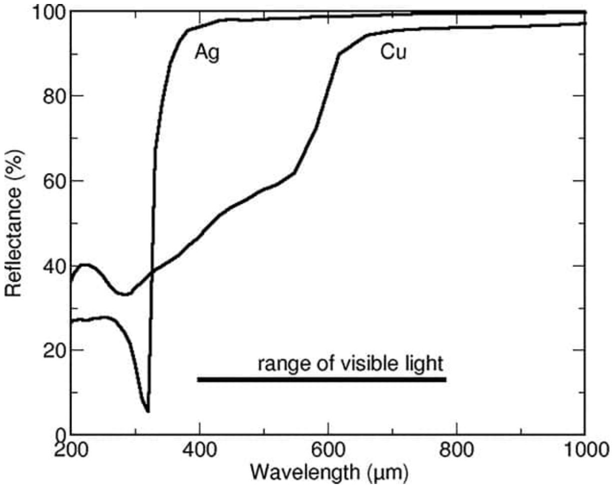

Fig. 4 The color of copper is a result of the dependence of reflectivity on wavelength. Data from Refractiveindex (2022) *Optical Constants of the Elements*. Available at: https://refractiveindex.info (Accessed: 18. April 2022).

wavelength of copper is shown in Fig. 4 in comparison to that of silver (Refractiveindex, 2022). Metals like copper (and gold) have a color because they have an adequate external electronic configuration $s^1d^{10} \leftrightarrow s^2d^9$ and the sublevels s and d are close enough to allow the mentioned transition to occur.

Deformation mechanisms

Copper is deformed predominantly by dislocation glide at room temperature. The slip system in copper, as in all other metals with a face centered cubic symmetry of the unit cell is {1 1 1} < 1 1 0>, while the critical shear stress for slip amounts to approx. 3–4 MPa. Failure of copper is ductile. Deformation may also be driven by other mechanisms upon altering surrounding conditions. Mechanical twinning occurs as soon as the critical stress for twinning is achieved, i.e., approx. 140 MPa. As in other materials with face centered cubic symmetry of the unit cell the twin system is {1 1 1} < 1 1 2>. This deformation mechanism is activated, e.g., at sufficient strain hardening, small grain sizes in the ultra-fine grained region, or at low temperatures, when dynamic recovery is suppressed. A grain-size in the nanometer region activates grain rotation and grain-boundary sliding as special deformation mechanisms. Ultra-fine grained copper exhibits high strengths and low ductility, and their ductility decreased with decreasing grain sizes, which limited their applications. The limited uniform deformation results from the restricted dislocation activities in the ultra-fine grains and localized deformation. A dominant surface feature of the localized deformation is the appearance of shear bands. Twinned copper shows an intense intrinsic size effect, i.e., thinner twin spacing causes larger strength. When the temperature is lowered below room temperature, the extent of work hardening increases as indicated in Fig. 5 (Blewitt et al., 1955).

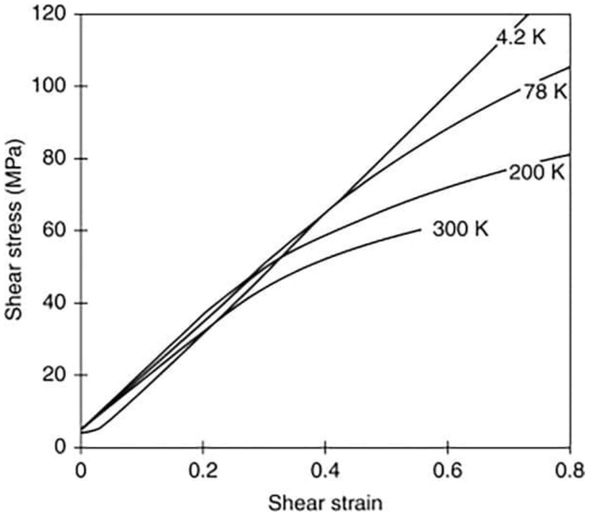

Fig. 5 Tensile stress–strain curves for copper crystals at temperatures down to 4.2 K. Adapted from Blewitt TH, Coltman RR, and Redman JK (1955) Proceedings of the Conference on Defects in Crystalline Solids, Bristol, p. 369. London: Physical Society.

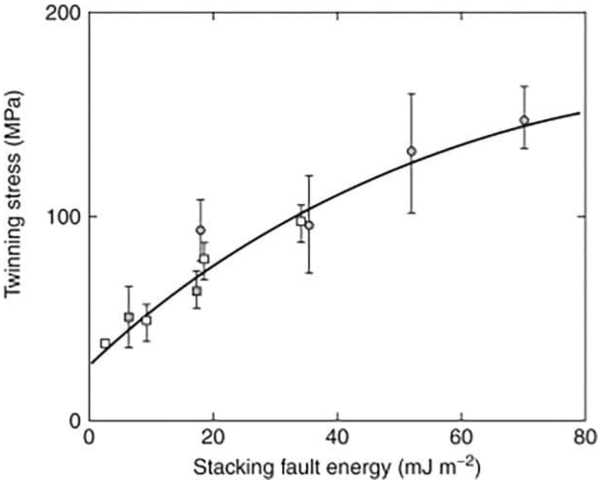

Fig. 6 The critical shear stress for twinning decreases with decreasing stacking fault energy (●, Cu–Zn; □, Cu–Al; ■, Cu-Ge). Adapted from Venables J.A. (1965) In: Hirth, Rogers (eds.) *Deformation Twinning*, *Proceedings of the Metallurgical Society Conference*, vol. 25, Reed-Hill, R.E., et al. AIME Physical Metallurgy Committee.

While the formation of mechanical twins is favored at low temperatures in copper it is also affected by the crystal orientation as well as the stacking fault energy. There is clear evidence that in metals with a high stacking fault energy, mechanical twinning virtually does not occur, while materials with a low stacking fault energy twin easily under a mechanic load. In copper alloys, twinning depends on the stacking fault energy. The critical resolved-shear stress for twinning is lowered by solid solutions that reduce the stacking fault energy (see Fig. 6) (Venables, 1965). It is significant that copper is not embrittled at low temperatures and does not fracture by cleavage, because of which copper finds use in cryogenic equipment.

Commercial grades of copper

There are several commercial grades of copper. The principal use of oxygen-free copper (C10100) with a minimum of 99.99% Cu is for wire. Also, chemical, or physical vapor deposition techniques, used in microelectronics, rely on highest purity. Fire-refined tough-pitch copper (C12500) is containing between 0.02% and 0.05% oxygen in the form of Cu_2O and ~0.5% other elements. Electrolytic tough-pitch copper (C11000) contains up to 0,04% oxygen. The copper–oxygen phase diagram is shown in Fig. 7 (ASM, 1973). There is a eutectic at 0.38% oxygen and 1066 °C. Fig. 8 is a typical microstructure of cast tough-pitch copper showing primary copper dendrites surrounded by a copper–copper oxide eutectic.

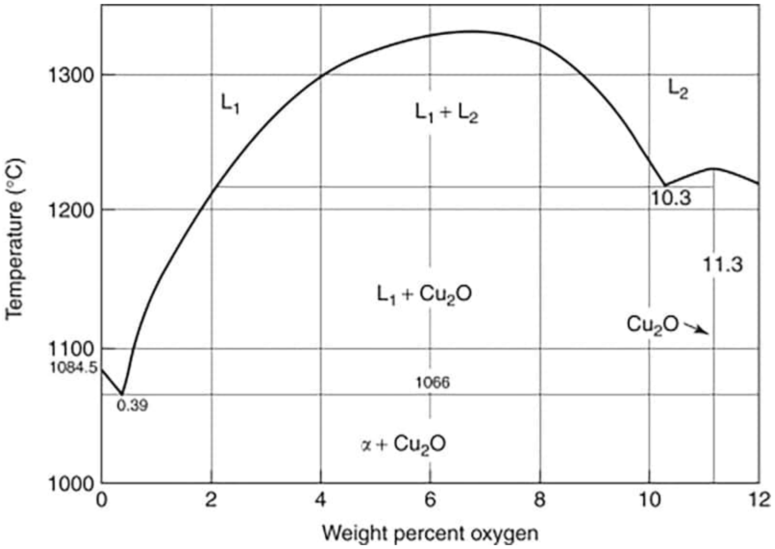

Fig. 7 The copper–oxygen phase diagram. Adapted from ASM (1973) *ASM Metals Handbook*, 8th edn., vol. VIII. Materials Park, OH: ASM.

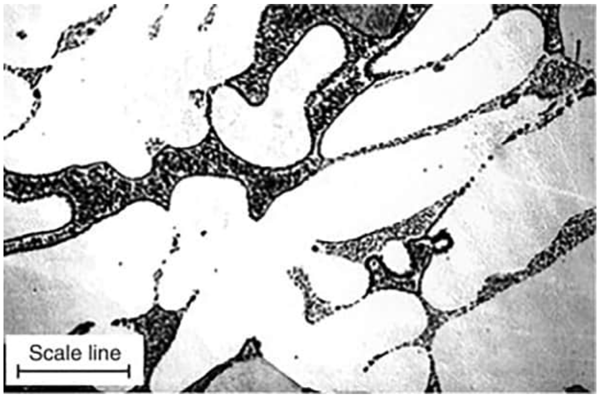

Fig. 8 The microstructure of cast tough pitch copper. The scale line is ~125 μm. Note the primary copper dendrites and the Cu–Cu_2O eutectic. Reproduced with permission of the Copper Development Association Inc.

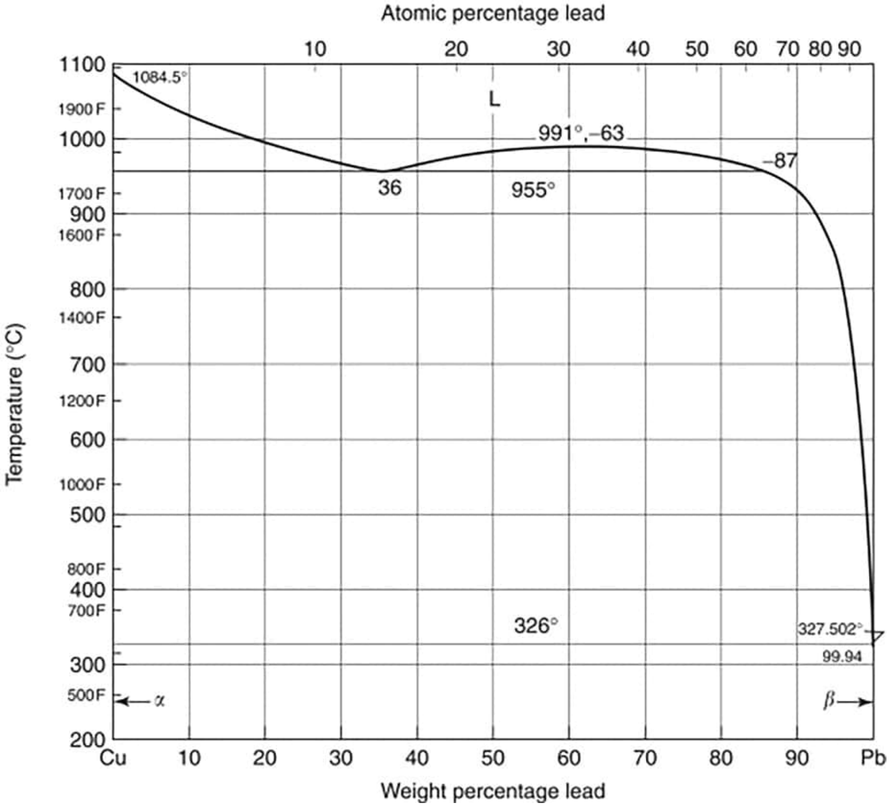

Fig. 9 The copper–lead phase diagram. Data from ASM (1973) *ASM Metals Handbook*, 8th edn., vol. VIII. Materials Park, OH: ASM.

Often tellurium (~0.5%) or sulfur (~0.5%) is added to copper to promote free machining. As oxygen presents in copper can be detrimental when processed at high temperature in hydrogen atmosphere (risk of hydrogen disease), several deoxidized, frequently done with phosphorus, commercial copper classes exist. Deoxidation leaves residual phosphorus in solid solution, which characterizes the class (0.015–0.04% for C12200). This lowers the conductivity to below that of oxygen-free and even tough pitch copper. If the deoxidized copper is to be used for conductivity reason, the residual phosphorus in solid solution is less than 0.01% as is the case for the deoxidized class C10300 with 0.001–0.005%P.

Lead is also added (up to 1%) to copper to form free machining characteristics. However, there are regulatory restrictions for the use of lead as alloying element. Lead is virtually insoluble in copper as shown by the copper–lead phase diagram (see Fig. 9). Lead particles appear as a separate phase in the grain boundaries (see Fig. 10).

Bismuth has a similar effect on the machinability like lead but is a very detrimental impurity. It completely wets the grain boundaries and because it is brittle, its presence renders copper brittle. It must be kept <0.003%.

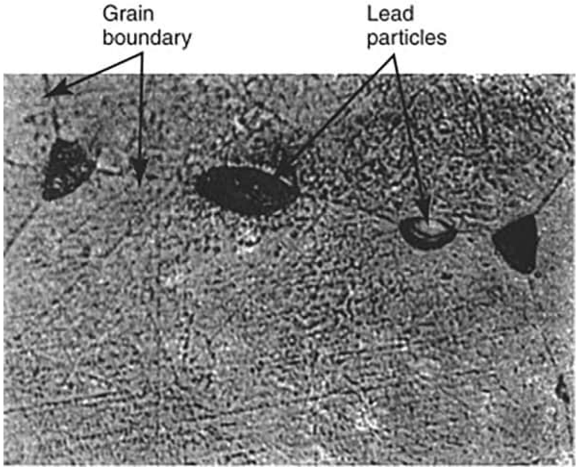

Fig. 10 Lead appears as a separate phase in copper alloys. Adapted from ASM (2001) *Copper and Copper Alloys*, *ASM Speciality Handbook*. ASM: Materials Park, OH.

Copper alloys

Copper is too soft for structural applications. Its strength is markedly increased by alloying. For dilute substitutional solutions (see Fig. 11) (Linde et al., 1950), the yield strength increases in proportion to the solute concentration. The rate of this increase is proportional to the 4/3 power of a misfit parameter defined as $\varepsilon = (da/a)/dc$, where da/a is the fractional change in the lattice parameter (a) with concentration c, expressed as an atomic fraction of solutes,

$$\Delta\tau/\Delta c = CG\varepsilon^{\frac{4}{3}}$$

where G is the shear modulus of copper and C is a constant. The misfit, ϵ, is the fractional difference of atomic diameters of copper and solute. Fig. 12 shows the misfits for several solutes. On an atomic basis Sb, Sn, and In are the most potent hardeners (Linde and Edwardson, 1954).

The stacking fault energy has a strong influence on the active deformation mode as well as on the capability of grain refinement, thus hardening. It is well promoted, that lowering the stacking fault energy (as well as lowering the temperature) follows the promotion of deformation twinning via dislocation slip. Although different measurements of the stacking fault energy of pure copper have ranges from 40 to 169 mJ m^{-2}, the best estimate is probably 45 mJ m^{-2}. Zinc, tin, and aluminum form solid solutions that lower the stacking fault energy to <5 mJ m^{-2} at high concentrations as shown in Fig. 13. A lower stacking fault energy leads to more strain hardening. The value of n in the power-law equation,

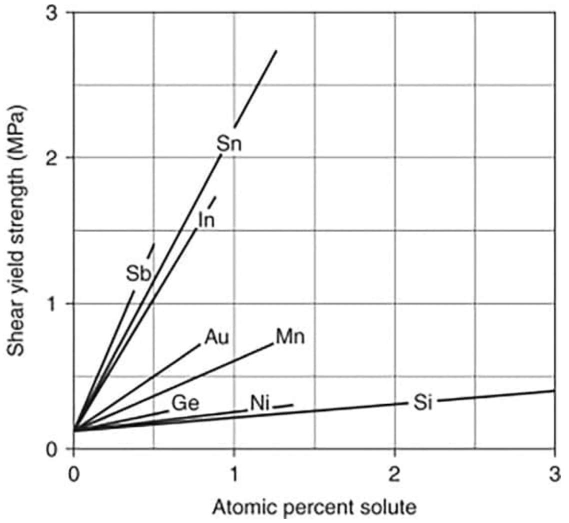

Fig. 11 Effect of solute concentration on shear yield strength of dilute copper base alloys. Note that the strength is proportional to concentration. Data from Linde JO, Lindell BO, and Stade CH (1950) Investigation of the critical shear stress for single crystals of metallic solid solutions 1. Arkiv für Fysik 2, 89.

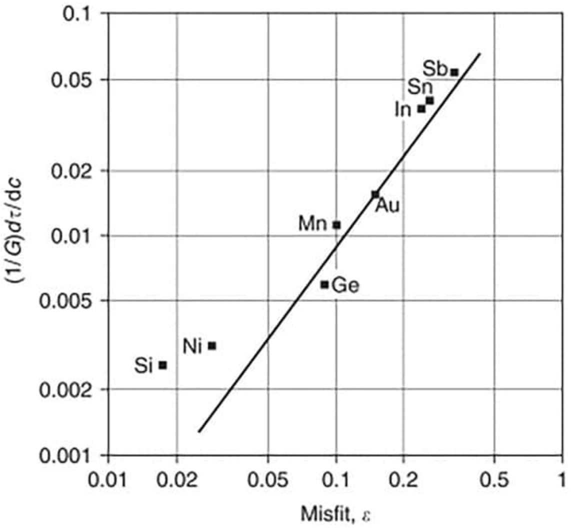

Fig. 12 The effect of the atomic misfit on the strengthening effect of the solute. Data from Linde JO and Edwardson S (1954) Investigation of the critical shear stress for single crystals of metallic solid solutions 2. Arkiv für Fysik 8, 511.

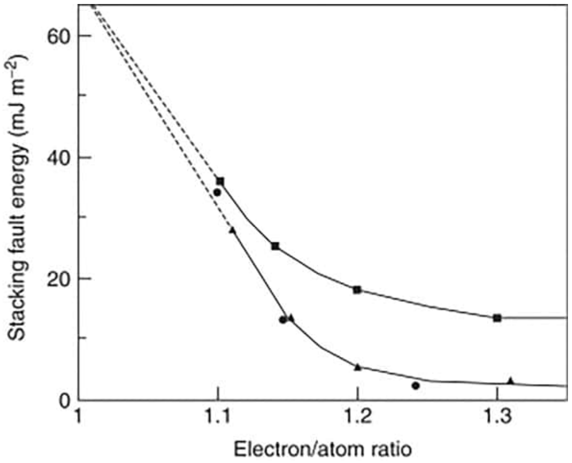

Fig. 13 The stacking fault energy of alloys (▪Cu–Zn, ▲Cu–Al, ● Cu-Ge). Adapted from Venables J.A. (1965) In: Hirth, Rogers (eds.) *Deformation Twinning, Proceedings of the Metallurgical Society Conference*, vol. 25, Reed-Hill, R.E., et al. AIME Physical Metallurgy Committee.

$$\sigma = K\varepsilon^n$$

increases from ~0.4 for pure copper to ~0.6 or 0.65 at 35% Zn. The greater strain hardening raises the tensile strength as shown in Fig. 14.

One reason for the hardening low stacking fault alloys is seen in the formation of deformation twins yielding a smaller grain size. Finer grain size also increases strength. The grain-size (D) dependence of the yield strength (σ_Y) follows the Hall–Petch relation

$$\sigma_Y = \sigma_0 + \frac{K_{HP}}{\sqrt{D}}$$

Here K_{HP} is the Hall-Petch constant. Besides the given solid-solution and grain size strengthening, copper alloys are also hardened by precipitation hardening, oxide dispersion strengthening and work hardening as discussed below.

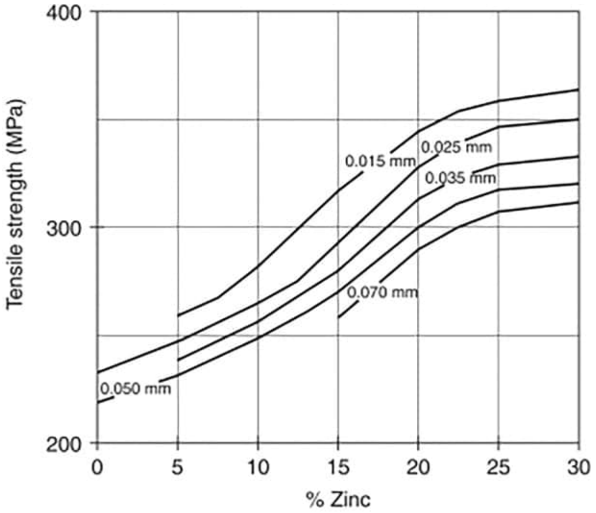

Fig. 14 The effect of zinc content on increasing the tensile strength. Finer grain size has a similar effect. Adapted from ASM (2001) *Copper and Copper Alloys*, *ASM Speciality Handbook*. Materials Park, OH: ASM.

High copper alloys

In some cases, however, the individual properties of pure copper may not be adequate for a particular application. Relatively small amounts of other elements can significantly improve one or more properties of pure copper, such as its strength, softening temperature and machinability, while other properties, such as electrical and thermal conductivity and workability are kept as high and good as possible. Alloying elements include beryllium, chromium, cobalt, iron, magnesium, manganese, nickel, phosphorus, silicon, silver, sulfur, tellurium, tin, titanium, zinc, zirconium, and can be used either individually or in combination. A number of these alloying elements, such as manganese and silicon, cause a relatively strong decrease in conductivity (Fig. 15), but they also improve the material's high-temperature stability, its suitability for welding and its resistance to corrosion. The extent to which the material's properties are modified also depends strongly on the quantity of alloying elements added. In most of these alloys the concentrations of the individual alloying elements remain below 1–2% and the cumulative concentration is under 5%. There are clusters of alloyed copper with their property range (see Fig. 32).

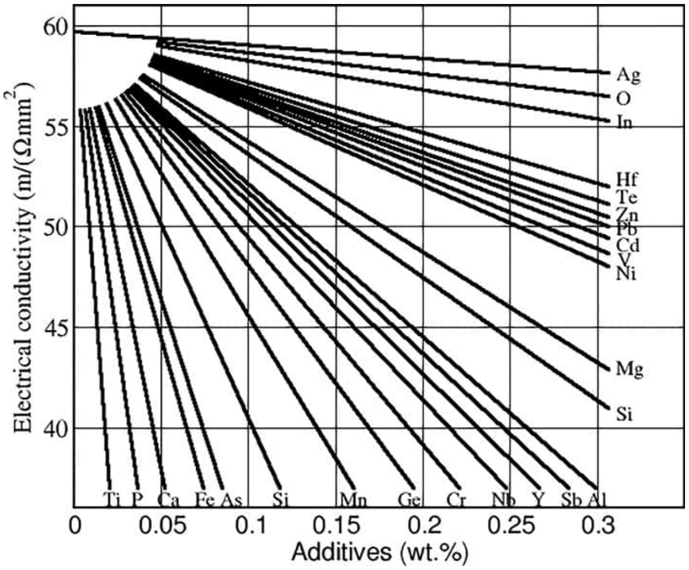

Fig. 15 Influence of alloying elements on the conductivity of copper (DKI, 2018). From Pawlek F., Reichel K. (1956) Der Einfluss von Verunreinigungen auf die elektrische Leitfähigkeit von Kupfer. *Zeitschrift für Metallkunde* 47: 347–351.

The response of these materials to changes in temperature is striking, as no embrittlement is observed even down to temperatures as low as −200 °C.

This class of materials, called in UNS "*high copper alloys*" do not fall into any other copper alloy group. It is essentially composed of a number of non-age-hardenable and age-hardenable alloys. Non-precipitation-hardenable alloys are those whose strength can only be improved by cold working. The strength of precipitation-hardenable alloys on the other hand can be improved by cold working and, in particular, by suitable precipitation heat treatment.

The age-hardening behavior is based on the fact that the solubility of the mentioned alloying elements in Cu decreases with decreasing temperature. On this basis, a heat treatment is applied that leads to age hardening. A high-temperature solution treatment is followed by a low-temperature aging treatment. This serves to precipitate a dispersion of small metastable or stable particles, which give rise to hardening by several hardening mechanisms that depend in detail on the microstructural, chemical, crystallographic and mechanical properties of the precipitated particles.

Copper silver alloys

Commercially available copper-silver alloys contain less than 1% Ag, between 0.03% and 0.12% Ag and exhibit a single-phase microstructure. Though they are not aged-hardenable. These silver concentrations already cause an increase of the softening temperatures vis-à-vis pure copper. Different classes of copper-silver alloys exist, subdivided in oxygen-containing, oxygen-free and phosphorous deoxidized containing varying concentrations of silver.

The copper-rich f.c.c phase has a maximum solubility of approx. 8% silver at the eutectic temperature of 779 °C, while the solubility vanishes at room temperature. Hence, copper-silver alloys with concentrations above approx. 2% are age-hardenable. With well-tuned precipitates, copper alloys with 7% silver and traces of Zr exhibit an ultimate tensile strength of up to 1.4 GPa while having an excellent conductivity approx. 80% IACS.

One of the benefits of copper-silver alloys compared to pure copper is that the hardness achieved through cold working the material can be maintained even at relatively high temperatures. The softening temperature of CuAg0.10 is around 300 °C. A further outstanding property of these materials is their relatively high creep rupture strength, which is of major significance in applications subjected to mechanical stress at elevated temperatures.

The main applications of copper-silver alloys are inter alia high-strength catenary wires (for high-speed trains); commutator segments and rotor windings in electric motors; transformers and generators that are subjected to high-temperature stresses.

Beryllium copper

Copper alloys containing 1.8–2.0% Be and 0.2–0.8% Ni + Co are precipitation-hardenable. The alloy C172000 is solution treated at ~800 °C and rapidly cooled. The precipitation is done between 300 °C and 400 °C. Fig. 16 shows the copper-rich end of the Cu-Be phase diagram. Precipitation hardening produces very high strengths. Even higher strengths can be achieved by cold working after the solution treatment and before precipitation as shown in Table 2. The principal drawback is that the toxicity of beryllium is an extreme danger in preparing this alloy.

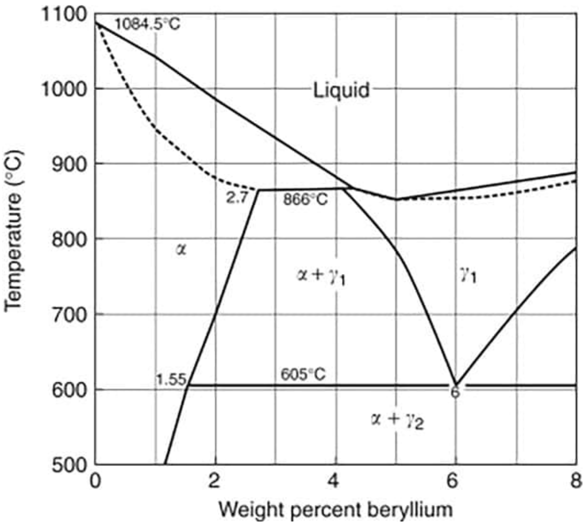

Fig. 16 The copper–beryllium phase diagram. Adapted from ASM (1973) *ASM Metals Handbook*, 8th edn., vol. VIII. Materials Park, OH: ASM.

Table 2 Strength of beryllium copper sheet (C17200).

Condition	*Yield strength (MPa)*	*Tensile strength (MPa)*
Annealed	250	465
1/4H	485	570
1/2H	555	605
H	690	730
Annealed & HT	1060	1260
1/4H & HT	1125	1290
1/2H & HT	1180	1325
H & HT	1195	1360

HT indicates age-hardening treatment. Solution treatments were done prior to work hardening.
Data from ASM (2001) *Copper and Copper Alloys*, *ASM Speciality Handbook.* ASM: Materials Park, OH.

Chromium and zirconium copper

Chromium copper (C18050) contains up to 1% Cr. The maximum solubility of chromium in copper is only 0.65% at the eutectic temperature of 1075 °C and this very low value decreases significantly with decreasing temperature. At 400 °C, the solubility of chromium in copper falls to below 0.03%. As a result of this temperature solubility dependence, the chromium can be precipitated and these alloys can therefore be age-hardened. Fully heat-treated chromium copper can reach a conductivity of 85% IACS.

Zirconium copper (C15000) contains 0.13–0.20% Zr. It can also be heat treated to yield strengths of 400 MPa while retaining a conductivity of 84% IACS.

The advantages of CuZr are its high softening temperature and creep rupture strength and its notch strength insensitivity at elevated temperatures. A disadvantage of copper-zirconium alloys is that they exhibit only minimal precipitation hardening. CuCr, in contrast, exhibits good strength parameters in its precipitation-hardened state. However, the relatively high notch sensitivity of CuCr at higher temperatures can be a disadvantage in certain situations. The beneficial properties of each of CuCr and CuZr can be usefully combined in the ternary copper-chromium-zirconium (CuCrZr) alloy system. The characteristics of CuCrZr are:

- high strength at room temperature
- high softening temperature
- improved creep rupture strength

even at elevated temperatures (Fig. 17).

Copper nickel silicon alloys (nickel-silicon bronze)

The high solubility of silicon in copper can be significantly reduced by the addition of nickel and the solubility decreases further with falling temperature. The temperature-dependent solubility of the intermetallic compounds Ni_2Si, Ni_5Si_2 (or $Ni_{31}Si_{12}$) means that copper-nickel-silicon alloys can be age-hardened. The crystal structures of the silicides are semi-coherent or incoherent with the matrix.

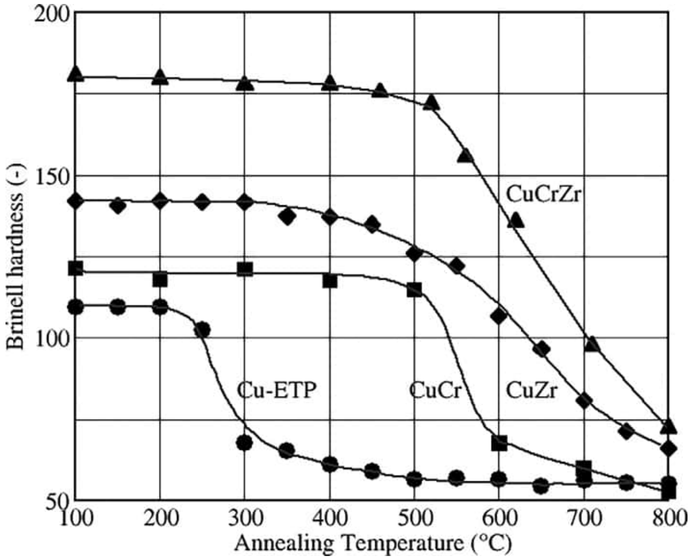

Fig. 17 Resistance to tempering of Cu compared to CuCr, CuZr and CuCrZr, all samples were cold worked before tempering (DKI, 2018).

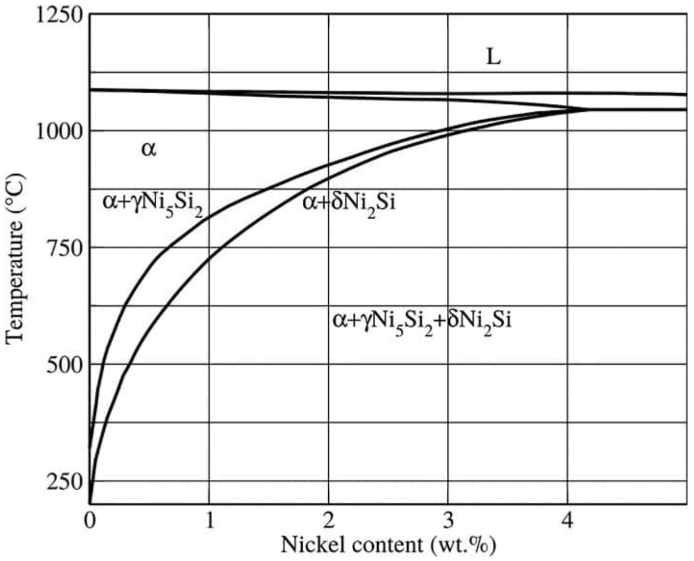

Fig. 18 Solution annealing temperature of Cu-Ni-Si as a function of the chemical composition of the alloy (MDT, 2006).

Copper-nickel-silicon alloys exhibit high tensile strengths (up to about 900 MPa), electrical conductivities of up to 50% IACS, good corrosion resistance and good workability. The excellent thermal stability of the higher nickel alloys makes them well suited for the manufacture of springs elements that will be used at temperatures above 150 °C. Adding small quantities of magnesium improves resistance to stress relaxation. Partial substitution of nickel by cobalt can increase mechanical strength by up to 100 MPa.

Age-hardened Cu-Ni-Si alloys are highly resistant to stress corrosion cracking. These alloys are particularly wear resistant due to their high hardness.

Solution annealing is performed at temperatures above 850 °C. The exact annealing temperature depends on the nickel content of the alloy: Ni_5Si_2 requires a higher temperature than Ni_2Si (Fig. 18). The material is then quenched to freeze-in the high-temperature microstructure.

Oxygen dispersion-strengthened (ODS) copper

As an additional type of high copper alloys, dispersion-strengthened coppers (ODS) contain 0.15–0.6% vol. of finely dispersed oxide particles, such as Al_2O_3, Y_2O_3, etc. ranging in size from 3 nm to 12 nm. They are produced using powder metallurgical, mechanical alloying or by internal oxidation methods and combine the high electrical conductivity of copper with the high strength due to the good stability of the oxides. Because of the way how these dispersoid materials are produced, they are best classified as composites materials.

ODS copper alloys have the benefit of keeping the strength and hardness even at high temperatures than the ones produced metallurgically. Copper dispersion strengthened by 0.2–0.7% Al_2O_3 retains reasonable strength at temperatures up to 1000 °C. It finds applications as electrodes for resistance welding.

Summarizing, there are four groups of elements that are used for the alloying of copper, depending on the desired use, as indicated in Fig. 19.

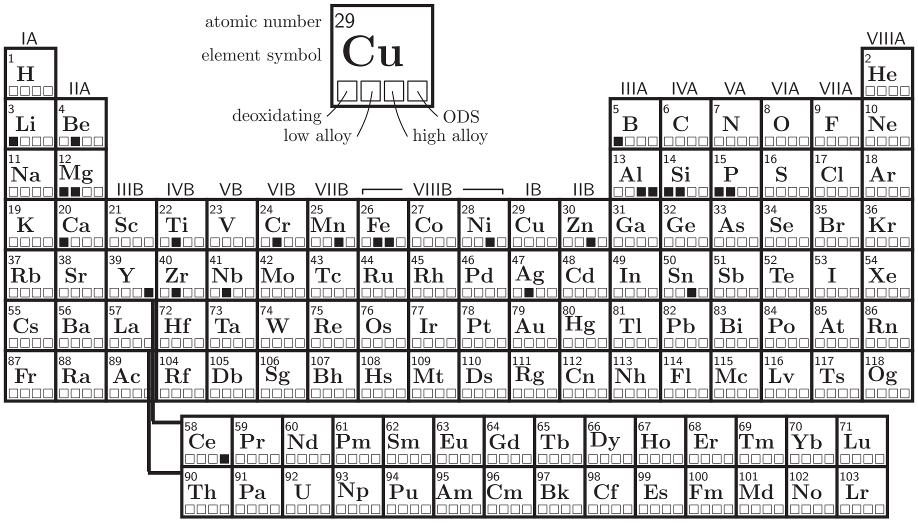

Fig. 19 Uses of elemental additions to copper. Indicated are elements for deoxidization, low- and high copper alloys and elements forming oxide dispersoids.

Commercial alloys

Copper and its alloys are classified as being either wrought alloys or casting alloys, depending on their usage. The unified numbering system (UNS) designations for copper material groups are listed in Table 3.

Sheets produced by cold rolling and rods or wire produced by drawing are sold with a temper designation indicating their state as defined in ASTM B 601. A synopsis of the system is outlined in Table 4.

Brass

Brasses are alloys of copper and zinc. Fig. 20 is the copper–zinc phase diagram. The solubility of zinc in the f.c.c. lattice of copper is $>35\%$. At nearly equal atomic percentages of copper and zinc, there is a b.c.c. intermetallic phase β, that has a wide range of solubility. At temperatures $<\sim 460\ ^\circ\mathrm{C}$, β-brass undergoes an ordering reaction to form an ordered b.c.c. phase β' with a B2 (CsCl) structure. Each copper atom is surrounded by eight zinc and eight copper atoms. A eutectoid transformation, $\beta' \rightarrow \alpha + \gamma$ at 250 °C has been reported. However, the transformation is rarely, if ever, encountered.

Zinc provides solid solution hardening to copper. Both the yield strength and the tensile strength increase with zinc content, as indicated in Figs. 21 and 22.

As the lower stacking fault energy increases the exponent n, (as explained in the section "Copper alloys") the uniform elongation also increases in the power-law approximation of the stress–strain curve. Another effect of the lower stacking fault energy is that

Table 3 Commercial copper alloy families (UNS Standard Designation for Wrought and Cast Copper (copper.org) and Unified Numbering System (UNS) for Copper and Copper Alloys (unscopperalloys.org)).

Group	*Description*	*Designation*
Coppers	Metals which have a designated minimum copper content of 99.3% or higher	Wrought o Coppers (C10100–C15999) o High Copper Alloys (C16000–C19999) o Brasses (C20000–C49999) o Bronzes (C50000–C69999) o Copper Nickels (C70000–C73499) o Nickel Silvers (C73500–C79999) Cast o Coppers (C80000–C81399) o High Copper Alloys (C81400–C83299) o Brasses (C83300–C89999) o Bronzes (C90000–C95999) o Copper Nickels (C96000–C96999) o Leaded Coppers (C98000–C98999) o Nickel Silvers (C97000–C97999) o Special Alloys (C99000–C99999)
High copper alloys	For the wrought products, these are alloys with designated copper contents less than 99.3% but more than 96% which do not fall into any other copper alloy group. The *cast high copper alloys* have designated copper contents in excess of 94%, to which silver may be added for special properties	
Brasses	These alloys contain zinc as the principal alloying element with or without other designated alloying elements such as iron, aluminum, nickel and silicon. The *wrought alloys* comprise three main families of brasses: copper-zinc alloys; copper-zinc-lead alloys (leaded brasses); and copper-zinc-tin alloys (tin brasses). The *cast alloys* comprise four main families of brasses: copper-tin-zinc alloys (red, semi-red and yellow brasses); "manganese bronze" alloys (high strength yellow brasses); leaded "manganese bronze" alloys (leaded high strength yellow brasses); copper-zinc-silicon alloys (silicon brasses and bronzes); and cast copper-bismuth and copper-bismuth-selenium alloys. Ingot for remelting for the manufacture of castings may vary slightly from the ranges shown	
Bronzes	Broadly speaking, bronzes are copper alloys in which the major alloying element is not zinc or nickel. Originally "bronze" described alloys with tin as the only or principal alloying element. Today, the term is generally used not by itself but with a modifying adjective. For *wrought alloys*, there are four main families of bronzes: copper-tin-phosphorus alloys (phosphor bronzes); copper-tin-lead-phosphorus alloys (leaded phosphor bronzes); copper-aluminum alloys (aluminum bronzes); and copper-silicon alloys (silicon bronzes) The *cast alloys* have four main families of bronzes: copper-tin alloys (tin bronzes); copper-tin-lead alloys (leaded and high leaded tin bronzes); copper-tin-nickel alloys (nickel-tin bronzes); and copper-aluminum alloys (aluminum bronzes) The family of alloys known as "manganese bronzes," in which zinc is the major alloying element, is included in the brasses, above	
Copper-nickels	These are alloys with nickel as the principal alloying element, with or without other designated alloying elements	
Copper-nickel-zinc alloys	Known commonly as "nickel silvers," these are alloys which contain zinc and nickel as the principal and secondary alloying elements, with or without other designated elements	
Leaded coppers	These comprise a series of *cast alloys* of copper with 20% or more lead, sometimes with a small amount of silver, but without tin or zinc	
Special alloys	Alloys whose chemical compositions do not fall into any of the above categories are combined in "special alloys"	

Table 4 Examples of temper designations for copper alloys (Fundamentals: Types of Copper and Properties).

Temper designation	*Temper name or condition*
Annealed	
O10	Cast and annealed
O20	Hot forged and annealed
O60	Soft annealed
O61	Annealed
O81	Annealed to Temper ¼ Hard
O5015	Average grain size: 15 μm
Cold worked tempers	
H01	¼ Hard
H02	½ Hard
H04	Hard
H08	Spring
Cold worked and stress relieved tempers	
HR01	H01 and stress relieved
HR04	H04 and stress relieved
Precipitation hardening	
TB00	Solution heat treated
TF00	TB00 and age hardened
TH92	TB00 and cold worked and aged
Manufactured tempers	
M01	As sand cast
M04	As pressure die cast
M06	As investment cast

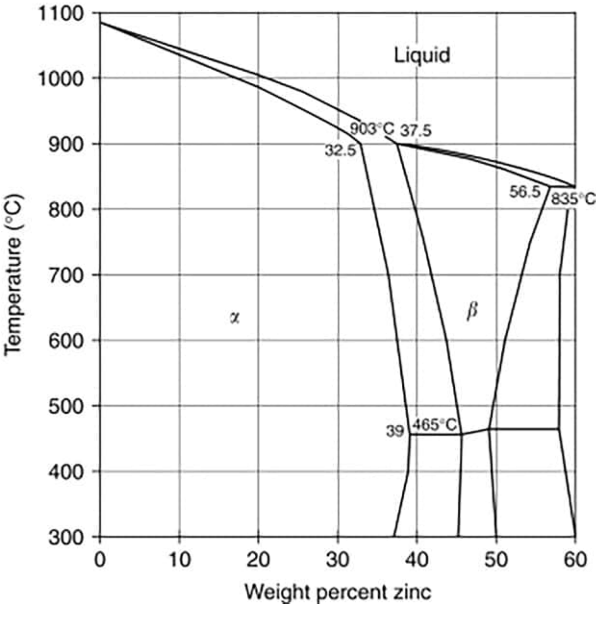

Fig. 20 The copper–zinc phase diagram. Adapted from ASM (2001) *Copper and Copper Alloys, ASM Speciality Handbook*. ASM: Materials Park, OH.

annealing twins are much more frequent. Fig. 23 compares the annealed microstructure of copper with brass containing 30% Zn (Hosford, 1993). The microstructures of brass containing 40% zinc or more consist of two phases, α and β. The two-phase microstructure of Muntz metal (40% Zn) is shown in Fig. 24. At 800 °C the microstructure is entirely β, but as the alloy is cooled, α precipitates. The effects of other alloying elements to brass on the solid solubility of zinc can be approximated by "*zinc equivalents*." A concentration of 1% tin is equivalent to 2% zinc, so tin has a zinc equivalent of 2. Table 5 lists the zinc equivalents of the common alloying elements. The relative values of the zinc equivalents of the elements can be understood in terms of the number of valence electrons per atom. Silicon and aluminum have high valencies (4 for silicon and 3 for aluminum) and low atomic masses (28 for silicon and 27 for aluminum), so 1 wt% causes a large increase of the electron-to-atom ratio. Magnesium, like

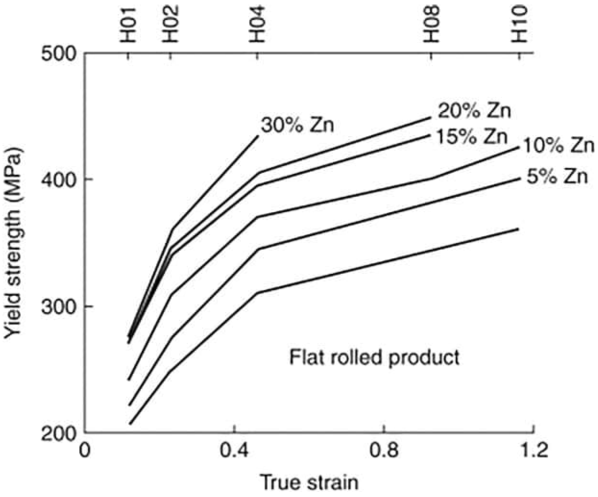

Fig. 21 The yield strength of brasses increases with the amount of cold work and the zinc content. The true strain, $\varepsilon = \ln(t_o/t)$ where t is the thickness and t_o is the thickness before cold rolling. Adapted from ASM (1979) *ASM Metals Handbook*, 9th edn. vol. II. Metals Park, OH: ASM.

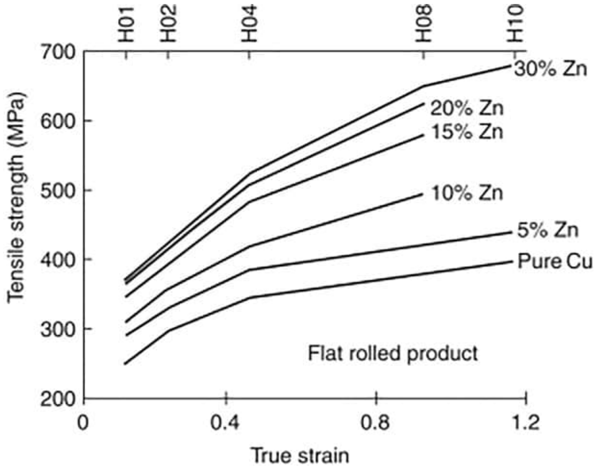

Fig. 22 The tensile strength of brasses increases with the amount of cold work and the zinc content. The true strain, $\varepsilon = \ln(t_o/t)$ where t is the thickness and t_o is the thickness before cold rolling. Data from ASM (1979) *ASM Metals Handbook*, 9th edn. vol. II. Metals Park, OH: ASM.

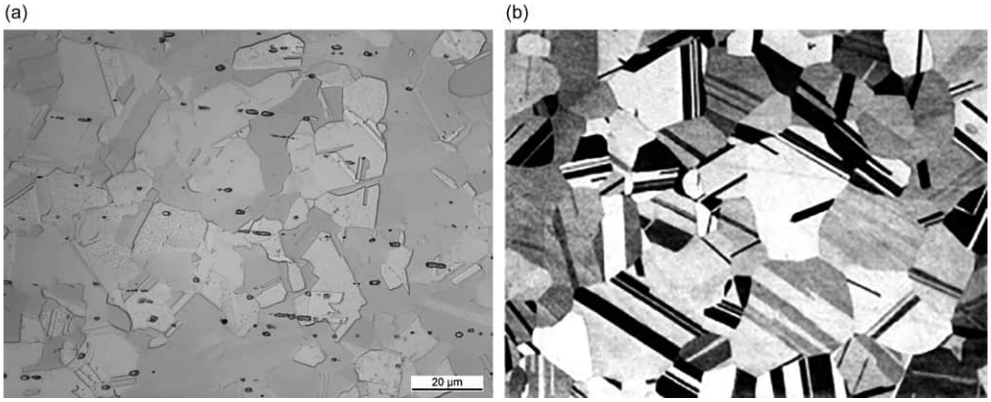

Fig. 23 Microstructures of (a) pure copper (C11000) and (b) 70/30 brass (200×). Note that the frequency of annealing twins is higher in the brass. (a) Adapted from ASM (1973) *ASM Metals Handbook*, 8th edn., vol. VIII. Materials Park, OH: ASM; source Kupferinstitut. (b) Adapted from Hosford W.F. (1993) *The Mechanics of Crystals and Textured Polycrystals*. London: Oxford Science Pub. (Courtesy A Graf).

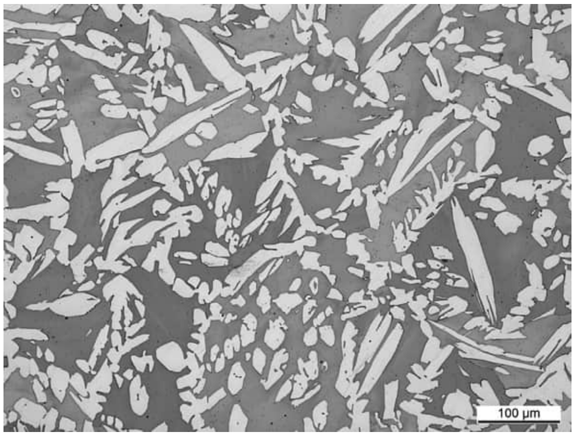

Fig. 24 Photomicrograph of a brass (42% Zn). The dark phase is β and the light phase is α, which has precipitated during cooling. Source Kupferinstitut.

Table 5 Zinc equivalents of several alloying elements in brass.

Element	*Zn equivalent*	*Element*	*Zn equivalent*
Si	10	Al	6
Mg	–2	Sn	2
Fe	0.9	Mn	0.5
Co	–0.8	Ni	–1.3

zinc has a valency of 2, but the atomic mass of magnesium is less than half that of zinc (24 for magnesium vs 65 for zinc), so 1 wt% Mg has over twice the effect of 1 wt% Zn. Tin has a valence of 4, but its atomic mass (119) is roughly twice that of zinc.

Free cutting brass has been alloyed with lead up to 3% (C36000) to enhance the machinability. Legislative restrictions of certain chemical elements assumed detrimental to human and environment, e.g., Cd, Pb, has led to the development of alternative lead free-cutting brass types in enhancing the zinc content (C28500) or replacing lead by silicon (C69300) or other elements. As lead confers multiple properties to copper alloys (good machinability, lubrication for dry-running, etc.) it is unlikely to find a one to one lead replacement. Not all properties of leaded alloys can be given by the lead free alternatives. Hence the free cutting properties of high silicon brass is given be the presence of a silicon rich phase acting as chip breaker.

Bronze

True bronzes are copper–tin alloys. Tin is much less soluble in copper than zinc as shown in the copper–tin phase diagram (see Fig. 25). The ϵ-phase is very sluggish to form and is rarely encountered. Tin is a potent solid solution strengthener. However, alloys

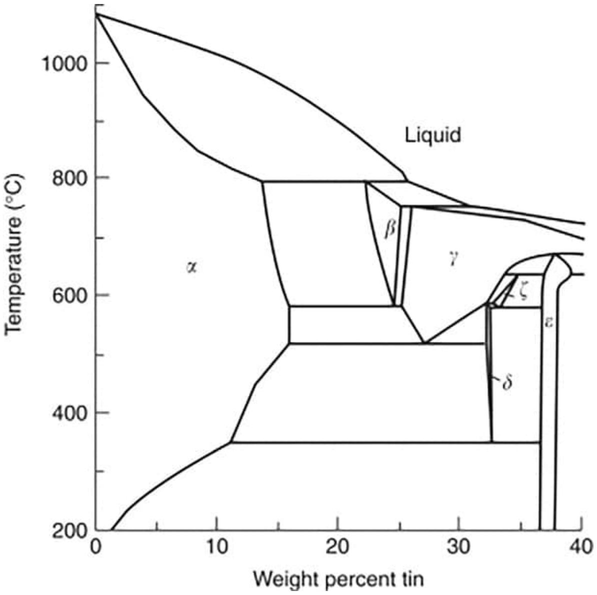

Fig. 25 The copper–tin phase diagram. β is a b.c.c. phase. In alloys containing $\sim$20% Sn, formation of the ϵ-phase is so sluggish that it is seldom encountered. Adapted from ASM (1973) *ASM Metals Handbook*, 8th edn., vol. VIII. Materials Park, OH: ASM.

with >8% Sn are too brittle to be formed mechanically. Because bronzes have a much greater difference of the liquidus and solidus temperatures than brass, they are much easier to cast. Casting alloys often contain up to 12% Sn, these are extensively for pipe fittings, pumps bodies and up to ~20% Sn for bells.

Wrought alloys contain up to 8–10% Sn. They are mainly used for connectors.

Aluminum bronze

Alloys of copper with aluminum called aluminum-bronze, even though they contain no tin. Aluminum-bronzes containing up to 7% Al behave much like brass. Above 7% a b.c.c β-phase occurs. The phase diagram (see Fig. 26) shows that a b.c.c. β-phase transformation into $(\alpha + \gamma_2)$ eutectoid occurs at ~12% Al.

This eutectoid transformation of $\beta \rightarrow \alpha + \gamma_2$ occurs at 565 °C and 11.8% Al. Fig. 27 shows the pearlite-like microstructure of alternating platelets of α and γ_2 in an alloy of Cu–11.8% Al after slowly cooling from 800 °C. With rapid cooling, the eutectoid transformation is suppressed and the alloy transforms by martensitic shear to a new hexagonal phase β'. Fig. 28 shows the martensitic β' needles in the same alloy after rapid cooling. The martensitic reaction is almost instantaneous. It starts when β is quenched below the M_s temperature and is virtually complete when the temperature is at the M_f. The M_s and M_f temperatures depend on the composition as shown in Fig. 29 (Flinn, 1961). The oxidation resistance of aluminum bronzes is somewhat superior to brass.

To enhance the strength and corrosion resistance of aluminum bronze it is alloyed with nickel and iron with a small amount of manganese. This extends the α-phase area and shifts the formation of the corrosion sensitive γ_2-phase to higher aluminum content (C63000, C95820). These alloys are used for ship propellers, pump bodies and other high-performance parts in the gas and oil industry.

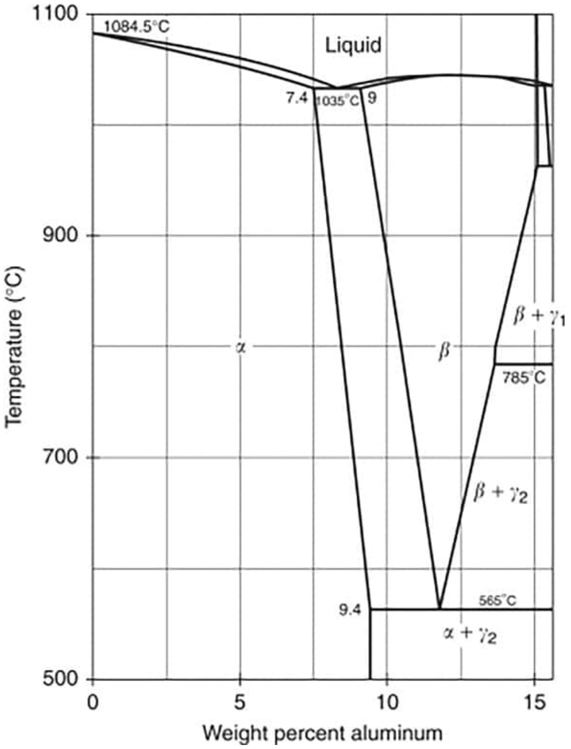

Fig. 26 The copper–aluminum phase diagram. β is a b.c.c. phase. Note that eutectoid transformation at 565 °C. Adapted from ASM (1973) *ASM Metals Handbook*, 8th edn., vol. VIII. Materials Park, OH: ASM.

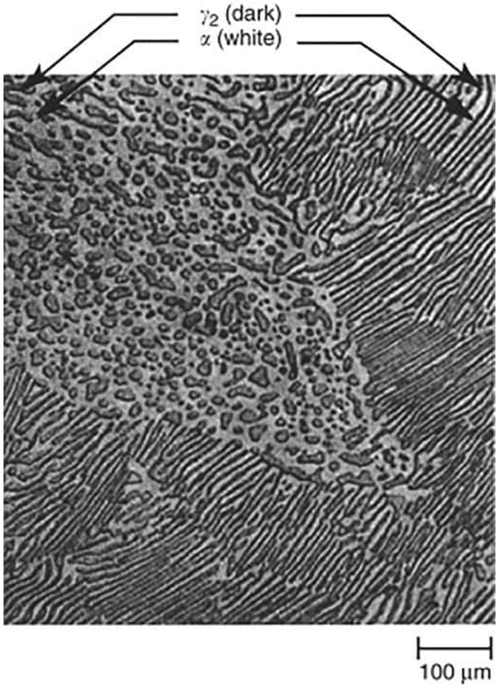

Fig. 27 Pearlite-like structure in Cu–11.8% Al after slow cooling from 800 °C. Adapted from ASM (2001) *Copper and Copper Alloys*, *ASM Speciality Handbook*. ASM: Materials Park, OH.

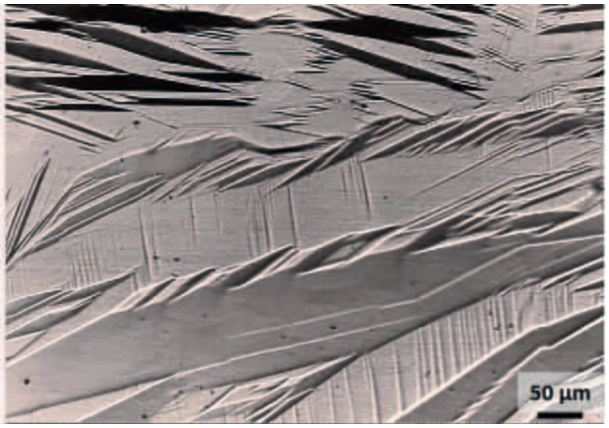

Fig. 28 Martensitic structure of Cu–6% Al–10% Mn after rapid cooling from 800 °C (Tikana et al., 2003).

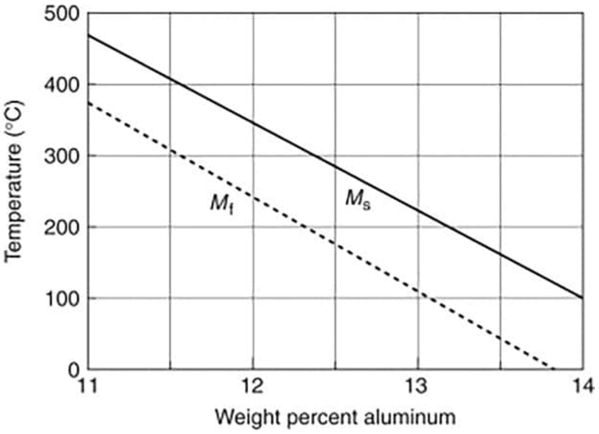

Fig. 29 The M_s and M_f temperatures of aluminum bronzes. Adapted from Flinn R.A. (1961) *The Non-Ferrous Copper, Brass, and Bronze Castings*. Cleveland, OH: Founders Society.

Copper nickel alloys

Copper and nickel are completely miscible in both the liquid and solid state as shown in the copper–nickel phase diagram (see Fig. 30). The low-temperature miscibility gap is rarely encountered.

Nickel imparts improved corrosion and oxidation resistance to copper. Cupronickels containing 10–30% Ni are widely used for tubes in offshore and marine area, heat exchangers and as plates to protect offshore pillars.

Alloying copper with 20% Ni causes a loss of the copper's familiar yellow–reddish color. Coinage accounts for ~1% of the consumption of copper. The five-cent pieces ("nickels") in the US and Canada are alloys of 75% copper and 25% nickel. The 10-cent ("dime") and 25-cent ("quarter") pieces are sandwiches of pure copper core clad with 75% copper–25% nickel alloy as shown in Fig. 31. The Susan B Anthony US dollar is a sandwich of pure copper clad with 77Cu–12 Zn–7 Mn–4 Ni. European coins are either copper-based alloys or combinations of two copper-based alloys. Constantan (45% Ni) has a nearly zero-temperature coefficient of resistivity, hence is useful in instruments.

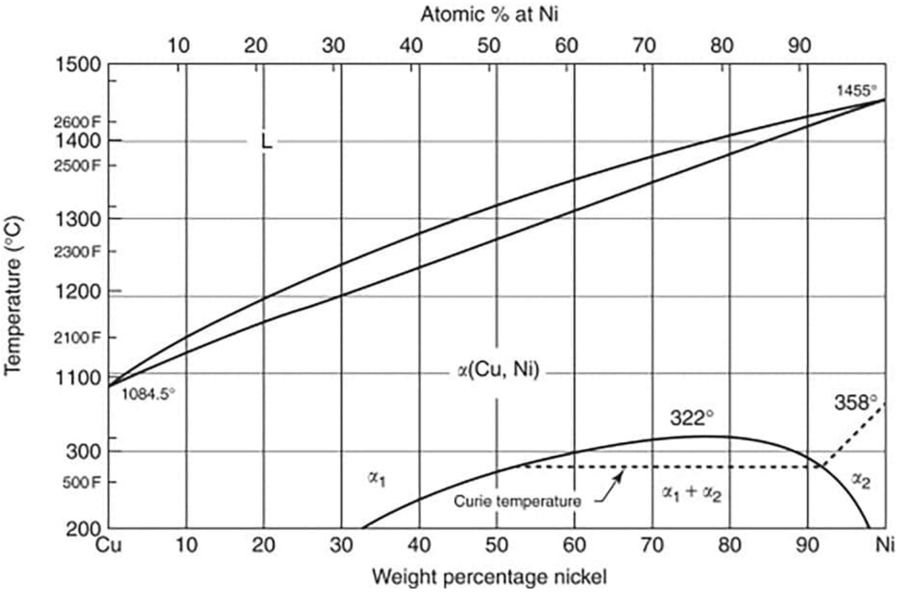

Fig. 30 The copper–nickel phase diagram shows complete miscibility. Adapted from ASM (1973) *ASM Metals Handbook*, 8th edn., vol. VIII. Materials Park, OH: ASM.

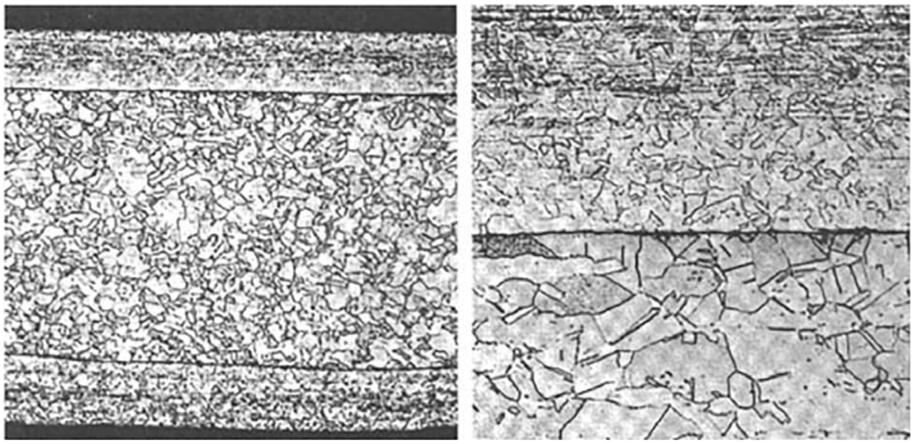

Fig. 31 Cross section of a US dime. Adapted from ASM (2001) *Copper and Copper Alloys*, *ASM Speciality Handbook*. ASM: Materials Park, OH.

Shape memory alloys

Cu-based shape memory alloys and among these copper–zinc (Cu-Zn), copper–aluminum (Cu-Al), and copper–tin (Cu-Sn) alloys have shown potential due to their good shape recovery. The martensitic transformation temperature is approx. 100 °C for the Cu-Al-Mn alloys. The exact temperatures depend on composition. The temperature hysteresis is in the range of 15–25 °C. They are considered as cost effective because they are easily produced using conventional processing routes. Further, they show a high electrical and thermal conductivity. However, their applications are still limited due to their low mechanical strength, brittleness and thermal stability. Unfortunately, the binary alloys suffer from bad cold workability and martensite stabilization; hence ternary and quaternary additions are used to improve the properties, which has successfully been done for Cu-Zn and Cu-Al alloys, only. The Cu-Zn-Al alloys with 10–30% Zn and 5–10% Al and the additions of other elements yield to improved mechanical properties, in particular plasticity, while the Cu-Al-Ni alloys with 11–15% Al and 3–4% Ni and the additions of other elements aim at higher transformation temperatures (approx. 230 °C). The Cu-Al-Ni alloys are the only available copper-based high-temperature shape memory alloys. They are, however, very brittle. The recoverable strain for both groups is approx. 4–6%. In addition to the shape memory, superelastic, and pseudoelastic effects, these alloys also present a temperature memory effect, a small hysteresis, and a high damping coefficient.

Property relationships

For all copper alloys, the Wiedemann–Franz law applies. This means that the ratio of the electronic contribution of the thermal conductivity (κ) to the electrical conductivity (σ) is proportional to the temperature. In principle all metallurgical effects that lower the conductivity, i.e., rise the resistance cause an increase in strength. Therefore, there is a balance between conductivity and strength in copper alloys as shown in Fig. 32.

Among the copper alloys, the precipitation hardenable alloys show slightly enhanced combination of strength and conductivity, i.e., they are closer to the upper right corner of this Asby diagram, than solid solutions. This is because the electrical resistance of these alloys is determined upon a parallel arrangement of the individual contributions, giving lower values than the serial arrangement characterizing the solid solution case. In both cases, the strength values are superimposed upon:

$$\tau = \tau_0 + \sqrt[k]{\sum_i \Delta\tau_i^k}$$

Where $\Delta\tau_i$ are the individual contributions to the strength, and k is an exponent ranging from 0.5 to 1 depending on whether the strengthening effects are of similar or dissimilar measure. Table 6 summarizs the composition and properties of characteristic copper alloys as presented before in representative selection.

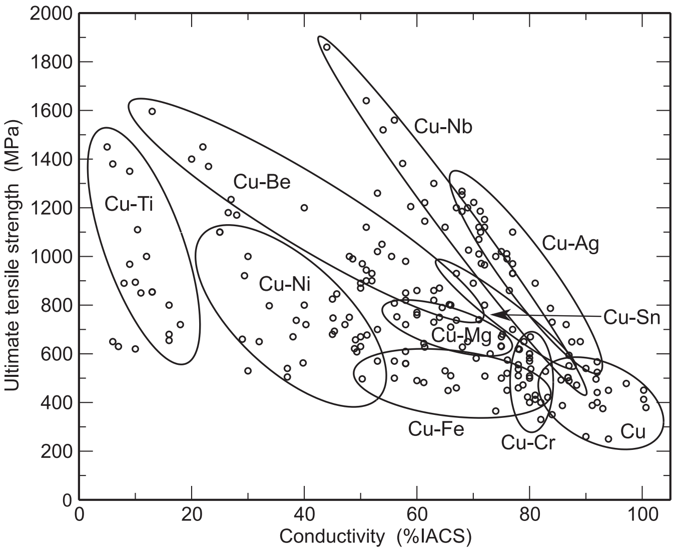

Fig. 32 Strength of selected copper alloys in relation to their conductivity. The most important groups of copper alloys are labeled.

Table 6 Composition and properties of characteristic copper alloys (Freudenberger and Warlimont, 2018).

Material	*UNS No.*	*Purity; other elements (wt%)*	*Yield strength (MPa)*	*Ultimate tensile strength (MPa)*	*Elongation to failure (%)*	*Thermal conductivity (Wm^{-1} K^{-1})*	*Electrical conductivity (Sm^{-1})*
Oxygen-free Cu	C10100	99.99 Cu	69–325	221–385	4–60	401	58.89
Oxygen-free Cu	C10200	99.95 Cu	69–325	221–385	4–60	399	58.58
Oxygen-free low phosphorus Cu	C10800	99.95 Cu, 0.009 P	69–345	250–379	4–50	350	49.31
Phosphorus deoxidized Cu	C14200	99.68 Cu, 0.35 As, 0.02 P	69–345	250–379	8–35	188	26.10
Beryllium copper	C17200	bal Cu, 0.2 Al, 2.0 Be, 0.2 Co	172–1344	469–1462	1–48	$\leq$95	24.94
Chromium copper	C18200	bal Cu, 1.2 Cr, 0.1 Fe, 0.05 Pb, 0.1 Si	479–531	232–593	14–60	188	26.10
Lead copper	C18700	bal Cu, 1.5 Pb	69–345	221–379	8–45	377	55.87
Silver-bearing copper	C11300	bal Cu, 0.027 Ag, 0.04 O	69–365	221–455	4–55	397	57.43
Zirconium copper	C15000	bal Cu, 0.2 Zr	41–496	200–524	2–54	367	54.95
Aluminum brass	C68700	77.5 Cu, 20.5 Zn, 2 Al	186	414	55	101	13.34
Cartridge brass	C68700	70 Cu, 30 Zn	76–448	303–896	3–66	121	15.49
Cap copper	C21000	95 Cu, 5 Zn	69–400	234–441	8–45	234	32.48
Low brass	C24000	80 Cu, 20 Zn	83–448	290–862	3–55	138	21.45
Muntz metal	C28000	60 Cu, 40 Zn	145–379	372–510	10–52	126	16.24
Naval brass	C46400	60 Cu, 39.25 Zn, 0.75 Sn	172–455	379–607	17–50	117	15.08
Red brass	C23000	85 Cu, 5 Zn	69–434	269–724	3–55	159	25.52
Yellow brass	C26800	65 Cu, 35 Zn	97–427	317–883	3–65	121	15.08

Manufacturing processes

Manufacturing is the process of converting raw materials into products, including all intermediate processes involved in the production and integration of a product components. The traditional production of semi-finished products can be structured into melting and casting, hot and cold work with heat treatments and finishing. Additive manufacturing processes overcome this queue. In the following the most important processes to produce copper-based semi-finished products are introduced.

Casting

A large variety of casting processes can be applied of producing copper base alloy castings, which are also commonly in use for iron and non-ferrous metals, as e.g., in particular (i) sand casting, (ii) mold casting, (iii) die casting, (iv) chill casting, (v) centrifugal casting and (vi) continuous casting. Due to the melting temperature and good conductivity, the metal is molten by an induction furnace rather than a combination of gas and electric oven. Permanent metal molds are used on a large scale as they provide enhanced dimensional accuracy and surface finish of the castings. In addition, the higher cooling rate causes grain refinement, and thus an improvement in the mechanical properties. Mainly used are the gravity die casting process and the centrifugal and continuous casting processes for near-net shape castings. The separation between the liquidus- and solidus line ranges from below 50 °C for, e.g., aluminum- and nickel bronzes via an intermediate freezing range of 50–100 °C for, e.g., silicon bronze and -brass to up to 170 °C for, e.g., tin bronzes. In general, alloys with a greater separation of liquidus and solidus are regarded as easier to cast. In a fixed thermal gradient, the length of dendrite L, arms is proportional to this temperature difference, ΔT. Also, the liquid-to-solid shrinkage is a measure to characterize the casting process. A higher shrinkage is seen, e.g., for aluminum- and silicon bronzes. They are more fluid, more easily poured and result in high-grade castings. However, careful design is necessary to promote directional solidification and avoid internal shrinkage and crack formation. The shrinkage during solidification can occur inter-dendritically, what simplifies risering. Lower liquidus temperatures are also beneficial.

Forming

Due to its enormous plasticity and formability, copper is capable of being formed into all types of semi-finished products such as sheet, strip, tube, rod, wire, and die and open die forgings. Cold working at room temperature is easily applied for copper in the recrystallized condition. As cast microstructures do not fulfill this requirement and are partly not easy to deform, hot working at 800 °C to 900 °C, depending on the technique, is applied to obtain a recrystallized microstructure in-situ. Forming processes, such as extrusion, forging, swaging, drawing, rolling and profile rolling, are used to produce semi-finished products without the necessity of cutting in near-final dimensions.

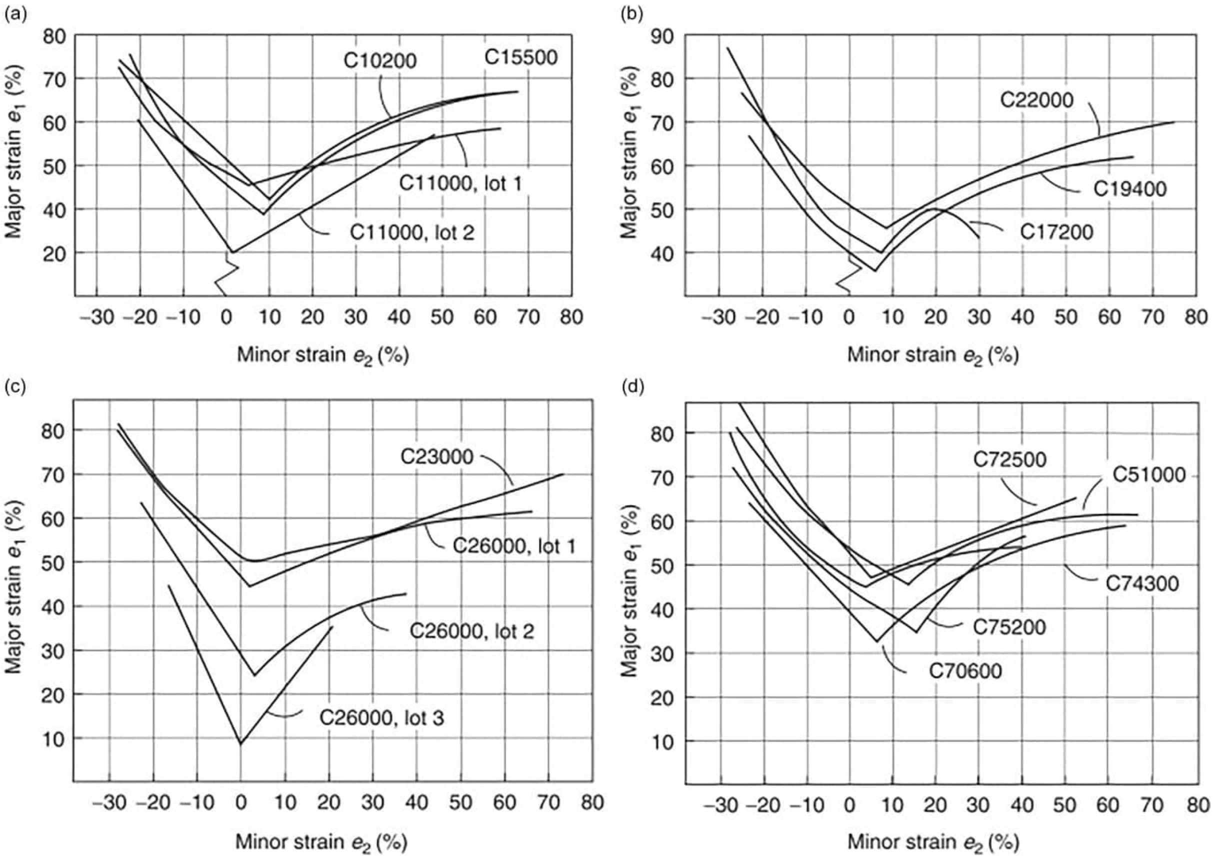

Fig. 33 Forming limit diagrams for copper and copper alloy sheets.

Sheet formability benefits from high strain-hardening exponents and high *R*-values. The R-value, which is also called the Lankford coefficient or the plastic strain ratio, is the ratio of the true width strain to the true thickness strain at a particular value of length strain, i.e.,

$$R = \varepsilon_W / \varepsilon_t$$

Forming limit diagrams (see Fig. 33) show the combinations of strains that lead to the formation of localized necks. Minima occur near plane strain, $\varepsilon_2 = 0$ (corresponding to e_2 in Fig. 33). The level of ϵ_1 at this point depends strongly on the strain-hardening exponent, n in $\sigma = K\varepsilon^n$. Cold-worked sheets tend to have lower forming limits. The forming limits tend to rise with sheet thickness. A high strain-rate exponent m, in

$$\sigma = C\varepsilon^m$$

is also useful in forming. However, it is found to be very low (0.002–0.005) for copper and brass at room temperature.

In deep drawing applied, e.g., for flat bottom cups, the limiting drawing ratio (LDR) which is the ratio between the maximum blank diameter and the punch diameter, depends mainly on the *R*-value of the sheet material. A large R-value represents resistance to thinning. Because the *R*-values of copper and brass sheets tend to be <1, the values of LDR tend to fall between 2.1 and 2.2. Formability in sheet forming that involve biaxial stretching depends mainly on the strain-hardening exponent n. Because of this, copper and especially brass have very good stretchability.

Extrusion and forging

Forging and extrusion are two reliable processes to manufacture copper parts and components, showing very similar results. Forging uses radial compressive forces to shape the material by a custom-made steel die, which can be open or closed. Forged copper parts are exceptionally strong, highly reliable and have tremendous structural integrity. The forging process is less labor-intensive and leaves less scraps behind than extrusion. In contrast, extrusion uses a high pressure to push the copper billet through a die, which can have differently-shaped cross-sections depending on the aimed cross section of the semi-finished product. Hot extrusion reduce pores and voids, breaks up the cast structure, and creates a more homogeneous microstructure, while cold extrusion gives the final shape a better finish on the surface and adds strength via work hardening. In addition, grains are elongated further increasing the strength. Extrusion is also beneficial with respect to creating long, tubular metal parts that require strict tolerance requirements. Forging of massive parts might show difficulties in meeting these requirements and, thus, cause secondary processing to successfully create the finished shape. Hot forging temperatures for most copper alloys lie in the range of 600–750 °C, while hot extrusion of copper takes place at up to 900 °C, i.e., above 80% of the melting temperature, which is commonly used.

Powder processing

Parts of copper and copper alloys are sometimes fabricated by conventional powder metallurgy that involves pressing powder to the desired shape and sintering to achieve nearly full density. Copper powder can be obtained from various techniques, such as atomization, electrolysis, hydrometallurgy and solid-state reduction. Each of them generates powder having certain inherent characteristics. While atomization generates powder particles having either spherical or irregular shape, electrolysis follows dendritic particles and solid-state reaction tends to porous particles of irregular shape. These powders are then further processed, either by additive manufacturing or sintering. For the later, powders are pressed into nearly the desired shapes at room temperature and sintered at high temperatures below the melting temperature at which the part is fully densified. For sintered parts made from alloys, suitable pre-alloyed powders are used. Alloying constituents with melting temperatures below the sintering temperature, such as lead, favor the sintering process. Besides conventional alloys, sintering techniques are applied to dispersion strengthened copper alloys. After sintering, the parts require calibration. Most sintered pats from copper alloys were used as oil-impregnated, self-lubricating bearings. These parts have a pore space of up to 30%, which is achieved by stopping the sintering before complete densification. These pores act as container for the lubricant.

Additive manufacturing

Traditional forming techniques have difficulties in realizing complex shapes, which can be overcome utilizing additive manufacturing. Selective laser melting (SLM) and selective electron beam melting (SEBM) are the main techniques used for additive manufacturing, besides binder jetting, laser metal deposition and ultrasonic additive manufacturing. Additive manufacturing has shown a strong development in recent years and is expected to become the dominant processing method for parts of complex geometry as well as individually shaped components, always in combination with computer aided design. Liquid copper has an extremely high reflectivity of approx. 98% for laser light with commonly applied wavelengths in the range of 1000–1100 nm. The absorption of the impacted energy can be raised to 25–40%, when wavelengths of 515 nm are utilized. In contrast, the SEBM technology is suitable for the processing of copper as the nature of reflexion differs for electrons and photons. Both, mechanical and physical properties of parts and components are directly influenced by the density of the metal, while a high density is beneficial. The major drawback of SLM against SEBM is related to this issue, since besides the used wavelength, an increasing laser power also causes a higher density of the build parts. When the applied energy density is in the region of 250–750 J/mm^3, parts with relatively high density can be obtained. With SEBM being applied, parts with a relative density of >99% can be built easily. Pure copper parts with a relative density of 99.95% build through SEBM have an electrical conductivity of 99% IACS and a thermal conductivity of 400 W/mK.

Deformation textures

During conventional drawing of copper mixed <1 1 1>/<1 0 0> fiber textures develop with a strong <1 1 1> fiber component develops, which is common for materials with a face centered cubic symmetry of the unit cell. The ratio of <1 0 0> to <1 1 1> increases with alloying. The compression texture of copper has <1 1 0> directions parallel to the axis of compression. The development of deformation textures in copper during rolling is different. Most orientations assemble along two incomplete fibers. The rolling texture of copper is described by two continuous fibers: (i) the α-fiber, which runs from the Goss orientation, {1 1 0} < 0 0 1>, to the brass orientation, {1 1 0} < 1 1 2>, and (ii) the β-fiber, which runs from the copper orientation, {1 1 2} < 1 1 1>, over S orientation, {1 2 3} < 6 3 4>, to the brass orientation, {1 1 0} < 1 1 2>.

The corresponding texture is represented schematically in Fig. 34 (Humphreys and Hatherly, 1995).

The rolling texture of low stacking fault energy alloys is different. Here, the brass orientation is much stronger and the fiber between the Goss and Brass orientations is more prominent. There are two additional fibers. Fiber γ corresponds to orientations having {111} aligned parallel to the rolling plane. It extends from {1 1 1} < 1 1 2>. Fiber τ consists of orientations with <1 1 0> parallel to the transverse direction. Fig. 35 is a schematic representation of the fibers. As the amount of deformation increases the α-fiber remains strong, the β-fiber increases, and the copper and S components decrease.

The relative amounts of these components change as the temperature of rolling decreases or as the copper is alloyed with zinc or another element that lowers its stacking fault energy. The transition from copper-type recrystallization texture to the Brass-type texture depends on the stacking fault energy of the alloy.

The rolling texture also depends on the rolling temperature.

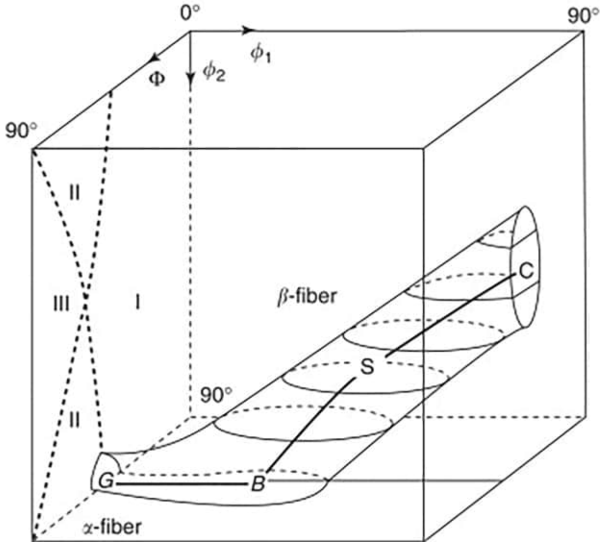

Fig. 34 Schematic representation of the ODF shown in Fig. 25. Adapted from Humphreys FJ and Hatherly M (1995) Recrystallization and Related Annealing Phenomena. London: Elsevier.

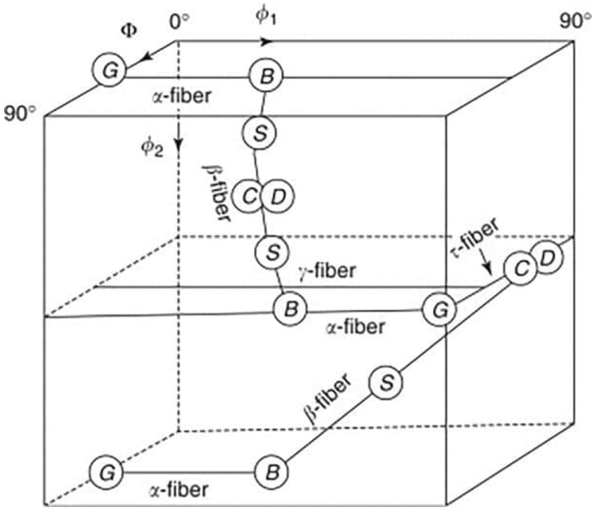

Fig. 35 Schematic representation of the ODF in Fig. 27. Adapted from Humphreys FJ and Hatherly M (1995) Recrystallization and Related Annealing Phenomena. London: Elsevier.

Thermal response

Annealing of copper and its alloys is done for homogenization, aging or recovery and recrystallization. Homogenization and aging focus on the targeted adjusting of the phases within the alloy, e.g., to obtain single-phase material and to resolve segregations, or to form precipitates with a well-adjusted size and distribution. Recovery and Recrystallization alter microstructural features that are not part of the thermodynamic equilibrium, such as dislocation- and grain boundary networks. In this case, the stored energy of cold work is the driving force for the transformation of the microstructure. The effects of annealing cold-worked metal are usually divided into three stages: recovery, recrystallization, and grain growth. These effects are strongly related to degree of cold work which is applied before annealing. On one side a certain minimum degree of cold work is required to store enough energy that is released during annealing and driving the mentioned processes. On the other side, if a certain degree of deformation is applied, the formability drops, and these processes need to be activated to allow further cold work.

Recovery

During recovery, the excess vacancies anneal out and dislocations are rearranged into lower-energy configurations. There are no major changes in hardness or strength. Fig. 36 shows the effect of foregone cold work as well as the subsequent thermal treatment on

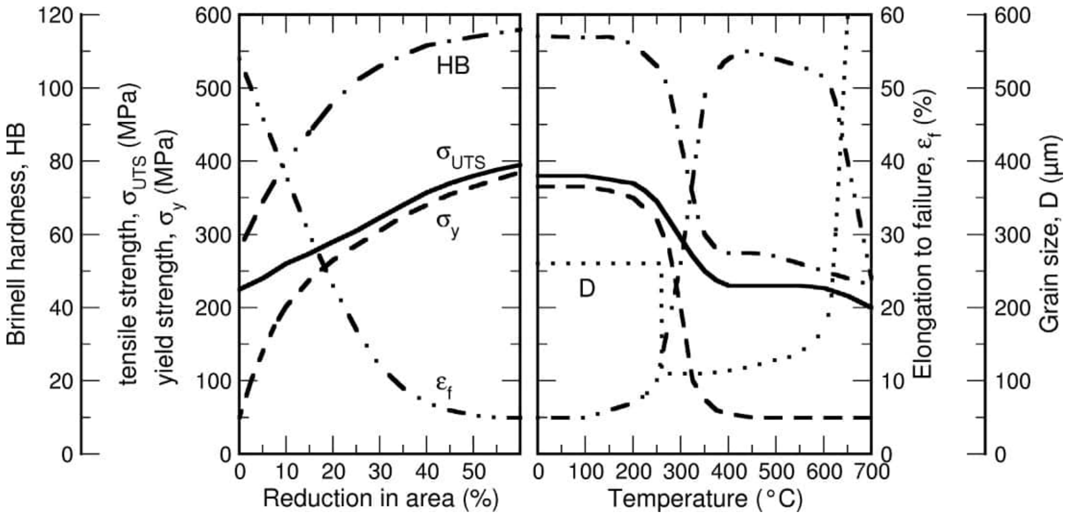

Fig. 36 Variation of mechanical properties during cold work of OF copper, left. Annealing of a sample that was deformed to an area reduction of 50% causes an energy release depending on the annealing temperature, right. The transition from recovery to recrystallization is most apparent from the change in grain size D, i.e., changes <250 °C are caused by annealing out of vacancies, changes >250 °C are a result of recrystallization and grain growth. Adapted from Wielandwerke (1999) *Wieland-Kupferwerkstoffe*, *Herstellung*, *Eigenschaften und Verarbeitung*. Wieland-Werke AG.

the mechanical properties of copper (Wielandwerke, 1999). During cold work, hardness HB, yield strength σ_y and ultimate tensile strength σ_{UTS} increase, while the strain to failure ε_f decreases. During recovery, the dislocations glide and re-arrange in energetically favored sites. During this process, the strength slightly decreases and the elongation slightly increases.

Recrystallization

During recrystallization after cold work, new strain-free grains are formed. The extent of recrystallization depends on both temperature and time. It is customary to define the recrystallization temperature as the temperature at which 63% of the grains will be recrystallized in 1 h. This originates from the Johnson Mehl Avrami Kolmogorov equation, in which the fraction f of the microstructure recrystallized at any temperature should be given by

$$f = 1 - \exp\left[-\left(\frac{t}{t_R}\right)^n\right]$$

Where t_R is the recrystallization time. At $t = t_R$: $f = 1 - (1/e) = 0.63$. For most metals of commercial purity, the recrystallization temperature is between 1/3 and 1/2 of the melting point on an absolute scale. However, the recrystallization temperature depends on purity, the extent of cold work before annealing, and the prior grain size. Fig. 37 shows the kinetics of recrystallization of copper that is 99.999% pure after cold reduction of 98% (Guy and Hren, 1974).

The fact that the recrystallization temperature of 113 °C in this case is only 28% of the melting temperature is explained by the extreme purity and very heavy reduction. The time, t, to achieve 63% recrystallization is given by the Arrhenius equation,

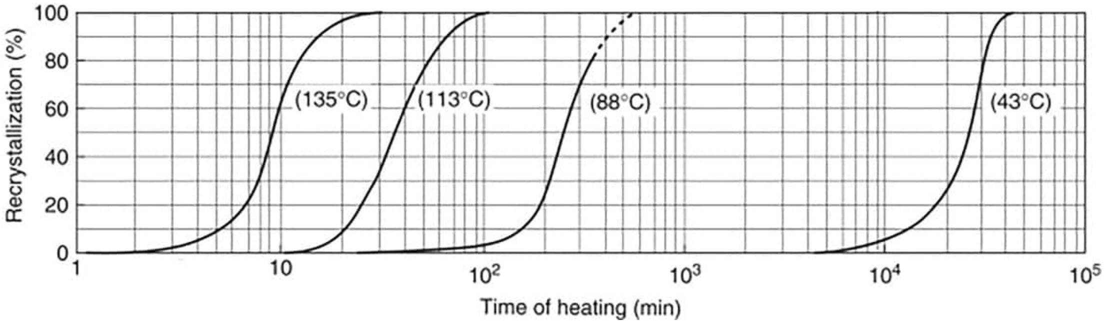

Fig. 37 Isothermal recrystallization of 99.999% pure copper cold-worked 98%. Adapted from Guy AA and Hren JJ (1974) Elements of Physical Metallurgy, 3rd edn. Reading, MA: Addison-Wesley Publishing Co.

$$t = t_0 \exp\left[\frac{Q}{RT}\right]$$

where Q is the activation energy, R is the gas constant, and T is the absolute temperature. Fig. 38 is an Arrhenius plot of the data in Fig. 37. The activation energy is 92.6 kJ mol^{-1}.

According to the Johnson–Mehl–Avrami-Kolmogorov equation, the exponent n is the sum of the contributions from nucleation n_n and growth n_g. If the nucleation rate is constant, $n_n = 1$ and if the growth rate is constant $n_g = 3$. Fig. 39 is a log–log plot of $\ln(1 - f)$ vs t of the data for Fig. 37 at 135 °C. The slope is close to 4, indicating constant nucleation and growth rates.

The effect of the amount of cold work that is applied prior to the recrystallization heat treatment on the evolution of the hardness with annealing temperature is illustrated in Fig. 40 for copper. It is obvious that with increasing cold work a decreasing recrystallization temperature is observed. This dependency is depicted in Fig. 41.

As already mentioned, the recrystallization temperature also depends on the size the grains have prior to annealing. The effect thereof is shown in Fig. 42 for copper being annealed at 225 °C. With increasing deformation strain, the recrystallization temperature seen at a subsequent heat treatment lowers or at a given temperature, recrystallization is faster in fine-grained material.

The grain size resulting from recrystallization depends on the relative rates of nucleation and growth of recrystallized grains. Increasing amounts of cold work before recrystallization decreases the resulting grain size because it increases the nucleation rate more than the growth rate. Solutes in solid solution decrease the recrystallized grain size because they decrease the growth rate by slowing grain-boundary motion. Second-phase particles have the same effect but they may increase the nucleation rate. Finally, the grain size before recrystallization affects the recrystallized grain size. With a finer prior grain size, there are more sites for nucleation, so the resulting grain size is also smaller.

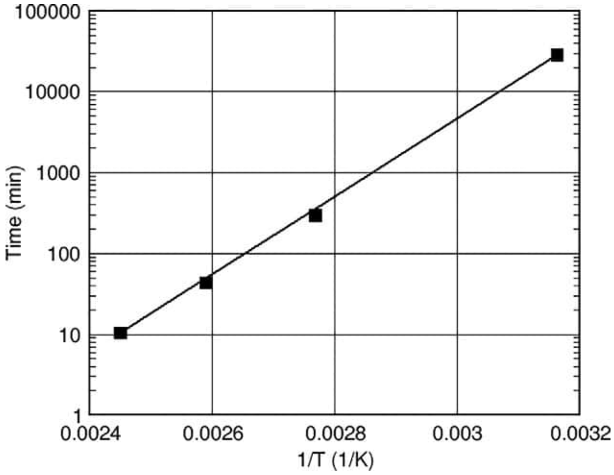

Fig. 38 An Arrhenius plot of the time–temperature relation for 63% recrystallization of the copper in Fig. 37.

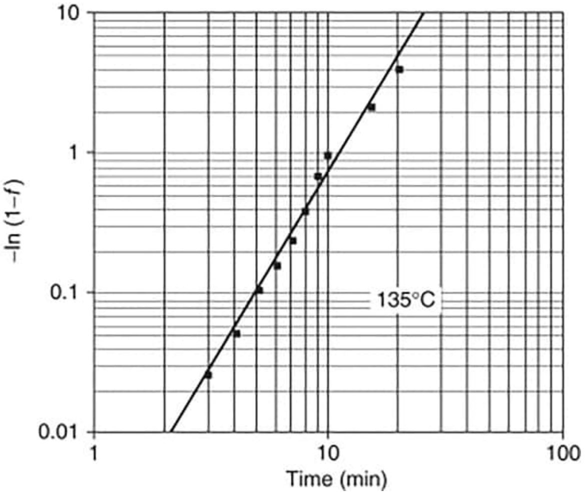

Fig. 39 A Johnson–Mehl–Avrami-Kolmogorov plot of the recrystallization of the copper in Fig. 34 at 135 °C. The slope is nearly 4, which indicates that the nucleation rate is constant and there is a constant rate of growth in three dimensions.

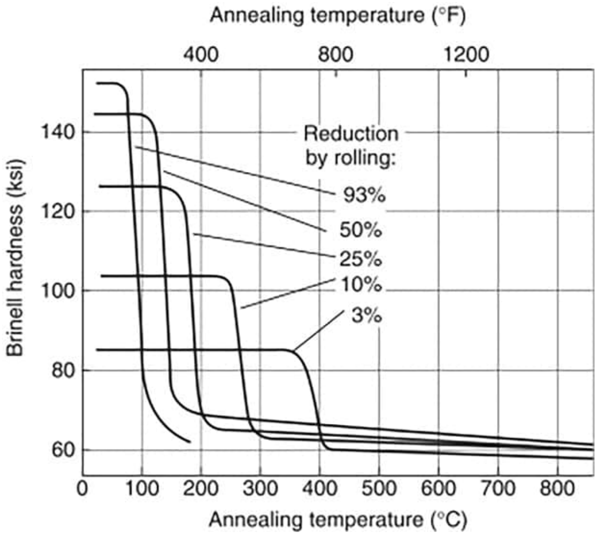

Fig. 40 The recrystallization temperature of copper depends on the amount of cold work. Adapted from ASM (2001) *Copper and Copper Alloys*, *ASM Speciality Handbook*. Materials Park, OH: ASM.

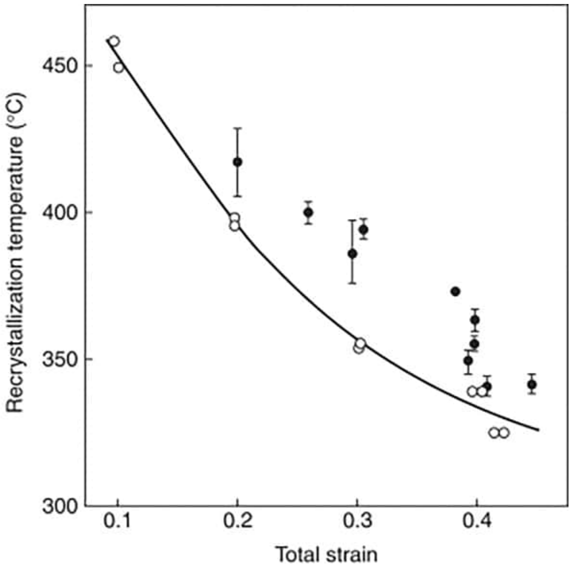

Fig. 41 The dependence of the recrystallization temperature on prior strain (○, simple tension, ● compression + tension). Adapted from Humphreys FJ and Hatherly M (1995) Recrystallization and Related Annealing Phenomena. London: Elsevier.

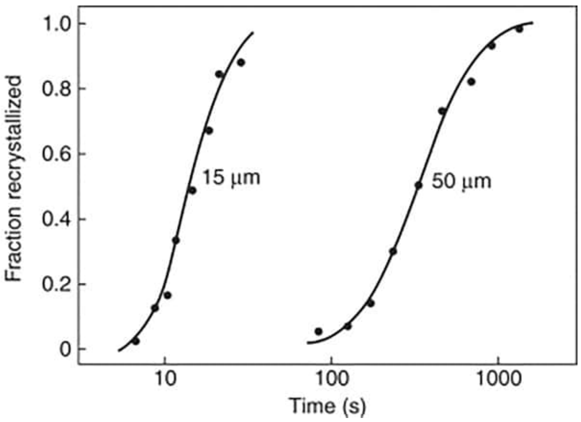

Fig. 42 Dependence of recrystallization kinetics on prior grain size. Copper cold-rolled 93% and recrystallized at 225 °C. Adapted from Humphreys FJ and Hatherly M (1995) Recrystallization and Related Annealing Phenomena. London: Elsevier.

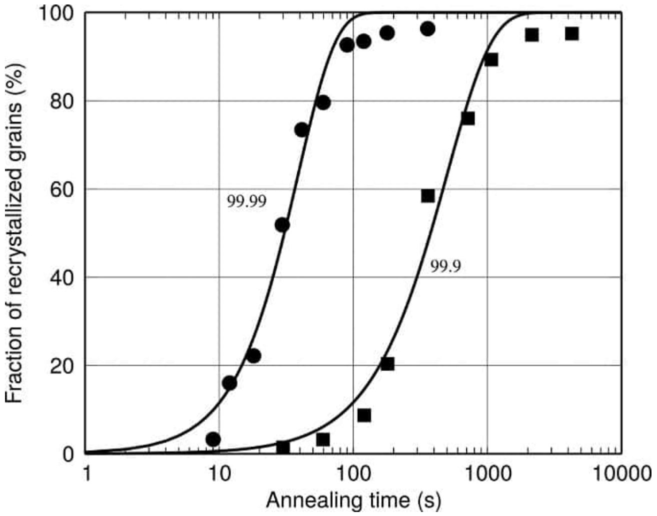

Fig. 43 Time dependence of recrystallization in 99.99% and 99.9% copper during isothermal annealing. Solid curves give their recrystallization fractions as a function of annealing time are fitted by using the classical JMAK model. Adapted from Yao (2021), https://doi.org/10.1016/j.msea.2021.141786.

The recrystallization kinetics are heavily influenced by the purity of the material. This causes the recrystallization time, observed at $T = 200\,^{\circ}\mathrm{C}$, to drop from approx. 1 h 22 min to approx. 6 min when the purity rises from 99.9% to 99.99%, as depicted in Fig. 43.

Depending on the purity, the recrystallization temperature for highly purified copper and commercially pure copper ranges from 80 °C to 300 °C. If a heavily cold worked copper is given enough time, it can even recrystallize at room temperature. Alloying elements raise the recrystallization temperature as shown in Fig. 44. 0.02 wt% Zr raises the recrystallization temperature to 540 °C (not shown here), while the effect of, e.g., Zn is low.

As mentioned before, the recrystallization temperature strongly depends on the purity of the material, for which reason the recrystallization temperatures discussed before differ. As shown in Table 7 (DKI, 1982), the recrystallization temperature in oxygen-free copper with just 20 ppm additions range between 140 °C and 222 °C, and in oxygen containing copper the range is up to 260 °C.

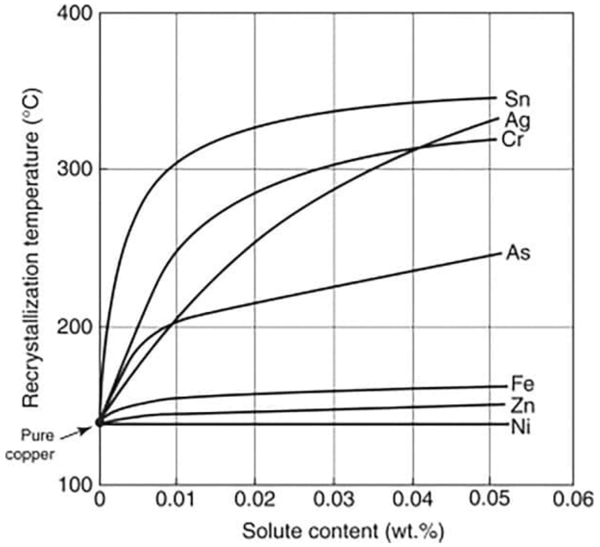

Fig. 44 The effect of various solutes on the recrystallization temperature of copper. Adapted from ASM (2001) *Copper and Copper Alloys*, *ASM Speciality Handbook*. Materials Park, OH: ASM.

Table 7 Recrystallization temperatures of copper (in °C) with respect to minor elemental additions.

Amount	*20 ppm*		*50 ppm*		*100 ppm*		*500 ppm*	
Alloying element	*C10100*	*C10200*	*C10100*	*C10200*	*C10100*	*C10200*	*C10100*	*C10200*
O_2	140		140		140		140	
Fe	140	146	140	153	140	155	148	167
Sb	180	192	258	282	296	314	336	336
As	168	168	198	189	205	205	242	242
Ni	140	140	140	140	140	140	140	140
Pb	146	250	146	270	146	247	146	286
Bi	210	260	247	300	275	328		
Ag	148	148	172	172	207	207	330	330
Sn	140	198	140	277	140	315	140	346
S	181	181	183	183	183	183		
Se	222	222	234	234	240	240	250	250
Te	212	212	228	228	238	238	250	250
P	140	258	140	284	140	300		
Si		161		181		198		242
Co		145		152		161		161
Cr		152		190		260		320
Zn		148		151		152		156
Cd		183		248	275	309	325	356

Data from DKI (1982) *Kupfer*. Deutsches Kupferinstitut.

Grain growth

With continued heating, the larger recrystallized grains grow at the expense of other smaller recrystallized grains, with the result that the grain size increases. In most theories of grain boundary motion, the growth rate is usually expressed by a product of the grain boundary mobility of the rate-determining process and the driving force. The increase of the average grain diameter during isothermal heat treatments can be described by an empirically established time law. Assuming that the mean radius of curvature of the grain boundary R is proportional to the diameter of the grain D, and that the mean grain boundary velocity v is proportional to the time variation of the grain diameter dD/dt, the law can be formulated as follows:

$$\frac{dD}{dt} = C_1 \frac{\gamma}{D} \; C_1 \sim \exp\left[-\frac{Q}{kT}\right]$$

From this, γ is the surface energy, follows by integration:

$$D^2 - D_0^2 = C_2 \gamma \, t$$

Assuming that the grain size has already increased considerably ($D \gg D_0$), the following applies:

$$D = C \cdot t^n$$

Here, $n = 0.5$, but this has been observed experimentally only for pure elements and for annealing temperatures close to the melting point. It was shown experimentally that the exponent n depends on purity and temperature and ranges from 0.1 to 0.5. It is obvious that the grain boundary mobility is higher for pure materials and secondary phases slow down the motion of grain boundaries. In consequence, oxide dispersion strengthened coppers, such as, e.g., Cu-Al_2O_3, are resistant to grain growth and, therefore, are suitable for high temperature applications.

Annealing textures

The texture of copper cold rolled 97% at room temperature and recrystallized at 200 °C consists almost entirely of cube texture and its twins. Other textural components of copper, rolled at lower temperatures and recrystallized at 400 °C, are indicated in Table 8. The recrystallization texture of copper rolled at −196 °C is very similar to the recrystallization texture of cold-rolled brass.

The transition from copper-type recrystallization texture to the brass-type texture depends on the stacking fault energy of the alloy. The strength of the cube texture is reduced by light rolling reductions, large grain sizes, and low recrystallization temperatures.

Table 8 Texture components of copper, rolled, and recrystallized at 400 °C.

Component	*Percentage of texture*		
	−80 °C	*−140 °C*	*−196 °C*
$(2\ 1\ 4)\left[\bar{5}\ \bar{2}\ 3\right]$	0	21.4	57.4
(3 1 0)[0 0 1]	0	8.1	21.3
(1 0 0)[0 0 1]	94.5	60.4	12.8
$(1\ 2\ 2)\left[\bar{2}\ \bar{1}\ 2\right]$	5.7	10.1	8.5

Adapted from Hu H., Goodman S.R. (1952) *Transactions of the Metallurgical Society of AIME* 277: 637.

Anisotropy

The anisotropy of plastic behavior of sheet material is conventionally documented by the Lankford parameter or R-value which is defined by the ratio of contractile strains during a tension test,

$$R = \frac{\varepsilon_w}{\varepsilon_t}$$

where w and t denote the width and thickness directions in a tension test. Because R changes with the direction of the tensile axis, it is common to measure the values at 0°, 45°, and 90° to the rolling direction and to define an average $\overline{R}$ as

$$\overline{R} = \frac{R_0 + 2\,R_{45} + R_{90}}{4}$$

Like all f.c.c. metals, copper and copper alloys have R-values considerably <1.0. For annealed copper, typically, $R_0 = 0.9$, $R_{45} = 0.4$, $R_{90} = 0.9$, and $\overline{R} = 0.6$ or 0.7 and for annealed 70:30 brass, typically, $R_0 = 0.9$, $R_{45} = 0.9$, $R_{90} = 0.8$, and $\overline{R} = 0.9$. The cube texture component lowers R_{45} considerably, while components with $\{1\ 1\ 1\}$ parallel to the sheet raise the R-values.

Corrosion

Many of the applications of copper and copper-based alloys depend on their generally good corrosion resistance. Due to its standard electrochemical potential +0.34 V for Cu/Cu^{2+} and +0.52 V for Cu/Cu^{+}, copper is chemically classified as noble metal, hence is in not oxidizing acids corrosion resistant.

Environments in which copper is susceptible to corrosion attack include certain soft, low-pH well waters, oxidizing acids, ammoniacal solutions, amines, cyanides, nitrates and nitrites, oxidizing heavy metal salts (formation of complex films/compounds), and certain sulfites. The corrosion of copper can also occur by specific microbiologic agents.

Depending on the use condition of the copper material (media, temperature, pH, velocity, etc.), the type and appearance of the corrosion can strongly differ (Table 9).

A few specific forms of corrosion are given below. One is pitting corrosion in which the attack is very localized. Pitting attacks cause much more damage than the same amount of metal loss uniformly spread over the corroded surface. A second type of corrosion is dezincification of brasses containing >15% Zn. Both copper and zinc atoms go into solution, but copper then

Table 9 Types of corrosion according to the conditions.

Surrounding medium	*Corrosion type*	*Corrosion type acc. to the appearance*
Electrolyte, water, humide gases, etc.	Electrochemical corrosion	Surface/uniform corrosion
Wet/hot gases, organic liquids (non conductive)	Chemical corrosion	Selective corrosion
Microorganism	Microbiological influence corrosion-MIC (mainly electrochemical processes)	Contact corrosion
		Pitting corrosion
		Stress corrosion
		Fatigue corrosion
		Inter-granular corrosion
		Erosion corrosion
		High temperature corrosion

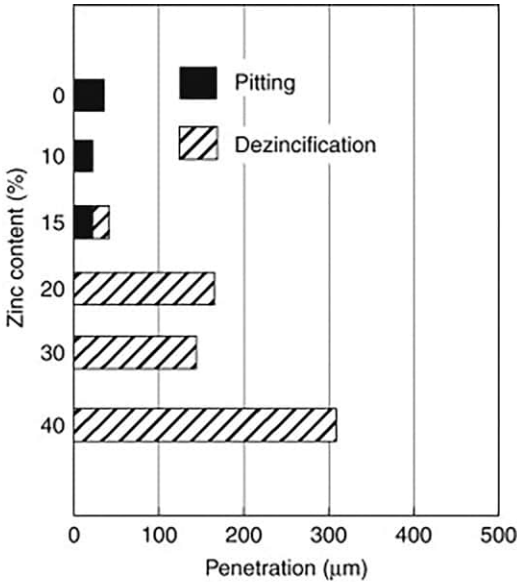

Fig. 45 The effect of zinc content on corrosion of brass when exposed to 0.01 M NH_4Cl at 45 °C for 60 days. Adapted from ASM (2001) *Copper and Copper Alloys*, *ASM Speciality Handbook*. ASM: Materials Park, OH.

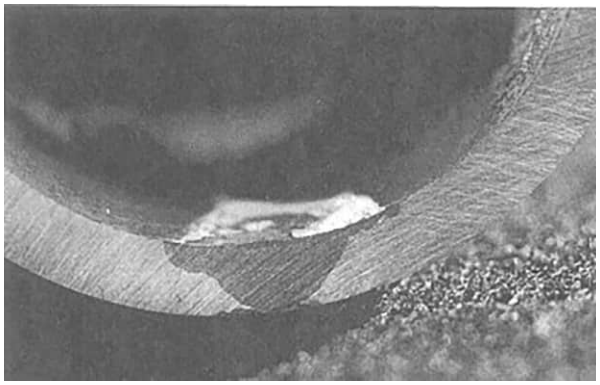

Fig. 46 A plug of dezincified metal on a brass pipe. Adapted from ASM (2001) *Copper and Copper Alloys*, *ASM Speciality Handbook*. ASM: Materials Park, OH.

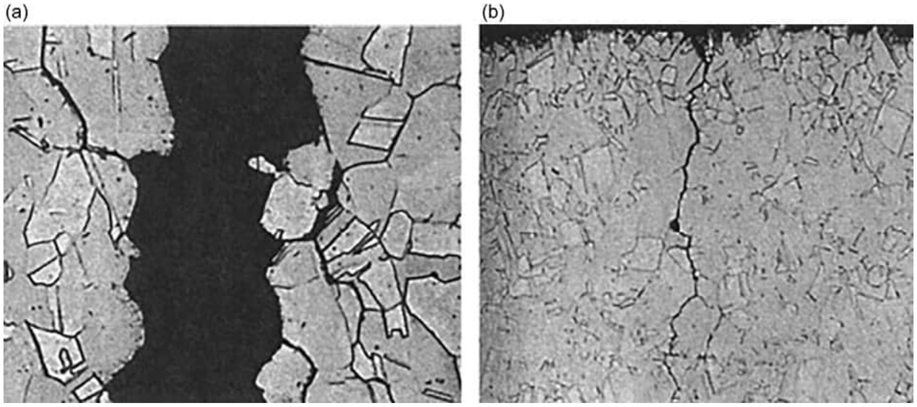

Fig. 47 Examples of stress-corrosion cracking in brass. Both condenser tubes of drawn C12200 copper. Adapted from ASM (2001) *Copper and Copper Alloys*, *ASM Speciality Handbook*. Materials Park, OH: ASM.

precipitates as a porous plug. Fig. 45 shows the effect of composition on the tendency to pitting and dezincification. An example of dezincification is shown in Fig. 46.

Brass containing ⩾15% Zn is susceptible to stress corrosion or season cracking. It occurs only when the brass is under tensile stresses and specific environments. For brass, ammonia is the most common agent. Fig. 47 shows examples of stress-corrosion cracking of brass. The propensity to stress corrosion increases with zinc content and temperature as shown in Fig. 48. Removal of residual stresses by stress-relief anneals is sufficient for many applications.

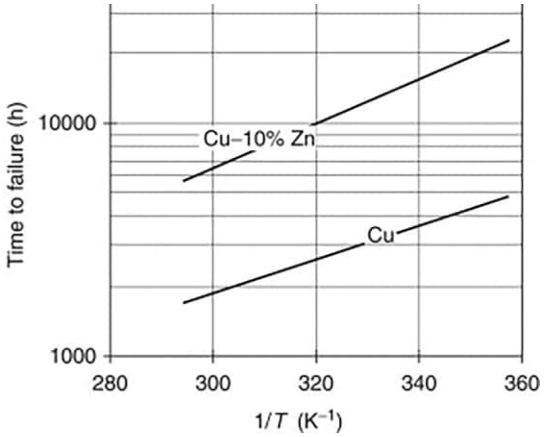

Fig. 48 Arrhenius plot of time to failure of copper and brass under constant load in NH_4OH in the temperature range of 40–70 °C. Adapted from ASM (2001) *Copper and Copper Alloys*, *ASM Speciality Handbook*. Materials Park, OH: ASM.

Hydrogen sickness

Hydrogen is not a problem for most copper alloys. However, if tough-pitch copper containing Cu_2O is exposed to hydrogen at high temperatures, severe embrittlement and crack formation is observed. This water vapor embrittlement is caused by hydrogen reduction of copper oxide inclusions and the formation of water $2H + Cu_2O \rightarrow H_2O + 2Cu$. Water is insolvable in copper, both in liquid and gaseous form, which forms pressurized bubbles and then causes fracture—typically at grain boundaries. At temperatures above the critical temperature for water, the steam pressure generated by the reaction exceeds the strength of copper and cause the grains to be literally forced away from each other. This can happen during casting, welding and heat treatments. Hydrogen formed in humid atmosphere and diffused into the metal. Further, the solubility of hydrogen, like other gases, is much greater in liquid copper than solid copper. Fig. 49 shows the solubility of hydrogen in copper and copper–aluminum alloys (Flinn, 1963). Alloying with aluminum and some other elements decreases the solubility.

Once the copper contains oxides, any contact to a hydrogen-containing atmosphere must be avoided at high temperatures. Problems relating to the occurrence of water vapor embrittlement can be avoided if (i) alloys chosen for hydrogen service are free of oxide inclusions, (ii) alloys contain sufficient amounts of deoxidizing elements, or (iii) alloys are not annealed/treated in hydrogen atmosphere.

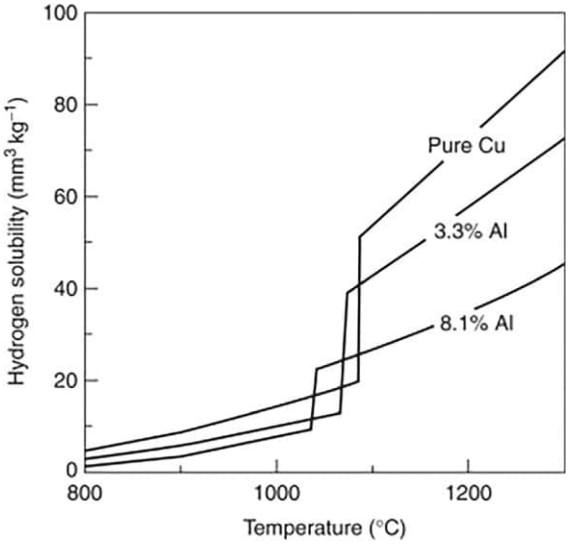

Fig. 49 Solubility of hydrogen in copper and Cu-Al alloys. Adapted from Flinn R.A. (1963) *Fundamentals of Metal Casting*. Reading, MA: Addison-Wesley.

Conclusion

Global copper refinery production amounts 24 Mt./a. One third of the total supply comes from recycling. Among the elements copper has the second-best conductivity, which is also reflected by the good conductivities of most copper alloys, ranging from 30 to 59 $M\Omega m^{-1}$ and 250 to 400 WmK^{-1}, respectively. Single-phase copper alloys are well deformable via dislocation slip ($\{1\ 1\ 1\}\ \langle 110 \rangle$) and in the case of low temperatures and/or low stacking fault energies via deformation twinning. The properties of copper strongly depends on the impurities, as, e.g., the conductivity is very sensitive to alloying and the recrystallization temperature rises from 140 °C to 250 °C by the addition of 20 ppm phosphorous, which is often added for deoxidation. Copper alloys are strengthened by various hardening mechanisms and can show a valuable combination of strength and conductivity of 1.4 GPa and approx. 80% IACS. Certain copper alloys are made for use at high temperatures, showing a softening temperature of approx. 500 °C in the case of CuCrZr. Brass and bronze are used due to their tuneable excellent structure-property relationships, including high strength, good formability, good corrosion resistance, and good wear resistance. Well established as well as novel processing techniques are presented alongside with their potential of widening the field of application of copper and its alloys.

References

ASM (1973) *ASM Metals Handbook*, 8th edn. vol. VIII. Materials Park, OH: ASM.
ASM (1979) *ASM Metals Handbook*, 9th edn. vol. II. Metals Park, OH: ASM.
ASM (2001) *Copper and Copper Alloys, ASM Speciality Handbook*. Materials Park, OH: ASM.
Blewitt TH, et al. (1955) *Proceedings of the Conference on Defects in Crystalline Solids, Bristol*. London: Physical Society. 369.
Bourassa RR and Lengeler B (1976) The formation and migration energies of vacancies in quenched copper. *Journal of Physics F: Metal Physics* 6: 1405.
Branicio PS, et al. (2013) Effect of strain on the stacking fault energy of copper: A first-principles study. *Physical Review B* 88: 064104.
Copperalliance (2022) Copper Environment Profile. Available at: https://copperalliance.org/sustainable-copper/about-copper/copper-environmental-profile/. Accessed: 18 April 2022.
DKI (1982) *Kupfer*. Deutsches Kupferinstitut.
DKI (2018) DKI Brochure i008: Low-Alloyed Copper Alloys. Available at: https://www.kupferinstitut.de/wp-content/uploads/2019/11/RZ_Niedriglegierte_Kupferwerkstoffe_i8_EN_Einzelseiten.pdf. Accessed: 18.04.2022.
Flinn RA (1961) *The Non-Ferrous Copper, Brass, and Bronze Castings*. Cleveland, OH: Founders Society.
Flinn RA (1963) *Fundamentals of Metal Casting*. Reading, MA: Addison-Wesley.
Freudenberger J and Warlimont H (2018) Copper and copper alloys. In: Warlinomt H and Martienssen W (eds.) *Springer Handbook of Materials Data*. Springer.
Guy AG and Hren JJ (1974) *Elements of Physical Metallurgy*. Reading, MA: Addison-Wesley.
Hosford WF (1993) *The Mechanics of Crystals and Textured Polycrystals*. London: Oxford Science Pub.
Humphreys FJ and Hatherly M (1995) *Recrystallization and Related Phenomena*. London: Elsevier.
ICSG (2021) *2021 ICSG Statistical Yearbook*. International Copper Study Group (ICSG).
Ledbetter HM and Naimon ER (1974) Elastic properties of metals and alloys. II. Copper. *Journal of Physical and Chemical Reference Data* 3: 897.
Linde JO and Edwardson S (1954) Investigation of the critical shear stress for single crystals of metallic solid solutions 2. *Arkiv für Fysik* 8: 511.
Linde JO, et al. (1950) Investigation of the critical shear stress for single crystals of metallic solid solutions 1. *Arkiv für Fysik* 2: 89.
MDT (2006) *Phase Diagrams of Cu-Ni-Si Base Alloys*. Tokyo, Japan: Materials Design Technology Co., Ltd.
Murr LE (1975) *Interfacial Phenomena in Metals and Alloys*. Addison-Wesley.
Refractiveindex (2022) Optical Constants of the Elements. Avialable at https://refractiveindex.info. Accessed: 18. April 2022.
Tikana L, et al. (2003) A laser remelted complex manganese bronze with shape memory. *Zeitschrift für Metallkunde* 94: 848.
USGS (2022) USGS Copper Statistics and Information. Available at https://pubs.usgs.gov/periodicals/mcs2022/mcs2022-copper.pdf. Accessed: 18. April 2022.
Venables JA (1965) In: Hirth and Rogers (eds.) *Deformation Twinning, Proceedings of the Metallurgical Society Conference*. vol. 25. AIME Physical Metallurgy Committee. Reed-Hill, R.E., et al.
Wielandwerke (1999) *Wieland-Kupferwerkstoffe, Herstellung, Eigenschaften und Verarbeitung*. Wieland-Werke AG1999.
Wolfram Research (2007) Element Data, Wolfram Language Function. https://reference.wolfram.com/language/ref/ElementData.html. (updated 2014).

Further reading

Brochures and Factsheets, Media Library–Deutsches Kupferinstitut. https://www.kupferinstitut.de/mediathek/?lang=en
Joseph G (1999) *Copper: It Trade, Manufacture, Use and Environmental Status*. Materials Park, OH: ASM.
Kupfer. Düsseldorf: Deutsches Kupfer-Institut.
Laughlin D and Hono K (eds.) (2014) *Physical Metallurgy*, 5th edn. Elsevier.
Meigh H (2000) *Cast and Wrought Aluminium Bronzes*. Copper Development Association.
Smithells CJ and Brandes EA (1983) *Smithells Metals Reference Book*. London: Butterworths.
Warlimont H and Martienssen W (eds.) (2018) *Springer Handbook of Materials Data*. Springer.
West EG (1882) *Copper and Its Alloys*. New York: Wiley.

Alloys: Titanium

TR Bieler, RM Trevino, and L Zeng, Michigan State University, East Lansing, MI, USA

© 2005 Elsevier Ltd. All rights reserved.

This is an update of T.R. Bieler, R.M. Trevino, L. Zeng, Alloys: Titanium, Editor(s): Franco Bassani, Gerald L. Liedl, Peter Wyder, Encyclopedia of Condensed Matter Physics, Elsevier, 2005, Pages 65–76, ISBN 9780123694010, https://doi.org/10.1016/B0-12-369401-9/00536-2.

Introduction 635
Crystallographic Structure of Phases in Titanium Alloys 635
Effects of Crystal Orientations on Mechanical Properties 637
The Classification of Titanium Alloys 638
Commercially Pure Titanium; 99–99.5% Ti 639
Near α and α Titanium Alloys; $\mathrm{Al_{equiv}}<8$ and $\mathrm{Mo_{equiv}}<1$ 639
Near-α Titanium Alloys; $6<\mathrm{Al_{equiv}}<10$ and $\mathrm{Mo_{equiv}}<2$ 639
α–β Titanium Alloys; $5<\mathrm{Al_{equiv}}<10$ and $2<\mathrm{Mo_{equiv}}<8$ 640
β Titanium Alloys; $\mathrm{Al_{equiv}}<6$ and $\mathrm{Mo_{equiv}}=15$–30 (Metastable β), >30 (Stable β) 640
Heat Treating of Titanium Alloys 641
Stress Relieving 645
Annealing 645
Solution Treating 645
Quenching 645
Aging 645
Welding of Titanium Alloys 646
Challenging and Problematic Issues with Titanium Alloys 646
Further Reading 646

Introduction

Titanium and titanium alloys offer a unique combination of physical and mechanical properties that makes titanium an excellent choice for applications that require high strength at temperatures below 550°C, good stiffness (104–133 GPa), toughness, and corrosion resistance. Another desirable characteristic of titanium is its relatively low density of 4.54 $\mathrm{g\,cm^{-3}}$, which is between iron (7.87 $\mathrm{g\,cm^{-3}}$) and aluminum (2.70 $\mathrm{g\,cm^{-3}}$). The high specific strength along with good corrosion resistance makes titanium an enabling material in the aerospace industry (e.g., airframe components, rotors, and compression blades in jet engines), and it is important in the growing biomedical engineering field due to its biocompatibility with living tissues. Titanium alloys have historically been too expensive for the auto industry, but titanium alloys have been recently used for exhaust systems, valves, and springs (its high-yield strength and moderate modulus value gives titanium alloys tremendous elastic resilience). Titanium aluminide intermetallic alloys are likely to become important in the future, due to their lower density and superior high-temperature capabilities.

Titanium ranks ninth as the most plentiful elements, and is the fourth most abundant structural metal in the Earth's crust exceeded only by aluminum, iron, and magnesium. Despite this abundance, the difficulty in processing titanium makes it expensive (~\$50/kg for Ti, compared to \$4/kg for Al and \$1/kg for Fe); yet it is a strategic metal due to which its corrosion resistance and specific strength outweigh its high cost. The cost is likely to drop in the next decade, as new processing methods that reduce the energy requirements and allow continuous processing are scaled up.

The crystallography is considered first, to establish how phase transformations between low- and high-temperature crystal structures occur. From this, the rationale and the complexity surrounding alloying and processing strategies can be appreciated. Finally, a few problematic issues associated with titanium alloys are noted.

Crystallographic Structure of Phases in Titanium Alloys

Titanium exists in two allotropic crystal forms, α, which is a hexagonal structure with a c/a ratio of ~1.59 (slightly squashed compared to the close packed ratio of 1.63), and β, which has the body-centered cubic (b.c.c.) crystal structure. In pure titanium, the α-phase is stable up to the β transus temperature (β_T), 883°C. The α-phase is transformed upon heating above 883°C to the b.c.c. β-phase. The idealized orientation relationship between α (thin lines) and β (dashed lines) is illustrated in Figure 1. However, the actual lattice spacings for α and β do not match perfectly. Figure 2 shows how the atomic positions of these phases are related to each other based on a common origin using lattice constants from a Ti–6Al–4 V alloy. With heating, the $\alpha \rightarrow \beta$ transformation requires lattice strains of ~10% expansion along $[2\,\bar{1}\,\bar{1}\,0]_\alpha$ to become a $[1\,0\,0]_\beta$ direction, ~10% contraction along the $[01\,\bar{1}\,0]_\alpha$ to become $[01\bar{1}]_\beta$, and ~1% contraction along $[0\,0\,0\,1]_\alpha$ that becomes $[01\bar{1}]_\beta$. Due to this imperfect geometrical relationship, one of the two

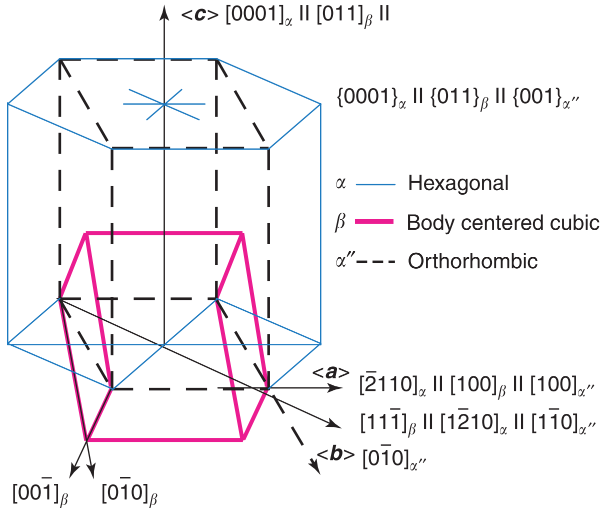
$<c>$ $[0001]_\alpha \parallel [011]_\beta \parallel$
$\{0001\}_\alpha \parallel \{011\}_\beta \parallel \{001\}_{\alpha''}$
α Hexagonal
β Body centered cubic
α'' Orthorhombic
$<a>$ $[\bar{2}110]_\alpha \parallel [100]_\beta \parallel [100]_{\alpha''}$
$[11\bar{1}]_\beta \parallel [1\bar{2}10]_\alpha \parallel [1\bar{1}0]_{\alpha''}$
$<b>$ $[0\bar{1}0]_{\alpha''}$
$[00\bar{1}]_\beta$
$[0\bar{1}0]_\beta$

Figure 1 Idealized orientation relationship between α, β, and α'' crystal structures.

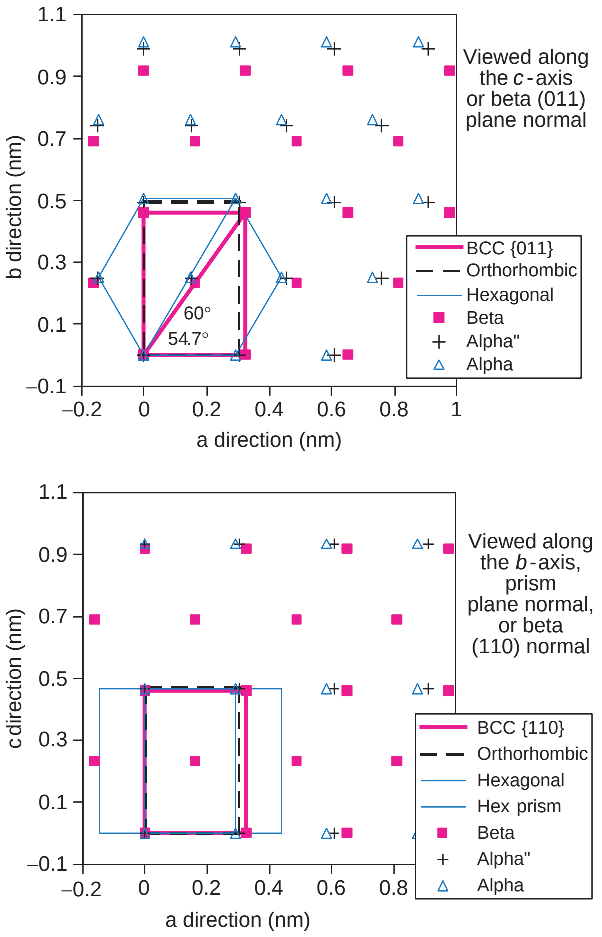

Figure 2 Atomic lattice positions of the α, β, and α'' crystal structures.

$\langle 1\,1\,1\rangle_\beta$ directions in the $\{1\,1\,0\}$ plane will be rotated ~5° to align itself with one of the $\langle \bar{2}\,110\rangle_\alpha$ directions, leading to six possible variants of β from one α orientation, as shown in Figure 3a. This means that two β variants can be misoriented from another by ~10°. Thus, β variants arising from one parent α crystal can be misoriented from each other by ~10°, 50°, 60°, or 70° rotation about a $\langle 0\,1\,1\rangle_\beta$ axis (a prior $\langle 0\,0\,0\,1\rangle_\alpha$ axis).

With the reverse $\beta \rightarrow \alpha$ transformation upon cooling, a $\langle -2\,1\,1\,0\rangle_\alpha$ vector can align with one of the two $\langle 1\,1\,1\rangle_\beta$ directions on each of the six $\{1\,1\,0\}$ planes in the β-phase. Since the angles between $\{1\,1\,0\}_\beta$ planes are either 60° or 90°, the c-axes of daughter α can

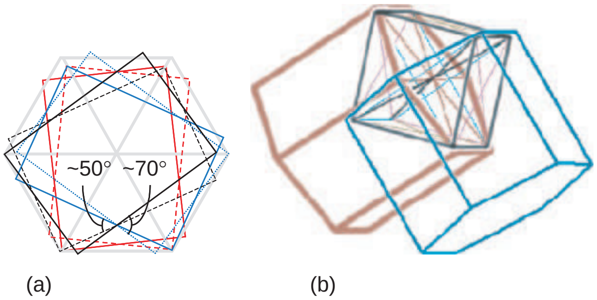

Figure 3 (a) Possible β {0 1 1} plane orientations based upon parent α during $\alpha \rightarrow \beta$ transformation, and (b) two possible α orientations based upon parent β during $\beta \rightarrow \alpha$ transformation.

point in as many as six directions, and each direction has two variants that are rotated ~10° about the *c*-axis. An example of a 90° misorientation from the same parent β crystal is shown in Figure 3b.

Although there are 12 variants of the α orientation possible for each parent β orientation, most prior β grains will only choose a few of the 12 α variants during the α–β transformation process. Recent research has shown that the preferred transformation variants are those that have higher populations of dislocations present on $\{1\,1\,0\}_\beta$ planes. Therefore, it is possible to control the transformation process by controlling the dislocation density in the β-phase. The dislocation density depends on dislocation generation (plastic deformation) and annihilation (recovery) processes that are sensitive to prior deformation history, heating rates, and time at temperature. The understanding of what controls variant selection is just emerging, and it is likely to be exploited profitably in the coming decade to allow the manufacturing processes to be designed to achieve optimized properties for a given application.

In addition to α-and β-phases, there are a number of subtle variations, including α' and α'' martensites that may form during quenching, and ordered phases such as α_2- and ω-phases. With quenching, there is no opportunity for diffusional segregation of alloying elements; so the resulting hexagonal supersaturated α' has lattice constants slightly different from equilibrium α. The α''-phase has an orthorhombic crystal structure, which is outlined in bold lines in Figure 1. This crystal structure is between the α and the β crystal lattice (Figure 2). The α_2-phase (Ti_3Al) is an ordered version of the hexagonal lattice with Al atoms spaced regularly on the hexagonal lattice, which increases the resistance to dislocation motion. There has been much interest in ordered orthorhombic intermetallic Ti–Al–Nb alloys in the past decade. The ω-phase is a different hexagonal ordered-crystal structure that could form in prior β-regions after long-term aging or in α-regions after stress-induced transformation from $\alpha \rightarrow \omega$. Ordered phases resist dislocation motion, which can increase the strength, but the continuous ω-phase is known to reduce the ductility and facilitate crack nucleation.

Figure 2 shows that the atomic arrangement of the α-, α''-, and β-phases are very similar; but small differences in atomic position lead to different crystal structures that have significantly different properties. Thus, phase boundaries in Ti alloys are typically coherent or semi-coherent. These phase boundaries are quite easily observed in polished and etched microstructures, often giving the impression of a fine grain size, but it is important to realize that the domains of similar orientations are often much larger than they appear, and these "invisible" mesotextural features can account for early dwell fatigue crack nucleation.

Unlike steels, the martensitic transformations in titanium result in small volume changes and modest shears, but the paradigm of using martensitic transformations in steels to manipulate microstructures and properties is also used in titanium alloys, though the details are completely different (e.g., α'' is softer than α). Ordered intermetallic alloys based on Ti_3Al and TiAl can also be manipulated with similar strategies as those used in titanium alloys, but again, the details differ. The technology of titanium alloys is highly dependent on the ability to control the phase transformation from the β- to the α-phase using strategic alloying and heat treatment history, which gives titanium alloys flexible and designable properties similar to that possible with steels.

Effects of Crystal Orientations on Mechanical Properties

The hexagonal crystal structure has considerable elastic and plastic anisotropy, which are strongly affected by processing history. Young's modulus is highest (143 GPa) along the *c*-axis, and lowest (104 GPa) in any direction in the basal plane. Titanium deforms with eight slip and twinning systems are illustrated in Figure 4. Each of these systems require different critical resolved shear stresses to operate, making the plastic deformation process much more complicated than cubic metals. Prism slip in $\langle a \rangle$ directions is the easiest, leading to plastic deformation that leaves the crystal dimension along the *c*-axis and the *c*-axis orientation unchanged. The next easiest slip system is basal slip in $\langle a \rangle$ directions, which also does not change the dimension of the crystal along the *c*-axis, but it causes crystal rotation about a prism plane normal axis. It is possible to have $\langle a \rangle$ slip on pyramidal planes as well.

To change the crystal dimension along the *c*-axis, twinning or $\langle c+a \rangle$ slip on pyramidal planes is required, but the critical resolved stress for $\langle c+a \rangle$ slip is high, so twinning systems are usually more easily activated. Consequently, Ti crystals are intrinsically hard when stressed along the *c*-axis. Furthermore, the relative strengths of these deformation systems change with temperature, for example, twinning does not occur at elevated temperatures. Consequently, the distribution of crystal orientations can have a large impact on both elastic and plastic properties. Even pure titanium behaves like a composite material; depending on the crystal orientation with respect to the resolved shear stresses, any crystal can be either hard or soft. In Figure 5, shades of gray represent the Taylor factor (proportional to the plastic flow stress of the crystal) in a rolled plate deformed in uniaxial tension.

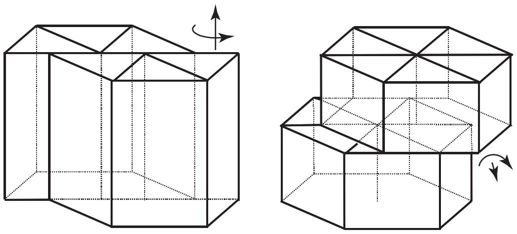

(a) $\{1\,0\,\bar{1}\,0\} < 1\,\bar{2}\,1\,0>$
Prism slip has 3 systems

(b) $\{0\,0\,0\,1\} <1\,\bar{2}\,1\,0>$
Basal slip has 3 systems

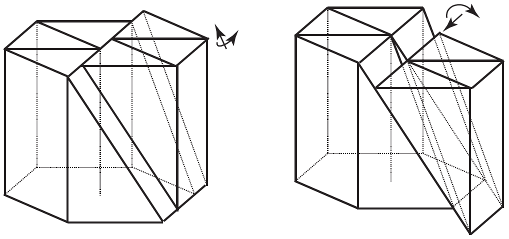

(c) $\{1\,0\,\bar{1}\,1\} < 1\,\bar{2}\,1\,0>$
3 systems

(d) $\{1\,0\,\bar{1}\,1\} < 2\,\bar{1}\,\bar{1}\,\bar{3}>$
6 systems

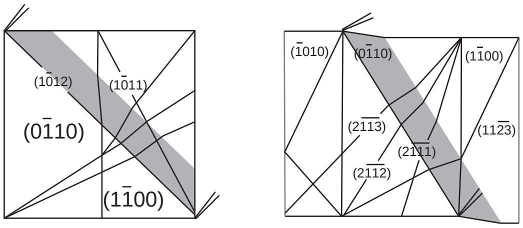

(e) $\{1\,0\,\bar{1}\,2\} <\bar{1}\,0\,1\,1\}>$
Tensile twinning
shear of 0.169
$= \tan^{-1}$ (9.6°)

(f) $\{2\,\bar{1}\,\bar{1}\,2\} <2\,\bar{1}\,\bar{1}\,\bar{3}>$
Compressive twinning
shear of 0.224
$= \tan^{-1}$ (12.6°)

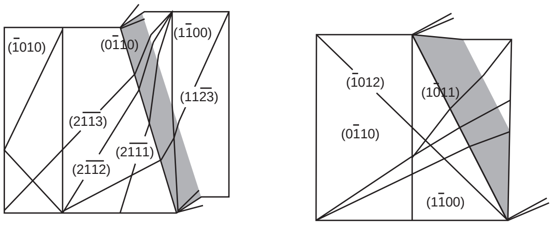

(g) $\{2\,\bar{1}\,\bar{1}\,1\} <\bar{2}\,1\,1\,6>$
Tensile twinning
shear of 0.628
$= \tan^{-1}$ (32.1°)

(h) $\{1\,0\,\bar{1}\,1\} <1\,0\,\bar{1}\,\bar{2}>$
Compressive twinning
shear of 0.103
$= \tan^{-1}$ (5.9°)

Figure 4 (a) Prism slip, (b) basal slip in the $\langle a\rangle$ direction, (c) $\langle a\rangle$ slip, (d) $\langle c+a\rangle$ slip on pyramidal planes, and (e–h) twinning systems; all types have 6 systems. Only $\langle c+a\rangle$ slip or twinning causes a change in crystal dimension in the *c* direction. Arrows illustrate axis of crystal rotation due to slip; only prism slip does not change the orientation of the *c*-axis.

The Classification of Titanium Alloys

Titanium alloys are classified according to the phases present within their microstructure. Alloys consisting of mainly α-phase are called α-alloys, but if small amounts of β-phase are present, the alloy is classified as a near-α alloy. Alloys consisting of a mixture of both α- and β-phases are termed α–β alloys. Finally, titanium alloys that have the majority of β-phase at room temperature are called β-alloys. Figure 6 shows the effects that several important alloying elements have on the phase diagram, indicating that the equilibrium between α, $\alpha+\beta$, and β phase fields (α and β transus lines) are highly sensitive to alloy composition. Aluminum is one of the most important alloying elements because it is a potent solid–solution strengthener and it reduces the density, so it is found in virtually all titanium alloys. Ti_3Al (α_2) forms with more than 6 wt.% Al, which can strengthen, but also embrittle the alloy. Molybdenum and vanadium are the two most popular β-stabilizing additives, which also provide strengthening of the β-phase. Tin

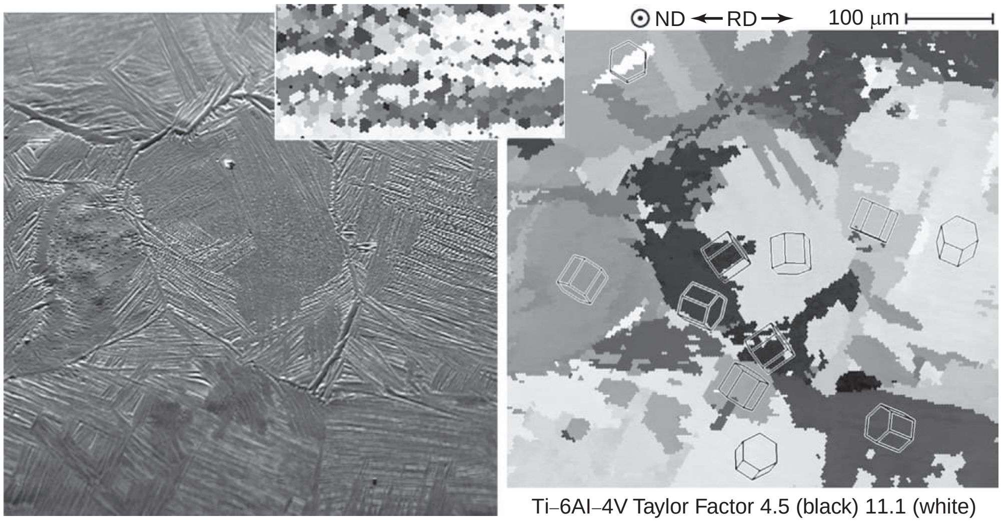

Figure 5 Rolled plate (rolling direction and plate normal are indicated) SEM and Orientation Imaging Microscopy Taylor factor maps before (inset) and after annealing above β transus, followed by controlled slow cooling. Taylor factor was computed based upon uniaxial deformation in the rolling direction with CRSS ratios of 0.7:1:3 for prism:basal:pyramidal $\langle c{+}a \rangle$ slip. (Images obtained at the Air Force Research Laboratory, WPAFB, OH.)

and zirconium are the only two alloying elements used which have neither an α-stabilizing nor β-stabilizing effect on the crystal structure (Figure 6a), but both provide solid–solution strengthening to the α-phase; also, Sn is known to improve weldability. All other elements either stabilize the α- or β-phase, as summarized in Table 1.

The aluminum equivalent and molybdenum equivalent equations (in wt.%) are used to describe the degree of stability of the α- and β-phases, and to define what class an alloy is in. Oxygen and nitrogen are potent α-stabilizers, and iron is the most potent β-stabilizer:

$$\mathrm{Al_{equiv}} = \%\mathrm{Al} + \frac{1}{3}(\%\mathrm{Sn}) + \frac{1}{6}(\%\mathrm{Zr}) + 10(\%\mathrm{O})$$

$$\mathrm{Mo_{equiv}} = \%\mathrm{Mo} + 0.67(\%\mathrm{V}) + 2.9(\%\mathrm{Fe}) + 1.6(\%\mathrm{Cr}) - \%\mathrm{Al}$$

$$\mathrm{O_{equiv}} = \%\mathrm{O} + 2(\%\mathrm{N}) + 0.67(\%\mathrm{C})$$

Commercially Pure Titanium; 99–99.5% Ti

Commercially pure (CP) titanium is considered an α-alloy, because the α-phase is the only phase present. Oxygen is the main alloying element that determines the grade and strength of the alloy (Figures 6b and 7). CP titanium has lower strength than other alloys, but it is the alloy of choice for applications requiring corrosion resistance, and it has better elevated temperature creep resistance, and is less expensive than the other titanium alloys. Figure 7 shows how the strength and hardness increase with interstitial element concentration. Since oxygen is the main alloying element in CP titanium, the $\mathrm{O_{equiv}}$ describes the strengthening effect of the interstitial elements O, N, and C. Each 0.1% $\mathrm{O_{equiv}}$ increases the strength of unalloyed titanium by ~120.5 MPa.

Near α and α Titanium Alloys; $\mathrm{Al_{equiv}} < 8$ and $\mathrm{Mo_{equiv}} < 1$

Alpha titanium alloys are primarily used in the chemical and processes engineering industry. These applications require excellent corrosion resistance and ductility. Aluminum is the most important alloying element in order to stabilize α-phase, add strength, and lower the density (Figure 6b, Table 2). Ti–5Al–2.5Sn is the most commonly used α alloy, and like most α alloys it cannot be age-hardened, but it does has excellent weldability.

Near-α Titanium Alloys; $6 < \mathrm{Al_{equiv}} < 10$ and $\mathrm{Mo_{equiv}} < 2$

Near-α alloys are ideal for high temperature applications ~500–550°C, where its excellent creep resistance can be combined with higher strength due to a small amount of dispersed β-phase. Small amounts of molybdenum and vanadium are added to retain some β-phase at room temperature. Ti–8Al–1Mo–1V is the most commonly used near-α alloy, however the high aluminum content can cause stress corrosion cracking (SCC) problems; therefore, most alloys used today are limited to 6 wt.% Al to avoid SCC problems. This alloy has good weldability, but a limited degree of hardenability due to a small amount of β-phase.

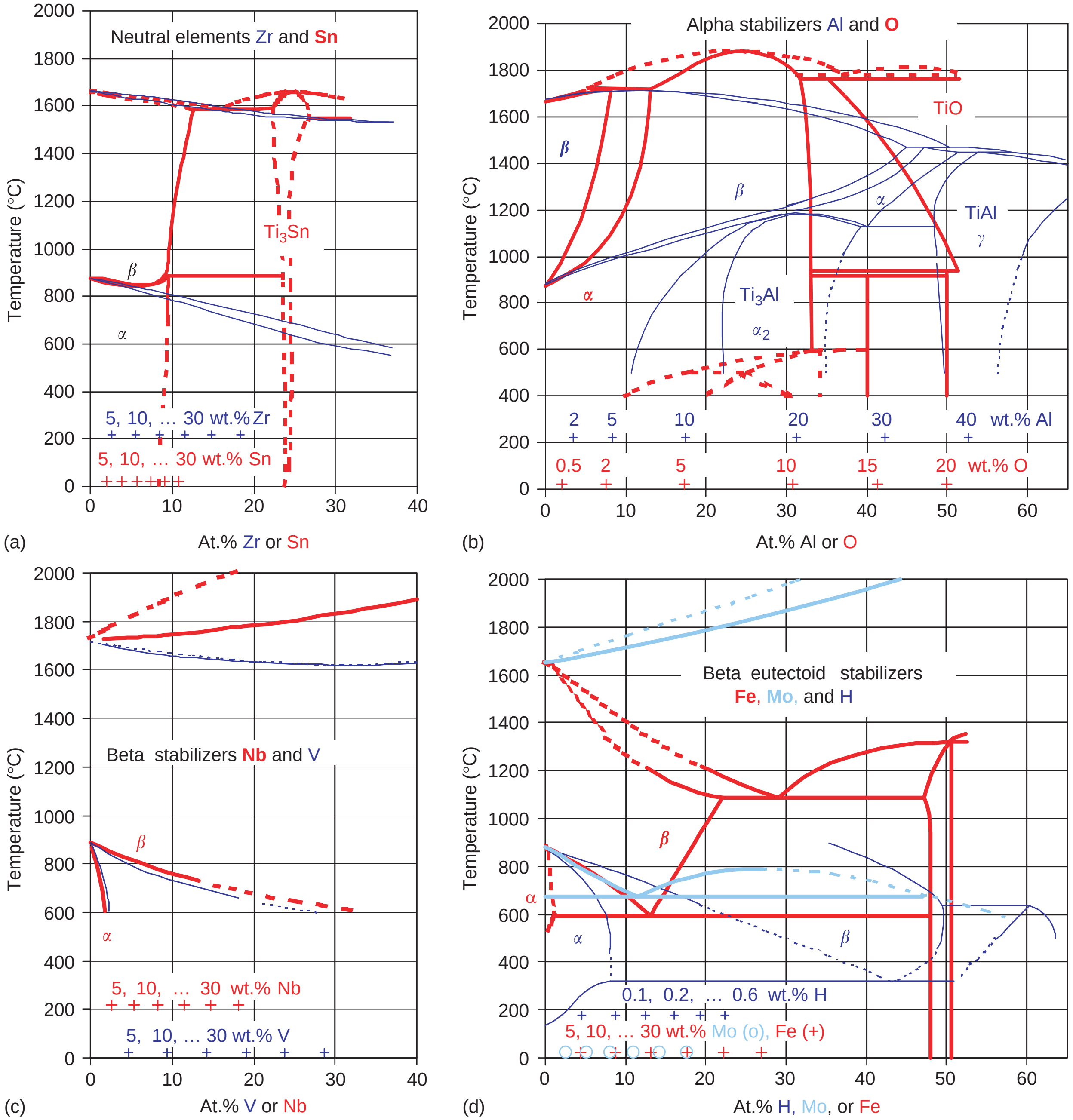

Figure 6 Exemplary phase diagrams for elements that have (a) neutral, (b) α stablizing, (c) β stabilizing, and (d) β eutectoid stablizing effects. (Adapted from Smithells Metals Reference Book, 7th edn., 1992, London: Butterworth. McCullough C, Valencia JJ, Levi CG, and Mehrabian R (1989) Phase equilibria and solidification in Ti–Al alloys. *Acta Metallurgica* 37(5): 1321–1336, for update of Ti–Al system.)

α–β Titanium Alloys; $5<\mathrm{Al}_{\mathrm{equiv}}<10$ and $2<\mathrm{Mo}_{\mathrm{equiv}}<8$

The α–β alloy Ti–6Al–4V is the most popular of all titanium alloys, representing more than 50% of the titanium market (Figures 6b and 6c). The α–β alloys can be solution heat-treated, quenched, and aged to medium-/high-strength levels and have good formability, but the creep resistance and weldability are lower than the α and near-α alloys, primarily due to the presence of the β-phase, which has a much higher diffusivity and more slip systems.

β Titanium Alloys; $\mathrm{Al}_{\mathrm{equiv}}<6$ and $\mathrm{Mo}_{\mathrm{equiv}}=15$–30 (Metastable β), >30 (Stable β)

The β titanium alloys are heat treatable, to achieve the highest strength levels of the five types of titanium alloys (Figures 6c and 6d). The high strength arises from precipitation of very fine α-phase during an aging heat treatment. The b.c.c. crystal structure also gives

Table 1 Effects of alloying elements

Alloying element	*Range (wt.%)*	*Effect on structure and properties*
Aluminum, Al	2–7	α-Stabilizer, solid solution strengthener, reduces density, improves oxidation resistance
Carbon, C	0.05–0.1	α-Stabilizer, interstitial element
Chromium, Cr	2–12	β-Eutectoid stabilizer
Cobalt, Co		β-Eutectoid stabilizer
Copper, Cu	2–6	β-Eutectoid stabilizer, improves weldability, α and β strengthener
Hydrogen, H	0.008–0.02	β-Eutectoid stabilizer, interstitial element
Iron, Fe		β-Eutectoid stabilizer
Manganese, Mn		β-Eutectoid stabilizer
Molybdenum, Mo	2–20	β-Isomorphous stabilizer, moderate solid solution strengthener of β phase
Nickel, Ni		β-Eutectoid stabilizer
Niobium, Nb		β-Isomorphous stabilizer, known to improve oxidation behavior of Ti alloys, moderate solid solution strengthener of β phase
Nitrogen, N	0.015–0.07	α-Stabilizer, interstitial element
Oxygen, O	0.1–0.4	α-Stabilizer, interstitial element, strengthens α phase
Silicon, Si	0.05–1	β-Eutectoid stabilizer, Si atoms tend to segregate at dislocations and thus effectively prevent dislocation climb, improving creep resistance, also strengthens α phase
Tantilum, Ta		β-Isomorphous stabilizer
Tin, Sn	2–6	Neutral stabilizer, improves weldability, solid solution strengthener of α phase
Vanadium, V	2–20	β-Isomorphous stabilizer, moderate solid solution strengthener of β phase
Zirconium, Zr	2–8	Neutral stabilizer, solid solution strengthener of α phase, Zr also tends to homogenize fine silicide precipitates

Various sources, including (1990) Properties and selection: nonferrous alloy and special-purpose materials. *ASM Metal Handbook*, vol. 2, p. 605. Metals Park, OH: ASM International.

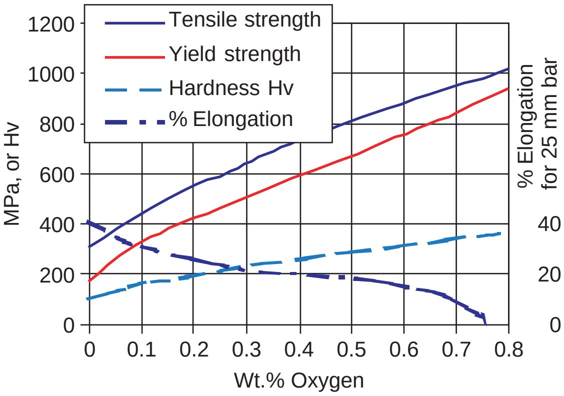

Figure 7 Effect of oxygen on strength and elongation in CP titanium. (Adapted from Jaffee RI (1958) The physical metallurgy of titanium alloys. *Progress in Metal Physics* 7:109.)

good formability properties prior to heat treatment. Beta titanium alloys contain large amounts of alloying elements such as Mo, Cr, V, and Fe which are needed to stabilize the β-phase. The high degree of alloying elements makes β alloys the densest of the five alloy types (Table 2).

Tables 2–4 provide further details, using normal font to identify CP, italics to identify near-α and α alloys, bold italics to identify α–β alloys, and bold to identify β alloys. Table 2 is sorted by density to illustrate the influence of alloying. Table 5 describes weldability issues, and Tables 3 and 4 describe heat treating methodologies, which are discussed next.

Heat Treating of Titanium Alloys

Titanium and titanium alloys are heat treated for a number of reasons: to reduce residual stresses from the many different fabrication processes (stress relieving), to obtain optimum combinations of ductility, machinability, and dimensional stability (annealing), to increase strength (solution treating and aging in α–β and β alloys), and finally to optimize specific properties such as fracture toughness, fatigue strength, and high-temperature creep resistance. In general, a heat treatment is used to rearrange phase–volume fractions, phase boundaries in strategic ways. A quench from high temperature is commonly used to provide a

Table 2 Effect of alloying on properties (sorted by density)

Titanium alloy – CP, near α and α,**α–β**, ***near β, metastable β, or β***	*Condition*	E *(Gpa)*	*Poisson's ratio*	*Density (g cm^{-3})*	*Room temperature properties*			*K(IC)(MPa $m^{1/2>}$)*	*V-notch (J)*
					Y.S. (MPa)	*T.S. (MPa)*	*% Elong.*		
Ti–8Al–1Mo–1V	*Duplex annealed*	*120*	*0.32*	*4.37*	*951*	*1000*	*15*	*82*	*32*
Ti–6Al–4V	***Annealed***	***110–140***	***0.342***	***4.43***	***924***	***993***	***14***	***33–110***	***19***
	Solution+age			***4.43***	***1103***	***1172***	***10***	***33–110***	
Ti–5Al–2.5Sn	*Annealed*	*115*	*0.31*	*4.48*	*807*	*862*	*16*	*96*	*26*
Ti–6Al–2Nb–1Ta–1Mo	*As rolled 2.5 cm plate*	*113.8*	*0.31*	*4.48*	*758*	*855*	*13*		*31*
Ti–3Al–2.5V	***Annealed***			***4.48***	***586***	***689***	***20***		
Ti–7Al–4Mo	***Solution+age***			***4.48***	***1034***	***1103***	***16***		***18***
99.5%Ti Grade 1	Annealed	102.7	0.34	4.51	241	331	30		
99.2%Ti Grade 2	Annealed	102.7	0.34	4.51	354	434	28		43
Ti–0.3Mo–0.8Ni (Ti Code 12)				*4.51*					
Ti–6Al–2Sn–4Zr–2Mo	*Duplex annealed*			*4.54*	*896*	*979*	*15*		
	Annealed	***110–117***		***4.54***	***1000***	***1069***	***14***	***30–70***	***18***
Ti–6Al–6V–2Sn (Cu+Fe)	***Solution+age***			***4.54***	***1172***	***1276***	***10***	***30–70***	
Ti–6Al–2Sn–2Zr–2Mo–2Cr–0.25Si	***Solution+age***	***110–120***	***0.327***	***4.57***	***1138***	***1276***	***11***	***65–110***	
Ti–6Al–2Sn–4Zr–6Mo	***Solution+age***	***114***		***4.65***	***1172***	***1269***	***10***	***30–60***	
Ti–5Al–2Sn–4Mo–2Zr–4Cr (Ti–17)		***112***		***4.65***	***1050***	***1100–1250***	***8–15***	***30–80***	
Ti–10V–2Fe–3Al		**110**		**4.65**	**1000–1200**	**1000–1400**	**6–16**	**30–100**	
Ti–15V–3Al–3Cr–3Sn		**80–100**		**4.78**	**800–1000**	**800–1100**	**10–20**	**40–100**	
Ti–13V–11Cr–3Al	**Solution+age**		**0.304**	**4.82**	**1172**	**1220**	**8**	**77**	**11**
Ti–3Al–8V–6Cr–4Zr–4Mo (β C)	**Solution+age**			**4.82**	**1379**	**1448**	**7**	**50–90**	**10**
	Annealed	**86–115**		**4.82**	**834**	**883**	**15**	**50–90**	
Ti–8Mo–8V–2Fe–3Al	**Solution+age**			**4.85**	**1241**	**1310**	**8**		
15Mo–3Al–0.3Fe–2.8Nb–0.2Si (β-21S)			**0.33**	**4.94**					
Ti–15Mo–5Zr–3Al				**5.01**					
Ti–11.5Mo–6Zr–4.5Sn (β III)	**Solution+age**	**83–103**		**5.06**	**1317**	**1386**	**11**	**50–100**	

Y.S.=Yield strength; T.S.=Tensile strength.

Sources: (1990) Properties and selection: Nonferrous alloys and special-purpose materials. *ASM Metals Handbook*, vol. 2, p. 621. Metals Park, OH: ASM International; (1993) *ASM Metals Reference Book*, 3rd edn. Metals Park, OH: ASM International.

Table 3 Heat treating of titanium alloys

Titanium alloy – CP, near α and α	T(β) °*C*±*15*	Stress–relief		Annealing			Solution treating			Aging	
α+β, near β, metastable β, β		°*C*	Time *(h)*	°*C*	Time *(h)*	Cooling	°*C*	Time *(h)*	Cooling	°*C*	Time *(h)*
99.5%Ti Grade 1	910	480–595	1/4–4	650–760	1/10–2	Air	N/A	N/A	N/A	N/A	N/A
99.2%Ti Grade 2	913	480–595	1/4–4	650–760	1/10–2	Air	N/A	N/A	N/A	N/A	N/A
α or near-α alloys											
Ti–5Al–2.5Sn	*1050*	*540–650*	*1/4–4*	*720–845*	*1/6–4*	*Air*	*N/A*	*N/A*	*N/A*	*N/A*	*N/A*
Ti–8Al–1Mo–1V	*1040*	*595–705*	*1/4–4*	*790*	*1–8*	*Air or furnace*	*980–1010*	*1*	*Oil or water*	*565–595*	. . .
Ti–6Al–2Sn–4Zr–2Mo	*995*	*595–705*	*1/4–4*	*900*	*1/2–1*	*Air*	*955–980*	*1*	*Air*	*595*	*8*
Ti–6Al–2Nb–1Ta–1Mo	*1015*	*595–650*	*1/4–2*	*790–900*	*1–4*	*Air*					
Ti–0.3Mo–0.8Ni (Ti code 12)	*880*	*480–595*	*1/4–4*								
α–β alloys											
Ti–6Al–4V	***1000 (±20)***	***480–650***	***1–4***	***705–790***	***1–4***	***Air or furnace***	***955–970***	***1***	***Water***	***480–595***	***4–8***
Ti–6Al–6V–2Sn (Cu+Fe)	***945***	***480–650***	***1–4***	***705–815***	***3/4–4***	***Air or furnace***	***885–910***	***1***	***Water***	***480–595***	***4–8***
Ti–3Al–2.5V	***935***	***540–650***	***1/2–2***	***650–760***	***1/2–2***	***Air***					
Ti–6Al–2Sn–4Zr–6Mo	***940***	***595–705***	***1/4–4***	***N/A***	***N/A***	***N/A***	***845–890***	***1***	***Air***	***580–605***	***4–8***
Ti–5Al–2Sn–4Mo–2Zr–4Cr (Ti–17)	***900***	***480–650***	***1–4***	***N/A***	***N/A***	***N/A***	***845–870***	***1***	***Air***	***580–605***	***4–8***
Ti–7Al–4Mo	***1000***	***480–705***	***1–8***	***705–790***	***1–8***	***Air***					
Ti–6Al–2Sn–2Zr–2Mo–2Cr–0.25Si	***970***	***480–650***	***1–4***	***705–815***	***1–2***	***Air***	***870–925***	***1***	***Water***	***900–1100***	***4–8***
β or near-β alloys											
Ti–13V–11Cr–3Al	**720**	**705–730**	**1/12–1/4**	**705–790**	**1/6–1**	**Air or water**	**775–800**	**1/4–1**	**Air or water**	**425–480**	**4–100**
Ti–11.5Mo–6Zr–4.5Sn (β III)	**760**	**720–730**	**1/12–1/4**	**690–760**	**1/6–2**	**Air or water**	**690–790**	**1/8–1**	**Air or water**	**480–595**	**8–32**
Ti–10V–2Fe–3Al	**805**	**675–705**	**1/2–2**	**N/A**	**N/A**	**N/A**	**760–780**	**1**	**Water**	**495–525**	**8**
Ti–15V–3Al–3Cr–3Sn	**760**	**790–815**	**1/12–1/4**	**790–815**	**1/12–1/4**	**Air or water**	**790–815**	**1/4**	**Air**	**510–595**	**8–24**
Ti–8Mo–8V–2Fe–3Al	**775**										
Ti–15Mo–5Zr–3Al	**785**										
15Mo–3Al–0.3Fe–2.8Nb–0.2Si (β-21S)	**800**										
Ti–3Al–8V–6Cr–4Zr–4Mo (β C)	**795**	**705–760**	**1/6–1/2**	**790–815**	**1/4–1**	**Air or water**	**815–925**	**1**	**Water**	**455–540**	**8–24**

Adapted from (1991) Heat treating. *ASM Metals Handbook*, vol. 4, pp. 914–917. Metals Park, OH: ASM International.

Table 4 Heat treating of α–β alloys

Heat treatment designation	*Heat treatment cycle*	*Microstructure*
Duplex anneal	Solution treat at 50–75°C below $T(\beta)$, air cool and age for 2–8 h at 540–675°C	Primary α, plus Widmanstätten α–β regions
Solution treat and age	Solution treat at ~40°C below $T(\beta)$, water quench(a) and age for 2–8 h at 535–675°C	Primary α, plus tempered α' or a β–α mixture
Beta anneal	Solution treat at ~15°C above $T(\beta)$, air cool and stabilize at 650–760°C	Widmanstätten α–β colony microstructure
Beta quench	Solution treat at ~15°C above $T(\beta)$, water quench and temper at 650–760°C for 2 h	Tempered α'
Recrystallization anneal	925°C for 4 h, cool at 50°C h^{-1} to 760°C, air cool	Equiaxed α with β at grain-boundary triple points
Mill anneal	α–β Hot work plus anneal at 705°C for 30 min to several hours and air cool	Incompletely recrystallized α with a small volume fraction of small β particles

In more heavily β-stabilized alloys such as Ti–6Al–2Sn–4Zr–6Mo or Ti–6Al–6V–2Sn, solution treatment is followed by air cooling. Subsequent aging causes precipitation of α-phase to form an α–β mixture.

Adapted from (1991) Heat treating. *ASM Metals Handbook*, vol. 4, p. 914. Metals Park, OH: ASM International.

Table 5 Welding of titanium alloys

Alloy type	*Condition*	*Description*
Unalloyed titanium	Annealed	Welding of cold-worked alloys anneals the HAZ and negates any strength produced by cold working
Alpha titanium alloys	Annealed	Ti–5Al–2.5Sn, Ti–6Al–2Sn–4Zr–2Mo, Ti–5Al–5Sn–2Zr–2Mo, Ti–6Al–2Nb–1Ta–1Mo, and Ti–8Al–1Mo–1V are always welded in annealed condition
Alpha–beta titanium alloys	Annealed or solution-treated and partially aged	Low weld ductility of most α–β alloys is caused by phase transformation in the weld zone or HAZ
Metastable beta titanium alloys	Annealed or solution heat treated	In as-welded condition, welds are low in strength but ductile; to obtain full strength the alloys are welded in annealed condition, the weld is cold worked by shot peening or planishing, and the weldament is then solution treated and aged
Weld type	*Thickness range*	*Description*
Gas–tungsten arc weld (GTAW)	Base metal up to 2.5 mm, for thicker base metal filler metal is required	
Gas–metal arc weld (GMAW)	More than 3 mm to greater than 13 mm	Applied using pulse current or spray mode and is less costly than GTAW
Plasma arc welding (PAW)	Plate up to 13 mm, filler metal may be used	Faster than GTAW and can be used on thicker sections
Electron-beam welding (EBW)	Plates 6 mm to more than 76 mm	Used in aircraft and aerospace industry for producing high quality welds; performed in high vacuum atmosphere therefore low contamination of weldament
Laser-beam welding (LBW)	Base metal usually cannot exceed 13 mm	
Friction welding (FRW)		Useful for joining tube, pipe, or rods
Resistance welding (RW)		Used to join titanium sheet by spot welds or continuous seam welds, also used to weld titanium sheet to dissimilar metals
Fluxes	N/A	Fluxes cannot be used because they combine with titanium to form brittleness and may reduce corrosion resistance

Excerpted from (1990) Welding brazing and soldering. *ASM Metals Handbook*, vol. 6, pp. 783–786. Metals Park, OH: ASM International.

thermodynamic driving force for nanoscale rearrangement at lower aging temperatures. More recently, benefits of rapid heating into the β-phase field to obtain desirable microstructures have been described. Standard practice is identified in Tables 3 and 4, and the preferred phase for alloying elements is in Table 1. However, alloy element local concentration is highly dependent on the history of the phase volume fraction and locations of phase boundaries in space and hence, on all prior heat treating and working history. For this reason, the same heat treatment on materials with different prior history can cause considerable variability in resulting properties.

Unalloyed α titanium alloys can be stress relieved and annealed, but cannot be heat treated to increase their strength. When the heat treatment of titanium alloys involves heating to temperatures near the β transus, it is important that T_β is known for each specific alloy. Table 3 illustrates how the β transus temperature (β_T) depends on alloy composition.

Stress Relieving

Stress relieving (SR) is used to remove residual stresses from prior fabrication steps, or even prior heat treatments. Unbalanced residual stresses can result in part distortion, and cause problems in those alloys susceptible to hydrogen embrittlement. SR can result in aging of all alloy types, α can be aged by α_2 precipitates, and if metastable β is present, α precipitation that provides strengthening can occur. For α and α–β alloys, the SR temperature will be in the range of 480–815°C, and if these alloys were β-annealed, more rearrangement of phase boundaries is needed and the SR temperature should be increased by $\sim$55°C. When stress-relieving β alloys, care must be taken to avoid interfering with the final age-hardening treatment. If a β alloy has not been heat treated, the SR temperature should be substantially below the β_T to prevent preferred α precipitation in grain boundaries (which embrittles the material). If the β alloy is in its final age-hardened condition, the SR temperature should be at or below the aging temperature to prevent strength reduction.

Annealing

Annealing is similar to SR but usually done at higher temperatures. The annealing of titanium and titanium alloys serves primarily to increase fracture toughness, room temperature ductility, dimensional stability, and high-temperature creep resistance. This is often the final heat treatment for α and α–β alloys, as it yields a good balance of properties. Care must be taken when using β alloys in the annealed condition in service temperatures up to 400°C, which could result in embrittlement, and service temperatures in the range of 400–600°C could age-harden the β alloy, resulting in a strength increase at the expense of ductility. Alpha and α–β alloys are typically annealed in the temperature range of 700–900°C, while β alloys are normally annealed in the temperature range of 690–815°C.

There are four commonly used annealing treatments, mill annealing (MA), duplex annealing (DA), recrystallization annealing (RA), and β annealing (BA). MA is a general-purpose heat treatment given to all mill products, but it is not a full anneal and the material may retain effects of prior working processes. DA is used for α and α–β alloys; it involves an initial anneal high in the α/β-phase field to generate significant fractions of both α and β with small grain/phase sizes near 10 μm, followed by an MA to provide thermal stability in the prior β regions. DA improves creep resistance and fracture toughness (resistance to crack nucleation) of the material. An RA is done at a temperature high enough in α/β-phase field to ensure recrystallization. It is then slowly cooled to form a high-volume fraction of equiaxed α with islands of retained β at triple points, and some interfacial β at α/α boundaries. RA provides high-damage tolerance properties (fracture toughness, crack growth resistance) that are crucial for fracture critical applications. Finally, BA is done at temperatures above the β_T, leading to a large grain size followed by a subsequent MA (Figure 5 shows how a BA converted a small grain size DA microstructure into large prior β grains that were transformed into several α variants during slow cooling). For α and α–β alloys, BA maximizes the damage tolerance properties, since resistance to crack propagation is best when there are fewer grain boundaries.

Solution Treating

Solution treating (ST) is used to transform a desired amount of α- to β-phase in near α and α–β alloys, by heating the material to a temperature near β_T and then cooling strategically to produce a higher ratio of β-phase in a desired morphology. Beta alloys are normally solution treated above the β_T (700–815°C), while α and α–β alloys are normally solution treated slightly below the β_T (850–1000°C) (Table 3). For most β alloys, the object of ST is to retain 100% β-phase upon quenching, so that upon subsequent aging, decomposition of the metastable β-phase occurs to generate second-phase precipitates that provide high strength.

Quenching

The rate of cooling from the ST temperature strongly affects the strength of the material. Slow cooling rates allow diffusion to occur, resulting in decomposition of the β-phase and may prevent effective strengthening during the aging process. Also the quench delay, which is the time from which the material is removed from the furnace and subsequently placed into the quenching media, can affect properties. Longer quench delays can lower strength; this reduced strength is ascribed to the formation of coarse acicular α prior to immersion in quenchant. Alpha–beta alloys are typically quenched in water, a 5% brine solution, or a caustic soda solution because the rate is sufficient to retain the β-phase obtained by ST. For highly β-stabilized alloys and small sections, an air or fan cooling may be adequate.

Aging

Aging is the final heat treatment step needed in order to achieve high-strength levels. Aging causes the decomposition of the supersaturated β-phase retained upon quenching, through α-precipitation within the β-matrix. Martensites also decompose in a manner that sharpens interfaces or boundaries that provide strengthening. The aging temperature controls the size and volume fraction of the α-precipitates, and determines the final strength of the material. Aging at or near the annealing temperature results in overaging, which is desirable if good toughness and dimensional stability are needed with only a modest increase in strength. For α

and α–β alloys, aging is usually done in the temperature range of 480–605°C, and β alloys are typically aged in the temperature range of 425–595°C.

Suggested heat treatments for various titanium alloys are listed in Tables 3 and 4. It is also important to note that not all heat treatments are applicable to all titanium alloys, because some alloys are designed for specific purposes, for example, Ti–5Al–2Sn–2Zr–4Mo–4Cr (Ti-17) and Ti–6Al–2Sn–4Zr–6Mo are designed for strength in heavy sections, Ti–5Al–2.5Sn and Ti–2.5Cu, for weldability, Ti–6Al–2Sn–4Zr–2Mo and Ti–6Al–5Zr–0.5Mo–0.2Si, for creep resistance.

Welding of Titanium Alloys

Table 5 provides relevant details for welding titanium alloys. Unalloyed titanium and α alloys are weldable. These alloys are typically welded in the annealed condition, and have good weldability because they are insensitive to heat treatments. Alpha–beta alloys and weakly β-stabilized alloys are also weldable, but should be welded in the annealed or solution-treated conditions prior to aging heat treatments. Most β alloys can be welded in annealed or solution-treated condition, but subsequent aging can cause the weld to become brittle. Most strongly β-stabilized alloys are embrittled by welding, since it is not possible to quench a weld (without quenching, second phases precipitate preferentially on grain boundaries).

Challenging and Problematic Issues with Titanium Alloys

Although titanium alloys have many desirable characteristics, they have problematic areas as well. These include their affinity to oxygen, hydrogen pickup, susceptibility to certain types of chemical attack, and damage generation arising from the elastic and plastic anisotropy of the hexagonal crystal structure.

Heat treating can cause contamination due to oxidation that causes an oxygen-rich brittle layer on the metal surface called "α case." Unless surface hardening is needed for wear resistance, this α case must be mechanically or chemically removed before the part can be put into service. Another concern is embrittlement due to very low levels of hydrogen, nitrogen, and carbon absorption at virtually every fabrication stage from casting to heat treating. Due to its great affinity to oxygen, alumina (Al_2O_3) cannot be used to machine titanium alloys, so WC tools (typically C-2 grades) are used for turning and face milling, while high-carbide, high-speed steels are appropriate for drilling, tapping, and end milling.

Though CP titanium is highly corrosion resistant, SCC is more likely with increasing alloy content, and in environments with red fuming nitric acid, N_2O_4, HF, methonal, HCl, and seawater. The susceptibility depends greatly on alloy elements, crystal orientation and misorientations at grain boundaries, and the details of microstructural evolution.

Due to its hexagonal crystal structure, slip in the $\langle a \rangle$ direction is much more facile than other directions, so heterogeneous deformation and shear banding is common. Combinations of working and heat treatment can generate highly preferred crystal orientations, so between the coherent phase boundaries with transformation shears, and the anisotropy of the thermal expansion coefficient (which is 20% higher in the $\langle c \rangle$ than $\langle a \rangle$ directions) substantial residual stresses are common even after a stress relief anneal. Though titanium alloys can be processed for excellent high-temperature creep resistance, room-temperature creep occurs in some microstructures and alloys, and hence dimensional stability can be a problem. To fully optimize material property design for particular applications, control of texture and microstructure with innovative processing strategies requires predictive understanding of the rules for variant selection during the $\alpha \rightarrow \beta \rightarrow \alpha$ transformations, which are not yet well established.

Further Reading

(1991) Heat treating. *ASM Handbook*, vol. 4. Metals Park, OH: ASM Publications.

Bondarchuk VI, Ivasishin OM, Moiseyeva IV, Okrainets PM, and Pishchak VK (2001) Effect of rapid heat treatment on the high-temperature deformation of refractory titanium alloys. *Metal Physics and Advanced Technologies (UK)* 19(5): 743–753.

Boyer RR and Lutjering G (1996) Heat treatment of titanium alloysoverview. In: Weiss I, Srinivasan R, Bania PJ, Eylon D, and Semiatin SL (eds.) *Titanium Alloy Processing*, pp. 349–367. Warrendale, PA: The Minerals, Metals and Materials Society.

Boyer R, Collings EW, and Welch G (eds.) (1994) *Materials Properties HandbookTitanium Alloys*. Materials Park, OH: ASM Publications.

Donachie MJ Jr. (2000) *TitaniumA Technical Guide*, 2nd edn. Metals Park, OH: ASM Publications.

Exner HE, Muller C, and Schmidt H (2004) Modification of titanium alloys for medical applications. *Zeitschrift fur Metallkunde* 95(7): 650–662.

Froes (Sam) FH, Imam MA, and Fray D (eds.) (2004) *Cost-Affordable Titanium*. Warrendale, PA: The Minerals, Metals and Materials Society.

http://doc.tms.org

http://www.asm-intl.org

http://www.matls.com

Leyens C and Peters M (2003) *Titanium and Titanium Alloys; Fundamentals and Applications*. Weinheim: Wiley-VCH Verlag GmbH & Co. KGaA.

Semiatin SL, Seetharaman V, and Weiss I (1996) Hot working of titanium alloys – an overview. In: Weiss I, Srinivasan R, Bania PJ, Eylon D, and Semiatin SL (eds.) *Titanium Alloy Processing*pp. 3–74. Warrendale, PA: The Minerals, Metals and Materials Society.

Smith WF (1993) *Structure and Properties of Engineering Alloys*, 2nd edn., pp. 433–484. New York: McGraw-Hill.

Veeck S, Lee D, and Tom T (2002) Titanium investment castings. *Advanced Materials & Processes* 160(1): 59–62.

High-entropy alloys: An overview on the fundamentals, development, and future perspective

Hung Yen[a,b], **An-Chou Yeh**[a,b], **and Jien-Wei Yeh**[a,b], [a]Department of Materials Science and Engineering, National Tsing Hua University, Hsinchu, Taiwan, ROC; [b]High Entropy Materials Center, National Tsing Hua University, Hsinchu, Taiwan, ROC

© 2024 Elsevier Ltd. All rights reserved.

Introduction 647
Concepts and definition of high-entropy alloys 648
The four core effects and related theories of high-entropy alloys 649
High entropy effect 649
Sluggish diffusion effect 650
Severe lattice distortion effect 651
Cocktail effect 653
Development of special high-entropy alloys 653
Low-stacking-fault-energy high-entropy alloys (LSF-HEAs) 653
High-entropy superalloys (HESAs) 653
Refractory high-entropy alloys (RHEAs) 654
High-entropy metallic glasses (HEMGs) 654
Eutectic high-entropy alloys (EHEAs) 654
High-entropy intermetallic compounds (HEICs) 655
High-entropy coatings (HE-Coatings) 655
Future perspective 655
Conclusion 655
Acknowledgments 656
References 656

Abstract

High-Entropy Alloys (HEAs) is a revolutionary concept of the alloy design field proposed in 2004. It provides a much greater scope of composition design than ever before. The four core effects of HEAs could lead to good combinations of properties and allow tuning the crystal structures and microstructures of the system. The fundamental physical metallurgy principles of HEAs are different from those of the conventional alloys in many aspects, and the deformation mechanisms of HEAs are particularly interesting to the community. Recently, a new mechanism of strengthening and toughening by high slip-plane density in HEAs has been proposed. Since HEAs possess great potentials for various applications, several types of HEAs have been developed, such as low stacking fault high-entropy alloys (LSF-HEAs), high-entropy superalloys (HESAs), refractory high-entropy alloys (RHEAs), high-entropy metallic glasses (HEMGs), eutectic high-entropy alloys (EHEAs), high-entropy intermetallic compounds (HEICs), and high-entropy Coatings (HE-Coatings). In this article, the basic concept and definition of HEAs are described. Furthermore, the four core effects are reviewed and clarified. The recent progresses of developing LSF-HEAs, HESA, HEMGs, RHEAs, EHEAs, HEICs, and HE-Coatings for potential applications are summarized.

Key points

- Fundamental concepts and developments of HEAs are introduced.
- The four core effects of HEAs are reviewed and clarified.
- The potential applications of HEAs in LSF-HEAs, HESAs, HEMGs, RHEAs, EHEAs, HEICs, and HE-Coatings are summarized.

Introduction

High-Entropy Alloys (HEAs) is a revolutionary concept of the alloy design; it provides a much greater scope of composition design than ever before. The four core effects of HEAs could lead to good combinations of properties and allow tuning the crystal structures and microstructures of the system. Since HEAs possess great potentials for various applications, several types of HEAs have been

https://doi.org/10.1016/B978-0-323-90800-9.00117-7

developed. In this article, the basic concept and definition of HEAs are described. Furthermore, the four core effects are reviewed and clarified. The recent progresses of developing LSF-HEAs, HESAs, HEMGs, RHEAs, EHEAs, HEICs, and HE-Coatings for potential applications are summarized.

Concepts and definition of high-entropy alloys

The human civilization has been defined by the development and applications of materials, such as stone, bronze, and iron; the development of rudimentary thermo-chemistry allowed the extraction of copper and iron, and led to the Bronze Age and the Iron Age. Cast iron technology in 1620s established the dominance of metal alloys in engineering at that time, followed by the development of steel technology in 1850 and other special alloys such as stellite alloys (mostly cobalt based with additions of Cr, C, W, and/or Mo), permalloys (nickel–iron magnetic alloy), copper-beryllium alloys, aluminum alloys, titanium alloys, magnesium alloys, and superalloys. The materials development in the timeline have been driven by the desire for greater performance; however, since 1950s, the rate of development of new metallic alloys has slowed down. This could be due to the limitation of composition design space based on one major solvent, as well as the competitions from other types of engineering materials.

High-Entropy Alloys (HEAs) is a novel concept in alloy design explored by Professor Jien-Wei Yeh since 1995 (Taiwan). After eight years of research, he and his team published the first five papers on HEAs in 2004 (Yeh et al., 2004a). Different from the conventional alloy design space, which restricts itself to the corner of the phase diagram, Professor Yeh and his group reported a new approach to design alloy by mixing elements in nonequimolar or equimolar proportions, forming multi-principal-component alloys. These new alloys possess higher configurational entropy than those of common commercial alloys which mainly based one element. According to the statistical thermodynamics, Boltzmann's equation can be used to calculate the configurational entropy of a system (Gaskell, 1995; Moore, 1962):

$$\Delta S_{conf} = k_B \ln w \tag{1}$$

where k_B is Boltzmann's constant and w is the number of available energies that can be mixed among the system. For a n-element alloy in the random solution state, the ideal configurational entropy can be expressed as:

$$\Delta S_{conf} = -R\sum\nolimits_{i=1}^{n} X_i \ln X_i \tag{2}$$

where R is the gas constant, 8.314 J/K ·mol, and X_i is the atom fraction of the ith element.

Based on Eq. (2), we can calculate the configurational entropy per mole for an equimolar alloy in regular solid solution state or liquid state by the following expression as Eq. (3) (Yeh et al., 2004a; Yeh, 2006):

$$\Delta S_{conf} = k_B \ln w = -R\left({}^{1}\!/_{n} \ln {}^{1}\!/_{n} + {}^{1}\!/_{n} \ln {}^{1}\!/_{n} + \ \ldots {}^{1}\!/_{n} \ln {}^{1}\!/_{n} \right) = -R \ \ln n \tag{3}$$

The ideal configurational entropies for equimolar alloys ($X_1 = X_2 = \ldots = X_n$ in Eq. 2) with different n-elements up to 13 are shown in Table 1. The ΔS_{conf} is increased as the number of elements in the system increases.

Professor Yeh proposed two definitions for HEAs (Yeh, 2013). One expression is based on the composition and shown in Eq. (4), and the other is based on the configurational entropy and shown in Eq. (5).

$$n_{major} \geq 5 \text{ and}, n_{minor} \geq 0$$

$$5\ at.\% \leq X_i \leq 35\text{at.}\%and, X_j \leq 5\ at.\% \tag{4}$$

$$\Delta S_{conf} \geq 1.5R \tag{5}$$

where n_{major} and n_{minor} are the number of major elements and minor elements, respectively. X_i and X_j are the atomic percentage of major elements i and minor elements j, respectively.

According to the definition given in Eq. (5), the medium-entropy alloys (MEAs) and the low-entropy alloys (LEAs) can be defined as well based on the configurational entropy (Yeh, 2013). Fig. 1 shows the composition scope of alloys based on the configurational entropy. This demonstrates that the HEAs can extend the design scope greater than those of LEAs and MEAs. Therefore, there should be more room to tune the compositions for a broad range of structures and properties (Yeh et al., 2004a; Huang et al., 2004; Chen et al., 2004).

Table 1 The ideal configurational entropies (ΔS_{conf}/R) for equimolar alloys with different n-elements up to 13 (Yeh, 2013).

n	1	2	3	4	5	6	7	8	9	10	11	12	13
$\Delta S_{conf}/R$	0	0.69	1.10	1.39	1.61	1.79	1.95	2.08	2.20	2.30	2.40	2.49	2.57

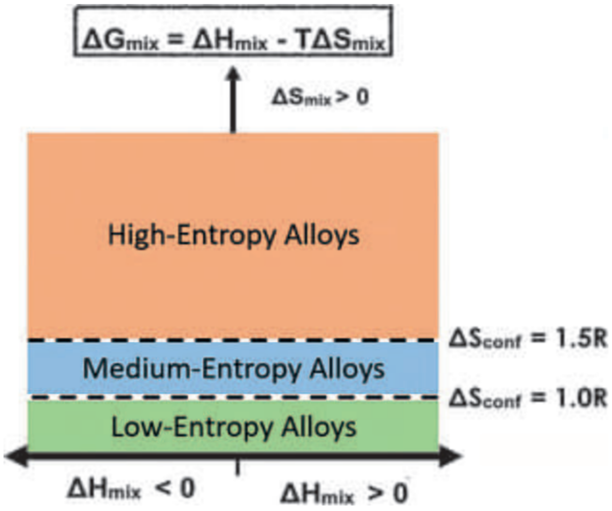

Fig. 1 Categories of alloys based on the configurational entropy, encompassing the range of mixing enthalpy from negative to positive.

Before Prof. Jien-Wei Yeh of Taiwan published the novel concept of "High-Entropy Alloys" in 2004, Professor Brian Cantor of the United Kingdom also carried out similar pioneering work. In 1981, Professor Brian Cantor initiated a research on equi-atomic multicomponent alloys with Alain Vincent (Cantor, 2014); it was found that only $Co_{20}Cr_{20}Fe_{20}Mn_{20}Ni_{20}$ possesses a single FCC phase, indicating that all these five elements are mixed into a solid solution. However, this work was unpublished until 2004 except in a thesis at Sussex University. Prof. Brian Cantor found that the total number of phases is always significantly less than the maximum equilibrium number allowed by the Gibbs phase rule and even less than the maximum number allowed under nonequilibrium solidification condition.

Professor Srinivasa Ranganathan of India is another significant scientist who assisted the launch of HEAs technology; Professor Ranganathan contributed to the understanding of the structure of interfaces, quasicrystals, bulk metallic glasses, nanostructured materials, and novel multicomponent alloys. After his communications and discussions about HEAs with Prof. Jien-Wei Yeh, Prof. Ranganathan's article entitled "Alloyed pleasures – multimetallic cocktails" was published in Current Science in November 2003 (Ranganathan, 2003). This article was the first journal publication mentioning HEAs. In this article, Prof. Ranganathan reviewed three alloy systems, that is, bulk metallic glasses, superelastic and superplastic alloys, and HEAs. Hence, Professor Ranganathan was the first person to introduce Professor Yeh's high-entropy alloy research to the world. The following section reviews the four core effects of HEA and deformation mechanisms in more details

The four core effects and related theories of high-entropy alloys

In the field of physical metallurgy, the relationships between composition, processing, structures, and properties are investigated and correlated (Reed-Hill, 1994). The design guideline of HEAs has been laid out by four core effects (Yeh, 2006; Murty et al., 2014). These are (1) high configurational entropy effect for thermodynamics (2) sluggish diffusion for kinetics v, (3) lattice distortion effect for structure, and (4) the cocktail effect for properties. Fig. 2 illustrates how four core effects influence the physical metallurgy of HEAs (Biswas et al., 2020); even until recently, these four core effects of HEAs are still under passionate debate.

High entropy effect

High entropy effect is associated with the enhanced thermodynamic stability of solid solution phases (Yeh, 2013), and the configurational entropy is the main consideration. The other entropy terms involved such as vibrational, electronic, and magnetic are relatively small and often neglected for convenience. According to the second law of thermodynamics shown in Eq. (6), a system reaches its thermodynamic equilibrium when its Gibbs free energy ΔG_{mix} is the lowest at a given temperature and pressure.

$$\Delta G_{mix} = \Delta H_{mix} - T\Delta S_{mix} \tag{6}$$

where ΔH_{mix} is the mixing enthalpy of the system, T is the given temperature, and ΔS_{mix} is the mixing entropy of the system.

The magnitude of mixing enthalpies with negative values indicates the tendency for the compounds or second phase formation. However, a large configurational entropy in near-equimolar alloys with 5 or more elements can counterbalance the effect of mixing

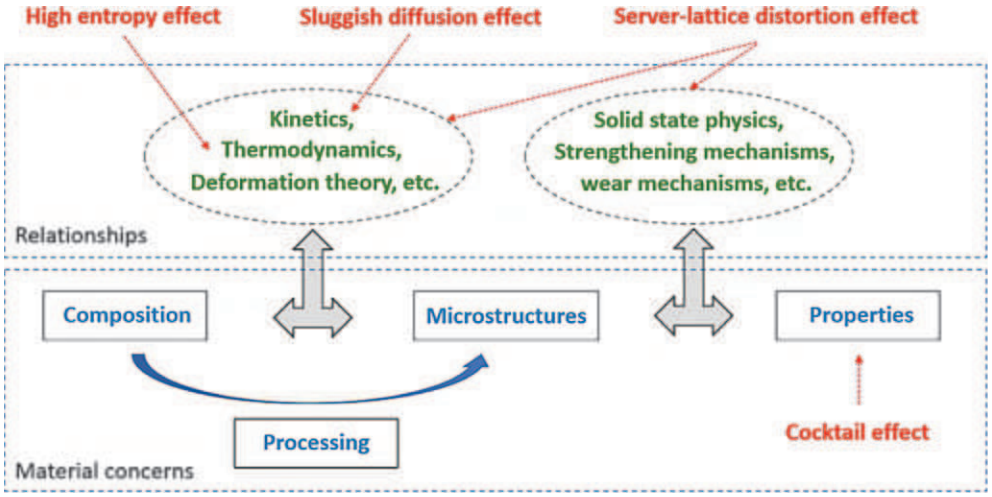
High entropy effect
Sluggish diffusion effect
Server-lattice distortion effect
Kinetics, Thermodynamics, Deformation theory, etc.
Solid state physics, Strengthening mechanisms, wear mechanisms, etc.
Relationships
Composition
Microstructures
Properties
Processing
Cocktail effect
Material concerns

Fig. 2 Four core effects of HEAs' influence on physical metallurgy.

enthalpy and promote the formation of solid solutions (SS) phases instead of pure elements segregations or compounds (Miracle et al., 2014). Zhang et al. (Zhang et al., 2008) also proposed the forming trend of disordered SS, ordered SS intermediate phases and bulk metallic glass (BMG) by comparing ΔS_{mix}, ΔH_{mix}, and atomic size difference, and found the significance of entropy effect. Moreover, Yang and Zhang (2012), Yeh (2009), and Guo and Liu (2013, 2011) clearly showed how the thermodynamic phase stability will be influenced by higher entropy, and provided a guideline for SS phase formation. The high entropy effect is definitely the most essential effect of HEAs. It emphasizes that mixing entropy term, which plays a critical role to further decrease the mixing free energy of the random state, could render greater stability for the SS phases of HEAs. This effect of entropy allows alloy designers to control the microstructure in order to design materials with promising properties. Furthermore, Cheng et al. (2017) reported that the mixing entropies of phases in HEAs can be higher than that in conventional alloys, and the higher entropy could counterbalance the strain energy and chemical energy increases due to mixing and guarantee the stable existence of lattice-distorted concentrated solid solutions (CSS).

Sluggish diffusion effect

Sluggish diffusion effect means that the diffusion rate becomes slower in the distorted lattice, and in addition, the rate of phase transformation is slowed down due to required cooperative diffusion of many elements for nucleation and growth of crystals or phases. A more positive enthalpy of formation and an excess amount of mixing entropy are both related to the formation of vacancy in crystalline HEAs (Moore, 1962). Since vacancy is the key control factor of substitutional diffusion, vacancy concentration and its mobility in the whole solute matrix are important diffusion issues in HEA systems. Different from the conventional alloys, either a vacancy or an atom of the HEAs would have a fluctuated diffusion path to migrate and have slower diffusion with higher activation energy. As a result, the phase transformation in HEAs would be slower and tend to form the nanostructure or even amorphous structure due to sluggish diffusion and cooperative diffusion. In other words, sluggish diffusion could better retain the properties of HEAs at elevated temperatures (Tsai et al., 2009; Senkov and Woodward, 2011; Senkov et al., 2011a). Cheng et al. (2017) reported sluggish diffusion phenomena in high-entropy concentrated solid solutions by observing slower phase transformation rate. This could be caused by lattice distortion, which could result in variations of lattice potential energy and higher activation energy along the diffusion path. Fig. 3 shows that atoms in the HEA lattice would experience fluctuated lattice potential energy due to different lattice distortion and coordination bonding along its diffusion path; hence atoms in HEAs lattice need higher activation energy to overcome deeper traps in order to migrate in the path (Gao et al., 2016). The direct evidence of sluggish diffusion in HEAs systems

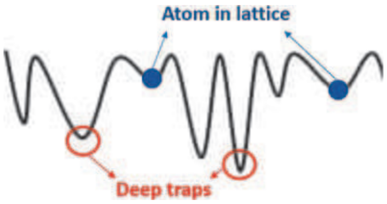

Fig. 3 Schematic diagram shows the fluctuation of lattice potential energy along the diffusion path for an atom jumping in the lattice. Adapted from Gao MC, Yeh JW, Liaw PK, and Zhang Y (2016) High-Entropy Alloys Fundamentals and Applications, Springer. IBSN 978-3-319-27011-1.

has been obtained by diffusion couple experiment. Tsai et al. (2013) conducted the diffusion experiment on diffusion couples that consisted of single-face-centered cubic Co—Cr—Fe—Mn—Ni systems. For each couple, only the concentrations of two elements were adjusted. The diffusion couples were annealed at various temperatures in order to determine the diffusion profile so that diffusion coefficients of each element and activation energy could be determined. The author measured the temperature dependence of the diffusion coefficients for Cr, Mn, Fe, Co, and Ni in different matrix including FCC pure metals and various stainless steels. The data showed that the diffusion coefficients for Cr, Mn, Fe, Co, and Ni in the HEA system are smaller than in the pure matrix. It is apparent that sluggish diffusion occurred in the HEA. In addition to this nonradiotracer method, radiotracer method has been conducted on CoCrFeMnNi alloy (Vaidya et al., 2016, 2018); an obvious decrease in bulk diffusion rates is confirmed when the homologous temperature is used for comparison. This demonstrates that higher lattice distortion could lead to slower atomic diffusion since homologous temperature used for comparison could reveal the main effect from lattice distortion on diffusion. Interestingly, sluggish diffusion has also been reported recently in the high-entropy ceramic systems (Li et al., 2022; Zhang et al., 2021). Thus, it appears that sluggish diffusion phenomenon is a genuine effect associated with lattice distortion in different high-entropy materials systems.

Severe lattice distortion effect

Lattice distortion caused by solute atoms is well known in traditional physical metallurgy; however, this effect in HEAs is more pronounced since the distortion is at every site and varies from one site to the next, that is, severe lattice distortion. Hence, it would have a profound influence on the properties of HEAs. The lattice distortion is nominally related to differences in atomic size (δ) in the Eq. (7) for multi-element system (Yang and Zhang, 2012).

$$\delta = 100\sqrt{\sum_{i=1}^{n} c_i(1 - r_i/\bar{r})^2} \tag{7}$$

where $\sum_{i=1}^{n} c_i r_i$ and c_i and r_i are the atomic percentage (%) and atomic radius of the ith element (nm), respectively, and $\bar{r}$ is the average radius (nm).

In addition to the atomic size difference, atomic bonding difference between atomic pairs also contributes to the distortion since an atom can have different neighboring atoms and hence has nonsymmetrical bonding with neighbors. However, the actual degree of lattice distortion would be smaller than the nominal difference because some relaxation of atomic configuration would occur in order to achieve smaller overall free energy of the whole alloy. Interactions will occur when dislocations, electrons, phonons, and X-ray beam pass through severe distorted lattice (Gao et al., 2016). Thus, dislocation movement would be more difficult and hence solution hardening could be achieved; electrons and phonons would be scattered, resulting in lower conductivities. X-ray beam would also be scattered remarkably in the distortion lattice and thus result in smaller peak intensity.

Lin et al. (2021) showed how severe lattice distortions' effect could influence mechanical properties in HEAs. Higher solution-hardening rates occurred in concentrated solutions due to high concentrations of lattice distortion sites in the whole-solute matrix (Fig. 4). Fig. 4 illustrates how dislocation lines move smoothly in the lattice of a pure metal (low entropy state), how they are dragged by small number of solutes encountered in the dilute solutions (medium entropy state), and how they are dragged by a large number of solutes encountered in the concentrated solutions (high entropy state). As a result, both the lattice friction and solution hardening are increased to enhance the yield strength of concentrated solid solutions. The authors measured the stress and strain curves of Ni (1A), Ni-2at%W (1A2W), Ni-4atwt%W (1A4W), CrFeNi (3A), and CoCrFeMnNi (5A) alloys and showed that the 3A alloy (CrFeNi MEA) and 5A alloy (CoCrFeMnNi HEA) have significantly higher strength than those of pure and dilute metals, 1A (Ni), 1A2W (Ni-2at%W), and 1A4W (Ni-4at%W), even though the nominal atomic size difference is in the following increasing order: Ni < CrFeNi < CoCrFeMnNi < Ni–2 at.% W < Ni–4 at.% W. It can be concluded that lattice distortion effect is significant in the dislocation behavior and mechanical properties for 3A and 5A due to the whole-solute lattice distortion.

Generally, high strength is achieved by hindering dislocation motion in crystalline solids; however it often decreases ductility in metal alloys. Therefore, metallurgists have long thought about how to overcome this tradeoff in between strength and ductility. In 2021, a mechanism of HEA was unveiled, in which both the strength and toughness of an alloy could be enhanced through high slip-plane density (Yeh, 2021). In fact, recent studies also support this theory (Stoudt et al., 2000; Yang et al., 2018; Pan et al., 2021). Edge dislocations could induce slip and cause deformation, but they could also pile up at grain boundaries and interfaces to induce crack. Fig. 5 shows the schematic diagram of reduced crack-forming tendency due to the increased density of activated slip plane (Yeh, 2021). The discrete slip bands (a group of activated slip planes) would cause a higher stress concentration against obstacles to initiate cracks than a more uniform slip planes under the same shear strain. Therefore, a concept of high accommodation strategy was proposed to increase the active slip planes and dislocation density, and this could increase both the strength and ductility during deformation. The article (Yeh, 2021) also mentioned that low SFE in a severely distorted lattice in HEAs could inherently enhance the density of active slip planes and can improve both strength and ductility. In addition, small grain size, dislocation cell structure, nanoprecipitates, dense stacking faults, and nanotwins could enhance the accommodation of higher densities of slip planes.

Heat conduction in metals could be affected by solutes and defects (Jain et al., 1969; Venkatasubramanian, 2000). Therefore, lattice distortion effect could also affect the thermal conductivity. The thermal conductivity $k(T)$ of a material at temperature T could

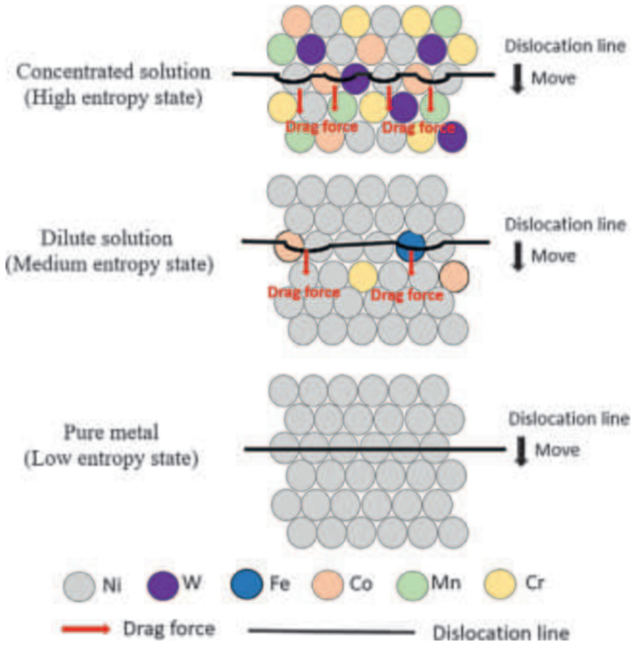
Concentrated solution
(High entropy state)
Dislocation line
Move
Drag force
Drag force
Dilute solution
(Medium entropy state)
Dislocation line
Move
Drag force
Drag force
Pure metal
(Low entropy state)
Dislocation line
Move
Ni
W
Fe
Co
Mn
Cr
Drag force
Dislocation line

Fig. 4 Schematics of the dislocation configurations in pure metal (below), dilute solution (middle), and concentrated solution (top).

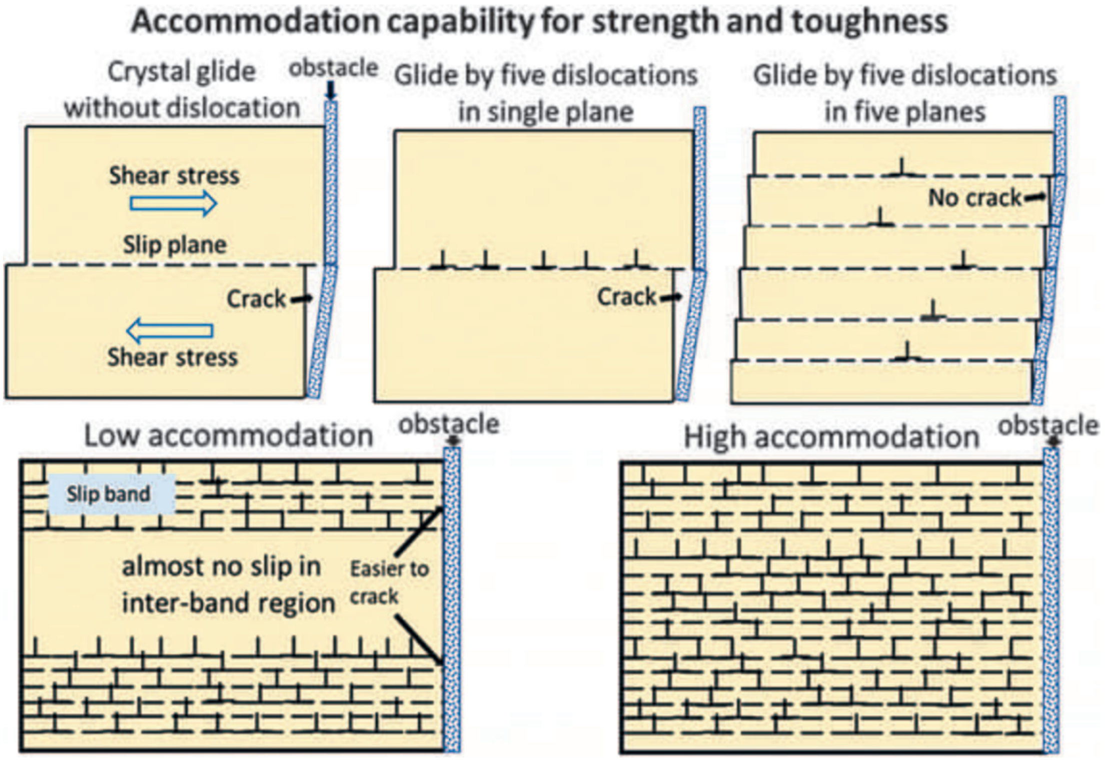
Accommodation capability for strength and toughness
Crystal glide without dislocation
obstacle
Shear stress
Slip plane
Crack
Shear stress
Glide by five dislocations in single plane
Crack
Glide by five dislocations in five planes
No crack
Low accommodation
obstacle
Slip band
almost no slip in inter-band region
Easier to crack
High accommodation
obstacle

Fig. 5 Schematic diagram of the reduced crack-forming tendency due to increased density of activated slip plane, and the high accommodation capacity strategy to increase the number of activated slip plane and thus increase the strength and ductility.

generally be described according to the relationships in Eqs. (8), (9) (Jain et al., 1969). Cheng et al. (2017) measured the thermal conductivities of as-homogenized Ni—Co—Fe—Cr—Mn alloy series and showed a drop of k with an increase in the number of elements due to more severe lattice distortion in the temperature range of 25°C to 400 °C.

$$k(T) = \alpha(T) * \rho(T) * C_P(T) \tag{8}$$

$$C_P = \sum X_i C_P^i \tag{9}$$

where $\alpha(T)$ is thermal diffusivity, $\rho(T)$ is density, $C_P(T)$ is specific heat, and X_i and C_P^i are the molar fraction and specific heat of constituent element i, respectively.

Cocktail effect

The term "multimetallic cocktails" was first proposed by Professor Ranganathan (Ranganathan, 2003). It is the overall effect of composition, structure, and microstructure. Properties of HEAs are not as simple as those predicted from the rule of mixture, but mutual interactions between unlike atoms, phase formation, and microstructures. Since HEAs contain at least five major elements in the system, the synergistic responses from the constituent elements can be important. The cocktail effects in HEAs have drawn lots of discussions (Pickering and Jones, 2016). The development of Refractory High Entropy Alloys (RHEAs) is the classic example of the use of cocktail effect. The concept of RHEAs was first reported by the US Air Force Research Laboratory. Senkov et al. (2011a, b, 2010) used the high melting point elements to design RHEAs in order to replace the Co-based and Ni-based alloys; the cocktails of different refractory elements have rendered new high-temperature alloys with not only high melting temperatures but also excellent mechanical properties. They also compared the temperature dependence of the yield strength of $Nb_{25}Mo_{25}Ta_{25}W_{25}$ and $V_{20}Nb_{20}Mo_{20}Ta_{20}W_{20}$ RHEAs and two superalloys, Inconel 718 and Haynes 230 (Senkov et al., 2011a). The data of these two RHEAs obvious show that RHEAs possess greater temperature capability than those of conventional superalloys.

Liu et al. (2021) also highlighted the cocktail effect by adding appropriate Cu content, which could increase the aspect ratio of the particular phase in $FeCoNiCr_{0.4}Cu_x$, resulting in enhanced megahertz electromagnetic wave absorption of magnetic properties. Moreover, the addition of Cr element has been reported to result excellent mechanical properties and corrosion resistance in other HEAs system (Lee et al., 2008; Zhang et al., 2019; Duan et al., 2020). To sum up, by utilizing the cocktail effect, that is, adding suitable elements in HEAs, better combinations of properties for engineering applications can be obtained, providing additional flexibility to HEAs properties design.

Development of special high-entropy alloys

Based on the concept of HEAs, several types of new alloy systems have been developed with promising properties for engineering applications. This section reviews the current state of the art of various special HEAs.

Low-stacking-fault-energy high-entropy alloys (LSF-HEAs)

CoCrFeMnNi and related FCC-type HEAs have been found to possess relatively low stacking fault energies, which generally attribute to both high strength and good ductility. Zaddach et al. (Youssef et al., 2015) reported that for CoCrFeMnNi, both its tensile strength and ductility can be increased at cryogenic temperatures, as deformation-induced twinning becomes a more prominent deformation mechanism (Zaddach et al., 2013). Generally, in low-SFE alloys, dissociation of partial dislocations with a wide spacing is more energetically favorable for the dislocations, cross-slip and climb. So, alloys are more likely to deform by twinning. The low-SFE increases the dislocation storage capacity, increases strain-hardening through the "dynamic Hall–Petch" effect of the deformation twins, and results in an increase of both strength and ductility (Jian et al., 2013). Sarma et al. (2010) described the change in deformation mechanisms in Cu—Al alloys as a function of temperature and SFE. As the Al content increases, the SFE decreases, making twinning as the predominant deformation mechanism. Zaddach et al. (2015) also reported $Ni_{18.5}Fe_{18.5}Cr_{18.5}Co_{26}Mn_{18.5}$, which contains cobalt to further reduce the SFE, had a 30% improvement in elongation comparing to the equiatomic alloy. Sathiaraj et al. (2020) reported that the mechanical twinning and shear banding at intermediate and high rolling reductions, respectively, are related to the formation of the brass-type rolling texture in the low SFE HEAs investigated.

High-entropy superalloys (HESAs)

Superalloys are important materials for gas turbine engines in aerospace and energy industries (Reed, 2006). Traditional superalloys have relied on ordered $Ni_3(Al,Ti)$-based $L1_2$-structured (γ') coherent precipitates to strengthen the FCC-structured (γ) matrix. During the development of advanced superalloys, Ru and Re elements are of interest due to their contributions to phase stability and creep resistance. In fact, the addition of these two elements in the Ni-based system can be seen as a "quasi-cocktail effect" (Yeh et al., 2004b, 2008; Yeh and Tin, 2005, 2006; Kawagishi et al., 2012). Although creep properties of Ni-based alloys can be improved by adding Ru and Re, high density and high cost prohibit a large scale of applications. Furthermore, the homologous temperature of superalloys has appeared to reach the limit, and efforts on superalloy development have focused on improving the cost performance by reducing the use of expensive elements. However, the Ni-based system actually constrains the composition design space to further reduce the cost and density. Therefore, the concept of HEAs, that is, $\Delta S_{conf} \geq 1.5R$, can open the window to exploit the vast composition space for superalloys development (Yeh et al., 2004a; Gao et al., 2016). The name of High Entropy Superalloys (HESAs) has been given to this class of materials. One of the first HESAs is $Al_xCo_{1.5}CrFeNi_{1.5}Ti_{(0.5\text{-}x)}$ with an FCC γ matrix and uniform dispersion of $L1_2$ γ' particles; this alloy can possess higher temperature capability than that of Inconel 718 (Yeh et al., 2014). Chen et al. (2020a) reported the new cast-type HESA system, low-cost element Fe was used to lower down the cost of material, and lightweight elements such as Al, Ti, and Cr could lower down the density. In addition, alloy design based on elemental partitioning characteristics could control not only the lattice parameters, but also the intrinsic properties of γ matrix and γ' precipitate. The substitution of 2.0 at% Ni by 2.0 at% Ti affected the partitioning characteristics for other elements, resulting in an increase in the entropy of γ matrix, and a decrease in the entropy for γ' phase, which in turn could enhance its thermal stability. Moreover, for oxidation and corrosion resistances of HESAs, the design concept also promoted the formation of protective Al_2O_3 or Cr_2O_3 layers. HESAs have shown superior cost-specific tensile yield strength than that of conventional superalloys. Chen et al. (2020b) also recently reported an interesting hierarchical microstructure strengthening mechanism in a single crystal high entropy superalloy—$Ni_{48.3}Co_{16.9}Al_{10.2}Fe_{8.9}Cr_{7.4}Ti_{5.8}Nb_{1.2}Mo_{0.9}W_{0.4}$ HESA. In addition to the FCC matrix and the $L1_2$-structured phase, there were high entropy FCC nanoparticles dispersion within the $L1_2$ phase. This hierarchical microstructure was achieved through a phase transformation pathway through metastability. Because of the hierarchical structure, HESAs have shown outstanding high-temperature mechanical properties; these materials are promising new alloys with better cost performance than conventional superalloys.

Refractory high-entropy alloys (RHEAs)

RHEAs were originated from the Air Force Research Laboratory (AFRL). Senkov et al. (2010, 2011b) proposed the MoNbTaW and MoNbTaVW RHEAs with a simple BCC solid solution phase. These two kinds of RHEAs possess high hardness and high temperature strength. To further improve the ductility, niobium and tantalum were retained; hafnium, titanium, and zirconium were added; and the result was HfNbTaTiZr RHEA, which is also a stable BCC solid solution. This RHEA possesses a superior room temperature strength and can retain the high hardness as well as the high temperature strength (Senkov et al., 2011b, 2012). Senkov at el. (Senkov and Woodward, 2011; Senkov et al., 2013a,b) developed $CrMo_{0.5}NbTa_{0.5}TiZr$ and CrNbTiVZr by adding the low-density elements Cr and V instead of the high-density elements Hf and Ta in order to retain the strength and reduce the density. The microstructure of $CrMo_{0.5}NbTa_{0.5}TiZr$ showed Zr-rich Laves phase; however, it can still possess high strength at 800 °C. The other RHEA, CrNbTiVZr, also possessed the same microstructure and property correlation, and the addition of V element could enhance the high temperature strength. The partial substitution of Al element with Cr element in RHEAs system could avoid the formation of laves phases and maintain the oxidation resistance with lower density. Al element could also enhance the strength of BCC SS by strong bonding with transition elements. $AlMo_{0.5}NbTa_{0.5}TiZr$ and $Al_{0.4}Hf_{0.6}NbTaTiZr$ were reported to possess twice the strength of HfNbTaTiZr at room temperature (Senkov et al., 2014, 2016). Stepanov et al. (Stepanov et al., 2015; Yurchenko et al., 2017) reported the light-weight RHEAs systems, including $AlCr_xNbTiV$, AlxNbTiVZr, and $AlNbTiVZr_x$. By adding a number of low-density elements such as Al, Cr, and Ti in the high entropy quantity, the density of RHEAs could be reduced significantly. These kinds of RHEAs possess high strength at room temperature and the microstructure often contains B2 precipitate or laves phase. Alloy design needs to consider the phase formations in RHEAs carefully since Al addition could easily lead to a decrease in melting point and soften the material at high temperatures. RHEAs possessing a low neutron absorption cross-section and a low decay cycle are potential candidates for application in nuclear industry. In summary, RHEAs can be applied to high-temperature applications beyond the temperature capability of nickel-based superalloys.

High-entropy metallic glasses (HEMGs)

The metallic glasses are regarded as promising materials due to high hardness, strength, and elasticity. However, the tensile brittleness after elastic deformation limits the use of metallic glasses as structural materials. Studies have reported that the HEAs can be fully amorphous without crystalline phases after solidification (Takeuchi et al., 2014). Interestingly, HEMGs could combine the features of both metallic glasses and high-entropy alloys, and may provide a new direction to develop materials with high strength and high ductility. Gong et al. (Gong et al., 2020) demonstrated that TiZrHfBeCu can possess excellent compressive plasticity. Li et al. (2019) reported that the $(Fe_{1/3}Co_{1/3}Ni_{1/3})_{80}(P_{1/2}B_{1/2})_{20}$ HEMGs have superior magneto-caloric property in a wide temperature range comparing with those of conventional crystalline materials. Chen et al. (2021) reported that the magnetic properties of HEMGs can be superior to conventional materials and might be promising candidates for the magnetic refrigeration application.

Eutectic high-entropy alloys (EHEAs)

Eutectic alloys are known to possess good castability and excellent mechanical strength (Otarawanna and Dahle, 2011). Since the eutectic reaction is associated with isothermal transformation, both chemical segregation and shrinkage cavity can be alleviated. Eutectic HEAs (EHEAs) with the composite FCC/BCC structures can possess the advantages of good mechanical properties and excellent castability. Lu et al. (2017) demonstrated the excellent corrosion resistance and strength of $AlCoCrFeNi_{2.1}$ comparing to those of commercial $CuZn_{25}Al_5$ copper alloys used in marine applications. Jiang et al. (2019) developed the $CoCrFeNiNb_{0.45}$ EHEA with an ultrafine lamellar microstructure; this as-cast alloy also showed outstanding thermal stability and hardness up to 1100 °C. Furthermore, Ding et al. (2017) reported that $AlCoCrFeNi_{2.1}$ EHEA possessed excellent mechanical properties and good corrosion resistance properties. There is limited studies on the solidification of EHEAs with complete eutectic microstructure; this could be due to the complicated solidification mechanism associated with HEA effects. The underlying mechanism of the solidification behaviors of EHEAs still needs to be further clarified in the future.

High-entropy intermetallic compounds (HEICs)

High-entropy intermetallic compounds (HEICs) are a new class of high-entropy materials, which may fill the knowledge gap between the metallic HEAs and intermetallic HEA compounds. These new HEICs are mostly metallic but also have crystal structures resembling the ionic solid. Zhou et al. (2019) fabricated the HEICs $(Fe_{0.2}Co_{0.2}Ni_{0.2}Mn_{0.2}Cu_{0.2})Al_1$ with a B2 structure and $(Ti_{0.25}Nb_{0.25}V_{0.25}Zr_{0.25})Al_3$ with a $D0_{22}$ structure. Yao et al. (2021) developed the HEICs $(Fe_{0.75}Co_{0.75}Ni_{0.75}Cu_{0.75}TiZrHf)$ with B2 ordering and showed an ultrahigh compressive yield strength of 2.25 GPa and a fracture strength of 2.52 GPa. Moreover, this HEICs possessed high thermal stability. The atomic-size dispersity δ, which is shown in Eq. (7), is one of the phase selection criteria. Furthermore, this work adapted previous concept (Gargarella et al., 2011) and proposed a new criteria to better describe how the electronegativity of the central atom could be affected by the neighboring atoms; a probability coefficient of direct electronegativity difference, μ, is then considered as shown in Eqs. (10), (11). Therefore, the atomic-size dispersity, δ, and the overall electronegativity difference, η, could be employed to reveal that HEICs are prone to form in the region of $\delta \geq 5.5$ and $0.2 \leq \eta \leq 0.4$.

$$\eta = \sqrt{\sum_{i=1}^{n} c_i \left[\sum_{0}^{\mu} (e_i - e_j)\right]} \tag{10}$$

$$\mu = c_j Vm_j^{2/3} \Big/ \sum_{0}^{c_j} Vm_j^{2/3} \tag{11}$$

where $e_i - e_j$ is the direct Pauling's electronegativity difference between central and neighbor atoms, μ is the probability coefficient, c_i and c_j are the atomic fractions for the corresponding element, and Vm is the molar volume.

High-entropy coatings (HE-Coatings)

The HE-Coatings can compose of HEAs and HEA-based materials, including metal, ceramics, and composites. Not only the materials of HE-Coatings are diverse, but also are the fabrication processes. The first two papers on HEA-based coatings were published by Prof. Jien-Wei Yeh's team (Huang et al., 2004; Chen et al., 2004); these included HEA nitride films with more than five elements fabricated by magnetron sputtering, and $AlSiTiCrFeCoNiMo_{0.5}$ and $AlSiTiCrFeNiMo_{0.5}$ coatings fabricated by thermal-spray technique. HEA-based coatings have the potential to be applied as diffusion barrier and high-temperature protective coating. Chang et al. (2014) reported the suppressed interdiffusion kinetics in high-entropy coating film and it could be a diffusion barrier to improve the Cu/TaN interface in the IC technology. Hsu et al. (2018, 2016) studied the $NiCo_{0.6}Fe_{0.2}Cr_xSiAlTi_y$ system as high-temperature protective coating. The results indicated that HE-Coatings could possess high hardness and excellent wear resistance due to the formation of Nb—Si compounds at the interface. In addition, the thermal conductivity of $NiCo_{0.6}Fe_{0.2}Cr_{1.5}SiAlTi_{0.2}$ was lower than commercial MCrAlY by 30% at elevated temperature and exhibited smaller thermal expansion than that of MCrAlY for better compatibility with the substrate turbine blade alloys.

Future perspective

There are still many challenges ahead to study and develop future HEA-based materials. For example, the cocktail effect allows more flexible alloy design to improve properties of HEAs; however, due to the complexity of HEAs systems, mechanisms of different cocktail effects can interact with each other and become very complex. There are ongoing efforts to develop CALPHAD-based tools to predict phases in HEAs, but lots of research works are still needed in order to improve the prediction capability and accuracy; artificial intelligence or machine learning may assist the effort to speed up the development of a prediction tool for the cocktail effects of HEAs in the future. Sluggish diffusion and lattice distortion have been proven in HEAs; however, how to employ these concepts in the actual alloy design has remained a challenge, and this clearly needs an accurate phase prediction tool for HEAs. Furthermore, research works on the deformation behaviors of HEAs have been conducted on polycrystalline samples, in order to study the effects of intrinsic HEA compositions, the fabrication of single crystal samples is of interest, especially for RHEAs. Nevertheless, "High-Entropy Alloys" have become one of the most important material research fields. The concept of HEAs has given the community a novel idea of material design, to develop new structural and functional materials for various applications. Nowadays, the research activities of HEAs are growing rapidly; we believe that in the near future, the concept of HEAs can have many positive impacts to our society and make the world more wonderful.

Conclusion

There are still many challenges ahead to study and develop future HEA-based materials. Due to the complexity of HEAs systems, mechanisms of different cocktail effects can interact with each other and become very complex; this should be a subject of interest for future study. There are ongoing efforts to develop CALPHAD-based tools to predict phases in HEAs, but lots of research works are still needed to improve the prediction capability and accuracy; artificial intelligence or machine learning may assist in the effort to speed up the development of a prediction tool for the cocktail effects of HEAs in the future. Sluggish diffusion and lattice distortion have been proven in HEAs; however, how to employ these concepts in the actual alloy design has remained a challenge.

Furthermore, research works on the deformation behaviors of HEAs have been conducted on polycrystalline samples, to study the effects of intrinsic HEA compositions, the fabrication of single crystal samples is of interest, especially for RHEAs. Nevertheless, "High-Entropy Alloys" have become one of the most important material research fields. The concept of HEAs has given the community a novel idea to develop new structural and functional materials for various applications. Nowadays, the research activities of HEAs are growing rapidly; we believe that in the near future, the concept of HEAs can have many positive impacts to our society and make the world more wonderful.

Acknowledgments

The financial support by the "High Entropy Materials Centre" from The Featured Areas Research Centre Program within the framework of the Higher Education Sprout Project by the Ministry of Education (MOE) and from the Project MOST107-2923-E-007-010-MY3, MOST109-2221-E-007-057, MOST110-2634-F-007-024, MOST110-2224-E-007-001, MOST110-2221-E-007-020-MY3 by Ministry of Science and Technology (MOST) in Taiwan.

References

Biswas K, et al. (2020) High entropy alloys: Key issues under passionate debate. *Scripta Materialia* 188: 54–58. https://doi.org/10.1016/j.scriptamat.2020.07.010.

Cantor B (2014) Multicomponent and high entropy alloys. *Entropy* 16(9): 4749–4768. https://doi.org/10.3390/e16094749.

Chang SY, et al. (2014) Structural and thermodynamic factors of suppressed interdiffusion kinetics in multi-component high-entropy materials. *Scientific Reports* 4. https://doi.org/10.1038/srep04162. ARTN 4162.

Chen TK, et al. (2004) Nanostructured nitride films of multi-element high-entropy alloys by reactive DC sputtering. *Surface & Coatings Technology* 188: 193–200. https://doi.org/10.1016/j.surfcoat.2004.08.023.

Chen YT, et al. (2020a) Designing high entropy superalloys for elevated temperature application. *Scripta Materialia* 187: 177–182. https://doi.org/10.1016/j.scriptamat.2020.06.002.

Chen YT, et al. (2020b) Hierarchical microstructure strengthening in a single crystal high entropy superalloy. *Scientific Reports* 10(1). https://doi.org/10.1016/j.scriptamat.2020.06.002.

Chen Y, et al. (2021) High entropy metallic glasses: Glass formation, crystallization and properties. *Journal of Alloys and Compounds* 866. https://doi.org/10.1016/j.jallcom.2021.158852. ARTN 158852.

Cheng CY, et al. (2017) Physical metallurgy of concentrated solid solutions from low-entropy to high-entropy alloys. *Current Opinion in Solid State and Materials Science* 21(6): 299–311. https://doi.org/10.1016/j.cossms.2017.09.002.

Ding PP, et al. (2017) Preparation, characterization and properties of multicomponent A1CoCrFeNi(2.1) powder by gas atomization method. *Journal of Alloys and Compounds* 721: 609–614. https://doi.org/10.1016/j.jallcom.2017.06.020.

Duan YP, et al. (2020) Optimizing the electromagnetic properties of the FeCoNiAlCrx high entropy alloy powders by composition adjustment and annealing treatment. *Journal of Magnetism and Magnetic Materials* 497. https://doi.org/10.1016/j.jmmm.2019.165947. ARTN 165947.

Gao MC, Yeh JW, Liaw PK, and Zhang Y (2016) *High-Entropy Alloys Fundamentals and Applications*. Springer. IBSN 978-3-319-27011-1.

Gargarella P, et al. (2011) Prediction of good glass formers in the Al-Ni-La and Al-Ni-Gd systems using topological instability and electronegativity. *Journal of Applied Physics* 109(9). https://doi.org/10.1063/1.3563099. Artn 093509.

Gaskell DR (1995) *Introduction to the Thermodynamics of Materials*, 3rd. Washington, D.C.: Taylor & Francis. ISBN: 978-1560324324.

Gong P, et al. (2020) Influence of deep cryogenic cycling on the rejuvenation and plasticization of TiZrHfBeCu high-entropy bulk metallic glass. *Materials Science and Engineering a-Structural Materials Properties Microstructure and Processing* 797. https://doi.org/10.1016/j.msea.2020.140078. ARTN 140078.

Guo S and Liu CT (2011) Phase stability in high entropy alloys: Formation of solid-solution phase or amorphous phase. *Progress in Natural Science: Materials International* 21(6): 433–446. https://doi.org/10.1016/S1002-0071(12)60080-X.

Guo S and Liu CT (2013) Phase selection rules for complex multi-component alloys with equiatomic or close-to-equiatomic compositions. *Chinese Journal of Natural Medicines* 35: 85–96.

Hsu WL, et al. (2016) A heat-resistant NiCo0.6Fe0.2Cr1.5SiAlTi0.2 overlay coating for high-temperature applications. *Journal of the Electrochemical Society* 163(13): C752–C758. https://doi.org/10.1149/2.0821613jes.

Hsu WL, et al. (2018) A study of NiCo0.6Fe0.2CrxSiAlTiy high-entropy alloys for applications as a high-temperature protective coating and a bond coat in thermal barrier coating systems. *Journal of the Electrochemical Society* 165(9): C524–C531. https://doi.org/10.1149/2.1191809jes.

Huang PK, et al. (2004) Multi-principal-element alloys with improved oxidation and wear resistance for thermal spray coating. *Advanced Engineering Materials* 6(1–2): 74–78. https://doi.org/10.1002/adem.200300507.

Jain SC, et al. (1969) Thermal conductivity of metals at high temperatures by the Jain and Krishnan method III. Platinum. *Journal of Physics D: Applied Physics* 2(1): 109–113. https://doi.org/10.1088/0022-3727/2/1/316.

Jian WW, et al. (2013) Physics and model of strengthening by parallel stacking faults. *Applied Physics Letters* 103(13). https://doi.org/10.1063/1.4822323. Artn 133108.

Jiang H, et al. (2019) Direct solidification of bulk ultrafine-microstructure eutectic high-entropy alloys with outstanding thermal stability. *Scripta Materialia* 165: 145–149. https://doi.org/10.1016/j.scriptamat.2019.02.035.

Kawagishi K, et al. (2012) Development of an Oxidation-Resistant High-Strength Sixth-Generation Single-Crystal Superalloy Tms-238. In: *Superalloys 2012*, pp. 189–195. [Online]. Available: <Go to ISI>://WOS:000324518300021.

Lee CP, et al. (2008) Enhancing pitting corrosion resistance of AlxCrFe1.5MnNi0.5 high-entropy alloys by anodic treatment in sulfuric acid. *Thin Solid Films* 517(3): 1301–1305. https://doi.org/10.1016/j.tsf.2008.06.014.

Li CZ, et al. (2019) New ferromagnetic (Fe1/3Co1/3Ni1/3)(80)(P1/2B1/2)(20) high entropy bulk metallic glass with superior magnetic and mechanical properties. *Journal of Alloys and Compounds* 791: 947–951. https://doi.org/10.1016/j.jallcom.2019.03.375.

Li Z, et al. (2022) Characterization of novel high-entropy (La0.2Nd0.2Sm0.2Dy0.2Yb0.2)2Zr2O7 electrospun ceramic nanofibers. *Ceramics International*. https://doi.org/10.1016/j.ceramint.2022.01.067.

Lin KH, et al. (2021) Different lattice distortion effects on the tensile properties of Ni-W dilute solutions and CrFeNi and CoCrFeMnNi concentrated solutions. *Acta Materialia* 221. https://doi.org/10.1016/j.actamat.2021.117399. ARTN117399.

Liu XJ, et al. (2021) Enhancement of magnetic properties in FeCoNiCr0.4Cux high entropy alloys through the cocktail effect for megahertz electromagnetic wave absorption. *Journal of Alloys and Compounds* 872. https://doi.org/10.1016/j.jallcom.2021.159602. ARTN 159602.

Lu YP, et al. (2017) Directly cast bulk eutectic and near-eutectic high entropy alloys with balanced strength and ductility in a wide temperature range. *Acta Materialia* 124: 143–150. https://doi.org/10.1016/j.actamat.2016.11.016.

Miracle DB, et al. (2014) Exploration and development of high entropy alloys for structural applications. *Entropy* 16(1): 494–525. https://doi.org/10.3390/e16010494.

Moore WJ (1962) Thermodynamics of solids (Swalin, Richard A.). *Journal of Chemical Education* 39(9): 488. https://doi.org/10.1021/ed039p488.3.

Murty BS, Yeh JW, and Ranganathan S (2014) *High-Entropy Alloys*, 1st edn, p. 2, ISBN: 9780128002513. https://doi.org/10.1016/B978-0-12-800251-3.00001-8.

Otarawanna S and Dahle AK (2011) 6 - Casting of aluminium alloys. In: Lumley R (ed.) *Fundamentals of Aluminium Metallurgy*, pp. 141–154. Woodhead Publishing.

Pan QS, et al. (2021) Gradient cell-structured high-entropy alloy with exceptional strength and ductility. *Science* 374(6570): 984. https://doi.org/10.1126/science.abj8114.

Pickering EJ and Jones NG (2016) High-entropy alloys: A critical assessment of their founding principles and future prospects. *International Materials Reviews* 61(3): 183–202. https://doi.org/10.1080/09506608.2016.1180020.

Ranganathan S (2003) Alloyed pleasures: Multimetallic cocktails. *Current Science* **85**(10): 1404–1406. [Online]. Available: <Go to ISI>://WOS:000187013600009.

Reed RC (2006) *The Superalloys: Fundamentals and Applications*. Cambridge: Cambridge University Press. https://doi.org/10.1017/CBO9780511541285. online ISBN 9780511541285.

Reed-Hill RE (1994) *Physical Metallurgy Principles*, 3rd edn. Boston, PWS Pub. Co. ISBN10: 0534921736.

Sarma VS, et al. (2010) Role of stacking fault energy in strengthening due to cryo-deformation of FCC metals. *Materials Science and Engineering a-Structural Materials Properties Microstructure and Processing* 527(29–30): 7624–7630. https://doi.org/10.1016/j.msea.2010.08.015.

Sathiaraj GD, et al. (2020) Effect of stacking fault energy on microstructure and texture evolution during the rolling of non-equiatomic CrMnFeCoNi high-entropy alloys. *Crystals* 10(7). https://doi.org/10.3390/cryst10070607. ARTN 607.

Senkov ON and Woodward CF (2011) Microstructure and properties of a refractory NbCrMo0.5Ta0.5TiZr alloy. *Materials Science and Engineering a-Structural Materials Properties Microstructure and Processing* 529: 311–320. https://doi.org/10.1016/j.msea.2011.09.033.

Senkov ON, et al. (2010) Refractory high-entropy alloys. *Intermetallics* 18(9): 1758–1765. https://doi.org/10.1016/j.intermet.2010.05.014.

Senkov ON, et al. (2011a) Mechanical properties of Nb25Mo25Ta25W25 and V20Nb20Mo20Ta20W20 refractory high entropy alloys. *Intermetallics* 19(5): 698–706. https://doi.org/10.1016/j.intermet.2011.01.004.

Senkov ON, et al. (2011b) Microstructure and room temperature properties of a high-entropy TaNbHfZrTi alloy. *Journal of Alloys and Compounds* 509(20): 6043–6048. https://doi.org/10.1016/j.jallcom.2011.02.171.

Senkov ON, et al. (2012) Microstructure and elevated temperature properties of a refractory TaNbHfZrTi alloy. *Journal of Materials Science* 47(9): 4062–4074. https://doi.org/10.1007/s10853-012-6260-2.

Senkov ON, et al. (2013a) Mechanical properties of low-density, refractory multi-principal element alloys of the Cr-Nb-Ti-V-Zr system. *Materials Science and Engineering a-Structural Materials Properties Microstructure and Processing* 565: 51–62. https://doi.org/10.1016/j.msea.2012.12.018.

Senkov ON, et al. (2013b) Low-density, refractory multi-principal element alloys of the Cr-Nb-Ti-V-Zr system: Microstructure and phase analysis. *Acta Materialia* 61(5): 1545–1557. https://doi.org/10.1016/j.actamat.2012.11.032.

Senkov ON, Senkova SV, and Woodward C (2014) Effect of aluminum on the microstructure and properties of two refractory high-entropy alloys. *Acta Materialia* 68: 214–228. https://doi.org/10.1016/j.actamat.2014.01.029.

Senkov ON, et al. (2016) Development of a refractory high entropy superalloy. *Entropy* 18(3). https://doi.org/10.3390/e18030102.

Stepanov ND, et al. (2015) Structure and mechanical properties of the AlCrxNbTiV (x=0, 0.5, 1, 1.5) high entropy alloys. *Journal of Alloys and Compounds* 652: 266–280. https://doi.org/10.1016/j.jallcom.2015.08.224.

Stoudt MR, et al. (2000) Suppression of fatigue cracking with nanometer-scale multilayered coatings. *Scripta Materialia* 43(6): 491–496. https://doi.org/10.1016/S1359-6462(00)00449-8.

Takeuchi A, et al. (2014) Alloy designs of high-entropy crystalline and bulk glassy alloys by evaluating mixing enthalpy and delta parameter for quinary to decimal equi-atomic alloys. *Materials Transactions* 55(1): 165–170. https://doi.org/10.2320/matertrans.M2013352.

Tsai CW, et al. (2009) Deformation and annealing behaviors of high-entropy alloy Al0.5CoCrCuFeNi. *Journal of Alloys and Compounds* 486(1–2): 427–435. https://doi.org/10.1016/j.jallcom.2009.06.182.

Tsai KY, et al. (2013) Sluggish diffusion in Co-Cr-Fe-Mn-Ni high-entropy alloys. *Acta Materialia* 61(13): 4887–4897. https://doi.org/10.1016/j.actamat.2013.04.058.

Vaidya M, et al. (2016) Ni tracer diffusion in CoCrFeNi and CoCrFeMnNi high entropy alloys. *Journal of Alloys and Compounds* 688: 994–1001. https://doi.org/10.1016/j.jallcom.2016.07.239.

Vaidya M, et al. (2018) Bulk tracer diffusion in CoCrFeNi and CoCrFeMnNi high entropy alloys. *Acta Materialia* 146: 211–224. https://doi.org/10.1016/j.actamat.2017.12.052.

Venkatasubramanian R (2000) Lattice thermal conductivity reduction and phonon localization-like behavior in superlattice structures. *Physical Review B* 61. https://doi.org/10.1103/PhysRevB.61.3091.

Yang X and Zhang Y (2012) Prediction of high-entropy stabilized solid-solution in multi-component alloys. *Materials Chemistry and Physics* 132(2–3): 233–238. https://doi.org/10.1016/j.matchemphys.2011.11.021.

Yang T, et al. (2018) Multicomponent intermetallic nanoparticles and superb mechanical behaviors of complex alloys. *Science* 362(6417): 933. https://doi.org/10.1126/science.aas8815.

Yao KD, et al. (2021) High-entropy intermetallic compound with ultra-high strength and thermal stability. *Scripta Materialia* 194. https://doi.org/10.1016/j.scriptamat.2020.113674. ARTN 113674.

Yeh JW (2006) Recent progress in high-entropy alloys. *Annales De Chimie-Science Des Materiaux* 31(6): 633–648. https://doi.org/10.3166/acsm.31.633-648.

Yeh JW (2009) Recent progress in high-entropy alloys. In: *The 2009 cross-strait conference on metallic glasses*. Taipei: National Taiwan University of Science and Technology.

Yeh JW (2013) Alloy design strategies and future trends in high-entropy alloys. *JOM* 65(12): 1759–1771. https://doi.org/10.1007/s11837-013-0761-6.

Yeh JW (2021) Strength through high slip-plane density. *Science* 374(6570): 940–941. https://doi.org/10.1126/science.abm0120.

Yeh AC and Tin S (2005) Effects of Ru and Re additions on the high temperature flow stresses of Ni-base single crystal superalloys. *Scripta Materialia* 52(6): 519–524. https://doi.org/10.1016/j.scriptamat.2004.10.039.

Yeh AC and Tin S (2006) Effects of Ru on the high-temperature phase stability of Ni-base single-crystal superalloys. *Metallurgical and Materials Transactions a-Physical Metallurgy and Materials. Science* **37a**(9): 2621–2631. https://doi.org/10.1007/Bf02586097.

Yeh JW, et al. (2004a) Nanostructured high-entropy alloys with multiple principal elements: Novel alloy design concepts and outcomes. *Advanced Engineering Materials* 6(5): 299–303. https://doi.org/10.1002/adem.200300567.

Yeh AC, et al. (2004b) High temperature creep of Ru-bearing Ni-base single crystal superalloys. In: *Superalloys 2004*, pp. 677–685. [Online]. Available: <Go to ISI>://WOS:000228231000077.

Yeh AC, et al. (2008) On the creep and phase stability of advanced Ni-base single crystal superalloys. *Materials Science and Engineering a-Structural Materials Properties Microstructure and Processing* 490(1–2): 445–451. https://doi.org/10.1016/j.msea.2008.02.008.

Yeh AC, et al. (2014) On the Solidification and Phase Stability of a Co-Cr-Fe-Ni-Ti High-Entropy Alloy. *Metallurgical and Materials Transactions a-Physical Metallurgy and Materials Science* **45a**(1): 184–190. https://doi.org/10.1007/s11661-013-2097-9.

Youssef KM, et al. (2015) A novel low-density, high-hardness, high-entropy alloy with close-packed single-phase nanocrystalline structures. *Materials Research Letters* 3(2): 95–99. https://doi.org/10.1080/21663831.2014.985855.

Yurchenko NY, et al. (2017) Structure and mechanical properties of B2 ordered refractory AlNbTiVZrx (x=0–1.5) high-entropy alloys. *Materials Science and Engineering a-Structural Materials Properties Microstructure and Processing* 704: 82–90. https://doi.org/10.1016/j.msea.2017.08.019.

Zaddach AJ, et al. (2013) Mechanical properties and stacking fault energies of NiFeCrCoMn high-entropy alloy. *JOM* 65(12): 1780–1789. https://doi.org/10.1007/s11837-013-0771-4.

Zaddach AJ, et al. (2015) Tensile properties of low-stacking fault energy high-entropy alloys. *Materials Science and Engineering a-Structural Materials Properties Microstructure and Processing* 636: 373–378. https://doi.org/10.1016/j.msea.2015.03.109.

Zhang Y, et al. (2008) Solid-solution phase formation rules for multi-component alloys. *Advanced Engineering Materials* 10(6): 534–538. https://doi.org/10.1002/adem.200700240.

Zhang XR, et al. (2019) Influence of remelting and annealing treatment on corrosion resistance of AlFeNiCoCuCr high entropy alloy in 3.5% NaCl solution. *Journal of Alloys and Compounds* 775: 565–570. https://doi.org/10.1016/j.jallcom.2018.10.081.

Zhang W, et al. (2021) Grain growth kinetics and densification mechanism of (TiZrHfVNbTa)C high-entropy ceramic under pressureless sintering. *Journal of Materials Science and Technology*.

Zhou NX, et al. (2019) Single-phase high-entropy intermetallic compounds (HEICs): bridging high-entropy alloys and ceramics. *Science Bulletin* 64(12): 856–864. https://doi.org/10.1016/j.scib.2019.05.007.

Halide perovskites: Properties, synthesis, and applications

Nathaniel P Gallop and Rebecca L Milot, Department of Physics, University of Warwick, Coventry, United Kingdom

© 2024 Elsevier Ltd. All rights reserved.

Introduction 659
Overview 660
Brief history of the field 660
Structure of MHPs and related materials 660
Synthesis 662
Physical, optical, and optoelectronic properties 663
Optical properties 664
Optoelectronic properties 667
Other physical properties 669
Applications 670
Photovoltaic cells 671
Water oxidation and other catalysis 672
Light emission 672
Other electronics 673
Thermoelectric generators 673
Key issues 673
Stability 673
Toxicity 674
Understanding fundamental properties 674
Conclusion 674
References 675

Abstract

Metal halide perovskites have been widely investigated for their potential to replace standard semiconductors in a range of applications including solar cells and light-emitting diodes because high-quality materials with high charge-carrier mobilities and long charge-carrier lifetimes can be relatively easily synthesized in a variety of morphologies using many different techniques. Furthermore, their optoelectronic properties including bandgap energy can be altered with simple chemical substitution, allowing for materials to be tuned for specific applications. Despite issues with stability and toxicity, some highly efficient devices have been fabricated, and the number of potential applications continues to grow.

Key points

- In recent years halide perovskites have attracted much attention due to their potential application in many optoelectronic devices, including photovoltaic cells.
- Their promise in a range of applications stems from their ease of synthesis and their unique set of optoelectronic and physical properties, including strong optical absorption and long charge-carrier diffusion lengths.
- The tunability of halide perovskite properties with chemical composition and morphology has resulted in the development of different types of materials and synthetic methods.
- However, two main obstacles, stability and toxicity, are currently hindering the realization of commercialization of perovskite-based devices, although a large research effort has been dedicated to address these issues.

Introduction

In the last decade, research on metal halide perovskites (MHPs) has increased dramatically due to their promising applications in photovoltaic (PV) cells and other devices. This meteoric rise has been enabled both by the superior optical and electronic properties of these materials and by their ease of synthesis, making them attractive alternatives to standard inorganic semiconductors for applications ranging from light-emitting diodes to nonvolatile memory devices (Jena et al., 2019). They are also intriguing due to their usual combination of physical properties, which includes high charge-carrier mobilities, low thermal conductivity, and defect tolerance among others. Due to all of this interest, thousands of publications about halide perovskites are added to the literature every year, and products are approaching commercialization, including silicon-perovskite tandem solar cells.

https://doi.org/10.1016/B978-0-323-90800-9.00204-3

This article provides a brief overview of what has made MHPs so interesting to many researchers, focusing on how their unique set of physical and chemical properties has enabled the development of devices. It is by no means an exhaustive review of the subject, and the reader is referred to the many more specific review articles cited in this overview.

Overview

Brief history of the field

The discovery of perovskites in general can be traced back to 1839, when mineralogist Gustav Rose identified the naturally-occurring, oxide perovskite $CaTiO_3$, naming it in honor of nobleman and amateur minerologist Lev Perovski (Jena et al., 2019). The synthesis of $CaTiO_3$ in 1851 led to the development of other oxide perovskites including $BaTiO_3$ and $LiNbO_3$, which have been evaluated since then for their ferroelectric, piezoelectric, dielectric properties, among others. Alongside these investigations for oxide perovskites, inorganic metal halide perovskites including $CsPbX_3(X = Cl^-, Br^-, \text{or } I^-)$ were first synthesized in the 1890s, with analogous materials incorporating organic species (for example $CH_3NH_3PbX_3$, $X = I^-,Br^-$) first reported about 80 years later in the 1970s. From this point, however, the tunable nature of the chemical structure was exploited by a couple of pioneering groups, who reported a greatly expanded range of materials with different organic and metal cation species. The potential application in light-emission, nonlinear optics, and thin-film transistors was also identified at this time (Kagan et al., 1999; Jena et al., 2019). While applications in PV were purportedly also discussed at this time, they were discounted due to concerns over lead toxicity, coupled with the tendency for tin-containing MHPs to degrade (Green et al., 2014).

The explosion of interest in MHPs that has shaped the field today did not come until after the first demonstration of a solar cell containing an MHP in 2009, however (Kojima et al., 2009). This solar cell was based on the working principles of a dye-sensitized solar cell (DSSC), where an MHP acted as the sensitizing layer on a metal-oxide surface. At the time, the DSSC field was well established, with many researchers focused on the topic world-wide, but the maximum reported efficiencies of cells had remained around 10% for about a decade (NREL, 2021). Although the first report of an MHP cell gave efficiencies of only 3.8% (Kojima et al., 2009), this value was improved to 10.9% by Lee et al. (2012), which rivaled the best performing DSSCs. Furthermore, concurrent studies of the fundamental properties of metal halide perovskites found that they have high charge-carrier mobilities, long charge-carrier lifetimes, and therefore long charge-carrier diffusion lengths, which suggested that perovskite solar cells could achieve much higher efficiencies (Johnston and Herz, 2016). Combined with their ease of synthesis, this success enabled the popularity of perovskites to grow rapidly. Over the next decade, solar cell efficiencies would exceed 25%, rivaling silicon technologies and approaching the fundamental limit for the efficiency of a single junction solar cell (NREL, 2021). Following this success, perovskites have also been investigated for a range of other optoelectronic applications including photodetection (Wang and Kim, 2017), photocatalysis (Ren et al., 2022), and light-emission (Otero-Martinez et al., 2022), and there are now several businesses looking to commercialize perovskite technologies.

Structure of MHPs and related materials

MHPs adopt the classic ABX_3 structure, where A is a monovalent cation, B is a divalent metal cation, and X is a halide anion (Fig. 1). This perovskite structure can be visualized as a set of corner-sharing BX_6 octahedra in which the A-site cation occupies the cuboctahedral cavities created by the three-dimensional network of octahedra.

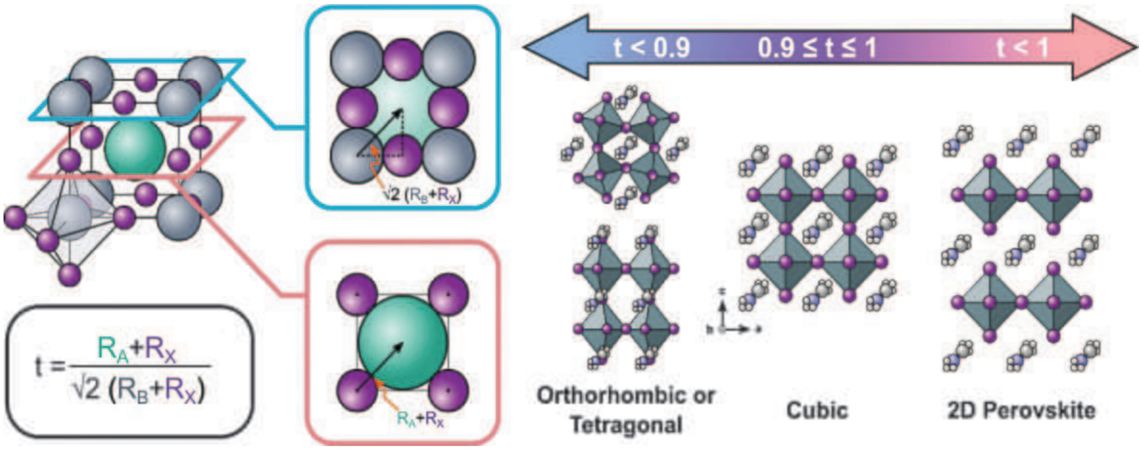

Fig. 1 The Goldschmidt Tolerance Factor and its influence on the structure of hybrid perovskites. (left) Illustration of the perovskite structure and a visualization of the geometric arguments that give rise to the Goldschmidt tolerance factor. (right) Cartoons illustrating the effects of non-ideal Goldschmidt tolerance factors on perovskite crystal structures.

Many different compositions of MHPs have been reported, and this tunability of structure is what makes these materials attractive for many different applications because the optoelectronic properties also tune with chemical composition. Commonly, a small organic alkylammonium cation such as methylammonium (MA, $CH_3NH_3^+$) or formamidinium (FA, $CH(NH_2)_2^+$) is used as the A-site cation. As this cation is not bonded to the metal covalently and therefore does not form an organo-metallic compound, metal hybrid perovskites are often given the additional classification as hybrid due to their mixed organic-inorganic components. However, all- inorganic varieties such as $CsPbI_3$ are included in the more general MHP classification. For both hybrid or all-inorganic varieties, the metal cation is typically lead (II) or tin (II), but a range of other divalent metal cations has been reported including germanium, copper, cobalt, palladium, and many more (Wang et al., 2019). Many other possible compositions have been also identified computationally (Filip and Giustino, 2018). Of the halides anions, iodide and bromide are most commonly used, but chlorine-based MHPs have also been synthesized. Pseudo-halides such as cyanide (CN-) or thiocyanide (SCN-) have also been reported and are sometimes discussed in the same context as MHPs.

With such a variety of options, it is important to discuss what the limits are to perovskite formation. The Goldschmidt tolerance factor (GTF) is often used to predict the formation of MHPs based solely on the sizes of their constituent ions. First proposed for metal oxide perovskites in 1926, the tolerance factor is defined as follows, where the subscripts A, B, and X correspond to the organic cation, metal cation, and halide, respectively, and r is the ionic radius.

$$t = \frac{r_A + r_X}{\sqrt{2}(r_B + r_X)}$$

The tolerance factor constitutes what is commonly referred to as the "no-rattling" principle of structural design which seeks to maximize the number of anions around a cation while ensuring that all the anions touch a cation (Filip and Giustino, 2018) and can be obtained from a simple geometric argument, which is outlined in Fig. 1. This argument can be understood by considering two 'slices' through the perovskite unit cell: one through a plane containing the metal and halide ions and another containing the divalent cation and halides (highlighted as red and blue in Fig. 1, respectively).

For a cubic perovskite, we expect the 'size' of these slices to be equal and for halide and metal ions to stack perfectly on top of each other. For this to be true, the distances from the atoms at the corners of the crystal to the center of each slice (given by the black arrows in the red and blue boxes) must also be equal. We can express this distance in terms of the ionic radii of the constituent ions in two different ways, as shown in Fig. 1. The tolerance factor is simply a ratio of these two lengths. If the two lengths are equal, then $t = 1$.

A tolerance factor of 1 thus indicates a perfect cubic structure as shown in Fig. 1, but cubic structures are possible for MHPs with values as low as about 0.9 (Wang et al., 2019). For example, $FAPbI_3$ has a tolerance factor of 0.89 at room temperature but still adopts a cubic crystal structure. For values of 0.7–0.89, structures which maintain the perovskite coordination are still possible, but are distorted from the cubic structure because of the poor 'fit' of the ions. For example, substituting the formamidinium cation with the smaller methylammonium decreases the tolerance factor to 0.84 and results in a tetragonal crystal structure at room temperature in which the Pb—I octahedra are tilted with respect to the ideal cubic structure, and the lattice constant is larger in one dimension than in the other two (Fig. 1).

Values of t greater than 1, where perovskite structures generally do not form, are most often obtained when the A-site cation is too large. However, stable perovskite-like structures are possible including 2D or layered perovskites, in which a layer or layers of metal-halide octahedra are separated by a layer of larger organic cations as shown in Fig. 1 (Sirbu et al., 2021).

The flexibility in the tolerance factor means that mixed or alloyed structures are also possible, increasing the synthetic space and tunability even more. One example is the so-called double perovskites in which the B-site divalent cation is replaced with a monovalent cation and trivalent cation in equal proportion, i.e., $CsInAgCl_6$ or Cu_2AgBiI_6. Non-stoichiometric mixtures, in which one or more of the components is mixed with an ion of the same valence in an arbitrary proportion, are also possible. Some common examples include mixed halides such as $FAPb(Br_yI_{1-y})_3$, where y can have any value between 0 and 1, mixed-cation compositions such as $FA_xCs_{1-x}PbI_3$, and mixed lead-tin materials. It is also possible to mix two or more of the components as in $FA_{0.75}Cs_{0.25}Sn_{0.5}Pb_{0.5}I_3$ or $FA_{0.83}Cs_{0.17}Pb(I_{0.5}Br_{0.5})_3$. Through careful selection of the ionic radii of the perovskite's constituents, the optical and structural properties of the material can be controlled, giving researchers a powerful tool to tune the desirable characteristics of the material, as will be discussed in more detail in later sections.

Although the Goldschmidt Tolerance Factor has been shown to predict 80% of possible perovskites (Filip and Giustino, 2018), it is not a perfect predictor of crystal structure in hybrid perovskites for several reasons:

1) The traditional implementation for GTFs assumes spherically symmetric A-site species. The organic cations in hybrid perovskites are clearly non-spherical, which makes assigning an ionic radius challenging.
2) The geometric arguments that give rise to the tolerance factor assume hard spheres for the ionic species. This assumption breaks down for the B-site species Pb and Sn, as well as for heavier halide ions, such as bromine and iodine.
3) Tolerance factors primarily apply to thermodynamic minima, however given the low temperatures at which hybrid perovskites are commonly synthesized, kinetic trapping of otherwise non-ideal states is possible.

As a result, there have been several attempts to modify the Goldschmidt tolerance factor to better apply to hybrid perovskites, for example through the use of data-mining and machine learning approaches (Filip and Giustino, 2018; Kieslich et al., 2015; Sato et al., 2016; Travis et al., 2016), by revising values for the ionic radii of the halide and organic cation species to account for bond covalency (Travis et al., 2016) or else by applying more sophisticated geometric models beyond the hard-sphere model initially proposed (Travis et al., 2016; Kieslich et al., 2015).

Synthesis

One of the most appealing properties of MHPs is that high quality materials can be synthesized at ambient temperatures and pressures. This ease of synthesis gives them an advantage over traditional inorganic semiconductors such as silicon whose syntheses typically require high temperatures of over 1000 °C (Jena et al., 2019). Furthermore, MHPs can be synthesized in many different morphologies including polycrystalline thin films, quantum dots, nanowires, nanoplatelets, single crystals, and powders, providing further opportunities to tune materials for device applications (Fig. 2).

Most MHP syntheses involve the combination of a metal halide salt and an organic (or cesium) halide salt in equal molar quantities to create the desired perovskite. For example,

$$PbI_2 + CH_3NH_3I \rightarrow CH_3NH_3PbI_3$$

While this basic equation dictates the main chemical composition of the perovskite material, the experimental conditions can further fine-tune the properties and morphology of the MHP that is created. Synthetic methods can roughly be divided into those that involve combining the starting materials in a solvent (for example spin-coating or ink-jet printing) and solvent-free methods (e.g., vapor deposition). Solvent-based methods have been the most popular to date due to their relative ease and the low cost of associated equipment, although solvent-free methods are also popular because of their potential for scalability.

MHPs are most commonly synthesized as polycrystalline thin films with thicknesses a few 100s of nanometers because this is the architecture most useful for devices such as solar cells and LEDs. A further benefit for devices, thin films can be prepared on a range of substrates by various methods including spin-coating, vapor deposition, or ink-jet printing. As a result, much research has been dedicated to optimizing the synthesis of thin films (Dunlap-Shohl et al., 2019).

The most basic and widely used solution-processing technique for metal halide thin films is spin-coating (Dunlap-Shohl et al., 2019). In a one-step procedure, the starting materials are dissolved in a polar, aprotic solvent such as dimethyl sulfoxide (DMSO), dimethylformamide (DMF), γ-butyrolactone (GBL), or mixtures of such solvents. These polar solvents are needed because of the low solubility of lead in other common organic solvents. The solution is then dropped unto a substrate (usually glass or coated glass) spinning at hundreds to thousands of revolutions per minute. Films with uniform thicknesses typically from 100 nm to 500 nm form spontaneously as the solvent evaporates and is driven off the substrate by spinning. While the substrate is spinning, an

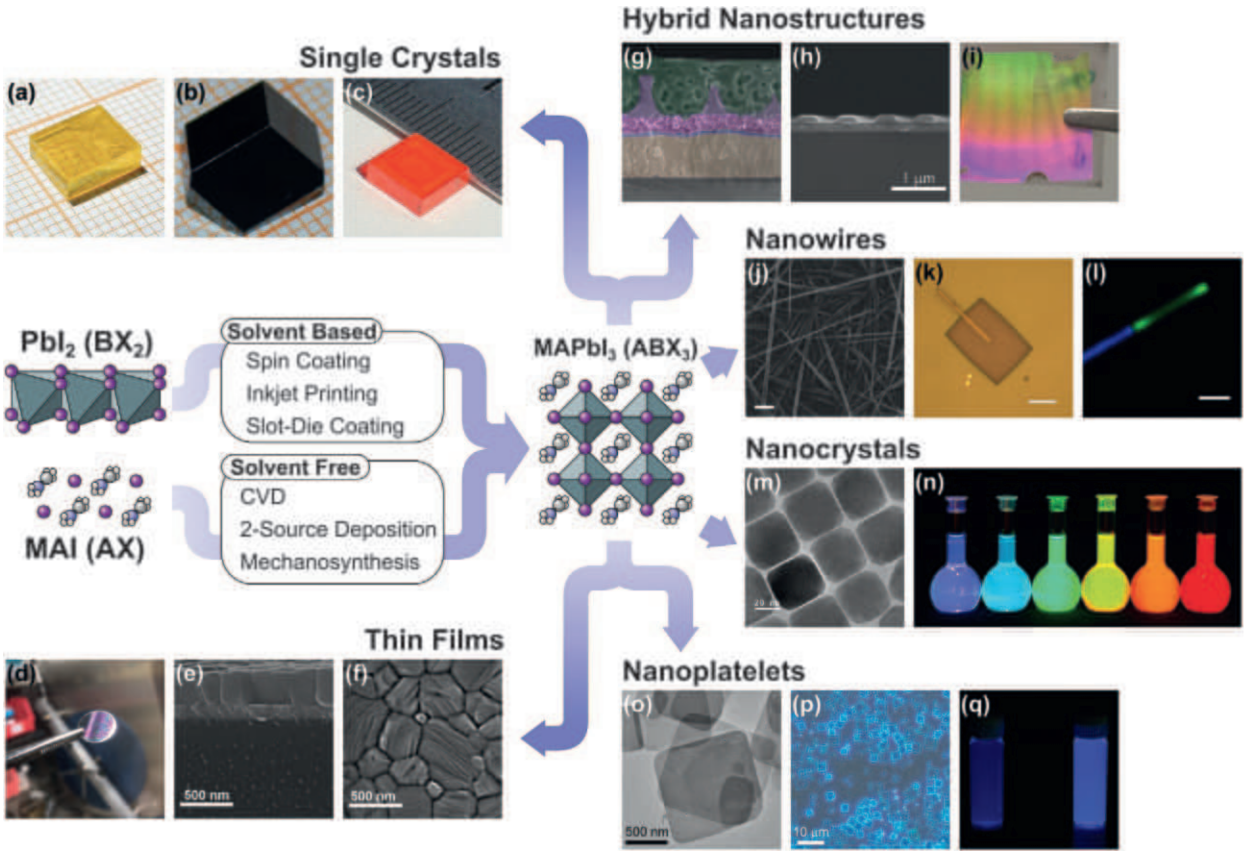

Fig. 2 The diversity of synthetic techniques and morphologies of hybrid perovskites, including single crystals (a–c) and thin films (d–f). A wide diversity of hybrid perovskite nanostructures also exist, including hybrid nanostructures (g–i), nanowires (j–l), nanocrystals (m and n), and nanoplatelets (o–q). Subfigures (a–c) adapted from Ma et al. (2021), (e and f) from Jia et al. (2021), (g) from Meng et al. (2016), (h and i) from Mao et al. (2017), (j) from Im et al. (2015), (k and l) from Dou et al. (2017), (m) from Bera et al. (2020), (n) from Protesescu et al. (2015), (o and q) from Weidman et al. (2016), and (p) from Dou et al. (2015).

"antisolvent" such as the non-polar toluene might also be applied to aid crystallization and the formation of uniform films. After spinning, the films are usually annealed at temperatures between 100 °C and 200 °C to drive off any remaining solvent and improve crystallinity and film morphology. In addition this one-step method, two-step methods are also common in which a metal halide film is deposited first and allowed to dry. The organic halide is then incorporated separately either in the solution, vapor, or solid phase. The perovskite film then forms as the organic halide ions diffuse through the metal halide film.

Much work has been done to tune spin-coating methods to optimize thin films for device applications. The ideal thin film for device applications should be highly crystalline, have large grain sizes, be free of pinholes, and have lower impurity or defect densities. Some common methods to achieve these goals include forming the films in an excess of starting material, including various additives into the starting solution, post treating with different solutions or gases, and many more. For a more complete overview of these strategies, see the review article by Dunlap-Shohl et al. (2019).

In addition to spin-coating, other solvent-based deposition techniques have been investigated for thin films, with the aim of making film synthesis more scalable in a manufacturing setting (Dunlap-Shohl et al., 2019). One example is blade-coating, where the solution of starting materials is drawn across the substrate using a blade at fixed height. Similarly, slot-die coating involves passing the starting solution through a narrow die at a fixed rate and then moving the die relative to the substrate in order to produce the desired film. Both blade-coating and slot die coating are important for the development of roll-to-roll processing methods. Another method identified for its commercial promise is spray-coating, where the solution is aerosolized through injection through a nozzle, which is then directed toward a substrate. Ink-jet printing is a variation on this method that enables patternable deposition of thin films.

Thin films can also be prepared by several solvent-free approaches. The more popular solvent-free approach is thermal evaporation (Xiang et al., 2022). In dual-source thermal evaporation, a substrate is placed in a chamber under high vacuum (typically 10^{-5} to 10^{-7} Torr). The solid starting materials are then evaporated in separate crucibles and directed toward the substrate where the vapors combine and form the perovskite film. The evaporation rates of the starting materials are controlled in order to tune the stoichiometry of the vapor. Similarly, chemical vapor deposition (CVD) methods have also been investigated (Raiford et al., 2020). In CVD, an inert flow gas such as nitrogen or argon transports the vaporized starting materials into a vacuum chamber where the components react and deposit on a substrate. As with solution processing, both one-step methods, where the all starting materials are introduced at once, and two-step methods, where the metal halide is deposited first, are possible. CVD chambers can operate at higher pressures than thermal evaporation systems (typically 10^{-3} Torr—i.e., atmospheric pressure).

Additionally, perovskite nanomaterials including quantum dots (Le et al., 2018; Xu et al., 2021), nanoplatelets (Otero-Martinez et al., 2022), nanowires (Zhang et al., 2022; Wang et al., 2022), and more have been synthesized. Nanomaterials can be formed through a variety of processes, many of which resemble synthetic methods for thin films (Le et al., 2018, Xu et al., 2021). As with thin films, the most popular methods for nanoparticle synthesis are solution-based. The difference between nanomaterial and thin film synthesis is that nanomaterials are formed in the presence of organic ligands such as oleic acid or oleylamine which serve to limit the growth of the particles and passivate surface defects (Xu et al., 2021; Le et al., 2018). In the commonly used hot injection method, a solution containing the A-site cation and ligands is prepared at room temperature. A separate solution of the metal halide and ligands is prepared and heated to temperatures from 100 °C to 200 °C and then added to the other solution. Typically, there is also a post processing step to remove some of the ligands to facilitate charge transport and make the particles more suitable for device applications. Some ligands are left, however, to prevent agglomeration and maintain defect passivation. For most solution-based syntheses, the size and shape of the nanomaterials is controlled by a range of factors including the temperature of the reaction, acid-base equilibrium of the ligands, ligand chain length, and ligand concentration.

Nanoparticle size and shape can also be controlled using templates. Although templated growth of perovskite quantum dots has been reported (Le et al., 2018), template methods are more often employed for nanowires (Zhang et al., 2022; Wang et al., 2022). In a blade-coating technique analogous to that for thin films, a solution of starting materials is deposited on a substrate templated with the desired dimensions of nanowires, and a blade is then drawn across the surface of the substrate to remove excess material, leaving the nanowires behind. Additionally, vapor deposition techniques can be used to grow nanowires vertically from a template both with and without a catalyst in an analogous fashion to more standard inorganic semiconductor nanowires. A template can also be applied following the deposition of a thin film, as with nanowires etched using a focused-ion beam (FIB).

In addition to thin films and nanomaterials, synthesis of bulk materials has also been a focus due to their perceived chemical purity. Large single crystals (with lengths ~1 cm) can be grown through a variety of solution based methods (Murali et al., 2020). These methods generally involve the saturation of a solution of starting materials, and slow growth of the crystal is controlled by temperature or solvent engineering. As many of the crystals formed through these methods are too thick for device applications, much research is focused on developing methods to control the growth of thinner crystals (Murali et al., 2020). Smaller crystals and powders can be prepared with similar methods but they can also be synthesized using mechanosynthesis, a solvent free technique in which the solid starting materials are mixed and ground together to form the desired perovskite (Kubicki et al., 2021; Rosales et al., 2019). This technique has the advantage that perovskites with clear chemical compositions can be synthesized and insolvent dopants can be incorporated. It is currently most used to create samples for detailed spectroscopic studies but is also being investigated for device applications (Prochowicz et al., 2019).

Physical, optical, and optoelectronic properties

Many of the unique features of hybrid perovskites, for instance the combination of organic and inorganic species within the same lattice, the use of large and polarizable B- and X-site species, as well as the diverse morphologies that can be adopted by these materials leads to a wide variety of interesting and exotic material properties. Exploring these properties remains a vibrant area of study, and is essential to improving their performances in existing applications (for example, as solar absorbers), as well as motivating and discovering new technological applications and use cases.

Optical properties

Optical absorption and photoluminescence

Most metal halide perovskites are semiconductors with bandgaps in the visible region of the electromagnetic spectrum (Fig. 3), which is one of the main features that makes them attractive for photovoltaic and other optoelectronic applications. Additionally, they normally have high absorption coefficients of ~10^4–10^5 cm^{-1} and exhibit high luminescence efficiencies. For example, the prototypical $MAPbI_3$ has a bandgap of 1.61 eV (770 nm) and an absorption coefficient which is 1×10^4 cm^{-1} at the band edge but which then increases above the bandgap to 3.8×10^4 at 2.0 eV (620 nm) and is even higher in the UV (Shirayama et al., 2016). As a result, the penetration depth for visible light in $MAPbI_3$ and similar materials is on the order of 1 μm or less.

The optical transitions in perovskites are strong due to the nature of the molecular orbitals which make up the conduction and valance bands. Density functional theory (DFT) calculations for lead-based MHPs suggest that the valance band maximum is

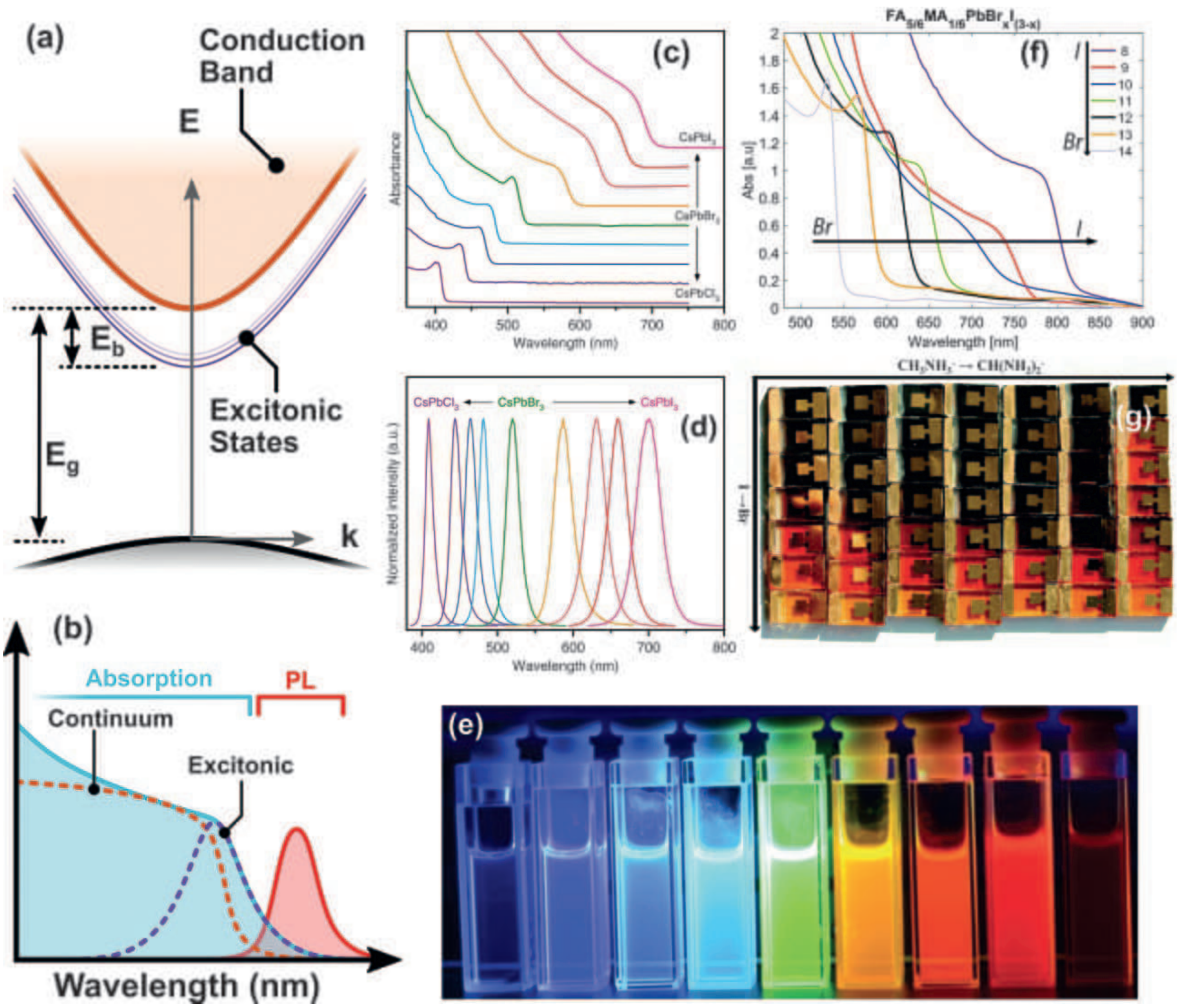

Fig. 3 Optical properties of hybrid perovskites. (a) Simplified band diagram of a perovskite, highlighting both the excitonic and continuum bands that give rise to distinct absorption features; (b) Schematic of a typical absorption spectrum of a halide perovskite highlighting the contributions from excitonic (blue dashed line) and continuum (orange dashed line) states—the photoluminescence spectrum is red-shifted relative to the absorption edge. (c–g) tuneability of the optical properties of halide perovskites: (c–e) absorption, PL spectra, and images of Subfigures (c–e) adapted from Zheng W, Huang P, Gong ZL, Tu D, Xu J, Zou QL, Li RF, You WW, Bunzli JCG and Chen XY (2018) Near-infrared-triggered photon upconversion tuning in all-inorganic cesium lead halide perovskite quantum dots. *Nature Communications* 9; subfigures (f) and (g) adapted from Jacobsson TJ, Correa-Baen JP, Pazoki M, Saliba M, Schenk K, Gratzel M and Hagfeldt A (2016) Exploration of the compositional space for mixed lead halogen perovskites for high efficiency solar cells. *Energy & Environmental Science* 9: 1706–1724.

formed by 6s orbitals of lead and 5p orbitals of iodide, and the conduction band minimum is made up of primarily the 6p orbitals of lead (Jena et al., 2019), and significant spin orbit coupling from the heavy atoms used in MHPs makes the bandgaps lower than they otherwise would be (Herz, 2016). Furthermore, the optical transition from the valence band to the conduction band involves the *p*-orbitals associated with both the halide and metal. As these orbitals create a higher density of states near the band edge than *s*-orbitals, perovskites have higher absorption coefficients as compared to semiconductors like GaAs whose conduction band is composed of *s*-orbitals (Manser et al., 2016).

Excitons also play a key role in the absorption properties of MHPs, even though the exciton binding energies of most 3D perovskites are on the order of 10–20 meV or less (Baranowski and Plochocka, 2020) and excitonic species are not present in large concentrations at ambient temperatures where kT ~25 meV. Fig. 3a and b highlights the position of the excitonic states relative to the valence and conduction bands of a typical hybrid perovskite. In general, so-called Wannier-Mott excitons are expected to be the dominant excitonic species within MHPs, and thus the energy levels of the excitons can be straightforwardly related to the bandgap of the material as follows

$$E_n = E_g - \frac{R_0 \mu}{m_0 \varepsilon_r^2 n^2},$$

where R_0 is the Rydberg constant, m_0 is the mass of an electron, ε_r is the dielectric constant, and μ is the reduced mass of the exciton ($1/\mu = 1/m_h + 1/m_e$, where m_e and m_h are the *effective* electron/hole masses). Combining this relationship with a suitable model for the band-to-band transitions of the material allows for the prediction of their band-edge absorption properties. For 3D hybrid perovskites, this is described by the Elliot Formula (Elliott, 1957; Baranowski and Plochocka, 2020), which takes the form

$$\alpha(\hbar\omega) = A \cdot \left(\Theta(\hbar\omega - E_g) \cdot D_{cv}(\hbar\omega) \cdot \frac{\pi x \cdot e^{\pi x}}{\sinh \pi x} \right) + \frac{A \cdot R_0 \mu}{m_0 \varepsilon_r^2} \sum_{n=1}^{\infty} \frac{4\pi}{n^3} \cdot \delta(\hbar\omega - E_n),$$

where A is a proportionality constant related to the transition matrix element, $\hbar\omega$ is the photon energy, Θ is the Heaviside (or step) function, δ is the Dirac delta function, D_{cv} is the joint density of states, and x is a parameter related to the photon energy by:

$$x = \sqrt{\frac{R_0 \mu}{m_0 \varepsilon_r^2} (\hbar\omega - E_g)}$$

A sketch showing the contribution of the excitonic progression and continuum to the overall absorption spectrum is given in Fig. 3b, where the excitonic and continuum contributions are given in blue and orange, respectively. It is important to note that the impulsive behavior of the Heaviside and delta functions only truly describe the absorption of the perovskite in the absence of instrument or other broadening effects; consequently, it is usually necessary to convolute the model with a suitable lineshape function. It is also important to note is that the Elliot Formula typically only accurately models the band-edge absorption of the perovskite within a few hundred meV of the absorption edge. This limit arises from several assumptions of the model, specifically that (i) only a single band-to-band transition is involved in the continuum, (ii) the transition matrix element (contained within the proportionality constant, A) is constant for all photon energies, and (iii) that the relevant bands are parabolic and isotropic (Davies et al., 2018). Nevertheless, fitting of absorption data with the Elliot Formula provides a (relatively) straightforward means of relating the optical properties of hybrid perovskites to their electronic dynamics. For a more detailed description of these processes, along with alternative methods of relating optical and excitonic dynamics of the perovskite, the reader is advised to consult (Baranowski and Plochocka, 2020) and (Davies et al., 2018).

As with many of the other properties discussed elsewhere in this chapter, alteration of the composition of the perovskite changes their absorption and emission properties. This is clearly demonstrated in Fig. 3c, d, f which highlights how alteration of the halide content of the perovskite results in a dramatic alteration of both the absorption onsets and the emission maxima (Jacobsson et al., 2016; Zheng et al., 2018). As the halide composition is changed from I to Br to Cl, the bandgap shits continuously over a range of several hundred nanometers when mixed halide compositions are included. In general, decreasing the atomic radius of the halide (e.g., Br – I) increases the bandgap energy due to the contribution of the halide to the density of states (DOS) of the valence band maximum (Wang et al., 2019).

For similar reasons as the halide, the identity of the B-site cation can also have an effect of the bandgap. However, changing the metal ion has a more complex effect on the bandgap energy due to both spin-orbit coupling effects associated with large cations such as lead and structural distortions of the lattice due to size changes of the ions (Herz, 2016). In $MAPbI_3$ for example, substituting lead for tin decreases the bandgap to 1.25 eV (990 nm) whereas switching to germanium increases the bandgap to 1.90 eV (652 nm) (Manser et al., 2016). Furthermore, mixed Pb—Sn perovskites exhibit an unusual bandgap bowing effect, where compositions with about 50–70% tin exhibit the narrowest bandgaps (Parrott et al., 2018).

Changing the cation can also alter the bandgap energy, but to a lesser extent than the halide and B-site cation. For example, $FAPbI_3$ and $MAPbI_3$ have band edges of 1.47 eV (843 nm) and (1.55 eV), respectively (Jena et al., 2019). This smaller change is because the A-site cation does not contribute significantly to the valence and conduction bands. However, the identity of the A-site cation can indirectly change the bandgap energy by altering the size and orientation of the network of metal-halide octahedra (Manser et al., 2016).

The presence of impurities or dopants can also alter the bandgap energy of MHPs. As such, reported bandgaps often vary depending on the preparation method or morphology of a MHP with a given composition. For highly doped materials such as p-doped tin perovskites, the Burstein-Moss effect can result in significant shifts in bandgap energy with doping density (Milot et al., 2018).

The excitonic component of the absorption is distinctly more pronounced in some perovskites than in others. In general, the dielectric constant of many perovskites is relatively large, meaning that their exciton binding energies are often quite small, sometimes even below the ambient thermal energy ($\sim$25 meV), as is the case with $MAPbI_3$ ($\sim$12 meV), which in turn suppresses the excitonic contribution to the band-edge absorption. One strategy to enhance the excitonic character of MHP absorption includes encouraging quantum confinement effects through the synthesis of perovskite nanocrystals or nanoplatelets or through compositional engineering. When the size of a particle is on the order of or smaller than the exciton Bohr diameter, the bandgap is blue shifted with decreasing particle size. For example, the bandgap of $CsPbCl_3$ increases from 2.4 to 2.7 eV as the particle diameter decreases from 12 nm to 3 nm (Protesescu et al., 2015). Another way to alter the excitonic character of perovskites is through compositional engineering. 2D layered perovskites, which experience increased confinement due to the dielectric mismatch between the conducting metal-halide octahedra and insulating organic layers, have exciton binding energies of up 100s of millielectronvolts and correspondingly blue-shifted absorption spectra (Sirbu et al., 2021). Their exciton binding energy and absorption can be further tuned through the mixture of long and short organic cations via the formation of Ruddlesden-Popper phases, in which it is possible to vary the thicknesses of the metal-halide layer between the insulating organic layers (Sirbu et al., 2021; Milot et al., 2016).

Changes in bandgap energy generally correspond to changes in the photoluminescence energy as highlighted in Fig. 3c, d. Typically, observed Stokes shifts are moderate, although highly doped materials exhibit larger shifts (Milot et al., 2018). For more specific information about the PL properties of MHPs, see the review article by Goetz et al. (2020).

Vibrational absorption and structural dynamics

The vibrational absorption properties of perovskites are key to understanding their structural dynamics, which carry important implications for the optoelectronic properties of the material and thus its performance in devices. These structural dynamics can be described in terms of two closely related regimes of motions: oscillations of the A and BX_3 sublattices and rotation of the A-site cations.

An example infrared/THz spectrum of the archetypal $MAPbI_3$ perovskite is given in Fig. 4. Hybrid perovskites exhibit a rich and complex vibrational structure owing to the interplay between the organic small-molecule A-site ions and the inorganic BX_3 cage. Broadly speaking, we can delineate four regimes of vibrational motion in these materials: (i) internal vibrations and rotations of the

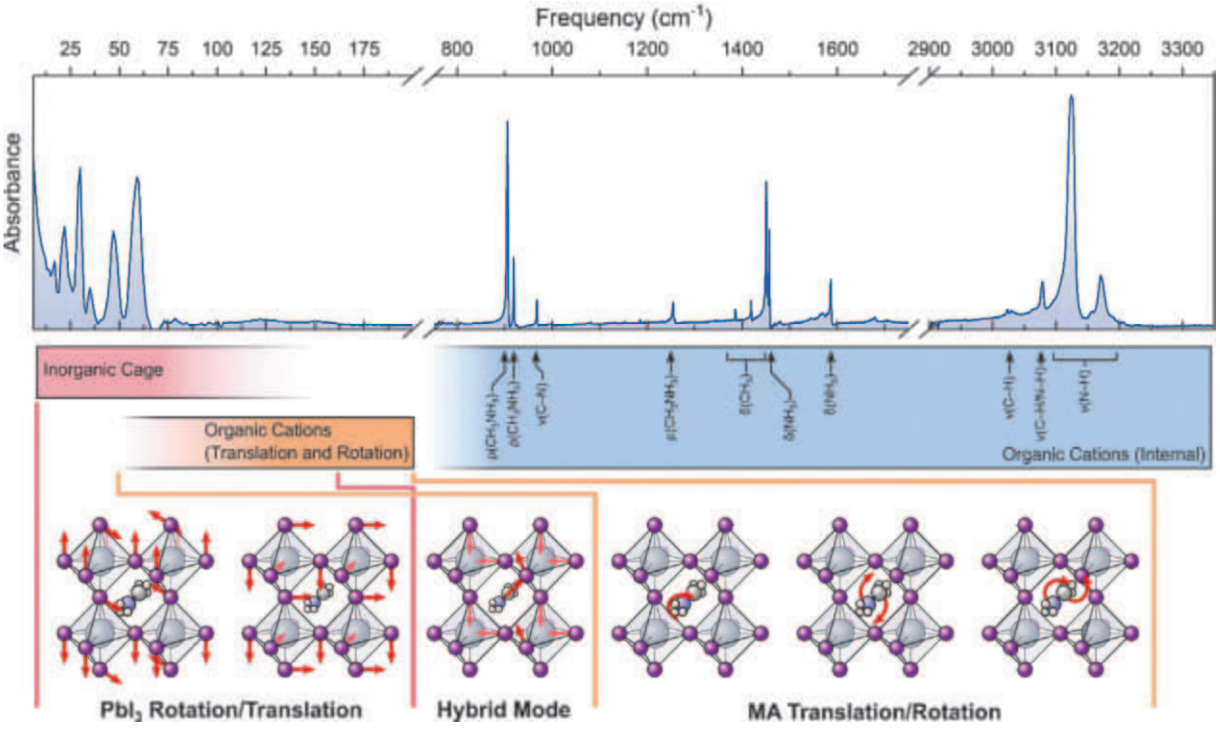

Fig. 4 Vibrational Properties of $MAPbI_3$. The top figure is a combined infrared and THz spectrum of MAPbI3 at $\sim$5 K, adapted from Perez-Osorio MA, Milot RL, Filip MR, Patel JB, Herz LM, Johnston MB and Giustino F (2015) Vibrational properties of the organic inorganic halide perovskite $CH_3NH_3PbI_3$ from theory and experiment: Factor group analysis, first-principles calculations, and low-temperature infrared spectra. *Journal of Physical Chemistry C* 119: 25703–25718. The vibrational structure of these materials can be understood as arising from three different regimes of vibrational motion which are visualized in the lower subfigures.

inorganic cage; (ii) rotations and vibrations of the organic cations; (iii) internal vibrational modes of the organic cations; (iv) so-called ‘mixed’ or ‘hybrid’ modes, where translations and rotations of the A-site ions and BX_3 sublattice occur in concert. Cartoons illustrating representative examples of these modes are given in Fig. 4; more detailed discussion and assignment of the vibrational structure of $MAPbX_3$ can be found in Perez-Osorio et al. (2015) and Leguy et al. (2016), while discussion of the vibrational structure of FA-containing perovskites can be found in Ibaceta-Jaña et al. (2020) and Kucharska et al. (2014). The complexity of this rich vibrational structure is further compounded by the relatively ‘soft’ nature of most hybrid perovskites—a term that describes both their mechanical properties (i.e., low bulk modulii), as well as the relative freedom of the ionic species to move around their equilibrium positions—which results in highly anharmonic and multi-well modes that are strongly populated at room temperature (Egger et al., 2018). This anharmonicity enables coupling between many different types of nuclear motion, leading to multi-mode vibrational bands in which the motions of both the organic and inorganic sublattices contribute to the overall mode. The behavior is most pronounced for the ‘hybrid’ modes mentioned previously, but theoretical calculations indicate that it is nevertheless present at some level for virtually all of the low-frequency ($>200\ \text{cm}^{-1}$) modes (Perez-Osorio et al., 2015).

Alongside these vibrations, rotations of the organic cations within their octahedral cages are well documented and have been extensively studied (Gallop et al., 2018). These studies have largely focused on methylammonium as an A-site species, although FA based perovskites have also attracted some attention (Ghosh et al., 2017; Taylor et al., 2018). These studies have identified two regimes of rotational motion: so-called ‘wobbling within a cone’ (also sometimes referred to as ‘frustrated liberations’), where the organic cations liberate around their local equilibrium positions but do not change their gross orientation, as well as ‘rotational diffusion’ where the organic cations reorient themselves along a different face of their octahedral cavity. The rapidity of these rotations is known to depend on a number of factors, including the crystalline phase (Wasylishen et al., 1985), the halide content of the inorganic lattice (Selig et al., 2017), the presence of multiple A-site species within the material (Gallop et al., 2022), and the proximity of the organic species to a material interface (Sung et al., 2020), among others. Many of these dependencies are driven by the interaction between the organic cations and the inorganic lattices; for example, the incorporation of multiple halide species and/or multiple A-site ions inhibits cation rotation, likely due to the creation of anisotropies within the cuboctahedral cavities and the alteration of the vibrational structure of the inorganic cage (Ghosh et al., 2017; Gallop et al., 2022).

The influence of the vibrational and rotational dynamics of perovskites remains an active area of investigation. The interplay between vibrational structure and carrier dynamics is particularly well documented, for example in the relaxation of hot carriers (Hopper et al., 2018) and in the modulation of charge mobilities (Munson et al., 2019). The exceptionally low phonon lifetimes of many perovskites also likely contributes the low thermal conductivity of these materials (Haeger et al., 2020). By contrast, significant debate still exists regarding the relevance of cation rotations to the optoelectronic properties of perovskites, and will likely remained unresolved in the absence of experimental techniques able to more directly probe the interaction between the organic cation and the inorganic cage (Gallop et al., 2018).

Non-linear optical properties

The non-linear optical (NLO) properties of many perovskites have also been investigated. Although this field is still developing, knowledge of the NLO properties is important for applications including lasers, photoelectric devices, and others that require high illumination intensities (Zhou et al., 2020; Xu et al., 2020). NLO properties can be distinguished by their dependence of the polarization **P** on the electric field **E** of the incident light as follows.

$$\mathbf{P} = \varepsilon_0 \chi^{(1)} \mathbf{E} + \varepsilon_0 \chi^{(2)} \mathbf{E}^2 + \varepsilon_0 \chi^{(3)} \mathbf{E}^3 + \ \ldots,$$

where, ε_0 is the dielectric constant and $\chi^{(n)}$ is the susceptibility tensor.

Second-order nonlinear processes or $\chi^{(2)}$ processes include effects such as second harmonic generation and optical rectification and require that a crystal lack inversion symmetry and thus be non-centrosymmetric. Since many perovskites have centrosymmetric cubic or tetragonal crystal structures, they do not exhibit strong second order effects. However, Ge and Sn perovskites (e.g., $MASnI_3$ and $MAGeI_3$) have shown second-order NLO effects including second harmonic generation (Zhou et al., 2020). Second order effects have also been demonstrated in perovskites which replace the B-site metal cation with a chiral organic cation that breaks the inversion symmetry of the perovskite structure (Xu et al., 2020). Centrosymmetricity can also be broken by defects or at surfaces, which means that second order NLO provides a way to study important surface effects for centrosymmetric crystals (Zhou et al., 2020).

Third-order $\chi^{(3)}$ processes do not have the same requirement for non-centrosymmetricity and have been more widely studied in MHPs (Zhou et al., 2020, Xu et al., 2020). The most commonly studied $\chi^{(3)}$ process in MHPs is two-photon absorption, although the optical Kerr effect, third harmonic generation, and four-wave mixing have also been observed. Generally, MHPs and especially layered perovskites have large two-phonon absorption coefficients, although reported values vary depending on sample morphology and excitation conditions, and more work is required to systematically understand the NLO properties of MHPs (Zhou et al., 2020).

Optoelectronic properties

Charge-carrier mobility

One of the benefits of metal halide perovskites for device applications is that they exhibit high charge-carrier mobilities at ambient temperatures typically on the order of 30–50 $\text{cm}^2\text{V}^{-1}\ \text{s}^{-1}$ as compared to other thin film materials such as metal oxides or organic semiconductors. As compared to III–V semiconductors which typically have mobilities over 1000 $cm^2V^{-1}\ s^{-1}$, however, charge carrier mobilities in metal halide perovskites are fairly low (Herz, 2017). Unlike many traditional semiconductors, perovskites exhibit very similar effective masses and thus mobilities for electrons and holes which enables ambipolar charge transport and facilitates charge separation (Herz, 2017). As with any semiconductor, however, the mobility of a given MHP material is sensitive to a number of extrinsic and intrinsic factors such as morphology (extrinsic) and electron-phonon interactions (intrinsic). As a result a wide range of mobilities have been reported even for films of similar compositions. However, these values can be rationalized by considering the material in its entirety with regard to both chemical composition and defect chemistry (Herz, 2017).

Extrinsic factors that affect the mobility of perovskites include its morphology, crystallinity, and defect density. For example, defects at grain boundaries have been shown to limit the mobility across thin films. As a result, local measurements of the mobility of $MAPbI_3$ thin films average (37 ± 18) $cm^2V^{-1}\ s^{-1}$, whereas long-range measurements across grain boundaries produce average values of (2.4 ± 1.1) $cm^2V^{-1}\ s^{-1}$ (Herz, 2017). Mobilities of 60–100 $cm^2V^{-1}\ s^{-1}$ have been reported for $MAPbI_3$ single crystals, which have lower defect densities and higher crystallinity than many thin films (Herz, 2017; Xia et al., 2021). Similarly, the mobility of $FASnI_3$ was found to be tunable with defect density from 23 to 67 $cm^2V^{-1}\ s^{-1}$ for films with doping densities of 7.2×10^{18} cm^{-3} to 2.2×10^{20} cm^{-3} (Milot et al., 2018).

Although most extrinsic limits to mobility can be mitigated with improved materials processing, charge-carrier mobilities in halide perovskites are also fundamentally limited due to their intrinsic properties and thus their chemical composition. Specifically, free charges in perovskites interact strongly with the perovskite lattice due to Fröhlich coupling interactions with longitudinal optical (LO) phonons (Herz, 2017). Because these interactions are relatively strong, charge-carriers in perovskites are considered to exist as large polarons (Buizza and Herz, 2021; Ghosh et al., 2020). Changing the chemical composition of the perovskite generally changes the LO phonon energy, which dictates the strength of the Fröhlich interaction and thus has a large effect on the mobility. Although changing the composition can also change the curvature of the conduction and valence band and thus the effective masses of carriers, electron-phonon interactions are believed to be the stronger determinant of charge-carrier mobility (Herz, 2017). For example, substituting lead for tin shifts the LO phonon energies to higher frequencies and thus increases the charge-carrier mobility (Milot et al., 2018).

For 2D layered perovskites and other quantum-confined materials, effective charge-carrier mobilities are lower than for 3D materials due to high exciton binding energies (Sirbu et al., 2021). For these materials, however, it is important to distinguish between the charge-carrier mobility of excitons and free charge-carriers, which exist in equilibrium at different rations depending on the exciton binding energy and the overall carrier density (Kober-Czerny et al., 2022; Milot et al., 2016). In a prototypical $PEAPbI_4$ (PEA = phenylethylammonium) thin film, mobility for free charges was determined to be 8 $cm^2V^{-1}\ s^{-1}$ and be less dependent on the polycrystalline nature of the thin film (Kober-Czerny et al., 2022). Similarly, excitons in 2D MHPs have been shown to exhibit good long-range diffusion (Sirbu et al., 2021).

Charge transport and charge-carrier recombination

Although high charge-carrier mobilities are important for efficient charge transport in a material, the diffusion length L_D of carriers in a material is also dependent on the charge-carrier lifetime $r(n)$ as follows

$$L_D(n) = \sqrt{\frac{\mu k_B T}{r(n) e}},$$

where μ is the charge-carrier mobility, k_B is the Boltzmann constant, T is temperature, and e is the electronic charge (Herz, 2016). Achieving efficient charge transport thus involves minimizing the recombination rate in addition to maximizing mobility. In typical 3D perovskites with mobilities on the order of 30 $cm^2\ V^{-1}\ s^{-1}$, diffusion lengths can be on the order of microns due to long charge-carrier recombination rates. It is important to note the dependence on the carrier concentration n of the overall recombination rate and thus the diffusion length. This dependence is generally expressed as

$$r(n)^{-} = k_3 n^2 + k_2 n + k_1,$$

where k_1 is the monomolecular recombination rate k_2 and k_3 are the rate constants for bimolecular and 3rd order or Auger recombination processes, respectively.

Monomolecular process typically involve recombination of electrons or holes with defects or traps in the MHP lattice. Reported values are thus highly sensitive to the preparation method of the perovskite material and have been shown to range from $10^9\ s^{-1}$ (lifetime, $\tau = 1$ ns) for highly doped tin-based perovskites to $10^6\ s^{-1}$ ($\tau = 1\ \mu s$) for higher quality thin films (Johnston and Herz, 2016). In general, however, MHPs exhibit a surprising defect tolerance which enables thin films to have low monomolecular recombination rates despite using synthetic techniques that would promote defect formation in other types of materials. Despite this defect tolerance, defects are still a major concern for devices which operate with low charge carrier densities (such as solar cells operating at densities $\sim 10^{14}$–10^{15} cm^{-3}) because they can limit charge transport and thus prevent devices from reaching their maximum theoretical efficiency. Although the nature of defect states in perovskites has been widely studied, uncertainties remain as to the chemical species and energetics responsible for various effects (Jin et al., 2020). One reason understanding these states is difficult is that it is common for a distribution of trap states to exist in a material (Wright et al., 2017). Additionally, defect densities are highly dependent on film processing procedures and have been shown to be influenced by the microstructure, with increased defect densities found at grain boundaries (Jin et al., 2020; Phung and Abate, 2018). A more detailed discussion of defects in perovskites can be found elsewhere (Singh et al., 2020; Stranks, 2017).

Bimolecular recombination between electrons and holes is the main mechanism for radiative recombination in perovskites. As a result, bimolecular recombination dictates the radiative efficiency $\Phi(n)$ as highlighted by the following equation.

$$\Phi(n) = \frac{r_{radiative}}{r_{total}} = \frac{nk_2}{k_1 + nk_2 + n^2k_3}$$

Values of k_2 for 3D perovskites are typically on the order of 10^{-10} cm^3 s^{-1} and are comparable to values for inorganic semiconductors including GaAs (Davies et al., 2018). Also similarly to inorganic semiconductors, bimolecular recombination has been found to be an inverse absorption process (Davies et al., 2018), so materials that exhibit strong optical absorption also have high radiative recombination rates. Due to the relationship between absorption and bimolecular radiation, differences with chemical composition are expected. However, these differences are not as dramatic as other properties as many perovskites exhibit similarly strong absorption. For example, k_2 for FASnI$_3$ was found to be 1×10^{-10}–2×10^{-10} cm^3 s^{-1} independent of doping density as compared to 6.8×10^{-10} for MAPbI$_3$ (Milot et al., 2018; Crothers et al., 2017) despite the band edge absorption energies and defect densities in these materials. However, larger differences are observed with quantum confined perovskites, as exciton formation encourages bimolecular recombination because electrons and holes are closer together, and increased k_2 values have been seen in 2D perovskites (Sirbu et al., 2021; Milot et al., 2016).

Of the three main recombination mechanisms in MHPs, Auger recombination is the least well characterized despite its importance for applications that require higher charge-carrier densities including LEDs and lasers. Reports of k_3 values for 3D perovskites are typically on the order of 0.1–10×10^{-28} cm^6 s^{-1} and have been found to vary significantly with structural phase and chemical composition (Herz, 2016). The difficulty in characterizing Auger recombination is that it can result from many different mechanisms including charge-carrier interactions with defects, phonons, and higher-lying excited states, and more work is needed to untangle these interactions (Herz, 2016).

Other physical properties

Ion mobility

Hybrid perovskites often contain large concentrations of ionic defects that are mobile under conditions relevant to the operation of many devices. This ion mobility presents a considerable hurdle to future development of perovskite materials, both in photovoltaics and in other applications. We delineate two separate types of mobile ions within perovskites, specifically intrinsic ions that result from the presence of charged defects, as well as extrinsic ions that result from mobile dopant species. Mobile dopant species can be introduced during synthesis (either deliberately or inadvertently) or may originate from other layers within a device stack (for example, from electron/hole transport layers in solar cells).

Of the two types of defects, the intrinsic ion migration remains more broadly studied; for any crystal at a temperature of >0 K, the increase in configurational entropy that results from the point defects makes their formation thermodynamically inevitable, which means that their mobility plays a strong role regardless of processing conditions and/or device implementation (Senocrate and Maier, 2019). The intrinsic defects of perovskite crystals are illustrated in Fig. 5 and almost exclusively consist of either vacancies or interstices of the A-, B- or X-site ionic species; anti-site defects are predicted to be unstable and to quickly collapse into a vacancy

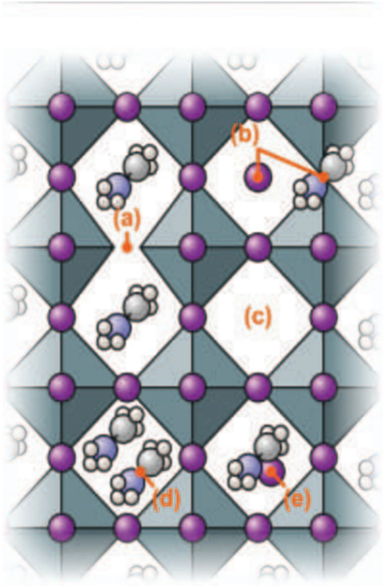

Fig. 5 Cartoon illustrating different defect types in hybrid perovskites, including an iodine vacancy (a), antisite defects (b), an MA vacancy (c), and MA and iodine interstitials (d and e). An identical set of defects could also be present for the Pb ions but are not displayed here for clarity.

and interstitial. The relative concentration(s) of these different defects can be estimated through application of mass-action laws combined with appropriate constraints to account for electroneutrality (Moia and Maier, 2021), while their mobilities can be estimated from *ab initio* calculations (Azpiroz et al., 2015; Eames et al., 2015). *Ab Initio* calculations typically extrapolate mobilities by treating the macroscopic movement of ionic defects as a sequence of thermally activated hops between adjacent sites, the frequency of which is related to an energetic barrier *via* an Arrhenius type relation. The results of these *ab initio* 'hopping' studies have implicated the migration of halide defects (both vacancies and interstitials) as the dominant cause of ionic mobility (Azpiroz et al., 2015, Eames et al., 2015). It is important to recognize however that a simple Arrhenius-type relation neglects other processes within the material (e.g., formation of defect complexes, temperature dependent charge carrier concentrations, etc.) (Senocrate and Maier, 2019). Nevertheless, subsequent experimental studies have further identified halide vacancies as the dominant mobile ionic species, validating earlier *ab initio* studies and demonstrating their utility in studying ionic mobility (Senocrate et al., 2017; Yang et al., 2015; Eames et al., 2015). Recent efforts have continued to build on these earlier findings by considering both electronic and ionic mobility, enabling links between ionic mobility and the performance of hybrid perovskite optoelectronics to be studied (Calado et al., 2022).

By contrast, while extrinsic mobile ions (such as Li^+) are also known to be important in the behavior of hybrid perovskite devices (Li et al., 2017b), they are less extensively studied and the thermodynamics and kinetics of their underlying processes is less well understood and more challenging to characterize, potentially owing to the diversity of different potential dopants (Senocrate et al., 2018; Park et al., 2018; Ceratti et al., 2020), as well as co-operative effects in which certain extrinsic species can act to enhance the mobility of ionic defects (Ceratti et al., 2020; Jong et al., 2018). Nevertheless, several studies have further highlighted the undesirable nature of extrinsic ions for solar cells containing perovskites and have emphasized the importance of further study of extrinsic ion migration with a view to either mitigating the amount of ion migration or else mitigating the effect of extrinsic ion migration (Domanski et al., 2016; Jong et al., 2018).

The most immediately apparent of these effects is the well-documented hysteresis of the J-V curves of certain hybrid perovskites, which is now known to be due at least partially to bias-induced migration of ionic defects. Hysteresis can lead to significant errors in the reporting of J-V characteristics and can even be exploited to artificially inflate solar cell performance figures; for this reason, it is essential to carefully control the conditions under which the J-V curves are acquired, including scan rate and direction, pre-biasing, and light soaking (Kim et al., 2015). Moreover, the formation of a space-charge layer close to the electron/hole contacts by mobile ions is known to strongly inhibit charge collection and so reduce device performance (Kim et al., 2020). Moreover, mobile ionic defects act as charge traps, leading to a strongly nonlinear relationship between carrier dynamics and the movement of intrinsic defects. Finally, ionic mobility can also lead to long-term degradation issues, for example through excorporation of halide species, or else through photoinduced demixing in mixed halide species, which further limits the lifetime of these materials (Moia and Maier, 2021). By contrast, the exotic switching physics that arise from ion migration is an avenue for new technological applications; for example, in next-generation hardware security (John et al., 2021) and biomimetic computing (Gogoi et al., 2021), among others.

Thermal properties

In addition to their optical and electronic properties, the thermal properties of perovskites are interesting to consider for device applications. In general, perovskites have low heat capacities, low thermal conductivities, and high thermal expansion coefficients at ambient temperature (Haeger et al., 2020). They don't behave like traditional semiconductors in this respect but instead have properties more similar to insulators like glass (Haque et al., 2020). Thermal conductivity is the parameter reported for the widest range of perovskite materials. Values for $MAPbI_3$ are on average $0.35\,Wm^{-1}\,K^{-1}$, and most materials fall in the range of $0.1–0.5\,Wm^{-1}\,K^{-1}$. These values are low because heat transport in perovskites occurs mainly via phonons, which exhibit strong phonon-phonon scattering interactions that limit heat transport, similarly to how electron-phonon interactions limit the transfer of charge (Haque et al., 2020). More specifically, the group velocity of acoustic phonons is low and the optical phonons have short lifetimes (<100 ps) and short mean free paths (<10 ps) in MHPs, resulting in inefficient heat transport.

As with most perovskite properties, the thermal properties are tunable with perovskite composition and morphology. Additionally, thermal properties are highly temperature dependent and also sensitive to structural phase changes (Haeger et al., 2020). For example, thermal conductivities can vary significantly due to phonon scattering by defects, which decreases the phonon mean free path. Accordingly, lower thermal conductivities have been observed at grain boundaries in thin-film MHPs. Halide perovskite nanomaterials including quantum dots also exhibit lower thermal conductivities because the mean free path of phonons is limited to ~100 nm by their geometry. 2D layered perovskites also have lower thermal conductivities than their 3D analogs because of both geometric confinement and decreased phonon propagation across the organic layers. An exception to the mean free path argument is the observation of increased thermal conductivities for the series $MAPbI_3—MAPbBr_3—MAPbCl_3$ as the mean free path of phonons in these materials is similar. In this case, the differences are likely the results of differences in the sound velocity and heat capacity of the materials. Although changes in thermal conductivity have been observed for A-site cation substitution, there is debate about origin of these changes, and results from theoretical studies and experiments often disagree (Haque et al., 2020).

Applications

The unique physical and chemical properties of MHPs have been the main driver for the interest in their development for devices. Due to their many similarities to inorganic semiconductors, the main areas of interest are those in which materials such as silicon and GaAs have traditionally dominated. These applications include solar cells (Ali et al., 2021; Green et al., 2014), light emission

(Lei et al., 2021; Veldhuis et al., 2016), and other electronics such as field-effect transistors (Younis et al., 2021). The following section summarizes some of these main applications of MHPs but also highlights some of the emerging applications including photocatalysis (Ren et al., 2022) and thermoelectric generators (Haque et al., 2020) in order to showcase the potential range of MHP applications.

Photovoltaic cells

The production of efficient photovoltaic cells is one of the biggest driving forces for MHP research. In just over a decade of development, perovskite solar cells rival market-leading silicon technologies; according to the best research-cell efficiency chart published by the US National Renewable Energy Lab (NREL), the current record power conversion efficiency (PCE) is 25.7% for a perovskite-based solar cell compared to 26.7% for a crystalline silicon cell (NREL, 2021; Min et al., 2021).

Due to their strong visible absorption and relatively high charge-carrier mobility, MHPs form the active layers solar cells and are thus responsible for solar light absorption and for facilitating initial charge separation. They are usually deposited as thin films in solar devices, but other morphologies have also been studied; examples of more exotic hybrid perovskite PV devices include solar cells that use perovskite nanowires (Im et al., 2015), as well as devices that employ sophisticated nanostructured architectures (Tooghi et al., 2020). A diagram and cross-sectional SEM of a typical perovskite solar cell is given in Fig. 6a and b which shows a perovskite layer sandwiched between a hole transport material (HTM) and electron transport material (ETM). In typical devices, the perovskite layer is on the order of 300–500 nm thick (Fig. 6b), which is sufficient to absorb most of the incoming solar radiation. Following light absorption by the perovskite, charges are separated by the energy gradient produced by the HTM and ETM on either side of the perovskite. This charge separation is possible without additional engineering of the perovskite film (e.g., a p-n junction as in silicon solar cells or a bulk heterojunction as in organic solar cells) because perovskites exhibit high, ambipolar mobilities and the diffusion length of carriers is greater than the thickness of the film. Following charge separation, the circuit is completed by metal

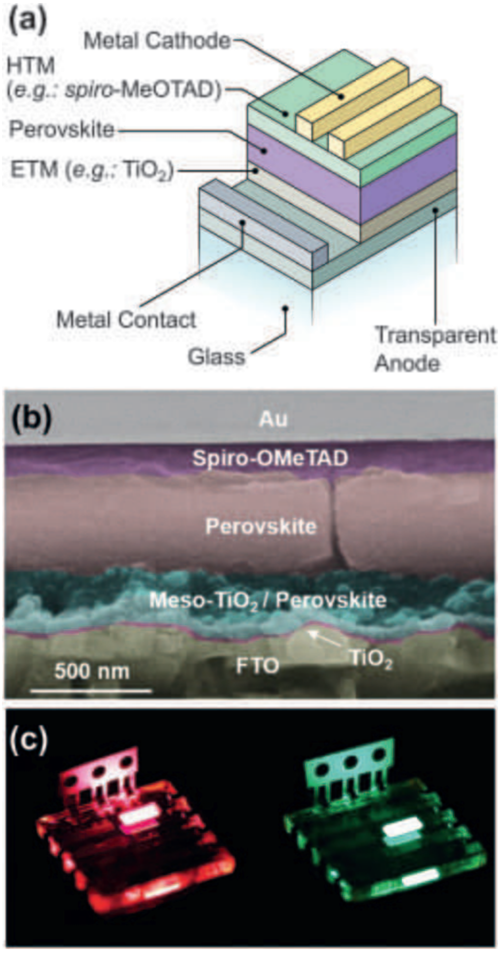

Fig. 6 Hybrid perovskite devices. (a and b) diagram (a) and SEM cross-section (b) of a hybrid perovskite solar cell. Similar device architectures find use in applications beyond solar cells, as in the hybrid perovskite LEDs shown in (c). Subfigure (b) reproduced with permission from Li CW, Zhou YY, Wang L, Chang Y, Zong YX, Etgar L, Cui GL, Padture NP and Pang SP (2017a) Methylammonium-mediated evolution of mixed-organic-cation perovskite thin films: A dynamic composition-tuning process. *Angewandte Chemie, International Edition* 56: 7674–7678.; (c) is adapted courtesy of Zhi-Kuang Tan/University of Cambridge.

and transparent conducting electrodes. Much research effort has been dedicated to optimizing materials synthesis and device fabrication techniques in order to enable high efficiency devices, and the reader is referred to several more specific reviews for further information (Ali et al., 2021; Green et al., 2014; Sirbu et al., 2021).

The theoretical limit for the efficiency of a single junction solar cell such the one described previously is ~33%, but this limit increases to 42% for a tandem solar cell which employs two absorbers with different bandgaps chosen to maximize solar absorption while minimizing thermalization losses (Li and Zhang, 2020). The bandgap tunability of perovskites over the visible region makes them attractive for the development of such tandem cells. For example, substituting bromide into $FAPbI_3$ to form mixed halide perovskites of the form $FAPb(I_yBr_{1-y})_3$ can tune the bandgap from 1.48–2.23 eV (Eperon et al., 2014), encompassing the optimum range for the wide bandgap materials for tandem solar cells. Similarly, replacing tin with lead pushes the bandgap closer to the optimized bandgap for a single junction (1.34 eV), and mixing tin and lead can further tune the bandgap between 1.2 eV and 1.4 eV, including the optimum value for the low bandgap absorber for a two-layer tandem solar cell (Moot et al., 2020; Konstantakou and Stergiopoulos, 2017). Accordingly, perovskite-perovskite tandem solar cells have been fabricated using such materials, although reported efficiencies are still below single-junction cells and more development is needed (Ho-Baillie et al., 2021). However, more progress has been made with perovskite-Si tandem cells due to their potential to be integrated with exiting manufacturing, and efficiencies up to 31.3% have been reported (NREL, 2021).

Water oxidation and other catalysis

Metal halide perovskites have also been investigated for their photocatalytic activity (Ren et al., 2022) due to their known ability to efficiently harness light energy and transport charge. One potential application is artificial photosynthesis, where sunlight is used to split water into molecular hydrogen and oxygen. In photoelectrochemical cells for water splitting, perovskites have incorporated into both the photo-cathode for oxygen generation and photo-anode for hydrogen generation. Analogously, perovskites have also been used for CO_2 reduction and for the reduction of HX to H_2. There have also been reports of using perovskites for other photochemical reactions such as the degradation of pollutants including methyl orange, methylene blue, and rhodamine B and organic synthesis including the oxidation of benzylic alcohols to aldehydes and C—H bond activation. Although some perovskite-based photocatalytic devices have shown good reactivity, stability has been limited to hours or days due to the stability of the perovskite material in aqueous environments (see "Key issues"). As compared to solar cells, perovskite photocatalysis is much a newer sub-field, and there is more opportunity for significant improvements in performance.

Light emission

The second most popular application for perovskites after solar cells is light emission for both light-emitting diodes (LEDs) and lasers.

LEDs are essentially a solar cell running in reverse, where charge-carriers are injected into a material and light is emitted as the carriers recombine radiatively. Therefore, factors which make perovskites suitable for solar cells, such as high charge-carrier mobilities and strong light absorption, mean that perovskites also make good LEDs. There is the additional qualification for LED materials to exhibit a high photoluminescence quantum yield (PLQY). A high PLQY can be achieved by minimizing nonradiative recombination processes included trap-assisted and Auger recombination processes, allowing the dominant recombination mechanism to be radiative, bimolecular recombination. In practice, this balance entails engineering materials with low monomolecular and Auger recombination rate constants and high bimolecular recombination rate constants. As the bimolecular rate constants for 3D perovskites are not particularly high (therefore putting a larger burden on minimizing monomolecular recombination), 2D layered perovskites and quantum dots have seen more application in perovskite LEDs (PeLEDs) as quantum confinement in these materials lowers the separation between electrons and holes, thus promoting bimolecular recombination.

For the best perovskite LEDs, external quantum efficiencies (EQEs) of over 23% have been reported, which make perovskites competitive with other semiconductor and organic LED technologies (Fakharuddin et al., 2022). Furthermore, the bandgap tunability of perovskites has resulted in the fabrication of devices emitting at wavelengths from the ultraviolet to near-infrared, with the most efficient devices emitting green and red wavelengths (Fig. 4). Perovskite LEDs also exhibit good color purity due to their relatively narrow emission spectra.

Lasing applications also rely on the promotion of bimolecular recombination over other charge deactivation processes (Lei et al., 2021). Again, factors including strong absorption and low defect densities are important for efficient lasing with the added requirement of high optical gain to promote population inversion in the material following the injection of charge-carriers (either through optical or electrical pumping). A simple measure of the potential for high optical gain is the threshold for amplified spontaneous emission, which manifests as a narrowing of the PL peak as population inversion is achieved. Perovskites have demonstrated ASE thresholds as low as 4 $\mu J/cm^2$, although they are highly dependent on a number of factors including the chemical composition, defect density, and morphology of the material. Most commonly pumped with ultrafast lasers, a number of perovskite laser resonators have been reported for a range of wavelengths throughout the visible spectrum and into the near-infrared. Additionally, optically pumped continuous wave (CW) lasers have been fabricated, which has historically been a challenge for solution-processed semiconductors. Although electrically driven lasers have not yet been demonstrated due to issues with heating and photoinduced defects, quasi-2D MHP materials show promise for this application due to their low ASE threshold and energy landscape beneficial to enabling population inversion (Lei et al., 2021).

Other electronics

MHPs have also been investigated for a range of other electronic applications including transistors and nonvolatile resistive switching (RS) memories (Younis et al., 2021). They are attractive for these applications for similar reasons as optoelectronics including high charge-carrier mobility, ambipolar charge transport, and low defect density. In fact transistors were one of the first applications investigated in the 1990s for 2D perovskites, and their development continues, benefiting from the compositional engineering used to optimize perovskite materials for other applications. Additionally, perovskites have shown promise for use in memory devices. These devices rely on a property of MHPs that is usually considered detrimental to device efficiency, namely the electrical hysteresis that exists due to their facile ion mobility. The most commonly used perovskites for resistive random-access memory (RRAM) devices are therefore 3D perovskites such as $MAPbI_3$ and $MAPbBr_3$ which exhibit strong ion migration. Although these devices are still at an early stage of development, their performance is already competitive with exiting devices, showing promise for the future development of this field.

Thermoelectric generators

Other applications use the unique heat and electrical transport properties of MHPs to their advantage to convert heat electrical energy in thermoelectric generators (Haeger et al., 2020; Haque et al., 2020). Although the performance of perovskite-based thermoelectric generators is on par with versions utilizing organic materials, efficiencies are still significantly lower than the best inorganic materials such as Bi_2Te_3 (Haque et al., 2020). However, MHPs remain promising for these applications because they have low thermal conductivities coupled with high charge-carrier mobilities and large Seebeck coefficients.

Key issues

Stability

Stability has been aptly called the Achilles heel of MHPs (Moot et al., 2020), as many materials can irreversibly degrade in the presence of four major environmental factors: moisture, oxygen, light, and heat (Wang et al., 2016). This degradation is a significant problem given their potential application in devices such as solar cells, which need to operate under a variety of conditions.

Degradation occurs in both dry air and moist O_2 free conditions, indicating that O_2 and H_2O mechanisms of degradation are separate—one does not require the other (Bryant et al., 2016). For $MAPbI_3$, the weakness is the organic cation, and degradation in both cases occurs through attack of the A-site ion. In the case of oxygen degradation, this occurs via the photocatalytic generation of superoxide ions (O_2^{*-}) (Aristidou et al., 2015). For water degradation, it is believed that attack of the A-site ion proceeds via deprotonation of the ammonium moiety, followed by transfer of the proton the iodine ion. For water induced degradation, this proceeds via:

$$CH_3NH_3PbI_3(s) \overset{H_2O}{\rightarrow} CH_3NH_2 + PbI_2 + HI$$

$MAPbI_3$ hydrates can also form through water ingress, disrupting the 3D crystal structure and facilitating further degradation as described above (Leguy et al., 2015).

Perovskites also degrade at moderately high temperatures not too far above ambient temperatures (Wang et al., 2016). Additionally, the low thermal conductivities of perovskites mean that the materials cannot easily dissipate heat (for example under prolonged solar irradiation), and local temperatures could be higher in the materials, further promoting degradation. Temperature changes can also alter many properties of perovskite materials including their charge-carrier mobilities and recombination dynamics (Milot et al., 2015). Having high temperature fluctuations in devices which have been optimized at a specific temperature could therefore decrease their efficiency operating under different conditions if heat dissipation is not properly managed.

Light sensitivity is not only a manifestation of poor thermal transport but is also a catalyst for chemical degradation processes. Furthermore, it has been shown to be related to a range of film characteristics including ion migration and defect density (Chen et al., 2021). For example, light sensitivity is a particular challenge for mixed-halide materials like $FAPb(I_yBr_{1-y})_3$ as illumination promotes halide segregation, leading to the formation of regions in the film which are either iodide or bromide rich (Hoke et al., 2015). This rearrangement alters the energy landscape such that charge-carriers are funneled to the lower energy iodide-rich regions inhibiting efficient charge transport in devices (Knight and Herz, 2020).

For device applications, some atmospheric instabilities, including degradation from humidity and oxygen exposure, can be avoided by encapsulating whole devices or device layers with a material that is impermeable to these species but does not significantly impeded device performance (Li et al., 2021b; He et al., 2020; Lin et al., 2018). Similarly, thermal instability could be improved via heat management techniques, although low thermal conductivities make this approach challenging (Haeger et al., 2020). Light instability is a bigger problem, however, since it is central to the operation of optoelectronic devices and thus requires careful materials engineering to resolve.

As a result, several strategies have been implemented to improve the stability of the perovskite layer itself including mixing A-site cations, increasing grain size, and treating with passivating agents (Knight and Herz, 2020). For example, perovskite stability to water can be improved partially by substitution with less acidic A-site species, such as formamidinium (Aristidou et al., 2015), and 2D layered perovskites are substantially more stable than their 3D counterparts due to the hydrophobic cations blocking water ingress and suppressing ion migration (Sirbu et al., 2021). Passivation of grain boundaries has also been shown to improve stability by reducing water ingress (Qin et al., 2020), and/or by passivating X-site vacancies that would otherwise drive defect-induced degradation processes discussed in previous sections (Li et al., 2021a). However, the exact mechanisms underlying many improvement strategies are still unclear largely because changing one aspect of the film can change a number of its properties including morphology, crystallinity, defect density, and band structure (Knight and Herz, 2020; Rehman et al., 2017; Rehman et al., 2015), and more research is needed to develop and understand stable perovskites for device applications.

Toxicity

Another key challenge for MHPs is that lead is a highly toxic substance. Although devices such as perovskite solar cells use very thin films with only a partial lead component, even these amounts could have environmental and health impacts when used on an industrial scale (Goetz et al., 2021; Babayigit et al., 2016). Lead leakage into the environment could be mitigated through encapsulation and recycling strategies (Li et al., 2021b; Goetz et al., 2021), but finding a non-toxic replacement would be a more permanent and reliable solution. Although a range of perovskite and perovskite-like materials have been identified to replace lead-based materials, these options tend to improve toxicity at the expense of either efficiency or facile processibility (Huang et al., 2021). For example, chalcogenide perovskites such as (e.g., $BaZnS_3$) have demonstrated good optoelectronic properties but complicated processing at high temperatures makes them unattractive for large scale commercialization. Among all of the options, tin-based perovskites have shown the most promise, despite some similar concerns about their toxicity and stability (Goetz et al., 2021).

Understanding fundamental properties

Because MHPs have been developed so rapidly for device applications, the understanding of their fundamental properties has lagged behind, especially since they exhibit a unique set of properties (e.g., high charge-carrier mobilities but low thermal conductivities) that makes characterization according to existing materials classes difficult. Furthermore, sample-to-samples variations and the dependence of properties on many extrinsic factors such as defect density make fundamental studies challenging. Although a range of properties are currently being discussed in the literature including ferroelectricity (Zhou et al., 2018), polarons (Ghosh et al., 2020), and entropy (Martiradonna, 2018), we have chosen to discuss just a couple of examples to highlight the main arguments at the heart of many of these disputes.

One unanswered question in MHP research is the relationship between the chemical composition of a perovskite material (including defects) and its optoelectronic properties. As a result, it is not unusual to see contrasting reports in the literature as the field attempts to pinpoint these underlying mechanisms. For example, halide migration in mixed halide perovskites has been attributed to both extrinsic factors such as crystallinity and crystal size and intrinsic factors related to coupling of charge-carriers to the crystal lattice (Knight and Herz, 2020). The difficulty with these analyses hinges on the fact that perovskite thin films, which are the most widely studied, are polycrystalline materials containing grain boundaries and grains. A high degree of heterogeneity can exist among grains both in terms of their defect concentration and crystallinity, and optoelectronic properties including the photoluminescence quantum yield and Raman vibrational modes have been shown to vary significantly from grain to grain (Petrus et al., 2017). Because the nanostructured properties can be difficult to characterize, the influence of this heterogeneity on bulk charge transport properties has remained elusive (Petrus et al., 2017).

Cation rotation—in particular its relevance toward the optoelectronic properties and device performances of hybrid perovskites— is also highly controversial. Early theoretical studies invoked the orientational disorder of the organic species in hybrid perovskites to explain their surprisingly low recombination velocities (Ma and Wang, 2015; Frost et al., 2014), however more recent experimental determinations of cation rotational mobility strongly indicate the that the long-lived orientational ordering necessary for effective segregation of electrons and holes was highly unlikely (Gallop et al., 2018). Other theoretical studies have suggested that orientationally mobile organic cations can act to 'solvate' electrons and holes, providing an additional barrier to carrier recombination and thus explaining the relatively large carrier diffusion lengths despite relatively low mobilities (Bonn et al., 2017; Zhu and Podzorov, 2015). However, these ideas appear incompatible with experimental observations of similar recombination rates in halide perovskites incorporating inorganic Cs ions as their A-site species (Zhu et al., 2017; Kulbak et al., 2015). More recently, ultrafast spectroscopy experiments have focused on the interactions between the organic cation and the inorganic lattice (Grechko et al., 2018), although the influence of this interaction on the electronic properties of the perovskite is yet to be fully understood.

Conclusion

Metal halide perovskites have attracted much attention in recent years due to their potential applications and their interesting physical properties. This interest has arisen because MHPs have electronic properties which resemble traditional semiconductors like GaAs and silicon but can be more easily synthesized using either solution processing or vapor-based techniques. Furthermore, they offer straightforward tunability of their optoelectronic properties so that they can be tailored for the specific application. As a result, many applications have been successfully developed, both based entirely on MHPs or using MHPs to boost the efficiency of existing devices (i.e., tandem solar cells). The list of applications is ever expanding from photocatalysis to memory devices and beyond.

However, perovskites have some major issues that need to be solved, namely their toxicity and stability, before they can realize their full potential. As such, solving these problems continues to be a major focus in the field. Alongside this effort, researchers are also seeking to better understand the fundamental properties of MHPs in order to better inform device design and better understand a material that defies characterization according to existing systems.

References

Ali N, Shehzad N, Uddin S, Ahmed R, Jabeen M, Kalam A, Al-Sehemi AG, Alrobei H, Kanoun MB, Khesro A, and Goumri-Said S (2021) A review on perovskite materials with solar cell prospective. *International Journal of Energy Research* 45: 19729–19745.

Aristidou N, Sanchez-Molina I, Chotchuangchutchaval T, Brown M, Martinez L, Rath T, and Haque SA (2015) The role of oxygen in the degradation of methylammonium lead trihalide perovskite photoactive layers. *Angewandte Chemie, International Edition* 54: 8208–8212.

Azpiroz JM, Mosconi E, Bisquert J, and De Angelis F (2015) Defect migration in methylammonium lead iodide and its role in perovskite solar cell operation. *Energy & Environmental Science* 8: 2118–2127.

Babayigit A, Ethirajan A, Muller M, and Conings B (2016) Toxicity of organometal halide perovskite solar cells. *Nature Materials* 15: 247–251.

Baranowski M and Plochocka P (2020) Excitons in metal-halide perovskites. *Advanced Energy Materials* 10.

Bera S, Behera RK, and Pradhan N (2020) Alpha-Halo ketone for polyhedral perovskite nanocrystals: Evolutions, shape conversions, ligand chemistry, and self-assembly. *Journal of the American Chemical Society* 142: 20865–20874.

Bonn M, Miyata K, Hendry E, and Zhu XY (2017) Role of dielectric drag in polaron mobility in lead halide perovskites. *ACS Energy Letters* 2: 2555–2562.

Bryant D, Aristidou N, Pont S, Sanchez-Molina I, Chotchunangatchaval T, Wheeler S, Durrant JR, and Haque SA (2016) Light and oxygen induced degradation limits the operational stability of methylammonium lead triiodide perovskite solar cells. *Energy & Environmental Science* 9: 1655–1660.

Buizza LRV and Herz LM (2021) Polarons and charge localization in metal-halide semiconductors for photovoltaic and light-emitting devices. *Advanced Materials* 33: 19.

Calado P, Gelmetti I, Hilton B, Azzouzi M, Nelson J, and Barnes PRF (2022) Driftfusion: An open source code for simulating ordered semiconductor devices with mixed ionic-electronic conducting materials in one dimension. *Journal of Computational Electronics* 21: 960–991.

Ceratti DR, Zohar A, Kozlov R, Dong H, Uraltsev G, Girshevitz O, Pinkas I, Avram L, Hodes G, and Cahen D (2020) Eppur si Muove: Proton diffusion in halide perovskite single crystals. *Advanced Materials* 32.

Chen WJ, Gan ZX, Green MA, Jia BH, and Wen XM (2021) Revealing dynamic effects of mobile ions in halide perovskite solar cells using time-resolved microspectroscopy. *Small Methods* 5: 2000731.

Crothers TW, Milot RL, Patel JB, Parrott ES, Schlipf J, Muller-Buschbaum P, Johnston MB, and Herz LM (2017) Photon reabsorption masks intrinsic bimolecular charge-carrier recombination in $CH_3NH_3PbI_3$ perovskite. *Nano Letters* 17: 5782–5789.

Davies CL, Filip MR, Patel JB, Crothers TW, Verdi C, Wright AD, Milot RL, Giustino F, Johnston MB, and Herz LM (2018) Bimolecular recombination in methylammonium lead triiodide perovskite is an inverse absorption process. *Nature Communications* 9: 293.

Domanski K, Correa-Baena JP, Mine N, Nazeeruddin MK, Abate A, Saliba M, Tress W, Hagfeldt A, and Gratzel M (2016) Not all that glitters is gold: Metal-migration-induced degradation in perovskite solar cells. *ACS Nano* 10: 6306–6314.

Dou LT, Wong AB, Yu Y, Lai ML, Kornienko N, Eaton SW, Fu A, Bischak CG, Ma J, Ding TN, Ginsberg NS, Wang LW, Alivisatos AP, and Yang PD (2015) Atomically thin two-dimensional organic-inorganic hybrid perovskites. *Science* 349: 1518–1521.

Dou L, Lai ML, Kley CS, Yang YM, Bischak CG, Zhang DD, Eaton SW, Ginsberg NS, and Yang PD (2017) Spatially resolved multicolor CsPbX3 nanowire heterojunctions via anion exchange. *Proceedings of the National Academy of Sciences of the United States of America* 114: 7216–7221.

Dunlap-Shohl WA, Zhou YY, Padture NP, and Mitzi DB (2019) Synthetic approaches for halide perovskite thin films. *Chemical Reviews* 119: 3193–3295.

Eames C, Frost JM, Barnes PRF, O'Regan BC, Walsh A, and Islam MS (2015) Ionic transport in hybrid lead iodide perovskite solar cells. *Nature Communications* 6: 7497.

Egger DA, Bera A, Cahen D, Hodes G, Kirchartz T, Kronik L, Lovrincic R, Rappe AM, Reichman DR, and Yaffe O (2018) What remains unexplained about the properties of halide perovskites? *Advanced Materials* 30: 1800691.

Elliott RJ (1957) Intensity of optical absorption by excitons. *Physical Review* 108: 1384–1389.

Eperon GE, Stranks SD, Menelaou C, Johnston MB, Herz LM, and Snaith HJ (2014) Formamidinium lead trihalide: A broadly tunable perovskite for efficient planar heterojunction solar cells. *Energy & Environmental Science* 7: 982–988.

Fakharuddin A, Gangishetty MK, Abdi-Jalebi M, Chin SH, Yusoff AB, Congreve DN, Tress W, Deschler F, Vasilopoulou M, and Bolink HJ (2022) Perovskite light-emitting diodes. *Nature Electronics* 5: 203–216.

Filip MR and Giustino F (2018) The geometric blueprint of perovskites. *Proceedings of the National Academy of Sciences of the United States of America* 115: 5397–5402.

Frost JM, Butler KT, Brivio F, Hendon CH, Van Schilfgaarde M, and Walsh A (2014) Atomistic origins of high-performance in hybrid halide perovskite solar cells. *Nano Letters* 14: 2584–2590.

Gallop NP, Selig O, Giubertoni G, Bakker HJ, Rezus YLA, Frost JM, Jansen TLC, Lovrincic R, and Bakulin AA (2018) Rotational cation dynamics in metal halide perovskites: Effect on phonons and material properties. *The Journal of Physical Chemistry Letters* 9: 5987–5997.

Gallop NP, Ye J, Greetham GM, Jansen TLC, Dai L, Zelewski SJ, Arul R, Baumberg JJ, Hoye RLZ, and Bakulin AA (2022) The effect of caesium alloying on the ultrafast structural dynamics of hybrid organic–inorganic halide perovskites. *Journal of Materials Chemistry A* 10: 22408–22418.

Ghosh D, Walsh Atkins P, Islam MS, Walker AB, and Eames C (2017) Good vibrations: Locking of octahedral tilting in mixed-cation iodide perovskites for solar cells. *ACS Energy Letters* 2: 2424–2429.

Ghosh D, Welch E, Neukirch AJ, Zakhidov A, and Tretiak S (2020) Polarons in halide perovskites: A perspective. *Journal of Physical Chemistry Letters* 11: 3271–3286.

Goetz KP, Taylor AD, Paulus F, and Vaynzof Y (2020) Shining light on the photoluminescence properties of metal halide perovskites. *Advanced Functional Materials* 30.

Goetz KP, Taylor AD, Hofstetter YJ, and Vaynzof Y (2021) Sustainability in perovskite solar cells. *ACS Applied Materials & Interfaces* 13: 1–17.

Gogoi HJ, Bajpai K, Mallajosyula AT, and Solanki A (2021) Advances in flexible memristors with hybrid perovskites. *The Journal of Physical Chemistry Letters* 12: 8798–8825.

Grechko M, Bretschneider SA, Vietze L, Kim H, and Bonn M (2018) Vibrational coupling between organic and inorganic sublattices of hybrid perovskites. *Angewandte Chemie, International Edition* 57: 13657–13661.

Green MA, Ho-Baillie A, and Snaith HJ (2014) The emergence of perovskite solar cells. *Nature Photonics* 8: 506–514.

Haeger T, Heiderhoff R, and Riedl T (2020) Thermal properties of metal-halide perovskites. *Journal of Materials Chemistry C* 8: 14289–14311.

Haque MA, Kee S, Villalva DR, Ong W-L, and Baran D (2020) Halide perovskites: Thermal transport and prospects for thermoelectricity. *Advanced Science* 7: 1903389.

He SS, Qiu LB, Ono LK, and Qi YB (2020) How far are we from attaining 10-year lifetime for metal halide perovskite solar cells? *Materials Science & Engineering R: Reports* 140: 100545.

Herz LM (2016) Charge-carrier dynamics in organic-inorganic metal halide perovskites. *Annual Review of Physical Chemistry* 67(1): 65–89.

Herz LM (2017) Charge-carrier mobilities in metal halide perovskites: Fundamental mechanisms and limits. *ACS Energy Letters* 2: 1539–1548.

Ho-Baillie AWY, Zheng JH, Mahmud MA, Ma FJ, McKenzie DR, and Green MA (2021) Recent progress and future prospects of perovskite tandem solar cells. *Applied Physics Reviews* 8.

Hoke ET, Slotcavage DJ, Dohner ER, Bowring AR, Karunadasa HI, and McGehee MD (2015) Reversible photo-induced trap formation in mixed-halide hybrid perovskites for photovoltaics. *Chemical Science* 6: 613–617.
Hopper TR, Gorodetsky A, Frost JM, Müller C, Lovrincic R, and Bakulin AA (2018) Ultrafast intraband spectroscopy of hot-carrier cooling in lead-halide perovskites. *ACS Energy Letters* 3: 2199–2205.
Huang YT, Kavanagh SR, Scanlon DO, Walsh A, and Hoye RLZ (2021) Perovskite-inspired materials for photovoltaics and beyond-from design to devices. *Nanotechnology* 32: 132004.
Ibaceta-Jaña J, Muydinov R, Rosado P, Mirhosseini H, Chugh M, Nazarenko O, Dirin DN, Heinrich D, Wagner MR, Kühne TD, Szyszka B, Kovalenko MV, and Hoffmann A (2020) Vibrational dynamics in lead halide hybrid perovskites investigated by Raman spectroscopy. *Physical Chemistry Chemical Physics* 22: 5604–5614.
Im JH, Luo JS, Franckevicius M, Pellet N, Gao P, Moehl T, Zakeeruddin SM, Nazeeruddin MK, Gratzel M, and Park NG (2015) Nanowire perovskite solar cell. *Nano Letters* 15: 2120–2126.
Jacobsson TJ, Correa-Baen JP, Pazoki M, Saliba M, Schenk K, Gratzel M, and Hagfeldt A (2016) Exploration of the compositional space for mixed lead halogen perovskites for high efficiency solar cells. *Energy & Environmental Science* 9: 1706–1724.
Jena AK, Kulkarni A, and Miyasaka T (2019) Halide perovskite photovoltaics: Background, status, and future prospects. *Chemical Reviews* 119: 3036–3103.
Jia PC, Qin L, Zhao D, Tang Y, Song B, Guo JH, Li XM, Li L, Cui QH, Hu YF, Lou ZD, Teng F, and Hou YB (2021) The trapped charges at grain boundaries in perovskite solar cells. *Advanced Functional Materials* 31: 2107125.
Jin HD, Debroye E, Keshavarz M, Scheblykin IG, Roeffaers MBJ, Hofkens J, and Steele JA (2020) It's a trap! On the nature of localised states and charge trapping in lead halide perovskites. *Materials Horizons* 7: 397–410.
John RA, Shah N, Vishwanath SK, Ng SE, Febriansyah B, Jagadeeswararao M, Chang C-H, Basu A, and Mathews N (2021) Halide perovskite memristors as flexible and reconfigurable physical unclonable functions. *Nature Communications* 12: 3681.
Johnston MB and Herz LM (2016) Hybrid perovskites for photovoltaics: Charge-carrier recombination, diffusion, and radiative efficiencies. *Accounts of Chemical Research* 49: 146–154.
Jong UG, Yu CJ, Ri GC, McMahon AP, Harrison NM, Barnes PRF, and Walsh A (2018) Influence of water intercalation and hydration on chemical decomposition and ion transport in methylammonium lead halide perovskites. *Journal of Materials Chemistry A* 6: 1067–1074.
Kagan CR, Mitzi DB, and Dimitrakopoulos CD (1999) Organic-inorganic hybrid materials as semiconducting channels in thin-film field-effect transistors. *Science* 286: 945–947.
Kieslich G, Sun SJ, and Cheetham AK (2015) An extended Tolerance Factor approach for organic-inorganic perovskites. *Chemical Science* 6: 3430–3433.
Kim H-S, Jang I-H, Ahn N, Choi M, Guerrero A, Bisquert J, and Park N-G (2015) Control of I–V hysteresis in $CH_3NH_3PbI_3$ perovskite solar cell. *The Journal of Physical Chemistry Letters* 6: 4633–4639.
Kim GY, Senocrate A, Moia D, and Maier J (2020) Ionically generated built-in equilibrium space charge zones-a paradigm change for lead halide perovskite interfaces. *Advanced Functional Materials* 30: 2002426.
Knight AJ and Herz LM (2020) Preventing phase segregation in mixed-halide perovskites: A perspective. *Energy & Environmental Science* 13: 2024–2046.
Kober-Czerny M, Motti SG, Holzhey P, Wenger B, Lim J, Herz LM, and Snaith HJ (2022) Excellent long-range charge-carrier mobility in 2D perovskites. *Advanced Functional Materials* 32: 2203064.
Kojima A, Teshima K, Shirai Y, and Miyasaka T (2009) Organometal halide perovskites as visible-light sensitizers for photovoltaic cells. *Journal of the American Chemical Society* 131: 6050.
Konstantakou M and Stergiopoulos T (2017) A critical review on tin halide perovskite solar cells. *Journal of Materials Chemistry A* 5: 11518–11549.
Kubicki DJ, Stranks SD, Grey CP, and Emsley L (2021) NMR spectroscopy probes microstructure, dynamics and doping of metal halide perovskites. *Nature Reviews Chemistry* 5: 624–645.
Kucharska E, Hanuza J, Ciupa A, Maczka M, and Macalik L (2014) Vibrational properties and DFT calculations of formamidine-templated Co and Fe formates. *Vibrational Spectroscopy* 75: 45–50.
Kulbak M, Cahen D, and Hodes G (2015) How important is the organic part of lead halide perovskite photovoltaic cells? Efficient $CsPbBr_3$ cells. *The Journal of Physical Chemistry Letters* 6: 2452–2456.
Le QV, Hong K, Jang HW, and Kim SY (2018) Halide perovskite quantum dots for light-emitting diodes: Properties, synthesis, applications, and outlooks. *Advanced Electronic Materials* 4: 1800335.
Lee MM, Teuscher J, Miyasaka T, Murakami TN, and Snaith HJ (2012) Efficient hybrid solar cells based on meso-superstructured organometal halide perovskites. *Science* 338: 643–647.
Leguy AMA, Hu Y, Campoy-Quiles M, Alonso MI, Weber OJ, Azarhoosh P, Van Schilfgaarde M, Weller MT, Bein T, Nelson J, Docampo P, and Barnes PRF (2015) Reversible hydration of CH(3)NH(3)PbI(3) in films, single crystals, and solar cells. *Chemistry of Materials* 27: 3397–3407.
Leguy AMA, Goñi AR, Frost JM, Skelton J, Brivio F, Rodríguez-Martínez X, Weber OJ, Pallipurath A, Alonso MI, Campoy-Quiles M, Weller MT, Nelson J, Walsh A, and Barnes PRF (2016) Dynamic disorder, phonon lifetimes, and the assignment of modes to the vibrational spectra of methylammonium lead halide perovskites. *Physical Chemistry Chemical Physics* 18: 27051–27066.
Lei L, Dong Q, Gundogdu K, and So F (2021) Metal halide perovskites for laser applications. *Advanced Functional Materials* 31: 2010144.
Li H and Zhang W (2020) Perovskite tandem solar cells: From fundamentals to commercial deployment. *Chemical Reviews* 120: 9835–9950.
Li CW, Zhou YY, Wang L, Chang Y, Zong YX, Etgar L, Cui GL, Padture NP, and Pang SP (2017a) Methylammonium-mediated evolution of mixed-organic-cation perovskite thin films: A dynamic composition-tuning process. *Angewandte Chemie, International Edition* 56: 7674–7678.
Li Z, Xiao CX, Yang Y, Harvey SP, Kim DH, Christians JA, Yang MJ, Schulz P, Nanayakkara SU, Jiang CS, Luther JM, Berry JJ, Beard MC, Al-Jassim MM, and Zhu K (2017b) Extrinsic ion migration in perovskite solar cells. *Energy & Environmental Science* 10: 1234–1242.
Li C, Li H, Zhu ZN, Cui NY, Tan ZA, and Yang RS (2021a) Perovskite passivation strategies for efficient and stable solar cells. *Solar RRL* 5: 2000579.
Li JL, Xia R, Qi WJ, Zhou X, Cheng J, Chen YF, Hou GF, Ding Y, Li YL, Zhao Y, and Zhang XD (2021b) Encapsulation of perovskite solar cells for enhanced stability: Structures, materials and characterization. *Journal of Power Sources* 485: 229313.
Lin CT, Pont S, Kim J, Du T, Xu SD, Li XE, Bryant D, McLachlan MA, and Durrant JR (2018) Passivation against oxygen and light induced degradation by the PCBM electron transport layer in planar perovskite solar cells. *Sustainable Energy & Fuels* 2: 1686–1692.
Ma J and Wang L-W (2015) Nanoscale charge localization induced by random orientations of organic molecules in hybrid perovskite $CH_3NH_3PbI_3$. *Nano Letters* 15: 248–253.
Ma L, Yan Z, Zhou X, et al. (2021) A polymer controlled nucleation route towards the generalized growth of organic-inorganic perovskite single crystals. *Nature Communications* 12: 2023. https://doi.org/10.1038/s41467-021-22193-1.
Manser JS, Christians JA, and Kamat PV (2016) Intriguing optoelectronic properties of metal halide perovskites. *Chemical Reviews* 116: 12956–13008.
Mao J, Sha WEI, Zhang H, Ren XG, Zhuang JQ, Roy VAL, Wong KS, and Choy WCH (2017) Novel direct nanopatterning approach to fabricate periodically nanostructured perovskite for optoelectronic applications. *Advanced Functional Materials* 27.
Martiradonna L (2018) Riddles in perovskite research. *Nature Materials* 17: 377.
Meng K, Gao SS, Wu LL, Wang G, Liu X, Chen G, Liu Z, and Chen G (2016) Two-dimensional organic-inorganic hybrid perovskite photonic films. *Nano Letters* 16: 4166–4173.
Milot RL, Eperon GE, Snaith HJ, Johnston MB, and Herz LM (2015) Temperature-dependent charge-carrier dynamics in $CH_3NH_3PbI_3$ perovskite thin films. *Advanced Functional Materials* 25: 6218–6227.
Milot RL, Sutton RJ, Eperon GE, Haghighirad AA, Hardigree JM, Miranda L, Snaith HJ, Johnston MB, and Herz LM (2016) Charge-carrier dynamics in 2D hybrid metal-halide perovskites. *Nano Letters* 16: 7001–7007.

Milot RL, Klug MT, Davies CL, Wang Z, Kraus H, Snaith HJ, Johnston MB, and Herz LM (2018) The effects of doping density and temperature on the optoelectronic properties of formamidinium tin triiodide thin films. *Advanced Materials* 30: 1804506.

Min H, Lee DY, Kim J, Kim G, Lee KS, Kim J, Paik MJ, Kim YK, Kim KS, Kim MG, Shin TJ, and Il Seok S (2021) Perovskite solar cells with atomically coherent interlayers on SnO_2 electrodes. *Nature* 598: 444–450.

Moia D and Maier J (2021) Ion transport, defect chemistry, and the device physics of hybrid perovskite solar cells. *ACS Energy Letters* 6: 1566–1576.

Moot T, Werner J, Eperon GE, Zhu K, Berry JJ, McGehee MD, and Luther JM (2020) Choose your own adventure: Fabrication of monolithic all-perovskite tandem photovoltaics. *Advanced Materials* 32: 2003312.

Munson KT, Swartzfager JR, and Asbury JB (2019) Lattice anharmonicity: A double-edged sword for 3D perovskite-based optoelectronics. *ACS Energy Letters* 4: 1888–1897.

Murali B, Kolli HK, Yin J, Ketavath R, Bakr OM, and Mohammed OF (2020) Single crystals: The next big wave of perovskite optoelectronics. *ACS Materials Letters* 2: 184–214.

NREL (2021) *NREL Best Research-Cell Efficiency Chart*. Available at: https://www.nrel.gov/pv/assets/pdfs/best-research-cell-efficiencies.20200104.pdf (Accessed March 15, 2021).

Otero-Martinez C, Ye JZ, Sung J, Pastoriza-Santos I, Perez-Juste J, Xia ZG, Rao A, Hoye RLZ, and Polavarapu L (2022) Colloidal metal-halide perovskite nanoplatelets: Thickness-controlled synthesis, properties, and application in light-emitting diodes. *Advanced Materials* 34: e2107105.

Park JS, Kim S, Xie ZJ, and Walsh A (2018) Point defect engineering in thin-film solar cells. *Nature Reviews Materials* 3: 194–210.

Parrott ES, Green T, Milot RL, Johnston MB, Snaith HJ, and Herz LM (2018) Interplay of structural and optoelectronic properties in formamidinium mixed tin–lead triiodide perovskites. *Advanced Functional Materials* 28: 1802803.

Perez-Osorio MA, Milot RL, Filip MR, Patel JB, Herz LM, Johnston MB, and Giustino F (2015) Vibrational properties of the organic inorganic halide perovskite $CH_3NH_3PbI_3$ from theory and experiment: Factor group analysis, first-principles calculations, and low-temperature infrared spectra. *Journal of Physical Chemistry C* 119: 25703–25718.

Petrus ML, Schlipf J, Li C, Gujar TP, Giesbrecht N, Muller-Buschbaum P, Thelakkat M, Bein T, Huttner S, and Docampo P (2017) Capturing the sun: A review of the challenges and perspectives of perovskite solar cells. *Advanced Energy Materials* 7: 1700264.

Phung N and Abate A (2018) The impact of nano- and microstructure on the stability of perovskite solar cells. *Small* 14: 1802573.

Prochowicz D, Saski M, Yadav P, Grätzel M, and Lewiński J (2019) Mechanoperovskites for photovoltaic applications: Preparation, characterization, and device fabrication. *Accounts of Chemical Research* 52: 3233–3243.

Protesescu L, Yakunin S, Bodnarchuk MI, Krieg F, Caputo R, Hendon CH, Yang RX, Walsh A, and Kovalenko MV (2015) Nanocrystals of cesium lead halide perovskites (CsPbX3, X = Cl, Br, and I): Novel optoelectronic materials showing bright emission with wide color gamut. *Nano Letters* 15: 3692–3696.

Qin PL, Wu T, Wang ZC, Xiao L, Ma L, Ye FH, Xiong L, Chen XB, Li HX, Yu XL, and Fang GJ (2020) Grain boundary and interface passivation with core-shell Au@CdS nanospheres for high-efficiency perovskite solar cells. *Advanced Functional Materials* 30: 1908408.

Raiford JA, Oyakhire ST, and Bent SF (2020) Applications of atomic layer deposition and chemical vapor deposition for perovskite solar cells. *Energy & Environmental Science* 13: 1997–2023.

Rehman W, Milot RL, Eperon GE, Wehrenfennig C, Boland JL, Snaith HJ, Johnston MB, and Herz LM (2015) Charge-carrier dynamics and mobilities in formamidinium lead mixed-halide perovskites. *Advanced Materials* 27: 7938–7944.

Rehman W, McMeekin DP, Patel JB, Milot RL, Johnston MB, Snaith HJ, and Herz LM (2017) Photovoltaic mixed-cation lead mixed-halide perovskites: Links between crystallinity, photo-stability and electronic properties. *Energy & Environmental Science* 10: 361–369.

Ren KK, Yue SZ, Li CH, Fang ZB, Gasem KAM, Leszczynski J, Qu SC, Wang ZJ, and Fan MH (2022) Metal halide perovskites for photocatalysis applications. *Journal of Materials Chemistry A* 10: 407–429.

Rosales BA, Wei L, and Vela J (2019) Synthesis and mixing of complex halide perovskites by solvent-free solid-state methods. *Journal of Solid State Chemistry* 271: 206–215.

Sato T, Takagi S, Deledda S, Hauback BC, and Orimo S (2016) Extending the applicability of the Goldschmidt tolerance factor to arbitrary ionic compounds. *Scientific Reports* 6: 23592.

Selig O, Sadhanala A, Müller C, Lovrincic R, Chen Z, Rezus YLA, Frost JM, Jansen TLC, and Bakulin AA (2017) Organic cation rotation and immobilization in pure and mixed methylammonium lead-halide perovskites. *Journal of the American Chemical Society* 139: 4068–4074.

Senocrate A and Maier J (2019) Solid-state ionics of hybrid halide perovskites. *Journal of the American Chemical Society* 141: 8382–8396.

Senocrate A, Moudrakovski I, Kim GY, Yang TY, Gregori G, Gratzel M, and Maier J (2017) The nature of ion conduction in methylammonium lead iodide: A multimethod approach. *Angewandte Chemie, International Edition* 56: 7755–7759.

Senocrate A, Acarturk T, Kim GY, Merkle R, Starke U, Gratzel M, and Maier J (2018) Interaction of oxygen with halide perovskites. *Journal of Materials Chemistry A* 6: 10847–10855.

Shirayama M, Kadowaki H, Miyadera T, Sugita T, Tamakoshi M, Kato M, Fujiseki T, Murata D, Hara S, Murakami TN, Fujimoto S, Chikamatsu M, and Fujiwara H (2016) Optical transitions in hybrid perovskite solar cells: Ellipsometry, density functional theory, and quantum efficiency analyses for $CH_3NH_3PbI_3$. *Physical Review Applied* 5.

Singh S, Laxmi, and Kabra D (2020) Defects in halide perovskite semiconductors: Impact on photo-physics and solar cell performance. *Journal of Physics D: Applied Physics* 53: 503003.

Sirbu D, Balogun FH, Milot RL, and Docampo P (2021) Layered perovskites in solar cells: Structure, optoelectronic properties, and device design. *Advanced Energy Materials* 11: 2003877.

Stranks SD (2017) Nonradiative losses in metal halide perovskites. *ACS Energy Letters* 2: 1515–1525.

Sung W, Muller C, Hietzschold S, Lovrincic R, Gallop NP, Bakulin AA, Nihonyanagi S, and Tahara T (2020) Preferred orientations of organic cations at lead-halide perovskite interfaces revealed using vibrational sum-frequency spectroscopy. *Materials Horizons* 7: 1348–1357.

Taylor VCA, Tiwari D, Duchi M, Donaldson PM, Clark IP, Fermin DJ, and Oliver TAA (2018) Investigating the role of the organic cation in formamidinium lead iodide perovskite using ultrafast spectroscopy. *The Journal of Physical Chemistry Letters* 9: 895–901.

Tooghi A, Fathi D, and Eskandari M (2020) High-performance perovskite solar cell using photonic-plasmonic nanostructure. *Scientific Reports* 10.

Travis W, Glover ENK, Bronstein H, Scanlon DO, and Palgrave RG (2016) On the application of the tolerance factor to inorganic and hybrid halide perovskites: A revised system. *Chemical Science* 7: 4548–4556.

Veldhuis SA, Boix PP, Yantara N, Li MJ, Sum TC, Mathews N, and Mhaisalkar SG (2016) Perovskite materials for light-emitting diodes and lasers. *Advanced Materials* 28: 6804–6834.

Wang H and Kim DH (2017) Perovskite-based photodetectors: Materials and devices. *Chemical Society Reviews* 46: 5204–5236.

Wang D, Wright M, Elumalai NK, and Uddin A (2016) Stability of perovskite solar cells. *Solar Energy Materials and Solar Cells* 147: 255–275.

Wang K, Yang D, Wu CC, Sanghadasa M, and Priya S (2019) Recent progress in fundamental understanding of halide perovskite semiconductors. *Progress in Materials Science* 106: 100580.

Wang M, Cao FR, and Li L (2022) Metal halide perovskite nano/microwires. *Small Structures* 3: 2100165.

Wasylishen RE, Knop O, and Macdonald JB (1985) Cation rotation in methylammonium lead halides. *Solid State Communications* 56: 581–582.

Weidman MC, Seitz M, Stranks SD, and Tisdale WA (2016) Highly tunable colloidal perovskite nanoplatelets through variable cation, metal, and halide composition. *ACS Nano* 10: 7830–7839.

Wright AD, Milot RL, Eperon GE, Snaith HJ, Johnston MB, and Herz LM (2017) Band-tail recombination in hybrid lead iodide perovskite. *Advanced Functional Materials* 27: 1700860.

Xia CQ, Peng J, Ponce S, Patel JB, Wright AD, Crothers TW, Rothmann MU, Borchert J, Milot RL, Kraus H, Lin Q, Giustino F, Herz LM, and Johnston MB (2021) Limits to electrical mobility in lead-halide perovskite semiconductors. *The Journal of Physical Chemistry Letters*. (Accepted).

Xiang Y, Mo XD, Li X, Huang KQ, He P, Dai GZ, and Yang JL (2022) Progress on growth of metal halide perovskites by vapor-phase synthesis and their applications. *Journal of Physics D: Applied Physics* 55: 073001.

Xu JL, Li XY, Xiong JB, Yuan CQ, Semin S, Rasing T, and Bu XH (2020) Halide perovskites for nonlinear optics. *Advanced Materials* 32.

Xu LM, Yuan SC, Ma L, Zhang BS, Fang T, Li XS, and Song JZ (2021) All-inorganic perovskite quantum dots as light-harvesting, interfacial, and light-converting layers toward solar cells. *Journal of Materials Chemistry A* 9: 18947–18973.

Yang TY, Gregori G, Pellet N, Gratzel M, and Maier J (2015) The significance of ion conduction in a hybrid organic-inorganic lead-iodide-based perovskite photosensitizer. *Angewandte Chemie, International Edition* 54: 7905–7910.

Younis A, Lin CH, Guan XW, Shahrokhi S, Huang CY, Wang YT, He TY, Singh S, Hu L, Retamal JRD, He JH, and Wu T (2021) Halide perovskites: A new era of solution-processed electronics. *Advanced Materials* 33.

Zhang DQ, Zhang QP, Zhu YY, Poddar S, Zhang YT, Gu LL, Zeng HB, and Fan ZY (2022) Metal halide perovskite nanowires: Synthesis, integration, properties, and applications in optoelectronics. *Advanced Energy Materials* 2022: 2201735.

Zheng W, Huang P, Gong ZL, Tu D, Xu J, Zou QL, Li RF, You WW, Bunzli JCG, and Chen XY (2018) Near-infrared-triggered photon upconversion tuning in all-inorganic cesium lead halide perovskite quantum dots. *Nature Communications* 9: 3462.

Zhou Y, Chen J, Bakr OM, and Sun HT (2018) Metal-doped lead halide perovskites: Synthesis, properties, and optoelectronic applications. *Chemistry of Materials* 30: 6589–6613.

Zhou YX, Huang YY, Xu XL, Fan ZY, Khurgin JB, and Xiong QH (2020) Nonlinear optical properties of halide perovskites and their applications. *Applied Physics Reviews* 7.

Zhu XY and Podzorov V (2015) Charge carriers in hybrid organic–inorganic lead halide perovskites might be protected as large polarons. *The Journal of Physical Chemistry Letters* 6: 4758–4761.

Zhu HM, Trinh MT, Wang J, Fu YP, Joshi PP, Miyata K, Jin S, and Zhu XY (2017) Organic cations might not be essential to the remarkable properties of band edge carriers in lead halide perovskites. *Advanced Materials* 29: 1603072.

Powder processing—Models and simulations

AB Yu, ARC Research Hub for Computational Particle Technology, Department of Chemical and Biological Engineering, Monash University, Clayton, VIC, Australia

© 2024 Elsevier Ltd. All rights reserved.

This is an update of A.B. Yu, Powder Processing: Models and Simulations, Editor(s): Franco Bassani, Gerald L. Liedl, Peter Wyder, Encyclopedia of Condensed Matter Physics, Elsevier, 2005, Pages 401–414, ISBN 9780123694010, https://doi.org/10.1016/B0-12-369401-9/00556-8.

Introduction **680**
Simulation method **681**
Governing equations 681
Models for particle-particle and particle-fluid interactions 681
Numerical solution and boundary treatments 683
Model validity and application **684**
Particle packing 684
Particle flow in a horizontal rotating drum 687
Gas fluidization of cohesive powders 690
Conclusion **693**
References **693**

Abstract

Particle science and technology is a rapidly developing interdisciplinary research area with its core being the understanding of the relationships between micro- and macro-scopic properties of granular matter—a state of matter that is widely encountered but poorly understood. The macroscopic behavior of particulate matter is controlled by the interactions between individual particles as well as interactions with surrounding gas, liquid and/or wall. Understanding the microscopic mechanisms in terms of these interaction forces is therefore key to leading to truly interdisciplinary research into particulate matter and producing results that can be generally used. This aim can be effectively achieved via particle scale research based on detailed microdynamic information such as the forces acting on and trajectories of individual particles in a considered system. In recent years, such research has been rapidly developed worldwide, mainly as a result of the rapid development of discrete particle simulation technique and computer technology. This chapter presents an overview of the work in this direction. It is demonstrated that simulation and modeling has emerged to be a powerful tool not only for fundamental research but also for engineering application.

Nomenclature

$\mathbf{C_n}$	Coordination number, dimensionless
$\mathbf{d}$	Diameter of particles, m
f	Force acting on a particle, N
g	Gravitational acceleration, ms^{-2}
$\mathbf{H}$	Hamaker constant, Nm
$\mathbf{I}$	Moment of inertia of a particle, defined as $I = 2/5$ mR^2, kgm^2
$\mathbf{k_c}$	Number of particles in a computational cell, dimensionless
$\mathbf{k_i}$	Number of particles interacting with particle i, dimensionless
$\mathbf{m}$	Mass of a particle, kg
$\mathbf{N}$	Total number of particles in a considered system, dimensionless
$\mathbf{p}$	Pressure, Pa
R	Radius vector of a particle, m
Re	Reynolds number, dimensionless
$\mathbf{t}$	Time, s
T	Torque acting on a particle, Nm
u	Fluid velocity, ms^{-1}
v	Translational velocity of a particle, ms^{-1}
$\mathbf{z}$	Separation distance between two interacting surfaces, m
$\mathbf{z_0}$	Smallest separation distance between two interacting surfaces, m
$\mathbf{\Delta V}$	Volume of a computational cell, m^3

Greek letters

δ	Displacement between two contacting particles, m
$\boldsymbol{\epsilon}$	Porosity, dimensionless
$\boldsymbol{\gamma}$	Friction coefficient, dimensionless
$\boldsymbol{\rho}$	Density, kgm^{-3}
τ	Fluid viscous stress tensor, $kgm^{-1}\ s^{-2}$
$\boldsymbol{\mu}$	Viscosity, $kgm^{-1}\ s^{-1}$
$\boldsymbol{\eta}$	Viscous contact damping coefficient of a particle, kgs^{-1}
$\boldsymbol{\kappa}$	Spring constant of a particle, Nm^{-1}
ω	Rotational velocity of a particle, s^{-1}
$\boldsymbol{\zeta}$	Arbitrary variable used in averaging operators

Subscripts

c	Contact
d	Damping
f	Fluid phase
i	Particle i
ij	Between particles i and j
n	Normal component
p	Particle phase
pf	Particle-fluid
pp.	Particle-particle
r	Rolling friction
s	Sliding friction
t	Tangential component
v	van der Waals

Averaging operator

$\langle\ \rangle$ Ensemble-average, defined as $\langle \zeta \rangle = \frac{1}{N}\sum_{i=1}^{N} \zeta_i$

Introduction

Granular materials, which can be either wet or dry and range in size from nanometers to centimeters, are widely encountered as particles or powder in industries and in nature (Bideau and Hansen, 1993; Herrmann et al., 1997; Mehta, 1993; Oda and Iwashita, 1999; Seville et al., 1997). As with solids, they can withstand deformation and form heaps; as with liquids, they can flow; as with gases, they exhibit compressibility. Corresponding to the fluid- and solid-like modes, they show different flow regimes: quasi-static regime, rapid flow regime and a transitional regime that lies in between. These features give rise to another state of matter that is poorly understood. Development of a general theory to describe the packing (statics) and flow (dynamics) of granular materials has been a problem challenging the scientific community for years.

Essentially, the existing approaches to modeling granular materials can be classified into two categories: the continuum approach at a macroscopic level and the discrete approach at a microscopic level. In the continuum approach, the macroscopic behavior is described by balance equations, e.g., mass and momentum as used in the Two Fluid Model (TFM), closed with constitutive relations together with initial and boundary conditions (Gidaspow, 1994; Crowe et al., 1998). This approach is preferred in process modeling and applied research because of its computational convenience. However, its effective use heavily depends on constitutive or closure relations and the momentum exchange between particles of different types. In the past, different theories have been devised for different materials and for different flow regimes. For example, models have been proposed to derive the constitutive equations for the rate-independent deformation of granular materials based on either the plasticity theory or the double shearing theory; rapid flow of granular materials has been described by extending the kinetic theory of dense gases; the transitional regime that involves both collisional and frictional mechanisms is studied by use of the kinetic theory combined with the Mohr-Coulomb quasi-static theory (Bideau and Hansen, 1993; Herrmann et al., 1997; Oda and Iwashita, 1999). However, to date, there is no accepted continuum theory applicable to all flow conditions. As a result, phenomenological assumptions have to be made to obtain the constitutive relations and boundary conditions, which have very limited application.

The discrete approach is based on the analysis of the motion of individual particles and has the advantage that there is no need for global assumptions on the solids such as steady-state behavior, uniform constituency, and/or constitutive relations. Various methods have been developed in the past. A major type of discrete approach is based on the so-called Discrete Element Method (DEM) originally developed for rock mechanics. The method considers a finite number of discrete particles interacting by means of contact and non-contact forces, and every particle in a considered system is described by Newton's equations of motion (Herrmann et al., 1997; Oda and Iwashita, 1999). In principle, it is similar to molecular dynamic simulation (MDS) but the forces involved differ because of the difference in time and length scales (Israelachvili, 1991; Xu and Yu, 1997). DEM-based simulation has been recognized as an effective method to study the fundamentals of granular materials and assess the performance of industrial processes. By means of a proper average method, it can also generate information to support continuum modeling.

This chapter is focused on the discrete approach. It first describes the principles and key features of the simulation method, and then discusses its application to the study of a few typical static and dynamic particle systems. Emphasis will be given to the validity analysis and the usefulness of the resulting particle scale information in elucidating the fundamentals of granular materials, achieved through illustrative examples.

Simulation method

Governing equations

A particle in a considered system can have two types of motion: translational and rotational, determined by Newton's second law of motion. During its movement, the particle may collide with its neighbor particles or wall at the contact points and interact with the surrounding fluid, through which the momentum and energy are exchanged. For the systems considered in this article, at any time t, the equations governing the translational and rotational motions of particle i are (Xu and Yu, 1997; Zhou et al., 1999; Yang et al., 2000)

$$\mathrm{m}_i \frac{\mathrm{d}v_i}{\mathrm{dt}} = \mathbf{f}_{pf,i} + \mathrm{m}_i\mathbf{g} + \sum_{j=1}^{k_i}\left(\mathbf{f}_{c,ij} + \mathbf{f}_{d,ij} + \mathbf{f}_{v,ij}\right) \tag{1}$$

and

$$\mathrm{I}_i \frac{\mathrm{d}\boldsymbol{\omega}_i}{\mathrm{dt}} = \sum_{j=1}^{k_i}\left(\mathbf{T}_{c,ij} + \mathbf{T}_{r,ij}\right) \tag{2}$$

where $\mathrm{m_i}$, $\mathrm{I_i}$, $\mathbf{v}_\mathrm{i}$ and $\boldsymbol{\omega}_\mathrm{i}$ are, respectively, the mass, moment of inertia, translational and rotational velocities of the particle. The forces involved are: the particle-fluid interaction force, $\mathbf{f}_\mathrm{pf,i}$, gravitational force, $\mathrm{m_i}\mathbf{g}$, and interparticle forces between particles i and j. The torques include the interparticle torque $\mathbf{T}_\mathrm{c,ij}$ and rolling friction torque $\mathbf{T}_\mathrm{r,ij}$. For multiple interactions, the interparticle forces and torques are summed for k_i particles interacting with particle i.

Particle flow is often coupled with fluid (gas and/or liquid) flow. Various approaches have been proposed to simulate such a coupled particle-fluid flow. The time and length scales for fluid flow can range from discrete (MDS, Lattice Boltzman (LB), Pseudo-particle (PP)) to continuum (Direct Numerical Simulation (DNS), Large Eddy Simulation (LES), and other conventional techniques like TFM) description. These methods have been widely used in Computational Fluid Dynamics (CFD) (Gidaspow, 1994; Crowe et al., 1998; Zhu et al., 2007; Rong et al., 2014; Wu et al., 2021). Relative to particle phase, they can also be categorized into three groups: sub-particle, pseudo-particle and computational cell. Table 1 lists a few representative combinations of different length scales for fluid and particle phases and their relative merits in different aspects.

At this stage of development, the difficulty in particle-fluid flow modeling is mainly related to solid phase rather than fluid phase. Therefore, the so-called combined continuum and discrete model (CCDM) or CFD-DEM is attractive because of its computational convenience as compared to DNS or LB-DEM and capability to capture the particle physics as compared to TFM. In CCDM, the continuum fluid field is calculated from the continuity and the Navier-Stokes equations based on the local mean variables over a computational cell, which are given by (Xu and Yu, 1997; Zhou et al., 2010)

$$\frac{\partial \varepsilon}{\partial \mathrm{t}} + \nabla\cdot(\varepsilon\mathbf{u}) = 0 \tag{3}$$

and

$$\frac{\partial\left(\rho_f\varepsilon\mathbf{u}\right)}{\partial\mathrm{t}} + \nabla\cdot\left(\rho_f\varepsilon\mathbf{uu}\right) = -\nabla\mathrm{p} - \mathbf{F}_{pf} + \nabla\cdot(\varepsilon\boldsymbol{\tau}) + \rho_f\varepsilon\mathbf{g} \tag{4}$$

where $\mathbf{u}$, p and $\boldsymbol{\tau}$ are, respectively, the fluid velocity, pressure and viscous stress tensor; $\boldsymbol{F}_{pf} = \left(\sum_{i=1}^{k_c} f_{pf,i}/\Delta\mathrm{V}\right)$ is the particle-fluid interaction force, and ε, $\triangle$V and $\mathrm{k_c}$ are respectively the porosity, volume and number of particles in a computational cell.

Models for particle-particle and particle-fluid interactions

The forces acting on a particle result from particle-particle and particle-fluid interactions. For particles, these interactions include the forces due to direct or non-direct contacts between particles, as shown in Fig. 1. The direct contact forces include the contact force and viscous contact damping force. The non-direct contact forces include the forces associated with fine particles such as the van der

Table 1 Typical models for particle-fluid flow and their relative merits.

Model type				*Closure of equations*	*Incorporation of distribution effects of dispersed, solid phase*	*Computational effort*	*Suitability for engineering application in relation to process modeling and control*	*Suitability for fundamental research in relation to fluid physics*
Length scale for fluid phase	*Length scale for particle phase*	*Nature of coupling*	*Example*					
Sub-particle (discrete or continuum)	Particle (discrete)	Discrete +discrete or continuum +discrete	LB-DEM or DNS	Yes (but may experience numerical difficulty for systems with strong particle-particle interactions)	Yes	Extremely demanding	Extremely difficult	Most acceptable (**$\mathbf{f}_{pf}$** can be used for CCDM)
Pseudo-particle (discrete)	Particle (discrete)	Discrete +discrete	PP-DEM	No (difficulty to determine physical properties of a pseudo-particle)	Yes	Very demanding	Very difficult	Acceptable (but only valid for well defined PP system)
Computational cell (continuum)	Particle (discrete)	Continuum + discrete	CCDM or CFD-DEM	Yes	Yes	Demanding	Difficult	Acceptable
Computational cell (continuum)	Computational cell (continuum)	Continuum + continuum	TFM	No (constitutive relation for solid phase and phase interactions not generally available)	No	Acceptable	Easy	No

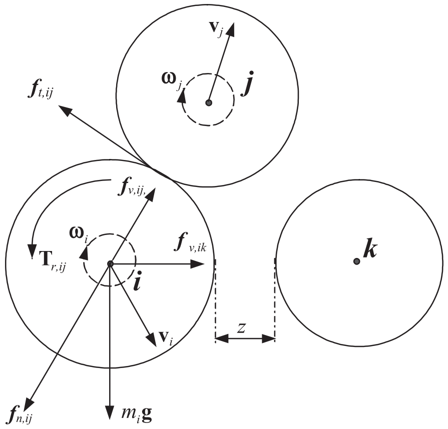

Fig. 1 Schematic illustration of the forces acting on particle *i* from contacting particle *j* and non-contacting particle *k* (Yang et al., 2000).

Table 2 Components of forces and torque acting on particle *i*.

Force or torque		*Symbol*	*Equation*
Normal forces	Contact	$\mathbf{f}_{cn,\ ij}$	$-\kappa_i\boldsymbol{\delta}_{c,\ ij}$
	Damping	$\mathbf{f}_{dn,\ ij}$	$-\eta_i v_{n,\ ij}$
Tangential forces	Contact	$\mathbf{f}_{ct,\ ij}$	$\min\left(\gamma_s f_{cn,ij},\ \kappa_i\boldsymbol{\delta}_{t,ij}\right)\frac{\boldsymbol{\delta}_{t,ij}}{\delta_{t,ij}}$
	Damping	$\mathbf{f}_{dt,\ ij}$	$-\eta_i\mathbf{v}_{t,\ ij}$
Torques	Interparticle	$\mathbf{T}_{c,\ ij}$	$\mathbf{R}_i\times(\mathbf{f}_{ct,\ ij}+\mathbf{f}_{dt,\ ij})$
	Rolling friction	$\mathbf{T}_{r,\ ij}$	$-\gamma_r R_i \mathbf{f}_{cn,ij}\ \hat{\boldsymbol{\omega}}_i$
Gravity force		$\mathbf{G}_i$	$m_i\mathbf{g}$
van der Waals force		$\mathbf{f}_{v,\ ij}$	$\frac{Hd}{6[\max(z,z_0)]^2}\frac{\mathbf{R}_i}{R_i}$
Fluid drag force		$\mathbf{f}_{pf,\ i}$	$0.5c_{d0,i}\rho_f\pi R_i^{\ 2}\varepsilon_i^2\lvert u_i-v_i\rvert(u_i-v_i)\varepsilon_i^{-(\chi+1)}$

where: $\boldsymbol{V}_{ij}=\boldsymbol{V}_j-\boldsymbol{V}_i+\boldsymbol{\omega}_j\times\boldsymbol{R}_j-\boldsymbol{\omega}_i\times\boldsymbol{R}_i$, $\mathbf{V}_{n,ij}=(\mathbf{V}_{ij}\bullet\mathbf{n})\bullet\mathbf{n}$, $\mathbf{V}_{t,ij}=(\mathbf{V}_{ij}\times\mathbf{n})\times\mathbf{n}$, $\widehat{\boldsymbol{\omega}}_i=\frac{\boldsymbol{\omega}_i}{\omega_i}$, $\mathbf{n}=\frac{\mathbf{R}_i}{R_i}$, $\chi=3.7-0.65\exp\left[-\frac{\left(1.5-\log_{10}Re_{p,i}\right)^2}{2}\right]$,
$c_{d0,i}=\left(0.63+\frac{4.8}{Re_{p,i}^{0.5}}\right)^2$, $Re_{p,i}=\frac{2\rho_f R_i\varepsilon_i\lvert\boldsymbol{u}_i-\boldsymbol{v}_i\rvert}{\mu_f}$

Waals force, electrostatic force, capillary and viscous forces, and solid bonding forces (Israelachvili, 1991; Sun et al., 2013). Particle-fluid interactions include buoyancy, drag force, and so on (Crowe et al., 1998; Rong et al., 2014; Wu et al., 2021; Zhou et al., 2010). These forces have been implemented by various investigators in various ways. To date, the equations to determine some of the forces are not fully developed. Therefore, to develop a more comprehensive theory and experimental techniques to quantify the interaction forces between particles and between particle and fluid under various conditions will continue to be an active research area for years to come. Table 2 lists the equations employed to calculate the forces and torques for the particle systems considered in this chapter; they are also commonly used in the literature (Xu and Yu, 1997; Zhou et al., 1999; Yang et al., 2000; Zhu et al., 2007; Rong et al., 2014; Wu et al., 2021; Zhou et al., 2010).

Numerical solution and boundary treatments

Eqs. (1) and (2) for solid flow can be solved by an explicit time integration method and Eqs. (3) and (4) for fluid flow by use of a standard CFD algorithm, facilitated with suitable boundary conditions. For the fluid phase, the no-slip boundary condition often applies to bed walls, together with other (inlet or outlet) conditions specified. For the particle phase, the interparticle force models are also applied to the interaction between a particle and a wall, with the corresponding wall properties used; however, the wall is assumed to be so rigid that no displacement and movement of the wall result from this interaction. Depending on the geometry and flow conditions, periodic boundary conditions can be implemented to reduce the computational effort. If fluid flow is negligible, simulations can be conducted without the need for solving Eqs. (3) and (4).

The modeling of the solid flow by DEM is at the individual particle level, while the gas flow by CFD is at the computational cell level. As shown in Fig. 2, their coupling is numerically achieved as follows. At each time step, DEM will give information, such as the positions and velocities of individual particles, for the evaluation of porosity and volumetric fluid drag force in a computational cell. CFD will then use these data to determine the gas flow field which then yields the fluid drag forces acting on individual particles. Incorporation of the resulting forces into DEM will produce information about the motion of individual particles for the next time step. The fluid drag force acting on individual particles will react on the fluid phase from the particles, so that Newton's third law of motion is satisfied (Xu and Yu, 1997; Zhu et al., 2007; Zhou et al., 2010).

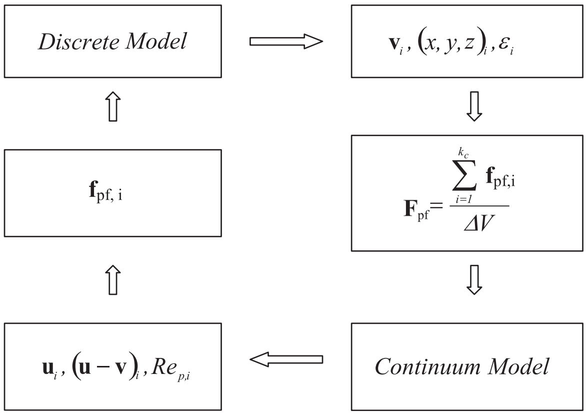
Discrete Model
$\mathbf{v}_i, (x,y,z)_i, \varepsilon_i$
$\mathbf{f}_{pf,i}$
$\mathbf{F}_{pf} = \frac{\sum_{i=1}^{k_c} \mathbf{f}_{pf,i}}{\Delta V}$
$\mathbf{u}_i, (\mathbf{u}-\mathbf{v})_i, Re_{p,i}$
Continuum Model

Fig. 2 Coupling and information exchange between continuum and discrete models (Xu and Yu, 1997).

Model validity and application

Particle packing

Random packing of particles, as a core research area in particle science and technology, is fundamental to many operations in powder processing and is useful in modeling some physical systems. Its formation is a dynamic process involving various interparticle forces as discussed above. Therefore, a successful simulation method must take into account all dynamic factors related to both geometry and force. Most of the previous methods only consider the former and ignore the latter, and hence fail to generate realistic packing structures, particularly when forces rather than the gravity are dominant. DEM-based simulation offers a promising way to overcome this difficulty (Yang et al., 2000; Yu et al., 2006; Zhu et al., 2007; Tian et al., 2014).

Simulation conditions can vary to represent different packing processes, e.g., the spherical growth of a packing under a centripetal force like that used in isotropic compression or the vertical growth under gravity and other forces. Treatment such as vibration or compaction can also be implemented in a simulation. Here we only consider packing with vertical growth, which is typically conducted as follows. First, particles are randomly generated without overlap in a cylindrical or rectangular container. Then, the particles are allowed to settle down under the gravity and other forces. This dynamic process proceeds until all particles reach stable positions with an essentially zero velocity as a result of the damping effect for energy dissipation. This packing process is equivalent to a physical operation to transform a gas-fluidized bed to a fixed bed by stopping gas supply. Periodical boundary conditions can be applied to avoid the effect of side walls. Table 3 lists the parameters normally used to simulate the packing of glass beads. Note that Young's modulus is smaller than the real one in order to reduce the computational effort.

The validity of the simulation technique can be assessed at both macroscopic and microscopic levels. Fig. 3 shows the relationship between porosity and particle size for mono-sized spheres. The good agreement between the measured and simulated results confirms macroscopically the validity of the DEM and the important role of the van der Waals force in governing the behavior of fine spheres ranging from 1 to 100 μm (Yang et al., 2000). The split second peak in the radial distribution function has been recognized as a key feature for coarse spheres with negligible effect of the van der Waals force. For years, many investigators have struggled to reproduce this feature by computer simulation. As shown in Fig. 4, it can be readily generated with the present simulation technique. The results also show that radial distribution function varies with particle size or porosity. Coordination number is a more sensitive parameter in characterizing the packing structure. Fig. 5 shows the simulated coordination number distributions for a particle mixture are quantitatively comparable to those measured, confirming the validity of the DEM approach from the viewpoint of microstructure.

Table 3 Parameters for glass beads.

Parameter	*Symbol*	*Base value*
Particle density	ρ_p	2.5×10^3 kg m^{-3}
Young's modulus	Y	1.0×10^7 N m^{-2}
Poisson's ratio	$\tilde{\sigma}$	0.29
Sliding friction coefficient	γ_s	0.3
Rolling friction coefficient	γ_r	0.005
Normal damping coefficient	η_i	2×10^{-5} s^{-1}
Hamaker constant	H	6.5×10^{-20} N m
Minimum separation	z_0	1×10^{-20} m

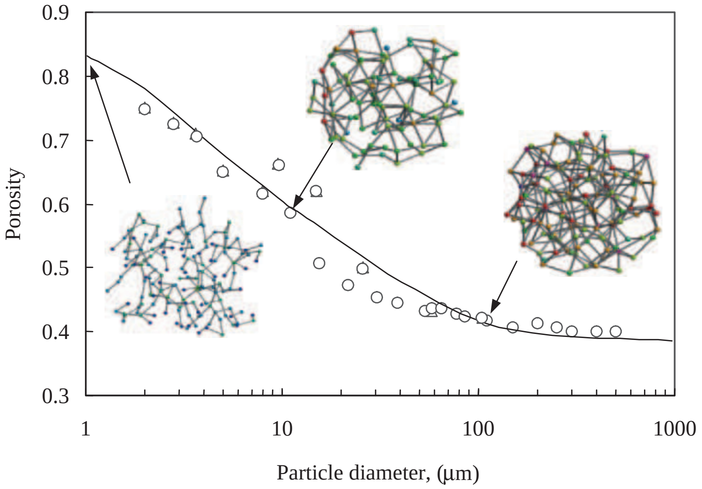

Fig. 3 Porosity vs particle size for glass beads: points, measured; line, simulated; and insets, packing structures taken from spherical samples for different sized spheres (Yang et al., 2000).

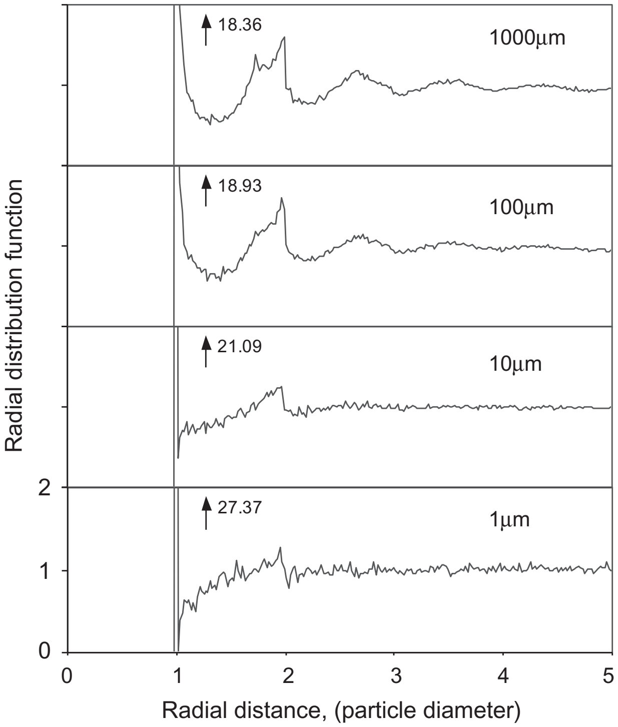

Fig. 4 The radial distribution function for packings of different sized particles, with the number showing the value of the first peak (Yang et al., 2000).

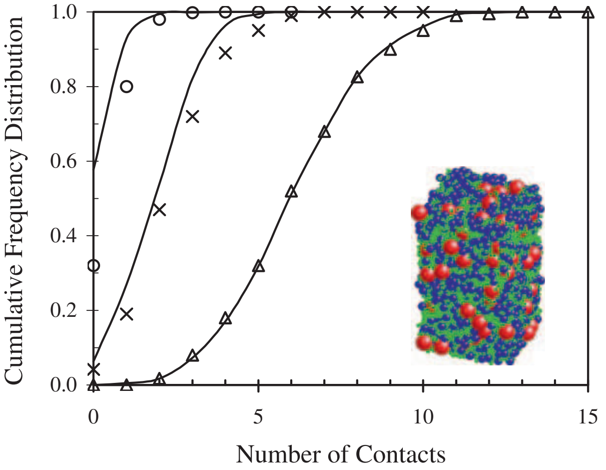

Fig. 5 Distribution of coordination numbers for the packing of a ternary mixtures of spheres (inset) when the size ratios are 4:2:1 and the volume fractions are 0.25, 0.50 and 0.25 for large (red), medium (purple) and small (green) components: o, measured contacts between medium and large components; x, measured contacts between medium and medium components; △, measured contacts between medium and small components; lines, simulated (Yi et al., 2011).

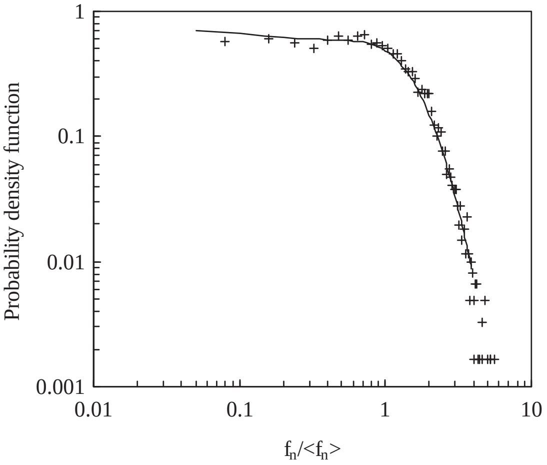

Fig. 6 Frequency probability distribution of normalized normal contact forces between particles for the packing of 1 mm spheres: +, simulated; —, measured (Yang et al., 2000).

Further comparison can be made in terms of interparticle forces. There is a good agreement between the simulated and measured distributions of normal contact forces between particles for a packing formed under gravity (Fig. 6). This demonstrates the capability of the DEM in generating quantitative force information which is difficult, if not impossible, to obtain with the current experimental technique.

The validated DEM model offers a convenient way to carry out controlled numerical experiments to study the packing of particles under various conditions. For example, it has been used to quantify the effects of material properties such as sliding and rolling friction coefficients related to the surface forces, Hamaker constant and particle density related to the body forces acting on a particle, as shown in Fig. 7. Correlations between macroscopic and microscopic or structural variables such as porosity, radial distribution function and coordination number can be established based on DEM simulations. An important finding from this type

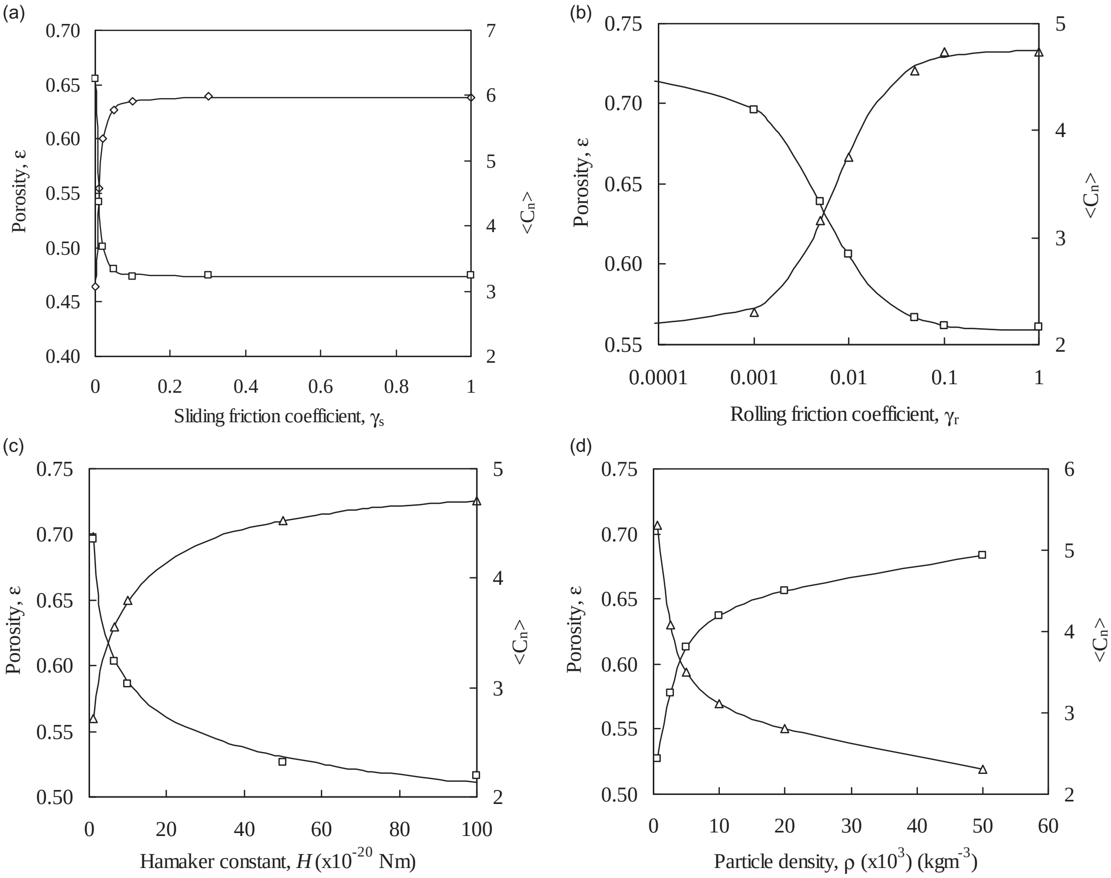

Fig. 7 The effect of material properties on porosity (-△-) and mean coordination number (-□-): (a), sliding friction coefficient; (b), rolling friction coefficient; (c), Hamaker constant; and (d), particle density (Yang et al., 2000).

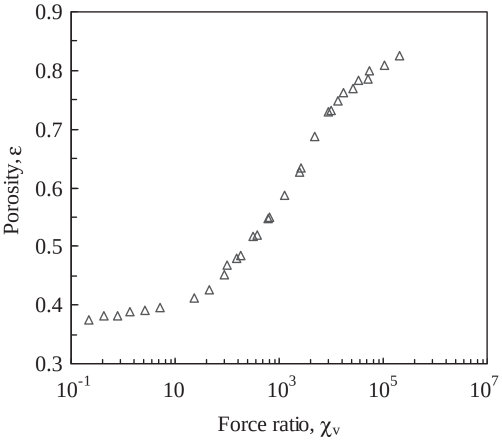

Fig. 8 The relationship between porosity and force ratio for glass beads, where $\chi_v = \frac{1}{N}|\sum_j \mathbf{F}_{v,ij}/m_i g|$ (Yang et al., 2000).

of studies is that macroscopic properties, e.g., porosity, can be described as a function of interparticle forces, i.e., the force ratio between the average van der Waals force and gravity force on a particle, as shown in Fig. 8. This relationship, as a state of equation, can be generalized in terms of cohesive force relative to effective gravity force, although further work is necessary to understand its dependence on variables related to surface forces.

Structural analysis is key to elucidating the packing mechanisms and the underlying physics. Realistic simulation of particle packing is crucial to such analysis. In fact, the resulting structural information can be directly used to study the structural properties of porous media, including, for example, permeability related to pore-to-pore connectivity and effective thermal conductivity related to particle-to-particle connectivity. DEM-based microstructural study will play a key role to quantify the governing mechanisms and generate reliable predictive methods for engineering application (Tian et al., 2014).

Particle flow in a horizontal rotating drum

Rotating drums are widely used in various industries for various purposes. A comprehensive understanding of the flow of particles in a drum under different conditions is essential for process control and optimization. It is also very much related to the physics of granular matter, e.g., particle avalanche in relation to heap formation or transition between fluid-like and solid-like modes. This example illustrates how such a process can be simulated and analyzed (Zhou et al., 1999; Zhu et al., 2007; Gan et al., 2020).

We have simulated the flow of glass beads in a horizontal drum of diameter 100 mm and thickness 16 mm (Yang et al., 2000). The drum is 35% filled with spheres of diameter 3 mm and rotates at various pre-set speeds. Periodic conditions apply axially to reduce the number of particles used; the analysis is for simplicity two-dimensional, achieved by averaging the data along the axial direction. Depending on the rotation speed, different flow regimes have been identified; but the cases considered here are in the so-called rolling regime that is commonly used in practice. The flow of particles in this regime has been well documented in the literature. Driven by the rotating drum, particles participate in collective solid rotation, reaching the filling surface inclined at an angle of repose from the rotating bulk at the bottom, pouring down this surface and getting mixed at the same time and then being re-trapped into the rotating bulk. This is indeed what is observed in the simulation, as shown in Fig. 9.

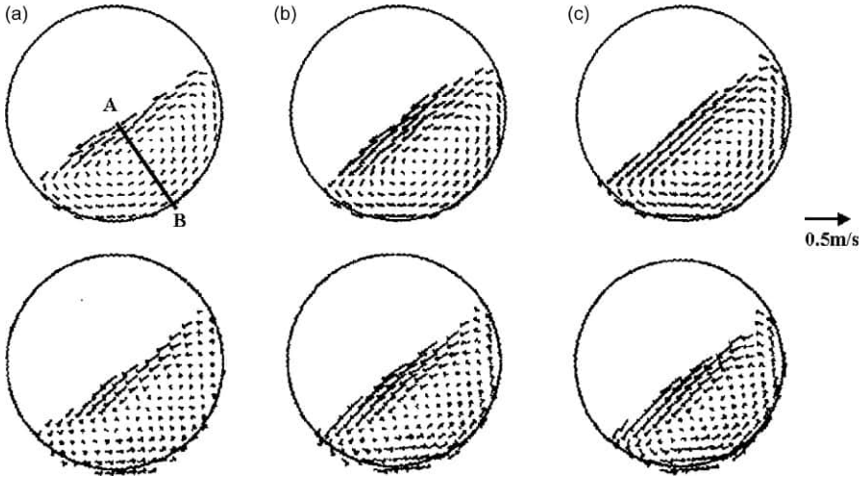

Fig. 9 Velocity fields in a plane section taken from DEM simulation (top) and PEPT experiment (bottom) at rotation speeds of: (a), 20 rpm; (b), 42 rpm; and (c), 65 rpm (Yang et al., 2003).

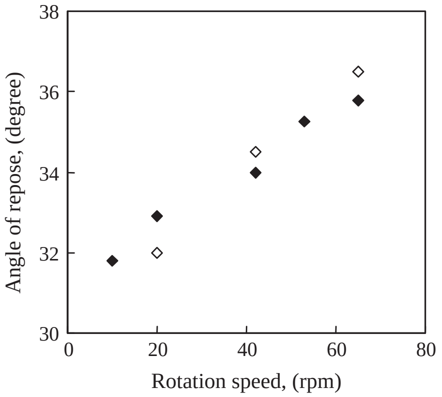

Fig. 10 Dynamic angle of repose as a function of rotation speed: ◇, PEPT measurement; □, DEM simulation (Yang et al., 2003).

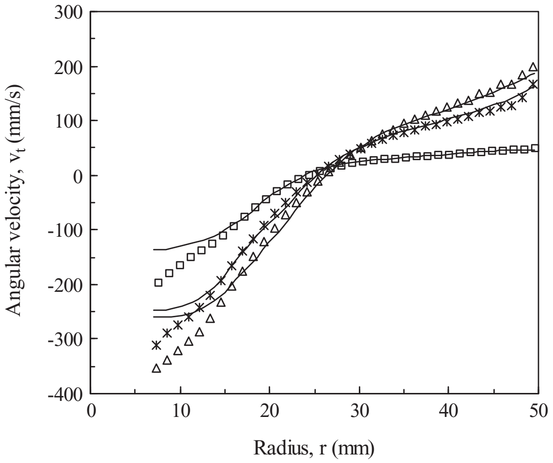

Fig. 11 Angular velocity along the radius perpendicular to the flowing surface at rotation speeds of: □, 20 rpm; ⁎, 42 rpm; and △, 65 rpm. Points are the PEPT measurements, and solid lines are the simulated results (Yang et al., 2003).

The validity of the simulation technique can be assessed by directly comparing the simulated and measured results. It is very useful to do so at a particle scale. One of the experimental techniques to produce such data is the so-called Positron Emission Particle Tracking (PEPT) (Zhou et al., 2004; Zhu et al., 2007). Fig. 10 shows the dependence of the dynamic angle of repose on rotation speed. The agreement between the DEM simulation and PEPT measurement is good, both indicating the angle increases linearly with the speed of rotation for the range considered.

Fig. 9 also shows the flow patterns produced by the DEM are comparable to those generated by PEPT at different rotation speeds. To be more quantitative, Fig. 11 plots the angular velocity along the radius perpendicular to the flowing surface, i.e., line $\overline{AB}$ AB in Fig. 9. Obviously, the agreement between the simulation and experiment is good. Satisfactory agreement between DEM and PEPT can also be observed for other processes such as bladed mixer and gas fluidization. It is noticed that the simulated velocity near the flow surface is higher than the PEPT velocity. This difference is mainly because the DEM simulation may not fully represent the PEPT experimental conditions, for example, the wall properties are simply assumed to be the same as those of particles in the DEM simulation. The selection of parameters for simulation is important to generate results matching physical experiment. The different sampling methods used in the simulation and experiment may also contribute to this observed discrepancy. Unlike the PEPT which determines the velocity field using the trajectory data of a single particle, the velocity field obtained from the DEM simulation is the average of the instantaneous velocities of all particles in the system.

The dynamics of particle flow includes at least three aspects: velocity, structure and force. Previous studies have to be largely limited to velocity field because of the difficulty in obtaining information for the other two. Consequently, there have been problems in probing the underlying mechanics and solving practical problems reliably. DEM is an effective technique that can overcome this problem. Its results can be readily used to establish the spatial and statistical distributions of important variables related to flow and force structures such as porosity, coordination number and various forces acting on particles. These variables can be treated as local average variables. As an example, Fig. 12 shows some typical results when the rotation speed is 42 rpm.

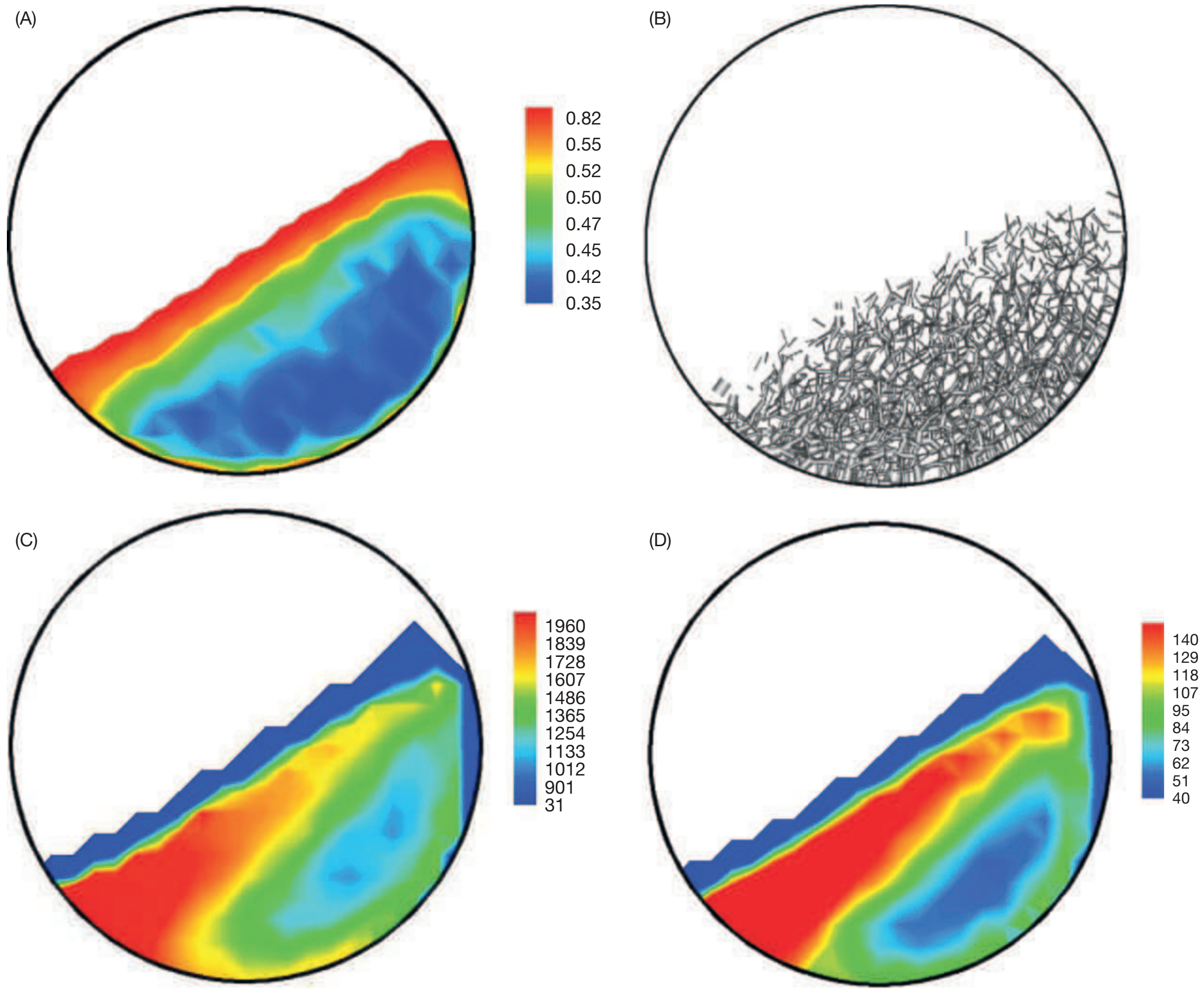

Fig. 12 Spatial distribution of: (a), porosity; (b), (snapshot) force network, total force (mg); (c), collision velocity (ms^{-1}); and (d), collision frequency (s^{-1}) when the rotation speed is 42 rpm (Yang et al., 2003).

Non-uniformity is obvious. For example, the bottom part, i.e., the rotating solid bed, has a lower porosity while the top part, i.e., flow layer, has a higher porosity (Fig. 12a). The normal contact force is important as other contact forces (e.g., tangential contact force) are directly related to it. Fig. 12b shows the force network in terms of this force, where each stick represents one connection between two particles with its thickness representing the magnitude of the force. As expected, large forces occur to particles at the bottom wall region to provide supports to the top particles. However, relatively large forces can also be found at the lower joint region between flow layer and rotating solid bed where particles of high velocity pouring down the bed surface impact the particles of low velocity waiting to start the bed rotation movement. Particles at the top have minimum contact forces. Notably, the force network actually also represents the flow structure of particles.

Understanding the interactions among particles is important for such a dynamic system (Zhou et al., 2004; Zhu et al., 2007). For example, the size enlargement or reduction process depends on two important factors: the effectiveness of a collision and the frequency of collisions between particles. The effectiveness is mainly related to the so-called initial kinetic energy or impact energy which is proportional to the square of the relative collision velocity between two particles v_{ij} $(=|\mathbf{v}_i - \mathbf{v}_j|)$. Fig. 12c shows the spatial distribution of relative collision velocity. It demonstrates the most vigorous interaction between particles is at the lower joint point between flow layer and rotation solid bed. It then propagates into the bed mainly along the shear band between the flow layer and rotation solid bed. As shown in Fig. 12d, the spatial distribution of collision frequency has a similar pattern. A region of high relative collision velocity corresponds to a region of high collision frequency, or vice versa. Note that the concept of collision differs from that of contact between particles. The contact or coordination number is determined by "freezing" the bed. In contrast, particle collision is a dynamic process and a collision must be from two non-contacting particles. Fig. 12d is obtained when two particles come to contact from a gap of at least 1% of particle diameter.

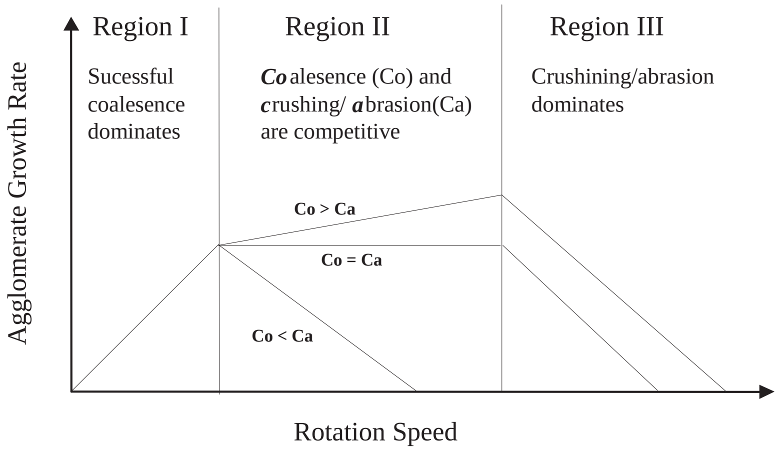
Region I
Region II
Region III
Sucessful coalesence dominates
Coalesence (Co) and crushing/ abrasion(Ca) are competitive
Crushining/abrasion dominates
Co > Ca
Co = Ca
Co < Ca
Agglomerate Growth Rate
Rotation Speed

Fig. 13 Schematic illustration of the effect of rotation speed on the growth kinetics of agglomerate size (Yang et al., 2003).

The resulting information can be used to understand the performance of industrial operations. We here take particle size enlargement by agglomeration as an example. Increasing rotation speed can increase the impact energy per collision and the collision frequency, giving two opposite effects on agglomeration in a drum. The increased kinetic energy will promote the breakage, crushing and abrasion of agglomerates, decreasing the growth rate. On the other hand, the increased collision frequency means more contacts or coalescences among particles within a given time period, leading to an increased growth rate. Consequently, as schematically shown in Fig. 13, depending on the rotation speed and operational conditions, various growth kinetics can result from the two opposite effects.

Gas fluidization of cohesive powders

It has long been recognized in practice that powders show four distinct behaviors, i.e., cohesive, aeratable, sand-like and spoutable, when fluidized. Theoretically, these behaviors must be related to particle-particle and particle-fluid interactions (Xu and Yu, 1997; Zhu et al., 2007; Zhou et al., 2009; Hou et al., 2012; Gan et al., 2016; Chen et al., 2012). Through controlled numerical experiments, the role of various interparticle forces can be examined. The simulations are carried out in a rectangular packed bed. Gas is then introduced uniformly at the bottom of the bed at a specified velocity to start a coupled gas-solid flow. Table 4 lists the physical parameters used in this work. Different from the above two examples, it is assumed that $\gamma_r = \sqrt{\mathrm{R}_i^2 - \left(\mathrm{R}_i - 0.5\delta_{ij}\right)^2}/\mathrm{R}_i$.

Fig. 14 summarizes the gas and solid flow patterns in the sequence of increasing gas velocity, with particles colored in a layered pattern according to their initial positions in the bed to demonstrate the particle rearrangement and mixing. Three states can be seen in this figure: fixed bed, expanded bed and fluidized bed. In the fixed bed, there is no observable structural change in the bed. Gas simply flows through interstices among stationary particles. In the expanded bed, cavities or large pores of different sizes and orientations are formed. Generally speaking, the cavities show an elongated shape and are predominantly horizontal. The expanded bed terminates at the so-called minimum bubbling velocity which is about 0.028 m/s from the simulation. In the fluidized bed, sustainable bubbles appear in the bed. The predicted trends are qualitatively in good agreement with those observed.

The analysis of the forces acting on individual particles is important to understand the phenomena observed. This can be demonstrated in the analysis of the origin of bed expansion. Fig. 15 shows the variation of the overall averaged contact force, the van der Waals force and fluid drag force relative to particle gravity during the transition from a fixed bed to an expanded bed when $u = 0.024$ m/s. Three stages, i.e., startup, transient and stable, can be identified in this figure. In the startup stage, both the contact and van der Waals forces increase sharply within a short time. The two forces reach their maximum and then the contact force fluctuates at this level while the van der Waals force decreases. In the transient stage, the fluctuation in contact force is attenuated and the van der Waals force starts to increase. In the stable stage, the contact force and van der Waals force balance each other. The fluid drag force is virtually maintained at a value just balancing the weight of the bed during all three stages, a fact that highlights the

Table 4 Parameters used for the present simulation.

Solid phase		*Gas phase*	
Particle shape	*Spherical*	*Type of gas*	*Air*
Number of particles, N	45,000	Viscosity, μ_f	1.8×10^{-5} kgm^{-1} s^{-1}
Particle diameter, d	1.0×10^{-4} m	Density, ρ_f	1.205 kgm^{-3}
Particle density, ρ_p	1440 kgm^{-3}	Bed width	2.5×10^{-2} m
Spring constant, κ	50 Nm^{-1}	Bed height	4.5×10^{-2} m
Sliding friction coefficient, γ_s	0.3	Bed thickness	1.0×10^{-4} m
Contact damping coefficient, η	1.65×10^{-5} kgs^{-1}	Cell width	1.0×10^{-3} m
Hamaker constant, H	2.10×10^{-20} Nm	Cell height	1.0×10^{-3} m

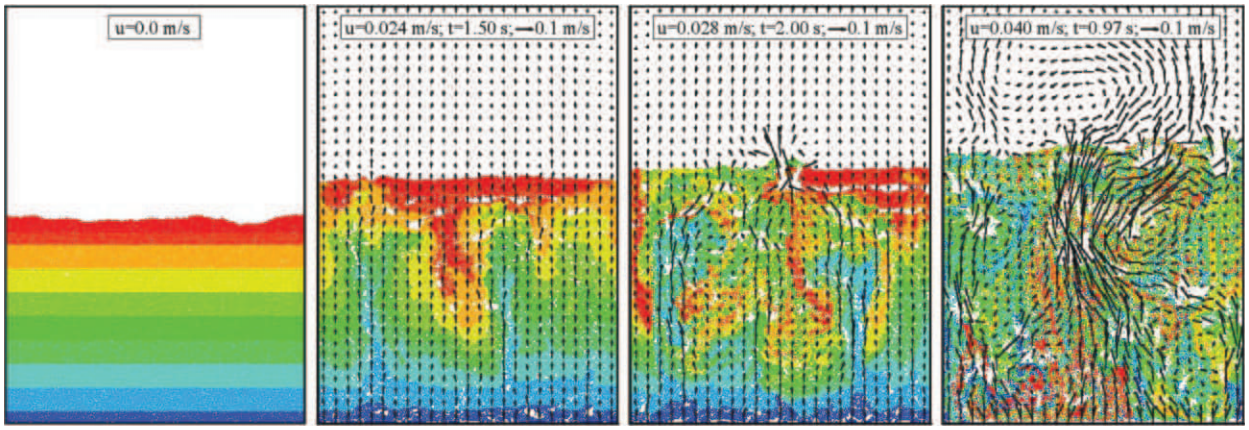

Fig. 14 Particle configurations and gas flow fields for different superficial gas velocities, showing the existence of fixed ($u = 0.0\ \mathrm{ms}^{-1}$), expanded ($u = 0.024\ \mathrm{ms}^{-1}$) and fluidized beds ($u \geq 0.028\ \mathrm{ms}^{-1}$) (Yu and Xu, 2003).

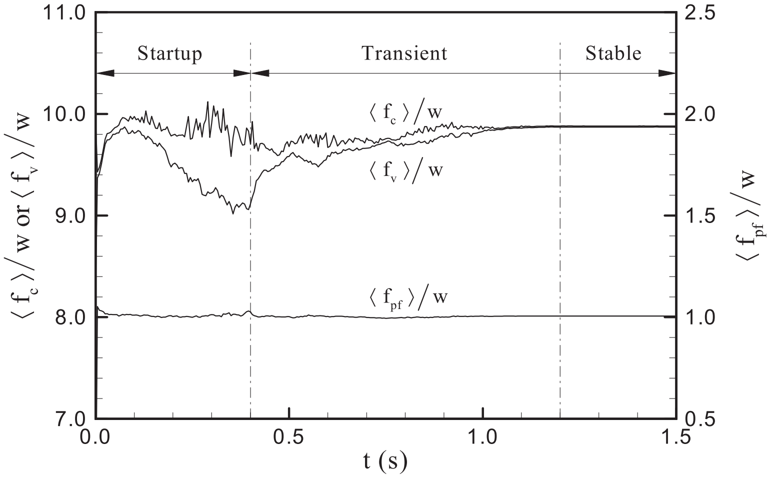

Fig. 15 Variation of dimensionless ensemble-averaged contact force, van der Waals force and fluid drag force with time when $u = 0.024\ \mathrm{ms}^{-1}$.

rapid response from the solid phase, by changing its porosity, to the fluid drag force induced by gas flow. Clearly, the contact force must be balanced by the van der Waals force to form a stable expanded bed. Further analysis of the spatial distributions of the two forces indicates that the balance between them is observed not only at a bulk average scale but also at an individual particle scale, as shown in Fig. 16. If the van der Waals force is unable to balance the contact force after initial disruption of the fixed bed, instability and then fluidization result.

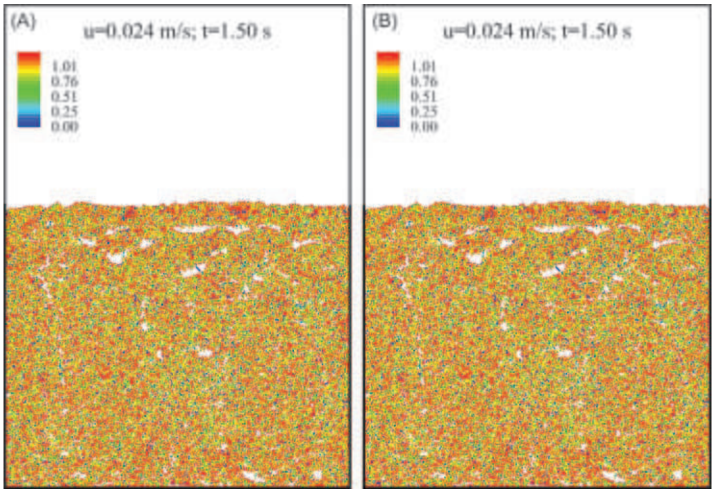

Fig. 16 Spatial distribution of the magnitudes of: (a), contact force; (b), van der Waals force acting on individual particles in an expanded bed when $u = 0.024\ \mathrm{ms}^{-1}$. The forces relative to the gravity of a particle are shown in a logarithm scale (Yu and Xu, 2003).

Fig. 17 shows the sequences of gas-solid flow patterns when increasing magnitude of the van der Waals force, where the change of the van der Waals force is achieved by adjusting the Hamaker constant. Three regimes of fluidization can be identified from this figure: good fluidization, quasi-fluidization and defluidization. When the ratio of the maximum van der Waals force (determined when $z = z_0$) to particle gravity is less than about 30, good fluidization is obtained with continuous bubbles of relatively small sizes rising through the bed. When the force ratio is in the range of about 40 to 100, the fluidization quality deteriorates significantly and severe channeling occurs although the bed is still fluidizable at higher gas velocities. When the force ratio is greater than about 300, the fluidization is impossible by normal means. The simulation well reproduces the phenomena experimentally observed, leading to the quantification of the roles of various particle-particle and particle-fluid interaction forces for this gas-solid flow system (Hou et al., 2012). This approach has been extended to more complicated particle-fluid flow systems including, for example, heat and mass transfer coupled with chemical reactions, and non-spherical particles such as ellipsoids (Gan et al., 2016; Zhou et al., 2011; Kuang et al., 2018, 2020).

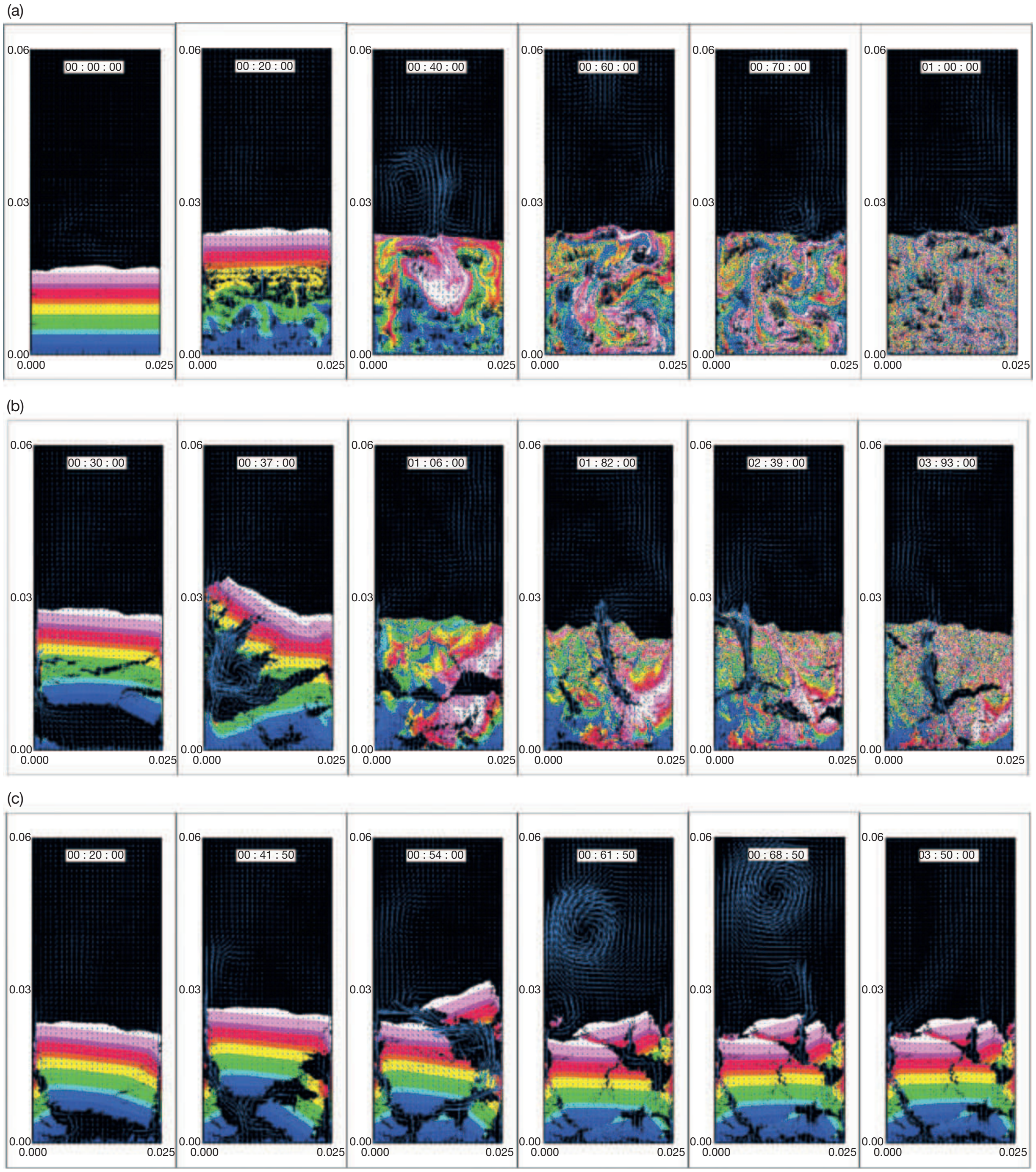

Fig. 17 Gas-solid flow patterns when the ratio of superficial gas velocity to minimum fluidization velocity is 4.8 and the ratio of van der Waals force to particle weight is (a) 10, (b) 70, and (c) 300. The particles are colored according to their initial heights in the bed to visualize the solid mixing (Yu and Xu, 2003).

Conclusion

The bulk behavior of granular materials depends on the collective interactions among individual particles. Particle scale modeling and analysis are therefore key to elucidating the underlying physics and linking fundamental to applied research, particularly in developing from know-how to know-why knowledge. The examples discussed in this article clearly demonstrate that discrete particle simulation, although not perfect at this stage of development, does capture the main features and is an effective way to achieve this goal. With the rapid development of computer technology, it offers a cost-effective way to meet the challenge of understanding the ever-changing particle science and technology resulting from the continuing development of new processes and products. Indeed, we have seen this development in the past two decades or so, leading to various breakthroughs or new developments in simulation and modeling of particulate systems. For example, facilitated with suitable constitutive relations, granular flows in different flow regimes can be simulated now (Zheng and Yu, 2017; Zheng et al., 2019).

References

Bideau D and Hansen A (eds.) (1993) *Disorder and Granular Media*. North-Holland: Elsevier Science.

Chen J, Chu KW, Zou RP, Yu AB, and Vince A (2012) Prediction of the performance of dense medium cyclones in coal preparation. *Minerals Engineering* 31: 59–70.

Crowe CT, Sommerfield M, and Tsuji Y (1998) *Multiphase Flows With Droplets and Particles*. CRC Press.

Gan JQ, Zhou ZY, and Yu AB (2016) CFD–DEM modeling of gas fluidization of fine ellipsoidal particles. *AICHE Journal* 62: 62–77.

Gan JQ, Evans T, and Yu AB (2020) Application of GPU-DEM simulation on large-scale granular handling and processing in ironmaking related industries. *Powder Technology* 361: 258–273.

Gidaspow D (1994) *Multiphase Flow and Fluidization: Continuum and Kinetic Theory Descriptions*. Academic Press.

Herrmann HJ, Hovi JP, and Luding S (1997) *Physics of Dry Granular Media*. Kluwer Academic Publishers.

Hou QF, Zhou ZY, and Yu AB (2012) Micromechanical modeling and analysis of different flow regimes in gas fluidization. *Chemical Engineering Science* 84: 449–468.

Israelachvili JN (1991) *Intermolecular and Surface Forces*, 2nd ed. Academic Press.

Kuang SB, Li ZY, and Yu AB (2018) Review on modelling and simulation of blast furnace. *Steel Research International* 89: 1700071-1/25.

Kuang SB, Zhou MM, and Yu AB (2020) CFD-DEM modelling and simulation of pneumatic conveying—A review. *Powder Technology* 365: 186–207.

Mehta A (ed.) (1993) *Granular Matter: An Interdiscilinary Approach*. Springer-Verlag.

Oda M and Iwashita K (eds.) (1999) *Mechanics of Granular Materials*. A. A: Balkema Publishers.

Rong LW, Dong KJ, and Yu AB (2014) Lattice-Boltzmann simulation of fluid flow through packed beds of spheres: Effect of particle size distribution. *Chemical Engineering Science* 116: 508–523.

Seville JPK, Tüzün U, and Clift R (1997) *Processing of Particulate Solids*. Blackie Academic & Professional.

Sun WF, Zeng QH, Yu AB, and Kendall K (2013) Calculation of normal contact forces between silica nanospheres. *Langmuir* 29: 7825–7837.

Tian ZA, Dong KJ, and Yu AB (2014) Structural evolution in the packing of uniform spheres. *Physical Review E* 89: 032202.

Wu YL, Hou QF, Qi Z, and Yu AB (2021) Particle–pore scale modelling of particle–fluid flows. *Chemical Engineering Science* 235: 116500.

Xu BH and Yu AB (1997) Numerical simulation of the gas-solid flow in a fluidized bed by combining discrete particle method with computational fluid dynamics. *Chemical Engineering Science* 52: 2785–2809.

Yang RY, Zou RP, and Yu AB (2000) Computer simulation of the packing of fine particles. *Physical Review E* 62: 3900–3908.

Yang RY, Zou RP, and Yu AB (2003) Microdynamic analysis of the flow of particles in horizontal rotating drum. *Powder Technology* 130: 138–146.

Yi LY, Dong KJ, Zou RP, and Yu AB (2011) Coordination number of the packing of ternary mixtures of spheres: DEM simulations vs. measurements. *Industrial and Engineering Chemistry Research* 50: 8773–8785.

Yu AB and Xu BH (2003) Particle scale modelling of particle-fluid flow in fluidization. *Journal of Chemical Technology and Biotechnology* 78: 111–121.

Yu AB, An XZ, Zou RP, Yang RY, and Kendall K (2006) Self-assembly of particles for densest packing by mechanical vibration. *Physical Review Letters* 97: 265501.

Zheng QJ and Yu AB (2017) Why have continuum theories previously failed to describe sandpile formation? *Physical Review Letters* 113: 068001.

Zheng QJ, Bai L, Yang LYM, and Yu AB (2019) Continuum modeling of granular mixing in a rotating drum. *Industrial & Engineering Chemistry Research* 58: 19251–19262.

Zhou ZY, Pinson D, Zou RP, and Yu AB (2011) Discrete particle simulation of gas fluidization of ellipsoidal particles. *Chemical Engineering Science* 66: 6128–6145.

Zhou YC, Wright BD, Yang RY, Xu BH, and Yu AB (1999) Rolling friction in the dynamic simulation of sandpile formation. *Physica A* 269: 536–553.

Zhou YC, Yu AB, Stewart R, and Bridgwater J (2004) Microdynamic analysis of particle flow in a bladed mixer. *Chemical Engineering Science* 59: 1343–1364.

Zhou ZY, Yu AB, and Zulli P (2009) Particle scale study of heat transfer in packed and bubbling fluidized beds. *AICHE Journal* 55: 868–884.

Zhou ZY, Kuang SB, Chu KW, and Yu AB (2010) Discrete particle simulation of particle–fluid flow: Model formulations and their applicability. *Journal of Fluid Mechanics* 661: 482–510.

Zhu HP, Zhou ZY, Yang RY, and Yu AB (2007) Discrete particle simulation of particulate systems. *Chemical Engineering Science* 62: 3378–3396.

Molecular clusters

Naoki Haruta[a] **and Kimihisa Yamamoto**[b], [a]Fukui Institute for Fundamental Chemistry, Kyoto University, Kyoto, Japan; [b]Institute of Innovative Research, Tokyo Institute of Technology, Tokyo, Japan

© 2024 Elsevier Ltd. All rights reserved.

This is an update of R.A. Broglia, Molecular Clusters, Editor(s): Franco Bassani, Gerald L. Liedl, Peter Wyder, Encyclopedia of Condensed Matter Physics, Elsevier, 2005, Pages 443–453, ISBN 9780123694010, https://doi.org/10.1016/B0-12-369401-9/01150-5.

Introduction 694
Theoretical principles 695
Syntheses and characterizations 697
Applications 699
Conclusion 699
References 700

Abstract

Clusters are ultrasmall particles with about 1 nm size composed of a dozen atoms and show peculiar catalytic, optical, and magnetic activities. In contrast to bulks and nanoparticles, adding or eliminating only a single atom drastically changes a cluster's properties due to its amorphous structure and quantum size effects. Interestingly, some clusters called superatoms have atom-mimic electronic configurations and characteristics; thus, the periodic table of clusters has been proposed. Recent developments allow us to obtain clusters in the gas, liquid, and solid phases and use them as materials. Clusters will be new building blocks in future science.

Key points

- Recent developments allow obtaining clusters in the gas, liquid, and solid phases.
- The addition or elimination of only a single atom drastically changes a cluster's properties.
- Clusters called superatoms have atom-mimic properties and could be new building blocks.

Introduction

In materials science, bulk materials, including crystal and amorphous ones, have a long history. Metal, semiconducting, and dielectric bulks provide a foundation for most modern technology. After the 1990s, nanoparticles received much attention as a novel material instead of the bulks. Nanoparticles are much smaller particles than the bulks, whose size is only ~10 nm or ~10^2 nm. They exhibit extraordinary optical, magnetic, and catalytic properties due to their small size and high surface area; therefore, they are being put to industrial use. Recently, there has appeared the third material, i.e., sub-nano particles. Sub-nano means a particle size of about 1 nm (Fig. 1). Such ultrasmall particles contain only a dozen atoms. Because of the difficulty in precisely synthesizing them, they have not been considered materials. However, recent experimental developments enable us to obtain them in the liquid and solid phases, thereby telling us that they differ entirely from the bulk and nano ones.

Sub-nano particles have unexpectedly been known for a long time. After the 1980s, in the fields of molecular physics and physical chemistry, they have been called clusters. A carbon material shaped like a soccer ball, i.e., fullerene, which is composed of 60 carbon atoms, is a typical example of a cluster (Kroto et al., 1985). Synthesizing clusters is quite simple. Suppose one irradiates an intense laser beam onto a bulk metal in a vacuum. Metal atoms and molecules with high energies evaporate from the surface. Such metal gases spontaneously aggregate to form polyatomic particles called clusters. They can be ionized and mass-separated under an electric field. Many clusters with various sizes have thus been synthesized and analyzed. However, this method faces a problem; the amount obtained at one time is very low on most picogram scales. Clusters are, therefore, difficult to be utilized as materials.

Recently, there appeared breakthroughs in the synthesis methods for clusters. The chemical reduction methods for nanoparticles (Cushing et al., 2004) help synthesize clusters. In a solution, a reducing agent converts metal salts into bare metal atoms, which aggregate into larger particles. To avoid the undesirable formation of bulks or nanoparticles, some sophisticated techniques are needed; i.e., polymer protection (Tsunoyama et al., 2004, 2008; Tsunoyama and Tsukuda, 2009), ligand protection (Bartlett et al., 1978; Zhang et al., 2004; Schmid et al., 1981; Brust et al., 1994), etching (Shichibu et al., 2007), or dendrimer-templated synthesis

https://doi.org/10.1016/B978-0-323-90800-9.00235-3

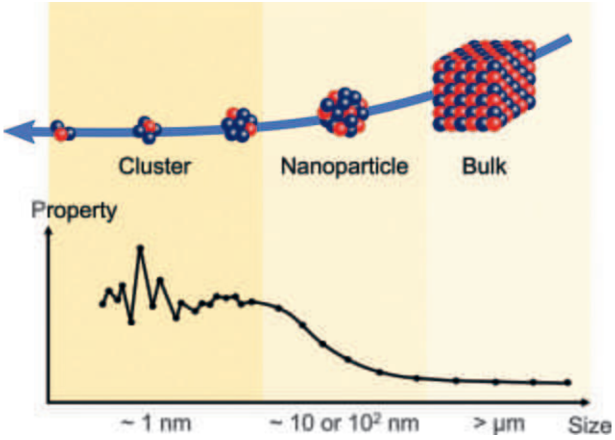

Fig. 1 Structural hierarchy in materials science.

(Zhao et al. (1998); Satoh et al., 2008; Yamamoto et al., 2009), as described later in detail. At the same time, size-separation techniques and conversions to the solid states are also being developed. These techniques enable us to obtain a cluster with a specific number of its constitutive atoms in the liquid and solid phases. With the help of these sophisticated methods, clusters can be used as materials.

With developing synthetic methods, many scientists have also studied applications of clusters (Liu and Corma, 2018). Since the discovery of the unexpected catalytic activity of nanoparticles by Haruta et al. (1987), it is well known that the nanoparticles' properties differ entirely from the bulks. Afterward, the difference between nanoparticles and clusters received much attention. Various properties of nanoparticles change smoothly as their size varies. For instance, the catalytic activity smoothly increases as the particle size decreases because the total surface area becomes more extensive. However, in the size range of clusters, the dependence of the catalytic activity on the size is zigzag (Imaoka et al., 2015), as shown in Fig. 1. Thus, their properties depend not on the diameter of the clusters but on the number of constitutive atoms. The bulk and nanoparticle favor close-packed structures in many cases, but clusters are intrinsically amorphous. For clusters, crystalline structures are unstable due to their large surface areas. As clusters become larger, i.e., with more than dozens of constitutive atoms, crystalline-like forms occasionally appear from the inside. The addition or elimination of only an atom, hence, drastically affects catalytic activity. This is a uniqueness of clusters. In other words, a cluster is considered an individual molecule that has long been challenging to find.

Remarkably, clusters offer a new science of superatoms instead the conventional science based on the elements. The superatom, meaning a specially stable cluster, is a novel, higher-order concept than an atom. It has electronic orbitals and an electronic configuration like an atom. Quantum mechanics can validate such an idea. For instance, a typical superatom, the Al_{13} cluster, resembles a chlorine atom (Bergeron et al., 2004). Due to its atom-mimic electronic configuration, a superatom has a chemical property like an atom and can be used as a building block for larger compounds. This is a modern kind of alchemy. Recent studies have shown that there could be a periodic table of clusters analogous to the periodic table of the elements (Tomalia and Khanna, 2016; Tsukamoto et al., 2019). While modern physics and chemistry are based on the elements, clusters could provide a foundation for future science.

In this article, we give the readers the theoretical and experimental essences of clusters. First, we look at the shell model describing the electronic states of clusters and explain their stability. In this context, we introduce the novel concept of the superatom and also the periodic table of clusters. We then review the experimental developments; i.e., various synthetic methods, separation techniques, characterizations, and applications. The reader can now overview the overall picture of clusters and their future perspectives.

Theoretical principles

In sub-nano science, the theoretical concept of superatoms appeared. First, let us look back on the conventional atom. This can be seen in an elementary quantum mechanics textbook, but it is essential and suggestive for considering the analogy of clusters and atoms. An atom is a positively charged massive nucleus surrounded by a cloud of negatively charged light electrons. The electronic states determine the materials' properties; i.e., stability, appearance, conductivity, magnetism, etc. Each one-electron state is called an orbital, especially an atomic orbital in this case. The orbital comes from the orbit, which is the traveling path of an astronomical object. Depending on the angular momenta, the shapes of the atomic orbitals are classified as s, p, d, f, ⋯; e.g., an s atomic orbital has a spherical shape, and p atomic orbitals have three dipolar shapes in the x, y, and z-directions. Different orbitals with the same energy are termed to be degenerate. The degrees of degeneracies are 1, 3, 5, 7, ⋯ for the s, p, d, f, ⋯ orbitals, respectively.

In general, different types of orbitals have different energy levels. The constitutive electrons of the atom occupy their atomic orbitals to minimize its total electronic energy based on the Pauli exclusion principle and Hund's rules. The former originates from the spin-statistics theorem and forbids the occupation of the same single orbital by more than two electrons. The latter comes from the potential exchange interaction and arranges the spins, which are magnetic dipoles intrinsic to electrons, as ferromagnetic as possible in the degenerate orbitals. For instance, a hydrogen atom has an electron partially occupying the 1s atomic orbital; a carbon atom has six electrons fully occupying the 1s and 2s atomic orbitals and partially occupying the 2p orbitals. Note that the 1s and 2s atomic orbitals are both s atomic orbitals, but their shapes in the radial direction are slightly different. How electrons occupy orbitals in an atom is called its electronic configuration, which is intrinsic to each atom.

Clusters also have electronic orbitals. A cluster is a molecule with multiple nuclei surrounded by electronic clouds composed of molecular orbitals. Interestingly, the molecular orbitals of clusters, especially highly-symmetrical clusters, have shapes just like the atomic orbitals. They are thus called superatomic orbitals (Fig. 2). Of course, superatomic orbitals are not localized at a single atom but delocalized over the cluster. A molecular orbital resembling an s atomic orbital is called an S superatomic orbital. This analogy can be understood based on the shell model (de Heer, 1993). The shell model originates from the electronic structure of an atom. Interestingly, it can also be used to describe the structure of an atomic nucleus in the field of nuclear physics. The shell model regards a cluster as the three-dimensional spherical potential with valence electrons and entirely ignores its detailed molecular structure. A potential that is easy to be analyzed is employed. For instance, the jellium model (the infinite/finite potential well), the harmonic potential, or their intermediates such as the Woods–Saxon potential. In any case, it is assumed that a cluster is spherical. This approximation is valid only for highly-symmetrical metal clusters. The electronic Schrödinger equation for this model can be solved and electronic orbitals can be obtained with their energy levels. The product of radial and spherical harmonic functions gives each superatomic orbital in the same manner as atomic orbitals.

As with atomic orbitals, the full occupation of superatomic orbitals by electrons is expected to result in stable closed shells. Recall the electronic configurations of noble gases. On the other hand, Hund's rules suggest that the arrangement of electronic spins in the degenerate orbitals could be ferromagnetic, leading to a high magnetism. Thus, in the case of clusters, their molecular properties can be understood and predicted in analogy to atoms. Furthermore, it is expected that there exists a cluster with nearly the same electronic configuration as an atom. The number of valence electrons necessary for the stable closed shell is termed the magic number. Here, core electrons are ignored. This simplification is valid since the core and valence orbitals can be separable in many cases. Many clusters satisfying the magic number requirement have been detected and characterized by gas-phase spectroscopic methods. A cluster with the atom-mimic electronic configuration is called a superatom. The same electronic configuration implies the analogy of various chemical properties. The most outstanding example is the aluminum cluster, Al_{13}, having an icosahedral symmetry. Indeed, Bergeron et al. (2004) reported that Al_{13} shows a chemical behavior resembling a halogen. Al_{13} had been synthesized on a picogram scale in the gas phase for fundamental research. Still, Kambe et al. (2017) succeeded in its synthesis on a large scale in the liquid phase. The molecular orbitals of this cluster are S, P, ⋯ superatomic orbitals, and a stable closed-shell structure is formed similar to that of a chlorine anion. Other examples have also been reported, including Au_{20} with a tetrahedral symmetry (Li et al., 2003).

Physicists and chemists have assembled various compounds using atoms, but from now on, they could use superatoms as building blocks for larger compounds. Qian et al. (2010) obtained a dimer of gold superatoms, which can be regarded as a higher-order molecule. Roy et al. (2013) obtained cocrystals of superatoms and fullerenes. The emergence of superatoms thus implies a new era of materials science. In 1869, Mendeleev proposed the periodic table of the elements. It has long been the foundation of the natural sciences and contributed to discovering many elements that obey the periodic rule. Thereafter, higher-order substances, including molecules, clusters, nanoparticles, and bulks, have received much attention. However, it still remains challenging to predict and design such higher-order substances. As with Mendeleev's periodic table, such a periodic table for higher-order substances would be valuable. Tomalia and Khanna (2016) pointed out the possibility of nano-periodicity in higher-order substances typified by superatoms.

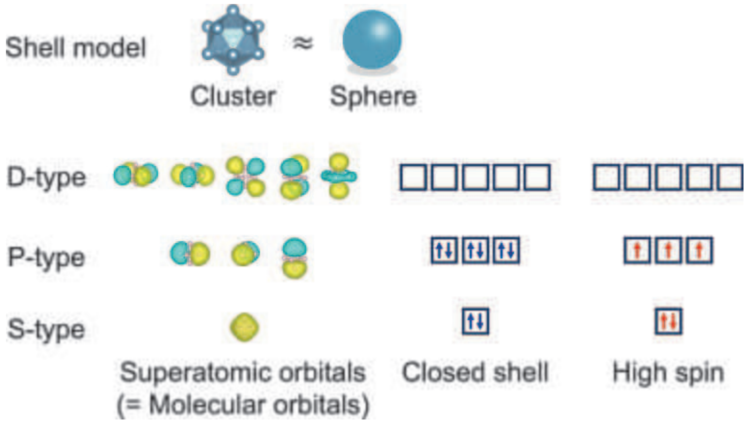

Fig. 2 The shell model and superatomic orbitals.

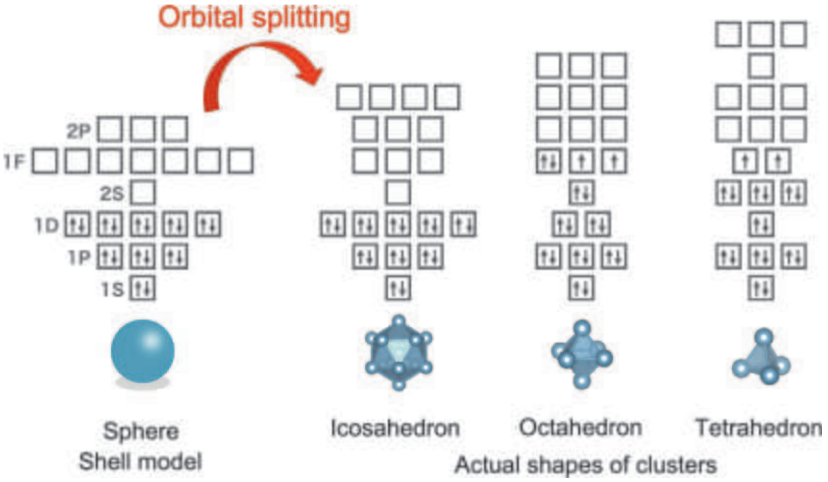

Fig. 3 The splitting of superatomic orbitals in actual shapes of clusters.

As described earlier, clusters have often been predicted based on the shell model which assumes that their structures have an approximately spherical symmetry. However, this spherical approximation is applicable especially for subglobular clusters like icosahedrons (Fig. 3). Indeed, the initially discovered superatom was the Al_{13} cluster with an icosahedral symmetry. A theoretical framework that describes a broader range of clusters is necessary to obtain a universal law. Though the shell model is a candidate for such a theory, most clusters are not quasi-spherical because the numbers of their constitutive atoms are inappropriate for constructing highly-symmetrical structures like icosahedrons. Even if they have icosahedral atomicities, many clusters exhibit a Jahn–Teller or pseudo-Jahn–Teller instability due to electronic reasons. The former states that the partial occupation of degenerate orbitals by electrons gives rise to spontaneous symmetry-breaking of the clusters' structures. The latter states that the pseudo-degeneracy, or near miss of energy, between occupied and unoccupied orbitals causes spontaneous symmetry-breaking of the clusters' structures.

Notice that exceptionally stable clusters with lower symmetries than icosahedrons have also been found, such as Au_{20} with a tetrahedral symmetry (Li et al., 2003). In such clusters, the validity of the shell model relatively decreases due to the split and shift of the superatomic orbital levels, implying that it is desirable to establish a more sophisticated method to find an abundance of stable clusters. To broaden the scope of the shell model, Tsukamoto et al. (2019) proposed the symmetry-adapted orbital model, which explicitly takes into account the level splittings of the electronic orbitals due to lower structural symmetries, as well as the number of valence electrons and the number of constitutive atoms. This model tells us there are different magic numbers for different cluster shapes. This refinement implies the possibility of an abundance of stable clusters with various shapes that obey a certain periodicity. The periodicity originates from the analogy of electronic configurations between superatoms and atoms. Consequently, all clusters with the same symmetry can be unified into a periodic framework analogous to the periodic table of the elements.

Syntheses and characterizations

In this section, we describe the experimental aspects. As stated in the Introduction, the cluster study starts in the gas phase. We here look at how to produce clusters in a laboratory. Laser ablation (Maruyama et al., 1990) and magnetron sputtering techniques (Xirouchaki and Palmer, 2004) are available. An intense laser or argon ion beam is irradiated onto a bulk metal in a vacuum. Metal atoms and molecules with high energies evaporate from the bulk surface. In the case of metals with low boiling points, heating can also cause evaporation (Baker et al., 2000). The vacuum chamber enables us to ignore collisions with background gases. Such metal gases spontaneously aggregate into clusters. However, various sizes of clusters are mixed at that time. For mass separation, the clusters should be ionized. Some ionization techniques have been developed; i.e., electron ionization (EI) (Jackschath et al., 1992) and photoionization (PI) (Letokhov, 1987). After ionization, applying an electric field accelerates ions, mass-separated clusters can be obtained by time-of-flight mass spectrometry (TOF-MS) or using a quadrupole mass analyzer (QMS) (Knight et al., 1986; Martin et al., 1991; Katakuse et al., 1985; Kim et al., 1994).

Mass separation can thus determine each cluster's mass, but its structure is yet unknown. The following techniques can estimate the structures of the clusters. One method is ultraviolet photoelectron spectroscopy (UPS) (Li et al., 2003; Lechtken et al., 2007; Huang et al., 2008, 2009; Häkkinen et al., 2003, 2004), which irradiates ultraviolet light into a cluster and detects the kinetic energy of the accompanying photoelectron. The energy difference between the incident light and photoelectron is the binding energy of the corresponding electron. The obtained spectrum reflects the density of states near the Fermi energy intrinsic to the cluster's structure. The structure reproducing the obtained spectrum can be found with the help of the first principles calculations. Photodissociation (PD) spectroscopy can also be used to estimate the structures of the clusters (Gilb et al., 2004). In this method, light is irradiated onto a cluster, and then its dissociated fragments, including atoms, are detected. If a cluster cannot be photo dissociated, one can use a messenger like a noble gas that is attached to the target cluster and dissociated after photoirradiation. The obtained spectrum can nearly be regarded as the photoabsorption spectrum intrinsic to the cluster's structure. As with photoelectron spectroscopy, comparison with theoretical calculations clarifies the cluster's structure. Also, gas chromatography (GC) is a vital tool for estimating a cluster's structure (Dugourd et al., 1997; Gilb et al., 2002). Under an electric field in a gas, the cluster moves along with a collision with gaseous atoms and molecules. The obtained ion mobility is related to the cluster's cross-section, reflecting its geometrical structure. Electron diffraction in an ion trap (TIED) can also be employed (Schooss et al., 2010; Xing et al., 2006). Comparing the diffraction patterns between experiments and calculations estimates the cluster's structure.

Recently, clusters in the gas phase can be captured onto solid surfaces. This capture is vital for characterization and applications because available analyses for gaseous clusters are limited. One method is to utilize the defects of metal oxide surfaces, which effectively form chemical bonds with clusters (Sanchez et al., 1999). In general, however, clusters fly rapidly (~keV) in the gas phase. The collision of clusters with solid surfaces destroys the clusters, violating the merit of in-advance mass separation. The clusters must be slow down before adsorption. For that purpose, Mitsui et al. (2006) introduced self-assembled monolayers on the surface as impact absorbers (soft-landing isolations).

We subsequently look at the syntheses in the liquid phase. Success in the liquid phase required more years of research than in the gas phase. The reason is the inevitable instability of clusters due to their high surface areas per molar amount, amorphous structures, and quantum size effects. In the conventional chemical reduction methods for nanoparticles (Cushing et al., 2004), metal salts are dissolved in a solution and a reducing agent is used, thus converting metal salts into bare metal atoms. The bare metal atoms quickly aggregate to form particles larger than clusters. The undesirable formation of bulks or nanoparticles must be avoided. For that purpose, various protection methods have been developed. One method uses polymers, including polyvinylpyrrolidone (PVP) (Tsunoyama et al., 2004, 2008; Tsunoyama and Tsukuda, 2009). For instance, gold clusters surrounded by a polymer can be separated in a solution. Another protection method is ligand protection. Organic ligands, including phosphine (Bartlett et al., 1978; Zhang et al., 2004; Schmid et al., 1981) and thiolate (Brust et al., 1994), can be introduced onto a cluster's surface. Some ligand-protected clusters can be crystallized.

Along with the ligand-protection method, an etching technique has also been developed (Shichibu et al., 2007). While mixing metal salts and reducing agents, an excessive amount of ligands are added to the solution. First, large clusters are formed and coordinated by some ligands. The clusters subsequently become smaller etched by ligands. Finally, only specific stable clusters with the magic number remain. Ligand protection methods can also synthesize Zintl ions; i.e., anionic clusters consisting of an alkali or alkaline earth metal and a post-transition metal or metalloid (Wilson et al., 2018). They are named after E. Zintl and have a more extended history than many other cluster compounds.

Liquid-phase syntheses are in the same situation as gas-phase syntheses. Since a mixture of clusters with various sizes is obtained when synthesized, size separation is indispensable. Size-exclusion chromatography (SEC) is a typical technique that transports clusters through the column packed with fine, porous beads (Murayama et al., 2004; Tsunoyama et al., 2007). The time for transporting depends on the clusters' sizes. Polyacrylamide gel electrophoresis (PAGE) is also used for size separation, in which cluster ions move in a gel under an electric field (Negishi et al., 2005; Tsunoyama et al., 2006). The measured electrophoretic mobility depends on the clusters' sizes and charges. Electrospray ionization mass spectrometry (ESI-MS) can be used for the same purpose (Negishi et al., 2005; Chaki et al., 2008). Applying an electric field allows a solution including clusters to be tiny charged droplets, then time-of-flight mass spectrometry enables us to separate them. Similarly, the matrix-assisted laser desorption/ionization (MALDI) technique embeds clusters into a laser-absorbing matrix and photoionizes the matrix (Tsunoyama et al., 2010).

In the ligand protection method, a single crystal of a cluster can be occasionally obtained. This is a fortunate case. If so, the single-crystal X-ray diffraction (SC-XRD) measurement gives direct information about the structure of a cluster (Heaven et al., 2008; Qian et al., 2010; Jadzinsky et al., 2007). If not, various techniques are usually combined to estimate the structure of a cluster. X-ray photoelectron spectroscopy (XPS) tells us the oxidation states of the constitutive atoms of the cluster (Inomata et al., 2018). It irradiates X-ray into a cluster and detects the kinetic energy of the accompanying photoelectron. The energy difference between the incident X-ray and photoelectron is the binding energy of the corresponding core electron, which is intrinsic to the atom's oxidation state. For a negatively-charged atom, the binding energy is lower. In contrast, the binding energy is higher for a positively-charged atom. The oxidation states of the constitutive atoms of the cluster can be determined by comparing them to the reference bulk samples whose atoms' oxidation states are already known. The extended X-ray absorption fine structures (EXAFS) analysis, which observes the scattering of photoelectrons by the adjacent atoms, estimates the coordination number around each constitutive atom (Yamazoe and Tsukuda, 2019). The high-resolution scanning transmission electron microscopy (HR-STEM) has been dramatically improved, and the number of its constitutive atoms can be visually counted (Imaoka et al., 2017). Energy-dispersive X-ray spectroscopy (EDS), though its resolution is not so high, tells us the elemental components of a cluster (Tsukamoto et al., 2018). This technique is essential for poly-elemental clusters.

Recently, there appeared a breakthrough in liquid-phase syntheses. This new method also utilizes the typical synthetic method for nanoparticles; i.e., the chemical reduction method (Cushing et al., 2004). The problem was that the obtained particles rapidly grow larger than the nanoscale ones. Zhao et al. (1998) proposed one idea to overcome this difficulty; they confined metal salts and reducing agents into small reaction fields in a solution. A typical reaction field is a dendrimer, a new type of polymer with many branches and specific molecular weight. If adsorption sites for metal salts are embedded into the dendrimer in advance, a certain amount of metal salts can be accumulated in a single dendrimer. By adding reducing agents, the metal salts form a cluster inside the dendrimer. Branches of the dendrimer prohibit the unfavorable aggregation of clusters.

Furthermore, Yamamoto et al. (2002) introduced a specially fine-tuned dendrimer, the phenylazomethine dendrimer (DPA), in which metal salts stepwise adsorb on its imine sites from the inner layers to the outer layers. Remarkably, the number of metal salts coordinated onto this dendrimer can be spectroscopically observed as the change in the isosbestic points. In this case, size separation of the clusters is unnecessary because the number of the constitutive atoms of a cluster is controlled at nearly one-atom precision when synthesized (Satoh et al., 2008; Yamamoto et al., 2009). With this sophisticated dendrimer-templated method, many clusters were successfully synthesized in a liquid (Kambe et al., 2017; Tsukamoto et al., 2018). Besides, the accumulation of different metal salts into the dendrimer even enables us to synthesize poly-elemental alloy clusters. Supporting the obtained clusters on substrates avoids aggregation and leads to various analyses and applications.

Applications

In the late 1980s, Haruta et al. (1987) showed that if inert gold bulk is made to be in a nanoscale, it provides a catalytic activity. This discovery is the beginning of nanoscience, and many physicists and chemists have studied nanoparticles. A typical example of a smaller particle than the bulks is a nanoparticle, while its extreme example is a cluster. One can easily imagine that clusters possess exceptional potential, including a catalytic activity. They have high surface areas, amorphous structures, and nontrivial quantum size effects. Indeed, many researchers reported their higher catalytic activity than the bulks and nanoparticles (Liu and Corma, 2018). That is, however, not all.

Imaoka et al. (2013) elucidated that the oxygen reduction catalytic activity discretely depends on the cluster's atomicity. The Pt_{12} and Pt_{13} clusters showed completely different catalytic activities. The oxygen reduction reaction was significantly enhanced when only one atom was removed from Pt_{13}. It was considered due to the contrast between the deformed coordination of Pt_{12} and the icosahedral coordination of Pt_{13}. In the sub-nano region, the addition or elimination of one atom drastically changes the catalytic activity. This discrete property is entirely different from the properties of the bulk and nano. Since the bulk and nano have many constitutive atoms, adding or eliminating one atom is not essential. In this context, each cluster can be considered an individual molecule with unique properties. Besides, poly-elemental clusters have more potential applications, including catalysis. Takahashi et al. (2017) reported that multimetallic clusters composed of copper, platinum, and gold with a specific composition ratio exhibit 24-times greater activity than that of a commercially available Pt catalyst for the aerobic oxidation of hydrocarbons. Such atom hybridization adds a new dimension to clusters (Tsukamoto et al., 2018).

In the case of ligand-protected clusters, there is the possibility that ligands prohibit catalytic reactions. This concern is natural because ligands are introduced to enhance the stability of clusters, in other words, to make them inert. However, some reports showed that ligand-protected clusters are still catalytically active. Thiolate-protected gold clusters, including $Au_{25}(SR)_{18}$ supported by titania or ceria, enhance selective hydrogenations (Zhu et al., 2010a), styrene's epoxidation (Zhu et al., 2010b), and carbon monoxide oxidation (Nie et al., 2012). These results are surprising because they are contrary to common sense that the catalytic activity of gold is lost by sulfur poisoning.

Grandjean et al. (2018) observed the bright luminescence of the hydrated Ag_4 cluster in zeolites. This luminescence is assigned to the electronic transition between superatomic orbitals. Some gold clusters with ligands including alkynyl (Wan et al., 2015) and N-heterocyclic carbenes (Narouz et al., 2019) also show a good luminescence. Fine-tuning the atomicity of clusters and the types of ligands could broaden the applications of clusters. The intense luminescence of gold clusters can also be observed when coordinated by dendrimers (Zheng et al., 2003, 2004), proteins (Xie et al., 2009), and tetraoctylammonium cations (Pyo et al., 2015). Wang et al. (2014) reported that doping silver atoms into gold clusters considerably enhances the luminescence of the gold clusters.

Using circular dichroism (CD) spectroscopy, which observes the absorption difference between left and right circularly polarized lights, the Cotton effect was observed for gold clusters protected by chiral ligands, including BINAP (Yanagimoto et al., 2006). The Cotton effect is the rapid change of circular dichroism in the absorption region and was named after A. Cotton. The observation of the Cotton effect implies that chiral information of the ligand is transferred into the cluster core. Furthermore, with the X-ray magnetic circular dichroism (XMCD), which observes the absorption difference between left and right circularly polarized X-rays under an external magnetic field, Negishi et al. (2006) investigated the magnetic moments of gold clusters protected by glutathione. They found that bonding at the gold/glutathione causes spin polarization of the gold clusters. The interaction of cluster cores and ligands is not totally clear, and its understanding and control could further broaden the potential use of clusters.

Recently, the cocrystallization of clusters with fullerene as well as the cocrystallization of different types of clusters were achieved (Roy et al., 2013; Pinkard et al., 2018; Doud et al., 2020). The success of synthesizing such new solid-state materials, called superatomic crystals, realized the emergence of novel collective properties; i.e. good electronic transport, thermal conductivity, and a magnetically ordered phase.

Conclusion

This article reviewed the history of a cluster, an ultrasmall particle on a sub-nano scale consisting of a dozen atoms. Its peculiar catalytic, optical, and magnetic characteristics are due to a high surface area, an amorphous structure, and quantum size effects. In the early stage, it could be synthesized only in the gas phase and could not be a material. Nowadays, it is the third material, an alternative to bulk and nano ones, due to the development of their liquid-phase syntheses and crystallization techniques.

Interestingly, some clusters have atom-mimic electronic configurations and chemical properties. Thus, they are called superatoms. The superatom is a higher-order concept than an atom. As with the conventional periodic table of the elements, a periodic table of superatoms has been proposed. Some superatoms have been synthesized in the liquid phase, and their cocrystals have also been obtained. Superatoms will be new building blocks in future science. Shortly, scientists could spread applications, including superatom-based devices, around the world.

References

Baker SH, Thornton SC, Edmonds KW, Maher MJ, Norris C, and Binns C (2000) The construction of a gas aggregation source for the preparation of size-selected nanoscale transition metal clusters. *The Review of Scientific Instruments* 71(8): 3178–3183.

Bartlett PA, Bauer B, and Singer SJ (1978) Synthesis of water-soluble undecagold cluster compounds of potential importance in electron microscopic and other studies of biological systems. *Journal of the American Chemical Society* 100(16): 5085–5089.

Bergeron DE, Castleman AW Jr, Morisato T, and Khanna SN (2004) Formation of $Al_{13}I^-$: Evidence for the superhalogen character of Al_{13}. *Science* 304(5667): 84–87.

Brust M, Walker M, Bethell D, Schiffrin DJ, and Whyman R (1994) Synthesis of thiol-derivatised gold nanoparticles in a two-phase liquid-liquid system. *Journal of the Chemical Society, Chemical Communications* 7: 801–802.

Chaki NK, Negishi Y, Tsunoyama H, Shichibu Y, and Tsukuda T (2008) Ubiquitous 8 and 29 kDa gold: Alkanethiolate cluster compounds: Mass-spectrometric determination of molecular formulas and structural implications. *Journal of the American Chemical Society* 130(27): 8608–8610.

Cushing BL, Kolesnichenko VL, and O'connor CJ (2004) Recent advances in the liquid-phase syntheses of inorganic nanoparticles. *Chemical Reviews* 104(9): 3893–3946.

de Heer WA (1993) The physics of simple metal clusters: Experimental aspects and simple models. *Reviews of Modern Physics* 65(3): 611.

Doud EA, Voevodin A, Hochuli TJ, Champsaur AM, Nuckolls C, and Roy X (2020) Superatoms in materials science. *Nature Reviews Materials* 5(5): 371–387.

Dugourd P, Hudgins RR, Clemmer DE, and Jarrold MF (1997) High-resolution ion mobility measurements. *The Review of Scientific Instruments* 68(2): 1122–1129.

Gilb S, Weis P, Furche F, Ahlrichs R, and Kappes MM (2002) Structures of small gold cluster cations (Au_n^+, $n < 14$): Ion mobility measurements versus density functional calculations. *The Journal of Chemical Physics* 116(10): 4094–4101.

Gilb S, Jacobsen K, Schooss D, Furche F, Ahlrichs R, and Kappes MM (2004) Electronic photodissociation spectroscopy of $Au_n^- \cdot Xe$ ($n = 7$-11) versus time-dependent density functional theory prediction. *The Journal of Chemical Physics* 121(10): 4619–4627.

Grandjean D, Coutiño-Gonzalez E, Cuong NT, Fron E, Baekelant W, Aghakhani S, Schlexer P, D'Acapito F, Banerjee D, Roeffaers MBJ, Nguyen MT, Hofkens J, and Lievens P (2018) Origin of the bright photoluminescence of few-atom silver clusters confined in LTA zeolites. *Science* 361(6403): 686–690.

Häkkinen H, Yoon B, Landman U, Li X, Zhai HJ, and Wang LS (2003) On the electronic and atomic structures of small Au_N^- ($N = 4$-14) clusters: A photoelectron spectroscopy and density-functional study. *The Journal of Physical Chemistry. A* 107(32): 6168–6175.

Häkkinen H, Moseler M, Kostko O, Morgner N, Hoffmann MA, and Issendorff BV (2004) Symmetry and electronic structure of noble-metal nanoparticles and the role of relativity. *Physical Review Letters* 93(9): 093401.

Haruta M, Kobayashi T, Sano H, and Yamada N (1987) Novel gold catalysts for the oxidation of carbon monoxide at a temperature far below 0°C. *Chemistry Letters* 36(1): 153–166.

Heaven MW, Dass A, White PS, Holt KM, and Murray RW (2008) Crystal structure of the gold nanoparticle $[N(C_8H_{17})_4][Au_{25}(SCH_2CH_2Ph)_{18}]$. *Journal of the American Chemical Society* 130(12): 3754–3755.

Huang W, Ji M, Dong CD, Gu X, Wang LM, Gong XG, and Wang LS (2008) Relativistic effects and the unique low-symmetry structures of gold nanoclusters. *ACS Nano* 2(5): 897–904.

Huang W, Bulusu S, Pal R, Zeng XC, and Wang LS (2009) Structural transition of gold nanoclusters: From the golden cage to the golden pyramid. *ACS Nano* 3(5): 1225–1230.

Imaoka T, Kitazawa H, Chun WJ, Omura S, Albrecht K, and Yamamoto K (2013) Magic number Pt_{13} and misshapen Pt_{12} clusters: Which one is the better catalyst? *Journal of the American Chemical Society* 135(35): 13089–13095.

Imaoka T, Kitazawa H, Chun WJ, and Yamamoto K (2015) Finding the most catalytically active platinum clusters with low atomicity. *Angewandte Chemie, International Edition* 54(34): 9810–9815.

Imaoka T, Akanuma Y, Haruta N, Tsuchiya S, Ishihara K, Okayasu T, Chun W-J, Takahashi M, and Yamamoto K (2017) Platinum clusters with precise numbers of atoms for preparative-scale catalysis. *Nature Communications* 8(1): 1–8.

Inomata Y, Albrecht K, and Yamamoto K (2018) Size-dependent oxidation state and CO oxidation activity of tin oxide clusters. *ACS Catalysis* 8(1): 451–456.

Jackschath C, Rabin I, and Schulze W (1992) Electron impact ionization of silver clusters Ag_n, $n \leqq 36$. *Zeitschrift fur Physik D* 22(2): 517–520.

Jadzinsky PD, Calero G, Ackerson CJ, Bushnell DA, and Kornberg RD (2007) Structure of a thiol monolayer-protected gold nanoparticle at 1.1 Å resolution. *Science* 318(5849): 430–433.

Kambe T, Haruta N, Imaoka T, and Yamamoto K (2017) Solution-phase synthesis of Al_{13}^- using a dendrimer template. *Nature Communications* 8(1): 2046.

Katakuse I, Ichihara T, Fujita Y, Matsuo T, Sakurai T, and Matsuda H (1985) Mass distributions of copper, silver and gold clusters and electronic shell structure. *International Journal of Mass Spectrometry and Ion Processes* 67(2): 229–236.

Kim HS, Wood TD, Marshall AG, and Lee J (1994) Production of gold cluster ions by laser desorption/ionization Fourier-transform ion cyclotron resonance mass spectrometry. *Chemical Physics Letters* 224(5–6): 589–594.

Knight WD, Walt AH, and Winston AS (1986) Shell structure and response properties of metal clusters. *Zeitschrift fur Physik D* 3(2–3): 109–114.

Kroto HW, Heath JR, O'Brien SC, Curl RF, and Smalley RE (1985) C_{60}: Buckminsterfullerene. *Nature* 318(6042): 162–163.

Lechtken A, Schooss D, Stairs JR, Blom MN, Furche F, Morgner N, Kostko O, von Issendorff B, and Kappes MM (2007) Au_{34}^-: A chiral gold cluster? *Angewandte Chemie, International Edition* 46(16): 2944–2948.

Letokhov V (1987) *Laser Photoionization Spectroscopy*. Orlando: Elsevier.

Li J, Li X, Zhai HJ, and Wang LS (2003) Au_{20}: A tetrahedral cluster. *Science* 299(5608): 864–867.

Liu L and Corma A (2018) Metal catalysts for heterogeneous catalysis: From single atoms to nanoclusters and nanoparticles. *Chemical Reviews* 118(10): 4981–5079.

Martin TP, Bergmann T, Göhlich H, and Lange T (1991) Shell structure of clusters. *The Journal of Physical Chemistry* 95(17): 6421–6429.

Maruyama S, Anderson LR, and Smalley RE (1990) Direct injection supersonic cluster beam source for FT-ICR studies of clusters. *The Review of Scientific Instruments* 61(12): 3686–3693.

Mitsui M, Nagaoka S, Matsumoto T, and Nakajima A (2006) Soft-landing isolation of vanadium-benzene sandwich clusters on a room-temperature substrate using n-alkanethiolate self-assembled monolayer matrixes. *The Journal of Physical Chemistry. B* 110(7): 2968–2971.

Murayama H, Narushima T, Negishi Y, and Tsukuda T (2004) Structures and stabilities of alkanethiolate monolayers on palladium clusters as studied by gel permeation chromatography. *The Journal of Physical Chemistry. B* 108(11): 3496–3503.

Narouz MR, Takano S, Lummis PA, Levchenko TI, Nazemi A, Kaappa Malola S, Yousefalizadeh G, Calhoun LA, Stamplecoskie KG, Häkkinen H, Tsukuda T, and Crudden CM (2019) Robust, highly luminescent Au_{13} superatoms protected by N-heterocyclic carbenes. *Journal of the American Chemical Society* 141(38): 14997–15002.

Negishi Y, Nobusada K, and Tsukuda T (2005) Glutathione-protected gold clusters revisited: Bridging the gap between gold (I)-thiolate complexes and thiolate-protected gold nanocrystals. *Journal of the American Chemical Society* 127(14): 5261–5270.

Negishi Y, Tsunoyama H, Suzuki M, Kawamura N, Matsushita MM, Maruyama K, Sugawara T, Yokoyama T, and Tsukuda T (2006) X-ray magnetic circular dichroism of size-selected, thiolated gold clusters. *Journal of the American Chemical Society* 128(37): 12034–12035.

Nie X, Qian H, Ge Q, Xu H, and Jin R (2012) CO oxidation catalyzed by oxide-supported $Au_{25}(SR)_{18}$ nanoclusters and identification of perimeter sites as active centers. *ACS Nano* 6(7): 6014–6022.

Pinkard A, Champsaur AM, and Roy X (2018) Molecular clusters: Nanoscale building blocks for solid-state materials. *Accounts of Chemical Research* 51(4): 919–929.

Pyo K, Thanthirige VD, Kwak K, Pandurangan P, Ramakrishna G, and Lee D (2015) Ultrabright luminescence from gold nanoclusters: Rigidifying the Au (I)-thiolate shell. *Journal of the American Chemical Society* 137(25): 8244–8250.

Qian H, Eckenhoff WT, Zhu Y, Pintauer T, and Jin R (2010) Total structure determination of thiolate-protected Au_{38} nanoparticles. *Journal of the American Chemical Society* 132(24): 8280–8281.

Roy X, Lee CH, Crowther AC, Schenck CL, Besara T, Lalancette RA, Siegrist T, Stephens PW, Brus LE, Kim P, Steigerwald ML, and Nuckolls C (2013) Nanoscale atoms in solid-state chemistry. *Science* 341(6142): 157–160.

Sanchez A, Abbet S, Heiz U, Schneider WD, Häkkinen H, Barnett RN, and Landman U (1999) When gold is not noble: Nanoscale gold catalysts. *The Journal of Physical Chemistry A* 103(48): 9573–9578.

Satoh N, Nakashima T, Kamikura K, and Yamamoto K (2008) Quantum size effect in TiO_2 nanoparticles prepared by finely controlled metal assembly on dendrimer templates. *Nature Nanotechnology* 3: 106–111.

Schmid G, Pfeil R, Boese R, Bandermann F, Meyer S, Calis GHM, and Vandervelden WA (1981) $Au_{55}[P(C_6H_5)_3]_{12}Cl_{6—A}$ gold cluster of an exceptional size. *Chemische Berichte* 114(11): 3634–3642.

Schooss D, Weis P, Hampe O, and Kappes MM (2010) Determining the size-dependent structure of ligand-free gold-cluster ions. *Philosophical Transactions of the Royal Society A* 368(1915): 1211–1243.

Shichibu Y, Negishi Y, Tsunoyama H, Kanehara M, Teranishi T, and Tsukuda T (2007) Extremely high stability of glutathionate-protected Au_{25} clusters against core etching. *Small* 3(5): 835–839.

Takahashi M, Koizumi H, Chun WJ, Kori M, Imaoka T, and Yamamoto K (2017) Finely controlled multimetallic nanocluster catalysts for solvent-free aerobic oxidation of hydrocarbons. *Science Advances* 3(7): e1700101.

Tomalia DA and Khanna SN (2016) A systematic framework and nanoperiodic concept for unifying nanoscience: Hard/soft nanoelements, superatoms, meta-atoms, new emerging properties, periodic property patterns, and predictive Mendeleev-like nanoperiodic tables. *Chemical Reviews* 116(4): 2705–2774.

Tsukamoto T, Kambe T, Nakao A, Imaoka T, and Yamamoto K (2018) Atom-hybridization for synthesis of polymetallic clusters. *Nature Communications* 9(1): 1–7.

Tsukamoto T, Haruta N, Kambe T, Kuzume A, and Yamamoto K (2019) Periodicity of molecular clusters based on symmetry-adapted orbital model. *Nature Communications* 10(1): 1–8.

Tsunoyama H and Tsukuda T (2009) Magic numbers of gold clusters stabilized by PVP. *Journal of the American Chemical Society* 131(51): 18216–18217.

Tsunoyama H, Sakurai H, Ichikuni N, Negishi Y, and Tsukuda T (2004) Colloidal gold nanoparticles as catalyst for carbon-carbon bond formation: Application to aerobic homocoupling of phenylboronic acid in water. *Langmuir* 20(26): 11293–11296.

Tsunoyama H, Negishi Y, and Tsukuda T (2006) Chromatographic isolation of “missing” Au_{55} clusters protected by alkanethiolates. *Journal of the American Chemical Society* 128(18): 6036–6037.

Tsunoyama H, Nickut P, Negishi Y, Al-Shamery K, Matsumoto Y, and Tsukuda T (2007) Formation of alkanethiolate-protected gold clusters with unprecedented core sizes in the thiolation of polymer-stabilized gold clusters. *Journal of Physical Chemistry C* 111(11): 4153–4158.

Tsunoyama H, Ichikuni N, and Tsukuda T (2008) Microfluidic synthesis and catalytic application of PVP-stabilized, ~ 1 nm gold clusters. *Langmuir* 24(20): 11327–11330.

Tsunoyama R, Tsunoyama H, Pannopard P, Limtrakul J, and Tsukuda T (2010) MALDI mass analysis of 11 kDa gold clusters protected by octadecanethiolate ligands. *Journal of Physical Chemistry C* 114(38): 16004–16009.

Wan XK, Xu WW, Yuan SF, Gao Y, Zeng XC, and Wang QM (2015) A Near-infrared-emissive alkynyl-protected Au_{24} nanocluster. *Angewandte Chemie, International Edition* 54(33): 9683–9686.

Wang S, Meng X, Das A, Li T, Song Y, Cao T, Zhu X, Zhu M, and Jin R (2014) A 200-fold quantum yield boost in the photoluminescence of silver-doped Ag_xAu_{25-x} nanoclusters: The 13th silver atom matters. *Angewandte Chemie* 126(9): 2408–2412.

Wilson RJ, Weinert B, and Dehnen S (2018) Recent developments in Zintl cluster chemistry. *Dalton Transactions* 47(42): 14861–14869.

Xie J, Zheng Y, and Ying JY (2009) Protein-directed synthesis of highly fluorescent gold nanoclusters. *Journal of the American Chemical Society* 131(3): 888–889.

Xing X, Yoon B, Landman U, and Parks JH (2006) Structural evolution of Au nanoclusters: From planar to cage to tubular motifs. *Physical Review B* 74(16): 165423.

Xirouchaki C and Palmer RE (2004) Deposition of size-selected metal clusters generated by magnetron sputtering and gas condensation: A progress review. *Philosophical Transactions of the Royal Society A* 362(1814): 117–124.

Yamamoto K, Higuchi M, Shiki S, Tsuruta M, and Chiba H (2002) Stepwise radial complexation of imine groups in phenylazomethine dendrimers. *Nature* 415(6871): 509–511.

Yamamoto K, Imaoka T, Chun WJ, Enoki O, Katoh H, Takenaga M, and Sonoi A (2009) Size-specific catalytic activity of platinum clusters enhances oxygen reduction reactions. *Nature Chemistry* 1(5): 397–402.

Yamazoe S and Tsukuda T (2019) X-ray absorption spectroscopy on atomically precise metal clusters. *Bulletin of the Chemical Society of Japan* 92(1): 193–204.

Yanagimoto Y, Negishi Y, Fujihara H, and Tsukuda T (2006) Chiroptical activity of BINAP-stabilized undecagold clusters. *The Journal of Physical Chemistry B* 110(24): 11611–11614.

Zhang HF, Stender M, Zhang R, Wang C, Li J, and Wang LS (2004) Toward the solution synthesis of the tetrahedral Au_{20} cluster. *The Journal of Physical Chemistry B* 108(33): 12259–12263.

Zhao M, Sun L, and Crooks RM (1998) Preparation of Cu nanoclusters within dendrimer templates. *Journal of the American Chemical Society* 120: 4877–4878.

Zheng J, Petty JT, and Dickson RM (2003) High quantum yield blue emission from water-soluble Au_8 nanodots. *Journal of the American Chemical Society* 125(26): 7780–7781.

Zheng J, Zhang C, and Dickson RM (2004) Highly fluorescent, water-soluble, size-tunable gold quantum dots. *Physical Review Letters* 93(7): 077402.

Zhu Y, Qian H, Drake BA, and Jin R (2010a) Atomically precise $Au_{25}(SR)_{18}$ nanoparticles as catalysts for the selective hydrogenation of α, β-unsaturated ketones and aldehydes. *Angewandte Chemie* 122(7): 1317–1320.

Zhu Y, Qian H, and Jin R (2010b) An atomic-level strategy for unraveling gold nanocatalysis from the perspective of $Au_n(SR)_m$ nanoclusters. *Chemistry—a European Journal* 16(37): 11455–11462.

Electronic states of carbon materials☆

S Latil[a] **and C Ewels**[b], [a]CEA, IRAMIS, SPEC, GMT, Gif-sur-Yvette, France; [b]Nantes Université, CNRS, Institut des Matériaux de Nantes Jean Rouxel, IMN, Nantes, France

© 2024 Elsevier Ltd. All rights reserved.

This is an update of P. Lambin, J. Fink, Carbon Materials, Electronic States of, Editor(s): Franco Bassani, Gerald L. Liedl, Peter Wyder, Encyclopedia of Condensed Matter Physics, Elsevier, 2005, Pages 143–151, ISBN 9780123694010, https://doi.org/10.1016/B0-12-369401-9/00463-0.

Introduction	702
Hybrid orbitals	703
Diamond	704
Graphene and graphite	706
Carbon nanotubes	708
Fullerenes and fullerites	711
Miscellaneous synthetic carbons	713
Disordered carbons	713
Conclusion	714
References	714

Abstract

This chapter explores the remarkably varied electronic behavior of pure carbon species, including fullerenes and fullerite, graphene and graphite, nanotubes, diamond, amorphous carbons, and miscellaneous synthetic carbons such as nanorings and graphyne. We show how their diverse electronic structure derives directly from the different hybridizations possible between the 2*s* and 2*p* Carbon orbitals, the capability in Carbon for strong π bonding between 2*p* orbitals of neighboring atoms, and the dimensionality and symmetry of the resultant carbon forms. We discuss the diverse consequences of this electronic structure including ultra-hardness, negative electron affinity and superconductivity, and how the electronic states of carbon materials can be controlled through doping.

Key points

This chapter introduces key concepts of Carbon electronic structure and demonstrates how these underpin the wide variety of carbon forms and their unique individual behavior.

- *Underlying electronic structure*: Carbon has the possibility to hybridize into sp, sp^2, and sp^3 configurations. When coupled with strongly overlapping p_z-orbitals creating π-bonds, this allows carbon atoms to form single, double and triple bonds with their neighbors.
- *Symmetry and dimensionality*: Depending on the atomic arrangements, carbon can form 0D molecules (fullerenes), 1D nanotubes, 2D graphene, and 3D structures such as graphite and diamond. Each shows distinct electronic properties resulting from the structural symmetry and dimensionality.
- *Materials Behavior*: We will draw on a range of practical examples, showing how the underlying electronic structure results directly in measureable material properties in carbon materials (such as transparency, superconductivity, hardness, and color).
- *Modifying Properties*: We will describe how the electronic structure of carbon materials can be modified and tuned, through doping, intercalation, and external stimuli such as electric fields and pressure.
- *Latest Advances*: We will highlight some of the latest discoveries and newest advances, including recently synthesized carbon materials such as carbyne nanorings and graphyne.

Introduction

Carbon is a remarkable element that shows a variety of stable and metastable structures, ranging from three-dimensional (3D) diamond via 2D graphene and 1D carbyne to 0D fullerenes. The different forms of carbon are the consequence of two important characteristics of its electronic $1s^2 2s^2 2p^2$ configuration. First, carbon may form different hybridizations, called sp^n, between its

---

☆*Change History*: April 2023. S. Latil and C. Ewels rewritten abstract, added objectives, updated text, added Miscellaneous Synthetic Carbons section, added new conclusion and summary, updated Table 1, Figures 4, 9, and added new Figures 5, 6, 7, 8, 9a, 10.

Table 1 Structural and electronic properties of the 3D carbon allotropes at room temperature.

	Diamond (Diamond: Mineral Information, Data and Localities, 2023)	*C_{60} fullerite (American Elements, 2023; Wikipedia, 2022a)*	*Graphite (Graphite Summary, 2023; Pisanty, 1991)*
σ-Bond hybridization	sp^3	$sp^{2+\epsilon}$	sp^2
Structure	f.c.c.	f.c.c.	hex
Lattice parameters (nm)	$a = 0.357$	$a = 1.420$	$a = 0.246$, $c = 0.671$
Density (g/cm^3)	3.52	1.65–1.72	2.27
C–C distance (nm)	0.154	0.140–0.146 (Hedberg et al., 1991)	0.142
Bandgap (eV)	5.48 (Clark et al., 1964)	1.9–2.3 (Lof et al., 1992; Rabenau et al., 1993)	−0.03
Type	Large-gap semiconductor	Semiconductor	Semimetal
Binding energy (eV/atom)	7.35	6.96	7.37

2*s* orbital and *n* of its 2*p* orbitals ($1 \leqslant n \leqslant 3$). Next, the C–C distance is small enough to allow for a large π bonding between 2*p* orbitals of neighboring atoms that are not hybridized with the 2*s* orbital (when $n < 3$). These two properties together give wide structural flexibility, thanks to which the chemistry of carbon is so rich.

Already with pure carbon, different structures exist which have very different electronic properties. The three three-dimensional allotropic crystalline forms of carbon are listed in Table 1. Beyond these, the hexagonal symmetry of a graphite monolayer, graphene, results in unique charge carrier behavior as described below. Other more exotic structures are covered briefly later.

Hybrid orbitals

A carbon atom has six electrons. The two electrons in the 1*s* shell are energetically stable and never participate in chemical bonds or electronic response. The remaining four electrons should organize like $[\mathrm{He}](2s^2)(2p^2)$, leading to an atomic triplet state $^3\mathrm{P}_0$, with two electrons embedded in a stable 2*s* orbital and only two valence electrons that can interact with neighboring species. However, the quintuplet state $^5\mathrm{S}_2$ coming from the $[\mathrm{He}](2s^1)(2p^3)$ configuration is less than 4 eV higher in energy, and explains why carbon can mobilize four electrons in chemical bonds. The way these four electrons are organized around the nucleus is the hybridization.

When two carbon atoms are brought together to form a C_2 molecule, the electrons move in an effective potential that has cylindrical symmetry around the line joining the two nuclei. A molecular wave function may be totally invariant under a rotation by an angle ϕ about this axis, thus forming a σ state, or it may transform like $\cos(m\phi)$, thus forming a π state ($m = 1$), a δ state ($m = 2$), etc. The ground state of the C_2 molecule is a σ state. Its expression can be written as a linear combination of atomic orbitals (LCAO) restricted to the 2*s* and $2p_z$ valence orbitals, which have full rotational symmetry about the molecular axis chosen as the *z* direction. In addition, the wave function of the ground state is even with respect to the inversion about the molecule center. This means $\psi\sigma_g = (\Phi_{A+} + \Phi_{B-})/\sqrt{2}$, where $\Phi_{A+} = \alpha\varphi_{As} + \beta\varphi_{Az}$ and $\Phi_{B-} = \alpha\varphi_{Bs} - \beta\varphi_{Bz}$. In that expression, φ_{As} and φ_{Az} are the 2*s* and $2p_z$ orbitals located on one carbon atom, either at location *A* or *B*. Φ_{A+} and Φ_{B-} are linear combinations of these orbitals, called sp^1 hybrids (see Fig. 1a). They are symmetric to each other with respect to the inversion center. The numerical coefficients α and β are determined by solving a secular LCAO equation.

In a C_2 molecule, two electrons occupy the σ_g ground state (see Fig. 1b) and form a strong σ bond. Two electrons occupy the next σ state, which is a nonbonding state with wavefunction $\psi\sigma_u = (\Phi_{A-} - \Phi_{B+})/\sqrt{2}$. It is a combination of sp^1 hybrids on A and B sites that point opposite to the other atom. These hybrid orbitals are ready to overlap with an H atom each, such as in the acetylene C_2H_2 molecule, or with other C atoms such as in carbyne, which is a 1D carbon chain. The last four electrons of the C_2 molecule occupy the doubly degenerate π_u bonding state (see Fig. 1b) obtained by combining the $2p_x$ orbitals and the $2p_y$ orbitals. These electrons form two π bonds.

Other hybridizations of the 2*s* and 2*p* valence orbitals may be formed. The most symmetric combinations correspond to the sp^2 and sp^3 hybrids illustrated in Fig. 2. In the first case, each carbon atom forms three sp^2 hybrids, by mixing the 2*s* orbital with $2p_x$ and $2p_y$ orbitals. In graphene and graphite, the sp^2 hybrid orbitals have maxima of probability density along three directions at 120° in the *xy* plane. They form σ bonds with neighboring atoms. sp^3 hybrids are combinations of all valence orbitals. In diamond, each atom forms four such hybrids along four directions at 109.5° in space with tetrahedral symmetry.

Dimensionality and system symmetry critically determine electronic behavior, and carbon in this respect shows more versatility than any other chemical element. This is seen in the electronic density of states around the Fermi level (E_F) for different carbon species. C_{60} is molecular and has localized electronic states giving sharp delta functions in the DoS (Fig. 11a), although these broaden somewhat in fullerite crystals due to inter-molecular coupling. Nanotubes have 1D-dispersed states along their lengths giving rise to characteristic spiked van Hove singularities (Fig. 8). The conjugated hexagonal 2D-lattice of graphene gives symmetric parabolic DOS around the Fermi level due to graphene's conical bands (Fig. 5e), while the DOS plots of graphite and diamond reflect their more complex 3D symmetry. These different electronic behaviors are now discussed in more detail.

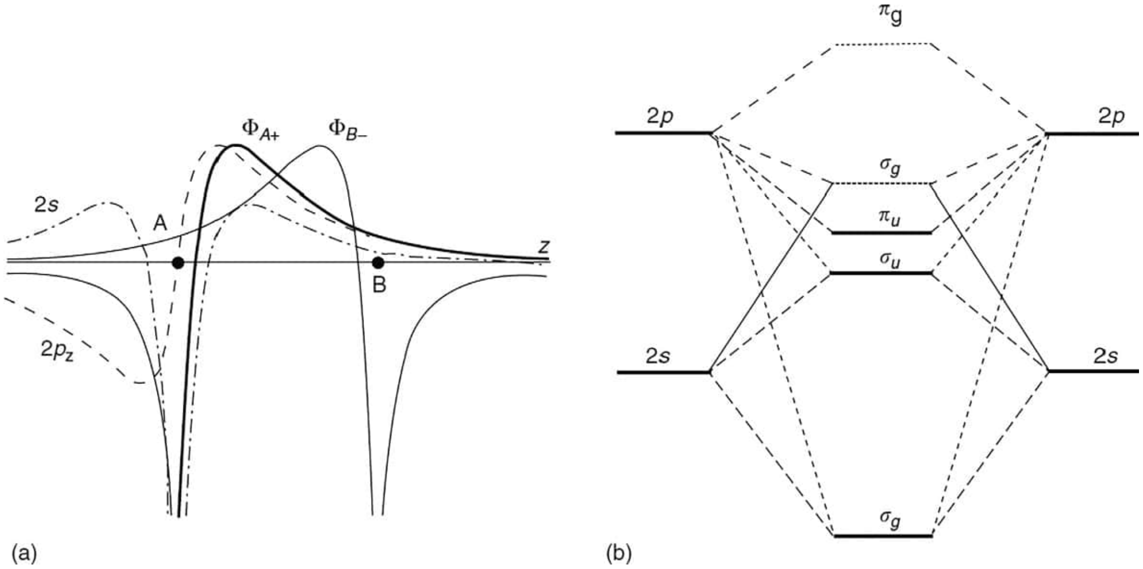

Fig. 1 (a) Variation of the 2*s* (dot-dashed line) and $2p_z$ (dashed line) atomic orbitals on site A along the axis *z* of the C_2 molecule. The solid line curves represent the Φ_{A+} (thick line) and Φ_{B-} (thin line) sp^1 hybrid orbitals, (b) Formation of the electronic levels of C_2 from the 2*s* and 2*p* levels of the atoms. The highest σ_g and the π_g levels are unoccupied.

Diamond

When carbon atoms are brought together to form a solid, their 2*s* and 2*p* levels broaden and form energy bands. The formation of these bands is illustrated in Fig. 3 for the case of diamond. At large interatomic distance, the bands are narrow and conserve most of the 2*s* and 2*p* characters of the individual atoms. When the distance decreases, the width of the bands increases and their *s* and *p* characters start to mix. At some distance, there is a crossing between the bottom of the band that originates from the 2*p* level, and the top of the band that originates from the 2*s* level. From now on, one may consider that the electronic states result from the σ overlapping of sp^3 hybrid orbitals. By reducing the interatomic distance further, a gap opens between σ bands that have acquired bonding and antibonding characters, respectively. There are four hybrid orbitals per atom, giving rise to two states in each of the bonding and antibonding bands. Each band may therefore accommodate four electrons, due to spin degeneracy. Since there are four electrons per atom, the bonding band is full, the antibonding band is empty, and the system is a semiconductor. The so-called hybridization gap that separates the bonding and antibonding σ bands increases with decreasing distance. Interestingly enough, this picture remains qualitatively correct for the tetrahedral *sp* semiconductors that adopt the same diamond structure. From the decreasing interatomic distance in going from Ge to Si to C, one may understand the increase of their band gap. The picture also remains qualitatively correct for tetrahedral amorphous carbon.

For a crystalline material, the most complete description of the electronic states is provided by its band structure. A theoretical band structure of diamond is shown in Fig. 4b for Bloch vectors parallel to a principal diagonal of the cubic cell (ΓL line) and parallel to an edge of the cubic cell (ΓX line). The valence band extends from −22.6 to 0 eV. The width of the hybridization gap at the Γ point is 7.4 eV. There are four branches in the valence band, the two atoms per unit cell of diamond (Fig. 4a) bringing two bonding σ states each. The symmetry of the wave function along the ΓL and ΓX lines is high enough to allow for a twofold degeneracy of the top valence branch and the bottom conduction branch. The computed minimum band gap is 5.6 eV. It is an indirect gap, corresponding to a transition between the Γ point and the minimum of the bottom conduction branch along ΓX. The gap is so large that diamond does not absorb any visible radiation. Pure diamond is transparent, as a consequence.

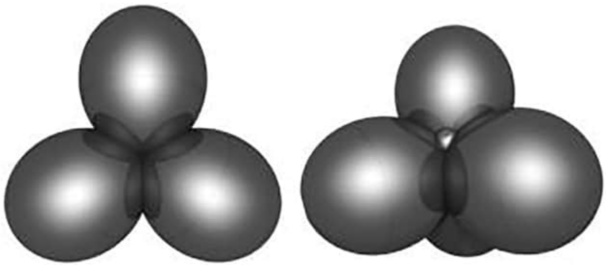

Fig. 2 Carbon sp^2 (left) and sp^3 (right) hybrid orbitals. Each orbital is represented by its angular probability distribution for an electron at 0.15 nm from the C nucleus.

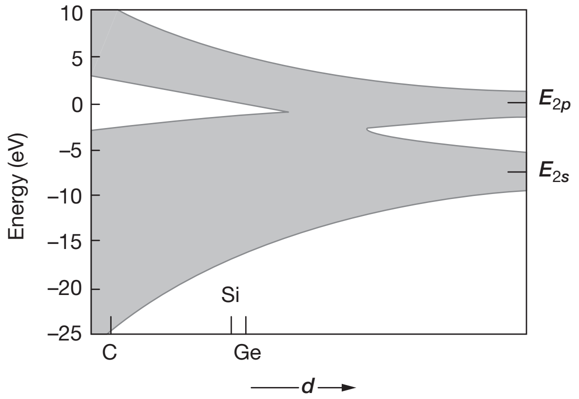

Fig. 3 Schematic illustration of the band formation in diamond structure as a function of the interatomic distance (tight-binding description). The positions of Ge, Si, and C are indicated.

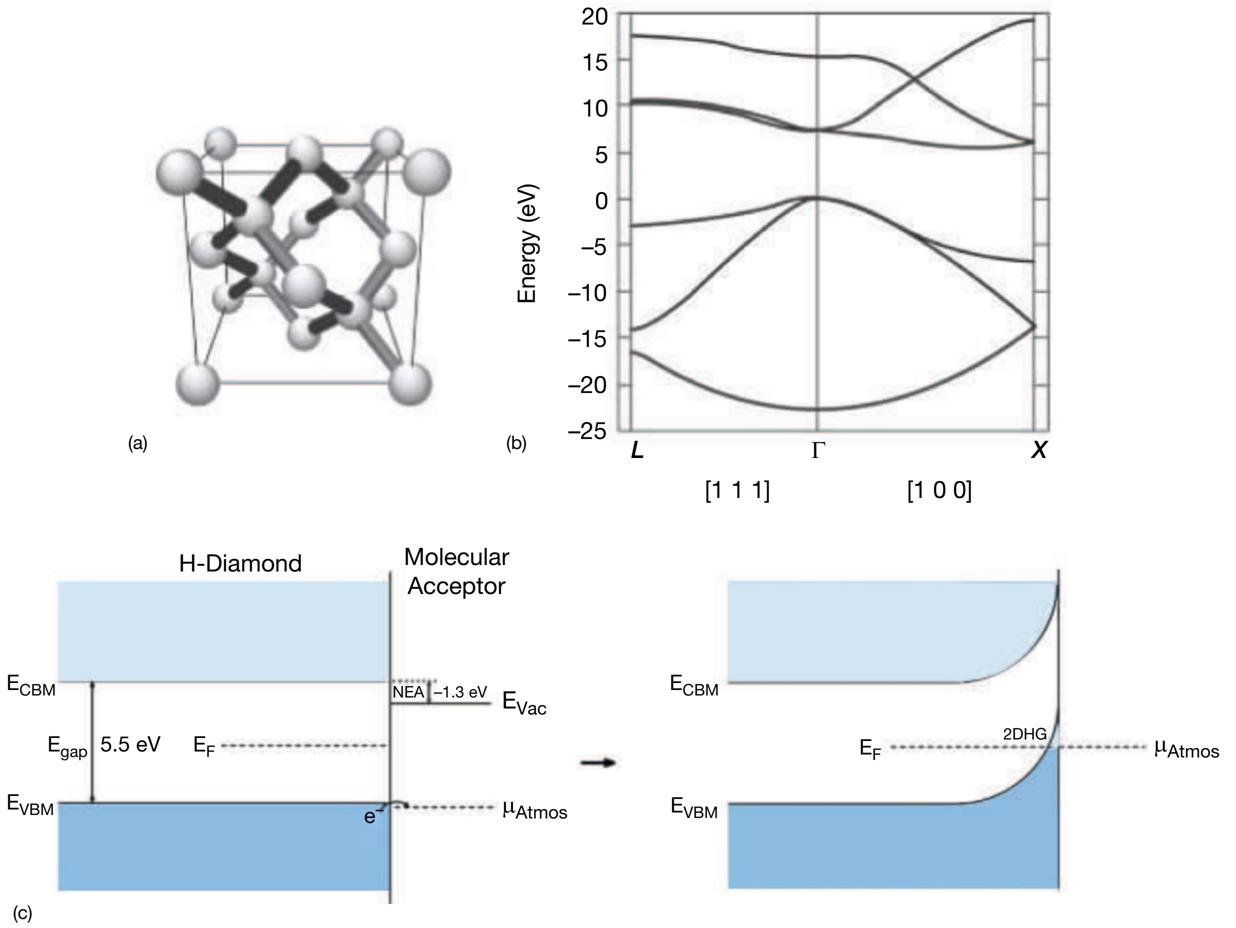

Fig. 4 (a) Cubic diamond crystal structure, (b) Band structure of diamond along high-symmetry lines calculated with the all-electron GW approximation. (Courtesy of M Alouani.) (c) Energy band diagram of a hydrogen-terminated diamond surface showing Negative Electron Affinity (NEA) of the surface and, upon exposure to ambient air, formation of a two-dimensional hole gas through Charge Transfer Doping. μ_{Atmos} is the electrochemical potential of adsorbed molecules that trap valence electrons from the diamond, causing upward band bending and creation of a two-dimensional hole gas (2DHG) just below the surface. Image (c) adapted from Crawford KG, Maini I, Macdonald DA, Moran DAJ (2021). Surface transfer doping of diamond: A review. *Progress in Surface Science 96*: 100613. doi:10.1016/j.progsurf.2021.100613.

The σ bonds in diamond are very strong. As a result, its Young modulus for uniaxial strain applied along a fourfold symmetry axis is 1.05 GPa, one of the hardest materials measured (see ultrahard fullerites below). Switching from AB-layer stacking in cubic diamond to ABC- lowers the symmetry and results in the rare hexagonal carbon phase, Lonsdaleite (De and Pryor, 2014; Kraus et al., 2016; Turneaure et al., 2017).

Diamond can be doped with other elements beside carbon to create donor and acceptor states, but this is difficult to achieve due to diamond's high density and strong σ bonds. Boron is the standard dopant for *p*-type conductivity, its optical activity giving a distinct blue color. While phosphorus and other elements such as arsenic show *n*-type character it remains difficult to *n*-dope diamond, which has limited diamond's development for devices. This is despite its high carrier mobilities (1945 cm V^{-1} s^{-1} for electrons and 2285 cm V^{-1} s^{-1} for holes (Gabrysch et al., 2011)) and breakdown field (13 MV/cm), rendering it interesting for high power devices (Umezawa, 2018). The most common natural dopant in diamond is nitrogen, and of particular note is the negative nitrogen-vacancy defect (NV^- center) in diamond, which has optically detectable spin transitions and allows highly sensitive local field measurements (Dolde et al., 2011).

Hydrogen terminated diamond surfaces show negative electron affinity (NEA), meaning the vacuum level lies below the conduction band minimum (Himpsel et al., 1979; van der Weide et al., 1994). As such, excited electrons spontaneously emit from the surface, of interest in applications such as cold cathodes for electron microscopy (Kleshch et al., 2016). Introducing cationic species to hydrogen-terminated diamond surfaces (such as CO_2 dissolved in surface water, NO_2, or molecules such as fullerenes or F4-TCNQ) results in shallow *p*-type conductive states in the diamond subsurface (surface transfer doping (Crawford et al., 2021), see Fig. 4c).

For further reading on diamond see the entry elsewhere in this encyclopedia on "CVD diamonds and superdiamonds".

Graphene and graphite

Graphite is the most common 3D allotrope of pure carbon. It is constructed from a stacking of atomically thin layers with a honeycomb structure named graphene (Fig. 5a). Graphene has another entry of the encyclopedia dedicated to it. The high cohesive energy of graphite (Table 1) comes almost exclusively from the strong σ interactions between the sp^2 hybrids and the less strong π interactions between the $2p_z$ orbitals (interatomic distance is 0.142 nm). The atomic layers are bound together by weak van der Waals forces (interlayer separation is in the range 0.33–0.36 nm). Consequently the electronic interactions between layers are weak and the electronic structure of the whole 3D crystal is mostly driven by that of the individual planes.

Graphene consists of a hexagonal array of carbon atoms in a plane. The repeat unit cell (Fig. 5a) is a rhombus containing two equivalent carbon atoms (same chemical environment). The electronic properties of isolated single graphene sheets are described in detail in other entries in the encyclopedia. A short summary of the very particular electronic properties of this atomically thin bi-dimensional crystal is made in Fig. 5. The planar geometry of the graphene layer implies that the symmetry group contains the $+z/-z$ mirror plane operation. The electronic band structure of a single graphene layer can then be sorted: σ states are symmetric under the mirror plane operation, and π bands are anti-symmetric.

Fig. 5c shows the calculated electronic band structure of graphene. Both σ and σ^* bands are plotted in black. The bonding σ states are formed by overlapping sp^2 hybrid orbitals oriented along the C–C bonds, with energy approximately in the range −21 to −5 eV. The anti-bonding σ^* states lie above +1 eV, i.e., ~6 eV above the bonding states. This is close to the band gap observed in diamond, which only has σ and no π-bonding. Unlike the case of diamond, in graphene this gap is bridged by the π and π^* states that originate from the $2p_z$ orbitals, perpendicular to the atomic layer. The dispersion of the bonding π states (from the bottom of the band to the Fermi level, in red in Fig. 5c and d) is quite large (~8 eV), symptomatic of a high degree of delocalization of the electrons. These delocalized electrons are associated with the electrical conductivity of graphene and graphite. The anti-bonding π^* band (in blue) has an energy above the Fermi level (close to −2 eV).

The π band and one π^* band cross at the corner K of the Brillouin zone (Fig. 5c and d). The Fermi level coincides with this crossing point, and since there are no electronic states exactly at the Fermi level, graphene is therefore technically a zero-gap semiconductor rather than a semi-metal. The low energy electronic properties are then totally controlled by these two π and π^* bands, and it is reasonable to describe the electronic properties of graphene with such a "two band model" (Fig. 5d). The states close to E_F have momentum located in the vicinity of the K point, at the boundary of the Brillouin zone. The bands in this area are linear, a behavior very peculiar to graphene which is responsible for much of its surprising electronic properties. The electronic density of states (Fig. 5e) shows van Hove singularities located around ~2.5 eV above and below E_F (corresponding to the shoulders at point M of the Brillouin zone) and a typical V-shaped density close to E_F (corresponding to regions close to K).

Different allotropes of graphite exist according to the stacking arrangement of the graphene planes. The most common crystalline form of graphite, discovered by J. D. Bernal in 1924 (Bernal and Bragg, 1924), has the stacking illustrated in Fig. 6a: alternate graphene layers are offset, with one of the two carbon atoms in the graphene unit cell lying above an atom in the sheet below, the other lying above a hexagon. These alternating layers are often labeled "A" and "B" and the Bernal geometry is often also called AB-stacked graphite for that reason. In Bernal graphite, there are four atoms per unit cell (two per layer), each of them forms three σ states and two π states, of which half have a bonding character. The major difference with graphene is that the four atoms are now in different chemical environments: two of them have atoms located directly above and below them, whereas the other two have the center of hexagons. The corresponding hexagonal Brillouin zone is sketched in Fig. 6b. Since the Bernal crystal is genuinely three-dimensional, the former K point of the reciprocal plane of graphene is now replaced with the axis along k_z in the corner of the zone: the H–K line.

As for graphene, the σ states of graphite are combinations of sp^2 hybrid orbitals and the π states are combinations of $2p_z$ orbitals. Since the interactions between planes are weak, the bonding σ and anti-bonding σ^* electronic bands of the two layers in the unit cell are quasi-degenerate and remain located far from the Fermi level (Fig. 6c). This means they participate only marginally to the

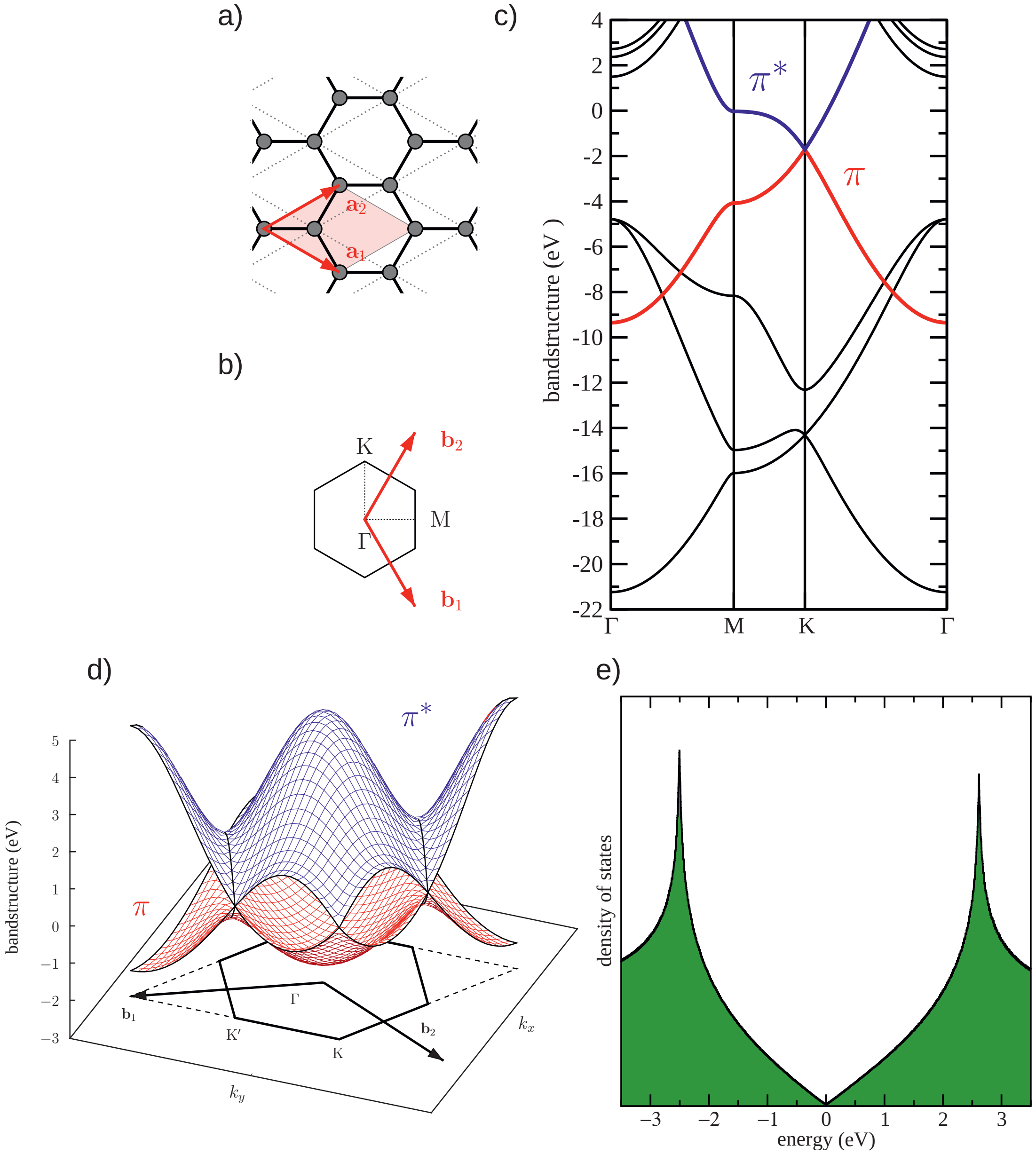

Fig. 5 (a) Graphene 2D hexagonal structure. The primitive cell, that contains two carbon atoms, is highlighted. The two atoms are equivalent (same chemical environment) (b) Brillouin zone of graphene in the reciprocal plane. The high-symmetry points K and M are specified. (c) The band structure of graphene calculated with the local-density approximation and plotted along the high-symmetry directions. The Fermi level is exactly at the crossing of the two bands π and π^* that are plotted in red and blue. The σ bands are in black. (d) 3D view of the pure p_z bands. They cross at the corner K of the Brillouin zone. The Fermi level coincides with the crossing energy. (e) Typical electronic density of states of graphene. The density is exactly zero at the Fermi level (set to 0 eV), which is why graphene is a zero-gap semiconductor.

electronic response of graphite. Electronic interaction between the graphene sheets is much more efficient with the out-of-plane $2p_z$ orbitals contained in the π-bonds, and these orbitals form two bonding bands and two antibonding bands. Consequently, they appear as two pairs of bands split around the Fermi level, by the interlayer coupling.

Fig. 6d shows this in more detail. Along the H–K line, there is a series of pockets of electronic (bands below E_F) and hole states (bands above E_F). The overlap is small (around ~30 meV) between the π and π^* bands. The consequence is that graphite is a semi-metal. It is a poor electrical conductor (room temperature resistivity of crystalline samples $\rho\| \approx 10-6\ \Omega\text{m}$) because the number of charge carriers (electrons and holes) is small, contributing to its use in resistance heaters (Okada et al., 2017).

Graphite intercalation compounds (GIC) are composed of planes of intercalant atoms or small molecules separated by a few graphitic sheets, in a sequence that repeats periodically along the *c*-axis as in a superlattice. The number of graphitic layers stacked between two successive intercalant planes is called the stage of the GIC. The intercalants can be electron donors (such as alkali

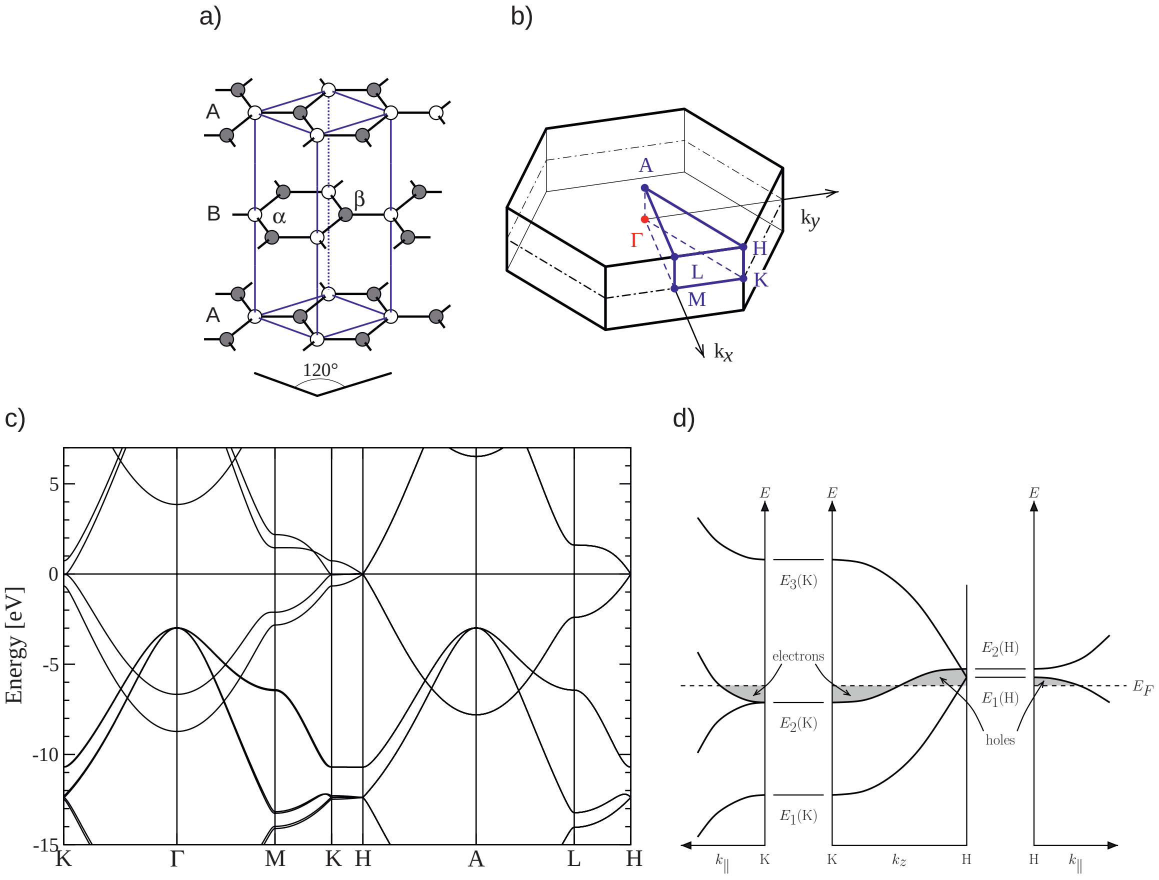

Fig. 6 (a) Graphite unit cell with Bernal AB-stacking. (b) First Brillouin zone of graphite with its high-symmetry points. (c) The band structure of Bernal graphite calculated with the local-density approximation and plotted along the high-symmetry directions. Four electronic π bands are in the vicinity of the Fermi level (set to zero). The σ bands (nearly doubly degenerate) lie below. (d) Schematic of the π bands in the vicinity of the H–K line orthogonal to the graphene layers, illustrating the coexistence of electrons and holes.

metals) or electron acceptors (such as bromine), shifting the graphite Fermi level up and down respectively. Depending on the intercalants used and their concentration, a huge class of GICs can be realized with tailored electronic properties, ranging from metals $\rho\| \approx 10 - 8$ Ωm to insulators (Ebert, 1976; Li et al., 2019).

Carbon nanotubes

Carbon nanotubes are cylindrical forms of graphene or graphite. A single-wall nanotube (SWNT) is composed of one graphene sheet rolled up into a cylinder. SWNTs preferentially pack together in the form of bundles of 10–200 tubes. The van der Waals attraction between the tubes has very little effect on the electronic density of states of the individual components. Multi-wall carbon nanotubes (MWNTs) are composed of several single-wall tubes arranged coaxially, with interlayer distance ~0.34 nm. The electronic structure of large multi-wall nanotubes is similar to that of graphite; roughly speaking, they behave like a semimetal. In principle, about one third of the coaxial layers are supposed to be metallic (see below), the remaining being semiconducting. Under high potential bias, each tubular layer of a multi-wall nanotube can transport a current ~20 μA before breaking (Collins et al., 2001), consistent with the capability of MWNTs to withstand high current densities of over 10^9 A/cm^2.

To understand the electronic properties of a single-wall nanotube, the zone folding model is very practical, based on a joint analysis of nanotube geometry and graphene electronic structure. The circumference of the nanotube is a direct lattice vector of graphite, wrapped around in such a way that its two ends coincide. This vector is commonly called the chiral vector. It is developed as $\mathbf{C}_h = n\mathbf{a}_1 + m\mathbf{a}_2$, where n and m are two integer numbers (the wrapping indices of the nanotube), and $\mathbf{a}_1$ and $\mathbf{a}_2$ are the two Bravais vectors of the graphene layer (Mintmire and White, 1995). This construction is illustrated in Fig. 7a and b. The diameter of the nanotube d is given by $d = \frac{\sqrt{3}a_{cc}}{\pi}\sqrt{n^2 + m^2 + n.m}$, and the chiral angle θ given by $\tan(\theta) = \frac{\sqrt{3}}{2m + n}$.

As in graphene, the electronic structure of a nanotube close to the Fermi energy is dominated by π and π^* states. A SWNT can be "metallic" or semiconducting, depending on its wrapping indices. When the radius is not too small, the rule is that the (n,m)

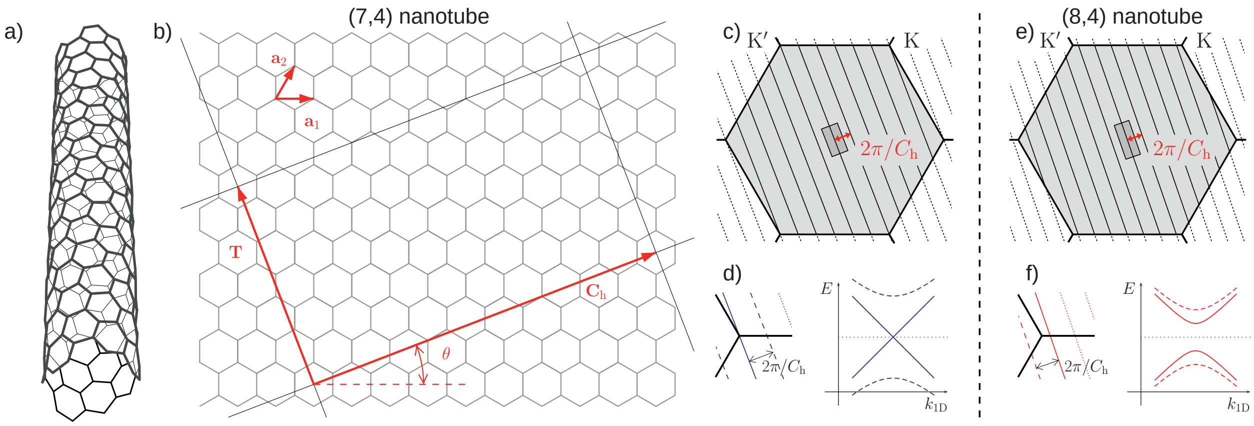

Fig. 7 (a) Schematic representation of a single-wall nanotube. The example is the (7,4) nanotube. (b) The unfolded canvas of the tube is a rectangular region, showing the construction of its chiral vector $\mathbf{C}_h = 7\ \mathbf{a}_1 + 4\ \mathbf{a}_2$. The translation symmetry vector **T** is perpendicular. The helical angle θ of the tube is indicated. (c) When *n*–*m* is a multiple of three the point K of the Brillouin zone of graphene is included in the selection of k-points of the zone folding model. (d) Consequently two bands with a nearly linear dispersion are crossing at E_F. The tube is "metallic." (e) When *n*–*m* is not a multiple of three the point K is not included in the selection. Bands are no longer crossing at E_F. (f) The nanotube is semiconducting.

Table 2 Electronic properties of single-wall (*n*, *m*) nanotubes.

"Zig-zag" if $m = 0$, otherwise "Chiral"		"Armchair"
$n - m \neq \mathcal{M}(3)$ Semiconductor	$n - m = \mathcal{M}(3) \neq 0$ Tiny gap ($E_g \sim \cos(3\theta)/d^2$)	$n - m = 0$ Truly metallic
$E_g = S_{11} = \frac{2\gamma_0 a_{cc}}{d}$ $S_{22} = 2S_{11}$	$M_{11} = 3S_{11}$	$\rho = \frac{2\sqrt{3}a_{cc}}{\pi^2\gamma_0 d}$

d is the diameter, θ is the chiral angle, $a_{CC} = 0.142$ nm, E_g is the bandgap of the semiconducting tubes, $\gamma_0 = 2.9$ eV is the π-electron interaction., and ρ is the density of states per atom at the Fermi level for the truly metallic tubes (or in the pseudogap plateau for the tubes exhibiting the tiny gap).

nanotube is metallic if *n*–*m* is a multiple of three, otherwise it is semiconducting (Table 2). The rolling of 2D graphene into a 1D tube results in the collapse of the 2D graphene band structure onto a series of 1D lines (Fig. 7c) whose spacing and orientation depends on the nanotube chirality. For metallic tubes, the Bloch vector at the point *K* (see Fig. 7c and d), where the π and π* bands of graphene meet, satisfies cyclic boundary conditions around the circumference: $C_h.K = q.2\pi$, with *q* an integer. Similarly to graphene, the electron bands close to E_F in a "metallic" nanotube are linear. They give rise to a plateau of density of states around the Fermi level (Fig. 8 left). At either sides of this plateau are spikes in the density of states, called van Hove singularities (vHs). These correspond to the top of the band located below the two linear bands, and the bottom of the next band above them. The energy separation of these two vHs is inversely proportional to the nanotube diameter, and is very useful for spectroscopic analysis (see below). Each band crossing the Fermi level contributes one quantum $2e^2/h$ to the conductance of the nanotube when it is connected to two macroscopic electrodes. This means that the minimum resistance of a metallic SWNT is $h/4e^2 = 6.45$ kΩ (two bands are crossing E_F). Below room temperature, the intrinsic resistance of an isolated nanotube increases upon cooling.

In the situation when *n*–*m* is a *not* multiple of three, the point *K* does not satisfy the cyclic conditions of the wrapping: the electronic bands of the nanotube never meet and a gap is opened (see Fig. 7e and f). Similarly to "metallic" nanotubes, the gap is flanked by two vHs (S_{11} in Fig. 8 right), and the value of this gap is inversely proportional to the tube diameter. In addition, a second pair of vHs is present in the density of states, separated by the energy S_{22}.

More reliable calculations of the electronic properties of nanotubes validate the predictions given by the zone folding model, as shown in Fig. 9. Only a small correction must be noted: in reality only the armchair (*n*,*n*) nanotubes are truly metallic, the "metallic" nanotubes with *n*–*m* a non-zero multiple of three exhibit a tiny gap that scales as $1/d^2$. The evolution of this secondary gap has been observed by scanning tunneling spectroscopy (Ouyang et al., 2001).

The most remarkable characteristic of the SWNTs, directly linked to their 1D periodicity, is the presence of the van Hove singularities (vHs) in the density of states. These spikes are fingerprints of the nanotube structure and can be probed by optical absorption, resonant Raman spectroscopy, electron-energy-loss spectroscopy (EELS), and scanning tunneling spectroscopy. An example of optical absorption spectrum of bundles of SWNTs with 1.3 nm average diameter is shown in Fig. 10a. The peaks ~0.7 and 1.3 eV are due to transitions between the first pair $E_{11}S$ and the second pair $E_{22}S$ of van Hove singularities that border the gap of the semiconducting nanotubes. The absorption peak ~1.9 eV is due to interband transitions $E_{11}M$ across the plateau of

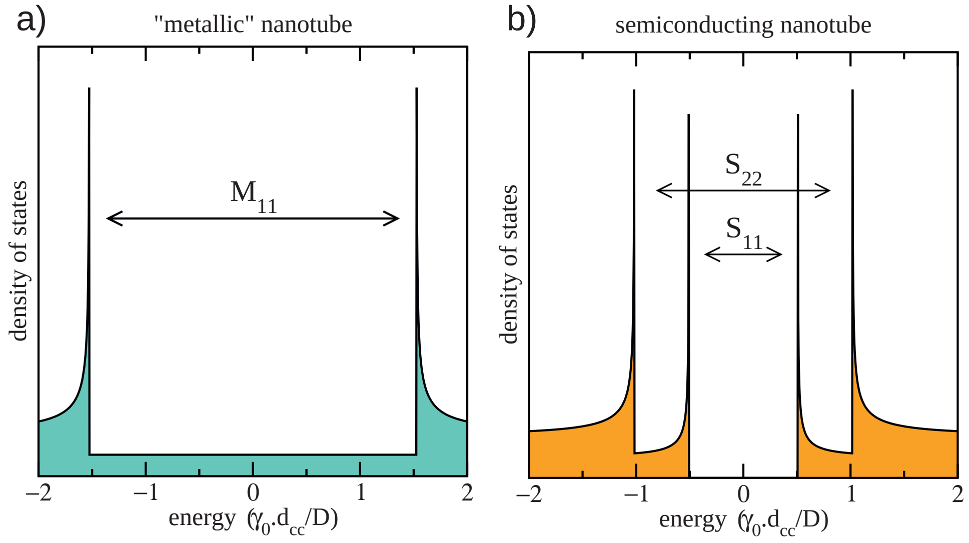

Fig. 8 (a) Typical shape of the electronic density of states of a "metallic" nanotube (the 7,4 nanotube in Fig. 7). It is constant over a wide energy range around E_F separated by two van Hove singularities (vHs). (b) Shape of the electronic density of states of a semiconductor nanotube. The gap (value S_{11}) is separated by a first couple of vHs. There is a second pair of vHs further from E_F with energy separation S_{22}.

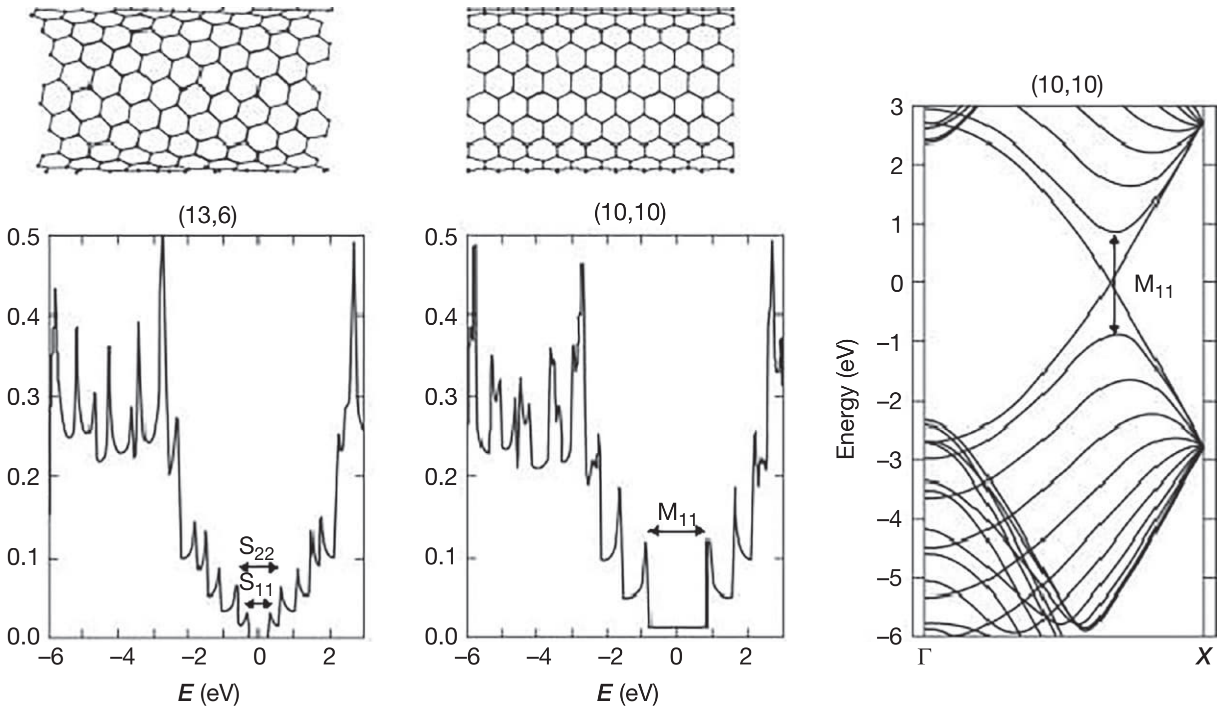

Fig. 9 Complete tight-binding ($\sigma + \pi$ electron) density of states of the semiconducting (13,6) chiral nanotube and the metallic armchair (10,10) nanotube. The atomic structures of these two nanotubes are illustrated on the top. The band structure of (10,10) is shown in the right-hand side panel. The Fermi level is set at zero energy.

density of states of the metallic nanotubes (see Fig. 7). In general, the spacing of the van Hove singularities is inversely related to the nanotube diameter, and plots of this are commonly referred to as Kataura plots (Kataura et al., 1999) (see Fig. 10b).

When performing resonant Raman spectroscopy, nanotubes with van Hove spacings corresponding closely to the energy of the exciting laser will have their signal enhanced by many orders of magnitude over non-resonant tubes. In practice this means that Raman spectroscopy of SWNTs only shows vibrational peaks for tubes which are in resonance. SWNTs have a low frequency vibrational mode detectable in Raman spectroscopy corresponding to a periodic change in the nanotube radius, called its radial

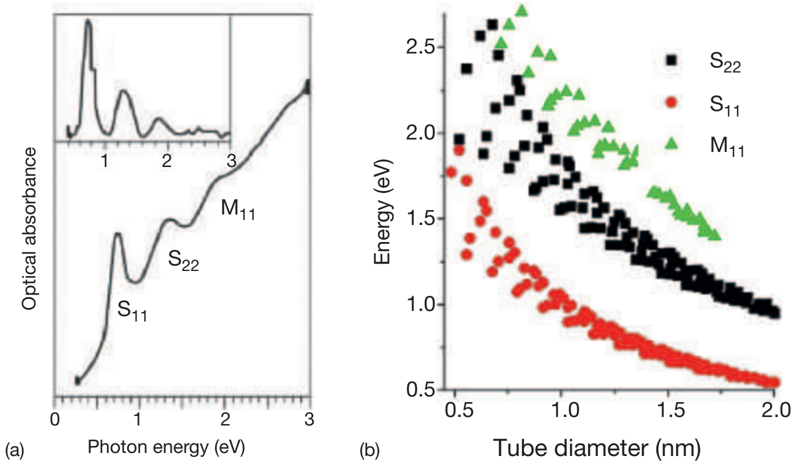

Fig. 10 (a) Optical absorption spectrum of bundles of SWNTs, with interband transition peaks superimposed on the wing of the broad π-plasmon absorption band. The same spectrum after removal of the plasmon background is shown in the inset. (b) Kataura plot showing spacing between van Hove singularities in the nanotube density of states for different tube diameters and chiralities as a function of their diameter. Image from Wikipedia.org.

breathing mode. The frequency of this mode is inversely proportional to the tube radius. It is therefore possible to modify the x-axis of the Kataura plot to show instead the radial breathing mode frequency. In this way, knowing the excitation laser energy used for the resonance Raman measurement and the frequency of detected radial breathing modes allows precise identification of the nanotubes present and in resonance in the sample.

Similar to graphite, bundles of single-wall carbon nanotubes can be doped by intercalation between and/or inside the tubes, using either electron acceptors (*p*-type doping (Grigorian et al., 1998)) or donors (*n*-type doping). In all cases, there is a charge transfer, a noticeable modification of the optical response of the nanotubes, and a strong reduction of the electrical resistance of the bundles. The Fermi level of the nanotube can be shifted by more than 1 eV by electron or hole doping. In the case of alkali intercalation, for instance, the Fermi level moves up across the conduction bands of the nanotubes. As a consequence, the lowest optical transitions S_{11}, S_{22}, and M_{11}, are progressively suppressed as their final states become occupied. The corresponding resonant behavior of the Raman cross section disappears at the same occasion. Other mechanisms to shift the Fermi level in nanotubes include molecular surface absorption, electrochemical gating, substitutional doping and defect formation (Monthioux, 2011).

For further reading see entries elsewhere in the encyclopedia covering "Electronic Properties of Rolled-up Nanoarchitectures" and "Optical Properties of Rolled-up Nanoarchitectures".

Fullerenes and fullerites

Fullerenes are hollow carbon cage molecules, the cages constructed from carbon atoms connected to three neighbors forming a closed or partially closed surface made up of polygons with carbon atoms at their vertices. Following Euler's formula, for a closed cage structure the number of pentagons minus number of heptagons must equal 12 (Anderson, 2023). C_{60} (Buckminsterfullerene) is the most abundant fullerene (Kroto et al., 1991). Its atoms are located on the surface of a sphere of ~0.7 nm diameter forming a truncated icosahedron. They sit at the vertices of 12 pentagons, the edges of which have a length of 0.145 nm, slightly longer than the 30 bonds (0.140 nm) shared by the hexagons that connect the pentagons. $2p$ orbitals locally normal to the molecular surface form π states, and $sp^{2+\epsilon}$ hybrids, which point along the C–C bonds form σ states, with some mixing of both characters due to the strong curvature of the molecule. The electronic levels of C_{60} are shown in Fig. 11a. In total there are 60 π states, of which 30 are occupied. Similarly, there are 90 σ occupied states. Due to the icosahedral symmetry of C_{60}, most of the electronic levels are degenerate. The highest occupied molecular orbital (HOMO) of C_{60} has h_u symmetry (fivefold degeneracy), and the lowest unoccupied molecular orbital (LUMO) has t_{1u} symmetry (threefold degeneracy). The HOMO–LUMO separation is 2 eV. The states near the HOMO–LUMO gap have a dominant π character. Because both the HOMO and LUMO wave functions are antisymmetric with respect to the inversion center of the molecule, the HOMO–LUMO transition is dipole forbidden. The lowest measured optical transition of the C_{60} molecule is ~3 eV. Due to its lower symmetry, the C_{70} molecule has eight different bonds, whose lengths vary between 0.137 and 0.147 nm. The one-electron states of C_{70} are singly or doubly degenerate, the HOMO–LUMO separation is 1.8 eV. The smallest fullerene, C_{20} consists of 12 pentagons and no hexagons, is almost entirely sp^3-bonding character due to the high local curvature, and as a result is extremely reactive and unstable (Prinzbach et al., 2000).

Fullerites are solids realized by close packing of fullerene molecules. The cohesion of these crystals is assured by van de Waals interactions between the fullerenes. In the solid, the electronic levels of the individual fullerene molecules are only weakly broadened by intermolecular coupling; they form bands with little dispersion, typically 0.5 eV. The C_{60} crystal (Fig. 11b) is a semiconductor with a 2.2 eV band gap, fcc at low temperatures but increasing in symmetry to simple cubic above 260 K when

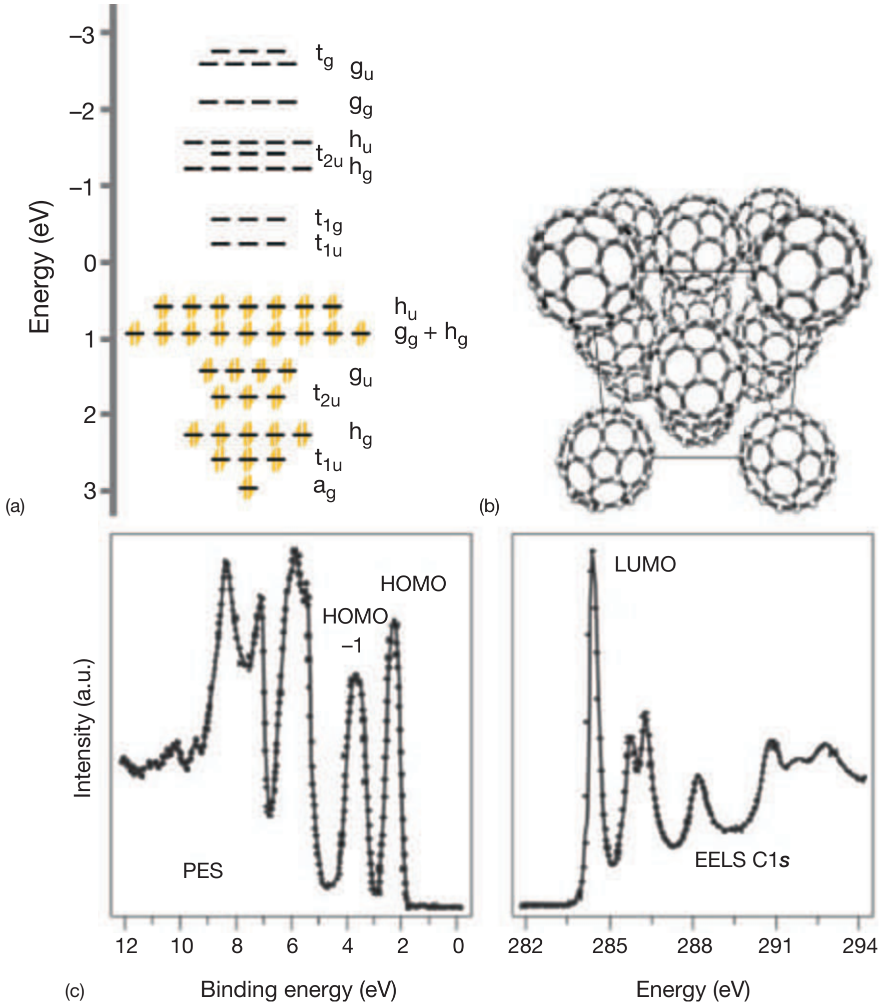

Fig. 11 (a) Electronic energy levels for isolated C_{60} (b) Conventional face-center cubic cell of the C_{60} fullerite, (c) Room temperature photoemission spectrum, and (d) C1s excitation EELS spectrum of C_{60} thin film, revealing the distribution of occupied and unoccupied electronic states, respectively.

individual C_{60} molecules freely rotate about their center of mass (Lubenets et al., 1997). The distribution of the occupied states in C_{60} fullerite is clearly revealed by photoemission spectroscopy (Fig. 11c), whereas the unoccupied states can be probed by inverse photoemission and also by EELS (Fig. 11d). High pressure compression of fullerites can result in polymerization and cross-linking between fullerene neighbors forming sp^3-bonds (Serebryanaya et al., 2001). The resultant ultra-hard fullerites are able to plastically deform diamond (Popov et al., 2014).

Like all molecules, the fullerenes are highly-correlated electronic systems. An effective Coulomb energy U can be estimated by $U = I - A - \Delta$, where I is the ionization energy (7.5 eV), A is the electron affinity (2.7 eV), and Δ is the HOMO–LUMO separation (2 eV). This gives $U \approx 2.8$ eV as the bare value for an isolated fullerene, although this can be reduced by 1 eV in the solid state due to screening effects.

Fullerenes can be doped, by incorporation of atoms endohedrally in the cage centers (Popov et al., 2013), e.g., Gd@C_{82} (Zhang et al., 2020), and by atomic substitution (heterofullerenes), such as $C_{59}N$ (Andreoni et al., 1996). X-ray photoemission provides valuable information on the electronic structure of these compounds (Erbahar et al., 2016). Inversely, various fullerenes and endohedral metallo-fullerenes can be encapsulated inside single-walled carbon nanotubes. In these remarkable structures, called carbon peapods, the encapsulated molecules form 1D chains (Smith et al., 1998). The fullerenes in a peapod can be more densely packed than in bulk fullerite. Their electronic levels form bands, which hybridize partly with the electronic states of the host nanotube.

Fullerites can be doped by intercalation of atoms and small molecules in the octahedral and tetragonal cavities of their crystal lattice. Since the electron affinity of the fullerene molecules is high, they easily accept electrons from the intercalants. In the case of C_{60}, the phase diagram of the A_xC_{60} compounds, with A an alkali metal, is remarkably rich. The x electrons given by the ionized alkali atoms fill in the t_{1u} LUMO-derived band, which may accommodate six electrons. This simple rigid band-structure picture predicts that all the A_xC_{60} compounds should be metallic except for $x = 0$ and 6. In fact, there are strong electron correlation effects in fullerites, as mentioned above, which invalidate this model, and only A_3C_{60} is metallic. Remarkably enough, most of the compounds having that composition are superconductors. The critical temperature T_c increases with increasing the ionic radius of the intercalant: 18 K in K_3C_{60} (Hebard et al., 1991), 30 K in Rb_3C_{60}, and 33 K in $RbCs_2C_{60}$ (Tanigaki et al., 1991). The raising of T_c is due to the narrowing of the LUMO-derived band with fullerene lattice spacing, and the resulting increase of density of states at the Fermi energy.

Miscellaneous synthetic carbons

Although many metastable pure carbon structures have been theoretically predicted, very few have been experimentally synthesized or isolated. Fully *sp*-hybridized carbon structures are notoriously unstable, but individual *sp*-bound C_{18} carbyne rings have been produced on surfaces and show alternating single-triple bond character (Kaiser et al., 2019; Scriven et al., 2020) (see Fig. 12a), while extended linear carbon chains have been successfully encapsulated inside carbon nanotubes (Shi et al., 2016). Localized triple carbon bonds (two carbons sharing one σ- and two orthogonal π-bonds) are short with a characteristically high vibrational frequency in the range 1800–2200 cm^{-1}.

Mixed sp/sp^2 layered structures, graphdiyne and graphynes, have been produced through organic synthesis routes (Hu et al., 2022; Leytham-Powell and University of Colorado Boulder, 2022; Li et al., 2010; Liu et al., 2022). Graphdiyne consists of a layered lattice of benzene rings, connected via triple-bonded C_2 pairs (see Fig. 12b). Since the back bonds on the benzene rings are single σ-bonds, there is no extended conjugation between the rings and the material behaves as a semiconductor.

Disordered carbons

Carbon may form different partially disordered solids depending on the preparation technique used and experimental conditions, all of which have considerable technological interest. Amorphous carbons form a wide range of structures intermediate between the two extreme allotropic forms, diamond and graphite. Each can be characterized by the sp^3/sp^2 ratio (there may be a small proportion of sp^1 states as well), and different degrees of local order and hydrogenation. The density of a carbon sample can be determined from the frequency of its $\sigma + \pi$ plasmon measured in EELS (Ferrari et al., 2000), by the formula $\omega_p = ne^2/\varepsilon_0 m^*$, where n is the valence-electron density, directly related to the atomic density, ϵ_0 is the dielectric permittivity, and m^* is the electron effective mass ($\approx 0.87\ m_e$) (LiBassi et al., 2000). EELS and C1*s* photoelectron spectroscopy give access to the sp^3/sp^2 fraction (Fallon et al., 1993; Grossman et al., 1996). Experiments indicate that the sp^3/sp^2 ratio increases linearly with the atomic density of the sample.

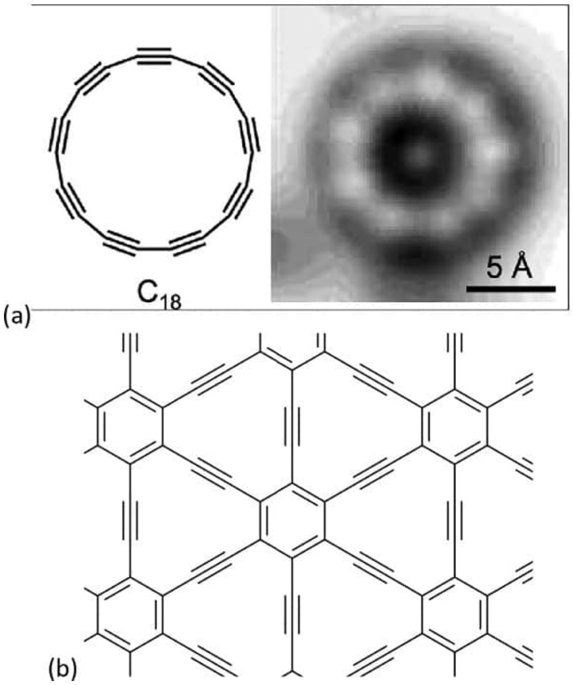

Fig. 12 (a) C_{18} *sp*-bound carbyne rings produced on substrates through debromination of $C_{18}Br_6$, and (b) γ-graphyne or graphdiyne structure consisting of *sp*-bonded C_2 units interconnecting hexagonal sp^2-rings. From Panel (a) Scriven LM, Kaiser K, Schulz F, Sterling AJ, Woltering SL, Gawel P, Christensen KE, Anderson HL, Gross L (2020). Synthesis of cyclo[18]carbon via debromination of C18Br6. *Journal of the American Chemical Society. 142*: 12921–12924. doi:10.1021/jacs.0c05033.

When the sp^2 and sp^3 sites are intermixed at the atomic scale, the electronic structure of amorphous carbon near the Fermi level is dominated by π and π^* states, arising from the sp^2 sites, and to a much lesser extent, by disorder-induced σ-band tails due to both sp^2 and sp^3 sites. When the sp^3/sp^2 ratio is large, as in most diamond-like carbons, one speaks of tetrahedral amorphous carbon. This material is hard, electrically insulating, and transparent. The minority sp^2 sites tend to form small clusters; they control the band gap, which can be reduced by a factor of 2 or more with respect to crystalline diamond. In sp^2-rich systems, the sp^3 sites can be randomly and uniformly distributed among the atoms, leading to a non-graphitic disordered structure. The electrical conductivity of such a sample is small and exhibits a semiconducting behavior. By heat treatment, and concomitant migration of the sp^3 defects, graphite-like amorphous carbon is obtained. It can be viewed as a random assembly of nanometer-sized turbostratic entities, partly embedded in a matrix of fourfold atoms. The electronic structure and the conductivity, then, depend critically on the size distribution of the turbostratic entities and on their degree of disorder.

Conclusion

In his 1975 short story collection "The Periodic Table," Primo Levi wrote that "Every element says something to someone (something different to each) like the mountain valleys or beaches visited in youth. One must perhaps make an exception for carbon, because it says everything to everyone" (Levi, 2000). Carbon is the earliest recorded non-metal chemical element in human history (approaching 4000BC charcoal was used for metal ore reduction by the Egyptians and Sumerians (CAER, 2012)), and yet continues to reveal new surprises, resulting in two Nobel prizes in the last 30 years. In this chapter we have shown that from only a few simple tools that carbon provides—the possibility of π-bonding, the capability to hybridize into sp, sp^2, and sp^3 configurations—a vast wealth of structures and electronic behaviors emerge, spanning the full range of condensed matter physics.

A key driver for the electronic behavior of carbon materials is local symmetry. In C_{60} the molecular icosahedral symmetry results in highly degenerate molecular states, the origin of superconductivity observed in doped fullerite crystals. The hexagonal 2D-lattice of conjugated p_z-orbitals in graphene results in conical electronic bands that touch at the Fermi level and give rise to the amazing Dirac fermionic behavior of electrons in graphene. The 1D-nature of nanotubes creates sharp van Hove singularities in their electronic density of states that dominates their optical response, with the tube symmetry determining whether it behaves as a metal, semi-metal or semiconductor.

The electronic behavior of carbons links directly to other material properties, such as the high thermal conductivity, optical transparency and toughness of diamond. As such the flexibility in geometry and electronic structure gives rise to carbon materials that span the range of materials parameters, representing some of the mechanically strongest and weakest materials known, the best insulators and conductors, and the most optically transparent to the blackest of blacks (Wikipedia, 2022b). Carbon continues to surprise (witness the discovery of superconductivity in twisted graphene bilayers (Cao et al., 2018)), and with continued advances in synthetic carbon chemistry and doping promising more to come, Primo Levi's words hold as true today as when they were first written.

References

American Elements, 2023. Fullerene-C60 American Elements. https://www.americanelements.com/fullerene-c60-99685-96-8 [WWW Document]. URL (accessed 9.21.22).

Anderson, O.K., 2023. Euler's Theorum (MPI-FKF) Educational. https://www2.fkf.mpg.de/andersen/fullerene/euler.html [WWW Document]. URL (accessed 9.21.22).

Andreoni W, Curioni A, Holczer K, Prassides K, Keshavarz-K. M, Hummelen J-C, and Wudl F (1996) Unconventional bonding of azafullerenes: Theory and experiment. *Journal of the American Chemical Society* 118: 11335–11336. https://doi.org/10.1021/ja962279i.

Bernal JD and Bragg WL (1924) The structure of graphite. *Proceedings of the Royal Society of London, Series A* 106: 749–773. https://doi.org/10.1098/rspa.1924.0101. Containing Papers of a Mathematical and Physical Character.

CAER K (2012) *University of Kentucky Center for Applied Energy Research—Carbon Materials—Carbon History and Timeline*. Educational. https://web.archive.org/web/20121101085829/http://www.caer.uky.edu/carbon/history/carbonhistory.shtml#. [WWW Document]. URL (accessed 9.21.22).

Cao Y, Fatemi V, Fang S, Watanabe K, Taniguchi T, Kaxiras E, and Jarillo-Herrero P (2018) Unconventional superconductivity in magic-angle graphene superlattices. *Nature* 556: 43–50. https://doi.org/10.1038/nature26160.

Clark CD, Dean PJ, Harris PV, and Price WC (1964) Intrinsic edge absorption in diamond. *Proceedings of the Royal Society of London. Series A: Mathematical and Physical Sciences* 277: 312–329. https://doi.org/10.1098/rspa.1964.0025.

Collins PG, Arnold MS, and Avouris P (2001) Engineering carbon nanotubes and nanotube circuits using electrical breakdown. *Science* 292: 706–709. https://doi.org/10.1126/science.1058782.

Crawford KG, Maini I, Macdonald DA, and Moran DAJ (2021) Surface transfer doping of diamond: A review. *Progress in Surface Science* 96: 100613. https://doi.org/10.1016/j.progsurf.2021.100613.

De A and Pryor CE (2014) Electronic structure and optical properties of Si, Ge and diamond in the lonsdaleite phase. *Journal of Physics: Condensed Matter* 26: 045801. https://doi.org/10.1088/0953-8984/26/4/045801.

Diamond: Mineral Information, Data and Localities. 2023. https://www.mindat.org/min-1282.html [WWW Document], URL (accessed 9.21.22).

Dolde F, Fedder H, Doherty MW, Nöbauer T, Rempp F, Balasubramanian G, Wolf T, Reinhard F, Hollenberg LCL, Jelezko F, and Wrachtrup J (2011) Electric-field sensing using single diamond spins. *Nature Physics* 7: 459–463. https://doi.org/10.1038/nphys1969.

Ebert LB (1976) Intercalation compounds of grpahite. *Annual Review of Materials Science* 181–211.

Erbahar D, Susi T, Rocquefelte X, Bittencourt C, Scardamaglia M, Blaha P, Guttmann P, Rotas G, Tagmatarchis N, Zhu X, Hitchcock AP, and Ewels CP (2016) Spectromicroscopy of C60 and azafullerene C59N: Identifying surface adsorbed water. *Scientific Reports* 6: 35605. https://doi.org/10.1038/srep35605.

Fallon PJ, Veerasamy VS, Davis CA, Robertson J, Amaratunga GAJ, Milne WI, and Koskinen J (1993) Properties of filtered-ion-beam-deposited diamondlike carbon as a function of ion energy. *Physical Review B* 48: 4777–4782. https://doi.org/10.1103/PhysRevB.48.4777.

Ferrari AC, Libassi A, Tanner BK, Stolojan V, Yuan J, Brown LM, Rodil SE, Kleinsorge B, and Robertson J (2000) Density, sp3 fraction, and cross-sectional structure of amorphous carbon films determined by x-ray reflectivity and electron energy-loss spectroscopy. *Physical Review B* 62: 11089–11103. https://doi.org/10.1103/PhysRevB.62.11089.

Gabrysch M, Majdi S, Twitchen DJ, and Isberg J (2011) Electron and hole drift velocity in chemical vapor deposition diamond. *Journal of Applied Physics* 109: 063719. https://doi.org/10.1063/1.3554721.

Graphite Summary 2023. mindat.org. https://www.mindat.org/min-1740.html [WWW Document], URL (accessed 9.21.22).

Grigorian L, Williams KA, Fang S, Sumanasekera GU, Loper AL, Dickey EC, Pennycook SJ, and Eklund PC (1998) Reversible intercalation of charged iodine chains into carbon nanotube ropes. *Physical Review Letters* 80: 5560–5563. https://doi.org/10.1103/PhysRevLett.80.5560.

Grossman E, Lempert GD, Kulik J, Marton D, Rabalais JW, and Lifshitz Y (1996) Role of ion energy in determination of the sp3 fraction of ion beam deposited carbon films. *Applied Physics Letters* 68: 1214–1216. https://doi.org/10.1063/1.115973.

Hebard AF, Rosseinsky MJ, Haddon RC, Murphy DW, Glarum SH, Palstra TTM, Ramirez AP, and Kortan AR (1991) Superconductivity at 18 K in potassium-doped C60. *Nature* 350: 600–601. https://doi.org/10.1038/350600a0.

Hedberg K, Hedberg L, Bethune DS, Brown CA, Dorn HC, Johnson RD, and De Vries M (1991) Bond lengths in free molecules of buckminsterfullerene, C60, from gas-phase electron diffraction. *Science* 254: 410–412. https://doi.org/10.1126/science.254.5030.410.

Himpsel FJ, Knapp JA, VanVechten JA, and Eastman DE (1979) Quantum photoyield of diamond(111)—A stable negative-affinity emitter. *Physical Review B* 20: 624–627. https://doi.org/10.1103/PhysRevB.20.624.

Hu Y, Wu C, Pan Q, Jin Y, Lyu R, Martinez V, Huang S, Wu J, Wayment LJ, Clark NA, Raschke MB, Zhao Y, and Zhang W (2022) Synthesis of γ-graphyne using dynamic covalent chemistry. *Nature Synthesis* 1: 449–454. https://doi.org/10.1038/s44160-022-00068-7.

Kaiser K, Scriven LM, Schulz F, Gawel P, Gross L, and Anderson HL (2019) An sp-hybridized molecular carbon allotrope, cyclo[18]carbon. *Science* 365: 1299–1301. https://doi.org/10.1126/science.aay1914.

Kataura H, Kumazawa Y, Maniwa Y, Umezu I, Suzuki S, Ohtsuka Y, and Achiba Y (1999) Optical properties of single-wall carbon nanotubes. *Synthetic Metals* 103: 2555–2558. International Conference on Science and Technology of Synthetic Metals https://doi.org/10.1016/S0379-6779(98)00278-1.

Kleshch VI, Purcell ST, and Obraztsov AN (2016) Single crystal diamond needle as point electron source. *Scientific Reports* 6: 35260. https://doi.org/10.1038/srep35260.

Kraus D, Ravasio A, Gauthier M, Gericke DO, Vorberger J, Frydrych S, Helfrich J, Fletcher LB, Schaumann G, Nagler B, Barbrel B, Bachmann B, Gamboa EJ, Göde S, Granados E, Gregori G, Lee HJ, Neumayer P, Schumaker W, Döppner T, Falcone RW, Glenzer SH, and Roth M (2016) Nanosecond formation of diamond and lonsdaleite by shock compression of graphite. *Nature Communications* 7: 10970. https://doi.org/10.1038/ncomms10970.

Kroto HW, Allaf AW, and Balm SP (1991) C60: Buckminsterfullerene. *Chemical Reviews* 91: 1213–1235. https://doi.org/10.1021/cr00006a005.

Levi P (2000) Carbon. In: *The Periodic Table*, 26th, p. 240. Penguin Classics. ISBN-10: 0141185147, ISBN-13: 978-0141185149.

Leytham-Powell C and University of Colorado Boulder (2022) Long-hypothesized “next generation wonder material” created for first time. https://phys.org/news/2022-05-long-hypothesized-material.html. [WWW Document]. URL (accessed 9.21.22).

Li G, Li Y, Liu H, Guo Y, Li Y, and Zhu D (2010) Architecture of graphdiyne nanoscale films. *Chemical Communications* 46: 3256–3258. https://doi.org/10.1039/B922733D.

Li Y, Lu Y, Adelhelm P, Titirici M-M, and Hu Y-S (2019) Intercalation chemistry of graphite: alkali metal ions and beyond. *Chemical Society Reviews* 48: 4655–4687. https://doi.org/10.1039/C9CS00162J.

LiBassi A, Ferrari AC, Stolojan V, Tanner BK, Robertson J, and Brown LM (2000) Density, sp3 content and internal layering of DLC films by X-ray reflectivity and electron energy loss spectroscopy. *Diamond and Related Materials* 9: 771–776. https://doi.org/10.1016/S0925-9635(99)00233-2.

Liu X, Cho SM, Lin S, Chen Z, Choi W, Kim Y-M, Yun E, Baek EH, Ryu DH, and Lee H (2022) Constructing two-dimensional holey graphyne with unusual annulative π-extension. *Matter* 5: 2306–2318. https://doi.org/10.1016/j.matt.2022.04.033.

Lof RW, van Veenendaal MA, Koopmans B, Jonkman HT, and Sawatzky GA (1992) Band gap, excitons, and Coulomb interaction in solid C60. *Physical Review Letters* 68: 3924–3927. https://doi.org/10.1103/PhysRevLett.68.3924.

Lubenets SV, Natsik VD, Fomenko LS, Isakina AP, Prokhvatilov AI, Strzhemechny MA, Aksenova NA, and Ruoff RS (1997) The structure, slip systems, and microhardness of C60 crystals. *Low Temperature Physics* 23: 251–261. https://doi.org/10.1063/1.593358.

Mintmire JW and White CT (1995) Electronic and structural properties of carbon nanotubes. *Carbon* 33: 893–902. https://doi.org/10.1016/0008-6223(95)00018-9.

Monthioux M (2011) *Carbon Meta-Nanotubes: Synthesis, Properties and Applications*, 1st edn. Wiley. Wiley.

Okada M, Ohta N, Yoshimoto O, Tatsumi M, and Inagaki M (2017) Review on the high-temperature resistance of graphite in inert atmospheres. *Carbon* 116: 737–743. https://doi.org/10.1016/j.carbon.2017.02.039.

Ouyang M, Huang J-L, Cheung CL, and Lieber CM (2001) Energy gaps in “metallic” single-walled carbon nanotubes. *Science* 292: 702–705. https://doi.org/10.1126/science.1058853.

Pisanty A (1991) *The Electronic Structure of Graphite: A Chemist’s Introduction to Band Theory*. [WWW Document] ACS Publicationshttps://doi.org/10.1021/ed068p804.

Popov AA, Yang S, and Dunsch L (2013) Endohedral fullerenes. *Chemical Reviews* 113: 5989–6113. https://doi.org/10.1021/cr300297r.

Popov M, Mordkovich V, Perfilov S, Kirichenko A, Kulnitskiy B, Perezhogin I, and Blank V (2014) Synthesis of ultrahard fullerite with a catalytic 3D polymerization reaction of C60. *Carbon* 76: 250–256. https://doi.org/10.1016/j.carbon.2014.04.075.

Prinzbach H, Weiler A, Landenberger P, Wahl F, Wörth J, Scott LT, Gelmont M, Olevano D, and v. Issendorff B (2000) Gas-phase production and photoelectron spectroscopy of the smallest fullerene, C20. *Nature* 407: 60–63. https://doi.org/10.1038/35024037.

Rabenau T, Simon A, Kremer RK, and Sohmen E (1993) The energy gaps of fullerene C60 and C70 determined from the temperature dependent microwave conductivity. *Zeitschrift fuer Physik B: Condensed Matter* 90: 69–72. https://doi.org/10.1007/BF01321034.

Scriven LM, Kaiser K, Schulz F, Sterling AJ, Woltering SL, Gawel P, Christensen KE, Anderson HL, and Gross L (2020) Synthesis of cyclo[18]carbon via debromination of C18Br6. *Journal of the American Chemical Society* 142: 12921–12924. https://doi.org/10.1021/jacs.0c05033.

Serebryanaya NR, Blank VD, Ivdenko VA, and Chernozatonskii LA (2001) Pressure-induced superhard phase of C60. *Solid State Communications* 118: 183–187. https://doi.org/10.1016/S0038-1098(01)00082-5.

Shi L, Rohringer P, Suenaga K, Niimi Y, Kotakoski J, Meyer JC, Peterlik H, Wanko M, Cahangirov S, Rubio A, Lapin ZJ, Novotny L, Ayala P, and Pichler T (2016) Confined linear carbon chains as a route to bulk carbyne. *Nature Materials* 15: 634–639. https://doi.org/10.1038/nmat4617.

Smith BW, Monthioux M, and Luzzi DE (1998) Encapsulated C60 in carbon nanotubes. *Nature* 396: 323–324. https://doi.org/10.1038/24521.

Tanigaki K, Ebbesen TW, Saito S, Mizuki J, Tsai JS, Kubo Y, and Kuroshima S (1991) Superconductivity at 33 K in CsxRbyC60. *Nature* 352: 222–223. https://doi.org/10.1038/352222a0.

Turneaure SJ, Sharma SM, Volz TJ, Winey JM, and Gupta YM (2017) Transformation of shock-compressed graphite to hexagonal diamond in nanoseconds. *Science Advances* 3: eaao3561. https://doi.org/10.1126/sciadv.aao3561.

Umezawa H (2018) Recent advances in diamond power semiconductor devices. *Materials Science in Semiconductor Processing* 78: 147–156. Wide band gap semiconductors technology for next generation of energy efficient power electronics. https://doi.org/10.1016/j.mssp.2018.01.007.

van der Weide J, Zhang Z, Baumann PK, Wensell MG, Bernholc J, and Nemanich RJ (1994) Negative-electron-affinity effects on the diamond (100) surface. *Physical Review B* 50: 5803–5806. https://doi.org/10.1103/PhysRevB.50.5803.

Wikipedia (2022a) *Buckminsterfullerene*. Wikipedia.

Wikipedia (2022b) *Vantablack*. Wikipedia.

Zhang K, Wang C, Zhang M, Bai Z, Xie F-F, Tan Y-Z, Guo Y, Hu K-J, Cao L, Zhang S, Tu X, Pan D, Kang L, Chen J, Wu P, Wang X, Wang J, Liu J, Song Y, Wang G, Song F, Ji W, Xie S-Y, Shi S-F, Reed MA, and Wang B (2020) A Gd@C82 single-molecule electret. *Nature Nanotechnology* 15: 1019–1024. https://doi.org/10.1038/s41565-020-00778-z.

Atomic layer deposition of materials

Jun Peng and Robert Zierold, Center for Hybrid Nanostructures, Universität Hamburg, Hamburg, Germany

© 2024 Elsevier Ltd. All rights reserved.

Introduction to and general principle of ALD **716**
Overview **718**
Thermal vs. plasma-enhanced ALD 718
Temporal vs. spatial ALD 720
ALD of oxides 721
ALD of nitrides 721
ALD of metals and elements 722
ALD of sulfides, phosphides, fluorides 722
ALD of ternary and quaternary components 723
In situ characterization of ALD processes 724
Nanostructures (high aspect ratio) 725
Conclusion **726**
Acknowledgments **727**
References **727**

Abstract

As a chemical vapor deposition technique that can achieve outstanding coating conformality on complex structures, atomic layer deposition (ALD) has received great attention in both academic research and industrial applications since its invention in the 1960s and 1970s. Herein, the basic principle of ALD—based on a sequence of self-limiting gas-solid-surface reactions—and different ALD approaches are summarized, namely temporal vs. spatial and thermal vs. plasma-enhanced. Subsequently, the variety of materials deposited by ALD is highlighted, and some ALD-coated nanostructures are presented. Finally, a short but comprehensive introduction is given to the most recent developments and achievements in ALD or closely related methods.

Introduction to and general principle of ALD

Atomic layer deposition (ALD) is a coating technique to deposit thin films and is closely related to the chemical vapor deposition (CVD) method. In contrast to normal CVD, where one or more precursors are decomposed or reacted in the gas phase, ALD bases on sequential, separated self-limiting gas-solid surface reactions of two or more gaseous precursor species. A binary ALD cycle consisting of two half-reactions is sketched in Fig. 1A.

Four steps can be identified:

1. *Pulse 1:* The substrate's surface is occupied by certain surface groups. Vapor of precursor α is brought to the substrate's surface.
2. *Purge 1:* After the completed, self-terminating surface reaction, the non-used precursor α molecules as well as the reaction by-products are pumped away, and the reaction chamber is purged.
3. *Pulse 2*: At this point, the substrate remains in an intermediate surface state. The second precursor β is pulsed into the ALD chamber and reacts in a self-limiting manner with the exposed parts of precursor α chemisorbed to the substrate.
4. *Purge 2*: After the completed gas-solid surface reaction, the reaction chamber is purged from the by-products and the non-used precursor β molecules.

If the two precursors α and β are well-chosen, the surface groups after one ALD cycle allow for repeating the cycle. In every ideal ALD cycle, the same amount of material—a fraction of the material's monolayer—is deposited depending on the accessible surface sites, the precursor size, and the precursor and substrate chemistry. Typical growth rates, usually defined as *growth per cycle* (GPC), observed for ALD processes range from 0.1 to 1.5 Angstrom per ALD cycle. Thus, the total deposited film thickness can be defined by the number of cycles during an ALD process (Fig. 1B). Note, the thin film growth via ideal ALD is not limited by the absolute mass transport of precursor molecules as long as self-termination of the surface reactions is reached. In general, ALD is diffusion-limited, which means, on the one hand, no line-of-sight from the precursor source to the substrate is required (Fig. 1C). On the other hand, the molecules need sufficient time for diffusion and surface site reaction. Consequently, homogeneous and conformal coatings with controlled sub-nm thickness can be achieved even on three-dimensional (3D) features at the expense of extended process times. Depending on the precursors chosen, a plethora of materials can be deposited by ALD, ranging from oxides, nitrides, fluorides, sulfides, and phosphides as well as selenides, tellurides to pure elements or mixtures of the aforementioned materials. In the "[. . .] case study for the trimethylaluminum/water process," Puurunen describes the most important features and main characteristics of ALD in detail in her review article in 2005 (Puurunen, 2005). An updated version of the review, including more than 2300

https://doi.org/10.1016/B978-0-323-90800-9.00206-7

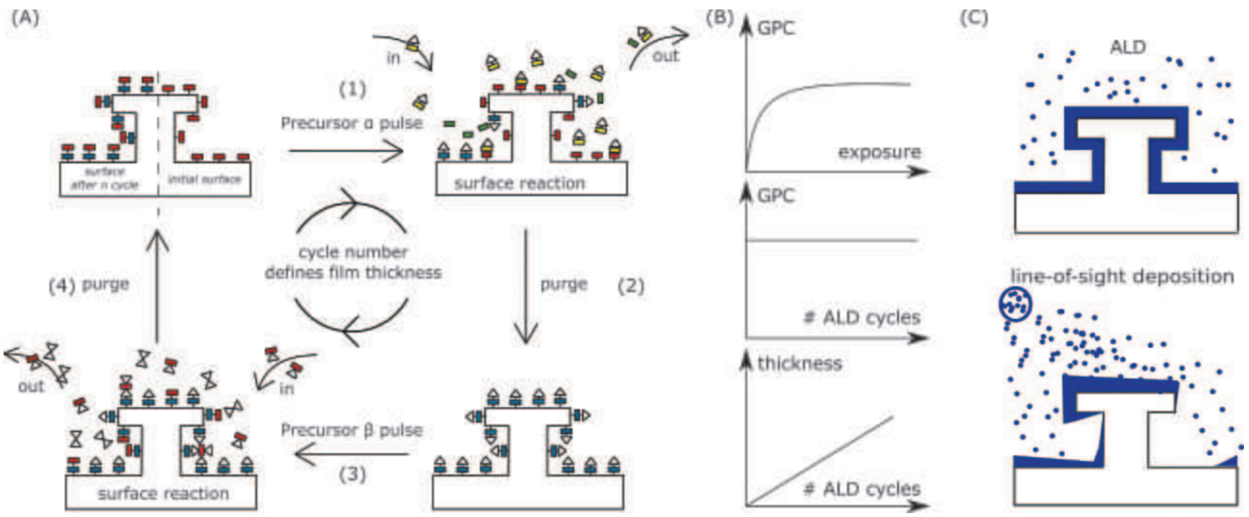

Fig. 1 (A) Schematic of an ALD cycle with two different precursor species. One ALD cycle consists of a pulse of precursor α which reacts in a self-limiting manner with surface groups. After purging the reaction chamber, the precursor β is brought to the substrate presenting an intermediated surface. Precursor β reacts there again in self-terminating behavior, and deposits the desired material. Subsequently, the reaction chamber is purged again. Since the (resulting) surface groups after one ALD cycle can react with precursor α again, a sequential deposition routine allows for exact thickness control by adjusting the number of cycles. (B) Due to the self-limiting nature of the ALD reactions, a constant GPC and thus a linear growth as the function of cycle number is achieved. (C) Schematic comparison of a conformal surface reaction-limited ALD process and a deposition process which is mass flux limited by a line-of-sight coating, e.g., sputtering.

references and focusing on the crystallinity of ALD deposited film was published in 2013 (Miikkulainen et al., 2013). In general, ALD has the capability to provide continuous, pinhole-free films with a low content of residual impurities. However, by employing the different surface chemistry of precursors on various materials, ALD can be tailored in such a way that the deposition of nanoparticles and clusters or in an area-selective fashion is feasible (Grillo et al., 2017; Mackus et al., 2014). Note, Steve George's review (George, 2010) summarizes in a short and comprehensive manner the major trends and developments in ALD in the last two decades. Specifically, the review addresses new ALD process technologies, such as plasma-enhanced ALD (PEALD), atmospheric-pressure ALD, spatial ALD, area-selective ALD (AS-ALD), and (polymer) molecular layer deposition (MLD), to name a few of them.

The origin of ALD dates back to the 1960s and 1970s when the principle of ALD was developed and investigated in parallel in the former Soviet Union and Finland under the name "Molecular layering" and "Atomic Layer Epitaxy," respectively. However, the initial ALD research activities in the Soviet Union went unnoticed for a long time and are still poorly cited compared to the fundamental studies in Finland (Puurunen, 2014). An ALD community-driven virtual project on the history of ALD (VPHA) (Ahvenniemi et al., 2017) summarizes 22 publications—voted by the community as significant early achievements in the field of ALD—in chronological order. Note, "early" is defined therein as before 1986 when a review article about ALD or atomic layer epitaxy was published by authors not treated as the pioneers of ALD. In detail, Shevjakov, Aleskovskii, and Kol'tsov reported on metal chloride reactions with water for the deposition of TiO_2, GeO_2, and later SiO_2 and PO_x from 1965 to 1975. At that time, Suntola and Antson (Suntola and Antson, 1977) patented the principle of atomic layer epitaxy for depositing compound films from elemental precursors, e.g., ZnS from Zn and S. However, other materials such as SnO_2 and GaP are listed, as well, and H_2S as a potential hydrogen source is suggested. In the follow-up patents and applications, molecular inorganic precursors were introduced, e.g., $TaCl_5$ and $AlCl_3$ with H_2O for depositing Ta_2O_5 and Al_2O_3, respectively, as well as ZnS from $ZnCl_2$ and H_2S. Note, the first industrial application of ALD or atomic layer epitaxy was in fact ZnS, which was used for the fabrication of thin film electroluminescence displays employed at Helsinki airport from 1982 until 1998. In the mid of the 80s, metal-organic precursors were introduced in ALD for the first time to deposit III-V semiconducting GaAs and AlAs by utilizing AsH_3 with $Ga(CH_3)_3$ and $Al(CH_3)_3$, respectively. In the early 1990s, the more general term ALD gained acceptance over atomic layer epitaxy because many ALD reactions did not result in epitaxial or even crystalline growth. Due to the high purity of the deposited materials, the ability to coat even complex structures without shadowing effect, and the precise control of the film thickness, ALD came into the focus of the semiconductor industry in the 1990s for the deposition of high-κ dielectrics. Using materials with higher dielectric constant than the classical silicon dioxide allowed for further miniaturization of metal-oxide-semiconductor field-effect transistors (MOSFET) structures. Together with the industrial interest in ALD, the research landscape also revived, and great progress was made in the last 20 years in precursor and reaction chemistry. As of 2022, a community-driven process database hosted and maintained by Kessel's group at Eindhoven University of Technology gives a tabular literature overview of the published processes.[1] Moreover, a regularly updated list of review articles related to ALD can also be found there. ALD is outstandingly suited for the coating of (nano) structures with high aspect ratios—the ratio of geometrical characteristic length and diameter—because of its self-limiting nature.

---

[1] https://www.atomiclimits.com [accessed 02.04.2022]

In such substrates, e.g., opals, nanoporous membranes, bio-materials, and nanoparticles, ALD is often the only suitable technique to reach a conformal coating without shadowing effects (Knez et al., 2007; Bae et al., 2011; Detavernier et al., 2011). Besides basic research in physics, chemistry, and material science, ALD is also a state-of-the-art technique in different industry fields, such as semiconductor and solar cell energy.

Overview

In order to offer a more comprehensive understanding of ALD, this section firstly presents several basic forms of ALD, namely thermal and plasma-enhanced ALD as well as temporal and spatial ALD in Sections "Thermal vs. plasma-enhanced ALD" and "Temporal vs. spatial ALD", respectively. Since ALD has received attention from basic research to industry in recent years, a variety of ALD processes utilizing various precursor types have been explored to deposit materials comprising the majority of elements in the periodic table as summarized in Fig. 2. However, one of the most important points for a successful ALD is the metal precursors used. A typical metal precursor contains one type of metal atom per precursor, and several characteristics, namely high reactivity, volatility, and good thermal stability over a wide temperature range, have to be fulfilled. State of aggregation, costs, ease of handling, and toxicity are side aspects but not to be neglected. Note, the ligands' properties determine the properties of the metal precursor and thus can be used to tailor the precursor chemistry. Although the potential advantages of organometallic precursors are their high volatility and low growth temperature, one of the disadvantages is that their thermal decomposition often takes place already at low temperatures, which may induce non-self-limiting CVD components besides the ALD growth and high impurity contents. Main material classes deposited by ALD are presented in Sections "ALD of oxides," "ALD of nitrides," "ALD of metals and elements," "ALD of sulfides, phosphides, fluorides." Subsequently, approaches synthesizing multi-component films (Section "ALD of ternary and quaternary components") and, following, in situ characterization methods in ALD processes (Section "In situ characterization of ALD processes") are discussed. Finally, a selection of applications profiting from the unrivaled ability of ALD to deposit conformal coatings on nanostructures will be presented.

Thermal vs. plasma-enhanced ALD

ALD bases on (at least) two binary reactions of a precursor α with a precursor β, often denoted as reactants, to prepare the desired material. A common example is the deposition of aluminum oxide by the reaction of trimethylaluminum (TMA, $Al(CH_3)_3$) with water. The two half-reactions can be written as:

$$(1\text{st half}-\text{reaction})\ \mathrm{AlOH}^* + \mathrm{Al(CH_3)_3} \rightarrow \mathrm{AlOAl(CH_3)_2}^* + \mathrm{CH_4}$$

$$(2\text{nd half}-\text{reaction})\ \mathrm{AlCH_3}^* + \mathrm{H_2O} \rightarrow \mathrm{AlOH}^* + \mathrm{CH_4}$$

$$\text{summing up to } 2\mathrm{Al(CH_3)_3} + 3\mathrm{H_2O} \rightarrow \mathrm{Al_2O_3} + 3\mathrm{CH_4}.$$

The driving force of this exothermic reaction is the formation of a strong Al-O chemical bond. Similarly, other thermal oxide processes, such as those for TiO_2 and ZnO, are also driven by a conducive change in the Gibbs free energy. However, other ALD reactions might require additional energy, such as heat, to overcome the energy barrier for the chemical reaction of the precursor with the surface. In the ideal ALD, a temperature range, the so-called *ALD window*, can be defined in which the growth per cycle is constant (Fig. 3). Below the ALD temperature window, either CVD caused by precursor condensation or a suppressed growth can be

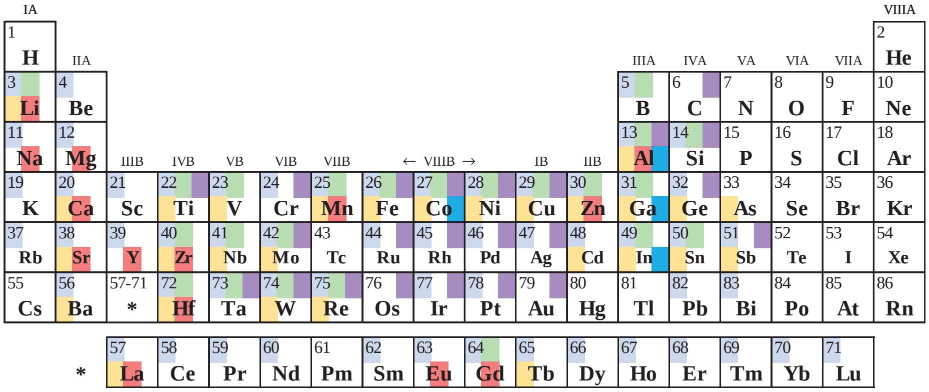
IA
VIIIA
IIA
IIIA
IVA
VA
VIA
VIIA
IIIB
IVB
VB
VIB
VIIB
← VIIIB →
IB
IIB
1 H
2 He
3 Li
4 Be
5 B
6 C
7 N
8 O
9 F
10 Ne
11 Na
12 Mg
13 Al
14 Si
15 P
16 S
17 Cl
18 Ar
19 K
20 Ca
21 Sc
22 Ti
23 V
24 Cr
25 Mn
26 Fe
27 Co
28 Ni
29 Cu
30 Zn
31 Ga
32 Ge
33 As
34 Se
35 Br
36 Kr
37 Rb
38 Sr
39 Y
40 Zr
41 Nb
42 Mo
43 Tc
44 Ru
45 Rh
46 Pd
47 Ag
48 Cd
49 In
50 Sn
51 Sb
52 Te
53 I
54 Xe
55 Cs
56 Ba
57-71 *
72 Hf
73 Ta
74 W
75 Re
76 Os
77 Ir
78 Pt
79 Au
80 Hg
81 Tl
82 Pb
83 Bi
84 Po
85 At
86 Rn
*
57 La
58 Ce
59 Pr
60 Nd
61 Pm
62 Sm
63 Eu
64 Gd
65 Tb
66 Dy
67 Ho
68 Er
69 Tm
70 Yb
71 Lu

Fig. 2 Periodic table illustrating the reported materials deposited by ALD. Oxides, nitrides, pure elements, sulfides, phosphides, and fluorides are displayed with cerulean, olive, purple, straw, red, and blue background squares, respectively, at the element's panel.

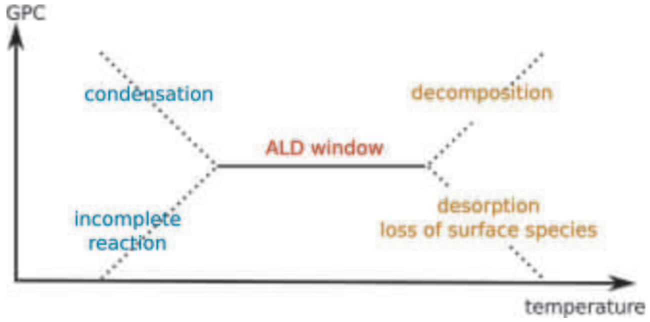

Fig. 3 Sketch of the ALD window including the processes when the ALD window is left to lower and higher temperatures.

identified; whereas, above the ALD window, precursor decomposition and desorption or loss of functional groups can lead to CVD and reduced growth, respectively. Note, the applicable reaction temperatures are generally limited by constraints in precursor vapor pressure and stability, reaction chamber design, and substrate. To overcome this thermodynamic obstacle without excessive heating, additional external energy is needed which can be provided, e.g., by a highly reactive species delivered from plasma or radical source in at least one half-cycle of the ALD reaction. In addition to the inherent higher reactivity of the plasma radical, the ions' kinetic energy, surface recombination rates and energies, and the total energy flux of the plasma radiation contribute to the additional energy term in a PEALD process.

Already in the first ALD review by Suntola and Hyvärinen in 1985 (Suntola and Hyvarinen, 1985), the authors predicted the occurrence of plasma-supported ALD to render new reaction pathways. Six years later, a first plasma-enhanced, also called plasma-activated, ALD process of GaAs employing hydrogen radicals prepared in a plasma source was reported. However, it lasted almost one decade until the ALD community took up the topic when PEALD was used for the deposition of Ti and Ta. From there, novel processes and precursors as well as plasma sources and reactor types have been developed, enabling ALD scientists to deposit materials hardly achievable by thermal ALD, e.g., elemental metals and semiconductors, or to improve the deposition quality and to reduce the impurity content of the deposited films. The reviews of Profijt in 2011 (Profijt et al., 2011) and Knoops in 2019 (Knoops et al., 2019) present a comprehensive summary of the development of PEALD in the past 20 years.

On the one hand, PEALD reveals several advantages compared to thermal ALD: First, as aforementioned, the plasma, with its highly reactive species, provides an additional energy contribution. Consequently, the thermal energy, i.e., temperature, needed to deposit an ALD thin film with the same properties as in a thermal ALD process can be lowered. Such a reduction in temperature is of particular interest if temperature-sensitive substrates, e.g., polymeric ones, need to be coated. Second, several publications report on improved material properties deposited by PEALD compared to thermal ALD, such as impurity content, density, and optical or electronic characteristics, to name a few. Third, some metal-organic precursors are not usable in thermal ALD; thus, novel ALD reaction pathways are conceivable. For instance, some metal-organic compounds with sufficient vapor pressure and thermal stability reveal a vanishing or negligible reactivity to water, rendering them unsuitable for thermal ALD. However, by utilizing a highly reactive oxygen plasma, these compounds can be employed as ALD precursors, opening new reaction schemes. Additionally, hydrogen plasma can provide highly reducing species to allow for depositing metals not feasible by thermal ALD reductants. Fourth, due to the highly reactive plasma species, more reactive surface sites can be prepared during the ALD plasma half-cycle leading to an overall increased growth rate for some processes.

On the other hand, PEALD also has some drawbacks compared to thermal ALD. The major disadvantage is the non-usability of PEALD to coat high aspect ratio nanostructures or highly porous substrates conformally. Recombination of radicals at the surface with other species or radicals is accompanied by losing their high reactivity. Since the probability of surface collision and, consequently, recombination is significantly increased for these kinds of high surface area substrates, the local flux of radicals inside the porous structure or at 3D structures is reduced as a function of the diffusion depth and geometry, respectively; thus, the deposition becomes non-conformal. By varying the plasma parameters, such as power, duration, and pressure, to name a few of them, the conformality of the PEALD process can be controlled and improved for aspect ratios up to ~30. However, PEALD cannot compete with thermal ALD where aspect ratios of 1000 and more or even branched porous substrates with non-ballistic transport paths can be coated conformally at sufficiently long diffusion and purge times. Another impediment of PEALD is the possibility of damage or surface alteration upon the plasma half-reaction. The highly reactive species of the reactant can alter the chemical properties of the substrate surface via oxidation and nitridation, leading to an unwanted interface. Energetic ions impinging on the surface during the plasma may lead to bond-breaking and defects in the deposited materials or on the substrate, as well as to charge accumulation in the thin film. Another source of plasma-induced damage is the highly energetic ultraviolet (UV) radiation occurring during the plasma. This radiation can alter the properties of polymeric substrates but also potentially introduce defects and degrade surface passivation. Lastly, the plasma source and the control of which render the ALD system much more complex, prone to error, and expensive. Furthermore, the parameter space for process optimization, e.g., temperature, (partial) pressure, and precursor dose, is expanded by the plasma parameters, e.g., power and duration.

Temporal vs. spatial ALD

The invention and development of ALD sparked several concepts of ALD reactor designs. The scientists in the former Soviet Union started their research on ALD in a reactor chamber with a stationary substrate exposed to a sequence of different precursors. In contrast, Suntola drafted in his initial patent (Suntola and Antson, 1977) a concept of a rotating disk holding the substrate which crosses areas of stationary precursor vapors during spinning. Thus, two different major operation modes can be defined, namely temporal and spatial ALD (Fig. 4).

In temporal ALD, a heated reactor is loaded with a stationary substrate, and stationary valves control the precursors flow by opening and closing one after the other, separated by a purge/pump time. Adjusting the duration of the individual steps in the ALD cycle is needed to achieve sufficient precursor doses to saturate all surface groups but also to remove all non-used precursors and reaction by-products to avoid reduced growth and CVD, respectively. Scale-up of thermal temporal ALD processes is achieved in so-called batch reactors in which several substrates are stacked over each other and coated simultaneously. Of course, precursor doses and purge times have to be increased according to the increased surface area of the reactor and substrate. Note, PEALD in batch reactors is hampered because of the stacked arrangements of the substrates (see Fig. 4). Specifically, the long diffusion paths without line-of-sight between substrate and plasma source increase the probability of surface collision and recombination; thus, reducing the number of reactive species deep inside the batch.

In spatial ALD, the substrate moves through different fixed and stationary precursor zones separated by a zone where the purging occurs. For instance, this could be a rotating substrate, as in the Suntola patent (Suntola and Antson, 1977). Still, it could also be a substrate transported (back and forth) through a line of different precursor zones separated by an inert gas zone (see Fig. 4). A fixed substrate with a movable precursor injection head is another concept of spatial ALD. Note, in all cases, not only thermal ALD but also PEALD operation is feasible. The main advantage of spatial ALD compared to temporal ALD is the absence of purge time needed to empty the reaction chamber. Since the chemical surface reaction typically occurs in the millisecond time range, only the mechanical transfer time between two separated precursor zones limits the total cycle time of ALD. Of course, at more complex structures, the exposure time—which is the time the substrate has to remain in one precursor zone—has to be extended to fulfill the ALD criterion of self-limitation at all available and accessible surface groups. A good overview of different concepts of spatial ALD, such as roll-to-roll reactors where a flexible substrate is moved from one roll to another roll by guide rollers running several times through two different precursor zones chamber, rotating disks reactors, and drum reactors, to name a few of them, is given by Poodt

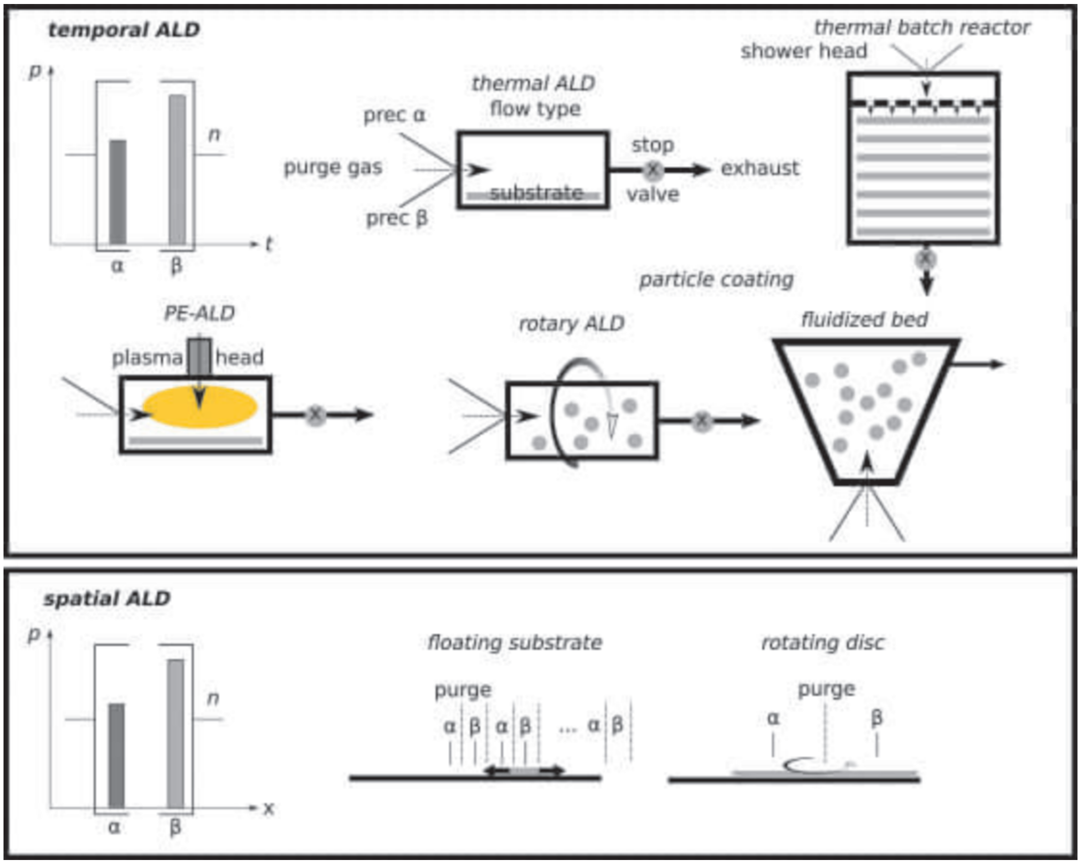

Fig. 4 Schematic overview for different reactor types. Upper box: Types of ALD reactors operating in a temporal fashion, e.g., thermal and thermal batch ALD, PEALD, but also ALD systems for particles coatings. Lower box: ALD reactor types working in the spatial regime, such as floating substrate or rotating disk reactors.

et al. (Poodt et al., 2011). In terms of economic aspects, spatial ALD comes with a more complex reactor design with mechanical parts compared to temporal ALD. On the other hand, the reactor wall is coated in temporal ALD, and usually, much more precursor than needed for the self-limiting surface reaction is provided. However, the precursor excess, which is not reacted, is then purged and thus wasted. In other words, the efficiency of precursor utilization is increased for spatial ALD concepts compared to temporal ones. Consequently, the running costs of the spatial ALD coating, namely the expenses for precursors, could be significantly reduced compared to temporal ALD. Moreover, complex gas abatement systems for cleaning the exhaust gas of non-used (and potentially explosive or toxic) precursor are superfluous.

ALD of oxides

Metal oxides have been deposited from a huge variety of inorganic and organic molecular precursors, such as halides, alkoxides, alkyls, amides, and beta-diketonates, just to name a few. As reactants, water, ozone, and oxygen plasma have been mainly used (Miikkulainen et al., 2013). Note, processes with water often bases on a protonation reaction of the precursor ligands, whereas reactions with ozone and oxygen plasma are often combustion-like. Alternative oxidant precursors, such as hydrogen peroxide, alcohols, and N_2O, have been reported in literature as well. Furthermore, special ALD processes have been explored which do not contain a separate dedicated oxygen reactant but use another metal precursor as oxygen source. Specifically, metal alkoxides or carboxylates have been employed for such processes that are treated as more gentle to the underlying substrate since a highly oxidizing reactant is waived.

Historically, the major driving force for ALD of oxides was the need for advanced high-κ dielectrics as gate oxides in MOSFET and as capacitor dielectrics in dynamic random-access memories (DRAM). Nowadays, ALD is recognized as a state-of-the-art deposition technique in the industrial fabrication of these complex logic and memory devices due to its inherent conformality and film thickness control, often outperforming other deposition techniques, such as CVD and sputter coat (Hwang, 2014). Within the last decades, the device structures changed from 2D to nanostructured 3D, rendering ALD the method of choice. The majority of the deposited dielectrics by ALD are binary oxides, e.g., HfO_2, Al_2O_3, ZrO_2, to name a few of them. Also, doped oxides, e.g., Sr- or Ba-doped TiO_2 ($SrTiO_3$, STO; $BaTiO_3$, BTO) or nanolaminates consisting of zirconia and alumina are of particular interest for DRAM applications (Coll and Napari, 2019).

Recently, ALD in general has aroused interest in more fields and applications: Special attention has been paid to moisture diffusion barrier layers, e.g., Al_2O_3, $ZrO_{2,}$ and SiO_2, to encapsulate and to protect organic-light emitting diodes (OLED). Other transition-metal oxides, namely MO_3, WO_3, and V_2O_5 have been employed as hole contact in OLEDs. Further, lithium oxide compounds have already been deposited for battery applications. Besides, in organic and flexible electronics and displays, ALD of transparent conducting oxides, for instance, Sn-doped In_2O_3 (ITO) and Al-doped ZnO (AZO), has taken hold in industry.

Other properties of oxide thin films, e.g., magnetism, ferroelectricity, or multiferroics, deposited by ALD have been investigated in detail in basic research but also for applications. For example, multiferroic (doped) hafnia layers have been studied as potential resistive RAM (ReRAM).

Apart from binary oxides, plenty of doped oxides, e.g., In_2O_3:Zr, SnO_2:Sb, ZnO:Ga, and other ternary or quaternary oxides (for further information see Section "ALD of ternary and quaternary components"), such as $PbTiO_3$, $SrTa_2O_6$, $SrBi_2Ta_2O_9$, $La_{1-x}Ca_xMnO_3$, to name a few of them, have also been produced via ALD.

ALD of nitrides

Typically, metal nitrides are hard, chemically resistant, sometimes catalytically active, and often electrically conductive materials. Since the pioneering work of ALD-deposited metal nitride published in 1988 (Hiltunen et al., 1988), they have become the material class with the 2nd most number of ALD publications after ALD oxides. Metal nitrides, such as Si_3N_4, TaN, TiN, and WN_x, are often used as diffusion barriers for water as well as oxygen and metal diffusion, respectively, in the microelectronics industry. Another increasing interest in ALD of nitrides exists in research on superconductivity, e.g., TiN, NbN, or mixtures of them. The reported nitrides deposited by ALD can be generally divided into two categories according to their electrical properties: (1) nitride dielectrics or semiconductors such as BN, AlN, GaN, Si_3N_4, Ta_3N_5, Cu_3N, InN, Zr_3N_4, Hf_3N_4, LaN, LuN; (2) metallic nitrides such as TiN, Ti-Si-N, TaN, NbN, MoN, Ti-Al-N, WN_x, WN_xC_y, Co_xN, Sn_xN.

The most typical ALD nitride processes are based on the reaction of metal chloride (or other halide) precursors with NH_3 as a reactant. A prime example is the reaction of $TiCl_4$ with NH_3 to deposit TiN. However, these processes need relatively high temperatures (typically in the range of 350–500 °C) and suffer from residual impurities of the respective halogens. Both issues can be addressed simultaneously by replacing the halide precursor with a metal-organic precursor. Specifically, metal-organic alkyl amide-based compounds can be used for metal nitride deposition, e.g., TiN, ZrN_x, MoN_x, HfN_x, TaN_x, and $WN_,$ at lower temperatures (150–250 °C) compared to the halide-based processes and avoiding halogen residues at the same time but at the cost of additional carbon impurities (Miikkulainen et al., 2013). To grow nitrides containing main Group III elements, namely Al, Ga, and In, by ALD, alkyls which contain a direct metal-carbon bond have been used.

NH_3 serves as a reductant of the metal center in the precursor during the ALD reaction. Generally, NH_3 leads to the stable nitride with the highest metal oxidation state. For instance, to achieve the conductive TaN over the dielectric Ta_3N_5 an additional reducing agent to NH_3, such as elemental Zn or Me_3Al needs to be implemented during the ALD process (Miikkulainen et al., 2013). Different reducing agents, such as hydrazine (Me_2NNH_2) and tert-butylamine, have been employed for the deposition of TaN and TiN as well.

PEALD can ease the deposition of metal nitrides with a lower oxidation state and often reduced amount of impurities compared to thermal ALD. The deposition temperature can be lowered, novel precursor chemistries could be used, e.g., $Nb(N^tBu)(NEtMe)_3$ instead $NbCl_5$ for depositing NbN, and the number of tunable process parameters, e.g., plasma power, pressure, and gases, can be increased to improve and tune the thin film properties. Instead of using gaseous NH_3, nitrogen-hydrogen mixtures with adjustable ratio have been exploited in PEALD. The hydrogen-plasma serves as reductant during the ALD process whereas the nitrogen-plasma resembles the nitrogen source. Note, amide compounds, i.e., $Ti[NMe_2]_4$, in combination with reducing hydrogen (plasma) have been studied to deposit the corresponding nitride, i.e., TiN, without the need of an additional nitrogen source.

ALD of metals and elements

Metals deposited by ALD are often more challenging to achieve in high quality compared to oxides and nitrides. Consequently, relatively less research—and even fewer industrial applications—utilizing metal ALD has been carried out compared to ALD of metal oxides in the past. However, in order to fulfill Moore's law, CMOS devices need to be further downs-scaled, and the architecture becomes more complex. Hence, increased demands for the precision and conformality of the deposition process are set. These requirements can be easily met by ALD leading to a number of potential applications in the device fabrication, not only for oxides and nitrides as aforementioned, but also for metal deposition. Tungsten and copper are essential metals for plugs and interconnects, respectively, in CMOS technology and have been in focus for ALD for a while. Whereas, tungsten layers can be deposited by the reducing WF_6 with diborane, silanes, or hydrogen (plasma) for years. The reliable deposition of metallic copper remained challenging until novel reaction pathways have been developed, e.g., $Cu(dmap)_2$ or $Cu(hfac)_2$, in combination with a plethora of reductants including H_2, H_2 plasma, diethyl zinc, formic acid, formaldehyde, etc. Other applications of metals (Ru, Co, Ta, Ni, and Ti) deposited by ALD in barriers and liners for interconnects or electrical contacts and gate electrodes are conceivable nowadays. Note, the introduction of 3D gate structures, such as fin- or nanowire-based gate-all-around FETs makes the use of ALD processes inevitable for reliable device fabrication (Hagen et al., 2019; Hwang, 2014).

Noble metals, especially in the form of (nano)particles, are of interest for catalysis applications. In contrast to electronic device preparation in which continuous—ideally pinhole-free—thin films are aimed for, isolated particles and islands are often preferred for maximum catalytic performance. By employing the difference in surface energy of the metal to be deposited and the substrate, the ALD process parameters can be tuned to adjust particle-size distribution. Especially, platinum-group metals, e.g., Pt, Ru, Pd, Ir, are comparably easy to reduce in their oxidation state—after precursor adsorption of the metal precursor at the substrate's surface—and thus can be deposited in their metallic state without the need of high temperatures or strong reducing agents.

Three different types of reaction schemes for the reduction step have been mainly explored: First, "normal" reducing agents, e.g., H_2, NH_3, and N_2/H_2 as well as plasma of which, have been applied not only on platinum group metals but also on some more reactive metals. Molecular H_2 has been widely used for the ALD of some highly reactive metals, e.g., Cu, Ta, Ti, and Sn, by reaction with their halides. NH_3 or nitrogen/hydrogen plasma was employed to deposit metallic films of cobalt and nickel. Second, metal deposition via an intermediated surface oxidation step by utilizing oxygen, ozone, water, or air as reactant for combustion of the adsorbed precursor. In other words, firstly, a metal oxide film is produced, followed by a subsequent reduction to metal by the next metal precursor pulse. This reaction is often supported by self-catalytic effects of the metallic thin films as well as a limited stability of the intermediated oxides. Third, other less common reducing agents have been investigated to deposit metals, such as zinc vapor, silanes, and boranes.

Note, further developing and optimizing processes for metals remain an important aspect of ALD. Specifically, metal-organic precursor development and the search for matching reductants are still ongoing for reliable metal deposition. Current materials of interest are the deposition of gold and silver. Moreover, understanding the interplay between substrate properties, e.g., surface energy, texture, and oxidation state, with the metal deposition process, specifically its initial nucleation, is essential to control and to tune the growth of metallic particles but also continuous thin films.

ALD of sulfides, phosphides, fluorides

Apart from the widely investigated oxides, nitrides, and metals discussed above, other binary compounds have also been explored and some of which have even been already put to applications.

As previously mentioned, the development of ALD was driven by the need for an optimized fabrication method for thin film electroluminescent displays containing ZnS. In detail, manganese- as well as rare and alkaline earth-doped ZnS films, have been used for monochromatic (yellow) and multi-color displays, respectively. Most recently, the development of advanced structures for "green" energy-related applications, such as photovoltaics or batteries, have been a driving force for ALD of sulfide materials. Especially the unique ability of ALD to conformally coat complex structures is advantageous to coat these (often porous) devices with a large surface area and to tailor the interfaces. For example, CdS and InS can be employed to deposit a buffer layer for energy band alignment in $Cu(In,Ga)Se_2$ (CIGS) solar cells. The first deposition of ZnS based on elemental Zn and S. However, halides and, much more prominent, metal-organic precursors can easily react with hydrogen sulfide (H_2S) to form a metal sulfide at lower temperatures than needed for elemental precursors.

ALD of phosphides has been rarely reported: Only CoP has been developed as a catalyst to enable efficient water splitting, whereas AlP, GaP, and InP have gotten their position in semiconductor applications. Phosphorus is customarily delivered by its hydrides, e.g., PH_3 plasma. However, PH_3 decomposes seriously during plasma treatment so that excess P remains, which is hard to eliminate in the following purge step and leads to an undesirable deposition. Therefore, the subsequent removal—for instance, by an additional H_2 plasma step—of the excess P would be the key to achieve ALD of phosphides (Zhang et al., 2020).

Metal fluorides, e.g., CaF_2, SrF_2, MgF_2, LaF_3, ZnF_2, are important optical coating materials because they possess not only a low refractive index but also a high transmission at both UV and infrared (IR) wavelengths. The conformal characteristic of ALD coating renders it a perfect method to produce three-dimensionally shaped optical components. Furthermore, other metal fluorides, e.g., AlF_3, have been employed as a protective coating on Li-ion battery electrodes. Similarly to phosphides, only a decent number of processes for ALD of fluorides has been reported because vaporous HF reacts with metal-organic precursors to form fluorides, e.g., AlF, MgF, NaF, ZrF_4, etc., but it is highly toxic and corrosive, and thus needs dedicated ALD and laboratory equipment with high safety requirements. Nonetheless, alternatives have been explored: On the one hand, the in situ thermal decomposition of NH_4F to only locally create the HF and to avoid handling dangerous HF vapor has been suggested. On the other hand, vaporous TiF_4 and TaF_5 have been used as fluorine reactants in combination with a variety of metal-thd precursors. Unlike HF, these reactants are low vapor pressure solids and can thus be handled and stored more safely with fewer restrictions. Note, even the reactant carries another metal center, the impurity content of Ti and Ta is reported to be of minor nature.

ALD of ternary and quaternary components

The basic principle of ALD is based on two half-reactions forming a binary material. Hence, traditional applications of ALD rely on binary oxides. However, the binary process can be combined to form complex tailor-made materials containing three, four, and more elements, often referred to as ternary, quaternary, and quinary materials, respectively. Strategies to synthesize such complex materials by ALD include so-called supercycle schemes, co-dosing approaches, and multistep approaches (Vandalon, 2020; Mackus et al., 2019b), as illustrated in Fig. 5.

A regular binary ALD cycle (Fig. 5A) usually consists of sequential precursor pulses, exposure, or carrier gas purge for each half-reaction to form one ALD cycle. In a so-called supercycle deposition scheme, two or more binary ALD processes (running *m*- and *n*-times, etc.) are put together into a "larger" loop which itself is then repeated *x*-times (Fig. 5B). Depending on the number of *m* and *n*, the achieved compound can be tailored and divided as follows:

(1) *m* and *n* are comparably small and equal (e.g., 1:1, 1:2, etc.): A ternary oxide, $A_xB_yC_z$, which is uniform and well-mixed in the deposited composition. The ratio between the different constituents can be slightly tailored.
(2) $m \gg n$, or vice versa (e.g., 1:20, 1:50): A doped material can be achieved.
(3) *m* and *n* are close but large (e.g., 20:20, 40:50, etc.): A so-called nanolaminate consisting of separated continuous thin layers is formed.

Accordingly, in the example of the reactions with diethylzinc (precursor β), trimethylaluminum (precursor γ), and water (precursor α) for depositing ZnO and Al_2O_3, one can deposit by varying *m* and *n*: (1) a $Zn_xAl_yO_z$ ternary oxide thin film with tailor-made stoichiometry, (2) an Al-doped ZnO thin film which can be employed as transparent conductive oxide, and (3) a multilayer film of separated Al_2O_3 and ZnO layers. Also, the accordingly management of trimethylaluminum (precursor β) and O_3 (precursor α_1) plus titan(*IV*)isopropoxide (precursor γ) and water (precursor α_2) can respectively lead to $Al_xTi_yO_z$, Al-doped TiO_2, "Al_2O_3 + TiO_2" nanolaminate too.

In the co-dosing approach, as shown in Fig. 5C, at least two precursors (e.g., β, γ) are injected simultaneously into the reaction chamber simultaneously. Alternatively, two precursors or reactants can be mixed in varying proportions in the precursor container or a dedicated volume and then injected together. A typical example of the co-dosing scheme is the ALD process for ZnO_xS_y. Both reactants, namely, H_2O and H_2S, are pulsed at the same time. By varying the concentration ratio of them, the resulting composition of the deposited materials can be tailored.

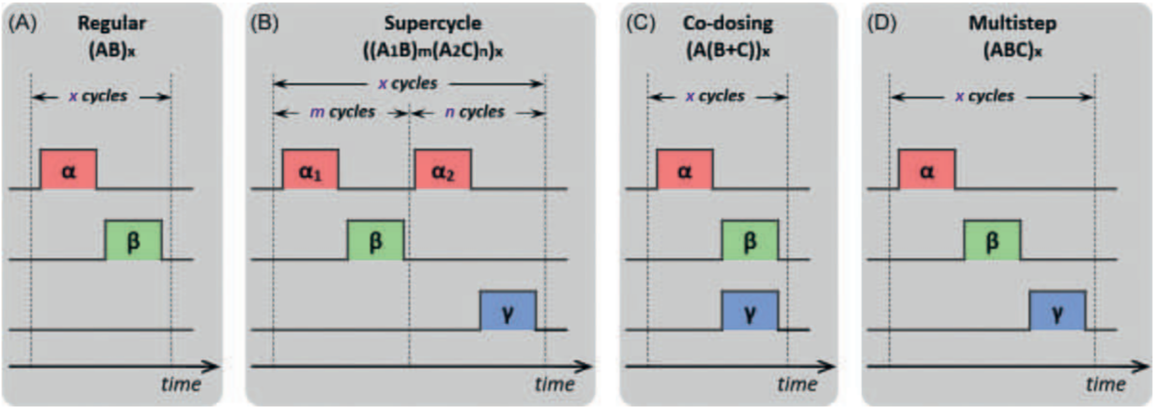

Fig. 5 Schematic overview of strategies leading to complex materials constituting more than two elements. Here, precursor α, β, γ are containing the target deposited elements A, B, C, respectively. Precursor α_1 and α_2 in the schematic diagram for supercycle can stand for the same precursor or two different precursors that contribute to the same deposited element A.

Supercycling and co-dosing can both be used for the deposition of multicomponent thin films. However, each of them has specific advantages and downsides. On the one hand, better mixing of the constituents in the sub-monolayer regime can be achieved by co-dosing compared to the supercycle approach. On the other hand, the simultaneous competing chemical reactions of the two precursors on the substrate—with different (and often not well-known) kinetics, reactivity, diffusivity, and adsorption behavior—complicate the prediction for process optimization and may vary in complex architectures like trenches. In contrast, such a potential drawback is avoided in the supercycle approach since the individual ALD reactions are separated. To which degree any of these effects play a role and to which extent they impact the properties of the prepared film varies from case to case.

The multistep approach (Fig. 5D) is also used to deposit multicomponent materials in ALD. Within this manner, a regular ALD process consisting of two half-cycle (AB-type) is extended by adding one or more steps (ABC-, ABCD-type, etc.). These additional steps can introduce an other constituent to the material, resulting in the deposition of a multicomponent material. Besides, the multistep scheme is often used to extend the operating window of ALD processes or modify the properties of a material. For example, in the low-temperature Pt ALD process using $PtMe_3CpMe$ and O_2 plasma, the regular ALD process results in PtO_x at low temperatures. Low-temperature deposition of metallic platinum can be achieved by a multistep approach adding an H_2 plasma as a third step to reduce the PtO_x to metallic Pt.

Note, different process schemes can be combined with each other, e.g., the plasma-enhanced deposition of TiNbN uses the supercycle approach for varying the Nb/Ti ratio and the co-dosing approach during the plasma half-reaction of nitrogen and hydrogen to replace NH_3.

In situ characterization of ALD processes

Optimization and characterization of ALD processes are typically performed as follows in daily lab routine: One of the ALD parameters, such as precursor or reactants, temperatures (chamber, precursor), characteristic times (pulse, exposure, purge), plasma parameters (power, duration), to name a few of them, is altered and a process of *x*-cycles is run. Subsequently, the properties of the deposited thin film, e.g., composition, morphology, thickness, and crystallinity, are ex situ characterized, and based on these results, the process is adapted. This procedure is repeated until the desired properties are achieved. However, such an approach could be rather time-consuming and the chemical reactions occurring at the surface during the process remain unknown.

Hence, in situ operation of characterization methods typically used afterward, but also other techniques not applied for thin film analysis can speed up the optimization process and may shed light onto the ALD reaction itself. Note, the self-limiting nature of the ALD half-reactions is beneficial for these kinds of studies since the surface remains for a long time in the same state allowing for long measuring/integration times without altering the surface. Most of the ex situ characterization methods used in the ALD community to characterize the deposited thin film or the process can also be employed in situ after modification of the ALD reaction chamber.

A summary of selected in situ methods and the targeted thin film and reaction analysis is given in Table 1 (Knapas and Ritala, 2013; Devloo-Casier et al., 2014; Dendooven and Detavernier, 2017).

Table 1 In situ methods and their targets.

Classification	*Method*	*Target*
Gravimetry/Mass	Quartz crystal microbalance to study the mass up-take/loss during half-reactions	• GPC • Conclusion to chemistry • Characteristic times (saturating and purging behavior) • Determination of precursor decomposition and surface etching reaction
Optical	Fourier-transform infrared spectroscopy	Molecular species during half-reactions in gas phase and on surface
	(Surface-enhanced) Raman	Molecular species on surface
	(Spectroscopic) Ellipsometry	Film thickness evolution and refractive index
	Optical emission spectroscopy	Only for PEALD: species during plasma pulse
X-ray Analysis	Absorption spectroscopy	Probing the local atomic environment
	Diffraction	Crystallinity and grain size
	Fluorescence	Film composition (and thickness)
	Grazing-incidence small-angle scattering	Surface morphology
	Photoelectron spectroscopy	Surface composition and oxidation state
	Reflectivity	Thickness, roughness, density
Charge/Mass	Quadrupole mass spectrometry	Gas phase molecules
Electron	Reflection high-energy electron diffraction	Growth mode and film thickness
Electrical/thermal	Resistance measurements	Conductivity and growth mode
	Thermopile	Heat, reaction enthalpy

Nanostructures (high aspect ratio)

The separated self-limiting gas-solid chemical reactions of ALD feature two important aspects: (1) thickness control in the sub-nm regime and (2) conformal deposition in a non-line-of-sight fashion. Hence, ALD is ideally suited to overcoat complexly shaped nano- and microstructures since the gaseous precursor can easily penetrate into complex substrates, and the same film thickness at any position of the sample is deposited. ALD has proven its value in applications of conformal thin film deposition inside complicated geometries and 3D nanostructures, e.g., deep trenches, grooves, narrow pores, aerogels, etc. All of which are difficult to coat conformally by other deposition techniques such as sputter, pulsed laser deposition, and CVD.

Depending on the template structure, which needs to be coated, ALD can be used in exposure/stop mode operation. In detail, a valve between chamber and vacuum pump is closed immediately before the precursor is pulsed into the chamber. Then the reaction chamber rests in this state, and the precursor molecule can diffuse into the template structure. After a time *t*, the valve is opened again, and the chamber is purged. Note, determining the minimum duration of *t*—which can span even to a few minutes—is not trivial since several aspects such as sticking probability, temperatures, pressures, precursor doses, and aspect ratio, to name a few of them, influence the time needed to achieve full coverage of the surface (Cremers et al., 2019).

A plethora of nanostructured templates such as free-standing nanowires and -tubes, porous membranes, 3D printed scaffolds, assembled spheres/blocks, polymeric networks, CNT forests, and even biological substrates, e.g., viruses and butterfly wings, have been coated by ALD for various applications (Knez et al., 2007; Bae et al., 2011; Detavernier et al., 2011; Harberts et al., 2020). A selection of templates is highlighted in Fig. 6. Moreover, prominent applications of ALD and nanostructures used therein are summarized in Table 2.

In general, ALD on these nanostructured templates can fulfill several tasks:

(i) Adding a "functional" layer to a non-active template that provides support, e.g., metal electrodes, photoactive layer, magnetic layers.
(ii) Stabilization of underlying substrate, e.g., resistive coating against harsh environments, increasing mechanical stability, encapsulation.
(iii) Changing the electrical nature of the surface, e.g., ionic conductivity, capacity enhancement, work function adaptation.
(iv) Spacer layer or sacrificial layer between functional layers of interest.

A conformal coating of individual particles which are assembled on a substrate is hampered by the contact points between the particles but also between particle and substrate. (Miniaturized) Fluidized bed and rotary reactors agitate the particles in such a way that surface reactions all around the particles are achieved during the exposure to the precursor gases (Weimer, 2019). The coated particles can be later assembled into composite materials for application in similar fields as aforementioned, e.g., catalysis, electrode materials, and encapsulation, to name a few of them.

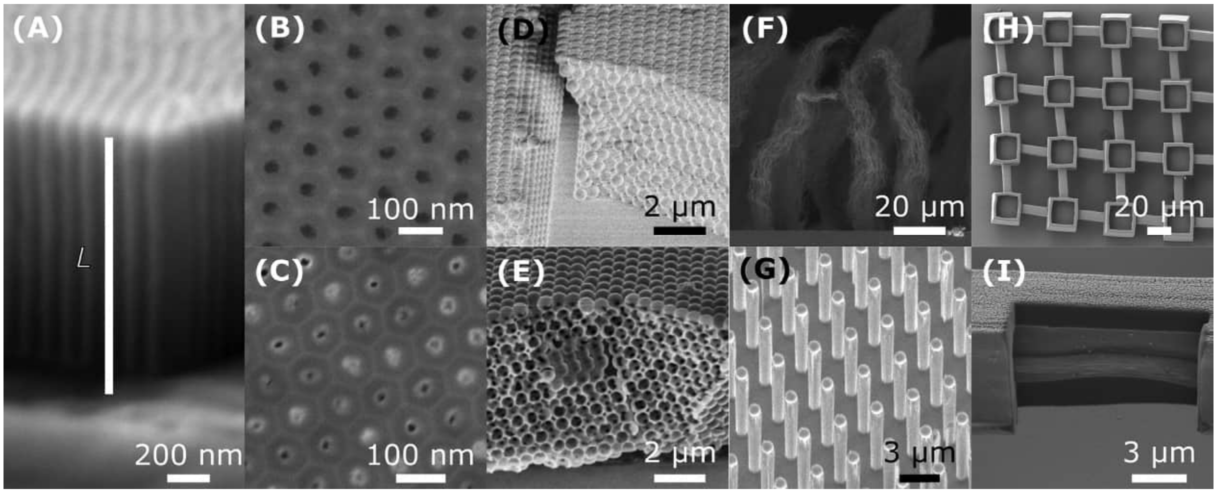

Fig. 6 Scanning electron microscopy (SEM) images of nanostructures that have been employed as templates for ALD. AAO facilitates the growth of nanotubes by ALD: The length, L, shown in the (A) cross-sectional image along the hole direction; the diameter and the interpore distance of the pore (B) can be controlled vy the anodization process; the bright ring inside the pores in (C) are ZnO nanotubes embedded in the AAO membrane after ALD and Ar^+ sputtering removing the interconnecting layer on top. Pores appearing blocked are filled by redeposited material during the sputtering process. (D) Opal template from self-assembled polystyrene beads and (E) inverse opal achieved after ALD and calcination of the opal template. (F) CVD-grown CNTs and (G) nanorods prepared by a combination of lithography and reactive ion etching have been employed as templates for ALD. SEM images of (H) a 3D-printed scaffold structure utilized for cell culturing after ALD coating and (I) a cross-sectional image after focused ion beam cutting of the connecting tunnel.

Table 2 Application overview of ALD-coated complex nanostructures.

Application	*Nanostructured templates*	*References*
Solar cells	• inorganic nanorod/-wires/-tubes • (inverse) opals • porous membranes (anodic aluminum oxide (AAO), anodized titania)	Niu et al. (2015)
Energy storage (supercaps, batteries, etc.)	• inorganic nanorod/-wires/-tubes • inverse opals • Ni foam, Pt/AAO • carbon nanotubes (CNTs) scaffold, multiwalled CNTs (MWCNTs) sponge, graphene foam & expanded graphite (GF)	Guan and Wang (2016)
Photocatalyst	• nanorod/-particles/-wires/-tubes • nanosheets, membranes • AAO • mesoporous silica • CNTs • zeolites	Eswar et al. (2019)
Solid oxide fuel cells	• nanostructured (porous) silicon • AAO • porous solid electrodes (LSC – LaSrCoO, LSCF-GDC – LaSrCoFeO, Ag)	Shim et al. (2019) and Karimaghaloo et al. (2019)
Gas sensing	• CNTs, CNT foams • polymeric fibers, nanocellulose • AAO • self-assembled porous block copolymer • porous Au, Si • inorganic nanorod/-wires • inverse opals	Marichy and Pinna (2016)
(Micro)Fluidics	• pores in SiN • nanochannels in Si • AAO • ion track-etched polymeric membranes • porous block copolymer	Wang et al. (2013) and Yang et al. (2018)
Bio-medical applications	• AAO • nanowires • nanoporous silicon nitride membrane • porous polymer particles • nanocellulose aerogels • porous biotemplates, i.e., tobacco mosaic virus, and ferritin • 3D-printed scaffolds	Skoog et al. (2013) and Harberts et al. (2020)

Conclusion

As discussed and shown above, ALD is a versatile tool that allows for the deposition of thin films of a plethora of materials, e.g., metals, oxides, nitrides, ternary ones, etc., with sub-nm precision even on complex nanostructures.

The conformality is an ALD-inherent property which is usually treated as an advantage of ALD. However, in industrial applications, deposition on specified areas and no growth on others would ease the processing much because complex further lithography-(deposition-)etching steps can be saved. Since ALD bases on chemical (gas-solid surface) reactions, one could locally tailor or can employ the given surface chemistry in a sense to enable or to inhibit the growth (Mackus et al., 2019a). Such an AS-ALD could be achieved by either selective precursor/reactant adsorption on the growth area or surface deactivation to define the non-growth area. A prime example of selective precursor adsorption is the different chemical nature of -OH and -H terminated surfaces, i.e., oxides can be easily deposited at -OH groups but hardly at -H terminated surface sites. On the other hand, self-assembled monolayers or small inhibitor molecules, such as acetylacetone (Hacac), could be used to deactivate surface sites for reaction with the precursor. However, none of these processes could fully suppress the growth in the non-growth areas leading to a reduced selectivity. Hence, correction steps are introduced into the AS-ALD cycle, similar to the supercycle ALD approach mentioned before. For instance, repeated functionalization of the non-growth area or a (selective) etching step which removes deposited material in the non-growth area are experimental pathways to tackle the selectivity problem.

Especially the combination of AS-ALD with atomic layer etching—the counterpart of atomic layer deposition—is a promising approach. Similar to ALD, an atomic layer etching process (abbreviated in literature with ALE but not to be confused with atomic layer epitaxy) consists of (at least) two self-limiting steps. The first step modifies the top surface layer in a way that the surface binding energy is weakened. In the 2nd half cycle—the etching step—the topmost layer is removed. Hence, a layer-by-layer etching is achieved. The etch rate per cycle is constant, and by setting the cycle number, the etched film thickness is defined. The lowered binding energy in the 1st step can be overcome by either using a plasma (ion bombardment) or a thermal chemical reaction in the 2nd step to remove the topmost layer. ALE was invented in the late 80s, but with further pushing Moore's law, an upswing has been taken in the last decade (Kanarik et al., 2015). A prime example of ALE is the etching of Si: Therein, the silicon surface is exposed to a chlorine species—either thermally or by plasma chlorination—forming Si-Cl bonds at the top. In the etching step, energy in the form of an Ar plasma is transferred to the substrate to form gaseous $SiCl_2$ with an evaporation energy of $\sim$2.3 eV, which is significantly lower than the binding energy of 4.7 eV for pure Si. The plasma energy has to be chosen in such a way that the ion bombardment does not harm the bulk silicon but only the chlorinated surface. Hence, the etching stops once all chlorine species have been removed. Since a plasma etching step is used, the etching behavior is directionally similar to reactive ion etching. Most recently, significant progress in the development of thermal ALE processes has been achieved by introducing the isotropic, conformal behavior well-known form ALD by employing thermally driven chemical reactions in the 2nd step. Note, other energy sources to remove the modified surface layers are conceivable as well, such as photons and temperature or a combination of both as well as neutral beams of Ne (Kanarik et al., 2018; Fischer et al., 2021). Up to now, a variety of materials ranging from semiconductors, such as Si or GaAs, to metals, nitrides, and oxides can be etched by ALE. A database for ALE processes is available on the atomic limits blog, similar to the ALD database.[2]

All the processes mentioned above target the deposition (and etching) of inorganic materials. However, the general principle of ALD based on separated self-limiting reaction steps can also be used to deposit organic thin films or even hybrid organic/inorganic structures in combination with ALD. These processes are then called MLD (Sundberg and Karppinen, 2014; Meng, 2017). Compared to ALD, MLD is much younger and dates back to the early 1990s. In combination with ALD, in the 2000s organic/inorganic hybrid materials—metal centers covalently bonded to organic molecules—could be prepared for the first time with versatile and tunable material properties. MLD allows for the deposition of polymeric thin films, such as amides, imides, ureas, urethanes, esters, etc.

By its origin and definition, ALD utilizes gaseous precursor molecules to conduct the self-limiting reaction. However, it has been shown that ALD can also be conducted from liquid precursors in fluidic reactors, so-called liquid- or solvent-based ALD (lALD/sALD (Graniel et al., 2021). Herein, the same prerequisites as for ALD from the gas phase have been defined, namely self-terminating, sequential surface reactions with a defined growth per cycle. On the one hand, lALD widens the field of applicable precursors and materials. Specifically, precursors which have no or only very few vapor pressures or are thermally not stable could be potentially employed to design lALD reactions. On the other hand, the setups as well as the purging step are more complex compared to the ALD based on gaseous precursors since the reaction chamber has to be rinsed with a solvent. As a consequence, the duration of the cycle times as well as consumptions costs for the purge medium, if not circulated, are higher than for conventional ALD but with the perspective of the utilization of cheaper precursors.

In summary, ALD and neighboring techniques, namely AS-ALD, MLD, ALE, and lALD, will be essential to push the limits in downscaling semiconductor devices further, to develop novel process schemes, to create and synthesize materials with tailor-made properties, and to open up new applications in various, such as 'green' energy, semiconductors, biology & medicine, optics, and sensors, to name a few of them.

Acknowledgments

We would like to thank the Deutsche Forschungsgemeinschaft (DFG, German Research Foundation)—Projektnummer 192346071—SFB 986 for support.

References

Ahvenniemi E, Akbashev AR, Ali S, Bechelany M, Berdova M, Boyadjiev S, Cameron DC, Chen R, Chubarov M, Cremers V, Devi A, Drozd V, Elnikova L, Gottardi G, Grigoras K, Hausmann DM, Hwang CS, Jen S-H, Kallio T, Kanervo J, Khmelnitskiy I, Kim DH, Klibanov L, Koshtyal Y, Krause AOI, Kuhs J, Kärkkänen I, Kääriäinen M-L, Kääriäinen T, Lamagna L, Łapicki AA, Leskelä M, Lipsanen H, Lyytinen J, Malkov A, Malygin A, Mennad A, Militzer C, Molarius J, Norek M, Özgit-Akgün Ç, Panov M, Pedersen H, Piallat F, Popov G, Puurunen RL, Rampelberg G, Ras RHA, Rauwel E, Roozeboom F, Sajavaara T, Salami H, Savin H, Schneider N, Seidel TE, Sundqvist J, Suyatin DB, Törndahl T, van Ommen JR, Wiemer C, Ylivaara OME, and Yurkevich O (2017) Review Article: Recommended reading list of early publications on atomic layer deposition—Outcome of the "Virtual Project on the History of ALD" *Journal of Vacuum Science & Technology A: Vacuum, Surfaces, and Films* 35.

Bae C, Shin H, and Nielsch K (2011) Surface modification and fabrication of 3D nanostructures by atomic layer deposition. *MRS Bulletin* 36: 887–897.

Coll M and Napari M (2019) Atomic layer deposition of functional multicomponent oxides. *APL Materials* 7: 110901.

Cremers V, Puurunen RL, and Dendooven J (2019) Conformality in atomic layer deposition: Current status overview of analysis and modelling. *Applied Physics Reviews* 6: 021302.

Dendooven J and Detavernier C (2017) Basics of atomic layer deposition: Growth characteristics and conformality. In: Bachmann J (ed.) *Atomic Layer Deposition in Energy Conversion Applications, Wiley Online Library*, https://doi.org/10.1002/9783527694822.ch1.

Detavernier C, Dendooven J, Pulinthanathu Sree S, Ludwig KF, and Martens JA (2011) Tailoring nanoporous materials by atomic layer deposition. *Chemical Society Reviews* 40: 5242–5253.

---

[2] https://www.atomiclimits.com/aledatabase/ [accessed, 02.03.2022]

Devloo-Casier K, Ludwig KF, Detavernier C, and Dendooven J (2014) In situ synchrotron based x-ray techniques as monitoring tools for atomic layer deposition. *Journal of Vacuum Science and Technology A Vacuum, Surfaces, and Films* 32: 010801.

Eswar NKR, Singh SA, and Heo J (2019) Atomic layer deposited photocatalysts: Comprehensive review on viable fabrication routes and reactor design approaches for photo-mediated redox reactions. *Journal of Materials Chemistry A* 7: 17703–17734.

Fischer A, Routzahn A, George SM, and Lill T (2021) Thermal atomic layer etching: A review. *Journal of Vacuum Science & Technology A* 39: 030801.

George SM (2010) Atomic layer deposition: An overview. *Chemical Reviews* 110: 111–131.

Graniel O, Puigmartí-Luis J, and Muñoz-Rojas D (2021) Liquid atomic layer deposition as emergent technology for the fabrication of thin films. *Dalton Transactions* 50: 6373–6381.

Grillo F, van Bui H, Moulijn JA, Kreutzer MT, and van Ommen JR (2017) Understanding and controlling the aggregative growth of platinum nanoparticles in atomic layer deposition: An avenue to size selection. *The Journal of Physical Chemistry Letters* 8: 975–983.

Guan C and Wang J (2016) Recent development of advanced electrode materials by atomic layer deposition for electrochemical energy storage. *Advanced Science* 3: 1500405.

Hagen DJ, Pemble ME, and Karppinen M (2019) Atomic layer deposition of metals: Precursors and film growth. *Applied Physics Reviews* 6: 041309.

Harberts J, Fendler C, Teuber J, Siegmund M, Silva A, Rieck N, Wolpert M, Zierold R, and Blick & Blick, R.H. (2020) Toward brain-on-a-chip: Human induced pluripotent stem cell-derived guided neuronal networks in tailor-made 3D nanoprinted microscaffolds. *ACS Nano* 14: 13091–13102.

Hiltunen L, Leskelä M, Mäkelä M, Niinistö L, Nykänen E, and Soininen P (1988) Nitrides of titanium, niobium, tantalum and molybdenum grown as thin films by the atomic layer epitaxy method. *Thin Solid Films* 166: 149–154.

Hwang CS (2014) *Atomic Layer Deposition for Semiconductors*. Boston, Ma: Springer US.

Kanarik KJ, Lill T, Hudson EA, Sriraman S, Tan S, Marks J, Vahedi V, and Gottscho RA (2015) Overview of atomic layer etching in the semiconductor industry. *Journal of Vacuum Science & Technology A* 33: 020802.

Kanarik KJ, Tan S, and Gottscho RA (2018) Atomic layer etching: Rethinking the art of etch. *The Journal of Physical Chemistry Letters* 9: 4814–4821.

Karimaghaloo A, Koo J, Kang H-S, Song SA, Shim JH, and Lee MH (2019) Nanoscale surface and interface engineering of solid oxide fuel cells by atomic layer deposition. *International Journal of Precision Engineering and Manufacturing-Green Technology* 6: 611–628.

Knapas K and Ritala M (2013) Situ studies on reaction mechanisms in atomic layer deposition. *Critical Reviews in Solid State and Materials Sciences* 38: 167–202.

Knez M, Nielsch K, and Niinistö L (2007) Synthesis and surface engineering of complex nanostructures by atomic layer deposition. *Advanced Materials* 19: 3425–3438.

Knoops HCM, Faraz T, Arts K, and Kessels WMM (2019) Status and prospects of plasma-assisted atomic layer deposition. *Journal of Vacuum Science & Technology A* 37: 030902.

Mackus AJM, Bol AA, and Kessels WMM (2014) The use of atomic layer deposition in advanced nanopatterning. *Nanoscale* 6: 10941–10960.

Mackus AJM, Merkx MJM, and Kessels WMM (2019a) From the bottom-up: Toward area-selective atomic layer deposition with high selectivity. *Chemistry of Materials* 31: 2.

Mackus AJM, Schneider JR, Macisaac C, Baker JG, and Bent SF (2019b) Synthesis of doped, ternary, and quaternary materials by atomic layer deposition: A review. *Chemistry of Materials* 31: 1142–1183.

Marichy C and Pinna N (2016) Atomic layer deposition to materials for gas sensing applications. *Advanced Materials Interfaces* 3: 1600335.

Meng X (2017) An overview of molecular layer deposition for organic and organic–inorganic hybrid materials: Mechanisms, growth characteristics, and promising applications. *Journal of Materials Chemistry A* 5: 18326–18378.

Miikkulainen V, Leskelä M, Ritala M, and Puurunen RL (2013) Crystallinity of inorganic films grown by atomic layer deposition: Overview and general trends. *Journal of Applied Physics* 113: 021301.

Niu W, Li X, Karuturi SK, Fam DW, Fan H, Shrestha S, Wong LH, and Tok AIY (2015) Applications of atomic layer deposition in solar cells. *Nanotechnology* 26: 064001.

Poodt P, Cameron DC, Dickey E, George SM, Kuznetsov V, Parsons GN, Roozeboom F, Sundaram G, and Vermeer A (2011) Spatial atomic layer deposition: A route towards further industrialization of atomic layer deposition. *Journal of Vacuum Science & Technology A* 30: 010802.

Profijt HB, Potts SE, van de Sanden MCM, and Kessels WMM (2011) Plasma-assisted atomic layer deposition: Basics, opportunities, and challenges. *Journal of Vacuum Science & Technology A* 29: 050801.

Puurunen RL (2005) Surface chemistry of atomic layer deposition: A case study for the trimethylaluminum/water process. *Journal of Applied Physics* 97: 121301.

Puurunen RL (2014) A short history of atomic layer deposition: Tuomo Suntola's atomic layer epitaxy. *Chemical Vapor Deposition* 20: 332–344.

Shim JH, Han GD, Choi HJ, Kim Y, Xu S, An J, Kim YB, Graf T, Schladt TD, Gür TM, and Prinz FB (2019) Atomic layer deposition for surface engineering of solid oxide fuel cell electrodes. *International Journal of Precision Engineering and Manufacturing-Green Technology* 6: 629–646.

Skoog SA, Elam JW, and Narayan RJ (2013) Atomic layer deposition: Medical and biological applications. *International Materials Review* 58: 113–129.

Sundberg P and Karppinen M (2014) Organic and inorganic–organic thin film structures by molecular layer deposition: A review. *Beilstein Journal of Nanotechnology* 5: 1104–1136.

Suntola T and Antson J (1977) *Method for Producing Compound Thin Films*. US patent application.

Suntola T and Hyvarinen J (1985) Atomic layer epitaxy. *Annual Review of Materials Science* 15: 177–195.

Vandalon V (2020) Ternary Materials and Multi-Step ALD Processes Are Trending!. [Online] https://www.atomiclimits.com Available: https://www.atomiclimits.com/2020/12/29/looking-back-on-the-ald-database-in-2020-towards-ternary-materials-and-multi-step-ald-processes/. [Accessed 01.04.2022].

Wang C-M, Kong D-L, Chen Q, and Xue J-M (2013) Surface engineering of synthetic nanopores by atomic layer deposition and their applications. *Frontiers of Materials Science* 7: 335–349.

Weimer AW (2019) Particle atomic layer deposition. *Journal of Nanoparticle Research* 21: 9.

Yang H-C, Waldman RZ, Chen Z, and Darling SB (2018) Atomic layer deposition for membrane interface engineering. *Nanoscale* 10: 20505–20513.

Zhang H, Hagen DJ, Li X, Graff A, Heyroth F, Fuhrmann B, Kostanovskiy I, Schweizer SL, Caddeo F, Maijenburg AW, Parkin S, and Wehrspohn RB (2020) Atomic layer deposition of cobalt phosphide for efficient water splitting. *Angewandte Chemie International Edition* 59: 17172–17176.

Relevant websites

https://www.atomiclimits.com—AtomicLimits
http://www.blog.baldengineering.com—BALD Engineering AB

Catalysts: Combinatorial heterogeneous catalysis

Weijie Zhang and Sen Zhang, Department of Chemistry, University of Virginia, Charlottesville, VA, United States

© 2024 Elsevier Ltd. All rights reserved.

This is an update of A. Hagemeyer, A. Volpe, Catalysts: Combinatorial Catalysis, Editor(s): Franco Bassani, Gerald L. Liedl, Peter Wyder, Encyclopedia of Condensed Matter Physics, Elsevier, 2005, Pages 151–158, ISBN 9780123694010, https://doi.org/10.1016/B0-12-369401-9/01128-1.

Introduction	729
The hierarchical workflow in heterogeneous catalysis	730
High-throughput synthesis technologies	731
High-throughput characterization and screening techniques	732
Applications	734
Conclusion	735
References	736

Abstract

Substantial progress has been made in the field of combinatorial heterogeneous catalysis in the past decade. Combinatorial heterogeneous catalysis involves the computation-assisted design of diverse, high-density assemblies or arrays of potential heterogeneous catalytic materials, and high-throughput synthesis, characterization, and screening techniques. This chapter focuses on representative high-throughput preparation, characterization, and testing workflows that have recently been developed and employed in heterogeneous catalysis. It not only provides an introduction to combinatorial heterogeneous catalysis and the recent examples, but also highlights the areas in which advances are needed in the future.

Key points

- An introduction to combinatorial heterogeneous catalysis;
- Recent examples of high-throughput synthesis, characterization, and screening techniques for heterogeneous catalysis;
- A summary and outlook of the applications of combinatorial heterogeneous catalysis.

Introduction

The use of combinatorial methodologies to accelerate the research and development process in heterogeneous catalysis is increasing at a rapid pace in both industrial and academic laboratories (Xiang et al., 1995; Cawse, 2001; Hagemeyer et al., 2001; Seh et al., 2017). As shown in Fig. 1, combinatorial heterogeneous catalysis is a systematic screening of large heterogeneous catalytic materials libraries in a high-throughput fashion. It consists of three elements: large-scale event management, large library, and high-throughput screening. At the core of the term “combinatorial” is the “high-throughput” ability to prepare, characterize, and examine heterogeneous catalysts. For industry, the key drivers include the need to reduce the time-to-market for new and optimized catalysts and processes, increased probability of success due to the ability to perform far greater numbers of experiments than in the past, better intellectual property protection made possible by the thoroughness with which a given technical area can be explored, shorter more projects possible per unit time, the benefits of “early failure,” and the increased organizational efficiency resulting from improved data storage, access, analysis, and sharing. Similar advantages have already been addressed by the pharmaceutical industry, where long development times and high research costs have forced the development of high-throughput approaches to accelerate the drug discovery process.

Traditional methods for the discovery of new heterogeneous catalysts are not very efficient because discovery protocols are primarily trial-and-error processes. The ability to predict the required catalyst composition, structure, and formulation for a given chemical transformation is low and, for complex multi-component catalysts, almost nonexistent. In addition, there are many variables that affect a catalyst, including not only the elemental composition but also metal precursor types used, wet synthesis variables, method of post-treatment such as calcination conditions, presence and type/shape of catalyst support, and operating conditions such as temperature, pressure space velocity, and reactant gas composition. These variables are too numerous to adequately explore using conventional methods, especially in discovery programs, but also in catalyst optimization work where there may be fewer variables but where catalyst complexity (catalysts are often multi-component systems) is high.

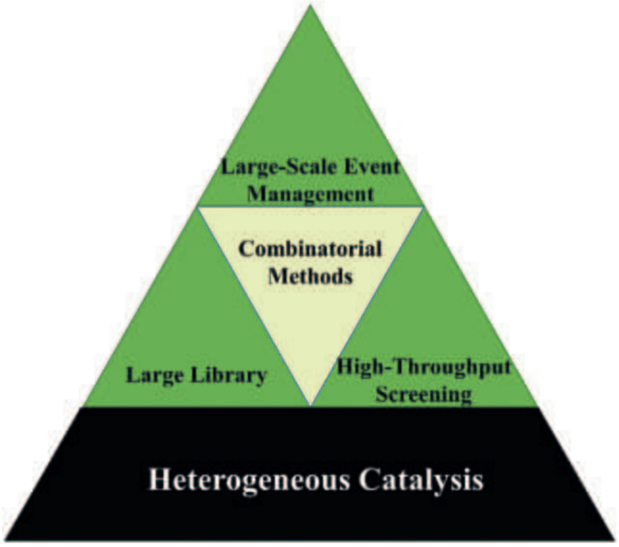

Fig. 1 Combinatorial heterogeneous catalysis.

The high-throughput experimental process in combinatorial heterogeneous catalysis involves the computation-assisted design of diverse, high-density assemblies or arrays of potential catalytic materials (known as "libraries"), and high-throughput synthesis, characterization, and screening techniques that are characterized by using robotics and advanced computation (Senkan, 2001; Busch et al., 2002; Song et al., 2002; Sun et al., 2002). The integrated synthesis and screening of a plurality of catalysts in library format have been recognized as essential factors. Equipment miniaturization and integrated data management systems are also key aspects of successful workflows. The development and implementation of these methods require the involvement of unconventional engineering and computation resources not commonly available at chemical, refining, and petrochemical companies where heterogeneous catalysis is practiced. High-throughput research is optimally performed by interdisciplinary teams typically made up of chemists, engineers, and programmers (Bergh et al., 2003; Liu et al., 2003; Muller et al., 2003; Murphy et al., 2003; Jahnisch et al., 2004; Schunk et al., 2007; Ludwig, 2019).

The number of experiments that can now be performed using state-of-the-art high-throughput workflows can be an order of magnitude or higher than was possible only a few years ago using conventional research. For example, a high-throughput program can yield 50,000 experiments per year compared to 500–1000 experiments using traditional methods. This chapter is updated from its previous version published in 2005 (Hagemeyer and Volpe, 2005), and describes representative high-throughput preparation, characterization, and testing workflows developed and employed in heterogeneous catalysis over the last 5 years.

The hierarchical workflow in heterogeneous catalysis

The research and scale-up phases leading to the commercialization of heterogeneous catalysts are illustrated in Fig. 2 (Ortega et al., 2021). The high-throughput workflow can be divided into primary, secondary, and, in some cases, tertiary screening. Primary screening approaches are typically very high throughput qualitative or semi-quantitative screens performed on small samples often using unconventional reactor designs and are most often focused on discovery. The objective during this phase is to broadly screen a large and diverse set of material types that may perform the desired catalytic reaction. Discoveries termed "hits," are then taken to the secondary screen, and, importantly, compositional space that is not useful is discarded. Although it is critical that primary screening results correlate with the real catalytic process, this can usually be accomplished by screening for qualitative trends and using relative performance rankings generated by using a simplified analog of the real process parameter. The primary screen must be designed to minimize both false positives and especially false negatives. Primary screening removes the key bottleneck in the R&D process.

Secondary screening is used for the confirmation and optimization of primary hits. In contrast to the primary screen, the catalyst form, reactor, and process analytics are designed to closely represent those of the real bench-scale material and reaction. The data quality and precision should be equivalent to that of a standard laboratory reactor since the goal is to observe small improvements in performance as a function of catalyst modification. Optimized hits, termed "leads," are taken to the tertiary screening phase to generate commercial development candidates. If necessary, tertiary screening can be performed using conventional fixed-bed micro-reactors with full reactant and product detection and full mass balance, and in some cases is also parallelized. Secondary synthesis and screening technology have, in many cases, evolved to the point where the quality of the data obtained is equivalent to

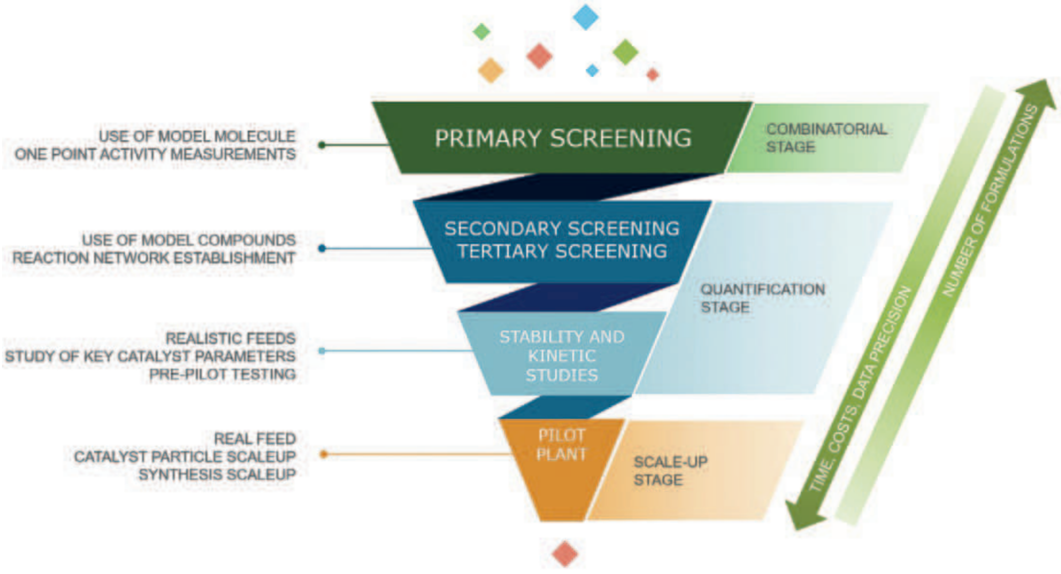
USE OF MODEL MOLECULE
ONE POINT ACTIVITY MEASUREMENTS
PRIMARY SCREENING
COMBINATORIAL STAGE
USE OF MODEL COMPOUNDS
REACTION NETWORK ESTABLISHMENT
SECONDARY SCREENING
TERTIARY SCREENING
QUANTIFICATION STAGE
REALISTIC FEEDS
STUDY OF KEY CATALYST PARAMETERS
PRE-PILOT TESTING
STABILITY AND KINETIC STUDIES
REAL FEED
CATALYST PARTICLE SCALEUP
SYNTHESIS SCALEUP
PILOT PLANT
SCALE-UP STAGE
TIME, COSTS, DATA PRECISION
NUMBER OF FORMULATIONS

Fig. 2 Schematic illustration of research and scale-up phases leading to commercialization in a heterogeneous catalyst development program (Ortega et al., 2021). From Ortega C, Otyuskaya D, Ras EJ, Virla LD, Patience GS, Dathe H (2021) Experimental methods in chemical engineering: High throughput catalyst testing - HTCT. *Canadian Journal of Chemical Engineering* 99: 1288–1306. Copyright 2021, John Wiley & Sons, Inc.

that obtained using conventional laboratory technologies. Accordingly, in some instances, pilot plant studies can proceed directly from secondary screening, without tertiary screening.

High-throughput synthesis technologies

The development of high-performance heterogeneous catalysts relies on the ability to control and optimize the catalyst's physical dimension and atomic structure, especially for nanocatalysts with large surface areas (Roy et al., 2021; Liu et al., 2021; Clayson et al., 2020). Synthetic advances to achieve high-quality nanomaterials with control over size, dispersity, phase, composition, and physical properties have driven progress toward heterogeneous catalysis. Multi-element nanomaterials hold great potential for various catalytic applications due to their widely tunable surface structures. However, conventional approaches are slow and rely on serendipity in search of optimized catalysts from complex multi-element nanomaterials. A general and robust synthetic strategy is highly desirable in investigating catalysts with increasingly complex compositions.

Recently, a high-throughput technique has been reported for combinatorial composition design and rapid synthesis of ultrafine multi-metallic nanoclusters (MMNCs) (Yao et al., 2020). They prepared and screened the PtPdRhRuIrFeCoNi compositional space using high-throughput rapid T shock synthesis coupled with scanning droplet cell electrochemistry (Fig. 3). The high-throughput synthesis includes two facile steps: (1) combinatorial composition design using metal precursors by formulation in solution phases; (2) uniform multimetallic nanoclusters synthesis by rapid thermal shock of the precursor-loaded carbon support. Then, the high-throughput electrochemistry was performed using a scanning droplet cell setup to rapidly screen for promising multimetallic nanocluster catalysts. This synthetic technique led to two promising catalysts, PtPdRhNi and PtPdFeCoNi, being quickly identified for the oxygen reduction reaction (ORR). The two nanoparticle catalysts were further carefully characterized using synchrotron X-ray diffraction (XRD) and transmission electron microscopy (TEM), and their catalytic properties were verified in a rotating disk setup (Fig. 3).

Due to its versatility and flexibility in energy saving, simplicity, and cost-effectiveness as well as the ability in controlling particle sizes, compositions, and structures, the wet-chemical technique has been well recognized to fulfill the mission of catalytic nanomaterial synthesis. However, conventional ways of high-throughput parallel synthesis require complex operation and costly equipment, which greatly restricts their further applications. In recent years, a microfluidic-based composition and temperature-controlling platform shows great promise in high-throughput wet-chemical synthesis. As shown in Fig. 4, a microfluidic-based composition and temperature-controlling platform was prepared to perform high-throughput wet-chemical synthesis (Hu et al., 2020). This platform employed 100-channel reactor arrays for wet-chemical synthesis with 5-level temperature gradients and utilized a microfluidic chip to prepare 20-level concentration gradients of the two reagents (50.85 mM of $CoCl_2$ water solution and 50.85 mM of $NiCl_2$ water solution) to generate CoNi bimetallic catalytic materials. They used X-ray photoelectron spectroscopy (XPS) to confirm the as-synthesized nanomaterials oxidation states. Scanning electron microscopy (SEM) and energy dispersive

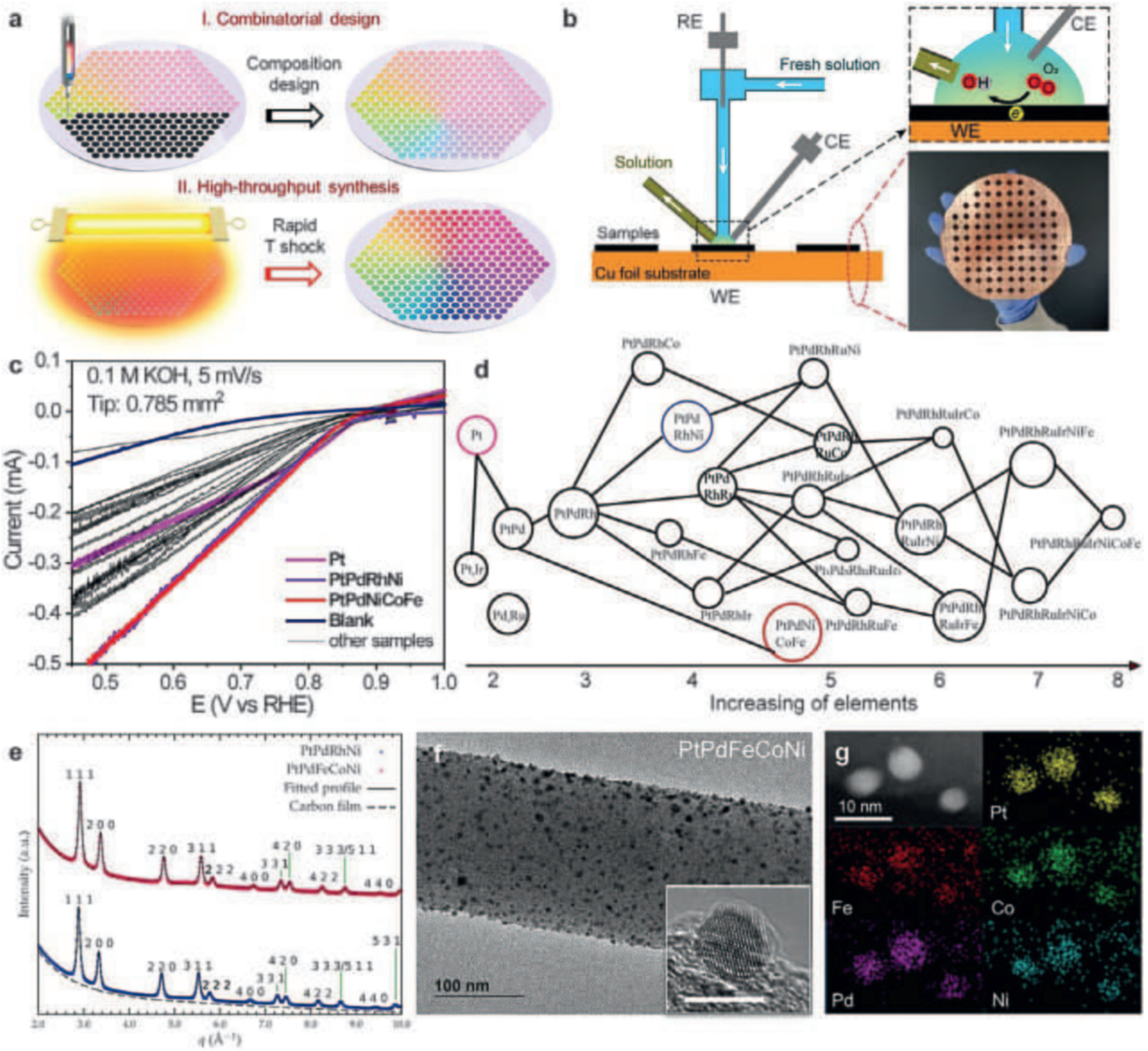

Fig. 3 The combinatorial and high-throughput synthesis and screening of multi-metallic nanoclusters for electrocatalysis. (A) Schematic illustration of the combinatorial and high-throughput synthesis of uniform MMNCs. (B) The scanning droplet cell setup and patterned samples on the copper substrate. (C) Fast screening of PtPd-based MMNCs for catalytic ORR. (D) The compositional designs and their corresponding ORR performances. (E) Synchrotron XRD profiles for PtPdRhNi and PtPdFeCoNi, showing the single-phase FCC structure. a.u., arbitrary units. (F and G) TEM image (F) and elemental maps (G) of PtPdFeCoNi (Yao et al., 2020). From Yao, Y, Huang Z, Li T, Wang H, Liu Y, Stein HS, Mao Y, Gao J, Jiao M, Dong Q, Dai J, Xie P, Xie H, Lacey SD, Takeuchi I, Gregoire JM, Jiang R, Wang C, Taylor AD, Shahbazian-Yassar R, and Hu L (2020) High-throughput, combinatorial synthesis of multimetallic nanoclusters. *Proceedings of the National Academy of Sciences* 117: 6316–6322. Copyright © 2020, National Academy of Science.

X-ray spectroscopy (EDS) were further applied to characterize Co-Ni bimetallic solid materials synthesized under different reaction conditions. This work not only provides a dramatic increase in efficiency compared with the conventional approach but also enables a one-step investigation of the mild synthetic conditions required for a wet-chemical technique.

High-throughput characterization and screening techniques

The high-throughput characterization techniques are also essential in screening heterogeneous catalysts (Steinmann et al., 2022; Taylor et al., 2021; Pluchinsky et al., 2020). The physical and chemical properties of catalytic materials need to be systematically characterized to establish structure-property relationships for refining the catalyst optimization principle. The comprehensive characterization includes surface area and porous structure by Brunauer-Emmett-Teller (BET) analysis, particle size distribution via light and X-ray scattering, morphology via SEM or TEM, phase and structure by XRD and extended X-ray absorption fine-structure spectra (EXAFS), electronic structure by XPS and X-ray absorption near edge structure (XANES), and elemental

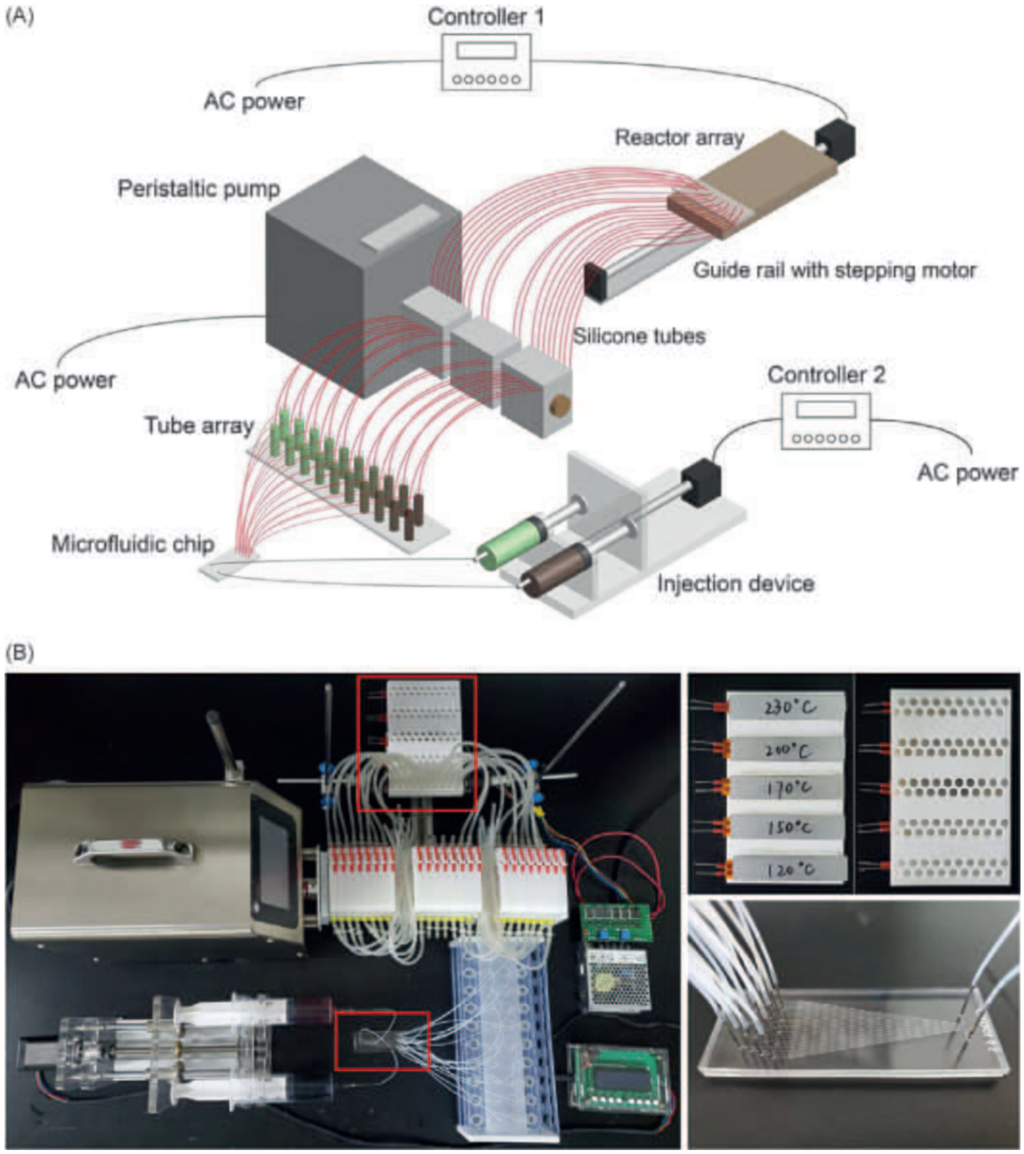

Fig. 4 (A) Schematic diagram of the microfluidic-based composition and temperature controlling platform; (B) photo of the high-throughput synthesis platform (Hu et al., 2020). From Hu Y, Liu B, Wu Y, Li M, Liu X, Ding J, Han X, Deng Y, Hu W, Zhong C (2020) Facile high throughput wet-chemical synthesis approach using a microfluidic-based composition and temperature controlling platform. *Frontiers in Chemistry* 8: 579828. Copyright © 2020 Hu, Liu, Wu, Li, Liu, Ding, Han, Deng, Hu and Zhong, Frontiers Media SA.

composition by inductively coupled plasma mass spectrometry (ICP-MS) and EDS, etc. Built on multichannel reactor design, sample automation, and large-scale data processing, high-throughput characterization by each of these techniques has become possible in recent years. More excitingly, some characterization techniques have been developed with *in-situ* or *operando* capability. For example, high-throughput *in-situ* EXAFS spectra was used to characterize a library of 91 catalyst precursors containing ternary combinations of Cu, Pt, and Au on γ-Al_2O_3 (Tsapatsaris et al., 2007). Valuable structure information was obtained by probing the local electronic structures, including coordination numbers, bond lengths, and static and thermal disorder. These results facilitated the understanding of CO oxidation rate over noble metal catalysts. 6 wt% Au on γ-Al_2O_3 displayed conversion rate oscillations related to reduction/oxidation cycles, indicating that its oxide or sub-surface layers deactivate the reactive surface.

One exciting advance in combinatorial heterogeneous catalysis over the past few years is high-throughput computational screening methods with high accuracy. In a typical example, Goddard et al. investigated the Haber-Bosch reaction mechanism ($N_2 + 3H_2 \rightarrow 2NH_3$) on two most active surfaces, Fe (111) and Fe (211) reconstructed surface. As shown in Fig. 5, they used density functional theory (DFT) to predict the free-energy barriers for the 34 most important 2×2 surface configurations and all 12 important reaction steps (Fuller et al., 2022). The predicted turnover frequencies were within experimental error. In order to make this strategy practical to screen more dopant candidates, they developed a hierarchical high-throughput catalysis screening (HHTCS) approach and then successfully identified the most important 4 reaction steps out of 12 for the two surfaces to examine

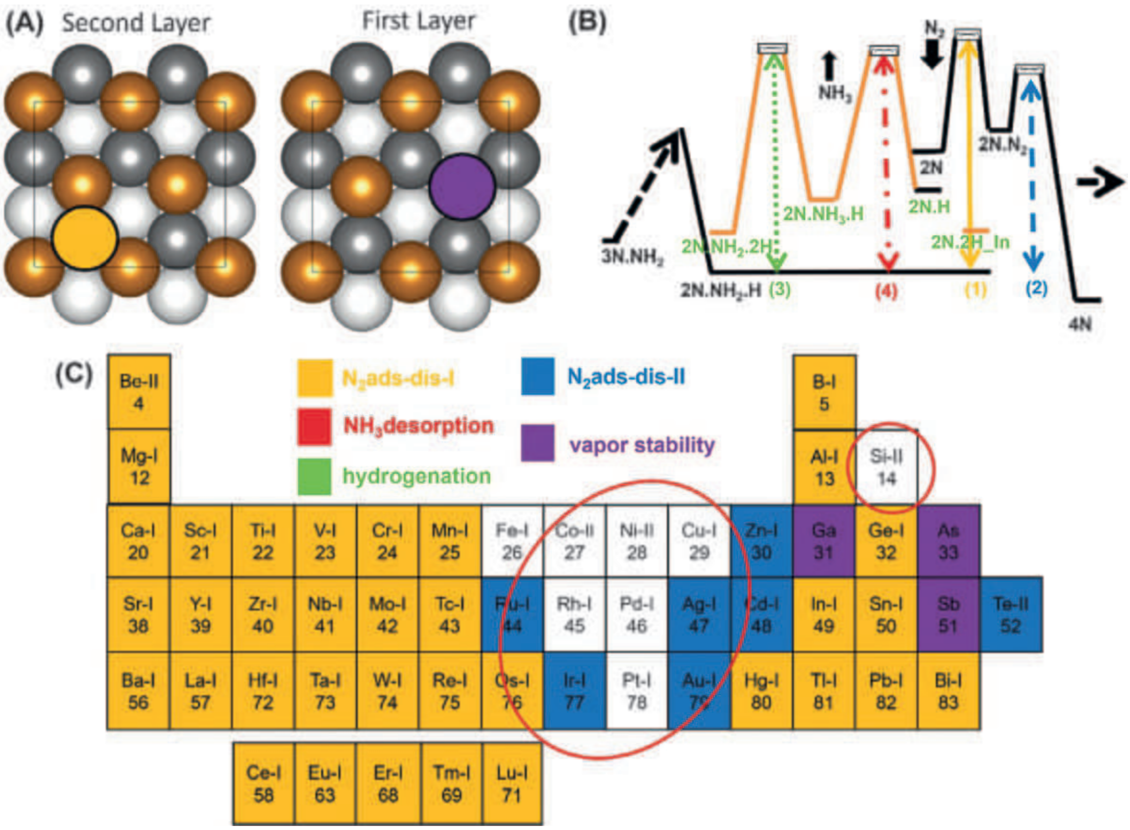
(A)
Second Layer
First Layer
(B)
N_2
NH_3
3N.NH$_2$
2N.NH$_2$.2H
2N.NH$_3$.H
2N
2N.N$_2$
2N.H
2N.2H_ln
2N.NH$_2$.H (3)
(4)
(1)
(2)
4N
(C)
N$_2$ads-dis-I
NH$_3$desorption
hydrogenation
N$_2$ads-dis-II
vapor stability
Be-II 4
Mg-I 12
Ca-I 20
Sc-I 21
Ti-I 22
V-I 23
Cr-I 24
Mn-I 25
Fe-I 26
Co-II 27
Ni-II 28
Cu-I 29
Zn-I 30
Ga 31
Ge-I 32
As 33
B-I 5
Al-I 13
Si-II 14
Sr-I 38
Y-I 39
Zr-I 40
Nb-I 41
Mo-I 42
Tc-I 43
Ru-I 44
Rh-I 45
Pd-I 46
Ag-I 47
Cd-I 48
In-I 49
Sn-I 50
Sb 51
Te-II 52
Ba-I 56
La-I 57
Hf-I 72
Ta-I 73
W-I 74
Re-I 75
Os-I 76
Ir-I 77
Pt-I 78
Au-I 79
Hg-I 80
Tl-I 81
Pb-I 82
Bi-I 83
Ce-I 58
Eu-I 63
Er-I 68
Tm-I 69
Lu-I 71

Fig. 5 Application of hierarchical high-throughput catalysis screening to Fe bcc (111) for Haber-Bosch NH_3 synthesis. (A) First layer (purple) and second layer (yellow) doping sites on the Fe-bcc (111) surface. (B) Free-energy landscape demonstrating the reaction barriers evaluated in HHTCS as colored lines. (C) Figure showing the results of the HHTCS screening sequence: candidates eliminated due to the vapor stability criterion are represented in purple, while those eliminated by the corresponding barriers shown in (B) are shaded in the same colors as in (B). Circles highlight the best dopant candidates (Fuller et al., 2022). From Fuller J, An Q, Fortunelli A, Goddard WA 3rd (2022) Reaction mechanisms, kinetics, and improved catalysts for ammonia synthesis from hierarchical high throughput catalyst design. *Accounts of Chemical Research* 55: 1124–1134. Copyright © 2022, American Chemical Society.

>50 dopant cases. Among the 34 transition-metal candidates and 17 non-transition metals (metalloids and main group metals), Co, Ni, and Si prefer subsurface sites. Ni doping was found to be the best, with a predicted 16-fold enhancement in the reaction rate. Finally, they proposed a new research direction to pursue increasing the accuracy via embedded correlated wave function techniques or *ad hoc* corrections.

The recent boom of machine-learning (ML) and deep-learning (DL) techniques has also advanced the high-throughput development of heterogeneous catalysts. As shown in Fig. 6, a Cu-Al catalyst has demonstrated for active and selective CO_2 electro-reduction to C_2H_4 with the aid of a ML-accelerated, high-throughput DFT framework (Zhong et al., 2020). The computational studies indicate that the Cu-Al catalyst provides multiple sites and surface orientations with near-optimal CO binding for both active and selective CO_2 electro-reduction. Guided by the computational prediction, Cu-Al electrocatalysts were synthesized and demonstrated efficient reduction of CO_2 to ethylene with the highest Faradaic efficiency in the reported literature. It clearly suggests the value of machine learning and computation in guiding the experimental design of complex multi-metallic heterogeneous catalysts.

Applications

Combinatorial heterogeneous catalysis is ideally suited for the discovery of novel noble metal and mixed metal oxide catalyst formulations for total combustion/volatile organic compound (VOC) removal, emissions control from stationary and mobile sources (NO_x abatement, CO oxidation, automotive three-way catalysis) due to the uncomplicated feeds and product mixes that often allows truly parallel detection and very high sample through-puts. Furthermore, combinatorial methods are advantageously applicable to multi-component catalysts (mixed metal oxides, alloys) for selective oxidation, hydrogenation, and dehydrogenation. The demand for higher sensitivities and efficiencies in refining has triggered the search for new zeolite structures by parallel hydrothermal synthesis. Additionally, improved fast analytical techniques are making it increasingly possible to perform high-throughput experimentation on complex real plant feeds. It is also promising for developing improved catalysts that are critical to clean energy-related

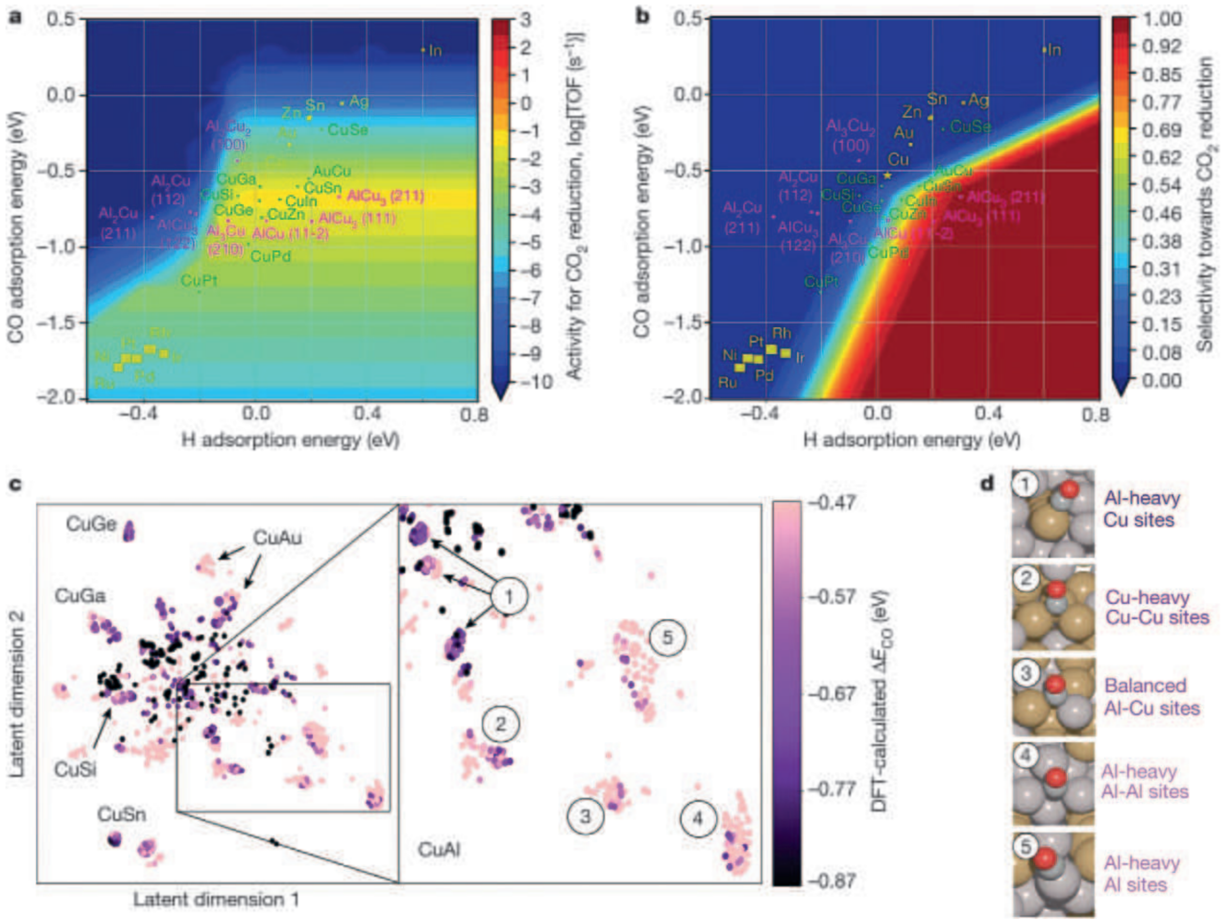

Fig. 6 Screening of Cu and Cu-based complexes using computational methods. (A) A two-dimensional activity volcano plot for CO_2 reduction. TOF. (B) A two-dimensional selectivity volcano plot for CO_2 reduction. CO and H adsorption energies in panels a and b were calculated using DFT. (C) t-SNE scheme representation of approximately 4000 adsorption sites on which they performed DFT calculations with Cu-containing alloys. The Cu-Al clusters are labeled numerically. (D) Representative coordination sites for each of the clusters labeled in the t-SNE scheme (Zhong et al., 2020). From Zhong M, Tran, K, Min Y, Wang C, Wang Z, Dinh CT, De Luna P, Yu Z, Rasouli AS, Brodersen P, Sun S, Voznyy O, Tan CS, Askerka M, Che F, Liu M, Seifitokaldani A, Pang Y, Lo SC, Ip A, Ulissi Z, Sargent EH (2020) Accelerated discovery of CO2 electrocatalysts using active machine learning. *Nature* 581: 178–183. Copyright 2020, Springer Nature.

electrochemical conversion processes, including water splitting, fuel cells, and CO_2 capture and conversion. These electrocatalytic processes enable to transform of small molecules (e.g., CO_2, and water) and renewable feedstocks (e.g., biomass) into higher-value products (e.g., hydrocarbons, oxygenates, hydrogen, and ammonia) by coupling to renewable energy, and plays ever-increasing roles in addressing the environmental issues of modern society.

Published examples of extended and comprehensive combinatorial screening programs include ethane oxidative dehydrogenation leading to the discovery of Mo-V-Nb catalysts (Cong et al., 1999; Botella et al., 2003), combustion catalysis due to the demand for better low-temperature activity (Maier, 2003; Wang et al., 2021) in exhaust gas and air cleaning, automotive emission, stoves, and explosion prevention sensors, the water gas shift reaction aiming at high activity non-pyrophoric catalysts for fuel processors in future fuel cell-driven vehicles (Grubert et al., 2006), preferential CO oxidation in excess hydrogen (Laveille et al., 2013), propylene oxidation over supported metals (Kalyoncu et al., 2015), isobutane oxidation over mixed metal oxides (Paul, 2004; Otroshchenko et al., 2021), low-temperature light paraffin isomerization catalysts (Serra et al., 2003; Naqvi et al., 2018), methanol synthesis catalysts (Schüth et al., 2002), ethylbenzene oxidative dehydrogenation (Urschey, 2003), HCN synthesis over supported noble metals (Yamasaki et al., 2022), new anode and cathode formulations for polymer electrolyte membrane (PEM) fuel cells (Djilali, 2007) and CO_2 conversion (Zhong et al., 2020), and diesel tailpipe emissions control (Reşitoğlu et al., 2014; Sundermann and Gerlach, 2016).

Conclusion

Substantial progress has been made on combinatorial heterogeneous catalysis in recent years. Looking forward, it is clear that the field of combinatorial heterogeneous catalysis will continue to advance and be applied at an ever-increasing rate. Areas in which advances are needed and are being pursued include: creating high-throughput synthetic methods for precision synthesis of catalytic materials with well-controlled atomic structures and nanoscale architectures, development of ML/DL-assisted computational methods with further improved accuracy and ability to predict catalysts in complex environments (especially for complicated liquid and electrochemical conditions), integration of multiple characterization tools with high-throughput *in-situ* and *operando* capability, acceleration of scale-up activities using commercial-sized catalysts (e.g., large commercial-size pellets with control overactive catalyst distribution in the support), performing process optimization in high-throughput reactors, development of new equipment that can handle harsher reaction feeds and conditions, including high temperature, pressure, corrosive and heavy feeds, improved and faster analytical methods for analyzing reaction products from screening (including analyzing complicated real plant feeds) and for faster/better-characterizing catalyst materials, and further miniaturization and automation.

References

Bergh S, Cong P, Ehnebuske B, Guan S, Hagemeyer A, et al. (2003) Combinatorial heterogeneous catalysis: oxidative dehydrogena tion of ethane to ethylene, selective oxidation of ethane to acetic acid, and selective ammoxidation of propane to acrylonitrile. *Topics in Catalysis* 23: 65–79.

Botella P, López Nieto JM, Dejoz A, Vázquez MI, and Martı´nez-Arias A (2003) Mo-V-Nb mixed oxides as catalysts in the selective oxidation of ethane. *Catalysis Today* 78: 507–512.

Busch OM, Hoffmann C, Johann TR, Schmidt HW, Strehlau W, et al. (2002) Application of a new color detection based method for the fast parallel screening of $DeNO_x$ catalysts. *Journal of the American Chemical Society* 124: 13527–13532.

Cawse JN (2001) Experimental strategies for combinatorial and high-throughput materials development. *Accounts of Chemical Research* 34: 213–221.

Clayson IG, Hewitt D, Hutereau M, Pope T, and Slater B (2020) High throughput methods in the synthesis, characterization, and optimization of porous materials. *Advanced Materials* 32: e2002780.

Cong P, Dehestani A, Doolen R, Giaquinta DM, Guan S, et al. (1999) Combinatorial discovery of oxidative dehydrogenation catalysts within the Mo-V-Nb-O system. *Proceedings of the National Academy of Sciences* 96: 11077–11080.

Djilali N (2007) Computational modelling of polymer electrolyte membrane (PEM) fuel cells: Challenges and opportunities. *Energy* 32: 269–280.

Fuller J, An Q, Fortunelli A, and Goddard WA III (2022) Reaction mechanisms, kinetics, and improved catalysts for ammonia synthesis from hierarchical high throughput catalyst design. *Accounts of Chemical Research* 55: 1124–1134.

Grubert G, Kolf S, Baerns M, Vauthey I, Farrusseng D, et al. (2006) Discovery of new catalytic materials for the water-gas shift reaction by high-throughput experimentation. *Applied Catalysis A: General* 306: 17–21.

Hagemeyer A and Volpe A Jr (2005) Catalysts: Combinatorial catalysis. In: Bassani F, Liedl G, and Wyder P (eds.) *Encyclopedia of Condensed Matter Physics*. Oxford: Elsevier Academic Press.

Hagemeyer A, Jandeleit B, Liu YM, Poojary DM, Turner HW, et al. (2001) Applications of combinatorial methods in catalysis. *Applied Catalysis A: General* 221: 23–43.

Hu Y, Liu B, Wu Y, Li M, Liu X, et al. (2020) Facile high throughput wet-chemical synthesis approach using a microfluidic-based composition and temperature controlling platform. *Frontiers in Chemistry* 8: 579828.

Jahnisch K, Hessel V, Lowe H, and Baerns M (2004) Chemistry in microstructured reactors. *Angewandte Chemie International Edition* 43: 406–446.

Kalyoncu Ş, Düzenli D, Onal I, Seubsai A, Noon D, et al. (2015) Direct epoxidation of propylene to propylene oxide on various catalytic systems: A combinatorial micro-reactor study. *Catalysis Communications* 61: 16–20.

Laveille P, Biausque G, Zhu H, Basset J-M, and Caps V (2013) A high-throughput study of the redox properties of Nb-Ni oxide catalysts by low temperature CO oxidation: Implications in ethane ODH. *Catalysis Today* 203: 3–9.

Liu YM, Cong PJ, Doolen RD, Guan SH, Markov V, et al. (2003) Discovery from combinatorial heterogeneous catalysis-A new class of catalyst for ethane oxidative dehydrogenation at low temperatures. *Applied Catalysis A: General* 254: 59–66.

Liu X, Liu B, Ding J, Deng Y, Han X, et al. (2021) Building a library for catalysts research using high-throughput approaches. *Advanced Functional Materials* 32: 2107862.

Ludwig A (2019) Discovery of new materials using combinatorial synthesis and high-throughput characterization of thin-film materials libraries combined with computational methods. *npj Computational Materials* 5: 70.

Maier WF (2003) *Combinatorial Chemistry*. Amsterdam: Elsevier B.V. Press.

Muller A, Drese K, Gnaser H, Hampe M, Hessel V, et al. (2003) Fast preparation and testing methods using a microstructured modular reactor for parallel gas phase catalyst screening. *Catalysis Today* 81: 377–391.

Murphy V, Volpe AFJ, and Weinberg WH (2003) High-throughput approaches to catalyst discovery. *Current Opinion in Chemical Biology* 7: 427–433.

Naqvi SR, Bibi A, Naqvi M, Noor T, Nizami A-S, et al. (2018) New trends in improving gasoline quality and octane through naphtha isomerization: A short review. *Applied Petrochemical Research* 8: 131–139.

Ortega C, Otyuskaya D, Ras EJ, Virla LD, Patience GS, et al. (2021) Experimental methods in chemical engineering: High throughput catalyst testing-HTCT. *Canadian Journal of Chemical Engineering* 99: 1288–1306.

Otroshchenko T, Jiang G, Kondratenko VA, Rodemerck U, and Kondratenko EV (2021) Current status and perspectives in oxidative, non-oxidative and CO_2-mediated dehydrogenation of propane and isobutane over metal oxide catalysts. *Chemical Society Reviews* 50: 473–527.

Paul J (2004) Combinatorial discovery of new catalysts for the selective oxidation of isobutane. *Applied Catalysis A: General* 265: 185–193.

Pluchinsky AJ, Wackelin DJ, Huang X, Arnold FH, and Mrksich M (2020) High throughput screening with SAMDI mass spectrometry for directed evolution. *Journal of the American Chemical Society* 142: 19804–19808.

Reşitoğlu İA, Altinişik K, and Keskin A (2014) The pollutant emissions from diesel-engine vehicles and exhaust after treatment systems. *Clean Technologies and Environmental Policy* 17: 15–27.

Roy D, Mandal SC, and Pathak B (2021) Machine learning-driven high-throughput screening of alloy-based catalysts for selective CO_2 hydrogenation to methanol. *ACS Applied Materials & Interfaces* 13: 56151–56163.

Schunk SA, Sundermann A, and Hibst H (2007) Retrospective hit-deconvolution of mixed metal oxides: spotting structure-property-relationships in gas phase oxidation catalysis through high throughput experimentation. *Combinatorial Chemistry & High Throughput Screening* 10: 51–57.

Schüth F, Busch O, Hoffmann C, Johann T, Kiener C, et al. (2002) High-throughput experimentation in oxidation catalysis. *Topics in Catalysis* 21: 55–66.

Seh ZW, Kibsgaard J, Dickens CF, Chorkendorff I, Norskov JK, et al. (2017) Combining theory and experiment in electrocatalysis: Insights into materials design. *Science* 355: eaad4998.

Senkan S (2001) Combinatorial heterogeneous catalysis-a new path in an old field. *Angewandte Chemie International Edition* 40: 312–329.

Serra JM, Chica A, and Corma A (2003) Development of a low temperature light paraffin isomerization catalysts with improved resistance to water and sulphur by combinatorial methods. *Applied Catalysis A: General* 239: 35–42.

Song Y, Yu J, Li G, Li Y, Wang Y, et al. (2002) Combinatorial approach for the hydrothermal syntheses of open-framework zinc phosphates. *Chemical Communications*: 1720–1721.

Steinmann SN, Hermawan A, Bin Jassar M, and Seh ZW (2022) Autonomous high-throughput computations in catalysis. *Chem Catalysis* 2: 940–956.

Sun Y, Chan BC, Ramnarayanan R, Leventry WM, Mallouk TE, et al. (2002) Split-pool method for synthesis of solid-state material combinatorial libraries. *Journal of Combinatorial Chemistry* 4: 569–575.

Sundermann A and Gerlach O (2016) High-throughput screening as a supplemental tool for the development of advanced emission control catalysts: Methodological approaches and data processing. *Catalysts* 6: 23.

Taylor AK, Nesvaderani F, Ovens JS, Campbell S, and Gates BD (2021) Enabling a high-throughput characterization of microscale interfaces within coated cathode particles. *ACS Applied Energy Materials* 4: 9731–9741.

Tsapatsaris N, Beesley AM, Weiher N, Tromp M, Evans J, et al. (2007) High throughput in situ EXAFS instrumentation for the automatic characterization of materials and catalysts. *AIP Conference Proceedings* 879: 1739–1742.

Urschey J (2003) Combinatorial and conventional development of novel dehydrogenation catalysts. *Applied Catalysis A: General* 252: 91–106.

Wang T, Qiu L, Li H, Zhang C, Sun Y, et al. (2021) Facile synthesis of palladium incorporated $NiCo_2O_4$ spinel for low temperature methane combustion: Activate lattice oxygen to promote activity. *Journal of Catalysis* 404: 400–410.

Xiang XD, Sun X, Briceno G, Lou Y, Wang KA, et al. (1995) A combinatorial approach to materials discovery. *Science* 268: 1738–1740.

Yamasaki T, Takagaki A, Shishido T, Bando KK, Kodaira T, et al. (2022) Particle size effect on hydrogen cyanide synthesis with CH_4 and NO over an alumina-supported platinum catalyst. *Journal of the Japan Petroleum Institute* 65: 184–191.

Yao Y, Huang Z, Li T, Wang H, Liu Y, et al. (2020) High-throughput, combinatorial synthesis of multimetallic nanoclusters. *Proceedings of the National Academy of Sciences* 117: 6316–6322.

Zhong M, Tran K, Min Y, Wang C, Wang Z, et al. (2020) Accelerated discovery of CO_2 electrocatalysts using active machine learning. *Nature* 581: 178–183.

Catalysts: Materials

Weijie Zhang and Sen Zhang, Department of Chemistry, University of Virginia, Charlottesville, VA, United States

© 2024 Elsevier Ltd. All rights reserved.

This is an update of A. Hagemeyer, A. Volpe, Catalysts: Materials, Editor(s): Franco Bassani, Gerald L. Liedl, Peter Wyder, Encyclopedia of Condensed Matter Physics, Elsevier, 2005, Pages 158–165, ISBN 9780123694010, https://doi.org/10.1016/B0-12-369401-9/00541-6.

Introduction 738
Applications of catalysis in chemical processes 740
Status of catalysis research and catalyst discovery 740
Kinetic considerations 740
Aspects of adsorption 741
Catalysis 741
The principle of Sabatier 741
Microkinetic modeling 742
Catalyst properties, shapes, and preparation 742
Precipitation (bulk catalysts) 743
Fusion (bulk, pre-molten alloys, and metal oxides) 743
Evaporative methods 744
Impregnation (supported catalysts) 744
Catalyst supports 744
Hydrothermal synthesis (zeolites) 744
Raney metals 744
Colloidal wet-chemical synthesis 744
Catalyst characterization 746
Catalyst deactivation 746
Sintering 746
Structure decomposition or structure collapse 746
Fouling and poisoning 746
Conclusion 747
References 748

Abstract

Heterogeneous catalysis is one of the pillars of modern chemical industries. Updated from its previous version published in 2005, the chapter first outlines the general concepts of heterogeneous catalysis and its critical role in chemical processes. It then provides a brief overview of design principles, including kinetics, aspects of adsorption, and microkinetic modeling of heterogeneous catalysts. The chapter then summarizes the representative strategies for catalyst preparation and characterization and the understanding of catalyst deactivation. It finally highlights the future trends in heterogeneous catalysis with an emphasis on sustainable and green chemistry, atomic precision catalysts, and emerging computational design of catalysts.

Key points

- Provides an introduction to fundamental principles of heterogeneous catalysis;
- Covers all aspects of heterogeneous catalytic materials: catalyst preparation, catalyst characterization, and catalyst deactivation;
- Outlines future trends in heterogeneous catalysis development.

Introduction

Catalysis is the process of accelerating the reaction rate by adding a compound known as a catalyst. Catalysts are not consumed in the reaction and remain unchanged after it. A catalyst does not, however, affect the thermodynamics of a reaction or the equilibrium composition of the reaction components (Augustine, 1995; Bowker, 1998; Cornils et al., 2003; Ertl et al., 1999; Farrauto and Bartholomew, 1998; Kamerlin and Warshel, 2010).

Catalysis is the cornerstone of modern chemical industries. More than 90% of the current chemical processes for the production of commodity and fine chemicals involve catalysis. Fig. 1 highlights the use of catalytic transformations to obtain a broad range of

https://doi.org/10.1016/B978-0-323-90800-9.00202-X

valuable chemicals from C1 gases (CH_4, CO, and CO_2) (Cui et al., 2019). The C1 sources are obtained from fossil fuels, biomass feedstocks, and organic wastes. Built on well-established catalytic processes, including water-gas shift reaction (WGSR), reversed WGSR (RWGSR), Fischer-Tropsch synthesis (FTS), hydrogenation (HYD), oxidation, oxidative coupling of methane (OCM), and methane dehydroaromatization (MDA), etc., the C1 sources are converted to fuels, olefins, alcohols, and aromatics that are all integral to the modern society (Gates, 1992; Satterfield, 1991; Rase, 2000; Morbidelli et al., 2010; Le Page, 1987; Hagemeyer and Volpe, 2005).

As shown in Fig. 2, three types of catalysts are utilized commercially, including heterogeneous catalysts (porous solids and supported nanoparticles), homogeneous catalysts (dissolved in the liquid reaction mixture), and biological catalysts (enzymes) (Liu and Corma, 2021). Catalytic processes include single-phase homogeneous liquid, two-phase heterogeneous liquid-solid and gas-solid (the most prevalent), and three-phase heterogeneous liquid-solid-gas, implemented using a variety of reactor types. Catalyst activity, selectivity, chemical, and mechanical stability, lifetime, and form determine the cost and the energy efficiency of each process. Control factors to tune catalyst properties are bulk chemical composition, surface composition, stability of active phases, active site structure and distribution, texture (i.e., surface area and porosity), and mass and heat transport. The method of preparation is also crucial to the final catalyst structure and performance (Szostak, 1989).

Catalytic processes are superior to noncatalytic synthetic routes mainly because of energy, raw material savings, and selectivity enhancements. Advantages of heterogeneous catalysis compared to homogeneous catalysis include easy separation of the catalyst and reaction products, minimized reactor corrosion, and larger ranges of possible reaction conditions, which is important when the equilibrium limits the reaction to extreme conditions. Typical heterogeneous catalysts comprise metals or metal oxides and inorganic microporous materials such as zeolites. This chapter is updated from its previous version published in 2005 (Hagemeyer and Volpe, 2005), and focuses on heterogeneous catalysis in the vapor phase.

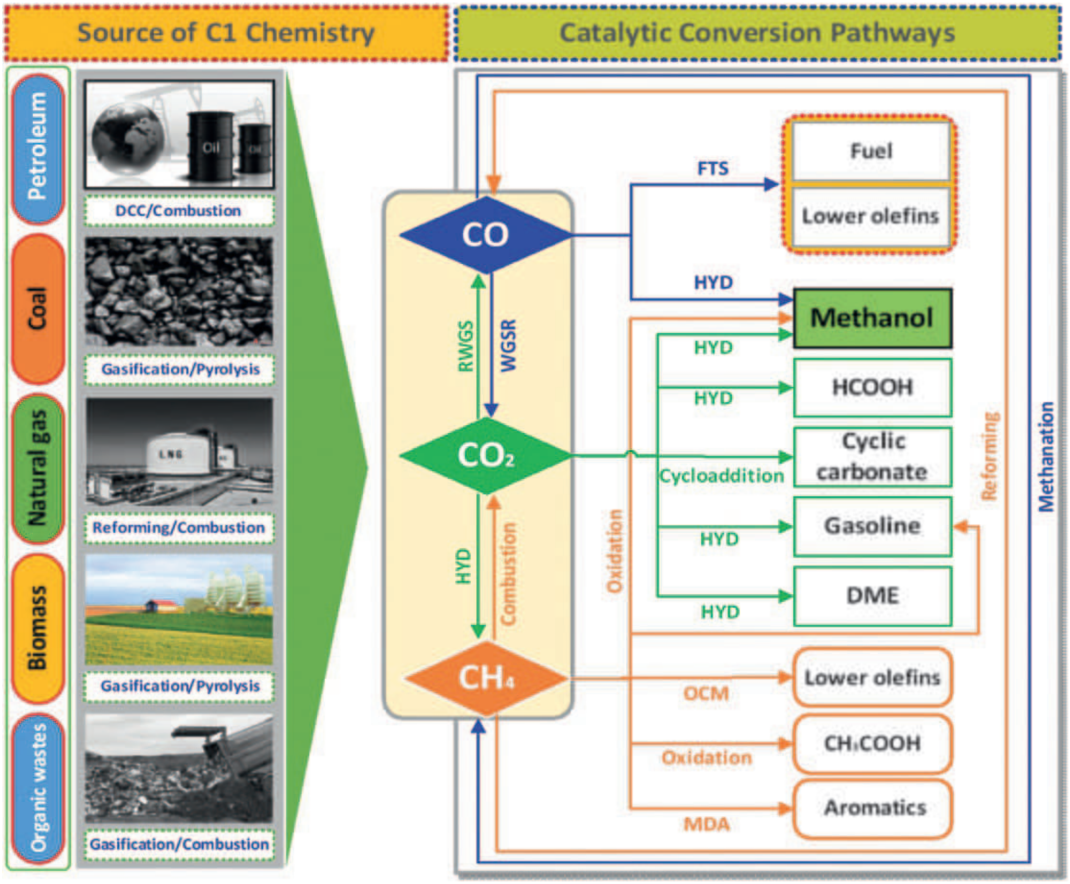
Source of C1 Chemistry
Catalytic Conversion Pathways
Petroleum
DCC/Combustion
Coal
Gasification/Pyrolysis
Natural gas
Reforming/Combustion
Biomass
Gasification/Pyrolysis
Organic wastes
Gasification/Combustion
CO
RWGS
WGSR
CO₂
HYD
Combustion
CH₄
FTS
Fuel
Lower olefins
HYD
Methanol
HYD
HCOOH
HYD
Cyclic carbonate
Cycloaddition
Gasoline
HYD
DME
HYD
Oxidation
Reforming
Methanation
Lower olefins
OCM
CH₃COOH
Oxidation
Aromatics
MDA

Fig. 1 Major source and catalytic transformation routes of CO, CO_2, and CH_4 (Cui et al., 2019). From Cui WG, Zhang GY, Hu TL, and Bu XH (2019) Metal-organic framework-based heterogeneous catalysts for the conversion of C1 chemistry: CO, CO_2 and CH_4. *Coordination Chemistry Reviews* 387: 79–120. Copyright 2019, Elsevier.

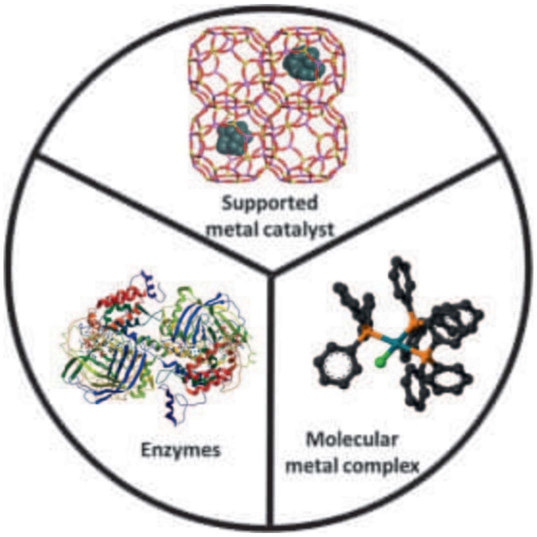

Fig. 2 Three types of catalysts (bio-, homogeneous, and heterogeneous catalysis).

Applications of catalysis in chemical processes

Thermodynamics frequently limits the concentration of the desired product(s) of a reaction, and conditions (temperature, pressure, space velocity, and reactant composition) must be optimized to maximize the equilibrium concentration of those products. The next step is to develop a catalyst to increase the reaction rate since it is frequently too slow to be practical. It might seem that the optimal catalyst should produce the highest possible reaction rate; however, this is not always the case since such a catalyst might exhibit mass and energy transfer limitations and could be unstable under feasible reaction conditions. The catalyst and the reactor form an integrated unit. Common reactor types (and associated catalyst formulations) are fixed beds (shaped millimeter-sized bodies), fluidized beds (50–150 mm diameter fluidizable particles), stirred tank reactors (slurried powders), and trickle beds (for three-phase reactions). Reactor operation can be continuous, semi-continuous, or batch, with adiabatic or isothermal temperature control. Consideration of mass and energy balance from the macroscopic catalyst bed scale down to the active center is needed to address the complexity of heterogeneous catalysis (Wijngaarden et al., 1998; Twigg, 1989; Thomas and Thomas, 1997).

Status of catalysis research and catalyst discovery

Current approaches used for the understanding and rational design of catalysts include various types of spectroscopies on catalysts and catalyst models, acquisition of kinetic data for catalytic reactions, quantum-chemical and thermodynamic calculations for the elementary steps and molecules involved in a reaction, micro-kinetic modeling, and machine-learning/deep-learning assisted catalyst search and optimization.

Kinetic considerations

The slow step in a reaction mechanism is known as the "rate-limiting step" since it determines the rate of the overall reaction. The rate-limiting step can usually be described as an energy barrier the system must cross. The rate constant has a temperature dependence:

$$k = A\ \exp\ (-E_A/RT)$$

where A is the pre-exponential factor and E_A is the activation energy. The activation energy can be determined graphically from the experimental determination of the rate constant as a function of reaction temperature through an Arrhenius plot. A catalyst provides an energetically easier reaction pathway to transform reactants into products that is characterized by lower activation energy.

The kinetics of a catalytic reaction is usually measured in a reactor under relevant process conditions and often power law equations such as $r = C_A^n C_B^m \ldots$ that are used to model the macro-kinetics (n, m are reaction orders for A and B).

Aspects of adsorption

Mass transport and adsorption are important aspects of catalysis. Mass transport exists between the fluid phase (gas, liquid) and catalyst particles, and within a catalyst particle. It is important to determine the influence of mass transport on the catalytic reaction rate and product selectivity. The first step in a catalytic event is the adsorption of reactant(s) onto a catalyst surface, followed by chemical reaction(s) at the surface and eventually desorption of products into the fluid phase. There are two main classes of adsorption: physisorption and chemisorption. In physisorption the attractive force is a weak *van der Waals* interaction with an adsorption energy of ~5–10 kJ mol^{-1} and the chemical bonds in the adsorbing molecules remain intact. Multiple layers of adsorbed molecules are possible. In chemisorption, the adsorption energy is comparable to that of a chemical bond, and the molecule may adsorb intact or it may dissociate. Chemisorption energies are ~30–70 kJ mol^{-1} for molecules and ~100–400 kJ mol^{-1} for atoms.

The number of adsorption sites on a catalyst is constant and the competition for those sites has important consequences for macroscopic kinetics and thus catalysis. This is the reason for treating the surface sites as if they were a reactant in the reaction equations. Measurements of adsorption isotherms are used to characterize catalyst porosities and surfaces, to model the reaction kinetics, and help in understanding reaction mechanisms. An isotherm is a coverage considered as a function of temperature and pressure, $\theta(T, p)$. The Brunauer-Emmett-Teller (BET) adsorption isotherm for multi-layer physisorption is used in the determination of catalyst surface areas and porosities. Let the surface area be given by

$$SA = \frac{\mathrm{V_m}}{22414}\mathrm{A_m}N$$

with SA = surface area, V_m = monolayer volume (cc STP), 22,414 = molar volume of ideal gas (cc STP), A_m = adsorbate molecular cross-sectional area, N = Avogadro's number. The BET model is applied to isotherm data from $P/P_0 = 0.05$–0.35 as follows:

$$\frac{P/P_0}{V_{ads}(1-P/P_0)} = \frac{1}{V_m} + \frac{(C-1)}{V_m C}\frac{P}{P_0}$$

and from the linear relationship, $V_m = 1/(\text{slope} + \text{intercept})$ and $C = \text{slope}/\text{intercept} + 1$ (the C value is related to the heat of adsorption). The Langmuir adsorption isotherm, on the other hand describes adsorption for single-layer chemisorption, i.e., when the adsorbate forms a monolayer with sites having the same adsorption energy. The Langmuir calculation is applicable only to microporous samples:

$$\frac{P/P_0}{V_{ads}} = \frac{1}{V_m B} + \frac{P/P_0}{V_m}$$

and from the linear relationship (typically for $P/P_0 < 0.05$), $V_m = 1/\text{slope}$.

Catalysis

In a catalytic reaction, active sites react and are regenerated and reused in a cyclic manner. The catalyst activity depends on "the number of active sites" and "the turnover frequency." The reaction mechanism consists of many different steps each of which may be of a different type. For example, the Langmuir-Hinshelwood mechanism consists of the following sequence of steps: (1) adsorption from the gas phase, (2) dissociation of molecules at the surface, (3) reactions between adsorbed molecules, and (4) desorption to the gas phase. The Eley-Rideal mechanism covers another important class of reactions and consists of: (1) adsorption from the gas phase, (2) dissociation of molecules at the surface, (3) reactions between gas and adsorbed molecules, and (4) desorption to the gas phase. The Mars-van Krevelen mechanism is often observed for selective oxidations over reducible metal oxide catalysts when lattice oxygen from the oxide is inserted into the hydrocarbon reactant and the lattice defect is subsequently re-oxidized by reaction with gaseous oxygen. The oxidation of the hydrocarbon is thus mediated by the catalyst which is the direct oxidizing agent providing nucleophilic lattice oxygen that is often more selective than molecular or chemisorbed oxygen species.

The principle of Sabatier

An ideal catalyst should bind products and reactants with a moderate strength: neither too strongly to desorb the products nor too weakly to activate the reactants. This leads to a volcano curve of the rate versus adsorption as illustrated in Fig. 3A, which is known as the "Principle of Sabatier" (Medford et al., 2015). In general, the activation energy for the catalyzed dissociation of diatomic molecules decreases when moving left from the noble metals in the periodic table. For example, taking CO as a simple model for adsorption, the *anti*-bonding $2\pi^*$ states are partially filled when chemisorbed and they fill further during dissociation. The *anti*-bonding molecular states must be close to the Fermi level of the metal, and when the metal has *d*-states close to the Fermi level, as in the transition metals, there is a strong covalent interaction between the anti-bonding states and the metal *d*-states. For the early transition metals with low *d* filling, the *anti*-bonding metal-C orbital is almost empty due to strong donation resulting in a stronger metal-CO bond, negative adsorption enthalpy, and dissociation (e.g., Fischer Tropsch metals Fe, Co, and Ru), whereas for

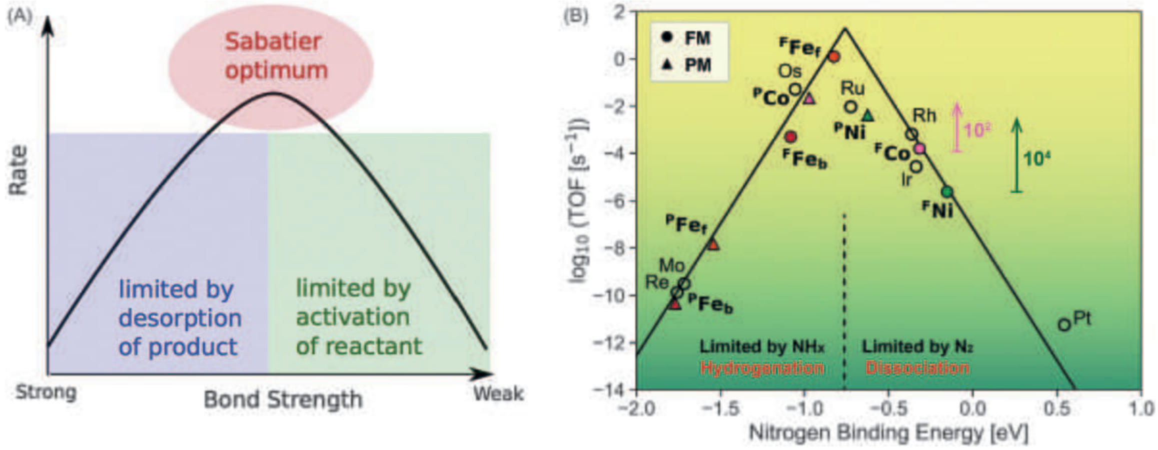

Fig. 3 (A) Schematic representation of the qualitative Sabatier principle (Medford et al., 2015). (B) Computationally established Sabatier principle for ammonia synthesis activity on the step sites of different transition metals (Xu et al., 2022). (A) From Medford AJ, Vojvodic A, Hummelshøj JS, Voss J, Abild-Pedersen F et al. (2015) From the Sabatier principle to a predictive theory of transition-metal heterogeneous catalysis. *Journal of Catalysis* 328: 36–42. Copyright 2015, Elsevier. (B) From Xu G, Cai C, and Wang T (2022) Toward sabatier optimal for ammonia synthesis with paramagnetic phase of ferromagnetic transition metal catalysts. *Journal of the American Chemical Society* 144: 23089–23095.Copyright 2022, ACS.

the late transition metals and noble metals with high *d* filling, the *anti*-bonding metal-C orbital is almost full due to strong back-donation resulting in weaker metal-CO bond, positive adsorption enthalpy, and no dissociation.

The Haber-Bosch process, converting hydrogen (H_2) and nitrogen (N_2) to ammonia (NH_3), is an important reaction in heterogeneous catalysis. In order to guide the new catalyst design, the volcano plot between nitrogen binding energy and ammonia synthesis activity among metals has been established. As shown in Fig. 3B, the activities of metals with low nitrogen binding energy are limited by the hydrogenation steps (the left), and those with high nitrogen binding energy will be hindered by the high transition state energy of N_2 dissociation (the right) (Xu et al., 2022). Therefore, the catalyst with a moderate nitrogen binding energy and small transition state energy of N_2 dissociation denotes the Sabatier optimal for the Haber-Bosch process. Additionally, Fig. 3B reveals that the TOF on the same catalytically active site, such as Fe, Co, and Ni metals, strongly depends on their metallic element.

Microkinetic modeling

The detailed microscopic description of a chemical reaction in terms of the motion of the individual atoms taking part in the event is known as the "reaction dynamics." The link between the microscopic description of the reaction dynamics and the macro-scopic kinetics that can be measured in a catalytic reactor is the micro-kinetic model. Such a model for a given reaction begins with binding energies and reaction rate constants deduced from surface science experiments on well-defined single-crystal surfaces and relates these to the macroscopic kinetics of the reaction. The aim is to identify the basic parameters of the reactants and the surface that determine the reaction dynamics (activation barriers, etc.) and relate them to factors determining the catalytic activity. The models are useful for understanding variations in the catalytic activity from one system to another. The stability of the intermediates and the activation barriers are among the input parameters for the micro-kinetic model, and it is straightforward to calculate the effects of changes in stability for some or all the intermediates.

Catalyst properties, shapes, and preparation

Catalysts for continuous-flow fix-bed processes must be shaped to allow the fluid reactant stream to freely pass through the packed bed with an acceptable pressure drop and come into contact with a surface area as large as possible. An example is illustrated in Fig. 4 where catalyst bodies of various sizes, shapes, and geometries (e.g., powder, 10-hole ring, multicore-shell, monolith, foam, core-shell and pellet) are used for biogas reforming. The shape determines the void fraction, packing density, and mechanical strength (Zhao et al., 2020). The fluid mechanics, flow characteristics and pressure drop, and diffusion restrictions are influenced by the shape and size of the catalyst bodies. Small bodies are often easier to manufacture but suffer from higher pressure drop.

Catalyst pellets used in commercial fixed-bed reactors range in diameter from 1.5 to 10 mm. Typical ring sizes are 6–20 mm. Extrudates are 1–5 mm in diameter and 10–30 mm long. Pellets can have several channels and are usually 20–40 mm in diameter and 10–20 mm long (compared to a ring, the use of several smaller channels gives improved mechanical strength with good mass- and heat-transport). Monoliths are used for high gas flow rates or dust (fly ash, soot) containing gas feeds. For the control of emissions in power plant exhaust gas steams, for instance, typical honeycombs are sized 150 mm in edge and 1 m in length,

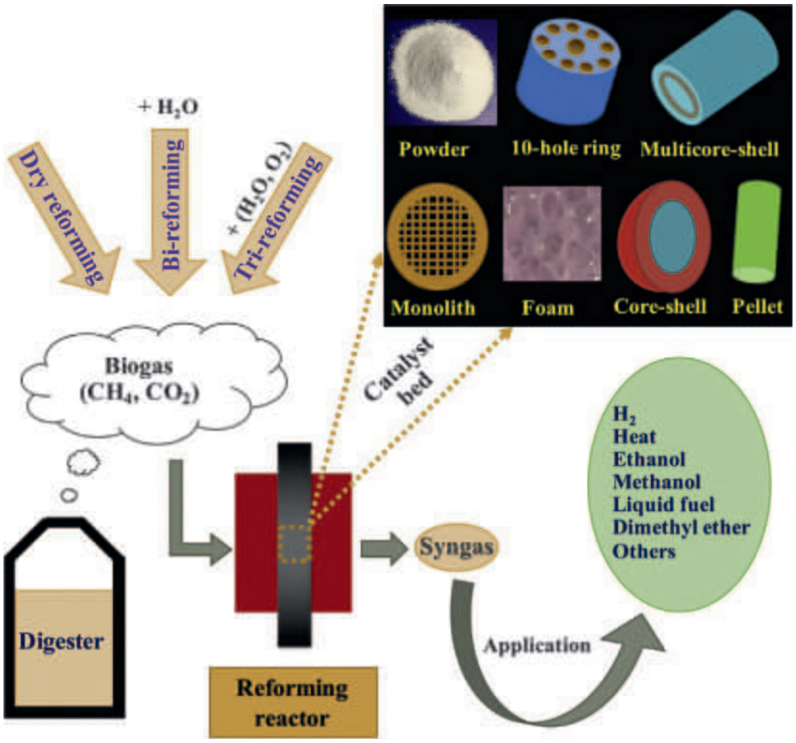

Fig. 4 Catalysts of various shapes are used in biogas reforming. Biogas is produced from the digestion process that breaks organic matter (e.g., wastewater). Through the reforming process, biogas gas can be converted to syngas (CO and H_2), which can be subsequently used to synthesize other chemicals (Zhao et al., 2020). From Zhao X, Joseph B, Kuhn J, and Ozcan S (2020) Biogas reforming to syngas: A review. *iScience* 23: 101082. Copyright 2020, Elsevier.

with ~1000 channels per monolith. A stack consists of two to three layers of several hundred honeycombs each. Solid catalysts can be entirely composed of the catalytically active material (bulk catalysts) or supported on porous carriers to improve the mechanical stability or finely distribute the active material thereby creating a large number of active sites.

High activity and selectivity, long-term stability (lifetime), resistance to poisons, tolerance to deviations from operating conditions such as temperature excursions (hot spots), good mechanical strength, and lack of toxic or hazardous ingredients-make high demands on technical catalysts. A variety of synthetic tools are available for the preparation of catalysts, and the performance often more strongly depends on the details of the synthetic route rather than the final composition.

Precipitation (bulk catalysts)

Catalysts are precipitated by mixing one solution with another solution or a suspension to form an insoluble compound. Typical precipitation agents are acids or bases to induce a pH change to a metal salt solution. The precipitate is filtered, washed, dried, calcined, and crushed to a fine powder. A binder is added, and the powder is tableted. The catalyst may also be shaped before calcination by extruding the filter cake. Typical binders are graphite or stearic acid. Common catalysts prepared by precipitation include alumina-supported Cu-Zn for methanol synthesis and the water gas shift reaction.

Fusion (bulk, pre-molten alloys, and metal oxides)

Catalysts based on metals and metal oxides may be prepared by fusion, crushing, and screening. The finished catalyst consists of irregular pieces of a narrow range of sizes. Fusion is only possible for catalysts that are conductors at high temperatures. During the preparative process, the catalyst powder is placed in an electro-furnace and heated by passing a large current through graphite electrodes. At the start of the cycle, a solid catalyst is added to the furnace and the electrodes are lowered. The voltage is fixed, and the current is regulated through the height of the electrodes. The molten mass is stirred by the electromagnetic fields generated by the current flowing between the electrodes. At the end of the process, the electrodes are raised, and the molten catalyst is poured out.

The catalyst has no porosity before reduction. The pore system is created when the metal oxide is reduced during the activation of the catalyst (the catalyst may also be supplied in pre-reduced form). The pre-reduced catalyst is first completely reduced then passivated by gentle oxidation to allow it to be transported and loaded safely. Common catalysts prepared by fusion include alloy catalysts (e.g., Pt-Rh gauze for ammonia oxidation) and oxides (e.g., Fe oxide for ammonia synthesis or Fischer-Tropsch synthesis), and fused V_2O_5-$K_2S_2O_7$ for sulfuric acid synthesis.

Evaporative methods

Wet mixing of (soluble or insoluble) metal precursors in water or organic solvents and subsequent removal of the solvent by evaporation, freeze drying, or spray drying may be used to produce mixed multi-metal oxide catalysts. Often, preformed catalyst powders are slurried and spray-dried once again to produce a fluffy and compactable powder for subsequent shaping by extrusion or tablet pressing.

Impregnation (supported catalysts)

Impregnated catalysts are prepared by impregnating (e.g., spraying) a solution of a metal salt or mixture onto pellets of a porous support. The metal loading in the finished catalyst is typically 1–5% but can be as low as 0.1%. When liquid is slowly added to a porous solid powder, the liquid is first absorbed in the pores and the powder flows as if it is dry. When the pores are filled, the outer surface of the granules suddenly becomes wet, the granules tend to stick together, and the powder forms lump instead of flowing freely. Incipient wetness is the point when the pores are filled, but the outer surface of the granules is dry, and can easily be determined by shaking or stirring the powder. Following impregnation to incipient wetness, the pellets are dried and calcined to transform the metal into an insoluble form. The metal salt can be deposited homogeneously through the pellet or most of the metal may be deposited near the outside of the pellet. The distribution of the metal is controlled through the interaction of the metal solution(s) with the support, e.g., through varying the metal counterion, through control of pH, or through the addition of chelating agents to the impregnation liquid. The impregnation method (wet versus dry, fast, and slow) and drying conditions can also affect distribution. Typical distributions include eggshell, egg white, and egg yolk. Shell catalysts are often used for selective oxidations to overcome pore diffusion limitations and suppress consecutive over-oxidation reactions, whereas egg-white catalysts are used in refining to protect the inner catalyst layer from feed poisons.

Compared to other catalyst preparation methods, impregnation offers several advantages. For example, the pellets may be shaped before the metal is added; the filtering and washing of the catalysts are not necessary; low metal loadings are easily achieved; and control over the distribution of the metal in pellets is possible.

Common catalysts prepared by impregnation include carbon-supported Pt and Pd for hydrogenations, ceria-zirconia supported Pt-Rh for the three-way catalytic converter, and titania-supported V_2O_5 for NO_x abatement.

Catalyst supports

Since the catalysis occurs at the surface of the metal particles, the catalysts are prepared so as to expose a large metal area, typically 10–100 $m^2\ g^{-1}$ of catalyst. The function of the support is primarily to increase and stabilize the area of the metal particles. The size of the metal particles may be reported as the total area of the metal surface, as the diameter of the metal particles (commonly 3–15 nm), and as the so-called metal dispersion (defined as the fraction of all metal atoms that are present at the metal particle surface, commonly from 20 up to ~80%).

Support contains pores having irregular shapes. These pores fall into two size ranges. Macro-pores have diameters of 100 nm or more and are formed from cracks/spaces between crystallites. Micro-pores have diameters of 1 nm or less and are due to the "roughness" of the solid surface itself, or the structure of the crystal lattice.

Hydrothermal synthesis (zeolites)

Typically, Si and Al precursors together with an organic structure-directing agent are heated up to 200 °C under autogenous pressure in autoclaves for up to several days to synthesize crystalline microporous zeolites or other molecular sieves such as aluminophosphates. These materials have well-defined pore structures (pore diameters ranging from ~3 to 8 Å) as compared to the broad pore size distributions found in traditional carrier materials. As catalysts, they may contain metal in the pore. Applications of zeolites as supports, solid acids or shape-selective catalysis are common. Zeolites are widely used in refining and petrochemicals, e.g., ultra-stabilized Y zeolite for fluid catalytic cracking and ZSM-5 for xylene isomerization.

Raney metals

Highly porous metal sponges can be made in aqueous solutions by the dissolution of aluminum alloys using a strong base. Metal sponges are typically used for hydrogenation in laboratory synthesis. Raney nickel is made by dissolving an (Al, Ni)-alloy containing 50% Ni in 20% NaOH in water. The surface area is 80–100 $m^2\ g^{-1}$. The most commonly used Raney metals are Ni, Co, Cu, and Fe.

Colloidal wet-chemical synthesis

Colloidal nanoparticles and clusters (1–20 nm) can be prepared by chemical reduction or decomposition of metal compounds in solution in the presence of surfactants or stabilizing polymers (Lee et al., 2013). The synthesized nanoparticles and clusters can be adsorbed onto high-surface-area supports (metal oxide or carbon) as the supported catalysts. A significant advantage of colloidal wet-chemical synthesis is the possibility to tune the nanoparticle physical dimensions (sizes and shapes), compositions (alloys or doping), atomic structures (crystal phases), and architectures (heterostructures, core/shell), which has been extensively studied in past two decades and demonstrated substantial success for metals and metal oxides nanocatalysts (Zhang et al., 2014, 2019; Wu et al., 2018; Shi et al., 2021). Once loaded onto supports, colloidal nanocatalysts are often surface activated by removing surfactants, as the surfactants may block the active surface for catalysis. The typical ligand removal methods include thermal calcination, UV-ozone cleaning, and ligand exchange and stripping (Dong et al., 2011; Luo et al., 2017; Cargnello et al., 2015; Li et al., 2012; Godbold et al., 2021).

Nanocatalysts produced through colloidal wet-chemical synthesis could present uniform size and structure (also called monodisperse nanoparticles or well-defined nanoparticles) and thus are beneficial to unambiguously understand the structure-property relationship in catalysis, which is unachievable by using ill-defined catalysts synthesized in other methods (Yan et al., 2018; Qin et al., 2018, 2020; Mitchell et al., 2021). Fig. 5A displays High-angle annular dark-field scanning transmission electron microscopy (HAADF-STEM) image of an ill-defined Fe oxide-supported Au catalyst, revealing the existence of small clusters and

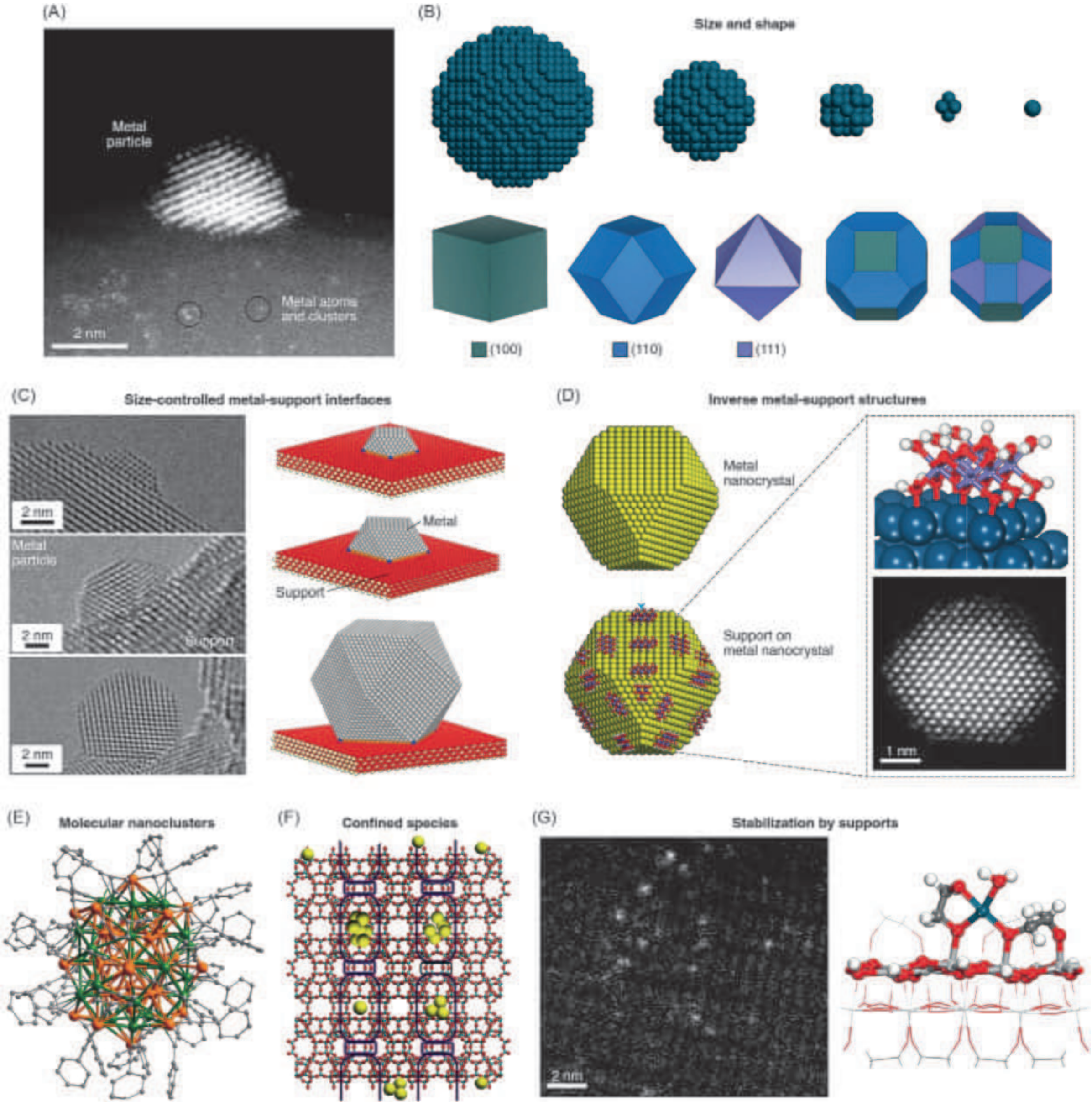
(A)
Metal particle
Metal atoms and clusters
2 nm
(B)
Size and shape
(100)
(110)
(111)
(C)
Size-controlled metal-support interfaces
2 nm
Metal particle
2 nm
Support
2 nm
Metal
Support
(D)
Inverse metal-support structures
Metal nanocrystal
Support on metal nanocrystal
1 nm
(E)
Molecular nanoclusters
(F)
Confined species
(G)
Stabilization by supports
2 nm

Fig. 5 Well-defined catalysts. (A) High-angle annular dark-field scanning transmission electron microscopy (HAADF-STEM) image of a typically ill-defined supported catalyst. (B) Schematic illustration showing the control of particle size or morphology. The exposed facets are color coded, highlighting the variation with particle shape. (C) Controllable metal-support interface by tuning the size of metal nanoparticles. (D) an inverse metal nanocatalyst with sub-monolayer support deposited on a metal nanocrystal. (E) Structural model of an atomically precise metal nanocluster showing the well-defined binding structure of surface ligands. (F) Schematics showing the engineering of atomically dispersed metal catalysts by confining single atoms or clusters in porous materials. (G) HAADF-STEM image and determined atomic-scale structure of Pd_1/TiO_2 (Mitchell et al., 2021). From Mitchell S, Qin R, Zheng Z, and Perez-Ramirez J (2021) Nanoscale engineering of catalytic materials for sustainable technologies. *Nature Nanotechnology* 16: 129–139. Copyright 2021, Springer Nature.

individual atoms in addition to nanoparticles (Mitchell et al., 2021; Allard et al., 2009). Using colloidal synthesis, well-defined nanoparticles can be created with controllable sizes and shapes (exposed surface facets), as illustrated in Fig. 5B and C (Cargnello et al., 2013). Besides nanoparticles loaded on metal oxide supports, colloidal synthesis also enables to generate inversed structure by modifying the nanoparticle surface with active metal oxide coverage (Fig. 5D) (Chen et al., 2014). The new opportunities presented by colloidal synthesis are built on the ability and the ease of modulating nanoparticle nucleation and growth kinetics in solution phase by tailoring reaction conditions and using functional surfactant ligands. As shown in Fig. 5E–G, this wet-chemical strategy has been expanded to synthesize well-define cluster catalysts, confined active sites in porous zeolite/Metal Organic Framework (MOF), and single-atom catalysts (Liu et al., 2017, 2016; Wang et al., 2016).

Catalyst characterization

Catalysts are characterized for chemical composition, atomic order (crystallinity), phase identification and distribution, porosity, and to identify deactivation mechanisms. Commonly applied techniques include inductively coupled plasma, X-ray fluorescence, physi/chemisorption measurements (BET, Hg porosimetry, various titration techniques), electron microscopy (SEM, TEM, and STEM), Auger spectroscopy, X-ray photoelectron spectroscopy, atomic force microscopy, secondary ion mass spectrometry, X-ray absorption, and X-ray diffraction. These methods are often combined to provide a more detailed analysis of the catalyst structures and physical and chemical properties. Over the past decades, *in-situ* and *operando* characterizations have been extensively pursued to reveal the reaction mechanism and the real active site structures and energetics during catalytic processes (Wu et al., 2018; Tsoukalou et al., 2019; Kovtunov et al., 2019; Beck et al., 2021).

Catalyst deactivation

A number of different processes that contribute to the loss of catalyst activity with time on stream are described below. This problem is most often dealt with commercially by slowly increasing the catalyst temperature over time to maintain constant activity/productivity. When it is no longer possible to achieve the necessary performance, the catalyst is replaced (Lin et al., 2021).

Sintering

For supported metal catalysts, the active component is present on the catalyst in the form of small particles which are inherently unstable. A catalyst slowly loses activity due to the growth of these particles (favored by the resulting decrease in surface energy) and the resulting loss of surface area. There are two mechanisms for sintering: atoms may detach from one particle and move to another (Ostwald ripening), or crystallites may move along the support surface and coalesce. Sintering depends on the nature of the metal, the support, the strength of the metal-support interaction, the gases present, temperature, pressure, and time. Catalyst sintering is irreversible.

Structure decomposition or structure collapse

Crystalline catalysts such as zeolites and multi-metal oxides can deactivate due to the destruction of the crystalline phase or lattice structure. Another problem can be the loss of elements from the catalyst (or volatile compounds such as Mo, Re, etc.). This can be solved in some cases by the slow addition of the volatile element to the catalyst bed. In the case of attrition losses (e.g., for fluid catalytic cracking (FCC) zeolite catalysts), it is necessary to add in new catalysts slowly over time to the riser.

Fouling and poisoning

Catalytic activity may also be lost due to the formation of carbon ("coking") or due to the deposition of impurities or of dust or other particulates in the reactant stream onto the catalyst surface. The formation of carbon in many cases is reversible. For example, the catalyst can be taken offline, and the carbon removed by oxidation ("catalyst regeneration").

Examples of fouling by particulates occur in the removal of NO_x from industrial flue gases or in catalytic converters used in automobiles. In these cases, the catalyst is manufactured in a shape that allows the particulates to pass through the reactor with minimum accumulation (e.g., a catalyst was coated onto a ceramic monolith). A serious problem with catalyst dust may occur if the catalyst bed is improperly loaded, if there is a problem with excessive vibration in the reactor, or if physically weak catalysts are used. In these cases, dust may be formed by attrition, leading to dust accumulation in the reactor or elsewhere in the process impeding or blocking the gas flow. The highly reactive catalyst dust presents a serious safety hazard since it can cause an explosion when pipes or heat exchangers are opened for maintenance.

Examples of poisons that can be present in feeds include metallic impurities such as V, Na, and Ni in FCC processes, metallo-organics in desulfurization processes, and thiophenic sulfur compounds in various refining processes such as reforming. These poisons react with the catalyst and reduce or destroy its activity. It is often necessary to remove the poisons with a guard bed or dedicated upstream catalytic process (as is done with hydrodesulfurization, for example). Sometimes, the impurity is completely absorbed in the first few percent of the catalyst bed due to its strong interaction with the catalyst.

Conclusion

Commercial catalysts are used in refining (e.g., alkylation, dimerization, disproportionation, isomerization, catalytic cracking, FCC, hydro-processing (e.g., hydrotreating, hydrodesulfurization, hydrocracking), hydrogen production, reforming), chemical catalysis (e.g., aromatics production, monomer synthesis, polymerization, organic synthesis, cyclic and acyclic intermediates, medical, flavors and perfumes, rubber processing, plasticizers, surface active agents, agricultural, using oxidation, hydrogenation, dehydrogenation, phase transfer catalysis), biocatalysis, and environmental applications (automobile and industrial pollution control). There are numerous references available covering these applications in detail. The competitive pressures of a mature industry, the trend toward simpler and less capital-intensive processes, access to cheaper and renewable feedstocks, and the desire for more environmentally benign processes drive the development of new, high-performance catalysts in the future. Meanwhile, the demand for sustainable energy and green chemistry requires to shift conventional thermal catalytic processes to electrocatalytic or photocatalytic processes that can effectively utilize renewable electrical and solar energies. This also leads to tremendous efforts in developing emerging materials that are suited to these new catalytic processes (e.g., electrocatalysts for water splitting to produce clean H_2, electrocatalysts for CO_2 reduction to CO, formate, methanol etc.) (Godbold et al., 2021; Yin et al., 2022; Zhang et al., 2018; Liu et al., 2020).

The design and construction of atomically precise catalytic sites will continue to be at the forefront of catalysis research and development. Colloidal synthesis of well-defined nanoparticles and cluster catalysts is a representative example. New opportunities also exist in the development of heterogeneous catalysts through the controlled assembly of functional building blocks (Sudarsanam et al., 2019; Bennett et al., 2021). As shown in Fig. 6, diverse assembling building units, covering both inorganic and organic units, have long been applied in a variety of catalytic applications, and their porosities and topological structures can greatly determine the reaction mechanisms, accessibility of specific active sites and the selectivity of target products (Bennett et al., 2021). New approaches to the discovery of potentially new catalytic hybrid materials, including innovative preparation methods and combinatorial/high-throughput catalysis, are having positive impacts on catalyst development.

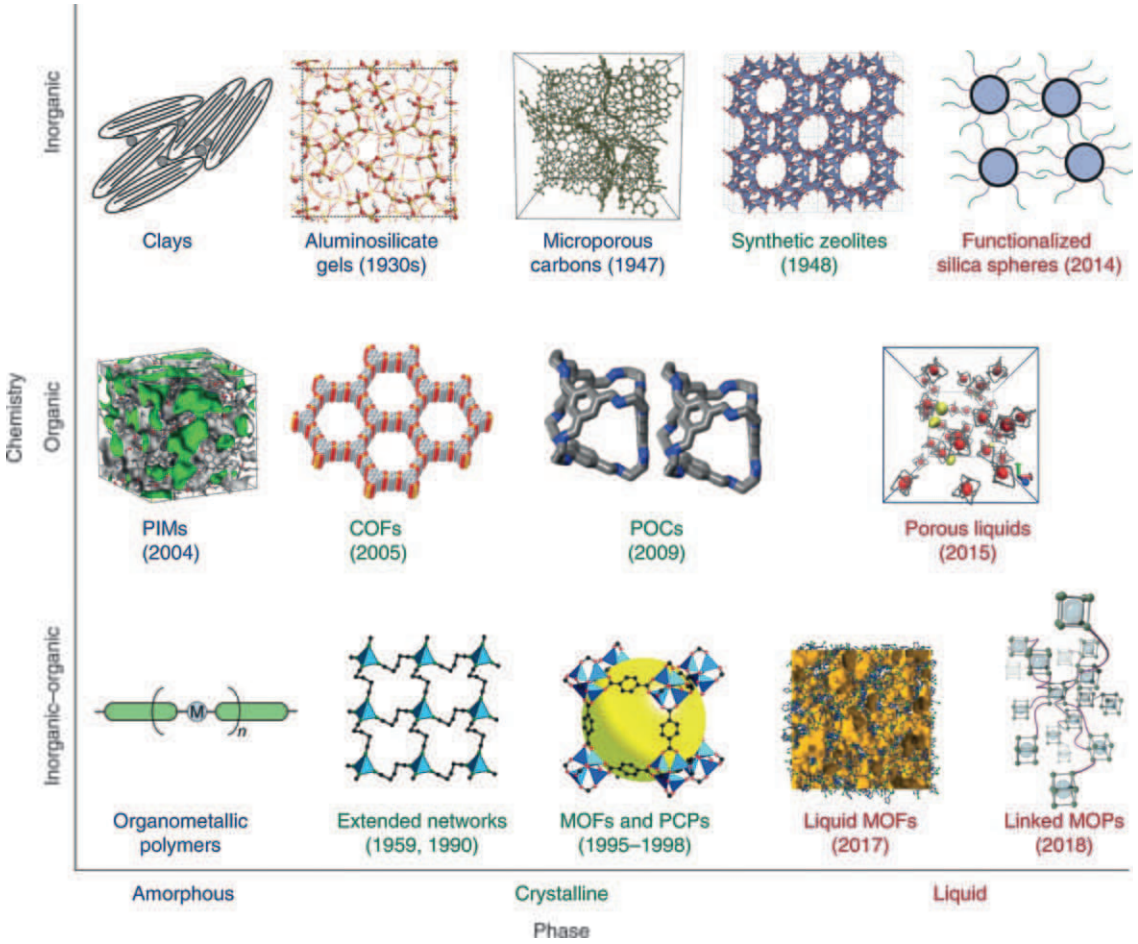
Inorganic
Clays
Aluminosilicate gels (1930s)
Microporous carbons (1947)
Synthetic zeolites (1948)
Functionalized silica spheres (2014)
Chemistry
Organic
PIMs (2004)
COFs (2005)
POCs (2009)
Porous liquids (2015)
Inorganic–organic
M
n
Organometallic polymers
Extended networks (1959, 1990)
MOFs and PCPs (1995–1998)
Liquid MOFs (2017)
Linked MOPs (2018)
Amorphous
Crystalline
Liquid
Phase

Fig. 6 Selected examples for the diverse assembling building units as potential heterogeneous catalysts (Bennett et al., 2021). From Bennett TD, Coudert FX, James SL, and Cooper AI (2021) The changing state of porous materials. *Nature Materials* 20: 1179–1187. Copyright 2021, Springer Nature.

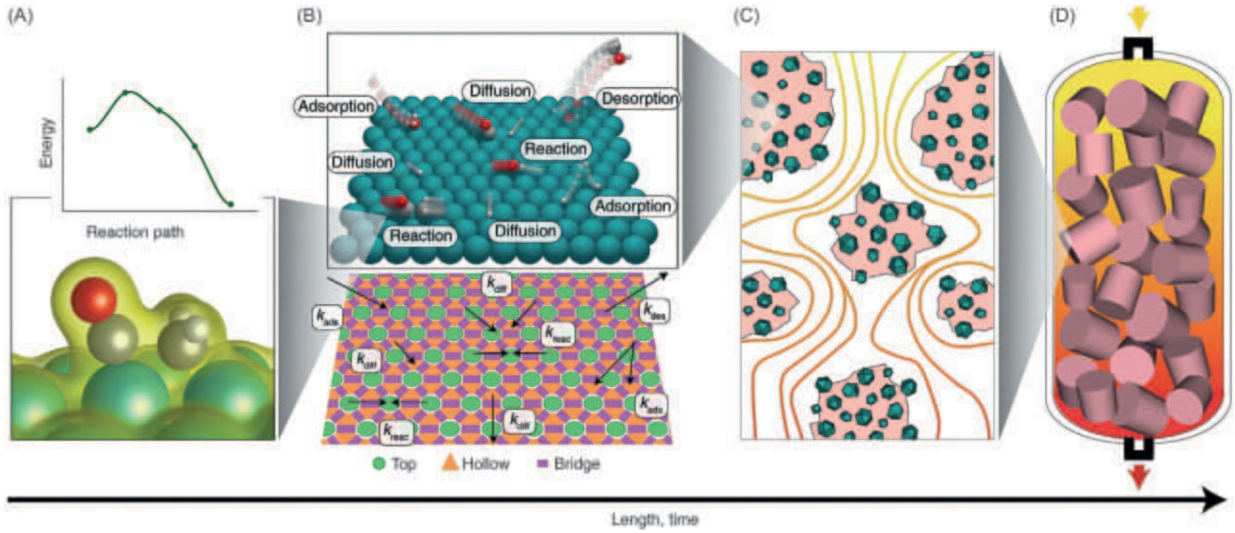

Fig. 7 Schematic illustration of a generic multiscale modeling framework for catalysts with complex working environments (Bruix et al., 2019). From Bruix A, Margraf JT, Andersen M, and Reuter K (2019) First-principles-based multiscale modelling of heterogeneous catalysis. *Nature Catalysis* 2: 659–670.Copyright 2019, Springer Nature.

Although catalysis has been used in industry for more than 150 years, the experimental techniques for investigating catalysis at the atomic level did not become routine until about 25 years ago, and the computational techniques not until 10 years ago. For this reason, the field has still been largely an empirical one. Fig. 7 highlights the complexity of the catalytic process at the scales ranging from atomic transformation at the catalyst surface to the complicated macroscale environment (heat, mass, and potential), which requires the rapid development of quantum mechanics and multiscale computational methods to further deepen the understanding of reaction mechanisms and catalyst designing principles (Bruix et al., 2019). The continued development of the computational method, especially emerging machine learning (ML) and artificial intelligence (AI)-guided catalyst design, will open new or additional opportunities in search of high-performance catalysts with complex multi-element compositions and structures that are impossible through conventional empirical strategies.

References

Allard LF, Borisevich A, Deng W, Si R, Flytzani-Stephanopoulos M, et al. (2009) Evolution of gold structure during thermal treatment of Au/FeO_x catalysts revealed by aberration-corrected electron microscopy. *Journal of Electron Microscopy* 58: 199–212.
Augustine R (1995) *Heterogeneous Catalysis for the Synthetic Chemist*. New York: Marcel Dekker.
Beck A, Zabilskiy M, Newton MA, Safonova O, Willinger MG, et al. (2021) Following the structure of copper-zinc-alumina across the pressure gap in carbon dioxide hydrogenation. *Nature Catalysis* 4: 488–497.
Bennett TD, Coudert FX, James SL, and Cooper AI (2021) The changing state of porous materials. *Nature Materials* 20: 1179–1187.
Bowker M (1998) *The Basis and Applications of Heterogeneous Catalysis*. New York: Oxford University.
Bruix A, Margraf JT, Andersen M, and Reuter K (2019) First-principles-based multiscale modelling of heterogeneous catalysis. *Nature Catalysis* 2: 659–670.
Cargnello M, Doan-Nguyen VV, Gordon TR, Diaz RE, Stach EA, et al. (2013) Control of metal nanocrystal size reveals metal-support interface role for ceria catalysts. *Science* 341: 771–773.
Cargnello M, Chen C, Diroll BT, Doan-Nguyen VV, Gorte RJ, et al. (2015) Efficient removal of organic ligands from supported nanocrystals by fast thermal annealing enables catalytic studies on well-defined active phases. *Journal of the American Chemical Society* 137: 6906–6911.
Chen G, Zhao Y, Fu G, Duchesne PN, Gu L, et al. (2014) Interfacial effects in iron-nickel hydroxide-platinum nanoparticles enhance catalytic oxidation. *Science* 344: 495–499.
Cornils B, Herrmann W, Schlogl R, and Wong C (2003) *Catalysis from A to Z: A Concise Encyclopedia*. Weinheim: WILEY-VCH.
Cui WG, Zhang GY, Hu TL, and Bu XH (2019) Metal-organic framework-based heterogeneous catalysts for the conversion of C1 chemistry: CO, CO_2 and CH_4. *Coordination Chemistry Reviews* 387: 79–120.
Dong A, Ye X, Chen J, Kang Y, Gordon T, et al. (2011) A generalized ligand-exchange strategy enabling sequential surface functionalization of colloidal nanocrystals. *Journal of the American Chemical Society* 133: 998–1006.
Ertl G, Knoezinger H, and Weitkamp J (1999) *Preparation of Solid Catalysts*. Weinheim: WILEY-VCH.
Farrauto R and Bartholomew C (1998) *Fundamentals of Industrial Catalytic Processes*. London: Blackie Academic and Professional.
Gates B (1992) *Catalytic Chemistry*. New York: WILEY-VCH.
Godbold P, Johnson G, Obi AD, Brown R, Hwang S, et al. (2021) Surfactant removal for colloidal nanocrystal catalysts mediated by N-heterocyclic carbenes. *Journal of the American Chemical Society* 143: 2644–2648.
Hagemeyer A and Volpe A Jr (2005) Catalysts: Materials. In: Bassani F, Liedl G, and Wyder P (eds.) *Encyclopedia of Condensed Matter Physics*. Oxford: Elsevier Academic Press.
Kamerlin SC and Warshel A (2010) At the dawn of the 21st century: Is dynamics the missing link for understanding enzyme catalysis? *Proteins* 78: 1339–1375.
Kovtunov KV, Lebedev D, Svyatova A, Pokochueva EV, Prosvirin IP, et al. (2019) Robust in situ magnetic resonance imaging of heterogeneous catalytic hydrogenation with and without hyperpolarization. *ChemCatChem* 11: 969–973.
Le Page J (1987) *Applied Heterogeneous Catalysis: Design, Manufacture, Use of Solid Catalysts*. Paris: Éditions Technip.
Lee J, Zhang S, and Sun SH (2013) High-temperature solution-phase syntheses of metal-oxide nanocrystals. *Chemistry of Materials* 25: 1293–1304.

Li D, Wang C, Tripkovic D, Sun S, Markovic NM, et al. (2012) Surfactant removal for colloidal nanoparticles from solution synthesis: The effect on catalytic performance. *ACS Catalysis* 2: 1358–1362.

Lin LL, Liu JJ, Liu X, Gao ZR, Rui N, et al. (2021) Reversing sintering effect of Ni particles on gamma-Mo_2N via strong metal support interaction. *Nature Communications* 12: 6978.

Liu LC and Corma A (2021) Isolated metal atoms and clusters for alkane activation: Translating knowledge from enzymatic and homogeneous to heterogeneous systems. *Chem* 7: 2347–2384.

Liu P, Zhao Y, Qin R, Mo S, Chen G, et al. (2016) Photochemical route for synthesizing atomically dispersed palladium catalysts. *Science* 352: 797–801.

Liu L, Diaz U, Arenal R, Agostini G, Concepcion P, et al. (2017) Generation of subnanometric platinum with high stability during transformation of a 2D zeolite into 3D. *Nature Materials* 16: 132–138.

Liu C, Qian J, Ye Y, Zhou H, Sun C-J, et al. (2020) Oxygen evolution reaction over catalytic single-site Co in a well-defined brookite TiO_2 nanorod surface. *Nature Catalysis* 4: 36–45.

Luo J, Monai M, Wang C, Lee JD, Duchoň T, et al. (2017) Unraveling the surface state and composition of highly selective nanocrystalline Ni-Cu alloy catalysts for hydrodeoxygenation of HMF. *Catalysis Science & Technology* 7: 1735–1743.

Medford AJ, Vojvodic A, Hummelshøj JS, Voss J, Abild-Pedersen F, et al. (2015) From the Sabatier principle to a predictive theory of transition-metal heterogeneous catalysis. *Journal of Catalysis* 328: 36–42.

Mitchell S, Qin R, Zheng N, and Perez-Ramirez J (2021) Nanoscale engineering of catalytic materials for sustainable technologies. *Nature Nanotechnology* 16: 129–139.

Morbidelli M, Gavriilidis A, and Varma A (2010) *Catalyst Design*. Cambridge: Cambridge University Press.

Qin RX, Liu PX, Fu G, and Zheng NF (2018) Strategies for stabilizing atomically dispersed metal catalysts. *Small Methods* 2: 1700286.

Qin R, Liu K, Wu Q, and Zheng N (2020) Surface coordination chemistry of atomically dispersed metal catalysts. *Chemical Reviews* 120: 11810–11899.

Rase H (2000) *Handbook of Commercial Catalysts: Heterogeneous Catalysts*. Boca Raton: CRC Press.

Satterfield C (1991) *Heterogeneous Catalysis in Industrial Practice*. New York: McGraw-Hill.

Shi Y, Lyu Z, Zhao M, Chen R, Nguyen QN, et al. (2021) Noble-metal nanocrystals with controlled shapes for catalytic and electrocatalytic applications. *Chemical Reviews* 121: 649–735.

Sudarsanam P, Peeters E, Makshina EV, Parvulescu VI, and Sels BF (2019) Advances in porous and nanoscale catalysts for viable biomass conversion. *Chemical Society Reviews* 48: 2366–2421.

Szostak R (1989) *Molecular Sieves*. London: Springer Dordrecht.

Thomas J and Thomas W (1997) *Principles and practice of heterogeneous catalysis*. Weinheim: Wiley-VCH.

Tsoukalou A, Abdala PM, Stoian D, Huang X, Willinger MG, et al. (2019) Structural evolution and dynamics of an In_2O_3 catalyst for CO_2 hydrogenation to methanol: An operando XAS-XRD and in situ TEM study. *Journal of the American Chemical Society* 141: 13497–13505.

Twigg M (1989) *Catalyst Handbook*. London: CRC Press LLC.

Wang Y, Wan XK, Ren L, Su H, Li G, et al. (2016) Atomically precise alkynyl-protected metal nanoclusters as a model catalyst: Observation of promoting effect of surface ligands on catalysis by metal nanoparticles. *Journal of the American Chemical Society* 138: 3278–3281.

Wijngaarden R, Kronberg A, and Westerterp K (1998) *Industrial Catalysis: Optimizing Catalysts and Processes*. Weinheim: Wiley-VCH.

Wu CH, Liu C, Su D, Xin HL, Fang H-T, et al. (2018) Bimetallic synergy in cobalt-palladium nanocatalysts for CO oxidation. *Nature Catalysis* 2: 78–85.

Xu G, Cai C, and Wang T (2022) Toward sabatier optimal for ammonia synthesis with paramagnetic phase of ferromagnetic transition metal catalysts. *Journal of the American Chemical Society* 144: 23089–23095.

Yan J, Teo BK, and Zheng N (2018) Surface chemistry of atomically precise coinage-metal nanoclusters: From structural control to surface reactivity and catalysis. *Accounts of Chemical Research* 51: 3084–3093.

Yin Z, Yu J, Xie Z, Yu SW, Zhang L, et al. (2022) Hybrid catalyst coupling single-atom Ni and nanoscale Cu for efficient CO_2 electroreduction to ethylene. *Journal of the American Chemical Society* 144: 20931–20938.

Zhang S, Zhang X, Jiang G, Zhu H, Guo S, et al. (2014) Tuning nanoparticle structure and surface strain for catalysis optimization. *Journal of the American Chemical Society* 136: 7734–7739.

Zhang W, Qin Q, Dai L, Qin R, Zhao X, et al. (2018) Electrochemical reduction of carbon dioxide to methanol on hierarchical Pd/SnO_2 nanosheets with abundant Pd-O-Sn interfaces. *Angewandte Chemie International Edition* 57: 9475–9479.

Zhang Z, Wu Q, Johnson G, Ye Y, Li X, et al. (2019) Generalized synthetic strategy for transition-metal-doped brookite-phase TiO_2 nanorods. *Journal of the American Chemical Society* 141: 16548–16552.

Zhao X, Joseph B, Kuhn J, and Ozcan S (2020) Biogas reforming to syngas: A review. *iScience* 23: 101082.

Numerical Approximation and Analysis

C Brezinski, Université des Sciences et Technologies de Lille, Villeneuve d'Ascq, France

© 2005 Elsevier Ltd. All rights reserved.

This is an update of C. Brezinski, Numerical Approximation and Analysis, Editor(s): Franco Bassani, Gerald L. Liedl, Peter Wyder, Encyclopedia of Condensed Matter Physics, Elsevier, 2005, Pages 132–134, ISBN 9780123694010, https://doi.org/10.1016/B0-12-369401-9/00563-5.

Introduction 750
Approximation of Functions 750
Ordinary Differential Equations 751
Integral Equations 751
Systems of Linear Equations 752
Further Reading 753

Introduction

When the solution of a mathematical problem cannot be obtained in an analytical form (e.g., the solution of a differential equation) or when it requires too many arithmetical operations (as the solution of a system of linear equations by Cramer's rule), then it is necessary to make use of a numerical method. Usually, such a method only provides an approximation of the solution. Numerical analysis is the branch of mathematics where constructive methods (that is methods able to construct effectively, numerically, the solution) are defined and studied.

Numerical approximation covers the approximation of functions in various senses (interpolation, best approximation, Padé approximation, etc.), the numerical solution of differential and integral equations, the computation of definite integrals, the solution of systems of linear and nonlinear equations, the computation of eigenelements, etc. It is beyond the scope of this article to enter into details and the aim of the article is to give a flavor of the domain and to describe the main ideas.

A numerical method is implemented on a computer. So, each arithmetical operation is affected by an error since computers work with numbers having a finite number of digits. So, the result which is finally obtained depends not only on the quality of the approximation used but also on the propagation of these rounding errors. Taking this point into account is fundamental when using a numerical method.

Approximation of Functions

In many situations, one needs to approximate a function f by another function g. The procedure to be used depends highly on the information on f and on the form of g. The function g can be a polynomial or a combination of given functions satisfying some conditions, or a rational function, or a spline (piecewise polynomials). If f is known at some given points x_i, then interpolation can be used. Interpolation determines the unknown parameters involved in g and provides approximations $g(x_i)$ of $f(x_i)$. If the numbers of parameters are less than the numbers of interpolation points, f can be approximated in the least squares sense. If the information on f is analytic, approximation in the sense of some norm can be used.

If the Taylor expansion of f around zero is known, a quite powerful procedure is Padé approximation. It is assumed that the formal expansion

$$f(z) = c_0 + c_1 z + c_2 z^2 + \cdots$$

is known. A rational approximation is derived with a numerator $N_p(z) = a_0 + \cdots + a_p z^p$ and a denominator $D_q(z) = b_0 + \cdots + b_q z^q$ so that the series expansion of $N_p(z)/D_q(z)$ agrees with the expansion of f as far as possible, which means

$$f(z)D_q(z) - N_p(z) = \mathcal{O}\left(z^{p+q+1}\right)$$

Such a rational function is called a Padé approximant and it is denoted by $[p/q]_f(z)$. The coefficients of N_p and D_q given by

$$\begin{aligned}
a_0 &= b_0 c_0 \\
a_1 &= b_0 c_1 + b_1 c_0 \\
&\vdots \\
a_p &= b_0 c_p + \cdots + b_q c_{p-q} \\
0 &= b_0 c_{p+1} + \cdots + b_q c_{p-q+1} \\
&\vdots \\
0 &= b_0 c_{p+q} + \cdots + b_q c_p a_0
\end{aligned}$$

with $c_i = 0$ for $i < 0$. Setting $b_0 = 1$ and solving the system formed by the last q equations gives the b_i. Then the a_i are directly obtained by the first p relations.

Padé approximants are widely used in many problems of mathematical physics.

Ordinary Differential Equations

Consider a Cauchy problem for a system of k ordinary differential equations

$$\begin{aligned} y'(x) &= f(x, y(x)),\ x \in [a, b] \\ y(a) &= y_0 \end{aligned}$$

where $f : \mathbb{R} \times \mathbb{R}^k \mapsto \mathbb{R}^k$, $y \in \mathbb{R}^k$, and $y_0 \in \mathbb{R}^k$ is given.

A numerical method for the integration of this system consists in constructing approximations y_n of the exact solution $y(x_n)$ at some chosen points $a = x_0 < x_1 < \cdots < x_n < \cdots < x_N = b$ in the interval of integration. There are two types of procedures for obtaining these approximations: one-step methods (where y_{n+1} is deduced only from y_n) and multistep methods (where y_{n+1} depends on $y_n, \ldots, y_{n-p}$).

First choose a fixed step size $\hbar(b - a)/N$ and set $x_n = a + nh$ for $n = 0, \ldots, N$. Of course, for $y_0, \ldots, y_N$ to be approximations of $y(x_0), \ldots, y(x_N)$, the formula for computing y_{n+1} has to satisfy some properties, namely the consistency, the stability, and the convergence which means that the error tends to zero when h tends to zero. Another quite important property of a method is its order r which explains the behavior of the error with h, $y_n - y(x_n) = O(h^r)$.

In a one-step method, the approximate solution is computed by

$$y_{n+1} = y_n + \hbar\Phi(x_n, y_n, h),\ n = 0, \ldots, N - 1$$

A Runge–Kutta method consists in

$$\begin{aligned} k_i &= f(x_n + \theta_i h, y_n + h\eta_i) \\ \eta_i &= a_{i1}k_1 + \cdots + a_{im}k_m \\ \Phi(x_n, y_n, \hbar) &= c_1 k_1 + \cdots + c_m k_m \end{aligned}$$

If $a_{ij} = 0$ for $j \geqslant i$, the method is explicit (which means that each k_i can be computed separately) while, if not, it is implicit and the k_i are given as the solution of a system of (nonlinear) equations. Of course, an implicit method is much more difficult to implement but, in the case of a stiff differential equation (that is an equation whose solution varies rapidly), such an implicit method has to be used.

In a multistep method, $y_0, \ldots, y_{p-1}$ have first to be computed by a one-step method and then $y_p, \ldots, y_N$ are obtained by

$$a_0 y_n + \cdots + a_p y_{n+p} = h\left(b_0 f_n + \cdots + b_p f_{n+p}\right)$$

for $n = 0, \ldots, N-p$, where $f_i = f(x_i, y_i)$. If $b_p = 0$ the method is explicit, otherwise it is implicit.

The main practical problem about the numerical integration of a differential equation concerns the precision of the approximate solution. If a desired precision has to be achieved, the first step is to choose the method. Then, h has to be chosen and adapted along the interval of integration in order to obtain the desired accuracy. This means, of course, that a procedure for estimating the error has to be implemented.

Integral Equations

Let g and K be two known functions. There are two kinds of integral equations depending whether the unknown function f appears only under the integral sign or also outside it. In these two kinds, two types arise depending on the interval of integration. If the interval of integration has fixed endpoints, a Fredholm equation is obtained.

$$\begin{aligned} \text{1st kind}: &\quad \int_a^b K(x, t) f(t) \mathrm{d}t = g(x) \\ \text{2nd kind}: &\quad f(x) - \lambda \int_a^b K(x, t) f(t) \mathrm{d}t = g(x) \end{aligned}$$

where $\lambda \neq 0$ is a parameter. If the right endpoint is a variable, a Volterra equation is obtained.

$$\begin{aligned} \text{1st kind}: &\quad \int_a^x K(x, t) f(t) \mathrm{d}t = g(x) \\ \text{2nd kind}: &\quad f(x) - \lambda \int_a^x K(x, t) f(t) \mathrm{d}t = g(x) \end{aligned}$$

Fredholm equations reduce to Volterra if the kernel K is such that $K(x,t) = 0$ for $x \leqslant t \leqslant b$.

To obtain approximations f_j of the function f at some points x_j, assume that the function g is known at some points x_i. So

$$g(x_i) = \int_a^b K(x_i, t) f(t) \mathrm{d}t, i = 1, \ldots, N$$

and similarly for the other integral equations. The definite integral is evaluated by a quadrature formula

$$\int_a^b K(x_i, t) f(t) \mathrm{d}t \simeq \sum_{j=1}^{M} \mathrm{a_{ij} f(t_j)}$$

Thus, the approximations $f_j \simeq f(t_j)$ is obtained by solving the system of linear equations

$$g(x_i) = \sum_{j=1}^{M} a_{ij} f_j, i = 1, \ldots, N$$

If $N \neq M$, the system is solved in the least squares sense. Otherwise, a square system is obtained. However, it must be noticed that this system is usually ill-conditioned and thus preconditioning and/or regularization have to be used (see the next section). This is the case with the inversion of the Laplace transform, one of the most important integral equations.

Fredholm equations of the second kind can be solved by the method of successive approximations. If $\mathcal{K}$ denotes the integral operator which maps f into $\int_a^b K(x, t) f(t)$, then this integral equation is $(I - \lambda \mathcal{K}) f = g$. So, f is given by its Neumann series

$$f = (I - \lambda \mathcal{K})^{-1} g = I + \sum_{i=0}^{\infty} \lambda^i \mathcal{K}^i g$$

In other terms, set $f_0 = g$ and then compute

$$f_i(x) = g(x) + \lambda \int_a^b K(x, t) f_{i-1}(t) \mathrm{d}t, \ \mathrm{i} = 1, 2, \ldots$$

This method converges if $\|\lambda \mathcal{K}\| > 1$.

Systems of Linear Equations

The choice of a method for solving a system of p linear equations in p unknowns, $Ax=b$, highly depends on the value of p. There are two classes of methods: direct methods and iterative methods.

When p is not too large (i.e., up to 10^4), an elimination procedure, such as Gaussian elimination, or Cholesky decomposition if the matrix is symmetric and positive definite, or Householder factorization, can be used. They all consist in transforming the system into an equivalent one (i.e., with the same solution) but with a matrix which is upper triangular. Then, such a system can be easily solved starting from the last equation.

When p is very large (several millions) and the matrix of the system comes out from the discretization, by finite differences or finite elements, of a partial differential equation, it is sparse (which means that most elements are zero). However, a direct method could not be used since the upper triangular matrix obtained by a direct method could be full. In that case, iterative methods are preferred. These methods split into two subclasses: relaxation methods and projection methods. Relaxation methods are nowadays mostly used as preconditioners (see below). Projection methods consist in generating a sequence of approximate solutions belonging to subspaces of increasing dimensions. Usually, these subspaces are Krylov subspaces and thus the name of such methods. Among them, the most popular are Lanczos method, the BiCGStab, and GMRES.

A fundamental topic of the solution of a system of linear equations is the condition number $\kappa(A) = \|A\| \cdot \|A^{-1}\|$ of the matrix A, a number greater than 1. If this number is large, then a small perturbation of the matrix A and/or the right-hand side b can produce a large variation in the exact solution of the system. The system is said to be ill-conditioned. Also, the speed of convergence of some Krylov subspace methods depends on the condition number: the larger it is the slower is the convergence. Thus, it is important, when a matrix is ill-conditioned to precondition the system, that is to consider the new system $M^{-1} Ax = M^{-1} b$, where the matrix M is an approximation of A easy to invert (or, equivalently, a system with M as its matrix is easy to solve) and chosen so that $\kappa(M^{-1} A)$ is smaller than $\kappa(A)$. There is no universal preconditioner and almost each system is a particular case.

Another procedure for solving an ill-conditioned system is to use regularization. It consists in solving a perturbed system. A vector x which minimizes

$$\|Ax - b\|_2 + \lambda \|Hx\|$$

is derived where λ is a parameter and H a matrix. The solution x_λ depends on $\lambda \geqslant 0$ (and also on H). When λ is close to 0, x_λ is close to $x = A^{-1} b$ but, since A is ill-conditioned, it is badly computed. If λ is large, x_λ will be correctly computed but it will not be a good approximation of x. So, there is a balance to find between large and small values of λ, and this is the main difficulty of regularization. It can be avoided by using an extrapolation technique.

Further Reading

Baker GA Jr. and Graves-Morris P (1996) *Padé Approximants*, 2nd edn Cambridge: Cambridge University Press.
Björck Å (1996) *Numerical Methods for Least Squares Problems*. Philadelphia: SIAM.
Brezinski C (1997) *Projection Methods for Systems of Equations*. Amsterdam: North-Holland.
Brezinski C and van Iseghem J (1994) Padé approximations. In: Ciarlet PG and Lions JL (eds.) *Handbook of Numerical Analysis*, vol. III, pp. 47–222. Amsterdam: North Holland.
Butcher JC (1987) *The Numerical Analysis of Ordinary Differential Equations*. Chichester: Wiley.
Davis PJ (1975) *Interpolation and Approximation*. New York: Dover.
Kythe PK and Puri P (2002) *Computational Methods for Linear Integral Equations*. Boston: Birkhäuser.
Meurant G (1999) *Computer Solution of Large Linear System*. Amsterdam: North-Holland.
Saad Y (1996) *Iterative Methods for Sparse Linear Systems*. Boston: PWS Publishing Company.

Computer Simulation Techniques in Condensed Matter Physics

K Binder, Johannes Gutenberg Universität Mainz, Mainz, Germany

© 2005 Elsevier Ltd. All rights reserved.

This is an update of K. Binder, Computer Simulation Techniques in Condensed Matter Physics, Editor(s): Franco Bassani, Gerald L. Liedl, Peter Wyder, Encyclopedia of Condensed Matter Physics, Elsevier, 2005, Pages 211–219, ISBN 9780123694010, https://doi.org/10.1016/B0-12-369401-9/00564-7.

Introduction 754
MD Algorithms 755
Importance Sampling Monte Carlo Methods 757
Path-Integral Monte Carlo (PIMC) 759
Conclusion 760
Further Reading 760

Introduction

Computer simulation techniques in condensed matter physics aim to compute the structure and the physical properties (including also dynamic response functions and transport) from atomistic input. The theoretical basis of these approaches are quantum mechanics and statistical thermodynamics. There exist many variants of these methods, and it depends on the nature of the problem to find out which variant is most appropriate. Such simulations can complement both analytical theory and experiment, and due to the availability of cheap computing power simulations have become an extremely widespread tool of research.

The conceptually simplest approach is the classical molecular dynamics (MD) method: one simply solves Newton's equations of motion numerically for the many-particle system (assuming that the N atoms or molecules in a volume V interact with effective potentials that are either phenomenologically assumed or fitted to electronic structure calculations). The basis of this method thus is classical mechanics, and one creates a deterministic trajectory in the phase space of the system. The idea is to take time averages of the observables of interest along this trajectory. The ergodicity hypothesis of statistical mechanics asserts that these time averages are equivalent to ensemble averages of the appropriate microcanonical (NVE) ensemble. Of course, Newton's equations of motion conserve the total energy E, and hence the conjugate intensive thermodynamic variables (temperature T, pressure p) can only be indirectly inferred and they exhibit statistical fluctuations. Since N is finite and sometimes even fairly small, such fluctuations cannot be neglected and need to be considered with care.

Sometimes one desires to directly realize other ensembles of statistical mechanics with a simulation, for example, the NVT or NpT ensemble. This is possible by introducing a coupling to suitable "thermostats" or "barostats."

An alternative way to carry out an MD simulation with $T = \text{const}$ introduces a weak friction force, together with random forces whose strengths are controlled by the fluctuation dissipation theorem. This method is closely related to the "Brownian Dynamics" (BD) method where one simulates Langevin equations (the inertial terms in the equations of motion being omitted). Clearly, this is a coarse-grained description of a physical system as only a subset of the degrees of freedom is explicitly considered, the remaining ones form the "heat bath." While this is not always a good description of the physical dynamics, such methods can be advantageous for the computation of static properties from averages along the stochastic trajectory in phase space.

A similar description applies to the importance sampling Monte Carlo (MC) method, where one creates a random walk-like trajectory in configuration space, controlled by transition probabilities that ensure the approach to thermal equilibrium through the detailed balance condition. Many of the practical limitations of simulations, such as "statistical errors," as well as systematic errors due to the finite size of the simulated system or the finite "length" of the simulated trajectory (or observation time, respectively) are common to all these simulation methods.

Of course, it is quantum mechanics and not classical mechanics that describes the basic physics of condensed matter. But attempting a numerical solution of the Schrödinger equation for a system of many nuclei and electrons is premature and still not feasible even with the fastest computers. Thus, approximations are needed: one very popular approach is the "*ab initio* MD" or "Car–Parrinello method" (CP), where some electronic degrees of freedom are included in MD via the density-functional theory (DFT). The huge advantage of this technique is that one no longer relies on effective interatomic potentials, which often are only phenomenologically chosen *ad hoc* assumptions, lacking any firm foundation in quantum chemistry. However, the disadvantage of this technique is that it is several orders of magnitude slower than classical MD, and hence only very short timescales and very small systems are accessible. Furthermore, the method cannot handle van der Waals-like forces well (e.g., in noble gases, one is still better off with the simple Lennard–Jones potential, amended by three-body forces).

In the standard CP method, the ionic motion is still treated classically. Alternatively, one can still use effective potentials between ions and/or neutral atoms as in classical MD or MC, but rely on quantum statistical mechanics for the ionic degrees of freedom. This is achieved by the path integral Monte Carlo (PIMC) or path integral molecular dynamics (PIMD). Such techniques are indeed crucial for a study of solids at low temperatures, to ensure that their thermal properties are compatible with the third law of thermodynamics. For most fluids, however, classical MD is sufficient (of course, quantum liquids such as helium are an exception).

Other variants of quantum Monte Carlo (QMC) have been developed in order to deal with electronic degrees of freedom on rigid lattices, desiring to describe magnetic systems (e.g., via the Heisenberg model where spin operators at neighboring lattice sites

https://doi.org/10.1016/B978-0-323-90800-9.00332-2

are coupled by exchange interactions), models for high T_c superconductors (e.g., using the Hubbard Hamiltonian, describing a hopping of electrons from site to site, and an on-site Coulomb repulsion), etc. These techniques ("diffusion Monte Carlo," "Green's function Monte Carlo," "variational Monte Carlo," "worldline Monte Carlo," etc.) are fairly specialized and complicated, and hence are not treated further here.

What information does one then wish to extract from the simulations? When systems in thermal equilibrium are considered, the first task is to calculate static properties. For example, in a fluid a basic property is the static structure factor $S(k), S(k) = \langle|\delta\rho(\boldsymbol{k})|^2\rangle_{\mathrm{T}}, \delta\rho(\boldsymbol{k})$ being a spatial Fourier transform of density fluctuations, $\boldsymbol{k}$ being the wave vector of a scattering experiment. In addition, one may want to calculate time-dependent correlation functions that describe the decay of small thermal fluctuations in equilibrium systems with time. A quantity of this type is the intermediate scattering function $S(k,t) = \langle\delta\rho(-\boldsymbol{k},0)\delta\rho(\boldsymbol{k},t)\rangle$ or its Fourier transform with respect to time, $S(k,\omega)$. This "dynamic structure factor" is accessible to inelastic scattering of neutrons, X-rays, or light (with energy transfer hω).

It is also possible to consider systems out of thermal equilibrium; for example, in solids under strong mechanical deformation, a crack may form and propagate. An important application of MD for fluids also is the study of systems exhibiting a steady state flow under shear deformation. The purpose of such nonequilibrium molecular dynamics (NEMD) work can be the estimation of transport coefficients (e.g., the shear viscosity) if the deformation is weak enough so that the system is still in the regime of linear response. However, the study of nonlinear phenomena also ("shear thinning," a decrease of the effective viscosity with increasing shear rate, or "shear melting" of colloidal crystals, etc.) may be of interest. In addition, one can study nonsteady state transient behavior, as it occurs, for example, after a sudden change from one thermodynamic state to another, and one wishes to study the approach of the system to its new thermal equilibrium. Classical examples of this problem are nucleation of fluid droplets in a supersaturated gas, or the kinetics of phase separation in a binary mixture ("spinodal decomposition") after a temperature quench. However, such processes are often too slow, and cannot be studied by NEMD, and one has to resort to a simulation of a coarse-grained model by nonequilibrium Monte Carlo (NEMC). This approach is suitable to deal also with irreversible growth processes far from equilibrium, such as diffusion-limited aggregation (DLA). This is an example of a mechanism of structure formation on mesoscopic scales of length and time that was discovered by simulations, and still lacks a good understanding in terms of the analytical theory.

In the following, the salient features of a few important simulation methods (classical MD, MC, PIMC) are briefly described. Also, limitations of simulations (e.g., due to the small size of the simulated system) are mentioned, and the extent to which these limitations can be overcome are discussed.

MD Algorithms

Consider a system of N particles (atoms) with Cartesian coordinates, $\boldsymbol{X} = \{\boldsymbol{r}_i\}, i = 1, \ldots, N$, in a d-dimensional space. The dynamics then is described by Newton's equations of motion, $m_i\ddot{r}_i = f_i = -\,\partial \mathrm{U}_{pot}/\partial r_i$, m_i being the mass of the ith particle, f_i the force acting on it. This force is assumed to be entirely due to interactions with other particles: $U_{\mathrm{pot}}(\boldsymbol{X}) = U_{\mathrm{pot}}(\boldsymbol{r}_1, \ldots, \boldsymbol{r}_N) = \sum u(|\boldsymbol{r}_i - \boldsymbol{r}_j|)$, where the sum extends once over each pair i, j of particles, and it has been assumed for simplicity that U_{pot} is pairwise additive. Then $\boldsymbol{f}_i = -\sum_j \partial\, u(|\boldsymbol{r}_i - \boldsymbol{r}_j|)/\partial \boldsymbol{r}_i$. Note that $E = E_{\mathrm{kin}} + U_{\mathrm{pot}} = \sum_i m_i \dot{r}_i^2/2 + U_{\mathrm{pot}}$ is a constant of motion $\left(\dot{E} = \mathrm{d}E/\mathrm{d}t = 0\right)$.

MD now means that Newton's equations of motion are integrated numerically, by a computationally efficient scheme, such as Verlet's algorithm

$$\boldsymbol{r}_i(t+\delta t) = 2\boldsymbol{r}_i(t) - \boldsymbol{r}_i(t-\delta t) + \frac{1}{m_i}(\delta t)^2 \boldsymbol{f}_i(t) + 0\{(\delta t)^4\} \qquad [1]$$

where δt is the MD time step, and the velocity $\boldsymbol{v}_i(t)$ is updated similarly,

$$\boldsymbol{v}_i(t) = [\boldsymbol{r}_i(t+\delta t) - \boldsymbol{r}_i(t-\delta t)]/[2(\delta t)] + 0\{(\delta t)^3\} \qquad [2]$$

This algorithm is manifestly time-reversible and in spite of inevitable errors due to the discreteness of the time step δt, it keeps an important symmetry property of Newton's equations. To understand how large δt can be chosen, consider argon as an example, where atoms interact with a Lennard–Jones potential, $u_{\mathrm{LJ}} = 4\varepsilon[(\sigma/r)^{12} - (\sigma/r)^6]$, with $\sigma \approx 3.4$ Å, $\varepsilon/k_{\mathrm{B}} \approx 120$ K (k_{B} = Boltzmann's constant), and $m \approx 6.6 \times 10^{-23}$ g. Rescaling coordinates ($\boldsymbol{r}^* \equiv \boldsymbol{r}/\sigma$) yields ($\boldsymbol{r}_{ij}^* \equiv \boldsymbol{r}_i^* - \boldsymbol{r}_j^*$)

$$\boldsymbol{r}^*(t+\delta t) = 2\boldsymbol{r}^*(t) - \boldsymbol{r}^*(t-\delta t) - (\delta t/\tau_0)^2 \frac{\boldsymbol{r}_{ij}^*}{|\boldsymbol{r}_{ij}^*|} \times \sum_{j(\neq i)} [(r_{ij}^*)^{-13} - (r_{ij}^*)^{-7}/2] \qquad [3]$$

where the natural time unit τ_0 of MD was defined as $\tau_0 = (m\sigma^2/48\varepsilon)^{1/2}$ which is roughly $\tau_0 \approx 3.1 \times 10^{-13}$ s for argon. In order to keep numerical errors small, one needs to choose $\delta t = 0.03\ \tau_0$ (or smaller), that is, $\delta t \approx 10^{-14}$ s. So even with a million time steps, one only reaches a real time of $\sim$10 ns.

As mentioned above, from a statistical mechanics point of view this algorithm realizes the microcanonical NVE ensemble. Temperature T is then inferred from the kinetic energy,

$$\begin{aligned} T &= \langle \hat{T} \rangle_{\mathrm{NVE}}, \\ \hat{T} &= 2E_{\mathrm{kin}}/(3k_{\mathrm{B}}N) \\ &= \sum_{i=1}^{N} m_i \boldsymbol{v}_i^2/(3k_{\mathrm{B}}N) \end{aligned} \qquad [4]$$

Note that N is finite (typically $10^2 \leqslant N \leqslant 10^6$) and hence temperature fluctuations are non-negligible. These fluctuations contain information on the specific heat C_V, since $[\langle \hat{T}^2 \rangle - \langle \hat{T} \rangle^2]/\langle \hat{T} \rangle^2 = 2(1-3k_B/2C_V)/(3N)$. Since the "length" of an MD run (i.e., its number of time steps) is finite, these fluctuations of T cause a statistical error in the estimation of temperature.

The pressure p can be estimated using the virial theorem,

$$p = \langle \hat{P} \rangle_{\mathrm{NVE}}, \quad \hat{P} = \left(2E_{\mathrm{Kin}} + \sum_i \boldsymbol{r}_i \cdot \boldsymbol{f}_i \right) / 3V \qquad [5]$$

and again statistical fluctuations need to be considered.

It is often desirable to realize the canonical (NVT) rather than the microcanonical (NVE) ensemble. In an MD framework, this can be done by extending the Lagrangian of the system by a variable, representing the thermostat which has a fictitious "mass" Q. This yields the Nose–Hoover algorithm, where Newton's equations of motion are extended by a "friction"-like term,

$$\ddot{\boldsymbol{r}}_i = \boldsymbol{f}_i/m_i - \zeta(t)\dot{\boldsymbol{r}}_i, \quad \dot{\zeta} = \left[\sum_i m_i \boldsymbol{v}_i^2 - 3Nk_{\mathrm{B}}T \right] / Q \qquad [6]$$

Thus the "friction coefficient" $\zeta(t)$ fluctuates around zero, responding to the imbalance between the instantaneous kinetic energy and the intended canonical average. The total energy no longer is conserved, and energy fluctuations are linked to the specific heat as ($\hat{H}$ is the Hamiltonian)

$$NC_V/k_{\mathrm{B}} = \left[\langle \hat{H}^2 \rangle_{\mathrm{NVT}} - \langle \hat{H} \rangle_{\mathrm{NVT}}^2 \right] / (k_{\mathrm{B}}T)^2 \qquad [7]$$

It is important to note, however, that dynamical correlation functions between observables such as $\langle A(0)A(t) \rangle$, where A is the observable of interest, are not precisely identical to the microcanonical ones. This is even more true for MD runs that realize the isothermal–isobaric (NpT) ensemble, where the pressure is given and the volume V rather fluctuates, by coupling to the so-called "Andersen barostat." Therefore, one often uses MD in NVT or NpT ensembles for equilibration (and the computations of static averages) only, generating a set of well-equilibrated system configurations, which are then used as initial states for runs where thermostats and/or barostats are switched off, realizing the runs in the NVE ensemble, where $\langle A(0)A(t) \rangle$ is computed as a time average, $\int_0^{t_{\mathrm{obs}}-t} \mathrm{d}t_0 [A(t_0)A(t_0+t)]/(t_{\mathrm{obs}}-t)$, t_{obs} being the total "observation time" over which the run is extended.

In order to judge whether t_{obs} is large enough, it is important to know what the slow observables in the system are. A typical reason for slow relaxation is the presence of large "objects" of correlated sets of particles in the systems, which show slow motions. An example is "critical slowing down" near second-order phase transitions, where large "clusters" of the variable representing the local order parameter occur. For example, near the liquid–gas critical point, large density fluctuations occur which are correlated over a correlation length ξ which diverges at criticality in the thermodynamic limit ($N \to \infty$), and then also the corresponding relaxation time τ diverges. Another example are polymer chains in solution or melt – a flexible polymer consisting of N monomers relaxes in the melt on a timescale $\tau \approx N^2$ in the Rouse limit (unentangled chains) or even $\tau \propto N^3$ in the reptation limit of entangled chains (i.e., a snakelike motion of the chains along their owncontour). Thus, MD simulations of critical phenomena as well as of polymeric systems or other soft matter systems with objects containing many subunits (membranes, microemulsions, etc.) are intrinsically difficult.

However, it should also be noted that another reason for slow relaxation are conservation laws. In the NVE and NVT ensembles, the average density $\langle \rho \rangle = N/V$ is strictly conserved. Assuming for local fluctuations in density $\delta\rho(\boldsymbol{r},t) - \langle \rho \rangle$ that Fick's law holds, a gradient $\nabla(\delta\rho(\boldsymbol{r},t))$ causes a density current $\boldsymbol{j}(\boldsymbol{r},t)$, D being a diffusion coefficient, $\boldsymbol{j}(\boldsymbol{r},t) = -D\nabla(\delta\rho(\boldsymbol{r},t))$. The conservation law implies the continuity equation $\partial\rho(\boldsymbol{r},t)/\partial t + \nabla \cdot \boldsymbol{j}(\boldsymbol{r},t) = 0$, and hence a diffusion equation for $\delta\rho(\boldsymbol{r},t)$ results, $\partial(\delta\rho(\boldsymbol{r},t))/\partial t = D\nabla^2(\delta\rho(\boldsymbol{r},t))$. The Fourier components $\delta\rho_{\boldsymbol{k}}(t)$ of $\delta\rho(\boldsymbol{r},t)$ then satisfy the equation

$$\begin{aligned} &\frac{\mathrm{d}}{\mathrm{d}t}\delta\rho_{\boldsymbol{k}}(t) = -Dk^2\delta\rho_{\boldsymbol{k}}, \\ &\delta\rho_{\boldsymbol{k}}(t) = \delta\rho_{\boldsymbol{k}}(0)\exp\left(-Dk^2 t\right) \end{aligned} \qquad [8]$$

Therefore, the dynamic correlation function of density fluctuations at long wavelengths decays very slowly,

$$S_\rho(\boldsymbol{k},t) \equiv \left\langle \delta_\rho(-\boldsymbol{k},0)\delta_\rho(\boldsymbol{k},0) \right\rangle = S(k)\exp\left(-t/\tau_{\boldsymbol{k}}\right), \tau_{\boldsymbol{k}} = \left(Dk^2\right)^{-1} \qquad [9]$$

Equation [9] demonstrates the "hydrodynamic slowing down" $\tau_k \to \infty$ for k→0. Of course, due to finite size effects, this divergence of the relaxation time is cut off; in a (hyper)cubic system of linear dimension L with periodic boundary conditions, the smallest wave number is $k_{\min} = (2\pi)/L$, and hence the largest relaxation time is $\tau_{\max} = L^2/(4\pi^2 D)$. Clearly, this phenomenon makes the equilibration of very large systems difficult.

A brief mention is made of the way transport coefficients are estimated from simulations. The simplest case are self-diffusion coefficients, where one can apply the Einstein relation, following the mean square displacements of "tagged" particles, $\left\langle [\boldsymbol{r}(t) - \boldsymbol{r}(0)]^2 \right\rangle = 2\mathrm{d}\,Dt$, $t \to \infty$. Transport coefficients relating to collective properties can be extracted from Green–Kubo relations, for example, the shear viscosity is related to time correlations of the off-diagonal components of the pressure tensor σ_{xy},

$$\eta = \int_0^\infty \mathrm{d}t \langle \sigma_{xy}(0)\sigma_{xy}(t)\rangle/(Vk_{\mathrm{B}}T) \qquad [10]$$

where

$$\sigma_{xy} = \sum_{i=1}^{N} \{ m_i \boldsymbol{v}_i^x \boldsymbol{v}_i^y + \frac{1}{2} \sum_{j(\neq i)} x_{ij} f_i^y (r_{ij}) \} \qquad [11]$$

Similar relations can be written down for thermal conductivity, electrical conductivity, interdiffusion coefficient in mixtures, etc. Alternatively, transport coefficients can be estimated from NEMD, creating via suitable boundary conditions, a steady state of the appropriate quantity (mass density of a particle species, heat, momentum density) through the system.

Importance Sampling Monte Carlo Methods

Most MC calculations aim at the estimation of thermodynamic averages by importance sampling methods. Considering a variable $A(\boldsymbol{X}$ where X denotes a point in phase space, such averages are defined in classical statistical mechanics by

$$\langle A \rangle = \int \mathrm{d}X P_{\mathrm{eq}}(X) A(X), P_{\mathrm{eq}}(X) = (1/Z) \exp\left[-\hat{H}(X)/k_{\mathrm{B}}T\right] \qquad [12]$$

where $\hat{H}(\boldsymbol{X})$ is the Hamiltonian of the system, and Z is the partition function

$$Z = \int \mathrm{d}X \exp\left[-\hat{H}(X)/k_{\mathrm{B}}T\right] \qquad [13]$$

Note that when one deals with the simulation of a fluid, momenta of the particles need not be included in $\boldsymbol{X}$ since they cancel out from all averages. In addition, $\boldsymbol{X}$ may denote any subset of variables only, for the problem of interest. For example, dealing with the phase transition of an anisotropic magnet, one may approximate the crystal lattice as rigid, and then each lattice site i carries as single degree of freedom an Ising spin, $S_i = \pm 1$. The Ising model Hamiltonian then is

$$\hat{H}_{\mathrm{Ising}} = -J \sum_{\langle i \neq i \rangle} S_i S_i - h \sum_i S_i \qquad [14]$$

assuming a nearest neighbor pairwise exchange energy J and a coupling to a magnetic field h (choosing units such that the magnetic moment per spin is unity). Here $\boldsymbol{X}$ stands for $S_1, S_2, \ldots, S_N$, that is, the phase space is discrete, and $\int \mathrm{d}\boldsymbol{X}$ stands symbolically for summation over all 2^N microstates of the system.

Now the basic idea of MC sampling is to consider the task of computing $\langle A \rangle$ as a problem of numerical integration over the phase space, where one would approximate $\langle A \rangle$ by an average $\bar{A}$ over M points only,

$$\bar{A} = \frac{1}{M} \sum_{v=1}^{M} P_{\mathrm{eq}}(\boldsymbol{X}_v) A(\boldsymbol{X}_v) \qquad [15]$$

The difficulty, of course, is that the integration space is very high dimensional, and it is a problem to choose the sample of M points $\boldsymbol{X}_v$ appropriately. It is easy to see that a regular grid of points $\boldsymbol{X}_v$ does not work, but a uniform random sampling of phase space ("simple sampling") does not work either in most cases. A notable exception, of course, is the sampling of nonthermal random distributions, for example, the random occupation of lattice sites in a mixed crystal $A_x B_{1-x}$ by A and B atoms can be simulated straightforwardly. Choosing random numbers η uniformly distributed between zero and unity, an A-atom is assigned to the considered lattice site if $\eta < x$, while otherwise the site is taken to be occupied by a B-atom. This straightforward use of MC sampling works only if the occupation probabilities of neighboring lattice sites are independent of each other, however. Other physically relevant problems where simple sampling works are the generation of random walks and (short) self-avoiding walks, the bond percolation problem (nearest neighbor links connecting lattice sites are chosen at random conducting or isolating, to understand the electrical conductivity of disordered solids), etc. However, simple sampling is not useful for the estimation of thermal averages when N is large. The reason is that it is only a very small region of phase space where the important contributions come from, and via simple sampling only very few points X_v would be drawn from this important region. This is seen when one considers the reduced distribution function $P_N(m)$ of the density m of some extensive variable, for example, the magnetization of the Ising magnet, $m = (1/N)\sum S_i$, where the sum runs over all lattice sites, or the internal energy, etc., $P_N(m) = \int \mathrm{d}\boldsymbol{X}\delta(m-(1/N)\sum S_i)P_{\mathrm{eq}}(\boldsymbol{X})$. Such distributions exhibit sharp peaks at the (*a priori* unknown) average value $\langle m \rangle$, of width proportional to $1/\sqrt{N}$. It is clear, however, that from simple sampling for large N, almost no states would be generated in the region where $P_N(m)$ has its peak; most of the computational effort would be wasted for exploring a completely uninteresting part of the phase space.

Thus a method is needed that leads one automatically to the important region of the phase space. Such a method is provided by the Metropolis importance sampling algorithm, which yields states $\boldsymbol{X}_\nu$, with a probability proportional to the Boltzmann factor. This is achieved by generating a Markov chain of states recursively one from the other, $\boldsymbol{X}_\nu \rightarrow \boldsymbol{X}_{\nu+1} \rightarrow \boldsymbol{X}_{\nu+2} \rightarrow \ldots$, using a properly chosen transition probability. For a fluid, the move from $\boldsymbol{X}$ to $\boldsymbol{X}'$ may mean a random displacement of a single randomly chosen particle; for an Ising model, it may mean a single spin is chosen at random and considered for a spin flip, or for exchange with one of its neighbors; but also flips of large clusters of spins in one move together may be carried out. Also moves that have no counterpart in reality are conceivable (e.g., in a dense polymer melt, one may select a pair of long chains that are close by each other, cut them in the middle, and reconnect the parts differently than previously). Even though such moves need not represent any physically plausible dynamics, they may provide an efficient sampling of the phase space. The great flexibility in the choice of such moves, adapted to the problem one wishes to study, is one of the particular strengths of the MC methods.

The states $\boldsymbol{X}_\nu$ are distributed according to the Boltzmann factor $P_{\mathrm{eq}}(\boldsymbol{X})$ if the transition probability $W(\boldsymbol{X}\text{–}\boldsymbol{X}')$ satisfies the condition of detailed balance

$$P_{\mathrm{eq}}(\boldsymbol{X})W(\boldsymbol{X} \rightarrow \boldsymbol{X}') = P_{\mathrm{eq}}(\boldsymbol{X}')W(\boldsymbol{X}' \rightarrow \boldsymbol{X}) \qquad [16]$$

For instance, a choice that satisfies eqn [16] is simply

$$W(\boldsymbol{X} \rightarrow \boldsymbol{X}') = \begin{cases} \tau_0^{-1}, \text{ if } \delta\hat{H} \equiv \hat{H}(\boldsymbol{X}') - \hat{H}(\boldsymbol{X}) < 0 \\ \tau_0^{-1} \exp\left(-\delta\hat{H}/k_{\mathrm{B}}T\right), \text{ if } \delta\hat{H} \geqslant 0 \end{cases}$$

Here, a constant τ_0 has been arbitrarily introduced to set a timescale, so that W gets the meaning of a transition probability per unit time (but one may choose $\tau_0 = 1$, of course, and normally one considers one Monte Carlo step (MCS) per degree of freedom as the natural unit of the MC "time"). This notion is useful, since MC sampling can be interpreted as "time averaging" along stochastic trajectories in phase space, described by a master equation for the probability $P(\boldsymbol{X}, t)$ that a state $\boldsymbol{X}$ occurs at time t,

$$\frac{\mathrm{d}}{\mathrm{d}t}P(\boldsymbol{X}, t) = -\sum_{\boldsymbol{X}'} W(\boldsymbol{X} \rightarrow \boldsymbol{X}')P(\boldsymbol{X}, t) + \sum_{\boldsymbol{X}'} W(\boldsymbol{X}' \rightarrow \boldsymbol{X})P(\boldsymbol{X}', t) \qquad [17]$$

This rate equation describes the balance between the loss of probability by all processes $\boldsymbol{X} \rightarrow \boldsymbol{X}'$ that lead away from the considered state and the gain of probability due to the inverse process. Obviously, $\mathrm{d}P/\mathrm{d}t = 0$ if $P = P_{\mathrm{eq}}(\boldsymbol{X})$, due to the detailed balance principle, eqn [16].

Of course, the dynamical properties of a system described by such a stochastic trajectory through phase space generated via MC will differ in general from dynamic properties deduced from the deterministic MD trajectories. In fact, the MC dynamics is of physical significance only when one deals with systems for which the considered degrees of freedom are a (slow!) subset weakly coupled to the remaining (fast!) degrees of freedom, that behave like a heat bath. This is the case for the Ising magnet and for diffusion in solid alloys A_xB_{1-x}, for instance. In both cases the phonons of the crystal act like a heat bath, causing random spin flips or random jumps of A or B atoms to vacant sites, respectively. Often the MC dynamics is considered as fairly realistic for random growth or aggregation phenomena on mesoscopic scales, such as diffusion-limited aggregation (DLA).

The dynamic interpretation of MC sampling in terms of a stochastic trajectory in phase space is important for the understanding of "statistical error," since the subsequently generated states $\{\mathrm{X}_\nu\}$ are highly correlated with each other. In fact, one can show that the expected mean square statistical error becomes

$$\left\langle (\delta A)^2 \right\rangle = \frac{1}{n}\left[\left\langle A^2 \right\rangle - \langle A \rangle^2\right](1 + 2\tau_{AA}/\delta t) \qquad [18]$$

where

$$\tau_{AA} = \int_0^\infty \Phi_{AA}(t)\mathrm{d}t, \quad \Phi_{AA}(t) \equiv [\langle A(0)A(t)\rangle - \langle A\rangle^2]/[\langle A^2\rangle - \langle A\rangle^2] \qquad [19]$$

if n observations $\{A_\mu\}$ of the observable A separated by time increment δt are taken. If these n observations were statistically independent, the enhancement by the "dynamic factor" $(1+2\tau_{AA}/\delta t)$ would be absent. As noted in the discussion of MD methods, relaxation times τ_{AA} get large near critical points, or when one considers long wavelength Fourier components of a conserved quantity ("critical slowing down," "hydrodynamic slowing down," also hamper MC!). Also the questions of whether or not an algorithm is ergodic, and how fast equilibrium is reached or whether hysteresis may occur, etc., are important for both MD and MC.

A further limitation of simulations that may need consideration are finite size effects. Considering Fourier components such as $\delta\rho_{\boldsymbol{k}}$ (eqns [8] and [9]), one must note that in a finite system with periodic boundary conditions $\boldsymbol{k}$–space is quantized. For example, if one has a cubic simulation cell $L \times L \times L$, the allowed wave vectors are $\boldsymbol{k}_n = (2\pi/L)\left(n_x, n_y, n_z\right)$ where n_α are integers. With respect to static phenomena, the gap in the spectrum of long wavelength modes affects physical properties for which these modes are important (e.g., long wavelength phonons cause the T^3 law for specific heats, if the crystal is treated by quantum statistical mechanics; long wavelength magnons in a Heisenberg ferromagnet cause a divergence of the longitudinal and transverse susceptibilities; capillary waves cause a divergence of interfacial widths, etc.). Thus for many physical properties, it is advisable to repeat the simulation for a range of values of L, and carry out a suitable extrapolation of the results to the thermodynamic limit, $L \to \infty$.

The problem of finite size effects is particularly cumbersome when one deals with phase transitions. However, the study of phase transitions is a problem for which simulations are often necessary, and, in fact, useful! One approach to overcome the limitation of finite size for such problems relies on the concept of finite size scaling. Consider, as a simple example, the transition of the Ising model {eqn [14]} from the paramagnetic phase at $T > T_\mathrm{c}$ to a ferromagnetic state at $T < T_\mathrm{c}$. Near the critical temperature T_c, spontaneous magnetization m_sp and susceptibility χ are singular in the thermodynamic limit, $m_\mathrm{sp} \propto (1-T/T_\mathrm{c})^\beta$, $\chi \propto |1-T/T_\mathrm{c}|^{-\gamma}$, where β, γ are "critical exponents." Varying H for $T < T_\mathrm{c}$, however, m at $H = 0$ has a jump singularity from $-m_\mathrm{sp}$ to $+m_\mathrm{sp}$, χ then has a delta-function singularity: this is a special case of a first-order transition.

In a finite system, however, these singularities are always rounded. For example, χ for $H = 0$ as a function of T does not diverge, there is a peak of finite height only, which also is shifted away from T_c. Thus, it is a nontrivial problem to estimate both T_c and other critical properties (such as exponents) with sufficient accuracy.

For critical phenomena, finite size scaling rests on a comparison of lengths: the linear dimension L scales with the correlation length $\xi \propto |1-T/T_\mathrm{c}|^{-\nu}$ of the system. As a consequence, near T_c moments of the order parameter distribution depend on L and ξ basically via a scaling function of the ratio L/ξ, apart from a power-law prefactor $\langle |m|^k \rangle = L^{-k\beta/\nu} \tilde{M}_k(L/\xi)$, $L \to \infty$, k integer, $\tilde{M}_k$ being a "scaling function"! Particularly useful are, thus, suitable ratios of moments where the power law prefactors cancel out, such as the reduced fourth-order cumulant

$$\begin{aligned} U_L(T) &= 1-\langle m^4 \rangle / \left[3\langle m^2 \rangle^2\right] \\ &= \tilde{U}(L/\xi), \quad L \to \infty \end{aligned} \qquad [20]$$

Since $\xi \to \infty$ as $T \to T_\mathrm{c}$, all curves $U_L(T)$ must intersect at $T = T_\mathrm{c}$ in a universal value $\tilde{U}(0)$; note that $U_L(T) \to 2/3$ for $T < T_\mathrm{c}$ as $L \to \infty$, while $U_L(T) \to 0$ for $T > T_\mathrm{c}$. If such a unique intersection point is found, it thus serves to find the location of T_c. If the intersections of different pairs $U_L(T)$, $U_{L'}(T)$ scatter, on the other hand, one can conclude that corrections to scaling are still pronounced, and the study of larger systems is required. At T_c, one also finds that $\langle |m| \rangle \propto L^{-\beta/\nu}$, $\chi \propto L^{\gamma/\nu}$, and thus one can estimate critical exponents.

Also, first-order transitions are rounded; while in the Ising model for $T < T_\mathrm{c}$, two phases with $\pm m_\mathrm{sp}$ occur precisely at $H = 0$, the distribution function of the magnetization simply is $P_\infty(m) = \left[\delta\left(m - m_\mathrm{sp}\right) + \delta\left(m + m_\mathrm{sp}\right)\right]/2$, and for finite L, one observes two broadened peaks not only at $H = 0$ but over a range ΔH of fields, with $\Delta H \propto L^{-d}$, inversely proportional to the volume of the system. But the location of the first-order transition is found accurately from the "equal weight rule" for the two peaks.

The sampling of $P_L(m)$ is very useful since one can show that for $T < T_\mathrm{c}$, one has $P_L(0)/P_L\left(m_\mathrm{sp}\right) \propto \exp\left(-2L^{d-1}\sigma/k_\mathrm{B}T\right)$, σ being the interfacial tension between the coexisting phases. Use of this formula, in fact, is one of the most powerful recipes to estimate interfacial free energies from simulations. Of course, $P_L(0)/P_L\left(m_\mathrm{sp}\right)$ for large L is extremely small, and thus this ratio cannot be sampled directly, but needs more advanced schemes that are not described here due to lack of space, such as "umbrella sampling" or "multicanonical MC."

Of course, the above comments discuss the study of phase transitions by simulations only in a nutshell, and the reader is directed to the "Further reading" section for further details.

Path-Integral Monte Carlo (PIMC)

Thermal averages for a quantum system are calculated, and thus eqns [12] and [13] are rewritten appropriately

$$\begin{aligned} \langle \hat{A} \rangle &= Z^{-1}\,\mathrm{Tr}\,\exp\left(-\hat{H}/k_\mathrm{B}T\right)\hat{A}, \\ Z &= \mathrm{Tr}\,\exp\left(-\hat{H}/k_\mathrm{B}T\right) \end{aligned} \qquad [21]$$

using a notation that emphasizes the operator character of the Hamiltonian $\hat{H}$ and observable $\hat{A}$. For simplicity, consider first the case of one particle in a potential $V(x)$ in one dimension, where $\hat{H} = -\left(\hbar^2/2m\right)\mathrm{d}^2/\mathrm{d}x^2 + V(x)$, m being the mass of the particle. In position representation $Z = \int \mathrm{d}x \langle x| \exp\left(-\hat{H}/k_\mathrm{B}T\right)|x\rangle$, $|x\rangle$ being an eigenvector of the position operator. The problem now is that $\hat{H} = \hat{E}_\mathrm{kin} + \hat{V}(x)$, where $\hat{E}_\mathrm{kin}$ and $\hat{V}(x)$ do not commute. Applying the Suzuki–Trotter formula, P being a positive integer

$$\begin{aligned} &\exp\left[-\left(\hat{E}_\mathrm{kin} + \hat{V}\right)/k_\mathrm{B}T\right] \\ &\quad = \lim_{P \to \infty}\left[\exp\left(-\hat{E}_\mathrm{kin}/k_\mathrm{B}TP\right)\exp\left(-\hat{V}/k_\mathrm{B}TP\right)\right]^P \end{aligned} \qquad [22]$$

one can reduce Z to $(x_{P+1} = x_1)$

$$Z = \lim_{P \to \infty} \left(\frac{k_{\mathrm{B}} T m P}{2\pi\hbar^2} \right)^{P/2} \int \mathrm{d}x_1 \ldots \int \mathrm{d}x_P \times \exp\left(\left[-\frac{\kappa}{2} \sum_{S=1}^{P} (x_s - x_{s+1})^2 - P^{-1} \sum_{S=1}^{P} V(x_s) \right] / k_{\mathrm{B}} TP \right) \qquad [23]$$

where $\kappa \equiv (k_{\mathrm{B}} T/\hbar)^2 mP$. Apart from the prefactor, eqn [23] is the configurational partition function of a ring polymer within the framework of classical statistical mechanics: P beads are coupled by harmonic springs with spring constant κ, and are exposed to a potential $V(x)/P$.

This approach is straightforwardly generalized to a system of N interacting quantum particles, if the quantum mechanical exchange is neglected: one ends up with a system of N classical cyclic "polymer chains." As a result of this isomorphism, methods for simulating classical systems (MC, MD) can be carried over to such quantum-mechanical problems, too. At high temperatures, κ gets very large, the cyclic chain contracts essentially to a point, while at low T the chains are spread out, representing zero-point motions. The lower the T is, the larger the P has to be: if σ is a characteristic distance over which the potential $V(x)$ changes, one must have $\hbar^2/m\sigma^2 \ll k_{\mathrm{B}} TP$ so that two neighbors along the "polymer chain" are at a distance much smaller than σ. The typical size of the ring polymer, of course, is of the order of the thermal de Broglie wavelength λ_{T}: at very low temperatures (or for very light particles such as He atoms) λ_{T} becomes comparable to the interparticle spacing, and the precise formulation of the problem requires the correct incorporation of the statistics of the particles (Bose–Einstein versus Fermi–Dirac) into the formalism. For fermions, this leads to the famous difficulty known as "minus sign problem" – the distribution to be sampled loses its interpretation as a probability distribution, because it is no longer non-negative everywhere. Thus the study of systems such as liquid ^{3}He (or fermions on a lattice, a problem to which a similar formulation based on the Suzuki–Trotter decomposition is applicable) is still an active area of research. However, one may stress that the simplified formulation of PIMC (or PIMD, respectively) that ignores the statistics of the particles is useful (and indispensable!) to study the thermal properties of crystals (such as solid Ne or Ar, SiO_2, polyethylene etc.) at low temperatures (and obtain temperature dependences of lattice parameters, elastic constants etc., that are compatible with the third law of thermodynamics).

Conclusion

In this article, the basic foundations of three important simulation methods (classical MD and MC, PIMC) have been briefly described, and some technical limitations as well as recipes of how they can be overcome have also been mentioned. However, there are many "tricks of the trade" that could not be described, due to lack of space: for example, one can switch on or off arbitrary perturbations or parts of the interparticle forces, and combine this with suitable thermodynamic integration methods to gain information on thermodynamic excess potentials, etc. Very important variations are also possible by a suitable choice of various boundary conditions (e.g., a combination of "tilted periodic" with "antiperiodic" boundary conditions allows the study of tilted interfaces in Ising systems). An important aspect also is that an analysis of conceptually important quantities (e.g., Voronoi polyhedra distributions in amorphous solids, ring statistics in molten silica, orientational order parameters in two-dimensional melting, etc.) is readily possible with simulations, while one can infer these quantities from experiment at best indirectly. Many such extensions of the techniques described here, as well as further simulation methods, and last but not the least, numerous application examples can be found in the "Further reading" section.

Further Reading

Allen MP and Tildesley DJ (1987) *Computer Simulation of Liquids*. Oxford: Clarendon Press.
Binder K (ed.) (1979) *Monte Carlo Methods in Statistical Physics*. Berlin: Springer.
Binder K (ed.) (1992) *The Monte Carlo Method in Condensed Matter Physics*. Berlin: Springer.
Binder K and Ciccotti G (eds.) (1996) *Monte Carlo and Molecular Dynamics of Condensed Matter Systems*. Bologna: Societa Italiana di Fisica.
Binder K and Heermann DW (2002) *Monte Carlo Simulation in Statistical Physics. An Introduction*, 4th edn Berlin: Springer.
Car R and Parrinello M (1985) Unified approach for molecular dynamics and density functional theory. *Physical Review Letters* 55: 2471–2474.
Doll JD and Gubernatis JE (eds.) (1990) *Quantum Simulations*. Singapore: World Scientific.
Frenkel D and Smit B (2002) *Understanding Molecular SimulationFrom Algorithms to Applications*, 2nd edn San Diego: Academic Press.
Grotendorst J, Marx D, and Muramatsu A (eds.) (2002) *Quantum Simulations of Complex Many-Body SystemsFrom Theory to Algorithms*. Jülich: NIC.
Landau DP and Binder K (2000) *A Guide to Monte Carlo Simulations in Statistical Physics*. Cambridge: Cambridge University Press.
Rapaport DC (1995) *The Art of Molecular Dynamics*. Cambridge: Cambridge University Press.
Suzuki M (ed.) (1992) *Quantum Monte Carlo Methods in Condensed Matter Physics*. Singapore: World Scientific.

Multicircle Diffractometry Methods

DA Walko, Argonne National Laboratory, Argonne, IL, USA

© 2005 Elsevier Ltd. All rights reserved.

This is an update of D.A. Walko, Multicircle Diffractometry Methods, Editor(s): Franco Bassani, Gerald L. Liedl, Peter Wyder, Encyclopedia of Condensed Matter Physics, Elsevier, 2005, Pages 32–41, ISBN 9780123694010, https://doi.org/10.1016/B0-12-369401-9/00638-0.

Introduction **761**
Four-Circle Eulerian Geometry **762**
Angle Calculations **764**
The Diffraction Equation 764
Determining the Orientation Matrix 765
Operating Modes 766
Equivalent Angle Settings 766
Alternative Four-Circle Geometries **767**
Kappa Geometry 767
Four-Circle General-Inclination Geometries 767
Five-Circle and Six-Circle Diffractometers **769**
Acknowledgments **769**
Further Reading **770**

Nomenclature

$\boldsymbol{a_i}$, $\boldsymbol{\alpha_i}$ $(\boldsymbol{i = 1\text{–}3})$	real-space lattice parameters (Å,°)
$\boldsymbol{b_i}$, $\boldsymbol{\beta_i}$ $(\boldsymbol{i = 1\text{–}3})$	reciprocal-space lattice parameters (Å,°)
B	matrix which produces a Cartesian coordinate system for reciprocal space ($Å^{-1}$)
$\boldsymbol{d}$	lattice-plane spacing (Å)
$\boldsymbol{h}$	reciprocal lattice vector (reciprocal lattice units)
$\boldsymbol{h}_c$	reciprocal lattice vector in Cartesian coordinates ($Å^{-1}$)
$\boldsymbol{h}_1$	reciprocal lattice vector in lab frame ($Å^{-1}$)
$\boldsymbol{h}_\varphi$	reciprocal lattice vector in frame of φ axis ($Å^{-1}$)
K	diffracted wave vector ($Å^{-1}$)
K_0	incident wave vector ($Å^{-1}$)
N	reference vector ($Å^{-1}$)
Q	scattering vector ($Å^{-1}$)
$R(\boldsymbol{\zeta})$	rotation matrix describing the effect of diffractometer axis ζ (unitless)
U	orientation matrix (unitless)
$\boldsymbol{\alpha_0}$	kappa diffractometer angle (°)
$\boldsymbol{\gamma}$, $\boldsymbol{\delta}$, $\boldsymbol{\eta}$, $\boldsymbol{\alpha}$	Z-axis diffractometer angles (°)
$\boldsymbol{\delta}$, $\boldsymbol{\nu}$, $\boldsymbol{\eta}$, $\boldsymbol{\mu}$	S2D2 diffractometer angles (°)
$\boldsymbol{2\theta}$	total scattering angle (°)
$\boldsymbol{2\theta}$, $\boldsymbol{\theta}$, $\boldsymbol{\chi}$, $\boldsymbol{\varphi}$	four-circle Eulerian diffractometer angles (°)
$\boldsymbol{2\theta}$, $\boldsymbol{\theta_\kappa}$, $\boldsymbol{\kappa}$, $\boldsymbol{\varphi_\kappa}$	kappa diffractometer angles (°)
$\boldsymbol{\lambda}$	wavelength (Å)
$\boldsymbol{\psi}$	azimuthal angle (°)

Introduction

When a monochromatic, collimated beam of radiation (X-rays or neutrons) is incident upon a stationary single crystal, the diffraction condition will probably be satisfied for few if any reflections, depending on a number of parameters such as the size of the unit cell, crystal mosaicity, and the energy spread of the radiation. It is even less likely that any particular reflection will be observed, and useful information, such as a reflection's integrated intensity, is not immediately available. Over the years, several methods of collecting scattering data have developed. The earliest X-ray experiments were performed with polychromatic radiation and a two-dimensional (2D) detector (photographic film); known as the Laue method, this technique has remained useful for quick sample alignment and has found new use in timing experiments in which an entire diffraction pattern is collected in a very short exposure. The powder-diffraction method consists of literally grinding the sample to a powder, effecting an ensemble average over all sample orientations; a powder-diffraction pattern is then collected with 1D scan of the detector. The rotation method consists of rotating a single-crystal sample through a given angle while measuring the pattern on a 2D detector with the use of modern image plates or charge-coupled device (CCD) detectors; this is the standard technique for macromolecular protein crystallography. While the above methods are practical for collecting integrated intensities of sharp, well-defined Bragg points, they may compromise on measurement of diffuse features. As an alternative, multicircle diffractometry uses computerized control of a high-precision goniometer (i.e., angle-positioning instrument) in order to hold both sample and detector at precise orientations, becoming a powerful tool to provide quantitative scattering data at well-defined positions in reciprocal space. Monochromatic radiation is used and, typically, observed by a point detector (a detector with a small, well-defined aperture).

Multicircle diffractometry is regularly applied to studies of systems in which orientational information cannot be sacrificed, such as measurement of pole figures for texture analysis or residual stress analysis; grazing-incidence or grazing-exit diffraction for studies of surfaces, thin films, and superlattices; and observation of diffuse scattering due to short-range order, defects such as twins or voids, or thermal diffuse scattering. Two examples of scattering data that require multicircle collection methods are shown in Figure 1. The reciprocal-space map in Figure 1a is from an Ni film grown on MgO(0 0 1); the peaks in the diffraction pattern are used to identify the various epitaxial orientations of the Ni crystal relative to the substrate, as well as the film's strain and mosaic spread. Figure 1b shows integrated intensities from two truncation rods of an epitaxial $SrTiO_3$ film on Si(0 0 1); the rods are continuous, diffuse features which can be analyzed to determine the atomic structure of the film and interface. The foremost drawback of multicircle diffractometer methods, compared to the other methods mentioned above, is that data are collected relatively slowly, often one point at a time rather than over a wide range of reciprocal space at once. The fairly involved calculations of the technique, described in some detail below, are no longer the issue that they once were, given the power and economy of modern computers; various diffractometer-control software packages are available.

In this article, several geometries of multicircle diffractometers, beginning with the standard four-circle Eulerian diffractometer, are reviewed. An overview of the transformation between reciprocal space and angle space is given, and various options in operating a diffractometer are described. Other diffractometer geometries will then be presented, including alternate four-circle geometries, then progressing to five- and six-circle geometries. Throughout the article, an attempt is made to point out potential sources of confusion, such as those caused by conflicting systems of nomenclature; correspondingly, the names of angles used here may differ from those in the literature or those implemented on various instruments. In that vein, it is to be noted that this article uses the term "multicircle diffractometers" to refer to instruments whose circles rotate the sample or detector; additional circles, which are used for polarization analysis or wavelength-dispersive analysis of the radiation, are not counted.

Four-Circle Eulerian Geometry

The basic four-circle diffractometer geometry is shown in Figure 2. The sample sits at the center of rotation on the φ circle, which rotates on the χ circle. The χ and φ circles together constitute a Eulerian cradle, for which this geometry is named. The Eulerian cradle then rotates on the θ circle. The detector rotates on the 2θ circle. The θ-axis is collinear with the 2θ axis; since both axes are perpendicular to the incident beam, this diffractometer is classified as normal-beam geometry. The scattering plane is defined as the plane that contains the diffracted wave vector $\boldsymbol{K}$ and the incident wave vector $\boldsymbol{K_0}$, as well as their difference, the scattering vector $\boldsymbol{Q}$, as shown in Figure 2b. The scattering plane is often horizontal for a laboratory-based X-ray diffractometer, so that the effects of gravity are minimized; at synchrotron sources the scattering plane is usually vertical, to take advantage of the (typically) *s*-polarization of the radiation and the higher degree of collimation in the vertical plane.

The correct operation of a diffractometer hinges on its being properly configured. Figure 2a shows the Eulerian four-circle diffractometer with all angles at their zero positions, in which case the direct beam travels along the axis of the χ circle, defining the zero position of θ; the detector intercepts the direct beam, defining the zero of 2θ; and the θ and φ axes are collinear, defining the zero of χ. The zero of φ is arbitrary. The sense of rotation, as shown in Figure 2b, is left-handed for all axes except χ.

The origin of the rather inelegant naming system is historical. In Bragg's original derivation of X-ray diffraction, the incident and exit X-ray beams both made an angle of θ with the diffracting planes, for a total scattering angle of 2θ. For normal-incidence diffractometers, the scattering angle is set by a single rotation typically labeled 2θ. The sample angle θ is not necessarily equal to one-half of 2θ, except in the special case of some three-circle diffractometers where the axes are mechanically coupled with a 1:2 gear ratio. Thus, although Bragg's law is often written as $\lambda = 2d\sin\theta$, it is better written as

$$\lambda = 2d\sin(2\theta/2) \qquad [1]$$

where λ is the wavelength and d is the lattice-plane spacing. The angle between θ and 2θ is ω, which is defined as

$$\omega = \theta\text{–}(2\theta)/2 \qquad [2]$$

The case of $\omega = 0$ is called the symmetric mode of diffraction. Unfortunately, there is no standard notation even for the most common type of diffractometer, and the θ circle is sometimes labeled ω.

Common angle scans performed on a four-circle Eulerian diffractometer include θ and $\theta/2\theta$ scans. A scan of the θ-axis probes the sample at a given magnitude of the scattering vector $|\boldsymbol{Q}|$ (defined below in eqn [9]). As an example, a θ scan might be used to probe a sample's mosaic spread; one possible source of instrumental broadening for this scan would be the beam divergence. In the $\theta/2\theta$ scan, the 2θ circle rotates at twice the rate of the θ circle. The trajectory of the $\theta/2\theta$ scan is radially outward from the origin of reciprocal space (i.e., $\boldsymbol{Q}$ increases in magnitude, with constant direction). This two-angle scan might be used to measure variations in a sample's lattice-parameter or strain; a source of instrumental broadening could be the radiation's band pass (i.e., the spread in

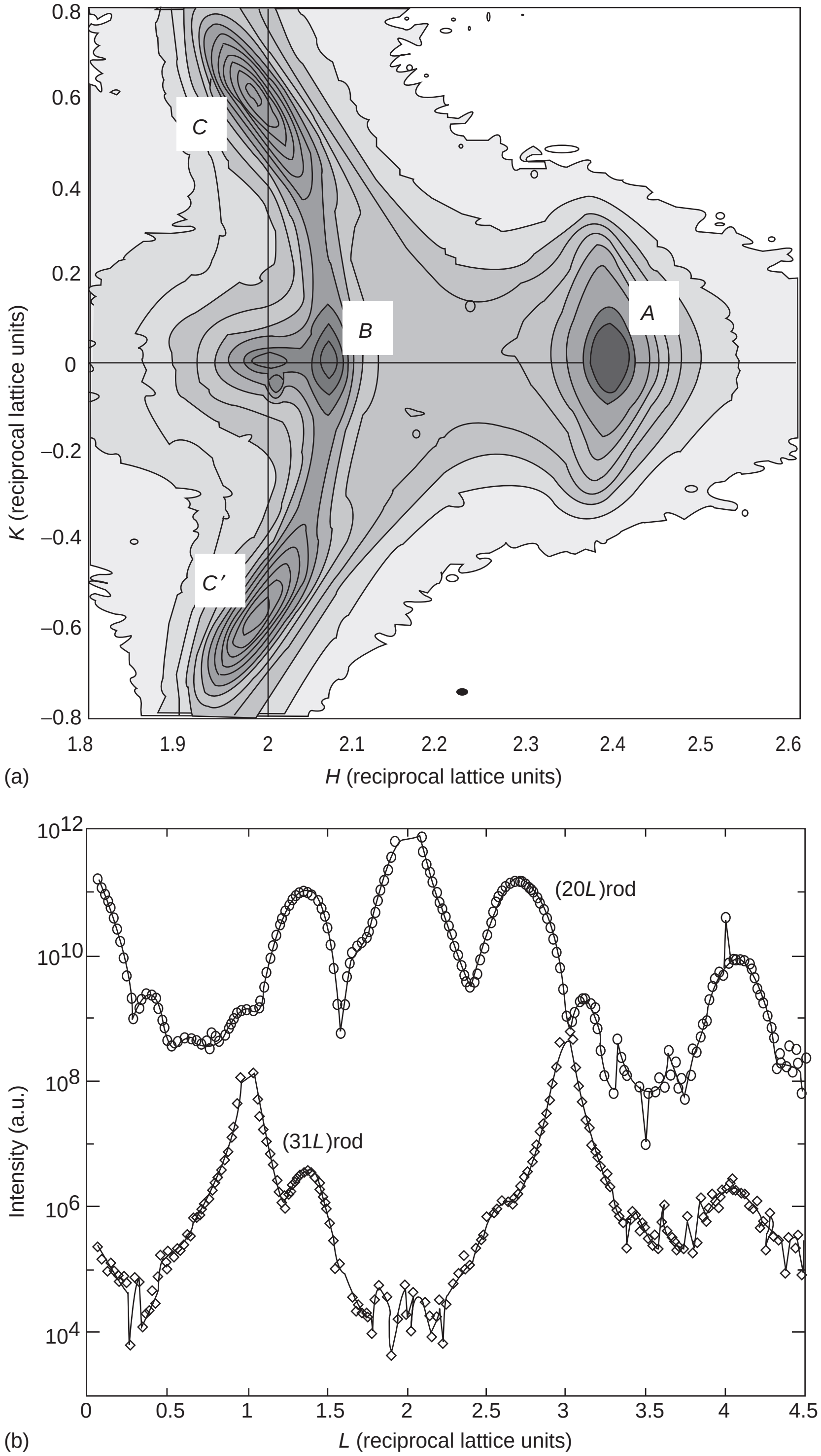

Figure 1 Two examples of thin-film diffraction data collected on a six-circle diffractometer. In both cases, the reciprocal lattice of the substrate material is used as a reference. (a) Reciprocal-space map of a 12 nm film of Ni grown at MgO(0 0 1). The map was made at $L = 0.05$ reciprocal lattice units, with the incident beam set at a grazing angle of 0.2°; the contours are spaced logarithmically. The sharp peak near the main MgO(0 0 2) peak at $H = 2$, $K = 0$ shows that the substrate is somewhat twinned. The peak marked *A* corresponds to an Ni(2 0 0) peak with relaxed cube-on-cube epitaxy. The peaks marked *B*, *C*, and *C*′ are Ni(1 1 1) peaks due to regions with the epitaxial relationship (1 1 0)Ni ∥ (0 0 1)MgO. (b) Truncation-rod data of five unit cells of $SrTiO_3$ grown on Si(0 0 1), collected with a fixed 0.3° angle of incidence. Circles indicate integrated intensities along the (20*L*) rod, and diamonds represent the (31*L*) rod (vertically offset for clarity). Data points very close to the bulk Bragg points (2 0 2), (3 1 1), and (3 1 3) were not measured, since they have very high intensities and no surface sensitivity.

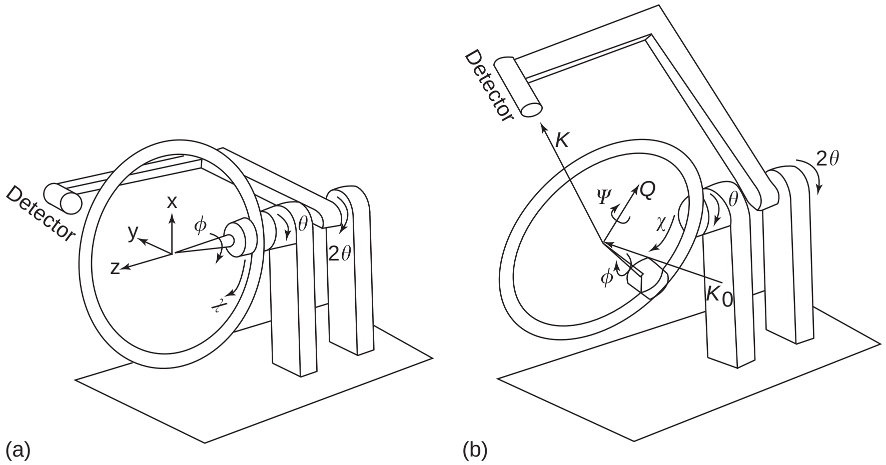

Figure 2 Diagram of a four-circle Eulerian diffractometer with (a) all angles at 0° and (b) all angles with positive displacements. The coordinate system is shown in (a), while incident wave vector $\boldsymbol{K}_0$, diffracted wave vector $\boldsymbol{K}$, scattering vector $\boldsymbol{Q}$, and azimuthal angle ψ are shown in (b).

wavelength). A $\theta/2\theta$ scan is preferable to a single-axis 2θ scan because the reciprocal-space trajectory of a $\theta/2\theta$ scan is simpler to interpret. However, the power of modern multicircle diffractometry is to move to arbitrary positions and scan in arbitrary directions of the reciprocal space; the following sections of this article show how this is accomplished.

Angle Calculations

The Diffraction Equation

The fundamental problem in multicircle diffractometry is to map a sample's reciprocal-space coordinates to the diffractometer's angles: to measure the scattered intensity at a certain point in reciprocal space, what values should the angles have? The solution to this question was worked out by Busing and Levy for the case of a four-circle diffractometer, with extensions by many authors to other geometries. Here, the principles for the ideal four-circle case are outlined; detailed calculations for a variety of geometries can be found in the literature.

The question of mapping from reciprocal space to angle space could be restated as how to set the scattering vector $\boldsymbol{Q}$ equal to a desired reciprocal-lattice point $\boldsymbol{h}$, that is,

$$\boldsymbol{h} = \boldsymbol{Q} \qquad [3]$$

The two sides of eqn [3] must be written in the same reference frame and in the same coordinates; here one may choose to transform eqn [3] to Å^{-1} units in the laboratory frame. Beginning with the left-hand side of eqn [3], the transformation of reciprocal-lattice vector $\boldsymbol{h}$ from reciprocal-lattice coordinates ($\boldsymbol{h}$, with no subscript) to lab coordinates ($\boldsymbol{h}_\mathrm{l}$) is achieved in a number of steps by successive application of a number of matrices. First, $\boldsymbol{h}$ in reciprocal-lattice units is transformed into Cartesian coordinates ($\boldsymbol{h}_\mathrm{c}$, in Å^{-1} units) via the matrix $\boldsymbol{B}$:

$$\boldsymbol{h}_\mathrm{c} = \boldsymbol{B}\boldsymbol{h} \qquad [4]$$

where $\boldsymbol{B}$ is constructed from the lattice parameters. The matrix $\boldsymbol{B}$ is most easily expressed as a combination of real-space lattice parameters a_i, α_i, and reciprocal-space lattice parameters b_i, β_i ($i = 1$–3):

$$\boldsymbol{B} = \begin{pmatrix} b_1 & b_2 \cos\beta_3 & b_3 \cos\beta_2 \\ 0 & b_2 \sin\beta_3 & -b_3 \cos\beta_2 \cos\alpha_1 \\ 0 & 0 & 2\pi/a_3 \end{pmatrix} \qquad [5]$$

where $a_i \cdot b_j = 2\pi\delta_{ij}$. Generally, $\boldsymbol{B}$ is not orthonormal, but the other matrices in this section are all orthonormal rotation matrices. The next step is to transform $\boldsymbol{h}_\mathrm{c}$ into the coordinate system of the diffractometer's φ axis:

$$\boldsymbol{h}_\phi = \boldsymbol{U}\boldsymbol{h}_\mathrm{c} \qquad [6]$$

where $\boldsymbol{U}$ describes the orientation of the crystal relative to the diffractometer, and as such, is known as the orientation matrix. The determination of $\boldsymbol{U}$ is a critical step in multicircle diffractometery and is described in the next section. $\boldsymbol{h}_\varphi$ is then transformed into laboratory coordinates by the successive application of the diffractometer-axes rotation matrices $\boldsymbol{R}$:

$$\boldsymbol{h}_\mathrm{l} = \boldsymbol{R}(\theta)\boldsymbol{R}(\chi)\boldsymbol{R}(\phi)\boldsymbol{h}_\phi \qquad [7]$$

where

$$\boldsymbol{R}(\theta) = \begin{pmatrix} \cos\theta & \sin\theta & 0 \\ -\sin\theta & \cos\theta & 0 \\ 0 & 0 & 1 \end{pmatrix}$$
$$\boldsymbol{R}(\chi) = \begin{pmatrix} \cos\chi & 0 & \sin\chi \\ 0 & 1 & 0 \\ -\sin\chi & 0 & \cos\chi \end{pmatrix} \qquad [8]$$
$$\boldsymbol{R}(\phi) = \begin{pmatrix} \cos\phi & \sin\phi & 0 \\ -\sin\phi & \cos\phi & 0 \\ 0 & 0 & 1 \end{pmatrix}$$

Turning to the right side of eqn [3], the scattering vector or momentum transfer, $\boldsymbol{Q}$, is defined as

$$\boldsymbol{Q} = \boldsymbol{K} - \boldsymbol{K}_0 \qquad [9]$$

where $\boldsymbol{K}$ and $\boldsymbol{K}_0$ are the diffracted and incident wave vectors, respectively. Their magnitudes are equal and defined as

$$|\boldsymbol{K}| = |\boldsymbol{K_0}| = K = 2\pi/\lambda \qquad [10]$$

The magnitude of $\boldsymbol{Q}$ is then

$$|\boldsymbol{Q}| = \frac{2\pi}{d} = \frac{4\pi \sin(2\theta/2)}{\lambda} \qquad [11]$$

It should be noted that numerous conventions exist for the definitions of eqns [9] and [10]. For example, the symbols $\boldsymbol{s}$ and $\boldsymbol{s_0}$ or $\boldsymbol{k}'$ and $\boldsymbol{k}$ may be used for the diffracted and incident wave vectors respectively. These wave vectors are often defined without the factor of 2π in eqn [10]; correspondingly, the factors of 2π are removed from eqns [5] and [11]. Other common symbols for the scattering vector include $\boldsymbol{G}$, $\boldsymbol{H}$, and $\boldsymbol{K}$.

In laboratory units, the incident wave vector is along the y-axis:

$$\boldsymbol{K_0} = \begin{pmatrix} 0 \\ K \\ 0 \end{pmatrix} \qquad [12]$$

The diffracted wave vector is along the y-axis of the detector frame, which can be transformed into the lab frame with a rotation matrix for the 2θ axis:

$$\boldsymbol{K} = \boldsymbol{R}(2\theta)\begin{pmatrix} 0 \\ K \\ 0 \end{pmatrix}, \qquad [13]$$
$$\boldsymbol{R}(2\theta) = \begin{pmatrix} \cos 2\theta & \sin 2\theta & 0 \\ -\sin 2\theta & \cos 2\theta & 0 \\ 0 & 0 & 1 \end{pmatrix}$$

The scattering vector $\boldsymbol{Q}$, then, equals $[\boldsymbol{R}(2\theta) - \boldsymbol{I}]\ \boldsymbol{K}_0$, where $\boldsymbol{I}$ is the identity matrix. Substitution into eqn [3] results in the basic diffractometer equation for a four-circle diffractometer:

$$\boldsymbol{R}(\theta)\boldsymbol{R}(\chi)\boldsymbol{R}(\phi)\boldsymbol{UBh} = [\boldsymbol{R}(2\theta) - \boldsymbol{I}]\begin{pmatrix} 0 \\ K \\ 0 \end{pmatrix} \qquad [14]$$

Several possible generalizations of the above procedure are fairly straightforward to derive. For another diffractometer geometry, one simply incorporates the appropriate rotation matrices $\boldsymbol{R}$ into eqn [14]. One can also measure the directions of a diffractometer's rotation axes with, for example, an autocollimator, creating empirical $\boldsymbol{R}$ matrices rather than the idealized ones of eqns [8] and [13]. One also need not assume that the incident beam is perfectly collinear with the y-axis but can generalize the beam's direction (eqn [12]). This can be very useful in situations where the incident beam is not level (e.g., deflected upwards by a grazing-incidence mirror), but the entire diffractometer cannot be tilted. Several authors have worked out the equations for completely general diffractometer geometries.

Determining the Orientation Matrix

With the diffraction equation (eqn [14]) otherwise solved, the orientation matrix $\boldsymbol{U}$ must be determined; $\boldsymbol{B}$ must also be found if the sample's lattice parameters are not precisely known. Busing and Levy demonstrated several methods of determining $\boldsymbol{U}$ that result in a 1D set of solutions in diffractometer-angle space. To uniquely determine $\boldsymbol{U}$, a constraint must be added; selection of constraints are discussed in the following section.

If the sample's lattice parameters are known, then two noncollinear orientation reflections, $\boldsymbol{h}_1$and $\boldsymbol{h}_2$, must be found to determine $\boldsymbol{U}$. Then, in principle, solving the following equations for $\boldsymbol{h}_1$ and $\boldsymbol{h}_2$ will determine $\boldsymbol{U}$:

$$\boldsymbol{h}_{i\phi} = \boldsymbol{U}\boldsymbol{B}\boldsymbol{h}_i \quad [15]$$

where $i = 1,2$ and the $\boldsymbol{h}_{i\varphi}$ vectors are calculated from the observed angular positions of $\boldsymbol{h}_i$. But in practice, experimental uncertainties prevent one $\boldsymbol{U}$ matrix from exactly satisfying eqn [15] for both $\boldsymbol{h}_{1\varphi}$ and $\boldsymbol{h}_{2\varphi}$. Errors can arise from effects such as mosaic spread, refraction, beam divergence, or mechanical imperfections in the diffractometer. Therefore, the following procedure is commonly used to determine $\boldsymbol{U}$: $\boldsymbol{h}_{1\varphi}$, called the primary reflection, exactly satisfies eqn [15], but $\boldsymbol{h}_{2\varphi}$, as the secondary reflection, only determines the rotation of the coordinate system about $\boldsymbol{h}_{1\varphi}$. Exchanging $\boldsymbol{h}_1$ and $\boldsymbol{h}_2$ generally results in slightly different solutions for $\boldsymbol{U}$. Generally, to minimize the effect of angular misalignment and achieve a more accurate solution of $\boldsymbol{U}$, the orientation reflections should be at fairly high angles (high $|\boldsymbol{Q}|$) and fairly far apart in angle (as a suggestion, the angle between $\boldsymbol{h}_1$ and $\boldsymbol{h}_2$ should be at least 40°). On the other hand, when a good alignment is not easily maintained, one could select orientation reflections that are close to each other and then probe only the nearby region of reciprocal space. Then, when another region is to be probed, a new set of orientation reflections can be chosen in the new region.

When the sample's lattice parameters are not known, the matrix $\boldsymbol{UB}$ must be determined; sometimes the $\boldsymbol{UB}$ matrix, rather than just $\boldsymbol{U}$, is known as the orientation matrix. In the unknown lattice-parameter case, three non-coplanar reflections ($\boldsymbol{h}_1$, $\boldsymbol{h}_2$, $\boldsymbol{h}_3$) with known (or assumed) Miller indices should be found that, with the selection of one constraint as discussed below, allows for a unique solution of $\boldsymbol{UB}$ in eqn [15]. With four or more reflections, a least-squares fitting method can be applied to eqn [15] to refine the lattice parameters. The resulting lattice parameters will not exactly reflect the symmetry of the crystal lattice but should be fairly close. For example, with a cubic crystal, the unit cell lengths should be nearly equal, and the angles should be within a few tenths of 90°. With a sufficiently large set of orientation reflections $\boldsymbol{h}_i$, still other parameters may also be refined, such as a displacement of the crystal from the diffractometer's center of rotation.

Operating Modes

As mentioned above, the calculation of diffractometer angles for a given reciprocal-lattice point is under-determined, since reciprocal space is three-dimensional while a four-circle diffractometer has, obviously, four degrees of freedom. An additional constraint is needed that is usually achieved by freezing one angle at a certain value. In the case of a four-circle normal-incidence diffractometer, the detector angle 2θ is determined by the magnitude of the scattering vector $\boldsymbol{Q}$; a constraint cannot be placed on 2θ without restricting the range of accessible reciprocal space to a single magnitude of $|\boldsymbol{Q}|$. Therefore, constraints in the four-circle Eulerian geometry should be applied only to a diffractometer's sample angle or to an appropriately defined azimuthal angle.

The simplest and perhaps most common four-circle mode is to constrain ω (see eqn [2]) at a fixed value. The constraint of $\omega = 0$ is called the symmetric or bisecting mode, since the incident and diffracted beams make the same angle to the plane of the χ circle; generally, this mode permits the greatest access to reciprocal space. Another mode based on sample angles is to constrain χ or φ to a fixed value; such a mode might be useful when a sample environmental cell (e.g., oven, cryostat, or vacuum chamber) has a small window that must be kept oriented to the incident beam, but is otherwise fairly limiting.

Another possible operating mode is to choose a zone, a plane of reciprocal space passing through the origin, as the scattering plane. A zone can be defined by two non-collinear Bragg points; appropriate values of χ and φ are then selected to place the two Bragg points in the scattering plane. This mode contains two constraints, that is, it freezes two sample angles. Thus, access to reciprocal space is reduced to a single plane, but data collection is simplified since the zone can be studied with movements of only 2θ and θ.

Instead of constraining a particular sample angle to a given value, one can also constrain the azimuthal rotation of the sample about the scattering vector. As shown in Figure 2b, ψ is the azimuthal rotation about $\boldsymbol{Q}$. In defining ψ, a reference vector $\boldsymbol{N}$ must be chosen. $\boldsymbol{N}$ can point in any direction except parallel to $\boldsymbol{Q}$, but is often a special direction for the sample, for example, the surface normal, a magnetic field direction, or the direction of polarization in a polar material. The definition of $\psi = 0°$ is when $\boldsymbol{N}$ lies in the scattering plane; $\psi = 90°$ when $\boldsymbol{N}$ lies in the plane defined by $\boldsymbol{Q}$ and the diffractometer's $\theta/2\theta$ axes. The constrained-ψ mode is particularly useful in surface diffraction when $\boldsymbol{N}$ is chosen to be the surface normal. Mochrie has shown how to calculate ψ for a given incident angle or exit angle, which provide particularly convenient modes for grazing-incidence or grazing-exit studies. The constraint of $\psi = 90°$ sets the incident angle equal to the exit angle.

Equivalent Angle Settings

In addition to selection of an operating mode, other choices of angle must be made in the operation of a diffractometer. Although any angle can theoretically be rotated by 360° without changing anything, the axes of most diffractometers have limited ranges of motion and cannot rotate indefinitely. The diffractometer-control software must determine, for example, whether a rotation from −170 to +170° will be done with a motion of −20 or +340°. Furthermore, symmetry operations make some sets of angle combinations equivalent. For example, for a given χ and φ, the pair of angles (2θ, ω) are equivalent to (-2θ, $\omega-180$), but both settings may not be equally practical or accessible on a given diffractometer. In general, seven sets of angles can substitute for the set of (2θ, θ, χ, φ), although not all of these sets are compatible with all operating modes. A diffractometer-control program must, implicitly or explicitly, select one of these sets. A convenient choice is to select angles that fall within the allowed range as set by software limits.

Alternative Four-Circle Geometries

Kappa Geometry

Several types of four-circle diffractometer geometries exist in addition to the Eulerian geometry described above. Perhaps the most common is the “kappa” geometry, originally developed by Enraf–Nonius. As shown in Figure 3, the χ circle of the Eulerian geometry is replaced by a κ-axis, which is built on an arm at an angle of α_0 to the θ_κ axis; typically, α_0 is nominally 50°. The κ-axis rotates another arm with another angle of α_0, upon which sits the φ_κ-axis. The “κ” subscripts on the θ_κ and φ_κ circles distinguish those circles of the kappa diffractometer from similar θ and φ circles of a standard Eulerian diffractometer, although not all systems of nomenclature make this explicit distinction. One could incorporate the rotation matrix of κ in deriving solutions to the diffraction equation (eqn [14]). However, it is often simpler to directly relate the kappa angles (θ_κ, κ, φ_κ) to the Eulerian angles (θ, χ, φ):

$$\begin{aligned}\theta &= \theta_\kappa - \cos(\kappa/2)/\cos(\chi/2)\\ \chi &= 2\arcsin[\sin(\kappa/2)\sin\alpha_0]\\ \phi &= \phi_\kappa - \cos(\kappa/2)/\cos(\chi/2)\end{aligned} \qquad [16]$$

The relations in eqn [16] are straightforward to be included in the diffractometer-control software after an appropriate solution to eqn [14] is computed in Eulerian geometry, with the advantage of allowing users to operate a kappa diffractometer just as the more familiar Eulerian diffractometer is. In doing so, (θ, χ, φ) are called “pseudoangles,” whereas the physically present (θ_κ, κ, φ_κ) are called “real” angles.

The foremost advantage of a kappa-geometry diffractometer is the elimination of the χ circle. The primary weakness of Eulerian geometry is the limited mechanical perfection of the χ circle; any deviation from a perfect circle will, for example, increase the sphere of confusion. This issue is often exacerbated for diffractometers with an open or split χ circle. On the other hand, a closed χ circle blocks the incident or diffracted beam for some values of θ; beam blockage is less of an issue with kappa geometry. A related advantage is the relative compactness of the κ arm compared to the χ circle, making kappa geometry popular for confined spaces or crowded experimental stations. One hypothetical drawback of the kappa geometry is its limited angular range. As seen in eqn [16], a kappa diffractometer whose κ-axis has a full range of ±180° emulates a Eulerian diffractometer with a maximum theoretical range of $\chi = \pm 2\alpha_0$ (i.e., typically ±100°). This issue can be dealt with by selection of a suitable angular setting, as discussed above, and should not generally pose a problem. A practical caution is that the asymmetric shape of the kappa arm, as it folds and unfolds, makes it particularly vulnerable to collisions with nearby objects (e.g., the input flight path or the detector arm); care should be taken to properly set hardware and software limit switches such that collisions cannot occur in any potential angular configuration.

Four-Circle General-Inclination Geometries

Another class of diffractometers, known as general-inclination geometries, is distinct from the normal-incidence geometries in that it provides more than one degree of freedom to the detector. Such geometries can significantly increase the range of accessible reciprocal space in situations where the angular range is limited by a sample cell. In contrast to the normal-incidence geometry, the

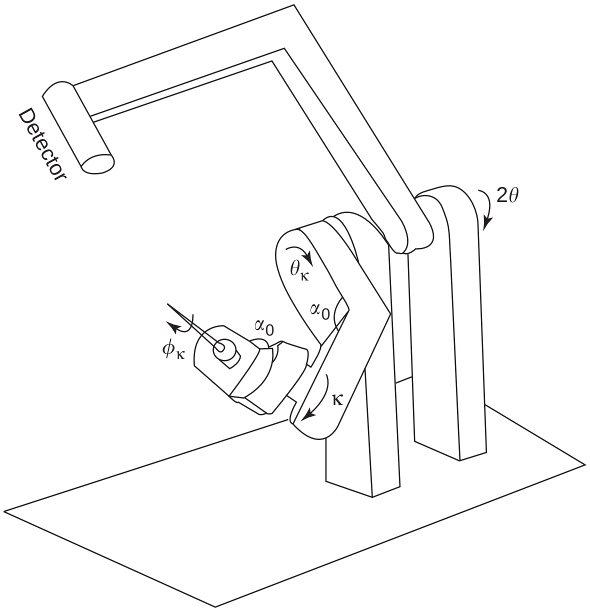

Figure 3 Diagram of a four-circle kappa diffractometer. The angles are chosen to hold a sample at the same place as the Eulerian diffractometer shown in Figure 2b, via the relations given eqn [16].

scattering plane (containing $\boldsymbol{K}$, $\boldsymbol{K}_0$, and $\boldsymbol{Q}$) of the general-inclination geometry is no longer fixed; there is no simple one-to-one correspondence between the general-inclination and normal-incidence geometries such as that which exists between the Eulerian and kappa geometries. Since the position of the detector in a general-inclination geometry is a compound motion of several angles, the total scattering angle 2θ must be calculated, and cannot be simply read from one dial on the instrument. In this article, the convention that 2θ is the total scattering angle is followed. As such, only the normal-incidence geometry has a single circle that can be properly labeled 2θ, although many systems of nomenclature use 2θ as the label for one of the detector circles.

Several variations of four-circle inclined-geometry diffractometers have been developed, two of which are illustrated in Figure 4. For the "*Z*-axis" diffractometer (Figure 4a), the sample sits on the η-axis and the detector on the δ and γ-axes; all three axes then rotate about the α-axis. It may be noted that many *Z*-axis diffractometers call the sample axis θ (or ω); here, this axis is labeled as η to emphasize that it is not equivalent to the Eulerian θ-axis, since the η-axis is not orthogonal to the X-ray beam when $\alpha \neq 0$. The *Z*-axis geometry is particularly useful in holding heavy sample equipment such as vacuum chambers, as it minimizes motions that must be coupled through the sample chamber. The total scattering angle 2θ is given by

$$2\theta_{Z-\mathrm{axis}} = \arccos(\cos\gamma\cos\delta\cos\alpha + \sin\alpha\sin\gamma) \qquad [17]$$

Another example of inclined geometry is the "S2D2" diffractometer. As shown in Figure 4b, the S2D2 geometry is composed of two pairs of orthogonal axes: the sample rotates on η and μ, while the detector rotates on δ and ν. Indeed, the name "S2D2" is meant to indicate that this geometry has two degrees of freedom for the sample ("S2") and two degrees of freedom for the detector ("D2"). In this nomenclature, the normal-incidence four-circle Eulerian and kappa diffractometers both have "S3D1" geometry. The *Z*-axis geometry does not exactly fit into this naming system, since one degree of freedom is shared between the sample and detector, but the designation (S1D2)*1 has been used, implying that a *Z*-axis diffractometer is an S1D2 (three-circle) diffractometer mounted upon a fourth circle. A practical advantage of the S2D2 geometry is the mechanical decoupling of the sample and detector motions, limiting the propagation of mechanical errors. The scattering angle of the S2D2 diffractometer is given by eqn [17] with γ set to zero:

$$2\theta_{\mathrm{S2D2}} = \arccos(\cos\nu\cos\delta) \qquad [18]$$

The orientation matrix $\boldsymbol{U}$ of a four-circle inclined geometry can be calculated in the same way as for the four-circle normal-incidence geometry case, and a mode with one constraint must be selected. The diffraction equations are similar to the normal-incidence case, but the appropriate rotation matrices for the sample and detector axes must be incorporated on both sides of eqn [14].

The *Z*-axis and S2D2 geometries are particularly useful for surface scattering when the surface normal is aligned parallel to the η-axis, since the angle of incidence is given simply by the diffractometer angle α or μ, respectively. However, sufficiently precise sample alignment is often not easy, especially in a vacuum environment, which leads naturally to the desire for additional degrees of freedom for the sample. Such diffractometer geometries are described in the next section.

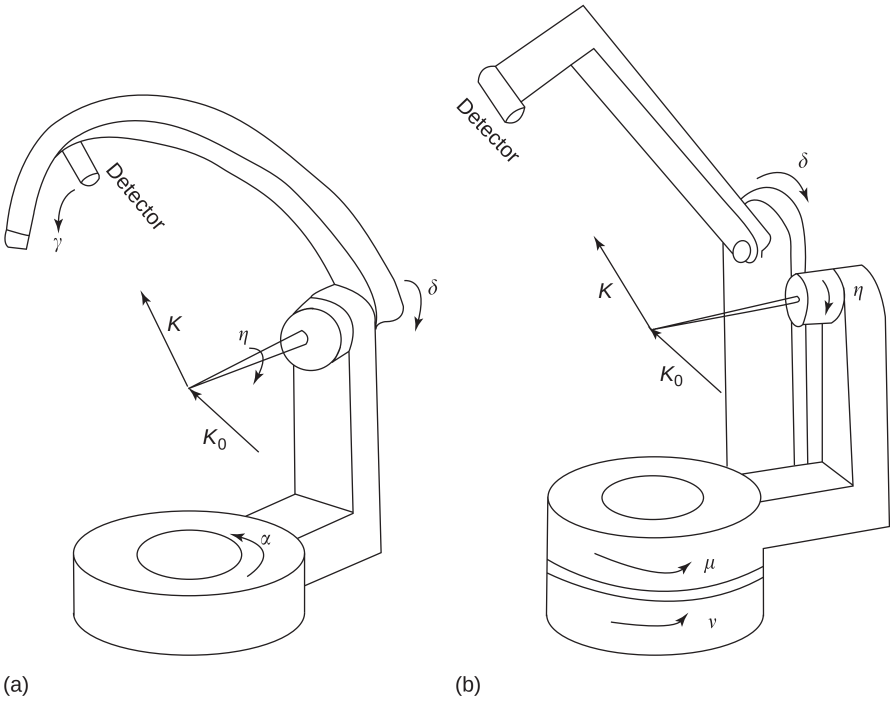

Figure 4 Two examples of general-inclination four-circle diffractometers: (a) *Z*-axis geometry; (b) S2D2 geometry.

Five-Circle and Six-Circle Diffractometers

Representing the next level of complexity and flexibility, five- and six-circle diffractometer geometries all fall into the class of inclined geometries. In general, such diffractometers have been developed to provide better access to larger ranges of reciprocal space or to provide greater flexibility in sample positioning, given the constraints of a particular experiment.

Several varieties of five- and six-circle diffractometers have been constructed. The basic five-circle diffractometer could be characterized as a four-circle normal-incidence diffractometer (either Eulerian or kappa) with the θ-axis horizontal, mounted on a fifth rotation stage whose axis is vertical. The sample and detector motions are coupled by the fifth circle, so this five-circle geometry could be labeled (S3D1)*1. This five-circle diffractometer can be converted into a six-circle instrument by the addition of another vertical axis, upon which sit the sample circles (θ, χ, and φ); the entire diffractometer rotates on the bottommost axis. Alternatively, one could add the χ and φ circles of a Eulerian cradle (or the κ and φ_κ circles of a kappa arm) to an S2D2 diffractometer (Figure 4b); this geometry decouples the sample and detector motions and would thus be labeled S4D2. Another six-circle geometry is formed by adding a Eulerian cradle to a Z-axis diffractometer (Figure 4a); the sample and detector motions of this geometry are coupled through the α-axis.

While the additional degrees of freedom in five- and six-circle diffractometers provide much greater flexibility in operation, the degree of complexity in operation increases correspondingly. On a practical level, five- and six-circle diffractometers are generally quite large, with more (and heavier) counterweights than four-circle diffractometers. The large size and extra degrees of freedom increase the possibility of collisions and the damage that a collision can cause; hardware and software limits must be carefully set to avoid a collision in any potential angular configuration. More fundamentally, the choice of a mode becomes more complicated. Each additional degree of freedom (rotation axis) requires an additional constraint in the transformation between angle space and reciprocal space. Specifically, to uniquely determine the angle settings for a reciprocal lattice point, a five-circle or six-circle diffractometer requires, respectively, two or three constraints. The number of possible operating modes becomes correspondingly larger, and the geometry calculations supported by the diffractometer-control software also grow in complexity.

Although the modes of a five- or six-circle diffractometer require selection of several constraints, the constraints cannot be chosen arbitrarily. For example, one could not constrain two detector circles, since that would limit reciprocal-space access to a single magnitude of $|\boldsymbol{Q}|$. In the case of surface diffraction, one could not choose both the incident angle and the exit angle since that would overconstrain the azimuthal angle; one could choose to make the incident and exit angles equal but could not select a specific value for both. In the particular case of S4D2 geometry, a system was developed by You to organize mode selection by categorizing the angles which could be subject to constraints. The three categories of angles are detector, azimuthal, and sample. A detector constraint would fix one of the angles upon which the detector rotates, or would fix the angle of $\boldsymbol{Q}$ or reference vector $\boldsymbol{N}$ with respect to the horizontal plane; for example, $\boldsymbol{Q}$ or $\boldsymbol{N}$ could be fixed to lie in the horizontal or vertical plane. Azimuthal constraints include fixing the incident or exit angle, or otherwise fixing the azimuthal angle ψ. Possible sample constraints include fixing a sample angle at a certain value or constraining it relative to another angle. The key to this method is that no more than one constraint may be placed on either detector angles or azimuthal angles; the remaining constraint(s) must be applied to sample angles. Both sets of data in Figure 1, for example, were collected on an S4D2 diffractometer with one detector constraint (fixed angle of $\boldsymbol{N}$), one azimuthal constraint (fixed angle of incidence), and one sample constraint (η was fixed to be half of δ). One could also select one detector or azimuthal constraint and two sample constraints, or one could select three sample constraints.

The development of five- and six-circle diffractometers was driven by the need for flexibility in diffractometer operation, especially for access to the widest possible range of reciprocal space, given the experimental constraints. While some future advances in this technique may lie in the area of new diffractometer geometries, more critical needs lie in the area of improved data-collection efficiency. For example, many experiments may benefit from detectors with the sometimes-conflicting qualities of better resolution, larger dynamic ranges, or parallel data collection by use of 1D or 2D detectors. The overhead expense of motor motion can be reduced by the so-called trajectory or on-the-fly scanning: rather than collect data point by point, the diffractometer axes rotate continuously and the incoming data are binned into multichannel counters. In general, just as modern computers have made multicircle diffractometry viable as a regular research tool, increased automation will improve the efficiency in all steps of a diffraction experiment.

Acknowledgments

Data in Figure 1 were collected at the Advanced Photon Source beamline 7ID, in collaboration with R Clarke and C Cionca (Figure 1a), and M J Bedzyk and D M Goodner (Figure 1b). Use of the Advanced Photon Source was supported by the US Department of Energy, Office of Science, Basic Energy Sciences, under Contract No. W-31-109-ENG-38.

Further Reading

Arndt UW and Willis BTM (1966) *Single Crystal Diffractometry.* Cambridge: Cambridge University Press.

Bloch JM (1985) Angle and index calculations for a '*z*-axis' x-ray diffractometer. *Journal of Applied Crystallography* 18: 33–36.

Busing WR and Levy HA (1967) Angle calculations for 3- and 4-circle x-ray and neutron diffractometers. *Acta Crystallographica* 22: 457–464.

Evans-Lutterodt KW and Tang M-T (1995) Angle calculations for a '2+2' surface x-ray diffractometer. *Journal of Applied Crystallography* 28: 318–326.

Hamilton WC (1989) Angle settings for four-circle diffractometers. In: Ibers JA and Hamilton WC (eds.) *International Tables for X-Ray Crystallography*, vol. 4, pp. 274–284. Dordrecht: Kluwer Academic.

Lohmeier M and Vlieg E (1993) Angle calculations for a six-circle x-ray diffractometer. *Journal of Applied Crystallography* 26: 706–716.

Mochrie SGJ (1988) Four-circle angle calculations for surface diffraction. *Journal of Applied Crystallography* 21: 1–3.

Sands DE (1982) *Vectors and Tensors in Crystallography*. Mineola: Dover Publications.

Vlieg E, Van der Veen JF, Macdonald JE, and Miller M (1987) Angle calculations for five-circle diffractometer used for surface x-ray diffraction. *Journal of Applied Crystallography* 20: 330–337.

You H (1999) Angle calculations for a '4S+2D' six-circle diffractometer. *Journal of Applied Crystallography* 32: 614–623.

Disorder and Localization Theory☆

A Harju[a], **EN Economou**[b], **and CM Soukoulis**[c], [a]Aalto University, Espoo, Finland; [b]University of Crete, Heraklion, Greece; [c]Iowa State University, Ames, IA, USA

© 2016 Elsevier Inc. All rights reserved.

This is an update of A. Harju, E.N. Economou, C.M. Soukoulis, Disorder and Localization Theory, Reference Module in Materials Science and Materials Engineering, Elsevier, 2016, ISBN 9780128035818, https://doi.org/10.1016/B978-0-12-803581-8.01034-1.

Introduction 771
'Classical' Treatment of Disorder 771
Weak Disorder and the Role of Interferences 772
Disorder, Density of States, and Wave Functions 774
Three-Dimensional Systems 774
Two-Dimensional Systems 775
One-Dimensional and Quasi-One-Dimensional Systems 776
Level Statistics 776
Transfer Matrix Techniques 777
Scaling Approach 777
Potential Well Analogy 777
Other Realizations 778
Further Reading 778

Introduction

When an electron is placed in solid material, it will scatter from the potential of the atoms. If the atoms are identical and ordered in a perfect lattice, the constructive interference compensates the scattering. In this case the eigenstates of the electron are plane-wave-like solutions, called Bloch waves. The Bloch states extend over the whole lattice and carry current. There are also regions in energy without eigenstates, corresponding to gaps. If the lattice of atoms is nearly perfect, the Bloch theorem is not mathematically valid anymore. However, a small imperfection could be treated as a weak perturbation that would mildly mix the Bloch states. With sufficient disorder, the transport becomes diffusive (ohmic). In this regime, a semiclassical picture of electrons bouncing from impurities might be sufficient to capture the essential physics. However, P.W. Anderson (1958) showed in his seminal paper that with sufficient amount of disorder, the electronic states at zero temperature do not diffuse but are localized in space. It means that a material that is metallic without defects would become an insulator at low temperatures when the amount of disorder is increased. Further, this case should not be mixed with the traditional insulators with a perfect lattice, where the Fermi energy happens to be within the gap region of energy.

'Classical' Treatment of Disorder

In actual solids, there are always static, chemical, and structural deviations from periodicity, located randomly within the solid; in other words, there is always disorder. The thermal vibrations of atoms (or ions), although dynamical in nature, can be treated for fast processes and high temperatures as additional sources of static disorder. However, at low temperatures, lattice vibrations and other dynamical processes lead to inelastic scatterings, which are clearly distinct from the elastic scatterings considered up to now; these inelastic scatterings are responsible for an energy uncertainty, ΔE, which in turn defines an inelastic dephasing time $\tau_\phi \sim \hbar/\Delta E$; for $t \gtrsim \tau_\phi$, the phase is randomized.

Disorder is crucial in determining important transport properties, such as electrical and thermal conductivities, magnetoresistances, photoconductivities, and metal–insulator transitions. Under normal conditions, the main role of disorder is to change the propagation of electrons (or more generally, of whatever carriers) from ballistic to diffusive; the latter involves a new characteristic quantity, the so-called transport mean free path, l, which is connected to the diffusion length $L_\mathrm{D} = (D\tau)^{1/2}$ by the relation $L_\mathrm{D} = l/\sqrt{d}$. D is the diffusion coefficient, $\tau = l/v$, v is the carrier velocity, and d is the space dimensionality. The transport mean free path, for low concentration, $n_\mathrm{s} = N_\mathrm{s}/V$, of scatterers is related to the transport cross section σ_{ti} of each scatterer by the relation

$$\frac{1}{l} = \frac{1}{V}\sum_{i=1}^{N_\mathrm{s}} \sigma_{ti} \qquad [1]$$

which means that over a length l, the N_s scatterers within the volume $V = Sl$ will intercept the whole cross section, S, of the incoming wave (i.e., $S = \sum_i \sigma_{ti}$).

☆*Change History*: June 2015. A. Harju carried out an overall improvement to the text. Most importantly, the role of P.W. Anderson is introduced.

The summation of σ_{ti}s in eqn [1] implies that interference effects have been omitted; thus the term 'classical' in the title of this subsection. Actually, a scattered wave from one scatterer can be scattered again by other scatterers; this is especially true when the σ_{ti}s are large and their concentration, n_s, is high. All these single and multiple scattered waves can, in principle, interfere with one another, possibly modifying the basic result in eqn [1]. The argument in support of eqn [1] is that constructive and destructive interference more or less cancel each other as a result of the interfering waves having random phase differences (associated with the random positions and phase shifts of the scatterers).

Weak Disorder and the Role of Interferences

Consider an electron initially ($t=0$) at the point $\boldsymbol{r}$. The probability density amplitude, $A(t)$, to again find the electron at $\boldsymbol{r}$, after time t, is given by $A(t)=\sum_\nu A_\nu(t)$, where the sum is over all directed path integrals, $A_\nu=\exp[(i/\hbar)\int_0^t L(r_\nu(t'))\,\mathrm{d}t']$, starting and ending at $\boldsymbol{r}$. The probability density, $\mathrm{d}P(\mathrm{t})/\mathrm{d}^3r$, to find the electron at $\boldsymbol{r}$ after time t is $\mathrm{d}P/\mathrm{d}^3r=|A(t)|^2=\sum_\nu|A_\nu(t)|^2+\sum_{\nu\neq\mu}A_\nu(t)A_\mu^*(t)$. Omitting the last double sum on the basis of random phases is equivalent to the approximation leading to eqn [1]. However, not all terms with $\mu\neq\nu$ have random phases; indeed, for each path $\mu=\bar{\nu}$, where $\bar{\nu}$ is the same as path ν but run in the opposite direction (the last equality stems from time-reversal symmetry), and consequently $\sum_{\gamma\neq\mu}A_\gamma A_\mu^*=\sum_\gamma A_\gamma A_{\bar{\gamma}}^*+\sum_{\mu\neq\gamma,\bar{\gamma}}A_\gamma A_\mu^*$. Thus, making the reasonable assumption that $\sum_{\mu\neq\nu,\bar{\nu}}A_\nu A_\mu^*$ is really zero because of random phases, one may come to the conclusion that $\mathrm{d}P/\mathrm{d}^3r$ is twice as big as the classical diffusion would predict, since $\sum_\gamma A_\gamma A_{\bar{\gamma}}^*=\sum_\gamma\left|A_\gamma\right|^2$. Actually, $\mathrm{d}P(t)/\mathrm{d}^3r$ is less than twice as large because the equality $A\bar{\nu}=A_\nu$ is not valid for very long paths, whose length far exceeds the inelastic dephasing length $L_\phi\equiv(D\tau_\phi)^{1/2}$; for such long paths, repeated inelastic scattering destroys the phase equality of $A\bar{\nu}$ and A_ν. In any case, the conclusion is that interference effects make quantum diffusion slower than classical diffusion, and lead to a decrease of the diffusion coefficient and the electrical conductivity. This decrease is proportional to the integral $\int\mathrm{d}t\sum_\gamma A_\gamma A_{\bar{\gamma}}^*$.

The latter can be estimated by taking into account that the paths which contribute are inside a tube of cross section λ^2 (or λ^{d-1} for a d-dimensional system, where λ is the wavelength) around the classical trajectory. Furthermore, the probability of returning is directly related to the probability of self-intersection of this orbital tube. Within time $\mathrm{d}t$, the wave would move by $v\mathrm{d}t$ and would sweep a volume $\mathrm{d}V=\lambda^{d-1}v\mathrm{d}t$; hence, the probability of self-intersection during the time interval $\mathrm{d}t$, after time t has elapsed, is equal to the ratio of the volume $\mathrm{d}V=\lambda^{d-1}v\mathrm{d}t$ over the total volume swept up to t; the latter is of the order of $L_D^d=(Dt)^{d/2}$. Hence, the probability of self-intersection at any time between $t=\tau$ and $t=\tau_\phi$ is proportional to $\int_\tau^{\tau_\phi}\mathrm{d}t\lambda^{d-1}v/(Dt)^{d/2}$. The elastic collision time, $\tau=l/v$, has been set as the lower limit because, for $t\ll\tau$, the motion is ballistic and the probability of self-intersection is zero; the inelastic dephasing time τ_ϕ is the upper limit since for $t\gtrsim\tau_\phi$, the phase equality of A_ν and $A\bar{\nu}$ is lost. Notice that at high temperatures, where $\tau_\phi\approx\tau$, the quantum corrections are negligible. On the other hand, for low temperatures, where $\tau_\phi\gg\tau$, there is an appreciable increase in the probability, p, of returning to the initial point and consequently an appreciable correction, $\delta\sigma=\sigma-\sigma_0$, to the classical conductivity, σ_0, as a result of interference effects:

$$\delta\sigma\sim-p\sim1-\left(\frac{\tau_\phi}{\tau}\right)^{1/2}\approx-\left(\frac{\tau_\phi}{\tau}\right)^{1/2}=-\frac{L_\phi}{L_D}\quad\text{(1D systems)}\qquad[2a]$$

$$\delta\sigma\sim-p\sim-\frac{\lambda}{L_D}\ln\frac{\tau_\phi}{\tau}=-\frac{2\lambda}{L_D}\ln\frac{L_\phi}{L_D}\quad\text{(2D systems)}\qquad[2b]$$

$$\delta\sigma\sim-p\sim-\frac{\lambda^2}{L_D^2}\left[1-\left(\frac{\tau}{\tau_\phi}\right)^{1/2}\right]=-\frac{\lambda^2}{L_D^2}\left(1-\frac{L_D}{L_\phi}\right)\approx0\quad\text{(3D systems)}\qquad[2c]$$

The above formulas are valid when the disorder is weak, so that $|\delta\sigma|$ is considerably smaller than σ_0, since otherwise, one could end up with negative conductivity $\sigma=\sigma_0+\delta\sigma$. The condition $|\delta\sigma|\ll\sigma_0$ implies that $\lambda\ll L_D$, which in turn means that under the present conditions, $\delta\sigma$ is negligible for 3D systems. On the other hand, for 1D and 2D systems, $\delta\sigma$ can become appreciable when $L_\phi\gg L_D$; furthermore, since τ_ϕ is proportional to T^{-1} for $2D$ and $T^{-2/3}$ for 1D systems, and for very low temperatures, T, it follows that σ for $d=1$ and $d=2$ decreases with decreasing T. Such a T-dependence suggests an insulating behavior as $T\to0$ K, and consequently, the nonexistence of one- and two-dimensional metallic behavior. In other words, the possibility is raised that in 1D and 2D systems, as $L_\phi\to\infty$, the conductivity may become zero, no matter how weak the disorder is. The possibility of $\sigma\to0$ as $L_\phi\to\infty$ may be realized even in 3D systems when the disorder is strong enough, so that $\lambda\gtrsim L_D$. This question is taken up again in the next subsection, in which formulas [2a]–[2c] are generalized to the strong disorder case.

This subsection is concluded by pointing out that the presence of a magnetic field, $\boldsymbol{B}$, breaks the time-reversal symmetry, and as a result, breaks the equality $A_\nu=A\bar{\nu}$, and consequently, reduces the magnitude of $|\delta\sigma|$, and thus, tends to restore the classical behavior. Actually, the magnetic field adds a term $q\boldsymbol{A}\cdot\boldsymbol{v}$ to the Lagrangian, where q is the charge of carriers ($-e$ for electrons), and $\boldsymbol{A}$ is the vector potential such that $\boldsymbol{B}=\nabla\times\boldsymbol{A}$. So the closed path integrals, $A_\nu, A\bar{\nu}$, in the presence of $\boldsymbol{B}$, acquire an extra phase, that is $A_\nu=A_{\nu0}\exp(i\phi_\nu), A\bar{\nu}=A_{\nu0}\exp(-i\phi_\nu)$, where $\phi_\nu=q\phi_\nu/\hbar h$, and ϕ_ν is the magnetic flux through the closed path. As a result $A_\gamma A_{\bar{\gamma}}^*+A_{\bar{\gamma}}A_{\bar{\gamma}}^*=2\left|A_{\gamma0}\right|^2\cos\left(2\phi_\gamma\right)$, instead of $2\left|A_{\nu0}\right|^2$ as in the case $\boldsymbol{B}=0$. This implies a periodic variation of the conductance as a function of the applied magnetic field if ϕ_ν is a constant independent of ν. Indeed, this phenomenon has been observed in cylindrical tubes of cross section S with very thin walls, and with the magnetic field parallel to the axis of the tube. The configuration is such that $\phi_\nu=nBS$, where $n=1, 2, \ldots$. Because L_ϕ^2 is not much larger than S, the dominant contribution comes from $n=1$ and the

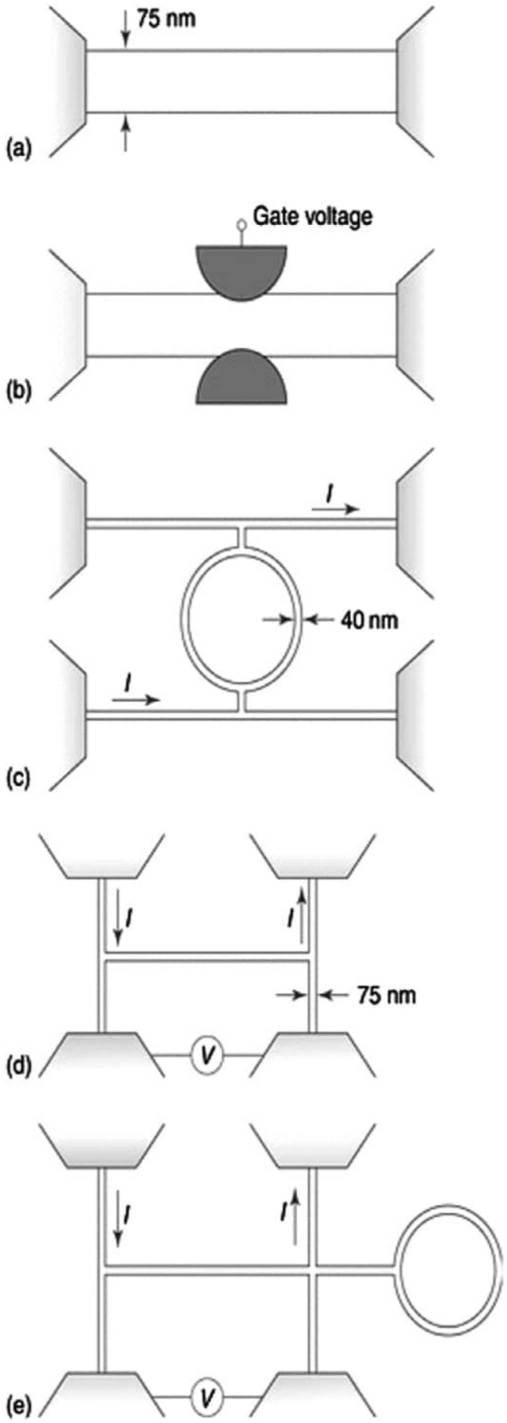

Figure 1 Various mesoscopic wires. (a) Simple quantum wire. (b) The gate voltage, V_G, creates a restriction which gradually, by changing V_G, leads to the 1D limit. (c) Four probe ring configuration which splits the current to the two semicircular paths. (d and e) Four probe configurations differing by the presence of the ring in case (e). The cross sections of the wires are $\sim 10^3$ nm^2, and their length $\sim\mu$m.

conductance, G, varies as $\delta G \sim \cos(2eBS/\hbar)$; this is the so-called $h/2e$ Aharonov–Bohm effect. In ring configurations, such as in Figure 1(c), where the conduction paths are between diametrically opposite points, the variation of the conductance, δG, is proportional to $\cos(eBS/\hbar)$; this is the so-called h/e Aharonov–Bohm effect. Notice that the Aharonov–Bohm effects can provide an operational definition of the length L_ϕ, since for lengths $L \gtrsim L_\phi$, the characteristic conductance oscillations gradually disappear. In thin wires, such as in Figures 1(d) and 1(e), the oscillatory magnetic field dependence of the conductance is more complicated as shown in Figure 2. It must be pointed out that these oscillations are reproducible (for the same system) and that their size is universal and $\sim e^2/\pi\hbar$. Furthermore, the conductance in the system of Figure 1(d) is different from that in the system of Figure 1(e),

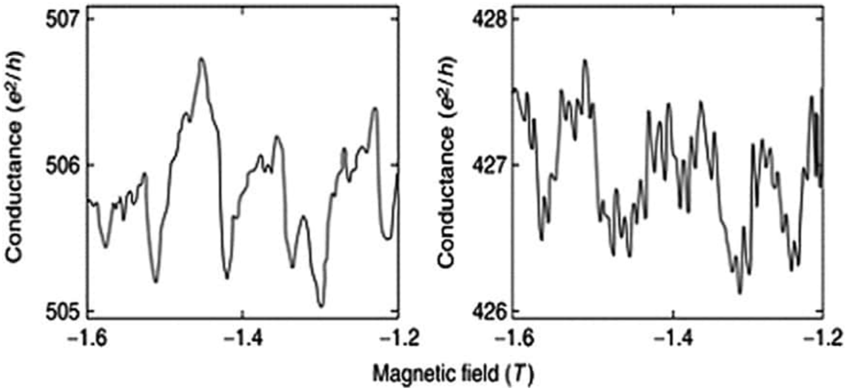

Figure 2 Electrical conductance versus applied magnetic field for the configuration of **Figure 1(d)** (left) and for that of **Figure 1(e)** (right). (Reproduced with permission from Webb, R.A., Washburn, S., 1988. Quantum interference fluctuations in disordered metals. Physics Today 41, 46. © American Institute of Physics.)

in spite of the classical current carrying paths being identical in the two configurations; this shows the wave nature of electronic propagation, the non-negligible role of interference effects associated with the existence of the ring in **Figure 1(e)**, and the nonlocal nature of the current–electric field relation.

Disorder, Density of States, and Wave Functions

Three-Dimensional Systems

In **Figure 3(a)**, the density of states (DOS) of a band associated with the *s*-level of identical atoms placed periodically in a simple cubic lattice is shown; the bandwidth is $12|V_2|$, where V_2 is the matrix element transferring electrons between two neighboring atoms. Disorder is introduced (**Figures 3(b)–3(d)**) by assuming that the *s*-levels of atoms are independent random variables possessing a Gaussian distribution of standard deviation w. The effects of the disorder are the following: (1) The analytical singularities shown in **Figure 3(a)** disappear. (2) The bandwidth increases as the band edges $\pm E_B^{(0)}$ move to new positions $\pm E_B$, where $E_B - E_B^{(0)} = c_1 w^2/|V_2|$ ($c_1 \approx 0.25$ in the present case). (3) Besides this widening of the band, tails in the DOS, $\rho(E)$, appear which are of exponential nature, $\rho(E) \sim \exp(-|E|/E_0)$ for $E_B \gtrapprox |E|$, where $E_0 = c_2 w^2/|V_2|$ ($c_2 \approx 0.12$ in the present case); these tails give rise to tails in the optical absorption of semiconductors for $\hbar\omega$ less than the gap (Urbach tails). (4) Two characteristic energies, $\pm E_c$, termed mobility edges, appear at which the nature of the eigenstates changes from propagating (or extended) to non-propagating (or localized, shaded regions in **Figures 3(b)–3(d)**). The localized eigenstates are trapped either around a cluster of atoms or around a single atom whose *s*-energy level is much different than the average. For low disorder ($w \lessapprox 2.5|V_2|$), the mobility edges follow the band edges closely, $|E_B| - |E_c| \sim w^4/|V_2|^3$. As the disorder increases, the mobility edges start moving toward the center of the band, and eventually they merge together making all eigenstates of the band localized; this is known as the Anderson transition (in the present case, this transition occurs when $w \simeq 6.2|V_2|$).

For weak disorders (e.g., **Figure 3(b)**), the states near the center of the band are quasi-Bloch characterized by the band index, j, the wave vector, $\boldsymbol{k}$, and the mean free path, which is connected to the phase $\phi(\mathbf{r})$ of the eigenfunction through the relation $\langle \exp[i\phi(r) - i\phi(0)] \rangle = \exp(-r/2l')$, where the symbol $\langle\rangle$ denotes the average value over all random variables. The mean free path l' satisfies eqn [1] with σ_i instead of σ_{ti}. As one moves from the center of the band toward the mobility edges, the amplitude of the eigenstates develops ever increasing fluctuations, both in magnitude and spatial extent up to a maximum length, ξ; for distances, r, such that $a \ll r \lessapprox \xi$, the eigenfunctions exhibit a statistically self-similar, fractal, behavior (a is the lattice spacing). As $|E| \to |E_c|$, ξ blows up, $\xi \to A/(|E_c| - |E|)^{\gamma}$, where γ has been estimated to be 1.58 (in the absence of a magnetic field) and 1.43 (in the presence of a magnetic field). On the localized sides of the spectrum, the eigenfunctions, $\psi(\mathbf{r})$, decay exponentially on the average, that is, $\langle|\psi(r)|\rangle_g \sim \exp(-r/L_c)$, as $r \to \infty$, where $\langle|\psi(r)|\rangle_g \equiv \exp[\langle \ln|\psi(r)|\rangle]$, and L_c is the so-called localization length. For distances, r, such that $a \ll r \lessapprox L_c$, the eigenfunctions exhibit fluctuations of statistically self-similar, fractal nature. As $|E| \to |E_c|$, L_c blows up: $L_c \to A'/(|E| - |E_c|)^{\gamma}$.

The contribution of a band to the conductivity, $\sigma(T)$, is given by $\sigma(T) = \int dE\sigma(E,T)(-\partial f/\partial E)$, where $f(E)$ is the Fermi–Dirac distribution, $\sigma(E,T)$ is proportional to the DOS $\rho(E)$ and the mobility $\mu(E)$ at E. The conductivity $\sigma(E,T)$ for a finite cube of length L at $T = 0$ K is given by

$$\sigma(E,0) = \frac{e^2}{\hbar}\left(\frac{0.066}{\xi} + \frac{A_1}{L}\right) \tag{3}$$

for E in the extended region (A_1 is ~ 0.05), $\sigma(E,0) \sim \exp(-2L/L_c)$ in the localized regime, and for $L_c \ll\ll L$. Actually, L, besides the length of the specimen, can be of any number of upper cut-off lengths such as L_ϕ or $R_B = (\hbar_c/eB)^{1/2}$, the cyclotron radius in the presence of a magnetic field, or $L_w = (D/\omega)^{1/2}$, the diffusion length in the presence of an AC field of frequency ω, etc. In the presence

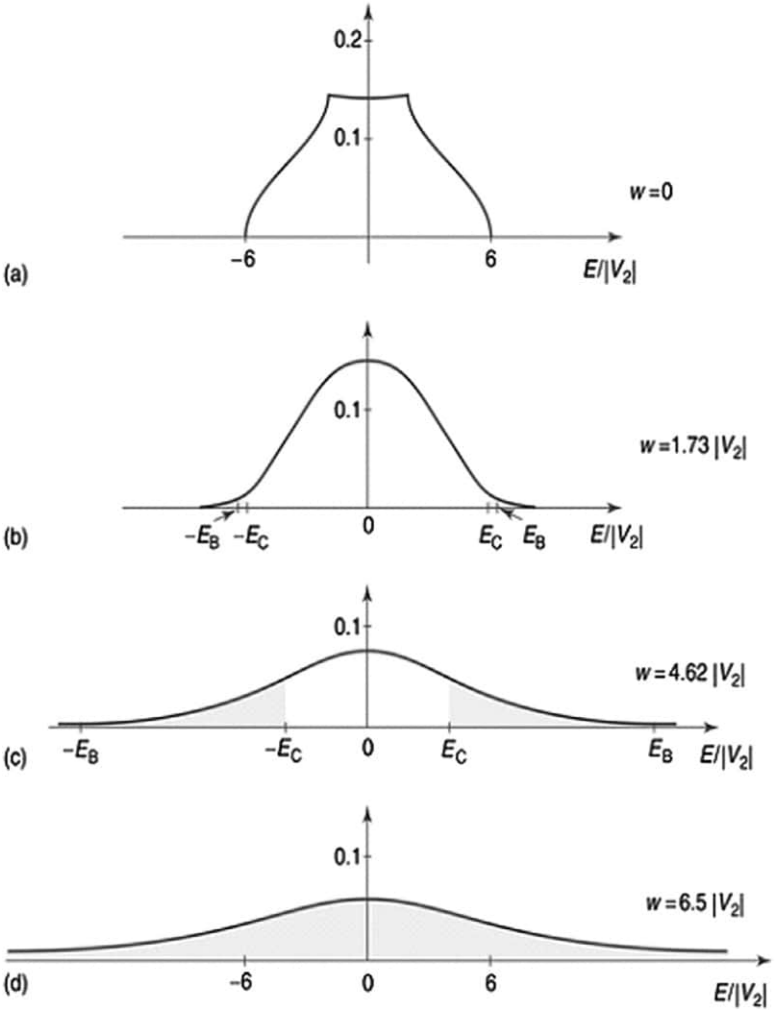

Figure 3 The density of states (DOS) of a band associated with the *s*-level of atoms placed periodically in a simple cubic lattice. The *s*-level of each atom is an independent random variable of Gaussian probability distribution with zero-average value and standard deviation equal to *w*, which goes from zero (case (a)) to 6.5 | V_2| (case (d)). The bandwidth at $w=0$ is 12 | V_2 | . Shaded regions correspond to localized eigenstates.

of all these upper cut-off lengths, L in the above formulas should be replaced by an effective length, $\tilde{L}$, probably of the form $\tilde{L}^{-2} = c_1L^{-2}+c_2L_{\phi}^{-2}+c_3L_{\omega}^{-2}+c_4R_{\mathrm{B}}^{-2}+\cdots$, where the weights c_i are of the order of unity.

Two-Dimensional Systems

2D systems of electrons trapped at the interface of Si/SiO$_2$ or GaAs/A1$_x$Ga$_{1-x}$As, are in a borderline as far as localization properties are concerned. In the absence of magnetic forces, all eigenstates are localized, no matter how weak the disorder is (exceptions do exist). In the presence of magnetic forces, the situation is qualitatively similar to that shown in Figures 3**(b)**–3**(d)** with an extremely narrow region of extended states at the center of the band. This picture has been employed to interpret the so-called integral quantum hall effect (IQHE), where as the Fermi level moves in the localized regime, the Hall resistance does not change until it enters the extended regime and a rather abrupt step is exhibited.

In the absence of magnetic forces, the localization length at E is related to the mean free path $l(E):L_c(E)\simeq 2.7l(E)\exp[S(E)l(E)/4]$, where $S(E)$ is the length of the line in $\boldsymbol{k}$-space satisfying the equation $E_k=E$. The conductivity $\sigma(E,0)$ is given by an approximate interpolation formula involving $\tilde{L}$ and L_c as well as a length $r_0\simeq\acute{c}l$. In the limit $\tilde{L}\ll L_c$,

$$\sigma \approx \sigma_0-\frac{e^2}{\pi^2\hbar}\ln\frac{\tilde{L}}{r_0} \qquad [4]$$

while for $L_c\ll\tilde{L}$, $\sigma=\left(2\sigma_0\tilde{L}/L_c\right)\exp\left(-2\tilde{L}/L_c\right)$. Equation [4] is similar to eqn [2b] and is known as a weak localization correction. For $\tilde{L}\simeq R_{\mathrm{B}}$, eqn [4] gives $\delta\sigma\equiv\sigma(B)-\sigma(0)=(e^2/2\pi^2\hbar)\ln[1+(eL_{\phi}^2B/1.78\hbar c)]$, that is a negative magnetoresistance, $\delta R/R\simeq-\delta\sigma/\sigma$, as

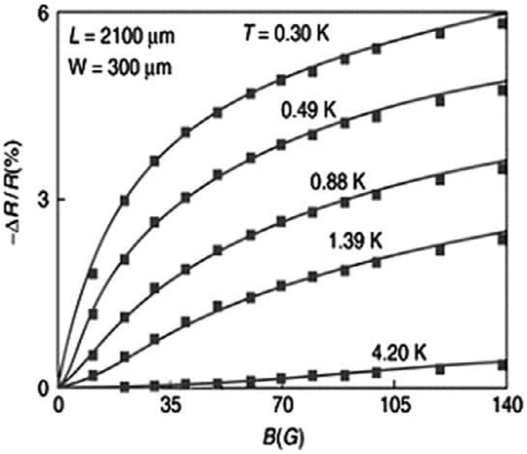

Figure 4 Experimental data (solid squares) and theoretical results (continuous lines) for the relative magnetoresistance $-\Delta R/R$, in a two-dimensional sample of electronic concentration $n = 1.6 \times 10^{11}$ cm^{-2} and mobility $\mu = 27000$ cm^2 V^{-1} s^{-1}. (Reproduced from Choi, K.K., *et al.*, 1987. Dephasing time and one-dimensional localization of two-dimensional electrons in GaAs/Al$_x$Ga$_{1-x}$As heterostructures. Physical Review B 36, 7751.)

shown in Figure 4. For $L \simeq L_\phi \sim T^{-1/2}$, the above formulas for the conductivity show that $\sigma \to 0$ as $T \to 0$ K. Notice, however, that electron–electron interactions produce a similar temperature dependence. Nevertheless, recent experiments at very low temperatures, in very clean interfaces GaAs/Al$_x$ Ga$_{1-x}$As or Si/SiO$_2$, have shown that $\sigma(T)$ stops decreasing and starts increasing with decreasing temperatures.

A second two-dimensional material of relevance here is graphene, a two-dimensional allotrope of carbon. The weak localization in graphene is more complicated than for the two-dimensional electron gas discussed above, as the Berry phase π in a closed trajectory can convert the weak localization to weak antilocalization, see Tikhonenko *et al.* (2009). For strong short-range disorder, strong localization is expected.

One-Dimensional and Quasi-One-Dimensional Systems

For 1D systems, such as the one shown in Figure 1**(b)**, all eigenstates are localized, no matter how small the disorder is (exceptions do exist); the localization length is proportional to the mean free path, $L_c = cl$, where the coefficient c equals 4 for not-so-strong a disorder. The conductivity, σ, is given by $\sigma = \left(e^2\tilde{L}/\pi\hbar\right)/\left[\exp\left(2\tilde{L}/L_c\right)-1\right]$. Thus in the limit $\tilde{L} \ll L_c$, $\sigma = \left(e^2L_c/2\pi\hbar\right)-\left(e^2\tilde{L}/2\pi\hbar\right)$; the first term gives the classical result $\sigma = 2e^2l/\pi\hbar$, since $L_c = 4l$, while the second is linear in $\tilde{L}$ as in eqn [2a]. Taking into account that the conductance G in 1D equals to $\sigma/\tilde{L}$ and that the geometrically averaged transmission coefficient, T, equals to $\exp\left(-2\tilde{L}/L_c\right)$, the formula for σ can be recast as $G = (e^2/\pi\hbar)T/(1-T)$. However, a direct calculation of G gives $G = (e^2/\pi\hbar)T$. This discrepancy is due to the fact that the first formula gives the conductance of the wire *per se* without taking into account the two contact resistances $2R_c = \pi\hbar/e^2$, and it requires a four-probe measurement for its determination; on the contrary, the result $G = (e^2/\pi\hbar)T$ is the outcome of a two-probe measurement and it includes the contact resistances, so that $1/G = 2R_c + R_w = (\pi\hbar/e^2) + (\pi\hbar/e^2)[(1-T)/T] = (\pi\hbar/e^2)/T$. In the presence of M coupled parallel to 1D channels in the limit where $\tilde{L} \ll l$ and $T \simeq 1$, the two-probe measurement will give $G = (e^2/\pi\hbar)M$ in agreement with the experimental results in Figure 5. The importance of the above formulas lies in their capability to be generalized to a multiterminal system; each terminal, i, is in contact with a reservoir at electrochemical potential $\mu_i = -|e|V_i$, and feeds the system with a net current I_i.

$$I_i = \frac{e^2}{\pi\hbar}\sum_i T_{i\leftarrow j}\left(V_i - V_j\right) \qquad [5]$$

Equation [5] is very useful in treating many mesoscopic systems, such as quantum dots exhibiting the phenomenon Coulomb blockade.

Level Statistics

Localized eigenstates belonging to neighboring energy levels of a very large system are, in general, far away from one another and hence, they have negligible overlap and as a result, negligible level repulsion. On the contrary, extended eigenstates always overlap, and thus always exhibit level repulsion. Hence, the probability distribution of the separation of two consecutive energy levels

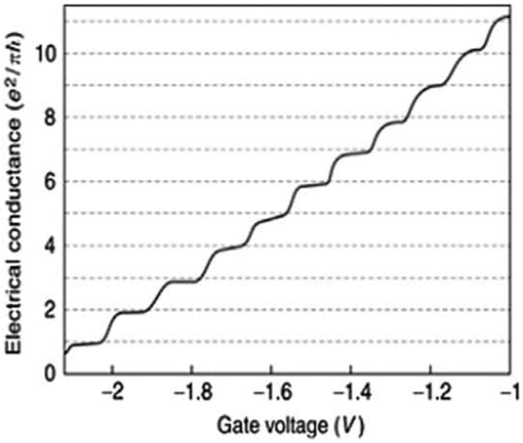

Figure 5 The electrical conductance of the configuration shown in **Figure 1(b)** vs. the gate voltage, V_g. The step-like dependence on V_g according to the formula $G=(e^2/\pi\hbar)M$, $M=1, 2, \ldots$, is shown. For $V_g<-2$ V, the 1D limit $M=1$ has been reached. (Reproduced from van Wees, B.J., *et al.*, 1988. Quantized conductance of point contacts in a two-dimensional electron gas. Physical Review Letters 60, 848.)

(which can be obtained numerically) is quite different for localized and extended eigenstates. This difference is an efficient way for determining regions of localized and extended states.

Transfer Matrix Techniques

A transfer matrix, t_{12}, propagates the general solution of the wave equation from point x_1 to point x_2 along 1D and quasi-1D systems. By multiplying transfer matrices, $t_{0L}=t_{12}t_{23}\ldots t_{NL}$, the solution at one end ($x=0$) can be connected to the solution at the other end ($x=L$). For disordered quasi-1D systems, the eigenvalues of t_{0L} come in pairs $(\mu_i, \overline{\mu}_i)$, such that $\mu_i \to \exp(L/L_{ci})$ and $\overline{\mu}_i \to \exp(-L/L_{ci})$ as $L\to\infty$, where $\pm L_{ci}^{-1}$ are the so-called Lyapunov exponents. The longest L_{ci}, L_c, determines the transmission coefficient, T, of the quasi-1D system of length L as $T=(-2L/L_c)$. By considering quasi-1D strips of M coupled channels arranged in a plane, or wires of square cross section with M^2 channels, $L_c(M)$ can be determined numerically; by employing a scaling property, the limit $M\to\infty$ can be taken, which determines L_c for the 2D case ($L_c=\lim L_c(M)$ as $M\to\infty$), and both L_c (when $L_c(M)$ converges as $M\to\infty$) and ξ (when $L_c(M)\sim M^2/\xi$) for the 3D case.

Scaling Approach

In the model considered in Figure 3, the only relevant parameter is the dimensionless ratio $w/|V_2|$. Then a cluster of p neighboring atoms of length $L_1=p^{1/d}a$ (where a is the lattice spacing) is examined and one may attempt to define a single dimensionless ratio, Q_1, which would play for the cluster the same role as $w/|V_2|$ plays for each atom. By repeating the rescaling n times, where n eventually approaches infinity, one finds that $Q_n=(\hbar/e^2)G$, where G is the conductance of a d-dimensional 'cube' of linear dimension $L=p^{n/d}a$. Since $Q_n\equiv Q(L)$ is the only relevant parameter, the occurrence or not of localization depends on whether $Q(L)$ tends to infinity or to zero respectively, as $L\to\infty$. To find this limit, the logarithmic derivative $\beta=d\ln Q/d\ln L$, which depends on the parameter Q, is defined. In the limit $Q\to\infty$, the classical behavior is approached, which gives that $Q\sim G\sim L^{d-2}$; hence $\beta\to d-2$, that is, negative for $d<2$ and positive for $d>2$. Assuming that β is a monotonically increasing function of Q, one can conclude that in the limit $L\to\infty$, $G\to 0$ for $d<2$. For $d>2$, $G\to\infty$ as $L\to\infty$ (in the region $\beta>0$), and $G\to 0$ as $L\to\infty$ (in the region $\beta<0$).

Potential Well Analogy

More sophisticated approximate analytical approaches for the calculation of σ permit one, under certain conditions, to map the localization question to that of an effective d-dimensional potential well (in the absence of magnetic forces) of depth $V_0(E)\sim[\sigma_0(E)]^{-1}[l(E)]^{-d}$ and linear extent $a\sim l(E)$. If this effective potential well sustains a bound state of decay length $L_c(E)$, then the states at E are localized with localization length equal to $L_c(E)$. If the effective potential well exhibits a resonance in the cross section at $E_r(E)$, then the eigenstates at E are extended with a length ξ given by $E_r(E)=\hbar^2/2m\xi^2(E)$, $\xi\gg l$. Using the fact that a potential well, no matter how shallow, always sustains a bound state for $d\ll 2$, while it must exceed a critical value of V_0a^2 to sustain a bound state for $d=3$, the basic picture presented before is recaptured, before including the expressions for the localization length in 1D and 2D systems. Furthermore, by employing the critical value of V_0a^2, one finds that localized states appear in 3D systems, when the product $lk \lesssim 0.85$ or $l/\lambda \lesssim 0.14$; this is the so-called Ioffe–Regel criterion.

Other Realizations

There is also evidence of Anderson localization of light, see Segev (2010), and cold atom gases, see Modugno (2010).

Further Reading

Abrahams E, Kravchenko S, and Sarachik MP (2001) Metallic behaviour and related phenomena in two dimensions. *Reviews of Modern Physics* 73: 251.
Anderson PW (1958) Absence of diffusion in certain random lattices. *Physical Review* 109: 1492.
Brandes T and Kettemann S (2003) *Anderson Localization and Its Ramifications*. Berlin: Springer.
Datta S (1995) *Electronic Transport in Mesoscopic Systems*. Cambridge: Cambridge University Press.
Economou EN (1983) *Green's Functions in Quantum Physics*, second ed Berlin: Springer.
Imry Y (2002) *Introduction to Mesoscopic Physics*, second ed Oxford: Oxford University Press.
Lifshits IM, Gredelkul SA, and Pastur LA (1998) *Introduction to the Theory of Disordered Systems*. New York: Wiley.
Modugno, G., 2010. Anderson localization in Bose–Einstein condensates. Reports on Progress in Physics 73, 102401.
Sakoda K (2004) *Optical Properties of Photonic Crystals*, second ed Berlin: Springer.
Segev M, Silberberg Y, and Christodoulides DN (2013) Anderson localization of light. *Nature Photonics* 7: 197–204.
Soukoulis CM (2001) *Photonic Crystals and Light Localization in the 21st Century*. Dordrecht: Kluwer.

Optical Properties of Insulators[☆]

Y Toyozawa[a] **and S Elsheikhi**[a,b], [a]University of Tokyo, Tokyo, Japan; [b]University of Benghazi, Benghazi, Libya

© 2016 Elsevier Inc. All rights reserved.

This is an update of Y. Toyozawa, S Elsheikhi, S. Elsheikhi, Optical Properties of Insulators, Reference Module in Materials Science and Materials Engineering, Elsevier, 2016, ISBN 9780128035818, https://doi.org/10.1016/B978-0-12-803581-8.01167-X.

Band Model and Optical Properties 779
Spin–Orbit Mott insulators 779
Topological Kondo Insulators 780
Exciton Model and the Optical Spectrum Near the Absorption Edge 780
Dipole–Dipole Interaction Contributing to the Translational Motion of an Exciton 781
The Effect of Spin and the Interplay of Exchange and Spin–Orbit Interactions 782
Participation of Phonons in the Electronic Excitation 782
Absorption Bands of Extrinsic Origin below the Band gap 784
Intrinsic Photoluminescence and Its Correlation with the Urbach Rule 784
Optical Excitation of Inner Shell Electrons 784
References 785
Further Reading 785

Band Model and Optical Properties

An insulator, also called a dielectric, is a material that resists the flow of electric current. An insulating material has atoms with tightly bonded valence electrons. These materials are used in parts of electrical equipment, also called insulators or insulation, intended to support or separate electrical conductors without passing current through themselves. Some materials such as glass, paper, or Teflon are very good electrical insulators.

Insulators are characterized, and contradistinguished from metals, by the existence of a forbidden energy band of finite width, a band gap, between the highest filled band (the valence band) and the lowest empty band (conduction band). The existence of a band gap can be confirmed by the optical transparency, that is, a vanishing absorption constant, up to a finite energy a little below the band gap ε_g, except in the lower energy region where the absorption due to lattice vibrations may arise.

The energy difference between the first absorption peak and the band gap ε_g, from where the continuous spectrum of band-to-band transitions starts, is due to the Coulomb binding energy between the excited electron in the conduction band and the positive hole left behind in the valence band, a typical example of 'configuration interaction' – a step beyond the one-electron approximation of the band model – or of 'final state interaction' in the optical spectrum. This bound electron–hole pair is called 'exciton,' which means a quantum of excitation.

Spin–Orbit Mott insulators

Mott insulators are the byproduct of strong electron correlations. Many of them are based on 3d transition metals (V2O3, cuprates, etc.) with narrow, half-filled bands. This situation favors insulating states via the Mott electron localization mechanism. In iridium oxides (iridates) 5d orbitals are more extended spatially than 3d orbitals leading to a strong reduction in the Coulombic repulsion. Furthermore taking into account the splitting of bands due to crystal field effects leads to the highest occupied electron band being far away from half-filling. Therefore taking into account both of the above effects one would expect the Mott states to be less favorable in the iridates. However, it turns out that many iridates are in fact insulators, and the currently accepted physical picture is that they realize a new form of insulator, so called spin-orbit Mott insulator (Kim *et al.*, 2008), where the spin–orbit interaction is essential in splitting the electron bands and opening up an insulating gap. The layered perovskite Sr_2IrO_4 is certainly the most studied case and is becoming a reference example. There are many questions that remain open about the properties of a SO-Mott insulator including its full spectrum of magnetic/electronic excitations which include magnons, spin-orbital excitons and interband transitions. Another key issue is the effect of charge doping. In many Mott insulators doping has been shown to bring about new exotic phases, such as high-temperature superconductivity in the layered cuprates.

Theoretical ideas (Wang and Senthil, 2011) have been put forward that high-temperature superconductivity of a different kind to the one in the cuprates could occur in doped pinorbits in Mott insulators, such as Sr_2IrO_4. Experimentally there are only a few reports (Ge *et al.*, 2011) so far on successful doping of Sr_2IrO_4 or Ba_2IrO_4. While these two materials apparently only differ in a local

---

[☆] *Change History*: August 2015. S. Elsheikhi added Abstract and Keywords, expanded text with additional review materials, updated the list of references, and provided an updated Change History section.

tilt of the IrO_6 octahedra, only the Ba one becomes metallic under pressure. Therefore the understanding of how to dope iridates and what happens in this case to SO Mott insulators is currently one of the priority challenges in the field.

Topological Kondo Insulators

Kondo insulators are a particularly simple type of a heavy fermion material where highly renormalized f-electrons, hybridized with conduction electrons, form a completely filled band of quasi particles with excitation gaps in the millivolt range. While these materials are strongly interacting electron systems, their excitations and their ground-states can be regarded as adiabatically connected to non-interacting band insulators.

It has been recently shown that most (time-reversal invariant) band-insulators can be classified by the topological structure of their ground-state wave functions (Fu *et al.*, 2007).

One of the dramatic consequences of this discovery is the existence of a new class of 'topological' band-insulators in which strong SO coupling leads to a ground-state that is topologically non-trivial, giving rise to gapless surface excitations. It has been recently proposed (Alexandrov *et al.*, 2013) that that the 'old' heavy fermion materials, longtime studied in the context of quantum criticality, represent indeed strong candidates to host new SO-driven topological phases, where the strong correlation may stabilize 'heavy' Dirac quasi particles.

Exciton Model and the Optical Spectrum Near the Absorption Edge

The relative motion of the electron and the positive hole with orbital radius larger than the interatomic distance can be described in the effective mass approximation, and if their effective masses m_e and m_h and hence the reduced mass $m_r=(m_e^{-1}+m_h^{-1})^{-1}$ are isotropic, the binding energies form a hydrogen-like series: $Bn=R\gamma_{ex}/n^2(n=1,2,\ldots)$, $R\gamma_{ex}=(m_r/m)(\varepsilon_0/\varepsilon_e)^2$ where $R\gamma=13.6$ eV is the Rydberg energy, m the electron mass in vacuum, $\grave{o}_0$ the dielectric constant of vacuum, and ε_e the electronic dielectric constant $\varepsilon(\omega)$ at $\hbar\omega\sim O(Ry_{ex})<<\varepsilon_g$ which is contributed only from electronic transitions except when B_n is as small as the phonon energies. The exciton radius is given by $a_n=a_{ex}n^2$, $a_{ex}=(m/m_r)(\varepsilon_e/\varepsilon_0)a_H$ where $a_H=0.052$ nm is the orbital radius of the electron in the ground state of a hydrogen atom. This Wannier model of an exciton is valid for insulators with relatively small bandgap (less than a few eV) and hence with large values of $(\varepsilon_e/\varepsilon_0)$ and a_{ex}/a_H of the order of 10. In insulators with a larger bandgap, the exciton radius is smaller than or comparable with the interatomic (intermolecular) distance, and the Frenkel model of intra-atomic (intramolecular) excitation (as in rare gas solids and aromatic molecular crystals), or the model of charge transfer to neighboring atoms (from an anion to neighboring cations as in ionic crystals) is more appropriate at least for an exciton in its ground state (n = 1).

In the Wannier model, the matrix element of the optical transition is given as a product of that for the inter band transition and the amplitude of the hydrogen-like wave function $F_n(\boldsymbol{R}_m)$ of the relative motion at the origin $\boldsymbol{R}_m=0$ (probability amplitude that the electron and the hole are found on the same site), which is non-vanishing only for the s-like states ($\ell=0$ where ℓ is the angular momentum). Thus, the intensity of the ns exciton line at $\hbar\omega=E_n=\varepsilon_g-B_n$ in the absorption spectrum is proportional to the square of the above amplitude, namely to $n^{-3}(n=1,2,\ldots)$ as known in the hydrogen atom. Noting that the product of the intensity and the number density of states $|dE_n/d_n|^{-1}\propto n^3$ is independent of n and hence of energy $\hbar\omega$, one finds that the absorption spectra consisting of higher exciton lines overlapping with each other (due to their finite widths) tends to a plateau of constant height as $n\to\infty$. It can also be shown analytically that this asymptotic height is in exact accordance with that of the continuous spectrum of band-to-band transition with the Coulomb-enhancement factor $(\hbar\omega-\varepsilon_g)^{-1/2}$ which cancels out the density of states effect $(\hbar\omega-\varepsilon_g)^{+1/2}$. The resulting absorption spectrum around the band edge is shown schematically in **Figure 1(a)** where the n-dependence of the width γ_n of discrete lines does not affect the above mentioned continuity.

In the case that the matrix element of band-to-band transition vanishes at the band edge ε_g due to a reason of symmetries of band wave functions, one has to consider its values above the edge. Correspondingly, one has to use the gradient $\nabla_R F_n(\boldsymbol{R}_m)$ of the

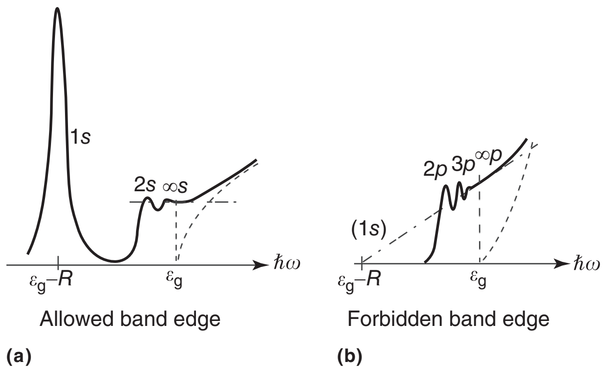

Allowed band edge

(a)

Forbidden band edge

(b)

Figure 1 The effect of Coulomb interaction on the fundamental absorption edge. The broken lines represent the interband absorption edge without the Coulomb effect. Reproduced with permission from Toyozawa, Y., 2003. Optical Processes in Solids. Cambridge: Cambridge University Press. © Cambridge University Press.

hydrogen wave function at the origin, which is nonvanishing only for the p-like states $\ell = 1$. Thus, np exciton lines ($n = 2, 3, \ldots$) appear at $\hbar\omega = E_n = \varepsilon_g - B_n$ of the absorption spectrum with intensities proportional to ($n^{-3} - n^{-5}$), with $n = 1$ missing. It can be shown, as before, that the broadened exciton lines asymptotically merge smoothly (inclusive of the finite slope extrapolating to the $n = 1$ position) to the continuous spectra of the Coulomb enhanced band-to-band transition around ϵ_g. The absorption spectra in this case of the forbidden band edge is schematically shown in **Figure 1(b)**. The intensity of the absorption spectra is smaller than that in the allowed band edge case mentioned above by a factor $(a/a_{ex})^2$, where a is the interatomic distance. Absorption spectra in alkali halides and cuprous oxides shown in **Figures 2(a)** and **2(b)** belong to the cases (a) and (b), respectively, of **Figure 1**.

Insulators with small band gaps become intrinsic semiconductors except at low temperatures. The existence of thermally excited free carriers causes a metallic screening of a long-range electron-hole Coulomb interaction into a short-range one, thus affecting the inter band optical spectra in such a way that the discrete exciton lines merge into the continuous spectra of inter band transition as temperature rises. Moreover, the free carriers give rise to their own optical absorption (intra band optical transition) in the infrared region.

Dipole–Dipole Interaction Contributing to the Translational Motion of an Exciton

As a composite particle consisting of an electron in the conduction band with effective mass m_e and a positive hole in the valence band with effective mass m_h, the exciton has effective mass $m_{ex} = m_c + m_h$ and translational kinetic energy $\hbar^2K^2/2m_{ex}$ near the bottom of the exciton band. Finite bandwidths of the valence, conduction, and hence exciton bands are due to the overlaps of wave functions between neighboring atoms.

The width of the exciton band is contributed by another type of interaction energy, the dipole–dipole interaction. Take the Frenkel exciton in which this interaction predominates, and consider how the intra-atomic excitation at the nth atom is transferred to the mth site. Consider the state $\Phi_n = \phi_p(r_n - R_n)\prod_{\ell(\neq n)}\phi_s(r_\ell - \boldsymbol{R}_\ell)$ where all atoms are in the s-like ground state except the nth atom which is in a p-like excited state. The excitation transfers to the mth atom through the matrix element

$$H_{nm} \equiv (\Phi_n, H\Phi_m) = \int\int \mathrm{d}r_n \mathrm{d}r_m \phi_p(\boldsymbol{r}_n - \boldsymbol{R}_n)\phi_s(\boldsymbol{r}_m - \boldsymbol{R}_m) \times v_{nm}\phi_s(\boldsymbol{r}_n - \boldsymbol{R}_n)\phi_p(\boldsymbol{r}_m - \boldsymbol{R}_m)$$

where H denotes the total Hamiltonian of the system consisting of N atoms with one electron per atom. Note that due to the orthogonality of atomic wave functions ϕ_s and ϕ_p and the neglect of overlaps of wave functions between different atoms, only

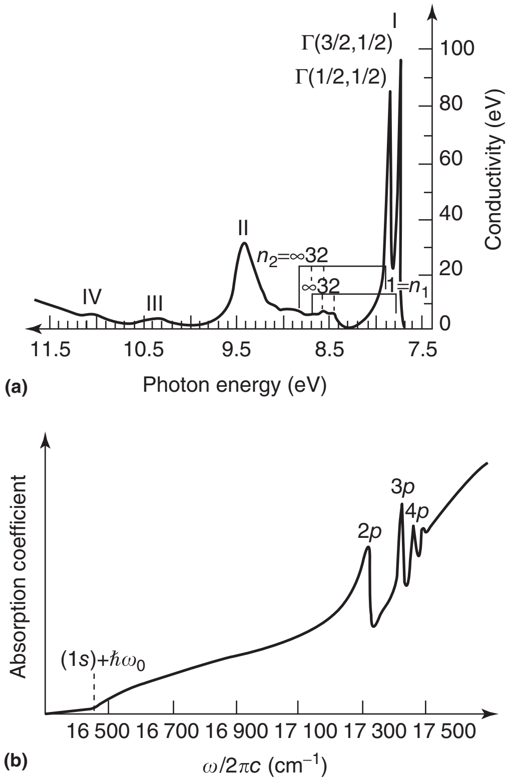

Figure 2 (a) Fundamental absorption spectrum of KCl crystal 10 K. Reproduced with permission from Tomiki, T., 1969. Journal of the Physical Society of Japan 26, 738. (b) The yellow series excitons at the fundamental absorption edge of Cu_2O crystal at 4.2 K. Reproduced from Nikitine, S., Grun, J.B., Sieskind, M.J., 1960. Journal of Physics and Chemistry of Solids 17, 296, with permission from Elsevier.

the Coulomb interaction $v_{nm} = e^2/4\pi\varepsilon_0 |r_n - r_m|$ remains among the total Hamiltonian H. Due to the same reasons, one can take only the lowest dipole–dipole terms in the multipole expansion of the long-range Coulomb interaction, namely $H_{nm} = (\boldsymbol{m}^2/\boldsymbol{R}_{nm}^3 - 3(m \cdot R_{nm})^2/R_{nm}^5)/4\pi\varepsilon_0 \equiv D(\boldsymbol{R}_{nm})$, where $\boldsymbol{m} \equiv \int \mathrm{d}r\phi_{\mathrm{p}}(r)(-er)\phi_{\mathrm{s}}(r)$ is the transition dipole moment. The Hamiltonian H is diagonalized with the wave function of the Frenkel exciton given by $\Psi_{\mathrm{K}}^{(e)} = N^{-1/2}\sum_n \exp(\mathrm{i}\boldsymbol{K} \cdot \boldsymbol{R}_n)\Phi_n$, namely $H_{KK'} = \delta_{KK'}E_K^{(e)}$, with diagonal energy being $E_K^{(e)} = (\Psi_K^{(e)}, H\Psi_K^{(e)}) = E^{(\mathrm{g})} + \varepsilon + D_K$ where $E^{(\mathrm{g})}$ is the ground-state energy of the entire system, $\varepsilon = \varepsilon_{\mathrm{p}} - \varepsilon_{\mathrm{s}}$ the atomic excitation energy in the crystal and $D_K \equiv \sum_{n(\neq 0)} D(R_n) \exp(-\mathrm{i}\mathrm{K} \cdot R_n)$. Thus, the dipole–dipole interaction contributes to the $\boldsymbol{K}$-dependence of the exciton energy.

One must be careful in summing up the long-range dipole-dipole interaction $D(\boldsymbol{R}_n) \propto R_n^{-3}$ because of the slow convergence, especially when K is much smaller than the reciprocal of the interatomic distance a. Dividing the summation into the inner region $R_{\mathrm{n}} < R_{\mathrm{c}}$ and the outer region $R_{\mathrm{n}} > R_{\mathrm{c}}$ where R_{c} is chosen so as $a \ll R_{\mathrm{c}} \ll K^{-1}$, and replacing the latter summation by integration, one obtains $D_K \equiv \sum_{n(\neq 0)}^{R_n} {}^{<R}{}_c D(R_n) - (N_0/3\varepsilon_0)[m^2 - 3(\boldsymbol{m} \cdot \boldsymbol{K})^2/K^2]$, which is singular at $\boldsymbol{K} = 0$ since it tends to different values depending on the direction in which K approaches 0. In a typical case that each atom is situated in the environment of cubic symmetry, the first summation vanishes. One has triply degenerate atomic p-states p_x, p_y, and p_z so that one has a 3 × 3 matrix of the K-dependent part: $(D_K')_{ij} = -(N_0\mu^2/3\varepsilon_0)[\delta_{ij} - 3K_iK_j/2]$. It is diagonalized by taking the coordinate system with the z-axis along the direction of k. In fact, one obtains a longitudinal wave $\boldsymbol{m}||\boldsymbol{K}$ with energy $(D_K')_{33} = (2/3)(N_0\mu^2/\varepsilon_0)$, and two transverse waves $\boldsymbol{m} \perp \boldsymbol{K}$ with energy $(D_K')_{11} = (D_K')_{22} = -(1/3)(N_0\mu^2/\varepsilon_0)$. Their energy difference, $N_0\mu^2/\varepsilon_0$, agrees with $\hbar$ times the longitudinal–transverse splitting $D_{1\mathrm{t}} = \omega_1 - \omega_{\mathrm{t}}$ of polarization waves which originates from the depolarizing field. Under the coexistence of many oscillators, ε_0, is to be replaced by the residual dielectric constant ε_j' which is contributed by the oscillators other than the one (j) under consideration. Note that this dielectric constant is different from ε_e, which governed the electron–hole relative motion.

The Effect of Spin and the Interplay of Exchange and Spin–Orbit Interactions

To be more realistic, one must consider the electron spin in addition to its orbital motion. Each atomic state characterized by (n,l,m) is doubly degenerate with up and down spins, $s = \pm 1/2$. The simplest closed shell atom consists of two ns electrons with configuration $(ns)^2$, and its optically allowed excited state consists of the configuration (ns) (np). The two electrons in the excited state can have either antiparallel (as in the ground state) or parallel spins, with energy difference $2\Delta_{\mathrm{exch}}(>0)$ where $\Delta_{\mathrm{exch}} = \int\int \mathrm{d}\boldsymbol{r}\mathrm{d}\boldsymbol{r}'\phi_p(\boldsymbol{r})\phi_s(\boldsymbol{r})(e^2/4\pi\varepsilon_0)|\boldsymbol{r} - \boldsymbol{r}'|^{-1}\phi_s(\boldsymbol{r}')\phi_p(\boldsymbol{r}')$ is the exchange energy. The singlet state is above the triplet state because one is concerned with the e–h (instead of the e–e) system. The optical transition to the triplet excited state is forbidden because of its total spin state $S = 1$ $(S \equiv s_1 + s_2)$ different from that of the ground state $S = 0$. Noting that Δ_{exch} is the special case $(n = m)$ of H_{nm} in the preceding section and that the dipole–dipole interactions vanish for the triplet state but are to be multiplied by 2 for the singlet state (because two electrons participate), one can incorporate the exchange and dipolar energy into a single form, $2\delta_{S,0}|F_n(0)|^2[\Delta_{\mathrm{exch}} + D_k]$, where multiplication by the squared amplitude of the wave function of e–h relative motion at the origin is required only where the interaction remains in the Wannier exciton. The total energy of the Wannier exciton with the principal quantum number n, spin quantum number S, and translational wave vector K is then given by $E_{n,S}(\boldsymbol{K}) = \varepsilon_{\mathrm{g}} - B_n + \hbar^2K^2/2m_{\mathrm{ex}} + 2\delta_{S,0}|F_n(0)|^2[\Delta_{\mathrm{exch}} + D_K]$. Another term to be considered is the spin–orbit interaction $H_{\mathrm{s.o.}} = \lambda\boldsymbol{l} \cdot \boldsymbol{s}$. One can diagonalize it together with the total angular momentum $\boldsymbol{j} = \boldsymbol{l} + \boldsymbol{s}$ by making use of the identity $2l \cdot s = (j^2 - l^2 - s^2) = j(j+1) - 1.2 - (1/2) \cdot (3/2)$. Thus, the atomic state with $\ell = 1$ are split into $j = 3/2$ and $j = 1/2$ with spin–orbit energies $+\lambda/3$ and-$\lambda/3$, respectively. According to this quasi-atomic model, the valence band of alkali halide which consists of p-orbitals of halogen is split to the upper $(j_{\mathrm{v}} = 3/2)$ and lower $(j_{\mathrm{v}} = 1/2)$ branches while the conduction band consisting of s-orbital of alkali is not split ($j_{\mathrm{v}} = 1/2$ only). Hence, the absorption edge of band-to-band transition appears at $\varepsilon_{\mathrm{g}} - \lambda/3$ and $\varepsilon_{\mathrm{g}} + 2\lambda/3$ with the intensity ratio 2:1 reflecting the degeneracy $2j_{\mathrm{v}} + 1$. This j–j coupling scheme is no more valid for exciton lines because of finite exchange-dipolar interaction, $\Delta_{\mathrm{n}} \equiv 2\delta_{S,0}|F_n(0)|^2[\Delta_{\mathrm{exch}} + D_0]$ mentioned above. As $\Delta_{\mathrm{n}}/\lambda$ increases the intensity ratio decreases, tending to 0 since the lower exciton state tends to a pure spin-triplet $(S = 1)$ which is optically forbidden (L–S coupling). In materials with small spin–orbit coupling constants as are realized with light atom constituents, the triplet exciton is optically almost forbidden. The continuous change from the j–j to L–S and again to j–j coupling schemes has been observed in the alloy system $\mathrm{CuCl}_{1-x}\mathrm{Br}_x$ in which λ varies continuously from negative to positive values with Δ_{exch} staying always small as composition x varies from 0 to 1, as is shown in Figure 3. The L–S coupling scheme is realized only around the composition x where λ changes sign, the j–j coupling scheme with intensity ratio 1:2 and 2:1 is observed on its left and right sides, respectively.

The quasi-atomic model mentioned above has been improved to the crystalline field model in which the symmetry of the crystal is fully taken into account. The anisotropic exchange energy introduced thereby as an independent material parameter has in fact been observed in some materials.

Participation of Phonons in the Electronic Excitation

The wave vector of a photon with energy enough for the electronic excitation across a band gap of 10 eV is $\sim 10^8$ m^{-1} which is much smaller than the reciprocal lattice $\sim 10^{10}$ m^{-1}. One can thus assume that the wave vector (pseudo or crystal momentum divided by $\hbar$) is conserved in the optical transition, namely $\boldsymbol{k}_{\mathrm{c}} - \boldsymbol{k}_{\mathrm{v}} = 0$ or $\boldsymbol{K}_{\mathrm{ex}} = 0$. In addition, it has been tacitly assumed so far that the bottom of the conduction band and the top of the valence band are at the origin, $\boldsymbol{k}_{\mathrm{c}}^m = 0$ and $\boldsymbol{k}_{\mathrm{v}}^m = 0$, which, however, is not always the case. If one or both of them are not at the origin, the absorption edge of band-to band transition appears around the indirect gap $\varepsilon_{\mathrm{g}} = \varepsilon_{\mathrm{c}}(k_{\mathrm{c}}^m) - \varepsilon_{\mathrm{v}}(k_{\mathrm{v}}^m)$, but with the participation of phonons with wave vector $\boldsymbol{K} = \boldsymbol{k}_{\mathrm{id}}$ and $\omega_{\mathrm{s}}(\boldsymbol{k})$ to satisfy the conservation of the wave

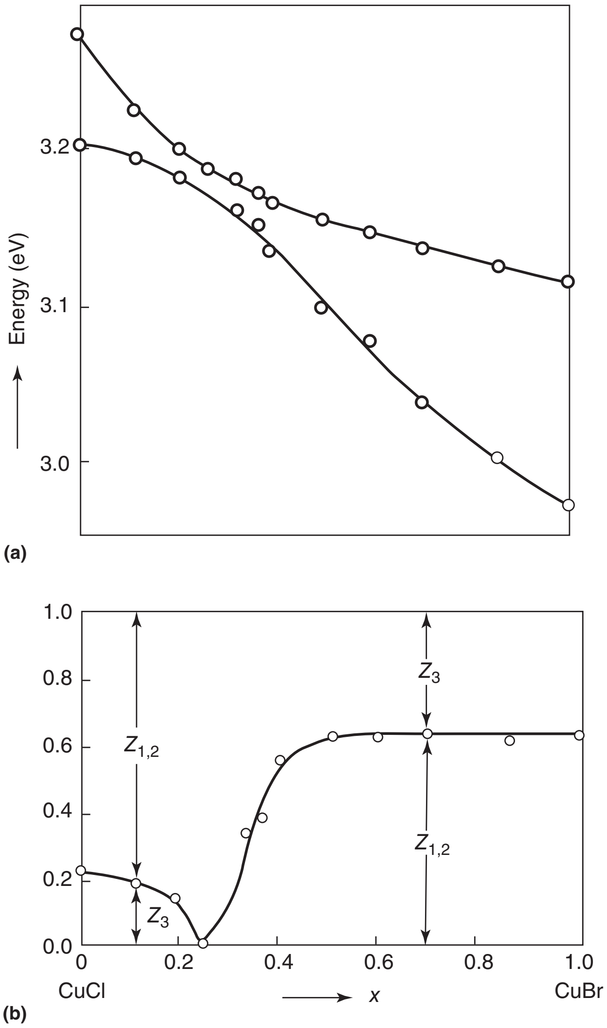

Figure 3 (a) Observed energies, and (b) intensity ratio of $Z_{1,\,2}$ and Z_3 excitons in mixed crystal: $\text{CuCl}_{1-x}\text{Br}_x$ as functions of the concentration *x*. Reproduced with permission from Kato, Y., Yu, C.I., Goto, T., 1970. Journal of the Physical Society of Japan 28, 104.

vector. Hence, the exact absorption edge appears at $\varepsilon_g - B_n' \pm \hbar\omega_s(\pm k_{id})$ according as a phonon is absorbed or emitted, where B_1' is the binding energy of the exciton formed at $K = k_{id}$ and $\omega_s(k)$ is the circular frequency of the sth mode lattice vibration with wave vector K. The absorption spectrum rises with the square root of energy from each edge reflecting the density of states of the exciton band, with the intensity proportional to the square of the indirect exciton–phonon interaction matrix element and the temperature dependent factor $\bar{n}_s$ and $\bar{n}_s + 1$ for absorption and emission of a phonon, respectively, where $\bar{n}_s = \left[\exp\{\hbar\omega_s(\pm k_{id})/k_B T\} - 1\right]^{-1}$ is the thermal average of the number of phonons. Such indirect exciton edges are observed in germanium and silicon ($\boldsymbol{k}_c^m \neq 0$), silver halides ($\boldsymbol{k}_v^m \neq 0$), and thallous halides ($0 \neq \boldsymbol{k}_c^m \neq \boldsymbol{k}_v^m \neq 0$). Similar phonon-mediated exciton edge arises even when $k_c^m = k_v^m = 0$, provided the exciton transition matrix element vanishes at $K_{ex} = 0$, as is realized with the 1*s* exciton in Cu_2O (see Figure 2(**b**)).

The widths γ of direct exciton absorption peaks, introduced phenomenologically as damping constants of oscillators, are microscopically attributed to the rate τ^{-1} of scattering of the optically created exciton $\boldsymbol{K}_{ex} = 0$ to $\boldsymbol{K}_{ex} \neq 0$ by absorbing or emitting a wave number conserving phonon, which is of the same origin as the indirect exciton transition mentioned above. An indirect exciton absorption band is, therefore, supposed to be the tail part of the broadened peaks of a direct exciton. As a second-order process, the $\boldsymbol{K} = 0$ exciton is the intermediate state which is resonant and non-resonant to the incident photon in the direct and indirect transitions, respectively.

In fact, one can incorporate both aspects in a unified expression for a multicomponent exciton absorption spectrum. For a multiband scheme of excitons with energy $E_{\lambda K}$, one can write the spectral line shape as the sum of asymmetric Lorentzians: $F(E) = \sum_\lambda \bar{f}_\lambda \pi^{-1}\left[\bar{\Gamma}_{\lambda 0} + \bar{A}_\lambda\left(E - \bar{E}_{\lambda 0}\right)\right] / \left[\left(E - \bar{E}_{\lambda 0}\right)^2 + \bar{\Gamma}_{\lambda 0}^2\right]$ which is in accordance with the result of the classical model of damped oscillators $\left(\hbar\gamma_\lambda \leftrightarrow \bar{\Gamma}_{\lambda 0}\right)$ for the direct exciton peaks, except for the asymmetry terms with $\bar{A}_\lambda$ (the degree of asymmetry) in the numerator, and the fact that the quantities crowned with bars are the renormalized (in the phonon field) quantities dependent on a variable E, the photon energy (though not shown explicitly). The shape of the indirect absorption edge is contained implicitly in the functional form of the width $\overline{\Gamma}_{\lambda 0}(E)$, which is proportional to the combined density of states of excitons and phonons in the final state of indirect transition. The asymmetry term $\overline{A}_{\lambda}\left(E - \overline{E}_{\lambda_0}\right)$ in the numerator originates from the interference of the direct exciton peak λ with its background continuum of indirect exciton transitions to other exciton bands $\lambda'(\neq\lambda)$ – a solid-state version of the Fano effect well known in atomic spectroscopy. Such multicomponent asymmetric Lorentzian peaks have, in fact, been observed as shown in Figure 2**(b)**. The asymmetry here is due to the interference of the direct exciton peak with the background continuum of phonon-assisted optical transition to the 1*s* exciton band to which the direct transition is forbidden. Phonon sidebands of the direct exciton peak (as are observed in some ionic crystals) are also contained implicitly in the functional form of $\overline{\Gamma}_{\lambda 0}(E)$.

Absorption Bands of Extrinsic Origin below the Band gap

While (chemically) pure and (physically) perfect insulators are transparent in the spectral region below the first exciton peak (in the direct band gap case), impure or imperfect insulators have various absorption bands due to the electronic transitions at impurity (guest) atoms or point defects of a lattice. The localized electron(s) is subject to a strong interaction with phonons (stronger than the mobile exciton is) particularly when its orbital radius is comparable with the lattice constant, and once excited, it causes significant displacements of nearby atoms to their new equilibrium positions (lattice relaxation). From this 'relaxed excited state,' the electron returns to the ground state emitting a photon (luminescence) or non-radiatively. The peak of the emission band is displaced from that of the absorption band (Stokes shift), both bands being more like Gaussian shapes as can be described by the configuration coordinate model. Examples are Tl-like atoms in alkali halides which are known as phosphorescence centers of high efficiency and the F-centers (an electron captured at an anion vacancy) in alkali halides which are subject to a variety of photochemical reactions resulting in the color changes of the crystal.

The impurities and imperfections sometimes give rise to bound excitons as can be confirmed by the optical absorption bands just below the intrinsic exciton absorption peaks. For example, the α and β absorption bands in alkali halides correspond to exciton formation around an anion vacancy and an F-center, respectively. Shallow bound excitons, as are realized at donors in direct gap semiconductors (such as CdS), have large oscillator strengths of the order of the number of host atoms covered by their extended wave functions, the effect known as 'giant oscillator strength.'

Intrinsic Photoluminescence and Its Correlation with the Urbach Rule

The optically created exciton will be thermalized around the bottom of the exciton band from where it will emit a photon with energy smaller (in the indirect case) than or equal (in the direct case) to the absorption edge. In the direct case, the exciton is gradually converted into a photon during its thermalization through the polariton bottleneck. In any case, the emission spectrum from this 'mobile exciton' is a sharp line.

In some materials, the exciton becomes self-trapped by the lattice distortion caused by itself. The emission spectrum of this selftrapped exciton is a broad Gaussian with a significant Stokes shift from the exciton absorption peak (direct gap case) or edge (indirect case), similar to the localized center mentioned before. In the configuration coordinate model, the self-trapped state is separated by a potential barrier from the free or mobile state, and which of them is more stable depends on whether the exciton–phonon coupling constant g, a material constant, is greater or smaller than a critical value g_c.

In contrast to different behaviors of the emission spectrum in the weak and strong coupling cases, the line shape of the exciton absorption band varies continuously as a function of g. For instance, the low energy tail of the exciton absorption spectrum in many insulators has been found to obey the Urbach rule: $\exp[-\sigma(E_0' - E)/k_B T]$ except at low temperatures where E_0' is the convergence point of semi-logarithmically plotted line contours at various temperatures T, and the steepness coefficient σ is the material constant. This exponential tail has been ascribed to momentarily localized exciton states under a fluctuating field of lattice vibrations, with σ being given by a constant (different values for direct and indirect gap cases) times g^{-1}. While empirical values of σ and g derived therefrom are rather evenly distributed over a variety of insulating materials, the observed emission spectrum of the exciton is distinctly different according as g is smaller (→ sharp line almost resonant to the absorption peak in the direct gap case) or larger (→ broadband with a significant Stokes shift) than the critical value g_c in accordance with the theoretical prediction from the observed value of σ.

Optical Excitation of Inner Shell Electrons

Synchrotron radiation has facilitated the spectroscopic studies over a vast energy range extending up to the X-ray, corresponding to electronic transitions from different inner atomic states (much deeper than the outermost orbital state responsible for the valence band) to the empty conduction band. Below the ionization continuum of each inner state, there appear exciton lines as in the valence band excitation. However, the exciton here can be viewed as a localized excitation since the width of the energy band formed by the inner atomic state is negligibly small. Moreover, the positive hole in the inner state is subject to decay processes such as (1) radiative recombination, and (2) Auger recombination with an electron in the upper filled band (inclusive of the valence band) which are the main causes of a lifetime broadening of the exciton line, except in shallow inner bands (next below the valence band)

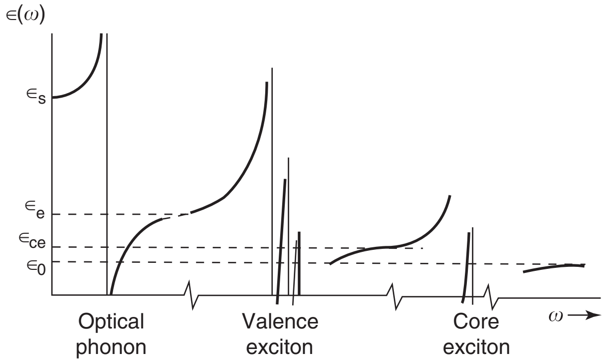

Figure 4 Typical dispersion of dielectric constant υ(ω) of an ionic crystal. At frequencies far higher than those of optical phonons but a little below the bandgap, dispersion appears due to excitons associated with the valence band hole. At even higher frequencies, dispersions appear due to excitons associated with the inner shell holes. Reproduced with permission from Toyozawa, Y., 2003. Optical Processes in Solids. Cambridge: Cambridge University Press. © Cambridge University Press.

in some materials in which (1) is insignificant and (2) is impossible because of insufficient energy of electronic recombination against the ionization of valence electrons. Whether the optical spectrum belongs to the band edge allowed or forbidden type, depends on the symmetry of the inner atomic state. The electron–hole exchange energy with its possible interplay with spin–orbit interaction appears here in the same way as before.

Typical dielectric dispersion in the entire ω-region of an ionic crystal is shown schematically in Figure 4, in the idealistic situation of no damping (vanishing line width).

References

Alexandrov V, Dzero M, and Coleman P (2013) Cubic Topological Kondo Insulators. *Phys. Rev.Lett.* 111: , 226403.
Fu L, Kane CL, and Mele EJ (2007) Topological insulators in three dimensions. *Phys. Rev.Lett.* 98: , 106803.
Ge M, Qi TF, Korneta OB, et al. (2011) Lattice-driven magnetoresistivity and metal-insulator transition in single-layered iridates. *Phys. Rev. B* 84: , 100402 (R).
Kim BJ, Jin H, Moon SJ, et al. (2008) Novel J eff = 1/2 mott state induced by relativistic spin-orbit coupling in Sr2Ir04. *Phys. Rev. Lett.* 101: , 076402.
Wang Fa and Senthil T (2011) Twisted Hubbard Model for Sr2Ir04: Magnetism and possible high temperature superconductivity. *Phys. Rev. Lett.* 106: , 136402.

Further Reading

Ashcroft NW and Mermin ND (1976) *Solid State Physics*. Philadelphia: Saunders College.
Broude VL, Rashba EI, and Sheka EF (1985) *Spectroscopy of Molecular Excitons*. Berlin: Springer.
Cho K (1979) Internal structure of excitons. In: Cho K (ed.) *Excitons*, pp. 15–53. Berlin: Springer. (Chapter 2).
Elliott RJ (1963) Theory of excitons – I (optical spectra of excitons). In: Kuper CG and Whitfield GD (eds.) *Polarons and Excitons*, pp. 269–293. Oliver and Boyd: Edinburgh, London.
Fowler WB (1968) *Physics of Color Centers*. New York: Academic Press.
Haken H (1963) Theory of excitons – II (polaron effect of excitons). In: Kuper CG and Whitfield GD (eds.) *Polarons and Excitons*, pp. 295–324. Oliver and Boyd: Edinburgh, London.
Knox RS (1953) Theory of excitons. In: Seitz F and Turnbull A (eds.) *Solid State Physics (Suppl).* vol. 5. New York: Academic Press.
Kotani A and Toyozawa Y (1979) Theoretical aspects of inner level spectroscopy. In: Kunz C (ed.) *Synchrotron Radiation, Technique and Applications*, pp. 169–229. Berlin: Springer.
Rashba EI and Sturge MD (1982) *Excitons*. Amsterdam: North-Holland.
Song KS and Williams RT (1993) *Self-Trapped Excitons*. Berlin: Springer.
Toyozawa Y (2003) *Optical Processes in Solids*. Cambridge: Cambridge University Press.
Ueta M, Kanzaki H, Kobayashi K, Toyozawa Y, and Hanamura E (1986) *Excitonic Processes in Solids*. Berlin: Springer.

Ruthenates☆

J-S Zhou[a], **JB Goodenough**[a], **and B Raveau**[b], [a]University of Texas at Austin, Austin, TX, USA; [b]Laboratoire de Cristallographie, ISMRA, Caen, France

© 2016 Elsevier Inc. All rights reserved.

This is an update of J.-S. Zhou, J.B. Goodenough, B. Raveau, Ruthenates, Reference Module in Materials Science and Materials Engineering, Elsevier, 2016, ISBN 9780128035818,https://doi.org/10.1016/B978-0-12-803581-8.01135-8.

Introduction 786
Ruthenate Perovskites and Post-Perovskites 786
Ruddlesden–Popper (RP) Ruthenates 792
Ruthenate Hexagonal Perovskite Polytypes 796
Pyrochlore Ruthenates 799
The Quasi-Two-Dimensional Ruthenates 801
The Quasi-One-Dimensional Ruthenates Ln_3RuO_7 803
Ruthenium as a Substituting Element in Oxides 803
References 805
Further Reading 806

Introduction

The structural properties of the ruthenium oxides are mainly governed by the strong octahedral-site preference of the Ru(IV) ion; in the Ru-O phase diagram, RuO_2 is the only stable oxide. However, in the presence of counter cations that lower the energy of the top of the O-2 p bands, as in the double perovskite structure of $A_2(Ln(III)Ru(V))O_6$, the Ru(V) oxidation state can be realized. Moreover, in doped ruthenates, both the Ru(V)/Ru(IV) and the Ru(IV)/Ru(III) redox couples may be accessed.

The electronic properties of the ruthenium oxides are governed by the occupancy and orbital ordering of the Ru-4d states. Strong bonding of the Ru to oxygen results in an octahedral-site low-spin Ru(IV) : t^4e^0 (Mullikan notation) outer-electron configuration in orbitals of 4d symmetry; the xy, (yz± izx) t orbitals π-bond to the oxygen and the (x^2-y^2), $(3z^2-r^2)$ e orbitals σ-bond. The cubic-field splitting of the t and e energies quenches the orbital angular momentum of quantum number L having $m_l=\pm 2$, but not that having $m_l=\pm 1$ of the (yz ± izx) orbitals. Therefore, a strong intraatomic spin–orbit coupling $\lambda(\mathbf{L}\bullet\mathbf{S})$ of a localized Ru(IV) : t^4e° configuration is not quenched where the site symmetry orders the minority-spin 4d electron into the (yz ± izx) orbitals. On the other hand, strong Ru-O π bonding creates Ru-O-Ru interatomic interactions that can be strong enough to render the 4d electrons itinerant, which suppresses the localized spin–orbit coupling. The $ARuO_3$ perovskites with A = Ca, Sr, Ba, and Pb illustrate a crossover from localized to itinerant 4d electronic behavior and the influence of strong spin–orbit coupling where the intraatomic 4d electron–electron interactions compete with the interatomic Ru-O-Ru interactions between the 4d electrons. In the rutile structure of RuO_2, orbital ordering fills the *c*-axis Ru(IV)-4d orbitals, which elongates the *c* axis; and the Ru-O-Ru π-bond interactions give metallic conductivity associated with a half-filled π^* band. RuO_2 is a catalyst for the oxygen-evolution reaction of an air electrode in an electrochemical cell.

The ruthenates containing other cations can be classified according to their structure into seven categories: perovskites, post-perovskites, Ruddlesden–Popper phases, hexagonal perovskite polytypes, pyrochlores, quasi-2D $SrRu_2O_6$, and 1D Ln_3RuO_7.

Ruthenate Perovskites and Post-Perovskites

The ideal AMO_3 perovskite structure, **Figure 3(a)**, consists of a cubic framework of corner-shared $MO_{6/2}$ octahedra with a larger A cation in the center of the framework. The $MO_{6/2}$ octahedra of the MO_3 framework may be rotated cooperatively to enhance the A-O bonding if the size of the A cation gives a geometric tolerance factor $t=(A-O)/[\sqrt{2}(B-O)]<1$; (A−O) and (M−O) are the equilibrium bond lengths. This structural flexibility allows stabilization of the perovskite system $Sr_{1-x}Ca_xRuO_3$ having a $t<1$ in which the cooperative rotations of the $RuO_{6/2}$ octahedra are primarily around the cubic [1 − 1 0] axis, **Figure 1(b)**, to give an orthorhombic structure; in space group *Pnma*, the rotation axis is the orthorhombic *a* axis. However, the site rotations also induce site distortions (Zhou and Goodenough, 2005, 2008) in which the O-Ru-O bond lengths within the (001) planes alternate short and long; and as t approaches t = 1, the Ru-O-Ru bond angle subtending the rotation axis decreases from 90° to render the orthorhombic structure pseudocubic in $SrRuO_3$ (Lee *et al.*, 2013). For $t>1$, the 180° Ru-O-Ru bonds of the cubic structure are stretched until, in $BaRuO_3$, an hexagonal polytype structure is stabilized. In addition, the O-2 P_π orbitals of the cubic framework σ-bond with the A cations, and the competition between A-O σ bonding and Ru-O π bonding with the same O-2 P_π orbital modifies the strength of the Ru-O-Ru interactions as well as the bending from 180° of the Ru-O-Ru interactions. The competition

---

☆*Change History*: July 2015. J.-S. Zhou and J.B. Goodenough have rewritten the introduction and updated most sections in the article to reflect new developments in this field in 2015.

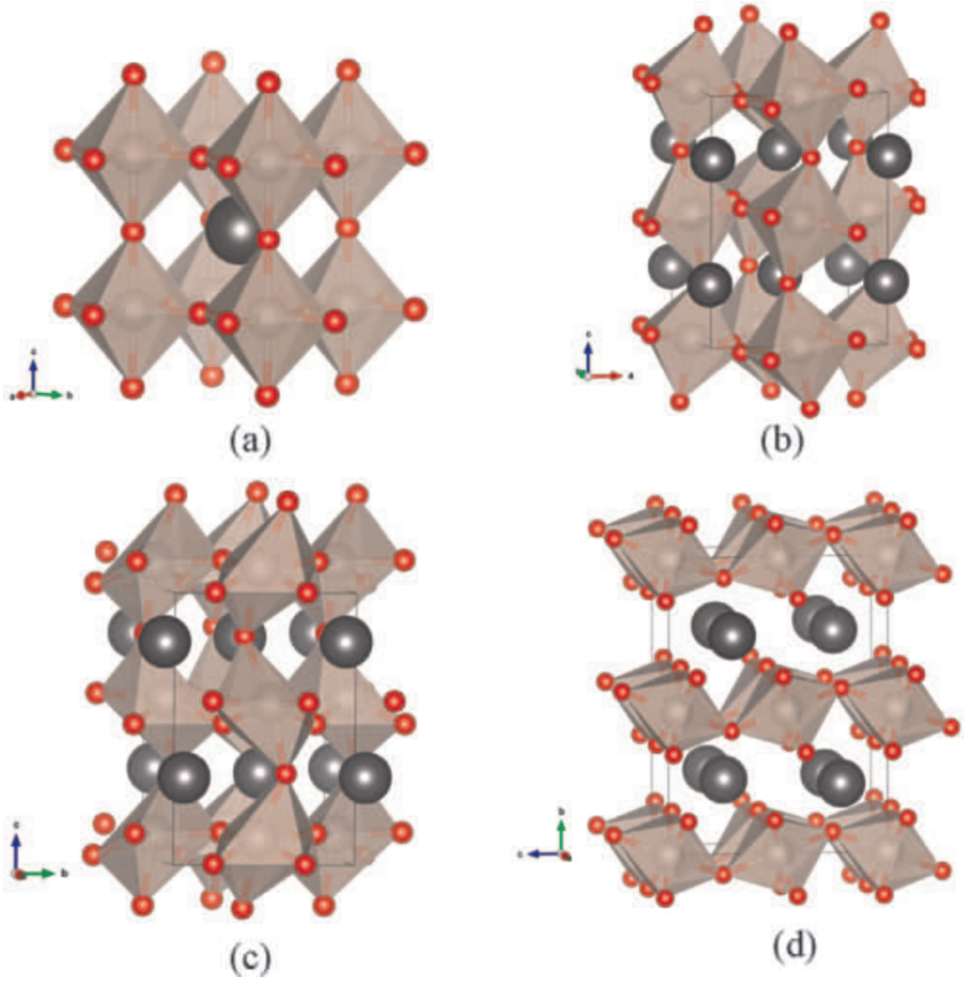

(a) (b) (c) (d)

Figure 1 Crystal structures of three perovskites: (a) *Pm-3 m*, (b) *Pnma*, (c) *Pbn/2*, and (d) post-perovskite *Cmcm*.

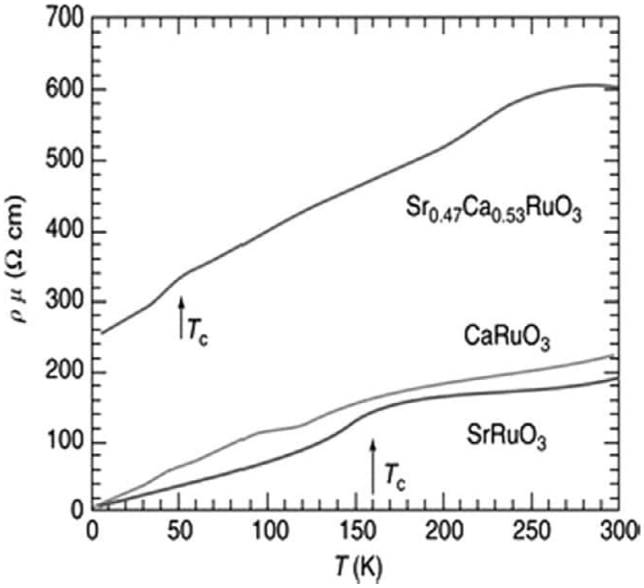

Figure 2 Resistivity vs. temperature for Sr$_{1-x}$Ca$_x$MnO$_3$ perovskites ($X = 0, 0.53, 1$). Reprinted with permission from Cao, G., McCall, S., Shepard, M., Crow, J.E., Guertin, R.P., 1997. Physical Review B 56, 321–329. © American Physical Society.

between intraatomic $\lambda(\mathbf{L}\bullet\mathbf{S})$ interactions and interatomic interactions of the minority-spin electrons is nearly balanced in $SrRuO_3$, but the interatomic Ru-O-Ru interactions are weakened relative to the intraatomic $\lambda(\mathbf{L}\bullet\mathbf{S})$ interactions in $CaRuO_3$. The transport properties of $CaRuO_3$ and $SrRuO_3$ perovskites are similar; they both exhibit bad-metal behavior (**Figure 2**) as a result of interatomic Ru-O-Ru interactions. Nevertheless, the magnetic properties of these oxides are very different: $SrRuO_3$ is ferromagnetic with a T_c of 165 K, whereas $CaRuO_3$ has been described for a long time as a paramagnetic metal involving antiferromagnetic interactions and is now believed by several authors to be nearly ferromagnetic, as supported by NMR observations. The different behavior of $SrRuO_3$ compared to $CaRuO_3$ is also observed; its $\rho(T)$ curve (**Figure 2**) shows a Fisher–Langer type anomaly at T_c. The highly correlated nature of the 4d-electron band in these perovskites is also confirmed by studies of their solid solution $Sr_{1-x}Ca_xRuO_3$. The peculiar magnetic behavior of $CaRuO_3$, and the fact that it sits on the verge of a ferromagnetic instability is also supported by studies, which show that the substitution of Ti(IV) for Ru(IV) in this phase induces ferromagnetism at a low Ti level (2%).

By taking advantage of the high-pressure technique developed in the area of geosciences, the perovskite structure of $BaRuO_3$ can be stabilized. At atmosphere pressure, $BaRuO_3$ with $t > 1$ crystallizes in the 9 R polytype. High pressure is needed to reduce the tolerance factor t at the synthesis temperature. The high-pressure cubic phase of $BaRuO_3$ (**Figure 1** **(a)**) stabilized at 18 GPa, is quenchable to ambient condition (Jin *et al.*, 2008). Two series of solid solutions $Ca_{1-x}Sr_xRuO_3$ and $Sr_{1-x}Ba_xRuO_3$ make it possible to map out T_c versus the averaged A cation size of the perovskite ruthenates. The maximum T_c is found for $SrRuO_3$. However, the size variance effect introduced in the solid solution alters the curve of T_c versus $\langle r_A\rangle$. After correcting for the size variance effect, the data of T_c^0 versus $\langle r_A\rangle$ can be fit with a parabolic curve. The new phase diagram of **Figure 3(a)** reveals important information: (1) T_c is extremely sensitive to the change of lattice parameters; (2) the optimum T_c occurs in the $ARuO_3$ with $t \approx 1$; (3) while T_c decreases on both sides of the dome, the temperature dependence of magnetization gives distinctly different behavior as T_c is approached in the paramagnetic phase. All samples in the $Sr_{1-x}Ba_xRuO_3$ series show a typical Curie–Weiss behavior of $\chi(T)$ (**Figure 3(c)**). In contrast, the concave curvature of inverse paramagnetic susceptibility versus T in $Ca_{1-x}Sr_xRuO_3$ (**Figure 3(b)**) as T_c is approached from higher temperatures, resembles that of a Griffiths phase. This observation indicates that the suppression of magnetism in Ca rich $Ca_{1-x}Sr_xRuO_3$ is caused by a dilution with a non-magnetic phase. The local distortion at Ru sites in $CaRuO_3$ supports preserving the orbital angular momentum and $\lambda(\mathbf{L}\bullet\mathbf{S})$ orders the possible moment parallel to the c axis, which is orthogonal to the magnetic easy axis found in $SrRuO_3$. The strong intraatomic spin–orbit coupling competes with the interatomic spin-spin interaction, which results in a non-magnetic ground state. A non-linear curve of inverse χ versus T of $CaRuO_3$ supports the argument of a strong spin–orbit coupling. In $Sr_{1-x}Ba_xRuO_3$, T_c decreases with x due to a bandwidth broadening. Suppression of T_c in $BaRuO_3$ can be made under high pressure; the ferromagnetic transition ends up with a quantum critical point (Zhou *et al.*, 2008).

$PbRuO_3$ prepared at ambient pressure has an oxygen deficient pyrochlore structure. Perovskite $PbRuO_3$ and the solid solution $Sr_{1-x}Pb_xRuO_3$ have been added into the *Pnma* perovskite family by using high-pressure synthesis. The paramagnetic metal $PbRuO_3$ undergoes an unusual metal–metal transition at $T_s \approx 90$ K (Cheng *et al.*, 2009) to the orthorhombic *Imma* phase in which an orbital ordering has been detected by neutron diffraction (Kimber *et al.*, 2009). The ferromagnetism of $SrRuO_3$ is progressively suppressed with Pb substitution in $Sr_{1-x}Pb_xRuO_3$ (**Figure 4**). On the $PbRuO_3$ side, the structural transition at T_s vanishes sharply with Sr substitution. T_s of $PbRuO_3$ can also be suppressed by applying a pressure of 5 GPa (Kusmartseva, *et al.*, 2013). At 30 GPa and room temperature, pressure induces a first-order structural transition to a highly distorted perovskite structure with the *Pbn/2* space group (**Figure 1(c)**). A hybridization between the Ru:4d and Pb: 6s/6p leads to an unprecedentedly short Pb-Ru bond length in the perovskite structure (Cheng *et al.*, 2013).

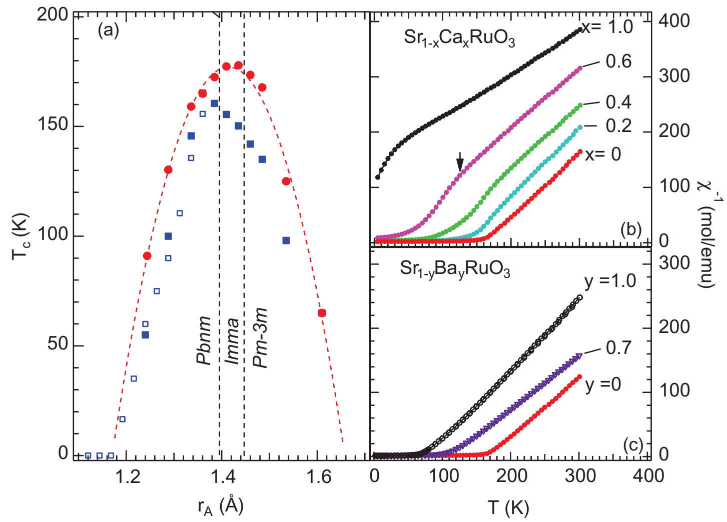

Figure 3 (a) Phase diagram of Curie temperature T_c vs. the averaged ionic size at A site; the symbol of solid circles represents T_c^0 after correcting for the size variance effect; the symbol of solid squares represent T_c of the samples synthesized under high pressure; the symbol of hollow squares: T_c of the samples made at ambient pressure. (b,c) Temperature dependence of inverse magnetic susceptibility for $Sr_{1-x}Ca_xRuO_3$ and $Sr_{1-y}Ba_yRuO_3$. After Cheng, J.-G., Zhou, J.-S., Goodenough, J.B., 2013. Proceedings of National Academy of Sciences USA 110, 13312–13315.

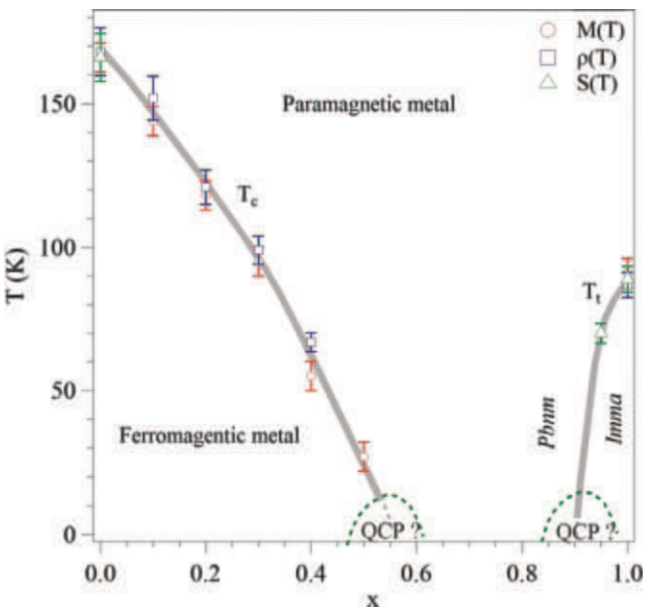

Figure 4 Phase diagram of transition temperature vs. Pb concentration x in $Sr_{1-x}Pb_xRuO_3$. M(T) stands for the result from the magnetization measurement; ρ(T) from the resistivity measurement; S(T) from thermoelectric power measurement. QCP stands for quantum critical point. After Cheng, J.-G., Zhou, J.-S., Goodenough, J.B., 2010. Physical Review B 81, 134412.

The family of A-site ordered perovskites $CaCu_3M_4O_{12}$ (M = Ti, Cr, Mn, Ge, Sn, Ru, Ir, Pt) has grown quickly helped by high-pressure synthesis. Most of the A-site ordered perovskites are insulators. Metallic $CaCu_3Ru_4O_{12}$ crystallizes in a cubic structure with $a \approx 7.42$ Å and *Im-3* (No.204) space group, which consists of 3D corner-shared RuO_6 octahedra and Cu in co-planar sites. Due to the strong hybridization between Cu:3d and Ru : 4 d, $CaCu_3Ru_4O_{12}$ has become well-known for its heavy Fermion behavior and a Kondo-like effect. The valence on the Cu site can be changed by substituting Na, La, or their combination for Ca. Figure 5 shows the relationship between the lattice parameters and the formal valence on the Cu site in $ACu_3Ru_4O_{12}$ (A = Na, Ca, La).

The perovskite $CaRuO_3$ can be converted into the post-perovskite structure (Figure 1**(d)**) at P = 23 GPa and 980° C (Kojitani *et al.*, 2007). A post-perovskite structure consists of layered octahedra in which the $RuO_{6/2}$ octahdra are corner-shared on the *c* axis and edge-shared on the *a* axis. The post-perovskite $CaRuO_3$ is an insulator and exhibits a complicated temperature dependence of magnetic susceptibility; a broad hump at 450 K indicates a quasi-1D magnetic coupling and the Néel temperature occurs at 270 K. Like the perovskite $CaRuO_3$, the local structural distortion at Ru sites orders the 4d-orbital occupancy so as to preserve the orbital angular momentum.

Besides, the Ru(IV) perovskites, a series of perovskites containing Ru(V) with the generic formulation A_2LnRuO_6 have been reported for A = Ca, Sr, or Ba and Ln = La, Nd, Y, Ho, Lu, or Er. The crystal symmetry of these phases is often monoclinic (P21/na, with $a \sim b \sim a_c\sqrt{2}$, $c \sim 2a_c$, $\beta \sim 90.2$) and more rarely cubic (Fm3m $a \sim 2a_c$). All these oxides exhibit a 1:1 ordering between Ru(V) and Ln(III) or Ca(II) on the octahedral sites. Thus, in this structural type (Figure 6), one $RuO_{6/2}$ octahedron alternates with one $LnO_{6/2}$ octahedron along the three crystallographic directions. In all these compounds, the Ru(V) lattice is antiferromagnetic at low temperature with T_N values ranging from 26 to 40 K. Most of them exhibit an A-type antiferromagnetic structure at low temperature (Figure 7**(a)**), except Ba_2LaRuO_6, which belongs to the third type (Figure 7**(b)**). Moreover, the lanthanide cations may be involved

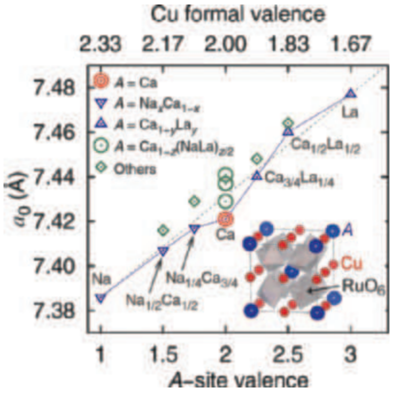

Figure 5 The phase diagram of lattice parameter vs. the valance on Cu and the A site of $ACu_3Ru_4O_{12}$. After Tanaka, S., Takatsu, H., Yonezawa, S., Maeno, Y., 2009. Physical Review B 80, 035113; inset: schematic drawing of the crystal structure.

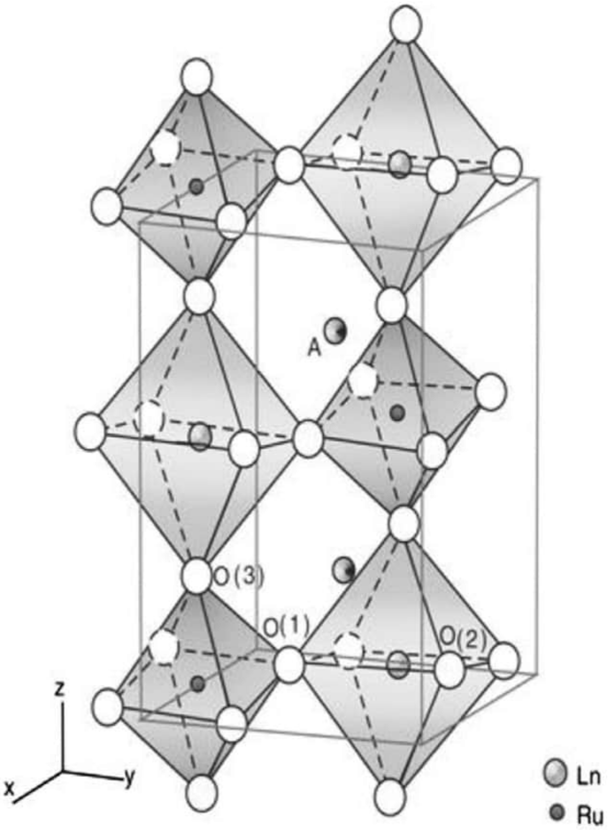

Figure 6 Crystal structure of the ordered perovskites A_2LnRuO_6. After Battle, P.D., Jones, C.W., Studer, F., 1991. Journal of Solid State Chemistry 90, 302–312.

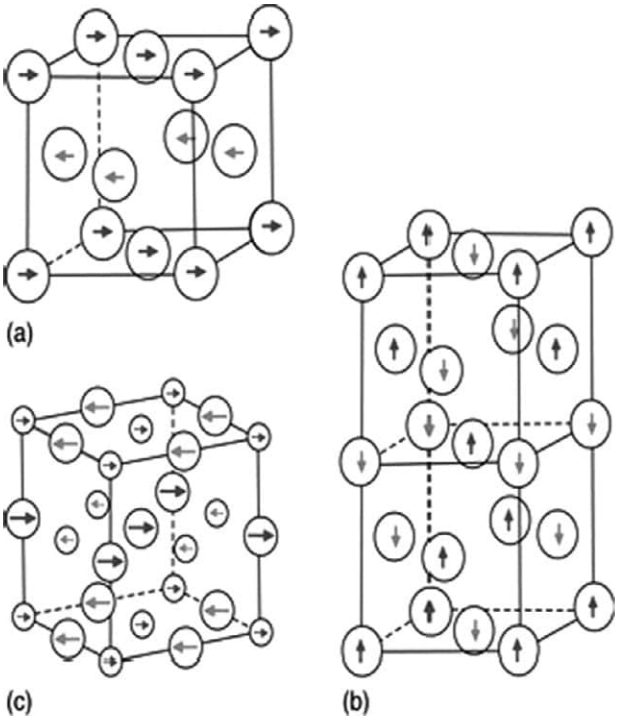

Figure 7 Antiferromagnetic structures of: (a) A-type A_2LnRuO_6 (Ln=Pr–Ln), (b) third-type Ba_2LaRuO_6, and (c) of Sr_2ErRuO_6 with two sublattices, Ru^{5+} (small circles) and Er^{3+} (large circles). After Battle, P.D., Jones, C.W., Studer, F., 1991. Journal of Solid State Chemistry 90, 302–312.

in the long-range antiferromagnetic order depending on their nature, as is illustrated, for example, for Sr_2ErRuO_6 (**Figure 7(c)**), which consists of two interpenetrating A-type antiferromagnetic sublattices on Ru(V) and Er^{3+} sites, respectively. High-temperature magnetic susceptibility measurements, carried out on Ba_2YRuO_6, Ba_2LuRuO_6, and Sr_2LuRuO_6, suggest that the Ru(V) d-electrons may be itinerant rather than localized. Such a feature may result from a direct overlap of the neighboring Ru orbitals via Ru-O-O-Ru interactions. Perovskites A_2MRuO_6 involving a disorder of ruthenium and of a transition element M over the same octahedral sites have also been synthesized for M = Ni, Co, Fe, Cu. This site disorder is indeed the case for the compounds $Sr_2MRuO_6\,(M=Fe, Co)$, $BaLaMRuO_6\,(M=Ni, Co)$, and $SrLaCoRuO_6$, all of which exhibit a monoclinic symmetry, either $I2/c$ or $I2/m$ or $P2_1/n$, with $a \sim b \sim a_c\sqrt{2}c \sim 2a_c$, and $\beta{\sim}90.1^\circ$, except $BaLaNiRuO_6$ which is triclinic. These oxides exhibit a complex magnetic behavior, because two alioelectronic cations are distributed randomly over the octahedral sites. This situation often results in a spin-glass behavior as shown from the magnetic susceptibility curves of $BaLaCoRuO_6$ (**Figure 8(a)**), and of Sr_2FeRuO_6 (**Figure 8(b)**) which exhibit a cusp around 50 and 40 K, respectively. This behavior is significantly different from that of the double perovskites $BaLaZnRuO_6$ and $BaLaMgRuO_6$, which exhibit an A-type antiferromagnetic ordering at low temperature; the Zn^{2+} and Mg^{2+} ions have no net spin.

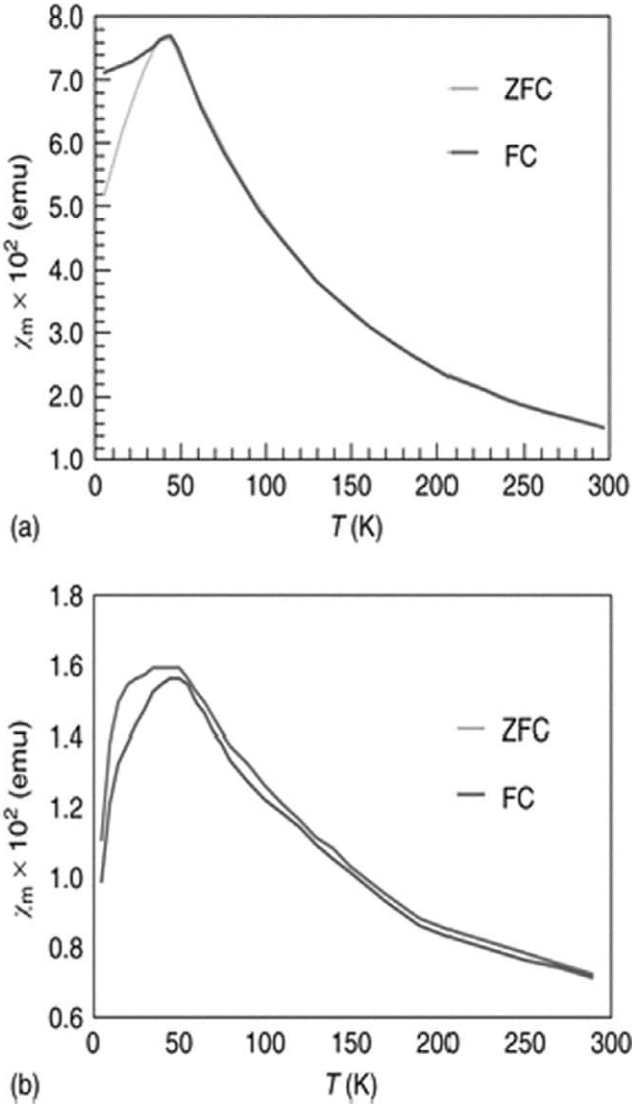

Figure 8 Magnetic susceptibility vs. temperature of (a) $BaLaCoRuO_6$ and (b) Sr_2FeRuO_6. (b) After Battle, P.D., Jones, C.W., Studer, F., 1991. Journal of Solid State Chemistry 90, 302–312.

Ruddlesden–Popper (RP) Ruthenates

The RP phases $A_{n+1}Ru_nO_{3n+1}$ with A = Ca or Sr have single CaO or SrO rock-salt phases separating n layers of $ARuO_3$ perovskite structure. These structures allow monitoring of the evolution of electronic properties with the thickness of the perovskite layers. Ca_2RuO_4 and Sr_2RuO_4 represent the first member n = 1 of the RP series; their structure (**Figure 9**(**a**)) consists of single perovskite layers '$SrRuO_3$' or '$CaRuO_3$' intergrown with single rock-salt layers 'SrO' or 'CaO.' In this structure, the Ru-O-Ru interactions are 2D rather than 3D, which reduces the π^* bandwidth associated with interatomic Ru-O-Ru interactions. These quasi-two-dimensional ruthenates exhibit different physical properties due to the different distortions of their structure. Ca_2RuO_4 exhibits a metal--insulator (MI) transition at $T_{MI}=357$ K (**Figure 10**(**a**)). This Mott insulator is antiferromagnetic below $T_N=110$ K. In contrast, Sr_2RuO_4 is a p-wave superconductor below $T_c=1.5$ K (Mackenzie and Maeno, 2003) and is paramagnetic above this temperature with a tendency toward ferromagnetism. A study of the system $Ca_{2-x}Sr_xRuO_3$ has shown that the system changes successively with decreasing x: from $x=2$ where it is a nonmagnetic Fermi liquid, to a ferromagnetic metal for $x = 0.5$, to an antiferromagnetically correlated metal for $0.2 < x < 0.5$, and to an antiferromagnetic insulator for $x < 0.2$. Neutron powder diffraction studies demonstrate that the magnetic state changes are associated with structural transitions as shown in the phase diagram of **Figure 11**. Based on structural distortions, a magnetic phase diagram can be calculated that demonstrates the rotation and the tilting of the RuO_6 octahedra being responsible for the ferro- and antiferromagnetism, respectively. The substitution of La^{3+} for Ca^{2+} in Ca_2RuO_4 shows that doping with very small amounts of lanthanum lowers the MI transition dramatically down to 100 K and, simultaneously, the resistivity at low temperature can be decreased by several orders of magnitude (**Figure 10**(**a**)). Concomitantly, ferromagnetism is induced in the material (**Figure 10**(**b**)). The Curie temperature can reach up to 100 K, but it remains lower than T_{MI}, suggesting that the metal–insulator transition is not driven by the magnetic instability. These results emphasize a competition between ferromagnetism and antiferromagnetism in these ruthenates with a π^* band 2/3 filled.

The $n = 2$ members of the RP series, $Ca_3Ru_2O_7$ and $Sr_3Ru_2O_7$, consist of double perovskite layers '$A_2Ru_2O_6$' intergrown with single rock-salt 'SrO or CaO' layers (**Figure 9** (**b**)). $Ca_3Ru_2O_7$ exhibits, like Ca_2RuO_4, a metal-to-insulator transition as T decreases, with $T_{MI}=48$ K (Cao *et al.*, 2013). Its magnetic phase diagram (**Figure 12**) shows that it is an antiferromagnetic Mott insulator below 48 K, and becomes a metallic ferromagnet between $T_{MI}=48$ K and $T_c=56$ K. Above T_c, this phase becomes paramagnetic and remains metallic. Remarkably, the antiferromagnetic phase becomes metallic as a magnetic field is increased beyond 6 T, suggesting that the system becomes a ferromagnetic metal (FMM). Note that the confluence of the limits at $T = 48$ K and $H = 4.1$ T lead to a multicritical point. Similar to $Ca_{2-x}La_xRuO_4$, the doping of $Ca_3Ru_2O_7$ at Ca sites changes the magnetism and transport properties of this oxide at low concentration. The resistivity decreases as x increases up to 0.04 in $Ca_{3-x}La_xRu_2O_7$ (**Figure 13**): finally, a metallic state to lowest temperatures is obtained for $x=0.05$. In contrast to $Ca_{2-x}La_xRuO_4$, no ferromagnetism is induced by doping; the antiferromagnetic metallic state characteristic of $Ca_3Ru_2O_7$ persists in zero applied magnetic-field. However, the application of even

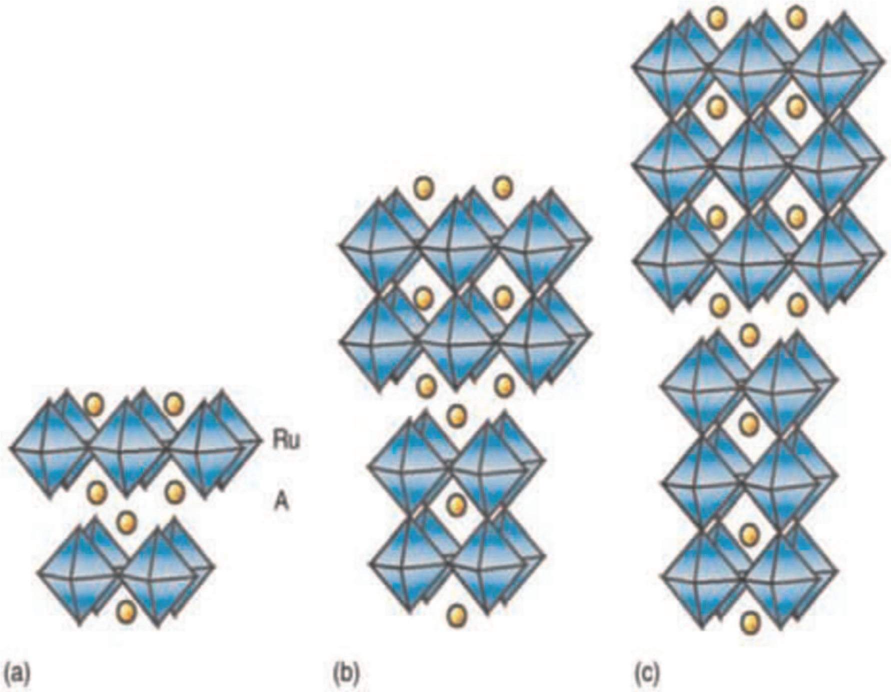

Figure 9 Structure of the RP ruthenates $A_{n+1}Ru_nO_{3n+1}$: (a) $n=1A_2RuO_4$, (b) $n=2A_3Ru_2O_7$, and (c) $n=3A_3Ru_4O_{10}$.

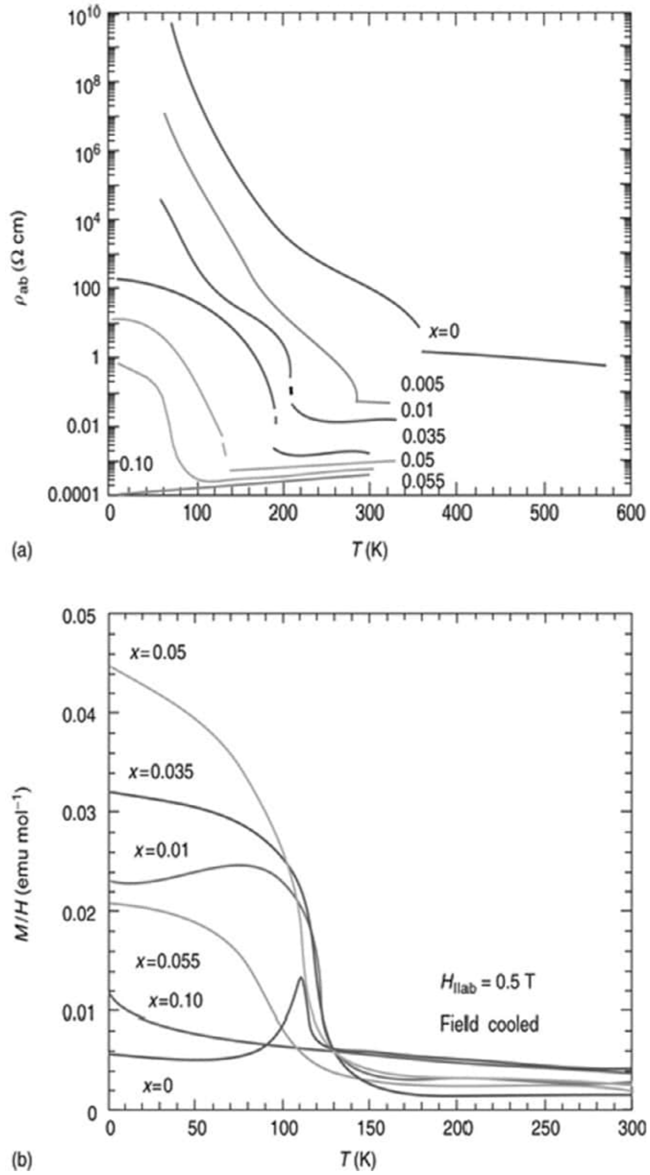

Figure 10 (a) Evolution of the resistivity and (b) of the magnetization vs. temperature for the oxides $Ca_{2-x}La_xRuO_4$. Reprinted with permission from Cao, G., McCall, S., Dobrosavljevic, V., *et al.*, 2000. Physical Review B 61, R5053–R5057. © American Physical Society.

a modest magnetic field induces a substantial ferromagnetism. The $M(H)$ curves (Figure 14) show that the saturation magnetization M_{sat} decreases sharply as x increases and disappears for $x = 0.04$, demonstrating that the metamagnetic transition is associated with the insulator-to-metal transition. La-doped or not, $Ca_3Ru_2O_7$ exhibits a negative magnetoresistance that can reach as high as 88%, depending on the temperature and magnetic field.

In contrast to $Ca_3Ru_2O_7$, $Sr_3Ru_2O_7$ is an itinerant-electron ferromagnet at low temperature. Single crystals of this compound have been grown. The zero-field-cooled (ZFC) and field-cooled (FC) $M(T)$ curves (Figure 15) of this oxide registered at low field show a large magnetic anisotropy below $T_c = 104$ K, the easy axis being near [0 0 1]. $Sr_3Ru_2O_7$ also shows a broad maximum below T_c with $H \perp (001)$ (inset Figure 15), suggesting the presence of a noncollinear spin structure in the ferromagnetic matrix. The M (H) curves for at $H \perp (001)$ in the low-temperature ranges show that the spin system undergoes a transition to a parallel spin configuration for a critical value of the magnetic field smaller than 3 T. This reorientation transition disappears at about 66 K in agreement with an additional transition observed at $T^* = 66$ K in the $M(T)$ curve (Figure 15). All these observations can be explained by a canting of the spins away from the [0 0 1] directions for $T < T^*$. The resistivity also exhibits a very large anisotropy as shown from the $\rho(T)$ curves (Figure 16); ρ_c/ρ_{ab} is indeed close to 3 at room temperature in accordance with the two-dimensional character of the structure, which favors the delocalization of the carriers within the basal plane of the $RuO_{6/2}$ octahedra. Note that besides the anomalies at T^* and T_c on the $\rho(T)$ curve, there exists a third anomaly at ~250 K whose origin is unknown. Like $SrRuO_3$, this oxide

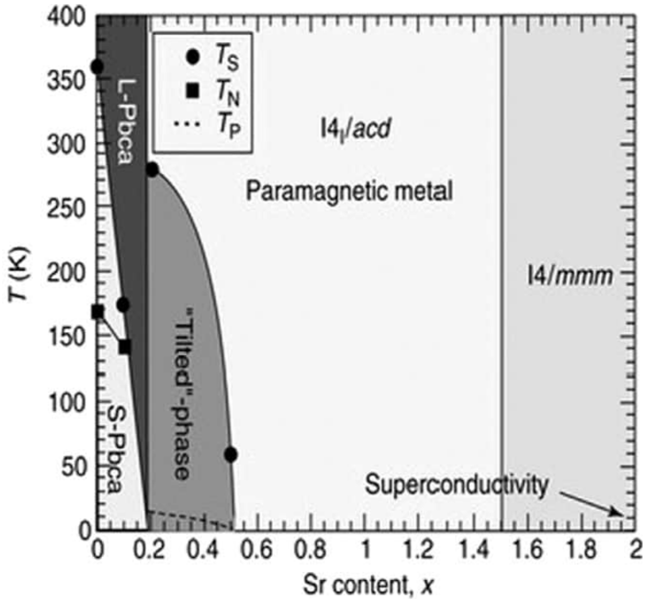

Figure 11 Phase diagram of $Ca_{2-x}Sr_xRuO_4$. Reprinted with permission from Friedt, O., Braden, M., André, G., *et al.*, 2001. Physical Review B 63, 174432. © American Physical Society.

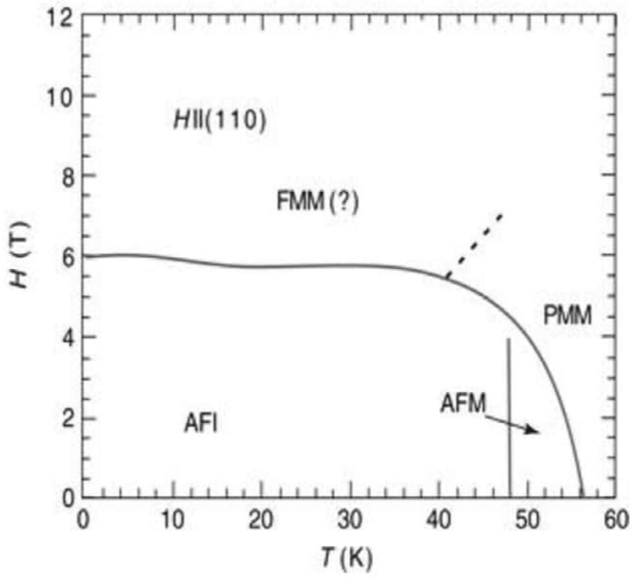

Figure 12 Magnetic phase diagram of $Ca_3Ru_2O_7$. Reprinted with permission from Cao, G., McCall, S., Crow, J.E., Guertin, R.P., 1997. Physical Review Letters 78, 1751–1754. © American Physical Society.

exhibits a negative magnetoresistance, as shown from the $MR(T)$ curve (**Figure 17**) with $MR = (\rho(0\,\mathrm{T}) - \rho\ (10\,\mathrm{T}))/\rho(0\,\mathrm{T})$. A peak of magnetoresistance of $\sim$ 15% observed below T^* suggests that the effect originates mainly from the spin reorientation under the magnetic field. In contrast, the effect at T_c is small compared to $SrRuO_3$, which exhibits a maximum MR of $\sim$ 10% at T_c.

The solid solution of $(Sr_{1-x}Ca_x)_3Ru_2O_7$ shows continuous changes of lattice parameters and a phase transition from *Bbcb* to $Bb2_1m$ at x=0.4. While the octahedral-site tilting in the basal plane increases with increasing x, the tilting seen in the ac plane onsets at x = 0.4 corresponding to the structural transition (Peng *et al.*, 2010). As shown in the resistivity ρ(T) (**Figure 18**), transitions at T_N and T_{MI} remain for $x > 0.4$; but they become much broader. The γ_e in the insulator phase of $x > 0.4$ is small relative to that of the metallic phase of x = 1. A much enhanced γ_e for the phase $0 < x < 0.4$ indicates strong quantum critical fluctuations below T_f in the regimes III and IV of the phase diagram (**Figure 19**).

The third member of the RP series, $Sr_4Ru_3O_{10}$ consists of triple perovskite layers 'Ru_3O_9' intergrown with single rock-salt 'SrO' layers. The single-crystal study of this compound shows that, like $Sr_3Ru_2O_7$, this oxide is ferromagnetic with a T_c of 148 K, intermediate between that of $SrRuO_3$ and $Sr_3Ru_2O_7$. The $M(T)$ curves (**Figure 20(a)**) show that, in contrast to $Sr_3Ru_2O_7$, the easy axis lies in the *ab* plane. Also different from the latter phase, there is no clear evidence for spin reorientation at low temperature. The

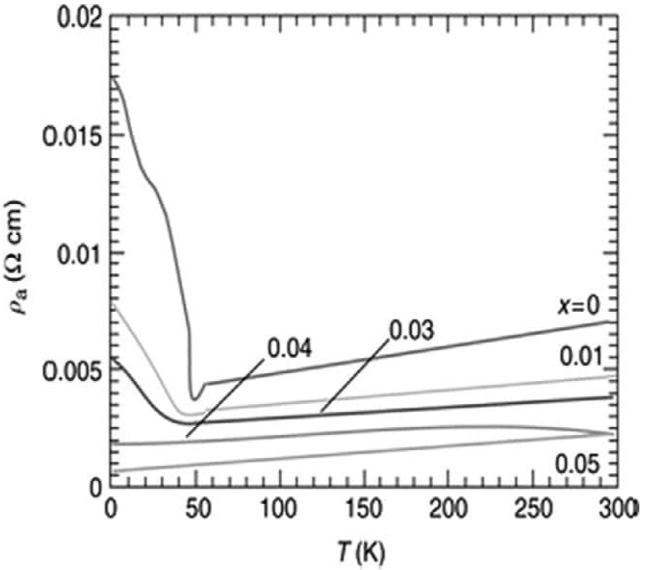

Figure 13 Resistivity vs. temperature for $(Ca_{1-x}La_x)_3Ru_2O_7$. Reprinted with permission from Cao, G., Abboud, K., McCall, S., Crow, J.E., Guertin, R.P, 2000. Physical Review B 62, 998–1003. © American Physical Society.

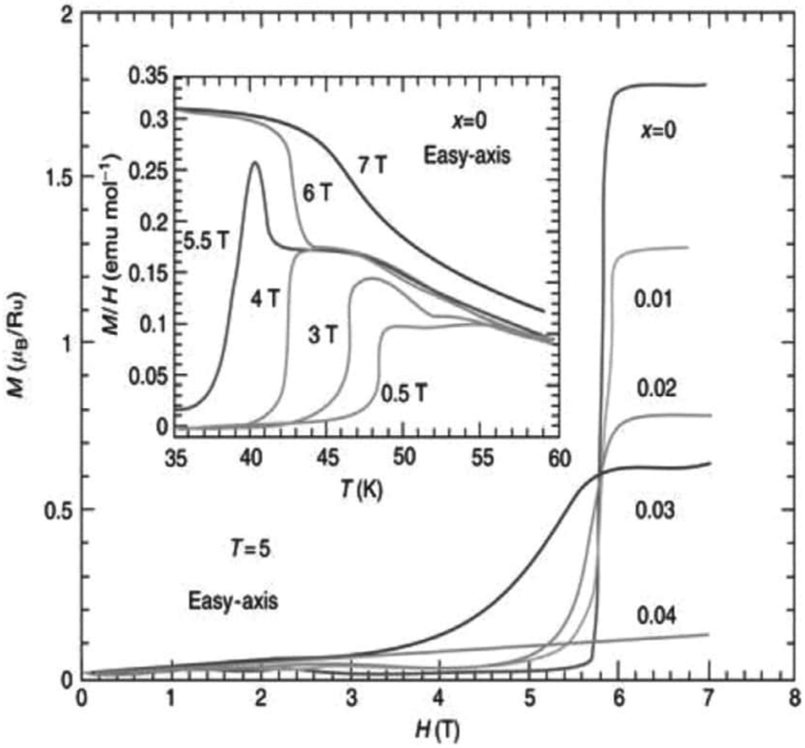

Figure 14 Magnetization vs. field at 5 K for $(Ca_{1-x}La_x)_3Ru_2O_7$. Reprinted with permission from Cao, G., Abboud, K., McCall, S., Crow, J.E., Guertin, R.P., 2000. Physical Review B 62, 998–1003. © American Physical Society.

saturation value of the magnetization, 1.75 μ_B per formula unit, is in agreement with the low-spin configuration generally observed for Ru(IV) d^4. The $\rho(T)$ curve (Figure 20(b)) of this phase is similar to that observed for $SrRuO_3$ with a Fisher–Langer anomaly at $T_c = 148$ K. As in $SrRuO_3$, a small magnetoresistance is maximum at T_c(~6% under 10 T) along with the disappearance of the Fisher–Langer anomaly under a magnetic field.

It is significant that in the Sr-RP series, the ferromagnetic T_c increases as the thickness n of the perovskite layers increase whereas in the Ca-RP series, the long-range magnetic-ordering temperature decreases with n, which is consistent with the observation that in the perovskites ($n = \infty$), $SrRuO_3$ is ferromagnetic and $CaRuO_3$ undergoes no long-range magnetic order to the lowest temperature.

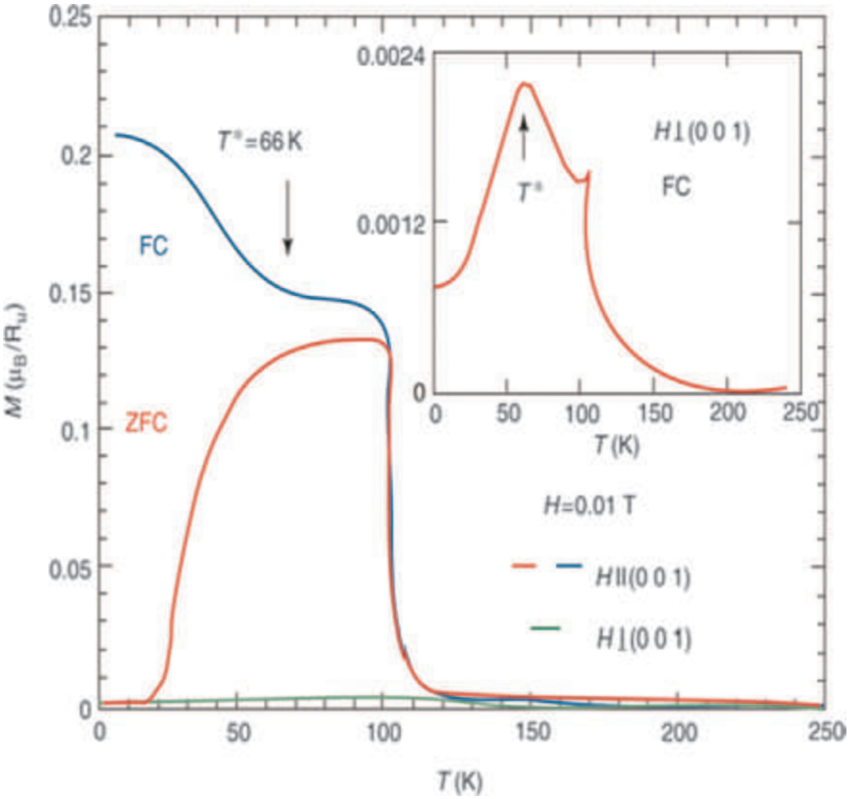

Figure 15 Magnetization vs. temperature at $H = 0.01$ T for $Sr_3Ru_2O_7$; red and blue lines: M vs. T with $H_{\|}(0 0 1)$ measured in a zero-field-cooled (ZFC) and field cooled (FC) sequence; green line: M vs. T with $H_{\perp}(0 0 1)$ after FC. Inset: M vs. T for FC at $H_{\perp}(0 0 1)$. Reprinted with permission from Cao, G., McCall, S., Crow, J.E., 1997. Physical Review B 55, R672–R675. © American Physical Society.

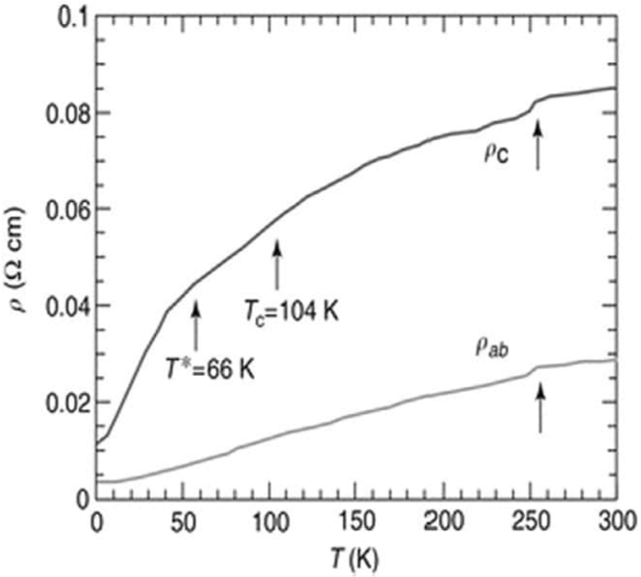

Figure 16 Resistivity vs. temperature T for $Sr_3Ru_2O_7$. Reprinted with permission from Cao, G., McCall, S., Crow, J.E., 1997. Physical Review B 55, R672–R675. © American Physical Society.

Ruthenate Hexagonal Perovskite Polytypes

Where large A cations make the perovskite tolerance factor $t > 1$, the cubic structure becomes unstable relative to a hexagonal polytype. In the cubic structure, the (111) AO_3 planes are cubically stacked; in the polytype, some hexagonal stacking of these planes are introduced periodically. Hexagonal stacking creates face-sharing octahedral sites as illustrated in Figure 21. Three polytypes of $BaRuO_3$ are known, 9 R, 4 H, and 6 H; the number refers to the number of AO_3 planes characterizing the *c*-axis periodicity of the

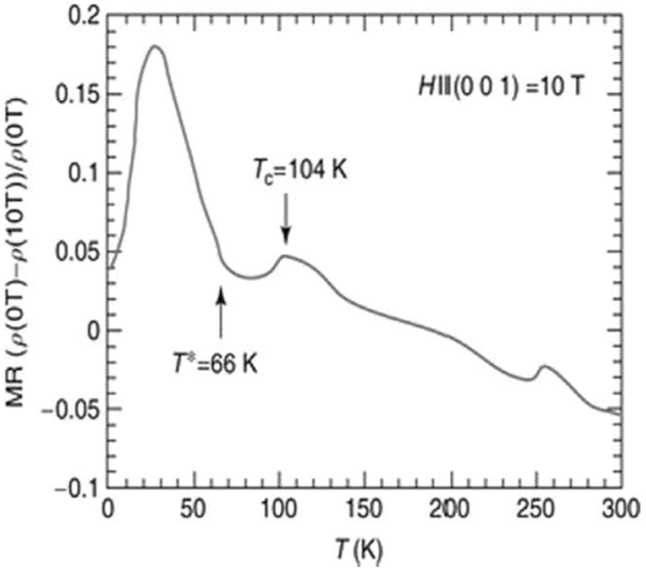

Figure 17 Magnetoresistance vs. temperature for $Sr_3Ru_2O_7$. Reprinted with permission from Cao, G., McCall, S., Crow, J.E., 1997. Physical Review B 55, R672–R675. © American Physical Society.

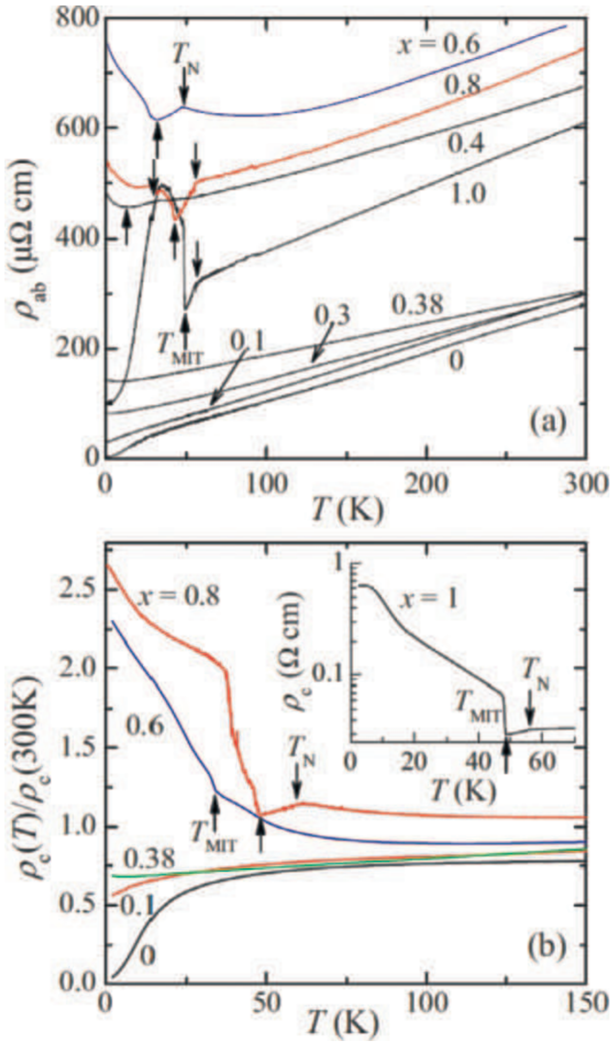

Figure 18 Temperature dependence of resistivity of $(Sr_{1-x}Ca_x)_3Ru_2O_7$. Reprinted with permission from Qu, Z., Peng, J., Liu, T., *et al.*, 2009. Physical Review B 80, 115130. © American Physical Society.

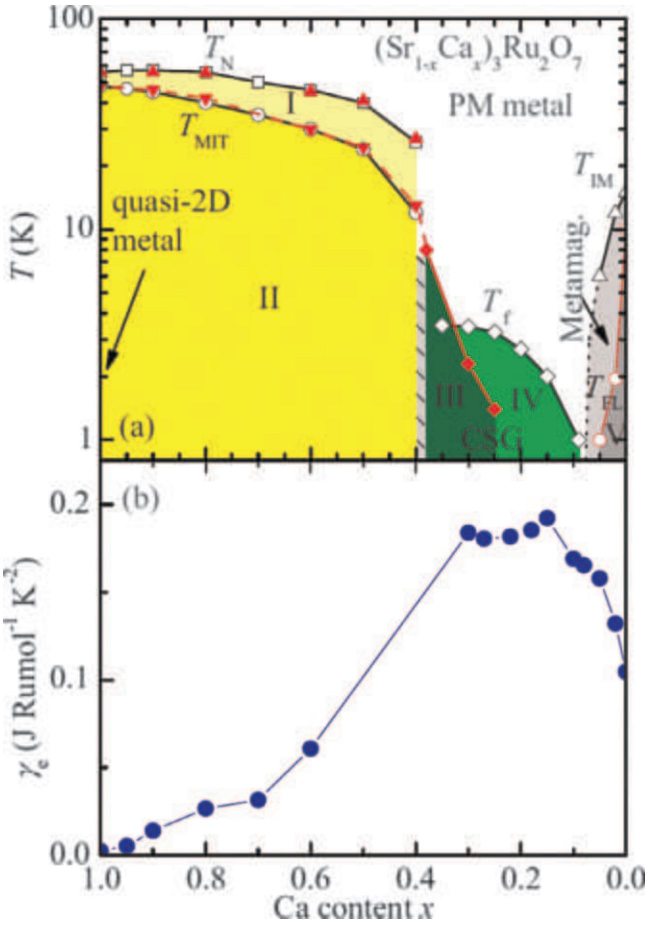

Figure 19 Phase diagram of $(Sr_{1-x}Ca_x)_3Ru_2O_7$. Reprinted with permission from Qu, Z., Peng, J., Liu T., *et al.*, 2009. Physical Review B 80, 115130. © American Physical Society. γ_e is the linear term coefficient in the temperature dependence of specific heat. A similar phase diagram has also reported by Iwata, K., *et al.*, 2008. Journal Physical Society Japan 77, 104716.

rhombohedral (R) or hexagonal (H) structure. Prepared under atmosphere pressure, $BaRuO_3$ has the 9 R structure of Figure 21(b). Prepared under successively higher pressure, the ratio of hexagonally stacked to cubically stacked AO_3 layers decreases from 2:1 in the 9 R phase to 1:1 in the 4 H (Figure 21(a)) to 1:2 in the 6 H (Figure 21(c)), and finally to the 3 C all-cubic stacking of the perovskite phase. All these structures remain stable at low temperatures if the pressure of synthesis is removed at room temperature. The polytypes are a compromise between all hexagonal and all cubic AO_3-plane stacking, the hexagonal stacking allowing an increased volume for A cations, but at the expense of a large coulomb repulsion across a shared face. Hexagonal stacking introduces a strong axial field that orders the t orbitals of the t^4e° Ru^{IV} configuration into a half-filled xy orbital and ¾-filled yz ± izx orbitals. As a result, the orbital angular momentum of the Ru^{IV} ions is maximized. Both the 9 R and 4 H phases of $BaRuO_3$ exhibit an almost temperature-independent paramagnetic susceptibility, signaling Pauli paramagnetism with no detectable local magnetic moment on the Ru(IV). The 4 H $BaRuO_3$ phase indeed exhibits a metallic-like resistivity in the range $4 \leq T \leq 300$ K (Figure 22). The 9 R $BaRuO_3$ phase, on the other hand, shows a metallic-like resistivity only above ~100 K; but an up-turn in the resistivity is found below ~100 K (Figure 22). Moreover, the resistivity of these materials is sensitive to annealing under different temperatures. The paramagnetic susceptibility of the 9 R phase does not follow the Curie–Weiss law due to strong spin–orbit coupling. The structural change from 9 R to 6 H and to 3 C (perovskite) leads to an evolution of $\chi(T)$ from a non-Curie–Weiss behavior in the 9 R phase to a typical Curie–Weiss behavior and ferromagnetism as illustrated in Figure 23.

The ruthenates $Ba_3MRu_2O_9$, with M = Fe, CO, Ni, Cu, In, all exhibit a 6 H structure built up of units of two-face shared octahedra occupied by Ru interconnected by single $MO_{6/2}$ octahedra (Figure 21(c)). In these phases, ruthenium is either pentavalent or mixed valent Ru(IV)–Ru(V). In contrast to $BaRuO_3$, all these oxides are semiconductors as a result of the Ru dimers separated by the M atoms. Magnetic susceptibility measurements show that the M-3*d* species have local moments below 400 K and that compounds with M = Co, Ni, Cu exhibit a magnetic transition near 100 K. The magnetic structure of these oxides varies with the nature of the M element. The oxides $Ba_3MRu_3O_9$ with M = Mg, Ca, Cd, Sr also exhibit the same 6 H structure with a similar ordering of the ruthenium ions into face-shared bioctahedra and of the M cations in the isolated corner-shared octahedra. These oxides are also semiconductors. The magnetic susceptibility behavior suggests that the d-electrons of the Ru(V) are delocalized between the two sites of the paired octahedra in agreement with the Heisenberg–Dirac–Van Vleck model.

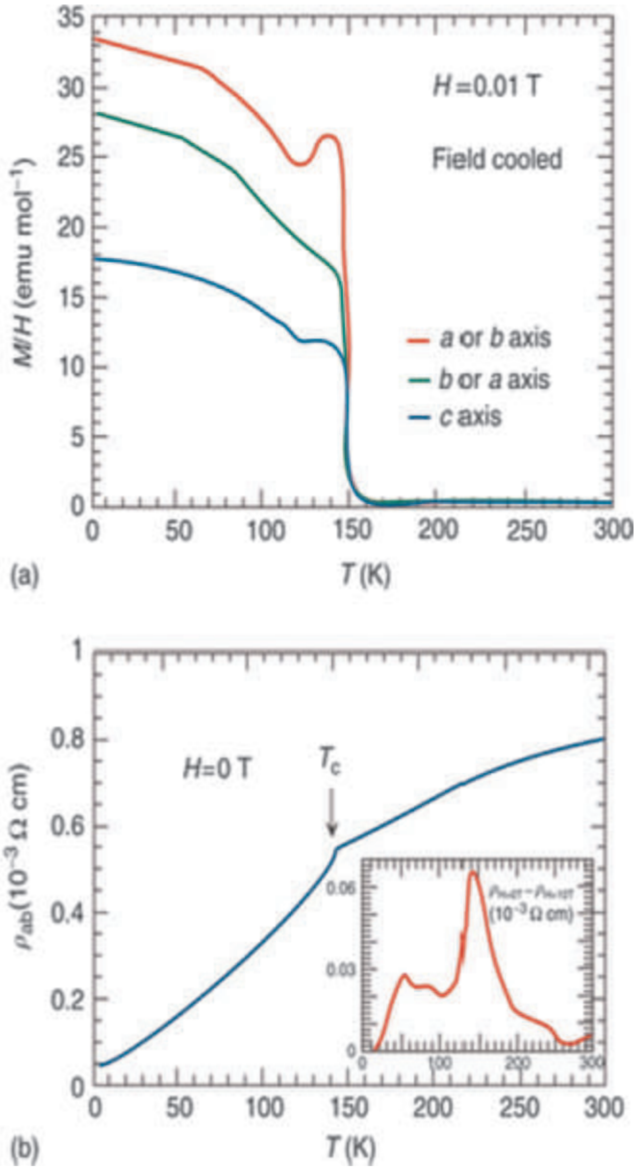

Figure 20 Magnetization (a) and resistivity (b) of $Sr_4Ru_3O_{10}$ vs. temperature. Reprinted with permission from Cao, G., McCall, S., Shepard, M., Crow, J.E., Guertin, R.P., 1997. Ferromagnetism in $Sr_4Ru_3O_{10}$: Relationship to other layered metallic oxides. Physical Review B 56, R5740–R5743. © American Physical Society.

Pyrochlore Ruthenates

The cubic $A_2B_2O_{7\text{-}x}$ pyrochlore structure (Figure 24) also has a B_2O_6 framework of corner-shared $BO_{6/2}$ octahedra; but this framework is penetrated by an $A_2O_{1\text{-}x}$ sublattice in which x may be as high as x = 1, but normally is x = 0. Ruthenates with the pyrochlore structure have been extensively studied, mainly for their transport properties, which are closely related to their oxygen nonstoichiometry. For instance, $Bi_2Ru_2O_7$ and $Pb_2Ru_2O_{6.5}$ were found to exhibit a metal-like behavior with a resistivity of $\sim 10^{-3}\,\Omega$ cm at room temperature and a Pauli paramagnetism. The nearly temperature-independent resistivity in the vicinity of room temperature has been exploited. Based on XPS, UPS, and EELS studies, it has been shown that the 6 *p* states of Bi and Pb hybridized with the Ru:4d states via shared O:2 p states. In contrast, rare-earth ruthenates $Ln_2Ru_2O_7$, Ln = Pr–Lu, Y, were found to be semiconductors with low activation energies. On the other hand, the difference in conductivity between $Ln_2Ru_2O_7$ and $Bi_2Ru_2O_7$ has been attributed to different bending of the Ru–O–Ru bond, which is 128° in $Ln_2Ru_2O_7$ and 138° in $Bi_2Ru_2O_7$. This viewpoint is supported by a study of the solid solution $La_{2-x}Cd_xRu_2O_7$, which also exhibits metallic conductivity and has Ru–O–Ru bond angles similar to that of $Bi_2Ru_2O_7$, but is characterized by large paramagnetic susceptibilities. Similarly, the studies of the solid solutions $Bi_{2-x}Ln_xRu_2O_7$ and $Pb_{2-x}Ln_xRu_2O_7$ with Ln = Y, Pr–Lu, clearly show that the metal–insulator crossover

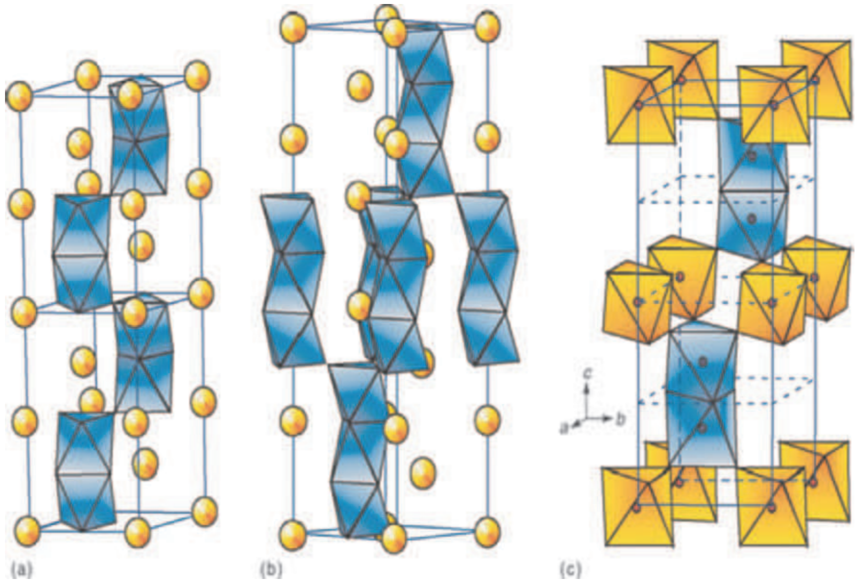

Figure 21 Structures of (a) 4H $BaRuO_3$, (b) 9R $BaRuO_3$, and (c) 6H $Ba_3MRu_2O_9$ where blue circles represent Ru and red circles M elements.

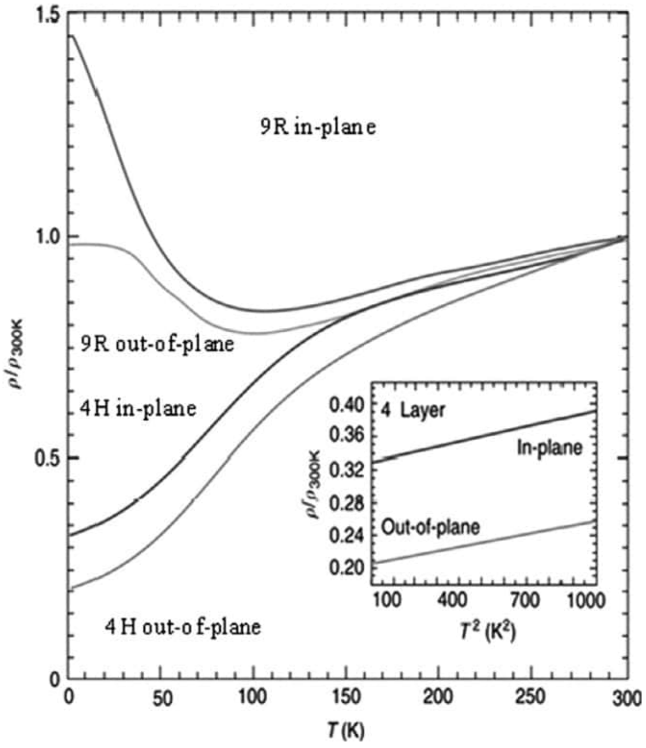

Figure 22 Resistivity vs. temperature for 4H and 9R $BaRuO_3$ forms. Reprinted with permission from Rijssenbeek, J.T., Jin, R., Zadorozhny, Yu, *et al.*, 1999. Electrical and magnetic properties of the two crystallographic forms of $BaRuO_3$. Physical Review B 59, 4561–4564. © American Physical Society.

observed for these oxides at temperatures ranging from 40 to 80 K is correlated to the bending of the Ru–O–Ru bond and to the distortion of the RuO_6 octahedra. Finally, the pyrochlore $Tl_{2-x}Ru_2O_{7-\delta}$, which was synthesized under high pressure, is a good example of the great influence of cationic and oxygen nonstoichiometry upon the transport properties of this structural family. Under reducing conditions, these phases exhibit a metallic behavior (Figure 25(a)) whereas in neutral atmosphere (Figure 25(b)) or under high oxygen pressure (Figure 25(c)), they show a metal-to-insulator transition at about 40 and 120 K, respectively. The latter transitions are correlated to structural changes versus temperature. The magnetic properties of these oxides are so far not completely characterized; their spin-glass behavior and magnetic anomalies at different temperatures (40 and 120 K) depends on

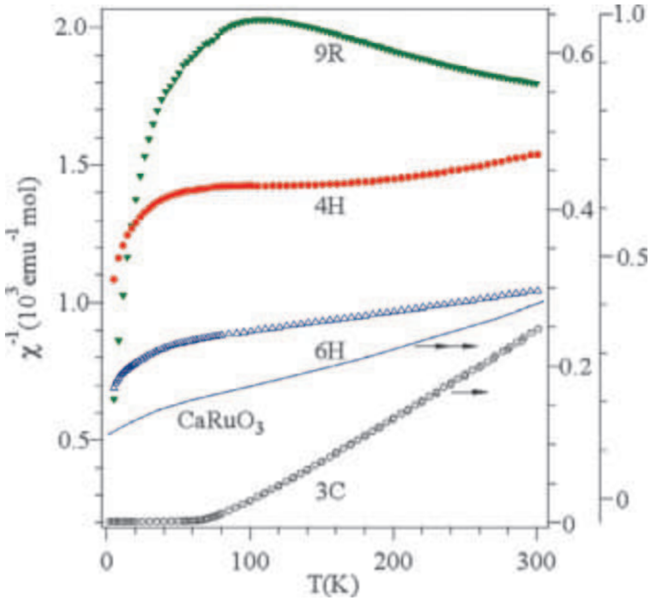

Figure 23 Inverse magnetic susceptibility vs. temperature of $BaRuO_3$. After Jin, C.-Q., Zhou, J.-S., Goodenough, J.B., *et al.*, 2008. Proceedings of National Academy of Sciences USA 105, 7115–7119.

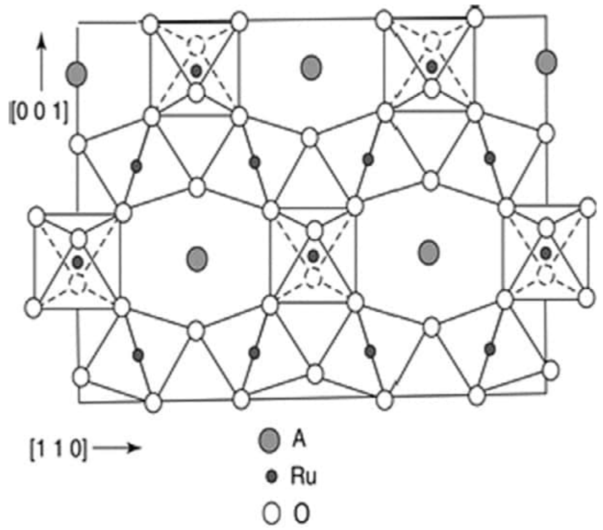

Figure 24 Pyrochlore structure of $A_2RU_2O_{7-\delta}$ ruthenates.

the conditions of synthesis, i.e., their oxygen content. A neutron powder diffraction study revealed in great detail the structural change on crossing the metal–insulator transition. On cooling through T_{MI}, the Ru–O bond length in the Ru_1 array shrinks sharply whereas that in the Ru_2 array expands (Figure 26). A DFT calculation indicates an orbital ordering in the insulator phase, which leads to the formation of quasi-1D chains.

The Quasi-Two-Dimensional Ruthenates

The ruthenate $SrRu_2O_6$ with the defect 3D $KSbO_3$ structure can be made if the synthesis is performed in a sealed Au tube at 700° C and 3000 atm pressure. The low-temperature hydrothermal synthesis can lead to a 2D $PbSb_2O_6$-type structure (Figure 27) with a = 5.20573 °A and c =10.46908 °A in the space group *P*-31 *c*. Spins on Ru(V) are coupled antiferromagnetically within the RuO_6 octahedra layers with a $T_N \approx 560$ K. A similar layered honeycomb structure with the *C*2/*m* space group has been found in Li_2RuO_3 ($a = 5.021$ °A, $b = 8.755$ °A) and Na_2RuO_3 ($a = 5.346$ °A, $b = 9.255$ °A). In sharp contrast to Ru(V) in $SrRu_2O_6$, the spins on Ru(IV) are ordered antiferromagnetically at 9 K in Li_2RuO_3 and 30 K in Na_2RuO_3 (Wang *et al.*, 2014).

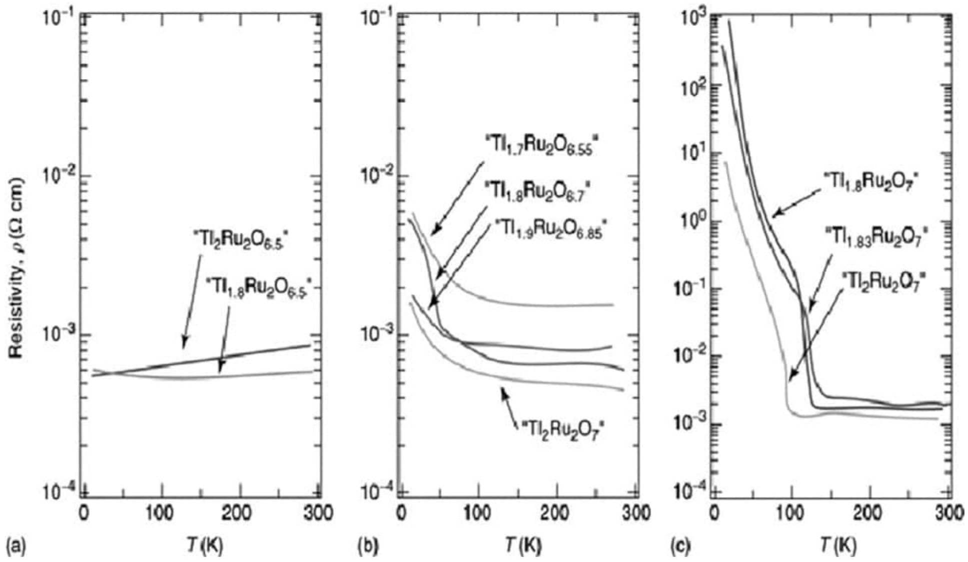

Figure 25 Temperature dependence of resistivity for thallium pyrochlores with various nominal compositions prepared under pressure (a) in reducing conditions (b) in neutral atmosphere, and (c) under high oxygen pressure. After Takeda, T., Nagata, M., Kobayashi, H., *et al.*, 1998. Journal of Solid State Chemistry 140, 182–193.

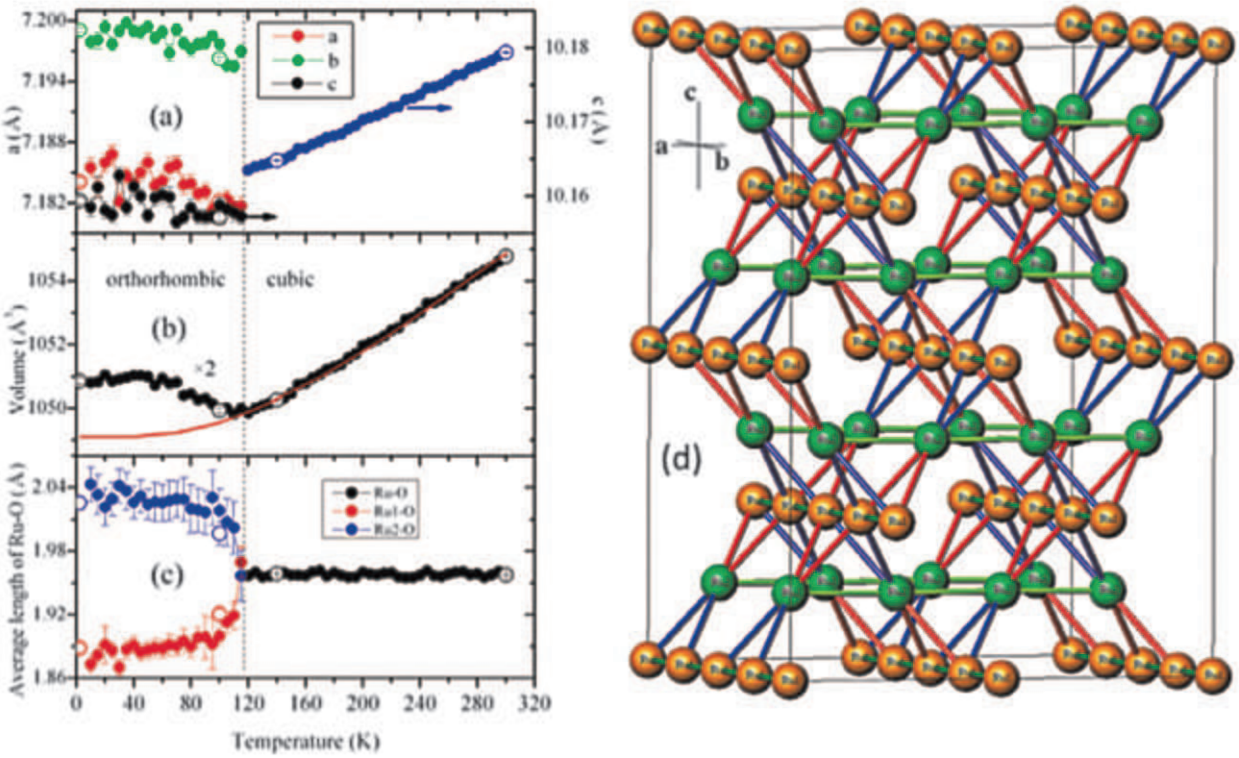

Figure 26 Temperature dependences of lattice parameters and Ru-O bond lengths of $Tl_2Ru_2O_7$ (a, b, c); Crystal structure below T_{MIT} (d). After Lee, S., Park, J.G., Adroja, D.T., *et al.*, 2006. Nature Materials 5, 471–476.

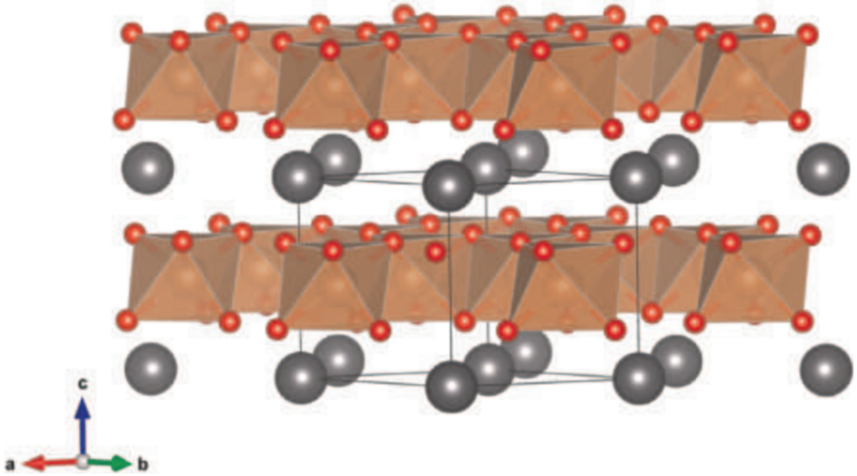

Figure 27 Crystal structure of $SrRu_2O_6$; dark grey balls, Sr; red balls, oxygen; Ru, inside octahedra.

The Quasi-One-Dimensional Ruthenates Ln_3RuO_7

The lanthanide ruthenates Ln_3RuO_7 (Ln = La-Sm) exhibit, from the viewpoint of the Ru arrangement, a 1D-type structure built up of chains of corner-sharing RuO_6 octahedra. The magnetic and transport properties of La_3RuO_7 reflect its 1D geometry. This phase is a semiconductor even along the chain, though the Ru–O–Ru angles of 145° are very similar to those observed for 3D pyrochlore ruthenates. The magnetic data show that this Ru(V) oxide exhibits a Curie–Weiss behavior above 50 K and an antiferromagnetic order below this temperature. In fact, a short-range antiferromagnetic order is observed in the range 20–50 K which becomes long range below 20 K.

Ruthenium as a Substituting Element in Oxides

The ability of ruthenium to adopt an octahedral coordination makes it possible to substitute it for transition elements in many oxides. As a consequence, its electronic configuration either as Ru(IV) or as Ru(V) and the large extension of its d orbitals, suggests that such an element is susceptible to induce new physical properties in already known materials. Two examples of this promising role of Ru to induce new properties are described.

The first example deals with the introduction of Ru into the 1212 structure of cuprates. It has been discovered that the ruthenium-doped 1212 cuprate $RuSr_2GdCu_2O_8$ is both a superconductor with a $T_c = 15-40$ K, and a ferromagnet with a $T_c =$ 133–136 K (Figure 28). The coexistence of superconductivity and ferromagnetism below 15–40 K appears most surprising since,

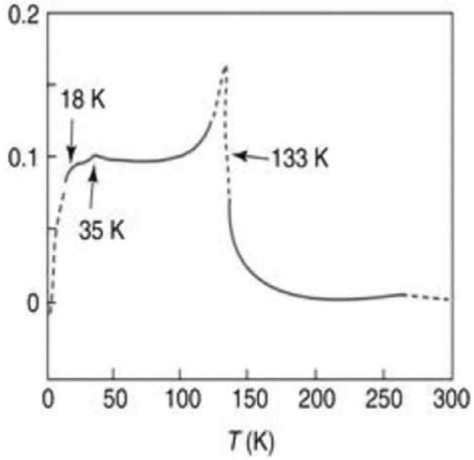

Figure 28 AC susceptibility measurements of $RuSr_2Cu_2O_8$, showing that superconductivity exists up to 35 K, with a superconductive $T_c = 18$ K and a Curie temperature $T_c = 133$ K. Reproduced figure with permission from Chmaissem, O., Jorgensen, J.D., Shaked, H., Dollar, P., Tallon, J.L. 2000. Physical Review B 61, 6401–6407. © American Physical Society.

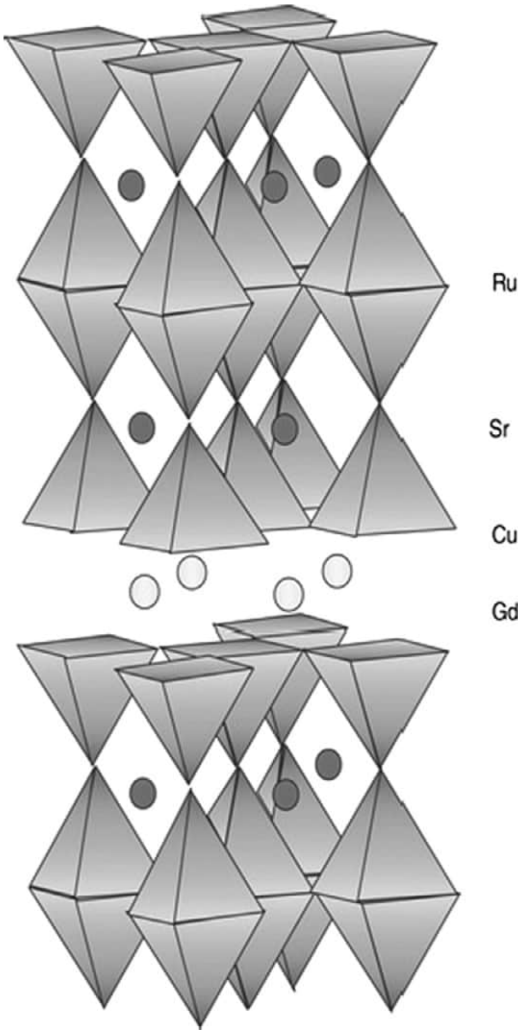

Figure 29 The 1212 structure of $RuSr_2GdCu_2O_8$ built up of layers of RuO_6 octahedra stacked with layers of CuO_5 pyramids.

according to Ginzburg, such a feature should not be possible at a microscopic scale. The particular layered structure of this compound (Figure 29), which consists of superconducting pyramidal copper layers stacked with octahedral ruthenium layers, is certainly the key to understanding this behavior since this structural separation should decrease the interactions between ferromagnetism and superconductivity dramatically. In any case, this extraordinary behavior has prompted numerous investigations still in progress to help understand the physics of these materials.

The second example deals with the doping of perovskite manganites with ruthenium. It has been shown that the partial substitution of ruthenium for manganese in charge-ordered manganites such as $Sm_{0.5}Ca_{0.5}MnO_3$, which are insulator ferromagnets, induces ferromagnetism and a metal–insulator transition with consequently, colossal magnetoresistance (CMR) effects. Thus, a very high T_c up to 220 K can be reached by Mn-site doping, changing completely the magnetic-phase diagram of the manganites. This situation is illustrated for $Sm_{1-x}Ca_xMnO_3$ (Figure 30(a)) doped with 12% Ru (Figure 30(b)). It can be seen that the T_c of the ferromagnetic insulating region is increased by Ru substitution; but more importantly, the broad charge-ordered antiferromagnetic domain (Figure 30(a)) is suppressed and replaced by a ferromagnetic metallic region with a T_c up to 200 K. This great ability of Ru to induce ferromagnetism and metal-like behavior can be explained by both its ability to couple ferromagnetically with manganese neighbors and the large extension of its d-orbitals allowing stronger interatomic interactions and, therefore, conduction paths to be enhanced.

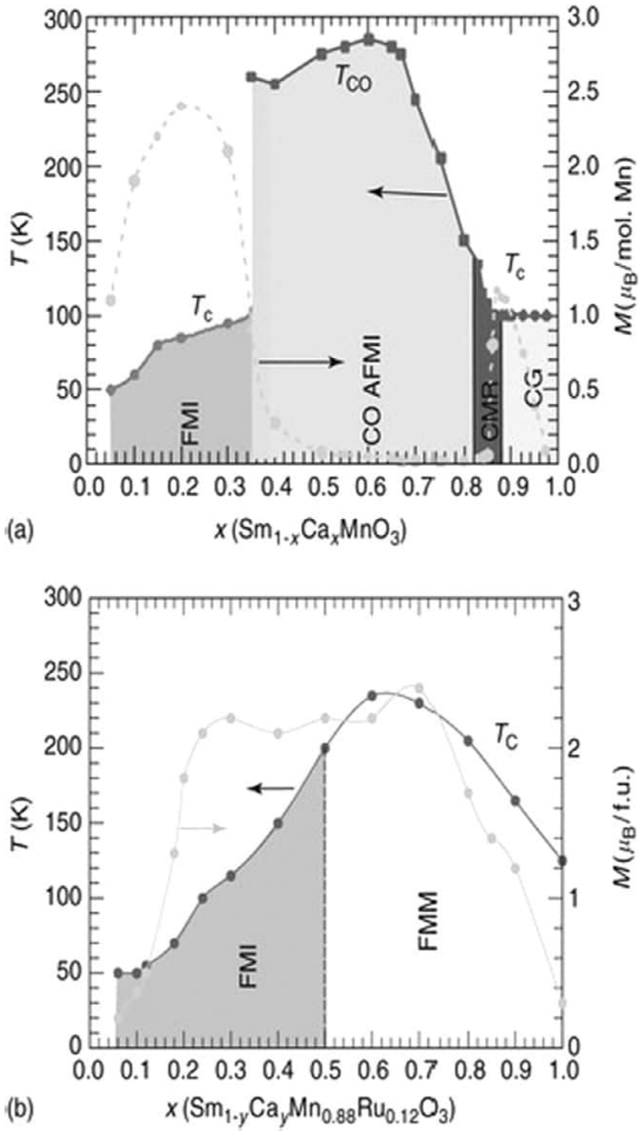

Figure 30 Magnetic phase diagrams of the manganites $Sm_{1-x}Ca_xMnO_3$ (a) and $Sm_{1-x}Ca_xMn_{0.88}Ru_{0.12}MnO_3$ (b).

References

Cao G, Delong LE, and Schlottmann P (2013) Frontiers of 4D-and 5D-Transition Metal Oxides. *World Scientific* 179–212.
Cheng J-G, Kweon KE, Zhou J-S, et al. (2013) *Proceedings of the National Academy of Sciences of the USA* 110: 20003–20007.
Cheng J-G, Zhou J-S, and Goodenough JB (2009) *Physical Review B* 80: 174426.
Jin C-Q, Zhou J-S, Goodenough JB, et al. (2008) *Proceedings of the National Academy of Sciences of the United States of America* 105: 7115–7119.
Kimber SA, Rodgers JA, Wu H, et al. (2009) *Physical Review Letters* 102: 046409.
Kojitani H, Shirako Y, and Akaogi M (2007) *Physics of the Earth and Planetary Interiors* 165: 127–134.
Kusmartseva AF, Sinclair A, Rodgers JA, Kimber SA, and Attield JP (2013) *Physical Review B* 87: 16513.
Lee S, Zhang JR, Torii S, et al. (2013) *Journal Physics Condensed Matter* 25: 465601.
Mackenzie AP and Maeno Y (2003) *Review of Modern Physics* 75: 657–712.
Peng J, Qu Z, Fobes D, et al. (2010) *Physical Review B* 82: 024417.
Wang JC, Terzic J, Qi TF, et al. (2014) *Physical Review* 90: 161110R.
Zhou J-S and Goodenough JB (2005) *Physical Review Letters* 94: 065501.
Zhou J-S and Goodenough JB (2008) *Physical Review* B77: 132104.
Zhou J-S, Matsubayashi K, Uwatoko Y, et al. (2008) *Physical Review Letters* 101: 077206.

Further Reading

André G, Nakatsuji S, et al. (2001) *Physical Review B* 63: 174432.
Battle PD, Gibb TC, Jones CW, and Studer F (1989) *Journal of Solid State Chemistry* 78: 281–293.
Battle PD and Jones CW (1989) *Journal of Solid State Chemistry* 78: 108.
Cao G, McCall SK, Crow JE, and Guertin RP (1997) *Physical Review B* 56: R5740–R5743.
Dang HT, Mravlje J, Georges A, and Millis AJ (2015) *Physical Review B* 91: 195149.
Goodenough JB (1971) *Metallic Oxides*. Pergamon Oxford.
Kanno R, Kawamoto Y, Izumi F, and Sleight AW (1998) *Journal of Solid State Chemistry* 140: 182–193.
Khalifah P, Erwin RW, Lynn JW, et al. (1999) *Physical Review B* 60: 9573–9578.
Kim SH and Battle PD (1995) *Journal of Solid State Chemistry* 114: 174–183.
Liu Y, Batlogg B, et al. (1999) *Physical Review B* 59: 4561–4564.
Martin C, Maignan A, Hervieu M, et al. (2001) *Physical Review B* 63: 174402.
Martin C, Maignan A, Hervieu M, and Raveau B (1999) *Physical Review B* 60: 12191–12199.
Rao CNR and Raveau B (1998) *Colossal and Magnetoresistance, Charge Ordering and Related Properties of Manganese Oxides*. Singapore: World Scientific.
Tallon JL, Loram JW, Williams GVM, and Bernhard C (2000) *Physical Review B* 61: R6471–R6474.
Tokura Y (1999) *Colossal Magnetoresistive Oxides*. New York, NY: Gordon and Breach.

Optical Fibers[☆]

V Degiorgio and I Cristiani, Università di Pavia, Pavia, Italy

© 2016 Elsevier Inc. All rights reserved.

This is an update of V. Degiorgio, I. Cristiani, Optical Fibers, Reference Module in Materials Science and Materials Engineering, Elsevier, 2016, ISBN 9780128035818, https://doi.org/10.1016/B978-0-12-803581-8.01133-4.

Introduction 807
Structure and Modes 807
Attenuation 809
Dispersion 810
Special Fibers 811
Fiber Bragg Gratings 812
Fiber Amplifiers and Lasers 812
Nonlinear Fiber Optics 813
Further Reading 814

Introduction

Immediately after the laser invention it was realized that laser beams, with a carrier frequency of some 10^{14} Hz, have the potential to transport information with a much larger frequency band than either radio or microwaves. Atmospheric transmission is limited to line-of-sight communications and is strongly dependent on visibility conditions. It was therefore natural to think about a waveguide having the function of creating a protected path for the light beam, and also of compensating diffraction by optical confinement. Indeed, an optical wave having a finite transversal size broadens during propagation in free space. If we consider the output of a typical laser working at the wavelength λ, this is represented by a Gaussian wave with a beam diameter d of the order of 1 mm. The diffraction angle θ (also called the divergence of the beam) is of the order of λ/d. Taking $\lambda = 1$ μm, we find that at the distance $L = 1$ km the beam diameter becomes 1 m. At present, guided-wave optics is an important technology with applications that are not limited to the transmission of optical signals, but also involve the fabrication of integrated optical and optoelectronic devices, such as lasers and modulators. The basic concept of optical confinement is simple. A dielectric medium of refractive index n_1, embedded in a medium of lower refractive index n_2, acts as a light trap within which optical rays remain confined by multiple internal reflections at the boundaries. The optical waveguide may have the shape of a slab, strip, or cylinder. The most widely used is the optical fiber, which is made of two concentric cylinders of glass or polymeric material. Silica glass fibers represent by far the most important family of fibers, because they can transmit optical pulses over long distances with small attenuation and limited pulse broadening. The fibers made of polymeric material, called plastic optical fibers (POF), although presenting much larger losses than silica fibers, have the advantage of a much cheaper fabrication process, and can be competitive for the short links required in a variety of applications, including communication networks inside a building or a vehicle.

Besides telecommunications, important applications of optical fibers are found in the areas of sensing and of biomedical imaging. Fiber sensors can measure temperature, pressure, strain, current flow along high-voltage power lines, and rotations in aircraft navigation. Fiber-optic endoscopy utilizes fiber bundles to guide light into the internal area under investigation and to transmit back the image.

Structure and Modes

The structure of an optical fiber is shown in Figure 1. Typically, the cladding is made of pure silica, whereas the core is doped with germania during manufacturing in order to increase its refractive index and introduce a positive index step between core and cladding. In many cases, instead of having a step in the refractive index profile, the refractive index of the core is graded from a maximum value at its center to a minimum value, corresponding to the refractive index of the cladding, at the core-cladding boundary. The fiber is then called a graded-index fiber, whereas the fiber shown in Figure 1 is called a step-index fiber. For optical-communication fibers, the cladding diameter is typically 125 μm, and the core diameter can vary from 9 to 50 μm depending on the application.

An elementary description of light trapping in the core of a step-index fiber can be based on total internal reflection: since $n_1 > n_2$, when the angle of incidence β on the core-cladding interface is larger than the limit angle $\beta_c = \arcsin(n_2/n_1)$, total internal reflection occurs, so that the beam can propagate for an indefinite distance within the fiber core without radiating outside any

---

[☆] *Change History*: June 2015. V. Degiorgio and I. Cristiani introduced small edits in the text of the article including a sentence about the fiber Raman laser and updated citations.

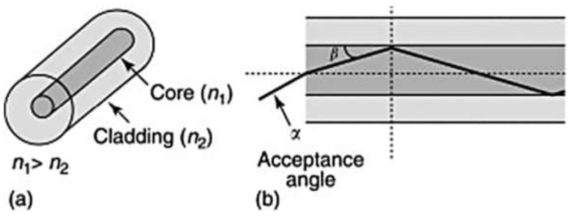

Figure 1 (a) Scheme of an optical fiber. (b) Waveguiding effect by total internal reflection.

optical power. If we consider an optical ray whose propagation direction forms an angle α with the axis of the fiber, it is easy to derive that the maximum acceptance angle, $\alpha_{\max}$, is given by:

$$\sin\alpha_{\max} = n_1\sqrt{1 - \sin^2\beta_c} = \sqrt{n_1^2 - n_2^2} \qquad [1]$$

The quantity $\sin\alpha_{\max}$ is called numerical aperture of the fiber, and is indicated with the symbol *NA*. Considering a realistic case in which $n_1 = 1.48$, $n_2 = 1.46$, we find that the numerical aperture is 0.24, and $\alpha_{\max} = 14°$.

The geometrical picture of light guidance by multiple reflections is not adequate to explain the propagation properties of the fiber. In particular, geometrical optics suggests a complete confinement of the light beam within the core, whereas wave optics predicts a non-zero intensity in the cladding region (evanescent wave). The general treatment requires solving the wave equation with the appropriate boundary conditions. Since it goes beyond the scope of this article to discuss such a treatment, we limit ourselves to a description of the main results. Assuming that the electromagnetic wave is monochromatic (that is, it contains a single frequency υ) and that nonlinear optical effects are negligible, it is found that there is a set of field configurations, called fiber modes, which can propagate without attenuation maintaining the same transversal distribution and the same polarization at all distances along the waveguide axis. In most practical cases the full set of modes can be approximated by a set of so-called 'linearly polarized' LP_{mn} modes, where the indices m and n are integer numbers. An LP_{mn} mode has n field maxima along a radius vector and $2m$ field maxima round a circumference. By calling E_{mn} the electric field associated to the mode mn, and choosing the z-axis coincident with the fiber axis, the fiber mode is characterized by a transversal field distribution $A_{mn}(x, y)$ and by a propagation constant β_{mn}, both depending on m and n:

$$E_{mn}(x, y, z, t) = A_{mn}(x, y)e^{i(\beta_{mn}z - \omega t)} \qquad [2]$$

where $\omega = 2\pi\upsilon$ is the angular frequency. We show in Figure 2 the amplitude profile of the fundamental mode LP_{01} that is approximately described by a Gaussian function:

$$A_{01}(r) = A_o \exp\left(-\frac{r^2}{w^2}\right) \qquad [3]$$

where $r = (x^2 + y^2)^{1/2}$ is the distance from the fiber axis. We see that the field amplitude $A_{01}(x, y)$ is mainly concentrated inside the core, but presents exponentially decaying tails extending into the cladding region. Higher-order modes present more complicated profiles extending more and more deeply into the cladding as the indices m and n become larger and larger.

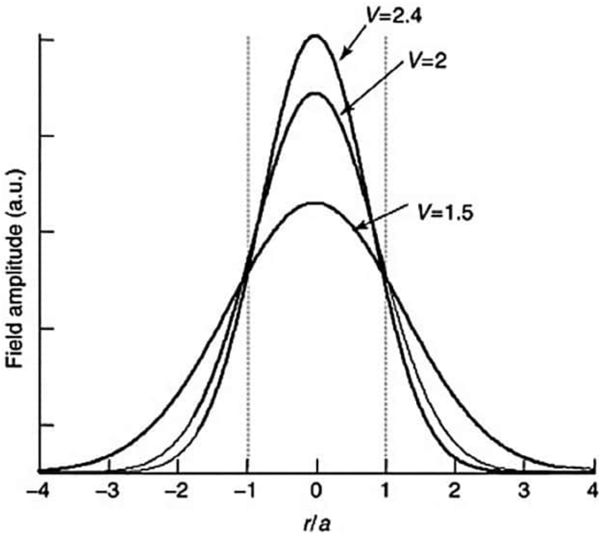

Figure 2 Field profile of the fundamental propagation mode LP_{01} for various values of the normalized frequency *V*.

In order to discuss fiber properties it is helpful to introduce the dimensionless parameter V, called normalized frequency, defined as:

$$V = \frac{2\pi a}{\lambda}\sqrt{n_1^2 - n_2^2} \qquad [4]$$

where $\lambda = c/\upsilon$ is the wavelength. The plots in **Figure 2** indicate that the beam size w is a decreasing function of V. This can be easily understood if we note that the beam is more tightly confined when the core size is large in comparison with the wavelength, and when the difference in refractive index between core and cladding is large.

From the propagation constant β_{mn} one can derive the effective index of refraction n_{mn} seen by the mode mn, by using the relation: $\beta_{mn} = 2\pi n_{mn}/\lambda$. The value of n_{mn} will be clearly intermediate between n_1 and n_2, approaching more closely n_1 when the field mode is more tightly confined.

A very important general property of waveguides is that, for a fixed waveguide configuration and a fixed λ, a fundamental mode always exists, whereas higher-order modes can be sustained only under specific conditions. In the case of optical fibers the parameter controlling the single-mode or multimode behavior is the normalized frequency V. If V is sufficiently small, the fiber is single-mode. When V becomes larger than a critical value V_c, also the second mode can be sustained. By progressively increasing V, more and more modes can be guided. For $V \gg 1$, the number N of guided modes is given by: $N \cong V^2/2$.

The value of V_c is dependent on the fiber structure. In the case of the step-index fiber, $V_c = 2.405$. Fibers that are single-mode at $\lambda = 1500$ nm are usually designed with values of V close to 2, by choosing a core radius around 5 μm and a difference $n_1 - n_2$ around 10^{-2}. Note that, since V is inversely proportional to λ, a fiber that is single-mode in the near infrared will be multi-mode in the visible.

Multi-mode fibers have typically a core diameter around 50 μm. They are easier to align and less expensive than single-mode ones. However, as discussed below in the Section dealing with dispersion, they are not fit for pulse transmission over long distances because pulse-broadening effects are large.

Attenuation

In principle a guided mode can propagate in an optical fiber for arbitrary distances without suffering radiation losses. In practice, however, the propagating wave is always attenuated. Assuming that the losses are linear, the optical power P_o launched into the fiber decays exponentially along the fiber following the law:

$$P(z) = P_o e^{-\alpha_o z} \qquad [5]$$

where α_o, expressed in km^{-1}, is the attenuation coefficient. In practice, the quantity given in fiber specifications is the coefficient $\alpha = 4.34\,\alpha_o$ expressing the attenuation in dB km^{-1}.

The attenuation is due to two phenomena: light scattering and absorption. Light scattering is originated by the microscopic in homogeneities that exist in the glass at the drawing temperature because of spontaneous thermal fluctuations. Such in homogeneities are frozen during the rapid cooling process, and give rise to spatial fluctuations of the refractive index over a sub-micrometric scale. Rayleigh scattering from these fluctuations has a cross-section that scales according to λ^{-4}. As a consequence, scattering losses rapidly decrease as a function of wavelength.

Optical fibers are usually made of fused silica glass (SiO_2). This material has two strong absorption bands, a ultraviolet band around 0.3 μm due to electronic transitions and an infrared band around 1.7 μm due to the vibrational mode of the Si–O bond. The presence of water impurities gives other absorption peaks due to vibrations of the OH^- ion, the most important one near 1370 nm. Because of the combined effect of scattering and absorption, the attenuation curve for silica glass, as shown in **Figure 3**, has an absolute minimum at 1550 nm and a secondary minimum around 1300 nm. The OH^- absorption peak no longer exists in recent fibers, because of improvements in the purification process. However, several networks using fibers with water impurities are still installed and in use.

The earliest optical communication schemes were working at about 800 nm, where the attenuation has a local minimum, not apparent in **Figure 3**. The value of the attenuation at the absolute minimum, $\alpha_{\min}$, is about 0.15 dB km^{-1}, corresponding to a reduction of the input power by a factor of two after a propagation length of 20 km. Optical communication systems operate around the wavelength corresponding to the minimum attenuation.

If different oxides are added to SiO_2, the position of $\alpha_{\min}$ is only slightly changed because essentially all oxides present vibrational transitions in the range 1.5–2 μm. A significant shift of the minimum attenuation can be obtained by using glasses made with mixtures of fluorides, such as the so-called ZBLAN glasses that contain Zr, Ba, La, Al, and Na fluorides. Since vibrational levels of fluorides are localized in the range 5–8 μm, ZBLAN glasses present the attenuation minimum around 3 μm, with a value of $\alpha_{\min}$ one order of magnitude smaller than that of silica glasses. It is, however, rather difficult to draw ZBLAN fibers of good optical quality.

It should be mentioned that fiber losses increase considerably if the fiber is curved. This can be easily understood in the frame of geometrical optics: if the fiber is curved, there is a change of the incidence angle at the core-cladding interface and some rays may be

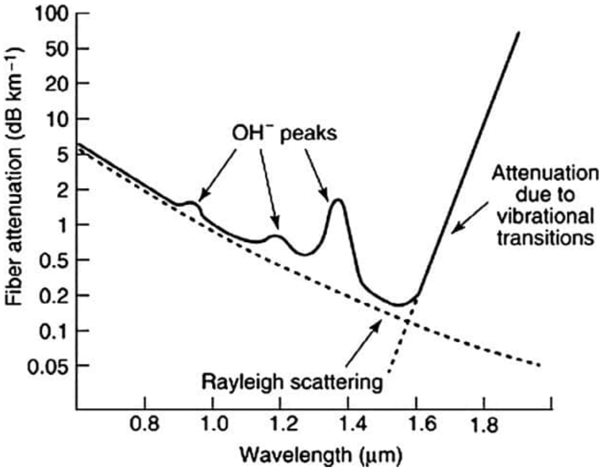

Figure 3 Dependence of the attenuation coefficient α of silica glass on the wavelength λ.

not totally reflected. Such a radiation loss affects in particular the modes presenting a field distribution that extends considerably into the cladding, as it happens when the normalized frequency V is small.

Dispersion

In Optics the term dispersion indicates that the index of refraction of the medium changes with the frequency of the propagating wave, $n = n(\omega)$. An optical pulse with duration Δt has a spectral broadening $\Delta\omega \geq \Delta t^{-1}$, and cannot be treated as a monochromatic wave. Each frequency component travels in the dispersive medium with a different phase velocity $\upsilon_\phi = c/n(\omega)$. As a consequence, the pulse shape changes during propagation. If we assume that the input pulse is transform-limited, which means that all the frequency components have the same phase, the effect of dispersion is a progressive increase of the pulse duration as the propagation length increases.

If the wave, instead of propagating in a homogeneous medium, propagates along an optical fiber, its velocity is determined by the effective index of refraction n_{mn} defined above. Note that, even in absence of material dispersion, the effective index of refraction changes with frequency because the mode profile is frequency-dependent. Therefore the fiber is dispersive even in absence of dispersion of the materials constituting the fiber. This results in a waveguide contribution that must be added to the material contribution to obtain the total fiber dispersion.

Laser pulses have a spectral broadening $\Delta\omega$ usually much smaller than the central frequency ω_o. This allows treating the wave propagation in a dispersive medium by using a perturbative approach. The propagation constant $\beta(\omega)$ is expanded in a power series around ω_o, and the series is truncated to the quadratic term:

$$\beta(\omega) = \beta_o + \beta_1(\omega - \omega_o) + \frac{1}{2}\beta_2(\omega - \omega_o)^2 \qquad [6]$$

where β_j is the j-th derivative of $\beta(\omega)$ evaluated at $\omega = \omega_0$. By using eqn [6] inside the propagation equation, it can be shown that the reciprocal of β_1 is the group velocity (that is, the velocity of the pulse peak) and that β_2 is the parameter responsible for pulse broadening, usually called group velocity dispersion (GVD). If we assume that the input pulse is a transform-limited Gaussian pulse having duration equal to Δt_o, the pulse duration Δt after a path-length z is given by:

$$\Delta t = \sqrt{(\Delta t_o)^2 + \left(\frac{|\beta_2|z}{\Delta t_o}\right)^2} = \Delta t_o\sqrt{1 + \left(\frac{z}{L_D}\right)^2} \qquad [7]$$

where $L_D = (\Delta t_o)^2/|\beta_2|$ is called the dispersion length. Equation 7 indicates that dispersion effects become more and more important as the pulse duration becomes shorter and shorter. Considering, for instance, a standard single-mode optical-communication fiber at 1550 nm, $\beta_2 = -20$ ps^2 km^{-1}, and $\Delta t_o = 10$ ps, we find $L_D = 5$ km. This means that the pulse duration is more than doubled when $z = 10$ km. Clearly, pulse broadening can be very detrimental in long communication links because it produces a smearing out of individual bits, leading to higher bit error rates. In order to reduce such an effect, fibers with low value of β_2 around 1550 nm have to be used. These special fibers, called dispersion-shifted fibers, are fabricated by an appropriate choice of refractive-index profile. We show in Figure 4 the behavior of β_2 as a function of λ for a standard single-mode fiber and for a dispersion-shifted fiber.

Multi-mode fibers present an additional dispersion mechanism due to the fact that different modes, even if operating at the same wavelength, have different field profiles, hence different effective refractive indices. Therefore, if the pulse input power is coupled

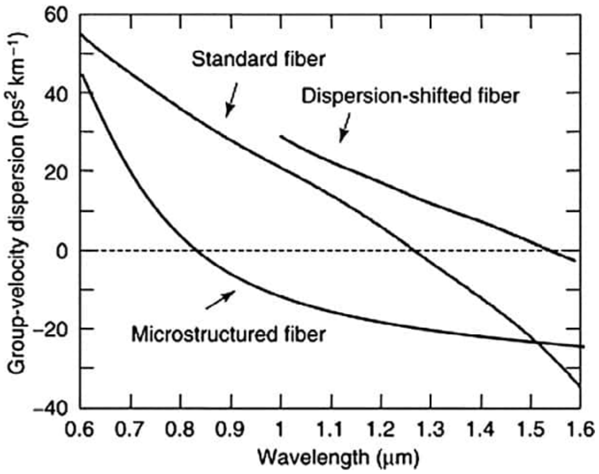

Figure 4 The dispersion parameter β_2 plotted as a function of wavelength for a standard single-mode fiber, a dispersion-shifted fiber, and a microstructured fiber.

simultaneously to several modes, modal dispersion gives a contribution to pulse broadening that can be larger than that due to material- and waveguide-dispersion.

Special Fibers

Besides step-index and graded-index fibers, other types of fibers having a more complicated index profile are used for special purposes. In the previous Section we have mentioned dispersion-shifted fibers, designed to present a reduced dispersion in a specific wavelength range. Another useful category is that of polarization-maintaining fibers, fibers presenting some anisotropy in the index profile that makes them birefringent. A very recent development consists in fibers presenting air holes running along the fiber axis. An example is shown in Figure 5. These are called micro structured fibers, and may have a variety of applications connected with the fact the air-silica structure allows single-mode behavior over a very wide wavelength range and gives more freedom in choosing the area of the propagating mode or the shape of the dispersion curve.

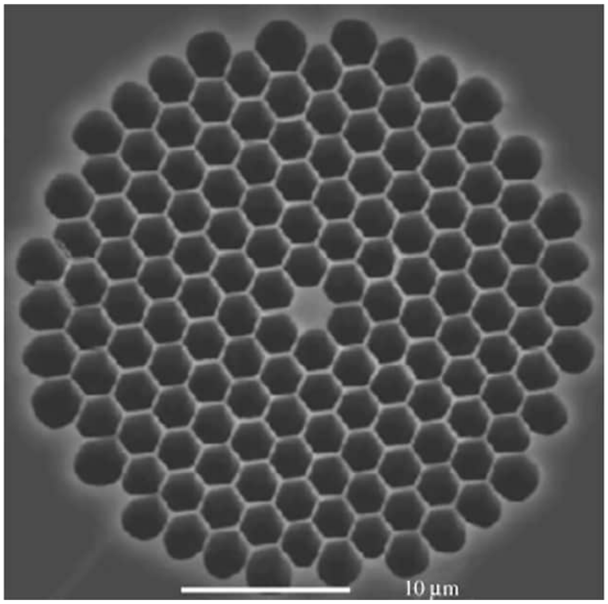

Figure 5 Cross-section of a microstructured fiber made of silica with air holes running along the fiber axis. The silica core has a diameter of about 2 μm.

Fiber Bragg Gratings

It is very helpful to be able to manipulate optical signals traveling inside fibers without extracting them from the fiber. This not only reduces losses, but also makes the optical system more flexible. Following the all-fiber approach, various optical components and devices have been conceived and built in order to perform a variety of functions, such as beam splitters and combiners, mirrors, filters, polarizers, amplifiers, and even lasers. In this Section we describe frequency-selective mirrors obtained by introducing inside the fiber core a longitudinal modulation of the refractive index with given periodicity. Such a modulation acts as a phase grating, the structure is indeed called 'fiber Bragg grating' (FBG). The behavior can be understood by similarity with a multilayer dielectric mirror: a sequence of weakly reflecting surfaces can become a high reflectivity structure if a constructive interference condition is established among all the reflected fields. Calling Λ the grating period, such a condition requires that the phase shift suffered by the field propagating over the distance Λ be π (or a multiple of π) – the condition is satisfied for the wavelength λ_o given by:

$$\lambda_o = 2n\Lambda \qquad [8]$$

where n is the average refractive index of the fiber core. If we call Δn the amplitude of the refractive-index modulation and N the number of grating periods, the peak reflectivity is given by:

$$R_{\max} = \tan h^2\left(N\frac{\Delta n}{n}\right) \qquad [9]$$

Typically the grating length L is of the order of millimeters, that is, $N = L/\Lambda$ is in the range $10^3 - 10^4$. Therefore $R_{\max}$ can be close to 100%, even if Δn is small. The bandwidth of the FBG mirror is a decreasing function of N, so that the reflectivity peak can become very narrow for large N.

FBGs are fabricated by exploiting the photosensitivity of the Ge-doped core of silica fibers. The presence of Ge atoms leads to the formation of oxygen-deficient bonds that represent defects in the silica matrix. The energy required to break the bond is about 5 eV. The absorption of a 244-nm photon from an excimer laser can break the defect-bond, resulting in a change of absorption spectrum and in a corresponding change in refractive index. Since index changes occur only in the spatial regions where ultraviolet light is absorbed, by illuminating the fiber core with a periodic intensity pattern an index-of-refraction grating is generated.

Fiber Amplifiers and Lasers

An important family of materials used for optical amplification is represented by dispersions of rare-earth ions, such as neodymium or erbium or ytterbium, in a solid matrix that can consist of a crystal or a glass. An interesting extension of the idea of the rare-earth solid-state optical amplifier is the fiber amplifier, which utilizes silica fibers doped with rare-earth ions. Optical amplification is extremely important in long-distance optical-communication links in order to compensate for fiber attenuation, so that the optical power can be maintained at sufficiently high levels along the path to ensure a satisfactory signal-to-noise ratio. Doped fibers can provide wide-band amplification at wavelengths around 1550 nm, corresponding to the attenuation minimum for silica fibers.

The most important fiber amplifier is based on Erbium-doped silica fibers and uses a transition of the Er^{3+} ion in a wavelength range extending from 1530 to 1560 nm. The energy level diagram of the ion Er^{3+} is shown in Figure 6. The upper level of the 1530-nm transition is metastable (with a lifetime of 12 ms), thus permitting to easily achieve population inversion by exciting the ion with radiation at 980 or 1480 nm. The pump field comes from a semiconductor laser, either GaAlAs (980 nm) or InGaAsP (1480 nm). A scheme of the amplifier configuration is shown in Figure 7. The pump field and the signal field are injected into the single-mode doped fiber by using a dichroic coupler. After the doped fiber an optical isolator is inserted in order to eliminate back-reflections. The length of the amplifying fiber is typically around 10 m, and the optical gain can be as large as 10 000. The efficiency

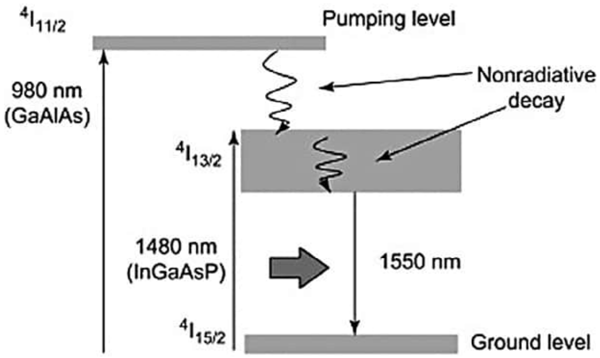

Figure 6 Energy levels of the Er^{3+} ion.

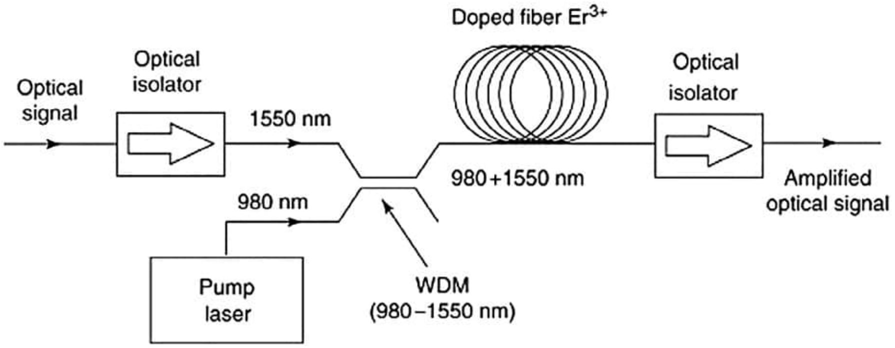

Figure 7 Scheme of an Erbium-doped fiber amplifier, pumped by a semiconductor laser. WDM (Wavelength Division Multiplexer) indicates a wavelength dependent combiner.

of the amplifier is large because the single-mode fiber ensures a very good spatial overlap between pump field and signal field. The conversion efficiency can be further improved by using a mixed erbium–ytterbium doping.

Any optical amplifier can be converted into a laser oscillator if a positive feedback scheme is provided. The fiber amplifier can become a fiber laser by placing the amplifier in between two mirrors, constituted, for instance, by two FBGs. Since the fiber is very thin, the surface to volume ratio is large, thus permitting very efficient heat dissipation without using the water-circulation cooling system typical of power lasers. When using a single-mode fiber, the output beam has a very smooth Gaussian profile, therefore it can be focused to a very small focal spot, at variance with the behavior of high-power semiconductor or Nd-YAG lasers. Fiber lasers can work either continuous or pulsed. Rare-earth-doped fibers with their broad gain bandwidth are convenient laser media for the generation of ultrashort optical pulses.

In order to improve the coupling between the semiconductor pump laser and the amplifier, a new fiber geometry involving a double cladding was introduced. A very successful fiber laser using such geometry is the ytterbium laser, which is pumped around 915 nm and can emit in a wide band centered around 1100 nm. Continuous-wave Yb fiber lasers with an output power as large as 1 kW and efficiency of 75–80% are now available. Because of its efficiency, compactness, and simplicity of cooling requirements, the Yb fiber laser is often used in industrial processes, such as marking, welding, and precision cutting.

Nonlinear Fiber Optics

Nonlinear optical effects are particularly efficient in single-mode optical fibers despite the relatively small third-order susceptibility of silica glass. The reason for this is that the spot size of the propagating beam is small and the interaction length can be very long, due to wave guiding and to low losses. A point of great conceptual relevance is that most of the treatments of nonlinear propagation are developed for plane waves, whereas experiments in bulk materials are performed with laser beams that can be considered as Gaussian waves. Therefore diffraction can play a significant role in the experiments, making the comparison with the plane-wave theory sometime difficult. The nonlinear propagation inside the optical fiber can be treated in most cases by assuming that the transversal field distribution is invariant along the propagation distance, so that the propagation problem becomes spatially unidimensional as in the case of the plane-wave approach. This makes much simpler the comparison between theory and experiment.

The two most important nonlinear phenomena in nonlinear fiber optics are the optical Kerr effect and stimulated Raman scattering (SRS).

The optical Kerr effect, that is, the linear dependence of the index of refraction on the beam intensity, gives rise to a self-induced phase shift experienced by the optical field during its propagation, called self-phase modulation (SPM). SPM is responsible for the spectral broadening of optical pulses. In normal dispersion the consequence is that SPM gives an additional contribution to the spreading out in time of the pulse. There is however an interesting situation, corresponding to positive Kerr effect and negative GVD, in which there is a compensation between the two effects, so that an optical pulse of appropriate intensity and shape (optical soliton) can propagate with constant shape and amplitude over a distance that is limited in practice only by the linear attenuation in the fiber. Indeed, several beautiful experiments showing the onset and development of solitonic propagation have been performed. With standard fibers the wavelength range of negative GVD is above 1.3 μm, but the new fibers presenting an air-silica microstructure (see the Section Special Fibers) can shift to lower wavelengths the negative GVD region, as shown in Figure 4, so that solitonic propagation in the visible can be observed.

Concerning SRS, we recall that, starting from a pump wave at frequency υ_p, the effect of SRS is that of generating a strong signal, called the Stokes wave, at a frequency $\upsilon_s = \upsilon_p - \upsilon_\nu$, where υ_ν is a vibrational frequency typical of the considered medium. In the case of silica fibers, the main effect is associated with vibrations of the Si–O bond, occurring at $\upsilon_\nu = 12$ THz. SRS can be used to amplify a weak signal at frequency υ_s in presence of a pump υ_p. Raman amplification is very attractive for applications in optical communications because, at variance with what happens in erbium-doped fiber amplifiers, it is non-resonant, so that it can be used for any υ_s, provided the appropriate pump is available.

SRS is a very interesting method not only to amplify signals, but also to generate new laser wavelengths by converting the Raman fiber amplifier into an oscillator. The availability of high-power diode lasers as pump sources and the development of high reflectivity FBGs makes it possible the realization of nested cavities in which several Stokes lines can simultaneously resonate. In this configuration the pump power can be very efficiently converted to the highest-order Stokes line.

Further Reading

Agrawal GP (2006) *Nonlinear Fiber Optics*, fourth ed New York, NY: Academic Press.
Bjarklev A, Broeng J, and Sanchez Bjarklev A (2003) *Photonic Crystal Fibers*. New York, NY: Springer.
Hecht J (2005) *Understanding Fiber Optics*, fifth ed Harlow: Prentice Hall.
Rini M, Cristiani I, and Degiorgio V (2000) Numerical modeling and optimization of cascaded CW Raman fiber laser. *IEEE Journal of Quantum Electronics* 36: 1117.
Saleh BEA and Teich MC (2007) *Fundamentals of Photonics*, second ed New York, NY: Wiley.
Wilson J and Hawkes J (1998) *Optoelectronics: An Introduction*. Harlow: Prentice Hall.

Light Emitting Diodes[☆]

E Fred Schubert[a], **Jaehee Cho**[b], **and Jong Kyu Kim**[c], [a]Rensselaer Polytechnic Institute, Troy, NY, United States; [b]Chonbuk National University, Jeonju, South Korea; [c]Pohang University of Science and Technology, Pohang, South Korea

© 2016 Elsevier Inc. All rights reserved.

This is an update of E. Fred Schubert, Jaehee Cho, Jong Kyu Kim, Light Emitting Diodes, Reference Module in Materials Science and Materials Engineering, Elsevier, 2016, ISBN 9780128035818, https://doi.org/10.1016/B978-0-12-803581-8.01081-X.

Introduction 815
Recombination in Direct-Gap and Indirect-Gap Semiconductors 815
Optical Emission Spectrum 816
Homostructures and Heterostructures 817
Light-Extraction in LEDs 819
White LEDs 820
DUV LEDs 824
LED Packaging 825
References 826

Introduction

During the past 100 years, light-emitting diodes (LEDs) have undergone a significant evolution. The first LED emitting in the visible wavelength region was based on a SiC compound semiconductor. The device had an external quantum efficiency (EQE) of much less than 1.0%. Today, the external efficiencies of red LEDs based on AlGaInP can exceed 50%; this semiconductor is also capable of emitting in the orange, amber, and yellow wavelength range. AlGaInN compounds can emit efficiently in the near ultraviolet (near UV), violet, blue, cyan, and green wavelength range. Thus, all colors of the visible spectrum are covered by semiconductor materials. This has opened up the use of LEDs in areas as diverse as indicator, signage, display, and lighting applications. In particular, as device output powers continuously increase, LED lamps have reached luminous flux levels of, for example, 800 lm, comparable to those of conventional incandescent and fluorescent lamps. Furthermore, LED lifetimes exceeding 20000 h compare favorably with incandescent sources (~ 500 h) and fluorescent sources (~ 5000 h) thereby contributing to the attractiveness of LEDs.

Inorganic LEDs are generally based on p–n junctions. However, in order to achieve high internal quantum efficiencies, free carriers need to be spatially confined. Furthermore to reduce reabsorption effects, the bandgap energy of the confinement layers should be greater than the bandgap energy of the active region. These requirements led to the development of heterostructure LEDs that employ different semiconductor materials (i.e., alloy compositions) for the light-emitting active region and the confinement regions. Particularly popular are multiple quantum wells (QWs) embedded into the active region. The light-extraction efficiency, which measures the fraction of photons leaving the semiconductor die (and thus become useful, i.e., visible photons), is strongly affected by the device shape and surface structure. For devices with high internal-efficiency, maximizing the light-extraction efficiency is a key challenge.

This article concerns inorganic LEDs and introduces the basic concepts of optical emission. Band diagrams of direct-gap and indirect-gap semiconductors and the spectral shape of spontaneous emission will be discussed along with electrical properties and current flow. Subsequently, strategies to improve light extraction out of the LED chip are presented including surface roughening and chip shaping. Due to total internal reflection at the surfaces of an LED chip, the light-extraction efficiency in standard devices is well below 100%. A particular challenge in achieving efficient emission is the minimization of optical absorption processes inside the semiconductor. This can be achieved by, for example, covering absorbing regions, such as absorbing substrates, with highly reflective mirrors. The development of white LEDs, including phosphor-based approaches and multiple-LED approaches, is presented and their properties, such as color rendering and luminous efficacy, are discussed. A short section will address the accomplishments and challenges in deep ultraviolet (DUV) LEDs. Finally, the current state of the art in LED packaging including packages with low thermal resistance, will be discussed.

Recombination in Direct-Gap and Indirect-Gap Semiconductors

The probability that electrons and holes recombine radiatively is proportional to the product of electron and hole concentration, that is, $R \propto np$. The recombination rate per unit time per unit volume can be written as

$$R = -\frac{\mathrm{d}n}{\mathrm{d}t} = -\frac{\mathrm{d}p}{\mathrm{d}t} = Bnp \tag{1}$$

[☆] *Change History*: March 2015. E.F. Schubert, J. Cho, and J.K. Kim completely rewrote the article.

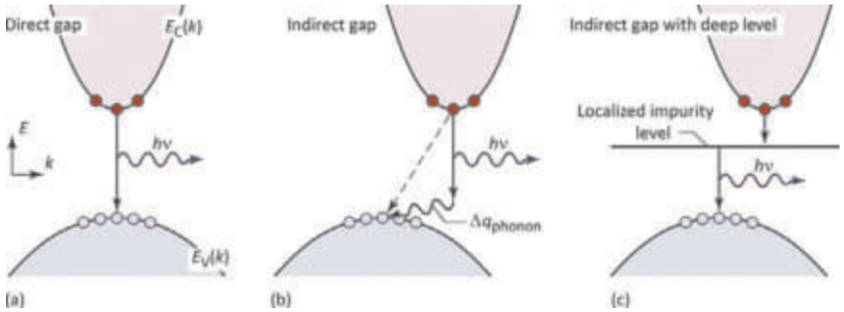

Figure 1 Semiconductor band structure for a (a) direct-gap semiconductor, (b) indirect-gap semiconductor, and (c) indirect-gap semiconductors with a deep isoelectronic impurity level. Indirect radiative transitions have a much smaller probability due to the requirement of a phonon.

where B is a proportionality constant, the bimolecular recombination coefficient, with a typical value of 10^{-10} cm^3 s^{-1} for direct-gap III–V semiconductors. Fundamental types of band structures and associated recombination processes are shown in Figure 1.

During the recombination process, the electron momentum ($p=(2m^*E)^{1/2}$) cannot change significantly because momentum must be conserved and the photon momentum ($p=h/\lambda$) is negligibly small. Thus optical transitions must be 'vertical' in nature, that is, electrons recombine only with holes that have the same k value as shown in Figure 1. Efficient recombination occurs in direct-gap semiconductors shown in Figure 1(a). However, the recombination probability is much lower in indirect-gap semiconductors because a phonon is required to satisfy momentum conservation, as shown in Figure 1(b). The radiative efficiency of indirect-gap semiconductors can be increased by isoelectronic impurities, for example, N in GaP. Isoelectronic impurities can form an optically active deep level that is localized in real space (small dx) but, according to the uncertainty relation, delocalized in k space (large dk), so that the impurity can satisfy the momentum conservation, as indicated in Figure 1(c). During nonradiative recombination, the electron energy is converted to vibrational energy of lattice atoms, that is, phonons. There are several physical mechanisms by which nonradiative recombination can occur with the most common ones being nonradiative recombination at point defects (impurities, vacancies, interstitials, anti-site defects, and impurity complexes) and spatially extended defects (screw and edge dislocations, cluster defects, and surfaces of structural cracks). It is quite common for such defects to form one or several energy levels within the forbidden gap. The defects act as efficient recombination centers (Shockley–Read–Hall or SRH recombination centers), particularly if the center's energy level is close to the middle of the gap.

Optical Emission Spectrum

The spectral line-width of spontaneous emission can be calculated to be 1.8 kT (see, e.g., Schubert, 2006). The theoretical emission spectrum is shown in Figure 2. The line-width of 1.8 kT is caused by the thermal energy of carriers and is therefore referred to as the 'thermal broadening.' It indicates that the line-width broadens with increasing temperature. It also indicates that the line-width becomes narrower at cryogenic temperatures. For example, at room temperature, the theoretical line-width of a GaAs LED emitting at 870 nm is $\Delta E=46$ meV or $\Delta\lambda=28$ nm.

The spectral line-width of LED emission is important in several respects. *Firstly*, the line-width of an LED emitting in the visible range is relatively narrow compared with the range of the entire visible spectrum. Furthermore, the LED emission is narrower than the spectral width of a single color as perceived by the human eye. For example, *red* colors range from 625 to 770 nm ($\Delta\lambda=105$ nm), which is much wider than the typical emission spectrum of a red LED ($\Delta\lambda\approx25$ nm). Therefore, LED emission is perceived (by the human eye) as *monochromatic*. *Secondly*, optical fibers are dispersive, which leads to a range of propagation velocities for a light pulse comprising a range of wavelengths. The material dispersion in optical fibers limits the '*bit rate × distance product*' achievable with LEDs. The spontaneous lifetime of carriers in LEDs in direct-gap semiconductors typically is on the order of 1–100 ns depending on the active region doping concentration (or carrier concentrations) and the material quality. Thus, modulation speeds up to 1 Gbit s^{-1} are attainable with LEDs.

In practice, the emission line-width is usually broader than the theoretical value of 1.8 kT. A spectral width of 1.8 kT is expected for the thermally broadened emission. However, due to other broadening mechanisms, the line-width can exceed the theoretical value. A prominent broadening mechanism among ternary and quaternary III–V alloy semiconductors is *alloy broadening*, i.e., the statistical fluctuation of the active region's alloy composition. Alloy broadening is independent of temperature and can broaden the line-width to 2 to 5 times of its thermally broadened value. For example, at room temperature, GaInN blue and green LEDs can have a line-width of 3–10 kT.

Figure 3 shows typical LED emission spectra at room temperature. The emission spectra include an AlGaInP/GaAs red, GaInN/GaN green, GaInN/GaN blue, GaInN/GaN UV, and an AlGaN/AlGaN DUV LED. The active region of visible-spectrum LEDs is typically comprised of a ternary or quaternary alloy, for example, $Ga_{1-x}In_xN$ or $(Al_xGa_{1-x})_{0.5}In_{0.5}P$. An idealized alloy-broadened emission spectrum has a Gaussian lineshape. It may be noted that deep UV LEDs are not yet as mature as visible-spectrum devices. For example, the emission spectrum of the 290 nm device shown in Figure 3 has a low energy shoulder that is due to an undesired parasitic emission, most likely a defect-related emission.

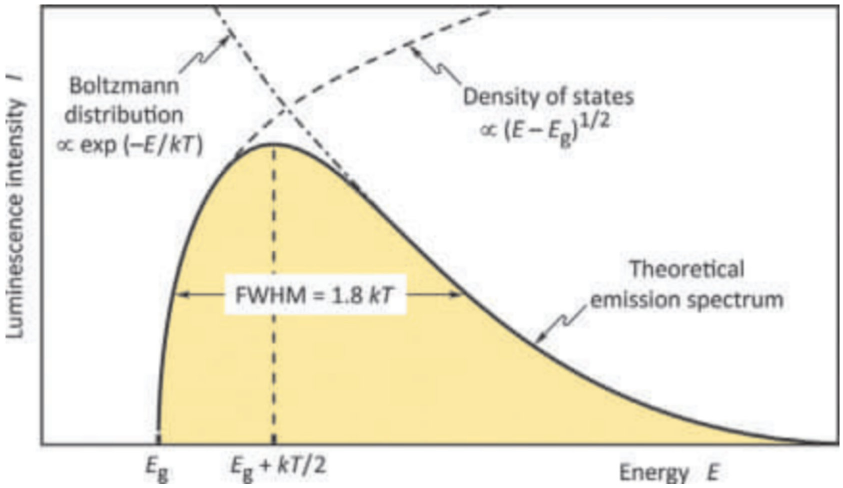

Figure 2 Theoretical emission spectrum of an LED. The full-width at half-maximum (FWHM) of the emission line is 1.8 *kT*.

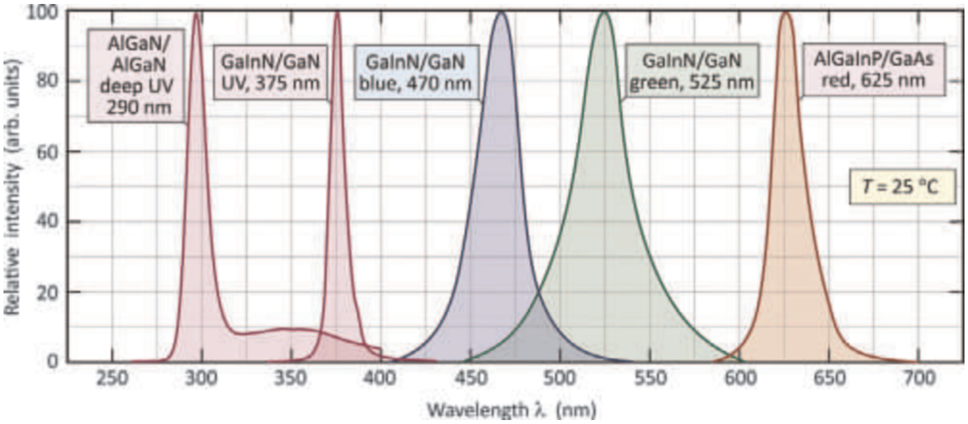

Figure 3 Emission spectra, at room temperature, of AlGaInP/GaAs red, GaInN/GaN green, GaInN/GaN blue, GaInN/GaN UV, and AlGaN/AlGaN DUV LEDs.

Homostructures and Heterostructures

In the vicinity of the unbiased p–n junction plane, electrons originating from donors on the n-type side diffuse to the p-type side where they recombine, as shown in the band diagram of Figure 4. A corresponding process occurs with holes. As a result, a region near the p–n junction, the *depletion region*, is depleted of free carriers. In the absence of free carriers, the types of charges in the depletion region are ionized donor and acceptor charges. The charges in the depletion region produce a potential, the *built-in potential*, V_{bi}, given by

$$V_{\mathrm{bi}} = \frac{kT}{e} \ln \frac{N_{\mathrm{A}} N_{\mathrm{D}}}{n_{\mathrm{i}}^2} \qquad [2]$$

where N_{A} and N_{D} is the acceptor and donor concentration, respectively, and n_{i} is the intrinsic carrier concentration of the semiconductor. The built-in voltage represents a barrier that free carriers must overcome in order to reach the neutral region of opposite conductivity type.

The width of the depletion region is given by

$$W_{\mathrm{D}} = \sqrt{\frac{2\varepsilon}{e}(V_{\mathrm{bi}} - V)\left(\frac{1}{N_{\mathrm{A}}} + \frac{1}{N_{\mathrm{D}}}\right)} \qquad [3]$$

where $\varepsilon = \varepsilon_{\mathrm{r}}\varepsilon_0$ is the dielectric permittivity of the semiconductor and V is the diode bias voltage.

An external bias applied to a p–n junction will drop across the depletion region, which is resistive due to the lack of free carriers. A forward bias decreases the p–n junction barrier causing electrons and holes to be injected into the neutral regions with

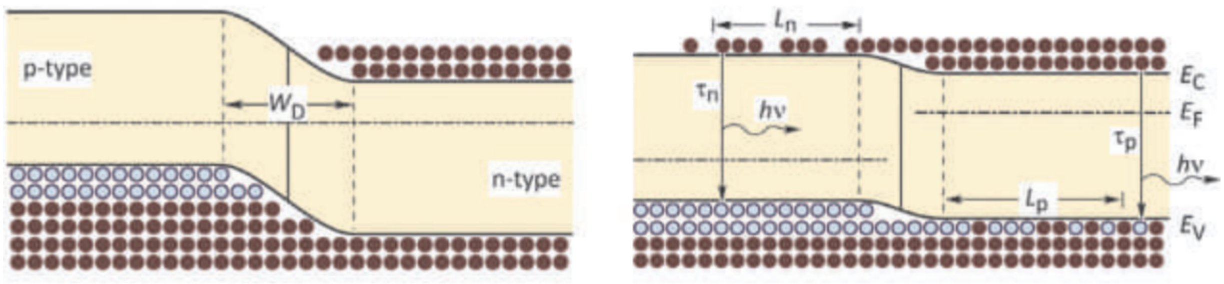

(a) Homojunction in equilibrium

(b) Homojunction under forward bias

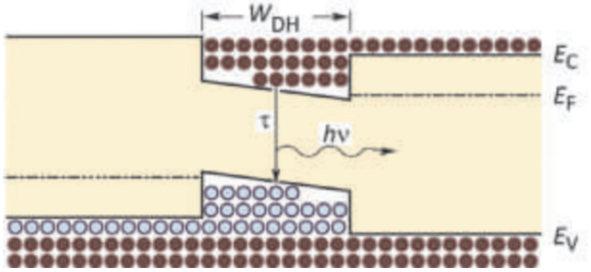

(c) Heterojunction under forward bias

Figure 4 Free carrier distribution in (a) homostructure under equilibrium conditions, (b) forward-biased homostructure, and (c) forward-biased double heterostructure (DH). $L_{n/p}$ and $\tau_{n/p}$ are the minority carrier diffusion lengths and lifetimes, respectively. W_D is the width of the depletion region. In the forward-biased homostructure, carriers are distributed over the diffusion length ($L_n + L_p$); in a DH, they are distributed over the thickness of the DH (W_{DH}). The carrier confinement provided by the DH reduces SRH recombination.

opposite conductivity type. As the injection current increases, carriers diffuse into the regions of opposite conductivity type and recombine, thereby emitting photons.

The theory of current transport in p–n junctions was first developed by William B. Shockley in the early 1950s and the equation describing the *I*–*V* characteristic is known as the *Shockley equation*

$$I = eA\left(\sqrt{\frac{D_p}{\tau_p}}\frac{n_i^2}{N_D} + \sqrt{\frac{D_n}{\tau_n}}\frac{n_i^2}{N_A}\right)\left(e^{eV/kT} - 1\right) \qquad [4]$$

where A is the junction area and $D_{n,\ p}$ and $\tau_{n,\ p}$ are the electron and hole diffusion constants and minority carrier lifetimes, respectively.

Under typical forward bias conditions, the diode voltage is $V \gg kT/e,$ and thus $[\exp\,(eV/kT) - 1] \approx \exp\,(eV/kT)$. For such forward bias conditions, the Shockley equation can be rewritten as

$$I = e\,A\left(\sqrt{\frac{D_p}{\tau_p}}N_A + \sqrt{\frac{D_n}{\tau_n}}N_D\right)e^{e\,(V - V_{bi})/kT} \qquad [5]$$

The exponent in the equation illustrates that the current strongly increases as the diode voltage approaches a *threshold*, which is about equal to the built-in voltage, i.e., $V_{th} \approx V_{bi}$.

In an ideal diode, every electron injected into the active region will generate a photon. Thus conservation of energy requires that the electron energy eV equals the photon energy $h\nu$, i.e.,

$$eV = h\nu \qquad [6]$$

Beyond turn-on, the diode becomes highly conductive and the diode voltage V is about the same as the threshold voltage V_{th}. The energy of photons emitted from a semiconductor with energy gap E_g is given by

$$h\nu = E_g + (1/2)kT \approx E_g \qquad [7]$$

Thus eqn [6] can be rewritten as

$$V_{th} \approx V_{bi} \approx E_g/e \qquad [8]$$

For example, a GaAs IR LED emitting at 870 nm has a threshold voltage of about 1.4 V; similarly, a GaInN blue LED has a threshold voltage of about 2.8 V.

Homojunction LEDs have significant drawbacks and hence are no longer used. At the present time, virtually all commercial devices are heterojunction LEDs. Heterojunction active regions have several advantages that will be discussed below.

The effect of a double heterostructure (DH) on the carrier concentration is illustrated in **Figure 4**. Under forward bias, carriers diffuse across the p–n junction. In the case of a homostructure under forward bias, minority carriers are distributed over the electron and hole diffusion lengths as illustrated in **Figure 4(b)**. In III–V semiconductors, diffusion lengths can be 10 μm or longer. The wide distribution of carriers and the correspondingly low carrier concentration (particularly toward the end of the diffusion tail) can be avoided by the employment of DHs. Carriers are confined to the active region of width W_{DH}, as shown in **Figure 4 (c)**. To attain good carrier confinement, the barrier heights should be much greater than the thermal energy kT.

An important advantage of the DH design is illustrated in **Figure 5**. The DH structure has a much smaller number of defects within the recombination region so that nonradiative SRH recombination via deep levels is much less significant in a DH and in QW active regions. As a result, DH or QW LEDs have a much higher efficiency than homostructure LEDs.

The term 'DHs' is frequently used for active layers with thickness of 100 to 500 nm. The term 'QW' active region is used for active layers with thickness of 2 to 100 nm. Single quantum well (SQW) and multi-quantum well (MQW) active regions provide additional carrier confinement, which can further improve the internal quantum efficiency. If a MQW active region is used, the barriers between the wells may impede the flow of carriers between adjacent wells. Thus the barriers in a MQW active region need to be sufficiently 'transparent' (low and/or thin barriers) in order to allow for efficient carrier transport between the wells and to avoid the inhomogeneous distribution of carriers within the active region.

Another advantage of DH and QW structures is the optical transparency of the barrier layers. That is, the two cladding layers (cladding the active region) have a wider bandgap than the active region. That is, light generated in the active region cannot be absorbed in the cladding layers because their bandgap energy is greater than the photon energy ($E_g > h\nu$).

Light-Extraction in LEDs

Owing to the high refractive index of semiconductors, light incident on a planar semiconductor–air interface is totally internally reflected, if the angle of incidence is sufficiently large. Snell's law gives the critical angle of total internal reflection. As a result of total internal reflection, light can be 'trapped' inside the semiconductor chip. Light trapped in the chip will eventually be reabsorbed, for example, by the substrate, active region, cladding layer, or by a metallic contact.

If the light is absorbed by the substrate, the electron–hole pair will most likely recombine non-radiatively due to the inherently low efficiency of substrates. If the light is absorbed by the active region, the electron–hole pair may re-emit a photon or recombine non-radiatively. For active regions with internal quantum efficiencies of less than 100%, any reabsorption event will reduce the efficiency of the LED. For this reason, light should be coupled out of the LED chip with the shorted possible path length inside the chip.

If the angle of incidence of a light ray is close to normal incidence, light can escape from the semiconductor. However, total internal reflection occurs for light rays with oblique and grazing-angle incidence. Total internal reflection reduces the EQE significantly, in particular for LEDs consisting of high-refractive-index materials.

Assume that the angle of incidence in the semiconductor at the semiconductor–air interface is given by ϕ. Then the critical angle of total internal reflection, ϕ_c, can be inferred from Snell's law and is given by

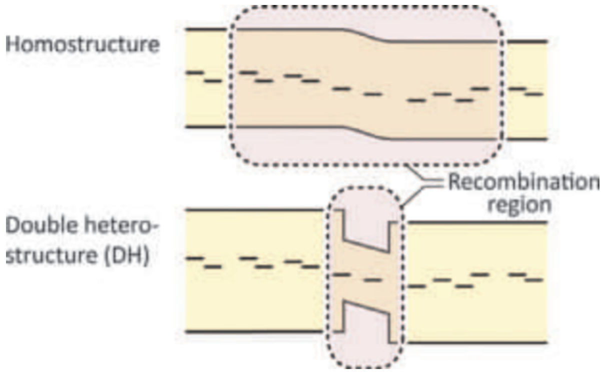

Figure 5 In a double heterostructure (or QW structure), the recombination region, and thus the number of defects contained in this region, is much smaller than in a homostructure. Therefore, nonradiative SRH recombination will play a much smaller role in DH active regions (as well as QW active regions).

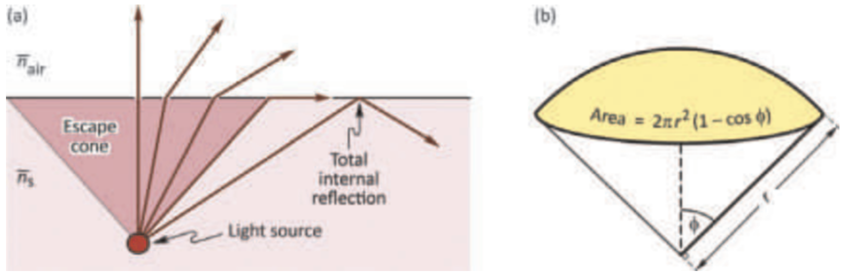
(a)
$\overline{n}_{\text{air}}$
Escape cone
$\overline{n}_{\text{s}}$
Total internal reflection
Light source
(b)
Area = $2\pi r^2(1-\cos\phi)$
ϕ
r

Figure 6 (a) Illustration of refraction and total internal reflection at a semiconductor–air interface. (b) Definition of the escape cone by the critical angle ϕ_c. Area of calotte-shaped section of the sphere defined by radius r and angle ϕ_c.

$$\phi_c = \arcsin\frac{\overline{n}_{\text{air}}}{\overline{n}_{\text{s}}} \qquad [9]$$

The refractive indices of semiconductors are usually quite high. For example, GaAs has a refractive index of 3.4. Thus, according to eqn [9], the critical angle for total internal reflection is quite small. In this case, we can use the approximation $\sin\phi_c \approx \phi_c$. The critical angle for total internal reflection is then given by

$$\phi_c \approx \frac{\overline{n}_{\text{air}}}{\overline{n}_{\text{s}}} \qquad [10]$$

The angle of total internal reflection defines the light escape cone, as shown in Figure 6(**a**). Light emitted into the cone can escape from the semiconductor, whereas light emitted outside the cone is subject to total internal reflection.

Calculating the surface area of the spherical cone with radius r allows one to determine the total fraction of light that is emitted into the light escape cone. The surface area of the calotte-shaped surface is shown in Figure 6(**b**). The fraction of the light emitted inside a semiconductor can escape from the semiconductor is given by

$$\frac{P_{\text{escape}}}{P_{\text{source}}} = \frac{1}{2}(1-\cos\phi_c) \approx \frac{1}{4}\frac{\overline{n}^2_{\text{air}}}{\overline{n}^2_{\text{s}}} \qquad [11]$$

The escape problem is a significant problem for high-efficiency LEDs. In most semiconductors, the refractive index is quite high ($\overline{n} \geq 2.5$) and thus only a small percentage of the light generated in the semiconductor can escape from a planar LED. The problem is less significant in semiconductors with a small refractive index and for polymers, which have refractive indices of the order of 1.5.

The light escape problem, illustrated in Figure 7 (**a**), has been known since the infancy of LED technology in the 1960s. It has also been known that the geometrical shape of the LED die plays a critical role. The optimum LED would be spherical in shape with a point-like light-emitting region in the center of the LED. Unfortunately, spherical LEDs with a point-like light source in the center of the LED are impractical. Semiconductor fabrication technology is, in view of the flat substrates used in epitaxial growth, a planar technology. Thus spherical LEDs would be exceedingly difficult to fabricate using conventional processing technologies.

More realistic alternatives include the resonant-cavity LED (see Figure 7(**b**)), surface-textured LEDs (see Figure 7 (**c**)), and chip-shaped LEDs (see Figure 7(**d**)).

A popular method to increase the light-extraction efficiency is the use of ***roughened*** or ***textured semiconductor surfaces***, first introduced by Bergh and Saul (1973) for GaP-based devices. The authors showed that, at the first instance the light is incident at the semiconductor–air interface, the same amount of light escapes from a rough surface plane as does from a smooth surface plane. However, since the reflections occur at random angles, a similar proportion of light will escape at the second and subsequent instances the light ray is incident on the roughened surface. This is in contrast to a smooth surface plane which preserves reflection angles and thus traps the reflected light. Figure 8(**a**) illustrates the enhanced out-coupling of a light ray through a roughened surface.

GaN textured surfaces created by crystallographic etching (Stocker *et al.*, 1998) are very well suited to enhance light extraction. Several publications reported an increase in light extraction in GaN-based LEDs with surface texturing achieved by crystallographic wet chemical etching (Gao *et al.*, 2004; Fujii *et al.*, 2004; Jung *et al.*, 2010; Horng *et al.*, 2011). The strongly textured GaN surfaces shown in Figure 8(**b**) reveal the exposure of a variety of crystal planes that are indicative of a crystallographic etch (Haerle, 2004; Jung *et al.*, 2010).

White LEDs

High-efficiency red, orange, and yellow devices (AlGaInP LEDs) had been developed in the 1980s. High-efficiency violet, blue, and green devices (GaInN LEDs) had been developed in the 1990s. Therefore, in the mid-1990s monochromatic high-efficiency devices, covering the entire visible spectrum, were available. As a result, the generation of white light by LEDs had been enabled. There are several approaches for white LEDs:

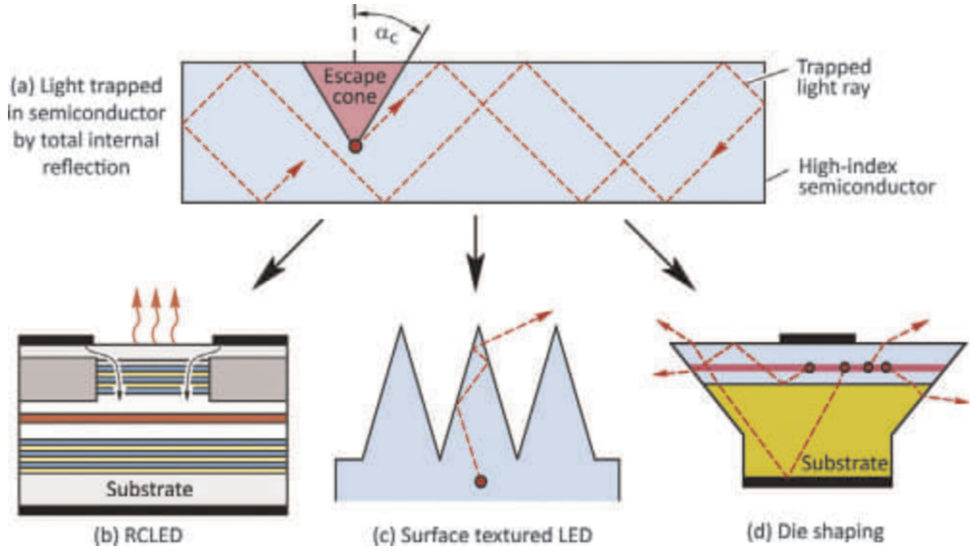
α_c
(a) Light trapped in semiconductor by total internal reflection
Escape cone
Trapped light ray
High-index semiconductor
Substrate
Substrate
(b) RCLED
(c) Surface textured LED
(d) Die shaping

Figure 7 (a) Light rays emanating from a point-like emitter are trapped inside the semiconductor due to total internal reflection. Only light rays with propagation directions falling within the escape cone can leave the semiconductor. Strategies increasing the extraction efficiency include the (b) resonant-cavity LED, (c) surface-textured LED, and (d) die-shaped LED.

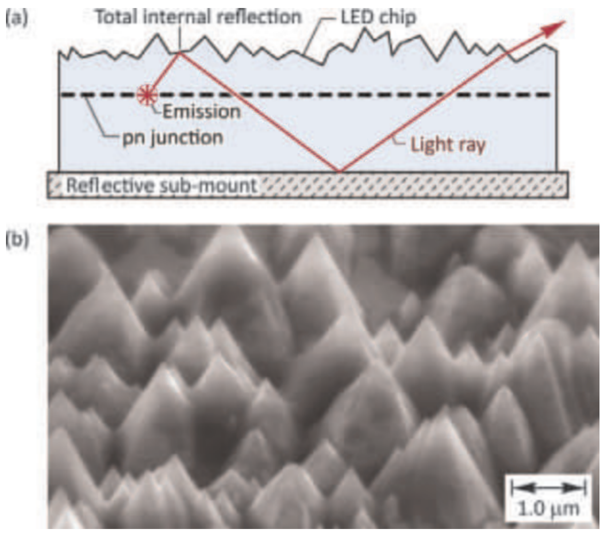
(a)
Total internal reflection
LED chip
Emission
pn junction
Light ray
Reflective sub-mount
(b)
1.0 µm

Figure 8 (a) LED chip with roughened surface enabling out-coupling of light (after Bergh and Saul, 1973). (b) Scanning electron micrograph (SEM) of N-face GaN surface after crystallographic wet chemical etching using a KOH-solution (after Jung *et al.*, 2010).

A *first* approach is a multi-LED approach in which the light from multiple LEDs emitting different colors is mixed to create white light. This approach became feasible with the demonstration of highly efficient blue and green LEDs (Nakamura *et al.*, 1994,1995). Nakamura *et al.* (1995) stated: "By combining high-power and high-brightness blue InGaN SQW LED, green InGaN SQW LED and red GaAlAs LED, many kinds of applications, such as LED full-color displays and LED white lamps for use in place of light bulbs or fluorescent lamps, are now possible with characteristics of high reliability, high durability and low energy consumption."

A *second* approach is a UV-LED-plus-multi-color-phosphor combination (Baretz and Tischler, 2003). However, this approach suffers from a lower efficiency compared with the multi-LED approach since UV light is converted to visible light whereby a significant fraction of the energy is being lost. We note that this approach is similar to a conventional fluorescent lamp; in both cases UV light is converted into visible light by means of a phosphor.

A *third* approach is a blue-LED-plus-yellow-phosphor combination. This approach is most efficient and most successful. Due to the complementary nature of blue and yellow light, white light can be created by the mixture of blue light from an LED chip, and yellow light from a yellow phosphor. Cerium-doped yttrium-aluminum garnet phosphor (Ce-doped YAG), a stable and highly

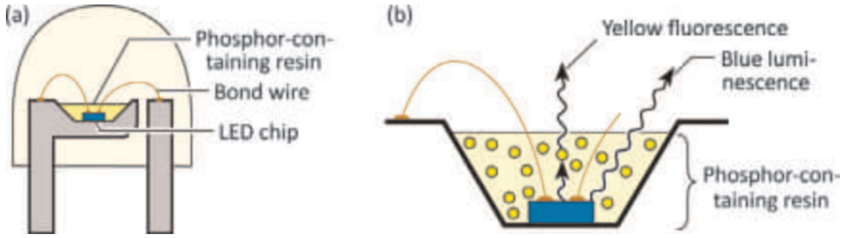

Figure 9 (a) White LED lamp consisting of a GaInN blue LED chip and a yellow YAG:Ce phosphor. (b) Blue luminescence and wavelength-converted yellow fluorescence (after Nakamura and Fasol, 1997).

efficient yellow phosphor, was first used for a white LED by Bando *et al.* (1996, 1998), as further described by Nakamura and Fasol (1997) and Shimizu *et al.* (1999).

The third approach evolved into a pervasive commercial success, in part due to its efficiency, simplicity, and the requirement of only one LED chip driven by only one power supply.

Indeed, on September 13, 1996, a new era in lighting began: An article in the Japanese newspaper Nikkei (1996) announced a new type of white light LED, based on a blue LED chip and a yellow Ce-doped YAG phosphor, as shown in **Figure 9**. The white LED was reported to be efficient (5 lm W^{-1}), low cost, and have a predicted lifespan of 50 000 h. What was announced in a relatively short newspaper article was a novel light source that was set to revolutionize the world of lighting.

In October 1996, full-scale production of the phosphor-converted white LED started at the Nichia Company in Anan, Japan. On November 29, 1996, technical details of Nichia's white LED were presented at a technical meeting of the Institute of Phosphor Society (Japan) and the associated 264th Proceedings of the Institute of Phosphor Society (Japan). The emission spectrum of the first phosphor-converted white LED is shown in **Figure 10** (Bando *et al.*, 1996). The emission spectrum is continuous covering nearly the entire visible wavelength range. Compared with the 'spiky' emission spectrum of the then-common compact fluorescent lamps (CFLs), the quality of the white light emitted by the LED was superior. Likewise, compared with the power consumption of the then-common incandescent light bulbs, the prospect of white LEDs, in terms of power consumption, was far superior. Thus, the foundation of a new LED white light source, that was poised to replace conventional white light sources, had been established.

Whereas organic phosphors (dyes having carbon ring molecules) had been initially used to generate white light, these organic phosphors simply were not sufficiently stable: When subjected to the high optical radiation density of an LED chip, the double bonds of the organic phosphor molecules break thereby degrading the phosphor molecule (frequently containing aromatic rings). The first successful and commercially viable white LED was based on a yellow garnet phosphor, $Y_3Al_5O_{12}$ doped with the optically active element Ce. Such YAG:Ce phosphors are characterized by (1) an optical absorption band in the blue spectral range, (2) an emission band that has a peak wavelength of about 550–580 nm, (3) high chemical stability, (4) high stability under high optical irradiance as encountered in proximity of a high-brightness blue LED chip, (5) short radiative lifetime (about 50–80 ns), and (6) tunability of the optical emission spectrum by chemical modifications of the YAG host material, for example, the substitution of Y atoms by Gd atoms and of Al atoms by Ga atoms yielding a phosphor with the general formula $(Y_{1-x}Gd_x)_3(Al_{1-x}Ga_x)_5O_{12}:Ce$. These favorable characteristics have made YAG:Ce the phosphor of choice for white LEDs.

At the present time, 'phosphor blends' are frequently employed. Such phosphor blends are a mixture of multiple phosphor materials. Common phosphors include the YAG:Ce family of phosphors, Eu-doped silicate phosphors emitting in the green spectral range and Eu-doped nitride phosphors emitting in the red spectral range. **Figure 11** shows typical emission spectra of white LEDs with low, medium, and high color temperatures. As the color temperature of the light source is decreased, (1) the relative phosphor emission increases and (2) a red phosphor with a peak wavelength of about 600–650 nm is added.

The temporal evolution of the luminous efficiency of light sources is shown in **Figure 12**. The figure shows the following light sources: Incandescent lamp with C filament demonstrated in 1879 by Thomas A. Edison; Incandescent lamp with ductile W filament demonstrated in 1911 by William D. Coolidge; Linear fluorescent lamp (LFL) introduced in 1937 at the New York World's

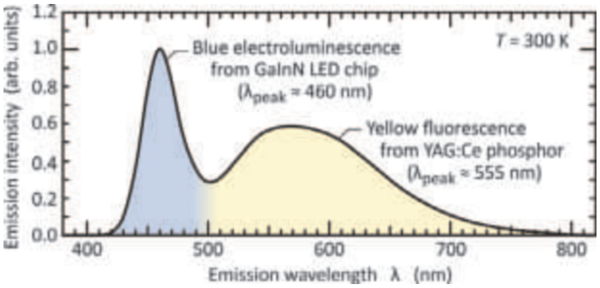

Figure 10 Emission spectrum of first phosphor-converted white LED. The LED consists of a GaInN blue LED chip and a YAG:Ce yellow phosphor (after Bando *et al.*, 1996).

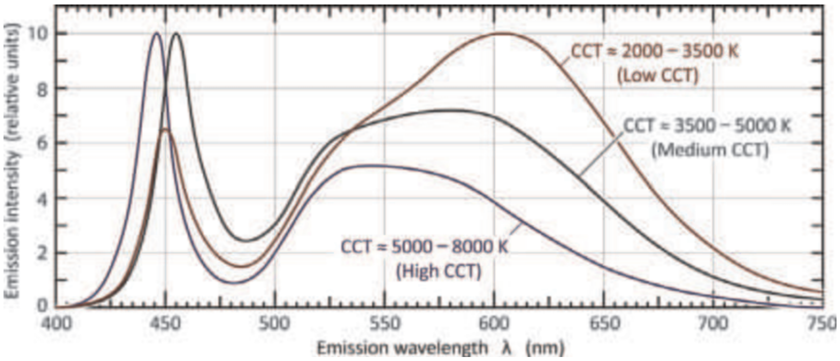

Figure 11 Emission spectra of phosphor-converted white LEDs having a low, medium, and high correlated color temperature (CCT). The relative intensities of the LED-chip emission and the phosphor emission allow one to tune the CCT within the ranges indicated.

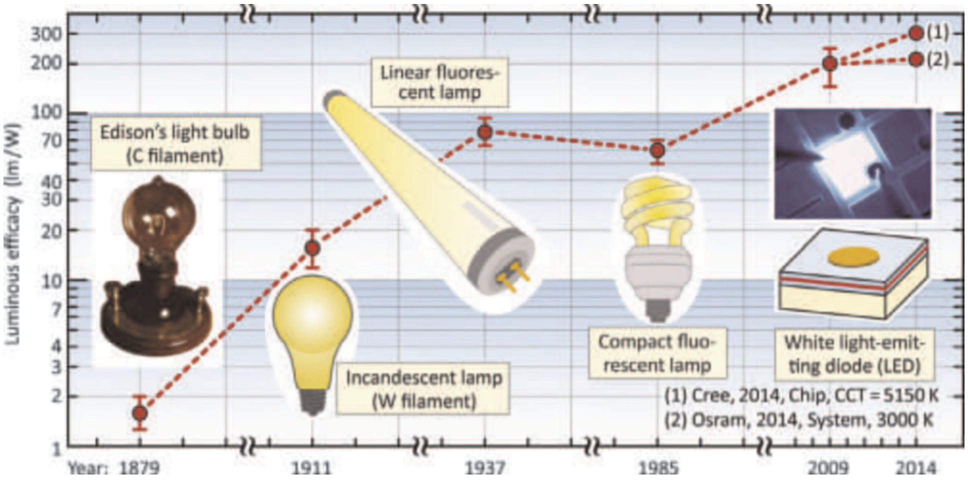

Figure 12 Temporal development of the luminous efficiency of different types of lamps. The 2014 points represent: (1) White LED device performance (Cree Company, 2014; 303 lm W^{-1}; CCT = 5150 K), and (2) White LED device and system performance (Osram Company, 2014; 215 lm W^{-1} (device); 205 lm W^{-1} (system); CCT = 3000 K).

Fair; CFL introduced in 1985 by Osram Company (after Kane and Sell, 2000). These conventional light sources and their typical efficiencies are as follows:

- Incandescent light bulb with C (carbon) filament: 1.2 – 2 lm W^{-1}
- Incandescent light bulb with W (tungsten) filament: 10 – 18 lm W^{-1}
- Incandescent halogen light bulb with W (tungsten) filament: 16 – 24 lm W^{-1}
- LFL: 65–95 lm W^{-1}
- CFL: 50 – 70 lm W^{-1}

In 2010, reported efficiencies of white LEDs were in the 150–250 lm W^{-1} range. Very high efficiencies were reported by several companies including the following: Nichia Company's Takashi Mukai announced a laboratory-result efficiency of 249 lm W^{-1} for a white LED injected with a low current (Mukai, 2009). The Cree Company announced a laboratory-result efficiency of 208 lm W^{-1} for a white LED with a CCT of about 4600 K at an injection current of 350mA (Cree, 2010). On March 26, 2014, the Cree Company announced a laboratory-result efficiency of 303 lm W^{-1} for a white LED lamp (excluding power supply) with a CCT of 5150 K at an injection current of 350 mA (Cree, 2014). On March 28, 2014, the Osram Company announced a lamp efficacy of 215 lm W^{-1} and a system efficiency (including power supply) of 205 lm W^{-1} for a white LED lamp system with a color temperature of 3000K (Osram Company, 2014).

DUV LEDs

III-Nitrides compound semiconductors such as AlN, GaN, and InN, and their alloys are known to produce light in a wide range of wavelengths from the near infrared, through the visible, down to the ultraviolet spectral range. The $Ga_{1-x}In_xN$ - based blue-LED-plus-yellow-phosphor combination has evolved into a commercial success for highly efficient, environmentally friendly white light sources for general illumination. $Al_xGa_{1-x}N$-based LEDs, covering the wide range of *DUV* wavelengths from about 360 nm (GaN) down to 210 nm (AlN), become increasingly attractive due to their promising potential in applications such as purification of air and water, sterilization in food processing, disinfection in hospitals, and medical applications (Khan *et al.*, 2007; Shur and Gaska, 2010). The promise of $Al_xGa_{1-x}N$ DUV LEDs goes far beyond just replacing the mercury lamps in existing applications and includes the creation of new market opportunities.

However, the reported EQE values of $Al_xGa_{1-x}N$ DUV LEDs are low, and decrease almost exponentially with increasing Al molar fraction x, as shown in **Figure 13**. The reasons for the decrease are related to intrinsic material properties of AlGaN: *Firstly*, increasing the Al composition generally leads to a high density of extended defects such as dislocations, grain boundaries, and cracks in the $Al_xGa_{1-x}N$ epilayer, which results in poor internal quantum efficiency. *Secondly*, doping, especially p-type doping, of $Al_xGa_{1-x}N$ films becomes difficult because the ionization energy of acceptor dopants (Mg) increases with Al composition ($\sim$170 meV for GaN, $\sim$630 meV for AlN), which causes multiple additional problems including (1) poor ohmic contact properties for both n- and p-type AlGaN thereby causing a high operating voltage, (2) poor hole-injection efficiency into the active region, and (3) high resistivity of the AlGaN layer causing non-uniform current injection into the active region, also referred to as 'current crowding' (Guo and Schubert, 2001). Although a p-type GaN layer is typically used as a contact and a hole-supplying layer to overcome (1) and (2), it causes poor light-extraction efficiency due to a strong absorption of UV photons by the p-type GaN. *Thirdly*, the light-extraction efficiency in AlGaN DUV LEDs grown on c-plane sapphire substrates is severely limited by strong TM-polarized anisotropic emission due to the unique valence band structure of $Al_xGa_{1-x}N$ for $x > \sim 0.25$ in which the topmost valence band is the crystal-field split-off hole band having a P_Z-orbital-like property (Taniyasu and Kasu, 2010). Conventional light-extracting-enhancing techniques, such as surface texturing and substrate pattering, favor extracting TE-polarized light, and thus have a negligible effect on AlGaN DUV LEDs. Accordingly, this calls for a totally new approach to deliver a real breakthrough in light extraction.

Despite the challenges originating from intrinsic material properties of AlGaN, impressive research efforts in the development of AlGaN DUV LEDs have advanced the EQE from less than 0.1% to about $1 \sim 10\%$ (depending on the emission wavelength) over the past 10 years. Various growth techniques including pulsed atomic-layer epitaxy and high-temperature growth, and stress-managing techniques such as the use of AlN/AlGaN superlattices (SLs) resulted in a strongly reduced dislocations density and crack formation, and thus enhanced internal quantum efficiency.

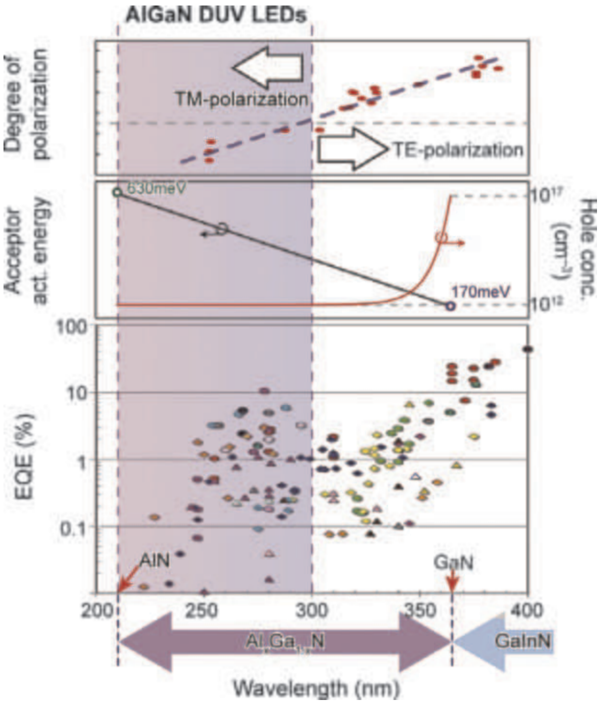

Figure 13 Maximum external quantum efficiencies (EQEs) attained by various research groups as compiled by Kneissl (2015), and acceptor activation energy and corresponding hole concentrations, and reported values of degree of polarization (Northrup *et al.*, 2012)

Another critical area that is in need of a major improvement is the p-type doping of AlGaN. One alternative way to achieve a highly conductive p-type AlGaN is to grow SLs that have been shown to enhance the free hole concentration in AlGaN by a factor of 10 (Goepfert *et al.*, 2000). The band modulation of SLs along with the modulation caused by the polarization fields enables a higher acceptor ionization ratio and thus a higher hole concentration. Another proposed alternative to overcome the p-type doping problem is the injection of holes by means of a polarization-charge-enhanced tunnel junction (Schubert, 2010). According to this concept, polarization-charge-enhanced tunnel junctions can improve the hole-injection efficiency by enabling a p-side-down structure and even reduce optical absorption in the p-type GaN contact layers. Finally, a new light-extraction-enhancing approach has been proposed to utilize the inherently strong TM-polarized light emitted from the AlGaN active region (Kim *et al.*, 2015). The side-emission-enhanced DUV LEDs show better electrical properties as well as much enhanced light output power with a strongly upward-directed emission due to an exposed sidewall of the active region and Al-coated selective-area-grown n-type GaN micro-reflectors.

Oto *et al.* (2010) proposed an alternative way to realize a highly efficient DUV emitter based on electron–hole generation by means of electron-beam excitation. In contrast to p–n junction devices (like an LED), electron-beam excitation uses highly accelerated electrons to generate electron–hole pairs inside the target material. At an acceleration voltage of 8 kV, a maximum power efficiency of 40% was reported for 240 nm emission; this is remarkable given the much lower efficiencies attained by conventional p–n junction DUV LEDs emitting at similar wavelengths.

LED Packaging

Virtually all LEDs are mounted in a package that provides two electrical leads, a transparent optical window for the light to escape, and, in high-power packages, a thermal path for heat dissipation. The chip-encapsulating material advantageously possesses high optical transparency, a high refractive index, chemical inertness, high-temperature stability, and hermeticity. The refractive index contrast between the semiconductor and air is reduced by including an encapsulant thereby increasing the light-extraction efficiency. Virtually all encapsulants are polymers with a typical refractive index of about 1.5 to 1.8. The reduced index contrast at the semiconductor-to-encapsulant interface increases the critical angle for total internal reflection thereby enlarging the light escape cone and the light-extraction efficiency.

A ***low-power package*** is shown in **Figure 14(a)**. The LED chip is die-bonded (e.g., attached by means of an adhesive) to the bottom of a cup-like depression ('reflector cup') located in one of the lead terminals (usually the cathode terminal). A bond wire connects the LED top contact to the other lead terminal (usually the anode terminal). The LED package shown in the figure is frequently referred to as a 'radial,' a '5 mm' or 'T1–3/4' package.

In low-power LEDs, the encapsulant has the shape of a hemisphere, as shown in **Figure 14(a)**, so that the angle of incidence at the encapsulant–air interface is always normal. As a result, total internal reflection does not occur at the encapsulant–air interface. There are types of LEDs that do *not* have a hemispherical shape for the encapsulant. Some LEDs have a rectangular or cylindrical shape with a planar front surface.

A ***high-power package*** is shown in **Figure 14(b)**. High-power packages have a *direct, thermally conductive path* from the LED chip, through a heat-sink, to, for example, a printed circuit board with a metal core. The high-power package shown in the figure has several advanced features. Firstly, the package contains an Al or Cu heat-sink slug with low thermal resistance to which the LED submount is attached by means of a metal-based adhesive material. Secondly, the chip is encapsulated with silicone. Because standard silicone retains mechanical softness when cured, the silicone encapsulant is covered with a plastic cover that also serves as lens. Thirdly, the chip is directly mounted on a Si submount that includes electrostatic discharge (ESD) protection.

Generally, packaging processes are associated with high costs. During the front-end epitaxial-wafer processing stage, many LED chips are processed at the same time (there are thousands of LED chips per epitaxial wafer). However, during the back-end

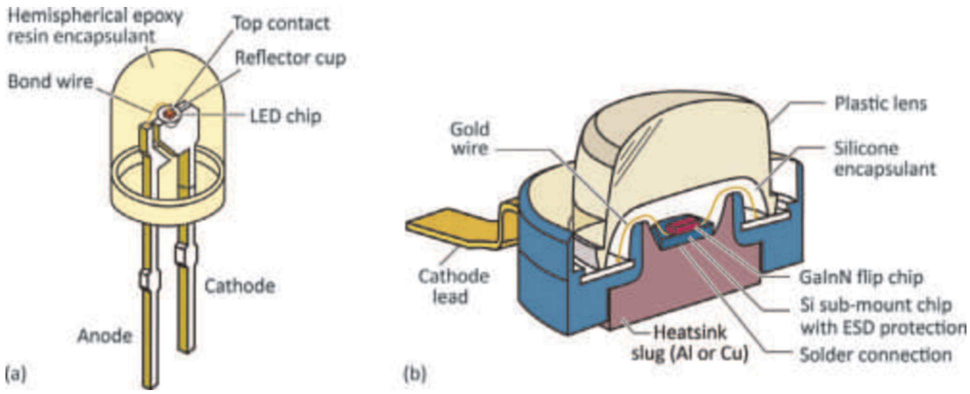

Figure 14 (a) Traditional LED package having radial miniature lamp configuration. (b) High-power surface-mount LED package having a dedicated heat path by means of a heat-sink slug.

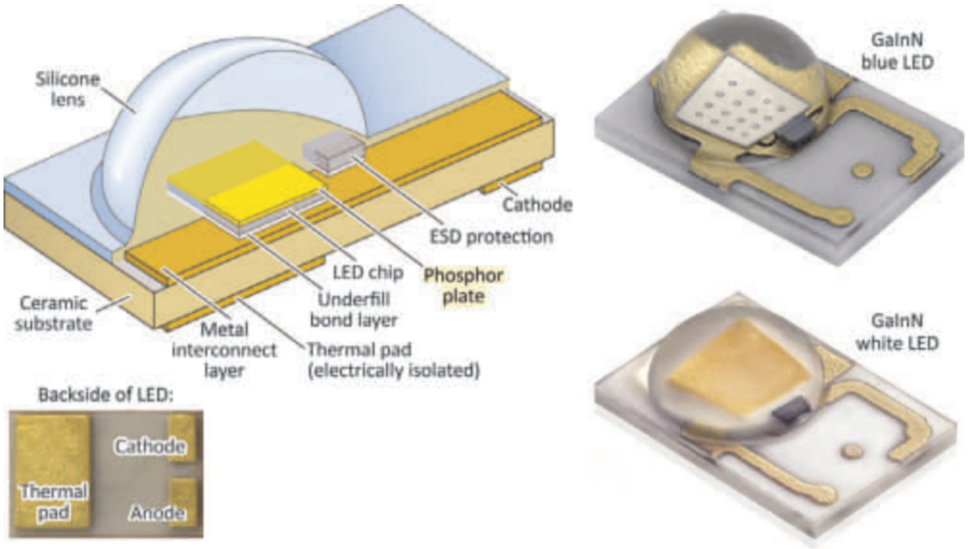

Figure 15 High-power LED package having a ceramic substrate for improved heat sinking and a dedicated thermal pad that is electrically insulated from the anode and cathode contact (adapted from Luxeon Rebel blue and white LED of the Philips Lumileds Company; Philips, 2014).

packaging process, packages may be processed one-at-a-time. Accordingly, the packaging process is a serial process and thus expensive. To reduce costs, the LED packaging process is 'parallelized,' that is, arrays of packages are processed, for example, in a 10×15 array. As one of the final steps in the process, the array of LED packages is 'singulated,' i.e., separated into single devices.

A singulated LED package is shown in Figure 15 (Luxeon Rebel blue and white LED of the Philips Lumileds Company; Philips, 2014). Inspection of the figure shows that the chip is mounted on a ceramic substrate. The ceramic substrate was originally an element of an array of devices that was singulated, for example, by sawing the ceramic board on which the array of devices is located. Ceramics have a high thermal conductivity that is close to that of metals. For example, AlN and Al have a thermal conductivity of 170–190 and 205 – 250 W m^{-1} K^{-1}, respectively.

References

Bergh AA and Saul RH (1973) *US Pat. 3,739,217 Surface Roughening of Electroluminescent Diodes*. .

Bando K, Noguchi Y, Sakano K, and Shimizu Y (1996) *Development and application of high-brightness white LEDs (in Japanese) Technical Digest, Phosphor Research Society*. 264th Meeting, November 29, 5–14.

Bando K, Sakano K, Noguchi Y, and Shimizu Y (1998) Development of high-bright and pure-white LED lamps. *Journal of Light and Visual Environments* 22: 2.

Baretz B and Tischler MA (2003) *US Pat. 6,600,175 B1 having a priority date of March 26, 1996 Solid-state white light emitter and display using the same*. .

Cree Company (press release; February 3, 2010) Cree breaks 200 lm W – 1 efficacy barrier.

Cree Company (press release; March 26, 2014) Cree first to break 300 lm-per-watt barrier. Available at: http://www.cree.com/News-and-Events/Cree-News/Press-Releases/2014/March/ 300LPW-LED-barrier (accessed 27.07.15).

Fujii T, Gao Y, Sharma R, et al. (2004) Increase in the extraction efficiency of GaN-based light-emitting diodes via surface roughening. *Applied Physics Letters* 84: 855.

Gao Y, Fujii T, Sharma R, et al. (2004) Roughening hexagonal surface morphology on laser lift-off (LLO) N-face GaN with simple photo-enhanced chemical wet etching. *Japanese Journal of Applied Physics* 43: L 637.

Goepfert ID, Schubert EF, Osinsky A, Norris PE, and Faleev NN (2000) Experimental and theoretical study of acceptor activation and transport properties in p-type $Al_xGa_{1-x}N$/GaN superlattices. *Journal of Applied Physics* 88: 2030.

Guo X and Schubert EF (2001) Current crowding and optical saturation effects in GaInN/GaN light-emitting diodes grown on insulating substrates. *Applied Physics Letters* 78: 3337.

Haerle V (2004) *Naturally textured GaN surface*. China: China Hi-Tech Fair (CHTF) Shenzhen, October. 12–17.

Horng R-H, Lu Y-A, and Wuu D-S (2011) Light extraction investigation for thin-film GaN light-emitting diodes with imbedded electrodes. *IEEE Photonics Technology Letters* 23: 54.

Jung Y, Baik KH, Ren F, Pearton SJ, and Kima J (2010) Effects of photo-electrochemical etching of N-polar and Ga-polar gallium nitride on sapphire substrates. *Journal of the Electrochemical Society* 157: H676.

Kane R and Sell H (eds.) (2000) *Revolution in Lamps: A Chronicle of 50 Years of Progress*, second ed Lilburn, Georgia: Fairmont Press.

Khan A, Balakrishnan K, and Katona T (2007) Ultraviolet light-emitting diodes based on group three nitrides. *Nature Photonics* 2: 77.

Kim DY, Park JH, Lee JW, et al. (2015) Overcoming the fundamental limitation in light-extraction efficiency of deep-UV LEDs by utilizing transverse-magnetic-dominant emission. *Light: Science & Applications* 4. , e263https://doi.org/10.1038/lsa.2015.36.

Kneissl, M. (press release, January 25, 2015) UV LED Efficiency 2015. Available at: http://www.Researchgate.net/publication/271302876_UV_LED_Efficiency_2015 (accessed 27.07.15).

Mukai, T. Presentation at SPIE Photonics West (January 29, 2009); see also Compound Semiconductor "Nichia's 249 lm W^{-1} LEDs mark tech shift" page 5 (March 2009)

Nakamura S and Fasol G (1997) *The Blue Laser Diode: GaN Based Light Emitters and Lasers*. Berlin, Germany: Springer-Verlag.

Nakamura S, Mukai T, and Senoh M (1994) Candela-class high-brightness InGaN/AlGaN double-heterostructure blue-light-emitting diodes. *Applied Physics Letters* 64: 1687.

Nakamura S, Senor M, Iwasa N, et al. (1995) Super-bright green InGaN single-quantum-well-structure light-emitting diodes. *Japanese Journal of Applied Physics* 34: 1332.

Nikkei, Japanese newspaper (September 13, 1996) "White LED lamp: Light emission with high luminous efficiency halving production costs."

Northrup JE, Chua CL, Yang Z, et al. (2012) Effect of strain and barrier composition on the polarization of light emission from AlGaN/AlN quantum wells. *Applied Physics Letters* 100: , 021101.

Osram Company (press release; March 28, 2014) Osram constructs the world's most efficient LED lamp [with 205 lm W^{-1} system efficiency]. Available at: http://www.osram.com/osram_com/press/press-releases/_trade_press/2014/osram-constructs-the-worlds-most-efficient-led-lamp/index.jsp (accessed 27.07.15)

Oto T, Banal RG, Kataoka K, Funato M, and Kawakami Y (2010) 100 mW deep-ultraviolet emission from aluminum-nitride-based quantum wells pumped by an electron beam. *Nature Photonics* 4: 767–770.

Philips, Luxeon Rebel blue and white LED of the Philips Lumileds Company (2014).

Schubert EF (2006) *Light-Emitting Diodes*, Second ed Cambridge UK: Cambridge University Press.

Schubert MF (2010) Polarization-charge tunnel junctions for ultraviolet light-emitters without p-type contact. *Applied Physics Letters* 96: 031102.

Shimizu, Y., Sakano, K., Noguchi, Y., Moriguchi T., 1999. US Pat. 5,998,925 Light-emitting device having a nitride compound semiconductor and a phosphor containing a garnet fluorescent material.

Shur MS and Gaska R (2010) Deep-ultraviolet light-emitting diodes. *IEEE Transactions on Electron Devices* 57: 12.

Stocker DA, Schubert EF, and Redwing JM (1998) Crystallographic wet chemical etching of GaN. *Applied Physics Letters* 73: 2654.

Taniyasu Y and Kasu M (2010) Improved emission efficiency of 210 nm deep-ultraviolet aluminum nitride light-emitting diode. *NTT Technical Review* 8: 1.

Diamond Anvil Cells☆

WA Bassett, Cornell University, Ithaca, NY, USA

© 2016 Elsevier Inc. All rights reserved.

This is an update of W.A. Bassett, Diamond Anvil Cells, Reference Module in Materials Science and Materials Engineering, Elsevier, 2016, ISBN 9780128035818, https://doi.org/10.1016/B978-0-12-803581-8.01079-1.

History and Background 828
Principles of the Diamond Anvil Cell 828
Gaskets 829
Heating a Sample in a DAC can be Achieved by 829
Pressure Measurement 831
Primary Pressure Measurement 831
Secondary Pressure Measurement 831
Temperature Measurement 832
Pressure Measurement at High Temperatures 832
Primary Pressure Measurement at High Temperature 832
Secondary Pressure Measurement at High Temperature 832
Analytical Methods 832
Recent Advances 837
Gasketless Sample Mounting 837
Polycrystalline Diamond Anvils 838
The Push to Ever Higher Pressures 838
Diffraction Peaks in X-ray Absorption Spectra 839
Conclusion 839
References 840
Further Reading 840

History and Background

In the late 1950s Alvin Van Valkenburg at the National Bureau of Standards (now the National Institute of Science and Technology) reasoned that he could make infrared absorption measurements on a sample under pressure by squeezing the sample between the flat faces of two diamond anvils. He did not know if the faces were perfectly parallel and so he placed his device on the stage of a microscope and looked through the diamonds at the sample. When he saw the sample, he immediately realized that he had something extraordinary. Although the diamond faces were in fact not very parallel, he could see that parts of the sample looked different because they were at high pressure (HP); and the diamond anvil cell was born. Visual observation continues to the present as the most important technique used with DACs. Van Valkenburg found that he could solidify water, alcohol, and other liquids by placing them in gaskets formed by drilling holes in metal foils and placing them between the diamond faces. He also found he could see phase transitions in single crystals of calcite and other solids when surrounded by a fluid in a gasket. The National Bureau of Standards group soon found they could examine samples under pressure by X-ray diffraction as well.

Since that time there have been more than a dozen additions to the list of analytical techniques successfully used to study samples at high pressures and temperatures (HPT) in the DAC. These include a variety of applications employing visible light, infrared, X-rays, electrical resistance, and magnetic susceptibility.

Principles of the Diamond Anvil Cell

Diamond has many properties that make it ideal for use as anvils in HP devices. It is the hardest material known, has elastic moduli with very large values, is transparent to large portions of the electromagnetic spectrum, is a good electric insulator, is an excellent thermal conductor, and is readily available as nearly perfect single crystals. Gem diamonds are available in high-quality, ready-cut shapes close to the most desirable shapes for anvils. Grinding and polishing the culet point on a brilliant-cut faceted diamond is all that is needed to turn it into an anvil face. Although metastable, diamond has a remarkable resistance to change with increased pressure and temperature up to hundreds of GPa and ~1500 K. Recently developed transparent polycrystalline diamond anvils have some valuable advantages in the pursuit of HP high-temperature research. See 'Recent Advances' below.

☆*Change History*: April 2015. W. Akers Bassett added the following new subsections under 'Recent Advances' above and references to this section are made throughout the text: (1) Gasketless Sample Mounting, (2) Polycrystalline Diamond Anvils, (3) The Push to Ever Higher Pressures, and (4) Diffraction Peaks in X-ray Absorption Spectra. The following figures have been added: (1) Figure 12 showing gasketless configuration, (2) Figure 13 showing two-stage diamond anvil cell, and (3) Figure 14 showing analytical techniques used with DACs.

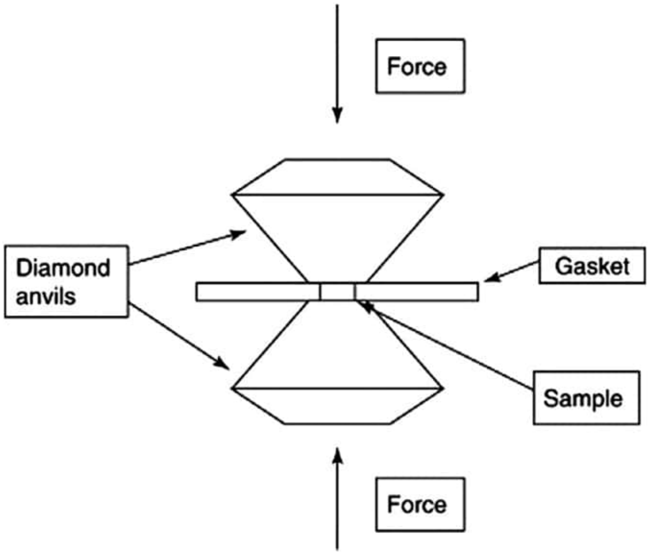

Figure 1 The diamond anvil cell (DAC) consists of two gem diamonds with their culet points ground and polished to form anvil faces. The diamonds are driven together against a sample contained in a gasket consisting of a hole drilled in a foil. This very versatile principle allows a wide variety of configurations depending on the type of analytical technique being applied.

Great versatility is possible because the principle of the diamond anvil cell is simple: two diamond anvils driven together with a sample trapped between them (Figure 1). Because pressure is defined as force divided by area, it can be increased by increasing force or decreasing area. The DAC clearly benefits from the latter. As analytical techniques have become miniaturized, diamond anvil faces have been reduced to dimensions only microns across while forces continue to be generated by screws, levers, and small hydraulic or pneumatic devices. Because such small anvil faces are needed for generating very HPs, precise parts with precise motions are essential for maintaining alignment. DACs need good support for the anvils, usually a hard material such as tungsten carbide or a ceramic such as Si_3N_4, while providing adequate access for analytical techniques, usually an opening in the support and/or in the plane of the sample. The principle is so simple that DACs can be adapted to the geometric needs of many analytical techniques. As a result, there are numerous DAC designs.

Gaskets

Gaskets play an important role in the many applications of DACs. The properties of gasket materials are crucial and are selected for specific applications. The rheologic properties of gasket materials are usually the most important. However, transparency to X-rays, electrical properties, and chemical properties are important as well. Gasket materials include rhenium, tungsten, iridium, spring steel, inconel, stainless steel, brass, boron–epoxy mixture, aluminum, and beryllium. Recently fluid samples have been sealed in a sample cavity in one of the diamond anvils by pressing the flat anvil faces together, i.e., with no gasket. See ‘Recent Advances‘ below.

Heating a Sample in a DAC can be Achieved by

1. external resistance heating including use of heaters that surround the whole cell, heaters that surround just the anvils, heaters that surround the seats that the anvils sit on (Figure 2), and graphite heaters that are imbedded within the anvils;
2. internal resistance heaters are heaters that are insulated from the anvils and therefore do not heat the anvils to temperatures as high as sample temperature (Figure 3). They consist of an electrically conducting sample wire, a metal strip with a hole to receive the sample, or graphite sandwich; and
3. laser heating also heats the sample without heating the anvils (Figure 4).

External resistance heating (Figure 2) requires careful choice of materials that will resist softening or deformation with temperature change. Because some of the materials, including diamond, readily oxidize at high temperature, an inert or slightly reducing gas is needed to prevent oxidation. The main advantage of external heating is the very constant and uniform temperatures that can be achieved. Pressures can also be held constant when the cell is designed to eliminate or minimize the effects of dimensional changes with temperature. Pneumatic devices and springs that are kept cool are especially important for achieving this. The main disadvantage is the upper limit of 1500 K at which diamond begins to graphitize.

Internal resistance heating (Figure 3) has the advantage that it heats only the sample and can, therefore, generate much higher temperatures than can be tolerated by the diamond anvils. The upper limit for internal resistance heating is imposed by the melting point of the resistor. However, that can be very high if Re or W is used.

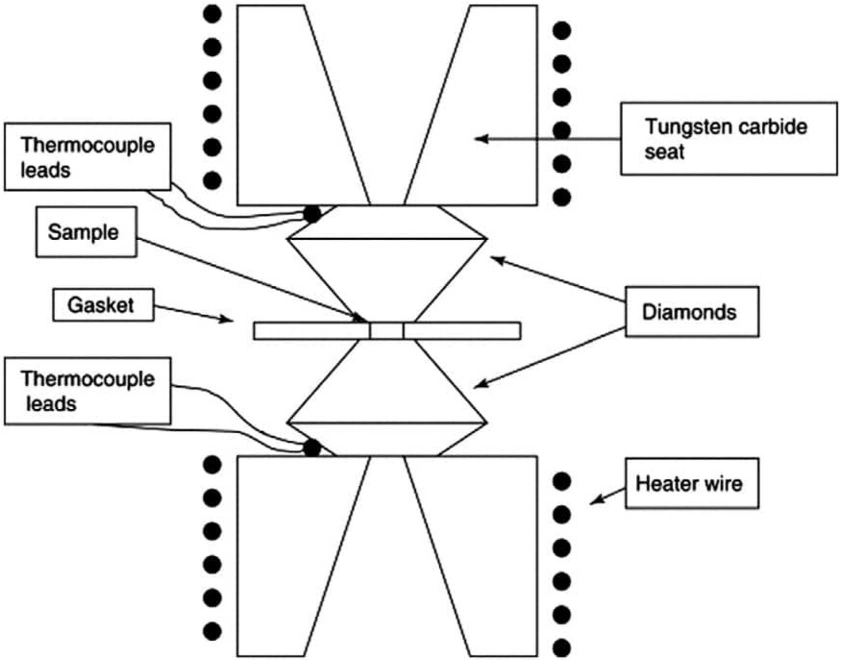

Figure 2 Samples can be heated to 1500 K while under pressure by means of resistance heaters wound around the seats supporting the diamond anvils. Thermocouples placed in contact with the diamond anvils measure temperatures to within a few kelvin. Corrections can be made by observing melting of standard materials in the sample chamber. Access can be through the diamonds or the gasket.

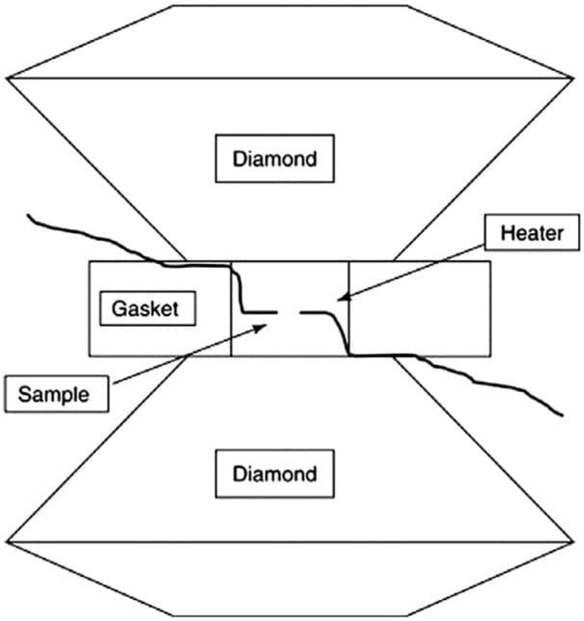

Figure 3 An internal resistance heater, usually constructed from rhenium, can be used to heat a sample to much higher temperatures (3000 K) than the diamonds can tolerate because it is insulated from them. Temperatures are measured by spectroradiometry.

Laser heating (Figure 4) has employed yttrium aluminum garnet (YAG), yttrium lithium fluoride (YLF), and CO_2 lasers with their beams focused through the anvils onto the sample. The sample must be thermally insulated from the diamond anvils by a transparent material, which protects the diamonds and serves as a pressure medium. Although continuous power delivered to both sides of the sample has yielded the best quantitative results, single-side and pulsed laser heating have been used extensively to overcome kinetic barriers and promote phase transitions. Temperatures of thousands of kelvin can be achieved, especially if very short pulses are used. Sample design for laser heating is much simpler than for internal resistance heating, but requires a rather large and complex optical system outside of the DAC.

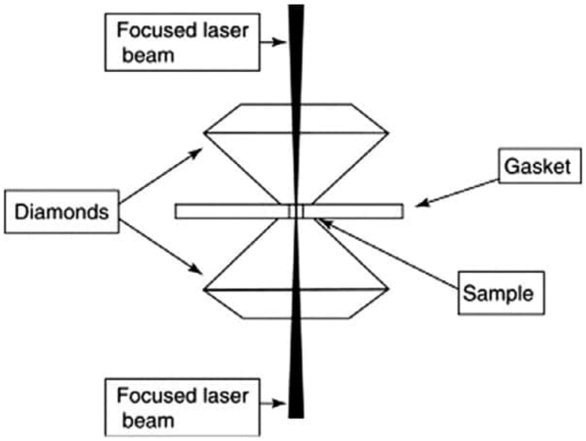

Figure 4 Laser heating can raise the temperatures of samples to several thousands of kelvin. When a laser beam is split and directed to the sample through both anvils, more uniform and constant temperatures can be achieved than heating from one side alone. Temperature gradients within the sample are minimized by using the larger TEM_{01} laser mode and focusing the probing X-ray beam to a very small spot within the heated area.

Low temperatures down to that of liquid helium can be achieved by passing cold gases through the DAC or injecting liquid nitrogen or liquid helium directly into the cell and letting it boil there. Another approach has been to completely immerse the DAC into liquid nitrogen or liquid helium.

Pressure Measurement

Accurate methods for determining pressure can be divided into two groups: (1) primary, those that are independent and (2) secondary, those that must be calibrated using a primary pressure scale.

Primary Pressure Measurement

Force divided by area can provide reliable, accurate pressure measurements but only if the pressure over the area is uniform as in piston-cylinder apparatus. However, piston-cylinder apparatus cannot generate pressures anywhere near what is possible using DACs. Phase transitions such as those in elemental bismuth were used as calibration points for transferring pressure measurements to other types of apparatus in which those same phase transitions could be observed.

One of the most significant advances was Decker's development of an equation of state (EoS) for NaCl from first principles. This could be applied directly when X-ray diffraction (XRD) was used and NaCl was mixed with the sample in a DAC. Its use for calibrating secondary pressure scales, such as the ruby fluorescent scale, was also very valuable.

Dynamic shock-wave measurements are also an important source of primary pressure determination but rely on corrections when data are converted from high-temperature Hugoniot measurements to isothermal EoS. Nonetheless, dynamic measurements on some metals have provided an important means for calibrating the secondary pressure scales, especially the ruby fluorescence scale, to higher pressures.

Recent primary pressure scales have been based on combining data from direct compression measurement using XRD and sound velocity measurements, which yield data related to the pressure derivative of compression. From the two sets of data, it is possible to derive completely independent values of pressure as a function of lattice parameters. Brillouin scattering in the DAC and sound interferometry have been used to measure sound velocities.

Secondary Pressure Measurement

A secondary pressure scale is one that offers an observable change as a function of pressure. There are many materials which display observable phase transitions at calibrated pressures – Bi, AgI, KCl, and NaCl, to mention a few. One or two of these can be included along with a sample as a pressure indicator. There are many materials whose EoS have been calibrated so that a measurement of their lattice parameters by XRD can be used for determining pressure. Sometimes the sample itself can be used in cases where its EoS is well defined and some other property is being investigated.

The most widely used secondary pressure scale is the ruby fluorescence scale. Ruby, when excited by some higher energy radiation, emits R1 and R2 peaks in the red end of the visible spectrum that shift monotonously with pressure. The fluorescence is typically excited by an argon ion laser and the emission is analyzed by a grating spectrometer. The positions of the R1 and R2 lines in the spectrum provide a convenient and inexpensive method for determining pressure. In addition, broadening and separation of the R1 and R2 peaks can be used as indicators of deviatoric stress and pressure gradient. Other fluorescent materials such as Cr: MgO and Sm:YAG have been used as well, but ruby continues to be the most popular.

Raman spectra of diamond show shifts with pressure and can be used as a secondary pressure scale. At lower pressures, diamond particles synthesized from ^{13}C are used to avoid interference from the diamond anvils. At higher pressures, natural diamond can be used.

Recent advances in DAC design have led to dramatic increases in sustained pressures that DACs are capable of achieving. Recent reduction of the size of samples that instrumental methods are capable of analyzing has provided a strong incentive to develop new DAC designs. See 'Recent Advances' below.

Temperature Measurement

Temperature measurements in externally heated DACs can be accomplished by placing thermocouples in contact with the diamond anvils. Because diamonds are such good thermal conductors, discrepancies between sample temperature and thermo-couple temperature are rarely more than a few degrees celsius even at the highest temperatures. Corrections to thermocouple readings can be determined by observing melting of standard materials such as $NaNO_3$ and NaCl placed in the sample chamber. The same thermocouples used for high-temperature measurements can be used for the low-temperature measurements.

Internal resistance heating and laser heating are utilized in order to achieve temperatures in excess of those that cause damage to the diamond anvils (~1500 K). The most commonly used method of temperature determination is spectroradiometry, which consists of fitting the spectrum of incandescent light from the hot sample to a blackbody or graybody curve. Steep temperature gradients and unknown emissivities can be sources of error. However, there are ways to correct for these errors.

Recently, the intensity ratio of stokes and anti-stokes peaks in X-ray Raman spectra has been used to determine temperatures. They were found to be in good agreement with those determined by spectroradiometry.

Pressure Measurement at High Temperatures

Primary Pressure Measurement at High Temperature

Accurate pressure measurement in samples at high temperature has been an area of much concern. Neither sample pressure (isobaric) nor sample volume (isochoric) can be assumed to remain constant as temperature is changed in most sample configurations. In these cases, an internal calibrant is needed. Decker's EoS for NaCl is a full EoS including the effect of temperature on molar volume and is, therefore, suitable for pressure measurement at high temperature. The full EoS of gold has also been determined and is desirable for samples in which only a small amount of pressure calibrant is wanted or where recrystallization needs to be avoided.

There are two configurations, however, that can greatly reduce or eliminate the effect of temperature on pressure. A very small opaque sample surrounded by a much larger volume of transparent pressure medium can be locally heated by laser and remain nearly isobaric because of the relative sizes. Isochoric conditions can be achieved at relatively low pressures by cycling a sample in a gasket, such as rhenium, to high temperature several times. If forces are not great, the gasket finishes relaxing on about the third cycle and the sample volume can be shown to remain constant with temperature within experimental error. If the full EoS of the contents is known, as with H_2O, the pressure can be calculated from the temperature. This approach has been especially valuable in fluid studies where the pressure is allowed to develop as a result of heating.

Secondary Pressure Measurement at High Temperature

Attempts to use ruby and Sm:YAG to measure pressure at high temperature have been less than satisfactory. The fluorescence emission from ruby fades with temperature and the emissions from Sm:YAG are complex to follow. There are several rapidly-running reversible phase transitions that have been calibrated, for example, $BaTiO_3$, $PbTiO_3$, $Pb_3(PO_4)_2$, and transition in quartz. These have specific trajectories in P–T space and, therefore, are not useful for determining pressure at just any location in the P–T space. They are, however, very useful for calibrating fluid EoS described above. Re and other metals have been calibrated for pressure measurement at very high temperatures using XRD.

Analytical Methods

Visual observation is the easiest and most useful method for studying a sample in a DAC. It requires only using a microscope to look at it through the diamond anvils. Visual observation is valuable for not only alignment and centering but can be used to observe phase transitions, coexistence of phases, and optical properties. Phase diagrams can be developed by observing phases as P and T are changed.

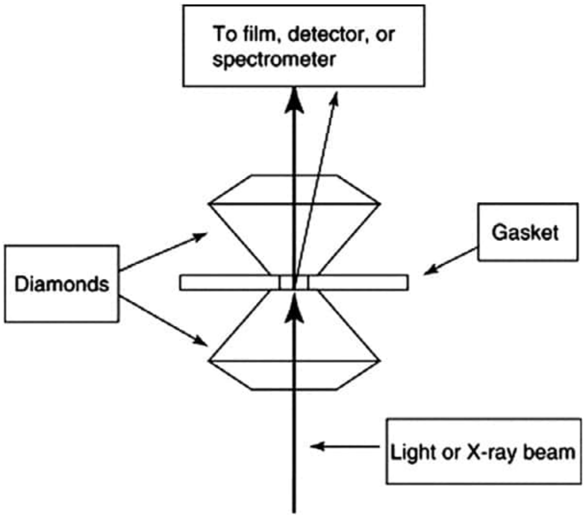

Figure 5 The most commonly used configuration is to pass electromagnetic radiation though one diamond anvil to the sample and to observe or analyze the radiation emerging through the other diamond anvil.

XRD of samples under pressure has been one of the most important applications of DACs. Angle dispersion X-ray diffraction (ADXD) using monochromatic radiation and energy-dispersion X-ray diffraction (EDXD) using white radiation are both used, usually by passing an X-ray beam through one anvil to the sample and collecting scattered X-rays through the other anvil (Figure 5). X-rays that pass through a transparent gasket can also be collected (Figure 6). Both polycrystalline and single-crystal samples can be studied. The advent of synchrotron radiation (SR) with its high intensities, very smooth white spectrum, and excellent collimation has reduced exposure times by orders of magnitude while improving resolution and offering a greater variety of configurations. Improved solid-state detectors have also played a major role.

Emitted visible light from a sample in a DAC can be spectrally analyzed. Fluorescence emission may be excited by X-rays, ultraviolet light, or visible light of shorter wavelength. The trajectory of an X-ray beam as it passes through a fluorescent diamond can be located visually by emission of visible light. The ruby method for determining pressure depends on the excitation of fluorescent emission in small ruby chips included in a sample. Incandescent light from a hot sample contained in a DAC can be spectrally analyzed and fit to a blackbody curve to determine the temperature. Sample fluorescence has been an important source of fundamental information, especially for studying the effect of pressure and temperature on organic compounds. Lasers are favored for stimulating fluorescence because of their high intensity and because they make it possible to pinpoint parts of the sample.

Absorption spectra of light passing through a sample (Figure 5) as well as spectra of reflected light (Figure 7) provide useful information about bonding and band gap changes as a function of pressure and temperature. Imaging can allow selected portions of a sample to be analyzed.

Infrared (IR) absorption spectroscopy requires carefully selected diamonds (usually type II) to be transparent over the desired range of IR-active frequencies. IR absorption at HP has been especially important for understanding the effects of pressure and temperature on organic materials.

Raman scattering has been a very important analytical technique for HPT samples. Light scattered from the sample can be analyzed to determine Raman active vibrational frequencies. Vibrational frequencies are an important source of information for identifying phases, examining bonding, and studying the relationships between vibration frequencies and phase transitions. Hyper-Raman spectroscopy employs a three-photon process and can detect not only far IR vibrational frequencies but can also detect frequencies ('silent' modes) that are not normally IR or Raman active.

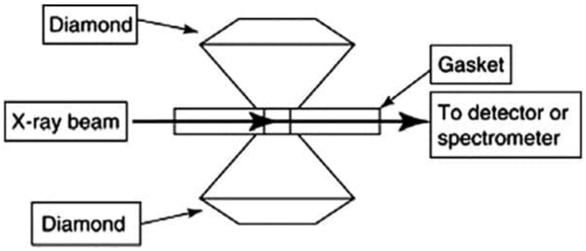

Figure 6 Gasket materials transparent to X-rays such as beryllium and boron–epoxy mixture allow incident X-rays to enter through one side of the gasket and scattered X-rays to be collected through the other side.

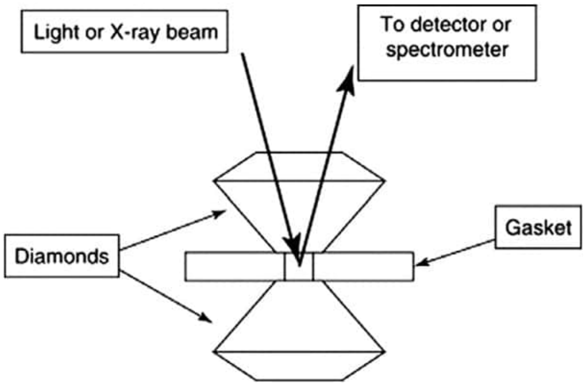

Figure 7 Observation and analysis of radiation scattered back through the same diamond it entered provide an important source of information for many types of studies.

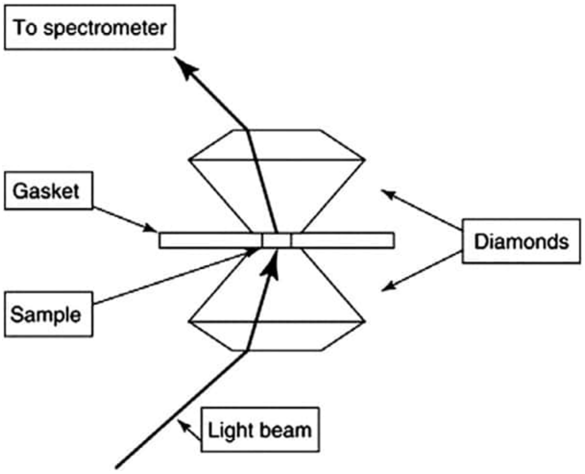

Figure 8 Brillouin scattering can be used to determine phonon velocities in high-pressure samples without making corrections for refractive indices if the anvil faces bisect the 90° angle between the incident and scattered light rays.

Brillouin scattering has been an important source of information on the effects of P and T on the elastic properties of single-crystal samples. A light beam from a laser, usually an Ar^+ laser, is directed through one of the diamond anvils onto an oriented single-crystal sample in a DAC. Light scattered by interaction with phonons in the sample contains frequency shifts (usually smaller than in Raman spectra) that can be used to calculate the velocities of the phonons. If the anvil faces exactly bisect a 90° angle between the incident beam and scattered light, no corrections need to be made for the refractive index of the sample, medium, and anvils (Figure 8). These phonon velocities, in turn, can be used to determine the effects of P and T on elastic moduli.

Impulsive stimulated scattering (ISS) is another technique that yields information about sound velocities and elastic moduli. Sound waves in the ISS method are generated within the sample by means of laser radiation. Laser light from a different source is Bragg reflected from these sound waves. Its intensity fluctuation can then be used to determine sound velocities.

X-ray spectroscopy (XRS) which includes emission, absorption, and scattering is an area of active development of new techniques and applications in HPT research. X-ray emission spectroscopy (XES) consists of analyzing spectra of radiation excited by an incident X-ray beam as it passes out through the anvils (Figures 5 and 7) or the gasket (Figure 6). Laser-machined diamond anvils and very transparent gaskets are two modifications that now make it possible to analyze all elements heavier than Ca. While elemental analysis is the most important application, newly developed sub-eV energy resolution makes it possible to show a line shape which can be used to provide valuable information on filled electronic states as well as valence and magnetic states such as high-spin to low-spin transition in Fe.

X-ray absorption spectroscopy (XAS) consists of analyzing the spectra of photons absorbed when their energies exceed the excitation energy of deep-core electrons. Laser-drilled holes in the diamond anvils (Figure 9) can reduce the amount of diamond in the beam to 0.3 mm. In these DACs, X-ray absorption fine structure (XAFS) spectra down to 4 keV permit analyses of the K edges of elements as light as Sc as well as L edges of rare-earth elements. Near-edge X-ray absorption fine structure (XANES) provides information on the symmetry-projected conduction band density of states (DOS), while the extended X-ray absorption fine structure (EXAFS) provides local structure information. These element-specific probes are able to reveal electronic and structural changes that take place at HPT conditions.

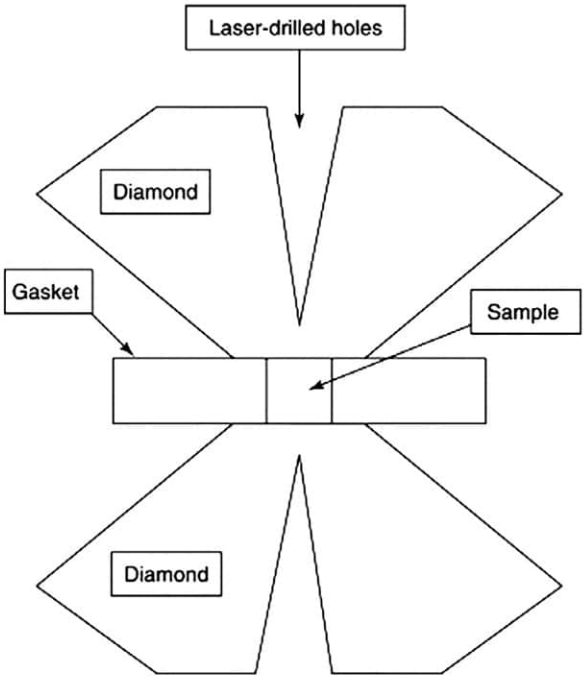

Figure 9 Holes laser-drilled to within 0.15 mm of the anvil face greatly reduce the absorption by diamond allowing X-ray absorption studies to be made at energies down to 4 keV.

An alternative and very successful way of obtaining absorption spectra is by measuring the intensity of fluorescence emission at the energy of one of the emission peaks while the energy of the incident beam is scanned over the absorption edge being studied. X-rays emerging through an X-ray transparent gasket (Figure 10) or side of one of the anvils (Figure 11) are collected and analyzed. The signal-to-noise ratio is much improved with this method due to reduced intensity of Rayleigh scattering at 90° to the X-ray beam.

Nuclear resonance X-ray spectroscopy (NRXS), also known as Mössbauer spectroscopy, deals with exceedingly narrow absorption peaks resulting from nuclear transitions. NRXS uses an in-line high-resolution monochromator (HRM) on an SR beam capable of narrowing the photon energy and fine-tuning the monochromatic X-ray beam with meV resolution. Avalanche photodiodes (APD) are used to collect signals from nuclear resonance absorption, and reject all other signals. HRM monochromators have made it possible to extend the Mössbauer method to other elements besides iron that have suitable isomer transitions.

Inelastic X-ray spectroscopy (IXS) represents a major breakthrough for HP research. As in Raman spectroscopy, the energies of the events being probed appear as differences in the energies of incident and scattered X-rays. For this reason, IXS is sometimes referred to as X-ray Raman spectroscopy. This principle makes it possible for experimenters to select X-ray energies that are high enough to easily penetrate diamond anvils and/or low-Z gaskets while probing low-energy phenomena. Recent advances in focusing of X-rays onto samples as small as 0.01 mm and dramatic improvements in monochromators and analyzers to achieve sub-eV resolution

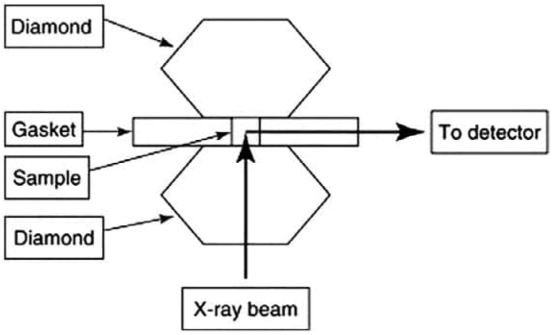

Figure 10 X-ray emission excited by an X-ray beam passing through one of the diamond anvils can pass out through a transparent gasket and be analyzed. Background due to Rayleigh and Compton scattering is minimized when the detector is located at 90° from the X-ray beam in the plane of polarization of an X-ray beam from a synchrotron source.

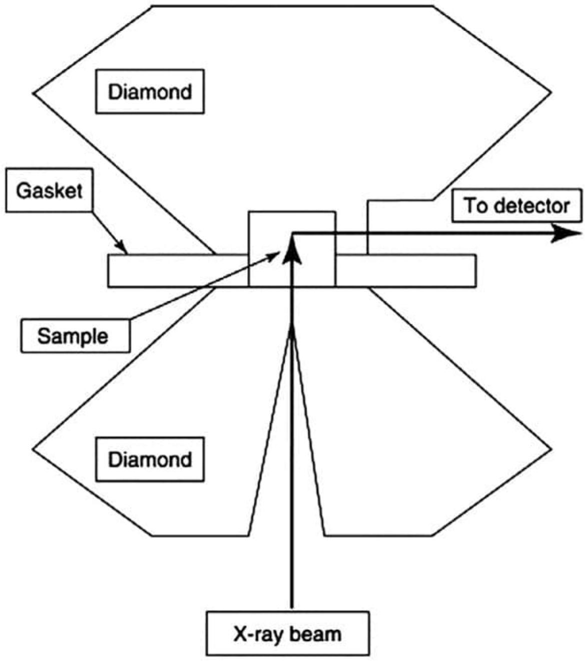

Figure 11 X-ray emission excited by an X-ray beam passing through one of the diamond anvils can pass out through the side of the other diamond anvil to be analyzed. Using a diamond with a laser-drilled hole for one anvil and a diamond with a thin-walled recess for the other greatly reduces absorption to permit high-pressure–temperature studies down to energies of 4 keV and less.

have opened the way for these techniques to be applied to investigations of a wide variety of low-energy events at HPT conditions. IXS comprises several techniques which yield different types of information. They are X-ray inelastic near-edge spectroscopy (XINES), electronic inelastic X-ray scattering (EIXS), resonant inelastic X-ray scattering (RIXS), nuclear resonant inelastic X-ray scattering (NRIXS), and phonon inelastic X-ray scattering (PIXS).

X-ray inelastic near-edge spectroscopy (XINES) is capable of making measurements that yield the same information as XANES on near core-electron absorption edge features. The principle is similar to that of electron energy loss spectroscopy (EELS). These techniques provide information about the nature of chemical bonding. Spectral features are particularly pronounced and the information particularly important for the very light elements. It is only since the development of XINES that such measurements can be made at HPT conditions because the low-energy X-ray and electron beams needed for XANES and EELS are completely blocked by any of the pressure vessels. Successful observations have been made on second-row elements from Li (56 eV) to O (543 eV) at HPs. This opens a wide new field of near K-edge spectroscopy of the very light elements.

Electronic inelastic X-ray scattering (EIXS), which is very similar to XINES in principle and instrumentation, can be used to investigate the drastic effect that pressure can have on the energy and dispersion of electronic bands. The IXS principle makes it possible to use a 10 keV X-ray beam for excitation and a monochromator capable of 0.3–1 eV resolution to probe high-energy electronic phenomena, including electronic band structure, Fermi surface, excitons, plasmons, and their dispersions at HP.

In resonant inelastic X-ray spectroscopy (RIXS) experiments, both incident and scattered X-ray energies need to be scanned. Of particular interest is the investigation of phase transitions driven by electron correlation effects that occur in transition elements and rare-earth elements and their compounds at HPs.

Nuclear resonant inelastic X-ray scattering (NRIXS) utilizes inelastic scattering to collect nuclear resonance or Mössbauer spectra. An APD directly downstream of the sample collects nuclear resonant forward scattering (NRFS) spectra which provide a precise determination of the hyperfine interaction parameter and Lamb–Mössbauer factor. APDs surrounding the sample collect NRIXS spectra. Isotopes that exhibit a nuclear resonant Mössbauer effect, for example ^{57}Fe, offer an extraordinary opportunity to make phonon DOS measurements on samples containing them, measurements that provide valuable information on dynamic, thermodynamic, and elastic properties.

PIXS requires detecting a very weak sample signal in the presence of a very strong background signal, especially when a HP vessel contains the sample. New novel HRMs which are being developed will improve the feasibility of making nonresonant PIXS measurements at HP. Such measurements would be a valuable source of information on phonon dynamics in highly compressed materials, information important for understanding vibrational thermodynamic properties, elasticity, and phase transition mechanisms.

Electrical resistance has been measured on samples as a function of pressure and at high temperature in DACs. For these experiments, fine electric leads are connected to the sample and four-lead systems have been employed for the most quantitative measurements. A particularly novel approach, dubbed designer diamonds, has employed diamonds in which the leads are imbedded in the anvils by vapor depositing single-crystal diamond over the leads.

Magnetic measurements have been made in DACs constructed of nonmagnetic materials such as beryllium–copper. Coils for generating and picking up signals are placed as close to the sample as possible.

Sound velocity measurements have been made by three important methods, Brillouin scattering, impulse stimulated scattering, and interferometry of GHz acoustic signals. The first two of these use interactions between photons and phonons while the third generates GHz sound by a transducer and uses interferometry of the acoustic signals to measure travel time in a crystal only ~0.1 mm across. Sound velocities are then calculated.

Gamma rays emitted by a radioactive sample in a DAC have been counted and the effect of pressure on the decay rate measured. Pressure has been shown to increase the decay rate of the electron-capture process of ^{7}Be in a beryllium oxide sample.

Recent Advances

Gasketless Sample Mounting

The earliest samples subjected to pressure between two diamond anvils were not gasketed as described in Bassett (2009). A solid sample would form its own gasket as it extruded from between the anvil faces leading to a pressure gradient from highest in the center to lowest at the edges. There are a number of experiments that can take advantage of such a pressure gradient, especially when there is reason to observe all of the HP phases simultaneously. The initial pressure distribution is roughly Gaussian but changes shape as force on the anvils is cycled. Such a sample also typically has a deviatoric elastic strain resulting from the uniaxial stress. The elastic strain can be calculated from the ellipticity of diffraction rings produced by a monochromatic X-ray beam traveling perpendicular to the uniaxial force. Strength of the sample as a function of pressure can be calculated from the largest observed ellipticity as pressure is increased as described by Bassett (2006).

A gasketless DAC with a laser-drilled recess in one of the anvils (**Figure 12**) is described by Chou *et al.* (2008). Such a configuration has some very important advantages. When a sample is placed in the recess and sealed there by pressing the otherwise flat anvil faces together, a fluid sample can be contained to pressures of several GPa. It differs from gasketed sample mounting in several important and beneficial ways. It preserves sample volume that undergoes negligible change during most experiments. Because volume is a thermodynamic parameter, isochoric observations can have advantages similar to those of isobaric or isothermal. Needless to say, the only pressure in a sample contained in a constant volume is that resulting from increased temperature and depends on the equations of state of the phases present in the sample. However, if the isochoric behavior of the dominant component is well characterized as in the case with H_2O in aqueous samples, the observed phases of H_2O, especially liquid and vapor, can provide a reliable method for determining pressure when temperature is measured. For some compositions it can pay to load the sample in the solid state and then take advantage of the ΔP of phase transitions with increased temperature to yield even higher pressures than possible with EoS alone. The gasketless approach also has the important advantage of containing the sample in a single-composition cavity, i.e., diamond which is a relatively inert material and one that is unavoidable in most diamond anvil cell research. Although reactions between samples and diamond have been observed, they generally present less of a complication than do reactions with a metal. All of the analytical methods used for gasketed samples can also be used with gasketless samples.

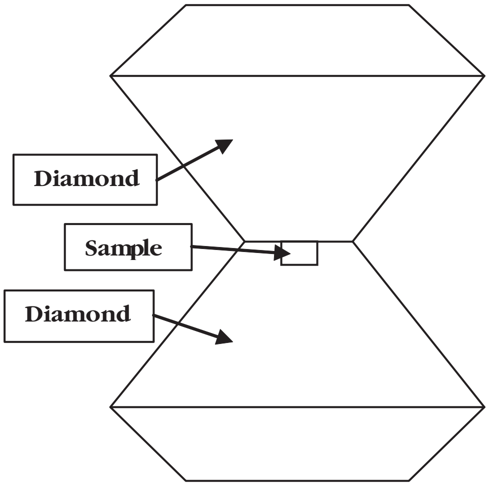

Figure 12 A sample can be placed in a laser-drilled recess in one of the anvil faces and sealed there by pressing the anvil faces together. If the anvil faces have a perfectly flat polish and they are pushed together with sufficient force, a fluid can be contained to pressures of several GPa. See Chou *et al.* (2008).

Polycrystalline Diamond Anvils

Polycrystalline diamond has some very important benefits that make it desirable for use as anvils. It is tougher than single-crystal diamond which can break along cleavage directions when subjected to directed stresses which are impossible to avoid in anvils. Because of these properties, polycrystalline diamond anvils have been used to dramatically extend the pressure range of DACs as described below.

While single-crystal anvils can be desirable for diffraction studies of polycrystalline samples, polycrystalline anvils can be desirable for single-crystal samples and especially for some spectroscopic analyses in which diffraction can cause interference as described below.

Early attempts to produce polycrystalline anvils resulted in opaque anvils but subsequently, routes to forming transparent nano-polycrystalline diamond (NPD) anvils were developed (Irifune *et al*., 2003; Sumiya and Harano, 2012). Transparency has played a key role in the history of DACs because of the need for good alignment and because so many pressure-induced changes are visible.

The Push to Ever Higher Pressures

The pressures that can be achieved with DACs have increased dramatically over the years. In the early days of DAC research pressure was measured in bars, and most DAC results were reported in the kilobar (Kbar) range. More recently, researchers have reported pressure in pascals and most DAC results are reported in gigapscals (GPa). But understandably, achieving sustained pressures over a megabar (Mbar), 100 GPa, took on a life of its own. Even after pressures reported in the literature were switched to GPa, the term megabar continued to be used when talking about higher pressures as a destination. Mao and Bell (1976) succeeded in passing the megabar goal by taking advantage of the properties of stainless steel gaskets and beveled anvils to distribute stress so as to preserve the diamond anvils to higher pressures.

A more recent important advance has been the two-stage diamond anvil cell described by Dubrovinsky *et al.* (2012). Spherical and hemispherical nanocrystalline diamond (NCD) anvils 20–50 μm in diameter have been synthesized from glassy carbon balls in a multi-anvil press also described by Dubrovinsky *et al.* (2012). These have been used as second-stage anvils using a conventional DAC for the first stage. In the two-stage cell shown in **Figure 13** the hemispherical NCD anvils are placed inside of a gasketed chamber squeezed between the 300 μm anvil faces of a conventional DAC. A shallow recess in one of the 300 μm anvil faces prevents sideways slippage. The medium, paraffin or solid neon, contained in the gasket provides support to the secondary anvils while force is transferred directly to the secondary anvils by direct contact with the primary anvils. The HP medium surrounding the secondary anvils plays an important role in providing support for achieving extremely HP between the secondary anvils. In a recent paper Sakai *et al.* (2015) describe a clever way to prepare beveled secondary polycrystalline anvils with 3 μm faces from a single block so that they remain in perfect alignment without the need for a recess in one of the primary anvils.

The portion of sample that is at the maximum pressure in both designs described above is very small, and obtaining diffraction data on it is possible only with the extremely small focused X-ray beams now available at synchrotron sources. On the basis of diffraction patterns of rhenium and gold obtained at these very HPs, Dubrovinsky *et al.* (2012) report achieving sample pressures in excess of 600 GPa. Now, teragapascal (TPa) takes on significance as a new destination that once belonged to the term megabar.

Although dynamic (shockwave) pressure studies yield pressures greater than those produced by DACs, data must be collected in fractions of a second at elevated temperatures due to heating caused by compression. On the other hand, DACs offer sustained pressure at any sustained temperature. Rather than being competitors, the two methods often complement each other and provide new insights.

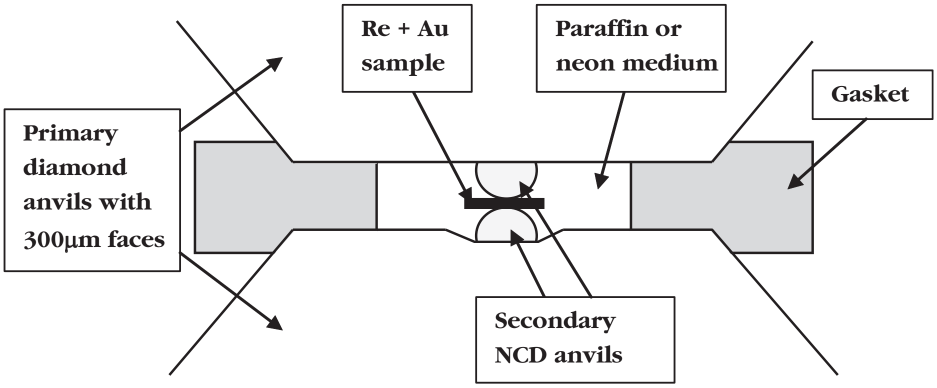

Figure 13 Two-stage diamond anvil cell capable of pressure in excess of 5 Mbar (500 GPa). The secondary anvils are made of polycrystalline diamond. Modified from **Figure 2** in Dubrovinsky *et al.* (2012).

Diffraction Peaks in X-ray Absorption Spectra

Unfortunately, strong attenuation of some wavelengths in a spectrum can occur due to Bragg diffraction as the X-rays pass through single-crystal diamond anvils leading to unwanted sharp peaks called glitches by Ishimatsu *et al.* (2012). There are presently two ways of dealing with this form of interference. One way is to shift the wavelengths of these unwanted peaks by changing the orientation of the DAC slightly, obtaining spectra at these different orientations, and then combining the spectra to reject the sharp peaks resulting from Bragg diffraction. The other way is to use the new polycrystalline NPD anvils described above to smooth the attenuation due to diffraction. The orientations of the crystallites in these anvils are so random that the smoothed attenuation can be considered little more than background. If a correction for the attenuation is warranted, it is easily applied. Details of this application of NPD anvils are given by Ishimatsu *et al.* (2012). In some neutron diffraction studies in which single-crystal phases are observed polycrystalline diamond anvils can serve the same purpose.

Conclusion

Diamond anvil cells combined with many analytical techniques (Figure 14) have been a valuable source of information on fundamental properties of materials since the late 1950s. Improvements in diamond anvil cell designs are leading to ever higher and more accurate sustained pressures and temperatures that make it possible to utilize the improvements in analytical methods for probing ever smaller samples. These improvements, in turn, open the way to better understanding of matter at extreme conditions, providing data for understanding planetary interiors, contributing to the search for superhard materials, aiding in understanding of

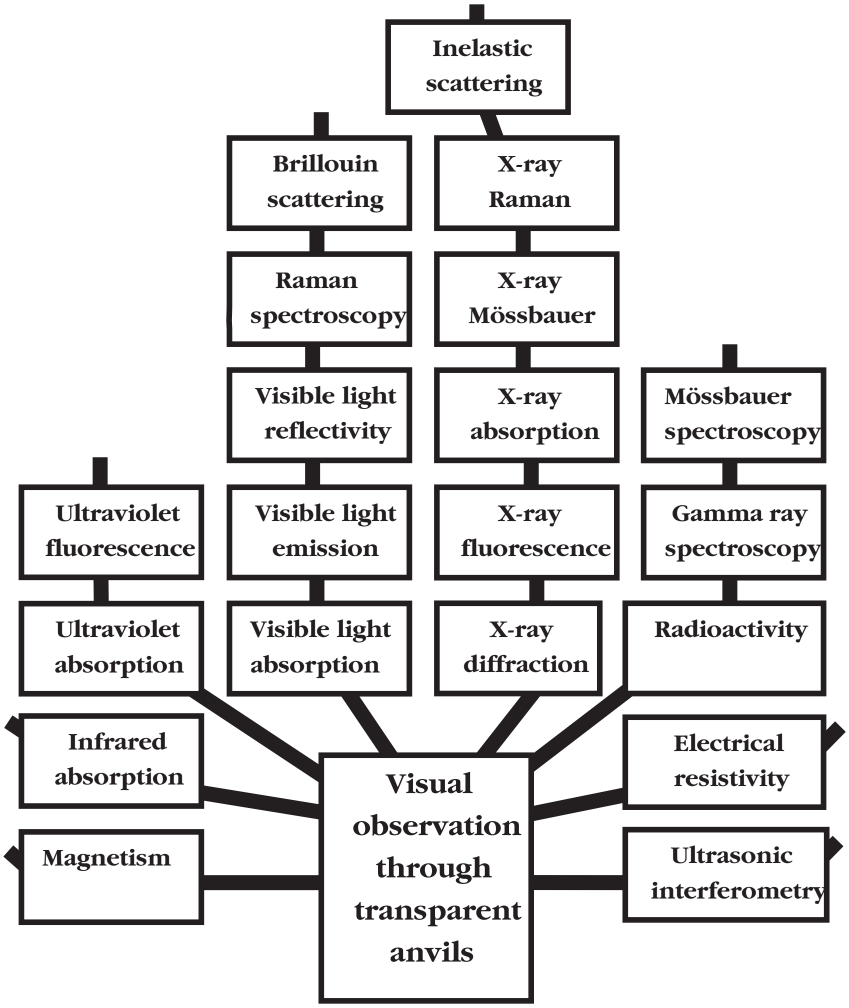
Inelastic scattering
Brillouin scattering
X-ray Raman
Raman spectroscopy
X-ray Mössbauer
Visible light reflectivity
X-ray absorption
Mössbauer spectroscopy
Ultraviolet fluorescence
Visible light emission
X-ray fluorescence
Gamma ray spectroscopy
Ultraviolet absorption
Visible light absorption
X-ray diffraction
Radioactivity
Infrared absorption
Electrical resistivity
Magnetism
Ultrasonic interferometry
Visual observation through transparent anvils

Figure 14 Virtually all diamond anvil cell experiments begin with visual observation. As advances are made in miniaturization of samples that instruments are capable of analyzing, diamond anvil cells are capable of providing ever higher pressures applied to those samples by reducing a in $P = f/a$.

hydrothermal reactions that play important roles in geological processes, shedding light on biological processes including properties of macromolecules and even organisms themselves. Future research with DACs is certain to yield important new results in all of the scientific disciplines.

References

Bassett WA (2006) Deviatoric stress: A nuisance or a gold mine? *J. Phys. Condens. Matter* 18: S921–S931.
Bassett WA (2009) Diamond anvil cell, 50th birthday. *High Pressure Res.* 29: 163–186.
Chou IM, Bassett WA, Anderson AJ, Mayanovic RA, and Shang L (2008) Containment of fluid samples in the hydrothermal diamond-anvil cell without the use of metal gaskets: performance and advantages for in situ analysis. *Rev. Sci. Instrum.* 79(11): 115103–1–115103–4.
Dubrovinsky L, Dubrovinskaia N, Prakapenka VB, and Abakumov AM (2012) Implementation of micro-ball nanodiamond anvils for high-pressure studies above 6 Mbar. *Nat. Commun.* 3: 1163. https://doi.org/10.1038/ncomms2160.
Irifune T, Kurio A, Sakamoto S, Inoue T, and Sumiya H (2003) Ultrahard polycrystalline diamond from graphite. *Nature* 421: 599–600.
Ishimatsu N, Matsumoto K, Maruyama H, et al. (2012) Glitch-free X-ray absorption spectrum under high pressure obtained using nano-polycrystalline diamond anvils. *J. Synchrotron Rad.* 19: 768–772.
Mao HK and Bell PM (1976) High-pressure physics: The 1-megabar mark on the ruby R1 static pressure scale. *Science* 191: 851–852.
Sakai T, Yagi T, Ohfuji H, et al. (2015) High-pressure generation using double stage micro-paired diamond anvils shaped by focused ion beam. *Rev. Sci. Instrum.* 86: 033905. https://doi.org/10.1063/1.4914844.
Sumiya H and Harano K (2012) Distinctive mechanical properties of nano-polycrystalline diamond synthesized by direct conversion sintering under HPHT. *Diamond Relat. Mater. Elsevier.* 24: 44–48.

Further Reading

Bridgman PW (1963) General outlook on the field of high pressure research. In: Paul W and Warschauer DM (eds.) *Solids under Pressure 1–13*. New York: McGraw-Hill.
Irifune T and Hemely RJ (2012) Synthetic diamond opens windows into the deep earth. *EOS, Trans., Am. Geophysical Union* 93(7): 65–66.
Paul W and Warschauer DM (eds.) (1963) In: *Solids under Pressure*, vols. 1–13. New York: McGraw-Hill.
Piermarini GJ and Block S (1975) Ultrahigh pressure diamond anvil cells and several semiconductor phase transitions pressure in relation to the fixed point pressure scale. *Rev. Sci. Instrum.* 46: 973–979.
Van Valkenburg A (1962) Visual observation of high pressure transitions. *Rev. Sci. Instrum.* 33: 1462.
Weinstein BA and Piermarini GJ (1975) Raman scattering and phonons dispersion in Si and GaP at very high pressure. *Phys. Rev. B* 12: 1172–1186.
Weir CE, Lippincott ER, Van Valkenburg A, and Buting EN (1959) Infrared studies in the 1–15 μm region to 30 000 atm. *J. Res. Natl. Bureau Stand. A* 63: 55–62.

INDEX

This index is in letter-by-letter order, whereby hyphens and spaces within index headings are ignored in the alphabetization, and it is arranged in set-out style, with a maximum of four levels of heading. Location references refer to the volume number, in bold, followed by the page number. Page numbers suffixed by *f* and *t* refers to figures and tables terms respectively. *vs.* indicates a comparison. **Bold locators** refers to main articles.

A

AA-stacked bilayer graphene
  crystal structure, **1**:618
  electronic band structure and tight-binding model, **1**:618–620
Abelian Chern–Simons gauge theory, **1**:67–69
Abelian Higgs model, **1**:45
Ab initio calculation, **2**:261
Ab initio molecular dynamics (AIMD), **4**:543, **4**:546, **5**:754
Ab initio phasing methods
  direct methods, **5**:34–36
  dual space iterative algorithms, **5**:36–38, **5**:37*f*
  Patterson function, **5**:33, **5**:33–34*f*
  phase determination in practice, **5**:36
  phasing of large structures, direct methods with density modification, **5**:36
  probability methods, **5**:35, **5**:35*f*
  structure invariants, **5**:34–35
Abrikosov parameter, **2**:696
Abrikosov vortex, **2**:654
Absorption, **4**:706, **5**:450–451
  excitonic component of, **5**:666
  and luminescence energies, **1**:857
  vibrational, **5**:666–667
Absorption coefficient, **5**:155, **5**:161–162
Accretion, **4**:434
AC-electrokinetic phenomena, **4**:704–705
Ac-field-driven Falicov–Kimball model, **1**:975, **1**:975*f*
Ac-field-driven Fermi–Hubbard model, **1**:976–977
Acoustic phonons, **4**:187
Acoustic theory
  application of, **3**:209
  basic, **3**:201–202
  for fluids, **3**:202–203
  to liquids, **3**:205–207
  quality factor, **3**:201–203
  to solids, **3**:207–208
  for solids and piezoelectrics, **3**:203–205
Acousto-optic beam splitter (AOBS), **4**:111
AC quantum voltmeter (AC-QVM), **1**:10
Acquisition function, machine learning, **4**:558
Action potential (AP), **3**:159, **4**:695–696
Active magnetic regenerator (AMR) cycle, **2**:90–92
Active metasurface, **5**:101, **5**:101*f*
Adam and Gibbs theory, **3**:176
Additional boundary condition (ABC), **3**:685
Additive manufactured (AM) components, **3**:832–833, **3**:833–834*t*
Additive manufacturing, **5**:624
  alloys, **5**:531, **5**:580–582
  of ceramics, **5**:419
  magnesium alloys, **5**:555
  plastics and ceramics, **3**:602–603
  THz NDE of, **3**:605–617
  THz optical components, **3**:604–605
  THz spectral characterization of materials, **3**:604
Adiabatic approximation. *See* Born–Oppenheimer approximation
Adiabatic continuity, **1**:342
Adiabatic potential energy surfaces (APES), **1**:798–799
A-DNA, **4**:667
Adsorption, catalysts, **5**:741
Advanced packaging materials, **5**:348*t*
Advanced work-hardening models, **3**:850–851
Aerosols, **4**:215
Age hardening, in Al-Cu alloys, **5**:574
Aggregation, protein, **4**:654–655
Aging, **2**:375–378, **2**:380–382
Aharonov–Bohm–Casher (ABC) interactions, **2**:806–807
Aharonov–Bohm effect, **1**:214, **1**:214–215*f*, **1**:219–224, **1**:492, **3**:415–416, **3**:716
  cold atoms physics, **1**:229
  electrons on ring, **1**:220
  energy eigenvalues *vs.* magnetic flux, **1**:221*f*
  gauge invariance, **1**:220
  interference, **1**:220
  periodicity in, **1**:220
  persistent current, **1**:221–222
  in quantum rings, **3**:433–434
  spectrum, **1**:220–221
Aharonov–Bohm flux, **1**:660–661
Aharonov–Bohm interference, **1**:219*f*
Aharonov–Bohm interferometer, **1**:222–224
Aharonov–Bohm period, **3**:410
Aharonov–Casher effect, **1**:218, **1**:224–229, **1**:224*f*, **1**:492
Aharonov–Casher spin interference, **2**:200–201
AHE. *See* Anomalous Hall effect (AHE)
Aircraft brakes, **5**:334–335, **5**:345
Alkali phosphate glasses, **3**:185
Alloy disorder, **3**:237, **3**:245–246, **3**:248
Alloys, **5**:459, **5**:460*f*
  additively manufactured metal, **3**:832–833
  additive manufacturing of, **5**:590–591
  Co-Al-W-based, **5**:592
  complex concentrated, **3**:828–832, **3**:830*f*
  crystal structures in, **5**:512
  directionally solidified, **5**:587
  element behavior in iron, **5**:534, **5**:535*t*
  ferromagnetic iron, **5**:548*t*
  high entropy, **3**:830*f*
  highly mismatched, **5**:460–463, **5**:462*f*
  interstitial elements, **5**:534–535, **5**:534*f*, **5**:535*t*
  iron-based, **5**:540*f*, **5**:545*t*
  magnesium, **5**:553
  medium entropy, **3**:830*f*
  metallic, **3**:166–167, **3**:166*f*
  and perovskites, **5**:466–467, **5**:467*f*
  processing, **5**:541–543
  silicon-germanium, **3**:538
  substitutional alloying elements, **5**:536
  for turbine disks, **5**:588–590
  Van der Waals semiconductors, **5**:465–466, **5**:466*f*
Al—Mn icosahedral quasicrystal, **5**:319, **5**:328
Almost-bosonic anyons, **1**:468–469
Almost-fermionic anyons, **1**:469–470
Almost Mathieu model, **1**:713–714

AlNiCo decagonal phase, electron diffraction pattern of, **5**:329, **5**:330*f*
Alnicos, **2**:82, **2**:82*t*
Al—Pd—Mn quasicrystal
  Bragg reflections, 2-D images of, **5**:323, **5**:323*f*
  fivefold axis Laue X-ray diffraction pattern of, **5**:319, **5**:320*f*
  phason diffuse scattering, **5**:330–331
  X-ray diffraction pattern, **5**:321, **5**:322*f*
AlphaFold2, **5**:45–46, **5**:46*f*
Altermagnets, **2**:164, **2**:169–174, **2**:171*f*
Altland–Zirnbauer classification, **2**:799–800
Alumina, **4**:742, **5**:438–439
Alumina-based fibers, **5**:338
Aluminum alloys
  for additive manufacturing, **5**:580–582
  alloying systems for, **5**:575*t*
  applications of, **5**:581–582
  deformation, **5**:575–576, **5**:578
  design, **5**:578
  features and classification of, **5**:574–576
  microstructural features, **5**:581
  microstructures, **5**:577*f*
  processing of, **5**:576–578
  property–microstructure relationships, **5**:579*t*
Aluminum bronze, **5**:618–619
Ambegaokar-Baratoff (AB) regime, **2**:623–624
Ambipolar electric field effect, **1**:608
Amino acid (AA), **4**:656–657
Amorphous alloys, **2**:80–81, **2**:81*t*, **5**:518–519
Amorphous carbons, **5**:713
Amorphous ice systems, **3**:177
Amorphous magnetic systems, **2**:23
Amorphous metal, **2**:22–23
Amplitude mode
  coherent dynamics of superconducting, **3**:702
  superfluid Fermi gas, **1**:194–195, **1**:195*f*
Amyloid, **4**:658
Analytical-type DOEs, **5**:96
Andersen barostat, **5**:756
Anderson–Bogoliubov mode, **1**:187–188, **1**:191–195, **1**:192–194*f*
Anderson–Higgs mechanism, **1**:159
Anderson localization, **1**:567
  and integer quantum Hall effect, **1**:568–570
  network model, **1**:570–572
  single-particle models for, **1**:567
Anderson model, **3**:383–385
AND plane, **3**:554, **3**:555*f*
Andreev reflection (AR), **1**:112, **2**:618
Anelastic behavior, thin films, **5**:265–266
Angell classification, of glasses, **3**:174
Angle-dependent magnetoresistance oscillations, **1**:821–822, **4**:128
Angle-resolved photoemission spectroscopy (ARPES), **1**:659, **1**:691–692, **1**:697, **1**:819–821, **1**:975, **1**:981–982, **1**:985–986, **2**:330, **2**:584–585, **4**:335, **5**:136
  correlated topological insulators, **4**:359–360
  dirac semimetals, **4**:345–347, **4**:348*f*
  kagome systems, **4**:350
  magnetic topological insulators, **4**:342–344
  magnetic Weyl semimetals, **4**:350
  nonmagnetic Weyl semimetals, **4**:347–350, **4**:349*f*
  topological chiral semimetals, **4**:357–359, **4**:358*f*
  topological crystalline insulators, **4**:345, **4**:346*f*
  topological insulators, **4**:335–342
  topological nodal-line semimetals, **4**:356–357, **4**:356*f*
  topological superconductors, **4**:360
  transition metal dichalcogenides, **4**:350–356, **4**:351*f*
  ultrafast experiments, **4**:360–362, **4**:361*f*
  weak topological insulators, **4**:345
Angle-resolved STEM (AR-STEM), **4**:97, **4**:104–105, **4**:105–106*f*
Angstrom-resolved Raman images, **4**:314*f*
Angular momentum of electron, **2**:9
Anharmonicity, **1**:876
Anharmonic oscillator, **5**:114–115
Anharmonic potential, **1**:646–650
Animal cell, cellular compartments of, **4**:690, **4**:691*f*
Animal models
  extremely low frequency fields, **4**:712–713
  intermediate frequency fields, **4**:714
  radiofrequency fields, **4**:715
  static fields, **4**:711
Anisotropic diffusion, **3**:349
Anisotropic magnetoresistance (AMR), **2**:160
Anisotropic susceptibility, **2**:41
Anisotropy, **2**:53, **2**:558–559, **2**:562, **3**:481–482, **3**:489, **3**:491–492, **3**:496–497, **3**:840–841, **5**:631
ANN. *See* Artificial neural networks (ANNs)
Annealing textures, **5**:630
Annihilation process, **3**:854–855
Anodization, **5**:351–352, **5**:354–355, **5**:360, **5**:442–445
Anomalous diffraction, **5**:47
Anomalous dispersion, **5**:145
Anomalous Floquet topological insulator, **1**:972
Anomalous Hall conductivity, **1**:675–676
Anomalous Hall effect (AHE), **1**:600
  charge transport description, **1**:594–598, **1**:595–596*f*
  definition, **1**:587
  ferromagnetism, **1**:590–591, **1**:591*f*
  history, **1**:588–590, **1**:588*f*
  measurements, **2**:385
  scalar scattering, role of, **1**:588
  spin-orbit coupling, **1**:587–588, **1**:592–593
  topological materials, **1**:594–599, **1**:595–596*f*, **1**:598*f*
Anomalous quantum Hall effect, **1**:79
Anomalous scattering, **5**:45
Anomalous skin effect, **1**:829, **4**:372
Antenna action, **4**:733–736
Anti-bunching, **1**:115
Anticommutation relation (ACR), **1**:132
Antiferroelectric liquid crystal, **5**:381, **5**:383*f*
Antiferromagnetic crystals, **5**:9
Antiferromagnetic quasicrystals, **5**:5*f*
Antiferromagnetism, **2**:29*f*, **2**:31, **2**:56–57, **5**:491
Antiferromagnets, **2**:19, **2**:22–23, **2**:146, **2**:170–171, **2**:174
  magnetizing process of, **2**:57–58
  ultrafast dynamics in, **3**:699–700
Anti-Kondo effect, **3**:391
Anti-Pfaffian state, **1**:296, **1**:332, **1**:550
  partial equilibration on, **1**:353–354
Antisites, **5**:185
Anti-Stokes scattering, **4**:300–301, **4**:301*f*
Antisymmetry groups, **5**:2
Anyon(s), **1**:271, **1**:290, **1**:485, **1**:501–512, **1**:503–504*f*, **1**:507*t*, **1**:509–511*f*
  almost-bosonic, **1**:468–469
  almost-fermionic, **1**:469–470
  applications, **1**:395
  braid group statistics, **1**:489–492
  braiding and fusing of, **1**:489–492
  composites/fusion rules, **1**:492
  and fractional quantum Hall effect, **1**:399–400, **1**:400*f*
  fractional statistics, **1**:485
  ground state degeneracy, **1**:495–496
  quantum statistics, **1**:485–489
  topological computation, **1**:493–494, **1**:496
Anyon collisions
  collider with random sources, **1**:405, **1**:406*f*
  elements of theory, **1**:408–411
  experimental results, **1**:411–413, **1**:411*f*
  fermion and boson collisions, **1**:404–405, **1**:404*f*
  random collisions of electrons, **1**:405–408, **1**:407–408*f*
  reverse tunneling process, **1**:409–410*f*
APD. *See* Avalanche photodiode (APD)
Aperiodically ordered solids, **5**:291
Aperiodic crystal, **4**:510, **4**:512–513, **4**:513*f*
Aperiodic crystals, **5**:68, **5**:291, **5**:319, **5**:330–331
Aperiodicity, **5**:25–28
Aperiodic media, **5**:269
  conductivity, **5**:275–276
  exponents, **5**:274–275
  Hull, **5**:270–272
  noncommutative Brillouin zone (NCBZ), **5**:272–273
  transport mechanisms, **5**:270
Aperiodic order, **5**:295
Aperiodic Schrödinger operators, **5**:295
Application-specific ICs (ASICs), **3**:756
Applied electric field, on colloidal crystal structure, **4**:113–114
Approximate exchange-correlation functionals, **1**:870–872
Approximation of functions, **5**:750
Aqueous electrolytes, **4**:702
Aqueous media, **4**:702

Aramid fibers, **5**:338
Arbitrary frequency domain waveform, **1**:12–13, **1**:13*f*
Arbitrary time domain waveform, **1**:12–13, **1**:13*f*
Architectural installations, ceramics, **5**:419, **5**:419*f*
Area-selective ALD (AS-ALD), **5**:717–718
Argand diagram, **5**:43–44
Arithmetic equivalence, **5**:65
Armchair nanoribbons, **2**:281–282
Aromatic polyamide fibers, **5**:338
ARPES. *See* Angle-resolved photoemission spectroscopy (ARPES)
Artificial atoms, **3**:325–326, **3**:329–332, **3**:331*f*, **3**:333*f*, **3**:426–427
Artificial intelligence (AI), **4**:91
Artificial molecules, **3**:325–326, **3**:331
Artificial neural networks (ANNs), **4**:549, **5**:240, **5**:240*f*
Artificial quantum systems, **1**:976
Artificial spin glass, **2**:126
Artificial spin ice, **2**:126
Assembly of moments, **2**:27
Astronomy, X-ray sources, **4**:434–438
Atom
  Bohr model of, **2**:40
  energy levels for, **3**:500–501, **3**:501*f*
Atomic Cluster Expansion framework, **4**:547
Atomic force microscopy (AFM), **2**:533, **3**:659–661, **4**:51, **4**:53, **4**:54*f*, **4**:310–312
  beam-deflection, **4**:55*f*
  bimodal AFM, **4**:57–58
  dissipation force microscopy, **4**:59
  friction force microscopy, **4**:58–59
  high-speed AFM, **4**:57
  Kelvin probe force microscopy, **4**:58
  magnetic force microscopy, **4**:59
  noncontact atomic force microscopy, **4**:54–55, **4**:56*f*
  phase imaging, **4**:57
  pulsed force mode, **4**:57
  tapping mode force microscopy, **4**:56–57, **4**:57*f*
Atomic form factor, **5**:43
Atomic layer deposition (ALD), **1**:14–15, **2**:535, **3**:562, **5**:256, **5**:716
  cycle, **5**:717*f*
  forms of, **5**:718
  in situ characterization, **5**:724, **5**:724*t*
  of metals and elements, **5**:722
  nanostructures (high aspect ratio), **5**:725, **5**:725*f*, **5**:726*t*
  origin of, **5**:717–718
  of oxides, **5**:721
  steps, **5**:716
  of sulfides, phosphides, fluorides, **5**:722–723
  temporal *vs.* spatial, **5**:720–721, **5**:720*f*
  of ternary and quaternary components, **5**:723–724, **5**:723*f*
  thermal *vs.* plasma-enhanced, **5**:718–719, **5**:718*f*
Atomic layer epitaxy (ALE), **5**:256
Atomic limit, **1**:916
Atomic magnetic moment, **2**:35–36
Atomic mass-related properties, semiconductors
  electronic structure, **2**:489–490
  local vibrational modes, **2**:492–493
  phonon dispersion, **2**:486–487
  self- and dopant diffusion, **2**:490–492
  structure, **2**:485–486
  thermal conductivity, **2**:488–489
Atomic physics, **3**:70
Atomic spin-orbit coupling, **1**:592
Atomic structure, of quasicrystals
  AlMn alloy, electron diffraction pattern of, **5**:319
  Al—Pd—Mn phase (*see* Al—Pd—Mn quasicrystal)
  aperiodic crystals, **5**:319, **5**:330–331
  CdYb icosahedral quasicrystalline phase, **5**:324–328
  decagonal phase, **5**:329, **5**:330*f*
  diffraction pattern, **5**:318–319
  diffuse scattering, **5**:319, **5**:329–330
  disorder, **5**:319
  dodecagonal symmetry, **5**:320
  icosahedral quasicrystals, **5**:328–329, **5**:329*f*
  incommensurate modulated phases and composites structures, **5**:319
  intermetallic quasicrystal, **5**:319–320
  oxide quasicrystals, **5**:320
  periodic atomic structures, **5**:318–319, **5**:329–330
  phason modes, **5**:330–331, **5**:331*f*
  structural quality of, **5**:323, **5**:323*f*
  superspace crystallography, **5**:321–323, **5**:321–322*f*
  ZnMgY icosahedral phase, single grain of, **5**:319–320, **5**:320*f*
Atomistic models, **2**:114
Atom probe tomography (APT), **3**:245
Atom trapping, **3**:70*f*
Atom tweezer array system, **3**:142
Attenuated total reflection (ATR), **3**:731–732, **3**:731*f*, **4**:374
Attenuation, **3**:206
Attractive contact interactions, **3**:130
Au-based amorphous alloys, **5**:519
Auger recombination, **3**:248
Au nanodots, **5**:363–364
Austenite, **5**:536
Autocorrelation analysis, **4**:325
Autocorrelation function (ACF), **4**:325
Automatic FLOW for Materials Discovery (AFLOW), **4**:553
Avalanche photodiode (APD), **3**:764
Avian magnetoreception, **4**:588–589
Avian navigation, **4**:598–599
Axial anomaly, **1**:85
Axion, **1**:674–675

B

Backgated structure, **3**:787, **3**:787*f*
Bainite, **5**:536–538
Balian-Werthamer (BW) state, **2**:798–799
Ballistic transport, **2**:301
Banana liquid crystal. *See* Bent-core liquid crystal
Band-anticrossing (BAC) model, **3**:236–237, **3**:247, **5**:463–464
Band bending, **2**:263, **2**:269
Band gap, **5**:453–461, **5**:458*f*, **5**:463–467
Band gap bowing, **3**:240–241, **3**:245–247
Band gap engineering, and strain, **5**:464–465, **5**:465–466*f*
Band-gap opening, graphene, **2**:353–354
Band-limited square waveform (BLSW), **1**:22, **1**:22*f*
Band structure, **2**:478–480, **5**:120–121
  of gallium arsenide, **2**:225
  twisted bilayer graphene, **2**:290–291
Band theory
  of antiferromagnetism, **2**:61–62
  of ferromagnetism, **2**:60
Bardeen–Cooper–Schrieffer (BCS) limit, **1**:188, **1**:192–194
Bardeen–Cooper–Schrieffer (BCS) theory, **2**:660–665, **2**:670, **2**:693, **3**:4, **3**:456, **3**:723
Bargmann space, **1**:540, **1**:543, **1**:642–643
Barnase, **4**:647–648
Battery material, **4**:185
Bayesian optimization (BO), machine learning, **4**:557, **4**:557*f*
BCS-BEC crossover
  density-controlled, **3**:33–34
  graphene-based systems, **3**:34
  iron-based systems, **3**:34–35
  organic systems, **3**:35–36
BD method. *See* “Brownian dynamics” (BD) method
B-DNA, **4**:665–667
Beam dynamics elements, **4**:461–462
Beam equivalent pressure (BEP), **2**:537
Beam flux monitor (BFM), **2**:537
Beam manipulation, **4**:462–463, **4**:467–468, **4**:467*f*, **4**:473
Beam modes, **4**:414–417
Beam properties, **3**:775–776
Beam splitter (BS), **1**:925–926, **5**:168, **5**:174, **5**:178–183, **5**:179–182*f*
BEC. *See* Bose–Einstein condensation (BEC)
BEC–BCS crossover, **1**:189, **1**:192, **1**:192*f*
  CFB model and BCS model, **3**:11–13
  crossover at T = 0, **3**:13
  Nambu–Goldstone mode, **3**:16–17
  neutron superfluid in the crust regime of neutron star, **3**:19–20
  Tan’s contact, **3**:17–18
  unitary Fermi gas and universal thermodynamics, **3**:18–19
Behler-Parrinello (BP) descriptors, **4**:547
Bending magnets, **4**:426–431, **4**:427*f*, **4**:438–439
Bending stiffness, **5**:393–394
Bent-core liquid crystal, **5**:383–388, **5**:385–387*f*
Bent DNA, **4**:672
Berezinskii–Kosterlitz–Thouless (BKT), **1**:910–911, **2**:584–585, **2**:587, **2**:670, **2**:806, **2**:808–812, **2**:810*f*, **3**:720–722

Bernal-stacked bilayer graphene, **1**:528
  band gap tunable with an electric field, **1**:616–618
  Berry phase 2π, **1**:615
  crystal structure, **1**:612
  effective-mass model, pseudospin and chirality, **1**:613–614
  electronic band structure and tight-binding model, **1**:612–613
  integer quantum Hall effect, **1**:618
  symmetries, **1**:615
  trigonal warping and other tight-binding parameters, **1**:615–616
Bernal stacking, **1**:769
Bernard and Duraffourg condition, **3**:771–772, **3**:772*f*
Bernoulli number, **1**:972
Berry connections, **1**:74, **1**:692–693, **2**:797–798, **5**:129
Berry curvature, **1**:74–75
Berry phase, **1**:39, **1**:476–477, **1**:607, **1**:610–611, **1**:666–668, **1**:670
Berry phase 2π, **1**:615
Beryllium copper, **5**:611
Berzelius, Joens J., **3**:792*f*
β-lacto-globulin, **4**:657
β-mercaptoethanol, **4**:657
Bethe ansatz (BA), **1**:909
Bethe–Salpeter equation, **1**:763, **4**:393, **4**:397
Beyond mean-field, **2**:366–367
BF gauge theory, **1**:67
Biased bilayer graphene, plasmons in, **1**:771–776
Biexcitons, **3**:708*f*
Big data, **4**:91
Bilayer graphene, **1**:374–377, **1**:769–771, **2**:249–251, **2**:249–250*f*, **2**:254, **2**:297–298, **2**:300
Bilayer systems, **1**:298–300
Binarization process, **5**:98
Bioactive ceramic scaffolds, **4**:742–743
Bioactive glass scaffolds, **4**:743, **4**:744*f*
Bioactive materials, **4**:740
  class A, **4**:740
  class B, **4**:740
  mechanism of bone bonding, **4**:740
Bioceramics, **5**:422–423
Biochemistry and life science, **1**:262
Biodegradable polymers, **4**:742
Bioeffects
  of extremely low frequency fields, **4**:711–713
  of intermediate frequency fields, **4**:713–714
  of radiofrequency fields, **4**:714–716
  of static fields, **4**:710–711
Biogenic magnetites, **4**:707
Bioglass®, **4**:740
Biohybrid microrobots, **3**:542
Biological context
  coherent transfer processes
    microtubules, **4**:598
    mitochondria, **4**:598
    photosynthesis, **4**:597
  new (and old) avenues of interest, **4**:600–601
  quantum tunnelling
    DNA, **4**:596
    enzymes, **4**:596
  spin dynamics
    avian navigation, **4**:598–599
    chirality, **4**:600
    phosphorus nuclear spin, **4**:599–600
    reactive oxygen species, **4**:599
    spin chemistry, **4**:598
Biological matter
  magnetic susceptibility, **4**:707, **4**:707*t*
  passive electric properties of, **4**:701
Biomedical materials, **4**:740–741
  bioactive materials, **4**:740
  composites, **4**:741
  need for, **4**:739
Biophotonics, **3**:313, **3**:320
  bio-Raman spectroscopy and, **4**:745, **4**:746*f*
  spectroscopy and, **4**:744–745
Bio-Raman spectroscopy, **4**:745, **4**:746*f*
Bioresorbable polymers, **4**:742
Bipolar, **3**:571
Bipolar transistors, **3**:758–761, **3**:760–761*f*, **3**:781–783
Bir-Aronov-Pikus mechanism, **2**:229
Birefringence, **3**:614–617, **3**:670–671
  optical materials, **5**:100
  phase matching, **4**:385, **4**:385*f*
Bit-line driven scheme, **3**:569
Black phosphorous, **2**:483*f*
Blast furnace process, **5**:541
Blister copper, **5**:602
Bloch acceleration theorem, **5**:129–130
Bloch bands, with high Chern numbers, **1**:527
Bloch electrons
  low magnetic fields, **1**:700–702
  and magnetic oscillations, **1**:702–703
  semiclassical methods, **1**:702–703, **1**:705–710
  strong magnetic fields, **1**:703–710
Bloch equation, **1**:692
Bloch functions, **1**:763, **5**:131, **5**:219–220, **5**:219*f*
Bloch geometry, **1**:671–673
Bloch-Gruneisen model, **3**:254
Bloch sphere representation, of single-qubit quantum computation, **1**:280*f*
Bloch theorem, **3**:740, **5**:319
  vs. Floquet's theorem, **1**:969, **1**:969*t*
Bloch wall, **2**:49–51, **2**:51*f*
Bloch wave function, **2**:517, **5**:129
Block selection transistors (BST), **3**:569
BLS. *See* Brillouin light scattering (BLS)
BMD. *See* Bone mineral density (BMD)
BN nanotubes, **1**:763–764
Bode plots, **4**:269, **4**:285–289, **4**:286–288*f*, **4**:290–291*f*
Bogoliubov-de Gennes (BdG) Hamiltonian, **2**:795–800
Bogoliubov energy, **1**:189–190
Bogoliubov quasiparticle, **1**:134
Bogoliubov transformation, **3**:126
Bohr magneton, **4**:231
Bohr model of atoms, **2**:40
Bohr–Sommerfeld model, **2**:41, **2**:653
Bohr–van Leeuwen theorem, **2**:36, **2**:39–40, **2**:42, **2**:71
Boltzmann constant, **3**:3, **3**:209, **4**:208, **4**:230
Boltzmann distribution, **2**:460, **4**:571, **4**:572*f*
Boltzmann equation, **1**:594–595, **4**:375
Boltzmann factor, **5**:169
Boltzmann statistics, **2**:71
Bonding states, **3**:331
Bond orientational order (BOO), **5**:278
Bone, **4**:739
  cancellous, **4**:739
  cortical, **4**:739
  defects, **4**:739–740
  mineral, **4**:739
Bone mineral density (BMD), **3**:841
Bone repair, scaffolds for, **4**:741–743
  bioactive ceramic scaffolds, **4**:742–743
  bioactive glass scaffolds, **4**:743, **4**:744*f*
  criteria for ideal scaffold, **4**:741–742
  polymer scaffolds, **4**:742
Boolean equations, **3**:555
Boolean rule, **4**:688
Boric oxide anomaly, **3**:183
Born approximation, **1**:597
Born model, **5**:208
Born–Oppenheimer approximation, **1**:868, **3**:503, **4**:544
Boron fibers, **5**:337
Bose distribution function, **2**:59
Bose–Einstein condensation (BEC), **1**:158–159, **1**:188–189, **1**:213, **1**:641, **2**:423–424, **2**:655, **3**:3, **3**:10, **3**:68–70, **3**:74*f*, **3**:76–77*f*, **3**:124, **3**:135–136, **3**:644, **3**:720–722, **5**:125
  coherence and superfluidity, **3**:75–78
  collision-induced loss, **3**:646–647
  in dilute atomic gases, **3**:70–71
  disorder, **3**:79
  excitonic Lyman spectroscopy, **3**:647, **3**:648*f*
  excitons in cuprous oxide, **3**:644–645
  experiments at sub-Kelvin temperatures, **3**:648–650, **3**:649–650*f*
  Fermi gases, **3**:73–75
  long-range interactions, **3**:81
  low-dimensional physics, **3**:81
  new macroscopic quantum state, imaging, **3**:71–72
  optical lattices, **3**:79
  quantum mixtures of ultracold atomic gases, **3**:78–79
  role of interactions, **3**:72–73
  supersolidity, **3**:81–82
  in 3-D ideal Bose particle system, **3**:645–646
  typical LO-phonon-assisted luminescence spectra, **3**:645*f*, **3**:647*f*
  visualization of, **3**:651*f*
Bose–Einstein condensed cold atoms, hopping amplitude of, **1**:976–977, **1**:976*f*
Bose–Einstein distribution, **5**:169, **5**:169*f*
Bose–Einstein statistics, **1**:485
Bose–Fermi mixtures, **1**:507, **1**:512
Bose gases
  dipolar, **3**:132*f*

  noninteracting, **3**:125–126
  unitary, **3**:129*f*
Bose–Hubbard model, **1**:976–977
Boson collisions, **1**:404–405, **1**:404*f*
Bosonization, **1**:52–62
  anomalies and duality, **1**:59–62
  in 2+1 dimensions, **1**:119–125
  of Dirac theory in 2+1 dimensions, **1**:120–124
  of Fermi surface, **1**:124–125
Boson peak, **5**:299–301
Bosons, **1**:279, **1**:485, **1**:487, **1**:946, **1**:952–953
Bottom electrode (BE), **3**:571
Bouchaud's trap model, **2**:381
Boundary conditions
  at metal–metal interface, **4**:376–377
  metal optics, **4**:371, **4**:373, **4**:376
Boundary layers (heterogeneous doping), **3**:153–156
Bound states, probability densities of, **2**:348*f*
Bound water, **4**:704
Bragg diffraction, **4**:400–401, **4**:404, **5**:93
Bragg gratings, **3**:778
Bragg's law, **4**:400
Braid group, **1**:65–66, **1**:72, **1**:395–396, **1**:397*f*, **1**:489–492, **1**:490*f*
Braiding
  anyons and anyon systems via, **1**:274–275
  non-Abelian anyons via, **1**:272
  non-degeneracy, **1**:274
  structure on fusion category, **1**:277
  universality, **1**:273–274
Braids and knots, **1**:269–270
Brass, **5**:614–617
Bravais classes, **5**:65–66, **5**:65*t*, **5**:66*f*
Bravais lattice, **1**:684, **5**:71*t*
Break junction technique, **4**:678*f*, **4**:679, **4**:680*f*, **4**:681
Bremsstrahlung, electromagnetic radiation, **4**:434–435
Brewster angle, **4**:373
Bridgman method, **1**:697
Bridgman–Stockbarger techniques, **5**:196–198
Bright excitons, **3**:708*f*, **3**:712–713
Brightness, **4**:461–462, **4**:464–467, **4**:473
Brillouin function, **2**:37, **2**:43, **2**:56
Brillouin light scattering (BLS)
  Co/Cu superlattice, **4**:191
  elastic constant determination of bulk crystal, **4**:188–190
  examples, **4**:188
  gases, **4**:191
  glasses, **4**:190
  history of, **4**:188
  origin of, **4**:188
  research directions, **4**:192
  scattering geometries and frequency analysis, **4**:188
  surface acoustic modes in thin layers, **4**:191
  from surface acoustic phonons, **4**:191*f*
Brillouin shift, **4**:390–391
Brillouin-Wigner perturbation theory, **1**:972
Brillouin zone (BZ), **1**:682, **2**:406, **2**:406*f*, **2**:457, **2**:476, **2**:476*f*, **2**:480–481, **5**:120–121, **5**:125, **5**:131, **5**:131*f*
Broadband pump-probe spectroscopy, **3**:697
Broken symmetry phases, **1**:290–291
Bronzes, **5**:617–618
"Brownian dynamics" (BD) method, **5**:754
Brownian motion, **3**:173–174, **3**:280–283, **4**:323
Brown-Twiss correlations
  beam splitter (BS), **5**:178
  Hanbury Brown–Twiss apparatus, **5**:178, **5**:178*f*
  Mandel Q-parameter, **5**:178
  photon antibunching, **5**:168, **5**:178–179, **5**:179*f*
  photon bunching, **5**:168, **5**:179, **5**:179*f*
  quasi-monochromatic radiation, **5**:178
Bulk-boundary correspondence, **2**:800–801
Bulk catalysts, **5**:743
Bulk collective excitations, **1**:335
Bulk diffusion effects, **3**:858
Bulk-edge correspondence, **1**:660
  quantum Hall effect to Chern insulators, **1**:662–664
  short-range entangled states, symmetry protection and edge states, **1**:666–668
  universality of, **1**:665–666
Bulk energy gap
  density dependence, **1**:346
  disorder, **1**:347–348
  in-plane magnetic field, **1**:348
  mobility, **1**:347–348
  optical probes of, **1**:348
  and sample design, **1**:347–348
Bulk inversion asymmetry (BIA), **1**:592
Bulk materials, **2**:577–578
Bulk semiconductor technology, **2**:513
Burau representation, **1**:475
Burgers vector, **5**:404–405
Butler–Volmer equation, **3**:146
B–Z transition, **4**:670

C

C$_{60}$, **1**:763
CaF$_2$-BaF$_2$ heterolayers, ionic conductivity of, **3**:155*f*
Cage effect, **3**:173–174
CaKFe$_4$As$_4$, superconductivity in, **2**:608–609
Calamitic liquid crystals, **5**:380–382
  antiferroelectric SmC* phase, **5**:381, **5**:383*f*
  ferroelectric SmC* phase, **5**:381, **5**:383*f*
  hexatic and crystal smectic phases, **5**:381
  smectic-A (SmA) phase, **5**:375, **5**:381, **5**:381*f*
  smectic-C (SmC) phase, **5**:381, **5**:382*f*
  twist-grain boundary (TGB) phase, **5**:381–382, **5**:384*f*
Calaverite, **4**:513–514
"Calculable" waveforms, **1**:12
Callan-Harvey effect, **1**:86–88
CALPHAD (CALculation of PHAse Diagrams) method, **5**:513–515
Cancellous bone, **4**:739
Canonical ensemble, **4**:563–564
Canonical partition function, **4**:563
CaO–Al$_2$O$_3$ glasses, **3**:183
Capture system, **4**:472–473
Carbide coatings, **5**:417
Carbon/carbon composites (CCCs), **5**:345–346
Carbon fibers, **5**:337
Carbon materials, electronic states of
  carbon nanotubes, **5**:708–711
  diamond, **5**:704–706
  disordered carbons, **5**:713–714
  fullerenes and fullerites, **5**:711–713
  graphene and graphite, **5**:706–708
  hybrid orbitals, **5**:703
  local symmetry, **5**:714
  synthetic carbons, **5**:713
Carbon matrix composites (CAMCs), **5**:345–346
Carbon nanotubes (CNTs), **2**:284–286, **4**:89*f*, **4**:679, **5**:708–711
Carbon peapods, **5**:712
Caret-like MCE, **2**:88–89
Carlson–Goldman mode, **1**:192–193
Carotenoids, **4**:732
Car–Parrinello method, **2**:261, **5**:754
Carrier confinement, **3**:773
Carrier density, **1**:587
Carrier mobility, **2**:461–463
Carriers concentration, **1**:853–854
Carriers of plastic strain, **3**:853
Casimir–Onsager conditions, **4**:495
Casting, **5**:553, **5**:576–577
Cast irons
  mechanical properties of, **5**:542*t*
  steel processing route, **5**:543*f*
Catalysts
  adsorption aspects, **5**:741
  applications, **5**:734–735, **5**:734*f*, **5**:740
  characterization, **5**:746
  colloidal wet-chemical synthesis, **5**:744–746
  deactivation, **5**:746
  evaporative methods, **5**:744
  fouling and poisoning, **5**:746
  fusion (bulk, pre-molten alloys, and metal oxides), **5**:743
  heterogeneous, **5**:730, **5**:747*f*
  high-throughput synthesis technologies, **5**:731–732, **5**:732*f*
  hydrothermal synthesis (zeolites), **5**:744
  impregnation (supported catalysts), **5**:744
  kinetic considerations, **5**:740
  microkinetic modeling, **5**:742
  nanocatalysts, **5**:745–746
  precipitation (bulk catalysts), **5**:743
  preparation, **5**:742–746
  principle of Sabatier, **5**:741–742
  properties, **5**:742–746
  raney metals, **5**:744
  research and discovery, **5**:740
  shapes, **5**:742–746, **5**:743*f*
  sintering, **5**:746
  structure decomposition, **5**:746

Catalysts *(Continued)*
  supports, **5**:744
  transformation routes of, **5**:739*f*
  well-defined, **5**:745*f*
Cathodes
  field emission, **4**:466–467
  photo, **4**:465–466, **4**:466*f*
  thermoionic, **4**:463–465, **4**:464*f*
Cauchy–Riemann dual of field, **1**:61
Cavity cooling schemes, **4**:328
Cavity green function, **3**:657–658
Cavity polaritons, **2**:503–505
Cavity spintronics, **2**:149–150
CBE. *See* Coulomb blockade effect (CBE)
CDW. *See* Charge density wave (CDW)
CdYb icosahedral quasicrystal
  atomic density of, **5**:327–328, **5**:328*f*
  data phasing, **5**:324–326, **5**:326*f*
  general structure determination principles and periodic approximant, **5**:324, **5**:324–325*f*
  modeling and refining, **5**:326–328, **5**:327*f*
Cell excitation, **4**:700
Cell membrane, **4**:695–698
Cell-oriented encoding, **5**:96
Cellular materials, **5**:390
Cellular models
  extremely low frequency fields, **4**:711–712
  intermediate frequency fields, **4**:714
  radiofrequency fields, **4**:715
  static fields, **4**:711
Celluloid, **5**:425
Central limit theorem, **4**:653
Ceramic capacitors, **5**:439
Ceramic matrix composites (CMCs), **5**:346–347
Ceramics, **4**:742, **5**:390, **5**:416
  additive manufacturing of, **5**:419
  architectural installations, **5**:419, **5**:419*f*
  defined, **5**:437
  diamond coatings, **5**:420, **5**:421*f*
  electrical, **5**:417–418
  mechanical/structural, **5**:417
  optical, **5**:418–419
  processing of, **5**:419
  properties, **5**:417
  sustainable processing, **5**:420–421
  thin film techniques, **5**:420
  toughness, **5**:417
  trends in, materials, **5**:422–423
Ceramic sensors, **5**:440
Ceramics, history of
  alumina (aluminum oxide) and substrate material, **5**:438–439
  ceramic sensors, **5**:440
  ceramic turbocharger and ceramic turbine, **5**:440
  development of ceramic capacitors, **5**:439
  ferrite materials and magnetic recording, **5**:440
  ion conductivity ceramics, **5**:439–440
  large-sized insulator and ceramic carrier, **5**:438
  optical fibers, **5**:440–441
  piezoelectric ceramics, **5**:439
  superconducting ceramic materials, **5**:440
Ceramic slurries, **4**:743
Ceramic turbine, **5**:440
Ceramic turbocharger, **5**:440
CE-type ordering, **2**:105
Chain FRAM (CFRAM), **3**:569
Chalcogenide glasses, **3**:185, **3**:188–189
Chalker-Coddington model, **1**:567
Chameleon sequence, **4**:658
Chaotic light, **5**:171
  single-mode/multi-mode laser, **5**:171
  spectroscopic source, **5**:170
  temporal evolution of, **5**:170–171, **5**:171*f*
  wave trains emitted, sequence of, **5**:170, **5**:170*f*
Charge carrier concentrations, **3**:146–149
Charge-carrier mobility, halide perovskites, **5**:667–668
Charge-carrier recombination, halide perovskites, **5**:668–669
Charge-coupled devices (CCDs), **4**:83, **4**:97
Charge density wave (CDW), **1**:55, **2**:585–588, **2**:590, **2**:605–606, **2**:608
  and lattice defects, **3**:443–445
Charged excitations, **1**:292
Charged impurity, **2**:300, **2**:303
Charged particle, **4**:434, **4**:438
Charge flipping, **5**:37–38, **5**:37*f*
Charge Kondo effect, **3**:394–395, **3**:395*f*
Charge order (CO), **2**:585
Charge recombination, **1**:857
Charge transfer, **2**:581, **4**:588, **5**:209–211, **5**:214–215
Charge transfer excitations, **4**:199–200
Charge transport
  halide perovskites, **5**:668–669
  in organic molecules, **4**:676, **4**:676*f*
Charge-trap flash (CTF), **3**:562, **3**:563*f*
Charging energy, **3**:328
Chemical bath deposition (CBD), **5**:257
Chemical bonding
  Heitler-London theory of, **2**:55
  in tetrahedrally coordinated crystals, **5**:454
Chemical capacitance, **3**:158
Chemical diffusion, in mixed conductors and battery storage, **3**:157–158
Chemical enhancement (CE), **4**:305–306
Chemical microrobots, **3**:542
Chemical potential, **1**:864, **1**:864*f*, **4**:563
Chemical precursor, CVD, **5**:254
Chemical reduction, **5**:694–695, **5**:698
Chemical shielding, **4**:636, **4**:637*f*
Chemical shift anisotropy (CSA), **4**:637
Chemical vapor deposition (CVD), **2**:534*f*, **3**:754, **5**:205, **5**:254–255, **5**:254*f*
  chemical precursor, **5**:254
  components, **2**:535
  energy-assisted, **5**:256
  epitaxy, **2**:534–535, **2**:534*f*
  graphene, **5**:255
  method, **5**:716
  plasma-assisted, **5**:256
  reactions, **5**:254
  reactor configurations, **5**:254*f*
  types, **2**:535
  UV-assisted and photo-assisted, **5**:256
Chemical vapor transport (CVT) method, **5**:205
Chern insulator, **1**:78, **1**:727–729, **2**:357–359, **2**:358*f*
Chern invariants, **1**:74–76
Chern number, **1**:663–667, **1**:679, **1**:690–693, **1**:696–698, **1**:971–972, **1**:975, **2**:353, **2**:795–796, **2**:798
Chern number matrix, **1**:625–627
Chern–Simons gauge theory, **1**:66–67, **1**:69, **1**:71, **1**:88–112, **1**:115
Chern–Simons term, **2**:806–807, **2**:814
Chiral anomaly, **1**:57–59, **1**:684–685
Chiral conformal field theory, **1**:110–112
Chirality, **3**:362, **3**:454, **4**:595, **4**:600
Chiral magnetic effect, in cosmology, **1**:441–442
Chiral Majorana fermions, **1**:698
Chiral polarization, **3**:692
Chiral spin liquid (CSL), **1**:627
Chiral superconductivity, **2**:637–638
Chiral symmetry, **1**:55–57, **2**:798–799
Chiral symmetry breaking, **1**:55–57
Chromium copper, **5**:612
Chymotrypsin inhibitor 2, **4**:651, **4**:652*f*
CI2 folds, **4**:647, **4**:648*f*
Cilia-based microrobots, **3**:543, **3**:543*f*
Circuit breaker contact pads, **5**:334–335, **5**:344
Circuit QED, **2**:626
Circular permutant, **4**:644–645
Cladding, **5**:577–578
Class A bioactive materials, **4**:740
Class B bioactive materials, **4**:740
Class C superconductors, **1**:573
Class D superconductors, **1**:573
Classical and quantum lattice systems, **1**:167–171
Classical critical phenomena
  order parameter field, **1**:30
  and phase transitions, **1**:30
Classical equilibrium statistical mechanics, **4**:560
Classical limit, **3**:329
Classical Monte Carlo simulation, **1**:880–881
Classical spin models, **4**:568
Classical statistical mechanics, **4**:560
  canonical ensemble, **4**:563–564
  classical spin models, **4**:568
  grand canonical ensemble, **4**:564–565
  macroscopic and microscopic variables, **4**:560
  microcanonical ensemble, **4**:561–563
  perfect gas, **4**:565–567
  phase space averages, **4**:561
  phase transitions ad universality classes, **4**:568
  statistical ensembles, **4**:561
  statistical models, **4**:567–569
  time averages, **4**:560
Classical thermodynamics, **2**:63
'Classical' treatment of disorder, **5**:771–772
Classical wave theory, **5**:175–176
Class I observables
  generalities, **1**:673

  - magnetoelectric response and axion, **1**:674–675
  - polarization, **1**:673
- Class II observables
  - generalities, **1**:675
  - time-reversal even observables, **1**:677–679
  - time-reversal odd observables, **1**:675–677
- Clathrate, **3**:207
- Clausius–Clapeyron equation, **2**:87
- Clausius inequality, **4**:478–479
- Clean surfaces, **2**:258
- Cluster DMFT, **1**:1000
- Cluster, energy levels for, **3**:500–501, **3**:501*f*
- Clustering, machine learning, **4**:555*f*
- Clusters, molecular
  - applications, **5**:699
  - syntheses and characterizations, **5**:697–699
  - theoretical principles, **5**:695–697, **5**:696–697*f*
- Cluster sputtering system, **1**:13–14
- CMOS detector, **5**:95
- Coarse grained (CG) models, **4**:660
- "Coarsening" process, **3**:858
- Coarser structural scale, **3**:857–858
- Coated conductors, **2**:578
- Cobalt
  - FEBID, **3**:454
  - FIBID, **3**:452–453
- Cobalt–samarium magnets, **2**:82–83, **2**:83*t*
- Co-based superalloy, **5**:591–592
- Cocktail effect, **5**:653
- Coefficient of thermal expansion (CTE), **5**:337, **5**:339, **5**:342, **5**:347
- Coercive field, **3**:285–286
- Coercivity, **2**:10–11, **2**:11*f*, **2**:16–17
- Coffin-Manson relationship, **3**:819
- Coherence, **3**:532
  - lengths, **2**:568
  - and superfluidity, **3**:75–78
- Coherence and population trapping (CPT), **5**:139–140
- Coherent and incoherent polaron transport, **2**:433–434
- Coherent energy and charge transfer processes, **4**:595
  - microtubules, **4**:598
  - mitochondria, **4**:598
  - photosynthesis, **4**:597
- Coherent lattice vibrations, **3**:513
- Coherent macroscopic dynamics, of order parameters, **3**:696
- Coherent magnetization dynamics, **3**:515
- Coherent potential approximation, **5**:569–571
- Coherent spin precession, **3**:59, **3**:64, **3**:66
- Coherent states, **1**:39, **1**:547–549
- Coherent superpositions of states, **4**:585–586
- Cold atom realization
  - of dissipative Hubbard model, **3**:139
  - of Thouless pump, **3**:139–140
- Cold atoms
  - fractional quantum Hall effect, **1**:633
  - integer quantum Hall effect, **1**:631–632
- Cold atom SU(N) fermion system, **3**:138–139
- Cold-atom systems, **1**:530, **3**:135–136, **3**:141
  - cold atom realization
    - of dissipative Hubbard model, **3**:139
    - of Thouless pump, **3**:139–140
  - key issues of, **3**:136
  - non-standard optical lattice system, as novel energy-band emulation, **3**:141–142
  - optical lattice minimum, **3**:137–138
  - overview of, **3**:136–137
  - two-orbital cold atom system, as quantum transport emulation, **3**:140–141
  - ultracold fermions as Fermi-Hubbard-Model emulation, **3**:138–139
- Cold deformation, **5**:528
- Cole-Cole relaxation, **4**:280
- Collagen, **4**:739
- Collective excitations, **1**:193*f*
- Collective modes
  - BEC–BCS crossover, **1**:192*f*
  - in Bose condensates, **1**:188–189
  - of Josephson-like nature, **3**:76
- Collective variables (CVs), **4**:661
- Collision-broadened chaotic light
  - first-order coherence degree, modulus of, **5**:173*f*, **5**:174
  - second-order coherence degree, **5**:175–176, **5**:176*f*
- Collision-induced loss, **3**:646–647
- Collodion, **5**:424
- Colloidal interactions, **4**:327–328
- Colloidal models, **4**:113
- Colloidal particles, **4**:110
- Colloidal quantum dots, **3**:328
- Colloidal suspension, **4**:110
- Colloidal system, **4**:327
- Colloidal wet-chemical synthesis, catalysts, **5**:744–746
- Colloids, **3**:206, **4**:215, **4**:227, **4**:306–309, **4**:312–313
- Color centers, **3**:677
- Colossal magneto-resistance, **1**:590, **2**:84, **2**:95
- Columnar microstucture, **3**:471, **3**:471*f*
- Commercially pure titanium, **5**:639
- Compass, **2**:2, **2**:3*f*, **2**:4
- Complex concentrated alloys (CCAs), **3**:828–832, **3**:830*f*
- Complex dielectric function, **3**:667–668, **3**:813, **5**:152–154
- Complexity, **1**:857
- Complex materials, **4**:184
- Complex pinning landscapes, **3**:374–375
- Complex plots, **4**:269, **4**:270*t*, **4**:286–288*f*, **4**:290–291*f*, **4**:292
- Complex refractive index, **5**:154–155
- Complimentary MOS (CMOS) configuration, **3**:761, **3**:763*f*
- Composite boson field theory, **1**:95–98, **1**:103
- Composite fermions theory, **1**:98–103, **1**:294–295, **1**:328–329
- Composite materials
  - aircraft structures, **5**:334–335
  - antennas, **5**:339
  - and applications, **5**:334–335
  - aramid fibers, **5**:338
  - automobile engine, **5**:334–336, **5**:340, **5**:344
  - boron fibers, **5**:337
  - brakes, **5**:334–335, **5**:345
  - carbon (graphite) fibers, **5**:337
  - carbon matrix composites, **5**:345–346
  - ceramic matrix composites, **5**:346–347
  - characteristics and properties of, **5**:338–339
  - classes of, **5**:334*t*
  - commercial and aerospace applications, **5**:335
  - cutting tools, **5**:333–335
  - electronic packaging, **5**:334–335
  - fibers based on alumina, **5**:338
  - fibers based silicon carbide, **5**:338
  - gas turbine engines, **5**:334–335
  - glass fibers, **5**:336–337
  - glass processing equipment, **5**:334–335
  - heat treatment furnaces, **5**:334–335
  - high-density polyethylene fibers, **5**:338
  - high-speed and precision machinery, **5**:334–335
  - instrument structures, **5**:339
  - launch vehicle, **5**:340
  - manufacturing processes, **5**:340
  - matrix materials, **5**:335*t*, **5**:336
  - mechanical properties, **5**:339–340
  - metal matrix composites, **5**:344–345
  - PBO fibers, **5**:338
  - physical properties, **5**:339–340
  - polymer matrix composites, **5**:340–344
  - reinforcements, **5**:336
  - rocket nozzles, **5**:334–335
  - spacecraft, **5**:339
  - thermal management materials, **5**:347
- Composite particle, **1**:492
- Compound nanotubes, **1**:763–764
- Compressible and incompressible regions, **1**:560–561
- Compressible ion model, **5**:208–209
- Compton profile, **4**:176–178, **4**:181
- Compton scattering, **1**:824–826
  - comparison with theory, **4**:181–185
  - instrumentation, **4**:178–180
  - multiple scattering, **4**:180
  - theory, **4**:174–178
- Computational fluid dynamics (CFD), **5**:239
- Computational imaging technique. *See* Ptychography
- Computer generated holography (CGH). *See* Diffractive optical element (DOE)
- Computer simulations, **3**:178–180
- Concrete, **5**:418–419
- Condensed matter physics, **1**:220–224, **1**:763, **4**:109, **4**:112
  - applications in, **4**:113–114
  - importance sampling Monte Carlo methods, **5**:757–759
  - MD algorithms, **5**:755–757
  - Path-Integral Monte Carlo (PIMC), **5**:759–760

Condensed matter physics emulation, cold-atom systems as, **3**:135–136
  cold atom realization
    of dissipative Hubbard model, **3**:139
    of Thouless pump, **3**:139–140
  key issues of, **3**:136
  non-standard optical lattice system, as novel energy-band emulation, **3**:141–142
  optical lattice minimum, **3**:137–138
  overview of, **3**:136–137
  two-orbital cold atom system, as quantum transport emulation, **3**:140–141
  ultracold fermions as Fermi-Hubbard-Model emulation, **3**:138–139
Condensed-phase reaction, **5**:257–258
Condon domains, **4**:233
Conducting atomic force microscopy (c-AFM), **4**:678–679, **4**:678*f*, **4**:680*f*
Conduction band, **2**:456–457, **2**:460
Conduction band edge (CBE), **3**:240–241, **3**:246
Conductivity, electrical, **2**:461–463
  of expanded fluid mercury, **3**:166*f*
  experimental temperature and impurity-concentration dependence, **3**:253–257
  measurements, **3**:251
  molten semiconductors, **3**:168
  pressure, **3**:258
  size effects (mean free path), **3**:258
  theoretical background, **3**:252–253
Conductivity tensor, **4**:379
Conductivity, thermal. *See* Thermal conductivity
Configurational entropy, **3**:176
Configurational weight in classical Monte Carlo simulation, **1**:880–881
Configurational weight in quantum Monte Carlo method
  determinant Quantum Monte Carlo, **1**:883–884
  stochastic series expansion (SSE) method, **1**:883
  world-line Monte Carlo, **1**:882–883
Confined excitons, **2**:421–422
Confined phonons, **4**:163, **4**:166–167
Confined vibration modes, **4**:163–167
Confinement, **2**:249, **2**:251, **2**:254–255
Confinement models and energy spectra
  effect of non-parabolicity and anisotropy, **3**:300–301
  parabolic well model, **3**:299–300
  square well model, **3**:298–299
Confocal imaging, **4**:112–113
  model materials for, **4**:113
  system, **4**:111
Confocal laser scanning microscopy, **4**:110–111
Confocal optical sectioning microscopy, **4**:109–110, **4**:114
Conformal Bootstrap methods, **1**:123
Conformal field theory, **1**:103–110
Conformational sampling method, protein folding, **4**:661
Confusion/garbage-can principle, **3**:186
Consciousness, **4**:598, **4**:600–601
Conservation of energy, **3**:201
Conservative dynamics, **1**:963–964
Conservative ensembles, **3**:158
Constant energy contour, **2**:334
Constituent particles, **5**:576
Constitutive equation, **3**:684–685, **3**:691–692
Contact potential difference (CPD), **4**:51, **4**:58
Contacts, **3**:750
Contact shift restraints, **4**:724–726, **4**:725*f*
Containerless confinement, liquids, **3**:207
Content-addressable memory, **3**:590
Continuous-cooling-transformation curves (CCT), **5**:513
Continuous Czochralski method (CCz), **5**:193–194
Continuous replica symmetry breaking, **2**:372
Continuous sheet casting, magnesium alloys, **5**:554
Continuous single-component atomic gases, **3**:109–110
Continuous variables, **1**:261–262
Continuous wave, **5**:168
Continuum-based approach, **3**:239–242
  band-anticrossing (BAC) models, **3**:240–241
  composition fluctuations and localization landscape approach, **3**:241–242
  crystal field split-off (CF)/C-band, **3**:240
  crystal field splitting energy, **3**:240
  direct band gap semiconductor, **3**:239–240
  heavy-hole (HH) and light-hole (LH) bands, **3**:240
  III-N nitride materials, bulk band structure in, **3**:239–240, **3**:239*f*
  k.p model, **3**:239–240
  QW and quantum dot (QD) structures, **3**:240
  single-band effective mass approximation, **3**:240
  wurtzite and zincblende structures, **3**:240
Contrast transfer function (CTF), **4**:74, **4**:88
Controllability of parameters, **3**:137
Control of hydrogenation, **2**:596
Conventional crystallographic coordinate systems, **5**:71–72, **5**:71*t*
Conventional two-level quantum computer, **1**:280–281
Convergent beam electron diffraction (CBED), **2**:398*f*
Cooperons, **3**:223–226, **3**:223*f*
Cooper pairs, **1**:214, **2**:646–651, **2**:678–680, **2**:703–704, **3**:4, **3**:514
Cooper pair tunneling, **2**:617
Coordination defects, **3**:193, **3**:198
Coplanar waveguide (CPW), **1**:11
Copper
  additive manufacturing, **5**:624
  alloys, **5**:608–609
  aluminum bronze, **5**:618–619
  anisotropy, **5**:631
  annealing textures, **5**:630
  beryllium copper, **5**:611
  brass, **5**:614–617
  bronzes, **5**:617–618
  casting processes, **5**:622
  chromium and zirconium copper, **5**:612
  color, **5**:604–605
  commercial alloys, **5**:614
  commercial grades of, **5**:606–607
  corrosion resistance, **5**:631–632
  deformation mechanisms, **5**:605–606
  deformation textures, **5**:624
  electrical properties, **5**:604
  extrusion and forging, **5**:623–624
  FEBID, **3**:454
  FIBID, **3**:452
  forming, **5**:622–623
  grain growth, **5**:630
  high copper alloys, **5**:610–611
  hydrogen sickness, **5**:633
  manufacturing processes, **5**:622
  oxygen dispersion-strengthened, **5**:613
  powder processing, **5**:624
  production, **5**:602
  properties of, **5**:603
  property relationships, **5**:621
  recovery, **5**:625–626
  recrystallization, **5**:626–629
  shape memory alloys, **5**:621
  thermal response, **5**:625
  uses, **5**:603–604
Copper nickel alloys, **5**:620
Copper nickel silicon alloys, **5**:612
Copper-oxide superconductor, **3**:368, **3**:371*f*
Copper silver alloys, **5**:611
Core–core Coulomb energy, **1**:760
Core electrons, resonant inelastic X-ray scattering, **4**:201
Core-level lineshape, **4**:240
Core photoemission from graphene to silicene
  C 1s and Si 2p core levels of graphene and kagome silicene, **4**:240–244
  C 1s of graphene on SiC(0001) and Ni(111), **4**:241–243
  photoemission spectroscopy experiment, **4**:238, **4**:238*f*
  Si 2p and Al 2p core-levels, **4**:243–244
  spectroscopy, **4**:239
Core-shell particles, **2**:123
Coriolis force, **1**:641
Correlated disorder, **3**:443–445
  and phase separation in $\mathrm{HgBa_2CuO_{4+y}}$, **3**:444–445, **3**:444–445*f*
  and phase separation in $\mathrm{La_2CuO_{4+y}}$, **3**:443, **3**:443–444*f*
Correlated-electron systems, **4**:121, **4**:128, **4**:130
Correlated materials, **3**:694–695, **3**:702
Correlated topological insulators, **4**:359–360
Correlation length, for spin-glass order, **2**:383–385
Corrosion, **5**:518
Corrosion resistance, **5**:631–632
Cortical bone, **4**:739
Cost-effective technology, **5**:365
Co-tunneling, **3**:268–270

Coulomb blockade, **3**:261, **3**:382–384
  applications, **3**:270–271
  charge quantization and charging energy, **3**:261
  co-tunneling, **3**:268–270
  Coulomb oscillations and staircase, **3**:265–266
  quantum effects, **3**:267–268
  single electron box, **3**:262
  single electron transistor, **3**:262–265
Coulomb blockade effect (CBE), **3**:328
  and single electronics, **3**:328–329
Coulomb energy, **2**:69–70
Coulomb integrals, **2**:75
Coulomb interaction, **1**:590–591, **1**:915, **2**:805–806, **2**:805*f*, **2**:809*f*, **2**:810, **2**:814–815, **3**:221–222, **3**:221*f*, **3**:229, **3**:233, **3**:672–677
Coulomb ion potential, **1**:758
Coulomb oscillations and staircase, **3**:265–266
Coulomb peaks, **3**:385–386
Coulomb potential, **2**:516
Coulomb repulsion, **2**:74–75
Coulomb screening effect, **1**:765
Counter flow, **3**:5–6
Counterflow superconductivity, **3**:723
Coupled chains, **1**:907–909, **1**:911–912
Coupled modes, **3**:658, **3**:662–663
Covalent bonds, **1**:756
Crack growth laws, **3**:823–824
CRISPR RNAs (crRNAs), **4**:668
Critical Assessment of Structure Prediction (CASP), **4**:659
Critical Casimir forces, **4**:328
Critical current density, **2**:554–563
Critical current fluctuations, in Josephson junctions
  moderately damped regime (MDR), **2**:728–730, **2**:728*f*, **2**:730*f*
  underdamped regime, phase dynamics in, **2**:726–728, **2**:727*f*
  very high critical current density regime, **2**:730–732, **2**:732*f*
Critical currents and flux pinning, **2**:573
Critical fields, **2**:569–570, **2**:694–695
Critical temperature, **2**:568
Critical velocity, **3**:8
Cr metal, Fermi surface of, **2**:62, **2**:62*f*
Cross entropy benchmarking (XEB), **1**:250
Cross section, **4**:209–210
Crrent-phase relation (CPR), **2**:620
Crucible-free zone melting technique, **5**:199–200
Cruciform, **4**:670
Crust regime, **3**:19–20
Cryo-electron ptychography (Cryo-EPty), **4**:84, **4**:86*f*
Cryogenic magnonics, **2**:748
Cryptochrome, **4**:580–581
Crystal binding (interatomic forces)
  band filling and metallic behavior, **5**:222–225
  band structure, **5**:218
  band structure in three dimensions, **5**:225–228
  basic second-order model, **5**:212
  dependence of metallic structure on density of states, **5**:228–229
  machine-learned potentials, **5**:214–215
  modeling deformable ions, **5**:213–214
  rigid ion model, **5**:209–212, **5**:210*f*, **5**:211*t*, **5**:212*f*
  tight binding approximation, **5**:218–222
  variable charge transfer models, **5**:214
Crystal defects, **5**:241–243
Crystal field split-off (CF)/C-band, **3**:240
Crystal field splitting energy, **3**:240
Crystal growth analysis
  defects, **5**:241–243
  morphological instability, **5**:244–245
  segregation, **5**:243–244
Crystal growth modeling
  continuum methods, **5**:235–239
  process engineering, **5**:239–241
Crystal growth theory
  kinetics, **5**:234–235
  thermodynamics, **5**:232–233
Crystal lattice accommodation, epitaxy, **2**:530*f*
Crystal lattice dynamics, **5**:411
  formulation of problem, **5**:411–412
  thermodynamics, **5**:412–413
Crystalline electric field (CEF), **2**:30
  interactions, **2**:71–73, **2**:72*f*
  theory, **2**:71
Crystalline organic metals, **4**:116, **4**:121–122
Crystalline symmetry, **5**:70
Crystalline thin films, **5**:263–264
Crystallization, **3**:470–471, **5**:232–233, **5**:237
Crystallographic coordinate systems, **5**:71–72
Crystallographic databases, **5**:14
Crystallographic orientation
  graphical descriptions, **3**:485–486
  orientation descriptions, **3**:483–484
  symmetry, **3**:484–485
Crystallographic phase determination, **5**:45–47
Crystallographic phase problem, **5**:30
Crystallographic point groups, **5**:51–52
  subgroups of, **5**:55–56
  symbols for, **5**:52
Crystallographic slip, **3**:844–846
Crystallographic symmetry elements, **5**:72–73, **5**:73–74*f*, **5**:75*t*
Crystallographic symmetry groups, **5**:70
Crystallographic symmetry operations, **5**:72
Crystallography, **5**:36–37, **5**:39, **5**:70
Crystal optics
  constitutive equation, **5**:81–82
  Fresnel equation, **5**:83
  Maxwell equations, **5**:80–81
  polarization devices based on, **5**:86–87
  and ray surface, **5**:83
  wave vector surface, **5**:83
Crystal orientations, titanium alloys, **5**:637
Crystal plasticity finite element model (CPFEM), **3**:594
Crystal pulling
  Bridgman-Stockbarger techniques, **5**:196–198
  Czochralski technique, **5**:191–194
  gradient freeze techniques, **5**:196–198
  Nacken Kyropulous method, **5**:194
  shaped crystal growth, **5**:194–196
  zone melting in crucibles, **5**:198–199
Crystals, **5**:61
  electrons in, **2**:405–408
  elementary jump mechanisms in, **3**:157*f*
  plastic deformation of, **3**:844–847
  structure analysis, **2**:593–594
Crystal structure, **2**:566–567
  crystallographic databases, **5**:14
  crystal symmetry, **5**:11–12
  derived geometric parameters, **5**:15
  measures of quality, **5**:14–15
  in metals and alloys, **5**:512
  refinement model, **5**:14
  unit cell contents, **5**:13–14
Crystal structure determination
  ab initio phasing methods, **5**:33–38
  classification of phasing methods, **5**:32
  direct methods, **5**:34–36
  direct space methods, **5**:38–39, **5**:38*f*
  dual space iterative algorithms, **5**:36–38, **5**:37*f*
  genetic algorithms, **5**:38–39
  low-resolution diffraction data, phasing methods for, **5**:39
  Patterson function, **5**:33, **5**:33–34*f*
  phase determination in practice, **5**:36
  phasing of large structures, direct methods with density modification, **5**:36
  probability methods, **5**:35, **5**:35*f*
  reflection statistics, **5**:32, **5**:32*f*
  simulated annealing, **5**:39
  structure factor normalization, **5**:31
  structure invariants, **5**:34–35
  types of input data, **5**:30–31, **5**:31*f*
Crystal systems, **5**:71*t*
Cuprates, **2**:581, **2**:582–584*f*, **2**:583–585, **2**:588–590, **2**:599, **2**:635–636, **4**:116
  pseudogap, **2**:582–583
  stripe order, **2**:586–587
  uniqueness of, **2**:581–582, **2**:582*f*
Cuprate superconductors, **2**:608
Cuprous oxide, excitons in, **3**:644–645
Curie constant, **2**:27
Curie law, **2**:27
Curie relaxation, cross-correlation between, **4**:723
Curie's law, **2**:37
Curie's principle, **5**:59–60
Curie temperature, **2**:29, **2**:44*t*, **2**:76
Curie–Weiss law, **2**:27, **2**:37–38, **2**:56, **2**:63, **2**:372
Current induced spin polarization, **2**:182–183
Current-perpendicular-to-plane (CPP), **2**:164
Current-voltage (I –V) characteristics, Josephson junctions, **2**:621–623
Curved surface, **3**:416
Curvilinear nanoarchitectures
  energy functionals, **2**:122
  Landau-Lifshitz equation, **2**:122
  mechanically ultrasoft magnets, **2**:122
Custom ICs, **3**:756
CVD. *See* Chemical vapor deposition (CVD)

Cycle-averaged intensity, **5**:170
Cyclotron frequency, **2**:650
Cyclotron motion, **1**:540
Cyclotron resonance, **1**:829
  in Ge, **2**:458*f*
Cyclotron resonance, in elemental metals and simple metallic alloys
  experimental considerations, **4**:118
  extraction of scattering rates, **4**:118–120
Cyclotron resonance, in metals
  effects related to cyclotron resonance, **4**:130
  elemental metals and simple metallic alloys, **4**:118–120
  Landau quantization, **4**:117–118
  layered metals and degenerate semiconductor systems, **4**:121–128
  many-body effects I, **4**:128–129
  many-body effects II, **4**:129
Cyclotron resonance, semiconductors
  effective mass measurements, **4**:141–143
  experimental techniques, **4**:135–141
  extraction of apparent scattering times, **4**:125–126
  field-orientation dependence, of cyclotron effective mass, **4**:141–142, **4**:141*f*
  Fourier transform spectroscopy, **4**:135–136, **4**:137*f*
  fractional quantum Hall effect (FQHE), **4**:146
  free-electron laser (FEL), **4**:138–139, **4**:139*f*
  frequency-shifted CR, **4**:144
  general considerations, **4**:133–134, **4**:134*f*
  Landau level hybridization, **4**:144–145
  magneto-excitons *vs.*, **4**:146–148, **4**:147–148*f*
  magnetoplasmon modes, **4**:134
  nonparabolicity, bandstructure, **4**:142, **4**:142*f*
  nonparabolicity, polaron coupling, **4**:143, **4**:143–144*f*
  optically detected cyclotron resonance (ODCR), **4**:139–141, **4**:140*f*
  pulsed measurements, **4**:125
  quasistatic measurements, **4**:123–125
  shifts and coupling of resonance, **4**:143–146
  spin splitting, **4**:145–146, **4**:145–146*f*
  subband structure, **4**:144
  swept field, fixed frequency, **4**:135
  terahertz time-domain spectroscopy (THz-TDS), **4**:136–138, **4**:137–138*f*
  very high (megagauss) and very low fields, **4**:135, **4**:136*f*
Cytoplasmic dispersion, **4**:701
Cytosolic proteins, **4**:702
Czochralski technique, **5**:191–194

D

DAC. *See* Diamond anvil cells (DAC)
d’Alembert equation, **5**:152
Damped harmonic oscillator, **3**:814–815
Dangling bonds, **2**:263
Dark excitons, **3**:708*f*, **3**:712–713
Dark matter detection, **1**:155
Dark resonances, **5**:139
Dark-state polaritons, in atomic gases, **2**:505
Darwin width, **4**:401
Data analysis, **4**:293
Data science and machine learning, applications, **3**:825–828, **3**:826*f*
Davidson-Cole relaxation, **4**:280
d-Block d^n configurations, **5**:487–490
DC sputter discharge, physical vapor deposition, **5**:251*f*
d–*d* interactions, **5**:473–477
Deactivation, catalysts, **5**:746
Dealloying, **5**:519–520
Debye dispersion, **4**:701
Debye-Hückel theory, **3**:152–153
Debye length, **2**:263
Debye oscillator model, **4**:372
Debye process with parallel leakage path, **4**:284
Debye relaxation, **3**:815, **4**:279–280
Debye temperature, **3**:274
Debye time constant, **4**:279–280
Debye-type dielectric polarization process, **4**:282
Debye–Waller factor, **5**:31, **5**:279
Decagonal quasicrystals, **5**:329, **5**:330*f*
Decimation methods, **3**:214–215
Decoherence, **1**:215, **1**:244
Deconvolution approach, **4**:74–75
Deep impurities
  energy levels, experimental determination of, **2**:519
  theory of the electronic states of, **2**:518–519
Deep level transient spectroscopy (DLTS), **2**:519
Deep ultraviolet (DUV) LEDs, **5**:824–825
Defect characterization, **1**:857–858
Defect models, **1**:857–858, **1**:858*f*
Defect states, **3**:744–746
Defocused-probe ptychography, **4**:81, **4**:81*f*
Deformable ion, **5**:213–214
Deformation fundamentals, **3**:845*f*
  crystallographic slip, **3**:844–846
  twinning, **3**:846–847
Deformation mechanisms, **5**:605–606
  magnesium, **5**:551–552
Deformation microstructure, **3**:847, **3**:851*f*
Deformations, measurement of, **5**:99, **5**:99*f*
Deformation textures, **5**:624
Degenerate four-wave mixing (DFWM) signal, **3**:660*f*
de Haas–van Alphen effect, **2**:42
de Haas–van Alphen (dHvA) technique, **4**:228, **4**:230–232
  pickup coil technique, **4**:235
  torque method, **4**:235, **4**:236*f*
Delamination, thin films, **5**:266–267, **5**:267*f*
Demagnetizing field, **2**:46
De Morgan’s theorem, **3**:554
Dendrimer-templated synthesis, **5**:694–695
Dendrite, **3**:476, **3**:476*f*
Density-controlled BCS-BEC crossover, **3**:33–34
Density correlation functions, **3**:175–176
Density-functional based methods
  functionals derived from DFT+*U*, **1**:992–993
  time-dependent density functional theory, **1**:992
Density-functional perturbation theory (DFPT), **1**:876
Density functional theory (DFT), **1**:756, **1**:758, **1**:859, **2**:468, **2**:511, **3**:238–239, **3**:247, **3**:503, **4**:305–306, **4**:397, **4**:546, **4**:553, **5**:208–209, **5**:211–212, **5**:214–215, **5**:455
  approximate exchange-correlation functionals, **1**:870–872
  basic formalism, **1**:868–870
  Born–Oppenheimer approximation, **1**:868
  electronic structure, **1**:872–875
  of electrons, **3**:163
  extensions, **1**:870
  halide perovskites, **5**:664–665
  Hohenberg-Kohn theorem, **1**:868–870
  Kohn-Sham equation, **1**:868–870
  nuclear dynamics, **1**:875–876
  program packages, **1**:877
  pseudopotential methods, **1**:840–846
  reproducibility, **1**:877
  time-dependent, **3**:163
Density matrix renormalization group (DMRG), **1**:909, **3**:216–217
Density, of dislocations, **5**:405
Density of states (DOS), **1**:853–854, **4**:152, **5**:299
  dependence of metallic structure on, **5**:228–229
Deoxyribonucleic acid (DNA), **4**:594–596, **4**:675–676
  A-DNA, **4**:667
  B-DNA, **4**:665–667
  B´-DNA, **4**:667
  bent, **4**:672
  biophysical methods to, **4**:673
  break junction technique, **4**:678*f*, **4**:679, **4**:680*f*, **4**:681
  B–Z transition, **4**:670
  charge transport in, **4**:680–681*f*
  conducting atomic force microscopy, **4**:678, **4**:678*f*
  contacting techniques for, **4**:677–679
  cruciform, **4**:670
  electrodes at fixed distances, **4**:679
  electronic properties, **4**:675–676
  gel electrophoresis, **4**:674
  knots of, **4**:668
  melting, **4**:670
  nanopores, **4**:682
  nanostructures and nanodevices from, **4**:672
  organic molecules, conductance in, **4**:676–677, **4**:676*f*
  origami method, **4**:682
  ps-DNA, **4**:667
  quadruplexes, **4**:671–672
  sequencing, **4**:651
  single-molecule experiments with, **4**:674

  single molecules, electrical properties of, **4**:679–682, **4**:680–681*f*
  structural transitions and unusual structures, **4**:670
  structures of, **4**:665
  supercoiling, **4**:669
  theoretical models, **4**:673
  topology, **4**:668
  triplexes, **4**:671
  Z-DNA, **4**:667
Deposition techniques, **3**:754
Derivative spectroscopy, **1**:762
Descriptors, **4**:546–548, **4**:547*f*
  machine learning, **4**:555–556
Detached solidification, **5**:198
Detailed balance, **4**:208
Determinant quantum Monte Carlo (DQMC), **1**:883–884
Deviations from Matthiessen's rule (DMR), **3**:256
Device fabricatoin, **3**:749–750
Device under test (DUT), **1**:21–22
De-wetting, **3**:432–433
DFT. *See* Density functional theory (DFT)
DFT local-density approximation (DFT-LDA), **4**:397–398
Diamagnetic proteins, paramagnetic tagging of, **4**:729
Diamagnetic susceptibility, **2**:41
Diamagnetic systems, magnetic susceptibility in, **4**:720, **4**:720*f*
Diamagnetism, **2**:39–42
Diamond, **5**:420
  acoustics to solids, **3**:207
  electronic states of, **5**:704–706
Diamond anvil cells (DAC), **2**:594, **2**:594*f*
  analytical methods, **5**:832–837
  diffraction peaks in X-ray absorption spectra, **5**:839
  gasketless sample mounting, **5**:837
  gaskets, **5**:829
  heating a sample in, **5**:829–831
  polycrystalline diamond anvils, **5**:838
  primary pressure measurement, **5**:831
  primary pressure measurement at high temperature, **5**:832
  principles of, **5**:828–829
  secondary pressure measurement, **5**:831–832
  secondary pressure measurement at high temperature, **5**:832
  temperature measurement, **5**:832
  two-stage, **5**:838
Diamond coatings, ceramics, **5**:420, **5**:421*f*
Diatomic molecules, **1**:214, **3**:331
Dichroism effects, in resonant inelastic X-ray scattering, **4**:201
Dichromated gelatin, **5**:94
Dichromatic groups, **5**:2
Dielectric confinement effect, **3**:637
Dielectric constant, **4**:280, **4**:293
Dielectric dispersion, **3**:814–815
Dielectric function, **1**:765–766, **1**:770, **1**:774, **1**:777, **4**:371–372, **5**:118–120, **5**:152–154
  definition and general properties of the dielectric susceptibility and permittivity, **3**:812–813
  dielectric response of homogeneous materials, **3**:815–816
  fluctuation-dissipation theorem, **3**:814
  of Ge, **2**:481*f*
  Kramers-Kronig relations, **3**:813
  physical mechanisms and models of dielectric dispersion, **3**:814–815
  polaritons, **3**:814
  of Si, **2**:482*f*
Dielectric response, **3**:806–807
Dielectric susceptibility, **3**:812–813
Dielectric tensor, **3**:804, **3**:806–807, **4**:379–380
Difference-frequency generation (DFG), **4**:386–387
Difference map (DM) algorithm, **4**:78–80, **4**:80*f*
Differential nonlinearity (DNL), **1**:21
Differential phase contrast (DPC) imaging, **4**:73, **4**:96, **4**:96*f*
Diffraction, **3**:598–599
  electron, **4**:63
Diffraction equation, **5**:764–765
Diffraction experiment, **5**:44–45
Diffraction pattern, of crystal, **5**:318–319
Diffraction topographic technique, **4**:404–405, **4**:405*f*
Diffractive optical element (DOE), **5**:95, **5**:102
  analytical-type, **5**:96
  applications sectors, **5**:99
  microlithography techniques, **5**:96
  numerical-type, **5**:96–99, **5**:97–99*f*
Diffractometers, five-circle and six-circle, **5**:769
Diffuse scattering, **5**:319, **5**:329–330
Diffusion, **4**:690
  point defects, **5**:186
Diffusion-limited aggregation (DLA), **5**:755
Diffusion mediated plasticity, **5**:265, **5**:266*f*
Diffusion Monte Carlo (DMC), **1**:940
Diffusive alloying, **3**:432–433
Diffusive regime, **3**:282
Diffusivity of fluorescent probes, **4**:110
Diffuson, **3**:223, **3**:223*f*
Digital holographic microscopy (DHM), **5**:100
Digital holography (DH), **5**:99–100, **5**:99*f*, **5**:102
Digital image correlation (DIC), **3**:595
Diluted ferromagnetic semiconductors, **2**:514
Dilution refrigerator, **3**:648–650
Dimensionality reduction techniques, **4**:550–551
Dimerization, **2**:264
Dimers-adatom-stacking fault (DAS) model, **2**:266
Dingle temperature, **4**:230
Diophantine equation, **1**:78
Diophantine regime, **1**:721
Diophantine relation, **1**:724
Dipolar Bose gases, **3**:132*f*
Dipolar coupling, **4**:636–637, **4**:637*f*
Dipolar interactions, **3**:131–132
Dipolar length, **2**:68
Dipolar truncation, **4**:639–640
Dipole approximation regime, **4**:320–321
Dipole coupling, **2**:424
Dipole–dipole interaction, **2**:73, **4**:721, **4**:721*f*, **4**:723
Dip-peak transition, **5**:182*f*, **5**:183
Dirac and Weyl semimetals, **4**:345–347, **4**:348*f*
  chiral anomaly, **1**:684–685
  magnetic Weyl semimetal, **1**:682–683
  topological magnetotransport phenomena, **1**:685–688
Dirac cones, **2**:330–333
Dirac electrons, **2**:356
Dirac equation, **2**:64, **2**:344, **2**:346
Dirac fermions, **1**:652, **1**:654
  in 2+1 dimensions, **1**:72–73
  in one space dimensions, **1**:53–55
  and topological insulators, **1**:73–74
Dirac fluid, **2**:308
Dirac gapless relativistic equation, **5**:131
Dirac Lagrangian, **1**:84–85
Dirac materials, beyond graphene
  buckled stanene grown on InSb(111), **2**:335–336
  flat stanene grown on Cu(111) substrate, **2**:336–337
  overview on, **2**:330–331
  silicene and multilayer silicene, **2**:331–334
  2D-TMDs, **2**:339
  1T′-WS2 on bilayer graphene/SiC(0001), **2**:339
  ultra-flat bismuthene on SiC(0001), **2**:338
Dirac points, **5**:129, **5**:131
Dirac quantization, **1**:229
Dirac semimetals, **1**:594
Dirac string, **1**:229, **1**:233
Dirac–Weyl equation, **2**:211–212
Direct and indirect excitons, **3**:708*f*
Direct band gap semiconductor, **3**:239–240
Direct binary search (DBS) algorithm, **5**:97–98
Direct current SQUID (DC SQUID), **2**:703–704
Direct exchange, **2**:75, **5**:493
Direct excitons, **3**:708*f*, **3**:718
Direct gap elemental semiconductors, **2**:482–483
Direct-gap semiconductor, **5**:121, **5**:815–816
Directional solidification, **5**:196–199
Direct methods, **5**:34–36, **5**:45, **5**:47
  phase determination in practice, **5**:36
  phasing of large structures, direct methods with density modification, **5**:36
  probability methods, **5**:35, **5**:35*f*
  structure invariants, **5**:34–35
Direct screening, **4**:553–554, **4**:554*f*
Direct space methods, **5**:38–39, **5**:38*f*
  genetic algorithms, **5**:38–39
  simulated annealing, **5**:39
Direct strip cast alloys, **5**:530
Disaccommodation, **2**:79
Discotic liquid crystal, **5**:382–383, **5**:385*f*
Discrete chiral transformation, **1**:56–57

Discrete element method (DEM), **5**:681
Dislocation dynamics model, **3**:851
Dislocation-induced strain glass, **2**:396
Dislocation mediated plasticity, **5**:264–265, **5**:264*f*
Dislocations, **5**:404
  cores, **5**:408–409, **5**:409*f*
  density of, **5**:405
  dissociation and stacking faults, **5**:407–408
  elastic fields and energy associated with, **5**:405
  forces on, **5**:405–406
  interaction between, **5**:405–406
  multiplication, **5**:406–407
  principal characteristics of, **5**:404–405
Dislocation theory, **3**:850–851
Disorder, **3**:79
Disorder and localization theory
  'classical' treatment of disorder, **5**:771–772
  disorder, density of states, and wave functions, **5**:774–775
  level statistics, **5**:776–777
  one-dimensional and quasi-one-dimensional systems, **5**:776
  potential well analogy, **5**:777–778
  scaling approach, **5**:777
  transfer matrix techniques, **5**:777
  two-dimensional systems, **5**:775–776
  weak disorder and the role of interferences, **5**:772–774
Disordered carbons, electronic states of, **5**:713–714
Disordered electron liquid
  non-linear sigma model, **3**:223–226
  scale-dependent theory of, **3**:223–226
Disordered Fermi-liquid, **3**:221–222*f*
Disordered magnetic systems
  amorphous magnetic systems, **2**:23
  magnetic materials, **2**:23
  models, **2**:19
  random field Ising model, **2**:22–23
  re-entrant spin glasses, **2**:22
  spin glasses, **2**:19–22
Disordered solids, **1**:857–858
Disordered solids and glasses, electronic structure of
  electronic density of states, **3**:195–198
  electronic wavefunction, **3**:198
  general aspects, **3**:194–195
  nature of disorder, **3**:192–193
Disordered systems, **5**:301
Disorder-induced small-polaron formation, **2**:433
Dispersion, **4**:701–702
Dispersion curve, **2**:405, **2**:407*f*, **2**:408
Dispersion hardening, **5**:581
Dispersion relations, **5**:153–154, **5**:159
Dispersoids, **5**:576
Displacive *vs.* order-disorder limits, **3**:290–291
Dissipation force microscopy, **4**:59
Dissipative Hubbard model, **3**:139, **3**:142
Dissociation and stacking faults, dislocations, **5**:407–408
Distance-preserving transformations, **5**:62
Distributed Bragg reflector (DBR), **3**:658, **3**:739
Distributed feedback (DFB) laser, **3**:777, **3**:778*f*
DMFT. *See* Dynamical mean field theory (DMFT)
DNA. *See* Deoxyribonucleic acid (DNA)
DOE. *See* Diffractive optical element (DOE)
Domain swapping, **4**:640
Domain walls, **2**:65–67, **2**:67*f*, **2**:120–121, **2**:143–145, **2**:144*f*
Doped graphene, **2**:637–638
  chiral superconductivity, **2**:637–638
  twisted bilayer graphene, **2**:638
Doped perovskite manganites, **2**:84
Doping, **2**:408–410, **3**:149–152
Doppler-broadened chaotic light
  first-order coherence degree, modulus of, **5**:173*f*, **5**:174
  second-order coherence degree, **5**:175–176, **5**:176*f*
Doppler effect, **5**:170
Doppler holography, **5**:100, **5**:100*f*
Doppler shift, **4**:390–391
Double bilayer graphene, **3**:45–46
Double Crucible Czochralski technique, **5**:193–194
Double exchange, **2**:75, **2**:76*f*, **2**:95, **5**:496
Double exposure holographic interferometry, **5**:95
Double heterostructure, **3**:772
Double monolayer graphene, **3**:44–45
  nanoribbons from, **3**:47
  in periodic magnetic field, **3**:47
Double quantum dot (DQD), **3**:394
Double transition metal dichalcogenide monolayers, **3**:46
Double van der Waals layers, **3**:48
Driven-dissipative condensation, in exciton-polariton systems, **3**:110–113
Driving free energy, **4**:498, **4**:503–504
Droplet-based self-assembly, **2**:550
Droplet epitaxy, **2**:545, **2**:547*f*
Drude, **2**:428–429, **2**:435, **2**:441, **2**:443, **2**:445
Drude-Lorentz models, **5**:164
Drude model, **1**:895, **4**:372, **4**:375
Drude response, **3**:815
Drude weight, **1**:678–679
Dry etching process, **3**:754
Drying techniques, **5**:445–446
d–(s)p interactions, **5**:477–483
Dual comb hyperspectral digital holography, **5**:100
Duality mapping, **1**:119
Dual space iterative algorithms, **5**:36–38, **5**:37*f*
Duplex microstucture, **3**:478–479
  by consolidation, **3**:474–475, **3**:475*f*
  by solidification, **3**:475–478, **3**:476–478*f*
  by transformation in solid phase, **3**:478–479
d-wave, **2**:582–587, **2**:584*f*, **2**:589–590
Dyakonov-Perel mechanism, **1**:592, **2**:229
Dye-sensitized solar cell (DSSC), **5**:660
Dynamical de-wetting & diffusive alloying, **3**:432–433
Dynamical mean field theory (DMFT), **1**:918, **1**:921–922, **1**:974–975, **1**:975*f*, **3**:702
  functionals derived from, **1**:993
  Mott–Hubbard transition, **1**:918–920, **1**:919*f*
  spin glasses (SGs), **2**:367–368
Dynamical phase transition stages, **3**:88–89
Dynamical synthetic gauge fields, **1**:633–635
Dynamical theory, **4**:401–402
Dynamical vector potentials, **1**:633–635
Dynamic holography, **5**:95
Dynamic light scattering (DLS), **4**:226
Dynamic random-access memory
  architecture, **3**:585–586
  asynchronous, **3**:586–587
  capacitorless cell, **3**:588–589
  cell array organization, **3**:583–585
  general considerations on volatile memories, **3**:589
  graphics applications, **3**:588
  one-transistor one-capacitor DRAM cell., **3**:582*f*
  Rambus, **3**:587–588
  sense amplifier, **3**:581
  synchronous, **3**:587
Dynamic Wannier–Stark ladder, **1**:971
Dyson equation, **1**:974–975
Dzialoshinsky–Moriya exchange, **2**:76
Dzyaloshinskii–Moriya interaction, **2**:114, **2**:353, **3**:400–401, **3**:699

E

Easy magnetization direction (EMD), **2**:48, **2**:53
Ebers–Moll model, **3**:760*f*
Eco-ceramics, **5**:421, **5**:421*f*
Edge-controlled FFI, in weak-pinning regime, **2**:743
Edge defects, as gates for fast-moving fluxons, **2**:743–744
Edge defined film fed growth (EFG) method, **5**:194*f*
Edge excitations, **1**:292
Edge states, **1**:110–112
Edge velocities, **1**:341
Edwards-Anderson model, **2**:384
e–e interaction, **3**:223
EEPROMs. *See* Electrically erasable and programmable read-only memories (EEPROMs)
Effective Brillouin zone (EBZ), **1**:625
Effective charges, **1**:856–857
Effective continuum model, **1**:518, **2**:289–290
Effective field theory, **1**:300–301
Effective gauge field, **2**:145–146
Effective magnetic moment, **2**:37
Effective mass, **2**:405–408, **2**:457, **2**:460
Effective masses
  band curvature and charge carriers types, **1**:850–851

  density of states, **1**:853–854
  electron dynamics, **1**:850
  heterostructures, **1**:852–853
  measurement methods, **1**:854–855
  parabolic band approximation, **1**:851–852
  of semiconductors, **1**:852*t*
  two-dimensional materials, **1**:854
Effective mass theory, **1**:852, **1**:858
Effective medium approximation (EMA), **3**:812, **3**:816
Effective number of bits (ENOB), **1**:21
Effective range, **3**:19
Effective spin Hamiltonian, **2**:74
Effective temperature, **3**:696
E-gun, **2**:537
Eigenstrain theory, **3**:593
Elastic behavior, **3**:838
  anisotropy, **3**:840–841
  fundamental nature of elastic constants, **3**:842
  hyperelasticity, **3**:842
  isotropic materials, **3**:838–840, **3**:839*t*
  measuring elastic constants, **3**:841–842
Elastic behavior, thin films, **5**:265–266
Elastic constants, **3**:203*f*, **3**:205, **3**:207
  of diamond and boron nitride, **4**:190*t*
  fundamental nature of, **3**:842
  measuring, **3**:841–842
  of porous materials, **5**:392–394
Elastic deformation, **5**:265
Elasticity, of vortex lattice, **2**:699–701
Elastic network models (ENMs), **4**:660
Elastic scattering, **5**:42
Elastic strain, **5**:265
Elber's model (crack-closure model), **3**:824
Electrical ceramics, **5**:417–418
Electrical conductivity. *See* Conductivity, electrical
Electrically erasable and programmable read-only memories (EEPROMs), **3**:553–554, **3**:556–558, **3**:557*f*
Electrically programmable read-only memories (EPROMs), **3**:553–556
  cell array organization, **3**:556, **3**:557*f*
  floating-gate EPROMs cell, **3**:555–556, **3**:556*f*
Electrical resistivity, **2**:595, **3**:253, **3**:259
Electric and magnetic fields, in cells and tissues
  absorption, **4**:706
  AC-electrokinetic phenomena, **4**:704–705
  aqueous media, properties of, **4**:702
  dispersions, **4**:701–702
  field generation and interaction, **4**:700–701
  impedance, **4**:704–705
  induced transmembrane potential, **4**:705–706
  passive electric properties, **4**:701
  passive magnetic properties, **4**:707
  passive membrane properties, **4**:703–704
  physiological transmembrane potential, **4**:706–707
Electric arc furnaces (EAFs), **5**:541
Electric charge polarization, **1**:87
Electric current inducing spin current, **2**:231
Electric displacement, **4**:701
Electric field gradient (EFG), **4**:211
Electric field mapping, **4**:101–102
Electric susceptibility, **3**:683–684
Electrochemical STM (ECSTM), **4**:60
Electrodeposition, **5**:257–258
Electromagnetically induced transparency (EIT), **1**:961
  analogs, **5**:145–147
  coherence and population trapping, **5**:139–140
  electromagnetic induced transparency, **5**:140–142
  fast and slow light, **5**:142–145
  light storage, **5**:145
Electromagnetic duality, **1**:116
Electromagnetic effect, **3**:728–729
Electromagnetic fields (EMFs), **4**:709–710
  amplification, **3**:728–729
  health risk assessment, **4**:716–717
  medical applications, **4**:716
  occupational exposures, **4**:716
Electromagnetic induced transparency (EIT), **5**:140–142
Electromagnetic radiation, X-ray sources, **4**:433, **4**:438, **4**:440–441
Electromagnetic revolution, **2**:7
Electromagnetic simulation software, **4**:293–295
Electromagnetic theory, **4**:321–322
Electromagnetic waves, **3**:509–510
  in solids, **3**:666–668
Electromagnon, **3**:700–701
Electromigration, **3**:369–370
Electron backscatter diffraction (EBSD), **3**:488–489, **3**:597, **3**:597*f*, **3**:599
Electron-beam lithography (EBL), **4**:310
Electron–core potentials. *See* Pseudopotentials
Electron crystals, **1**:319–320
Electron density, **5**:30
Electron density equation, **5**:44–45
Electron dynamics, **5**:129
Electronegativity, **5**:454–455, **5**:459–461, **5**:464, **5**:467
Electron–electron interactions, **1**:681, **1**:758, **1**:915–916, **2**:40, **2**:476–477, **2**:633, **4**:145–148
  in QDs, **3**:304–306
Electron–electron potentials, **1**:759
Electron emission, terahertz light and, **3**:515–516
Electron energies, **5**:498–499
Electron energy loss spectroscopy (EELS), **4**:64, **4**:81
Electron gas (theory)
  dynamical screening and plasmons, **1**:787–789
  electron correlations, **1**:783–784
  electron gas and density functional theory, **1**:785
  electron gas in reduced dimensionality, **1**:789–790
  ideal Fermi gas and Fermi liquid theory, **1**:780–782
  spin-orbit interaction, **1**:795
  static screening, **1**:785–787
  transport coefficients, **1**:794–795
  two-dimensional electron gas at high magnetic field, **1**:793–794
  two-dimensional electron gas in graphene, **1**:790–793
  weakly interacting electron gas, **1**:782–783
  Wigner crystallization, **1**:789
Electron gas behavior, **3**:162
Electron gun, **4**:462–469, **4**:464*f*
  field emission cathodes, **4**:466–467
  photo cathodes, **4**:465–466, **4**:466*f*
  thermoionic cathodes, **4**:463–465, **4**:464*f*
Electron-hole complexes, **2**:463–464
Electron–hole interactions, **1**:763, **4**:392–393, **4**:397–398
Electron-hole liquid, **2**:422–423
Electron-hole propagator, **1**:765–766, **1**:772, **1**:774
Electron-hole superfluidity
  crossover physics, **3**:41–42
  double bilayer graphene, **3**:45–46
  double monolayer graphene, **3**:44–45
  double transition metal dichalcogenide monolayers, **3**:46
  equations, **3**:40
  gallium arsenide double quantum wells, **3**:44
  gap and onset density, **3**:42
  identifying, **3**:43–44
  indium arsenide–gallium antimonide double quantum wells, **3**:46
  screening in, **3**:40–41
  transition temperature, **3**:42–43
Electron holography, **4**:72
Electronically controlled optical sampling (ECOPS), **4**:138
Electronic bands, **2**:478–480
Electronic band structure, **5**:455–457, **5**:456–457*f*, **5**:460–461, **5**:463–464, **5**:466–467
Electronic correlations, **1**:312–313, **2**:609
Electronic density of states, **3**:195–198
  quasicrystals, **5**:293–295
Electronic digital semiconductors memories, **5**:95
Electronic mechanisms
  electron-electron interaction, **2**:633
  lattice systems, **2**:633–639
  quantum-critical point, **2**:641–642
  renormalization group analysis, **2**:639–640
  spin and charge fluctuations, **2**:640–642
  strong coupling, **2**:639–642
Electronic nematic, **2**:608
Electronic signatures, relativistic spin–orbit coupled transport phenomena, **2**:213
Electronic states
  crystal structure and symmetry, **2**:476
  direct gap elemental semiconductors, **2**:482–483
  energy band calculations, **2**:476–478
  experimental data, **2**:480–482

Electronic states *(Continued)*
  in intermetallic compounds, **5**:472–473
  pseudopotential approach, **2**:478
  quantum rings, **3**:419–420, **3**:419–420*f*
  Si, Ge and α-tin band structures, **2**:478–480
Electronic structure, **4**:8
  coherent potential approximation, **5**:569–571
  coupling of electrons and lattice deformation, **1**:860–862
  defects in disordered materials, **1**:863
  density functional theory, **1**:872–875
  extensions and approximations, **5**:572
  Green's function, **5**:566–567
  metals impurities in, **5**:567–568
  order-N methods, **5**:571–572
  outlook, **1**:865
  pure metals, **5**:567
  self-trapping and localization, **1**:862–863
  surfaces and interfaces, **1**:863–865
  theoretical methods for defect, **1**:858–860
Electronic structure, of quasicrystals
  aperiodically ordered solids, **5**:291
  electronic density of states, **5**:293–295
  magnetic properties, **5**:292–293
  nature of electronic states, **5**:295
  quasicrystal surfaces, **5**:291
  role of clusters, **5**:296
  transport properties, **5**:291–292
Electronic structure problem, approximations to, **3**:503–504
Electronic surface states, **2**:260–263
Electronic wavefunction, **3**:198
Electron injector, **4**:462*f*
Electron–ion correlations, **3**:167–168
Electron lithography, **2**:525–526
Electron microscopy, **4**:72, **4**:76, **4**:83
Electron momentum density (EMD), **4**:176–177
Electron momentum distribution (EMD)
  Compton scattering, **1**:824–826
  positron annihilation, **1**:826–827
  spin-resolved measurements, **1**:828
Electron-optics, **2**:301, **4**:33
Electron–phonon coupling, **2**:489, **4**:167, **4**:171, **4**:199–200
Electron–phonon coupling and polarons, in low-dimensional structures
  discretization of the electron and/or phonon bulk state, **2**:468–469
  first-principles calculations, **2**:470–471
  historical models, **2**:466–467
  microscopic ab initio formalism, **2**:467–468
  new phonons and couplings, **2**:469–470
  treatment of, **2**:471
Electron-phonon interactions, **4**:142*f*, **4**:143, **4**:144*f*
Electron pockets
  in Ge, **2**:458*f*
  in Si, **2**:459*f*
Electron ptychography (ET)
  advantage of, **4**:73
  algorithms, **4**:73–80, **4**:73*f*
  applications, **4**:83–84, **4**:83–86*f*
  defocused-probe ptychography, **4**:81, **4**:81*f*
  difference map (DM) algorithm, **4**:78–80, **4**:80*f*
  electron detectors, **4**:73
  focused-probe ptychography, **4**:81, **4**:81*f*
  Fourier ptychography, **4**:81–82, **4**:82*f*
  iterative algorithms, **4**:76–80, **4**:77*f*
  low-frequency information transfer, **4**:88, **4**:90*f*
  multidimensional ptychography, **4**:88–91, **4**:91*f*
  multiple scattering, **4**:88, **4**:89*f*
  multiple states, **4**:86–87, **4**:87*f*
  optical configuration, **4**:80–82, **4**:87*f*
  probe position errors, **4**:81*f*, **4**:87–88
  ptychographic iterative engine, **4**:77–79, **4**:78–79*f*
  single side band (SSB) method, **4**:74, **4**:75–77*f*
  technical development, advances in, **4**:85–88
  Wigner distribution deconvolution (WDD) approach, **4**:74–76, **4**:77*f*
  workflow of, **4**:72, **4**:72*f*
Electron quantum optics (EQO), **1**:924
  beam-splitters, **1**:925–926
  on-demand single-electron sources, **1**:925–926
  wave-guides, **1**:925–926
Electrons, **2**:405–408
  angular momentum of, **2**:9
  in crystal, **2**:405–408
  random collisions of, **1**:405–408, **1**:407–408*f*
Electrons and holes
  carrier mobility and electrical conductivity, **2**:461–463
  donors and acceptors, **2**:459–460
  doping, **2**:457, **2**:460–462
  electron-hole complexes, **2**:463–464
  free carrier density, **2**:460
  pockets, **2**:457–458
  valence band, **2**:456–458, **2**:460
Electron sources, **4**:462–463, **4**:462*f*
  beam manipulation systems, **4**:467–468, **4**:467–468*f*
  development, **4**:468–469
  electron guns, **4**:463–467
  field emission cathodes, **4**:466–467
  photo cathodes, **4**:465–466, **4**:466*f*
  thermoionic cathodes, **4**:463–465, **4**:464*f*
  time structure of electron beams, **4**:463
Electron spin kinetics, **3**:678
Electron spin relaxation, **2**:143–144
Electron spin resonance (ESR), **2**:493
  spin-orbit interaction, **2**:202–203
Electron spin resonance STM (ESR-STM), **4**:61
Electrophoretic effect, **3**:156
Electrostatic force microscopy (EFM), **4**:58
Electrostatic screening, **1**:560
Elemental hops, **2**:435–437
Elementary excitations, **1**:947–948, **1**:948*f*, **1**:951
Elementary pinning mechanisms, **2**:555–556
Elements, of space group, **5**:64
Eliashberg theory, **1**:762, **2**:642
Elinvar effect, **2**:396
Elliott-Yafet mechanism, **2**:229
Ellipsometric functions, **5**:157–159
Ellipsometry, **2**:533, **4**:396
Elzerman read-out scheme, **2**:253
Embedded cluster model, **1**:859–860, **1**:859*f*
Emission Mössbauer spectroscopy (eMS), **4**:24–25
Emission spectrum, **3**:775–776
Emittance, **4**:462–468, **4**:471–473
Empirical pseudopotential method (EPM), **1**:758–759, **1**:762, **3**:243, **3**:247
Empirical tight-binding model (ETBM), **3**:242–243, **3**:243*f*, **3**:247
Empty lattice band, **2**:478*f*
Enantiomorphism, **5**:58–59
Energy-assisted chemical vapor deposition, **5**:256
Energy balance equation, **4**:490
Energy bands, **2**:476–478
  1D stripes, **2**:354
  and redox couples, **5**:498–499
Energy conversion and storage, **4**:736–737, **4**:737*f*
Energy diagram, **1**:860, **1**:860*f*, **1**:864*f*, **1**:865
Energy dispersive X-ray spectroscopy (EDS), **2**:533, **4**:65, **5**:698
Energy gaps, **2**:475, **2**:478
  high-temperature superconductors, **2**:571
  realistic effects on, **1**:338
Energy landscape theory, **4**:610–612
Energy level quantization, **2**:622–623
Energy-level statistics, **3**:215
Energy-loss near-edge fine structure (ELNES), **4**:155–156, **4**:157*f*, **4**:159
Energy spectrum, **3**:419–420
Energy transfer, **4**:733–736, **4**:734*f*
  between two different regions, **4**:489
Entanglement, **1**:238, **4**:594–596
  and quantum gates, **3**:331–332
Entanglement-based approaches, **1**:301
Entanglement entropy, **1**:340–341
Entropy balance relations, **4**:490–491
Envelope function approximation, **1**:852–853
Enzymes, **4**:594–597
Epitaxial strains, **5**:261–263
Epitaxy, **3**:754
  chemical vapor deposition, **2**:534–535, **2**:534*f*
  crystal lattice accommodation, **2**:530*f*
  definition, **2**:528
  E-gun, **2**:537
  flux measurement and stoichiometry, **2**:537
  gaseous sources, **2**:537
  laser, **2**:537
  liquid-phase, **2**:535, **5**:258
  material characterization, **2**:533–534
  material evaporation source, **2**:537
  metal organic vapor phase, **5**:255–256
  modes of film growth, **2**:530–533, **2**:531*f*
  molecular beam, **2**:536–539, **2**:536*f*, **2**:545–546

  nucleation and epitaxial growth modes, **2**:546–548, **2**:546–547*f*
  oxide compound, **2**:538–539
  pulsed laser deposition, **2**:539–541, **2**:539–540*f*
  pumping system, **2**:536
  in situ growth monitoring, **2**:551–552, **2**:551*f*
  solid-phase, **2**:535
  sputtering, **2**:541
  strain in, **2**:548, **2**:548*f*
  substrate and lattice matching, **2**:529–530
  techniques, **2**:534–541
  in technology, **2**:545–546
  vapor-phase, **2**:529*f*
Equation of state (EoS), **3**:205–206
Equilibrium, **4**:498
Equilibrium statistical mechanics, **1**:158–159, **4**:560
Equilibrium stripe width, **2**:69–70
Equipartition theorem, **4**:324–325
Equivalent circuits, **4**:269–270
Erasable holographic materials, **5**:94
Ergodic hypothesis, **4**:562
Ergodic problem, **4**:562
Ergodic theorem, **2**:40
Error diffusion encoding, **5**:97, **5**:97*f*
Eshelby expression, **5**:396
ETBM. *See* Empirical tight-binding model (ETBM)
Etching, **5**:694–695, **5**:698
Ettingshausen effect, **4**:494
Euclidean field theories, Goldstone theorem for, **1**:164–167
Euclidean space, **1**:487
Euclidean transformations, **5**:62–63, **5**:67
Euler equation, **2**:65
Eutectic high-entropy alloys (EHEAs), **5**:654
Eutectic microstructure, **3**:476, **3**:478*f*
Evaporation
  catalysts, **5**:744
  physical vapor deposition, **5**:250
Evaporative cooling, **3**:71
Exact diagonalization, **3**:213
Excess electrons, **3**:168–169
Exchange bias effect, **2**:123
Exchange-enhanced paramagnetic susceptibility, **2**:38
Exchange interactions, **2**:29–30, **2**:45, **2**:48, **2**:73–77
Exchange spring magnets, **2**:83
Exchange statistics, **1**:485–486
Exchange stiffness constant, **2**:58–59
Excitation energy, **4**:733–735, **4**:734–735*f*
Excitation gaps
  neutral fermion gap, **1**:338
  neutral gap, **1**:338
  realistic effects on energy gaps, **1**:338
  transport gap, **1**:338
Excitation transfer, in biological systems, **4**:735, **4**:735*f*
Excitation wave, **3**:707
Exciton, **1**:856–857
Exciton delocalization, **4**:735
Exciton fine structure, **3**:641
Excitonic complexes, **3**:716–718
Excitonic devices, **3**:723–724
Excitonic matter, **3**:719–720
Excitonium, **3**:719–720
Exciton-polaritons, **2**:424–426, **3**:675, **3**:708*f*, **3**:713–714
Exciton-polaron, **3**:714
Excitons, **1**:855, **4**:199–201, **5**:123–125
  BEC and superfluids, **3**:720–722
  in cuprous oxide, **3**:644–645
  direct and indirect, **3**:718
  existence of, **3**:707–709
  Frankel & Wannier-Mott excitons, **3**:707
  halide perovskites, **5**:665
  in heterostructures, **3**:715–716
  interactions, **3**:714–715
  Lyman spectroscopy, **3**:647, **3**:648*f*
  quantum dots, **3**:716–718
  in quantum Hall bilayers, **3**:719
  Rydberg, **3**:718–719
  spin structure, **3**:712–713
  theory of, **3**:709–711
  in various materials, **3**:711–712
Excitons, in nanoscale semiconductor structures
  effect of dielectric confinement on electron-hole energy spectra, **3**:637–638
  one dimensional excitons in nanorods and nanowires, **3**:639–640
  optical properties of anisotropic semiconductor nanostructures, **3**:637
  optical properties of spherical nanocrystals, **3**:632–636
  photoluminescence of excitons in nanoscale semiconductor structures, **3**:640–641
  spatial confinement of carriers in, **3**:632
  transmission electron microscopy (TEM) images, **3**:630, **3**:630*f*
  two dimensional excitons in nanoplatelets, **3**:638–639
Exciton theory
  basic ideas, **2**:418–419
  coherence and Bose-Einstein condensation, **2**:423–424
  confined excitons, **2**:421–422
  dipole coupling, **2**:424
  electron-hole liquid, **2**:422–423
  excitonic molecules and complexes, **2**:422
  exciton polaritons, **2**:424–426
  Frenkel excitons, **2**:419
  hydrogenic excitons, **2**:419–420
  indirect excitons, **2**:421
Exotic smectics, **5**:381
Extended anyon gas, **1**:467–468
Extended DMFT (EDMFT), **1**:1000–1001
Extended energy-loss fine structure (EELFS), **4**:155
Extended PIE (ePIE) algorithm, **4**:78–79, **4**:78–79*f*, **4**:87–88
Extended X-ray absorption fine structures (EXAFS), **4**:155, **5**:698
Extinction rules, **5**:66–67
Extreme learning machine (ELM), **3**:828
Extremely low frequency fields (ELF), **4**:709
  bioeffects of, **4**:711–713
Extrinsic surface states, **2**:263
Extrusion, **5**:623–624
  magnesium alloys, **5**:558–560

F

Fabry–Perot interferometer, **1**:404, **4**:187
Face-centered cubic lattice, **2**:476
Factor group, **5**:63
Fano-Kondo effect, **3**:391
Faraday geometry, **4**:116, **4**:133–134, **4**:137–138
Faraday rotation, **4**:380
Faraday's law of induction, **2**:41
Far infrared modulated photoluminescence (FIRM-PL), **4**:140*f*
Fast dynamics, of vortices in superconductors
  cryogenic magnonics and magnon fluxonics, **2**:748
  flux-flow instability mechanisms, **2**:737
  from global to local instability models, **2**:741–744
  high-T_c superconductors and ultraclean regime, **2**:739
  Larkin-Ovchinnikov model, **2**:737–738
  under a microwave ac stimulus, **2**:744–747
  pinning effects on the flux-flow instability, **2**:739–741
  quasiparticle relaxation in dirty and clean regimes, **2**:739
  quasiparticle scattering mechanisms, **2**:737
  refinements of Larkin-Ovchinnikov model, **2**:738
  superconductivity in curved 3D nanoarchitectures, **2**:747
Fast Fourier transform (FFT), **1**:11–12
Fast single-photon detectors, **3**:459
Fast vortex dynamics, under microwave ac stimulus
  braking of instabilities by microwave stimulus, **2**:746–747
  condensate and quasiparticles under dc/ac biasing, **2**:744–745
  enhancement of superconductivity at microwaves, **2**:744
  microwave stimulation in vortex state, **2**:745–746
Fatigue
  additively manufactured metals/alloys, **3**:832–833
  combined striations and static fracture modes, **3**:825
  of complex concentrated alloys, **3**:828–832
  crack growth, **3**:822
  crack initiation, **3**:820
  crack propagation, **3**:820, **3**:821*f*
  data science and machine learning, applications, **3**:825–828, **3**:826*f*
  empirical approaches, **3**:820–821
  fracture modes, **3**:824–825
  LEFM approaches, **3**:822–823
  life prediction, **3**:829*f*

Fatigue *(Continued)*
  machine and deep learning approaches, mechanical property estimation, **3**:827*t*
  machine learning techniques, **3**:827
  material development and mechanical property estimation, **3**:826*f*
  mechanisms of, **3**:820
  physics-guided modeling of, **3**:827
  short crack problem, **3**:825, **3**:825*f*
  strain-based, **3**:821
  stress-based, **3**:820–821
  striations, **3**:825
  transgranular cleavage, **3**:824–825
  types of, **3**:819
  variable-amplitude fatigue, **3**:821–822
Fe-based superconductors, **2**:598–599, **2**:633
Feedback processes, **4**:527–528
Femtosecond-laser-induced plasma formation, **3**:511
Femtosecond lasers, **3**:695
Fenna-Mathews-Olson complex, **4**:579, **4**:579*f*
Fe-pnictides, **2**:633
Fermi and Bose systems, **4**:572–573
Fermi–Dirac distribution, **1**:897*f*, **5**:774
Fermi–Dirac distribution function, **4**:572, **4**:572*f*
Fermi–Dirac function, **1**:595, **2**:405, **2**:405*f*, **2**:408–409, **4**:230
Fermi–Dirac statistics, **1**:485, **2**:41
Fermi distribution function, **2**:60
Fermi energy, **3**:384, **4**:572–573, **4**:572*f*
Fermi gases, **3**:73–75, **4**:572–573
Fermi-Hubbard-Model emulation, ultracold fermions as, **3**:138–139
Fermi-hyperneted chain, **1**:939–940
Fermi level, **2**:263, **2**:267, **2**:269
Fermi liquid, **1**:781, **1**:790, **3**:389
Fermi-liquid theory, **1**:213, **3**:4, **3**:220, **3**:223–226
Fermion collisions, **1**:404–405, **1**:404*f*
Fermion doubling theorem, **2**:800–801
Fermionic cold-atom systems, **1**:977
Fermions, **1**:279, **1**:485, **1**:489, **1**:494–496, **1**:500–512, **1**:946, **1**:952
Fermi sea, **1**:213
  for spin and charge, **1**:902*f*
Fermi's golden rule, **4**:162, **4**:209
Fermi sphere, **1**:213, **5**:292
Fermi superfluid, **3**:10–11, **3**:16
Fermi surface, **2**:62, **2**:62*f*, **4**:178, **4**:183, **4**:228, **4**:230, **4**:233–234
Fermi surface measurements
  angle-dependent magnetoresistance oscillations, **1**:821–822
  angle-resolved photoemission spectroscopy, **1**:819–821
  anomalous skin effect, **1**:829
  bulk sensitivity, **1**:829
  cyclotron resonance, **1**:829
  dimensionality, **1**:828
  electron momentum distribution, **1**:822–828
  Friedel oscillations, **1**:829–830
  Kohn anomalies, **1**:829–830
  k-space resolution, **1**:828
  quantum oscillations, **1**:816–819
  Ruderman-Kittel-Kasuya-Yosida (RKKY) interaction, **1**:829–830
  sample purity, **1**:828
  sensitivity to correlations, **1**:828
  temperature, **1**:828
Fermi surface nesting, **2**:448–449
Fermi systems, in dimensions, **1**:119–120
Ferrimagnetic iron garnets, **2**:80
Ferrimagnetism, **2**:10, **2**:29*f*, **2**:31, **5**:491–493
Ferrimagnets, ultrafast dynamics in, **3**:698
Ferrite, **2**:80, **2**:82, **5**:537
Ferrite materials and magnetic recording, **5**:440
Ferroelastics, **2**:389–391, **2**:389*t*
Ferroelectric FETs (FeFET), **3**:569–570, **3**:570*f*
Ferroelectricity, **1**:805–806, **5**:57–58
  beyond the Landau paradigm, **3**:294–295
  displacive *vs.* order-disorder limits, **3**:290–291
  domains, domain walls and ferroelectric textures, **3**:292–293
  dynamics, **3**:291–292
  improper ferroelectricity, **3**:293
  Landau-Ginzburg-Devonshire framework, **3**:287–290
  in liquid crystals and incommensurate ferroelectrics, **3**:293
  multiferroics, **3**:294
  probing ferroelectricity, **3**:285–287
Ferroelectric liquid crystal, **5**:381, **5**:383*f*
Ferroelectric RAM (FRAM), **3**:554, **3**:564, **3**:574
  bit-line driven scheme, **3**:569
  cell array organization, **3**:569, **3**:569*f*
  cell region and capacitor, **3**:567–568, **3**:568*f*
  electric polarization *vs.* field, **3**:567–568, **3**:568*f*
  22 nm SOI CMOS technology, fabricated in, **3**:569–570, **3**:570*f*
  one transistor and one capacitor (1T-1C) cell, **3**:567, **3**:568*f*
  peripheral memory region, **3**:567–568, **3**:568*f*
  R/W scheme, **3**:569
  two transistors and two capacitors (2T-2C) cell, **3**:567
Ferroelectrics, **2**:389–390, **2**:389*t*, **2**:397–398, **2**:399–400*f*, **2**:402, **3**:814–816
  ultrafast dynamics in, **3**:700
Ferroelectric transition, **2**:390, **2**:402
Ferroic glasses
  crossover relaxor, **2**:398
  definition, classification and physical nature, **2**:389–390, **2**:389*t*
  ferroic LRO and ferroic frozen SRO, **2**:391, **2**:391*f*
  ferromagnetic strain glass, **2**:399, **2**:401*f*
  history, **2**:390–391, **2**:390*f*
  isothermal "crystallization" of strain glass, **2**:400–402, **2**:401*f*
  novel properties and potential applications, **2**:395–402
  origin and theoretical models, **2**:391–392, **2**:392–393*f*
  re-entrant strain glass, low modulus and high damping, **2**:398–399, **2**:400*f*
  relaxors, **2**:397–398, **2**:398*f*
  signatures, **2**:392–394, **2**:393–395*f*
  strain glasses, **2**:396–397, **2**:397*f*
Ferroic material, **2**:389, **2**:402
Ferroic transition, **2**:391–393, **2**:400–401
Ferromagnet, **2**:143–144
Ferromagnetic bilayer, **2**:144
Ferromagnetic core-shell coaxial GaAs/Fe nanostructures, **5**:365
Ferromagnetic iron alloys, **5**:548*t*
Ferromagnetic order, **2**:26–28
Ferromagnetic resonance (FMR) experiments, **4**:191
Ferromagnetism, **1**:590–591, **1**:591*f*, **2**:4, **2**:29*f*, **2**:43–53, **2**:55–56, **5**:491
Ferromagnets
  magnetization curve of, **2**:51, **2**:52*f*
  ultrafast dynamics in, **3**:697–698
Feshbach resonance, **3**:10–12, **3**:73–74, **3**:73*f*, **3**:135–140
FETs. *See* Field effect transistors (FETs)
Feynman diagrams, **1**:29, **1**:765–766
  and correlation functions, **1**:29–30
Feynman-Hellman theorem, **1**:221–222
Feynman-Vernon-Caldeira-Leggett influence functional technique, **2**:672
FFI. *See* Flux-flow instability (FFI)
Fiber Bragg gratings (FBG), **5**:96
Fiber bundle, **1**:74–75
Fiber-reinforced polymer composite materials, **3**:841
Fibers
  alumina-based, **5**:338
  based silicon carbide, **5**:338
  carbon (graphite), **5**:337
Fibonacci anyon model, **1**:281
Fibonacci chain, **5**:321, **5**:321–322*f*
Fibonacci sequence, **1**:475
Fibonacci topological quantum computer
  braiding rules, **1**:282
  fusion rules, **1**:281
  topological qubit, **1**:281
  universality, **1**:283
Fictive temperature, **3**:187
Field-driven electron emission, **3**:515–516
Field-effect transistors, **2**:412–413
Field effect transistors (FETs), **3**:759–761, **3**:762*f*, **3**:783–787, **3**:784*f*, **3**:786*f*, **3**:799
Field emission cathodes, **4**:466–467
Field emissions (FE), **4**:437
Field-induced metamagnetic transition, **2**:58
Field-induced spin-density waves, **2**:453–454
Field-programmable chips, **3**:756
Filling factor, **1**:541, **1**:550–551, **3**:719
Film growth and epitaxy methods
  atomic layer deposition, **5**:256
  chemical bath deposition, **5**:257

  chemical vapor deposition, **5**:254–255, **5**:254*f*
  by condensed-phase reaction, **5**:257–258
  electrodeposition, **5**:257–258
  Langmuir-Blodgett deposition, **5**:257, **5**:258*f*
  metal organic vapor phase epitaxy, **5**:255–256
  molecular beam epitaxy, **5**:252–253, **5**:253*f*
  physical vapor deposition, **5**:249–252
  sol-gel deposition, **5**:257, **5**:257*f*
Film growth, modes of, **2**:530–533, **2**:531*f*
Fine-grained film, **5**:263–264
Fine structure constant, **1**:2–3
Fine structure of exciton levels, **3**:673
Finite-size scaling, **3**:216
First Brillouin zone, **3**:239
First law of thermodynamics, **4**:476–477
First-moment scanning transmission electron microscopy (FM-STEM), **4**:96, **4**:98–100
  mapping charges and potentials, **4**:102–103
  partial coherence, **4**:102
  polarization and meso-scale electric fields, **4**:103–104
First-order coherence, **5**:167
  beam splitter, **5**:168, **5**:174
  degree of, **5**:173–174, **5**:173*f*
  first-order correlation function, of electric field, **5**:172–173
  first order interference phenomena, **5**:175
  first-order temporal coherence, degree of, **5**:173
  interference optical phenomena, **5**:172
  light sources, coherence times and lengths of, **5**:174, **5**:174*t*
  Mach–Zehnder interferometer, **5**:174, **5**:174*f*
  optical coherence theory, **5**:172
  optical interference, **5**:175
First-order correlation function, **5**:172–173
First order interference phenomena, **5**:175
First-order perturbation theory, **2**:71
First-order temporal coherence, degree of, **5**:173
First-principle density functional theory, **3**:237
First-principles calculation, **4**:553, **4**:554*f*
First-principles methods, **1**:858
Five-circle diffractometer, **5**:769
Fixed radius
  two dimensional configuration space with, **1**:488*f*
  three dimensional configuration space with, **1**:487*f*
Flash EEPROMs, **3**:554, **3**:558–563
  charge-trap flash (CTF), **3**:562
  ETOX flash cell, **3**:558, **3**:558*f*
  flash array architecture, **3**:558–560, **3**:559–560*f*
  multi-bit memory storage, **3**:562
  reliability, **3**:560–562, **3**:561*f*
  three-dimensional (3D) V-NAND flash memories, **3**:562–563, **3**:563*f*
Flash memories, **3**:553
Flat band, **3**:141–142
Flexoelectricity, **1**:808–809
Floating-gate EPROMs cell, **3**:555–556, **3**:556*f*
Floating zone technique, **5**:199–200, **5**:201*f*
Floquet–Bloch solutions, **1**:719–720
Floquet DMFT, **1**:999–1000
Floquet-Magnus expansion, **1**:972
Floquet prethermalization, **1**:967–968
Floquet states, **1**:977
  definition, **1**:967
  Dirac electrons, quasienergy spectrum of, **1**:971, **1**:971*f*
  examples, **1**:970–972
  experimental observations, **1**:975–977, **1**:976*f*
  Floquet theory, **1**:967–970
  high-frequency expansion, **1**:972–973
  nontrivial time-periodic stationary states, **1**:968
  one-dimensional lattice, quasienergy spectrum of noninteracting electrons on, **1**:971, **1**:971*f*
  origin, **1**:967
  periodically driven isolated quantum systems, **1**:967–968, **1**:968*f*
  periodically driven open quantum systems, **1**:967–968, **1**:968*f*, **1**:973–975
  physical properties, **1**:967
  time-periodic nonequilibrium steady state, **1**:967–968, **1**:968*f*
Floquet's theorem, **1**:969, **1**:969*t*
Floquet theory, **1**:967–970
Floquet topological insulator, **1**:971
FLOTOX device, **3**:556–558, **3**:557*f*
Fluctuation-dissipation relation, **3**:281–282
Fluctuation-dissipation theorem (FDT), **2**:376, **3**:814
Fluid mixtures, **4**:217–219
Fluid permeability, highly porous materials, **5**:399–401, **5**:399–400*f*
Fluorescent resonance energy transfer (FRET), **4**:660
Fluoride
  atomic layer deposition of, **5**:722–723
  glasses, **3**:188
Fluorophore, **4**:109
Flux-charge duality, **2**:680
Flux creep, **2**:560, **2**:574–575
Flux diodes, **3**:375–376
Flux-flow instability (FFI), **2**:736–737
  high-T_c superconductors and ultraclean regime, **2**:739
  Larkin-Ovchinnikov model of, **2**:737–738
  mechanisms, **2**:737
  quasiparticle relaxation in dirty and clean regimes, **2**:739
  quasiparticle scattering mechanisms, **2**:737
  refinements of the Larkin-Ovchinnikov model, **2**:738
Fluxonics, **2**:748, **3**:369
Fluxon speed limits, edge barrier effects on, **2**:743
Flux quantization, **2**:653–654, **3**:6
Flux vortex, **2**:802
Fock-Darwin states, Landau levels *vs.*, **3**:301–303
Fock space, **1**:870
Focused electron beam induced deposition (FEBID), **3**:449*f*
  binary compounds, **3**:455
  fundamentals of, **3**:449–452
  planar superconducting nanostructures, **3**:456–457
  single element, **3**:454
  ternary compounds, **3**:455
Focused ion beam-digital image correlation (FIB-DIC), **3**:596–598, **3**:596–597*f*, **3**:600
Focused ion beam induced deposition (FIBID), **3**:449*f*
  fundamentals of, **3**:449–452
  materials grown with, **3**:452–454
  nanostructures, **3**:453*t*
  planar superconducting nanostructures, **3**:455–456
  vortex dynamics, **3**:456
Focused ion beam-scanning electron microscope (FIB-SEM), **3**:596, **3**:598
Focused-probe ptychography, **4**:81, **4**:81*f*
Focusing mirrors, **4**:31–32
Fokker-Planck approach, **3**:282–283
Folded vibration modes, **4**:168–170
Folding effect, **4**:163
Forces, on dislocations, **5**:405–406
Forging, **5**:623–624
Formal charges, **5**:210–211
Forman's model, **3**:824
Form factor, **4**:222–223
Forming, **5**:622–623
Fouling, catalysts, **5**:746
Four-circle diffractometer geometries
  general-inclination geometries, **5**:767–768
  kappa geometry, **5**:767
Four-circle Eulerian geometry, **5**:762–764
4D STEM, **4**:72, **4**:72*f*, **4**:74, **4**:97
4D topological systems, **1**:692
Fourier analysis, **5**:43
Fourier constraint set (FCS), **4**:79–80
Fourier hologram
  diffraction pattern, **5**:92–93
  reconstruction, **5**:92, **5**:92*f*
  recording, **5**:91–92, **5**:92*f*
Fourier module, lattice dynamics, **5**:279
Fourier ptychography, **4**:81–82, **4**:82*f*
Fourier's law, **4**:489
Fourier synthesis, **5**:45
Fourier transform, **4**:76, **5**:153, **5**:318–319
Fourier transform infrared (FTIR) spectroscopy, **4**:135–138, **4**:137*f*, **4**:744
Fourier transform spectroscopy, **4**:135–136, **4**:137*f*
Four-wave-mixing (FWM), **4**:388–389
Fowler-Nordheim tunneling, **3**:557, **3**:560
Fractional charge, **1**:62–64
  experimental evidence, **1**:113–114
Fractional Chern insulators (FCI)
  band requirements, **1**:519–520
  Bernal-stacked bilayer graphene, **1**:528

Fractional Chern insulators (FCI) *(Continued)*
  Bloch bands with high Chern numbers, **1**:527
  cold-atom systems, **1**:530
  competing phases of, **1**:526–527
  effective continuum model, **1**:518
  interaction requirements, **1**:520
  numerical evidence of, **1**:524–526
  particle-hole asymmetry, **1**:520–521
  tight-binding formalism, **1**:517–518
  twisted bilayer graphene, **1**:523–527, **1**:529–530
Fractional exchange statistics (FES), **1**:501–507, **1**:504*f*, **1**:507*t*, **1**:509–512, **1**:510*f*
Fractionally charged quasihole, **1**:93
Fractionally charged solitons, **1**:63–64
Fractional quantum Hall effect (FQHE), **1**:4, **1**:88–112, **1**:367–373, **1**:386, **1**:403, **1**:485, **1**:564–565, **1**:629–630, **1**:641, **4**:146. *See also* Quantum Hall effect
  adiabatic continuity, **1**:342
  anti-Pfaffian state, **1**:332
  bulk collective excitations, **1**:335
  in cold atoms, **1**:633
  competing phases and Landau level mixing, **1**:342–345
  composite fermions theory, **1**:328–329
  and conformal field theory, **1**:103–110
  edge velocities, **1**:341
  entanglement entropy and spectra, **1**:340–341
  excitation gaps, **1**:336–338
  ground state degeneracy, **1**:340
  Haldane pseudo-potentials, **1**:388–389
  incompressibility estimates, **1**:391–392
  integer quantum Hall effect, **1**:386
  interaction's singularity, **1**:387
  interferometry experiments, **1**:356
  Kitaev's 16-fold way, **1**:333–334
  Landau levels, **1**:386
  Laughlin phase stability, **1**:388, **1**:390–391
  Laughlin quasi-holes, **1**:387–388
  many-body quantum Hamiltonian, **1**:385
  multi-terminal thermal conductance experiment, **1**:355–356
  non-Abelian quasiparticles, **1**:341–342
  numerical methods and geometries, **1**:335–336
  paired quantum hall states, **1**:329
  pairing evidence, **1**:339–340
  Pfaffian state, **1**:330–331
  phenomenology of, **1**:383–385
  PH-Pfaffian state, **1**:332–333
  quantum Hall plateaux, **1**:385
  restriction to lowest Landau level, **1**:386
  spectral gap conjecture, **1**:390
  spin polarization, **1**:336–338
  topological shift, **1**:340
  unexpected experimental results and PH-Pfaffian, **1**:345
  wave function overlap, **1**:340
Fractional quantum Hall effect, in semiconductor systems
  effective field theory, **1**:300–301
  entanglement-based approaches, **1**:301
  half-filled Landau level, **1**:295–296
  hierarchy and composite fermions, **1**:293–295
  Laughlin states, **1**:291–293
  multicomponent fractional quantum Hall effect, **1**:297–300
  non-Abelian states, **1**:296–297
  Parton theory, **1**:300
  phenomenology of, **1**:287–291
Fractional quantum Hall regime, crystallization of levitons, **1**:930–931
Fractional quantum Hall states
  CF series p/(2sp + 1) in graphene, **1**:318–319
  even-denominator states, **1**:319
  1/3-family of, **1**:317–318
Fractional quantum spin Hall effect (FQSHE), **1**:626–627
Fractional statistics, **1**:65–72
  anyons and fractional quantum Hall effect, **1**:399–400, **1**:399–400*f*
  basics of, **1**:65–66
  and braids, **1**:70–72
  in 1D, **1**:396–399, **1**:398*f*
  in 2D, **1**:395–396, **1**:395–397*f*
Fracture
  combined striations and static, **3**:825
  mechanics and LEFM approaches, **3**:823
  mechanics-based techniques, **3**:833
  modes, **3**:824–825
  thin films, **5**:266–267, **5**:267*f*
Fragile liquids, **3**:174
Fragility, **3**:187
FRAM. *See* Ferroelectric RAM (FRAM)
Frankel excitons, **3**:707
Frank–Read dislocation sources, **5**:406–407, **5**:406*f*
Frank-van der Merwe mode, **2**:547–548, **2**:548*f*
Free carrier density, **2**:460
Free electron laser (FEL), **3**:511, **4**:138–139, **4**:139*f*, **4**:430–431
  X-ray sources, **4**:440
Free electrons, **1**:895*f*
Free electron systems, **2**:77, **2**:77*f*
Free energy, **2**:697
Free-fermion bath model, **1**:974
Free layer (FL), **3**:565
Freezing, critical dynamics of, **2**:373–374
Frenkel defect, **5**:185
Frenkel excitons, **2**:419
Frequency dependence, **4**:271
Frequency-shifting scheme, **4**:389
Fresnel equation, **5**:83
Fresnel zone plates, **4**:32
Friction force microscopy (FFM), **4**:58–59
Friedel oscillations, **1**:829–830
Friedel sum rule, **3**:391
Frohlich model, **2**:467–468
Frozen core approximation, **3**:243
Frozen-orbital approximation, **4**:239
Frozen phonon, **1**:761, **1**:876
Frustrated spin systems, **1**:627
Frustrated systems, **5**:493
Frustration, **2**:372
Fuel cells, **5**:418
Fullerenes, electronic states of, **5**:711–713
Fullerites, electronic states of, **5**:711–713
Fully disordered system, **2**:32–33
Functional integral, **1**:32
Function approximation, **5**:750
Fundamental laws of thermodynamics, in heat and work transfer
  application of thermodynamic concepts, **4**:483
  Clausius inequality, **4**:478–479
  deficit functions and their use in setting up functions of state, **4**:479–480
  force, heat, work, and the first law of thermodynamics, **4**:476–477
  heat transfer, entropy, and the second law of thermodynamics, **4**:477–478
  Kelvin and Planck statements, **4**:479
  Maxwell relations, **4**:480–481
  performance of work, **4**:485–486
  reprise and extension of fundamentals, **4**:484–486
  third law of thermodynamics, **4**:481–482
  zeroth law, temperature, and equations of state, **4**:475–476
Fusion, catalysts, **5**:743
Fusion categories, **1**:277
Fusion rules, **1**:492
  of chiral Ising CFT, **1**:106–107
  for non-Abelian vortex anyons
    in D2-BN, **2**:776–777
    in spin-2 BECs, **2**:777

G

GaAs quantum dots
  crystalline density of states, **3**:507, **3**:508*f*
  energy gap *vs.* size of dot, **3**:506–507, **3**:507*f*
  energy levels of, **3**:506, **3**:507*f*
Gabor hologram. *See* In-line hologram
Ga^+ FIB, **3**:449–450, **3**:452, **3**:457
Gallium aluminum arsenide, **3**:236–237
Gallium arsenide (GaAs), **3**:337–349, **3**:340–341*f*, **3**:350–351*f*, **3**:350*t*, **3**:352
  band structure of, **2**:225
  double quantum wells, **3**:44
Galvano-thermomagnetic effects, **4**:496*t*
Gamete/zygote transport, **3**:545
  egg/zygote cells, transportation of, **3**:546–547, **3**:546*f*
  navigating reproductive system barriers, **3**:547–548
  sperm cells, transportation of, **3**:545–546, **3**:545*f*
Gamma-irradiation, **4**:700
GaN/InGaN HBT structure, **3**:783*f*
Gap function, **2**:636
Gapless graphene, **2**:355
Gapped graphene-like material
  conduction band population distribution, **5**:133, **5**:134–135*f*, **5**:135–136
  valley polarization, **5**:135–136
Garnets, **2**:80
Gas chromatography (GC), **5**:697–698

Gaseous sources, epitaxy, **2**:537
Gases
  Brillouin light scattering, **4**:191
  Fermi, **3**:73–75, **4**:572–573
Gate fidelity, **1**:280
Gate insulator, **3**:750
Gauge invariance, **1**:660, **1**:665, **3**:689
Gauge-invariant Bloch projector, **1**:672
Gauge theory of states of matter, **1**:418–421
  chiral anomaly, **1**:421–425
  chiral magnetic effect, **1**:440–442
  chiral spin currents, **1**:438–440
  conduction quantization in quantum wires, **1**:424–425
  effective actions and their properties, **1**:420–421
  fractional or braid statistics, **1**:425–429
  Hall effect and axion electrodynamics, **1**:442–444
  induced Chern–Simons, **1**:437–438
  2D quantum Hall effect, **1**:429–437
  3D topological insulators and axions, **1**:444–446
Gauge transformations, **1**:220, **1**:969
Gauging translations, in crystal lattice
  emerging of Goldstone modes, **1**:200
  gauging spatial translations, **1**:201–202
  optical phonons remain still undescribed, **1**:204–205
  peculiarities of spatial translations, **1**:202
  pseudo-relativistic metric, **1**:201
  Yang–Mills theory of acoustic phonons in crystal, **1**:202–204
Gaussian approximation, **1**:189–190
Gaussian approximation potentials (GAP), **4**:548–549
Gaussian distribution, **5**:168, **5**:173–174
Gaussian fluctuations, of pair field, **1**:190–192, **1**:192*f*
Gaussian pair fluctuation approach, **1**:192–193
Gaussian process regression (GPR), **4**:548–549, **4**:557–558
  machine learning, **4**:557–558
Ge islands
  regular alignment of, **2**:526*f*
  vertical stacking, **2**:523, **2**:523*f*
Gelatine, **2**:382
Gel-casting method, **4**:743
Gel electrophoresis, **4**:674
Gell-Mann–Low beta function, **1**:33
General Hartree–Fock (GHF), **1**:133
Generalized chiral magnetic effect, **1**:443–444
Generalized ensemble (GE) method, **4**:661
Generalized exclusion statistics (GES), **1**:501–508, **1**:507*t*, **1**:510–512
Generalized gradient approximation (GGA), **1**:871
Generalized Kadanoff-Baym ansatz (GKBA)
  equation of motion, **1**:996
  linear-scaling algorithm, **1**:996–997
Generalized random energy model, **2**:381
Generalized stacking fault, **5**:407, **5**:407*f*
General point groups, **5**:51
Genetic algorithms, **5**:38–39
Genetic algorithms, for biological systems
  evolution model, **4**:688–689
  genetic regulatory networks, **4**:684–688, **4**:686–688*f*
Genetic regulatory networks, **4**:684–688, **4**:686–688*f*
Geometrically equivalent, **5**:65
Geometrical ray optics regime, **4**:319–320
Geometric interpretation, of symmetry matrices, **5**:76–78, **5**:77*t*
Gerchberg–Saxton algorithm, **5**:98
Germanene, **5**:129, **5**:131–132
Germanium, **2**:413–414
$Ge_2Sb_2Te_5$ (GST), **3**:570–571
g-factor, **4**:133, **4**:145, **4**:147
Giant electrostriction, **1**:810
Giant magnetoimpedance effect (GMI), **2**:81
Giant magnetoresistance (GMR), **2**:160–161, **2**:161*f*, **2**:164
Giant magnetostrictive materials, **2**:83–84
Giant permittivity, **3**:812
Gibbs free energy, **3**:172
Gibbs measure, N-particle density as, **1**:648–649
Ginzburg–Landau approach, **1**:206
Ginzburg–Landau (GL) equation, **2**:704
Ginzburg–Landau (GL) theory, **2**:647, **2**:693–694
Ginzburg number, **2**:671
Glass ceramics, **3**:185–186, **3**:188
Glasses, **3**:274
  Angell classification of, **3**:174
  applications, **3**:181
  bonding and electronic defects, **3**:185
  Brillouin light scattering, **4**:190
  crystal growth and phase separation, **3**:185–186, **3**:185*f*
  definition, **3**:182
  diffusion and electrical behavior, **3**:189, **3**:189*f*
  formation, **3**:186
  holographic grating in, **5**:94
  mechanical behavior, **3**:188
  medium-range order, **3**:183–184, **3**:184*f*
  nonsilicate glass-forming systems, **3**:185
  optical instrumentation, components in, **3**:181
  optical properties, **3**:188
  phase separation, **3**:186
  processing, **3**:187
  production routes, **3**:182
  properties, **3**:182
  short-range structure, **3**:182–183, **3**:182–183*f*
  from solids, **3**:182
  structure, **3**:182–184
  thermal properties, **3**:187
  transformation range effects, **3**:187
  viscosity, **3**:186–187, **3**:186*f*
Glass fibers, **5**:336–337
Glass forming ability (GFA), **5**:519
Glass transition, **3**:176, **3**:178
Glassy states of water, **3**:177–178
Glide operation, **5**:64
Glide plane, **5**:64, **5**:64*f*
Gold
  FEBID, **3**:454
  FIBID, **3**:452
Goldman equation, **4**:707
Gold nanoparticles, **3**:735
Goldschmidt tolerance factor, **5**:660*f*, **5**:661
Goldstone and Higgs modes
  dark matter detection, **1**:155
  Higgs mechanism, **1**:154
  Higgs modes, **1**:152–153
  Nambu–Goldstone modes, **1**:149–152
  topological phases and emergent quasiparticles, **1**:155
Goldstone modes, **1**:187–189, **1**:315–316
Goldstone theorem, **1**:158, **1**:160
  for Euclidean field theories, **1**:164–167
Goldstone–Wilczek formula, **1**:64
Gottesman-Kitaev-Preskill (GKP) bosonic code, **1**:261
Governing equations, **5**:235, **5**:237
G-protein-coupled receptors (GPCRs), **4**:641
GP zones, **5**:580
G-quadruplex structures, **4**:681
Gradient-descent-based algorithm, **4**:87–88
Gradient expansion, **1**:870
Gradient forces, **4**:319–321
Gradient freeze techniques, **5**:196–198
Grain boundaries (GBs), **2**:555–556, **2**:559–560, **2**:562–563, **2**:619–620
Grain-boundary strengthening, **3**:857
Grand canonical ensemble, **4**:564–565
Grand-unified theories (GUTs), **2**:805
Granularity, **3**:802–803, **3**:809
Graphdiyne, **5**:713
Graphene, **2**:248, **2**:250–252, **2**:251–252*f*, **2**:344, **2**:347, **3**:712, **4**:74, **4**:76*f*
  analytical results, **2**:355
  applications, **1**:604
  band-gap opening, **2**:353–354
  bilayer, **2**:249, **2**:249*f*
  calculation methods, **2**:354–355
  charge polarization, **2**:280–281
  chemical vapor deposition, **5**:255
  Chern insulator and QSH phases, **2**:357–359, **2**:358*f*
  correlated electronic phases in partially filled Landau levels, **1**:313–320
  double trilayer and quadlayer, **3**:48
  edges and edge states, **2**:351
  electronic state of, **2**:274–277, **5**:706–708
  electrons in single Landau level, **1**:311–313
  energy bands, 1D stripes, **2**:354
  fabrication, **1**:603
  gapless, **2**:355
  Green’s function, **2**:354–355
  high quality quantum dots, **2**:250–251
  history, **1**:603
  Landau levels, **1**:310–311
  one-dimensional systems, **2**:249–250, **2**:249–250*f*
  Pauli blockade, in graphene double quantum dots, **2**:252–253, **2**:253*f*
  properties of, **1**:603–604, **2**:350–351
  quantum Hall phase, **2**:356–357, **2**:357*f*, **2**:359*f*
  qubits, **2**:254–255
  ribbon, **2**:354–357, **2**:357*f*

Graphene *(Continued)*
  spin lifetimes, in graphene quantum dots, **2**:253–254, **2**:254*f*
  spinor wavefunction of, **2**:345
  topological, **2**:355–359
  topological properties of, **2**:277–278
  2D electron gas in, **1**:790–793
  in 2D honeycomb lattices, **2**:351–354
  in two dimensions, **2**:351–353
  and van der Waals heterostructures, **2**:207–213
  and Zak phase, **2**:280–281
Graphene/hBN heterostructures, **2**:319
Graphene/hBN superlattice, **1**:726–727
Graphene layers
  counting, **2**:237
  Raman spectroscopy, **2**:236–244
Graphene-like systems, **2**:351
Graphene-like topological materials
  Brillouin zone of, **5**:131, **5**:131*f*
  broken inversion symmetry, **5**:132, **5**:136
  Dirac points, **5**:131
  effective interband dipole coupling, properties of, **5**:132
  Hamiltonian, energy spectrum of, **5**:131
  honeycomb crystal structure of, **5**:131, **5**:131*f*
  interband coupling, magnitude of, **5**:132
  intraband and interband Berry connections, **5**:132
  inversion symmetry, **5**:131, **5**:136
  low energy effective model, **5**:131–132
  nearest-neighbor tight-binding model, **5**:131
  topological resonance, **5**:132
  transition metal dichalcogenide (TMDC) monolayers, **5**:129, **5**:131
  two-dimensional (2D), **5**:131–132
  wave functions, **5**:131
Graphene nanoribbons, **2**:278–280
  armchair nanoribbons, **2**:281–282
  zigzag nanoribbons, **2**:282–284
Graphene oxide (GO), **3**:735
Graphene qubits, **2**:254–255
Graphene superlattices, **1**:725–726, **1**:725*f*
Graphene, transport
  ballistic transport and electron optics, **2**:301
  carrier scattering in graphene devices, **2**:298–301
  electronic structures of, **2**:296–297
  hydrodynamic transport, **2**:307–308
  nonlocal transport and edge transport, **2**:304–306
  topological properties, **2**:297–298
  valley hall transport, **2**:302–303
Graphene, valley currents in
  future directions, **1**:656
  key issues, **1**:655–656
  overview, **1**:652–655
Graphics processing units (GPUs), **4**:661
Graphite, electronic states of, **5**:706–708
Graphite fibers, **5**:337
Graphite intercalation compounds (GIC), **5**:707–708
Graphynes, **5**:713
Green-function approach, **2**:518–519
Green's function Monte Carlo (GFMC), **1**:940
Green's functions, **1**:29, **1**:191, **1**:763, **1**:973–975, **2**:354–355, **3**:656, **3**:658
  of cavity polariton, **3**:658–659
  for elastodynamics, **3**:524–525
  Hartree approximation, **1**:995–996
  from multiple scattering theory, **5**:566–567
  nonequilibrium Green's function (NEGF) method, **1**:993–994
  observables, **1**:994
  self-energy approximations, **1**:994–995
Green's function theory, **1**:873–874
Greenspan viscometer, **3**:206
Gross–Pitaevskii equation, **1**:188, **3**:3, **3**:130
Ground state degeneracy, **1**:271, **1**:340
Ground-state projector, **1**:672
Group elements, **5**:70
Group IV and chemical trends, **5**:455–456, **5**:457*f*
Group multiplication, **1**:490*f*
Group theory, **2**:476, **5**:70
Group velocity, **2**:407–408, **2**:407*f*
Growth from an Element of Shape (GES), **5**:195
Growth modes, nucleation and epitaxial, **2**:546–548, **2**:546–547*f*
Guided vortex motion, **3**:376
Guide RNAs (gRNAs), **4**:668
Guiding center variables, **1**:549
Guinier–Preston zones, **5**:574
Guncotton, **5**:424
GW+EDMFT, **1**:1001

H

Hadamard gate, **1**:280, **1**:283
Hagen–Rubens relation, **4**:372
Haldane-Halperin hierarchy, **1**:293–294
Haldane model, **1**:665, **1**:973, **1**:977, **2**:353
Haldane pseudo-potentials, **1**:388–389
Half-filled Landau level, **1**:295–296, **1**:372–373, **1**:377, **1**:380
Half quantum vortex, in D4-BN state
  axisymmetric singly quantized vortex, **2**:782
  HQVs, **2**:782–784
  isolated HQV, **2**:784–785
  molecule of HQVs, **2**:785
  nonaxisymmetric singly quantized vortex, **2**:782
  vortices in D4-BN state, **2**:781–782
Half-quantum vortices (HQV), **1**:135, **1**:137
Half-vortex, **1**:107
Halide glasses, **3**:188
Halide perovskites
  applications, **5**:670–673
  charge-carrier mobility, **5**:667–668
  charge-carrier recombination, **5**:668–669
  charge transport, **5**:668–669
  fundamental properties, **5**:674
  ion mobility, **5**:669–670
  light emission, **5**:672
  metal, **5**:660–663
  non-linear optical properties, **5**:667
  optical absorption and photoluminescence, **5**:664–666, **5**:664*f*
  optical properties, **5**:663–670
  optoelectronic properties, **5**:663–670
  photovoltaic cells, **5**:671–672, **5**:671*f*
  physical properties, **5**:663–670
  resistive switching, **5**:673
  stability, **5**:673–674
  synthetic techniques and morphologies of, **5**:662*f*
  thermal properties, **5**:670
  thermoelectric generators, **5**:673
  toxicity, **5**:674
  water oxidation, **5**:672
Hall coefficient, **1**:587, **2**:462–463
Hall effect, **1**:555–556, **5**:292
  isothermal, **4**:494
  on two-dimensional charge carrier system, **1**:557–559
Hall mobilities, **2**:439–440
Hall–Petch relationship, **5**:515–516
Hamiltonian, **2**:94–95
Hamiltonian gauge, **1**:672
Hanbury Brown-Twiss apparatus, **5**:178, **5**:178*f*
Hanbury-Brown-Twiss (HBT) intensity interferometer, **1**:924–928
Haneman's model, **4**:392–393
Hanle effect, **2**:230–231
Hardening behavior, **3**:847–848
Hard magnetic materials, **2**:82–83
Harmonic confinement, **3**:72
Harmonic generation frequency conversion, **4**:246–255
Harmonic oscillator, **3**:684
Harmonic oscillator approximation (HOA), **5**:162
Harper equation, **1**:662–663, **1**:663*f*
Harper model, **1**:713–714
Harper's equation, **1**:77, **1**:724
Hartree approximation, **1**:995–996
Hartree–Fock expression, **3**:504
Hartree–Fock theory, **3**:239
Harvesting light, **4**:732–733, **4**:733*f*
Havriliak-Negami relaxation, **4**:280
HCA layer, on bioactive glasses, **4**:740, **4**:741*f*
Heat carriers
  kinetic theory of, **3**:274
  magnetic excitations as, **3**:276
Heat conduction, **3**:535
Heat exchanger method (HEM), **5**:197
Heat flux, **4**:488–489, **4**:494
Heating events, **2**:732
Heat transfer
  equations, **4**:489
  between two different systems, **4**:488
Heat transport
  elementary description of, **4**:488–489
  superconductivity and, **3**:275–276
Heat-treatable alloys, **5**:579–580
Heat treating, of titanium alloys
  aging, **5**:645–646

  annealing, **5**:645
  quenching, **5**:645
  solution treating, **5**:645
  stress relieving, **5**:645
Heesch groups, **5**:2
^{3}He in 3D, **1**:951–953
^{4}He in 3D, **1**:947–951
^{3}He in reduced dimensions, **1**:955
^{4}He in reduced dimensions, **1**:953–954
Heisenberg–Dirac Hamiltonian, **2**:45
Heisenberg exchange energy, **2**:58–59
Heisenberg exchange interactions, **2**:9
Heisenberg Hamiltonian, **1**:590–591, **2**:74
Heisenberg model, **1**:151–152
Heisenberg theory, **2**:30
Heisenberg uncertainty principle, **3**:501
Heitler–London theory of chemical bonding, **2**:55
Helical microrobots, **3**:543
Helical wigglers, **4**:430
Helimagnetism, **2**:29*f*, **2**:31–32
Helium, **3**:1–2
Helium ion microscope (HIM), **3**:371–372*f*, **3**:372, **3**:377*f*, **3**:451*f*, **3**:457
Helium liquids, **1**:946–947
Hellmann–Feynman forces, **1**:760–761
Helmholtz equation, **4**:303
Helmholtz free energy, **4**:563–564
HEMT. *See* High-electron-mobility transistor (HEMT)
^{3}He refrigerator, **3**:648
Hermann–Mauguin (international) symbols, **5**:78–79
Hetero-bipolar transistors, **3**:781–783
Heteroepitaxial growth, **3**:427–428, **3**:428*f*
Heteroepitaxy, **2**:526–527
Heterogeneous catalysts, **5**:730, **5**:747*f*
Heterogeneous-elasticity theory (HET), **5**:303, **5**:313
Heterojunctions, **2**:269, **2**:269*f*, **2**:412–413
Heterovalent semiconductor heterojunctions, **2**:512, **2**:513*f*
Heusler compounds (HC), **2**:163, **2**:167–168, **2**:174
Hexagonal boron nitride (hBN), **2**:249
Hexagonal boron nitride (hBN) superlattice, **1**:726–727
Hexagonal ferrites, **2**:82, **2**:82*t*
Hexagonal perovskite polytypes, **5**:796–798
Hexagonal warping, **4**:336–340, **4**:339*f*
Heyd-Scuseria-Ernzerhof (HSE) ansatz, **3**:239
Hidden Jahn-Teller effects (h-JTE), **1**:798–799
Higgs and Goldstone modes, in crystalline solids
  gauging translations in crystal lattice, **1**:200–205
  notation, **1**:198
  spontaneous symmetry breaking and order parameter, **1**:205–210
  symmetry and invariance, **1**:199–200
  symmetry of states, **1**:199
  symmetry of the physical laws, **1**:199–200
Higgs and Nambu–Goldstone (NG) modes
  in atomic Fermi gases, **1**:179–181
  in other systems, **1**:181–183
  in superconductors, **1**:176–179
Higgs mechanism, **1**:154, **1**:158–160
Higgs mode, **1**:152–153, **1**:188–191, **1**:192*f*, **1**:194
High-angle annular dark-field scanning transmission electron microscopy (HAADF-STEM), **5**:745–746
High charge carrier concentrations, **3**:152–153
High copper alloys, **5**:610–611
High critical temperature superconductors, **2**:617–618
High damping, **2**:399, **2**:400*f*
High density liquid (HDL), **3**:178–179
High-density polyethylene fibers, **5**:338
High-electron-mobility transistor (HEMT), **3**:785
High-energy physics, **1**:56–57
High-entropy alloys (HEAs), **3**:830*f*
  cocktail effect, **5**:653
  concepts of, **5**:648–649
  definition of, **5**:648–649
  eutectic, **5**:654
  high-entropy coatings (HE-Coatings), **5**:655
  high entropy effect, **5**:649–650
  high-entropy intermetallic compounds, **5**:655
  high-entropy metallic glasses (HEMGs), **5**:654
  high-entropy superalloys (HESAs), **5**:653–654
  low-stacking-fault-energy high-entropy alloys (LSF-HEAs), **5**:653
  refractory, **5**:654
  severe lattice distortion effect, **5**:651–653
  sluggish diffusion effect, **5**:650–651
High-entropy coatings (HE-Coatings), **5**:655
High entropy effect, **5**:649–650
High-entropy intermetallic compounds (HEICs), **5**:655
High-entropy metallic glasses (HEMGs), **5**:654
High-entropy superalloys (HESAs), **5**:653–654
Higher-lying crystal-field states, **2**:37
Higher-order 1D replica modes, **1**:902*f*
Higher-order topological insulators, **1**:690, **1**:696
Higher-spin pairing, **3**:28
Highest occupied molecular orbital (HOMO), **3**:736, **4**:53
Highly disordered superconductors, **2**:609
Highly mismatched alloys (HMAs), **5**:460–463, **5**:462*f*, **5**:467
Highly porous materials, **5**:390–391
  cell structures, **5**:391, **5**:392*f*
  electrical characteristics, **5**:396–399
  energy-absorbing structures, **5**:394–395
  fluid permeability, **5**:399–401
  fracture mechanics, **5**:394–395, **5**:395*f*
  magnetic actuation, **5**:401–402
  magnetomechanical devices, **5**:401–402
  mechanical properties, **5**:392–395
  multifunctional applications, **5**:396–402
  performance requirements, **5**:392–395
  properties of, **5**:391–392
  specific surface area, **5**:399–401
  strength, **5**:394–395
  thermal insulation characteristics, **5**:396–399, **5**:397–398*f*
  transport properties, **5**:396–402
High magnetic fields, **4**:137*f*, **4**:138–139, **4**:142*f*, **4**:144*f*, **4**:147–148, **4**:147*f*
High molecular compounds, **5**:426
High-order harmonic generation, **4**:252–253
  phase-matching in, **4**:254–255
High-power package, **5**:825
High pressure, **2**:593, **2**:594*f*
High-pressure die cast magnesium alloys, **5**:555–556
High-resolution electron energy-loss spectroscopy (HREELS), **4**:152, **4**:153*f*
High-resolution electron microscopy (HREM), **2**:398*f*
High-resolution scanning transmission electron microscopy (HR-STEM), **5**:698
High-resolution solid-state NMR (HR-SSNMR) technique, **4**:636
High-T_c superconductors and ultraclean regime, **2**:739
High temperature solution growth, **5**:202–203
High-temperature superconductivity, **2**:633, **3**:437, **3**:445*f*
High-temperature superconductors, **3**:437–438
  bulk materials, **2**:577–578
  coated conductors, **2**:578
  coherence lengths, **2**:568
  critical currents and flux pinning, **2**:573
  critical fields, **2**:569–570
  critical temperature, **2**:568
  crystal structures, **2**:566–567
  energy gap, **2**:571
  experimental methods, **2**:576–577
  flux creep, **2**:574–575
  iron-based superconductor, **2**:577
  irreversibility field, **2**:573
  Josephson effects, **2**:717–719
  magnesium diboride, **2**:577
  mixed-state phase diagram, **2**:575
  normal-state properties, **2**:576
  overview, **2**:566
  pairing symmetry, **2**:570
  penetration depth, **2**:568–569
  phase diagram, **2**:567
  in quantum circuits, **2**:719–721
  role of oxygen dopants, **2**:714–715
  superconducting properties, **2**:567
  tapes and wires, **2**:578
  thin films, **2**:577
  twistronics, **2**:716–719
  type-II superconductivity, **2**:572
  van der Waals nature of, **2**:714–715
  vortex lattice melting of, **2**:575
  vortex structures, **2**:572
High-throughput synthesis technologies, catalysts, **5**:731–732, **5**:732*f*
Hilbert space, **1**:494
Hodgkin and Huxley (HH) model, **4**:696

Hofstadter butterfly, **1**:724, **1**:725*f*
  band topology, **1**:729
  graphene superlattices, **1**:725–726, **1**:725*f*
  hBN superlattice, **1**:726–727
  in twisted bilayer graphene, **1**:727–729
Hofstadter's butterfly, **2**:292
Hohenberg-Kohn approach, **3**:238
Hohenberg-Kohn theorem, **1**:868–870
Hole-doped cuprates, **2**:582–583*f*, **2**:583, **2**:589–590
Holes, **2**:405–408
Hollow particles, **2**:123
"Hollow"-type ptychography, **4**:91
Holographic interferometry, **5**:95
Holographic memories, **5**:95
Holographic optical elements (HOEs), **5**:95
Holographic recording materials, **5**:94–95
Holography
  applications, **5**:88–89
  artificial surfaces, **5**:100–102
  characteristics and recording procedure, **5**:93–95
  computer-generated holograms and diffractive optics (*see* Diffractive optical element (DOE))
  definition, **5**:88–89
  digital, **5**:99–100, **5**:99*f*, **5**:102
  Fourier hologram, **5**:91–93, **5**:92*f*
  history, **5**:88–89
  in-line hologram, **5**:89–90, **5**:90*f*
  in nonlinear and microwave optics, **5**:102
  off-axis hologram, **5**:90–91, **5**:91*f*
  optical, **5**:95–96, **5**:102
  principal setups, **5**:89–93
  principle of, **5**:89
  purpose of, **5**:89
  speckle noise, **5**:93
  3D imaging, application in, **5**:88–89
Holohedries, **5**:70
Holomorphic wave functions, **1**:546, **1**:551
Holy Grail, **2**:593
Homoepitaxy, **2**:526–527
Homogeneous nucleation, **3**:185–186
HOMO–LUMO separation, **5**:711
Honeycomb lattice, **2**:329, **2**:331, **2**:335–336
  graphene, **2**:350–351
  2D, **2**:351–354
Honeycomb monolayers
  with proximity-induced SOC, **2**:211–213
  SOC interactions, **2**:210–211
  tight-binding description, **2**:209–210
Hong-Ou-Mandel (HOM) collisional interferometer, **1**:924–928
Hong-Ou-Mandel (HOM) dipNoise measurements, **1**:405, **1**:415
Hong-Ou-Mandel (HOM) effect, **1**:501–502, **1**:512
Hong-Ou-Mandel experiment, **5**:181, **5**:182*f*
Hooke's law, **3**:839
Hopping electrodeposition, **5**:363–364
Hopping process, **3**:145–146
Horizontal Bridgman (HB) method, **5**:196
Horizontal rotating drum, **5**:687–690
Hot deformation, **5**:528–529
Houston functions, **5**:130
HPC-centric approach, **1**:258–259
Hubbard Hamiltonian, **2**:77
Hubbard model, **1**:914–922, **1**:919*f*, **3**:136–139, **3**:142
Hubbard–Stratonovich field, **1**:46–47
Hubbard–Stratonovich identity, **1**:189–190
Hubbard–Stratonovich transformation, **1**:44
Human studies
  extremely low frequency fields, **4**:713
  radiofrequency fields, **4**:715–716
  static fields, **4**:711
Hume–Rothery alloys, **5**:290
Hume–Rothery electronic stabilization, **5**:319–320
Hund's coupling, **1**:915, **1**:920–921
Hund's rule, **1**:807, **2**:26, **2**:30, **2**:35–38, **2**:74, **2**:76
Husimi function, **1**:242*f*
Hybridization
  of double bilayer graphene, **3**:47–48
  optoplasmonic, **3**:363
Hybrid Josephson junctions
  coplanar junction configuration, **2**:627
  ferromagnetic barrier, **2**:628
  semiconducting barrier, **2**:627
  topological insulators, **2**:627–628
  van der Waals crystals integration, **2**:628
Hybrid magnonic platforms
  magnon–phonon system, **2**:156
  magnon–photon system, **2**:152–153
  magnon-qubit system, **2**:153–156
Hydrated silicon, **4**:743
Hydride, **2**:592–594, **2**:594*t*
  near room-temperature superconductivity in, **2**:595–596
  superconducting hydrides, **2**:594–595
Hydrodynamic approximation, **4**:375
Hydrodynamic effective field theory, **1**:94–95
Hydrodynamic fluctuations, **4**:217
Hydrodynamics, **3**:5–6
Hydrogen, **2**:593–596
  element and, **2**:595
Hydrogenation, control of, **2**:596
Hydrogen atom model, **2**:516
Hydrogen-bonded molecular glasses, **3**:185
Hydrogenic excitons, **2**:419–420
Hydrogen-rich compounds, **2**:593
Hydrogen sickness, **5**:633
Hydrogen sulfide (H_2S), **2**:595
Hydrogen terminated diamond surfaces, **5**:706
Hydrothermal growth, **5**:203–204
Hydrothermal synthesis (zeolites), catalysts, **5**:744
Hyperbolic dispersion, **3**:366
Hyperelasticity, **3**:842
Hyperfine interactions
  angular dependence of absorption and emission, **4**:24
  isomer shift, **4**:21
  magnetic splitting, **4**:22
  mixed hyperfine interaction, **4**:22–23
  quadrupole splitting, **4**:22
Hyperfine interaction with nuclear spins, **2**:226
Hyperfine shift restraints, **4**:724–726, **4**:725*f*
Hysteresis cycle, **2**:51–53, **2**:53*f*

I

Icosahedral quasicrystal
  Al—Mn icosahedral quasicrystal, **5**:319, **5**:328
  CdYb icosahedral quasicrystalline phase (*see* CdYb icosahedral quasicrystal)
  Mackay-type, Bergman-type and Tsai-type, **5**:328
  ZnMgY phase, single grain of, **5**:319–320, **5**:320*f*
  Zn—Sc icosahedral quasicrystal, **5**:328–331, **5**:329*f*, **5**:331*f*
Icosahedral symmetry, **5**:291
ICs. *See* Integrated circuits (ICs)
Ideal anyon gas
  braid group, **1**:455
  density functionals for, **1**:461–462
  exchange *vs.* exclusion, **1**:459–461
  kinetic energy, **1**:456–457
  local exclusion principle and degeneracy pressure for, **1**:462–465
  quantum statistics, **1**:453–455
  states of particular interest, **1**:465–466
  statistics transmutation in 2D, **1**:457–459
Iinteger quantum Hall effect, **1**:559–564
Image processing methods, **4**:113
Imbalanced pairing, **3**:24–25
Impedance spectroscopy and mobility spectra
  data analysis, **4**:293
  electromagnetic simulation software, **4**:293–295
  equivalent circuits, **4**:269–270
  microscopic interpretation, **4**:276
  multimedia, **4**:296
  multiplane analysis of several multiple process combinations, **4**:282
  multiple parallel processes, **4**:274–276
  polarization mechanisms, **4**:276–279
  recent advances, **4**:295
  relaxation and resonance frequency spectra, **4**:279–282
  temperature dependence, **4**:282–293
  temperature dependence and conductivity curves, **4**:271–274
  time constants and frequency dependence, **4**:271
Impregnation (supported catalysts), **5**:744
Impurities and crystal defects, structural and electrical properties of, **2**:516
Impurity solvers, **1**:998–999
InAs/GaAs quantum rings
  dynamical de-wetting & diffusive alloying, **3**:432–433
  formation and optical properties, **3**:430–432
  MBE with in-situ characterization, **3**:427–428
  quantum dots, **3**:429–430
  stress-induced melted indium, **3**:428–429
Incommensurate composites, lattice dynamics, **5**:281
Incommensurate modulated structures, lattice dynamics, **5**:280–281*f*
Incommensurate phases
  aperiodic structures, **4**:510–513

  habit of calaverite, **4**:513–514
  luminescence of europium containing scheelites, **4**:516–518
  organic perovskite $CH_3NH_3PbI_3$, **4**:518–520
  sodium carbonate (Na_2CO_3), **4**:514–516
Incompressible fluids, **1**:289–290
Index of refraction, **4**:212–213
Indirect exchange
  in insulators, **2**:75
  in metals, **2**:75–77
Indirect excitons, **2**:421, **3**:708*f*, **3**:718
Indirect-gap semiconductors, **5**:815–816
Indium arsenide–gallium antimonide double quantum wells, **3**:46
Indium composition, role of, **3**:346–348, **3**:346–347*t*, **3**:346–347*f*
Induced field, **3**:803–804
Induced moment, temperature and field dependences of, **2**:58–59*f*
Induced transmembrane potential, **4**:705–706
Inelastic Brillouin light scattering, **4**:192–193. *See also* Brillouin light scattering (BLS)
Inelastic electron scattering, **4**:150–151
  cross-section for, **4**:151
  excitation of core electrons, **4**:155–156, **4**:156–157*f*
  interband transitions, **4**:151–152
  plasmon excitations, **4**:152–153, **4**:153–154*f*
  $(e^-, 2e^-)$ scattering, **4**:156–158, **4**:158*f*
  vibrations at surfaces, **4**:153–154, **4**:155*f*
Inelastic neutron scattering (INS), **2**:588, **4**:195–196, **5**:301, **5**:305, **5**:306*f*, **5**:307–308
Inelastic scattering, **4**:106–107, **5**:431–432
Inelastic X-ray scattering (IXS), **5**:309–312
  adiabatic approximation, **4**:197
  compton scattering, **4**:195–196
  from core electrons (X-ray Raman scattering), **4**:198–199, **4**:199*f*
  deep, **4**:203
  from electronic excitations, **4**:197–201
  high-frequency dynamics in liquids and glasses, **4**:203
  inelastic neutron scattering, **4**:195–196
  kinematics, scattering process, **4**:196*f*
  from phonons, **4**:202–203, **4**:202*f*
  resonant, **4**:195, **4**:199–201
  theoretical aspects, **4**:196–197
  from valence electrons, **4**:198
Infinite time-evolving block decimation (iTEBD) method, **1**:991–992
Information engines, **4**:532
Information extraction, **1**:239
Information flows, **4**:532–533
Infrared, **3**:187
Infrared bounds, **1**:168–170
Infrared-resonant Raman scattering (IRRS), **3**:513
InGaAs, **3**:337–338, **3**:340–342, **3**:342*f*, **3**:345–349, **3**:346–348*f*, **3**:350–351*f*
Inhomogeneous materials, effective dielectric function of, **3**:816–817
In-line hologram
  application of, **5**:90
  intensity distribution, **5**:89
  reconstruction, **5**:90, **5**:90*f*
  recording, **5**:89, **5**:90*f*
  transmitted wave, **5**:89
  uniform coherent parallel beam, **5**:89
In-memory computing (IMC), **3**:564, **3**:573–574
Inorganic crystals
  melt growth, **5**:191–200
  solution growth, **5**:200–204
  vapor growth, **5**:204–205
In-plane-gate transistor, **3**:787, **3**:788*f*
In situ characterization, atomic layer deposition, **5**:724, **5**:724*t*
Insulating crystals, thermal transport in, **3**:274
Insulator(s)
  higher-order topological, **1**:690, **1**:696
  indirect exchange in, **2**:75
  point defects in, **5**:187–188
Insulator-metal transitions, **2**:107–109
Insulator, optical properties
  absorption bands of extrinsic origin below the band gap, **5**:784
  band model, **5**:779
  dipole–dipole interaction, **5**:781–782
  effect of spin and the interplay of exchange and spin–orbit interactions, **5**:782
  exciton model and the optical spectrum near the absorption edge, **5**:780–781
  intrinsic photoluminescence and its correlation with the Urbach rule, **5**:784
  optical excitation of inner shell electrons, **5**:784–785
  participation of phonons in the electronic excitation, **5**:782–784
  spin–orbit mott insulators, **5**:779
  topological Kondo insulators, **5**:780
Insulator-to-metal transition, **3**:701
Integer quantum Hall effect (IQHE), **1**:308–309, **1**:386, **1**:567, **1**:629–633
  and Anderson localization, **1**:568–570
  bernal-stacked bilayer graphene, electronic properties of, **1**:618
  in cold atoms, **1**:631–632
  edge states in, **1**:569*f*
  extension of, **1**:632–633
  monolayer graphene, electrical properties of, **1**:610
  scaling flow, **1**:569–570, **1**:570*f*
  single-particle eigenstates, properties of, **1**:568*f*
  universality, **1**:571
Integral equations, **5**:751–752
Integral kernels, **1**:548
Integral nonlinearity (INL), **1**:21
Integral quantum Hall effect (IQHE), **3**:531, **5**:775
Integrated circuits (ICs), **3**:748, **3**:749*f*, **3**:785–786
  applications
    random-access memory (RAM), **3**:755
    read-only memory (ROM), **3**:755
  custom, **3**:756
  materials, **3**:748–749
  microprocessors, **3**:756
  physics of
    Moore's Law, **3**:754–755
    speed and power, **3**:755
  processing techniques
    deposition techniques, **3**:754
    dry etching process, **3**:754
    photolithography, **3**:753–754
  technology, **3**:749–753
    device fabricatoin, **3**:749–750
    interconnects, **3**:750–751
    packaging, **3**:752–753
Integrated MOS transistor, **3**:752*f*
Integration density, **3**:754–755
Intense terahertz pulse generation, **1**:986–987
Interacting Bose mixtures, **3**:131
Interacting Dirac fermions
  bilayer graphene, **1**:374–377
  fractional quantum Hall effect, **1**:367–373
  graphene monolayer, **1**:373–374
  Pfaffian states in graphene, **1**:377–380
Interacting quantum Hall edge channels, **1**:928–929
Interatomic exchange interaction, **2**:55
Interatomic force constants, **1**:875–876
Interatomic forces
  band filling and metallic behavior, **5**:222–225
  band structure, **5**:218
  band structure in three dimensions, **5**:225–228
  dependence of metallic structure on density of states, **5**:228–229
  tight binding approximation, **5**:218–222
Interband absorption, **3**:668–669
Interband Berry connection, **5**:129–132
Interband electron dynamics, **5**:130
Interband electron-hole continuum, **1**:766
Inter-band scattering, **1**:768
Interband transitions, **4**:151–152, **4**:155, **4**:159, **5**:120–121, **5**:160, **5**:162
Intercell connectivity, **5**:390–391
Interconnects, **3**:750–751, **3**:752*f*
Intercrystalline diffusion effects, **3**:859
Interfaces, **2**:267–270
Interface vibration modes, **4**:167
Interferometry
  and braiding, **1**:351–352
  and charge, **1**:351
Interlayer exciton (ILX), **3**:708*f*, **3**:718
Intermediate frequency (IF) fields, **4**:713–714
Intermetallic compounds, electronic states of, **5**:469–471
  classifying electronic states in, **5**:472–473
  electronic interactions between different metallic types, **5**:473–477
Intermetallic quasicrystal, **5**:319–320
International Alloy Designation System (IADS), **5**:574–575
International System of Units, **1**:2, **1**:555
Interstitial alloy elements, **5**:534–535, **5**:534*f*, **5**:535*t*
Interstitial alloys, **5**:524–526
Intertwined order, **2**:588, **2**:590
Intra-atomic exchange interaction, **2**:64

Intraband absorption, **3**:669
Intraband adiabatic dynamics, **5**:129
Intra-band backward scattering, **1**:766
Intraband Berry connection, **5**:129, **5**:131–132
Intraband transition, **5**:164
Intralayer excitons, **3**:708*f*
Intrinsically disordered proteins (IDPs), **4**:659
Intrinsically unfolded proteins (IUPs), **4**:659
Intrinsic inhomogeneity, **2**:97
Intrinsic surface states, **2**:263
Invar, **2**:396
Invariant functions, **5**:66–67
Inverse DM effect, **2**:103
Inverse Fourier transform, **4**:74–75
Inverse multislice (invMS) ptychography, **4**:88
"Inverse opal" structure, **3**:741
Inverse pole figure, **3**:485, **3**:486*f*, **3**:493, **3**:494*f*
Inverse spin galvanic effect, **2**:216–218
Iodine, vacancy, **5**:669*f*
Ion-beam milling, **3**:369
Ion conductivity ceramics, **5**:439–440
Ionicity, **5**:455
Ionic Raman scattering (IRS), **3**:513
Ion-induced nanostructures, **3**:370–373
Ion irradiation, **3**:371–372
Ionizing spectrum of radiations, **4**:709, **4**:710*f*
Ion mobility, halide perovskites, **5**:669–670
Ion-permeating pathway, **4**:694–695
Ion plating, physical vapor deposition, **5**:252
Ion transport
  in biology, **3**:159
  membrane voltage, complex changes of, **4**:695–698, **4**:695*f*, **4**:697*f*
  transport proteins, **4**:693–695
Iron, **2**:79, **5**:533–534
  categories of, **5**:538–541
  chemical properties, **5**:547
  FEBID, **3**:454
  functional properties, **5**:547
Iron alloys
  additive manufactured alloys, **5**:531
  advanced high strength steels, **5**:531
  cold deformation, **5**:528
  direct strip cast alloys, **5**:530
  hot deformation, **5**:528–529
  intermetallic compounds, **5**:530
  interstitial alloys, **5**:524–526
  magnetic alloys, **5**:529–530
  phase transformations in, **5**:527
  production of, **5**:523
  shape memory alloys, **5**:530
  static annealing, **5**:529
  structure and properties of, **5**:524
  substitutional alloys, **5**:526–527
Iron-based superconductor, **2**:577
Iron–cobalt alloys, **2**:80
Irreversibility field, **2**:554–555, **2**:555*f*, **2**:560–561, **2**:561*f*, **2**:563–564
Irreversible thermodynamics, **4**:488
  energy balance equation, **4**:490
  entropy balance relations, **4**:490–491
  heat and mass transport, **4**:488–489
  mass balance equation, **4**:490
  Peltier effects, **4**:493
  phenomenological coefficients, **4**:495
  phenomenological equations, **4**:491, **4**:493–494
  thermoelectric phenomena, **4**:491–492
  thermoelectric transport coefficients, **4**:492
  Thomson effects, **4**:493
  transport coefficients for thermomagnetic phenomena, **4**:494–495
  transport effects in magnetic fields, **4**:493
Ising anyons, **1**:135
Ising gas, **1**:475
Ising models
  duality, **1**:49–52
  in transverse field, **1**:36–38
  2D classical model, **1**:49–50
  3D duality, **1**:50–52
Isolated quantum dot approximation, **3**:383–384
Isometries, **5**:70
Isomorphous replacement, **5**:45–47
Isothermal Hall effect, **4**:494
Isotope superlattices, **2**:486, **2**:490
Isotropic materials, **3**:838–840, **3**:839*t*
Isovalent semiconductor heterojunctions, **2**:512
Iterative algorithms, **4**:76–80, **4**:77*f*
  difference map (DM) algorithm, **4**:78–80, **4**:80*f*
  ptychographic iterative engine (PIE), **4**:77–79, **4**:78–79*f*
Iterative Fourier transform algorithm (IFTA), **5**:98, **5**:98*f*
Itinerant-electron model, **2**:55, **2**:59–63
Itinerant exchange, **2**:77

J

Jackiw–Rebbi result, **1**:64
Jahn–Teller effect (JTE), **1**:798, **2**:95–96
  adiabatic potentials *vs.* observables, **1**:798–801
  cooperative, ferroelectricity, **1**:805–806
  crystal sublattices, **1**:810–811
  flexoelectricity, **1**:808–809
  giant electrostriction, **1**:810
  in local properties of solids, **1**:801–804
  multiferroicity, **1**:807–808
  orientational polarization of solids, **1**:808–810
  permittivity, **1**:809
  puckered two-dimensional systems, **1**:811
  quantum information devices, **1**:804
  solids and 2D systems, **1**:810–811
  ultrasonic exploration, **1**:801–804
Janus microrobots, **3**:542
JAWS. *See* Josephson arbitrary waveform synthesizer (JAWS)
Jellium, **2**:261–263
Jellium model, **1**:779–780, **1**:784, **1**:795, **5**:696
Johnson-noise thermometry (JNT), **1**:25
Jordan–Wigner transformation, **1**:505
Josephson arbitrary waveform synthesizer (JAWS)
  applications, **1**:21–25
  arbitrary frequency domain waveform, **1**:12–13, **1**:13*f*
  arbitrary time domain waveform, **1**:12–13, **1**:13*f*
  band-limited square waveform (BLSW), **1**:22, **1**:22*f*
  chip circuit layout, example of, **1**:11, **1**:11*f*
  CIFB modulator topology, **1**:11–12
  critical current density *vs.* characteristic voltage of SNS junctions, **1**:13–14, **1**:14*f*
  current-voltage characteristic *vs.* pulse repetition frequency, **1**:19–20, **1**:20*f*
  eight-channel PTB JAWS setup, **1**:15–16, **1**:16*f*
  "electrical" *vs.* "optical" JAWS setup, **1**:16–17, **1**:17*f*
  features, **1**:12, **1**:21
  fundamental elements of, **1**:10–13
  high-quality Sigma Delta modulation, **1**:11–12
  for metrological applications, **1**:12–13
  one-stage three-section Wilkinson divider, layout and photograph of, **1**:19, **1**:19*f*
  one-stage Wilkinson divider, current-voltage characteristic of, **1**:19, **1**:19*f*
  one-stage Wilkinson divider, time and frequency domain of sine waveform, **1**:20, **1**:20*f*
  optical pulse drive and on-chip power divider, **1**:16–20
  pulse-tube cryocooler, **1**:16, **1**:17*f*
  quantized waveforms, practical realization of, **1**:11–12, **1**:11*f*
  Si-carrier chip, PDs mounted on, **1**:17–18, **1**:18*f*
  sine waveforms, frequency and time domain of, **1**:15, **1**:16*f*
  sine waveforms, frequency spectra of, **1**:12, **1**:12–13*f*
  SNS junctions, current-voltage characteristics of, **1**:10, **1**:10*f*
  5-stacked Josephson junctions, cross-section SEM image of, **1**:14–15, **1**:15*f*
  5-stacked SNS junctions, multilayer sequence of, **1**:14, **1**:14*f*
  technology, **1**:13–15
  unipolar sine waveform, frequency spectrum and time domain of, **1**:18–19, **1**:18*f*
Josephson effect, **2**:618, **2**:717–719, **3**:8, **3**:76, **3**:77*f*
  coupling between macroscopic quantum systems and equations of, **2**:617–620
Josephson equations, **1**:10, **2**:726
Josephson junction arrays (JJA), **2**:808
Josephson junctions, **2**:616, **2**:702–704, **2**:709, **3**:376–377, **3**:459–460, **3**:532. *See also* Hybrid Josephson junctions
  current-voltage (I –V) characteristics, **2**:621–623

  - essential parameters, **2**:620
  - Hamiltonian of, **2**:623
  - magnetic dependence of critical current, **2**:624–626
  - properties of, **2**:621–626
  - for qubits, quantum circuits and superconducting electronics, low temperature, **2**:626–627
  - temperature dependence of I–V curves, **2**:623–624
- Josephson plasmons, **3**:514
- Josephson weak link, **2**:618–619
- JTEs. *See* Jahn–Teller effect (JTE)
- Junction diodes, **3**:757, **3**:758*f*

K

- Kagome systems, **4**:350
- Kane–Mele coupling, **2**:358*f*
- Kane–Mele model, **1**:691
- Kane models, **1**:852
- Kappa geometry, **5**:767
- Kataura plots, **5**:709–710
- Kato’s fringes, **4**:404
- Kauzmann paradox, **3**:187
- Kauzmann temperature, **3**:173
- Keldysh path integral technique, **2**:676–677
- Kelvin probe force microscopy (KPFM), **4**:51, **4**:58
- Kernel-extreme learning machine (KELM), **3**:828, **3**:828*f*
- Kernel method, **4**:548–549
- Kibble balance, **1**:5–6
- Kibble–Zurek scaling law, **3**:97–99
  - criticality at equilibrium, **3**:95
  - criticality in dynamical setting, **3**:95–97
  - early ideas, **3**:93
  - in elongated ultracold atomic system, **3**:99–102
  - homogeneous, **3**:102–104
  - numerical phase transition model, **3**:94–95
- Kinetic theory, **3**:278–280, **3**:282
- Kinetic theory of heat carriers, **3**:274
- Kitaev chain, **2**:796–797
- Kitaev model, in one dimension, **1**:494–496
- Kitaev’s 16-fold way, **1**:333–334
  - anyons, properties of, **1**:334
  - edge theory, **1**:334
- Klein tunneling, **1**:608–610, **2**:301, **2**:344–345
- K-NN model, **3**:828
- Knudsen cells (K-cells), **5**:252–253, **5**:253*f*
- Kohn anomalies, **1**:829–830
- Kohn–Sham equation, **1**:868–870, **3**:238, **3**:504–506
- Kohn–Sham states, **1**:873–875
- Kohn’s theorem, **4**:133–134, **4**:145
- Kondo cloud, **3**:389
  - observation of, **3**:392, **3**:393*f*
  - spatial extension of, **3**:392
- Kondo-correlated quantum dot
  - phase shift through spin 1/2, **3**:391–392
  - transport through, **3**:389–390
  - varieties of, **3**:392–395
- Kondo effect, **3**:259
  - emulation, two-orbital two-electron atom system as, **3**:140
  - history of, **3**:388
  - multi-channel, **3**:396–397
  - overview, **3**:389
  - with superconductivity, **3**:397
  - in unitary limit and universal scaling, **3**:390*f*
- Kondo effects, in quantum dots
  - Anderson model for, **3**:383–385
  - Coulomb peaks to Kondo plateau, **3**:385–386
  - emergence of, **3**:385
  - isolated quantum dot approximation, **3**:383–384
  - linear response conductance, **3**:383
  - magnetic impurity in metal, **3**:384–385
  - non-interacting approximation, **3**:384
  - quantum dot model, **3**:382–383
- Kondo peak, **3**:385
- Kondo plateau, **3**:385–386
- Kondo problem, **1**:34
- Kondo resonance, **3**:389–391
- Kondo temperature, **3**:385–386
- Korshunov instanton, **3**:268
- Kosterlitz–Thouless transition, **1**:45, **1**:170
- Kramers–Kronig relations, **3**:512, **3**:813, **4**:151–152, **5**:119, **5**:154
  - anharmonic oscillator, **5**:114–115
  - data analysis, **5**:116
  - description of nonlinear optical functions, **5**:111–112
  - dispersion relations, **5**:107–108
  - harmonic generation, **5**:113
  - and linear sum rules, **5**:108–110
  - pump and probe, **5**:114
  - relativistic and spatial dependent corrections, **5**:110–111
  - second-harmonic generation, **5**:115–116
- Kramers theorem, **1**:691
- Kramer’s theory, **4**:651
- Kretschmann configuration, **3**:732
- Kriging/black box optimization, **4**:557
- Kröger-Vink diagrams, **3**:148, **3**:150*f*
- Kronig-Penney potential, **2**:260
- *k*-space resolution, **1**:828

L

- Lagrangian of Dirac theory, **1**:72
- Lambert–Beer law, **5**:155
- Lamb–Mössbauer factor, **4**:212
- Lamellar microstructure, **3**:478, **3**:478*f*
- Landau criterion, **3**:52, **3**:54, **3**:65
- Landau cylinder, **4**:229–230, **4**:229*f*
- Landau diamagnetism, **2**:42
- Landauer’s principle, **4**:529–530
- Landau–Ginzburg–Devonshire framework, **3**:287–290
- Landau–Ginzburg theory, **1**:30–32, **1**:96
- Landau-level fan-diagram analysis, **1**:697
- Landau level mixing, **1**:551
  - competing phases and, **1**:342–345
  - non-perturbative treatment I, **1**:343
  - non-perturbative treatment II, **1**:343
  - perturbative treatment I, **1**:343
  - perturbative treatment II, **1**:343
  - perturbative treatment III, **1**:344–345
  - perturbative treatment IV, **1**:345
- Landau levels (LLs), **1**:386, **1**:540, **1**:559, **1**:610, **1**:661, **1**:724, **1**:726, **2**:356–357, **4**:133, **4**:142–145, **4**:148*f*
  - cyclotron motion, **1**:540
  - *vs.* Fock-Darwin states, **3**:301–303
  - and integer Hall effect, **1**:89–92
  - lowest level, **1**:543
  - magnetic Hamiltonian, **1**:540–541
  - unitary maps between, **1**:544
- Landau–Lifshitz constant, **2**:58–59, **2**:63
- Landau–Lifshitz equation, **2**:122
- Landau–Lifshitz–Gilbert (LLG) equation, **2**:145, **3**:400–401
- Landau–Placzek ratio, **4**:190
- Landau quantization, **4**:117–118, **4**:229–230
- Landau theory, **2**:60–61
- Langevin approach, **3**:281–282
- Langevin function, **2**:27, **2**:37, **2**:44
- Langmuir–Blodgett deposition, **5**:257, **5**:258*f*
- Langmuir–Blodgett trough, **5**:258*f*
- Langmuir frequency, **4**:152
- Lankford coefficient, **5**:623
- Lanthanum hydride, **2**:595–596
- Laplace equation, **4**:303
- Large- and small-bipolaron formation, **2**:431–432
- Large-polaron transport, **2**:434–435
- Large-signal pulse modulation, **3**:777
- Large-sized insulator and ceramic carrier, **5**:438
- Larkin–Ovchinnikov model of FFI, **2**:737–738
- Laser
  - ablation, **5**:697
  - amplifier, **4**:413–414
  - cooling and atom trapping, **3**:70
  - epitaxy, **2**:537
  - manufacturing, **5**:102
  - materials, **4**:411, **4**:413, **4**:418
  - oscillator, **4**:409–410, **4**:417
  - resonators, **4**:414–417
- Laser diodes (LD), **3**:766–768, **3**:767–768*f*, **3**:776–777, **3**:777*f*
- Laser Doppler holography, **5**:100
- Laser plasma, X-ray sources, **4**:441
- Laser radiation sources
  - interaction of light with matter, **4**:411–412
  - laser active media, **4**:418–419
  - laser resonators and beam modes, **4**:414–417
  - laser transients, **4**:420–423
  - optical laser, **4**:409, **4**:410*f*
  - population inversion and laser beam properties, **4**:410–411
  - rate-equation approximation and laser amplifier, **4**:413–414
  - single mode continuous laser operation, **4**:417–418
  - thermal population distribution, **4**:409*f*
- Laser transients
  - mode-locking and ultra-short pulse generation, **4**:421–423

Laser transients *(Continued)*
  Q-switching pulse generation, **4**:420–421
Lateral resolution, **4**:112
Lateral waveguiding, **3**:774*f*
Lattice, **2**:633–639
  and Bravais classes, **5**:7–8
  conductivity, **3**:537
  cuprates, **2**:635–636
  doped graphene, **2**:637–638
  Fe-pnictides, **2**:633
  periodicity, **5**:61–62
  point symmetries, **5**:70, **5**:71*t*
  s-wave superconductivity from repulsion, **2**:638–639
  and symmetries, **5**:70, **5**:78–79, **5**:79*t*
  types, **5**:11–13, **5**:12*t*
  vibrations, **3**:535
Lattice dynamics
  atomic dynamics and cluster structure, **5**:285
  bond orientational order (BOO), **5**:278
  characteristic property of, **5**:282
  Fourier module, **5**:279
  generalized vibrational density-of-states, **5**:284–285
  incommensurate composites, **5**:281
  incommensurate modulated structures, **5**:280–281, **5**:280–281*f*
  long-range order (LRO), **5**:278
  phason flips, **5**:288
  phonon dispersions, **5**:282–284, **5**:283–284*f*
  quasicrystals, **5**:278–279, **5**:282, **5**:285–286
  temperature dependence, atomic dynamics, **5**:286–288, **5**:287*f*
Lattice gauge theory, **1**:635
Lattice heat capacity, at high temperatures, **5**:413
Lattice-matched semiconductor interface, **2**:512
Lattice-mismatched semiconductor interface, **2**:513
Lattice-periodic Bloch function, **5**:129
Lattice preferred orientation (LPO), **3**:483
Laue conditions, **5**:43–44, **5**:44*f*
Laughlin phase stability, **1**:388, **1**:390–391
Laughlin quasi-holes, **1**:387–388
Laughlin states, **1**:549–550, **1**:646
Laughlin's wave function, **1**:92–93, **1**:291–292
Layered metals and degenerate semiconductor systems
  apparent scattering rate in layered metals, **4**:126–128
  cyclotron resonance in semiconductors, candidate topological insulators and low carrier-density system, **4**:123–126
  extraction of apparent scattering rates in layered metals, **4**:123
  Fermi surfaces and resonant cavity techniques, **4**:121–123
LD. *See* Laser diodes (LD)
Lead-alloy technology, **2**:617–618
LED. *See* Light-emitting diodes (LEDs)
LEED. *See* Low-energy electron diffraction (LEED)
LEEM. *See* Low-energy electron microscopy (LEEM)
Lee–Yang theorem, **1**:166
LEFM approaches, fatigue
  crack growth laws, **3**:823–824
  crack propagation models, **3**:834
  Elber's model (crack-closure model), **3**:824
  Forman's model, **3**:824
  formulation, **3**:822
  fracture mechanics and, **3**:823
  fundamentals, **3**:822
  multiparameter law, **3**:824
  Paris' model, **3**:824
  Walker's model, **3**:824
Lefschetz thimble, **1**:890
Left-handed material (LHM)
  optics with, **4**:380–381
  refraction at, **4**:381, **4**:381*f*
Lennard–Jones potential, **4**:545–546, **5**:755
Lenz's law of induction, **2**:39, **2**:41
Levitons, **1**:926
  crystallization, **1**:930–931
  interaction effect in HOM profile, **1**:930
Lieb lattice, **3**:136–137, **3**:141–142
Lifshitz–Kosevich (LK) formula, **4**:230–231, **4**:231*f*
Ligand protection, **5**:694–695, **5**:698
Light diffusion and scattering, **5**:448
Light emission, halide perovskites, **5**:672
Light-emitting diodes (LEDs), **3**:237, **3**:766, **3**:766*f*
  direct-gap semiconductors, **5**:815–816
  DUV, **5**:824–825
  homostructures and heterostructures, **5**:817–819
  indirect-gap semiconductors, **5**:815–816
  light-extraction in, **5**:819–820
  mechanism, **2**:416–417
  optical emission spectrum, **5**:816
  packaging, **5**:825–826
  white, **5**:820–823
Light-excitons, **3**:713–714
Light-harvesting (LH), **4**:578–580
  complexes, **4**:731
  in photosynthesis and energy transport, **4**:586–588
Lindblad operators, **1**:973
Linear combination of atomic orbitals (LCAO), **1**:732–733, **2**:74–75, **5**:703
Linear dispersion, **4**:377
Linear Invar effect, **2**:396
Linear magnetoresistance, **4**:128
Linear response conductance, **3**:383
Linear response theory, **3**:383
Linear-scaling algorithm, **1**:996–997
Liouville regime, **1**:721–722
Liouville's theorem, **4**:462
Liquid crystal (LC)
  antiferroelectric SmC* phase, **5**:381, **5**:383*f*
  bent-core mesophases, **5**:383–388, **5**:385–387*f*
  calamitic mesophases, **5**:380–382
  definition, **5**:375
  discotic/columnar mesophases, **5**:382–383, **5**:385*f*
  ferroelectric SmC* phase, **5**:381, **5**:383*f*
  hexagonal (D_h) columnar mesophases, **5**:383, **5**:385*f*
  hexatic and crystal smectic phases, **5**:381
  nematic (N) phase, **5**:375–380
  rectangular (D_r) columnar mesophases, **5**:383, **5**:385*f*
  smectic-A (SmA) phase, **5**:375, **5**:381, **5**:381*f*
  smectic-C (SmC) phase, **5**:381, **5**:382*f*
  twist-grain boundary (TGB) phase, **5**:381–382, **5**:384*f*
Liquid crystal on silicon (LCoS) SLMs, **5**:98–99, **5**:99*f*
Liquid crystals, **3**:206
Liquid Encapsulated Czochralski method (LEC), **5**:194
Liquid helium
  early approaches, **1**:934–935
  microscopic theories, **1**:935–940
  quantum Monte Carlo methods, **1**:940–943
Liquid indium, **3**:427, **3**:429–430, **3**:429*f*, **3**:432
Liquid-liquid critical point (LLCP), **3**:178–179
Liquid metals and alloys. *See* Metallic liquids
Liquid-phase epitaxy (LPE), **2**:535, **2**:545, **5**:258
Liquids
  acoustics to, **3**:205–207
  containerless confinement, **3**:207
  electron–ion correlations, **3**:167–168
  experimental and theoretical methods, **3**:163
  fragile and strong, **3**:174
  metallic, **3**:164–167, **3**:164–166*f*
  semiconductors and insulators, **3**:168–169
  spectral features measurement, **4**:190
Lithography, **2**:525–527, **3**:369
Load-sharing mechanism, **3**:858
Local CPD (LCPD), **4**:58
Local density approximation (LDA), **1**:756, **1**:758, **1**:763, **1**:871, **3**:238, **3**:503–504, **3**:809
Local density of states (LDOS), **2**:260–261, **4**:51
Local elementary structures (LESs), **4**:653–654
Local Fermi liquid, **3**:391
Local FFI model, for thin films near Tc, **2**:741–742
Local field effects
  application, **3**:809–810
  dielectric response, **3**:806–807
  exchange and correlation, **3**:807
  induced field, **3**:803–804
  macroscopic fields, **3**:804–806
  nonlocal dielectric response, **3**:808–809
  photoemission from layered crystals, **3**:807–808
Localization landscape approach, **3**:237, **3**:241–242

Localization length, **1**:568–570, **1**:572
Localized-electron model, **2**:55–59
Localized interface states, **2**:514
Localized surface plasmon (LSP), **4**:301–303
Localized surface plasmon-polaritons, **3**:659
Localized surface plasmon resonance (LSPR), **4**:302–304
Local magnetic interaction, **2**:115–116
Local spin density approximation (LSDA), **2**:75, **3**:504
Local vibrational modes (LVM), **2**:492–493
Lodestones, **2**:2–4, **2**:3*f*
Lohmann hologram, **5**:96, **5**:97*f*
London penetration depth, **2**:650
London theory, **2**:693, **2**:697–698
Longitudinal conductivity, **1**:677
Longitudinal mode, **4**:417, **4**:420–421
Longitudinal-transverse (LT) splitting, **3**:687
Long-range electron-phonon interactions, **2**:429
Long-range interaction, **3**:81
Long-range magnetic order, **2**:73–77
Long-range scattering, **2**:299–300
Long wavelength approximation (LWA), **3**:654–655, **3**:685, **3**:687
Loop braid group, **1**:275–276
Lorentz force, **4**:379–380
Lorentzian distribution, **4**:230
Lorentz invariant quantum field theory, **1**:32
Lorentz-Lorenz formula, **3**:803
Lorentz oscillator model, **3**:655
Lorenz-Mie theory, **4**:318
Low density liquid (LDL), **3**:178–179
Low-dimensional materials, **2**:468–469
Low-dimensional physics, **3**:81
Low energy effective model, **5**:131–132
Low-energy electron diffraction (LEED), **4**:1, **4**:5–7, **4**:10
Low-energy electron microscopy (LEEM)
  band structure analysis, **4**:10–12
  chemisorption, chemical reactions and oxidation, **4**:7
  clean surfaces, **4**:6–7
  electron–specimen interaction, **4**:2–3
  instrumentation, **4**:4–5
  spin-polarized, **4**:12–13
  thin film growth, **4**:7–10
Lowest Landau level (LLL)
  anyons, **1**:473
  as Bargmann space of holomorphic functions, **1**:543
  mapping Hamiltonians to, **1**:546–547
Lowest unoccupied molecular orbital (LUMO), **4**:53
Low-stacking-fault-energy high-entropy alloys (LSF-HEAs), **5**:653
Low-temperature continuum-level strengthening, **3**:857–858
Low-temperature dislocation, **3**:853–857
  grain-boundary strengthening, **3**:857
  particle strengthening, **3**:855–856, **3**:856*f*
  solid solution strengthening, **3**:855, **3**:855*f*
  work hardening, **3**:854–855
Low temperature solution growth, **5**:202
L-particle densities, **1**:545–546
Luminescence of Europium containing scheelites, **4**:516–518
Luttinger–Kohn model, **1**:852
Luttinger liquid, **1**:928–929
Lyman spectroscopy, **3**:647, **3**:648*f*

M

Machine learned interatomic potential, **4**:551
  amorphous silicon, **4**:550
  applications, **4**:549–550
  data generation, **4**:549
  organic molecules, **4**:550
  regression, **4**:548–549
  representations, **4**:546–548
  water, **4**:550
Machine learning (ML), **3**:217, **4**:544, **4**:554–555, **5**:209, **5**:214–215, **5**:239–240
  acquisition function, **4**:558
  applications, **3**:826*f*
  Bayesian optimization (BO), **4**:557, **4**:557*f*
  classification, **4**:554
  clustering, **4**:555*f*
  descriptors, **4**:555–556
  first-principles calculation, **4**:553
  Gaussian process regression, **4**:557–558
  potentials, **4**:556, **4**:556*f*
  regression, **4**:554–555
  techniques, **3**:827
Mach–Zehnder interferometer (MZI), **1**:356, **5**:174, **5**:174*f*, **5**:179, **5**:180*f*
Mach–Zehnder modulator (MZM), **1**:17–18
Mackay type quasicrystals, **5**:328
Macromolecular crystallography
  model building and refinement, **5**:48
  scattering equation, **5**:42–43 (*see also* Scattering)
Macroscopic and microscopic variables, **4**:560
Macroscopic fields, **3**:804–806
Macroscopic polarizability, **3**:684
Macroscopic quantum systems, and equations of Josephson effect, **2**:617–620
Macroscopic quantum tunneling (MQT), **1**:216, **2**:622–623, **2**:725, **2**:727–730, **2**:727–728*f*, **2**:730*f*
Macroscopic susceptibility, **3**:690–691
Macroscopic wave function, **3**:3
Macrostructure, definition, **3**:465
Madelung constants for ionic crystals, **5**:211*t*
Madelung energy, **5**:210–211
Magic-angle spinning (MAS), **4**:637
Magic numbers, **3**:304–306
Magma, **1**:276–277
Magnesium alloys
  additive manufacturing, **5**:555
  alloying, **5**:553
  applications, **5**:562
  casting, **5**:553
  continuous sheet casting, **5**:554
  extrusion, **5**:558–560
  high-pressure die cast, **5**:555–556
  issues, **5**:562–563
  machining, **5**:554
  processing, **5**:553–555
  sand cast/permanent mold cast, **5**:557–558
  thermomechanical processing, **5**:554
  welding and joining, **5**:555
Magnesium deformation, **5**:551–552
Magnesium diboride, **2**:577
Magnesium plate/sheet alloys, **5**:560–562
Magnetic actuation, **5**:401–402, **5**:401–402*f*
Magnetic alloys, **5**:529–530
Magnetic anisotropy, **2**:30, **2**:46–49, **2**:64
Magnetic annealing, **2**:49
Magnetic Bragg peaks, **5**:2, **5**:7–8, **5**:9*f*
Magnetic breakdown, **4**:233–234
Magnetic bubbles, **2**:121
Magnetic-charges avoidance rule, **2**:65
Magnetic circular polarization, of exciton photoluminescence, **3**:679
Magnetic Compton scattering, **4**:174, **4**:177, **4**:180, **4**:184
Magnetic coupling, **2**:30–31
Magnetic domains, **2**:49–51, **2**:50*f*, **2**:64–65, **2**:67–70
Magnetic energy density, **2**:28, **2**:30
Magnetic excitation, as heat carriers, **3**:276
Magnetic field, **3**:678, **4**:235
  effects, **3**:329–332, **4**:707–708
  generation, **4**:707–708
  Schrödinger equation for free electrons in, **4**:229
Magnetic fluctuations, **2**:29
Magnetic flux quanta, **2**:741
Magnetic force microscopy (MFM), **4**:59
Magnetic free energy, **2**:63
Magnetic groups, generalization of, **5**:10
Magnetic Hamiltonian
  complex notation, **1**:542
  eigenfunctions, **1**:543
  factorization, **1**:543
  Landau levels, **1**:540–541
  oscillators, **1**:541–542
Magnetic induction, **4**:707
Magnetic insulator, **2**:169, **2**:172–173
  interaction of magnons with carriers of information, **2**:173
  magnons as carriers of information, **2**:172
  non-linear magnonic devices, **2**:173
Magnetic interaction, **2**:227, **4**:233
Magnetic materials, **2**:23
Magnetic moment, **2**:26, **2**:372, **4**:719, **4**:719*f*
Magnetic monopole, **1**:45–47, **1**:229
Magnetic nanostructures
  core-shell particles, **2**:123
  critical phenomena, **2**:117–118
  curvilinear magnetism, **2**:122
  curvilinear nanoarchitectures, **2**:122
  curvilinear shape, **2**:124
  exchange bias effect, **2**:123
  hollow particles, **2**:123
  magnetic materials and topological insulators, **2**:124
  magnetoelectric and multiferroic particles, **2**:123
  nanoscaled magnets, **2**:124–126

Magnetic nanostructures *(Continued)*
  ordering and theoretical description, **2**:113–117
  single domain particles, **2**:118–119
  3D magnetism, **2**:125
  topological magnetic textures, **2**:119–122
  2D magnetic materials, **2**:124
Magnetic noise, **2**:376–378
Magnetic order, **2**:87–90
  atomistic models, **2**:114
  local magnetic interactions, **2**:115–116
  micromagnetic equations of state, **2**:116–117
  non-local magnetic interactions, **2**:116
  phenomenological description, **2**:114–115
Magnetic orientation Mössbauer spectroscopy, **4**:27
Magnetic oxide
  exchange interaction, **2**:102–103
  frustrated magnetism, **2**:103–104
  insulator-metal transitions, **2**:107–109
  intersite effects, **2**:101–102
  isolated magnetic ions in crystal, **2**:99–101
  magnetoelectrics, **2**:106–107
  metallic oxides, **2**:107–109
  multiferroics, **2**:106–107
  orderings, **2**:105
  properties and applications, **2**:110–111
  spin ice, **2**:103–104
  spin liquids, **2**:103–104
  superconductivity, **2**:109–110
Magnetic phase diagram, **2**:590
Magnetic phase transition, **2**:113, **2**:118, **2**:124
Magnetic point groups, **5**:2–5
  of crystals, **5**:4–5
  of finite objects, **5**:4
  orthorhombic, **5**:3*t*
Magnetic proximity effect
  F/S/F spin valves, **2**:689
  superconductor-ferromagnetic insulator structures, **2**:688–689
Magnetic random-access memory (MRAM), **2**:160–161, **2**:163–167, **2**:169, **3**:554
Magnetic recording, **2**:12, **2**:14–16, **2**:15*f*
Magnetic sensors, **2**:160, **2**:163
Magnetic skyrmions, **1**:591, **1**:591*f*
Magnetic space group, **5**:5–9
  one-dimensional, **5**:2*f*
  types, **5**:6
Magnetic structure
  experimental studies of, **2**:33–34
  smooth, spin-transfer mechanism, **2**:144
Magnetic susceptibility, **2**:44–45
  biological matter, **4**:707, **4**:707*t*
  diamagnetic and paramagnetic systems, **4**:720, **4**:720*f*
Magnetic symmetry
  of periodic crystals, **5**:6–7
  of quasiperiodic crystals, **5**:7–9
Magnetic Thomas–Fermi theory, **1**:470–472
Magnetic topological insulators (TIs), **2**:113, **4**:342–344, **4**:344*f*
Magnetic topological solitons, **2**:119–120
Magnetic tunnel junction (MTJ), **2**:161, **2**:167, **3**:554, **3**:565–566, **3**:565–566*f*
Magnetic vortices, **2**:121, **3**:52, **3**:54*f*, **3**:58–59
Magnetic Weyl semimetal, **1**:682–683, **4**:350
Magnetic X-ray circular dichroism, **2**:34
Magnetism, **2**:26
  early history, **2**:2–4
  experimental methods, **2**:13–14
  fundamentals, **2**:8–10
  magnetic phenomenology and materials, **2**:10–12
  materials and technology, **2**:14–16
  modern developments, **2**:12–16
  from navigation to industry, **2**:4–7
  numerical simulations, **2**:13
  theory, **2**:12–13
  units, **2**:7–8
Magnetization, **2**:27–28, **2**:36–37, **2**:43
  curves, **2**:51–53, **2**:695*f*
  dynamics, **2**:125
  quantum rings, **3**:420–422, **3**:421*f*
  rotation, **2**:53
Magneto- and electro-optical effects, **3**:671
Magnetocaloric effect (MCE)
  discovery and application, **2**:85
  fundamentals, **2**:86–87
  future, **2**:92
  magnetic order, **2**:87–90
Magnetocrystalline anisotropy, **2**:48, **2**:48*f*
Magnetoelectrics, **2**:106–107, **2**:123, **3**:700–701
Magneto-excitons, **3**:719
Magnetomechanical device, **5**:401–402, **5**:401–402*f*
Magnetooptical Kerr effect (MOKE), **4**:380
Magneto-optical sum rule, **1**:676
Magnetooptics, **4**:379–380
Magnetophononics, **3**:514
Magnetoplasmon modes, **4**:134
Magnetoreception, with radical pairs, **4**:580–581
Magnetoresistance (MR), **2**:95, **3**:259, **3**:565
Magnetoroton excitation, **1**:292
Magneto spectrum, **2**:292–293
Magnetostatic energy, **2**:46, **2**:64, **2**:68–69
Magnetostatics, **2**:29
Magnetostriction, **2**:399, **2**:401*f*
Magnetotransport effects in 2DEGs, **3**:531
Magnetron sputtering, **5**:251*f*, **5**:252, **5**:697
Magnon. *See* Spin waves
Magnonics, **2**:163–164, **2**:172
Magnons, **1**:315–316, **4**:199–201
  collective excitations, **2**:452–453
  fluxonics, **2**:748
  phonon system, **2**:152–153, **2**:156
  qubit system, **2**:153–156
  squeezing, **2**:152
Majorana fermion (MF), **2**:796–797
  experimental realizations, **1**:144–145
  fingerprint, **1**:143–144
  Ising anyons, **1**:135
  in Kitaev model, **1**:140–142
  Kitaev quantum wire, **1**:136*f*
  p + *ip* state, **1**:135
  topological quantum computing, **1**:135
Majorana modes, **1**:495–498
Majorana zero modes (MZMs), **1**:274, **1**:697–698, **2**:627
Maksym–Chakraborty effect, **3**:304–306
Mandel Q-parameter, **5**:178
Manganites, **2**:84
  chemical composition, **2**:93
  colossal magnetoresistance effect (CMR), **2**:95
  doping, **2**:93
  insulating state, **2**:96
  interactions, **2**:94–95
  metallic phase, **2**:95
  percolative transition, **2**:96–97
  phase diagram, **2**:93
  structure, **2**:93, **2**:94*f*
Manipulation of matter, terahertz light and, **3**:510
Many-body effects I, **4**:128–129
Many-body effects II, **4**:129
Many-body Hilbert space scarring, **1**:256
Many-body localization (MBL), **2**:805
Many-body quantum Hamiltonian, **1**:385
Many body states, **1**:545–546
Many-electron treatment, **1**:858
Many-particle correlations, **1**:559
Markov state model (MSM), **4**:661
Martensite, **2**:389–391, **2**:396, **2**:398–402, **5**:536, **5**:538
Martensitic transformation, **2**:396, **2**:400–402, **2**:401*f*
Masked ion irradiation of thin films, **3**:371–372
Mass balance equation, **4**:490
Massless Goldstone modes, **1**:170–171
Mass transfer, **4**:489
Mass transport
  elementary description, **4**:488–489
  in ionic materials, **3**:159
Materials for microelectromechanical systems (MEMS), **5**:505–506
Materials informatics, **4**:553–554
Mathematical constructs
  basic equations, **3**:489
  harmonic method, **3**:491–492
  MTEX method, **3**:493
  ODF estimation from diffraction pole figure measurements, **3**:491
  ODF estimation from individual orientations, **3**:489–490
  WIMV-method, **3**:492–493
Matrix formulation, **1**:716
Matrix representation, of symmetry operations, **5**:74–78
Matsubara frequency, **2**:639
Matter, topological phases, **1**:72–115
Matthiessen's rule, **2**:461–462
Maxwell–Boltzmann (MB) distribution, **4**:463
Maxwell boundary conditions, **3**:683–684
Maxwell demon, **4**:522–523, **4**:523*f*
Maxwell's equation, **2**:68, **2**:86–87, **3**:658, **3**:803, **4**:370, **4**:375, **4**:377–378, **5**:80–81, **5**:151–152
Maxwell's fish-eye lens and bound states, **2**:346–347
Maxwell–Wagner dispersion, **4**:701
MBE. *See* Molecular beam epitaxy (MBE)

- MCBJs. *See* Mechanically controllable break junctions (MCBJs)
- McCumber–Stewart parameter, **2**:622
- MCE. *See* Magnetocaloric effect (MCE)
- McMillan equation, **1**:761
- Mean field approximation, **2**:74
- Mean field density, **1**:649
- Mean-field Ising spin glass, **2**:375
- Mean field theory, **5**:302–303
- Mean free path (MFP), **3**:258, **3**:279, **5**:249–250
- Mean square displacement (MSD), **3**:173, **4**:325
- Measurement methods, **3**:137–138
- Measuring elastic constants, **3**:841–842
- Mechanically controllable break junctions (MCBJs), **4**:678*f*, **4**:679–680
- Mechanical properties
  - elastic behavior, **3**:838
    - anisotropy, **3**:840–841
    - fundamental nature of elastic constants, **3**:842
    - hyperelasticity, **3**:842
    - isotropic materials, **3**:838–840, **3**:839*t*
    - measuring elastic constants, **3**:841–842
  - plastic behavior
    - applications, **3**:851–852
    - deformation fundamentals, **3**:844–847, **3**:845*f*
    - deformation microstructure, **3**:847
    - hardening behavior, **3**:847–848
    - modeling, **3**:850–851
    - recovery and recrystallization, **3**:848–850
    - texture, **3**:848
  - strengthening mechanisms due to thermal activation, **3**:858–859
  - strengthening mechanisms in metals, **3**:853
    - low-temperature continuum-level, **3**:857–858
    - low-temperature dislocation, **3**:853–857
- Mechanical/structural ceramics, **5**:417
- Medical microrobots, **3**:544, **3**:548
- Medium entropy alloys (MEAs), **3**:830*f*
- Megaexcitons, **3**:707
- Meissner effect, **2**:645
- Meissner state (MS)
  - Cooper pairs, **2**:646–651
  - definitions, **2**:645–646
  - microscopic whirls, **2**:651–652
  - penetration depth, **2**:652
  - temperature, **2**:652–653
- Membrane voltage, **4**:695–698
- Memory, **3**:755, **3**:762–763, **3**:764*f*
  - applications, **3**:329
  - classification, **3**:577–578
  - dip, **2**:380
- Memristors, **3**:554, **3**:564
- Mermin-Ho relation, **3**:402–403
- Mermin–Wagner–Hohenberg theorem, **1**:158, **1**:160, **1**:170, **2**:670
- Mermin–Wagner theorem, **1**:45
- Mesoscopic channels, **1**:924–926
- Mesoscopic effects, **3**:259
- Mesoscopic physics, **1**:220
- Mesoscopic quantum transport emulation, **3**:141
- Messenger RNA (mRNA), **4**:665
- Meta-dynamics (MetaD) simulation, **4**:661
- Metal halide perovskites (MHPs), **5**:659–663. *See also* Halide perovskites
  - structure, **5**:660–661
  - synthesis, **5**:662–663
- Metal-induced gap states (MIGS), **2**:268
- Metal–insulator–controlled semiconductor FETs (MISFETs), **3**:783–784, **3**:784*f*
- Metal-insulator-metal (MIM) device, **3**:554, **3**:564, **3**:571
- Metal-insulator transition, **1**:914, **1**:916–917, **2**:96
  - scaling theory, **3**:226–228
  - in two-dimensional system, **3**:229–231
- Metallic alloys, **5**:511
  - chemical bonds and crystal structures, **5**:512
  - chemical properties, **5**:518
  - electrical and magnetic properties, **5**:517–518
  - free energy and phase diagrams, **5**:513–515
  - intermediate phases, **5**:512
  - magnetooptics, **4**:379–380
  - materials selection, **5**:518
  - mechanical properties, **5**:516–517
  - microstructure, **5**:515–516
  - phase stability and transformations, **5**:512–516
  - phase transformations, thermodynamics and kinetics of, **5**:512–513
  - plasma waves in optics, **4**:375–378
  - reflection and transmission, **4**:370–373
  - solid solutions, **5**:512
  - surface plasmon polaritons, **4**:373–375, **4**:374*f*
- Metallic bonding, **5**:217
- Metallic crystal structures, slip systems of, **3**:845*t*
- Metallic liquids, **3**:164–167, **3**:164–166*f*
  - electron–ion correlations, **3**:167–168
  - metallic alloys, **3**:166–167, **3**:166*f*
  - M/NM transition, **3**:166
  - polyvalent metals, **3**:165–166, **3**:165*f*
  - simple metals, **3**:164–165, **3**:164–165*f*
- Metallic S/F structures, **2**:683–686
- Metallic superlattices, bulk and surface spin waves in, **4**:191–192
- Metal–ligand interactions, **5**:486–487
- Metallization, **3**:168–169
- Metalloproteins, **4**:719
  - collecting paramagnetism-based restraints, **4**:726–727, **4**:726–728*f*, **4**:727*t*
  - contact shift restraints, **4**:724–726, **4**:725*f*
  - Curie and dipole–dipole relaxation restraints, **4**:723
  - diamagnetic and paramagnetic systems, **4**:720
  - dipole–dipole interaction, **4**:721
  - paramagnetic tagging of diamagnetic proteins, **4**:729
  - pseudocontact shift restraints, **4**:721–722
  - recovering information on structure heterogeneity, **4**:728–729
  - relaxation enhancement restraints, **4**:722–723
  - self-orientation residual dipolar coupling restraints, **4**:723–724, **4**:724*f*
  - solution structure of, **4**:728, **4**:728*f*
- Metal matrix composites (MMCs), **5**:344–345
- Metal–metal interactions, **5**:490–497
- Metal optics
  - magnetooptics, **4**:379–380
  - plasma waves in optics, **4**:375–378
  - reflection and transmission, **4**:370–373
  - surface plasmon polaritons, **4**:373–375, **4**:374*f*
- Metal organic chemical vapor deposition (MOCVD), **2**:535, **4**:393, **5**:255–256
- Metal organic vapor phase epitaxy (MOVPE), **2**:535, **5**:255–256, **5**:255*f*
- Metals
  - contact, **1**:563
  - crystal structures, **5**:512
  - and elements, atomic layer deposition, **5**:722
  - impurities, **5**:567–568
  - indirect exchange in, **2**:75–77
  - point defects, **5**:186
- Metamagnetism, **5**:493
- Metamaterials, **3**:672
- Metastability, **3**:172–173, **4**:504–505
- Metasurface holography, **5**:101
- Metrology, **1**:555, **1**:559, **1**:562*f*, **1**:563
- Mg-Al based alloys, **5**:558–560
- MgB_2, two-gap superconductor in, **2**:604, **2**:605*f*
- Mg-Li based alloys, **5**:562
- Mg-Mn-RE based alloys, **5**:560
- Mg-RE based alloys, **5**:560–562
- Mg-Zn based alloys, **5**:559, **5**:561
- Microactuators, **5**:506
- Microcanonical ensemble, **4**:561–563
- Microcavity devices, **1**:962–963
- Micro-electromechanical systems (MEMS), **5**:422, **5**:422*f*
- Microkinetic modeling, catalysts, **5**:742
- Microlithography, **5**:96, **5**:98–99
- Micromachining, **5**:504–505
- Micromagnetic equations of state, **2**:116–117
- Micromagnetism, **2**:10, **2**:13, **2**:115
- Micromechanical devices and systems
  - chemistry and biomedical applications, **5**:509–510
  - future development, **5**:510
  - materials for, **5**:505–506
  - microactuators, **5**:506
  - micromachining, **5**:504–505
  - optical devices, **5**:508–509
  - printers, **5**:508
  - sensors, **5**:507–508
- Microprocessors, **3**:756
- Microrobots, **3**:540–541, **3**:548
  - alternative geometries, **3**:544
  - biocompatibility and immunological response, **3**:544–545
  - biohybrid, **3**:542
  - chemical, **3**:542
  - cilia-based, **3**:543, **3**:543*f*

Microrobots *(Continued)*
  gamete/zygote transport, **3**:545–548
  helical, **3**:543
  Janus, **3**:542
  optimization of microrobots efficiency, **3**:541–544
  physically-driven, **3**:542–544
  physical principles of microrobots motion at low Reynolds numbers, **3**:541
  tubular, **3**:542
Microscopic polarizability, **3**:684–687
  microscopic response determination, **3**:685–686
  nonlocal response, **3**:685
  oscillator strength, **3**:686–687
  polariton dispersion equation, **3**:686
Microscopic theory, **2**:449–450
Microstructure
  backscatter electron contrast image, **3**:474*f*
  columnar, **3**:471, **3**:471*f*
  columnar thin film multilayer, **3**:472*f*
  definition, **3**:465
  duplex, **3**:478–479
  grain boundaries in single phase, **3**:472–474, **3**:473*f*
  grain boundary character distribution, **3**:472*f*
  grain size distributions, **3**:469*f*
  lamellar, **3**:479
  phase transformations and, **5**:536–538, **5**:537*f*
  polycrystalline, **3**:465–466
  prototypical, **3**:465–466
  single phase, **3**:466–474, **3**:467*f*
  steels, **5**:539*f*
  tabular alumina, **3**:470*f*
Microtexture, **3**:496
Microtubules, **4**:598, **4**:600–601
Micro-whirls (MW) model, **2**:651–652
Mie scattering, **4**:215, **4**:223, **4**:304
Miller indices, **2**:258, **5**:44
Miner's rule, **3**:821
Miniaturization, **1**:237
Minimum free energy pathway (MFEP), **4**:661
Misorientation, **3**:495
Mitochondria, **4**:598
Mixed-state phase diagram, **2**:575
Mixed-state ptychography, **4**:86–87
ML. *See* Machine learning (ML)
ML-based neural networks, **3**:828
MnO$_6$ octahedron, **2**:94*f*
Mobile charge carriers, **2**:516
Mobility, **2**:408, **3**:156
M$_2$O–B$_2$O$_3$ glasses, **3**:183
Mode coupling theory, **3**:176
Mode-locking, **4**:421–423
Model of particle, quantum rings, **3**:417–419
Models of dielectric dispersion, **3**:814–815
Moderately damped regime (MDR), **2**:728–730, **2**:728*f*
Modular isotopes, **1**:275
Modular tensor, **1**:271
Modulated or derivative reflectivity spectrum, of Ge, **1**:762, **1**:762*f*
Modulation spectroscopy, **5**:125
Moiré Brillouin zone, **2**:288–289
Moiré excitons, **3**:708*f*, **3**:722
Moiré pattern, **2**:288–289, **2**:314–315
Moiré superlattice, **1**:725–726, **2**:292–293
Molecular beam epitaxy (MBE), **1**:697, **2**:536–539, **2**:536*f*, **2**:545–546, **3**:338, **3**:339*f*, **3**:426–427, **5**:249–250, **5**:252–253, **5**:253*f*
  growth chamber, **3**:339*f*
  growth modes, **3**:339–340, **3**:339–340*f*
Molecular clusters
  applications, **5**:699
  syntheses and characterizations, **5**:697–699
  theoretical principles, **5**:695–697, **5**:696–697*f*
Molecular dynamics (MD), **1**:733, **4**:543–544, **4**:550–551, **4**:658, **5**:312–313, **5**:755–757
Molecular excitons, **3**:707
Molecular field model, **2**:27–29, **2**:31–32, **2**:43–46, **2**:55–56
Molecular liquids, **3**:168–169
Molecular orbital theory, **2**:72
Molecular replacement method, **5**:45–46
Molecular transform, **5**:43
Molten semiconductors, **3**:168
Moment alignment, **2**:27
Momentum-resolved scanning transmission electron microscopy (MR-STEM), **4**:98, **4**:106–107
Monoid, **1**:276–277
Monolayer graphene
  ambipolar electric field effect, **1**:608
  band structure and tight-binding model, **1**:605
  Berry phase, **1**:607
  crystal structure, **1**:604–605
  Dirac effective-mass model, pseudospin and chirality, **1**:606
  integer quantum Hall effect, **1**:610
  Klein tunneling, **1**:608–610
  plasmons in, **1**:766–769
  symmetries, **1**:606–607
  trigonal warping and tight-binding parameters, **1**:607–608
Monte Carlo (MC) method, **4**:538–539, **5**:97–98, **5**:754
Mooij–Schön plasma modes, **2**:673
Moore-Read state, **1**:330–331, **1**:550–551
Moore's law, **1**:237, **3**:754–755, **3**:756*f*
Morphisms, **1**:276
Morphological instability, **5**:244–245
Mössbauer effect, **4**:209
Mössbauer spectroscopy, **4**:206, **4**:210, **4**:214
  emission, **4**:24–25
  hyperfine interactions, **4**:21–24
  internal conversion, **4**:20–21
  magnetic orientation, **4**:27
  nucleus and nuclear radiation, **4**:16–18
  phase analysis, **4**:26
  site determination, **4**:26–27
  synchrotron based methods, **4**:24
Mott–Hubbard metal–insulator transition, **1**:916–918, **1**:917*f*
Mott–Hubbard transition, **1**:914–921, **1**:919*f*, **5**:486
Mott insulator, **1**:914–916, **1**:920–921, **2**:101, **3**:137–139, **3**:701–702
Mott transition, **1**:910–911, **1**:911*f*
MQT. *See* Macroscopic quantum tunneling (MQT)
MRAM. *See* Magnetic random-access memory (MRAM)
MTJ. *See* Magnetic tunnel junction (MTJ)
Multiband superconductors, **2**:605*f*
Multicanonical MD (McMD) simulation, **4**:661
Multi-channel Kondo effect, **3**:396–397
Multicircle diffractometry
  diffraction equation, **5**:764–765
  equivalent angle settings, **5**:766
  five-circle and six-circle diffractometers, **5**:769
  four-circle diffractometers, **5**:767–768
  four-circle Eulerian geometry, **5**:762–764
  operating modes, **5**:766
  orientation matrix determination, **5**:765–766
  scattering data, **5**:762, **5**:763*f*
Multi-component catalysts, **5**:729
Multicomponent fractional quantum Hall effect, **1**:297–300
Multidimensional ptychography, **4**:88–91, **4**:91*f*
Multiexcitons, **3**:708*f*, **3**:715–718
Multiferroics, **1**:807–808
  particles, **2**:123
  ultrafast dynamics in, **3**:700–701
Multi-fractal analysis, **3**:215–216
Multigap superconductors, **2**:599
Multilayer paint stacks
  accelerated corrosion protocols, **3**:621–622
  terahertz NDE of multilayer paints, **3**:618–620
  terahertz NDE of paint corrosion, **3**:620–621
Multiorbital Hubbard model, **1**:920–921
Multiple Andreev reflection (MAR), **2**:627–628
Multiple electron beam system, **4**:91
Multiple memories, **2**:380
Multiple pulling technique, **5**:193–194
Multiple scattering theory, **5**:566–567
Multiple wavelength anomalous diffraction (MAD), **5**:47
Multiplication, dislocations, **5**:406–407
Multislice ptychography, **4**:88, **4**:89*f*
Multi-terminal thermal conductance experiment, **1**:355–356
Multivariate statistics (MS), **4**:661
Multi-wall carbon nanotube (MWNT), **5**:708
Muon-spin rotation (μSR), **2**:33
Muscle contraction, **4**:696
Mutual information, **4**:524–525
MZMs. *See* Majorana zero modes (MZMs)

N

Nacken Kyropulous method, **5**:194
Nambu–Goldstone modes, **1**:149–152
Nanocatalysts, **5**:745–746

Nanocrystalline alloys, **2**:81, **2**:81*t*
Nanocrystals, **1**:763
Nanodimensional superconducting quantum interference devices (nanoSQUIDs)
  applications, **2**:708
  cantilevers, **2**:706, **2**:708
  definition, **2**:702
  $I(V)$-characteristics, **2**:705
  limitations, **2**:702–703
  long-term stability, **2**:709
  operating temperature, **2**:703
  scanning system, **2**:703, **2**:709–710
  spin sensitivity, **2**:706
  stationary applications, **2**:708
Nanoelectro mechanical system (NEMS), **2**:706
Nano-ionics, **3**:154–156
Nanoparticles (NPs), **5**:694–696, **5**:698–699
  metal immobilized, **4**:309
  metallic suspension, **4**:308–309
Nanopatterned superconductors, **3**:373–377
Nanopores, **4**:682
Nanoporous gold (NPG), **5**:519–520
Nanoscaled magnets
  magnetization dynamics studies, **2**:125
  magnetometry studies, **2**:124–125
  nanostructure tomographic imaging, **2**:125–126
  spintronic and spinorbitronic characterization, **2**:126
Nanoscale phase separation, **3**:437–438, **3**:445*f*
Nanosculpturing, **2**:702–703, **2**:708–709
Nanostructured superconductors
  electromigration, **3**:369–370
  ion-induced nanostructures, **3**:370–373
  lithography and ion-beam milling, **3**:369
  templating strategies, **3**:370
Nanostructures, **3**:325–327, **3**:326*f*, **3**:329
  atomic layer deposition, **5**:725, **5**:725*f*, **5**:726*t*
  calculated electronic levels, **3**:506–507
  cavity green function, **3**:657–658
  cavity polariton, **3**:658–659
  computational approaches, **3**:505–506
  droplet-based self-assembly, **2**:550
  EM Green function, **3**:658–659
  microscopic response, **3**:655–657
  nondipole-type excited states, **3**:662
  nonlocality-enhanced electric quadrupole transition, **3**:659–661
  self-assembly, **2**:549–550
  strain-induced self-assembly, **2**:549
  ultrafast radiative decay, **3**:663
  vapor–liquid–solid (VLS) growth of nanowires, **2**:550
Nano-superconductivity, **3**:457, **3**:460
Nanotechnology, **5**:422, **5**:422*f*
Nanotubes, **1**:763
$Na_2O–SiO_2$ glass
  modified random network model for, **3**:183–184, **3**:184*f*
  structure of, **3**:182, **3**:183*f*
Narrow bands, **1**:914–915
Natural optical activity, **3**:671–672
Natural organic polymers, **5**:424
Natural to artificial photosynthesis, **4**:737, **4**:738*f*
Nature of disorder, **3**:192–193
Nature's novel materials, **4**:594–596
  biological context
    coherent transfer processes, **4**:597–598
    new (and old) avenues of interest, **4**:600–601
    quantum tunnelling, **4**:596–597
    spin dynamics, **4**:598–600
  history of, **4**:594
  methods and models, **4**:595–596
  non trivial quantum effects, **4**:594–595
NbN-based nanoSQUIDs, **2**:710
Near-α titanium alloys, **5**:639
Nearest-neighbor tight-binding model, **5**:131
Nearly free-electron model, **1**:756
Near-room-temperature magnetic refrigeration, **2**:85, **2**:90–92
Necklace braid group, **1**:276
Néel temperature, **2**:31
Nematic (N) phase, LC
  biaxial nematic phase, **5**:376–377, **5**:377*f*
  blue phases (BPs), **5**:378, **5**:379*f*
  cholesteric phase, **5**:377, **5**:378*f*
  director, **5**:375–376
  ferroelectric nematic (N_F) phase, **5**:379–380, **5**:380*f*
  twist-bend nematic (N_{tb}) phase, **5**:378–379, **5**:380*f*
  uniaxial N phase, **5**:376–377, **5**:376*f*
Neodymium–iron–boron alloys, **2**:83, **2**:83*t*
Nernst effect, **4**:494
Nernst equation, **4**:696, **4**:707
Nernst–Planck equation, **3**:146
Network-based models (NMs), **4**:661
Network formers, **3**:183
Network model, **1**:570–573
Network modifiers, **3**:183
Neumann's principle, **5**:57
Neuronal exocytosis, **4**:696
Neutral fermion gap, **1**:338
Neutral gap, **1**:338
Neutrino physics, **2**:796
Neutron, **4**:444–446
  beam transport, **4**:454–455
  compact neutron sources, **4**:449–450
  conceptual foundations, **5**:429–430
  diffraction, **2**:26, **2**:33–34, **2**:34*f*, **5**:9, **5**:430–431
  energies and properties, **4**:451
  fission sources, **4**:447–448
  halo neutrons, **4**:450–451
  historical evolution, **4**:446
  inelastic scattering, **5**:431–432
  moderation of, **4**:452–453
  optics, **5**:435–436
  polarization analysis, **5**:433–434
  polarized, **5**:432–433
  scattering, **1**:948–950, **1**:949*f*, **4**:444–446
  spallation sources, **4**:448–449
  spin echo, **5**:434
  steady-state and pulsed neutron sources, **5**:434–435
  transmutation doping, **2**:494–495
Neutron gap, **3**:27
Neutron stars
  flux tubes and domains in, **3**:26–27
  higher-spin pairing, **3**:28
  imbalanced pairing, **3**:24–25
  induced interactions, **3**:27
  microscopic theories, **3**:23–24
  neutron gap, **3**:27
  non-adiabatic effects, **3**:27
  proton gap, **3**:27–28
  quantized vorticity and rotation of, **3**:25–26
  superfluid fraction, **3**:28
  thermal evolution, **3**:27
New macroscopic quantum state, imaging, **3**:71–72
Newton's law, **3**:201
Nickel
  blade alloys, **5**:584*t*
  disk alloys, **5**:585*t*
  superalloy, **5**:587–591
Nickel borocarbides, **2**:606, **2**:607*f*
Nickel–iron alloys, **2**:80
Nickel–iron-based superalloy, **5**:585–586, **5**:586*f*
Niobium, **3**:454
Nipkow spinning disc confocal microscopy, **4**:111
Nitride-based alloys, **3**:237
Nitride superconductors, **2**:703, **2**:709
Niu–Thouless–Wu formula, **1**:91, **1**:662
NLSM. *See* Nonlinear sigma model (NLSM)
Noise, **3**:776–777
  and loss of information, **1**:256–257
  spectroscopy, **1**:1013
Noise measurements, **1**:403*f*
  shot noise in dc transport, **1**:355
  thermal tunneling noise, **1**:355
Noisy intermediate-scale quantum (NISQ), **1**:259–260
Non-Abelian anyon collider, **1**:356
Non-Abelian anyon in non-Abelian vortex
  discrete symmetry of vortices, **2**:786–787
  existence of zero energy states, **2**:785–786
  topology of vortex-bound states, **2**:787–788
Non-Abelian anyons, **1**:272, **1**:279
  braid group and quantum statistics, **2**:757–758
  Burau, **1**:475
  Fibonacci sequence, **1**:475, **2**:759–760
  generalities, **1**:493–494
  HQVs in SCs, **2**:765–767
  HQVs with Majorana zero modes in SF^3He, **2**:763–765
  Ising anyons, **2**:759
  Ising gas, **1**:475
  Kitaev model in one dimension, **1**:494–496
  Majorana modes, **1**:496–497
  Majorana zero modes as Ising anyons, **2**:761–763
  superconducting nanowires, **2**:767
  symmetry-protected, **2**:768–771
  topological quantum computation, **1**:296–297, **2**:768
  vortex anyons, **2**:760–761

Non-Abelian anyons *(Continued)*
  vortices in Fe(Se,Te), **2**:768
  Yang-Lee anyons, **2**:760
Non-Abelian Berry connection, **1**:673
Non-Abelian gauge theory, **1**:34
Non-Abelian quasiparticles, **1**:341–342
Non-Abelian states, **1**:296–297
  bulk energy gap, **1**:346–348
  quasiparticle charge and braiding, **1**:351–352
  quasiparticle charge and edge exponents, **1**:350–351
  spin polarization, **1**:348–350
  upstream neutral mode, **1**:351
Non-Abelian statistics, **1**:371, **1**:380
Non-Abelian vortex anyons
  BN phases in spin-2 BEC, **2**:774–775
  cyclic phase in spin-2 BEC, **2**:775–776
  D_2-BN liquid crystals, **2**:773–774
  D_4-BN liquid crystals, **2**:774
  fusion rules for, **2**:776–777
  nematic liquid crystals, **2**:772
  spinor BEC, **2**:774
Non-adiabatic effects, **3**:27
Non adiabatic torque, **2**:143–144
Non-capillary Shaping (NCS) method, **5**:194–195
Noncommutative Brillouin zone (NCBZ), **5**:272–273
Noncontact atomic force microscopy (nc-AFM), **4**:54–55, **4**:56*f*
Nondestructive evaluation (NDE) methods, **3**:602
Nondipole-type excited states, **3**:662
Nondisruptive deletion, **4**:645
Nonepitaxial films, **5**:263–264
Nonequilibrium dynamical mean field theory
  cluster DMFT, **1**:1000
  extended DMFT (EDMFT) formalism, **1**:1000–1001
  Floquet DMFT, **1**:999–1000
  formalism, **1**:997–998
  GW+EDMFT, **1**:1001
  impurity solvers, **1**:998–999
Non-equilibrium Green's function (NEGF) method, **1**:993–994
Non-equilibrium Kondo effect, **3**:396
Non-equilibrium Monte Carlo (NEMC), **5**:755
Non-equilibrium physics, **1**:962–963
Non-equilibrium statistical mechanics, **4**:560
Non-equilibrium steady state (NESS), **1**:967–968
Nonferromagnetic types of magnetic orders, **2**:31
Non-heat-treatable alloys, **5**:578–579
Non-Hermitian photonics, **3**:360–363
Nonideal anyon gas
  almost-bosonic anyons, **1**:468–469
  almost-fermionic anyons, **1**:469–470
  extended anyon gas, **1**:467–468
  interactions and fields, **1**:472–473
  lowest Landau level (LLL) anyons, **1**:473
  magnetic Thomas–Fermi theory, **1**:470–472
  point-interacting anyons, **1**:472
Noninteracting Bose gases, **3**:125–126
Noninteracting limit, **1**:916
Non-ionizing spectrum of radiations, **4**:709, **4**:710*f*
Nonlinear electron dynamics, **5**:128
Nonlinearity, physical origin of, **4**:383–384
Nonlinear magnonic devices, **2**:173
Nonlinear optical (NLO) method, **3**:696, **5**:667
Nonlinear optics, **1**:959, **3**:680–681
  physical origin, **4**:383–384
  second-order nonlinear effects, **4**:384–387
  stimulated Brillouin scattering (SBS), **4**:391
  stimulated Raman scattering (SRS), **4**:389–391
  third-order nonlinear effects, **4**:388–389
Nonlinear phononics effect, **3**:513
Nonlinear polarization and susceptibilities, **4**:247–248
Nonlinear-resistive (RSJN) model, **2**:622
Nonlinear sigma model (NLSM), **1**:35, **1**:38–41, **1**:47–48, **3**:223–226
Nonlocal dielectric response, **3**:808–809
Nonlocality-enhanced electric quadrupole transition, **3**:659–661
Nonlocal magnetic interactions, **2**:116
Nonlocal transport, **2**:304–306
Nonmagnetic Weyl semimetals, **4**:347–350, **4**:349*f*
Nonnaturally derived fields, **4**:709
Nonparabolicity, **4**:134–136, **4**:145
  bandstructure, **4**:142, **4**:142*f*
  polaron coupling, **4**:143
Nonradiative decay, **1**:861–862
Nonresonant chemical effect, **4**:306
Nonresonant inelastic X-ray scattering (NIXS), **4**:197–199, **4**:198*f*
Nonresonant XES, **4**:201
Nonsilicate glass-forming systems, **3**:185
Non-standard optical lattice system, **3**:141–142
Nonsymmorphic space groups, **5**:64, **5**:66
Nonthermal pathways, laser excitation, **3**:512*f*
Nontrivial quantum effects, **4**:594
Nonuniform perpendicular spin configuration, **2**:68
Non-volatile memory (NVM)
  classification, **3**:553–554, **3**:553*f*
  commodities and consumer products, use in, **3**:552–553
  electrically erasable and programmable read-only memories (EEPROMs), **3**:553–554, **3**:556–558, **3**:557*f*
  electrically programmable read-only memories (EPROMs), **3**:553–556, **3**:556–557*f*
  ferroelectric RAM (FRAM), **3**:554, **3**:564, **3**:567–570, **3**:568–570*f*, **3**:574
  flash EEPROMs (*see* Flash EEPROMs)
  flash memories, **3**:553
  in-memory computing (IMC), **3**:564, **3**:573–574
  magnetic RAM (MRAM), **3**:554, **3**:564–567, **3**:564*f*, **3**:574
  non-volatile random-access memories (NV-RAM), **3**:553–554, **3**:564–573
  phase-change memories (PCMs), **3**:554, **3**:564, **3**:570–571, **3**:570–571*f*, **3**:574
  professional systems, use in, **3**:552–553
  read-only memories (ROMs), **3**:553–555, **3**:555*f*
  resistive RAM (RRAM), **3**:554, **3**:564, **3**:571–575, **3**:572–573*f*
Non-volatile random-access memories (NV-RAM), **3**:553–554
  chalcogenide materials, **3**:564
  ferroelectric RAMs (FRAM), **3**:564, **3**:567–570, **3**:568–570*f*, **3**:574
  magnetic RAMs (MRAM), **3**:564–567, **3**:564*f*, **3**:574
  phase-change memories (PCM), **3**:554, **3**:564, **3**:570–571, **3**:570–571*f*, **3**:574
  resistive memories (RRAM), **3**:564, **3**:571–575, **3**:572–573*f*
Non-volatile thin film memory, **2**:15
Normalized root-mean-square-error (NRMSE), **4**:87–88
Novel flat-band emulator, **3**:141–142
NPs. *See* Nanoparticles (NPs)
Nuclear dynamics, **1**:875–876
  forces acting on nuclei, **1**:875
  interatomic force constants, **1**:875–876
Nuclear magnetic resonance (NMR) spectroscopy
  limitations, **4**:629–630
  principles, **4**:621–622
  protein folding, **4**:623–629
Nuclear resonance, **4**:206–207
Nuclear resonant inelastic x-ray scattering (NRIXS), **4**:206, **4**:208–213
Nuclear resonant scattering (NRS)
  cross section, **4**:209–210
  experimental procedure, **4**:213, **4**:214*f*
  index of refraction, **4**:212–213
  level splitting, **4**:211
  NRIXS, **4**:208–213
  observation, **4**:210
  phonon density of states, **4**:210–211
  properties of, **4**:206–207
  scattering processes, **4**:207–208
  SMS, **4**:211
Nuclear spin, **2**:226, **2**:485, **2**:493–494
Nucleation
  crystal, **3**:465–466, **3**:470
  and epitaxial growth modes, **2**:546–548, **2**:546–547*f*
  heterogenous, **3**:471
  homogeneous, **3**:471
Nucleation–condensation mechanism, **4**:647
Nuclei of strain, **3**:593
Nucleus–nucleus Coulomb repulsion, **5**:209–210
Null-model random network, **4**:687
Numerical aperture (NA), **4**:111–112
Numerical approximation and analysis
  approximation of functions, **5**:750
  integral equations, **5**:751–752
  ordinary differential equations, **5**:751
  systems of linear equations, **5**:752
Numerical methods for localization

  diagonalization, **3**:213
  energy-level statistics, **3**:215
  finite-size scaling, **3**:216
  localization and many-body interactions, **3**:216–217
  machine learning, **3**:217
  quasi 1D methods, **3**:213–214
  renormalization and decimation methods, **3**:214–215
  wavefunction statistics and multi-fractal analysis, **3**:215–216
Numerical phase transition model, **3**:94–95
Numerical renormalization group (NRG) method, **3**:384
Numerical-type DOEs, **5**:96–99, **5**:97–99*f*
Nyquist plots, **4**:269, **4**:271

O

Object beam, **5**:89
Odd-rank tensors
  ferroelectricity, **5**:57–58
  piezoelectricity, **5**:58
  pyroelectricity, **5**:57–58
Off-axis hologram
  reconstruction, **5**:91, **5**:91*f*
  recording, **5**:90, **5**:91*f*
Off-axis reference beam optical holography, **5**:88–89
Ohm's law, **1**:686, **3**:251, **3**:273, **4**:494, **4**:695–696
Olfaction and tunneling, **4**:589–590
On-chip power divider, for JAWS, **1**:16–20
On-demand single-electron sources, **1**:925–926
One-dimensional (1D) Fibonacci quasicrystal
  1D diffraction pattern, **5**:321, **5**:322*f*
  2D description, **5**:321, **5**:321*f*
  2D diffraction pattern, **5**:321, **5**:322*f*
One-dimensional (1D) quantum physics, **1**:906–907, **1**:906*f*, **1**:912–913
  collective excitations, **1**:907–908, **1**:908*f*
  complications, **1**:910–912
  coupled chains, **1**:911–912
  effect of disorder/quasiperiodic potentials, **1**:911
  fundamental concepts, **1**:906–910
  methods, **1**:909–910, **1**:910*f*
  Mott transition, **1**:910–911, **1**:911*f*
One-dimensional (1D) statistical anyons, **1**:508–509, **1**:509*f*
One-dimensional (1D) systems, **1**:896
  ballistic channels, conductance quantization, **1**:898*f*
  electrostatically-defined, **1**:898*f*
  experimental realization, **1**:896–899
  interaction effects, **1**:899–902
  quantum transport and electron-electron interactions, **1**:894–903
One-dimensional (1D) topological superconductors, **2**:796–797
One-electron energy, **2**:61, **2**:61*f*
One-stage Wilkinson divider
  current-voltage characteristic of, **1**:19, **1**:19*f*
  sine waveform, time and frequency domain of, **1**:20, **1**:20*f*
One transistor and one capacitor (1T-1C) memory cell, **3**:567
Onsager-Casimir symmetry relation, **3**:146
Onsager's reciprocity condition, **4**:491
Open integer-spin chains, **1**:48–49
Open-network materials, **5**:390
Open Quantum Materials Database (OQMD), **4**:553
Open quantum system, **1**:967–968, **1**:968*f*, **1**:973–975, **3**:139
Operator product expansion, **1**:31–32
Optical absorption, **3**:668–669, **5**:664–666, **5**:664*f*
Optical ceramics, **5**:418–419
Optical coherence theory, **5**:172
Optical confinement, **3**:773
Optical conjugation, **4**:388–389
Optical density, **4**:109
Optical emission, from SAD's and CD's, **3**:332–333
Optical fibers, **5**:440–441
  attenuation, **5**:809–810
  dispersion, **5**:810–811
  fiber amplifiers and lasers, **5**:812–813
  fiber Bragg gratings, **5**:812
  nonlinear fiber optics, **5**:813–814
  special fibers, **5**:811
  structure and modes, **5**:807–809
Optical holography, **5**:95–96, **5**:102
Optical Kerr effect, **4**:388, **5**:95, **5**:813
  optical switch, **4**:388
  self-focusing, **4**:388
  self-phase modulation, **4**:388
Optical lattices, **3**:79
  minimum, **3**:137–138
  quantum annealer, **4**:540–541
  quantum emulation, **3**:136–137*f*
Optical Lieb lattice system, **3**:141–142
Optically detected cyclotron resonance (ODCR), **4**:139–141, **4**:140*f*
Optically induced spin-galvanic effect
  basic experiments, **2**:180–181
  SIA/BIA spin splitting ratio, **2**:181–182
Optical metasurface, **5**:100
Optical microscopy, **4**:109
Optical modification of superconductivity, **3**:701
Optical orientation of electron spins, **3**:678–679
Optical orientation of spins in semiconductors
  band structure of gallium arsenide, **2**:225
  exchange interaction, **2**:226
  Hanle effect, **2**:230–231
  historical background, **2**:224
  hyperfine interaction with nuclear spins, **2**:226
  interconnections between spin and charge, **2**:231
  magnetic interaction, **2**:227
  optical spin orientation and detection, **2**:227–228
  Pauli principle, **2**:225–226
  photo-generation of carriers and luminescence, **2**:227
  spin interactions, **2**:225–227
  spin-orbit interaction, **2**:226
  spin relaxation, **2**:228–230
Optical path, **4**:109
Optical phonon response, **5**:160, **5**:164
Optical properties
  biaxial crystals, **5**:85
  halide perovskites, **5**:663–670
  two-dimensional systems, **3**:673–674
  uniaxial crystals, **5**:83–85
Optical properties of dielectrics and semiconductors
  Coulomb interaction effects, **3**:672–677
  electromagnetic waves in solids, **3**:666–668
  nonlinear optics, **3**:680–681
  optical absorption, **3**:668–669
  optical reflection and transmission, **3**:668
  photoluminescence, **3**:677–680
  tensor nature of permittivity, **3**:669–672
Optical properties of materials
  complex dielectric function, **5**:152–154
  complex refractive index, **5**:154–155
  Maxwell's equations in medium, **5**:151–152
  optical spectra, **5**:159–160
  polarized light, **5**:156–157
  reflection and transmission property, **5**:155–159
  theoretical models, **5**:160–164
  unpolarized light, **5**:155–156
Optical pulse drive, for JAWS, **1**:16–20
Optical rectification, **3**:511
Optical reflection and transmission, **3**:668
Optical resolution, limits of, **4**:112
Optical spectra, **5**:159–160
Optical spin orientation, **2**:189
Optical switch, **4**:388
Optical theorem (OT), **4**:219–220
Optical transitions, **1**:857, **1**:860*f*, **2**:227, **2**:478, **2**:480–481
Optical trapping, **4**:318–323
Optical tweezers, **4**:215, **4**:317–318
  in air and vacuum, **4**:328–329
  applications, **4**:326–329
  autocorrelation analysis, **4**:325
  Brownian motion in, **4**:323
  equipartition theorem, **4**:324–325
  experimental setup and calibration techniques, **4**:323–325
  mean square displacement analysis, **4**:325
  potential analysis, **4**:325
  single molecule and single cell mechanics, **4**:326–327
  statistical physics and colloidal interactions, **4**:327–328
Optoelectronic properties, halide perovskites, **5**:663–670
Optoplasmonic hybridization, **3**:363
Orbital Kondo effect, **3**:393
Orbital magnetization, **1**:676–677
Orbital moment, **2**:26
Ordered self-assembled quantum ring arrays, **3**:349–352, **3**:350*t*, **3**:350–352*f*
Order-N methods, **5**:571–572

Orders of magnitude, **4**:234–235
Ordinary differential equations, **5**:751
Organic materials, **5**:94
Organic perovskite ($CH_3NH_3PbI_3$), **4**:518–520
Organic semiconductors, **2**:414
Orientational polarization of solids, **1**:808–810
Orientation distribution function (ODF), **3**:489
OR plane, **3**:554–555, **3**:555*f*
Oscillator strength, **3**:686–687
Oscillatory quantity, **4**:231–232
Osteoclasts, **4**:739
Osteoporosis, **4**:739
Osteoproduction, **4**:740, **4**:741*f*
Overdoped regime, **2**:588
Overlap constraint set (OCS), **4**:79–80
Ovonic threshold switch (OTS) device, **3**:571
Oxidation, **5**:446–447
Oxide quasicrystals, **5**:320
Oxides, atomic layer deposition of, **5**:721
Oxygen dispersion-strengthened (ODS) copper, **5**:613

P

Packaging, **3**:752–753, **3**:753*f*
Padé approximation, **5**:750
Pair correlation function, **1**:783–784
Paired quantum hall states, **1**:329
Pairing evidence, **1**:339–340
Pairing fluctuation, **3**:14–15, **3**:18
Pairing symmetry, **2**:570
Parabolic band approximation, **1**:851–852
Parabolic well model, **3**:299–300
Parallel pores, **5**:356
Paramagnetic Curie temperature, **2**:29
Paramagnetic systems, magnetic susceptibility in, **4**:720, **4**:720*f*
Paramagnetic tagging, of diamagnetic proteins, **4**:729
Paramagnetism, **2**:27, **2**:35–38
Paramagnetism-based restraints, **4**:719, **4**:726–727, **4**:726*f*
Paramagnons, **3**:276
Parent Hamiltonian and Haldane pseudopotentials, **1**:293
Paris' model, **3**:824
Parity anomaly, **1**:79–83
Partial coherence, **4**:86–87
Particle-fluid interactions, **5**:681–683
Particle flux, **4**:489
Particle-hole asymmetry, **1**:520–521
Particle packing, **5**:684–687
Particle-particle interactions, **5**:681–683
Particle strengthening, **3**:855–856, **3**:856*f*
Particle-vortex duality, **1**:119
  3D XY model, **1**:116–118
  in 2+1 dimensions, **1**:116–125
Partition noise, **5**:179–180
Parton theory, **1**:300
Passive membrane
  bound water, **4**:704
  lipid region, **4**:704
  membrane proteins, **4**:704
  sectoral capacitance, **4**:703
Patch clamp technique, **4**:690, **4**:693
Path integral formulation for ferromagnets and antiferromagnets, **1**:39
Path integral Monte Carlo (PIMC) method, **1**:941–942, **5**:759–760
Pauli blockade, in graphene double quantum dots, **2**:252–253, **2**:253*f*
Pauli exclusion principle, **1**:590–591, **1**:758, **1**:780–781, **1**:886, **1**:895, **2**:73, **2**:75, **3**:3
Pauli SO coupling, **2**:186–187
Pauli spin susceptibility, **2**:60
Pauli–Villars scheme, **1**:84
PCMs. *See* Phase-change memories (PCMs)
PCTFs. *See* Phase contrast transfer functions (PCTFs)
Pearlite, **5**:537
Peierls phases, **1**:633–635
Peltier effects, **4**:493
Penetration depth, **2**:568–569
Penrose–Onsager condensation, **3**:90–92
Penrose tiling, **5**:291, **5**:292*f*, **5**:295, **5**:296*f*
Percolative transition, **2**:96–97, **2**:96*f*
Perfect gas, **4**:565–567
Periodically driven quantum systems, **1**:967–968, **1**:968*f*, **1**:973–975
Periodic antiferromagnets, **5**:4*f*
Periodic crystals, **5**:318–319, **5**:329–330
Periodicity and lattices
  lattices in two and three dimensions, **5**:17–22
  reciprocal lattice, diffraction, and electronic band structure, **5**:22–25
  variations of periodicity, superstructures and aperiodicity, **5**:25–28
Periodic soil model, **3**:521–523
Periodic table, **2**:799–800, **2**:800*t*, **5**:210*f*, **5**:695–697, **5**:699–700
Permalloys. *See* Nickel–iron alloys
Permanent magnet, **2**:2, **2**:4–6, **2**:19, **2**:23
Permanent mold cast, **5**:557–558
Permittivity, **1**:809, **3**:812–813
Perovskites, **5**:466–467, **5**:467*f*. *See also* Halide perovskites
Perovskite-type crystals, **3**:513
Perpendicular magnetic anisotropy (PMA), **2**:115–116, **2**:163
Persistent current, **3**:6, **3**:422
Persistent spin helix (PSH) state, **2**:195–197, **2**:195*f*, **2**:198*f*
Perturbation theory, **1**:29, **2**:61–62
Perturbative correction, **3**:229
Pfaffian function, **1**:369–373
Pfaffian state, **1**:330–331
  bilayer graphene, **1**:377–380
  composite fermions weak pairing, **1**:331
  conformal field theory description, **1**:330–331
  edge theory, **1**:331
  graphene monolayer, **1**:377
Phase-change memories (PCMs), **3**:554, **3**:564, **3**:574
  advantages, **3**:571
  cells, cross section of, **3**:570, **3**:570*f*
  chalcogenide selector device, **3**:571, **3**:571*f*
  cross-point array sandwiched between M2 and M3 metal layers, **3**:571, **3**:571*f*
  $Ge_2Sb_2Te_5$ (GST), **3**:570–571
  X-point, **3**:571
Phase-charge duality, **2**:675–676
Phase-conjugate mirror, **4**:389
Phase contrast, **4**:65, **4**:66*f*
Phase contrast transfer functions (PCTFs), **4**:83–84, **4**:88, **4**:90*f*
Phase-detour encoding, **5**:96
Phase diagrams, of high-temperature superconductors
  CDW fluctuations, **2**:585
  charge order, **2**:585
  magnetic phase diagram, **2**:590
  overdoped regime, **2**:588
  precursor pairing, **2**:584–585
  pseudogap regime, **2**:586
  spectroscopy and hidden orders, **2**:590
  spin fluctuations, **2**:583–584
  spin order, **2**:583
  strange metal regime, **2**:588–589, **2**:589*f*
  stripe order, **2**:586–588, **2**:587*f*
  temperature-doping phase diagram, **2**:582–583
  unconventional superconductivity, **2**:584, **2**:584*f*
  uniqueness of cuprates, **2**:581–582, **2**:582*f*
Phase diffusion (PD), **2**:729
Phase dynamics, **2**:725–730, **2**:727–728*f*, **2**:732–733
Phase functions, **5**:8–9
Phase locked loop (PLL), **4**:55
Phase-matching, **4**:249–251, **4**:254–255, **4**:385–386, **4**:385*f*
Phase-ordering dynamics
  evolution around nonthermal fixed points, **3**:106–109
  scaling hypothesis and late-time coarsening, **3**:104–106
Phase problem, in crystallography, **5**:45
Phase retrapping, **2**:729
Phase separation (PS), **2**:96–97, **3**:437
Phase shifting digital holography, **5**:99–100
Phase slip, **3**:8
Phase space averages, **4**:561
Phase stability, **1**:735–738
  alloy solutions, **4**:501–503
  classification of phase transformations, **4**:499–500
  competitive phase selection and metastability, **4**:504–505
  constrained equilibrium, **4**:505–506
  equilibrium, **4**:498
  in metallic alloys, **5**:512–516
  nucleation—controlled reactions, **4**:504
  phase transformation energetics, **4**:503–504
  pure components, **4**:498–499
Phase transformations
  in metallic alloys, **5**:512–516
  and microstructures, **5**:536–538, **5**:537*f*
  thermodynamics and kinetics, **5**:512–513
Phase transitions, **1**:158–159, **2**:583, **2**:586, **2**:587*f*

Phase volume holograms, **5**:93
Phasons
  collective excitations, **2**:450–452
  diffuse scattering, **5**:330–331
  flips, **5**:288
  modes, **5**:330–331
Phenolic resins, **5**:425
Phenomenological equations, **4**:489
  for thermoelectric effects, **4**:491
  for thermomagnetic phenomena, **4**:493–494
φ-value analysis, protein folding, **4**:645–647
Phillips–Kleinman cancellation theorem, **1**:834–836
Phonomagnetism, **3**:514
Phonons, **1**:947–954, **1**:950*f*, **3**:274, **3**:513
  assisted transitions, **5**:122–123
  confined vibration modes, **4**:163–167
  in crystalline materials, **4**:203
  damping, **5**:414–415
  density of states, **4**:210–211
  dispersion, **2**:486–487, **5**:282–284, **5**:283–284*f*
  fluctuations, **5**:330–331
  folded vibration modes, **4**:168–170
  heat transport, **3**:276
  interface vibration modes, **4**:167
  IXS methodology, **4**:202–203, **4**:202*f*
  polaritons, **3**:674–675
  spectra and damping, **5**:413–415
  surface vibration modes, **4**:167–168
Phosphides, atomic layer deposition of, **5**:722–723
Phosphorus nuclear spin, **4**:599–600
Photo cathodes, **4**:465–466, **4**:466*f*
Photoconducting antennas (PCA), **3**:510–511, **3**:602
Photodetection, **5**:167, **5**:172
Photodetectors, **3**:763–765
Photodiodes (PD), **1**:16–17, **3**:763–765
Photoelectron spectromicroscopy
  development, **4**:30
  electron-optics approach, **4**:33
  performance, **4**:33–34
  photon-focusing approach, **4**:31–32
  recent developments, **4**:35
  resolution and sensitivity, **4**:34–35
  two approaches to, **4**:30–31
Photoemission from layered crystals, **3**:807–808
Photoemission Si, **2**:481–482
Photo-generation of carriers and luminescence, **2**:227
Photo-induced force microscopy (PIFM), **3**:659–661, **4**:60
Photo-induced phase transition, **1**:986
Photolithography, **3**:753–754
Photoluminescence, **3**:237, **3**:313–315, **3**:677–680
Photomultiplier tube, **4**:110
Photon antibunching, **5**:168, **5**:178–179, **5**:179*f*
Photon blockade effect, **1**:961
Photon bunching, **5**:168, **5**:179, **5**:179*f*
Photon correlation, **4**:226
Photon-focusing approach
  focusing mirrors, **4**:31–32
  Fresnel zone plates, **4**:32
  refractive lenses and compound refractive lenses, **4**:32
  Schwarzschild objectives, **4**:32
Photon gun, **3**:532
Photonic bands, **3**:739
  defect states, **3**:744–746
  measurement, **3**:746–747
  photonic crystal slabs, **3**:743–744
  properties, **3**:739–740
  theoretical methods, **3**:740–741
  three-dimensional photonic crystals, **3**:741–742
  two-dimensional photonic crystals, **3**:743
Photonic crystal slabs, **3**:743–744
Photonic force microscopy, **4**:318
Photonic gap, **3**:739
Photonic quantum Hall (QH) effects
  losses and non-Hermitian topological phases, **1**:580
  optical nonlinearities, **1**:581
  pre-quantum Hall era, **1**:576
  quantum Hall era, **1**:576–577
  routes to topological bands, **1**:578–580
  Schrödinger formalism for electromagnetism, **1**:578
  symmetry-breaking perturbations, **1**:580–581
  topological lasers, **1**:582–583
  topological photonics era, **1**:577
  topological waveguides and cavities, **1**:581–582
Photon number distribution, **5**:171–172
Photon-phonon coupling, **3**:514
Photon polarization, **3**:332–333
Photon statistics and coherence theory
  beam splitter (BS), **5**:168, **5**:174, **5**:178–183, **5**:179–182*f*
  Brown–Twiss correlations, **5**:168, **5**:178–179, **5**:178–179*f*
  first-order coherence, **5**:172–175, **5**:173–174*f*
  Poissonian statistics, **5**:167–168
  second-order correlation, **5**:167, **5**:175–177, **5**:176–177*f*
  sub Poissonian statistics, **5**:167–168, **5**:171–172
  super Poissonian statistics, **5**:169–171
Photophysics, **4**:731
Photopolymers films, **5**:94
Photoproduction, **4**:471
Photorefractive crystals, **5**:94
Photosynthesis, **4**:578–580, **4**:594–598, **4**:731–732, **4**:732*f*
  antenna action, **4**:733–736
  components, **4**:731
  energy conversion and storage, **4**:736–737, **4**:737*f*
  energy transfer, **4**:733–736, **4**:734*f*
  harvesting light, **4**:732–733, **4**:733*f*
  natural to artificial, **4**:737, **4**:738*f*
  photosynthetic machinery, **4**:731–732, **4**:732*f*
  physics of, **4**:731
  pigments of, **4**:732
Photosystems, **4**:733, **4**:734*f*
Photovoltaic (PV) cells, **5**:659, **5**:671–672, **5**:671*f*
PH-Pfaffian state, **1**:332–333
  bulk edge correspondence, **1**:353
  disorder induced Pf-APf domain walls, **1**:353
Physically-driven microrobots, **3**:542–544
Physical metallurgy, **5**:592–593, **5**:593*f*
Physical vapor deposition (PVD), **2**:545, **3**:754, **5**:249–252
  DC sputter discharge, **5**:251*f*
  electron beam heated evaporation source, **5**:250*f*
  evaporation, **5**:250
  ion plating, **5**:252
  sputtering, **5**:250–252
  thermal-spraying, **5**:252
Physical vapor transport (PVT), **5**:205
Physics of integrated circuits
  Moore’s Law, **3**:754–755
  speed and power, **3**:755
Physics of quantum dots, **3**:325–326, **3**:336
  artificial atoms, **3**:329–332
  artificial molecules, **3**:329–332
  colloidal quantum dots, **3**:328
  Coulomb blockade and single electronics, **3**:328–329
  entanglement and quantum gates, **3**:331–332
  magnetic field effects, **3**:329–332
  memory applications, **3**:329
  modeling and simulation, **3**:333–336
  optical emission, from SAD’s and CD’s, **3**:332–333
  planar quantum dots, **3**:326
  self-assembled quantum dots, **3**:327
  silicon nanocrystals, **3**:327–328
  single electronics, **3**:328
  vertical quantum dots, **3**:326
Physikalisch-Technische Bundesanstalt (PTB)
  history, **1**:9
  tasks of, **1**:9
Physiological transmembrane potential, **4**:706–707
Pickup coil technique, **4**:235
Piezoelectrics, **2**:400*f*, **5**:58
  acoustics to solids, **3**:208
  acoustic theory for, **3**:203–205
  ceramics, **5**:439
  polarization vector field, **3**:238
  tube scanners, **4**:52
Piezospectroscopy, **3**:671
Pigments of photosynthesis, **4**:732
Pinhole, **4**:110, **4**:112*f*
Pinned layer (PL), **3**:565
Pinning effects, on flux-flow instability
  effects of uncorrelated disorder, **2**:739–740
  fast dynamics of guided magnetic flux quanta, **2**:741
  low-field crossover in instability velocity, **2**:740
  on self-heating, **2**:740–741
  vortex lattice commensurability effects, **2**:741

Pixel reassignment, **4**:112, **4**:114
Planar dislocation core, **5**:408–409
Planar lipid bilayer, **4**:690
Planar nanoSQUID, **2**:708–710
Planar quantum dots (QDs), **3**:326
  confinement models and energy spectra, **3**:298–301
  electron-electron interactions in QDs, **3**:304–306
  Landau levels *vs.* Fock-Darwin states, **3**:301–303
Planck constant, **1**:555
Plane-wave pseudopotential method (PWPM), **1**:758–762
Plane waves, **1**:756, **4**:405, **4**:405*f*
Plasma analogy and mean field limit, **1**:648–649
Plasma enhanced chemical vapor deposition (PECVD), **1**:14–15, **2**:535, **5**:256
Plasma waves, in metal optics, **4**:375–378
Plasmon-enhanced Raman spectroscopy (PERS), **4**:301–302
  applications, **4**:312–314
  chemical enhancement, **4**:305–306
  electromagnetic enhancement, **4**:302–305
  nanostructures, bulk metal substrates, **4**:310
  plasmonic enhancement, **4**:306–307
  quasi-static approximation, **4**:303–304
  sensitive analytes detection, **4**:307–310
  SERS (*see* Surface enhanced Raman scattering (SERS))
  spatial resolution, **4**:307
  TERS (*see* Tip-enhanced Raman spectroscopy (TERS))
Plasmonic dimer, **4**:305
Plasmons, **4**:198–201
  in biased bilayer graphene, **1**:771–776
  in bilayer graphene, **1**:769–771
  excitation, **4**:152–153, **4**:153–154*f*
  in monolayer graphene, **1**:766–769
Plastic behavior
  applications, **3**:851–852
  deformation fundamentals, **3**:844–847, **3**:845*f*
  deformation microstructure, **3**:847
  hardening behavior, **3**:847–848
  modeling, **3**:850–851
  recovery and recrystallization, **3**:848–850
  texture, **3**:848
  of thin films, **5**:263–265
Plastic deformation of crystals, **3**:844–847
Plasticity, **3**:851
Platinum
  FEBID, **3**:454
  FIBID, **3**:452–454
Plutonium, **3**:207
P/M superalloy, **5**:589–590
Pnictide- and Fe-based superconductors, **2**:608–609
p-n junctions, **2**:410–411
Point charge model, **2**:71
Point contact tunneling, **1**:112–115
Point defect, **1**:856, **3**:156
  control, **5**:185–186
  diffusion, **5**:186
  in insulators, **5**:187–188
  in normal metals and superconductors, **5**:186
  for quantum computing, **5**:189
  in semiconductors, **5**:187
  types, **5**:185
Point groups
  crystallographic, **5**:51–52
  description, **5**:52–54
  general, **5**:51
  symbols for, **5**:78–79
Point-interacting anyons, **1**:472
Point-oriented encoding methods, **5**:96–97
Point spread function, **4**:112
Pointwise scanning of CLSM, **4**:111
Poisson equation, **2**:68–69
Poissonian statistics, **5**:167–168
Poisson noise. *See* Shot noise
Poisson's ratio, **3**:838–839, **3**:841, **5**:392, **5**:393*f*
Polaritons, **3**:674–676, **3**:814, **5**:123–125
  anisotropic media, **2**:500
  in bulk, **2**:499–501
  cavity, **2**:503–505
  dark-state, **2**:505
  definition, **2**:497–498
  dispersion equation, **2**:499–500, **3**:686
  in nanostructures with reduced dimensionality, **2**:503
  in quantum microcavities, **3**:676
  spatial dispersion and additional waves, **2**:500–501
  strong coupling, **2**:499
  surface, **2**:501–503
  theoretical approach, **2**:498–499
  ultrastrong coupling, **2**:499
  weak coupling, **2**:499
Polarity, **5**:455
Polarizability
  cancellation problem, **3**:688
  definitions, **3**:687
  generalization, **3**:688–692
  macroscopic, **3**:684
  microscopic, **3**:684–687
  point ions, **1**:858
  single susceptibility theory (*see* Single susceptibility theory)
  traditional aspects, **3**:683–688
Polarization, **1**:673, **3**:802–805, **3**:803*f*, **4**:276–279, **4**:370, **5**:433–434
Polarized light, **5**:156–157
Polarized neutrons, **5**:432–433
Polarized Raman scattering, **1**:356–357
Polaron absorption, **2**:440–441
Polaron coupling, **4**:143, **4**:144*f*
Polarons in condensed matter
  coherent and incoherent polaron transport, **2**:433–434
  disorder-induced small-polaron formation, **2**:433
  Hall mobilities, **2**:439–440
  interactions between polarons, **2**:441–442
  large- and small-bipolaron formation, **2**:431–432
  large-polaron transport, **2**:434–435
  long-range electron-phonon interactions, **2**:429
  polaron absorption, **2**:440–441
  Seebeck coefficients, **2**:438–439
  self-trapping, **2**:430–431
  short-range electron-phonon interactions, **2**:429
  small-polaron relaxation phenomena, **2**:437–438
  small-polaron transport, **2**:435–437
  superconductivity of large-bipolaron liquid, **2**:442–443
Polyacetylene, **1**:62–63
Polycrystalline diamond anvils, **5**:838
Polycrystals, **3**:465–466
  atomic force microscopy of, **3**:470*f*
  microstructure of, **3**:469*f*
Polymerase chain reaction (PCR), **4**:644–645
Polymer matrix composites (PMCs), **5**:340–344, **5**:341*t*, **5**:344*t*
Polymers, **4**:742
  dawn of understanding, **5**:426
  developments in nineteenth century, **5**:424–425
  first synthetic plastic, **5**:425–426
  networks, **4**:110
  post 1930s, **5**:427
  protection, **5**:694–695
  scaffolds, **4**:742
Polymethyl methacrylate (PMMA), **5**:94
Polymorphism, **5**:453–454, **5**:460
Poly(p-phenylenebenzobisoxazole (PBO) fibers, **5**:338
Polyvalent metals, **3**:165–166, **3**:165*f*
Pontryagin index, **3**:402–403
Population inversion, **3**:771–772
Pore architecture, **5**:390–391, **5**:391*f*
Porous cellular metals, **5**:390
Porous silicon
  absorption, **5**:450–451
  anodization, **5**:442–445
  chemical properties, **5**:447
  drying techniques, **5**:445–446
  electrical properties, **5**:448
  electronic properties, **5**:447
  generalities and definitions, **5**:442
  LEDs, **5**:451
  light diffusion and scattering, **5**:448
  oxidation techniques, **5**:446–447
  S-band, **5**:449–450
  sensors, biosensors, medical applications, **5**:452
  structural properties, **5**:447
Position-correcting ptychographic iterative engine (pcPIE), **4**:87–88
Positron
  annihilation, **1**:826–827
  capture, **4**:471–472
  generation by lasers, **4**:473
  moderation, **4**:470–471, **4**:471*f*
  photon production separation, **4**:472–473, **4**:472*f*
  photoproduction, **4**:471
  slow, **4**:469–471, **4**:469*f*
Posner molecules, **4**:599–600
Potassium ions, **4**:694

Potential energy surfaces, **4**:544–545
Potentiometer method, **1**:23, **1**:24*f*
Powder processing
  and boundary treatments, **5**:683
  gas fluidization of, **5**:690–692
  governing equations, **5**:681
  horizontal rotating drum, **5**:687–690
  numerical solution, **5**:683
  particle-fluid interactions, **5**:681–683
  particle packing, **5**:684–687
  particle-particle interactions, **5**:681–683
Power, **3**:755
Poynting's theorem, **4**:376
Precipitation
  catalysts, **5**:743
  hardening, **5**:574
Pressure, **2**:592–595
  generation and measurement technique, **2**:594
Primitive crystallographic coordinate system, **5**:71
Principal component analysis (PCA), **4**:661
Principle angle of incidence, **4**:373
Principle of Sabatier, catalysts, **5**:741–742
Printed circuit board (PCB), **1**:11
Pristine graphene, **5**:129, **5**:131–133, **5**:131*f*, **5**:134*f*, **5**:136
Probing ferroelectricity, **3**:285–287
Processing techniques, ICs
  deposition techniques, **3**:754
  dry etching process, **3**:754
  photolithography, **3**:753–754
Programmable Josephson voltage standard (PJVS) chips, **1**:10
Programmable ROMs (PROMs), **3**:554
Propulsion system, **5**:594–595
Protein
  as catalysts, **4**:644
  CI2 folds, **4**:647, **4**:648*f*
  cytosolic, **4**:702
  denaturation, **4**:651
  engineering, **4**:644–645
  evolution, **4**:659
  FKBP12, **4**:646–647, **4**:647*f*
  lattice model, **4**:653
  local elementary structures (LESs), **4**:653–654
  membrane, **4**:704
  molten globule states, **4**:657
  point mutation, **4**:645
  receptor, **4**:684
  role in biological functions, **4**:656
  solid-state NMR structural studies of, **4**:636–641
  structure, **4**:656–657
  structure prediction, **4**:658–659
  transport, **4**:693–695
Protein Data Bank (PDB), **4**:656, **5**:42
Protein folding, **4**:623–629
  aggregation, **4**:654–655
  barnase, **4**:647–648, **4**:648*f*
  CI2 folds, **4**:647, **4**:648*f*
  complexity, **4**:658
  computational approaches, **4**:649–650
  conformational sampling methods, **4**:661
  early studies on, **4**:657–658
  energy landscape theory, **4**:610–612
  engrailed homeodomain, **4**:648
  exchange-domain mechanism, **4**:654
  and funnels, **4**:610–612
  hierarchical folding mechanisms, **4**:606–607, **4**:647–648
  kinetics, **4**:613–614
  knotting, **4**:608, **4**:614–615
  lock-and-key mechanism, **4**:654
  models for, **4**:651–654
  nucleation–condensation mechanism, **4**:647
  and paradox of Levinthal, **4**:609–610
  pathways, **4**:645
  φ-value analysis, **4**:645–647
  and physical interactions, **4**:606–607
  recent topics in, **4**:659–662
  recent trends in hardware, **4**:660–661
  robust analysis, **4**:661
  simulations
    in cellular environments, **4**:662
    developmental models, **4**:660
  single protein folding experiments, **4**:660
  thermodynamic hypothesis, **4**:609–610
  transition, **4**:608–609
  ultrafast folders, **4**:648
  unifying mechanism, **4**:649
Proton gap, **3**:27–28
Proton superconductor, **3**:26–27
Proximity effect (PE), **2**:618
Pseudo-Brillouin zone, **5**:292–293
Pseudocontact shift restraints, **4**:721–722, **4**:722*f*
Pseudo-contact shifts (PCSs), **4**:721–722, **4**:726, **4**:726–727*f*, **4**:727*t*
Pseudogap (PG) regime, **2**:586
Pseudo-Jahn–Teller effect (PJTE), **1**:798
Pseudomonas auriginosa, **4**:684
Pseudopotentials, **1**:757–758, **1**:757–758*f*
  condensed matter, **3**:503, **3**:504*f*
  density-functional theory, **1**:840–846
  empirical, **1**:838–840
  model potentials, **1**:836–838
  Phillips–Kleinman cancellation theorem, **1**:834–836
Pseudospin, **1**:606, **1**:613–614, **2**:345
Pseudo-spin valve (PSV) MRAM, **3**:565
$^3P_2$ topological SFs
  cyclic state, **2**:780
  ferromagnetic state, **2**:780
  half quantum vortex in D4-BN state, **2**:781–785
  magnetized nematic state, **2**:780
  nematic state, **2**:779–780
  vortices in, **2**:780–781
Ptychographic iterative engine (PIE), **4**:77–79, **4**:78–79*f*
Ptychographic matched illumination detector interferometry STEM (PMIDI-STEM), **4**:88, **4**:90*f*
Ptychography
  advantage of, **4**:73
  algorithms, **4**:73–80, **4**:73*f*
  applications, **4**:83–84, **4**:83–86*f*
  defocused-probe, **4**:81, **4**:81*f*
  difference map (DM) algorithm, **4**:78–80, **4**:80*f*
  electron detectors, **4**:73
  focused-probe, **4**:81, **4**:81*f*
  Fourier, **4**:81–82, **4**:82*f*
  iterative algorithms, **4**:76–80, **4**:77*f*
  low-frequency information transfer, **4**:88, **4**:90*f*
  multidimensional, **4**:88–91, **4**:91*f*
  multiple scattering, **4**:88, **4**:89*f*
  multiple states, **4**:86–87, **4**:87*f*
  optical configuration, **4**:80–82, **4**:87*f*
  probe position errors, **4**:81*f*, **4**:87–88
  ptychographic iterative engine (PIE), **4**:77–79, **4**:78–79*f*
  single side band (SSB) method, **4**:74, **4**:75–77*f*
  technical development, advances in, **4**:85–88
  Wigner distribution deconvolution (WDD) approach, **4**:74–76, **4**:77*f*
  workflow of, **4**:72, **4**:72*f*
Pulsed laser deposition, **2**:539–541, **2**:539–540*f*
Pulse-driven AC Josephson voltage standard. *See* Josephson arbitrary waveform synthesizer (JAWS)
Pulse pattern generator (PPG), **1**:10
Pulse-tube cryocooler, **1**:16, **1**:17*f*
Pulse width modulation technique, **5**:97
Pumping system, **2**:536
Pump-probe micro-spectroscopy, **3**:681
Pump-probe spectroscopy, **1**:982–987, **3**:681
Purcell effect, **3**:679
Pure metals, **5**:567
Pure phase LCoS SLM, **5**:99, **5**:99*f*
PVD. *See* Physical vapor deposition (PVD)
Pyrochlore ruthenates, **5**:799–801
Pyroelectricity, **5**:57–58

Q

QAHE. *See* Quantum anomalous Hall effect (QAHE)
QAOA. *See* Quantum approximate optimization algorithm (QAOA)
QD. *See* Quantum dots (QDs)
QHE. *See* Quantum Hall effect (QHE)
Qiskit simulator, **1**:243–244
QPCs. *See* Quantum point contacts (QPCs)
QPU-centric approach, **1**:258
Q-switching pulse generation, **4**:420–421
Quadruplex, **4**:671–672
Quadrupolar coupling, **4**:636–637, **4**:637*f*
Quantitative image processing, **4**:113
Quantization
  of circulation, **3**:6
  of conductance, **1**:896–899
  in potential wells, **3**:530
Quantized anomalous Hall effect (QAH), **1**:728
Quantized vorticity and rotation, **3**:25–26
Quantum, **4**:571–575
Quantum algorithms, **1**:239, **1**:248–249

Quantum annealing and computation
  analog computation, **4**:536
  cost function, **4**:536
  D-wave annealer, **4**:541–542
  energy landscape, **4**:536–537
  entanglement, **4**:540–541
  ergodic, **4**:538–540
  escape probability, **4**:537
  fidelity, **4**:541*f*
  free energy, **4**:539
  logic gates, **4**:536
  non-ergodic, **4**:537, **4**:539–540
  photon cavity, **4**:541*f*
  quantum tunneling, **4**:537–538
  simulated (classical) annealing, **4**:536–537
  in spin glasses, **4**:538–540
  using optical lattice in cavity, **4**:540–541
Quantum anomalous Hall effect (QAHE), **1**:4, **1**:682, **1**:697–698. *See also* Quantum Hall effect
Quantum antiferromagnets, **1**:38–41
Quantum approximate optimization algorithm (QAOA)
  air transportation, **1**:252–253
  basics, **1**:251–252
Quantum biology, **4**:594–596
  advantage, **4**:577–578
  avian magnetoreception, **4**:588–589
  biological context
    coherent transfer processes, **4**:597–598
    new (and old) avenues of interest, **4**:600–601
    quantum tunnelling, **4**:596–597
    spin dynamics, **4**:598–600
  coherent superpositions of states, **4**:585–586
  contenders, **4**:581–582
  entanglement, **4**:585–586
  history of, **4**:585, **4**:594
  light-harvesting in photosynthesis and energy transport, **4**:586–588
  magnetoreception with radical pairs, **4**:580–581
  methods and models, **4**:595–596
  non trivial quantum effects, **4**:594–595
  olfaction and tunneling, **4**:589–590
  photosynthesis, **4**:578–580
  quantum features of organisms, **4**:590
  tunneling, **4**:585–586
Quantum cascade Lasers (QCL), **3**:511
Quantum circuits
  high-temperature superconductors in, **2**:719–721
  low temperature Josephson junctions for, **2**:626–627
  noise in, **1**:1008–1009
Quantum computing, point defects for, **5**:189
Quantum computing schemes based on cellular automata (QCA), **3**:532
Quantum confined Stark effect, **3**:718
Quantum confinement, **3**:309–310, **3**:501–502
  in Dirac-like nanostructures, **2**:344–349
  in two-dimensions, **2**:345–346
Quantum criticality, **1**:36–41
  dynamic scaling, **1**:36
  scale invariance, **1**:36
Quantum depletion, **3**:127
Quantum device
  definition, **3**:529
  of reduced dimensionality, **3**:529–531
Quantum dot molecules (QDMs), **3**:718
Quantum dots (QDs), **2**:548*f*, **2**:549, **3**:325–326, **3**:337–338, **3**:341–342, **3**:352, **3**:388–389, **3**:403–407, **3**:429–430, **3**:531–532. *See also* Kondo effects, in quantum dots
  effects of shells and impurities, **3**:316–319
  for electron transport, **3**:382*f*
  energy levels, **3**:500–501, **3**:501*f*
  excitons, **3**:716–718
  in graphene (*see* Graphene)
  helium, **3**:406–407
  of hydrogenated silicon, ball and stick model for, **3**:501–502, **3**:502*f*
  InGaAs, **3**:342, **3**:342*f*
  inhomogeneous magnetic field, **3**:404–406
  model of, **3**:382–383
  optical absorption, **3**:310–313
  optoelectronic and biomedical applications, **3**:320–323
  photoluminescence, **3**:313–315
  quantum confinement effect, **3**:309–310
  spin textures, **3**:403–404
Quantum droplets, in Bose mixtures, **3**:131*f*
Quantum effects, **3**:267–268
Quantum efficiency (QE), **4**:465
Quantum electrodynamics (QED), **1**:5, **3**:654, **3**:688
Quantum emulation system, **3**:135–136, **3**:136*f*, **3**:138, **3**:140–142
Quantum error correction, **1**:258
Quantum error mitigation, **1**:257–258
Quantum error suppression, **1**:257
Quantum ferromagnet, **1**:40
Quantum field theory, **1**:29, **2**:800–801
Quantum fluctuations in superconducting nanowires
  dissipative transport and noise, **2**:676–678
  insulating regime, **2**:678–680
  localization of Cooper pairs, **2**:678–680
  phase-charge duality, **2**:675–676
  quantum phase slips, **2**:672–674
  quantum phase transition, **2**:674
  superconducting fluctuations, **2**:671–672
  superconducting regime, **2**:676–678
Quantum fluids, dynamics of
  ^{3}He in 3D, **1**:951–953
  ^{4}He in 3D, **1**:947–951
  ^{3}He in reduced dimensions, **1**:955
  ^{4}He in reduced dimensions, **1**:953–954
  He liquids, **1**:946–947
Quantum fluids of light (QFL)
  concept of, **1**:959
  microcavity devices, **1**:962–963
  photon-photon interactions, **1**:960–961, **1**:961*f*
  propagating geometries, **1**:963–964
  strongly correlated fluids and topological states of photonic matter, **1**:964–965
Quantum gas microscopy, **3**:136–138, **3**:140
Quantum gates, entanglement and, **3**:331–332
Quantum Hall bilayers, excitons in, **3**:719
Quantum Hall effect (QHE), **1**:79, **1**:81–82, **1**:629, **1**:691, **1**:725, **2**:292–293, **2**:795–796, **2**:815
  anyons, **1**:399–400, **1**:400*f*
  fractional, **1**:399–400, **1**:564–565
  integer, **1**:559–564
  on lattice, **1**:76–78
  Laughlin argument, **1**:660–661
  role of edge states, **1**:661
  theoretical models, **1**:559
  TKNN integer, **1**:661–662
  two-dimensional charge carrier system, **1**:556–559
  universality of, **1**:2–4
Quantum Hall ferromagnetism, **1**:310
Quantum Hall phases, of cold Bose gases
  anharmonic potential, **1**:646–650
  Bargmann space, **1**:642–643
  basic Hamiltonian, **1**:641–646
  complex notation, **1**:642–643
  fully correlated states, **1**:647–648
  Laughlin state, **1**:646
  lowest Landau level confinement, **1**:642–644
  mean field density, **1**:649
  N-particle case, contact interaction, **1**:643–644
  N-particle density as Gibbs measure, **1**:648–649
  1-particle case, **1**:642
  plasma analogy and mean field limit, **1**:648–649
  spectral gaps, **1**:644–645
  uncorrelated (Gross-Piaevskii) regime, **1**:645–646
  yrast curve, **1**:644–646
Quantum Hall plateaux, **1**:385
Quantum Hall resistance (QHR), **1**:24–25, **1**:24*f*
Quantum Hall (QH) setting
  Berry phases, **1**:476–477
  transmuted Hamiltonian, **1**:477–478
Quantum hardware, **1**:243–244
Quantum information device, **1**:804
Quantum information scrambling, **1**:255–256
Quantum information theory, **3**:325–326, **3**:332–333, **3**:336, **4**:575
Quantum interference, **4**:233–234
Quantum interferometer, **1**:114–115
Quantum light detection, **5**:167, **5**:171–172
Quantum logic, **1**:238–239
Quantum magnetism, **3**:139
Quantum magnonics
  hybrid magnonic platforms, **2**:152–156
  quantum states of magnons, **2**:150–152
  spin waves and magnons, **2**:148–150
Quantum many-body systems, **4**:575
Quantum Master equation, **1**:973
Quantum mechanics, **2**:9–10, **3**:530
  Aharonov–Bohm effect, **1**:214
  exchange interaction, **2**:55–56

  quantum statistics, **1**:212–214
  validity of, **1**:215–217
Quantum microcavities, **3**:676
Quantum mixtures of ultracold atomic gases, **3**:78–79
Quantum Monte Carlo (QMC) method, **5**:754–755
  configurational weight, **1**:881–884
    in classical Monte Carlo simulation, **1**:880–881
  sign bound theory, **1**:888–889
  sign problem (*see* Sign problem in quantum Monte Carlo simulations)
  split orthogonal group, Majorana representation and Majorana positivity, **1**:887–888
  symmetry, **1**:887
Quantum nanoscience
  artificial atoms, **1**:1009–1011
  noise in quantum circuits, **1**:1008–1009
  quantum sensing, **1**:1011–1013
  theoretical overview, **1**:1005–1006
Quantum oscillations, **1**:816–819
Quantum phase slips (QPS), **2**:672–674
Quantum phase transition (QPT), **2**:674, **2**:797, **3**:80*f*, **4**:574–575
Quantum physics, **1**:237
Quantum point contacts (QPCs), **1**:403–404, **1**:403*f*, **1**:899, **1**:924, **2**:249, **3**:392, **3**:397
Quantum processor systems, **1**:248
Quantum rings (QRs), **3**:407–412, **3**:716
  Aharonov–Bohm Period, **3**:410
  arrays, **3**:349–352, **3**:350*t*, **3**:350–352*f*
  electronic states, **3**:419–420, **3**:419–420*f*
  magnetization, **3**:420–422, **3**:421*f*
  model of particle, **3**:417–419
  persistent current, **3**:422
  radial potential, **3**:416–417
  spin textures in, **3**:407–410
Quantum sawtooth map, **1**:241
Quantum sensing, **1**:1011–1013
Quantum simulation, **1**:240–243, **3**:79–80, **3**:82
Quantum spin Hall effect, **2**:203
  fractional, **1**:626–627
  frustrated spin systems, **1**:627
  insulator, **1**:691, **1**:693
  interaction, **1**:625–627
  many-body Chern number matrix, **1**:625–626
  time-reversal symmetry, **1**:623–624
  topological characterization, **1**:624
  topological insulator and, **1**:624
  Z_2 characterization, **1**:625
Quantum states of magnons
  magnon antibunching, **2**:150–151
  magnon BEC and spin superfluidity, **2**:152
  squeezed states, **2**:151–152
Quantum statistics, **1**:212–214, **1**:394, **1**:485–489, **4**:560, **4**:571–575
Quantum supremacy, **1**:249–250
Quantum theory of magnetism, **2**:55
Quantum transport
  emulation, two-orbital cold atom system as, **3**:140–141
  and localization, **1**:255
Quantum tunneling, **4**:537–538, **4**:594–597
  DNA, **4**:596
  enzymes, **4**:596
Quantum volume (QV), **1**:244, **1**:250–251
Quantum wells (QWs), **3**:46–47, **3**:247, **3**:531, **3**:716
Quantum wires, **1**:424–425, **3**:531, **3**:716
Quarter wave transformer (QWT), **4**:471–472
Quartz crystal microbalance (QCM), **2**:537
Quartz microbalance, **3**:206
Quasi-condensation, **3**:90–92
Quasicrystals
  antiferromagnetic, **5**:5*f*
  electronic density of states, **5**:293–295
  lattice dynamics, **5**:278–279, **5**:282, **5**:285–286
  low-energy modes in, **5**:286
  magnetic properties, **5**:292–293
  nature of electronic states, **5**:295
  phason fluctuation in, **5**:288–289
  surfaces, **5**:291
  transport properties, **5**:291–292
Quasiholes
  fractionally charged, **1**:93
  fractional statistics, **1**:94
Quasi-linear superelasticity, **2**:396
Quasimaterials, **5**:390–391
Quasi-monochromatic radiation, **5**:178
Quasi-one-dimensional ruthenates Ln3RuO7, **5**:803
Quasi-one-dimensional (1D) wires, **2**:670
Quasiparticles, **1**:279, **1**:860, **3**:707
  Andreev bound states, **2**:620
  and braiding, **1**:351–352
  and edge exponents, **1**:350–351
  QPC tunneling, **1**:350–351
  relaxation in dirty and clean regimes, **2**:739
  scattering mechanisms, **2**:737
  SETs, **1**:351
  spectroscopy, **3**:707–709
  tunneling conductance, **1**:351
Quasiperiodic potentials, **1**:911
Quasi phase-matching (QPM), **4**:251
Quasi-relativistic phenomena, **2**:344
Quasi-static approximation, **4**:303–304
Quasi-two-dimensional ruthenates, **5**:801–802
Quasi-unit cell approach, **5**:329
Quaternary alloys, **5**:464
Quaternary components, atomic layer deposition of, **5**:723*f*
Qubits, **1**:238, **1**:280, **1**:804, **2**:626–627
Quenched turbulence dynamics, **3**:108–109
Quenching, **5**:580
Quintuple layers (QLs), **1**:695–696

R

Radial potential, quantum rings, **3**:416–417
Radiation
  beam of normal laser-diodes, **3**:776
  from charged particles, **3**:511
  pressure, **4**:321
Radiative shift, **3**:656–657, **3**:662
Radiative width, **3**:658, **3**:664
Radical-pair-based reaction, **4**:580
Radioactive sources, **4**:469–470
Rainbow/color holograms, **5**:95
RAM. *See* Random-access memory (RAM)
Raman gain, **4**:390
Raman intensity, **3**:728–729
Raman–Nath diffraction regime, **5**:93
Raman scattering, **3**:728–729, **4**:160–162, **4**:170–171, **4**:389–390, **5**:307–308
Raman spectroscopy (RS), **4**:300–301, **4**:745
  basics, **4**:161–163
  counting graphene layers, **2**:237
  of defected graphene, **2**:242–244
  of doped graphene, **2**:241–242
  of graphene and graphene layers, **2**:236–244
  of light scattering, **2**:233–234
  magnetic fields, **2**:244
  phonons in nanostructures, **4**:163–170
  process, **2**:234–236
  resonance Raman scattering in nanostructures, **4**:170–171
  of strained graphene, **2**:238–240
Ramsey-type quantum interferometer method, **1**:242, **1**:243*f*
Random-access memory (RAM), **3**:755
Random fatigue-limit model, **3**:827
Random field Ising model, **2**:22–23
Random matrix theory, **2**:800
Random phase approximation (RPA), **1**:765, **3**:802–803
Random wave functions (RWF), **3**:241, **3**:247
Raney metals, catalysts, **5**:744
Rapid solidification (RS), **5**:581
Rare-earth compounds, **5**:499–500
Rare-earth $4f^n$ configurations, **5**:487
Rare-earth materials, magnetostriction constants for, **2**:83–84, **2**:84*t*
RAS. *See* Reflectance anisotropy spectroscopy (RAS)
Rashba interaction, **1**:592, **1**:596
Rashba semiconductors, **1**:593, **1**:593*f*
Rate-equation approximation, **4**:413–414
Rational approximation, **1**:718
Rayleigh resolution criterion, **4**:112
Rayleigh scattering (RS), **4**:300–301, **4**:301*f*
  complex refractive index, **4**:225
  dispersed particles, **4**:219–225
  dynamic, **4**:226
  interacting particles, **4**:224–225
  liquid mixtures and solutions, **4**:218
  molecular, **4**:216
  optical theorem, **4**:219–220
  problem statement, **4**:219
  quantum fluids, **4**:218–219
  scattering and fluctuations, **4**:216–217
  scattering regimes, **4**:220–224
  simple liquids, **4**:217–218
  structure factor, **4**:217
Rayleigh waves, 1D soil model for, **3**:522
Reaction centers (RCs), **4**:731
Reactive ion etching with inductive coupled plasma (RIE-ICP), **1**:14–15
Reactive oxygen species (ROS), **4**:598–599

Read-only memories (ROMs), **3**:553–555, **3**:555*f*, **3**:755
Receptors, **4**:596–597
Reciprocal lattice, **5**:66–67
Reciprocal space, **5**:45
Reciprocal susceptibility, **2**:27, **2**:28*f*
Recombinant DNA technology, **4**:644–645
Recrystallization, **3**:848–850, **5**:574, **5**:576–579, **5**:581, **5**:626–629
Redox couples f^n/d^n, **5**:486–487
Reduced dimensionality, **4**:142, **4**:144
Reduced graphene-oxide (rGO) materials, **5**:101, **5**:101*f*
Re-entrant relaxor-ferroelectric composite (RRFC), **2**:398
Re-entrant spin glasses, **2**:22
Reference beam, **5**:89
Refinement model, **5**:14, **5**:48
Refinements of Larkin–Ovchinnikov model, **2**:738
Reflectance anisotropy spectroscopy (RAS), **4**:393–396, **4**:395*f*
Reflection CLSM, **4**:111
Reflection high-energy electron diffraction (RHEED), **2**:533, **2**:549, **5**:253*f*
Reflection positivity, **1**:160, **1**:169–170
Reflection statistics, **5**:32, **5**:32*f*
Refractive index, **3**:772*f*, **4**:109, **4**:113, **5**:154–155, **5**:164
Refractory high-entropy alloys (RHEAs), **5**:654
Regression, machine learning, **4**:554–555
Reinforcement fibers, **5**:336, **5**:336*t*
Reinforcement learning, **3**:826–827, **3**:826*f*
Rejuvenation, **2**:379–381, **2**:380*f*, **2**:384–385
Relativistic quantum field theory (RQFT), **1**:159
Relativistic spin–orbit coupled transport phenomena
  electronic signatures, **2**:213
  inverse spin galvanic effect, **2**:216–218
  spin–charge interconversion, **2**:218–219
  Spin Hall effect, **2**:214–216, **2**:214*f*
Relaxation and resonance frequency spectra, **4**:279–282
Relaxation enhancement restraints, **4**:722–723
Relaxation rates, **4**:727
Remanence/remanent magnetization, **2**:52–53
Renormalization group (RG), **1**:31–36, **2**:29, **3**:224
  fixed points, **1**:32–33
  universality classes, **1**:33
Replica exchange MD (REMD) simulation, **4**:661
Reprogrammable multi-level phase holography, **5**:101, **5**:101*f*
Residual dipolar couplings (RDCs), **4**:724, **4**:726–727, **4**:727*f*
Residual stress and strain evaluation
  diffraction, **3**:598–599
  digital image correlation (DIC), **3**:595
  eigenstrain theory, **3**:593
  experimental techniques, **3**:596–599, **3**:596*f*
  focused ion beam-digital image correlation (FIB-DIC), **3**:596–598, **3**:596–597*f*
  influence of residual stress on structural integrity, **3**:599
  live *vs.* residual strains and stresses, **3**:594–595
  rich tomography of strain and stress, **3**:599
  statistical considerations, **3**:594, **3**:595*f*
  stress and strain multi-scaling, **3**:593, **3**:594*f*
Resistively shunted junction (RSJ) model, **2**:621
Resistive RAM (RRAM), **3**:554, **3**:564, **3**:574–575
  bipolar, **3**:571
  bottom electrode (BE), **3**:571
  cross-point architecture, **3**:572, **3**:572*f*
  read operation, **3**:572, **3**:573*f*
  top electrode (TE), **3**:571
  two-layer concept, **3**:572, **3**:572*f*
  writing scheme of, **3**:572, **3**:573*f*
Resistive switching, halide perovskites, **5**:673
Resonance behavior, **4**:280
Resonance electronic transition, **4**:160–161
Resonance frequency, **3**:201, **3**:203, **3**:205
Resonance Raman scattering (RRS), **4**:170–171, **4**:301
Resonant charge transfer chemical effect, **4**:306
Resonant inelastic X-ray scattering (RIXS), **2**:585, **4**:199–201, **4**:200*f*
  from core electrons, **4**:201
  dichroism effects in, **4**:201
  spin selective, **4**:201
  from valence electrons, **4**:201
Resonant photonic crystals, **3**:676–677
Resonant state, **2**:260
Resonant ultrasound spectroscopy (RUS), **3**:203
Resonator, **3**:201–203
Resorbable polymers, **4**:742
Response function, **1**:873
Reststrahlen band, **4**:143, **4**:145*f*
Reststrahlen region, **5**:160
Retina vessels, **5**:100, **5**:100*f*
Reverse Watson–Crick, **4**:667
Ribbon, graphene, **2**:354–357, **2**:357*f*
Ribonuclease A (RNase), **4**:657
Ribonucleic acid (RNA)
  biophysical methods to, **4**:673
  contacting techniques for, **4**:677–679
  electronic properties, **4**:675–676
  and function, **4**:667–668
  gel electrophoresis, **4**:674
  nanostructures and nanodevices from, **4**:672
  organic molecules, conductance in, **4**:676–677, **4**:676*f*
  single molecules, electrical properties of, **4**:679–682, **4**:680–681*f*
  structure and function, **4**:667–668
  theoretical models, **4**:673
  unusual structure, **4**:672
Righi–Leduc effect, **3**:277, **4**:494–495
Rigid ion model, **5**:208–212, **5**:210*f*, **5**:211*t*, **5**:212*f*
Rigid motions, **5**:70
Ripplons, **1**:954
R-martensite, **2**:401*f*
RNA. *See* Ribonucleic acid (RNA)
RNA polymerase (RNAp), **4**:684, **4**:685*f*
Robust analysis, protein folding, **4**:661
Rokhsar–Wright–Mermin (RWM) formalism, **5**:6
Rolled sheet, **3**:493–494
Rolled-up structures, optical properties
  mode responses with weak external perturbations, **3**:360
  mode splitting and non-Hermitian photonics, **3**:360–363
  optoplasmonic hybridization in metal/dielectric rolled-up structures, **3**:363
  rolled-up metamaterials, **3**:366
  rolled-up microtubes as optically active and passive devices, **3**:358–360
  spin-orbit coupling in rolled-up cavities, **3**:363–366
  split axial modes in 3D microtube cavities, **3**:357–358
ROM. *See* Read-only memories (ROMs)
Room-temperature superconductivity, in hydrides
  lanthanum hydride, **2**:595–596
  unidentified superconducting objects (USOs), **2**:596
Rotating-wave approximation, **1**:973
Rotons, **1**:950–951, **1**:953–954
RQFT. *See* Relativistic quantum field theory (RQFT)
Ruddlesden–Popper (RP) ruthenates, **5**:792–795
Ruderman–Kittel–Kasuya–Yosida (RKKY) interaction, **1**:590–591, **1**:829–830, **2**:75–77, **2**:114, **2**:372, **3**:398
Rule of angular-momentum quantization, **2**:39
Ruthenates
  hexagonal perovskite polytypes, **5**:796–798
  perovskites and post-perovskites, **5**:786–791
  pyrochlore, **5**:799–801
  quasi-one-dimensional ruthenates Ln3RuO7, **5**:803
  quasi-two-dimensional, **5**:801–802
  Ruddlesden–Popper (RP), **5**:792–795
  ruthenium as substituting element in oxides, **5**:803–804
Ruthenium, **3**:454
Rutiles, **5**:497–498
Rydberg excitons, **3**:718–719
Rydberg states, **5**:123

S

Saccromyces cerevisia, **4**:684, **4**:686*f*
Sachdev-Ye-Kitaev (SYK), **2**:642
Sand cast alloys, **5**:557–558
Saturable absorber, **4**:421, **4**:423
Saturation magnetization, **1**:587, **2**:44, **2**:44*t*, **2**:46
Sayre's equation, **5**:34

S-band, **5**:449–450
Scalar coupling, **4**:636–637, **4**:637*f*
Scalar electrodynamics, **1**:118–119
Scalar field theory, **1**:149–151
Scale-dependent theory, of disordered electron liquid, **3**:223–226
Scaling theory, of metal-insulator transition, **3**:226–228
Scanning capacitance microscopy (SCM), **4**:61
Scanning electrochemical microscopy (SECM), **4**:60
Scanning electron microscopy (SEM), **2**:533
  electron optical figures of merit, **4**:40–49
  principles, **4**:37–40
Scanning ion conductance microscopy (SICM), **4**:60
Scanning nanoSQUID microscopy, **2**:708
Scanning nearfield acoustic microscopy (SNAM), **4**:60
Scanning nearfield optical microscopy (SNOM), **4**:59
Scanning noise microscopy (SNM), **4**:60
Scanning potentiometry microscopy (SPotM), **4**:60
Scanning probe microscopy (SPM), **4**:51, **4**:60*f*, **4**:61, **4**:302, **4**:310
Scanning spreading resistance microscopy (SSRM), **4**:61
Scanning thermal microscopy (SThM), **4**:60
Scanning transmission electron microscopy (STEM), **4**:71, **4**:72*f*
  advantages of, **4**:65
  angle-resolved, **4**:104–105
  annular detector, **4**:68*f*
  first-moment, **4**:98–100
  modes, **4**:70*f*
  momentum-resolved, **4**:97
  multidimensionality in, **4**:96
  primary motivation for, **4**:65
  reciprocity, **4**:65
  setup and detection schemes, **4**:96*f*
  vs. TEM, **4**:64–65, **4**:64*f*
Scanning tunneling induced luminescence microscopy (STlM), **4**:60
Scanning tunneling microscopy (STM), **2**:601–603, **2**:602*f*, **2**:607–608, **2**:610, **4**:51–53, **4**:53*f*, **4**:310–311, **4**:678*f*, **4**:679, **4**:680*f*, **4**:681
Scanning tunneling spectroscopy (STS), **1**:697
Scanning X-ray diffraction microscopy (SXDM), **4**:79–80, **4**:80*f*
Scattering, **4**:156–158, **4**:158*f*
  by atoms and molecules, **5**:43
  cross-section, **4**:151–152
  by crystal, **5**:43–44
  equation, **5**:42–43
  force, **4**:319, **4**:321
  length, **3**:10–11
  matrix method, **3**:741
  rate, **4**:134–135
Schoenflies symbols, **5**:78
Schottky barrier, **2**:263, **2**:268, **2**:268*f*
Schottky capacitance, **2**:519
Schottky diodes and p-n junctions, **2**:410–411
Schrodinger–Poisson methods, **1**:592
Schrödinger's equation, **1**:695, **1**:724, **1**:756, **1**:867, **2**:42, **2**:518, **3**:241, **3**:247, **3**:416, **3**:503, **3**:689, **4**:229, **4**:537, **5**:130
Schwarzschild objectives, **4**:32
Screened Coulomb interaction, **3**:221*f*
SDR. *See* Surface differential reflectivity (SDR)
SDW. *See* Spin-density wave (SDW)
Secondary beams, **4**:473
Secondary ion mass spectroscopy (SIMS), **2**:490, **2**:533
Second harmonic generation (SHG), **4**:246–249, **4**:384–385, **4**:384–385*f*, **5**:115–116
Second law for feedback processes, **4**:527–528
Second law of thermodynamics, **4**:477–478
Second-order correlation, **5**:167, **5**:175–177, **5**:176–177*f*
Second-order nonlinear effects
  nonlinear optical materials, **4**:387
  parametric amplification and oscillation, **4**:386–387, **4**:386–387*f*
  phase matching, **4**:385–386, **4**:385*f*
  second-harmonic generation, **4**:384–385, **4**:384–385*f*
Second-order perturbation theory, **2**:75
Seebeck coefficient, **2**:438–439, **3**:536, **4**:492, **4**:495–496
Seismic metamaterials
  classification, **3**:524
  in earthquake engineering, **3**:523
  elasticity hypothesis, **3**:521
  extracting information, **3**:525–526
  full-scale structured ground, **3**:521
  periodic soil model, **3**:521–523
  and seismic site effects, **3**:520–521
  seismic wave amplification, **3**:520–521
  superficial soil, **3**:524
Selection rules, **4**:154, **4**:159
Selection transistor, **3**:557–558
Self amplified spontaneous emission (SASE), **4**:440–441
Self-assembled quantum dot (QDs), **3**:327, **3**:426
Self-assembled quantum rings, **3**:340–341, **3**:340–341*f*
Self-assembly, of origami structures, **4**:682
Self-energy approximations, **1**:994–995
Self-ordering, **5**:351
Self-organized porous semiconductor compounds
  applications of self-organized ordered arrays, **5**:365–368
  hopping electrodeposition, **5**:363–364
  parallel to crystal surface, **5**:356–360
  perpendicular to crystal surface, **5**:354–356
  three-dimensional modulation of porous layer, **5**:360–362
  TiO_2 nanotubes, **5**:351–354
Self-organized semiconductor nanostructures
  array of quantum dots, **3**:341–349
  growth of, **3**:338–341
  indium composition, role of, **3**:346–348, **3**:346–347*t*, **3**:346–347*f*
  InGaAs quantum dots, lateral ordering of, **3**:342, **3**:342*f*
  low indium composition, As_2, **3**:348–349, **3**:348*t*, **3**:348–349*f*
  molecular beam epitaxy (MBE), **3**:338–340, **3**:339–340*f*
  ordered self-assembled quantum ring arrays, **3**:349–352, **3**:350*t*, **3**:350–352*f*
  ordering evolution from single layer, vertically stacked QDs layers, **3**:343–346, **3**:343–345*f*
  self-assembled quantum rings, **3**:340–341, **3**:340–341*f*
Self-orientation residual dipolar coupling restraints, **4**:723–724, **4**:724*f*
Self-trapping, **2**:430–431
Sellmeier dispersion model, **5**:164
Semi-classical model, **1**:594–595
Semiclassical quantization and Berry phase, **1**:610–611
Semiconducting oxides, **5**:188
Semiconductor heterojunctions
  band alignments, **2**:509, **2**:510*f*
  band offsets
    engineering, **2**:511–514
    measurement, **2**:509–510, **2**:510*f*
    trends, **2**:512–513
  electronic bands, spatial profile of, **2**:507, **2**:508*f*
  electronic properties, **2**:509
  energy gaps *vs.* lattice constants, **2**:508, **2**:509*f*
  localized interface states, **2**:514
  spintronics, **2**:514
  stick-and-ball model, **2**:507, **2**:508*f*
Semiconductor lasers, **3**:771, **3**:777
  dynamic properties and noise, **3**:776–777
  emission spectrum and beam properties, **3**:775–776
  heterostructures, **3**:772–773, **3**:772*f*
  output power *vs.* current characteristic, **3**:775, **3**:775*f*
  population inversion, **3**:771–772
  single-frequency semiconductor lasers, **3**:777–779, **3**:778*f*
  stripe laser diodes, **3**:773–774
  vertical-cavity surface-emitting lasers (VCSELs), **3**:779–780, **3**:779*f*
  waveguiding, **3**:774–775
Semiconductor nanoislands
  lateral positioning, **2**:522
  vertical stacking, **2**:523, **2**:523*f*, **2**:527*f*
Semiconductors, **2**:413–414, **2**:456, **3**:757, **5**:659
  absorption, **5**:118–120
  alloys, **5**:453–455, **5**:459–461, **5**:467
  atomic mass-related properties, **2**:485–493
  bipolar transistors, **3**:758, **3**:760–761*f*
  coupled QD, **3**:331–332
  current rectification by Schottky diodes and p–n junctions, **2**:410–411
  dielectric function, **5**:118–120
  doping, **2**:408–410
  double heterostructure, **3**:772*f*
  effective mass, electrons, and holes, **2**:405–408

Semiconductors *(Continued)*
  excess electrons, molecular liquids, and metallization under pressure, **3**:168–169
  excitons and polaritons, **5**:123–125
  facetted surfaces, **2**:523, **2**:524*f*
  field effect transistors (FET), **3**:759–761, **3**:762*f*
  free-standing nanowires, **2**:524–525
  heterojunctions and field-effect transistors, **2**:412–413
  heterostructure, **3**:764*f*, **3**:772–773, **3**:772*f*, **4**:142, **4**:146*f*
  interband transitions, **5**:120–121
  junction diodes, **3**:757, **3**:758*f*
  laser diodes (LD), **3**:766–768, **3**:767–768*f*
  light emitting diodes (LED), **2**:416–417, **3**:766, **3**:766*f*, **5**:126
  liquids, **3**:168–169
  memories, **3**:762–763, **3**:764*f*
  mobilities, **2**:408
  modulation spectroscopy, **5**:125
  molten salts, **3**:168
  monolayer thick wires, at step edges, **2**:523, **2**:524*f*
  nanoislands, **2**:521–523, **2**:521*f*
  neutron transmutation doping, **2**:494–495
  optical properties and applications, **2**:414–416
  phonon-assisted transitions, **5**:122–123
  photodetectors and photodiodes, **3**:763–765
  point defects in, **5**:187
  population inversion and gain in, **3**:771–772
  reflectivity, **5**:118–119, **5**:125
  self-organized growth, physical principles of, **2**:520–521
  solar cells, **3**:765–766, **3**:765*f*
  spin-related properties, **2**:493–494
  superlattice, **4**:164*f*
  thermoelements, **3**:536–537, **3**:536*f*
  III-V, **1**:556, **5**:457–458, **5**:458*f*
  transport properties of, **2**:457
  II-VI, **5**:458–459, **5**:458*f*
  wide bandgap materials, **3**:768–769
Semiconductors, simulations and carrier localization effects in
  (Al,Ga)N systems, **3**:246–248
  (Al, In)N alloys, **3**:237, **3**:243, **3**:245–247
  (Al,Ga)As alloys, **3**:237–238
  band-anticrossing (BAC) models, **3**:236–237, **3**:240–241, **3**:247
  classical III-V materials, **3**:237–238
  composition fluctuations and localization landscape approach, **3**:241–242
  continuum-based approach, **3**:239–242
  density functional theory (DFT), **3**:238–239, **3**:247
  empirical pseudo-potential method (EPM), **3**:243, **3**:247
  empirical tight-binding model (ETBM), **3**:242–243, **3**:243*f*, **3**:247
  first-principle density functional theory, **3**:237
  gallium aluminum arsenide, **3**:236–237
  III-nitride alloys, **3**:237–238
  (In, Ga)N alloys and heterostructures, **3**:237–238, **3**:243–245, **3**:244–245*f*, **3**:247
  (In,Ga)N/GaN QW systems, **3**:237, **3**:245, **3**:248
  localization landscape approach, **3**:237
  modified continuum approaches, **3**:237
  nitride-based alloys, **3**:237
  piezoelectric polarization vector field, **3**:238
  semi-empirical atomistic approaches, **3**:237, **3**:242–243
  spontaneous built-in electric polarization vector field, **3**:237–238, **3**:238*f*
  tight-binding (TB) model, **3**:242–243, **3**:243*f*
  virtual crystal approximation (VCA), **3**:236–237
Semiconductor surface reconstruction
  Si(100)2 x 1, **2**:264
  Si(111)2 x 1, **2**:264–265
  Si(111)7 x 7, **2**:266–267
Semicovalent exchange, **5**:495
Semi-empirical atomistic approach, **3**:237
  empirical pseudo-potential method (EPM), **3**:243, **3**:247
  empirical tight-binding theory, **3**:242–243, **3**:243*f*
  tight-binding (TB) model, **3**:242–243, **3**:243*f*
SET. *See* Single–electron transistor (SET)
Severe lattice distortion effect, **5**:651–653
Shallow impurities
  energy levels, experimental determination of, **2**:518, **2**:518*t*
  theory of electronic states, **2**:516–517, **2**:518*f*
Shannon entropy, **4**:525–527
Shape anisotropy, **2**:48–49
Shaped crystal growth, **5**:194–196
Shape dependence, **3**:655, **3**:659
Shape memory alloy, **2**:390–391, **2**:396, **2**:398–399, **5**:530, **5**:621
Shape memory effect, **2**:396, **2**:396*f*
Shear stress, **3**:839–840
Shear waves, **3**:522, **3**:842
Sheet-forming process, **3**:851*f*
Shell model, **5**:208–209, **5**:213–215, **5**:695–697, **5**:696*f*
Sherrington-Kirkpatrick (SK) model, **4**:536
Short-circuit diffusion paths, **3**:859
Short-range electron-phonon interactions, **2**:429
Short-range entangled states, **1**:666–668
Shot noise, **5**:172
Shubnikov–de Haas (SdH) technique, **1**:697, **4**:228, **4**:232, **4**:234, **4**:236
Side jump, **1**:589, **1**:589*f*, **1**:593
Si/Ge core-shell nanowires, **2**:525, **2**:525*f*
Signal-to-noise and distortion ratio (SINAD), **1**:21
Signal-to-noise ratio (SNR), **5**:97
Sign bound theory, **1**:880, **1**:887–890
Sign problem in quantum Monte Carlo simulations
  Aharonov-Anandan phase, **1**:886–887
  basis-dependent, **1**:885–886
  definition, **1**:884–887
  geometric frustration, **1**:886
  Pauli exclusion principle, **1**:886
Silicene, **5**:129, **5**:131–132
Silicon (Si), **2**:413–414, **3**:791–794, **3**:792–801*f*, **3**:796–801, **4**:83*f*
  absorption constant *vs.* photon energy, **4**:392, **4**:393*f*
  differential reflectivity spectra, **4**:392–393, **4**:394*f*
  nanocrystals, **3**:327–328
  reflectance anisotropy spectra, **4**:393, **4**:395*f*
  surface contribution to reflectance of, **4**:393, **4**:394*f*
Silicon carbide-based fibers, **5**:338
Silicon-germanium alloys, **3**:538
Silicon-germanium double quantum wells, **3**:46–47
Silicon-oxide-nitride-oxide-silicon (SONOS), **3**:562
Silver
  electroreflection on, **4**:378, **4**:379*f*
  FEBID, **3**:454
Silver halide emulsions, **5**:94
Simple liquids, **4**:217–218
Simple shear deformation, **3**:848
Simplified molecular input line entry system (SMILES), **4**:556
Simulated annealing, **5**:39
Simulations, protein folding
  in cellular environments, **4**:662
  developmental models, **4**:660
Sine-Gordon field theory, **1**:44–45, **1**:61–62
Sine waveforms
  frequency and time domain of, **1**:15, **1**:16*f*
  frequency spectra of, **1**:12, **1**:12–13*f*
Single-band effective mass approximation, **3**:240
Single beam optical tweezers, **4**:322–323
Single cell polarization, **4**:704
Single-color pump-probe spectroscopy, **3**:696
Single-component glass-forming systems, **3**:182
Single-crystal films, **5**:263–264
Single-crystal X-ray diffraction (SC-XRD), **5**:698
Single domain particles, **2**:118
  nonuniform nontopological magnetization pattern, **2**:119
  Stoner–Wohlfarth model, **2**:119
  superparamagnetism, **2**:118
Single electronics, **3**:325–326, **3**:328–329, **3**:336
Single–electron transistor (SET), **3**:262–265, **3**:788–789, **3**:788*f*
Single electron tunneling device, **1**:1009
Single-electron turnstile, **3**:271
Single flux quantum (SFQ) digital logic, **2**:626

Single-frequency semiconductor lasers, **3**:777–779, **3**:778*f*
Single-molecule fluorescence with force-measurement techniques, **4**:326
Single particle analysis (SPA), **4**:84
Single-particle spectrum, **1**:559, **1**:872–873
Single phase microstructures, **3**:466–474
  by crystallization, **3**:470–471
  by sintering, **3**:466–470
Single protein folding, **4**:660
Single quantum objects, **3**:336
Single-shot ptychography, **4**:91
Single side band (SSB) method, **4**:74, **4**:75–77*f*
Single susceptibility theory
  basics of, **3**:688–692
  chiral polarization phenomenology, **3**:692
  components of, **3**:692
  macroscopic susceptibility, **3**:690–691
  three different polarizations, **3**:688
Single-vortex and collective pinning by point defects, **2**:557–559
Single-walled carbon nanotubes (SWCNTs), **3**:659
Single-wall nanotube (SWNT), **5**:708–711, **5**:711*f*
Single wavelength anomalous diffraction (SAD), **5**:47
Sintering
  catalysts, **5**:746
  single phase microstructures by, **3**:466–470
Si 3s pseudo-wave-function, **1**:757–758, **1**:757*f*
Size dependence, **3**:655, **3**:657, **3**:662–663
Size parameter of particle, **4**:319
Skew scattering mechanism, **1**:588–589, **1**:589*f*, **1**:593
Skin effect, **4**:372
Skyrmion, **1**:316–317, **1**:590, **3**:58–59
Skyrmion bubbles, **2**:121
Slip systems, of metallic crystal structures, **3**:845*t*
Slonczewski mechanism, **2**:117
Sluggish diffusion effect, **5**:650–651
Small magnetic systems, **2**:703
Small-polaron relaxation phenomena, **2**:437–438
Small-polaron transport, **2**:435–437
Snell law, **5**:157
SNS-type Josephson junctions, **1**:10, **1**:13–14, **1**:14*f*
SOC. *See* Spin-orbital coupling (SOC)
Sodium carbonate (Na$_2$CO$_3$), **4**:514–516
Sodium ions, **4**:694
Softening, **3**:848–850
Soft ferrites, **2**:80
Soft ferromagnet, **2**:19
Soft-landing isolations, **5**:698
Soft magnetic alloys, **5**:517–518
Soft magnets, **2**:11, **2**:78–81, **2**:79*t*
Soft steels, **2**:79
Solar cells, **3**:765–766, **3**:765*f*
Sol-gel deposition, **5**:257, **5**:257*f*
Solid crystalline materials, **1**:681
Solid oxide fuel cells (SOFC), **5**:418
Solid-phase epitaxy (SPE), **2**:535, **2**:545
Solids, **3**:203–205
  aperiodically ordered, **5**:291
  electromagnetic waves in, **3**:666–668
  optical properties of, **3**:713
  ultrashort optical pulses, **5**:128–130
Solid solution strengthening, **3**:855, **3**:855*f*
Solid-state diffusion, **2**:495
Solid-state NMR structural studies, of proteins
  applications, **4**:640–641, **4**:641–642*f*
  chemical shielding, **4**:636, **4**:637*f*
  dipolar coupling, **4**:636–637, **4**:637*f*
  dynamics, **4**:640
  interactions, **4**:636–637, **4**:637*f*, **4**:640
  orientations, **4**:640
  quadrupolar coupling, **4**:636–637, **4**:637*f*
  sample preparation, **4**:637–638
  scalar coupling, **4**:636–637, **4**:637*f*
  secondary structure, **4**:639, **4**:640*f*
  spectral assignment, **4**:638–639, **4**:638–639*f*
  tertiary structure, **4**:639–640
Solitons in one dimensions, **1**:62
Solution growth
  extreme high pressure, **5**:204
  high temperature, **5**:202–203
  hydrothermal growth, **5**:203–204
  low temperature, **5**:202
  principle of, **5**:202
Solution structure determination programs, **4**:728, **4**:728*f*
Sommerfeld number, **3**:275
Souza–Wilkens–Martin (SWM) sum rule, **1**:675, **1**:677–679
Space groups, **5**:61, **5**:63
  classification, **5**:64–65
  elements, **5**:64
  notation, **5**:65–66
  representations, **5**:67–68
  structure, **5**:63–64
  symbols for, **5**:78–79
  types, **5**:11–12
  unit cells for, **5**:63–64, **5**:63*f*
Space Shuttle Orbiter, **5**:334–335
Sparse matrix methods, **3**:213
Spatial dispersion, **2**:500–501
Spatial light modulator (SLM), **5**:98–99
Spatially direct and indirect excitons, **3**:708*f*
Spatial profiles of bandgap energy, **3**:772*f*
Spatial resolution, **4**:307
Specific energy, **4**:562
Specific heat, **5**:305
Specific surface area, highly porous materials, **5**:399–401, **5**:399–400*f*
Speckle noise, in holographic imaging, **5**:93
Spectral continuity, **1**:718–719
Spectral gap conjecture, **1**:390, **1**:644–645, **1**:647
Spectral gaps, **1**:644–645
Spectroscopy, **4**:744–745, **5**:125
Speed, **3**:755
Sphericity, **1**:277
Spin and valley optical orientation, in transition metal dichalcogenides, **3**:679
Spin–charge interconversion, **2**:218–219
Spin chemistry, **4**:598–599
Spin Chern number, **1**:624–626
Spin chirality mechanism, **1**:590
Spin coherent states, **1**:38–39
Spin crossover (SCO), **1**:807
Spin-curl force, **4**:321
Spin current density, **2**:143–144
Spin-density wave (SDW), **2**:583, **2**:585–588, **2**:590, **2**:633, **5**:493
  basic static properties, **2**:450
  fermi surface nesting and, **2**:448–449
  field-induced, **2**:453–454
  magnons, collective excitations, **2**:452–453
  microscopic theory, **2**:449–450
  phasons, collective excitations, **2**:450–452
Spin detection, **2**:198–200
Spin dynamics
  avian navigation, **4**:598–599
  chirality, **4**:600
  phosphorus nuclear spin, **4**:599–600
  reactive oxygen species, **4**:599
  spin chemistry, **4**:598
Spinels, **5**:497
Spin Faraday and Kerr rotation, **3**:681
Spin fluctuations, **2**:62–63, **2**:583–584, **3**:276
Spinful systems, **1**:298
Spin galvanic effect
  current induced spin polarization, **2**:182–183
  kinetic mechanism, **2**:178–179
  mechanism due to spin injection, **2**:180
  optically induced, **2**:180–182
  phenomenological description, **2**:178
  relaxational mechanism, **2**:179–180
  in transport experiments, **2**:182
Spin generation, **2**:198–200
Spin glasses (SGs), **2**:19–22, **2**:32–33, **2**:33*f*, **2**:372, **3**:185, **4**:538–540, **5**:493
  cavity method, **2**:366–367
  critical dynamics of freezing, **2**:373–374
  domain growth and hierarchy of states, **2**:380–382
  dynamical mean-field theory (DMFT), **2**:367–368
  experimental, **2**:362
  frozen disorder, **2**:372
  frozen state, **2**:372–373
  in low dimensions, **2**:368–369
  magnetic characterization of, **2**:373*f*
  magnetic noise, **2**:376–378
  multiple memories, **2**:380
  numerical methods, **2**:368
  order parameter, **2**:363
  phase, **2**:372–375
  relaxation of magnetization, **2**:375–376
  replica method, **2**:363–365
  self-averaging, **2**:362–363
  slow dynamics and aging in, **2**:375–378
  spatial correlations, **2**:368
  temperature step experiments, **2**:379–380
  thermodynamic phase transition, **2**:374–375
  Thouless–Anderson–Palmer (TAP) approach, **2**:365–366

Spin glasses (SGs) *(Continued)*
  transition, **2**:375, **2**:390, **2**:394
Spin glass order, correlation length for, **2**:383–385
Spin groups, **5**:10
Spin Hall effect, **1**:691, **1**:696, **2**:231
  experiments, **2**:136–137
  instructive example and general framework, **2**:138–139
  Onsager reciprocity and non-Abelian gauge field point of view, **2**:139–140
  relativistic spin–orbit coupled transport phenomena, **2**:214–216, **2**:214*f*
  role of spin-orbit coupling, **2**:134
  size and form of (effective) spin-orbit coupling, **2**:134–135
  spin currents, **2**:135–136
Spin Hall insulator, **1**:691
Spin Hall magnetoresistance (SMR), **2**:163
Spin-independent Hamiltonian, **2**:74
Spin manipulations
  by Aharonov–Casher spin interference, **2**:200–201
  by SOI-based ESR, **2**:202–203
Spin moment, **2**:26
Spin-momentum locking, **1**:593, **1**:691, **1**:691*f*, **1**:695, **1**:697
Spin-orbital coupling (SOC), **1**:587–588, **1**:592–593, **1**:623–624, **1**:801, **1**:804, **2**:72–73, **2**:687, **3**:400–401
  and band structure of solids, **2**:190–191
  group theory of, **2**:187–188
  mechanisms of, **2**:188–189
  optical spin orientation, **2**:189
  Pauli SO coupling, **2**:186–187
  in rolled-up cavities, **3**:363–366
  spin precession and spin relaxation, **2**:189–190
Spin-orbit interaction (SOI), **1**:903, **2**:226, **3**:689, **3**:693
  gate controlled Rashba, **2**:195–196
  origin of, **2**:194–195
  spin generation and detection, **2**:198–200
  spin manipulation by Aharonov–Casher spin interference, **2**:200–201
  spin manipulation by SOI-based ESR, **2**:202–203
  spin relaxation and suppression for long spin coherence, **2**:197–198
Spin-orbit Mott insulator, **5**:779
Spin-orbit torque (SOT), **2**:117, **2**:146, **2**:219, **3**:567
Spinor Bose–Einstein condensates, **2**:757
Spin order, **2**:583
Spin photoexcitation, **3**:678
Spin polarization, **1**:336–338, **1**:348–350, **2**:231
Spin precession, **2**:189–190
Spin pumping, **1**:625–626
Spin relaxation, **2**:189–190, **2**:197–198, **2**:228–230
Spin reorientation transition (SRT), **2**:48
Spin-resolved measurements, **1**:828
Spin-S degree of freedom, **1**:39
Spin selective, resonant inelastic X-ray scattering, **4**:201
Spin splitting, **4**:133, **4**:145–146, **4**:145–146*f*, **4**:231, **4**:233
Spin structure, **3**:712–713
Spin superfluidity, **2**:152
  in antiferromagnets, **3**:59–62
  concept of, **3**:52–56
  experiments on detection of spin superfluidity, **3**:64–65
  in ferromagnets, **3**:56–59
  long-distance superfluid spin transport, **3**:63–64
  superfluid spin transport without spin conservation law, **3**:62–63
Spin textures
  Aharonov–Bohm Period of QR, **3**:410
  higher topological charge, **3**:411–412
  index characterizing topology, **3**:402–403
  inhomogeneous magnetic field, **3**:404–406
  models, **3**:401–402
  in QRs, **3**:407–410
  in quantum dot helium, **3**:406–407
  in quantum dots, **3**:403–407
  in quantum rings, **3**:407–412
  topological charges of, **3**:403–404
Spin-transfer torque (STT), **2**:143, **2**:161, **3**:565–567, **3**:567*f*
  equation of motion, **2**:145
  microscopic theory, **2**:145–146
  spin-orbit torque, **2**:146
  spin-transfer mechanism, **2**:144–145
Spintronics, **2**:14, **2**:139–140, **2**:514, **3**:325–326
  altermagnets, **2**:171–172, **2**:171*f*
  antiferromagnets, **2**:170–171
  conventional materials and current applications, **2**:164–167
  emitters, **3**:511
  giant magnetoresistance (GMR), **2**:164
  Heusler compounds (HC), **2**:167–168
  historical overview, **2**:162–164, **2**:162*f*
  honeycomb monolayers, **2**:209–210
  interaction of magnons with carriers of information, **2**:173
  magnetic insulators, **2**:172–173
  magnons as carriers of information, **2**:172
  non-linear magnonic devices, **2**:173
  SOT-MRAM, **2**:165–166
  STT-MRAM, **2**:165
  tunnel magnetoresistance (TMR), **2**:164–165
  in 2D van der Waals materials, **2**:168–170, **2**:168*t*
  voltage-control of magnetic anisotropy (VCMA), **2**:166–167
Spin-valley quantum Hall ferromagnets, **1**:314–317
Spin-valve MRAM, **3**:565
Spin waves, **2**:58–59, **2**:59*f*, **2**:148–150
Spin Zeeman interaction, **3**:689
Spin-zero, **4**:231
Split-charge separation, **1**:900*f*
Split-gate device, **1**:896*f*
Spontaneous breaking of (continuous) symmetries, **1**:158–160, **1**:162–163, **1**:169–170
Spontaneous magnetization, **2**:27–29
Spontaneous symmetry breaking (SSB), **1**:148–149, **1**:798
  in crystalline solids, **1**:206–209
  Ginzburg–Landau approach, **1**:206
  in structural phase transitions in metals, **1**:209–210
Sp–Sp interactions, **5**:479–483
Sputtering, **2**:541, **5**:250–252
Square well model, **3**:298–299
Squeezed vacuum state, **5**:177, **5**:177*f*
"SQUID-on-tip" 3D configuration, **2**:708
SrBi$_2$Ta$_2$O$_9$ (SBT), **3**:569
Stability, halide perovskites, **5**:673–674
Stainless steels, **5**:547*t*
Standard model of solids, **1**:756, **1**:757*f*
State-of-the-art semiconductor technology, **3**:775–776
Static annealing, **5**:529
Static fields (SF), **4**:709–711
Static power dissipation, **3**:755
Static random-access memory (SRAM)
  applications, **3**:581
  cell array organization, **3**:580
  cell reading and writing, **3**:580–581
  sense amplifier, **3**:581
Statistical anyons, **1**:502–507, **1**:503–504*f*, **1**:512
  equilibrium thermodynamics, **1**:507–511
  and generalized exclusion statistics, **1**:506–507
  1D, **1**:508–509, **1**:509*f*
  in second quantization, **1**:505
  thermodynamic equivalence, **1**:511, **1**:511*f*
  2D, **1**:509–510, **1**:510*f*
  2D FES anyons, **1**:510–511, **1**:510*f*
  wavefunction, **1**:504–505
Statistical ensembles, **4**:561
Statistical entropy, **4**:562
Statistical mechanics, **4**:110, **4**:571–575
Steady-state and pulsed neutron sources, **5**:434–435
Steels
  advanced high strength, **5**:531
  austenitic, **5**:543
  categories, **5**:538–541
  chemical properties, **5**:547
  functional properties, **5**:547
  mechanical properties, **5**:542*t*, **5**:544–546, **5**:544*f*
  microstructures, **5**:539*f*
Stellar activity, **4**:434
Stellar remnants, **4**:434
STEM. *See* Scanning transmission electron microscopy (STEM)
Stern–Gerlach effect, **2**:199–200
Stevens operator, **2**:71–73
Stillinger-Weber potential, **4**:546
Stimulated Brillouin scattering (SBS), **4**:391
Stimulated Raman scattering (SRS), **4**:389–391, **5**:813
STM with inverse Photoemission (STMiP), **4**:60
Stochastic series expansion (SSE) method, **1**:883
Stochastic thermodynamics, **4**:327
Stokes field, **4**:390

Stokes scattering, **4**:300–301, **4**:301*f*
Stokes' theorem, **1**:692, **2**:654
Stoner enhancement yielding, **2**:77
Stoner theory, **2**:60, **2**:63
Stoner–Wohlfarth model, **2**:77, **2**:119
Strain engineering, **5**:464–465, **5**:465–466*f*, **5**:467
Strain glass, **2**:389–394, **2**:390–397*f*, **2**:396–402, **2**:400–401*f*
Strain-induced self-assembly, **2**:549
Strain-life approach, **3**:821
Strange metal regime, **2**:588–589, **2**:589*f*
Stranski–Krastanov (S-K) growth mode, **2**:521–522, **2**:532, **3**:339
Strengthening mechanisms, **5**:544
  in metals, **3**:853
    low-temperature continuum-level, **3**:857–858
    low-temperature dislocation, **3**:853–857
  thermal activation, limitations of, **3**:858–859
    bulk diffusion effects, **3**:858
    intercrystalline diffusion effects, **3**:859
Stress anisotropy, **2**:49
Stress-induced leakage current (SILC), **3**:561–562
Stress-induced melted indium, **3**:428–429
Stress–strain curves, **3**:850*f*
Stress *vs.* strain behavior, **3**:839*f*
Stripe laser diodes, **3**:773–774
Stripe order, **2**:586–588, **2**:587*f*
Stripes, **2**:67–68, **2**:68*f*
Stroboscopic topograph, **4**:406, **4**:406*f*
Strong-coupling polaron, **2**:430–431
Strong liquids, **3**:174
Strong magnetic field
  bilayer graphene, **1**:374–377
  graphene monolayer, **1**:373–374
Structure heterogeneity, **4**:728–729
Structure inversion asymmetry (SIA), **1**:592
Structures (orientation texture)
  crystallographic orientation, **3**:483–486
  mathematical constructs, **3**:489–493
  microtexture, **3**:496
  misorientation, **3**:495
  modelling, **3**:497–498
  rolled sheet, **3**:493–494
  tensor averaging, **3**:496–497
  texture measurement techniques, **3**:487–489
  thin films, **3**:493
STT. *See* Spin-transfer torque (STT)
Subbands, **4**:135–136, **4**:139, **4**:144
Sublattice, **2**:26, **2**:31, **5**:26
Sub-nano particles, **5**:694
Sub Poissonian statistics, **5**:167–168, **5**:171–172
Substitutional alloys, **5**:526–527
Substitutional impurities, **5**:185
Substrate and lattice matching, **2**:529–530
Sudden-approximation, **4**:239
Sulfides, atomic layer deposition of, **5**:722–723
Sum rules
  elementary description, **5**:106–107
  Kramers–Kronig relations and linear, **5**:108–110
  in non-linear optics, **5**:113–114
Superalloy
  chemical element arrangement, **5**:586*f*
  classification and key phases in, **5**:585–592
  Co-based, **5**:591–592
  definition, **5**:583
  development, **5**:584*f*
  element cost, **5**:596
  element production rates, **5**:596–598
  embodied carbon, **5**:595–596
  Ni-based, **5**:587–591
  Ni-Fe-based, **5**:585–586, **5**:586*f*
  physical metallurgy, **5**:592–593, **5**:593*f*
  P/M, **5**:589–590
  propulsion systems, **5**:594–595
  strengthening mechanisms in, **5**:594*t*
  sustainability considerations, **5**:593–598
  for turbine blades, **5**:587–588
Superatom, **5**:695–697, **5**:699–700
Superatomic orbitals, **5**:696–697, **5**:696–697*f*
Superconducting ceramic materials, **5**:440
Superconducting density of states, **2**:600–601, **2**:601*f*
  cuprate superconductors, **2**:608
  free electrons, dispersion relation for, **2**:601, **2**:601*f*
  highly disordered superconductors, **2**:609
  measuring probes, **2**:601
  pnictide- and Fe-based superconductors, **2**:608–609
  topological superconductors, **2**:609
  tunneling conductance (*see* Tunneling conductance)
  unconventional superconductivity, **2**:607–608
Superconducting devices
  direct-writing of, **3**:455–458
  planar superconducting nanostructure, **3**:458–460
  3D superconducting nanostructures, **3**:460
Superconducting field effect transistor (S-FET), **3**:459
Superconducting films, **2**:807
Superconducting fluctuations, **2**:671–672
Superconducting hydrides, synthesis of
  direct synthesis from element and hydrogen, **2**:595
  pressure generation and measurement technique, **2**:594
Superconducting quantum interference devices (SQUIDs), **1**:1008–1009, **2**:118, **2**:123, **3**:459
Superconducting qubits, **1**:260
Superconducting transition temperatures, **2**:593*f*
Superconductivity (SC), **1**:761, **2**:592, **2**:644–645, **2**:693, **3**:3, **3**:10, **3**:11*f*, **3**:17, **3**:73–74, **3**:79
  Bardeen–Cooper–Schrieffer theory of, **1**:29
  Cooper pairs, **2**:646–651
  and correlated phenomena, **2**:292
  in curved 3D nanoarchitectures, **2**:747
  electron-electron interaction, **2**:633
  elementary pinning mechanisms, **2**:555–556
  flux quantization, **2**:653–654
  global critical currents of superconductors, **2**:560–563
  and heat transport, **3**:275–276
  incoherence, **2**:641–642
  Kondo effect with, **3**:397
  of large-bipolaron liquid, **2**:442–443
  lattice systems, **2**:633–639
  Meissner state, **2**:645–646
  microscopic whirls, **2**:651–652
  non-Fermi liquid, **2**:633, **2**:641–642
  pairing vertex, **2**:633, **2**:642
  penetration depth, **2**:652
  pinning and current blocking by extended defects, **2**:559–560
  quantum-critical point, **2**:641–642
  renormalization group analysis, **2**:639–640
  self-energy, **2**:641–642
  single-vortex and collective pinning by point defects, **2**:557–559
  spin and charge fluctuations, **2**:640–642
  strong coupling, **2**:639–642
  temperature, **2**:652–653
  terahertz light, **3**:514
  total current, **2**:655
  vertex function, **2**:634, **2**:641
Superconductor/ferromagnet (S/F) structures
  magnetic proximity effect, **2**:687–689
  metallic, **2**:683–686
  non-equilibrium properties of, **2**:689–691
  odd-frequency triplet superconductivity in, **2**:686–687
Superconductor–insulator transition (SIT), **2**:805–806, **2**:808–809, **2**:809*f*, **2**:814–815
Superconductors, **2**:592
  control of hydrogenation, **2**:596
  critical fields of, **2**:694–695
  cuprate, **2**:608
  global critical currents of, **2**:560–563
  high pressure, **2**:593
  Holy Grail, **2**:593
  hydrogen-rich compounds, **2**:593
  point defects in, **5**:186
  room-temperature superconductivity in hydrides
    lanthanum hydride, **2**:595–596
    unidentified superconducting objects (USOs), **2**:596
  synthesis of superconducting hydrides
    direct synthesis from element and hydrogen, **2**:595
    pressure generation and measurement technique, **2**:594
  theoretical predictions, **2**:594
  topological, **4**:360
  ultrafast charge dynamics in, **3**:701–702
Supercontinuum, **3**:697
Supercooled liquids, **3**:171–172
  diffusion, **3**:173–174
  dynamics of, **3**:173–177
  fragile and strong liquids, **3**:174
  slow dynamics, **3**:175–177
  supercooled water, **3**:177–179

Supercritical-thickness strained silicon-on-insulator (SC-sSOI) wafers, **4**:405–406
Superelasticity, **2**:396–397, **2**:396–397*f*
Superexchange, **2**:75, **2**:76*f*, **5**:494
Superfluid Fermi gas
  amplitude mode, **1**:194–195, **1**:195*f*
  Anderson–Bogoliubov mode, **1**:192–194, **1**:193–194*f*
  order parameter, **1**:189–190
Superfluid fraction, **3**:28
Superfluidity, **3**:69
  circulation of, **3**:1, **3**:2*f*
  coherence and, **3**:75–78
  effects, **3**:27
  hydrodynamics, **3**:5–6
  microscopic origin, **3**:3–5
  occurrence, **3**:1–3
  phase slip, Josephson effect and critical velocity, **3**:8
  quantization of circulation, **3**:6
  rotating superfluid, **3**:6–8
  vortex lines, **3**:6–8
Superinsulation, **2**:804–806
  asymptotic freedom and size effects, **2**:811, **2**:812*f*
  dynamical exponents and linear potential, **2**:813, **2**:813*f*
  electric Meissner effect, **2**:811–812, **2**:812*f*
  finite temperature phase diagram, **2**:809, **2**:810*f*
  gauge theories of planar superconductors, **2**:806–808
  Josephson junction arrays, **2**:808
  nature of superinsulator, **2**:809–813, **2**:811*f*
  oblique superinsulators, in 3D, **2**:813–814
  quantum phase diagram, at T = 0, **2**:808–809, **2**:809*f*
  quantum phases, SIT, **2**:808–809, **2**:809*f*
  role of disorder, **2**:814–815
  superconducting films, **2**:807
Superparamagnetism, **2**:118
Super Poissonian statistics, **5**:167–168
  chaotic light, **5**:170–171, **5**:170–171*f*
  thermal light, **5**:169–170, **5**:169*f*
Superposition principle, **1**:238
Super-resolution ptychography, **4**:83
Supersolid, **3**:81–82, **3**:208
Superspace crystallography and quasicrystals, **5**:321–323, **5**:321–322*f*
Superspace group, **4**:513, **4**:520
Superspace theory, **5**:319
Superspin glass, **2**:22, **2**:374
Superstripes landscape, in perovskites high Tc superconductors
  charge density waves and lattice defects, **3**:443–445
  Hg1201, **3**:444–445, **3**:444–445*f*
  LCO, **3**:443, **3**:443–444*f*
  oxygen order, in cuprates systems, **3**:438–442
  scale free distribution of oxygen wires, in YBCO, **3**:442, **3**:442*f*
  superlattices, in YBCO, **3**:438–442, **3**:439–441*f*
Superstructures, **5**:25–28
Supervised learning, **3**:826, **3**:826*f*
Support vector machine (SVM), **3**:828
Support vector regression (SVR), **3**:828
Surface acoustic modes, in thin layers, **4**:191
Surface acoustic waves
  and geometric resonance, **1**:348–349
  knight shift, **1**:350
  light scattering, **1**:349–350
  transport experiments, **1**:349
Surface differential reflectivity (SDR), **4**:392–393, **4**:393–394*f*
Surface electromagnetic waves, **3**:730–732
Surface enhanced Raman scattering (SERS), **3**:735–738, **5**:520
  electromagnetic enhancement to metal particles, **3**:733–734
  flat metal surface, **3**:729–730
  nanostructures, **3**:735
  plasmonic nanostructures for, **4**:308–310
  Raman intensity, **3**:728–729
  roughness, **3**:736
  sensitive analytes detection, **4**:307–310
  surface electromagnetic waves, **3**:730–732
  surface plasmons, **3**:730–732
  surface selection rules, **3**:729–730
Surface plasmon polaritons (SPP), **4**:373–375, **4**:374*f*, **4**:377–378
Surface plasmons, **3**:730–732
Surface polaritons, **2**:501–503
Surface reconstruction
  and relaxation, **2**:258–259
  semiconductor surfaces, **2**:263–267
Surfaces, optical properties of
  ellipsometry, **4**:396
  reflectance anisotropy spectroscopy (RAS), **4**:393–396, **4**:395*f*
  surface differential reflectivity (SDR), **4**:392–393, **4**:393–394*f*
  theory, **4**:396–398
Surface states, **2**:260
  electronic, **2**:260–263
  extrinsic, **2**:263
  intrinsic, **2**:263
Surface (interface) stresses, **5**:261–263
Surface vibration modes, **4**:167–168
Surface waves, **4**:374–375
Surfactants, **4**:743
Surrogate models, **4**:545–546
Sustainable aviation fuels (SAF), **5**:594–595
S-wave superconductivity, **2**:638–639
Switching current distributions (SCDs), **2**:725–726, **2**:730–733, **2**:730*f*, **2**:732*f*
Symmetric gradient domain machine learning (sGDML), **4**:548–549
Symmetry-protected non-Abelian anyons
  mirror and unitary symmetries, **2**:769–770
  multiple majorana zero modes and coxeter group, **2**:770–771
Symmetry protection and edge states, **1**:666–668
Symmorphic space groups, **5**:63–64, **5**:65*t*, **5**:66
Synchrotron Mössbauer spectroscopy (SMS), **4**:206, **4**:211
Synchrotron radiation (SR), **3**:511, **4**:180, **4**:205–206, **4**:214
  bending magnets, **4**:438–439
  free-electron lasers, **4**:430–431
  helical wigglers, **4**:430
  practical use of, **4**:431–432
  relativistic basis of synchrotron sources, **4**:426–427
  sources, **4**:438–440
  topography, **4**:405–406, **4**:406*f*
  undulators, **4**:429–430, **4**:439–440
  wiggler, **4**:429, **4**:439
  X-ray sources, **4**:425–426
Synthetic magnetic field, **1**:629–631
Systems of linear equations, **5**:752
Szilárd engine, **4**:523*f*

T

Tangent formula, **5**:47
Tapes and wires, **2**:578
Tapping mode force microscopy, **4**:56–57, **4**:57*f*
TCI. *See* Topological crystalline insulator (TCI)
TDSE. *See* Time dependent Schrödinger equation (TDSE)
TEC. *See* Thermal expansion coefficient (TEC)
Technology, ICs, **3**:749–753
  device fabrication, **3**:749–750
  interconnects, **3**:750–751
  packaging, **3**:752–753
Temperature dependence, **4**:282–293
  and conductivity curves, **4**:271–274
  of elastic moduli, **5**:413
  lattice dynamics, **5**:286–288, **5**:287*f*
  of phonon frequencies, **5**:413–414, **5**:414*f*
Temperature-doping phase diagram, **2**:582–583
Temperature gradient solution growth technique, **5**:203*f*
Temperature-microscope effect, **2**:382
Temperature step experiments, **2**:379–380
Templating strategies, **3**:370
Temporal *vs.* spatial atomic layer deposition, **5**:720–721, **5**:720*f*
Ten Martini problem
  Diophantine regime, **1**:721
  gap opening, **1**:716–717
  Harper and almost Mathieu models, **1**:713–714
  Liouville regime, **1**:721–722
  matrix formulation, **1**:716
  rational approximation, **1**:718
  spectral continuity, **1**:718–719
  transfer matrix, **1**:715–716, **1**:719–720
Tensor averaging, **3**:496–497
Tensor nature of permittivity, **3**:669–672
Tensor symmetry, definition of, **5**:56–57
Terahertz-dressed electronic state, **3**:516
Terahertz (THz) light
  coherent magnetization dynamics, **3**:515
  control over matter, **3**:513–516
  electron dynamics, control of, **3**:515–516
  equilibrium, **3**:512

  excitation path, **3**:510
  ferroelectric phase transition, **3**:516
  field emission, **3**:515–516
  Franz–Keldysh effect, **3**:516
  high-field carrier generation, **3**:515
  incoherent ultrafast demagnetization, **3**:515
  insulator-to-metal phase transition, **3**:516
  lattice, control over, **3**:513
  magnetic degree of freedom, **3**:514
  magnetic field component, **3**:515
  magnetic phase transition, **3**:516
  magnetization switching, **3**:515
  and manipulation of matter, **3**:510
  matter interaction and experimental tools, **3**:512–513
  non-resonant control, **3**:515–516
  nonthermal pathways, laser excitation, **3**:512*f*
  out-of-equilibrium, **3**:512–513
  phase transitions and hidden orders driven, **3**:516
  prototype antiferromagnet, **3**:514
  resonant control, **3**:513–514
  sources, **3**:510–511
  structural phase transitions, **3**:516
  superconductive phase transition, **3**:516
  superconductivity, control over, **3**:514
  topological phase transition, **3**:516
  weak sources, **3**:510–511
Terahertz nondestructive evaluation, **3**:602
Terahertz time-domain spectroscopy (THz-TDS), **4**:136–138, **4**:137–138*f*, **4**:147
Terfenol, **2**:83–84
Terfenol-D alloys, **2**:83–84
Ternary components, atomic layer deposition of, **5**:723–724, **5**:723*f*
Tersoff's model, **2**:511
Tetrahedrally coordinated crystals, **5**:454
Texture, **3**:848
Texture measurement techniques
  electron backscatter diffraction, **3**:488–489
  X-ray diffraction, **3**:487
Theory of Fermi liquid, **1**:29
Thermal activation (TA), **2**:727*f*, **3**:858–859
  bulk diffusion effects, **3**:858
  intercrystalline diffusion effects, **3**:859
Thermal conductivity, **2**:488–489, **5**:305
  definition, **3**:273
  measurement, **3**:277
  of metals, **3**:275
  and thermal diffusivity, **3**:273–274
Thermal de Broglie wavelength, **3**:68–69
Thermal diffusivity, **3**:273–274
Thermal expansion, **5**:412–413
Thermal expansion coefficient (TEC), **3**:182, **3**:187
Thermal fluctuations, **2**:561–562
Thermal Hall conductivity, **2**:798
Thermal light, **5**:169–170, **5**:169*f*
Thermally activated phase slips (TAPS), **2**:672
Thermal magnetoresistivity, **3**:277
Thermal management materials, **5**:347
Thermal power, **1**:356–357
Thermal response, **5**:625
Thermal-spraying, physical vapor deposition, **5**:252
Thermal strains, **5**:261–263
Thermal transport, in insulating crystals, **3**:274
Thermal *vs.* plasma-enhanced atomic layer deposition, **5**:718–719, **5**:718*f*
Thermionic emission (TE), **4**:437
Thermodynamics, **3**:79, **5**:412–413
  advances in analysis, **4**:507–508
  autonomous pressure Maxwell demon, **4**:523*f*
  entropy, **4**:562
  information, **4**:524–525
  informational states and Landauer's principle, **4**:529–530
  information flows, **4**:532–533
  of nanoscale systems, **4**:506–507
  phase stability, **4**:498–506
  phase transition, **2**:374–375
  second law, **4**:527–528, **4**:530–532
  Shannon and thermodynamic entropies, **4**:525–527
  Szilárd engine, **4**:523*f*
Thermoelectric devices, **3**:207
Thermoelectric energy conversion devices
  lattice conductivity, **3**:537
  modules, **3**:538
  Seebeck coefficient, **3**:536
  semiconductor thermoelements, **3**:536–537, **3**:536*f*
  thermoelectric figure of merit, **3**:535–536
  thermoelectric materials, **3**:537–538
Thermoelectric generators, **5**:673
Thermoionic cathodes, **4**:463–465, **4**:464*f*
Thermomagnetic phenomena
  phenomenological equations for, **4**:493–494
  transport coefficients for, **4**:494–495
Thermomechanical processing, **5**:554
Thermo-remanent magnetization (TRM), **2**:375, **2**:376*f*
Theta terms, and domain walls, **1**:86–88
Thin films, **2**:577, **3**:493, **3**:668
  deformation, measurements of, **5**:263, **5**:264*f*
  deposition, **5**:249*f*
  elastic and anelastic behavior, **5**:265–266
  focused ion beam modification of, **3**:372–373
  fracture and delamination, **5**:266–267, **5**:267*f*
  growth, **4**:7–10
  mechanical properties of, **5**:261
  plastic behavior of, **5**:263–265
  stack with magnetic tunnel junction, **2**:15*f*
  stresses, **5**:261–263, **5**:262*f*
Thin-layer quantization, **3**:416–417
Thin limit
  topological insulators, **4**:342, **4**:343*f*
  transition metal dichalcogenides (TMDs), **4**:354–356, **4**:355*f*
Third law of thermodynamics, **4**:481–482
Third-order nonlinear effects
  four-wave-mixing and optical conjugation, **4**:388–389, **4**:389*f*
  optical Kerr effect, **4**:388
Thirring model, **1**:56–57
Thomson effects, **4**:493
Thomson scattering, **4**:206–207, **5**:42
Thouless–Anderson–Palmer (TAP) approach, **2**:365–366
Thouless–Kohmoto–Nightingale–den Nijs (TKNN) formula, **1**:623, **2**:798
Thouless pump, **3**:136–140, **3**:142
Three-channel Kondo effect, **3**:395*f*, **3**:397
Three-dimensional (3D) nanoprinting, **3**:460
Three-dimensional (3D) photonic crystals, **3**:741–742
Three-dimensional (3D) printed components, **3**:832–833
Three-dimensional (3D) quasicrystalline model, **5**:326–327, **5**:327*f*
Three-dimensional (3D) superconducting nanostructures, **3**:457–458, **3**:460
Three-dimensional (3D) systems, **5**:774–775
Three-dimensional (3D) topological insulators, **1**:690–691, **1**:694
  Bi_2Se_3, Bi_2Te_3, Sb_2Te_3, **1**:695–696
  HgTe, **1**:695
  higher-order topological insulators, **1**:696
  model Hamiltonian of, **1**:694–695
  SmB_6, **1**:696
  synthesis of materials, **1**:697
  time-reversal-invariant 3D TIs, **1**:696
  $TlBiSe_2$ and its variants, **1**:696
  topological surface states, spin-momentum locking in, **1**:691, **1**:691*f*, **1**:697
Three-dimensional (3D) topological superconductors, **2**:798–799
Three-dimensional (3D) V-NAND flash memories, **3**:562–563, **3**:563*f*
Three-dimensional (3D) Z_2 topological insulators, **1**:83–88
THz computed tomography, **3**:610–614
THz NDE of additively manufactured components
  birefringence, **3**:614–617
  effect of 3D printing parameters on FDM printed components, **3**:608–609
  of infill structures, **3**:607
  refractive effects, **3**:610
  THz computed tomography, **3**:610–614
  THz imaging of defects, **3**:607–608
THz NDE of multilayer paint stacks, **3**:603
Tight-binding (TB) model, **3**:242–243, **3**:243*f*
  approximation, **5**:218–222
  elastic constants, **1**:738–740
  finite temperature properties from molecular dynamics, **1**:746
  formalism, **1**:517–518
  ground-state behavior and phase stability, **1**:735–738
  multicomponent systems, **1**:746–747
  NRL tight-binding method, **1**:734–735
  one- and two-dimensional structures, **1**:748–753
  phonons, **1**:742–745
  point defects, **1**:745
  stacking faults, **1**:742
  surfaces, **1**:742
  technical procedure, **1**:735

Tight-binding (TB) model *(Continued)*
  vacancies, **1**:740–742
Time averages, **4**:560
Time constants and frequency dependence, **4**:271
Time-dependent density functional theory (TDDFT), **3**:163, **3**:702
Time-dependent DMRG, **1**:991–992
Time dependent Schrödinger equation (TDSE), **1**:967–968, **1**:970, **1**:973, **5**:129–130
Time-domain THZ spectroscopy, **3**:697
Time-of-flight (TOF) method, **3**:137
Time-perturbed angular correlation (TPAC), **4**:206
Time-resolved ARPES, **1**:975, **1**:976*f*
Time-resolved electron and X-ray diffraction, **3**:697
Time-resolved photoemission, **3**:697
Time-resolved spectroscopy, **1**:981
Time-reversal even observables, **1**:677–679
Time-reversal invariance (TRI), **1**:135
Time-reversal-invariant insulators, **1**:690–692
Time-reversal-invariant momenta, **1**:691, **1**:693–694, **1**:693*f*
Time-reversal odd observables, **1**:675–677
Time-reversal symmetry (TRS), **1**:691, **2**:796
Time–temperature–transformation curves, **5**:513
Tip-enhanced Raman spectroscopy (TERS), **4**:60
  detection geometries for, **4**:311*f*
  hot spot on demand, **4**:310–312
  principle of, **4**:310*f*
  probes nanofabrication and preservation, **4**:311–312
Tissues, **4**:739
Titanium alloys
  challenging and problematic issues with, **5**:646
  classification, **5**:638–641
  commercially pure, **5**:639
  crystallographic structure of phases in, **5**:635–637
  effects of crystal orientations on mechanical properties, **5**:637
  heat treating of, **5**:641–646
  welding of, **5**:646
TMDCs. *See* Transition metal dichalcogenides (TMDCs)
TMD heterostructures, **2**:319–322
Tomography, **3**:595, **3**:599–600
Tomonaga–Luttinger liquid (TLL), **1**:899, **1**:907–911, **1**:913
Top electrode (TE), **3**:571
Topological chiral semimetals, **4**:357–359, **4**:358*f*
Topological crystalline insulator (TCI), **1**:690, **1**:696, **4**:345, **4**:346*f*
Topological disorder, **3**:193, **3**:194*f*
Topological excitations, **1**:41–49
  and open integer-spin chains, **1**:48–49
  vortices and magnetic monopoles, **1**:41–47
Topological field theory, **1**:66
Topological graphene, **2**:355–359
Topological insulators (TIs), **1**:72–83, **1**:134–135, **1**:555, **1**:593, **1**:593*f*, **2**:267, **2**:267*f*, **3**:669, **4**:123–126
  angle-resolved photoemission spectroscopy (ARPES) experiments, **1**:697
  correlated, **4**:359–360
  definition, **1**:690
  hexagonal warping, **4**:336–340, **4**:339*f*
  higher-order topological insulators, **1**:690, **1**:696
  historical perspective, **1**:691–692
  magnetic, **4**:342–344
  Majorana zero modes (MZMs), **1**:697–698
  nontrivial topology of, **1**:690–691
  quantum anomalous Hall effect (QAHE), **1**:697–698
  quantum spin Hall effect, **1**:624
  representative materials, **1**:695–696
  scanning tunneling epectroscopy (STS) experiments, **1**:697
  spin and orbital texture, **4**:340–341, **4**:341*f*
  strong, **4**:335–336, **4**:337–338*f*
  synthesis of materials, **1**:697
  theory of, **1**:692–694
  thin limit, **4**:342, **4**:343*f*
  three-dimensional (3D) (*see* Three-dimensional (3D) topological insulators)
  time-reversal-invariant insulators, **1**:690
  topological crystalline insulator (TCI), **1**:690, **1**:696
  topological superconductivity, **1**:697–698
  transport experiments, **1**:696–697
  two-dimensional (2D) topological insulators, **1**:690–691, **1**:693, **1**:695
  weak, **4**:345
  Z_2 characterization, **1**:625
Topological invariance, **1**:70–71
Topological magnetic textures
  domain walls, **2**:120–121
  magnetic topological solitons, **2**:119–120
  magnetic vortices, **2**:121
  skyrmions and magnetic bubbles, **2**:121
  3D textures, **2**:121–122
Topological magnetotransport phenomena, **1**:685–688
Topological nodal-line semimetals, **4**:356–357, **4**:356*f*
Topological phase, **1**:659, **1**:666
Topological pump, **1**:666
Topological quantum computation, **1**:296–297
  braid group, **1**:269
  modeling topological phases with categories, **1**:271–272
  objectives, **1**:268–269
  origins of, **1**:270
  role of braid group, **1**:272–275
Topological quantum computer, **1**:279
  Fibonacci (*see* Fibonacci topological quantum computer)
  hardware error sources, **1**:283
  leakage error, **1**:283
  quantum compilation error, **1**:283
Topological quantum computing (TQC), **1**:135–136
Topological quantum field theories (TQFTs), **1**:270
Topological qubit, **1**:281
Topological resonance, **5**:135–136, **5**:135*f*
Topological semimeta, **1**:681–683, **1**:688
Topological shift, **1**:340
Topological superconductivity, **1**:697–698
Topological superconductor (TS), **1**:109, **1**:132, **1**:134–135, **2**:609, **2**:801–802, **4**:360
  bosonic Cooper pairs, **2**:795–796
  bulk-boundary correspondence and effect of disorder, **2**:800–801
  fermionic Bogoliubov quasiparticles, **2**:795–796
  gapped topological (ground) states, **2**:796
  interactions, effect of, **2**:801
  Majorana fermions, **2**:796
  one-dimensional, **2**:796–797
  quantum Hall effect, **2**:795–796
  three-dimensional, **2**:798–799
  and topological insulators, **2**:799–800, **2**:800*t*
  two-dimensional, **2**:798
Torque method, **4**:235, **4**:236*f*
Torsional stiffness, **5**:393–394
Toughened, scratch resistant glass for screens, **5**:417
Toughness, **5**:538, **5**:540
Toxicity, halide perovskites, **5**:674
Trabecular bone, **4**:739
Traditional packaging materials, **5**:348*t*
Trajectory analysis, **4**:113
Transfer matrices and gaps
  Floquet–Bloch solutions, **1**:719–720
  reducibility to constant coefficients, **1**:720
  rotation number, **1**:719
Transfer-matrix method (TMM), **1**:715–716, **3**:213–214, **3**:741
Transfer RNA (tRNA), **4**:665
Transformation routes, of catalysts, **5**:739*f*
Transient CT mechanism, **4**:306
Transient Schottky capacitance, **2**:519
Transistors, **3**:781
  backgated structure, **3**:787, **3**:787*f*
  bipolar and hetero-bipolar transistors, **3**:781–783
  field effect transistors (FETs), **3**:783–787, **3**:784*f*, **3**:786*f*
  in-plane-gate transistor, **3**:787, **3**:788*f*
  single–electron transistor (SET), **3**:788–789, **3**:788*f*
  well, **3**:749–750
Transition-metal compounds
  d-Block d^n configurations, **5**:487–490
  energy bands and redox couples, **5**:498–499
  metal–ligand interactions, **5**:486–487
  metal–metal interactions, **5**:490–497
  rare-earth compounds, **5**:499–500
  rutiles, **5**:497–498
  spinels, **5**:497

  transition-metal *d*-block compounds, **5**:500–501
Transition metal dichalcogenides (TMDCs), **1**:594, **2**:168, **2**:207, **2**:255, **2**:605–606, **2**:606*f*, **3**:48, **5**:126, **5**:129, **5**:131, **5**:136
  dirac cones in inversion symmetrics, **4**:351–353, **4**:352*f*
  thin limit, **4**:354–356, **4**:355*f*
  Weyl phases in inversion asymmetrics, **4**:353–354
Transition metals, **2**:35–36, **2**:36*t*, **2**:164, **2**:174
Translational invariance, **3**:739
Translational symmetry, **2**:476
Translation subgroup, **5**:63
Translucent concrete, **5**:418–419, **5**:418*f*
Transmission, **1**:228–229, **1**:228*f*, **4**:134*f*, **4**:135–136, **4**:136*f*
Transmission electron microscopy (TEM), **2**:533, **4**:71
  aberrations of, **4**:63, **4**:65
  coherent imaging, **4**:65–67, **4**:66*f*
  contrast transfer function, **4**:66*f*, **4**:67, **4**:69
  electron optics of, **4**:64–65
  incoherent imaging, **4**:67–69
  as nano-laboratory, **4**:69
  principles of image formation, **4**:65–69
  reciprocity, **4**:65
  role of, **4**:63
  STEM *vs.*, **4**:64–65, **4**:64*f*
Transmuted Hamiltonian, **1**:477–478
Transport coefficients, **3**:278–280
  for thermomagnetic phenomena, **4**:494–495
  use of constraints, **4**:495–496
Transport gaps, **1**:338
Transport properties
  Brownian motion, **3**:280–283
  crystal lattice dynamics, **5**:415
  quasicrystals, **5**:291–292
  transport in presence of gradient, **3**:279–280
Transport proteins
  gating, **4**:694–695, **4**:695*f*
  selectivity, **4**:694, **4**:694*f*
  structure and function, **4**:693–695
Transverse double heterostructure, **3**:774
Transverse relaxation rates, **4**:727
Traveling Salesman Problem, **4**:536–537
Tricalcium phosphate, **4**:740
Trigonal warping, **1**:607–608, **1**:615–616
Triplet superconductivity, **2**:598
Triplexes, **4**:671
Tripositive rare-earth ions, **2**:35–36, **2**:36*t*
True stress–strain behavior, **3**:847, **3**:848*f*
Tubular microrobots, **3**:542
Tungsten
  FEBID, **3**:454
  FIBID, **3**:452
Tungsten carbide, **5**:344
Tunneling, **4**:589–590
Tunneling conductance
  Bardeen's formalism, **2**:601–602
  β-Bi$_2$Pd and AuSn$_4$, **2**:604, **2**:605*f*
  behavior at defects and impurities, **2**:603–604
  bias voltage, **2**:602
  distribution of values of superconducting gap, **2**:601*f*, **2**:602–603
  Fermi function, **2**:601–602
  2H-NbSe$_2$, 2H-NbS$_2$, and 2H-TaS$_2$, superconductivity in, **2**:605–606, **2**:606*f*
  nickel borocarbides, **2**:606, **2**:607*f*
  superconducting Al and Pb, **2**:604, **2**:604*f*
  S-wave BCS single gap, **2**:601*f*, **2**:602
  tip and sample, tunneling between, **2**:601–602, **2**:602*f*
  tunneling current, **2**:601–602
  two-gap superconductor, in MgB$_2$, **2**:604, **2**:605*f*
Tunneling density of states (TDOS), **3**:228–229
Tunneling effects in JTE, **1**:803
Tunnel-Junction-Microscopic (TJM) model, **2**:622
Tunnel magnetoresistance (TMR), **2**:160–161, **2**:161*f*, **2**:164–165
Turbine blades, superalloy for, **5**:587–588
Twinning, **3**:846–847
Twisted bilayer graphene (TBG), **1**:523–527, **1**:529–530, **1**:727–729, **2**:638
  atomic structures of, **2**:289*f*
  band structure, **2**:290–291
  effective continuum model, **2**:289–290
  magneto spectra and quantum hall effect, **2**:292–293
  moiré Brillouin zone, **2**:288–289
  Moiré pattern, **2**:288–289
  superconductivity and correlated phenomena, **2**:292
  2D material, **2**:293
Twisted graphene multilayer, **1**:726, **1**:729
Twisted HTS JJs, **2**:628
Twist-grain boundary (TGB) phase, **5**:381–382, **5**:384*f*
Twistronics, **2**:314–315, **2**:716–719
Two-band (electron–hole) conductors transport, **4**:495
Two-channel Kondo effect, **3**:395*f*
Two-dimensional (2D) anyon gas properties
  ideal anyon gas, **1**:453–466
  non-Abelian anyon gas, **1**:473–475
  nonideal anyon gas, **1**:466–473
  one-dimensional anyons, **1**:452
  plane and polarons impurities, **1**:478–480
  precursor ideas, **1**:452
  quantum Hall (QH) setting, **1**:476–478
  sphere and angulons impurities, **1**:480
  three perspectives on, **1**:451–452
Two-dimensional (2D) carrier gases, **3**:530–531
Two-dimensional (2D) charge carrier system, **1**:556–557
Two-dimensional (2D) Dirac equation, **1**:695
Two-dimensional (2D) electron gas, **3**:530–531
  in graphene, **1**:790–793
  at high magnetic field, **1**:793–794
Two-dimensional (2D) electron system, **1**:560–561
Two-dimensional (2D) FES anyons, **1**:510–511, **1**:510*f*
Two-dimensional (2D) photonic crystals, **3**:743
Two-dimensional (2D) quantum Hall effect (QHE)
  Abelian Hall fluids classification, **1**:433–437
  anomalous chiral edge currents, **1**:430–433
Two-dimensional (2D) statistical anyons, **1**:509–510, **1**:510*f*
Two-dimensional (2D) topological insulators, **1**:690–691, **1**:693, **1**:695
Two-dimensional (2D) topological superconductors, **2**:798
Two-dimensional (2D) van der Waals materials, **2**:168–170, **2**:168*t*
Two-electron system, **2**:74
Two-fluid model, **3**:5
Two-gap superconductors, **2**:603–604, **2**:605*f*, **2**:608–609
Two-orbital cold atom system, as quantum transport emulation, **3**:140–141
Two-orbital two-electron atom system, **3**:140
Two-particle scattering, **3**:396
Two-photon entanglement, **3**:679–680
Two transistors and two capacitors (2T-2C), **3**:567
Type-II superconductivity, **2**:572
Type-I superconductors, **2**:694–695
Typical pressure–temperature phase diagram, **3**:69*f*

U

Ultracold atomic gas, **3**:78–79
Ultracold fermions, **3**:138–139
Ultrafast dynamics
  in antiferromagnets, **3**:699–700
  of correlated materials, **3**:702
  in ferrimagnets, **3**:698
  in ferroelectrics, **3**:700
  in ferromagnets, **3**:697–698
  interference effects, **5**:133–135, **5**:133–134*f*
  in magnetoelectrics and multiferroics, **3**:700–701
  topological resonance, **5**:135–136, **5**:135*f*
Ultrafast magnetism, **3**:697–698
Ultrafast optics, of topological materials, **5**:128
  graphene-like materials, **5**:129, **5**:131–132, **5**:131*f*
  solids, **5**:128–130
Ultrafast phono-magnetism, **3**:701
Ultrahigh modulus (UHM), **5**:337
Ultra-high vacuum (UHV) equipment, **2**:545, **5**:249–250
Ultra-short pulse generation, **4**:421–423
Ultraviolet photoelectron spectroscopy (UPS), **5**:697–698
Unconventional superconductivity, **2**:584, **2**:584*f*, **2**:598–599, **2**:607–608

Uncorrelated (Gross-Piaevskii) regime, **1**:645–646
Undamped mode, **1**:767, **1**:776
Undercooling, **4**:497–498
Underdamped regime, **2**:726–728, **2**:727*f*, **2**:732
Undulators, **4**:439–440
Uniaxial anisotropy, **2**:82
Unidentified superconducting objects (USOs), **2**:596
Unidirectional spin Hall magnetoresistance (USMR), **2**:163
Unitary Bose gas, **3**:129*f*
Unitary contact interactions, **3**:129–130
Unitary Fermi gas, **3**:18–19
Unitary maps, **1**:544, **1**:548
Unitary modular category (UMC), **1**:271
Unit cell, **5**:13–14, **5**:62–64, **5**:63*f*, **5**:70
Universality of Bose–Einstein condensation (BEC), **3**:85–88
  on astrophysical/cosmological scales, **3**:114–116
  continuous single-component atomic gases, **3**:109–110
  correlation functions, **3**:89–90
  driven-dissipative condensation in, **3**:110–113
  dynamical phase transition stages, **3**:88–89
  Kibble–Zurek scaling law, **3**:93–104
  Penrose–Onsager condensation *vs.* quasi-condensation, **3**:90–92
  during phase-ordering dynamics, **3**:104–109
  workhorse model of, **3**:92–93
Universal Lindblad equation, **1**:973
Universal low-pass filter (ULF), **3**:241, **3**:247
Universal scaling, **3**:389–390
Universal thermodynamics, **3**:18–19
Unsupervised learning, **3**:826–827, **3**:826*f*
Upstream neutral mode, **1**:351
Urbach-Tauc model, **5**:162
USOs. *See* Unidentified superconducting objects (USOs)
UV-assisted and photo-assisted chemical vapor deposition, **5**:256

V

Vacuum degeneracy, **1**:69–70
Valence electron density, for silicon, **1**:758, **1**:759–760*f*
Valence electrons, **4**:201
Valence force field (VFF) models, **3**:242
Valence photoemission
  of correlated systems, **4**:262–263
  high-brightness synchrotron sources, **4**:262
  with synchrotron sources, **4**:259–262
Valley currents in graphene, **1**:652–656
Valley excitons, **3**:708*f*, **3**:712
Valley Hall effect, **2**:298, **2**:302–305
Valley polarization, **5**:135–136
Vanadium-triisopropoxide (VTIP), **2**:538
Vandermonde determinant, **1**:110
Van der Waals (vdW) heterostructures
  assembly and growth of, **2**:312–313
  atomic reconstruction, **2**:316–317
  characterization, **2**:323–327
  clean interlayer interfaces, **2**:313–314
  graphene and, **2**:207–213
  graphene/hBN heterostructures, **2**:319
  layered materials, **2**:311–312
  Moiré patterns and twistronics, **2**:314–315
  superlubricity and self-rotation of layers, **2**:315–316
  TMD heterostructures, **2**:319–322
  twisted bilayer graphene and superconductivity, **2**:317–319
  2D heterostructures by intercalation, **2**:322–323
Van der Waals semiconductors and alloys, **5**:465–466, **5**:466*f*
Van Hove doping, **2**:637
Van Hove singularities (vHs), **1**:762, **2**:330, **5**:120, **5**:703, **5**:708–710
Van Vleck mechanism, **1**:591, **1**:598
Van Vleck paramagnetic susceptibility, **2**:35, **2**:37–38
Van Vleck perturbation expansion, **1**:972
Vapor growth, **5**:204–205
  chemical vapor transport and deposition, **5**:205
  sublimation technique, **5**:205
Vapor liquid solid (VLS) technique, **1**:697, **2**:524–525, **2**:550
Vapor-phase epitaxy, **2**:529, **2**:529*f*
Vapor transport method, **1**:697
Variable charge transfer models, **5**:214
Variational quantum eigensolver (VQE), **1**:253–255
VCSELs. *See* Vertical-cavity surface-emitting lasers (VCSELs)
Verlet's algorithm, **5**:755
Verneuil technique, **5**:200, **5**:201*f*
Vertical Bridgman (HB) method, **5**:196
Vertical-cavity surface-emitting lasers (VCSELs), **3**:779–780, **3**:779*f*
Vertical gradient freeze (VGF) method, **5**:196
Vertical quantum dots, **3**:326
V-grooves, **2**:527, **2**:527*f*
Vibrating sample magnetometers (VSM), **2**:123
Vibrational excitations in disordered solids
  boson peak, **5**:299–301
  BP anomalies, **5**:301–305
  density of states (DOS), **5**:299
  inelastic X-ray scattering, **5**:309–312
  specific heat and thermal conductivity, **5**:305
  spectroscopic methods, **5**:306–309
Vibrational spectroscopy, **4**:744
Violaxanthin, **4**:736
Virtual crystal approximation (VCA), **3**:236–237, **3**:245–246
Virtual imaged phased array (VIPA), **4**:192
Virtual screening, **4**:554*f*
Viscosity, **3**:206
Viscous friction, **3**:282
Vogel–Tammann–Fulcher equation (VTF), **3**:174, **3**:186–187
Void aspect ratio, **5**:392, **5**:393*f*
Volatile memories
  dynamic random-access memory, **3**:581–589
  static random-access memory, **3**:578–581
Voltage-control of magnetic anisotropy (VCMA), **2**:163, **2**:166–167
Volume holograms, **5**:93
von Klitzing constant, **1**:3*f*, **1**:5, **1**:5*f*, **1**:555
von Neumann equation, **1**:973
Vortex lattice, **2**:695–697, **2**:699–701
  commensurability effects on FFI, **2**:741
  melting, **2**:575
Vortex lines, **3**:6–8
Vortex pinning arrays, **3**:373–374
Vortex ratchets, **3**:375–376
Vortices, **2**:572
  duality transformation, **1**:44
  in films, **2**:698–699
  homotopy group, **1**:42
  and magnetic monopoles, **1**:41–47
  near surfaces, **2**:698–699
  in two dimensions, **1**:42–45

W

Walker's model, **3**:824
Wannier function, **1**:763
Wannier–Mott excitons, **3**:707, **5**:123
Washboard potential, **2**:622–623
Water
  glassy states of, **3**:177–178
  oxidation, **5**:672
  permittivity, **4**:702
Wave function, **3**:212
  diagonalization, **1**:991
  overlap, **1**:340
  statistics, **3**:215–216
  time-dependent DMRG and iTEBD, **1**:991–992
Wave-guides, **1**:925–926, **3**:774–775
Weak perturbation regime, **3**:696
Weak phase object approximation (WPOA), **4**:74–75
Weak repulsive contact interactions
  effects near T_c, **3**:128
  excitations and sound, **3**:126–127
  quantum depletion, **3**:127
Weiss' molecular-field hypothesis, **2**:45
Welding
  magnesium alloys, **5**:555
  titanium alloys, **5**:646
Wentzel–Kramers–Brillouin (WKB), **3**:403–404
Weston cell, **1**:10
Weyl semimetals, **1**:445–446, **1**:594, **5**:136

magnetic, **4**:350
nonmagnetic, **4**:347–350, **4**:349*f*
Whispering gallery mode (WGM), **2**:347, **3**:355
White-beam X-ray topography (WBXRT), **4**:404
White light emitting diodes, **5**:820–823
Wick's theorem, **1**:107
Wide bandgap materials, **3**:768–769
Widefield microscopy, **4**:109–110, **4**:114
Wiedemann–Franz law (WFL), **3**:231–232, **3**:275
Wiggler, **4**:429, **4**:439
Wigner crystallization, **1**:789
Wigner crystals, **1**:290–291
Wigner distribution deconvolution (WDD) approach, **4**:74–76, **4**:77*f*
Wigner–Weisskopf dissipation, **3**:713–714
Wilson–Fisher (WF) fixed point, **1**:34, **1**:123
Wilson ratio, **3**:396
Winding number, **3**:402–403
Work hardening, **3**:854–855
Workhorse model, **3**:92–93
World-line Monte Carlo, **1**:882–883

X

XEB. *See* Cross entropy benchmarking (XEB)
X-ray crystallography, **5**:42
X-ray diffraction (XRD), **2**:533, **2**:595, **3**:487, **5**:36, **5**:376–377, **5**:377*f*, **5**:381–382, **5**:386, **5**:388
X-ray inelastic scattering (XIS), **5**:279
X-ray magnetic circular dichroism (XMCD), **1**:676
X-ray photoelectron spectroscopy (XPS), **2**:533, **5**:698
X-ray Raman scattering, **4**:198–199, **4**:199*f*
X-ray sources, **4**:425–426
conventional (astronomy), **4**:434–438
fourth generation light, **4**:440–441
laser plasma, **4**:441
natural (astronomy), **4**:434
sealed tube and rotating anode sources, **4**:436–437, **4**:437*f*
synchrotron, **4**:438–440
X-ray tube, **4**:434–435
X-ray topography
Borrmann triangle ABC, **4**:401–402, **4**:401*f*
contrast mechanisms, **4**:402–404
diffraction technique, **4**:404–405
dislocations, **4**:400, **4**:400*f*
flux-grown Ga–YIG crystal, **4**:400, **4**:401*f*
imperfections effect, **4**:402–404, **4**:403*f*
principle, **4**:400–401, **4**:400–401*f*
simulations, **4**:406, **4**:407*f*
synchrotron radiation topography, **4**:405–406
X-ray tube, **4**:437–438
XRD. *See* X-ray diffraction (XRD)

Y

Yang–Mills coupling constant, **1**:35
Yang–Mills theory of acoustic phonons in crystal, **1**:202–204
Yee algorithm, **3**:741
Young's modulus, **3**:838–839, **3**:840*f*, **3**:841, **5**:390–392, **5**:393*f*
Yrast curve, **1**:644–646

Z

Zak phase, **2**:280–281, **2**:355
Z-contrast, **4**:68–69, **4**:69*f*
Z-DNA, **4**:667
Zeaxanthin, **4**:736
Zeeman coupling, **1**:39
Zeeman effect, **1**:189, **1**:592
Zeeman energy, **2**:27, **2**:31, **2**:49, **2**:53, **2**:55–56, **2**:119, **3**:401
Zeeman Hamiltonian, **1**:224–225
Zehner exchange, **2**:75
Zener's double-exchange mechanism, **2**:96
Zero-bias anomaly, **1**:901*f*
Zero-dimensional systems, **3**:336
Zero-energy bound states, **2**:347
Zero group velocity, **1**:776–777
Z_2 gauge theory, **1**:50–52
Zigzag edge states, graphene, **2**:355
Zigzag nanoribbons, **2**:282–284
Z_2 index, **1**:690–695
Zirconium copper, **5**:612
Zn—Sc icosahedral quasicrystal
phason diffuse scattering, **5**:330–331, **5**:331*f*
structure determination, **5**:328–329, **5**:329*f*
Zone melting in crucibles, **5**:198–199
Z_2 topological index, **1**:625

This page intentionally left blank

Encyclopedia of Condensed Matter Physics

Second Edition

EDITOR-IN-CHIEF:
Tapash Chakraborty
University of Manitoba, Winnipeg, Manitoba, Canada

SECTION EDITORS:
Ana M. Sanchez
Department of Physics, University of Warwick, Coventry, United Kingdom

Hideo Aoki
Department of Physics, University of Tokyo, Tokyo, Japan

Robert H. Blick
Center for Hybrid Nanostructures, University of Hamburg & DESY, Hamburg, Germany

Roberto Raimondi
Mathematics and Physics Department, Roma Tre University, Rome, Italy

Rudolf A. Roemer
Department of Physics, University of Warwick, Coventry, United Kingdom

Vladimir Mihajlovic Fomin
Leibniz Institute for Solid State and Materials Research (IFW), Dresden, Germany

ELSEVIER

ACADEMIC PRESS
An imprint of Elsevier
elsevier.com/books-and-journals

Volume ISBN
ISBN 978-0-443-21827-9
9 780443 218279

Set ISBN
ISBN 978-0-323-90800-9
9 780323 908009